SPRINGER
REFERENCE

Dongqing Li
Editor-in-Chief

Encyclopedia of Microfluidics and Nanofluidics

Springer

Encyclopedia of Microfluidics and Nanofluidics

Dongqing Li (Ed.)

Encyclopedia of Microfluidics and Nanofluidics

With 1636 Figures and 152 Tables

Springer

Prof. Dongqing Li
Department of Mechanical Engineering
Vanderbilt University
VU Station B 351592
2301 Vanderbilt Place
Nashville, TN. 37235-1592
USA
dongqing.li@vanderbilt.edu

Library of Congress Control Number: 2008927465

ISBN: 978-0-387-48998-8

The print version of the whole set will be available under ISBN 978-0-387-32468-5.
The print and electronic bundle of the whole set will be available under ISBN 978-0-387-49000-7.

© 2008 Springer Science+Business Media, LLC.

All rights reserved. This work may not be translated or copied in whole or in part without the written permission of the publisher (Springer Science+Business Media, LLC., 233 Spring Street, New York, NY 10013, USA), except for brief excerpts in connection with reviews or scholarly analysis. Use in connection with any form of information storage and retrieval, electronic adaptation, computer software, or by similar or dissimilar methodology now known or hereafter developed is forbidden.

The use in this publication of trade names, trademarks, service marks, and similar terms, even if they are not identified as such, is not to be taken as an expression of opinion as to whether or not they are subject to proprietary rights.

springer.com

Editor: Steven Elliot, Norwell / Kerstin Kindler, Heidelberg
Development Editor: Sylvia Blago, Heidelberg
Typesetting and Production: le-tex publishing services oHG, Leipzig
Cover Design: Frido Steinen-Broo, Spain

Printed on acid-free paper SPIN: 11601296 2109 — 5 4 3 2 1 0

Preface

Microfluidics and nanofluidics are among the most rapidly growing fields of scientific research and technology development. Over the past 15 years, the research activities in these fields have been increasing exponentially as evidenced by the number of published papers in the literature. Microfluidics and nanofluidics not only bring exciting opportunities to study the new phenomena unique to these small scales, but also enable the development of many new and high-impact technologies from handheld biomedical laboratory (Lab-on-a-Chip) to detection and manipulation of single molecules. While these exciting and inter-disciplinary research fields attract more and more researchers, one major challenge is the lack of a single reference resource providing up-to-date reviews and overviews of various directions in the field of microfluidics and nanofluidics. This is the motivation behind the development of the Encyclopedia of Microfluidics and Nanofluidics. As a comprehensive resource, no single review paper or several books focused on specific topics can replace the role of an Encyclopedia.

This is the first Encyclopedia of Microfluidics and Nanofluidics for the scientific community. It covers the fundamentals, latest developments and cutting-edge experimental techniques, including electrical double-layers; optofluidics; DNA lab-on-a-chip; nanosensors; and much more. The high technical quality of the Encyclopedia has been ensured by our International Editorial Board consisting of leading scientists in these fields, and the over 250 experts in microfluidics and nanofluidics. The carefully selected entries deliver relevant and comprehensive information, and are fully illustrated with thousands of diagrams, photos, line art, many in full color.

The Encyclopedia provides basic information on all fundamental and applied aspects of microfluidics and nanofluidics by covering two decades of research. It is the only scientific work of its kind in the field of microfluidics and nanofluidics bringing together core knowledge and the very latest advances. Written for a wide audience with different levels of experience, it provides valuable information to graduate students and scientists who may be new to these fields of microfluidics and nanofluidics while providing up-to-date information to active scientists and experts in the field. This outstanding encyclopedia is an indispensable source for research professionals, technology investors and developers seeking the most up-to-date information on microfluidics and nanofluidics among a wide range of disciplines from science to engineering to medicine.

It takes two years of hard work of many people for this Encyclopedia to come to live. I would like to give my sincere thanks the Editorial Board members and many specially invited experts for helping me to review so many manuscripts to ensure the highest quality. I would like to thank and congratulate all contributing authors. This is your Encyclopedia and you made the great contribution to these fields. Finally, my heartfelt appreciation goes to the colleagues at Springer, Steven Elliot, Oona Schmid, Sylvia Blago, and Simone Giesler-Güllich; without their persistent efforts and hard work everyday, it is not possible to complete this Encyclopedia.

Dongqing Li
(Editor-in-Chief)

Nashville, March 2008

Editor-in-Chief

DONGQING LI
Department of Mechanical Engineering
Vanderbilt University
VU Station B 351592
2301 Vanderbilt Place
Nashville, TN. 37235-1592
USA
dongqing.li@vanderbilt.edu

Section Editors

Chong H. Ahn
Department of Electrical and Computer Engineering
University of Cincinnati
Cincinnati, OH, USA
chong.ahn@uc.edu

Martin Gijs
Swiss Federal Institute of Technology (EPFL)
Institute of Microelectronic & Microsystems (IMM)
Lausanne, Switzerland
martin.gijs@epfl.ch

Steffen Hardt
Institute for Nano- and Micro Process Technology
University of Hannover
Hannover, Germany
hardt@nmp.uni-hannover.de

Satish G. Kandlikar
Mechanical Engineering Department
Rochester Institute of Technology
Rochester, NY, USA
sgkeme@rit.edu

James P. Landers
Department of Chemistry
University of Virginia
Charlottesville, VA, USA
landers@virginia.edu

Yuehe Lin
Environmental Molecular Sciences Laboratory
Pacific Northwest National Laboratory
Richland, WA, USA
Yuehe.Lin@pnl.gov

Andrew de Mello
Department of Chemistry
Imperial College of Science, Technology and Medicine
London, UK
a.demello@ic.ac.uk

Hywel Morgan
School of Electronics and Computer Science
University of Southampton
Southampton, UK
hm@ecs.soton.ac.uk

Nico F. de Rooij
The Institute of Microtechnology
University of Neuchâtel
Neuchâtel, Switzerland
Nico.deRooij@unine.ch

Steve Wereley
School of Mechanical Engineering
Purdue University
West Lafayette, IN, USA
wereley@purdue.edu

Ruey-Jen Yang
Department of Engineering Science
National Cheng Kung University
Tainan City, Taiwan
rjyang@mail.ncku.edu.tw

Contributors

ABRAHAM, JOHN
Department of Mechanical Engineering
Purdue University
West Lafayette, IN
USA
jabraham@ecn.purdue.edu

AGARWAL, RAMESH
Aerospace Research and Education Center (AeREC)
and Aerospace Engineering Program
Washington University
St. Louis, MO
USA
rka@me.wustl.edu

AI, LISONG
Department of Biomedical Engineering
& Cardiovascular Medicine
School of Engineering & School of Medicine
University of Southern California
Los Angles, CA
USA

AKHMECHET, ROMAN
Sibley School of Mechanical Engineering
Cornell University
Ithaca, NY
USA
ra224@cornell.edu

ANGELI, PANAGIOTA
Department of Chemical Engineering
University College London
London
UK
p.angeli@ucl.ac.uk

ANNA, SHELLEY L.
Department of Mechanical Engineering
Carnegie Mellon University
Pittsburgh, PA
USA
sanna@cmu.edu

ARNOLD, MARKUS
HSG-IMAT, Hahn-Schickard-Gesellschaft
Institute for Microassembly Technology
Stuttgart
Germany
arnold@hsg-imat.de

ASFER, MOHAMMED
Department of Mechanical Engineering
IIT Kanpur
Kanpur
India

ASHGRIZ, NASSER
Department of Mechanical and Industrial Engineering
University of Toronto
Toronto, ON
Canada
ashgriz@mie.utoronto.ca

AUERSWALD, JANKO
Division Microrobotics
Centre Suisse d'Electronique et de Microtechnique
(CSEM S.A.)
Alpnach
Switzerland
janko.auerswald@csem.ch

BAKAJIN, OLGICA
Lawrence Livermore National Laboratory
Livermore, CA
USA
bakajin1@llnl.gov

BALDWIN, RICHARD P.
Department of Chemistry
University of Louisville
Louisville, KY
USA
rick.baldwin@louisville.edu

BAMIRO, OLUYINKA O.
Western Michigan University
Kalamazoo, MI
USA
oluyinka.o.bamiro@wmich.edu

BARBULOVIC-NAD, IRENA
Terrence Donnelly Centre for Cellular and Biomolecular Research
University of Toronto
Toronto, ON
Canada

BAROUD, CHARLES N.
LadHyX and Departement de Mécanique
Ecole Polytechnique
Palaiseau
France
baroud@ladhyx.polytechnique.fr

BARRETT, LOUISE M.
Sandia National Laboratories
Livermore, CA
USA
lmbarre@sandia.gov

BAYAZITOGLU, YILDIZ
Rice University
Houston, TX
USA
bayaz@rice.edu

BAZANT, MARTIN Z.
Department of Mathematics and Institute for Soldier Nanotechnologies
Massachusetts Institute of Technology
Cambridge, MA
USA
bazant@math.mit.edu

BEDEAUX, DICK
Department of Chemistry
Norwegian University of Science and Technology
Trondheim
Norway

BEDEKAR, ADITYA S.
CFD Research Corporation
Huntsville, AL
USA

BERG, JORDAN M.
Nano Tech Center & Department of Mechanical Engineering
Texas Tech University
Lubbock, TX
USA

BHAGAT, ALI ASGAR S.
Department of Electrical and Computer Engineering
University of Cincinnati
Cincinnati, OH
USA

BHATTACHARYA, SMITI
C. Eugene Bennett Department of Chemistry
West Virginia University
Morgantown, WV
USA

BHATTACHARYYA, ARPITA
Biomedical Engineering Department
Boston University
Boston, MA
USA
abhatta@bu.edu

BINDER, KURT
Institut für Physik
Johannes Gutenberg Universität Mainz
Mainz
Germany
kurt.binder@uni-mainz.de

BREUER, KENNETH S.
Division of Engineering
Brown University
Providence, RI
USA
kbreuer@brown.edu

BRUTIN, DAVID
IUSTI Laboratory
Poytech'Marseille
Marseille
France
david.brutin@polytech.univ-mrs.fr

BUTLER, DAVID LEE
School of Mechanical & Aerospace Engineering
Nanyang Technological University
Singapore
Singapore
mdlbutler@ntu.edu.sg

BÜTTNER, LARS
Professorship of Measuring and Testing Techniques
Dresden University of Technology
Dresden
Germany

CAO, JINHUA
Department of Mechanical Engineering
Purdue University
West Lafayette, IN
USA

CETIN, BARBAROS
Department of Mechanical Engineering
Vanderbilt University
Nashville, TN
USA
barbaros.cetin@vanderbilt.edu

CHAI, JOHN C.
School of Mechanical & Aerospace Engineering
Nanyang Technological University
Singapore
Singapore

CHAKRABORTY, SUMAN
Department of Mechanical Engineering
Indian Institute of Technology
Kharagpur
India
suman@mech.iitkgp.ernet.in

CHAMARTHY, PRAMOD
Department of Mechanical Engineering
Purdue University
West Lafayette, IN
USA
pramodc@purdue.edu

CHANG, CHIH-CHANG
Department of Engineering Science
National Cheng Kung University
Tainan
Taiwan

CHANG, HSUEH-CHIA
Department of Chemical and Biomolecular Engineering
Center for Microfluidic and Medical Diagnostics
University of Notre Dame
Notre Dame, IN
USA
hchang@nd.edu

CHANG, JUN KEUN
NanoEnTek Inc. & Digital Bio Technology Co., Inc.
Seoul
Korea
jkchang@digital-bio.com

CHARON, LUC
Department of Medical Biophysics
University of Toronto
Toronto, ON
Canada

CHEN, GANG
School of Pharmacy
Fudan University
Shanghai
China
gangchen@fudan.edu.cn

CHEN, JIA-KUN
Department of Engineering Science
National Cheng Kung University
Tainan
Taiwan

CHEN, RONGSHENG
Department of Biology and Chemistry
City University of Hong Kong
Kowloon
Hong Kong

CHEN, XIAOHONG
School of Pharmacy
Fudan University
Shanghai
China

CHEN, ZHONGPING
Department of Biomedical Engineering
University of California
Irvine, CA
USA
z2chen@uci.edu

CHEN, ZILIN
Department of Chemical and Biomolecular Engineering
Center for Microfluidic and Medical Diagnostics
University of Notre Dame
Notre Dame, IN
USA
zchen@nd.edu

CHENG, JI-YEN
Research Center for Applied Sciences
Academia Sinica
Taipei
Taiwan
jycheng@gate.sinica.edu.tw

CHENG, PING
School of Mechanical and Power Engineering
Shanghai Jiaotong University
Shanghai
China
pingcheng@sjtu.edu.cn

CHEREMISIN, FELIX G.
Russian Academy of Science
Moscow
Russia
cherem@ocas.ru

CHIAO, MU
Department of Mechanical Engineering
University of British Columbia
Vancouver, British Columbia
Canada
muchiao@mech.ubc.ca

CHON, CHAN HEE
Department of Mechanical Engineering
Vanderbilt University
Nashville, TN
USA
Chanhee.chon@vanderbilt.edu

CHOO, JAEBUM
Department of Applied Chemistry
Hanyang University
Ansan, Kyunggi-do
South Korea
jbchoo@hanyang.ac.kr

CHRISTENSEN, KENNETH T.
Department of Mechanical Science and Engineering
University of Illinois
Urbana, IL
USA
ktc@uiuc.edu

CHUN, YANG
School of Mechanical and Aerospace Engineering
Nanyang Technological University
Singapore
Singapore

CHUNG, CHEN-KUEI
Department of Mechanical Engineering
National Cheng Kung University
Tainan City
Taiwan (R.O.C.)
ckchung@mail.ncku.edu.tw

CLICQ, DAVID
Transport Modeling & (Bio)analytical Separation Science Group (TMAS2)
Vrije Universiteit Brussel
Brussel
Belgium

COLIN, STÉPHANE
National Institute of Applied Sciences of Toulouse (INSAT)
Toulouse Cedex 4
France
stephane.colin@insa-toulouse.fr

COLLINS, JOHN
Maxwell Sensors Inc.
Fullerton, CA
USA
Collins.biomint@gmail.com

CROSS, MICHAEL
Electrical & Computer Engineering Program
School of Engineering
The University of Vermont
Burlington, VT
USA
mcross@cems.uvm.edu

CUI, ZHENG
Rutherford Appleton Laboratory
Oxford
UK
z.cui@rl.ac.uk

CZARSKE, JÜRGEN
Professorship of Measuring and Testing Techniques
Dresden University of Technology
Dresden
Germany
juergen.czarske@tu-dresden.de

DALLAS, TIM
Nano Tech Center & Department of Electrical & Computer Engineering
Texas Tech University
Lubbock, TX
USA

DAMES, CHRIS
Department of Mechanical Engineering
University of California
Riverside, CA
USA
cdames@engr.ucr.edu

DANG, KHANH
Harvard-MIT Division of Health Sciences
and Technology
Massachusetts Institute of Technology
Cambridge, MA
USA

DAUB, MARTINA
Laboratory for MEMS Applications
Department of Microsystems Engineering (IMTEK)
University of Freiburg
Freiburg
Germany
daub@imtek.de

DE SILVA, MAURIS
Bascom Palmer Eye Institute
University of Miami
Miami, FL
USA
mdesilva@med.miami.edu

DEMIRCI, UTKAN
Harvard-MIT Division of Health Sciences
and Technology
Massachusetts Institute of Technology
Cambridge, MA
USA

DENG, PEIGANG
MEMS Department
China Resources Semiconductor (HK) Co., Ltd.
Hong Kong
China

DERMICI, DENIZ
Department of Economics
Bogazici University
Istanbul
Turkey

DESMET, GERT
Transport Modeling & (Bio)analytical Separation Science
Group (TMAS2)
Vrije Universiteit Brussel
Brussel
Belgium

DIAS, FRANCISCO
HE-Arc
Institut des Microtechnologies
La Chaux-de-Fonds
Switzerland

DJILALI, NED
Institute for Integrated Energy Systems (IESVic)
and Department of Mechanical Engineering
University of Victoria
Victoria, BC
Canada

DORFMAN, KEVIN D.
Department of Chemical Engineering and Materials
Science
University of Minnesota
Minneapolis, MN
USA
dorfman@umn.edu

DUCRÉE, JENS
HSG-IMIT, c/o IMTEK
University of Freiburg
Freiburg
Germany
jens.ducree@hsg-imit.de

DURMUS, N. GOZDE
Department of Molecular Biology and Genetics
Middle East Technical University
Ankara
Turkey

DUTTA, DEBASHIS
Department of Chemistry
University of Wyoming
Laramie, WY
USA
ddutta@uwyo.edu

DUTTA, PRASHANTA
School of Mechanical and Materials Engineering
Washington State University
Pullman, WA
USA
dutta@mail.wsu.edu

ERICKSON, DAVID
Sibley School of Mechanical and Aerospace Engineering
Cornell University
Ithaca, New York
USA
de54@cornell.edu

EWING, ANDREW H.
Department of Mechanical Engineering
Purdue University
West Lafayette, IN
USA

EIJKEL, JAN C. T.
BIOS, Lab-on-a-Chip Group
MESA+ Institute for Nanotechnology
Enschede
Netherlands

FAN, TONGXIANG
State Key Lab of Metal Matrix Composites
Shanghai Jiaotong University
Shanghai
China
txfan@sjtu.edu.cn

FANG, JI
Institute for Micromanufacturing
Louisiana Tech University
Ruston, LA
USA
jfang@latech.edu

FEKETE, VERONIKA
Transport Modeling & (Bio)analytical Separation Science Group (TMAS2)
Vrije Universiteit Brussel
Brussel
Belgium

FRANSSILA, SAMI
Helsinki University of Technology
Helsinki
Finland
sami.franssila@tkk.fi

FREIRE, SERGIO
Department of Chemistry
University of Toronto
Toronto, ON
Canada

FRIEND, JAMES
Micro/Nanophysics Research Laboratory
Monash University
Clayton, VIC
Australia
james.friend@eng.monash.edu.au

FRÉCHETTE, LUC G.
Department of Mechanical Engineering
Université de Sherbrooke
Sherbrooke, QC
Canada
Luc.Frechette@USherbrooke.ca

FU, JIANPING
Department of Mechanical Engineering
Massachusetts Institute of Technology
Cambridge, MA
USA
jpfu@mit.edu

FU, LUNG-MING
Department of Materials Engineering
National Pingtung University of Science and Technology
Pingtung
Taiwan, ROC
loudyfu@mail.npust.edu.tw

GAN, HIONG YAP
Division of Manufacturing Engineering School of Mechanical and Aerospace Engineering
Nanyang Technological University
Singapore
Singapore
ganh0002@ntu.edu.sg

GAO, YANDONG
Department of Mechanical Engineering
Vanderbilt University
Nashville, TN
USA
yandong.gao@vanderbilt.edu

GARCIA-CORDERO, JOSE L.
Biomedical Diagnostics Institute
National Centre for Sensor Research
Dublin City University
Dublin
Ireland

GARRELL, ROBIN L.
Department of Chemistry & Biochemistry
University of California
Los Angeles, CA
USA

GAVRIILIDIS, ASTERIOS
Department of Chemical Engineering
University College London
London
UK
a.gavriilidis@ucl.ac.uk

GEELHOED, PETER
Laboratory for Aero- & Hydrodynamics
Delft University of Technology
Delft
Netherlands
p.f.geelhoed@tudelft.nl

GHEBER, LEVI A.
Department of Biotechnology Engineering
Ben-Gurion
University of the Negev
Beer-Sheva
Israel
glevi@bgu.ac.il

GHOSAL, SANDIP
Department of Mechanical Engineering
Northwestern University
Evanston, IL
USA
s-ghosal@northwestern.edu

GLAWDEL, TOM
Department of Mechanical and Mechatronics Engineering
University of Waterloo
Waterloo, ON
Canada
tglawdel@engmail.uwaterloo.ca

GRAY, BONNIE
School of Engineering Science
Simon Fraser University
Burnaby, BC
Canada
bgray@sfu.ca

GREEN, NICOLAS
School of Electronics and Computer Science
University of Southampton
Southampton
UK

GUASTO, JEFFREY S.
Division of Engineering
Brown University
Providence, RI
USA
jguasto@brown.edu

GUI, LIN
Department of Mechanical and Mechatronics Engineering
University of Waterloo
Waterloo, ON
Canada

GUISEPPI-ELIE, ANTHONY
Center for Bioelectronics, Biosensors, and Biochips (C3B)
Department of Chemical and Biomolecular Engineering,
and Department of Bioengineering
Clemson University
Clemson, SC
USA
guiseppi@clemson.edu

HALL, JEREMIAH
Department of Aerospace Engineering Sciences
University of Colorado
Boulder, CO
USA

HAN, JONGYOON
Department of Electrical Engineering and Computer
Science and Department of Biological Engineering
Massachusetts Institute of Technology
Cambridge, MA
USA
jyhan@mit.edu

HAQUETTE, HENRI
HE-Arc
Institut des Microtechnologies
La Chaux-de-Fonds
Switzerland

HARRIS, NICK R.
School of Electronics and Computer Science
University of Southampton
Highfield, Southampton
UK
nrh@ecs.soton.ac.uk

HASHIM, AHMAD YUSAIRI BANI
Faculty of Manufacturing Engineering
Universiti Teknikal Malaysia Melaka
Melaka
Malaysia
yusairi@utem.edu.my

HAU, WINKY L. W.
IMTEK
University of Freiburg
Freiburg
Germany
winky.hau@imtek.de

HENDERSON, CLIFFORD L.
School of Chemical and Biomolecular Engineering
Georgia Institute of Technology
Atlanta, GA
USA
cliff.henderson@chbe.gatech.edu

HEO, CHUL-JOON
National CRI Center for Integrated Optofluidic Systems
and Department of Chemical and Biomolecular
Engineering
Korea Advanced Institute of Science and Technology
Daejeon
Korea

HILL, MARTYN
School of Engineering Sciences
University of Southampton
Highfield, Southampton
UK

HILL JR., HERBERT H.
Department of Chemistry
Washington State University
Pullman, WA
USA

HINRICHS, KARSTEN
ISAS - Institute for Analytical Sciences
Berlin
Germany
hinrichs@isas.de

HITT, DARREN L.
Mechanical Engineering Program, School of Engineering
The University of Vermont
Burlington, VT
USA
darren.hitt@uvm.edu

HONG, JONGIN
Department of Chemistry
Imperial College London, South Kensington Campus
London
UK
hong.jongin@gmail.com

HORIUCHI, KEISUKE
Mechanical Engineering Research Laboratory
Hitachi, Ltd.
Hitachinaka, Ibaraki
Japan

HOUSE, DUSTIN
Department of Mechanical Engineering
Vanderbilt University
Nashville, TN
USA
dustin.l.house@vanderbilt.edu

HSIAI, TZUNG K.
Department of Biomedical Engineering
& Cardiovascular Medicine
School of Engineering & School of Medicine
University of Southern California
Los Angles, CA
USA

HSIEH, CHENG-CHIEH
Intel Corporation
Chandler, AZ
USA
cheng-chieh.hsieh@intel.com

HSIEH, YI-CHENG
Department of Biomedical Engineering
Rutgers, The State University of New Jersey
Piscataway, NJ
USA

HU, GUOQING
Department of Mechanical Engineering
Vanderbilt University
Nashville, TN
USA

HUANG, PETER
Department of Biomedical Engineering
Tufts University
Medford, MA
USA

HUANG, XIAOYANG
School of Mechanical and Aerospace Engineering
Nanyang Technological University
Singapore
Singapore

HWANG, EUN-SOO
Microsystems Laboratory
School of Mechanical Engineering
Yonsei University
Seoul
Republic of Korea

IANCU, FLORIN
Michigan State University
East Lansing, MI
USA
ihuin@egr.msu.edu

ILES, ALEXANDER
Department of Chemistry
The University of Hull
Hull
UK
n.pamme@hull.ac.uk

IRIMIA, DANIEL
Massachusetts General Hospital
Harvard Medical School
Boston, VA
USA
dirimia@partners.org

IYER, SRINIVAS
Bioscience Division
Los Alamos National Laboratory
Los Alamos, NM
USA
siyer@lanl.gov

JACKSON, DOUGLAS J.
Department of Electrical and Computer Engineering
University of Louisville
Louisville, KY
USA
doug.jackson@louisville.edu

JAFARI, ALI
Department of Mechanical and Industrial Engineering
University of Toronto
Toronto, ON
Canada

JANG, SE GYU
National CRI Center for Integrated Optofluidic Systems and Department of Chemical and Biomolecular Engineering
Korea Advanced Institute of Science and Technology
Daejeon
Korea

JEON, NOO LI
Department of Biomedical Engineering
University of California
Irvine, CA
USA

JIANG, HONG
GraceFlow Technology
Columbia, SC
USA
ajiangca2@yahoo.com

JIAO, ZHENJUN
School of Mechanical and Aerospace Engineering
Nanyang Technological University
Singapore
Singapore

JO, KYOO DONG
C. Eugene Bennett Department of Chemistry
West Virginia University
Morgantown, WV
USA
atimperm@wvu.edu

JUBERY, TALUKDER Z.
School of Mechanical and Materials Engineering
Washington State University
Pullman, WA
USA

KANDLIKAR, SATISH G.
Department of Mechanical Engineering
Rochester Institute of Technology
Rochester, NY
USA
sgkeme@rit.edu

KANG, KWAN HYOUNG
Department of Mechanical Engineering
Pohang University of Science and Technology
Pohang
South Korea
khkang@postech.edu

KANG, SANGMO
Dong-A University
Busan
Korea

KANG, YUEJUN
Department of Mechanical Engineering
Vanderbilt University
Nashville, TN
USA
yuejun.kang@vanderbilt.edu

KARNIK, ROHIT
Department of Mechanical Engineering
Massachusetts Institute of Technology
Cambridge, MA
USA
karnik@mit.edu

KASSEGNE, SAMUEL K.
MEMS Research Laboratory
Department of Mechanical Engineering
College of Engineering
San Diego State University
San Diego, CA
USA
kassegne@mail.sdsu.edu

KEH, HUAN J.
Department of Chemical Engineering
National Taiwan University
Taipei
Taiwan
huan@ntu.edu.tw

KELLY, KATHLEEN
C. Eugene Bennett Department of Chemistry
West Virginia University
Morgantown, WV
USA

KEPPNER, HERBERT
HE-Arc
Institut des Microtechnologies
La Chaux-de-Fonds
Switzerland

KEYNTON, ROBERT S.
Department of Bioengineering
University of Louisville
Louisville, KY
USA
rob.keynton@louisville.edu

KHADEMHOSSEINI, ALI
Harvard-MIT Division of Health Sciences and Technology
Massachusetts Institute of Technology
Cambridge, MA
USA
alik@mit.edu

KIM, HYUNG JOON
Department of Biomedical Engineering
University of California
Irvine, CA
USA

KIM, SE-HEON
National CRI Center for Integrated Optofluidic Systems and Department of Chemical and Biomolecular Engineering
Korea Advanced Institute of Science and Technology
Daejeon
Korea

KIM, YONG-HO
Microsystems Laboratory
School of Mechanical Engineering
Yonsei University
Seoul
Republic of Korea

KIM, YONG-JUN
Microsystems Laboratory
School of Mechanical Engineering
Yonsei University
Seoul
Republic of Korea
yjk@yonsei.ac.kr

KIM, YOUNG JO
Department of Chemical Engineering
Center for Surface Science and Plasma Technology
University of Missouri-Columbia
Columbia, MO
USA
yuq@missouri.edu

KING, MICHAEL R.
University of Rochester
Rochester, NY
USA
mike_king@urmc.rochester.edu

KITAMORI, TAKEHIKO
Department of Applied Chemistry
School of Engineering
The University of Tokyo
Tokyo
Japan
kitamori@icl.t.u-tokyo.ac.jp

KJEANG, ERIK
Institute for Integrated Energy Systems (IESVic) and Department of Mechanical Engineering
University of Victoria
Victoria, BC
Canada

KJELSTRUP, SIGNE
Department of Chemistry
Norwegian University of Science and Technology
Trondheim
Norway

KLAPPERICH, CATHERINE M.
Biomedical and Manufacturing Engineering Departments
Boston University
Boston, MA
USA
catherin@bu.edu

KLEINSTREUER, CLEMENT
Mechanical and Aerospace Engineering
North Carolina State University
Raleigh, NC
USA
ck@eos.ncsu.edu

KNAPP, HELMUT F.
Division Microrobotics
Centre Suisse d'Electronique et de Microtechnique (CSEM S.A.)
Alpnach
Switzerland

KOCKMANN, NORBERT
Laboratory for Design of Microsystems
Department of Microsystems Engineering – IMTEK
Albert-Ludwig University of Freiburg
Freiburg
Germany
kockmann@imtek.de

KONG, LINGXUE
Center for Material and Fiber Innovation
Deakin University
Geelong, VIC
Australia
lingxue.kong@deakin.edu.au

KOZBERG, MARIEL
Department of Chemical Engineering
Massachusetts Institute of Technology
Cambridge, MA
USA

KRISHNAMOORTHY, SIVA
Baxter Healthcare Corporation
Round Lake, IL
USA

KUMAR, ALOKE
Department of Mechanical Engineering
Purdue University
West Lafayette, IN
USA

KUMAR, HARIBALAN
Seamans Center for the Engineering Arts and Sciences
University of Iowa
Iowa City, IA
USA
haribalan-kumar@uiowa.edu

KWOK, DANIEL Y.
Department of Mechanical Engineering
Schulich School of Engineering
University of Calgary
Calgary, AB
Canada
daniel.kwok@ucalgary.ca

KÖHLER, MICHAEL
Stiftungslehrstuhl der Deutschen Bundesstiftung Umwelt,
Institut für Physik
Technische Universität Ilmenau
Ilmenau
Germany
michael.koehler@tu-ilmenau.de

KÜCK, HEINZ
HSG-IMAT, Hahn-Schickard-Gesellschaft
Institute for Microassembly Technology
Stuttgart
Germany
kueck@hsg-imat.de

LAM, YEE CHEONG
Division of Manufacturing Engineering School
of Mechanical and Aerospace Engineering
Nanyang Technological University
Singapore
Singapore

LEE, ABRAHAM P.
Department of Biomedical Engineering and Department
of Mechanical Aerospace
University of California
Irvine, CA
USA
aplee@uci.edu

LEE, CHIA-YEN
Department of Mechanical and Automation Engineering
Da-Yeh University
Chung-Hua
Taiwan, ROC

LEE, JAESUNG
LG Material & Parts R&D Center
LG Micron
Korea
jaesung@lgmicron.com

LEE, SEUNG-KON
National CRI Center for Integrated Optofluidic Systems
and Department of Chemical and Biomolecular
Engineering
Korea Advanced Institute of Science and Technology
Daejeon
Korea

LEE, YI-KUEN
Department of Mechanical Engineering
Hong Kong University of Science and Technology
Hong Kong
China

LI, CHEUK-WING
Department of Biology and Chemistry
City University of Hong Kong
Hong Kong
China

LI, DEYU
Department of Mechanical Engineering
Vanderbilt University
Nashville, TN
USA
deyu.li@vanderbilt.edu

LI, DONGQING
Department of Mechanical Engineering
Vanderbilt University
Nashville, TN
USA

LI, JIE
Mechanical and Aerospace Engineering
North Carolina State University
Raleigh, NC
USA

LI, ZHIXIN
Department of Engineering Mechanics
Tsinghua University
Beijing
China

LILGE, LOTHAR
Department of Medical Biophysics
University of Toronto
Toronto, ON
Canada

LIM, JONG-MIN
National CRI Center for Integrated Optofluidic Systems and Department of Chemical and Biomolecular Engineering
Korea Advanced Institute of Science and Technology
Daejeon
Korea

LIM, TEIK-CHENG
School of Science and Technology
SIM University
Singapore
Singapore
tclim@unisim.edu.sg

LIN, BINGCHENG
Dalian Institute of Chemical Physics
Chinese Academy of Sciences
Dalian
China
bclin@dicp.ac.cn

LIN, CHE-HSIN
Department of Mechanical and Electromechanical Engineering
National Sun Yat-sen University
Kaohsiung
Taiwan
chehsin@mail.nsysu.edu.tw

LIN, RICHARD L.
Department of Materials Science and Engineering
Massachusetts Institute of Technology
Cambridge, MA
USA

LIN, YUEHE
Pacific Northwest National Laboratory
Richland, WA
USA
yuehe.lin@pnl.gov

LINDEMANN, TIMO
Laboratory for MEMS Applications
Department of Microsystems Engineering
University of Freiburg
Freiburg
Germany

LIOU, WILLIAM W.
Western Michigan University
Kalamazoo, MI
USA
William.liou@wmich.edu

LIU, CHENG-HSIEN
Department of Power Mechanical Engineering
National Tsing Hua University
Hsinchu
Taiwan
Liuch@pme.nthu.edu.tw

LIU, JING
Cryogenic Lab, Technical Institute of Physics and Chemistry
Chinese Academy of Sciences
Beijing
China
jliu@cl.cryo.ac.cn

LIU, XIN
Dalian Institute of Chemical Physics
Chinese Academy of Sciences
Dalian
China

LO, WIN-JET
Department of Refrigeration and Air-Conditioning
National Chin-Yi University of Technology
Taichung
Taiwan

LOUISOS, WILLIAM F.
Mechanical Engineering Program, School of Engineering
University of Vermont
Burlington, VT
USA

LUCAS, LONNIE J.
Department of Agricultural & Biosystems Engineering
The University of Arizona
Tucson, AZ
USA

LUKES, JENNIFER R.
Department of Chemistry
Imperial College London, South Kensington Campus
London
UK
jrlukes@seas.upenn.edu

LUO, HAOXIANG
Department of Mechanical Engineering
Vanderbilt University
Nashville, TN
USA
haoxiang.luo@vanderbilt.edu

MA, HONGBIN
Department of Mechanical & Aerospace Engineering
University of Missouri-Columbia
Columbia, MO
USA

MAEDA, HIDEAKI
Nanotechnology Research Institute
National Institute of Advanced Industrial Science
and Technology (AIST)
Tosu, Saga
Japan
maeda-h@aist.go.jp

MANDAL, SUDEEP
Sibley School of Mechanical and Aerospace Engineering
Cornell University
Ithaca, NY
USA
sm445@cornell.edu

MANN, J. ADIN
Department of Chemical Engineering
Case Western Reserve University
Cleveland, OH
USA

MANZARI, MEHRDAD T.
Sharif University of Technology
Tehran
Iran
mtmanzari@sharif.edu

MAO, XIAOLE
Department of Bioengineering
The Pennsylvania State University
University Park, PA
USA

MAWATARI, KAZUMA
Microchemistry Group
Kanagawa Academy of Science and Technology (KAST)
Kanagawa
Japan
kmawatari@world.odn.ne.jp

MIAO, JIANMIN
Micromachines Centre, School of Mechanical
and Aerospace Engineering
Nanyang Technological University
Singapore
Singapore
mjmmiao@ntu.edu.sg

MILLER, ELIZABETH M.
Terrence Donnelly Centre for Cellular
and Biomolecular Research
University of Toronto
Toronto, ON
Canada

MINAS, GRACA
Department of Industrial Electronics
University of Minho
Guimaraes
Portugal
gminas@dei.uminho.pt

MINC, NICOLAS
Department of Microbiology
Columbia University
NYC, NY
USA
nm2268@columbia.edu

MINERICK, ADRIENNE R.
Dave C Swalm School of Chemical Engineering
Mississippi State University
Starkville, MS
USA
minerick@che.msstate.edu

MINTEER, SHELLEY D.
Department of Chemistry
Saint Louis University
St. Louis, Missouri
USA
minteers@slu.edu

MIRAGHAIE, REZA
Keck Graduate Institute
Claremont, CA
USA
reza_miraghaie@kgi.edu

MITRA, SUSHANTA K.
Department of Mechanical Engineering
Indian Institute of Technology Bombay
Mumbai
India
skmitra@me.iitb.ac.in

MIYAZAKI, MASAYA
Nanotechnology Research Institute
National Institute of Advanced Industrial Science
and Technology (AIST)
Tosu, Saga
Japan
m.miyazaki@aist.go.jp

MOHSENI, KAMRAN
Department of Aerospace Engineering Sciences
University of Colorado
Boulder, CO
USA
mohseni@colorado.edu

MORGAN, HYWEL
School of Electronics and Computer Science
University of Southampton
Southampton
UK
hm@ecs.soton.ac.uk

MORINI, GIAN LUCA
Institute of Physics
DIENCA Università di Bologna
Bologna
Italy
gianluca.morini@mail.ing.unibo.it

MORRISON, DAVID W. G.
Harvard-MIT Division of Health Sciences
and Technology
Massachusetts Institute of Technology
Cambridge, MA
USA

MURTHY, SHASHI K.
Department of Chemical Engineering
Northeastern University
Boston, MA
USA
smurthy@coe.neu.edu

MÜLLER, NORBERT
Michigan State University
East Lansing, MI
USA

NADIM, ALI
Keck Graduate Institute
Claremont, CA
USA
nadim@kgi.edu

NAKAMURA, HIROYUKI
Nanotechnology Research Institute
National Institute of Advanced Industrial Science
and Technology (AIST)
Tosu
Japan
nakamura-hiroyuki@aist.go.jp

NAM-TRUNG, NGUYEN
School of Mechanical and Aerospace Engineering
Nanyang Technological University
Singapore
Singapore
mntnguyen@ntu.edu.sg

NASAREK, R.
Technical Thermodynamics
Mechanical Engineering Faculty
Darmstadt University of Technology
Darmstadt
Germany
nasarek@ttd.tu-darmstadt.de

NATRAJAN, VINAY K.
Department of Mechanical Science and Engineering
University of Illinois
Urbana, IL
USA

NGUYEN, BAO
MEMS Research Laboratory Department of Mechanical Engineering
College of Engineering
San Diego State University
San Diego, CA
USA
mntnguyen@ntu.edu.sg

NGUYEN, NAM-TRUNG
School of Mechanical & Aerospace Engineering
Nanyang Technological University
Singapore
Singapore
mntnguyen@ntu.edu.sg

NIEDERMANN, PHILIPPE
Division Microrobotics
Centre Suisse d'Electronique et de Microtechnique (CSEM S.A.)
Alpnach
Switzerland

O'KENNEDY, RICHARD
Applied Biochemistry Group
School of Biotechnology and Biomedical Diagnostics
Institute National Centre for Sensor Research
Dublin City University
Dublin
Ireland
richard.okennedy@dcu.ie

OLSEN, MICHAEL G.
Department of Mechanical Engineering
Iowa State University
Ames, IA
USA
mgolsen@iastate.edu

OOI, KIM TIOW
School of Mechanical and Aerospace Engineering
Nanyang Technological University
Singapore
Singapore

PAIS, ANDREA
Department of Electrical and Computer Engineering
University of Cincinnati
Cincinnati, OH
USA

PAMME, NICOLE
Department of Chemistry
The University of Hull
Hull
UK

PAN, YU-JEN
Department of Engineering Science
National Cheng Kung University
Tainan
Taiwan

PANDA, SIDDHARTHA
Department of Chemical Engineering
IIT Kanpur
Kanpur
India
spanda@iitk.ac.in

PANIGRAHI, PRADIPTA KUMAR
Department of Mechanical Engineering
IIT Kanpur
Kanpur
India
panig@iitk.ac.in

PAPAUTSKY, IAN
Department of Electrical and Computer Engineering
University of Cincinnati
Cincinnati, OH
USA
Ian.Papautsky@uc.edu

PAPPAERT, KRIS
Transport Modeling & (Bio)analytical Separation Science Group (TMAS2)
Vrije Universiteit Brussel
Brussel
Belgium
kris.pappaert@gmail.com

PARIKESIT, GEA O. F.
Quantitative Imaging Group
Delft University of Technology
Delft
The Netherlands
g.o.f.parikesit@tudelft.nl

PARK, HYUNG GYU
Lawrence Livermore National Laboratory
Livermore, CA
USA

PARK, JEONG WON
Department of Biomedical Engineering
University of California
Irvine, CA
USA
njeon@uci.edu

PARK, SECHUL
Microsystems Laboratory
School of Mechanical Engineering
Yonsei University
Seoul
Republic of Korea

PELES, YOAV
Department of Mechanical, Aerospace and Nuclear Engineering
Rensselaer Polytechnic Institute
Troy, NY
USA
pelesy@rpi.edu

PETERSON, DOMINIC S.
Chemistry Division
Los Alamos National Laboratory
Los Alamos, NM
USA
DominicP@lanl.gov

PETERSON, ERIK T. K.
Department of Electrical and Computer Engineering
University of Cincinnati
Cincinnati, OH
USA

POPA, DAN
Automation & Robotics Research Institute
The University of Texas at Arlington
Fort Worth, TX
USA
popa@uta.edu

PYARAJAN, SAIJU
Department of Pathology and NYU Cancer Institute
New York University School of Medicine
New York, NY
USA
Saiju.Pyarajan@med.nyu.edu

QI, SUIJIAN
Department of Biology and Chemistry
City University of Hong Kong
Kowloon Tong
Hong Kong SAR

QIN, JIANHUA
Department of Biotechnology
Dalian Institute of Chemical Physics
Chinese Academy of Sciences
Dalian
China
jhqin@dicp.ac.cn

QUAN, XIAOJUN
School of Mechanical and Power Engineering
Shanghai Jiaotong University
Shanghai
China

RADADIA, ADARSH D.
University of Illinois at Urbana-Champaign
Urbana, IL
USA
radadia@uiuc.edu

RADISIC, MILICA
Department of Chemical Engineering and Applied Chemistry
Institute of Biomaterials and Biomedical Engineering
University of Toronto
Toronto, ON
Canada

RAUSCHER, MARKUS
Max-Planck-Institut für Metallforschung
Stuttgart
Germany
rauscher@mf.mpg.de

REDDY, VARUN
Department of Bioengineering
The Pennsylvania State University
University Park, PA
USA

REN, CAROLYN
Department of Mechanical and Mechatronics Engineering
University of Waterloo
Waterloo, ON
Canada
c3ren@mecheng1.uwaterloo.ca

RESCHKE, BRENT
C. Eugene Bennett Department of Chemistry
West Virginia University
Morgantown, WV
USA

RICCO, ANTONIO J.
Biomedical Diagnostics Institute National Centre for Sensor Research
Dublin City University
Dublin
Ireland
ajricco@alum.mit.edu

ROUHANIZADEH, MAHSA
Department of Biomedical Engineering
& Cardiovascular Medicine
School of Engineering & School of Medicine
University of Southern California
Los Angles, CA
USA
rouhaniz@usc.edu

ROUSSEL, THOMAS J.
Department of Bioengineering
University of Louisville
Louisville, KY
USA
thomas.roussel@louisville.edu

ROY, SUBRATA
Department of Mechanical and Aerospace Engineering
University of Florida
Gainesville, IA
USA
roy@ufl.edu

SAGGERE, LAXMAN
University of Illinois at Chicago
Chicago, IL
USA
saggere@uic.edu

SAHA, AURO ASHISH
Department of Mechanical Engineering
Indian Institute of Technology Bombay
Mumbai
India

SAINIEMI, LAURI
Helsinki University of Technology
Helsinki
Finland
lauri.sainiemi@tkk.fi

SCHAEFER, LAURA
Mechanical Engineering and Materials Science
Department
University of Pittsburgh
Pittsburgh, PA
USA
las149@pitt.edu

SCHMIDT, HOLGER
University of California
Santa Cruz, CA
USA
hschmidt@soe.ucsc.edu

SCHÖNFELD, FRIEDHELM
Institut für Mikrotechnik Mainz GmbH
Mainz
Germany
Schoenfeld@imm-mainz.de

SENGUPTA, SHRAMIK
Department of Chemical and Biomolecular Engineering
University of Notre Dame
Notre Dame, IN
USA

SETHU, PALANIAPPAN
Department of Bioengineering
University of Louisville
Louisville, KY
USA
p.sethu@louisville.edu

SHAPIRO, BENJAMIN
Aerospace Engineering; joint appointments with
Bio-engineering, Institute of Systems Research; affiliated
with Applied Mathematics and Scientific Computation
program
University of Maryland
College Park, MD
USA
benshap@eng.umd.edu

SHARIPOV, FELIX
Departamento de Física
Universidade Federal do Paraná
Curitiba
Brazil
sharipov@fisica.ufpr.br

SHIN, HWA SUNG
Department of Biomedical Engineering
University of California
Irvine, CA
USA

SHUI, LINGLING
BIOS, Lab-on-a-Chip Group
MESA+ Institute for Nanotechnology
Enschede
Netherlands
L.shui@ewi.utwente.nl

SILBER-LI, ZHANHUA
LNM, Institute of Mechanics
Chinese Academy of Sciences
Beijing
China
lili@imech.ac.cn

SIMMONS, BLAKE A.
Sandia National Laboratories
Livermore, CA
USA

SINGH, ANUP K.
Sandia National Laboratories
Livermore, CA
USA
aksingh@sandia.gov

SINGHAL, ASHOK K.
CFD Research Corporation
Huntsville, AL
USA

SINTON, DAVID
Department of Mechanical Engineering
University of Victoria
Victoria, BC
Canada
dongqing.li@vanderbilt.edu
dsinton@me.uvic.ca

SONG, YONG-AK
Department of Mechanical Engineering
Massachusetts Institute of Technology
Cambridge, MA
USA
yongak@mit.edu

STAROV, VICTOR M.
Department of Chemical Engineering
Loughborough University
Loughborough, Leicestershire
UK
V.M.Starov@lboro.ac.uk

STEPHAN, PETER
Technical Thermodynamics
Mechanical Engineering Faculty
Darmstadt University of Technology
Darmstadt
Germany
pstephan@ttd.tu-darmstadt.de

STERLING, JAMES D.
Keck Graduate Institute
Claremont, CA
USA

STREMLER, MARK A.
Department of Engineering Science and Mechanics
Virginia Polytechnic Institute and State University
Blacksburg, VA
USA
mark.stremler@vt.edu

SU, CHUN-MIN
Flow Measurement Laboratory
Center for Measurement Standards
Industrial Technology Research Institute
Hsinchu
Taiwan

SUGUMAR, DHARMALINGAM
Faculty of Manufacturing Engineering
Universiti Teknikal Malaysia Melaka
Melaka
Malaysia
sugumar@utem.edu.my

SUH, YONG KWEON
Dong-A University
Busan
Korea
yksuh@dau.ac.kr

SUN, TAO
Nanoscale Systems Integration Group
School of Electronics and Computer Science
University of Southampton
Highfield, Southampton
UK
ts5@ecs.soton.ac.uk

SUNDARAM, SHIVSHANKAR
CFD Research Corporation
Huntsville, AL
USA

SWICKRATH, MICHAEL J.
Department of Chemical Engineering
Case Western Reserve University
Cleveland, OH
USA
michael.swickrath@case.edu

SYMS, RICHARD R. A.
Electrical and Electronic Engineering Department
Imperial College London
London
UK
r.syms@imperial.ac.uk

TAM, MAGGIE
Department of Chemistry
Washington State University
Pullman, WA
USA

TANG, GONGYUE
School of Mechanical and Aerospace Engineering
Nanyang Technological University
Singapore
Singapore

TATSUMA, TETSU
Institute of Industrial Science
University of Tokyo
Tokyo
Japan
tatsuma@iis.u-tokyo.ac.jp

TESAŘ, VÁCLAV
Department of Thermodynamics,
Institute of Thermomechanics
Academy of Sciences of the Czech Republic
Prague
Czech Republic
tesar@it.cas.cz

THIBAUDEAU, GISELLE
Electron Microscopy Center
Mississippi State University
Mississippi State, MS
USA
giselle@emcenter.msstate.edu

TIMPERMAN, AARON T.
C. Eugene Bennett Department of Chemistry
West Virginia University
Morgantown, WV
USA
atimperm@wvu.edu

TSAI, CHIEN-HSIUNG
Department of Vehicle Engineering
National Pingtung University of Science and Technology
Pingtung
Taiwan
chtsai@mail.npust.edu.tw

TULLY, ELIZABETH
Applied Biochemistry Group
School of Biotechnology and Biomedical Diagnostics
Institute
National Centre for Sensor Research
Dublin City University
Dublin
Ireland

VAN DEN BERG, ALBERT
BIOS, Lab-on-a-Chip Group
MESA+ Institute for Nanotechnology
Enschede
Netherlands

VAN DER LINDEN, HEIKO
Laboratory for Aero- and Hydrodynamics
Faculty of Mechanical, Maritime and Materials
Engineering
TU Delft
Delft
Netherlands
heiko.vanderlinden@tudelft.nl

VARHUE, W.J.
Electrical & Computer Engineering Program
School of Engineering
The University of Vermont
Burlington, VT
USA
varhue@cems.uvm.edu

VENDITTI, ROBERTO
Department of Mechanical and Industrial Engineering
University of Toronto
Toronto, ON
Canada
roberto.venditti@gmail.com

WAGNER, E.
Technical Thermodynamics
Mechanical Engineering Faculty
Darmstadt University of Technology
Darmstadt
Germany

WALKER, GREG
Department of Mechanical Engineering
Vanderbilt University
Nashville, TN
USA
greg.walker@vanderbilt.edu

WAN, WEIJIE
Department of Systems Design Engineering
University of Waterloo
Waterloo, ON
Canada
wwan@engmail.uwaterloo.ca

WANG, CHENG
School of Mechanical and Aerospace Engineering
Nanyang Technological University
Singapore
Singapore

WANG, GUIREN
Department of Mechanical Engineering
University of South Carolina
Columbia, SC
USA
wanggu@engr.sc.edu

WANG, MORAN
NEAT, Department of Biological & Agricultural Engineering
University of California Davis
Davis, CA
USA
mmwang@ucdavis.edu

WANG, WEISONG
Department of Astronomy
University of Texas at Austin
Austin, TX
USA
weisong@astro.as.utexas.edu

WANG, YI
CFD Research Corporation
Huntsville, AL
USA
yxw@cfdrc.com

WANG, YING-CHIH
Department of Mechanical Engineering
Massachusetts Institute of Technology
Cambridge, MA
USA
ycwang@mit.edu

WERELEY, STEVEN T.
Department of Mechanical Engineering
Purdue University
West Lafayette, IN
USA
wereley@purdue.edu

WESTERWEEL, JERRY
Laboratory for Aero- & Hydrodynamics
Delft University of Technology
Delft
Netherlands

WHEELER, AARON R.
Department of Chemistry
University of Toronto
Toronto, ON
Canada
awheeler@chem.utoronto.ca

WILLIAMS, STUART
Mechanical Engineering
Purdue University
West Lafayette, IN
USA
swilliams@purdue.edu

WNEK, GARY E.
Department of Macromolecular Science and Engineering
Case Western Reserve University
Cleveland, OH
USA

WONG, STEVEN
MEMS Research Laboratory Department of Mechanical Engineering College of Engineering
San Diego State University
San Diego, CA
USA

WONG, TECK NENG
School of Mechanical & Aerospace Engineering
Nanyang Technological University
Singapore
Singapore
mtnwong@ntu.edu.sg

WU, HONGKAI
Department of Chemistry
Tsinghua University
Beijing
P. R. China
hkwu@mail.tsinghua.edu.cn

WU, HUIYING
School of Mechanical and Power Engineering
Shanghai Jiaotong University
Shanghai
China

WU, JIE
Department of Electrical Engineering and Computer Science
The University of Tennessee
Knoxville, TN
USA
jaynewu@utk.edu

WU, ZHEMIN
Department of Mechanical Engineering
Vanderbilt University
Nashville, TN
USA
zhemin.wu@vanderbilt.edu

XU, DONGYAN
Department of Mechanical Engineering
Vanderbilt University
Nashville, TN
USA
dongyan.xu@vanderbilt.edu

XU, JENNIFER
Department of Biomedical Engineering
& Cardiovascular Medicine
School of Engineering & School of Medicine
University of Southern California
Los Angles, CA
USA

XUAN, XIANGCHUN
Department of Mechanical Engineering
Clemson University
Clemson, SC
USA
xchxuan@mie.utoronto.ca

YAN, DEGUANG
Nanyang Technological University
Singapore
Singapore

YAN, HUI
Department of Chemistry
Tsinghua University
Beijing
P. R. China

YANDONG, GAO
School of Mechanical and Aerospace Engineering
Nanyang Technological University
Singapore
Singapore

YANG, ALLEN
Sibley School of Mechanical Engineering
Cornell University
Ithaca, NY
USA
ay38@cornell.edu

YANG, CHENG-TSAIR
Flow Measurement Laboratory
Center for Measurement Standards
Industrial Technology Research Institute
Hsinchu
Taiwan
ctyang@itri.org.tw

YANG, CHUN
School of Mechanical and Aerospace Engineering
Nanyang Technological University
Singapore
Singapore
mcyang@ntu.edu.sg

YANG, EUI-HYEOK
Department of Mechanical Engineering
Stevens Institute of Technology
Hoboken, NJ
USA
eyang@stevens.edu

YANG, JUN
Bioengineering College
Chongqing University
Chongqing
China
yjun1999@hotmail.com

YANG, LIJU
Biomanufacturing Research Institute & Technology
Enterprise, and Department of Pharmaceutical Sciences
North Carolina Central University
Durham, NC
USA
lyang@nccu.edu

YANG, MENGSU
Department of Biology and Chemistry
City University of Hong Kong
Kowloon Tong
Hong Kong SAR
bhmyang@cityu.edu.hk

YANG, RUEY-JEN
Department of Engineering Science
National Cheng Kung University
Tainan
Taiwan
rjyang@mail.ncku.edu.tw

YANG, SEUNG-MAN
National CRI Center for Integrated Optofluidic Systems
and Department of Chemical and Biomolecular
Engineering
Korea Advanced Institute of Science and Technology
Daejeon
Korea
smyang@kaist.ac.kr

Yang, Shu
Materials Science and Engineering
University of Pennsylvania
Philadelphia, PA
USA

Yang, Sung
Department of Mechatronics, School of Information and Mechatronics
Gwangju Institute of Science and Technology (GIST)
Gwangju, Buk-gu
Republic of Korea
syang@gist.ac.kr

Yap, Y. F.
School of Mechanical & Aerospace Engineering
Nanyang Technological University
Singapore
Singapore

Yasuda, Kenji
Department of Biomedical Information, Division of Biosystems
Institute of Biomaterials and Bioengineering
Tokyo Medical and Dental University
Tokyo
Japan
yasuda.bmi@tmd.ac.jp

Ye, Nannan
Department of Biotechnology
Dalian Institute of Chemical Physics
Chinese Academy of Sciences
Dalian
China

Ye, Wenjing
Department of Mechanical Engineering
Hong Kong University of Science and Technology
Hong Kong
China
mewye@ust.hk

Yeo, Leslie
Micro/Nanophysics Research Laboratory
Monash University
Clayton, VIC
Australia

Yeow, John T.W.
Department of Systems Design Engineering
University of Waterloo
Waterloo, ON
Canada
jyeow@engmail.uwaterloo.ca

Yi, Changqing
Department of Biology and Chemistry
City University of Hong Kong
Kowloon Tong
Hong Kong SAR

Yoon, Jeong-Yeol
Department of Agricultural & Biosystems Engineering
The University of Arizona
Tucson, AZ
USA
jyyoon@email.arizona.edu

Yoon, Seung-Il
Microsystems Laboratory
School of Mechanical Engineering
Yonsei University
Seoul
Republic of Korea

Yu, Hongyu
Department of Biomedical Engineering & Cardiovascular Medicine
School of Engineering & School of Medicine
University of Southern California
Los Angles, CA
USA

Yu, Qingsong
Department of Chemical Engineering
Center for Surface Science and Plasma Technology
University of Missouri-Columbia
Columbia, MO
USA

Zahn, Jeffrey D.
Department of Biomedical Engineering
Rutgers, The State University of New Jersey
Piscataway, NJ
USA
jdzahn@rci.rutgers.edu

Zengerle, Roland
Laboratory for MEMS Applications
Department of Microsystems Engineering
University of Freiburg
Freiburg
Germany
zengerle@imtek.uni-freiburg.de

ZHANG, DI
State Key Lab of Metal Matrix Composites
Shanghai Jiaotong University
Shanghai
China

ZHANG, JUNFENG
School of Engineering
Laurentian Universtiy
Sudbury, ON
Canada
jzhang@laurentian.ca

ZHANG, YALI
School of Mechanical & Aerospace Engineering
Nanyang Technological University
Singapore
Singapore

ZHAO, SHIHUAI
Center for Microfibrous Materials Manufacturing
Chemical Engineering
Auburn University
Auburn, AL
USA
szhao@auburn.edu

ZHENG, XIAOLIN
Bioengineering College
Chongqing University
Chongqing
China

ZHOU, HAN
State Key Lab of Metal Matrix Composites
Shanghai Jiaotong University
Shanghai
China

Absolute Pressure

► Pressure

Absorption

► Photometer

AC Dielectrophoresis Lab-on-Chip Devices

Stuart Williams
Mechanical Engineering, Purdue University,
West Lafayette, IN, USA
swilliams@purdue.edu

Synonyms

Dielectrophoretic force; DEP

Definition

Dielectrophoresis is the translational motion of a neutral particle by induced polarization in a nonuniform electric field. The magnitude and direction of the induced dielectrophoretic force are dependent on the characteristics of the applied electric field as well as the dielectric properties of the surrounding medium and of the particle itself.

Overview

Herbert Pohl was one of the first to study particle electrokinetics in the 1950s, particularly the manipulation of polarizable particles with nonuniform fields. He coined the term ►dielectrophoresis, and details of his investigations can be found in his classic text [1]. The advancement of microfabrication techniques and the demand of Lab-on-a-Chip technologies have led to the development of dielectrophoresis techniques for particulate, biological and pharmaceutical applications. Dielectrophoresis was initially used to manipulate particles and cells in the micrometer range (1 μm to 1 mm). Since the early 1990s, nanotechnology has incorporated dielectrophoresis for the manipulation of viruses, DNA, protein molecules and other nanoparticles (diameters of 1 nm to 1 μm). This article provides a brief background of dielectrophoresis followed by its basic manipulation of particles using translation, rotation (electrorotation), orientation (electro-orientation) and traveling wave dielectrophoresis. This article approaches design considerations and modeling techniques for the micrometer length scale; it does not specifically address all dielectrophoresis complexities at the nanometer scale. The majority of this article deals with popular applications of dielectrophoresis including novel techniques to induce these forces; by no means does it cover all of the existing applications. For a more extensive explanation of dielectrophoresis the reader is referred to texts by Jones [2], Morgan and Green [3], and Hughes [4], the latter of which addresses techniques for nanometer-sized particles.

For most dielectrophoresis cases, the applied electric field is an alternating current (AC) signal, created with a common frequency generator. In typical experimentation, frequencies are generally greater than 100 kHz with magnitudes below 20 V peak-to-peak. The shape of the signal is typically sinusoidal, but pulse signals have also been used in dielectrophoresis applications. This signal is applied to electrode geometries, the micrometer-sized features of which can be created using simple microfabrication techniques. Electrodes are typically fabricated on the surface of silicon wafers or glass substrates, including microscope slides. For most biological applications it is recommended that the species of interest be visually observed by optical means, which leaves glass or other transparent materials as favorable substrates. In the case where the electrodes themselves hinder visual observation they are patterned out of indium tin oxide (ITO), a transparent conducting material. Microfluidic channels and other fabricated features can easily be incorporated into the system. It is pos-

sible to manipulate, separate or group targeted cells with novel electrode geometry design and fabrication. Due to its simplicity in fabrication and its susceptibility to visual observation and analysis, dielectrophoresis is a favorable technique for biological experimentation.

Dielectrophoretic forces, though, can be induced by means other than an applied electric signal through electrodes. Optical tools can be implemented to modify an applied electric field, making these methods more susceptible for dynamic as opposed to static manipulation of electric fields with surface electrodes. Dielectrophoresis applications are not limited to particulate manipulation either. With properly configured surface-electrode geometry, it is possible to induce fluid motion and create nanoliter-sized droplets. Additionally, dielectrophoretic forces can be utilized to manipulate particles to build micro- and nano-structures such as wires.

Basic Methodology

Before we can incorporate dielectrophoresis into Lab-on-a-Chip systems it is important to have a grasp of the theory behind dielectrophoresis. Basic theory, common experimental parameters, typical dielectrophoretic manipulation techniques, particle modeling considerations and dielectrophoresis-induced effects are discussed below.

Dielectrophoresis

Dielectrophoresis is the translational motion of a particle by induced polarization in a nonuniform electric field. When conductive, uncharged particles are exposed to an electric field they will polarize, inducing a dipole on the particle. The magnitude and charge orientation of the induced dipole are dependent on the permittivities and conductivities of the medium and of the particle. If the electric field is uniform the induced charges on both sides of the particle are equal, creating no net force on the particle. However, if the electric field is nonuniform (Fig. 1) there will be a net force greater than zero. The general expression for the dielectrophoretic force of a homogeneous sphere is expressed as

$$F_{\mathrm{DEP}} = 2\pi \varepsilon_0 \varepsilon_{\mathrm{m}} r^3 \mathrm{Re}\big[K(\omega)\big] \nabla E^2 \quad (1)$$

where ε_0 is the permittivity of free space, ε_{m} is the relative permittivity of the medium, r is the radius of the particle, $\mathrm{Re}\,[K(\omega)]$ is the real part of the Clausius–Mossotti factor and ∇E^2 is the gradient of the magnitude of the electric field squared. This equation assumes that the there is no applied phase gradients to the electric field. The Clausius–

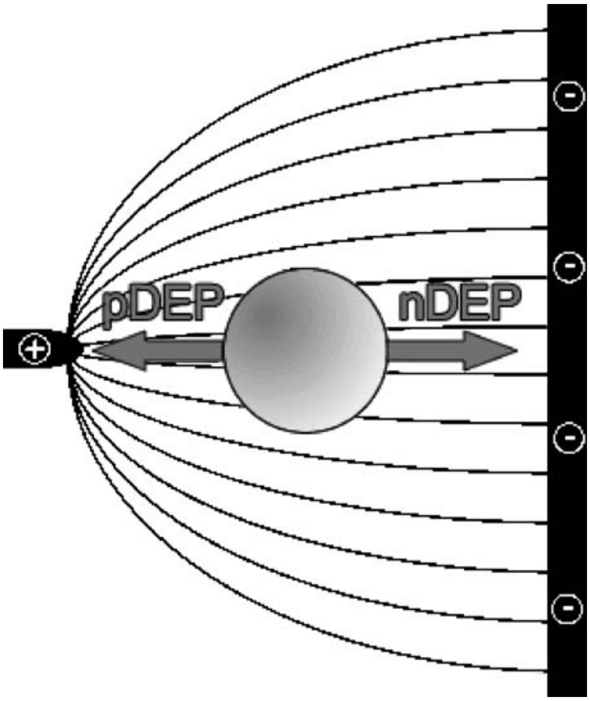

AC Dielectrophoresis Lab-on-Chip Devices, Figure 1 A polarizable particle in a nonuniform electric field

Mossotti factor is defined as

$$K(\omega) = \frac{\varepsilon_{\mathrm{p}}^* - \varepsilon_{\mathrm{m}}^*}{\varepsilon_{\mathrm{p}}^* + 2\varepsilon_{\mathrm{m}}^*} \quad (2)$$

where subscripts p and m are assigned to the particle and medium, respectively, and ε^* is called the complex permittivity. The complex permittivity is

$$\varepsilon^* = \varepsilon_0 \varepsilon_{\mathrm{r}} - j\frac{\sigma}{\omega} \quad (3)$$

where j is $\sqrt{-1}$, ε_{r} is the material's relative permittivity, σ is the material's conductivity and $\omega = 2\pi f$ (where f is the applied frequency). The Clausius–Mossotti factor is a function of frequency and, depending on the dielectric properties of the medium and particle, this factor can be either positive or negative with a possible range of $+1.0$ to -0.5. If $\mathrm{Re}\,[K(\omega)]$ is negative, the particle experiences negative dielectrophoresis (nDEP) and is repelled from gradients in the nonuniform electric field (Fig. 1). For a positive value of $\mathrm{Re}\,[K(\omega)]$, the particle is attracted to high electric field gradients with positive dielectrophoresis (pDEP). With dielectrophoresis it is possible to manipulate particles using a variety of techniques and applications.

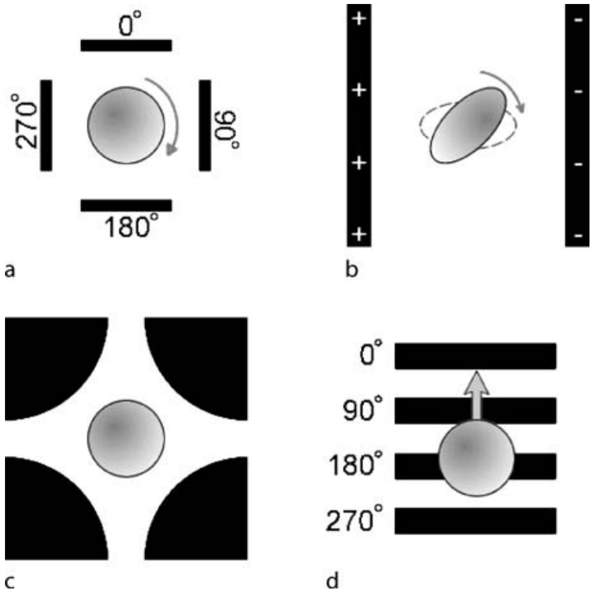

AC Dielectrophoresis Lab-on-Chip Devices, Figure 2 Dielectrophoretic manipulation techniques: (**a**) electrorotation, (**b**) electro-orientation, (**c**) particle trapping and (**d**) traveling wave dielectrophoresis

Particle Manipulation

The majority of dielectrophoretic manipulation of particles includes translating (dielectrophoresis), rotating (electrorotation), orienting (electro-orientation), trapping and using traveling wave dielectrophoresis. Figure 2 provides an illustrative representation of each technique. In electrorotation a torque is applied to a particle that is subjected to a rotating electric field (Fig. 2a). The induced dipole takes a finite amount of time to polarize in a neutral dielectric particle, which attempts to orient itself with the direction of the electric field. This dipole, though, lags behind the applied rotating electric field. The reorientation of the dipole with the electric field induces a torque on the particle, rotating it. Next, electro-orientation involves the alignment of a nonspherical particle in a uniform electric field (Fig. 2b). When an ellipsoidal particle polarizes, the dipole moment will align the particle with its longest nondispersed dipole parallel to the field lines. Its orientation is a function of the electric field frequency and the dielectric properties of the medium and particle.

Dielectrophoretic forces, though, can be used to not only rotate a particle, but trap it as well. There are two types of particle trapping, those that utilize pDEP or nDEP forces. For example, four electrodes can be positioned in a quadrupole arrangement and, when the appropriate electric field is applied, a particle or particles are trapped in the electric field null at its center (Fig. 2c). Particle trapping will be revisited later in this article. Traveling wave dielectrophoresis is the linear application of electrorotation (Fig. 2d). An AC electric wave is produced by applying an electric field that travels linearly along a series of electrodes. The particle will translate in the same or opposite direction as the traveling wave depending on the properties of the applied signal frequency and the dielectrics of the particle and medium.

Modeling and Dielectrophoretic Effects

When incorporating dielectrophoresis in Lab-on-a-Chip systems, additional modeling parameters and electrophysiological interactions need to be considered. Obviously, biological cells and some particulates are not all completely spherical nor are they homogeneous. Typically cells are modeled as multi-shelled particles with each shell having its own respective conductivity and permittivity. Additionally, nonspherical particles are modeled as ellipsoids. For each of these situations the Clausius–Mossotti factor is extended to include these geometrical and layered effects by applying polarization factors. These modifications are described in detail elsewhere [2–4]. The dielectric properties of some particles and cells are unknown; however, dielectric techniques can be applied to determine these characteristics. For example, when an induced particle changes from pDEP to nDEP, or vice versa, this is called its crossover frequency. Similarly, a particle in electrorotation that changes in rotational velocity or direction under different conditions will give insight into its dielectric properties. Many of the previously mentioned dielectrophoretic manipulation techniques can be applied to determine particle dielectric characteristics. By varying both the medium conductivity and the applied frequency, the changes in a particle's induced dielectrophoretic behavior can be visually observed.

The electric field can induce higher order poles, called multipoles, instead of the assumed dipole. This occurs when the electric field is highly nonuniform; for example, when the electrode geometry is on the same length scale as the particle or when a particle is in a field null. For most applications, though, the dipole assumption accurately depicts the behavior of the particle. However, multipoles can effect the particle's interaction with the electric field and will react differently from an induced dipole. The electric field can also induce some negative physiological effects to the cell by inducing cell heating and influencing transmembrane voltage. Transmembrane voltage can affect ion movement and damage voltage-sensitive proteins. The electric field itself can heat the surrounding medium in what is called *Joule heating*. Joule heating creates temperature gradients that can directly heat the cell or create localized convection currents. By working at the

micrometer length scale some of these negative effects are minimized; however, they may still influence the system and cannot be ignored.

Key Research Findings

This dielectrophoresis background only serves as a brief overview; these technologies need to be explored in more detail before incorporating them into a Lab-on-a-Chip system. Lab-on-a-Chip systems integrate techniques of small fluid and sample handling with detection or process capabilities. Dielectrophoresis can be incorporated into these systems to manipulate, separate or trap cells as well as control small amounts of fluid. This technology can be used to trap cells for additional analysis, separate cell types based on dielectric properties, dispense picoliter droplets or used for similar manipulative applications. However, dielectrophoresis itself cannot be used as a sensor, except to determine dielectric properties of cells or detect such changes in response to stimuli. The integration of sensory technologies with dielectrophoresis is not discussed. Instead, specific novel dielectrophoresis applications are addressed in detail.

Trapping Particles

One of the more popular dielectrophoretic manipulation techniques involves the trapping of individual or groups of cells. Dielectrophoresis can be thought of as *electrical tweezers* that will grab onto and position cells. Trapping can be accomplished by means of novel electrode geometries that utilize pDEP or nDEP forces to selectively capture a particle or cell. Some electrode geometries induce both types of forces simultaneously; an example of such an arrangement involves interdigitated electrodes (Fig. 3). Planar electrode fingers, whose width and gap separation are a few times larger than the diameter of the particles of interest, have alternating applied voltages (either 180° out of phase or alternating $+V/\text{ground}$). This geometry creates a strong pDEP force at the edges of the electrodes and a field null above the center of each electrode strip. This arrangement provides both trapping capabilities and the ability to determine unknown particle dielectric properties from visual observation. For example, at a particular frequency and medium conductivity a particle will experience a pDEP force. However, for a different applied frequency and/or a change in medium conductivity the same particle could undergo nDEP. The strength of the dielectrophoretic trapping force can be estimated with the hydrodynamic drag necessary to release the particle. Similarly, interdigitated electrodes can be used to separate two cells that experience opposite pDEP/nDEP forces due to their different dielectric characteristics. Interdigitated electrodes are one of the simpler electrode geometries, compared to other trapping arrangements.

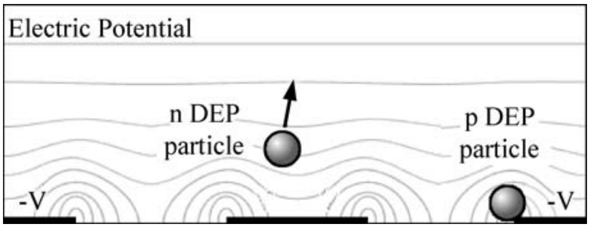

AC Dielectrophoresis Lab-on-Chip Devices, Figure 3 Dielectrophoresis of particles with interdigitated electrodes (side view). Particles experiencing pDEP are attracted to the edges of the electrode while nDEP forces repel the particle to the middle of the electrode

Other electrode geometries have been designed to capture individual cells using either pDEP or nDEP forces. A number of these geometries have been explored by Voldman and his research group [5] and will be discussed here. For pDEP, geometries are created that generate extreme electric field gradients in the trapping region. A geometry that creates such a field gradient is illustrated in Fig. 4a. An electrode smaller than the diameter of the particle has the signal applied through it to a larger, receiving electrode. The generated electric field would be similar to that illustrated in Fig. 1, with a high gradient in proximity to the smaller electrode. Electric field nulls have also been generated with electrode geometries for nDEP traps. Recall the quadrupole geometry in Fig. 2c. When an appropriate electric field is applied a field null is created in the center of the trap. The trapped particle is repelled from the surrounding regions of field gradients. Another nDEP trap is illustrated in Fig. 4b. The electric field is applied from the trapping electrode to the receiving electrode strip. A particle is trapped within the generated null inside the "boxed" electrode geometry. These previous geometries will trap a particle near the surface of the substrate. Electrodes, though, can be arranged three-dimensionally to create traps that capture particles and cells in suspension. One example is a nDEP trap using two stacked quadrupole geometries, resulting in an octopole trap (Fig. 4c). The electric field null is generated in the midplane between these two electrode substrates and thus a particle experiencing nDEP is captured in suspension. These are just a few examples of established trapping geometries, as others could be designed to suit a particular trapping application.
There are numerous trap geometries that exist for both pDEP and nDEP. These electrode arrangements and cell concentration can be varied to trap both single cells and groups of cells alike. However, there are dielectrophoretic interactions that cannot be ignored for trapping applications. Multipoles may need to be considered for single-

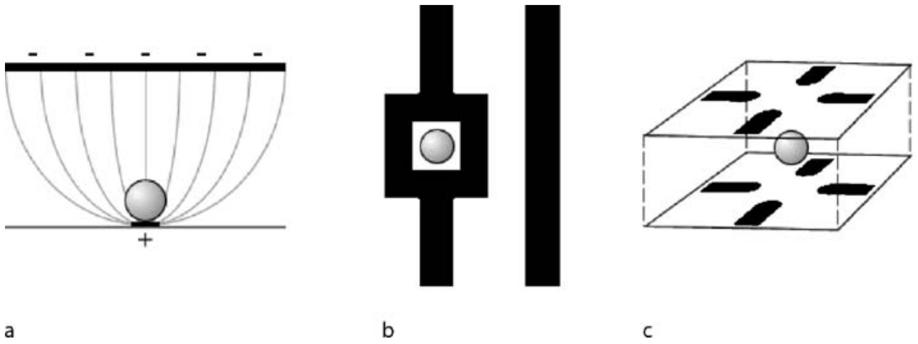

AC Dielectrophoresis Lab-on-Chip Devices, Figure 4 Various electrode geometries for dielectrophoretic traps: (**a**) pDEN trap (side view), (**b**) nDEP planar trap (top view), and (**c**) nDEP octopolar trap

particle traps since the generated field will have inhomogeneities on the scale of the particle itself. Also, particle–particle dielectrophoretic interactions will influence the capabilities of multi-particulate traps. Dielectrophoresis, therefore, needs to be accurately modeled and thoroughly investigated prior to use in a specific application.

Electrode-Based Systems

Microsystems have incorporated dielectrophoretic forces into microchannels to manipulate particles and cells with various electrode geometries. Electrodes can be used to align target cells or separate particulate cells from the rest of the sample, an example of which is illustrated in Fig. 5. These systems use a three-dimensional arrangement of electrodes, with mirrored electrode geometries aligned and separated by microfluidic structures. Thus the electrodes in Fig. 5 are on the top and bottom surfaces of the microchannel and do not significantly impede or manipulate the fluid flow. This system is optimized for a particular set of cells such that the applied signals generate the strongest dielectrophoretic forces; this system will operate with the maximum possible applied flow rate for more effective processing. The system, though, will be selective to a set of cells with the same or similar dielectric properties. This process is obviously advantageous for an application that selectively separates cells based on their dielectric properties. Additionally, this system can simultaneously separate and trap targeted cells for selective biological investigations. An example of a dielectrophoresis system and a description of its potential for biological analysis is explained in [6]. These dielectrophoresis techniques can be coupled with a variety of existing biological tools for innovative applications including fluorescence evaluation of cells in small populations, cell sorting, long-term investigations of single cells, cellular kinetics and other similar Lab-on-a-Chip analyses.

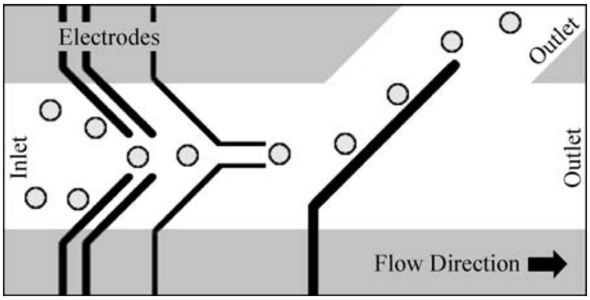

AC Dielectrophoresis Lab-on-Chip Devices, Figure 5 An illustration of a dielectrophoretic microsystem that can selectively sort particles (top view). Recall that the electrodes are on the top and bottom surfaces of the microchannel and to not mechanically manipulate the particles

Insulating Dielectrophoresis

Conventionally, the nonuniform electric fields for dielectrophoresis applications are produced directly with an arrangement of conductive electrodes. However, a nonuniform electric field can be generated in microchannels without direct interaction with electrodes. For example, Cummings generated nonuniform electric fields using remote electrodes placed at the inlet and outlet of the microchannel [7]. The electric field is applied across the channel and is deformed by the variations in the channel geometry or by insulating structures or posts within the microchannel. These mechanical structures within the channel will affect the generated electric field as well as dynamically change the flow field; these can be successfully coupled to produce an efficient particle concentrator within the channel. By using remote electrodes, electrochemical reactions and other unwanted dielectrophoretic effects will not occur within the section of particle collection or concentration. However, this technique relies on the application of higher voltages to produce the necessary electric field gradient, with magnitudes in the hundreds to thousands of volts

(outside the range of conventional waveform generators). The driving mechanism for fluid flow for these systems is electrokinetic in that it combines features of electroosmotic and electrophoretic flows. Insulating dielectrophoresis Lab-on-a-Chip systems use a coupled arrangement of electrokinetic and dielectrophoretic phenomena to separate or capture targeted particles. Consider such a dielectrophoresis system that has an array of insulating posts within a microchannel. At a low applied electric field there will be induced electrokinetic motion but minimal particle manipulation effects from dielectrophoresis. However, at higher magnitudes the influence of insulating posts becomes apparent, inducing dielectrophoretic forces on the particles. At a certain threshold in the applied electric field dielectrophoresis forces on the particles are greater than the electrokinetic forces, resulting in captured targeted particles at the insulating posts. Releasing these particles is just a simple decrease in signal magnitude. Structures other than posts have been successfully used to similarly manipulate and separate particles of different dielectric properties.

Optical Dielectrophoresis

An electrode-less approach to induce localized dielectrophoretic forces can be created by light illumination in optically induced dielectrophoresis. This technique utilizes low-power optical beams to manipulate particles and cells. Consider an AC electric signal applied across two parallel electrodes with a film of photoconductive layer in between. This generates a uniform electric field across the film; however, the photoconductive layers have higher conductivities under illumination, thus distorting the otherwise uniform electric field. An illustration of a simplified optically induced dielectrophoresis system is shown in Fig. 6. The illumination of the photoconductive layer produces a virtual electrode and locally induced dielectrophoretic forces. These forces can be used in pDEP or nDEP applications and have the distinct advantage of being temporary, as opposed to permanent microfabricated electrode features. For example, trapped particles can be moved with the translation of the illumination pattern and released by simply turning off the light.

These optical methods, though, have been developed to include image projectors to manipulate cells using larger, patterned illumination areas. For example, virtual structures can be used to direct cells or can be alternatively used to pattern trapped cells. An investigation of optically induced dielectrophoresis for cellular manipulation is found in detail elsewhere [8]. This investigation characterizes the controllability of these optical techniques. This technique, though, should not be confused with optical tweezers (also called optical traps), which manipulate cells with forces generated by a highly focused laser beam. Optical tweezers use high optical intensity that may cause damage to the cell or induce localized heating. In contrast, optically induced dielectrophoretic techniques have about 1000 times less optical intensity.

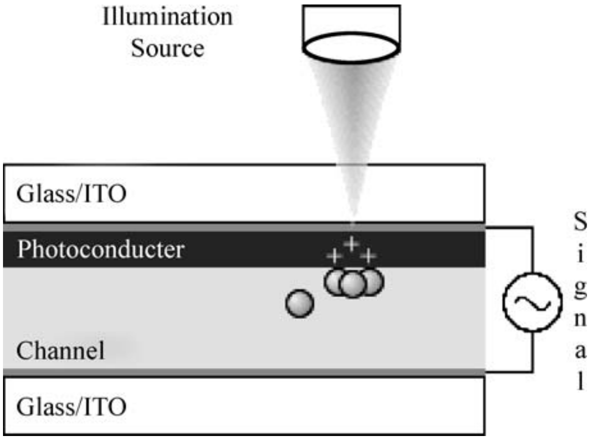

AC Dielectrophoresis Lab-on-Chip Devices, Figure 6 An example for a simple setup for optically induced dielectrophoresis. The optical source is illuminated through the ITO/glass substrate onto the photoconductive layer, creating an electric field gradient in which particles experiencing pDEP are attracted

Liquid Manipulation

Outside of particle manipulation, dielectrophoresis has also been used to control small volumes of liquid [9]. Liquids themselves also polarize and will, therefore, respond to nonuniform electric fields by being attracted to high-field-intensity regions. Liquid dielectrophoresis influences hydrostatic equilibrium and does not directly manipulate the fluid using dynamic mechanisms typically associated with electro-osmotic flow, electroconvection or other electrohydrodynamic methods. As with all dielectrophoresis techniques, liquid dielectrophoretic forces become stronger at smaller length scales, typically the micrometer length scale. Simple applications of this technique require a fluid running between two closely spaced planar electrodes (Fig. 7). A signal is applied between these two electrodes inducing the collection of individual molecules to the area of highest field intensity, along the edges of the electrodes. The liquid will translate and fill the area along these electrode “fingers” until equilibrium is achieved.

When the signal is removed the liquid will retract and return to its original hydrostatic equilibrium form. This retraction can be coupled together with surface structures to generate nanoliter droplets. However, typical voltage magnitudes are in the hundreds of volts, resulting in Joule

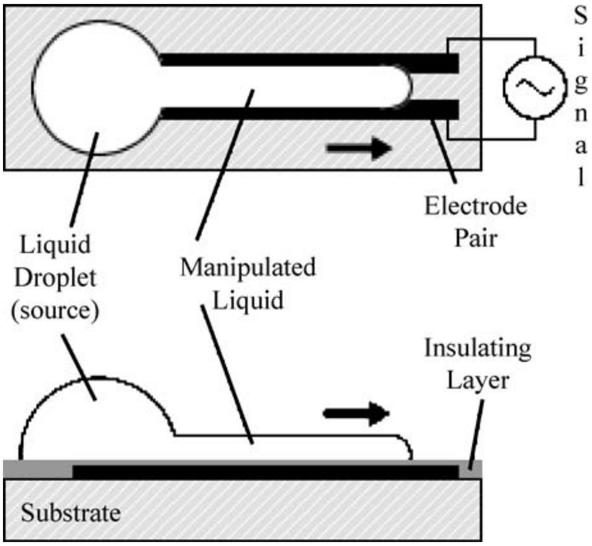

AC Dielectrophoresis Lab-on-Chip Devices, Figure 7 Liquid dielectrophoresis with a set of planar electrode fingers with an insulating layer (top view and side view). A signal is applied to manipulate the liquid to travel along the gap between the electrodes

heating and electrolysis. Electrolysis can be easily avoided by coating the electrode surface with an insulating layer. Heating is typically insignificant when liquids are nonconductive; however, water and other highly conductive liquids will undergo Joule heating. To cope with these issues in present liquid dielectrophoresis systems, very short applications of voltage (< 0.1 s) are applied to avoid heating. Liquid dielectrophoresis involves a complex relationship between electrohydrodynamics, fluid dynamics, surface effects, Joule heating and dielectrophoresis but this technique provides a rapid actuation of liquid that can be utilized in Lab-on-a-Chip systems.

Molecular Dielectrophoresis

Dielectrophoresis has also been used to manipulate macromolecules such as DNA, viruses, proteins and carbon nanotubes. The term *colloids* will be used here to generally describe a particle between 1 nm and 1000 nm. At this scale we need to take into consideration additional parameters that will affect the efficiency and application of dielectrophoresis. The first is Brownian motion, or the random chaotic movement of molecules, which will introduce another destabilizing variable if we were to trap colloids. Second, electrostatic effects at the surface of colloids, created by the electrical double layer, will influence particle–particle interactions. Factors such as hydrodynamic drag, buoyancy, electrothermal effects and a particle's double layer interactions need to be considered when applying dielectrophoresis to colloids.

The importance of mechanically controlling these structures in Lab-on-a-Chip systems with dielectrophoretic techniques will aid in the understanding of their biological interactions with other subcellular entities. For example, miniature quadrupole traps can be used to determine the crossover frequency of specific proteins and viruses. Capturing viruses at a particular set of experimental parameters will give insight into their identification as well as provide a means to concentrate or separate these particles. The crossover frequency of a protein is not only a function of medium conductivity, but it is dependent on the pH as well. Thus, dielectrophoresis can be coupled with chemistry-oriented techniques in order to approach the experimentation of single molecules. DNA has also been manipulated using dielectrophoresis. In one study [10], DNA was uncoiled from its natural bundled condition and stretched between two electrodes, aligning itself along the field lines. It was shown that it took about one-third of one second to uncoil a 48,500 base-pair DNA to a length of 17 μm. The applications of DNA manipulation include electrical measurements between electrodes and positioning of DNA for structural purposes or modification. Carbon nanotubes have also been manipulated similarly. These manipulative techniques have contributed to the assembly of nanometer-sized structures.

Dielectrophoretic Assembly

Dielectrophoresis can be utilized in assembly procedures to induce particle–particle interactions or to use attractive forces between electrodes to position a component and complete a circuit. When two polarized particles come into close proximity to each other they will undergo an attractive force due to their dipole interactions. This is referred to as dipole–dipole interaction, mutual dielectrophoresis or pearl chaining because this phenomenon creates strings of particles. Recall that a particle's induced dipole aligns itself to the electric field and that like particles will always have the same dipole orientation. These particles will have an attractive force since their opposite charges are aligned facing each other. Additionally, these particle chain formations can also be attributed to the distorted electric field caused by the particle's induced dipole. These field disturbances can cause a localized dielectrophoretic force, increasing the strength of these particle–particle interactions. Pearl chains are typically observed near electrode edges where the strength of the electric field is the greatest.

Pearl chains of nanoparticles can be arranged and fused together to create a nanowire or other similar struc-

tures. However, other dielectrophoresis techniques can be utilized to assemble a variety of geometries. Dielectrophoretic traps and optical dielectrophoresis can assemble groups of like particles. Electro-orientation techniques have been used to align and connect nanowires between electrodes. Functionalized particles can be implemented with dielectrophoresis Lab-on-a-Chip systems to create biological sensory or assembly systems. Dielectrophoresis, therefore, is a very versatile engineering tool.

Future Directions for Research

As a nonmechanical and minimally invasive process, dielectrophoresis presents as a tool to be used in Lab-on-a-Chip systems to manipulate particles and cells. These techniques will continue to evolve as the size of microfabricated features continue to decrease past the nanometer scale. This miniaturization will give rise into more comprehensive, subcellular microsystems which need novel methods to manipulate specific entities to suit a biological, chemical or sensory purpose. Dielectrophoresis phenomena at these decreasing length scales will continue to be characterized, leading to newly developed dielectrophoresis phenomena and subsequent innovative manipulation techniques. The future of dielectrophoresis is with the continued investigation and development of novel applications of dielectrophoresis techniques. With the integration of these technologies, a complete dielectrophoresis-driven Lab-on-a-Chip diagnostics system is possible.

Cross References

- ► AC Electro-Osmotic Flow
- ► Dielectrophoresis
- ► Dielectrophoretic Motion of Particles and Cells
- ► Electrokinetic Motion of Cells and Nonpolarizable Particles
- ► Electroosmotic Flow (DC)
- ► Electrophoresis
- ► Electrothermal Effects
- ► Joule Heating in Electrokinetic Flow: Theoretical Methods
- ► Lab-on-a-Chip (General Philosophy)
- ► Lab-on-Chip Devices for Particle and Cell Separation
- ► Techniques for Manipulating Cells

References

1. Pohl HA (1978) Dielectrophoresis. Cambridge University Press, Cambridge
2. Jones TB (1995) Electromechanics of Particles. Cambridge University Press, Cambridge
3. Morgan H, Green N (2003) AC Electrokinetics: Colloids and Nanoparticles. Research Studies Press, Baldock
4. Hughes MP (2003) Nanoelectromechanics in Engineering and Biology. CRC Press, Boca Raton, Florida
5. Rosenthal A, Taff BM, Voldman J (2006) Quantitative modeling of dielectrophoretic traps. Lab Chip 6:508–515
6. Muller T, Pfennig A, Klein P, Gradl G, Jager M, Schnelle T (2003) The potential of dielectrophoresis for single-cell experiments. IEEE Eng Med Biol Mag 22:51–61
7. Cummings EB (2003) Streaming dielectrophoresis for continuous-flow microfluidic devices. IEEE Eng Med and Biol Mag 22:75–84
8. Chiou PY, Ohta AT, Wu MC (2005) Massively parallel manipulation of single cells and microparticles using optical images. Nature 436:370–372
9. Jones TB (2001) Liquid dielectrophoresis on the microscale. J Electrostat 51–52:290–299
10. Washizu M and Kurosawa O (1990) Electrostatic manipulation of DNA in microfabricated structures. IEEE Trans Ind Appl 26:1165–1172

AC Electrokinetics

► Dielectrophoresis

AC Electro-Osmosis (ACEO)

► Nonlinear Electrokinetic Phenomena

AC Electro-Osmotic Flow

MARTIN Z. BAZANT[1,2]
[1] Department of Mathematics and Institute of Soldier Nanotechnologies, Massachusetts Institute of Technology, Cambridge, MA, USA
[2] Ecole Superieure de Physique et Chimie Industrielles, Paris, France
bazant@math.mit.edu

Synonyms

AC pumping of liquids; Traveling-wave electro-osmosis

Definition

AC electro-osmosis (ACEO) is a ►nonlinear electrokinetic phenomenon of induced-charge electro-osmotic flow around electrodes applying an alternating voltage.

Overview

Classical electrokinetic phenomena, such as ►electro-osmotic flow and ►electrophoresis, are linear in the applied voltage and thus cannot produce any net flow under alternating current (AC) conditions. A variety of

► nonlinear electrokinetic phenomena, which persist in AC fields, have been known for decades in colloid science, but the focus has been on electrophoretic mobility and particle interactions. The advent of microfluidics has stimulated interest in the use of electric fields to drive fluid flows, without any moving parts. In this context, nonlinear electrokinetics offers some unique advantages, such as the reduction of unwanted electrochemical reactions (using AC voltages) and the ability to drive fast, programmable flows at low voltages (using closely spaced micro-electrodes).

In the late 1990s, Ramos et al. discovered steady electro-osmotic flow over a pair of micro-electrodes applying an AC voltage and dubbed the effect *AC electro-osmosis* [1]. Around the same time, Ajdari predicted ACEO flow over periodic electrode arrays and showed how the effect could be used for long-range pumping [2]. As the performance of ACEO pumps has advanced [3, 4], ACEO has also been exploited, in conjunction with ► dielectrophoresis (DEP), in different geometries to manipulate particles and cells in microfluidic devices [5–7].

Basic Methodology

Local Flow Generation

ACEO is a phenomenon of ► induced-charge electro-osmosis (ICEO), where flow is generated by the action of an electric field on its own induced diffuse charge near a polarizable surface. The main difference with other examples of ICEO, such as flows around metal colloids, is that ACEO involves electrode surfaces, which supply both the electric field and the induced screening charge, in different regions at different times. For this reason, ACEO is inherently time-dependent (as the name implies) and tied to the dynamics of diffuse charge, as ions move to screen the electrodes.

Perhaps the easiest way to understand ACEO is to consider a pair of planar electrodes applying a sudden DC voltage (which is analogous to ICEO flow around a polarizable particle in an sudden electric field). As shown in Fig. 1, charge relaxation can initially be described by an equivalent RC circuit, where the diffuse layers act as capacitors, connected to "current-tube" resistors of varying length through the bulk solution. Since the resistance is smaller (and the field larger) near the gap, the inner portions of double layers on the electrodes charge more quickly than the outer portions. As shown in Fig. 2, this causes ICEO flow to occur, directed outward from the gap, only when the electrodes are partially screened, as the tangential field from the unscreened outer portions acts on induced charge on the inner portions. Note that the flow is independent of the sign of the applied voltage: If the polarity were reversed, then the field and induced charges would both change sign, resulting in the same ICEO flow.

Under AC forcing, the flow peaks when the oscillation period is comparable to the charging time (Fig. 2b). ACEO flow decays at higher frequencies, since there is not enough time for charge relaxation (Fig. 2a). It also decays at lower frequencies, since there is enough time to completely screen the bulk electric field (Fig. 2c).

Mathematical models of ACEO follow other examples of ICEO, as described in the article on ► nonlinear electrokinetic phenomena. A major simplification in the case of small voltages is to assume sinusoidal response to sinusoidal AC forcing and solve only for the complex amplitudes of the potential and velocity components at a single frequency ω (Fourier mode) [2]. In this regime, the basic scaling of time-averaged ACEO flow is

$$\langle u \rangle \propto \frac{\varepsilon V^2}{\eta(1+\delta)L\left[\frac{\omega}{\omega_c}+\frac{\omega_c}{\omega}\right]^2} \tag{1}$$

where V is the applied voltage, ε and η are the permittivity and viscosity of the liquid (both assumed constant), L is electrode spacing (roughly center to center), δ is the ratio of the diffuse-layer to compact-layer capacitances (both assumed constant). The peak frequency is at the scale of the RC charging time

$$\omega_c \propto \frac{D\,(1+\delta)}{\lambda L} \tag{2}$$

where λ is the Debye screening length and D is a characteristic ionic diffusivity.

The relevant case of a large applied voltage, $V \gg kT/e = 25\,\mathrm{mV}$, is not yet fully understood. A variety of new effects could become important, such as steric effects of finite molecular sizes, viscoelectric effects, discrete electrostatic correlations, dissociation and de-solvation kinetics, and/or Faradaic electrochemical reactions passing current through the surface. In particular, *Faradaic charging* (as opposed to *capacitive charging*, described above) has been proposed to explain experimentally observed flow reversal at high voltage [7], although this has not yet been borne out in a complete mathematical model of ACEO. Standard models of Faradaic reactions mainly predict suppression of the flow (by short-circuiting of the double layer charging process) and flow reversal only in certain cases, at lower frequencies than in the experiments [2, 8]. Although reactions surely play a role in ACEO, high-frequency flow reversal may be attributable to other effects, such as ion crowding in the diffuse layer [9].

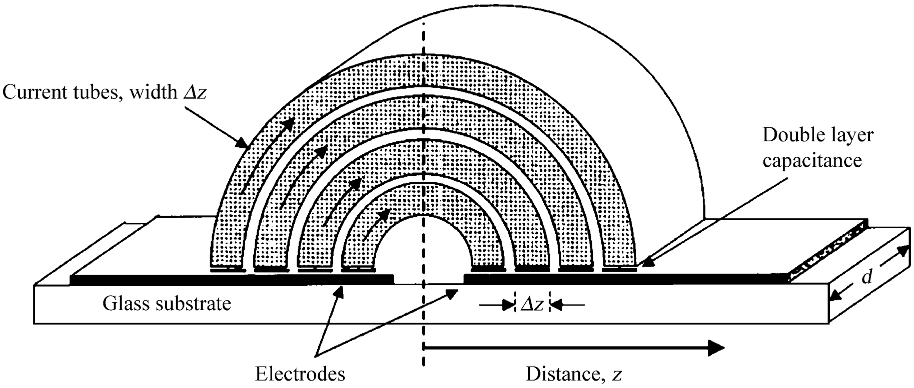

AC Electro-Osmotic Flow, Figure 1 Equivalent RC circuit model for double-layer charging over a pair of electrodes. The inner edges of the electrodes encounter less bulk resistance (due to shorter "current tubes") and thus charge more quickly than the outer edges (reproduced from [1]

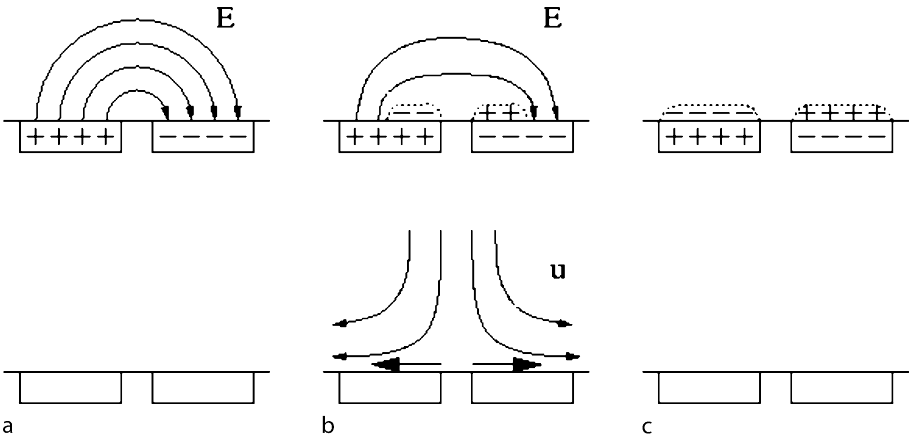

AC Electro-Osmotic Flow, Figure 2 The basic mechanism of AC electro-osmosis: Electrochemical relaxation (top) and induced -charge electro-osmotic flow (bottom) in response to a suddenly applied voltage across an electrode pair. (**a**) At first the electric field has no tangential component on the electrodes, since they are equipotential surfaces, and thus there is no electro-osmotic flow. (**b**) Capacitive double-layer charging begins near the gap where the initial normal current is strongest and causes the unscreened field lines dip down and provide tangential components over the induced charge; the result is ICEO flow directed away from the electrode gap. (**c**) After the charging time passes, the electrodes are fully screened, leaving no electric field and thus no flow. An AC voltage can drive a steady time-averaged flow, similar to (**b**), if its period is comparable to the charging time

Fluid Pumping

Regardless of the details of flow generation, there are some useful general principles to guide the development of microfluidic pumps. ACEO flow over a small set of electrodes can be used for local fluid mixing or particle trapping at stagnation points, but the flow decays quickly away from the electrode surfaces. A symmetric, periodic array of many inter-digitated electrodes (of alternating polarity at each moment in time) similarly produces an array of counter-rotating convection rolls, but no net pumping of the fluid in one direction. Instead, long-range pumping over an electrode array requires broken symmetry within each spatial period to rectify the AC forcing.

There are several ways to design ACEO pumps by breaking symmetry in a periodic electrode array. Ajdari originally suggested modulating either the electrode capacitance via a dielectric coating (Fig. 3a) or the surface height (Fig. 3b) with half the spatial period of the array, so that the one side of each electrode drives stronger ACEO flow compared to the other side and thus "wins" to produce net pumping over the array [2]. In the first implementation of an ACEO pump, Brown, Smith and Rennie opted instead to break symmetry by using planar electrodes of different widths and gaps [10], and, until recently, this design was the only one studied experimentally [3] or theoretically [8].

The performance of ACEO pumps can be greatly enhanced by designing appropriate non-planar electrode geometries.

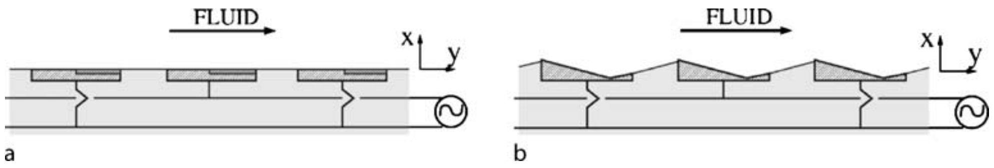

AC Electro-Osmotic Flow, Figure 3 Sketches of local broken symmetries in a periodic electrode array which lead to global time-averaged ACEO pumping: (**a**) non-uniform surface coatings; (**b**) non-uniform surface height (reproduced from [2])

As recently predicted by Bazant and Ben [11], various *3D ACEO* designs exhibit dramatically increased flow rate without flow reversal, due to a special geometry in which the non-uniform slip profile on the electrodes all contributes to flow in the same direction. The basic idea is to create a *fluid conveyor belt* with electrodes each having steps of two different heights: On each electrode, the region of desired forward flow is raised up, while the region of reverse flow is recessed below, so as to recirculate in a vortex aiding the forward flow (rather than fighting it, as in planar designs). This can be accomplished with electrodes having electroplated metal steps, as shown in Fig. 4, although other designs are possible, such as flat electrode steps deposited on a grooved surface (without the vertical metal surfaces). Simulations predict that 3D ACEO pumps are faster than planar pumps by more than an order of magnitude, at the same voltage and minimum feature size, and thus can achieve mm/s velocities with only a few volts. This suggests using 3D ACEO pumps to drive flows in battery-powered, portable or implantable microfluidic devices.

Fluid pumping over electrode arrays can also be achieved by applying a traveling wave of voltage. At low frequency, a similar induced-charge electro-osmotic mechanism, which peaks at the RC frequency (2), is responsible for the flow [12]. At high frequency (or with a thick dielectric coating on the electrodes), the classical Erlich–Melcher effect used to pump dielectric liquids, which peaks at the Debye frequency, $\sigma/\varepsilon = D/\lambda^2$, can also be observed [13]. Although traveling-wave ACEO seems to produce slower flow than standing-wave ACEO with planar electrodes, the possibility of designing suitable non-planar electrodes has not yet been considered.

Key Research Findings

The groups of Ramos [1] and Green [15] have pioneered the study of ACEO by developing theoretical models and measuring flows around pairs of micro-electrodes in dilute KCl. Their work has ruled out ▶electrothermal effects (below 5 V in dilute electrolytes) and clarified the capacitive charging mechanism described above. The basic model successfully predicts the scaling of ACEO flow at low voltage and low salt concentration, although it tends to over-estimate velocities.

Following Ajdari [2], there has been extensive experimental [3, 4, 10, 12, 13] and theoretical [8, 9, 11] work on ACEO flows driven by periodic inter-digitated electrode arrays. Velocities exceeding 100 μm/s have been demonstrated in water [4, 10] and dilute KCl [3] by applying several volts at 1 – 100 kHz frequencies using asymmetric arrays of planar electrodes with unequal widths and gaps, at the scale of several microns. Somewhat slower flows have also been achieved by applying traveling-wave voltages with inter-digitated planar electrodes [12, 13], although the electrical connections are more complicated.

A puzzling feature of ACEO in many situations with planar electrodes is that the flow direction can reverse (compared to the theory) with increasing voltage, typically above 2 V. For example, high-voltage flow reversal has been observed in dilute KCl for AC forcing [3] and traveling-wave forcing [13] and in tap water for AC forcing with a DC offset [7]. As shown in Fig. 5a, the reverse flow is eventually faster than the forward flow and seems to grow more quickly with voltage than the expected scaling $u \propto V^2$.

Another puzzling feature of ACEO is the strong decay of the flow with increasing salt concentration. For this reason, all experiments in the literature have used either very dilute solutions (mostly KCl) or water (de-ionized or from the tap). A few groups have studied the concentration dependence of ACEO in aqueous KCl solutions [3, 15, 16]. These experiments and recent work on ▶electrokinetic motion of heterogeneous particles suggest that flows due to ▶induced-charge electro-osmosis exhibit a universal decay with concentration like $u \propto \log(c_{\max}/c)$ at large voltage [9]. As shown in Fig. 5b, the flow effectively vanishes above a bulk salt concentration of only $c_{\max} \approx 10$ mM, which is an order of magnitude smaller than most biological solutions.

Nevertheless, advances have been made in applying ACEO flows to pumping, mixing, and trapping particles in microfluidic devices. Experiments on 3D ACEO pumps with non-planar stepped electrode arrays have demonstrated an order of magnitude increase in flow rate versus the fastest planar design, due to the robust fluid-conveyor-

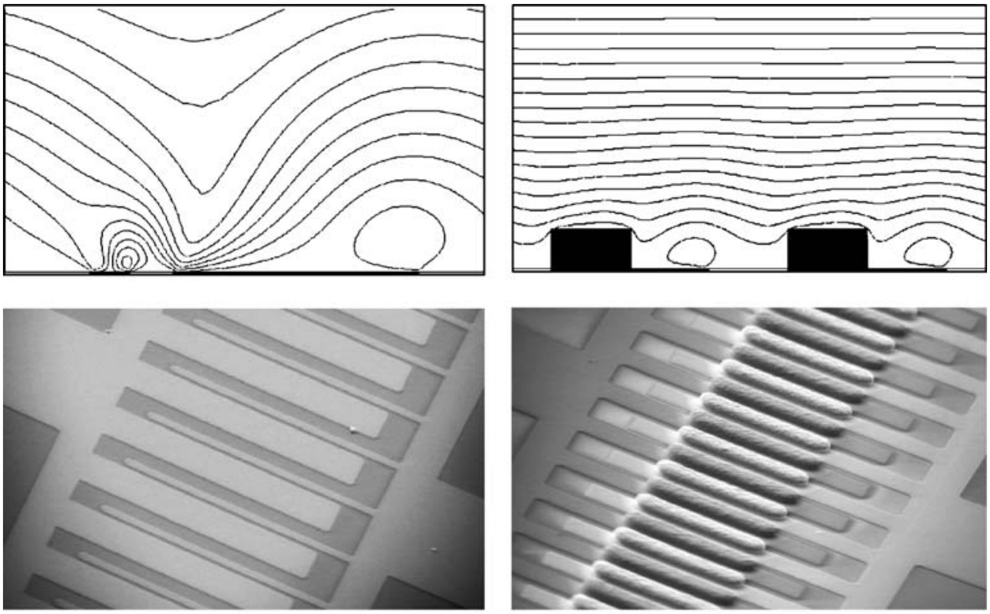

a b

AC Electro-Osmotic Flow, Figure 4 Top: Simulations of ACEO microfluidic pumps, showing the time-averaged flow over a pair of micro-electrodes (dark regions) in one spatial period of an interdigitated-electrode array. (**a**) A nearly optimal planar design with different electrode sizes and gaps; the smaller electrode has the largest local slip velocity, but the larger electrode "wins" in overall pumping from left to right. (**b**) A much faster 3D ACEO design with stepped electrodes having a symmetric footprint and the same minimum feature size; the reverse slip now recirculates in a vortex to create a *fluid conveyor belt* for the raised pumping flow from left to right (reproduced from [11]). Bottom: Scanning electron microscopy images of each design fabricated in gold on glass with minimum feature size (gap) of 5 μm (unpublished, courtesy of J. P. Urbanski using the methods of [4, 14])

belt mechanism [4]. For a wide range of near-optimal step heights, there is also no observed flow reversal [14]. Therefore, it is now possible to drive fast, reliable mm/s flows in water or dilute electrolytes with less than 3 V, which can be provided by a small lithium battery.

Progress has also been made in exploiting ACEO flows to manipulate colloidal particles and biological cells in microfluidic devices [5–7]. The basic strategy is to use ACEO flow to draw particles to stagnation points on the electrodes, where they are trapped, presumably by DEP (although the classical theory does not seem to predict this effect). By increasing the voltage, the ACEO flow can be reversed, and particles are observed to move away from the stagnation lines, overcoming any remaining trapping force. In this way, it is possible to "write" and "erase" suspended particles, bacteria, or micro-algae on microelectrodes, as shown in Fig. 7a. This effect can be enhanced by added a DC bias voltage to the low-frequency AC voltage (50 – 100 Hz) between adjacent electrodes [7]. Particles are observed to collect only on the positively biased electrode, as shown in Fig. 7b. It has been suggested that opposing ACEO flows are produced by the competition between Faradaic charging on one electrode (positive bias) and capacitive charging on the other (negative bias), but a quantitative theory remains to be developed and confirmed systematically by experiments.

Future Directions for Research

ACEO is attractive to exploit in microfluidics since it offers precise local flow control without moving parts, using standard fabrication methods from the electronics industry. Device operation requires only the voltage (few Volts), power (mW), and current (mA) of a small battery, and Faradaic reactions are reduced or eliminated. These features make ACEO a promising route to portable or implantable microfluidic systems. In contrast, DC electro-osmotic pumps, such as those exploiting electroosmotic flow in porous media, typically require several 100 V and produce bubbling at the electrodes due to electrolysis, which can require a catalytic gas management system. On the other hand, ACEO pumps have so far only produced very small pressures (< 10 Pa) far below those of porous-plug DC pumps (> 100 kPa), but new designs could close this gap. In any case, the ability to tune flows and particle motion by ACEO at the micron scale by modulating relatively small AC voltages could have many uses, e. g. for

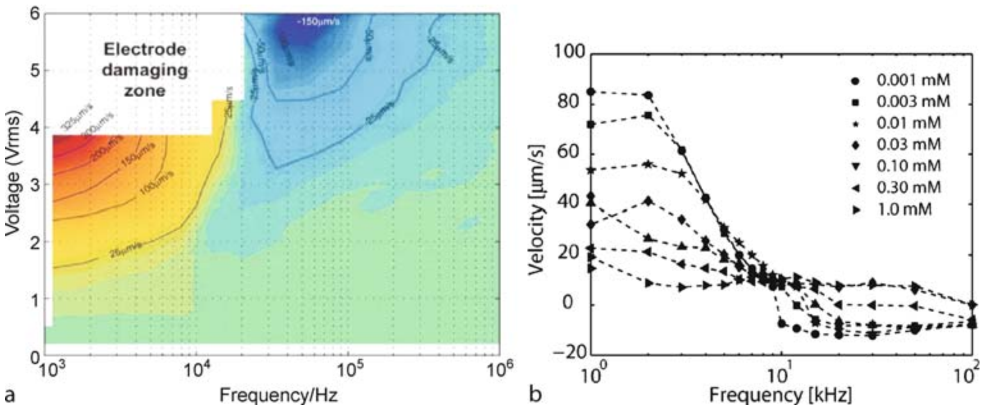

AC Electro-Osmotic Flow, Figure 5 Experimental data for ACEO pumping of KCl around a microfluidic loop, one-fifth covered by the asymmetric planar electrode array of Fig. 4a. (**a**) Contour plot of mean velocity versus AC frequency and RMS voltage at a bulk salt concentration of 0.1 mM (reproduced from [3]), where *electrode damaging* refers to bubble formation and inability to observe consistent flows. (**b**) Velocity versus AC frequency at 2 V peak-to-peak for different concentrations (reproduced from [16]). Both show high-voltage, high-frequency flow reversal, and the latter shows the strong decay with salt concentration

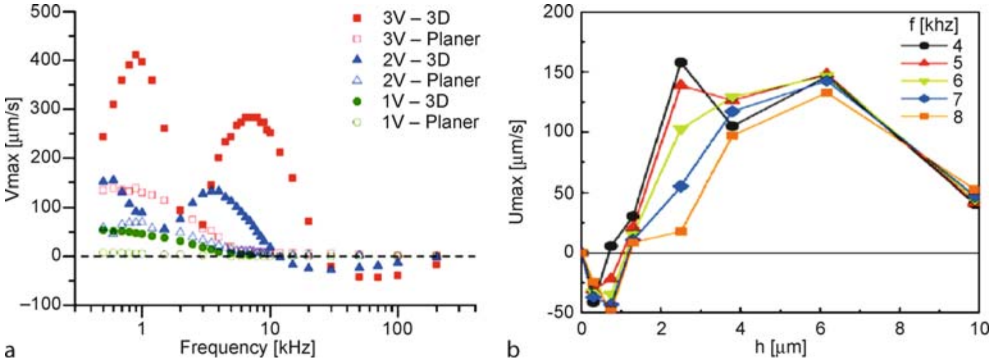

AC Electro-Osmotic Flow, Figure 6 (**a**) Comparison of ACEO pumping of water around a microfluidic loop by planar and (non-optimal) 3D electrode arrays with similar 5 μm minimum feature size (reproduced from [4]). (**b**) Experimental optimization of the step height for 3D ACEO pumping of dilute KCl (reproduced from [15])

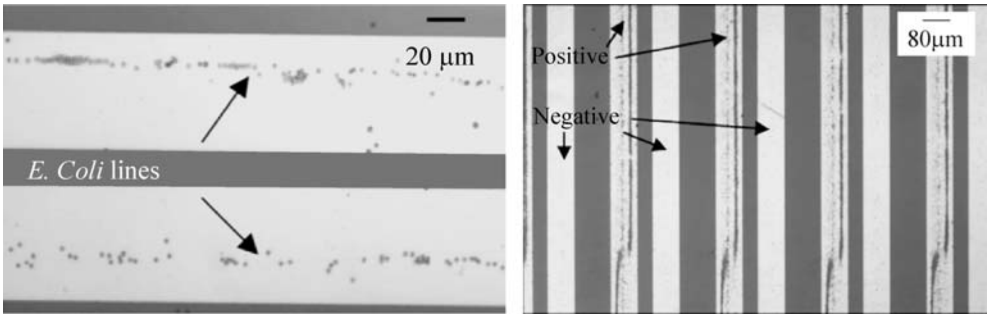

AC Electro-Osmotic Flow, Figure 7 (**a**) Collection of *E. Coli* bacteria in tap water along the stagnation lines of ACEO flow on Au microelectrodes at low frequency (100 Hz) and moderate voltage (1 V). (**b**) Preferential particle trapping by asymmetric polarization ACEO on electrodes with positive DC bias at higher voltage ($>$ 3 V) (reproduced from [7])

mixing, flow fragmentation, or manipulation of colloids and cells.

Understanding flow reversal in ACEO is an important open question, from both fundamental and practical points of view. As noted above, it has been attributed to Faradaic reactions, using theoretical arguments suggesting a scaling $u \propto e^V$ [7]. Simulations of ACEO pumps using standard Butler–Volmer reaction kinetics have failed to predict any flow reversal, except at low frequencies below 100 Hz [2, 8], although this may be consistent with experiments showing low-frequency flow reversal with a DC bias [7]. In contrast, high-voltage flow reversal with unbiased AC forcing in electrode-array pumps tends to occur at high frequency (> 10 kHz), as shown in Fig. 5. An alternative hypothesis, which predicts high-frequency, high-voltage flow reversal due to capacitive charging alone, is based on the reduction of double-layer capacitance due to ion crowding effects [9]. The question is far from settled, however, and more theoretical and experimental work is needed.

Another important open question concerns the dependence of ACEO flow on the solution chemistry (concentration, ionic species, solvent characteristics, etc.). The suppression of ACEO above 10 mM bulk salt concentration limits its use in biological applications and points to possible new physics of the double layer at large voltages, such as a dramatic increase in the diffuse-layer viscosity upon ion crowding [9]. Very few electrolytes have been studied experimentally, but current work suggests that varying the ionic species can also substantially alter the flow. An interesting direction for future research would be to develop surface coatings, electrode materials, and buffer solutions to mitigate or manipulate these complex interfacial phenomena.

Cross References

- ▶ Dielectrophoresis
- ▶ Dielectrophoretic Motion of Particles and Cells
- ▶ Electrical Double Layers
- ▶ Electrokinetic Motion of Polarizable Particles
- ▶ Electrokinetic Motion of Heterogeneous Particles
- ▶ Electroosmotic Flow (DC)
- ▶ Electrokinetic Flow in Porous Media
- ▶ Induced-Charge Electro-Osmosis
- ▶ Nonlinear Electrokinetic Phenomena

References

1. Ramos A, Morgan H, Green NG, Castellanos A (1999) AC electric-field-induced fluid flow in microelectrodes, J Colloid Interface Sci 217:420–422
2. Ajdari A (2000) Pumping liquids using asymmetric electrode arrays. Phys Rev E 61:R45–R48
3. Studer V, Pepin A, Chen Y, Ajdari A (2004) An integrated AC electrokinetic pump in a microfluidic loop for fast tunable flow control, Analyst 129:944–949
4. Urbanski JP, Thorsen T, Levitan JA, Bazant MZ (2006) Fast ac electo-osmotic pumps with non-planar electrodes, Appl Phys Lett 89:143508
5. Green NG, Ramos A, Morgan H (2000) AC electrokinetics: a survey of sub-micrometre particle dynamics, J Appl Phys D 33:632–641
6. Wong PK, Wang TH, Deval JH, Ho CM (2004) Electrokinetics in micro devices for biotechnology applications, IEEE/AMSE Transactions on Mechatronics 9:366–376
7. Wu J (2006) Biased AC electro-osmosis for on-chip bioparticle processing, IEEE Transactions on Nanotechnology 5:84–88
8. Olesen LH, Bruus H, Ajdari A (2006) AC electrokinetic micropumps: The effect of geometrical confinement, Faradaic current injection, and nonlinear surface capacitance, Phys Rev E 73:056313
9. Bazant MZ, Kilic MS, Storey B, Ajdari A (2007) Nonlinear electrokinetics at large applied voltages. Preprint. (http://www.arxiv.org/abs/cond-mat/0703035)
10. Brown ABD, Smith CG, Rennie AR (2000) Pumping of water with AC electric fields applied to asymmetric pairs of microelectrods. Phys Rev E 63:016305
11. Bazant MZ, Ben Y (2006) Theoretical prediction of fast 3D ACEO pumps, Lab Chip 6:1455–1461
12. Cahill BP, Heyderman LJ, Gobrecht J, Stemmer A (2004) Electro-osmotic streaming on application of traveling-wave electric fields. Phys Rev E 70:036305
13. Ramos A, Morgan H, Green NG, Gonzalez A, Castellanos A (2005) Pumping of liquids with traveling-wave electroosmosis. J Appl Phys 97:084906
14. Urbanski JP, Levitan JA, Burch DN, Thorsen T, Bazant MZ (2006) The effect of step height on the performance of AC electro-osmotic microfluidic pumps, J Colloid Interface Sci 309:332–341
15. Green NG, Ramos A, Gonzalez A, Morgan H, Castellanos A (2000) Fluid flow induced by nonuniform ac electric fields in electrolytes on microelectrodes. I. Experimental measurements. Phys Rev E 61:4011–018
16. Bazant MZ, Urbanski JP, Levitan JA, Subramanian K, Kilic MS, Jones A, Thorsen T (2007) Electrolyte dependence of AC electro-osmosis. In: Proceedings of 11th International Conference on Miniaturized Systems for Chemistry and Life Sciences (MicroTAS), 2007, pp 285–2878

Acoustic Droplet Ejection

▶ Transport of Droplets by Acoustics

Acoustic Levitation of Droplets

▶ Transport of Droplets by Acoustics

Acoustic Particle Concentration

▶ Transport of Droplets by Acoustics

Acoustics Based Biosensors

N. Gozde Durmus[1], Richard L. Lin[2], Mariel Kozberg[3], Deniz Dermici[4], Ali Khademhosseini[5,6], Utkan Demirci[5,6]
[1] Department of Molecular Biology and Genetics, Middle East Technical University, Ankara, Turkey
[2] Department of Materials Science and Engineering, Massachusetts Institute of Technology, Cambridge, MA, USA
[3] Department of Chemical Engineering, Massachusetts Institute of Technology, Cambridge, MA, USA
[4] Department of Economics, Bogazici University, Istanbul, Turkey
[5] Harvard-MIT Division of Health Sciences and Technology, Massachusetts Institute of Technology, Cambridge, MA, USA
[6] Center for Biomedical Engineering, Department of Medicine, Brigham and Women's Hospital and Harvard Medical School, Cambridge, MA, USA
udemirci@partners.org

Synonyms

Acoustic waves; Medical imaging; CMUTs

Definitions

A biosensor is defined as an analytical device that uses a biological recognition system to target molecules or macromolecules. Biosensors use a physio-chemical transducer to convert the signal from the bio-recognition system into a detectable signal [1]. Biosensors consist of three components: 1) the detector, which identifies the stimulus; 2) the transducer, which converts this stimulus to an output; and 3) the output system, which involves amplification and display of the output in an appropriate format [1].
Piezoelectricity is a phenomenon displayed in certain crystals, such as quartz and Rochelle salt, where mechanical stress induces voltage generation and vice versa.

Overview

There is an increasing demand for small, reliable, disposable, and inexpensive sensors in industrial, medical, and a variety of other science and engineering fields. Sensors are one of the fastest growing markets, with annual growth of about 18%. In particular, the market for biosensors is increasingly promising due to their application in progressing areas of healthcare, biotechnology, and medicine. For instance, the use of biosensors in personal glucose testing, HIV, and early cancer detection are areas with great medical relevance [1]. In addition, the ability to detect pathogenic and physiologically relevant molecules in the body with high sensitivity and selectivity offers a powerful tool in early diagnosis and treatment of diseases [1].
An acoustic wave biosensor utilizes acoustic or mechanical waves as a detection mechanism to obtain medical, biochemical, biophysical information about the analyte of interest [1, 2]. It detects changes in mass, elasticity, conductivity and dielectric properties from mechanical or electrical variations. These devices also employ the piezoelectric effect to excite acoustic waves electrically at an input transducer and to receive the waves at the output transducer [2].
The first scientific experiment of piezoelectricity was conducted in 1880 by Pierre and Paul Jacques Curie, who found that compression of various crystals leads to voltage production on their surface. They showed the converse effect the following year by demonstrating the elongation of certain crystals when injected with electric current. Although these observations intrigued the scientific community, piezoelectricity remained much of a laboratory technology until Paul Langevin used piezoelectric transducers to construct sonar for submarine detection in 1915 [3]. Acoustic biosensors can be made with piezoelectric crystals such as quartz, lithium niobiate or lithium tantalate since they are robust and environmentally stable. In addition, such sensors are versatile and can detect, in principle, various biomolecules [1]. Acoustic wave sensors can be categorized according to the waves they generate, such as bulk or surface acoustic waves (Fig. 1). Each of these wave mechanisms have various advantages and disadvantages depending on their specific applications [1].
The goal of this review is to categorize and describe the mainstream acoustic wave biosensors. We will begin by discussing biosensors that utilize bulk acoustic waves and subsequently analyze devices that employ surface acoustic waves. We will also examine sensors that employ capacitive micromachined ultrasound transducers, a novel technology that does not require piezoelectric substrates. For each type of these sensors, we will present an overview of their scientific mechanisms and fabrication techniques in the Basic Methodology section. We will then go on to discuss the advantages and applications in biology and medicine in the Key Research Findings and Future Direction for Research sections.

Basic Methodology

Bulk Acoustic Wave (BAW) Devices

Bulk acoustic wave (BAW) biosensors employ either longitudinal or shear waves, although the latter is often preferred to reduce acoustic radiation in the medium of

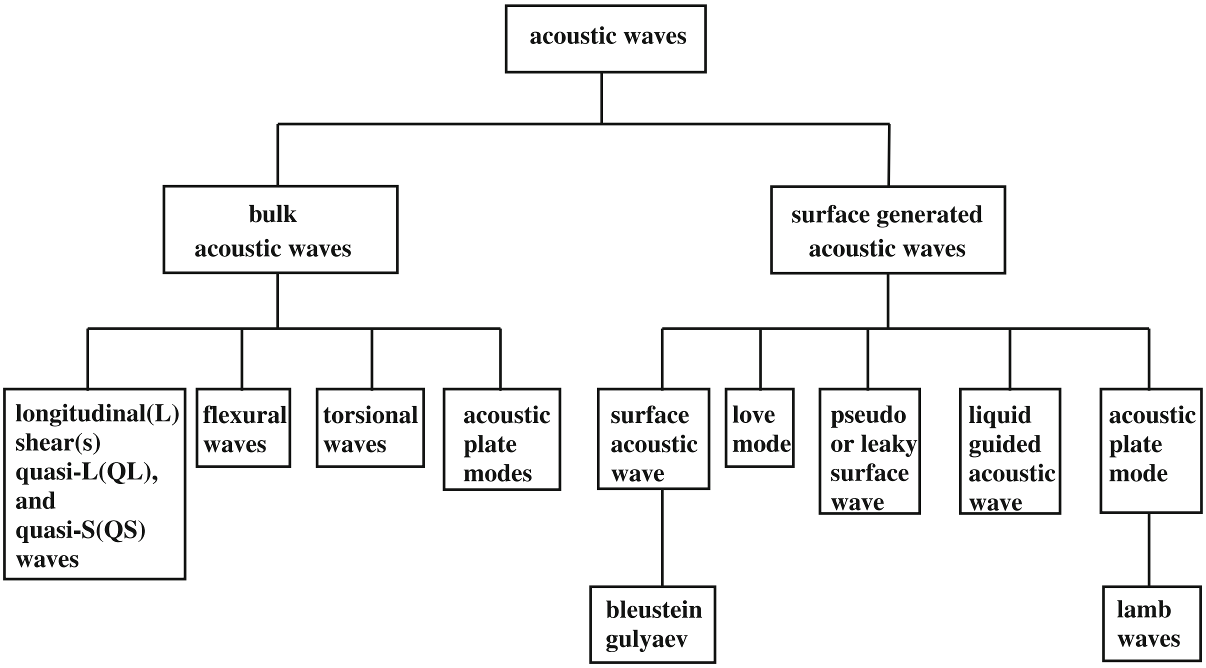

Acoustics Based Biosensors, Figure 1 Classification of acoustic waves [1]

interest. They are the oldest and the simplest acoustic wave devices. BAW devices consist of a parallel electrode placed on both sides of the thin piece of crystal. A BAW sensor can technically employ any piezoelectric element and typically quartz is used, as it is an inexpensive material readily available in nature and easily synthesizable in abundant quantities. In addition, thin disks of quartz are more stable at high temperatures than other piezoelectric elements. When an alternating electric field is applied, it results in a potential difference between the two electrodes and the shear deformation of the crystal. As a result, there is mechanical oscillation of a standing wave across the bulk of the quartz. The frequency of the vibrations is dependent on quartz properties such as density, size, and phase in contact with the crystal surface [4]. Currently, thickness shear mode (TSM) resonator and shear-horizontal acoustic plate mode (SH-APM) sensors remain the most widespread BAW sensors. The other two common BAW sensors that lie beyond the scope of this article are the thin rod acoustic wave sensors and the flexural plate wave devices [4].

BAW Device – Thickness Shear Mode (TSM) Resonator

TSM resonator, also known as quartz crystal microbalance (QCM), is the simplest and most widespread acoustic wave device today. TSM typically composes of a quartz plate sandwiched by electrodes on opposite faces. Electric field crosses through this plate when voltage is applied to the electrodes, resulting in a shear mechanical strain or displacement in the quartz. By oscillating the voltage frequency, a mechanical resonance can be generated, where the maximum displacement of crystal occurs at the surfaces. The resonant frequency, F_r, and the quality factor, Q, are the two resonance parameters. While F_r is the mechanical thickness shear resonance as mentioned before, it is also defined as the frequency of the maximum value of the electrical conductance, G_{el}. Q is approximated mathematically from the electrical conductance resonance spectrum as $Q = F_r/\Delta F_{BW}$, or the ratio of resonant frequency to the half bandwidth [5] (1).

Coupling of molecules in solid, liquid, or gas phase to the TSM resonator changes the resonance parameters. When mass attaches onto the crystal face, it raises the quartz's overall weight and reduces F_r. Saurbrey first derived the mathematical relationship between loading mass and F_r to be:

$$\Delta f = -\frac{2f_0^2 \Delta m}{A_{piezo}(u_q p_q)^{1/2}}$$

(1) The variables $\Delta f, f_0$, Δm, A_{piezo}, u_q, and p_q represent, respectively, the crystal's measured frequency shift, initial resonant frequency, mass change, surface area, shear mod-

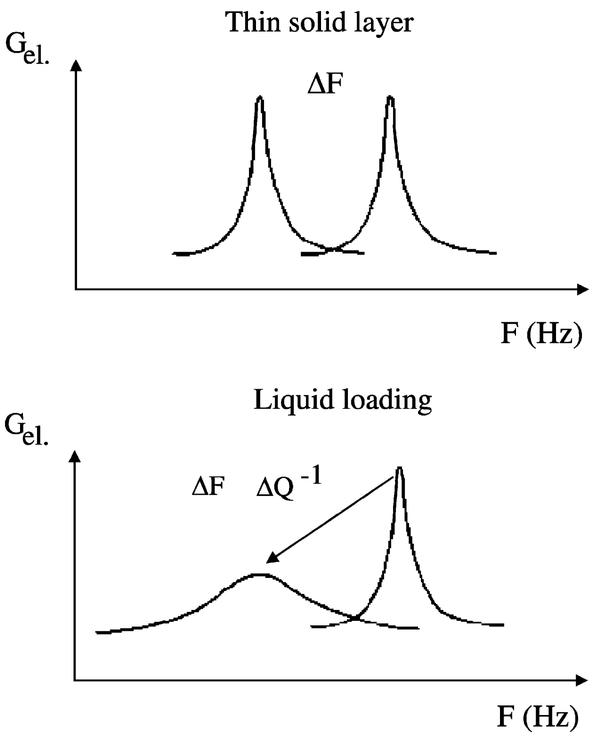

Acoustics Based Biosensors, Figure 2 Changes to the resonance peaks due to a thin solid layer (top) and liquid (bottom). Note the decrease in Q for TSM resonator in liquid [22]

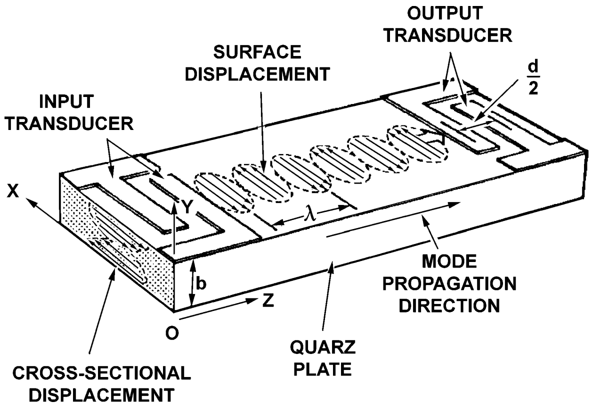

Acoustics Based Biosensors, Figure 3 SH-APM can sense on either side of the device because waves travel between the upper and lower surfaces of the plate [2]

ulus, and density [6]. TSM resonators immersed in liquid present a special case because acoustic energy dissipation through the fluid lowers Q as well. Additional formulas need to be applied to account for the liquid's viscosity and loading [6]. Figure 2 shows a comparison between shifts induced by solid and liquid loading on resonators.

TSM resonators possess lower mass sensitivity than most acoustic wave sensors that employ other mechanisms since they typically operate between only 5 and 30 MHz. Thinner devices can be used to increase frequencies that result in increased mass sensitivity, they are more fragile and harder to manufacture and handle [5]. Recent research on this topic has been on creating high-frequency TSM resonators with piezoelectric films and bulk silicon micromachining techniques.

TSM Fabrication

TSM resonator fabrication usually utilizes photolithography [2]. The resonance frequency of the quartz crystal depends on the shear modulus, density, and material thickness [1]. After polishing the quartz, photoresist is deposited and the device is exposed to UV light through a mask, which determines the active areas that have to be metalized on the devices. On a TSM resonator, they represent the location of the electrode plates. A chemical interface is then added to the remaining crystal surface, where molecules in the liquid can bond to and be detected [2].

BAW Device – Shear-Horizontal Acoustic Plate Mode (SH-APM) Sensor

First introduced in the 1980s, SH-APM sensors use a thin piezoelectric substrate, or a plate, to guide the acoustic wave and to confine its energy within the plate's top and bottom surfaces. Most of the production and analysis principles employed in SH-APM sensors are used in a TSM resonator. Their most striking difference is that SH-APM sensors employ interdigital transducers (IDT) rather than electrode plates. IDTs are deposited on opposite ends of a surface, where one IDT generates displacement waves through application of an oscillating voltage and the other receives it (Fig. 3) [2]. The surface without IDT is immersed in the targeted liquid and acts as the sensor, so the device will not suffer from corrosion problems as electrode plates do in biological solutions [7].

Like TSM resonators, SH-APM sensors prevent the acoustic waves from gaining a shear vertical component and thus lessening energy radiation in the form of compression waves into the liquid. They achieve this by restraining particle displacement within the plate plane. However, given a SH-APM and a TSM device of similar plate thickness, the former usually attains higher mass sensitivity than the latter because IDT is much smaller and precise than the electrode plates on TSM. In general, SH-APM devices generate waves with a frequency ranging from 100 to 150 MHz, but they are also more complex and expensive than their TSM relatives [2].

SH-APM Fabrication

Although the crystals and substrates may be different, SH-APM sensors are fabricated in a similar fashion as TSM resonators. One difference that must be noted is the use of IDTs in SH-APM fabrication, which is not present in TSM resonators. Depending on the application, the optimization of sensor performance can be achieved through adjustments of the length, width, position, and thickness of the IDTs. These parameters can be altered by varying the design of the masks, amount of photoresist and other chemicals used in the fabrication process [2, 7].

Moreover, SH-APM devices require additional processing during their fabrication of the thin plates with respect to the IDT periodicity. Thin slices of piezoelectric materials such as quartz are often used. The whole procedure permits researchers to choose the correct crystallographic orientation for generating the desired shear waves. Despite this improvement, SH-APM devices remain less sensitive than SAW devices for two reasons. First, energy of the wave does not reach a maximum at the surface. Second, similar to TSM, SH-APM is restrained by a minimum thickness of piezoelectric plate [2, 7].

Surface Acoustic Wave Sensors (SAW)

Surface acoustic wave (SAW) sensors have been used for years in measuring temperature, pressure, viscosity, acceleration, concentration and chemical/biological entities [3]. They are also used to perform signal-processing operations and are sensitive to their environment [8]. This type of acoustic wave sensors consists of basic components such as piezoelectric substrate (crystals such as quartz, GaAs, or $LiNbO_3$), micrometallization patterns (electrodes), interdigital transducers (IDT) and active thin films. Unlike BAW, which only interacts with the environment at the opposite surface of the material by traversing through it, SAW travels along or near the surface of the piezoelectric material [3]. The piezoelectric device detects small mass changes at the surface of the sensor as a frequency response, as the electrodes on the surface of the piezoelectric substrate transmit and receive acoustic waves [8]. The acoustic wave is confined to the surface of the piezoelectric substrate and the excited wave is propagated along the crystal surface. The surface wave velocity changes due to the mass or the viscosity changes due to the binding reactions on the sensor surface. The range that SAW device operates depends on the acoustic velocity of the crystal substrate and IDT wavelength, and it usually lies between lower MHz range to the GHz range [8]. These devices are commonly used because of their ability to directly sense the changes in mechanical and mass properties and they have a broad range of applications such as pressure, temperature, viscosity, mass, chemical and biological sensing [8]. SAW sensors coated with organic and/or inorganic materials can be used to analyze absorption on the surface of a device [9]. For chemical sensing, the chemoselective material must be tailored to the analyte of interest. During its operation, SAW sensor responds to a gas or vapor exposure in air by a shift in resonant signal frequency, and then recovers to the original signal frequency, when the sensor is exposed to ambient air free of the responding analyte [8]. The SAW velocity changes according to the absorbed chemical substance and it results in the alternation of the mass load, the elastic stress and the conductivity of the polymer coating on the SAW device.

SAW devices are also considered as "electronic noses." An electronic nose is a device that is composed of a chemical-sensing system and a pattern-recognition system. Electronic noses mostly have the ability to detect very low vapor concentrations [8]. If there is vapor on the piezoelectric surface of the SAW device, the chemical substances in the vapor and in the acoustic wave interact and the properties of the wave changes. Sensitivity of the SAW detector is dependent on the temperature of the piezoelectric crystal and the vapor-pressure of the analyte. Chemical concentration of analyte of interest can be tested by monitoring the frequency. The SAW chemical sensor requires no special support gases and no consumables other than electrical power. Many of the SAW devices have been produced for military and defense applications. They are used for on-the-spot vapor detection of plastic explosives containing nitro groups such as trinitrotoluene (TNT) and cyclotrimethylenetrinitramine (RDX) [8]. As a result, SAW sensors are attractive for real-time detection and monitoring of toxic or hazardous gases, vapors and they are used in biology as a sensitive method for detection of biochemicals and biomolecular interactions [9].

SAW devices operate at high frequencies, which lead to smaller, more sensitive devices that have limits in the picogram range [8]. SAW devices can be miniaturized by using photolithographic techniques and complex circuits can be present on the substrate surface. Miniaturization makes them advantageous since the smaller dimensions increases the sensing surface area and binding properties [6]. Moreover, there is a dual-delay system with SAW sensors (Fig. 4). It is a layered structure and has three fundamental advantages. First, it compensates the influence of temperature on the differential frequency and the air pressure. Second, it reduces the measured frequency of the system from MHz range to kHz range [6]. Third, SAW devices have the ability to directly sense mass and mechanical changes in an environment, which makes them more sensitive than other electrical and thermal biosensors. Furthermore, they have numerous advantages in bio-

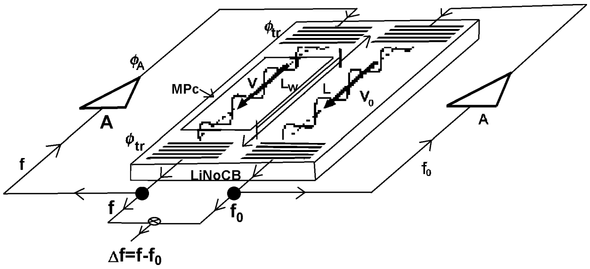

Acoustics Based Biosensors, Figure 4 SAW device dual delay line structure and its principal of operation [21]

logical applications [6]. These devices are also more cost-efficient than the optical biosensors and easier to handle. They are employed to study biomolecular interactions and allow easy and direct detection of analyte of interest [8]. In summary, SAW technology is a cost-effective method of label-free detection of biomolecular interactions and allows direct monitoring on the surface of a transducer in real time [10].

SAW Device Fabrication

Various lithographic techniques are used in the fabrication of interdigital transducers (IDT's) for surface acoustic wave sensors. The most widely used and least costly photolithographic technique to fabricate SAW devices is conventional contact printing. It uses rigid or conformable glass plates bearing the photographic image, which can be negative or positive depending on the fabrication steps of the IDT pattern [11]. Mass production of acoustic devices is done by optical lithography. Excitation of the SAW harmonics depends on the metallization ratio between the gaps and the electrodes of the SAW device. A lithography method especially suited for the fabrication of small gaps is the near-field phase shift technique. In this technique, a transparent mask with a pattern on its surface is brought into contact with the substrate. The phase of the exposing light is modulated at the edges of the patterned relief. High frequency, low-loss SAW devices can be fabricated by depositing thin piezoelectric films on substrates. These include ZnO, GaN, AlN, and $Al_xGa_{1-x}N$ thin films on sapphire, SiC and diamond substrates. The SiO_2/ZnO/diamond structure can provide a high acoustic velocity and a zero temperature coefficient of frequency. Extremely high velocity SAW modes with moderate coupling coefficient in AlN and GaN thin films are deposited on SiC, diamond, or sapphire substrates [12]. In addition, imprint lithography is a commercial method to fabricate SAW devices, especially for simple pattern, one-mask-level applications, where large areas can be patterned with nanometer-scale critical dimensions and high fidelity. Moreover, nanoimprint lithography is becoming a popular lithographic method. SAW filters and SAW correlators, present ideal structures to be fabricated using this method.

Capacitive Micromachined Ultrasonic Transducers (CMUTs)

Electrostatic transducers have been used for sound wave excitation and detection as an alternative to piezoelectric devices that are used widely for nondestructive evolution and medical-related applications. The vibration of a thin plate under electrostatic forces is the main acoustic actuation and sensing mechanism of these devices. These devices are based on the electrostatic attraction force between the backplate and the metallized membrane. The simplest forms of this device consists of a thin metal membrane that is stretched above a back electrode forming a small gap [13]. Upon exposure to sound waves, the gap height is modulated at the frequency of the incoming pressure field that induces a change in the device capacitance, which generates an output voltage proportional to the amplitude of the field. The capacitor is also used to generate sound waves. The advantage of the electrostatic devices compared to the other types of transducers is the impedance matching between the transducer and the surrounding medium. Advances in the silicon micromachining techniques enabled the fabrication of micro electro-mechanical systems (MEMS) based electrostatic transducers. These devices use the ultrasonic waves due to the miniaturization capacity of the silicon machining techniques and are called, capacitive micromachined ultrasonic transducers (CMUTs) [13].

CMUT are made of small and thin transducer membranes that are suspended over a conductive silicon substrate (Fig. 5). The two plates of the capacitor, substrate and the membrane are separated by a vacuum-sealed cavity. Two-dimensional (2D) arrays of miniaturized electrostatic cells are micro-scale cells that operate in parallel and driven in phase. Surface silicon micromachining is used for their microfabrication [13]. The operation principle of these devices is based on the capacitance modulation of a micro-condenser. Between the metalized membrane and the substrate, a direct current voltage is applied. The membrane is attracted toward the bulk by the electrostatic force, and induced stress within the membrane resists the attraction. If the membrane is exposed to ultrasound, a current output is generated as the capacitance changes under constant bias voltage. The amplitude of the current output is a function of the frequency of the incident wave, the bias voltage, and the capacitance of the device. CMUTs perform operation in the megahertz range. The lateral dimensions of each cell are in the order of tens of microns [13]. The gap

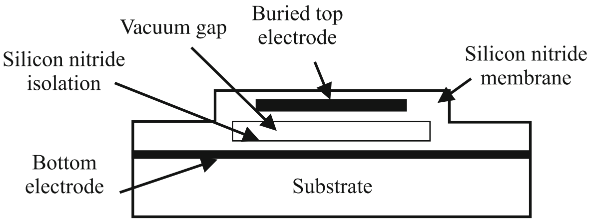

Acoustics Based Biosensors, Figure 5 Schematic cross section of a CMUT transducer membrane [23]

between the membrane and the substrate vacuum-sealed or unsealed can be as small as 500 Å. The membranes may be conductive or coated with a conductive electrode. This structure results in very efficient transducers that can compete with their piezoelectric counterparts in terms of efficiency and bandwidth. The small and thin membranes that constitute the CMUT transducer are micromachined onto a silicon substrate [13].

CMUT Fabrication

There are two conventional methods to fabricate CMUT; sacrificial release process and wafer-bonding method. The first CMUT was created by using a sacrificial release process and this method has become the standard CMUT fabrication for many years. In the sacrificial release process, a cavity underneath the membrane is created by depositing or growing a sacrificial layer on the carrier substrate. The sacrificial layer is removed with an etchant after the membrane deposition. However, there are some problems associated with this technology. The surface micromachining process causes limitation on the cavity and membrane size of a CMUT device. In addition, it is hard to batch produce surface micromachined CMUTs to tight quality specifications [14]. On the other hand, wafer-bonding method is a new fabrication technique that combines bulk and surface micromachining techniques. The transducer membrane and cavity are defined on a SOI wafer and on a prime wafer, respectively. Two wafers are then bonded by using silicon direct bonding in a vacuum environment, together forming the transducer (Fig. 6) [14]. This new method improves CMUT performance since it decreases the number of process steps, device turn-around time, and increases the overall uniformity, reliability, repeatability.

Key Research Findings

Advantages of BAW Devices over SAW Devices

Acoustic biosensors generally employ BAW rather than SAW because BAW devices generate waves that mainly propagate in the shear horizontal motion. Since shear horizontal wave does not radiate significant amount of energy into liquids, it minimizes damping in the liquid operation. Besides few exceptions, the SAW sensor induces considerable surface-normal displacement that radiates compression waves into the liquid and causes excessive damping. Since biosensors detect chemicals in liquid solutions, BAW is often preferred over SAW for many biosensing applications [2].

Biological Applications of SH-APM Sensors

SH-APM sensors have been utilized in various biological applications. For example, Liren et al. [15] presented a urease biosensor in which a 0.5 mm thick ZX-$LiNbO_3$ substrate was used and a resonant frequency approximately centered at 50 MHz. APM was generated and detected by IDTs, with a period of 88 um and a center distance of 10 mm, on the same PZ crystal. The group also fabricated two pairs of IDTs on the substrate so that one would conduct biochemical reactions while the other acted as a reference. Using this device, they successfully measured urea concentrations by detecting variations in the resonant frequency [15].

SH-APM sensors have also been applied in immunochemical reactions. In order to observe antigen-antibody reactions through mass loading on the crystal surface, Dahint et al. [7] constructed an immunosensor using a 150 MHz APM device on a ZX-$LiNbO_3$ plate with a thickness of 0.5 mm. These sensors, which could detect mass as small as to 200 pg/mm^2 of crystal surface, marked a shift in resonant frequency of around 1 kHz upon antigen adsorption [7].

Biological Applications of TSM Resonators

Many biosensors that employ TSM resonators are available on the market today. Depending on their design, they can detect biological entities such as nucleic acids, viruses, bacteria, and cells. An example of TSM-based biosensor was presented by Davis et al. [16]. They used a coating of human IgG and subsequently used a TSM resonator to detect the presence of sheep antihuman IgG as marked by the decrease in the resonant frequency, signifying an increase in the mass loading from the attachment of the antibodies [16].

TSM sensors can also be used as DNA-based sensors. Okahata et al. [28] studied the use of oscillatory driven 9 or 27 MHz quartz to quantify DNA–DNA and DNA–protein interactions. They used quartz with one side specifically coated and the other side rubber cased, which was dipped into a stirred and thermostated solution of the target. Binding amounts were evaluated quantitatively as mass per unit area. Effects of probe immobilization tech-

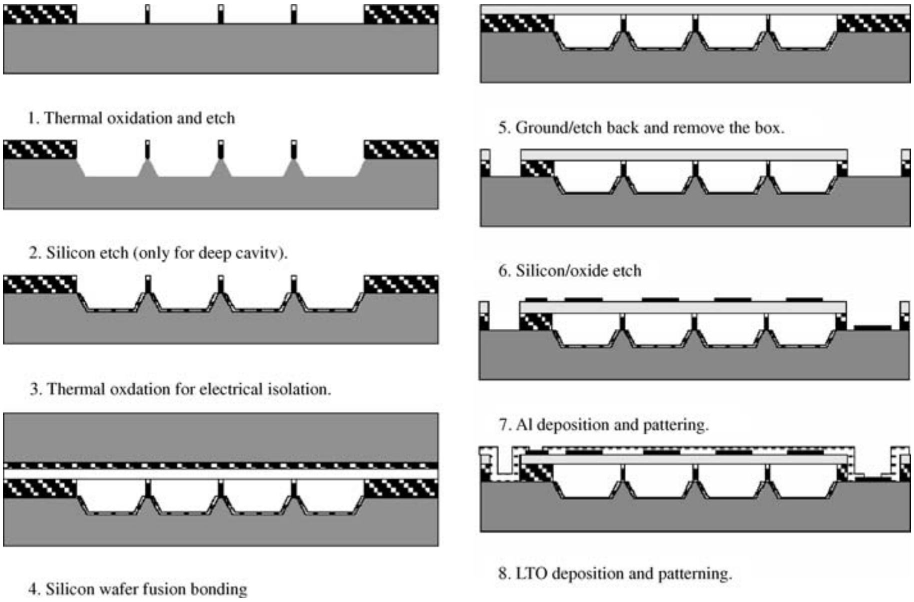

Acoustics Based Biosensors, Figure 6 Major steps of CMUT fabrication with wafer bonding method. (Reprinted with permission from Ergun et al.[24])

niques, chain lengths, ionic strengths, temperatures and mismatches on hybridization, regulatory protein binding, and electrostatic effects in DNA-binding properties of lysine containing oligopeptides were evaluated quantitatively. In addition, Tessier et al. [22] used a TSM sensor, or specifically an antibody functionalized quartz sensor, to detect human erythrocytes. Adsorption and desorption studies of antibody conjugated phages at antigen immobilized TSM resonator-surfaces in a high-throughput set-up were also performed [4].

Biological Applications of SAW

SAW devices are useful in industrial and commercial applications of chemical and biological sensing. In biological applications, these devices can be used to detect molecules by mass. A potential application of SAW devices in biology is in building immunosensors. In a study, immunosensor SAW devices were first coated with a parylene thin film to create a chemically homogeneous layer. Then, photoactive and functional groups containing dextran were immobilized and antibodies were bonded. This sensor consisted of lithium tantalate substrate with gold transducers and used to monitor urease binding [10]. This sensor was applied to monitor the amount of the urea in human urine to diagnose the onset of liver and kidney diseases [10]. In addition, another study immobilized polysaccharides to a silicon oxide surface intended for SAW. The pneumococcal polysaccharide (PPS) vaccine can immobilize via Protein A after pre-treatment of the surface with hydrochloric acid. The results show that the immobilization of PPS via Protein A increased the sensitivity of Streptococcus pneumoniae antibodies detection in human serum when compared with ELISA [17]. This study shows that SAW sensors can be used in detection of microbial contaminants in the environment.

Advantages of CMUT Devices

Piezoelectric ultrasonic transducers are used to generate and detect ultrasound over the last 30 years. This technology gives a bandwidth as high as 60–80% and a high sensitivity [18]. Nevertheless, the piezoelectric transducers have disadvantages in air or fluid-coupled applications due to the impedance mismatch between the medium and the piezoceramic material. Moreover, it is an expensive technique and shows some restrictions for the 2D arrays. On the other hand, CMUT devices became an attractive alternative to piezoelectric transducers as they have inherently low mechanical impedance associated with a thin vibrating membrane. Thin membranes that are fully supported with insulating posts on all sides and these devices have the advantage of the good mechanical properties of silicone and silicone nitride [19]. As the mechanical impedance of such thin membranes is much closer to those of fluids in a wide frequency range, CMUTs are better in immersion applications than piezoelectric devices. Moreover, CMUTs are fabricated using standard micromachining processes and provide ease of fabrication, batch production, very high level of integration and repeatability. Tak-

ing advantage of the microfabrication techniques, these devices can provide the broad bandwidth and coupling efficiency required for high performance. Furthermore, this kind of ultrasonic transducers have the ability to make complex array designs using standard photolithographic techniques that makes them usable for imaging applications [19]. A transducer with a wider band increases the resolution as well as enabling the design of the image processed. In addition, CMUTs are an alternative for intravascular imaging systems as they can be microfabricated as small 2D imaging arrays and maintain electroacoustic performance [19].

Biological Applications of CMUTS

Today's ultrasound technology has a wide range of applications in industrial and medical field, from distance measurement to medical diagnostic imaging. The fields such as dermatology, ophthalmology, and cardiovascular medicine require ultrasonic imaging systems. CMUTs enable in vivo medical imaging at high frequencies. They are also used in the microfluidics and acoustic sensing, which have applications in the biomedical engineering.

Intravascular ultrasound (IVUS) is a medical imaging technique that uses ultrasound equipment with long, thin catheters and enables visualization of blood vessels through the blood column and inner wall of blood vessels. This gives information about cardiovascular diseases. In addition, a pulse-echo phased array B-scan sector, 1D linear CMUT array was produced by Demirci et al. [19] to demonstrate the viability of CMUTs for ultrasound imaging for medical applications. 64- and 128-element 1D CMUT arrays with 100% yield and uniform element response were fabricated. For imaging experiments, resolution test phantom was used to mimic the attenuation properties of soft tissue. The image quality was found in order to show the practicality of using CMUT devices for ultrasound medical imaging due to its wide bandwidth and high sensitivity. Current l-dimensional (1D) side looking ultrasound imaging probes do not have the forward viewing capability. Demirci et al. [19] showed forward-viewing annular CMUT arrays can be used for medical imaging applications. 64-element, forward-viewing annular arrays were fabricated and designed for imaging applications in the 20 MHz range. The devices operate in the 5–26 MHz range with a fractional bandwidth of 135%. These forward-viewing annular CMUT arrays are promising tools for measuring blood flow and imaging upon being mounted on the front surface of a cylindrical catheter probe [19]. Forward-viewing IVUS enables new procedures in cardiac medicine such as viewing blood vessels, guiding stent placement, and monitoring operations in the heart [20]. In addition, researchers focused on developing a forward-looking 2D imaging arrays that can be microfabricated and integrated with electronics. CMUTs are alternative tools for 2D medical imaging arrays. In a study, ring annular CMUT was used for forward-looking IVUS imaging at 16 MHz. This 1 mm diamater arrayed CMUT device was used for volumetric imaging and they were found to have potential use in IVUS imaging catheters [20]. Another study by Knight et al. [29] modeled and designed the CMUT membranes for performance in forward looking IVUS. They used finite element analysis to calculate the electromechanical coupling coefficient, k^2 and showed that the CMUT geometry can be optimized for maximum coupling coefficient, allowing CMUT IVUS array elements to be designed with more than 60 dB/V dynamic range with 10 MHz bandwidth around 20 MHz by fabricating a 1.02 mm diameter 64-element array [20]. A recent improvent in CMUT technology produces a three dimensional ultrasound imaging system using a forward-looking ring array with a diameter of 2 mm and 64 elements each 100 μm × 100 μm in size. 3D images of several wire targets and Palmaz–Schatz stents indicate the potential of imaging with such a device. In addition, further improvements point to a promising future for forward-viewing CMUT ring arrays in intravascular imaging [21]. CMUT devices are used in the real time in vivo imaging applications with an improved performance over the existing medical ultrasound transducers. A wafer bonded CMUT probe showed a bandwidth of 130 % (3–13 MHz), which covers nearly the entire frequency range for medical ultrasound applications. Carotid artery and thyroid gland were imaged with surface and bulk-micromachined CMUT arrays and real time in vivo images were compared with a PZT array. The bandwidth and resolution performance of the surface micromachined arrays were slightly better than PZT. However, depth of penetration was not as good as in PZT. Bulk micromachined CMUT arrays showed the first real-time in-vivo images and had improved resolution and bandwidth but less depth of penetration. As a result, improved axial resolution and extremely broad bandwidth are achieved by CMUTs. Improved axial resolution will allow smaller targets to be resolved in tissue for such applications as imaging micro-calcifications in the breast, small abnormalities in the thyroid, or better delineation of the intimal linings of blood vessels to search for plaque build-up [22].

Future Directions for Research

Advancements made over the past decades have culminated in the initiation and development of acoustic wave biosensors. The ability to detect biological molecules by

these sensors may contribute to treatment of many diseases such as HIV and cancer. In addition, these devices are promising in medical imaging given their ability to generate high-resolution pictures in real time. However, there are still limitations to some of these devices that can be surmounted through future research and though the potential of the application of these devices to biological situations has been recognized, more work is left to be done in order to employ them on a wider scale. Below are some limitations and potentials of the devices.

SAW Devices

There are a number of potential limitations with the SAW sensors as they are today. One limitation is that SAW sensors are sensitive to a variety of parameters [8]. In addition, the intensity of an acoustic wave can decrease in biological solution such that the sensing system may not work efficiently. Furthermore, many SAW devices that are used in the gas-sensing applications may not be used to detect molecules in the liquid phase. When a fluid contacts the SAW surface, the longitudinal wave component pumps a compression wave into the fluid [2]. In air, the energy losses are not too effective. However, in many liquids, all the energy is pumped out of the acoustic wave before it reaches the device's receiving transducer. SAW devices can perform well in liquids when they rely on surface waves with no longitudinal components like horizontally polarized shear waves, surface transverse waves, and the guided acoustic waves called "Love waves" [2]. Recent advances in liquid sensors and immunoassays improved the detection limits. In addition, surface technologies like functionalization with fluorescent probes, DNA, and enzymes increased the use of SAW devices in liquid samples [7]. There are also radar-type SAW sensors for high-voltage applications that detect at long distances. These sensors cannot be used scans of wider areas due to two main limitations. According to the radar equation, the radiofrequency signal changes with the fourth power of the distance between the radar unit and SAW sensor. As a result, high signal attenuation is governed by this equation. Second, only a few echo sounds can be distinguished because all sensors in the detection range respond immediately. Attaining this requires differentiated sensors that responds within different time slots, and multiple sensors can be used with a limited number of reflectors and limited identity-code capacity [25].

In addition, generation of acoustic waves in microstructures requires various processes and technologies, with compatibility as one of the main limitations in the development of smart sensors. Restrictions of manual handling and fabrication process limit minimum thickness of the devices to be about 100 microns. Adoption of silicon fabrication opens the possibility for the integration of the acoustic devices and electronic driving circuitry, leading to the development of smart sensors. This technique involves localization of specific fabrication steps to common areas to minimize the total number of process steps in the fabrication process as well as to maintain SAW and Lamb wave device integrity and quality [26].

Most of today's acoustic wave generation and focusing apparatus suffer from these further limitations: The piezoelectric arrays are expensive, and it is hard to get high-level, well-distributed intensities. In addition, shocks are generated at a rate of one or two shocks per second, whereas extracorporeal shockwave treatment (ESWT) typically requires thousands of shocks per treatment. Acoustic lenses are mostly fragile and non-effective for larger apertures. Moreover, electrohydraulic approach has disadvantages of non-uniform discharges, pain and high noise level.

BAW Devices – TSM Resonator

The limitations of TSM resonators are mostly related with the experimental setup, accuracy in modeling the sensor and physical behavior of a viscoelastic polymer. Researchers should be careful in model approximations, parameter estimations, and measurement errors. For acoustically thin polymers, the thickness can be calculated with a small error, but the shear moduli can hardly be extracted from measurements due to negligible influence on the sensor behavior. On the other hand, the coating thickness should be known because of the existence of multipleidentical solutions for acoustically thick polymers [27]. In addition, for detailed interpretation of sensor response in liquid requires more sophisticated experimental setup [4]. In addition, mechanical, optical, and electrochemical properties are helpful to characterize interactions at biological surfaces and interfaces. However, the needed equipment are expensive. While miniaturized quarts arrays seem to present a solution for low cost sensor setups, miniaturization has its limitations because small electrode areas can load enough molecules to achieve measurable frequency shifts. As a solution, combination of automatized pipetting systems, microfluidics, integrated sensor arrays and multicomponent data analysis may open the way towards high throughput screening with acoustic wave sensors [4].

Two major challenges are present in the application of TSM resonator as a biosensor. First, cross reactions such as unspecific protein adsorption affects the accuracy of the results. This limits the resonator's use to binding sites that specifically bond to the targeted biological molecules

and poses a significant disadvantage in environments containing various compounds. Second, since the resonator only responds to mass loadings, the analysis cannot differentiate this signal from other factors that can affect the resonant frequency such as viscoelasticity and acoustic coupling effect. This leads to a disagreement between the experimental and theoretical values of mass uptake, an error that needs to be accounted for by researchers [4]. Immunochemical analyzes or nucleic acid hybridization results of TSM resonators should always be coupled with a reference analysis method. In addition, dry- and wet-coated TSM resonators may not give the same results due to changes in viscoelasticity, so calibration should be done in the sensing medium during nucleic acid analyzes. Complexation of DNA may limit the flexibility of the molecule strands and ionic strength changes or interaction with the surface might vary extension and shape of the molecule. These may change viscoelastic behavior and produce erroneous results from TSM resonators [4].

CMUTs

CMUTs have the potential to make ultrasound a far more versatile and important imaging modality. This technology has made advances in acoustic matching and the micro-miniaturization of electronics. It enables higher frequency imaging, allows clinicians to view small features in the body, and is useful for ultrasound imaging especially in the area of volumetric in vivo imaging, intravascular, and intracardiac research.

Cross References

► Biosensors Using Atomic Force Microscopes
► Biosensors Using Lasers
► Biosensors Using Magnetics
► Biosensors Using Surface-Enhanced Raman Scattering
► Biosensor
► Piezoelectric

References

1. Lec RM, Lewin PA (1999) Acoustic wave biosensors, Engineering in Medicine and Biology Society, 1998. Proceedings of the 20th Annual International Conference of the IEEE. 6:2779–2784
2. Drafts B (2001) Acoustic wave technology sensors, Microwave Theory and Techniques, IEEE Transactions on 49(4):795–802
3. piezoelectricity Encyclopædia Britannica. (2006) EncyclopædiaBritannica Online, 25 Aug. 2006, http://search.eb.com/eb/article-9059986
4. Kaspar M et al (2000) Thickness shear mode resonators ('mass-sensitive devices') in bioanalysis. Fresenius' J Anal Chem 366(6–7):602–10
5. Sauerbrey G (1959) Use of Quartz Crystal Vibrator for Weighting Thin Films on a Microbalance. Z Phys 155:206
6. Lin Z, Yip CM, Joseph IS, Ward MD (1993) Operation of an Ultrasensitive 30-MHz Quartz Crystal Microbalance in Liquids. Anal Chem 65:1546–1551
7. Dahint R et al (1994) Acoustic Plate Mode Sensor for Immunochemical Reactions. Anal Chem 66(18):2888–92
8. Milstein L, Das P (1977) Spread Spectrum Receiver Using Surface Acoustic Wave Technology. Communications, IEEE Trans 25(8):841–847
9. McGill RA, Chung R, Chrisey DB, Dorsey PC, Matthews P, Pique A, Mlsna TE, Stepnowski JL (1998) Performance optimization of surface acoustic wave chemical sensors. Ultrasonics, Ferroelectrics and Frequency Control, IEEE Trans 45(5):1370–1380
10. Lange K, Bender F, Voight A, Gao H, Rapp M (2003) A Surface Acoustic Wave Biosensor Concept with Low Flow Cell Volumes for Label-Free Detection. Anal Chem 75(20):5561–5566
11. Campbell CK (1984) Simplified Computer-Aided Fabrication of SAW Transducer Pattern Masks. Sonics and Ultrasonics, IEEE Trans 31(3):185–186
12. Chen Y, Emanetoglu NW, Saraf G, Wu P, Lu Y, Parekh A, Merai V, Udovich E, Lu D, Lee DS, Armour EA, Pophristic M (2005) Analysis of SAW properties in ZnO/Al/sub x/Ga/sub 1-x/N/c-Al/sub 2/O/sub 3/ structures. Ultrasonics, Ferroelectrics and Frequency Control, IEEE Trans 52(7):1161–1169
13. Ergun AS, Yaralioglu GG, Khuri-Yakub BT (2003) Capacitive micromachined ultrasonic transducers: theory and technology. J Aerosp Eng 16:76–84
14. Huang Y, Ergun AS, Hæggström E, Badi MH, and Khuri-Yakub BT (2003) Fabricating capacitive micromachined ultrasonic transducers with wafer-bonding technology. J Microelectromech Syst 12:128–37
15. Liren W, Xue W, Sixin W, Xuesong Y, Yuquan C (1996) A two-acoustic-waveguide-channel SH-APM urease biosensor. Engineering in Medicine and Biology Society. 1:85–86
16. Davis KA, Leary TR (1989) Continuous liquid-phase piezoelectric biosensor for kinetic immunoassays. Anal Chem 61(11):1227 – 1230
17. Dutra RF, Castro CMHB, Azevedo CR, Vinhas E, Malague E, Melo EHM, Lima Filho JL, Kennedy JF (2000) Immobilization of pneumococcal polysaccharide vaccine on silicon oxide wafer for an acoustical biosensor. Biosens Bioelectron 15(9–10):511–514
18. Caliano G, Carotenuto R, Cianci E, Foglietti V, Caronti A, Iula A, Pappalardo M (2005) Design, fabrication and characterization of a capacitive micromachined ultrasonic probe for medical imaging. IEEE Trans 52(12):2259–2269
19. Demirci U, Ergun AS, Oralkan O, Karaman M, Khuri-Yakub BT (2004), Forward-Viewing CMUT arrays for medical imaging. IEEE Trans Ultrason Ferroelect Freq Contr 55:887–895
20. Yeh DT, Oralkan O, Wygant IO, O'Donnell M, Khuri-Yakub BT (2006) 3-D ultrasound imaging using a forward-looking CMUT ring array for intravascular/intracardiac applications. IEEE Trans Ultrason Ferroelectr Freq Control 53(6):1202–11
21. Jakubik W, Urbanczyk M, Opilski A (2001) Sensor properties of lead phthalocyanine in a surface acoustic wave system. Ultrasonics 39(3):227–232
22. Tessier L et al (1997) Potential of the thickness shear mode acoustic immunosensors for biological analysis. Analytica Chimica Acta 347:207–17
23. Degertekin LF, Guldiken OR, Karaman M (2005) Micromachined capacitive transducer arrays for intravascular ultrasound. Proc SPIE Int Soc Opt Eng 5721:104

24. Huang Y, Ergun AS, Hæggström E, Badi MH, Khuri-Yakub BT (2003) Fabricating capacitive micromachined ultrasonic transducers with wafer-bonding technology. J Microelectromech Syst 12:128–37
25. Scholl G, Schmidt F, Wolff U (2001) Surface Acoustic Wave Devices for Sensor Applications. Phys Stat Sol (a) 185(1):47–58
26. Hoummady M, Campitelli A, Wlodarski W (1997) Acoustic wave sensors: design, sensing mechanisms and applications. Smart Mater Struct 6:647–657
27. Behling C, Lucklum R, Hauptmann P (1997) Possibilities and limitations in quantitative determination of polymer shear parameters by TSM resonators. Sens Actuators A 61:260–266
28. Okahata Y, Matsunobu Y, Ijiro K, Mukae M, Murakami, Makino K (1992) Hybridization of Nucleic Acids Immobilized on a Quartz Crystal Microbalance. J Am Chem Soc 114:8299–8300
29. Knight JG, Degertekin FL (2002) Capacitive micromachined ultrasonic transducers for forward looking intravascular imaging arrays. Ultrasonics Symposium, 2002, Proceedings. 2:1079–1082

Acoustic Separation

► Particle Manipulation Using Ultrasonic Fields

Acoustic Streaming

Yong Kweon Suh, Sangmo Kang
Dong-A University, Busan, Korea
yksuh@dau.ac.kr

Synonyms

Steady streaming; Eulerian streaming

Definition

Acoustic streaming is a secondary steady flow generated from the primary oscillatory flow. It includes not only the Eulerian streaming flow caused by the fluid dynamical interaction but also the Stokes drift flow which arises from a purely kinematic viewpoint.

Overview

Acoustic streaming originates from the acoustics. When the compressible fluid experiences a high-frequency oscillation driven by a certain source of sound, the nonlinear interaction causes a steady current in the field. This phenomenon is usually referred to as acoustic streaming. However, it was found that even an incompressible fluid can produce such steady streaming when the fluid oscillates adjacent to a certain obstacle or an interface. So, as pointed out by Riley [1], the term *acoustic streaming* is misleading. Instead of acoustic streaming he insisted on using *steady streaming* to encompass the case of incompressible fluid. *Acoustic streaming* in this article means both of these effects.

Another important issue that must be addressed is, whether or not the Stokes drift flow should be included in the streaming flow category. The Stokes drift flow is purely kinematic and so it is basically different from the Eulerian streaming flow, which is driven by the time average of the Reynolds stress term. However, the mass-transport effect given by the Stokes drift flow is not weaker than the Eulerian streaming. On the contrary, in the case of a progressive wave, the Stokes drift flow plays a dominant role (e. g., application of flexural plate waves to pumping and mixing in microfluidics [2]). Therefore, the Stokes drift flow must be understood as a kind of streaming flow.

Unfortunately, little is known about the historical background to the study of acoustic streaming. Therefore, instead of trying to give the historical background of the general concept, we will briefly survey the modeling and applications of acoustic streaming in microfluidics. A survey of steady streaming flow has been given by Riley [1].

In the early period, study mainly focused on the acoustic streaming of compressible fluids. The simplest and seminal phenomenon associated with acoustic streaming is the *quartz wind*. When the air experiences a high-frequency oscillation given by an ultrasound source, a progressive wave is established in the air. Due to the attenuation of the wave, a nonzero time averaged Reynolds stress is built in the region close to the sound source, and this stress pushes the air in the direction of wave propagation. The resultant wind is called a quartz wind. Lighthill [3] has provided a physical and simple analytical treatment of this steady streaming flow. Another important phenomenon is the so-called Kundt's dust pattern. When the air within a duct receives a standing wave, a nonzero time average of the Reynolds stress is built inside the duct. Due to the interaction between the air and the duct wall, a steady recirculating flow takes place within the duct. The net effect is that dust or particles accumulate at nodes.

On the other hand, researchers interested in mass transport in water waves have shown that a similar phenomenon occurs for incompressible flow (see [4] for an example). The salient feature is when an obstacle oscillates with high frequency in the quiescent viscous fluid. In this case the steady streaming emerges from both sides of the obstacle along the oscillating direction at small viscosity [5].

In this article, we will describe in some detail the fundamentals of three types of streaming flows associated with the microfluidic applications. First, the quartz wind which corresponds to the one-dimensional compressible flow will be introduced. Second, the Eulerian streaming flow

in two-dimensional space will be considered. Kundt's dust phenomenon will also be explained. Finally, we address the flexural plate wave and its net effect, i.e., the Stokes drift flow.

Basic Methodology

One-Dimensional Compressible Flow Model – Quartz Wind

In this and next subsections we closely follow the review by Riley [1] to describe the physical mechanism of acoustic streaming. We first consider the case when the sound is generated from a source and travels along a certain direction, say the x^*-direction, in a space. The governing equation for the motion of the compressible fluid is

$$\frac{\partial \rho^*}{\partial t^*} + \frac{\partial \rho^* u^*}{\partial x^*} = 0 \tag{1a}$$

$$\frac{\partial u^*}{\partial t^*} + u^* \frac{\partial u^*}{\partial x^*} = -\frac{1}{\rho^*}\frac{\partial p^*}{\partial x^*} + \frac{4}{3}\nu \frac{\partial^2 u^*}{\partial x^{*2}} \tag{1b}$$

where u^* is the flow velocity, p^* the pressure, t^* the time, ρ^* the density of the fluid and ν the kinematic viscosity of the fluid. The fluid particle is assumed to oscillate back and forth with amplitude A_0, frequency ω, and wavelength λ. We then take $1/\omega$, $\lambda/2\pi$, $A_0\omega$, and $\rho_0^* A_0 \omega^2(\lambda/2\pi)$ as the reference quantities for the time, length, velocity, and pressure, respectively. Further, we expand the density as

$$\rho^* = \rho_0^* (1 + \varepsilon\rho_0 + \varepsilon^2 \rho_1 + \ldots) \tag{2}$$

where ρ_0^* corresponds to the undisturbed fluid density. We also expand the dimensionless velocity and pressure, respectively, as

$$u = u_0 + \varepsilon u_1 + \varepsilon^2 u_2 + \ldots \tag{3a}$$

$$p = p_0 + \varepsilon p_1 + \varepsilon^2 p_2 + \ldots \tag{3b}$$

Then the leading-order equations of Eqs. (1a) and (1b) for the small value of the parameter ε become

$$\frac{\partial \rho_0}{\partial t} + \frac{\partial u_0}{\partial x} = 0 \tag{4a}$$

$$\frac{\partial u_0}{\partial t} = -\frac{\partial p_0}{\partial x} + \frac{4}{3}\delta \frac{\partial^2 u_0}{\partial x^2} \tag{4b}$$

where the variables without an asterisk are dimensionless. Here, the two dimensionless parameters are

$$\varepsilon = \frac{A_0}{\lambda/2\pi}, \quad \delta = \frac{\nu}{\omega(\lambda/2\pi)^2} \tag{5}$$

which can be considered as the dimensionless amplitude of the flow motion and the inverse of the Reynolds number, respectively. As usual, these parameters are assumed to be small. To solve this system of equations we eliminate the perturbed density in Eq. (4a) and the pressure in Eq. (4b) by using the definition of sound

$$\frac{\partial p^*}{\partial \rho^*} = c^{*2} = \omega^2 (\lambda/2\pi)^2 \tag{6}$$

We then have

$$\frac{\partial^2 u_0}{\partial t^2} - \frac{\partial^2 u_0}{\partial x^2} - \frac{4}{3}\delta \frac{\partial^3 u_0}{\partial t \partial x^2} = 0 \tag{7}$$

The solution of this equation is

$$u_0 = \exp(-2\delta x/3)\cos(x - t) \tag{8}$$

Notice that the basic mode is progressive. We need the next higher-order equation of Eq. (1b), which is

$$\frac{\partial u_1}{\partial t} + \frac{\partial p_1}{\partial x} - \frac{4}{3}\delta \frac{\partial^2 u_1}{\partial x^2} = -u_0 \frac{\partial u_0}{\partial x} \tag{9}$$

The right-hand side term can be understood as a dimensionless force per unit mass. Substituting Eq. (8) into the right-hand side gives

$$-u_0 \frac{\partial u_0}{\partial x} = \exp(-4\delta x/3) \left[\frac{\delta}{3} + \frac{\delta}{3}\cos 2(x-t) + \frac{1}{2}\sin 2(x-t)\right]$$

Taking the time average over one period (the operation to be denoted as $\langle\rangle$) of this provides

$$-\left\langle u_0 \frac{\partial u_0}{\partial x}\right\rangle = \frac{\delta}{3}\exp(-4\delta x/3) \tag{10}$$

which plays a role as the driving force for the generation of the steady flow $\overline{u}_1$. Taking the time average of Eq. (9) results in

$$\frac{\partial \overline{p}_1}{\partial x} - \frac{4}{3}\delta \frac{\partial^2 \overline{u}_1}{\partial x^2} = -\left\langle u_0 \frac{\partial u_0}{\partial x}\right\rangle \tag{11}$$

It should be noted that the term (10) can be understood as a kind of body force. Lighthill [3] has presented solutions of this system of equations for the case in which the force (10) acts as a point source in an infinite space. It is seen that when the viscosity is low enough (at high streaming Reynolds numbers) the flow from the source is like a jet as shown in Fig. 1. This flow is sometimes called the *quartz wind*. The term *acoustic streaming* refers

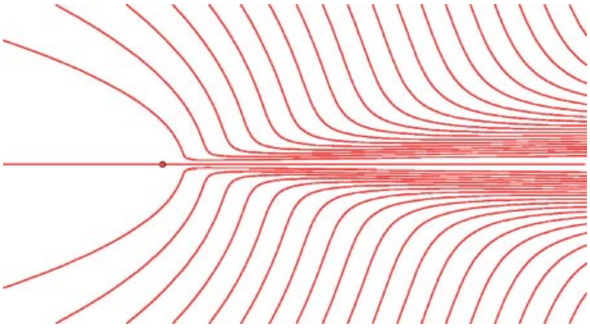

Acoustic Streaming, Figure 1 Acoustic streaming *quartz wind* generated from a point source of ultrasound

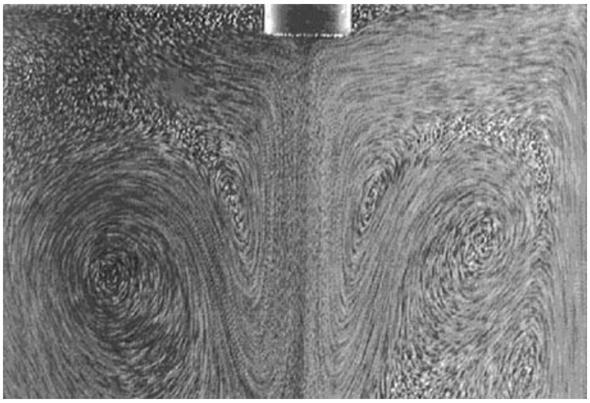

Acoustic Streaming, Figure 2 Acoustic streaming generated from an actual ultrasonic transducer

to this flow in the case of ultrasound. As can be seen from Eq. (10), the driving force for this current vanishes when there is no attenuation, i. e., when $\delta = 0$. Therefore we can say that the acoustic streaming in for the case of ultrasound in a compressible fluid is attributed to the attenuation of sound. The photograph in Fig. 2 clearly shows the streaming flow ejected by the transducer that creates the ultrasound.

On the other hand, we can also calculate the Stokes drift velocity from the solution of Eq. (8). We can follow a certain fluid particle's path $x(x_0, t)$, where x_0 is a reference point independent of the time. From the definition of the flow velocity we can write

$$\frac{dx}{dt} = \varepsilon u \tag{12}$$

We substitute Eq. (8) into the right-hand side of this and let $x = x_0 + \varepsilon x_1(t)$. We then have

$$x_1 = -\exp(-2\delta x_0/3)\sin(x_0 - t) \tag{13}$$

and

$$u_0 = -\exp(-2\delta x_0/3)\cos(x_0 - t) + \left(\frac{\partial u_0}{\partial x}\right)_{x=x_0} \varepsilon x_1 \tag{14}$$

Here again the last term contains the steady component and it becomes

$$\varepsilon u_{\mathrm{d}} = \frac{1}{2}\varepsilon \exp(-4\delta x_0/3) \tag{15}$$

which is known as the Stokes drift velocity. The steady streaming flow $\varepsilon \overline{u}_1$ given by the solution of Eq. (11) is called the Eulerian streaming flow. Compared with the Eulerian streaming flow, the Stokes drift flow is confined in a region close to the sound source, i. e., within the region $x = O(1/\delta)$. Actually this region corresponds to the one that the force (10) acts upon. That is, within this region the steady flow velocity is composed of the Eulerian streaming velocity and the Stokes drift velocity

$$u_{\mathrm{L}} = \varepsilon \overline{u}_1 + \varepsilon u_{\mathrm{d}} \tag{16}$$

which is known as the Lagrangian velocity. Beyond this region the Stokes drift flow vanishes and only the Eulerian streaming exists. In many cases the Stokes drift velocity is ignored, but when the location of interest is not far from the sound source it should be considered. In general, the Stokes flow is expected to occur only when the primary wave is progressive, not when it is standing.

Eulerian Streaming

Even the incompressible fluid can also give rise to Eulerian streaming flow when a solid obstacle is in contact with the oscillating fluid. Consider a two-dimensional incompressible flow around a solid body governed by the following dimensionless equations:

$$\nabla \cdot \mathbf{u} = 0 \tag{17a}$$

$$\frac{\partial \mathbf{u}}{\partial t} + \varepsilon \mathbf{u} \cdot \nabla \mathbf{u} = -\nabla p + \frac{1}{\mathrm{Re}}\nabla^2 \mathbf{u} \tag{17b}$$

where $\mathbf{u} = (u, v)$ and ∇ is the two-dimensional gradient operator. We use $1/\omega$, L, $A_0\omega$ and $\rho^* A_0 \omega^2 L$ as the reference quantities for the time, length, velocity and pressure, respectively. Note that the reference length L used here represents a typical dimension of the obstacle. The Reynolds number Re defined as

$$\mathrm{Re} = \frac{\omega L^2}{\nu}$$

is assumed to be large. For the small value of ε, we expand

$$(\mathbf{u}, p) = (\mathbf{u}_0, p_0) + \varepsilon(\mathbf{u}_1, p_1) + \dots . \tag{18}$$

The leading-order equation of Eq. (17b) is then

$$\frac{\partial \mathbf{u}_0}{\partial t} = -\nabla p_0 \tag{19}$$

Therefore the leading-order solution is of potential flow. Moreover the solutions can take a separable form, e. g.

$$\mathbf{u}_0 = \mathbf{f}(x, y)\exp(\mathrm{i}t) \tag{20}$$

where the complex functions $\mathbf{f}$ must satisfy the continuity equation (17a) and $\mathrm{i} = \sqrt{-1}$ denotes the imaginary unit. Note that the inviscid region governed by these equations comprises most of the flow domain except the thin layer near the solid boundary.

Since the potential flow solution (Eq. (20)) does not satisfy the no-slip condition on the solid surface, we must consider a thin layer (called the Stokes layer) adjacent to the surface $n = 0$, where n refers to the local coordinate normal to the wall. In this thin layer, we use the strained coordinate Y defined as

$$n = \sqrt{2/\mathrm{Re}}\, Y$$

We also use the velocity components U and V along the local coordinates s and n, respectively (the coordinate s is along the surface). Then the boundary layer equation becomes

$$\frac{\partial U}{\partial t} - \frac{\partial u_\mathrm{e}}{\partial t} = \frac{1}{2}\frac{\partial^2 U}{\partial Y^2} - \varepsilon\left(U\frac{\partial U}{\partial s} + V\frac{\partial U}{\partial n}\right) \tag{21}$$

where $u_\mathrm{e}(s)$ denotes the tangential component of the potential flow velocity evaluated at the solid surface. We expand the velocity components as before.

$$(U, V) = \left(U_0, \sqrt{2/\mathrm{Re}}V_0\right) + \varepsilon\left(U_1, \sqrt{2/\mathrm{Re}}V_1\right) + \dots \tag{22}$$

The leading-order equation is

$$\frac{\partial U_0}{\partial t} - \frac{\partial u_{0\mathrm{e}}}{\partial t} = \frac{1}{2}\frac{\partial^2 U_0}{\partial Y^2}$$

whose solution takes the following form:

$$U_0 = u_{0\mathrm{e}}(s)\left[1 - \exp(-(1+\mathrm{i})Y)\right]\exp(\mathrm{i}t) \tag{23}$$

The normal component V_0 can also be obtained from the continuity equation. Note that this flow is still time periodic. The $O(\varepsilon)$ equation (21) then becomes

$$\frac{\partial U_1}{\partial t} - \frac{\partial u_{1\mathrm{e}}}{\partial t} = \frac{1}{2}\frac{\partial^2 U_1}{\partial Y^2} - \left(U_0\frac{\partial U_0}{\partial s} + V_0\frac{\partial U_0}{\partial Y}\right) \tag{24}$$

Here our interest is the time independent flow. Taking the time average of the above equation over one period of oscillation gives

$$\frac{1}{2}\frac{\partial^2 \overline{U}_1}{\partial Y^2} = \left\langle U_0\frac{\partial U_0}{\partial s} + V_0\frac{\partial U_0}{\partial Y}\right\rangle \tag{25}$$

The solution of this equation yields the streaming velocity at the edge of the boundary layer,

$$\overline{U}_{1\infty} = -\frac{3}{8}\left[(1-\mathrm{i})u_{0\mathrm{e}}^{\#}\frac{\mathrm{d}u_{0\mathrm{e}}}{\mathrm{d}s} + (1+\mathrm{i})u_{0\mathrm{e}}\frac{\mathrm{d}u_{0\mathrm{e}}^{\#}}{\mathrm{d}s}\right] \tag{26}$$

where the superscript # denotes the complex conjugate. This velocity then acts as a boundary condition for the exterior bulk region. The governing equation of the steady streaming flow takes the following form [1]:

$$(\overline{\mathbf{u}} + \overline{\mathbf{u}}_\mathrm{d})\cdot\nabla\overline{\mathbf{u}} = -\nabla\overline{p} + \frac{1}{\mathrm{Re}_\mathrm{s}}\nabla^2\overline{\mathbf{u}} \tag{27}$$

where Re_s is the streaming Reynolds number based on the streaming velocity at the edge of the Stokes layer; $\mathrm{Re}_\mathrm{s} = \varepsilon^2\mathrm{Re}$. This equation looks very similar to the Navier–Stokes equation, but here the convective velocity is replaced by the Lagrangian velocity $\overline{\mathbf{u}}_\mathrm{L} = \overline{\mathbf{u}} + \overline{\mathbf{u}}_d$.

The above formulation is effective and suitable when the streaming Reynolds number is large so that the Reynolds stress action is confined within the thin Stokes layer. In the microfluidic application, however, Re_s is usually small. So, the Reynolds stress term may be added to the streaming-flow equation (27) so that

$$(\overline{\mathbf{u}} + \overline{\mathbf{u}}_\mathrm{d})\cdot\nabla\overline{\mathbf{u}} = -\nabla\overline{p} + \frac{1}{\mathrm{Re}_\mathrm{s}}\nabla^2\overline{\mathbf{u}} - \mathbf{F} \tag{28a}$$

$$\mathbf{F} = \langle\, (\mathbf{U}_0\cdot\nabla)\mathbf{U}_0 + \mathbf{U}_0(\nabla\cdot\mathbf{U}_0)\,\rangle \tag{28b}$$

where the second term within $\langle\,\rangle$ on the right-hand side is nonzero for the compressible fluid case; for the compressible fluid case Eq. (28a) itself must be modified. This means that for the case with a low streaming Reynolds number, Eq. (28a) must be solved over the whole domain including the Stokes layer. Another important point for the incompressible flow is that the Reynolds stress vanishes when the primary oscillating flow is of the progressive-wave type. On the other hand, it should be noted that in

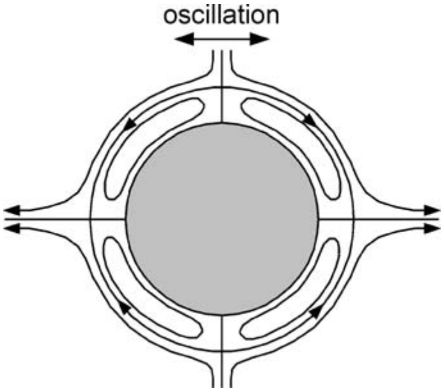

Acoustic Streaming, Figure 3 Sketch of the flow structure of the Eulerian streaming around a circular cylinder oscillating at a high frequency in a viscous fluid

the microfluidic area no literature has taken into account the Stokes drift flow in the convecting velocity (i. e., the velocity $(\overline{\mathbf{u}}+\overline{\mathbf{u}}_{\mathrm{d}})$ in Eq. (28a)) in the numerical simulation of the streaming flow.

We can experience a typical example of the Eulerian streaming flow around a circular cylinder [5]. Here, the fluid surrounding the cylinder oscillates with high frequency; or the cylinder may oscillate in the otherwise quiescent fluid without fundamental difference in the results. The steady flow within the Stokes layer at high streaming Reynolds numbers shows four-cell structure around the circular cylinder as shown in Fig. 3. There are two streams coming out of the cylinder from both sides in the direction of oscillation.

Kundt's dust pattern manifests another simple example of the Eulerian streaming flow given by the two-dimensional standing wave in a duct. When an acoustic standing wave is established in the duct with a compressible fluid, the steady streaming reveals four-cell structure over a half wavelength (or over the space between two neighboring nodes) as shown in Fig. 4. Near the duct wall, the steady streaming is toward the nodes, and near the duct center it is coming out of the nodes. Therefore dust within the duct should cluster near the nodal points of the standing wave. The detailed solution for this case has been given by Riley [1].

Stokes Drift Flow

Usually, by acoustic streaming we mean *Eulerian* streaming. However, the recent application of the flexural plate wave in microfluidics implies that the Stokes drift flow should also be considered as a type of steady streaming flow, because the net effect in the fluid transport is not discernable between the two. Here we derive the equations

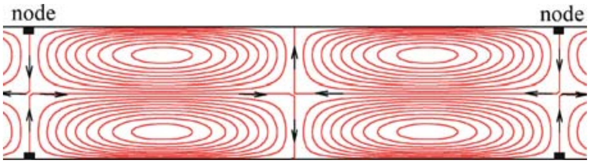

Acoustic Streaming, Figure 4 Eulerian streaming flow occurring between two parallel plates when a standing wave takes place inside the duct. Distance between the nodes corresponds to a half wavelength of the standing wave

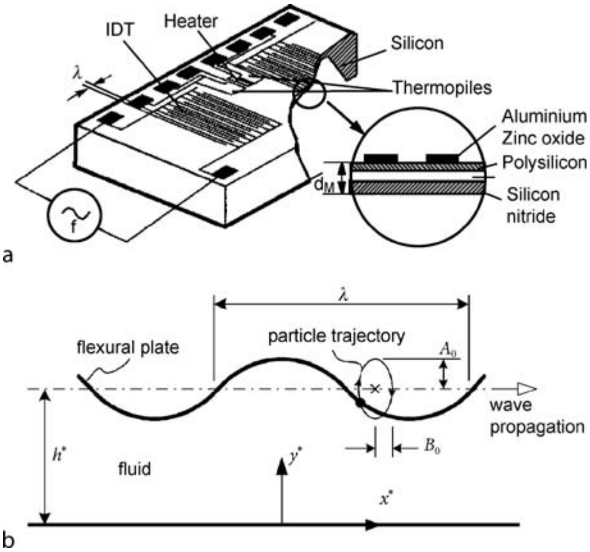

Acoustic Streaming, Figure 5 Microfluidic device utilizing the flexural plate wave. (**a**) Fabricated device; (**b**) shape of the flexural plate and the coordinates for analysis

as well as the solutions for the Stokes drift flow given by the flexural plate wave. The case of one-dimensional compressible flow has already been treated in this article.

Consider a viscous fluid confined between a flat wall at $y^* = 0$ and a flexural plate at $y^* = h^*$. The flexural plate oscillates showing a traveling wave with a high frequency ω by a well established piezoelectric vibration system. Fig. 5 illustrates the geometry of the flow model investigated in this article. The wavelength is λ and the wave propagation speed is $c^* = \omega\lambda/2\pi$. A particle attached on the flexural plate describes an ellipse with major A_0 and minor $B_0 = rA_0$ rotating clockwise when the wave travels toward the right-hand side as shown in Fig. 5 [2]. The ratio r is given from $r = \pi d/\lambda$, where d is the membrane thickness. A typical value of r is 0.1. The spatial coordinate x^* is along the wave propagation direction and y^* normal to it.

As before we use $1/\omega$ as the time scale, $\lambda/2\pi$ as the length scale, $A_0\omega$ as the velocity scale and $\rho A_0\omega^2\lambda/2\pi$ as

the pressure scale, then the dimensionless continuity and momentum equations take the form given in Eqs. (17a) and (17b). The equations for the particle motion on the flexural plate are

$$\delta x = -r\varepsilon \sin(x_0 - t) \tag{29a}$$

$$\delta y = \varepsilon \cos(x_0 - t) \tag{29b}$$

As a typical example, for $\lambda = 100\,\mu\text{m}$, $d = 3\,\mu\text{m}$, $A_0 = 6\,\text{nm}$, and the frequency $\omega/2\pi = 3\,\text{MHz}$, we have $A_0\omega = 113\,\text{mm/s}$, $\varepsilon = 3.8\times10^{-4}$, and $\text{Re} = 4760$. The boundary conditions are

$$u = 0 \qquad \text{at } y = 0 \tag{30a}$$

$$v = 0 \qquad \text{at } y = 0 \tag{30b}$$

$$u = r\cos(x - t) \qquad \text{at } y = h \tag{30c}$$

$$v = \sin(x - t) \qquad \text{at } y = h \tag{30d}$$

where h is the dimensionless depth of the fluid layer. The velocity conditions, Eqs. (30c) and (30d), are derived from Eqs. (29a) and (29b), respectively. In this derivation we simply replaced x_0 by x, which is valid for small r; later we will consider the higher-order effect.

As before, we neglect the nonlinear term in Eq. (17b). We also assume that Re is very large. Equation. (17b) then becomes

$$\frac{\partial \mathbf{u}}{\partial t} = -\nabla p \tag{31}$$

This indicates that the velocity field can be described by a potential function $\phi(x, y, t)$ in such a way that $\mathbf{u} = \nabla\phi$. As usual, this inviscid solution must satisfy the boundary condition for the normal component of the velocity at each of the walls but not the tangential component. This is the most important part of the analysis, because otherwise the leading-order solution is not of the progressive-wave type. Applying the conditions given in Eqs. (30b) and (30d) to the Laplace equation $\nabla^2\phi = 0$ and solving for ϕ, we obtain $\phi = (\cosh y/\sinh h)\sin(x - t)$ and

$$u = \frac{\cosh y}{\sinh h}\cos(x - t) \tag{32a}$$

$$v = \frac{\sinh y}{\sinh h}\sin(x - t) \tag{32b}$$

The bulk flow solution given by Eqs. (32a) and (32b) does not satisfy the condition for the tangential component of the velocity on the walls. So, we must expect boundary layers near each of the walls. First, near the top wall, $y = h$, we use the strained variable $Z = (h - y)\sqrt{\text{Re}/2}$. Then we obtain the appropriate x-momentum equation and solve for u to obtain

$$u = \coth h\,\cos(x - t) + (r - \coth h)\exp(-Z)\cos(x + Z - t) \tag{33}$$

A similar process leads to the following solution for u in the bottom boundary layer:

$$u = \frac{1}{\sinh h}\left[\cos(x - t) - \exp(-Y)\cos(x + Y - t)\right] \tag{34}$$

where $Y = y\sqrt{\text{Re}/2}$.

The analytical solutions obtained so far imply that the flow field driven by the oscillating flexural plate is progressive. This means that the Reynolds stress should vanish and so there should be no Eulerian streaming. On the other hand, it produces the nonzero Stokes drift flow. First we consider the bulk flow. Into the definition of the velocity components u and v, i. e., $\mathrm{d}x/\mathrm{d}t = \varepsilon u$ and $\mathrm{d}y/\mathrm{d}t = \varepsilon v$, we substitute Eqs. (32a) and (32b). Assuming the variables x and y on the right-hand side are constant, i. e. $x = x_0$ and $y = y_0$, we can integrate the equations to obtain

$$x = x_0 - \varepsilon\frac{\cosh y_0}{\sinh h}\sin(x_0 - t) \tag{35a}$$

$$y = y_0 + \varepsilon\frac{\sinh y_0}{\sinh h}\cos(x_0 - t) \tag{35b}$$

Now we substitute Eqs. (35a) and (35b) into Taylor expansions for u and v, i. e., Eqs. (32a) and (32b) about $(x, y) = (x_0, y_0)$ and take the time average over one period to obtain the steady velocity components $\overline{v} = 0$ and

$$\overline{u} = \frac{\varepsilon}{2\sinh^2 h}(\cosh^2 y + \sinh^2 y) \tag{36}$$

Next, we consider the top boundary layer. After some algebra we obtain $\overline{v} = 0$ and

$$\begin{aligned}\overline{u} = \frac{\varepsilon}{2}\Bigg\{&\left[\frac{\cosh y}{\sinh h}(1 - A) + rA\right]^2 \\ &+ \frac{\sinh y}{\sinh h}(1 - A)\left[\frac{\sinh y}{\sinh h}(1 - A) + A + r(y - h)A\right] \\ &+ B^2\left(r - \frac{\cosh y}{\sinh h}\right)^2 \\ &+ B^2\frac{\sinh y}{\sinh h}\left[\frac{\sinh y}{\sinh h} - r(y - h)\right]\Bigg\}\end{aligned} \tag{37}$$

where functions A and B are

$$(A, B) = \exp(-Z)(\cos Z, \sin Z)$$

Similar treatment can be done for the bottom boundary layer and we obtain $\overline{v} = 0$ and

$$\overline{u} = \frac{\varepsilon}{2\sinh^2 h}\left[1 - 2\exp(-Y)\cos Y + \exp(-2Y)\right] \quad (38)$$

Now, the complete formula for the streaming velocity applicable to all the regions including the two boundary layers is $\overline{v} = 0$ and

$$\begin{aligned}\overline{u} = \frac{\varepsilon}{2}\Bigg\{&\left[\frac{\cosh y}{\sinh h}(1-A) + rA\right]^2 \\ &+ \frac{\sinh y}{\sinh h}(1-A)\left[\frac{\sinh y}{\sinh h}(1-A) + A + r(y-h)A\right] \\ &+ B^2\left(r - \frac{\cosh y}{\sinh h}\right)^2 \\ &+ B^2\frac{\sinh y}{\sinh h}\left[\frac{\sinh y}{\sinh h} - r(y-h)\right] \\ &+ \frac{1}{\sinh^2 h}\left[\exp(-2Y) - 2\exp(-Y)\cos Y\right] - r^2\frac{y}{h}\Bigg\}\end{aligned} \quad (39)$$

As a typical example, for the case with $\lambda = 100\,\mu\text{m}$ and $h^* = 50\,\mu\text{m}$, we have $h = \pi$, and for $\varepsilon = 3.8 \times 10^{-4}$ and $\text{Re} = 4760$ we evaluate $\overline{u} = 3.8 \times 10^{-4}$ as the approximately maximum streaming velocity obtained from the bulk-flow solution (Eq. (36)) at $y = h$. When the velocity scale is $A_0\omega = 113\,\mu\text{m}$, this becomes $\overline{u}^* = 43\,\mu\text{m/s}$. This is not much different from the measured velocity (less than $100\,\mu\text{m/s}$) reported by Nguyen et al. [2], considering that the numerical result $1000\,\mu\text{m/s}$ obtained by them is more than 10 times the measured value for the same parameter set.

Figure 6 shows distributions of the streaming velocity for three depths of the fluid layer with the parameter set presented previously. The magnitude of streaming velocity increases on the whole as the depth decreases. Further decrease of h results in the overlap of the top and bottom boundary layers, and so the analytical solutions presented so far may not hold in that case.

The flow rate through the channel is given by

$$q = \int_0^h \overline{u}\,\mathrm{d}y$$

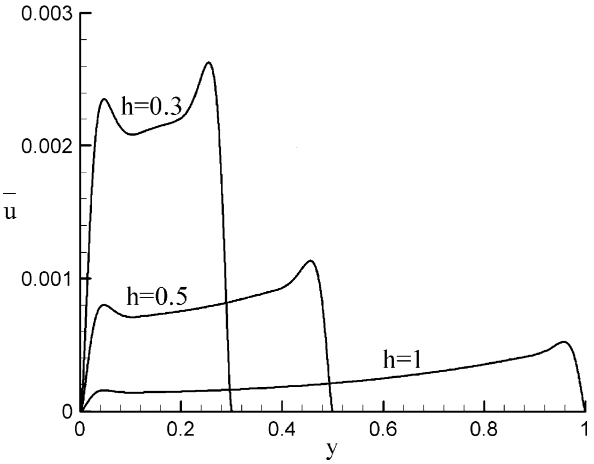

Acoustic Streaming, Figure 6 Distributions of the Stokes drift velocity across the fluid layer for three channel depths given by the flexural plate wave

Substituting the streaming velocity distribution (Eq. (39)) into this yields the following formula.

$$q = \frac{\varepsilon}{2\sinh^2 h}\left[\sinh h \cosh h - \sqrt{2/\text{Re}}\left(1 + \frac{7}{8}\sinh^2 h\right)\right] \quad (40)$$

At high Reynolds numbers, the second term within [ ] on the right-hand side of the above equation can be neglected and so the flow rate increases as the channel depth decreases, in line with the numerical result of Nguyen et al. [2]. On the other hand, when the second term is considered the flow rate shows a maximum value at a critical depth. Figure 7 shows the dependence of the flow rate on the depth at three Reynolds numbers and at the other parameter values the same as those presented previously. It indeed shows that at each of the critical depths, the flow rate has a maximum value. The critical depth increases as the Reynolds number decreases. It can be shown that the critical depth is given by the formula

$$h_c = \sinh^{-1}\left(\sqrt{\frac{8}{\text{Re} - 8}}\right) \quad (41)$$

For instance, at $\text{Re} = 4760$ we obtain $h_c = 0.041$ which corresponds to $h_c^* = 0.65\,\mu\text{m}$ at $\lambda = 100\,\mu\text{m}$. This is very small compared with the wavelength, but it is still far larger than the amplitude of the oscillation of the plate, $A_0 = 6\,\text{nm}$.

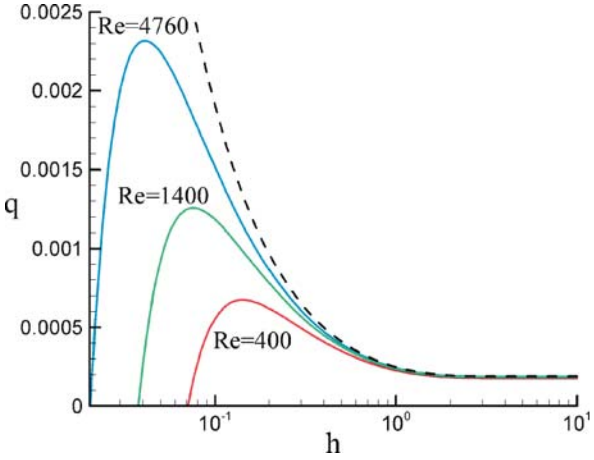

Acoustic Streaming, Figure 7 Effect of the channel depth on the flow rate at three Reynolds numbers for the flexural-plate-wave pumping. Dashed line corresponds to $\mathrm{Re} = \infty$

Key Research Findings

Acoustic streaming has been applied to various microfluidic areas. White's group [2] have developed micropumps that utilize the flexural plate wave as the actuator. They have conducted a numerical simulation but the deviation was significant; their simulation results had to be corrected by a factor of 7 in order to fit the measurement data. To date, no report has been given of a satisfactory agreement between the experimental measurements and numerical or theoretical predictions. The numerical computation for acoustic streaming is not as simple as it looks. There are two key factors which may degrade the numerical results: one arises from the thin Stokes layer and the other from the extremely low levels of the streaming velocity compared with the primary flow. These can be overcome when we put very fine grids near the Stokes layer and simultaneously use high-precision numerical values.

In order to apply acoustic streaming to fluid mixing, Yaralioglu et al. [7] designed patterns of piezoelectric transducers on the bottom wall of a microchannel. They verified experimentally that the transducers, by generating acoustic streaming inside the channel normal to the main flow, enhanced the mixing. The mixing effect was, of course, affected by the configuration of the electrode patterning. They also asserted that the fundamental problem of the formation of bubbles and unintended heating of the fluid was not expected to occur in their system.

Acoustic streaming has also been applied to electrochemistry. Compton's group [8] has tested the use of ultrasound to study the effect of the various configurations of the acoustic streaming on the limiting current from an electrode. It was shown that there was a critical diffusion layer thickness below which the layer no longer became thinner. Recently they performed a numerical simulation on the acoustic streaming over an electrode within an axisymmetric space. The streaming flow was generated by the Reynolds stress terms formulated by other investigators. They successfully verified the previous experimental results that acoustic streaming was the principle mechanism of enhanced mass transport in sono-electrochemical cells.

Ultrasonics and its universal effect (acoustic streaming) have been used to manipulate particles in microfluidic devices, e. g., trapping, collection, separation, and deposition. For instance, Petersson et al. [9] employed a microchannel system with one center and two side channels at the inlet and outlet, respectively, of the channel. Through the side inlet channels they put a medium, say fluid A, containing particles, and through the center inlet channel the fluid B containing no particles. They then applied ultrasound normal to the channel in such a way that a standing wave was established in the main channel where the two media contacted each other. Due to the Reynolds stress and recirculating streaming flows, particles were collected near the channel center and this pattern persisted all the way through the main channel. At the outlet, the particles flow with the fluid B. They implied that such a medium-exchange effect could be applied to blood washing.

Marmottant and Hilgenfeldt [10] have considered bubble-driven microfluidic transport for bioengineering applications. In their experiment, bubbles were adsorbed on the bottom wall of the microchannel. When the standing ultrasound wave was introduced within the channel, steady streaming flow was generated. They stressed that the flow pattern in bubble streaming was quite different from that induced by an oscillating solid object. More interestingly, close contact of a foreign solid particle to the bubble showed a significant effect in the overall steady-flow field due to superposition of the bubble and particle streaming fields.

Future Directions for Research

To date no numerical simulation of the acoustic streaming flow associated with application to the microfluidics has been successfully performed. The simulation can be performed only with the streaming flow by using the governing equation given as Eq. (27), but we also need to solve the full unsteady Navier–Stokes equations including not only the primary oscillatory flow component but also the secondary steady flow component. In this case locally fine grids must be adopted to deal with the thin Stokes layer adjacent to the solid surface.

We also need to analyze the case for the flexural-plate-wave flow in more detail and to simultaneously perform numerical simulations of the resultant flows. The results of the full numerical simulation may be used to prove that the steady flow components are generated by the mechanism known as the Stokes drift flow.

We also need to study the dissipation effect caused by the oscillatory flow. At present, in Lab-on-a-Chip design, we are usually interested in the feasibility of the functions provided by the transducers, but sooner or later the energy consumption may be one of the most important factors.

Cross References

- ► Acoustic-Based Biosensors
- ► Piezoelectric Microdispenser
- ► Transport of Droplets by Acoustics
- ► Ultrasonic Pump

References

1. Riley N (2001) Steady streaming. Ann Rev Fluid Mech 33:43–65
2. Nguyen NT, Meng AH, Black J, White RM (2000) Integrated flow sensor for in situ measurement and control of acoustic streaming in flexural plate wave micropumps. Sens Actuators A 79:115–121
3. Lighthill J (1978) Waves in Fluids. Cambridge University Press, Cambridge
4. Iskandarani M, Liu PLF (1991) Mass transport in three-dimensional water waves. J Fluid Mech 231:417–437
5. Schlichting H, Gersten K (2003) Boundary Layer Theory. Springer, Berlin
6. Frampton KD, Martin SE, Minor K (2003) The scaling of acoustic streaming for application in micro-fluidic devices. Appl Acoust 64:681–692
7. Yaralioglu GG, Wygant IO, Marentis TC, Khuri-Yakub BT (2004) Ultrasonic mixing in microfluidic channels using integrated transducers. Anal Chem 76:3694–3698
8. Marken F, Akkermans RP, Compton RG (1996) Voltammetry in the presence of ultrasound: the limit of acoustic streaming induced diffusion layer thinning and the effect of solvent viscosity. J Electroanal Chem 415:55–63
9. Petersson F, Nilsson A, Jonsson H, Laurell T (2005) Carrier medium exchange through ultrasonic particles switching in microfluidic channels. Anal Chem 77:1216–1221
10. Marmottant P, Hilgenfeldt S (2004) A bubble-driven microfluidic transport element for bioengineering. Proc Nat Acad Sci 101(26):9523–9527

Acoustic Streaming Pumps

► Ultrasonic Pumps

Acoustic Waves

► Acoustics Based Biosensors

AC Pumping of Liquids

► AC Electro-Osmotic Flow

Active Mixer

CHIH-CHANG CHANG[1], LUNG-MING FU[2], RUEY-JEN YANG[1]

[1] Department of Engineering Science, National Cheng Kung University, Tainan, Taiwan

[2] Department of Materials Engineering, National Pingtun University of Science and Technology, Pingtun, Taiwan

rjyang@mail.ncku.edu.tw

Synonyms

Dynamic mixing; Active mixing

Definition

The term “active mixer” or “active micromixer” refers to a microfluidic device in which species mixing is enhanced by the application of some form of external energy disturbance. Typically, this disturbance is generated either by moving components within the micromixer itself, e. g. magnetically-actuated stirrers, or by the application of an external force field, e. g. pressure, ultrasound, acoustic, electrohydrodynamic, electrokinetic, dielectrophoretic, magneto-hydrodynamic, thermal, and so forth [1].

Overview

Mixing occurs in many natural phenomena, including geophysical, ocean and atmospheric flows, and is also an important step in industrial processes involving chemical reactions, fermentation reactions, combustion, and so forth. Traditionally, industrial mixing applications have always been performed using large-scale apparatus. However, in recent years, micro-scale devices (commonly referred to as microfluidic devices) have been proposed as a means of constructing micro-total analysis systems (μ-TAS) and Lab-on-a-Chip (LOC) devices. However, achieving a rapid and efficient mixing of different reactants when performing chemical and biological analyzes in such microfluidic devices is highly challenging. Therefore, the problem of developing enhanced micromixing schemes suitable for microfluidic applications has attracted significant interest within industrial and academic circles in recent years. As a result, the literature now

contains a large number of studies concerning micromixers implemented using a variety of mixing strategies [1].
The characteristic size of the microchannels in microfluidic devices is very small (typically of the order of several hundred micrometers), and hence the flow is dominated by viscous forces. As a result, the flow is restricted to the low Reynolds number regime, and thus turbulence does not occur. The Reynolds number of microfluidic flows in a conventional straight microchannel is typically less than unity, and the resulting Stokes flow is unidirectional. Even in curved or twisted microchannels, the transverse component of the flow (i. e. the secondary flow) is very small compared to the streamwise component since the inertial effects induced by the microchannel geometry are very weak. Therefore, when the microchannels contain two or more fluid streams, mixing of the different streams is dominated by molecular diffusion effects. In microscale channels, the diffusive mixing process is very slow compared with the rate at which the fluid is convected along the channel. Typically, microfluidic flows have a high Péclet number, i. e. $\mathrm{Pe} = Ul/D$, where U is the average flow velocity, l is the channel dimension and D is the molecular diffusivity. The diffusive mixing time is given by $t_\mathrm{D} \sim l^2/D$ and the mixing channel length required to achieve an adequate species mixing increases linearly with the Péclet number ($L_\mathrm{m} \sim \mathrm{Pe} \times l$). For example, for an average flow velocity of $500\,\mu\mathrm{m/s}$, a channel dimension of $100\,\mu\mathrm{m}$ and a molecular diffusivity of $10\,\mu\mathrm{m}^2/\mathrm{s}$, the mixing time and length required to achieve a complete species mixing are of the order of 1000 sec and 0.5 m, respectively. However, many practical biochemical applications, e. g. immunoassays and DNA hybridization, require the rapid mixing of macromolecules characterized by relatively low molecular diffusivity. Therefore, the mixing performance obtained in typical microchannels is unsuitable for biochemical analysis applications. Accordingly, a requirement exists for enhanced microfluidic mixing schemes to support the development of μ-TAS and LOC devices. Typically, such schemes involve reducing the diffusion length (i. e. l) and the diffusion time by increasing the interfacial contact area between the mixing species.
Although it is difficult to induce turbulence (so-called Eulerian chaos) in microchannels, the mixing performance obtained in low Reynolds number flow regimes can be enhanced via the chaotic advection mechanism (or so-called Lagrangian chaos). Chaotic advection occurs in regular, "smooth" (from a Eulerian viewpoint) flows [2] and provides an effective increase in both the interfacial contact area and the concentration gradient by inducing a reduction in the striation thickness, and hence in the diffusion length. As a result, both the mixing time and the mixing length are considerably reduced. In the case of a linear reduction in the striation thickness within the flow path, the mixing time and mixing length exhibit a sub-linear dependence on Pe. The two parameters can be reduced to as much as $t_\mathrm{m} \sim \ln(\mathrm{Pe})$ and $L_\mathrm{m} \sim \ln(\mathrm{Pe})$, respectively, for chaotic flows in the limit of large Pe [2, 3]. Importantly, chaotic advection cannot occur in steady, two-dimensional flows, but is restricted to time-dependent two-dimensional and three-dimensional flows. Accordingly, a small cylindrical rotor spinning about its centre with a uniform angular frequency (i. e. Couette flow) fails to provide an efficient micromixing performance, whereas two such rotors turned on and off alternatively create a blinking vortex phenomenon which yields a powerful mixing effect [2]. In Couette flow, the fluid streams are only stretched. Hence, chaotic advection cannot be induced, and thus the mixing effect is very poor. However, in the two-rotor arrangement, the fluid streams are repeatedly stretched around one rotor and then folded around the other. As a result, chaotic advection is induced and a good mixing performance is obtained. In general, achieving an effective mixing of two or more fluid streams always requires a repeated stretching and folding of the fluid elements. In recent years, various active mixing approaches have been proposed using chaotic advection to enhance the mixing effect. The chaotic flows induced by such active approaches are time-dependent and are easily controlled using external mechanisms. As such, active mixers are eminently suitable components for reconfigurable microfluidic systems.

Basic Methodology

Flow Field

Applying the continuum assumption, microfluidic flows can be modeled by the continuity equation and by a momentum equation modified to include the body force term, i. e.

$$\nabla \cdot \boldsymbol{u} = 0 \tag{1}$$

and

$$\rho_f \left(\frac{\partial \boldsymbol{u}}{\partial t} + \boldsymbol{u} \cdot \nabla \boldsymbol{u} \right) = -\nabla p + \mu \nabla^2 \boldsymbol{u} + \boldsymbol{F} \quad , \tag{2}$$

where t, $\boldsymbol{u}$, p, ρ_f and μ denote the time, the fluid velocity, the pressure, the fluid density and the fluid viscosity, respectively. In Eq. (2), $\boldsymbol{F}$ represents the external driving force (i. e. the external energy source) associated with the specific active micromixer. For example, in an electrohydrodynamic/electrokinetic-based active mixer, $\boldsymbol{F}$ represents the Coulombic force produced by the presence of a free space charge, $\rho_e E$, where ρ_e is the net free charge

density in the bulk liquid or at the solid-liquid interface (i. e. the electrical double layer) and $\boldsymbol{E}$ is the intensity of the externally applied DC or AC electrical field. Meanwhile, for a magneto-hydrodynamic mixer, $\boldsymbol{F}$ is the Lorentz force induced by the coupling between the magnetic field $\boldsymbol{B}$ and the electrical field $\boldsymbol{E}$, ($\boldsymbol{J} \times \boldsymbol{B}$, where $\boldsymbol{J}$ is the current density). In the literature, Eqs. (1) and (2) are generally solved using well-known numerical methods such as the finite difference method (FDM), the finite volume method (FVM), the finite element method (FEM), and so forth.

In typical microfluidic applications, the Reynolds number is much lower than unity (i. e. $\mathrm{Re} = \rho_f Ul/\mu \ll 1$), and hence the flow can be approximated as a creeping flow (i. e. Stokes flow). Therefore, the convection term in Eq. (2) can be neglected, and the time-dependent flows in active micromixers are then governed by Eq. (1) and Eq. (3), i. e.

$$\rho_\mathrm{f} \frac{\partial \boldsymbol{u}}{\partial t} = -\nabla p + \mu \nabla^2 \boldsymbol{u} + \boldsymbol{F}. \tag{3}$$

Additionally, provided that the time required to reach the viscous diffusion time scale is much less than the oscillation time scale (ω^{-1}), i. e. $\rho_\mathrm{f} \omega l^2/\mu \ll 1$, the time derivative term in Eq.(3) can be neglected, and therefore the unsteady flow fields in active micromixers can be regarded as quasi-steady Stokes flow described by Eqs. (1) and (4), i. e.

$$0 = -\nabla p + \mu \nabla^2 \boldsymbol{u} + \boldsymbol{F} \quad . \tag{4}$$

Visualization of Mixing Process

Numerical studies relating to active micromixers generally visualize the mixing process and evaluate the mixing performance by solving the following convection-diffusion equation:

$$\frac{\partial C}{\partial t} + \boldsymbol{u} \cdot \nabla C = D \nabla^2 C \tag{5}$$

in which C and D represent the sample concentration and the diffusion coefficient, respectively. However, there are several drawbacks to this approach. For example, if the deformation of the species interface is complex and the mixing channel is very long, the equation solution may fail to identify the interface precisely due to numerical diffusion and natural species diffusion. Furthermore, in large Péclet number flows, convective transport dominates the diffusive mechanism and the sample dispersion in the flow field can be greatly enhanced by promoting the convective transport. In such diffusion-limited cases, the diffusion effects can be neglected, and the sample simply convects with the fluid along the local instantaneous streamlines. Under these conditions, the Lagrangian particle tracing technique, which introduces mass-less, non-interacting passive particles into the flow fields, provides a satisfactory means of observing the advection phenomenon within the fluid streams without solving Eq. (5). The motion of a tracer particle can be tracked by the following kinematic equation (dynamic system):

$$\frac{\mathrm{d}\boldsymbol{r}}{\mathrm{d}t} = \boldsymbol{u}\,(\boldsymbol{r}, t)\,, \tag{6}$$

where $\boldsymbol{r}$ is the location of the tracer particle and $\boldsymbol{u}\,(\boldsymbol{r}, t)$ is the Eulerian velocity field. The tracer particle position in the unsteady flow field at different times can be obtained simply by integrating Eq. (6). Many suitable integration methods are presented in the literature, ranging from the simple first-order Euler method to the fourth-order Runge–Kutta method, or even higher-order methods. Besides simulating the dispersion of a blob of samples, the particle tracing method also enables the stretching and folding of fluid elements in an unsteady flow field to be clearly observed.

Characterization of Chaotic Mixing

In order to optimize the fluid deformation phenomena in active micromixers during the mixing process, it is first necessary to understand the fluid stretching and folding mechanisms which take place, and to evaluate them in a quantitative manner. Over the past few decades, dynamic system analysis techniques such as Poincaré maps and Lyapunov exponents have revealed that the repeated stretching and folding of fluid elements results in a chaotic mixing effect. (Interested readers are referred to the text edited by Ottino [2] for details regarding the application of Poincaré maps and Lyapunov exponents to the exploration of mixing kinematics). The information provided by Poincaré maps and Lyapunov exponent analysis enables a thorough understanding of the characteristics of micro-active mixing systems. Specifically, Poincaré maps can be used to explain the transitions of the mixing system behavior from periodic or quasi-periodic to chaotic motion, while the Lyapunov exponents provide an indication of the strength of the chaotic behavior and can be used to quantify the effects of the amplitude and frequency of the perturbations on the chaotic response. Collectively, the data provided by Poincaré maps and Lyapunov exponents provide sufficient information to optimize the design and operation of micro-active mixing devices.

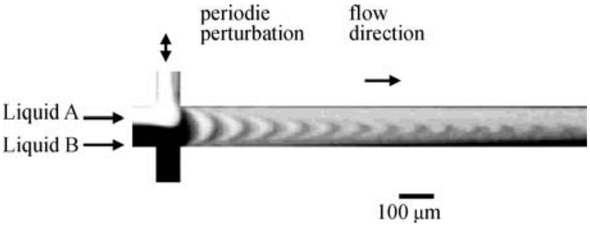

Active Mixer, Figure 1 Pressure perturbations induce lobe-like distortions of the interface and facilitate rapid mixing in the device with one pair of side channel

Key Research Findings

Many active mixing approaches have been proposed in recent years. Broadly speaking these approaches can be classified in terms of whether or not they use moving parts to generate a mixing effect. In those micromixers which do use moving parts, mixing is commonly achieved using micro stirrer bars, piezoelectric membranes, gas bubbles, and so forth. However, since the integration of these moving parts within the overall microfluidic system is challenging, and therefore expensive, researchers have paid increasing attention to active micromixers containing no moving elements. Numerous proposals for active mixing approaches have been presented in recent years, and space constraints prevent their detailed discussion here. Hence, the following provides no more than a high-level review of some of the more fundamental techniques. For a comprehensive discussion of active mixing schemes, interested readers are directed to the review presented by Nguyen and Wu in [1].

Pressure Perturbation Mixer

In pressure perturbation mixers, the species are perturbed by pulsing their velocities in some way. For example, Niu and Lee [4] presented an active mixer comprising a main channel and multiple side channels, in which the mixing species were stirred by pulsing the velocities of the fluids introduced through the side channels, as shown in Fig. 1. The resulting stretching and folding of the fluid elements in the main and side channels induced a chaotic advection mixing effect. A detailed particle simulation study was performed to examine the respective effects of the amplitude and frequency of the flow perturbations on the species mixing performance. Poincaré maps, constructed using the simulation data, showed that for a given parameter set, the fluid flow exhibited both chaotic and quasi-periodic responses. Additionally, Lyapunov exponent data were applied as mixing indices to evaluate the intensity of the chaotic mixing effect. The optimal operating parameters were then determined by plotting the Lyapunov exponent data against the amplitude and frequency of the perturbation.

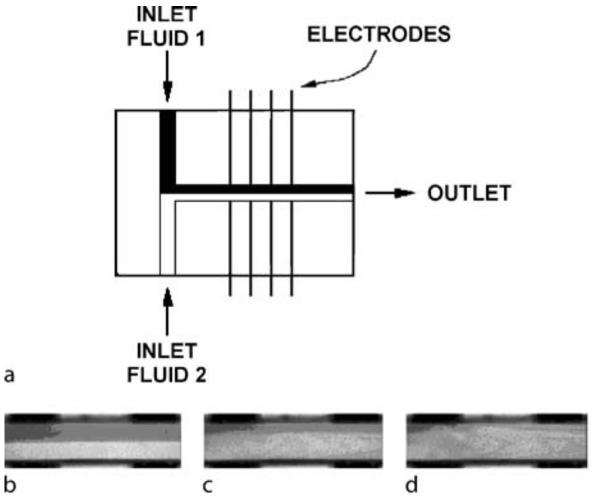

Active Mixer, Figure 2 (**a**) Configuration of electrohydrodynamic mixer. Experimental images of mixing (**b**) initial condition, (**c**) after the application of a DC electric field of intensity $E = 4 \times 10^5\ V/m$ and (**d**) $E = 6 \times 10^5$ V/m

Electrohydrodynamic (EHD) Mixer

In electrohydrodynamic (EDH) mixers, a mixing effect is created by applying an external electrical field to a bulk flow containing both an electrical conductivity gradient and a permittivity gradient. In the micromixer proposed by Moctar et al. [5], two fluids with identical viscosity and density but different electrical properties were injected into the mixing channel by syringe pumps, and the electrodes were arranged in such a way that the electrical field was perpendicular to the species interface, as shown in Fig. 2(a), creating a transversal secondary flow. The mixing effects induced by both DC and AC electrical fields were explored in a series of experimental investigations. From Fig. 2(b), (c) and (d), it can be seen that the mixing becomes more chaotic as the intensity of DC electric field increases. The results revealed that the application of an appropriate voltage and frequency to the electrodes, yielded a satisfactory mixing performance within less than 0.1 sec over a short mixing distance, even at Reynolds numbers as low as 0.02.

Electrokinetic-Based Mixer

Oddy et al. [6] presented a micromixer in which AC electrical fields were used to induce the electrokinetic instability (EKI) phenomenon in microscale channels at very low Reynolds numbers, as shown in Fig. 3. EKI is similar

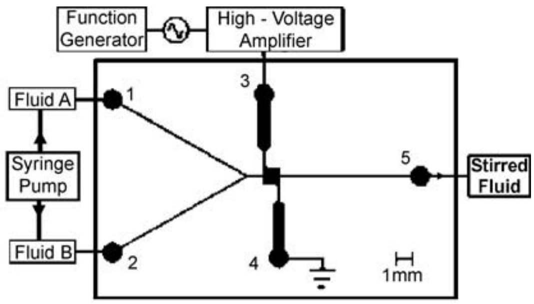

a

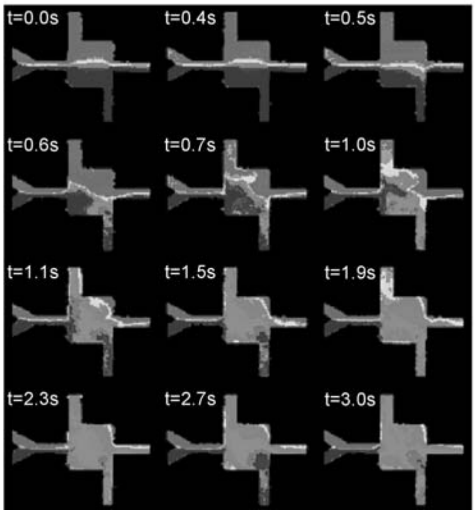

b

Active Mixer, Figure 3 (**a**) Configuration of electrokinetic instability mixer and (**b**) time-stamped experimental images of mixing process

to electrohydrodynamic instability, which can be induced by either AC or DC electrical fields when an electrical conductivity gradient exists in the bulk flow. The results showed that for a flow rate of 0.5 μl/min, the EKI flow field resulted in a rapid stretching and folding of the fluid and achieved an effective mixing performance within 3 seconds, corresponding to less than 1% of the time required to achieve mixing via diffusion effects in a conventional straight microchannel.

Fu et al. [7] periodically switched an external electrical field to carry out species mixing in a T-form electrokinetic microfluidic mixer by generating electrokinetic perturbation forces. The authors showed that the mixing performance of the microfluidic mixer was enhanced by increasing the contact area and contact time of the mixing fluids, and by creating irregular flow fields in the mixing channel. However, the results also indicated that an adequate switching frequency was required to achieve a satisfactory mixing performance, as shown in Fig. 4.

Qian and Bau [8] applied time-wise periodic alterations of the zeta potential along the microchannel walls to induce

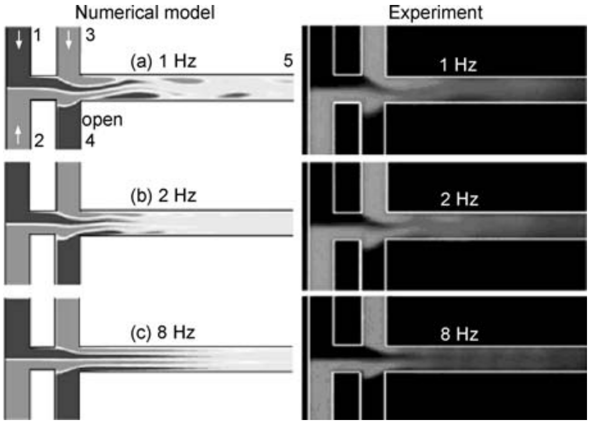

Active Mixer, Figure 4 Numerical and experimental images of mixing for different switching frequencies for a constant driving electric field of 100 V/cm

an electroosmotic chaotic advection effect. It was shown that both a spatial and a temporal control of the zeta potential could be achieved by applying a field effect (i. e. a capacitive effect). The effect of periodically switching between several different flow fields at various periods was analyzed by performing particle tracking simulations (i. e. Poincaré maps). The results indicated that a more chaotic mixing effect was achieved at lower values of the switching frequency.

Magneto-Hydrodynamic (MHD) Mixer

Various researchers have employed the magneto-hydrodynamic (MHD) effect to implement micromixers. For example, Bau et al. [9] developed an active micromixer which used either DC or AC electrical and magnetic fields to generate Lorentz forces with which to stretch and fold the species fluids in a mixing chamber. The results indicated that an adequate mixing result was achieved within several seconds. A more sophisticated MHD mixer was developed by Yi et al. [10] based upon the two blinking-vortex arrangement used to induce chaotic advection. The proposed micromixer comprised a small cylindrical mixing chamber with an electrode deposited on its side wall and two copper-wire electrodes positioned eccentrically on the lower surface of the chamber. The chamber was orientated such that its axis was parallel to the direction of an applied magnetic field, and a mixing effect was generated by applying a potential difference of period T alternately between one of the wire electrodes and the circular side-wall electrode and between the second wire electrode and the side-wall electrode, as shown in Fig. 5. The particle tracing results revealed that the intensity of the chaotic mixing effect increased with increasing

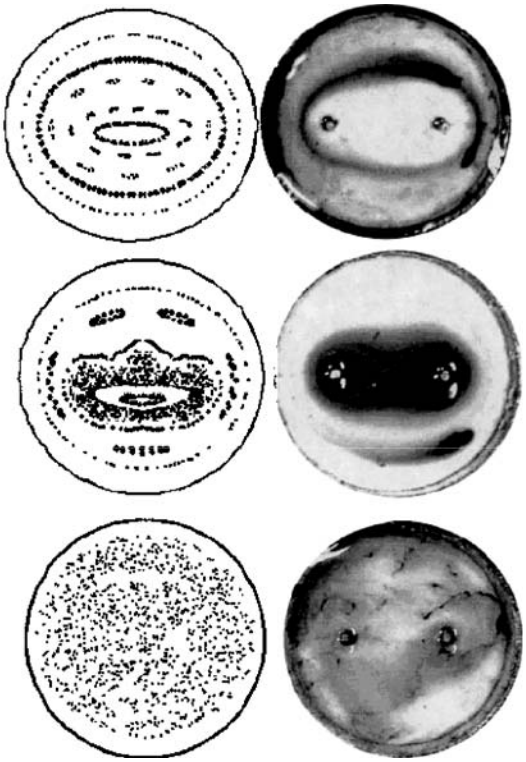

a

b

c

Active Mixer, Figure 5 Poincare maps (left column) and flow visualization photographs (co-rotating). For different periods of (**a**) $T = 4$, (**b**) $T = 10$ and (**c**) $T = 40$

T, resulting in a satisfactory mixing result within 40 periods.

Future Directions for Research

It seems likely that future micromixer designs will continue the current trend for implementing species mixing without the use of moving mechanical parts. Furthermore, it seems reasonable to speculate that the use of electrokinetic forces to induce a mixing effect will become increasingly common since this technique greatly simplifies the microfabrication process and reduces the cost and complexity involved in embedding active mixers within microfluidic systems. Electrokinetic forces have been widely employed in active mixing schemes in recent years, a case in point being the EKI mixer presented by Oddy et al. in [6]. However, current EKI-based mixers suffer the drawback of a high electrical voltage requirement. Accordingly, low-voltage, AC electrokinetic techniques are expected to receive increasing attention in coming years. Finally, it is known that the high flow rates required to achieve species mixing can be produced through various nonlinear electrokinetic phenomena. Therefore, the application of nonlinear electrokinetic techniques to realize active mixers is likely to emerge as a major research topic in the microfluidics community in the near future.

Cross References

► AC Electro-Osmotic Flow
► Chaotic Flow
► Electroosmotic Flow (DC)
► Electrokinetic/Hydrodynamic Flow Instability
► Microfluidic Mixing

References

1. Nguyen NT and Wu Z (2005) Micromixers – a review. J Micromech Microeng 15:R1–16
2. Ottino JM (1989) The Kinematics of Mixing: Stretching, Chaos, and Transport. Cambridge University Press, Cambridge
3. Stroock AD, Dertinger SKW, Ajdari A, Mezic I, Stone HA, Whitesides GM (2002) Chaotic mixer for microchannels. Science 295:647–651
4. Niu X, Lee YK (2003) Efficient spatial-temporal chaotic mixing in microchannels. J Micromech Microeng 13:454–62
5. El Moctar AO, Aubry N, Batton J (2003) Electro-hydrodynamic micro-fluidic mixer. Lab Chip 3:273–280
6. Oddy MH, Santiago JG, Mikkelsen JC (2001) Electrokinetic instability micromixing Anal Chem 73:5822–5832
7. Fu LM, Yang RJ, Lin CH, Chien YS (2005) A novel microfluidic mixer utilizing electrokinetic driving forces under low switching frequency. Electrophoresis 26:1814–1824
8. Qian S and Bau HH (2002) A chaotic electroosmotic stirrer Anal Chem 74:3616–3625
9. Bau HH, Zhong J, Yi M (2001) A minute magneto hydro dynamic (MHD) mixer. Sens Actuators B 79:207–215
10. Yi M, Qian S, Bau HH (2002) A minute magneto hydro dynamic (MHD) chaotic stirrer. J Fluid Mech 468:153–177

Active Mixing

► Active Mixer

Active Particle Flows

► Simulating Migration of Polymer Chains, Methods

Advanced Silicon Etching (ASE)

► ICP Etching
► Plasma Etching

AFM

Definition

The *atomic force microscope* (AFM) is a very high-resolution type of scanning probe microscope, with demonstrated resolution of fractions of an Angstrom, more than a 1000 times better than the optical diffraction limit. The AFM is one of the foremost tools for imaging, measuring and manipulating matter at the nanoscale. The AFM consists of a microscale cantilever with a sharp tip (probe) at its end that is used to scan the specimen surface. When the tip is brought into proximity of a sample surface, forces between the tip and the sample lead to a deflection of the cantilever according to Hooke's law. Depending on the situation, forces that are measured in AFM include mechanical contact force, Van der Waals forces, capillary forces, chemical bonding, electrostatic forces, magnetic forces, etc. Typically, the deflection is measured using a laser spot reflected from the top of the cantilever into an array of photodiodes. Other methods that are used include optical interferometry, capacitive sensing or piezoresistive AFM probes.

Cross References

- ► Atomic Force Microscope (AFM)
- ► Biosensor
- ► Biosensors Using Atomic Force Microscopes
- ► Scanning Probe Microscope

AFM Biosensors

► Biosensors Using Atomic Force Microscopes

Aggregation of Nanoparticles

► Nano-Particle Controllable Assembly

Aging

Definition

Aging is known in material science as material fatigue. It is a permanent structural damage that occurs when a material is subjected to cyclic or fluctuating strains at nominal stresses that have maximum values less than (often much less than) the static yield strength of the material. These damages can although be effected by thermal stresses due to continuous heating and cooling.

AIN

► Piezoelectric Materials for Microfluidics

Amperometric Detection

- ► Amperometric Techniques
- ► Electrochemical Techniques

Amperometric Techniques

THOMAS J. ROUSSEL[1,3], DOUGLAS J. JACKSON[2], RICHARD P. BALDWIN[3], ROBERT S. KEYNTON[1]
[1] Department of Bioengineering, University of Louisville, Louisville, KY, USA
[2] Department of Electrical and Computer Engineering, University of Louisville, Louisville, KY, USA
[3] Department of Chemistry, University of Louisville, Louisville, KY, USA
thomas.roussel@louisville.edu,
doug.jackson@louisville.edu,
rick.baldwin@louisville.edu, rob.keynton@louisville.edu

Synonyms

Amperometric detection; Controlled-potential instrumentation; Electrochemical detection; Oxidation/reduction

Definition

Amperometry is one of a family of electrochemical methods in which the potential applied to a sensing electrode is controlled instrumentally and the current occurring as a consequence of oxidation/reduction at the electrode surface is recorded as the analytical signal. In its simplest form, the applied potential is stepped to and then held at a constant value; and resulting current is measured as a function of time. When *amperometric detection* is used in conjunction with separation techniques such as capillary electrophoresis or liquid chromatography, the sensing (or "working") electrode is placed at the end of the separation stream so as to permit detection of sample components as they emerge and pass over the electrode surface. The applied potential must be sufficient to cause facile oxidation or reduction of the target analytes; and, in general, the magnitude of the measured current is directly proportional to the analyte concentration.

Overview

Amperometric electrochemical (EC) detection was initially developed in the 1970s for conventional sized high performance liquid chromatography (HPLC) instrumentation [1]. However, as the principal micro/nanofluidic applications of the approach are most directly related to capillary electrophoresis (CE), it is the development of these latter systems that is of greatest relevance here. Amperometric detection was first introduced in conventional bench-scale CE in 1987 by Wallingford and Ewing [2] for the determination of catecholamine-based neurotransmitters. The detection was carried out by carefully placing a small carbon fiber electrode at the outlet of the separation capillary and recording the current transient caused by oxidation of each catecholamine as it emerged from the capillary outlet and passed over the fiber. Subsequently, dozens of papers have appeared both on novel instrument designs in CE/EC and on a wide range of CE/EC applications [3]. During the course of this work, amperometric CE/EC has been carried out on a variety of carbon and metallic electrodes and has been shown to offer both the high sensitivity (μM–nM) required by CE and a unique selectivity determined by the potential applied and the specific electrode used. In general, this detection approach is applicable to several important families of organics. In addition to catechols, these include carbohydrates, amino acids, thiols, phenols, and aromatic amines, as well as a variety of specific compounds of biological or pharmaceutical interest.

In amperometry, quantification of species concentration is possible because the magnitude of the current generated in any given experiment is determined by the number of molecules, of that species, oxidized or reduced at the surface of the sensing electrode and therefore is directly proportional to the concentration of the molecule detected as defined by Faraday's law (Eq. (1)).

$$i_t = \frac{\mathrm{d}Q}{\mathrm{d}t} = \eta F \frac{\mathrm{dN}}{\mathrm{d}t} \tag{1}$$

Where i_t is the current generated at the surface of the sensing electrode at time $= t$, Q is the charge at the surface of the sensing electrode, η is the number of moles of electrons transferred per mole of analyte, N is the number of moles of analyte oxidized or reduced, and F is the Faraday constant (96,487 $\mathrm{C mol}^{-1}$). Detection limits have been reported at the attomole and femtomole levels [4, 5], roughly corresponding to micromolar concentrations in the carrier fluid. Because this form of detection is coupled to the liberation or consumption of electrons, the application of this detection technique is limited to those species that are electroactive, i. e., those that can be oxidized or reduced at an electrode surface. While amperometry has been used for decades in benchtop scale analytical systems, the greatest attractiveness of this particular detection approach lies with the ability to miniaturize the necessary electrodes (working, reference, and auxiliary or counter) and incorporate them into miniaturized *Lab-on-a-Chip* devices. The simplicity of the supporting electronics for amperometry provides advantages as well compared to other detection systems (e. g., UV-visible absorbance, laser-induced fluorescence, mass spectrometry, etc.) that require a considerably larger ensemble of supporting equipment.

The specific fluidic system involved, while not the main topic of this chapter, is closely linked to the detection system and warrants a brief explanation. Separation techniques such as CE and HPLC utilize channels or columns that pass a fluidic medium carrying the analytes of interest. Bulk flow is actuated using either gravity or pressure, in the case of LC, or electroosmotic forces, in the case of CE. Separation of analytes occurs due to physical or chemical interactions with what is incorporated into the column (a packing material that completely fills the column or is coated onto the inner walls) for HPLC or differential electrical migration of the charged analytes toward the electrokinetic "drive" electrodes for CE. Many of these separation techniques are being downsized using microfabrication methods, referred to collectively as *microfluidics*.

Basic Methodology

In a redox reaction (Eq. (2)), electrons are removed from a solution species (oxidation) at one electrode and transferred to a solute (reduction) at the other:

$$\begin{aligned} &\alpha A \rightarrow \chi C + ne^- && \text{(anode)} \\ &\beta B + ne^- \rightarrow \delta D && \text{(cathode)} \end{aligned} \tag{2}$$

where A, B, C, and D are the reactants and products of the reaction α, β, χ, and δ are their stoichiometric coefficients, and n is the number of electrons. To carry out and monitor such a reaction, an electrochemical *cell* is used. These *cells* typically consist of three electrodes – the working, auxiliary, and reference electrodes – placed in electrolyte solution. Amperometric sensing is controlled by application of the desired potential or voltage solely to the working electrode. This is the electrode at which the redox reaction (either oxidation or reduction) of the analyte of interest occurs, and therefore it is the current flowing at this electrode that constitutes the analytical signal (Fig. 1). The function of the reference electrode is to provide a contact

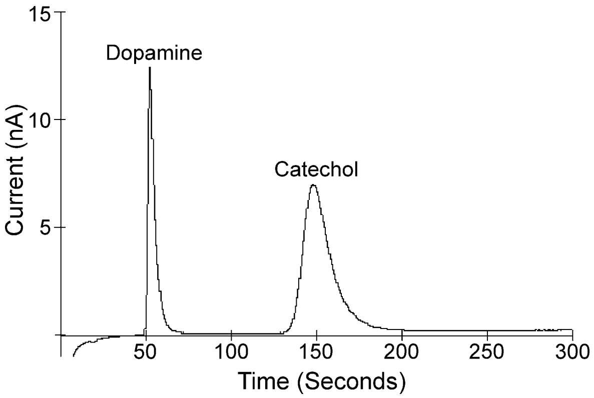

Amperometric Techniques, Figure 1 Typical electropherogram for catechol and dopamine using amperometric detection on a microchip platform

whose potential remains constant during the amperometry experiment, and its chemical composition (saturated calomel, Ag/AgCl, etc.) is purposely selected to facilitate this. The role of the counter electrode is to provide a current path that completes the electrical circuit. Thus, the redox reaction occurring here is equal in size but opposite in direction (i. e., reduction or oxidation). Normally, this electrode consists of a simple metallic contact, most commonly platinum.

The chemical composition/structure of the working electrode can vary considerably, and a proper selection is often critical to achieving success in a given application. The minimum requirements are reasonable degrees of chemical inertness and electrical conductivity. Commonly encountered electrodes include metals, such as Pt, Au, or Hg, and carbon. In addition, the surface of these electrode materials can also be modified chemically by a number of different approaches in order to optimize performance for a specific electrochemical process [6]. For example, the charge, polarity, porosity, and specific chemical and biochemical reactivity can be adjusted by the addition of appropriate functional groups, self-assembled mono- and bi-layers, and polymer coatings.

The function of the external electronic circuitry – or the "potentiostat" – in amperometric experiments is to supply the desired voltage difference between the working and reference electrodes and measure the resulting redox current instantaneously. The magnitude of the working electrode potential necessary to initiate the oxidation or reduction is ideally determined by the Nernst equation (shown in Eq. (3)) but can also be affected by factors such as the conductivity of the carrier fluid, the electron-transfer kinetics of the specific redox reaction, the composition of the detection electrode, and the relative distance between the working and reference electrodes.

$$E = E^0 - \frac{0.059}{|n|} \log \left(\frac{a_C^\chi a_D^\delta}{a_A^\alpha a_B^\beta} \right) \tag{3}$$

where E is the potential of the working electrode, E^0 is the standard potential for the redox reaction of interest, n is the number of electrons involved, and the a's represent the activities of the reactants and products. It follows from the Nernst equation that making the working electrode potential more negative favors the reduction process and is therefore said to be more "reducing" or "cathodic" while application of a more positive potential would be "oxidizing" or "anodic". Thus, in practice, amperometric detection involving analyte reduction is generally carried out by application of negative potentials, while analyte oxidation requires use of relatively positive applied potentials. Successful bench-scale CE/EC in the amperometric mode requires the accurate maintenance of EC potentials on the order of roughly ± 1 V at working electrodes placed in CE fields on the order of 5 – 30 kV and the measurement of EC currents typically pA in magnitude in the presence of μA-level background CE currents.

A representative three-electrode amperometric detection configuration and a simplified potentiostat circuit are shown in Fig. 1. The working and reference electrodes are placed in the amplifier feedback loops so that the voltage difference between them must match an adjustable external voltage source. Because the composition of the reference electrode is designed to maintain its potential at a constant value, the working electrode potential is just the selected external voltage compared to or "vs." the specific reference electrode used. The reference electrode is connected to a high input impedance buffer amplifier, which serves to limit the current flow through it to a negligible level, which in turn serves to keep its composition unchanged and its potential at its starting value. The working electrode is connected to an ammeter circuit, typically a sensitive transimpedance amplifier (current-to-voltage converter). The oxidation or reduction reaction occurring when an electroactive analyte passes the working electrode produces current flow in the ammeter that is then converted to a proportional voltage for display.

A simple electrical model of the solution as seen by the electrodes is shown in Fig. 3. Resistances are primarily determined by the ionic content of the electrolyte solution, which is typically in the 0.01 – 0.10 M range. When the electrodes are placed in an electrolyte solution, a charge separation or "double layer" forms spontaneously at the electrode-solution interface. This produces a capacitance, commonly referred to as the double-layer

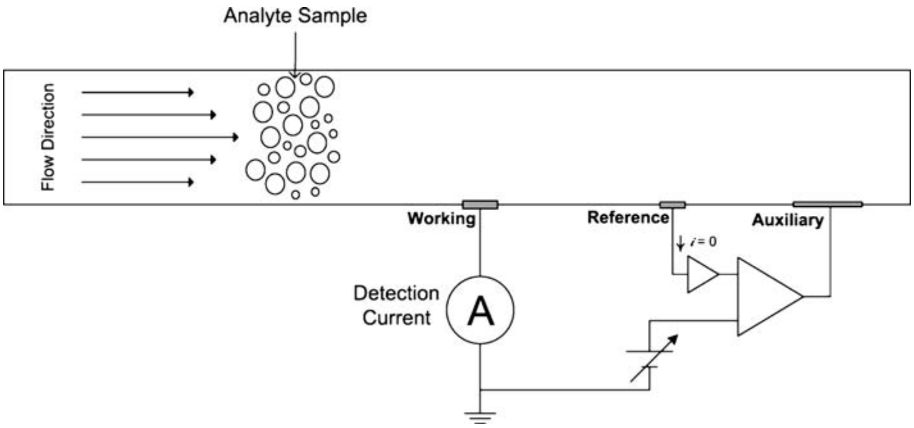

Amperometric Techniques, Figure 2 Schematic of amperometric detection cell (general representation for Lab-on-a-Chip (LOC) applications

capacitance, C_{DL}. The size of this capacitance is a function of electrode area, electrode-to-solution potential, electrode material, and the ion concentration in solution. The potentiostat compensates only for capacitance, impedance, and resistance (C_{DLA}, R_c, Z_{FA}) within its control loop and allows these to be largely ignored experimentally. Therefore, the uncompensated resistor, R_u, which is outside the loop, causes an error in the working electrode potential, iR_u, as a result. However, given the very small amplitude currents usually involved in microfluidic systems and the relatively low resistivities of the aqueous electrolyte solutions normally employed, this error is seldom of any practical concern for amperometric measurements. Of course, the product $R_u C_{DL}$ represents the cell time-constant and largely determines the speed of response of the cell to any change in the applied potential. For typical amperometric detection applications where the applied potential is kept constant throughout the entire experiment, this also is of no concern; but, for the relatively few cases in which the potential is systematically scanned during the CE separation, limitations in accurate control of the working electrode potential due to charging of C_{DLW} must be considered.

Application of amperometric detection to HPLC instrumentation is usually straightforward, involving the placement of conventional size electrodes downstream from the column exit. Care must be given to keep the dead-volume entailed by the detection cell and connecting tubing small enough to avoid compromising the separation efficiency. For CE/EC systems, however, there are two specific issues that must be addressed experimentally: 1) physical alignment of the electrodes with the capillary or channel outlet; and, 2) electrical decoupling of the EC detection from the high-voltage CE field. The need to optimize capillary/electrode alignment arises from the very small dimensions involved – with the widths of both CE channels and EC electrodes typically in the 10 – 100 μ range. Thus, optimum sensitivity dictates that the working electrode is placed very near the channel outlet while acceptable reproducibility requires that this positioning, once established, be maintained throughout extended sets of experiments. With bench-top CE instrumentation, this usually requires the use of microscopes and 3D micro-positioners to align the fiber or wire with respect to the capillary. Alternative arrangements to ease this problem have been suggested such as the use of planar "wall-jet" electrodes that can be somewhat larger in size or the incorporation of the EC electrode onto the capillary by deposition of an appropriate metallic film onto its outside tip. Of course, one of the attractive features of Lab-on-a-Chip CE/EC systems is that the specific location, size, and shape of the EC electrodes can be absolutely controlled during the microfabrication process.

In amperometric detection, the placement of the working electrode in CE/EC detection systems can be divided into three different categories, *off-channel (or column)*, end-*channel (or column)* and in-*channel detection.* The purpose of this distinction is to indicate the location of the EC electrodes with respect to the CE electrodes and field (Fig. 4). This is an important consideration because of the possible interactions that might occur, as mentioned above, between the EC and much larger CE electric fields. "Off-channel" EC detection refers to the situation in which an electrically conducting "fracture" or thin crack, opening, or hole is created in the capillary or channel wall a short distance before the exit. This fracture allows the CE voltage and current to be dropped before the actual physical end of the system and permits the EC electrodes to be placed near or even inside the capillary exit for efficient analyte detection but nevertheless to remain

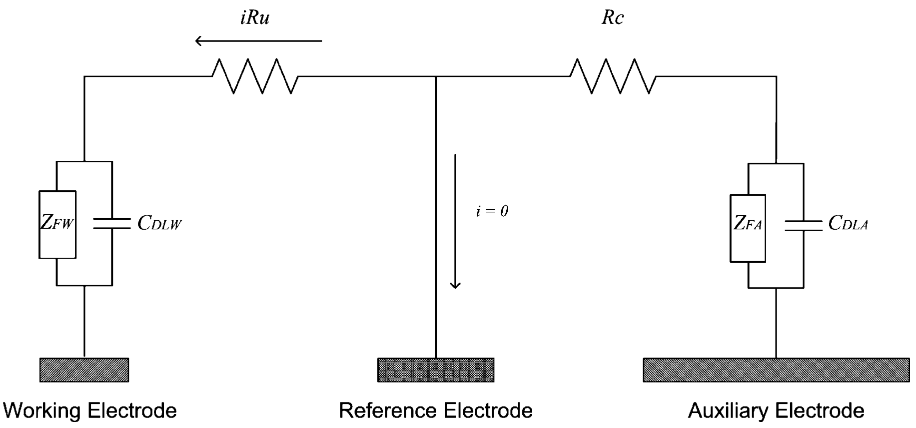

Amperometric Techniques, Figure 3 Electrical model of three-electrode cell (Z_{FW} is the faradaic impedance at the working electrode; C_{DLW} is the double-layer capacitance at the working electrode; Z_{FA} is the faradaic impedance at the auxilary electrode; C_{DLA} is the double-layer capacitance at the auxilary electrode; R_C is the resistance of the electrochemical cell; R_u is the uncompensated resistance; and, i is the current)

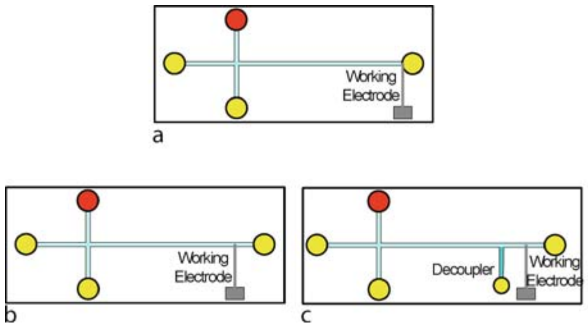

Amperometric Techniques, Figure 4 Schematic of EC electrode placement for the different detection electrode configurations: (**a**) end-channel detection; (**b**) in-channel detection; and, (**c**) off-channel detection

"off" or outside the influence of the CE field, commonly referred to as "decoupling" [7, 8]. The off-channel approach, which often may pose significant technical difficulties to implement, offers the possibility of very efficient detection of the analyte while it is still contained within the confines of the narrow separation channel and remains in the form of a relatively concentrated plug. "End-channel" detection refers to the more convenient placement of the EC detection electrode just beyond the end of the separation channel in the CE buffer reservoir. Thus, the EC cell is located within the high-voltage CE field, and electrical interactions between the two are still possible. However, as long as the CE capillary or channel width is sufficiently small, its ohmic resistance is high enough that the CE current is negligibly small and only a very small portion of the CE voltage extends beyond the exit and into the much larger volume detection compartment. Of course, an inherent problem with this technique is that the well-defined analyte plugs maintained within the capillary immediately begin to spread radially upon exiting and moving into the much larger volume detection reservoir. Therefore, care must be taken that the detection electrode, in this case, is located close to the exit of the channel, typically 25 – 100 μm, but not so close as to interact unduly with the residual CE voltage that does extend slightly beyond the separation channel. A detailed study of the residual post-capillary CE field, and the effect of end-channel electrode placement, has been reported by Klett et al. [9]. The in-*channel* approach has been employed by researchers, however, this approach is limited due to bubble generation in the channel, which can significantly decrease the signal-to-noise (S/N) ratio of the electrochemical signal, as well as the high electric field can significantly effect the resting background current generated at the surface of the working electrode.

In regards to electrode geometry, the EC detector response is proportional to electron generation (or consumption) during the desired redox reaction. Therefore, increasing the area of the detection electrode will increase the detection signal. The tradeoff is that the background noise increases linearly as well. Due to the confined geometry of the microchannel, in-channel electrodes are limited to simple rectangular shapes determined by the channel width and exposed electrode area. This configuration is sufficient to maximize the contact of the analyte with the electrode surface. For an end-channel electrode configuration, however, a simple rectangular planar electrode is not the only option. The conventional planar geometry can be altered to match the shape of the radially migrating analyte so as to maximize the delivery of the sample to the detection electrode surface.

Key Research Findings

The first microfluidic *Lab-on-a-Chip* (LOC) devices were reported by Harrison and Manz in the early 1990s. These devices consisted of simple channels, several cm in length and 10 – 100 μm in width and depth, etched into glass microscope slides or silica plates via conventional micromachining techniques [10]. In this work, samples were injected onto the chip and moved as required through the channel network by electroosmotic flow; separations were carried out by electrophoretic mechanisms common to bench-scale CE instrumentation; and target analytes were detected and quantitated via fluorescence detection. Subsequent studies by these and other groups demonstrated unique advantages for the Lab-on-a-Chip approach: high separation efficiencies, short analysis times, minute sample and reagent consumption, high sample throughput, and easy automation.

In 1996, the first use of amperometric detection in microchip CE devices was reported by Wooley, Lao, Glazer and Mathies [11] who used off-chip CE driving electrodes together with a photolithographically patterned Pt electrode placed just outside the CE channel for on-chip detection of catechol neurotransmitters by direct oxidation and DNA fragments and PCR products indirectly by EC monitoring of an electroactive intercalating agent. In another end-channel approach, Baldwin and colleagues [12] were the first to demonstrate a Lab-on-a-Chip device that incorporated both CE high-voltage electrodes and all amperometric EC detection electrodes directly onto an integrated, microchip platform. Key features of their device were the formation of a "shelf or ledge" at the end of the separation channel to restrict the height of the detection reservoir near the working electrode and the radial pattern of the working electrodes. These features enabled optimization of EC detection by decreasing the electrical resistance and CE voltage drop in the detection region and increasing the residence/contact time of the analytes with the working electrode, respectively. Another novel CE microchip end-column approach has been reported by Ertl et al. [13], which integrates sheath-flow into the CEEC system to increase analyte velocity in the detection reservoir as it exits the CE separation channel. Their study further elucidated the importance of the spacing between the working and reference electrodes, with optimum detector performance achieved for a spacing of $\sim 20\,\mu m$. Using an electrically isolated potentiostat with a floating working electrode, Martin and coworkers [14] successfully detected catechol with minimum band-broadening effects by placing the working electrode just inside the separation channel but without any decoupling. Off-channel EC detection approaches have been also explored in microchip platforms. For example, the Lunte groups demonstrated two different methods for decoupling the CE field from the EC detection system. In the first, decoupling was achieved by laser-cutting a series of 20, 30 μm holes in the roof of the CE channel into the upper glass coverplate and then filling them with cellulose acetate [8]. In the second, a 500 μm wide Pd decoupler strip was fabricated via photolithography and sputter-coated onto the glass substrate that formed the bottom of the CE channels [15]. When placed directly in the CE channel and used as the CE cathode, the Pd was able to absorb the H_2 gas that is generated during normal CE operation and leads to the formation of bubbles in the channel. The key advantages of these approaches (and others like them) are that they allow microchips to operate at higher field strengths (up to 1700 V/cm) with superior limits of detection (~ 25 nM for dopamine with a carbon fiber electrode) and allow the EC working electrode to be placed in-channel where higher efficiency separations can be realized. Similarly, Lai et al. [16] integrated a Pd-film decoupler with a series-dual electrode to significantly enhance the oxidation current when switching between the single electrode mode and dual-series mode. In other work, Wu et al. [17] electrodeposited Pt nanoparticles on a Au ground electrode to construct the decoupler and achieved a limit of detection of 0.125 μM at a $S/N = 4$ for dopamine with a Au working electrode.

Compared to alternative detection approaches, amperometric methods are ideally suited to microfabrication processes since the electrodes themselves have the ideal dimensions (1 to 10 μm) for incorporation onto a microchip. Most importantly, patterning and construction of EC microelectrodes is extremely compatible with mainstream microfabrication technologies such as photolithography and sputter-coating. As a result, electrodes (and electrochemical cells) of different shape, size, location, and composition can be patterned directly onto glass, silica, and other substrates with a high degree of accuracy using the same photolithographic techniques employed to fabricate the microchip's CE channels, thereby allowing the detection operation to be fully integrated onto the chip (Fig. 5). In addition, multiple electrodes in different CE channels or multiple electrodes with different response characteristics can be created to allow the device to fit the intended application optimally (Fig. 5b). This level of integration does not exist with other detection approaches and has several performance and applications advantages. For example, with LIF, multi-channel detection requires either the use of multiple fluorescence systems or a means of scanning a single fluorometer across multiple spots on the chip.

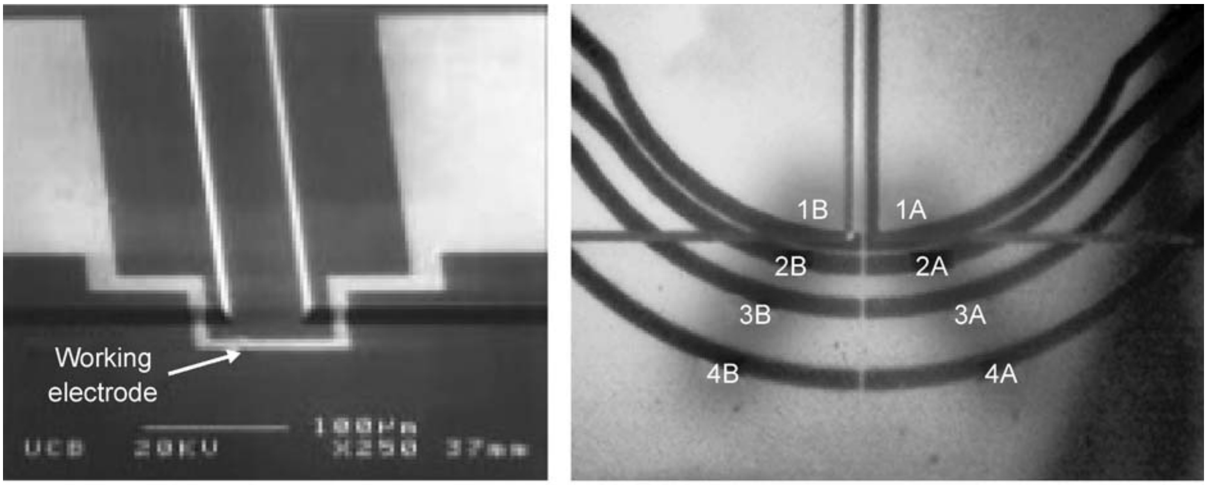

a b

Amperometric Techniques, Figure 5 Examples of different electrode geometries that can be fabricated via photolithographic techniques: (**a**) rectangular working electrodes (Reprinted with permission from [11]); and, (**b**) multiple radial working electrodes (Reprinted with permission from [18])

Chip-based amperometric EC detection techniques have been utilized in several noteworthy analysis situations – most commonly in clinical (e. g., immunoassays and protein analysis) and environmental sensing. A recent review by Vandaveer et al. [19] provides an excellent overview of these applications.

Future Directions for Research

Considering the relative ease with which prototypes can be developed on the micro-scale, custom EC electrode configurations mated perfectly to the CE separation platform are possible. For example, devices with multiple separation channels may be outfitted with multiple EC cells, each identical to the other to establish redundancy for fail-safe detection. Each channel could run simultaneously and statistical calculations (running averages, standard deviations, etc.) could be used to enhance both the reliability of detection and the robustness of the detection system. The development of such advanced LOC instruments is expected to be central to their practical utilization in applications involving remote and unattended sensing.

Another possibility would be for each channel of a multiple channel CE/EC system to be configured with an EC cell specifically designed to detect a different analyte or analyte group. This could be accomplished, for instance, by maintaining each EC electrode at a different potential, fabricating each detection electrode out of a different substrate, or modifying each electrode chemically or biochemically. In this case, there would be no redundancy; however, a single experiment could yield results for a range of analyte components. Furthermore, alternative microfabrication techniques can be developed to create electrodes with alternative geometries, such as flow through or three-dimensional, large surface area detection electrodes. Increased surface area electrodes allow for a more complete interaction between the analyte and the detector which should be expected to enhance the signal-to-noise ratio and sensitivity.

A relatively new area which is likely to grow in importance is the construction/functionalization of the EC electrodes with alternative materials to enhance the reactivity toward the analyte or to allow detection of analytes that do not oxidize or reduce ideally at simple electrodes. For example, Marwan et al. [20] reported the functionalization of glassy carbon electrodes with metal-based species in order to elicit the electrochemical reduction of nitrates and oxidation of hydrogen peroxide. Similarly, Sarapuu et al. [21] have shown the modification of boron-doped diamond and highly oriented pyrolytic graphite electrodes with quinones to greatly enhance the rate of oxygen reduction, thereby allowing a highly sensitive determination of hydrogen peroxide. Biological molecules (DNA, antigens, etc.) which are often not inherently electroactive can be detected electrochemically by approaches such as Kavanagh's [22] in which a redox polymer and a single-stranded DNA probe were attached to a gold electrode; hybridization and formation of the double-stranded probe DNA altered the electrochemistry of the polymer and thereby permitted detection of the complementary DNA species. Continuing research into further functionalization of traditional and modified electrode materials will further enhance sensitivity and promote selectivity between ana-

lytes, especially in the areas of clinical and biochemical analysis.

An alternative approach gaining widespread attention is the addition of an electrochemically active tag or label to an electro-inactive biomolecule such as DNA, SNPs, etc. Similarly to fluorescence detection, in which a sample is treated with a natively fluorescent chemical marker in order to render it optically detectable, this technique tags the sample at a specific site with a molecule that undergoes oxidation/reduction at a well-characterized electrode system. Wooley, et al. [11] first proposed this promising approach in 1998. Since then, others have demonstrated the ability to carry out this technique on a microchip platform. Hebert and colleagues [23, 24] have detected a specific SNP (Single Nucleotide Polymorphism) site using an electrochemically active taggant in conjunction with sinusoidal voltammetry, while Wang and coworkers [25] labeled amino acids with electrochemically active 1-cyanobenz(f)isoindole derivatives to permit the detection of arginine, lysine, phenylalanine, glycine and cysteine. Given the inherent sensitivity of EC and the flexibility of microfabrication, this line of research is expected to have a major impact on the detection of many important biomolecules.

Cross References

► Capillary Electrophoresis
► Electroosmotic Flow (DC)
► Electrophoresis
► Surface Conductivity Measurement
► Potentiometry

References

1. Kissinger PT, Ridgway TH (1996) Small-Amplitude Controlled-Potential Techniques. In: Kissinger PT, Heineman WR (eds) Laboratory Techniques in Electroanalytical Chemistry, 2nd edn. Dekker, New York
2. Wallingford RA, Ewing AG, (1987) Capillary zone electrophoresis with electrochemical detection. Anal Chem 59:1762–1766
3. Haber C (1996) In: Landers JP (ed) Electrochemical detection in capillary electrophoresis. Handbook of Capillary Electrophoresis, 2nd edn. CRC, Boca Raton
4. Sloss S, Ewing AG (1993) Improved method for end-column amperometric detection for capillary electrophoresis. Anal Chem 65:577–581
5. Wang J (2000) Analytical Electrochemistry, 2nd edn. Wiley-VCH, New York
6. Bard AJ, and Faulkner LR (2001) Electrochemical Methods: Fundamentals and Applications, Chapter 13, 2nd edn. Wiley, Hoboken, p 580
7. Osbourn DM, Lunte CE (2001) Cellulose acetate decoupler for on-column electrochemical detection in capillary electrophoresis. Anal Chem 73:5961–5964
8. Osbourn DM, Lunte CE (2003) On-column electrochemical detection for microchip capillary electrophoresis. Anal Chem 75:2710–2714
9. Klett O, Björefors F, Nyholm L (2001) Elimination of high-voltage field effects in end-column electrochemical detection in capillary electrophoresis by use of on-chip microband electrodes. Anal Chem 73:1909–1915
10. Harrison DJ, Manz A, Fan Z, Ludi H, Widmer HM (1992) Capillary electrophoresis and sample injection systems integrated on a planar glass chip. Anal Chem 64:1926–1932
11. Woolley AT, Lao K, Glazer AN, Mathies RA (1998) Capillary electrophoresis chips with integrated electrochemical detection. Anal Chem 70:684–688
12. Baldwin RP, Roussel Jr. TJ, Crain MM, Bathlagunda V, Jackson DJ, Gullapalli J, Conklin JA, Pai R, Naber JN, Walsh KM, Keynton RS (2002) Fully-integrated on-chip electrochemical detection for capillary electrophoresis in a microfabricated device. Anal Chem 74:3690–3697
13. Ertl P, Emrich CA, Singhai P, Mathies RA, (2004) Capillary electrophoresis chips with a sheath-flow supported electrochemical detection system. Anal Chem 76:3749–3755
14. Martin RS, Ratzlaff KL, Huynh BH, Lunte SM (2002) In-channel electrochemical detection for microchip capillary electrophoresis using an electrically isolated potentiostat. Anal Chem 74:1136–1143
15. Lacher NA, Lunte SM, Martin RS (2004) Development of a microfabricated palladium decoupler/electrochemical detector for microchip capillary electrophoresis using a hybrid glass/poly(dimethylsiloxane) device. Anal Chem 76:2482–2491
16. Lai CCJ, Chen CH, Ko FH (2004) In-channel dual-electrode amperometric detection in electrophoretic chips with a palladium film decoupler. J Chromatogr A 1023:143–150
17. Wu CC, Wu RG, Huang JG, Lin YC, Chang HC (2003) Three-electrode electrochemical detector and platinum film decoupler integrated with a capillary electrophoresis microchip for amperometric detection. Anal Chem 75:947–952
18. Keynton RS, Roussel TJ, Crain MM, Jackson DJ, Franco DB, Naber JF, Walsh KM, and Baldwin RP (2004) Design and development of microfabricated capillary electrophoresis devices with electrochemical detection. Anal Chim Acta 507:95–105
19. Vandaveer IV WR, Pasas-Farmer SA, Fischer DJ, Frankenfeld CN, Lunte SM (2004) Recent developments in electrochemical detection for microchip capillary electrophoresis. Electrophoresis 25:3528–3549
20. Marwan J, Addou T, Belanger D (2005) Functionalization of glassy carbon electrodes with metal-based species. Chem Mater 17:2395–2403
21. Sarapuu A, Helstein K, Schiffrin DJ, Tammeveski K (2005) Kinetics of oxygen reduction on quinone-modified HOPG and BDD electrodes in alkaline solution. Electrochem Sol State Lett 8:E30–E33
22. Kavanagh P, Leech D (2006) Redox polymer and probe DNA tethered to gold electrodes for enzyme-amplified amperometric detection of DNA hybridization. Anal Chem 78:2710–2716
23. Hebert NE, Snyder B, McCreery RL, Kuhr WG, Brazill SA (2003) Performance of pyrolyzed photoresist carbon films in a microchip capillary electrophoresis device with sinusoidal voltammetric detection. Anal Chem 75:4265–4271
24. Hebert NE, Kuhr WG, Brazill SA (2003) A microchip electrophoresis device with integrated electrochemical detection: A direct comparison of constant potential amperometry and sinusoidal voltammetry. Anal Chem 75:3301–3307

25. Wang J, Chen G, Pumera M (2003) Microchip separation and electrochemical detection of amino acids and peptides following precolumn derivatization with naphthalene-2,3-dicarboxyaldehyde. Electroanalysis 15:862–865

Amphoteric Ion Exchange Membrane

Definition

An ion exchange membrane which includes both a weak anioin exchange and a weak cation exchange functionality in to the same membrane. This type of membrane has the ion exchange functionalities distributed randomly throughout the membrane.

Cross References

► Ion Exchange Membranes

Analysis/Design

► Control of Micro-Fluidics

Analysis of Individual Cell Contents

► Single Cell Analysis in Microfluidic Devices

Analyte

Definition

An *analyte* is the substance or chemical constituent that is undergoing analysis. It is the substance being measured in an analytical procedure. For instance, in an immunoassay, the analyte may be the ligand or the binder.

Cross References

► Biosensor
► Chemical Analysis
► Bio-Analysis

Analytical Method

► Analytical Modeling

Analytical Modeling

Synonyms

Analytical method

Definition

Analytical modeling is to seek for mathematical functions and equations that are obtained from the closed-form (exact or approximate) solution to the original physics-governing equations. The outcome of analytical modeling is behavioral models.

Cross References

► Behavioral Model

Anion

Definition

Negatively charged ion that moves towards the anode in electrophoresis.

Cross References

► Electrophoresis

Anion Exchange Membrane

Definition

An ion exchange membrane that interacts with anions and typically consist of amine functionalities ($-NH_3^+$, $-NRH_2^+$, etc). These functionalities allow anions to pass through the membrane and prevents cations from passing through the membrane. The ability of the membrane to bind ions is greatly dependant on the pH of the solution and the ions of intrest.

Cross References

► Ion Exchange Membranes

Anisotropic Etching

Dustin House, Dongqing Li
Department of Mechanical Engineering,
Vanderbilt University, Nashville, TN, USA
dustin.l.house@vanderbilt.edu

Synonyms

Silicon etching; Etching single crystalline materials; Potassium hydroxide (KOH) etching; Deep reactive-ion etching (DRIE); Bosch process; Physical-chemical etching

Definition

Anisotropic etching is a subtractive microfabrication technique that aims to preferentially remove a material in specific directions to obtain intricate and often flat shapes. Wet techniques exploit the crystalline properties of a structure to etch in directions governed by crystallographic orientation. Dry techniques utilize an inhibitor to protect the sidewalls of a cavity during ion bombardment to obtain high aspect ratios.

Overview

In contrast to isotropic etching, anisotropic etching is a fabrication technique that removes material in specific directions allowing for the production of geometric characteristics such as sharp corners, flat surfaces, and deep cavities. Relative to microfabrication, selectivity can be defined as the ratio of the etch rate of the target material to the etch rate of other materials. The definition can also be applied more specifically to single crystalline materials such as silicon where it would be considered the ratio of the etch rate in the target direction to the etch rate in other directions.

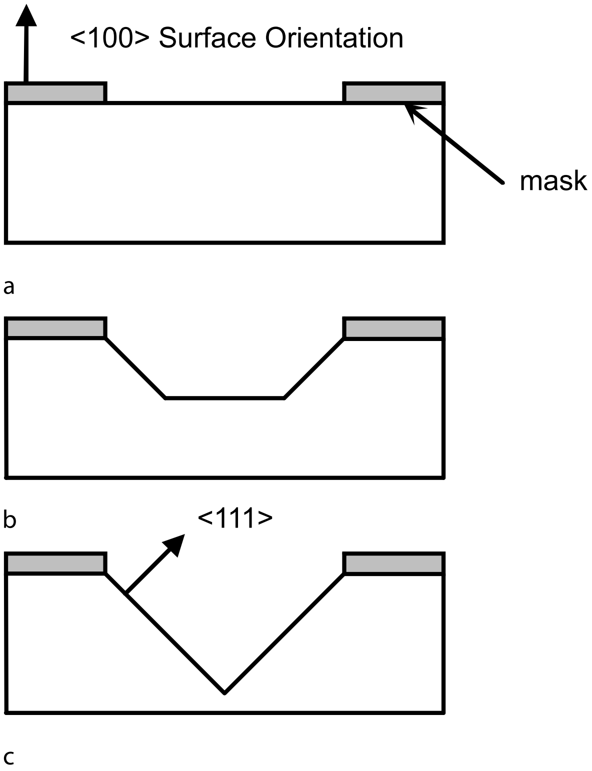

Anisotropic Etching, Figure 1 Example of a masked silicon wafer with a ⟨100⟩ surface orientation (**a**) before, (**b**) during, (**c**) and after exposure to a potassium hydroxide etch

Different etchants used in anisotropic wet etching have specific etch rates for each crystallographic plane in the material being removed. It is the difference in etch rates between planes that produce shapes within the material being etched that appear to follow the planes within the crystalline structure as seen in Fig. 1. For more information on the crystalline structure of silicon and how miller indices are used in designating crystal planes, see The MEMS Handbook [1]. It is commonly accepted that the ⟨111⟩ plane etches the slowest regardless of the etchant used. However, the crystal plane that etches the fastest depends on the etchant composition [2]. Ammonium hydroxide etchants (NH_4OH and TMAH) are frequently used to etch silicon due to their compatibility with certain metals involved in on-chip circuitry, whereas alkali hydroxide etchants (NaOH, CsOH) are used for their faster etch rates [3]. A commonly used alkali hydroxide etchant for silicon is potassium hydroxide (KOH) which provides a high level of selectivity between the ⟨100⟩ and ⟨111⟩ planes. Materials that are highly resistant to these etchants, such as silicon nitride and silicon dioxide are often utilized as etch stops in more complex designs. Detailed specifications for each etchant including etch rates in specific crystal planes, and recommended temperatures, concentrations and etch stops is available in the literature such as those of Nguyen and Wereley [2].

Careful design and alignment of the mask must be ensured when involving directional dependence in the etching process. Because the planes will continue indefinitely until they reach a surface or another plane, undercutting of the masking material is possible. A shape that does not align with the correct planes can produce an opening that circumscribes the original shape if etched long enough as seen in Fig. 2. The angle produced between the slow-etch plane and the surface after etching is clearly dependent on surface orientation and the crystalline structure of the material. Such angles are found in the literature and are utilized in design to achieve accurate depths and specific slopes (including vertical). Equipment used in wet etching can be easily obtained in most laboratories. The material being etched is suspended within a beaker containing the etchant while a magnetic stirrer ensures continuous transport of reactants to and products from the surface of the material. A simple temperature-controlled hot-

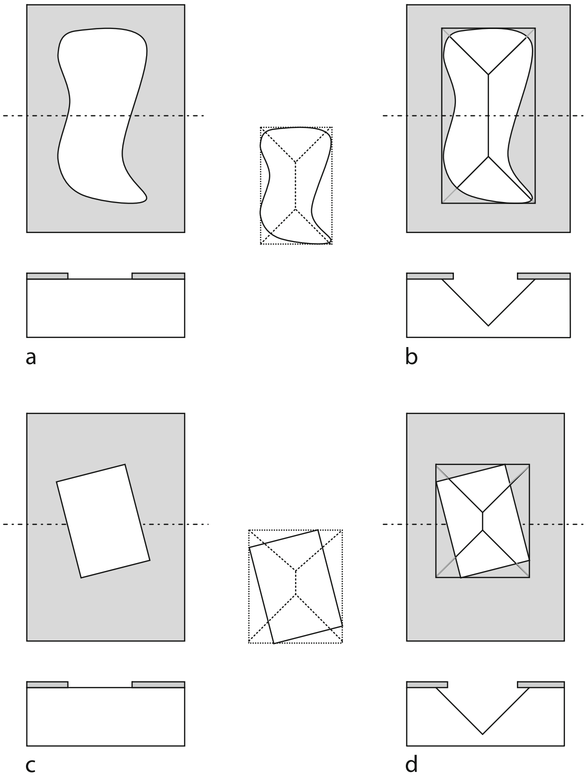

Anisotropic Etching, Figure 2 Examples of undercutting that is possible for (**a**,**b**) odd shaped masks and (**c**,**d**) misaligned masks relative to crystal planes

plate regulates the optimum temperature.

Anisotropic dry etching is a method for creating high aspect ratio trenches with nearly vertical walls. The two common techniques utilize a protective coating along the vertical walls of an etched trench such that the bottom of the trench etches at a faster rate allowing for large aspect ratios. Each is independent of crystal orientation. The first method forces the reactant gases to condense on the sidewalls of the trench by lowering the temperature of the materials with liquid nitrogen. Ions are then accelerated toward the trench by means of an electric field. This physical shower of ions results in an etching effect. After ion bombardment removes the bottom layer, it can be etched further while the sidewalls are protected by the cryogenically frozen inhibitor. Another novel approach, commonly referred to as the Bosch process (named after its inventor, Robert Bosch) alternates additive and subtractive microfabrication techniques. During the additive stage, chemical vapor deposition is used to coat the sidewalls of the trench with a polymeric passivation layer. Similarly to the previous method, ion bombardment is then used to sputter off the trench bottom, exposing the substrate to the chemical etchant [4]. Several companies specialize in the production of microfabrication equipment for various reactive ion etching processes. These processes, commonly referred to as deep reactive ion etching (DRIE) are capable of producing channels with a depth on the order of 500 μm and aspect ratios on the order of 30 : 1 [5].

Cross References

► Bulk Micromachining
► Dry Chemical Etch
► Fabrication of 3D Microfluidics Structures
► Isotropic Etching
► Microfabrication Techniques
► Plasma Etching
► Reactive Ion Etching (RIE)
► Silicon Micromachining
► Sputter Etching
► Wet Chemical Etch

References

1. Gad-el-Hak M (2002) The MEMS Handbook. CRC Press, Florida
2. Nguyen N, Wereley S (2002) Fundamentals and Applications of Microfluidics. Artech House, Inc., Massachusetts
3. Lobontiu N, Ephrahim G (2005) Mechanics of Microelectromechanical Sytems. Springer Science + Business Media, Inc., Massachusetts
4. Franssila S (2004) Introduction to Microfabrication. Wiley, West Sussex
5. Tabeling P (2006) Introduction to Microfluidics. Oxford University Press, Oxford

Anisotropic Silicon Etching

► Silicon Micromachining

Anisotropic Silicon Micromachining

► Bulk Micromachining

Anisotropy

Definition

The directional dependency of a measurable property of a material.

Cross References

► Sputtering for Film Deposition

ANN

► Artificial Neural Networks

Anode

Definition

Positively charged electrode.

Cross References

► Electrophoresis

Anodic Bonding

ZHENG CUI
Rutherford Appleton Laboratory, Oxford, UK
z.cui@rl.ac.uk

Synonyms

Field assisted bonding; Electrostatic bonding

Definition

Anodic bonding is a technique to produce hermetic seals between metals and glass insulators. Anodic bonding is mostly used for hermetic sealing of silicon and glass. Different from other sealing techniques, anodic bonding involves heating and applying an electrical field to a bonding pair.

Overview

The anodic bonding technique was first reported in 1969, with the name of field assisted glass–metal sealing [1]. It has since been developed into a widely used hermetic sealing technique for a variety of MEMS devices and microfluidic devices. The equipment for anodic bonding can be simply a hot plate on which the bonding parts are heated to the sealing temperature between 300 and 600 °C and a DC power supply to apply a high voltage from 200 V up to 2000 V to the bonding parts. The bonding process takes only a few minutes. Figure 1 shows schematically the setup for anodic bonding, where the conductive part, in this case a silicon wafer, is connected positively to the applied voltage. The essential conditions for anodic bonding are:

1. The bonding surfaces should be flat and well polished to less than 5 nm in surface roughness. When the bonding pair is put together, the two parts are in intimate contact at the polished surfaces.
2. The materials of the bonding pair must have well matched thermal expansion coefficients.
3. Anodic bonding only occurs between conductive materials and glass materials.

The mechanism of anodic bonding is believed to be both physical and chemical. The physical mechanism is electrostatic force. At the typical bonding temperature, most glass materials contain mobile positive ions compensated by almost immobile negative ions. Upon applying high voltage, these positive ions migrate to the negative electrode connected to the glass and become largely neutralized, leaving a depletion layer with negative space charge at the contact interface. Figure 2 shows the typical electrical current profile during anodic bonding [2]. The initial rise of current represents the migration and neutralization positive ions at the electrode. Then the current drops and a depletion layer is built up at the interface. The contact interface, although well polished at both sides, initially has only a few points of physical contact. Therefore, there is a high electrostatic field generated from the negative charge layer at the gaps. The high electrostatic attractive force then pulls the surfaces into direct contact, which explains why the bonding always starts at the point contact of electrode and spreads radially. The radial spreading of the bonding front makes it impossible for air to become trapped between the bonding surfaces. The electrostatic force depends on a number of factors, such as the total applied voltage, the width of the gap, the concentration and distribution of ions in the glass, whether under the high field the negative ions will drift out of the glass or the positive ions will drift into the glass and possible formation of surface charge on the glass (the effect of such charge would partially shield the charge in the glass, thus reducing the field in the gap).

The chemistry of anodic bonding is an oxidation process at the interface. Due to the high electrostatic field, oxygen anions leave the glass and create Si–O–Si bonds, i.e., a thin layer of SiO_2 is formed. This gives the strong bond between silicon and glass, and the bonding becomes irreversible. The formation of thin SiO_2 layer at the bonding interface has been verified by Rutherford backscattering spectroscopy. It has also been demonstrated that the rate of oxygen release is directly proportional to the average current passing through the bonding area. In areas where silicon and glass are in direct contact due to electrostatic attractive force, the oxygen anions will oxidize the silicon into SiO_2 and form the anodic bond. The oxygen is therefore totally consumed. However, in areas where silicon is

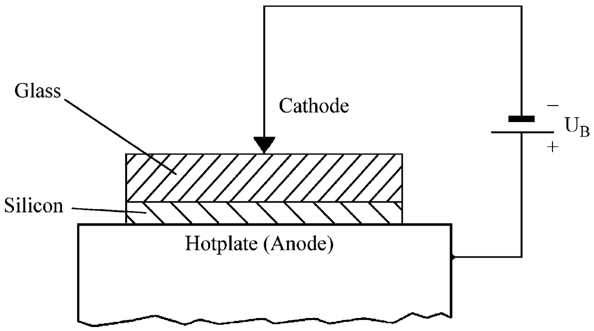

Anodic Bonding, Figure 1 Schematic setup for anodic bonding of silicon to glass

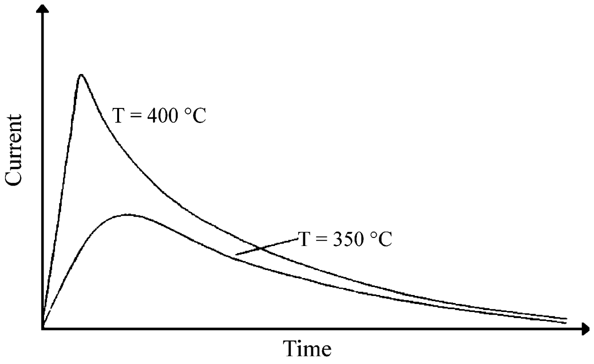

Anodic Bonding, Figure 2 Current profiles during anodic bonding at different temperatures

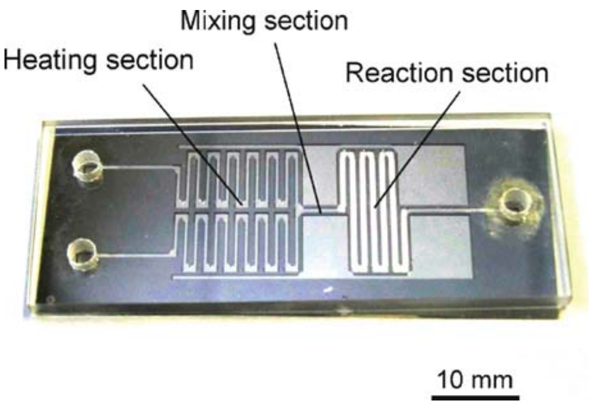

Anodic Bonding, Figure 3 Microreactor chip assembly by anodic bonding of silicon and glass

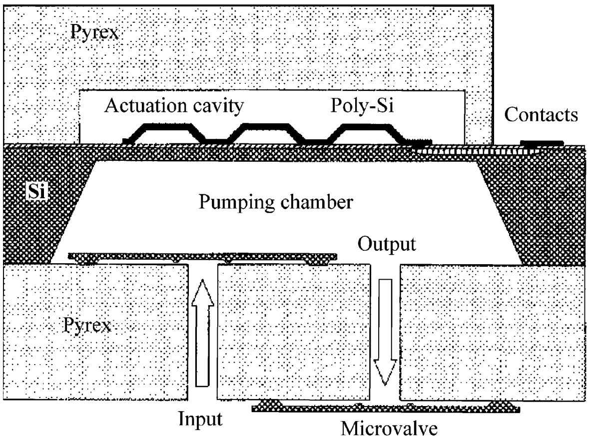

Anodic Bonding, Figure 4 Schematic cross-section of a micropump assembled by anodic bonding of glass–silicon–glass

not in direct contact with glass, for example in the case of an etched cavity into the glass or silicon, oxygen evolution into the cavity can occur. This may have detrimental effects in some device applications [3].

The bonding strength for silicon–glass anodic bonding is measured typically at 10 – 20 MPa. Some have reported between 30 MPa and 40 MPa at higher bonding voltage [2]. The pull test has demonstrated that bonding strength is higher than the fracture strength of the glass, i.e., the break in the pull test occurs only in the glass and not at the silicon–glass interface.

Anodic bonding of glass and silicon has found many applications in microsystems, MEMS and microfluidics, including the fabrication of pressure sensors, accelerometers, micropumps and other fluid handling devices. A typical microfluidic device is shown in Fig. 3, which is a microreactor chip to perform chemical synthetic reactions [4]. The microreactor was made by wet or dry etching of silicon to form microchannels and sealed by anodic bonding of a glass slide on top with inlet and outlet holes. Anodic bonding can provide an airtight seal to ensure proper function of fluidic flow in the microchannels. Silicon is a preferred material in microfluidic systems because micromachining of silicon is the most mature fabrication technique. Complex structures can be made in silicon by either wet chemical or reactive ion etching. Anodic bonding of silicon with glass can also help in the building of multistack microsystems to perform complicated functions. Figure 4 shows an example of a micropump made by silicon/glass micromachining and anodic bonding [5]. This is a glass–silicon–glass multistack system. The top Pyrex glass provides a hermetically sealed cavity so that the polysilicon heater can heat up the air in the cavity. Expansion of the hot air in the cavity will compress the silicon membrane to perform a pumping action in the pumping chamber. The bottom Pyrex glass seals the pump chamber as well as provides the input and output holes for fluid flow in and out of the pump chamber.

Anodic bonding is the primary method for packaging silicon microstructures, for example packaging of pressure sensors, accelerometers and solar cell panels, because of

its relatively low bonding temperature. With bonding temperature being below the glass transition point, the glass thermal expansion coefficient remains constant, which enables stress-free packaging of silicon microstructures (provided the glass has a good thermal expansion match with silicon over the process temperature range). In addition, with the low bonding temperature there is no measurable flow of glass, which ensures sealing around silicon microstructures without any loss of dimensional tolerances. Apart from low bonding temperature, there are other attractive features of anodic bonding:

- Since glass is an electrical insulator, parasitic capacitances are extremely small.
- The bonding process can be readily performed in vacuum, allowing hermetic sealing or zero pressure reference cavity to be formed (or sealing with special gas mixtures).
- The transparency of glass allows optical inspection or detection of fluidic flow/reaction in microfluidic devices. It also facilitates alignment of microstructures in glass with microstructures in silicon.

Although glass–silicon sealing or assembly is the most common form of anodic bonding, the technique can also be applied to the sealing of many metals with a variety of glasses. Successful seals have been made with borosilicate glass, soda lime glass, potash soda glass, aluminosilicate glass, fused silica and fiber optical glass [1]. Strong seals have also been made to some ceramic materials. For those metals and alloys whose thermal expansion coefficients are matched to the above glasses, successful anodic bonding have also been made, such as tantalum, titanium, Kovar, Niromet 44, and to semiconductors such as germanium and gallium arsenide, in addition to silicon [1].

Basic Methodology

Although the principle of anodic bonding is simple, successful bonding depends on appropriate selection of bonding materials, good preparation of bonding surfaces, optimization of bonding conditions and inspection of bonded samples. These are explained in the example of silicon–glass anodic bonding.

Material Selection

Silicon material is normally of standard wafer sizes and thicknesses. As the anode part of the bonding pair, the silicon should be low in resistivity. However, some applications require an insulating layer to prevent electrical leakage in silicon. In this case, a thin layer of silicon dioxide or silicon nitride should be deposited on the silicon surface. The insulating layer does not prevent anodic bonding of silicon with glass. However, a thicker insulating layer can increase the bonding time dramatically. For example, for a 0.5 μm thick oxide layer a bonding time of approximately five times longer is required [2]. For anodic bonding with glass, p-type silicon wafers (boron doped) are preferred, as a high electrostatic field is much easier to build up, particularly at low temperature, at the silicon side of a silicon–glass interface for p-type silicon than for n-type silicon (phosphor doped) [6]. However, for high-temperature anodic bonding ($> 400\,^{\circ}$C) the doping type of silicon is no longer a factor.

Borosilicate glasses such as Corning 7740 Pyrex glass, Schott Borofloat 33 glass and Hoya SD-2 glass are commonly used for anodic bonding with silicon. They are of almost the same coefficient of thermal expansion (CTE) as that of silicon. They also have the necessary electrical conductivity at the bonding temperature. However, some special applications require the glass to be high in resistivity (Corning 7070 glass) or high in spectral transmission (Pilkington CMZ glass). Glasses that have a CTE different from silicon or a low concentration of mobile positive ions are still able to be anodically bonded with silicon, but with special process conditions. For example, to bond Corning 7070 glass with silicon, much higher temperature and voltage are needed. To bond a Fisher glass slide whose CTE is very different from that of silicon, the bonding temperature has to be much lower (150 °C) and bonding time is much longer (60 min) [6].

Preparation of Bonding Surfaces

A well-polished surface is essential for a successful bonding. The average surface roughness (R_a) should be less than 5 nm. Commercial silicon wafers and glass substrates are normally polished to this standard. Although anodic bonding is fairly tolerant to particles and contaminations on the bonding surfaces, they still need to be cleaned prior to anodic bonding, unless the wafers are straight out of the box. A study has demonstrated that a $H_2SO_4 + H_2O_2$ acidic clean of bonding surface can significantly reduce the bonding time compared to a simple cleaning with acetone [6]. Thorough cleaning is even more important for structured wafers. Whether the bonding surfaces are hydrophobic or hydrophilic can also have an influence on bonding. At low temperature, a hydrophilic surface is easier to bond than a hydrophobic surface. However, such difference disappears at high bonding temperature [7].

Process Parameters

The basic process parameters for anodic bonding are temperature, voltage, clamping pressure, environment and bonding time.

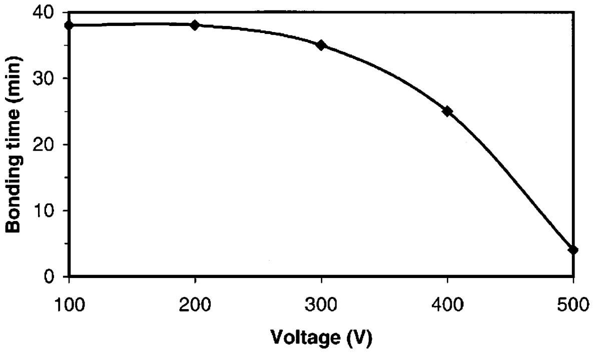

Anodic Bonding, Figure 5 Bonding time as a function of applied voltage for silicon–glass anodic bonding

- Bonding temperature is normally in the range 300 – 500 °C. Higher temperature promotes better mobility of positive ions in glass, resulting in a faster bonding process. However, the temperature must be below the softening point of glass (glass transition temperature).
- Typical bonding voltage is in the range of 200 to 2000 V. High voltage helps to drive the positive ions in glass towards the cathode, leaving a negatively charged region at the bonding interface. The electrostatic force at the interface pulls the silicon and glass in direct contact, resulting in oxygen ions in glass oxidizing the silicon to form strong chemical bonds. Figure 5 shows the bonding time as a function of bonding voltage for anodic bonding of Corning 7740 glass with silicon [6]. It is apparent that higher voltage results in a shorter bonding time. For glasses with low concentration of sodium ions (Na^+), both high temperature and high voltage are necessary for a successful bonding. Higher voltage is also needed for thicker glass. High voltage also helps to reduce the temperature necessary for a good bonding.
- Standard silicon wafers are not completely flat but with $\pm 20 - 40$ μm bowing and wrapping. In order to make sure the silicon wafer is in intimate contact with the glass, a pressurized clamping is necessary. The clamping pressure is normally below 50 N.
- Anodic bonding can be carried out either in vacuum, or in a gaseous or atmospheric environment. However, bonding in air is much faster than in vacuum or in an inert gas environment [7]. This may be due to the oxygen in air which helps the oxidation process during anodic bonding. However, many applications require anodic bonding to be carried out in vacuum.
- Bonding time is typically 1–5 min for Corning 7740 glass and silicon. For special glasses, the bonding time may be longer. As mentioned before, both bonding temperature and voltage can influence the bonding time. After bonding, there is a cooling time. The cooling can be a few minutes with the help of purging inert gas. However, the cooling should be slow for materials with large difference in CTE.

Inspection and Testing

The bonding process can be visually monitored through the glass. Initially there will be an interference fringe pattern when the silicon and glass are in contact because of the microscopic gaps between them. As the bonding progresses the interference pattern recedes gradually, until a uniform color is seen across the whole bonding surface. Any defects in the bonding will show as voids at the bonding interface. Better inspection of bonding quality can be achieved by scanning acoustic microscopy (SAM). SAM can detect any loose contact at the bonding interface independent of visual errors.

The bonding strength can be tested in different ways, such as pressure testing, pull testing, shear testing and bending testing [2]. The pull test has demonstrated bonding strength in the range 10 – 20 MPa, which is greater than the fracture strength of glass. The upper limit of bonding strength is difficult to estimate, as the break in the pull test always occurs in the glass, not at the silicon–glass interface. However, for imperfect bonding, the bonding strength is poor and the glass often breaks along the boundary of voids.

Although anodic bonding can be done simply with a hot plate and a DC power supply, reliable and reproducible anodic bonding can only be performed with purpose-built systems. There are commercially available wafer bonders. With commercial systems, the bonding process can be either manual or automatic. The bonding is performed in a chamber of either vacuum or filled with gases. One of the key issues in anodic bonding is the alignment when both the silicon and glass have some fabricated microstructures. The alignment process in a commercial wafer bonder can be carried out either off-line or in situ. The in situ alignment is advantageous because high-accuracy alignment (± 5 μm) occurs only when the process temperature is reached, thus avoiding differential thermal expansion effects which can compromise alignment. It enables the user to make in situ adjustments and visual confirmation before finally committing to making the bond.

Key Research Findings

Anodic bonding is relatively simple in principle and has been well developed over the last few decades. Research in this area has been very much focused on solving practical and application-specific issues. One of the practi-

cal issues is dealing with anodic bonding of silicon–glass assemblies with shallow cavities. This is often encountered in microfluidic systems where microchannels are of high lateral-to-depth aspect ratio. Anodic bonding can cause the microchannels to collapse due to high electrostatic force at the bonding interface. Theoretical and experimental study indicated that the collapse can be avoided as long as the following condition is satisfied [8]:

$$\varepsilon_a V^2 a / E_{eff} d^3 < 1$$

where ε_a is the permittivity of air, V is the applied voltage for anodic bonding, E_{eff} is a material constant which characterizes the elastic stiffness of the materials, a is the half width of the channel and d is the channel depth. A similar problem happens when packaging pressure sensors, micropumps and accelerometers by anodic bonding. Most of these devices have micromachined silicon membranes, diaphragms or suspended beams. These micromechanical structures may stick to the glass when they are too flexible and too close to the bonding interface.

Although anodic bonding is a low-temperature process compared to fusion bonding which requires temperatures up to 1200 °C, the bonding process can still induce thermal residual stress in the silicon–glass assembly, causing bowing of the bonded wafer. The thermal expansion of Pyrex glass is not a constant but changes with temperature. The higher the bonding temperature the larger the mismatch between silicon and glass. For Corning 7740 Pyrex glass, the crossover point with silicon (where the thermal expansion of silicon is exactly the same as that of Corning 7740 glass) is around 300 °C. Experiments showed that bonding made at this temperature can be maintained flat within $\pm 5\,\mu m$ [3]. The crossover point is also dependent on the thickness of glass. Experiments indicated that for 0.5 mm thick glass (Corning 7740) the crossover temperature is at ~ 315 °C, while it becomes ~ 260 °C for 1.5 mm thick glass [7].

It is known that glass cannot be anodically bonded to glass. However, research has found that this can be realized by depositing an intermediate layer. The intermediate layer can be polysilicon, amorphous silicon, silicon nitride or silicon carbide [9]. This has opened an easy route to construct glass-based microfluidic systems which are widely used for capillary electrophoresis. Other investigations into anodic bonding have been on oxygen release into sealed cavities during bonding or proper seals for thin metal films which act as lead through electrodes [3].

Future Directions for Research

Anodic bonding is a fairly mature technique. Many basic issues have been dealt with. Future researches will mostly focus on widening its applications, particularly in microelectronic and microsystem (MEMS) packaging. Packaging can significantly influence the performance of final devices and systems. Therefore, anodic bonding has to be integrated as part of the manufacturing process and its influence should be fully taken into account at the design and manufacturing stages.

Cross References

► Wafer Bonding

References

1. Wallis G, Pomerantz DI (1969) Field assisted glass–metal sealing. J Appl Phys 40(10):3946–3949
2. Obermeier E (1995) Anodic wafer bonding. Electrochem Soc Proc 95-7:212–220
3. Roger T, Kowal J (1995) Selection of glass, anodic bonding conditions and material compatibility for silicon–glass capacitive sensors. Sens Actuators A46–47:113–120
4. Cao E, Gavriilidis A, Cui Z (2002) Application of micro-engineered reactors in chemical engineering. MST News 3/02: 14–16
5. Acero MC, Plaza JA, Esteve J, Carmona M, Marco S, Samitier J (1997) Design of a modular micropump based on anodic bonding. J Micromech Microeng 7:179–182
6. Lee TMH, Lee DHY, Liaw CYN, Lao AIK, Hsing IM (2000) Detailed characterisation of anodic bonding process between glass and thin-film coated silicon substrates. Sens Actuators 86:103–107
7. Cozma A, Puers B (1995) Characterization of the electrostatic bonding of silicon and Pyrex glass. J Micromech Microeng 5:98–102
8. Shih WP, Hui CY, Tien NC (2004) Collapse of microchannels during anodic bonding: theory and experiments. J Appl Phys 95(5):2800–2808
9. Berthold A, Nicola L, Sarro PM, Vellekoop MJ (2000) Glass-to-glass anodic bonding with standard IC technology thin films as intermediate layers. Sens Actuators A82(1-3):224–228

Anthrax

Definition

Anthrax is an acute infectious disease caused by the spore-forming bacterium *Bacillus anthracis*. Anthrax most commonly occurs in wild and domestic lower vertebrates (cattle, sheep, goats, camels, antelopes, and other herbivores), but it can also occur in humans when they are exposed to infected animals or tissue from infected animals.

Antibody

Definition

Antibodies are immune system-related proteins called immunoglobulins. An important component of the immune system, antibodies are found in the blood of all vertebrates. The synthesis, or manufacture, of antibodies is initiated when a foreign substance, referred to as an antigen, enters the body. Lymphocyte cells respond to the foreign substance by making an antibody with a molecular arrangement that fits the shape of molecules on the surface of the substance so that the antibody combines with it. Common antigens are the protein components of bacteria and viruses.

Antigen

Definition

An antigen is any substance that causes the immune system to produce antibodies against it. An antigen may be a foreign substance from the environment such as chemicals, bacteria, viruses, or pollen. An antigen may also be formed within the body, as with bacterial toxins or tissue cells.

Aperiodic AC Field

► Unbalanced AC field

Aperiodic Electrophoresis

Synonyms

Nonlinear electrophoresis; Field-dependent electrophoretic mobility

Definition

Aperiodic electrophoresis refers to the use of an unbalanced AC field to separate charged polarizable particles due to the Stotz–Wien effect of field-dependent electrophoretic mobility.

Cross References

► Electrokinetic Motion of Polarizable Particles
► Electroosmotic Flow (DC)
► AC Electro-Osmotic Flow
► Electrophoresis
► Induced-Charge Electrophoresis
► Nonlinear Electrokinetic Phenomena
► Unbalanced AC field
► Stotz–Wien Effect

Apoptosis

► Microfluidics for Studies of Apoptosis

Apparent Slip

► Boundary Slip of Liquids

ARDE

► Aspect Ratio Dependent Etching

Arnoldi Algorithm

► Arnoldi-Based Model Order Reduction

Arnoldi-Based Macromodeling

► Arnoldi-Based Model Order Reduction

Arnoldi-Based Model Order Reduction

Synonyms

Arnoldi-based macromodeling; Arnoldi algorithm

Definition

Arnoldi-based algorithm is a classical Krylov-subspace-based Model Order Reduction technique. It reduces the dimension of the spatially semi-discretized form of the original governing PDEs using moment-matching of transfer functions.

Cross References

► Model Order Reduction (MOR)
► Macromodels
► Macromodel

Artificial Atom

► Quantum Dot

Artificial Muscle Materials

► Piezoelectric Materials for Microfluidics

Artificial Neural Networks

Synonyms

ANN

Definition

An artificial neural network is an information processing paradigm inspired by way the human nervous system processes information. It consists of an interconnected group of processing elements (neurons) which can exhibit a complex global behavior, determined by the network topology (the scheme used to connect elements together), and the algorithm (the rules) employed to specify the values of the weights connecting the nodes, the connections between the neurons. Based on *training rules* (whereby the weights of connections are adjusted on the basis of presented patterns), ANNs can be trained to generate an arbitrary number of outputs in response to an arbitrary number of inputs.

Cross References

► Model Order Reduction (MOR)
► Neural Network

Aspect Ratio Dependent Etching

Synonyms

ARDE

Definition

ARDE is the phenomenon of the etching rate related to the aspect ratio. The larger the aspect ratio, the lower the etching rate.

Cross References

► RIE Lag
► Anisotropic Etching
► Reactive Ion Etching (RIE)
► Plasma Etching

Assay

Synonyms

Test

Definition

A method for the determination of the level of a given analyte in a given sample or set of samples.

Cross References

► Lab-on-a-Chip Device for Chemical Analysis

Assembly of Nanoparticles Into Controlled Nanostructures

► Nano-Particle Controllable Assembly

Atomic Force Microscope (AFM)

Definition

Material characterization technique which uses a tip (typically silicon) on the end of a cantilever to determine the surface profile of a material. As the cantilever is moved across the surface, a laser is reflected off of the backside. As the cantilever is deflected, the change in laser beam position is detected by a photodetector. This information is then used to create a three-dimensional image of the surface, with atomic-scale resolution.

Cross References

► AFM
► Fabrication of Self-Assembled Catalytic Nanostructures

Atomistic Computer Simulation

► Molecular Dynamics Simulation Method

Atomistic Deposition

► Chemical Vapor Deposition for Film Deposition

Atwood Number

Definition

A dimensionless number that describes the density difference between two adjacent fluids with a common interface.

Cross References

► Piezoelectric Microdispenser

Background Subtraction

Definition

With background subtraction the background in an image is removed. Thus it is done when a very uniform background is needed (e. g. for ►PIV algorithms). Hereby only relatively sharp objects remain and the background is removed with morphological algorithms. A non-uniform background results from non-uniform illumination and/or image capturing.

Backpressure

► Pump Head

Band Broadening

► Hydrodynamic Dispersion

Bead Based Assays

► Bead Based Microfluidic Platforms

Bead Based Microfluidic Platforms

SUNG YANG[1], JEFFREY D. ZAHN[2]
[1] Department of Mechatronics, School of Information and Mechatronics, Gwangju Institute of Science and Technology (GIST), Gwangju, Buk-gu, Republic of Korea
[2] Department of Biomedical Engineering, The State University of New Jersey, Piscataway, NJ, USA
syang@gist.ac.kr, jdzahn@rci.rutgers.edu

Synonyms

Bead based assays; Cytometric bead immunoassay; Particle manipulation

Definition

Bead based microfluidic platforms may be used for either particle manipulation or bead based sensing especially in cytometric bead based immunoassays. Bead based microfluidic platforms are often geared to biomedical research and diagnostics particularly in protein diagnostics through immunosorbent assays. For instance, in bead based immunosorbent assays, antigen–antibody reactions are induced on the surface of the bead in the solution and then, the binding event of the antigen–antibody is monitored by fluorescent labeling of either a secondary antigen or antibody. These assays are used to detect biomolecules by utilizing specific ligand-receptor binding reactions. The ligand-receptor binding events may then be quantified by quantifying changes in bead properties using either optical or physical sensing mechanisms. In order to optimize bead based reactions, there has also been considerable interest in developing microfluidic systems for efficient bead handling and manipulation.

Overview

Recently, there have been enormous efforts to transform conventional biological analysis methods into more efficient or sensitive assays through the use of Lab-on-a-Chip platforms. One of these representative efforts is found in the increased development of bead based microfluidic platforms [1]. The majority of bead based microfluidic platforms have been developed to detect specific biomolecules in an unknown sample by utilizing a ligand-receptor binding event. Bead based platforms have several potential advantages over conventional techniques. Bead based microfluidic platforms provide a larger binding surface area to sample volume ratio and thus may yield an improvement in the detection limit of a specific biomolecule over conventional techniques by allow-

ing more available binding surface area per unit volume. This change in relative surface to volume ratio may also limit nonspecific binding and background interference due to other contaminating molecules which may also lead to improvements in detection limits of the desired analyte. In addition, bead based microfluidic platforms require less consumption of analyte sample as well as reagent volumes which may lead to less expensive assay platforms. There have been several reports which describe bead based microfluidic platforms for biomolecule detections [2–6] as well as novel methods which may be used for multiple particle manipulation and steering [7] within microfluidic environments. In the basic methodology section, the standard enzyme-linked immunosorbent assay (ELISA) is briefly introduced as a working principle for bead based microfluidic sensing platforms and the fundamentals of enzyme kinetics for ligand-receptor binding is also discussed as a theoretical background. Detailed discussions of case studies are presented in the Key Research Finding section.

Basic Methodology

ELISA (Enzyme-Linked Immunosorbent Assay)

The enzyme-linked immunosorbent assay (ELISA or EIA) is one of the most commonly utilized methods used in protein detection and analysis. An ELISA can provide quantitative information about antigen or antibody concentrations in solution by comparing the results of an unknown sample assay to a calibration curve based on known standard concentrations of the antibody or antigen of interest. Although, there are many variations in how ELISA may be performed, three of the most commonly used representative methods are discussed here (Fig. 1). The choice of which ELISA technique is used often depends on the nature of the antigen or antibody of interest, the availability of appropriate binding pairs, and the specificity of only the antigen of interest to a monoclonal antibody.

1. Indirect ELISA
   The concentration of an antibody (especially in blood plasma) can be quantitatively determined through the use of the indirect ELISA technique. In the indirect ELISA, an antigen is pre-coated within a microtiter well. Then a solution (e. g., blood plasma) containing the primary antibody of interest is added to the antigen coated microtiter well and allowed to incubate so that the two components may bind with each other. Afterwards a washing step removes any free primary antibody. Next, an enzyme-linked secondary antibody is added to produce a binding between the primary and secondary antibodies. The enzyme linked antibody often contains the catalytic protein of a horseradish peroxidase which cleaves a colorimetric substrate (such as *o*-phenylenediamine dihydrochloride) causing a color change in the substrate solution which may be monitored in a spectrophotometer by the optical density of the transmission spectra at the appropriate wavelength of light. Since the substrate produces a color change which is proportional to the amount of enzyme present through the binding reactions, the measured color change may be correlated with the concentration of the antibody of interest initially present in the solution which was analyzed. The concentration of antibody of interest can be determined by comparing the color change of the unknown sample against standards of known concentration.
2. Sandwich ELISA
   In a related technique, an antigen concentration can be determined by using a sandwich ELISA. In this technique, the antibody which binds to the antigen of interest is pre-coated in the microtiter well. Next, the sample containing the antigen of interest is added and allowed to bind with the pre-coated antibody. After the well is washed, an enzyme-linked secondary antibody specific to the antigen of interest is added and allowed to bind with the bound antigen. After washing any free secondary antibody away, the colormetric substrate for the enzyme is added. Again, by measuring the change of color in the enzyme reaction, as discussed before, the concentration of antigen can be determined by comparison with the color shifts of a predetermined standard calibration curve.
3. Competitive ELISA
   Another method to determine the concentration of an antigen is through the use of a competitive ELISA. In the competitive ELISA, a primary antibody is first incubated in a solution containing the antigen of interest. Through antibody-antigen binding the free antigen is captured by the antibody in solution. The larger the antigen concentration in the initial solution, the less free primary antibody that will be left after the antigen–antibody binding reaction. Next, the antigen–primary antibody mixture is added into an antigen pre-coated microtiter well. Now, only the free primary antibody left in the mixture will be able to bind with the antigen within the microtiter well. After a washing step, the antigen–primary antibody complex in the solution is removed and an enzyme-linked secondary antibody is added to produce a binding between the primary and secondary antibodies. As a final step, the colormetric substrate is added to the microtiter well and the amount of color change is measured and correlated to the known calibration curve. In the competitive assay, however, the concentration of the antigen of interest

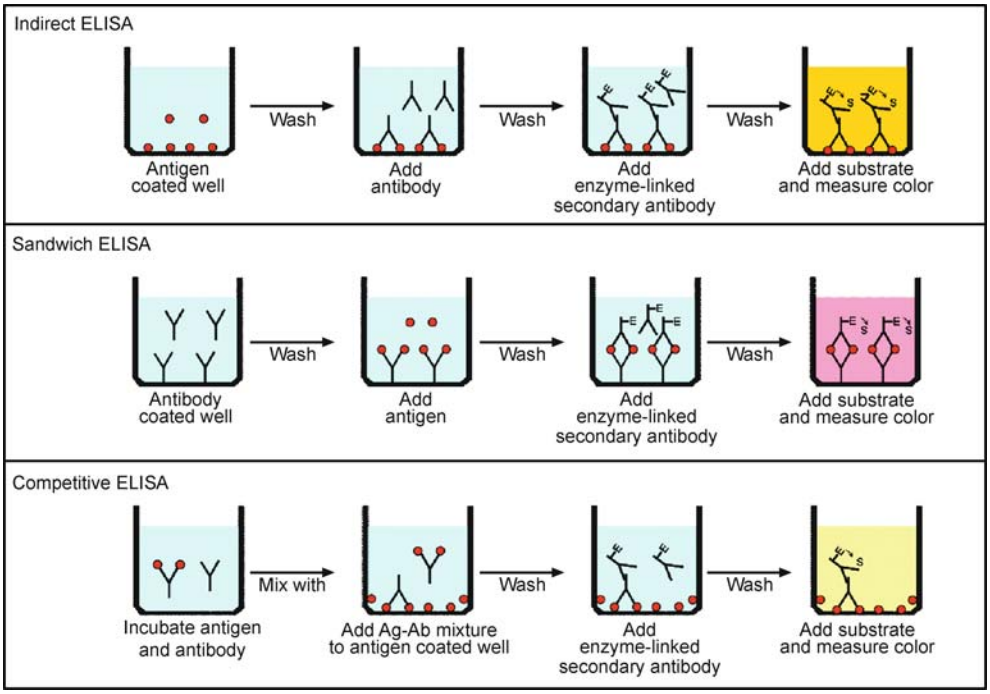

Bead Based Microfluidic Platforms, Figure 1 Variations in the ELISA technique. Each assay can be used not only for qualitative but also for quantitative determination of the presence of antigen or antibody by comparison with standard curves prepared with known concentrations of antibody or antigen. The indirect ELISA is useful to determine antibody concentrations in solution. On the other hand, the sandwich ELISA is useful in determining antigen concentrations. In the competitive ELISA, the concentration of antigen is inversely proportional to the color produced by the substrate because the competitive ELISA is an inhibition-type assay

in the original sample is inversely proportional to the amount of color change because the antigen in solution reduces the amount of free antibody which is able to bind to the antigen coated in the microtiter well.

Key Research Findings

Many research groups have pursued bead based immunosorbent assays within microfluidic platforms. Here, instead of coating antigen or antibodies within microtiter wells, they are coated onto the surface of micron sized beads which act as the reaction vessels. Sato et al. [2] demonstrated a bead based immunosorbent microfluidic platform (Fig. 2). In their system, they used polystyrene beads for the solid phase reaction in order to maximize the available surface area for antigen–antibody binding. First, the beads were introduced into the microfluidic channel, which was designed with a barrier to trap the beads at a specific location within the device and create a packed bed. Next, an antigen (human secretory immunoglobulin A (s-IgA)) was infused through the microdevice to allow nonspecific adsorption of the antigen to the packed beads. After the unbound antigen is washed away, an antibody (anti-s-IgA) which had been conjugated with colloidal gold was infused to produce the antigen–antibody binding reaction. After a final wash step to remove the unbound antibody, the amount of binding between the antigen and antibody was detected by a thermal lens microscope (TLM). The TLM uses an excitation laser and a probe laser which is focused through the objective lens. The colloidal gold absorbs some of the excitation light and the rest of the energy is dissipated in the solution as thermal energy. The temperature change is monitored by a change in the solution refractive index monitored through a thermal lens. The larger the amount of colloidal gold, the lower the temperature change in the solution and thus a smaller change in the refractive index of the solution so the initial antigen concentration may be correlated to the temperature change in the solution monitored by the thermal lens. Based on this procedure, they were able to obtain a thermal lens signal down to 1 μg/ml of antigen (s-IgA) concentration with a linear dependency of thermal lens signal on the initial antigen concentration. In addition, the time needed for the antigen–antibody binding reaction was reduced by 90 fold which resulted in a shortening of the overall analysis time to less than 1 hr compared to 24 h for the standard procedure.

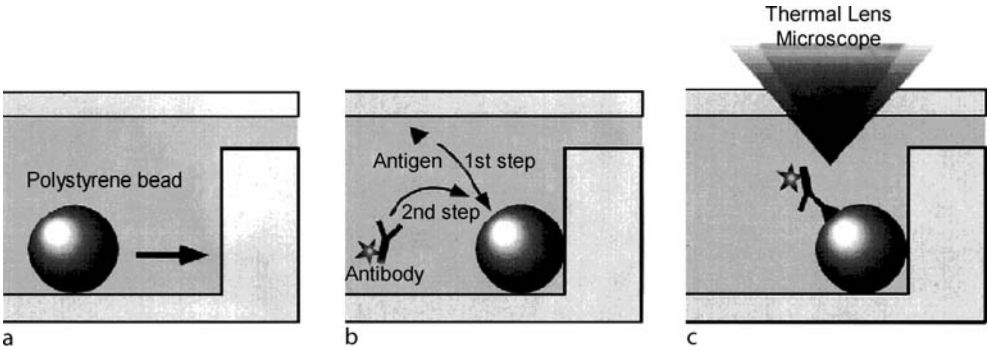

Bead Based Microfluidic Platforms, Figure 2 Schematic illustrations of integrated immunosorbent assay. (**a**) bead in (**b**) antigen and antibody binding (**c**) measurement [2]

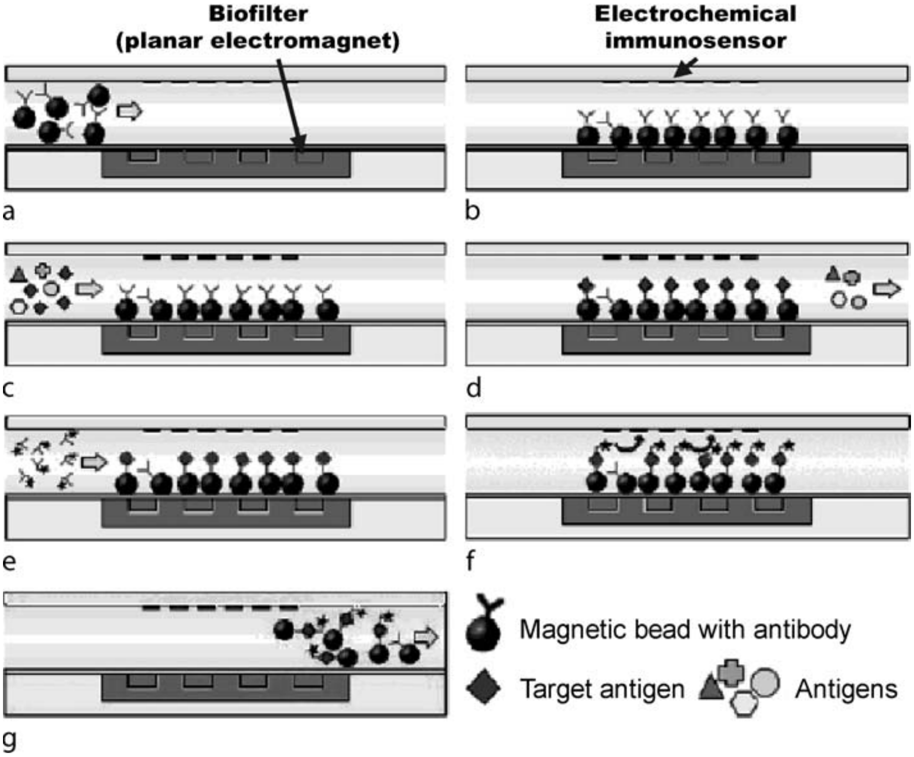

Bead Based Microfluidic Platforms, Figure 3 Conceptual illustration of bio-sampling and immunoassay procedure using magnetic bead approach: (**a**) injection of magnetic beads; (**b**) separation and holding of beads; (**c**) flowing sample; (**d**) immobilization of target antigen; (**e**) flowing labeled antibody; (**f**) electrochemical detection after adding enzyme substrate; and (**g**) washing out magnetic beads and ready for another immunoassay [3]

Next, Choi et al. [3] reported an integrated microfluidic biochemical detection system for rapid low-volume immunoassays. They utilized magnetic core beads as the solid support phase for the capture antibodies, and as carriers of captured target antigens. In order to detect target antigens, the working principle is based on a sandwich ELISA (Fig. 3). The antibody coated beads are first infused into the microfluidic channel with an integrated electromagnet. Once the magnetic beads are introduced, then they are attracted to the electromagnet and held in place. While holding the primary antibody coated magnetic beads within the magnetic field, target antigens are infused into the microfluidic channel. The antigen–antibody binding occurs while other free antigens not specific to the antibody used are washed away with the continuous flow. Next, enzyme-linked secondary antibodies are infused to produce a binding event between the bound antigen and secondary antibodies. The microfluidic channel is

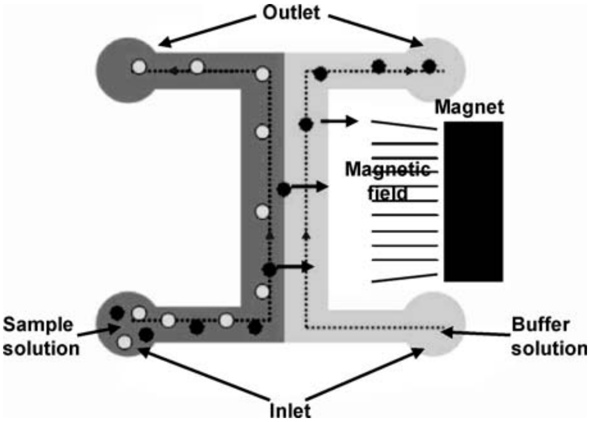

Bead Based Microfluidic Platforms, Figure 4 Proposed detection principle. Microbead conjugated with superparamagnetic nanoparticles (•). Unconjugated microbead (○) [4]

then washed to remove all unbound secondary antibodies. As a final step, a substrate solution, which reacts with the conjugated enzyme on the secondary antibody, is injected into the microfluidic channel. Electrochemistry is used as a detection method. To demonstrate this concept, they have used alkaline phosphatase (AP) and *p*-aminophenyl phosphate (PAPP) as the antibody bound enzyme and electrochemical substrate, respectively. AP converts PAPP to *p*-aminophenol (PAP). Thus, by applying an oxidizing potential to the patterned detection electrodes, PAP is converted into 4-quinoneimine (4-QI) by a 2-electron oxidation reaction. Therefore, by measuring the electrical current change by amperometry, it is possible to determine the concentration of the enzyme (AP) bound to the magnetic beads. By using mouse IgG as an analyte and applying the electrochemical detection principle, they were able to show a detection limit within their device of around 100 ng/ml of mouse IgG. Also, the total time required for an immunoassay was less than 20 min including sample incubation time, and sample volume wasted was less than 50 μl during five repeated assays.

Another good example of a bead based immunoassay is based on superparamagnetic nanoparticles (50 nm diameter) handling in microfluidic environments which was reported by Kim et al. [4]. In their report, the binding of antigen conjugated with superparamagnetic nanoparticles to antibody coated fluorescent microbeads (1 μm diameter) and the subsequent deflection of the magnetic nanoparticle bound fluorescent microbeads within a magnetic field were used as the signal for measuring the presence of analyte. To test their principle, the target analyte sample was conjugated with the superparamagnetic nanoparticles. The fluorescent microbeads were conjugated with antibodies to the analyte of interest by nonspecific adsorption. Then, the target nanoparticle conjugated analyte and the antibody coated microbeads are mixed together to produce antigen–antibody binding. Since the target analyte molecules are conjugated with the superparamagnetic nanoparticles, the fluorescent microbeads will be indirectly conjugated with the nanoparticles. The total amount of the superparamagnetic nanoparticles bound with the microbeads depends on the concentration of the target antigen. As shown in Fig. 4, a buffer and sample solution are both infused into a converging channel geometry where the sample solution contains the fluorescent microbeads with the bound superparamagnetic nanoparticles. A permanent magnet is placed on the buffer side of the microchannel geometry. Due to the presence of the magnetic field gradient, the nanoparticle bound microbead will be deflected towards the magnet and the deflection force will depend on the number of superparamagnetic nanoparticles presented on the microbeads. In this study, Kim, et al., assumed that if the concentration of the superparamagnetic nanoparticles bound to the fluorescent microbead increases, the velocity of the bead towards the magnet will increase. This implies that the bead velocity in the microchannel may be correlated back to the initial concentration of the target analyte. In addition, since the microbeads have specific optical properties, a multiplex analysis is also possible. Using this method, the magnetic force-based microfluidic immunoassay was successfully applied to detect both rabbit IgG and mouse IgG as model analytes. The detection limit of the system was determined to be 244 pg/ml and 15.6 ng/ml for rabbit IgG and mouse IgG, respectively.

Yang et al. [5] reported a novel concept in bead handling and serial reaction processing using a technique named "particle cross over" in microfluidic channels to accomplish continuous cytometric bead processing within a microfluidic device for bead based sensing platforms. The operating principle of the continuous biosensing is based on adapting the Zweifach–Fung effect [8, 9] in a novel manner. The Zweifach–Fung effect has shown that when a particle approaches a bifurcating region that all particles will flow into the daughter branch with the higher flow rate if the flow rate ratio between the two branches are greater than 2.5 : 1 when the particle diameter approaches the vessel diameter. Utilizing this mechanism involves moving cytometric beads through different regions within the microfluidic device where the bead is exposed to different solution environments so that antigen–antibody binding, washing and detection can occur without any significant sample dilution. When a micron-sized bead approaches a bifurcating region of microfluidic channel, it is possible for the bead to cross over from a carrier

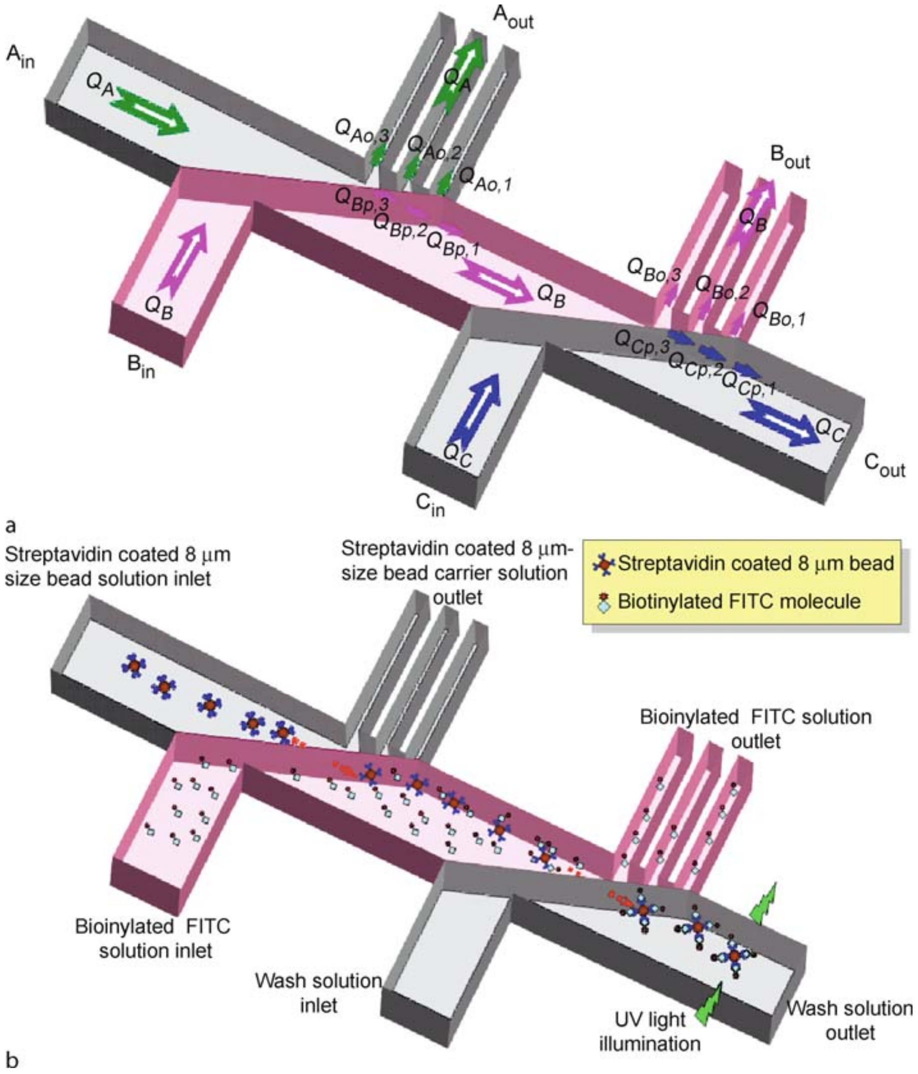

Bead Based Microfluidic Platforms, Figure 5 (**a**) Conceptual drawing of microflow structures within a microfluidic network for the particle cross over within microfluidic channels. It is possible to achieve the particle cross over from one to another fluid streams without losing particles into multiple parallel channels. (**b**) Schematic sketch of a representative example of continuous biosensing using the particle cross over mechanism. The concentration of biotinylated FITC molecules can be determined by measuring the fluorescence intensity of the biotinylated FITC bound streptavidin coated 8 μm-diameter particle at the detection window using an epifluorescence microscope [5]

fluid into a recipient fluid streams by precisely controlling flow rate ratio between the two downstream channels. For instance, as shown in Fig. 5a, a microfluidic device can be designed to have a 1 to 1 of total flow rate ratio ($Q_A = Q_B = Q_C$) at each bifurcation region. Thus, all three fluid streams which are infused from each inlet can be transported into each designated outlet ($A_{in} \rightarrow A_{out}$, $B_{in} \rightarrow B_{out}$, $C_{in} \rightarrow C_{out}$). At the same time, it is also possible to design the outlets as a series of multiple parallel channels at each bifurcation region so that a micron-sized particle infused from the inlet is not able to follow its original fluid stream of the carrier fluid into the outlet and will cross over into the recipient fluid stream (A→B) because of the Zweifach–Fung effect. In this study, a streptavidin coated 8 μm-diameter particles and biotinylated FITC dye were used as a test system for demonstrating continuous biosensing in microfluidic channels. The biotinylated FITC molecules produce fluorescence light (532 nm) under UV light exposure due to the presence of the FITC (fluorescence dye). Thus, the higher concentration of biotinylated FITC in solution, the more biotinylated FITC which is bound to a bead through biotin-streptavidin binding, the higher the fluorescence intensity which can be detected. Figure 5b represents a concep-

tual sketch of continuous biosensing based on the particle cross over mechanism. Once the streptavidin coated 8 μm-diameter beads in buffer media travel toward the 1st bifurcation region, then they can cross over into the biotinylated FITC solution without significant mixing of the two fluid streams. Once the streptavidin coated bead enters into the biotinylated FITC solution, the binding between the biotinylated FITC molecules and the streptavidin coated 8 μm-diameter beads occurs within the main channel. In addition, no significant serial dilution effect on biotinylated FITC solution is expected as would be expected by simply mixing the fluids together through a converging channel geometry and passive micromixing region because the old fluid infused from upstream of the main channel is removed at the bifurcation by maintaining a 1 to 1 total flow rate ratio between the two fluid streams. At the 2nd bifurcation, the biotinylated FITC bound streptavidin beads can then cross over to a wash solution by producing the same microflow structures. Finally, the fluorescence intensity of the biotinylated FITC bound streptavidin beads can be measured at a downstream detection window by an epifluorescence microscope. The fluorescence intensity of the beads can be assumed to be proportional to the concentration of biotinylated FITC dye in the solution. Since beads are continuously infused into the device from the bead inlet, it is expected that the bead fluorescence intensity will change in response to changes in biotinylated FITC dye concentration which can be tracked by plotting the bead fluorescence intensity as a function of time. Thus, the system can dynamically respond to changes in analyte concentration allowing continuous biosensing. Based on this concept, Yang, et al. demonstrated that the fluorescence intensity of the bead measured is linearly proportional to the analyte (biotinylated-FITC) concentration. The detection limit of the device was determined as a 50 ng/ml of biotinylated FITC concentration.

Another application area of bead based microfluidic platforms includes bead based DNA detections. Han et al. [6] reported quantum-dot-tagged microbeads for multiplexed optical coding of DNAs. Multicolor optical coding for DNA hybridization assays has been achieved by embedding different-sized quantum dots into polymeric microbeads at precisely controlled ratios. And then, as shown in Fig. 6, probe oligos were conjugated to the beads by cross linking. The target oligos were detected with Cascade Blue. After hybridization, nonspecifically bonded molecules and excess reagents were removed by a washing process. For multiplexed assays, they have optimized the oligo lengths and sequences so that all probes had similar melting temperatures ($T_m = 66\,°C - 99\,°C$) and hybridization kinetics (30 min). As a result, they have shown that the coding and target signals can be simultaneously read at the single-bead level with high uniformity and reproducibility. Also, they have shown that bead identification accuracies were as high as 99.99 % under favorable conditions.

A final example of bead based microfluidic platforms is a novel concept in particle handling and steering. Armani et al. [7] recently reported very attractive results on steering multiple particles simultaneously within microfluidic environments. They combined electrokinetic based microfluidic platforms with vision-based feedback control to independently steer multiple particles with micrometer accuracy in two spatial dimensions. In their method, they have steered particles by creating an electroosmotic flow field that carries all the particles from where the particles are to where particles should be at the next time step. The flow is created by the biasing of multiple electrodes arranged around the active test area. In order to steer each particle independently, they constructed a vision-based feedback loop comprised of sensing, computation, and actuation to steer particles along user-input trajectories. Particle locations were identified in real-time by an optical system and transferred to a control algorithm that then determined each electrode voltage necessary to create the proper electroosmotic flow pattern to carry all the particles to their next desired locations. They have experimentally demonstrated that it is possible to steer not only neutral particles but also charged particles simultaneously by precisely controlling electroosmotic flow patterns. The neutral particles can be carried by the electroosmotic flow by controlling voltage applied on each electrode. The charged particles can be also steered by both electroosmotic and electrophoretic forces by controlling voltage applied on each electrode. For instance, as shown in Fig. 7, they were able to steer three yeast cells (5 μm diameter), which have a small surface charge (electrophoretic mobility $c = -23.3 \pm 6.9 \times 10^{-9}\,\mathrm{m^2V^{-1}s^{-1}}$) within an accuracy of less than 1 μm by controlling the potentials of eight electrodes. Since this type of particle steering permits noninvasive steering of any visible particle regardless of the charge status of particles, it is expected that this technique is useful for navigating beads and particles to localized sensors for cell sorting, sample preparation, and for combinatory testing of particle interactions with other particles, chemical species, and distributed sensors.

Future Directions for Research

Although a variety of technologies related to bead based microfluidic platforms are introduced here, there are still many challenges to producing efficient Lab-on-a-Chip bead based sensor technologies over the conven-

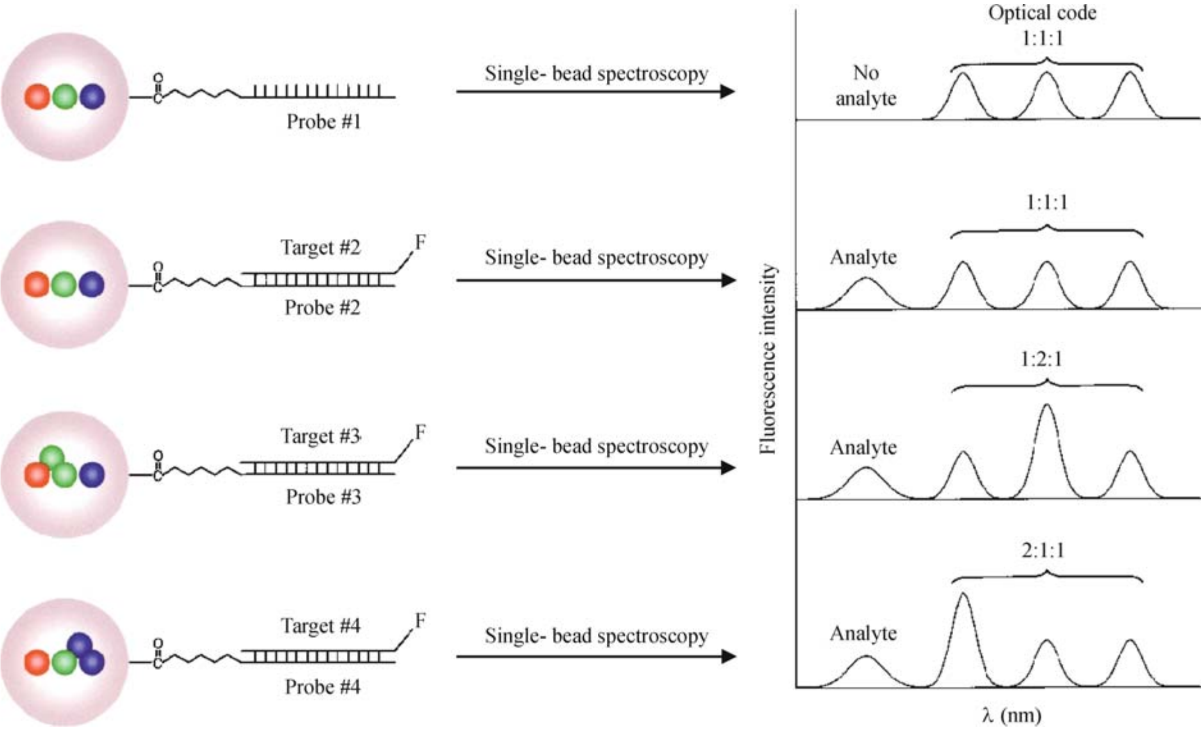

Bead Based Microfluidic Platforms, Figure 6 Schematic illustration of DNA hybridization assays using QD-tagged beads [6]

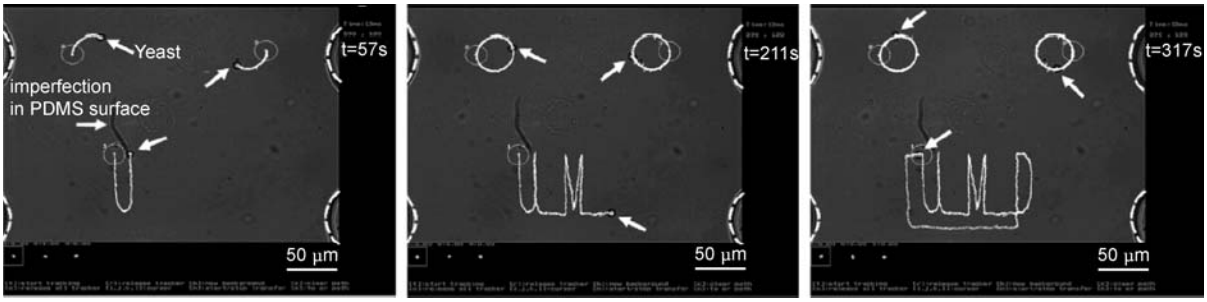

Bead Based Microfluidic Platforms, Figure 7 Steering of three yeast cells (5 μm diameter, Red Star, Giant Food) with small surface charge (electrophoretic mobility, $c = -23.3 \pm 6.9 \times 10^{-9}\ \mathrm{m^2V^{-1}s^{-1}}$) around two circles and a *UMD* path. The yeast cells are visible as small black dots with a white center (the three target cells are marked with a white arrow in each image), and the white curves are the trajectories that the target cells have traced out. The three beads are being steered to within an accuracy of one pixel (corresponding to less than 1 μm) [7]

tional sensing methods. For instance, although many bead based microfluidic immunosensing technologies have been demonstrated with faster throughput over conventional methods, these microdevices often still have higher concentration detection limits and higher variability when compared with the conventional macroscale methods. Thus, most laboratories still utilize standard ELISA protocols or more recently cytometric bead based flow cytometry assays. This implies that there still needs to be substantial improvement and standardization in the future development of these bead based platforms for truly realizing the promise of Lab-on-a-Chip bead based microfluidic sensing and handling platforms which can outperform the standard macroscale technologies.

Cross References

- ► Biosensors Using Magnetics
- ► Cell Sorting
- ► Lab-on-Chip Devices for Immunoassay
- ► Lab-on-Chip Devices for Particle and Cell Separation
- ► Sample Purification Using Magnetic Particles

References

1. Verpoorte E (2003) Beads and Chips: new recipes for analysis. Lab Chip 3:60N–68N
2. Sato K, Tokeshi M, Odake T, Kimura H, Ooi T, Nakao M, Kitamori T (2000) Integration of an Immunosorbent Assay System: Analysis of Secretory Human Immunoglobulin A on Polystyrene Beads in a Microchip. Anal Chem 72:1144–1147
3. Choi J-W, Oh KW, Thomas JH, Heineman WR, Halsall HB, Nevin JH, Helmicki AJ, Henderson HT, Ahn CH (2002) An integrated microfluidic biochemical detection system for protein analysis with magnetic bead-based sampling capabilities. Lab Chip 2:27–30
4. Kim KS, Park J-K (2005) Magnetic force-based multiplexed immunoassay using superparamagnetic nanoparticles in microfluidic channel. Lab Chip 5:657–664
5. Yang S, Ündar A, Zahn JD (2007) Continuous cytometric bead processing within a microfluidic device for bead based sensing platforms. Lab Chip 7(5):588–595
6. Han M, Gao X, Su JZ, Nie S (2001) Quantum-dot-tagged microbeads for multiplexed optical coding of biomolecules. Nature Biotechnol 19:631–635
7. Armani MD, Chaudhary SV, Probst R, Shapiro B (2006) Using Feedback Control of Microflows to Independently Steer Multiple Particles. J MEMS 15(4):945–956
8. Yen RT, Fung YC (1978) Effects of Velocity Distribution on Red Cell Distribution in Capillary Blood Vessel. Am J Physiol 235(2):H251–H257
9. Fung YC (1973) Stochastic Flow in Capillary Blood Vessels. Microvasc Res 5:34–48

Behavioral Model

Definition

The behavioral models are a set of equations derived directly from the underlying domain-physics. They are the most generic and effective forms describing the response of the system.

Bias Voltage

Definition

The application of a steady voltage to a system to improve its performance.

Cross References

► Sputtering for Film Deposition

Bifurcating Microchannel

► Flow Bifurcation in Microchannel

Bimorph

Definition

A structure composed of two active layers and one or more passive layers. Typically the active layers work through either thermal expansion, hygrothermal expansion, or piezoelectric expansion via an externally-applied electrical field. Bimorphs are used in the latter case to amplify the low maximum strain possible in piezoelectric materials while reducing the output force.

Cross References

► Unimorph
► Piezoelectric Valves

Biocatalytic Fuel Cell

► Biofuel Cell

Biochip

Synonyms

DNA array; Protein array; Cell array

Definition

► Microarray

Cross References

► Cell Culture (2D and 3D) on Chip
► Cell Patterning on Chip
► DNA Micro-arrays
► Droplet Dispensing
► Droplet Evaporation
► Evanescent-Wave Sensing
► Fluorescence Measurements
► Fluorescent Labeling
► Hydrophilic/Hydrophobic Patterning
► Lab-on-Chip Devices for Protein Analysis
► Methods for Surface Modification
► Microarray
► Supersonic Micro-Nozzles
► Proteomics in Microfluidic Devices
► Surface Tension, Capillarity and Contact Angle
► Van der Waals Interaction Forces

Biochip Printing

► Bioprinting on Chip

Bioengineering

► Biomimetics

Biofuel Cell

Synonyms

Biocatalytic fuel cell; Enzymatic fuel cell; Microbial fuel cell

Definition

Conceptually similar to a battery, a fuel cell is an electrochemical device that converts chemical energy stored in a fuel and an oxidant into electrical energy. The fundamental difference between a fuel cell and a battery is that fuel and oxidant are supplied from outside the reaction chamber and waste products are removed. Fuel cells that utilize biological catalysts are collectively termed biofuel cells. There is a common misinterpretation that biofuel cells are named as such because they use biological fuels, which is ambiguous as the same fuel (e.g., methanol) may originate from both biological and non-biological sources. A biofuel cell mimics electrochemical processes occurring in nature to harvest a useful electrical current, without the use of precious electrocatalysts such as platinum. There are two main categories of biofuel cells: microbial biofuel cells and enzymatic biofuel cells. Microbial biofuel cells utilize entire living cells or microorganisms combined with redox intermediates to catalyze the oxidation of a fuel. Enzymatic biofuel cells, on the other hand, catalyze the chemical reactions using biological redox enzymes that can be isolated and purified from suitable organisms, thus extracting the core part of the cell that enables catalytic activity.

Cross References

► Microfluidic Fuel Cells
► MEMS-Based Biosensor

Biognosis

► Biomimetics

Bioimmobilization

Definition

Bioimmobilization is the process of immobilizing biomolecules onto sensor surface to provide the biospecificity to the biosensor. Biospecificty is the property of the biorecognition membrane of the biotransducer that is conferred by the purposeful use of a bioactive receptor. The major purpose of bioimmobilization is to confer the molecular recognition and specificity inherent to the bioactive receptor to the biotransducer in a manner that maximizes the sensitivity of the physicochemical transducer that lies beneath. Amongst the various bioimmobilization approaches are:

- adsorption (physical, chemical and electrostatic),
- adsorption followed by covalent cross-linking,
- covalent tethering, and
- entrapment (physical or covalent) within host matrices (e. g. polymers, polymeric hydrogels and sol-gels).

Regardless of the specific linking chemistry and substrate employed, the key goals in all biomolecule immobilization strategies are:

- reproducible, high density coverage of the biomolecule on the substrate,
- the orientation of the biomolecule for efficient kinetics of the biological reaction,
- minimal background and non-specific adsorption to the support or substrate,
- improved sensitivity, and
- long term stability (retained bioactivity) of the immobilized biomolecule.

Cross References

► Impedimetric Biosensors for Micro and Nano Fluidics

Bio-Inspired Design

► Biomimetics

Biological Sensors

► Impedimetric Biosensors for Nano- and Microfluidics

Biomedical Microdevices

► Integrated Microdevices for Medical Diagnostics

B

Bio-MicroElectroMechanical Systems (BioMEMS)

► Droplet Based Lab-on-Chip Devices

Biomicrofluidics

► Electrokinetic Transport with Biochemical Reactions

Biomimesis

► Biomimetics

Biomimetics

DUSTIN HOUSE , DONGQING LI
Department of Mechanical Engineering,
Vanderbilt University, Nashville, TN, USA
dustin.l.house@vanderbilt.edu

Synonyms

Biomimicry; Bionics; Biognosis; Biotechnology; Bioengineering; Biophysics; Bio-inspired design; Biomimesis

Definition

Biomimetics is the study of how to apply the methods and principles found in nature to modern science and engineering.

Overview

Biomimetics has become a more modern approach in various fields of engineering design. Advocates of the field believe optimized solutions for ecological systems resulting from thousands of years of natural evolution can provide today's engineers with limitless applicable technologies. Julian Vincent, a well-established researcher and the director of the Centre for Biomimetics and Natural Technologies proclaims that there is only a 10% overlap between biology and technology in terms of the mechanisms used [1]. This vast technological potential has resulted in many innovative creations throughout history.
Possibly the most well-known application of biomimetics was by a Swiss inventor, George de Mestral, who observed the efficient manner in which cocklebures adhered themselves to clothing and fur and designed a material capable of mimicking the plant's trait, ultimately leading to the patent of VELCRO® [2]. Another familiar application can been seen in the parallel field of bionics which focuses heavily on the anatomy and physiology of humans and animals in the design of robotic components to obtain stable fluid-like motions while reducing energy expenditure [3, 4]. In the area of computer science, many forms of imitating nature to optimize engineering systems are utilized. Genetic algorithms utilize evolutionary theories formulated by Charles Darwin that force a program to iterate toward optimal solutions. Often used concurrently with genetic algorithms are artificial neural networks. Modeled after biological neural networks, this form of software design can adapt to closely model relationships between inputs and outputs of a system. On a smaller scale, biomimetics is used in the area of nanostructured materials as Wendell et al. observe cellular processes and apply novel phenomena to synthetic polymer membrane systems [5]. In the field of BioMEMS, the physiological process of hemostasis is being recreated chemically in a microfluidic system to design self-repairing devices [6]. Another area that is having significant influences on microfluidics is electrowetting-based actuation. The idea of optimizing the wetting properties of a surface to control a fluid is utilized by the lotus plant to self-clean itself as water droplets roll off the leaves [7].

Cross References

► Self-Assembly Fabrication

References

1. Hooper R (2004) Ideas Stolen Right From Nature. Wired Nov 9. http://www.wired.com/science/discoveries/news/2004/11/65642. Accessed 27 Nov 2007
2. Vincent F, Bogatyreva O, Bogatyrev N, Bowyer A, Pahl A (2006) Biomimetics: its practice and theory. J R Soc Interface 3:471–482
3. Clark J, Cham J, Bailey S, Froehlich E, Nahata P, Full R, Cutkosky M (2001) Biomimetic Design and Fabrication of a Hexapedal Running Robot. Proc IEEE Int Conf Robot Automat 4:3643–3649
4. Menciassi A, Accoto D, Gorini S, Dario P (2006) Development of a biomimetic miniature robotic crawler. Auton Robot 21:155–163
5. Wendell D, Patti J, Montemagno C (2006) Using Biological Inspiration to Engineer Functional Nanostructured Materials. Small 2(11):1324–1329
6. Runyon M, Johnson-Kerner B, Ismagilov R (2004) Minimal functional model of Hemostasis in a Biomimetic Microfluidic System. Angew Chem Int Ed 43:1531–1536
7. Cho S, Moon H, Kim C (2003) Creating, Transporting, Cutting, and Merging Liquid Droplets by Electrowetting-Based Actuation for Digital Microfluidic Circuits. J MEMS 12(1):70–80

Biomimicry

► Biomimetics

Biomolecular Adsorption in Microfluidics

Jeong-Yeol Yoon[1], Robin L. Garrell[2]
[1] Department of Agricultural & Biosystems Engineering, The University of Arizona, Tucson, AZ, USA
[2] Department of Chemistry & Biochemistry, University of California, Los Angeles, CA, USA
jyyoon@email.arizona.edu

Synonyms

Protein adsorption; Cell adhesion; Lab on a Chip

Definition

Biomolecular adsorption in microfluidics usually refers to the *nonspecific* adsorption of biomolecules (amino acids, peptides, DNA, RNA, proteins, and cells) onto the surfaces of microfluidic devices. In this sense, this is often referred as *biofouling in microfluidics*. This causes many problems including reduced device sensitivity, poorer detection limits and selectivity, and diminished device lifetime. Among the above adsorbing species, proteins (including protective proteins of cells) cause the biggest problems resulting from irreversible adsorption and subsequent denaturation.

Overview

The microfluidic device is probably the most popular lab-on-a-chip, and major breakthroughs have been made for its development over the last five years. Microfluidic devices have been demonstrated for many chemical and biological assays [1]. In the early 1990s, several problems in microfluidic actuation were identified. One problem was water stiction: the adhesion of water to microchannel walls made of hydrophilic materials such as glass, which perturbs the desired flow and prevents the channels from being rinsed for reuse [2]. This problem can be solved by passivating the channel walls, typically through modifications that alter the wettability of the surface [2]. Another serious problem is that biomolecules tend to adsorb from solution onto many of the materials commonly used for microfluidic devices [3]. The adsorbing species may include amino acids, peptides, proteins, DNA, RNA, and cells. Among these species, proteins cause the biggest problems, because they often denature and become very difficult to remove [3].

This entry reviews the physicochemical properties of microfluidic devices, mechanisms of biomolecular adsorption and denaturation at microfluidic device interfaces, and methods to minimize or to prevent biomolecular adsorption. The trade-offs between methods to reduce water stiction will also be discussed.

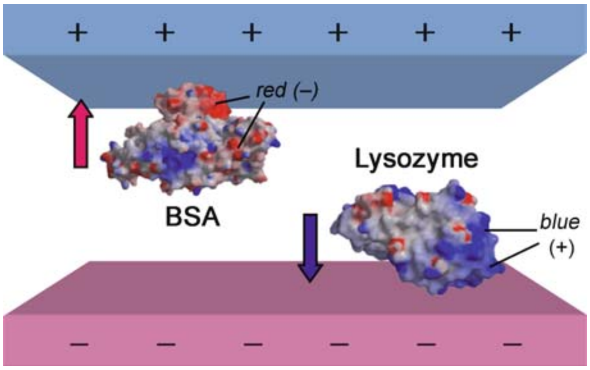

Biomolecular Adsorption in Microfluidics, Figure 1 At pH 7.2, bovine serum albumin (BSA) has negative net charge and is electrostatically attracted to the positively charged top surface. At that pH, lysozyme has positive net charge and is attracted to the negatively charged bottom surface

Basic Methodology

The interactions between protein molecules and solid surfaces can be classified into: hydrophobic interactions, electrostatic interactions, hydrogen bonding (a special type of electrostatic interactions), and van der Waals interactions [4].

Van der Waals and Electrostatic Interactions

Van der Waals interactions are a combination of several types of very weak, short-range interactions: dipole–dipole, induced dipole–induced dipole (London dispersion forces), dipole–induced dipole, and the Born repulsion. Van der Waals interactions are weak compared with electrostatic interactions, and are difficult to control through the choice of experimental conditions [4]. Hydrogen bonds, a special type of dipole–dipole interaction, are stronger and play important roles in protein folding, solvation, and adsorption. Electrostatic interactions arise from Coulombic attraction or repulsion between charged groups. Portions of protein surfaces are positively charged from terminal or side chain ammonium groups (colored blue in Fig. 1), while other portions are negatively charged from terminal or side chain carboxyl groups (colored red in Fig. 1) [4]. Depending on the pH, the net charge on a protein molecule can be positive or negative, or neutral at the isoelectric point (pI). Charged protein molecules adsorb on surfaces having the opposite charge, as illustrated in Fig. 1 [3].

Hydrophobic Interactions

In general, nonpolar substances such as hydrocarbon oils and polyethylene are considered hydrophobic. The hydrophobic effect refers to the phenomena that such species are more soluble in nonpolar solvents than in water. The effect is at least partly due to the tendency of water to form a hydrogen-bonded network structure that excludes nonpolar or non-hydrogen-bonding moieties. An attempt to transfer nonpolar moieties into the hydrogen-bonded water structure results in a decrease in entropy ($\Delta S < 0$) and almost no change in enthalpy ($\Delta H \approx 0$ at room temperature), thus leading to an increase in Gibbs free energy ($\Delta G > 0$), corresponding to a nonspontaneous process. The hydrophobic effect is especially important in biological systems. When a protein folds, the interior consists predominantly of hydrophobic domains, while the exterior is more hydrophilic.

In water, nonpolar and non-hydrogen-bonding moieties associate through hydrophobic interactions. Hydrophobic interactions can cause protein molecules to aggregate (even to the point of precipitating out of solution), and also play a major role in protein adsorption from water onto hydrophobic surfaces. At room temperature, protein molecules in solution diffuse by Brownian motion. When they come in contact with hydrophobic surfaces, they tend to remain there, adsorbing, unfolding, and eventually denaturing. Protein aggregation in solution and protein-surface hydrophobic interactions are maximized at the isoelectric point of a protein (pI), while electrostatic interactions with water are minimized at that pH [4].

Surface Wettability of Materials Used for Microfluidic Device Surfaces

Whether a surface is hydrophilic or hydrophobic, surface wettability can be assessed by measuring the contact angle, θ, of a sessile water droplet on a smooth surface. The contact angle is a consequence of the surface tensions (γ) at the liquid–vapor (LV), solid–vapor (SV), and solid–liquid (SL) interfaces, as shown by the Young equation,

$$\gamma_{SL} = \gamma_{SV} - \gamma_{LV} \cos\theta \,. \quad (1)$$

Figure 2 illustrates how static, advancing, and receding contact angles are defined. A larger contact angle indicates the surface is more hydrophobic than a reference surface.

Table 1 summarizes contact angles for water on various materials that are frequently used in direct contact with liquids for microfluidic devices. The values shown in this table are not definitive, as surface treatments such as plasma etching can dramatically change the contact angle. The advancing contact angle $\theta_{advancing}$, obtained by tilting

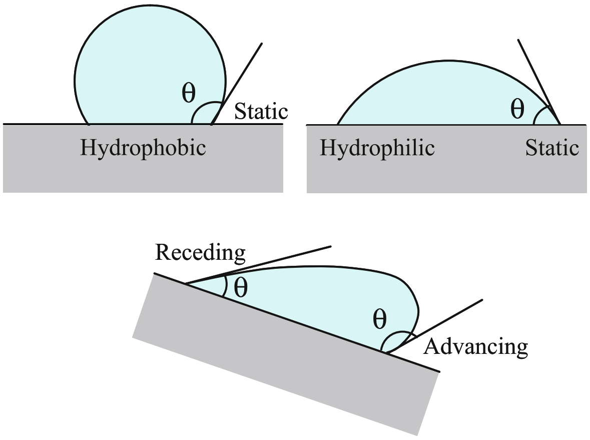

Biomolecular Adsorption in Microfluidics, Figure 2 Static, advancing, and receding contact angle as measures of surface wettability

the surface, by adding more liquid to a droplet, or by using the Wilhelmy plate method, is generally larger than the static contact angle θ_{static}; the difference depends on the surface homogeneity and roughness (Fig. 2). In general, on etching or roughening a surface, the contact angle θ typically increases, but it may decrease.

Glass, silicon dioxide (SiO_2), and poly(ethylene glycol) (PEG) are hydrophilic. Their static water contact angles are $\leqslant 30°$ as shown in Table 1. Many clean metal surfaces, including gold, show contact angles close to 0° [5]. Ordinarily, metal surfaces are contaminated, resulting in higher contact angles ($\sim 60°$ for gold) [6]. Polystyrene (PS), alkane-terminated self-assembled monolayers (SAMs), polydimethylsiloxane (PDMS), and Teflon are hydrophobic, with static water contact angles $\geqslant 90°$. All the other materials shown in Table 1, including ordinary gold, protein films, polyesters such as poly(methyl methacrylate) (PMMA), and polycarbonate (PC), can be considered as intermediate between hydrophilic and hydrophobic.

Nonspecific Protein Adsorption on the Surfaces of Microfluidic Devices

Proteins such as antibodies and enzymes can be deliberately anchored on microfluidic device surfaces by covalent bonds or molecular recognition in order to fabricate array biosensors. Nonspecific adsorption is the (usually) undesirable adsorption of molecules on the surface, and it ends up with loss of analyte. In nonspecific adsorption, the molecule–surface interactions are initially weaker, so the adsorption process is both slower and more difficult to control. Subsequent denaturation leads to stronger adhesion [7], as well as to changes in the surface hydrophilicity and roughness [8]. It is important to understand the mech-

Biomolecular Adsorption in Microfluidics, Table 1 Advancing and static water contact angles on common materials used for microfluidic device surfaces [18–43]

Materials	θ_{static} (deg)	$\theta_{advancing}$ (deg)
Glass (clean)	0	0
Glass (ordinary)	14–51	60
Gold (clean)		0
Gold (ordinary)	61–65	
Si wafer	22	
SiO_2		27
Poly(ethylene glycol) (PEG)	18	39–46
Albumin film	64–70	
Lysozyme film	58	
Polycarbonate (PC)	70	86
Poly(methyl methacrylate) (PMMA)	70–74	
Polystyrene (PS)	87–91	97
Alkanethiolate or alkylsilane self-assembled monolayers (SAMs)	108–115	110–116
Polydimethylsiloxane (PDMS)	108–113	118
Fluorohydrocarbon	115	
Teflon	112–118	

anisms of nonspecific protein adsorption in order to minimize the problems it can create.

Analyzing Protein Adsorption

Although protein adsorption from aqueous solutions onto various types of surfaces has been studied for several decades, no models accurately describe the process in detail [4]. Protein adsorption is typically analyzed by measuring a series of surface coverage data (Γ, usually in $mg \cdot m^{-2}$) against either the equilibrium protein concentration (C_{eq}, usually in $mg \cdot mL^{-1}$) or the time elapsed (t). Γ can be evaluated by measuring the amount of protein remaining in solution in contact with a particulate surface in a series of test tubes or in a stirred cell. Alternatively, the amount of protein adsorbed to an ordinary (non-particulate) surface can be measured directly by total internal reflection fluorescence (TIRF), surface plasmon resonance (SPR), ellipsometry, optical waveguide lightmode spectroscopy (OWLS), or a thickness shear mode (TSM) resonator.

A plot of Γ vs. C_{eq} is an adsorption isotherm. Data for protein adsorption are frequently modeled by the Langmuir equation, although the validity of using this equation for

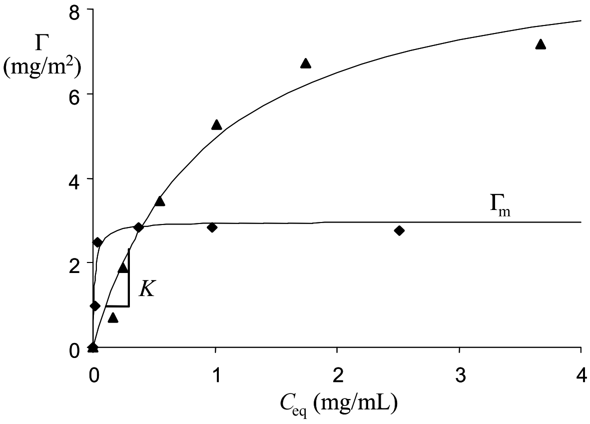

Biomolecular Adsorption in Microfluidics, Figure 3 A typical Langmuir-type adsorption isotherm, for bovine hemoglobin adsorbing from 10 mM phosphate buffer (pH 6.8) onto sulfonated polystyrene microparticles: ♦ = 0.14 sulfonate groups nm^{-2}, ▲ = 2.1 sulfonate groups nm^{-2}

protein adsorption remains an open question:

$$\Gamma = \Gamma_m \frac{KC_{eq}}{1 + KC_{eq}} \,. \tag{2}$$

This isotherm is characterized by the linear rise at low concentrations (slope $= K$, the equilibrium constant for adsorption) and the subsequent plateau ($\Gamma_m =$ the saturated surface coverage of protein), as shown in Fig. 3. K is associated with the ratio of the adsorption to desorption rates, and is related to the work of adhesion: the energy required to desorb the protein from the surface. A larger K indicates slower desorption than adsorption, leading to irreversible adsorption.

To get some control over protein adsorption, one has to understand the protein-surface interactions in advance. To this end, adsorption isotherms have been obtained for a wide variety of surfaces, from hydrophilic to hydrophobic. Techniques for controlling the surface wettability include varying the terminating groups of SAMs or the ratio of monomers in copolymers. The effects on protein adsorption of factors such as liquid polarity, temperature, pH, solute type (e. g. electrolyte), and solute concentration have been widely studied [4].

Several adsorption isotherm studies [9] have shown that K, associated with the ratio of the adsorption to desorption rate, is larger for hydrophobic surfaces than for hydrophilic surfaces, indicating proteins adsorbs irreversibly to hydrophobic surfaces. This irreversibility is closely associated with the extent of structural changes of proteins adsorbed on surfaces, which will be discussed in the following section.

Structural Changes of Protein Molecules at Water–Solid Interfaces

Once a protein molecule makes contact with a hydrophobic surface, conformational fluctuations at the outside of protein molecule cause hydrophobic residues to be exposed, some of which adhere to the surface, ultimately leading to unfolding and/or flattening [4]. This conformational change is a spontaneous process ($\Delta G < 0$), driven in part by entropy gain ($\Delta S > 0$). This unfolding has been shown through circular dichroism (CD) experiments to involve a decrease in α-helix and increase in β-sheet and unordered conformations [7]. This denaturation is, for the most part, responsible for the irreversibility of adsorption through hydrophobic interactions. Protein adsorption leads to the formation of a bumpy layer, or even to the formation of irregular aggregates of protein molecules adsorbed on the surface. For example, Locascio et al. have identified large, irregular aggregates of protein molecules adsorbed on the microchannel surface in a capillary electrophoresis system [8].

Association and dissociation of protein molecules on hydrophobic surfaces may also take place. Small proteins comprised of a single polypeptide chain, such as lysozyme, associate to form dimers upon adsorption on hydrophobic surfaces, especially near the pI of 11. Proteins that have a quaternary structure, such as hemoglobin, can dissociate into subunits upon contacting a hydrophobic surface, as the subunits are held together by hydrophobic interactions.

However, such structural changes have also been found for hydrophilic surfaces, when the surface is fully covered with proteins [7] and when the proteins are in contact with the surface for a long period of time (more than several hours) [3], indicating the participation of other interactions towards structural changes.

Key Research Findings

Small Solute, DNA, and Cell Adhesion to Microfluidic Device Surfaces

DNA is a negatively charged polyelectrolyte, and so sticks to positively charged surfaces, but not hydrophobic surfaces. Ions and water-soluble polymers also do not stick to hydrophobic surfaces.

The adhesion of cells to surfaces is different from that of proteins and DNA. Cell adhesion and spreading are believed to depend primarily on the hydrophobicity of both cells and surfaces. Cell surface hydrophobicity is usually associated with the presence of fibrillar structures on cell surfaces and specific cell wall proteins. Adhesion, spreading, and growth of mammalian cells are generally promoted on hydrophilic surfaces ($\theta_{\text{static}} \approx 30-40°$) [10], while those of bacterial cells are generally promoted on hydrophobic surfaces [11]. The latter can be distinguished from mammalian cells by the existence of fibrils and a large number of cell wall proteins. Other factors that affect cell adhesion include surface topography [10] and the presence of certain proteins (especially albumin and fibrinogen) that may interact with cell wall proteins.

Surface Materials Used in Microfluidic Applications

To prevent biomolecular adsorption and water stiction, the surface materials for a microfluidic device should be carefully chosen with consideration of the actuation method (hydrodynamic or electrokinetic) and analytes to be manipulated (small solutes, DNA, proteins, and/or cells). Tables 2 and 3 summarize the surface materials that have been used in microfluidic applications.

Minimizing Biomolecular Adsorption with Hydrodynamic Actuation

Hydrodynamic actuation methods include pressurizing a microchannel with a syringe pump or from a nitrogen tank (pumping), applying different pressures for inlets and outlets of microchannels (ΔP), centrifuging the microchannel tubes, and utilizing gravity or osmosis. In the absence of externally applied electrical potentials, hydrophobic interactions become dominant over electrostatic interactions, unless the surface is highly polarized. Since charged analytes (ion, dye, water-soluble polymer, and DNA) and mammalian cells do not have hydrophobic interactions, all types of surfaces, including hydrophilic (glass, SiO_2, and PEG), intermediate (PC and PMMA), and hydrophobic surfaces (PDMS), can be used for hydrodynamic actuation of these species, as shown in Table 2. Among these surfaces, PDMS can prevent water stiction that leads to fluctuation in the flow rate in microchannels. However, PDMS is not the optimal choice for the solutions of proteins or bacterial cells, because they adsorb on PDMS surfaces through hydrophobic interactions. PDMS also has some swelling issues, especially with nonpolar solvents.

Minimizing Biomolecular Adsorption with Electrokinetic Actuation: Electroosmotic Flow

The most common method of electrokinetic actuation is capillary electrophoresis (CE), in which electrophoresis of analytes and electroosmotic flow (EOF) of bulk fluid usually occur at the same time. Figure 4 illustrates the working principle of CE. The surface of fused silica capillaries is negatively charged at the pH values commonly used

Biomolecular Adsorption in Microfluidics, Table 2 Surface materials used for hydrodynamic actuation

Actuation method	Analyte	Surface materials	References
ΔP / pumping	Dye	PDMS	Anal. Chem. 75, 967–972
	Water-soluble polymer	SiO_2	Sens. Actuators B 82, 111–116
		Glass	Anal. Chem. 74, 3972–3976
	DNA	PEG	Anal. Chem. 74, 3372–3377
		Glass	Anal. Chem. 74, 3972–3976
		PC	Anal. Biochem. 311, 40–49
		PDMS	Talanta 55, 909–918
	Protein	PEG	Electrophoresis 23, 799–804
		PDMS	Anal. Chem. 73, 165–169 Anal. Chem. 74, 5243–5250 Anal. Chem. 74, 379–385 Anal. Chim. Acta 468, 143–152
	Mammalian cell	PDMS	Anal. Chem. 74, 3991–4001
Centrifugation / gravity	Ion	PMMA	Anal. Chem. 73, 3940–3946
	Protein	PDMS	Sens. Actuators B 72, 129–133 Anal. Chem. 73, 5207–5213
Self-filling / capillary osmosis	Protein	PEG	Langmuir 17, 4090–4095
		PDMS	Science 276, 779–781

Note. References taken from the period 2000–2003.

in CE. A diffuse double layer of cations is attracted to the stationary negative changes on the wall. EOF occurs when an electric field is applied, which causes the outer layer of cations to migrate towards the cathode, dragging along the bulk buffer solution. In many cases, the electroosmotic force is stronger than the electrophoretic force, which causes all analytes to migrate toward the cathode, regardless of their charge. Under these conditions, as shown in Fig. 4, analyte molecules are separated according to their charge.

Because the surfaces of microchannel walls have to be ionized for EOF, they may have electrostatic interactions with charged analytes. That is, charged protein molecule could adsorb through Coulombic interactions. Because EOF scales with the charge density on the channel walls, biomolecular adsorption originating from electrostatic interactions also depends on the rate of EOF [12]; whether the surface is originally hydrophilic or hydrophobic is less important. This explains why many materials ranging from glass (hydrophilic) to PDMS (hydrophobic) can be used for chip-based CE systems, as shown in Table 3.

CE-based methods that do not utilize electrophoresis include capillary electrochromatography (CEC) or micellar electrokinetic chromatography (MEKC). In CEC, EOF acts as a pump to move analytes past a stationary phase; analytes partition into the stationary phase with different affinities, enabling separation. Other CE-based methods that do not utilize EOF include capillary isoelectric focusing (CIEF) or capillary gel electrophoresis (CGE). CIEF works on the same basic principle as IEF. The capillary is treated with polyacrylamide or methylcellulose, so there is no EOF, ensuring that the relative movement of proteins depends solely on differences in their pI values. There are no electrostatic interactions between charged analytes and the microchannel surface, so hydrophobic interactions are

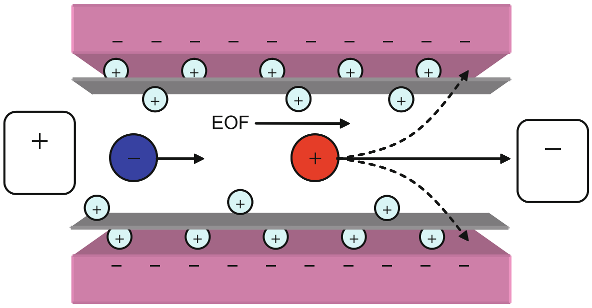

Biomolecular Adsorption in Microfluidics, Figure 4 Capillary electrophoresis (CE). Cations on a microchannel wall are pulled toward the anode, generating electroosmotic flow (EOF); positively and negatively charged analytes are separated by their differences in their electrophoretic mobilities. Depending on the rate of EOF, analytes may be attracted to a microchannel wall through electrostatic attraction, shown as dashed arrows

Biomolecular Adsorption in Microfluidics, Table 3 Surface materials used for electrokinetic actuation

Actuation method	Analytes	Surface materials	References
CE (electrophoresis and EOF)	Dye	PC	Anal. Chem. 74, 2556–2564
	Ion	PMMA	Anal. Chem. 74, 2407–2415 Anal. Chem. 74, 1968–1971
	Amino acids and sugar	Glass	Sens. Actuators B 81, 369–376
		PC	Anal. Chem. 74, 2556–2564
		PDMS	Electrophoresis 23, 3558–3566 Analyst 127, 1021–1023 Electrophoresis 23, 2347–2354 Electroanalysis 14, 1251–1255
	DNA	SiO_2	Fresenius J. Anal. Chem. 371, 112–119
		PEG	Anal. Biochem. 311, 40–49
		PC	Anal. Chem. 74, 2556–2564 Electrophoresis 21, 165–170 Electrophoresis 23, 2477–2484 Electrophoresis 22, 3939–3948
		PMMA	Electrophoresis 21, 165–170 Electrophoresis 22, 3939–3948 Sens. Actuators B 75, 142–148 Microsyst. Technol. 7, 265–268 Lab Chip 2, 88–95 Anal. Chim. Acta 470, 87–99
		SAM	Anal. Chem. 74, 1436–1441
	Protein	Protein film	Anal. Chem. 73, 4181–4189
		PC	Anal. Chem. 74, 2556–2564
		PMMA	Electrophoresis 22, 3972–3977
		PDMS	Anal. Chem. 73, 4491–4498 Anal. Chem. 74, 1772–1778 Electrophoresis 23, 740–749
CIEF (electrophoresis only)	Protein	Gold	Anal. Chem. 73, 1627–1633 Anal. Chem. 73, 658–666 Electrophoresis 23, 3638–3645
		PMMA	Electrophoresis 23, 3638–3645
CEC or other EOF-based microfluidics (EOF only)	Dye	PC	Anal. Chem. 74, 45–51
		PDMS	Sens. Actuators A 102, 223–233
	Protein	Glass	Anal. Chem. 73, 3400–3409
		PMMA	J. Chromatogr. A 857, 275–284
		PS	J. Chromatogr. A 857, 275–284
		PDMS	Sens. Actuators A 102, 223–233 Anal. Chem. 73, 5645–5650
Electrowetting	Ion	Teflon	Appl. Phys. Lett. 77, 1725–1726
	Protein	Teflon	Lab Chip 2, 19-23

Note. References taken from the period 2000–2003.

the dominant factor for separation. Materials commonly used for CIEF include polyacrylamide, cellulose, gold, and PMMA, as shown in Table 3. These materials are either hydrophilic or intermediate, and are capable of minimizing protein adsorption through hydrophobic interactions.

Surfaces of intermediate hydrophobicity, such as PC, PMMA, and protein film, are most commonly used for CE-based microfluidic chips, as they minimize water stiction as well as protein adsorption through hydrophobic interactions to some extent. The popularity of PDMS is

attributable to its ease of fabrication. However, PDMS has several problems for electrokinetic actuation. One is that CE in a PDMS channel supports lower EOF than glass or quartz because there is little negative charge on the surface. A more serious problem is that PDMS is gas permeable, allowing water vapor formed by Joule heating to permeate into the bulk material, changing the buffer concentration and the EOF rate. Salts may precipitate in PDMS channels, and affected devices have to be discarded. Another significant problem is that proteins adsorb to hydrophobic PDMS through hydrophobic interactions, leading to unstable EOF, peak tailing, and loss of sample [13].

To summarize, there is no definitive surface to be used for all types of analytes. Surfaces should be carefully chosen or modified, depending on the type of analyte and the method of actuation.

Modifying Surfaces to Prevent Biomolecular Adsorption and Water Stiction

Several microfabrication processes limit the choice of materials, and sometimes one is forced to use hydrophobic materials such as PS and PDMS. These hydrophobic surfaces can be made more hydrophilic by copolymerizing with hydrophilic monomers or coating with PEG or poly(ethylene oxide) (PEO) films [14]. The common feature of these hydrophilic modifications is the absence of functional groups that can act as hydrogen bond donors. Coating with protein films that resist certain biomolecules has also been demonstrated [15].

Water stiction on hydrophilic materials such as glass or silicon wafers can also be prevented. The surfaces can be passivated by depositing thin hydrophobic layers such as hydrocarbon/perfluorocarbon SAMs or Teflon. The nonstick nature of Teflon coatings found in many household products refers to the prevention of water stiction; the coatings do not prevent protein adsorption. Micropatterning these passivated hydrophobic layers can also be utilized to achieve microfluidic actuation of water. Zhao et al. [2] and Kataoka and Troian [16], for example, have patterned the hydrophobic surface to have a gradient from hydrophobic to hydrophilic, or alternating surfaces of hydrophobic and hydrophilic structures, to let the liquid flow over these surfaces. This *surface-directed* flow has thus far been demonstrated only for pure water. There are potential problems with protein solutions since proteins adsorb preferentially on rough rather than smooth surfaces.

Preventing Protein Adsorption in Electrowetting-Based Actuation

In several types of microfluidic actuation, hydrophobic surfaces have been used to control the rate of EOF or to manipulate droplets [3]. As noted earlier, however, it has not been possible to prevent protein adsorption that occurs through hydrophobic interactions. One way around this problem is to make the surface hydrophobic to prevent water stiction, while utilizing electrostatic repulsion to prevent biomolecular adsorption. We have recently demonstrated this strategy in electrowetting-based microfluidic actuation [3].

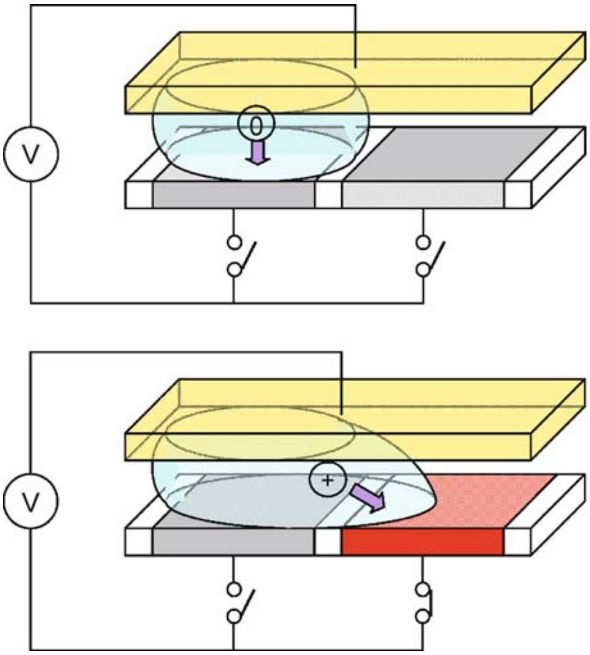

Biomolecular Adsorption in Microfluidics, Figure 5 Electrowetting-based actuation. Illustration of fluid motion induced by applying an electrical potential across dielectric-coated electrodes below a liquid droplet. By switching on the voltage at an electrode adjacent to the droplet, the surface tension is lowered, causing the droplet to move to the right. Biomolecules with neutral net charge may be attracted to electrodes while no voltage is applied. Biomolecules with positive (or negative) net charge may be attracted to electrodes while voltage is applied

Electrowetting-on-dielectric (EWOD) is a new method for moving liquids in biofluidic chips through electrical modification of the surface hydrophobicity (Fig. 5) [3]. We have demonstrated prevention of protein and DNA adsorption by minimizing hydrophobic interactions through careful choice of the bias, magnitude, and duration of the applied voltage, and by introducing electrostatic repulsions between charged proteins and the device surfaces.

Future Directions for Research

Summary of Current Approaches

The surfaces of microfluidic devices can be classified into three groups based on their surface wettability: glass, gold, Si wafer, SiO_2, and PEG as hydrophilic; PS, SAM,

PDMS, and Teflon as hydrophobic; and protein films, PMMA, and PC as intermediate. The common analytes in microfluidic devices can be classified into two groups based on their type of interactions with surfaces: small charged solutes and DNA interact primarily through electrostatic interactions, while proteins exhibit both electrostatic and hydrophobic interactions. In hydrodynamic actuation, biomolecules adsorb on surfaces largely through hydrophobic interactions. Hence small charged solute and DNA solutions are relatively easy to manipulate, as they have negligible hydrophobic interactions. For actuating protein solutions, the surface should be modified so as to be hydrophilic. In electrokinetic actuation, however, hydrophilic modification cannot be used since there are both hydrophobic and electrostatic interactions. An intermediate surface can be one possible solution, but a better way appears to be faster actuation (e. g. high EOF rate), utilizing electrostatic repulsion or changing device configuration, which have been demonstrated for electrowetting-based actuation.

Future of Biomolecular Adsorption in Microfluidics

The above summary addresses the adsorption of individual biomolecules in microfluidics. Biomolecular adsorption from real-world liquid samples such as blood will be much more complicated and probably almost impossible to prevent or control. However, we need to remember that biomolecular adsorption is not a problem unique to microfluidics; people have been working on antifouling coatings since the 1950s [17]. The future direction of this research will be related to or inspired by the research on biomaterials (e. g., prosthetic devices). Collaborations with orthopedic surgeons, dentists, and cell biologists are expected, which scientists are not really exploiting at this stage [17].

Cross References

- ► Surface Tension Driven Flow
- ► Capillary Electrophoresis (CE)
- ► Electroosmotic Flow (DC)
- ► Electrowetting

References

1. Verpoorte E, de Rooij NF (2003) Microfluidics meets MEMS. Proc. IEEE 91:930–953
2. Zhao B, Moore JS, Beebe DJ (2001) Surface-directed liquid flow inside microchannels. Science 291:1023–1026
3. Yoon JY, Garrell RL (2003) Preventing biomolecular adsorption in electrowetting-based biofluidic chips. Anal Chem 75:5097–5102
4. Kim JH, Yoon JY (2002) Protein adsorption on polymer particles. In: Hubbard A (ed) Encyclopedia of surface and colloid science. Marcel Dekker, New York
5. Adamson AW, Gast AP (1997) Physical chemistry of surfaces, 6th edn. John Wiley & Sons, New York
6. Smith T (1980) The hydrophilic nature of a clean gold surface. J Colloid Interface Sci 75:51–55
7. Horbett TA, Brash JL (1995) Proteins at interfaces II: fundamentals and applications. American Chemical Society, Washington, DC
8. Locascio LE, Hong JS, Gaitan M (2002) Liposomes as signal amplification reagents for bioassays in microfluidic channels. Electrophoresis 23:799–804
9. Yoon JY, Kim JH, Kim WS (1999) The relationship of interaction forces in the protein adsorption onto polymeric microspheres. Colloids Surf A 153:413–420
10. Ruardy TG, Schakenraad JM, van der Mei HC, Busscher HJ (1997) Preparation and characterization of chemical gradient surfaces and their application for the study of cellular interaction phenomena. Surf Sci Rep 29:3–30
11. Tsuneda S, Aikawa H, Hayashi H, Yuasa A, Hirata A (2003) Extracellular polymeric substances responsible for bacterial adhesion onto solid surface. FEMS Microbiol Lett 223:287–292
12. Locascio LE, Perso CE, Lee CS (1999) Measurement of electroosmotic flow in plastic imprinted microfluid devices and the effect of protein adsorption on flow rate. J Chromatogr A 857:275–284
13. Lee JN, Park C, Whitesides GM (2003) Solvent compatibility of poly(dimethylsiloxane)-based microfluidic devices. Anal Chem 75:6544–6554
14. Cox JD, Curry MS, Skirboll SK, Gourley PL, Sasaki DY (2002) Surface passivation of a microfluidic device to glial cell adhesion: a comparison of hydrophobic and hydrophilic SAM coatings. Biomaterials 23:929–935
15. Kingshott P, Griesser HJ (1999) Surfaces that resist bioadhesion. Curr Opin Solid State Mater Sci 4:403–412
16. Kataoka DE, Troian SM (1999) Patterning liquid flow on the microscopic scale. Nature 402:794–797
17. Mukhopadhyay R (2005) When microfluidic devices go bad. Anal Chem 77:429A–432A
18. Davies J, Nunnerley CS, Brisley AC, Edwards JC, Finlayson SD (1996) Use of dynamic contact angle profile analysis in studying the kinetics of protein removal from steel, glass, polytetrafluoroethylene, polypropylene, ethylene-propylene rubber, and silicone surfaces. J Colloid Interface Sci 182:437–443
19. Woodward RP (2000) Cleanliness measurement using contact angles. First Ten Angstroms, Portsmouth
20. Clint JH, Wicks AC (2001) Adhesion under water: surface energy considerations. Int J Adhes Adhes 21:267–273
21. Sklodowska A, Wozniak M, Matlakowska R (1999) The method of contact angle measurements and estimation of work of adhesion in bioleaching of metals. Biol Proc Online 1:114–121
22. Adamson AW, Gast AP (1997) Physical chemistry of surfaces, 6th edn. Wiley, Hoboken
23. Biederman H, Slavinska D, Boldyreva H, Lehmberg H, Takaoka G, Matsuo J, Kinpara H, Zemek J (2001) Modification of polycarbonate and polypropylene surfaces by argon ion cluster beams. J Vac Sci Technol B 19:2050–2056
24. Du YZ, Wood LL, Saavedra SS (2000) Growth behavior and structure of alkyltrichlorosilane monolayers bearing thioacetate and acetate tailgroups. Mater Sci Eng C 7:161–169

25. Klintberg L, Svedberg M, Nikolajeff F, Thornell G (2003) Fabrication of a paraffin actuator using hot embossing of polycarbonate. Sens Actuators A 103:307–316
26. van Oss CJ, Good RJ, Chaudhury MK (1988) Additive and nonadditive surface tension components and the interpretation of contact angles. Langmuir 4:884–891
27. Papra A, Bernard A, Juncker D, Larsen NB, Michel B, Delamarche E (2001) Microfluidic networks made of poly(dimethylsiloxane), Si, and Au coated with polyethylene glycol for patterning proteins onto surfaces. Langmuir 17:4090–4095
28. van der Vegt W, van der Mei HC, Busscher HJ (1994) A comparison of different approaches to calculate surface free energies of protein-coated substrata from measured contact angles of liquids. Langmuir 10:1314–1318
29. Kwok DY, Leung A, Lam CNC, Li A, Wu R, Neumann AW (1998) Low-rate dynamic contact angles on poly(methylmethacrylate) and the determination of solid surface tensions. J Colloid Interface Sci 206:44–51
30. Kwok DY, Neumann AW (1999) Contact angle measurement and contact angle interpretation. Adv Colloid Interface Sci 81:167–249
31. Aizawa H, Kurosawa S, Kobayashi K, Kashima K, Hirokawa T, Yoshimi Y, Yoshimoto M, Hirotsu T, Miyake J, Tanaka H (2000) Turning of contact angle on glass plates coated with plasma-polymerized styrene, allylamine and acrylic acid. Mater Sci Eng C 12:49–54
32. Sapsford KE, Ligler FS (2004) Real-time analysis of protein adsorption to a variety of thin films. Biosens Bioelectron 19:1045–1055
33. Clear SC, Nealey PF (1999) Chemical force microscopy study of adhesion and friction between surfaces functionalized with self-assembled monolayers and immersed in solvents. J Colloid Interface Sci 213:238–250
34. Srinivasan U, Houston MR, Howe RT, Maboudian R (1997) Self-assembled fluorocarbon films for enhanced stiction reduction. Transducers'97, pp 1399–1402
35. Abbott NL, Whitesides GM (1994) Potential-dependent wetting of aqueous solutions on self-assembled monolayers formed from 15-(ferrocenylcarbonyl)pentadecanethiol on gold. Langmuir 10:1493–1497
36. Appelhans D, Ferse D, Adler HJP, Plieth W, Fikus A, Grundke K, Schmitt FJ, Bayer T, Adolphi B (2000) Self-assembled monolayers prepared from ω-thiophene-functionalized n-alkyltrichlorosilane on silicon substrates. Colloids Surf A 161: 203–212
37. Ostuni E, Yan L, Whitesides GM (1999) The interaction of proteins and cells with self-assembled monolayers of alkanethiolates on gold and silver. Colloids Surf B 15:3–30
38. Sondag-Huethorst JAM, Fokkink LGJ (1992) Potential-dependent wetting of octadecanethiol-modified polycrystalline gold electrodes. Langmuir 8:2560–2566
39. Gillmor SD, Larson BJ, Braun JM, Mason CE, Cruz-Barba LE, Denes F, Lagally MG (2002) Low-contact-angle polydimethyl siloxane (PDMS) membranes for fabricating micro-bioarrays. IEEE-EMBS Microtechnologies in Medicine and Biology 2002, pp 51–56
40. Uilk JM, Mera AE, Fox RB, Wynne KJ (2003) Hydrosilation-cured poly(dimethylsiloxane) networks: intrinsic contact angles via dynamic contact angle analysis. Macromolecules 36:3689–3694
41. Grundke K, Werner C, Pöschel K, Jacobasch HJ (1999) Characterization of adsorbed protein layers by low-rate dynamic liquid-fluid contact angle measurements using axisymmetric drop shape analysis (part II). Colloids Surf A 156:19–31
42. Oh SJ, Jung JC, Zin WC (2001) Synthesis and surface property variations of polypropylene-graft-poly(ethylene glycol). J Colloid Interface Sci 238:43–47
43. Smith T (1980) The hydrophilic nature of a clean gold surface. J Colloid Interface Sci 75:51–55

Further Reading

Protein adsorption in general:

- Horbett TA, Brash JL (1995) Proteins at interfaces II: fundamentals and applications. American Chemical Society, Washington
- Dee KC, Puleo DA, Bizios R (2002) An introduction to tissue–biomaterial interactions. Wiley-Liss, Hoboken
- Andrade JD (1985) Surface and interfacial aspects of biomedical polymers volume 2: protein adsorption. Plenum, New York

Contact angle and hydrophobicity:

- Adamson AW, Gast AP (1997) Physical chemistry of surfaces, 6th edn. John Wiley & Sons, New York
- Shaw DJ (1992) Introduction to colloid and surface chemistry, 4th edn. Butterworth-Heinemann, Oxford

Biological and medical applications of microfluidic devices:

- Saliterman SS (2006) Fundamentals of bioMEMS and medical microdevices. Wiley Interscience and SPIE, Bellingham

Biomolecular Synthesis in Microfluids

MASAYA MIYAZAKI[1,2], HIDEAKI MAEDA[1,2,3]
[1] Nanotechnology Research Institute, National Institute of Advanced Industrial Science and Technology (AIST), Tosu, Saga, Japan
[2] Department of Molecular and Material Science, Interdisciplinary Graduate School of Engineering Sciences, Kyushu University, Kasuga, Fukuoka, Japan
[3] CREST, Japan Science and Technology Agency (JST), Kawaguchi, Saitama, Japan
m.miyazaki@aist.go.jp, maeda-h@aist.go.jp

Synonyms

Synthesis of biological molecules in microfluidics; Microfluidic reactor for biomolecular synthesis; Microreactor for synthesis of biomolecules

Definition

Biological molecules, such as proteins and peptides, oligosaccharides, nucleic acids, lipids and their related

compounds are widely used for biomaterial and pharmaceutical applications. These compounds are expensive, not so stable for long-term storage and do not require extremely large-scale synthesis. Also, the use of hazardous compounds is required in many cases. Therefore, the microreaction process is considered as a new approach which can overcome these restrictions in the synthesis of biomolecules. Several organic and biochemical syntheses have been performed using the microfluidic platform.

Overview

Biomolecules, fine chemicals and pharmaceuticals are high-value products that are produced in modest quantities. They are usually seasonal products that are customer specific and have a short shelf life. These characteristics usually place significant constraints in their production, such that it is not uncommon to see labor-intensive batch processes being used instead of the more efficient continuous process. This usually leads to a significant waste generation during the scale-up from the laboratory to production scale. In addition, the use of hazardous and often toxic homogeneous catalysts makes product purification and waste disposal important issues as regards today's stringent environmental regulations.

The microfluidic reaction system for biochemical synthesis was developed as miniaturization system of conventional synthetic chemistry. The development of microreaction processes has been much slower than that of μTAS. Lab-on-a-chip for synthetic applications is still a young research field as compared to the mature μTAS. To date, a number of gas- and liquid-phase reactions have been carried out in microfluidic systems and such microfluidic-based reactions are increasing tremendously. In this article, typical examples of biochemical syntheses within a microfluidic reactor are presented and discussed.

Peptide and Protein Synthesis

Peptide synthesis using a microfluidic reactor was reported by Watts et al. [1]. The synthesis of β-peptides has been successfully performed using a borosilicate glass microreactor (Fig. 1), in which a network of channels was produced using photolithographic and wet etching methods. The reagents were mobilized by electroosmotic flow (EOF). The microreactor was initially evaluated using a carbodiimide coupling reaction to form a dipeptide. The methodology has been extended such that the peptides may also be produced via the pentafluorophenyl ester derivatives of amino acids. It was found that performing the pentafluorophenyl ester reactions in the microreactor resulted in an increase in the reaction efficiency over the traditional batch method. Watts et al. postulated that the enhancement in the rate of reaction is an electrochemical phenomenon, due to the reaction being performed in an electric field, which is unique to microreactor systems. It has also been demonstrated that selective deprotection of the resultant dipeptides can be achieved. This approach has been used in the synthesis of a tripeptide.

Synthesis of another β-peptide was also performed. Seeberger et al. performed the synthesis of oligo β-amino acid using amino acid fluoride in a silicon microreactor [2]. They developed a method for high-efficiency synthesis that is capable of large-scale production.

Miyazaki et al. reported possible use of a microreactor as an active reaction vessel for carrying out biochemical reactions [3]. An important feature of the microchannel systems is their superior controllability of fluids, which cannot be achieved in the batchwise reactions using large reaction apparatus. The effects of a microfluidic system on chemical reactions of two different miscible solutions were examined using amino acid substitution as a model reaction. Substitution of phenylalanine in a microreaction system using separate solutions was more efficient than the batchwise reaction and microchannel reaction using a homogeneous solution. Substitution of other amino acids showed that this enhancement is caused by localization of hydrophobic amino acids at the dimethylformamide (DMF) – H_2O interface. By using the rapid Michael addition reaction of the SH group of cysteine to a maleimide group, it was demonstrated that such reaction involving hydrophilic compounds diminished in a microfluidic system. These results show that the microreaction system is a novel apparatus for regulating chemical reactions, depending on the structure of the reactant molecules, by controlling the mixing of two different solutions.

In addition to these organic syntheses, biochemical production of compounds in microreactors has also been performed. A microreactor array which enables high-throughput cell-free protein synthesis was developed [4]. The microreactor array is composed of a temperature control chip and a reaction chamber chip. The temperature control chip is a glass-made chip on which temperature control devices, heaters and temperature sensors are fabricated with an indium tin oxide (ITO) resistive material. The reaction chamber chip is fabricated by micromolding of polydimethylsiloxane (PDMS), and is designed to have an array of reaction chambers and flow channels for liquid introduction. The microreactor array is assembled by placing the reaction chamber chip on the temperature control chip. The small thermal mass of the reaction chamber resulted in a short thermal time constant of 170 ms for heating and 3 s for cooling. The performance of the microreactor array was examined through experiments on cell-free protein synthesis. By measuring

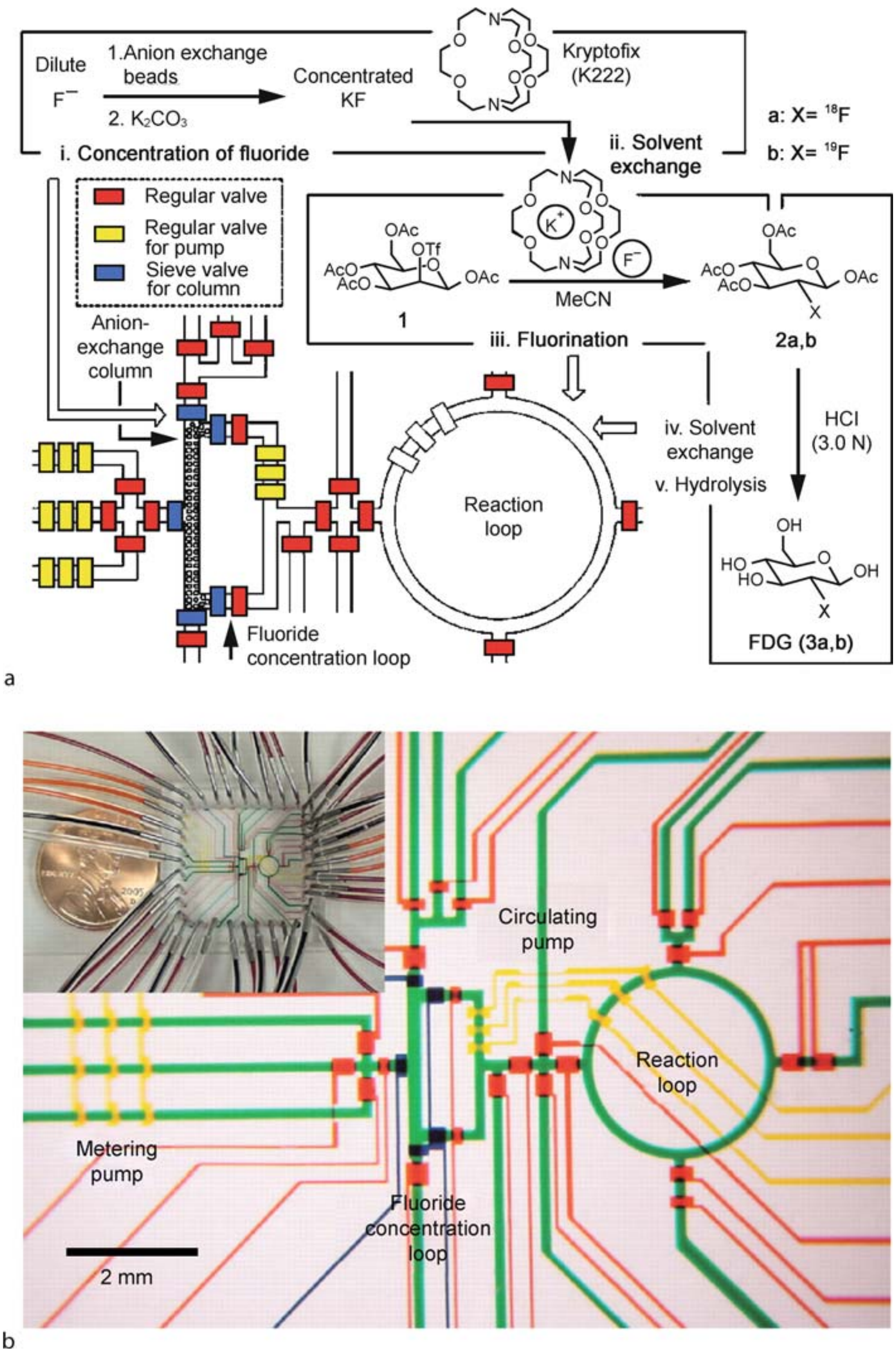

Biomolecular Synthesis in Microfluids, Figure 1 (**a**) Schematic representation of a chemical reaction circuit used in the production of 2-deoxy-2-fluoro-D-glucose (FDG). Five sequential processes are shown: (i) concentration of dilute fluoride ion with the use of a miniaturized anion exchange column located in a rectangle-shaped fluoride concentration loop, (ii) solvent exchange from water to dry MeCN, (iii) fluorination of the D-mannose triflate precursor 1, (iv) solvent exchange back to water, and (v) acidic hydrolysis of the fluorinated intermediate 2a (or 2b) in a ring-shaped reaction loop. Nanogram amounts of FDG (3a, 3b) are the final product. The operation of the circuit is controlled by pressure-driven valves, with their delegated responsibilities illustrated by their colors: red for regular valves (for isolation), yellow for pump valves (for fluidic metering circulation) and blue for sieve valves (for trapping anion exchange beads in the column module). (**b**) Optical micrograph of the central area of the circuit. The various channels have been loaded with food dyes to help visualize the different components of the microfluidic chip; colors are as in (**a**), plus green for fluidic channels. The inset shows an actual view of the device; a penny (diameter 18.9 mm) is shown for comparison. (Reproduced from [5])

the fluorescence emission from the products, it was confirmed that green fluorescent protein (GFP) and blue fluorescent protein (BFP) were successfully synthesized using *Escherichia coli* extract.

Synthesis of Sugar and Oligosaccharides

Synthesis of radiolabeled glucose has been achieved (Fig. 2) [5]. Quake et al. reported the synthesis of an [^{18}F]fluoride-radiolabeled molecular imaging probe, 2-deoxy-2-[^{18}F]fluoro-D-glucose ([^{18}F]FDG), in an integrated microfluidic device. Five sequential processes – [^{18}F]fluoride concentration, water evaporation, radiofluorination, solvent exchange and hydrolytic deprotection – proceeded with high radiochemical yield and purity and with shorter synthesis time relative to conventional automated synthesis. Multiple doses of [^{18}F]FDG for positron emission tomography imaging studies in mice were prepared. These results, which constitute a proof of principle for automated multistep syntheses at the nanogram to microgram scale, could be generalized to a range of radiolabeled substrates. Synthesis of oligosaccharides is one of the challenges in the field of synthetic organic chemistry. Generally, glycoside formation depends on the conformation, sterics and electronics of both reaction partners. The challenge in accurately predicting the reactivity of the coupling partners makes it difficult to foresee the outcome of the reaction. In addition, reaction variables such as concentration, stoichiometry, temperature, reaction time and activator play indisputable roles in the outcome of a given glycosylation. Jensen and Seeberger used continuous flow microreactors to systematically study the glycosylation reaction as an example of a challenging organic transformation (Fig. 3) [6]. A five-port silicon microreactor was designed with three primary inlets to mix and react glycosylating agent, nucleophile (acceptor) and activator (Fig. 4). Glycosylation reactions were performed rapidly over a wide range of conditions using this microreaction system. This microfluidic system enables easy handling of hazardous reagents such as trimethylsilyl trifluoromethanesulfonate at microliter scale.

In a different approach, transgalactosylation, which is the reverse reaction of the hydrolysis reaction by ►glycosidase, was carried out in organic solvent–buffer system as a reaction solvent to reduce the water concentration, and consequently the equilibrium of the reverse reaction was shifted [8]. The reaction was performed in a poly(methyl methacrylate) microreactor with two different inlets. The enzyme and reagents were loaded from these inlets by simple syringe pumping, and the reaction was terminated by heating. The reaction gave three kinds of stereoisomers, i. e. *p*-nitrophenyl-2-acetamide-2-deoxy-3-*O*-(β-D-galactopyranosyl)-β-D-glucopyranoside, *p*-nitrophenyl-2-acetamide-2-deoxy-4-*O*-(β-D-galactopyranosyl)-β-D-glucopyranoside and *p*-nitrophenyl-2-acetamide-2-deoxy-6-*O*-(β-D-galactopyranosyl)-β-D-glucopyranoside. The ratios between those isomers in the products were not determined, but the total amount of the disaccharide mixture (galactosylated *p*-nitrophenyl-2-acetamide-2-deoxy-6-*O*-(β-D-galactopyranosyl)-β-D-glucopyranoside; Gal-GlcNAcPNP) gave better yield when the reaction was conducted in the microreaction channel compared with that in the micro-test tube. This result suggests that the microreactor is an effective device for enzymatic transglycosylation.

Oligonucleotide Synthesis

The polymerase chain reaction (PCR) is the most widely used technique for oligonucleotide synthesis. Microchips/microdevices for PCR are studied extensively, and thus great progress has been made in the development and scope of microchip components of microchip-based PCR analyzers such as on-chip micromachining (fabrication, bonding and sealing), choice of substrate materials, surface chemistry and architecture of reaction vessel, handling of necessary sample fluid, control of three- or two-step temperature thermocycling, detection of amplified nucleic acid products, integration with other analytical functional units such as sample preparation, capillary electrophoresis (CE), DNA microarray hybridization, etc. The two general strategies for microchip-based PCR are flow-through and stationary chamber formats. The topic of microchip-based PCR, however, is well summarized in another article.

Chemical synthesis of oligonucleotide was also performed using a microfluidic platform. A microfluidic DNA oligonucleotide synthesizer made of PFPE which performs reaction cycles adopted from the widely used phosphoramidite method was reported [8]. PFPE is an elastomer with excellent chemical compatibility which makes it pos-

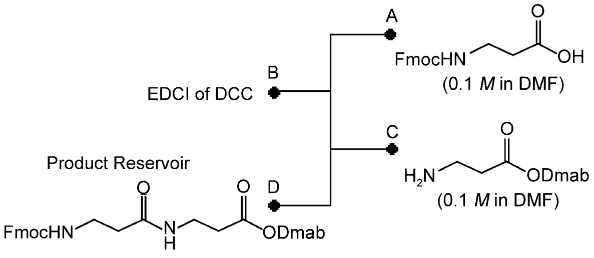

Biomolecular Synthesis in Microfluids, Figure 2 Schematic of the microreactor used in carbodiimide coupling reactions performed in [1]. (Reproduced from [1])

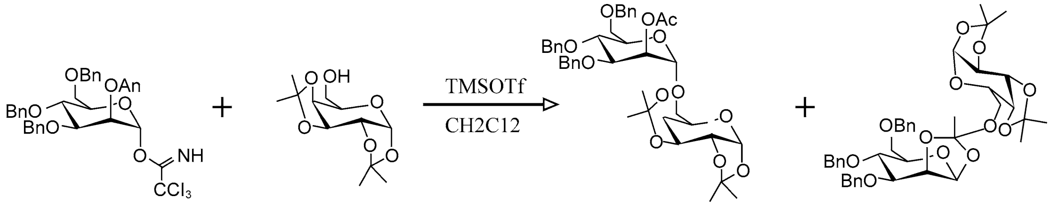

Glycosyl Donor **2** Glycosyl Acceptor **1** Desired Product **3** Orthoester **4**

a

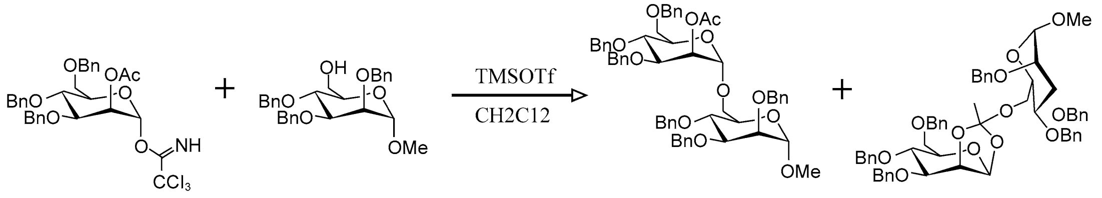

Glycosyl Donor **2** Glycosyl Acceptor **5** Desired Product **6** Orthoester Side Product **7**

b

Biomolecular Synthesis in Microfluids, Figure 3 (**a**) Sample glycosylation of glycosyl donor 2 and nucleophile (acceptor) 1 to fashion disaccharide 3. Formation of orthoester 4 is also often observed. (**b**) Glycosylation reaction involving glycosylating agent 2 (mannosyl donor) and nucleophile 5 (acceptor) to fashion disaccharide 6. Formation of orthoester 7 is also often observed. (Reproduced from [6])

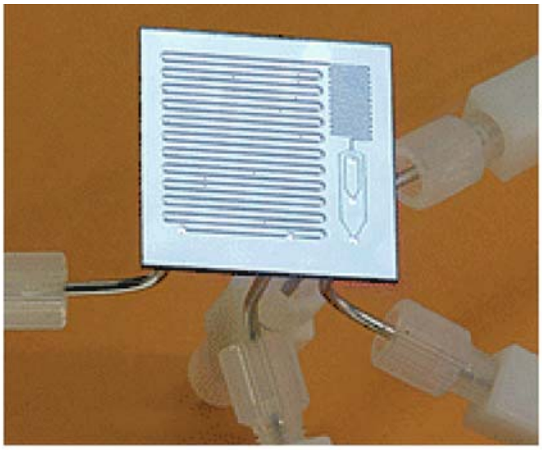

a

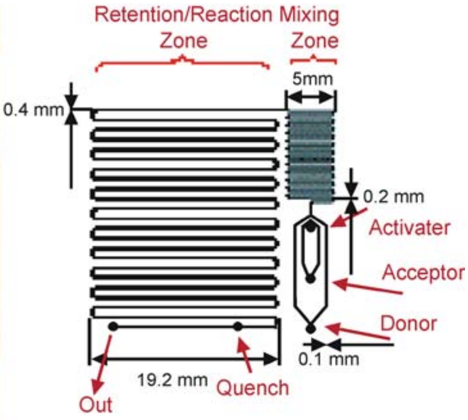

b

c

Biomolecular Synthesis in Microfluids, Figure 4 (**a**) Silicon microfluidic microreactor. (**b**) Schematic of microreactor system, comprised of three primary inlets, a mixing and reaction zone, a secondary inlet for quench and an outlet for analysis/collection. (**c**) Soldered joints of the microreactor; also perspective of the device from the side. (Reproduced from [6])

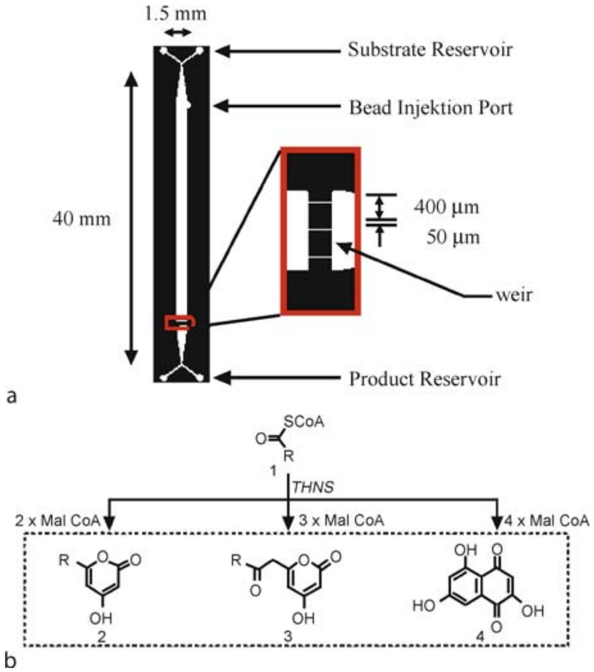

Biomolecular Synthesis in Microfluids, Figure 5 Schematic of the microreactor for polyketide synthesis. (**a**) biochip design used in this study. (**b**) Biosynthesis of flaviolin 4 and pyrone-based polyketides 2 and 3 from THNS with different starter CoA esters. (Reproduced from [11])

sible to perform organic chemical reactions. The device is capable of synthesizing 60 pmol of DNA oligonucleotides while consuming less than 500 nL of 0.1 mol L^{-1} phosphoramidite solution in each reaction cycle. The reduction of reagent consumption is significant: a 60-fold reduction over conventional automation. This approach demonstrates the usefulness of integrated micromechanical valves for complicated multistep organic synthetic reactions and enables automated chemical experiments with a wide variety of solvents.

Synthesis of Prodrugs and Other Bioactive Compounds

A microfluidic reaction system has also been used for the production of prodrugs. A multichannel membrane microreactor was fabricated and tested for ▶ Knoevenagel condensation of benzaldehyde and ethyl cyanoacetate to produce α-cyanocinnamic acid ethyl ester, a known intermediate for the production of an antihypertensive drug [9]. Knoevenagel condensations of carbonylic compounds and malonic esters yield several important key products such as nitriles used in anionic polymerization, and the α,β-unsaturated ester intermediates employed in the synthesis of several therapeutic drugs that include niphendipine and nitrendipine. Unlike most condensation reactions, Knoevenagel condensation is base-catalyzed. Strong bases such as sodium and potassium hydroxides and piperidine are traditionally used for these reactions. However, basic zeolites such as Cs-exchanged faujasite NaX and faujasite GeX, as well as amino-modified mesoporous silica are also able to catalyze these reactions. The use of heterogeneous catalysts significantly simplifies product separation and purification. It also eliminates the need for solvents. However, the water formed by the reaction is a poison for zeolite catalysts, and its removal is a must if we are to expect optimum catalyst performance. The removal of water has the added benefit of increasing the conversion for this equilibrium-limited reaction. By using Cs-exchanged faujasite NaX as the catalyst, the membrane microreactor could achieve supra-equilibrium conversion at higher product purity.

Another prodrug synthesis using a microfluidic reaction system is that of the antibiotic ciprofloacin [10]. A microreaction system developed by CPC systems (CYTOS) was used as a reaction apparatus. This system is the size of a videotape with a hold-up of 1.8 ml. The high surface-to-volume ratio for the mixing section as well as for the temperature-controlled reaction channels allow heat transfer coefficients of up to 2000 $W m^{-2} K^{-1}$. The synthesis has demonstrated the potential for faster development, particularly in the preparation of relevant quantities for development studies, such as clinical trials, using the microreaction systems.

Enzymatic syntheses within the microfluidic platform were also reported. The construction and novel compound synthesis from a synthetic metabolic pathway consisting of a type III polyketide synthase (PKS) known as 1,3,6,8-tetrahydroxynaphthalene synthase (THNS) from *Streptomyces coelicolor* and soybean peroxidase (SBP) in a microreactor were performed (Fig. 5) [11]. THNS immobilized to Ni-NTA agarose beads was prepacked into a microfluidic channel, while SBP was covalently attached to the walls of a second microfluidic channel precoated with a reactive poly(maleic anhydride) derivative. The result was a tandem, two-step biochip that enabled synthesis of novel polyketide derivatives. The first microchannel, consisting of THNS, resulted in the conversion of malonyl-CoA to flaviolin in yields of up to 40% with a residence time of 6 min. This conversion is similar to that obtained in several-milliliter batch reactions after 2 h. Linking this microchannel to the SBP microchannel results in biflaviolin synthesis. During the course of this work, we discovered that the substrate specificity of THNS could be manipulated by simply changing the reaction pH. As a result, the starter acyl-CoA specificity can be broadened to yield a series of truncated pyrone products. When combined with variations in the ratio of acyl-CoA and

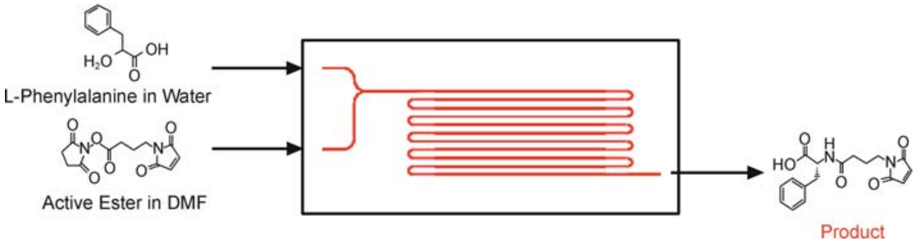

Biomolecular Synthesis in Microfluids, Figure 6 Microreactor setup used in the reaction of amino acid with active ester [3]

malonyl-CoA (extender substrate) feed rates, high yields of the pyrone products could be achieved, which is further structurally diversified from self- and cross-coupling in the SBP microchannel. The ability to rapidly evaluate the effects of reaction conditions and synthetic multienzyme pathways on a microfludic platform provides a new paradigm for performing metabolic pathway engineering, such as reconstruction of pathways for use in new compound discovery.

A monolith entrapped enzyme process was also applied to the microfluidic platform [12]. Several 10 cm long capillary tubes (made of poly(ether ether ketone) (PEEK)) with inside diameters of 0.1 – 2.0 mm were filled with silica monolith-immobilized protease derived by in situ sol–gel transition from a 1 : 4 mixture of tetramethoxysilane and methyltrimethoxysilane. ▶ Transesterification between 20 mM (*S*)-(−)-glycidol and 0.4 M vinyl *n*-butyrate in an organic solvent was used as the test reaction. The substrate solution flowed through the column at a flow rate of 0.0004 – 5.0 ml min^{-1}. The substrate conversion in the microbioreactor was higher than that in the batch reactor at high liquid flow rate. When three tubes were connected in series, the conversion at a fixed ratio of the mass of the enzyme to the liquid flow rate was increased by approximately 50% because of the tripling of the flow rate as compared to the setup with only a single tube. Changes in the tube diameter had no influence on the conversion at a fixed superficial liquid velocity. Further, the conversion increased with a decrease in the enzyme content. These results were ascribed to the apparent effect of liquid–solid mass transfer and were analyzed quantitatively using a simple mathematical model.

Basic Methodology

Basically, biomolecular synthesis reaction in a microreaction system was performed by organic synthesis or biochemical conversion. The reaction was performed by simple loading of substrate and enzyme solutions into separate inlets using syringe pumps.

Preparation of Microreaction Device

A brief overview of device fabrication was summarized to help readers, particularly the would-be microreactor users. Details can be found in other articles of this encyclopedia. From hard lithographic techniques to soft lithography and in-house-built devices, a concise description is given, and readers should refer to the appropriate articles for more details.

The foundations of microfluidic fabrication techniques lie in the well-established field of semiconductor microelectronics. For instance, the microfabrication tools of lithography, resist layers and wet and dry etching have been instrumental in the fabrication of many microfluidic systems. These methods have been used to create microfluidic systems through both direct and indirect ways. In the direct method, the microfabricated component is used directly as a channel in a device. Direct methods have the disadvantage of producing only one device for one completed fabrication. However, if the fabrication is fast, this can allow rapid prototyping of many designs. On the other hand, indirect methods use the microfabricated component as a master to transfer the design to a secondary material in a replication step. This molded material is then used as the final device. Indirect methods have the advantage of needing only one master to create many (up to hundreds) of final devices. In biomolecular synthesis, the reactions are mainly performed in organic media; therefore, silicon or glass has been widely used as the material for device preparation. These are mainly fabricated by direct method such as lithography or milling.

Performing a Microreaction

Generally, chemical syntheses using microreaction devices are performed by simple loading of reagents into the microchannel. Biomolecular synthesis depends on the molecular conformation, steric hindrance and electronics of both reaction partners. The challenge in accurately predicting the reactivity of the coupling partners makes it difficult to foresee the outcome of the reaction.

In addition, reaction variables such as concentration, stoichiometry, temperature, reaction time and activator play an indisputable role in the outcome of a given synthesis. In this article, the reaction of amino acid with active ester is shown as an example [3]. This reaction was a simple condensation reaction between amino group of amino acid and carboxyl group of active ester.

A ceramic microreaction device with a microchannel (width 400 μm × depth 400 μm × length 40 cm) was fabricated by micromachining. From two separate inlets, the solutions of active ester in DMF and amino acid with triethylamine (added for deprotonation of amino group of amino acid) in water were loaded separately by syringe pumping (Fig. 6). The resulting solution was collected and directly analyzed by HPLC to estimate the conversion rate. Each peak obtained by HPLC was confirmed by ESI-TOFMS. In the case of reaction between phenylalanine with *N*-(4-maleimidobutyloxy)succinimide (GMBS), the reaction did not proceed at higher flow rates (< 1 min, $> 50\,\text{ml min}^{-1}$). However, the reaction yield increased at slower flow rate and even exceeded 90% in a 10 min reaction time. This result indicates that the reaction rate in the microdevice is improved dramatically over batchwise reaction which gave 80% yield after 12 h.

Key Research Findings

In the last decade, many reactions for biomolecular synthesis were performed within microfluidic reactors. The use of microreactors provides several advantages over conventional reaction systems. A microfluidic reactor allows control of mixing reagents and reaction time. This can be achieved by controlling the length of the microchannel or integrating a micromixing device. Such control of fluid enables regulation of reaction by mixing. Generally, rapid micromixing enhances the reaction yield in a microfluidic system. However, some biomolecules such as peptides are amphiphilic, and these molecules prefer the interface of organic solvent and water. In a laminar flow system, mixing of two miscible solutions occurs gradually in a straight microchannel. Construction of mixing devices enhances mixing. Also, creation of repeating tight turns produces Dean vortices and disrupts the interface. Addition of these structures in a microreaction system strongly affects the reaction yield in the synthesis of biomolecules, as in the amino acid substitution [3]. Therefore, a proper design of the microchannel structure and precise fluid control are essential for the development of efficient microreaction systems for biomolecular synthesis.

Control over thermal or concentration gradients within the microreactor allows new methods for efficient chemical transformations with high space–time yields. PCR for oligonucleotide synthesis is a typical case. Also, in most cases, chemical reaction is sensitive for factors like temperature and concentration of reactant molecules. The narrow dimension of microfluidics brings attractive mass transfer and heat flow advantages. These attributes contribute to achieving efficient chemical synthesis. Often, reactions performed within a microreactor invariably generate relatively pure products in high yield, in comparison to the equivalent bulk reactions, in much shorter times and in sufficient quantities to perform full structural characterization. These are advantageous for the optimization of reaction conditions, especially biomolecular synthesis, which is expensive in most cases. Overall, microfluidic reactors are perceived as a useful tool for the synthesis of biomolecules.

Future Directions for Research

As noted above, the great advantages of microfluidic technology have been identified as ability to achieve higher yields and selectivities, more effective use of resources and much enhanced reaction control compared with conventional systems. Most biomolecules are expensive, and therefore high reaction yield and efficiency are desired for their synthesis. To achieve this, the technology of microreaction synthesis offers a wide range of solutions. Some biomolecules and their related compounds are bioactive molecules which are important for drug development. The development of a single microreactor enables small-scale production by numbering-up; therefore, the development of synthetic microreaction processes may become a popular area of research for drug development.

In addition, a microreaction device can be constructed by an integration of various components for chemical reactions such as synthesis, analysis, extraction, separation and concentration. This possibility opens access to elegant combined reactor arrangements. The development of integrated microreaction devices is an emerging field in biomolecular synthesis.

Cross References

- ► Microfluidic Bioreactors
- ► Lab-on-a-Chip Devices for Chemical Analysis
- ► Microfluidics for Bio- and Chemical Reactions
- ► Droplet Microreactors
- ► PCR Lab-on-chip Devices

References

1. Watts P, Wiles C, Haswell SJ, Pombo-Villar E (2002) Solution phase synthesis of β-peptides using micro reactors. Tetrahedron 58:5427–5439

2. Flögel O, Codée JDC, Seebach D, Seeberger PH, (2006) Microreactor Synthesis of β-Peptides. Angew Chem Int Ed 45:7000–7003
3. Miyazaki M, Yamashita K, Yamaguchi Y, Honda T, Nakamura H, Fujii M, Maeda H (2004) Differential regulation of chemical reaction in microfluidic system. New J Chem 28:1622–1626
4. Yamamoto T, Nojima T, Fujii T, (2002) PDMS-glass hybrid microreactor array with embedded temperature control device. Application to cell-free protein synthesis. Lab Chip 2:197–202
5. Lee CC, Sui G, Elizarov A, Shu CJ, Shin YS, Dooley AN, Huang J, Daridon A, Wyatt P, Stout D, Kolb HC, Witte ON, Satyamurthy N, Heath JR, Phelps ME, Quake SR, Tseng HR (2005) Multistep synthesis of a radiolabeled imaging probe using integrated microfluidics. Science 310:1793–1796
6. Ratner DM, Murphy ER, Jhunjhunwala M, Snyder DA, Jensen KF, Seeberger PH (2005) Microreactor-based reaction optimization in organic chemistry – glycosylation as a challenge. Chem Commun 5:578–580
7. Kanno K, Maeda H, Izumo S, Ikuno M, Takeshita K, Tashiro A, Fujii M (2002) Rapid enzymatic transglycosylation and oligosaccharide synthesis in a microchip reactor. Lab Chip 2:15–18
8. Huang Y, Castrataro P, Lee CC, Quake SR (2007) Solvent resistant microfluidic DNA synthesizer. Lab Chip 7:24–26
9. Lai SM, Martin-Aranda R, Yeung KL (2003) Knoevenagel condensation reaction in a membrane microreactor. Chem Commun 22:218–219
10. Taghavi-Moghadam S, Kleeman A, Golbig KG (2001) Microreaction technology as a novel approach to drug design, process development and reliability. Org Process Res Dev 5:652–658
11. Ku B, Cha J, Srinivasan A, Kwon SJ, Jeong JC, Sherman DH, Dordick JS (2006) Chip-based polyketide biosynthesis and functionalization. Biotechnol Prog 22:1102–1107
12. Kawakami K, Sera Y, Sakai S, Ono T, Ijima H (2005) Development and characterization of a silica monolith immobilized enzyme micro-bioreactors. Ind Eng Chem Res 44:236–240

Biomolecule Detection

► Fluorescent Labeling

Bionics

► Biomimetics

Biophysics

► Biomimetics

Bioprinting on Chip

Martina Daub, Roland Zengerle
Laboratory for MEMS Applications
Department of Microsystems Engineering (IMTEK),
University of Freiburg, Freiburg, Germany
daub@imtek.de, zengerle@imtek.de

Synonyms

Biochip printing; Microarray fabrication; DNA array; Protein array; Cell array

Definition

Bioprinting on chip concerns the fabrication of so-called ►microarrays or ►biochips. It comprises the deposition of a multitude of fluidic or dissolved biological agents onto solid substrates with subsequent coupling, i. e. fixation, of the organic molecules on the substrate surface. The biological substances are arranged as hundreds to hundreds of thousands of small chemical reaction areas, so-called spots, in a predetermined spatial order (ranging from the hundreds of micrometre down to the submicrometre range) to provide a 2D array. *Bioprinting on chip* involves printing techniques, microarrayers and criteria that comply with the requirements for high-quality microarray fabrication.

Overview

Generally, microarrays can be regarded as highly parallel sensors used in biomedical applications, chemical sciences, life sciences or drug discovery for studying a multitude of complex biological interactions simultaneously to determine the presence and/or amount of nucleic acids (e. g. oligonucleotides, genes, gene fragments) or proteins (e. g. antibodies, antigenes) in biological samples, e. g. in blood, cell extract or tissue extract, to investigate, for example, gene expression levels or for proteomics studies [1, 2]. Key technical challenges in creating high-content microarrays include advances in array fabrication. Additionally, to address those versatile applications, high-quality microarrays as well as high-quality microarray processing and data analysis are crucial to produce meaningful results. Quality control is needed for the whole process, including definition of microarray content, biological sample preparation, sample purification, sample quality, printing, coupling, washing, microarray quality, hybridisation, scanning, data acquisition, image analysis and data analysis [3–5]. This article focuses only on the transfer of biological molecules onto substrates.

The basic idea of all microarrays is a spatially, miniaturised arrangement of a multitude of different unique immobilised capture molecules on a two-dimensional substrate. Figure 1 shows the typical life cycle of a microarray experiment. One microarray contains hundreds to hundreds of thousands of spots. Typical substrates are glass, membranes or silicon wafers. The arranged multitude of biological agents acts as capture probes to bind molecules out of a complex biomedical sample to be

analysed in a high-throughput and parallel manner. The complex biological interactions are identified by mapping the binding event at a certain location to the specific capture molecules that were previously immobilised at that place. After hybridisation of labelled complementary molecules, i. e. binding of sterically compatible molecules, a scanning microscope detects the bound, labelled sample and measures the visualised probe to ascertain the presence and/or amount of the specific type of complementary molecule in the complex sample. Detection methods are mainly fluorescence based, but chemiluminescence, radioactivity, mass spectrometry or electrochemistry are also used.

In principle there are three main types of microarrays: DNA, protein and cell microarrays. Historically DNA microarrays were the first focus of research and gained a key position in medical and biological research. Typical applications are gene expression profiling, genotyping, sequence analysis and further gene investigations on their localisation, structure, modifications, interactions and function [6]. The proteome is the functional entity of encoded proteins by the genome. Proteins are the true targets of medicine and thus the pharmaceutical industry. Thus protein microarrays are powerful tools to provide quantitative data on a large number of samples to perform proteomics studies. The third type of microarrays, cell microarrays, provides additional functionalities not available through protein arrays where full protein functionality is only given in living organisms, e. g. through posttranslational modifications or for transmembranal proteins. Cell microarrays are intended to detect environmental toxins, to identify potential drug targets or to evaluate the specificity of drug leads by functionally characterising large numbers of gene products in cell-based assays.

The high impact of microarrays as a large-scale and high-throughput tool for biomedical applications in basic research, diagnostics and drug discovery as well as their commercial success have led to enormous efforts of different companies to provide the most suitable microarrayer system. Because of the extensive and time-consuming preparation of the precious printing agents, the reliable and effective processing of microarrayer systems is imperative. The bases for high-quality microarray printing are standardised biological and technological processes to guarantee robust biochip printing and with it reproducible microarray fabrication. Additionally, the multitude of samples shows different liquid properties which greatly influence the deposition behaviour. In contrast to the commercialized ink-jet technology, where the ink as printing medium is adapted to the printer, an ideal microarrayer would be able to deposit any liquid sample with arbitrary liquid properties. Not only the samples but also the solid substrates onto which the samples have to be deposited vary in a wide range.

Depending on the specific application, the general needs that a microarrayer should fulfil are

- to enable uniform, identical and reproducible spots in a regular array pattern with exact controllability of microarray position,
- reliable exclusion of cross-contamination (between samples) and carry-over (between successive printing processes),
- fast microarray production (speed, frequency, parallelism of printing, automation capability, short machine down times for washing steps and machine movements),
- flexibility of printing (chip layout, medium property independence, adjustability of spot size),
- minimum consumption of sample and of substrate area,
- cost-effective microarray production,
- avoid damaging of microarrayer, sample and surface chemistry of substrate,
- integrated quality control and
- robust, automated systems that are easy to handle and to maintain.

Preconditioned that the microarrayer printing properties lead to optimal results, other characteristics are crucial for high-quality microarray production. High coupling efficiency and homogeneity of the biological agent on the substrate are essential. To obtain high-quality microarrays with homogeneous spots, a further feature is homogeneous surface modification of the substrate. Environmental operation requirements include dust-free fabrication, control of temperature and relative humidity whilst printing and subsequent drying process. Associated with the wide variety of different microarray types in combination with very heterogeneous biological agents (e. g. nucleic acids, proteins, cells) there is a vast complexity of coupling types depending on coupling chemistries for the fixation of diverse biological molecules. For each application all interacting parameters have to be optimised to each other. For high binding efficiency of printed molecules onto different microarray surfaces the printing buffer has to be adapted to the kind of biological molecules and to the substrate surface chemistry. When an adequate parameter set is found, standard operating procedures enable robust microarray fabrication.

Basic Methodology

For the production of different types of microarrays a wide variety of microarray production techniques and specialised microarrayers are available. This article will focus on the three basic techniques commonly used: on-chip

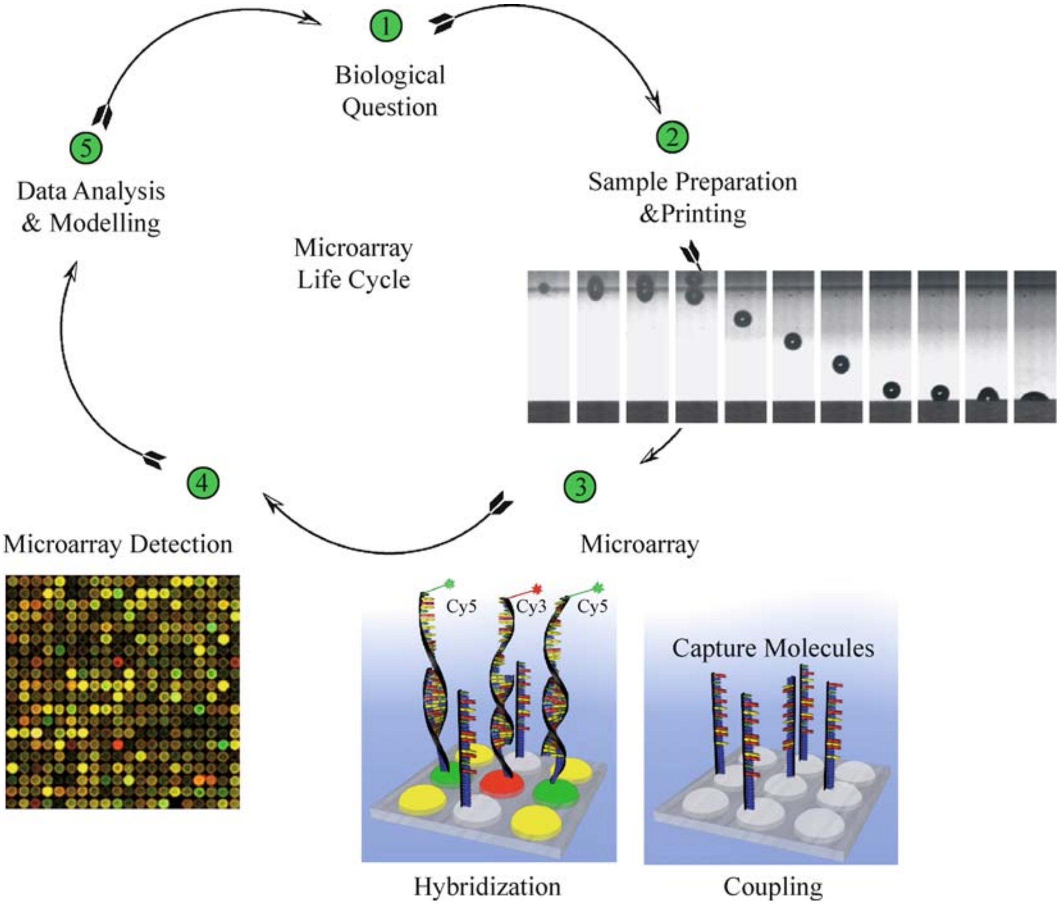

Bioprinting on Chip, Figure 1 Principle of microarray experiment. The microarray life cycle shows the five main steps needed for a microarray experiment [2]. (1) The biological question is the first step followed by (2) sample preparation including printing of the biomolecules onto the substrate. (3) The coupling of the capture molecules localised at predefined positions – so-called spots – finalises the microarray fabrication followed by the microarray reaction. A complex analyte liquid (sample) is brought into contact with the fixed capture molecules where hybridisation of matching molecules takes place. (4) In most instances the microarray analysis is fluorescence-based detection. (5) The last step includes data analysis and modelling by employing bioinformatic tools

synthesis and contact and non-contact printing techniques. In the following, currently available microarray production methods are presented, but the discussion does not claim to be exhaustive.

On-Chip Synthesis of Biomolecules

For the on-chip approaches the features of the microarray are synthesised directly on the substrate (Fig. 2). Oligonucleotides are assembled using sequential printing of oligonucleotide precursors or by photolithography approaches. On-chip approaches using printing are used exclusively by *Agilent Technologies* and called *SurePrint* technology [7]. Instead of printing the readily synthesised oligonucleotides onto the microarray surface, they are actually synthesised base by base in repeating print layers using standard phosphoramidite chemistry. An inkjet print cartridge with four heads is used, each one filled with one of the four different phosphoramidite nucleotides (A, C, G, T), the building blocks of in situ nucleic acid synthesis. The iterative oligonucleotide synthesis loop starts when the first nucleotide of each oligonucleotide is printed onto an activated glass surface. The protective 5′-hydroxyl group of the printed nucleotide is removed chemically and oxidised to activate it enabling it to react with the 3′-group of the nucleotide printed in the next print layer. The excess of unbound nucleotides is washed away so that they will not randomly react later in the synthesis. The process of printing a nucleotide followed by de-protection, activation and washing is repeated 60 times resulting in 60 mer oligonucleotide arrays. Available microarray formats on 1 in. by 3 in. microarray glass slides

include various content microarrays, e. g. whole genome microarrays of different model organisms, as well as fully customised microarrays. Microarray densities range from 1.9 K to 244 K (K means kilo features) per array; microarray formats for multiplexed arrays on single slides include 1×244 K, 2×105 K or 4×44 K, 4×22 K, and 8×15 K features. The printing process involves multiple real-time quality control feedback mechanisms of each printed layer of nucleotides. This guarantees the proper synthesis of the desired oligonucleotide sequence.

In an on-chip approach using photolithography *Affymetrix* uses a process to produce high-density oligonucleotide microarrays by a combinatorial on-chip approach. Affymetrix floods the phosphoramidites and uses light-activated deprotection by the use of masks. For each oligonucleotide synthesis step another photolithographic mask is needed. Oligomers with a length of up to 25 bases and a minimum feature size of 5 µm can be produced. Up to 100 masks have to be used for the fabrication of so-called *GeneChips*. *Affymetrix* offers a multitude of high-density microarrays for whole genome, targeted genotyping, sequencing analysis, quantification and regulation of gene expression and clinical applications. The product catalogue includes microarrays from various species like human, mouse, rat, and non-mammalian model species (e. g. yeast, plants, worms). Customised arrays are also available.

For higher flexibility *NimbleGen* and *Febit* use controllable micromirror arrays instead of masks for selective deprotection. The *NimbleGen* system is based on the Digital Micromirror Device (DMD), a solid-state array of micromirrors, which are able to pattern up to 786,000 individual pixels of light, enabling minimum feature sizes of 17 µm. These flexible virtual masks replace the physical chromium masks of the *Affymetrix* approach. This on-chip approach enables a more flexible production of small batches of high-density microarrays with different array layouts. *NimbleGen* was taken over by *Affymetrix* that now is offering both technologies.

Another company called *Febit* has integrated the DMD approach providing a highly versatile platform using a set of eight microchannel structures called *DNA processor*™. A freely user designable oligonucleotide microarray is built up inside these meandering microfluidic channels overnight in their *Geniom* device. After the oligomer building process, the hybridisation and analysis by fluorescence detection is also done in the same device. It allows the synthesis of up to eight times 6000 oligonucleotides. The major applications of *Geniom* are SNP genotyping (single nucleotide polymorphism) and gene expression profiling. Others include sequencing by hybridisation, de novo genotyping and epigenetic analysis.

Advantages of the on-chip approaches are that the systems are well established and very uniform processing is practicable. But these approaches can only be applied for the production of oligonucleotide microarrays. So far, only scientific but no commercial approaches hav been undertaken to produce peptide microarrays by an on-chip approach. Additionally, depending on the specific application, low-density microarrays and only low microarray numbers are sufficient to answer particular biological questions; thus, often small batches (hundreds) of microarrays with low density (a few hundred spots) are needed. In research applications the array layout needs to be flexible. The production of protein or cell microarrays is in high demand as well.

Contact Printing

The more commonly used approach for microarray fabrication is the deposition of pre-synthesised molecules by a microarray printer onto substrate, so-called contact and non-contact microarray printing (Fig. 3a,b). Contact arrayers use different shaped steel pins for direct deposition of droplets onto the substrate by touching the surface with the pins. Non-contact arrayers are similar to commercial piezo-driven ink-jet printers and deposit a droplet onto the substrate without coming into contact with the substrate surface. Microarrayers which use other technical approaches are also commercially available and will also be discussed.

Contact printing technologies were used from the beginning of microarray technology. They are based on pin tools, which are dipped into the sample solution and take up a small volume of sample. Then they are brought in contact with the slide surface where they deliver the sample as a small spot. Whilst moving the pins away from the surface, the adhesion forces between sample and substrate lead to retention of small volumes on the substrate. In this system the spot volume metering is determined by the interaction between the pin, the transferred fluid and the substrate. *TeleChem International* is one of the major pin suppliers for contact printing [8]. The catalogue includes pins and printheads of different brands like *ChipMaker, Stealth, ArrayIt* and printheads for *BioRobotics, Robodesign, Genetix* and *NanoPrint* robots. Their pins deliver spot volumes from 0.5 nl to 12 nl, resulting in spot diameters from 62.5 µm up to 600 µm. After each deposition solid pins need to be re-dipped for sample loading. Thus, specially shaped pins were developed to allow several depositions with one dipping action, e. g. capillary tubes, tweezers, microspotting pins or split pins. They are available with reservoir capacities from 0.25 µl to 1.25 µl of sample solution. Another way to circumvent re-dipping

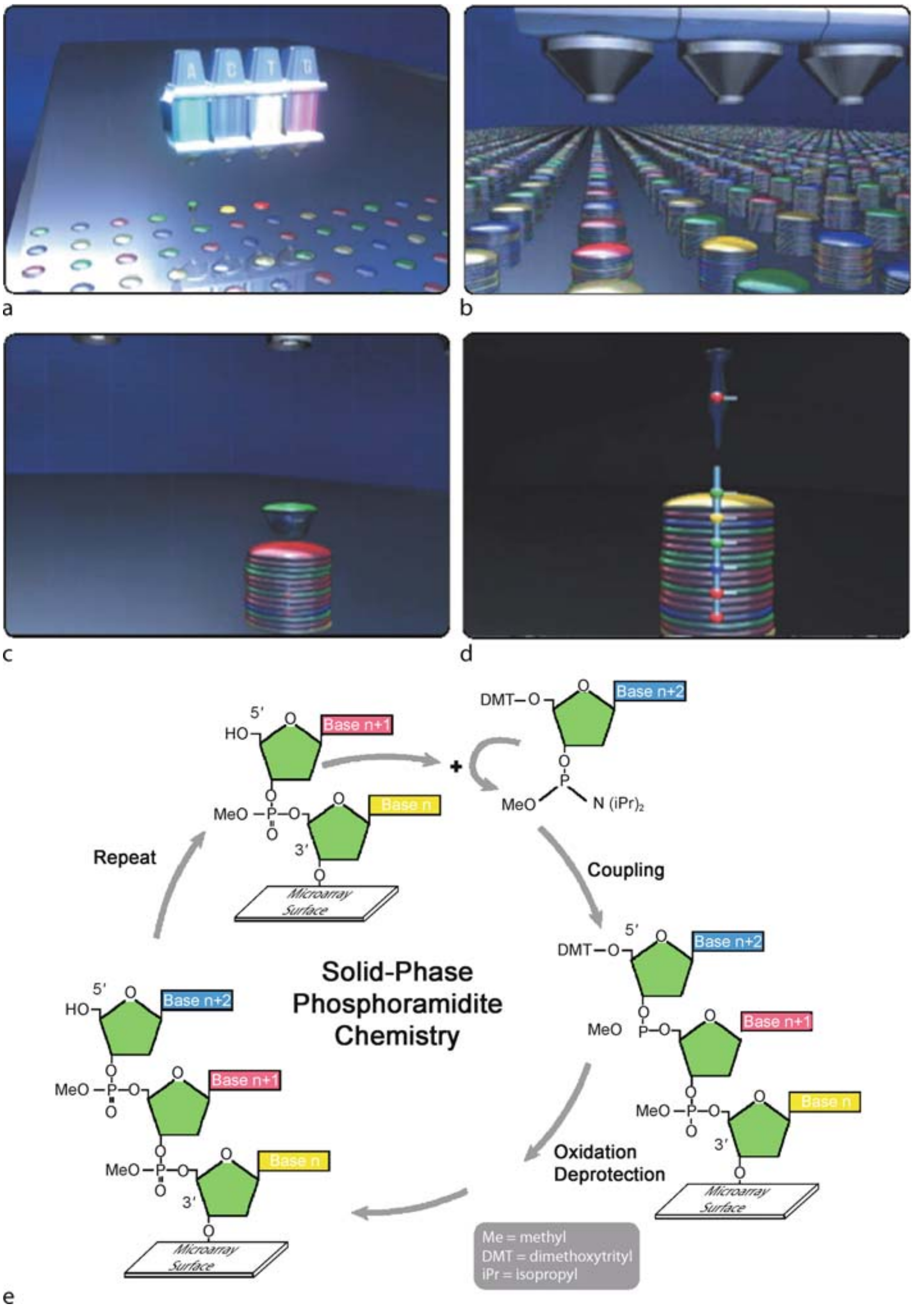

Bioprinting on Chip, Figure 2 On-chip synthesis of oligonucleotide microarrays using *SurePrint* technology of *Agilent Technologies* [7]. A schematic of the general mechanism via ink-jet printing shows (**a**) the first layer of nucleotides being deposited on the activated microarray surface. (**b**) The growth of the oligonucleotides after multiple layers of nucleotides have been precisely printed. (**c**) A close-up of one oligonucleotide as a new base is being added to the chain, which is shown in (**d**). (**e**) The general cycle of oligonucleotide synthesis via phosphoramidite chemistry (courtesy of *Agilent Technologies*)

is the pin-and-ring technology. A small ring is dipped into the sample solution. The surface tension of sample is used to form a fluid layer within the ring. A solid pin is pushed through the fluid layer and the trapped sample is deposited onto the surface. After retraction of the pin the fluid film is still intact and fluid is replenished from the ring. Commercially available contact printers are offered, for example, by *Genemachines*.

The contact printing technology is currently most commonly used to produce DNA microarrays. The advantage of pin-based printing technologies is the robust transfer of liquid by direct contact of the tip of the pin with the surface to be printed on. But this implies the risk of damaging the substrate surface by mechanical load during printing. To avoid this, the microspotting pins deposit samples without touching the pin to the substrate. Spots are produced with a 25 μm distance between pin and substrate surface. To produce a high number of arrays in a reasonable time, it is necessary to use many pins in parallel, typically up to 48. An accurate and precise volume deposition depends on the interaction between the pins, the sample and the slide surface. Therefore only mechanically very precisely produced pins will deliver the same volume consistently and reliably. Additionally, a careful pre-selection process of the pins combined with an accurate adjustment is needed to obtain a set of pins that are uniform in size, shape and height. Due to the adhesion force dependence of the contact printing process the printing media should be similar in media properties to produce equal spot sizes.

Non-Contact Printing

In non-contact printing techniques the liquid metering is not determined by the complex interplay of the pin, the liquid and substrate, but is separated from the substrate, because no contact between the printing tool and the substrate occurs (Fig. 3c–e). The fluid is ejected as a flying droplet or jet towards the surface from a certain distance, which makes metering more precise in many cases. Usually the dispensing units of non-contact printers come with a reservoir, enabling the dispensing of thousands of droplets without the need of interim refilling. Capillary forces or active pumping mechanisms are used to transport the liquid through microchannels or tubes from reservoirs to the dispensing orifices.

One concept of non-contact printing is based on syringe–solenoid-driven printers. In the syringe–solenoid concept a reservoir and a high-speed microsolenoid valve are connected to a high-resolution syringe (e. g. *synQUAD* system provided by *Genomic Solutions*). Within the *synQUAD* dispensing platform *PreSys 4040XL* containing an eight channel dispense head the system is filled with system liquid. Operating the syringe causes the sample to move into the tip. The syringe pressurises the system and if the microsolenoid valve is opened, droplets are dispensed out of the tip. This system delivers volumes from 20 nl to 20 μl per ejection process.

Further non-contact microarrayers are piezoelectrically driven. Companies like *MicroDrop*, *PerkinElmer*, *Scienion* and *GeSim* use a technology that is similar to ink-jet printer technology. The printers of *MicroDrop, PerkinElmer* and *Scienion* are based on glass tips. Each glass tip is surrounded by a piezo actuator. The dispenser tip of *GeSim* consists of bonded silicon and glass layers. A piezo actuator is fixed at the top of the dispenser tip. In all piezo tip systems the samples are aspirated into the tip by applying a slight vacuum at the back end of the capillary. The squeezing of the tip forced by the piezo actuation induces droplet ejection out of the capillary. The fast response time of the piezoelectric crystal permits fast dispensing rates (kilohertz range). The small deflection of the crystal generates droplet volumes from hundreds of picolitres to a few nanolitres.

For higher throughput, parallel systems were built with four (*PerkinElmer Piezorray*) and sixteen piezo tips (*GeSim Nano-Plotter NP 2.0*). Horizontal alignment of all tips to the substrate surface is not as critical as for contact printers. However, each tip has its own specific piezo actuator necessitating calibration of each tip to enable homogeneous droplet ejection. Usually the tips are produced in small batches in a handmade process, so an accurate quality control of tips is needed to ensure the high precision of tip geometries. Overall non-contact printing approaches provide less spot-to-spot and chip-to-chip variability than contact printing methods.

Another non-contact microarrayer using the *TopSpot* technology is offered by *Biofluidix* [9]. This technology enables high-throughput printing of microarrays. The *TopSpot* technology can be applied to the production of custom made low- to mid-density microarrays containing up to several thousands of different probes on a substrate. A key element of the *TopSpot* technology is the micromachined printhead which can be loaded with 24, 96, or up to 384 different samples. The reservoirs comprise one to several microlitres of printing medium. All liquids are printed onto a substrate simultaneously by a micronozzle array contained in the printhead. The microarray is then formed by the individual droplets on the substrate having a pitch of 500 μm. For each droplet only about one nanolitre of liquid is consumed. Therefore a printhead can create several thousand microarrays with one filling. The printhead is operated in the so-called print module, which is designed to apply a pressure pulse to the printhead via a piston such that droplet generation is initiated. For this purpose the piston is driven with a high velocity by a piezo actuator. The major advantage of the *TopSpot* technology over other nanolitre dispensing systems (e. g. an ink-jet printer) is that each nozzle can be supplied with another printing medium. The inherent parallelisation of the printhead increases the speed without the need of complicated automation systems. By using only one actuator unit to generate the pneumatic driven droplet dispensing out of

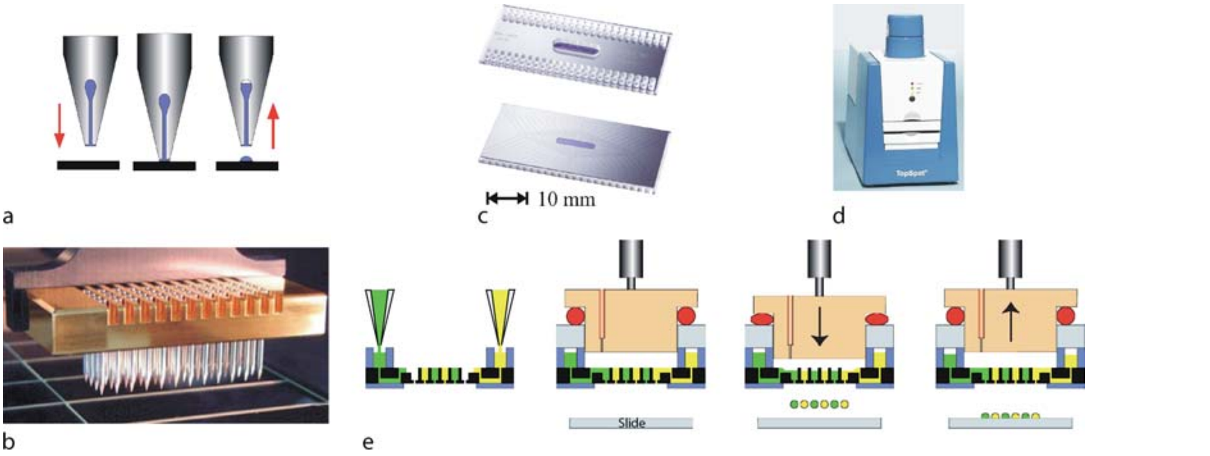

Bioprinting on Chip, Figure 3 Contact and non-contact printing. Contact printing mechanism of *TeleChem International Inc.* [8]. (**a**) *Micro-spotting pins* enable high-speed manufacture of microarrays. The pins have flat tips and defined uptake channels, which allows a thin (25 μm) layer of sample to form at the end of the pin, and printing to proceed by gentle surface contact. Printing occurs as a simple three-step *ink-stamping* process as follows: (left) downstroke, (centre) contact, and (right) upstroke. (**b**) Printing with 48 pins in parallel using the *ArrayIt*® microarray technology equipped with a *Stealth 48 printhead* fitted with *48 SMP3 microarray spotting pins* ((**a**), (**b**) by courtesy of *TeleChem*). Non-contact printing of microarrays using *TopSpot*® technology of *Biofluidix GmbH*. (**c**) Core of the *TopSpot*® technology [9] is the microfabricated printhead ((top) top view, (bottom) bottom view of a 96 position printhead) allowing highly parallel microarray fabrication. (**d**) The benchtop *TopSpot*® machine operating one printhead within a print module. (**e**) Schematic cross-section of the operating principle in four steps starting with filling of the printhead reservoirs. Via a piezostack actuator an air pressure is generated within the actuation chamber above the nozzle array that simultaneously affects all nozzles resulting in droplet ejection of 96 droplets ((**c**), (**d**), (**e**) by courtesy of *Biofluidix*)

all nozzles simultaneously, no calibration of multiple actuator units is needed. Several printheads can be lined up to generate microarrays with higher content.

Other Deposition Methods

In addition to on-chip approaches and contact and non-contact printing of agents onto microarrays there are further methods for microarray fabrication. Two examples are the protein profiling chips offered by the company *Zyomyx* and the electronic microarrays offered by the company *NanoGen*.

Zyomyx offers an all-in-one system for protein profiling. The system is provided as a comprehensive package that includes an assay workstation, a biochip scanner, data analysis software, assay reagents containing the calibration analytes and internally validated biochips. Each biochip is designed to assay up to 200 different proteins in each one of six separate flow cells. Every flow cell can be run with a sample volume of 25 μl. The chips are provided ready-to-use, and fully loaded with specified capture antibodies. The protein profiling biochips are fabricated by silicon micromachining. Every flow cell contains an ordered array of 200 micropillars, each one with a height of 150 μm and a diameter of 50 μm. Specific capture agents are directionally bound to the top of each pillar.

The core of *NanoGens* technology is the *NanoChip Electronic Microarray*. It consists of a silicon chip capable of rapid identification and analysis of biological molecules. The technology utilises the natural positive or negative charge of most biological molecules. Applying an electric current to individual test sites on the *NanoChip* enables rapid movement and concentration of the molecules. Molecular binding onto the test sites is accelerated 1000 times compared to traditional passive methods. Currently *NanoChips* with 100 or 400 test sites for DNA and RNA analysis are commercially available. The sites have diameters of 80 μm and a pitch of 200 μm. The *NanoChip* microarray technology provides an open platform that allows customers to run common assays as well as customise their own assays. Applications include SNP analysis, and insertion, deletion and mutation analyses.

Another deposition method for fabricating microarrays containing functional proteins for surface immunoassays is so-called microcontact printing. The Delamarche group [10] uses a microfluidic chip that comprises a number of independent capillary systems, each of which is composed of a filling port, an appended microchannel and a capillary pump. Each capillary system fills spontaneously driven by capillary forces, the flow through the channels being driven by evaporation employing Peltier-controlled cooling and heating. The sandwich fluores-

cence immunoassay takes place on the surface of a polydimethylsiloxane (PDMS) slab, which is placed across the microchannels. After precoating of the PDMS surface with capture antibodies the binding sites of analyte molecules are localised by using the chip, then the captured analyte molecules are bound to a second fluorescently labelled antibody using a second chip that is directed orthogonally to the first chip. The assay results in a mosaic of fluorescence signals on the PDMS surface which are measured using a fluorescence scanner.

Coupling of Capture Biomolecules

An indispensable factor for high-quality microarray fabrication performed with contact or non-contact printing is the efficient and homogeneous fixation of biological molecules on the substrate surface, so-called coupling. The printing system in combination with other interacting parameters like substrate surface chemistry, type of biological agents, printing buffer composition, immobilisation protocols and washing procedures have to be optimised to each other. It is important to distinguish between, for example, nucleic acid or protein or cell microarrays.

Nucleic Acid Microarrays

Within the above mentioned microarray categories further partition into sub-categories makes it even more complex. Nucleic acids comprise various configurations and lengths, e. g. oligonucleotides, cDNA, RNA and plasmids, with diverse properties leading to different coupling requirements. First of all the choice of substrate combined with adequate surface chemistry is relevant to couple nucleic acids onto the substrate surface. For high-sensitivity measurements an important precondition is the low autofluorescence of substrate and coating and the absence of non-specific background to ensure high signal-to-noise ratios. Most commonly used are glass substrates on which functional aminosilanes are deposited to form layers on the substrate to which the capture molecules can be bound. Some examples of such functionalised organosilane compounds are APTES (3-aminopropyltriethoxysilane), AEA (*N*-(2-aminoethyl)-3-aminopropyltrimethoxysilane), AEEA (3-(2-(2-aminoethyl)-ethylamino)-propyltrimethoxysilane) and GOPS (3-glycidoxypropyltrimethoxysilane). These monovalent and multivalent cations are known to condense DNA into higher ordered structures. Another glass substrate modification is the NHS ester modification to couple the proteins by EDC-NHS chemistry (EDC is *N*-(3-dimethylaminopropyl)-N'-ethylcarbodiimide; NHS is *N*-hydroxysuccinimide). Thereby NHS-esters react with amines to form amide bonds. EDC is a cross-linker that effects direct coupling between carboxylates (−COOH) and primary amines ($-NH_2$). A third method is the coating of glass substrates with functional epoxy groups to react with amino-functionalised biomolecules. Substrates other than glass are nitrocellulose, nylon or cellulose acetate membranes, and polymer substrates such as COC (cyclo-olefin copolymer) or PMMA (poly(methyl methacrylate)). As for all kinds of microarrays, the coupling chemistry used has to be optimised relating to all interacting parameters like capture molecules, substrate, printing buffer, immobilisation protocol, etc. Besides a stable, reproducible and established production process, strict internal manufacturing controls are crucial for low batch-to-batch variations. The quality of biomolecule coupling onto the slide surface depends on coupling chemistry of the substrate surface and the reproducibility of the surface properties.

Parameters that have to be adapted to the specific application are printing buffer, including buffer system (e. g. phosphate, carbonate, borate based; corresponding acid–base pair; salt components), concentration, pH value and additional supplements such as DMSO (dimethylsulfoxide) and betaine. The printing buffer composition has to be optimised according to the printing molecules, the substrate surface and the immobilisation protocol used. Within this protocol varying parameters that have to be adapted are, for example, incubation times, temperature curves and relative humidity. Commonly used approaches for immobilisation are incubation in a heated water bath or in an oven. Additionally the washing procedure to remove unbound molecules after coupling has to be adapted.

Protein Microarrays

Proteomic profiling will yield more direct answers to the current biological and pharmacological questions, because the majority of known biological effector molecules, diagnostic markers and pharmaceutical targets are proteins, not mRNA or DNA. Protein microarrays are expected to significantly expedite the discovery of new markers and targets of pharmaceutical interest, and to have the potential for high-throughput applications. In particular, antibody and cell lysate microarrays have the potential to revolutionise protein expression profiling. Where functionality is only given in living cells, also cell microarrays become relevant. The main precondition for protein and cell microarrays is that the capture proteins or cells are kept in a functional state after being immobilised to the microarray substrate by exclusion of protein denaturation or cell lysis.

Protein microarrays can be classified into three general categories regarding their applications: expression profiling, interaction profiling and functional identification. Protein expression profiles reflect the concentration profile

of proteins depending on the cell or tissue status (e. g. cell type, age, environmental conditions, disease state). Antibody arrays are the main tool to perform protein expression profiling. Protein interaction profiling is most critical to drug discovery since many drugs and toxins affect protein–protein interactions. With so-called proteome arrays, which are microarrays with the whole proteome or a subset of it immobilised to the substrate surface, protein interactions can be categorised at a large scale. At the same time more precisely specific domain–domain interactions can be identified. Besides purified proteomes and proteome subsets, interaction profiling can be based on various other immobilised capture molecules, e. g. antibodies, antibody fragments, engineered binding proteins or even aptamers. Also microarrays of immobilised antigens have been developed, e. g. for profiling the reactivity of antisera. The spots of protein microarrays can also consist of complex samples, such as blood sera or cell lysates, which can be probed, for example, against a single antibody. The microarrays of this approach are termed reverse phase microarrays. The most seminal field is the decoding of protein function. At present only for a small population of proteins is the function known. The identification of the particular function for each protein connected with manifold interactions among each other is the goal of proteomics studies and to utilise the knowledge gained about regulatory processes for the healthcare and pharmacological industry.

In contrast to DNA microarrays, production of protein microarrays is an immense technological challenge. The first challenge derives from the limited availability of proteins for the fabrication of vast amounts of protein microarrays. Whereas for DNA with the *polymerase chain reaction (PCR)* a routine method exists to enormously increase the number of DNA copies and automated processes are established for oligonucleotide synthesis, for proteins such methods are missing; hence, proteins are produced in very small quantities. Furthermore, the biochemistry of proteins is orders of magnitude more complex than DNA biochemistry, so that the production of protein microarrays is much more difficult. Whereas DNA is a relatively simple polyanion and can be modified and easily immobilised on solid surfaces based on electrostatic interactions or covalent bonding, protein bonding is much more delicate. The complexity derives from a multitude of biochemical properties. Protein molecules possess particular three-dimensional structures, varying chemical and physical properties (e. g. hydrophilic and hydrophobic domains, ionic interactions) and the activity and function as well as the partial charge of domains depend on the local physical and chemical microenvironment. Additionally, complexity is further increased by posttranscriptional modifications of protein conformation; hence the well-established on-chip approaches of oligonucleotide microarrays are not applicable to protein microarrays. For protein microarray production four major requirements have to be fulfilled:

- speed of protein production and accurate purification,
- minimisation of background caused by unspecific protein binding to obtain high signal-to-noise ratios,
- native protein conformation and orientation on substrate surface and
- protein detection and identification.

A protein interacts with other molecules through specific functional domains. Hence, native conformation and orientation of the immobilised capture molecules are indispensable for meaningful results from protein microarrays. The most problematic factor is the potential of inadvertent masking or degradation of epitopes of antibodies, active sites of enzymes or binding sites of receptors. Thus surface chemistry plays a critical role in protein microarrays where the surface chemistry should provide an inherently inert surface that resists non-specific binding in combination with integrated functional groups that ensure facile, highly specific and oriented immobilisation of native proteins.

For protein immobilisation the most commonly used method is the EDC–NHS affinity ligand coupling chemistry as described for DNA bonding to glass substrates. An advanced surface coating method for protein microarrays was developed by the company *MicroSurfaces*. A *poly(ethylene glycol)* (PEG) surface coating, arranged as a high-density brush to provide a zero background surface, is functionalised with molecules that mediate biomolecular binding. The kind of molecules depends on the interaction mode and the application. Surfaces are functionalised with biotin or streptavidin, chelated copper, epoxy functional groups or NHS to mediate binding of streptavidin- or biotin-labelled proteins, polyhistidine-tagged proteins (with Cu^{2+}). The epoxy functional groups are used to covalently attach proteins in purified form via amine groups.

Cell Microarrays

For cell microarray printing additional elementary demands have to be addressed by the printing technology. A highly reproducible number of living cells per spot on microarray slides and an optimised printing process that is qualified for reproducible production of cell microarrays along with keeping their vitality and function for analysis are essential. There are two fundamental methods to produce cell microarrays. The indirect method was developed by J. Ziauddin and D.M. Sabbatini (2001) [11]. To produce

transfected cell microarrays a mixture of gelatine, acting as an anchor, containing different DNA molecules for transfection purposes is printed onto a glass substrate using a standard pin printing arrayer. After drying of gelatine–DNA spots the substrate is incubated with a cell suspension containing the transfective agent. This induces incorporation of DNA into the cells, resulting in cell microarrays of differently transfected cells. In the direct method the different cell types themselves are printed onto the substrate. In some publications contact-based microarrayers are used, but more often non-contact-based devices like modified ink-jet printers or piezo-driven tips are used.

The construction of chemically modified solid supports is of particular importance in cell-based microarrays. For cell immobilisation on substrates the most commonly used method is the binding to poly-L-lysine-coated slides. Binding of cells results from ionic interactions between the cell membrane and the positively charged poly-L-lysine surface. This method is most effective for adherent cell types. To promote cell adhesion, surfaces coated with extracellular matrix (ECM) proteins such as collagen or fibronectin have also been employed. In some cases, polymer-treated surfaces are used in conjunction with the above mentioned compounds to reduce non-specific adhesion.

Companies that offer microarrays and associated services are *Affymetrix, Agilent Technologies, GE Healthcare Bio-Sciences, Applied Biosystems Applera, BD Biosciences Clontech, BF-BIOlabs, BioCat, Biomol, Biozym Scientific, Cambrex Bio Science, Chemicon, Chipron, CLONDIAG chip technologies, Clontech Laboratories, Eppendorf, Gene Expression Center, Genetix, Greiner Bio-One, Hypromatrix, Invitrogen, KFB, Merck Biosciences, Miltenyi Biotec, MoBiTec, MWG Biotech, Panomics, Randox Laboratories, Schleicher&Schuell BioScience, Scienion, Sigma-Aldrich Chemie, SIRS-Lab* and *VBC-GENOMICS*, to name just a few.

Key Research Findings

Accelerated Molecule Interaction Research

After more than fifteen years of microarray research the technology holds a momentous position ranging from fundamental screening to clinical diagnostics. The first paper reporting the use of microarrays was published in 1989 by Ekins and co-workers. The microarray technology has since undergone numerous refinements, iterations and adaptations regarding the steadily increasing number of applications. The number of interactions to be measured and with it the variety and diversity of microarrays steadily increases. Fields of application include the investigation and treatment of various diseases (e. g. cancer, infectious diseases, autoimmune responses) to improve diagnostic accuracy and to predict treatment efficiency. This is supported by advanced elucidation of regulatory processes including cell signalling pathways, molecular interaction studies and regulation of transcription and replication where malfunction may also lead to disease development. Advanced identification of biomarkers and pharmacological target discovery accelerates pharma research and development.

Gene Expression Profiling, Deciphering Whole Genomes and the First Clinically Accredited Arrays

Most early microarrays provided gene expression profiling studies in order to identify genes of interest that may be over- or underexpressed in some defined biological condition. Fabrication of those microarrays required cloning of complementary DNA (cDNA) sequences copied from isolated messenger RNA (mRNA) out of cells or tissues, followed by subsequent amplification by PCR. The PCR product from each clone was then deposited on microarrays. The subsequent concept of oligonucleotide arrays allowed scientists a higher degree of flexibility for microarray design because of the independence of available clone sequences. Further advantages of oligonucleotide arrays vs. cDNA arrays are better reproducibility, streamlined workflow and lower fabrication costs. In combination with the complete mapping of the human genome early in 2001 (further refining of sequencing is still ongoing) and other genomes of various model organisms (e. g. the bacterium *Escherichia coli*, the yeast *Saccharomyces cerevisiae*, the roundworm *Caenorhabditis elegans*, the fruitfly *Drosophila melanogaster*, the laboratory rat *Rattus norvegicus* and the laboratory mouse *Mus musculus*) the microarray technology has opened new perspectives. Nowadays several companies (e. g. *Agilent Technologies, Affymetrix, TeleChem/ArrayIt, Applied Biosystems*) offer products that enable scientists to probe gene expression from entire genomes on one single microarray. The knowledge gained improves DNA diagnostics, genotyping, proteomics as well as pharmacogenetics studies. By data analysis using clustering tools, the resulting signatures allow typing of genes linked with, for example, cancer pathogenesis and metastasis and with it to guide treatment options and to avoid ineffective treatment. *Agendia* (based on *Agilent Technologies'* custom microarray) is the first company worldwide to be granted the ISO 17025 accreditation (2005) for its *MammaPrint* gene expression service to classify breast cancer patients as at low or high risk of developing distant metastasis in a ten-year period. In 2006 a further accreditation for *Agendias CupPrint,* to identify cancer of unknown primary that concerns 4% of all cancer diseases, was granted.

Encoded Proteins Manifest Gene Function

Additionally, research has greatly benefited from the post-genomic era. Despite the success of DNA microarrays in gene expression profiling or mutation mapping, it is the activity of encoded proteins that directly manifests the gene function. So protein microarrays have been applied in biomarker discovery, protein profiling, protein–protein interaction analysis and peptide mapping applications. It seems that especially antibody microarrays have the potential to revolutionise the progress in protein expression profiling. With it, for example in drug discovery, one seeks to develop a biological or chemical entity that will improve the disease symptomatology or actually treat the underlying pathophysiological basis of the particular disease state. Protein expression profiling in cell or tissue extracts enables one to elucidate pathways and to identify mechanisms involved in gene regulation. Antibody arrays are available from various companies (e. g. *Sigma-Aldrich, Invitrogen, Genetix, Clontech Laboratories, Hypromatrix, Chemicon, Panomics*).

To identify splicing variants of mRNA by exon-level expression profiling, exon microarrays are offered by, for example, *Affymetrix, ExonHit Therapeutics* together with *Agilent Technologies*. This approach takes into account that one gene encodes for multiple different proteins by alternative splicing, i. e. small blocks of transcribed mRNA can be rearranged in multiple various combinations to form different transcripts from the same gene. Splicing variants of proteins cannot be detected on the DNA level and are supposed to be involved in several diseases.

Cell Arrays for Interaction Studies in Life Processes

In similar fashion to DNA and protein microarrays the ability to create arrays of cells and even tissues at high-density offers the potential for the development of cell-based sensors with extremely high throughput and multiplex capability. Research on biomolecular interactions on the genomic, the proteomic and the cellular level paves the way for advanced understanding of the function of the human genome and to unravel the complexity of biological pathways and cellular networks that control life processes.

Progress in Microarray Fabrication Techniques

These advances in life science research using the highly parallel microarray technology would not have been possible without enormous progress in bioprinting on chips. For microarray fabrication the on-chip approach to synthesise capture molecules on chips is well established and highly reproducible. But it is only applicable to oligonucleotide arrays. The deposition of cDNA by contact and non-contact printing is also highly developed, and integrated quality control mechanisms guarantee high-quality microarray fabrication. The higher complexity of protein microarrays compared to nucleic acid microarrays leads to greater demands regarding bioprinting on chip. This implies correct folding of the capture molecules on the microarray surface to achieve reproducible results. Binding sites of bound proteins need to be accessible and in native conformation to act as functional capture molecules to deliver valid results. Additionally, posttranslational modifications, e. g. phosphorylation, methylation or farnesylation, might play an important role for reliable molecular interactions with other proteins as well as with nucleic acids.

Cell microarray printing implies the exclusion of shear forces during the printing process to keep the cells on the chip alive. Additional specific supplements within the printing buffer can prevent cells from breaking during the printing process. There are different approaches to couple living cells on a substrate surface. First of all – for adherent cells – the cellular adhesion can be used to keep the cells at the spot positions. This could be aided or mediated by binding of discrete areas of *poly-l-lysine* or *extracellular matrix protein* acting as kind of adhesive agent within the spot areas. An application of recent cell microarray studies is the parallel investigation of cell adhesion forces of different permanent cell lines on different polymer substrates. To couple non-adherent cells to generate a microarray containing living cells could be mediated by specific anchor molecules that are located within spots on the surface. One end of these anchor molecules binds to the substrate surface and the other end is a transmembranal region that incorporates into the cell membrane, connected by a spacer in between.

Future Directions for Research

Clinical Diagnosis and Treatment Prediction

With the progressive development of the capabilities that microarrays provide, comprehensive investigations lead to new insights into regulatory processes within cells to elucidate cellular processes like transcription and replication as well as protein expression. With the complete sets of genes of organisms available, studies of gene regulation and interactions are available for scientists. Using this technology, coherences of cellular processes and health can be discovered and used to develop new drugs and to improve healthcare by advanced diagnostics and treatment prediction by assessing related gene signatures. The first steps towards diagnostic microarrays and treatment prediction are being taken with the ISO accreditation of *MammaPrint* and *CupPrint* arrays by *Agendia*. Another

step forward into the clinic was the approval of *AmpliChip (Roche Diagnostics)* by the *FDA (US Food and Drug Administration)* in 2005. The pharmacogenetic *AmpliChip* helps physicians to tailor patient dosages of drugs that are metabolised differentially by cytochrome P450 enzyme variants. These real medical applications of microarrays will lead to a gathering of momentum towards the wide field of medical applications that was anticipated years ago. Commercialisation towards real medical application beyond pure research breaks into new markets.

Reliability of Microarray Data, Standardisation and Terminology

Currently the progress to utilise microarray studies for clinical practice is further supported by the *FDA*. Under the auspices of *FDA* scientists, combined community-wide efforts are ongoing within the *MAQC project (MicroArray Quality Control)* dealing with the objective assessment of seven microarray platforms to experimentally address the key issues surrounding the reliability of DNA microarray data. The project aims at the set-up of guidelines for using microarrays in clinical practice and regulatory decision-making. Studies aiming at intraplatform reproducibility and analytical consistency across microarray platforms that are indispensable to translate the technology from pure research to clinical application are the main subject.

An important starting point to perform reliable microarray experiments and to gain meaningful information is the biological question and with it choosing the optimal microarray type (nucleic acid vs. protein vs. cell vs. any other kind) and information content (low-, mid-, high-density array) together with an adequate platform for each experiment. Furthermore a range of quality control for all successive processes and protocols is required.

In the very beginning of making sense out of microarray experiments enormous discrepancies between microarray results appeared. Furthermore standard formats for microarray data to share data and results were missing. One effort towards standard generation in microarray data handling started in 2001. Brazma et al. published in 2001 the *Minimum Information About a Microarray Experiment (MIAME)* that describes the minimum information that is needed to enable the interpretation of the results of the experiment unambiguously and potentially to reproduce the experiment and is aimed at facilitating the dissemination of those data [12]. The *Microarray Gene Expression Data Society* (MGED) further refined those efforts in 2002 with a publication of Spellmann et al. [13] with the design and implementation of *MicroArray Gene Expression Markup Language* (MAGE-ML), followed by the set-up of standards and ontologies for microarray databases and for high-throughput data sharing. Those efforts towards standardisation and community-wide usability of generated data and results lead to the accord that with careful experimental design and appropriate data transformation and analysis, microarray data can indeed be reproducible and comparable among different formats and laboratories. One major outcome is that statistical analysis in regulatory submissions and clinical diagnostics is likely to be different from that used in basic research and discovery. This study can be used as a solid foundation for combining other microarray studies to realise the comprehensive potential by accumulating microarray results to enlarge understanding of biological processes and with it pave the way for new healthcare uses.

Microarray Evolution

DNA sequencing is another challenge to unravel coherences between DNA sequence and DNA function. Deciphering the whole genome of organisms leads to new possibilities by comparison of sequence differences interacting with their resulting phenotypes. The differences between human beings are small and the unique DNA sequences differ by only about 0.1%, regardless of ethic origin. These genetic differences encode for how humans look and to what diseases they are susceptible. Furthermore they can be used for evolution studies as well as for historical migration patterns of humans across the world.

The numerous different types of microarrays in combination with the widespread fields of applications claim for advanced microarray fabrication technologies that are adapted to the specific needs regarding speed and flexibility. For all technologies reproducibility and robust processing as well as accuracy and printing precision should be taken for granted. With the ongoing and shifting usage of this tool further innovative platforms will appear.

Taken together these various capabilities that microarrays provide make high demands on bioprinting on chip technologies and therewith coupling chemistries. The important conclusion is that the microarray technology will continue to dramatically change over time as our picture of regulatory processes becomes more sophisticated and complete. With it the relevant microarray fabrication technologies and microarray platforms have to develop further associated with the increasing requirements.

Cross References

- ► Capillary Filling
- ► Cell Culture (2D and 3D) on Chip
- ► Cell Patterning on Chip
- ► DNA Micro-arrays
- ► Droplet Dispensing
- ► Droplet Evaporation

- ► Evanescent-Wave Sensing
- ► Fluorescence Measurements
- ► Fluorescent Labelling
- ► Hydrophilic/Hydrophobic Patterning
- ► Methods for Surface Modification
- ► Supersonic Micro-Nozzles
- ► Proteomics in Microfluidic Devices
- ► Surface Tension Driven Flow
- ► Capillarity and Contact Angle
- ► Van der Waals Interaction Forces

References

1. Hardiman G (2003) Microarray technologies - an overview. Pharmacogenomics 4(3):251–256
2. Schena M (2000) Microarray Biochip Technology, 1st edn. Eaton Publishing Company/Biotechniques Books, Natick
3. Allison DB, Page GP, Beasley TM, Edwards JW (eds) (2006) DNA Microarrays and Related Genomics Techniques: Design, Analysis, and Interpretation of Experiments. Chapman and Hall/CRC Press, Boca Raton
4. Zhang W, Shmulevich I, Astola J (2004) Microarray Quality Control. Wiley, New Jersey
5. Simon RM, Korn EL, McShane LM, Radmacher MD, Wright GW, Zhao Y (2004) Design and Analysis of DNA Microarray Investigations. Springer, New York, Berlin, Heidelberg, Hong Kong, London, Milan, Paris, Tokyo
6. Kronick MN (2004) Creation of the whole human genome microarray. Expert Rev Proteomics 1(1):19–28
7. Agilent Technologies, Inc. (2003) Agilent SurePrint Technology. http://www.chem.agilent.com/temp/radADA68/00039489.pdf. Accessed 17 Nov 2006
8. TeleChem International, Inc. (1998–2005) Stealth Microarray Spotting Pins and Printheads, Products, Printing Technology. http://arrayit.com/Products/Printing/Stealth/stealth.html. Accessed 17 Nov 2006
9. Biofluidix GmbH (2005–2006) http://www.biofluidix.com. Accessed 17 Nov 2006
10. Cesaro-Tadic S, Dernick G, Juncker D, Buurmann G, Kropshofer H, Michel B, Fattinger C, Delamarche E (2004) High-sensitivity miniaturized immunoassays for tumor necrosis factor alpha using microfluidic systems. Lab Chip 4(6):563–569
11. Ziauddin J, Sabatini DM (2001) Microarrays of cells expressing defined cDNAs. Nature 411(6833):107–110
12. Brazma A, Hingamp P, Quackenbush J, Sherlock G, Spellman P, Stoeckert C, Aach J, Ansorge W, Ball CA, Causton HC, Gaasterland T, Glenisson P, Holstege FC, Kim IF, Markowitz V, Matese JC, Parkinson H, Robinson A, Sarkans U, Schulze-Kremer S, Stewart J, Taylor R, Vilo J, Vingron M (2001) Minimum information about a microarray experiment (MIAME)-toward standards for microarray data. Nat Genet 29(4):365-371
13. Spellman PT, Miller M, Stewart J, Troup C, Sarkans U, Chervitz S, Bernhart D, Sherlock G, Ball C, Lepage M, Swiatek M, Marks WL, Goncalves J, Markel S, Iordan D, Shojatalab M, Pizarro A, White J, Hubley R, Deutsch E, Senger M, Aronow BJ, Robinson A, Bassett D, Stoeckert CJ Jr, Brazma A (2002) Design and implementation of microarray gene expression markup language (MAGE-ML). Genome Biol 23;3(9)

Biorecognition

Definition

Biorecognition is the ability of a biologically derived entity (molecule or pathway) to reproducibly identify an analyte target and to generate a predictable response commensurate with that recognition reaction.

Cross References

- ► Impedimetric Biosensors for Micro and Nano Fluidics

Biosafety

- ► Lab-on-Chip Devices for Biodefense Applications

Biosample Preparation by Lab-on-a-Chip Devices

Jongyoon Han[1], Jianping Fu[2], Ying-Chih Wang[2], Yong-Ak Song[2]

[1] Department of Electrical Engineering and Computer Science and Department of Biological Engineering, Massachusetts Institute of Technology, Cambridge, MA, USA

[2] Department of Mechanical Engineering, Massachusetts Institute of Technology, Cambridge, MA, USA

jyhan@mit.edu, jpfu@mit.edu, ycwang@mit.edu, yongak@mit.edu

Synonyms

Sample pre-fractionation; Preparatory separation; Microfluidic devices; Microsystems

Definition

Sample preparation is usually defined as a series of molecular separation/fractionation steps required or recommended in order to obtain higher sensitivity and selectivity of downstream biosensing or bioanalysis.

Overview

Given the complexity of most biological samples, sample preparation has been, and will be, one of the critical challenges in bioanalysis. Typically, most biosensing involves detection of low-concentration target molecules over molecular backgrounds with much higher concentrations. In genomic biosensing, this problem is largely

resolved by polymerase chain reaction (PCR), which can be used to increase the number of nucleotides with a specific sequence by several orders of magnitudes. However, in proteomic biosensing and bioanalysis, the issue of sample preparation still remains as a serious technical bottleneck, since there is no PCR equivalent for proteins and other biomolecules. For example, blood plasma or serum from any source is valuable for proteomics-based discovery of biomarkers for diseases or for discovery of novel drug targets. Detection of these proteins has potential diagnostic values; however, the major challenge is the complexity of common biomolecule samples. It is estimated that there are more than 10 000 protein species present in a serum sample. Moreover, most biomarker proteins are generally present at very low concentrations ($\ll$ pg/ml), while others, such as albumin and immunoglobulins, are present in very large amounts ($\gg$ mg/ml). This large concentration variation poses a formidable challenge to currently existing biomolecule detection techniques, most of which do not have low enough detection sensitivity and large enough dynamic range. It is expected, therefore, that the detection of low-abundance protein species or biomarkers would be possible only by better sample preparation and sorting. Conventionally, two dimensional (2D) protein gel electrophoresis, coupled with mass spectrometry (MS) has been the norm of proteomics research for decades, while multidimensional liquid chromatography coupled with MS is getting wider use due to ease of automation. Both techniques demonstrate similar separation peak capacity (up to ~ 3000) and dynamic range of detection ($\sim 10^4$) when coupled with MS.

Microfluidic engineering has the potential to improve the proteomic sample preparation processes significantly, by the automation and integration of many, laborious fractionation steps on a chip. While microfluidic devices for 2D protein separation [1] have already been demonstrated, the following technical issues still need to be addressed before the wider application of microfluidic 2D protein separation devices.

1. Preparatory separation should be able to process large sample volume. While small sample consumption is beneficial for some applications (such as single-cell analysis), most proteomic samples (blood, for example) are available in the volume larger than $\sim 1\,\mu L$. Most microfluidic separation systems are based on miniaturized capillary electrophoresis, which is essentially an analytic (not preparatory) technique. Therefore, the overall sample throughput and the detection sensitivity in such separation are limited.
2. Any preparatory separation device should be designed with the downstream sensing in mind. Many capillary electrophoresis separations utilize polymeric sieving media or reagents like carrier ampholytes, which are detrimental to most downstream detection systems (such as MS) by causing huge background and nonspecific binding.
3. Since there is no *PCR-like signal amplification* process for proteins or peptides, there must be efficient sample pre-concentration steps in the overall process. The low-abundance molecules could be efficiently separated, but in order to cover several-order-of-magnitude concentration ranges, one needs to concentrate these purified dilute, low-abundance species into higher concentration.
4. Usually, more than one separation strategy would be needed to deal with the complexity of proteome. However, there is a need for developing separation techniques by pI (isoelectric point) or size (kD), rather than other properties such as hydrophobicity. One reason is that size-based separation would be an ideal method to eliminate most abundant proteins (albumin/globulin) from a given sample, which are typically larger than signaling molecules. Also, fractionation based on size (kD) or pI values will significantly reduce database searching time at the end of MS (or tandem MS)-based proteomic analysis.

The above issues come from the fact that technical requirements for preparatory separation are quite different from those of analytic separation. For the last decade, many microchip-based separation processes have been developed, demonstrating high resolution and speed. However, the requirement for preparatory separation/fractionation is different from that of analytical separation. Generally speaking, resolution is less stressed while sample throughput becomes more important. Accordingly, to meet the demand for high throughput, continuous-phase separation (free-flow electrophoresis, transverse electrophoresis) has been gaining increasing popularity. In this continuous-flow mode separation, molecules are fractionated continuously into different streams, based on different molecular properties (size, charge, electrophoretic mobility, etc.). As a result, the biomolecules are separated and flow to different output channels at the end of the main separation chamber, where the fractionated samples can be collected continuously, as shown in Fig. 1. This eliminates the need for careful sample loading and ensures higher throughput. Typical biosample analysis could involve many (up to ~ 10) steps, which are currently of manual operation. Therefore, integration of different separation and fractionation steps is highly important, in order to build meaningful sample preparation microsystems. Two main challenges are buffer exchange and flow rate (volume) matching between each component. Some of the techniques that are very useful for analytical separation are

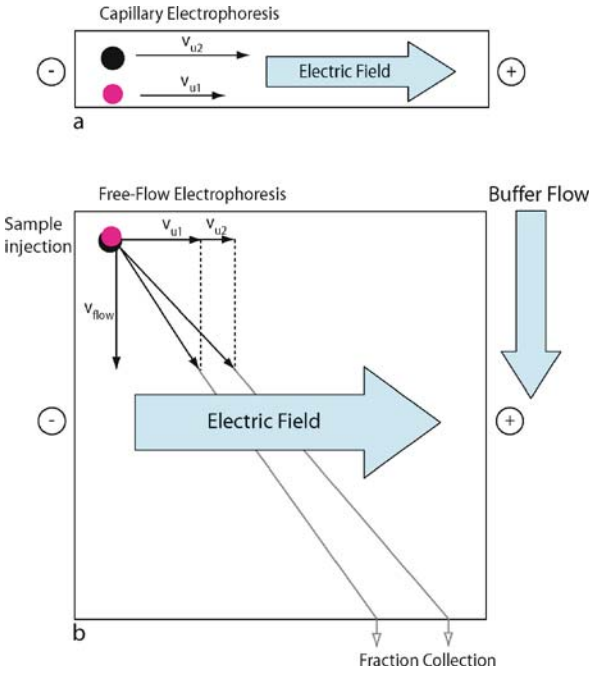

Biosample Preparation by Lab-on-a-Chip Devices, Figure 1 Comparison between (**a**) batch-mode capillary electrophoresis and (**b**) continuous-mode free-flow electrophoresis

not adequate for preparatory separation, because of specific buffer requirements or reagents to be used. Efficient buffer exchange methods in a microfluidic system have not been fully explored yet, as well as desalting of the sample (required for MS-based biosensing).

Basic Methodology

Filtration and Size-Based Separation

Gel filtration chromatography and gel electrophoresis are the two most commonly used techniques for separation of biologically relevant macromolecules (such as nucleic acids and proteins) based on size. Both techniques use gelatinous materials consisting of cross-linked three-dimensional pore networks, where the sieving interactions with the migrating biomolecules determine the separation efficiency. Depending on the relative size of the macromolecule compared with the gel mean pore size (e.g., the ratio of the radius of gyration R_g of the molecule to the gel mean pore size a), three basic separation mechanisms [2] have emerged to explain how flexible macromolecules migrate though a constraining gel medium – Ogston sieving ($R_g/a < 1$), entropic trapping ($R_g/a \sim 1$), and reptation ($R_g/a > 1$). In Ogston sieving, the macromolecule is smaller than the gel pores or constrictions, and the molecular sieving occurs because of steric interactions of the macromolecules with the gel pore network. Since $R_g/a < 1$, the molecules move rather freely through the gel matrix, assuming their unperturbed conformations. Entropic trapping applies when $R_g/a \sim 1$, and the conformation of the flexible macromolecule must deform or fluctuate to pass through the gel medium's spatial constrains. At each point, the number of accessible conformations defines the molecule's local entropy. Entropy differences derived from the gel medium's spatial heterogeneity drive molecules to partition or localize preferentially in less constrictive spaces, where their enhanced conformational freedom raises entropy. Reptation can be envisioned as a long flexible macromolecule occupying multiple pores threading its way through the gel in a snake-like fashion, which is very similar to the *reptation in a tube* process proposed by deGennes for entangled synthetic polymers. In reptation, only the end segments can escape as the molecule undergoes random curvilinear motion along the tube axis.

Both gel filtration chromatography and gel electrophoresis represent the current standard for size-based separation of biomolecules in laboratories. However, poor separation resolution in gel filtration chromatography and difficult sample recovery with gel electrophoresis make neither method optimal in separating complex mixtures for downstream analysis. Various microchip-based separation systems have been developed by using liquid or solid polymeric materials as sieving media contained in microchannels, and such systems have demonstrated fast separation of various biomolecules (e.g., DNA, proteins and carbohydrates) with rather high resolution [3, 4]. However, the foreign sieving matrices pose intrinsic difficulties for the integration of automated multistep bioanalysis microsystems. Furthermore, these microchip-based systems are limited to analytical separation of biomolecules, due to the difficulty of harvesting purified biomolecules for downstream analysis.

Recently, there has been great interest in switching from disordered porous gel media to patterned regular sieving structures, in the hope of achieving more efficient separation than gels in terms of separation speed and resolution [5]. While there are many different techniques to fabricate micrometer- or nanometer-sized sieving pores, it is sometimes more important to consider and understand the detailed molecular interaction with micro- or nanopore sieves before designing a molecular filter. Biomolecule interaction with molecular filters or sieves can be quite complicated, especially for the case of biopolymers such as long DNA. Intuitions based on filtration process of macroscopic objects can be quite misleading for the interaction between nanosized molecular sieves and nanometer-sized biomolecules in liquid environments.

Charge-Based (pI-Based) Separation

The charge density of biomolecules is related to their electrophoretic mobility; therefore electrophoresis in a free solution (*capillary zone electrophoresis (CZE)*) can be a method to separate biomolecules based on the charge density. The free solution electrophoretic mobility μ_e is a characteristic feature of each analyte, which is determined by the complicated balance among the electrical driving force on the analyte, electrical driving force on the counterions within the Debye layer on the analyte backbone and the frictional force from the surrounding fluid. Therefore, it is not a trivial matter to determine or calculate the electrophoretic mobility of a given protein/peptide *a priori* from the sequence information. Also, electrophoretic mobilities of many proteins among a given proteome can be similar. Therefore, the CZE is not an ideal technique for separating a very complex protein mixture for sample preparation purposes.

The most powerful variant for charge-based separation is *isoelectric focusing (IEF)*. To perform this separation technique, a linear pH gradient has to be established first either in the gel or in the microchannel. Once the pH gradient has been established, the biomolecules such as proteins and peptides migrate to the position where the pH equals their specific isoelectric point (pI). At this specific position, the net charge of the molecules becomes zero and they stop migrating. Molecules with different pI values focus at different positions with the pH gradient, thus allowing an effective charge-based separation of the molecules. This is a powerful fractionation technique because pI of a given target protein can be easily and accurately estimated from amino acid sequences; therefore one can collect and analyze only the pI region of interest. This could significantly cut down database searching time after MS detection, which can be quite time-consuming.

Because of its utility, IEF has been employed in many different forms even at macroscopic scales. Miniaturization of IEF would have benefits of employing small potentials. In IEF, the separation resolution does not depend of the length of the channel. The focused peak width σ can be given as the following equation:

$$\sigma = \sqrt{\frac{D\left(dx/d(\mathrm{pH})\right)}{E\left(d\mu/d(\mathrm{pH})\right)}} \sim \frac{L}{\sqrt{V}} \qquad (1)$$

Here, D is the diffusion constant of the protein, E $(= V/L$, L is the channel length) is the electric field and μ is the mobility of the protein. While $\mathrm{d}\mu/\mathrm{d(pH)}$ is an inherent property of the protein, $\mathrm{d}x/\mathrm{d(pH)}$ (pH gradient in length) scales as $\sim L$ for a given pH range determined by the ampholyte used in the experiment. The separation resolution R_S is given as $\sim d/\sigma$, where d is the separation distance in the microchannel between the two peaks of interest. Since d also scales as $\sim L$, R_S is only proportional to $V^{1/2}$, independent of the length of the channel L. In other words, for a given applied potential, the separation resolution does not change as the channel length is decreased, because of increased field strength in the channel makes the focused peak narrower. However, the time it takes to achieve IEF in the channel is decreased, because of shorter channel length as well as higher electric field strength.

One important consideration for the miniaturization would be the ways to achieve a pH gradient. The best resolution can be achieved by immobiline gel, where ampholyte chemical groups are polymerized into a gel. The other method to obtain a pH gradient is to use carrier ampholytes in solution form. The ampholytes are small buffer molecules with a wide range of isoelectric points that form a pH gradient when an electric field is applied. Typically, the electric field is generated between a basic solution (catholyte) such as ammonium hydroxide at the cathode and an acidic solution (anolyte), e.g. phosphoric acid, at the anode. It is possible to establish a natural pH gradient, relying on reduction–oxidation process near the electrode [6]. However, such a natural pH gradient is not stable enough for practical applications. Instead, adding carrier is preferred, in order to obtain more stable pH gradient. This is true even when immobiline gel is used. More stable separation is achieved by adding carrier ampholytes to the gel solution. Therefore, the use of carrier ampholytes has been the method of choice for microfluidic IEF devices. This, however, can interfere with subsequent analysis such as MS.

Isotachophoresis utilizes two different buffer systems, one as the leading electrolyte and the other as the trailing electrolyte. The leading electrolyte has a higher mobility than that of the analytes while the trailing electrolyte has a lower mobility. When an electric field is applied, the ions of the leading electrolyte migrate fastest and those of the trailing electrolyte slowest. Then, the ions of the analytes spread into the gradient of the electrical strength set by the mobilities of the terminating electrolytes. However, for practical applications, it is often difficult to find the appropriate terminating electrolytes with the required mobilities. The other limiting factor for this separation technique is that the ions have to be of the same polarity in order to be separated.

Affinity-Based Separation

The affinity-based sample preparation method on microchips is another powerful tool for separation of biomolecules. Conventional affinity-based separation

B

methods such as liquid chromatography or affinity chromatography have been successfully implemented in microfluidic chip format. The way the chromatography works in the microchannel is essentially the same as in the conventional method. In capillary electrochromatography (CEC), which combines the separation power of both liquid chromatography and capillary electrophoresis, the analyte is forced through a column of the stationary phase by electroosmosis instead of pressure. After this step, the gradient elution with a varying solvent composition, for instance 5% to 50% methanol, flows across the column and separates the analyte mixture depending on how well it mobilizes the analyte. The more hydrophobic component will elute first if the methanol content is high. However, when the methanol concentration is low, the hydrophilic analyte will elute more readily. The affinity chromatography is based on the specific interaction between an immobilized ligand and the target protein to be separated.

The last two variants of affinity-based separation are *micellar electrokinetic chromatography (MEKC)* and *electrochromatography (EC)*. MEKC uses surfactants which form micelles as pseudo-stationary phase in the microchannel. During electrophoresis, the analytes partition into the micelles depending on their hydrophobicity. Through the interaction with the micelles, the retention time of the molecules can be increased. In this way, even neural molecules can be separated. Electrochromatography utilizes an electrokinetic flow instead of pressure-driven flow to bring the mobile phase through a packed bed consisting of silica with a large negative surface charge. This induces an electro-osmotic flow (EOF) which drives the separation. A plug-like velocity profile brings a higher efficiency than HPLC.

Signal Amplification and Preconcentration

Several research groups have reported ways to preconcentrate samples in "Lab-on-a-Chip" devices. While most on-chip preconcentration approaches evolve from conventional capillary electrophoresis and chromatographic column techniques, these preconcentration techniques play an increasingly important role in chip-based system. The basic preconcentration strategies applied on microfluidic devices can be classified into three large categories: electrokinetic preconcentration, chromatographic preconcentration and membrane preconcentration.

Electrokinetic Preconcentration

Field-amplified stacking (FAS) (Fig. 2a) is a technique with a long history, first introduced by Mikkers et al. in the late 1970s [7].

The mechanism relies on manipulating buffer concentration to achieve local field amplification. The relation between the electrical field (E) and buffer concentration (C) can be defined by the relative conductive (γ) as:

$$\gamma = \frac{c_L}{c_H} = \frac{\sigma_L}{\sigma_H} = \frac{E_{\text{buffer}}}{E_{\text{sample}}} \tag{2}$$

As a result, when we introduce low conductivity (σ_L) sample plug into capillaries or microfluidic channels with high conductivity running buffer, most of the potential drop will be applied onto the injected sample. This locally amplified field will therefore drive/stack sample to the ends of the plug by electrophoretic force. With a given plug size, one can increase the enhancement factor by increasing the relative conductivity. Even though FAS is one of the simplest preconcentration schemes to implement on microchips, the band broadening at the stacking boundary caused by hydrodynamic mixing from both flow injection and mismatched EOF makes it difficult to have highly focused peak.

Transient isotachophoresis and *micellar electrokinetic sweeping* can be viewed as extensions of the stacking concept of FAS. In the case of isotachophoresis, with the understanding of a sample's electrophoretic mobilities, the sample plug is sandwiched by leading electrolyte (LE) and terminating electrolyte (TE) instead of the same high conductivity buffer. Based on the order of descending mobilities, the constituents will separate into distinct zones between high mobility LE and low mobility TE (relative to sample constituents) upon the application of the separation voltage. Moreover, once the steady-state gradient is achieved, the boundaries between samples can be maintained by a self-focusing mechanism which alleviates the dispersion problem from which FAS suffers. Both FAS and isotachophoresis use buffer manipulation to achieve local field enhancement that helps sample stacking. Micellar electrokinetic sweeping, on the other hand, works on changing the electrophoretic mobilities of samples by labeling them with micelle compounds (surfactants). Once the correct compound is chosen, one can use a small plug of fast moving micelle compounds to sweep samples rapidly out of the sample zone by hydrophobic interaction. The enhancement factor of micellar electrokinetic sweeping can be further improved by coupling with FAS, however, it is still limited by analytes' affinity to the micellar compounds.

While FAS and its related techniques are well-established, their merit for sample preparation device is limited since these techniques usually require special buffer arrangements or reagents in the system. *Electrofocusing* (Fig.2b) is another class of techniques used to collect and concen-

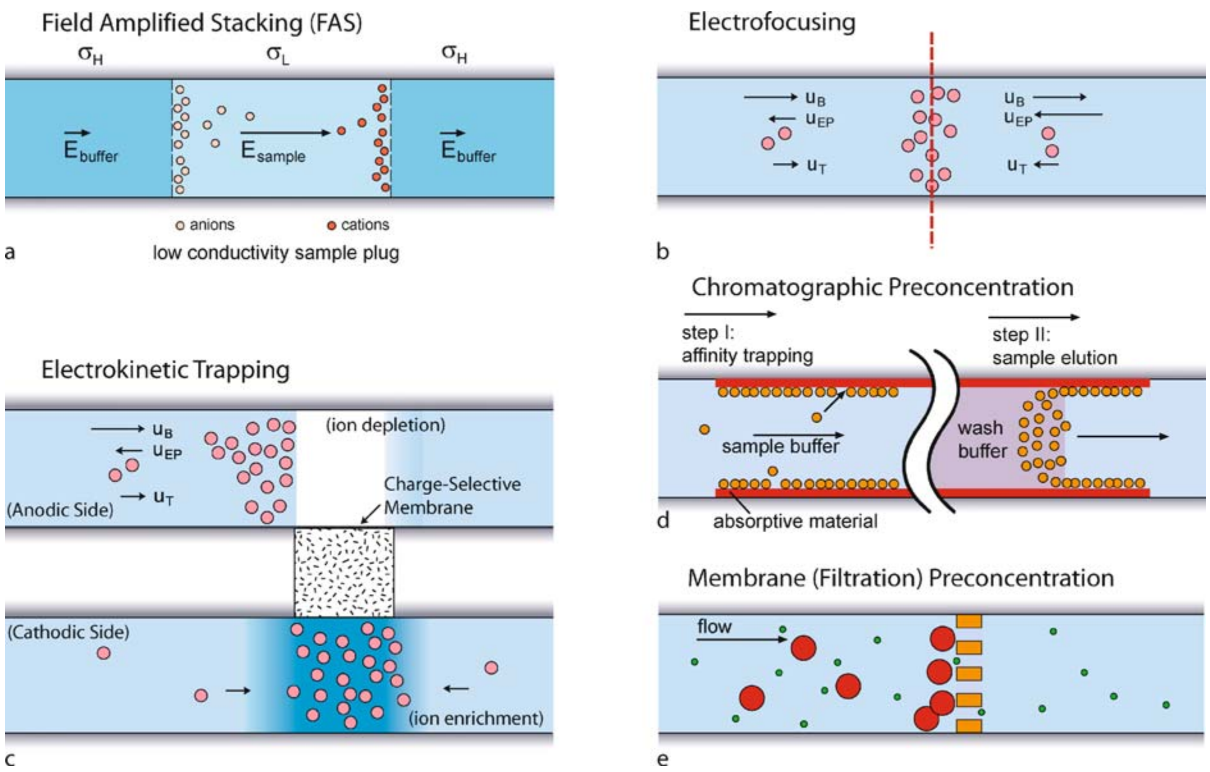

Biosample Preparation by Lab-on-a-Chip Devices, Figure 2 Various types of preconcentration strategies. (**a**) Field amplified stacking, (**b**) electrofocusing (various types), (**c**) electrokinetic trapping (both anodic and cathodic side), (**d**) chromatographic preconcentration and (**e**) membrane preconcentration

trate analytes by manipulating both hydraulic and electrophoretic driving forces in the microchannel. Electrofocusing can occur whenever the net molecular velocity profile is converging, as shown in Fig.2b, by either controlling the flow and/or electric field of the two zones. Such a condition can be obtained by changing channel geometry, electric field of each zone or temperature of each zone. Electrofocusing can be achieved in a continuous fashion (collection of molecules until enough concentration is reached), and does not require any special buffers or ionic strength arrangements. However, the collection would be critically dependent on the specific electrophoretic mobility of the target.

Another novel electrokinetic preconcentration technique is *electrokinetic trapping* (Fig.2c), utilizing unique electrokinetic properties of perm-selective membranes. As a perm-selective membrane, one can use traditional membranes (such as Nafion®), nanochannels or charged polymer monoliths. When a current is applied through such a perm-selective membrane/nanochannel, concentration polarization of ions can occur (even at moderate buffer concentrations), causing the ion concentration of anodic side to decrease (ion depletion) and that of cathodic side to increase (ion enrichment). Both phenomena can be (and have been) utilized for concentrating biomolecules. In the cathodic side, biomolecules and ions can be enriched due to the ion enrichment process. In the anodic side, ion depletion region can be used in a similar manner as a *stacking boundary*, although the physical mechanism in this case is different from FAS. Unlike FAS, both cations and anions are collected at the same boundary. This is because both ionic species are *repelled* by concentration polarization process from the membrane/nanochannel. The advantage of electrokinetic trapping is that the preconcentration can be less sensitive to specific molecular electrokinetic properties (such as electrophoretic mobility), therefore providing a generic way for various types of molecules. However, concentration polarization and related phenomena are generally poorly understood, and the linearity and stability of the trapping is sometimes an issue.

Chromatographic Preconcentration

Chromatographic preconcentration (Fig.2d) is also called solid-phase extraction. It usually involves two steps. First, analytes are retained by affinity binding force onto an

appropriate stationary subject. Then, with the application of elution buffer, the analytes can be eluted into a more concentrated form. Non-microfluidic examples of this strategy are widely used, such as commercially available trap column for mass spectrometry and SELDI (surface-enhanced laser desorption and ionization)-MS. Affinity reagents and bead systems are well-developed for trapping proteins and peptides and commercially available, which makes its implementation to microfluidic format rather straightforward. Also, chromatographic preconcentration techniques can also desalt biosamples, which is another important benefit especially for MS. One of the drawbacks of chromatographic preconcentrations, however, is that the preconcentration can be biased (hydrophobic vs. hydrophilic), and the washing (elution) step could potentially re-dilute the concentrated plugs. In addition, chromatographic preconcentration can be limited by the number of binding sites (binding surface area) in the systems.

Membrane Preconcentration

In membrane preconcentration (Fig.2e), gel or porous membranes are used to concentrate molecules bigger than the size of the pores. By adjusting the pore size, one can allow the passage of buffer ions and small molecules but exclude larger molecules of interest. With the formation of nanofilters or nanoporous membranes within the microfluidic systems, this strategy can be implemented easily. Membrane (filtration)-based preconcentration will not have any chemical bias (mainly dependent on the size of the molecule), but continuous membrane filtration could generate eventual clogging of the system, which is one of the main problems in this technique.

Key Research Findings

Filtration and Size-Based Separation

For size-separation of biomolecules, it is imperative to have a molecular sieving structure incorporated in the system. Formation of polyacrylamide gel in a microchannel is one viable option, but solid-state, artificial sieving systems are much preferred due to their mechanical and chemical stability. Artificial molecular sieving systems can be fabricated using a variety of techniques [8–13], such as colloidal templating, anodized alumina pore fabrication, packed nanospheres, superparamagnetic particle arraying, standard photolithography and e-beam lithography.

Regular arrays of micrometer- or nanometer-sized pillars have been fabricated by different groups with either photolithography (with pillar diameter and spacing down to 1 μm) or e-beam lithography (with pillar diameter and spacing down to 100 nm) on silicon substrates. The advantages of such microlithographically fabricated devices include the precise control over the sieving matrix geometry and the design flexibility. By applying two alternating electric fields of different directions and different magnitudes, Huang et al. recently devised a *DNA prism* device that can continuously separate long DNA molecules with high speed [14]. In this design, the longer DNA molecules only follow the strong electric field component while the shorter ones migrate in the direction of the sum electric field vector. However, their application was largely limited to rather large biomolecules (long DNA).

The concept of Brownian ratchets has been applied to construct asymmetric obstacle courses that provide a spatially asymmetric steric potential for biomolecule separation [15, 16]. The basic idea is to use such asymmetric obstacles to rectify the Brownian motion laterally and thereby to deflect diffusing biomolecules based on their sizes. So far, the Brownian ratchet systems have been successfully demonstrated for long DNA and phospholipids [15, 16], even though the separation resolution reported so far was not ideal.

More recently, a microfabricated nanofilter array system was developed, which can be used for separating various biomolecules such DNA molecules and proteins [17, 18]. The unique feature of this class of molecular filters is that only standard photolithography is needed to create ∼ 10 nm sized molecular filters. Using the same system, one can employ different sieving mechanism. For long DNA molecules, entropic trapping mechanism is used, while small DNA and proteins can be separated by Ogston sieving mechanism. These devices demonstrated speed and resolution comparable to or better than the conventional techniques (i. e. pulsed field gel electrophoresis for long DNA, and capillary gel electrophoresis for proteins). One important advantage of a nanofilter array system is that the separation efficiency could be further improved by increasing the nanofilter density, by using advanced high-resolution (photo or e-beam) lithography techniques.

In terms of sample preparation, continuous-flow separation is also highly desirable for micro-/nanofluidic devices because of the low sample throughput. We choose two recent developments here that we believe represent the current advance of this particular exciting area: the *Tango* device (or the bump array) (by Huang et al. [19]) that separates long DNA molecules by asymmetric bifurcation of laminar flow [19], and the anisotropic nanofilter array (ANA) (by Fu et al.) that separates DNA and proteins based on the different sieving characteristics along two orthogonal directions within the ANA structure [18]. The Tango device employed arrays of micrometer-sized pillars and spacing, with each pillar column slightly shifted with respect to the previous one in a direction perpendicular to

the flow direction. Longer DNA molecules are displaced as they flow through the pillar array while shorter DNA molecules remain in the feeding streamlines (i. e. the deterministic lateral displacement), leading to efficient separation. It is believed that as the gap size of pillar array is reduced using nanofabrication, the Tango device can be used to fractionate biologically relevant molecules. The design of the ANA consists of a 2D periodic nanofilter array, and the designed structural anisotropy in the ANA causes different sized biomolecules to follow radically different trajectories leading to separation. So far, continuous-flow Ogston sieving-based separation of short DNA and proteins as well as entropic trapping-based separation of long DNA molecules have been demonstrated with the ANA structure. The design of the structural anisotropy is the key for the continuous-flow biomolecule separation, and it can be applied to any sieving mechanism across the nanofluidic sieving structure along the orthogonal direction (size-, charge- or hydrophobicity-based) that can lead to differential transport across the nanofilters. Highly efficient, continuous-flow molecular separation would be possible as long as one can create a separation system that is *anisotropic* in nature.

Charge-Based Separation

IEF-based sample fractionation devices have been developed and commercialized, but miniaturizing them into a microfluidic format is being studied actively. Especially, there have been tremendous efforts to increase the throughput of charge-based separation by operating the microfluidic device in a continuous mode. The Yager group from the University of Washington fabricated a multi-stacked Mylar continuous-flow separation device with palladium electrodes in direct contact with the solution. Since the electrodes were in direct contact with the solution, only a small voltage, 2.3 V, could be applied over a 1.27 mm wide channel [6]. Because of the small distance, however, it generated sufficient electric field, ~ 18 V/cm, for the separation of a binary mixture of proteins. The same group used the electrolysis of the buffer, H^+ at the anode and OH^- at the cathode, to generate a natural pH gradient across the microchannel without using any carrier ampholytes [6]. This low-voltage approach, however, requires a significant amount of time for separation at around 4 minutes. To reduce the separation time, Zhang et al. developed a high-voltage μ-FFE (free flow electrophoresis) device by isolating the separation channel from the electrode reservoirs using narrow (4 μm wide) microchannels [20]. Their FFE microchip with 10 μm deep channels in a polydimethylsiloxane (PDMS) substrate allowed an electric field up to 270 V/cm and they could successfully separate two fluorescent dyes, rhodamine 110 and fluorescein, as well as two amino acids in 2 s. However, the high voltage induced a strong EOF which deteriorated the separation result. The μ-FFE device developed by Kohlheyer incorporates two new improvements compared to the previous ones [21]. First, it is a multifunctional μ-FFE device which can perform free-flow zone electrophoresis and free-flow IEF. Depending on the separation method to be used, the only parameter to be changed is the width of the sample by hydrodynamic focusing. This can be performed easily on the run by changing the flow rates in the two side channels. Second, they implemented a polymerized acrylamide as the salt bridge between the main separation channel and the electrode reservoirs. This proved to be more effective in suppressing the EOF than the microchannel as the salt bridge. Isotachophoresis (ITP) has been also realized in microchip format for the free-flow electrophoresis [22]. A sample mixture of fluorescein, eosin G and acetylsalicylic was separated in less than a minute. Song et al. developed a novel ampholyte- and gel-free pI-based continuous-flow sorting technique [23]. Their method differs from previous approaches in that this continuous sorting process involves no external power supply and no special ampholytes. Instead, they utilized the diffusion potential generated by the diffusion of different ionic species in situ at the laminar flow junction.

Free-flow electrophoresis has also been successfully applied to separate subcellular particles such as organelles (mitochondria) [24]. This is facilitated by the fact that these particles contain many different proteins and amphoretic molecules. The sorting in microscale devices offers obvious advantages compared to the conventional ones. Less heat is generated by using only ~ 2 V compared to 2000 V of conventional devices and this causes less damage of organelles. The result shows that free-flow electrophoresis can be applied to various organelles, even for organelles that are larger and do not have uniform pI values.

Affinity-Based Separation

While the technology for affinity-based separation is very well developed for capillary-based separation, chromatography in microchips has not been as popular as electrophoresis, mainly due to the difficulty in packing microchannels with beads. In particular, if the channels are not straight but are curved into serpentine configurations, it is quite a challenge to achieve a uniform packing of the channels. Instead of packing affinity beads, creating a polymer monolith [25, 26] is much preferred, with controlled, relatively uniform pore sizes, variety of chemical groups one can incorporate into the system, and covalent

linkage to the channel wall (therefore no need of frits to hold the monolith stationary).

Often, fittings for microfluidic systems cannot handle the high pressure required for chromatographic separation, and electrokinetic flow can be used in lieu of pressure-driven flow. Using the microchip chromatography, driven either by elecroosmosis or pressure, a separation of low-molecular-weight neutral and basic compounds and acidic proteins has been demonstrated. He et al. demonstrated CEC of peptides in a microfabricated system [27]. They mimicked the packed bed by etching an array of support structures into a quartz substrate, the so-called collocate monolith support structures. These columns were prepared with polystyrene sulfate for stationary phase. A mixture of tryptic peptides from ovalbumin was separated in the CEC isocratically as opposed to the gradient elution mode.

In capillary-based separations, technologies based on microbeads with specific chemistry are well-developed and mature, and utilizing such bead systems in microfluidic channels would be of tremendous value. Oleschuk et al. developed a design that allows exchange of packing materials [28]. This can be utilized for solid-phase extraction (SPE) and CEC. Using CEC, a separation of BODIPY and fluorescein could be achieved with a mobile-phase composition of 30% acetonitrile / 70% aqueous 50 mM ammonium acetate. The BODIPY is hydrophobic and has a higher affinity for the column than the fluorescein, causing slower elution of BODIPY. In addition to affinity-based separations, microchannels with packed beads could provide other functionalities for microfluidic sample preparation systems, such as peptide digestions [29, 30], removal of majority proteins and extraction of DNA from cells [31]. It was shown that peptide digestion reaction can be significantly expedited ($\sim$ 10 min) compared with solution-phase digestion process.

Signal Amplification and Preconcentration

Given the importance of sample preconcentration in many biosensing applications, several sample preconcentration techniques, including field-amplified sample stacking (FAS), isotachophoresis (ITP), electrokinetic trapping, micellar electrokinetic sweeping, chromatographic preconcentration, electrofocusing (various types) and membrane filtration preconcentration have been developed. Each technique has its own advantages and disadvantages.

Field-Amplified Stacking and Other Related Techniques

FAS can be implemented on microchips in a very similar manner as capillary electrophoresis. However, the requirement of low ionic strength sample buffer for FAS puts limitation on its use as general preconcentration technique. Variations of the technique, such as transient isotachophoresis and micellar electrokinetic sweeping, have been more successfully used. Jung et al. reported on-chip transient isotachophoresis by introducing TE and LE into a T-junction simultaneously to achieve fast sample loading, preconcentration and separation [32]. Micellar electrokinetic sweeping, pioneered by the Terabe group, combines field-amplified stacking with affinity concentration using micelles [33], and provides very high concentration factors. These techniques were originally developed for capillary electrophoresis; therefore they are well suited for enhancing the sensitivity of microchip-based separation and detection. However, they require special arrangements of buffers with different ionic concentrations, which makes the coupling to the downstream biosensing challenging, limiting their use as sample preparation devices. For example, micellar electrokinetic sweeping relies on a detergent additive (sodium dodecyl sulfate), which has a negative impact on the downstream analysis.

Electrofocusing and Electrokinetic Trapping

Newer techniques such as electrofocusing and electrokinetic trapping could be ideal alternatives for proteomic sample preconcentration. One of the benefits electrofocusing offers is that the collection can be run continuously, and therefore, concentration can be arbitrarily increased (with a limitation imposed by crystallization and other technical issues). Electrofocusing can continuously collect molecules by applying two different (electrophoretic and hydraulic, typically) driving forces in the opposite direction in a microchannel or capillary to trap molecules. Various types of electrofocusing [34–37], which differ in the method to generate a gradient in electrophoretic mobility (temperature, electric field, etc.), have been demonstrated in microfluidic and capillary systems. Depending on the focusing time, these techniques can achieve typically up to $\sim 10^5$-fold concentration enhancement.

Electrokinetic trapping techniques [38–41] have been recently demonstrated as an efficient way of concentrating protein samples. Different membrane materials can be used, such as polymer monolith (Singh and coworkers), Nafion® (Swerdlow and coworkers), nanochannels (Han and coworkers) and even PDMS (Kim et al.). These techniques demonstrate impressive concentration factors (up to $\sim 10^6$) as well as the flexibility to be coupled to downstream analysis. These techniques are dependent on the ion depletion and concentration polarization, which as a generic process are quite common to most nanoporous membrane systems. Therefore, there is no specific buffer

requirement, as long as the ionic strength is moderate (∼ 10 mM or less).

Chromatographic Preconcentration/Membrane Preconcentration

Several groups [42, 43] have demonstrated affinity-based molecular preconcentration systems in a microfluidic format. Affinity chemical groups can be directly coated to the surface of the glass microchannel, although techniques using microbeads (Harrison and coworkers) and polymer monoliths (Frechet and coworkers) provide better functionality, larger binding surface area and flexibility in fabrication and integration. The concentration factor in these systems is eventually determined by the surface binding area. For efficient capturing from larger sample volume (∼ 1 μL or more), a larger microchannel is required.
Membrane preconcentration [44, 45] is a microscale version of membrane filtration and dialysis, which is well established. Typically gel or other polymeric materials (Singh and coworkers) as well as nanofluidic channels/solid membranes (Ramsey and coworkers) are used as a molecular filter. An advantage of this technique is that one can combine preconcentration with filtration/separation in a single step. A disadvantage of this technique would be that it becomes progressively more difficult for smaller proteins and peptides, and it is also limited by the ambiguity of the molecular weight cut-off of the nanoporous filter membrane materials. Even in the case of regular nanofilters, molecular size filtration of biomolecules can be quite complicated due to conformation changes of biomolecules.

Future Directions for Research

The importance of sample preparation in bioanalysis is expected to draw more attention in the future, since this is currently one of the major bottlenecks in biosensing. For preparatory separation, continuous-flow fractionation is much preferred over elution-type separation, due to the flexibility of integration and higher sample processing rates. More and more fractionation techniques would be made into a continuous-flow format, possibly by adopting anisotropic sieving system designs. Since typical sample preparation could easily involve many (up to ∼ 10) different separation/reaction/preconcentration processes, integration of these individual steps on a single device would be highly desirable for practical application. Recent developments in sample preconcentration devices have the potential to enhance any new and existing biosensors in terms of sensitivity and selectivity, if properly integrated with preparatory separation steps.

Cross References

► Isoelectric Focusing
► Electrokinetic Flow and Ion Transport in Nanochannels

B

References

1. Rocklin RD et al (2000) A microfabricated fluidic device for performing two-dimensional liquid-phase separations. Anal Chem 72:5244–5249
2. Viovy JL (2000) Electrophoresis of DNA and other polyelectrolytes: Physical mechanisms. Rev Mod Phys 72:813–872
3. Woolley AT et al (1994) Ultra-high-speed DNA fragment separations using microfabricated capillary array electrophoresis chips. Proc Natl Acad Sci USA 91:11348–11352
4. Yao S et al (1999) SDS capillary gel electrophoresis of proteins in microfabricated channels. Proc Natl Acad Sci USA 96:5372–5377
5. Volkmuth WD et al (1992) DNA Electrophoresis in Microlithographic Arrays. Nature (London) 358:600–602
6. Macounova K et al (2000) Generation of Natural pH Gradients in Microfluidic Channels for Use in Isoelectric Focusing. Anal Chem 72:3745–3751
7. Mikkers FEP et al (1979) High-performance zone electrophoresis. J Chromatogr 169:11–20
8. Turner SW et al (1998) Monolithic nanofluid sieving structures for DNA manipulation. J Vac Sci Technol B 16:3835–3840
9. Han J et al (1999) Entropic trapping and sieving of long DNA molecules in a nanofluidic channel. J Vac Sci Technol A 17:2142–2147
10. Doyle PS et al (2002) Self-assembled magnetic matrices for DNA separation chips. Science 295:2237
11. Sano T et al (2003) Size-exclusion chromatography using self-organized nanopores in anodic porous alumina. Appl Phys Lett 83:4438–4440
12. Baba M et al (2003) DNA size separation using artificially nanostructured matrix. Appl Phys Lett 83:1468–1470
13. Tabuchi M et al (2004) Nanospheres for DNA separation chips. Nat Biotechnol 22:337–340
14. Huang LR et al (2002) A DNA prism for high-speed continuous fractionation of large DNA molecules. Nat Biotechnol 20:1048–1051
15. Chou C-F et al (1999) Sorting by diffusion: An asymmetric obstacle course for continuous molecular separation. Proc Natl Acad Sci USA 96:13762–13765
16. van Oudenaarden A et al (1999) Brownian Ratchets: Molecular Separations in Lipid Bilayers Supported on Patterned Arrays. Science 285:1046–1048
17. Han J et al (2000) Separation of Long DNA Molecules in a Microfabricated Entropic Trap Array. Science 288:1026–1029
18. Fu J et al (2006) Patterned anisotropic nanofluidic sieving structure for continuous-flow separation of DNA and protein. Nat Nanotech 2 121–128
19. Huang LR et al (2004) Continuous particle separation through deterministic lateral displacement. Science 304:987–990
20. Zhang C-X et al (2003) High-Speed Free-Flow Electrophoresis on Chip. Anal Chem 75:5759–5766
21. Kohlheyer D et al (2006) Free-flow zone electrophoresis and isoelectric focusing using a microfabricated glass device with ion permeable membranes. Lab Chip 6:374–380
22. Janasek D et al (2006) Isotachophoresis in Free-Flow Using a Miniaturized Device. Anal Chem 78:3815–3819

23. Song Y-A et al (2006) Continuous-Flow pI-Based Sorting of Proteins and Peptides in a Microfluidic Chip Using Diffusion Potential. Anal Chem 78:3528–3536
24. Lu H et al (2004) A Microfabricated Device for Subcellular Organelle Sorting. Anal Chem 76:5705–5712
25. Yu C et al (2000) Towards stationary phases for chromatography on a microchip: Modeled porous polymer monoliths prepared in capillaries by photoinitiated in situ polymerization as separation media for electrochromatography. Electrophoresis 21:120–127
26. Ericson C et al (2000) Electroosmosis- and Pressure-Driven Chromatography in Chips Using Continuous Beds. Anal Chem 72:81–87
27. He B et al (1999) Capillary electrochromatography of peptides in a microfabricated system. J Chromatogr A 853:257–262
28. Oleschuk RD et al (2000) Trapping of Bead-Based Reagents within Microfluidic Systems: On-Chip Solid-Phase Extraction and Electrochromatography. Anal Chem 72:585–590
29. Wang C et al (2000) Integration of immobilized trypsin bead bed for protein digestion within a microfluidic chip incorporating capillary electrophoresis separations and an electrospray mass spectrometry interface. Rapid Commun Mass Spectrom 14:1377–1383
30. Jin LJ et al (2003) A microchip-based proteolytic digestion system driven by electroosmotic pumping. Lab Chip 3:11–18
31. Tian H et al (2000) Evaluation of Silica Resins for Direct and Efficient Extraction of DNA from Complex Biological Matrices in a Miniaturized Format. Anal Biochem 283:175–191
32. Jung B et al (2006) On-chip Millionfold Sample Stacking Using Transient Isotachophoresis. Anal Chem 78:2319–2327
33. Quirion JP et al (1998) Exceeding 5000-Fold Concentration of Dilute Analytes in Micellar Electrokinetic Chromatography. Science 282:465–468
34. Hori A et al (1993) Electroconcentration by Using Countercurrent due to Pressurized Flow and Electrophoretic Mobility. Anal Chem 65:2882–2886
35. Huang Z et al (1999) Digitally Controlled Electrophoretic Focusing. Anal Chem 71:1628–1632
36. Ross D et al (2002) Microfluidic Temperature Gradient Focusing. Anal Chem 74:2556–2564
37. Humble PH et al (2004) Electric Field Gradient Focusing of Proteins Based on Shaped Ionically Conductive Acrylic Polymer. Anal Chem 76:5641–5648
38. Singh AK et al (2002) In: Micro Total Analysis Systems, vol 1. Kluwer, Nara, Japan, pp 347–349
39. Astorga-Wells J et al (2003) Fluidic Preconcentrator Device for Capillary Electrophoresis of Proteins. Anal Chem 75:5207–5212
40. Wang Y-C et al (2005) Million-fold Preconcentration of Proteins and Peptides by Nanofluidic Filter. Anal Chem 77:4293–4299
41. Kim SM et al (2006) Electrokinetic Protein Preconcentration Using a Simple Glass/Poly(dimethylsiloxane) Microfluidic Chip. Anal Chem 78:4779–4785
42. Li J et al (2001) Integrated system for high throughput protein identification using a microfabricated device coupled to capillary electrophoresis/nanoelectrospray mass spectrometry. Proteomics 1:975–986
43. Yu C et al (2001) Monolithic Porous Polymer for On-Chip Solid-Phase Extraction and Preconcentration Prepared by Photoinitiated in Situ Polymerization within a Microfluidic Device. Anal Chem 73:5088–5096
44. Khandurina J et al (1999) Microfabricated Porous Membrane Structure for Sample Concentration and Electrophoretic Analysis. Anal Chem 71:1815–1819
45. Song S et al (2004) Electrophoretic Concentration of Proteins at Laser-Patterned Nanoporous Membranes in Microchips. Anal Chem 76:4589–4592

Biosecurity

► Lab-on-Chip Devices for Biodefense Applications

Biosensor

Definition

A *biosensor* is a device for the detection of an analyte that combines a biological component with a physicochemical detector component.

It consists of 3 parts:

- the *sensitive biological element* , including biological material (eg. tissue, microorganisms, organelles, cell receptors, enzymes, antibodies, nucleic acids etc) and a biologically derived material or biomimic).
- the *transducer* in between (associates both components)
- the *detector element* (works in a physicochemical way; optical, piezoelectric electrochemical, thermometric, or magnetic.)

Cross References

► Biosensor
► Acoustics Based Biosensors
► Impedimetric Biosensors for Nano- and Microfluidics

Biosensors Using Atomic Force Microscopes

Suijian Qi, Changqing Yi, Mengsu Yang
Department of Biology and Chemistry, City University of Hong Kong, Kowloon Tong, Hong Kong SAR
bhmyang@cityu.edu.hk

Synonyms

Biosensors using scanning force microscope; Cantilever biosensors; Force-based biosensors; AFM biosensors; Force biosensors

Definition

Biosensors using ►atomic force microscopes (AFMs) are devices which employ an atomic force microscope for biological recognition events. The principle of biosensors

using atomic force microscopy is mainly based on the mass-sensitive detection of binding events that change the deflection of a ►cantilever whose surface is modified with immobilized bioreceptors.

Overview

A ►biosensor, which exploits a biological detection or recognition system for target molecules, typically consists of three components: the transducer, the detector and the signal output. The core of a biosensor is the physico-chemical transducer which converts the biological recognition event into a useable output signal. There are numerous studies that integrate various detection schemes with biosensors, which can be categorized into optical detectors (for example, UV-Vis absorption, fluorescence, and chemiluminescence), electrochemical detectors (for example, amperometry, potentiometry, and conductometry) and mass spectrometric (MS) detectors according to the different detection principles. Recently, state-of-the-art AFMs have also entered into the biosensing area as highly sensitive detectors.

AFM is a type of scanning probe microscope with very high resolution, and is one of the foremost tools for imaging, measuring and manipulating matter at nanoscale level. An AFM mainly consists of a microscale cantilever (with a sharp tip), an optical deflection system and a sample stage (Fig. 1a). AFM has basically been used as a high-resolution imaging tool to "feel" the topography of a sample and it has the ability to visualize the atomic and molecular structure of sample surfaces. In the imaging mode of AFM, the sharp tip at the end of the cantilever is raster-scanned over the surface of a sample. As the tip approaches the surface, the cantilever deflects as a result of the interaction forces between the tip and the surface of the sample, and its deflections are monitored by a laser and a photodiode and then used to reconstruct the topography of the sample [1, 2]. Besides its imaging mode, AFM is also a powerful tool for measuring the force between a single bio-molecule pair interaction with nanometer resolution, as AFM is able to measure intermolecular forces as small as a few piconewtons (as weak as a single hydrogen bond interaction). As a biosensor AFM is able to directly probe the adhesion or rupture (unbinding) force interactions between molecules, such as ligands and receptors, antibody and antigen pairs; and strength of chemical bonds, such as hydrogen bonds [3].

When AFM operates as a force sensor, the interaction force between the tip and the substrate surface can be measured by moving the tip perpendicular to the surface while measuring the force on the tip. The working principle is as follows: one type of molecule, i. e., an

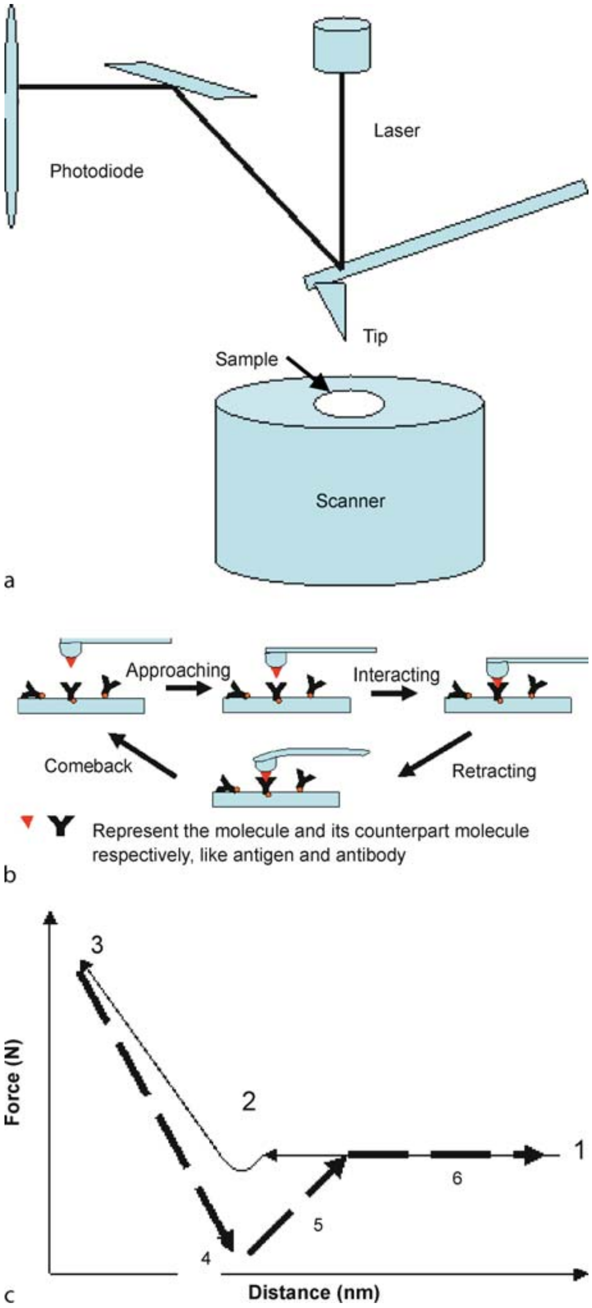

Biosensors Using Atomic Force Microscopes, Figure 1 (**a**) Basic components and working principle of AFM. A sharp tip fixed at the end of a flexible cantilever is raster-scanned over the surface of a sample. As the tip interacts with the surface, the cantilever deflects and its deflections are monitored by a laser and a photodiode and then used to reconstruct the topography of the sample. (**b**) A schematic diagram of AFM as a biosensor in detecting the force interaction between biological molecules. (**c**) Force–distance curve. During the tip (immobilized with one type of molecule, i. e., antigen) of the cantilever approaches to the substrate (immobilized with the counterpart of molecule, i. e., antibody), the *line* 1–3 is followed. By retracting the tip back, the cantilever bends downward as a function of the unbinding force between the two molecules, the line 4–6 (*dash*) is followed

antibody is attached to the tip of the cantilever and its counterpart molecule, i. e., an antigen is attached on the substrate surface. When the tip and substrate approach to each other, the two molecules interact and bonds are formed. Thus, their adhesion force can be measured. By retracting the tip back, the cantilever bends downward as a function of the unbinding force between the two molecules. Thus, the unbinding force, defined as the maximum force at the point of separation of the samples, can be recorded and measured. The force is monitored by the deflection of the cantilever and the deflection is directly proportional to the force. The schematic diagram of such an experiment and the force–distance curve are illustrated in Fig. 1b and 1c.

There have been several other powerful techniques for probing the molecular interaction between biosurfaces, including the use of shear flow detachment, surface force apparatus, biomembrane force probe, and optical tweezers [4]. The main advantages of using AFM are its high resolution, easy sample preparation, and its ability to manipulate in aqueous medium. AFM is currently the only force technique that makes mapping and analyzing single receptors with nanoscale lateral resolution possible [4]. Up to now, researchers have successfully used this system to measure interaction force between biotin and streptavidin, avidin and biotin, antibodies and their antigens, and single pairs of DNA nucleotides.

Basic Methodology

The first studies using AFM as a detection tool for intra- or intermolecular force can only measure discrete force. As the techniques for tip and sample preparation improve, single molecular interaction force detection will become the focus of AFM biosensors.

Major Factors for Single Molecular Interaction Force Detection

For real measurements of interactions between single molecules, very strict conditions are needed. Several important factors should be considered. First, the density of molecules distributed on both tip and sample should be sufficiently low to allow the formation of single molecular interactions. Second, to prevent unwanted detachment, covalent bonding of the molecules to the tip and the sample is critical. Generally, the binding between the surfaces and the molecules should be much stronger than the intermolecular force being studied. Third, a suitable molecular crosslinker (spacer) is a good choice to attach the molecules to the surfaces so that the molecules can interact with their counterparts with sufficient mobility. Forth, unspecific adsorption on the modified surfaces should be blocked to minimize the contribution of unspecific adhesion to the measured forces. Fifth, for oriented systems, site-directed coupling in which the molecule has a defined orientation may be desired [4]. Moreover, the rupture forces measured in an interaction force experiment are highly dependent on the conditions of the experiment, i. e., the spring constant of the cantilevers and the retraction rate of the cantilevers, and these factors will affect the result of the measurement.

Basic Procedures for Preparing AFM Tips and Samples

The coupling of biomolecules to the tip and to the surface has proved to be essential in the measurement of single molecular interaction force. The quality and reproducibility of the functionalization steps are the key factors leading to the success and reliability of a single-molecule experiment.

Preparing AFM Tips

Two types of surface chemistries have been developed for the functionalization of tips, they are based either on the strong chemisorption of thiols on gold surfaces or on the covalent attachment of silanes or alcohol on silicon oxide surfaces [4].

Strong Chemisorption of Thiols on Gold Surfaces The gold coating techniques can be used to functionalize the tip. When the tip has been coated by a thin adhesive layer of gold (gold tip), proteins, oligonucleotides or carbohydrates that bear thiol groups can be attached directly onto the gold surfaces. We can also functionalize the gold tip with alkanethiols which can attach biomolecules by self-assembled monolayers (SAMs). SAMs are easily obtained by immersing gold surfaces in dilute (typically 1 mM) ethanol solutions of the interested alkanethiols. The alkanethiols may be terminated by carboxyl group or amino group. The former can be reacted with amino groups of proteins using 1-ethyl-3-(3-dimethylaminopropyl) carbodiimide (EDC) and N-hydroxysuccinimide (NHS) in aqueous solution. This method can provide both firm attachment and molecular mobility, but is restricted by the multiple attachment points which lead to broad unbinding force distributions. The latter can also be used to attach proteins [4].

When the gold tip is functionalized with alkanethiols terminated with nitrilotriacetate (NTA) group, recombinant histidine-tagged proteins can attach to it via their carboxy or amino group. This method allows the optimal exposure of the C-terminal or N-terminal domains. Moreover, it can orient the attached molecules in the same way and minimize nonspecific protein adsorption and allows low density coupling to ensure single molecule recognition. But

the binding strength between NTA and histidine-tagged protein is ten times lower than that of the covalent bond. Therefore this method is not suitable for studying strong receptor–ligand bonds [4].

Covalent Attachment of Silanes or Alcohol on Silicon Oxide Surfaces The method does not require a gold coating tip, and can be applied directly to silicon tips. Proteins can be linked to the silicon tip through a crosslinker which carries heterobifunctional group, for example, a polyethylene glycol (PEG) crosslinker with an amine-reactive NHS group on one end and 2-pyridyldithiopropionyl (PDP) on the other end. The NHS group reacts with amines on the silicon tip forming a stable amide bond while the PDP group reacts with free thiols presented by cysteines in the protein forming a stable disulfide bond.

Preparing Samples

The receptors or ligands recognized by the functionalized tip need to be firmly attached to a solid support using appropriate, nondestructive approaches. Mica, glass and silicon have proved to be excellent supports for immobilizing purified receptors. The surface of mica is negatively charged at neutral pH, positively charged proteins can adsorb to it forming a strong enough binding to withstand the pulling force during the force detection experiments. The surface chemistries that are often used to prepare the samples are the same as those for preparing the tips, including strong chemisorption of thiols on gold surfaces and covalent attachment of silanes or alcohol on silicon oxide surfaces [4].
Besides molecules and biomolecules, cells can also be attached to the tips or sample supports. It makes the detection of cell–cell, cell–support interactions possible. The most important factor when attaching cells is that the attaching methods should retain the integrity and viability of the cells while at the same the binding between the cell and tip, cell and support should firm enough. Chemical fixation using crosslinking or attaching through adhesive coating proteins (collagen, fibronectin) can be applied to the cell attachment.

Other Features for the Single Molecular Interaction Force Detection

When the tips and samples have been functionalized, the quality of the tip and sample modifications should be evaluated. A control experiment is necessary to ensure that the bonds being formed during the tip or sample preparation processes will not break during the force experiment. A block experiment is important to address the specificity of the interaction force being detected. A block experiment can be performed by masking the receptor sites with free ligands.

Key Research Findings

Detection of the Forces of Discrete Bonds

Several investigations have demonstrated the measurement of inter- or intra-molecular interactions using AFM. Lee and co-workers were the first to use AFM to measure discrete and biologically specific rupture forces between biotin and streptavidin which are one of the strongest ►noncovalent interactions in nature. The schematic diagram was similar to Fig. 1b. First, the force probe (a glass microsphere glued to a cantilever) and the surface were coated with bovine serum albumin (BSA) by nonspecific adsorption; then, biotin was covalently coupled to BAS-coated force probe and surface; subsequently, the biotin-functionalized surface was incubated with the counterpart molecule, streptavidin, resulting in a monolayer of streptavidin bound to the biotinylated BSA on the glass surface. When the force probe and surface approached each other, the biotin on the probe could interact with the streptavidin and bonds were formed. When retracting the cantilever, the bonds formed could be disrupted. This rupture occurs when the gradient of the cantilever potential exceeds the highest gradient in the unbinding pathway of the ligand–receptor interaction potential. By registering the deflection of the cantilever at rupture, the rupture force could be measured. After blocking the streptavidin by free biotin, no rupture force was measured, which showed the specificity of the interactions.

Detection of Single Molecular Interaction Force

Lee's work was very useful for measuring the unbinding forces of discrete bonds, but not for measuring the single molecular interaction force. To successfully detect the single molecular interaction force, several techniques have been developed to modify the tips and the samples, e. g., crosslinker system, intrilotriacetate (NTA)-Ni^{2+}-His system. Whatever technique is used, the key point is to make the density of the molecules distributed on both the tip and the sample sufficiently low to allow the formation of single molecular interactions. Kienberger et al. [5] have successfully detected the single molecular interaction force between abotin and avidin.

Detection of the Force Interactions of DNA in the Aqueous Medium

The most significant point of AFM is that it can be applied to detect the force interactions in aqueous medium. The

measurements are not as straightforward as those between the tips and the solid surfaces. Cengiz and co-workers [6] have constructed a biosensor for quantitative measurements of molecular nucleic acid in aqueous medium. Only an AFM head with a cantilever, a sensitive approaching unit (to control the approach of the target solution to the AFM tips) and a CCD camera were needed in such a system. The sensitive approaching unit was in fact an inchworm motor that provides precise approach positioning in the Z-direction with high stiffness and holds position even with the power turned off. This type of motor has a resolution of 1 nm and a speed range of 1 nm/s to 0.5 mm/s when used as its own controller. When using this system, a model single strand DNA (ssDNA) molecule was covalently attached onto the tips (cantilevers) of the AFM as a specific ligand. Buffer solutions with and without free ssDNA molecules were approaching to the tip ($+Z$-direction) by the inchworm motor until the tip touched to the solution. The tips interacted with the target ssDNAs in the buffer solution for about 10 min to complete hybridization and then the buffer solution was driven at the opposite direction ($-Z$-direction) and meanwhile the *separation distance* (L, in nm) that the tip got rid of the solution was measured to follow the interaction between the ligand molecules attached on the cantilever (the tip) and the target molecules in the buffer solution. The percentage separation distance (PSD) was calculated from the following equation and used as the main variable:

$$(\mathrm{PSD})(\%) = \left\{(L_2 - L_1)\right\} \times 100 \qquad (1)$$

Where L_1 is the separation distance for the buffer solution without ssDNA (nm), and L_2 is the separation distance for the same buffer solution containing the target ssDNA (nm). Note that the negative value shows the decrease in the interaction between the AFM tip and the liquid phase. And in order to show the specificity of these AFM sensors, buffer solutions with the non-complementary ssDNA were also measured. The results showed that after hybridization with its complementary ssDNA, the PSD values were significantly increased when compared with the PSD values for the buffer solutions, while the PSD values for the non-complementary ssDNA increased slightly (specificity of the method). The PSD values also decreased with the concentration of the target ssDNA in the medium. It seemed that there was a correlation between the concentration of the complementary target ssDNA in the medium and the PSD value, although it was not linear.

Force Amplified Biological Sensor (FABS)

AFM biosensors have been used by researchers to measure binding or rupture forces between biological molecules.

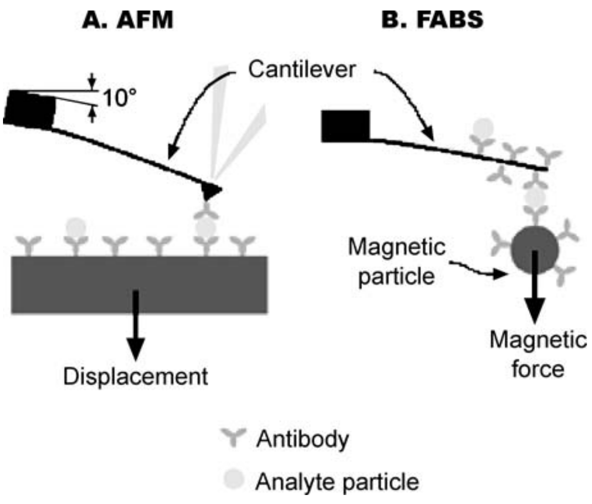

Biosensors Using Atomic Force Microscopes, Figure 2 Detection of antibody–antigen interaction forces with AFM and with FABS. (**a**) In AFM, a piezoceramic translator moves an antibody-derivitized surface away from a cantilever until a single antibody–antigen bond breaks. (**b**) In FABS, a magnetic field pulls on antibody-derivitized magnetic particles. The cantilever can bear thousands of particles, although the figure only shows one. (reproduced from [7])

However, they have a few drawbacks, for example, the nonideal geometry of AFM can produce artifacts, the result of measurement is affected by many factors and in order to obtain good results, very strict experimental conditions are required. Improvements of the AFM biosensors are being studied.

A FABS, whose working principle was very similar to that of the AFM biosensor, was a cantilever-based immunosensor [7]. However, its configuration was much simpler than that of the AFM. Rather than using a piezoceramic translator to pull on intermolecular bonds, it used magnetic particles, which eliminated the need to manually position a tip and sample next to each other with picometer precision and stability. The cantilever-beam force transducer was the only element of the AFM retained by the FABS.

Here, the measurement of antibody–antigen interactions was used to illustrate the working mechanism of a FABS (Fig. 2): one or more cantilevers with attached antibodies will capture antigen from a sample solution; 2 μm magnetic particles that also have attached antibodies will then bind to the captured antigen (at this stage the particles are not magnetized); after they have bound to the cantilever, a large magnetic field will magnetize the particles while a modulated field gradient exerts force on them. This force will cause particles bound via antibody–antigen bonds to pull on and bend the cantilever, while dislodging nonspecifically bound particles (*force discrimination*). The amount that the cantilever bends will indicate the

number of particles bound to the cantilever and, therefore, the concentration of analyte (antigen) in the sample. The FABS is capable of detecting a single bound particle, potentially corresponding to a single antigen molecule. A second detection mode might involve gradually increasing the force on the magnetic particles and determining the number of particles that detach at the expected antibody–antigen interaction force.

As can be seen from above, the magnetic particles, the Helmholtz coils, and cantilevers are the critical components of the FABS. The force generated by each magnetic particle is

$$F = 0.524Md^3(\mathrm{d}B/\mathrm{d}Z) \quad (2)$$

Where M is the volume magnetization of the magnetic material, d is the particle diameter, and $\mathrm{d}B/\mathrm{d}Z$ is the field gradient generated by the Helmholtz coils.

With its ability to detect a single bound molecule and to distinguish specific from nonspecific interactions, FABS could potentially have 6 – 8 orders of magnitude more sensitivity than commonly used immunoassays. This ability would be of value for environmental monitoring. Testing for airborne bacteria or viruses, for example, can presently require several days of air collection to accumulate detectable amounts of analyte. The high sensitivity of FABS could dramatically reduce sampling times and speed the detection of dangerous microorganisms or chemicals.

Combination of AFM and Other Techniques: AFM-Tip-Integrated Biosensors

Kueng et al. [8] have developed an AFM-tip-integrated biosensor to map molecular transport across membranes. Actually, this biosensor was a combined AFM-SECM (scanning electrochemical microscopy) probe which retained the integrity of both techniques and could be applied in dynamic-mode operation on soft biological samples. The combined AFM-SECM probe was fabricated as shown in Fig. 3a. An electroactive area with defined geometry, which was recessed from the apex of the AFM tip, allowed integration of the SECM functionality into AFM by correlating the current measured at the integrated electrode with the topographical information obtained by the AFM tip. Biological recognition elements, such as enzymes were then immobilized to the combined AFM-SECM probe as shown in Fig. 3b. In this integrated biosensor, AFM worked in its imaging dynamic mode, which was different from the above described biosensors which used AFM in a nonimaging mode.

To demonstrate the ability of this AFM-tip-integrated biosensor to study glucose membrane transport, a porous polycarbonate membrane (200 nm pore size) was mounted in a vertical diffusion cell that separated aqueous solutions in the donor and receptor compartments to mimic glucose transport through cellular membranes (Fig. 3c) and the glucose oxidase containing polymer layer was immobilized onto the probe (Fig. 3b). The combined AFM-SECM glucose oxidase electrode acted as a sensor that established concentration profiles of individual species near the sample surface. When the AFM tip was scanning in the X-direction above a synthetic membrane with 200 nm pores, the expected qualitative height and current signals were recorded (Fig. 3c). At the position of the pores, the height signal decreased, and glucose diffused through the pores toward the immobilized glucose oxidase layer, which catalyzed the conversion of glucose into gluconolactone (Fig. 4a). The current recorded at this glucose biosensor during the imaging of the pores increased as a result of the localized production of H_2O_2 when glucose diffused from the donor into the receptor compartment. Fig. 4c and 4d show AFM topography, SECM current images in the presence and absence of glucose in the donor compartment and exemplary line scans of the height and current response, respectively. The glucose signal response in the electrochemical image corresponded to the topography measured simultaneously with the AFM tip. The SECM current image of the porous membrane represented a contour map of the glucose concentration after emergence of the aqueous solution of glucose from the membrane pore and free diffusion into the receptor-compartment solution. While in the control experiment without glucose in the donor compartment, the measured current was negligible (Fig. 4f).

The glucose transport rate could be obtained by using Fick's law at appropriate boundary conditions, assuming that the pore opening was hemispherical. The concentration profile $C(r)$ at a radius r above the hemispherical pore opening could be described by Eqs. (3) and (4).

$$C(r) = (r_0/r)C_S \quad (3)$$

$$r_0 = 2a/\pi \quad (4)$$

Where C_S was the molecule concentration at the surface of the pore opening.

Earlier results showed that the radial divergence of the diffusive flux from a microscopic pore, regardless of its real shape, results in the pore appearing as if it were hemispherical in shape. For a disk-shaped pore with radius a, the radius of the corresponding hemispherical pore r_0 could be described by Eq. (4) [8].

Based on this approach, the theoretical glucose concentration at a distance (r) of 310 nm, which corresponds to

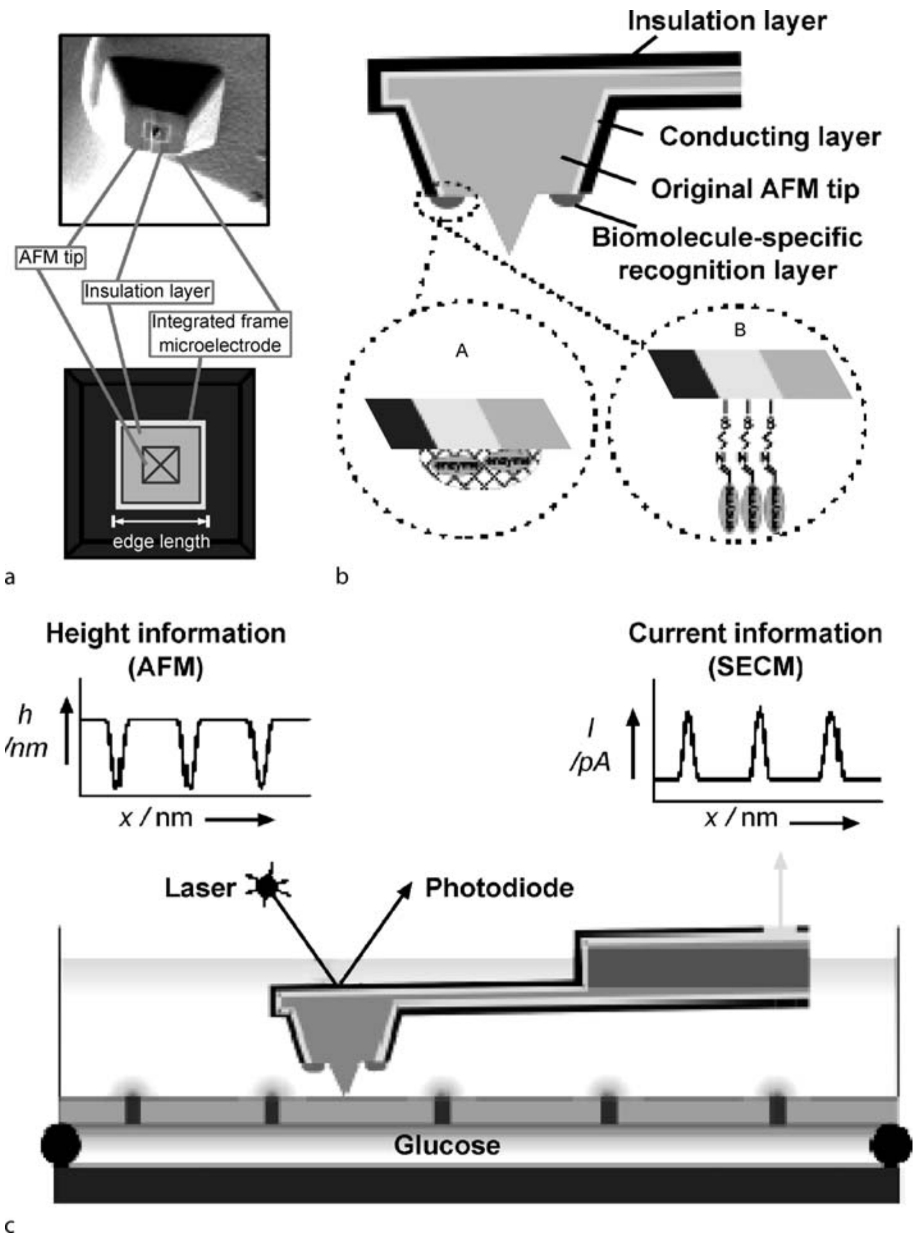

Biosensors Using Atomic Force Microscopes, Figure 3 (**a**) SEM image and schematic top view of an AFM-tip-integrated frame electrode; (**b**) schematic cross-section of an AFM-tip integrated biosensor. Enzymes can be immobilized at the surface of the scanning-probe tip-integrated electrode through self-assembled thiol monolayers with functionalized headgroups (A) or through electrochemical deposition of enzyme-containing polymer films (B). (**c**) Schematic cross-section of the experimental setup for imaging glucose transport through a porous membrane during simultaneous AFM mapping. (reproduced from [8])

the reshaped AFM tip height, above a pore opening with a radius (a) of 100 nm was estimated to be 0.62 mM for a 3 mM glucose solution. The evaluation of the current response in the SECM image (Fig. 4d) resulted in an average peak current of 1.5 ± 0.3 pA. According to the linear regression of the glucose calibration obtained at the integrated electrode (Fig. 4b), the measured glucose concentration was estimated to be 0.66 ± 0.13 mM. This semi-quantitative value corresponded well to the theoretically estimated concentration of 0.62 mM.

Glucose biosensors fabricated with this technology exhibit excellent sensitivity, response time, reproducibility, and long-term stability. This technology has a wide range of applications for biological specimens and processes.

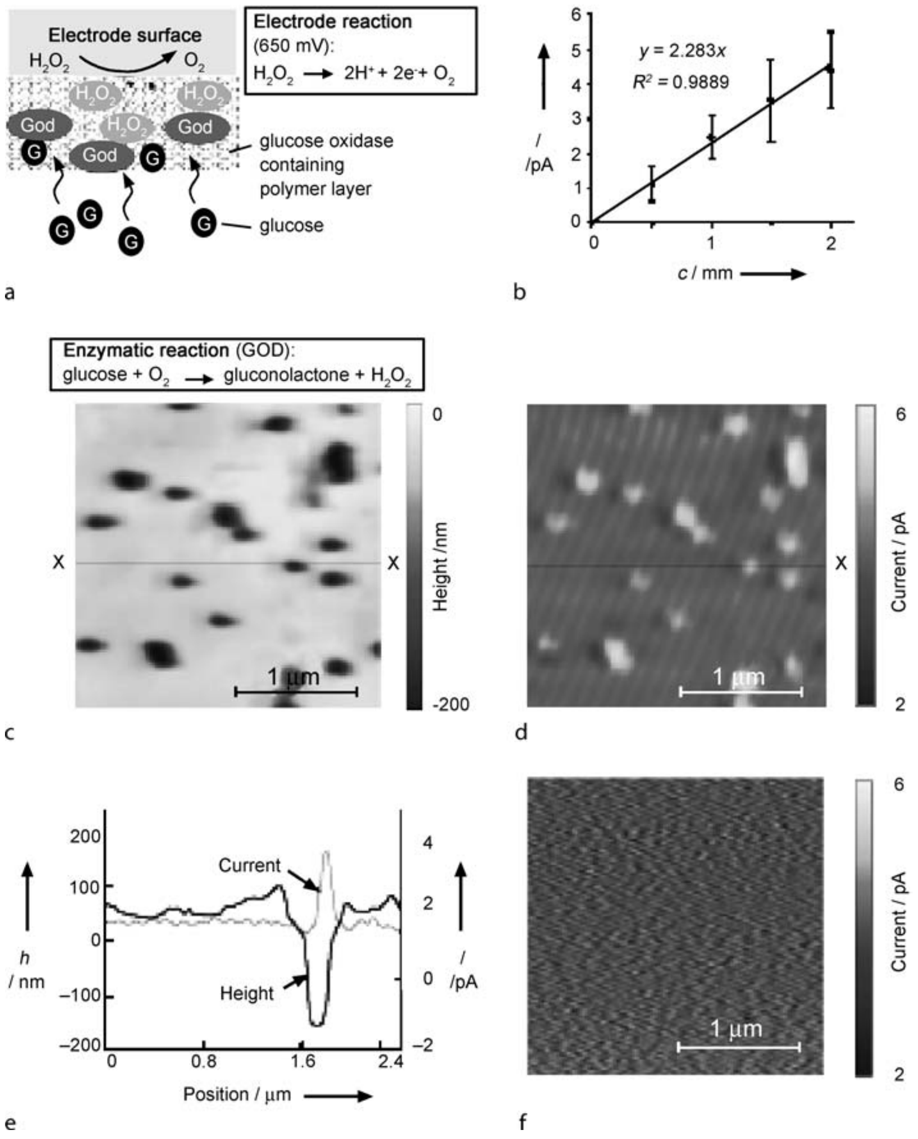

Biosensors Using Atomic Force Microscopes, Figure 4 (**a**) Reactions for glucose detection with a biosensor based on glucose oxidase (GOD). (**b**) Glucose calibration of an AFM-tip-integrated biosensor (edge length: 800 nm) fabricated by entrapment of glucose oxidase within a polymer film. Simultaneously recorded (**c**) height and (**d**) current images of glucose diffusion through a porous polycarbonate membrane (pore size: 200 nm); images recorded in AFM dynamic mode. (**e**) Exemplary corresponding line scans of height and current. (**f**) Current image recorded without glucose in the donor compartment. (reproduced from [8])

Future Directions for Research

The development of AFM and its use in detecting molecular interactions has led to the understanding of molecular recognition on a variety of biological surfaces. Researchers will continue to find more suitable surface chemistries to functionalize the AFM tip for the more precise measurement of single molecule interaction force and individual bond strength, and eventually use the AFM as a biosensor in the medical profession to screen samples for a particular chemical or biological agent. Second, the ability of the AFM to acquire movies (sequential images) under aqueous environments can be used to follow biological processes, dynamics and macromolecular assembly occurring in real time. Finally, the combination of AFM and other techniques to develop multifunctional, highly sensitive, easy operating devices for the purpose of molecular interactions study will be among future research interests.

Cross References

► Biosensor
► Atomic Force Microscope (AFM)

References

1. Kasaa S, Thomson NH, Smith BL, Hansma PK, Miklossy J, Hansma HG (1997) Biological applications of the AFM: from single molecules to organs. Int J Imag Sys Technol 8:151–161
2. Reich Z, Kapon R, Nevo R, Pilpel Y, Zmora S, Scolnik Y (2001) Scanning force microscopy in the applied biological sciences. Biotechnol Adv 19:451–485
3. Willemsen OH, Snel MME, Cambi A, Greve J, Grooth BGD, Figdor CG (2000) Biomolecular interactions measured by atomic force microscopy. Biophys J 79:3267–3281
4. Hinterdorfer P, Dufrene YF (2006) Detection and localization of single molecular recognition events using atomic force microscopy. Nature Methods 3:347–355
5. Kienberger F, Ebner A, Gruber HJ, Hinterdorfer P (2006) Molecular recognition imaging and force spectroscopy of single biomolecules. Acc Chem Res 39:29–36
6. Kocum C, Ulgen SD, Cubukcu E, Piskin E (2006) Atomic force microscopy tips (cantilevers) as molecular nucleic acid sensors. Ultramicroscopy 106:326–333
7. Baselt DR, Lee GU, Hansen KM, Chrisey LA, Colton RJ (1997) A high-sensitivity micromachined biosensor. Proc IEEE 85:672–680
8. Kueng A, Kranz C, Lugstein A, Bertagnolli E, Mizaikoff B (2005) AFM-tip-integrated amperometric microbiosensors: high-resolution imaging of membrane transport. Angew Chem (Int Ed) 44:3419–3422
9. Ebner A, Kienberger F, Kada G, Stroh CM, Geretschlager M, Kamruzzahan ASM, Wildling L, Johnson WT, Ashcroft B, Nelson J, Lindsay SM, Gruber HJ, Hinterdorfer P (2005) Localization of single avidin–biotin interactions using simultaneous topography and molecular recognition imaging. Chem Phys Chem 6:897–900

Biosensors Using Infrared Imaging

► Infrared Imaging and Mapping for Biosensors

Biosensors Using Lasers

JUN YANG, XIAOLIN ZHENG
Bioengineering College, Chongqing University, Chongqing, China
yjun1999@hotmail.com

Synonyms

Laser-based biosensors

Definition

Biosensors using lasers are defined as sensors for biological applications which are based on laser technology. There is a series of biosensors which use laser-based detection methods such as: surface plasmon resonance, fiber optics, waveguides, microcantilevers, and so on. Due to their high sensitivity and precision, laser-based biosensors have been widely used in many fields, including immunoassays and drug screening.

Overview

Biological sensing is a process which obtains selected information about biological macromolecular interactions in real time. Biosensors are miniaturized analytical devices based on biological sensing technology, which commonly comprise a biorecognition molecular layer immobilized on the interface between the analyte solution and a signal transducer (Fig. 1) [1]. The main part of a typical biosensor is this biologically sensitive layer that converts the biological change into a detectable signal, which is subsequently translated into a digital electronic result. The sensitive substances on the interface, which can include enzymes, antibodies, DNA segments, peptides or even a microorganism, provide the biosensor with its selectivity for the target analyte so that the molecule that is of interest can be picked out by the biosensor from a mixture of many different molecules. The extent of the biorecognition event is determined by the signal transducer and converted into an electronic signal for the end user. Popular transducers in biosensors include electrical, optical, or piezoelectric devices.

Optical biosensors are the most popular because of their high sensitivity, fast response time, in situ monitoring, and the absence of electrical interference. Due to its outstanding advantages in monochromaticity, coherence, low beam divergence, and strong irradiance, the laser is widely used as the light source in optical biosensors. For a wide range of biological systems, biosensors using lasers can be used to provide qualitative information, such as whether or not two molecules interact, and quantitative information, such as kinetic and equilibrium constants for macromolecular interactions. In a typical experiment, one molecule is attached to a surface and the other molecule, which is in solution, flows over the surface. Their interaction is transferred to a recognizable optical signal under the laser irradiation and converted to an electronic signal by optoelectronic components such as the charge coupled device (CCD) and the photomultiplier tube.

Many laser-based biosensors are derived from traditional detection methods. For example, traditional enzyme-based biological sensing analyses use the photometric detection

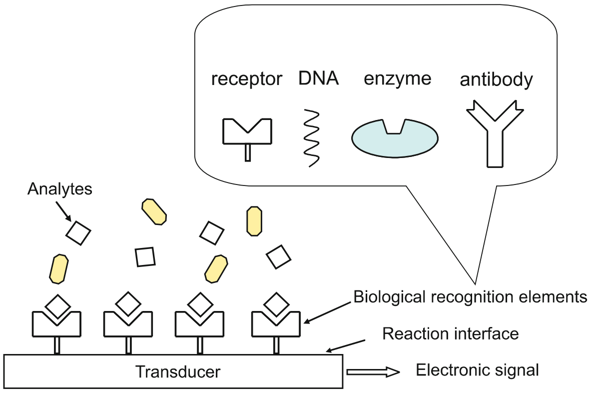

Biosensors Using Lasers, Figure 1 The biosensor comprises a biorecognition molecular layer immobilized on the interface of a signal transducer. Biological change on this interface is converted into a detectable signal and subsequently translated into a digital electronic result. Many types of sensitive molecules including enzymes, antibodies, a DNA segment, peptides or even a microorganism can be immobilized on the interface

method, where the enzyme reaction is linked to a colorimetric or fluorescent indicator. Some of these assay methods can be miniaturized and converted to solid-state systems, which were the early laser-based biosensors. This concept is now being applied to absorbance measurements by using evanescent wave detection, where the optical fiber, or in more general terms, the waveguide, itself forms the sensor surface. The binding of the immobilized biorecognition molecule and the analyte has an impact on the light propagating through the waveguide. The evanescent wave decays exponentially away from the surface of the waveguide, so that recognizable molecular interaction is limited to the layer immediately adjacent to the sensor surface, which is not affected by changes in the bulk solution.

Direct reading unlabeled immunoassay has also been sought through laser-based optoelectronics. In order to monitor the physico-chemical change produced by the interaction between an antibody and an antigen, without the secondary labels which are used in traditional biochemical assay methods, exploration of new detection techniques is required. Surface plasmon resonance (SPR) is the most outstanding of these techniques, with a sensitivity as high as 10^{-8} g/l [2]. The SPR biosensor is now the most popular optical biosensor. The microcantilever is another laser-based biological sensing method for the detection of analyte without labeling, where biological changes are monitored by using a laser optical beam deflection technique which detects the reflection of a microcantilever induced by biological interaction.

Several popular laser-based biosensors, SPR, optic fibers, waveguides, and microcantilever biosensors, will be summarized below.

Basic Methodology

Surface Plasmon Resonance

As a laser-based optical biosensor technique, SPR can measure molecular binding events at a metal surface by detecting changes in the local refractive index. The depth probed at the metal–aqueous interface is typically 200 nm, making SPR a surface-sensitive technique ideal for studying interactions between immobilized biological molecules and a solution-phase analyte.

SPR is an optical phenomenon that arises under conditions of total internal reflection of p-polarized light at an interface between a metal film and a liquid/gas phase, where a prism or grating is used as a coupling component (Fig. 2) [2]. Total internal reflection of light occurs when light traversing a medium of high refractive index (commonly a glass prism) encounters an interface with a medium of lower refractive index (usually an aqueous or gaseous environment). During total internal reflection, the energy and momentum of incident light can be transferred into the surface of the metal to create a surface plasmon. This excitation of plasmons generates an evanescent wave which propagates along the glass–metal surface, but decays exponentially over about one wavelength from the interface. For a fixed excitation wavelength, variation of the incident angle (θ) allows detection of the optimal angle associated with SPR, where most incident light is absorbed by the surface plasmon wave. This unique angle for minimal reflected light intensity is called the SPR angle (θ_{SPR}). Measurement of the intensity of reflected light as a function of the incident angle generates a SPR spectrum (Fig. 3a), which depends upon the refractive index and the thickness of the dielectric medium in the immediate vicinity of the interface. Although the evanescent field extends some 300 nm into the medium of low refractive index, the exponential decay of its amplitude gives rise to a rapidly decreasing sensitivity of response with increasing distance from the metal surface. As the detection method based on SPR angle, for a fixed incident angle, variation of the excitation wavelength allows the wavelength associated with optimal conditions for SPR to be detected. The incident angle and excitation wavelength scan are commonly used as detection methods in SPR biosensors.

The incident angle (or wavelength) where the resonance occurs strongly depends on the refractive index close to the metal surface. In a SPR biosensor, the interaction between immobilized biomolecules on the surface and analytes in solution changes the local refractive index, which results

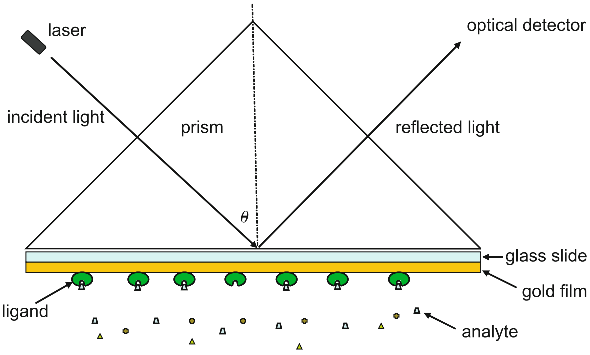

Biosensors Using Lasers, Figure 2 Schematic representation of a SPR biosensor. Laser and prism are used as the emitted light source and coupling component, respectively. Receptor molecules immobilized on the gold surface interact with analytes in solution, which induce the change in the refractive index in the immediate vicinity of the interface. This change can be detected by the SPR signal monitoring on the gold surface

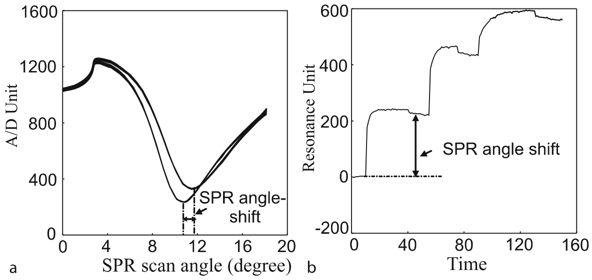

Biosensors Using Lasers, Figure 3 (a), SPR curve of a detection method based on incident angle scan. SPR angle shifts with the change in refractive index. (b), monitoring the shift of SPR angle in real time

in a shift in the SPR angle. By monitoring changes in the shift process of the SPR angle, it is possible to measure the interaction on the surface in real time (Fig. 3b). Here no label is needed. Typical biological systems examined using these instruments include antibody–antigen, ligand–receptor, and protein–nucleic acid interactions.

Traditional SPR spectroscopy biosensors, which measure the entire SPR curve as a function of the angle or wavelength, have been widely used, but offer limited throughput. The development of SPR imaging (microscopy (SPM)) allows for the simultaneous measurement of thousands of biomolecular interactions [3]. Typically, a SPM consists of a highly coherent p-polarized light source expanded by a beam expander and consequently reflected from an SPR active medium (sensing surface) to a detector. The CCD camera is frequently used as the detector in this system, which collects the reflected light intensity in an image. SPM imaging measurements are performed at a fixed incident angle that falls within a linear region of the SPR curve, so that changes in light intensity are proportional to the changes in refractive index caused by the biomolecular interaction on the surface. Thus, the gray-level intensity of the SPM image correlates with the amount of material bound to the sensing region. When combined with protein arrays, SPM imaging technology has the potential to become an invaluable tool for a broad range of applications that require high-throughput analysis of biomolecular interactions, such as proteomic analysis, drug screening, and immunoassay.

SPR offers several advantages over conventional techniques such as fluorescence or enzyme-linked immunosorbent assay. Here the analyte does not require any special characteristics or labels and can be detected directly; the measurements can be performed in real time to collect kinetic data; it is a versatile technique, capable of detecting analytes over a wide range of molecular weights and binding affinities. Because of its unique features, SPR has become a powerful tool for studying biomolecular interactions.

Fiber Optics

Fiber optic biosensors, which often use a laser as the light source are based on several different detection principles. Most existing laser-based detection methods used in large-scale instruments can be miniaturized by using optical fibers. For example, fluorescence and absorbance detection have been miniaturized by this way. In the case of absorption, the detector measures the reduction in the intensity of light from the source. This reduction is caused by an absorbent product arising from the reaction between the immobilized substance and the analyte. Absorption measurements are generally made using monochromatic wavelength light, and both the incidence and emitted beams have the same wavelength. At least two fibers are necessary in this system, one for the inward beam and one for the outward beam, because the intensities of these two beams cannot be separated at the same wavelength (Fig. 4a). The use of white light, however, can yield a complete absorption spectrum with the help of photodiode matrices or arrays. The wavelength of the rescence emission is different from its excitation wavelength, and a single fiber is sufficient to transport both the excitation and the emission radiation (Fig. 4b). A single fiber can also be used to measure fluorescence quenching, which occurs when a compound that absorbs in the same spectral region as the emission is present.

Some optical phenomena (e. g., evanescent waves) within the microscale optical environment are used to construct fiber optic biosensors [4]. In fiber optic biosensors for photometric detection, the light between the sample and the source or detector is transported along the interior of

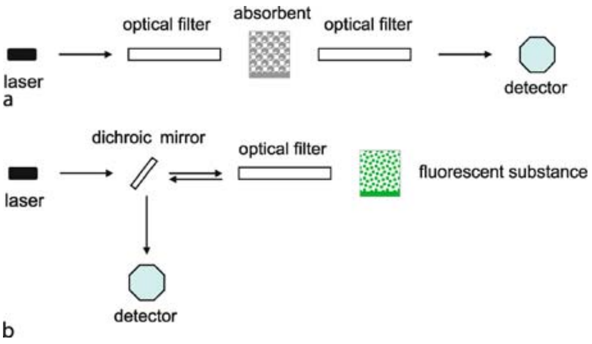

Biosensors Using Lasers, Figure 4 Fiber optic biosensors based on (a) absorbance, and (b) fluorescence detection methods

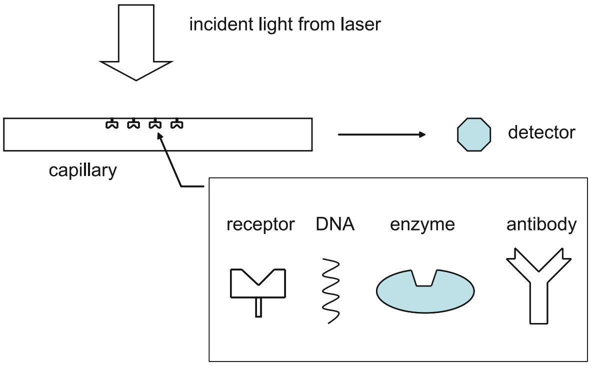

Biosensors Using Lasers, Figure 5 A capillary is used as an optical waveguide for evanescent wave-based biological sensing detection. The waveguide is perpendicularly illuminated by laser light, and the detection signal is subsequently collected from one end of the waveguide

the fibers following the principle of total reflection. The total reflection in a fiber is not perfect and some electromagnetic radiation penetrates the sheath covering the fiber. This is called the evanescent wave, and its intensity diminishes exponentially with the perpendicular distance from the interface as the surface wave in SPR. It can be used to detect the variations in optical properties of chemical and biological films placed around the fiber [5]. The laser optical detection method based on evanescent waves is widely used in biosensors. For example, a tapered optical fiber is used to analyze the total internal reflectance fluorescence. As light is propagated down the fiber, an evanescent wave excites fluorescent tracers bound to the fiber surface. Because the evanescent wave decays exponentially with the distance from the fiber surface, the excitation radius only extends about 100 nm into the buffer medium. A portion of the emission is captured and propagated back through the fiber to the detector.

Waveguides

A waveguide works on a similar principle to optical fibers, so most fiber optic detection methods can be transplanted to waveguide-based biosensors [6]. Compared with optical fibers, the waveguide is more easily integrated with other optical components (e. g., grating, interferometer) and can be integrated into miniaturized detection devices such as microfluidic chips.

The fiber optic biosensor, based on an evanescent wave, is the most popular of the biosensors using waveguides. In the early stage, a capillary is used as the waveguide to collect free propagating fluorescence [7]. For biosensor applications, probe molecules can be covalently bonded to the interior surface of the capillary to detect target molecules flowing through the capillary. Placing the probe coating on the interior surface also facilitates handling and protects against accidental damage. One detection method is achieved by illuminating the capillary (waveguide) at a 90° angle relative to the length of the waveguide and subsequently collecting the emitted fluorescence from the end of the waveguide (Fig. 5).

A waveguide can be integrated with a ating to form an optical waveguide grating coupler sensor, which responds to the change in optical refractive index of the liquid or gas cover medium. As in SPR detection, the optical refractive index in the immediate vicinity of the interface is directly related to the adsorption or binding of molecules on the surface. The optical waveguide grating coupler sensor chip is based on a fine optical grating prepared on a thin waveguide layer on a glass substrate. The optical grating couples the light of a laser at a given resonance angle into the waveguide layer. This resonance angle is very sensitive to the presence of adsorbed molecules and to any change in the refractive index of the medium covering the surface of the chip.

A planar waveguide with a corrugated surface, which can be tuned to be a resonant Bragg reflector, is also a laser-based biosensor (Fig. 6) [8]. The reflection coefficient of the light propagating through the waveguide depends on the depth of the corrugation as well as on the length of the corrugated region. A specially prepared layer, which selectively adsorbs the target biomolecules, is only covered on the surface of higher parts of the corrugation. When solution flows over this corrugation, some target biomolecules bind with the cover layer, the corrugation depth rises and the reflection coefficient changes. This change is proportional to the difference between the dielectric permittivities of the analyte and solution, and can be used to monitor the dynamics of the surface reaction. The presence and concentration of the target biomolecules in the solution can also be inferred by this method.

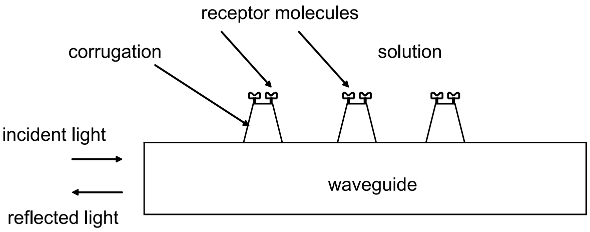

Biosensors Using Lasers, Figure 6 Schematic of a laser-based biosensor using the resonant Bragg reflector principle. A receptor molecular layer covers the surface of some corrugation that is used as sensing materials. After some target molecules bind with the receptor molecular layer, the corrugation amplitude rises and coupling coefficient changes

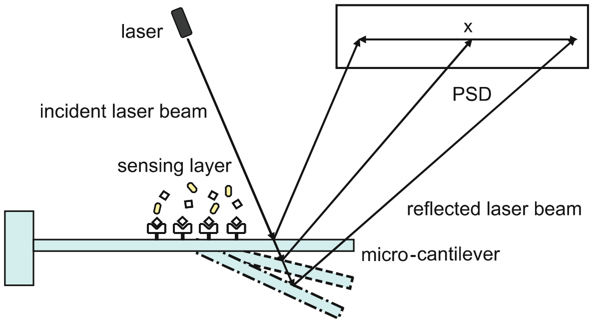

Biosensors Using Lasers, Figure 7 Scheme of the optical read-out method for a microcantilever bending evaluation. The displacement of the free end of the cantilever is measured by monitoring the optical deflection of an incident laser beam on a position-sensitive detector

Microcantilevers

Biosensors using microcantilevers have attracted considerable interest in the last few years [9, 10]. The microcantilevers transduce the recognition event from their receptor-coated surface into a mechanical deflection. As the ligands interact with the receptors, the adsorption stress leads the bending of the cantilever toward or away from the receptor side depending on the nature of the chemical bonding of the molecules. The deflection of the microcantilever can be measured using the optical beam deflection technique, which is highly sensitive and widely used in atomic force microscopy. The displacement of the free end of the cantilever is measured by detecting the optical deflection of an incident laser beam on a position-sensitive detector (PSD), which allows the absolute value of the cantilever displacement to be calculated (Fig. 7). This method provides sub-angstrom resolution and can easily be implemented. High sensitivity biological sensing thus becomes possible.

The defection (δ) of a microcantilever, which is caused by the surface stress difference of the top (receptor-coated) and the bottom surfaces, can be estimated according to

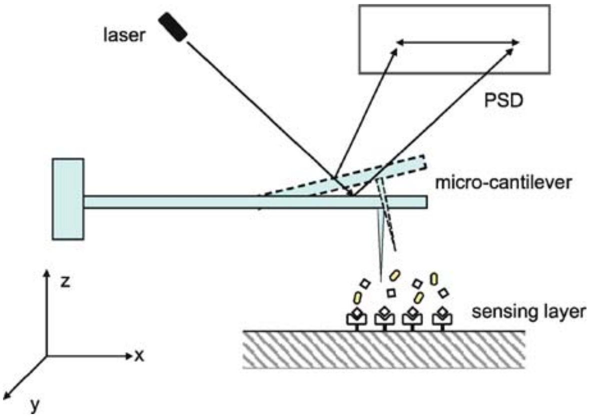

Biosensors Using Lasers, Figure 8 Working principle of the microcantilever atomic force biosensor

Stoney's formula:

$$\delta = \frac{3\,(1-v)\,(\sigma_1-\sigma_2)\,L^2}{Ed^2}$$

where v is the Poisson ratio of the cantilever material; σ_1 and σ_2 represent the surface stress of the top and bottom surfaces, respectively. L and d are the length and the thickness of the cantilever, respectively, and E is Young's modulus of the cantilever material.

The microcantilever atomic force biosensor is another type of microcantilever-based biosensor. Its working principle is similar to that of the microcantilever biosensor. However, receptor molecules are covered on a planar other than the surface of cantilever. Biological changes are also monitored using an optical beam deflection technique. The laser illuminates the end of the microcantilever and changes in position are detected using a matching PSD. This sensor works like a profilometer by moving a microfabricated tip held at the end of a microcantilever across the sample while recording the x-, y-, and z-coordinates of the preparation being scanned (Fig. 8). The z-coordinate is calculated by detecting the laser beam reflected off the surface of the cantilever. These microcantilever biosensors are able to detect many biological systems such as single-strand DNA hybridization, and protein–protein/DNA binding, pH variations.

Future Directions for Research

In recent years, laser-based biosensors have become important tools in many fields such as analytical biochemistry, pharmaceutical research and development, and food/environmental monitoring. However, the volumes of the optic components in these biosensors limit their application in portable microdevices. In order to obtain

more powerful, miniaturized, and cheaper biosensors using lasers, novel biological sensing principles, detection means and fabrication methods need to be sought. The integration of biosensors and microfluidic chips will be an important direction for developments in laser-based biosensors. Biosensors can be used as microscale detection tools in lab-on-a-chip for the research and development of miniaturized detection devices, i. e., micro-total analysis systems.

Cross References

- ► Biosensors Using Atomic Force Microscopes
- ► Fluorescence Measurements
- ► Nanoscale Biosensors
- ► On-chip Waveguides
- ► Surface Modification
- ► Surface Plasmon Resonance Sensors

References

1. Ziegler C, Gopel W (1998) Biosensor development. Curr Opin Chem Biol 2:585–591
2. Boozer C, Kim G, Cong SX, Guan HW, Londergan T (2006) Looking towards label-free biomolecular interaction analysis in a high-throughput format: a review of new surface plasmon resonance technologies. Curr Opin Biotechnol 17:400–405
3. Rothenhausler B, Knoll W (1988) Surface-plasmon microscopy. Nature 332:615–617
4. Shriverlake LC, Breslin KA, Charles PT, Conrad DW, Golden JP, Ligler FS (1995) Detection of TNT in water using an evanescent-wave fiberoptic biosensor. Anal Chem 67:2431–2435
5. Rogers KR, Apostol A, Madsen SJ, Spencer CW (2001) Fiber optic biosensor for detection of DNA damage. Anal Chim Acta 444:51–60
6. Dhadwal HS, Kemp P, Aller J, Dantzler MM (2004) Capillary waveguide nucleic acid based biosensor. Anal Chim Acta 501:205–217
7. Zhu PX, Shelton DR, Karns JS, Sundaram A, Li SH, Amstutz P, Tang CM (2005) Detection of water-borne E-coli O157 using the integrating waveguide biosensor. Biosens Bioelectron 21:678–683
8. Dotsenko AV, Diikov AL, Vartanyan TA (2003) Label-free biosensor using an optical waveguide with induced Bragg grating of variable strength. Sens Actuators B 94:116–121
9. Zhang XR, Xu XF (2004) Development of a biosensor based on laser-fabricated polymer microcantilevers. Appl Phys Lett 85:2423–2425
10. Carrascosa LG, Moreno M, Alvarez M, Lechuga LM (2006) Nanomechanical biosensors: a new sensing tool. TRAC 25: 196–206

Biosensors Using Magnetics

Chan Hee Chon, Dongqing Li
Department of Mechanical Engineering,
Vanderbilt University, Nashville, TN, USA
Chanhee.chon@vanderbilt.edu

Synonyms

Magnetic biosensors; Magnetic-based biosensors

Definition

Biosensors are analytical devices incorporating biological or biologically derived sensing elements with physicochemical transducers to produce digital electronic signals [1]. These biosensors determine the concentration of substances and other parameters of biological interest. The detecting elements of biosensors work in different physicochemical ways: optical, piezoelectric, electrochemical, thermometric, and magnetic. Biosensors using magnetics utilize the magnetic field created by magnetic particles that bind to target molecules in a biological assay (Fig. 1).

Overview

There is an increasing need for higher sensitivity and specificity of detection for biosensors. Magnetic particles, by the use of the magnetoresistive (MR) effect, have been developed as labels for biosensing. These magnetic biosensors have several advantages compared to optical and electrical biosensors. The properties of magnetic particles are not affected by reagent chemistry so that they are very stable over time. Magnetic fields are also not screened by aqueous reagents or biomaterials. In addition, magnetism may be used to remotely manipulate the magnetic particles [2]. Therefore, magnetic biosensors using MR materials have been proposed as a new technology to detect low concentrations of targets in biofluids [3].

The target biomolecules in a biofluid are attached on magnetic particles. When these magnetically labeled

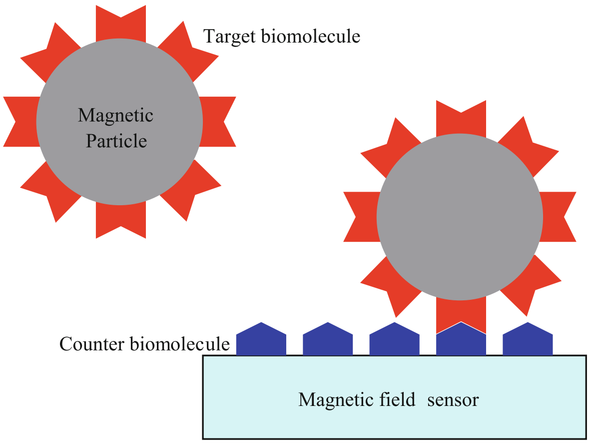

Biosensors Using Magnetics, Figure 1 Schematic of magnetically labeled biomolecule detection in a biosensor. Target biomolecules bound with a magnetic particle interact with magnetoresistive sensor-bound counter biomolecules to be detected

target biomolecules pass over the magnetic biosensor with counter biomolecules bound on its surface, these biomolecules interact with each other and the biosensor generates detecting electronic signals (Fig. 1).

A number of sensitive magnetic field detection devices have been developed as biosensors: giant magnetoresistive (GMR) sensors [4], piezoresistive cantilevers [5], inductive sensors [6], superconducting quantum interference devices (SQUIDs) [7, 8], anisotropic magnetoresistive (AMR) rings [9], and miniature Hall crosses [10].

Cross References

- ► Magnetic Field-based Lap-on-Chip Devices
- ► Biosensors Using Atomic Force Microscopes
- ► Biosensors Using Laser
- ► Infrared Imaging and Mapping for Biosensors
- ► Biosensors Using Surface-enhanced Raman Scattering

References

1. Turner APF, Karube I, Wilson GS (1987) In: Biosensors: Fundamentals and Applications. Oxford University Press, Oxford, p 770
2. Rife JC et al (2003) Design and performance of GMR sensors for the detection of magnetic microbeads in biosensors. Sens Actuators A 107:209–218
3. Graham DL, Ferreira HA, Freitas PP (2004) Magnetoresistive-based biosensors and biochip. Trends Biotechnol 22:455–462
4. Baselt DR, Lee GU, Natesan M, Metzger SW, Sheehan PE, Colton RJ (1998) A biosensor based on magnetoresistance technology. Biosens Bioelectron 13:731–739
5. Baselt DR, Lee GU, Natesan M, Hansen KM, Chrisey LA, Colton RJ (1995) A high-sensitive micromachined biosensor. Proc IEEE 85:672–680
6. Richardson J, Hill A, Luxton R, Hawkins P (2001) A novel measuring system for the determination of paramagnetic particle labels for use in magneto-immunoassays. Biosens Bioelectron 16:1127–1132
7. Lee S, Myers WR, Grossman HL, Cho HM, Chemla YR, Clarke J (2002) Magnetic gradiometer based on a high-transition temperature superconducting quantum interference device for improved sensitivity of a biosensor. Appl Phys Lett 81:3094–3096
8. Enpuku K, Hotta M, Nakahodo A (2001) High-T_c SQUID system for biological immunoassays. Physica C 357–360: 1462–1465
9. Miller MM, Prinz GA, Cheng SF, Bounnak S (2002) Detection of a micron-sized magnetic sphere using a ring-shaped anisotropic magnetoresistance-based sensor: A model for a magnetoresistance-based biosensor. Appl Phys Lett 81:2211–2213
10. Besse PA, Boero G, Demierre M, Pott V, Potovic R (2002) Detection of a single magnetic microbead using a miniaturized silicon Hall sensor. Appl Phys Lett 80:4199–4201

Biosensors Using Scanning Force Microscope

► Biosensors Using Atomic Force Microscopes

Biosensors Using Surface-Enhanced Raman Scattering

JAEBUM CHOO
Department of Applied Chemistry, Hanyang University, Ansan, Kyunggi-do, South Korea
jbchoo@hanyang.ac.kr

Synonyms

SERS-based biosensors

Definition

Devices for the highly sensitive detection of biological analytes using surface enhanced Raman scattering (SERS) spectroscopy. SERS is a highly sensitive optical detection technique in which lasers are used to excite vibrational transitions in molecule adsorbed on a metal nanoparticle surface. As a result of large optical fields, the Raman cross section for a molecule on a surface is enhanced by factors of $10^6 – 10^{10}$.

Overview

Microfluidic technology has recently been developed to perform a variety of biological or environmental trace analyses. These devices have several advantages compared with conventional techniques, such as minimal sample requirement, reduced reaction time, ease-of-use, improved product conversion, and reduced waste generation. It has long been realized that the system used for detection of the progress of the reaction is a key issue in determining the applicability of the microfluidic system. Because of the extremely small volume in a microfluidic channel, a highly sensitive detection method is essential in order to monitor the progress of the reaction. At the early development stage of a microfluidic detection, off-chip detection methods, such as high performance liquid chromatography or mass spectrometry, have been widely used to detect the small volumes of chemical species in a microfluidic channel. However, off-chip detection is very inconvenient for continuous monitoring of reactions since the sample must be removed from the reservoir of a chip on each detection occasion.

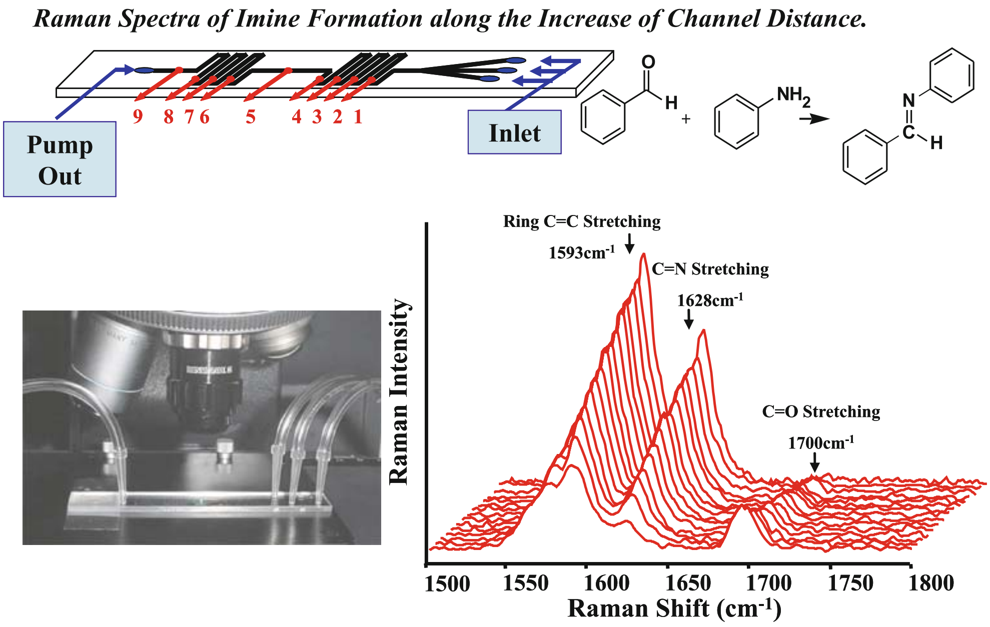

Biosensors Using Surface-Enhanced Raman Scattering, Figure 1 In situ Raman monitoring of imine formation reaction in a glass microfluidic sensor. The change in Raman spectra corresponds to the peak changes caused by the imine formation at various points along the channel

On the other hand, spectroscopic detection methods, such as laser induced fluorescence (LIF), UV/Vis absorption, chemiluminescence and thermal lens microscopy (TLM), have been used for on-chip detection. Among these methods, the fluorescence detection method has been most widely used because of its high sensitivity and low detection limits for biologically relevant species. However, the fluorescence detection technique has some disadvantages. Many chemical species do not fluoresce and so need to be treated with fluorescence tags to allow on-chip detection. Furthermore, it may have drawbacks such as a photobleaching and overlapping peaks caused by broad fluorescence emission profiles in multiplexed biological detection. Raman spectroscopy is another well-known analytical method, which offers great advantages for probing the biological and structural properties of a compound on a microscopic scale. The detection and identification of non-fluorescent samples is possible using this technique. Photodecomposition is reduced compared with fluorescent samples since the excited states are rapidly quenched and the excitation energy does not have to be in resonance with electronic transitions.

However, Raman scattering is an extremely inefficient process with low scattering cross-sections that are approximately fourteen orders of magnitude smaller than the absorption cross sections of fluorescent dye molecules. In order to achieve a high sensitivity of a biological sample, the scattering intensity should be greatly increased. Surface enhanced Raman scattering (SERS) spectroscopy, using silver nanoparticles, has shown promise in overcoming the low sensitivity problems inherent in Raman spectroscopy. Using the SERS technique, the detection sensitivity is enhanced up to 6 – 10 orders of magnitude over conventional Raman spectroscopy. As a result, the SERS technique provides a comparable sensitivity with fluorescence detection. In order to understand the enhancement mechanisms, it is instructive to refer to the following equation:

$$P = \alpha E \tag{1}$$

where P is the induced dipole moment, α is the molecular polarizability, and E is the incident electric field. The Raman scattering intensity (I) is proportional to the square of the induced dipole moment (P).

$$I = P^2 \tag{2}$$

Raman enhancement can take place by either increasing the electric field (E) experienced by the molecule (electromagnetic enhancement) or by changing the molecular polarizability of the adsorbate (chemical enhancement). The electromagnetic enhancement mechanism is explained by a phenomenon known as surface plasmon resonance. Surface plasmons are oscillations of conduction band electrons at a metal surface. At the surface

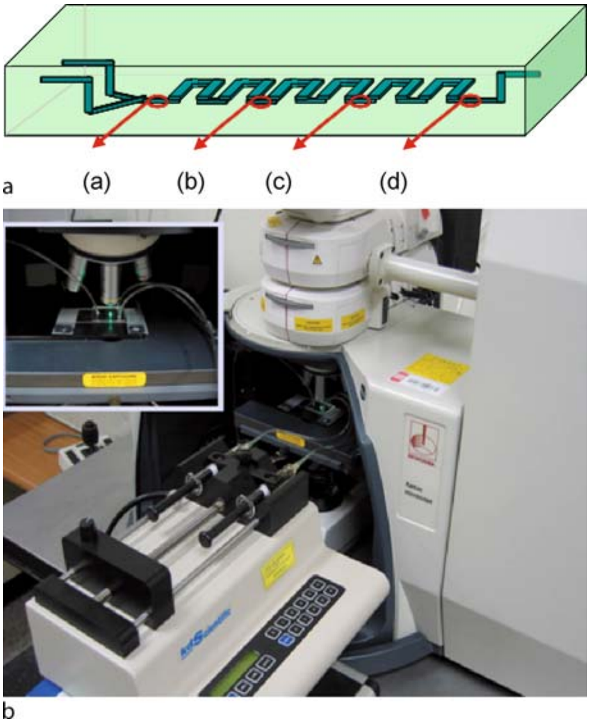

Biosensors Using Surface-Enhanced Raman Scattering, Figure 2 Schematic diagram of the experimental set-ups comprising a PDMS microfluidic channel and a microstage: (**a**) A schematic view of a 3D serpentine PDMS channel and four measurement spots along the channel distance: (a) at 0.15 mm, (b) at 28.5 mm, (c) at 68.4 mm, and (d) at 105.7 mm. (**b**) the optical arrangements for focusing the laser on the PDMS channel on the stage of confocal Raman microscope

plasmon resonance frequency, conduction band electrons move easily producing a large oscillation in the local electric field intensity. The surface plasmon frequency strongly depends on surface morphology (size and shape of particles), the dielectric properties of the metal, and the wavelength of the incident light. Electromagnetic effects are known to be decreased as a function of $1/r^3$ distance from the surface. Chemical enhancement involves the bond formation between the analyte and the metal surface. This bond makes it possible to transfer charge from the metal surface to the adsorbate molecule and this effect increases the molecular polarizability of the molecule. There have been many experimental evidences that both effects play a key role on the SERS effects. However, it is generally believed that electromagnetic enhancement may have a greater part to play than chemical enhancement. The main analytical advantages of SERS are enhanced sensitivity, surface specificity, and fluorescence noise reduction. Furthermore, it is possible to simultaneously detect multiplex analytes using SERS since its signals are much narrower than fluorescence bands.

However, the quantitative application of SERS is known to be very difficult because it is very hard to control the experimental conditions such as the degree of aggregation, the particle sizes of metal colloids, and the inhomogeneous distributions of molecules on the metal surface. As a result, under ordinary sampling conditions, the precision expected from a SERS experiment is very poor. On the other hand, a highly precise quantitative measurement can be obtained if continuous flow and homogeneous mixing conditions between analytes and silver nanoparticles are maintained. For this purpose, a functional microfluidic channel for the efficient mixing of analytes and aggregated silver colloids. Under the optimum conditions of using an an efficiently designed mixing channel and flow velocity, the quantitative SERS detection of analytes can be achieved under flowing conditions. This analytical method provides fast and reproducible results for the quantitative measurement of analytes at low detection levels. For example, the GC/MS or HPLC analysis requires longer than ten minutes for the sample pretreatments and measurements. On the other hand, only thirty seconds are needed when the SERS detection technique is applied. The SERS detection, in combination with microfluidic technology, can applied to the highly sensitive biological/environmental trace analyses.

Basic Methodology

Fabrication of an Alligator Teeth-Shaped PDMS Channel

Microfluidic channels are fabricated by stacking two PDMS layers that have upper and lower teeth patterns. These layers are produced by the pattern replication from mould masters. Two epoxy-based photoresist (EPON) mould masters, including upper and lower teeth patterns, were fabricated. By pouring the mixture of PDMS prepolymer and curing agent in a 10 : 1 ratio onto the lower mould master and by curing for 2 h on the hot plate at 80 °C, the patterned thick layer (thickness: 1.0 cm) with a lower pattern is constructed. The layer with upper teeth pattern is fabricated by the compression micro-moulding of PDMS elastomer. The PDMS pre-polymer is poured onto the mould master and compressed with transparent film and an aluminum disk. Then it is cured for 2 h. The thin upper layer (thickness: 200 μm) is produced by separating it from the mould master. For the bonding of upper and lower layers, the surfaces of both layers are activated in the oxygen plasma. Then it is aligned using the house-made aligner. Methanol is used as a surfactant between both layers. Finally, the cover glass is stacked onto the upper layer.

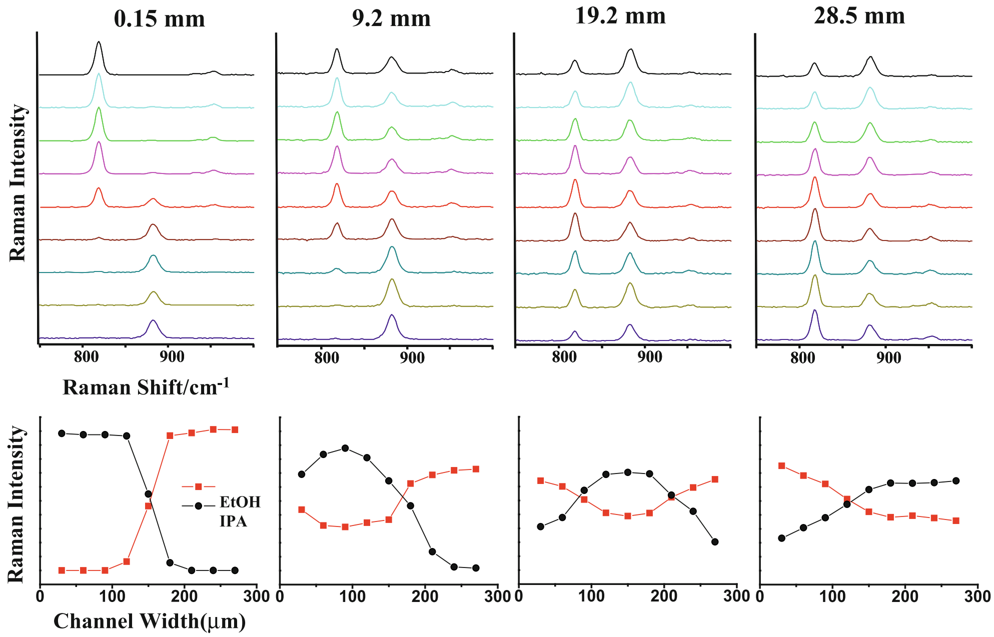

Biosensors Using Surface-Enhanced Raman Scattering, Figure 3 Raman profiling spectra and corresponding peak area changes for the C – O/C – C stretching modes of an ethanol-isopropanol mixture in a 3D serpentine channel. The upper number denotes the channel distance beyond the T-junction spot of the channel

Preparation of Silver Nanocolloids

Silver colloids are prepared by the method, as is recently reported by Leopold and Lendl. Here silver nitrate is reduced by hydroxylamine hydrochloride. The advantages of the hydroxylamine hydrochloride-reduced silver colloid are in its fast preparation at room temperature and its immediate applicability for SERS. First, 5 mL of hydroxylamine hydrochloride (3.0×10^{-2} M) is dissolved in 84 mL of triply distilled water and then 1 mL of sodium hydroxide (1.7×10^{-3} M) is added to maintain an alkaline pH condition. Next, 10 mL of silver nitrate solution (1.0×10^{-3} M) is added dropwise to the solution with continuous stirring. The solution is continuously stirred for additional 20 min. UV/Vis spectroscopy and TEM were used to characterize the particle size of produced colloids. Figure 1 shows the TEM, AFM images and UV/Vis absorption and Raman spectra of SERS-active colloidal nanoparticles.

SERS Detection

SERS measurements are performed using a Raman microscope system. An argon ion laser operating at $\lambda = 514.5$ nm is generally used as the excitation source. The Rayleigh line is removed from the collected Raman scattering by a holographic notch filter located in the collection path. Raman scattering signal is detected using a charge-coupled device (CCD) camera or photomultiplier tube (PMT). In Raman microscope, an additional CCD camera is fitted to an optical microscope to obtain optical images. A two-slit confocal arrangement is used to reduce the background Raman scattering from the unfocused laser beams. Although the laser beam is focused on the middle of the micro channel, i. e., the section between the top and the bottom in the z direction, the Raman signal from a small volume of chemicals in the micro channel cannot be completely separated from the signals originating from the surrounding PDMS material. To resolve this problem, all the Raman spectra are measured in the confocal mode. In the Raman system, the function of the pinhole is replaced by the cooperation of the entrance slit and the pixels in the CCD detector. Using the confocal technique, the background stray light, due to any out-of-focus regions of the PDMS, is effectively removed. The silver colloids and biological analytes are introduced into the channel from microsyringes connected by tubes to the inlet pipettes. The flow rate is controlled by using a microsyringe pump. The confocal SERS is measured after the analytes are effectively adsorbed on the silver nanoparticles by traveling the upper and lower alligator teeth-shaped microfluidic channel. Confocal SERS microscopy can be used as a highly sensitive sensing technique for the detection of non-fluorescent biological samples in a PDMS microfluidic channel.

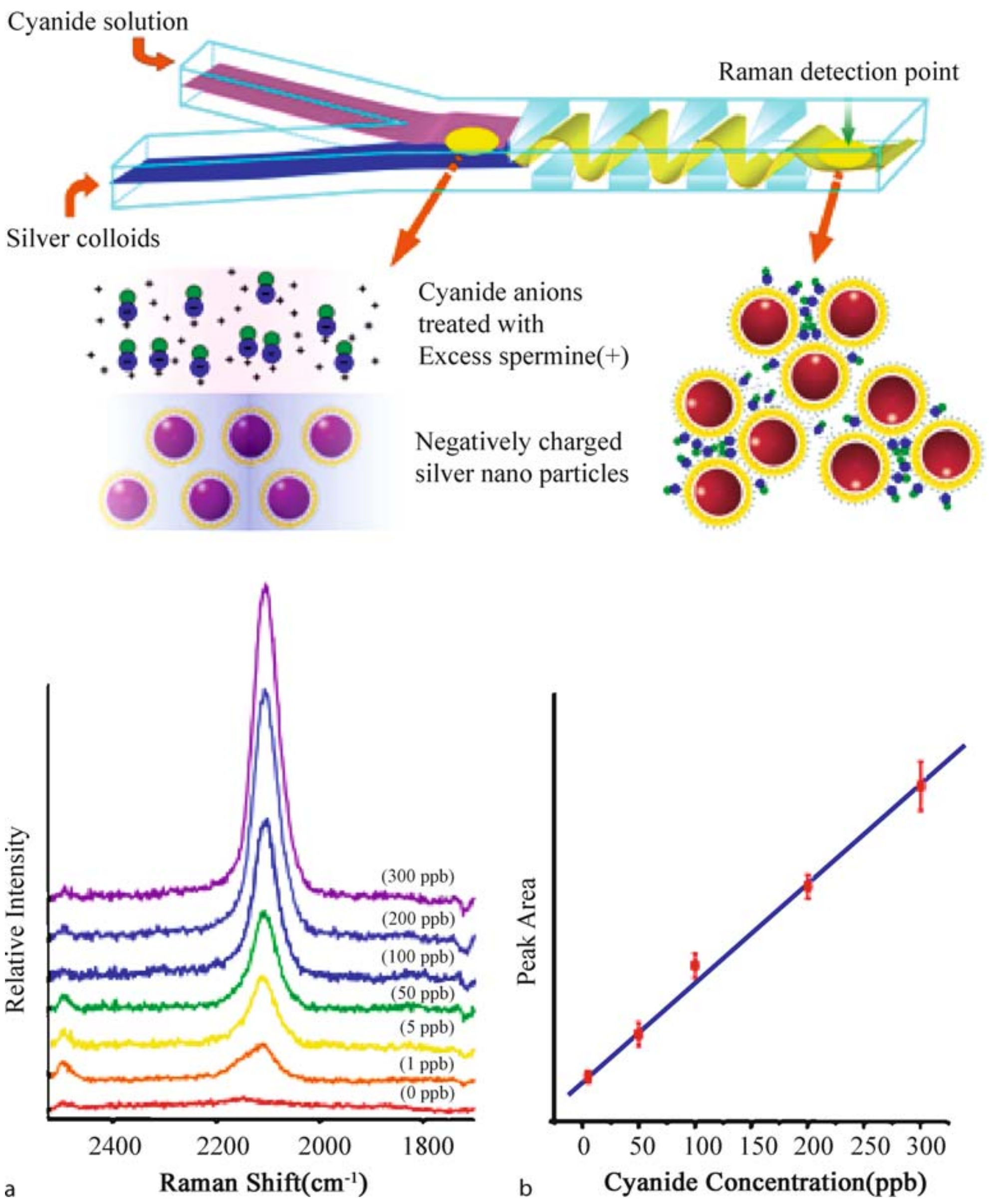

Biosensors Using Surface-Enhanced Raman Scattering, Figure 4 Schematic illustration of the alligator teeth-shaped microfluidic channel. The confluent streams of silver colloids and trace analytes were effectively mixed in the channel through the triangular structures, which are located on the upper and lower surfaces of the channel in a zigzag manner. The flow rate was 5 μL/min. (**a**) SER spectra for increasing concentrations of cyanide ion in the microfluidic channel: (a) 0 ppb, (b) 1 ppb, (c) 5 ppb, (d) 50 ppb, (e) 100 ppb, (f) 200 ppb, and (g) 300 ppb. (**b**) Variation of $C \equiv N$ stretching peak area as a function of cynide ion concentration. (correlation coefficient, $R = 0.991$)

Key Research Findings

In situ Monitoring of Chemical Reaction Using Raman Microscopy

Laser-induced Raman microscopy can be used to monitor a chemical reaction in a microfluidic channel. In situ monitoring of imine formation reaction in a glass microfluidic chip was previously performed. In order to monitor the diffusion process in a microfluidic channel, the Raman spectra are measured at various points along the channel with a constant flow rate. Time-dependent Raman spectra are also measured without flow in order to monitor the variation of Raman peaks to a complete conversion. The disappearance of the $C=O$ stretching peak at 1700 cm^{-1} of the reactant, benzaldehyde, and the appearance of the Raman peak for the product, an imine, at

B

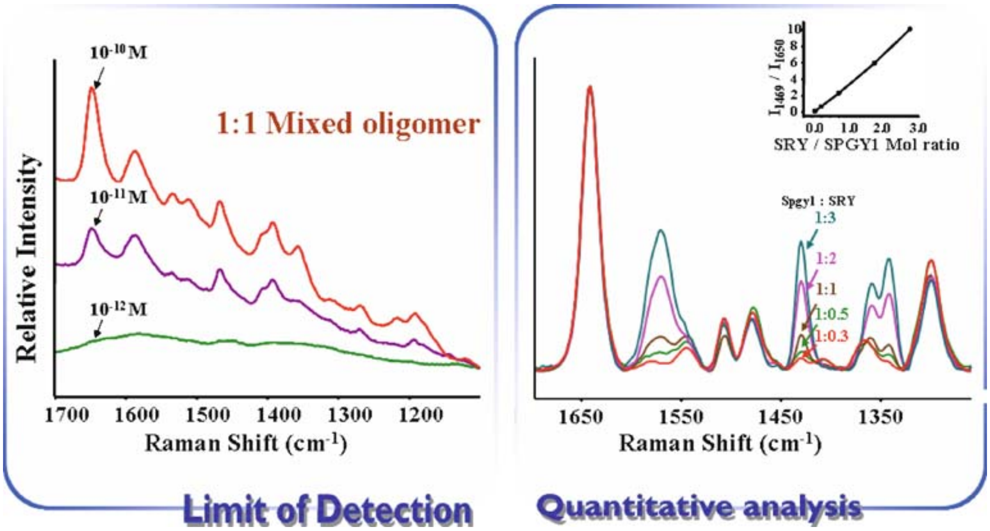

Biosensors Using Surface-Enhanced Raman Scattering, Figure 5 (**a**) Confocal SER spectra of 1 : 1 duplex DNA oligomer mixtures (Cy3-labeled SRY and TAMRA-labelled SPGY1) measured at different concentrations. The flow velocity was 74.08 mm/sec. (*b*) Confocal SER spectra of different molar ratios of duplex DNA oligomer mixtures. The molar ratio between Cy3-labeled SRY and TAMRA-labelled SPGY1 is (a) 1 : 3, (b) 1 : 2, (c) 1 : 1, (d) 2 : 1, and (e) 3 : 1, respectively. The flow velocity was 74.08 mm/sec. The insert shows the variation of peak area ratio (I_{1469}/I_{1650}) as a function of SRY/SPYG1 molar ratio

1628 cm^{-1} have been successfully monitored. In addition, the intensity increases of three phenyl-stretching modes in the 1550–1630 cm^{-1} region have also been observed. The increase of Raman intensity for this vibrational mode is caused by an effective π electron conjugation between two phenyl rings through the $-C=N-$ bridging group of the product. Laser-induced Raman microscopy enables us to monitor in situ product formation as well as to get detailed structural information in a microfluidic channel. Laser-induced Raman microscopy is considered as a very sensitive detection technique with a high spatial resolution for the in situ monitoring of organic reaction in a microfluidic channel system. Figure 1 shows in situ Raman monitoring of imine formation reaction in a microfluidic sensor and the optical arrangement for laser focusing on the microfluidic channel of the channel.

Analysis of Passive Mixing Behavior in a PDMS Microfluidic Channel Using Confocal Raman Microscopy

A rapid mixing of the fluids flowing through a microfluidic channel is very important for various applications of microfluidic systems, and a number of devices have been designed to enhance the mixing on the microscale. To use this channel as a microchemical reactor, it is very important to continuously monitor the chemical changes of reaction mixtures in the channel. Confocal Raman Microscopy (CRM) offers a promising route to achieve this goal, since it provides a direct measurement of the conversion process from reactant to product. The applicability of CRM for effective evaluation of the mixing efficiency in a recently developed 3D serpentine channel has been studied. Figure 2a shows a schematic view of a 3D serpentine PDMS channel and four measurement spots along the channel distance. Figure 2b shows the experimental set-up for the confocal Raman measurements on the confluent streams in the microfluidic channels. These two streams were introduced into the PDMS channel from micro syringes connected by tubes to the inlet pipettes. The flow rates were controlled simultaneously using a KD Science micro syringe pump. For the confocal Raman spectroscopic measurements, no fluorescence dye was used during the signal measurements. Figure 3 shows the changes of profiling Raman spectra along the channel distance in the 3D serpentine channel. Ethanol and isopropanol were used for the test of mixing process in the Raman spectroscopy. The results show that the fast mixing behavior of the confluent laminar streams in the 3D serpentine channel that are driven by chaotic advection can be successfully evaluated using the confocal Raman profiling technique.

Ultra-Sensitive Trace Analysis of Cyanide Ion Water Pollutant in a PDMS Microfluidic Channel Using SERS Microscopy

Cyanide ion is one of the most hazardous toxic pollutants in ground waters. It is mainly discharged from the industries such as gold mining, electroplating, printing, tex-

tiles and leather manufacturing. Thus, it is very important to develop a highly sensitive detection system for monitoring trace amounts of cyanide ion in ground waters. SERS spectroscopic technique for a rapid and sensitive trace analysis if cyanide ion water pollutant in an alligator-teeth shaped PDMS microfluidic channel. The confluent streams of silver colloids and trace analytes were effectively mixed in the channel through the triangular structures, which are located on the upper and lower surfaces of the channel in a zigzag manner. The flow rate was controlled using a microsyringe pump. In this work, an alligator teeth-shaped PDMS channel has been fabricated and the SERS detection method has been used to achieve highly sensitive analyte detection. SERS detection, in combination with Lab-on-a-Chip technology, has been applied to the trace analysis of cyanide ion water pollutant. Compared with other methods for the trace analysis of cyanide ions, the detection sensitivity was enhanced by several orders of magnitude. Figure 4 shows the adsorption process of cyanide ions on the silver nanoparticles in a PDMS microfluidic channel. The limit of detection (LOD) is determined to be in the 0.5 – 1.0 ppb range from three standard deviations above the backgrounds.

Quantitative Analysis of Methyl Parathion Pesticides Using Confocal SERS

A quantitative analysis of the methyl parathion pesticides is performed based on the measured SERS peak height at 1246 cm^{-1}. This method has a detection limit of 0.1 ppm. This value satisfies the requirement recommended by the Collaborative International Pesticides Analytical Council (CIPAC) for the determination of methyl parathion in pesticide formulations. This study demonstrates the feasibility of using confocal SERS for the highly sensitive detection of methyl parathion pesticides in a PDMS microfluidic channel. Raman peak, centered at 1246 cm^{-1}, is used as a quantitative evaluation of methyl parathion pesticides. A very good linear response is found in the concentration range 0.1 – 1 ppm. The limit of detection (LOD) is determined to be 0.1 ppm assessed from five standard deviations above background. Compared to other methods for the trace analysis of methyl parathion pesticides, the LOD is enhanced by several orders of magnitude. We expect this analytical technique can be successfully applied to highly sensitive bioanalysis as well as to other trace analysis.

Quantitative Analysis of Duplex Dye-labelled DNA Oligonucleotides in a PDMS Microfluidic Sensor Using Confocal SERS

Rapid and highly sensitive detection of duplex dye-labelled DNA sequences in a PDMS microfluidic channel is investigated using confocal SERS microscopy. This method does not need either an immobilization procedure or a PCR amplification procedure, which are essential for a DNA microarray chip. Furthermore, Raman peaks of each dye-labelled DNA can be easily resolved since they are much narrower than the corresponding broad fluorescence bands. To find the potential applicability of confocal SERS for sensitive bio-detection in a microfluidic channel, the mixture of two different dye-labelled (TAMRA and Cy3) sex determining Y genes, SRY and SPGY1, is adsorbed on silver colloids in the alligator-teeth shaped PDMS microfluidic channel and its SERS signals are measured under flowing conditions. Its major SERS peaks were observable down to the concentration of 10^{-11} M. In the present study, we explore the feasibility of confocal SERS for the highly sensitive detection of duplex dye-labelled DNA oligonucleotides in a PDMS microfluidic channel. Figure 5a shows the confocal SERS spectra of 1 : 1 DNA oligomer mixture adsorbed on colloidal silver at the constant flow velocity. According to our spectral data, the LOD of duplex oligomer mixture is estimated to be 10^{-11} M. Figure 5b also illustrates the confocal SERS spectra for different molar ratios of two oligonucleotides in a microfluidic channel. Different amounts of Cy3-labeled SRY (from 1.65×10^{-10} to 1.5×10^{-9} M) are added to the constant concentration of TAMRA-labelled SPGY1 (5.0×10^{-10} M) to control the molar ratio between SRY and SPGY1 to be 1 : 3, 1 : 2, 1 : 1, 2 : 1, and 3 : 1, respectively. The TAMRA peak at 1650 cm^{-1} is used as an internal standard and the variations of Cy-3 Raman peaks at 1588, 1469 and 1393 cm^{-1} are monitored for their different molar ratios. The intensities of those Raman peaks increase concomitantly with the increase in the concentration of Cy3-labeled SRY. In particular, the Raman peak at 1469 cm^{-1} can be used for the quantitative evaluation of SRY since it does not overlap with any Raman peaks of SPGY1. The insert in Fig. 5b shows the linear response of peak area ratio (I_{1469}/I_{1560}) with the changes in the molar ratio of duplex DNA oligonucleotides. This means that the highly sensitive quantitative detection of duplex DNA oligonucleotide mixtures in a microfluidic channel is possible using the confocal SERS microscopic technique.

Future Directions for Research

In order to apply the SERS sensor to biological analysis, the problem for high throughput screening (HTS) should be solved. In the case of DNA microarray, the throughput is around 16 h for 1 mill oligonucleotide hybridizations. There are two possible ways to apply the microfluidic system to a high-throughput screening (HTS) of biological analysis. First, a multi-parallelization microfluidic channel

can be used for this purpose. Second, a biological assay can be performed in series by rapidly injecting the sample solutions one after the other. In this case, several thousand assays are possible within a period of a few hours if the injection time is less than 1 s.

Cross References

- ► Nanoparticles
- ► Microfluidic Optical Devices

References

1. Ruperez A, Laserna JJ (1996) Surface Enhanced Raman Spectrocopy. In: Laserna JJ (ed) Modern Techniques in Raman Spectroscopy. Wiley, Chichester
2. Pelletier MJ (1999) Introduction to Applied Raman Spectroscopy. In: Pelletier MJ (ed) Analytical Applications of Raman Spectroscopy. Blackwell Science, Oxford
3. Smith E, Dent G (2005) Surface Enhanced Raman Scattering and Surface Enhanced Resonance Raman Scattering. In: Smith E (ed) Modern Raman Spectroscopy. Wiley, Chichester
4. Zhao J, Zhang XY, Yonzon CR, Haes AJ, Van Duyne RP (2006) Localized Surface Plasmon Resonance Biosensors. Nanomedicine 1:219–228
5. Zhang XY, Young MA, Lyandres O, Van Duyne RP (2005) Rapid Detection of an Anthrax Biomarkers by Surface-enhanced Raman Spectroscopy. J Am Chem Soc 127:4484–4489
6. Lee M, Lee JP, Rhee H, Choo J, Chai YG, Lee EK (2003) Applicability of Laser-Induced Raman Microscopy for In-Situ Monitoring of Imine Formation in a Glass Microfluidic Chip. J Raman Spectrosc 34:737–742
7. Lee D, Lee S, Seong GH, Choo J, Lee EK, Gweon DG, Lee S (2006) Quantitative Analysis of Methyl Parathion Pesticides in a PDMS Microfluidic Channel Using Confocal Surface-Enhanced Raman Spectroscopy. Appl Spectrosc 60:373–377
8. Yea GH, Lee S, Kyong JB, Choo J, Lee EK, Joo SW, Lee S (2005) Ultra-Sensitive Trace Analysis of Cyanide Water Pollutant in a PDMS Microfluidic Channel Using Surface-Enhanced Raman Spectroscopy. Analyst 130:1009–1011
9. Yea GH, Lee S, Choo J, Oh CH, Lee S (2006) Fast and Sensitive Analysis of DNA Hybridization in a PDMS Microfluidic Channel Using Fluorescence Resonance Energy Transfer. Chemical Communication of RSC, UK 1509–1511
10. Park T, Lee S, Seong GH, Choo J, Lee EK, Kim YS, Ji WH, Hwang SY, Gweon DG, Lee S (2005) Highly Sensitive Signal Detection of Duplex Dye-labelled DNA Oligonucleotides in a PDMS Microfluidic Chip: Confocal Surface-Enhanced Raman Spectroscopic Study. Lab Chip 5:437–442

Biotechnology

► Biomimetics

Bioterrorism

► Lab-on-Chip Devices for Biodefense Applications

Biothreat

► Lab-on-Chip Devices for Biodefense Applications

Biotransducer

Definition

The biotransducer is the functional heart of a biosensor system. The biotransducer comprises the molecular biospecificity of the biorecognition membrane layer and the signal generating capability of the physicochemical transducer. The reproducible, intimate linking of these two parts across an interface is a key distinguishing quality of biotransducers.

Cross References

► Impedimetric Biosensors for Micro and Nano Fluidics

Bipolar Membrane

Definition

An ion-exchange membrane that consists of a layered ion structure. This typically consists of a cation exchange layer and an anion exchange layer. The use of a bipolar membrane enables many functionalities to be used such as antifouling, water dissociation, and the separation of ions. Bipolar membranes are typically unstable in high current environments.

Cross References

► Ion Exchange Membranes

Bistability

Definition

Capability to remain, without an external control action, in either one of two different stable states.

Bistability is a useful property in diverter valves with two outlets when operating in two alternative regimes, the supplied fluid leaving in each regime mainly through one of them. If the microfluidic valve operates at Reynolds numbers – related to the conditions in the inlet – higher than ~ 1000, the bistability may be obtained without use of any movable components in the valve, using the Coanda effect of alternative attachment of a fluid jet to one of two mutually opposed attachment walls. The bistable valves may be

a very useful part of sampling units used in microfluidic systems for combinatorial chemistry testing.

Cross References

► Microfluidic Systems for Combinatorial Chemistry
► Sampling Unit

Blending

► Microfluidic Mixing

Block Copolymerization

Synonyms

Block heteropolymerization

Definition

Polymerization reaction of blocks of different polymerized monomers.

Cross References

► Polymer Synthesis within Microfluidic Reactor

Block Heteropolymerization

► Block Copolymerization

Blood Analysis

► Integrated Microdevices for Medical Diagnostics

Blood–Plasma Separators

► Microfilters

Boiling and Evaporation in Microchannels

Satish G. Kandlikar
Rochester Institute of Technology, Rochester, NY, USA
sgkeme@rit.edu

Synonyms

Flow boiling in microchannels; Flow boiling in narrow channels

Definition

Flow boiling in a microchannel refers to the boiling of a liquid, caused by the addition of heat through the channel walls, as it flows through a microchannel resulting in a net vapor generation at the exit.

Overview

► Microchannels are defined on the basis of the following definition by Kandlikar and Grande [1]:

Conventional channels:	$D > 3$ mm
Minichannels:	$3\text{ mm} \geqslant D > 200\,\mu\text{m}$
Microchannels:	$200\,\mu\text{m} \geqslant D > 10\,\mu\text{m}$
Transitional channels:	$10\,\mu\text{m} \geqslant D > 0.1\,\mu\text{m}$
Transitional microchannels:	$10\,\mu\text{m} \geqslant D > 1\,\mu\text{m}$
Transitional nanochannels:	$1\,\mu\text{m} \geqslant D > 0.1\,\mu\text{m}$
Nanochannels:	$0.1\,\mu\text{m} \geqslant D$

where D is the minimum channel dimension. This article deals with the change of phase of a liquid due to heat transfer from the channels walls while it flows through a microchannel.

The boiling process refers to nucleation of vapor bubbles and their growth resulting from heat transfer from a heated wall. Evaporation refers to change of phase from liquid to vapor at the liquid–vapor interface. Boiling is further classified as pool boiling, which refers to boiling in a pool of liquid, and flow boiling, which refers to boiling with an impressed flow.

Flow boiling in microchannels is essentially similar to the flow boiling process in ► conventional sized channels. Some differences are noted due to the effect of small channel dimensions on the flow boiling process resulting in a large surface area to flow volume ratio [2]. The surface tension forces become important at these scales as compared to the gravitational forces. This makes the boiling process in microchannels less dependent on gravity and orientation. Flow boiling in microchannels is therefore seen as a desirable heat transfer mode in ► microgravity environments.

Applications of microchannel boiling process using low-pressure water [3] or a dielectric hold great promise for chip cooling applications. The high heat transfer coefficients coupled with large heat-carrying capacity due to latent heat removal present an attractive cooling option.

The smaller channel dimensions also shift the flow towards lower Reynolds number. In general, there is a lack of available experimental data for heat transfer in microchannels and a need exists to generate new experimental data to cover the overall shift in the Reynolds numbers, heat flux and mass flux in practical applications.

Basic Methodology

Flow boiling in microchannels is currently at the research stage. The experimental methods employed are evolving as temperature and pressure measurements in the microchannels require deployment of sensors that are microfabricated. For this reason, silicon microchannels with embedded pressure and temperature sensors are being pursued. This is an area where further research is needed to establish the measurement techniques. Metal and ceramic heat exchanger devices are also being fabricated using advanced micromachining and chemical/laser etching and machining processes.

Key Research Findings

Heat Transfer During Flow Boiling in Microchannels

A limited number of experimental studies are available on flow boiling in microchannels using copper and silicon as the substrate over a limited range of heat and mass fluxes for a few fluids (water being the most widely used working fluid), e. g. Pokharna et al. [3], Lee and Mudawar [4], Kosar et al.[5], Hetsroni, et al.[6]. Early studies indicated that the heat transfer at lower mass flux and lower quality conditions is dominated by the nucleate boiling process as in the case of pool boiling. As more data become available, it is seen that the heat transfer exhibits the nucleate boiling dominant mode under low mass flux, low quality conditions, while it appears to be dependent on mass flux and independent of heat flux at higher mass fluxes and higher qualities, as in the case of the convective boiling dominant mode. However, the experimental data are seen to have a larger uncertainty band as compared to the flow boiling data in conventional sized channels due to difficulties in measuring local temperature, pressure and channel dimensions accurately. As the instrumentation, measuring techniques and experimental procedures are refined, more reliable data are expected to become available in the coming years. Further information on the research needs in this area is given by Kandlikar [2].

Heat Transfer Correlations for Flow Boiling in Minichannels and Microchannels

The flow boiling process in microchannels and minichannels has been studied over a limited range of heat and mass fluxes (mostly at the lower ends of their respective ranges employed in macroscale channels). In this range, some authors have found pool boiling type correlations to work well, while others have found the influence of convective effects. The following correlation is an extension of the Kandlikar correlation for large-diameter tubes that is derived from the low mass flux data available in the literature. In the higher mass flux regions, corresponding to the higher all-liquid Reynolds number, the correlation is expected to follow the trends in larger diameter tubes. The overall correlations for microchannels in different regions are given below [7].

Terminology

h_{TP} – two-phase heat transfer coefficient, x – quality, q – heat flux, G – mass flux, h_{LV} – latent heat of vaporization, ρ – density, k – thermal conductivity, D_h – hydraulic diameter, and $\mathrm{Co} = [(1-x)/x]^{0.8}[\rho_V/\rho_L]^{0.5}$, $\mathrm{Bo} = q''/(Gh_{LV})$, $\mathrm{Re}_{LO} = G(1-x)D_h/\mu_L$, $\mathrm{Fr}_{LO} = G^2/(\rho_L^2 g D_h)$ and $\mathrm{Nu}_{LO} = (h_{LO}D_h/k)$. Subscripts CBD and NBD refer to nucleate boiling dominant and convective boiling dominant regions respectively, and L and V refer to liquid and vapor, respectively.

For flow boiling in microchannels and minichannels, heat transfer correlations in the NBD and CBD regions are given below:

$$h_{TP,NBD} = 0.6683\,\mathrm{Co}^{-0.2}(1-x)^{0.8} f_2(\mathrm{Fr}_{LO})\,h_{LO} + 1058\,\mathrm{Bo}^{0.7}(1-x)^{0.8}\,h_{LO}F_{FL} \quad (1)$$

$$h_{TP,CBD} = 1.136\,\mathrm{Co}^{-0.9}(1-x)^{0.8} f_2(\mathrm{Fr}_{LO})\,h_{LO} + 667.2\,\mathrm{Bo}^{0.7}(1-x)^{0.8} h_{LO}F_{FL} \quad (2)$$

The flow boiling heat transfer coefficient h_{TP} is then related to $h_{TP,NBD}$ and $h_{TP,CBD}$ depending on the flow regions under all-liquid flow conditions as described below.

Region I

Turbulent flow region: $\mathrm{Re}_{LO} \geqslant 3000$

$$h_{TP} = \text{larger of } \left(h_{TP,NBD}, h_{TP,CBD}\right) \quad (3)$$

h_{LO} is given by:

For $10^4 \leqslant \mathrm{Re}_{LO} \leqslant 5\times10^6$, Petukhov and Popov correlation:

$$h_{LO} = \frac{\mathrm{Re}_{LO}\,\mathrm{Pr}_L(f/2)(k_L/D)}{1+12.7\left(\mathrm{Pr}_L^{2/3}-1\right)(f/2)^{0.5}} \quad (4)$$

For $3000 \leqslant \mathrm{Re_{LO}} < 10^4$, Gnielinski correlation:

$$h_{\mathrm{LO}} = \frac{(\mathrm{Re_{LO}} - 1000)\,\mathrm{Pr_L}(f/2)(k_\mathrm{L}/D)}{1 + 12.7\left(\mathrm{Pr_L^{2/3}} - 1\right)(f/2)^{0.5}} \qquad (5)$$

The friction factor f in the above equations is given by

$$f = \left[1.58\ln(\mathrm{Re_{LO}}) - 3.28\right]^{-2} \qquad (6)$$

Region II

Transition region: $1600 \leqslant \mathrm{Re_{LO}} < 3000$

$$h_{\mathrm{TP}} = \text{larger of } (h_{\mathrm{TP,NBD}}, h_{\mathrm{TP,CBD}}) \qquad (7)$$

With h_{LO} taken from linear interpolation between the turbulent value using the Gnielinski correlation (given under Region I above) and the appropriate laminar value (for $q'' = C$ or $T = C$) using $h_{\mathrm{LO}} = (\mathrm{Nu_{LO}}k/D_\mathrm{h})$.

Region III

Laminar flow region: $100 \leqslant \mathrm{Re_{LO}} < 1600$

$$h_{\mathrm{TP}} = \text{larger of } (h_{\mathrm{TP,NBD}}, h_{\mathrm{TP,CBD}}) \qquad (8)$$

With h_{LO} taken from the appropriate laminar value (for $q'' = C$ or $T = C$) using $h_{\mathrm{LO}} = (\mathrm{Nu_{LO}}k/D_\mathrm{h})$.

Region IV

Deep laminar flow region: $\mathrm{Re_{LO}} < 100$

$$h_{\mathrm{TP}} = h_{\mathrm{TP,NBD}} \qquad (9)$$

Fluid-Surface Parameter, F_{FL}

The fluid surface parameters in Eqs. (1) and (2) are given in Table 1, with h_{LO} taken from the appropriate laminar value (for $q'' = C$ or $T = C$) using $h_{\mathrm{LO}} = (\mathrm{Nu_{LO}}k/D_\mathrm{h})$.

Boiling and Evaporation in Microchannels, Table 1 Values of F_{Fl} (fluid-surface parameter) in the flow boiling correlations (Eqs. (1) and (2))

Fluid	F_{Fl}
Water	1.00
R-11	1.30
R-12	1.50
R-13B1	1.31
R-22	2.20
R-113	1.30
R-114	1.24
R-134a	1.63
R-152a	1.10
R-32/R-132	3.30
R-141b	1.80
R-124	1.00
Kerosene	0.488

Critical Heat Flux

During the flow boiling process, the walls of the channel are generally covered with liquid or a liquid film, occasionally exposing the walls to the vapor phase followed by rewetting with the liquid. At certain conditions, the liquid fails to rewet the walls leading to the condition of *dryout*. Since the vapor is unable to cool the wall as effectively as a liquid-covered wall, the local wall temperature may rise uncontrollably with further addition of heat.

The heat flux at this condition is referred to as the ►critical heat flux, or ►CHF. It depends on the flow conditions, channel geometry, local quality, fluid properties, channel material and flow history. Bergles and Kandlikar [8] discuss the CHF in microchannels from a systems perspective. It is important to establish CHF condition as a function of the mass flux and quality for a given system to ensure its safe operation. Qu and Mudawar [9] presented CHF data with water in 21 parallel minichannels of $215\,\mu\mathrm{m} \times 821\,\mu\mathrm{m}$ cross-section over a range of $G = 86 - 268\,\mathrm{kg/(m^2 s)}$ and $q'' = 264 - 542\,\mathrm{kW/m^2}$, $x = 0.0 - 0.56$, and $P_{\mathrm{in}} = 121.3 - 139.8\,\mathrm{kPa}$. Kosar et al. [5] present low-pressure water data in microchannels enhanced with reentrant cavities. Also, the correlation by Katto [10] developed for large channels may be applied for approximate CHF estimation in the absence of an established CHF correlation for microchannels.

Future Directions for Research

Flow boiling in microchannels is currently in the research phase. Its applications include high heat flux removal in advanced computer chips and high-power electronics and electrical systems, pulsed power weapons systems, solid-state lasers and phased-array radars and sensor arrays. Microchannel heat exchangers for phase change applications offer the advantages of very compact design with large volumetric energy transfer densities. It is especially suited for the future 3D computer chip architecture by incorporating the microchannels in multiple parallel configurations. Other cooling arrangements which rely on the surface cooling techniques, such as spray or jet cooling, may not be suitable to the 3D configuration. Hot spot cooling and integration with the device architecture is also a possible application.

Another area that is expected to benefit by incorporation of microchannels is the refrigeration industry where

the potential benefits resulting from material and space savings will be quite significant. The high heat transfer coefficients and compact design makes flow boiling in microchannels very attractive in air liquefaction and cryogenic industries as well. It is expected that significant innovations and new developments will occur in this field in the near future.

One of the challenges faced in microchannel flow boiling systems is the limit posed by the critical heat flux (CHF). Establishing the CHF limits of the plain microchannels and developing new enhanced geometries with higher CHF limits is a priority that needs to be addressed in the future before widespread application of microchannel flow boiling systems can be considered.

Cross References

- ▶ Bubble Actuated Microfluidic Switch
- ▶ Bubble Dynamics in Microchannels
- ▶ Cavitation in Microdomains
- ▶ Droplet Dispensing
- ▶ Flow Boiling Instability
- ▶ Heat Transfer in Microchannel Flows

References

1. Kandlikar SG, Grande WJ (2003) Evolution of Microchannel Flow Passages – Thermohydraulic Performance and Fabrication Technology. Heat Trans Eng 24(1):3–17
2. Kandlikar SG (2002) Fundamental Issues Related to Flow Boiling in Minichannels and Microchannels. Exp Thermal Fluid Sci 26(2–4):389–407
3. Pokharna H, Masahiro K, DiStefano E, Mongia R, Barry J, Crowley C, Chen W, Izenson M (2004) Microchannel Cooling in Computing Platforms: Performance Needs and Challenges in Implementation. 2nd Int Conf Microchannels Minichannels (ICNMM2004), ASME, 109–118
4. Lee J, Mudawar I (2005) Two-Phase Flow in High-Heat Flux Micro-channel Heat Sink for Refrigeration Cooling Applications, Part II: Heat Transfer Characteristics. Int J Heat Mass Trans 48:941–955
5. Kosar A, Kuo C, Peles Y (2005) Reduced Pressure Boiling Heat Transfer in Rectangular Microchannels with Interconnected Reentrant Cavities. J Heat Trans 127:1106–1114
6. Hetsroni G, Klein D, Mosyak A, Segal Z, Pogrebnyak E (2004) Convective Boiling in Parallel Microchannels. Microscale Thermophys Eng 8:403–421
7. Kandlikar SG, Balasubramanian P (2004) An Extension of the Flow Boiling Correlation to Transition, Laminar and Deep Laminar Flows in Minichannels and Microchannels. Heat Trans Eng 25(3):86–93
8. Bergles AE, Kandlikar SG (2005) On the Nature of Critical Heat Flux in Microchannels. J Heat Trans 127(1):101–107
9. Qu WL, Mudawar I (2004) Transport Phenomena in Two-Phase Micro-channel Heat Sinks. J Electron Packag 126(2):213–22
10. Katto Y (1981) General Features of CHF of Forced Convection Boiling in Uniformly Heated Rectangular Channels. Int J Heat Mass Trans 24:1413–1419

Boltzmann Equation

Definition

Boltzmann equation determines the evolution of the velocity distribution function and reads as where $Q(ff)$ is the collision integral.

Cross References

- ▶ Gas Flow in Nanochannels
- ▶ Heat Transfer in Microchannel Flows
- ▶ Supersonic Micro-Nozzles
- ▶ Micro - and Nanoscale in Gas Dynamics
- ▶ Lattice Poisson-Boltzmann Method, Analysis of Electroosmotic Microfluidics

Boltzmann's Constant

Definition

A constant that relates temperature of a body to the thermal energy retained within it; $k = 1.3806504 \times 10^{-23}$ J/K.

Cross References

- ▶ Piezoelectric Microdispenser

Bonding of Non-Metallic Inorganic Surfaces and Polymers

- ▶ Glass-Polymer Bonding

Bosch Process

- ▶ Anisotropic Etching
- ▶ ICP Etching

Boundary Condition at Interface

- ▶ Boundary Slip of Liquids

Boundary Element Method

- ▶ Boundary Element Method and its Applications to the Modeling of MEMS Devices

Boundary Element Method and its Applications to the Modeling of MEMS Devices

WENJING YE
Department of Mechanical Engineering,
Hong Kong University of Science and Technology,
Hong Kong, China
mewye@ust.hk

Synonyms

Boundary element method; Boundary integral approaches

Definition

The boundary element method is a numerical method for solving integral equations. These integral equations are the integral representations of the governing equations of the underlying physical problems, often formulated based on the fundamental solutions of the problems.

Overview

The boundary element method (BEM) has been established as a powerful numerical method for solving engineering problems. Applications include, but are not limit to, electromagnetics, elasticity, acoustics, potential and viscous flow. In contrast to other numerical techniques, the governing equations are cast into a set of integral equations that are solved by collocation or Galerkin discretization. A detailed description of this method can be found in [1]. One major advantage of the BEM is that it reduces the dimensionality of the problem by one. Thus for the majority of practical cases the simple boundary discretization leads to a much smaller system of algebraic equations than any domain method. Another advantage of the BEM is that it can handle rapid transitions and steep gradients of fields since the formulation only involves unknowns on surfaces. Given the reduced complexity of data preprocessing (meshing) and smaller size of the resulting systems, the BEM is an efficient method for solving many engineering problems, especially for exterior problems and problems with free surfaces or moving boundaries.

One disadvantage of the conventional BEM is that it generates a fully populated system matrix. Also, the computation of matrix entries involves singular and nearly singular surface integrals, which are difficult to compute. This offsets some of the computer time saved by the much reduced matrix size. The recently developed accelerated BEM approaches have overcome this difficulty by combining matrix sparsification techniques, such as the fast multipole method (FMM) [2] and the precorrected-FFT technique [3], with iterative solvers. A central idea in acceleration techniques is to approximate the matrix-vector product by some computationally efficient means. In the FMM, multipole and local expansion is used to calculate the long-range interactions. In the precorrected-FFT method, a uniform grid is used to represent the long-range interactions. This grid representation allows the fast Fourier transform to be used to efficiently perform the computation. With these accelerated techniques, the BEM has emerged as one of the most efficient numerical methods for large-scale problems particularly those with complex 3D geometry. Fast BEM codes have been developed and applied successfully in a variety of applications including the modeling of complex MEMS devices, for example, the prediction of air damping in micro-resonators [4].

Basic Methodology

Boundary Integral Formulation

The BEM starts with an integral formulation of the governing equation. As an illustration, consider the potential problem governed by the Laplace equation:

$$\nabla^2 u = 0 \tag{1}$$

An integral formulation of the Laplace equation reads

$$c(\boldsymbol{x})u(\boldsymbol{x}) = -\int_{\partial\Omega} G(\boldsymbol{x},\boldsymbol{y})\frac{\partial u(\boldsymbol{y})}{\partial n(\boldsymbol{y})}\,\mathrm{d}S(\boldsymbol{y}) + \int_{\partial\Omega} \frac{\partial G(\boldsymbol{x},\boldsymbol{y})}{\partial n(\boldsymbol{y})}u(\boldsymbol{y})\,\mathrm{d}S(\boldsymbol{y}) \tag{2}$$

where

$$c(\boldsymbol{x}) = \begin{cases} 1, \boldsymbol{x} \in \Omega \\ 0, \boldsymbol{x} \notin (\Omega \cup \partial\Omega) \\ \alpha, \boldsymbol{x} \in \partial\Omega \end{cases}$$

In Eq. (2), Ω is the domain of the problem with boundary $\partial\Omega$, $n(\boldsymbol{y})$ is the outward normal vector at the field point $\boldsymbol{y}$, $\boldsymbol{x}$ is the evaluation point and α is the solid angle at $\boldsymbol{x}$ (it equals $1/2$ when $\boldsymbol{x}$ is a smooth surface point). $G(\boldsymbol{x},\boldsymbol{y})$ is the Green's function of the Laplace operator which, in a 3D space, is given by

$$G(\boldsymbol{x},\boldsymbol{y}) = \frac{1}{4\pi r}\,,\ \text{where } r = |\boldsymbol{x}-\boldsymbol{y}|\ .$$

Note that all integrals in Eq. (2) are boundary integrals, i. e., they involve only the boundary values of the dependent variable and its derivatives. As such, this integral

equation can be employed to obtain the unknown boundary quantities based on the given boundary conditions. For example, for Dirichlet problems, the unknown boundary values are the normal derivatives of the potential, which can be calculated by solving Eq. (2) with evaluation points being on the boundary. Once all the boundary quantities are obtained, the potential at any point inside the domain is calculated again using Eq. (2) but with $c(\boldsymbol{x}) = 1$.

Discretization

To numerically solve Eq. (2), one can employ either the Galerkin scheme or the collocation scheme. In the Galerkin scheme, Eq. (2) is satisfies in a weighted integral sense while in the collocation scheme, the integral equation is satisfied at the chosen collocation points. For simplicity, the collocation scheme is used to illustrate the numerical implementation of the BEM.

First, the boundary of the problem domain is discretized into a collection of elements. On each element, quantities are assumed to be simple functions, often polynomials, which are fully determined by their nodal values. For example, a constant element has only one node located at its centroid. Over this element, quantities are assumed to be constant determined by their values at the centroid. For a general case at the i-th element

$$u = \sum_{j=1}^{p} N_j u_j^{(i)} \tag{3}$$

$$q = \frac{\partial u}{\partial n} = \sum_{j=1}^{p} N_j q_j^{(i)} \tag{4}$$

where N_j is the interpolation function, p is the number of nodes of this element and $u_j^{(i)}$ and $q_j^{(i)}$ are the nodal values at the j-th node of the i-th element. Substituting Eqs. (3) and (4) into the integral formulation (2) and enforcing Eq. (2) is satisfied at each node, a set of discretized equations in the form of Eq. (5) can be obtained:

$$\begin{aligned} c(\boldsymbol{x}_k)u(\boldsymbol{x}_k) = &-\sum_{i=1}^{n}\int_{\Gamma_i} G(\boldsymbol{x}_k,\boldsymbol{y})\sum_{j=1}^{p} N_j(\boldsymbol{y})q_j^{(i)}\,\mathrm{d}S(\boldsymbol{y}) \\ &+\sum_{i=1}^{n}\int_{\Gamma_i}\frac{\partial G(\boldsymbol{x}_k,\boldsymbol{y})}{\partial n(\boldsymbol{y})}\sum_{j=1}^{p} N_j(\boldsymbol{y})u_j^{(i)}\,\mathrm{d}S(\boldsymbol{y}), \\ k = 1, 2, \cdots m \end{aligned} \tag{5}$$

In Eq. (5), n is the number of elements, Γ_i denotes the i-th element and m is the total number of nodes. This set of equations can be rearranged into a matrix form:

$$[\mathbf{G}]\{\boldsymbol{q}\} - [\mathbf{H}]\{\boldsymbol{u}\} = \mathbf{0} \tag{6}$$

where $\mathbf{G}$, $\mathbf{H}$ are matrices with entries being the element-wise integrals of the product of the kernel function (G and $\partial G/\partial n$) and the interpolation functions, and $\boldsymbol{u}$ and $\boldsymbol{q}$ are vectors comprised of nodal values of the potential and its normal derivative respectively. Equation (6) is a linear system that can be solved to obtain the unknown boundary values at each node. These values together with the given boundary conditions can be substituted into Eq. (2) to obtain potentials at interior points.

Key Research Findings

Air Damping of Laterally Oscillating Micro-Resonators

Air-packaged micro-resonators are widely used in a variety of low-frequency applications such as accelerometers, gyroscopes and sensors. In many of these applications, the quality factor of the resonator, defined as the ratio of total energy to energy dissipated per cycle, is a key performance variable but is very difficult to predict. The problem is that the dominant loss mechanism for many air-packaged resonators is viscous drag, and to predict drag it is necessary to accurately determine the detailed air flow in these typically very complicated three-dimensional resonators.

A number of approximate analytic models for drag have been developed, typically based on one-dimensional Couette or Stokes flow [5]. Such models give a good rough estimate of the drag force but they can be insufficiently accurate to correctly predict geometrical sensitivities. In particular, these one-dimensional models do not account for important finite size and edge effects. To account for these effects accurately, a detailed 3D analysis of air flow surrounding the resonators is necessary. This leads to a problem with a domain which is bounded by the complex resonator at one end and extends to infinity at the other end. For such a problem, domain methods such as the finite element method and the finite volume method, etc., could be very inefficient and are not suitable. The accelerated BEM, on the other hand, is a perfect method for handling this problem.

Micro-Resonator

The comb drive micro-resonator used for this study is shown in top and side view in Fig. 1. The main components of the resonator are a shuttle structure comprised of the connected back-to-back combs, two suspended folder beams with one end anchored to the substrate, and fixed

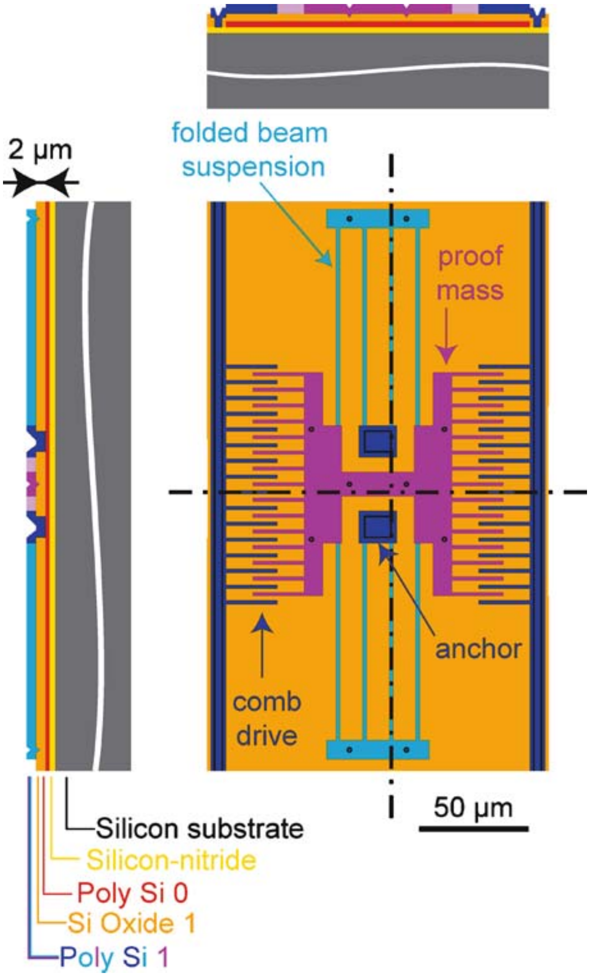

Boundary Element Method and its Applications to the Modeling of MEMS Devices, Figure 1 Schematic view of a laterally oscillating resonator

Boundary Element Method and its Applications to the Modeling of MEMS Devices, Table 1 Resonator dimensions

Finger gap	2.88 µm
Finger length	40.05 µm
Finger overlap	19.44 µm
Beam length	151 µm
Beam width	1.1 µm
Center plate Side plate1 × 2 Side plate2 × 4	54.9 × 19.26 µm^2 28.26 × 89.6 µm^2 11.3 × 40.5 µm^2
Thickness	1.96 µm
Substrate gap	2 µm
Truss length	78 µm
Truss width	13 µm

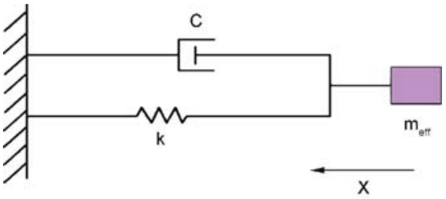

Boundary Element Method and its Applications to the Modeling of MEMS Devices, Figure 2 Spring–mass–dashpot model of a resonator

comb drives. Table 1 lists some key dimensions of the resonator.

The shuttle structure can be moved to the left or right using electrostatic forces generated by creating a potential difference between the shuttle and either the left or the right fixed combs (shown in dark blue in Fig. 1). Once the shuttle moves away, the folded beams, acting as springs, bring it back to its equilibrium position. This results in an oscillating motion.

Macro Model

Based on its operation principle, the resonator can be modeled as a simple spring–mass–dashpot system, as shown in Fig. 2, with the shuttle being the proof mass, folder beams being the spring and the surrounding air being the dashport damper. The displacement of the proof mass can then be obtained by solving the second-order differential equation

$$m_{\text{eff}}\ddot{x} + c\dot{x} + kx = F_{\text{applied}} \tag{7}$$

where x is the mass displacement measured from the equilibrium position, m_{eff} is the effective mass, c is the damping coefficient, k is the stiffness of the spring and F_{applied} is the externally applied electrostatic force.

The frequency and the quality factor of the resonator are related to the parameters as

$$f_0 = \frac{1}{2\pi}\sqrt{\frac{k}{m_{\text{eff}}}} \tag{8}$$

and

$$Q = \frac{\sqrt{km_{eff}}}{c} \tag{9}$$

The effective mass for the micro-resonator is easily determined from the geometry, given fabrication process information and the density of the structure material which is polysilicon in this case. Uncertainties in polysilicon's elastic material properties and manufacturing-induced residual stress make it difficult to predict the spring constant, though the measured resonant frequency data can be

combined with the computed effective mass to determine a spring constant. What has been most difficult to determine from geometry and process information is the loss in an air-packaged micromachined device, or equivalently the dashpot constant for the spring–mass–dashpot model. The difficulty is that loss in air-packaged microresonators is primarily due to viscous drag, which in turn depends on a very complicated air flow pattern. These issues will be considered in more detail in subsequent sections, with particular emphasis given to the issue of loss prediction.

Determination of Parameters

The effective mass for a spring–mass–dashpot model of the resonator is related to geometry and the density of the polysilicon. In particular, energy considerations and an application of beam theory lead to a resonator effective mass given by

$$m_{\text{eff}} = m_{\text{p}} + m_{\text{f}} + \frac{12}{35} m_{\text{b}} + \frac{1}{4} m_{\text{t}} \qquad (10)$$

where m_{p}, m_{f} are the masses of the shuttle and the moving fingers respectively, m_{b} is the mass of the beams and m_{t} is the mass of the connecting truss. With the dimensions shown in Table 1 and the density of $\rho = 2300\,\text{kg/m}^3$ for polysilicon, the effective mass of the system is 5.61×10^{-11} kg.

A simple approach to computing the spring constant for the resonator is to assume that the trusses joining the folded beam segments (shown in light blue in Fig. 2) are rigid. If there is no residual stress, beam theory predicts a spring constant of

$$k = 4Eh \left(\frac{w}{L}\right)^3 \qquad (11)$$

where E is the Young's modulus of polysilicon, and h, w and L are the thickness, the width and the length of the beam respectively. If E is chosen to be 150 GPa, the calculated stiffness of the beam in our resonator is $0.454\,\text{N/m}$. This value, together with the effective mass, would predict a natural resonant frequency of 14,321 Hz which is far from the measured value of 19,200 Hz. This indicates that either the stiffness or the mass was predicted wrong. Because stiffness is more sensitive to measurement error than mass (mass is linearly proportional to the beam width, but stiffness is proportional to the cube of width) and it also depends on residual stress and Young's modulus of polysilicon that are difficult to predict, it is reasonable to assume that mass is more accurate than the prediction of the stiffness. In addition, since the focus is on the issue of modeling damping, the semi-empirically determined value of $0.816\,\text{N/m}$, obtained from Eq. (8) using the effective mass from Eq. (10) and the measured resonant frequency, was used as the stiffness in this work.

The damping coefficient, c, caused by the drag force exerted on the resonator by the air, can only be determined if the air flow velocities are known. This requires the modeling of the fluid field surrounding the resonator. In the following section several of the flow models that have been used to compute resonator drag are discussed.

Flow Models

The frequency of operation is so slow that the open air surrounding the resonator can be regarded as an incompressible fluid. In addition, the characteristic length (micrometers) and oscillation amplitude (35 nm) are both small, resulting in a small Reynolds number (8×10^{-5}, $\text{Re} = \rho UL/\mu$, where ρ and μ are the density and viscosity of the fluid, U is a characteristic velocity and L is a characteristic length, 2 μm in the resonator under study), so the nonlinear inertial force will be negligible compared to the viscous force. Finally, rarefaction effects are unlikely to be significant, as the Knudsen number (Kn) for this resonator is small (0.03, $\text{Kn} = \lambda/L$; λ is the mean free path of the gas molecules, 0.065 μm). Thus, the fluid behavior is expected to be accurately described by solutions of the incompressible Stokes equations with no-slip boundary conditions.

For the oscillating resonator, the velocity is in sinusoidal steady state and therefore the velocity $\boldsymbol{u}$ and the pressure P of the fluid satisfy the frequency domain Stokes equation. The Stokes equation consists of the continuity equation and the linear momentum equation

$$\mathrm{i}2\pi f \rho \boldsymbol{u}(f) = -\nabla P(f) + \mu \nabla^2 \boldsymbol{u}(f) \qquad (12)$$

$$\nabla \cdot \boldsymbol{u}(f) = 0 \qquad (13)$$

where $\boldsymbol{u}(f)$ and $P(f)$ are complex amplitudes. For notational convenience, in the following the dependence on frequency will be assumed, and not stated explicitly. Note that in the case of steady flow, the only frequency-dependent term, the inertial term on the left side of Eq. (8), is zero.

To solve Eqs. (12) and (13) with oscillating velocity boundary conditions, simple models such as the Couette flow model and 1D Stokes model have been used. These models ignore the finite size and edge effects, as both of them model the device as two infinitely large parallel plates with one (the proof mass) oscillating on the top of the other (substrate). The Couette model further assumes a steady flow, resulting in a linear velocity profile between the plates. As shown later, the quality factor obtained by these two models is over-predicted by a factor of two, indicating the importance of 3D effects.

To account properly for all the edge and finite size effects and possible pressure gradients created by the motion of plates, a full 3D analysis is required. With the infinite domain and rather complicated resonator geometry, the BEM accelerated with the precorrected-FFT technique is chosen to numerically solve the 3D Stokes problem. To do so, an integral formulation must be introduced first:

$$u_j(\boldsymbol{x}) = -\frac{1}{8\pi\mu}\int_{\partial\Omega} G_{ij}(\boldsymbol{x},\boldsymbol{y}) f_j(\boldsymbol{y})\,\mathrm{d}S(\boldsymbol{y}) \tag{14}$$

where $\partial\Omega$ is the surface of the resonator, and the Greens function is given by

$$G_{ij}(\boldsymbol{x},\boldsymbol{y}) = \frac{\delta_{ij}}{r}A(R) + \frac{\hat{x}_i\hat{x}_j}{r^3}B(R) \tag{15}$$

$$A(R) = 2\,\mathrm{e}^{-R}\left(1+\frac{1}{R}+\frac{1}{R^2}\right) - \frac{2}{R^2}$$

$$B(R) = -2\,\mathrm{e}^{-R}\left(1+\frac{3}{R}+\frac{3}{R^2}\right) + \frac{6}{R^2}$$

$$R = \lambda r\,.$$

In Eq. (14), $u_j(\boldsymbol{x})$ is the j-th component of the velocity vector at the evaluation point $\boldsymbol{x}$, $\boldsymbol{f}$ is the Stokeslet density function, and the real part of $\boldsymbol{f}$ corresponds to the real part of the surface traction if there is a single moving object that rigidly moves in the fluid, $\hat{x}_i$ is the i-th component of the relative position vector between the evaluation point and the field point, i.e., $\hat{x}_i = y_i - x_i$, and λ is the frequency parameter which is defined as

$$\lambda^2 = i\frac{2\pi f\rho}{\mu}$$

Numerical Solution of 3D Stokes Model

The surface of the resonator is discretized into n small elements. A collocation scheme and constant elements were employed. A system of equations for the unknowns is derived by insisting that the integral Eq. (4) is satisfied exactly at each element centroid. The result is a linear system which relates the known quantities (velocity $\boldsymbol{u}$) to the unknown quantities (traction force $\boldsymbol{f}$), as in

$$\begin{Bmatrix} \boldsymbol{u}^1 \\ \boldsymbol{u}^2 \\ \vdots \\ \boldsymbol{u}^n \end{Bmatrix} = P(\omega) \begin{Bmatrix} \boldsymbol{f}^1 \\ \boldsymbol{f}^2 \\ \vdots \\ \boldsymbol{f}^n \end{Bmatrix} \tag{16}$$

where $\boldsymbol{u}^i$ and $\boldsymbol{f}^i$ are the velocity and traction force for the i-th element, and P is a $3n \times 3n$ dense matrix whose elements are given by

$$P^{ij}_{kl} = \int_{\Gamma_j}\left[\frac{\delta_{kl}A(R)}{r} + \frac{(x^i_k - y_k)(x^i_l - y_l)B(R)}{r^3}\right]\mathrm{d}s$$

$$k,l = 1,2,3\,. \tag{17}$$

Here, $\boldsymbol{x}^i$ denotes the centroid of the i-th element and Γ_j denotes the surface of the j-th element.

The dense linear system in Eq. (16), without any sparsification, could be very expensive to solve for large-scale systems. The computational time of a direct solver, for example, the Gaussian elimination, grows as the cube of the number of unknowns. For the resonator example, there are near 60,000 unknowns in the discretization shown in Fig. 3. Gaussian elimination would require more than 300,000 gigaflops to solve. In addition, the memory required to store the matrix grows as the square of the number of unknowns, and for the resonator example it would require more than 40 gigabytes.

Even with an iterative method which does not use the entries of the matrix P explicitly, but only requires matrix-vector products, the cost of computing dense matrix-vector products grows with the square of the number of unknowns. So just using an iterative method still results in a computationally expensive algorithm. However, there are a number of techniques for quickly computing approximate matrix-vector products for matrices associated with discretized integral equations.

The FastStokes program [6, 7] was used to compute the drag forces on the micro-resonator shown schematically in Fig. 2. FastStokes combines the iterative method GMRES [8] with the precorrected-FFT [3] technique for computing fast matrix-vector products. The discretized, or meshed, structure is shown in Fig. 3. Note that both the

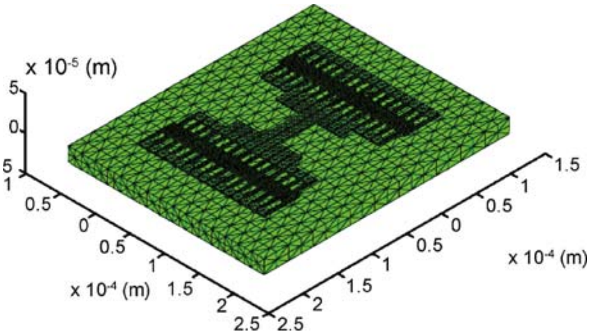

Boundary Element Method and its Applications to the Modeling of MEMS Devices, Figure 3 The meshed resonator

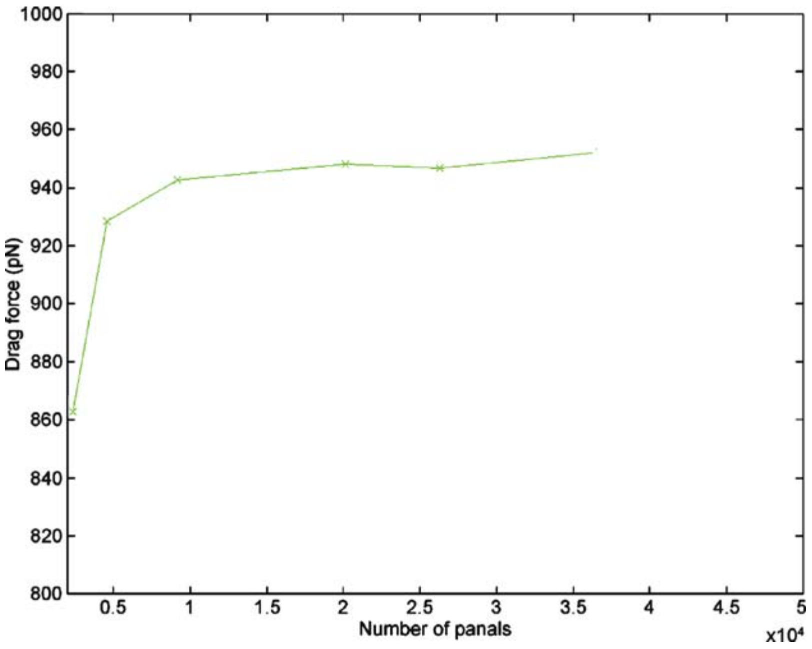

Boundary Element Method and its Applications to the Modeling of MEMS Devices, Figure 4 A convergence plot of the simulated drag force

Boundary Element Method and its Applications to the Modeling of MEMS Devices, Table 2 A comparison of drag force

Drag (pN)	Bottom	Side	Top
Couette	424.37	57.33	0
1D Stokes	437.93	57.37	52.67
FastStokes	510.72	294.50	142.80

polysilicon structures and the substrate are discretized, for a total of 20,148 panels.

The viscous drag forces on the resonator oscillating at $f = 19{,}200$ Hz were computed using progressively finer discretizations, to ensure that the discretization error was sufficiently small. Figure 4 is a plot of how the drag force converges with discretization refinement. As is clear from the plot, the results have converged to within 1% with as few as 10,000 panels. For these simulations, the kinematic viscosity and the density of air were assumed to be $0.157\ \text{cm}^2/\text{s}$ and $1.177\ \text{kg/m}^3$ respectively.

Table 2 shows the distribution of drag forces obtained from FastStokes (with a total of 36,700 panels) together with results obtained from the Couette model and the 1D Stokes model.

The contribution to the drag from the fluid between the resonator and the substrate (denoted as the bottom force) is predicted reasonably well by two simple 1D models. It is not surprising that the two 1D models are in such close agreement. The small gap ($g = 2\ \mu\text{m}$) and slow motion imply that the penetration depth, defined as the distance over which the motion amplitude has dropped to 1% of its maximum value, is 37 times larger than the gap. This indicates that the flow between the resonator and the substrate is fully developed and the velocity profile will be reasonably predicted by the Couette model. That the two 1D models are so close also suggests that the difference between the drag forces obtained from the 1D and 3D models is mostly due to the finite size effects.

Both 1D models seriously underestimate the drag force coming from the side. Due to the infinite-long plate assumption, only drag coming from the fluid between fingers is included in the 1D models. Result from the 3D calculation indicates that side forces are a significant contributor to resonator drag.

In the Couette model, in order to satisfy zero velocity at infinity, the velocity gradient at the top plate is zero. Thus there is no drag force from the top flow. By including the inertial term, the 1D Stokes model predicted about 52.67 pN of drag due to the fluid on the top. However, this value is much smaller than the drag predicted from the 3D Stokes model. This fact, again, indicates the significance of the finite size effects on the drag force.

Results

Quality Factor The quality factor, Q, of the resonator was calculated based on the computed drag force, the

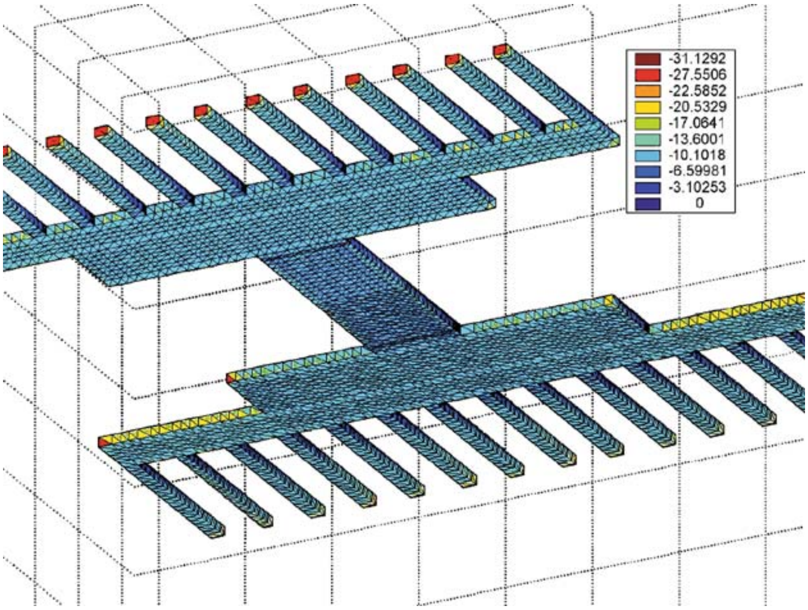

Boundary Element Method and its Applications to the Modeling of MEMS Devices, Figure 5 Drag force distribution on the resonator, bottom view

effective mass and the spring stiffness (9). Results are shown in Table 3 together with the measurement data.

It is clear that both the Couette model and the 1D Stokes model fail to predict the quality factor correctly. They overestimated the value of the quality factor by a factor of two. On the other hand, results from the 3D analysis agree well with the experimental result, with an error of 10%. This indicates that 3D effects are profound in this resonator. Figure 5 shows the detailed drag force distribution for the resonator. The drag force from the ambient air on the top of the resonator contributes 15.7% to the total drag, and the drag force from the air between the resonator and the substrate contributes 55% to the total drag. Side forces contribute almost 29.3%.

Impact of Frequency on Drag Force It is of interest to find out if the unsteady Stokes solver is necessary for computing drag forces on resonators because the unsteady Stokes solver is more expensive than a steady Stokes solver. The integrals in the matrix elements in a unsteady Stokes solver are more expensive to evaluate and both the matrix and vectors are complex. To study the impact of frequency on the drag force, a plot of drag force versus the frequency is shown in Fig. 6. The number of elements used in this simulation is 20,148. At $f = 19{,}200$ Hz, the difference in drag force obtained from the steady Stokes solver and the unsteady Stokes solver is under 6% (see Table 4). As an examination of Table 4 indicates, ignoring the inertial term results in under-predicting top force by nearly one third. Therefore, even at these low frequencies, it is necessary to include the inertial term.

Sensitivity of Drag Force on the Film Thickness A sensitivity test has been performed by varying the film thickness and simulating the drag force on the resonator. Results (obtained by using 20,148 panels) are shown in Table 5.

Boundary Element Method and its Applications to the Modeling of MEMS Devices, Table 3 Quality factor of the resonator: simulation results and experimental data

Method	Total drag (pN)	*Q*
Couette	481.70	58.9
1D Stokes	547.97	51.8
FastStokes	948.02	29.7
Measurement		27

Boundary Element Method and its Applications to the Modeling of MEMS Devices, Table 4 Distribution of drag force: steady versus unsteady

Drag force (pN)	Steady	Unsteady
Bottom	508.75	510.72
Side	284.84	294.50
Top	102.31	142.8
Total	895.9	948.02

Boundary Element Method and its Applications to the Modeling of MEMS Devices, Table 5 Sensitivity of drag force on the film thickness

Film thickness (% change compared with 2 μm)	Drag force (nN) (% change compared with that of 2 μm)
2 μm (0%)	948.02 (0%)
2.01 μm (0.5%)	945.26 (0.28%)
2.02 μm (1%)	942.70 (0.56%)
2.04 μm (2%)	937.57 (1.1%)
2.06 μm (3%)	932.59 (1.6%)
2.2 μm (10%)	900.10 (5.1%)

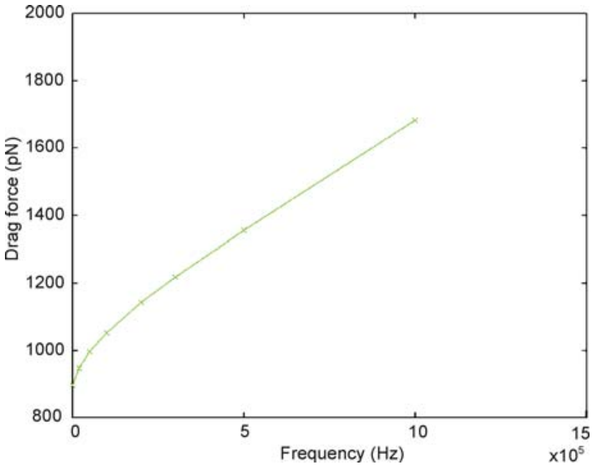

Boundary Element Method and its Applications to the Modeling of MEMS Devices, Figure 6 Drag force as a function of frequency

It has been found from the simulations that the perturbation of the drag force is roughly proportional to the perturbation of the film thickness times a factor of 0.55 for small perturbations. This can be explained using the Couette model because

- the bottom force (drag force coming from air between the resonator and the substrate) is affected the most by changes in gap and
- the Couette model predicts the bottom force pretty well for small gaps (as indicated in Table 2).

In the Couette model, the bottom force is inversely proportional to the gap. Thus, the relative change in bottom force is the same as the relative change in gap. However, the bottom force contributes only 55% of the total drag force. Therefore the relative change in total drag force is 0.55 times the relative change in gap.

Future Directions for Research

To date, most successful applications of the BEM are limited to linear and homogeneous problems. The extension to nonlinear problems is hindered by the existence of the volume integrals in the integral formulations of nonlinear problems. The evaluation of these volume integrals requires a volume discretization of the nonlinear region if standard methods are employed. As such, the boundary-only nature of the method is lost and the BEM loses its advantage in mesh generation as compared to domain methods. An efficient treatment of volume integrals would greatly expand the application scope of the BEM as many practical problems such as those encountered in MEMS devices and systems are inherently nonlinear. Research efforts have been made [9, 10] in this direction, but need to be continued and expanded.

Cross References

- ▶ Boundary Slip of Liquids
- ▶ Combined Pressure-Driven Flow and Electroosmotic Flow
- ▶ Electroosmotic Flow (DC)
- ▶ AC Electro-Osmotic Flow
- ▶ Volume and Finite Difference Method for Modeling and Simulation
- ▶ Finite Volume and Finite Difference Methods for Modeling and Simulation
- ▶ Gas Flow in Nanochannels
- ▶ Heat Transfer in Microchannel Flows
- ▶ Immersed Boundary Method
- ▶ Lattice Boltzmann Method (LBM)
- ▶ Meshless Methods
- ▶ Model Order Reduction (MOR)
- ▶ Molecular Dynamics Simulation Method
- ▶ Multiscale Modeling and Numerical Simulations
- ▶ Non-Continuous Approaches
- ▶ Pressure Driven Single Phase Gas Flows
- ▶ Spectral Methods

References

1. Banerjee PK (1994) The Boundary Element Methods in Engineering. McGraw-Hill, England
2. Greengard L, Rokhlin V (1997) A New Version of the Fast Multipole Method for the Laplace Equation in Three Dimensions. Acta Numerica 229–269
3. Phillips JR, White JA (1997) Precorrected-FFT Method for Electrostatic Analysis of Complicated 3D Structures. IEEE Trans Computer-Aided Des Integrated Circ Syst 16(10):1059–1072
4. Ye W, Wang X, Hemmert W, Freeman D, White J (2003) Air Damping in Lateral Oscillating Micro Resonators: a Numerical and Experimental Study. J Microelectromech Syst 12(5):557–566
5. Cho YH, Pisano AP, Howe RT (1994) Viscous damping model for laterally oscillating microstructures. J Microelectromech Syst 3(2):81–87

6. Aluru NR, White J (1998) A Fast integral equation technique for analysis of microflow sensors based on drag force calculations. Proc. of the International Conference on Modeling and Simulation of Microsystems, Semiconductors, Sensors and Actuators, 283–286, Santa Clara
7. Ye W, Wang X, White J (1999) A fast 3D solver for unsteady Stokes flow with applications to Micro-Electro-Mechanical Systems. Proc. of the International Conference on Modeling and Simulation of Microsystems, Semiconductors, Sensors and Actuators, 518–521, Puerto Rico
8. Saad Y, Schultz M (1986) GMRES: A generalized minimal residual algorithm for solving symmetric linear systems, SIAM. J Sci Statis Comput 7:856–869
9. Partridge PW, Brebbia CA, Wrobel LC (1992) The Dual Reciprocity Boundary Element Method. Elsevier, London
10. Ding J, Ye W (2006) A Grid Based Integral Approach for Quasilinear Problems. Comput Mech 38(2):114–118

Boundary Integral Approaches

► Boundary Element Method and its Applications to the Modeling of MEMS Devices

Boundary Slip of Liquids

Pradipta Kumar Panigrahi, Mohammed Asfer
Department of Mechanical Engineering, IIT Kanpur, Kanpur, India
panig@iitk.ac.in

Synonyms

Perfect slip; Apparent slip; Boundary condition at interface

Definition

The Navier–Stokes equation is one of the basic governing equations for study of fluid flow related to various disciplines of engineering and sciences. It is a partial differential equation whose integration leads to the appearance of some constants. These constants need to be evaluated for exact solutions of the flow field, which are obtained by imposing suitable boundary conditions. These boundary conditions have been proposed based on physical observation or theoretical analysis. One of the important boundary conditions is the no-slip condition, which states that the velocity of the fluid at the boundary is the same as that of the boundary. Accordingly, the velocity of the fluid adjacent to the wall is zero if the boundary surface is stationary and it is equal to the velocity of the surface if the surface is moving. This boundary condition is successful in representing a wide range of fluid flow problems. However, it has been observed that the no-slip boundary condition is not valid for all situations and there is a difference between velocity of the surface and the fluid particles near the boundary. This boundary condition is termed as slip condition.

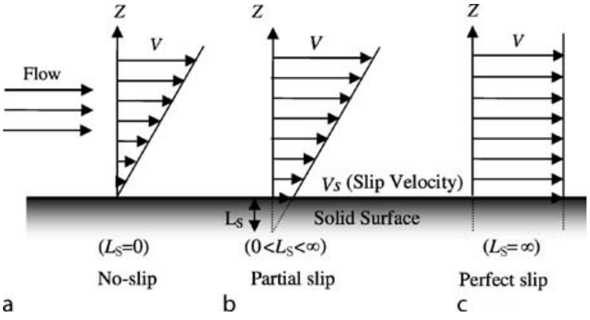

Boundary Slip of Liquids, Figure 1 Schematic representation of the no-slip, partial slip and perfect slip boundary conditions. Under no-slip boundary condition the relative velocity, V_S, between the fluid and the solid wall is zero at the wall. When slip occurs at the wall V_S is finite. The extent of slip is characterized by the slip length L_S (see text)

Overview

Three possible velocity profiles near a solid boundary are shown in Fig. 1. Figure 1a shows that the velocity of fluid particles near the stationary solid wall is equal to zero and represents the no-slip boundary condition. Figure 1b shows that the velocity near the stationary solid wall is non-zero with a relative velocity between the two and represents the slip boundary condition. Figure 1c shows the perfect slip condition, for which there is no influence of the boundary surface on the velocity profile. The velocity when extrapolated towards the wall matches that of the wall at some distance L_s away from it (Fig. 1b), which is known as the slip length and is used as a measure of the slip. The slip length is a fictitious distance below the surface at which the velocity would be equal to zero if extrapolated linearly. The velocity difference between the boundary surface and the adjacent fluid particles is known as the slip velocity, V_s, and is related to the velocity gradient $(\delta V/\delta y)$ near the solid boundary as [1]

$$V_s = \frac{\mu}{C_s}\frac{\delta V(y)}{\delta y} \tag{1}$$

where C_s is the coefficient of slip and μ is the coefficient of viscosity of the fluid. The slip length L_s is the ratio of coefficient of viscosity (μ) to the coefficient of slip (C_s). The no-slip boundary condition is equivalent to $C_s = \infty$ and the perfect slip condition is equivalent to $C_s = 0$.

The slip flow near the boundary surface can be analysed based on the type of fluid, i. e. gas, Newtonian and non-Newtonian liquids. The slip flow in gases has been derived based on Maxwell's kinetic theory. In gases, the concept of mean free path is well defined. Slip flow is observed when characteristic flow length scale is of the order of the mean free path of the gas molecules. An estimate of the mean free path of ideal gas is $l_{\mathrm{m}} \approx 1/(\sqrt{2}\pi\sigma^2\rho)$, where ρ is the gas density (here taken as the number of molecules per unit volume) and σ is the molecular diameter. The mean free path l_{m} depends strongly on pressure and temperature due to density variation. The Knudsen number is defined as the ratio of the mean free path to the characteristic length scale, i. e. $\mathrm{Kn} = l_{\mathrm{m}}/L$. The characteristic length scale (L) can be the overall dimension of the flow or scale of a macroscopic quantity ($L = \rho\ /\ |\delta\rho/\delta y|$). The slip velocity is expressed as a function of the Knudsen number and the velocity gradient at the wall as

$$V_{\mathrm{s}} = \frac{2-\sigma_{\mathrm{v}}}{\sigma_{\mathrm{v}}}\left(\mathrm{Kn}\left(\frac{\delta V}{\delta n}\right)_{\mathrm{s}} + \mathrm{Kn}^2\left(\frac{\delta^2 V}{\delta n^2}\right)_{\mathrm{s}} + \ldots\right) \quad (2)$$

where σ_{v} is the momentum accommodation coefficient, which is a function of the wall and gas interaction. The slip velocity is zero when the Knudsen number is small, i. e. the no-slip boundary condition is valid. The slip condition is valid for large Knudsen number, i. e. when $\mathrm{Kn} \geqslant 0.1$.

Liquid slip has implications to various macroscopic applications, i. e. flow through porous media, particle aggregation, liquid coating and lubrication, etc., in addition to small-scale, i. e. MEMS and bio-MEMS, applications. The movement of a three-phase contact line between two immiscible fluids and solid on a substrate during the advancing or receding film motion indicates the importance of the slip flow boundary condition. The visible contact angle from measurement differs from that predicted using the Young–Laplace equation. The buoyancy and Marangoni effect due to temperature and composition distribution is attributed to the slip flow nature of contact line movement. The conventional hydrodynamics with classical no-slip condition on the substrate generates multi-valued velocity and infinite drag force near the contact line. The imposition of slip condition eliminates this viscous stress singularity at the contact line. Molecular dynamics simulation has also confirmed the local slip near the contact line. Similarly, flows of polymer solutions also show significant apparent slip. Therefore, for liquids, the slip flow characteristics are different from those of gases and need a different explanation.

The liquid slip phenomenon is presented in the following sections. The experimental investigation quantifying the liquid slip is discussed to begin with followed by the results from molecular dynamics simulation. Subsequently, the factors responsible for liquid slip and possible mechanism responsible for liquid slip are discussed.

Basic Methodology

The applicability of slip flow is not well accepted to date by the academic community. One of the problems is the small length scale of the slip flow regime (if present) in comparison to the length scale of the flow or system. The hydrodynamic boundary condition appears to be one of no-slip, unless the flow is examined on a length scale comparable to the slip length. Hence, very accurate techniques with high spatial resolution capable of interfacial flow measurements are required to detect the effects of slip. Some of the experimental techniques for quantification of liquid slip are presented in the following sections.

Flow Rate

Macroscopic quantities, i. e. flow rate and pressure drop measurement, can be used for indirect determination of liquid slip. In this approach, a known pressure gradient ΔP is applied between the two ends of a capillary or a microchannel and the flow rate Q is measured. The flow rate for the slip flow condition is higher than that predicted from the no-slip boundary condition. For Poiseuille flow of fluid with viscosity μ through a narrow cylindrical channel of radius R and length L, the flow rate assuming no-slip boundary condition is

$$Q_{\mathrm{th}} = \left(\frac{\Delta P \pi R^4}{8\mu L}\right) \quad (3)$$

If there is slip at the walls of the channel, the Poiseuille flow velocity profile will be modified to

$$u(r) = \left(\frac{\Delta P}{4\mu}\right)\left[(R + L_{\mathrm{s}})^2 - r^2\right] \quad (4)$$

The flow rate can be obtained using the above slip flow boundary condition, and (assuming $L_{\mathrm{s}}/R \ll 1$) it can be derived that

$$Q_{\mathrm{slip}} = Q_{\mathrm{th}}\left(1 + \frac{4L_{\mathrm{s}}}{R}\right) \quad (5)$$

For any particular slip length of fluid flow, the slip flow rate increases with decreasing radius of the cylindrical channel. For the slip length $L_{\mathrm{s}} = 200\,\mathrm{nm}$, the flow rate with slip (Q_{slip}) is about 6% and 23% higher than the theoretical flow rate with no-slip (Q_{th}) for capillary radii of 13.3 μm and 3.48 μm respectively.

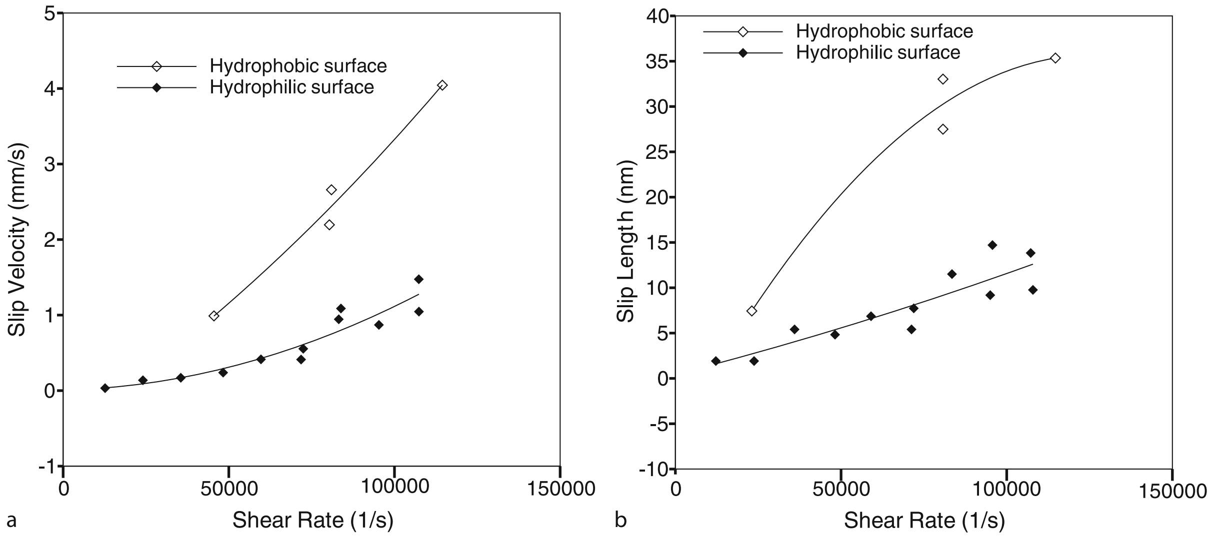

Boundary Slip of Liquids, Figure 2 Comparison of slip velocity and slip length between hydrophilic and hydrophobic surfaces as a function of shear rate

Choi et al. [4] presented the slip velocity and slip length of hydrophilic and hydrophobic microchannels (1 and 2 μm depth) based on flow rate and pressure drop measurements. Sample results from their study are compiled in Fig. 2. The flow rate for the hydrophobic surface is higher than that for the hydrophilic surface. The corresponding slip velocity and slip length for the hydrophobic surface are also higher than those for the hydrophilic surface. The slip velocity and slip length increase with strain rate.

Cheng and Giordano [5] reported the slip length data for different Newtonian fluids, i. e. silicone oil, hexane, decane and hexadecane (fluids having different molecular diameter), as a function of channel height (see Fig. 3). They observed the no-slip condition to be valid when water is the working fluid. However, the slip length is definite for other working fluids. The slip flow effect is insignificant for channel size greater than about 140 nm. Their study indicates the dependence of slip flow on the molecular diameter of the fluid and the fluid–channel wall interaction.

Hydrodynamic Force

The motion (steady or oscillatory) of a sphere towards a flat surface experiences a resistance to the motion. This resistance is due to the combined contribution from Stokes drag on the sphere, the drainage force and the drag force on the cantilever attached between the sphere and the force measuring apparatus, i. e. atomic force microscopy (AFM) or surface force apparatus (SFA). The exact hydrodynamic solutions of this resistance force for a sphere of radius a, approach velocity V, viscosity μ and closest separation distance h can be derived as [3]

$$F = f_{\text{slip}} \frac{6\pi \mu a^2 V}{h} \qquad (6)$$

For the no-slip boundary condition, $f_{\text{slip}} = 1$. Otherwise when there is slip, $f_{\text{slip}} < 1$, i. e.

$$f_{\text{slip}} = \frac{h}{3L_{\text{s}}}\left[\left(1+\frac{h}{6L_{\text{s}}}\right)\ln\left(1+\frac{6L_{\text{s}}}{h}\right)-1\right] \qquad (7)$$

Thus the hydrodynamic force for the slip flow case is smaller in magnitude than that for the no-slip case.

Figure 4a shows a schematic of the device for drainage force measurement. Fig. 4b shows the hydrodynamic force versus inverse separation distance for fluids of different viscosity based on the measurements by Neto et al. [3]. The predicted drainage force based on the no-slip flow condition is also compared in Fig. 4b. It is clearly evident that the no-slip boundary condition is unable to describe the experimental data. The slip length obtained based on Eq. (6) and (7) is equal to 4 nm and 12 nm for lower and higher viscosity values respectively. Figure 4c shows the slip length as a function of the approach velocity and fluid viscosity indicating that slip length is a function of both the fluid type, i. e. viscosity, and strain rate, i. e. the approach velocity.

Particle Image Velocimetry (PIV)

Micrometre-resolution particle image velocimetry (PIV) can also be used for direct observation of slip length by

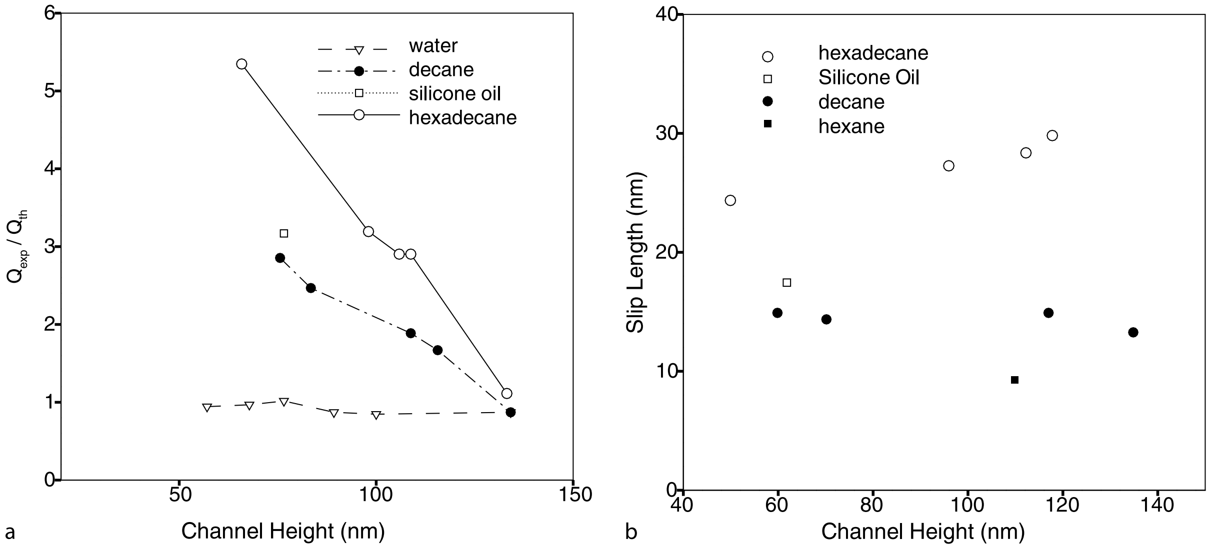

Boundary Slip of Liquids, Figure 3 (**a**) The ratio of experimental flow rate (Q_{exp}) to theoretical flow rate (Q_{th}) based on no-slip boundary condition and (**b**) the slip length as a function of channel height for different fluids (water, silicone oil, decane, hexane and hexadecane)

measuring the velocity profile in the near-wall region. Figure 5a shows a typical μ-PIV setup for microchannel velocity measurement. The velocity measurement in hydrophilic (uncoated glass) and hydrophobic (octadecyltrichlorosilane (OTS) coating) channels adopted from Trethway and Meinhart [6] is shown in Fig. 5b. Fluorescently dyed polystyrene particle of 300 nm diameter absorbs green (532 nm) Nd:YAG laser light which emits red (575 nm) light. The emitted light from the particles is collected by a CCD camera through an epi-fluorescent filter. The cross correlation between pair of particle images provides the velocity field information. The near-wall velocity field measurement of the microchannel (30 μm deep and 300 μm wide) shown in Fig. 5b indicates different velocity profile behaviour between the hydrophilic and hydrophobic channel. The hydrophobic channel shows a shifting of the velocity profile towards higher value and a finite non-zero velocity near the bottom wall, i. e. at about 450 nm from the wall surface, indicating slip flow behaviour.

Other Techniques

Sedimentation velocity and streaming potential measurements also provide indirect information about the slip length.

The sedimentation velocity of particles under gravity can be measured and compared with the predicted values based on no-slip and slip flow boundary conditions. The ratio of the sedimentation velocity as a function of slip length can be derived as

$$\frac{V_{\text{slip}}}{V_{\text{NS}}} = \frac{1 + 3L_{\text{s}}/a}{1 + 2L_{\text{s}}/a} \tag{8}$$

For small particles with radius a, the sedimentation velocity with slip (V_{slip}) for slip length L_{s} is larger than that with no-slip (V_{NS}). The comparison of actual velocity with the predicted velocity based on no-slip condition provides the slip length.

Streaming potential measurement of electrolyte flow inside a capillary depends on the slip length. The surface of the capillary acquires a net charge in contact with the electrolyte. The pressure-driven flow of the capillary creates an advection of charges resulting in surplus ions at one end of the capillary compared to the other end. If the two ends of the capillary are not short-circuited, a net steady-state potential difference, termed the streaming potential, develops. The streaming potential depends on the extent of slip. The ratio of streaming potential for slip (ΔV_{slip}) and no-slip (ΔV_{NS}) is given by

$$\frac{\Delta V_{\text{slip}}}{\Delta V_{\text{NS}}} = 1 + L_{\text{s}}\kappa \tag{9}$$

where κ is the Debye screening parameter, which gives the typical distance close to the surface where there is a net charge density in the liquid and $\kappa^{-1} = \left(\varepsilon_r \varepsilon_0 k_{\text{B}} T / 2e^2 n_0\right)^{1/2}$. Here ε_r is the dielectric constant of the liquid, ε_0 the permittivity of the vacuum, k_{B} Boltzmann's constant, T the temperature, e the electron charge

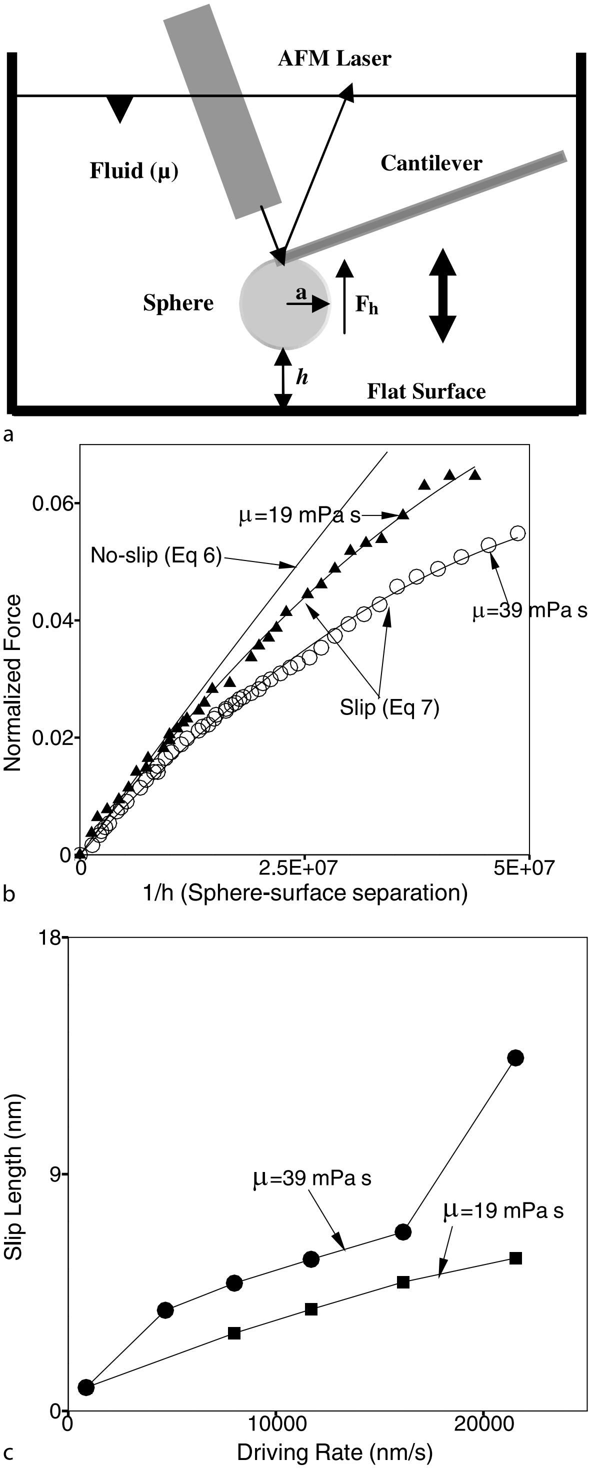

Boundary Slip of Liquids, Figure 4 (**a**) Schematic of the arrangement for slip length characterization, (**b**) the normalized hydrodynamic force versus inverse of separation for fluid of different viscosities and comparison with no-slip flow calculation and (**c**) slip length as a function of viscosity and driving rate

and n_0 the number density of ions in the bulk of the solution.

Molecular Dynamics Simulation

Molecular dynamics (MD) simulation is a useful tool for studying small-scale fluid flows. Numerical integration of Newton's law of motion for particles (atoms or molecules) is carried out:

$$m_i \frac{d^2 r_i}{dt^2} = \sum_j F_{ij} \tag{10}$$

where m_i is the particle mass, r_i the position of particle i and F_{ij} the interatomic or intermolecular force between particles i and j ($F_{ij} = -\nabla_i V_{ij}$). The Lennard-Jones two-body potential (V_{ij}) between particles is frequently used which is given by

$$V_{ij} = \varepsilon \left[\left(\frac{\sigma}{r_{ij}} \right)^{12} - c_{ij} \left(\frac{\sigma}{r_{ij}} \right)^{6} \right] \tag{11}$$

where ε is an energy scale, σ the particle size and r_{ij} the distance between particles i and j. The constants c_{ij} allow variation of the relative intermolecular attraction between liquids and solids, which therefore represents wetting behaviour.

Barrat and Bocquet [7] carried out the molecular dynamics simulation of Couette and Poiseuille flows. In Couette flow, the upper wall is moved with a constant velocity and in Poiseuille flow an external force drives the flow. Sample results from molecular dynamics simulation are reproduced in Fig. 6. The application of no-slip boundary condition leads to the expected linear and parabolic velocity profile respectively for Couette and Poiseuille flow. However, the velocity profile obtained from molecular dynamics simulation shows a sudden change of velocity in the near-wall region indicating slip flow. The velocity profile for Couette flow away from the solid surface is linear with slope different from that of the no-slip case. The velocity for the slip flow case is higher than that observed for the no-slip case for Poiseuille flow. For both Couette and Poiseuille flow, the partial slip boundary condition at the wall predict similar bulk flow as that observed by molecular dynamics simulation. Some discrepancy in the velocity profile is observed in the near-wall region.

Physical Parameters Affecting Slip

The results reported in the previous section have established the occurrence of slip flow from both experimental and simulation studies. It is important to know various physical parameters affecting slip. The physical

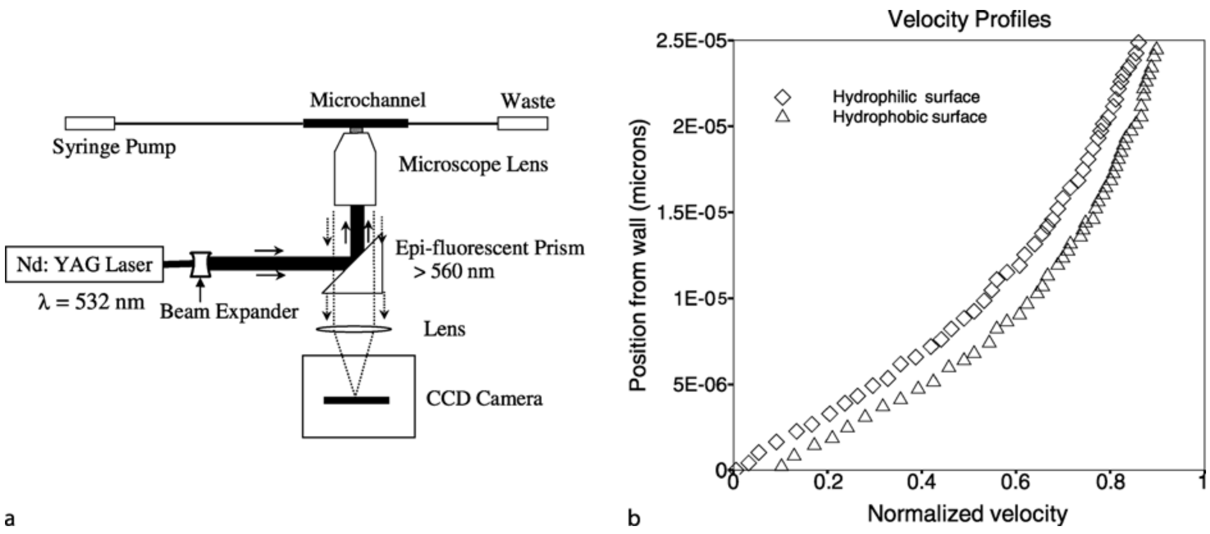

Boundary Slip of Liquids, Figure 5 (**a**) Experimental arrangement for μ-PIV measurement and (**b**) velocity profile for hydrophobic and hydrophilic surfaces obtained from μ-PIV measurement

parameters affecting slip are summarized in the following sections.

Surface Roughness

Roughness influences the behaviour at liquid–solid interfaces. Roughness induces flow around it that leads to dissipation of the mechanical energy. Therefore, there is an increase in the overall resistance to flow and the tendency of slip decreases due to surface roughness. The roughness also influences the dewetting behaviour of the liquid. A high contact angle is indicative of a weak interaction between liquid and solid, and thus causing the fluid molecules to slide across the solid. Roughness can increase the tendency to produce a gas–liquid interface at the solid boundary. The surface behaves like a super-hydrophobic surface and the slip tendency increases.
However, systematic study of surface roughness is not easy to implement. It is difficult to produce suitable surfaces of controlled roughness. Most efforts to alter the surface roughness result in additional undesired changes to the interface properties.

Surface Wettability

It is generally believed that a liquid has a larger slip tendency for poorly wetted surfaces. Higher contact angle indicates weak interaction between the solid and liquid and therefore is easy to overcome. Many experiments and molecular dynamic simulations have confirmed that the level of hydrophobicity is one of the primary factors determining the level of slip.

Shear Rate

The slip length also depends on the shear rate imposed on the fluid particles. Thompson and Troian [2] have reported the molecular dynamics simulation of Couette flow at different shear rates. At lower shear rate, the velocity profile follows the no-slip boundary condition. The slip length increases with increase in shear rate. The critical shear rate for slip is very high for simple liquids, i. e. 10^{11} s^{-1} for water, indicating that slip flow can be achieved experimentally in very small devices at very high speeds. Experiments performed with SFA and AFM have also showed shear dependence slip in the hydrodynamic force measurements.

Dissolved Gas and Bubbles

Dissolved gases or bubbles near a solid also influence the slip flow behaviour. It has been observed experimentally that the amount of slip depends on the type and quantity of dissolved gas in the fluid. From sedimentation studies it has been reported that slip is not observed in vacuum conditions while there is a clear slip when a liquid sample is in contact with air. Slip in non-wetting systems depends strongly on the environment in which the experiment is performed. Dissolved gases or nano-bubbles in the near-wall region are thought to create localized defects increasing the possibility of slip.

Polarity

For electrolyte solutions and polar liquids, the amount of slip depends on the electrical properties of the liquid. Sed-

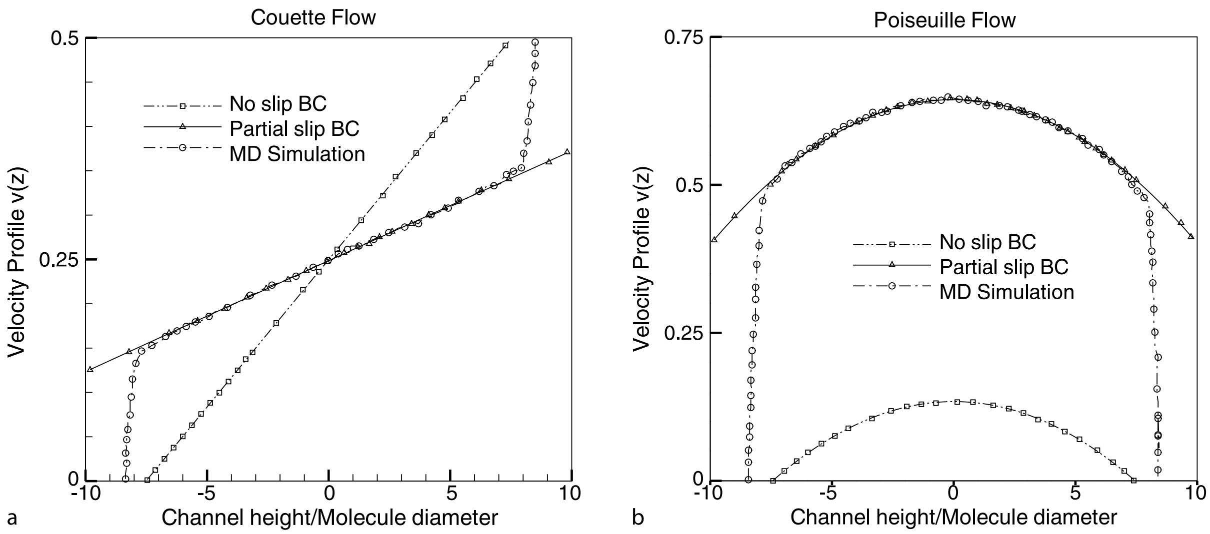

Boundary Slip of Liquids, Figure 6 Velocity profile for (**a**) Couette and (**b**) Poiseuille flow. Comparison between molecular dynamics simulation, no-slip boundary condition and partial slip boundary condition

imentation experiments report that slip is only observed for polar liquids. Drainage force experiments report slip to increase with increase in the dipolar moment of the liquid when liquids are polar. This phenomenon is attributed to the super-lattice structure in liquids due to the dipole–dipole interactions.

Possible Liquid Slip Mechanism

Slip flow phenomena can be explained by some possible mechanism. The fluid slip can be described as true or apparent slip. The true slip occurs at a molecular level, where liquid molecules are effectively sliding on the solid surface. The apparent slip occurs not at the solid–fluid interface but at the fluid–fluid interface where a thin layer of liquid/gas molecules is tightly bound to the solid surface. For apparent slip the velocity gradient close to the solid surface is so high that the bulk molecules beyond the layer of liquid/gas molecules appear to slide on the surface.

The true slip phenomena can be attributed to the liquid–liquid and liquid–solid interaction. If the viscous friction between liquid molecules at the interface is stronger than between molecules of the liquid and molecules of the solid, then the molecules can slide on the surface. This is true for hydrophobic surfaces but might also hold for hydrophilic surfaces. If the dimensions of the liquid molecules are of comparable size as the corrugation on the solid surface, then the molecules are trapped in the pits on the surface giving no-slip boundary conditions. But if their size is much smaller or much larger, they can slide on the surface.

For apparent slip, thin gas/liquid layers with a modified viscosity and/or mobility are created near the solid surface. At room temperature and pressure, there is always some residual gas dissolved in a liquid. Critical level of shear might induce cavitations in a liquid and the generated gas bubbles might adhere to the solid surface forming a thin gas layer at the solid surface onto which the liquid can slip. The other factor can be the critical shear rate at which a microscopic surface roughness or corrugation can favour the generation of turbulent flow layer at the interface, and thus modify the viscosity of this layer with respect to the bulk, even if the overall flow is laminar.

Key Research Findings

The correct specification of boundary condition of fluid flow near an interface or solid boundary is essential to obtain the analytical and numerical solution of fluid flow problems. The no-slip boundary condition is successful in describing a class of fluid flow problems. The applicability of the slip flow condition and the condition at which the no-slip boundary condition is invalid is of both academic interest and of practical interest. The recent developments of small-scale microfluidic systems have raised the importance of the specification of the correct boundary condition.

Barrat and Bocquet [7] reported slip in Couette and Poiseuille flow using molecular dynamics simulation (Fig. 6). Tretheway and Meinhart [6] reported a micrometre-resolution velocity profile in hydrophilic and hydrophobic microchannels of cross-section $30 \times 300\,\mu m^2$ using the μ-PIV technique (Fig. 5). Their

results showed significant fluid velocity near a hydrophobic (octadecyltrichlorosilane or OTS coated) microchannel wall and no-slip for a hydrophilic surface. Cheng and Giordano [5] reported pressure-driven flow of several classical fluids (hexane, decane, hexadecane and silicon oil) through lithographically produced channels. The results for water agree well with the theoretical prediction of no-slip boundary condition, for a channel height as small as 40 nm. However, for hexane, decane, hexadecane and silicone oil slip flow is observed when channel separation is reduced below about 100 nm (Fig. 3).

Choi et al. [4] examined the apparent slip effects of water in hydrophobic and hydrophilic microchannels experimentally using precision measurements of flow rate versus pressure drop. They compared their experimental results to that from analytical solution of flow through a channel with slip velocity at the wall. There was a clear difference between the flow of water on a hydrophilic and hydrophobic surface indicating the effect of slip flow (Fig. 2). Craig et al. [3] have reported clear evidence of boundary slip for a sphere–flat geometry from drainage force measurements using atomic force microscopy. The degree of slip is observed to be a function of both liquid viscosity and shear rate (Fig. 4).

Yang and Kwok [8] presented the analytical solution of fully developed electrokinetic flow subjected to sinusoidal pressure gradient or sinusoidal external electric field. The combined effect of slip flow and electrokinetics was demonstrated on the velocity profile in confined geometries. The velocity profile was observed to be a function of both slip coefficient and external electric field. They observed that both these effects play important roles for flow inside microchannels.

Ou and Rothstein [9] developed an ultra-hydrophobic surface with micrometre-sized ridges (20 – 30 μm wide) placed 20 – 120 μm apart aligned in the flow direction. They demonstrated maximum 25% drag reduction for flow inside these channels. From μ-PIV measurements, they showed the existence of slip flow at the air–water interface between the ridges, while the flow over the ridges obeys the no-slip condition. They attributed the existence of slip flow for drag reduction.

Future Directions for Research

The studies carried out so far have explained the slip flow phenomena to a great extent. However, the use of slip phenomena for analysis of different fluid flow problems is limited. The effect of various flow parameters, i. e. roughness, wettabilty, polarity and presence of nanobubbles or residual gases, on slip flow phenomena needs to be conclusively and systematically studied. The effect of temperature and concentration gradient on slip flow parameters needs to be properly characterized based on both molecular dynamics simulation and experiments. The effect of slip flow on turbulence production mechanism needs to be established. The development of advanced micro-/nano-manufacturing and measurement technology is expected to facilitate the systematic study of these parameters.

Manipulation of conditions required for generation of slip flow can have many practical applications. This will be beneficial in development of drag reduction and mixing enhancement technologies. This is particularly important for micro- and nanotechnologies, where the pressure penalty is very high and mixing is difficult due to the difficulty in generation of turbulent flow.

Cross References

► μ-PIV
► Molecular Dynamics Simulation
► Atomic Force Microscope (AFM)

References

1. Blake TD (1990) Slip between a liquid and a solid: D. M. Tolstoi's theory reconsidered. Colloids surf, 135–145
2. Thompson PA, Troian SM (1997) A general boundary condition for liquid flow at solid surfaces. Nature 389:360–362
3. Neto C, Craig VSJ, Williams DRM (2003) Evidence of shear-dependent boundary slip in Newtonian liquids. Eur Phys J E 12:71–74
4. Choi CH, Westin JA, Breuer KS (2003) Apparent slip flows in hydrophilic and hydrophobic micro channels. Phys Fluids 15:2897–2902
5. Cheng JT, Giordano N (2002) Fluid flow through nanometer-scale channels. Phys Rev E 65:1–5
6. Tretheway D, Meinhart C (2002) Apparent Fluid Slip at Hydrophobic Microchannel Walls. Phys Fluids 14:9–12
7. Barrat J, Bocquet L (1999) Large slip effect at a nonwetting fluid–solid interface. Phys Rev Lett 82:4671–4674
8. Yang J, Kwok DY (2003) Effect of liquid slip in electrokinetic parallel-plate microchannel flow. J Colloid Interf Sci 260:225–233
9. Ou J, Rothstein JP (2005) Direct velocity measurements of the flow past drag-reducing ultrahydrophobic surfaces. Phys Fluids 17:103606–10

Bragg Diffraction Equation or Bragg's Law

Definition

If a crystal is irradiated with x-ray radiation most of the radiation passes through unhindered. But some part of the radiation will be deflected by the crystal, which is called Raylight scattering and can be visualized on photographic plates. But the equation can only be achieved (and thereby the reflection be observed), if the pitch length

(which is although the phase shift of the radiation before and after the deflection) is an integer multiple of the wavelength. The Bragg diffraction equation was developed by William Henry Bragg and his son William Lawrence Bragg in 1912.

Bridging Instability

► Interfacial Instability

Brownian Diffusion

► Brownian Motion

Brownian Dynamics

► Simulating Migration of Polymer Chains, Methods

Brownian Motion

Synonyms

Brownian diffusion

Definition

Brownian motion refers to the random thermal diffusion of a particle suspended in a fluid due to collisions between the particle and the fluid molecules that are in continual, random motion.

Cross References

► Temperature Measurement, Methods

Brownian Noise

► Micro-PIV-Based Diffusometry

Bubble Actuated Microfluidic Switch

CHENG-HSIEN LIU
Department of Power Mechanical Engineering,
National Tsing Hua University, Hsinchu, Taiwan
Liuch@pme.nthu.edu.tw

Synonyms

Microflow switch; Multi-channel micro switch pumping; Capillarity-driven stop valve and sample injection switch; Multi-channel micro liquid dosing system

Definition

The bubble actuated microfluidic switch is actuated by either thermal bubble or electrolysis bubble. The microfluid is driven by capillary force and stop by design of hydrophobic property in the microchannels. The switch function of the microfluidic system is to control the fluid sample into the individual desired outlet reservoir for the applications such as selective on-chip sample dosing, microfluidic/bio-sample on-chip transportation and Lab-on-a-Chip microsystem integration.

Overview

Some design concepts and prototypes of microfluidic switches have been demonstrated over the past decade. Doring et al. [1] demonstrated that a laminar flow could be steered into one of two outlet ports using a thermal bimorph cantilever, which was made by a bimetal structure and used as an active component for flow switching. Blankenstein et al. [2] reported that the differential hydrodynamic pressures, which were generated by external pumps, between the inlet ports were used to guide specific fluid sample stream into the desired outlet port. The sample injection into one of the five outlet ports has been demonstrated in their study. Gebhard et al. [3] demonstrated a fluidic oscillator employing a V-shaped fluidic circuit with feedback micro channels, in which a part of the output flow was fed back into the inlet region to control the main flow to be redirected to the other desired microchannel. Gebhard's work demonstrated that the fluid could be switched between two output microchannels via their design. Lee et al. [4] reported that $M \times N$ pre-focused microfluidic switches have been successfully demonstrated with several external pumps to switch continuous liquid from an inlet channel to any desired outlet channel in multi-ported outlet microchannels. In their studies, the theoretical model based on the potential flow theory was built to predict the performance of single and multiple flow switching. Also, Lemoff and Lee [5] reported an AC magnetohydrodynamic (MHD) microfluidic switch, in which the Lorentz force was used to propel an electrolytic solution. Their switch took advantage of integrating two AC MHD pumps into different arms of a fluidic Y-channel to make the fluid switch into or out of either arm. In these proposed research studies, various microfluidic switches have been successfully

demonstrated. Anyway, most proposed studies still suffer from the disadvantages such as the need of several external pumps and mechanical moving parts inside the fluidic chip. In addition, most of them could not perform precise fluidic switch into tiny microchannels due to leakage problems.

Some MEMS technologies have been drawn toward taking advantage of surface tension, which becomes a dominant force in microscale. The continuous electrowetting (CEW) requires a liquid metal in a filler liquid, limiting the medium that can be driven. A droplet movement of aqueous liquid based on electrical control of surface tension has been demonstrated with an electrolyte droplet in a filler fluid [6], still requiring two liquids in the system. In addition, the electrowetting (EW) [7] and electrowetting on dielectric (EWOD) [8] can be used to handle aqueous liquid in microscale without any second liquid medium. In these cases, the change in contact angle or the wettability shift is caused by the change in the solid-liquid surface tension.

A novel microfluidic switch based on surface tension and distributed hydrophobic-patch design was just developed and reported in our group [9]. Both the capillary force and the barrier pressure are utilized in our proposed design to achieve the switching function. The trigger driving actuator in our reported concept-proof prototype relies only on the embedded heater, which generates thermal actuation bubbles, with time-sequence power control. The bubble actuator could be replaced by the electrolysis bubble actuator in a modified chip design. This kind of proposed fluidic switch devices could resolve the disadvantages in early proposed various microfluidic switches, such as the complicated electrical connections, the need of several external pumps, the mechanical moving parts inside the fluidic chip, and the leakage problems. Compared with other actuation mechanisms, the bubble actuator has the features of simple structure, no moving parts and being easy to be integrated with the control circuitry. However, for bio-applications by using thermal bubble actuation, the bio-samples might be broken or degraded either by the shear-stress acting on them due to the hydrodynamic movement of the fluids when the bubble grows and collapses, or by the local high temperature induced by the transient generation of the thermal bubble. It has been found that some pretreatment of the bioactive samples could lower these kinds of damage. For example, Okamoto et al. [10] successfully ejected DNA segments in a DNA micro-array device by using the thermal bubble jet-printing technology. To avoid the high temperature and high shear-stress damage from the thermal bubble, they optimized the DNA ejection solvent to improve volatility, solubility, wettability, viscosity and surface tension of DNA solution, and to promote spot separation by adding some additional chemicals. Maxwell et al. [11] also reported a microbubble bioparticle actuator that uses the micro thermal bubble actuation to manipulate the bioparticles. So far, they have demonstrated that bubble actuation could be used to actuate cell-sized particles and will use the bioparticle actuator to capture living cells. Besides, our group also successfully demonstrated cell sorting feature for liver cells by using electrolysis bubble actuator to actuate MEMS T-shape structure [12]. The MEMS design gets rid of PH value actuation to get high survival rate for delicate sorted liver cells. All of these results demonstrate promising research efforts for the MEMS bubble actuation technique to be integrated in biochips for bio-applications. In the following sections, we focus on the thermal-bubble actuated microfluidic switch based on surface tension and distributed hydrophobic-patch design. This device is taken as an example to understand the details about design concept, basic theory, operation principle as well as take a look at the function demonstration.

Basic Methodology

Design Concept of Bubble Actuated Microfluidic Switch

To introduce the concept and design details, a schematic representation of the 1×4 microfluidic switch with one inlet port and four outlet ports as shown in Fig. 1 is taken as a case study here. This case-study device, as shown in Fig. 1, consists of an embedded heater, a capillary system with hydrophilic microchannels, and a specific arrangement of hydrophobic patches. This device could be expanded to $1 \times N$ microfluidic switch via the similar design. Also the embedded heater could be replaced by electrolysis electrodes. In Fig. 1, L_i represents the length of each hydrophobic patch in the microchannel #*i*. From microchannel #1 to #4, L_i decreases with an increase of patch number in each microchannel. For the device design shown in Fig. 1, there are 1, 2, 3, and 4 separated hydrophobic patches in microchannel #1, #2, #3, and #4, respectively. These distributed patches have the same length in each microchannel.

In the $1 \times N$ microfluidic switch design, the switch mechanism among different microchannels is dominated by controlling the format and the timing of power input that generates thermal bubble actuation. During the growing process of the thermal bubble, the meniscus of the liquid in each microchannel stopping at the edges of the hydrophobic patches will be pushed forward as shown in Fig. 2. When the thermal bubble begins collapsing, the meniscus of the liquid in each microchannel will flow back till leaving the hydrophobic patch due to the barrier pressure if it stays on a hydrophobic patch. On the contrary, it will

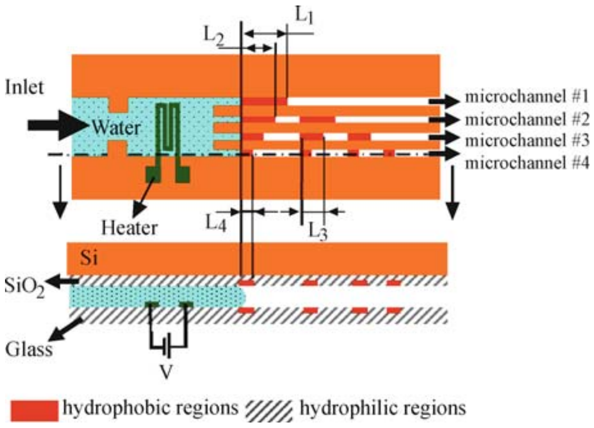

Bubble Actuated Microfluidic Switch, Figure 1 The design concept of the microfluidic switches where $L_i > L_{i+1}$, i. e. $L_1 > L_2 > L_3 > L_4$. L_i represents the length of each hydrophobic patch in microchannel #*i*. All other regions in the microchannels are hydrophilic

flow forward till reaching the edge of the next hydrophobic patch region due to the capillary force if it stays on a hydrophilic region.

Figure 2 illustrates the operation principles of a 1×4 microfluidic switch based on the proposed design concept by using specific separated hydrophobic patches in microchannels. As a fluid sample is first introduced into the inlet from the left, the fluid is driven forward to the right by the capillary force and then stops at the edges of the first hydrophobic patches of each microchannel as shown in Fig. 1. For instance, if we want to control and guide the continuous liquid into the microchannel #1, the volume control of the actuating bubble is required to push the fluid to pass through the first hydrophobic patch region of the microchannel #1 but not to pass through all the second hydrophobic patches in other microchannels. Because the length of the hydrophobic patch in microchannel #1 is the longest, the fluid could pass through all the first patches of all microchannels if the volume of the actuating bubble could push the fluid to pass through the first hydrophobic patch region in the microchannel #1. Then, the continuous liquid could be driven along the microchannel #1 by the capillary force, and stopped at second patches of other microchannels by the barrier pressure, as shown in Fig. 2a. One challenge on this capillary system design, for this case, is to drive the fluid through the microchannel #1 and precisely stop the fluid before the second hydrophobic patches in the other microchannels via the micro design of the separation gaps between hydrophobic patches and the time-sequence control of bubble volume.

For another example, if we want to control the liquid to flow into the microchannel #3 only, we could control the bubble volume via heater power control to overcome the barrier pressures of all the hydrophobic patches in microchannel #3 step by step. As soon as the fluid passes through each one of hydrophobic patches of the microchannel #3, the thermal bubble immediately begins collapsing via the voltage control on the heater. At this moment, the meniscuses of fluid staying on the hydrophilic region will flow forward due to capillary force till reaching the next hydrophobic patch in the microchannel #3 and #4. However, the meniscuses staying on the hydrophobic patches will flow back due to barrier pressure till leaving the hydrophobic patch in the microchannel #1 and #2. After we generate the growth and collapse of the thermal bubble three times, the continuous liquid could be driven through the microchannel #3 due to the capillary force, as shown in Fig. 2b. Based on the similar operation principles, the fluid could be controlled and guided into any desired microchannel or multiple microchannels based on the needs. As shown in Fig. 2c, the fluid is simultaneously switched into two desired outlet ports, the microchannel #2 and #4. Firstly, we generate the large bubble twice to make the fluid pass through all hydrophobic patch regions of microchannel #2. Afterwards, we generate the small bubble twice to make the fluid pass through the last two of the hydrophobic patch regions in microchannel #4. Based on the hydrophobic-patch design and programmed time-sequence bubble actuation, the fluid could be switched into desired outlet ports in the capillary system without the need of external pumps and complicated MEMS moving parts.

Microfabrication of Case-Study Microfluidic Switch Prototype

The micro fabrication of our capillary system with microfluidic switch function is a four-mask process, as illustrated in Fig. 3. A standard p-type <100> silicon wafer is grown with 5000 Å thermal oxide that is patterned and etched as the oxide mask, and then etched by KOH solution to define 20 μm-depth microchannels. Then, this silicon substrate is grown with another 7000 Å thermal oxide to form the hydrophilic layer. Next, the 1% Teflon solution is spin-coated on the oxide layer to define our designed hydrophobic patch regions by a lift-off process. On the Pyrex glass substrate, photoresist and HF solution are used to define the patterns and form the recesses of 1 μm-depth. A 5000 Å aluminum layer is, then, evaporated and patterned as the heater and electrodes by another lift-off process. Next, another 1% Teflon solution is also spin-coated on the Pyrex glass to define the hydrophobic pattern regions by another lift-off process. Finally, the silicon wafer and Pyrex glass are aligned for the anodic bonding process.

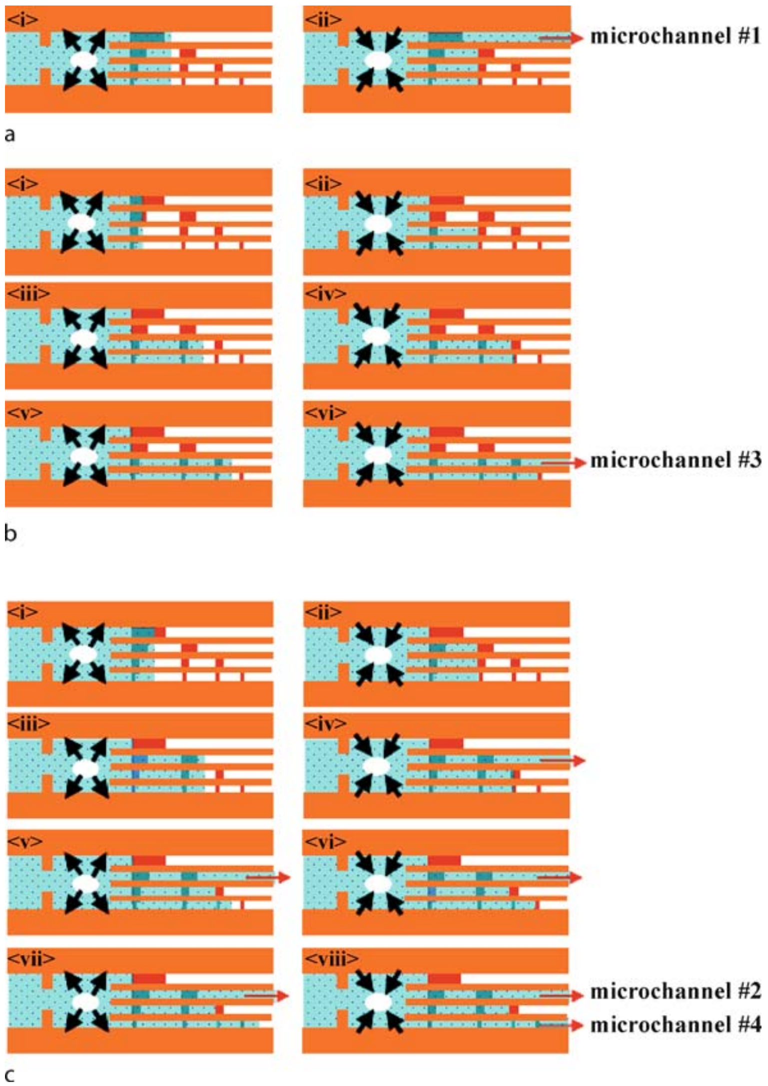

Bubble Actuated Microfluidic Switch, Figure 2 Illustration of design concept and operation principles for a 1×4 microfluidic switch via bubble actuator control, capillary force and hydrophobic patch distribution design. The liquid is controlled and switched into (**a**) microchannel #1, (**b**) microchannel #3, (**c**) microchannel #2 and #4 simultaneously

Background and Theory

Barrier Pressure Analysis

To study and design the capillary system with $1 \times N$ microfluidic switches, a theoretical model based on early literatures is proposed. The liquid actuation and control in the capillary system with microfluidic switch function is dominated by both barrier pressure and capillary force. Here, we model the liquid motion by using the total surface energy approach [13]. The surface energies are related to the equilibrium contact angle θ_c by Young's equation

$$\gamma_{sa} = \gamma_{sl} + \gamma_{la} \cos\theta_c \tag{1}$$

The total interfacial energy of the system could be modeled as

$$\begin{aligned} U_T &= A_{sl}\gamma_{sl} + A_{sa}\gamma_{sa} + A_{la}\gamma_{la} \\ &= (A_{sl} + A_{sa})\gamma_{sa} - A_{sl}\gamma_{la}\cos\theta_c + A_{la}\gamma_{la} \\ &= U_0 - A_{sl}\gamma_{la}\cos\theta_c + A_{la}\gamma_{la} \end{aligned} \tag{2}$$

where A_{sl}, A_{sa} and A_{la} are interface areas of solid-liquid, solid-air, and liquid-air, respectively, and γ_{sl}, γ_{sa}, and γ_{la} are the surface energies per unit area. The sum of $(A_{sl} + A_{sa})$ is invariant, so U_0 is a constant value.

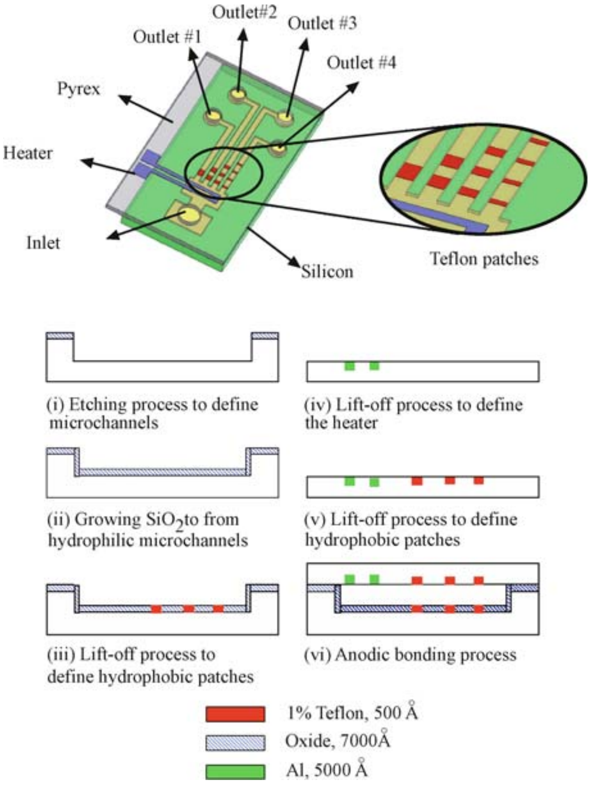

Bubble Actuated Microfluidic Switch, Figure 3 Microfabrication processes for the capillary system

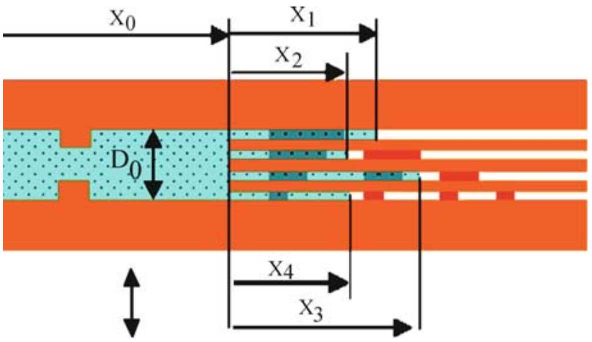

Bubble Actuated Microfluidic Switch, Figure 4 The meniscuses of the liquid stay at position x_1, x_2, x_3, x_4 in microchannel 1, 2, 3, 4, respectively, for a transient state. This is a general case for the analysis of pulling force and backward barrier pressure in the capillary system

When a liquid sample is introduced into the capillary system with a 1×4 microfluidic switch as shown in Fig. 1, it wicks by the capillary force and stops at the edges of hydrophobic patches due to the barrier pressure. To study the pulling force and backward barrier pressure in each microchannel, Fig. 4 illustrates a general case for the transient state with the liquid positions at x_1, x_2, x_3, and x_4 in microchannel #1, #2, #3, #4, respectively. The width of each outlet microchannel is much larger than the microchannel height, h, in the device, so the meniscus shape could be simplified as a one dimension problem. The effect of gravity is neglected because of shallow microchannels in the device. The meniscus is assumed to be a circular arc with a 2α angle where α is equal to $\pi/2-\theta_c$, as shown in Fig. 5. The total energy U_T is a function of the injected liquid volume V_L. The total energy U_T and the pressure P could be derived as follows [13].

$$U_T = U_0^* + \sum_{i=1}^{4}\left[-2D_i x_i \gamma_{la}\cos\theta_{c,i} + \gamma_{la}\frac{D_i h \alpha_i}{\sin\alpha_i}\right] \quad (3)$$

$$V_L = D_0 x_0 h + \sum_{i=1}^{4}\left[D_i x_i h - \frac{D_i h^2}{4\sin\alpha_i}\left(\frac{\alpha_i}{\sin\alpha_i} - \cos\alpha_i\right)\right] \quad (4)$$

where U_0^* is a constant value, D_i is the width of the microchannel #i, x_i is the meniscus in the microchannel #i, and $\theta_{c,i}$ is the contact angle between liquid and microchannel wall in microchannel #i. The pressure on the liquid is hence

$$P_1 = \frac{\partial U_T/\partial x_1}{\partial V_L/\partial x_1} = \frac{-2\gamma_{la}\cos\theta_{c,1}}{h},$$

$$P_2 = \frac{\partial U_T/\partial x_2}{\partial V_L/\partial x_2} = \frac{-2\gamma_{la}\cos\theta_{c,2}}{h},$$

$$P_3 = \frac{\partial U_T/\partial x_3}{\partial V_L/\partial x_3} = \frac{-2\gamma_{la}\cos\theta_{c,3}}{h},$$

$$P_4 = \frac{\partial U_T/\partial x_4}{\partial V_L/\partial x_4} = \frac{-2\gamma_{la}\cos\theta_{c,4}}{h} \quad (5)$$

$$P = \frac{dU_T}{dV_L} = \sum_{i=1}^{4} P_i = \sum_{i=1}^{4}\left[\frac{\partial U_T/\partial x_i}{\partial V_L/\partial x_i}\right] = -\sum_{i=1}^{4}\frac{2\gamma_{la}\cos\theta_{c,i}}{h} \quad (6)$$

where P_1, P_2, P_3, and P_4 are the individual forward/backward pressure in the microchannel #1, #2, #3, and #4, respectively. P is the total pressure applied to the fluid due to capillary force and barrier pressure. When all the fluid in each microchannel stays at the hydrophobic regions, $P_1=P_2=P_3=P_4$ with the same contact angle θ_c.

In the device design, the sample liquid is DI water, the height is 20 µm and the width of each microchannel is 100 µm. According to Eq. (5), the internal liquid pressure is a function of the contact angle, which is related

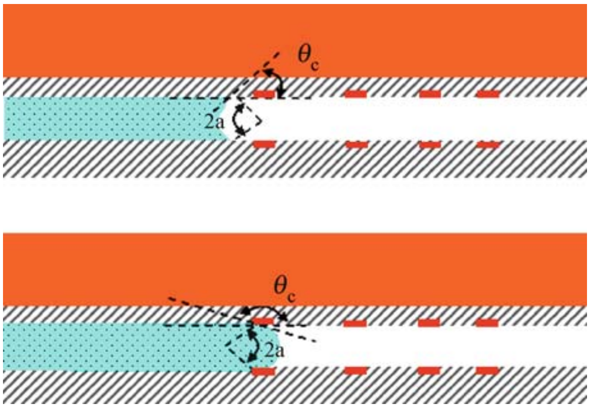

Bubble Actuated Microfluidic Switch, Figure 5 The definition for the angles of meniscus shape stayed at (**a**) hydrophilic region (**b**) hydrophobic region

to the meniscus positions, x_1, x_2, x_3 and x_4. The contact angle $\theta_c = 20°$ of hydrophilic microchannels could produce a negative pressure of nearly 7 kPa to make the liquid flow forward. The contact angle $\theta_c = 120°$ of hydrophobic patches could generate a positive barrier pressure of nearly 4 kPa to stop the liquid. Figure 6 shows the pressure distribution in each microchannel of the device based on the above contact angle parameters. The positive sign on the pressure means a backward barrier pressure on the hydrophobic patch regions. The negative sign means a forward pulling pressure on the hydrophilic region in the capillary microchannels.

Based on the above, we could extend 1×4 microfluidic switch system to $1\times N$ microfluidic switch system with similar derivation to obtain the mathematical models for the injected volume, the total energy and the total pressure as follows.

$$U_T = U_0^* + \sum_{i=1}^{N}\left[-2D_i x_i \gamma_{la}\cos\theta_{c,i} + \gamma_{la}\frac{D_i h\alpha_i}{\sin\alpha_i}\right] \quad (7)$$

$$V_L = Dx_0 h + \sum_{i=1}^{N}\left[D_i x_i h - \frac{D_i h^2}{4\sin\alpha_i}\left(\frac{\alpha_i}{\sin\alpha_i} - \cos\alpha_i\right)\right] \quad (8)$$

$$P = \frac{dU_T}{dV_L} = \sum_{i=1}^{N} P_i = \sum_{i=1}^{N}\left[\frac{\partial U_T/\partial x_i}{\partial V_L/\partial x_i}\right] = -\sum_{i=1}^{N}\frac{2\gamma_{la}\cos\theta_{c,i}}{h} \quad (9)$$

Thermal Bubble Nucleation

The growth and collapse of a micro-bubble via a micro-heater actuator, with the applications to ink-jet printers, have been studied extensively in the decades. It has been demonstrated that the pressure inside the bubble could reach several MPa during the initial bubble growth period, with the heating duration of within several microseconds. It should be highlighted that most previous researches regarding the bubble generation under a pulse heating show a nearly symmetric bubble growth and collapse periods, where the width of heating pulse was kept at several microseconds. In other words, the bubble growth velocity is nearly equal to the bubble collapse velocity, so there will be no net fluid flow after one cycle of bubble growth and collapse period. Recently, P. Deng et al. [14] have studied the bubble behavior under pulse heating with pulse width in the range from microseconds to milliseconds. They report that a relatively long pulse heating duration could change the near-symmetric bubble growth-collapse pattern by prolonging the vapor bubble condensation process.

Thermal Bubble Volume

The thermal bubble growth could be mainly classified into two modes in macro-scale bubble nucleation experiments, as described in an early literature report [15]. The first mode occurs at the initial stage of bubble growth that is hydrodynamically controlled and dominated by liquid inertia. For this first mode, the bubble diameter increases proportionally with heating time. The second mode occurs at the later stage of bubble growth that is dominated by the heat diffusion. The bubble grows at a slower rate and is proportional to the square root of heating time in this second mode. Recently, Tsai et al. [16] have investigated the transient bubble formation experiments on polysilicon micro-resistors. These studies demonstrate that the micro bubble nucleation processes could be classified into three groups depending on the input current. When the input current is low, no bubble is nucleated. For the middle range of the input current, a single spherical bubble is nucleated with a waiting period up to 2 s depending on the magnitude of the input current. After the resister temperature rises and reaches a steady state, the bubble growth rate is found proportional to the square root of heating time that is similar to the heat diffusion dominant model as proposed for the macro scale boiling experiments. From the experimental data, it is found that the bubble diameter, D, could be represented as $D = 2Ct^{1/2}$, where t is the heating time, and C is the bubble growth rate constant and determined by the heating rate.

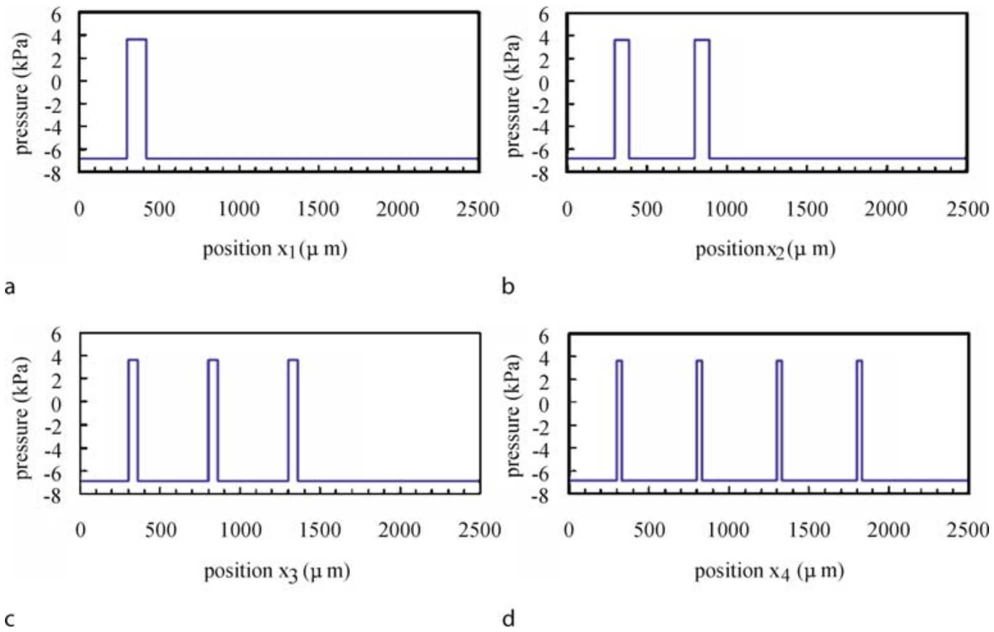

Bubble Actuated Microfluidic Switch, Figure 6 Hydrophobic barrier pressure distribution versus meniscus positions x_1, x_2, x_3, x_4 along (**a**) microchannel #1 (**b**) microchannel #2 (**c**) microchannel #3 (**d**) microchannel #4, respectively. The positive sign on pressure means a backward barrier pressure. The negative sign means a forward pulling pressure on the hydrophilic region in the capillary microchannels

Furthermore, a further assumption of a perfectly spherical bubble is made for the shape of the vapor layer generated on a thin-film heater surface, the bubble volume, V, could be modeled as [17]

$$V(t) = \frac{\pi D^3}{6} = \frac{4\pi}{3} C^3 t^{3/2} \tag{10}$$

In the design, the width of each microchannel is much larger than its height, so the bubble volume could be simplified as a two-dimension problem.

$$V(t) = \frac{\pi D^2}{4} h = \pi h C^2 t \tag{11}$$

The bubble volume increases linearly with time in the case, so we could control the bubble volume via the time of applied voltage to control the liquid positions through hydrophobic patches of different length. In addition, the bubble growth rate is also affected by the amplitude of the applied regulation voltage, so we could shorten the heating duration by increasing the amplitude of the applied voltage. Thus, the bubble volume could be controlled by the heating duration and the applied-voltage amplitude.

Thermal Energy

In fact, the heating rate is not fixed even if the heater is applied with a constant voltage. The power input to the heater is not constant because the heater resistance is continuously increasing with the temperature during the application of the heating pulse. For the square electrical voltage pulse with a time period, the thermal energy, Q, which is produced via a thin-film micro heater, could be derived by the following equation.

$$\begin{aligned} Q &= \int_0^{t_N} V_e I_e(t)\,dt = \int_0^{t_N} \frac{V_e^2}{R(T)}\,dt \\ &= \int_0^{t_N} \frac{V_e^2}{R_0(1+\alpha_T(T(t)-T_0))}\,dt \end{aligned} \tag{12}$$

where V_e, I_e, R and T are the applied voltage, the applied current, the heater resistance and temperature, respectively, α_T is the temperature coefficient of the Al wire resistor, t_N is the duration of the applied voltage pulse, and R_0 is the heater resistance at a reference temperature T_0. In the concept-proof prototype devices, the micro-heaters, as shown in Fig. 12a, are 30 μm wide Al wires with different resistances. In the following experimental demonstration, the micro-heater that we use for thermal bubble generation is characterized and has the resistance of 64.6 Ω at room temperature.

The relationship between thermal energy and the pulse duration would change due to the temperature effect. However, the thermal energy would increase with the applied heating duration. To characterize heater temperature, the

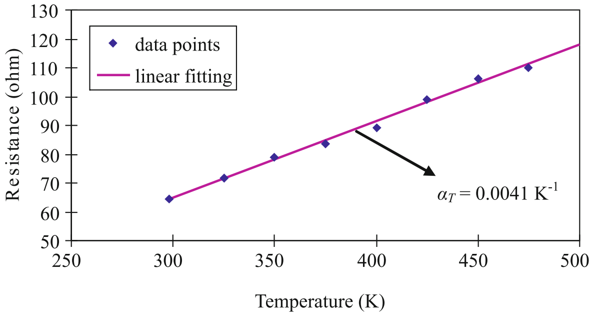

Bubble Actuated Microfluidic Switch, Figure 7 The characterized resistance for the micro heater versus the heater temperature. The Al micro heater has a nominal resistance of 64.6 Ω at the room temperature

relationship between the electric resistance and the temperature of the micro Al heater is studied. First, the heater is calibrated to obtain the temperature coefficient, α_{T}. The fluidic chip with the Al wire resistor is placed on a hot plate, whose temperature is controlled by a controller, and then the pad of the heater are connected to the input ports of a HP3457A multimeter. The resistance of the heater versus the temperature is characterized and recorded, as shown in Fig. 7. The temperature coefficient of the heater $\alpha_{\mathrm{T}}=0.0041\ \mathrm{K}^{-1}$is obtained by a linear fitting of the measured data which could help us to approach the real-time heater maximum temperature during the pulse heating process.

Mechanical Work

While a bubble expands or contracts in a liquid, mechanical work is transferred between the bubble and the surrounding liquid. The kinetic energy transferred from the expanding vapor microlayer on a thin-film heater surface could be used, in principle, to drive electromechanical microdevices such as micro actuators and micro pumps. The useful work converted from the thermal energy on the surface of a microheater is critical for these applications. The mechanical work, E_m, done by a vapor volume expansion on the surrounding liquid is [16]

$$E_m = \int P_{\mathrm{v}}\,\mathrm{d}V = \int_0^t P_{\mathrm{v}} \frac{\mathrm{d}V(t)}{\mathrm{d}t}\,\mathrm{d}t \qquad (13)$$

where P_{v} is the pressure within a bubble and $V(t)$ is the bubble volume. The microfluidic switch is activated to drive fluid forward when the bubble pressure overcomes the total barrier pressure, $P_{\mathrm{v}} > P$. Therefore, the mechanical work is used to overcome the barrier pressure and to increase the bubble volume. For reliability and controllability, we have to keep the total barrier pressure constant before the thermal bubble is activated each time, to make the mechanical work completely dominated by the bubble volume. The best way to keep the total barrier pressure constant is that the fluid must simultaneously pass all last hydrophobic patches at the desired turn-on microchannels. This is related to the operation principles that we will address next.

Bubble Actuated Microfluidic Switch, Table 1 Fifteen operation modes for the capillary system with a 1×4 microfluidic switch

Number of outlet ports on	Desired outlet ports (microchannel #*i*) on
One	1; 2; 3; 4
Two	1,2; 1,3; 1,4; 2,3; 2,4; 3,4
Three	1,2,3; 1,2,4; 1,3,4; 2,3,4
Fthe	1,2,3,4

Operation Principles

There are 15 operation modes for the capillary system with a 1×4 microfluidic switch, which could simultaneously switch the liquid into the desired outlet ports, as listed in Table 1. The operation modes could be divided into two parts, namely single and multiple output modes. We will discuss the required time-sequence power control for the bubble nucleation to function the fluidic switch appropriately for the capillary system as follows.

Single Output Modes

The sample liquid is assumed to be able to be pushed and pass the lengths of hydrophobic patches L_1, L_2, L_3 and L_4 in each microchannel, as shown in Fig. 1, with the voltage pulse widths T_1, T_2, T_3 and T_4 on the heater in capillary micro system. According to Eq. (11), the bubble volume increases proportionally to the heating time under a constant applied voltage. Thus, the relationship $T_1 > T_2 > T_3 > T_4$ is reasonably predicted. Therefore, we could control the fluid into one of microchannels by controlling the format and timing of heater power input, as shown in Fig. 8. For a $1 \times N$ microfluidic switch, if we desire to guide the liquid into the microchannel #i, the voltage pulse width t applied on the heater to generate actuating bubble must be $T_i \leqq t < T_{i-1}$ and the times of the bubble nucleation, i, is required to pass through all hydrophobic patches of microchannel #i. Also, the design on the separation gap between adjacent hydrophobic patches must be far enough to prohibit the fluid from passing through the microchannel #$i-1$ when we only intend to turn on microchannel #i.

Multiple Output Modes

Appling the similar principles, we could control the fluid into multiple microchannels based on the needs. For such multiple output modes, there are three different operation methods, as shown in Fig. 9, to control the fluid into the microchannel #2 and #4, for example, in the capillary system with a 1×4 microfluidic switch. The time-sequence actuation as shown in Fig. 9a, we would generate the growth and collapse of the thermal bubble six times to control the fluid to pass through the microchannel #4 and #2. The bubble pressure overcomes the barrier pressure to make the fluid pass through all hydrophobic patches of microchannel #2 and #4. Then, the capillary force pulls the fluid through to turn on microchannel #2 and #4. However, Fig. 9b demonstrates the same switch function with only four-time thermal-bubble actuation. These two methods have the common point which is firstly to control the fluid to pass through one of desired microchannels. According

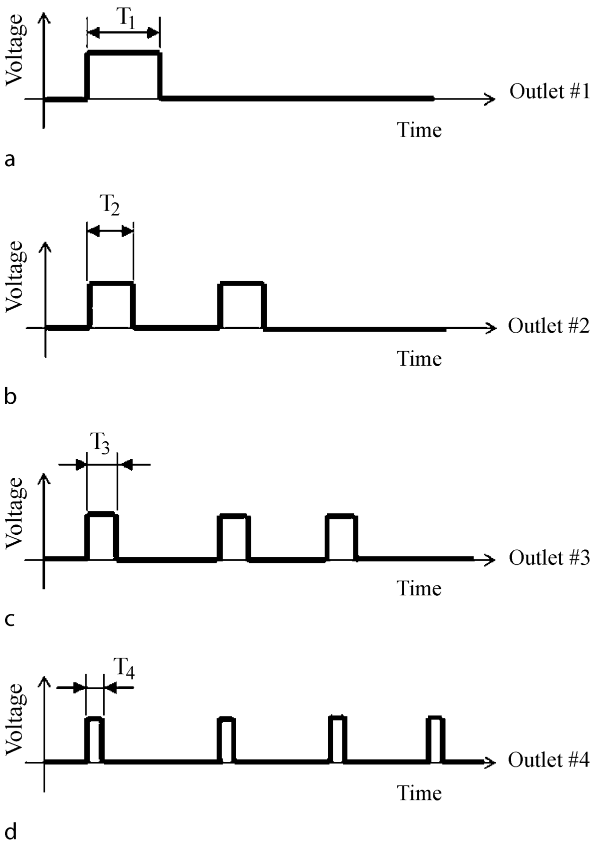

Bubble Actuated Microfluidic Switch, Figure 8 Pulse widths and the times of bubble nucleation management in a single output mode (**a**) for the power control to turn on microchannel #1 only (**b**) for the power control to turn on microchannel #2 only (**c**) for the power control to turn on microchannel #3 only (**d**) for the power control to turn on microchannel #4 only

to Eq. (6), the total barrier pressure would decrease due to the effect of the capillary force which would produce a negative pressure. Hence, the magnitude of the total barrier pressure would be affected after the fluid pass through one of the microchannels. The total barrier pressure would decrease with the number of the turn-on microchannels which the fluid has passed through via capillary force.

To ensure the controllability and reliability of the microfluidic switches, the same total barrier pressure is set as the requirement in the design when the thermal bubble is activated each time. This means that the fluid has to be steady-state and stop at hydrophobic patches of each microchannels before each bubble starts being generated. For example, if we desire to control the fluid into the microchannel #2 and #4 simultaneously, we could follow the third method, as illustrated in Fig. 9c, which makes the microchannel #2 and #4 turned on simultaneously on the last time of bubble growth actuation. This procedure could also minimize the times of the bubble nucleation for the same fluidic switch purpose.

For a $1 \times N$ general microfluidic switch, we want the fluid liquid to be controlled into five specific outlet ports, for example, which are connected with microchannels #*X*, #*Y*, #*Z*, #*V* and #*W*. The lengths of hydrophobic patches in these five microchannels have the relationship of $L_X > L_Y > L_Z > L_V > L_W$. Here, L_X, L_Y, L_Z, L_V and L_W represent the length of hydrophobic patches in microchannel #*X*, #*Y*, #*Z*, #*V* and #*W*, respectively. Then, we could design the required time-sequence power control logics to control the thermal bubble actuator via the control of voltage pulse width and bubble-actuation times. The control logics for the voltage pulse width and the bubble actuation times is described and optimized as follows.

Step 1: $T_X \leqq t_1 < T_{X-1}$, and $(X-1)$ times bubble actuation with the voltage pulse time width t_1.

Step 2: $T_Y \leqq t_2 < T_{Y-1}$, and $[(Y-1)-(X-1))] = (Y-X)$ times bubble actuation with the voltage pulse time width t_2.

Step 3: $T_Z \leqq t_3 < T_{Z-1}$, and $[(Z-1)-(Y-1)] = (Z-Y)$ times bubble actuation with the voltage pulse time width t_3.

Step 4: $T_V \leqq t_4 < T_{V-1}$, and $[(V-1)-(Z-1)] = (V-Z)$ times bubble actuation with the voltage pulse time width t_4.

Step 5: $T_W \leqq t_5 < T_{W-1}$, and $[(W-1)-(V-1)] = (W-V)$ times bubble actuation with the voltage pulse time width t_5.

Step 6: $T_X \leqq t_6 < T_{X-1}$, and one more time bubble actuation with the voltage pulse time width t_6,

where t_i represents the required voltage pulse time width at each step; T_i is the required voltage pulse time width

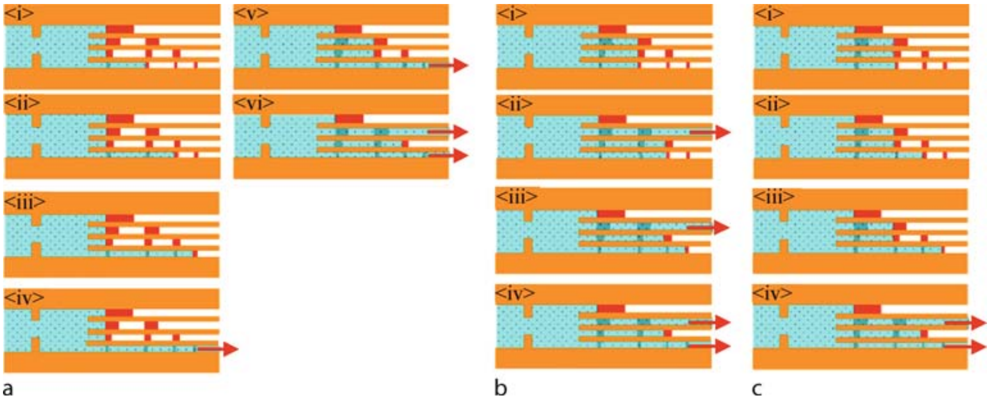

Bubble Actuated Microfluidic Switch, Figure 9 The three different time-sequence power control logics to turn on microchannel #2 and #4 in the capillary system with the 1 × 4 microfluidic switch function

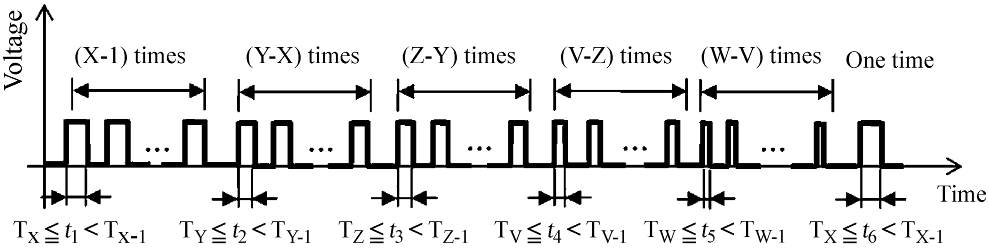

Bubble Actuated Microfluidic Switch, Figure 10 The optimized control logics to turn on microchannel #*X*, #*Y*, #*Z*, #*V* and #*W*. The t_i represents the required power pulse time width at each step. T_i is the required voltage pulse width on the heater to push the fluid to pass the first hydrophobic patch region in microchannel #*i*

on the heater to make the fluid pass through the first hydrophobic patch region in microchannel #*i*; *X*, *Y*, *Z*, *V* and *W* represent the desired turned-on microchannels. Therefore, we could simultaneously guide the fluid into specific desired microchannels by controlling the format and timing of power input based on the above generalized optimal operation steps, which are also summarized and shown in Fig. 10. The control logics could be applied to the capillary system with $1 \times N$ microfluidic switch function.

Experimental Results

Experimental Setup

The experimental setup which is utilized to observe the switch function is schematically represented in Fig. 11a. The volume of thermal bubble is controlled by the input pulse power of the heater with a preset duration which is programmed by the controller, composed of the Complex Programmable Logic Devices (CPLD) card, a buck circuit, and adaptors, as shown in Fig. 11a. In Fig. 11b, the programmable CPLD card is utilized to control the duration of the heating and to regulate the voltage amplitude by means of a buck circuit and a pulse width modulation (PWM) method. An optical microscope with a CCD camera is utilized to observe and record the switching process of the capillary system with $1 \times N$ microfluidic switches.

Experimental Demonstration

There are 15 operation modes, as shown in Table 1, for the controller design to operate the capillary system with a 1×4 microfluidic switch. In Fig. 12, two kinds of operation modes were recorded to demonstrate the fluidic switch functions for the capillary system with a 1×4 microfluidic switch. In Table 2, these designed dimensions of the hydrophobic patches are shown. The dyed DI water is introduced into the inlet, as shown in Fig. 12a, driven forward by the capillary force and finally stops at the edge of first hydrophobic patch in each microchannel, as shown in Fig. 12b. Figures 12c–f shows the results of the single-output mode demonstration – the continuous liquid is switched into the single desired outlet port via the control of the programmed bubble volume and the time sequence power control. Figure 12g demonstrates

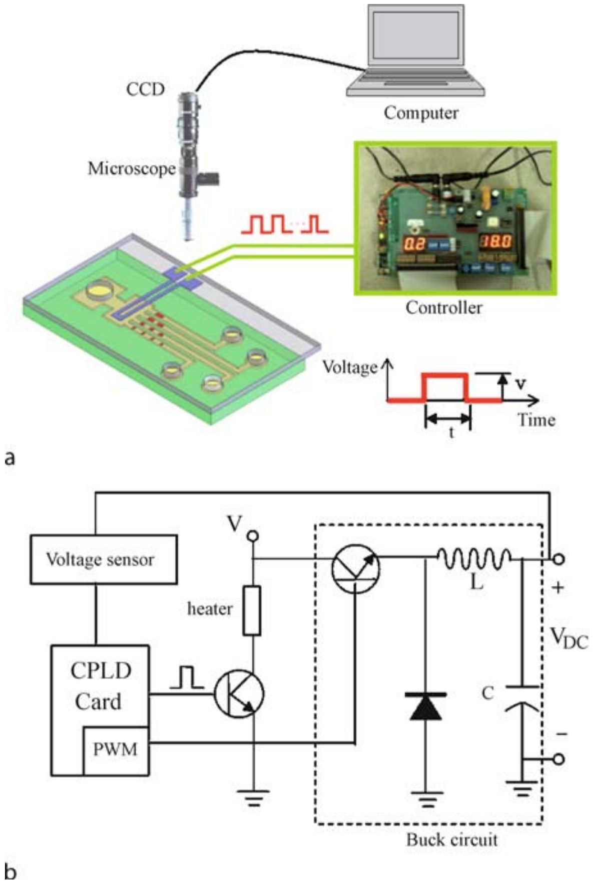

Bubble Actuated Microfluidic Switch, Figure 11 (**a**) Schematic diagram of the experimental setup (**b**) the control circuit of the micro heater for a square voltage pulse with a preset duration

Bubble Actuated Microfluidic Switch, Table 2 Geometry parameters of the 1×4 microfluidic switch (unit: μm)

	Geometry parameters
Hydrophobic length	$L_1 = 120$; $L_2 = 90$; $L_3 = 60$; $L_4 = 30$
Microchannel width	$D_1 = D_2 = D_3 = D_4 = 100$
Microchannel depth	$h = 20$

the result of the multiple-output modes – the continuous liquid is simultaneously switched into two desired outlet ports, microchannel #1 and #4. This operation mode in the controller breaks the barrier pressures of all hydrophobic patches in microchannel #1 and #4 to continuously drive liquid forward by the capillary force.

According to Eq. (11), the relationship between bubble volume and heating duration is linear for the case. Here, the bubble volume is characterized via the captured images by a CCD camera, and recorded along with the heating time under two different applied voltages, 5 V and 10 V, on the 30 μm wide micro heater, as shown in Fig. 13. The bubble growth rate constant, C, could be experimentally determined by the slope of the fitting curve. The bubble growth rate constants are characterized to be 56 and 105 $\mu m/s^{1/2}$ for the applied voltage of 5 V and 10 V, respectively. These experimental results imply that the bubble volume could be controlled by the heating duration and the applied-voltage amplitude. Therefore, the bubble volume can be controlled via the time of applied voltage to control the liquid positions through hydrophobic patches of different length in the device design.

The experimental results in Fig. 14a show the pulse width versus the length of hydrophobic patches in a 1×4 microfluidic switch under different applied voltages, 5 V and 10 V. The required voltage pulse width could be shortened by the lager voltage or the shorter hydrophobic patches. Thus, the magnitude of the applied voltage on heater and the dimension design of the hydrophobic patches would dominate the operation speed of the microfluidic switches. Besides, the relationship between the length of hydrophobic patch and the required voltage pulse width is nearly linear. However, the required pulse width must be increasing with the length of hydrophobic patch. Therefore, the bubble volume can be controlled to push the fluid through the hydrophobic patches with different length by managing the voltage pulse width, and then to drive the continuous fluid into specific outlet ports based on the operational rules and control logics. Also, the maximum temperature of the heater during the heating period can be derived by means of measuring the resistance of the heater at the end of heating based on the curve shown in Fig. 7. The relationship between the heating-pulse width and the maximum temperature is shown in Fig. 14b.

The design in this case-study prototype device remains an issue for the reversible motion of the liquid. This case-study prototype device could be effectively used for the one shot of liquid in both single-output and multi-output modes on demand. For continuous random switch function, another problem appears if we turn on microchannel $\#X$ first and desire to next turn on only microchannel $\#Y$ where $X > Y$. In this continuous switch function, the microchannel $\#(X+1)$ will be also turned on in this case-study prototype device. Anyway, above issues could be resolved via the two-way bubble actuator design [18, 19], which could make the fluid flow backwards in the unwanted microchannel. In addition, this micro fluidic switch has the potential to be integrated into a wider fluidic network system with stop valves or micro flow discretizers which could be used for separation of liquid segments from a continuous source.

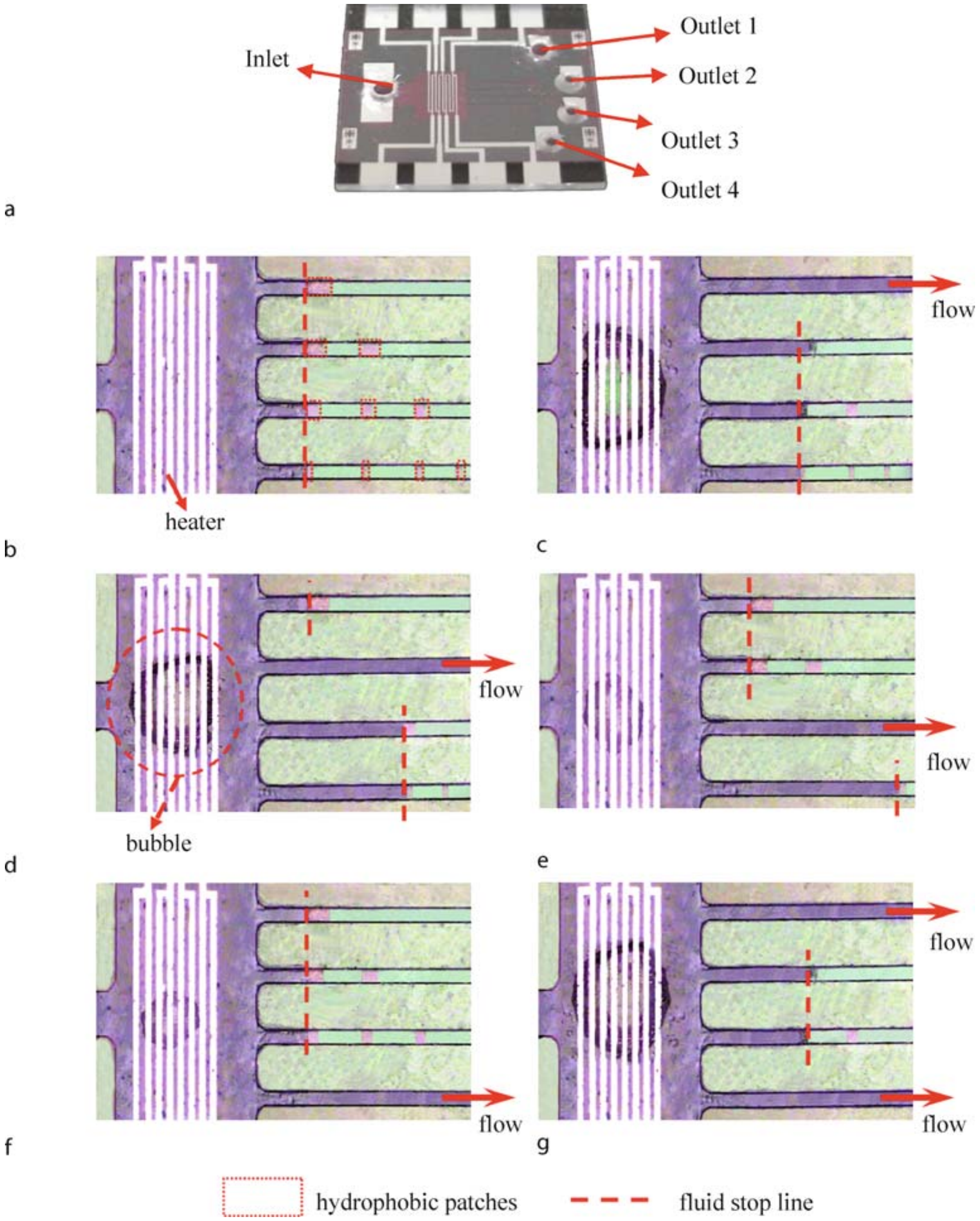

Bubble Actuated Microfluidic Switch, Figure 12 Experimental demonstration for different switch modes. (**a**) The 1×4 microfluidic switch prototype device. (**b**) DI water starts being ejected. (**c**)–(**f**) show the single-output switch mode to single desired outlet, microchannel #1, microchannel #2, microchannel #3 and microchannel #4, respectively. (**g**) shows simultaneous multiple- output mode to two desired outlets, microchannel #1 and #4

Key Research Findings

A capillary system with the appropriate design of bubble-actuated $1\times N$ microfluidic switches is successfully demonstrated to control continuous liquid into the desired outlets without the need of external pumps and MEMS mechanical moving parts. Theoretical models are proposed to study the liquid motion, which is dominated by both the barrier pressure and the capillary force in the device. This capillary micro-fluidic switch system is a valveless switch by means of the triggering bubble-actuator, the capillary force, the design of the distributed hydrophobic patches in the microchannels, and the time-sequence power control. The switch mechanism among

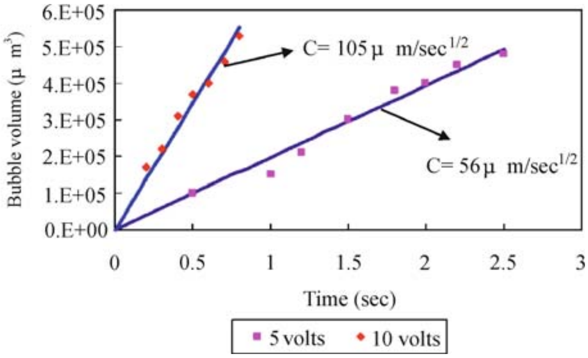

Bubble Actuated Microfluidic Switch, Figure 13 The bubble volume versus the heating period (pulse width) for a 1 × 4 microfluidic switch with the applied voltage of 5 V and 10 V

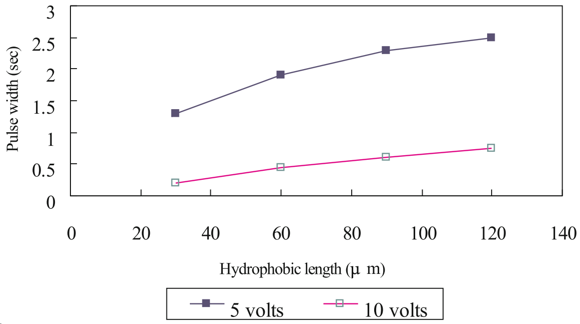

a

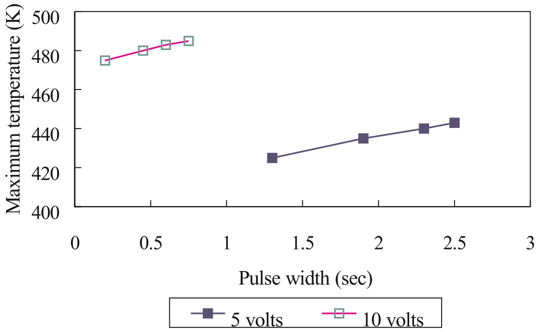

b

Bubble Actuated Microfluidic Switch, Figure 14 (**a**) Heating-pulse width versus length of hydrophobic patches (**b**) Maximum temperature versus heating-pulse width for the capillary system with a 1 × 4 microfluidic switch with the applied voltage of 5 V and 10 V

different microchannels in the case-study device is dominated by controlling the format and timing of power input that generates actuation bubbles. The design, synthesis and bubble control with its time-sequence control logics are presented via a case-study example of 1 × 4 thermal-bubble actuated microfluidic switches.

Future Directions for Research

This bubble actuated microfluidic switch could be effectively used for the one shot of liquid in both single-output and multi-output modes on demand. The reversible motion of the liquid is one further research direction. The long-term goal of this research work could be to develop integrated bio-analytical devices with the functions for specific flow guiding, specific flow injection, and precise liquid volume control.

Cross References

- ▶ Bubble Jet
- ▶ Surface Tension Driven Flow
- ▶ Hydrophilic/Hydrophobic Patterning
- ▶ Thermal Bubbles
- ▶ Bubble Dynamics in Microchannels
- ▶ Bubble Actuated Microfluidic Switch

References

1. Doring C, Grauer T, Marek J, Mettner MS, Trah HP, Willmann M (1992) Micromachined Thermoelectrically driven cantilever structures for fluid jet deflection. In: IEEE Micro Electro Mechanical Systems Workshop (MEM'92), pp 12–18
2. Blankenstein G, Larsen UD (1998) Modular concept of a laboratory on a chip for chemical and biochemical analysis. Biosens Bioelectron 13(3–4):427–438
3. Gebhard U, Hein H, Just E, Ruther P (1997) Combination of a fluidic micro-oscillator and micro-actuator in LIGA-technique for medical application. In: Solid-State Sensors and Actuators (Transducers'97), pp 761–764
4. Lee GB, Hwei BH, Huang GR (2001) Micromachined pre-focused M×N flow switches for continuous multi-sample injection. J Micromech Microeng 11:654–661
5. Lemoff AV, Lee AP (2003) An AC Magnetohydrodynamic Microfluidic Switch for Micro Total Analysis Systems. Biomed Microdevices 5(1):55–60
6. Pollack MG, Fair RB, Shenderov AD (2000) Electrowetting-based microactuation of liquid droplets for microfluidic applications. Appl Phys Lett 77(11):1725–1726
7. Matsumoto H, Colgate JE (1990) Preliminary investigation of micropumping based on electrical control of interfacial tension. In: Proc MEMS, Napa Valley, pp 105–110
8. Verheijen HJJ, Prins MWJ (1999) Reversible electrowetting and trapping of charge: model and experiments. Langmuir 15(20):6616–6620
9. Cheng CM, Liu CH (2006) A Capillary System with Thermal-Bubble-Actuated 1×N Micro Fluidic Switches via Time-Sequence Power Control for Continuous Liquid Handling. J MEMS 15(2):296–307
10. Okamoto T, Suzuki T, Yamamoto N (2000) Microarray fabrication with covalent attachment of DNA using bubble jet technology. Nat Biotechnol 18(4):438–441
11. Maxwell RB, Gerhardt AL, Schmidt MA, Toner M (2003) A Microbubble Powered Bioparticle Actuator. J MEMS 12(5):630–640

12. Ho CT, Lin RZ, Chang HY, Liu CH (2005) Micromachined Electrochemical T-switches for cell sorting applications. Lab Chip 5(11):1248–1258
13. Man PF, Mastrangelo CH, Burns MA, Burke DT (1999) Microfabricated Plastic Capillary Systems With Photo-Definable Hydrophilic and Hydrophobic Regions. In: Solid-State Sensors and Actuators (Transducers'99), pp 738–741
14. Deng P, Lee YK, Cheng P (2003) The growth and collapse of a micro-bubble under pulse heating. J Heat Mass Transf 46(21):4041–4050
15. Stralen SV, Cole R (1979) Boiling Phenomena, vol 1. Hemisphere, Bristol, pp 454–456
16. Tsai JH, Lin LW (2002) Transient thermal bubble formation on polysilicon micro-resisters. J Heat Transf 124(2):375–382
17. Zhao Z, Glod S, Poulikakos D (2000) Pressure and power generation during explosive vaporization on a thin-film microheater. J Heat Mass Transf 43:281–296
18. Jun TK, Kim CJ (1998) Valveless Pumping using Traversing Vapor Bubbles in Microchannels. J Appl Phys 83:5658–5664
19. Bohm S, Olthuis W, Bergveld P (2000) A bi-directional electrochemically driven micro liquid dosing system with integrated sensor/actuator electrodes. In: IEEE MEMS Workshop (MEM'00), pp 92–95

Bubble Dynamics in Microchannels

SATISH G. KANDLIKAR
Gleason Professor of Mechanical Engineering, Rochester Institute of Technology, Rochester, NY, USA
sgkeme@rit.edu

Synonyms

Bubble growth; Explosive Boiling in Microchannels; Confined bubble growth

Definition

Bubble dynamics in a microchannel refers to the nucleation of a bubble on heated flow channel walls and its subsequent interaction with the single-phase or two-phase flow field. ►Subcooled flow boiling refers to the boiling process with the mean flow enthalpy below the saturated liquid enthalpy at the local pressure, while ►saturated flow boiling refers to the boiling process with the mean flow enthalpy at or above the saturated liquid enthalpy but below saturated vapor enthalpy at the local pressure.

Overview

The formation and subsequent growth of a vapor bubble on a heated wall covered with a liquid is controlled by the forces arising from the excess pressure inside the bubble, the surface tension forces at the liquid–vapor interface and at the ►contact line formed by the interface at the heater surface, and the inertia forces resulting from the motion of the flow as well as the interface. The resistance to the phase change process at the liquid–vapor interface is quite small in comparison to the conduction resistance in the liquid surrounding a bubble and is generally neglected in analyzing the bubble dynamics.

Basic Methodology

The bubble dynamics during flow boiling in microchannels has been studied using high-speed video imaging and numerical techniques. The ►nucleation of a bubble and its growth leading to a confined bubble, vapor plug and annular flow have been analyzed under flow boiling studies. The research has primarily been conducted with water and several refrigerants such as R-123 and FC72 as the working fluids.

Key Research Findings

►Nucleation and *bubble growth*. Liquid enters a microchannel in a subcooled state and experiences a rise in temperature, while the local pressure falls due to frictional pressure drop along the channel in the flow direction. At some point downstream, the local saturation condition is reached. However, bubble nucleation will not occur immediately at this location as a certain degree of wall superheat is needed to activate a cavity according to the conditions originally suggested by Hsu [1]. The effect of the receding contact angle and the local flow field in front of a bubble was incorporated and the following equation is recommended [2] for nucleation of minimum and maximum cavity radii, $r_{c,min}$ and $r_{c,max}$:

$$\{r_{c,min}, r_{c,max}\} = \frac{\delta_t \sin\theta_r}{2.2}\left(\frac{\Delta T_{Sat}}{\Delta T_{Sat}+\Delta T_{Sub}}\right) \cdot \left[1 \mp \sqrt{1 - \frac{8.8\sigma T_{Sat}(\Delta T_{Sat}+\Delta T_{Sub})}{\rho_V h_{LV}\delta_t \Delta T_{Sat}^2}}\right] \quad (1)$$

where $\delta_t = k/h$; k – thermal conductivity of the fluid, $W/(mK)$; h – single-phase heat transfer coefficient prior to nucleation; θ_r – receding contact angle of the bubble interface on the microchannel wall; ΔT_{sat} – local wall superheat ($= T_{wall} - T_{sat}$), °C; ΔT_{sub} – local liquid subcooling ($= T_{sat} - T_{fluid}$), °C; σ – surface tension, N/m; h_{LV} – latent heat of vaporization, J/kg; and ρ_V – vapor density, kg/m^3.

The experimental studies of Zhang et al. [3] and Li et al. [4], among others, confirm that the conventional nucleation theories of nucleation and bubble growth are valid for microchannel flows as well. The complex interactions due to nucleation, bubble growth and local heat transfer in

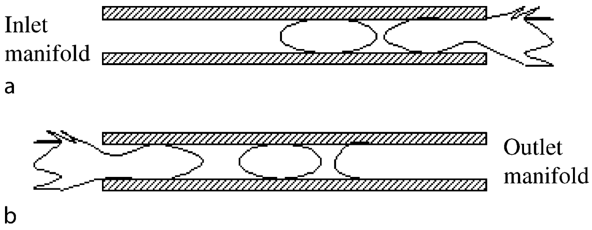

Bubble Dynamics in Microchannels, Figure 1 Flow boiling in microchannels with rapid evaporation leading to reversed flow in (**b**) [2]

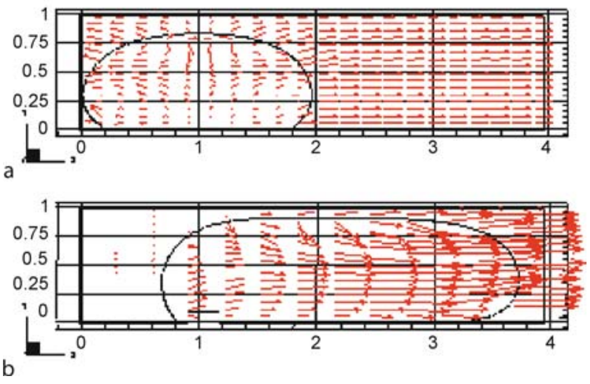

Bubble Dynamics in Microchannels, Figure 2 Bubble interface movement (**a**) without and (**b**) with a flow restrictor on the left side in a 200 μm square microchannel [9]

smooth circular and rectangular glass channels were studied by Yen et al. [5]. Their results showed that the corners in a rectangular microchannel provided nucleation cavities that initiated the boiling process at lower qualities and resulted in a higher heat transfer coefficient.

As a result of the very high single-phase heat transfer coefficients in microchannels, combined with the small radii of available nucleation cavities on the channel walls, the local liquid subcooling could be very low at the inception of nucleation. Under low flow conditions, it may even be negative, indicating that the bulk liquid is in a superheated state at the location of bubble nucleation [2]. The resulting rapid evaporation at the bubble interface raises the local pressure, creating a condition for fluid backflow. Experimental and numerical studies available in the literature indicate that the instability is predominant at the low heat fluxes [6, 7]. Figure 1 shows the effects of the explosive nature of the bubble growth under high liquid superheat conditions at the onset of nucleate boiling. If the nucleation occurs near the entrance region, the liquid vapor mixture is pushed back into the inlet manifold causing flow instabilities due to vapor condensation in the inlet manifold. If the nucleation occurs near the exit of the channel, the explosive growth propels the forward interface of the expanding bubble into the exit manifold. Backflow is prevented because of the inertia and frictional resistance in the microchannel prior to the nucleation site.

The flow instabilities due to nucleation and explosive bubble growth can be prevented by incorporating a flow restrictor at the inlet to each channel [2, 8]. Mukherjee and Kandlikar [9] analyzed the bubble growth process numerically. Their results, shown in Fig. 2, confirmed that the backflow of the interface can be substantially reduced by controlling the flow resistance at the inlet of the microchannel.

The ▶flow patterns observed in the microchannels are largely similar to those observed in the conventional sized channels. However, the range of conditions and their transitions are somewhat different in microchannels than those observed in conventional sized channels. The influence of heat flux is more apparent during flow boiling in microchannels as compared to the adiabatic two-phase flows. As the bubbles are nucleated, they grow rapidly because surrounding liquid is superheated and the volume of the subcooled or lower temperature bulk core is limited due to small channel dimensions. The bubbly flow therefore does not exist for any appreciable length. The rapid growth of a bubble following its nucleation causes a succession of expanding vapor plugs that are separated by thinning liquid slugs. Eventually the flow assumes an annular flow pattern. Kandlikar [10] modeled the heat transfer process as an extension of pool boiling, in which the microchannel surfaces act as a bubble base that is periodically swept by rapidly moving liquid–vapor interface. This model is supported by the strong dependence of heat transfer coefficient on the heat flux experimentally observed at lower mass fluxes. Several investigators have applied the annular flow model, but prediction of the liquid film thickness poses considerable difficulties. There is a need for experimental data covering wider ranges of heat and mass fluxes and channel geometries for validating these models before they can be successfully applied to practical cases of interest.

Future Directions for Research

Bubble dynamics in microchannels is of great interest in a number of applications, including microchannel evaporators, high-flux heat removal systems for chip cooling applications, ink-jet printers, atomization nozzles and bubble pumps. The high heat transfer coupled with multidimensional heat conduction in the channel wall, and the rapid growth of the bubble at the microscale make it difficult to verify the analytical models. Future research is needed in understanding the heat transfer mechanism

during bubble growth. In this regard, the presence of a ► microlayer, if present, and its thickness and evaporation rate are areas where fundamental understanding is lacking.

Cross References

- ► Boiling and Evaporation in Microchannels
- ► Bubble Actuated Microfluidic Switch
- ► Cavitation in Microdomains
- ► Droplet Dispensing
- ► Flow Boiling Instability
- ► Heat Transfer in Microchannel Flows

References

1. Hsu YY (1962) On the Size Range of Active Nucleation Cavities on a Heating Surface. J Heat Transf 84:207–216
2. Kandlikar SG (2006) Nucleation Characteristics and Stability Considerations during Flow Boiling in Microchannels. Exp Thermal Fluid Sci 30:441–447
3. Zhang L, Wang EN, Goodson KE, Kenney TW (2005) Phase Change Phenomena in Silicon Microchannels. Int J Heat Mass Transf 48:1572–1582
4. Li HY, Tseng FG, Pan C (2004) Bubble Dynamics in Microchannels. Part II: Two Parallel Microchannels. Int J Heat Mass Transf 47:5591–5601
5. Yen T-H, Shoji M, Takemura F, Suzuki Y, Kasagi N (2006) Visualization of Convective Heat Transfer in Single Microchannels with different Shaped Cross-sections. Int J Heat Mass Transf 49:3884–3894
6. Kandlikar SG, Steinke ME, Tian S, Campbell LA (2001) High-Speed Photographic Observation of Flow Boiling of Water in Parallel Minichannels. In: 35th Proceedings of National Heat Transfer Conference, June 2001, Anaheim, CA. Paper # NHTC01-11262. ASME Publications, New York
7. Qu WL, Mudawar I (2004) Transport Phenomena in Two-Phase Micro-channel Heat Sinks. J Electron Packag 126(2):213–224
8. Kosar A, Kuo C, Peles Y (2005) Reduced Pressure Boiling Heat Transfer in Rectangular Microchannels with Interconnected Reentrant Cavities. J Heat Transf 127:1106–1114
9. Mukherjee A, Kandlikar SG (2005) Numerical simulation of growth of a vapor bubble during flow boiling of water in a microchannel. Microfluid Nanofluid 1(2):137–145
10. Kandlikar SG (2002) Fundamental Issues Related to Flow Boiling in Minichannels and Microchannels. Exp Thermal Fluid Sci 26(2-4):389–407

Further Reading

- Kandlikar SG, Garimella S, Li D, Colin S, King MR (2005) Heat Transfer and Fluid Flow in Minichannels in Minichannels and Microchannels. Elsevier, Oxford
- Zhang L, Goodson KE, Kenny TW (2004) Silicon Microchannel Heat Sinks. Springer, Berlin/Heidelberg

Bubble Formation

► Cavitation

Bubble Growth

► Bubble Dynamics in Microchannels

Bubble Jet

Definition

The functional principle of a thermal *bubble jet* printhead is based on a current pulse applied to a microheater which leads to a very short heating pulse at the solid–liquid interface. This heating pulse leads to a small vapor bubble which expands explosively. The increasing vapor bubble leads to a volume displacement of the ink towards the nozzle and finally to a droplet ejection. The detaching of the vapor bubble from the hot surface results in a concurrent cooling down of the bubble which results in condensation and collapse of the bubble. The suction of the collapsing bubble and the capillary forces inside the printhead lead to refilling of the nozzle chamber that it is finished before the next shot after approximately 10 μs. The fast explosion of the bubble leads to a characteristic pressure behavior inside the liquid. Starting instantaneously with a very high pressure of about 7 MPa to 9 MPa right at the beginning of the vaporization, the pressure decreases exponentially during a few microseconds.

Cross References

- ► Bioprinting on Chip
- ► DNA Micro-arrays
- ► Droplet and Bubble Formation in Microchannels
- ► Droplet Based Lab-on-Chip Devices
- ► Electrowetting and Droplets
- ► Inkjet
- ► Piezoelectric Microdispenser
- ► Thermal Bubble

Bubble Train Flow

► Taylor Flow in Microchannels

Bulk Materials

► Materials Used in Microfluidic Devices

Bulk Micromachining

CHE-HSIN LIN
Department of Mechanical and Electromechanical Engineering, National Sun Yat-sen University, Kaohsiung, Taiwan
chehsin@mail.nsysu.edu.tw

Synonyms

Bulk micromachining of silicon; Anisotropic silicon micromachining

Definition

Bulk micromachining (BMM) is a set of processes that enable the 3D sculpting of various materials (mainly silicon) to make small structures that serve as components for MEMS devices. Bulk micromachining builds mechanical elements by starting with a bulk material, and then etching away unwanted parts, and being left with useful mechanical devices. Typically, the substrate is ▶ photo–patterned, leaving a protective layer on the parts of the substrate that are to be retained. The substrate is then etched using a ▶ wet chemical etch process, ▶ dry chemical etch process, reactive plasma etch process or photo-etch process. The etch process "eats away" any exposed substrate material on the substrate. Bulk micromachining is a relatively simple and inexpensive fabrication technology to fabricate a micromachined device. It is especially well suited for applications that require only simple microstructures like microchannels, microcavities and free-standing microstructures such as micro-pit or micro-tip.

Overview

Bulk micromachining makes 3D micromechanical devices by etching deeply into a bulk material such as silicon, quartz, glass, plastic or even metal, where silicon and glass are the most common materials used in MEMS technology. These processes have been broadly applied in the fabrication of micromachined sensors, actuators, transducers and some functional structures. In practical applications, single-crystalline silicon is the most popular substrate to be used as the bulk material for bulk micromachining processes. The excellent electrical and mechanical properties of single-crystalline silicon make it a desirable material in the MEMS field and semiconductor industry. On the other hand, glass-based materials have also been extensively used in fabricating microfluidic channels for bioanalytical applications due to their low price and excellent material properties. These two materials have become the major materials for microfluidic and nanofluidic applications. They have also led to a focus on the development of different machining technologies to fabricate functional microfluidic devices in these two materials.

Table 1 summarizes the basic fabrication characteristics for these materials. Because of the rapid growth of the semiconductor industry, silicon has become one of the best-known materials in the world and can be obtained as a single-crystal structure at a reasonable price. The rapid growth of the demand for miniaturized devices also makes single-crystalline silicon the most popular material for bulk micromachining processes. However, silicon substrate is opaque in the UV-visible wavelength range such that it is difficult to observe micro- or nanofluids inside the fabricated microdevices. Also, the fabrication process is comparatively delicate and expensive even though the techniques for machining silicon substrates have been well developed, and there are plenty of tools to machine silicon into various kinds of structures.

Alternatively, silica-based devices are also important in micro- and nanofluidics since they provide advantages over other materials, including high chemical resistance and mechanical strength, large optical transmission range and good electrical insulation. Silica-based materials also have good biocompatibilities for most living cells. These materials in their native state have Si–OH functional groups on their surface, which provide an easy way to chemically modify the surface properties. However, silica-based materials such as quartz and borofloat glass are relatively expensive and rare in compare with general-purpose glass slides. These materials also have a low etch rate in hydrofluoric acid (HF)-based etchants. They also require expensive etching masks such as metal/polysilicon/nitride layer. Alternatively, soda-lime glass has several advantages over borofloat glass and quartz. The cost is much lower and the fabrication process is also much simpler and cheaper. The only drawback is that the impurities in the soda-lime glass is much more than the quartz and borofloat glasses, which may produce insoluble precipitates during etching process. In general, the amorphous structure of glass-based results in an isotropic etching pattern during wet chemical etching. As a result, the aspect ratio of the patterned structures is typically less than 0.5, which could limit their use for high-aspect-ratio microfluidic applications. Microfabrication of miniature analytical instruments on glass substrates for chemical and biomedical application has recently been widely studied. Various microfluidic devices have been fabricated on planar glass and quartz chips for μ-TAS such as capillary electrophoresis, electrochromatagraphy, DNA separations and semen testing. Planar glass chips fabricated by micromachining technologies meet the requirements of miniaturized total analysis

Bulk Micromachining, Table 1 Characteristics of typical materials for bulk micromachining in MEMS field

	Silicon	Quartz	Glass
Transparency	No	Yes	Yes
Cost	High	High	Low
Fabrication technique	Delicate	Cheap but difficult	Cheap, easy
Bonding method	Anodic, Fusion	HF, Adhesive, Sodium silicate	Fusion, Adhesive, Sodium silicate
Surface modification	Moderate – Easy	Easy	Easy
Biocompatibility	Fair	Good	Good
Surface property	Hydrophobic	Hydrophilic	Hydrophilic
Structure aspect ratio	Wide range	Typically < 0.5	Typically < 0.5

systems. Considerable attention is now directed towards how to simplify, reduce the cost and reduce the time of the manufacturing processes.

In this article, bulk micromachining techniques for fabricating microfluidic devices in silicon and glass materials are summarized. The details of the fabrication characteristics and fabrication protocols are described.

Basic Methodology

Bulk Micromachining of Silicon-Based Materials

Bulk micromachining of silicon uses wet- or dry-etching techniques in conjunction with etch masks and etch-stop techniques to sculpt a microstructure from the silicon substrate. The purpose of silicon bulk micromachining is to selectively remove significant amounts of silicon from a substrate to fabricate 3D structures in bulk micromachined silicon. The available etching methods fall into three categories in terms of the state of the etchant: wet, vapor and plasma. Wet chemical etch is the most popular method among these techniques due to the process being cheap and easy. However, the geometries of etched features using the wet chemical etching technique are usually greatly corresponding to the crystal orientation of the silicon substrate. The etch rate of dry etching may depend on the selected etching recipe and the etching mechanism of the equipment. In general, silicon wafers are usually cut to give top surfaces that roughly correspond to the main crystal planes in silicon given by the Miller indices (100), (110) and (111). Figure 1 shows the geometrical shape of a wafer and the crystal direction and polarity. For microfluidic and nanofluidic purposes, (100) wafers are the most popular because of the possibilities for the crystallographic-dependent wet etching.

Wet bulk micromachining was first developed in the Bell Telephone Laboratories in the mid-1960s. Anisotropic etching of silicon was achieved in a wet chemical solution composed of KOH, alcohol and water. Bulk micromachining using chemical and electrochemical etching processes

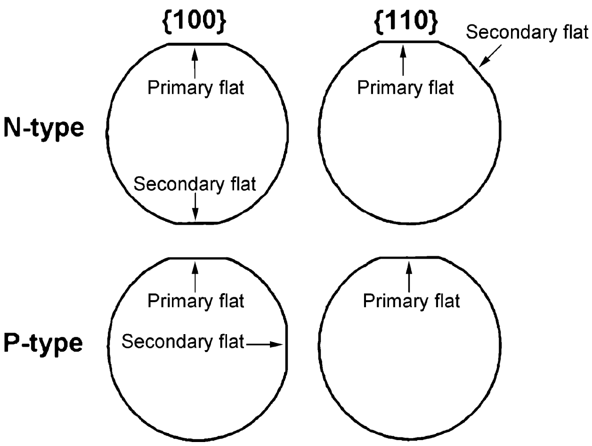

Bulk Micromachining, Figure 1 The geometrical shape of a wafer reveals the crystal direction and polarity

was pursued and became an extension of IC technology for the fabrication of 3D structures [1]. There are two major strategies, isotropic etching (crystal orientation independent) and anisotropic etching (crystal orientation dependent), adopted for this process. Figure 2 illustrates the possible features of the cross-section of a water substrate created using isotropic (Fig. 2a) and anisotropic (Fig. 2b) etching techniques. In general, the etched side wall is in round feature for a channel fabricated using ►isotropic etching since the etch rates in all directions are equal. However, a shallow dish-like feature would be obtained if the agitation during etching process is poor. On the other hand, the features created using ►anisotropic etching typically exhibit perfectly flat surfaces and are well defined. V-groove, U-groove and pyramidal pits can be fabricated with this approach. One can also form a famous feature of 54.74° sidewall while anisotropic etching (100) silicon. Figure 3 presents the typical structures which can be fabricated in (100) silicon using the anisotropic etching technique. The chemical reactions of wet etching rely on the oxidation of silicon to form compounds that can be physi-

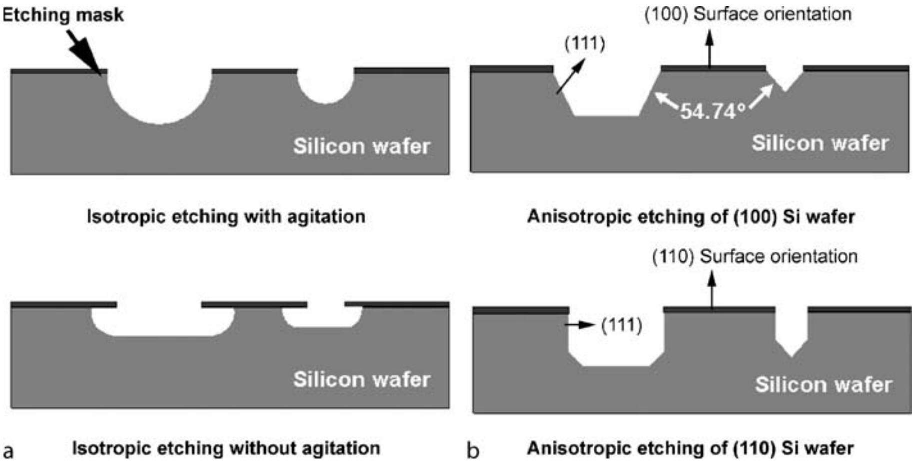

Bulk Micromachining, Figure 2 The possible features of the cross-section of a water substrate created using isotropic (**a**) and anisotropic (**b**) etching techniques

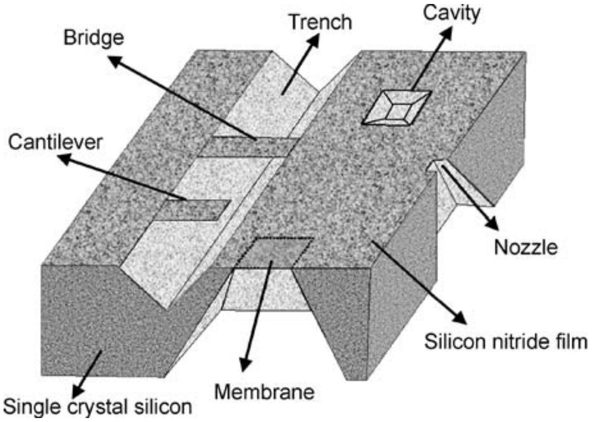

Bulk Micromachining, Figure 3 Typical structures which can be fabricated in single-crystal silicon using the anisotropic etching technique

cally removed from the substrate. The etching characteristics of the etching result are defined by the compositions of the etching chemicals, the material exchange rate of reactants and products, and some other minor factors. These include the temperature of the etching solution, the existence of additives and the shapes of the masks used to define the etched regions [2]. Table 2 provides a generalized comparison of the various etchants in terms of many of these important properties [3]. An excellent review article describing the techniques for silicon bulk micromachining can be found in Ref. [3].

Isotropic Etching of Silicon

HNA is the most popular etchant for silicon isotropic etching. The etchant is usually composed of hydrofluoric acid (HF)/nitric acid (HNO_3)/acetic acid (CH_3COOH) with a volume ratio of 1:3:8. Regarding the chemical reaction mechanism, silicon is firstly oxidized by nitric acid to form silicon oxide which is then etched away by hydrofluoric acid. Acetic acid in the recipe acts as the diluent which is essential for achieving the reaction. Water can also be used to dilute the mixture of HF and HNO_3, but this leads to dissociation of nitric acid and significantly reduces the etching speed. The rate-determining reaction of the HNA etching process is the oxidation of silicon. Therefore, increasing the ratio of nitric acid in the HNA solution will increase the reaction rate of the process. However, the surface will be slightly rougher in comparison with the surface etched using a normal HNA solution. Some negatively charged additives such as bromide, iodine or CrO_3^- can be used to reduce the surface roughness. Note also that the HNA isotropic etch is sensitive to the doping concentration of the silicon substrate. The etch process is slowed down in rate about 150 times by regions of light doping ($10^{17}\,cm^{-3}$ n- or p-type) relative to more heavily doped regions [4, 5]. The overall reaction can be expressed as:

$$6HF + HNO_3 + Si \rightarrow H_2SiF_6 + HNO_2 + H_2O + H_2$$

Anisotropic Etching of Silicon

The most often used etchant for silicon anisotropic etching is KOH. The recipe is often mixed with isopropyl alcohol (IPA) to saturate the solution to increase the etch selectivity for (111) versus (100) planes. Generally, the etch selectivity on the (111) plane can be up to 400 times slower than on the (100) plane while using alkali hydroxide solutions as etchants for silicon anisotropic etching. In addition, the etch rate for KOH anisotropic etching

Bulk Micromachining, Table 2 Basic fabrication characteristics of typical materials in MEMS field

	Comparison of Example Bulk Silicon Etchants						
	HNA (HF + HNO_3 + Acetic Acid)	Alkali-OH	EDP (ethylene diamine pyrochatechol)	TMAH (tetramethylammonium hydroxide)	XeF_2	SF_6 Plasma	DRIE (Deep Reactive Ion Etch)
Etch Type	wet	wet	wet	wet	dry[1]	dry	dry
Anisotropic	no	yes	yes	yes	no	varies	yes
Availability	common	common	moderate	moderate	limited	common	limited
Si Etch Rate $\mu m/min$	1 to 3	1 to 2	0.02 to 1	~ 1	1 to 3	~ 1	~ 1
Si Roughness	low	low	low	variable[2]	high[3]	variable	low
Nitride Etch	low	low	low	1 to 10 nm/min	?	low	low
Oxide Etch	10 to 30 nm/min	1 to 10 nm/min	1 to 80 nm/min	~ 1 nm/min	low	low	low
Al Selective	no	no	no[4]	yes[5]	yes	yes	yes
Au Selective	likely	yes	yes	yes	yes	yes	yes
P^{++} Etch Stop?	no (n slows)	yes	yes	yes	no	no (some dopant effects)	no
Electrochemical Stop?	?	yes	yes	yes	no	no	no
CMOS Compatible?[6]	no	no	yes	yes	yes	yes	yes
Cost[7]	low	low	moderate	moderate	moderate	high	high
Disposal	low	easy	difficult	moderate	N/A	N/A	N/A
Safety	moderate	moderate	low	high	moderate	high	high

[1] Sublimation from solid source.
[2] Varies with wt% TMAH, can be controlled to yield very low roughness.
[3] Addition of Xe to vary stoichiometry in F or Br etch systems can yield optically smooth surfaces.
[4] Some formulations do not attack Al, but are not common.
[5] With added Si, polysilicic acid or pH control.
[6] Defined as 1) allowing wafer to be immersed directly with no special measures and 2) no alkali ions.
[7] Includes cost of equipment.

of silicon is highly dependent on the concentration and the temperature of KOH. A concentration in the range of 40–[%wt]50 and temperature in the range of $70-80\,°C$ are typically adopted for the KOH etch process. Note that concentrations below [%wt]20 are not used due to high surface roughness and the formation of potential insoluble precipitates.

The reaction mechanism of the etch process is not fully clear. Several researchers proposed physical models for silicon anisotropic etching from the viewpoints of energy band gap [4, 5] and Gibbs free energy [6]. Over these models, one equation describing the simplified reaction mechanism is addressed as follow:

$$Si + 2OH^- + 2H_2O \rightarrow SiO_2(OH)_2^{2-} + 2H_2$$

Impurity doping can also be applied for slowing down the etch rate for silicon anisotropic etching in alkali hydroxide solutions. The etch rate was drastically slowed down in regions doped with boron to a concentration of $2\times10^{19}\,cm^{-3}$ [7]. However, fabricating microstructures of complex and arbitrary geometry is very difficult since the geometry of the microstructure fabricated using anisotropic etching process is limited by the crystal orientation. In order to overcome this drawback, an advanced deep etching technique utilizing high-density plasma and a wafer bonding process were developed. Reactive ions can perform consecutive etching of Si wafers up to a depth of a few hundred micrometers, while maintaining smooth vertical sidewall profiles. The other technology, wafer bonding, permits a Si substrate to be attached to another substrate, typically Si or glass. Three-dimensional complex microstructures can be achieved with this combination [3].

Figure 4a presents photo images of a micro gas sensor array fabricated using wet bulk micromachining, a typi-

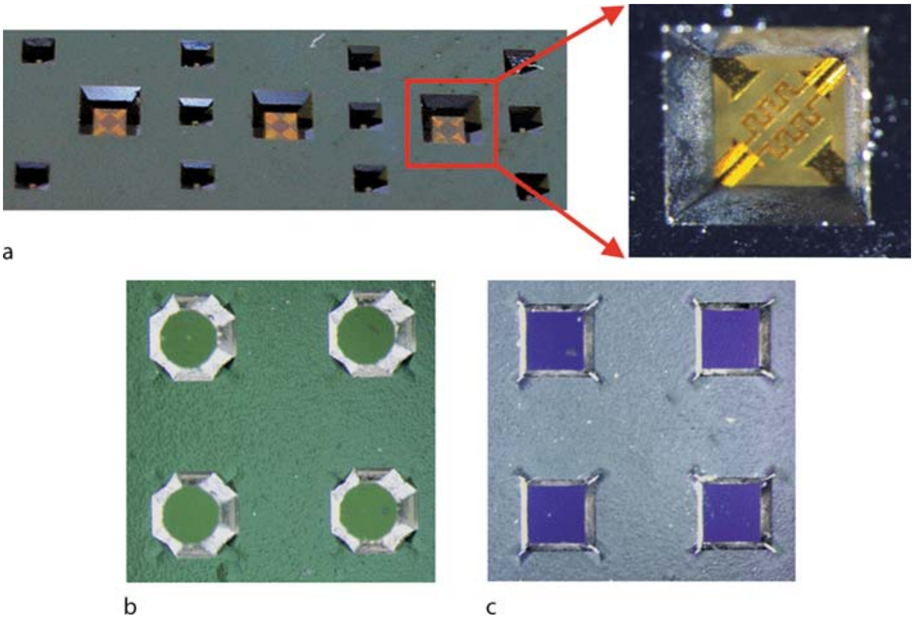

Bulk Micromachining, Figure 4 (**a**) Micro gas sensor array comprising micro-hotplates. (**b**) Etched mesa structures without convex corner compensation mask. (**c**) Etched mesa structures with convex corner compensation mask

cal application of silicon bulk micromachining. A micro gas sensor array comprising micro-hotplates with Pt resistance heaters was fabricated on a suspension silicon nitride film of 2 μm in thickness. The inset shows a close-up picture of a micro gas sensor. A wet bulk micromachining process was used to sculpt the silicon structure under the suspension micro-hotplates in order to eliminate thermal conduction and reduce thermal budget during operation. In addition to the cavity structure, mesa structures with convex corners are usually fabricated using wet bulk micromachining. However, convex corners where (111) planes meet are not stable during silicon anisotropic etching. These convex corners are rapidly undercut along {212} planes and other exposed unstable planes. Figure 4b shows the etched mesa structures with convex corner attacking features. This problem can be easily solved using corner compensation masks which preserve convex corners during the wet etching process. Figure 4c shows the etched mesa structures with the corner compensation design. A sharp convex corner was preserved after the etching process. On the other hand, undercut at convex corners also permits the creation of suspended structures such as cantilever beam and bridge structure. One special case for undercut of silicon substrate in anisotropic etch is mask misalignment. Mask misalignment with respect to the crystal lattice will result in uneven undercutting since the etching will proceed along crystal planes. The effect of misalignment is to enlarge the etched region. In general, if etched long enough, any mask-layer feature will result in a rectangular V-groove pit beneath a rectangular shape that is tangent to the mask features. Furthermore, the edges of the formed rectangular are oriented along ⟨110⟩ directions. A number of commercial and home-built computer simulation software packages have been developed to predict the etched pattern for silicon anisotropic etch [8].

Bulk Micromachining of Glass-Based Materials

Bulk micromachining of glass-based materials is a simple, fast and low-cost way to fabricate planar microfluidic devices. Here we present a fast process for bulk micromachining the glass-based materials especially for ►soda-lime glass. Rather than using a time-consuming vacuum deposition process to fabricate the mask required to etch the plates in an HF-based etchant, a 3 μm thick AZ4620 photoresist layer can be used as the masking material in the wet chemical etching process. An excellent surface quality can be obtained by an improved etching procedure. We also describe a shorter thermal bonding process without sophisticated polishing and cleaning procedures. A high bonding yield is obtained by using sintered alumina flats as the upper and underlying supports. This simple fabrication method will enable fabrication of microfluidic structures in an efficient way. The major contributions of the method is a novel process to remove the formed participant during the wet etching pro-

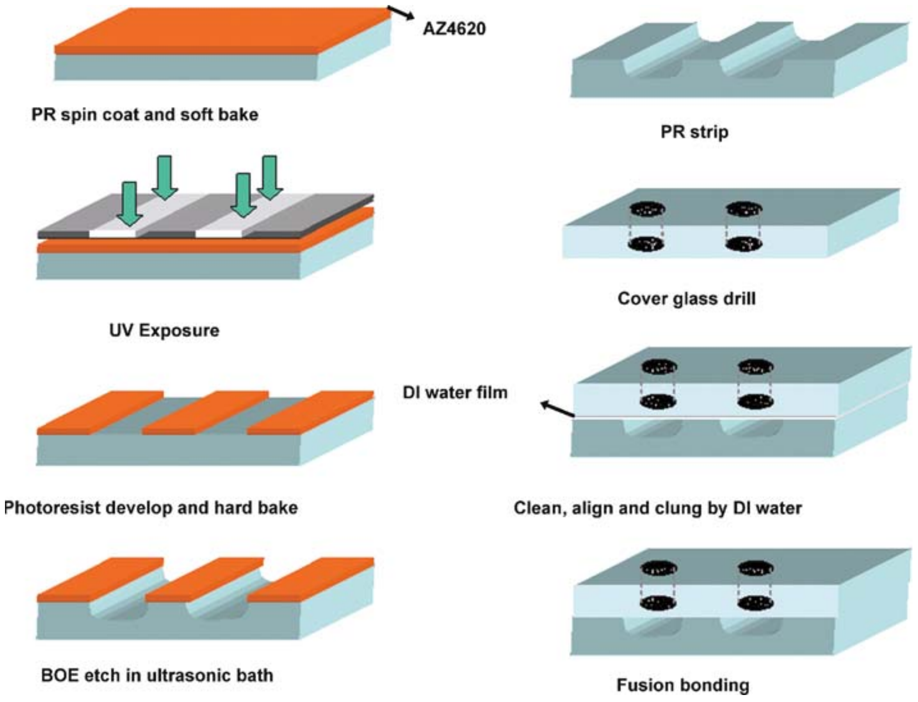

Bulk Micromachining, Figure 5 A simplified overview of the fabrication process which was used to form planar microfluidic channels on glass substrates

cess and a two-step baking process to prolong the survival time of the photoresist etch mask in the etchant. In the following we describe the details of the proposed method.

Soda-lime glass is a multicomponent mixture of SiO_2 (72.8%), Na_2O (13.7%), CaO (8.8%), MgO (4.0%) and small amounts of Fe_2O_3 (0.12%) and Al_2O_3 (0.1%). Insoluble products will be present and crystalline precipitates will be formed while etching soda-lime glass in HF-containing solution [10]. Since K_{sp} (solubility product constant at 25 °C) values of CaF_2 and MgF_2 are 4.0×10^{-11} and 6.4×10^{-9}, respectively, it is believed that most insoluble products are mainly CaF_2 and MgF_2. In order to solve the problem, 1 M HCl solution can be used to turn the precipitates into soluble products of $CaCl_2$ and $MgCl_2$. The equation below describes the chemical reaction for glass-based materials etched using HF-based etchants. The etch rate is about 0.9 µm/min for soda-lime glass etched in buffered HF solution (BOE, buffered oxide etchant) at room temperature and, with undoubtedly, the etching is isotropic inherently:

$$6HF + SiO_2 \rightarrow H_2SiF_6 + 2H_2O$$

In general, polished soda-lime glass or commercial microscope glass slides are preferred for this process. Note that the glass slides need to be annealed at 400 °C for 4 hours to relieve the residual stress inside the slides prior to the fabrication process. Otherwise, needle-like structures may form on the etched surface due to the stress corrosion effect, which may blur the glass and result in a rough surface. The simplified schematic for the fabrication process is shown in Fig. 5. The following describes the details of the fabrication process for wet bulk micromachining of microfluidic device in soda-lime glass [9].

Substrate Cleaning The glass substrates were firstly cleaned in a boiling Piranha solution (H_2SO_4 [%] : H_2O_2 [%] = 3 : 1; *Caution: Piranha solution is a very strong oxidant and is severely exothermic during reaction: it should be handled with extreme care*) for 10 min, then rinsed in DI water and blown-dry with nitrogen gas or CDA (clean dry air). The dehydration process was done by baking the glasses on a hot plate (100 °C) for 3 min to remove residual water molecules.

Lithography The glasses were then spin-coated with HMDS solution and baked on a hot plate (100 °C) for 3 min in order to improve the adhesion of the PR. The primer-treated substrates were coated with AZ 4620 positive PR, and a novel two-step baking process was used in this study. First, a soft-baking process was carried out

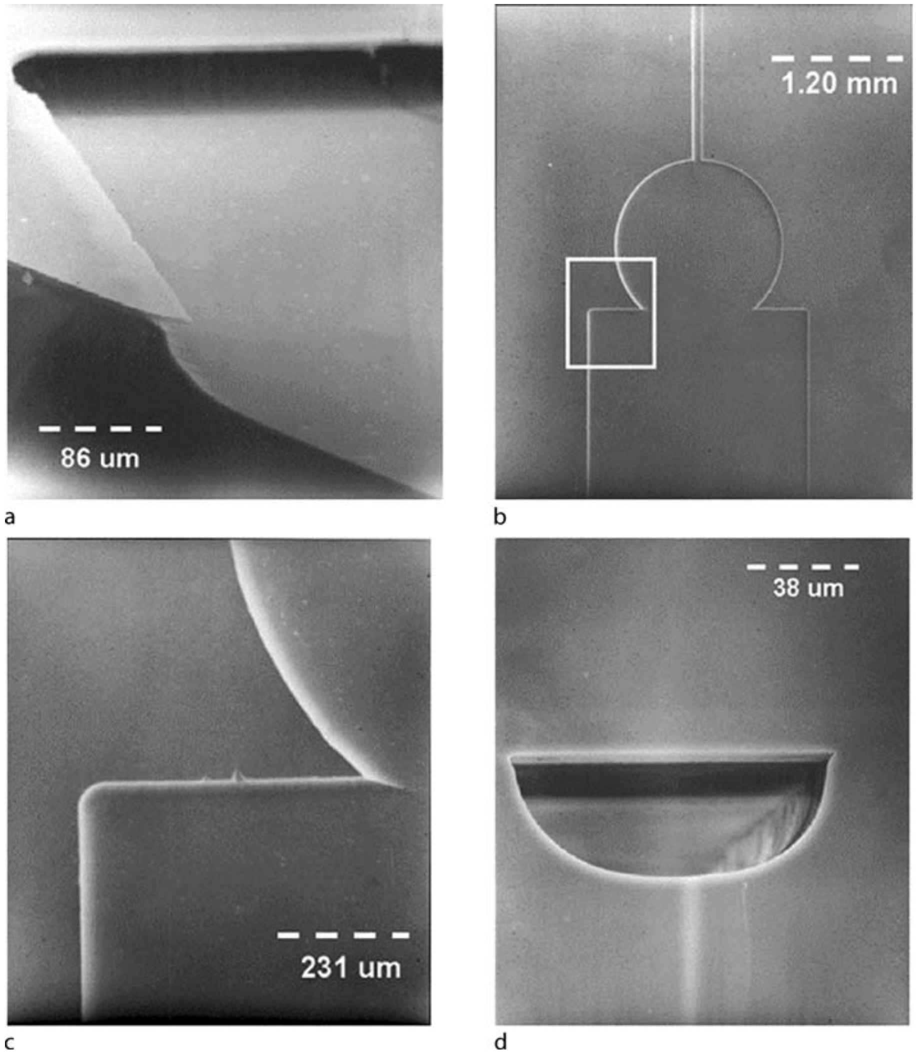

Bulk Micromachining, Figure 6 SEM images of the fabrication results of the proposed method. (**a**) Etched glass surface with PR etch mask. (**b**) After removing the PR mask. (**c**) Close-up view of a sharp corner. (**d**) Cross-sectional view of the sealed microfluidic channel after fusion bonding

at 100 °C for 1 min, 120 °C for 1.5 min, and then maintained at 100 °C for another 1 min. This two-step process can reduce the thermal stress between the glass substrate and the PR, resulting in longer survival time of the positive PR in BOE etchant. The thickness of the PR was approximately 3 μm after soft-baking. The UV lithography was carried out using a mask aligner and exposure dose was 180 mJ/cm^2. The developing of the PR was accomplished in 70 s by immersing the exposed substrate into the developer (one part AZ A400K developer : three parts DI water). After rinsing with DI water and blown-dry by N_2 gas, hard-baking of the PR was carried out at 120 °C for 1 min, 145 °C for 10 min, and then returned to 120 °C for 1 min.

Glass Etching After baking of the PR, the glass substrates were immersed in the BOE (6:1) etchant. The etching was done in an ultrasonic bath. In order to remove precipitated particles, we interrupted the etching process every 5 min and dipped the substrates in a 1 M HCl solution for 10 s during the etching process. After the HCl dipping, the substrates were then cleaned by dipping in DI water and then immersed into BOE etchant again. The etching and de-precipitation processes were iterated until the etching process was finished.

Glass Bonding The etched glass substrate and another cover glass with drilled via-holes were cleaned using boiling Piranha solution for 10 min and then rinsed by DI

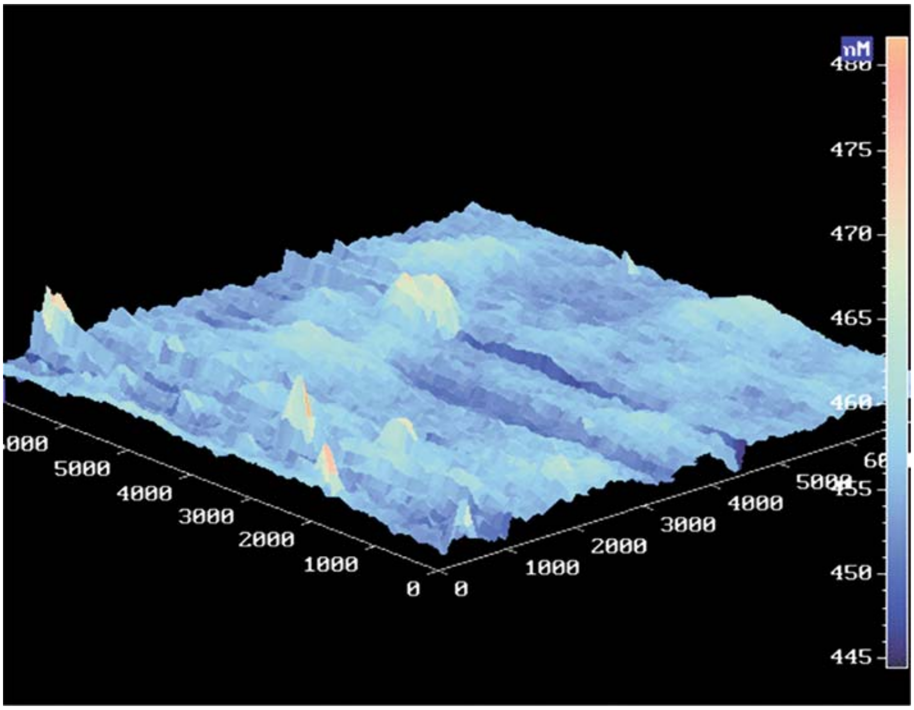

Bulk Micromachining, Figure 7 The surface profile of an etched glass substrate by using an atomic force microscope

water in ultrasonic bath for 3 min. The two glass flats were then carefully aligned and clung to each other by DI water. The atmospheric pressure will hold the two glasses tightly prior to ► thermal fusion bonding process. Bonding was performed by fusing the two glass substrates in a sintering oven at 580 °C for 20 min with a ramp rate of 5 °C/min. Polished alumina flats were stacked as upper and underlying plates which prevented the formation of fusion between glass substrate and alumina flats and kept the glass surface smooth. A sealed microfluidic device could be formed after bonding of the two glass plates.

Figure 6 shows SEM images of the fabrication results of the proposed method. Figure 6a is the etched glass substrate with PR etch mask. The feature of isotropic etching with an undercut structure of the glass substrate can be clearly seen. An etched microfluidic channel and a reservoir structure after removing the PR etch mask are shown in Fig. 6b. An etched microfluidic channel with a sharp geometry and smooth etched surface structures was observed. The close-up image of the inset in Fig. 6b is shown in Fig. 6c. It indicates that the edge of the sidewall is well defined due to good adhesion of PR on the glass substrate. Figure 6d shows a cross-sectional view of the bonded channel. The etched channel remained its original shape and the interface between the two glass substrates disappeared after the fusion bonding process. The bonding process can seal microfluidic channels of up to 3 mm in width without collapsing. It is also found that bonding temperature and holding time are the major factors for the fusion bonding process. Applied pressure and temperature ramping procedure only have minor effects on bonding quality. Temperature below 570 °C caused an incomplete bonding even though two plates were held for a long period of time. While temperature was higher than 580 °C and holding time was longer than 30 min, it resulted in fusion of the glass substrates and the alumina plates, causing cracking of the device due to the difference of the thermal expansion coefficients of the two materials. The bonding process can reduce the operation time, and, more importantly, preserve the original geometry of the etched channel with large area.

The depth and the surface roughness of the etched glass substrates were measured using a surface profilometer (Alpha-step 500). Three different locations on each glass substrate were measured. The average depth of the etched channels is 35.95 μm and the standard deviation is 0.39 μm for all 30 measured values. The etch rate is about 0.9 μm/min at room temperature and the etching is isotropic inherently. The high etch rate and uniformity of the wet etching process was due to the

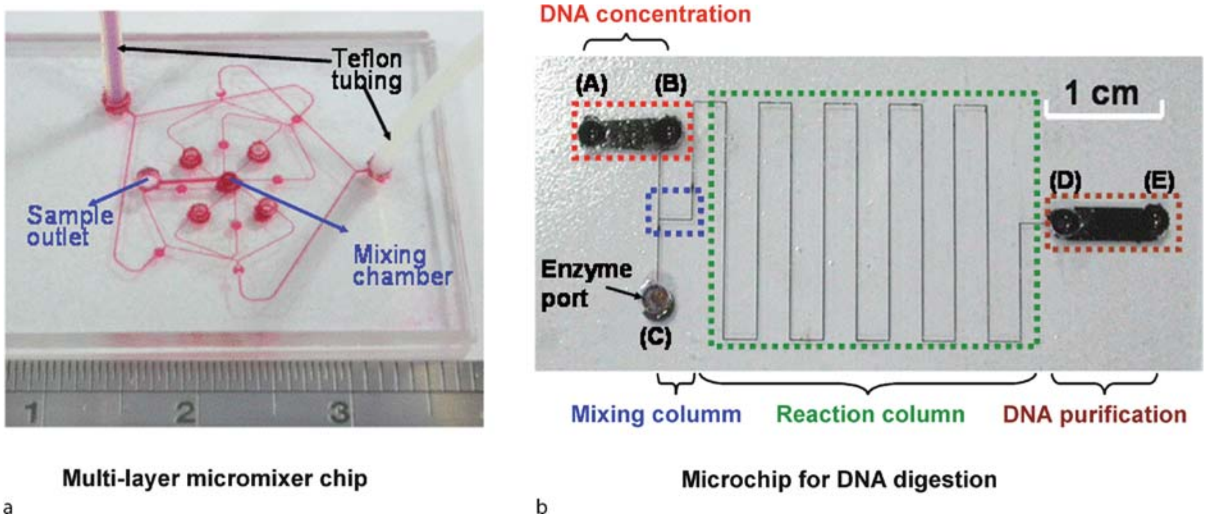

Bulk Micromachining, Figure 8 Optical images of two microfluidic devices fabricated using the proposed fabrication process. (**a**) Microfluidic vortex mixer. (**b**) Microfluidic chip for rapid DNA digestion and purification

fact that appropriate agitation was achieved by performing the etching process in an ultrasonic bath. Furthermore, ultrasonic agitation will make the insoluble precipitate, such as Al_2O_3, suspend in the solution instead of being deposited on the glass substrates. Figure 7 shows the surface profile of an etched glass substrate by using a scanning probe microscope (Solver P7LS). The maximum peak-to-peak roughness is around 0.71 Å and the average surface roughness (R_a) is less than 0.1 Å inside a 3.0 μm × 5.0 μm scanned area. Figure 8 shows the optical images of two microfluidic devices fabricated using the proposed fabrication process. Figure 8a is a microfluidic vortex mixer fabricated in a three-layer glass substrate and Fig. 8b shows a microfluidic chip for rapid DNA digestion and purification. It is observed that the fabricated microfluidic devices have good surface flatness and good optical transmittance which are beneficial for optical detection afterwards. This simple fabrication process is suitable for fast prototyping and mass production of the microfluidic systems in low-cost glass substrates.

Future Directions for Research

The anisotropic wet etching of silicon is a unique fabrication process in the MEMS field. The need to develop new processes to fabricate functional 3D microstructures in various materials is urgent for progress in microfluidic systems, micro-sensors, micro-actuators and micro-instrumentation. At present, to integrate surface micromachined devices and standard IC devices with bulk micromachined structures to demonstrate a new functional MEMS application is still a challenge for researchers who work in this field. The cooperation of multidisciplinary researchers will be required to develop miniature systems with the most appropriate building philosophy and the best operation performance.

Cross References

- ► Anisotropic Etching
- ► Isotropic Etching
- ► Laser Based Micromachining
- ► Micromolding
- ► Silicon Micromachining

References

1. Madou MJ (2002) Chapter 4 Fundamentals of Microfabrication: The Science of Miniaturization. CRC Press LLC, Florida
2. Petersen KE (1982) Silicon as a mechanical material. Proc IEEE 70(5):420–457
3. Kovacs GTA, Maluf NI, Petersen KE (1998) Bulk Micromachining of Silicon. Proc IEEE 86(8):1536–1551
4. Seidel H, Csepregi L, Heuberger A, Baumgartel H (1990) Anisotropic etching of crystalline silicon in alkaline solutions I: Orientation dependence and behavior of passivation layers. J Electrochem Soc 137(11):3612–3626
5. Seidel H, Csepregi L, Heuberger A, Baumgartel H (1990) Anisotropic etching of crystalline silicon in alkaline solutions II: Influence of dopants. J Electrochem Soc 137(11):3626–3632
6. Elwenspoek M (1996) The form of etch rate minima in wet chemical anisotropic etching of silicon. J Micromech Microeng 6:405–409
7. Williams KR, Muller RS (1996) Etch rates for Micromachining Processing. IEEE/ASME J Microelectromech Syst 5(4):256–269

8. Zhu Z, Liu C (2000) Micromachining process simulation using a continous cellular method. IEEE/ASME J Microelectromech Syst 9(2):252–261
9. Lin CH, Lee GB, Lin YH, Chang GL (2001) A Fast Prototyping Process for Fabrication of Microfluidic Systems on Soda-Lime Glass. J Micromech Microeng 11(6):726–732
10. Spierings G, Van D (1987) The dissolution of Na_2O-MgO-CaO-SiO_2 glass in aqueous HF solutions. J Mat Sci 22:1869–1874

Bulk Micromachining of Silicon

► Bulk Micromachining

Buried Channel Waveguides

► On Chip Waveguides

Calcium Titanium Oxide

► Perovskite

Cantilever

Definition

A cantilever is a beam anchored at one end and projecting into space.

Cross References

► Biosensor
► Atomic Force Microscope (AFM)

Cantilever Biosensors

► Biosensors Using Atomic Force Microscopes

Capacitance Cytometry

► Capacitance Method

Capacitance Method

YUEJUN KANG, DONGQING LI
Department of Mechanical Engineering, Vanderbilt University, Nashville, TN, USA
yuejun.kang@vanderbilt.edu

Synonyms

Capacitance cytometry; Capacitive sensing

Definition

A sensing method for detection, counting, or characterizing of the nanoliter droplets, cells or other microparticles by measuring the capacitance change between a pair of electrically charged and isolated conductors.

Overview

Capacitive sensors have been extensively applied in sensing pressure, acceleration, deformation, displacement, and position. In recent decades, capacitance methods have found new applications in biomedical analysis. By monitoring the cellular membrane capacitance, one can assay cell cycle progression [1], or differentiate normal and malignant cells [2]. With the latest development of microfluidics, capacitance sensors have been successfully integrated in Lab-on-a-Chip devices. Capacitance method renders an attractive option for detection because they are non-intrusive, highly sensitive and compatible with electrically conducting or insulating liquids.

Sohn and co-workers reported a novel device which can quantify the DNA content within the nucleus of single eukaryotic cells [3]. Since DNA molecules are highly charged in intracellular environment, they will be polarized in an applied low-frequency AC electric field. This polarization response can be measured as a change in total capacitance ΔC_T, across a pair of microelectrodes as individual cells suspended in buffer solution flow one by one through a microchannel (as shown in Fig. 1 and Fig. 2).

They found that there is a linear relationship between the capacitance and the DNA content of a cell. And they further showed that this relationship is not species-dependent. This innovative technique is termed as *capacitance cytometry*, which helps to reveal changes in cellular internal properties and determine the phase of individual cell in cell-cycle.

Chen et al. demonstrated a miniaturized coplanar capacitive sensor which can be integrated with microfluidic platform for detection of droplet position, size, and composition [4]. The inter-digitated, variable width design increases the capacitive signal for liquid structures with

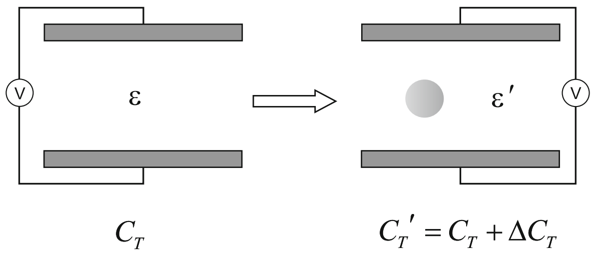

Capacitance Method, Figure 1 Schematics of the capacitive sensing method. When a microparticle, like a cell, passes between a pair of electrodes, the capacitance of the system will be changed

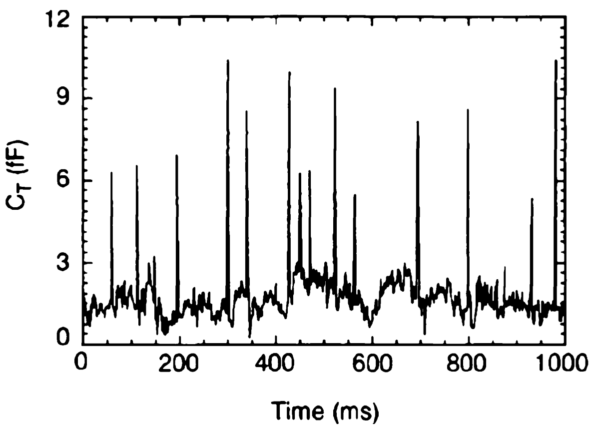

Capacitance Method, Figure 2 Capacitance change because of cells flowing past the electrodes. Each peak corresponds to the presence of a single cell [3]

non-uniform height profiles. The capacitive resolution and time response are 0.3 pF and 10 ms, respectively, allowing for accurate and fast sensing functions.

Based on a charge-based capacitance measurement method (CBCM), Ghafar–Zadeh and Sawan designed an accurate and simple topology circuit for measuring very small percentage of differential capacitance variations [5]. The simplified architecture and measurement linearity are highly advantageous in developing capacitive sensors for bio-particle detection.

Cross References

► Thermocapacitive Flow Sensor

References

1. Asami K, Gheorghiu E, Yonezawa T (1999) Real-time monitoring of yeast cell division by dielectric spectroscopy. Biophys J 76:3345–3348
2. Polevaya Y, Ermolina I, Schlesinger M, Ginzburg BZ, Feldman Y (1999) Time domain dielectric spectroscopy study of human cells: II. Normal and malignant white blood cells. Biochimica Biophysica Acta 1419:257–271
3. Sohn LL, Saleh OA, Facer GR, Beavis A J, Allan RS, Notterman DA (2000) Capacitance cytometry: measuring biological cells one by one. Proc Nat Acad Sci 97:10687–10690
4. Chen JZ, Darhuber A A, Troian SM, Wagner S (2004) Capacitive sensing of droplets for microfluidic devices based on thermocapillary actuation. Lab Chip 4:473–480
5. Ghafar-Zadeh E, Sawan M (2005) A high precision and linearity differential capacitive sensor circuit dedicated to bioparticles detection. 3rd Int IEEE-NEWCAS Conf 299–302

Capacitive Sensing

► Capacitance Method

Capillarity

► Wetting and Spreading

Capillarity-Driven Stop Valve and Sample Injection Switch

► Bubble Actuated Microfluidic Switch

Capillary-Based Microfluidics

► Surface-Directed Capillary Flow Systems

Capillary Electrochromatography

Synonyms

CEC

Definition

capillary electrochromatography (CEC) is a hybrid separation technique of capillary electrophoresis (CE) and capillary liquid chromatography (μ-LC), and combines both separation mechanism of CE and μ-LC. Capillary chromatographic column with a typical stationary phase is employed as the separation bed. The mobile phase is driven by electroosmotic flow. The separation selectivity results from differences in the retentions on the stationary phase and the electrophoretic mobilities of analytes.

Capillary Electrochromatography–Electrospray Ionization–Mass Spectrometry: An Integrated Electrokinetic Analytical Technique

Zilin Chen[1,2], Hsueh-Chia Chang[1]
[1] Department of Chemical and Biomolecular Engineering Center for Microfluidic and Medical Diagnostics, University of Notre Dame, Notre Dame, IN, USA
[2] College of Pharmacy, Wuhan University, Wuhan, China
zchen@nd.edu, hchang@nd.edu

Synonyms

CEC–ESI–MS

Definition

Capillary electrochromatography–electrospray ionization–mass spectrometry (CEC–ESI–MS) is an analytical technique combining electrochromatographic separation and mass spectrometric detection with an electrospray ionization interface.

Overview

► Capillary electrochromatography (CEC) is a hybrid separation technique that combines features of both capillary electrophoresis (CE) and high-performance liquid chromatography employing capillary columns (micro-HPLC). Like HPLC, the chromatographic resolution in CEC is based on the interaction between the analytes and stationary phases. However, in CEC, the analytes move through the separation bed of the column, driven by the electroosmotic flow (EOF), which drives the mobile phase, as well as the self-electrophoretic mobility when charged analytes are separated. Because of the flat pluglike profile of the EOF, CEC offers greatly enhanced separation efficiency compared to HPLC. With the advancement in column technologies, CEC has become a powerful separation technique for the separation of both neutral and charged analytes.

► Mass spectrometry (MS) is one of most useful detection methods for CEC, because it offers many advantages over other conventional detection methods. Most importantly, MS provides information about the chemical structures and molecular weights of analytes. ► Electrospray ionization (ESI) that generates gas-phase ions from analytes dissolved in a liquid phase is a soft ionization interface technique for coupling CEC separation with MS. Thus, CEC–ESI–MS is a promising simultaneous separation and detection technique for biomolecules, because it integrates advantages of high separation efficiency and chromatographic selectivity in CEC and high sensitivity and chemical and molecular mass information in MS detection.

Basic Methodology

The two major parts of a CEC–MS instrumental system are a capillary electrochromatograph and mass spectrometer, which are coupled together by an ESI interface. A schematic diagram of a CEC–MS instrumental system is shown in Fig. 1. Electrochromatographic separation column and ESI interface are two key technologies in CEC–ESI–MS, which are described in the following.

Electrochromatographic Column Technology

Electrochromatographic separation of analytes is performed on stationary phase in electrochromatographic columns. As shown in Fig. 2, three types of columns, namely open tubular, packed and monolithic columns, are used in CEC. In the open tubular column, the stationary phase is bonded or coated on the inner wall of a capillary column. In the packed columns, the particles bonded with chromatographic stationary phases are packed inside the capillary. Frits at the ends of capillary are used for preventing the movement of particles; sol–gel silicate or organic polymer as well as tapered capillary are used to embed the particles so that they do not move during the separation. The monolithic columns, also known as continuous bed with continuous skeleton and micro-scaled throughpores, include polymer-based and silica-based monoliths. Polymeric monolith columns are prepared by in situ polymerization of organic monomers in the presence of a porogen reagent using various initiator techniques such as free radical polymerization or photopolymerization. Silica monoliths are prepared by a sol–gel process including hydrolysis and polycondensation of precursors in a defined solvent in situ to produce a hydrogel, which is then converted to a xerogel upon drying. In the monolith columns, the stationary phases are bonded on the monolithic matrix by in situ copolymerization or post-modifications of bare monolith. In recent years, monolithic columns have received much attention, because monolithic columns offer many advantages over conventional open-tubular and packed columns, including in-capillary preparation, fritless design, high sample capacity and the absence of bubbles during CEC operation. Chen and co-authors developed a series of chiral silica monolithic columns for the enantioseparation of amino acids, peptides and pharmaceutical compounds by CEC

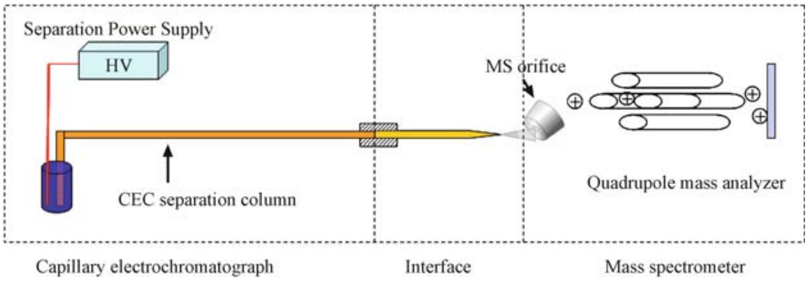

Capillary Electrochromatography–Electrospray Ionization–Mass Spectrometry: An Integrated Electrokinetic Analytical Technique, Figure 1 Schematic CEC-ESI-MS instrumental arrangement

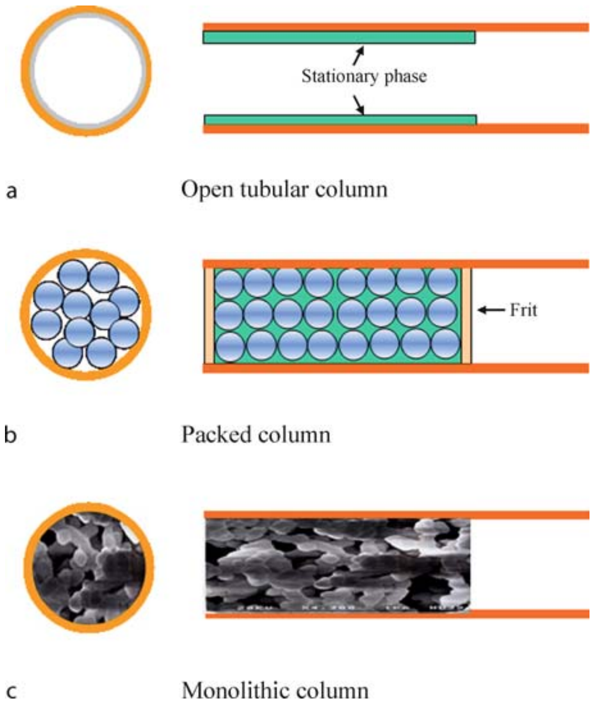

Capillary Electrochromatography–Electrospray Ionization–Mass Spectrometry: An Integrated Electrokinetic Analytical Technique, Figure 2 Schematic of three types of CEC columns

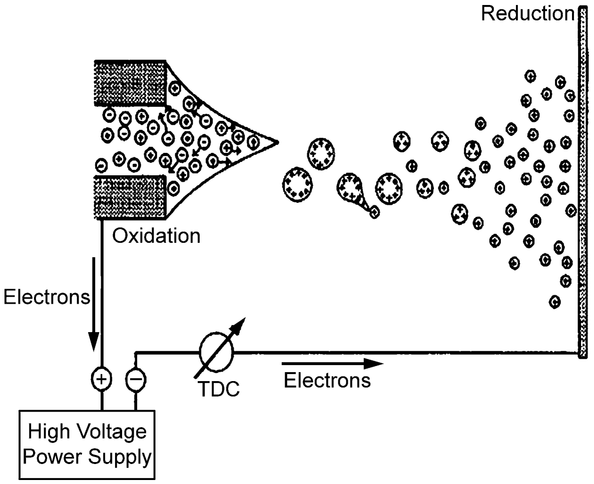

Capillary Electrochromatography–Electrospray Ionization–Mass Spectrometry: An Integrated Electrokinetic Analytical Technique, Figure 3 Schematic of major processes occurring in electrospray (from [4])

and micro-LC [1–3]. These chiral monolithic columns are expected to be used in CEC–ESI–MS for chiral separation. In the design of the electrochromatographic column for CEC–MS, three important factors, namely chromatographic selectivity to analytes, the magnitude and direction of electroosmotic flow and the compatibility with the mobile phases, must be taken into account. The flow rate of EOF is a very important factor, because it not only drives mobile phase and analytes, but also supports the generation of electrospray. A suitable flow rate of EOF for CEC–ESI is in the range of 50 to 300 nL/min. For achieving high efficiency of ionization compatible with MS detection, a minimum concentration of salts, surfactants and other additives in the mobile phase is necessary.

Electrospray Ionization Interface Technology

An ESI interface is an on-line combined interface of CEC and MS. ESI can be used for the analysis of almost all kinds of biomolecules which are polar and soluble in a solvent system, as well as capable of generating spray. ESI-MS has been used for the analysis of peptides, proteins, carbohydrates, DNA fragments and lipids. Figure 3 shows a schematic of major processes occurring in electrospray [4, 5]. The electrospray processes include:

- penetration of imposed electric field into liquid leads to formation of electric double layer in liquid;
- enrichment of surface of liquid by positive electrolyte ions leads to destabilization of meniscus and formation of cone and jet emitting droplets with excesses of positive ions; and

- charged droplets shrink by evaporation and split into smaller droplets and finally gas-phase ions [4, 5].

Figure 4 shows an image of an electrospray obtained at a silica capillary tip. A characteristic feature of electrospray ionization is the generation of multiple charged ions, which allow MS to be used in the analysis of large biomolecules of molecular masses far beyond 100 000. A series of signals including $[M+H]^{+}$, $[M+2H]^{2+}$, $[M+3H]^{3+}$ to $[M+nH]^{n+}$ can obtained from larger biomolecules. Samples used for ESI must be soluble, stable in solution and relatively clean. Salts and additives in the buffers must be kept at low concentration because they may reduce the ionization efficiency.

A suitable electrical connection between the CEC separation and the ESI emitter is a key for the CEC–ESI–MS coupling. Three main interfaces including coaxial sheath-flow interface, liquid junction interface and sheathless interface have been used in CE/CEC–ESI–MS. The main advantages of the sheath-flow interface are the wide flexibility in selection of separation electrolyte solutions, its reliability and the existence of several commercial designs which make it the most widely used interface in CE–ESI–MS routine analysis [6]. However, due to sample dilution and additional background noise from the sheath liquid, the sensitivity in the sheath-flow interface reduces in some cases. The liquid junction interface needs tedious capillary alignment and precise end-to-end butting of the separation capillary and spray tip [7]. Poor alignment causes low sensitivity and separation efficiency due to spreading of sample in the relatively large dead volume of the liquid junction.

The development of sheathless interfaces has attracted much attention because of the compatible flow rates of each technique, which leads to high desorption and ionization efficiency and, consequently, high sensitivity. Several sheathless designs have been reported including (1) the use of a single capillary where electrical contact is established by coating the capillary outlet with a conductive metal or polymer or by inserting a conductive wire into the outlet of the capillary or through a small pinhole in the wall of capillary, and (2) the use of two pieces of capillary where the CE capillary is connected to a short spray tip via a sleeve. The sleeves include a piece of microdialysis tubing, stainless steel tubing, a micro-tee and etched capillary widow [7].

Recently, we developed a chip-scale electroosmotic pump/electrospray coupling device using monolithic silica as EOF-generating material and Nafion tubing as the connection for pumping and electrospray capillaries. This device can generate a very stable electrospray with the support of electroosmotic flow [8, 9]. With the modifications, this device can be used for the CEC–MS interface [10]. Figure 5 shows a schematic sheathless ESI interface of CEC-MS. An open-tubular capillary separation column and a sharply tapered spray capillary (4.5 cm in length) were butted together inside Nafion tubing (5 mm in length). Epoxy was applied around the outside of the Nafion tubing/capillary boundaries. After the epoxy dried, the connected capillary was mounted on a glass slide (2 cm × 5 cm). A PVC tube (5 mm i.d., 8 mm in height) was glued on the top of the Nafion junction to form a reservoir. The reservoir was filled with the same running electrolyte as employed in the separation, and electrospray voltage was applied through a platinum wire dipped into the reservoir and connected to the MS power supply (HV1). The use of an open reservoir rather than an enclosed/limited reservoir avoids problems due to gas bubbles in the liquid circuit. A common ground connection was also formed between the external power supply for CEC separation (HV2), the shielding of the ESI power supply (HV1) lead cable, and the mass spectrometer. Figure 6 shows a sheathless CE/CEC–ESI–MS interface mounted on PicoView nanoelectrospray assembly for Micromass QuattroLC MS. This device offers many advantages, such as ease of fabrication, ruggedness, durability and no dilution effects, over existing devices which require a sheath flow or liquid junction interface.

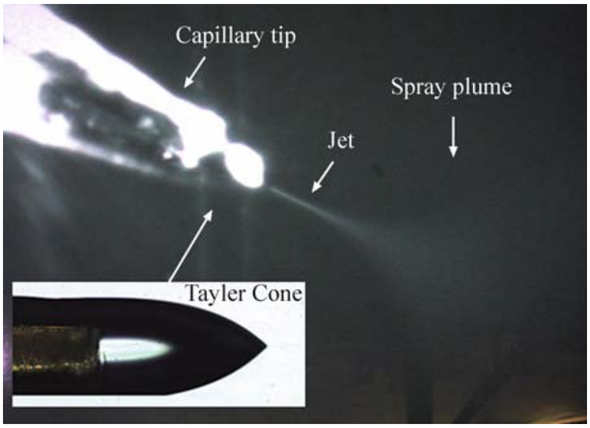

Capillary Electrochromatography–Electrospray Ionization–Mass Spectrometry: An Integrated Electrokinetic Analytical Technique, Figure 4 Image of nanoelectrospray

Mobile Phase in CEC–ESI–MS

In addition to CEC column and ESI interface technologies, the mobile phase is also an important factor for CEC–ESI–MS analysis. Electrochromatographic separation selectivity relies not only on the stationary phase, but also on the mobile phase. In the choice of mobile phase for CEC–ESI–

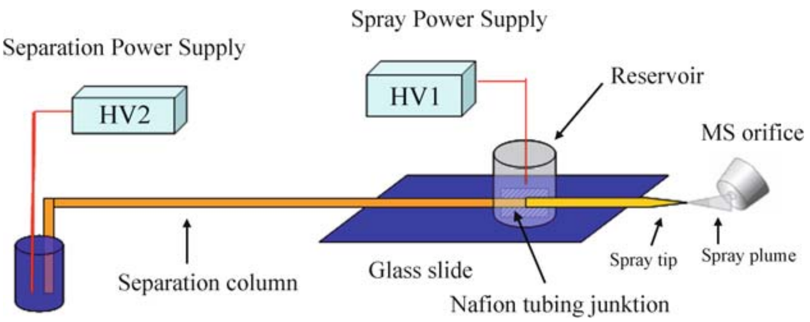

Capillary Electrochromatography–Electrospray Ionization–Mass Spectrometry: An Integrated Electrokinetic Analytical Technique, Figure 5 Sheathless ESI interface of CEC–MS (from [10])

MS analysis, both CEC separation selectivity and compatibility with ESI–MS detection should be taken into account. An ideal mobile phase for CEC–ESI–MS should meet various requirements:

- offering high electrochromatographic selectivity for the stationary phase,
- generating sufficient flow rate of EOF for driving the mobile phase and supporting a stable electrospray,
- producing highly efficient gas-phase ions of analytes for ESI, and
- offering high sensitivity and low contamination for MS detection.

Therefore, mobile phases used in CE/CEC–MS often contain exclusively volatile buffer additives, such as formic acid, acetic acid, trifluoroacetic acid, ammonium formate, ammonium acetate, ammonia or volatile organic amines. The mobile phase must be kept at the lowest level of conductivity. Salts, surfactants and other additives should be avoided or eliminated at the lowest level.

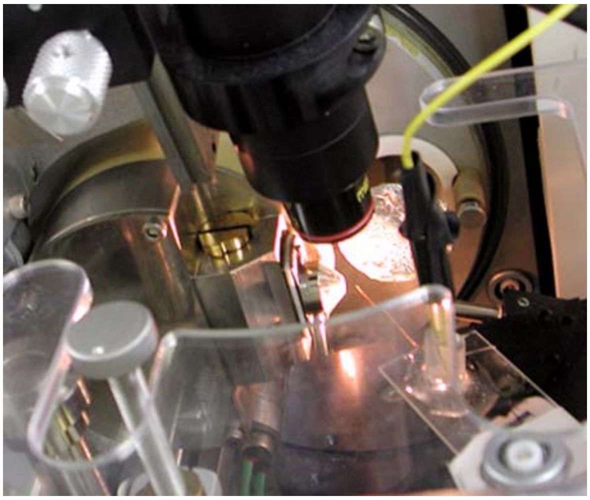

Capillary Electrochromatography–Electrospray Ionization–Mass Spectrometry: An Integrated Electrokinetic Analytical Technique, Figure 6 Image of sheathless nanoelectrospray interface mounted to mass spectrometer (from [10])

Key Research Findings

CEC–MS Applications

Although the number of papers reporting CEC–ESI–MS is not very many, CEC–ESI–MS has been applied to the analysis of a wide range of species from small ions to biomolecules. Several typical examples of applications are selected for review in the following.

CEC–MS Analysis of Chiral Compounds

CEC–ESI–MS has been successfully used for the analysis of chiral compounds. Coupling of CEC to MS offers many advantages for enantioseparation.

- Since the chiral selector is immobilized on the column matrix, there is no problem that the presence of nonvolatile chiral additives in CE–MS or MEKC–MS results in significant loss of electrospray efficiency and ion source contamination.
- MS detection provides high sensitivity and both molecular mass and structural information. Meanwhile, the CEC separation renders different retention times for enantiomers, as the enantiomers have the same molecular weight for MS detection.
- The nanoliter-scaled flow rates of EOF in CEC are suitable for an ESI source.

Mayer et al. reported open-tubular CEC–ESI–MS analysis of enantiomers of the chiral sedative–hypnotic drug hexobarbital by coupling a short Chirasil-Dex-coated capillary (15 and 25 cm × 50 μm i.d.) via a sheath liquid interface to a quadrupole mass spectrometer [11]. The mobile phase was 10 mM ammonium acetate buffer at pH 7, and the composition of the sheath liquid was 2-propanol/10 mM ammonium acetate at pH 7 (9:1, v/v). Schurig's group reported an on-line coupling of packed CEC with ESI–MS

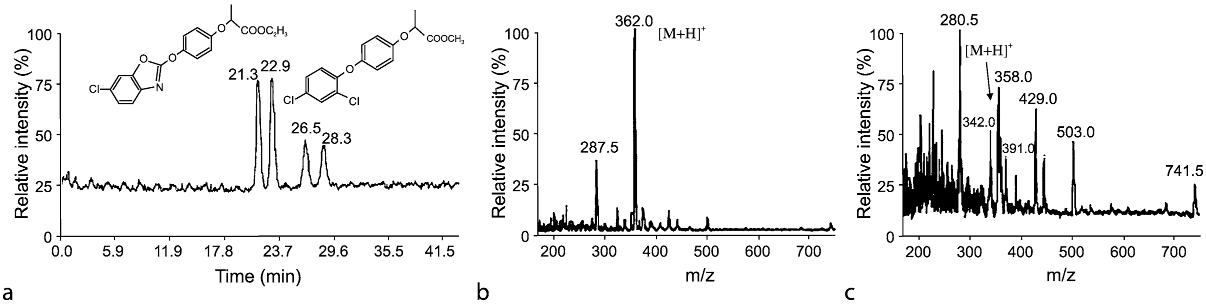

Capillary Electrochromatography–Electrospray Ionization–Mass Spectrometry: An Integrated Electrokinetic Analytical Technique, Figure 7
Separation of the enantiomers of fenoxaprop ethyl (21.3 and 22.9 min) and diclofop methyl (26.5 and 28.3 min) on a 30 cm × 100 µm i.d. capillary packed with Chira-Dex-silica. Conditions: 20.5 kV; 10 bar; 0.5 mM ammonium acetate buffer in water/methanol (40:60) at pH 6.6. (**a**) Total ion chromatogram in the positive mode. TIC was acquired scanning from m/z 170 to 750. Sheath liquid flow of water was kept at 3 µL/min. Corresponding mass spectra of fenoxaprop ethyl (**b**) and diclofop methyl (**c**) of the peaks in (**a**). (From [12])

and coordination ion spray (CIS)–MS for the analysis of chiral model compounds including barbiturates and chlorinated alkyl phenoxypropanoates [12]. The separation of enantiomers by pressure-supported CEC is performed in capillaries packed with permethylated β-cyclodextrin-modified silica (Chira-Dex-silica). Figure 7 shows the electrochromatogram and mass spectra. It is interesting that silver(I), cobalt(II), copper(II) and lithium(I) ions have been used for the postcolumn conversion of the analytes to charged coordination compounds which were detected in the CIS–MS mode. In the CIS detection mode, the sensitivity was significantly improved with the addition of $CoCl_2$ in the sheath flow.

Zhang and Shamsi reported the combination of a chiral column tapered at the outlet end and coupled to ESI–MS for simultaneous analysis of (±)-warfarin and (±)-coumachlor [13]. The chiral CEC was performed in capillaries packed with 5.0 µm (3R, 4S)-Whelk-O1 chiral stationary phase. Acetonitrile/5 mM ammonium acetate (pH 4.0) (70:30, v/v) and methanol/5 mM ammonium acetate (pH 8.5) (70:30, v/v) were used as mobile phase and sheath liquid, respectively. It was found that the externally tapered column showed much more reproducible retention time compared to the untapered column. However, because of the fragile outlet end of the external taper, the tip tended to break during the voltage ramp or due to arcing in the spray chamber. To overcome this problem, the same group developed an internally tapered column technology [14], and recently used it in simultaneous enantioseparation and sensitive detection of eight β-blockers by CEC–ESI–MS packed with vancomycin chiral stationary phase [15]. A mixture containing mehanol/acetonitrile/acetic acid/triethylamine at 70:30:1.6:0.2 (v/v/v/v) was selected as optimum mobile phase.

CEC–MS Analysis of Amino Acids, Peptides and Proteins

Studies on proteomics need rapid identification and characterization of large numbers of components such as amino acids and peptides in protein digests. CEC–ESI–MS is a powerful technique for such proteomic studies. Several papers reported pressurized CEC (pCEC) coupled with ESI–MS for the analysis of peptides and/or protein digests, where C_{18} silicagel or mixed-mode C_{18}/strong anion-exchange stationary phase [16] packed column was used as reversed-phase CEC separation and a mixture of water and acetonitrile containing 5–20 mM ammonium acetate was used as a mobile phase. In pCEC, both pressure and electric field are applied across a capillary column simultaneously; the flow profile in the column is a combination of parabolic flow induced by the pressure and flat

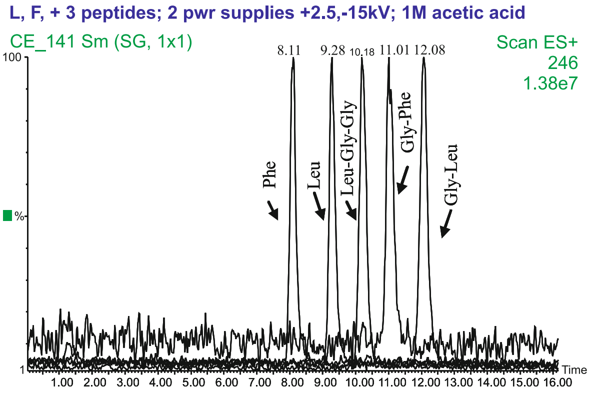

Capillary Electrochromatography–Electrospray Ionization–Mass Spectrometry: An Integrated Electrokinetic Analytical Technique, Figure 8 Extracted ion electrochromatograms of m/z [M+H$^+$] 166 (Phe), 132 (Leu), 246 (Leu-Gly-Gly), 223 (Gly-Phe) and 189 (Gly-Leu). Running electrolyte: 1 M acetic acid, Lupamin-coated capillary column, 2.5 kV spray voltage, and −15 kV separation voltages. (From [10])

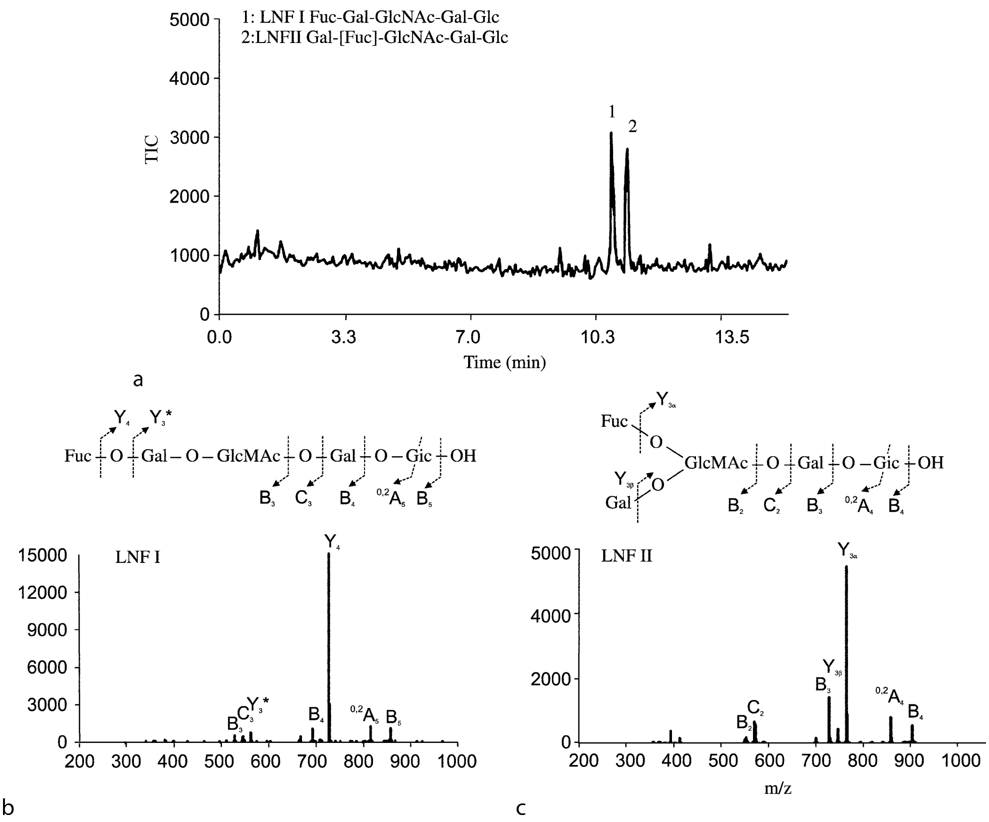

Capillary Electrochromatography–Electrospray Ionization–Mass Spectrometry: An Integrated Electrokinetic Analytical Technique, Figure 9
Mass electrochromatogram of a mixture of branching isomers (**a**). Experimental conditions: cyano column 22 cm, mobile phase acetonitrile/water/ammonium formate buffer (240 mM, pH 3.0, 65:34:1, v/v/v), field strength 600 V/cm, injection 4 kV, 10 s; sample: each sugar at 0.2 mg/mL. MS/MS of LNFI (**b**) and LNFII (**c**). (From [23])

flow caused by the EOF. In pCEC, pressure is not only used to minimize bubble formation, but it also provides a means of tuning selectivity for the separation of charged analytes by varying the electric field. The disadvantage is that the instrumental setup is relatively complicated. Karger's group reported high-efficiency peptide analysis on monolithic polymeric column by pCEC–ESI–MS [17]. The monolithic column was prepared from a mixture of methacrylates, porogens and an initiator with thermally induced in situ polymerization. The monolithic media have properties of fast mass transfer and low pressure resistance, enabling fast separation and coupling to ESI–MS. The same group also reported a microfabricated device that integrates a monolithic polymeric separation channel, an injector and an interface for ESI–MS [18].

Gucek et al. [19] succeeded in the coupling of CEC to an ion trap MS via nanoelectrospray for attomole characterization of peptides. It was demonstrated that it was possible to obtain a stable spray without a sheath liquid being employed by using a conductively coated tip butted to the end of a CEC column packed with 3 μm Hypersil C_8 or C_{18} bonded silica particles. The mobile phase was 3.2 mM ammonium acetate in 50% acetonitrile. In this sheathless interface the maximum sensitivity was obtained at low operating voltages, the best performances were achieved if the system operated at a CEC current of 2 μA, with electric field strength not higher than 500 V/cm because of insufficient flow to sustain the spray or air bubble formation at the spray tip. However, when using the sheath flow interface in the following work of the same group, the setup could bear electric field up to 1000 V/cm and CEC currents in the range 15–20 μA without showing a decrease in performance [20]. Electroosmotically driven solvent gradients were employed for the separation of 12 phenylthiohydantoin (PTH)-amino acids by reversed-phase CEC using Zorbax ODS particle-packed column with a time-of-flight MS detection [21].

We recently reported an open-tubular CEC coupling with a sheathless ESI–MS for analysis of some amino acids and peptides [10]. We employed Lupamin, a high molecular

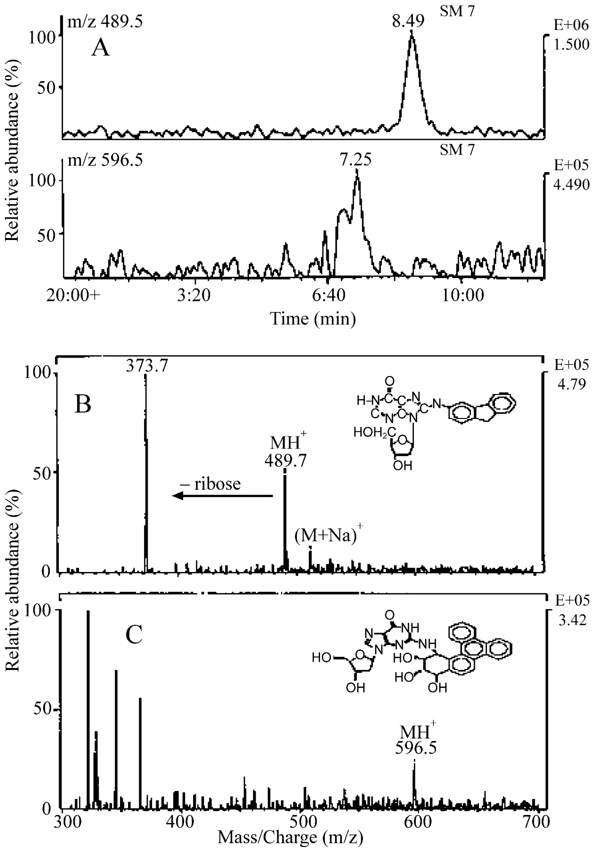

Capillary Electrochromatography–Electrospray Ionization–Mass Spectrometry: An Integrated Electrokinetic Analytical Technique, Figure 10 Extracted ion electrochromatograms of AAF-dG (m/z 489.5) and benzo[g]chrysene-dG (m/z 596.5) (**a**), and mass spectra of AAF-dG (**b**) and benzo[g]chrysene-dG (**c**) acquired from the 10^{-6} M concentration solution. (From [24])

weight linear polyvinylamine polymer, as stationary phase coated on the inner wall of an open-tubular capillary column. This column has several merits including easy preparation, low cost and good reliability. Positively charged amino groups in polyvinylamine in acidic conditions play three important roles:

- provide a strong reversed EOF for driving mobile phase and analytes from the inlet end of the separation capillary to the electrospray tip,
- function as a stationary phase by allowing specific chromatographic selectivity for resolving amino acids and peptides, and
- eliminate the adsorption of analyte resulting from the electrostatic adsorption in the case of bare silica capillary.

Figure 8 shows the selected ion electrochromatogram of a mixture of amino acids and peptides, in which a baseline separation was achieved.

CEC–MS Analysis of Carbohydrates

Novotny's group published several papers on CEC–MS analysis of carbohydrate mixtures [22, 23]. Ion trap tandem MS was coupled with CEC separation for separation and characterization of oligosaccharides [22, 23]. It was demonstrated that polar monolithic CEC columns containing either cyano or amino functional groups efficiently separated complex mixtures of carbohydrates with the use of mobile phases containing acetonitrile/dilute ammonium formate buffers. The separation of carbohydrate mixtures on both the cyano and amino columns is based on normal-phase mechanism. MS/MS detection mode can provide reliable data on the structural detail of glycans separated by CEC. Figure 9 shows electrochromatograms and MS/MS spectra of a mixture of oligosaccharide isomers [23].

CEC–MS Analysis of DNA Adducts

Human exposures to chemicals found in certain foods or environmental pollutants are linked to a higher risk for cancer. It is known that the initial step in chemical carcinogenesis is the covalent attachment of the chemical to DNA to produce DNA adducts. The structure identification of these DNA adducts is very important in cancer research. CEC–ESI–MS with shealth liquid interface has been demonstrated as a good tool for the analysis of DNA adducts as well as nucleosides with styrene oxide by Vouros and co-authors [24, 25]. Two common DNA adducts, acetylaminofluorene deoxyguanosine (AAF-dG) and an isomer of anti-benzo[g]chrysene 11,12-dihydrodiol 13,14-epoxide, were employed as model compounds. CEC separation was performed on a C_{18} silica gel-packed column and used a mixture of 60% acetonitrile and 5 mM ammonium acetate as the mobile phase. Figure 10 shows the extracted ion electrochromatograms and mass spectra of AAF-dG and benzo[g]chrysene-dG [25].

CEC–MS for Drug Analysis

CEC–MS is used as an analytical tool for pharmaceutical analysis. The CEC–ESI–MS analysis and quantification of a potential drug candidate from 13 structurally related compounds in extracted plasma were reported by Paterson et al. [26]. The CEC column was packed with an experimental 'mixed mode' stationary phase containing both C_{18} and sulfonic acid ligands. These phases promote stable electroosmotic flow across a wide range of pH values and allow a greater choice of buffer pH values. The mobile phase was acetonitrile/25 mM ammonium acetate (75:25) at pH 3.5 adjusted with acetic acid. Taylor et al. reported a CEC–ESI–MS analysis of mixtures of benzodiazepines, corticosteroids and thiazide diuretic drugs [27].

Separations were performed on a fused-silica capillary column packed with Hypersil ODS (3 μm) and Apex ODS (3 μm) particles and interfaced to a Platform MS using a triaxial inlet probe. Strickmann et al. [28] reported the separation of the non-steroidal anti-inflammatory drug etodolac and its phase I metabolites, 6-hydroxy etodolac, 7-hydroxy etodolac and 8-(1'-hydroxyethyl) etodolac, by pCEC coupled with ESI-MS detection. LiChrospher 100 RP-18, 5 μm particles were packed inside a 100 μm i.d. capillary and served as stationary phase. Ammonium formate (10 mM; pH 3.0)/acetonitrile (50:50) was used as the mobile phase. An automated CEC–MS(/MS) using mixed modes of reversed-phase (C_{18}/C_6) and ion-exchange (strong cation exchange, SCX) chromatography columns was used for the separation and detection of drug standards: salbutamol and salmeterol [29], as well as corticosteroids [30].

Future Research Directions

CEC–ESI–MS is a new integrated separation and detection technique for the analysis of biomolecules. It is still in the development stage. The following topics are considered as future research directions including

- new CEC column technology,
- new interface technology coupling CEC with ESI–MS,
- new electrospray principle and instrumental technology,
- microfluidic CEC–ESI devices coupled with MS and
- new applications of CEC–ESI–MS in bioanalysis.

References

1. Chen Z, Hobo T (2001) Chemically L-phenylalaninamide-modified monolithic silica column prepared by a sol-gel process for enantioseparation of dansyl amino acids by ligand exchange-capillary electrochromatography. Anal Chem 73:3348–3357
2. Chen Z, Hobo T (2001) Chemically L-prolinamide-modified monolithic silica column for enantiomeric separation of dansyl amino acids and hydroxyl acids by capillary electrochromatography. Electrophoresis 22:3339–3346
3. Chen Z, Ozawa H, Uchiyama K, Hobo T (2003) Cyclodextrin-modified monolithic columns for resolving dansyl amino acid enantiomers and positional isomers by capillary electrochromatography. Electrophoresis 24:2550–2558
4. Kebarle P, Tang T (1993) From ions in solution to ions in the gas phase. Anal Chem 65:972A–986A
5. Cole RB (ed) (1997) Electrospray ionization mass spectrometry: fundamentals, instrumentation, and applications. Wiley, New York.
6. Sanz-Nebot V, Balaguer E, Benavente F, Barbosa J (2005) Comparison of sheath-flow electrospray interfaces for the capillary electrophoresis-electrospray ionization-mass spectrometry analysis of peptides. Electrophoresis 26:1457–1465
7. Janini GM, Conrads TP, Wilkens KL, Issaq HJ, Veenstra TD (2003) A sheathless nanoflow electrospray interface for on-line capillary electrophoresis mass spectrometry. Anal Chem 75:1615–1619
8. Chen Z, Wang P, Chang HC (2005), An electroosmotic micropump based on monolithic silica for microflow analysis and electrospray. Anal Bioanal Chem 382:817–824
9. Wang P, Chen Z, Chang H-C (2006) A porous electrospray emitter assisted by an integrated electrokinetic pump based on silica monoliths. Electrophoresis, 27:3964–3970
10. Chen Z, Boggess B, Chang HC (2007) Open-tubular capillary electrochromatography-mass spectrometry with sheathless nanoflow electrospray ionization for the analysis of amino acids and peptides. J Mass Spectrometry, in press.
11. Schurig V, Mayer SJ (2001) Separation of enantiomers by open capillary electrochromatography on polysiloxane-bonded permethyl-β-cyclodextrin. Biochem Biophys Methods 48:117–141
12. Brocke A, Wistuba D, Gfrorer P, Stahl M, Schurig V, Bayer E (2001) On-line coupling of paced capillary electrochromatography with coordination ion spray-mass spectrometry for the separation of enantiomer. Electrophoresis 23:2963–2972
13. Zhang J, Shamsi S (2003) Combination of chiral capillary electrochromatography with electrospray ionization mass spectrometry: method development and assay of warfarin enantiomers in human plasma. Anal Chem 75:6295–6305
14. Zhang J, Norton D, Shamsi S (2006) Fabrication of internally tapered capillaries for capillary electrochromatography electrospray ionization mass spectrometry. Anal Chem 78:1323–1330
15. Zhang J, Shamsi S (2006) Simultaneous enantioseparation and sensitive detection of eight β-blockers using capillary electrochromatography-electrospray ionization-mass spectrometry. Electrophoresis, 27:2139–2151
16. Huang P, Jin X, Chen Y, Srinivasan JR, Lubman DM (1999) Use of a mixed-mode packing and voltage tuning for peptide mixture separation in pressurized capillary electrochromatography with an ion trap storage/reflection time-of-flight mass spectrometer detector. Anal Chem 71:1786–1791
17. Ivanov AR, Horvath C, Karger BL (2003) High-efficiency peptide analysis on monolithic multimode capillary columns: pressure-assisted capillary electrochromatography/capillary electrophoresis coupled to UV and electrospray ionization-mass spectrometry. Electrophoresis 24:3663–3673
18. Lazar IM, Li L, Yang Y, Karger BL (2003) Microfluidic device for capillary electrochromatography-mass spectrometry. Electrophoresis 24:3655–3662
19. Gucek M, Gaspari M, Walhagen K, Vreeken RJ, Verheij ER, van der Greef J (2000) Capillary electrochromatography/nanoelectrospray mass spectrometry for attomole characterization of peptides. Rapid Commun. Mass Spectrom. 14:1448–1454
20. Gaspari M, Gucek M, Walhagen K, Vreeken RJ, Verheij ER, Tjaden UR, van der Greef J (2001) Ion trap mass spectrometry as detector for capillary electrochromatography of peptides: possibilities and limitations. J Microcolumn Sep 13:243–249
21. Choudhary G, Horvath C, Banks JF (1998) Capillary electrochromatography of biomolecules with on-line electrospray ionization and time-of-flight mass spectrometry. J Chromatogr A 828:469–480
22. Que AH, Konse T, Baker AG, Novotny MV (2000) Analysis of bile acids and their conjugates by capillary electrochromatography/electrospray ion trap mass spectrometry. Anal Chem 72:2703–2710

23. Que AH, Novotny MV (2003) Structural characterization of neutral oligosaccharide mixtures through a combination of capillary electrochromatography and ion trap tandem mass spectrometry. Anal Bioanal Chem 375:599–608
24. Ding J, Vouros P (1999) Capillary electrochromatography and capillary electrochromatography-mass spectrometry for the analysis of DNA adduct mixtures. Anal Chem 69:379–384
25. Ding J, Barlow T, Dipple A, Vouros P (1998) Separation and identification of positively charged and neutral nucleoside adducts by capillary electrochromatography-microelectrospray mass spectrometry. J Am Soc Mass Spectrom 9:823–829
26. Paterson CJ, Boughtflower RJ, Higton D, Palmer E (1997) An investigation into the application of capillary electrochromatography-mass spectrometry for the analysis and quantification of a potential drug candidate in extracted plasma. Chromatographia 46:599–604
27. Taylor MR, Teale P (1997) Gradient capillary electrochromatography of drug mixtures with UV and electrospray ionization mass spectrometric detection. J Chromatogr A 768:89–95
28. Strickmann DB, Chankvetadze B, Blaschke G, Desiderio C, Fanali S (2000) Separation and identification of etodolac and its urinary phase I metabolites using capillary electrochromatography and on-line capillary electrochromatography-electrospray ionization mass spectrometry coupling. J Chromatogr A 887:393–407
29. Spikmans V, Lane SJ, Tjaden UR, van der Greef J (1999) Automated capillary electrochromatography tandem mass spectrometry using mixed mode reversed-phase ion-exchange chromatography column. Rapid Commun Mass Spectrom 13:141–149
30. Lane SJ, Tucker MG (1998) An automated electroosmotic sample introduction/separation interface for automated electroosmotic flow flow-injection mass spectrometry, infusion MS and CEC MS. Rapid Commun Mass Spectrom 12:947–954

Capillary Electrophoresis

Synonyms

Capillary zone electrophoresis; Capillary electrophoretic separation

Definition

Capillary electrophoresis (CE) is a routine analytical technique for fast and efficient separation of charged species. Under the influence of an electric field, the ionic species in a sample that is introduced as a plug (or zone) into an electrolyte at one end of a capillary will be separated into discrete bands when they migrate to the other end of the capillary at different electrophoretic velocities. However, Joule heating is an inevitable phenomenon in CE that limits the performance of electrophoretic separation.

Cross References

► Electrochemical Techniques
► Electrophoresis
► Electroosmotic Flow (DC)
► AC Electro-Osmotic Flow
► Hydrodynamic Dispersion
► Joule Heating in Electrokinetic Flow: Theoretical Methods

Capillary Electrophoretic Separation

► Capillary Electrophoresis

Capillary Filling

SUMAN CHAKRABORTY
Department of Mechanical Engineering, Indian Institute of Technology, Kharagpur, INDIA
suman@mech.iitkgp.ernet.in

Synonyms

Surface tension driven filling

Definition

Capillary filling refers to the filling of an open or closed conduit or a reservoir with the aid of capillary (surface tension) actuation mechanisms.

Overview

Capillary-driven filling of microchannels finds important applications in the Micro-Electrical-Mechanical-Systems (MEMS) and micro-total analysis systems for bio-medical and biotechnological applications. A comprehensive theoretical understanding of the capillary filling process can guide the designer to optimize the internal structure of the chip, such as the chambers, binding pillars, splits, valves, etc, in order to avoid any potential filling problem (including air-bubble entrapment and clogging) and to achieve high throughputs.

Basic Methodology

In a generic form, one can write the equation of motion describing the advancement of a liquid meniscus in a gas-filled capillary as

$$\frac{\mathrm{d}}{\mathrm{d}t}(MV_c) = \sum F \qquad (1)$$

where M is the fluid mass being transported, V_c is the velocity of its center of mass and $\sum F = F_{\text{surface tension}} + F_{\text{viscous}} + F_{\text{gravity}}$. Microchannel flows are typically characterized with low Bond numbers (which are indicators of

Capillary Filling, Table 1 Simplistic estimates of various forces for capillary filling in circular and rectangular microchannels

	Circular microchannel of radius R	Rectangular microchannels of width w and height h
$\frac{d}{dt}(MV_c)$	$\rho\pi R^2\left[s\frac{d^2s}{dt^2}+\left(\frac{ds}{dt}\right)^2\right]$	$\rho wh\left[s\frac{d^2s}{dt^2}+\left(\frac{ds}{dt}\right)^2\right]$
$F_{\text{surface tension}}$	$2\pi R\gamma_{lv}\cos\theta$	$2(w+h)\gamma_{lv}\cos\theta$
F_{viscous}	$8\pi\eta s\frac{ds}{dt}$	$\frac{\pi^4\eta}{8\left\{1-\frac{2h}{\pi w}\tanh\left(\frac{\pi w}{2h}\right)\right\}}\frac{w}{h}s\frac{ds}{dt}$

Capillary Filling, Table 2 Various non-dimensional parameters for circular and rectangular microchannels

	Circular microchannel of radius R	Rectangular microchannels of width w and height h
t^*	$\frac{8t\eta}{\rho R^2}$	$\frac{t\pi^4\eta}{8\rho w^2\varepsilon^2\left\{1-\frac{2\varepsilon}{\pi}\tanh\left(\frac{\pi}{2\varepsilon}\right)\right\}}$, where $\varepsilon=\frac{h}{w}$
s^*	$\sqrt{\frac{\eta^2}{\gamma_{lv}\rho R}}\frac{4s}{R}$	$\frac{s\pi^3\eta}{16\varepsilon^2\left\{1-\frac{2\varepsilon}{\pi}\tanh\left(\frac{\pi}{2\varepsilon}\right)\right\}}\sqrt{\frac{\varepsilon}{(1+\varepsilon)\gamma_{lv}\rho w^3}}$
D	$\cos\theta+\frac{Bo}{4}$, where $Bo=\frac{2\rho gRz_0}{\gamma_{lv}}$	$\cos\theta+\frac{\varepsilon}{2(1+\varepsilon)}Bo$, where $Bo=\frac{\rho gwz_0}{\gamma_{lv}}$

the ratio of gravity to surface tension force), and therefore the gravity force is neglected in this analysis. For a capillary advancement by a distance s, simple estimates of various terms appearing in eq. (1) can be made for circular and rectangular microchannels, as summarized in Table 1. In Table 1, ρ is the fluid density, γ_{lv} is the liquid-vapour interfacial tension, η is the fluid viscosity and θ is the contact angle at the interface. In case the fluid is supplied to the capillary channel with the aid of a hydrostatic head, z_0, then there is an additional driving force because of the hydrostatic pressure, which is equal to $\rho g\pi R^2 z_0$ for the circular tube and $\rho gwhz_0$ for the rectangular channel. With the initial conditions of $ds/dt=0$ at $t=0$ and $s=s_0$ at $t=0$, eq. (1) can be solved with the above specification of forces, to yield a general non-dimensional form of the solution as

$$s^{*2}-s_0^{*2}=D\left(t^*-1+\exp(-t^*)\right) \tag{2}$$

where the various non-dimensional parameters are defined as described in Table 2.

Although quite simplistic in nature, the solution given by eq. (2) may be far from being practical, because of certain unrealistic conditions in-built with the same. In reality, these simplifications can be relaxed to some extent, with the following considerations:

(i) Eq. (1) suffers from a fundamental drawback that as $t\to 0$, $M\to 0$ (since $s\to 0$), giving rise to an ill-posed problem with infinite initial acceleration. This ambiguity can be physically resolved by referring to the equation of continuity, based on which it can be inferred that in the onset of the capillary motion, the liquid present in the dipped portion of the capillary and/or the bulk reservoir to which it is connected also starts moving at the same time. This additional mass of fluid inducted into the motion initially is known as the added mass, m_0. This added mass can be approximated by executing a potential flow analysis for an incoming spherical liquid element that moves with a velocity ds/dt. Executing this analysis, one can obtain the following approximate expressions [1]:

$$\begin{aligned} m_0 &\approx \frac{3\rho\pi R^3}{8} && \text{for a cylindrical tube} \\ &\approx \frac{\rho\pi H^2}{8} && \text{for a rectangular channel of height } H \text{ and unit width} \end{aligned} \tag{3}$$

The above is equivalent to the introduction of an additional term in the left hand side of eq. (1), which eliminates the prediction of an unrealistic initial burst as $t\to 0^+$.

(ii) The consideration of fully developed Poiseuillean flow for drag force calculations may not be practically valid. Classically, the flow through any closed conduit is expected to pass through an entrance region of length L_1, followed by a fully developed regime of length L_2 (which is characterized by a so-called Poiseuillean velocity profile). However, since surface effects tend to dominate in microfluidic channels, a third regime also comes into play, unlike the cases with their macroscale counterparts. This third regime physically originates due to a deviation of the velocity profile from a classical Poiseuillean velocity profile, on account of strong interplay of adhesion and cohesion forces, which gives rise to a dynamically evolving contact angle between the interface and the channel wall. This regime (of length L_3, say) is the so-called menis-

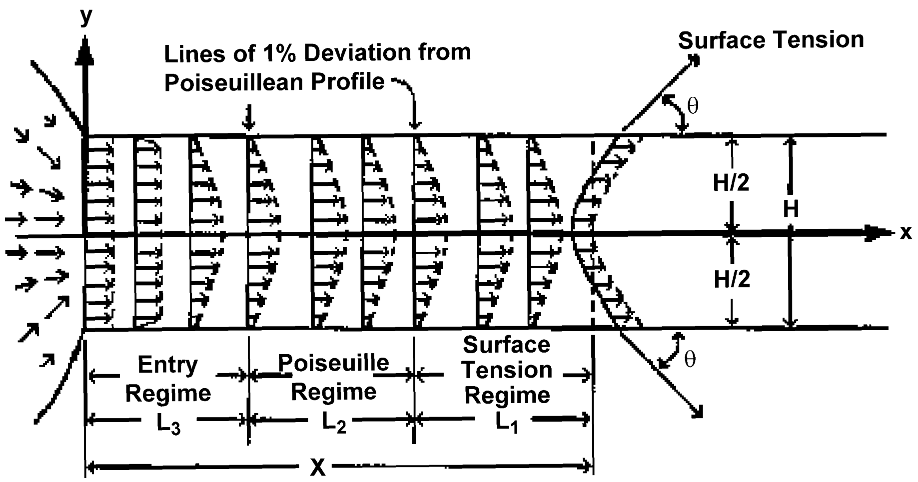

Capillary Filling, Figure 1 Velocity profiles corresponding to the flow into a capillary tube from a droplet

Capillary Filling, Table 3 Coefficients of the fitted polynomial depicting an enhanced flow resistance (as per eq. 5)

Coefficient	Value for $0 \leq \frac{x}{r_h} < 0.25$	Value for $0.25 \leq \frac{x}{r_h} < 0.35$	Value for $0.35 \leq \frac{x}{r_h} < 1$
a_0	2.36	4.88	1.29
a_1	0.95	−22.4	−2.89
a_2	−24.93	28.0	1.61

cus traction regime (refer to Fig. 1) [2, 3]. In reality, the total length of the fluid column (s_1, say) may vary, as the fluid advances inside the conduit. In case $s_1 < L_1 + L_3$, one has $L_2 = 0$, and hence, the entrance region and the meniscus traction region interact directly. The additional resistances because of the presence of these regimes, in practice, cannot be represented by simple mathematical expressions. However, experimental and/or full-scale computational results can be utilized to a good effect for specification of this enhanced resistance. For example, for the entrance regime, the numerical work of Lew and Fung [4] can be effectively utilized to express the net drag force gradient ($\mathrm{d}F_{\text{viscous}}/\mathrm{d}x$), in terms of its fully developed counterpart ($\mathrm{d}F^*_{\text{viscous}}/\mathrm{d}x$) as

$$\frac{\mathrm{d}F_{\text{viscous}}}{\mathrm{d}x} = \left[1 + f\left(\frac{x}{r_\mathrm{h}}\right)\right] \frac{\mathrm{d}F^*_{\text{viscous}}}{\mathrm{d}x} \quad (4)$$

where r_h is the hydraulic radius of the conduit and the function $f(x/r_\mathrm{h})$ takes care of the enhanced flow resistance in the entry region. Using the numerical results reported in Lew and Fung [4], the function $f(x/r_\mathrm{h})$ can be fitted in the following form:

$$f\left(\frac{x}{r_\mathrm{h}}\right) = a_0 + a_1\left(\frac{x}{r_\mathrm{h}}\right) + a_2\left(\frac{x}{r_\mathrm{h}}\right)^2 \quad (5)$$

where the coefficients a_0, a_1, and a_2 are tabulated in Table 3. It is interesting to observe from the above numerical data that $f(x/r_\mathrm{h})$ is positive everywhere, and becomes zero for $f(x/r_\mathrm{h})$ greater than 0.7 (i.e., when the flow becomes almost fully developed). Equation (4) can subsequently be integrated to obtain the drag force in the entrance regime (per unit width), as

$$F_{D,e} = \left[\int_0^X \frac{\mathrm{d}F^*_{\text{viscous}}}{\mathrm{d}x}\mathrm{d}x + \int_0^X f\left(\frac{x}{r_\mathrm{h}}\right)\frac{\mathrm{d}F^*_{\text{viscous}}}{\mathrm{d}x}\mathrm{d}x\right]$$
$$= r_\mathrm{h}\left[\frac{X}{r_\mathrm{h}} + \int_0^{X/r_\mathrm{h}} f\left(\frac{x}{r_\mathrm{h}}\right) d\left(\frac{x}{r_\mathrm{h}}\right)\right]\frac{\mathrm{d}F^*_{\text{viscous}}}{\mathrm{d}x} \quad (6)$$

where X is the axial length of the entry region under concern. It can be noted here that the term appearing in the above expression can also be expressed as a polynomial function (on integration of expression 5), which may be symbolically represented as $f_1(x/r_\mathrm{h})$ (say). It is extremely critical to recognize here that the net frictional resistance force needs to be quantified using distinctive mathematical expressions, depending on the different flow regimes existing within the channel. For instance, in situations where only the entrance and surface traction regimes exist, they

interact directly with each other. In that case, no Poiseuille flow regime exists, and the net resistance is a combination of the resistances offered by the entrance region and meniscus traction regime. For this, one needs to evaluate the flow resistance offered by the meniscus traction regime separately, based on the corresponding velocity profile. Without any further calculations, it may be concluded at this point that the surface traction regime must have near wall velocity components perpendicular to the wall, so that fluid sticks to the wall. This implies that local axial component of velocity also should increase, in order to satisfy the equation of continuity. If meniscus shape is maintained, the axial velocity component would then become gradually independent of y at the end of the meniscus traction regime. This implies that the boundary conditions for meniscus traction regime are just the inverse of those corresponding to the entry regime (i. e., inlet boundary condition for the entrance regime is same as exit boundary condition for the meniscus traction regime, and vise versa). Therefore, gradient of drag force for the meniscus traction regime can be expressed as (drawing analogy from equation 6)

$$\frac{\mathrm{d}F_{\mathrm{viscous}}}{\mathrm{d}x} = \left[1 + f\left(\frac{x_1 - x}{r_\mathrm{h}}\right)\right]\frac{\mathrm{d}F^*_{\mathrm{viscous}}}{\mathrm{d}x} \tag{7}$$

where x_1 is the total axial length of flow within the channel. A typical situation may be of interest in this regard, when $(x_{\max}/r_\mathrm{h})$ is less than or equal to 2×0.7, (that is, 1.4), i. e., when the Poiseuille flow regime does not exist, and the net drag force is given by a superposition as:

$$\begin{aligned} F_{\mathrm{viscous}} &= w r_\mathrm{h}\left[\frac{\bar{x}_1}{r_\mathrm{h}} + \int_0^{\bar{x}_1/2r_\mathrm{h}} f\left(\frac{x}{r_\mathrm{h}}\right) d\left(\frac{x}{r_\mathrm{h}}\right)\right. \\ &\quad \left. + \int_{\bar{x}_1/2r_\mathrm{h}}^{\bar{x}_1/r_\mathrm{h}} f\left(\frac{\bar{x}_1 - x}{r_\mathrm{h}}\right) d\left(\frac{x}{r_\mathrm{h}}\right)\right]\frac{dF^*_{\mathrm{viscous}}}{dx} \\ &= w r_\mathrm{h}\left[\frac{\bar{x}_1}{r_\mathrm{h}} + 2 f_1\left(\frac{\bar{x}_1}{2r_\mathrm{h}}\right)\right]\frac{dF^*_{\mathrm{viscous}}}{dx} \end{aligned} \tag{8}$$

where $\bar{x}_1$ is the total instantaneous axial length (averaged over the cross section) occupied by the fluid (which is equivalent to the parameter s as introduced earlier). In the most general situation, however, all the three regimes exist (when $(x_{\max}/r_\mathrm{h})$ is greater than 1.4), and the net drag force can be expressed as

$$F_{\mathrm{viscous}} = w r_\mathrm{h}\left[\frac{\bar{x}_1}{r_\mathrm{h}} + 2 f_1|_{\max}\right]\frac{\mathrm{d}F^*_{\mathrm{viscous}}}{\mathrm{d}x} \tag{9}$$

Overall, a realistic estimation of the drag force appearing in equation (1) can be obtained as

$$\begin{aligned} F_{\mathrm{viscous}} &= w r_\mathrm{h}\left[\frac{\bar{x}_1}{r_\mathrm{h}} + 2 f_1\left(\frac{\bar{x}_1}{r_\mathrm{h}}\right)\right]\frac{\mathrm{d}F^*_{\mathrm{viscous}}}{\mathrm{d}x} \\ &\qquad \textit{for} \quad 0 \le \frac{\bar{x}_1}{r_\mathrm{h}} \le 1.4 \\ &= w r_\mathrm{h}\left[\frac{\bar{x}_1}{r_\mathrm{h}} + 2 f_1|_{\max}\right]\frac{\mathrm{d}F^*_{\mathrm{viscous}}}{\mathrm{d}x} \\ &\qquad \textit{for} \quad \frac{\bar{x}_1}{r_\mathrm{h}} > 1.4 \end{aligned} \tag{10}$$

where $\mathrm{d}F^*_{\mathrm{viscous}}/\mathrm{d}x$ is described as

$$\begin{aligned} \frac{\mathrm{d}F^*_{\mathrm{viscous}}}{\mathrm{d}x} &= 8\pi\mu U && \text{for cylindrical microchannels} \\ &= 12\mu U/H && \text{for rectangular microchannels of unit width} \end{aligned}$$

(iii) The contact angle, θ, as appearing in the description of the surface tension, does not remain as fixed during the capillary advancement. Rather, it may undergo a dynamic evolution; on account of capillary slip mechanisms. On a microscopic scale, a possible mechanism in which such slip phenomena might occur on rough solid surfaces could be explained from the perspective that the contact line 'jumps' across indentations while moving along the solid boundary. This effectively leads a generalized expression of the variation of the effective contact angle with the con-

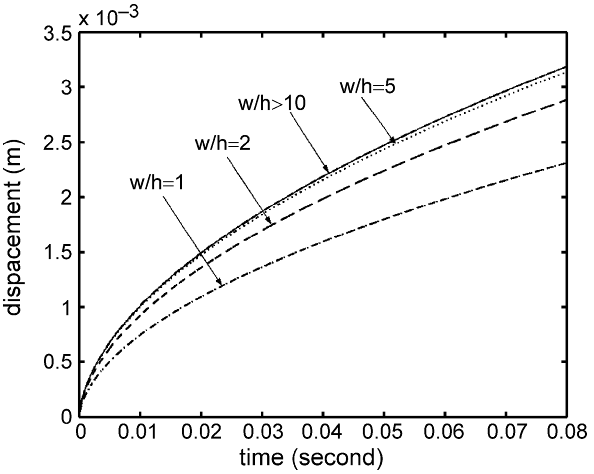

Capillary Filling, Figure 2 Typical displacement characteristics of the capillary meniscus, with variations in the channel aspect ratio (for simulation data, see Chakraborty [3])

tact line velocity in the following form [5]:

$$G(\theta) = G(\theta_0) + Ca \ln\left(\frac{K}{l_d}\right) + Ca \ln Ca \tag{11}$$

where Ca is the capillary number ($Ca = \frac{\eta U}{\gamma_{lv}}$), U being the cross-sectional-averaged axial speed of flow. In eq. (11), θ_0 is the microscopic static contact angle, K is a slipping model dependent constant, l_d denotes the scale of wall roughness and G(θ) is defined as [5]

$$G(\theta) = \int_0^\theta [f(\phi)]^{-1} d\phi \tag{12a}$$

$$\begin{aligned} f(\phi) = 2\sin\phi \Big\{ & q^2\left(\phi^2 - \sin^2\phi\right) \\ & + 2q\left[\phi(\pi-\phi) + \sin^2\phi\right] \\ & + (\pi-\phi)^2 - \sin^2\phi \Big\} \\ & \Big/ \Big\{ \left(\phi^2 - \sin^2\phi\right) \\ & \times [(\pi-\phi) + \sin\phi\cos\phi] \\ & + (\phi - \sin\phi\cos\phi)\left[(\pi-\phi)^2 - \sin^2\phi\right] \Big\} \end{aligned} \tag{12b}$$

where q is the viscosity ratio of the two fluids forming the capillary. Moreover, in reality, the microscopic contact angle, θ_0, can itself be dependent on the capillary flow velocity [6]. This gives rise to an additional velocity dependent frictional force, as appearing in eq. (7). The source of this frictional force is the excitation of damped capillary waves at the liquid-vapour interface due the contact line motions over the wall roughness elements. From experimentally obtained data [6], this can be modeled approximately in the following form:

$$F = 2\gamma_{lv}(w + h) BCa^x \tag{13}$$

where B and x are experimentally fitted constants. Some typical values of the various parameters pertinent to the specific slip model presented above are as follows [6]: $K = 0.3$, $l_d = 5000$Å, $B = 2.5$, $x = 0.3$. A physical basis of the introduction of the Ca-dependent and slip-modulated frictional force, F, can be provided as follows. As mentioned earlier, the contact line jumps across the indentations on the solid boundaries, as the contact line moves forward. During the jump, the liquid-vapour interface is pulled forward by the interfacial tension and is retarded by the liquid viscosity. The jump speed is therefore of the order of γ_{lv}/η, i. e., $Ca{\sim}1$. Because of the restoring effects, the liquid-vapour interface actually executes a time-periodic motion on a local scale. Further, the contact line actually slips during the jump process, and the corresponding dissipative effects associated with this jump are responsible for the additional frictional force, which gives rise to a velocity dependent θ_0. One potential slip scenario is that the contact line actually leaves the solid surface on one side of the indentation and reattaches itself on the other side of the indentation, since, without that detachment, the large viscous stress near the contact line would retard the movement the same significantly, so that local jump speeds with $Ca{\sim}1$ would not be realizable.

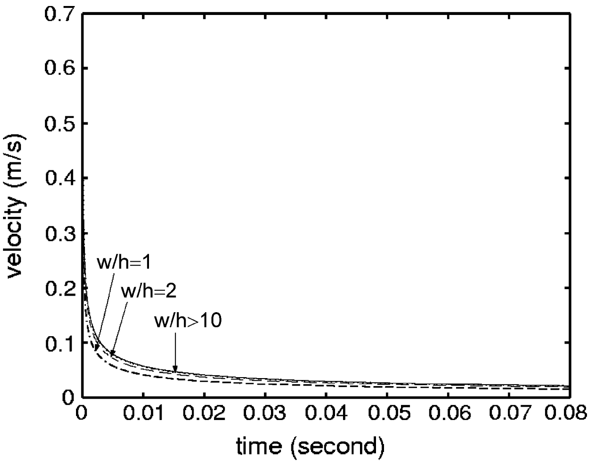

Capillary Filling, Figure 3 Typical displacement characteristics of the capillary meniscus, with variations in the channel aspect ratio (for simulation data, see Chakraborty [3])

Figures 2 and 3 depict typical displacement and velocity characteristics of the capillary meniscus, as a parametric function of the aspect ratio (w/h) of the microchannel. For more detailed explanations of the pertinent quantitative variations, one may refer to the work of Chakraborty [3].

Key Research Findings

The capillary filling model described as above is somewhat generic in nature and the effects of other driving forces (electric or magnetic fields, for instance) can conveniently be accommodated in the pertinent description of equation of motion. As a first example, one may refer to the capillary flow between parallel plates in the presence of an electromagnetic field [7], with the components of the electric and the magnetic field as $(0, 0, -E)$ and $(B\cos\alpha, B\sin\alpha, 0)$, respectively, where α is the inclination angle of the magnetic field relative to the channel axis. The separation between the two plates, h, is assumed to be much narrower in comparison to the channel width. Axial length of the channel is L. The angle between the direction of gravitational acceleration and the axial direc-

tion of motion is taken to be ϕ. For simplicity, the flow is assumed to be hydrodynamically fully developed, for which the velocity profile can be obtained by introducing the Lorentz (electromagnetic) force term in the linear momentum conservation equation, as

$$-\frac{\mathrm{d}p}{\mathrm{d}x}+\eta\frac{\mathrm{d}^2u}{\mathrm{d}y^2}-B^2\sigma_e\sin^2\alpha u+B\sigma_e E\sin\alpha+\rho g\sin\phi=0 \tag{14}$$

where σ_e is the electrical conductivity of the fluid and y represents the transverse direction in the plane of flow. The no-slip condition is assumed to prevail at the solid boundaries, i. e., $u(\pm h/2=0)$. The pressure boundary conditions are as follows: $p|_{x=0}=0$, and $p|_{x=s}=-\Delta p$ (which represents the pressure at the convex side of the interface), where Δp is the pressure drop across the meniscus, given by $\Delta p=(2\gamma_{lv}\cos\theta)/h$. With the aid of these boundary conditions and noting that $\mathrm{d}s/\mathrm{d}t=\frac{1}{h}\int_{-h/2}^{h/2}u\,\mathrm{d}y$, one can obtain an expression for the capillary filling time as (with $s=0$ at $t=0$)

$$\begin{aligned}t^*=&\left\{\frac{A}{(D_1+D_2)\left(\left(1-2D_4/\sqrt{A}\right)\sinh\left(\sqrt{A}/2\right)\right)}\right\}\\&-\left\{\frac{WeD_3}{(D_1+D_2)^2\left(\left(1-2D_4/\sqrt{A}\right)\sinh\left(\sqrt{A}/2\right)\right)}\right\}\\&\times\ln\left[1+\frac{D_1+D_2}{WeD_3}\frac{s}{L}\right]\end{aligned} \tag{15}$$

The various non-dimensional parameters appearing in eq. (15) are defined as follows: $t^*=tc_0/L$ (where $c_0=(\rho gh^2\sin\phi)/(3\eta)$), $D_1=aHa^2\sin\alpha$ (where $a=E/(c_0B)$, $Ha=Bh\sqrt{\sigma_e/\eta}$), $D_2=3$, $D_3=(-(\mathrm{d}p)/(\mathrm{d}x))\,(h^2/L^2)\mathrm{Re}$ (where $\mathrm{Re}=(Lc_0\rho^2)/\eta^2$), $A=Ha^2\sin^2\alpha$, $D_4=\left(2\exp(\sqrt{A}/2)\right)/\left(\exp(\sqrt{A})+1\right)$, $We=(2\gamma_{\mathrm{lv}}\cos\alpha)/\left(\rho c_0^2h\right)$. The percentage reduction in filling time because of

$$\psi=1-\frac{\text{filling time with EMF}}{\text{filling time without EMF}} \tag{16}$$

The above theoretical model has been numerically simulated in the work of Tso and Sundndaravadivelu [7]. Some major conclusions drawn from their studies can be summarized as follows:

1. The presence of electric field aids the flow, and thereby reduces the flow time for relatively large values of Ha. However, this effect is not unbounded, as it attains an asymptotic saturation with $a\approx 5$. Beyond this limit, any practical filling time reduction cannot be effectively realized by increasing the electric field strength, for a given magnetic field strength.
2. Effect of the angle α on the value of ψ is more significant for small values of a $(0\le a\le 5)$ only.

It needs to be noted here that the above results should better be interpreted from a qualitative viewpoint rather than an accurate quantitative viewpoint, since this analysis neglects the influences of dynamic contact angle, surface roughness, long range molecular forces, EDL effects and the electrical control of surface tension forces.

Dynamic interfacial effects due to capillary advancement in the presence of electroosmotic flows in hydrophobic circular microchannels have recently been investigated by Yang et al. [8]. In a general sense, their theoretical development is based on the prototype equation of motion of the form of eq. (1), with an additional term appearing in the right hand side to model the electroosmotic body force. Not only that, the quantification of the viscous drag force is also adapted to accommodate the influences of electroosmotic slip. To address these issues carefully, one may first derive an expression for electroosmotic flow velocity in presence of an axial electric field strength of E_1 in the solution, as

$$v_x=-\frac{\varepsilon_1\zeta E_1}{\eta}\left[1-\frac{J_0(j\kappa r)}{J_0(j\kappa R)}+j\beta\kappa\frac{J_0(j\kappa R)}{j\kappa R}\right] \tag{17}$$

where ε_1 is the permittivity of the electrolye being transported, ζ is the zeta-potential (see the article on 'Electric double layer fundamentals' for further details), J_0 is the zeroth-order Bessel function of the first kind, $j=\sqrt{-1}$, κ is the inverse of the characteristic electric double layer thickness and β is the slip coefficient (such that $v_z(R)=\beta\left((\partial v_z(R))/\partial r\right)$). The electrical charge density, as obtained by solving the Poisson–Boltzmann equation, can also be expressed in terms of the above-mentioned parameters, as

$$\rho_e=-\varepsilon_1\kappa^2\zeta\frac{J_0(j\kappa r)}{J_0(j\kappa R)} \tag{18}$$

It needs to be noted here that since the surface tension is fundamentally originated from the intermolecular forces and can be related to the thermodynamic work of adhesion and cohesion, the slip length can be estimated by appealing to the pertinent molecular theories as [8]

$$\beta=-\delta\left[\exp\{\alpha A\gamma_{lv}(1-\cos\theta)/k_BT\}-1\right] \tag{19}$$

where δ, A and α, respectively, are the average distances between the centers of the adjacent liquid molecules, the

effective surface area and the fraction of A composed of solid surface. For simplistic estimates, one may assume the liquid molecules to be spherical, with $A = \pi\delta^2$. Typical values of these parameters are $\delta = O\left(10^{-1}\right)$ nm and $\alpha = 1/6$ [8]. Based on these considerations, the electrosmotic body force and the viscous drag force can be estimated as

$$\begin{aligned} F_{\text{electroosmotic}} &= 2\pi s E_1 \int_0^R \rho_e r\,\mathrm{d}r \\ &= -2\pi s E_1 \varepsilon_1 \kappa^2 \zeta \frac{R}{j\kappa} \frac{J_1(j\kappa R)}{J_0(j\kappa R)} \end{aligned} \tag{20}$$

where J_1 is the zeroth-order Bessel function of the first kind.

$$\begin{aligned} F_{\text{viscous}} &= 2\pi R s \left(\eta \frac{\partial v_z(R)}{\partial r}\right) \\ &= 2\pi R \eta s \frac{\mathrm{d}s}{\mathrm{d}t} \frac{j\kappa \frac{J_1(j\kappa R)}{J_0(j\kappa R)}}{1 + j\beta\kappa \frac{J_1(j\kappa R)}{J_0(j\kappa R)} - \frac{2}{j\kappa R} \frac{J_1(j\kappa R)}{J_0(j\kappa R)}} \end{aligned} \tag{21}$$

Noting further that for thin electric double layers, κR is normally larger than 1000, which implies that $-j\left(\left(J_1(j\kappa R)\right)/\left(J_0(j\kappa R)\right)\right) \approx 1$, a simplified expression for eq. (1) can be obtained for this case as

$$\begin{aligned} &\rho\pi R^2 \left[s \frac{d^2 s}{dt^2} + \left(\frac{\mathrm{d}s}{\mathrm{d}t}\right)^2 \right] \\ &= 2\pi R \gamma_{lv} \cos\theta - 2\pi s E_1 \varepsilon_1 \kappa^2 \zeta \frac{R}{\kappa} + 2\pi R \eta \frac{\kappa}{1 - \beta\kappa} s \frac{\mathrm{d}s}{\mathrm{d}t} \end{aligned} \tag{22}$$

It is extremely important to note at this point the electric field E_1 is not the net axial electric field imposed on the capillary, but only the axial electric field acting on the electrolyte (remaining part of the capillary being occupied by a gas of permittivity ε_2, which is displaced by the electrolyte during its capillary advancement). If the electric field acting on the gas phase is E_2, then one can write: $\varepsilon_1 E_1 = \varepsilon_2 E_2$. If V_0 is the net axial voltage that acts on the capillary of total length L, then one can write

$$E_1 = \frac{V_0 \varepsilon_2}{\varepsilon_1 L + (\varepsilon_2 - \varepsilon_1) s} \tag{23}$$

With the initial conditions of $\mathrm{d}s/\mathrm{d}t = 0$ at $t = 0$ and $s = s_0$ at $t = 0$, eq. (23) can be numerically solved, to yield the displacement and velocity characteristics of the advancing capillary meniscus. Since the effect of added mass in not incorporated in eq. (22), a non-zero value of s_0 is required to avoid the prediction of an unrealistic initial burst at $t = 0$, as explained earlier. One major conclusion that can be drawn from the numerical simulation studies of Yang et al. [8], based on the above model, that while liquid slip on hydrophobic surfaces may increase the flow velocity, the presence of a capillary pressure across the liquid-vapour interface can suppress the electroosmotic flow and significantly decrease the flow performance.

The marching velocity of a capillary meniscus can also be obtained from the surface energy considerations, by relating the instantaneous position or velocity of the capillary front with the gradients of the net interfacial energy. The final forms of the governing equations, as expected, turn out to be of identical nature as the equations of capillary motion described earlier. For the mathematical details, one may refer to the recent work of Yang et al. [9].

Future Directions for Research

Although capillary filling of microchannels have been extensively investigated over the past few years, studies on capillary filling of nanochannels have only been very few. Tas et al. [10], in a recent study, investigated the capillary filling speed of water in nanochannels. In their studies, the above authors experimentally measured the capillary filling speed of water in nanochannels with a rectangular cross section and a height of the order of 100 nm, over a length of 1 cm. In a qualitative sense, the measured position of the meniscus as a function of time was found to qualitatively follow the Washburn model (refer to the article on 'Surface Tension Driven Flow', for details of this model). Quantitatively, however, a lowering of capillary filling speed could be noted, which might be attributed to the electro-viscous effects and stronger surface influences over nanoscopic length scales. Future efforts need to be directed to develop more rigorous mathematical models to predict the quantitative trends of capillary filling in nanofluidic channels, to resolve these issues.

Cross References

- ► Applications Based on Electrowetting
- ► Boundary Slip of Liquids
- ► Bubble Dynamics in Microchannel
- ► Droplet and Bubble Formation in Microchannels
- ► Droplet Based Lab-on-chip Devices
- ► Droplet Despensing
- ► Droplet Dynamics in Microchannels
- ► Droplet Evaporation
- ► Droplet Microreactors
- ► Electrocapillary
- ► Electrowetting and Droplets
- ► Surface Tension Driven Flow
- ► Transport of Droplets by Acoustics

► Transport of Droplets by Thermal Capillarity
► Wetting and Spreading

References

1. Yih CH (1995) Kinetic-energy mass, momentum mass, and drift mass in steady irrotational subsonic flow. J Fluid Mechanics 297:29–36
2. Huang W, Bhullar RS, Fung YC (2001) The surface-tension-driven flow of blood from a droplet into a capillary tube. ASME J Biomedical Eng 123:446–454
3. Chakraborty S (2005) Dynamics of capillary flow of blood into a microfluidic channel. Lab Chip 5:421–430
4. Law HS, Fung YC (1970) Entry flow into blood vessels at arbitrary Reynolds number. J Biomechanics 3:23–38
5. Hoffman RL (1975) A study of the advancing interface I. Interface shape in liquid-gas systems. J Colloid Interface Sci 50:228–235
6. Sheng P, Zhou M (1992) Immiscible-fluid displacement: contact-line dynamics and the velocity-dependent capillary pressure. Phys Rev A 45:5694–5708
7. Tso CP, Sundaravadivelu K (2001) Capillary flow between parallel plates in the presence of an electromagnetic field. J Phys D 34:3522–3527
8. Yang J, Lu F, Kwok DY (2004) Dynamic interfacial effect of electroosmotic slip flow with a moving capillary front in hydrophobic circular microchannels. J Chem Phys 121:7443–7448
9. Yang L-J, Yao T-J, Tai Y-C (2004) The marching velocity of the capillary meniscus in a microchannel. J Micromech Microeng 14:220–225
10. Tas NR, Haneveld J, Jansen HV, Elwenapoek, van den Berg A (2004) Capillary filling speed of water in nanochannels. Appl Phys Lett 18:3274–3276

Capillary Flow

► Surface Tension Driven Flow

Capillary Force Valves

DANIEL IRIMIA
Massachusetts General Hospital,
Harvard Medical School, Boston, MA, USA
dirimia@partners.org

Synonyms

Capillary valves

Definition

Capillary force valves are fluid control structures that use superficial tension at the interface between different fluids to block and/or restore the entrance of fluids in microchannels filled with a second immiscible fluid. For most of the microfluidic applications the second fluid is air, and the liquid–air interface at a narrow hydrophobic stricture is used to prevent the liquid from entering a capillary.

Overview

Capillary forces result from the interaction of liquid, gas and solid surfaces, at the interface between them. In the liquid phase, molecules are held together by cohesive forces. In the bulk of the liquid, the cohesive forces between one molecule and the surrounding molecules are balanced. However, for the same molecule at the edge of the liquid, the cohesive forces with other liquid molecules are larger than the interaction with air molecules (Fig. 1). As a result, the liquid molecules at the interface are pulled together towards the liquid. The overall effect of these forces is to minimize the free surface of the liquid that is exposed to air. The proportionality between the decrease in energy of the surface that results from decreasing the surface is described by the *surface tension*:

$$\gamma = \frac{\mathrm{d}G}{\mathrm{d}A}$$

where dG is the change in energy [N m], dA is the change in area [m^2] and γ is the surface tension or surface energy [N/m].

Of interest for capillary forces is the contact between three phases: liquid, solid and vapor (air). Three forces are present, trying simultaneously to minimize the contact area between the three phases. At equilibrium, the forces at the triple interface are balanced (Fig. 2) and the relationship between them is described by the Young–Dupree

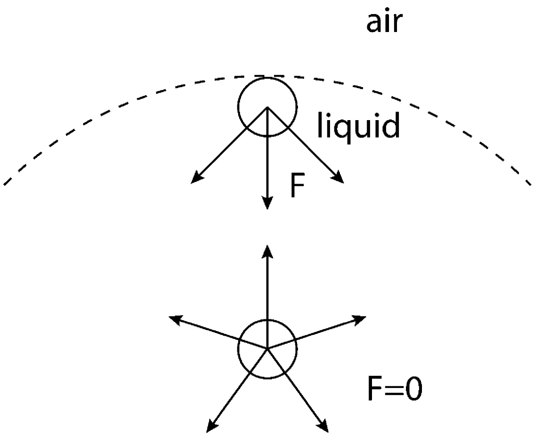

Capillary Force Valves, Figure 1 Superficial tension forces at the interface between a liquid and air. For molecules in the liquid there is a balance of the cohesive forces ($F = 0$), while for molecules closer to the interface, the cohesive forces with other molecules in the liquid are larger than the interaction with air molecules (resultant force F towards the bulk of the liquid)

equation:

$$\gamma_{AS}L = \gamma_{LS}L + \gamma_{LA}L \times \cos\Theta$$

where L is the length of the triple contact line and Θ is the contact angle between the liquid and the solid. It is interesting to observe the vertical component pulling on the solid surface in the case of wetting and pushing in the case of non-wetting surfaces.

Capillary forces are critical at the microscale. The surface tension is responsible for the increased pressure in a bubble trapped in a capillary, and for the increased pressure required to push liquid into an empty non-wetting capillary (Fig. 3). The relation between surface tension and pressure is given by the Laplace equation:

$$\Delta P = \gamma C$$

where C is the curvature of the liquid surface. Depending of the shape of the capillary, different formulas for the curvature are available:

$$C = \frac{2}{R}$$

$$C = \frac{1}{R_1} + \frac{1}{R_2}$$

where R is the curvature radius for the liquid in a circular capillary and R_1 and R_2 are the curvatures in a non-circular capillary.

Basic Methodology

The behavior of air and liquids in capillaries is of critical importance at the microscale. After their fabrication, most of the channels in microfluidic devices are filled with air. In general, before the microfluidic devices are used for their designed purpose, the air inside the microfluidic channels has to be replaced by the working fluid. However, there are many applications where not all the air is replaced at once, and the advance of fluid inside the microfluidic channels is controlled through capillary force valves.

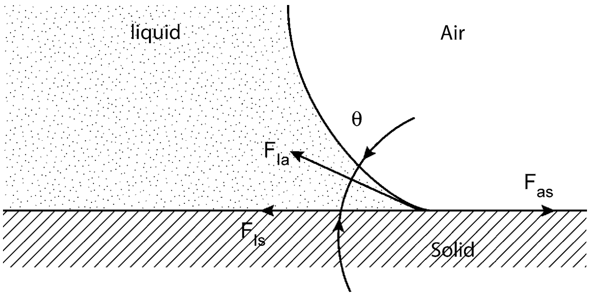

Capillary Force Valves, Figure 2 Capillary forces at the interaction between air, liquid and solid surfaces. Each of these forces works to minimize the energy of the interface between liquid and solid, air and solid, liquid and air: F_{ls}, F_{as}, F_{la}, respectively. At equilibrium, the horizontal projection of F_{la} and F_{ls} and F_{as} cancel each other. The corresponding angle between F_{la} and F_{ls} is the contact angle between liquid and solid (Θ)

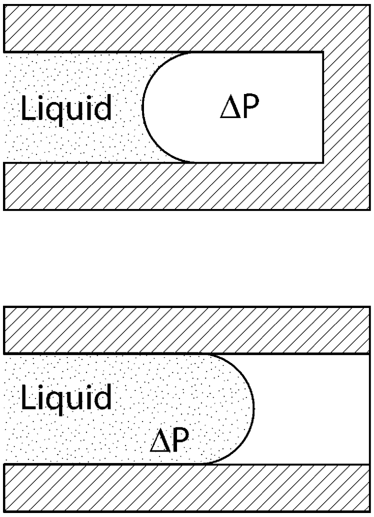

Capillary Force Valves, Figure 3 Capillary forces in hydrophilic capillaries result in increased pressure in trapped air bubbles. Capillary forces in hydrophobic capillaries prevent liquid from entering the capillary, and can be overcome by larger pressure

Two major strategies for making valves using the capillary forces are through the use of (a) local changes of contact angle and (b) local changes of surface geometry.

(a) The use of hydrophobic patches in a capillary relies on the increased pressure that is required to push the liquid over the area of larger contact angle (Fig. 4). The increased contact angle between the liquid and the capillary in the region of the hydrophobic patch results in a larger pressure necessary for moving the liquid over that region. After passing the patch, the pressure required for moving the liquid returns to pre-patch values. The combination of hydrophobic patches on the bottom of the channel is of interest for microfluidic devices where precise valving is required, or for liquids with different characteristics.

One other particular effect of practical interest whenever capillary forces are used is the difference between advancing and receding angles for the same fluid in the same capillary. This phenomenon is also known as hysteresis and manifests itself as larger contact angle at the advancing edge of a liquid–solid interface compared to the equilibrium contact angle which is itself larger than the contact angle at the receding edge of the liquid–solid interface (Fig. 5). The origin of this is partially in the roughness of the surface and can have interesting effects when moving columns of liquids through capillaries [1].

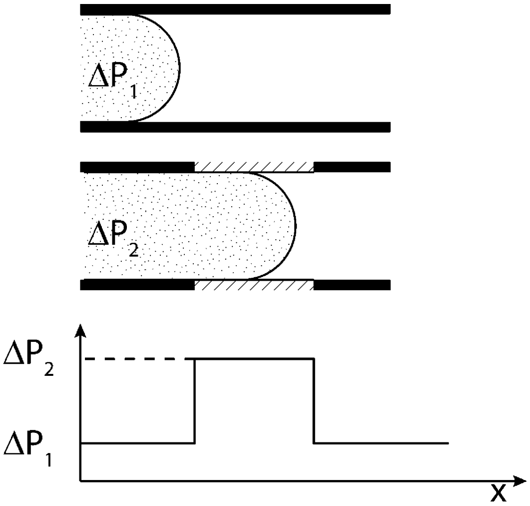

Capillary Force Valves, Figure 4 Schematics of a capillary valve using a hydrophobic patch. The pressure required to move the liquid (ΔP_1) is higher when the liquid–air interface reaches the region of increased hydrophobicity (ΔP_2)

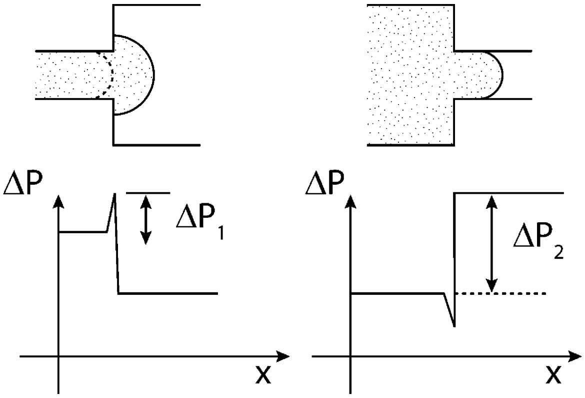

Capillary Force Valves, Figure 6 Schematics of capillary valves using changes in the diameter of the capillary. Rapid enlargement of a capillary changes the physical angle between the liquid interface and the solid surface and can form a temporary barrier for the advancing liquid (ΔP_1). Reducing the diameter of a hydrophobic capillary reduces the radius of curvature of the interface and requires larger pressure (ΔP_2) to move the liquid and could also function as a valving mechanism

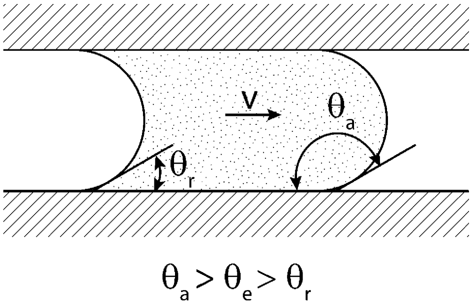

Capillary Force Valves, Figure 5 Hysteresis in contact angle. The contact angle at the advancing interface (Θ_a) is usually larger than the equilibrium contact angle (Θ_e), and larger than the contact angle at the trailing interface (Θ_t)

(b) The larger contact angle at advancing interfaces can be used in capillary valves as well, in combination with local change of the shape of the surface or the change in the diameter of the capillary (Fig. 6). This approach to controlling a liquid–air interface can be used alone or in combination with the hydrophobic patches. Although the fluid control is usually less precise for valves using changes in diameter compared to valves using hydrophobic patches, their implementation in microfluidic devices is overall easier.

Key Research Findings

For the majority of microfluidic devices the initial filling (priming) of the device with liquid or the formation of air bubbles inside can render the device unusable. However, there are numerous examples that use the liquid–air interfaces to control the flow of liquid for different applications. Wall-less control of the flow of liquid streams has been demonstrated on micropatterned hydrophobic surfaces (Fig. 7) [2]. Micropatterned patches have been used to precisely stop the liquid flow at a certain position inside a channel without the need for moving parts (Fig. 8) [3], and for the accurate metering of nanoliter volumes of liquids in microchannels [4, 5]. Handling of minute volumes of fluids and mixing inside a capillary have been reported. Through the use of passive valves to control the flow of fluid and air bubbles expanded from side chambers, volumes of liquids down to 25 pL can be handled precisely (Fig. 9) [6]. The hydrophobic nature of the liquid–wall interaction was critical for stable and complete separation of picoliter volumes of fluid [7].

Capillary valves are burst valves, i. e. once the liquid passes through them they no longer function as valves. Resetting a capillary valve requires the formation of the liquid–liquid or liquid–gas interface at the location of hydrophobic interaction. This can be achieved by the injection of gas or liquid, usually in a small volume, from a reservoir or generated on the chip [6, 8].

Future Directions for Research

Capillary valves have no moving parts, are simple and easy to implement and thus are very attractive for low-cost microfluidic devices. At the same time, several areas of improvement are under scrutiny, to increase the performance of the valve, to improve the integration and to

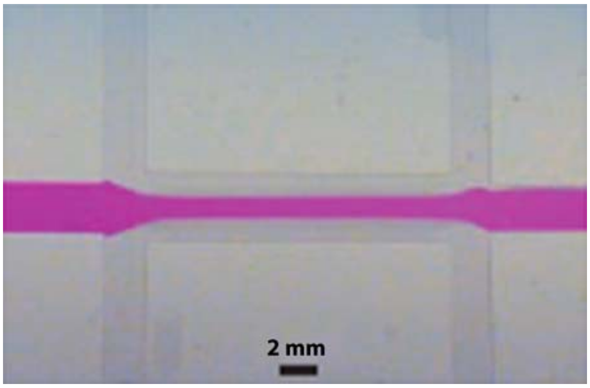

Capillary Force Valves, Figure 7 Hydrophilic and hydrophobic patches are used to control the flow of liquid streams (here rhodamine in water) in a wall-less configuration, just by relying on the surface tension of the liquid [2]

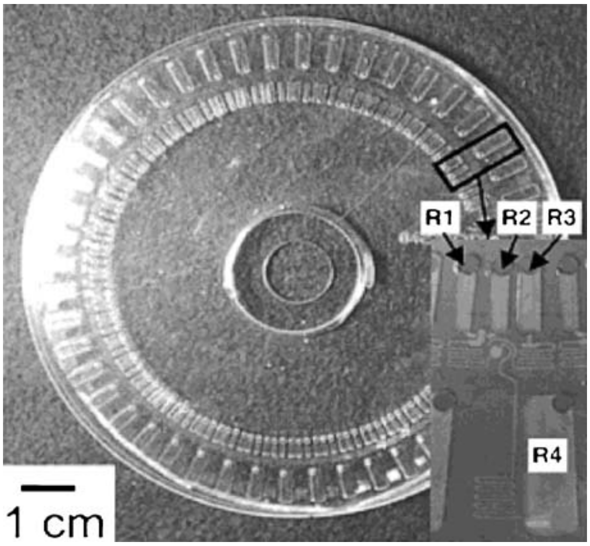

Capillary Force Valves, Figure 8 Capillary burst valves are used to control the sequential mixing of reagents in a Lab-on-a-CD type device. The solutions of enzyme, inhibitor and substrate were loaded in reservoirs that were connected to channels labeled R1, R2 and R3, respectively. R4 is a reservoir for waste collection. The rotation of the disk at different speeds controls the opening of the valves, and the sequence of mixing the enzyme with the inhibitor, followed by mixing with the substrate, and detection [3]

expand the range of applications. Continuous efforts are made to enlarge the variety of liquids that can be handled by new approaches to surface patterning in microcapillaries. The integration of an increasing number of valves for the implementation of complex reaction protocols is also an area of active research, especially, but not limited to, Lab-on-a-CD type devices [9]. Finally, while microfluidic devices are developed for applications outside the laboratory, it becomes increasingly important to

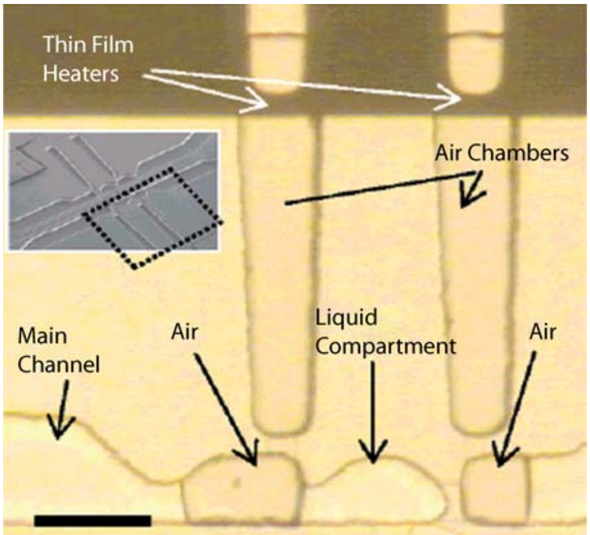

Capillary Force Valves, Figure 9 A volume of 25 pL is isolated by the creation of two new liquid–air interfaces, through the use of two thermal actuators. Two air bubbles isolate the separated volume from the rest of the liquid in the main channel [6]

provide robust valve designs that would ensure functioning over a wider range of temperatures, storage conditions and operator training, etc.

Cross References

- ► Lab-on-a-Chip (General Philosophy)
- ► Centrifugal Microfluidics
- ► Applications Based on Electrowetting
- ► Electrowetting
- ► Biosample Preparation Lab-on-a-Chip Devices
- ► Boiling and Evaporation in Microchannels
- ► Bubble Actuated Microfluidic Switch
- ► Capillary Filling
- ► Control of Microfluidics
- ► Droplet and Bubble Formation in Microchannels
- ► Electrocapillary
- ► Electrochemical Valves
- ► Electrowetting
- ► Fabrication of 3D Microfluidic Structures
- ► Fluid Metering
- ► Integrated Microfluidic Systems for Medical Diagnostics
- ► Lab-on-Chip Devices for Chemical Analysis
- ► Marangoni Convection
- ► Microfluidic Circuits
- ► Microfluidic Sample Manipulation
- ► Surface Tension, Capillarity and Contact Angle
- ► Transport of Droplets by Thermal Capillarity
- ► Water Management in Micro DMFCs

References

1. de Gennes P-G, Brochard-Wyart F, Quéré D (2004) Capillarity and wetting phenomena: drops, bubbles, pearls, waves; translated by Axel Reisinger. Springer, New York
2. Zhao B, Moore JS, Beebe DJ (2001) Surface-directed liquid flow inside microchannels. Science 291:1023–1026
3. Duffy DC, Gillis HL, Lin J, Sheppard NF, Kellogg GJ (1999) Microfabricated Centrifugal Microfluidic Systems: Characterization and Multiple Enzymatic Assays. Anal Chem 71:4669–4678
4. Handique K, Burke DT, Mastrangelo CH, Burns MA (2001) On-chip thermopneumatic pressure for discrete drop pumping. Anal Chem 73:1831–1838
5. Lee SH, Lee CS, Kim BG, Kim YK (2003) Quantitatively controlled nanoliter liquid manipulation using hydrophobic valving and control of surface wettability. J Micromech Microeng 13:89–97
6. Irimia D, Tompkins RG, Toner M (2004) Single-cell chemical lysis in picoliter-scale closed volumes using a microfabricated device. Anal Chem 76:6137–6143
7. Ajaev VS, Homsy GM (2001) Steady Vapor Bubbles in Rectangular Microchannels. J Colloid Interface Sci 240:259–271
8. Oh KW, Ahn CH (2006) A review of microvalves. J Micromech Microeng 16:R13–R39
9. Madou M, Zoval J, Jia G, Kido H, Kim J, Kim N (2006) Lab on a CD. Annu Rev Biomed Eng 8:601–628

Capillary Magnetophoresis

► Magnetophoresis

Capillary Reactor

► Droplet Microreactor

Capillary Valves

► Capillary Force Valves

Capillary Zone Electrophoresis

► Capillary Electrophoresis

Caspase Activation

► Microfluidics for Studies of Apoptosis

Cast-in-Place Polymeric Media

► Stationary Phases in Microchannels

Catalyst Testing

Definition

A branch of combinatorial chemistry used for developin develop in an empirical or semi-empirical manner new and more efficient catalysts.

Most often, in the heterogeneous catalysis the catalysts are solids–usually metals, very often precious metals–while the reactants are liquid or gaseous. The catalysts are usually composed of a number of (metal) components in various combinations. The tests are performed in parallel under the otherwise equal temperature and pressure conditions in a large number of microreactors. In each microreactor the combination of the tested catalyst components is different and this results in a different yield or selectivity of the test reaction. This is usually evaluated by composition analysis of the reaction products. The results are stored in a combinatorial library and processed mathematically to determine the optimum combination.

Cross References

► Microfluidic Systems for Combinatorial Chemistry
► Combinatorial Library

Cataphoresis

► Electrokinetic Motion of Cells and Nonpolarizable Particles

Cathode

Definition

Negatively charged electrode.

Cross References

► Electrophoresis

Cathode Sputtering

► Sputtering for Film Deposition

Cation

Definition

Positively charged ion that moves towards the cathode in electrophoresis.

Cross References

► Electrophoresis

Cation Exchange Membrane

Definition

An ion-exchange membrane that interacts with cations and have a variety of anion functional groups affixed to the membrane ($-COO^-$, $-SO_3^-$, $-PO_3^{2-}$, $-C_6H_4O^-$, etc). These functionalities allow cations to pass through the membrane and prevents anions from passing through the membrane. The ability of the membrane to bind ions is greatly dependant on the pH of the solution and the ions of interest.

Cross References

► Ion Exchange Membranes

Cavitation

Synonyms

Bubble formation

Definition

Formation of a vapor phase within a liquid or solid due to an extreme and rapid reduction in pressure and commonly exhibited in propellers and high-power acoustic systems.

Cross References

► Piezoelectric Microdispenser

Cavitation in Microdomains

Yoav Peles
Department of Mechanical, Aerospace and Nuclear Engineering, Rensselaer Polytechnic Institute, Troy, NY, USA
pelesy@rpi.edu

Synonyms

Liquid–vapor phase change; Multiphase flows

Definition

Cavitation is the process of nucleation in a liquid and subsequent formation of gas/vapor phase when the pressure falls below a critical value. Researchers studying cavitation address topics ranging from the initial appearance of cavities in liquids (cavitation inception) to the development of large-scale cavities (supercavitation).

Overview

Cavitation, the phenomenon that causes liquids to rupture and to form vaporous/gas cavities when subjected to sufficiently low pressures, can occur in any machine handling liquid when requisite hydrodynamic conditions develop (Fig. 1). Cavitation, in many cases, is an undesirable phenomenon in hydraulic machinery that can limit performance, lower efficiency, introduce sever structural vibration, generate acoustic noise, choke flow and cause catastrophic damage [1]. The pernicious effects of hydrodynamic cavitation on conventional fluid machinery have been recognized and actively researched in the last century. Present knowledge (experimental and analytical) of cavitation has contributed immensely towards improving the design of conventional scale fluid machinery.

Recent developments in microelectromechanical systems (MEMS) have enabled the integration and fabrication of numerous micro components such as pumps, valves and nozzles into complex high-speed microfluidic machines. These systems posses geometrical dimensions in the range $1-1000\,\mu m$, which are 10^3-10^4 times less than conventional machines, and operate at liquid flow speeds up to $300\,m/s$. It has been confirmed that microfluidic systems, like their large-scale counterparts, are susceptible to the deleterious effects of cavitation when appropriate hydro-

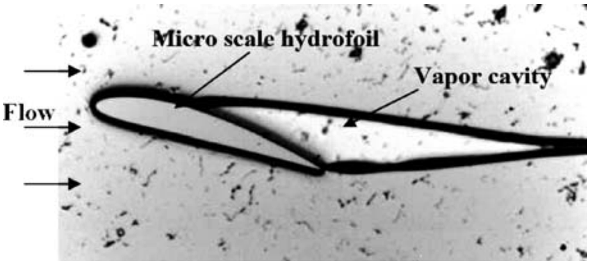

Cavitation in Microdomains, Figure 1 Cavitation in hydrofoils (flow is from left to right). Vapor cavity forms downstream of a NACA 4412 hydrofoil (angle of attach 16°, 1 mm, 100 µm height)

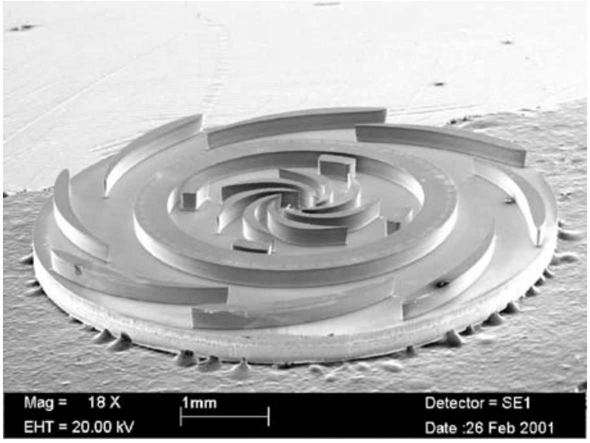

Cavitation in Microdomains, Figure 2 The MIT micro turbopump rotor [3]

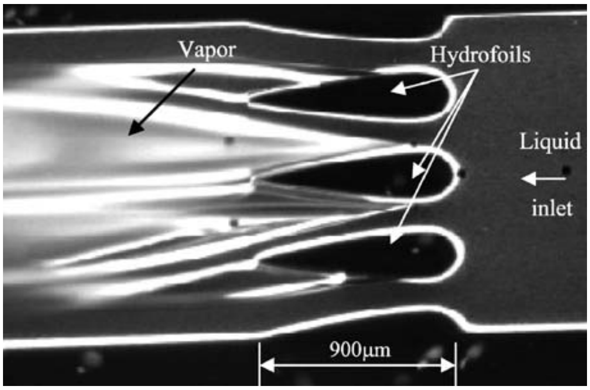

Cavitation in Microdomains, Figure 3 Cavitation in micro hydrofoils [3]

dynamic conditions develop. Cavitation damage in micro-orifices has been reported by Mishra and Peles [2]. Small pits on the silicon surface have been detected after only 7 – 8 hours of operation under cavitating flow.

Hydrodynamic cavitation, in the context of high-speed (750,000 – 1,200,000 rpm) MEMS turbopumps (Fig. 2) being developed for millimeter-scale, liquid bipropellant, high-pressure rocket engines, has been experimentally investigated for working fluids like water and ethanol by Pennathur et al. [3] with 900 µm hydrofoil cascades, which are characteristic of the centrifugal MIT micro turbopump. It was found that cavitation can seriously affect the efficiency and performance of the pump. The above investigation instigated two main design changes wherein the pump inlet pressure was raised, and a secondary boost pump was added in series with the main pump to produce the required pumping power. The experimental part of this research demonstrated that cavitation is clearly part of the engineering environment of MEMS fluid devices as exemplified by Fig. 3, and cavitation concerns are as important as they are in large-scale fluid devices.

Basic Methodology

A very useful parameter for quantifying cavitating flows of various intensities is the cavitation number, σ, given by

$$\sigma = \frac{P_\infty - P_\mathrm{v}}{\frac{1}{2}\rho V_\infty^2} \tag{1}$$

where P_∞ is the free stream pressure (or some characteristic pressure), P_v is the vapor pressure, ρ is the density and V_∞ is the velocity of the free stream. Of particular importance in the study of cavitation inception is the minimum pressure coefficient ($C_{\mathrm{p_{min}}}$) given by

$$C_{\mathrm{p_{min}}} = \frac{P_\mathrm{min} - P_\infty}{\frac{1}{2}\rho V_\infty^2} \tag{2}$$

where P_min is the minimum pressure in the liquid. Classical theory for scaling cavitation states that the cavitation number at inception cavitation equals $-C_{\mathrm{p_{min}}}$ and the cavitation number is sufficient to link one cavitation flow state to another provided the form of the flow field and its boundaries remain geometrically and kinematically similar. However, it has long been known that real flows often do not obey the classical theory because of so called scale effects, which arise from changes in velocity, size, fluid properties, nuclei size and distribution, etc. [1]. It has also been reported that nuclei and viscous effects are responsible for most scaling effects. As a direct result, several studies have been conducted that clearly demonstrate the role of viscous and nuclei effects on the excitation (inception) of cavitation. Nevertheless, due to the complexity of the scaling effect, serious questions remain as to how to scale cavitation.

Scaling Cavitation at the Microscale

Various known factors affecting cavitation in conventional scale systems are altered in microscale systems, such as flow dimensionless parameters, component geometries, liquid contaminants (nuclei sources) and surface roughness and chemistry (surface energy). The differences arise from various causes including microfabrication constraints, typical choice of device materials and the Reynolds number. Subsequent sections will discuss each effect in detail.

Geometrical Effects

Even when ignoring all scaling effects, conventional scale knowledge cannot be used to model cavitation in microsystems simply because scaling requires the model and prototype to be geometrically similar. However, microfabricated devices usually possess geometries that are considerably different from their conventional-sized counterparts.

The deep reactive ion etching (DRIE) technique, first presented in the mid- to late 1990s, facilitated the fabrication of numerous innovative microsystems, especially power-MEMS systems. Since most MEMS devices involve some form of lithography-based microfabrication, the use of flat substrates is required. Often, these flat substrates involve the use of DRIE methods and result in structures characterized by extrusion of two-dimensional features into the third dimension as illustrated in Fig. 2. Therefore, microfluidic components are often limited in their geometrical appearance, which precludes full three-dimensional shapes commonly found in many large-scale fluidic devices such as pumps hydrofoils, turbine blades and vanes, mixers, etc.

Nuclei Effects

The term nuclei refers to the impurities that cause weak spots in the liquid and, thus, promote cavitation events. Generally, nuclei can be categorized into two groups: stream nuclei and surface nuclei. Stream nuclei consist of undissolved gases or uncondensed vapor trapped in solid particles or in microbubbles moving with the flow, while surface nuclei originate in the solid–fluid boundary in the cracks, crevices and other surface imperfections. The importance of nuclei in dictating cavitation events has drawn considerable attention and resulted in various technical investigations.

Various mechanisms by which nuclei are formed have been suggested over the years. Holl [6] argued that the nuclei sources best applicable to most pragmatic engineering situations are non-condensable gases in crevices, either on particles flowing with the stream (stream nuclei) or on the solid boundaries of a body (surface nuclei). Billet [7] listed several experimental investigations that show stream nuclei to be the dominant source of cavitation nuclei in conventional scale systems. However, Holl [6] suggested that the source of cavitation depends on the surface energy characteristics of the system (i. e., hydrophobic vs. hydrophilic) and on the system size scale. Systems made of hydrophobic surfaces are very dependent upon surface nuclei, whereas systems made of hydrophilic surfaces depend upon stream nuclei.

In microsystems, the dimension, shape and chemistry of surface nuclei and relative size of the stream nuclei are altered. Microscale hydraulic devices are primarily fabricated from silicon by various microfabrication etching processes (primarily by DRIE processes), and possess vastly different surface chemistry (different material) and surface topography (different fabrication methods from those used in the construction of large-scale hydraulic devices). For example, the DRIE process forms deep trenches on the silicon wafer with a characteristic scalloped sidewall possessing a peak-to-peak roughness of $\sim 0.3\ \mu$m. Furthermore, the surface nuclei become increasingly important with respect to the stream nuclei as the length scale diminishes. This can be better understood by considering the time available for the stream nuclei growth. As system size is reduced (for a given velocity value), the dwell-time of a nucleus in the low-pressure region diminishes. Consequently, the nucleus has insufficient time to grow and become active. On the other hand, the time available for growth of the surface nuclei is not necessarily hampered as the system dimensions drop. The bubble conveniently dwells in the low-pressure region before it is torn from the surface due to the action of drag forces.

It should be noted that most conventional-scale investigations have been carried out with tap or natural water, in which the stream nuclei are mainly in the $10-100\ \mu$m size range. As stated by the specialist committee on water quality and cavitation, one key criterion for cavitation inception testing is the availability of a sufficient number of microbubbles in that size range. However, for microscale devices the applications typically dictate stringent requirement for stream contaminants not larger than $\sim 1\ \mu$m. It follows that most experimental data on stream nuclei size and distribution are not in the range applicable to the working fluid employed in microscale devices.

In light of the importance of the stream nuclei in conventional-scale cavitation, the problem of identifying cavitation nuclei size and concentration in the working fluid has received considerable attention. Photography, holography, acoustical and optical scattering, coulter counters and acoustical attenuation have all been used to detect and measure the size concentrations/distributions of cavitation nuclei. However, these methods do not directly measure the tensile strength of most nuclei and, therefore, provide limited information on the critical tension that makes a nucleus unstable. The cavitation susceptibility meter (CSM) was intended to directly measure the active nuclei concentration as a function of applied tension in a flow through a small venturi tube, where cavitation was induced by carefully controlled conditions. However,

stringent operational limitations in the form of laminar flow separation and surface nuclei effects, which are difficult to eliminate, bring into question the practical utility of CSMs over a wide range of applied tension [8]. Nevertheless, as long as CSMs are used for measuring relative differences of nuclei between different water sources they could be quite useful for direct water quality measurements.

Dimensionless Flow Parameters

Three main dimensionless parameters most likely dominating cavitation in microsystems are the cavitation (σ), Reynolds (Re), and Weber (We) numbers. Although early work on cavitation scaling [6] has suggested the We number as a possible parameter affecting cavitation, it has been found that nuclei together with viscous effects are responsible for most scaling effects in conventional-scale systems, and, therefore, the primary dimensionless parameters in large-scale systems are the Reynolds and cCavitation numbers (although in some circumstances other dimensionless parameters such as the Froude, Strouhal and Weber numbers are important).

High-velocity microsystems operate at considerably lower Reynolds numbers than their large-scale counterparts. For example, the maximum hydrofoil-based Reynolds number of the exceptionally high-speed MIT micro turbopump [3] is no more than $\sim 10{,}000$, while at conventional scale typical Reynolds numbers are of the order of $\sim 10^5$ to $\sim 10^8$. The vast majority of available data on limited and developed cavitation are for Reynolds number much higher than the range observed/attainable in microsystems. This has important consequences on the extension of conventional data to microsystems because it has long been recognized that viscous effects are significant for both inception and developed cavitation. For hydrofoils the problem becomes even more significant since different chord lengths yielded different cavitation inception–Reynolds number curves [1]. This suggests that there is an additional size or speed effect separate from the Reynolds number. Although Brennen [1] speculated that the ratio of nuclei size to hydrofoil length is the missing parameter, no definite conclusion could be reached in the absence of information on the nuclei.

Although the surface tension force is important in the excitation and initial growth stages of a cavitating bubble, surface forces hardly have any affect on the global flow field once the individual bubble has matured to a substantial macro size. In microdomains, on the other hand, a bubble is unable to grow beyond the microdevice domain and continues to be influenced by surface tension forces since they are dominant at those length scales. It follows that the Weber number (or/and the capillary number) assumes an increasingly important position as system size diminishes.

Key Research Findings

Unlike flow boiling, cavitation has not received considerable attention at the microscale. Nevertheless, several reports have been recently published that clearly show that conventional-scale knowledge and data cannot be simply employed to predict cavitation in microdomains. Mishra and Peles [2, 4, 5] studied hydrodynamic cavitation through micro-orifice entranced in microchannels. Their results revealed several key deviations in respect to macroscale systems. It was shown that the orifice size influences cavitation inception. An increase in the orifice size for a fixed microchannel width resulted in an increase in the cavitation inception number. Such a size scale effect has been observed by various authors even at the macroscale. The cavitation inception data presented by [9] for a fixed β (orifice-to-channel hydraulic diameter ratio) are smaller in magnitude than the results of [10] suggesting that the pipe diameter influences cavitation inception. It was shown that the cavitation number at inception (σ_i) varies with area (orifice-to-channel) aspect ratio (A_0/A_p) and a higher A_0/A_p results in a larger σ_i. The data indicate the presence of a dominant size scale effect on cavitation inception even at the microscale. Moreover, the σ_i values obtained from the Mishra and Peles experiments are considerably lower than any previous studies with larger orifices [9, 10]. This can be attributed to the small nuclei residence time and the surface tension forces, which are significant at the microscale and can aid in delaying the rupture of the liquid.

When they continued to reduce the cavitation number by reducing the exit pressure the *Vena Contracta* (the location where the static pressure drops to its minimum and the velocity rises to its maximum) static pressure approached the vapor pressure of water and caused flow rate choking irrespective of the inlet pressures. Although flow rate choking has been reported even in macroscale studies [9, 10], microflows readily transition from incipient to choking conditions since even a single vapor bubble in the microchannel is sufficient to choke the flow. In experiments conducted on larger orifices inside larger pipes, the cavitation number had to be reduced significantly beyond inception before flow rate choking is detected [9, 10]. Tullis [10] reported a 59% increase in the flow rate beyond inception to cause choking, whereas in the study of Mishra and Peles only a $1-2\%$ increase in the flow rate beyond inception was sufficient to cause choking in all microdevices. Similarly, Pennathur et al. [3] indicated a sharp transition into large attached supercavities and flow chocking

from cavitation inception in the investigation of flow over a 900 μm chord hydrofoil cascade. This phenomenon has not been reported for large-scale hydraulic equipment and it appears to be characteristic of microcavitating flows.

Mishra and Peles [5] performed a cavitating flow visualization study of a 40 μm wide micro-orifice entranced inside a 200 μm wide microchannel. They revealed various cavitating flow morphologies depending on the cavitation number and longitudinal position downstream of the orifice. At cavitation number slightly lower than σ_i inchoate cavitation bubbles appears immediately downstream of the orifice which collapse within a few microchannel diameters downstream. Further reduction in the cavitation number resulted in the emergence of a thin liquid jet from the micro-orifice. The jet appeared to be surrounded by two elongated bubbles at the top and the bottom, which stretched for a few microchannel diameters downstream (Fig. 4).

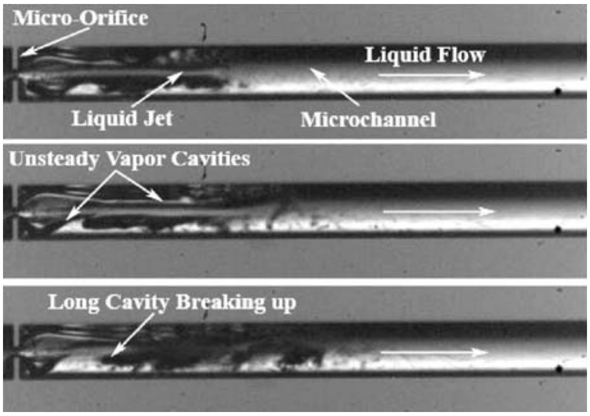

Cavitation in Microdomains, Figure 4 Developed cavitation with shedding ($\sigma = 0.227$)

Desinent cavitation is defined as the threshold cavitation number when the flow returns back to single-phase flows from cavitating conditions. The desinent cavitation number was considerably higher than the incipient cavitation number. Although the cavitation hysteresis (difference between incipient and desinent cavitation) phenomenon has been observed in macroscale [9, 10] its effects seem to be ameliorated with decrease in size of the system [5].

Future Directions for Research

In the future the microfluidics community will need to seriously address cavitation in order to enable the practical realization of many high-velocity microscale fluid machines. While the last decade has witnessed significant advances in power-MEMS technology, one of the most deleterious phenomena effecting hydraulic system, cavitation, is not very well understood at the microscale. Better knowledge of surface and stream nuclei effects at diminishing lengths and other scaling effects like viscous and surface tension will require careful study.

Cross References

► Boiling and Evaporation in Microchannels
► Bubble Dynamics in Microchannels
► Droplet and Bubble Formation in Microchannels
► Microfluidic Circuits

References

1. Brennen CE (1995) Cavitation and Bubble Dynamics. Oxford University Press, Oxford, UK
2. Mishra C, Peles Y (2005) Cavitation in Flow Through a Micro-Orifice Inside a Silicon Microchannel. Phys Fluid 17(1):013601–013616
3. Pennathur S, Peles Y, Epstein AH (2002) Cavitation at Micro-Scale in MEMS Fluid Machinery. In: Proceeding of IMECE'02, ASME International Mechanical Engineering Congress & Exposition, New Orleans, Louisiana, 17–22 November 2002
4. Mishra C, Peles Y (2005) Size Scale Effects on Cavitating Flows Through Micro-Orifices Entrenched in Rectangular Microchannels. J Microelectromech Syst 14(5):987–999
5. Mishra C, Peles Y (2005) Flow visualization of cavitating flows through a rectangular slot micro-orifice ingrained in a microchannel. Phys Fluid 17(11):113602–113616
6. Holl JW (1970) Nucli and cavitation. J Basic Eng 92:681
7. Billet ML (1986) Cavitation nuclei measurements with an optical system. J Fluid Eng 108:366
8. d'Agostino L, Acosta AJ (1991) Separation and surface nuclei effects in a cavitation susceptibility meter. J Fluid Eng 113:695
9. Yan Y, Thorpe RB (1990) Flow regime transitions due to cavitation in the flow through an orifice. Int J Multiphase Flow, 16:1023–1045
10. Tullis JP (1989) Hydraulics of Pipelines. Wiley, New York

Cavity Resonance

► Hemholtz Resonance

C-Axis

Definition

Crystal direction perpendicular to the substrate surface.

Cross References

► Fabrication of Self-Assembled Catalytic Nanostructures

CCD-Camera

► Charge Coupled Device (CCD) Camera
► Color Cameras

CEC

► Capillary Electrochromatography

CEC–ESI–MS

► Capillary Electrochromatography–Electrospray Ionization–Mass Spectrometry: An Integrated Electrokinetic Analytical Technique

Cell Adhesion

► Biomolecular Adsorption in Microfluidics

Cell Adhesion and Detachment

SHASHI K. MURTHY[1], MILICA RADISIC[2]
[1] Department of Chemical Engineering, Northeastern University, Boston, MA, USA
[2] Department of Chemical Engineering and Applied Chemistry
Institute of Biomaterials and Biomedical Engineering, University of Toronto, Toronto, ON, Canada
smurthy@coe.neu.edu

Synonyms

Cell capture; Cell attachment; Cell binding; Cell release

Definition

Cell adhesion results from specific attractive interactions between molecules on the cell surface and a substrate, which may be coated with more than one kind of molecule. Cell detachment represents the termination of these interactions by physical, chemical, electrical, optical, or other means.

Overview

Cells adhere to surfaces when attractive forces exist between the cell surface and the substrate of interest. In vivo, cells in animal tissues adhere to the extracellular matrix, by binding of adhesion receptors in the cell's membrane to the proteins of the extracellular matrix. Extracellular matrix is an interdigitating network of proteins and polysaccharides secreted by the cells themselves. For successful cultivation of anchorage dependent cells in a microfluidic device, it is necessary to provide means for the cells to attach to the device surface. Some surfaces, such as glass or poly(methyl methacrylate) (PMMA), may be naturally adhesive to certain cell types. It is generally accepted that the natural adhesiveness of these materials comes from their ability to support adsorption of serum proteins added to the culture medium, or extracellular matrix proteins secreted by the cells. In general, weakly hydrophobic surfaces will support adsorption of proteins, which are also hydrophobic, resulting in the cell attachment mediated by the adhesion receptors. In contrast, highly hydrophilic materials such as poly(ehtylene glycol) (PEG) will prevent protein adsorption and as a result prevent cell attachment.

More effective and specific cell adhesion can be achieved by taking advantage of unique receptors present on the cell surface and the specific attractive interactions that these receptors have with certain biomolecules called ligands. Often, cells of different types have different receptors on their surfaces and hence the ligand-receptor bond is like a lock and key connection. One cell type may have receptors that bind to a particular ligand but another cell type may be lacking that kind of receptor. A ligand-coated substrate will therefore bind cells of the former type, but not of the latter type.

Specifically, integrins are a group of adhesion receptors that mediate a large number of cell-matrix interactions. They are heterodimers, consisting of an α and β subunit. In vertebrates, at least 18 types of α subuntis and 8 types of β subunits are known. The differential adhesion properties of different cell types, come from the fact that different combinations of αβ sub-units are present in different cell types. Many cells contain integrins (e. g. α5β1) that can bind to an extracellular matrix protein, fibronectin. These integrins will bind to the type III repeats of fibronectin, specifically recognizing the Arg-Gly-Asp (RGD) peptide sequence.

Specific interactions between the cell surface receptors and their ligands (proteins or peptides) form the basis of cell adhesion in microfluidic devices. This entry will review methods of immobilizing ligands in microfluidic devices to achieve selective cell adhesion.

The detachment of cells from a substrate requires the disruption of the bonds that exist between cell surface receptors and ligands on the substrate. As such, cell detachment is difficult to achieve within microfluidic devices since receptor-ligand bonds tend to be strong. For example, although the dissociation constants (K_d) for a sin-

gle integrin receptor is relatively low (between 10^{-6} and 10^{-8} mol/l), binding of thousands of integrins present in the single cell to their ligands results in a firm anchoring of the cell to the surface. Thus, another factor that influences cell release is the density of receptors on the surfaces of a given cell. A higher receptor density will result in more receptor-ligand bonds forming, making it more difficult to detach the cell from the substrate. However, depending on the cell type and on the way the ligand is tethered to the substrate, cells can be detached using physical or chemical methods. Some examples of cell detachment techniques will also be described in this entry.

Basic Methodology

Cell Adhesion

The attachment of cells to surfaces is inherently a function of surface composition. The most commonly used materials in microfluidic device fabrication are silicon dioxide (glass), poly(dimethyl siloxane) (PDMS), and silicon. PDMS and silicon are hydrophobic and this characteristic can be exploited to coat these surfaces with ligands by adsorption. An alternative approach is to bind ligands covalently to surfaces. This approach is preferred when a strong adhesive force between targeted cells and the microfluidic device surface is required. This approach also results in highly reproducible surface coatings that are not affected by fluid flow, thus enabling application of high flow rates over prolonged times. Silicon, silicon dioxide, and PDMS surfaces are capable of chemically binding to a family of molecules known as alkoxysilanes. These molecules are comprised of one silicon atom bonded to three alkoxy groups and a fourth functional group capable of binding to other molecules. One approach to tether ligands to alkoxysilane molecules involves a coupling agent, namely the N-y-maleimidobutyryloxy succinimide ester, more commonly known as GMBS. This molecule contains two N-hyroxysuccinimide (NHS) ester groups that can bind to sulfhydryl groups (SH) and primary amine groups (NH_2). Hence, a silane containing a sulfhdryl group can be first attached to the microfluidic device surface, GMBS can then be attached to the silane, and finally any molecule with a primary amine group can be attached to the GMBS. Since primary amine groups are found on virtually all biomolecules (amino acids, antibodies, polypeptides, etc.), this three step technique is very versatile.

The binding of silanes to silicon, silicon dioxide, or PDMS surfaces requires activation of these surfaces with an oxygen plasma. For microfluidic devices made of glass and PDMS, oxygen plasmas are typically used to activate these surfaces prior to bonding them together, hence the silane treatment can immediately follow the bonding step. The oxygen plasma treatment disrupts the silicon-silicon and silicon-oxygen bonds in these surfaces, making them susceptible to bonding with alkoxysilanes, as illustrated in Fig. 1. The silane molecules are typically dissolved in an organic solvent such as ethanol in low concentrations (typically around 4 – 5% by volume) and the solution is injected directly into the microfluidic device and allowed to react for 30 min. Care must be taken while handling silanes because they are hazardous and moisture sensitive. Unreacted silane must be removed by rinsing the device with ethanol prior to introducing GMBS. GMBS is also dissolved in ethanol (a typical concentration is 28% by volume) and requires a 15 min reaction time period. After removing the unreacted GMBS, the device is rinsed with phosphate buffered saline (PBS) and finally, a solution of the ligand in PBS can be injected into the device. After 30 min of reaction time, the device is rinsed once again with PBS and is thereafter ready to capture cells by adhesion.

The concentration of ligand in the final step determines the ligand surface density that is ultimately achieved on the microfluidic device surface. This concentration can either be adjusted to ensure complete coverage of the surface or modulated when other molecules also need to be bound to the surface. An example of such a situation is when non-specific adhesive interactions between cells and the microfluidic device surface must be minimized. This type of *screening* can be accomplished by attaching poly(ethylene glycol) (also known as PEG) to the device surface in addition to the ligand molecules. The biological non-adhesiveness of PEG is very well known and its incorporation into the surface modification process described above can be readily accomplished using commercially available PEG that is functionalized with amine groups. The incorporation of PEG ensures that the only adhesive interactions that occur between cells and the microfluidic device are those between receptors on the cells and ligands on the device surface.

For microfluidic devices made with polymers such as poly(methyl methacrylate) (PMMA) and polycarbonate (PC), a different approach must be used to bind ligands to the device surface. The most common approach is the use of carbodiimide chemistry. For PMMA devices, a layer of carboxylic acid groups must first be generated by exposing the devices to an oxygen plasma or to ultraviolet light [1]. This step is not required for PC since the polymer already contains carboxylic acid groups. The next step is the attachment of the carbodiimide molecule to the surface over a 4 h time period, followed by a rinse with PBS and introduction of the ligand solution in PBS for an overnight coupling reaction (Fig. 2). Reagents and protocols for this process can be obtained commercially as kits.

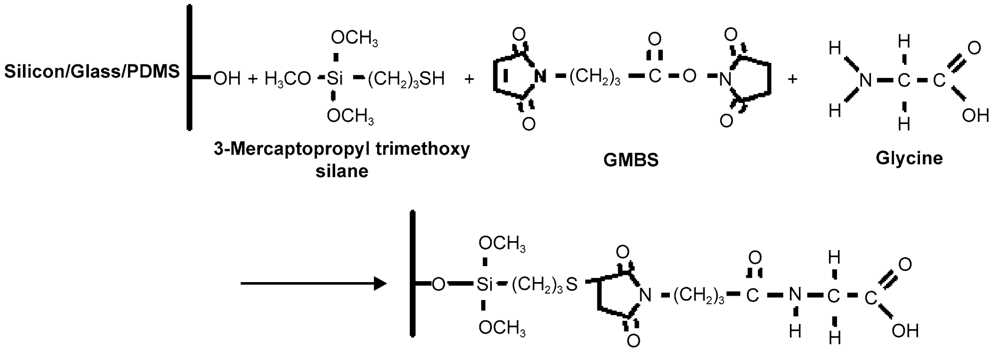

Cell Adhesion and Detachment, Figure 1 Chemical reaction scheme for the attachment of any molecule with a primary amine group to a silicon, glass, or PDMS surface

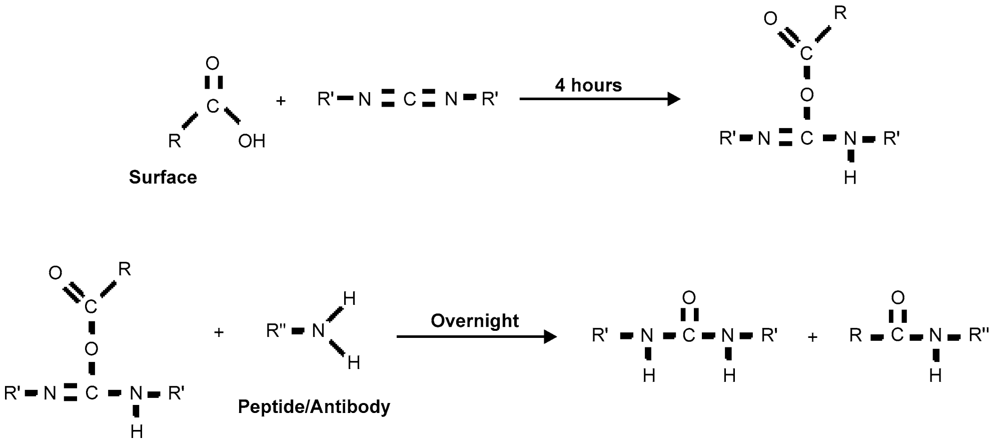

Cell Adhesion and Detachment, Figure 2 Chemical reaction scheme for the attachment of a biomolecule to the surface of polymeric microfluidic devices made of PMMA or PC. The carbodiimide coupling process starts with a reaction with carboxylic acid groups on the surface

Cell Detachment

The detachment of cells adhered to any surface requires the application of a force that is greater in magnitude to the force of adhesion. In standard monolayer, culture cells are detached by application of a proteolytic enzyme, trypsin. This is often impractical in microfluidic devices since it requires application of a rinsing solution, followed by incubation in a trypsin solution and finally the serum containing quenching solution.

For cells adhered within microfluidic devices, the easiest mode of detachment is by means of fluid flow. As demonstrated by Murthy et al. [5] (Fig. 3), the cell adhesion within microfluidic devices is dependent on the magnitude of flow-induced fluid shear forces. Under most conditions, increasing the magnitude of fluid shear forces (by, for example, increasing the flow rate) will result in lower cell adhesion. Therefore it is possible to design a system wherein cells are captured selectively while flowing through the device at a slow rate, and these captured cells can then be detached from the surface by flushing the device at a faster flow rate [2]. The main advantage of this approach is its simplicity; however the main limitation is that if the ligand-receptor bonds between the device surface and the cells are very strong, then it may be impossible to detach the cells without using very high shear forces that would almost certainly damage the cells.

An alternative approach is to design surface coatings that can facilitate cell detachment when an external stimulus is applied, such as an electrical potential or a small temperature change. An example of the former is a surface coating that consists of ligands bound to the surface via an electroactive chemical functional group [3]. The electroactive group, which is a quinone ester, is such that it undergoes a chemical change to a lactone upon the application of an electrical potential of −700 mV. When this change occurs, the ligand that was originally bound to the quinone ester is released, as shown in Fig. 4. Any cells that are attached to the surface via the ligand, would also then be released. From a microfabrication stand-

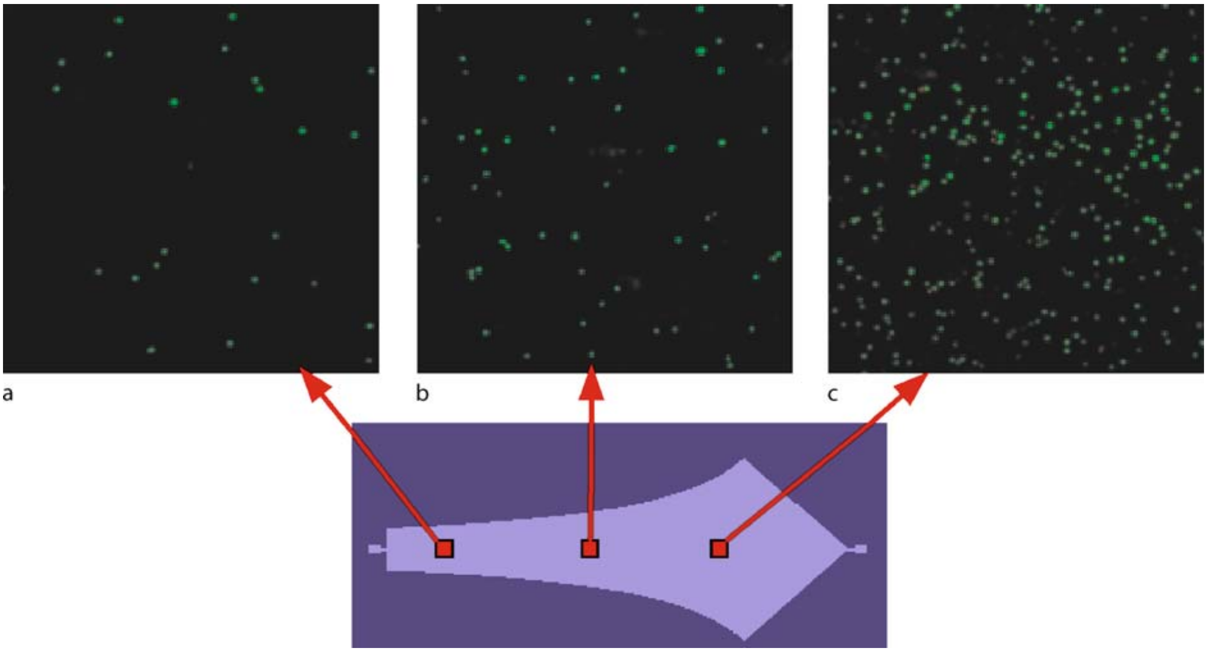

Cell Adhesion and Detachment, Figure 3 Selective adhesion of T lymphocytes in a microfluidic device as a function of shear stress. The device geometry, shown in blue, is such that the fluid shear stress decreases along the length of the device. This device was coated with the anti-CD5 antibody, which adheres to certain T lymphocytes. A mixture of T lymphocytes (stained green), and B lymphocytes (stained red) was passed through the device and the adhered cells were essentially all T lymphocytes (97% purity)

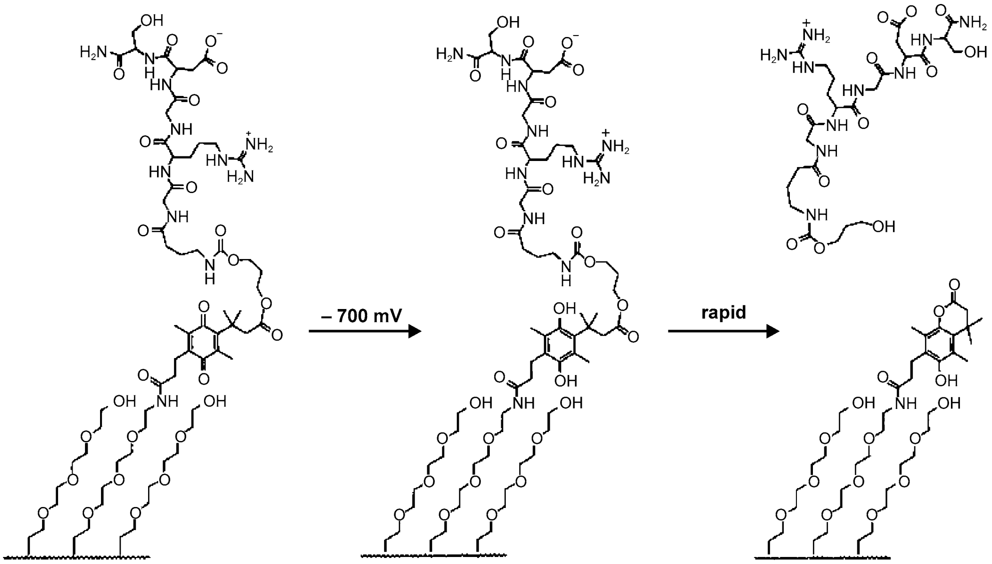

Cell Adhesion and Detachment, Figure 4 A self-assembled monolayer with an electroactive functional group bound to the RGD peptide. This quinine group is converted into a lactone group upon the application of an electrical potential and this change releases the RGD group from the surface. Taken from [3]

point, this approach is slightly more complex because it requires the incorporation of electrodes into the device structure.

Poly(N-isopropylacrylamide) (also known as PNIPAM) is a material that undergoes a physical change when its temperature is changed from 37°C to 20°C [4]. This change

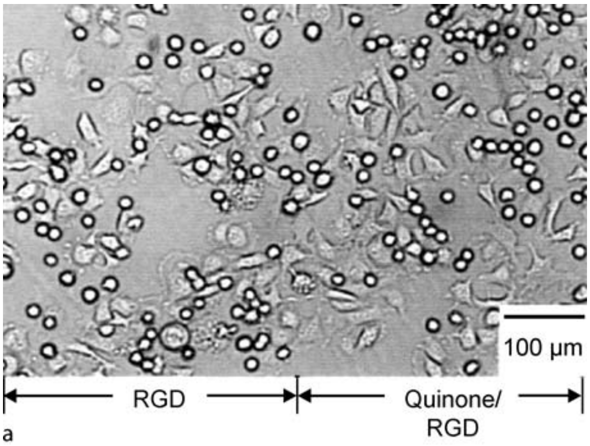

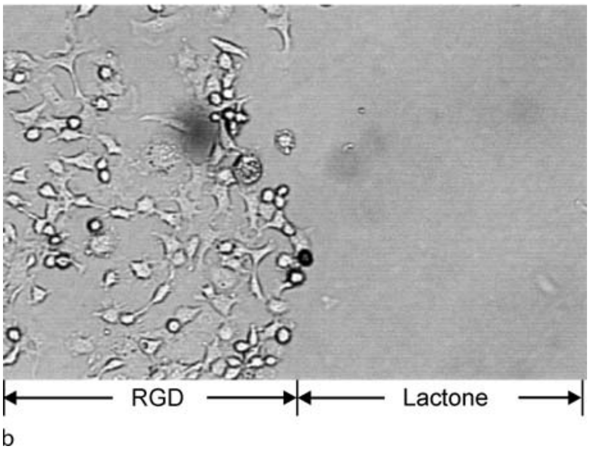

Cell Adhesion and Detachment, Figure 5 Release of cells from a surface coated with self assembled monolayers coupled to the RGD peptide. The left side of the surface has a monolayer that is not electroactive and the right side of the surface has a monolayer that contains the electroactive quinone group. Fibroblast cells initially adhere on both sides of the surface (**a**). Upon the application of an electrical potential, the quinone groups are converted to lactone groups and release the RGD groups along with the cells attached to these groups (**b**). Taken from [3]

is a phase transformation caused by rearrangements at the molecular level and results in a macroscopically observable change in hydrophobicity. PNIPAM is hydrophobic at 37°C and becomes hydrophilic at 20°C. This change can be reversed by raising the temperature back to 37°C. The hydrophobic PNIPAM surface at 37°C allows cell adhesion because the proteins on the cell surface are also moderately hydrophobic. The adhered cells can then be released by lowering the temperature to 20°C. The advantages of this technique include the ability to create PNIPAM surface by either solution chemistry techniques or vapor deposition, and the ability to form patterns of PNIPAM on any surface.

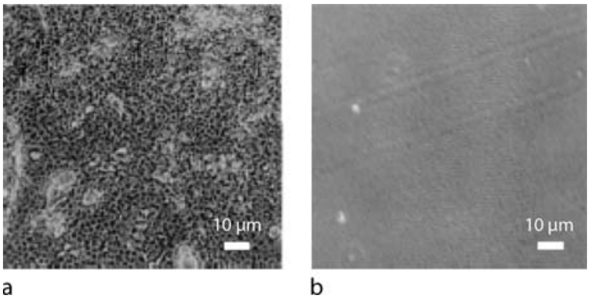

Cell Adhesion and Detachment, Figure 6 Cell detachment using the thermally responsive polymer PNIPAM. A surface coated with the polymer is seeded with human keratinocytes cells which form a sheet-like layer at 37°C (**a**). When the temperature is lowered to 20°C, the cells are released from the surface (**b**) as a sheet. Taken from [9]

Key Research Findings

The use of silane chemistry and coupling with GMBS was recently applied to the attachment of antibodies to the surfaces of glass/PDMS microfluidic devices by Murthy et al. [5]. These antibodies were selected based on their known affinity for two sub-types of white blood cells, T and B lymphocytes. The anti-CD5 antibody was selected based on its affinity for the T lymphocytes used in this work, and the anti-CD19 antibody was chosen based on its affinity for B lymphocytes. In addition to the antibody, Murthy et al. further functionalized their microfluidic devices with PEG to eliminate non-specific cell binding. Starting with mixed suspensions containing varying concentrations of each cell type, these investigators observed high purity capture ($> 97\%$) of the target cells, namely T lymphocytes in anti-CD5-coated devices and B lymphocytes in anti-CD19-coated devices (Fig. 3).

This design concept was further refined by Cheng et al. in the development of a microfluidic system designed to count T lymphocytes expressing the CD4 antigen for HIV diagnostics [6]. In HIV-positive patients the number of T lymphocytes expressing CD4 drops dramatically, and counting the number of CD4-positive T lymphocytes per unit volume of blood forms the basis of standard tests for HIV infection. The microfluidic system developed by Cheng et al. is a portable, point-of-care diagnostic device that requires only 10 µl of a blood sample for an accurate diagnostic measurement. Another example of a microfluidic diagnostic device based on antibody-mediated capture of cells has been described by Du et al. [7]. This device is designed to capture cervical cancer cells that are known to express the α6-integrin receptor by attachment to antibodies bound to the microfluidic device surface.

More recently, Plouffe et al. reported how peptides bound to the surface of a microfluidic device can be utilized

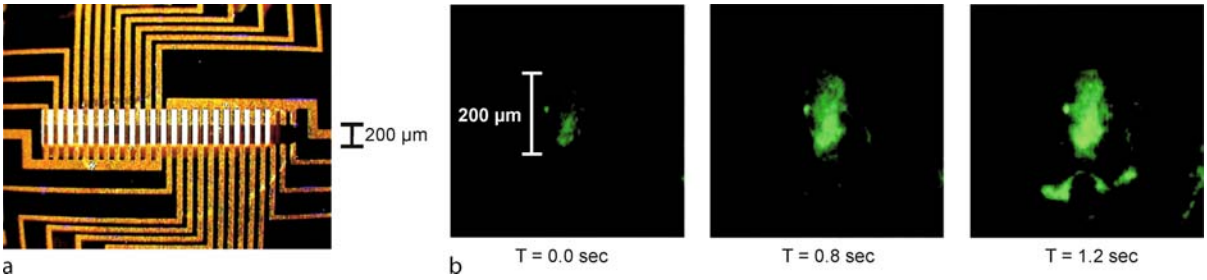

Cell Adhesion and Detachment, Figure 7 Biomolecule release within a microfluidic device using PNIPAM films and microfabricated heaters (**a**). The release of fluorescently labeled protein from a PNIPAM-coated region within the device when the heaters are turned off and the temperature falls below 37°C (**b**). From [10]

to selectively capture smooth muscle cells and endothelial cells from mixed suspensions containing both cell types along with fibroblasts [8]. The peptides used in this work were the sequences valine-alanine-proline-glycine (VAPG) and arginine-glutamic acid-aspartic acid-valine (REDV). VAPG is known to bind preferentially to smooth muscle cells and REDV is known to bind to endothelial cells. Smooth muscle cells and endothelial cells were captured by adhesion on the device surface with purity levels as high as 86 %. The captured cells remained viable after the flow and capture process, over a range of shear stresses between 1.3 – 4.3 dyn/cm^2.

The use of electroactive molecules to release cells was demonstrated by Yeo et al. [3] with the RGD peptide and fibroblast cells. The RGD peptide, which consists of three amino acids, arginine, glycine, and aspartic acid, linked together, is a ligand that binds to many different types of cells. Yeo et al. created a monolayer of alkanethiolate molecules on a gold surface. These molecules have a sulfhydryl group at one end which forms a bond with the gold surface; these molecules *self-assemble* on the surface to form a layer that is only one molecule thick (i. e. a *monolayer*). The other end of these molecules usually contain functional groups that can be utilized in subsequent reactions or processes, such as electroactive quinone groups connected to RGD units. As shown in Fig. 4, upon application of a −700 mV potential, the quinone groups undergo reduction to lactone, with the release of the RGD groups. Figure 5 shows the attachment of fibroblasts to a surface modified such that the left half contains RGD units tethered to a non-electroactive alkanethiolate monolayer. The right half of the surface contains RGD units attached to an alkanethiolate monolayer via electroactive quinone groups. In the absence of any electrical potential, fibroblasts do not distinguish between the two types of monolayers, perceiving only the RGD units and therefore becoming adhered to the surface. When the electrical potential is applied, the RGD units on the electroactive monolayer (right hand side of the surface) detach, causing detachment of the fibroblasts. This transition can be clearly seen by comparing Fig. 5a and Fig. 5b.

An example of cell detachment using the thermally responsive polymer PNIPAM has been described by Yamato et al. [9]. These investigators created a layer of PNIPAM by irradiating a polystyrene surface with an electron beam and allowing PNIPAM molecules in solution to bind covalently to the activated surface. A layer of human keratinocytes was cultured on this surface at 37°C. As shown in Fig. 6, lowering the temperature to 20°C resulted in detachment of the keratinocytes from the surface. The authors further observed that the keratinocytes detached as sheets, indicating that the cell detachment was uniform throughout the PNIPAM region.

The use of PNIPAM films within a microfluidic device has been described by Huber et al. [10]. This device, shown in Fig. 7a, consist of an array of microfabricated heaters over which a layer of silicon oxide and PNIPAM are deposited. Figure 7b shows the progressive release of fluorescently labeled protein from a location on this device. Initially, the PNIPAM is held at a temperature of 37°C and allows adsorption of the protein (the fluorescence is restricted to the PNIPAM-coated region). At the 0 s time point, the heaters are turned off, and as the PNIPAM cools, the protein is progressively detached, producing a fluorescent smear as it spreads away from the PNIPAM-coated region. Although this study by Huber et al. examined the release of protein molecules, the work of Yamato et al. suggests that a similar design concept could be utilized to detach cells within a microfluidic device.

Future Directions for Research

The ability to selectively adhere cells of different types within microfluidic devices is well developed. Knowledge of specific ligand-receptor interactions unique to any given cell type can readily be extended to a microfluidic applica-

tion, as illustrated in the examples above. However, more work needs to be done to better understand the mechanisms of cell-ligand interactions within the context of microfluidic systems. For example, it is known that the number of receptors on a cell may change based on exposure to fluid shear stress; such a change would impact the adhesion characteristics of the cells. In the area of cell detachment, future research must be directed at finding biologically specific release strategies that can be implemented easily within microfluidic devices.

Cross References

- ► Biomimetics
- ► Biomolecular Adsorption in Microfluidics
- ► Cell Culture (2D and 3D) on Chip
- ► Cell Patterning on Chip
- ► Cell Sorting
- ► Cell-Based Assays using Microfluidics
- ► Hydrophilic/Hydrophobic Patterning
- ► Microfluidics for Stem Cell Therapy

References

1. Feng J, Soper SA, McCarley RL, Murphy MC (2004) Separation of breast cancer cells from peripherally circulating blood using antibodies fixed in microchannels. Proc Int Soc Opt Eng 5312:278
2. Wankhede SP, Du ZQ, Berg JM, Vaughn MW, Dallas T, Cheng KH, Gollahon L (2006) Cell detachment model for an antibody-based microfluidic cancer screening system. Biotech Prog 22(5):1426–1433
3. Yeo WS, Hodneland CD, Mrksich M (2001) Electroactive monolayer substrates that selectively release adherent cells. Chembiochem 2(7–8):590–593
4. Yamato M, Konno C, Utsumi M, Kikuchi A, Okano T (2002) Thermally responsive polymer-grafted surfaces facilitate patterned cell seeding and co-culture. Biomaterials 23(2):561–567
5. Murthy SK, Sin A, Tompkins RG, Toner M (2004) Effect of Flow and Surface Conditions on Human Lymphocyte Isolation Using Microfluidic Chambers. Langmuir 20(26):11649–11655
6. Cheng X, Irimia D, Dixon M, Sekine K, Demirci U, Zamir L, Tompkins RG, Rodriguez W, Toner M (2007) A microfluidic device for practical label-free CD4+ T cell counting of HIV-infected subjects. Lab Chip 7:170–178
7. Du Z, Colls N, Cheng KH, Vaughn MW, Gollahon L (2006) Microfluidic-based diagnostics for cervical cancer cells. Biosens Bioelectron 21(10):1991–1995
8. Plouffe BD, Njoka D, Harris J, Liao J, Horick NK, Radisic M, Murthy SK (2007) Peptide-Mediated Selective Adhesion of Smooth Muscle and Endothelial Cells in Microfluidic Shear Flow. Langmuir 23(9):5050–5055
9. Yamato M, Utsumi M, Kushida A, Konno C, Kikuchi A, Okano T (2001) Thermo-responsive culture dishes allow the intact harvest of multilayered keratinocyte sheets without dispase by reducing temperature. Tissue Eng 7(4):473–480
10. Huber DL, Manginell RP, Samara MA, Kim BI, Bunker BC (2003) Programmed adsorption and release of proteins in a microfluidic device. Science 301(5631):352–354

Cell Analysis/Testing in Microfluidic Devices

► Cell Assays in Microfluidics

Cell Array

- ► Biochip
- ► Bioprinting on Chip

Cell Arraying

► Cell Patterning on Chip

Cell Assays

Synonyms

Phenotypic assay

Definition

A cell assay is the measurement and analysis of cellular response to chemical and/or physical stimulus. Cellular responses are diverse, including alterations of intracellular and extracellular biochemistry, cell morphology, motility, and growth properties. These responses characterize the cell phenotype.

Cross References

- ► Electrokinetic Motion of Cells and Nonpolarizable Particles
- ► Single-Cell Analysis in Microfluidics
- ► Patch-clamp Measurements on-Chip
- ► Cell Assays in Microfluidics

Cell Assays/Analysis/Testing on-Chip

► Cell Assays in Microfluidics

Cell Assays in Microfluidics

IRENA BARBULOVIC-NAD[1], AARON R. WHEELER[2]
[1] Terrence Donnelly Centre for Cellular and Biomolecular Research, University of Toronto, Toronto, ON, Canada
[2] Department of Chemistry, University of Toronto, Toronto, ON, Canada
awheeler@chem.utoronto.ca

Synonyms

Cell analysis/testing in microfluidic devices; Cell assays/ analysis/testing on-chip; Phenotypic screening in microfluidic devices/on-chip

Definition

A *cell assay* is defined as measurement and analysis of cellular response to chemical and/or physical stimulus. Cellular responses are diverse: alterations of intracellular and extracellular biochemistry, cell morphology, motility, and growth properties. These responses characterize the cell *phenotype*, and are typically monitored in a culture dish or a multiwell plate, while more recently microfluidic devices have been employed. A cell assay performed in a microfluidic device is sometimes termed an *on-chip* assay.

► High throughput screening (HTS) is a class of analytical techniques in which many different assays are performed in parallel, or very rapidly in succession. Currently, there is great interest in performing cell assays in a HTS format.

Overview

Introduction to Cell Assays

The cell is the irreducible element of life and is often studied as a living model of complex biological systems. Some studies, such as analysis of cell morphology and growth, can only be evaluated by means of cell assays. Other studies, such as the analysis of cellular biochemistry, can also be performed by simpler, molecular assays, that is, measuring molecular interactions in cell-free systems. Molecular assays are faster and less complicated to perform but can result in misleading conclusions as it is impossible to mimic the complex and unique properties of the intracellular environment (organelle compartmentalization of reagents, spatially localized receptors, varying temporal expression, etc.). Thus, cell assays are preferable for study of living systems. Nevertheless, they have several disadvantages, including being expensive, time-consuming, and much more complex than other kinds of analyses. An additional drawback is that many cells, such as mammalian cell culture lines, require strict adherence to sterile operating conditions.

Cell assays are conventionally performed in culture dishes or in multiwell plates (plastic trays containing 96, 384, etc. wells). While culture dishes require milliliter volumes of media and reagents, multiwell plates contain microliter volumes and enable simultaneous analysis of multiple cell types or stimuli. Cell responses in microwell plates are often evaluated using microplate readers, which are specialized optical detection instruments designed to rapidly analyze all of the samples on a plate, making use of techniques such as fluorescence intensity and polarization, luminescence, or absorbance. Multiwell plates and plate readers have become the standard means for medium- and high-throughput screening in cell and biomolecular assays. In these experiments, the plates, the plate reader, the fluid handling apparatus, and other miscellaneous equipment are typically integrated in a robotic analysis platform. Two major drawbacks of robotic platforms are the expense of the instrumentation (over $500,000), and the cost of experimental consumables (e. g., plates, pipette tips, reagents, and cells), which can be prohibitive. (This is true in general, but even more so for cell assays). Hence, applications requiring high-throughput cell assays are out of reach of all but the wealthiest of laboratories.

Miniaturization of Cell Assays in Microfluidics

Microfluidics, a technology characterized by devices containing networks of micron-dimension channels, enables integration of multiple processes on a single platform while reducing reagent consumption and analysis time. As such, microfluidics has been touted as a solution for the challenges inherent in conducting cell assays in HTS format [1].

In addition to the potential for facilitating HTS, microfluidic devices are advantageous for cell assays for a variety of reasons, the most obvious of which is the similarity in dimensions of cells and microchannels (10 – 100 μm widths and depths). Another important advantage is flow: channels with this size are characterized by laminar flow where diffusion is the only source of non-axial mass transport. Although diffusion-based transport is slow for delivering reagents across long distances, in microchannels, diffusion enables rapid and repeatable reagent delivery. In addition, the combination of laminar flow and diffusion makes possible the formation of highly resolved chemical gradients across small distances; this feature is particularly useful for cell assays as such gradients are common in living systems but difficult to implement in macroscale setups. A fourth advantage of microfluidic devices is the increased surface-to-volume ratio which facilitates

favorable scaling of heat and mass transfer, as well as favorable scaling of electrical and magnetic fields that are often used in cell analysis. A final consequence of the size regime is in concentration of analytes: as cells in microchannels are confined in sub-microliter volumes, relevant analytes do not become too dilute and can thus be more readily detected.

Microfluidics does have some disadvantages for cell assays. One limitation is the difficulty inherent in controlling many reagents simultaneously. A potential solution to this limitation is the use of *digital* or droplet-based microfluidics (▶ digital microfluidics). A second limitation is that the high surface-to-volume ratio of microchannels enhances the adsorption of molecules onto channel walls, reducing the effective concentration of reagents, and potentially causing problems related to cross-contamination. Finally, a major challenge for microfluidic applications in general is the macro-to-micro interface. To take a full advantage of the reduced scale, new technologies are needed to enable delivery of very low volumes of cells and reagents into microfluidic devices.

Key Examples

Li and Harrison carried out the first cell assay in microchannels [2]. This seminal work made use of electrokinetically driven flow (electroosmosis and electrophoresis) to transport bacteria, yeast, and mammalian cells in channels and to implement low-volume chemical lysis (cell death). This theme of microfluidics-based cell transport, sorting, and lysis, has continued to be a popular application, as well as related work in using microfluidics to culture cells and to pattern them into structures. We acknowledge the utility of these methods (and note that they are featured in several good reviews – see El-Ali et al. [1] and other entries in the *Encyclopedia*), but focus here on describing microfluidics-based cell assays that fit the definition described above – application of a stimulus and measurement of a response. These assays fall into four broad themes sorted as a function of the type of response to be measured: intracellular biochemistry, extracellular biochemistry, mechanical properties, and electrical properties. Prior to discussing these kinds of assays, we describe the basic methodology common to all forms of cell assays in microfluidics devices.

Basic Methodology

Cell Culture

In a microfluidic device for cell-based assays, adequate culture conditions must be maintained for the duration of the experiment, which can span hours or days. While being cultured, cells must be continuously perfused with nutrients and oxygen; in addition, constant temperature and pH must be maintained. Cell populations exist either in suspension (dispersed in liquid media) or as adherent layers grown on surfaces presenting an appropriate matrix, (Fig. 1a). In practice, adherent cells must be detached from culture flasks and seeded into a microfluidic device while sufficient time has to be allowed to achieve proper cell attachment and reduction of stress induced by the transfer [3]. Mobile cells in suspension are easier to handle and require less time to adapt to the new environment.

Cell assays are either performed on cell populations or on single cells. Being naturally heterogeneous, cell populations are more physiologically relevant and observation of populations allows for analysis of intercellular signaling. However, some cell phenotypes are not observable in an averaged signal produced by the population, so these assays can only be implemented by studying single cells. This chapter deals mainly with analysis of cell populations in microfluidic devices; we refer the reader to other entries of the *Encyclopedia* that discuss single cell analysis (▶ single-cell analysis in microfluidics).

Microflow Design

With typical flow rates usually smaller than 10 μl/min, a microflow has to be capable of continuous and uniform perfusion of media as well as steady culturing conditions. The flow must have a distribution such that adherent cells are not exposed to significant shear stress. Cells in suspension are either assayed while carried by bulk microflow or, more often, after immobilization in the chip. Common immobilization techniques are hydrodynamic trapping [4, 5] and adsorbing cells to a chemically treated surface [6].

Microflow is realized either as electroosmotic flow (EOF) or pressure driven flow. EOF is in many cases not suitable for transport of cell media due to its high ionic strength; additionally, the electrical fields may cause adverse effects on a cell population. Thus, pressure driven flow generated by off-chip or on-chip pumps is preferable for cell assays. On-chip pumps are particularly convenient – of note, pumps formed by multilayer soft-lithography have been applied to analyzing T-cell behavior in microfluidic devices [4].

Materials

Microchannels are generally fabricated in silicon, glass or poly(dimethyl siloxane) (PDMS). Glass and PDMS provide transparency for optical monitoring, and the latter is also permeable to the oxygen and carbon dioxide that is

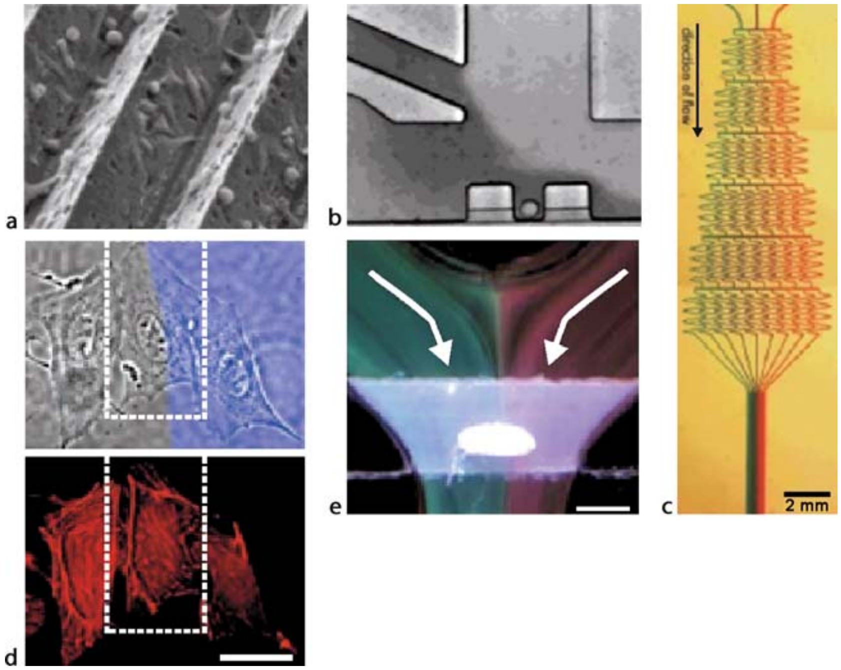

Cell Assays in Microfluidics, Figure 1 (**a**) HFF11 cell line grown in microfluidic V-channels for monitoring intracellular reporter gene activity. (Image reproduced, with permission, from [3]) (**b**) Cell from suspension hydrodynamically trapped in a perfusion chamber. (Image reproduced, with permission [4]) (**c**) A device for creating controlled linear, parabolic and periodic concentration gradients based on diffusive mixing (Image reproduced, with permission, from [7]) (**d**) Treatment of one part of an immobilized cell with latrunculin A and consequent disruption of actin filaments. (Image reproduced, with permission, from [10]) (**e**) *Drosophila* embryo developing while being exposed to two laminar streams of different temperature. (Image reproduced, with permission, from [11])

necessary for cell culture. For long-term assays, thorough sterilization of channels is recommended to prevent cell contamination [3]. Assays involving adherent cells require microchannel walls to be pretreated usually by attaching extracellular matrix proteins (e. g., fibronectin, collagen, or laminin) to enhance adhesion. On the other hand, when transporting cells in suspension, channel walls are often coated with bovine serum albumin (BSA) to prevent non-specific adhesion [4].

Types of Stimuli

Stimuli used for cell assays in microfluidic devices can be categorized into two main groups:

- chemical stimuli, including drugs and other reagents, antibodies and gene transfection agents, and
- physical stimuli, including topographical features and other mechanical and electrical forces.

Both kinds of stimuli are translated by cell signaling networks into a diverse range of responses, including growth and proliferation, migration, activation of metabolic pathways, production and release of proteins and other biomolecules, and the initiation of apoptosis (programmed cell death).

Detection Methods

Cell responses to physical or chemical cues are measured in microfluidic devices primarily via optical or electrochemical means. Fluorescence is the most widely used optical detection technique, because absorbance detection (commonly used for macro-scale assays) is of limited value in microchannels because of the short path lengths. Fluorescence detection, characterized by its unparalleled sensitivity, is easy to implement in microfluidic systems. Chemiluminescence and bioluminescence also offer low detection limits and have less background noise than fluorescence [6]. Electrochemical detectors are even more easily integrated with microfluidic devices and often are much less expensive than optical systems. However, fabrication of electrodes is a technical challenge and the electrical fields used in detection can interfere with on-chip processes such as electrophoresis. Electrochemical techniques include potentiometry, amperometry and con-

ductometry. Recently, mass spectrometry detectors and nuclear magnetic resonance detectors have been interfaced with microfluidics as well.

Key Research Findings

Cell assays in microfluidics can be classified into four themes: intracellular biochemistry, extracellular biochemistry, mechanical properties, and electrical properties.

Intracellular Biochemistry

Intracellular biochemistry assays were the first, and continue to be the most common cell assays performed in microfluidic devices. Controllable and highly resolved delivery of reagents to cells and facile integration with optical and electrochemical detection techniques has sparked research in many areas, ranging from metabolism to gene expression analysis. We categorize these assays in terms of the type of chemical stimuli (homogeneous vs. heterogenous), as well as by assay duration and throughput.

Homogeneous Stimuli

In the most straightforward form of intracellular biochemistry assays, a homogeneous stimulus is applied to cells, after which various indicators of metabolism or signaling are measured. Wheeler et al [4] performed cell viability assays and measured intracellular Ca^{2+} flux in Jurkat T-cells and U937 cells. A suspension of cells was hydrodynamically manipulated and focused onto a dock at a T-junction stagnation point (Fig. 1b). The integrated device, which relied on multiple on-chip valves and pumps, enabled a high degree of control of reagent delivery while facilitating complete solution change in approximately 100 ms.

Heterogeneous Stimuli

While homogeneous stimulus-response assays are more straightforward, a particularly useful kind of assay relies on heterogenous stimuli in the form of chemical gradients. A device for creating controlled linear, parabolic and periodic concentration gradients was developed by Dertinger et al. [7], employing diffusive mixing in a complex network of serpentine microchannels (Fig. 1c). This kind of structure has been exploited widely in microfluidic cell-based assays. For example, Thompson et al. [8] stimulated HeLa S3 cells with 8 different concentrations of the inflammatory cytokine TNF-α (an intercellular chemical messenger protein), and monitored the resulting dynamic expression of the NF-κB transcription factor with a fluorescent reporter. Another promising application of controllable concentration gradients was reported in studies of stem cells [9] – this is particularly relevant, as stem cell differentiation is highly dependent on microenvironmental cues.

In addition to forming gradients, multiple laminar streams can provide stimuli selectively to subcellular domains. In a striking example of this phenomenon, Takayama et al. [10] delivered a fluorescent dye specific for mitochondria to a designated portion of a cell. After staining, the migration of labeled mitochondria was observed within few hours. In the same study, local cytoskeletal structures were similarly effected by delivering latrunculin A (an agent that promotes dissolution of actin filaments), which resulted in localized disruption of cell morphology (Fig. 1d). Similarly, different temperature stimuli were applied using laminar streams to deliver fluid to immobilized *Drosophila* embryos (Fig. 1e) [11]. Posterior and anterior parts of embryos treated in this manner exhibited different development as a function of the different temperatures applied.

Long-Term Assays

Most of the aforementioned work describes short-term assays that were largely independent of cell response to the microfluidic environment. A thorough investigation of a microfluidic system for long-term experiments was performed by Davidsson et al. [3] using luciferase (an enzyme that catalyzes bioluminescent reactions) reporter gene activity in the cell line HFF11. Cells were immobilized on silicon chips at 37 °C (Fig. 1a), incubated in CO_2-independent cell media, and monitored for up to 30 hours. The authors observed that cell stress and consequent non-specific gene expression were caused by

- detachment and transfer of adherent cells from culture flask to the chip,
- a change of environment from static to flow, and
- changes in chemical environment (e. g., addition of fresh cell media.)

By allowing cells to incubate and adapt to new conditions for several hours, non-specific gene expression decreased to a low, steady level.

HTS Assays

Although a few studies have described medium-throughput microfluidic cell assays, the potential of this application has not yet been fully realized. Quake and coworkers [12] developed a device comprising hundreds of reaction chambers, a complex network of microchannels, and multiplexed valves. The utility of the device was illustrated by detecting a recombinant cytochrome c peroxidase (an enzyme used for chemiluminescent detection) expressed in *E. coli*. This device, which houses 256 725 nL chambers, demonstrates the potential for high-throughput

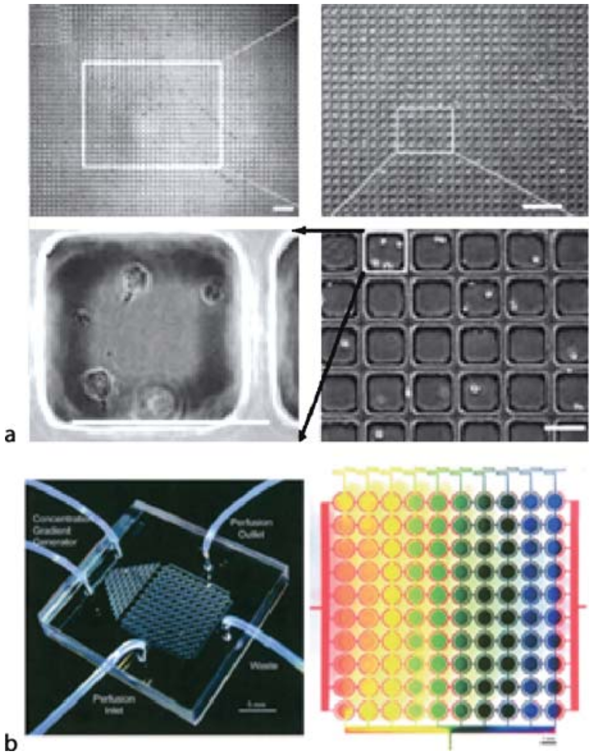

Cell Assays in Microfluidics, Figure 2 (**a**) Microfabricated array of cell chambers for high-throughput screening. (Image reproduced, with permission, from [13]) (**b**) Microfluidic array for high-throughput cell assays with concentration gradients formed across ten columns. (Image reproduced, with permission, from [14])

cell assays with minimal reagent use. A similar platform was developed by Chin et al. [13], and contains 10,000 microwells (Fig. 2a). Rat neural stem cells were seeded in the wells and enclosed in a microfluidic system such that all cells shared the same media, including any chemicals secreted by the cells. Proliferation of over 3,000 individual cells was monitored over period of days in single-, two- and three-cell-per-well assays. Hung et al. [14] developed a device for conducting cell assays in 100 chambers (Fig. 2b). In addition to perfusing cells with fresh media and assay reagents, the device was capable of passaging cells, i.e., growing multiple generations after cell division. Although these studies are promising, microfluidic systems capable of achieving throughput similar to conventional robotic platforms have not yet been realized.

Extracellular Biochemistry

Cells secrete signaling molecules (e.g., hormones and neurotransmitters), growth factors, and metabolic products. Measurements of the secreted molecules are required for studying cell–cell communication and regulation of cell secretory processes. Conventionally, these measurements are implemented by perfusing cells with chemical stimuli, collecting the perfusate, and analyzing it by *immunoassays* or other means. Integration of these processes on-chip enables continuous, automated monitoring and analysis of cellular secretion with high temporal resolution. This capacity is required to observe a complete secretion profile of system with complex kinetics. For example, insulin secretion goes through several phases, including initial burst, plateau and oscillations, all within seconds.

Understanding the mechanism of insulin secretion is tremendously important in diabetes research. In response to this challenge, an on-chip system for monitoring insulin secretion from islets of Langerhans (groups of pancreatic beta cells) was developed by Kennedy and coworkers [15]. The device enables a fully integrated cell assay with continuous on-chip cell perfusion, sampling of secretions, downstream mixing of labeling reagents, and separation and analysis with high temporal resolution (Fig. 3a). Islets were stimulated with glucose and extracellular fluid was sampled and analyzed every 6 s by means of an electrophoresis-based immunoassay having a 0.8 nM detection limit. Cells exhibited no morphological changes during the two-hour assay.

While the methods and devices developed by the Kennedy group for analysis of insulin secretion are the most comprehensive of this type, several on-chip methods have been reported for other analytes. For example, Davidsson et al. [6] designed a system for quantitative analysis of secreted glucose and ethanol. The allergic response of rat leukemia cells was monitored in a microfluidic device [16] by measuring fluorescence from a dye released along with histamine after stimulation. Lee et al. [5] investigated cell–cell communication via gap junction interactions on single cell pairs. The authors trapped two different mouse fibroblast populations at opposite sides of a microchannel and detected the interaction between cells by monitoring dye transfer between them. If the trapped cells were in contact, the dye was transferred within 16 h (Fig. 3b).

As these studies demonstrate, microfluidic devices are a useful and in some cases unique platform for dynamic, high-resolution measurements of cell secretory profiles. Relative to conventional tools, these on-chip methods enable superior control of perfusion, high-frequency analyte sampling, and integration of various processes on a single device.

Mechanical Response

Mechanical responses of cells to physical or chemical stimuli include cell growth patterns, morphology, adhesion and motility. Many mammalian cells grown in culture are adherent. For such cells, the adhesive interactions with the

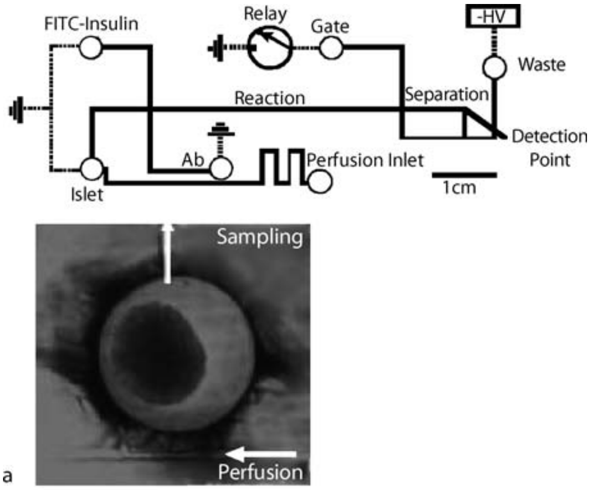

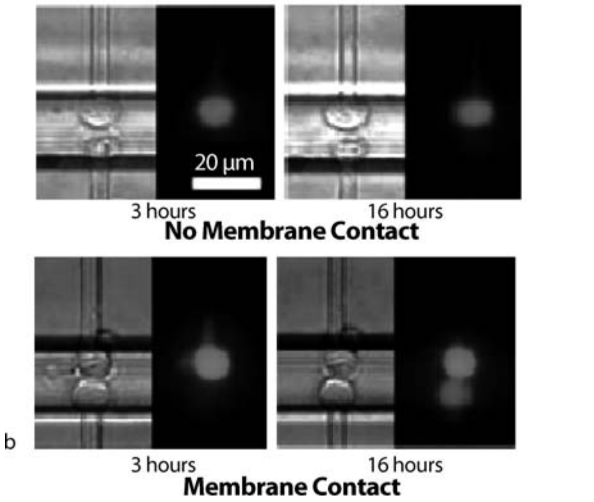

Cell Assays in Microfluidics, Figure 3 (**a**) Schematic of a device for continuous perfusion of pancreatic cell islets and stimulation with glucose, and monitoring of insulin release (top). Perfusion chamber with an islet (bottom). (Image reproduced, with permission, from [15]) (**b**) Microfluidic device for monitoring cell–cell communication via gap junctions. Fluorescent dye transfers from one cell to another only when cells are in contact. (Image reproduced, with permission, from [5])

physical environment (extracellular matrix or other cells) are a critical determinant of their biochemistry and behavior. Microfluidics has become a useful tool for studying these interactions. Many of these studies are reviewed elsewhere (▶ cell adhesion and detachment), so we focus here on assays that evaluate the effects of physical or chemical cues on cell morphology or motility.

Cell Morphology

Cell morphology, or shape, is important for survival, differentiation and migration. A few microfluidic cell assays have been conducted to characterize cell elongation, contraction and other morphological changes in response to mechanical forces and chemical cues. Gray et al. [17] studied endothelial cell shape in microchannels under static and dynamic flow conditions. Under both conditions significant cell elongation in the direction of a microchannel/flow was observed after 12 h. In other study, Li et al. [18] used a microfluidic platform and an acoustic wave sensor to monitor contractions of heart muscle cells. In addition to the effects of chemical stimuli, alterations in contractions were observed to be a function of electrode size, presence of the microchannel plate, and liquid loading onto the sensor.

Cell Motility

In cell motility and migration studies, special attention has been paid to chemotaxis, or migration of cells in response to gradients of chemicals known as chemokines. Chemotaxis of human neutrophils (immune cells that migrate to sites of infection or injury) was evaluated in seminal work by Jeon et al. [19]. Complex gradients of the chemokine interleukin-8 were generated in microchannels and maintained at a steady state using the pyramidal branched microchannel structure [7] described above. Others have noted that when generating chemokine gradients, care should be taken to moderate flow rates as a bias in cell migration is observed under high shear flow [20]. Beebe and coworkers [21] monitored neutrophil chemotaxis under concentration gradients formed statically, i. e., without flowing fluid. Chemical species diffused into a cell microchamber through a membrane which imposed high fluid resistance to minimize convective flows. In this manner, soluble cues including autocrine factors (secreted by a cell itself) and paracrine factors (secreted by other cells) were not washed away with a laminar flow but rather accumulated in the microenvironment. This design allows for examining the influence of cell–cell communication on chemotaxis or on other cell responses to chemical stimuli. While movement of cells in response to chemical factors has been a popular research topic, only a few studies have evaluated the effects on cell motility of mechanical stimuli. In one important study [22], neutrophil morphology, rheology and viscoelasticity were monitored when cells were seeded in microchannels of smaller dimensions than cell diameter (Fig. 4a). An important observation was made in that mechanical deformation of neutrophils is not passive, but rather active, as migration capabilities are enhanced through the formation of pseudopods and a reduction in cell stiffness. Undoubtedly, these findings encourage further research in this field.

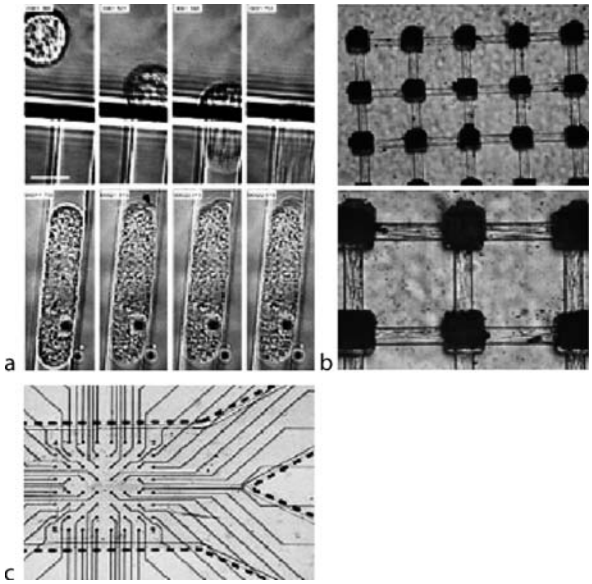

Cell Assays in Microfluidics, Figure 4 (**a**) A neutrophil flowing into a microchannel and becoming deformed. After entering the channel, the cell forms a pseudopod (arrow) that facilitates movement. (Image reproduced, with permission, from [22]) (**b**) Neurons seeded in chambers on top of patterned electrodes, with cell structures protruding into microchannels. (Image reproduced, with permission, from [24]) (**c**) Microfluidic channel (dashed lines) fabricated on top of patterned electrodes for recording neuronal activity. (Image reproduced, with permission, from [25])

True cell mechanical stimuli can hardly be implemented in macro-scale assays. Therefore, most of the work prior to the advent of microfluidics was focused on cellular response to chemicals or soluble signals. In contrast, as illustrated by the studies above, microfluidic devices are capable of mimicking in vivo physical conditions including topography and shear stress, which enables new research focused on mechanical response of cells to mechanical stimuli in combination with chemical cues.

Electrical Response

Electrical measurements on cells are discussed in other entries in the *Encyclopedia* (►cell electrical measurements, ►patch-clamp measurements on-chip). We focus here on the basic cell electrical responses assayed in microchannels, most of which have been developed in the context of cell-based biosensors. These studies typically evaluate cell action potential which is a net electrical change in cells resulting from changing concentrations of intracellular ions. Action potentials are important physiologically because they result in the transmission of signals between nerve cells and contraction of muscle cells. These electrogenic cells are very sensitive to chemical changes in the cell microenvironment and changes in action potential are detectable much sooner than any morphological changes.

DeBusschere and Kovacs [23] developed a portable microfluidic platform integrated with a complementary metal-oxide semiconductor (CMOS) chip which enables control of temperature as well as the capacity to measure action potentials in cardiomyocytes. When cells were stimulated with nifedipine (a calcium channel blocker), action potential activity was interrupted. Morin et al. [24] seeded neurons in an array of chambers in a microfluidic network integrated with an array of electrodes (Fig. 4b). The electrical activity of cells triggered with an electrical stimulus was monitored for several weeks. Cells in all chambers responded asynchronously to the stimulus. This device illustrates the utility of microfluidic tools that can investigate structure, function and organization of biological neural networks. A similar study probed the electrical characteristics of neurons as they responded to thermal stimulation [25] in a microfluidic laminar flow. Neurons were seeded on an array of electrodes (Fig. 4c) which allowed for measurements of variations in action potentials when cells were exposed to different temperatures.

By combining facile electrical measurements with controllable physical and chemical stimuli at the micron level, microfluidic devices are developing into a versatile platform for cell-based biosensors, drug discovery, genetic analysis and diagnostics.

Future Directions for Research

The studies summarized here were selected to demonstrate the potential of microfluidics for use in cell-based assays. We do note that the majority of the methods described are in a proof-of-principle stage. For real-world application in both academic and industrial research, a few hurdles must be overcome including device reliability, integration and automation, throughput, and macro-to-micro interfacing. We believe these challenges are solvable, and given the trajectory of interest and innovation in this area, we speculate that microfluidic cell assay tools will soon become irreplaceable in biosensing, diagnostics, drug screening and other biomedical applications.

Cross References

- ► Cell Adhesion and Detachment
- ► Cell Culture (2D and 3D) On Chip
- ► Electrokinetic Motion of Cells and Nonpolarizable Particles
- ► Cell Patterning on Chip
- ► Cell Sorting
- ► Single-Cell Analysis in Microfluidics

References

1. El-Ali J, Sorger PK, Jensen KF (2006) Cells on chips. Nature 442:403–411
2. Li PC, Harrison DJ (1997) Transport, Manipulation, and Reaction of Biological Cells On-Chip Using Electrokinetic Effects. Anal Chem 69:1564–1568
3. Davidsson R, Boketoft A, Bristulf J, Kotarsky K, Olde B, Owman C, Bengtsson M, Laurell T, Emneus J (2004) Developments toward a microfluidic system for long-term monitoring of dynamic cellular events in immobilized human cells. Anal Chem 76:4715–4720
4. Wheeler AR, Throndset W, Whelan RJ, Leach AM, Zare RN, Liau Y-H, Farrell K, Manger I, Daridon A (2003) Microfluidic Device for Single Cell Analysis. Anal Chem 75:3581–3586
5. Lee PJ, Hung PJ, Shaw R, Jan L, Lee LP (2005) Microfluidic application-specific integrated device for monitoring direct cell–cell communication via gap junctions between individual cell pairs. Appl Phys Lett 86:223902
6. Davidsson R, Johansson B, Passoth V, Bengtsson M, Laurell T, Emneus J (2004) Microfluidic biosensing systems - Part II. Monitoring the dynamic production of glucose and ethanol from microchip-immobilised yeast cells using enzymatic chemiluminescent mu-biosensors. Lab Chip 4:488–494
7. Dertinger SKW, Chiu DT, Jeon NL, Whitesides GM (2001) Generation of gradients having complex shapes using microfluidic networks. Anal Chem 73:1240–1246
8. Thompson DM, King KR, Wieder KJ, Toner M, Yarmush ML, Jayaraman A (2004) Dynamic gene expression profiling using a microfabricated living cell array. Anal Chem 76:4098–4103
9. Chung BG, Flanagan LA, Rhee SW, Schwartz PH, Lee AP, Monuki ES, Jeon NL (2005) Human neural stem cell growth and differentiation in a gradient-generating microfluidic device. Lab Chip 5:401–406
10. Takayama S, Ostuni E, LeDuc P, Naruse K, Ingber DE, Whitesides GM (2001) Subcellular positioning of small molecules. Nature 411:1016–1016
11. Lucchetta EM, Lee JH, Fu LA, Patel NH, Ismagilov RF (2005) Dynamics of Drosophila embryonic patterning network perturbed in space and time using microfluidics. Nature 434:1134–1138
12. Thorsen T, Maerkl SJ, Quake SR (2002) Microfluidic large-scale integration. Science 298:580–584
13. Chin VI, Taupin P, Sanga S, Scheel J, Gage FH, Bhatia SN (2004) Microfabricated platform for studying stem cell fates. Biotechnol Bioeng 88:399–415
14. Hung PJ, Lee PJ, Sabounchi P, Lin R, Lee LP (2005) Continuous perfusion microfluidic cell culture array for high-throughput cell-based assays. Biotechnol Bioeng 89:1–8
15. Shackman JG, Dahlgren GM, Peters JL, Kennedy RT (2005) Perfusion and chemical monitoring of living cells on a microfluidic chip. Lab Chip 5:56–63
16. Matsubara Y, Murakami Y, Kobayashi M, Morita Y, Tamiya E (2004) Application of on-chip cell cultures for the detection of allergic response. Biosens Bioelectron 19:741–747
17. Gray BL, Lieu DK, Collins SD, Smith RL, Barakat AI (2002) Microchannel platform for the study of endothelial cell shape and function. Biomed Microdevices 4:9–16
18. Li PCH, Wang WJ, Parameswaran M (2003) An acoustic wave sensor incorporated with a microfluidic chip for analyzing muscle cell contraction. Analyst 128:225–231
19. Jeon NL, Baskaran H, Dertinger SKW, Whitesides GM, Van De Water L, Toner M (2002) Neutrophil chemotaxis in linear and complex gradients of interleukin-8 formed in a microfabricated device. Nature Biotechnol 20:826–830
20. Walker GM, Sai JQ, Richmond A, Stremler M, Chung CY, Wikswo JP (2005) Effects of flow and diffusion on chemotaxis studies in a microfabricated gradient generator. Lab Chip 5:611–618
21. Abhyankar VV, Lokuta MA, Huttenlocher A, Beebe DJ (2006) Characterization of a membrane-based gradient generator for use in cell-signaling studies. Lab Chip 6:389–393
22. Yap B, Kamm RD (2005) Mechanical deformation of neutrophils into narrow channels induces pseudopod projection and changes in biomechanical properties. J Appl Phys 98:1930–1939
23. DeBusschere BD, Kovacs GTA (2001) Portable cell-based biosensor system using integrated CMOS cell-cartridges. Biosens Bioelectron 16:543–556
24. Morin F, Nishimura N, Griscom L, LePioufle B, Fujita H, Takamura Y, Tamiya E (2006) Constraining the connectivity of neuronal networks cultured on microelectrode arrays with microfluidic techniques: A step towards neuron-based functional chips. Biosens Bioelectron 21:1093–1100
25. Pearce TM, Wilson JA, Oakes SG, Chiu SY, Williams JC (2005) Integrated microelectrode array and microfluidics for temperature clamp of sensory neurons in culture. Lab Chip 5:97–101

Cell-Attached (Single-Channel) Voltage Clamp

► Patch Clamp Measurements On-Chip

Cell Attachment

► Cell Adhesion and Detachment

Cell-Based High-Throughput Assays

► Microfluidic Systems for High-Throughput Screening

Cell Binding

► Cell Adhesion and Detachment

Cell Capture

► Cell Adhesion and Detachment

Cell Culture (2D and 3D) on Chip

JUN YANG, XIAOLIN ZHENG
Bioengineering College, Chongqing University,
Chongqing, China
yjun1999@hotmail.com

Synonyms

On-Chip Cell Culture; Cell Culture on a Chip

Definition

Cell culture on chip is defined as those methods to cultivate biological living cells on two- and three-dimensional (2D and 3D) chip devices. Microchip techniques can provide many advantages for cell culture systems because the scale of the cultivated environment inside the microchip is fitted to the size of the cells. The integration of microfabrication and cell culture technologies promises great advances in basic biological research, diagnostics, biosensors, high-throughput drug screening, and so on.

Overview

Cultivating cells in vitro is one of the cornerstones of modern biology. Cell culture is an essential tool in biological science and clinical analysis, with some applications such as drug screening and biosensors. Many advances have been made in developing automated high-throughput cell culture systems. However, high cost and large size limit their application. It is therefore highly desirable to produce a miniaturized, inexpensive platform for *cell-culture-on-a-chip* to enable high-throughput cell experiments.

In their normal physiological environment, cells are subject to multiple cues varying in time and space. Here a cell or cell layer is a complex system with appropriate response to a variety of external physical and chemical excitations from neighboring cells and extracellular matrix. Microfabrication technology creates new opportunities for the spatial and temporal control of cell growth and stimuli by combining surface modification and microfluidic transportation methods. Microfabricated systems can present cells with different cues in a controllable and reproducible fashion that cannot easily be achieved by standard macroscopic cell culture methods. They can also be used to integrate cell culture with analytical devices to probe cellular behavior. Further integration with other analytic microsystems results in multifunctional platforms for basic biological research and cell-based biosensors. Among existing cell culture microsystems, some simply represent miniaturized versions of conventional laboratory techniques, whereas other devices exploit the advantages of small scales and low Reynolds numbers. Stable long-term cell culture is necessary and difficult in the realization of microchip-based cellular systems.

The integration of cell culture and microfabrication technologies provides some advantages for cell culture microsystems, because microfluidics allow the creation of culture systems on a size scale similar to the characteristic size of biological objects and their local in vivo environment. Much cell culture microsystems research takes place within a *Lab-on-a-Chip* or *micro total analysis system* (μTAS) framework that seeks to create microsystems incorporating several steps of an assay into a single system. Microfluidics can provide suitable environments for cell culture because of the large surface-to-volume ratio and fluidic behavior similar to the environments in vivo. Such microfluidic environments are now used to investigate cell–cell interactions and behaviors in vitro, emulating situations observed in vivo. Compared to traditional culture tools, microfluidic platforms should provide much greater control over cell microenvironments and rapid optimization of media composition using relatively small numbers of cells. The ability to perform multiple steps of a biological cell assay on a single self-contained microchip promises significant advantages in analysis speed, separation efficiency, cost reduction, reduced sample/reagent consumption, elimination of contamination, fewer wasted reagents, more detailed control of the cellular environment, and faster response time. Automated high-throughput experiments may be performed in a large number of repeating functional microstructures fabricated on a single chip. These microsystems can also monitor the time course of the release, which is difficult to measure by conventional batch cell culture methods.

Basic Methodology

Cells and the Extracellular Matrix

Cellular patterning using microfabrication techniques is essential for most on-chip cell culture methods. It is possible to reproducibly create a cell microenvironment at cellular resolution. Recent advances in microfabrication and microfluidics have allowed highly controlled cellular micropatterning, high-density sample characterization, and multiple experiments on one array. Surface patterning of microscale features allows micrometer-sized control over cell and extracellular matrix interactions, and the generation of ensembles of cells with defined geometry. Lam-

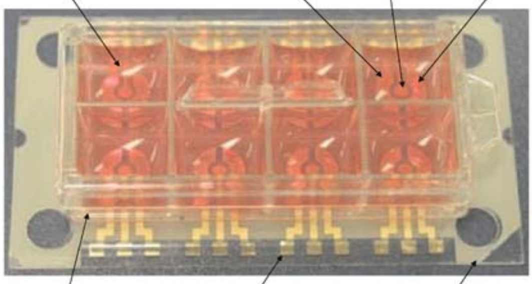

Cell Culture (2D and 3D) on Chip, Figure 1 Configuration of the microfabricated cell culture chip integrated with the electrochemical impedance measurement method. The cell chip consists of an eight-well cell culture chamber incorporated with a three-electrode system on each well. The gold electrode for impedance measurements is fabricated by sputtering on polycarbonate film

ination, molding, and photopolymerization techniques all allow fabrication of 3D scaffolds with feature sizes in the sub-micrometer range. The cellular micropatterning techniques have been employed to understand fundamental cell biology, especially cell–cell, cell–surface, and cell–medium interactions.

Among a large number of surface-patterning techniques available, the photolithographic technique is highly developed and has been widely used to control cell–cell interactions in co-cultures by using specific and nonspecific adhesion. In the microcontact printing method, the size and shape of a cell-adhesive region can be manipulated on the surface of a cell culture substrate. Consequently, the size and shape of the cells can be controlled by manipulating the adhesive regions, which affect many aspect of cellular activity such as protein secretion, cell growth, apoptosis, and differentiation. The microfluidic patterning technique using microchannels can generate patterns of thin lines containing various ligands on the cell culture substrate. With this technique, cell adhesion and spreading are spatially controlled on patterned lines containing specific peptides. The stencil method can be used for patterning virtually any adherent cell type on various materials, ranging from polystyrene Petri dishes to a microelectrode circuit or a gel.

Cellular micropatterning techniques have been used to understand questions in fundamental cell biology. The precise control of the cellular environment has been made possible by microtechnology, which provides new opportunities for understanding biochemical and mechanical processes responsible for changes in cellular behavior. Adhesive extracellular matrix patches can also be designed so that the shape of patterned cells can be controlled.

2D Cell Culture on Chip

2D Cell Culture on Patterned Surfaces

Patterned surfaces are widely used in 2D cell culture methods, where some receptor proteins or extracellular matrix are patterned on a surface for subsequent cell docking. Many microfabrication techniques described above can be used to form patterned surfaces. They allow a high degree of geometrical control over microscale features of a substrate. Micropatterned cell cultures are ideal to address fundamental issues of cell–cell and cell–surface interactions in confined geometries, as well as subcellular processes.

2D Cell Microarray

2D cell microarray technology is widely used in high-throughput cell-based research such as biosensors and drug screening. Surface patterning, soft lithography, and photolithography have been used to realize cell microarrays.

3D Cell Culture on Chip

Cell Culture in Microchambers

Microchamber-based cell culture is a common 3D cell culture method where cells are cultivated in a microscale chamber structure. This microchamber can easily be fabricated using existing microfabrication technology. It is similar to a miniaturized model of a traditional macroscopic cell culture well (Fig. 1). Microchambers are used for long-term culture and monitoring of extremely small populations of cells with single-cell resolution.

Agar Microculture Chip

A cell culture system based on photothermal etching has been developed for on-chip cultivation of living cells using an agarose microchamber array. The method can be used to flexibly change the chamber structure by photothermal etching, even during the cultivation of cells, depending upon the progress in cell growth. By using photothermal etching with adequate laser power, narrow tunnel-shaped channels can easily be fabricated between the microchambers at the bottom of the agar layer (Fig. 2). Photothermal etching occurs only in the area where an absorbing material is used, which means that it is possible to photothermally etch lines without damaging the cells in the microchambers. The advantages of this system are that it can control the positions and numbers of cells for cultivation by using agar-based microchambers, and it can change the tunnel network between adjacent chambers during cultivation by photothermal melting a portion of agar at the

focal point of an infrared laser beam. The results suggest that the agar–microchamber cell culture system in combination with photothermal etching can potentially be used for the next stage of single-cell culture including the real-time control of the interaction of cells during cell culture.

On-Chip Single-Cell Culture

Most current on-chip culture methods are carried out in a batch mode, without keeping tracking of a single cell, and only for adherent cells. Dynamic monitoring of a single cell is important for individual cell analysis without the influence of neighboring cells in independently controlled environments. Thus, single-cell culture chips are attracting wide attention. An ideal microchip for single-cell experiments should allow one to culture cells, to select any desired single cell from a group, to retain the cell for convenient cellular signal detection, and to deliver any buffer or reagent directly to the cell at any time during continual detection and observation. Most importantly, any negative impact on the live cell should be minimized.

Cell Culture on 3D Surfaces

Cell culture on 3D surfaces is similar to that on 2D surfaces despite the former being more complex surfaces. Cell patterning on 3D surfaces is rather difficult. Some microfabrication methods have been developed for 3D surface patterning. For example, a plasma-based dry etching method enables patterned cell culture inside microfluidic devices by allowing patterning, bonding, and sterilization steps to be carried out in a single step. This plasma-based dry etching method is used to pattern cell adhesive and non-adhesive areas on glass and polystyrene substrates. The surface patterning method offers a convenient way of micropatterning biomaterials for selective attachment of cells on substrates, and enables cultivation of patterned cells in microchannels.

One important application of cell culture on 3D surfaces is microtissue engineering. It is increasingly important to control cell growth into and within artificial scaffolds. Tissues such as skin, blood vessels, and cartilage have multilayer structures with different cells in each layer. With the aid of microfabrication technology, scaffolding methods for biodegradable polymers such as polylactic acid, polyglycolic acid, and the copolymer poly(lactide-*co*-glycolide) are developed to construct 3D multilayer microfluidic tissue scaffolds. Construction of complex microfluidic structures within and across the layers of multilayered scaffolds is demonstrated for modulation of cell growth.

Cell Culture in Microchannels

Microchannel systems can be used to generate continuous gradient of some growth factors in order to study the optimal proliferation and differentiation conditions of some cells. They can also be used to micropattern the cell culture surface area. Cells cultivated in microchannels are used to study cellular properties within fluidic environments, especially the impact from shear stress. For example, the geometry of the microchannel affects cell growth, orientation, and phenotype control of vascular smooth muscle cells. Smooth muscle cells cultured in wider microchannels (80 – 160 μm wide) switch from fibroblast morphology and random orientation to spindle-shaped morphology, and align along the direction of the microchannel nearing confluence at common cell density. They proliferate at low cell density and shift from a synthetic to a more contractile phenotype and random to unidirectional cellular orientation at high cell density nearing confluence. The wider microchannels also allow cells to grow to a higher cell density comparable to that of flat surfaces compared to narrower microchannels (10 and 40 μm wide).

3D Cell Microarray

A 3D cell microarray is similar to a 2D cell microarray except that cells are cultivated in arrays of microchambers. Cells in a 3D microarray can live longer than those in 2D culture style for medium perfusion and a temperature control unit can be integrated in this system. The microfluidic cell culture array can potentially offer an affordable platform for a wide range of applications in high-throughput cell-based screening, bioinformatics, synthetic biology, quantitative cell biology, and systems biology. As for the mono-microchamber cell culture style, detection components such as microelectrodes can also be fabricated in microchamber arrays for on-chip cellular analysis.

Cell Culture on Microcarrier Beads

In this mode, cells are grown on microcarrier beads and kept thermostatted while their metabolism is probed in real time. Several microanalytical systems are integrated in this cell culture device for real-time measurement of cellular activity.

Continuous Perfusion Cell Culture

Cultivating cells up to higher density and larger numbers is one of the most important tasks to achieve physiologically meaningful functions. It is also required for tissue engineering. To reach this goal, continuous nutrition

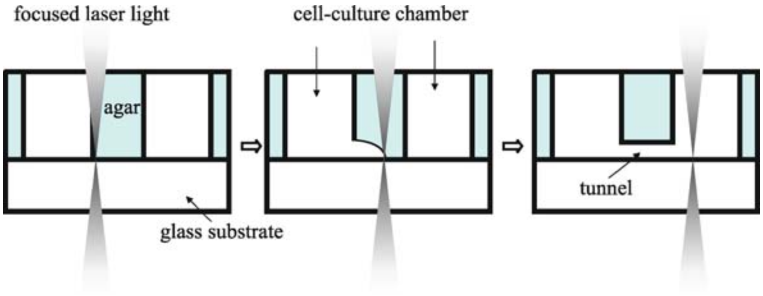

Cell Culture (2D and 3D) on Chip, Figure 2 A schematic of photothermal etching. First, an infrared laser beam is focused on the chromium layer on the glass slide; second, the focused beam is moved to the agar wall and a portion of agar at the spot-heated point melts and diffuses into water; finally, after the heated spot has been moved, two microchambers are connected by a tunnel

and oxygen supply and waste removal through the culture medium have to be ensured. Another important physiological function of cultivated cells is the secretion of chemical products. A variety of chemicals are released from cells, including signaling molecules such as hormones or neurotransmitters, trophic factors, and metabolic products. Temporally resolved measurements of materials released from cells are important in studying the regulation of the secretory process as well as technological pursuits such as drug development. Such measurements are typically performed by perfusing cells, collecting fractions, and then performing off-line analysis by immunoassays or other appropriate methods. Perfusion cell culture is believed to provide a stable culture environment due to the continuous supply of nutrients and removal of waste. However, the culture scales used in most cases are large, where the culture conditions cannot be regarded as homogenous because of chemical gradients. To improve this, the concept of miniaturization is applied to 3D cell culture. The development of a microfabricated device that can miniaturize and automate such measurements will be valuable in physiological studies. With the help of recent advances in microfabrication and μ-TAS, a continuous perfusion cell culture system can be miniaturized into a microfluidic device, which not only largely minimizes the chemical gradients existing in culture environments and cultured constructs, but also provides better control over the microenvironment of cells. It also reduces the required cell numbers, the volumes of culture medium, and the need for costly reagent. As a combination of microchamber and microchannel cell culture method, it uses a microscale perfusion system to provide a relatively stable culture environment, because of the continuous supply of nutrients and removal of waste, to realize longer-term cell culture.

Continuous-perfusion cell culture results in some advantages: it can allow one obtain truly dynamic measurements of secretion because the secreted products do not like those within traditional chamber-based methods where they continually increase in concentration; it can allow rapid raising and lowering of concentration of drugs or secretagogues on the cell as required for many experiments; and it can continually provide fresh nutrients to the cells, which decides the time that cells can be viable on the chip. The continuous-perfusion cell culture system can also enable vastly improved temporal resolution for monitoring, facile control of the cellular environment, and compatibility with longer-term measurements. A microfluidic system provides accurate control of the perfusion rates and biochemical composition of the environment surrounding the cells. It can serve as an improved in vitro model for studying muscle cell differentiation and for characterizing extracellular molecules and mechanisms involved in neuromuscular differentiation. Reliable fluidic control is particularly paramount for perfusion-based cell differentiation studies because differentiation processes are biochemically delicate and they take several days to complete. Thus, some elaborate micropumps and microvalves have been used in these systems for accurate fluidic control. Long-term viability is of great interest not only for differentiation studies but also for a variety of applications encompassing cell-based biosensors, high-throughput assays, and basic cell biology research. Long-term perfusion at low flow rates does not interfere with cell differentiation and is not observed to affect cell morphology or growth.

Key Research Findings

In 2D cell culture on chip, cell adhesion has been extensively studied on patterned surfaces for it is critical to cellular functions. Micropatterns have been used to study the cellular interactions with various materials such as metals, polymers, self-assembled monolayers, extracellular matrix proteins, cell-adhesion peptides, and other bioactive molecules. The physical and chemical proper-

ties of a substrate affect the attachment and growth of cells on it, and many studies have demonstrated that different topographical features of a surface affect cell attachment. Glass, silicon, and polydimethylsiloxane (PDMS) are widely used as substrate materials of cell culture microchips. The influence of these materials on the attachment and growth of several different types of cells has been studied. For example, PDMS substrate often requires oxidation of the surfaces to seal the device irreversibly. These hydrophilic surfaces may result in poor initial attachment, and detachment of certain cell types. In some cases, excess curing agent in the polymer may cause detachment of certain types of cells and prevent cells from reaching confluence. Some surface modification of PDMS substrate such as fibronectin coating is suitable for culturing various types of cells. There are many advantages of fabricating devices made of PDMS rather than conventional materials such as glass, silicon, and polystyrene.

Recently, cell spheroid microarrays have become a hotspot in cell microarray research. A 2D microarray of spherical multicellular aggregates (spheroids) are fabricated on a PDMS chip by a photolithography-based technique, which consists of thousands of cylindrical microcavities. Most cells on the PDMS chip gradually gather and subsequently form a single spheroid in each cavity until several days of culture. A part of the spheroid is attached to the bottom or wall surface of the microcavity, and the spheroid configuration is maintained for long-term culture. Spheroid microarrays can also be microfabricated on hydrogels. Photo-crosslinkable chitosan is synthesized and utilized for fabricating hydrogel microstructures through a micromolding process. The chitosan surface is initially cell repellent but becomes increasingly cell adhesive over time. By using this unique property of chitosan hydrogels, it is possible to generate patterned co-cultures of spheroids and support cells. This spatially controlled spheroid co-culture system can potentially provide a useful tool for fabricating biomimetic cellular microenvironments, for studies of cell–cell interactions, and for tissue engineering applications. Another spheroid culture device with an array of pyramid-like microholes is constructed in a silicon chip that is equipped with elastomeric microchannels. A cell suspension is introduced via the microfluidic channel into the microstructure that comprises silicon microholes and elastomeric microwells. A single spheroid can be formed and localized precisely within each microstructure. Since the culture medium can be replaced via the microchannels, a long-term culture is available on the chip.

Nanoporous polycarbonate membrane, which is used for macroscopic cell tissue culture and measurements, can be sandwiched between two structured wafers (silicon, glass, or PDMS) for cell patterning and culture. This method allows cell nutrition and exposure to various chemicals from either side of the membrane (Fig. 3). To realize a more efficient assay, a local temperature control device is designed and fabricated to keep different optimum temperatures in different areas on a microchip. Some detection methods such as electrochemical impedance or potential measurement electrodes can be integrated in microchambers for on-chip cell analysis (Fig. 1). Surface plasmon resonance (SPR) can also be integrated on microchamber cell culture devices for real-time monitoring of express proteins. As the surface patterned cell culture method, surface-modified PDMS is widely used in cell cultivation chambers. It has excellent air permeability, and air can be directly delivered to a PDMS microchamber without any external air supplying system. The microchamber can easily be integrated with other microfluidic components to form a whole cell-Lab-on-a-Chip.

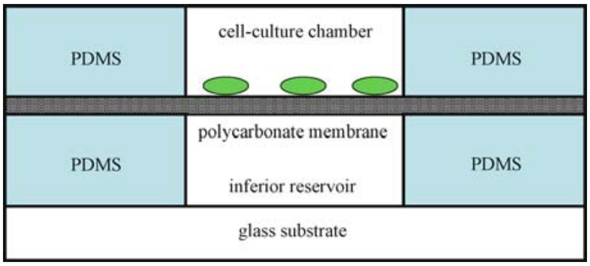

Cell Culture (2D and 3D) on Chip, Figure 3 Schematic cross-section of a cell culture microchamber device showing the PDMS sandwiched nanoporous polycarbonate membrane, assembled with top and bottom microfluidic reservoirs

In a single-cell culture chip model, a zero-speed point is controlled to retain the cell for 3D cell balancing and cell scanning in order to prevent damage of the cell by mechanical force. A dispersive flow delivers reagents at a high speed to very near the cell and provides them to the cell at a low speed. No force stronger than its gravitational force is exerted on the cell, which can be balanced on different positions on an arc-sloping wall, thus minimizing any negative impact on the cell due to strong liquid flows.

Protoplasts in a PDMS channel showed cell division and microcolony formation within several weeks. In embryo culture study, the results suggest that the microchannel culture systems may provide a culture environment that more closely mimics the in vivo environment. The microfluidic systems can enhance assisted reproduction efficiencies. The flow rate affects the cellular behavior of myoblasts, as well as differences in cell density of undifferentiated myoblasts and differentiation patterns. Shear stress brings some effects on hepatocyte activity. The shear flows cause hepatocytes to change morphology and functions accord-

ing to their exposed value of shear stress. The metabolic activities of hepatocytes under higher shear stress are lower. Morphologic observation reveals that hepatocytes change their shape like vascular endothelial cells do.

Microscale blood vessels can also be modeled by microfluidic channels. This work may be applicable to studies of blood vessels and endothelia. As in the microchamber cell culture method, detection devices such as microelectrodes can be fabricated in microchannels for on-chip cellular analysis.

In a 3D stem cell culture microarray platform, a high-density array of microwells is integrated into a fluidic chamber to guide deposition of adult neural stem cells and confine their progeny. This platform enables parallel, automated, long-term, live-cell microscopy of single cells in culture; tracking of individual cell fates over time; and correlation of differentiated progeny with founder clones. Using this microarray platform, one can further interrogate the response of distinct stem cell subpopulations to microenvironmental cues (mitogens, cell–cell interactions, and cell–extracellular matrix interactions) that govern their behavior. It enables parallel, quantitative analysis of stem cell proliferation and differentiation. In addition, unlike multiwell plate platforms, large numbers of live cells may be observed using conventional microscopy and correlated with differentiated progeny by high-magnification immunofluorescence in a rapid and efficient manner. In some cases, some drug containers can be integrated in 3D cell culture microarrays for high-throughput drug screening. This realizes a simultaneous evaluation of the effects of multiple chemical stimuli on the cells arrayed in the chip. Another novel platform technology creates arrays of microwells on chips for hosting cells in a local microenvironment characterized by controlled shape and surface chemistry. This 3D cell culturing combining 2D chemical patterning with topographical microstructuring presents to the cells a local 3D host structure. Using the inverted microcontact printing method, the plateau surface between the microwells is successfully passivated to block adsorption of proteins and prevent cell attachment by transfer of a graft copolymer. This novel platform is useful for fundamental cell biological studies and applications in the area of cell-based sensing.

A perfusion microbioreactor has been developed based on mass transport simulation to find out reasonable culture scales with relatively low chemical gradients. Here a PDMS surface is treated with surfactant solution to reduce nonspecific serum protein adsorption, which keeps the culture conditions steady. As described above, to achieve physiologically meaningful functions in vitro, a culture with a larger number of cells and higher density must be obtained. This will require bioreactors with larger surface areas for cell attachment and sufficient amounts of oxygen and nutrition supply. For these purposes, this bioreactor is fabricated by stacking tens of PDMS layers together. Several cell culture microchambers are fabricated on each PDMS layer. The high gas permeability of PDMS allows oxygen supply to the microfluidic channels through the thin walls. Consequently, by stacking single culture chambers and oxygen chambers in between, one can realize a microfluidic bioreactor for large-scale cell cultures. Continuous-perfusion microdevices can easily be integrated with other microfluidic analytical methods such as electrophoresis. Cellular activity under shear stress can also be monitored using continuous-perfusion systems. In some cases, a polymer membrane is used as scaffold for the attachment of cells in the perfusion system.

Future Directions for Research

Many cell culture microsystems available today are still in the proof-of-concept phase. Typical on-chip cell growth has been demonstrated, but robust approaches to fabrication, integration, and packaging remain major research areas. Integration and automation are important goals that also remain considerable hurdles. The rationales for integration include greater accuracy and reproducibility, smaller sample sizes, and higher throughput. Though on-chip cultivated cells can live longer and longer, long-term cell culture and perfect preservation of cellular activity are still very difficult. The growing emphasis in molecular biology on single-cell analysis derives from increasing and accurate appreciation of phenotypic heterogeneity among cells in a population. Physicochemical modeling of biological processes also demands single-cell data, or at least information about the distributions of key parameters. Thus, single-cell manipulation will be a future research hotspot. Although significant challenges face routine applications of *cell culture on chip*, tremendous advances have been realized over the past decade, and a future in which chips effectively compete with laboratory-scale technologies in the analysis of complex biological phenomena is clearly in sight. Highly integrated microdevices will find application in basic biomedical and pharmaceutical research, whereas robust and portable point-of-care devices will be used in clinical and point-of-care analysis.

Cross References

► Cell Adhesion and Detachment
► Cell Patterning on Chip
► Cell-based Assays Using Microfluidics
► Droplet Microreactors

References

1. Yeon JH, Park JK (2005) Cytotoxicity test based on electrochemical impedance measurement of HepG2 cultured in microfabricated cell chip. Analyt Biochem 341:308–315
2. Hediger S, Sayah A, Horisberger JD, et al (2001) Modular microsystem for epithelial cell culture and electrical characterization. Biosens Bioelectron 16:689–694
3. Moriguchi H, Wakamoto Y, Sugio Y, et al (2002) An agar-microchamber cell-cultivation system: flexible change of microchamber shapes during cultivation by photo-thermal etching. Lab Chip 2:125–130
4. El-Ali J, Sorger PK, Jensen KF (2006) Cells on chips. Nature 442:403–411
5. Andersson H, van den Berg A (2003) Microfluidic devices for cellomics: a review. Sens Actuators B-Chem 92:315–325
6. Balagadde FK, You LC, Hansen CL, et al (2005) Long-term monitoring of bacteria undergoing programmed population control in a microchemostat. Science 309:137–140
7. Gu W, Zhu XY, Futai N, et al (2004) Computerized microfluidic cell culture using elastomeric channels and Braille displays. Proceedings of the National Academy of the United States of America 101:15861–15866
8. Song JW, Gu W, Futai N, et al (2005) Computer-controlled microcirculatory support system for endothelial cell culture and shearing. Anal Chem 77:3993–3999
9. Goto M, Sato K, Murakami A, et al (2005) Development of a microchip-based bioassay system using cultured cells. Anal Chem 77:2125–2131
10. Chung BG, Flanagan LA, Rhee SW, et al (2005) Human neural stem cell growth and differentiation in a gradient-generating microfluidic device. Lab Chip 5:401–406

Cell Culture on a Chip

► Cell Culture (2D and 3D) on Chip

Cell Disruption

► On-Chip Cell Lysis

Cell Fractionation

► Cell Sorting

Cell Handling

► Manipulating Cells, Techniques

Cell Membrane Changes

► Microfluidics for Studies of Apoptosis

Cell Patterning on Chip

Ji-Yen Cheng
Research Center for Applied Sciences, Academia Sinica, Taipei, Taiwan
jycheng@gate.sinica.edu.tw

Synonyms

Cell arraying; Cell positioning

Definition

Cell patterning is a process to position cells on a substrate, especially in a microfluidic chip, with defined spatial selection and in turn to keep stable cell growth on the substrate.

Overview

Predefined patterning or network of cells is important for cellular/tissue function and neuronal activities. Cell patterning has a wide range of applications such as tissue engineering, wound healing, biosensors, and cell migration studies.

Early studies for patterning cells were reported in 1914 [1] in which the interaction between spiders' webs and embryonic cells was studied. Similarly, other artificial microstructures used for cell patterning have been reported. These structures include grooved structures, micro-stamps, and micro-agarose chambers. Another approach is to use patterned surface coatings, e. g. metal, self-assembled monolayer, protein, or other chemicals, to guide cell growth. These coatings either promote or inhibit cell adhesion so that a cell pattern is defined. The search for competent coating material is not trivial for a specific cell type. Therefore studies of biocompatible polymers, extracellular matrix protein, and new coating materials have regularly been reported. An alternative patterning approach that *actively* confines cells is to utilize dielectrophoresis force to trap cells near electrodes.

For all of the above approaches, the transfer of an artificial pattern onto a cell growth substrate is commonly accomplished by photolithography or laser director writing. Recently even ink-jet printers have been utilized for pattern transfer. Using a layer-by-layer approach, a microfluidic chip has been able to generate three-dimensional cell patterns [2].

Cross References

► Dielectrophoresis

References

1. Harrison RG (1914) The reaction of embryonic cells to solid structures. J Exp Zool 17:521–544
2. Tan W, Desai TA (2004) Layer-by-layer microfluidics for biomimetic three-dimensional structures. Biomaterials 25:1355–1364

Cell Positioning

► Cell Patterning on Chip

Cell Release

► Cell Adhesion and Detachment

Cell Separation

► Cell Sorting

Cell Sorting

Louise M. Barrett, Blake A. Simmons
Sandia National Laboratories, Livermore, CA, USA
lmbarre@sandia.gov

Synonyms

Cell separation; Cell fractionation

Definition

Cell sorting is defined as the separation of a heterogeneous mixture of cells into purified fractions of homogeneous cells. In this context it will also include the isolation of individual cell types from a heterogeneous mixture of cells. In this context *cell* refers to prokaryotic and eukaryotic cells.

Overview

Methods for processing microliter samples containing cells are in high demand for a wide range of applications in areas such as biomedical research, clinical diagnostics, counter-terrorism, environmental analysis, and biotechnology. Development of a cell-based screening assay often requires identification and isolation of particular cells from a mixture of various kinds of cells in various stages of development. Moreover, in order to obtain reproducible data on cells, reliable and nondestructive purification of cells is essential. However, the efficient separation of cells is a nontrivial task. In addition to the typical difficulties inherent to any analytical separation, the process is often further complicated by the physical and chemical heterogeneity and complexity of both the cells and the sample matrix. Cells, human cells in particular, are mechanically more fragile and more deformable than other cells. They are also biologically more sensitive and quicker to respond to changes in their environment.

Efficient and rapid sorting of cells on the macroscale has been accomplished with techniques such as flow cytometry, differential centrifugation, and filtration, but these conventional methods for sorting cells often result in dilution and dispersion and have disadvantages with regard to their cost, efficiency, response speed, resolution, and adaptability. Efforts to reduce volume and power requirements for particle separation have resulted in a number of miniaturized devices that take advantage of microfluidics and microfabrication. Advantages offered by microfluidic cell sorting techniques include more precise control over cellular microenvironments; significantly less reagent volumes and shorter reaction times in biochemical cell assays which in turn reduces space requirements and operational costs; single cells or rare cells can be manipulated in a non-invasive manner; massively parallel configurations with very high throughputs using arrays of microfluidic channels are possible; automation is more easily achieved; and processes are more easily integrated with further analysis steps.

This article highlights the most commonly used methods to perform cell sorting in microfluidic devices. Some of the microfluidic techniques presented here are a miniaturized version of conventional laboratory analysis techniques and devices, and take advantage of the reduced sample volumes and increased speed of analysis. Many other types of devices have successfully exploited the novel effects that arise in a microfabricated environment that are not evident on the macroscale.

Basic Methodology

Flow Cytometry

Flow cytometry is a conventional technique for counting, examining, and sorting microscopic particles suspended in a stream of fluid. It allows simultaneous multi-parametric analysis of the physical and/or chemical characteristics of single cells flowing through an optical and/or electrical detection apparatus. State-of-the-art conventional flow cytometry systems provide rapid and reliable analytical capacities; however, they are bulky, expensive, mechanically complex, and require trained dedicated staff, multiple sample pre-treatment steps, and a high volume of the sample. These facts have all motivated efforts to take advan-

tage of microfabrication technologies and microfluidics to achieve smaller, simpler, more innovative and inexpensive instrumentation. An excellent review of microfluidics for flow cytometry was recently published by Huh et al. [1].
Flow cytometry works in the following way. Specific cells in a sample are labeled with antibodies, fluorescent dye, or magnetic label. The cells are then focused to flow one by one in a single line passing the detection region. Particle focusing can be achieved using two approaches: passive focusing uses converging channels to confine cells without additional energy sources and active focusing using hydrodynamic, electrical, magnetic, or acoustic forces to confine the sample stream. Hydrodynamic focusing is a commonly used method for focusing the sample stream. Typically, the sample fluid stream is driven along the central channel of a cross-shaped channel. As the sample enters the intersection the three fluid streams meet and the sample stream is focused into narrow stream. The main advantage of this technique is that particle velocities are independent of the fluid composition or particle properties and the channel material. The disadvantages of hydrodynamic focusing are that accurate control of differential fluid flow rates or pressure on each channel is necessary to ensure efficient focusing; focusing acts on the fluid rather than the particles and therefore small particles and molecules can diffuse from the sample stream into the sheath fluid; however, it requires supplementary buffer inlets and precise flow control. Maintaining focusing whilst switching fluids into different channels is also problematic.

An alternative method is electrokinetic focusing, which uses a direct current electric field (at high voltages of $\sim$1 kV) to focus particles and liquids into a narrow stream. Typically, the sample fluid stream is driven along the central channel of a cross-shaped channel. As the sample enters the intersection, three fluid streams meet and the sample stream is focused into narrow stream. Dielectrophoresis (DEP) can also be used for sample focusing. DEP is the movement of polarized particles in a nonuniform electric field. This phenomenon is explained further in the next section. The main advantage of this method is that the focusing force acts on the particles rather than on the fluid, allowing particles to be focused within a single stream, and addition side streams are not necessary for focusing.

Targeted cells are then deflected or sorted from the sample stream for subsequent analysis. This cell sorting is commonly achieved by the active control of either the fluid flow or the particle/cell motion itself. The switch of flow is implemented by either electrokinetic or hydrodynamic means or by a combination of the two. In addition to this cell motion can be control by optical forces.

Filtration

This is another conventional technique which can be successfully miniaturized. Microscale filters work on the same principle as macroscale filters in that they separate cells based on size. Using microfabrication techniques, arrays of posts, comb-shaped filters, weir-type filters, and membranes (Fig. 2a) have been fabricated for mechanical filtration of heterogeneous cell samples. An advantage

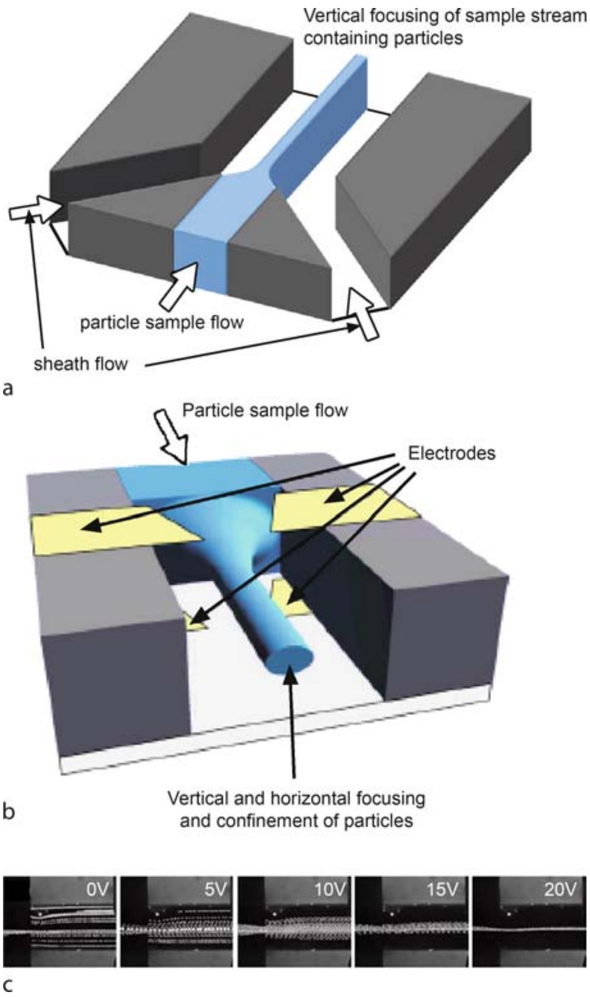

Cell Sorting, Figure 1 (**a**) Schematic diagram showing the principle of one-dimensional hydrodynamic focusing. The input particle stream is confined on both sides by sheath flow resulting in a focusing of the sample stream, and, as a result, of the suspended particles. (**b**) Schematic diagram showing how DEP can be used to focus particles in two dimensions. Thin microelectrodes on the top and bottom of the channel push the particles into the centre of the channel. The electrodes do not influence the fluid flow. (**c**) Sequence showing how increasing the applied voltage causes the particles to focus into a tight band at 20 V, with significantly poorer focusing at lower voltages. The dark region on the left of each image is the electrodes, which obscure the particles. (Adapted from [7])

of microfiltration is that it does not require specific buffer conditions. However, fabrication of microfluidic filtering components is not trivial. Trapping of the cells tends to be irreversible and clogging of filter and pressure build up is very common as operation time or sample volume is increased. Attempts have been made to overcome filter clogging using a filter parallel to the fluid flow as shown in Fig. 2b. The cell sample or feed stream flows down the center of the device. Smaller particles are transported into the lateral stream through the filtration barriers by high tangential rates, while larger particles will be still suspended in the feed stream. This dramatically avoids the problems of clogging. However, even after removing the problem of clogging due to the heterogeneity of cell size and deformability, the separation specificity of this filtration technique can be poor.

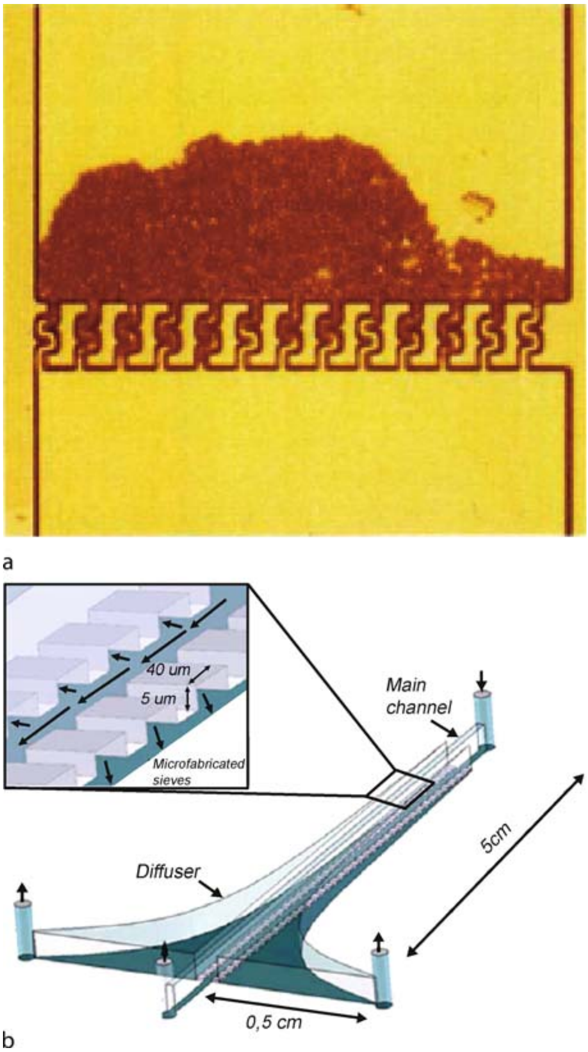

Cell Sorting, Figure 2 (**a**) Filtration of 5.78 μm diameter beads in 500 μm wide channel by a filter with 5 mm spacings. This device has also been used to separate blood cells. (Adapted from [8]) (**b**) Schematic of a microfluidic diffusive filter for cell enrichment. (Adapted from [9])

Electric Forces

Electrical forces that are used for cell sorting applications at the microscale include electrophoresis and DEP. Electrophoretic forces arise from the interaction of a cell's charge and an electric field, whereas DEP arises from a cell's polarizability [2]. Both forces can be used to create microsystems that separate cell mixtures into their component cell types. The advantage of using electric forces is that electrodes can be created in a microdevice using the standard microdevice fabrication techniques and they can be easy controlled using low-cost high-voltage power supplies which are often programmable. Electrophoresis enables the charge-based separation of suspended particles. This method has been used to separate and characterize bacteria and mammalian cells and has proven to be very useful for some applications. However, mixtures of different cell types or live and dead cells could not always be successfully separated since separation is solely based on the charge to size ratio. DEP was first described by Pohl [3] and a good review of its application in microfluidics was written by Hughes [4] DEP is the electrokinetic motion of dielectrically polarized particles in non-uniform electric fields. When particles approach a field gradient, they experience a selective force owing to DEP that is proportional to the particle volume and the difference in complex conductivity of the particle and the fluid. Unlike electrophoresis which depends primarily on the charge to size ratio of the particle, DEP depends on a set of both structural and chemical properties of the particle itself and the conductivity of the suspension media. This enhances selectivity and sensitivity of the technique. Depending on the relative magnitude of the particle conductivity and that of the fluid, the DEP force can act to drive particles towards regions of either high electric field strength or low electric field strengths. These types of DEP are termed positive and negative, respectively. Since most biological cells behave as dielectric particles in an external electric field, the generated DEP forces allow the manipulation of the cells in a liquid suspension.

There are two forms of DEP being used in the micro-/nanofluidic community. Most commonly, DEP is driven by electric field non-uniformities arising from multiple electrodes embedded throughout a fluidic system. Recently considerable interest has been shown in insulator-based dielectrophoresis (IDEP), an alternative approach to conventional DEP. IDEP has also been called *electrodeless*

DEP or *multigradient DEP*. In IDEP, insulating structures (i. e. packing material, posts, ridges, oil droplets) result in gradients in a local electric field (Figs. 3a and c), which is imparted using electrodes located only at the channel inlet and channel outlet. If the applied field has a DC component, this field can also produce an electrokinetic flow through the channel so external forces for fluid flow are not required.

The most popular mode of DEP operation for sorting cells in microsystems is in batch mode. DEP forces are used to trap and hold the cells of interest while allowing other cells and particles to pass through the device (Figs 3a and b). The trapped cells can then be released for further handling. However, operation in a batch mode can make the fluidic control of the microsystem and further cell processing difficult. Therefore, a great effort has been put into the development of continuous cell sorting techniques. Methods for continuous mode DEP are shown in Figs. 3c–e. In Fig. 3c native DEP mobilities of cells are used for separation of particles. In an alternative approach, Fig. 3e uses DEP labels to sort rare *Escherichia coli* that display a specific surface marker from an excess of nontarget bacteria of the same species. The label in this case is a polymeric bead with an antibody for the specific marker. Another commonly used method of continuous separation is called dielectrophoretic field flow fractionation (DEP-FFF). Cells are injected into a carrier flow that passes through the separation chamber where a DEP force is applied perpendicular to the flow. Negative DEP levitates flowing cells into different regions of a parabolic flow profile, achieving a spatial dispersion reflecting the dielectric properties of the cells. Negative DEP has also been used to deflect cells traveling in one laminar flow into another, or into side channels.

DEP is very attractive for sorting and separating cells of interest because the DEP force is created using electrode components without any moving parts. It can handle large numbers of cells and lends itself particularly well to cell handling since comparatively low voltages can produce significant and contactless forces. However, the main advantage of DEP is that it allows for label-free separation of cells allowing cells to remain in their native states. An important disadvantage to using DEP is that low-conductivity buffer is required so solvent exchange or dilution of sample is often necessary.

Magnetic Forces

Magnetoquasistatic fields are used to manipulate cells either due to an intrinsic magnetizability, such as the iron in red blood cells, or by attaching magnetic materials to the cells for magnetically activated cell sorting. The use of magnetic particles has attracted considerable interest since many functionalized magnetic beads (an iron oxide core surrounded by a polymer shell) are now commercially available. Magnetophoresis, the separation of particles based on different magnetic susceptibility, has the important attribute of being highly specific because the vast majority of material does not respond strongly to magnetic fields. Like DEP, magnetophoresis can be operated in batch and continuous mode. On application of a magnetic field the magnetically labeled cells can be retained in the reaction vessel while the remainder of the sample mixture is removed. Alternatively magnetic forces can also be used to create immunocapture beds to isolate cells as shown in Fig. 4a. The advantage of this technique is that beds can be formed and then released into large channels that do not clog easily. Continuous flow separation involves the application of an inhomogeneous magnetic field perpendicular to the direction of laminar flow, which forms a magnetic field gradient over the separation chamber. A mixture of magnetic particles and nonmagnetic particles can be injected continuously into the system through the sample inlet channel. The nonmagnetic particles are not influenced by the magnetic field and leave the chamber at the exit opposite the sample inlet. Magnetic particles, however, become magnetized and are hence dragged into the inhomogeneous magnetic field. Particles that are either different in size, or different in their magnetic susceptibility, will be deflected from the direction of laminar flow to a different degree and it is therefore possible to separate particles.

Ultrasonic Forces

Ultrasonic standing wave (USW) manipulation is a simple and useful method for handling, separating, and concentrating large groups of cells. An USW creates a pressure node that will attract particles or cells. As with DEP, a cell can experience either an attractive or repulsive acoustic force depending on its material parameters. This can be used either to trap objects locally over an ultrasonic transducer, concentrate them within a fluidic channel, or separate different types of objects from each other. Successful separation of human erythrocytes from human lipid vesicles has been reported (Fig. 5).

Optical Forces

Optical tweezers were developed by Ashkin and coworkers in the 1970s [5, 6]. Optical tweezers use the radiation pressure from a focused laser beam to trap, hold, and manipulate a particle or cell. The trapped object can be translated with extremely high precision, by rapidly scanning the laser beam between different positions and several

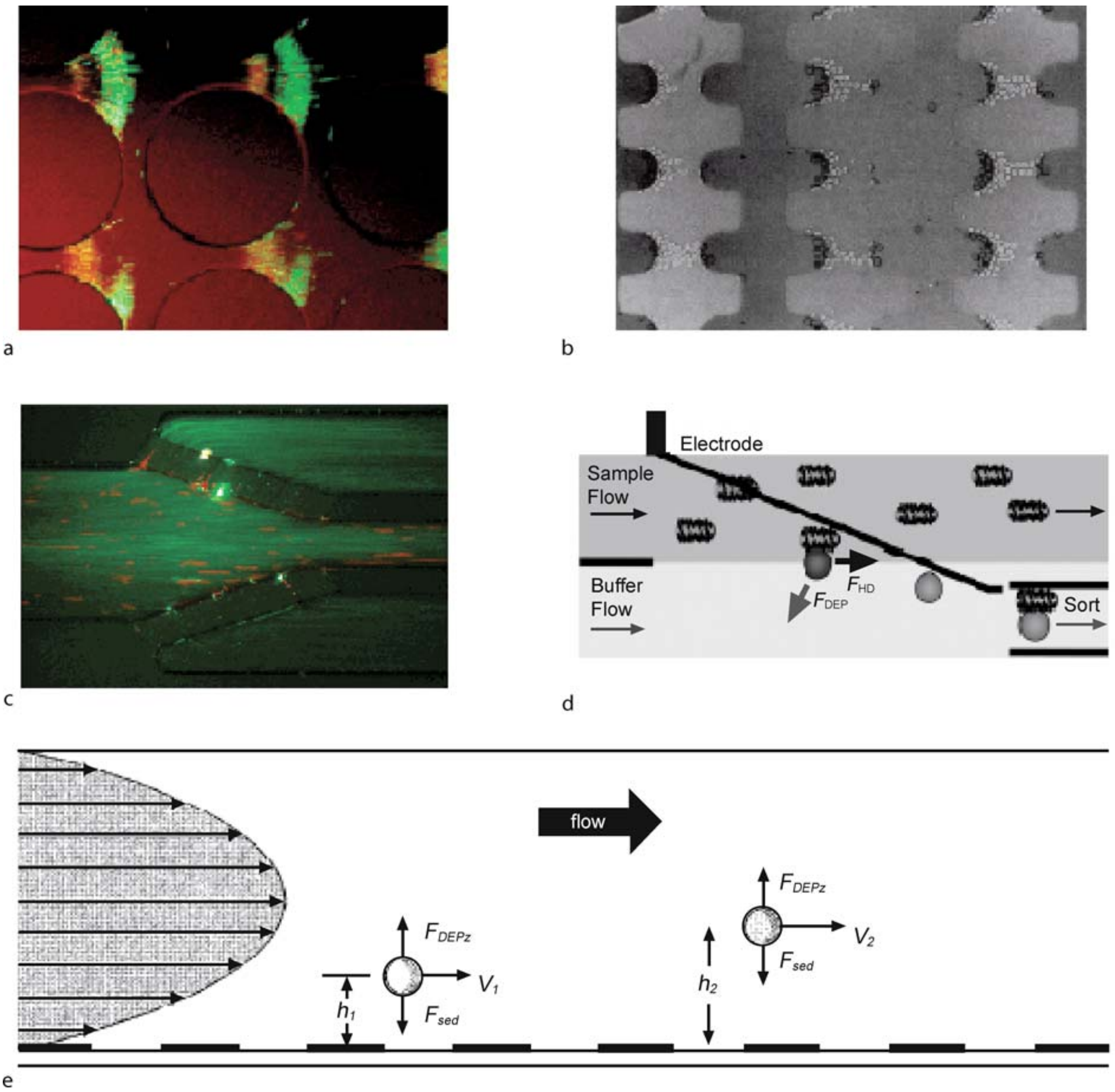

Cell Sorting, Figure 3 (**a**) Differential trapping of live and dead *Escherichia coli* cells using IDEP is shown by two separate bands of different color. Live cells (green) are trapped at the wider regions between the circular posts (negative DEP) and dead cells (red) exhibit less negative DEP since they are trapped at the narrower regions between circular posts. (Adapted from [10]) (**b**) Cancer cells, human breast cancer cell line MDA231, remain on the electrode tips after blood cells had been swept downstream. (Adapted from [11]) (**c**) Two-component sample of *Bacillus subtilis* and 200 nm particles; *Bacillus subtilis* cells are confined to the central channel due to the dielectrophoretic force created by ridges. (Adapted from [12]) (**d**) Schematic of rare cells separated from bulk cell sample. Cells entering in the sample stream are only deflected into the collection stream if they are labeled with a dielectrophoretically responsive label. (Adapted from [13]) (**e**) DEP-FFF principle and experimental setup. A thin, rectangular chamber was constructed with microfabricated, interdigitated electrodes on its bottom wall. Different cell types were levitated to different equilibrium heights under the influence of the opposing DEP (F_{DEPz}) and sedimentation (F_{sed}) forces. With a flow-velocity profile established in the chamber from the injection syringe pump, the cells at different heights ($h_2 > h_1$) were carried through the chamber at different velocities ($V_2 > V_1$) and thereby separated. Cells exited the chamber from the bottom outlet port and were detected and counted by an on-line flow cytometer. (Adapted from [14])

particles or cells can be held by a single laser beam. The use of optical forces for cell sorting is extremely attractive in that it is a noninvasive, noncontact, label-free technique. The nature of the interaction between a particle and the light field depends on the particle's size, shape, composition, and refractive index giving a range of criteria

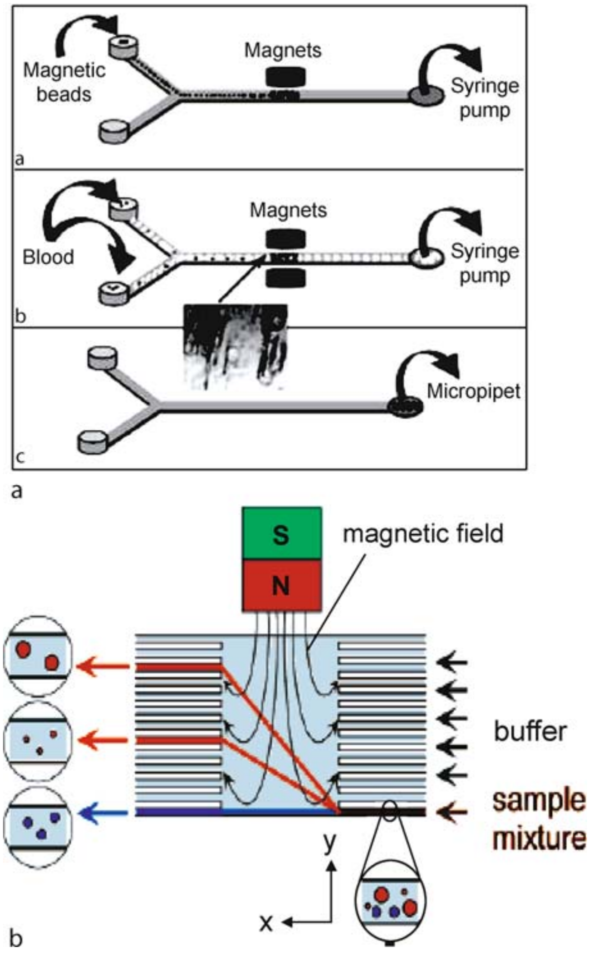

Cell Sorting, Figure 4 (**a**) Immunomagnetic separation of T cells: (a) syringe pump draws protein A/anti-human CD3 magnetic beads into the channel for capture with a magnet; (b) blood samples are introduced from both channels, T cells are captured with magnets above and below, then washed with RPMI 1640; (c) magnets were removed and captured cells and magnetic beads were transferred from the outlet with a micropipet. Inset shows T cells captured by beads in a magnetic field. Beads show as dark streaks, cells as translucent circles. (Adapted from [15]) (**b**) Concept of free-flow magnetophoresis. Magnetic particles are pumped into a laminar flow chamber; a magnetic field is applied perpendicular to the direction of flow. Particles deviate from the direction of laminar flow according to their size and magnetic susceptibility and are thus separated from each other and from nonmagnetic material. (Adapted from [16])

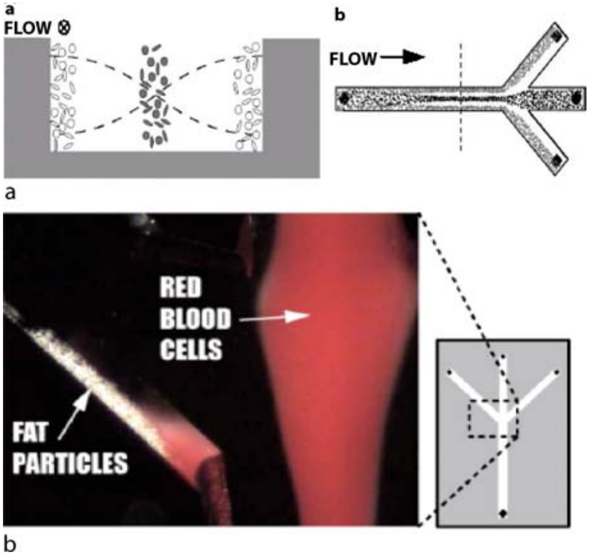

Cell Sorting, Figure 5 (**a**) Two particle types positioned, by acoustic forces, in the pressure nodal and anti-nodal planes of a standing wave. (Cross-section of the channel in (b), dashed line.) (b) Top view of a continuous separation of two particle types from each other and/or a fraction of their medium. (Adapted from [17]) (**b**) Human lipid particles separated from human erythrocytes at the trifurcation of 350 mm separation chip with ultrasound turned on. (Adapted from [18])

to sort a particle solely by tailoring the interference pattern to the particles one wishes to sort. The throughput is low since only a limited number of cells can be processed at one time, scale-up is difficult, and the position of the cell needs to be known in advance. Optical tweezers are custom built instruments usually starting with a commercial optical microscope with extensive modifications. The laser and optics required are very expensive. These instruments require specialized personnel to run. In addition one of the main concerns for laser tweezers is the cell viability/damage due to high laser power in long-term operation. In order to overcome the problems of throughput there has been a lot of interest in creating multiple optical traps using a single laser. This can be achieved using a diffractive beamsplitter which converts a single input beam into several beams, each of which forms a separate optical trap. The diffractive beamsplitter can be a computer-generated hologram, and therefore in the literature this technique has been coined *holographic optical tweezers* (HOT). These HOT devices can control hundreds of optical traps in a three-dimensional microscopic volume. Individual traps may be independently translated, eliminated, and created, but even a static array of traps is useful for particle separation as shown in Fig. 6a. Another approach has been to use a scanning laser beam while the light intensity levels were varied (as shown in the grayscale inset in Fig. 6b). Initial results showing the separation of polystyrene spheres were promising; however, the separation of cells has yet to demonstrated.

Another approach called optoelectronic tweezers shows great promised for cell sorting. Optoelectronic tweezers use direct optical images to create high-resolution DEP electrodes. The optoelectronic tweezers are constructed by assembling a ground layer (indium tin oxide (ITO)-

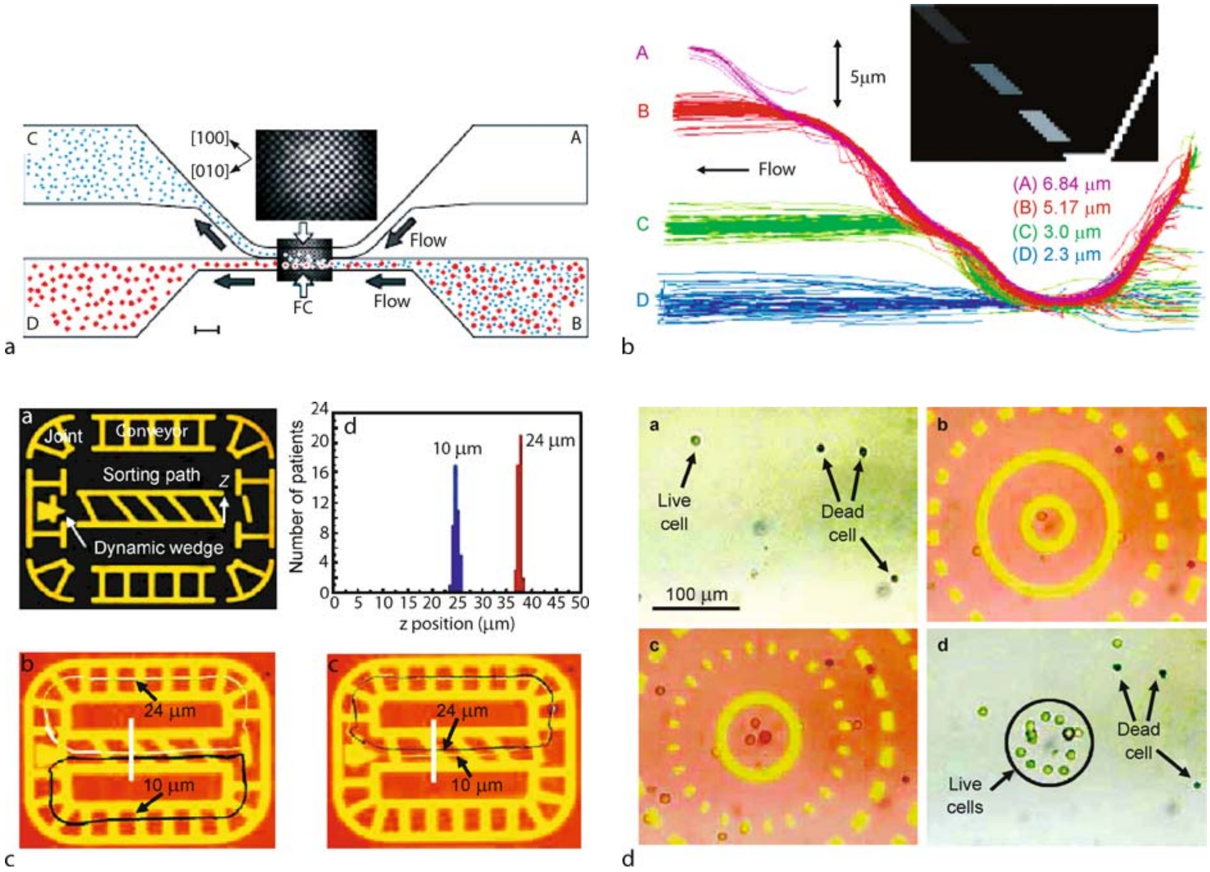

Cell Sorting, Figure 6 (**a**) Without an actuator all particles from chamber B would flow into chamber D. Chamber A would typically introduce a blank flow stream. The three-dimensional optical lattice into the fractionation chamber (FC) selectively deflects one species of particle into the upper flow field. The reconfigurability of the optical lattice allows for dynamic updating of selection criteria. The scale bar is 40 μm. (Adapted from [19]) (**b**) Separation of particles based on size using optical forces. (Adapted from [20]) (**c**) (a) Integration of virtual components, including an optical sorter path, conveyors, joints, and a wedge. The motion of different components is synchronized. (b, c) Two polystyrene particles with sizes of 10 μm and 24 μm pass through the sorter path and are fractionated in the *z*direction owing to the asymmetrical optical patterns. The particle trajectories can be switched at the end of the sorter path by the optical wedge. (d) Optical sorting repeatability test. The white and black loops in (b) and (c) represent the particle traces after 43 cycles. The trace broadening at the white bar has a standard deviation of 0.5 μm for the 10 μm bead and 0.15 μm for the 24 μm bead. (Adapted from [21]) (**d**) Selective collection of live cells from a mixture of live and dead human B cells. (a) Randomly positioned cells before OET. (b, c) Cell sorting. The live cells experience positive OET, trapping them in the bright areas, and pulling the live cells into the pattern's centre. The dead cells (stained with Trypan blue dye) leak out through the dark gaps and are not collected. The optical pattern appears light, while weak background scattered light results in a darker hue in the non-patterned areas. (d) Sorted cells. (Adapted from [22])

coated glass), a liquid chamber, and a photoconductive layer (glass substrate coated with an aluminum layer, photoconductive amorphous silicon layer, and silicon nitride layer). An electrical bias is applied between the top (ITO) and bottom (aluminum) electrodes. In the dark state, most of the voltage drops across the photoconductor due to its high electrical impedance. This results in a very weak electric field in the liquid layer. When the light source is focused on the photoconductive layer, the local photoconductivity in the illuminated region is greatly increased. This light-defined microelectrode creates a highly non-uniform field in the liquid layer. Since the field is non-uniform field, a DEP force is created and can be used to manipulate particles.

The main advantages of optoelectronic tweezers over optical tweezers is that the required optical power is orders of magnitudes lower (since light is used to switch the voltage drop between the photoconductive layer and the liquid layer and not to directly trap the particles) than that of conventional optical tweezers. This allows the use of a digital optical projector with an incoherent light source or light emitting diodes. As a result one can take advantage of projected real-time moving images which in turn produce addressable or moving electrodes. This has

allowed the creation of conveyor belts, moving deflecting wedges and shrinking circles (Figs. 6c and d). This makes the system very adaptable and vastly less expensive than optical tweezers.

Hydrodynamic Forces

A system that does not require outer field controls or any moving parts is an attractive option for cell sorting. The first attempts to used hydrodynamic forces for cell separation were based on macroscale separation using chromatographic media. Microfabrication techniques were used to create microscale *lattices* and *asymmetric obstacles* which would act to exploit the diffusion variation of particles of different size (Fig. 7). The devices were shown to be effective at separating blood into its separate components. Recently, there have been a few reports concerning continuous and hydrodynamic particle separation in microfluidic devices using only the laminar flow profile and channel geometry. This technique has been called *hydrodynamic filtration*, *pinched flow fractionation*, and *asymmetric pinched flow fractionation*. The principle of hydrodynamic particle movement is that small particles can be present near the inner surface of a microchannel, while large particles cannot fully access the low flow rate region near the surface. The most basic form of these devices (Figure 8a) allows particle streams to be separated according to their size using sections of different widths. Two fluid streams with/without particles a pumped through the narrow or "pinched" channel segment. The stream containing particles is focused on one sidewall in the narrow segment by controlling flow rates from both inlets. At the intersection between the narrow and wide segments the particles feel a force that is dependent on their size. The slight difference of the particle positions in the pinched segment is significantly amplified in the broadened segment, so the particles are separated perpendicularly to the flow direction according to their sizes. Larger particles are confined to the center of the microchannel due to the spreading flow profile. Smaller particles, however, are deflected towards the sidewall. The technique was further advanced to incorporate side channels which allow the particle collection as shown in Figs. 8b–d.

Key Research Findings

It is clear from examination of the literature that microfluidic techniques have advanced the field of cell sorting. Several macroscopic methods such as flow cytometry and filtration have been successfully miniaturized to give enhanced separation performance with a reduced sample volume. For example, in conventional macroscale sorting,

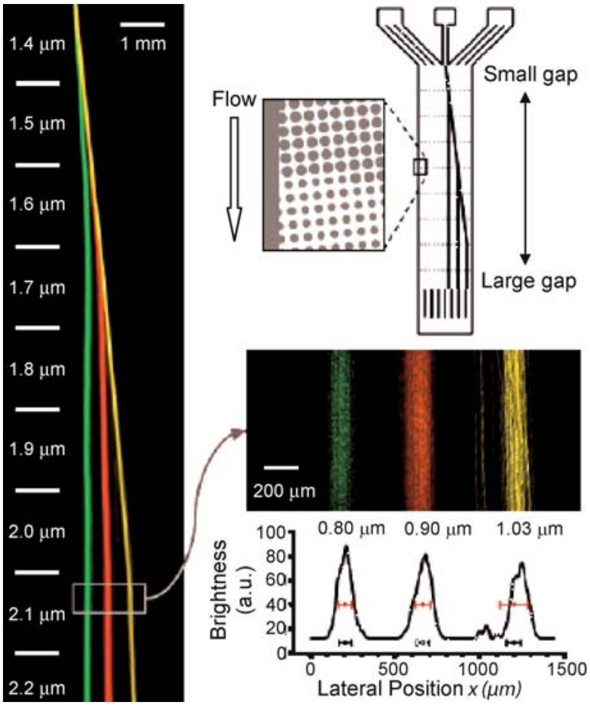

Cell Sorting, Figure 7 High-resolution separation of fluorescent microspheres with diameters of 0.80 µm (green), 0.90 µm (red), and 1.03 µm (yellow), with a matrix of varying gap size. (Adapted from [23])

using hydrodynamic focusing, a large amount of sheath liquid (of the order of liters) is necessary to processing a small amount of sample (of the order of milliliters) which has prevented a further reduction in the size and volume of the whole system. Microfluidic techniques have reduced the volume or even the need for a sheath fluid. In addition microfabricated filters have reduced the problems with clogging in conventional filters using laminar diffusion and microfilters parallel to the sample flow. However, macroscale cell sorting, using flow cytometry, remains faster (50,000 cells per second) than microfluidic cell sorting ($\leqslant$ 14,000 cells per second).

It is important to note at this point that cell sorting performance should not be judged solely on speed. Conventional flow cytometers are very expensive to purchase and operate, and are therefore only found in large research facilities or hospitals. Microfluidics has demonstrated that cell sorting, in multiple formats geared for tailored applications, can become available to all researchers and clinicians since these devices can be made cheaply and configured with commercially available instrumentation. In addition many of the microfluidic technologies allow for disposability which reduces the problem with sample cross-contamination, sterility, and biosafety (when

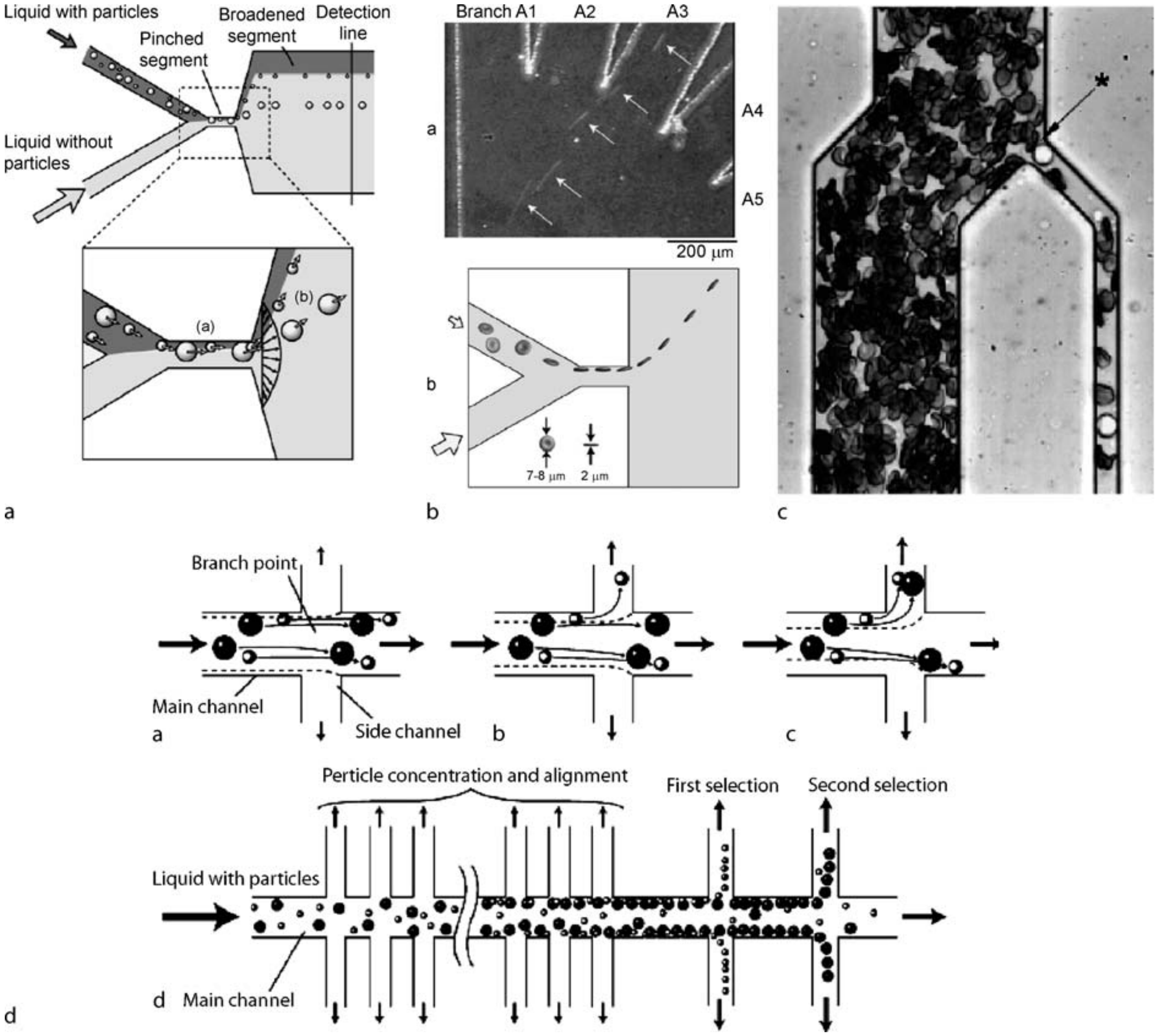

Cell Sorting, Figure 8 (**a**) Principle of pinched flow fractionation. (a) In the pinched segment, particles are aligned to one sidewall regardless of their sizes by controlling the flow rates from two inlets; (b) particles are separated according to their sizes by the spreading flow profile at the boundary of the pinched and the broadened segments. The dark-colored liquid contains particles. (Adapted from [24]) (**b**) Separation of erythrocytes. (a) A photograph of separated erythrocytes, indicated by white arrows. (b) Schematic diagram of the erythrocyte alignment and separation. (Adapted from [25]) (**c**) Leukocyte enrichment from whole blood. As smaller, more flexible erythrocytes seek the faster flow region in the center of the channel lumen, collide with leukocytes forcing them to migrate toward the sidewalls. Therefore, before the first bifurcation is reached, the leukocyte distribution across the channel changes considerably, with most of the leukocytes traveling near the channel sidewalls (Adapted from [26]) (**d**) Principle of hydrodynamic filtration. (a–c) Schematic diagrams showing particle behavior at a branch point; the relative flow rates distributed into side channels are (a) low, (b) medium, and (c) high. Broken lines show the virtual boundaries of the flows distributed into side and main channels. (d) Schematic diagram showing particle concentration and classification in a microchannel having multiple branch points and side channels. (Adapted from [27])

handling pathogenic samples). Microdevices also compare favorably with conventional techniques on cell purity and have shown increased cell viability which is very important when further analysis is necessary or long-term experiments are performed. In addition to this, entirely novel microdevices and techniques have been developed using acoustic, optical, dielectrophoretic, and hydrodynamic forces to sort cells. These forces cannot be harnessed on the macroscale. This has led to the ability to sort particles based on a widening set of parameters including size, charge, conductivity, shape, deformability, and life stage. An array of these devices operating in parallel will allow an increase in quantitative measurements which could allow the discovery of entirely new subpopulations

of cells from heterogeneous populations. These capabilities are very important in the realm of clinical diagnostics, presymptomatic disease detection, and biomedical applications.

Finally the most important point to be noted is that microfluidic techniques should be judged as complementary to rather than a replacement for conventional techniques which will continue to have a significant role in cell sorting. Most of the successful examples in adapting microfluidic devices for cell sorting have been those in which the microfluidic device is used as either sample preparation module or downstream processing and detection module after the conventional technique has processed the sample.

Future Directions for Research

It is clear that, great progress has been made in the field of cell sorting. However the key issues still to be addressed are parallelization, throughput, and integration. Parallelization will lead to higher throughput which at times is necessary because large sample volumes have to be processed such as in the sorting of rare cells, e. g. circulating tumor cells or in water analysis. Also as stated previously parallelization will allow multi-parameter sorting. Issues such as transport of cells to downstream analysis and how different cells types might be identified will also have to be addressed.

Cross References

- ► Biosample Preparation Lab-on-a-Chip Devices
- ► DC-Dielectrophoresis Lab-on-Chip Devices
- ► Dielectrophoresis
- ► Dielectrophoretic Motion of Particles and Cells
- ► Electrokinetic Motion of Cells and Nonpolarizable Particles
- ► Flow Cytometer Lab-on-Chip Devices
- ► Lab-on-a-Chip Devices for Particle and Cell Separation
- ► Magnetophoresis
- ► Microfilters
- ► Optical Tweezers for Manipulating Cells and Particles
- ► Single-Cell Analysis in Microfluidics
- ► Techniques of Manipulating Cells

References

1. Huh D, Gu W, Kamotani Y, Grotberg JB, Takayama S (2005) Microfluidics for flow cytometric analysis of cells and particles. Physiol Meas 26:R73–R98
2. Voldman J (2006) Electrical Forces For Microscale Cell Manipulation. Annu Rev Biomed Eng 8:425–454
3. Pohl HA (1978) Dielectrophoresis. Cambridge University Press, London
4. Hughes MP (2002) Strategies for dielectrophoretic separation in laboratory-on-a-chip systems. Electrophoresis 23:2569–2582
5. Ashkin A (1970) Accelerating and trapping of particles by radiation pressure. Phys Rev Lett 24:156–159
6. Ashkin A, Dziedzic JM, Bjorkholm JE, Chu S (1986) Observation of a Single-Beam Gradient Force Optical Trap for Dielectric Particles. Opt Lett 11:288–290
7. Holmes D, Morgan H, Green NG (2006) High throughput particle analysis: combining dielectrophoretic particle focusing with confocal optical detection. Biosens Bioelectron 21:1621–1630
8. Wilding P, Pfahier J, Bau HH, Zemel JN, Kricka LJ (1994) Manipulation and flow of biological fluids in straight channels micromachined in silicon. Clin Chem 40:43–47
9. Murthy SK, Sethu P, Vunjak-Novakovic G, Toner M, Radisic M (2006) Size-based microfluidic enrichment of neonatal rat cardiac cell populations. Biomed Microdev 8:231–237
10. Lapizco-Encinas BH, Simmons BA, Cummings EB, Fintschenko Y (2004) Dielectrophoretic concentration and separation of live and dead bacteria in an array of insulators. Anal Chem 76:1571–1579
11. Becker FF, Wang XB, Huang Y, Pething R, Vykoukal J, Gascoyne PR (1995) Separation of human breast cancer cells from blood by differential dielectric affinity. PNAS 92:860–864
12. Barrett LM, Skulan AJ, Singh AK, Cummings EB, Fiechtner GJ (2005) Dielectrophoretic manipulation of particles and cells using insulating ridges in faceted prism microchannels. Anal Chem 77:6798–6804
13. Hu X, Bessette PH, Qian J, Meinhart CD, Daugherty PS, Soh HT (2005) Marker-specific sorting of rare cells using dielectrophoresis. PNAS 102:15757–15761
14. Wang X, Yang J, Huang Y, Vykoukal J, Becker FF, Gascoyne PRC (2000) Cell separation by dielectrophoretic field-flow-fractionation. Anal Chem 72:832–839
15. Furdui VI, Harrison DJ (2004) Immunomagnetic T cell capture from blood for PCR analysis using microfluidic systems. Lab Chip 4:614–618
16. Pamme N, Manz A (2004) On-chip free-flow magnetophoresis: continuous flow separation of magnetic particles and agglomerates. Anal Chem 76:7250–7256
17. Petersson F, Nilsson A, Holm C, Jonsson H, Laurell T (2004) Separation of lipids from blood utilizing ultrasonic standing waves in microfluidic channels. Analyst 129:938–943
18. Petersson F, Nilsson A, Holm C, Jonsson H, Laurell T (2005) Continuous separation of lipid particles from erythrocytes by means of laminar flow and acoustic standing wave forces. Lab Chip 5:20–22
19. MacDonald MP, Spalding GC, Dholakia K (2003) Microfluidic sorting in an optical lattice. Nature 426:421–424
20. Milne G, Rhodes D, MacDonald M, Dholakia K (2007) Fractionation of polydisperse colloid with acousto-optically generated potential energy landscapes. Opt Lett 32:1144–1146
21. Chiou PY, Ohta AT, Wu MC (2005) Massively parallel manipulation of single cells and microparticles using optical images. Nature 436:370–372
22. Chiou PY, Ohta AT, Wu MC (2005) Massively parallel manipulation of single cells and microparticles using optical images. Nature 436:370–372
23. Huang LR, Cox EC, Austin RH, Sturm JC (2004) Continuous particle separation through deterministic lateral displacement. Science 304:987–990

24. Yamada M, Nakashima M, Seki M (2004) Pinched flow fractionation: continuous size separation of particles utilizing a laminar flow profile in a pinched microchannel. Anal Chem 76:5465–5471
25. Takagi J, Yamada M, Masahiro M, Yasuda M, Seki M (2005) Continuous particle separation in a microchannel having asymmetrically arranged multiple branches. Lab Chip 5:778–784
26. Shevkoplyas SS, Yoshida T, Munn LL, Bitensky MW (2005) Biomimetic autoseparation of leukocytes from whole blood in a microfluidic device. Anal Chem 77:933–937
27. Yamada M, Seki M (2005) Hydrodynamic filtration for on-chip particle concentration and classification utilizing microfluidics. Lab Chip 5:1233–1239

Cell and Tissue Culture

► Microfluidic Devices in Tissue Engineering

Cellular Microenvironments

► Microfluidic Devices in Tissue Engineering

Centrifugal Flow

► Centrifugal Microfluidics

Centrifugal Microfluidics

JENS DUCRÉE
HSG-IMIT, c/o IMTEK, University of Freiburg,
Freiburg, Germany
jens.ducree@hsg-imit.de

Synonyms

Centrifugal flow; Lab-on-a-disk; Lab-cd; Lab-disk; Microfluidics on a CD; Rotating channel flow

Definition

Centrifugal microfluidic technologies use the inertial pseudo forces experienced in a rotating reference frame to transport and manipulate fluids, overwhelmingly liquids, through networks of microchannels and chambers on substrates which are often in the format of a disk. These density-dependent pseudo forces are the centrifugal force scaling with the square of the frequency of rotation, the Euler force which is associated with an accelerated rotational motion and the Coriolis force acting on flows through rotating channels. Unit operations such as valving, routing, metering and mixing often results from the interplay of the rotational forces, capillary flow control and/or siphon-like structures. Centrifugal microfluidic systems typically comprise a polymeric substrate with the size of a compact disk incorporating a planar microchannel network and an actuation unit exhibiting a rotational drive, a detection unit and/or a dispenser. Most applications aim for the process integration, automation, parallelization and miniaturization of analytical, diagnostic and preparative protocols in life sciences.

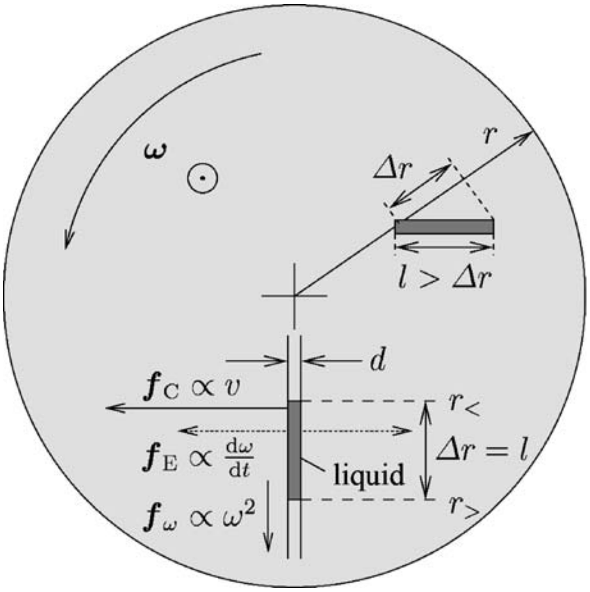

Centrifugal Microfluidics, Figure 1 Geometry and forces on a disk spinning at the angular velocity vector $\boldsymbol{\omega}$ pointing out of the paper plane towards the reader. The radial coordinate is given by r. The liquid plug of diameter d and absolute length l extends between its inner and outer radial positions $r_<$ and $r_>$, respectively, with $\Delta r = r_> - r_<$ and $\bar{r} = 0.5(r_< + r_>)$. For a radially oriented plug, $\Delta r = l$, otherwise $\Delta r < l$. The liquid traveling at a speed $\boldsymbol{v}$ down the channel is exposed to the centrifugal force density $\boldsymbol{f}_\omega \sim \omega^2$ (2), the Euler force density $f_{\mathrm{E}} \sim d\omega/dt$ (3) and to the Coriolis force density $\boldsymbol{f}_{\mathrm{C}} \sim \boldsymbol{v}$ (4)

Overview

Hydrodynamic Equation of Motion

In centrifugal microfluidic systems, the Navier–Stokes equation is most conveniently expressed within the reference frame where the substrate rotating at a frequency $\omega = 2\pi\nu$ is at rest (Fig. 1). Due to the non-inertial nature of this frame of reference, the centrifugal force density f_ω, the Euler force density f_{E} and the Coriolis force density f_{C} additionally appear in the hydrodynamic equation

of motion

$$\varrho\left[\frac{\partial}{\partial t}\boldsymbol{v}+(\boldsymbol{v}\cdot\nabla)\boldsymbol{v}\right]=-\nabla p+\eta\nabla^2\boldsymbol{v}\underbrace{-\varrho\boldsymbol{\omega}\times(\boldsymbol{\omega}\times\boldsymbol{r})}_{f_\omega}$$
$$\underbrace{-\varrho\frac{\mathrm{d}\boldsymbol{\omega}}{\mathrm{d}t}\times\boldsymbol{r}}_{f_\mathrm{E}}\underbrace{-2\varrho\boldsymbol{\omega}\times\boldsymbol{v}}_{f_\mathrm{C}} \quad (1)$$

where $\boldsymbol{r}$ denotes the radial position, ϱ the mass density and $\boldsymbol{v}$ the velocity of the fluid. For the common situation where the vector $\boldsymbol{\omega}$ is perpendicular to the vectors $\boldsymbol{r}$ and $\boldsymbol{v}$, the absolute values of the densities of the three pseudo forces in (1) reduce to

$$f_\omega=\varrho\omega^2 r \quad (2)$$

for the centrifugal force (density),

$$f_\mathrm{E}=\varrho r\frac{\mathrm{d}\omega}{\mathrm{d}t} \quad (3)$$

for the Euler force (density) and

$$f_\mathrm{C}=2\varrho\omega v \quad (4)$$

for the Coriolis force (density).

Centrifugal Flow

We consider the analytically simple case of a centrifugally driven flow through straight channel with round cross section of diameter d. A continuous liquid plug of length l within the channel possesses menisci at the radial positions $r_<$ and $r_>$ at its upstream and downstream end, respectively. The channel exhibits a mean radial position

$$\bar{r}=\frac{r_>+r_<}{2} \quad (5)$$

and covers a height

$$\Delta r=r_>-r_< \quad (6)$$

in radial direction.

To investigate the flow, we consider stationary conditions, discard fringe effects at the boundaries of the plug and look at the quasi-static case where ω is constant and the product $\boldsymbol{v}\omega$ is small so the Euler force f_E and the Coriolis force f_C can be neglected in (1). Further excluding external pressure differences $\Delta p=0$ between the inlet and the outlet, we can solve the Navier-Stokes equation (1) to obtain a parabolic flow profile exhibiting a mean velocity

$$\bar{v}=\frac{\varrho}{32\eta}\frac{\Delta r}{l}\bar{r}d^2\omega^2 \quad (7)$$

peaking at the center of the tube. For a radially oriented channel, Δr equals l to eliminate their ratio $\Delta r/l$ and hence, contrasting pressure-driven flows, the average flow velocity $\bar{v}$ becomes independent of the channel length l. Apart from the scaling with the properties of the liquid, we obtain $\bar{v}\sim\bar{r}d^2\omega^2$.

Using the material properties of water ($\varrho\approx 1000\,\mathrm{kg\,m^{-3}}$, $\eta\approx 1\,\mathrm{mPa\,s}$), a typical channel diameter $d=200\,\mu\mathrm{m}$, $\Delta r=l$ and a mean position of the liquid plug $\bar{r}=3\,\mathrm{cm}$, a scaling

$$\bar{v}\approx(\nu[\mathrm{Hz}])^2\cdot 1.48\times10^{-3}\mathrm{ms^{-1}} \quad (8)$$

is derived. At a frequency $\nu=30\,\mathrm{Hz}=1800\,\mathrm{rpm}$, the flow velocity $\bar{v}\approx 1.3\,\mathrm{m\,s^{-1}}$, implying a residence time of about 1.5 ms, only, in a 2 cm long radial channel which can easily be accommodated on a disk of the size of a standard Compact Disc™ (CD). Note that due to the parabolically shaped laminar flow, the residence time distribution varies across the channel.

The overall discharge

$$Q=\bar{v}A=\frac{\pi\varrho}{128\eta}\frac{\Delta r}{l}\bar{r}d^4\omega^2 \quad (9)$$

of the centrifugal flow scales with the mean radial position $\bar{r}$ and the square of the rotational frequency ω. Similar to a pressure driven Poiseuille flow, the discharge Q is proportional to the square of the channel cross section $A=\pi d^2/4$ and inversely proportional to the viscosity η. Note that similar to $\bar{v}$ in (7), the discharge Q is independent of the length of the liquid plug flowing through the channel as long as $\Delta r=l$.

For the liquid characteristics of water, a microchannel with a lateral extension of $d=200\,\mu\mathrm{m}$ and a mean radial plug position of $\bar{r}=3\,\mathrm{cm}$, we obtain a discharge

$$Q\approx(\nu[\mathrm{Hz}])^2\cdot 2.72\times10^{-3}\mathrm{ml\,min^{-1}} \quad (10)$$

yielding $Q\approx 2.45\,\mathrm{ml\,min^{-1}}$ at $\nu=30\,\mathrm{Hz}=1800\,\mathrm{rpm}$. This means that, for instance, a single disk featuring about hundred channels in parallel can process more than 100 ml per minute!

Also an equivalent (external) pressure head

$$\Delta p_\omega=\varrho\bar{r}\Delta r\omega^2 \quad (11)$$

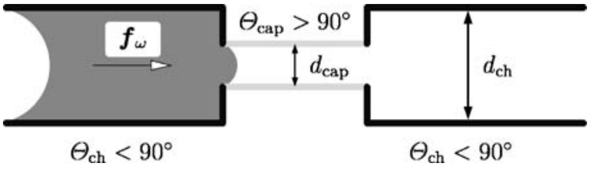

Centrifugal Microfluidics, Figure 2 A capillary barrier in made up of a geometrical constriction from the channel diameter d_{ch} to a narrow capillary of diameter $d_{cap} \ll d_{ch}$. In a hydrophobic barrier, the contact angles are $\Theta_{cap} > 90° > \Theta_{ch}$. The capability to stop the flow up to a certain frequency threshold ω^* (15) is determined by the capillary pressure Δp_Θ (14) scaling with the curvature d^{-1} as well as the inertia of the impinging flow

can be defined which would establish the same discharge Q as a centrifugal flow at an angular frequency ω. Note that in contrast to Q in (10), Δp_ω scales with the radial length of the plug Δr (6). Inserting again typical numbers for the liquid (water) and the geometry ($\bar{r} = 3$ cm, $\Delta r = 2$ cm), we arrive at

$$\Delta p_\omega \approx (\nu[\text{Hz}])^2 \cdot 2.4 \times 10^{-2}\,\text{kPa} \tag{12}$$

yielding a hydrostatic pressure head of $\Delta p_\omega \approx 21.6\,\text{kPa} \approx 0.2\,\text{atm}$ for $\nu = 30\,\text{Hz} = 1800\,\text{rpm}$.

In order to study secondary components of the centrifugal flow field, it is also interesting to look at the ratio

$$\frac{f_\omega}{f_C} \approx \frac{16\eta}{\varrho d^2}\frac{1}{\omega} \tag{13}$$

between the (radial) centrifugal force density f_ω and the (transversal) Coriolis force density f_C using $\bar{\nu}$ from (7) as the characteristic velocity. The scaling of the ratio with ω^{-1} implies that a threshold frequency exists beyond which f_C supersedes f_ω. Setting the ratio (13) to unity and inserting again the liquid characteristics of water for a channel measuring $d = 200\,\mu\text{m}$, f_ω already balances f_C at rather moderate centrifugal frequencies of about $64\,\text{Hz} \approx 3820\,\text{rpm}$.

Capillary Flow Control

Valving is an important unit operation in microfluidics. To assure a cost-efficient manufacturing, the substrate in centrifugal microfluidics ought to be made of passive components, only. Flow control is therefore commonly implemented by capillary forces. While a global hydrophilization of the substrate assures self-priming of narrow channel networks, selective hydrophobization of constrictions can generate a pressure difference opposing the further progression of a liquid meniscus (Fig. 2).

This capillary pressure

$$\Delta p_\Theta = 4\sigma\left[\frac{1}{d_{ch}}\cos\Theta_{ch} - \frac{1}{d_{cap}}\cos\Theta_{cap}\right] \tag{14}$$

depends on the surface tension σ of the liquid as well as the diameters d_{ch} and d_{cap} and the contact angles Θ_{ch} and Θ_{cap} at the channel and at the capillary constriction, respectively. For water ($\sigma \approx 10^{-1} Nm^{-1}$), a narrow constriction ($d_{cap}/d_{ch} \ll 1$) with $d_{cap} = 20\,\mu\text{m}$ and $\Theta_{cap} = 120°$, a pressure difference $\Delta p_\Theta = 0.2/d = 10\,\text{kPa}$ is found.

Setting Δp_Θ (14) equal to Δp_ω (11), such a capillary barrier breaks at frequencies

$$\nu\,[\text{Hz}] = \frac{1}{\pi}\sqrt{\frac{\sigma\,|\cos\Theta_{cap}|}{\varrho\bar{r}\Delta r d}} \tag{15}$$

resulting to roughly $\nu \approx 20$ Hz for the above specified conditions. A capillary barrier can be regarded as a high-pass valve with respect to the frequency of rotation ω.

Siphoning

The centrifugal field can also be deemed an artificial gravity with an acceleration $g = r\omega^2$. Therefore, also the siphoning effect can also be applied as sketched in Fig. 3. As long as the siphon tube which is submerged in the liquid within the reservoir stays empty, the liquid is retained at all frequencies ω. Once the tube is filled with a continuous liquid column and the liquid meniscus at $r_>$ has protruded farther outside than the liquid level in the reservoir at $r_<$, a hydrostatic pressure Δp_ω develops according to (11).

The flow out of the reservoir ceases as soon as $r_< = r_>$ or air disrupts the continuous columns, e. g. in case the reservoir is entirely empty. The priming of the tube can either proceed by adding water to the reservoir until its liquid level exceeds the crest point r_{crest} or by capillary action enabled by a hydrophilized inner surface of the tube. In contrast to the capillary barrier, the siphon represents a low-pass filter with respect to the frequency of rotation ω.

Sacrificial Valves

The previously introduced capillary and siphon-based valve structures are switched by the frequency of rotation ω. However, some applications demand vapor-proof valves for long-term liquid storage or programmability of the valves independent of the frequency of rotation ω.

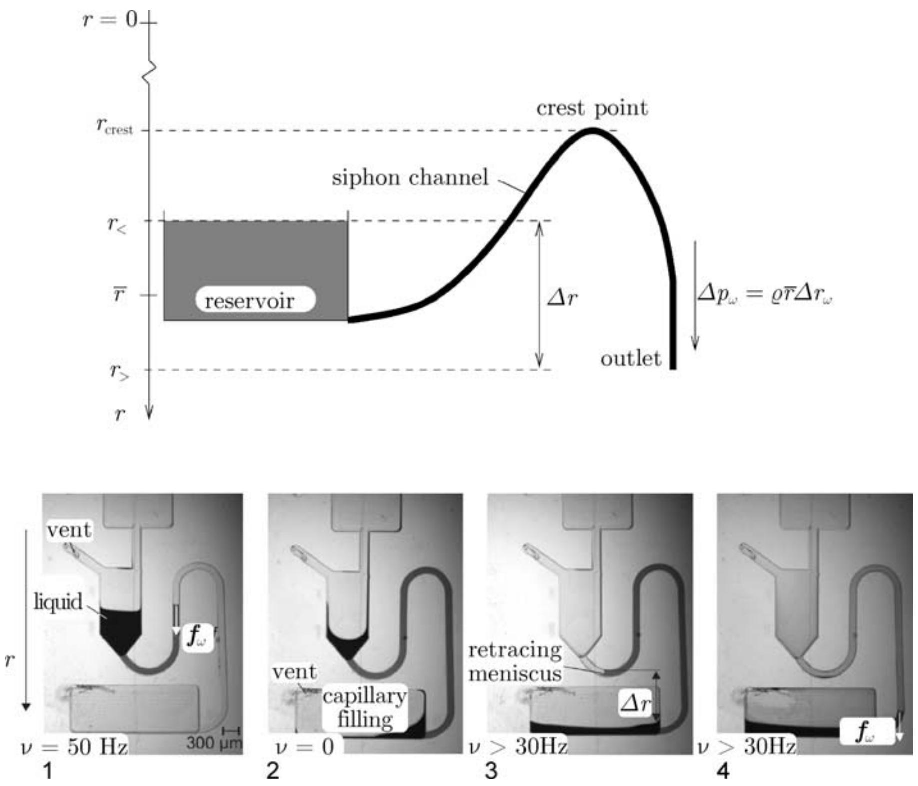

Centrifugal Microfluidics, Figure 3 A siphon structure consists of a reservoir and an outlet which are connected by a completely filled tube passing the crest point r_{crest}. The radial boundaries of the liquid volume are $r_<$ and $r_>$. For $\Delta r = r_> - r_< > 0$, a flow propelled by the hydrostatic pressure $\Delta p_\omega \sim \Delta r$ (11) drains from the reservoir over the crest point to the outlet without an external pump

In these cases, sacrificial valves may be employed. These valves are characterized by a disposable physical barrier such as a foil or polymer structure which is typically installed during manufacturing. For opening, these normally closed valves are, for instance, destroyed by punching with a spike or by laser ablation. Also regenerative valves, e. g. based on UV-polymerization, have been shown in Lab-on-a-Chip systems.

Sedimentation

A density difference between a liquid and suspended particles leads to a sedimentation in a centrifugal field (Fig. 4). The speed of sedimentation in radial direction

$$v_r = Sr\omega^2 \tag{16}$$

is governed by the centrifugal acceleration $g = r\omega^2$ as well as the sedimentation coefficient

$$S = \frac{m}{\bar{f}}\left(1 - \frac{\varrho_{\text{liquid}}}{\varrho_{\text{part}}}\right) \tag{17}$$

depending on the mass of the particle m, its hydrodynamic friction coefficient $\bar{f}$ and the ratio of the densities of the liquid ϱ_{liquid} and the particle ϱpart. This means that the speed of sedimentation v_{r} (16) is highest for heavy particles displaying a low drag coefficient $\bar{f}$ and a much higher density ϱ_{part} than the suspending liquid ϱ_{liquid}.
In an initially homogeneously distributed suspension, a shock interface forms traveling at a radial speed

$$r(t) = r_< \,\mathrm{e}^{S\omega^2 t} \tag{18}$$

from the inner liquid surface located at $r_<$. At a given instance in time t, the space between $r_<$ and r is cleared of particles.

System Aspects

Most present centrifugal microfluidic systems are networks of chambers communicating via interconnecting channels. Discrete liquid volumes are transferred between the chambers as the system seeks the hydrostatic equilibrium in the artificial gravity set by the frequency of rotation ω.

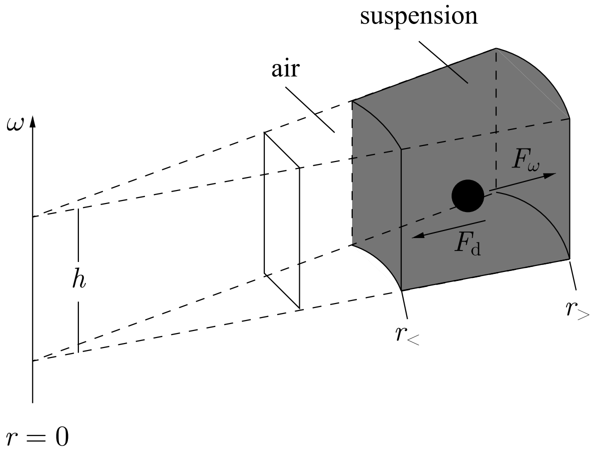

Centrifugal Microfluidics, Figure 4 Sedimentation of a particle suspended in a liquid volume under the impact of a centrifugal field f_ω (2). The volume of height h is confined by the inner and outer radial boundaries $r_<$ and $r_>$, respectively. The motion of the particle follows the buoyancy corrected force f_ω accounting for the mass difference Δm between the particle and the displaced liquid volume. The centrifugal motion is counteracted by the viscous drag F_d

In the majority of centrifugally controlled systems, the liquid handling proceeds in a pseudo-hydrostatic fashion governed by statically defined overflow, siphon and capillary principles. Highly dynamic break-up phenomena which are common, for instance, in contact-free liquid dispensers, are also possible, but rarely used. This means that the liquid handling performance can be made widely independent of the flow properties, in particular the viscosity of the processed liquid. Within the chambers, centrifugally induced buoyancy efficiently supports the removal of gas bubbles from the liquid bulk.

Furthermore, the ability to supersede capillary and surface tension related forces by raising the frequency of rotation ω also means that undesirable effects can virtually be 'switched off'. This refers the transient suppression of unwanted capillary filling as, for example, implemented by a hydrophilically primed siphon (Fig. 3). Also the surface-tension induced bending of surfaces may be compensated by a strong centrifugal field, thus allowing to shape flat menisci. The liquid handling performance may hence be made widely independent of the surface tension σ.

Another ubiquitous topic in Lab-on-a-Chip technology is the parallelization of processes. The centrifugal field suggests to replicate identical structures according to the rotational symmetry in a spoke-wheel like pattern. While such a highly symmetric layout has also be used in a pressure driven approach with a single pump pressurizing a central feed channel, only the centrifugal force transmission suppresses *hydrodynamic cross talk* between the parallel channels, e. g. the increase of the flow rate due to the clogging of a neighboring channel.

In summary, the quasi-hydrostatic implementation of liquid handling under the impact of the frequency controlled centrifugal field makes processes widely independent of the liquid properties. The symmetry as well as the volume force nature of the centrifugal field also improve the parallelization of processes.

Basic Methodology

Volume Metering

Most centrifugal microfluidic systems are networks of vessels and interconnecting channels performing assays, chemical synthesis or preparative protocols at the downstream end. To provide quantitative results, a metering of the volumes is required. However, an accurate and precise metering is not only essential for the chemistry, but it is also of key relevance for the centrifugal flow control via the radial coordinates $r_<$, $r_>$ and $\bar{r}$ of the volume within the channel network, see for instance (7), (9), (11) and (13).

Volume metering is predominantly realized by overflow principles. If, for instance, an excess volume is filled into a bucket, the liquid level lowers to its upper edge, thus metering the initial volume to the geometrically defined (smaller) volume of the bucket. In centrifugal microfluidics, the overflow corresponds to an outlet connected to a radially inward position (Fig. 5).

To interface with succeeding process steps, the volume often has to be forwarded to another chamber. To this end, another outlet channel located radially below than the first 'hole' is connected to the metering chamber. To avoid

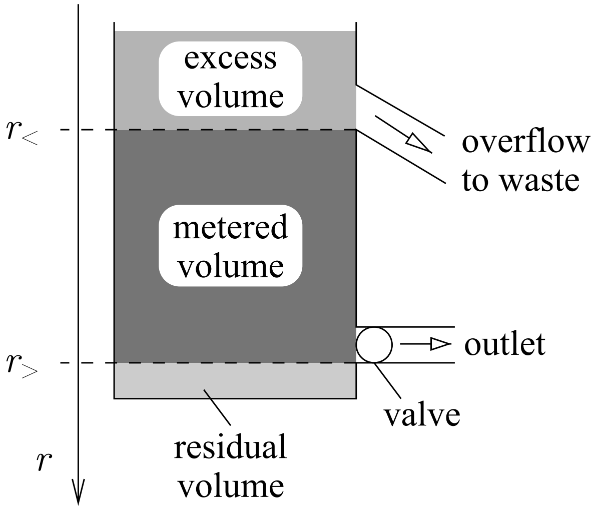

Centrifugal Microfluidics, Figure 5 Metering by an overflow connected at a radially inward position $r_<$. As long as the valve blocking the exit channel at $r_>$ is closed, excess liquid depletes via the overflow to a waste. After the liquid surface has reached $r_<$, the valve is opened and a volume geometrically defined by $\Delta r = r_> - r_<$ is forwarded via the outlet to downstream structures. The valve can, for instance, be represented by a hydrophobic constriction (Fig. 2) of a hydrophilic siphon (Fig. 3)

depletion of liquid during the metering phase, the passage is blocked by a capillary barrier (Fig. 2) or a siphon (Fig. 3) yielding upon changes of the rotational frequency ω.

Volume Splitting

In case an initial volume has to be split into several (metered) aliquots, a hydrophilic zigzag structure with hydrophobic patches confining the conduits connected to each jag has been used (Fig. 6). The upper jags are vents avoiding underpressure during the exit phase of the liquid. The outward pointing jags forward the geometrically defined volume retained in each V to the downstream areas. Key factors for a proper functioning are a complete initial capillary filling of the zigzag, the compensation of boundary effects at the two laterally outermost Vs, as well as synchronous *cutting* of the liquid column at the upper edges.

Batch-Mode Mixing

As in other microfluidic devices, strictly laminar conditions prevail at experimentally reasonable operating conditions. While smaller volumes of roughly a few nanoliters allow *spontaneous*, merely diffusive mixing within seconds and below, an efficient mixing of larger volumes, e. g. on the microliter range, requires an active reduction of diffusion distances and a simultaneous increase or interfacial surface area, also known as chaotic advection.

A broad scope of passive and active mixing schemes for Lab-on-a-Chip systems has been published in the literature. Many of these schemes may also be applied to centrifugal microfluidic systems. However, due to the technical and economical burden imposed by integrating active components onto the rotating, typically disposable substrate, passive mixing schemes are preferred. In this contribution we focus on schemes that make explicit nature of the rotational motion.

In a rotating chamber, mixing can be induced by rapid changes of the speed of rotation. The resulting the Euler force $f_E \sim d\omega/dt$ (3) leads to internal advection currents which accelerate mixing (Fig. 7, left). The efficiency of the mixing process is governed by the steepness and the magnitude of the frequency ramps $\omega(t)$ as well as by the shape and the size of the chamber. Due to the competition between favorable inertial effects and counteracting viscous dampening, chambers exhibiting aspect ratios near unity and containing large liquid volumes are preferable for this *shake-mode* mixing. By introducing paramagnetic beads which are deflected by stationary permanent magnets aligned with alternating polarization along the orbit of the chamber, a reversed *magnetic stirring* can be realized (Fig. 7, right).

Mixing of Flows

In case large *macroscopic* volumes have to be mixed which cannot be contained in a single chamber or when the volumes are too small for implementing mixing effects based on the Euler force f_E (3), continuous-flow mixing schemes may be applied. The aim is to contact the reagents with a large interfacial contact surface and short diffusion distances. A plethora of schemes to optimize micromixing between concurrent streams has been presented the literature for pressure driven flows. These schemes have often been enhanced by imposing secondary, transversal flow components or turbulent flow, e. g. via bends, impeller walls, grooves or stationary phases. The particular choice depends on parameters like the Reynolds number during operation and the constraints on the manufacturability and the durability of the system.

Due to the similarity of the flow profiles, most of these passive, continuous-flow schemes can, in principle, also be adopted for centrifugally driven flows. In addition, the availability of the Coriolis pseudo force f_C (4) offers an intrinsic means for the generation transversal flow components, even in straight radial channels exhibiting a constant cross section (Fig. 8). Due to the scaling of forces $f_\omega/f_C \sim \omega^{-1}$ (13), the Coriolis-force induced mixing is most efficient towards high frequencies of rotation ω, i. e. high flow rates Q (9).

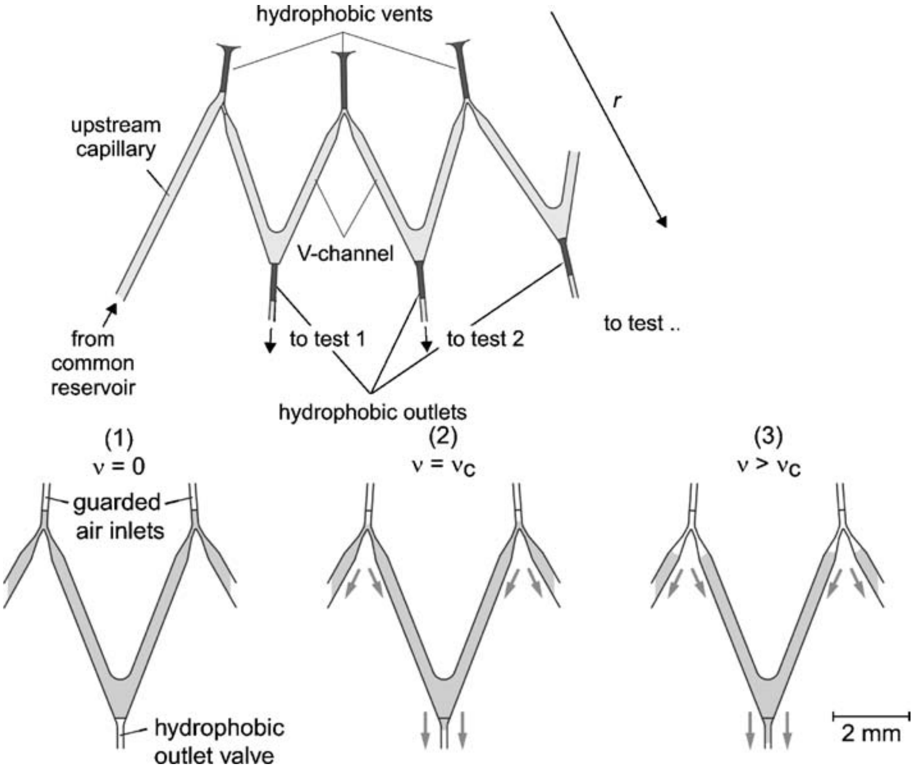

Centrifugal Microfluidics, Figure 6 (Top) Schematic of the structure for parallel metering comprising a zigzag channel which features hydrophobically blocked valves and vents. (Bottom) By elevating the rotational frequency above the burst frequency of the outer hydrophobic barriers, the volume contained in each V is released into attached test units. The precision of metering is linked to the symmetry of the break-up process [8]

Routing

The routing of a sequence of discrete volumes to designated outlets is a common task, e. g. in preparative protocols where sample, wash and elution buffers have to be directed to the waste or a receiving vessel after passing a common stationary phase. While different strategies such as flow focusing concepts have been pursued for Lab-on-a-Chip systems, we here consider on concepts connected to the rotational motion of centrifugal microfluidic systems.

In the first approach in Fig. 9, the incoming liquid stream disintegrates at the orifice on the upper left side of a large chamber. The individual droplets preferentially stick to the left hand wall where the centrifugal field guides them towards a hydrophobic patch at the entry of the first outlet channel. At high frequencies of rotation ω, the droplets overcome the capillary barrier. At lower frequencies ω, the interfacial force supersedes the centrifugal field to deflect the droplet towards the second outlet at the right hand side of the chamber.

Another routing scheme presented in Fig. 10 is primarily based on the Coriolis force f_C (4). In an inverse Y-channel geometry, the common radial inlet splits into two symmetric outlets. As the Coriolis force f_C prevails the centrifugal force ω towards elevated frequencies of rotation f_ω (13), a critical frequency ω^* exists above which binary switching occurs. Ideally, individual droplets pass the chamber interspersed between the inlet and the outlets in a free flight. The performance of this *Coriolis switch* is tightly linked to the dimensions and surface properties of the channels and the chamber. Attachment to the upper and lower walls by capillary forces tends to deteriorate the performance of binary switching. Note that a similar switching behavior could also be achieved by (solely or additionally) using the Euler force f_E (3).

Control of Flow Rate

The centrifugally driven flow rate Q (9) is governed by the mean radial position $\bar{r} \sim [r_< + r_>]$ (5) of the liquid volume and the frequency of rotation ω. In typical assay protocols, a metered volume such as a reagent or a wash buffer is driven from an upstream chamber by the centrifugal force through a stationary phase such as a biosensitive layer immobilized on the channel wall, aggregated beads or a membrane.

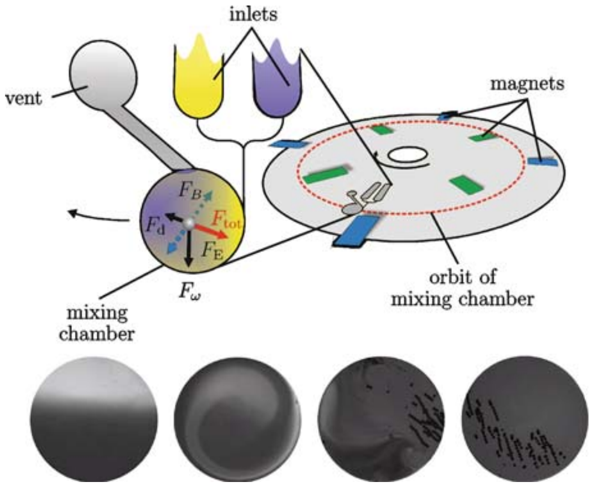

Centrifugal Microfluidics, Figure 7 (Top) Concept of the rotating microfluidic disk and the forces acting on a paramagnetic bead: a set of permanent magnets is aligned in the lab-frame at radial positions which are positioned inbound and outbound relative to the mean orbit followed by the rotating mixing chamber (dashed circle). Thus, a confined magnetic bead experiences an alternating radial driving force F_B which deflects the bead and induces advection via the viscous drag force F_d. The centrifugal force F_ω constantly points away from the center of rotation. Rapid changes of the sense of rotation lead to a Euler force F_E (3) on the bead and the liquid. (Bottom) Flow patterns induced by F_{tot} and f_E in the mixing chamber [7]

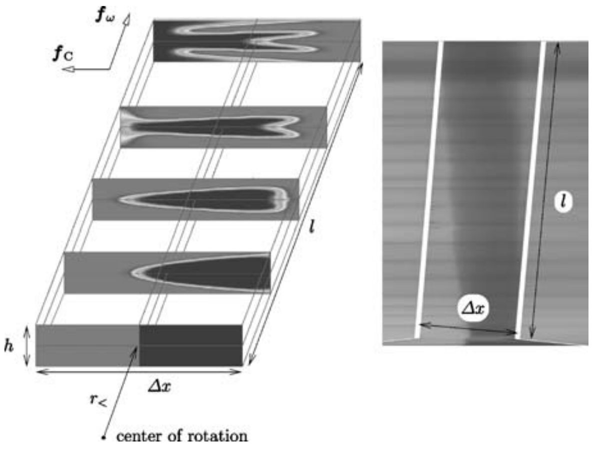

Centrifugal Microfluidics, Figure 8 Lateral spreading of two concurrent centrifugal flows A (clear) and B (dark) due to the Coriolis force f_C (4) for an angular frequency $\omega = 300\ \text{rad}\,\text{s}^{-1}$ in a rectangular radial channel of length $l = 2.1$ cm, height $h = 65\ \mu\text{m}$ and width $\Delta x = 320\ \mu\text{m}$ starting at $r_< = 3$ cm. The right hand side shows a top-view photography of the lateral spreading in the corresponding experiment. (Note that different length scales apply to the x- and y-axis.)

In many cases, the variation of the flow rate Q due to changes in $\bar{r}$ during the depletion of the upstream chamber ought to be minimized to homogenize incubation times. Looking at (9), the flow rate Q can be stabilized by an online adjustment of ω. Such a dynamic adjustment of ω either requires a very well reproducible flow behavior or a closed loop control of $\bar{r}$, e. g. via continuous tracking of the transient positions of the menisci $r_<$ and $r_>$.

An alternative to the adjustment of ω is to pinpoint $r_<$ and $r_>$ as far as possible during the flow interval. Regarding the downstream end at $r_>$, the continuous liquid column can, for example, be disrupted at a hydrophobic orifice leading into a large receiving vessel (Fig. 11). The fixed radial position of the orifice then coincides with $r_>$. For the upstream meniscus, the radial change of the inner meniscus $r_>$ can be minimized by maximizing the lateral dimensions of the issuing reservoir.

For other applications such as the simultaneous sedimentation at large ω (17), the overall minimization of the flow rate Q may be required. Resorting again to (9), we can also reduce the quotient $\Delta r d^4/l$ to throttle the flow rate. This geometric factor reflects the ratio of the hydrostatic pressure head ($\sim \Delta r$) to the hydrodynamic resistance ($\sim l/d^4$). So a radially shallow channel with a high tilt angle between the channel axis and the radial direction, i. e. $\Delta r \ll l$, diminishes Q (Fig. 1). A further reduction of Q can be accomplished by increasing the flow resistance, e. g. by a narrow, meander-like flow channel with an embedded stationary phase.

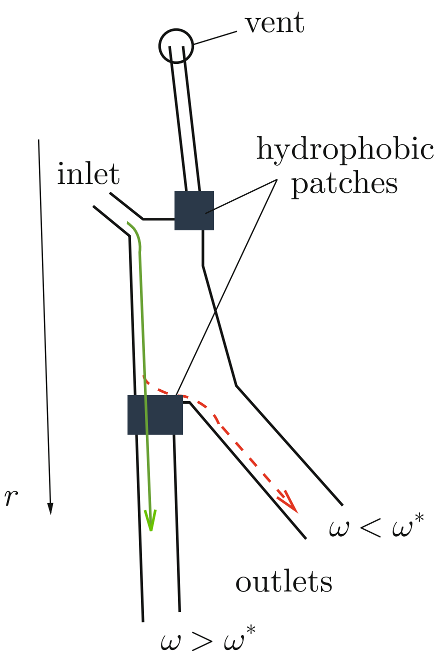

Centrifugal Microfluidics, Figure 9 Liquid router. Liquid is introduced via the upper left inlet and follows the left hand chamber walls towards a hydrophobic region at the entrance of the first outlet. Depending on the centrifugal field and thus the frequency ω, the droplet can either pass the capillary barrier or proceed to the second outlet [5]

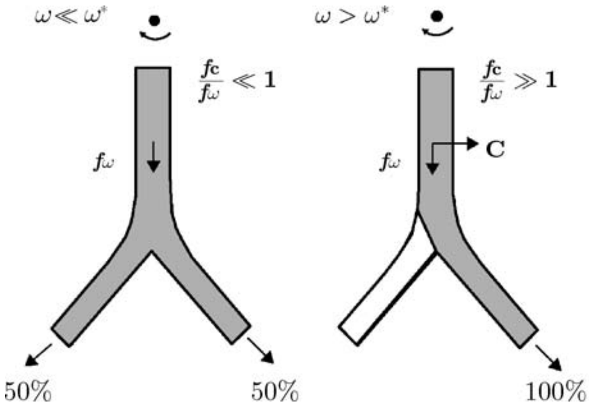

Centrifugal Microfluidics, Figure 10 Flow through a symmetric, inverse Y-structure. (Left) At low frequencies ω where the Coriolis force f_C (2) is still negligible compared to f_ω (3), the flow is symmetrically divided between both outlets. (Right) The Coriolis force f_C dominating beyond a critical frequency ω^* (13) diverts 100% of the flow into an outlet addressed by the sense of of rotation [9]

Particle Sedimentation

As the rotary drive offers the function of a customary centrifuge, also sedimentation processes can be enforced, see, for instance, the hematocrit measurement in Fig. 12. However, in typical applications based on centrifugal microfluidics, the sedimentation usually only constitutes one upstream unit step in an integrated process chain to which the supernatant has to be forwarded.

Figure 13 shows an integrated sedimentation structure based on hydrophobic valving for the initial, overflow based metering, a radially flat and narrow transfer channel to throttle the flow such that the suspension has sufficient time to sediment in the separation chamber before pure supernatant is passed on to the plasma chamber. From there, the plasma can, for instance, be forwarded downstream structures by a hydrophilic capillary while halting the rotation.

Fabrication

Compared to other Lab-on-a-Chip systems, similar criteria apply to the selection of the fabrication process. Usually a master is made by conventional microstructuring or, in particular during prototyping, by well-established *soft lithography*. Polymer replication of smaller lots is often done by hot embossing while mass fabrication can resort to injection molding. After the structuring of the bulk material, postprocessing such as surface modification (e. g. hydrophilic, hydrophobic, biosensitive, anti-fouling), sealing (e. g. thermal bonding, gluing), integration of stationary phases (e. g. aggregated beads, membranes) and reagent loading (e. g. lyophilized, liquid storage in pouch) may be required.

The main distinction to common, credit-card sized Lab-on-a-Chips is the high lateral extension of the substrate, e. g. with a diameter of 12 cm when using CD-like formats. Across such a large surface area, it is usually harder to guarantee homogeneity of all microstructuring and post-processing steps. In addition, the substrate has to be mechanically balanced to minimize the load of the spindle. As for most microfluidic substrates, the transfer from prototyping technologies to mass fabrication may be accompanied by significant deviations in the performance. These deviations often root in the change of the replication process, resulting in significant differences in the surface characteristics, e. g. affecting its texture or chemical composition. This may directly influence the behavior of capillary flow or the resistance to bio-fouling, but it may also alter the adherence of coatings and the sealing process.

Device Technology

The core element is a frequency-controlled motor and a holder for the rotating substrates (e. g. disks). Depending on the application, liquid, optical and possibly electrical interfacing between rotating *on-board* components and stationary *lab-frame* components such as dispensers or detection units have to be incorporated. A process control software has to synchronize events such as liquid handling or optical readout to the periodic motion of the substrate. Figure 14 shows device concept of the LabCD™ platform.

Development Tools

For the development of centrifugal microfluidic technologies, it is very useful to capture the dynamic processes during high-speed rotation. This is commonly done by a stroboscopic measurement setup comprising a microscope mounted CCD camera with a short exposure time and a flash light which are synchronized to the rotational motion (Fig. 15). Regarding simulation, the majority of commercially available computational fluid dynamic (CFD) packages is able to cope with rotating channels.

Key Research Findings

Since the early 1990s, several commercial and academic groups have launched activities to port various analytical or preparative protocols on centrifugal microfluidic systems. Companies such as Abaxis, Gyros, Gamera/Tecan, Eppendorf and SpinX have developed proprietary substrate formats and corresponding workstations incorporating actuation, liquid interfacing and detection units as well as various means for quality control. First full-fledged products have been available on the market.

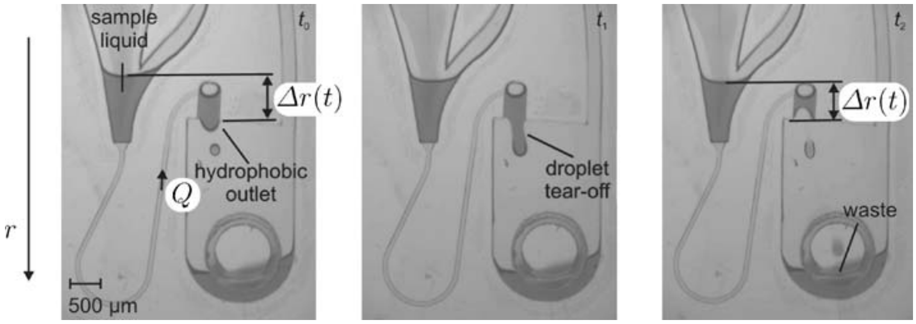

Centrifugal Microfluidics, Figure 11 Course of liquid break-off at the hydrophobic outlet of the drain channel in a structure designed to stabilize the flow rate Q (9). The liquid tears off into a waste reservoir. This way, the outer radial position of the liquid plug $r_>$ is kept constant and is fluidically decoupled from the filling height in the waste reservoir and other parasitic effects. The variation of inner plug position $r_<$ is minimized by the large lateral extension of the upstream chamber [8]

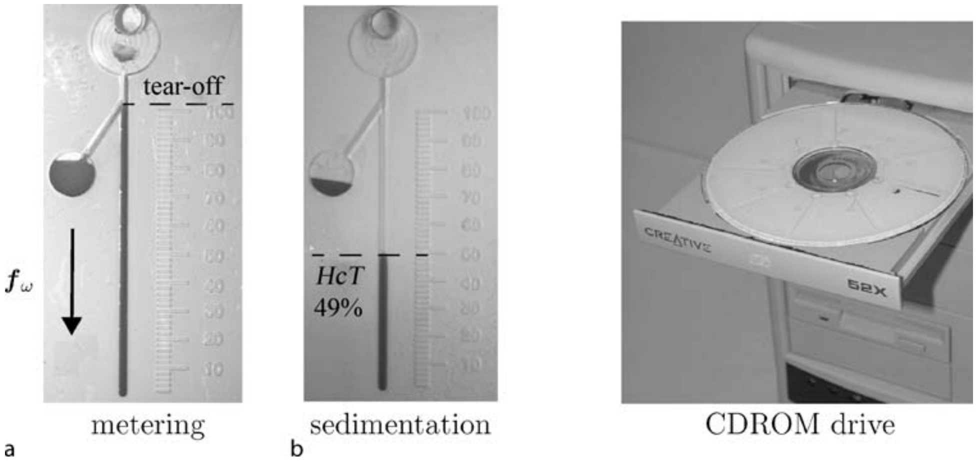

Centrifugal Microfluidics, Figure 12 (**a**) After an unmetered volume of whole blood is applied to the inlet reservoir, the capillary is primed and a precise volume of whole blood is metered during rotation. (**b**) Following sedimentation, the absolute hematocrit can be determined with the calibrated scale imprinted along the channel [7]

The present emphasis is put on general chemistry testing and immunoassays based on absorption, agglutination or fluorescence detection. Also the preparation of protein samples for subsequent analysis by MALDI-MS has been commercialized. For the rapidly emerging field of nucleic acid testing, key steps such as cell lysis, DNA isolation and thermocycling for polymerase chain reaction (PCR) have been demonstrated. In the mid-term future, it seems feasible to integrate an entire process chain comprising all steps between the take-up of real-world samples to displaying the analytical result on a centrifugal microfluidic nucleic acid workstation.

Another branch of centrifugal microfluidics forks into the field of micro process engineering. By making designated use of the frequency dependent artificial gravity conditions and the pseudo forces on the rotating substrate, applications such as ultra-fast mixing at high discharges, e. g. for chemical reacting, have been demonstrated. Also the centrifugally induced generation of multiphase systems such as highly monodisperse emulsions, segmented liquid-liquid and gas-liquid flow and air-to-liquid sampling has been shown.

Future Directions for Research

Most conventional Lab-on-a-Chip technologies may, in principle, be transferred to the *Lab-on-a-Disk*, in particular when they are active only while halting the rotation. The feasibility of the incorporation of these technologies to the rotating platform will be a trade-off between an enhancement of process integration, automation, control and variety of application protocols on the one side, and the increased complexity of the device (‘overengineering’) on the other.

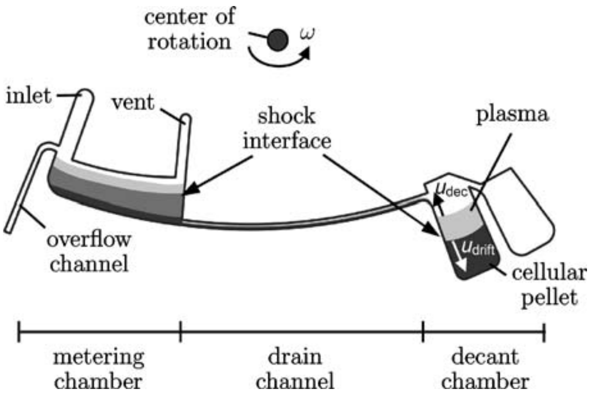

Centrifugal Microfluidics, Figure 13 Flow scheme of a decanting structure for plasma separation from whole blood. A metered volume of the blood sample is defined between hydrophobic stop and overflow channel. Upon breaking the outlet valve, a metered volume flows via the drain channel into the decant structure. A shock interface separating plasma from the cellular pellet builds out in all parts of the network and proceeds radially outwards at a speed u_{drift}. The filling height of the decant chamber rises at counter-current speed u_{dec} before the plasma overflows into the plasma collection chamber. The speed u_{dec} of the filling height in the cell reservoir is adjusted by the hydrodynamic resistance of the drain channel so that only purified plasma advances to the plasma reservoir [8]

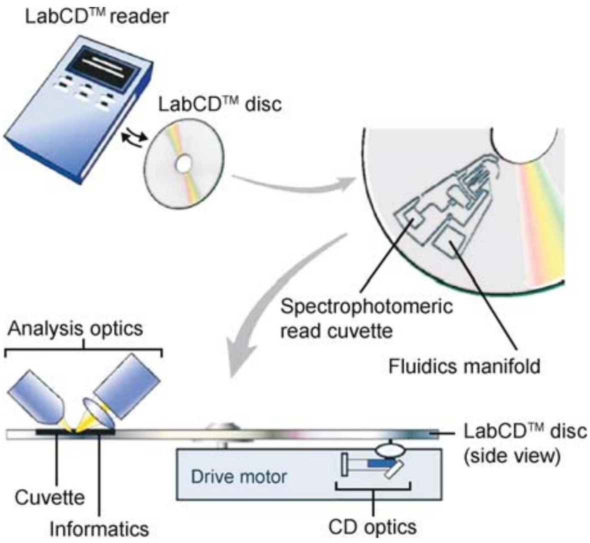

Centrifugal Microfluidics, Figure 14 LabCD™ instrument and disposable disk. Here, the analytical result is obtained through reflection spectrophotometry [3]

Future initiatives ought to start out with a look at the inherent advantages of centrifugal microfluidic systems:

- Modular setup
  - Centrifuge drive – passive microfluidic substrate
  - Easy exchange of disposable cartridge
  - Flexibility of substrate formats (disk, slide, ...)

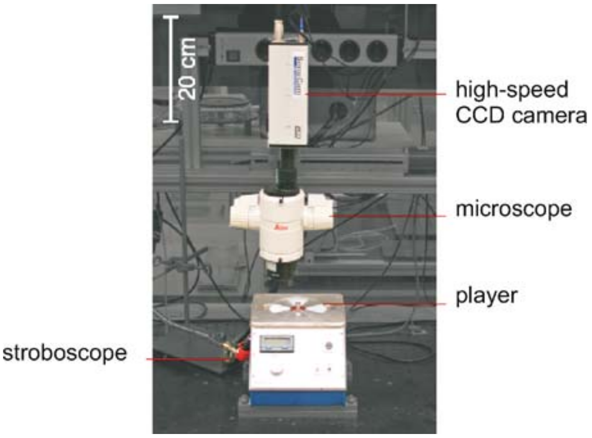

Centrifugal Microfluidics, Figure 15 Centrifugal test and development stand [7]

- Centrifugal field
  - Pulse-free pumping
  - No pressure-tight interfaces needed
  - Low pressure load on lids
  - Standard operation in sample prep
  - Robust liquid handling widely decoupled from viscosity and surface tension
  - Intrinsic, buoyancy-based bubble removal
  - Coriolis force manipulates flows
- Rotational symmetry
  - Replication of identical process channels
  - Simultaneous processing of parallel channels
  - Sequential channel-by-channel processing
- Full process integration and automation

and carefully weigh them against potential drawbacks such as

- Interfacing with lab-frame components
  - Pipettes and dispensers
  - Quality control units
  - Detection units
- On-board components
  - Exposure to centrifugal force
  - Need for mechanical balancing
  - Difficult wiring, e. g. for electrical power, liquids and signal transmission

which are primarily associated with the rotating motion of the substrate.

On behalf of research, the scope of unit operations should be extended. A key factor constitutes the availability of on-board detectors which will enable a truly continuous monitoring of processes taking place along the entire orbit to appreciable enhance the sensitivity. A similar effect may

be achieved by lab-frame optical systems which are able to track rotating reaction chambers.

Also an on-board electrical power supply, e. g. by photovoltaic cells or thermogenerators connected to a lab-frame irradiation source, would introduce additional, frequency independent degrees of freedom, enabling a multi-force manipulation of the processed liquids. Another extension of present centrifugal systems is the (wireless) data communication with the lab-frame workstation for an improved process control and analysis.

Regarding commercialization, it is expected that researchers will continue to further augment the level of process integration, automation, parallelization and miniaturization. Multi-purpose workstations which can run a set of different applications, each represented by a designated substrate (disk), will certainly be a strong selling point. The largest markets for centrifugal microfluidic technologies are expected for decentralized systems for medical diagnostics and (bio-)chemical analysis as well as research tools for pharmaceutical drug discovery.

Apart from reliability, sensitivity, interfacing with established standards and regulatory issues, the main hurdle to pass for a successful commercialization is clearly the price per assay or preparation compared to presently established or other emerging technologies. This concerns the polymer substrate as well as the device for which important lessons may, for instance, be learnt from the massive cost erosion of Compact Disc™ technology over the last decades. Patients autonomously performing complex diagnostic assay protocols by simply introducing a body liquid into a $1 disk which is automatically 'played' by a $10 discman remains a truly tantalizing vision for centrifugal microfluidic technologies.

Cross References

- ► Active Mixer
- ► Bead-Based Microfluidic Platform
- ► Biosample Preparation Lab-on-a-Chip Devices
- ► Capillary Filling
- ► Capillary Force Valves
- ► Fluid Metering
- ► Hydrophilic/Hydrophobic Patterning
- ► Integrated Micro Devices for Biological Applications
- ► Lab-on-a-Chip (General Philosophy)
- ► Lab-on-Chip Devices for Biodefense Applications
- ► Lab-on-Chip Devices for Chemical Analysis
- ► Lab-on-Chip Devices for Immunoassay
- ► Lab-on-Chip Devices for Particle and Cell Separation
- ► Lab-on-Chip Devices for Protein Analysis
- ► Lab-on-Chip Devices for Sample Extraction
- ► Microfabrication Techniques
- ► Lab-on-a-Chip Devices for Chemical Analysis
- ► Microfluidic Mixing
- ► Microfluidic Sample Manipulation
- ► Microfluidic Systems for Combinatorial Chemistry
- ► Microfluidic Systems for High-throughput Screening
- ► Microfluidics for Bio- and Chemical Reactions
- ► N-Chip Cell Lysis
- ► PCR Lab-on-Chip Devices
- ► Stationary Phases in Microchannels

References

1. Schembri CT, Ostoich V, Lingane PJ, Burd TL, Buhl SN (1992) Portable simultaneous multiple analyte whole-blood analyzer point-of-care testing. Clinical Chem 38(9):1665–1670
2. Madou MJ, Kellogg GJ (1998) LabCD: A centrifuge-based microfluidic platform diagnostics. In: Cohn GE, Katzir A (eds) Proc SPIE – Systems & Tech Clinical Diagnostics Drug Discovery 3259:80–93
3. Madou M, Zoval J, Jia G, Kido H, Kim J, Kim N (2006) Lab on a CD. Ann Rev Biomed Eng 8:601–628
4. Gustafsson M, Hirschberg D, Palmberg C, Jörnvall H, Bergman T (2004) Integrated sample preparation and MALDI mass spectrometry on a microfluidic compact disk. Anal Chem 76(2):345–350
5. Inganäs M, Dérand H, Eckersten A, Ekstrand G, Honerud AK, Jesson G, Thorsén G, Söderman T, Andersson P (2005) Integrated microfluidic compact disc device with potential use in both centralized and point-of-care laboratory settings. Clinical Chem 51(10):1985–1987
6. Pugia MJ, Blankenstein G, Peters RP, Profitt JA, Kadel K, Willms T, Sommer R, Kuo HH, Schulman LS (2005) Microfluidic tool box as technology platform for hand-held diagnostics. Clinical Chem 51(10):1923–1932
7. Steigert J, Grumann M, Brenner T, Mittenbühler K, Nann T, Rühe J, Moser I, Haeberle S, Riegger L, Riegler J, Bessler W, Zengerle R, Ducrée J (2005) Integrated sample preparation, reacting and detection on a high-frequency centrifugal microfluidic platform. J Assoc Labor Autom 10(5):331-341
8. Brenner T, Glatzel T, Zengerle R, Ducrée J (2005) Frequency-dependent transversal flow control in centrifugal microfluidics. Lab Chip 5(2):146–150
9. Haeberle S, Brenner T, Schlosser H-P, Zengerle R, Ducrée J (2005) Centrifugal micromixer. Chem Eng Tech 28(5):613–616
10. Felton M (2003) CD simplicity. Anal Chem 75(13):302A–306A

Ceramics

► Non-Metallic Inorganic Materials

Changes of Caspase Activity

► Microfluidics for Studies of Apoptosis

Chaotic

► Chaotic Mixing Based on Viscoelasticity

Chaotic Flows

William W. Liou
Western Michigan University, Kalamazoo, MI, USA
William.liou@wmich.edu

Synonyms

Turbulent flows; Turbulence

Definition

There is no universally recognized definition of chaotic flows. Flows with properties that are neither constant in time nor presenting any regular periodicity are normally referred as chaotic. Fluid turbulence is generally found to be chaotic. It is also random, dissipative, and multiple scaled in time and space. It is a complex system of infinite degrees of freedom.

Overview

Noises are due to random thermal fluctuations or other environmental factors and can be completely unpredictable except for statistical sense. Chaos arises from deterministic systems [1, 2]. Normally the nonlinearity in the system can produce high sensitivity to the initial state of the system such that even a small error will be exponentially amplified as the system evolves in time.
A simple differentiable dynamical system of dimension n can be written as

$$\frac{\mathrm{d}\boldsymbol{x}(t)}{\mathrm{d}t} = f(\boldsymbol{x}(t)) \text{ where } \boldsymbol{x} \in R^n$$

The solution of the system produces a time series of the value of $\boldsymbol{x}$ in time t with the initial value of $\boldsymbol{x}$ given at time $t = 0$ or $\boldsymbol{x}(t = 0) = \boldsymbol{x}_0$. The space $\boldsymbol{x}$ (R^n) with t as a parameter is termed a phase space. The function f determines the time evolution of the system. The dynamic system is nonlinear with nonlinear term in the function f. One example in fluid dynamics is the Navier–Stokes equations for Newtonian fluids. The nonlinearity of the system comes mainly from the convective motion of the fluid flow. The fluid motion can develop unpredictable, yet observable behavior with the proper choice of the initial conditions.
One example of such a system is the Lorenz system [3] with $n = 3$. The system can be written as

$$\frac{\mathrm{d}x}{\mathrm{d}t} = -\sigma x + \sigma y$$

$$\frac{\mathrm{d}y}{\mathrm{d}t} = -xy + rx - y$$

$$\frac{\mathrm{d}z}{\mathrm{d}t} = xy - bz$$

The system is a simplified form of the Navier–Stokes equations. The solution of the system ($x(t)$, $y(t)$, $z(t)$) in the phase space or trajectory with an initial condition near (0, 0, 0) and $\sigma = 10$, $r = 28$, $b = 3/8$ is shown in Fig. 1 [4].
Discrete equations, such as finite difference equations, can also produce chaos. Henon [5] proposed a system of discrete time evolution equations

$$x(t + 1) = y(t) + 1 - a[x(t)]^2$$

$$y(t + 1) = bx(t)$$

which exhibits the same essential properties as the Lorenz system for certain values of the parameters in the equations.
In practice, the identification of chaos is difficult. The noise of a physical system interferes with the dynamics that are determined by the governing equations. The components in a measurement device will also present noise. Several possible measures of chaos include the use of the power spectrum, the Poincare map and the Liapunov number.
The power spectrum is probably the most frequently used measure. The power spectrum decomposes a complex time

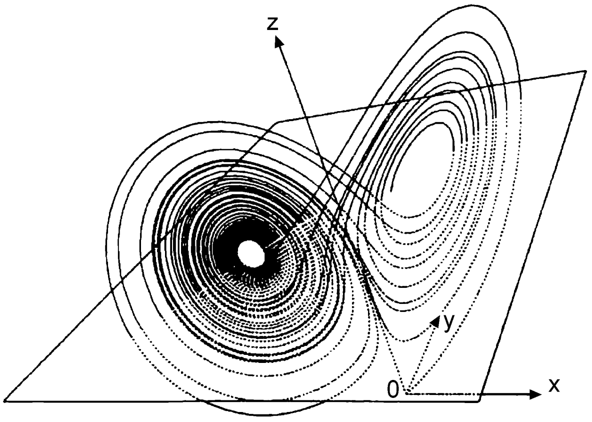

Chaotic Flows, Figure 1 Trajectory of the Lorenz system

series or system behavior into a series of sine waves of a range of frequency. The power spectrum of a chaotic time series is normally a continuous power spectrum. The power associated with a particular frequency is the square of the amplitude of that sine function. A time series is chaotic with a broad band of continuous frequency with appreciable power.

A Poincare map is established by cutting across the trajectories in a certain region in the phase space, say with dimension n, with a surface that is one dimension less than the dimension of the phase space, $n-1$. One such cut is also shown in Fig. 1. The equation that produces the return to the crossing the next time is a discrete evolution equation and is called the Poincare map. The dynamics of the continuous system that creates the Poincare map can be analyzed by the discrete equation. Therefore, chaotic behavior of the Poincare map can be used to identify chaos in the continuous system. For example, for certain parameters, the Henon discrete evolution equation is the Poincare map for the Lorenz systems.

The Liapunov number can be used as a quantitative measure for chaos. The connection between chaos and the Liapunov number is through attractors. An attractor is a set of points S such that for nearly any point surrounding S, the dynamics will approach S as the time approaches infinity. The steady state of a fluid flow can be termed an attractor with dimension zero and a stable limit cycle dimension one. There are attractors that do not have integer dimensions and are often called strange attractors. There is no universally acceptable definition for strange attractors. The Liapunov number is determined by the principle axes of the ellipsoidal in the phase space, which originates from a ball of points in the phase space. The relationship between the Liapnuv number and the characterization of chaos is not universal and is an area of intensive research.

Fluid turbulence has had many descriptions. It is random, chaotic, dissipative, and multiple scaled. The turbulent flows describable by the Navier–Stokes equations present these properties when the nonlinear terms, which represent the convective effect of fluid motion, become relatively large compared with the other terms, such as the viscous forces. The Reynolds number can be regarded as one such measure for the ratio. At small Reynolds numbers, or when the viscous effects dominate the nonlinearity in the system, the solutions of the Navier–Stokes equations are regular and smooth, a state commonly referred to as laminar flow. Chaotic time series of the flow begins to appear as the Reynolds number increases, or when the nonlinearity becomes dominant. As the time series of the behavior at large Reynolds number can present quite large oscillations, methods using averaging have been applied so that the smooth, averaged flow behaviors are more amendable to studies. This process, however, naturally produces additional unknowns that do not have the corresponding unaveraged quantities in the Navier–Stokes equations. This is referred to as the turbulence closure problem.

Basic Methodology

The averaging method for a turbulent flow divides the time series into an averaged value and a fluctuation with respect to that average [6]. Or,

$$u = U + u'$$

$$\text{where } U = \bar{u} = \lim_{(\zeta_b - \zeta_a)\to\infty} \frac{1}{\zeta_b - \zeta_a} \int_{\zeta_b}^{\zeta_u} u d\zeta$$

The quantity U can be obtained in a few different ways. The average can be taken over time or space variables. It can also be obtained by ensembling. When the three averaging procedures lead to the same result, the system is ergodic. The equations for the averaged quantities can be obtained by exercising the averaging procedure on the Navier–Stokes equations. u' represents the deviation of the time series from the average value, or fluctuation. The intensity of the fluctuation or $|u'|$ is a measure of the deviation. The decomposition or averaging has facilitated the development of most of the current understanding of turbulent flows theoretically, experimentally, and numerically. However, as described earlier, the averaging also introduces the closure problem. For example, for a and b being turbulent flow quantities, or $a = A + a'$, $b = B + b'$ the nonlinear convective terms of the averaged Navier–Stokes equations produce terms like

$$\overline{ab} = \bar{a}\,\bar{b} + \overline{a'b'}$$

The second-order correlation of the fluctuations $\overline{a'b'}$ is not known and does not appear in the Navier–Stokes equations. Additional equations need to be provided, therefore giving rise to the closure problem. The closures are provided for an area called turbulence modeling for RANS (Reynolds-averaged Navier–Stokes) and LES (large eddy simulation) methodologies.

With the exponential increase of computing speed, numerically solving the Navier–Stokes equations has been conducted for turbulent flows of increasingly high Reynolds numbers. This belongs to a subject called direct numerical simulation or DNS.

In micro- and nanoscaled devices, the particle nature of fluid becomes important. For a gaseous fluid, the ratio of the molecular mean free path λ and the system length scale

L is termed the Knudsen number Kn:

$$\mathrm{Kn} = \lambda/L$$

For micro- and nanoscale gaseous flows with large Knudsen number, say 0.1, the equilibrium assumption inherent in the Navier–Stokes equations becomes invalid and a discrete approach has to be used. This is also true for liquids, although the Knudsen number is not an appropriate parameter to measure deviation from continuum for liquid flows. Given the observations made from macroscaled devices and the known fluid properties, the Reynolds numbers for the flows in micro- and nanoscaled devices are very small due to the small length scales.

Key Research Findings

Arguably the most significant finding that has redirected turbulent flow research is the identification of the so-called coherent structures in experiments and in numerical studies. They are observable by using conditional sampling or phase averaging, particularly in flows that are somewhat excited. The structures are generally coherent in their appearance and vorticity. The structures are often of large scale, for example of the same order as that of the mean flow. They have been found to be responsible for mechanisms that relate to the transport and the production in almost all commonly observed turbulent flows. Findings show the existence of the underlying orderliness in the apparent chaos of turbulent flows and have fostered many modifications to the traditional thinking of turbulence, such as the turbulent gradient transport hypothesis. Weakly nonlinear analysis has been shown to reproduce the large-scale phenomena in simple flows.

Future Directions for Research

Chaotic flows remain one of the most challenging problems in sciences and engineering. At micro- and nanoscales, the behaviors of fluid flows are yet to be fully investigated. On the other hand, nano- and microscaled devices have brought new opportunities to the study of chaotic flows. Molecular tagging and many other new techniques are emerging every day. They also bring possibilities of new control methodologies of chaotic turbulent flows.

Cross References

► Micro- and Nanoscale Gas Dynamics
► Monte Carlo Method

References

1. Devaney RL (1986) An introduction to chaotic dynamical systems. Benjamin/Cummins, Menlo Park
2. Schuster HG (1984) Deterministic chaos: an introduction. Physik-Verlag, Weinheim
3. Lorenz EN (1963) Deterministic nonperiodic flow. J Atmos Sci 20:130
4. Lanford OE (1977) In: Turbulence Seminar. Springer Lecture Notes in Mathematics 615:113
5. Henon M (1976) A two-dimensional mapping with a strange attractor. Comm Math Phys 50:69
6. Tennekes H, Lumley JL (2001) A first course in turbulence. MIT Press

Chaotic Mixing Based on Viscoelasticity

Yee Cheong Lam, Hiong Yap Gan
School of Mechanical and Production Engineering, Nanyang Technological University, Singapore, Singapore
ganh0002@ntu.edu.sg

Synonyms

Non-Newtonian; Flow instabilities; Chaotic; Vortices

Definition

Due to the small characteristic dimensions of a microfluidic channel, flow in a microfluidic channel has a small Reynolds number. For aqueous solutions, this leads to laminar flow which is not conducive to mixing flow streams, particularly in the passive mixing approach. However, the viscoelasticity of fluids can be exploited to enhance mixing. Aqueous solutions, which are Newtonian fluids, could be made viscoelastic by the addition of a small amount of high molecular weight polymers to the solutions. These solutions with polymeric additives are known as non-Newtonian viscoelastic fluids. Through proper design of the microfluidic channels to exploit the viscoelastic nature of these fluids, flow instability and chaotic flow can be induced. This chaotic flow behavior will lead to efficient mixing. Viscoelastic mixing, can lead to efficient mixing even at small Reynolds number and large Péclet number.

Overview

Chaotic and turbulent flow instabilities are recognized as effective mechanisms for mixing. However, the microscale dimensions of microfluidic devices lead to small Reynolds numbers (small ratio of inertial to viscous forces). This impedes turbulent flow instabilities and promotes laminar flow due to the domination of viscous effects. For liquid flows in a microchannel, interaction between a fluid

and the channel wall will dominate, and the surface to volume ratio increases tremendously compared to that at macroscopic-length scales. For laminar flow, the primary means of mixing multiple streams in microfluidic channels is through the molecular diffusion mechanism. However, diffusion is small over the timescales of interest. Therefore mixing enhancement is one of the key challenges for microfluidic devices. Generally, passive mixers, which include lamination micromixers and chaotic advection mixers, rely on the diffusive mixing mechanism. They require long and complicated channels, and relatively slow flow rates. Although active mixers might be employed, they require external actuators [1]. Both approaches lead to complex and expensive fabrication processes. A different approach that bypasses the low Reynolds number limitation yet provides efficient mixing will be a significant improvement for microfluidic system design.

It is known that a viscoelastic fluid, e. g., a solution with a trace amount of highly deformable polymers, can lead to elastic flow instability at Reynolds number well below the transition number ($\mathrm{Re} \approx 2000$) for turbulence flow. Such chaotic flow behavior has been referred to as elastic turbulence by Tordella [2]. Indeed, the proper characterization of viscoelastic flows requires an additional non dimensional parameter, namely the Deborah number, De, which is the ratio of elastic to viscous forces. Viscoelastic fluids, which are ► non-Newtonian fluids, have a complex internal microstructure which can lead to counterintuitive flow and stress responses. The properties of these complex fluids can be varied through the length scales and timescales of the associated flows [3]. Typically the elastic stress, by shear and/or elongational strains, experienced by these fluids will not immediately become zero with the cessation of fluid motion and driving forces, but will decay with a characteristic time due to its elasticity. Therefore, through the high deformation rates achievable in microlength-scale devices, strong viscoelastic effects can be generated even in dilute aqueous polymeric solutions.

Hitherto little attention has been paid to microfluidic flow involving viscoelastic fluids with the notable exception of ink-jet printing. Ink-jet printing applications, whose typical dimensions are on the order of 50 μm or less, utilize aqueous fluids containing low concentrations of high molecular weight polymers. A prototypical geometry that captures a number of features in an ink-jet print head is the converging entry flow through abrupt contraction–expansion geometry. This geometry has been used extensively to study the nonlinear flow phenomenon associated with *non-Newtonian fluid* elasticity in converging flows at macrolength scales. The recirculating flow vortices have been comprehensively documented for a large number of polymeric solutions and polymer melts [4]. Lately, distinct similarities in these early works at macrolength scale were demonstrated qualitatively in a microlength-scale planar contraction by Rodd et al. [4], and in flip-flop memory devices by Groisman et al. [5].

Much less research has been conducted on the enhancement of mixing through viscoelastically induced flow instability in microfluidic devices. Groisman and Steinberg [6] have presented the use of a polymeric liquid for enhanced mixing in small geometries of millimeter scale. Moderate shear rates were generated in small channels to induce elastic flow instabilities. Using repeated half-ring flow geometry with a uniform cross-section, mixing was achieved with a relatively long mixing path at a moderate flow rate.

Indeed, to exploit effectively the viscoelasticity of fluids for chaotic flow instability, and thus mixing, sharper and smaller geometries should be employed. Stress singularities developed at such corners have been the source of elastic instabilities in many macroscale experiments [3], while rounded corners tend to suppress elastic behavior. From a practical standpoint, it is necessary to understand the rheological nature of such flow in order to optimize the use of viscoelastic effects in microfluidic mixing applications. The complex interplay that arises between the elasticity and viscosity of the fluids, and the ratio of contraction of the channel is the key to efficient mixing of fluid streams in microfluidic channels.

Basic Methodology

In the last few decades, understanding and controlling contraction flow or entry flow behavior has been one of the classical problems of fluid mechanics. Reviews of investigations published prior to 1987 can be found in Boger [7] and White et al. [8], and a brief summary of more recent works is given in Rodd et al. [4].

Dimensionless Parameters

For mixing in laminar flow, diffusion is an important mechanism. The Péclet number, Pe, indicates the relative importance of advection to diffusion, and is given by

$$\mathrm{Pe} = \frac{\bar{v} L_{\mathrm{char}}}{D} \tag{1}$$

where $\bar{v}$ is the average velocity, L_{char} is the upstream channel width and D is the diffusion coefficient. The higher the Pe, the less significant is the diffusion.

For an aqueous or a viscous solution, the onset of flow instability can be characterized by the Reynolds number, Re, which measures the relative importance of inertial and

viscous effects in a fluid flow. It can be defined as

$$\mathrm{Re} = \frac{\rho \bar{v} d_\mathrm{c}}{\mu_0} \qquad (2)$$

where d_c is the characteristic dimension of the geometry. ρ and μ_0 are the fluid density and viscosity, respectively.
For a given geometry, the viscoelastic effects of a fluid flow can be characterized by the Deborah number, De. The Deborah number is a dimensionless parameter which typifies the relative importance of the elastic stresses of the fluid with the timescale of the flow system [3]. Generally, a smaller dimension results in a higher characteristic deformation rate for the same flow rate, resulting in higher elastic effects and a higher De.
Based on the characteristic shear rate, the Deborah number can be expressed as

$$\mathrm{De} = \lambda \dot{\gamma}_\mathrm{char} = \lambda \left(\frac{2\bar{v}}{d_\mathrm{c}} \right) = \frac{2\lambda \bar{v}}{d_\mathrm{c}} \qquad (3)$$

The characteristic shear rate may be expressed as $\dot{\gamma}_\mathrm{char} = (\bar{v})/(d_c/2) = 2\bar{v}/d_c$, where λ is the *relaxation time of the viscoelastic fluid* measured in shear.
It should be noted that for some problems, more than one characteristic time for the flow can be identified [3]. Thus, a second dimensionless group, the Weissenberg number, Wi, is sometimes used in polymeric fluid dynamics. It can be defined as

$$\mathrm{Wi} = \lambda \kappa \qquad (4)$$

where κ is a characteristic strain rate in the flow. For problems where there is only one identifiable characteristic time, the Deborah number should be preferred. Indeed, in a steady channel flow De and Wi are interchangeable. However, there are debates about the most appropriate terminology for more complex flows that are associated with the unsteadiness of the process, see Bird et al. [3] and Metzner et al. [9] for further discussion of this topic.
A smaller channel has a smaller flow characteristic length and time. Thus, Re is smaller and it is difficult to have inertia/viscous flow instability. Conversely, De becomes larger and it is easier to have elastic/viscous instability. The relative dominance of elastic to inertial effects is typified by the Elasticity number, El, i. e., the ratio of fluid elasticity to fluid inertia. El is expressed as

$$\mathrm{El} = \frac{\mathrm{De}}{\mathrm{Re}} = \frac{2\lambda \mu_0}{\rho d_\mathrm{c}^2} \qquad (5)$$

El is a function of the given fluid and geometry. It is dependent on the fluid properties and the inverse of the characteristic cross-sectional area.

The contraction ratio (α) is another key parameter in determining the entry flow behavior. It is defined as

$$\alpha = \frac{W}{d_\mathrm{c}} \qquad (6)$$

where W is the upstream channel dimension and d_c is the characteristic dimension of the contraction channel.
However, in general the rheological properties of a viscoelastic fluid are shear rate ($\dot{\gamma}$) dependent. Thus the various dimensionless parameters are also shear rate dependent. For example, the Elasticity number El is now dependent on the change in shear rate $\dot{\gamma}$, which could be written as

$$\mathrm{El}(\dot{\gamma}) = \frac{2\lambda(\dot{\gamma})\mu(\dot{\gamma})}{\rho d_\mathrm{c}^2} \qquad (7)$$

However, as $\dot{\gamma}$ is a function of flow rate, it implies that both λ and μ are functions of flow rate. Thus, in contrast to Eq. (4), Eq. (7) indicates that El is also a function of the flow rate.

Contraction–Expansion Flow Behavior

The flow phenomena of viscoelastic entry flow for macro channels have been explored more comprehensively for axisymmetric geometries as compared to planar geometries in the past few decades. Details of the complex interplay between the elasticity and inertia of viscoelastic fluids for macro channels with axisymmetric geometries can be found in Cable and Boger [10, 11], who employed a number of shear thinning viscoelastic fluids in axisymmetric contractions, spanning a wide range of the De–Re operating space.
However, planar geometrical configurations will be the main focus here, as they are commonly found in microfluidic devices due to their ease of fabrication. Rodd et al. [4] have summarized the nonlinear flow phenomena in microfluidic channels in the De–Re space (see Fig. 1). Care should be taken when relating various phenomena from axisymmetric to planar geometries at similar De–Re regimes. For example, the formation and changes of the vortical flow pattern can be qualitatively different as a result of the difference in total strains and strain-rate histories experienced by the fluid elements in the two geometries [4, 12].

Contraction Flow Behavior

Contraction flow is commonly known as converging entry flow. Interesting flow phenomena have been observed with increasing Deborah number in an entry flow. Flow structures observed in converging entry flows, for viscoelastic

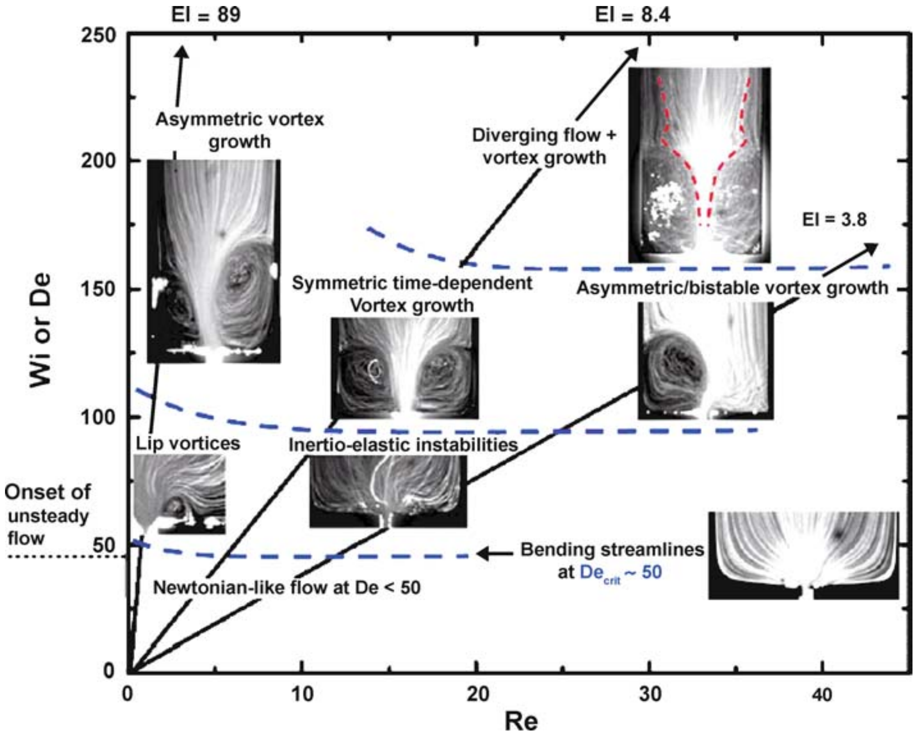

Chaotic Mixing Based on Viscoelasticity, Figure 1 Flow regimes in De–Re space for dilute aqueous PEO solutions through microlength scale contraction geometries [4]

fluids, can be categorized into three distinct regimes: vortex growth, diverging flow and unstable flow.

Vortex Growth The formation and growth of the vortex upstream of the contraction is proportional to the De value, which increases with an increase in flow rate (see Eq. (3)). This implies that the elastic forces become more dominant as the flow rate increases. When the elastic effects are large enough to suppress the inertial effects, a viscoelastic fluid undergoes transitions from the Newtonian-like behavior (low flow rate structure) to regimes with vortex formation and enhanced vortex size. This competition between elastic and inertial forces within the flow becomes violent with further increments in the flow rate. At a high enough flow rate, the large vortex observed in many viscoelastic entry flows ultimately becomes unstable, resulting in large fluctuations in the flow field and gross distortion of the viscoelastic fluid downstream of the contraction.

According to the convention in macro scale entry flow study, the vortex length has been widely used to characterize the vortical flow pattern observed in viscoelastic converging entry flow (see Eq. (8)). The dimensionless vortex length is defined as the axial distance from the upstream contraction plane at which the primary flow first detaches from the wall to the upstream channel width. It can be expressed as

$$\chi_L = \frac{L_v}{W} \tag{8}$$

where L_v is the vortex length and W is the upstream channel width.

For similar geometrical dimensions and flow conditions, a difference in the observations between planar and axisymmetric entry flows is the size of the salient corner vortex. This difference is believed to be caused by the difference in the total Hencky strain imposed on the macromolecules during the converging entry flow, which is less for planar entry flows than for axisymmetric entry flows [4].

Diverging Flows Diverging streamlines upstream at the contraction are a feature of contraction flows, which are mainly controlled by both elasticity and inertia. When the flow system reaches a critical value of Re, inertial effects cause a reduction in the size of the vortex and are often accompanied by diverging flow patterns at the interface region between the main stream flow and the secondary stream flow (corner vortices), (see Fig. 1) as indicated by the dashed line at De ≈ 240. A comprehensive illustration

of this flow regime can be found in Cable and Boger [10]. These flow structures have also been predicted numerically in the presence of both elasticity and inertia, for shear-thinning fluids, by the PTT or FENE-P models [4]. However, the precise dynamical mechanisms that lead to the development of the diverging streamlines upstream of the contraction are yet to be fully elucidated.

Unstable Flow Steady viscoelastic converging entry flows could become unstable at moderate Deborah and Reynolds numbers in both axisymmetric and planar geometries [4]. It has been found that viscoelastic fluids experience regimes consisting of diverging flow with unstable salient vortices, and regimes with Goertler-like and lip vortices [13].

Expansion Flow Behavior

Less research has been performed on the exit behavior of fluids from the contraction. Generally, the elasticity of a viscoelastic fluid has the opposite effects to fluid inertia. As a result, the large viscoelastic forces that generate vortex behavior upstream work in an opposite fashion downstream of the contraction, and thus suppress downstream vortex growth. These flow behaviors were reported by Townsend and Walters [14]. They investigated the expansion of viscoelastic and Newtonian fluids in an identical channel. They found that at a high Reynolds number, Newtonian fluids generated large circulation zones or corner vortices downstream of the contraction, which are a feature of the expansion flow behavior for Newtonian flow [15]. However, for a viscoelastic fluid with the same Reynolds number and a low Deborah number, the exit vortex behavior was completely suppressed.

Key Research Findings

Lately, the work of Groisman and Steinberg had been extended to micrometer-length scales [16]. By utilizing high molecular weight polyacrylamide, with a mean molecular weight (M_{wt}) = 1.8×10^7 g/mol, dissolved in two different Newtonian solvents with different viscosities, Burghelea et al. [16] demonstrated a chaotic flow through a flat curvilinear microchannel with a uniform square cross-section of 100 μm, as shown in Fig. 2. The characteristic mixing distance was estimated to be 7.3 segments of the curvilinear channel (two half-rings form one segment) or a nominal flow length of 6.88 mm. Characteristic mixing times were approximately 40 s. They showed that the stirring behavior induced in the flow by these viscoelastic dilute polymeric solutions results in efficient mixing in the microchannel with the characteristic mixing length significantly shorter than that of the herringbone

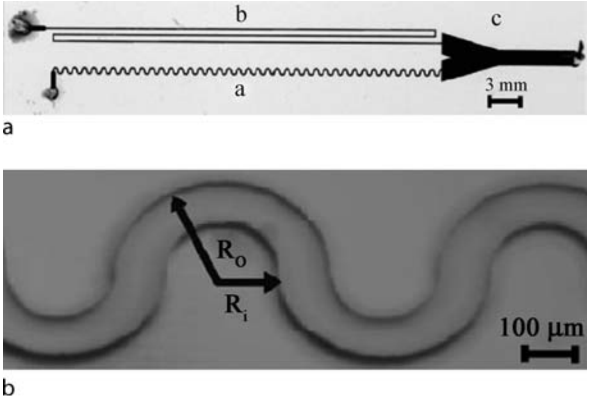

Chaotic Mixing Based on Viscoelasticity, Figure 2 (a) Curvilinear microfluidic device. (b) Zoom-in image of a section of the functional curvilinear channel [16]

patterning method for laminar flow of aqueous solutions. The characteristic mixing times for these viscoelastic fluids were reduced by approximately three to four orders of magnitude compared to the mixing mechanism based on molecular diffusion.

The promotion of viscoelastic instability by utilizing microchannels with abrupt contraction/expansion geometry for mixing has been exploited by Gan et al. [17, 18]. They employed a microchannel with a depth of 150 μm and an abrupt contraction/expansion of 1000 μm : 125 μm : 1000 μm to introduce the convergent/divergent flow. The viscoelastic fluids utilized consisted of 1 wt% poly(ethylene-oxide) (PEO) in 55 wt% glycerol water and green fluorescent dye for the main stream, and 0.1 wt% PEO in water and 3-μm red fluorescent microspheres for the side streams. The mean molecular weight (M_{wt}) of PEO is approximately 2×10^6 g/mol. These different viscoelastic fluids were mixed experimentally at very low Reynolds number ($Re < O(0.1)$), but large Péclet number ($Pe \sim O(10^6)$) and Elasticity number ($El > O(10^2)$). Rapid mixing with negligible diffusion was achieved with a characteristic mixing length of less than 5 mm and characteristic mixing time of the order of milliseconds. However, this microfluidic device requires high pressure to achieve a fast flow rate for mixing liquids of comparatively high viscosity and elasticity.

At such a large Elasticity number, the inertial effects were negligible. Thus, the Reynolds number is no longer relevant in describing the flow behaviors. The flow dynamics of these dissimilar viscoelastic fluids were mainly governed by the competition of the dominant viscous and elastic forces in the flow field. As such, the Deborah number would be the dominant governing parameter. They observed experimentally that with increasing

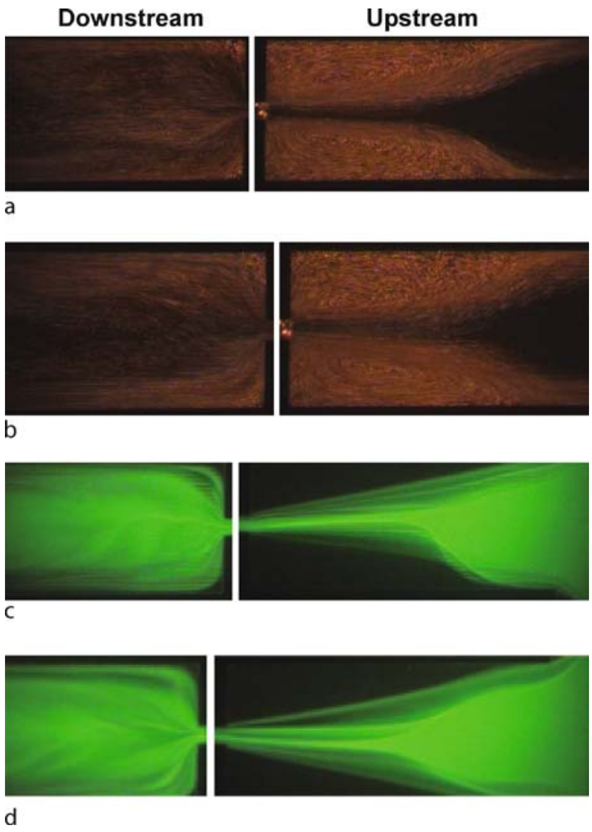

Chaotic Mixing Based on Viscoelasticity, Figure 3 Consecutive snapshots of viscoelastic fluids flow at $\dot{Q} = 12\,\text{ml/h}$. Each fluorescenttracer' snapshots, (a) and (b) or (c) and (d), were collected at 50 ms interval. Viscoelastic instability (whipping) upstream and downstream is highlighted. Significant and extensive mixing is illustrated clearly by extensive overlapping of the main stream (fluorescent dye) and side streams (microspheres) [18]

Deborah number, which increases with flow rate, the flow fields became increasingly unstable. At high enough Deborah number, unstable converging entry flows (unstable salient corner vortices) with large fluctuations of the central mainstream at upstream of the contraction were observed [18], which facilitated the subsequent mixing of the flow streams, as shown in Fig. 3. It is believed that the upstream viscoelastic whipping resulted in flow instability downstream of the contraction. This flow instability, together with the expansion-flow effects of the mainstream promoted effective mixing downstream. The mixing efficiency was found to be 22 % when upstream of the contraction and improved significantly to 68 % when downstream of the contraction. Gan et al. [18] further examined the flow of viscous fluid streams with no measurable elastic effects in an identical channel, but with the same viscosity ratio as the viscoelastic fluid streams. No mixing of the streams was observed. Thus, the necessity of fluid elasticity for flow instability and mixing was demonstrated.

Future Directions for Research

Chaotic mixing based on viscoelastic flow instability in rather simple microfluidic channel geometries was successfully demonstrated. These viscoelastic micromixers bypass the limitation of low Reynolds number in microfluidic flows and could potentially be implemented in a Lab-on-a-Chip platform with minimum requirements for design and fabrication. However, this type of micromixer is yet to be optimized.

In addition, there is a lack of a clear in-depth understanding of the nonlinear interaction between the shear and extensional rheology of the fluids with the generation of viscoelastic instability and mixing for a multiple streams flow in microfluidic channels. At a microlength scale, flow regimes not previously achievable at a macrolength scale could be explored. For example, with proper design of the channel and flow conditions, viscoelastic flows with devoid of inertial effects could be achieved. This type of flow can be characterized by the Deborah number alone. This provides an opportunity to investigate the critical Deborah number for the onset of flow instability, and thus for mixing. It could also facilitate the investigation of viscoelastic effects on the evolution of the various flow structures for single-stream and multiple streams flows.

Cross References

- ► Active Mixer
- ► Chaotic Flow
- ► Combined Pressure-driven Flow and Electroosmostic Flow
- ► Compute Mixing Efficiency
- ► Control of Microfluidics
- ► Curved Microchannel Flow
- ► Microfluidic Mixing
- ► Microfluidic Sample Manipulation
- ► Transition to Turbulence in Microchannels
- ► Turbulence in Microchannels
- ► Viscoelasticity
- ► Non-Newtonian Fluids in Microchannel
- ► Non-Newtonian Fluids in Microfluidics

References

1. Nguyen NT, Wu Z (2005) Micromixers – A review. J Micromechanics Microeng 15:1–16
2. Tordella JP (1969) Rheology: Theory and Applications. 5 In: Eirich FR (ed.) Academic Press, New York

3. Bird RB, Armstrong RC, Hassager O (1987) Dynamics of Polymeric Liquids, Vol 1. Wiley, New York
4. Rodd LE, Scott TP, Boger DV, Cooper-White JJ, McKinley GH (2005) The inertio-elastic planar entry flow of low-viscosity elastic fluids in micro-fabricated geometries. J Non-Newtonian Fluid Mech 129:1–22
5. Groisman A, Enzelberger M, Quake SR (2003) Microfluidic memory and control devices. Science 300:955–958
6. Groisman A, Steinberg V (2001) Efficient mixing at low Reynolds numbers using polymer additives. Nature 410:905–908
7. Boger DV (1987) Viscoelastic flows through contractions. Annu Rev Fluid Mech 19:157–182
8. White SA, Gotsis AD, Baird DG (1987) Review of the entry flow problem: experimental and numerical. J Non-Newtonian Fluid Mech 24:121–160
9. Metzner A, White JL, Denn MM (1966) Constitutive equations for viscoelastic fluids for short deformation periods and for rapidly changing flows: significance of the Deborah number. AIChE J 12:863–866
10. Cable PJ, Boger DV (1978) A comprehensive experimental investigation of tubular entry flow of viscoelastic fluids Part I: Vortex characteristics in stable flow. AIChE J 24:869–879
11. Cable PJ, Boger DV (1979) A comprehensive experimental investigation of tubular entry flow of viscoelastic fluids Part III: Unstable flow. AIChE J 25:152–159
12. Nigen S, Walters K (2002) Viscoelastic contractions flows: comparison of axisymmetry and planar configurations. J Non-Newtonian Fluid Mech 102:343–359
13. Chiba K, Sakatani T, Nakamura K (1990) Anomalous flow patterns in viscoelastic entry flow through a planar contraction. J Non-Newtonian Fluid Mechn 36:193–203
14. Townsend P, Walters K (1994) Expansion flows of non-Newtonian liquids. Chemical Eng Sci 49:749–763
15. Hawa T, Rusak Z (2001) The dynamics of a laminar flow in a symmetric channel with a sudden expansion. J Fluid Mech 436:283–320
16. Burghelea T, Segre E, Bar-Joseph I, Groisman A, Steinberg V (2004) Chaotic flow and efficient mixing in a microchannel with a polymer solution. Phys Rev E 69:066305–066308
17. Gan HY, Lam YC, Nguyen NT (2006) Polymer-based device for efficient mixing of viscoelastic fluids. App Phys Lett 88:224103
18. Gan HY, Lam YC, Nguyen NT, Tam KC, Yang C (2006) Efficient mixing of viscoelastic fluids in a microchannel at low Reynolds number. Microfluidics Nanofluidics 3:101–108

Charge Coupled Device (CCD) Camera

Synonyms

CCD-Camera

Definition

A charge-coupled device (CCD) is an image sensor, consisting of an integrated circuit containing an array of linked, or coupled, light-sensitive capacitors. CCD's are used in digital photography and astronomy (particularly in photometry, sensors, optical and UV spectroscopy and high speed video capture techniques).

Chemical Bond

Definition

A *chemical bond* is the physical phenomenon responsible for the attractive interactions between atoms that confers stability to di- and polyatomic chemical compounds. There are mainly three kinds of chemical bonds: covalent bonds, ionic bonds and hydrogen bonds. Generally covalent and ionic bonds are often described as strong, whereas hydrogen bonds and van der Waals are generally considered to be weaker.

Cross References

► Biosensor

Chemical Cytometry

Definition

Chemical cytometry is a highly specialized class of analytical techniques in which the contents of individual biological cells are evaluated by chemical separations (e.g., capillary electrophoresis). In contrast to the more conventional technique of flow cytometry, in which intact cells are evaluated for the presence of one or a few markers, in chemical cytometry, each cell to be analyzed is lysed, such that (theoretically) all of the chemical constituents can be detected, identified, and quantified.

Cross References

► Single Cell Analysis in Microfluidics

Chemical Etching

Synonyms

Chemical volatilization

Definition

A purely chemical process caused by neutral species generated in the plasma, which react with the etched layer to form volatile compounds. Chemical etching is typically isotropic and is characterized by high etch rates, usually good etch selectivity, and low substrate damage.

Cross References

► Anisotropic Etching
► Isotropic Etching

► Reactive Ion Etching (RIE)
► Plasma Etching
► Silicon Micromachining

Chemical Patterning

Definition

Method of generating drastic and abrupt discontinuities in wettability with materials of dissimilar chemical nature; utilized in promoting spontaneous capillary flow.

Cross References

► Surface-Directed Capillary Flow Systems

Chemical Vapor Deposition for Film Deposition

DHARMALINGAM SUGUMAR[1], LINGXUE KONG[2]
[1] Faculty of Manufacturing Engineering, Universiti Teknikal Malaysia Melaka, Ayer Keroh, Melaka, Malaysia
[2] Center for Material and Fiber Innovation, Deakin University, Geelong, VIC, Australia
sugumar@utem.edu.my, lingxue.kong@deakin.edu.au

Synonyms

CVD; Film coating; Atomistic deposition

Definition

Chemical vapor deposition (CVD) is a method of forming dense and stable structural parts or coatings using the decomposition of relatively high vapor pressure gases. Gaseous compounds of the materials to be deposited are transported to a substrate surface where a thermal reaction/deposition occurs. Reaction byproducts are then exhausted out of the system.

Overview

Chemical vapor deposition or CVD is a generic name for a group of processes that involve depositing a solid material from a gaseous phase and is similar in some respects to physical vapor deposition (PVD). PVD is different in that the precursors are solid, with the material to be deposited being vaporized from a solid target and deposited onto the substrate.

CVD is relatively a mature and well-defined process and its application in industries has gained widespread usage over the last 40 years. CVD process has evolved from simple extraction into more complex techniques that involve coating technology for thin-film production and for surface treatment or improvement. In the early years, CVD was mainly used in semiconductor manufacturing and protective coatings of electronic components. The CVD technology now has rapidly and extensively been applied in more advanced processes such as in ceramic processing for high-temperature cutting tool bits and turbine blades, among others. More recently, the CVD technology has been explored in the field of microfluidics and nanofluidics.

Advantages of the Chemical Vapor Deposition Technique

Although CVD is a complex process, it has many distinct advantages [1]:

- Highly dense and pure substances can be produced.
- Uniform thin films with high adhesion and good reproducibility can be formed.
- Films with good conformal thickness can be deposited on the surface of complex shapes.
- The crystalline structure, surface morphology and orientation can be controlled by controlling CVD process parameters.
- The rate of deposition can be easily controlled.
- The cost of operation is lower for a typical conventional CVD.
- A variety of ►precursor materials including halides, hydrides and organometallics can be used, which enables deposition of metals, carbides, nitrides and oxides.
- It can operate at relatively low deposition temperatures enabling the deposition of refractory materials at a small fraction of their melting temperatures.

Disadvantages of the Chemical Vapor Deposition Technique

- The extremely hazardous precursor gases cause chemical and safety hazards.
- Difficulty in depositing different types of materials using multi-source precursors because different precursors have different vaporization rates.
- The cost of fabrication increases for the variant CVD processes such as PACVD and PCVD.

Basic Methodology

CVD process can be performed either in a closed or open system. The differences between the two methods are that, in the former, the reactants and products are reused or recycled. The application of closed systems is losing popularity nowadays due to the inherently expensive method

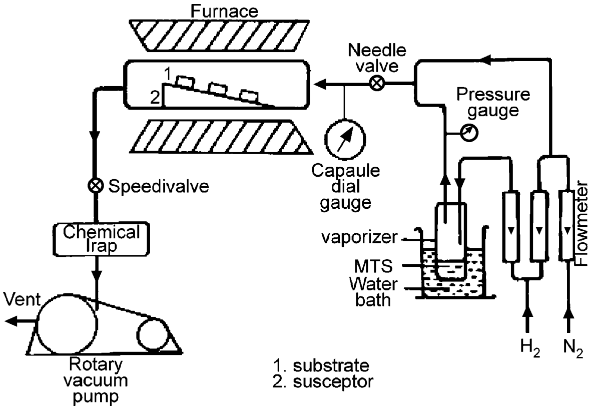

Chemical Vapor Deposition for Film Deposition, Figure 1 Schematic of a typical laboratory CVD equipment for the deposition of SiC coatings [1]

of recovering the reactants being not justifiable. Therefore, the usage of open system CVD processes is preferred, where, after the deposition process, the chemicals are removed from the system.

CVD Apparatus

There is no standard CVD system. Each system is individually tailored for a specific material and component. In general, a CVD apparatus consists of several basic components, for example as shown in Fig. 1.

Gas Delivery System

This component generates and supplies the vapor precursors that will be delivered to the reactor chamber. The delivery of precursors depends on the source temperature, carrier gas flow rate and pressure of the reaction chamber.

Reactor Chamber

The deposition takes place within this chamber. The design of this reactor depends on whether the starting material is solid, liquid or gas. The main function of the CVD reactor is to heat the substrate to deposition temperature. The reaction chamber wall can be either a hot wall or a cold wall.

Substrate Loading Mechanism

A system for introducing and removing substrates, mandrels, etc.

Energy Source

The energy source provides energy or heat required for precursors to react. For a hot-walled reactor system, heated furnaces are used for indirect heating of the substrate. The drawback of this mechanism is that the wall of the reactor chamber is also coated which lowers deposition efficiency and increases maintenance costs. For a cold-wall reactor system, only the substrate is heated, either inductively or resistively, and the wall of the chamber remains cold. Since most CVD processes are ►endothermic, the deposition process will occur on the heated substrate only and minimal deposition occurs on the cold chamber wall.

Vacuum System

This system is used to reduce the pressure in the reaction chamber for the CVD process that needs low pressure or high vacuum during deposition. A low-pressure CVD system requires a simpler vacuum system than that required in a PVD system.

Exhaust System

The main function of the exhaust system is to remove volatile byproducts from the reaction chamber.

Exhaust Treatment Systems

In some instances, exhaust gases may not be suitable for release into the atmosphere and may require treatment or conversion to safe/harmless compounds. Un-reacted precursors can be collected at the outlet and recycled.

Process Control Equipment

They include gauges and controlling units to monitor process parameters such as pressure, temperature and time. Alarms and safety devices would also be included in this category.

Chemical Precursors and Reaction Chemistry

Materials are deposited from gaseous state during CVD. Thus precursors for CVD processes must be volatile, but at the same time stable enough to be delivered to the reactor. Generally precursor compounds will only provide a single element to the deposited material, with others being volatilized during the CVD process. However, precursors may sometimes provide more than one element. Such materials simplify the delivery system, as they reduce the number of reactants required to produce a given compound.

When selecting a suitable precursor for coating applications, some characteristics should be considered as regards the precursor. It is necessary that the precursor [2]:

- is stable at room temperature;
- has suitable deposition rate;
- is safe to handle, has low toxicity, and is inflammable and not explosive;

- is cost effective for relatively low-cost deposition process;
- can generate vapor that is stable at low temperature;
- has low vaporization temperature and high saturation of vapor pressure.

Typical *Precursor Materials*

CVD *precursor materials* fall into a number of categories such as:

- Halides – $TiCl_4$, $TaCl_5$, WF_6
- Hydrides – SiH_4, GeH_4, $AlH_3(NMe_3)_2$, NH_3
- Metal organic compounds
- Metal alkyls – $AlMe_3$, $Ti(CH_2tBu)_4$
- Metal alkoxides – $Ti(OiPr)_4$, etc.
- Metal dialylamides – $Ti(NMe_2)_4$
- Metal diketonates – $Cu(acac)_2$
- Metal carbonyls – $Ni(CO)_4$
- Others which include a range of metal organic compounds, complexes and ligands.

Applications

CVD has applications across a wide range of industries such as [3, 4]:

- Coatings – for a variety of applications requiring specific properties including wear resistance, corrosion resistance, high-temperature protection, erosion protection and combinations thereof.
- Semiconductors and related devices – integrated circuits, sensors and optoelectronic devices.
- Dense structural parts – CVD can be used to produce components that are difficult or uneconomical to produce using conventional fabrication techniques. Dense parts produced via CVD are generally thin walled and maybe deposited onto a mandrel or former.
- Optical fibers – for telecommunications.
- Composites – preforms can be infiltrated using CVD techniques to produce ceramic matrix composites such as carbon–carbon, carbon–silicon carbide and silicon carbide–silicon carbide composites. This process is sometimes called chemical vapor infiltration or CVI.
- Surface modification for microchannels in microfluidic and nanofluidic devices.
- Powder production – production of novel powders and fibers.
- Catalysts.
- Micromachines and nanomachines.

Different CVD Methods

The conventional CVD method uses thermal energy to activate chemical reactions, which is commonly known as thermally activated CVD (TACVD). CVD reactions can be initiated by using different energy sources. Plasma and light energy are currently being used to activate the chemical reactions. Other types of CVD include atomic layer epitaxy, metalorganic CVD, flame-assisted CVD, and electrochemical vapor deposition. They are briefly discussed herewith [1, 5].

Thermally Activated CVD (TACVD)

TACVD is a conventional CVD technique which uses thermal energy to activate chemical reactions in a hot-wall or a cold-wall reactor using chemical precursors. The heating energy is derived usually from RF heating, infrared radiation or resistive heating. The TACVD technique can be further classified according to the pressure range in which it operates, that is, atmospheric pressure CVD (APCVD), low-pressure CVD (LPCVD) and ultrahigh-vacuum CVD (UHVCVD). Basically the operation of different pressure CVDs is the same except that the different pressure ratings alter the rate-limiting steps during the deposition. Thermally activated CVD is used both for thin-film applications and also for coating applications.

Metalorganic CVD (MOCVD)

MOCVD is a method of ►epitaxial growth of materials, especially semiconductors from the surface reaction of organic compounds and metal hydrides containing the required chemical elements. For example, indium phosphide could be grown in a reactor on a substrate by introducing trimethylindium ($(CH_3)_3In$) and phosphine (PH_3). Alternative names for this process are organometallic vapor phase epitaxy (OMVPE), metalorganic chemical vapor deposition (MOCVD) and metalorganic vapor phase epitaxy (MOVPE). Formation of the *epitaxial* layer occurs by final pyrolysis of the constituent chemicals on the substrate surface. The MOCVD technique has been widely employed in the semiconductor industry for various thin-film growth processes, which is one of the most critical steps in high technical microfabrications.

Plasma-assisted CVD (PACVD)

PACVD is employed to deposit hard and colorful coatings at low temperatures. Active species are created when the vapors of organic and organometallic compounds are introduced in the plasma. These active species interact with the surface of the substrate, which results in the deposition of a coating. The properties of the coating can be tailored by varying process parameters like substrate temperature, power density, pressure, and diluting gas. Different colors are achieved by changing the composition

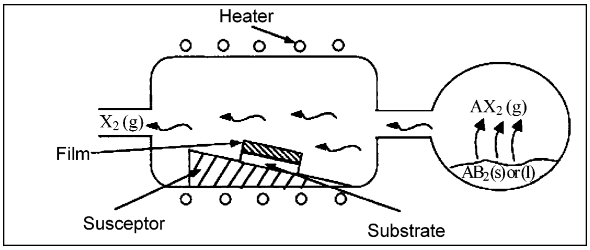

Chemical Vapor Deposition for Film Deposition, Figure 2 An illustration of a simple CVD process [1]

of metals and non-metals in the coating. Work has been initiated to develop hard coatings like Ti(O, C, N), TiO_2, Si(C, N), ZrO_2, etc. These coatings are being developed for various substrates like tools, optical components, artificial jewelry, high-temperature electronics, and automotive components.

Plasma-enhanced CVD (PECVD)

PECVD is a technique commonly used in microfabrication to deposit layers of insulating materials and amorphous or polycrystalline silicon. The plasma is used to help stimulate a reaction on the substrate surface of two or more species from the gas phase. The plasma helps break down the parent molecules and allows the reaction to occur at a lower temperature than conventional CVD. The major advantage of PECVD, in fact, is its capability of working at a lower temperature with respect to other conventional CVD systems. For example, while deposition temperatures of 700 – 900 °C are required for silicon deposition in CVD, a temperature range of 250 – 350 °C is sufficient in the PECVD systems.

Laser CVD (LCVD)

Laser-induced decomposition of a reactive gas is a well-known approach for depositing a material onto a surface. In this technique, a laser beam is directed through a vapor which contains a chemically reactive species. The energy of the laser beam activates the chemical reaction or decomposition of the reactive species, causing the formation of a reaction product. If the conditions are appropriate, the reaction product deposits upon the surface of interest. The deposition of coatings or layers by this approach is typically accomplished within a deposition chamber. The target surface is placed into the deposition chamber, which is partially evacuated prior to commencing the deposition. Partial evacuation is usually required because the reaction product is likely to recombine prior to deposition if the ambient pressure is too high.

Photochemical CVD (PCVD)

PCVD is a process wherein a source gas is in the vicinity of a substrate and is subjected to photolysis. Subsequently, the resulting active chemical species are deposited onto the substrate. It is an important low-temperature process as it does not cause damage to the substrate and does not induce unnecessary interdiffusion at the surface. The light source for the PCVD process can generally be either continuous light or discontinuous light (pulse beam). The former includes a low-pressure mercury lamp, a high-pressure mercury lamp, a deuterium lamp, a xenon lamp, an Ar ion laser and the like. These continuous light sources have a drawback that the deposition rate is very slow because a light of absorption range which induces excitation causing photolytic process inherent to the source gas is not emitted, or if the light of a wavelength existing in this absorption range is emitted, the power thereof is weak. The PCVD process is capable of forming films in a low-temperature process, which is never achieved in the other film forming processes, but there are problems to be solved, such as small deposition rate and poor film quality in the PCVD process using continuous light.

Chemical Beam Epitaxy (CBE)

CBE is a powerful growth technique which has come to prominence over the last ten years. Together with the longer established molecular beam epitaxy (MBE) and metalorganic vapor phase epitaxy (MOVPE), CBE provides a capability for the *epitaxial* growth of semiconductors and other advanced materials with control at the atomic limit. CBE is a hybrid form of molecular beam epitaxy where, instead of a solid source, a gas source is used. It is also called gas source molecular beam epitaxy. CBE uses room temperature gases as the source materials, thus avoiding significant contamination problems and the necessary higher substrate temperatures that can cause segregation of dopant atoms. The material is carried into a high-vacuum reaction chamber as a gaseous compound, typically as a hydride or a metalorganic.

Key Research Findings

Driven by major advances in microfluidic biosystems, such as the development of micro total analysis systems, microfabricated cell sorters, microseparators for DNA and proteins, and cell-based assays, the microfabrication of biologically meaningful microenvironments is within the scope of recent activities. Bioassays that exploit miniaturized formats are intrinsically advantageous (in part because of their small sample volumes and massively parallel processing), but they heavily rely on defined sur-

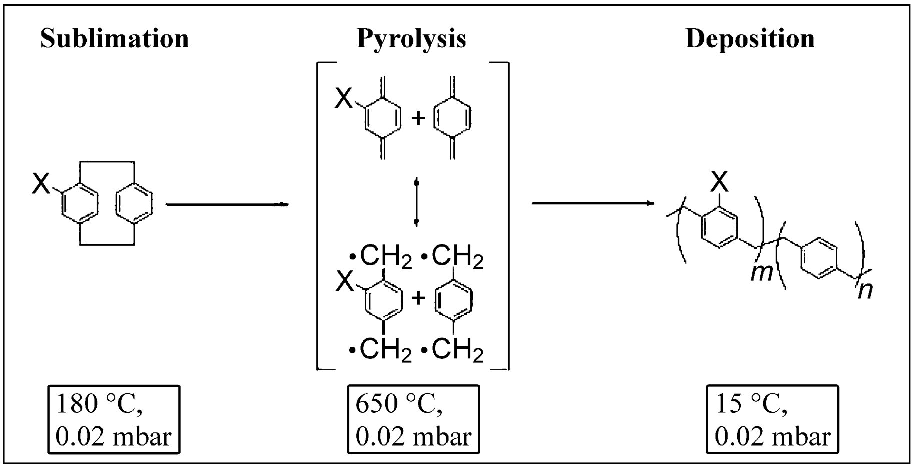

Chemical Vapor Deposition for Film Deposition, Figure 3 Chemical vapor deposition polymerization of reactive coatings, such as PPX-PPF [10]

face characteristics, such as wettability, surface topology, and interfacial charge distribution. Therefore, well-defined and stable surface properties along with the capability of immobilizing active biomolecules in the luminal surfaces of microfluidic devices are keys to their use as analytical tools. Often in the past, microfluidic devices have been made of silicon or glass, but these materials may not be the first choice for many special microfluidic applications, especially in biology or medicine. Several properties of silicon and glass could limit their use in microfluidic devices, including limited biocompatibility, intrinsic stiffness, unfavorable geometry, and incompatibility with soft materials needed, for example, for the incorporation of valves. The high surface-to-volume ratio in microfluidic devices implies that slight inhomogeneities in the surface can cause device malfunction. Polydimethylsiloxane (PDMS), a type of polymer, is often seen as an alternative because of its favorable mechanical properties and its straightforward manufacturing by rapid prototyping. However, PDMS is hydrophobic and allows nonspecific protein adhesion. The absence of functional groups at the PDMS surface prevents covalent immobilization of proteins, enzymes, or antibodies. PDMS also suffers from the lack of defined and constant surface properties under ambient conditions. Although surface modification of glass substrates via silane chemistry has been well established, simple but well-defined surface modification protocols for polymers, such as PDMS, are still being developed. The deposition of thin polymer films to establish chemically defined interfaces offers a unique way to overcome these limitations. Functionalized poly(*p*-xylylene)s are currently under investigation for protein attachment or for patterning of polymer brushes [6]. Thin film deposition is usually conducted by CVD polymerization, a room temperature process that requires no catalyst, solvent, or initiator. Recently, this approach was extended to the deposition of reactive coatings (Fig. 3) [7], that is, poly(*p*-xylylene carboxylic acid pentafluorophenolester-*co*-*p*-xylylene) (PPX-PPF) [8] and poly(*p*−xylylene-2,3-dicarboxylic acid anhydride) [9]. Without the need for further activation, the high chemical reactivity of their functional groups supported conversion with biological ligands or proteins and was used for surface patterning using microcontact printing.

Future Directions for Research

The CVD method is an important method for the deposition of highly pure thin-layer films for microfluidic and nanofluidic devices. The most common use of CVD techniques in microfluidic and nanofluidic devices is for surface modification. With the rapid development in microfluidic and nanofluidic research, the application of CVD will gain more momentum, especially in the process of surface modification.

Cross References

- ► Hydrophilic/Hydrophobic Patterning
- ► Plasma-Treatment Physics
- ► Surface Tension Driven Flow
- ► Capillarity and Contact Angle

References

1. Choy KL (2003) Chemical vapour deposition of coatings. Prog Mater Sci 48(2):57–170
2. Hampden-Smith MJ, Kodas TT (1995) Chemical vapor deposition of metals: Part 1. An overview of CVD processes. Chem Vapor Disposition 1(1):8–23
3. Pierson HO (1992) Handbook of chemical vapor deposition principles, technology and applications. Noyes Publications, Mill Road, Park Ridge
4. Wu Y, Kuroda M, Sugimura H, Inoue Y, Takai O (2003) Nanotextures fabricated by microwave plasma CVD: application to ultra water-repellent surface. Surf Coat Technol 174–175:867–871
5. Werner K, Richard SR (1977) Advances in deposition processes for passivation films. J Vacuum Sci Technol 14(5):1082–1099
6. Lahann J, Langer R (2001) Surface-Initiated Ring-Opening Polymerization of E-Caprolactone from a Patterned Poly(hydroxymethyl-p-xylylene). Macromol Rapid Commun 22(12):968–971
7. Henry AC, Tutt TJ, Galloway M, Davidson YY, McWhorter CS, Soper SA, McCarley RL (2000) Surface Modification of Poly(methyl methacrylate) Used in the Fabrication of Microanalytical Devices. Anal Chem 72(21):5331–5337
8. Lahann J, Choi IS, Lee J, Jensen KF, Langer R (2001) A New Method toward Microengineered Surfaces Based on Reactive Coating. Angew Chem (Int Ed) 40(17):3166–3169
9. Lahann J, Balcells M, Rodon T, Lee J, Choi IS, Jensen KF, Langer R (2002) Reactive Polymer Coatings: A Platform for Patterning Proteins and Mammalian Cells onto a Broad Range of Materials. Langmuir 18(9):3632–3638
10. Lahann J, Balcells M, Lu H, Rodon T, Jensen KF, Langer R (2003) Reactive Polymer Coatings: A First Step toward Surface Engineering of Microfluidic Devices. Anal Chem 75(9):2117–2122

Chemical Volatilization

► Chemical Etching

Chemiluminescence

Definition

Chemiluminescence is the emission of light (luminescence) without emission of heat as the result of a chemical reaction.

Chemiphoresis

► Diffusiophoresis

Chip-Based Systems

► Lab-on-Chip Devices for Protein Analysis

Chip Bonding

Definition

The process of joining a micro- or nano-structured substrate to a sealing layer to produce an enclosed device.

Cross References

► Sputtering for Film Deposition

Chip Electrospray Mass Spectrometry

► On-Chip Electrospray

Chip Thermocyclers

► PCR Lab-on-Chip Devices

Chiral Nematic

Definition

The name *nematic* comes from Greek and means *like a fibre* because of the elongated molecular structure. Chiral nematic formulations comprised entrirely of non-sterol based chemicals.

Cholesteric

Definition

The name *cholesteric* has a historical background since the first chemicals which showed the typical optical activity were esters of cholesterol. Cholesteric formulations comprised entirely of cholesterol and other sterol derived chemicals.

Chromatographic Chip Devices

Olgica Bakajin
Chemistry, Materials Earth and Life Sciences Directorate, Lawrence Livermore National Laboratory, Livermore, CA, USA
bakajin1@llnl.gov

Synonyms

Micro gas and liquid chromatography; μGC; Micro-LC

Definition

Chromatography is one of the most widely used molecular separation techniques. The separation occurs because the compounds within a complex mixture distribute between two phases differently: liquid and stationary phases in the case of liquid chromatography (LC) and gas and stationary phases in the case of gas chromatography (GC). Chromatographic chip devices aim to miniaturize chromatographic systems with the goal not only of size reduction, but also of improved function.

Overview

During a chromatographic separation process, different components of a mixture go through the system at different rates. Repeated sorption/desorption processes that take place during the movement of the sample over the stationary bed determine the rates at which the components are transported. The smaller the affinity a molecule has for the stationary phase, the shorter the time spent in a column. In principle, chromatography can purify basically any soluble or volatile substance if the right adsorbent material, carrier fluid and operating conditions are employed. Chromatography can accomplish separation, purification, detection and quantification of most molecules and is, thus, important for pharmaceutics, forensics and diagnostics.

The most common types of chromatography are:

- ►Gas chromatography
- ►High performance liquid chromatography (HPLC)
- Ion exchange chromatography
- Affinity chromatography

The initial theoretical work on open-tubular gas chromatography (Golay) and on packed-column liquid chromatography (van Deemter) was published as early as the 1950s. These papers led to the development of commercial gas chromatographs using capillaries with micrometer diameters, and liquid chromatographs with micrometer-scale particles for the stationary phase.

The development of chip-based GC systems has been motivated by the performance gains facilitated by miniaturization and integration and by the potential of creating portable and robust instruments for *in-the-field* and *on-site* chemical measurements.

Basic Methodology

A typical high-performance liquid chromatography (HPLC) system consists of two pumps, a mixer, an injector, a guard column, a separation column, a detector, an electrospray nozzle and a mass spectrometer. The two pumps and the mixer allow establishment of desired solvent gradients. The injector is used to inject a small amount of sample into the column. In all separation techniques, definition of a small volume of injected sample is crucial in preventing adverse broadening of peaks and a consequent loss in component resolution. The injected compounds are separated in the separation column and then detected via a simple detector or a mass spectrometer. All of the parts of the HPLC system have been miniaturized and several research groups have been able to demonstrate on-chip HPLC separations.

Key Research Findings

Over the past several decades many macroscale separation techniques have been transferred to planar chip formats. The first microfabricated chromatography system was reported by Terry et al. [1] in 1979. Their micro-GC system consisted of a sample injection system, a 1.5 m column and a thermal conductivity detector.

The development of micro-chromatography systems has been motivated by the fact that as the system size is reduced, its performance is improved. The improvements that include reduction in analysis time and increase in separation efficiencies are a direct consequence of miniaturization as described in Janasek et al. (see Further Reading) and summarized here. The benefits of miniaturization can be demonstrated considering proportionalities within the system. We assume that miniaturization is a three-dimensional downscaling process characterized by a typical length parameter d. The separation system is a diffusion-related system in which hydrodynamic, heat and molecular diffusion behave exactly

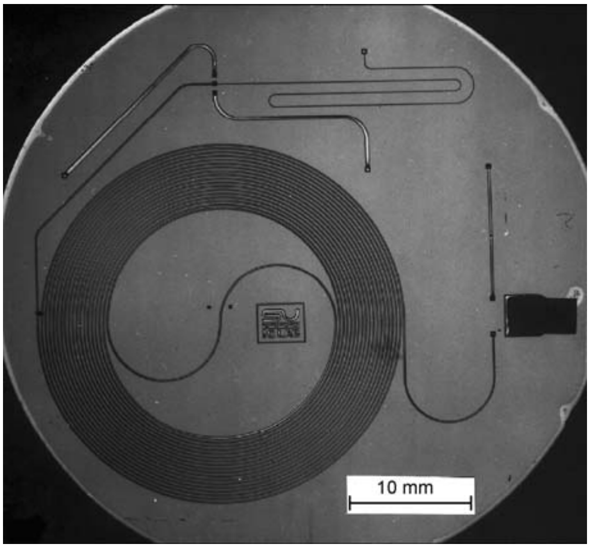

Chromatographic Chip Devices, Figure 1 The first microchromatographic device developed by Terry et al. [1].

the same in the miniaturized as in the original system, while the time variables decrease by a factor of d^2. This means that as the tube diameter gets reduced by a factor of 10, the analysis time and the detector response time get reduced by a factor of 100. The pressure drop requirements increase by a factor of 100, while the voltage requirements (for electrophoresis or electro-osmosis) remain the same. Therefore a miniaturized system can achieve faster separations while maintaining comparable separation efficiency.

Examples of recent micro-chromatography systems are shown in Figs. 1–4.

Micro Gas Chromatography

Sandia National Laboratories was one of the institutions that led the development by establishing the *Microanalytical Systems* program in 1997. The goal of the program was to develop highly portable micro total analysis systems for detection of chemical warfare agents and explosives. The *μChemlab* gas analysis system developed at Sandia consists of a microfabricated sample pre-concentrator, a chromatographic column and polymer-coated, surface acoustic wave (SAW) detectors. The sample pre-concentrator incorporates a thermally isolated (and sol–gel coated) membrane and resistive heater to effect rapid sample heating. Since, the membrane has a small thermal mass it can be heated to 200 °C within 10 ms, resulting in concentration enhancements of over two orders of magnitude and the creation of well-defined injection volumes. The entire, integrated system has been shown to successfully separate and detect a wide range of chemical species at parts-per-billion concentrations. Despite the problems associated with packing microfabricated chromatography columns, the Sandia group has also demonstrated the successful operation of packed, microfabricated GC columns.

Although successful operation of microfabricated GC systems has clearly been demonstrated, performance variability has been poor when compared to conventional GC technology. This is often associated with the ability to deposit or pack stationary phase materials in a homogeneous fashion, especially in the rectangular cross-sectional geometries of typical microfabricated channels.

Injection of extremely small volumes of gaseous samples into microfabricated GC columns is also crucial for microscale separations. Usually this is accomplished by integration of valves on chips. Although successful, these methods increase the complexity of the fabrication process. Injection of samples by rapid thermal desorption or by introducing the sample through a plasma are some of the alternatives. Manz et al. proposed a novel method to inject gaseous samples onto microfabricated columns in which a sample is continuously introduced into a chromatographic column and passed through a plasma generator. If the plasma is then interrupted for a brief period, a short unmodified sample plug is introduced into the separation column and subsequently separated.

Micro Liquid-Phase Chromatography

One of the first chip-based LC structures was developed by A. Manz and colleagues as early as in 1990. The device incorporated a micromachined open-tubular separation column and an integrated platinum electrode detector. Although not all realized in that initial study, the potential advantages that miniaturization could achieve included superior efficiency per unit time when compared to conventional LC, facile positioning of detection cells and low unit cost. The more common approach to LC is through the use of columns packed with particles. The particles (which are normally porous) support the stationary phase, provide a large interfacial area for analyte partitioning and form a homogeneous medium for the transport of mobile phase. In conventional systems, this approach is generally more effective since in open-tubular methods ultra-small column widths are required to counteract the limited rates of mobile phase transfer. These small dimensions lead to reduced loading capacities and a propensity to blockages. Several microsystems that use microfabricated channels filled with conventional packed beads phase have been developed. Although packed columns may be desirable, the introduction of stationary-phase material into microfabricated channels is a non-trivial process. Frits must be fabricated within the channel structure to retain the packing, and a high-pressure interface between the chip and an external pump must be made. In addition, due to the reduced channel dimensions and the complexities of the manifold pattern, the packing process is difficult and can often lead to non-uniform particle densities at channel walls and thus reduced separation efficiencies. Consequently, several chromatographic methods within microfabricated columns also employ an open-tubular approach. The primary difficulties associated with packing microfabricated channels can be eliminated if the packed bed is replaced by a continuous, porous bed, sometimes also referred to as the *monolithic* phases. The advantages of this approach are that the polymerization of the porous bed is easy and that the continuous polymer bed is attached to the channels walls, making a retaining frit redundant. In recent years there has also been considerable development of stationary phases with controlled porosity and the ability to attach desired chemistry to the phase [5].

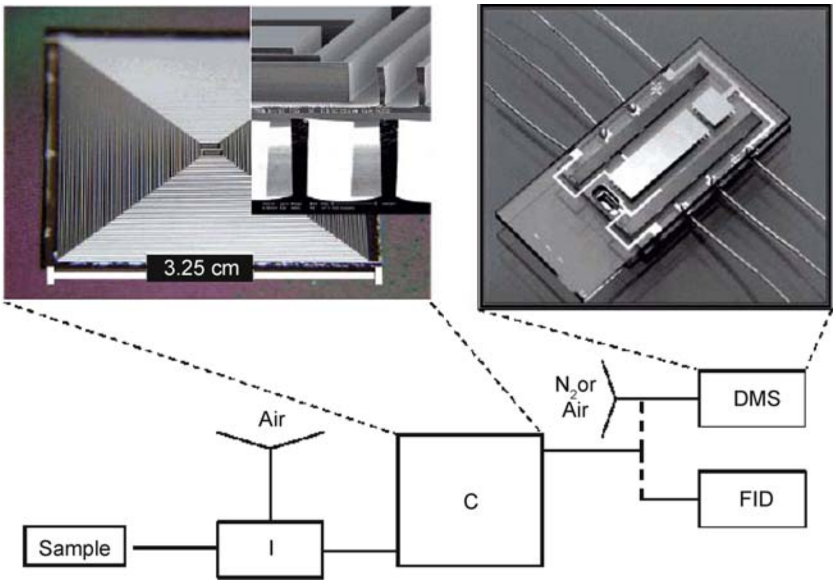

Chromatographic Chip Devices, Figure 2 Apparatus showing details of the microfabricated column (*upper left inset*) and the microfabricated DMS cell (*upper right inset*). A Varian 3400 GC is used as a platform. I, split inlet; FID, flame ionization detector; C, microfabricated column. The two detectors can be used alternately [2]

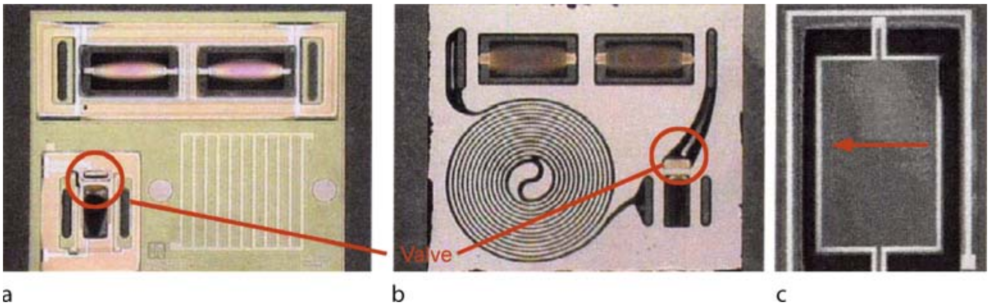

Chromatographic Chip Devices, Figure 3 Photographs of Sandia's Micro-Chem Lab system for gas chromatography integrated using surface micromachining with integrated fluidic technology (SwIFT) [3]

It is also worth noting that the use of electro-osmotic flow to pump the mobile phase during separation has been a major breakthrough, since it allows generation of high pressure in microfabricated channels.

Future Directions for Research

The transfer of macroscale chromatographic methods to chip-based formats, although advantageous, is not trivial and imaginative solutions to the problems of stationary phase introduction are required. It seems likely that future chromatographic chip systems will incorporate monolithic stationary phases due to the ease of their fabrication and localization within microchannels. Other nanoporous materials may also be of use.

Although several systems have been demonstrated, the big challenge in the development of micro-chromatography systems is still integration. The dead volume between different individual parts introduces a large amount of band broadening, which worsens the device performance.

As far as applications of on-chip chromatography go, we will most likely see developments geared towards two areas: miniature portable analysis systems and highly multiplexed systems. The benefits of miniaturization will enable the creation of detection and diagnostic instruments that are small and easy to use for point of care and military applications. Micro-chromatography devices will also enable development of systems of unprecedented complexity that will allow analysis of highly complex samples with compounds of interest in trace amounts. With

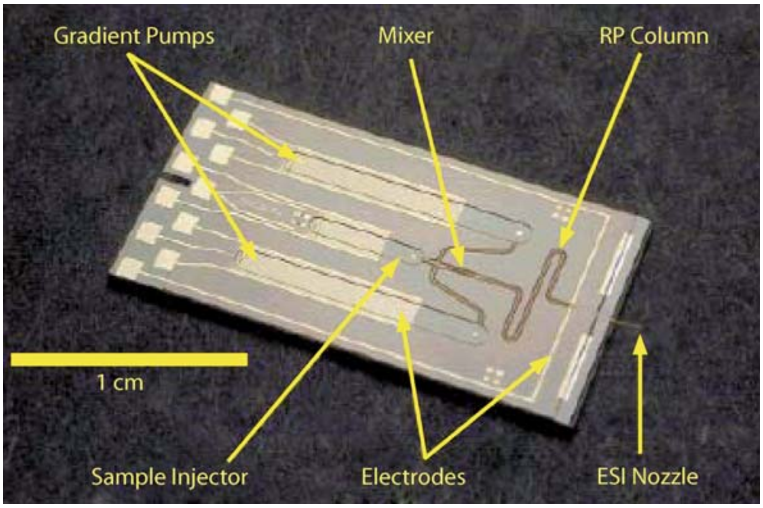

Chromatographic Chip Devices, Figure 4 Photograph of a microfluidic chip that integrates all the fluidic components of a gradient liquid chromatograph developed by Xie et al. [4]

such systems presymptomatic diagnosis of various diseases may become a reality.

Cross References

► Gas Chromatography

References

1. Terry SC, Jerman JH, Angell JB (1979) Ieee Tans Electron Devices 26:1880
2. Lambertus et al (2005) Anal Chem 77:7563
3. Lewis PR et al (2006) Ieee Sens J 6:784
4. Xie J, Miao YN, Shih J, Tai YC, Lee TD (2005) Anal Chem 77:6947
5. Geiser L, et al. (2007) J Chromatogr A 1140:140–146

Further Reading

- Eiceman GA, Gardea-Torresdey J, Dorman F, Overton E, Bhushan A, Dharmasena HP (2006) Anal Chem 78(12):3985
- Gross GM, Reid VR, Synovec RE (2005) Curr Anal Chem 1(2):135
- Eijkel JCT, van den Berg A (2006) Electrophoresis 27:677–685
- Dittrich PS, Tachikawa K, Manz A (2006) Anal Chem 78:3887–3907
- de Mello A (2002) Lab Chip 2:48N–54
- Nanasek D, Franzke J, Manz A (2006) Nature 442:374–380

Chromatography

Definition

General term defining a diverse group of techniques used to separate a sample mixture. The separation is based on differences in the relative affinities of the sample components for two different media, the mobile phase (a moving fluid) and the stationary phase (a porous solid or gel or a liquid coated on a solid support). The velocity at which each component is carried along with the mobile phase depends on its solubility and on its affinity for the stationary phase.

Closed-Loop

► Control of Micro-Fluidics

Closing Pressure

Definition

Closing pressure is the maximum pressure against which a valve or actuator can close completely.

Cross References

► Electromagnetic Valves
► Electrostatic Valves
► Magnetic Pumps
► Membrane Actuation for Micropumps
► Microactuators
► Peristaltic Pumps
► Piezoelectric Valves
► Pneumatic Valves
► Positive Displacement Pump
► Thermomechanical Valves
► Thermopneumatic Valves

Clusters

► Nanoparticles
► Nanoparticle Synthesis in Microreactors

CMOS-Camera

► Color Cameras

CMUTs

► Acoustics Based Biosensors

Coarse-Grained Particle Methods

► Dissipative Particle Dynamics

Coarse-Graining

Definition

A technique to reduce the complexity of a system while maintaining the physical behavior.

Co-Ions

Definition

Ions in solution with the same charge as the macroion or the charge of the channel wall.

Cross References

► Electrophoresis

Cold Light Sources

Definition

Cold light sources are used when strong illumination is needed, but drastic heat input into the object must be avoided, e. g. during microscopic observations. Usually a halogen lamp is installed with a concave mirror in the back and a system of lenses in the front. Unwanted IR and UV radiation are removed through glass filters. The lamp, all filters and lenses are fan cooled. The white light released from heat radiation is leaded through fiber optic cables to the object to be observed.

Colloidal Forces

► Disjoining Pressure

Color Cameras

Definition

In the main there are two kinds of technologies for digital color cameras, the CCD (Charged Coupled Devices) and the CMOS (Complementary Metal Oxide Semiconductor). While CCD cameras deliver images with a better quality and are more sensitive for low emittance, CMOS cameras are often used as high speed cameras. Today, common CMOS high speed cameras are able to record up to 32,000 images in a second.

Color Temperature

Definition

The color temperature is used to characterize the color of a light source. Its unit is Kelvin which is referred to the temperature a black body must have to emit light with the according color. It is directly related to the Planck's law of the black body radiation. Sun light for example has a color temperature of 5500 K. Light with a lower color temperature appears more red while light with a higher color temperature gets into blue.

Combinatorial Library

Definition

A collection of results of combinatorial chemistry tests.
The library is built by performing a number of parallel chemical reactions under nominally identical conditions, each of them differing in only one or a small number of variable parameters. The library may consist of the reaction products themselves, which makes them available for additional testing, or the library is virtual, consisting of only sets of numerical data. The data is needed in either case, because the are used as inputs into sometimes very sophisticated optimum seeking mathematical algorithms yielding as its result the optimum value of the variable parameter.

Cross References

► Microfluidic Systems for Combinatorial Chemistry

Combined Pressure-Driven Flow and Electroosmotic Flow

CHUN YANG, DEGUANG YAN
Nanyang Technological University, Singapore, Singapore
mcyang@ntu.edu.sg

Synonyms

Microchannel flow

Definition

Pressure-driven flow is bulk fluid motion resulting from either a globally applied difference (gradient) or an internally induced hydraulic pressure difference (gradient). Electroosmotic flow is the bulk liquid motion due to the interaction between an external electric field applied tangentially along a charged surface and the excess net charges in the electric double layer of such a charged surface. Specifically, the focus of this entry will be on the electroosmotic flow generated by an applied DC electric field only. In addition, the analysis of this entry is based on an assumption that the order of magnitude of the electroosmotic flow velocity is the same as that of the pressure-driven flow velocity. In the field of micro- and nanofluidics, the term *combined pressure-driven flow and electroosmotic flow* is referred to as the bulk liquid flow that is generated as a result of both pressure gradient and applied electric field.

Overview

The rapid development of microfluidics is mainly due to its promising applications as a well-controllable tool for studying fundamental physical and biochemical processes and a platform for performing chemical and biological assays. Advanced microfluidic devices can perform complete biochemical analyses in a single fabricated chip. The generic microfluidic systems involve buffer fluid and sample manipulations such as pumping, valving, mixing, injection, dispensing, etc. Fundamental understanding of the liquid flow characteristics in microchannels is thus essential for optimum design and precise control of microfluidic devices.

In general, liquid motion can be generated by either applying a pressure gradient or imposing an electric field, leading to, respectively, pressure-driven flow or electrokinetically driven flow. Traditionally, in large-sized channels flow is often driven by pressure that is usually generated by mechanical pumps. In microchannels however it becomes increasingly difficult to utilize the pressure-driven flow mode as the channel size shrinks, especially down to submicrometer range. Moreover, some systems like microvalves and micropumps with moving components are difficult to fabricate, and they are prone to mechanical failure due to fatigue and fabrication defects. Alternatively, electroosmotic flow enjoys numerous advantages (over pressure-driven flow), including ease of fabrication and control, no need for moving parts, high reliability, no noise, etc. Specifically, a plug-like velocity profile in electroosmotic flow can result in reduced dispersion of sample species, making capillary electrophoresis one of the most successful technologies for chemical and biomedical analyses.

The necessary condition for development of electroosmotic flow is the presence of electrostatic charges at the solid channel–liquid interface. The charging mechanisms of the solid–liquid interface are complex, possibly including the asymmetric dipoles of water molecules residing at the solid–liquid interface, adsorption of ions, disassociation of ionic groups, charge separation, etc. Such surface charges influence the distribution of nearby ions in the solution. Counter-ions (i. e. ions of opposite charge) are attracted towards the surface, while co-ions (i. e. ions of like charge) are repelled from the surface. This electrostatic interaction together with the random thermal motion of the ions leads to the formation of the so-called *electric double layer* (*EDL*). The model of the EDL was developed by Gouy and Chapman in 1906, and then improved by Stern in 1924 [1]. According to Stern's model, the EDL consists of a compact layer and a diffuse layer. The compact layer, usually less than 1 nm, exists immediately next to the solid surface, where counter-ions are strongly attracted to the solid surface thus immobile. The diffuse layer of the EDL is the layer from the compact layer to the bulk liquid, and its thickness ranges from several nanometers to micrometers, depending on liquid properties. Compared to the ions in the Stern layer, the ions in the diffuse layer are less influenced by the charged surface and hence are mobile. A review of modern EDL theory including recent descriptions and formulations of the basic structure (and component regions) of the EDL is given by Dukhin and Deryaguin [2].

Within the diffuse layer of the EDL, there is an excess of counter-ions over co-ions, and thus the net charge density is not zero so as to neutralize the surface charge. If an electric field is applied tangentially along a charged surface, the electric field will exert a Columbic force on the ions in the diffuse layer, resulting in a net migration of the liquid in the EDL region. This is called *electroosmosis* (*EO*). In a charged microcapillary, due to viscous forces the flow can be developed beyond the EDL region

to the rest of the liquid in the microcapillary, leading to a bulk *electroosmotic flow* (*EOF*). EOF is widely utilized in microfluidic devices to transport buffer solutions and to manipulate sample solutes. Examples include microfluidic pumping, flow control, mixing and reacting reagents, injecting or dispensing samples, capillary electrophoresis-based chemical separations, chromatography, etc. A recent review by Chang [3] demonstrates the viability of using electrokinetic flow in microfluidic platforms for miniature diagnostic kits.

Basic Methodology

Liquid Flow Field

Consider combined pressure-driven liquid flow and electroosmotic flow in a microfluidic channel. The liquid in the microchannel is assumed to be an incompressible, Newtonian, symmetric electrolyte with valence of $z_+ = -z_- = z$. Furthermore, if the Joule heating effect is negligible, the electrolyte is also assumed to have constant thermophysical and electrical properties including density, ρ, dynamic viscosity, μ, electrical conductivity, σ, and dielectric constant, ε_r. The channel wall is uniformly charged with a zeta potential, ζ. When an external DC electric field E is applied along the channel axial direction, the liquid starts to move due to electroosmosis that results from the interaction between the net charge density in the EDL of the channel and the applied electric field. The order of magnitude of the EOF velocity is assumed to be of the same order as that of the pressure-driven flow velocity. The governing equations for the combined pressure-driven flow and electroosmotic flow can be non-dimensionalized by using

$$\bar{\boldsymbol{r}} = \boldsymbol{r}/D_\mathrm{h} \qquad \bar{\boldsymbol{t}} = \boldsymbol{t}/\tau \qquad \bar{\boldsymbol{V}} = \boldsymbol{V}/U \tag{1a}$$

$$\bar{\boldsymbol{p}} = \boldsymbol{p}D_\mathrm{h}/(\mu U) \qquad \bar{\nabla} = D_\mathrm{h}\nabla \qquad \bar{\nabla}^2 = D_\mathrm{h}^2\nabla^2 \tag{1b}$$

where $\boldsymbol{r}$, $\boldsymbol{t}$, $\boldsymbol{V}$ and $\boldsymbol{p}$ are the position vector, time, local velocity vector and pressure, respectively. These quantities are normalized using D_h, τ, U and $\Pi = \mu U/D_\mathrm{h}$, which are the microchannel hydraulic diameter, characteristic time scale, characteristic flow velocity and characteristic pressure, respectively. Then we can write down the continuity equation

$$\bar{\nabla}\cdot\bar{\boldsymbol{V}} = 0 \tag{2}$$

and the Navier–Stokes equation

$$\mathrm{Re}\left(\frac{1}{\mathrm{St}}\frac{\partial\bar{\boldsymbol{V}}}{\partial\bar{\boldsymbol{t}}} + \bar{\boldsymbol{V}}\cdot\bar{\nabla}\bar{\boldsymbol{V}}\right) = -\bar{\nabla}\bar{\boldsymbol{p}} + \bar{F}_\mathrm{e} + \bar{\nabla}^2\bar{\boldsymbol{V}} \tag{3}$$

where $\mathrm{Re} = \rho U D_\mathrm{h}/\mu$ is the Reynolds number that characterizes the ratio of inertial force to viscous force, $\mathrm{St} = \tau U/D_\mathrm{h}$ is the Strouhal number that represents the ratio of characteristic process time, τ, to convective time, $\tau_\mathrm{c} = D_\mathrm{h}/U$ [4], and $\bar{F}_\mathrm{e} = D_\mathrm{h}^2\rho_\mathrm{e}E/\mu U$ is the dimensionless electrostatic body force due to the interaction between the net charge density in the EDL of the channel ρ_e and the applied electric field, E. Considering that usually the microchannel hydraulic diameter and the characteristic flow velocity respectively are of the order $D_\mathrm{h} = 10^2$ μm and $U = 1$ mm/s, we can estimate Re of the order of 10^{-1}, showing a low Reynolds number flow and thus a negligible inertial term, $\mathrm{Re}\bar{\boldsymbol{V}}\cdot\bar{\nabla}\bar{\boldsymbol{V}}$ in Eq. (3). Furthermore, for most microfluidic applications, the pumping time is of the order of $10^0 - 10^1$ s, the characteristic convective time scale is $\tau_\mathrm{c} = D_\mathrm{h}/U = 10^{-1}$ s, leading to the Strouhal number of the order of $\mathrm{St} = 10^1 - 10^2$. As a result, we can assume a pseudosteady flow by ignoring the transient term $(\mathrm{Re}/\mathrm{St})(\partial\bar{\boldsymbol{V}}/\partial\bar{t})$ [4]. Hence, Eq. (3) reduces to the Stokes equation expressed as

$$-\bar{\nabla}\bar{\boldsymbol{p}} + \bar{F}_\mathrm{e} + \bar{\nabla}^2\bar{\boldsymbol{V}} = 0 \tag{4}$$

Since the Stokes equation and its corresponding no-slip velocity boundary conditions are linear, we can treat the flow field as a linear superposition of two parts including the electroosmotic flow due to $\bar{F}_\mathrm{e}$ and the pressure-driven flow generated by $\bar{\nabla}\bar{p}$ resulting from either globally applied pressure or internally induced pressure (for instance due to geometry change of the microfluidic channel). Clearly, it is through the electrostatic body force $\bar{F}_\mathrm{e}$ that the Stokes equation is coupled with the governing equations for the net charge density in the EDL of channel, ρ_e, and for the externally applied electrical field, $E = -\nabla\phi$ (where ϕ is the local applied electrical potential).

Electric Double Layer Potential and Net Charge Density

According to the theory of electrostatics, the net charge density in the EDL of channel, ρ_e, is related to the EDL potential that is described by the Poisson equation, which in dimensionless form is expressed as [1]

$$\bar{\nabla}^2\bar{\psi} = -(D_\mathrm{h}\kappa)^2\bar{\rho}_\mathrm{e} \tag{5}$$

where the non-dimensional electric double layer potential is defined as $\bar{\psi} = ze\psi/(k_\mathrm{B}T)$. κ is the Debye–Hückel parameter defined as

$$\kappa = (2z^2e^2n_0/\varepsilon_r\varepsilon_0 k_\mathrm{B}T)^{1/2} \tag{6}$$

where k_b is the Boltzmann constant, T is the absolute temperature, ε_r is the dielectric constant of the fluid and ε_0 is the permittivity of vacuum. Physically, κ^{-1} represents the characteristic thickness of the EDL [1].

Therefore, the dimensionless net charge density is associated with the number concentration of N ions through

$$\bar{\rho}_e = \sum_{i=1}^{N} \frac{z_i}{z} \bar{n}_i \tag{7}$$

where the ionic concentration, n_i, and the net charge density, ρ_e, are normalized using the ionic number concentration in the bulk phase, n_0, and the quantity ezn_0, respectively.

Ionic Concentration Distributions

The Nernst–Planck Equation

Obviously, a full formulation of governing equations should also include the mass transfer equation for each type of ions in the system. The ionic concentration distribution, $n_i(r)$, is generally described by the Nernst–Planck equation. According to Dukhin and Deryaguin [2], the time scale related to electromigration within the EDL is characterized by $(\kappa^{-1})^2 / D_i$, which is of the order of $O(10^{-7} - 10^{-5})$ s, by assuming the reciprocal Debye–Hückel parameter, $\kappa^{-1} \approx 10 - 10^2$ nm (corresponding to an electrolyte of typical concentration $10^{-3} - 10^{-5}$ M) and the ion mass diffusion coefficient, $D_i = 10^{-9}$ m^2/s. This suggests a negligible transient effect of the EDL *relaxation*, i. e. $\partial n_i / \partial t = 0$, and thus the Nernst–Planck equation that governs the concentration of two most concentrated cations and anions in the buffer solution takes the convective-diffusion form as

$$\mathrm{Pe}_+ \bar{\nabla} \cdot (\bar{\boldsymbol{V}} \bar{n}_+) = \bar{\nabla}^2 \bar{n}_+ + \bar{\nabla} \cdot (\bar{n}_+ \bar{\nabla} \bar{\psi}) \tag{8a}$$

$$\mathrm{Pe}_- \bar{\nabla} \cdot (\bar{\boldsymbol{V}} \bar{n}_-) = \bar{\nabla}^2 \bar{n}_- - \bar{\nabla} \cdot (\bar{n}_- \bar{\nabla} \bar{\psi}) \tag{8b}$$

where $\mathrm{Pe}_i = U\kappa^{-1}/D_i$ is the Peclet number of type i ions. The gradient, ∇, and Laplacian operator, ∇^2, are scaled with respect to the reciprocal Debye–Hückel parameter, κ^{-1}.

The Boltzmann Distribution

Substituting typical values of $U = 1$ mm/s, $D_i = 10^{-9}$ m^2/s and $\kappa^{-1} = 10 - 10^2$ nm, we can estimate the Peclet number of order $\mathrm{Pe}_i = 10^{-2} - 10^{-1}$, indicating a negligible convection effect in Eq. (8b). Therefore, Eq. (8b) can be written as

$$\bar{\nabla}^2 \bar{n}_i = \bar{\nabla} \cdot \left(-\frac{z_i}{z} \bar{n}_i \bar{\nabla} \bar{\psi} \right) \tag{9}$$

We can readily solve Eq. (9), and obtain its solution, which is

$$\bar{n}_i = \exp\left(-\frac{z_i}{z} \bar{\psi} \right) \quad \text{or} \quad n_i = n_0 \exp\left(-\frac{z_i e \psi}{k_B T} \right) \tag{10}$$

This is the well-known Boltzmann distribution. In fact, Tang et al. [5] have performed a full numerical simulation, and their findings show that when the EDL is thin compared to the characteristic channel dimension, both the Nernst–Planck equation and the Boltzmann distribution predict identical ionic concentration distributions in the microchannel flow. Therefore, it can be concluded that from a microfluidic applications viewpoint, the Boltzmann distribution is adequate to describe the ionic concentration distributions in electrokinetic flow.

Externally Applied Electrical Potential

Since the electroosmotic flow is driven by an externally applied electric field, the applied electrical potential distribution needs to be formulated, and is governed by the conservation of charges equation, which is written as

$$\frac{\partial \rho_e}{\partial t} = -\nabla \cdot i \tag{11}$$

The electric current, i, is a result of the motion of all the ions in the electrolyte solution, and consists of three contributions, the convection current, i_{conv}, the diffusion current, i_{diff}, and the electromigration current, i_{cond} : $i = i_{conv} + i_{diff} + i_{cond}$. The expressions for each current are given by

$$\begin{aligned} i_{conv} &= \rho_e \boldsymbol{V} \\ i_{diff} &= -e \sum_{i}^{N} D_i z_i \nabla n_i \\ i_{cond} &= -\frac{e^2}{k_B T} \sum_{i}^{N} z_i^2 D_i n_i \nabla \phi = -\sigma \nabla \phi \end{aligned} \tag{12}$$

where $\boldsymbol{V}$ is the liquid velocity vector, $\sigma = -e^2 \sum_i^N z_i^2 D_i n_i / k_B T$ is the temperature-dependent electrical conductivity of the electrolyte solution and ϕ is the externally applied electrical potential.

In microfluidic systems where the EDL is thin compared to the characteristic microfluidic channel dimension, it can be approximated that the net charge density is zero and the ionic concentration is uniform throughout the channel domain. Furthermore, if the Joule heating effect is not concerned, we have $i_{conv} \approx 0$, $i_{diff} \approx 0$ and $\sigma \approx$ const. In addition, as discussed earlier the ion relaxation effect is

neglected, namely $\partial \rho_e / \partial t = 0$. Therefore, the conservation of charges equation reduces to

$$\nabla^2 \phi = 0 \tag{13}$$

which shows that the distribution of the externally applied electrical potential, ϕ, is governed by the Laplace equation. Thus, the local applied electrical field strength, E, can be calculated using

$$E = -\nabla \phi \tag{14}$$

Key Research Findings

General Model for Combined Pressure-Driven and Electroosmotic Flow

So far, all governing equations are presented. It can be seen that a closed mathematical model of the combined pressure-driven flow and electroosmotic flow in microfluidic channels should include the continuity equation, the Stokes equation, the Poisson equation, the Boltzmann distribution and the Laplace equation. A set of the governing equations for such combined pressure-driven flow and electroosmotic flow can be rewritten in dimensional form as

$$\nabla \cdot \boldsymbol{V} = 0 \tag{15}$$

$$-\nabla p - \rho_e \nabla \phi + \mu \nabla^2 \boldsymbol{V} = 0 \tag{16}$$

$$\nabla^2 \psi = -\kappa^2 \rho_e \tag{17}$$

$$\rho_e = \sum_{i=1}^{N} z_i n_i \tag{18}$$

$$n_i = n_0 \exp\left(-\frac{z_i e \psi}{k_B T}\right) \tag{19}$$

$$\nabla^2 \phi = 0 \tag{20}$$

The appropriate boundary conditions for solving these governing equations are specified as follows. The liquid velocity tangential and normal to all the channel walls must obey the no-slip and impermeable conditions. The EDL potential at the solid–liquid interface is specified as the zeta potential, which depends on channel material and electrolyte solution chemistry such as ionic strength, pH, etc. The externally applied electrical potential is generally specified by prescribed potentials imposed on inlet and outlet boundaries, and the electrical insulation condition is usually implemented to the channel walls. The prescribed global pressure values (if any) are provided on both inlet and outlet boundaries.

Obviously, in general no analytical solutions are available because of the complex governing equations, geometric domains and boundary conditions. A computational fluid dynamics (CFD) technique usually has to be applied in order to solve the governing equations together with the aforementioned boundary conditions. However, due to low Reynolds number flow, the Stokes equation is linear, and thus there is almost no challenge encountered when using numerical techniques to solve such kinds of single-phase flow problems. A more detailed discussion of numerical simulation of electroosmotic flow in microchannel geometries can be found elsewhere [6].

Simplified Model for Combined Pressure-Driven and Electroosmotic Flow

In microfluidic systems, due to the very thin EDL compared to the microchannel dimension, the electroosmotic velocity distribution and EDL potential profile inside the EDL region become insignificant. Thus we do not need to solve the Poisson equation together with the Boltzmann distribution. Instead the electroosmotic flow velocity at the edge of the EDL (i. e. from the diffuse layer to the bulk phase) is given by the Smoluchowski equation [1], expressed as

$$\boldsymbol{V}_{eo} = -\frac{\varepsilon_0 \varepsilon_r \zeta E}{\mu} \tag{21}$$

where ζ is the zeta potential of channel wall. As a result, when modeling two and three dimensional flow in microfluidic systems, it is usual practice to apply the Smoluchowski velocity to the tangential direction of the channel wall such that the EOF field can be considered as flow induced by a moving wall with such velocity. Since electrically neutral condition is assured outside the EDL region, namely the net charge density $\rho_e = 0$, the Columbic body force term in equation (16) becomes zero, and thus we can obtain a simplified model for the combined pressure-driven flow and electroosmotic flow. Such a model only involves the continuity equation and the simplified Stokes equation (i. e. without the presence of the Columbic body force):

$$\nabla \cdot \boldsymbol{V} = 0 \tag{22}$$

$$-\nabla p + \mu \nabla^2 \boldsymbol{V} = 0 \tag{23}$$

All the boundary conditions are the same as those described earlier except the no-slip condition is replaced by assigning the Smoluchowski velocity as a velocity tangential to the channel walls.

In the literature, this approximation, referred to as the slip velocity approach, in fact can provide a good estimation of the flow field in microfluidic geometries. Using the simplified model with the slip velocity boundary conditions, two case studies are considered. Case I considers electroosmotic flow in a T-shaped microgeometry of uniform zeta potential. The simulation results of the velocity field in vector form are shown in Fig. 1. It can be seen from Fig. 1 that the presence of the T-junction causes the flow to become two dimensional while inducing a local pressure gradient. As a result, the velocity field in the neighborhood of the T-junction exhibits a combined pressure-driven and electroosmosis-driven flow. However, the flow in the inlet and outlet regions still exhibits the usual *plug-like* EOF velocity pattern. In case II, EOF in a suddenly changed microchannel with height $2H_1$ and $2H_2$, and length L_1 and L_2 as shown in Fig. 2 is considered. Due to symmetry, only a half channel domain is computed. Specifically, the two channel walls are assumed to have different zeta potential values. Figure 3a presents the velocity vector of electroosmotic flow and Fig. 3b the streamtrace of electroosmotic flow in the microchannel shown in Fig. 2. It can be noted that the profiles of the EOF velocity deviate from the normal *plug-like* EOF shape due to internal pressure gradient induced by a sudden change in cross-section and zeta potential. Moreover, Fig. 3 also shows that the complex secondary flow near the step region is generated.

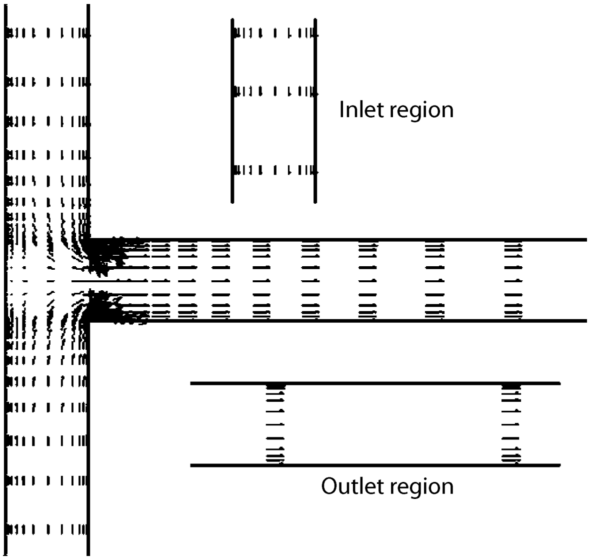

Combined Pressure-Driven Flow and Electroosmotic Flow, Figure 1 Simulation results of the velocity vector of EOF in a T-shaped microgeometry of uniform zeta potential. The parameters used in computation are: cross-section dimensions of the microchannels 100 μm × 100 μm; concentration of $NaHCO_3$ electrolyte 1 mM; zeta potential 70 mV; applied electric field strength 120 V/cm

Further Simplification for Combined Pressure-Driven and Electroosmotic Flow in Straight Microchannels

As a straight microchannel constitutes the basic segment in microfluidic structures, several examples of the combined pressure-driven and electroosmosis-driven flow in straight microchannels are demonstrated in this entry. Usually a microchannel length dimension is much larger than its lateral dimensions, and the flow in such a channel can be considered as unidirectional; this implies that the flow can be modeled as a fully developed flow, namely $\partial u/\partial x = 0$, $v = 0$ and $w = 0$ in terms of Cartesian coordinates. Furthermore, the following analyses are restricted to microchannels of a rectangular cross-section, $2w \times 2h$ (width by height), which is close to the real shape of microchannels made using the microfabrication technologies. With these considerations, the model, based on the slip velocity approach, describing the velocity field of such flow can be further simplified to

$$\frac{\partial^2 u}{\partial x^2} + \frac{\partial^2 u}{\partial y^2} = \frac{1}{\mu}\frac{\mathrm{d}p}{\mathrm{d}z} \tag{24}$$

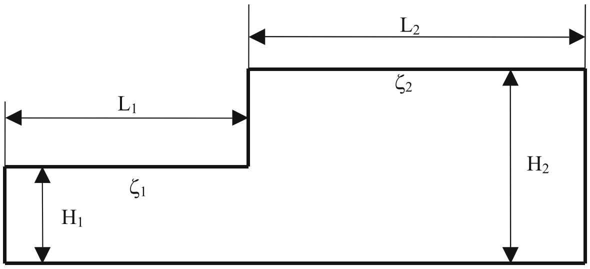

Combined Pressure-Driven Flow and Electroosmotic Flow, Figure 2 Schematic of a microchannel with sudden change in cross-section and zeta potential

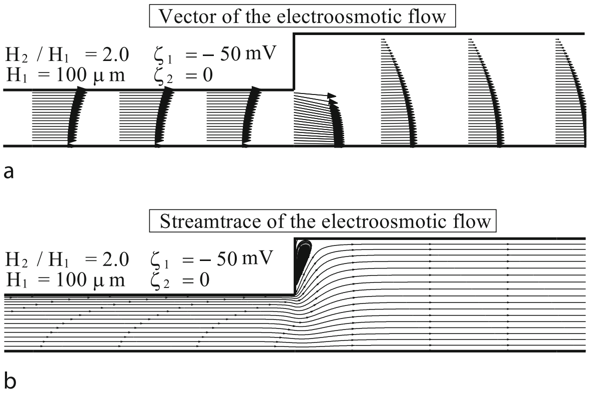

Combined Pressure-Driven Flow and Electroosmotic Flow, Figure 3 Simulation results of the velocity vector and streamline of EOF in the microchannel shown in Fig. 2

Because of linearity, the resultant velocity field is a linear superposition of the EOF velocity and the pressure-driven flow velocity, and is given by

$$u(x, y) = u_{\mathrm{eo}} \pm u_{\mathrm{p}}(x, y) \tag{25}$$

Here the choice of sign depends on the relative direction of the EOF and the pressure-driven flow. The EOF velocity is specified by the Smoluchowski velocity as

$$u_{\mathrm{eo}} = \frac{\varepsilon_0 \varepsilon_{\mathrm{r}} \zeta E_z}{\mu} \tag{26}$$

The pressure-driven flow velocity profile is described by the well-known Poiseuille flow which in a rectangular channel is expressed as

$$u_{\mathrm{p}}(x, y) = -\frac{h^2}{2\mu}\frac{\mathrm{d}p}{\mathrm{d}z} \times \left[1 - \left(\frac{y}{h}\right)^2 + 4\sum_{k=1}^{\infty}\frac{(-1)^k}{\alpha_k^3}\frac{\cosh\left(\frac{\alpha_k x}{h}\right)}{\cosh\left(\frac{\alpha_k w}{h}\right)}\cos\left(\frac{\alpha_k y}{h}\right)\right] \tag{27}$$

where $\alpha_k = (2k-1)\frac{\pi}{2}$ (here $k = 1, 2, \ldots$).
Recently, Xuan and Li [7] formulated a comprehensive model to describe AC or DC field-driven EOF in a straight channel with arbitrary cross-sectional shape.

Liquid Flow in a Straight Microchannel under Applied Pressure and Electrical Potential Difference

In this case, the global pressure values are specified, and we have $\mathrm{d}p/\mathrm{d}z = -\Delta p/l$ (where Δp is the pressure difference between inlet and outlet of the channel and l is the channel length along the flow direction). Therefore, if both the electric field and the pressure difference are imposed along the same direction, the velocity distribution can be obtained as

$$u(x, y) = \frac{\varepsilon_0 \varepsilon_{\mathrm{r}} \zeta E}{\mu} + \frac{h^2}{2\mu}\frac{\Delta p}{l} \times \left[1 - \left(\frac{y}{h}\right)^2 + 4\sum_{k=1}^{\infty}\frac{(-1)^k}{\alpha_k^3}\frac{\cosh\left(\frac{\alpha_k x}{h}\right)}{\cosh\left(\frac{\alpha_k w}{h}\right)}\cos\left(\frac{\alpha_k y}{h}\right)\right] \tag{28}$$

Electroosmotic Flow in a Straight Microchannel with two Closed Ends

Due to the closed-end structure, an inner backpressure gradient $\mathrm{d}p/\mathrm{d}z$ is induced to fulfill the condition of the zero net flow rates, which mathematically is expressed as

$$\int_0^{2w}\int_0^{2h} u(x, y)\mathrm{d}x\mathrm{d}y = 0 \tag{29}$$

Substituting Eqs. (25–27) into Eq. (29) yields

$$\frac{\mathrm{d}p}{\mathrm{d}z} = \frac{3\mu}{h^2}\frac{u_{\mathrm{eo}}}{\left[1 - \frac{6h}{w}\sum_{k=1}^{\infty}\frac{1}{\alpha_k^5}\tanh\left(\frac{\alpha_k w}{h}\right)\right]} \tag{30}$$

Therefore, we can obtain the electroosmotic velocity distribution in a closed-end rectangular microchannel:

$$u(x, y) = \frac{\varepsilon_0 \varepsilon_{\mathrm{r}} \zeta E_z}{\mu}\left[1 - \frac{3/2}{\left[1 - \frac{6h}{w}\sum_{k=1}^{\infty}\frac{1}{\alpha_k^5}\tanh\left(\frac{\alpha_k w}{h}\right)\right]}\right] \times \left[1 - \left(\frac{y}{h}\right)^2 + 4\sum_{k=1}^{\infty}\frac{(-1)^k}{\alpha_k^3}\frac{\cosh\left(\frac{\alpha_k x}{h}\right)}{\cosh\left(\frac{\alpha_k w}{h}\right)}\cos\left(\frac{\alpha_k y}{h}\right)\right] \tag{31}$$

Such a velocity distribution given by Eq. (31) was verified experimentally by Yan et al. [8] in which a method is proposed to simultaneously determine the zeta potentials of the channel surface and the tracer particles in aqueous solutions. This is achieved by carrying out microscale particle image velocimetry (micro-PIV) measurements of the electrokinetic velocity distributions of tracer particles in both open- and closed-end microchannels under the same water chemistry condition.

Electroosmotic Flow in a Straight Microchannel with Finite Reservoir Size Effect

In electrokinetically driven microfluidic applications, reservoirs are indispensable and have finite sizes. During operating processes, as the liquid level in reservoirs keeps changing as time elapses, a backpressure is generated. Thus, the flow in microfluidic channels actually exhibits a combination of the steady EOF and the time-dependent induced backpressure-driven flow. Yan et al. [9] developed a model to describe the effect of the finite reservoir size on EOF in a rectangular microchannel in connect with two identical cylindrical reservoirs of radius R. It can be shown that the induced backpressure gradient along the channel can be expressed as (see [9] for details)

$$\frac{\Delta p(t)}{l} = -\frac{\varepsilon_0 \varepsilon_{\mathrm{r}} \zeta E_z}{\mu}\frac{8\rho g w h}{\pi R^2 l}\left[1 - \exp(-Ct)\right] \tag{32}$$

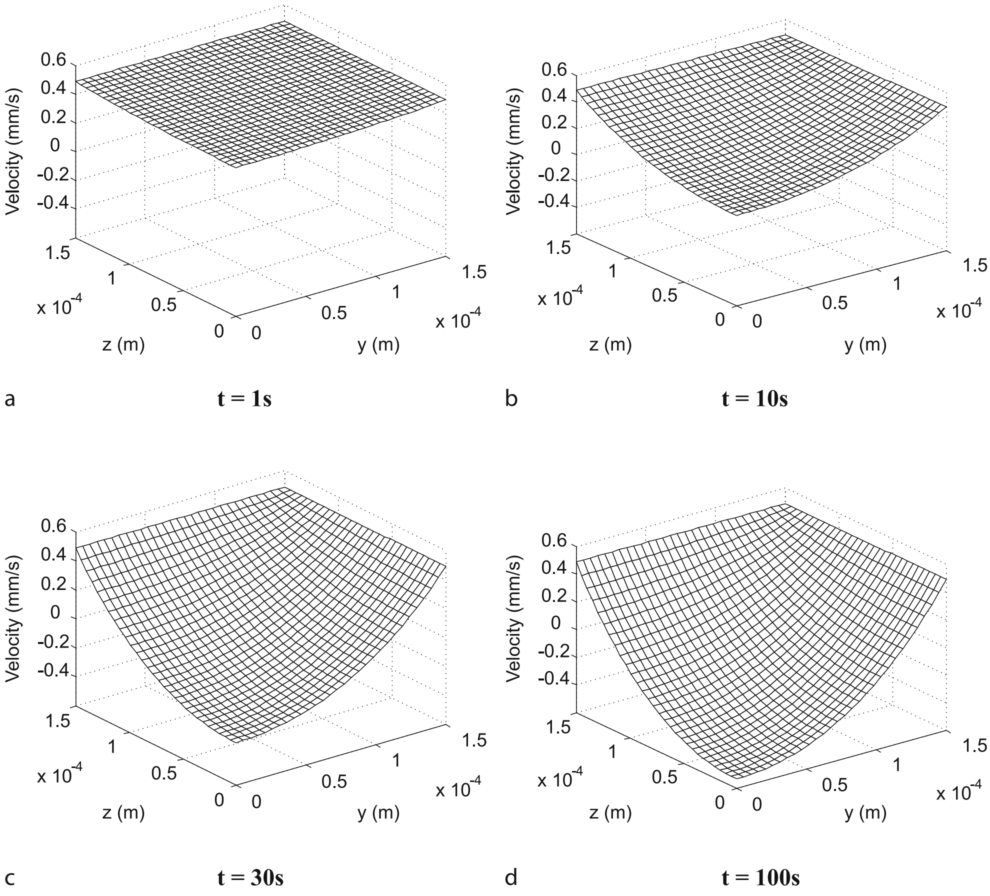

Combined Pressure-Driven Flow and Electroosmotic Flow, Figure 4 Simulation results of the time evolution of EOF velocity distributions due to finite reservoir size effects: (**a**) t = 1 s, (**b**) t = 10 s, (**c**) t = 30 s and (**d**) t = 100 s. The parameters used in computation are: cross-section dimensions of the microchannels 300 μm × 300 μm; channel length l = 4 cm; zeta potential 62 mV; applied electric field strength 100 V/cm; reservoir radii $R_1 = R_2$ = 1 mm

where

$$C = \frac{8wh^3\rho g}{3\pi\mu R^2 l}\left[1 - \frac{6h}{w}\sum_{k=1}^{\infty}\frac{1}{\alpha_k^5}\tanh\left(\frac{\alpha_k w}{h}\right)\right]$$

Therefore, the velocity distribution of EOF in a straight rectangular microchannel with finite reservoir size effect is expressed as

$$u(x, y, t) = \frac{\varepsilon_0\varepsilon_r\zeta E}{\mu}\left[1 - \frac{4\rho g w h^3}{\pi\mu C R^2 l}\left(1 - \exp(-Ct)\right)\right] \times \left[1 - \left(\frac{y}{h}\right)^2 + 4\sum_{k=1}^{\infty}\frac{(-1)^k}{\alpha_k^3}\frac{\cosh\left(\frac{\alpha_k x}{h}\right)}{\cosh\left(\frac{\alpha_k w}{h}\right)}\cos\left(\frac{\alpha_k y}{h}\right)\right] \tag{33}$$

It should be pointed out here that the velocity given by Eq. (33) now becomes time dependent because of the change of the liquid level in the two reservoirs. The evolution of the velocity distribution with time is simulated using Eq. (33), and the simulation results are shown in Fig. 4. It is noted in Fig. 4a that the velocity field keeps the *plug flow* during the period of EOF effective pumping. Afterwards the fluid velocity profile starts changing its shape due to the induced backpressure resulting from the difference of fluid level in the two reservoirs (see Fig. 4b). As time elapses, the induced backpressure-driven flow becomes stronger by showing a parabolic velocity distribution in Fig. 4c. In Fig. 4d, it is observed that the flow velocity field finally reaches a stage that the total volumetric flow rate is zero due to a counterbalance between the EOF velocity upward in the near wall region and the induced backpressure-driven flow downward in the central region of the channel.

In addition, a new concept termed *effective pumping period* is introduced to characterize the reservoir size

effect, and an analytical expression for such effective pumping time is given by

$$\Delta t_{\mathrm{eff}} \approx \frac{0.05}{C} \tag{34}$$

This time scale, Δt_{eff}, usually is of the order of about $O(10-10^2)$ s depending on channel and reservoir sizes, and is much larger than that of start-up EOF which is of the order of $O(D_{\mathrm{h}}^2\rho/\mu) \sim O(10^{-3})$ s. The proposed model was verified experimentally using the micro-PIV technique [9].

Electroosmotic Flow in a Straight Microchannel with a Step Change in Zeta Potential

Consider EOF in a straight microchannel consisting of two parts, segment I and segment II, with different lengths l_1 and l_2, respectively. Two segment are made from different material, and thus are uniformly charged with zeta potentials ζ_1 and ζ_2, respectively. As a result, the flow rates of pure EOF in the two segments are different. Since the liquid fluid is incompressible, the real flow rate going through segment I should be equal to that through segment II. Hence, the unbalance of the electroosmotic flow rate will induce a positive pressure gradient, $-(\mathrm{d}p/\mathrm{d}z)_1 > 0$, in segment I and a negative pressure gradient, $-(\mathrm{d}p/\mathrm{d}z)_2 < 0$, in segment II if $\zeta_1 < \zeta_2$, and vise versa. Mathematically, the equal flow rate condition reads

$$\int_0^{2w}\int_0^{2h} u_1\,(x,y)\mathrm{d}x\mathrm{d}y = \int_0^{2w}\int_0^{2h} u_2\,(x,y)\mathrm{d}x\mathrm{d}y \tag{35}$$

where the velocity profile in each segment is expressed as

$$u_i\,(x,y) = \frac{\varepsilon_0\varepsilon_{\mathrm{r}}\zeta_i E_z}{\mu} - \frac{h^2}{2\mu}\left(\frac{\mathrm{d}p}{\mathrm{d}z}\right)_i \times \left[1-\left(\frac{y}{h}\right)^2 + 4\sum_{k=1}^{\infty}\frac{(-1)^k}{\alpha_k^3}\frac{\cosh\left(\frac{\alpha_k x}{h}\right)}{\cosh\left(\frac{\alpha_k w}{h}\right)}\cos\left(\frac{\alpha_k y}{h}\right)\right] \quad (i = 1 \text{ or } 2) \tag{36}$$

Furthermore, since there is no applied pressure gradient across the entire length of the channel, the induced pressure should also fulfill the following relationship:

$$\left(\frac{\mathrm{d}p}{\mathrm{d}z}\right)_1 l_1 + \left(\frac{\mathrm{d}p}{\mathrm{d}z}\right)_2 l_2 = 0 \tag{37}$$

Therefore, the two induced pressure gradients in each segment can be determined by simultaneously solving Eqs. (35) and (37). The final velocity profile in each segment can be obtained by substituting the induced pressure gradient into Eq. (36). Using the caged-fluorescence technique, Herr et al. [10] carried out experiments, and found that such a velocity pattern is in agreement with their measured results.

Future Directions for Research

Fundamental understanding of the liquid flow characteristics in microfluidic geometries is the key to achieving optimum design and precise control of microfluidic devices used for chemical analyses and biomedical diagnoses. Based on the continuity mechanics approach, the theoretical framework of pressure-driven flow and electroosmotic flow in microfluidic channels has been well established. It is the author's opinion that the challenges we are now facing are multi-physics and multi-scale modeling and characterization. For example, the theoretical model presented in this entry assumes negligible Joule heating effect. However, when the applied electrical field is large and the buffer concentration is high, the Joule heating becomes significant. The presence of such Joule heat will cause a temperature rise, leading to a change of the electrical and thermophysical properties such as electrical conductivity, dielectric constant, zeta potential, viscosity, etc. The interplay or coupling among electrical, hydrodynamic and thermal phenomena will alter the flow characteristics, which will affect the pumping of buffer solution and manipulation of sample species.

The fast development of nanotechnology will lead to the emergence of nanofluidic technology. It is expected that the transport of ions and macromolecules and the control of liquid in nanofluidic channels and structures will still likely involve the use of an electrical field. This will open a completely new territory for nanofluidics-based electrokinetic phenomena which will be the main focus of the next decade of research.

Cross References

- ▶ Pressure-Driven Flow
- ▶ Electrical Double Layers
- ▶ Electroosmotic Flow (DC)
- ▶ AC Electro-Osmotic Flow
- ▶ Streaming Current and Electroviscosity
- ▶ Electrophoresis

References

1. Probstein RF (1994) Physiochemical Hydrodynamics, An Introduction. Wiley, New York
2. Dukhin SS, Deryaguin BV (1974) Electrokinetic Phenomena In: Matijevic E (ed) Surface and Colloid Science. Wiley, New York

3. Chang HC (2006) Electro-kinetics: A viable micro-fluidic platform for miniature diagnostic kits. Can J Chem Eng 84(1):1–15
4. Deen WM (1998) Analysis of Transport Phenomena. Oxford University Press, New York
5. Tang GY, Yang C, Chai JC, Gong HQ (2003) Modeling of electoosmotic flow and capillary electrophoresis with the Joule heating effect: the Nernst-Planck equation versus the Boltzmann distribution. Langmuir 19:10975–10984
6. Patankar NA, Hu HH (1998) Numerical simulation of electroosmotic flow. Analytical Chemistry 70(11):1870–1881
7. Xuan XC, Li D (2005) Electroosmotic flow in microchannels with arbitrary geometry and arbitrary distribution of wall charge. J Colloid Interface Sci 289(1):291–303
8. Yan DG, Yang C, Nguyen NT, Huang XY (2006) A method for simultaneously determining the zeta potentials of the channel surface and the tracer particles using microparticle image velocimetry technique. Electrophoresis 27(4):620–627
9. Yan DG, Yang C, Huang XY (2007) Effect of finite reservoir size on electroosmotic flow in microchannels. Microfluid Nanofluid 3(4):333–340
10. Herr AE, Molho JI, Santiago JG, Mungal MG, Kenny TW (2000) Electroosmotic capillary flow with nonuniform zeta potential. Anal Chem 72(6):1053–1057

Compactness

► Viscosity

Compact Support

Definition

A function is said to have compact support if its value vanishes outside a certain distance. In other words, the function is non-zero only within a certain region. In the finite element method, compact support ensures that the solution inside an element depends only on its nodal points. In meshless methods, the notion of compact support ensures that the number of neighbouring nodes or particles affecting the solution at a certain point is finite.

Cross References

► Meshless Methods
► Volume and Finite Difference Method for Modeling and Simulation

Complex Fluids

► Non-Newtonian Fluids in Microfluidics

Composite Nanoparticles

Synonyms

Core-shell Nanoparticles; Quantum-dot Quantum Well (QDQW nanoparticles)

Definition

A composite nanoparticle is a ► nanoparticle of composite structure, including core-shell structure, onion like structure and gladiate composition.

Cross References

► Nanoparticle Synthesis in Microreactor

Compression Molding

► Micromolding
► Micromolding (Injection and Compression Molding)

Compression Ratio

Definition

In a positive displacement pump a moving boundary changes the volume of a pump chamber. The compression ratio is the ratio of the difference between the maximum and minimum volume (also called the stroke volume), and the minimum volume (or dead volume).

Cross References

► Dead Volume
► Electromagnetic Valves
► Electrostatic Valves
► Magnetic Pumps
► Membrane Actuation for Micropumps
► Microactuators
► Peristaltic Pumps
► Piezoelectric Valves
► Pneumatic Valves
► Positive Displacement Pump
► Stroke Volume
► Thermomechanical Valves
► Thermopneumatic Valves

Computational Domain

Synonyms

Computational region

Definition

The computational domain refers to a simplified form of the physical domain both in terms of geometrical representation and boundary condition imposition. This simplified form should retain all physically important features of the problem but can ignore minor details. For example, when simulating fluid flow about a car, one can ignore gaps between doors while the actual boundary of the fluid flow domain may be replaced by a simple box-like boundary.

Cross References

- ► Meshless Methods
- ► Volume and Finite Difference Method for Modeling and Simulation

Computational Fluid Dynamics (CFD)

- ► Finite Volume and Finite Difference Methods for Modeling and Simulation

Computational Region

- ► Computational Domain

Concentration Control

- ► Reaction Condition Control

Concentration Gradient Generation and Control

JEONG WON PARK, HWA SUNG SHIN,
HYUNG JOON KIM, NOO LI JEON
Department of Biomedical Engineering, University of California, Irvine, CA, USA
njeon@uci.edu

Synonyms

Diffusion-based mixing

Definition

The concentration gradient of a solute is the change of concentration per unit distance in a solution. A concentration gradient is generated by diffusion between two regions where the concentration of a substance differs; diffusion proceeds until the concentrations in the two regions become equal.

Overview

Concentration gradients of diffusible molecules play an important role in many biological and chemical processes, such as chemotaxis, nerve growth cone guidance, surface patterning, and microfabrication. Traditional approaches (e. g., the Boyden chamber [1], micropipettes [2], generation under agarose [3], and derivatives of these approaches [4, 5]) are mainly used to release factors and investigate cell behavior subject to a concentration gradient. Although instrumental in furthering many biological studies, none of these methods are effective for generating stable gradients of complex shape, owing to the unbalanced flux of soluble factor into and from the region of interest. An alternative approach to generating and maintaining predictable and stable concentration gradients with control over the shape of the profile is needed for a number of applications in biology and chemistry. Recently, microfluidic microchannel networks have been extensively utilized for concentration-related analysis since they allow accurate and reproducible manipulation of the locations and quantities of samples released into the system. A "Christmas tree"-like microfluidic network for generating concentration gradients of complex shape (e. g., linear, parabolic, and periodic) along the width of a channel has been proposed by Jeon et al. [6] and Dertinger et al. [7]. Sample solutions with different concentrations were supplied at multiple inlets, and then mixed, split, and recombined in branch channels, which eventually converged to the main channel to yield a complex transverse profile (i. e., across the channel width). This device was later improved by integration of a simple *mixer module* with the gradient-generating network to enable on-chip dilution of initial samples and obtain dynamically controlled temporal and spatial gradients [8]. In spite of the many advantages of this "Christmas tree"-like gradient generator, the device has several drawbacks.

- The device can only generate gradients under fluid flow, which induces shear and drag forces that may alter intracellular signaling or cause changes in cell shape and attachment that may lead to migrational bias.
- The gradient evolves as the fluid flows downstream, such that the cells in the microchannel do not all experience the same concentration gradient.
- Under typical experimental flow rates, any autocrine/paracrine factors that are secreted by the cells will be washed away.

To compensate for these weakness, free-diffusion-based gradient generators have been developed. These devices have improved on conventional assays such as those done with a Boyden chamber or micropipette. This free-diffusion-based approach is less amenable to flexible manipulation of the gradients compared with the continuous-flow mixing approach, but generates gradients with no external control, allowing easier design of high-throughput experimental apparatus. The ladder chamber, as the name implies, consists of two main channels connected by several bridge microchannels. The purpose behind this design is to establish gradients in the bridge channels by allowing diffusion of molecules between the two main streams. The molecules diffuse across the microchannels and this results in the establishment of a linear gradient in the steady state [9]. If on-chip valves are incorporated into the device, the temporal delivery of the gradient can be flexibly regulated, allowing 2D or 3D gradients to be generated [10]. Flow-free gradients do not induce shear stress, and thus minimize mechanical disturbance to cells. Because of these advantages, these devices form a unique class of microfluidic gradient generator, and have been applied to studies of cell migration, drug delivery, and intracellular responses. When valves and micro/nanofabricated apertures are used to control the release of chemicals on-chip, a local chemical gradient near the source can be generated and controlled. This approach allows precise manipulation of local stimulation.

Two methods to generate concentration gradients in microfluidic devices, one based on laminar flow, and the other on free diffusion, will be summarized below.

Basic Methodology

Flow-Based Concentration Gradient Generation

A simple method for generating gradients is to continuously infuse two or more streams of different species into a simple microfluidic channel. Diffusion between the streams generates a gradient across the channel, perpendicular to the flow direction, having a diffusive profile that is stable at any fixed position in the channel but evolves along the channel. The upstream gradient has a step-like profile with a clear concentration interface, while the downstream gradient has a more continuous profile, resulting from diffusion. The process of mixing of laminar streams in microfluidic channels is governed by a diffusion model and has been well characterized by theory and experiments. On the basis of the well-characterized mixing process of continuous-flow streams in simple microfluidic channels, concentration gradients can be manipulated more flexibly by use of microfluidic networks.

Figure 1a shows the schematic design of a representative gradient-generating microfluidic network. This network consists of three inlets and one outlet. Each inlet is connected to syringes which contain solutions of chemicals of different concentration. When they are simultaneously infused into the microfluidic device, the three solutions are split, mixed, and recombined, resulting in different proportions of the solutions in each branch. Finally, the solutions in each branch are brought together into a single channel, establishing a gradient perpendicular to the flow direction.

The concentration gradient profile depends on the splitting ratio of the flow at each branch point. An electronic-circuit model was introduced to understand the splitting ratio in a pyramidal microfluidic network. As shown in Fig. 1b, the part of the network containing n vertical channels is defined as an nth-order branched system ($B = n$), and each vertical channel (V) is labeled from left to right by $V = i$, where i is an integer between 0 and $B - 1$. As the horizontal channels are shorter (by ~ 20 times) than the vertical ones, the resistance of the horizontal channels (R_H) is negligible compared with the resistance of the vertical ones (R_V). The flow rates are $[B - V]/[B + 1]$ and $[V + 1]/[B + 1]$ to the left and right, respectively. For instance, at the point P in Fig. 1b ($B = 4, V = 0$), the relative volumetric flows to the left and right are $4/5$ and $1/5$, respectively. This splitting characteristic determines the shape of the concentration gradient in the single channel where all branches join together.

To guarantee a spatially equilibrated concentration in each channel as a result of diffusive mixing between laminar streams, the two flows must spend a sufficiently long time in the serpentine channel that equilibrium is reached. An analytical solution for the concentration at any time in one dimension can give the approximate time required to reach the equilibrium state:

$$C(t,x) = \frac{1}{2}C_0 \sum_{n=-\infty}^{\infty} \left\{ \operatorname{erf}\frac{h + 2nl - x}{2\sqrt{Dt}} + \operatorname{erf}\frac{h - 2nl + x}{2\sqrt{Dt}} \right\} \tag{1}$$

where $C(t,x)$ is the concentration at point x and time t, C_0 is the initial concentration in the channel, h is the width of the initial distribution, l is the width of the channel, and D is the diffusion coefficient. The percentage mixing across a channel of width l at time t is defined as

$$\%\,\text{mixing}\,(t) = \left(1 - \frac{\int_0^l |C(t) - C(\infty)|\,\mathrm{d}x}{\int_0^l |C(0) - C(\infty)|\,\mathrm{d}x}\right) \times 100\% \tag{2}$$

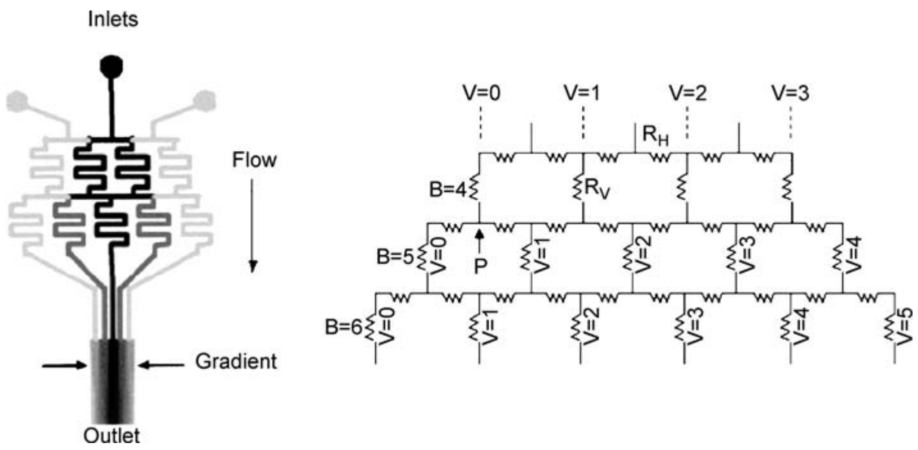

Concentration Gradient Generation and Control, Figure 1 (**a**) Schematic design of a representative gradient-generating microfluidic network. (**b**) Equivalent electronic-circuit model of a pyramidal microfluidic network

where $C(t)$, $C(\infty)$, and $C(0)$ are the concentrations across the width of the channel at times t, ∞, and 0, respectively.

Shape of Concentration Gradient

The shape of the concentration gradient created at the junction in the broad channel is governed by the splitting ratios of the streams at the individual nodes in the pyramidal network and depends on the number of inlets in the network and the relative concentrations of the solutions that are fed into the network. In general, the larger the number of inlets, the broader the range of accessible shapes. The number of outputs determines the number of steps that compose a profile. The width of the broad channel defines the overall width of the profile. Changing the number of outputs does not affect the overall shape of the profile.

Owing to the varying splitting ratios at the branching points in the network, streams injected from different inlets are mixed in different ways with neighboring streams while flowing through the network. As a result, different concentration gradients are generated. In general, all accessible concentration profiles that can be generated using an n-input network can be expressed as a linear combination of the profiles generated by using the individual inputs. All calculated concentration profiles generated by a microfluidic device with n inlets lie on a curve described by a polynomial of order $n-1$.

Generation of Periodic Gradients

There are two ways to generate periodic gradients. One way is to use a microfluidic network with an appropriately large number of inlets. It is more convenient, however, to generate the concentration profile by combining multiple pyramidal networks in a parallel way. By following this latter approach, a broad range of concentration profiles can be generated using a small number of inlets. A variety of sawtooth gradients can be established when the individual linear concentration gradients which are independently generated are brought together in the broad channel [7]. Increasing the number of inlets from two to three in the individual networks extends the accessible range of profiles, since composite gradients with parabolic parts can be generated. Figure 2b shows a symmetric gradient consisting of three parabolic parts. Since linear gradients are accessible with networks that have three inlets, mixed gradients consisting of both linear and parabolic parts can be generated (Fig. 2).

Generation of Dynamic Concentration Gradients

Although useful for many applications, an important limitation of the methods described above is that the shape of the gradient is fixed for each device, limiting application to a single static experiment. Moreover, these methods cannot be applied in applications requiring temporal variations in concentration. The following section describes a method of generating dynamically controlled temporal and spatial gradients using a single microfluidic device, by integrating a simple *mixer module* with individually controlled fluidic inputs with a gradient-generating network.

Mixer Module A simple microfluidic mixer module (Fig. 3a) was designed to generate controlled mixtures of two fluidic inputs. Buffer and FITC–dextran solutions, individually controlled by separate syringe pumps, were introduced into the microfluidic device via two inputs. The mixing channel was 40 mm long, to allow complete mixing in the range of flow rates tested for this experimental configuration. The final concentration in the obser-

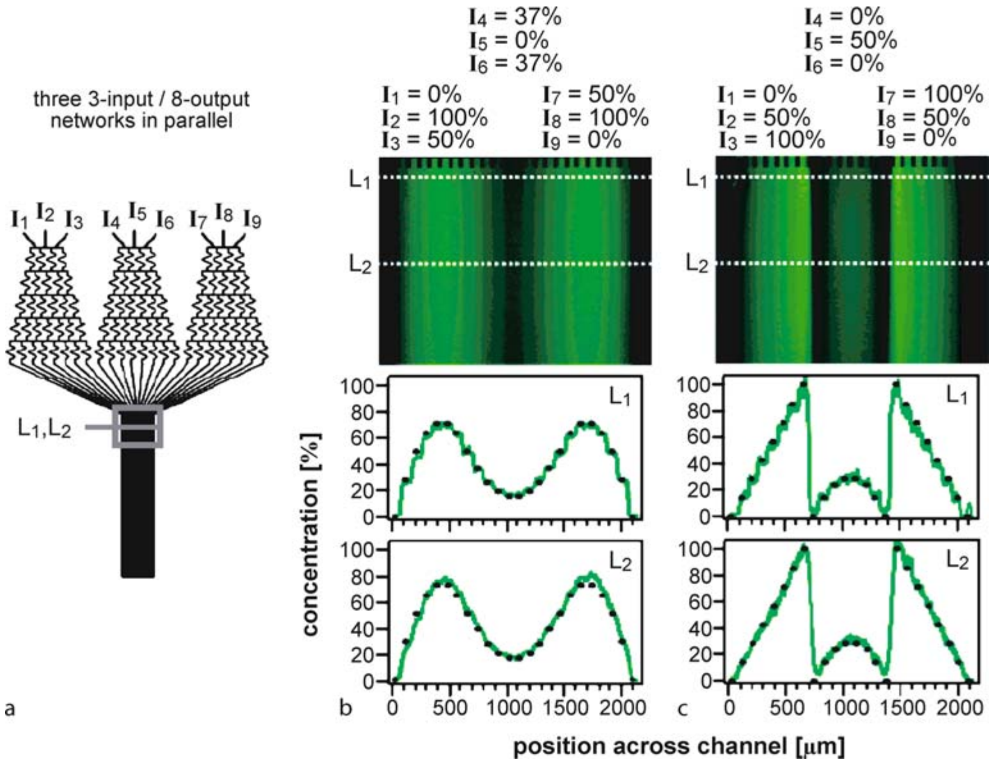

Concentration Gradient Generation and Control, Figure 2 (**a**) Schematic of the microfluidic network used (**b, c**) Fluorescence micrographs of two different periodic gradients, (**b**) consisting of parabolic parts and (**c**) a mixture of parabolic and linear parts

vation area, 40 mm downstream of the inputs, was spatially homogeneous. The final concentration is controlled by varying the ratio (k) of the flow rates of buffer (V_{buffer}) and FITC–dextran ($V_{\text{FITC–dextran}}$), where

$$k = \frac{V_{\text{buffer}}}{V_{\text{FITC–dextran}}} \tag{3}$$

If the portion of the mixing channel occupied by a fluidic input is proportional to its flow rate, the relationship between the normalized final concentration of FITC–dextran (c) in the observation channel and the flow rate ratio(k) is given by

$$c = \frac{1}{1+k} \tag{4}$$

If the total flow rate in the observation channel is kept constant (as in this experiment),

$$V_{\text{buffer}} + V_{\text{FITC–dextran}} = V_0 \tag{5}$$

The flow rates of buffer and FITC–dextran as a function of the normalized FITC–dextran concentration c and the total flow rate V_0 can then be readily determined:

$$V_{\text{FITC–dextran}} = cV_0$$
$$V_{\text{buffer}} = (1-c)V_0 \tag{6}$$

Since the FITC–dextran concentrations for $k = 0$ (FITC–dextran only) and $k = \infty$ (buffer only) are known, and their fluorescence intensities can be measured, these values were used as reference points to test the proposed mixing strategy by examining whether the relative fluorescence intensity was linearly proportional to the FITC–dextran concentration at other k values. Plotting the normalized fluorescence intensity versus the normalized FITC–dextran concentration gave a straight line, indicating that the strategy was valid (Fig. 3b).

Generation of Dynamic Linear Gradients To generate dynamically controlled spatial and temporal linear gradients with varying slope, baseline, and direction, the outlet of the mixer module described in the previous section was connected to the inlets of a gradient-generating device. By adjusting the relative flow rates of the buffer and the FITC–dextran inputs, while maintaining a constant total

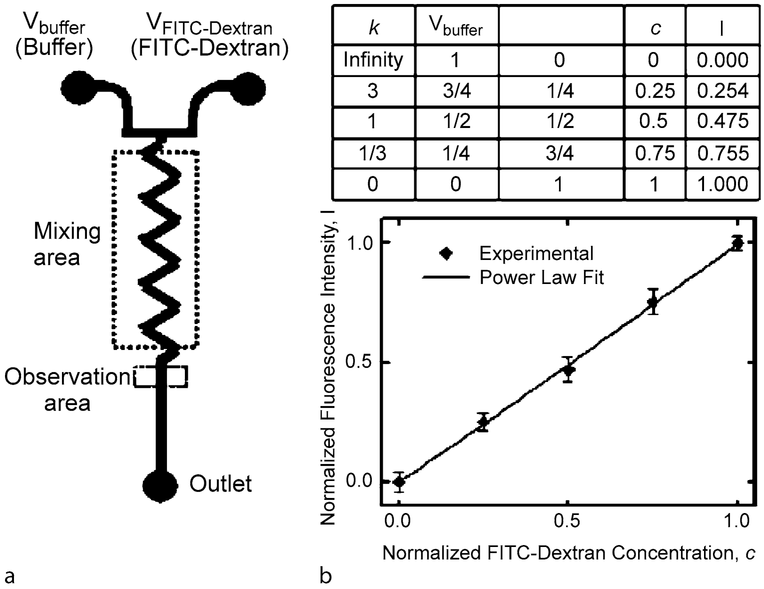

k	V_{buffer}		c	I
Infinity	1	0	0	0.000
3	3/4	1/4	0.25	0.254
1	1/2	1/2	0.5	0.475
1/3	1/4	3/4	0.75	0.755
0	0	1	1	1.000

Concentration Gradient Generation and Control, Figure 3 (**a**) Two-input mixer module. (**b**) Schematic of the microfluidic chamber. (**c**) Normalized fluorescence intensity (*I*) in the observation channel measured at different FITC–dextran concentrations

flow rate, the concentration of FITC–dextran injected into each inlet can be dynamically varied to change the slope, baseline, and direction of the linear gradients. Keeping the left inlet constant, the slope can be changed by changing the concentration of FITC–dextran in the right inlet. The linear gradient is represented by the normalized change in the FITC–dextran concentration from the left edge to the right edge of a 350 μm wide microchannel.

Generation of Dynamic Nonlinear Gradients A three-inlet nonlinear spatial-gradient generator has been demonstrated in earlier work [6, 7]. In that device, the gradient was described by the equation $c = ax^b + O(x)$, where c is the concentration, x is the position in the channel, a and b are the proportionality coefficient and the power of the major term, respectively, and $O(x)$ represents the remaining terms. The nonlinearity (or power) of the gradient was modified by adjusting the relative chemical concentration at the middle inlet. To change the concentration at the middle inlet, the experiment had to be stopped and the solution being pumped into the inlet had to be manually replaced with another solution. This section describes the incorporation of a mixer module into the middle inlet to allow dynamic control of the nonlinearity of the gradient (Fig. 4a). A mixer module with a buffer input and an FITC–dextran input was used. The gradient profile was of the power-law form

$$c(x) = ax^b \tag{7}$$

where c is the normalized FITC–dextran concentration as a function of the position (x) in the observation channel (the origin is at the left edge of the channel), and was directly proportional to the fluorescence intensity; a and b are fitting parameters. The power b varied from ~ 0.5 to ~ 2, depending on the FITC–dextran concentration at the middle inlet, and was in agreement with simulations (Fig. 4b). The gradient profiles were simulated by calculating the spatial distribution of the FITC–dextran concentration resulting from the repeated splitting and mixing of FITC–dextran and buffer flowing through the microchannel network from the inlets.

Free-Diffusion-Based Concentration Gradient Generation

Ladder Chamber

Design and Layout of Ladder Chamber A ladder chamber, as the name implies, consists of two main channels connected by several bridge channels. An inlet feeds into each of the main channels, which converge to a common outlet (Fig. 5).

The purpose behind this design is to establish gradients in the bridge channels by allowing diffusion of molecules between the two main streams. Diffusion across the bridge channels is theoretically equivalent to diffusion in a thin film, in which a linear gradient is established at steady state. The chamber can thus be seen as a source/sink diffusion system, with the key feature that the source and

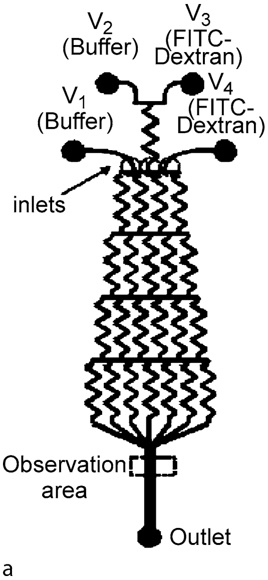

Gradient \ Relative Input Flow Rate	V_1	V_2	V_3	V_4	b
(0, 0.1, 1)	1/3	9/30	1/30	1/3	1.75
(0, 0.5, 1)	1/3	1/6	1/6	1/3	1.03
(0, 0.9, 1)	1/3	1/30	9/30	1/3	0.66

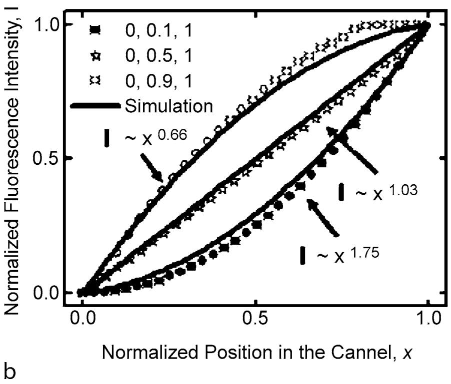

Concentration Gradient Generation and Control, Figure 4 Generation of dynamic nonlinear gradients. (**a**) Schematic of the microfluidic device. A mixer module was connected to the middle inlet of a three-inlet gradient device that generates nonlinear gradients. (**b**) Nonlinear gradients are represented by a combination of the three inlet concentrations and are in power-law form ($I = ax^b$). The graph shows gradient profiles for $(0, 0.1, 1)$, $(0, 0.5, 1)$ and $(0, 0.9, 1)$ obtained from experiments and simulations

sink are fluidic, rather than static; continuous flow provides constant replenishment of the solutions and ensures that the concentrations remain constant.

Flow Dynamics in Microgrooves In order to generate stable linear gradients, the fluid in the bridge channels must be static, such that only diffusion takes place, confining bulk fluid flow to the main channels. The bridge channels were thus designed in the form of microgrooves, having substantially smaller dimensions than the main channels, and consequently a higher fluidic resistance. To determine the optimum relative dimensions that satisfied these requirements, a finite element model was used to predict the flow dynamics in ladder chambers of various dimensions. To simplify the simulation, one main channel and one bridge channel were used, and the flow dynamics was examined when equal pressure differences existed across the bridge channel and along the main channel. When the height of the bridge channel was equal to that of the main channel (1 : 1 height ratio), part of the flow was diverted at a higher velocity into the bridge channel. When the ratio was 1 : 10, the flow was confined to the main channel, and no flow was able to enter the bridge channel. On the basis of these results, only ratios $\geqslant 1 : 10$ can successfully maintain a flow-free environment and ensure that diffusion is the only mode of transport in the microgrooves.

Gradient Generation in Microgrooves The ladder chamber was designed with two inlets and a common outlet to facilitate the loading of solutions and allow a constant flow to be easily maintained. Using the inlets as reservoirs, and withdrawing solution from the outlet using a syringe pump, flow was generated in both of the main channels simultaneously. By loading FITC–dextran and PBS into the reservoirs, a fluorescence gradient was generated across the microgrooves. Figure 6 shows the evolution of the gradient in a 400 μm long microgroove, going from its initial nonlinear profile to a linear steady state in 18 min. The gradient remained constant at 40 min, and was still stable at 90 min. It must be emphasized that the gradient stability is dependent on the flow, and remains stable as long as the flow is maintained.

Microfluidic Multiinjector (MMI)

MMI Design

The MMI was designed to integrate the functionality of pressure-actuated glass micropipettes on a single device using microfabrication and multilayer soft lithography. To generate a microscopic gradient, a device was fabricated with a network of fluidic channels that was controlled with a set of pressure control channels. Steady ejection of chemical solution from a microchannel-based orifice into a large reservoir resulted in gradients similar to

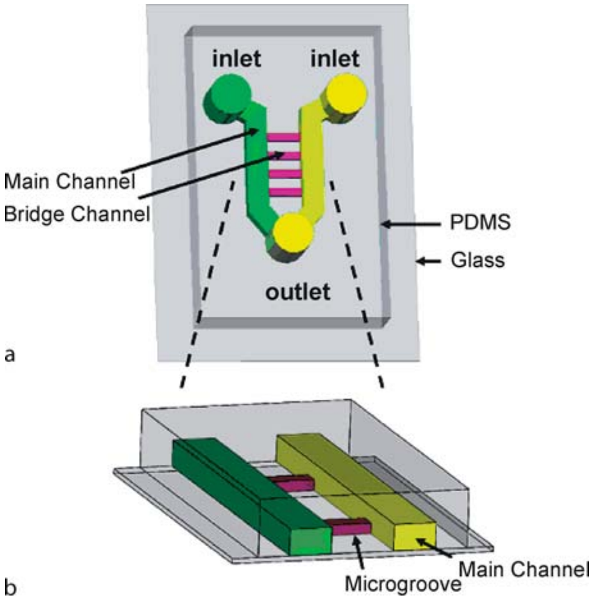

Concentration Gradient Generation and Control, Figure 5 Design and layout of the ladder chamber. (**a**) The chamber was fabricated from PDMS bonded to glass and consists of two main channels connected by bridge channels. (**b**) Constant flow in the main channels allows steady-state diffusion in the microgrooves

those produced by micropipettes. In the MMI, the macroscopic pressure tubing and valves were replaced with pressure control channels and on-chip barrier valves, while the glass micropipette was replaced with a fluidic channel with a 10 μm orifice. Figure 7a shows a schematic of a representative MMI device. The device consists of fluidic channels and valves made from PDMS that are separated by a 25 μm thick membrane. These valves were actuated by applying positive pressure (10 psi) to the control channel. The pressure caused the membrane between the channels to deform and close the fluidic channel. Venting the pressure channel opened the underlying fluidic channel to fluid flow. Repetitive actuation of the barrier valve allowed ejection of picoliter amounts of fluorescent solution into the reservoir. Similarly to a micropipette, steady pulsatile release of solution from an orifice resulted in stable gradients around the orifice.

Generation of Steady-State Concentration Gradient

The release volume must be accurately controlled with the valves to minimize macroscopic fluid flow and fluctuations in the gradient profile. Building on the results described in the previous section, the valve opening times and frequency were optimized to avoid rippling fluctuations in the gradients. Figure 7b shows the development of a stable gradient as a function of time for valve actuation at 0.67 Hz with 1 s opening. To quantitatively analyze the concentration gradient of the ejected substance, the fluorescence intensity was measured near the microfluidic orifice. Figure 7c shows 2D fluorescence intensity profiles at various times after the start of pulsatile release. The profile was governed by diffusion from a point source and reached steady state after 10 min. The measured fluorescence intensity profiles after 10 and 30 min fit well with the diffusion profile predicted by simulation. The concentration gradient produced by repetitive ejection of the solution was calculated by summing the concentration profiles from each pulse. The concentration profile after n injections was expressed as

$$C(r, t) = \sum_{i}^{n} \frac{r e^{\frac{-r^2}{4D(t-it_0)}}}{4[\pi D(t - it_0)]^{\frac{3}{2}}} \tag{8}$$

where $C(r, t)$ is the concentration at a position r relative to the injector and at time t after the onset of ejection, i is an integer from 0 to n, t_0 is the inverse of the ejection frequency, and D is the diffusion constant. From Fig. 7a, the volume of a single ejection is approximately 66.5 pl for $t_0 = 1.5$ s (valve-opening duration = 1 s). D for FITC–dextran was approximated as 1.7×10^{-6} cm^2/s for a dilute solution at room temperature. Because the injector is located at the bottom of the reservoir, the gradient formed around the injector tip is radial. The fluorescence profile is a sum of the fluorescence over the entire depth of the reservoir ($h = 2.5$ mm) and may differ slightly from the actual gradient that is present immediately above the substrate.

Generation of Overlapping Gradients using MMI

To demonstrate the potential of integrating multiple injectors to produce complex superimposed gradients, we fabricated a dual injector on a single chip. This device is capable of producing two identical gradients or two different competing gradients simultaneously. Figure 8a shows the schematic design of this MMI device that can produce overlapping gradients. Different, overlapping gradient profiles can be generated by fabricating multiple injectors on a single chip for high-throughput experiments. Figure 8b shows a 2D fluorescence intensity profile of overlapping gradients. Symmetric, overlapping gradients were formed simultaneously. The fluorescence intensity of the overlapping gradients was visualized by 3D fluorescence intensity plots, as shown in Fig. 8c.

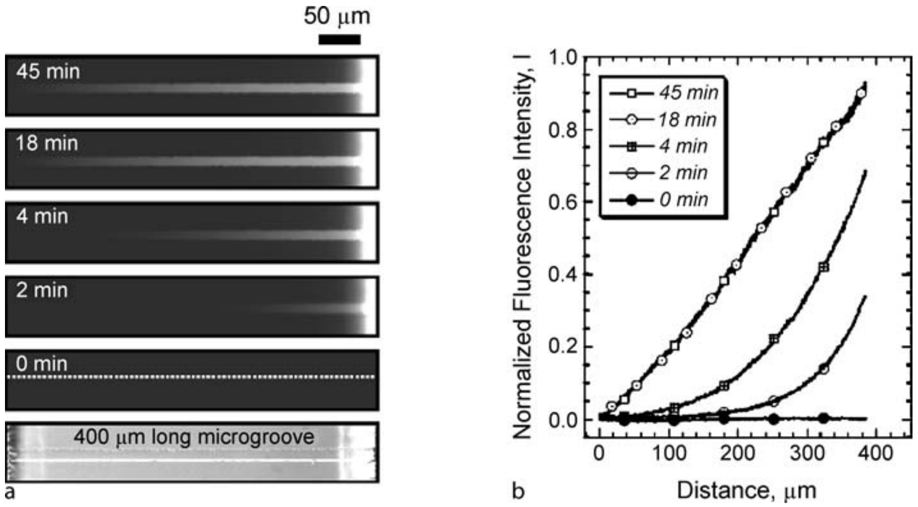

Concentration Gradient Generation and Control, Figure 6 Development of fluorescence gradients in microgrooves. (**a**) Right and left inlets loaded with FITC–dextran and PBS, respectively. (**b**) Plot of the fluorescence intensity profile across the microgroove as a function of time. A linear steady-state gradient was established after 18 min

Key Research Findings

There are a number of advantages in using microfluidic networks to generate gradients. First, a variety of gradients can be generated by using appropriate fluids or solutions. These gradients, in principle, can be used to generate gradients in topology, medium, and surface, all in the same channel. Second, it is possible to generate gradients with a resolution from several microns to several hundreds of microns; the larger channels are the right size to be relevant to studying cell biology. Third, gradients of different shapes (symmetric and asymmetric), types (smooth, step, and with multiple peaks), and kinds (static and dynamic) can be obtained with modification of the design of the microfluidic network or modification of the implementation of the experiment (i. e. the relative flow rates).

Jeon et al. [6] reported a microchannel network method for generating defined concentration gradients in a microfluidic device. Solutions of different concentrations were introduced into the microfluidic device by syringe pumps at separate inlets and repeatedly mixed and split through the microchannel network, producing multiple diluted streams with predictable concentrations. These streams flowed side by side in a common channel and generated a soluble or surface gradient across the channel. Dertinger et al. [7] developed the network method further to create concentration gradients with complex profiles. By configuring the inlet concentrations, gradients with various shapes such as linear, periodic, and parabolic gradients were produced. If multiple microchannel networks are arranged side by side in a single chip and the output streams are connected to a common gradient channel, the individual gradients produced by each network can be aligned to configure complex gradients. Superimposed gradients of two or more species could be also formed using the same approach. Lin et al. [8] improved the network approach to generate dynamically controlled temporal and spatial gradients. A two-inlet *mixing module* was developed to control the resulting concentration by varying the relative input flow rates. When mixing modules were incorporated into the microchannel network device, linear gradients with different slopes, baselines, and directions, as well as nonlinear gradients with different nonlinearities, could be produced, and altered dynamically.

In contrast to the generation of microfluidic gradients by continuous-flow mixing, the other method for gradient generation is the free diffusion of molecules in miniaturized flow-free microenvironments. Two methods have introduced to generate a flow-free concentration gradient of molecules. One method is the ladder chamber, which consists of two main channels connected by several microchannels. Using the inlets as reservoirs, and withdrawing solution from the outlet using a syringe pump, flow is generated in both of the main channels simultaneously. The concentration gradient in microgrooves has been found to reach to a linear steady state in 18 min. The duration of the gradient was limited only by the size of the reservoirs [9].

Another method is based on a microfluidic multiinjector (MMI) that combines the functionality of glass micropipette-based assays with integrated microfluidic valves on a single chip. Pulsatile release of solution using

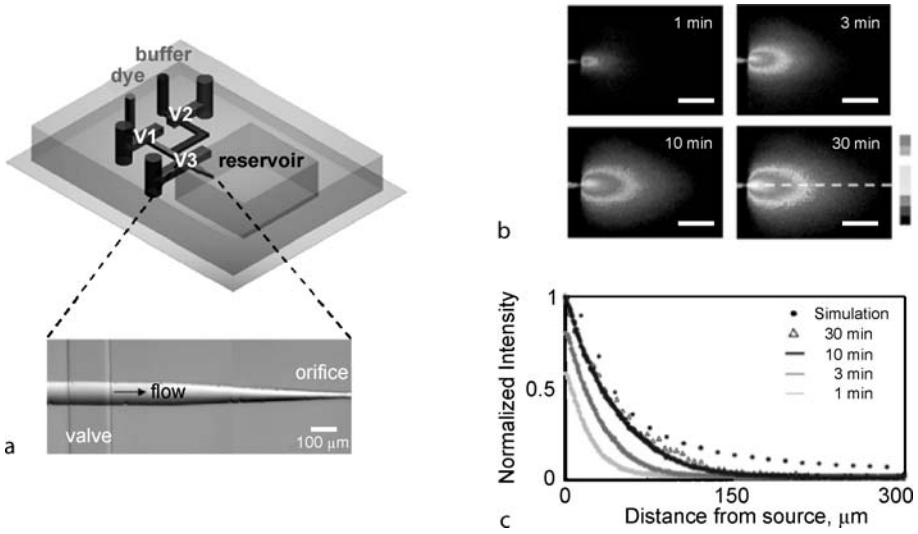

Concentration Gradient Generation and Control, Figure 7 (**a**) Schematic design of the microfluidic multiinjector (MMI). Crossings of control channels and fluidic channels make up the on-chip barrier valves ($V1, V2, V3$). These valves were actuated by pressurizing the control channel and deforming the membrane between the channels to close the fluidic channel. These valves controlled the pulsatile release of solution into the reservoir to generate a gradient. (**b**) 2D intensity profiles showing the gradient of FITC–dextran and its evolution with time. The barrier valve was actuated at 0.67 Hz and opened for 1 s. (**c**) 1D normalized fluorescence intensity profile along a horizontal line in Fig. 7b. Steady-state gradients were achieved within 10 min. The experimental measurements agreed closely with simulations. The scale bars represent 50 µm

integrated valves made from PDMS has produced microscopic chemical gradients near the orifice. Dynamic temporal and spatial gradients have been achieved reliably using this MMI [10]. Overlapping gradients have also been obtained. Miniaturized integration of multiple injectors on a single device will allow reproducible, high-throughput experiments with spatiotemporal gradients, with potential applications in basic and applied studies in chemotaxis and axon guidance.

Future Directions for Research

Gradient-generating microfluidic devices are an enabling experimental platform for fundamental research into a number of physiological and pathological processes that range from immune response through cancer cell migration to axon guidance. Compared with conventional macroscale devices, microfluidic devices allow precise control and manipulation of cellular microenvironments. Generation of stable and well-defined gradient profiles affords more accurate and reproducible quantitative analysis of cellular behavior. Although a microfluidic microchannel network can generate flexible shapes of concentration gradients using a single microfluidic device, this requires integration of computer-controlled syringe pumps that add complexity and limit the shapes obtainable, owing to the pulsatile nature of the stepper-motor-driven syringe pump. To overcome this limitation, pulse-free pumps or gravity-based pumps may be used. In spite of these limitations, the added flexibility in the gradient shape and the capacity to generate dynamic temporal and spatial gradients will be very useful in many areas of application where flexible gradient generation is needed.

The ladder chamber provides a powerful yet simple approach for generating and maintaining stable gradients on two-dimensional substrates. With its simple source-and-sink design, the chamber can generate steady-state gradients in a straightforward manner, without the need for specialized equipment. The chamber's microfluidic nature ensures precise and constant delivery of soluble factors, preventing depletion or accumulation of molecules in the streams, and thus maintaining gradient stability. This combination of characteristics has been lacking among previous chemotaxis assays. The simplicity of the ladder chamber is also complemented by its high throughput. The *ladder* design enables multiple experiments to be performed in parallel. Using a large number of parallel grooves of varying length, gradients of different steepness can be generated simultaneously in a single chamber. Consequently, the influence of gradient steepness on chemotaxis can be rapidly characterized in a single experiment, whereas most other assays, including those using a microfluidic chemotaxis chamber, would require multiple experimental runs. Moreover, it may be possible to generate gradients of several different concentrations in a single chamber by increasing the number of inputs. Since the inlet reservoirs

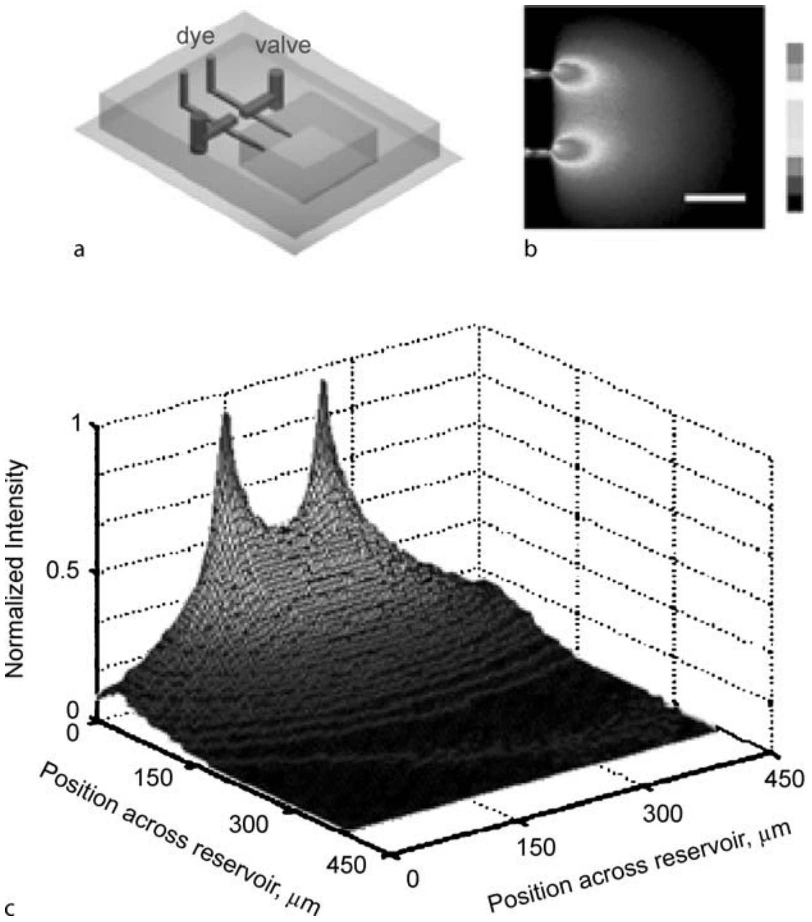

Concentration Gradient Generation and Control, Figure 8 Generation of overlapping gradients in the MMI. (**a**) Schematic design of a parallel MMI on a single chip. Two parallel microinjectors, 120 μm apart, were simultaneously controlled by valves actuated at 0.67 Hz with 1 s opening. (**b**) 2D intensity profile of the fluorescence image, showing symmetric overlapping gradients of FITC–dextran. (**c**) 3D normalized fluorescence intensity profile. The scale bar represents 100 μm

are open to access, the solutions can also be easily replaced and exchanged to allow dynamic control of the gradient during the course of the experiment.

One of the main advantages of the microfluidic multi-injector is that generation of dynamic temporal and spatial gradients can be achieved reliably using a simple experimental setup. Since each injector can be controlled independently, it is possible to generate dynamic spatiotemporal gradients, with potential applications in basic and applied studies of chemotaxis, axon guidance, and yeast polarization. For example, the direction and shape of the concentration gradient can be switched easily by controlling appropriate injectors in an array. When opposing microinjectors are alternately turned on and off, cells can be stimulated by competing gradients of chemoattractants and chemorepellents.

Cross References

► Cell-Based Assays Using Microfluidics
► Microfluidic Mixing
► Microfluidics for Biochemical and Chemical Reactions

References

1. Boyden S (1962) Chemotactic effect of mixtures of antibody and antigen on polymorphonuclear leucocytes. J Exp Med 115:453–466
2. Weiner OD, Servant G, Welch MD, Mitchison TJ, Sedat JW, Bourne HR (1999) Spatial control of actin polymerization during neutrophil chemotaxis. Nature Cell Biol 1:75–81
3. Wilkinson PC, Lackie JM (1983) The influence of contact guidance on chemotaxis of human neutrophil leukocytes. Exp Cell Res 145:255–264
4. Zicha D, Dunn GA, Brown AF (1991) A new directviewing chemotaxis chamber. J Cell Sci 99:769–775

5. Zigmond SH (1977) Ability of polymorphonuclear leukocytes to orient in gradients of chemotactic factors. J Cell Biol 75:606–616
6. Jeon NL, Dertinger SKW, Chiu DT, Choi IS, Stroock AD, Whitesides GM (2000) Generation of solution and surface gradients using microfluidic systems. Langmuir 16:8311–8316
7. Dertinger SKW, Chiu DT, Jeon NL, Whitesides GM (2001) Generation of gradients having complex shapes using microfluidic networks. Anal Chem 73:1240–1246
8. Lin F, Saadi W, Rhee SW, Wang SJ, Mittal S, Jeon NL (2004) Generation of dynamic temporal and spatial concentration gradients using microfluidic devices. Lab Chip 3:164–167
9. Saadi W (2005) Development and application of microfluidic devices for cancer cell chemotaxis. Ph.D. Thesis. University of California, Irvine
10. Chung BG, Lin F, Jeon NL (2006) A microfluidic multi-injector for gradient generation. Lab Chip 6:764–768

Condensation in Microchannels

PING CHENG , XIAOJUN QUAN , HUIYING WU
School of Mechanical and Power Engineering, Shanghai Jiaotong University, Shanghai, China
pingcheng@sjtu.edu.cn

Synonyms

Phase-change heat transfer in microchannels

Definition

Condensation is a heat transfer process in which vapor is cooled below its saturation temperature while it undergoes a change of phase from vapor to liquid.

Overview

Recently, condensation in microchannels having cross-sectional areas of different shapes, such as circular, triangular, square, trapezoidal, and rectangular, has received a great deal of attention because of its important application to micro heat exchangers [1, 2]. It has been found that mist flow, annular flow, injection flow, plug/slug flow, and bubbly flow may occur in different locations in a microchannel, depending on the local vapor quality and mass flux. Injection flow occurs where the shearing force is overcome by the surface tension force. The occurrence frequency of injection flow depends on the condensation heat transfer rate, the mass flux of vapor, and the cross-sectional shape of microchannels. At the same mass flux, it has been found that the average condensation heat transfer coefficient in microchannels is higher than that in a minichannel due to the thinning of the liquid film [3].

Microchannel Classification

Based on the analytical results of Li and Wang [4] on gravitational effects on condensation in channels, Cheng and Wu [2] proposed the classification of condensation heat transfer in channels according to the Bond number which is defined as

$$\mathrm{Bo} = \left(\frac{D_\mathrm{h}}{\ell_\mathrm{c}}\right)^2 = \frac{g\,(\rho_\mathrm{l} - \rho_\mathrm{v})\,D_\mathrm{h}^2}{\sigma} \quad (1)$$

where $\ell_\mathrm{c} = \left[\sigma/(\rho_\mathrm{l} - \rho_\mathrm{v})\,g\right]^{1/2}$ is the capillary length; D_h is the hydraulic diameter of the channel; g is the gravitational acceleration; σ is the surface tension; and ρ_l and ρ_v are density of the saturated liquid and the saturation vapor at a particular temperature (or pressure), respectively. Equation (1) shows that the Bond number is a ratio of the hydraulic diameter to the capillary length, which is also a measure of the relative importance of the buoyancy force to surface tension force. Furthermore, Cheng and Wu proposed the classifications of microchannels, minichannels, and macrochannels as follows [2]:

- Microchannel: if $\mathrm{Bo} < 0.05$ where the gravity effect can be neglected.
- Minichannel: if $0.05 < \mathrm{Bo} < 3.0$ where the surface tension effect becomes dominant and the gravitational effect is small.
- Macrochannel: if $\mathrm{Bo} > 3.0$ where the surface tension is small in comparison with the gravitational force.

According to the above classification, a channel with its hydraulic diameter less than 490 μm (at 450 K) is considered to be a microchannel if water is used as a working medium.

Basic Methodology

Figure 1 shows the experimental setup for the study of condensation in a microchannel [5]. The deionized water in the water tank was pumped into the electric boiler where water was vaporized. Saturated steam from the boiler flowed successively through the valve, filter, and test section and was finally collected by a container at atmospheric pressure. Figure 2 shows the test section of the parallel microchannels etched in a silicon wafer, which was cooled by circulation of cooling water from the bottom of the wafer. Temperature and pressure of steam at the inlet and the condensate at the outlet were measured by thermocouples and pressure transducers, respectively. Wall temperature distribution along the bottom of the microchannels was measured by thermocouples embedded in the silicon wafer substrate. The microchannels were then covered with thin transparent Pyrex glass from the top. To visualize condensation flow patterns

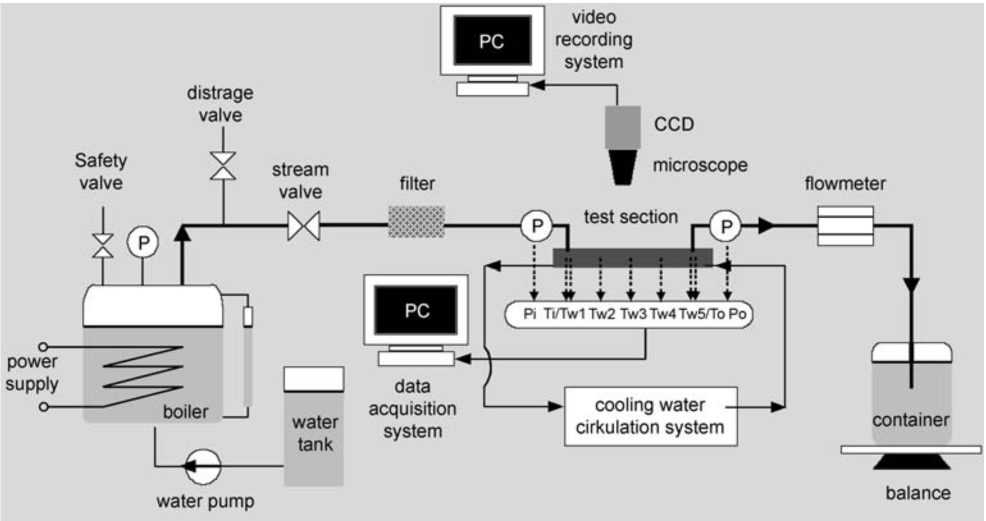

Condensation in Microchannels, Figure 1 Experimental system [5]

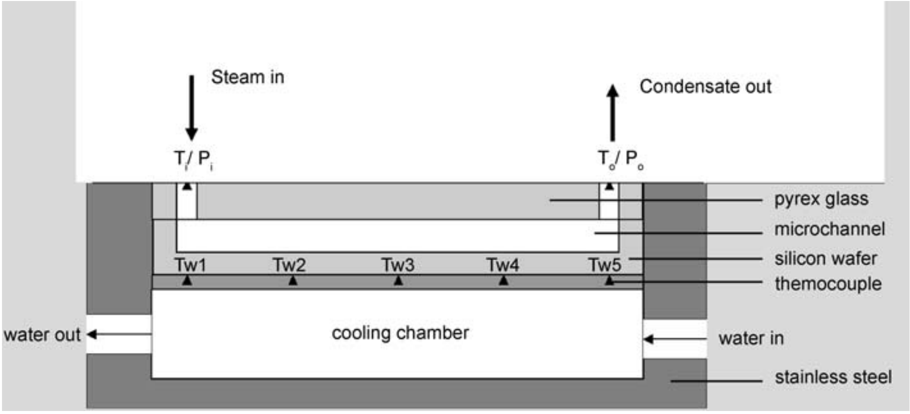

Condensation in Microchannels, Figure 2 Test section [5]

in the microchannels, a high-speed video recording system connected with a microscope was located above the microchannels (see Fig. 1).

Key Research Findings

Experimental Investigations

Flow Patterns and Transition Criteria

To study condensation flow patterns of refrigerant R134a in circular tubes and in *minichannels* having hydraulic diameters of 1 mm $< D_h <$ 5 mm, Garimella [6] used digitized frames of video and categorized four major flow regimes as annular, intermittent, wavy, and dispersed, which were further subdivided into 16 flow patterns. With decreasing hydraulic diameter ($D_h <$ 3 mm), it was found that (i) the overall range of the annular flow regime increases, (ii) the wavy regime decreases and thoroughly disappears at $D_h = 1$ mm, and (iii) the intermittent regime (plug/slug flow) increases. Wu and Cheng [5] carried out a series of simultaneous visualization and measurement experiments on saturated steam condensing in parallel silicon microchannels, having a trapezoidal cross-section with a hydraulic diameter of 83 μm and a length of 30 mm. Figure 3 shows that mist flow, annular flow, plug/slug flow, and bubbly flow occurred at different locations in the microchannel, depending on the local vapor quality. They observed for the first time the so-called "injection flow", which is a transition process from annular flow (where shearing force is predominant) to plug/slug flow (where the surface force is predominant).

C

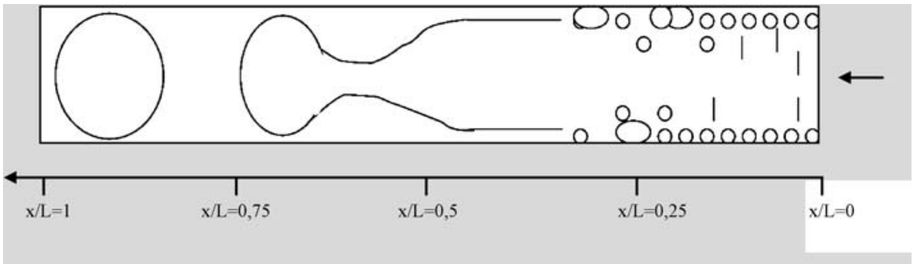

Condensation in Microchannels, Figure 3 Schematic of condensation flow pattern [5]

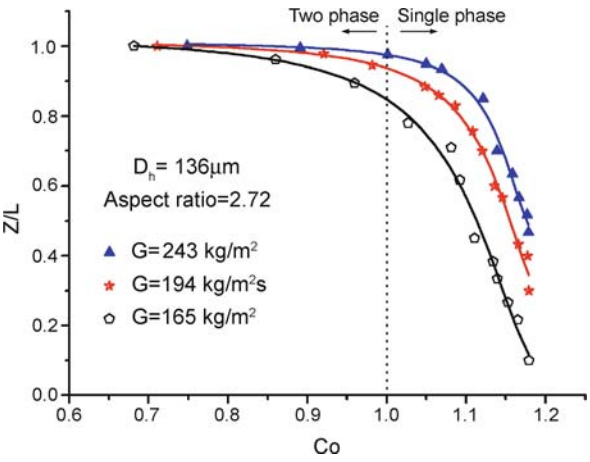

Condensation in Microchannels, Figure 4 Effects of mass flux on the dimensionless distance Z/L at different Co in microchannels having a hydraulic diameter of 136 μm [7]

Quan et al. [7] carried out further studies on the transition from annular flow to plug/slug flow in condensation of saturated steam in microchannels with trapezoidal cross-sections, having two different aspect ratios of 2.72 and 8 (where the aspect ratio is defined as the microchannel top width to height ratio) and two different hydraulic diameters of 136 and 128 μm, both having a length of 60 mm. Figure 4 shows the location of the dimensionless distance Z/L (with L being the length of the microchannel) along the microchannel (with $D_h = 136$ μm and aspect ratio $A = 2.72$) where the transition takes place versus the condensation number Co at three different mass fluxes of steam $G = 165$, 194, and 243 kg/m^{2}s respectively. The condensation number, Co, is defined as

$$\mathrm{Co} = \frac{Q}{m_v h_{fg}} \tag{2}$$

where Q is the amount of condensation heat transfer rate in the microchannel, m_v is the mass rate of steam, and h_{fg} is the latent heat of vapor. Note that $Z/L = 0$ means that the microchannel is fully occupied by plug/slug flow and single-phase liquid while $Z/L = 1$ means that the microchannel is fully occupied by annular flow in the microchannels. It can be seen from Fig. 4 that (i) at a constant Co, Z/L increases with the increase in mass flux (G), indicating that the location of the breakup point of injection flow will move toward the outlet, i.e. the annular flow regime in microchannels will be expanded and the slug/bubbly flow regime will shrink as the value of G increases; (ii) at a constant G, Z/L increases with the decrease in the condensation number, indicating that injection flow occurs further downstream, and the annular flow regime is expanded; (iii) at $Z/L = 1$, Co increases with increasing G; and (iv) Co = 1 is the criterion whether two-phase flow or liquid phase exists at the outlet: Co < 1 means that two-phase flow exists at the outlet while Co > 1 means that steam is completely condensed at the outlet. It is seen from Fig. 4 that the transition from annular flow to plug/slug flow takes place further upstream in the microchannels as dimensionless Co increases, or as the mass flux decreases. A flow pattern map in terms of heat transfer rate versus mass flux for condensation in microchannels having $D_h = 136$ μm and $A = 2.72$ is presented in Fig. 5, where the annular flow regime exists below the curve while the slug/bubbly flow regime exists above the curve. Figure 6 shows that the occurrence frequency of the injection flow in a microchannel (having $D_h = 128$ μm and $A = 8$) increases as the steam mass flux increases because of higher interface instability. At the same mass flux, it is shown that higher cooling rate leads to lower occurrence frequency because interfacial condensation tends to reduce instability.

Heat Transfer

Shin and Kim [3] carried out an experiment on condensation of R134a in single circular tubes ($D_h = 493$, 691, 1067 μm) and in mini-/microchannels having rectangular cross-sections ($D_h = 494$, 658, 972 μm) with mass flux in the range of $100 < G < 600$ kg/m^{2}s. It was

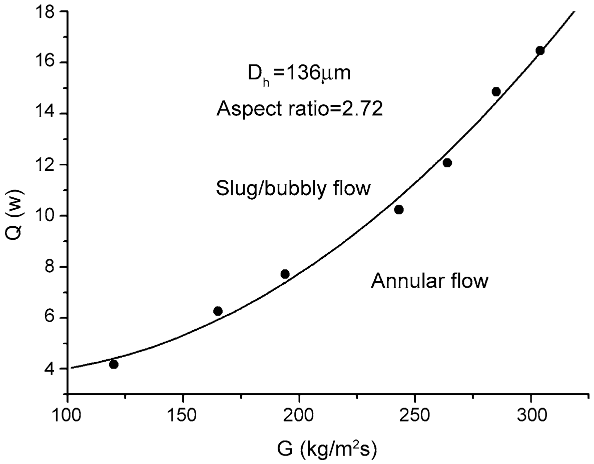

Condensation in Microchannels, Figure 5 Flow patterns of annular flow and slug/bubbly flow in a microchannel [7]

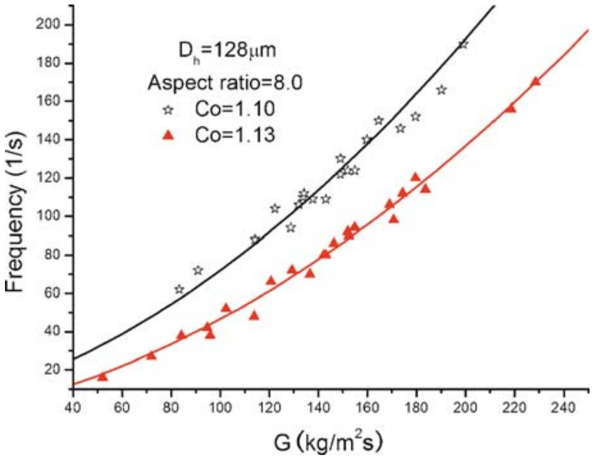

Condensation in Microchannels, Figure 6 The effects of mass flux on occurrence frequency of injection flow at different cooling rates [7]

reported that the heat transfer coefficient was independent of the heat flux and the values of the Nusselt number increased with the vapor quality. Also, it was found that Nusslet numbers at low mass fluxes ($G \leq 200\,\text{kg/m}^2\text{s}$) were higher than existing correlations for condensation in macrochannels (Fig. 7a) whereas those at high mass fluxes ($G = 400\,\text{kg/m}^2\text{s}$, for example) agreed well with some existing correlations (Fig. 7b). The average condensation heat transfer coefficient of a microchannel was found to be higher than that of a minichannel at the same mass flux. Also, it was found that the condensation heat transfer coefficients for channels with rectangular cross-sections at low mass fluxes were slightly higher than those for circular shape, and the whole situation would reverse at high mass fluxes of the refrigerant.

Pressure Drop

Shin and Kim [8] obtained pressure drop measurements for condensation flow of R134a in a microtube having a hydraulic diameter of 691 µm. Figure 8 shows a comparison of their pressure drop measurements with available correlation equations for macrochannels. Figure 8a shows that the pressure drop in condensation flow at low mass flux ($G \leq 200\,\text{kg/m}^2\text{s}$) in a microchannel is lower than that predicted by Friedel's correlation for macrotubes [9]. At higher mass fluxes ($G = 400\,\text{kg/m}^2\text{s}$, for example), however, their pressure drop measurements for condensation flow in a microchannel can be predicted well by Friedel's correlation, as shown in Fig. 8b.

Theoretical Studies

Teng et al. [10] investigated the effects of surface tension and shear force on interface instability of condensate film that resulted in a capillary bubbly flow. They pointed out that the surface tension effect on film instability depended on the wavenumber: surface tension stabilizes the interface if the dimensionless wavenumber is greater than 1; otherwise, it has a destabilizing effect. In contrast, the shear force always has a destabilizing effect on film instability.

Tabatabai and Faghri [11] put forward a new flow map to emphasize the importance of surface tension in condensation flow including annular, slug, plug, and bubble flow patterns in horizontal mini-/microtubes ($D_h < 4\,\text{mm}$). They noticed that the interface instability could result in ripple formation on the liquid surface, leading to the formation of collars that grow to form a bridge to establish slug, plug, and bubble flow regimes. However, in a macrotube, due to high gravitational pull on the liquid film, the bridge was not formed.

An analysis of droplet condensation heat transfer in a microchannel was carried out by Chen and Cheng [12], who found that droplet condensation heat flux increased as the hydraulic diameter decreased. Taking into account effects of surface tension (σ), interfacial shear stress (τ), and gravity (g) and assuming laminar condensate flow, Wang and Rose [13] presented a theoretical model to predict film condensation heat transfer for vapor flowing in horizontal noncircular micro-/minichannels. When the model is applied to channel sizes (side of square or triangle) in the range 0.5 – 5 mm and for refrigerants R134a, R22, and R410A, the results show that the initial enhancement is higher in smaller channels but falls off after a shorter distance along the channel; higher mass velocities result in increased length of enhanced heat transfer. Heat transfer coefficients of R22 and R134a are almost the same whereas those of R410A are somewhat smaller.

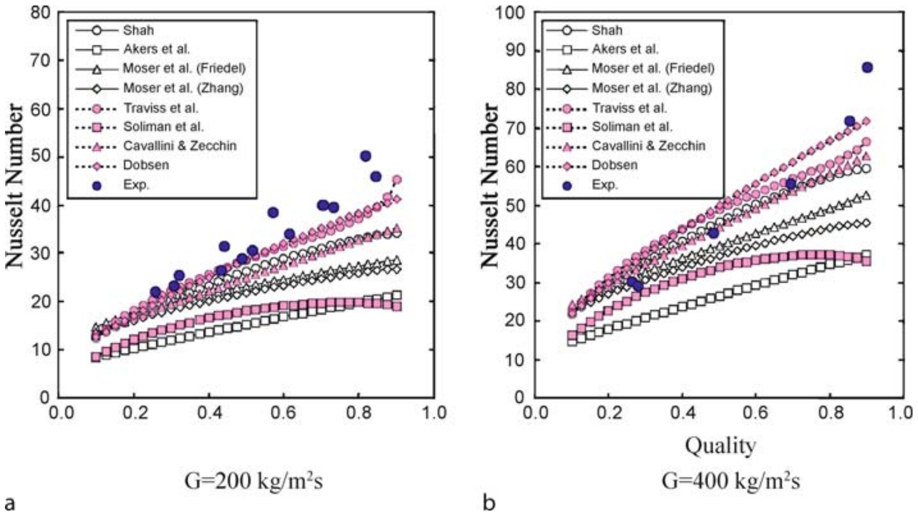

Condensation in Microchannels, Figure 7 Nusselt number versus quality at different mass fluxes for a microchannel having a hydraulic diameter of 493 μm [3]

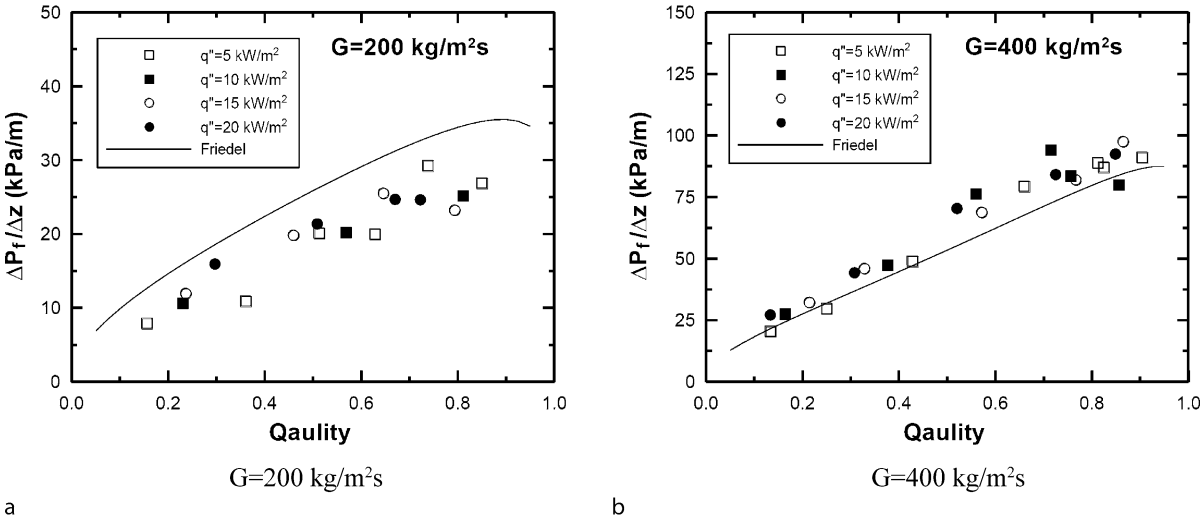

Condensation in Microchannels, Figure 8 Comparison of pressure drop for condensation in microchannels with existing correlations for condensation in macrochannels [8]

Figure 9 shows the profile of film thickness along the circumference of the triangular cross-section of the channel, where b is the side length of the channel, T_S is the vapor saturation temperature, ΔT is the temperature difference between vapor and channel wall, and G is the mass flux. It is shown that the film is substantially thicker at the corners of the triangular channel (at $x = 0$ mm, 1 mm). At the inlet, the thinnest film occurs near the corners. This location moves towards the center of the wall (at $x = 0.5$ mm) downstream. Figure 10 shows the local heat transfer coefficient along the circumference of the triangular cross-section of the channel. It is shown that low values of the heat transfer coefficient occur where the film is thick and high values occur where the film is thin. The maximum heat transfer coefficient becomes smaller, and its location moves towards the center of the sides, downstream along the channel. At the same time, the average heat transfer coefficient decreases because of the increase of liquid film thickness, as shown in Fig. 11. In the entry region of the channel, the heat transfer coefficient is higher for smaller channels because of the surface tension enhancement effect. However, the heat transfer coefficient becomes lower for smaller channels further along the channel because the meniscus zone increases more rapidly.

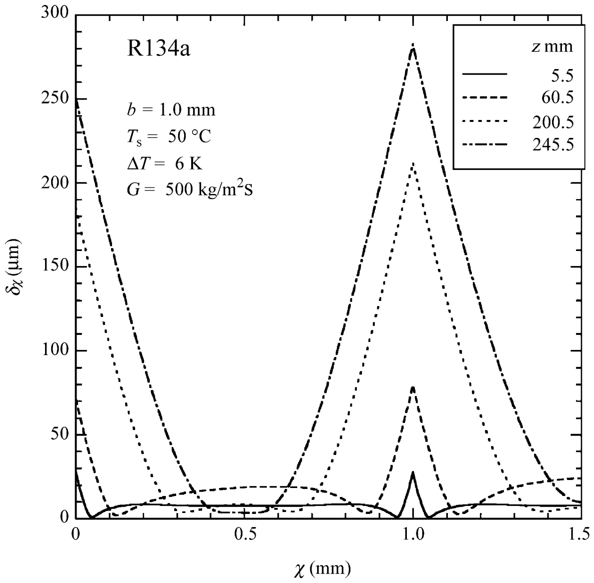

Condensation in Microchannels, Figure 9 Film thickness along sides of a triangular microchannel [13]

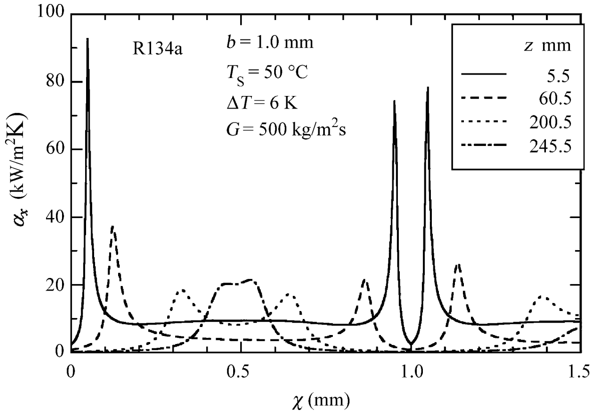

Condensation in Microchannels, Figure 10 Heat transfer coefficient along sides of a triangular microchannel [13]

Future Directions for Research

Although some experimental work has recently been carried out to study condensation flow patterns, and transition from annular to plug/slug flow in microchannels, the basic mechanisms of two-phase instability in condensing flow in microchannels are still not well understood. More experimental work is needed to investigate pressure drop and heat transfer characteristics in condensation in microchannels. Furthermore, the effects of hydrophilic and hydrophobic surface properties on condensation heat transfer in microchannels remain to be investigated experimentally. Improved experimental techniques, using integrated temperatures and pressure transducers for temperature and pressure drop measurements in condensing flow in microchannels are needed. Numerical simulations have yet to be carried out to study condensation flow patterns from mist flow, annular flow, injection flow, plug/slug flow to bubbly flow along microchannels.

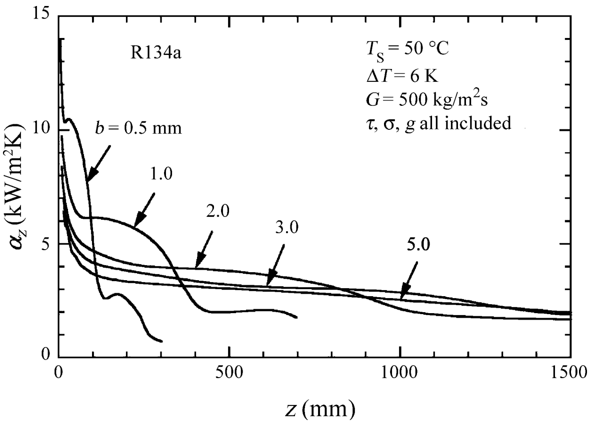

Condensation in Microchannels, Figure 11 Effect of sizes of hydraulic diameter on the cross-sectional averaged heat transfer coefficient [13]

Cross References

- ► Injection Flow
- ► Bubble Dynamics in Microchannels
- ► Microchannel

References

1. Mehendal SS, Jacobi AM, Shah RK (2000) Fluid flow and heat transfer at micro- and meso-scales with application to heat exchanger design. Appl Mech Rev 53(7):175–193
2. Cheng P, Wu HY (2006) Mesoscale and Microscale Phase-Change Heat Transfer. Adv Heat Transf 39:469–573
3. Shin JS, Kim MH (2005) An Experimental Study of Flow Condensation Heat Transfer inside Circular and Rectangular Mini-Channels. Heat Transf Eng 26(2):36–44
4. Li JM, Wang BX (2003) Size effect on two-phase regime for condensation in micro/mini tubes. Heat Transf Asian Res 32:65–71
5. Wu HY, Cheng P (2005) Condensation flow patterns in silicon microchannels. Int J Heat Mass Transf 48:2186–2197
6. Garimella S (2004) Condensation flow mechanisms in microchannels: basis for pressure drop and heat transfer models. Heat Transf Eng 25:104–116
7. Quan XJ, Cheng P, Wu HY (2007) Transition from Annular to Plug/Slug Flow in Condensation in Microchannels. Int J Heat Mass Transf (in press)
8. Shin JS, Kim MH (2004) An Experimental Study of Condensation Heat Transfer inside a Mini-Channel with a New Measurement Technique. Int J Multiph Flow 30:311–325
9. Friedel L (1979) Improved friction pressure drop correlation for horizontal and vertical two-phase pipe flow. European two-phase flow group meeting, paper No 2. Ispra

10. Teng H, Cheng P, Zhao TS (1999) Instability of condensation film and capillary blocking in small-diameter-thermosyphon condensers. Int J Heat Mass Transf 42:3071–3083
11. Tabatabai A, Faghri A (2001) A New Two-Phase Flow Map and Transition Boundary Accounting for Surface Tension Effects in Horizontal Miniature and Micro Tubes. Trans ASME 123:958–968
12. Chen YP, Cheng P (2005) Condensation of steam in a silicon microchannel. Int Comm Heat Mass Transf 32:175–183
13. Wang HS, Rose JW (2005) A theory of film condensation in horizontal noncircular section microchannels. J Heat Transf 127:1096–1105

Conductivity Detection

► Electrochemical Techniques

Confined Bubble Growth

► Bubble Dynamics in Microchannels

Confocal Microscope

Definition

A confocal microscope is a special kind of a microscope where the optical elements are arranged in such a way that the out-of-focus light is obstructed and only the light coming from the focal plane is used for the image. As a result, it is possible to obtain thin optical sections without physically damaging the specimen. These thin optical slices can be digitally processed to construct a 3D image of the specimen. Confocal microscopes are widely used in biological applications to observe processes inside living cells.

Confocal Microscopy, Detection

Adrienne R. Minerick[1], Giselle Thibaudeau[2]
[1] Dave C. Swalm School of Chemical Engineering, Mississippi State University, Mississippi State, MS, USA
[2] Electron Microscopy Center, Mississippi State University, Mississippi State, MS, USA
minerick@che.msstate.edu,
giselle@emcenter.msstate.edu

Synonyms

Laser scanning confocal microscopy (LSCM); Spinning-disk confocal microscopy

Definition

Confocal microscopy is a form of light microscopy that allows for high contrast imaging, and three-dimensional reconstruction. A confocal microscope employs laser excitation sources focused through pinhole(s) to excite fluorophores in a thin plane of a sample while rejecting out-of-focus light. The result is increased contrast and selective imaging at relatively high resolution across a wide range of wavelengths. Major advantages of confocal microscopy over conventional light microscopy include the availability of laser light sources in a broad range of wavelengths, the shallow depth of field, elimination of out-of-focus flare generated by fluorescence, noninvasive (optical) sectioning ability from relatively thick sections, and marginal improvement in axial and lateral resolution. With regards to micro- and nanofluidics, many of the current detection schemes utilized in fluidic devices would not be possible without confocal microscopy techniques.

Overview

The principle of confocal imaging was patented by Marvin Minsky in 1957 and is employed, at least in part, in modern confocal microscopes. The confocal microscope uses a laser light source, combined with sensitive photomultiplier tubes (PMTs) and scanning mirrors, all computer controlled to facilitate image acquisition, display, digital storage, and analysis. A confocal microscope uses point-by-point illumination within one fine focal plane and eliminates out-of-focus information, resulting in image quality that is significantly better than that of conventional (wide-field) microscopes. It is important to note that while confocal microscopy affords improved resolution of samples, it is still a form of light microscopy and is therefore limited by the wavelength of light. The resolution achieved by confocal microscopy is collectively determined by the individual specimen properties, the wavelength of light, and the objective lens being used. The fundamental optics of light microscopes, including the confocal microscope, have remained unchanged since the 1950s. What have improved significantly are other technologies associated with microscopy and the molecular labels (dyes) used to tag molecules, structures, and/or cells of interest.

The most useful molecular labels for confocal applications are fluorescent dyes. These molecules absorb light at a higher energy (shorter wavelengths) and emit light at a lower energy (longer wavelengths). The energy lost between absorption and emission is due to thermal, vibrational energy internal to the molecule. This phenomenon is particularly useful in confocal microscopy because one can attach one color fluorophore to a specific portion of the sample, a second color fluorophore to another portion of

the sample, and so forth, to gain spatial and higher quality resolution of sample characteristics.

Confocal microscopy can be a valuable tool for studies involving microfluidics, but poses significant limitations for nanofluidics. Because the resolution obtained with any sample is limited, fluorescent emission amplifiers will be required to improve the resolution to the degree needed for confocal microscopy at the nanoscale. The best horizontal resolution typically attained via confocal microscopy is approximately 0.2 μm, while the best vertically resolution is 0.5 μm [1]. This entry of the encyclopedia focuses on fluorescence detection using confocal microscopy as adapted for micro-/nanofluidics research.

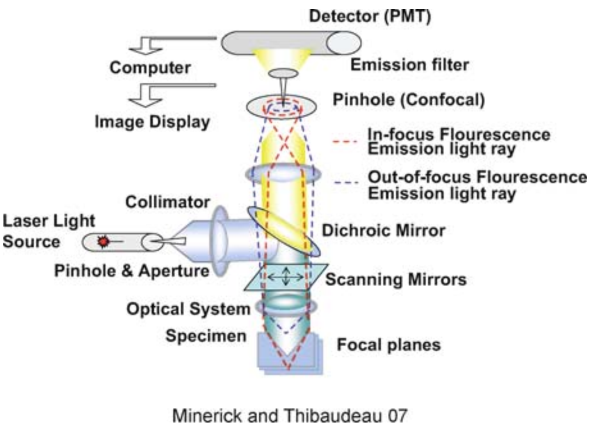

Confocal Microscopy, Detection, Figure 1 Schematic representing the optical pathway and image information flow of the laser scanning confocal microscopy (LSCM) technique. All principle components of generic LSCM are labeled. (Redrawn in part from Carl Zeiss *The Confocal Laser Scanning Microscope*)

Basic Methodology

This section is broken into two main parts. The first outlines the basic methodologies and techniques available with confocal microscopes (laser scanning confocal microscopy or LSCM). The second describes the adaptation of these technologies to a variety of microscale imaging devices involving everything from single cells to single molecules.

When the light source is transmitted through the sample and light is collected via an objective on the other side of the sample, this is known as trans-fluorescence. At times, it is advantageous to use the objective to not only deliver the excitation light, but to also collect emission light from a fluorophore. This is known as epi-fluorescence, and due to the expense of equipment, this technique is more common. A dichroic (dichromatic) mirror is used to separate the excitation light from the emission light, in order to reflect the excitation light and to pass light of wavelength longer than the excitation wavelength (emitted light) to a detector.

The basic optical pathway for the confocal microscope is shown in Fig. 1. This schematic diagram represents the optical pathway and image information flow of LSCM. All principle components of a generic LSCM system are labeled.

Light is focused through a pinhole in order to create a point source of light (or more appropriately, an Airy disk of light), which is then refocused down onto the sample with a lens. Recall that information does not have to be exactly at the focal point of an optical lens for the lens to transmit the light information. Therefore, it is necessary to utilize a second pinhole just before the detector in order to exclude light information that is not exactly at the focal point. Hence the name confocal has been used to describe this microscopy technique.

This exclusion of out-of-focus information gives confocal microscopy a distinct advantage over regular fluorescence microscopy. The surrounding sample is not uniformly illuminated, so widely scattered background fluorescence is minimized. Further, fluorescent light emitted from sample regions just outside of the point of focus are filtered through use of the pinhole in front of the detector.

One of the limitations created by focusing through a pinhole and rejecting out-of-focus light however is that there are fewer emitted photons to collect at any given time, resulting in the need for long collection times. One solution, the one used for confocal microscopes, is to use a laser light source, which adds the benefit of delivering a large number of photons in a dense stream of light and is available in a wide range of wavelengths (Table 1).

In order to reconstruct an image of a large area from information at single points, two main methods are used to scan the region of interest:

- fixed beam with sample stage moving to enable scanning in the *xy* plane; and
- fixed sample stage with the illuminated beam moved to scan in the *xy* plane.

Biological confocal microscopes have moved away from scanning the sample stage. However, with micro-/nanofluidic devices, scanning the stage has once again become a popular methodology because precise *xy* coordinates can be used to track to sample chambers or channel locations.

Within the class of techniques involving scanning the illumination beam, single or multiple beam scanning can be used. Single beam scanning involves controlling a single beam with computer-controlled mirrors or utilizing oscillating mirrors (also known as acousto-optical deflectors). Either way, a single beam is precisely directed in an *xy*

Confocal Microscopy, Detection, Table 1 Laser and comparable wavelengths (nm) available for widefield and confocal microscopy [2]

Laser Type	UV	Violet	Blue	Green	Yellow	Orange	Red
Argon Ion	351, 364	–	457, 477, 488	514	–	–	–
Blue Diode	–	405, 440	–	–	–	–	–
Diode-Pumped Solid State	355	430, 442	457, 473	532	561	–	–
Helium–Cadmium	322, 354	442	–	–	–	–	–
Krypton–Argon	–	–	488	–	568	–	647
Green Helium–Neon	–	–	–	543	–	–	–
Yellow Helium–Neon	–	–	–	–	594	–	–
Orange Helium–Neon	–	–	–	–	–	612	–
Red Helium–Neon	–	–	–	–	–	–	633
Red Diode	–	–	–	–	–	–	635, 650
Mercury Arc	365	405, 436	546	–	579	–	–
Xenon Arc	–	467	–	–	–	–	–

plane of the sample. This is relatively slow and in order to speed up the process to near real time, multiple beam scanning can be used. The most common method utilized is to direct a spread laser beam over a microlens array in the shape of a Nipkow disk (also termed spinning disk) to create multiple focused beams of light. A corresponding Nipkow disk perfectly aligned with the first can be used to create focal points of the multiple beams of light, which are all simultaneously focused onto the sample. Epi-fluorescent detection can occur by using the same objective and a dichroic mirror leading to a detector (i. e. a photomultiplier tube). This detector feeds information to a computer, which reconstructs the image, one pixel at a time [1].

The focused laser beam not only enhances the clarity of light information in the *xy* plane, but also can section through a sample in the *z*-direction. By scanning sections at increasing heights in a sample, it is possible to stack the two-dimensional images into a three-dimensional reconstruction of the sample. Therefore, confocal microscopy has gained popularity because three-dimensional renditions of cells or even microchannels can be created. Further, particle tracking in three dimensions has led to interesting particle velocity measurements. The main concepts involved in confocal microscopy have been adapted and permutated for a variety of microscope applications. A number of common types of specialized confocal microscopy are outlined here.

Two-Photon Excited Fluorescence or Two-Photon Confocal Microscopy

This method has the advantage that it increases the signal-to-noise ratio and the resulting image quality is much improved. This technique is similar to LSCM minus the need for pinholes. A mode-locked titanium:sapphire laser generates light in the near infrared. The laser is pulsed at a frequency about twice that of the absorption wavelength of the sample. This is done so that only a couple of photons hit at a single point of the sample to produce an emission signal. This is possible because the precise optics ensure that the energy from the photons occurs only in the plane of focus [3]. Sample penetration is increased with the greater laser power and out-of-focus photobleaching is avoided with this technique.

Near-Field Scanning Optical Microscopy

Near-field scanning optical microscopy (NSOM) is a type of microscopy where a sub-wavelength light source is used as a scanning probe. This fiber optic probe is coated with metal except for a small region at the tapered fiber tip and is used to deliver light to precise locations of the sample. Fluorescent photons emitted by the sample are collected by the same fiber optic. This is possible because fluorophores always emit light at a longer wavelength and the two wavelengths of light are able to propagate independently within the fiber optic. The tip is then rastered across the sample surface via the same mechanism as in atomic force microscopy (AFM) and a fluorescent image of the surface is digitally compiled. NSOM fiber optics require high-power lasers due to the loss of energy at all stages of the process. However, this tool can obtain resolutions well beyond the usual “diffraction limit” down to about 50 nm. Some examples of the uses of NSOM in the literature include its use in the field of magneto-optics and to investigate polymer blends and composites.

Pseudo-Confocal Technology (Deconvolution)

The Zeiss ApoTome is a less expensive alternative to confocal microscopy and can be added as an attachment to

motorized fluorescent microscopes. This technique uses a rapidly sliding grid (which cannot be seen in observed images) and a computer algorithm to subtract light that is bouncing off of structures outside of the focal plane. Image quality is greater than traditional light microscopy, but not as clear or rapid as confocal laser scanning microscopy.

Fluorescence Correlation Spectroscopy (FCS)

FCS is a type of spectroscopy that is based on the measurement of fluorescence intensity and the analysis of its fluctuations, which result from diffusion of the observed fluorophore in the excitation volume or changes in the fluorescence quantum yield arising from chemical reactions. Measurements are usually made on only a few molecules at a time, of the order of 10 ms. This is achieved by illuminating tiny volumes (~1 femtoliter) by employing two-photon excitation microscopy or confocal microscopy. FCS is used to measure translational diffusion coefficients of macromolecules, the number of fluorescent molecules under observation, and the relative fluorescence yield of different molecules in a (inhomogeneous) solution, which gives the amount of each species.

Fluorescence Recovery After Photobleaching (FRAP)

FRAP is an optical technique capable of quantifying the two-dimensional lateral diffusion of a molecularly thin film containing fluorescently labeled probes. The sample is first exposed to a very high energy laser beam which destroys fluorophores in that region. New, undamaged fluorophores then begin diffusing into that region and are imaged. This technique provides great utility in biological studies of cell membrane diffusion and protein binding. In addition, surface deposition of a fluorescing phospholipid bilayer (or monolayer) allows the characterization of hydrophilic or surfaces in terms of surface structure and free energy.

Total Internal Reflection Fluorescence (TIRF) Microscopy

TIRF microscopy is one of the more complicated techniques for more advanced users of fluorescence microscopy. In order to obtain fluorescent information about a very small feature, this technique uses decaying evanescent waves to probe a focal volume below the diffraction limit of light.

Programmable Array Microscopy

One step of sophistication above the multibeam scanning in confocal microscopy is the programmable array microscopy (PAM) technique, which uses a spatial light modulator (SLM) to generate a pattern of conjugated illumination and detection elements. The advantages of PAM include the ability to generate full-scale images rapidly. In addition, it can be combined with fluorescent quantification techniques such as fluorescence lifetime imaging, Forster resonance energy transfer (FRET), and other photoreactions.

Confocal Infrared (IR) Laser Microscopy

Confocal IR laser microscopy is very useful for the microelectronics industry because IR light is at ~1300 nm, which passes through silicon wafers (and other inorganic substrates). Further, the confocal technique reduces light flare and other image-enhancing behaviors. Given that many micro- and nanofluidic devices utilize silicon-derived fabrication techniques, confocal IR laser microscopy will likely gain popularity [4].

Adaptation of Confocal Techniques for Microdevice Applications

The largest challenge in adapting micro- or nanofluidic devices for confocal detection is in designing the device for thin sample cross-sections. Many fabrication techniques utilize thick sheets of poly(methyl methacrylate) (PMMA) or polydimethylsiloxane (PDMS) annealed to microscope slides or additional sheets of optically amenable polymers. However, the working distance of many confocal objectives is quite short and requires a maximum thickness of a 0.01 coverslip between the objective and the sample of interest. Laser light sources improve this, but the challenge still exists. A large number of novel and exciting fluidic schemes exist to enable mixing and the in situ tagging of specific molecules for fluorescent applications.

Key Research Findings

Even though the concept of confocal microscopy was invented and patented by M. Minsky in the 1950s, it took until the 1980s for technology to progress to the point where confocal microscopy was a widely used tool. A comprehensive summary of the historical progression of confocal video microscopy is available elsewhere [5]. Further, the 1990s saw an explosion in microfluidics built upon the technology developed for computer microchips. The integration of these areas is a natural extension from their foundations. The following discussion is a brief highlight of the current state of confocal microscopy in micro- and nanofluidics.

By nature, fluidics at small length scales transports a small number of cells or analytes of interest. Therefore, it is necessary for optical detection technology to be sensitive enough to detect these small numbers of cells or analytes. The current phase of research is seeing exciting results in accomplishing this very goal. LSCM coupled with poly-

merization techniques and microchannel device fabrication has been used to detect and analyze electrophoretic migration of DNA in three dimensions [6]. Such studies will enable the more efficient design of polymerization and detection systems for both biological and non-biological materials.

Just as LSCM became very useful for biologists requiring real-time monitoring of cell processes in three spatial dimensions, laser confocal microscopy has become a very popular solution for many micro- and nanofluidics researchers working to detect single cells and single molecules flowing past a fixed location (i. e. at the end of a separation channel). On the single cell detection front, recent work with single-cell time-correlated single-photon counting (scTCSPC) has enabled the recognition for cell sorting purposes of single-cell populations of green, cyano, and yellow fluorescent protein-tagged E. coli cells. This ultrahigh-sensitivity detection is accomplished via confocal focusing of light across a microchannel [7].

Moving to smaller scales, fluorescent confocal microscopy has been used to detect and count individual protein molecules in a cell within the construct of a PDMS microfluidic chip. The confocal laser beam was modified and focused to span the width of the microfluidic channel. The setup detects approximately 60% of the molecules flowing down the microchannel [8].

The challenge then becomes having a photomultiplier tube that can detect and amplify fewer and fewer photons of light for separate events. Technological advances in the area of nanolenses may be the answer to this challenge. For example, nanofabricated structures of 10 – 100 nm are now being utilized to allow for single-molecule experiments [9].

Future Directions for Research

Technological advances continue to equip life and materials scientists with the capability to probe the detailed nature of materials (biological and non-biological) at an ever-decreasing scale and have led to a great deal of excitement in new areas of research (e. g. nanoscience and nanotechnology). Given the well-known limitations of light microscopy, one might be hesitant to consider confocal microscopy a technology of the future. However, advances in optical collection techniques and fluorescent probe technologies have allowed significant progress in detection using confocal microscopy. Progress has been twofold: amplification (magnification) of the light emitted (captured) and/or amplification of the fluorescence signal to be detected.

Plasmon-based superlens [10] and/or hyperlens refract light in unconventional ways to allow the optics of a light microscope to see beyond the normal limit, i. e. magnify light and prevent the loss of so much information in the sub-wavelength features.

The ability to detect smaller and smaller amounts of analytes (small and large molecules alike) is needed in order to increase the sensitivity of Lab-on-a-Chip devices. One of the challenges with low concentration fluorescence is delivering enough light energy to a sample to then have enough light emitted that it is possible to collect a measurable amount with a given uni-directional detector. Therefore, at very low concentrations, amplification of single photons of light will need to be accomplished. Advances in the speed of spatial scanning will enable more applications. However, imaging at a single point along the time dimension will enable continuous screening in micro- and nanochannels as process streams flow past the detectors.

Key advances in this area will continue to be in the development of specialized microscopes utilizing combinations of the optical techniques discussed here. Increasing the reliability and reproducibility of such systems is important. Once developed, engineering systems for widespread use as (a) laboratory-scale commercial units and (b) microscale for portable Lab-on-a-Chip units will need to occur.

To fully integrate the confocal concept with portable, stand-alone micro-/nanodevices, inexpensive, yet functionally equivalent miniature microscopes are required. Diode lasers, microlenses, pinhole structures, and PMT detectors must be reliably fabricated, then aligned with precise focal lengths and pinhole apertures to focus directly into micro-/nanochannels or chambers. The task seems daunting, but the idea of seamlessly integrating all of these technological leaps in fluorescent microscopy is exciting!

Cross References

- ► Cell-Based Assays Using Microfluidics
- ► Detection Using Near Field Microscopy
- ► Detection Using TIRF Microscopy
- ► Lab-on-a-Chip (General Philosophy)
- ► Methods for Flow Rate Measurements
- ► Microchannel
- ► Nanofluidic Systems for Single Molecule Detection
- ► Optofluidics – Applications
- ► Single Cell Analysis in Microfluidics

References

1. Semwogerere D, Weeks ER (2005) Confocal Microscopy. Encyclopedia of Biomaterials and Biomedical Engineering. Taylor & Francis, London

2. Claxton, NS, Fellers, TJ, and Davidson, MW Laser Scanning Confocal Microscopy. http://www.olympusfluoview.com/theory/LSCMIntro.pdf. Accessed May 2007
3. Matsumoto B (ed) (2002) Cell Biological Applications of Confocal Microscopy, 2nd edn. Academic Press, San Diego
4. Rideout D (2007) Non-destructive Microelectronics Inspection. Micro Nano 12(2):1–6
5. Pawley JB (ed) (2006) Handbook of Biological Confocal Microscopy, 3rd edn. Springer, New York
6. Chen Z, Burke DT, Burns MA (2006) Confocal Laser Scanning Microscopy of DNA Electrophoresis in Microchannels. American Electrophoresis Society & American Institute of Chemical Engineers Annual Conference (Abstr)
7. Edel JB, Lahoud P, Cass AEG, de Mello AJ (2007) Discrimination between Single E. coli Cells using Time-Resolved Confocal Spectroscopy. J Phys Chem B 111:1129–1134
8. Huang B, Wu H, Bhaya D, Grossman A, Granier S, Kobilika BK, Zare RN (2007) Counting Low-copy Number Proteins in a Single Cell. Science 315:81–84
9. Mannion JT, Craighead HG (2006) Nanofluidic Structures for Single Biomolecule Fluorescent Detection. Biopolymers 85(2):131–143
10. Smolyaninov II, Hung YJ, Davis CC (2007) Magnifying Superlens in the Visible Frequency Range. Science 315:1699–1701

Constricted Flow Dimensions

Definition

Channel dimensions based on the constricted cross-sectional area caused by the presence of surface roughness.

Contact Line

Definition

The line formed by the liquid-vapor interface at the solid wall.

Cross References

► Bubble Dynamics in Microchannels

Contact Temperature Sensors

Synonyms

Temperature probes; Temperature sensors; Thermistors

Definition

Contact temperature sensors represent a class of temperature probes that are used to determine the temperature of a medium through the thermal equilibrium attained between the sensor and the medium when in contact. The change in the medium temperature is inferred from a corresponding variation in the sensor resistance or output voltage that can be used to obtain the temperature difference via an *a priori* calibration of the sensor output with temperature. The commonly implemented contact temperature sensors include thermocouples, resistance temperature detectors (RTDs) and thermistors.

Cross References

► Methods for Temperature Measurement
► Resistance Temperature Detectors
► Thermocouples

Continuous Model

► Transmission-Line Model

Contraphilic

Definition

The ability of a material to exhibit both hydrophilic and hydrophobic states dependent upon the material's environment.

Cross References

► Surface-Directed Capillary Flow Systems

Control

Definition

The use of decision algorithms and ►feedback in engineered systems to achieve desired performance. An autopilot is an example of feedback control, it uses decision algorithms and feedback to control the flight of an airplane. In this entry, the engineering systems are micro-fluidic systems.

Controlled-Potential Instrumentation

► Amperometric Techniques

Controlled System

Definition

A dynamical system that is controlled via feedback.

Control of Micro-Flows

► Control of Micro-Fluidics

Control of Micro-Fluidics

Benjamin Shapiro
Aerospace Engineering; joint appointments
with Bio-engineering, Institute of Systems Research;
affiliated with Applied Mathematics
and Scientific Computation program, University
of Maryland, College Park, MD, USA
benshap@eng.umd.edu

Synonyms

Control of micro-flows; Microfluidics; Closed-loop; Analysis/design; Sensing and actuation

Definition

►Control, or more fully ►feedback control, refers to using measurements from system sensors to decide what actions should be taken by system actuators to perform a system task. So sensing, algorithm decisions, and actuation are performed in feedback, in a closed-loop, in real time. Feedback is ubiquitous in biology and in complex engineering systems: sensing and correcting for errors enables systems to carry out high performance tasks in the presence of uncertainty and noise. The theory and practice of feedback control is a research area in its own right.

This entry discusses applications and extensions of feedback control as applied to micro-fluidic systems. Broadly speaking, feedback control has been developed for electronic systems and mechanical, fluid, and chemical systems on the macro-scale, but not for micro-fluidic systems.

Chemical and Physical Principles

The basic principle of feedback control is shown schematically below. A system is observed by sensors that produce measurements (y) at each time; these measurements are compared to the desired performance of the system (r); and the difference between the desired (r) and actual state (y) is used to create an error ($e = r - y$); a controller, usually implemented on a computer or via analog circuitry, operates on this error to decide which actuation actions (u) should be applied to the system to change its state from where it is to where it should be.

This feedback (y to e to u to y to ...) repeats at each time and, if the controller is successfully designed, drives the system dynamics to their desired performance. Sensing and correcting for errors fundamentally enables high performance and complex robust behavior in the face of uncertainty. This is familiar to those who study engineering and biological systems. Feedback regulatory mechanisms enable cells to correct for and carry out their functions even when their environmental conditions change dramatically [1]. In complex engineering systems, closed-loop behavior can track desired performance even if system dynamics are incompletely known, there are system uncertainties, and there is noise in the measurements and the actuation actions [2, 3].

An introduction to ►control theory; with sample applications in biological, electronic, quantum, information, mechanical and aerospace systems, and robotics; and a discussion of the modeling that is necessary for control algorithm design can be found in Astrom and Murray [2]. A more limited discussion of implementing control for systems well described by linear dynamics can be found in [4]. Modern and future high-impact applications for control theory are discussed in the report [5]. Directions for and challenges in control of micro- and nano-scale systems are reviewed in the March 2004 NSF report [6, 7], organized and directed by the author of this entry.

Control theory is well-developed for systems well-described by linear models (see, for example, Zhou [8]). (A linear model is, essentially, one in which doubling the inputs, the actuator actions, will double the outputs, the measurements.) All systems are nonlinear, but for small excursions about equilibria or prescribed trajectories, many systems can be linearized and effectively controlled using linear control techniques. For systems that cannot be approximated as linear, nonlinear control techniques [9] are available to varying degrees of success for sub-classes of systems: for Hamiltonian systems (e. g., [10]), for nonlinear systems that can be made linear by a clever choice of variable transformation (e. g., [11], chapter 10 in [12]), or other system sub-classes. Nonlinear control design has been motivated by systems that commonly appear in applications: these have traditionally been in electronic circuits and mechanical, fluid, and chemical systems on the macro-scale.

Fundamental principles for effective control of MEMS, including micro-fluidic systems, have not yet been established. In micro-fluidics, there is a need to control the

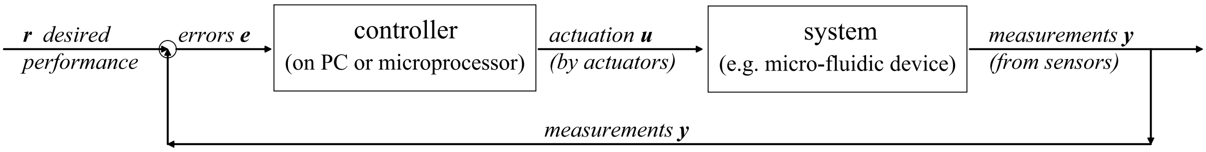

Control of Micro-Fluidics, Figure 1 A simple and classic feedback loop example. The system and controller are connected in a closed-loop by measurements $y(t)$, errors $e(t)$, and resulting actuator actions $u(t)$. At each time t, errors are continually corrected by the actuation actions to drive the system to its desired performance $r(t)$

motion of bulk flows usually actuated through physical effects at fluid boundaries. For example, electroosmotic and electrowetting bulk flows are actuated by an electric field acting on a thin electrical double layer and modulating the surface tension forces at the edges of the bulk liquid respectively. Such scenarios are best modeled by ►partial differential equations (PDEs) for the fluid bulk flow, with system specific models for the actuation effects on the fluid boundaries. Hence the control design question is control of PDEs through their boundary conditions – a mathematically technical and difficult problem. Further, there is a need to control the behavior, distributions, and interactions of objects (cells, DNA fragments) and chemicals inside micro-fluidic systems, both in the bulk and at surfaces. Chemical species are described by diffusion, convection, and reaction PDEs, but chemical species and discrete objects may be described by other means: by random walk equations superposed on the flow (for particles in a flow), by thermo/mechanical equations appropriate for DNA chains, or by adsorption/ desorption equations at surfaces. So the control question is control of PDEs, coupled to PDE or other equations that describe objects and chemicals inside the liquid, all actuated through the PDE boundary conditions.

There is a community of researchers that focus on control of PDEs, see for example [13], but they have been motivated by applications in macro-scale fluid dynamics and chemical processes, and although their research contains valuable insights and technical results, their methods cannot be directly applied to micro-fluidic systems.

Key Research Findings

The broad key finding can be simply summarized: there is no general micro-fluidic controls tool yet, instead it is necessary to phrase each application task as a tractable control-design mathematical question, to find an implement an answer, and then to validate this answer experimentally.

For example, splitting of droplets accurately in an electrowetting system or steering of cells by flow control, both systems tasks described in words, must be phrased as a mathematics control-design questions in-line with the feedback diagram of Fig. 1. This requires quantifying the actuation (electrowetting or elecroosmotic), choosing and describing the sensing (e. g., vision based sensing), modeling the physics of the system, and then phrasing and solving the control design question.

Specific research findings are described within the context of two sample applications next.

Examples of Application

Independently Steering Multiple Cells by Routine Electroosmotic Actuation and Feedback Control

Exploiting feedback control we can use electroosmotic actuation, which is routine and easy to implement in micro-fluidic devices, to steer cells – a task usually reserved for expensive, delicate, and large laser-tweezer systems. Our results in this area are described in [14–18] and the text below is adapted from these sources.

Our approach uses vision-based micro-flow control to steer particles by correcting for particle deviations – at each time we create a fluid flow to move the particles from where they are to where they should be. Figure 2 shows the basic control idea for a single particle: a micro-fluidic device, an optical observation system, and a computer with a control algorithm, are connected in a feedback loop. The vision system locates the position of the particle in real time, the computer then compares the current position of the particle with the desired (user input) particle position, the control algorithm computes the necessary actuator voltages that will create the electric field, or the fluid flow, that will carry the particle from where it is to where it should be, and these voltages are applied at electrodes in the micro-fluidic device. For example, if the particle is currently North/West of its desired location, then a South/East flow must be created. The process repeats at each time instant and forces the particle to follow the desired path.

Experimental steering of a bead along a figure ‘8’ path in a simple 4-channel PDMS device is shown in Fig. 3 (from [18]).

C

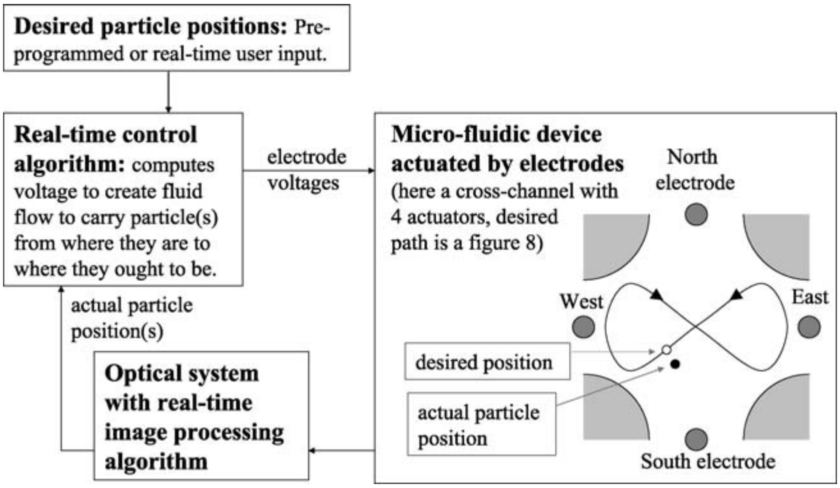

Control of Micro-Fluidics, Figure 2 Feedback control particle steering approach for a single particle. A micro-fluidic device with standard electroosmotic actuation is observed by a vision system that informs the control algorithm of the current particle position. The control algorithm compares the actual position against the desired position and finds the actuator voltages that will create a fluid flow, at the particle location, to steer the particles from where it is to where it should be. The process repeats continuously to steer the particle along its desired path

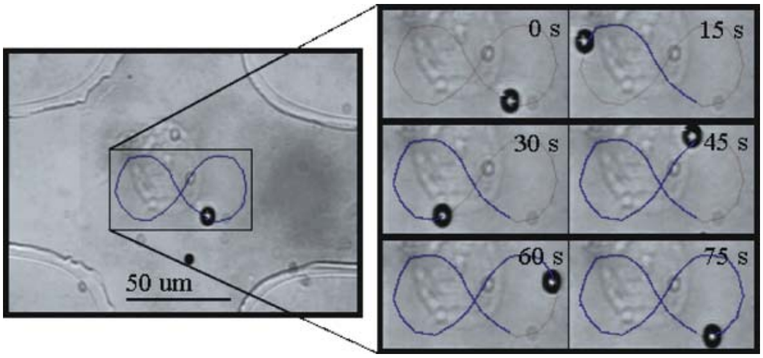

Control of Micro-Fluidics, Figure 3 Control of a bead with significant surface charge along a figure '8'. The bead has an approximate electrophoretic mobility of $c = (-57.3 \pm 5.6) \times 10^{-9} \mathrm{m}^2\mathrm{V}^{-1}\mathrm{s}^{-1}$. (By comparison, the electroosmotic mobility of our PDMS devices is $u = (36.5 \pm 3.6) \times 10^{-9} \mathrm{m}^2\mathrm{V}^{-1}\mathrm{s}^{-1}$.) Left: Photograph of the micro-fluidic devices with the figure '8' path super-imposed on the image. Right: The actual path of the chosen 5 μm polystyrene bead (Polysciences Inc.) (black circle) in the feedback control experiment. Snapshots are shown at 6 equally spaced times. The bead follows the required trajectory to within 3 μm

It is also possible to independently steer multiple particles at once. This requires a model of the electroosmotic actuation and fluid dynamics, and a more sophisticated control algorithm that essentially inverts the model at each moment: given desired velocities at each particle locations, it find the set of actuator voltages that will create a fluid flow that most nearly achieves those velocities. For an 8-channel device, where there are 7 fluid modes available for actuation (one of the electrodes acts as ground so only 7 degrees of freedom remain), different modes force particles at different locations in different directions. By intelligently actuating a combination of modes, we can force all the particles towards the right locations at each instant in time. Figure 4 shows steering of 3 yeast cells independently using such an 8-electrode PDMS device. It is also possible to trap all 3 cells, or to steer 1 or 2 while holding 2 or 1 cells stationary.

Modeling, control design, and experimental details are provided in [16, 18].

Control of Flows Driven by Electrically Actuated Surface Tension

In electrowetting-on-dielectric (EWOD) systems, the overall goal is precise and robust control of liquid motion. The following results are taken from [17, 19, 20].

In simulation, we have demonstrated the possibility of using the available electrodes in an EWOD system to actu-

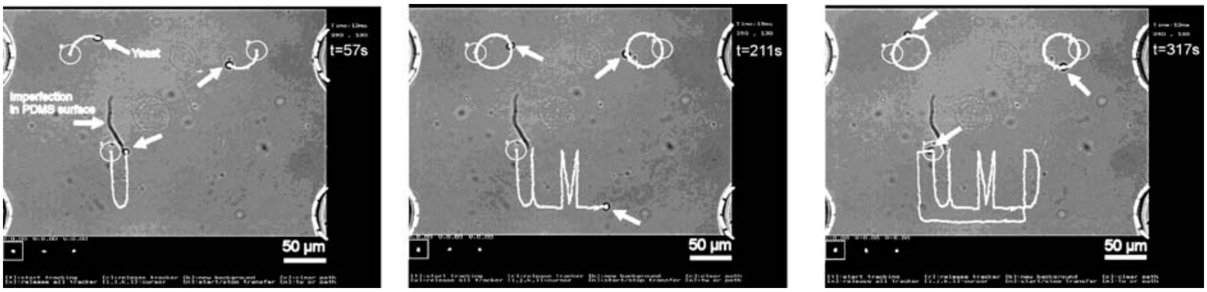

Control of Micro-Fluidics, Figure 4 Steering of 3 yeast cells (5 µm diameter, Red Star, Giant Food) with small surface charge (electrophoretic mobility $c = (-23.3 \pm 6.9)10^{-9}\ \mathrm{m^2V^{-1}s^{-1}}$) around two circles and a 'UMD' path (for 'University of Maryland'). The yeast cells are visible as small black dots with a white center (the three target cells are marked with a white arrow in each image), and the white curves are the trajectories that the target cells have traced out. The three beads are being steered to within an accuracy of one pixel (corresponding to less than 1 µm)

ate a single droplet in such a way that the resulting fluid flow inside the drop will carry a particle around a figure 8 path or carry two particles along separating trajectories. Steering particles inside droplets introduces another level of functionality into electro-wetting systems. For example, cells can be precisely placed over local sensors or moved from one location to another at rates much faster than those created by diffusion. In addition, particles can be sorted inside a droplet and then separated by controlled splitting of the droplet.

Our steering results are demonstrated using an experimentally validated numerical model [20] of droplet motion inside the UCLA electrowetting system [21, 22]. This model of EWOD fluid dynamics includes surface tension and electrowetting interface forces, viscous low Reynolds 2-phase fluid flow, and the essential loss mechanisms due to contact angle saturation, triple point line pinning, and the related mechanism of contact angle hysteresis.

The electrode voltages in an EWOD device directly influence the pressure gradient field inside a droplet which, in turn, controls the velocity field [20, 23, 24]. This allows us to steer multiple particles inside droplets by manipulating the fluid flow field through the voltages. Therefore, the control problem is to find an electrode voltage sequence that creates a temporally and spatially varying flow field that will carry all the particles along their desired trajectories.

However, the particle motion depends on the droplet shape and the number of electrodes that the droplet overlays at any given moment. Since this is not known a priori, we use local estimation and control at each time step of our simulation to compute the pressure boundary conditions needed to realize the desired flow field. At each instant in time, the control algorithm is provided with the droplet shape and particle locations, as would be available through a vision sensing system. Any deviation of the particles from their desired trajectories that may arise from thermal fluctuations, external disturbances, and actuation errors is corrected using feedback of the particle positions. We now give an overview of our algorithm.

1. *Initialization*: Represent the desired trajectory of each particle as a set of points connected by straight line segments.
2. *Sensing*: Feed back the particle position data and the location of the droplet boundary to the control algorithm (as would be provided by the vision sensing system).
3. *Control algorithm part A*: Choose the desired velocity directions of each particle so that the particles will move towards and then along the desired trajectories.
4. *Control algorithm part B*: Solve a least squares problem for the necessary voltage actuations to induce a pressure gradient field that will create a flow field that will carry the particles along the desired directions obtained in step 3.
5. *Actuate*: Apply the computed control voltages at the current time step of our simulation and advance the simulation to the next time step. This updates the droplet shape and particle positions. Then go back to step 2 and repeat the feedback control loop.

Step 4 of the algorithm requires more elaboration. Since the pressure field obeys Laplace's equation, which is linear, we can consider linear combinations of pressure boundary conditions due to voltage actuation at the electrodes (see Fig. 6). The problem of computing the necessary boundary conditions to create a pressure gradient field to move the particles in the directions we want, leads to a least squares problem.

This least squares problem is defined next. First, knowing the current droplet configuration, we solve Laplace's equation for the pressure field inside the droplet due to a single active electrode. The pressure boundary conditions are defined to be one on the droplet boundary that lies over the active electrode and zero everywhere else (see Fig. 6).

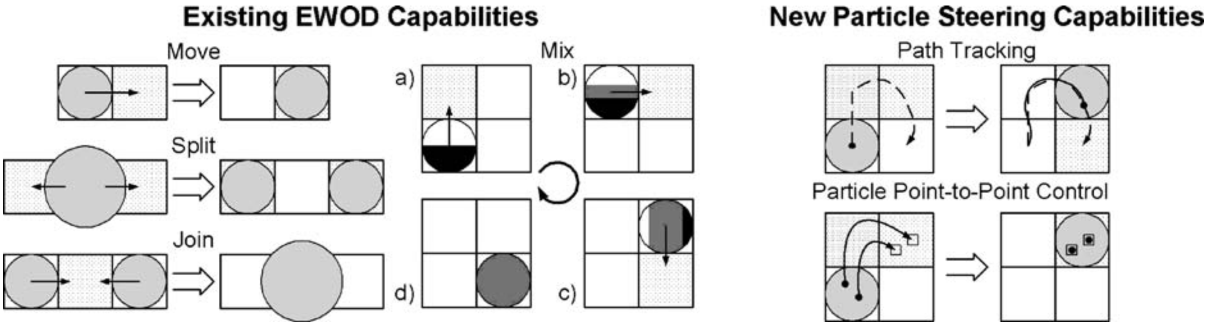

Control of Micro-Fluidics, Figure 5 The EWOD system manipulates fluids by charging a dielectric layer underneath the liquid that effectively changes the local surface tension properties of the liquid/gas interface creating liquid motion. Existing (move, split, join, and mix) capabilities of electrowetting devices are shown schematically above alongside the new particle steering capability discussed in this entry. The view is from the top of the EWOD device. Shaded circles represent droplets of liquid. Squares are electrodes where the dotted hatching indicates the electrode is on. Directed lines specify the direction of motion. The multi-shaded droplet shows the diffusion and mixing of two chemicals, here mixing is enhanced by the fluid dynamics created inside the droplet due to its imposed motion

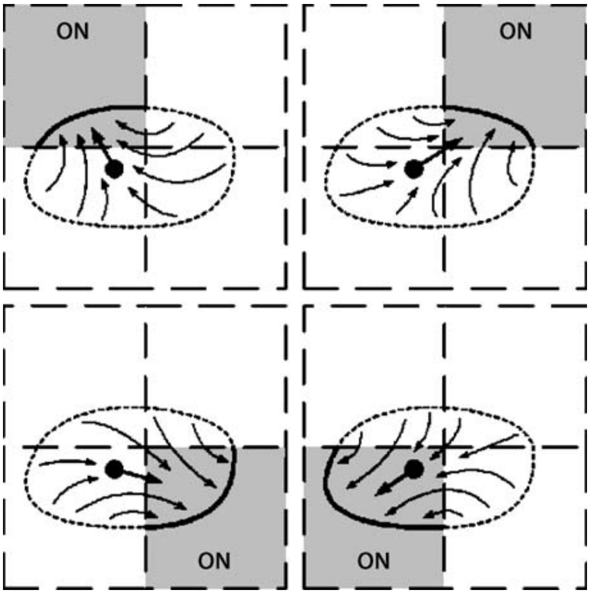

Control of Micro-Fluidics, Figure 6 Linear combination of pressure gradients for a single droplet overlaying four electrodes (small dashed squares). The diagram above shows a droplet in an EWOD system with four different instances of voltage actuation. In each instance, only one of the four electrodes is on. The particle floating inside the droplet (black dot) has a thick arrow indicating its direction of motion for each single electrode actuation. These arrows actually represent the opposite direction of the pressure gradient when a unit pressure boundary condition is set on the thick curve that overlays the shaded electrode, with zero pressure boundary conditions everywhere else. The thin curvy arrows show the fluid flow inside the droplet. Since the pressure field obeys Laplace's equation, it is linear and we can make the particle move in any desired direction by taking an appropriate linear combination of the four possible boundary conditions given above

From the pressure solution, the pressure gradient at each particle's position is computed. After repeating this for each electrode, we obtain a matrix of pressure gradients

$$G = -\begin{bmatrix} \nabla P_1(x_1, y_1) & \cdots & \nabla P_{\mathrm{N}}(x_1, y_1) \\ \vdots & \ddots & \vdots \\ \nabla P_1(x_{\mathrm{m}}, y_{\mathrm{m}}) & \cdots & \nabla P_{\mathrm{N}}(x_{\mathrm{m}}, y_{\mathrm{m}}) \end{bmatrix}, \qquad (1)$$

where $(x_{\mathrm{j}}, y_{\mathrm{j}})$ are the coordinates for the jth particle. Each column of pressure gradients $\nabla P_{\mathrm{k}}(x_{\mathrm{j}}, y_{\mathrm{j}})$ in the matrix corresponds to a single active electrode; each row to a single particle. The total number of particles is m and the number of available electrodes is N. The minus sign accounts for the direction of particle motion. (In the example of Fig. 6 the droplet overlays 4 electrodes and there is one particle, so $N = 4$ and $m = 1$.)

Next, we set the desired pressure gradient at particle j, $\nabla P_{\mathrm{D}}(x_j, y_j)$, equal to the desired velocity direction (denoted b) obtained in step 3 of our algorithm. This gives the following linear system

$$G\alpha = b\,, \quad \alpha = \begin{bmatrix} \alpha_1 \\ \vdots \\ \alpha_{\mathrm{N}} \end{bmatrix}, \quad b = \begin{bmatrix} \nabla P_{\mathrm{D}}(x_1, y_1) \\ \vdots \\ \nabla P_{\mathrm{D}}(x_{\mathrm{m}}, y_{\mathrm{m}}) \end{bmatrix}, \qquad (2)$$

where α is the vector of pressure boundary values that will achieve b. If $2m \geq N$, the number of particle degrees of freedom is greater than the available actuators and (in general) Eq. (2) cannot be solved exactly. A least squares solution is needed to obtain the best fit of actuations α. Otherwise, it is a pseudo-inverse problem, which has a solution as long as the matrix G has full row rank [25].

We solve Eq. (2) for α using the singular value decomposition (SVD) [25]. However, the range of boundary pressure actuations is limited by contact angle saturation. Using experimental data on the saturation characteristics for the

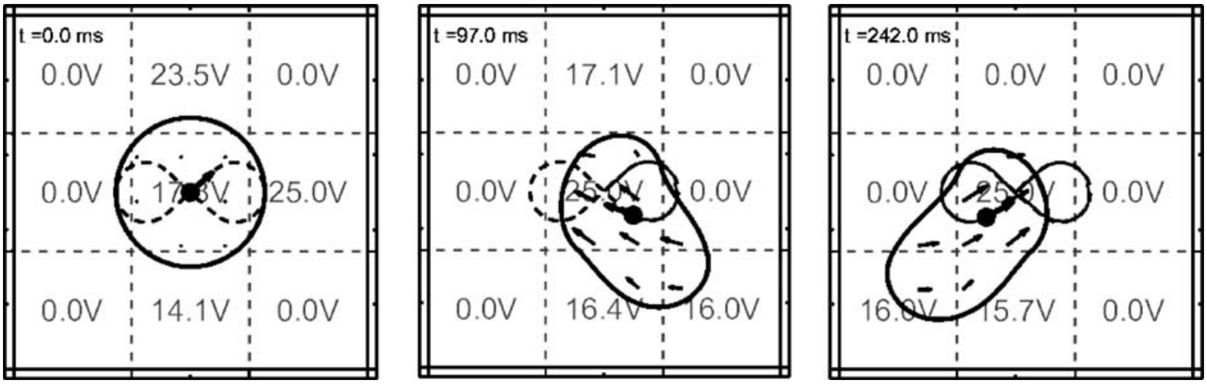

Control of Micro-Fluidics, Figure 7 Particle following a figure '8' path. In the simulation results above, we have a droplet (denoted by the thick black curve) lying on a 3×3 grid of electrodes (denoted by the dashed lines). The blue dashed curve is the desired figure '8' path and a black dot represents the particle with a thick red arrow pointing in the desired direction of travel. The red curve is the actual path of the particle. The black arrows inside the droplet denote the fluid velocity field inside the droplet. The voltages on the grid are time varying in such a way as to keep the particle moving along the desired path with less than 20 μm deviation

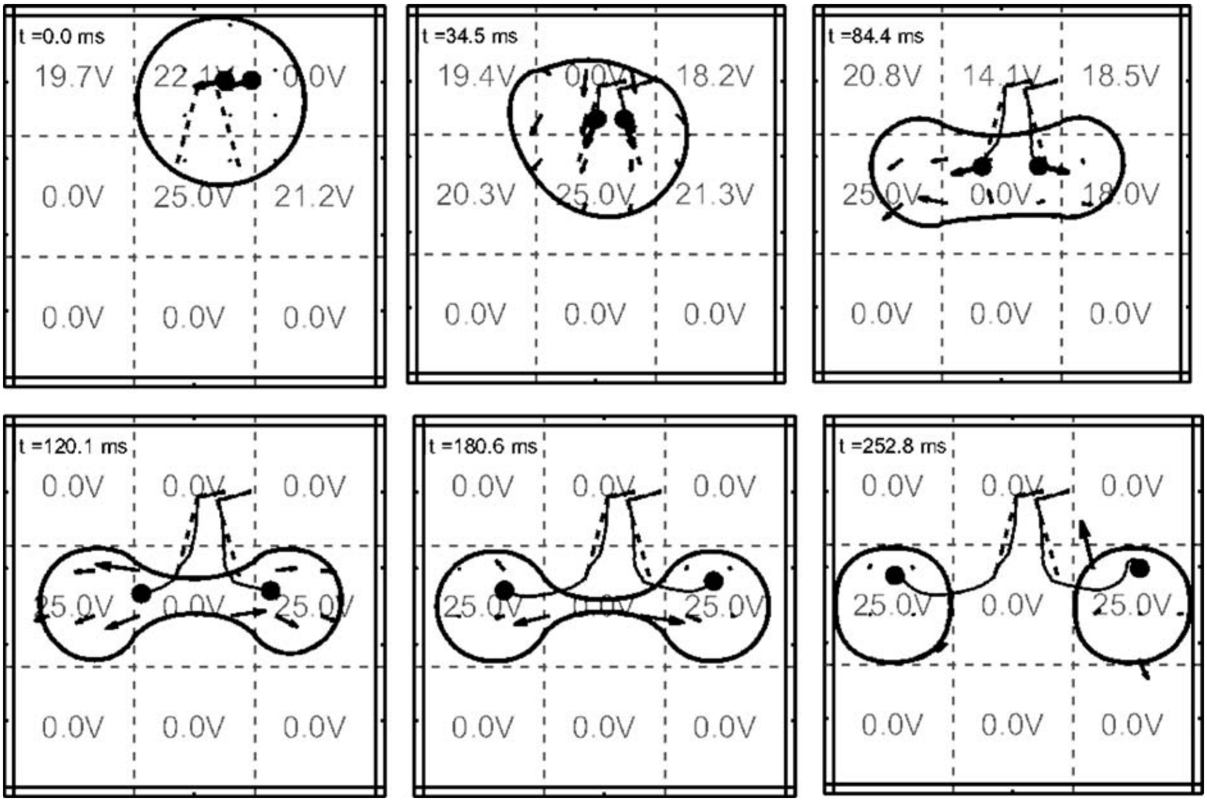

Control of Micro-Fluidics, Figure 8 Two-particle separation into two satellite drops (same format as in Fig. 7). Each particle first follows a trajectory that takes them away from each other. When there is sufficient distance between the two particles, our control algorithm turns off and the separation is completed by applying open loop voltages that split the droplet

UCLA EWOD device [22], we linearly map each component of the solution vector α so that these constraints are satisfied. As far as the steering algorithm is concerned, this mapping effectively changes the magnitude of b, which only affects the speed, and not the direction, of the particle motions. Hence, we choose the mapping so that the full dynamic range of boundary actuation is utilized, therefore maximizing the speed of the particles.

Finally, given that pressure on the boundary is directly related to the local contact angle [20], we again use experi-

mental data for the contact angle versus voltage characteristics of the EWOD device [22] to compute the electrode voltages needed to achieve the boundary pressures α. In general, there will be some uncertainty about the device parameters.

Simulations were run assuming the device characteristics described in [22]. A 3×3 electrode grid was used to actuate and control the droplet where each square electrode is 1.4 mm on a side. All voltage actuations in these simulations are within the limits of the UCLA EWOD device.

In Fig. 7, a droplet is shown moving in a way that makes a particle floating inside follow a figure '8' path. The droplet starts as a circle on the center electrode with a particle resting in its center. The voltages on the electrode grid are actuated using our algorithm and, throughout the motion, the droplet always overlaps enough electrodes to allow it to be controlled in a way that keeps the particle moving forward on the desired trajectory.

In Fig. 8, we demonstrate particle separation. A droplet starts in the first panel with two particles spaced 0.31 mm apart. Both particles follow separate diverging trajectories designed to stretch the droplet and separate the particles. Once the particles near the ends of their trajectories (see the third frame), our control algorithm turns off and we command an open loop voltage of 25 V on the middle left and right electrodes and zero volts everywhere else. This causes the droplet to split into two smaller drops, each of which contains a single particle. The reason for not using our control algorithm to complete the split is because of numerical instability. When both particles are in the lobes of the dumbbell shape of the pinching droplet, the available forcing at the particles' positions is fairly weak. This causes the condition number of the G matrix in Eq. (2) to degenerate and produce errors in the least squares solution. Therefore, we avoid this by commanding open loop voltages that will split the droplet [22].

Our simulations demonstrate the potential for performing particle placement and separation in the current UCLA EWOD devices with a reasonable number of electrodes. It is interesting to note that existing EWOD systems have enough control authority to steer a single particle along complex trajectories and to steer two particles along simple paths.

Cross References

- ► Electroosmotic Flow (DC)
- ► AC Electro-Osmotic Flow
- ► Electroosmotic Flow in Heterogeneous Microchannels
- ► Electrowetting
- ► Electrowetting and Droplets

References

1. Alberts B, Johnson A, Lewis J, Raff M, Roberts K, Walter P (2002) Molecular biology of the cell, 4th edn. Garland Science, New York
2. Murray RM, Astrom KJ (2008) Feedback Systems: An Introduction for Scientists and Engineers. To be published by Princeton Univ. Press, Princeton. (The most complete information on this book is acailable at: http://www.cds.caltech.edu/~murray/amwiki/Main_Page)
3. Doyle JC, Francis BA, Tannenbaum AR (1992) Feedback Control Theory. Macmillan, New York
4. Abramovici A, Chapsky J (2000) Feedback Control Systems: A Fast-Track Guide for Scientists and Engineerings. Kluwer, Boston
5. Murray RM, Astrom KJ, Boyd SP, Banda SS, Brockett RW, Burns JA, Dahleh MA, Doyle JC, Guckenheimer J, Holland CJ, Khargonekar PP, Kumar PR, Krishnaprasad PS, McRae GJ, Marsden JE, Meyer G, Powers WF, Stein G, Varaiya P (2002) Control in an Information Rich World. Air Force Office of Scientific Research (AFOSR). SIAM, Philadelphia
6. Shapiro B (2004) Website for the NSF workshop on 'Control and System Integration of Micro- and Nano-Scale Systems': http://www.isr.umd.edu/CMN-NSFwkshp/
7. Shapiro B (2005) Workshop on control of micro- and nano-scale systems. IEEE Contr Syst Magazine 25:82–88
8. Zhou K, Doyle JC, Glover K (1996) Robust and Optimal Control. Prentice Hall, New Jersey
9. Isidori A (1995) Nonlinear Control Systems, 3rd edn. Springer, New York
10. Leonard NE, Ortega R (2000) Lagrangian and hamiltonian methods for nonlinear control 2000. IFAC Workshop, Princeton
11. Yang B (2006) Output Feedback Control of Nonlinear Systems with Unstabilizable/Undetectable Linearization. In: Systems and Control Engineering. PhD thesis, Case Western Reserve, Cleveland
12. Marquez HJ (2003) Nonlinear Control Systems: Analysis and Design. Wiley-Interscience, Hoboken
13. Christofides PD (2001) Nonlinear and Robust Control of PDE Systems. Birkhauser, Boston
14. Armani M, Chaudhary S, Probst R, Shapiro B (2004) Micro flow control particle tweezers. Proc mTAS, Malmo
15. Armani M, Chaudhary S, Probst R, Shapiro B (2005) Using feedback control and micro-fluidics to steer individual particles. Proc 18th IEEE Int Conf MEMS, Miami
16. Chaudhary S, Shapiro B (2006) Arbitrary steering of multiple particles at once in an electroosmotically driven microfluidic system. IEEE Trans Contr Syst Technol 14:669–680
17. Armani M, Chaudhary S, Probst R, Walker S, Shapiro B (2005) Control of micro-fluidic systems: two examples, results, and challenges. Int J Robust Nonlinear Contr 15:785–803
18. Armani M, Chaudhary S, Probst R, Shapiro B (2006) Using feedback control and micro-fluidics to independently steer multiple particles. J MEMS 15:945–956
19. Walker S, Shapiro B (2005) A control method for steering individual particles inside liquid droplets actuated by electrowetting. Lab Chip 12:1404–1407
20. Walker S, Shapiro B (2006) Modeling the fluid dynamics of electrowetting on dielectric (EWOD). J MEMS 15:986–1000
21. Lee J, Moon H, Fowler J, Schoellhammer T, Kim CJ (2002) Electrowetting and electrowetting-on-dielectric for microscale liquid handling. Sens Actuators A 95:259–268

22. Cho SK, Moon H, Kim CJ (2003) Creating, transporting, cutting, and merging liquid droplets by electrowetting-based actuation for digital microfluidic circuits. J MEMS 12:70–80
23. Panton RL (1996) Incompressible Flow, 2nd edn. Wiley New York
24. Batchelor GK (1967) An Introduction to Fluid Dynamics. Cambridge University Press, Cambridge
25. Strang G (1988) Linear Algebra and Its Applications, 3rd edn. Brooks Cole, New York

Control Theory

Definition

The mathematical theory of designing controllers to achieve desired performance of the ► controlled system.

Control Volume Based Finite Difference Method

► Finite Volume and Finite Difference Methods for Modeling and Simulation

Control Volume Method

► Finite Volume and Finite Difference Methods for Modeling and Simulation

Convective Dispersion

► Hydrodynamic Dispersion

Convective Heat Transfer in Microchannels

GIAN LUCA MORINI
DIENCA Università di Bologna, Bologna, Italy
gianluca.morini@mail.ing.unibo.it

Synonyms

Single-phase forced convection in microchannels; Single-phase convective flows in microchannels; Heat transfer in microchannel flow

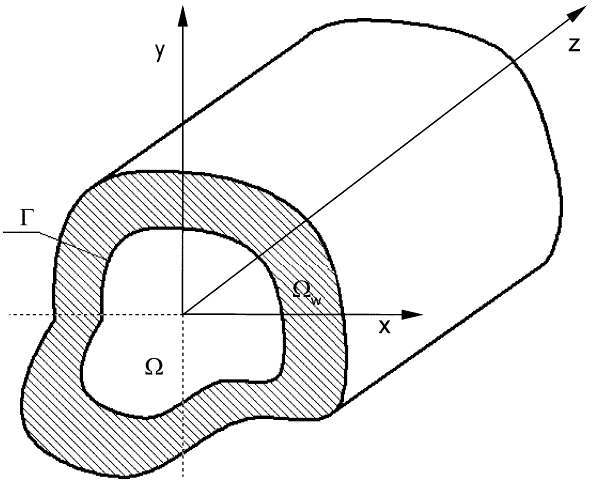

Convective Heat Transfer in Microchannels, Figure 1 Sketch of a straight microchannel with constant cross-section and Cartesian coordinate system

Definition

Convective heat transfer in microchannels is a process involving a forced mass movement of fluids through channels having hydraulic diameters less than 1 mm. The temperature difference between the microchannel walls and the fluid produces a net heat transfer that depends on the velocity and temperature gradient near the heated walls.

Overview

Single-phase forced convection through microchannels can be studied by determining the velocity distribution and the temperature field in the fluid region with the aid of the mass conservation principle (*continuity equation*), the fluid momentum balance equations and the energy balance equation [1]:

$$\begin{aligned} -\frac{1}{\rho}\frac{\mathrm{d}\rho}{\mathrm{d}t} &= \nabla\cdot\boldsymbol{v} \\ \rho\frac{\mathrm{d}\boldsymbol{v}}{\mathrm{d}t} &= -\nabla p + \rho\boldsymbol{g} - \nabla\cdot\tau - \boldsymbol{f}_{\mathrm{ext}} \\ \rho\frac{\mathrm{d}U}{\mathrm{d}t} &= -\nabla\cdot\boldsymbol{q} - p\ (\nabla\cdot\boldsymbol{v}) - \tau : \nabla\boldsymbol{v} + S_{\mathrm{g}} \end{aligned} \quad (1)$$

in which $\boldsymbol{v}$ is the velocity vector, ρ is the fluid density, t is the time, p is the pressure, $\mathrm{d}/\mathrm{d}t$ is the total derivative, τ is the viscous tensor, $\boldsymbol{f}_{\mathrm{ext}}$ denotes an external force per unit of volume, U is the specific internal energy of the fluid, S_{g} indicates a generic internal thermal source and $\boldsymbol{q}$ is the heat flux.
If we consider a steady-state, laminar, constant property (i. e. dynamic viscosity μ, specific heat c_{p}, thermal con-

ductivity k) flow in a straight microchannel of constant cross-sectional area (see Fig. 1), in the absence of free convection, mass diffusion and change of phase, the governing equations can be written as follows:

$$\mu\nabla^2 v_z = \frac{dp}{dz} + f_{ext,z} \tag{2}$$

$$\rho c_p v_z \frac{\partial T}{\partial z} = k\nabla^2 T + v_z \frac{\partial p}{\partial z} + \mu\Phi'_{inc} + S_g \text{ (ideal gases)} \tag{3}$$

$$\rho c_p v_z \frac{\partial T}{\partial z} = k\nabla^2 T + \beta T v_z \frac{\partial p}{\partial z} + \mu\Phi'_{inc} + S_g \text{ (liquids)} \tag{4}$$

Details about these balance equations can be found in the sections on ▶ viscous dissipation and ▶ pressure-driven single-phase liquid flow.

The expression of the viscous dissipation term for an incompressible fluid (Φ'_{inc}) with constant properties for different geometry coordinates can be found in the ▶ viscous dissipation entry.

Equations (3) and (4) differ only for the term related to the reversible work done by the fluid against the external pressure field (*flow work*). In general, Eq. (4) is written for liquids by neglecting the flow work term; this means considering $\beta = 0$ for liquids. This hypothesis is critically evaluated in the viscous dissipation entry; in fact, in microchannels, for liquids and gases, the flow work term can be important because the pressure gradient along the tube is in general very large, namely inversely proportional to the square of the hydraulic diameter of the channel.

In general $f_{ext,z}$ and S_g can be neglected in Eq. (2)–(4) if the external forces (i. e. electric forces), chemical and/or nuclear reactions are absent. On the contrary, for electro-osmotic flows these terms must be considered in the balance equations and they assume the following forms:

$$\begin{aligned} f_{ext,z} &= \rho_e E_z \\ S_g &= \lambda_0 E_z^2 \end{aligned} \tag{5}$$

in which E_z is the imposed electric potential gradient between the electrodes (expressed in V/m), ρ_e is the density of charge, λ_0 is the electrical conductivity (▶ electro-osmotic flow). These expressions underline that in an electro-osmotic flow where the fluid is moved by means of an imposed external electric potential gradient E_z there is a volumetric heat generation within the fluid linked to the Joule heating which is in turn related to the electric current induced in the fluid region.

Basic Methodology

Boundary Conditions

Velocity Problem

The boundary condition for the velocity problem (Eq. (2)) can be of three different kinds:

- The *no-slip condition*, valid for Newtonian liquids and for gases when the Knudsen number is less than 0.001 (▶ pressure-driven single-phase gas flows):

$$v_z|_\Gamma = 0 \tag{6}$$

  where Γ indicates the perimeter of the microchannel.
- The *slip condition*, valid for non-Newtonian liquids, like polymer solutions and surfactants, and for gases when the Knudsen number is greater than 0.001 (▶ pressure-driven single-phase gas flows):

$$v_{z,slip} = v_z|_\Gamma - v_{wall} = \xi \left.\frac{\partial v_z}{\partial n}\right|_\Gamma \tag{7}$$

  where ξ is a length commonly called the *coefficient of slip* and n is the normal direction, exiting the wall. The coefficient of slip is related to the nature of the fluid, to the status of the walls and to the temperature near the wall. For rarefied gases the slip condition can be written as follows:

$$v_z|_\Gamma - v_{wall} = \alpha \frac{2-\sigma_v}{\sigma_v}\lambda \left.\frac{\partial v_z}{\partial n}\right|_\Gamma \tag{8}$$

  in which σ_v is the momentum accommodation coefficient, λ is the molecular mean free path and α is a coefficient introduced by Cercignani to correct the original results of Maxwell. There exist more complicated expressions of this boundary condition (the so-called *second order slip boundary conditions*) but in this section these expressions are not taken into account.
- The *slug flow* condition for which the velocity field is considered as uniform in the whole cross-section:

$$v_z = W = const. \tag{9}$$

  This condition is particularly appropriate to analyze the convective heat transfer for ▶ electro-osmotic flows for which the velocity tends to become uniform on the cross-section.

Thermal Problem

In the *pure convection problem*, heat transfer through the wall is characterized by an appropriate thermal boundary condition directly or indirectly specified at the wall–fluid interface. In a pure convection problem the solution of the

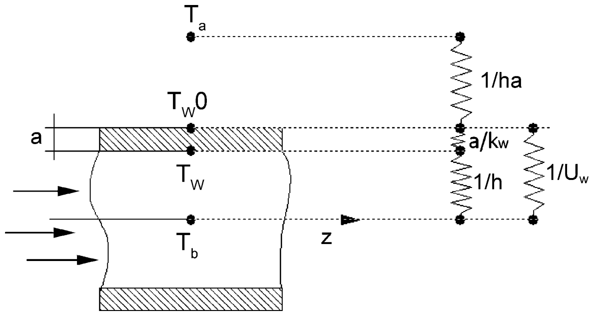

Convective Heat Transfer in Microchannels, Figure 2 Thermal circuit representation of the resistance in a microchannel between the bulk temperature (T_b) and the outside temperature (T_a)

temperature problem for the solid wall is not needed: the velocity and temperature are determined only in the fluid region. However, the heat transfer through the solid walls of the microchannel by conduction may have significant normal and/or peripheral as well as axial components; or the wall may be of non-uniform thickness. In these cases the temperature problem for the solid wall needs to be analyzed simultaneously with that for the fluid in order to calculate the real wall–fluid interface heat flux distribution. In this case the wall–fluid heat transfer is referred to as *conjugate heat transfer*.

In a pure convection problem the thermal boundary conditions are the set of specifications describing temperature and/or heat flux at the inner wall of the microchannel.

The peripheral average heat transfer flux is strongly dependent on the thermal boundary conditions in the laminar regime, typical of microchannels, while very much less dependent in the turbulent flow regime. For this reason, for microchannels is very important to classify the thermal boundary conditions in order to model correctly the internal convective heat transfer.

In this work, the classification of the thermal boundary conditions proposed by Shah and London [2] will be used.

T Boundary Conditions

The thermal boundary condition in which the wall temperature is considered as axially constant and peripherally uniform is referred as the **T** boundary condition. In this case the boundary condition can be written as follows:

$$T|_{\Gamma} = T_{\mathrm{w}} = \text{const.} \tag{10}$$

This condition can be applied for micro-condensers and for micro-evaporators where an external two-phase flow sets as constant the wall temperature of the microchannels inside which a single-phase fluid flows.

With reference to Fig. 2, the thermal boundary condition for which the outer wall temperature ($T_{\mathrm{w},0}$) is considered axially constant while the wall heat flux is considered as linearly proportional to wall temperature peripherally is referred to as the **T3** boundary condition:

$$k\left.\frac{\partial T}{\partial n}\right|_{\Gamma} = U_{\mathrm{w}}\left(T_{\mathrm{w},0} - T|_{\Gamma}\right) \tag{11}$$

where U_{w} is the wall thermal transmittance. For a straight thin wall of uniform thickness a and thermal conductivity equal to k_{w}, U_{w} is given by

$$U_{\mathrm{w}} = \frac{k_{\mathrm{w}}}{a} \tag{12}$$

This boundary condition allows the analysis of micro-condensers and micro-evaporators with finite wall thermal resistance. It is evident that when U_{w} tends to infinity the **T3** boundary condition reduces to the **T** boundary condition.

With reference to Fig. 2, when the outer fluid (or the environment temperature) T_{a} can be considered axially constant while the wall heat flux is nonlinearly proportional to the wall temperature (*radiative heat transfer*) the boundary condition is referred to as **T4**:

$$k\left.\frac{\partial T}{\partial n}\right|_{\Gamma} = \varepsilon_{\mathrm{w}}\sigma_0\left(T|_{\Gamma}^4 - T_{\mathrm{a}}^4\right) \tag{13}$$

where ε_{w} is the emissivity of the external wall and σ_0 is the Stefan–Boltzmann constant.

In this case, the wall thermal resistance is considered negligible. This kind of thermal boundary condition can be used, for example, for micro-radiators working in space and manufactured with materials having a large value of thermal conductivity.

H Boundary Conditions

The thermal boundary conditions of approximately constant axial heat flow rate per unit length of the microchannel are referred as to **H** boundary conditions.

When the wall heat transfer rate is constant axially while the wall temperature at any cross-section z is constant in the peripheral direction, the boundary condition is referred to as **H1**:

$$\begin{aligned} q' &= \dot{m}c_{\mathrm{p}}\frac{\mathrm{d}T_{\mathrm{b}}}{\mathrm{d}z} = \text{const.} && \text{independent of z} \\ T|_{\Gamma} &= T_{\mathrm{w}} = \text{const.} && \text{independent of (x,y)} \end{aligned} \tag{14}$$

where $\dot{m}$ is the mass flow rate in the microchannel, q' is the wall heat transfer rate per unit of length of the microchannel and T_b is the bulk temperature defined as

$$T_b = \frac{1}{\dot{m}c_p} \int_{\Omega} \rho v_z c_p T \mathrm{d}\Omega \tag{15}$$

with Ω being the cross-sectional area of the microchannel (see Fig. 1).

This kind of boundary condition is very common in microchannels heated by means of electrical resistances and made of highly conductive materials like copper or silicon.

When the wall heat flux per unit of heat transfer area (q'') is constant in the axial as well the peripheral direction the boundary condition is referred to as **H2**:

$$\begin{aligned} q''\Gamma_h &= \dot{m}c_p \frac{\mathrm{d}T_b}{\mathrm{d}z} = \text{const.} \qquad && \text{independent of z} \\ k\frac{\partial T}{\partial n}\bigg|_{\Gamma} &= q'' = \text{const.} && \text{independent of (x,y,z)} \end{aligned} \tag{16}$$

where Γ_h is the heated perimeter of the microchannel. In this case the wall temperature is not constant peripherally but assumes the maximum value near the corner of the cross-section (if any).

This kind of boundary condition enables one to model the convective heat transfer for microchannels heated electrically and made with very low conductive materials, like PMDS and so on, and with a uniform wall thickness.

For a constant wall heat transfer rate in the axial direction and the heat flux linearly proportional to the wall temperature in the peripheral direction the boundary condition is referred to as **H3**:

$$\begin{aligned} q' &= \dot{m}c_p \frac{\mathrm{d}T_b}{\mathrm{d}z} = \text{const.} \qquad && \text{independent of } z \\ k\frac{\partial T}{\partial n}\bigg|_{\Gamma} &= U_w \left(T_{w,0} - T|_{\Gamma}\right) \end{aligned} \tag{17}$$

The **H3** boundary condition contains the **H1** and **H2** boundary conditions as particular cases: in fact, when the wall transmittance U_w tends to zero the **H3** boundary condition reproduces the **H2** boundary condition. On the contrary, when the wall transmittance U_w tends to infinity the **H3** boundary condition approaches the **H1** boundary condition.

This kind of boundary condition is employed in modeling the convective heat transfer for microchannels heated electrically by taking into account a finite normal wall thermal resistance and negligible peripheral wall heat conduction.

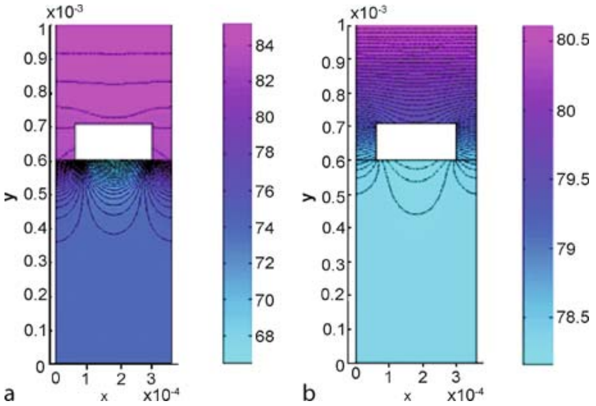

Convective Heat Transfer in Microchannels, Figure 3 Temperature distributions in a ⟨110⟩ silicon wafer with a Pyrex glass cover (a) or a silicon cover (b)

When the axial wall heat flux varies exponentially along the flow length while the peripheral wall temperature is constant at a particular section z the boundary condition is referred to as **H5**:

$$\begin{aligned} q' &= q'_0 e^{m'z} \\ T|_{\Gamma} &= T_w = \text{const.} \qquad \text{independent of } (x, y) \end{aligned} \tag{18}$$

The **H5** boundary condition can be used to approximate parallel and counterflow micro-heat exchangers in which the fluid bulk temperature varies exponentially along the microchannel.

The thermal boundary conditions described above are schematically summarized in Tab. 1.

Temperature Jump Condition

For rarefied gases there exists a temperature discontinuity between the fluid and the walls of the channel. This temperature jump can be expressed as follows (*first-order condition*):

$$T|_{\Gamma} - T_w = \alpha_t \frac{2-\sigma_t}{\sigma_t} \frac{2\left(\frac{c_p}{c_v}\right)}{\left(\frac{c_p}{c_v}\right)+1} \frac{\lambda}{\Pr} \frac{\partial T}{\partial n}\bigg|_{\Gamma} \tag{19}$$

where α_t is a coefficient introduced by Cercignani to correct the original results of Maxwell and σ_t is the thermal accommodation coefficient that depends on the fluid and on the wall characteristics. This boundary condition has been used in order to study **T**, **H1** and **H2** boundary problems.

Convective Heat Transfer in Microchannels, Table 1 Thermal boundary conditions for internal forced convection in microchannels

	Description	Equations	Applications
T	Constant wall temperature peripherally as well as axially	$T\|_\Gamma = T_w = \text{const.}$	Micro-condensers, Micro-evaporators with negligible wall thermal resistance
T3	Constant axial wall temperature with finite normal wall thermal resistance	$k\left.\frac{\partial T}{\partial n}\right\|_\Gamma = U_w\left(T_{w,0} - T\|_\Gamma\right);\quad T_{w,0} = \text{const.}$	Micro-condensers, Micro-evaporators with finite wall thermal resistance
T4	Non linear radiant-flux	$k\left.\frac{\partial T}{\partial n}\right\|_\Gamma = \varepsilon\sigma_0\left(T\|_\Gamma^4 - T_a^4\right);\quad T_a = \text{const.}$	Micro-radiators in space power systems with negligible normal wall resistance
H1	Constant axial wall heat flux with constant peripheral wall temperature	$q' = \dot{m}c_p\frac{dT_b}{dz} = \text{const.}$ ind of z $T\|_\Gamma = T_w = \text{const.}$ ind of (x, y)	Microchannels heated by means of electrical resistances and made with highly conductive materials, like copper or silicon.
H2	Constant axial wall heat flux with uniform peripheral wall heat flux	$q''\Gamma = \dot{m}c_p\frac{dT_b}{dz} = \text{const.}$ ind of z $k\left.\frac{\partial T}{\partial n}\right\|_\Gamma = q'' = \text{const.}$ ind of (x, y, z)	Microchannels heated electrically and made with very low conductive materials, like PMDS and so on, and with a uniform wall thickness.
H3	Constant axial wall heat flux with finite normal wall thermal resistance	$q' = \dot{m}c_p\frac{dT_b}{dz} = \text{const.}$ ind of z $k\left.\frac{\partial T}{\partial n}\right\|_\Gamma = U_w\left(T_{w,0} - T\|_\Gamma\right)$	Microchannels heated electrically by taking into account a finite normal wall thermal resistance and a negligible peripheral wall heat conduction.
H5	Exponential axial wall heat flux	$q' = q_0' e^{mz}$ $T\|_\Gamma = T_w = \text{const.}$ ind of (x, y)	Parallel and counterflow micro heat-exchangers in which the fluid bulk mean temperature varies exponentially along the microchannel.

Heated Perimeter

The thermal boundary conditions can vary along the perimeter of a microchannel and the heated perimeter can differ for the wetted perimeter of the microchannel because some parts of it can be considered as adiabatic. In Fig. 3 the temperature distribution in a silicon substrate (k_s = 148 W/(m K)) having a thickness of 400 μm with a rectangular microchannel is depicted. The half distance between two adjacent microchannels is equal to 60 μm. The microchannel has a height (h) of 110 μm and a width (a) of 237 μm. Water (k = 0.607 W/(m K)) with a bulk temperature of 60° C flows through the channels in the laminar regime. The microchannels have an axially unchanging cross-section. A uniform wall heat flux q'' of 640 kW/m^2 is imposed as a boundary condition on the top of the silicon substrate while all the other outer walls are taken as adiabatic. In Fig. 3 are shown the temperature distributions in this device when the microchannel is closed by a cover with a thickness of 600 μm in Pyrex glass ($k_p = 1.13\, W/(m K)$) (Fig. 3a) or in silicon (Fig. 3b). As is evident, owing to the high thermal conductivity of the silicon, the temperature gradient in the silicon substrate is very limited and the temperature field is close to isothermal (see Fig. 3a). On the contrary, it is possible to observe that the isothermal lines in the Pyrex cover tend to become orthogonal to the microchannel wall; this means that the Pyrex wall of the rectangular microchannel can be considered *quasi-adiabatic* (Fig. 3a).

In conclusion, if a Pyrex cover is used to close silicon microchannels the silicon walls of the microchannels tend to work at constant temperature with an imposed constant heat flux; on the contrary, the Pyrex side can be considered adiabatic. Due to the high ratio between the thermal conductivity of the silicon and of the fluid (in this case $k_s/k = 247$) and its small hydraulic diameter, the microchannel can be conveniently studied as a *long duct* under a classical **H1** thermal boundary condition (theoretically valid for $k_s/k = \infty$). On the other hand, when a silicon cover is used to close the microchannel, all the boundaries can be considered as isothermal (see Fig. 3b); it is possible to use the **H1** thermal boundary condition, with the four sides at an imposed uniform temperature.

In Fig. 4 the most common combinations of adiabatic and heated walls in microchannels of different cross-sections (rectangular, trapezoidal and double trapezoidal) are depicted. Each combination is classified by means of a number that corresponds to the number of the heated sides of the microchannel.

Dimensionless Equations and Boundary Conditions

As highlighted by Shah and London [2], a natural tendency exists to use in convection problems a large num-

ber of different sets of dimensionless groups based on the analyst's particular normalization of the differential equations and boundary conditions. An effort to standardize the definitions of dimensionless groups for laminar flows through channels was made by Shah and London [2] some years ago. In this section, the normalization of the convection problems proposed by Shah and London will be followed.

The balance equations for steady-state, laminar, constant property (i. e. dynamic viscosity μ, specific heat c_p, thermal conductivity k) flow in a microchannel of constant cross-sectional area (see Fig. 1), in the absence of free convection, mass diffusion and change of phase, can be written in a dimensionless form by using the following dimensionless quantity:

$$\begin{aligned} &x^* = \frac{x}{D_\mathrm{h}};\; y^* = \frac{y}{D_\mathrm{h}};\; z^* = \frac{z}{D_\mathrm{h}\mathrm{RePr}} = \frac{z}{D_\mathrm{h}\mathrm{Pe}};\\ &v_z^* = \frac{v_z}{W};\; T^* = \frac{(T-T_0)}{\Delta T_\mathrm{ref}};\\ &\mathrm{Re} = \frac{\rho W D_\mathrm{h}}{\mu};\; \mathrm{Pr} = \frac{\mu c_\mathrm{p}}{k};\; f\mathrm{Re} = -\frac{D_\mathrm{h}^2}{2\mu W}\frac{\mathrm{d}p}{\mathrm{d}z};\\ &\mathrm{Br} = \frac{\mu W^2}{k\Delta T_\mathrm{ref}} \end{aligned} \tag{20}$$

in which Re is the Reynolds number, Pr the Prandtl number, Pe the Péclet number (= RePr), fRe is the Poiseuille number (defined as the product of the Fanning friction factor f and the Reynolds number Re, see ▶ pressure-driven single-phase liquid flows), Br is the Brinkman number, D_h is the hydraulic diameter $(= 4\Omega/\Gamma)$, and W is the average fluid velocity:

$$W = \frac{1}{\Omega}\int_\Omega v_z \,\mathrm{d}\Omega\,. \tag{21}$$

The dimensionless form of the momentum and of the energy balance is the following:

$$\nabla^{*2} v_z^* = -2f\mathrm{Re} + f^* \tag{22}$$

$$\begin{aligned} v_z^*\frac{\partial T^*}{\partial z^*} &= \frac{1}{\mathrm{Pe}^2}\frac{\partial^2 T^*}{\partial z^{*2}} + \nabla^{*2}T^*\\ &\quad - 2\mathrm{Br}f\mathrm{Re}\,v_z^* + \mathrm{Br}\Phi_\mathrm{inc}'^* + S_\mathrm{g}^* \quad \text{(ideal gases)} \end{aligned} \tag{23a}$$

$$\begin{aligned} v_z^*\frac{\partial T^*}{\partial z^*} &= \frac{1}{\mathrm{Pe}^2}\frac{\partial^2 T^*}{\partial z^{*2}}\\ &\quad + \nabla^{*2}T^* - 2\left(\beta\Delta T_\mathrm{ref}T^* + \beta T_0\right)\\ &\quad \times \mathrm{Br}f\mathrm{Re}\,v_z^* + \mathrm{Br}\Phi_\mathrm{inc}'^* + S_\mathrm{g}^* \quad \text{(liquids)} \end{aligned} \tag{23b}$$

where

$$\nabla^{*2} = \frac{\partial^2}{\partial x^{*2}} + \frac{\partial^2}{\partial y^{*2}};\quad S_\mathrm{g}^* = \frac{S_\mathrm{g}D_\mathrm{h}^2}{k\Delta T_\mathrm{ref}};\quad f^* = \frac{f_{\mathrm{ext},z}D_\mathrm{h}^2}{\mu W}. \tag{24}$$

The choice of ΔT_ref used to define the dimensionless temperature (T^*) and the Brinkman number is different for **T** and **H** thermal boundary conditions:

$$\Delta T_\mathrm{ref} = \begin{cases} (T_\mathrm{c} - T_0) & \text{with } T_\mathrm{c} = T_\mathrm{w} \quad [T]\,;\\ & \phantom{\text{with }} T_\mathrm{c} = T_{\mathrm{w},0} \quad [T3]\,;\\ & \phantom{\text{with }} T_\mathrm{c} = T_\mathrm{a} \quad [T4]\\ \frac{q_\mathrm{c}}{k} & \text{with } q_\mathrm{c} = q' \quad [H1, H3, H5]\,;\\ & \phantom{\text{with }} q_\mathrm{c} = q''D_\mathrm{h} \quad [H2] \end{cases} \tag{25}$$

As an example, by combining Eqs. (24) and (5) it is possible to demonstrate that a new dimensionless group must be introduced to study the velocity field for electro-osmotic flows:

$$F = \frac{\rho_e E_z D_\mathrm{h}^2}{\mu W} \tag{26}$$

where ρ_e is a characteristic value of the density of the electric charge $(\rho_e = ezn_0)$, and in order to study forced convection of electro-osmotic flows the source term in Eqs. (23a) and (23b) suggests the introduction of the following new dimensionless group:

$$M_z = \frac{E_z^2\lambda_0 D_\mathrm{h}^2}{k\Delta T_\mathrm{ref}} \tag{27}$$

in which ΔT_ref depends on the thermal boundary conditions by following Eq. (25).

By using the dimensionless quantities of Eq. (20), it is possible to demonstrate that the boundary conditions written in dimensionless form introduce new dimensionless groups:

- The *slip flow* condition introduces the following dimensionless group:

$$\xi^* = \frac{\xi}{D_\mathrm{h}} \tag{28}$$

For rarefied gases, by using Eq. (8), it is possible to demonstrate that the slip flow condition leads to the Knudsen number, defined as the ratio between the molecular mean free path (λ) and the hydraulic diameter of the channel $(\mathrm{Kn} = \lambda/D_\mathrm{h})$.

C

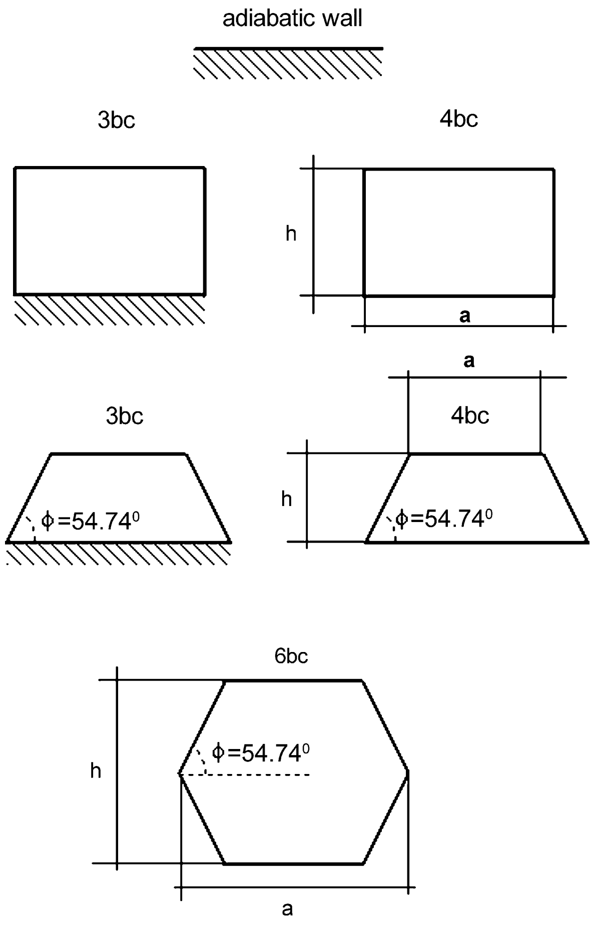

Convective Heat Transfer in Microchannels, Figure 4 Combination of heated and adiabatic walls considered for each geometry investigated

- The **T3** and **H3** boundary conditions introduce the dimensionless wall thermal resistance:

$$R_{\mathrm{w}} = \frac{k}{U_{\mathrm{w}} D_{\mathrm{h}}} \tag{29}$$

- The **T4** boundary condition introduces the following dimensionless group:

$$\gamma = \varepsilon_{\mathrm{w}} \sigma_0 T_{\mathrm{e}}^3 D_{\mathrm{h}} / k \tag{30}$$

  where T_{e} is the absolute fluid inlet temperature.
- The **H5** boundary condition introduces the following dimensionless group:

$$m = m' D_{\mathrm{h}} \mathrm{RePr} = m' D_{\mathrm{h}} \mathrm{Pe} \tag{31}$$

The Nusselt Number

The main goal of the solution of the balance equations described above is to calculate the convective heat transfer coefficient defined as follows:

$$q'' = -k \left.\frac{\partial T}{\partial n}\right|_{\Gamma} = h \left(T|_{\Gamma} - T_{\mathrm{b}} \right) \tag{32}$$

in which T_{b} is the bulk temperature defined by Eq. (13) and $T|_{\Gamma}$ and $\partial T/\partial n|_{\Gamma}$ are the local values of the fluid temperature and the normal gradient at the wall respectively. The convective heat transfer coefficient makes it possible to describe the heat flux at a local point on the heated perimeter. The ratio of the convective heat transfer coefficient and the pure molecular thermal conductance is defined as Nusselt number:

$$\mathrm{Nu} = \frac{h}{k/D_{\mathrm{h}}} \tag{33}$$

If one knows the dimensionless temperature distribution in the fluid region, the local value of the Nusselt number in a point on the heated perimeter can be calculated from its operational definition:

$$\mathrm{Nu} = -\frac{\left.\frac{\partial T^*}{\partial n^*}\right|_{\Gamma^*}}{T^*|_{\Gamma^*} - T_{\mathrm{b}}^*} \tag{34}$$

where $\Gamma_{\mathrm{h}}^* = \Gamma_{\mathrm{h}}/D_{\mathrm{h}}$ is the dimensionless heated perimeter. The peripherally average, but axially local, Nusselt number is defined by

$$\overline{\mathrm{Nu}} = -\frac{\int_{\Gamma_{\mathrm{h}}^*} \left.\frac{\partial T^*}{\partial n^*}\right|_{\Gamma^*} \mathrm{d}\Gamma^*}{\Gamma_{\mathrm{h}}^* \left(T_{\mathrm{wm}}^* - T_{\mathrm{b}}^* \right)} \tag{35}$$

in which the dimensionless peripheral mean wall temperature T_{wm}^* has been used with

$$T_{\mathrm{wm}}^* = \frac{\int_{\Gamma_{\mathrm{h}}^*} T^*|_{\Gamma^*} \mathrm{d}\Gamma^*}{\Gamma_{\mathrm{h}}^*} \tag{36}$$

By observing the dimensionless form of the balance equations (Eqs. (22), (23)) and bearing in mind the dimensionless groups that can be introduced by the boundary conditions it is easy to demonstrate that the average Nusselt number in the laminar regime can be considered, for a fixed cross-sectional geometry, as a function of the following dimensionless quantities:

$$\overline{\mathrm{Nu}} = \overline{\mathrm{Nu}}(z^*, \mathrm{Br}, \mathrm{Pe}, \beta \Delta T_{\mathrm{ref}}, S_{\mathrm{g}}^*, f^*, \xi^*, R_{\mathrm{w}} |\, m |\, \gamma) \tag{37}$$

For example, for an incompressible liquid ($\beta = 0$) with negligible viscous dissipation ($\mathrm{Br} = 0$) and no-slip condition at the walls ($\xi^* = 0$) without significant fixed external forces ($f^* = 0$) and internal heat sources ($S_{\mathrm{g}}^* = 0$) under an **H3** thermal boundary condition, the average Nusselt

number can be considered as a function of the following dimensionless quantities:

$$\overline{\mathrm{Nu}} = \overline{\mathrm{Nu}}(z^*, \mathrm{Pe}, R_\mathrm{w}) \tag{38}$$

The laminar flow inside a microchannel is considered *thermally fully developed* when the following equation is satisfied by the fluid temperature:

$$\frac{\partial}{\partial z^*}\left[\frac{T^*_\mathrm{wm} - T^*}{T^*_\mathrm{wm} - T^*_\mathrm{b}}\right] = 0\,. \tag{39}$$

In this case $\overline{\mathrm{Nu}}$ becomes independent to z^*. It is important to remark that the flow is always thermally developing for *conjugate problems*.

The effects related to the thermal entrance region are not considered in this section *entrance Region and developing flows*.

For a thermally fully developed laminar flow, for a fixed dynamic and thermal boundary condition and by neglecting the fluid axial conduction ($\mathrm{Pe} \to \infty$), viscous dissipation ($\mathrm{Br} = 0$), the flow work ($\beta = 0$) and electro-osmotic phenomena ($S^*_\mathrm{g} = f^* = 0$), the Nusselt number depends on the cross-sectional geometry (through the Poiseuille number $f\mathrm{Re}$) only.

The Nusselt number (Nu) can be used in order to optimize the thermal performances of microchannels with different cross-section together with the Poiseuille number ($f\mathrm{Re}$); for this comparison, Shah and London have introduced the *area goodness factor* defined as follows:

$$\frac{j}{f} = \frac{\mathrm{Nu}\,\mathrm{Pr}^{-1/3}}{f\mathrm{Re}} \tag{40}$$

Under the hypotheses that $\mathrm{Pe} = \mathrm{Br} = \beta = S^*_\mathrm{g} = f^* = 0$, from the equality in Eq. (40) it is evident that this factor is a constant for the fully developed laminar flow of a specified fluid. Since the dimensionless quantities j and f are independent of the scale of the geometry (D_h), the area goodness factor j/f for different microchannels represents the influence of the geometric factors on the pressure losses and the heat transfer and allows the comparison of the thermal hydraulic performances of microchannels having different cross-sections. In the viscous dissipation section a comparison of the thermal performances of rectangular and trapezoidal microchannels by means of the *area goodness factor* is presented.

Laminar Flow

The solution of Eqs. (22)–(23) with the appropriate dynamic and thermal boundary conditions allows one to obtain the velocity and temperature distribution inside the microchannel for laminar fully developed flows. The analytical solution of Eqs. (22)–(23) has been obtained only for a few cross-sectional geometries. The numerical approach enables the calculation of the local and the average Nusselt number by means of which the internal convective heat transfer coefficients in microchannels can be computed.

Circular Cross-Section

T Boundary Conditions

For circular cross-sections the average value of the Nusselt number has been computed for different thermal boundary conditions. The value of the average Nusselt number for the **T** boundary condition can be found in many textbooks; $\overline{\mathrm{Nu}}_\mathrm{T} = 3.656735$ for the case of pressure driven with negligible external volume forces ($f_{\mathrm{ext,z}} = 0$), axial heat conduction ($\mathrm{Pe} \to \infty$), viscous dissipation ($\mathrm{Br} = 0$), flow work ($\beta = 0$) and thermal energy sources ($S_\mathrm{g} = 0$) within the fluid. In the same conditions but for a slug flow the value of the average Nusselt number is $\overline{\mathrm{Nu}}_{\mathrm{T,sf}} = 5.783$. By including the effect of axial conduction in the fluid the fully developed average Nusselt number becomes a function of the Péclet number. An approximate relation by means of which $\overline{\mathrm{Nu}}_\mathrm{T}$ can be calculated as a function of Péclet number is the following:

$$\overline{\mathrm{Nu}}_\mathrm{T} = \begin{cases} 3.6568\left(1 + \frac{1.227}{\mathrm{Pe}^2}\right) & \mathrm{Pe} > 5 \\ 4.1807\,(1 - 0.0439Pe) & \mathrm{Pe} < 1.5 \end{cases} \tag{41}$$

For the **T3** boundary condition the average Nusselt number for fully developed laminar flow with negligible external volume forces ($f_{\mathrm{ext,z}} = 0$), axial heat conduction ($\mathrm{Pe} \to \infty$), viscous dissipation ($\mathrm{Br} = 0$), flow work ($\beta = 0$) and thermal energy sources ($S_\mathrm{g} = 0$) within the fluid is a function of the dimensionless wall thermal resistance R_w; the values of $\overline{\mathrm{Nu}}_{\mathrm{T3}}$ as a function of R_w are quoted in Tab. 2. When R_w tends to zero the Nusselt number tends to the value taken under **T** boundary conditions. On the contrary, for $R_\mathrm{w} \to \infty$ the Nusselt number tends to the value of the **H** boundary condition (48/11). In Tab. 3 the values of $\overline{\mathrm{Nu}}_{\mathrm{T3}}$ are tabulated as a function of the dimensionless wall thermal resistance R_w and the Péclet number by taking into account the axial conduction in the fluid.

For radiant flux boundary condition **T4** the average value of the Nusselt number can be calculated by using the following relation:

$$\overline{\mathrm{Nu}}_{\mathrm{T4}} = \frac{8.728 + 3.66\gamma\left(\dfrac{T_\mathrm{a}}{T_\mathrm{e}}\right)^3}{2 + \gamma\left(\dfrac{T_\mathrm{a}}{T_\mathrm{e}}\right)^3} \tag{42}$$

Convective Heat Transfer in Microchannels, Table 2 Nusselt numbers for laminar fully developed flow as a function of the dimensionless wall thermal resistance for the **T3** boundary condition

R_W	$\overline{\mathrm{Nu}}_{T3}$
0	3.657
0.005	3.669
0.025	3.713
0.05	3.763
0.1	3.844
0.15	3.908
0.25	4.000
0.5	4.124
1	4.223
∞	4.364

where T_a is the absolute outer fluid temperature (see Fig. 2), γ is defined by Eq. (30) and T_e is the absolute fluid inlet temperature.

Tunc and Bayazitoglu [3] have calculated for the **T** case the fully developed Nusselt numbers for microtubes through which a rarefied gas flows by taking into account the viscous dissipation but neglecting axial conduction in the fluid and the flow work. They defined the Brinkman number (Eq. (20)) with $\Delta T_{ref} = T_e - T|_\Gamma$ and used in the slip boundary conditions (Eqs. (8) and (19)) $\alpha = \sigma_v = \alpha_t = \sigma_t = 1$. The values of the Nusselt number for fully developed laminar flow determined by Tunc and Bayazitoglu [3] are quoted in Tab. 4 for $\mathrm{Br} = 0$ and $\mathrm{Br} = 0.01$ as a function of the Prandlt number and of the Knudsen number.

From the data it is clear that the Nusselt number decreases when the Knudsen number increases for a fixed Prandlt number. The rarefaction of the gas decreases the intensity of the heat transfer. When the Prandlt number increases for a fixed Knudsen number, the Nusselt number increases; this means that the convective heat transfer is enhanced for gases with larger Prandlt numbers. When the viscous dissipation increases the Nusselt number tends to increase. In fact, the increase of the viscous dissipation tends to increase the bulk temperature of the fluid. For a **T** boundary condition, since the Nusselt number is linked to the inverse of the difference between the wall temperature and the bulk temperature, an increase of the bulk temperature reduces this difference and increases the Nusselt number.

H Boundary Conditions

In the circular geometry there are no differences between **H1**, **H2** and **H3** boundary conditions in terms of Nusselt numbers. The Nusselt number can be expressed as

$$\overline{\mathrm{Nu}}_H = \frac{48}{11}\left(\frac{1}{1 + (3/44)\, S_g^* + (48/11)\,\mathrm{Br}}\right) \tag{43}$$

where S_g^* and Br are defined by Eqs. (24) and (20) respectively with ΔT_{ref} equal to $q'' D_h/k$. Axial conduction within the fluid is constant for the **H** boundary condition and consequently it does not affect the Nusselt number. Thus, in this case the Nusselt number is independent of the Péclet number.

The values of the Nusselt number for the **H5** boundary condition are quoted in Tab. 5 as a function of the parameter m defined by Eqs. (18) and (31). The data of Tab. 5 highlight how the **T** and **H** boundary conditions can be seen as particular cases of the H5 boundary condition for $m = -4\overline{\mathrm{Nu}}_T = -14.627$ and $m = 0$ respectively.

For slug flow the Nusselt number in the case of pressure-driven flow with negligible external volume forces ($f_{ext,z} = 0$), axial heat conduction ($\mathrm{Pe} \to \infty$), viscous dissipation ($\mathrm{Br} = 0$), flow work ($\beta = 0$) and thermal energy sources ($S_g = 0$) within the fluid is $\overline{\mathrm{Nu}}_{H,sf} = 8$.

Tunc and Bayazitoglu [3] have calculated in the **H** case the fully developed Nusselt numbers for microtubes through which a rarefied gas flows by taking into account the viscous dissipation but neglecting axial conduction in the fluid and flow work. They defined the Brinkman number (Eq. (20)) with $\Delta T_{ref} = q'' D_h/k$ and used in the slip boundary conditions (Eq. (8) and (19)) $\alpha = \sigma_v = \alpha_t = \sigma_t = 1$. The values of the Nusselt number for fully developed laminar flow determined by Tunc and Bayazitoglu [3] are quoted in Tab. 6 for $\mathrm{Br} = 0$, $\mathrm{Br} = -0.01$ and $\mathrm{Br} = 0.01$ as a function of the Prandlt number and of the Knudsen number. Negative values of the Brinkman number mean that the microchannel is cooled. By observing these data it is evident that the Nusselt number decreases when the Knudsen number increases for a fixed Prandlt number. The rarefaction of the gas decreases the intensity of the heat transfer. When the Prandlt number increases for a fixed Knudsen number the Nusselt number increases. The convective heat transfer is enhanced for gases with larger Prandlt numbers. When the viscous dissipation increases the Nusselt number tends to decrease; this trend is in disagreement with the behavior evidenced when the microtube is subjected to the **T** boundary condition.

Rectangular Cross-Section

T Boundary Conditions

For a rectangular microchannel the fully developed value of the Nusselt number $\overline{\mathrm{Nu}}_T$ in the case of pressure-driven

Convective Heat Transfer in Microchannels, Table 3 Nusselt numbers $\overline{\mathrm{Nu}}_{T3}$ for laminar fully developed flow as a function of the dimensionless wall thermal resistance and of the Péclet number for the T3 boundary condition

	$\overline{\mathrm{Nu}}_{T3}$							
R_W	Pe = 1	Pe = 5	Pe = 10	Pe = 20	Pe = 30	Pe = 50	Pe = 100	Pe = ∞
0	4.030	3.769	3.697	3.670	3.663	3.660	3.658	3.657
0.005	4.058	3.784	3.709	3.680	3.674	3.671	3.669	3.669
0.05	4.296	3.911	3.813	3.777	3.769	3.765	3.763	3.763
0.25	–	4.179	4.056	4.015	4.007	4.002	4.001	4.000
∞	4.364	4.364	4.364	4.364	4.364	4.364	4.364	4.364

C

Convective Heat Transfer in Microchannels, Table 4 Nusselt numbers $\overline{\mathrm{Nu}}_T$ for laminar fully developed flow as a function of the Knudsen number and the Prandtl number for Br = 0 and Br = 0.01 for the **T** boundary condition

	$\overline{\mathrm{Nu}}_T$				
Br = 0	Pr = 0.6	Pr = 0.7	Pr = 0.8	Pr = 0.9	Pr = 1
Kn = 0	3.657	3.657	3.657	3.657	3.657
Kn = 0.02	3.368	3.432	3.481	3.521	3.554
Kn = 0.04	3.075	3.183	3.270	3.341	3.400
Kn = 0.06	2.810	2.948	3.061	3.155	3.234
Kn = 0.08	2.577	2.733	2.864	2.974	3.069
Kn = 0.1	2.372	2.540	2.682	2.803	2.909
Kn = 0.12	2.194	2.367	2.516	2.645	2.758
Br = 0.01	**Pr = 0.6**	**Pr = 0.7**	**Pr = 0.8**	**Pr = 0.9**	**Pr = 1**
Kn = 0	6.423	6.423	6.423	6.423	6.423
Kn = 0.02	5.397	5.564	5.696	5.803	5.892
Kn = 0.04	4.597	4.845	5.048	5.129	5.364
Kn = 0.06	3.977	4.259	4.499	4.704	4.883
Kn = 0.08	3.490	3.784	4.039	4.262	4.459
Kn = 0.1	3.102	3.395	3.653	3.883	4.089
Kn = 0.12	2.782	3.073	3.286	3.559	3.768

Convective Heat Transfer in Microchannels, Table 5 Nusselt numbers $\overline{\mathrm{Nu}}_{H5}$ for laminar fully developed flow as a function of the m parameter defined by Eqs. (18) and (31) for the **H5** boundary condition

m	$\overline{\mathrm{Nu}}_{H5}$	m	$\overline{\mathrm{Nu}}_{H5}$
−70	−8.84	10	4.77
−60	−2.29	20	5.11
−50	0.256	30	5.42
−40	1.68	40	5.71
−30	2.64	50	5.97
−20	3.34	60	6.21
−14.63	3.657	70	6.43
−10	3.9	80	6.64
0	4.364	90	6.84
		100	7.02

Convective Heat Transfer in Microchannels, Table 6 Nusselt numbers $\overline{\mathrm{Nu}}_H$ for laminar fully developed flow as a function of the Knudsen number and the Prandtl number for Br = 0, Br = 0.01 and Br = -0.01 for the **H** boundary condition

	$\overline{\mathrm{Nu}}_H$				
Br = 0	Pr = 0.6	Pr = 0.7	Pr = 0.8	Pr = 0.9	Pr = 1
Kn = 0	4.364	4.364	4.364	4.364	4.364
Kn = 0.02	3.980	4.070	4.140	4.197	4.243
Kn = 0.04	3.598	3.748	3.869	3.969	4.052
Kn = 0.06	3.252	3.438	3.593	3.723	3.834
Kn = 0.08	2.949	3.155	3.331	3.481	3.611
Kn = 0.1	2.687	2.904	3.090	3.253	3.397
Kn = 0.12	2.461	2.681	2.874	3.044	3.195
Br = 0.01	**Pr = 0.6**	**Pr = 0.7**	**Pr = 0.8**	**Pr = 0.9**	**Pr = 1**
Kn = 0	4.035	4.035	4.035	4.035	4.035
Kn = 0.02	3.791	3.872	3.936	3.986	4.028
Kn = 0.04	3.486	3.627	3.740	3.833	3.910
Kn = 0.06	3.183	3.362	3.509	3.633	3.739
Kn = 0.08	2.905	3.106	3.275	3.420	3.546
Kn = 0.1	2.658	2.870	3.053	3.212	3.351
Kn = 0.12	2.442	2.658	2.848	3.014	3.163
Br = -0.01	**Pr = 0.6**	**Pr = 0.7**	**Pr = 0.8**	**Pr = 0.9**	**Pr = 1**
Kn = 0	4.748	4.748	4.748	4.748	4.748
Kn = 0.02	4.190	4.290	4.368	4.430	4.482
Kn = 0.04	3.718	3.878	4.008	4.115	4.204
Kn = 0.06	3.324	3.934	3.519	3.680	3.817
Kn = 0.08	2.994	3.207	3.388	3.544	3.679
Kn = 0.1	2.716	2.938	3.129	3.296	3.443
Kn = 0.12	2.481	2.705	2.901	3.074	3.229

flow with negligible external volume forces ($f_{\mathrm{ext},z} = 0$), axial heat conduction ($\mathrm{Pe} \to \infty$), viscous dissipation ($\mathrm{Br} = 0$), flow work ($\beta = 0$) and thermal energy sources ($S_g = 0$) within the fluid is reported as a function of the aspect ratio δ (defined as h/a ratio, see Fig. 4) in Tab. 7 for the 3bc and 4bc boundary condition (see Fig. 4).

Convective Heat Transfer in Microchannels, Table 7 Nusselt numbers $\overline{\mathrm{Nu}}_T$ for laminar fully developed flow for a rectangular cross-section with three (3bc) and four (4bc) heated sides as a function of the aspect ratio δ for the **T** boundary condition

	$\overline{\mathrm{Nu}}_T$	
δ	4bc	3bc
0	7.541	4.861
0.1	5.858	3.59
0.2	4.803	2.982
0.3	4.114	2.703
0.4	3.67	2.603
0.5	3.383	2.602
0.6	3.198	–
0.7	3.083	2.734
0.8	3.014	–
0.9	2.98	–
1	2.97	3.018
1.43	3.083	3.408
2	3.383	3.842
2.5	3.67	4.153
3.33	4.114	4.579
5	4.803	5.195
10	5.858	6.095
∞	7.541	7.541

The value of the Nusselt numbers obtained for the same conditions mentioned above but for slug flow can be calculated analytically as a function of the aspect ratio by means of the following relations for three and four heated walls:

$$\overline{\mathrm{Nu}}_{\mathrm{T,3bc,sf}} = \frac{\pi^2\left(4\delta^2+1\right)}{2\,(1+\delta)\,(1+2\delta)}$$
$$\overline{\mathrm{Nu}}_{\mathrm{T,4bc,sf}} = \frac{\pi^2\left(\delta^2+1\right)}{(1+\delta)^2} \qquad (44)$$

No data exist for **T3** and **T4** boundary conditions in the fully developed region.

H Boundary Conditions

In Tab. 8 the values of the Nusselt number for **H1** and **H2** boundary conditions (with three (3bc) and four (4bc) heated walls) in the case of pressure-driven flow with negligible external volume forces ($f_{\mathrm{ext,z}} = 0$), axial heat conduction ($\mathrm{Pe} \to \infty$), viscous dissipation ($\mathrm{Br} = 0$), flow work ($\beta = 0$) and thermal energy sources ($S_{\mathrm{g}} = 0$) within the fluid is quoted as a function of the aspect ratio δu.

For slug flow under **H1** boundary condition, in the case of pressure-driven flow with negligible external volume forces ($f_{\mathrm{ext,z}} = 0$), axial heat conduction ($\mathrm{Pe} \to \infty$), viscous dissipation ($\mathrm{Br} = 0$), flow work ($\beta = 0$) and thermal energy sources ($S_{\mathrm{g}} = 0$) within the fluid the Nusselt number can be calculated analytically as a function of the aspect ratio:

$$\overline{\mathrm{Nu}}_{\mathrm{H1,3bc,sf}} = \pi^6 \Big/ \left[128\,(1+\delta)\,(2\delta+1) \times \sum_{n=1,\mathrm{odd}}^{\infty} \sum_{m=1,\mathrm{odd}}^{\infty} \frac{1}{n^2 m^2\left(4m^2+\delta^2 n^2\right)}\right] \qquad (45)$$

$$\overline{\mathrm{Nu}}_{\mathrm{H1,4bc,sf}} = \pi^6 \Big/ \left[64\,(1+\delta)^2 \times \sum_{n=1,\mathrm{odd}}^{\infty} \sum_{m=1,\mathrm{odd}}^{\infty} \frac{1}{n^2 m^2\left(m^2+\delta^2 n^2\right)}\right] \qquad (46)$$

For slug flow under **H2** boundary conditions it is possible to demonstrate that the Nusselt number in the 4bc case (four heated sides) is independent of the aspect ratio and its value is 6. The Nusselt number for slug flow with three heated sides can be calculated by means of the following analytical expression:

$$\mathrm{Nu}_{\mathrm{H2,3bc,sf}} = 3\frac{(2\delta+1)}{(1+\delta)} \qquad (47)$$

In Tab. 9 the fully developed Nusselt numbers for rectangular microchannels in which rarefied gases flow under the **H1** boundary condition with four heated sides (4bc) are quoted. These values are obtained for a gas having $\mathrm{Pr} = 0.7$ by neglecting viscous dissipation, axial conduction and flow work and using in the slip boundary conditions (Eqs. (8) and (19)) $\alpha = \sigma_v = \alpha_t = \sigma_t = 1$. It is evident that the Nusselt number decreases when the Knudsen number increases and it tends to increase when the aspect ratio decreases.

Tunc and Bayazitoglu [4] have calculated in the case **H2** (4bc) the fully developed Nusselt numbers for rectangular microchannels through which a rarefied gas flows by neglecting the viscous dissipation, axial conduction in the fluid and the flow work. They used in the slip boundary conditions (Eqs. (8) and (19)) $\alpha = \sigma_v = \alpha_t = \sigma_t = 1$. The values of the Nusselt number for fully developed laminar flow determined by Tunc and Bayazitoglu [4] are quoted in Tab. 10 as a function of the aspect ratio δ, of the Prandlt number and of the Knudsen number for four sides heated (4bc). By observing these data it is evident that

Convective Heat Transfer in Microchannels, Table 8 Nusselt numbers $\overline{Nu}_{H1}$ and $\overline{Nu}_{H2}$ for laminar fully developed flow for a rectangular cross-section with three (3bc) and four (4bc) heated sides as a function of the aspect ratio δ for the **H1** and **H2** boundary conditions

	$\overline{Nu}_{H1}$		$\overline{Nu}_{H2}$	
δ	*4bc*	*3bc*	*4bc*	*3bc*
0	8.235	5.385	–	–
0.1	6.785	4.283	2.907	2.24
0.125	–	–	2.909	2.27
0.2	5.738	3.639	2.922	2.354
0.25	–	–	2.935	2.408
0.3	4.99	3.302	–	–
0.333	–	–	2.964	2.494
0.4	4.472	3.163	–	–
0.5	4.123	3.14	3.022	2.648
0.6	3.895	3.182	–	–
0.666	–	–	3.064	2.824
0.7	3.75	3.259	–	–
0.75	–	–	3.077	2.824
0.8	3.664	3.355	–	–
0.8333	–	–	3.085	2.869
0.9	3.62	3.46	–	–
1	3.608	3.568	3.091	2.943
1.11111	3.62	3.688	–	–
1.2	–	–	3.085	3.009
1.25	3.664	3.836	–	–
1.33	–	–	3.077	3.042
1.42857	3.75	4.018	–	–
1.5	–	–	3.064	3.076
1.66667	3.895	4.246	–	–
2	4.123	4.539	3.022	3.14
2.5	4.472	4.923	–	–
3	–	–	2.964	3.204
3.33333	4.99	5.439	–	–
4	–	–	2.935	3.241
5	5.738	6.131	2.922	3.268
8	–	–	2.909	3.319
10	6.785	7.044	2.907	3.339
∞	8.235	8.235	–	–

the Nusselt number decreases when the Knudsen number increases for a fixed Prandlt number. The rarefaction of the gas decreases the intensity of the heat transfer. When the Prandlt number increases for a fixed Knudsen number, the Nusselt number increases. The convective heat transfer is enhanced for gases with larger Prandlt numbers and for square microchannels ($\delta \to 1$). By comparing Tab. 9 with Tab. 10 it is evident that the Nusselt number for the **H1** boundary condition is larger than those calculated for the **H2** boundary condition.

The values of the fully developed Nusselt number for electro-osmotic flows under **H1** boundary condition for

Convective Heat Transfer in Microchannels, Table 9 Nusselt numbers $\overline{Nu}_{H1}$ for a rarefied gas with Pr = 0.7 in laminar fully developed flow in a rectangular microchannel with four sides heated as a function of the Knudsen number and of the aspect ratio δ for the **H1** boundary condition

	$\overline{Nu}_{H1}$			
Kn	$\delta = 1$	$\delta = 0.75$	$\delta = 0.5$	$\delta = 0.25$
0.02	3.38	3.45	3.76	4.66
0.04	3.14	3.19	3.41	4.09
0.06	2.91	2.94	3.11	3.62
0.08	2.70	2.72	2.85	3.24
0.1	2.51	2.53	2.62	2.93

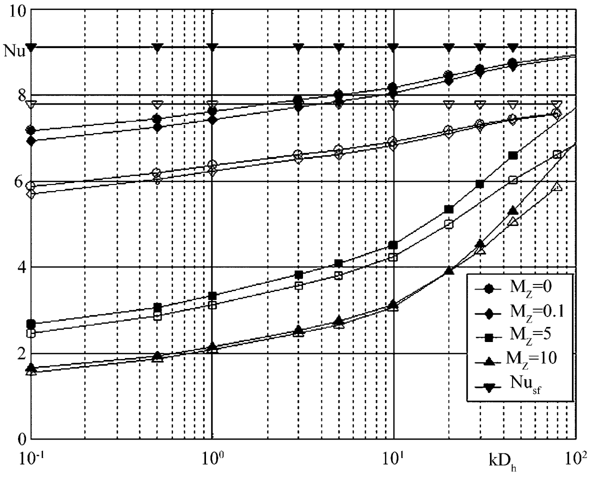

Convective Heat Transfer in Microchannels, Figure 5 Nusselt numbers as a function of the electro-osmotic diameter (kD_h) for rectangular microchannels. The filled symbols denote an aspect ratio $\delta = 0.25$, whereas the open symbols are for $\delta = 0.50$.The superscript sf stands for 'slug flow'

a rectangular cross-section with four sides heated (4bc) are depicted in Fig. 5 as a function of M_z (*Joule heating*) and the dimensionless electro-osmotic diameter:

$$kD_h = D_h \sqrt{\frac{2 n_0 z^2 e^2}{\varepsilon_r \varepsilon_0 k_B T}} \tag{48}$$

This parameter gives the magnitude of the diffuse layer thickness. It can be demonstrated that the value of the dimensionless electrokinetic potential for a given cross-section is strongly dependent on the product kD_h. Viscous dissipation, axial conduction and flow work are considered negligible.

It can be noticed how the presence of Joule heating reduces the value of the Nusselt number dramatically, while a decrease in the value of the aspect ratio δ dampens this effect. The value of the Nusselt number for a perfectly flat velocity profile (*slug flow*) for a rectangular duct, Nu_{sf}, is also plotted in Fig. 5 for the rectangular cross-section

Convective Heat Transfer in Microchannels, Table 10 Nusselt numbers $\overline{\mathrm{Nu}}_{\mathrm{H2}}$ for rarefied gases in laminar fully developed flow in a rectangular microchannel with four sides heated as a function of the Knudsen number, of the Prandtl number and of the aspect ratio δ for the **H2** boundary condition

		$\overline{\mathrm{Nu}}_{\mathrm{H2}}$									
Kn	Pr	$\delta = 1$	$\delta = 0.84$	$\delta = 0.75$	$\delta = 0.67$	$\delta = 0.5$	$\delta = 0.34$	$\delta = 0.25$	$\delta = 0.2$	$\delta = 0.125$	$\delta = 0.1$
0.02	0.6	2.95	2.93	2.92	2.90	2.85	2.76	2.67	2.59	2.35	2.19
	0.7	2.99	2.98	2.98	2.97	2.92	2.85	2.78	2.71	2.49	2.34
	0.9	3.07	3.06	3.58	3.05	3.02	2.97	2.93	2.88	2.72	2.59
0.04	0.6	2.76	2.73	2.71	2.68	2.59	2.42	2.27	2.12	1.75	1.56
	0.7	2.85	2.82	2.81	2.79	2.71	2.56	2.42	2.28	1.92	1.72
	0.9	2.98	2.97	2.96	2.94	2.88	2.77	2.66	2.54	2.20	2
0.06	0.6	2.58	2.53	2.5	2.46	2.33	2.11	1.92	1.75	1.37	1.19
	0.7	2.69	2.65	2.62	2.59	2.48	2.27	2.09	1.91	1.52	1.33
	0.9	2.86	2.84	2.82	2.79	2.70	2.53	2.36	2.2	1.79	1.59
0.08	0.6	2.4	2.34	2.30	2.25	2.10	1.85	1.64	1.47	1.11	0.95
	0.7	2.53	2.48	2.44	2.40	2.26	2.02	1.81	1.63	1.25	1.08
	0.9	2.74	2.70	2.67	2.63	2.52	2.29	2.09	1.91	1.5	1.31
0.1	0.6	2.23	2.17	2.12	2.06	1.91	1.64	1.43	1.27	0.94	0.79
	0.7	2.38	2.32	2.28	2.22	2.07	1.81	1.59	1.42	1.06	0.9
	0.9	2.61	2.56	2.52	2.48	2.34	2.09	1.87	1.68	1.29	1.11
0.12	0.6	2.05	2.01	1.96	1.9	1.74	1.47	1.27	1.11	0.81	0.69
	0.7	2.24	2.17	2.12	2.06	1.90	1.63	1.42	1.25	0.92	0.78
	0.9	2.49	2.43	2.38	2.33	2.18	1.90	1.68	1.50	1.12	0.96

considered. It is evident that the values of the Nusselt number approach the corresponding $\mathrm{Nu_{sf}}$ when kD_h increases, so much more so the lower the value of M_z.

Trapezoidal Cross-Section

It is well known that with photo-lithographic-based process one can obtain microchannels having a cross-section fixed by the orientation of the wafer crystal planes; for example, the microchannels etched in ⟨100⟩ silicon using a KOH solution have a trapezoidal cross-section with an apex angle of 54.74° imposed by the crystallographic morphology of the ⟨100⟩ silicon. By gluing together two KOH-etched trapezoidal silicon microchannels one can obtain microchannels having a double-trapezoidal cross-section (see Fig. 4). This kind of microchannel is investigated in this section.

Only numerical solutions have been published in the open literature for this kind of geometry.

T Boundary Conditions

Nonino et al. [5] computed numerically the value of the laminar fully developed average Nusselt number for trapezoidal and double trapezoidal KOH-etched microchannels under the **T** boundary condition with four and six heated sides respectively. They found that $\overline{\mathrm{Nu}}_\mathrm{T} = 2.7701$ for a trapezoidal microchannel with $\delta = 1$ and $\overline{\mathrm{Nu}}_\mathrm{T} = 3.3247$ for a double trapezoidal microchannel with $\delta = 0.828$. Further numerical investigations are required in order to investigate the role of the aspect ratio on the Nusselt number.

H Boundary Conditions

In Tab. 11 the values assumed by the Nusselt number for **H1** boundary conditions with three (3bc) and four (4bc) heated walls in the case of pressure-driven flow with negligible external volume forces ($f_{\mathrm{ext,z}} = 0$), axial heat conduction ($\mathrm{Pe} \to \infty$), viscous dissipation ($\mathrm{Br} = 0$), flow work ($\beta = 0$) and thermal energy sources ($S_\mathrm{g} = 0$) within the fluid is quoted as a function of the aspect ratio δ defined as h/a ratio (see Fig. 4).

In Tab. 12 the fully developed value of the Nusselt number for double-trapezoidal KOH-etched microchannels with six sides heated (6bc) are presented as a function of the aspect ratio δ defined as h/a ratio (see Fig. 4). For slug flow under **H1** boundary conditions, in the case of pressure-driven flow with negligible external volume forces ($f_{\mathrm{ext,z}} = 0$), axial heat conduction ($\mathrm{Pe} \to \infty$), viscous dissipation ($\mathrm{Br} = 0$), flow work ($\beta = 0$) and thermal energy sources ($S_\mathrm{g} = 0$) within the fluid the Nusselt numbers for KOH-etched trapezoidal and double-trapezoidal

Convective Heat Transfer in Microchannels, Table 11 Nusselt numbers $\overline{Nu}_{H1}$ for laminar fully developed flow for a KOH-etched trapezoidal cross-section with three (3bc) and four (4bc) heated sides as a function of the aspect ratio δ for the **H1** boundary condition

	$\overline{Nu}_{H1}$	
δ	4bc	3bc
0	8.235	5.385
0.05	7.302	4.752
0.1	6.575	4.283
0.2	5.536	3.666
0.3	4.852	3.315
0.4	4.391	3.116
0.5	4.073	3.002
0.6	3.850	2.939
0.7	3.691	2.906
0.8	3.577	2.889
0.9	3.493	2.883
1	3.431	2.883
10/9	3.381	2.889
5/4	3.338	2.898
10/7	3.303	2.912
5/3	3.277	2.930
2	3.261	2.948
2.5	3.255	2.964
10/3	3.251	2.968
5	3.236	2.946
10	3.188	2.880
∞	3.093	2.765

microchannels are quoted in Tab. 13 and 14 respectively as a function of the aspect ratio δ.

In Tab. 15 the fully developed Nusselt numbers for trapezoidal microchannels in which rarefied gases flow under the H1 boundary condition with four heated sides (4bc) are quoted. These values are obtained for a gas having $\mathrm{Pr} = 0.7$ by neglecting viscous dissipation, axial conduction and flow work and using in the slip boundary conditions (Eq. (8) and (19)) $\alpha = \sigma_v = \alpha_t = \sigma_t = 1$.

Laminar-to-Turbulent Transition

Heat transfer results are uncertain in the transition region because of the large number of parameters which determine when and how transition occurs (wall roughness, cross-sectional geometry, compressibility, Reynolds number and so on). Experimental results indicate that in smooth microchannels below Reynolds numbers of 1800–2000 the heat transfer results will be laminar and above 10 000 the results will be normally turbulent. The results in between are difficult to predict (see ▶ pressure-driven single-phase flow): unfortunately, this region is largely used when microchannels having hydraulic diameters less than 500 μm are considered (Re < 30 000).

Convective Heat Transfer in Microchannels, Table 12 Nusselt numbers $\overline{Nu}_{H1}$ for laminar fully developed flow for a KOH-etched double-trapezoidal cross-section with six (6bc) heated sides as a function of the aspect ratio δ for the **H1** boundary condition

	$\overline{Nu}_{H1}$
δ	6bc
0	8.235
0.1	6.93
0.2	5.909
0.4	4.63
0.5	4.302
0.6	4.113
0.7	4.02
0.8	3.988
0.9	3.987
1	3.988
1.2	3.876
1.3	3.73
1.414	3.506

Convective Heat Transfer in Microchannels, Table 13 Nusselt numbers $\overline{Nu}_{H1}$ for slug flow in a KOH-etched trapezoidal microchannel with three (3bc) and four (4bc) heated sides as a function of the aspect ratio δ for the **H1** boundary condition

	$\overline{Nu}_{H1,sf}$	
δ	4bc	3bc
0.010	11.796	5.895
0.054	11.027	5.513
0.116	10.165	5.116
0.279	8.75	4.58
0.387	8.188	4.437
0.521	7.723	4.369
0.693	7.357	4.362
0.921	7.09	4.401
1.237	6.92	4.472
1.707	6.839	4.555
3.959	6.845	4.664
8.039	6.846	4.627
∞	6.655	4.457

Turbulent Regime

The thermal behavior of turbulent flows in a microchannel, under conditions of constant properties and moderate velocity can be described by means of the Nusselt number. Under certain thermal boundary conditions the Nusselt number in the turbulent regime becomes independent on the channel length. As in the case of laminar flow the

Convective Heat Transfer in Microchannels, Table 14 Nusselt numbers $\overline{\mathrm{Nu}}_{\mathrm{H1}}$ for slug flow in a KOH-etched double-trapezoidal cross-section with six (6bc) heated sides as a function of the aspect ratio δ for the **H1** boundary condition

	$\overline{\mathrm{Nu}}_{\mathrm{H1,sf}}$
δ	6bc
0.02	11.729
0.1	10.754
0.2	9.751
0.4	8.374
0.5	7.962
0.6	7.702
0.7	7.563
0.8	7.541
0.9	7.522
1	7.556
1.2	7.541
1.3	7.393
1.414	7.03

two thermal boundary conditions of most technical interest for which such an asymptotical Nusselt number is obtained are for a constant heat flux (**H** boundary conditions) and for a constant surface temperature (**T** boundary condition). In the turbulent regime as well as in the laminar regime the **H** Nusselt numbers are always greater than **T** Nusselt numbers but in turbulent regime the difference is generally much smaller than for laminar flow and becomes negligible for fluids having $\mathrm{Pr} > 1$ (e. g. water).

For turbulent flow the thermal entrance region is shorter than for laminar flow (with the exception of liquid metals which have a very low Prandtl number) and thus the fully developed values of the Nusselt number are frequently used directly in heat transfer design without reference to the thermal entrance effects. The turbulent fully developed Nusselt number in a smooth channel can be expressed as a function of the Reynolds number and of the Prandtl number.

Algebraic correlations are used extensively to represent turbulent convective heat transfer data. One of the earliest correlations used for fully developed turbulent flow heat transfer is the *Dittus–Boelter correlation*:

$$\overline{\mathrm{Nu}} = 0.023\ \mathrm{Re}^{0.8}\mathrm{Pr}^{n} \tag{49}$$

where $n = 0.4$ for heating and $n = 0.3$ for cooling. This correlation can be employed for both **H** and **T** boundary conditions when $\mathrm{Re} > 10\,000$, $0.7 < \mathrm{Pr} < 160$ and $L/D_{\mathrm{h}} > 10$.

For fluids with Prandtl numbers less than 1 (e. g. gases) the difference among the thermal boundary conditions becomes important and the Nusselt number has to be calculated in a different way for **H** and **T** problems. In the range of the Prandtl number between 0.5 and 1 the turbulent fully developed Nusselt number can be calculated by using the following correlations:

$$\begin{aligned}\overline{\mathrm{Nu}}_{\mathrm{T}} &= 0.021\ \mathrm{Re}^{0.8}\mathrm{Pr}^{0.6}\\ \overline{\mathrm{Nu}}_{\mathrm{H}} &= 0.022\ \mathrm{Re}^{0.8}\mathrm{Pr}^{0.6}\end{aligned} \tag{50}$$

Another very common correlation used in order to predict the turbulent convective heat transfer in channels is the *Sieder and Tate correlation*:

$$\overline{\mathrm{Nu}} = 0.027\ \mathrm{Re}^{0.8}\mathrm{Pr}^{\frac{1}{3}}\left(\frac{\mu}{\mu_{\mathrm{w}}}\right)^{0.14} \tag{51}$$

The use of this correlation is recommended when the temperature variation inside the microchannel is large; in this case it is not possible to consider the thermophysical properties of the fluid as constant, and in particular it is necessary to take into account the variation of the viscosity with temperature. In this correlation all the properties must be computed at the average fluid bulk temperature except μ_{w} that is evaluated at the wall temperature. This correlation is valid for $\mathrm{Re} > 10\,000$; this range of Reynolds numbers is not commonly encountered when microchannels having a hydraulic diameter less than 500 μm are considered. For this reason, in many experimental works conducted with microchannels the data obtained in the turbulent regime have been compared with the predictions of the *Gnielnski correlation*:

$$\overline{\mathrm{Nu}} = \frac{(f/2)(\mathrm{Re}-1000)\mathrm{Pr}}{1+12.7(f/2)^{1/2}(\mathrm{Pr}^{2/3}-1)} \tag{52}$$

where f is the Fanning friction factor (see ► pressure–driven single-phase flow).

This correlation is valid for moderate Reynolds number ($3000 < \mathrm{Re} < 5\times10^{6}$) and for this reason can be considered as appropriate for microchannels where larger Reynolds numbers are hard to obtain. The experimental data obtained by Celata et al. [6] confirmed that this kind of correlation agrees well with the data obtained with microtubes having an inner diameter between 500 and 120 μm.

Experimental Determination of the Nusselt Number

Since the local value of the bulk temperature is not easy to measure along a microchannel, the local value of the Nusselt number cannot be calculated in general. Only the

mean value of the Nusselt number can be gained from the experimental data by means of the following equation:

$$\mathrm{Nu}_{\mathrm{m}} = \frac{Q}{k\Gamma_{\mathrm{h}}^{*} L(T_{\mathrm{m,w}} - T_{\mathrm{m,b}})} \tag{53}$$

in which Q is the power removed by the working fluid, Γ_{h}^{*} is the dimensionless heated perimeter of the microchannel ($\Gamma_{\mathrm{h}}/D_{\mathrm{h}}$) and L the microchannel length.

The average wall temperature ($T_{\mathrm{m,w}}$) is in general calculated as the mean of N temperature measures made along the microchannel and the average bulk temperature ($T_{\mathrm{m,b}}$) is usually interpolated by using the inlet and outlet temperatures because it is hard to provide local measurements of bulk temperature along the microchannel.

It is necessary to remark that a large number of comparisons between experimental and theoretical results for microchannels have revealed a deep mismatch in the thermal boundary and inlet conditions that can preclude the use of the conventional correlations. In addition, in experiments on flow and heat transfer in microchannels, some parameters, like the channel dimensions, the average roughness, the local convective heat transfer, the local value of the static pressure along a microchannel, and so on, are difficult to measure accurately. For this reason, a large number of inconsistencies in published data are very likely to be due to experimental inaccuracies.

In this section, the main effects that can be invoked in order to justify the eventual discrepancies between the theoretical and the experimental results in terms of Nusselt numbers are listed and systematically discussed.

Entrance Effects

First of all, the difference between the theoretical values of the Nusselt number and the experimental ones evaluated by means of Eq. (53) can be eliminated by taking into account the effects related to the entrance region. Since the length of the thermal entrance region can be very short for turbulent flow, the entrance effects become more important in microchannels in which the flow is laminar but with large Reynolds numbers ($\mathrm{Re} > 1500$). Theoretically, the mean Nusselt number along a channel having a length equal to L can be predicted by means of the following generalized *Hausen correlation*, valid for $\mathrm{Re} < 3000$:

$$\mathrm{Nu}_{\mathrm{m}} = \overline{\mathrm{Nu}} + K_1 \frac{\left(\frac{\mathrm{Re}\,\mathrm{Pr}\,D_{\mathrm{h}}}{L}\right)}{\left(1 + K_2\left(\frac{\mathrm{Re}\,\mathrm{Pr}\,D_{\mathrm{h}}}{L}\right)^{b}\right)} \tag{54}$$

In the *Hausen correlation* the mean Nusselt number is calculated as a sum of two terms: the first term ($\overline{\mathrm{Nu}}$) is the fully developed value of the Nusselt number; its value can be calculated by using the data quoted in the above sections. The second term takes into account the effects of the thermal **entrance region**. Rosehnow and Choi [7] give the value of the coefficients K_1, K_2 and b for circular channels; in the case of prescribed wall heat flux (**H** boundary condition) and developed profile of velocity, $\overline{\mathrm{Nu}}$ is equal to 48/11 (see Eq. (43)) with $\mathrm{Br} = S_{\mathrm{g}}^{*} = 0$, $K_1 = 0.023$, $K_2 = 0.0012$ and $b = 1$. Recently Li et al. [8] proposed to use in Eq. (54) for rectangular microchannels with four sides heated the following values: $K_1 = 0.14$, $K_2 = 0.05$ and $b = 2/3$. Equation (54) brings to the fore the effect of the entrance region on the mean value of the Nusselt number along a channel. If the Reynolds number increases, the length of the entrance region increases and the second term in Eq. (54) increases too. It is possible to demonstrate that the entrance effects in tubes become negligible if the following inequality is satisfied:

$$\frac{\mathrm{RePr}D_{\mathrm{h}}}{L} < 10 \tag{55}$$

Viscous Dissipation

When the Reynolds number increases the Brinkman number increases too; this means that the effect of the ▶ viscous dissipation gains in importance. When the fluid is heated by viscous dissipation the fully developed value of the Nusselt number tends to decrease for **H1** boundary condition; in fact, its value depends on the Brinkman number as follows:

$$\overline{\mathrm{Nu}}_{\mathrm{H1}}(\mathrm{Br}) = \frac{\overline{\mathrm{Nu}}_{\mathrm{H1}}}{1 + \sigma\,\mathrm{Br}} \tag{56}$$

where $\overline{\mathrm{Nu}}_{\mathrm{H1}}$ is the fully developed Nusselt number when $\mathrm{Br} = 0$ and σ is a parameter depending on the geometry of the channel cross-section and on the combination of heated and adiabatic sides of the channel. The values assumed by σ for rectangular, circular and KOH-etched trapezoidal cross-sections are quoted in the section on viscous dissipation.

Equation (56) states that when the Brinkman number increases the Nusselt number decreases; in other words, the viscous dissipation tends to reduce significantly the value of the convective heat transfer at large Reynolds numbers when the hydraulic diameter decreases. On the contrary, for low values of the Reynolds number, the mean value of the Nusselt number coincides theoretically with the fully developed value of the Nusselt number because the entrance region is very short and the effects of the viscous dissipation are unimportant in this region.

A theoretical criterion to draw the limit of significance of the viscous dissipation in adiabatic and in heated

microchannels is described in the section on viscous dissipation.

Wall–Fluid Conjugate Heat Transfer

In the region of low Reynolds numbers the effects of the *conjugated heat transfer* on the mean value of the Nusselt number are very important because the conduction along the walls (especially for silicon microchannels) becomes a competitive mechanism of heat transfer as compared to internal convection. As evidenced theoretically by Maranzana et al. [9], when the effects of conjugate heat transfer are predominant, the bulk temperature distribution along the microchannel is not linear at all even in the **H1** boundary condition. For this reason, the Nusselt number calculated by using Eq. (53) is underestimated because the mean value of the bulk temperature ($T_{m,b}$) along the microchannel is underestimated. For this reason if the experimental values of the Nusselt number calculated by means of Eq. (53) are compared with their theoretical fully developed value a difference can be noted. This difference decreases when the Reynolds number increases because the effects of conjugate heat transfer are limited for large Reynolds numbers. This fact explains the dependence of the Nusselt number evaluated by means of Eq. (53) on the Reynolds number especially when low values of the latter are considered. In other words, the mean Nusselt number evaluated through Eq. (53) can exhibit a dependence on the Reynolds number even in the laminar regime due to the axial conduction along the solid walls of the microchannel. The conjugate wall-fluid effects are predominant for low Reynolds numbers and therefore not in direct competition with the effects related to viscous heating.

The limit of significance of the wall axial heat conduction in comparison with the convective heat transfer can be drawn by using the following inequality:

$$\left(\frac{\lambda_s}{\lambda_f}\right)\left(\frac{D_h}{L}\right)\left(\frac{\Omega_w}{\Omega}-1\right)\frac{1}{\mathrm{RePr}} > 0.01 \qquad (57)$$

in which Ω and Ω_w are the areas depicted in Fig. 1. This dimensionless quantity allows the comparison of the heat transfer by axial conduction in the wall with the convective heat transfer in the flow. When Eq. (57) is satisfied the wall axial heat conduction cannot be neglected.

Temperature-Dependent Fluid Properties

Since the temperature rise along the microchannel can be very large at very low values of the Reynolds number, for a fixed value of the wall heat flux, the thermophysical properties cannot be considered as constants; in other words, the effects related to the *variation of the thermophysical properties with temperature* tend to be in general coupled with conjugate effects. It has been numerically demonstrated that in microchannel flows it becomes very important to take into account the variation of the fluid viscosity with the temperature; in contrast, the other thermophysical properties can be considered as constant.

In addition, for large Reynolds numbers and very small diameters, the pressure drop along the microchannel can be very high. In this case, the effect of the pressure on the thermophysical properties has to be taken into account. Since the viscosity tends to increase with pressure, the effect of a large pressure drop along a microchannel is similar to a temperature rise: the viscosity decreases along the microchannel. This means that the effects of the pressure on the fluid viscosity can be coupled with viscous dissipation effects at large Reynolds numbers. Experimentally it has been demonstrated that the variation of the thermophysical properties with the pressure can in general be considered negligible for pressure differences less than 50 MPa between the inlet and the outlet.

Convective Heat Transfer in Microchannels, Table 15 Nusselt numbers $\overline{\mathrm{Nu}}_{H1}$ for a rarefied gas with Pr = 0.7 in laminar fully developed flow in a KOH-etched trapezoidal microchannel with four sides heated as a function of the Knudsen number and of the aspect ratio δ for the **H1** boundary condition

	$\overline{\mathrm{Nu}}_{H1}$				
Kn	$\delta = 10$	$\delta = 5$	$\delta = 1$	$\delta = 0.5$	$\delta = 0.1$
0.02	2.98	3.02	3.18	3.68	5.59
0.04	2.76	2.80	2.93	3.31	4.78
0.06	2.56	2.60	2.70	3.00	4.16
0.08	2.38	2.41	2.50	2.73	3.66
0.1	2.22	2.24	2.32	2.50	3.26

Surface Roughness

It is well known that the friction factor and the convective heat transfer coefficient can be influenced by the relative roughness of the walls of a channel. For microchannels the relative roughness, defined as the ratio between the mean height of the surface asperities and the hydraulic diameter of the channel, can assume large values. Especially for stainless steel commercial microtubes the relative roughness can reach values equal to 2–8%.

Numerical works have demonstrated that the effect of the roughness on the Nusselt number is in general less pronounced than its effect on the friction factor: its influence on the heat transfer is mostly of the same order of magnitude as the accepted experimental uncertainty. A large relative roughness can increase or decrease the

value of the Nusselt number as compared to the value of Nu in a smooth microchannel and the effect of the roughness seems to be highly dependent on the channel shape.

Rarefaction Effects

A very accurate and recent review of the main results on this topic has been published [10]. In that review it is demonstrated that the slip-flow regime has been much studied in the last few years from theoretical and experimental points of view. The gas rarefaction decreases the value of the convective heat transfer, as evidenced by the results quoted in Tab. 6, 9, 10 and 15. The convective heat transfer for rarefied gases in microchannels depends on the kind of interactions between the gas and the walls; in fact, these interactions determine the value of the finite 'temperature jump' between walls and gas (see ▶ pressure-driven single phase gas flows). Rarefaction effects tend to influence the heat transfer for Knudsen numbers greater than 0.001.

Compressibility Effects

The conventional theory states that if the average value of the Mach number (Ma_m, defined as the ratio between the fluid velocity and the speed of sound) along a channel is less than 0.3 the flow can be modeled locally as incompressible. In addition, when the pressure drop along the tube length is lower than 5% of the inlet pressure, the effect of the acceleration of the gas flow in the axial direction can be neglected (in other words, the variation of the gas density along the channel can be neglected).

Since the pressure drop along the tube length is much larger in microchannels than in conventional-sized tubes, the effects of the gas acceleration cannot in general be neglected, even for very low values of the Mach numbers as observed theoretically and experimentally by several authors.

When $Ma_m > 0.3$ the hypothesis of incompressibility no longer holds and the gas acceleration leads to changes in the velocity profile not only in magnitude but also in shape. The magnitude increments produce additional pressure drop while the shape changes alter the friction factor at the walls. The continuous variation in shape of the velocity profile means that neither fully developed nor locally fully developed flows occur. This fact influences the convective heat transfer coefficient since no fully developed temperature profiles can occur if the flow is developing and the experimental Nusselt numbers differ by the theoretical values for fully developed flow. It is possible to demonstrate numerically that when the Mach number increases the Nusselt number decreases along the tube and it can become negative if the resulting temperature decrease along the microchannel is large enough.

Electric Double Layer Effects

One aspect which has been evidenced in numerical and experimental works is the influence of electrostatic interaction between fluid and channel walls on the friction factor and on the Nusselt number. In particular, it has been observed that in the presence of an electric double layer the Nusselt number increases because the temperature and the velocity gradients at the walls tend to be increased. The electro-osmotic interactions between the fluid and the walls could explain, for microchannels with a hydraulic diameter less than 20 μm, the dependence of the Nusselt number on the Reynolds number, even in the laminar regime.

Future Directions for Research

Convective heat transfer in microchannels has been studied extensively in the last decade both experimentally and theoretically. From a chronological analysis of these experimental works it is possible to note that the discrepancy between the experimental data obtained for microchannels and the predictions of the conventional theory is decreasing. This fact can be partially explained by considering the dramatic improvements in microfabrication techniques with the consequent more appropriate control of the roughness and geometry of the microchannel and with the increase in the accuracy of the experimental tests made. For this reason the results of the older studies are sometimes fraught with errors and can be misleading.

In the future it will be very important to study the role played by the main scaling effects (i. e. viscous dissipation, flow work, compressibility) and micro-effects (rarefaction, electric double layer effects) on the convective heat transfer for single-phase flows in microchannels with the aim to explain that many experimental results published in the open literature can be justified by using correctly the conventional theory.

Cross References

- ▶ Pressure-Driven Single-Phase Liquid Flow
- ▶ Pressure-Driven Single-Phase Gas Flows
- ▶ Viscous Dissipation
- ▶ Viscous Heating
- ▶ Electrical Double Layers
- ▶ Electroosmotic Flow (DC)
- ▶ AC Electro-Osmotic Flow
- ▶ Entrance Region
- ▶ Developing Flow

References

1. Bird RB, Stewart WE, Lighfoot EN (1960) Transport Phenomena. Wiley, New York
2. Shah RK, London A (1978) Laminar Flow Forced Convection in Ducts. Adv Heat Transf 14:1–468
3. Tunc G, Bayazitoglu Y (2001) Heat Transfer in Microtubes with Viscous Dissipation. Int J Heat Mass Transf 44:2395–2403
4. Tunc G, Bayazitoglu Y (2002) Heat Transfer in Rectangular Microchannels. Int J Heat Mass Transf 45:765–773
5. Nonino C, Del Giudice S, Savino S (2006) Temperature Dependent Viscosity Effects on Laminar Forced Convection in the Entrance Region of Straight Ducts. Int J Heat Mass Transf 49:4469–4481
6. Celata GP, Cumo M, Marconi V, McPhail SJ, Zummo G (2006) Single Phase Laminar and Turbulent Heat Transfer in Smooth and Rough Microtubes. 3rd Colloque SHF Microfluidique 2006, Toulouse (France) December 12–14
7. Rohsenow WM, Choi HY (1961) Heat, Mass and Momentum Transfer. Prentice-Hall, New York
8. Li J, Peterson GP, Cheng P (2004) Three-dimensional Analysis of Heat Transfer in a Micro-heat sink with Single Phase Flow. Int J Heat Mass Transf 47:4215–4231
9. Maranzana G, Perry I, Maillet D (2004) Mini- and microchannels influence of axial conduction in the walls. Int J Heat Mass Transf 47:3993–4004
10. Kandlikar SG, Garimella SV, Li D, Colin S, King M (2006) Heat Transfer and Fluid Flow in Minichannels and Microchannels. Elsevier, Amsterdam. Chap 2

Conventional Sized Channels

Channels with minimum passage dimension larger than 1 mm

Cross References

► Boiling and Evaporation in Microchannels

Core-Shell Nanoparticles

► Composite Nanoparticles

Counterions

Definition

Ions in solution with the opposite charge as the macroion or the charge of the channel wall.

Cross References

► Electrophoresis

Coupling Microfluidic Devices to Mass Spectrometers

► Interfaces between Microfluidics and Mass Spectrometry

Covalent Bonding

Definition

Covalent bonding is a description of chemical bonding that is characterized by the sharing of one or more electrons between two atoms. In general, bonds are defined by a mutual attraction that holds the resultant molecule together. Often, bonding occurs in such a way that the outer electron shells of the participating atoms become filled. In contrast to electrostatic interactions labeled as "ionic bonds,"the strength of covalent bond depends on the angular relation between atoms in polyatomic molecules. Covalent bonding is most important between atoms with similar electronegativities. Covalent bonding is often delocalized. Covalent bonding is a broad concept and includes many kinds of interactions, including σ-bonding, π-bonding, metal-metal bonding, agostic interactions, and three-center two-electron bonds.

Cross References

► Biosensor
► Chemical Bonds

Critical Heat Flux (CHF)

Definition

Condition where the channel walls are no longer wetted by the flowing liquid, a transition to the dry wall condition as a result of high heat flux imposed at the wall during microchannel flow boiling conditions

Cross References

► Boiling and Evaporation in Microchannels

Critical Reynolds Number

► Transition to Turbulence in Microchannels

Crossed Field Filter

Synonyms

Wien filter; Crossed-field mass spectrometer

Definition

A mass filter that separates ions according to their trajectories in a combined field consisting of perpendicular magnetic and electrostatic fields. Can also be used as a velocity filter.

Cross References

► Mass Spectrometry

Crossed-Field Mass Spectrometer

► Crossed Field Filter

Crosslinked Gels

► Stationary Phases in Microchannels

Crystallizaiton

► Nucleation and Growth

Cunningham's Correction

Synonyms

Millikan's resistance factor; Cunningham slip correction

Definition

Represents a correction to Stokes' drag and the friction between objects due to the breakdown of the continuum assumption for very small objects.

Cross References

► Piezoelectric Microdispenser

Cunningham Slip Correction

► Cunningham's Correction

Curie Temperature

Definition

The temperature at which a ferroelectric material undergoes a first-order polar-nonpolar transition. Not the same as the Curie–Weiss temperature.

Cross References

► Curie–Weiss Temperature

Curie–Weiss Temperature

Definition

The temperature at which the dielectric constant is a maximum, which may be different than the *Curie* temperature for ferroelectric materials that undergo a first-order polar-nonpolar transition at this particular temperature.

Cross References

► Curie Temperature

Current Monitoring Method

► Electrical Current Monitoring Methods

Current Monitoring Technique

► Electrical Current Monitoring Methods

Curvature

Synonyms

Mean curvature

Definition

Profile of the surface of a fluid front. This shape relates directly to capillary associated pressure drop and can be manipulated to induce capillary flow.

Cross References

► Surface-Directed Capillary Flow Systems

Curved Microchannel Flow

WIN-JET LO[1], RUEY-JEN YANG[2]
[1] Department of Refrigeration and Air-Conditioning, National Chin-Yi University of Technology, Taichung, Taiwan
[2] Department of Engineering Science, National Cheng Kung University, Tainan, Taiwan
riyang@mail.ncku.edu.tw

Synonyms

Serpentine microchannel flow; Helical microchannel flow; Spiral microchannel flow

Definition

It is often necessary to drive fluids from one part of a microfluidic device to another, to control the fluid motion, to enhance mixing, or to separate fluids. The fluids are transported through channels with characteristic cross-section dimensions in the micrometer range. A channel of this size is called microchannel. If the channels are not in a straight line, then they are called a curved microchannel.

Overview

The channel geometry of a microfluidic device is commonly characterized by a rectangular curved microchannel. The flow field conditions within such a microchannel have a significant influence upon the performance of the device when conducting the separation, extraction, and mixing of chemical or biological components.

Compared to the classical flow phenomena observed in macroscopic devices, microfluidic systems generally involve laminar flows. Schönfeld and Hardt [1] developed a simple micromixer. They showed that the secondary flows (known as "Dean vortices") induced in a curved microchannel generate a mixing effect in micro devices. They analyzed the secondary flow patterns in curved square channels of various dimensions and compared the relative transverse flows of bas-relief structured channels with those of curved square channels. Particular attention was paid to the formation of additional vortices close to the center of the outer channel wall. Based on the analytical results, a novel micromixer was proposed whose mixing action was generated by transitions of the secondary flow pattern. Jiang et al. [2] investigated helical flows and chaotic mixing in curved microchannels and performed a series of experimental evaluations to verify the predicted mixing results. The experimental and numerical results both revealed that the mixing performance was highly dependent on the structure of the helical flow patterns formed within the microchannels. Howell et al. [3] used a similar helical structure of microchannel to develop a Dean vortex-based micromixer. In their design, Dean vortices appeared at Reynolds numbers between 1 and 10 which became stronger with the increase in flow velocity. The vortex formation was investigated in various microchannels with different aspect ratios. Yamaguchi et al. [4] performed three-dimensional computational fluid dynamics simulations to investigate fluidic behavior in a microchannel containing hairpin curves. The authors also performed an experimental study to observe the 3-D flow patterns generated in a hairpin microchannel fabricated on a PMMA plate. The experimental data were found to be in good agreement with the numerical results. Yamaguchi et al. [5] investigated the interface configuration of two-layered laminar flow in a curved microchannel and showed that the configuration is heavily distorted by the curved structure, leading to an increased interfacial area and hence an improved mixing performance. They reported that the interface configuration of the two liquids was affected by the secondary flows induced by inertial forces acting at the corners of the microchannel. The results showed that the interface configuration was also dependent on the velocity, the density and the viscosity of the fluid, as well as on the curvature radius and aspect ratio of the cross-sectional plane of the channel. Ookawara et al. [6] proposed a novel application for curved microchannels in which the curved channels were used to classify contained particles. The feasibility of the proposed micro-separator/classifier was verified both numerically and experimentally. Ueda et al. [7] investigated the curvature effect on the dynamics of long DNA in microfluidic devices. It was shown that under weak hydrodynamic flow,

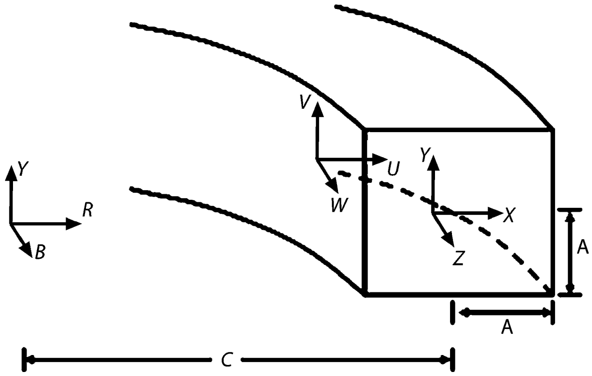

Curved Microchannel Flow, Figure 1 Geometry and related coordinate system of curved microchannel. Note that u, v, and w denote the velocities in the X-, Y-, and Z-directions, respectively

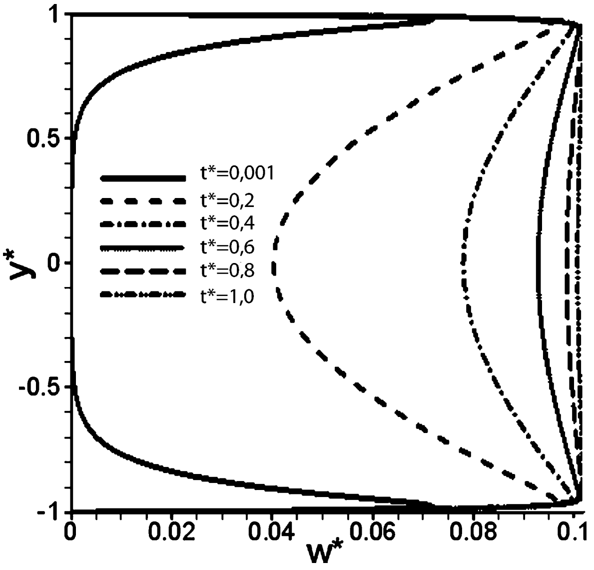

Curved Microchannel Flow, Figure 2 Axial velocity distribution along Y-direction. (The microchannel has a curvature ratio of C/A=50. The applied DC electric field has an intensity of 450 V/cm

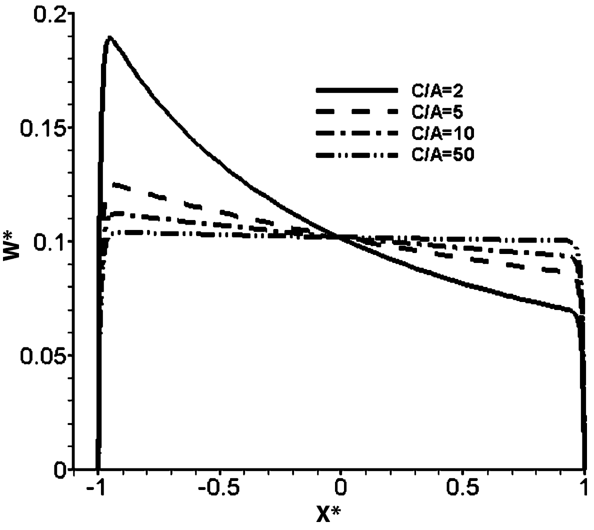

Curved Microchannel Flow, Figure 3 Velocity distributions along X-direction in microchannels with different curvature ratios. (The DC electric field intensity is 450 V/cm

long DNA exhibited a curvature entropy trapping effect. However, this effect disappeared as the hydrodynamic flow was increased.

Most studies mentioned above focus on the pressure-driven microfluidic flow in the microchannels. Recently, electrokinetically driven flows in curved microchannels have received much attention. Luo et al. [8, 9] investigated the transient electro-osmotic secondary flows which provide evidence of the growth and decay of vortices in the transverse section in a curved microchannel. They explored the small vortices that appear in each corner of the micro-channel as the AC electric field intensity is applied. Both upper and lower corner vortices gradually grow in size and strength and finally merge to form a single vortex, which compresses the original recirculation in the upper and lower half of the transverse section. Chen et al. [10] investigated the velocity distribution and secondary flow patterns induced by a DC electric field or an AC electric field in microchannels with various curvature ratios and driving frequencies.

Basic Methodology

This section focuses on the electrokinetically-driven flow in a rectangular curved microchannel. It is assumed that the fluid in the microchannel is filled with an incompressible Newtonian electrolyte of uniform dielectric constant, ε, and viscosity, μ. A fully developed flow field is then established in which the flow is driven by an applied DC or by an AC electric field. Since the characteristic length of the microchannel is of the order of magnitude of 10 microns, the interaction of the fluid and the wall is significant and must therefore be considered in the theoretical model. A review of the related literature reveals the widespread use of a theoretical microchannel model in previous studies. This model is described by the following set of equations: the Poisson–Boltzmann equation and the Navier–Stokes equation, which comprises the body force terms from the Guoy–Chapman model. When applying this model, it is convenient to transform the toroidal coordinate system (R, Y, θ) to the related coordinate system $(\boldsymbol{X}, \boldsymbol{Y}, \boldsymbol{Z})$, where $X = R - C$, $\mathrm{d}Z = C\mathrm{d}\theta$, and C is the radius of, as shown in Fig. 1.

When an external electric field is applied, the liquid flow induced by electroosmosis is governed by the general incompressible the equations of motion, i. e.

$$\nabla \cdot \boldsymbol{V} = 0 \tag{1}$$

and

$$\rho \frac{\partial \boldsymbol{V}}{\partial t} + \rho\,(\boldsymbol{V} \cdot \nabla)\,\boldsymbol{V} = -\nabla P + \boldsymbol{F} + \mu \nabla^2 \boldsymbol{V} \tag{2}$$

where $\boldsymbol{V}$ is the velocity, ρ is the fluid density, p is the static pressure, μ is the fluid viscosity, $\boldsymbol{F} = \rho_e \boldsymbol{E}$, If the gravity effect is neglected, the body force, $\boldsymbol{F}$, occurs only as a result of the action of the applied electric field on the free ions within the EDL. This body force induces a bulk fluid motion generally referred to as electroosmotic flow.

ρ_e is the net electric charge density and $\boldsymbol{E}$ is the electric field, which is given by

$$\boldsymbol{E} = -\nabla\Psi \tag{3}$$

where Ψ is the electric potential.
According to electrostatics theory, the potential is governed by the Poisson equation, i. e.

$$\nabla^2\Psi = -\frac{\rho_e}{\varepsilon\varepsilon_0} \tag{4}$$

where ε is the dielectric constant of the electrolyte solution and ε_0 is the permittivity of vacuum. Since, the Debye length of the EDL is typically very small compared to the microchannelwidth, the ion distribution is influenced primarily by the ζ potential. It is reasonable to assume that the electric potential, Ψ, is given by the linear superposition of the electrical double layer potential and the externally applied potential, i. e. $\Psi = \psi + \phi$. Therefore, equation (4) can be represented as

$$\nabla^2\psi = -\frac{\rho_e}{\varepsilon\varepsilon_0} \tag{5}$$

and

$$\nabla^2\phi = 0 \tag{6}$$

Under conditions of thermodynamic equilibrium, the ion concentration is described by the Boltzmann distribution. The electric potential distribution in the EDL can be described by the nonlinear Poisson–Boltzmann equation,

$$\nabla^2\psi = \frac{2n_0 ze}{\varepsilon\varepsilon_0}\sinh\left(\frac{ze\psi}{k_b T}\right) \tag{7}$$

The momentum expression of Eq. (2) can be rewritten in the following form:

$$\rho\frac{\partial \boldsymbol{V}}{\partial t} + \rho\left(\boldsymbol{V}\cdot\nabla\right)\boldsymbol{V} = -\nabla P + 2n_0 ze \sin\text{h}\left(\frac{ze\psi}{k_b T}\right) \times \left[\nabla\left(\psi+\phi\right)\right] + \mu\nabla^2\boldsymbol{V} \tag{8}$$

For fully developed flow field in the curved micro-channel, the Eqs. (1), (7) and (8) were transformed the toroidal coordinate system (R, Y, θ) to the related coordinate system $(\boldsymbol{X}, \boldsymbol{Y}, \boldsymbol{Z})$ and can be expressed as:

$$\frac{1}{(x+c)}\frac{\partial}{\partial x}\left[(x+c)\,u\right] + \frac{\partial v}{\partial y} = 0 \tag{9}$$

and

$$\frac{1}{(x+c)}\frac{\partial}{\partial x}\left[(x+c)\frac{\partial\psi}{\partial x}\right] + \frac{\partial^2\psi}{\partial y^2} = \frac{2n_0 ze}{\varepsilon}\sin\text{h}\left(\frac{ze\psi}{k_b T}\right) \tag{10}$$

and

$$\frac{\partial u}{\partial t} + u\frac{\partial u}{\partial x} + v\frac{\partial u}{\partial y} - \frac{w^2}{(x+c)} = -\frac{1}{\rho}\frac{\partial p}{\partial(x+c)} + \frac{\mu}{\rho}\left[\frac{\partial^2 u}{\partial\,(x+c)^2} + \frac{1}{(x+c)}\frac{\partial u}{\partial\,(x+c)} + \frac{\partial^2 u}{\partial y^2} - \frac{u}{(x+c)^2}\right] + \frac{1}{\rho}2n_0 ze\sin\text{h}\left[\frac{ze\psi}{k_b T}\right]\left[\frac{\partial\psi}{\partial\,(x+c)}\right] \tag{11a}$$

$$\frac{\partial v}{\partial t} + u\frac{\partial v}{\partial x} + v\frac{\partial u}{\partial y} = -\frac{1}{\rho}\frac{\partial p}{\partial y} + \frac{\mu}{\rho}\left[\frac{\partial^2 v}{\partial\,(x+c)^2} + \frac{1}{(x+c)}\frac{\partial v}{\partial\,(x+c)} + \frac{\partial^2 v}{\partial y^2}\right] + \frac{1}{\rho}2n_0 ze\sinh\left[\frac{ze\psi}{k_b T}\right]\left[\frac{\partial\psi}{\partial y}\right] \tag{11b}$$

$$\frac{\partial w}{\partial t} + u\frac{\partial w}{\partial x} + v\frac{\partial w}{\partial y} - \frac{uw}{(x+c)} = -\frac{1}{\rho}\frac{\partial p}{\partial z} + \frac{\mu}{\rho}\left[\frac{\partial^2 w}{\partial\,(x+c)^2} + \frac{1}{(x+c)}\frac{\partial w}{\partial\,(x+c)} + \frac{\partial^2 w}{\partial y^2} - \frac{w}{(x+c)^2}\right] + \frac{1}{\rho}2n_0 ze\sinh\left[\frac{ze\psi}{k_b T}\right]\left[\frac{\partial\phi}{\partial z}\right] \tag{11c}$$

The following non-dimensional parameters are introduced: $x^* = x/A$, $y^* = y/A$, $\psi^* = (ze\psi)/(k_b T)$, $\phi^* = (ze\phi)/(k_b T)$, $\Lambda^* = \left(A^2\Lambda\right)/\upsilon$, $u^* = u/\left(\upsilon/A\right)$, $v^* = v/\left(\upsilon/A\right)$, $t^* = t/(A/\upsilon)$, $p^* = (p - p_{\text{ref}})/\left(\rho\upsilon^2/A^2\right)$ where A is the height of the rectangular cross section of the microchannel, P_{ref} is the atmospheric pressure, υ is the kinetic viscosity of the electrolyte, t is time, and Λ is the frequency of the applied electric field, i. e. $\Lambda = 2\pi f$. The

eqs. (9), (10), (11a), (11b) and (11c) (omit the asterisks) can be rewritten in terms of the dimensionless parameters given above, i. e.

$$\frac{1}{(x+\beta)}\frac{\partial}{\partial x}[(x+\beta)\,u]+\frac{\partial v}{\partial y}=0 \tag{12}$$

and

$$\frac{1}{(x+\beta)}\frac{\partial}{\partial x}\left[(x+\beta)\frac{\partial\psi}{\partial x}\right]+\frac{\partial^2\psi}{\partial y^2}\kappa\,\sinh(\psi) \tag{13}$$

and

$$\frac{\partial u}{\partial t}+u\frac{\partial u}{\partial x}+v\frac{\partial u}{\partial y}-\frac{w^2}{(x+\beta)}+\frac{u}{(x+\beta)^2}$$
$$+\frac{\partial p}{\partial x}-\frac{1}{(x+\beta)}\frac{\partial}{\partial x}\left[(x+\beta)\frac{\partial u}{\partial x}\right]-\frac{\partial^2 u}{\partial y^2}$$
$$-G_x\cdot\sinh\psi\left(\frac{\partial\psi}{\partial x}\right)=0 \tag{14a}$$

$$\frac{\partial v}{\partial t}+u\frac{\partial v}{\partial x}+v\frac{\partial v}{\partial y}+\frac{\partial p}{\partial y}$$
$$-\frac{1}{(x+\beta)}\frac{\partial}{\partial x}\left[(x+\beta)\frac{\partial v}{\partial x}\right]$$
$$-\frac{\partial^2 v}{\partial y^2}-G_x\cdot\sinh\psi\left(\frac{\partial\psi}{\partial y}\right)=0 \tag{14b}$$

$$\frac{\partial w}{\partial t}+u\frac{\partial w}{\partial x}+v\frac{\partial w}{\partial y}+\frac{uw}{(x+\beta)}+\frac{w}{(x+\beta)^2}$$
$$+\frac{\beta}{(x+\beta)}\frac{\partial p}{\partial z}-\frac{1}{(x+\beta)}\frac{\partial}{\partial x}\left[(x+\beta)\frac{\partial w}{\partial x}\right]-\frac{\partial^2 w}{\partial y^2}$$
$$-G_x\cdot\sinh\psi\left(\frac{\beta}{(x+\beta)}\frac{\partial\phi}{\partial z}\right)=0 \tag{14c}$$

where $\kappa=AK$, $K=\left(2n_0z^2e^2/\varepsilon\varepsilon_0k_bT\right)^{1/2}$ is the Debye–Huckel parameter, the curvature ratio is given by $\beta=C/A$ and $Gx=2n_0k_bT/\left(\rho v^2/A^2\right)$ is the ratio of the EDL energy to the mechanical kinetic energy.

Key Research Findings

Figure 1 illustrates the geometry and related coordinate system of a curved microchannel. Figure 2 shows the axial velocity component distributions along the Y-direction of a microchannel with a curvature ratio of $C/A=50$ when a DC electric field with an intensity of 450 V/cm is applied. It can be seen that the axial velocity stabilizes after a dimensionless time of $t^*=1.0$. At this particular curvature ratio, the radius of curvature is so large that the curved channel approximates a straight channel, and hence the flat velocity profile is similar to that of the electro-osmotic flow observed in a straight microchannel. Figure 3 illustrates the axial velocity component distributions along the X-direction of microchannels with various curvature ratios $\left(2\le C/A\le 50\right)$. Due to the shorter turning arc-length along the inner wall, the electric field strength along the inner wall is much larger than that along the outer wall. Consequently, the electrokinetic force is larger along the inner wall resulting in a faster axial velocity w^* near the inner wall. A ratio of C/A=2 implies that the curvature of the microchannel resembles that of a hairpin curve, and hence the velocity near the inner wall is 2 times that near the outer wall of the microchannel. In the case of $C/A>10$, the velocity profile of the electro-osmotic flow is nearly flat. Figure 4 shows the secondary flow patterns in microchannels with different curvature ratios. The Dean number D_n, is defined as $\mathrm{D}_n=\mathrm{Re}\beta^{-\frac{1}{2}}$, where $\mathrm{Re}=(\mathrm{D}\bar{w})/A$ is the Reynolds number. $\mathrm{D}=(4AB)/(A+B)$, $A=B$, D is the hydraulic diameter, and $\bar{w}$ is the non-dimensional mean axial velocity, where $\bar{w}=\left(\int w(x,y)(x+\beta)\mathrm{d}x\mathrm{d}y\right)/\left(\int(x+\beta)\,\mathrm{d}x\mathrm{d}y\right)$, and $\beta=C/A$ is the radius of curvature. It is evident from Fig. 4 that when the ratio of C/A is smaller, the microchannel becomes more of a hairpin. When the secondary flows increase in strength the result is that vortices are induced near the inner walls. When the ratio of C/A is larger than 4, the curvature effect becomes weaker, and the inner vortices almost disappear. Figure 5 shows the velocity responses of the electro-osmotic flows induced by an AC electric field with an increasing Wo in curved microchannels. A dimensionless parameter, the Womersley number ($\mathrm{Wo}=(A/2)\sqrt{n/\upsilon}$, A is the characteristic length of the curved channel, n is the angular velocity of the applied electric field ($n=2\pi f$ where $f$is frequency in cycle/sec), υ is the kinematic viscosity of the fluid), is used to describe the transient fluid phenomena in an AC electric field. For a higher AC frequency (i. e., a larger Wo number), the fluid in the channel has nearly no effect due to the dragging force from the channel walls. This is because for a higher frequency the faster forward and backward electrokinetic force reverses itself and does not have sufficient time to diffuse to the center of the channel. Under this condition the w^* velocity in the center behaves with a very small amplitude of oscillation. Figure 6 shows the streamlined contours for the half-periods of applied sinusoidal electric fields with frequencies of 1.0 kHz (Wo = 0.50). The cyclic nature of the electro-osmotic flow evolution results

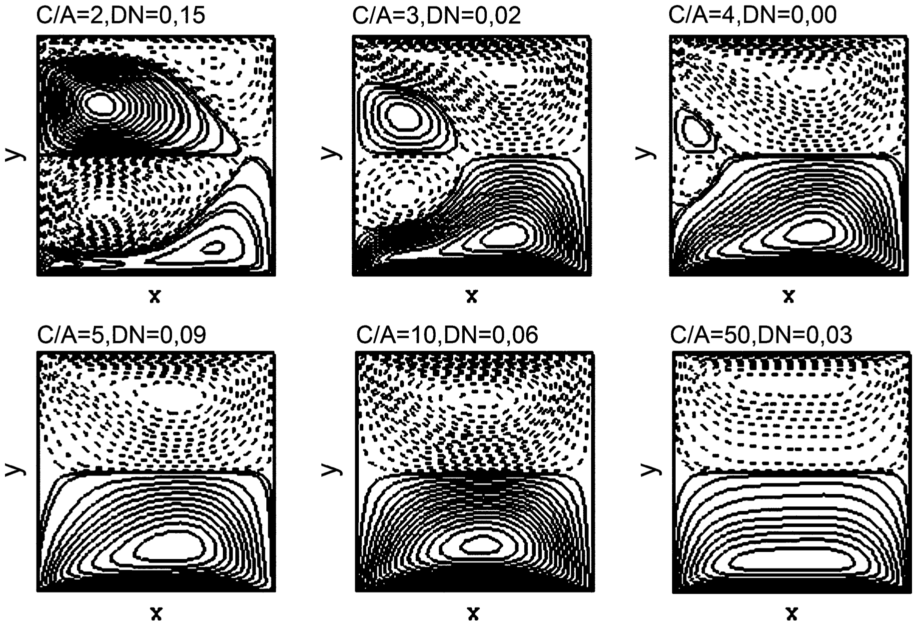

Curved Microchannel Flow, Figure 4 Secondary flow contours in microchannels with different curvature ratios. (The DC electric field intensity is 450 V/cm)

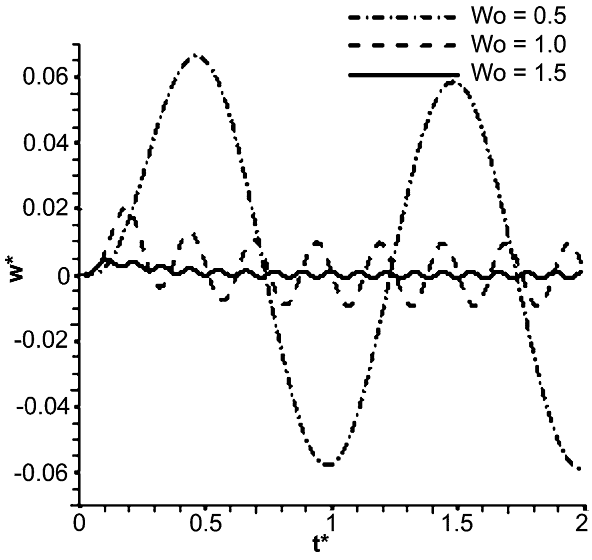

Curved Microchannel Flow, Figure 5 Transient velocity response in center of microchannel with Wo = 0.5, 1.0, and 1.5

in the growth and subsequent decay of vortices in each half of the transverse section. The greater net charge density within the double layer of the microchannel results in local maximum or minimum axial velocities near the upper and lower walls as the intensity of the applied electric field increases or decreases in either the positive or negative direction. The peak values of the axial velocity increase the force drops between the flows near the upper and lower walls as well as those in the central region, and hence prompt the formation of small vortices near the upper and lower walls. The force drops increase as the electric field intensity increases in either the positive or negative direction. Therefore, these vortices increase in size and strength as the intensity of the electric field increases, and finally merge to form one vortex in the upper half of the microchannel and a second vortex in the lower half. These vortices compress their respective neighboring recirculations as they continue to expand. Once the maximum, or minimum, electric field intensity has been attained, the original recirculations are compressed to such an extent that they vanish completely, and consequently the flow reverts to a two-vortex state. In the case with a higher applied electric field frequency 3.0 kHz (Wo = 0.87), during one period of the sinusoidal electric field, the momentum resulting from electro-osmosis near the walls has only enough time to affect a finite region near the corners of the microchannel. The induced vortices near the corners are very weak and are not strong enough or large enough to compress the original circulations. These vortices appear for a short period of time only.

Future Directions for Research

Microfluidic devices require a mixing operation for complex chemical synthesis and analysis. However, diffusive

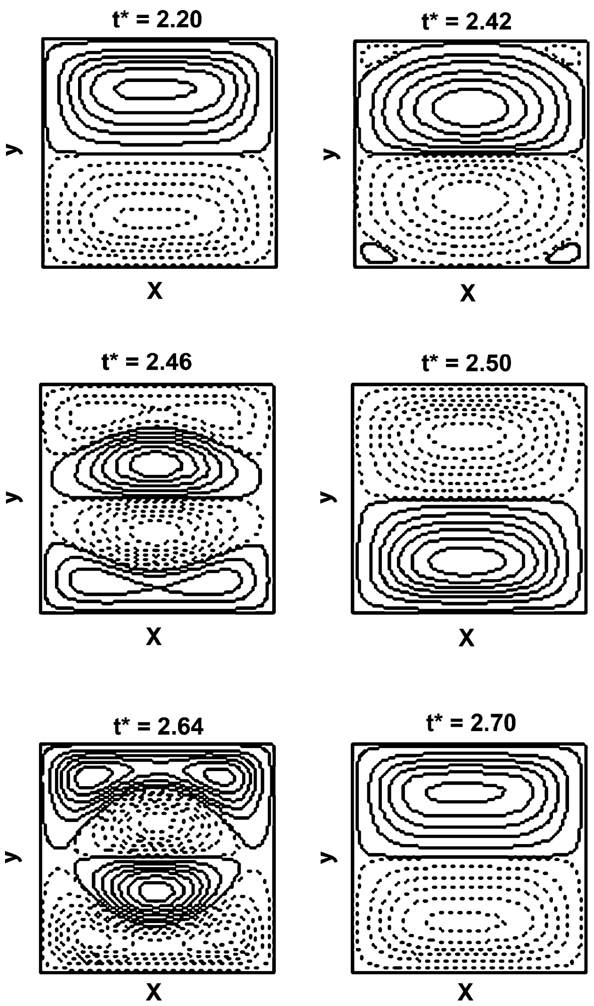

Curved Microchannel Flow, Figure 6 Streamline contours in transverse section of curved microchannel over half-period from t* = 2.20 to 2.70 for driving frequency of 1.0 kHz (Wo = 0.50)

mixing tends to be slow, and hence requires a relatively long mixing channel. A curved microchannel can be fabricated to save chip material. The formation of the vortices in the curved microchannel can be crated by the application of a periodic external electric field, which to increase the contact area of the different fluids in order to accelerate the mixing process. The induced secondary flow field in the curved microchannel may provide a rapid stirring mechanism or increase unwanted dispersion of the sample. The geometry of a microfluidic device is commonly characterized by a helical rectangular curved microchannel. In the future, 3-D induced electro-osmotic helical flows and chaotic mixing in curved microchannels should be investigated with a series of experimental evaluations and numerical analysis in order to further understanding of the relationship between the mixing performance and the structure of the helical flow patterns formed within microchannels.

Cross References

- ► Chaotic Flow
- ► Electrical Double Layers
- ► Electroosmotic Flow (DC)
- ► AC Electro-Osmotic Flow
- ► Microfluidic Mixing

References

1. Schönfeld F, Hardt S (2004) AIChE J 50:771
2. Jiang F, Drese KS, Hardt S, Küpper M, Schönfeld F (2004) AIChE J 50:2297
3. Howell PB, Mott DR, Golden JP, Ligler FS (2004) Lab Chip 4:663
4. Yamguchi Y, Takagi F, Yamashita K, Nakamura H, Maeda H, Sotowa K, Kusakabe K, Yamasaki Y, Morooka S (2004) AIChE J 50:1530
5. Yamaguchi Y, Takagi F, Watari T, Yamashita K, Nakamura H, Shimizu H, Maeda H (2004) Chem Eng J 101:367
6. Ookawara S, Higashi R, Street D, Qgawa K (2004) Chem Eng J 101:171.
7. Ueda M, Hayama T, Takamura Y, Horiike Y, Dotera T, Baba Y (2004) Jpn J Appl Phys 43:1649
8. Luo WJ (2004) J Colloid Interface Sci 278:497
9. Luo WJ, Pan PJ, Yang RJ (2005) J Micromech Microeng 15:463
10. Chen JK, Luo WJ, Yang RJ (2006) Jpn J Appl Phys 45(10A):7983

CVD

► Chemical Vapor Deposition for Film Deposition

Cy3/Cy5-Dye

Definition

These two dye molecules of the cyanine dye family are the most frequently used fluorescent dyes for DNA microarray analysis. Cy3 (green color) is exited at 550 nm and emits at 570 nm, Cy5 (red color) is exited at 649 nm and emits at 670 nm. However, the microarray scanners that are used to detect these dyes use different laser emission wavelengths (typically 532 nm and 635 nm) and filter wavelengths (550-600 nm and 655-695 nm) to avoid background contamination.

Cytometric Bead Immunoassay

► Bead Based Microfluidic Platforms

DC Capacitance

► Shunt Capacitance

DC Dielectrophoresis in Lab-on-a-Chip Devices

Adrienne R. Minerick
Dave C Swalm School of Chemical Engineering,
Mississippi State University, Starkville, MS, USA
minerick@che.msstate.edu

Synonyms

Electrodeless dielectrophoresis; Direct current dielectrophoresis (DC-DEP); Streaming dielectrophoresis; Trapping dielectrophoresis; Insulator-based dielectrophoresis (iDEP); Insulating post dielectrophoresis

Definition

Direct current (DC) dielectrophoresis (DEP) is an efficient means to move and thus separate particles or cells with the force of a stationary electric field. This is accomplished with a nonuniform electric field, which is created using insulator objects as obstacles in the path of the DC field. DC-DEP is then the induced motion of polarizable, dielectric objects of micron and smaller size, in a DC electric field that is modified by Lab-on-a-Chip geometry (or other means) to be spatially nonuniform.

Overview

Dielectrophoresis has a number of advantages over linear electrophoresis. Electrophoresis only works for samples having a narrow range of properties (significant surface charge, electrically conductive, measurably dense or with discernable radius). However, DEP enables precise manipulation of particles with widely varying electrical properties (particle only needs to be polarizable) while still interfacing with electronically controllable, microfluidics based applications. Dielectrophoresis can also directly manipulate native, unlabeled cells, thus eliminating the expense, labor, and time of labeling and tagging, as well as the development and validation of such labels and tags. The same basic DEP method has the capability of isolating and analyzing a wide range of particle types (polymer microparticles, metallic particles, cells, bacteria, viruses, DNA and proteins) using one basic procedure.

The field of dielectrophoresis is relatively recent. Herbert Pohl did dielectrophoretic research in the 1950s although this area did not gain visibility until his groundbreaking book was published in 1978 [1]. In this book, the two main components of the electric field in alternating current (AC) dielectrophoresis were extensively discussed, namely (i) a spatially nonuniform electric field and (ii) an alternating current electric field, both of which contribute to the nonlinear DEP force. Within the last 5 years, direct current dielectrophoresis has been explored. DC-DEP only utilizes the spatially nonuniform electric field component (part i), thus creating gradients in the electric field and enacting motion of cells. A brief background on the dielectrophoretic force is provided here followed by the contributing term for frequency dependent AC-DEP and then non-frequency dependent DC-DEP.

A significant boom in AC dielectrophoretic research occurred when microfabrication became widely available. This enabled precise fabrication of electrode systems (interdigitated electrodes, etc.), which created very symmetric, reproducible nonuniform electric fields enabling cellular responses to such fields to be more precisely quantified. It became apparent that at radio frequencies, cells were selectively controlled due to their inherent intra membrane polarizability characteristics. This attribute was exploited to sort cells because one cell type responded in a unique fashion from other cells at specific AC frequencies. Genetically or geometrically similar cells were found to have more similar, but still distinct, responses at given frequencies [2].

In AC and DC dielectrophoresis, the dielectrophoretic force acting on the polarized cell causes it to move either up or down the induced electric field gradient. This electric field gradient is created by a nonuniform electrode geometry in AC fields, or by a nonuniform insulator geometry of obstacles in an otherwise uniform DC field. This nonuniform field force can be derived from the net dielectric force:

$$\boldsymbol{F} = (\boldsymbol{p} \cdot \nabla)\,\boldsymbol{E} \tag{1}$$

Where $\boldsymbol{p}$, the dipole moment vector, can be broken down into the particle's effective polarizability, α, volume, v, of the particle, and the applied electric field, $\boldsymbol{E}$ ($\boldsymbol{p} = \alpha v \boldsymbol{E}$). This effective polarizability term is most commonly estimated using the Clausius–Mosotti factor for perfectly spherical particles as follows [1, 2]:

$$\mathrm{K}(\omega) = \frac{\tilde{\varepsilon}_\mathrm{p} - \tilde{\varepsilon}_\mathrm{m}}{\tilde{\varepsilon}_\mathrm{p} + 2\tilde{\varepsilon}_\mathrm{m}} \tag{2}$$

This frequency, ω, dependent factor, $\mathrm{K}(\omega)$, dynamically reflects the polarizability of a particle (subscript p) in a conductive medium (subscript m). The Clausius–Mosotti factor is a ratio of complex permittivities, $\tilde{\varepsilon}$, of the form $\tilde{\varepsilon} = \varepsilon - i\sigma/\omega$, where ω is the frequency, ε is the dielectric constant, and σ is the electrical conductivity of the medium. As can be seen, the complex $\mathrm{K}(\omega)$ factor has an imaginary component, which is out of phase with the applied electric field while the real component is in phase [2]. The imaginary component manifests itself as a torque on the particle and is detected in electrorotation or impendence measurements. However, the traditional dielectrophoretic force is dependent on the in-phase, or real component of the Clausius–Mosotti factor. In order to examine the special case when no frequency component is involved, DC-DEP can be estimated as the residual of this factor when frequency goes to zero [3]:

$$\lim_{\omega \to 0} \mathrm{K}(\omega) = \frac{\sigma_\mathrm{p} - \sigma_\mathrm{m}}{\sigma_\mathrm{p} + 2\sigma_\mathrm{m}} \tag{3}$$

Combining this all together and simplifying the gradient, one obtains an expression for the dielectrophoretic force:

$$\boldsymbol{F}_\mathrm{DEP} = \frac{1}{2} v \frac{\sigma_\mathrm{p} - \sigma_\mathrm{m}}{\sigma_\mathrm{p} + 2\sigma_\mathrm{m}} \nabla \boldsymbol{E}^2 \tag{4}$$

This dielectric force pushes particles toward regions of high field density or low field density depending on whether the Clausius–Mosotti factor is positive or negative, respectively. In other words, if $\sigma_\mathrm{p} < \sigma_\mathrm{m}$, then negative dielectrophoretic motion away from sharp points in electrodes or insulator obstacles is observed; the converse is true for positive dielectrophoresis. For a truly insulating particle, $\sigma_\mathrm{p} = 0$, the Clausius–Mosotti factor is simply $-1/2$, and motion away from high field density regions is observed [4]. Limiting further to a spherical particle yields:

$$\boldsymbol{F}_\mathrm{DEP} = -\frac{1}{3} \pi r^3 \nabla \boldsymbol{E}^2 \tag{5}$$

As a result of the complexity of this dielectric force phenomenon, many configurations and electric field operating conditions are possible. Specifically in DC fields, the nonuniform insulator geometry of obstacles results in a dielectrophoretic force acting on the polarized cell, which causes the cell to move either towards or away from electric field intensity without having the cells in direct contact with the electrode. Kang et al. noted the following advantages to direct current dielectrophoretic techniques [4]:

- insulators are less prone to fouling, thus they generally retain their function despite surface changes;
- no metal components are involved which greatly reduces the complexity of fabrication ...
- the structure is mechanically robust and chemically inert; and
- gas evolution due to electrolysis around the metal electrodes is avoided inside the channel.

Further, it is possible to simultaneously manipulate the particles via DC-DEP as well as linear electrophoresis in the same DC field. It should be noted that non-uniformities in the electric field are most effective when they occur over length scales comparable to a cell ($< 10\,\mu$m) in order for the cell to experience a significant dielectrophoretic force. Methods to embed insulators in the path of direct current electric field lines have varied. The next section will discuss these strategies.

Basic Methodology

Spatial non-uniformities in the electric field (i. e. gradients) can be created using any number of insulating protrusions or obstacles into a Lab-on-a-Chip device channel or chamber through which a DC field is being conducted. An insulator is a material that has a high resistance to flow of electrical current. DC field lines will naturally follow paths of least resistance through conducting fluid in channels and chambers. A characteristic of DC fields is that the field lines (paths of equal current) are parallel and follow a linear path with the flow of free electrons going from negative to positive. When an insulator is placed in the path of a DC field, the electric field lines diverge around the insulator and thus are densely compressed around insulator points and sharp edges. This results in a varying den-

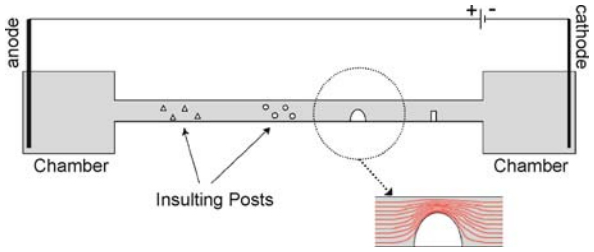

DC Dielectrophoresis in Lab-on-a-Chip Devices, Figure 1 The diagram depicts chambers holding a reservoir of fluid (shaded) at either end of a Lab-on-a-Chip linear channel. The electrodes are immersed in the chamber liquid and deliver a linear DC electric field. Insulating posts or protrusions of varying geometries (triangular posts, cylindrical posts, protruding oil menisci, or rectangular protrusion) are depicted. The bottom inset shows the equally spaced parallel field lines diverging around a protruding oil meniscus. Highest field density occurs where the field lines are most densely packed

sity of the electric field and thus what is termed an electric field gradient.

A number of creative ways have been developed to create non-uniformities in an electric field using insulators. Initial efforts simply used prefabricated posts embedded in the channels or rectangular protrusions into the channels. These were typically made out of polydimethylsiloxane (PDMS), or polymethylmethacrylate (PMMA), which are common polymers for photolithography or hot embossing fabrication techniques, respectively [4]. More recently, oil menisci have been used. Please see Fig. 1.

The shapes of such insulator protrusions have varied enabling slightly modified electric field gradients. In all cases, highest field intensity occurs at sharp points or areas of highest curvature on the insulator as well as through areas of constriction in channels. A key attribute of direct current dielectrophoresis is that the electrodes supplying the electric field can be located more remotely on the Lab-on-a-Chip device. Electrodes can be immersed in fluid in chambers at either end of the test channel (Fig. 1).

Key Research Findings

Initial work in this area was conducted by Cummings and Singh and is described in their seminal paper [5]. In this work, two operating regimes were observed. The first, named *streaming DEP* occurred when the dielectrophoretic forces from the spatially non-uniform field dominated over diffusive forces, but not over electrophoresis or electroosmotic flow. In this case, the particle motion observed was due to dielectrophoretic motion into specified streamlines of electrokinetic flows. The second regime was titled *trapping DEP*; the dielectrophoretic force in this regime was greater than the diffusive forces and electrokinetic forces combined and as a result, particles were trapped at the insulating post surfaces. It is noted that this regime allows for *inexpensive and embedded batch filter/concentrator devices* [5].

Insulating post dielectrophoresis was then adopted in 2004 to concentrate and sort live and dead *E.coli* [3]. The batch concentrator strategy was employed for this work; results showed that at a DC fields of 16 V/mm, live *E.Coli* cells were concentrated between insulating posts. Bands of dead cells and then live cells were accomplished at 60 V/mm with the dead cells preferentially concentrating at the electric field maxima region [3]. Particle trajectories were carefully explored via experiments and simulations and elucidated repulsive effects to due dielectric wall/particle interactions. It was shown in this work that changes in the conductivity of the aqueous media did not effect changes in the trajectory of the particles while particle size did effect trajectories [6]. This is supported by Eq. (5) above.

Efforts then turned to exploring other insulative materials for electrodeless DEP. Cyclo-olefin polymers (Zeonor®) were used as the construction materials for microchannels and the resulting wall zeta potentials were correlated with DC-DEP particle behaviors [7]. It was found that DC-DEP trapping voltages for polystyrene beads were lower with this polymeric insulating post array than with previously explored glass posts [3, 5]. The next major advance in insulator materials for this class of devices was an oil droplet obstacle [8]. This was accomplished by pushing oil through an intersecting channel such that it protruded into the main channel to create an oil meniscus as depicted in Fig. 1. This strategy resulted in an insulating barrier without a sharp point, and it was shown to be effective at modifying the electric field to be nonuniform. Thus particles of different sizes were separated into different trajectories as they passed by the oil obstacle [8]. The newest unique accomplishment at this date is the extension of DC-DEP from aqueous media to a viscous media of silicone oil [9]. This work found that joule heating let to density gradients in the liquid and buoyancy forces, which significantly effected particle and water droplet velocities. It was found that these velocities increased with particle/droplet size. Research in this area continues to net interesting results applicable to future Lab-on-a-Chip devices [9].

Future Directions for Research

Insulator materials and configurations, which may be tailored to the given application, are the basis for future research in this area. Since traditional AC dielectrophoresis requires precise metallization of embedded electrodes, a DC dielectrophoretic approach eliminates this time consuming and expensive process. This will facilitate rapid

prototyping of ideas and streamlined fruition of devices to the marketplace. Further, the use of oil as insulating barriers in the chambers will allow for dynamic control of the electric field gradient within the channel. This opens up opportunities for separations or sorting of cells via feedback control mechanisms.

Of course, as this avenue of research progresses, further work on how various cell populations respond to field nonuniformities will also be explored. Integration of this technique within a complete Lab-on-a-Chip device capable of sample preparation, dilution, mixing, quantified sensing, etc. is another major milestone to be attained. One thing is clear, there is significant promise in this area because of the wide applications of dielectrophoresis and the advantages that arise when embedded electrodes are no longer a concern in Lab-on-a-Chip devices.

Cross References

- ► AC Dielectrophoresis Lab-on-a-chip Devices
- ► Cell Sorting
- ► Dielectrophoresis
- ► Dielectrophoretic Motion of Particles and Cells
- ► Electrical Double Layers
- ► Electrokinetic Motion of Cells and Nonpolarizable Particles
- ► Electrokinetic Motion of Polarizable Particles
- ► Lab-on-a-Chip (General Philosophy)
- ► Lab-on-a-chip Devices for Particle and Cell Separation
- ► Nonlinear Electrokinetic Phenomena
- ► Techniques of Manipulating Cells

References

1. Pohl HA (1978) Dielectrophoresis: The behavior of neutral matter in nonuniform electric fields. Cambridge University Press, Cambridge
2. Gascoyne PRC, Vykoukal J (2002) Particle separation by dielectrophoresis. Electrophoresis 23:1973–1983
3. Lapizco-Encinas BH, Simmons BA, Cummings EB, Fintschenko Y (2004) Dielectrophoretic Concentration and Separation of Live and Dead Bacteria in an Array of Insulators. Anal Chem 76:1571–1579
4. Kang KW, Kang Y, Xuan X, Li D (2006) Continuous separation of microparticles by size with Direct current-dielectrophoresis. Electrophoresis 27:694–702
5. Cummings EB, Singh AK (2003) Dielectrophoresis in Microchips Containing Arrays of Insulating Posts: Theoretical and Experimental Results. Anal Chem 75:4724–4731
6. Kang KH, Xuan X, Kang Y, Li D (2006) Effects of DC-dielectrophoretic force on particle trajectories in microchannels. J Appl Phys 99:064702-1–064702-8
7. Mela P, van den Berg A, Fintschenko Y, Cummings EB, Simmons BA, Kirby BJ (2005) The zeta potential of cyclo-olefin polymer microchannels and its effects on insulative (electrodeless) dielectrophoresis particle trapping devices. Electrophoresis 26:1792–1799
8. Barbulovic-Nad I, Xuan X, Lee JSH, Li D (2006) DC-dielectrophoretic separation of microparticles using an oil droplet obstacle. Lab Chip 6:274–279
9. Du F, Baune M, Thoming J (2007) Insulator-based dielectrophoresis in viscous media – Simulation of particle and droplet velocity. J Electrost 65:452–458

Dead Volume

Definition

In a positive displacement pump a moving boundary changes the volume of a pump chamber. The *dead volume* is the minimum chamber volume.

Cross References

- ► Compression Ratio
- ► Electromagnetic Valves
- ► Electrostatic Valves
- ► Magnetic Pumps
- ► Membrane Actuation for Micropumps
- ► Microactuators
- ► Peristaltic Pumps
- ► Piezoelectric Valves
- ► Pneumatic Valves
- ► Positive Displacement Pump
- ► Stroke Volume
- ► Thermomechanical Valves
- ► Thermopneumatic Valves

Debye-Hückel Approximation

Definition

The process of linearizing the equation for the electric potential; valid if the potential energy of ions is small compared to their average kinetic energy due to thermal motion.

Cross References

- ► Electrokinetic Flow and Ion Transport in Nanochannels

Debye Layer

Definition

A cloud of counterions surrounding the macroion.

Cross References

- ► Electrophoresis
- ► Electrical Double Layers

Debye Length

Definition

A measure of the thickness of the Debye layer.

Cross References

- ► Electrokinetic Flow and Ion Transport in Nanochannels
- ► Electroosmotic Flow (DC)
- ► AC Electro-Osmotic Flow
- ► Electrical Double Layers

Deep Lithography

► LIGA

Deep Reactive-Ion Etching (DRIE)

► Anisotropic Etching

Deep Reactive Ion Silicon Etching

► Silicon Micromachining

Degree of Mixing

► Mixing Measures

De Laval Nozzle

Definition

A contoured or 'bell-shaped' converging/diverging nozzle geometry which both expands and aligns the supersonic portion of the nozzle flow; specifically, the exiting flow is aligned with the nozzle axis thus maximizing thrust production. The geometry of the de Laval nozzle is typically calculated using the method of characteristics for the supersonic nozzle flow so that the nozzle wall coincides with a streamline in the flow.

Delta Function

► Dirac Delta Function

Demixing

KURT BINDER
Institut für Physik, Johannes Gutenberg Universität
Mainz, Mainz, Germany
kurt.binder@uni-mainz.de

Synonyms

Phase separation kinetics; Unmixing; Spinodal decomposition

Definition

When a binary (or multicomponent) mixture by some fast change of external conditions (e. g. rapid change of temperature or pressure, etc.) is brought from the one-phase region into a state inside the miscibility gap of the equilibrium phase diagram, demixing occurs. That is, the system develops from a homogeneous state towards an arrangement of (macroscopic) domains of different chemical composition.

Overview

The basic mechanisms of phase separation of bulk binary fluid mixtures are either nucleation and growth, if the initial state from which the process starts is close to one of the branches of the coexistence curve which describe the concentrations of the phases coexisting in thermal equilibrium, or spinodal decomposition and subsequent coarsening, if the process starts from a state inside the unstable region of the equilibrium phase diagram. *Spinodal decomposition* means the spontaneous growth of long-wavelength concentration fluctuations, which are already present in the initial state. However, the so-called *spinodal curve*, separating the *metastable* region of the phase diagram (where phase separation starts by nucleation) from the *unstable* region, is not a well-defined concept, and the transition between these two mechanisms describing how concentration inhomogeneities develop is completely gradual.

After a brief review of these concepts, the effects of external boundaries on phase separation will be discussed. Confining a fluid mixture into a slit pore already modifies the static phase diagram of the system, precursors of wetting layers (surface layers where one component gets enriched)

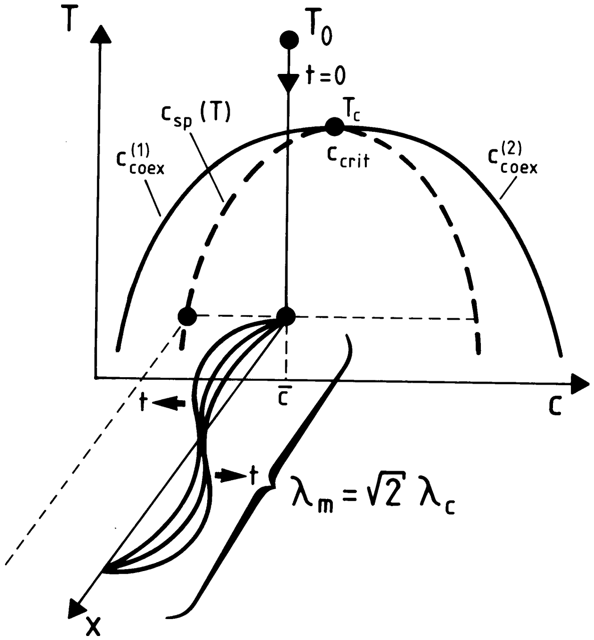

Demixing, Figure 1 Schematic description of a quenching experiment which leads to spinodal decomposition of a binary mixture: one starts at a temperature T_c such that the system is in thermal equilibrium for times $t < 0$ at the chosen average concentration $\bar{c}$ of one species (say, B). At time $t = 0$ the system is *quenched* (i. e. suddenly cooled) to a temperature T underneath the coexistence curve (consisting of two branches $c_{coex}^{(1)}$, $c_{coex}^{(2)}$ which merge at an upper critical solution point T_c, c_{crit}). If the state point $(\bar{c}, T)$ at which the quench ends lies inside of the spinodal curve $c_{sp}(T)$, then the linear theory of spinodal decomposition predicts that in the bulk of the system long-wavelength concentration fluctuations which exceed a critical wavelength λ_c are unstable, their amplitude grows spontaneously with time t after the quench. Initially the maximum growth rate occurs for a wavelength $\lambda_m = \sqrt{2}\lambda_c$. This spontaneous amplification of concentration fluctuations is schematically indicated in the figure, where a growth of a single concentration wave in the x-direction is shown

may form at the walls of the pore, and in the direction normal to the confining walls the system always is inhomogeneous. *Surface-directed spinodal decomposition* (i. e. a concentration variation like a damped sinusoidal wave with wavevector oriented normal to the surface) then occurs as a transient initial stage before lateral phase separation sets in. Additional complications arise for demixing of fluid mixtures inside porous materials due to the randomness of the structure.

Basic Methodology

Spinodal Decomposition

For simplicity, we consider here only a binary mixtures (A,B), and do not discuss the complications posed by extensions to multicomponent systems. Figure 1 shows a schematic phase diagram in the plane of variables temperature T and concentration c of species B. Kinetics of phase separation in bulk fluid mixtures is triggered by a rapid quench (at time $t = 0$) from the one-phase region into the miscibility gap. The initial equilibrium state ($t \leqslant 0$) is spatially homogeneous, apart from small-scale concentration inhomogeneities. The final equilibrium state towards which the system ultimately evolves ($t \to \infty$) consists of macroscopic domains of the two coexisting phases, with concentrations $c_{coex}^{(1)}(T)$ and $c_{coex}^{(2)}(T)$, given by the coexistence curve. The relative amounts X, $1 - X$ are given by the lever rule,

$$\bar{c} = c_{coex}^{(1)}(T)X + c_{coex}^{(2)}(T)(1 - X) \qquad (1)$$

We are interested in the time evolution of the system from the initial homogeneous state to the final segregated state. According to the most simple-minded theoretical concepts on this process, the initial stages of phase separation depend on the question whether the considered state point $(T, \bar{c})$ to which the quench leads lies inside or outside a special curve in the phase diagram, the so-called spinodal $c_{sp}(T)$, which will be defined below. If the state point falls in between the spinodal and the coexistence curve, phase separation is started by (homogeneous or heterogeneous) nucleation [1], i. e. a nanoscopically small droplet of the new phase appears on the background of the old phase. If the state point falls underneath the spinodal curve, however, phase separation does not need to be triggered by such *heterophase fluctuations* but long-wavelength fluctuations with arbitrarily small amplitudes (so-called *homophase fluctuations*) suffice to start the phase separation (see Fig. 1). Of course, one should not misunderstand this figure assuming that a periodic concentration distribution forms in the system: there is a whole *wave packet* of unstable *concentration waves*, with wavelengths $\lambda_c < \lambda < \infty$, and random orientations of their wavevectors, and so the concentration pattern which forms rather has the character of a randomly interconnected structure, like in a sponge or in a seaweed [2].

Assuming that one can associate with the initial homogeneous but unstable state a free energy $F'(c)$, the instability of this state is attributed to a negative second derivative, $\left(\partial^2 F'(c)/\partial c^2\right)_T < 0$. In the metastable region, on the other hand, one has $\left(\partial^2 F'(c)/\partial c^2\right)_T > 0$, while the curve in the (T, c) plane where $\left(\partial^2 F'(c)/\partial c^2\right)_T = 0$ defines the spinodal (or *limit of metastability*). This notion is familiar also from the van der Waals theory of the vapor–liquid transition of a simple fluid.

At the outset we emphasize, however, that $F'(c)$ is not a well-defined quantity: thermodynamic potentials are well defined for thermal equilibrium states only, states

with $\left(\partial^2 F'(c)/\partial c^2\right)_T < 0$ violate the basis laws of statistical thermodynamics. For $c_{\text{coex}}^{(1)} < c < c_{\text{coex}}^{(2)}$ the only well-defined free energy is the free energy which corresponds to the lever rule, i. e. $F(c) = F\left(c_{\text{coex}}^{(1)}(T)\right)X + F\left(c_{\text{coex}}^{(2)}(T)\right)(1-X)$, i. e. a linear function of the concentration. The double-well shape of $F(c)$ obtained from mean-field theories, such as the Bragg–Williams approximation of binary mixtures, is an artifact of an uncontrolled approximation. So the singular behavior resulting at the spinodal should not be taken seriously.

Nevertheless, the linearized theory of spinodal decomposition, based on the assumption that $\left(\partial^2 F'(c)/\partial c^2\right)_T < 0$ inside of the spinodal curve, provides a useful first orientation, and shall be described here. One considers the dynamics of a time-dependent local concentration field $c(\boldsymbol{x}, t)$. Since the average concentration $\bar{c} = (1/V)\int dx c(\vec{x}, t)$ is conserved, $c(\boldsymbol{x}, t)$ satisfies a continuity equation:

$$\frac{\partial c(\boldsymbol{x}, t)}{\partial t} + \nabla \cdot \boldsymbol{j}(\boldsymbol{x}, t) = 0 \tag{2}$$

where $\boldsymbol{j}(\boldsymbol{x}, t)$ is the concentration current density. Following standard nonequilibrium thermodynamics, $\boldsymbol{j}(\boldsymbol{x}, t)$ is set proportional to the gradient of the local chemical potential difference $\mu(\boldsymbol{x}, t)$,

$$\boldsymbol{j}(\boldsymbol{x}, t) = -M\nabla\mu(\boldsymbol{x}, t) \tag{3}$$

where M is a mobility. Since in thermal equilibrium $\mu = (\partial F/\partial c)_T$, we generalize this relation for an inhomogeneous situation out of equilibrium in terms of a functional derivative,

$$\mu(\boldsymbol{x}, t) = \delta\Delta F\left[c(\boldsymbol{x}, t)\right]/\delta c(\boldsymbol{x}, t) \tag{4}$$

where the free energy functional describing the inhomogeneous situation out of equilibrium is given as follows ($f' = F'/V$):

$$\Delta F\left[c(\boldsymbol{x}, t)\right] = \int dx \left\{ f'\left[c(\boldsymbol{x}, t)\right] + \frac{1}{2} r^2 k_{\mathrm{B}} T \left[\nabla c(\boldsymbol{x}, t)\right]^2 \right\} \tag{5}$$

Here the *gradient square* term describes the extra free energy cost due to concentration inhomogeneities. Boltzmann's constant is denoted as k_{B}, and the parameter r then has dimensions of length (in microscopic models, e. g. lattice models of binary mixtures treated in mean field approximation, r has the meaning of the range of pairwise interactions among the particles).

Equations (4) and (5) lead to

$$\mu(\boldsymbol{x}, t) = (\partial f'/\partial c)_T - r^2 k_{\mathrm{B}} T \nabla^2 c(\boldsymbol{x}, t) \tag{6}$$

and using this result in the continuity equation one obtains a generalized nonlinear diffusion equation [3]:

$$\frac{\partial c(\boldsymbol{x}, t)}{\partial t} = M\nabla^2 \left\{ \left(\frac{\partial f'\left[c(\boldsymbol{x}, t)\right]}{\partial c} \right)_T - r^2 k_{\mathrm{B}} T \nabla^2 c(\boldsymbol{x}, t) \right\} \tag{7}$$

Now it is assumed that in the initial state the fluctuation $\delta c(\boldsymbol{x}, t) = c(x, t) - \bar{c}$ is very small everywhere in the system (since on small length scales fluctuations can be large, this assumption typically is not true, but it is necessary to allow a simple analysis of Eq. (7)). Linearizing then Eq. (7) in $\delta c(\boldsymbol{x}, t)$ yields the equation

$$\frac{\partial \delta c(\boldsymbol{x}, t)}{\partial t} = M\nabla^2 \left\{ \left(\frac{\partial^2 f'\left[c(\boldsymbol{x}, t)\right]}{\partial c^2} \right)_{T,\bar{c}} - r^2 k_{\mathrm{B}} T \nabla^2 \right\} \delta c(\boldsymbol{x}, t) \tag{8}$$

which is solved by introducing Fourier transforms ($\boldsymbol{k}$ is the wavevector):

$$\delta c_k(t) = \int \mathrm{d}\boldsymbol{x} \exp(i\boldsymbol{k} \cdot \boldsymbol{x}) \delta c(\boldsymbol{x}, t) \tag{9}$$

to obtain

$$\delta c_k(t) = \delta c_k(0) \exp\left[A(k)t\right] \tag{10}$$

with the rate factor for the amplification of fluctuations

$$A(k) = -Mk^2 \left[\left(\partial^2 f'/\partial c^2 \right)_{T,\bar{c}} + r^2 k_{\mathrm{B}} T k^2 \right] \tag{11}$$

The equal-time structure factor $S(k, t)$ at the time t after the quench is

$$S(k, t) \equiv \left\langle \delta c_{-k}(t) \delta c_k(t) \right\rangle_T \tag{12}$$

where $\langle \ldots \rangle_T$ denotes a thermal average. Note that $S(k, t)$ is readily found experimentally by scattering of neutrons, X-rays or light, depending on the length scales of interest. Equations (10)–(12) imply that $S(k, t)$ has a simple exponential variation with time:

$$S(k, t) = S_{T_0}(k) \exp\left[2A(k)t\right] \tag{13}$$

where $S_{T_0}(k) = \left\langle \delta c_{-k}(0) \delta c_k(0) \right\rangle_T = \left\langle \delta c_{-k} \delta c_k \right\rangle_{T_0}$ is simply the equal-time structure factor in thermal equilibrium at temperature T_0 before the quench.

Note that $A(k)$ is positive for $0 < k < k_c$, with

$$k_c = 2\pi/\lambda_c = \left[-\left(\partial^2 f'(c)/\partial c^2\right)_{T,\bar{c}} / \left(r^2 k_B T\right)\right]^{1/2} \quad (14)$$

and hence the structure factor during the initial stages of phase separation (where the above linearization approximation is hoped to work) grows exponentially with time. This mechanism of phase separation, spontaneous amplification of fluctuations, is termed *spinodal decomposition*. Of course, this exponential growth is limited by nonlinear effects, which imply that the linearization of Eq. (7) yielding Eq. (8) no longer is valid, and those nonlinear effects cause an onset of *coarsening*: rather than observing a peak of $S(k,t)$ growing at a fixed wavenumber $k_m = 2\pi/\lambda_m$, where $A(k)$ is maximal (note $k_m = k_c/\sqrt{2}$ is easily derived from Eq. (9), with $dA(k)/dk = 0$ for $k = k_m$), the position $k_m(t)$ of the peak of $S(k,t)$ shrinks to zero as time $t \to \infty$, $k_m(t) \propto t^{-a}$, where a is a characteristic exponent describing this domain growth. The physical interpretation is that the growing concentration inhomogeneities develop into domains, separated by interfaces, and the length scale $\ell(t)$ of these domains increases with time: $\ell(t) \propto 1/k_m(t) \propto t^a$. The driving force of this *coarsening* of the domains which have formed is the reduction of total interfacial area and thus interfacial free energy cost in the system.

Another spectacular prediction of this linear theory, Eqs. (8)–(13), would originate from the presence of a special wavenumber k_c where $S(k = k_c, t)$ is strictly independent of time since $A(k = k_c) = 0$. Such a behavior is not at all observed, and the reason is that Eqs. (2) and (3) are completely deterministic, and lack the presence of statistical thermal fluctuations that physically should occur for the system in its states at the temperature $T > 0$. This problem can be remedied by adding a suitable random force term at the right-hand side of Eq. (3).

Finally, we draw attention to the special role played by the spinodal $c_{sp}(T)$. We expect that $-(\partial^2 f'(c)/\partial^2 c)_{T,\bar{c}} \propto \bar{c} - c_{sp}(T)$ for $\bar{c}$ close to $c_{sp}(T)$, and hence k_c exhibits for $\bar{c} \to c_{sp}(T)$ a critical vanishing, $k_c \propto [c - c_{sp}(T)]^{1/2}$, implying a divergence of the critical wavelength $\lambda_c = 2\pi/k_c$ (Fig. 2a). Similarly, when one approaches the spinodal from the metastable region of the phase diagram, the prediction of the mean-field theory of nucleation is that the radius R^* of the *critical droplet* (necessary to effect the creation of a nucleus of the stable phase on the background of the metastable phase) exhibits a similar critical divergence (Fig. 2a), $R^* \propto [c_{sp}(T) - \bar{c}]^{-1/2}$. However, there is no clear evidence for such a divergent length scale when one carries out quenches into the region of the phase diagram where the spinodal is expected to occur [3]. Rather, there is compelling evidence from both experiments and computer simulations that the transition from nucleation to spinodal decomposition is completely gradual [3] (Fig. 2a).

Nucleation and the Spinodal Curve

Before we comment on the reasons for this lack of a nonexistence of singularities associated with the spinodal, we recall the basic ideas about nucleation. One assumes that the critical fluctuation to consider is a spherical droplet (of the B-rich phase on the background of the A-rich metastable phase), and this droplet is described like a macroscopic object despite its nanoscopic size. Thus, considering the droplet formation free energy $\Delta F(R)$ as a function of droplet radius R,

$$\Delta F(R) = \Delta g(\bar{c})\left(4\pi R^3/3\right) + \gamma_{int}\left(4\pi R^2\right), \quad (15)$$

where the first term describes the contribution proportional to the droplet volume and the second term is a surface correction, γ_{int} being the interfacial free energy per unit area, taken for a flat planar interface. If $\bar{c}$ exceeds $c^{(1)}_{coex}$ only slightly, we may write

$$\Delta g(\bar{c}) = -\left(c^{(2)}_{coex} - c^{(1)}_{coex}\right)\left(\mu - \mu_{coex}\right) \quad (16)$$

μ_{coex} being the chemical potential difference at the coexistence curve. Minimizing now $\Delta F(R)$ with respect to R yields that the maximum value occurs at

$$R^* = 2\gamma_{int} / \left[\left(c^{(2)}_{coex} - c^{(1)}_{coex}\right)\left(\mu - \mu_{coex}\right)\right] \quad (17)$$

and the free energy barrier against homogeneous nucleation becomes

$$\Delta F^*(R = R^*) = \frac{(16\pi/3)\gamma^3_{int}}{\left[\left(c^{(2)}_{coex} - c^{(1)}_{coex}\right)\left(\mu - \mu_{coex}\right)\right]^2} \quad (18)$$

According to this formula, ΔF^* decreases monotonically with increasing concentration $\bar{c}$, but one can trust this result near the coexistence curve only, of course. The nucleation rate (number of nuclei formed per unit volume and unit time) then is estimated from the Arrhenius formula, $J = \nu^* \exp(-\Delta F^*/k_B T)$, ν^* being the so-called *attempt frequency*.

A treatment of the nucleation barrier that is not restricted to the neighborhood of the coexistence curve is also based on the free energy functional, Eq. (5). In fact, using such an approach for an *order parameter* $\psi(z)$ designed such that for $z \to -\infty$ one has a phase characterized by $\psi(z \to -\infty) \to -\psi_{coex}$, while for $z \to +\infty$ one has a phase characterized by $\psi(z \to +\infty) = +\psi_{coex}$, Fig. 3a,

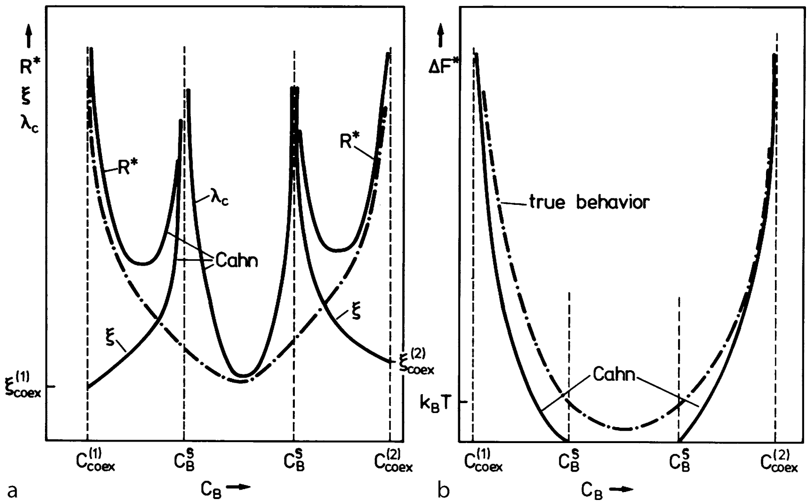

Demixing, Figure 2 (**a**) Characteristic lengths (a) and (b) nucleation barrier ΔF^* plotted vs. concentration c_B. *Full curves* show the predictions of the Cahn–Hillard mean-field theory of nucleation and spinodal decomposition for the critical wavelength λ_c and the correlation length ξ of concentration fluctuations in a metastable state, the radius R^* of a *critical droplet* (a) and the free energy barrier ΔF^* (**b**) *Dash-dotted curves* show, *on a different scale*, the conjectured smooth behavior of a system with short range interaction, for which the spinodal singularities at c^S_B are completely washed out

one can compute the interfacial profile $\psi(z)$ and associated interfacial tension by minimizing this free energy functional $\Delta F[\psi(z)]$ subject to the constraint that the specified boundary conditions are obeyed. Near the critical temperature T_c in Fig. 1 one obtains [4]

$$\psi(z) = \psi_{coes} \tanh\left[z/(2\xi_{coex})\right] ;$$
$$\xi_{coes} \propto r\left(1 - T/T_c\right)^{1/2} \qquad (19)$$

and $\gamma_{int} \propto r\left(1 - T/T_c\right)^{3/2}$. Since the range of the interaction (r) enters as a prefactor both in the correlation length ξ_{coex} at the coexistence curve, the *intrinsic width* $\ell_0 = 2\xi_{coex}$ of the interfacial profile, and the interfacial free energy, and hence ΔF^* scales as r^3 (Eq. (18)), we already see that r is a key parameter controlling the behavior of the system. In fact, for $r \to \infty$ it becomes too costly to form interfaces in the system, and so homogeneous nucleation is suppressed altogether, and then the spinodal curve and the singularities associated with it become well defined [3, 4].

This mean-field theory to calculate the interfacial profile and interfacial free energy can be extended to compute also for a critical droplet the order parameter profile (for a binary mixture near the critical point, $\psi_{coex} = c^{(2)}_{coex} - c_{crit}$, $-\psi_{coex} = c^{(1)}_{coex} - c_{crit}$, cf. Fig. 1). Qualitatively, the results are sketched in Figs. 3b and c: one simply imposes spherical symmetry to $\Delta F[\psi(\rho)]$ and minimizes this free energy functional subject to the constraint that $\psi(\rho \to \infty) \to \psi_{ms}$, the order parameter in the metastable phase surrounding the droplet. If ψ_{ms} is close to ψ_{coex}, the resulting profile $\psi(\rho)$ closely resembles the profile $\psi(z)$ of a flat interface; only the center of the interface now occurs at $\rho = R$, the droplet radius. In fact, this behavior is very well consistent with the separation of the excess free energy in bulk and interfacial terms, as written in Eq. (15). However, if ψ_{ms} is close to the spindodal, ψ_{sp}, Fig. 3c, the behavior is very different. There is no longer any clear-cut distinction between the droplet interior and its interface, and the amplitude of the whole order parameter variation across the droplet vanishes as $\psi_{ms} \to \psi_{sp}$. Physically, such a droplet profile can be interpreted as the spherical average of a ramified cluster, unlike the compact droplet assumed in Eq. (15) and found for ψ_{ms} near ψ_{coex} (Fig. 3b). Actually, the free energy cost to form such a droplet also is rather small, one finds $\Delta F^*(\psi_{ms} \to \psi_{sp}) \propto r^3(\psi_{sp} - \psi_{ms})^{3/2}$.

Now, although this mean field theory of nucleation can be executed throughout the full metastable region, from the coexistence curve all the way to the spinodal, it clearly makes sense only if the resulting free energy barrier against nucleation by far exceeds the thermal energy scale, $\Delta F^*(R = R^*) \gg k_BT$. If ΔF^* gets down to the order of k_BT, critical droplets could form everywhere in the system simultaneously, and the idea that far from the droplet one still has the homogeneous metastable phase fails. The condition that $\Delta F^* = 1$ yields then the ultimate limit of metastability, not $\Delta F^* = 0$ (the actual spinodal), and hence the condition $\Delta F^* = 1$, or equivalently $(\psi_{sp} - \psi_{ms}) \propto r^{-2}$, shows how close one can approach

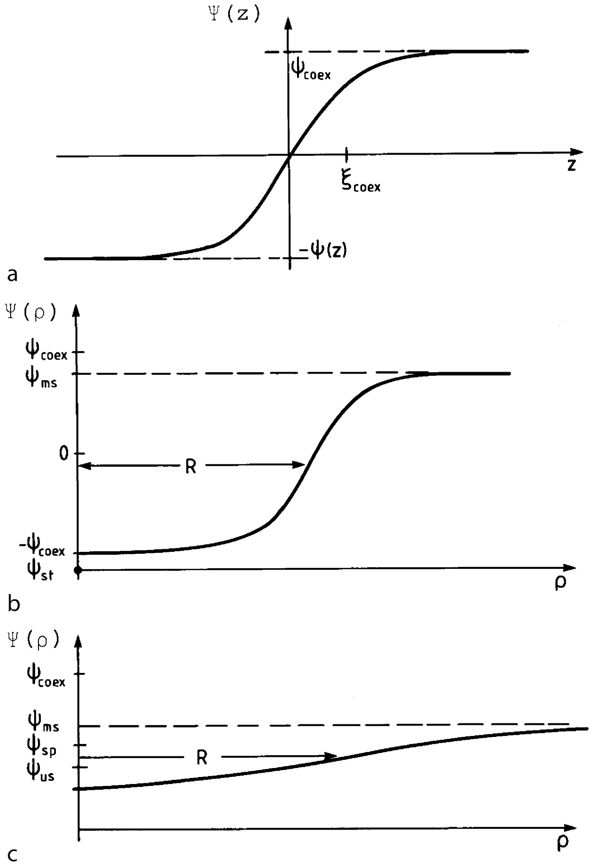

Demixing, Figure 3 (**a**) Order parameter profile $\psi(z)$ across an interface between two coexisting bulk phases with order parameters $\pm\psi_{\text{coex}}$, the interface being oriented perpendicular to the z-direction and centered at $z = 0$ (**b**) Radial order parameter profile for a marginally stable droplet of radius R. In the center of the droplet the order parameter takes the value of the stable phase at coexistence, $-\psi_{\text{coex}}$, while for radial distances $\rho \to \infty$, $\psi(\rho) \to \psi_{\text{ms}}$, the order parameter of the considered metastable state, for ψ_{ms} close to ψ_{coex}. (**c**) Same as (**b**), but for ψ_{ms} close to the spinodal, ψ_{sp}. Then $\psi(\rho = 0)$ does not reach $-\psi_{\text{coex}}$, but rather stays close to the unstable extremum of the free energy $f'(\psi)$, ψ_{us}

the spinodal before the crossover from nucleation to spinodal decomposition sets in. Actually, the situation is even more unfavorable when one includes the dependence on temperature distance from the critical point into the consideration (cf. Eq. (17)), and then one concludes that for mean-field theory to be self-consistent one requires first that $r^3(1 - T/T_c)^{1/2} \gg 1$ and [3, 4]

$$1 \ll r^3\left(1 - T/T_c\right)^{1/2}\left[1 - \bar{c}/c_{\text{sp}}(T)\right]^{\frac{3}{2}} \tag{20}$$

Similarly, exponential growth of the structure factor in spinodal decomposition with time t is predicted to occur when [3]

$$\exp(2A(k_m)t) \ll r^3\left(1 - T/T_c\right)^{1/2}\left[\bar{c}/c_{\text{sp}}(T) - 1\right]^{\frac{3}{2}} \tag{21}$$

These results explain why it is so difficult to verify experimentally the predictions of the linear theory of spinodal decomposition quantitatively.

Spinodals in Nanosystems

In the previous sections, a macroscopically large volume ($V \to \infty$) was tacitly assumed. Only then does the lever role hold, Eq. (1), which is based on ignoring interfacial contributions to the thermodynamic potential in the description of phase coexistence in thermal equilibrium.

If one considers a finite volume, say a box $L \times L \times L$, with periodic boundary conditions (or with *neutral* surfaces that do not prefer any of the coexisting phases), the situation is different: in a discussion of the thermodynamic equilibrium state of such a system, for conditions where for $L \to \infty$ one would have a two-phase coexistence, interfacial free energy contributions must not be neglected. And while for $L = \infty$ phase coexistence is described by a horizontal curve $\mu(c) = \mu_{\text{coex}}$, for $c^{(1)}_{\text{coex}} < c < c^{(2)}_{\text{coex}}$, for finite L one encounters a loop [5], with a maximum and a minimum (Fig. 4a). Actually, the example shown there does not refer to a fluid binary mixture, it rather refers to the demixing of a simple fluid into low-density vapor and high-density liquid, but we emphasize that the behavior of the fluid mixtures should be fully analogous. However, while in the regime of densities $\rho < \rho^{(1)}_{\text{coex}}$ (stable vapor) and $\rho > \rho^{(2)}_{\text{coex}}$ (stable liquid) the simulation data shown in this example rapidly converge with increasing L towards their limiting behavior, for $\rho^{(1)}_{\text{coex}} < \rho < \rho^{(2)}_{\text{coex}}$ the convergence is very slow: While for small L the loop is van der Waals-like, with increasing L the loop gets smaller, and the locations of the extrema $\rho^{(1)}_{\text{sp}}$, $\rho^{(2)}_{\text{sp}}$ slightly shift towards $\rho^{(1)}_{\text{sp}}$ and $\rho^{(2)}_{\text{sp}}$. Although, at first sight, these curves resemble van der Waals loops, their interpretation is completely different: the extrema are due to transitions from the homogeneous vapor and liquid phases (for $\rho < \rho^{(1)}_{\text{sp}}$ or $\rho > \rho^{(2)}_{\text{sp}}$, respectively) to a mixed state where vapor and liquid coexist (for $\rho^{(1)}_{\text{sp}} < \rho < \rho^{(2)}_{\text{sp}}$). As an example, Fig. 4b presents a more detailed study of these loops near $\rho_c \equiv \rho^{(1)}_{\text{coex}}$ at a lower temperature, where the behavior is more clearly seen. As L increases, a rather sharp transition from the supersaturated vapor (part of the curve where $\Delta\mu$ rises with increasing density ρ) to a less supersaturated vapor plus a liquid droplet occurs. This droplet evaporation/condensation transition becomes sharp only in the limit $L \to \infty$ where it disappears at the same time [5],

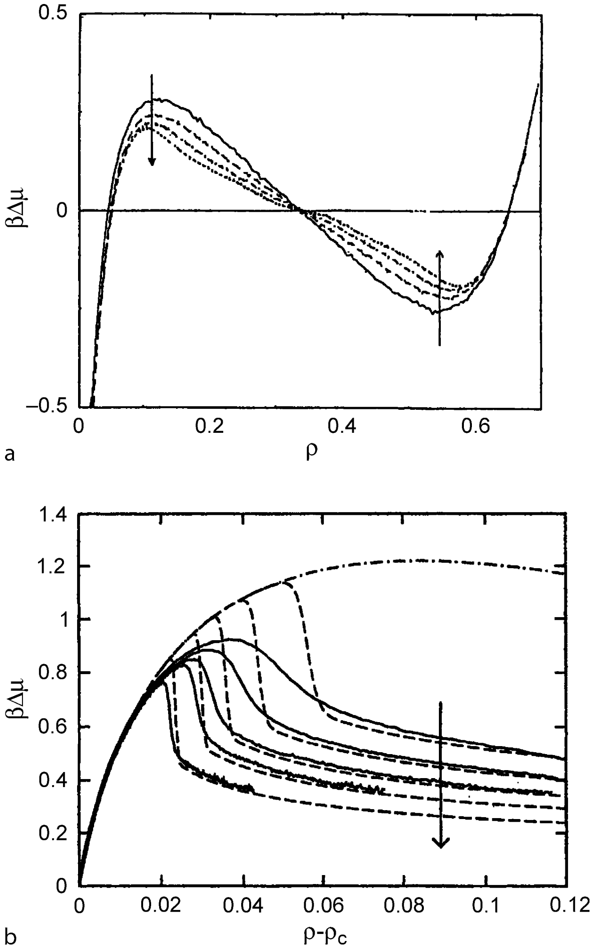

Demixing, Figure 4 (**a**) Normalized chemical potential difference $\beta\Delta\mu$ ($\beta = 1/(k_B T)$) of a simple Lennard-Jones fluid (particles interacting with a potential $u(r) = 4\varepsilon[(\sigma/r)^{12} - (\sigma/r)^6]$) plotted versus density ρ at a temperature $T = 0.85437$ (choosing units such that $\varepsilon = 1$). Here, μ_{coex} is the chemical potential of the fluid at which vapor–liquid coexistence occurs in the thermodynamic limit. Monte Carlo simulation *data* are shown, choosing cubic boxes of linear dimension $L \times L \times L$, with periodic boundary conditions in all three directions of space, and four sizes, $L = 6.74$, 9.0, 11.3 and 13.5, respectively (the arrows indicate increasing system size). (**b**) Same as (**a**), but for $T = 0.68$ and larger system sizes ($L = 11.3$, 13.5, 15.8, 18.3, and 22.5, from above to below, full curves). Dashed curves are corresponding predictions from an approximate analytical theory, describing the equilibrium of a liquid droplet with surrounding supersaturated vapor in a finite box, using Eq. (15). Dash-dotted curve represents the mean-field equation of state as given by the mean spherical approximation. From MacDowell et al. [5]

since then $\rho_{\text{sp}}^{(1)}$ coincides with $\rho_{\text{coex}}^{(1)}$. It is important to realize that these *loops* in Fig. 4 do not contain metastable and unstable parts, as are attributed to a van der Waals-like loop, but rather the whole loop, for the finite system, represents the true thermal equilibrium behavior. Thus, in a finite box for $\rho_{\text{coex}}^{(1)} < \rho < \rho_{\text{sp}}^{(1)}$ there is no possibility for the supersaturated vapor to decay, simply the total particle number contained in the box is too small to allow the nucleation of a stable droplet.

Of course, if the box is very small, e. g. $L \leqslant 3\xi_{\text{coex}}$ [4], then no phase separation within a box is possible at all, and then the state of the system is homogeneous irrespective of density. Thus, the mean field free energy density $f'(c)$ discussed above can be given a well-defined meaning when we re-interpret it as a coarse-grained free energy density $f_L(c)$ of a coarse-graining cell which has a linear dimension L of the order of ξ_{coex} or smaller. Note, however, that ξ_{coex} is typically only of the order of a Lennard-Jones diameter, except in the immediate vicinity of the critical point.

Coarsening: Dynamics of Phase Separation During the Late Stages

Irrespective of whether demixing has started by nucleation and growth or by spinodal decomposition, in the later stages of the process the state of the system is a heterogeneous arrangement of domains of the minority phase on the background of the majority phase. In cases where the volume fraction X of the minority phase is small enough, these domains are well separated from each other, while for large enough X the minority domains also form a percolating interconnected structure. It often is said that the morphology of well-separated droplets is evidence that phase separation has started by nucleation, but such an inference, in fact, is not conclusive: in reality there is no simple connection between the morphology of the late stages and the initial growth mechanism, and examples exist when an initially percolating rather ramified structure later breaks up into more compact separated droplets.

A comprehensive theory for the coarsening of such domains which are formed as a result of demixing is a formidable problem [2, 6, 7]. Here we only give a brief summary of some of the main mechanisms proposed in the literature.

The first mechanism proposed by Lifshitz and Slyozov (LS), also called the evaporation–condensation mechanism, is derived [6–8] for the situation where a *population* of droplets of the minority phase is in local equilibrium with the surrounding majority phase, which is slightly supersaturated because of the Gibbs–Thompson effect. Since in this droplet population more B-atoms *condense* on the larger B-rich droplets than *evaporate* into the supersaturated A-rich background, while for the smaller B-rich droplets the reverse is true, the diffusion of the B-atoms in the A-rich matrix maintain concentration gradients by which the smaller droplets shrink and finally dissolve in the matrix and the larger droplets grow. This mechanism

leads to a growth law $\ell(t) \propto t^{1/3}$ with time t after the quench, for $t \to \infty$, where $\ell(t)$ is the linear dimension of the growing droplets. This law holds in all dimensionalities $d \geqslant 2$. Although the original derivation [8] only holds for the limit of vanishing volume fraction of the B-rich phase, one now believes [6, 7] that the *LS* $t^{1/3}$ law holds for arbitrary volume fractions, but only in purely diffusive systems (i. e. solid rather than fluid binary mixtures, but in the latter it may also appear as a competing mechanism).

The droplet diffusion and coagulation mechanism [9] was the first proposal specifically addressing fluid mixtures, and is based on Stokes' law for the diffusion of droplets. That is, one assumes a diffusion constant $D(R)$ scaling with droplet radius R as $D(R) \propto \eta^{-1}R^{2-d}$, η being the shear viscosity of the fluid. The time τ for a droplet to travel a distance R then is estimated from the Einstein relation: $\tau D(R) = 2dR^2$, i. e. $\tau \propto \eta R^d$. At not too low volume fractions the average distance between droplets is of the order of R, and when two droplets collide they will coalesce. This leads to a volume change of the droplet of order $\Delta V \propto R^d$. So $\Delta V/\tau \propto \eta^{-1}$, and equating this to $\mathrm{d}V/\mathrm{d}t \propto R^{d-1}\,\mathrm{d}R/\mathrm{d}t$ yields $\mathrm{d}R/\mathrm{d}t \propto R^{1-d}/\eta$ or $R(t) \propto (t/\eta)^{1/d}$.

A faster mechanism of domain growth was proposed for the coarsening of interconnected domain structures [10], for $d = 3$, when the volume fraction of the minority phase is sufficiently large to maintain such a percolating structure. The key mechanism then is the deformation and break-up of tube-like regions in the domain structure. The characteristic velocity field v_ℓ around domains having linear dimensions ℓ is determined by a balance between the surface tension force density of order γ/ℓ, and the viscous stress of order $6\pi\eta v_\ell/\ell$. This leads to $v_\ell \propto \gamma/\eta$ and a growth law $\ell(t) \propto v_\ell t \propto (\gamma/\eta)t$, in $d = 3$ [10]. In $d = 2$, the analogue of this hydrodynamic mechanism is somewhat controversial, predictions range from $\ell(t) \propto t^{1/2}$ to $\ell(t) \propto t$, but it also has been suggested that different characteristic length scales may exhibit different growth exponents, and hence there would be no simple *dynamical scaling* [2, 6, 7] for domain growth in $d = 2$ at all. If dynamical scaling holds one expects that the equal-time structure factor $S(k,t)$ does not depend on both variables k and t in a completely general form, but essentially it depends on a single scaled variable $\zeta = k\ell(t)$ only

$$S(k,t) = [\ell(t)]^d \quad \tilde{S}(k\ell(t)) \,, \tag{22}$$

where $\tilde{S}(\zeta)$ is a *scaling function*. Prediction of $\tilde{S}(\zeta)$ is difficult even if the growth law $\ell(t) \propto t^a$ is known [2, 6, 7].

Finally, we note that the growth laws mentioned above hold only for low enough Reynolds numbers. On the scale of the domain size, the Reynolds number can be estimated as $\mathrm{Re}(\ell) = nv_\ell/\eta$, where n is the density, and hence $\mathrm{Re}(\ell)$ increases with time as the domain size grows. When $\ell(t)$ exceeds the so-called *inertial length* $\ell_{\mathrm{in}} \approx 10\eta^2/(n\gamma)$, one encounters both in $d = 2$ and $d = 3$ a regime where the surface energy density γ/ℓ is balanced with the kinetic energy density nv_ℓ^2. By setting $\ell = v_\ell t$ one obtains in this so-called *inertial regime* a growth law $\ell(t) \propto (\gamma/n)^{1/3}t^{2/3}$ [7].

From the above considerations it is clear that our discussion of spinodal decomposition in terms of a generalized nonlinear diffusion equation (Eq. (5)) was very incomplete, since there it was tacitly assumed that the concentration field $c(\boldsymbol{x},t)$ is the only relevant slow variable in the problems while in reality a second slow variable, the velocity field $v(\boldsymbol{x},t)$, needs to be included, even if the fluid on average is at rest. A particularly interesting complication arises for fluids exposed to shear flow, where the direction of $\boldsymbol{k}$ (relative to the flow direction) matters [11], while for fluids at rest $S(\boldsymbol{k},t)$ is isotropic. This problem is beyond our scope here, as are the subtleties which arise when the two constituents of a binary mixture have vastly different viscosity (*viscoelastic phase separation* [12]).

Binary Mixtures Confined Between Walls in Slit Pores: Equilibrium Behavior

In the context of microfluidics and nanofluidics, demixing of fluid binary mixtures confined in narrow pores is a particularly relevant issue. An important facet of this behavior is that the concentration of such confined mixtures is typically rather inhomogeneous in the z-direction perpendicular to the walls of a pore, and the equilibrium phase behavior due to the confinement which differs from that of the corresponding bulk mixture. The understanding of these phenomena is a prerequisite for a discussion of demixing kinetics in pores or narrow channels.

Figure 5 summarizes these effects in a qualitative way for a binary symmetric mixture [13]. Near the critical temperature T_c, the coexistence curve in the bulk is described by a power law for the concentrations x_A of A at the coexistence curve, $x_{\mathrm{A,coex}}^{(1,2)} - x_{\mathrm{A}}^{\mathrm{crit}} \hat{\to} \pm B(1 - T/T_c)^\beta$, where $x_{\mathrm{A}}^{\mathrm{crit}} = 1/2$ for a symmetric mixture, B is a system-dependent *critical amplitude* and the critical exponent $\beta \approx 0.325$, the universal value for the *universality class* of the $d = 3$ Ising model [2, 13]. At the surface of a semi-infinite mixture one may encounter a wetting transition [14]. This wetting transition implies a singular behavior of the surface excess free energy F_s, which is defined as (for a film between two walls at distance D) $F_{\mathrm{film}} = F_{\mathrm{bulk}} + (2/D)F_s$, $D \to \infty$, F_{bulk} being the bulk free energy of the system. Assuming, as done in figure 5, that the wetting transition occurs at the surface of B-rich mixtures (caused by the preferential attraction of A-particles to the walls), the transition is char-

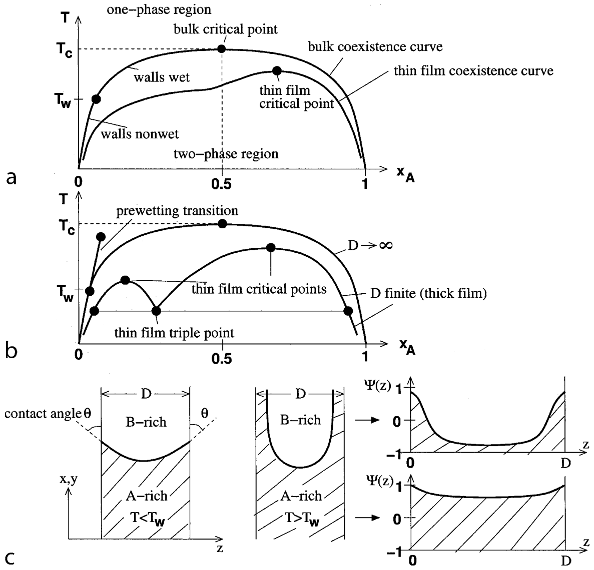

Demixing, Figure 5 Schematic phase diagrams (**a**), (**b**) and corresponding state (**c**) of a symmetric A, B mixture in a thin film of thickness D, using temperature T and concentration x_A of A as variable. The film is symmetric, i. e. both walls attract the A-particles with the same strength. In the limit $D \to \infty$ a wetting transition occurs at a temperature T_W, while for finite D the transition of the walls from *nonwet* (or *partially wet*) to *wet* (or *completely wet*) is rounded into a smooth gradual change. The wetting transition is assumed to be of second order in (**a**), while (**b**) refers to a first-order wetting transition. In (**b**), a prewetting transition line exists in the one-phase region, with one end being a prewetting critical point at high temperatures. The other end of this line is at the wetting transition temperature T_W, at the coexistence curve that separates the two-phase region from the one-phase region. Note that the critical concentration of a symmetric binary mixture is $x_A^{crit} = 0.5$ in the bulk, but is shifted to a larger value x_A in the thin film. Further, the critical temperature of the thin film typically is lower than in the bulk, $T_C(D) < T_C(\infty) = T_C$. For the case of first-order wetting and large enough D, a thin-film analog of the prewetting transition exists, as evidenced by the thin-film critical point at the left side of the phase diagram. When the thin enrichment layer segregation meets the lateral segregation of the *thick* film, a thin film triple point occurs at a temperature close to T_W. In (**c**) we provide schematic pictures of the thin-film states in the case of lateral phase segregation

acterized by a divergence of the surface excess concentration of A, x_A^{surf}. This surface excess concentration can either be found from F_s via suitable derivatives, or, equivalently, by integrating the concentration profile, $x_A^{surf} = \int_0^{D/2} \left[x_A(z) - x_{A,coex}^{(1)}\right] dz$, $D \to \infty$, z being the distance from the left wall, which is oriented perpendicular to the z-axis at $z = 0$. If the wall is *nonwet* (also called *incompletely wet*), x_A^{surf} tends to a finite value, $x_{A,coex}^{surf}$, when $x_A \to x_{A,coex}^{(1)}$ from the one-phase region. For a *wet* wall, on the other hand, $x_{A,coex}^{surf} = \infty$ (corresponding to an infinitely thick A-rich wetting layer coating the wall, separated from the B-rich bulk by a flat interface).

This situation (*complete wetting*) implies a divergence of x_A^{surf} when $x_A \to x_{A,coex}^{(1)}$ at constant temperature. For short-range forces between the walls and the particles this divergence is only logarithmic, $x_A^{surf} \propto \left|\ln(x_{A,coex}^{(1)} - x_A)\right|$, while for attractive forces which decay with distance z like a power law (e. g. van der Waals forces) one also obtains a power law divergence of x_A^{surf} [14]. At the coexistence curve $x_{A,coex}^{(1)}$, the surface excess free energy thus is that of a B-rich phase $F_{s,coex}^{B\text{-rich}}$ if the wall is non-wet, while for a wet wall we have $F_s = F_{s,coex}^{A\text{-rich}} + \gamma$, γ being (as above) the interfacial tension between coexisting bulk A-rich and B-rich phases. These quantities also determine the contact angle θ under which an A–B interface in the non-wet region meets the wall, $\cos\theta = (F_{s,coex}^{B\text{-rich}} - F_{s,coex}^{A\text{-rich}})/\gamma$, if $F_{s,coex}^{B\text{-rich}} < F_{s,coex}^{A\text{-rich}} + \gamma$ (see Fig. 5).

If one changes the state of the system such that one increases the temperature but stays always at the coexistence curve $x_{A,coex}^{(1)}$, one may encounter a wetting transition at T_W where the state of the wall changes from non-wet ($T < T_W$) to wet ($T > T_W$). This transition may be of first order (Fig. 5b) or second order (Fig. 5a). In the latter case, x_A^{surf} diverges continuously when $T \to T_W$ from below, while otherwise there is a discontinuous jump from a finite value at T_W to infinity. In this latter case, there is also a prewetting transition occurring in the one-phase region, where the thickness of the A-rich surface layer jumps from a smaller value to a larger (but finite) value. This line of prewetting transitions ends in a prewetting critical point.

This brief review of wetting phenomena now is the basis of understanding the equilibrium behavior of a thin film [15]. If the wall would be *neutral* (i. e., same attractive forces to both types of particles A, B), the critical concentration would still be $x_A^{crit} = 1/2$, but the critical temperature $T_c(D)$ of the film would be somewhat depressed, relative to the bulk $\{T_c(D \to \infty) \equiv T_c\}$, $T_c - T_c(D) \propto D^{-1/\nu}$, where $\nu \approx 0.629$ is the critical exponent of the correlation length ξ of the concentration fluctuations, in the universality class of the $d = 3$ Ising model [15]. Note, however, that critical correlations at fixed finite D can attain arbitrarily long range only in the lateral direction parallel to the film, so the transition at $T_c(D)$ then belongs to the class of the $d = 2$ Ising model ($\beta = 1/8$, but as $D \to \infty$ there is a crossover to $d = 3$, of course, reflected in a singular dependence of the critical amplitude $B(D)$ in the power law describing the coexistence curve). This means that the shape of the coexistence curve of the thin film is ultimately much flatter than the coexistence curve of the bulk. This effect cannot be described by mean-field theories, of course: mean-field theories neglect statistical fluctuations and imply $\beta = 1/2$ in all dimensions. The states underneath the coexistence curve of the thin film always imply two-phase equilibria

characterized by *lateral* phase separation. The development of a *stratified* structure with surface enrichment layers at the walls (right upper part of Fig. 2c) develops in a smooth gradual manner when one reaches $T \approx T_c$ and does *not* imply a *phase transition* in the sense of thermodynamics.

When there is a preferential attraction of A particles by walls, as assumed here, the phase diagram of the thin film is no longer symmetric with respect to $x_A = 1/2$, although we did assume such a symmetry in the bulk. This shift of x_A^{crit}, for which scaling arguments predict $x_A^{crit}(D) - x_A^{crit} \propto D^{-\beta/\nu}$ [15], and the resulting change of the coexistence curve is the analog of *capillary condensation* of gases for binary mixtures.

The phases that coexist with each other in the region below the coexistence curve of the thin film are inhomogeneous in the direction perpendicular to the walls (Fig. 5c). In the A-rich phase, we typically expect only a slight enhancement of the order parameter $\psi(z)$, which here is defined in terms of the densities $n_A(z)$, $n_B(z)$ of A(B) particles as $\psi(z) = [n_A(z) - n_B(z)]/[n_A(z) + n_B(z)]$, near the walls. In the B-rich phase, however, we expect more or less pronounced enrichment layers. As $D \to \infty$, the thickness of these layers diverges for $T > T_w$ but stays finite for $T < T_w$: in a film of finite thickness, the width of A-rich surface layers also stays finite (e. g. for $T > T_w$ for short-range surface forces $x_A^{surf} \propto \ln D$). Thus, the wetting transition always is rounded off in a thin film, while the prewetting line (Fig. 5b) does have an analog in films of finite thickness D, for large enough D [15]. This transition causes the two-phase coexistence region at small x_A in between the thin-film triple point and the thin-film critical point at the B-rich side. This two-phase coexistence region corresponds to a coexistence between B-rich phases with A-rich surface layers which both have finite (but different) thickness. As $D \to \infty$, this thin-film critical point on the B-rich side moves into the prewetting critical point, while the thin-film triple point merges with the first-order wetting transition. On the other hand, when D becomes very small, this thin-film critical point and the thin-film triple point may merge and annihilate each other [15]. For still smaller D the thin-film phase diagram then has the shape as shown in figure 5a, although one has a first-order wetting scenario in the semi-infinite bulk (Fig. 5b).

Finally, we comment on the state of the thin film encountered below the coexistence curve of the bulk but above the coexistence curve of the thin film. When one crosses the bulk coexistence curve, one encounters a *rounded transition* towards a layered (*stratified*) structure with two A-rich layers at the walls and a B-rich layer in the middle. The temperature region over which this transition is smeared out also is of order $\Delta T \propto D^{-1/\nu}$ around T_c, and hence for large D this phase separation in the direction normal to the walls may easily be mistaken (in experiments or simulations) as a true (sharp) phase transition, but it is not: one is still in the one-phase region of the thin film although the structure is strongly inhomogeneous. Such A-rich layers at the walls have a thickness varying proportional to D when D is varied at fixed D, unlike true wetting layers at the surface of a B-rich phase which vary much more weakly than linear with D (logarithmic, in the case of short-range forces). Actually, if the thickness of the domain walls between the domains could be neglected, the thickness ℓ of these domains would simply be given by the lever rule, i. e. in this case by $\ell = (D/2)\big(x_{A,coex}^{(2)} - x_A\big)/\big(x_{A,coex}^{(2)} - x_{A,coex}^{(1)}\big)$. However, since the interfacial width close to T_c diverges in the bulk (see Eq. (16)), the interfacial width in the z-direction in the thin film near T_c also scales proportional to D, and so the thickness of the domain walls in the stratified structure is never negligible. Unfortunately, these layers in the stratified structure are often referred to in the literature as *wetting layers*, which is completely misleading.

When one considers slit pores with different types of walls, the situation can become much more complicated [15]. The extreme situation is often referred to as *competing walls*, i. e. one wall (e. g., the left one) attracts A particles, the other wall (the right one) B particles, with the same absolute strength. In this case near T_c a gradual transition occurs to a stratified structure with a single domain wall between the A-rich domain on the left and the B-rich domain on the right. At $T_c(D)$, then, an *interface localization* transition occurs [15], the domain wall gets bound to the left wall in one part of the system and to the right wall in another part (see [15] for a discussion of the corresponding phase diagrams).

Surface-Directed Spinodal Decomposition

We are now again concerned with the demixing kinetics following temperature quenches, but rather than in the bulk as in Fig. 1 we now assume a thin-film geometry, with a phase diagram in equilibrium as shown in Fig. 5. Again one wishes to derive a phenomenological description, similar as for spinodal decomposition in the bulk (Eqs. (2)–(12)). Using a local order parameter $\psi(\rho, z)$, defined in analogy to $\psi(z)$ of the above section, but allowing now an inhomogeneity in the lateral directions (ρ), we amend the free energy functional $\Delta F[\psi(\rho, z, t)]$ (cf. Eq. (5)) by surface terms. Normalizing ψ by the order parameter ψ_{coex} describing the bulk coexistence curve and measuring distances $\vec{\rho}, z, D$ in units of the corresponding correlation length in the bulk, ξ_{coex}, the free energy functional

becomes ($\phi \equiv \psi/\psi_{\rm coex}$)

$$\Delta F[\phi] = F_{\rm bulk}[\phi] + F_{\rm s,1}[\phi] + F_{\rm s,2}[\phi] \tag{23}$$

where one often assumes a Ginzburg–Landau ϕ^4 form for the bulk [16]:

$$F_{\rm bulk}[\phi(\rho,z)] = \int d\rho \int_0^D dz[-\frac{\phi^2}{2} + \frac{\phi^2}{4} + \frac{1}{4}(\nabla\phi)^2 + V(z)\phi] \tag{24}$$

where $V(z)$ describes a long-range surface potential, e. g. $V(z) = -V_0\big[(z+1)^{-3} + (D+1-z)^{-3}\big]$, where the divergence at $z = 0$, $z = D$ was cut off by adding ± 1 at the locations of both walls [13, 16], to avoid problems with the numerical solutions of the resulting equations [16]. The surface terms $F_{\rm s,1}[\phi]$, $F_{\rm s,2}[\phi]$ are extended over the surfaces 1, 2 only:

$$F_{\rm s,1}[\phi] = \int_1 d\rho \left\{-\frac{g}{2}\big[\phi(\rho,0)\big]^2 - h_1\phi(\rho,0) - g'\phi(\rho,0)\frac{\partial\phi}{\partial z}\Big|_{z=0}\right\} \tag{25}$$

and

$$F_{\rm s,2}[\phi] = \int_2 d\rho \left\{-\frac{g}{2}\big[\phi(\rho,D)\big]^2 - h_D\phi(\rho,D) + g'\phi(\rho,D)\frac{\partial\phi}{\partial z}\Big|_{z=D}\right\} \tag{26}$$

The terms $F_{\rm s,1}, F_{\rm s,2}$ represent the *bare* surface excess free energy contributions due to local effects at and near the walls: additional short-range forces are included in the terms $-h_1\phi(\rho,0)$, $-h_D\phi(\rho,D)$; the other terms may represent physical effects such as the fact that a particle close to a wall has less neighbors to interact with (*missing neighbor effect*). Anyway, in the following the constants g, g', and $h_1 = h_D$ are treated as phenomenological parameters. Depending on the parameters g/g' and h_1/g', one may encounter first- or second-order wetting transitions in the limit $D \to \infty$ [15, 16] when $V_0 = 0$, and for finite D phase diagrams as shown in Fig. 5 result.

The extension to dynamics is again based on equations similar to Eqs. (2)–(4); however, in addition to an equation similar to Eq. (7) one now has to satisfy two boundary conditions resulting from the surfaces. Since the local order parameter at the surface is not a conserved quantity, Eq. (25) leads to [16]

$$\tau_0\frac{\partial}{\partial t}\phi(\rho,z=0,t) = -\delta F/\delta\phi(\rho,z=0,t) = h_1 + g\phi(\rho,0,t) + g'\partial\phi/\partial z|_{z=0} \tag{27}$$

and a similar equation for $\phi(\rho,D,t)$ results from Eq. (26). Another boundary condition expresses the physical requirement that the z-component of the flux at the surfaces must vanish,

$$J_z(\rho,0,t) = -\left\{\frac{\partial}{\partial z}\left[-\phi+\phi^3-\frac{1}{2}\nabla^2\phi+V(z)\right]+\theta_z\right\}_{z=0} = 0 \tag{28}$$

$\theta(\boldsymbol{r},t)$ being a random force which also enters the analog of Eq. (7) [16].

During the early stages, the fast relaxation of the nonconserved order parameter at the surfaces provides a boundary condition for the phase of the concentration waves which grow in the thin film. While in the bulk the random orientations and phases of these growing waves do not yield a time evolution of the average order parameter, these surface-directed concentration waves add up to an average oscillatory concentration profile near the surfaces of a thin film [16]. However, for a quantitative description extensive numerical calculations solving Eqs. (2)–(7), (27), and (28) are required [16].

Key Research Findings

Kinetics of demixing of fluid and solid mixtures in the bulk has been intensively studied for decades [2, 17]. A general conclusion of these studies is that the linearized Cahn theory of spinodal decomposition is not quantitatively valid (with the exception of symmetrical mixtures of polymers with high molecular weight [18]), but – within a factor of two or so – predicts the correct order of magnitude of the characteristic wavenumber $k_{\rm m}$ at which the peak of the equal-time structure factor first develops. No evidence of any singular behavior associated with the spinodal has been found, as expected in view of the theoretical arguments summarized above. The fact that for polymers with very large chain length N the initial exponential growth of $S(k,t)$, cf. Eq. (13), can be observed, and that the growth rate $A(k)$ agrees with Eq. (11), can be explained in terms of the self-consistency criterion for the linear theory, Eq. (21), since one can show [2, 19] that for polymers in $d = 3$ one needs to replace the factor r^3 in Eq. (28) by $\sqrt{N}$, and hence symmetrical ($N_{\rm A} = N_{\rm B} = N$) polymer mixtures

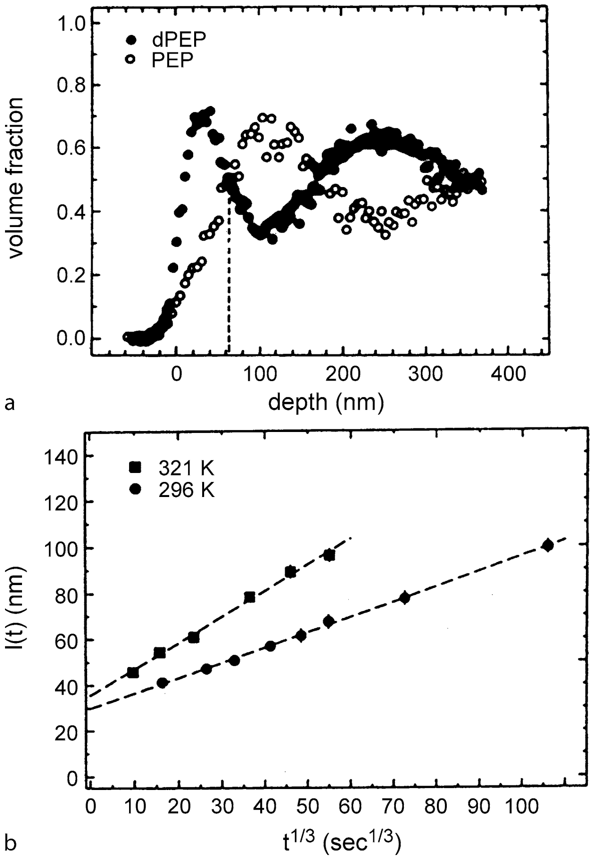

Demixing, Figure 6 (**a**) Volume fraction of deuterated poly(ethylene propylene), dPEP (full dots), and protonated PEP (open circles) versus depth, for a degree of polymerization $N \approx 2300$ for both constituents, after a 4 h quench to $T = 294$ K ($T_c = 365$ K). Profiles are obtained with time-of-flight forward recoil spectroscopy. The dashed line indicates the surface domain thickness $\ell(t)$. (**b**) Plot showing the growth of the surface domain thickness $\ell(t) \propto t^{1/3}$. From Krausch et al. [20]

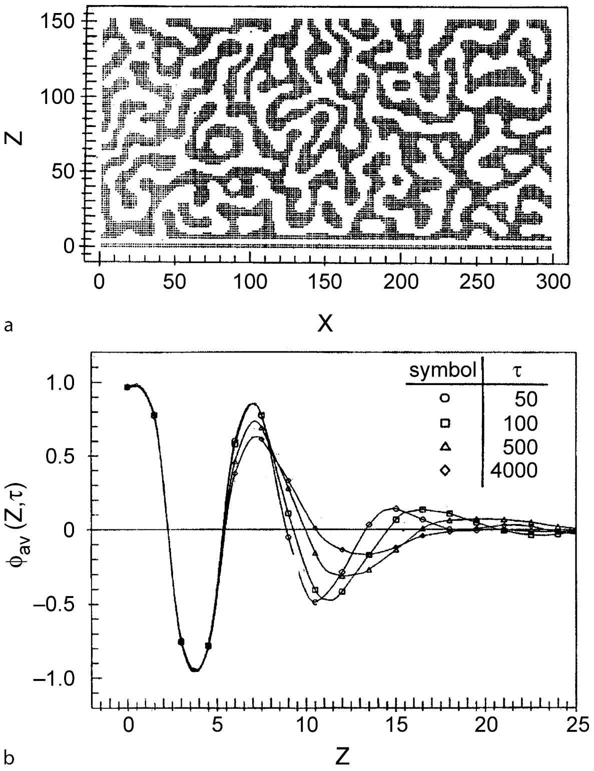

Demixing, Figure 7 (**a**) Snapshot picture of a two-dimensional system with a wall at $z = 0$ undergoing spinodal decomposition, starting at time $t = 0$ from a random configuration, with average order parameter $\phi = 0$. Using the model of Eqs. (7), (23)–(28) for $V_0 = 0$, $h_1 = 4$, $g = -4$, $g' = 4$, a discrete implementation using a lattice of size 150 × 300 was used. The cells with order parameter ϕ near $\phi = +1$ are shown in black, cells with order parameter $\phi = -1$ are left white. The snapshot refers to a scaled time $\tau = 500$. Note that at the wall an enrichment layer, followed by depletion layer, has formed. From Puri and Binder [21]. (**b**) Laterally averaged profiles $\phi_{av}(z, \tau)$ as a function of the scaled distance z from the surface, for four scaled times as indicated, obtained from the same calculation as (**a**). From Puri and Binder [21]

satisfy the theory during their initial stages, if N is large enough.

With respect to late stages of phase separation in the bulk, rather convincing and broad evidence for scaling in the late stages, Eq. (20), has been obtained [2, 6, 7, 17]. For off-critical quenches in binary fluid mixtures, one normally finds a growth law $\ell(t) \propto t^{1/3}$ in the last stages, compatible with the droplet diffusion–coalescence mechanism [2, 9]. For critical quenches, a slow crossover to the law [10] $\ell(t) \propto t$ has been seen, while experimental evidence for the growth law of the inertial regime [7], $\ell(t) \propto t^{2/3}$, is still lacking.

All the above statements refer to relatively simple, approximately symmetric, mixtures. For very asymmetric cases, in particular when one fluid is close to its glass transition while the other component of the mixture is much more mobile, no simple scaling behavior occurs [12] and the morphology of the domain pattern may change its character during the coarsening. The details of this behavior still are only poorly understood.

For systems quenched only slightly inside of their coexistence curve also nucleation behavior has been studied. Quantitative tests of homogeneous nucleation theory (as outlined in Eqs. (15)–(17)) turned out to be difficult, and different conclusions emerged for different systems: sometimes the *classical formula*, Eq. (18), fails dramatically, sometimes it gives reasonable estimates.

In the last two decades a lot of effort has been directed towards phase separation of fluid mixtures confined in thin films [16, 19]. Qualitative evidence for surface-directed spinodal decomposition has been found both experimentally [19, 20], see e. g. Fig. 6, and from numerical simula-

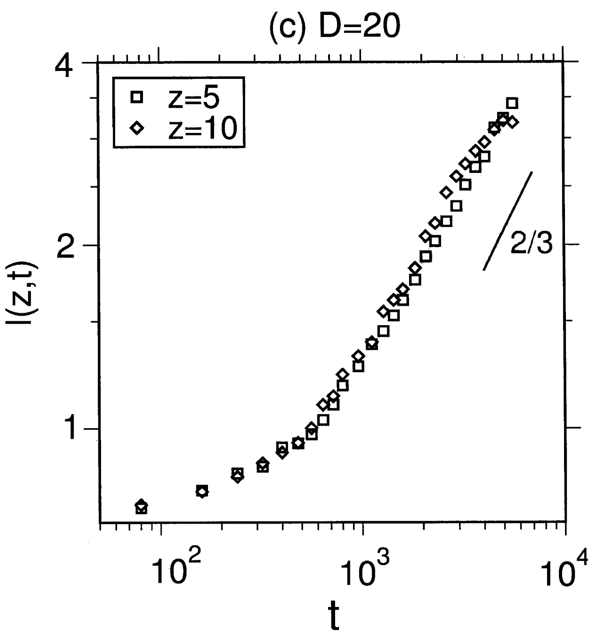

Demixing, Figure 8 Log–log plot of the length scale $\ell(z,t)$ of a thin film of a binary Lennard-Jones mixture between two flat planar walls $D=20$ Lennard-Jones parameters apart plotted versus time, for two different values of z. Lennard-Jones parameters were chosen $\sigma_{AA}=\sigma_{AB}=\sigma_{BB}=\sigma=1$, $\varepsilon_{AA}=\varepsilon_{BB}=\varepsilon=1$, $\varepsilon_{AB}=\varepsilon/2$, and masses of the particles are chosen to be equal, $m_A=m_B=1$. Time is measured in units of $t_0=(m\sigma^2/48\varepsilon)^{1/2}$. The density was chosen $n=1$, and a quench was performed (using $n_A=n_B=n/2$) from $T=5$ to $T=1.1$, far below $T_c(=1.638)$. At both walls, a potential $u_W(z)=(2\pi n\sigma^3/3)\varepsilon_W[(2/15)(\sigma/z')^9-\delta_\alpha(\sigma/z')^3]$ acts, where $z'=z+\sigma/2$ or $z'=D+\sigma/2-z$, respectively, $\delta_A=1$, $\delta_B=0$, $\varepsilon_W=0.005$ (yielding an incompletely wet wall). From Das et al. [13]

tion of Eqs. (5), (23)–(21), see e. g. Fig. 7 [21]. Note that this theory does ignore the coupling to the velocity field, and hence it yields in the late stages the LS growth law [8] $\ell(t)\propto t^{1/3}$. While some experiments observe the same growth law (Fig. 6b), other experiments observe faster growth, however. A full account of hydrodynamics can be obtained by molecular dynamics simulation of demixing of binary fluid mixtures, however. Figure 8 shows that in such a model fluid binary mixture indeed [13] a faster growth law than the LS growth is obtained, $\ell(t)\propto t^{2/3}$. While this law is reminiscent of domain growth in the inertial regime, the accessible length scales are too small by far to reach this regime, and hence a theoretical explanation for this finding is still lacking.

Thus while for demixing in the bulk, at least for *simple* symmetric mixtures, the theoretical results are to some extent supported by experiments and simulations, demixing kinetics in pores is still much less understood in detail.

Future Directions for Research

Particularly interesting future research should include systematic studies of phase separation in thin slit pores under flow, varying the slit widths and boundary conditions at the walls.

Cross References

- ► Brownian Motion and Diffusion
- ► Diffusion
- ► Droplet and Bubble Formation in Microchannel
- ► Molecular Dynamics Simulation Method
- ► Surface Tension Driven Flow
- ► Surface Tension, Capillarity, and Contact Angle
- ► Van der Waals Interaction Forces
- ► Viscoelasticity
- ► Wetting and Spreading

References

1. Binder K, Stauffer D (1976) Statistical theory of nucleation, condensation and coagulation. Adv Phys 25:343–396
2. Binder K, Fratzl P (2001) Chapter 6 Spinodal decomposition. In: Kostorz G (ed) Phase Transitions of Materials. Wiley-VCH, Weinheim, Germany, pp 409–480
3. Cahn JW (1961) On spinodal decomposition. Acta Metall 9:795–801
4. Binder K (1987) Theory of first order phase transitions. Rep Progr Phys 50:783–859
5. MacDowell LG, Virnau P, Müller M, Binder K (2004) The Evaporation/Condensation Transition of Liquid Droplets. J Chem Phys 120:5293–5308
6. Bray AJ (1994) Theory of phase ordering kinetics. Adv Phys 43:357–459
7. Onuki A (2002) Phase Transition Dynamics, Cambridge Univ. Press, Cambridge
8. Lifshitz IM, Slezov VV (1961) The kinetics of precipitation from supersaturated solid solutions. J Phys Chem Solids 19:35–50
9. Binder K, Stauffer D (1974) Theory for the slowing down of the relaxation and spinodal decomposition of binary mixtures. Phys Rev Lett 33:1006–1010
10. Siggia E (1979) Late stages of spinodal decomposition in binary mixtures. Phys Rev A20:595–605
11. Onuki A (1997) Phase transitions of fluids in shear flow. J Phys Condens Matter 9:6107–6157
12. Tanaka H (2000) Viscoelastic phase separation. J Phys Condens Matter 12:R207–R264
13. Das SK, Puri S, Horbach J, Binder K (2006) Spinodal decomposition in thin films: Molecular Dynamics simulations of a binary Lennard-Jones fluid mixture. Phys Rev E73(031604):1–15
14. Dietrich S (1988) Wetting Phenomena. In: Domb C, Lebowitz JL (eds) Phase Transitions and Critical Phenomena, vol 12, Academic Press, London, pp 1–218
15. Binder K, Landau DP, Müller M (2003) Monte Carlo Studies of Wetting, Interface Localization and Capillary Condensation. J Statist Phys 110:1411–1514
16. Puri S (2005) Surface-directed spinodal decomposition. J Phys Condens Matter 17:R1–R42

17. Komura S, Furukawa H (eds) (1988) Dynamics of Ordering Processes in Condensed Matter. Plenum Press, New York
18. Bates FS, Wiltzius P (1989) Spinodal decomposition of a symmetrical critical mixture of deuterated and protonated polymer. J Chem Phys 91:3258–3274
19. Krausch G (1995) Surface-induced self-assembly in thin polymer films. Mat Sci Eng Rep 14:1–94
20. Krausch G, Dai C-A, Kramer EJ, Bates FS (1993). Real space observation of dynamics scaling in a critical polymer mixture. Phys Rev Lett 71:3669–3672
21. Puri S, Binder K (1994) Surface effects on spinodal decomposition in binary mixtures and the interplay with wetting phenomena. Phys Rev E49:5359–5377

DEP

► AC Dielectrophoresis Lab-on-Chip Devices
► Dielectrophoresis

Deposition

► Nucleation and Growth

Depth of Field

Definition

The depth of field defines the distance to the focal plane an object can have to still appear sharp. For example in ►PIV/PIT measurements particles which are not within the depth of field appear blurred and with a bigger diameter. The depth of field depends on the wavelength of the illuminating light, the optics and the surrounding medium (e. g. air).

Detection Groove

Definition

The detection groove is a feature etched into a microchannel perpendicular to the fluid flow. The groove is very small, but much deeper than the channel itself, accumulating and mixing the fluid that passes through the channel. This feature can be used to improve the detection sensitivity for shear driven chromatography.

Developing Flows

Gian Luca Morini
DIENCA Università di Bologna, Bologna, Italy
gianluca.morini@mail.ing.unibo.it

Synonyms

Entrance flows; Establishing flows

Definition

When a fluid runs through a channel and its velocity and/or the temperature profile changes axially, the flow is said to be a developing flow.

Overview

In any type of flow (laminar or turbulent), the particles of a nonrarefied fluid immediately adjacent to the walls of a microchannel are always at zero velocity and in thermal equilibrium with the walls. Consider a fluid with a uniform velocity and temperature profile, entering a channel with walls maintained at a different value of temperature (lower or higher than the inlet fluid temperature). Upon entering the channel, therefore, the fluid particles that come into contact with the walls are slowed down and the temperature of the fluid at the walls becomes coincident with the wall temperature. For this reason, velocity and/or temperature gradients appear in the fluid near the walls, and the velocity and temperature profiles tend to change axially along the channel. The flow in this region is said to be a *developing flow*, and the part of the microchannel in which the velocity and/or the temperature field is not completely developed is named the *entrance region*.

In this region, a dynamic and a thermal boundary layer are thus formed, in which large velocity and temperature gradients exist. In the first part of the dynamic boundary layer the flow is laminar, but after a certain distance from the leading edge a transition to turbulent conditions can take place in the flow, with only a laminar sublayer remaining very close to the walls. The dynamic and thermal boundary layers increase in thickness in the entrance region until a fully developed condition is reached across the channel (see ► entrance region).

The development of the thermal and dynamic boundary layers can be either coupled or uncoupled. When the thermal and dynamic boundary layers develop together, the flow is said to be a *simultaneously developing flow*. When only the dynamic boundary layer develops, with the fluid in thermal equilibrium with the walls, the flow is said to be a *hydrodynamically developing flow*. When the flow is hydrodynamically fully developed but the thermal boundary layer develops, the flow is said to be a *hydrodynamically fully developed* and *thermally developing flow*: this situation can be obtained in a microchannel with adiabatic walls in the region near the entrance (*adiabatic preparation*) and where heating at the walls starts beyond the hydrodynamic entrance region.

The development of the velocity and temperature fields has a marked effect on the friction factor and the heat transfer coefficient near the channel entrance region. Correlations for the calculation of the friction factor and of the convective heat transfer coefficients in the entrance region of a microchannel are given in ► entrance region.

In general, the values of the friction factor and of the convective heat transfer increase near the beginning of the entrance region. For the convective heat transfer coefficient, from a physical point of view, this fact can be explained by observing that at the beginning of the thermal entrance region, a finite heat flux exists but only a near-zero temperature difference between the fluid and the wall, and the convective heat transfer coefficient would tend theoretically to infinity. However, because of axial heat conduction through the wall toward the entrance, the wall temperature actually rises above the temperature of the adjacent fluid and the heat transfer coefficient, though large, is finite. As the temperature profile develops, the local heat transfer coefficient decreases until, at a distance from the entrance-defined thermal entrance length (see ► entrance region), the change in the local coefficient becomes negligible and it reaches its fully developed value (see ► heat transfer in microchannels).

It should be added here that rounded or square-edged entrances can influence the values assumed by the convective heat transfer coefficient and, especially, the values assumed by the friction factor in the entrance region [1, 2]. Since the data cover only a few simple entrance geometries, the designer must exercise judgment in the application of the correlations proposed for calculating the friction factor and the convective heat transfer coefficient in the entrance region.

Since it is customary to use the simplified technique of assuming average, constant values for the friction factor and convective heat transfer coefficient along the entire microchannel, equal to their fully developed values, it is important to highlight the fact that this assumption holds only for microchannels for which the total channel length is larger (by three to four times at least) than the dynamic and thermal entrance lengths. These lengths can be calculated by using the correlations quoted in ► entrance region.

In microchannels, care must be used in order to analyze the dynamic and thermal behavior of developing flows under the following conditions:

- *Compressible flows*: in this case the velocity profile has a continuous variation in shape. This fact influences the convective heat transfer coefficient, since no fully developed temperature profile can occur if the flow is developing (see ► heat transfer in microchannels).
- *Electroosmotic flows* in microchannels subjected to an axial variation of the *zeta potential* (see ► electroosmotic flows and ► zeta potential).
- *Nonnegligible wall–fluid conjugate heat transfer*: when the conduction heat transfer at the walls of a microchannel is comparable to the wall–fluid convection heat transfer (see ► heat transfer in microchannels), thermally fully developed conditions cannot be reached along the microchannel.
- *Rarefied flows*: in the slip flow regime, rarefaction increases the hydrodynamic and thermal entrance lengths owing to slip at the walls (see ► pressure-driven single phase gas flows).

Future Directions for Research

Further investigations are required in order to highlight the roles of wall–fluid conjugate heat transfer, temperature-dependent fluid properties (i. e. viscosity), rarefaction, compressibility, and axial variation of the zeta potential in electroosmotic flows in developing flows for the most common microchannel cross-sectional geometries.

Cross References

► Entrance Region
► Convective Heat Transfer in Microchannels
► Electroosmotic Flow (DC)
► AC Electro-Osmotic Flow
► Zeta-Potential
► Pressure Driven Single Phase Gas Flows

References

1. Bird RB, Stewart WE, Lightfoot EN (1960) Transport Phenomena. Wiley, New York
2. Shah RK, London AL (1978) Laminar flow forced convection in ducts. Adv Heat Transf 14:196

Developing Region

► Entrance Region

Device Substrates

► Materials Used in Microfluidic Devices

Diagnostic Biochip

► Impedimetric Biosensors for Nano- and Microfluidics

D

Diamond Like Carbon (DLC)

Definition

A term that refers to the various different forms of amorphous carbon materials that exhibit some of the properties of diamond.

Cross References

► Sputtering for Film Deposition

Diamond Nanoparticles

► Plasma Treatment of Nanoparticles for Nanofluids

Diaphragm Actuation

► Membrane Actuation for Micropumps

Diaphragm Pump

► Peristaltic Pumps
► Positive Displacement Pump

Dielectric Spectroscopy

► Impedance Measurements of Cells

Dielectrophoresis

Hywel Morgan, Nicolas Green
School of Electronics and Computer Science, University of Southampton, Southampton, UK
hm@ecs.soton.ac.uk

Synonyms

AC electrokinetics; DEP

Definition

Dielectrophoresis is defined as the motion of an electrically polarisable particle in a non-uniform electric field.

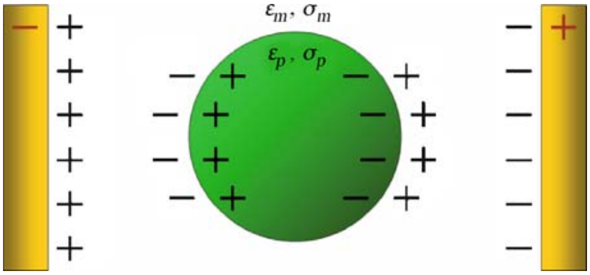

Dielectrophoresis, Figure 1 Schematic diagram of how a dielectric particle suspended in a dielectric fluid polarises in a uniform applied electric field ***E***

Chemical and Physical Principles

The key to understanding dielectrophoresis is the charge distribution at the interface between two materials of different conductivity and/or permittivity. The two materials might be for example a particle (e. g. latex bead or cell) and an electrolyte (such as potassium chloride). When an electric field is applied, charge moves and accumulates at the interface between the particle and the electrolyte as shown in Fig. 1. The amount of charge at the interface depends on the field strength and the electrical properties (conductivity and permittivity) of the particle and the electrolyte. However, a slight asymmetry in the charge density on the particle can occur as shown in Fig. 2. This produces an *induced* dipole across the particle. (Note that if the field is removed the dipole disappears). The magnitude of the dipole moment depends on the amount of charge moved and the size of the particle. For a spherical particle in an electrolyte subject to a uniform applied electric field, three cases can be considered:

1. If the polarisability of the particle is much greater than the electrolyte, more charge accumulates inside the interface than outside (Fig. 2a). Here the dipole is aligned with the applied field. This could be a conducting particle in an insulating medium or a particle with a high dielectric constant (permittivity) in an insulating medium with low dielectric constant.
2. When the particle polarisability is much less than the electrolyte, the net dipole points in the opposite direction (Fig. 2b). This case is an insulating sphere suspended in a liquid with a high dielectric constant or a high conductivity.
3. The third case is where the polarisability of the particle and electrolyte are the same and there is no net dipole (not shown).

These figures show the charge distribution at one instant in time. If we reverse the direction of the applied field and wait long enough, the opposite charge distribution is established, with the dipole in the same relative direction

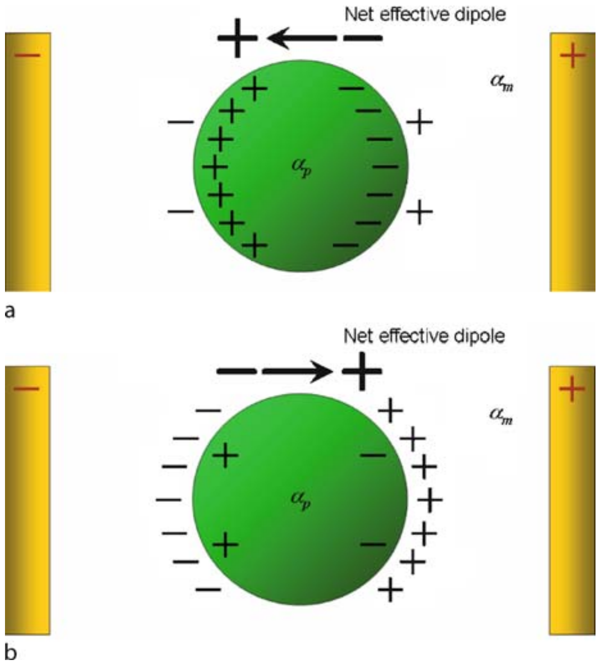

Dielectrophoresis, Figure 2 Schematic diagram of how different dielectric particles polarise if they have a much higher (**a**) or much lower (**b**) polarisability than the suspending fluid medium. If the polarisability is higher, more charges are produced on the inside of the particle/fluid interface and there is a net dipole across the particle that is parallel to the applied field. If the polarisability is lower, more charges are produced on the outside of the interface and the net dipole points in the opposite direction, against the field

with respect to the applied field. Following application of the field, charges do not move instantaneously; they take a few microseconds to reach equilibrium. At low frequencies, the movement of free charge keeps pace with the changing field. However, as the field frequency increases there comes a point where the charges no longer have sufficient time to respond. At high frequencies, free charge movement is no longer the dominant mechanism responsible for charging the interface, instead the polarisation of the bound charges (permittivity) dominates. The difference between these two states is termed a dielectric dispersion.

Extend this picture to consider a particle subjected to a **non-uniform** electric field. Figure 3a shows a particle with polarisability greater than the suspending medium where the electric field lines bend towards the particle, meeting the surface at right angles as if it were a metal sphere (note the field inside the particle is nearly zero). The converse (Fig. 3b) is where the particle polarisability is less than the electrolyte. The field lines now bend around the particle as if it were an insulator. The field inside is similar to that outside. When the polarisability of the particle and electrolyte are the same it is as if the particle does not exist and the field lines are parallel and continuous everywhere.

The figures also show that the field strength on one side of the particle is greater than the other. This leads to an imbalance of forces on the induced dipole, giving rise to particle movement. This effect is called *dielectrophoresis*, a term first coined by Pohl [1], [2]. When the polarisability of the particle is greater than its surrounding medium, the direction of the dipole is with the field and the particle experiences a force called *positive* DEP: the particle moves towards the high field region, Fig. 3a. The opposite situation gives rise to *negative* DEP, Fig. 3b; and the particle moves away from regions of high electric fields. The induced dipole is also a function of frequency. Therefore, the direction in which the particle moves is not only a function of the properties of the particle and the suspending medium, but also the frequency of the applied field. It is because of this that AC electrokinetics is such a useful tool for the manipulation and separation of particles.

Frequency Dependence of the Force

An example of the DEP force experienced by two different (solid homogeneous) polystyrene particles with different conductivities suspended in an electrolyte is plotted in Fig. 4. The force is constant at low frequencies for both particles, since the free charge has ample time to respond to the field. At high frequencies, the force is again constant but opposite in sign, since the dielectric constant of the fluid is much higher than that of particle, (80 for water, compared with 2.5 for polystyrene). At the intermediate frequency range there is a transition in the force spectrum so that the particle's behaviour switches from positive DEP to negative DEP. At one particular frequency, the polarisability of the particle is identical to the suspending medium, there is no induced dipole and the force is zero. This frequency is the cross-over frequency and can be used to characterise particles. As shown in the figure, for different particles there is a frequency band over which one particle experiences positive DEP and the other negative as shown by the shaded region in the figure so that binary separation is possible.

This illustrates two of the main features of dielectrophoresis for particle manipulation and separation:

- in a non-uniform field, the intrinsic electrical properties can give rise to a force which varies with the applied frequency of the (non-uniform) AC field.
- two different particles can exhibit quite different force-frequency spectra. The force could not only be different in magnitude but also in direction, so that the particles move in opposite directions in the same field with the

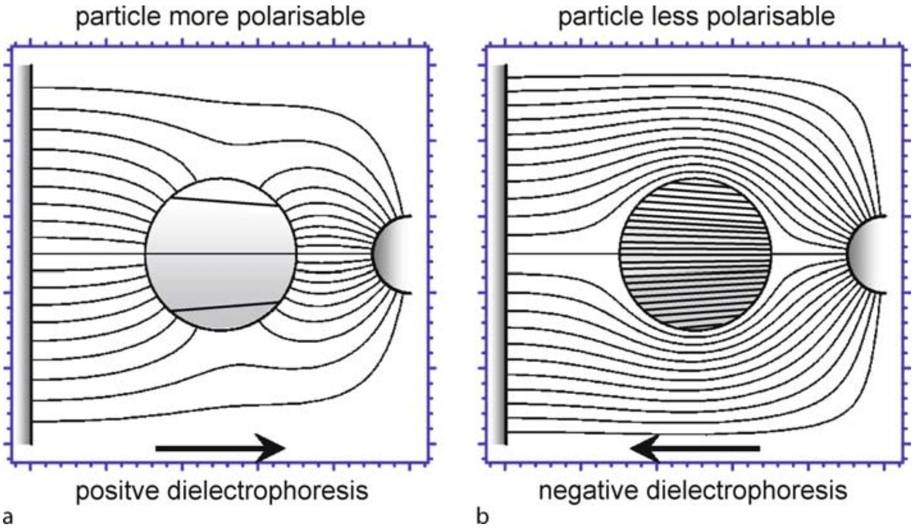

Dielectrophoresis, Figure 3 Electric field lines for a particle in a non-uniform field. (**a**) particle more polarisable than the suspending medium and (**b**) less polarisable than the suspending medium. The arrows show the direction of the force and movement in each case

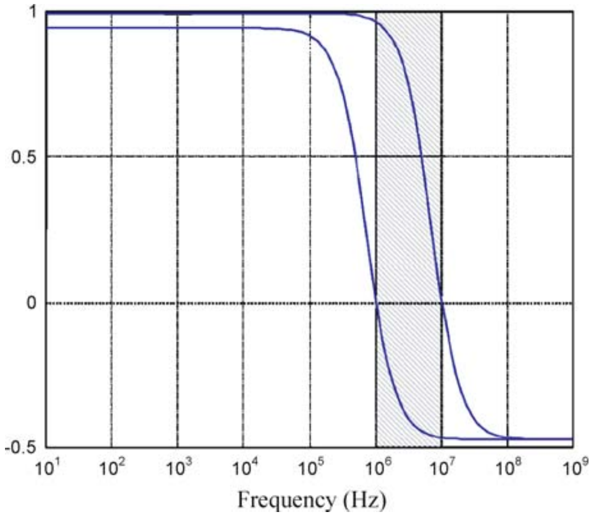

Dielectrophoresis, Figure 4 Plot of the Clausius Mossotti factor against frequency for two different solid particles. In the shaded area one particle experiences positive dielectrophoresis and the other negative dielectrophoresis, enabling separation in this frequency window

same frequency and thus dynamic separation of particles is possible.

Theory

From classical electrostatics the effective dipole moment $\boldsymbol{p}$ of homogenous dielectric sphere (volume v) in an electric field $\boldsymbol{E}$ is given by:

$$\boldsymbol{p} = v\tilde{\alpha}\boldsymbol{E} \tag{1}$$

where complex effective polarisability $\tilde{\alpha}$ is:

$$\tilde{\alpha} = 3\varepsilon_{\mathrm{m}} \left(\frac{\tilde{\varepsilon}_{\mathrm{p}} - \tilde{\varepsilon}_{\mathrm{m}}}{\tilde{\varepsilon}_{\mathrm{p}} + 2\tilde{\varepsilon}_{\mathrm{m}}} \right) = 3\varepsilon_{\mathrm{m}} \tilde{f}_{\mathrm{CM}} , \tag{2}$$

In this equation the factor, $\tilde{f}_{\mathrm{CM}}$ is called the Clausius–Mossotti factor and describes the frequency dependence of the polarisability. Combining Eqs. (1) and (2) leads to the expression for the dipole in terms of the complex permittivity of the particle and the suspending medium (subscript p and m respectively):

$$\boldsymbol{p} = 4\pi\varepsilon_{\mathrm{m}} \left(\frac{\tilde{\varepsilon}_{\mathrm{p}} - \tilde{\varepsilon}_{\mathrm{m}}}{\tilde{\varepsilon}_{\mathrm{p}} + 2\tilde{\varepsilon}_{\mathrm{m}}} \right) a^3 \boldsymbol{E} \tag{3}$$

where a is the particle radius, and a general complex permittivity is defined as: $\tilde{\varepsilon} = \varepsilon - j\sigma/\omega$, with permittivity ε, conductivity σ, angular frequency $\omega = 2\pi f$, and $j^2 = -1$ The magnitude of the polarisability, and therefore the effective dipole moment of the particle, is frequency dependent, described by the Clausius–Mossotti factor:

$$\tilde{f}_{\mathrm{CM}}(\tilde{\varepsilon}_{\mathrm{p}}, \tilde{\varepsilon}_{\mathrm{m}}) = \frac{\tilde{\varepsilon}_{\mathrm{p}} - \tilde{\varepsilon}_{\mathrm{m}}}{\tilde{\varepsilon}_{\mathrm{p}} + 2\tilde{\varepsilon}_{\mathrm{m}}} \tag{4}$$

This expression characterises the relaxation in the polarisability of the particle with a relaxation time of

$$\tau_{\mathrm{MW}} = \frac{\varepsilon_{\mathrm{p}} + 2\varepsilon_{\mathrm{m}}}{\sigma_{\mathrm{p}} + 2\sigma_{\mathrm{m}}} \tag{5}$$

The angular frequency $\omega_{MW} = 2\pi f_{MW} = 1/\tau_{MW}$ is the Maxwell–Wagner relaxation frequency since the dispersion in the dipole moment is caused by interfacial polarisation. The real part of the Clausius–Mossotti factor reaches a low frequency limiting value of $(\sigma_p - \sigma_m)/(\sigma_p + 2\sigma_m)$, i. e. it depends solely on the conductivity of the particle and suspending medium. Conversely the high frequency limiting value is $(\varepsilon_p - \varepsilon_m)/(\varepsilon_p + 2\varepsilon_m)$, dominated by the permittivity of the particle and suspending medium. Note that for a solid particle there is one dispersion in the dipole because there is one interface between particle and medium. In general there is one dispersion for each interface.

Derivation of the DEP Force

Consider an electric field with spatially varying field magnitude but no phase variation. Define an arbitrary, harmonic potential as $\phi(\boldsymbol{x}, t) = \mathrm{Re}\left[\tilde{\phi}(\boldsymbol{x})\,\mathrm{e}^{j\omega t}\right]$ where $\boldsymbol{x}$ is the position, the tilde indicates the complex phasor $\tilde{\phi} = \phi_R + j\phi_I$ and Re[...] indicates the real part of. The electric field is then given by $\boldsymbol{E}(\boldsymbol{x}, t) = \mathrm{Re}\left[\tilde{\boldsymbol{E}}(\boldsymbol{x})\,\mathrm{e}^{j\omega t}\right]$ where the vector $\tilde{\boldsymbol{E}} = -\nabla\tilde{\phi} = -(\nabla\phi_R + j\nabla\phi_I)$ is the corresponding phasor. The dipole moment of the particle is therefore $\boldsymbol{p} = v\tilde{\alpha}\boldsymbol{E}\,\mathrm{e}^{j\omega t}$ and the time-averaged force on the particle is (from Eq. (2))

$$\langle \boldsymbol{F}_{\mathrm{DEP}} \rangle = \frac{1}{2}\mathrm{Re}\left[(\boldsymbol{p}\cdot\nabla)\,\boldsymbol{E}^*\right] \tag{6}$$

where * indicates a complex conjugate. Since the phasors are real, the time-averaged force is

$$\langle \boldsymbol{F}_{\mathrm{DEP}} \rangle = \frac{1}{2}v\mathrm{Re}\left[\tilde{\alpha}\right](\boldsymbol{E}\cdot\nabla)\,\boldsymbol{E} = \frac{1}{4}v\mathrm{Re}\left[\tilde{\alpha}\right]\nabla(\boldsymbol{E}\cdot\boldsymbol{E}) \tag{7}$$

Using vector identities, the DEP force can be written as

$$\langle \boldsymbol{F}_{\mathrm{DEP}} \rangle = \frac{1}{4}v\mathrm{Re}\left[\tilde{\alpha}\right]\nabla\,|\boldsymbol{E}|^2 \tag{8}$$

or using *root-mean-square* (*rms*) values the DEP becomes

$$\langle \boldsymbol{F}_{\mathrm{DEP}} \rangle = \frac{1}{2}v\mathrm{Re}\left[\tilde{\alpha}\right]\nabla\,|\boldsymbol{E}_{\mathrm{rms}}|^2 \tag{9}$$

Substituting for the volume of the particle and the dipole moment, we obtain the widely used general expression for the DEP force on a spherical particle:

$$\langle \boldsymbol{F}_{DEP} \rangle = \pi\varepsilon_m a^3 \mathrm{Re}\left[\frac{\tilde{\varepsilon}_p - \tilde{\varepsilon}_m}{\tilde{\varepsilon}_p + 2\tilde{\varepsilon}_m}\right]\nabla\,|\mathbf{E}|^2 \tag{10}$$

Similar expressions can be obtained for particles of non-spherical shape, such as rods and ellipsoids [3].

This equation shows that the dielectrophoretic force depends on:

- the particle radius a (more correctly volume)
- the frequency of the applied field, through the real part of Clausius–Mossotti factor
- the energy density of the electric field and degree of non-uniformity of the electric field.

D

Key Research Findings

Dielectrophoresis has many applications such as trapping single particles, manipulating and separating large numbers of cells, creating ordered arrays of particles etc. However, all of these technological uses rely on being able to generate well defined electric field gradients. This is generally performed using microelectrodes fabricated onto insulating substrates (e. g. glass) as part of a microfluidic or Lab on a Chip system. Modern techniques allow fabrication of micro-electrodes with precise sizes and dimensions, enabling accurate control of the electric field geometry and therefore particle position. The DEP force is generated with AC fields, avoiding problems associated with electrolysis which occur with DC fields and electrophoresis. Dielectrophoretic manipulation of particles can be performed with almost any shape of electrode that produces a non-uniform electric field. An example of a microelectrode array is shown in Fig. 5a. This is a castellated microelectrode, made from metal typically 100 nm thick, and was first introduced by Pethig and coworkers [4]. The electric field map shown in Fig. 5b indicates where the regions of high and low electric field occur and therefore where particles move under either positive or negative DEP-shown schematically in Fig. 5c.

The DEP force is a short range force, this is because the electric field gradient decays rapidly from an electrode edge. Contrast this with electrophoresis where the force on the particle is constant wherever the electric field is present. The short range behaviour of DEP can be illustrated using the following example. A simple interdigitated electrode structure is shown in Fig. 6a, showing a semi-infinite array of electrode fingers. The electrodes are typically 10 to 50 μm wide (with similar gaps) and are connected alternately to a low voltage source of variable frequency. The space above the electrodes is filled with conducting electrolyte. When the voltage is applied the electrodes generate a field gradient, with force vectors shown in Fig. 6b. These vectors are drawn for a particle experiencing positive DEP; and point in the opposite direction for particles experiencing negative DEP. Far from the electrodes, the vectors point directly down towards the surface. Approaching the surface, the vectors point towards the electrode edges, where the field is highest. Although

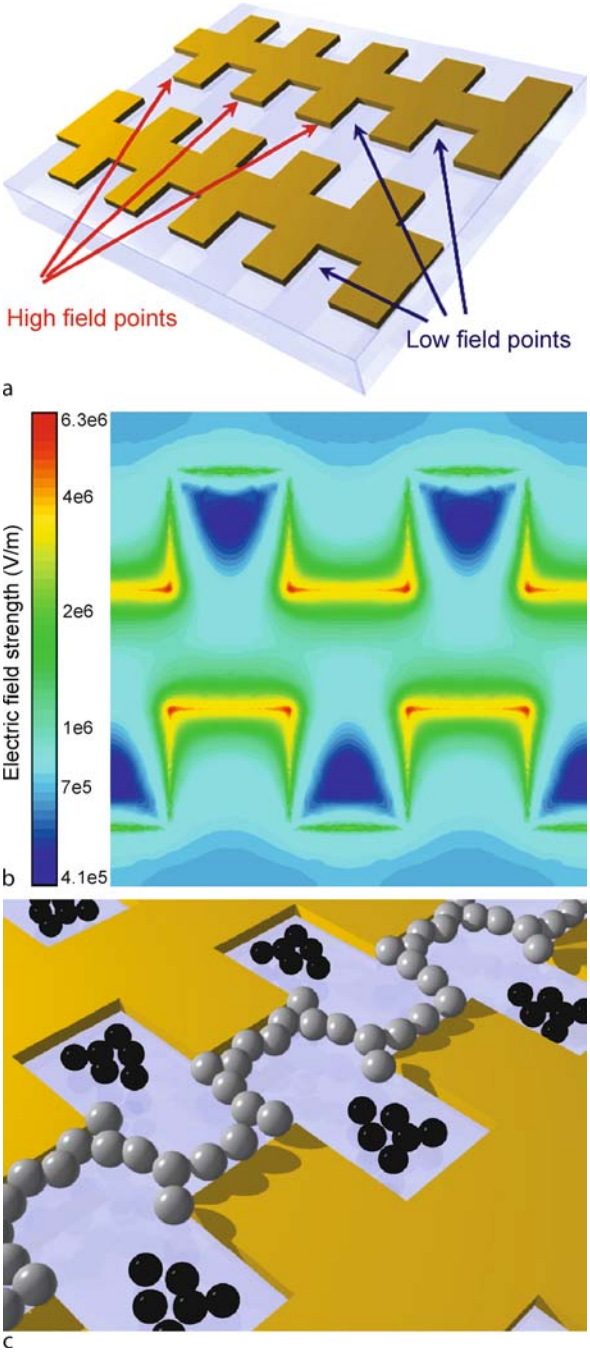

Dielectrophoresis, Figure 5 (**a**) Schematic diagram of the "castellated"electrode design, which consists of square features on parallel interdigitated electrodes; (**b**) Plot of the numerically calculated electric field magnitude for the castellated electrode design a horizontal plane 100 nm above the upper surface of the electrodes; (**c**) Schematic diagram showing where particles move on the microelectrodes under positive or negative DEP

the vectors show the direction of the force, the magnitude of the force is quite different, as shown in Fig. 6c.

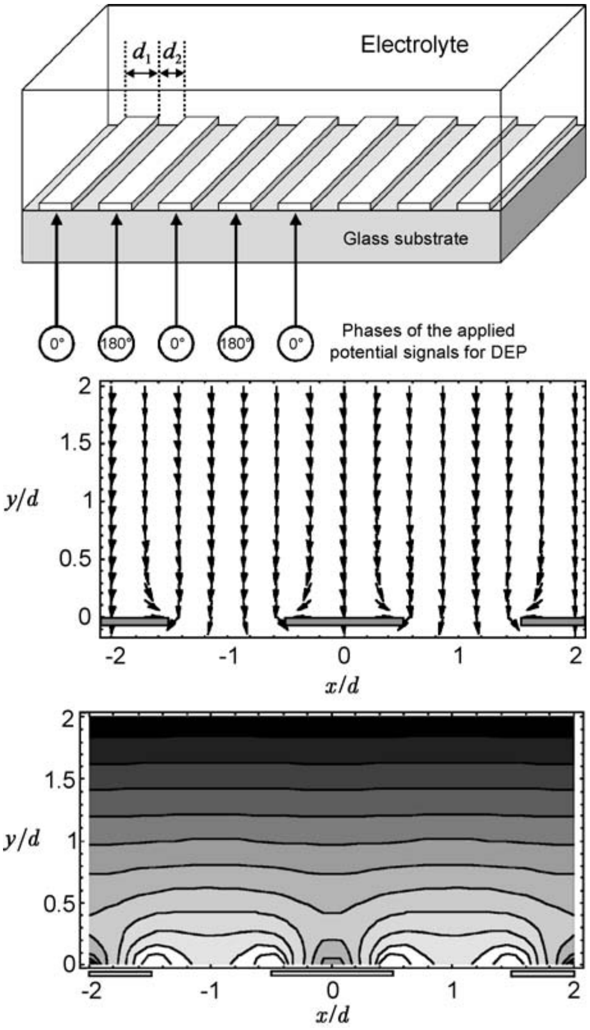

Dielectrophoresis, Figure 6 (**a**) Schematic diagram of the interdigitated electrode array in a microfluidic system; (**b**) Plot of the direction of the dielectrophoretic force for the interdigitated electrode array; (**c**) Plot of the magnitude of the dielectrophoretic force (Log_{10}) for the interdigitated electrode array

Here the force is maximum at the electrode surface (as expected), but it very quickly decays exponentially into the space above the electrodes. Therefore, particles at some distance from the electrodes experience very little force. For an electrode with width and gap d, and applied voltage V, (with y the vertical direction), the DEP force is proportional to the field gradient according to

$$\nabla|\boldsymbol{E}|^2 \approx \frac{V^2}{d^3} \exp\left(-\frac{\pi y}{d}\right) \tag{11}$$

This expression shows that the characteristic decay length of the force is $y = d/\pi$, and at this height the magnitude

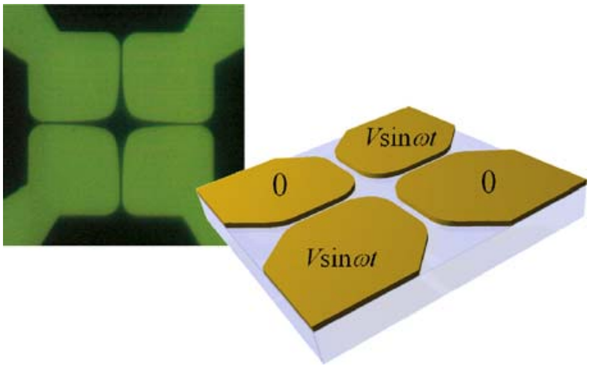

Dielectrophoresis, Figure 7 Schematic drawing of a quadrupole electrode set

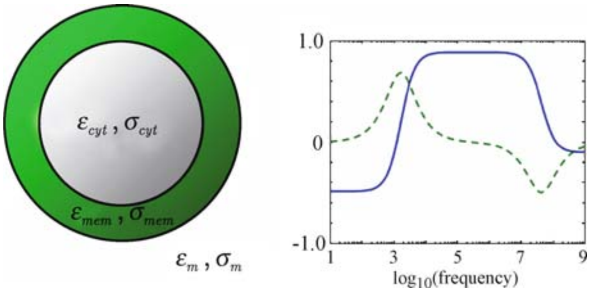

Dielectrophoresis, Figure 8 Schematic diagram of a cell represented by the shell model, together with a plot of the real and imaginary part of the Clausius–Mossotti factor for a single shelled object

of the field gradient will be 37% of its maximum. For an electrode with width and gap of 20 μm, this height is only 6.4 μm. Also we see that the force scales with the square of the voltage and the inverse third power of electrode gap. Changing the electrode gap by a factor of two can therefore change the force by a factor of 8. For further details of scaling in these systems see [5].

DEP characterisation of particles can be performed with a number of different electrode designs. One common design consists of four separate electrodes pointing towards a central region, called a quadrupole electrode (see Fig. 7) [6]. These electrodes generate an electric field gradient with a minimum in the centre and maximum at the edge. They are used for trapping single particles and also for electrorotation studies. A pair of quadrupole electrode arrays facing each other (on the top and bottom of a microfluidic channel) can form a *closed* electric field cage used for trapping single particles, for further details see [7].

Biological Particles

The theoretical analysis presented above assumes a solid homogeneous spherical dielectric particle; e. g. a polystyrene bead. Biological cells are neither perfect spheres nor completely homogenous dielectrics. However, their DEP properties can be predicted by treating the cell as a series of shells, with the first shell representing the cell membrane, as shown in Fig. 8. The cell membrane is extremely thin, and has very low conductivity and high capacitance. Because there are now two interfaces (membrane to outside and membrane to inside), the Clausisus–Mossotti factor has two dispersions. At low frequencies the cell is less polarisable than the medium and undergoes negative DEP. There is a region at intermediate frequencies where positive DEP is observed, at high frequencies negative DEP dominates because of the lower polarisability of the cell cytoplasm compared with the suspending medium. Different cells exhibit different DEP force-frequency profiles and can therefore be separated, see [8] for a review.

The position of the lower of the two cross over frequencies is dominated by the properties of the cell membrane (and also cell size) and measurement of this parameter is often used to characterise the dielectrophoretic properties of cells. The membrane capacitance of a cell can be determined by measuring the dielectrophoretic cross over frequency as a function of suspending medium conductivity [9]. The cross over frequency is as a function of membrane capacitance and membrane conductance according to:

$$f_{\text{Cross}} = \frac{\sqrt{2}}{8\pi r C_{\text{Mem}}} \sqrt{(4\sigma_m - rG_{\text{Mem}})^2 - 9r^2 G_{\text{Mem}}^2} \quad (12)$$

where G_{Mem} is the specific conductance of the membrane, C_{Mem} the specific membrane capacitance, σ_m the conductivity of the suspending medium and r the cell radius. Assuming that the particle has a very low membrane conductivity (i. e. $G_{\text{Mem}} = 0$), the specific membrane capacitance is given by the following simplified expression:

$$C_{\text{Mem}} = \frac{\sigma_m}{\pi \sqrt{2} f_{\text{Cross}} r} \quad (13)$$

Therefore measurement of both the cross over frequency and cell radius can be used to calculate an average membrane capacitance. Values of cell membrane capacitances per unit area range from 0.7 μF/cm^2 to over 2 μF/cm^2 indicating that the DEP cross over frequencies can differ substantially – one of the reasons why DEP has been used to fractionate different cell types. Measurement of the cell capacitance is also used to predict the DEP response of different cell populations and aid in the design and operation of DEP-based cell separation devices [10].

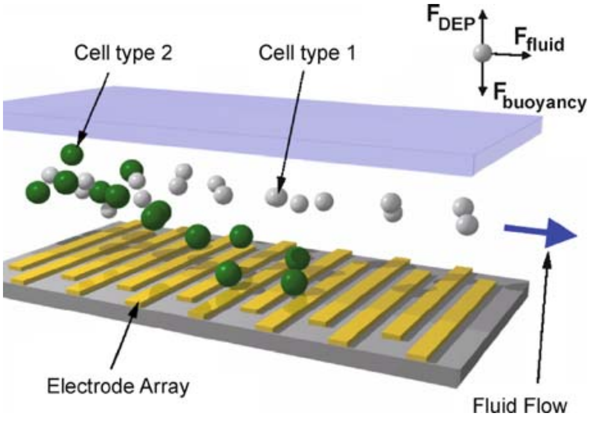

Dielectrophoresis, Figure 9 Diagram showing the working principle of a DEP-based flow-through microdevice which can be used to separate or fractionate cells and other particles

Examples of Applications

Cell Analysis and Separation Technologies

Because different cells exhibit different responses, one of the attractions of DEP is that it is could be used not only to manipulate cells, but also to trap and separate cells. There are many papers in this field, references [8], [9], [10], [11] provide excellent reviews. In general different types of cells may exhibit different dielectric properties, which, when particle size is also considered gives rise to differences in DEP force. These differences are exploited to effect cell separation. One of the simplest practical dielectrophoretic separators is based on flow separation. A mixture of cells moves through a microfluidic chamber with an electrode array fabricated on the bottom of the chamber – see Fig. 9. The cell or particle mixture is pumped across the electrode using a syringe pump. Correct choice of voltage and frequency on the electrodes leads to binary separation one population experiences positive dielectrophoresis and is attracted to the electrodes, whilst the other particles are repelled by negative dielectrophoresis. When all the cells are trapped, the electric field is switched off and the trapped cells released for collection down stream. The same electrode structure can also be used to fractionate particles along the device. In this case, the frequency of the electric field is chosen to attract all the particles to the electrodes, but the trajectory of each particle type will differ (depending on size and polarisability). The end result is a distribution of particles along the electrode array.

Cell-based DEP separation devices that utilise positive DEP forces suffer from one major drawback, which is that the cells must be suspended in a low-conductivity buffer. Although the buffer has to be iso-osmotic to prevent cell damage, this process is undesirable from the point of view of a Lab on a Chip system and furthermore causes considerable stress on the cells. One technique, developed by Gascoyne et al. [8], that uses negative DEP is a method called DEP-Field Flow Fractionation (FFF). In this technique, the particles are suspended in a medium above an interdigitated microelectrode array (e. g. Fig. 9). A voltage is applied to the electrodes at a frequency such that all the particles experience negative DEP. The DEP force induces levitation of the particles above the electrodes, and each particle reaches an equilibrium position where the upward DEP force is balanced by a downward (negative) buoyancy force. A fluid is now pumped through the device, and owing to the parabolic flow profile of the fluid, particles at different equilibrium heights are eluted at different times. The particles whose equilibrium height corresponds to the centre of the channel are carried through by the fastest flowing stream line and are the first to exit the system and so on.

These few examples serve to illustrate the wide range of methods that can be used to separate particles according to their polarisability. Many methods have not been discussed; the literature on DEP technologies is growing steadily and the reader is urged to refer to this for further examples.

Nano-Particle Manipulation and Characterisation

During the last 15 years, many developments in both the understanding and technology has lead to DEP being used to manipulate nano-scale objects, including macromolecules (particularly DNA), viruses, latex particles and carbon nanotubes. During manipulation of nano-particles, Brownian motion can dominate the behaviour of the particles. As shown by Eq. (10), the DEP force scales with particle volume. Therefore, in order for the DEP force to be sufficiently large to overcome the randomising effects of Brownian motion, the magnitude of the field gradient must be increased proportionally. Equation (11) shows that the factor $\nabla|\boldsymbol{E}|^2$ (which controls the DEP force) scales with the square of the voltage, and the inverse cube of the electrode gap. Therefore, the simplest way to increase the force is to reduce the electrode dimensions, which can be done fairly easily with modern microfabrication methods. One major obstacle to the manipulation of very small particles is that the large electric fields that are required also induce other effects in the liquid, notably AC electroosmosis and electrothermally driven fluid flow. For further details see [12].

Cross References

- ► AC Dielectrophoresis Lab-on-Chip Devices
- ► AC Electro-Osmotic Flow

► Dielectrophoretic Motion of Particles and Cells
► Electrokinetic Motion of Polarizable Particles
► Electrothermal Effects
► Lab-on-chip Devices for Particle and Cell Separation

References

1. Pohl HA (1958) Some Effects of Non-uniform Fields on Dielectrics. J Appl Phys 29:1182–1188
2. Pohl HA (1978) Dielectrophoresis. Cambridge Univ Press, Cambridge
3. Jones TB (1995) Electromechanics of particles. Cambridge Univ Press, Cambridge
4. Wang X-B, Huang Y, Burt JPH, Markx GH, Pethig R (1993) Selective Dielectrophoretic Confinement of Bioparticles in Potential Energy Wells. J Phys D Appl Phys 26:1278–1285
5. Castellanos A, Ramos A, Gonzalez A, Green NG, Morgan H (2003) Electrohydrodynamics and dielectrophoresis in microsystems: scaling laws. J Phys D Appl Phys 36:2584–2597
6. Huang Y, Pethig R (1991) Electrode design for negative dielectrophoresis applications. Meas Sci Technol 2:1142–1146
7. Schnelle T, Muller T, Fuhr G (2000) Trapping in AC octode field cage. J Electrostat 50:17–29
8. Gascoyne PRC, Vykoukal JV (2004) Dielectrophoresis-Based Sample Handling in General-Purpose Programmable Diagnostic Instruments. Proc IEEE 92:22–42
9. Huang Y, Wang XB, Becker FF, Gascoyne PRC (1996) Membrane changes associated with the temperatur-sensitive P85(gag-mos)-dependent transformation of rat kidney cells as determined by dielectrophoresis and electrorotation. Biochim Biophys Acta Biomembr 1282:76–84
10. Pethig R, Markx GH (1997) Applications of dielectrophoresis in biotechnology. Trends Biotech 15:426–432
11. Voldman J (2006) Electrical forces for microscale cell manipulation. Ann Rev Biomed Eng 8:425–454
12. Morgan H, Green NG (2003) AC Electrokinetics: Colloids and Nanoparticles. Research Studies, Herts

Dielectrophoretic Force

► AC Dielectrophoresis Lab-on-Chip Devices
► Dielectrophoretic Motion of Particles and Cells

Dielectrophoretic Motion of Particles and Cells

STUART WILLIAMS
Mechanical Engineering, Purdue University, West Lafayette, IN, USA
swilliams@purdue.edu

Synonyms

Dielectrophoretic force

Definition

Dielectrophoresis is the translational motion of an electrically neutral particle by induced polarization in a nonuniform electric field. The magnitude and direction of the induced dielectrophoretic force is dependant on the characteristics of the applied electric field as well as the dielectric properties of the surrounding medium and of the particle itself.

Overview

Herbert Pohl was the first to study particle electrokinetics in the 1950's, particularly the manipulation of uncharged particles with nonuniform electric fields. He coined the term *dielectrophoresis*, details of his investigations can be found in his classic text [1]. The advancement of microfabrication techniques and the demand of Lab-on-a-Chip technologies have led to the development of dielectrophoresis techniques for particulate, biological and pharmaceutical applications. Dielectrophoresis was initially used to manipulate particles and cells in the micrometer range (1 μm to 1 mm). Since the early 1990's, nanotechnology has incorporated dielectrophoresis for the manipulation of viruses, DNA, protein molecules and other nanoparticles (diameters of 1 nm to 1 μm). This article provides a brief background necessary for the development of dielectrophoresis followed by the theory of the basic dielectrophoretic manipulation techniques of translation, rotation (electrorotation) and orientation (electroorientation). Simulation and design considerations will be discussed for the micrometer length scale; this article will not specifically address all dielectrophoresis complexities at the nanometer scale. For a more extensive explanation of dielectrophoretic manipulation of particles it is suggested that the reader consults texts by T.B. Jones [2], Morgan and Green [3], and M.P. Hughes [4], the latter of which addresses these techniques for nanometer-sized particles.

It is important to note the differences between electrophoresis and dielectrophoresis. Both technologies manipulate particles with their interaction to an applied electric field. In electrophoresis, a force is created on a charged particle by its attraction to a potential with the opposite polarity. The speed at which a particle moves through a stagnant fluid under applied electrophoresis forces is proportional to its size and electrical charge. The applied electric field for electrophoresis is typically a direct-current (DC) signal. Dielectrophoresis utilizes a nonuniform electric field to induce a dipole or higher moments in a neutral particle. The magnitude and orientation of the induced dipole is a function of the dielectric properties of the particle and the surrounding medium. These induced moments in a nonuniform electric field can create a translational

and/or rotational force on a particle. The applied electric field for dielectrophoresis can be either direct-current or alternating-current (AC), but it is typically the latter of the two.

For most dielectrophoresis cases, the applied electric field can be created with a common frequency generator with frequencies typically greater than 100 kHz and magnitudes below 20 V peak-to-peak. Electrode geometries with features below 1mm can be created using simple microfabrication techniques. Electrodes are typically fabricated on the surface of silicon wafers or glass substrates, including microscope slides. For most biological applications it is recommended that the species of interest be visually observed by optical means, which leaves glass or other transparent materials as favorable substrates. In the case where the electrodes themselves hinder visual observation they are patterned with indium tin oxide (ITO), a transparent conducting material. Microfluidic channels and other fabricated features can easily be incorporated into the system. Due to its simple fabrication and its susceptibility to visual observation and analysis, dielectrophoresis is a favorable technique for biological experimentation.

There are several disadvantages when working with dielectrophoresis. This technique does not work at larger scales (>1 mm) based on the shear magnitude generated voltage necessary to apply an electric field to manipulate larger particles. This would require voltages greater than hundreds of volts (which is difficult to generate at high AC frequencies) and generate undesirable effects such as electrochemical reactions and Joule heating. By working at the micrometer length scale the required voltage decreases and some of these negative effects are minimized, however they may slightly influence the system and cannot be ignored. There are other forces that will work against the dielectrophoretic force including gravity, hydrodynamic drag and electrothermal forces. Additionally, the electric field itself can affect the physiology of a biological cell by inducing cell heating and influencing transmembrane voltage. These effects will be discussed later in this article.

Basic Methodology

Electrostatics

Capacitance is a measure of the electric charge stored for an applied electric potential. The simplest case for a capacitor consists of a dielectric material between two parallel, conductive plates (Fig. 1). When a potential is applied across the plates (+V and −V) a charge will accumulate on the plates due to the effects of the electric field and applied charge. On either side of the sandwiched material are accumulations of opposite charges, which induces a dipole and polarize the capacitor. It takes a finite amount of time for the dipole to accumulate and, when the potential is removed, it takes a finite amount of time for the induced dipole to dissipate. Capacitance of a material is typically expressed as

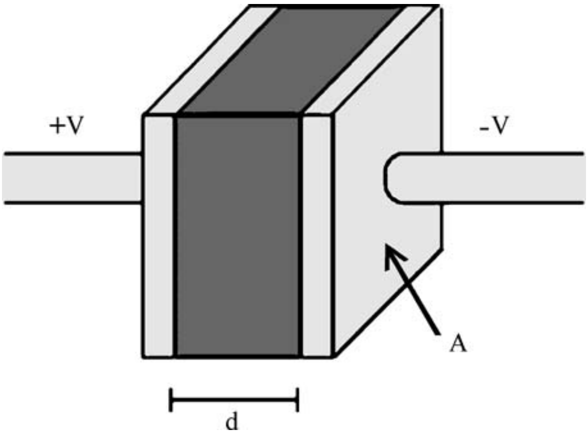

Dielectrophoretic Motion of Particles and Cells, Figure 1 A parallel plate capacitor

$$C = \frac{\varepsilon_0 \varepsilon_r A}{d} \quad (1)$$

where d is the distance between the plates, A is the cross-sectional area of the material, ε_0 is the permittivity of free space (8.854×10^{-12} F/m) and ε_r is the material's relative permittivity (a dimensionless quantity). When a capacitor is used in an AC circuit it will restrict the flow of current through the dielectric material for an applied electric potential. This out-of-phase impedance component can be incorporated into Eq. (1) to describe the dielectric properties of a material in terms of its conductivity and permittivity:

$$C = \frac{\varepsilon^* A}{d} \quad (2)$$

where ε^*, called the complex permittivity, replaces the $\varepsilon_0\varepsilon_r$ term in (1) and is expressed by

$$\varepsilon^* = \varepsilon_0 \varepsilon_r - j\frac{\sigma}{\omega} \quad (3)$$

where j is $\sqrt{-1}$, $\omega = 2\pi f$ and f is the applied frequency in Hertz. It is important to note that this term is frequency dependent. At very high frequencies the imaginary term is minimized and the complex permittivity is dominated by the material's permittivity. However, for very low frequencies the conductivity term dominates.

The dipole across the parallel plate capacitor is induced and does not hold a permanent charge. This induced dipole will align itself along the electric field lines. The ability of a material to polarize is dependent on its dielectric properties (conductivity and permittivity) and the applied electric potential magnitude and frequency. Additionally, there are other polarization effects that should be noted. The Debye relaxation is associated with the inability for a dipole to reorient with the applied electric field. This orientation lag of the induced dipole occurs due to the fact that it takes a finite time to form and unform, known as the relaxation time. For high applied AC frequencies the dipole will not have enough time to form, resulting in the inability to transfer charge. The Debye relaxation occurs within the dielectric material while a second relaxation, called the Maxwell–Wagner relaxation, occurs at the interface between two separate materials. Consider a parallel plate capacitor with two different materials in series between the plates with separate conductivities and permittivities. At the interface between these materials Maxwell–Wagner polarization occurs, which is a function of their dielectric properties. Both of these materials transfer charge differently, creating an accumulation of charge and inducing a dipole at their interface.

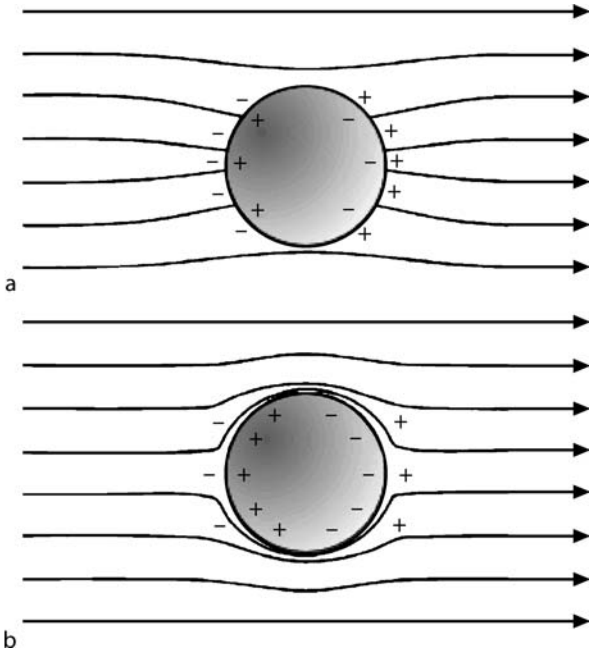

Dielectrophoretic Motion of Particles and Cells, Figure 2 A uniform electric field interacting with (**a**) a particle more polarizable than the medium and (**b**) a particle less polarizable than the medium

Dielectrophoresis

These previously mentioned principles will now be applied to a homogeneous dielectric sphere suspended in a conductive medium and exposed to an electric field. The magnitude of a dipole moment ($\boldsymbol{m}$) of a spherical particle is

$$\boldsymbol{m} = 4\pi r^3 \varepsilon_0 K(\omega) \boldsymbol{E} \tag{4}$$

where r is the radius of the particle and $K(\omega)$ is the Clausius–Mossotti factor defined by

$$K(\omega) = \frac{\varepsilon_{\mathrm{p}}^* - \varepsilon_{\mathrm{m}}^*}{\varepsilon_{\mathrm{p}}^* + 2\varepsilon_{\mathrm{m}}^*} \tag{5}$$

where the subscripts p and m refer to the particle and medium, respectively. The dipole is a function of the complex permittivities of the particle and medium which determine its magnitude and charge orientation. Consider a suspended particle in a uniform electric field (Fig. 2). For a particle which is more polarizable than the surrounding medium, there will be a greater accumulation of charge on the medium side of its interface and result in Fig. 2a. If the surrounding medium is more polarizable than the particle then the greater accumulation of charge will occur within the particle and result in Fig. 2b. Note the distorted electric fields in each figure, the induced dipole itself will affect the surrounding electric field accordingly. In a uniform electric field, though, the induced charges on both sides of the particle are equal, creating no net force on the particle. However, if it were placed in a nonuniform electric field, dielectrophoretic forces would be present.

Let's now consider a polarizable particle placed in a nonuniform electric field (Fig. 3). The nonuniform electric field is created by the electrode geometry shown. The general expression for the dielectrophoretic force of a homogenous sphere is expressed as

$$F_{\mathrm{DEP}} = 2\pi \varepsilon_0 \varepsilon_{\mathrm{m}} r^3 \mathrm{Re}\left[K(\omega)\right] \nabla E^2 \tag{6}$$

where $\mathrm{Re}\left[K(\omega)\right]$ is the real part of the Clausius–Mossotti factor and ∇E^2 is the gradient of the magnitude of the square of the electric field. This equation assumes that the there is no applied phase gradients to the electric field. The Clausius–Mossotti factor is a function of frequency and, depending on the dielectric properties of the medium and particle, this factor can be either positive or negative. If $\mathrm{Re}\left[K(\omega)\right]$ is negative, then the particle experiences negative dielectrophoresis (nDEP) and is repelled from gradients in the nonuniform electric field (Fig. 3). For positive $\mathrm{Re}\left[K(\omega)\right]$, the particle is attracted to high electric field gradients with positive dielectrophoresis (pDEP). The frequencies at which the particle changes from pDEP to

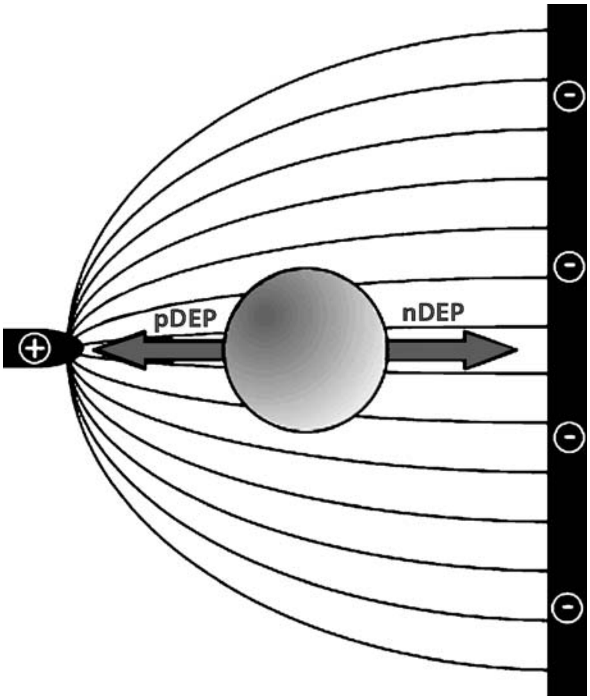

Dielectrophoretic Motion of Particles and Cells, Figure 3 A polarizable particle in a nonuniform electric field

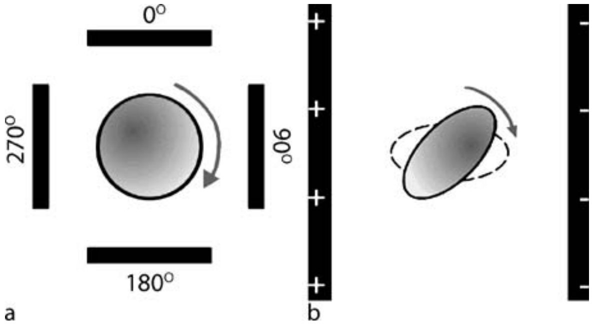

Dielectrophoretic Motion of Particles and Cells, Figure 4 Illustrations of (**a**) electrorotation and (**b**) electro-orientation

nDEP, or vice versa, is called its *crossover frequency*. By looking at (5), the maximum range of values for the Clausius–Mossotti factor is between +1 ($\varepsilon_p^* \gg \varepsilon_m^*$) and −0.5 ($\varepsilon_p^* \ll \varepsilon_m^*$). This demonstrates that the maximum induced pDEP force can be twice as strong as the nDEP force. The conductivity of the experimental medium and the applied frequency can be manipulated to induce either pDEP or nDEP forces on a particle. Effective manipulation of cells using dielectrophoretic forces requires novel electrode geometry design and applied signaling. A number of these techniques have been established including electrorotation and electro-orientation (Fig. 4).

Electrorotation

In brief, electrorotation involves an induced torque on a particle that is subjected to a rotating electric field (Fig. 4a). The electric field induces a dipole in the particle and, as the field rotates, the dipole attempts to rotate with the electric field. As the dipole lags behind the rotating field it attempts to reorient itself and a torque is induced on the particle. This dipole orientation lag is due to its relaxation time. The general equation for the electrorotational torque induced on a homogenous spherical particle is

$$\Gamma = -4\pi\varepsilon_0\varepsilon_m r^3 \mathrm{Im}\,[K(\omega)]\,E^2 \qquad (7)$$

The direction and rate of rotation relative to the electric field is dependent on the imaginary component of the Clausius–Mossotti factor ($\mathrm{Im}\,[K(\omega)]$). When this component is positive the direction of rotation is opposite of the direction of the rotating field and vice versa for a negative value of $\mathrm{Im}\,[K(\omega)]$. By properly applying a nonuniform electric field and controlling the real and imaginary parts of the Clausius–Mossotti factor, a particle can be simultaneously manipulated by dielectrophoresis and electrorotation.

Electro-Orientation

Electro-orientation involves the alignment of a nonspherical particle in a uniform electric field (Fig. 4b). When an ellipsoidal particle polarizes, the dipole moment will align the particle parallel with the electric field. Typically this alignment occurs with the nonspherical particle's longest axis, as this is the location of the longest dipole moment. However, one or more of their axes may become dispersed, resulting in its orientation with its longest nondispersed dipole parallel to the field lines. Its orientation is a function of the dielectric properties of the medium and the particle as well as the frequency of the applied electric field. A plot of a particle's preferred orientation with varied medium conductivities and applied frequencies is known as its *orientation spectrum*. The orientation spectrum includes the particle's turnover frequencies, or the conditions at which the particle reorients itself to the electric field. A particle's dielectric properties can be derived from these graphs, examples of which can be found in literature [5]. Similarly, electrorotation can be used to determine unknown dielectric properties of cells.

Modeling Particles and Cells

Obviously, biological cells and other particulates are not all completely spherical nor are they homogeneous. Typically cells are modeled as multi-shelled particles with each

shell having its own respective conductivity and permittivity. If the dielectric properties of each layer and the interior of the particle are known then it can be modeled with an effective conductivity and permittivity. This simplified model, however, is valid for only pointlike particles whose axes are small relative to electrode geometry features. It is also possible to adapt dielectrophoretic effects for nonspherical cells by modeling the particles as ellipsoids. For each of these situations the Clausius–Mossotti factor is extended to include these geometrical and layered effects by applying polarization factors. These modifications are beyond the scope of this article and are described in detail elsewhere [2–4]. Additionally, a comprehensive approach to apply dielectrophoresis, electrorotation and other dielectrophoretic techniques to ellipsoidal particles is detailed by J. Gimsa [6].

Particle Chains

When two polarized particles come into close proximity with each other they will undergo an attractive force due to their dipole interactions. This is referred to as dipole-dipole interactions, mutual dielectrophoresis or more commonly known as pearl chaining because this phenomenon creates strings of particles. Recall that a particle's induced dipole aligns itself to the electric field and that like particles will always have the same dipole orientation. These particles will have an attractive force since their opposite charges are aligned facing each other. Additionally, these particle chain formations can also be attributed to the distorted electric field caused by the particle's induced dipole (recall the modified, otherwise-uniform electric field lines in Fig. 2). These field disturbances can cause a localized dielectrophoretic force, increasing the strength of these particle-particle interactions. Pearl chains are typically observed near electrode edges where the strength of the electric field is the greatest. The measurement of chain length in experiments has been used to characterize the Clausius–Mossotti factor as well as create micro- and nanostructures.

Multipoles

The dielectrophoresis theory is based on the approximation that a sole dipole is induced in a particle. For most applications this assumption accurately depicts the behavior of a spherical particle; however, higher order poles (called multipoles) can be induced. A finite-sized particle in a uniform electric field will have higher multipole moments than a pure dipole moment. This is due to the mathematical nature of the multipole expansion which assumes pointlike particles. As soon as a particle is no longer pointlike, the higher multipoles start to contribute. This occurs when the electrode geometry is on the same length scale as the particle or when a particle is in an electric field null. Multipoles have multiple charge centers contained within the particle which interact with the electric field differently than the assumed dipole. Multipoles have been extensively investigated [7] and have been incorporated into various dielectrophoresis models.

D

Modeling Electric Fields

In order to determine the magnitude of the applied dielectrophoretic force it is necessary to quantify the gradient of the electric field squared (∇E^2). The nonuniformity of the generated electric field is the foundation for the dielectrophoretic manipulation of particles. A 3D electric field profile is typically created using a geometrical arrangement of surface electrodes. Mathematical models exist that have derived the electric field gradients of common electrode geometries. However, it is necessary to model the electric field of novel electrode geometries. By utilizing finite element computer programs such as ANSYS or COMSOL, a user can simulate the electric field for a defined electrode geometry. This data can be analyzed further by a postprocessing program that computes the gradient of the nonuniform field. For example, MATLAB has been used to determine these gradients from electric field input data [8].

Considerations

Outside of multipole theory, there are other electrokinetic effects that need to be considered when using dielectrophoresis to manipulate cells. Joule heating occurs when a current passes through a liquid medium, heating the solution due to the rapid movement of electrons. The thermal gradient across the solution causes convective circulation. Additionally, the dielectric properties of the medium are a function of temperature. These medium conductivity gradients are manipulated by the electric field to induce unwanted fluid flow. These induced temperature changes can affect cell physiology and, at temperatures above physiological conditions, can cause cell death. These temperature variations are more noticeable at larger length scales as the change in temperature (ΔT) is proportional to the applied voltage (V) by

$$\Delta T \approx \sigma V^2 L^3 \tag{8}$$

where L is the length scale of the system. These effects are obviously minimized at smaller length scales. Scaling effects that are commonly associated with dielectrophoretic techniques, including electrothermal heating, are discussed in detail elsewhere [9].

The electric field itself can directly interact and affect the cell. It can impose a transmembrane voltage across the cell, which can effect ion movement and damage voltage-sensitive proteins. There have been numerous investigations to correlate cell viability and their exposure to electric fields. Typically these experimentations involve monitoring the cell growth rate after exposure to the electric field and compare these results to a control. These negative physiological effects can be avoided, but dielectrophoretic techniques should still be used with caution.

The particles of interest can also interact with the surrounding medium due to hydrodynamic drag. This drag force is directly related to the particle shape and the fluid flow profile, which is determined by the incorporated channel geometry and pumping methods. Brownian motion refers to the random chaotic movement of particles and it plays a significant role in dielectrophoresis applications for nanometer-sized particles. Since most biological cells are micrometers in length, Brownian motion effects can be neglected. However, to manipulate proteins, viruses, or other molecules it is necessary to account for Brownian effects.

Key Research Findings

The major application of dielectrophoresis in micro- and nanofluidic systems continues to be the manipulation of particles and cells. Popular applications include particle trapping, dielectrophoretic microsystems, traveling wave dielectrophoresis and determination of cell dielectric properties. The specific dielectrophoretic techniques used in existing applications are too numerous to cover in this article. This article does provide a brief overview of some of the established manipulation techniques.

Particle Trapping

One of the more popular dielectrophoretic manipulation techniques involves the trapping of individual or groups of particles. Dielectrophoresis can be thought of as *electrical tweezers* that will grab onto and position particles. Trapping can be accomplished by means of novel electrode geometries that utilize pDEP or nDEP forces to selectively capture a particle or cell. For example, four electrodes can be positioned in a quadrupole arrangement and, when the proper electric field is applied to the electrode, a particle or particles are trapped in the electric field null in the center of the electrodes with nDEP forces (Fig. 5). Additionally, two sets of quadrupole electrodes can be placed and aligned on the top and bottom microchannel surfaces to create an octopole trap and capture a particle in suspension. One novel geometry that can capture particles with either pDEP or nDEP forces is with interdigitated electrodes. Planar electrode fingers, whose width and gap separation is a few times larger than the diameter of the particles of interest, have alternating applied AC signals (either 180° out of phase or alternating signal/ground). This geometry creates a strong pDEP force at the edges of the electrodes and a field null above the center of each electrode strip. Besides trapping, this geometry has been used to separate particles of different dielectric characteristics as they would be experiencing opposite dielectrophoretic forces (nDEP or pDEP). There are numerous other trap geometries that exist for both pDEP and nDEP.

There are a number or parameters that need to be addressed when attempting to trap a particle with dielectrophoresis. First, and most obvious, the dielectrophoretic force needs to be calculated for the respective electrode geometry. Electric field gradients are modeled and the resulting dielectrophoretic force is calculated with computer software. Forces generated by induced multipoles need to be considered and implemented into the dielectrophoresis calculations. The additional forces that need to be considered include the hydrodynamic drag force, the hydrodynamic lift force and sedimentation force. With all of these forces it is assumed that the fluid is under low Reynolds number flow due to dimensions typical with these microsystems and particles of interest. Hydrodynamic drag is directly proportional with the radius of the particle and the applied fluid velocity which is determined by the flow profile. For a particle near a planar surface a shear flow approximation can be used; the resultant force is similar to Stoke's drag. If the particle is held in suspension, as in nDEP octopole traps, the fluid flow can be modeled with a parabolic profile known as Poiseuille flow. The flow profile, though, is ultimately determined by the microchannel geometry and additional parameters will need to be addressed for a complete hydrodynamic drag assessment. There is hydrodynamic lifting force associated with a particle near the surface of a substrate and

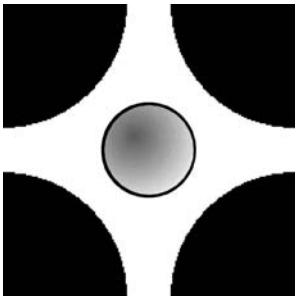

Dielectrophoretic Motion of Particles and Cells, Figure 5 A particle trapped by a negative dielectrophoresis quadrupole trap

under applied fluid flow. This is expressed with

$$F_{\text{lift}} = 9.22\left(36\,Q^2/w^2h^4\right)\rho r^4 \tag{9}$$

where Q is the volumetric flow rate, w and h are the microchannel dimensions, ρ is the density of the fluid and r is the radius of the particle [10]. As shown in (9), the lifting force significantly increases for larger particles and higher flow rates. Last, the sedimentation force is caused by gravity (g) and, for a spherical particle, is given by

$$F_{\text{sed}} = -\frac{4}{3}\pi r^3\left(\rho_{\text{p}} - \rho_{\text{m}}\right)g \tag{10}$$

A more in-depth explanation of dielectrophoretic trapping, including these additional modeling parameters, are shown elsewhere [8].

Electrode-Based Microsystems

Microsystems have incorporated dielectrophoretic forces into microchannels to manipulate particles and cells with various electrode geometries. Electrodes can be used to align target cells or separate particulate cells from the rest of the sample, an example of which is illustrated in Fig. 6. These systems use a 3D arrangement of electrodes, with mirrored electrode geometries aligned and separated by a thin film with microfluidic structures. Thus the electrodes in Fig. 6 are on the top and bottom surfaces of the microchannel and do not significantly impede or manipulate the flow field. This system is optimized for a particular set of cells such that the applied signals generate the strongest dielectrophoretic forces; this system will operate with the maximum possible applied flow rate for more effective processing. The system, though, will be selective to a set of cells with the same or similar dielectric properties. This process is obviously advantageous for an application that selectively separates cells based on their dielectric properties. Additionally, these systems can simultaneously separate and trap targeted cells for selective biological investigations. These dielectrophoresis techniques can be coupled with a variety of existing biological tools for innovative applications including fluorescence evaluation of cells in small populations, cell sorting, long-term investigations of single cells, cellular kinetics and other similar Lab-on-a-Chip analyses.

Traveling Wave Dielectrophoresis

Traveling wave dielectrophoresis is simply a linear application of electrorotation. An AC electric wave is produced by applying an electric field that travels linearly along a series of electrodes. An example of a traveling wave dielectrophoresis system with a 90° phase shift between electrodes is shown in Fig. 7. The expression for the traveling wave dielectrophoresis force for a homogeneous spherical particle is given by

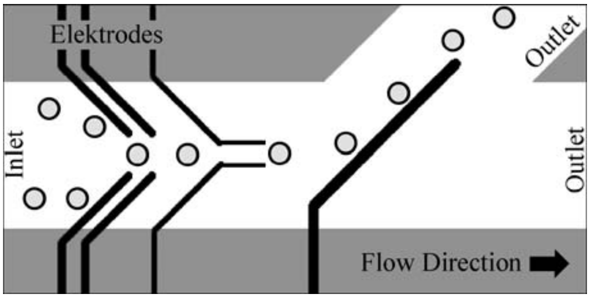

Dielectrophoretic Motion of Particles and Cells, Figure 6 An illustration of a dielectrophoretic microsystem that can selectively sort particles (top view). Recall that the electrodes are on the top and bottom surfaces of the microchannel and to not mechanically manipulate the particles

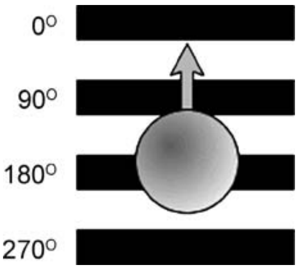

Dielectrophoretic Motion of Particles and Cells, Figure 7 Traveling wave dielectrophoresis

$$F_{\text{tw}} = \frac{-4\pi^2\varepsilon_0\varepsilon_{\text{m}}r^3\text{Im}\left[K(\omega)\right]E^2}{\lambda} \tag{11}$$

where λ is the wavelength of the applied signal. This is very similar to the electro-rotation force (7) including the incorporation of the imaginary part of the Clausius–Mossotti factor; the direction of the particle with respect to the traveling wave is dependent on this factor. The particle will translate in the same direction as the traveling wave if the dipole lags within one-half of a cycle of the electric field. For a lag greater than this the particle will travel in the opposite direction. Traveling wave dielectrophoresis can do more than just induce controlled translational motion, including separating particles of different dielectric properties. A geometry using a spiral electrode arrangement can concentrate particles towards its center while repelling unlike particles.

Dielectric Properties

Dielectric extraction for biological particles is complicated due to their unknown electrical properties and nonuniform geometries. However, dielectrophoretic techniques have been used to determine the dielectric properties of particles and cells. For non-spherical particles an orientation spectra can be obtained from electro-orientation experimentation and utilized to determine dielectric properties. Additionally, a particle's crossover frequency can be obtained through a visual observation when, at a given frequency, the cell of interest translates from an area of high electric field gradients to a field null (or vice versa). This can be observed for electrodes of various dimensions; for example, in an interdigitated electrode geometry as a dielectrophoretically-induced particle undergoes a change from pDEP to nDEP, it will translate from the electrode edge to above the center of the electrode strip. With careful experimentation and observation, the dielectric properties of unknown layers of multi-shelled particles can be determined. Dielectric properties have also been extracted from experiments measuring the translational speed of a particle under a dielectrophoretic force as well as counting and comparing dielectrophoresis-captured population spectra. Also, electrorotation and traveling wave dielectrophoresis experiments have been used to determine dielectric properties. There are a variety of ways to extract dielectric characteristics of particles and cells and, once determined, optimal dielectrophoresis systems can be designed.

Future Directions for Research

Dielectrophoretic techniques have continued to evolve from primitive, macroscale experimentation of Pohl to nanometer-sized particulate manipulation. This evolution is brought in part by the decreasing length scale of microfabrication techniques. As the feature size of fabricated electrodes become smaller and smaller, nanometer dielectrophoresis experimentations and phenomena will continue to unfold. The use of dielectrophoresis as a tool for micro- and nano-assembly has only recently emerged and these applications will continue to be developed. As a nonmechanical and minimally invasive process, dielectrophoresis presents itself for continued investigation as a constructive tool, including integration with sub-cellular biological entities.

As the number of applications of dielectrophoresis continues to increase, an accurate, comprehensive model becomes a necessary tool for optimal design. Although models exist describing individual dielectrophoretic manipulation techniques (especially for dielectrophoretic trap geometries), few exist for dynamic systems incorporating multiple dielectrophoresis applications with hydrodynamic, electrohydrodynamic and electrothermal phenomena. Additionally, these models need to incorporate non-spherical and non-rigid particle variables as well as fluid behaviors as you reach the nanometer length scale (such as Brownian motion) without ignoring important dielectric parameters such as particle–particle interactions and multipole theory.

Cross References

- ► AC Dielectrophoresis Lab-on-Chip Devices
- ► AC Electro-Osmotic Flow
- ► Dielectrophoresis
- ► Electrokinetic Motion of Cells and Nonpolarizable Particles
- ► Electroosmotic Flow (DC)
- ► Electrophoresis
- ► Electrothermal Effects
- ► Joule Heating in Electrokinetic Flow: Theoretical Methods
- ► Lab-on-a-Chip (General Philosophy)
- ► Lab-on-Chip Devices for Particle and Cell Separation
- ► Techniques for Manipulating Cells

References

1. Pohl HA (1978) Dielectrophoresis. Cambridge University Press, Cambridge
2. Jones TB (1995) Electromechanics of Particles. Cambridge University Press, Cambridge
3. Morgan H, Green N (2003) AC Electrokinetics: Colloids and Nanoparticles. Research Studies Press, Baldock, Hertfordshire
4. Hughes MP (2003) Nanoelectromechanics in Engineering and Biology. CRC Press, Boca Raton, Florida
5. Miller RD, Jones TB (1993) Electro-orientation of ellipsoidal erythrocytes. Biophys J 64:1588–1595
6. Gimsa J (2001) A comprehensive approach to electro-orientation, electrodeformation, dielectrophoresis, and electrorotation of ellipsoidal particles and biological cells. Bioelectrochemistry 54:23–31
7. Washizu M, Jones TB (1994) Multipolar dielectrophoretic force calculation. J Electrostat 33:187–198
8. Rosenthal A, Taff BM, Voldman J (2006) Quantitative modeling of dielectrophoretic traps. Lab on a Chip 6:508–515
9. Castellanos A, Ramos A, Gonzalez A, Green NG, Morgan H (2003) Electrohydrodynamic and dielectrophoresis in microsystems: scaling laws. J Phys D: Appl Phys 36:2584–2597
10. Cherukat P, McLaughlin JB (1994) The inertial lift on a rigid sphere in a linear shear-flow field near a flat wall. J Fluid Mech 263:1–18

Differential Ion Mobility Spectrometry

► Miniaturized Ion Mobility Spectrometry

Differential Pressure

► Pressure
► Pump Head

Diffuse Double Layer

► Electrical Double Layers

Diffuse Interface Model

► Interface Capturing Schemes for Free-Surface Flows

Diffusion

Definition

Diffusion is a process in which ions or molecules move from a more concentrated part of a solution to a more dilute part of the solution.

Cross References

► Lab-on-a-Chip Device for Chemical Analysis
► Microfluidic Mixing

Diffusion-Based Mixing

► Concentration Gradient Generation and Control

Diffusiophoresis

HUAN J. KEH
Department of Chemical Engineering, National Taiwan University, Taipei, Taiwan
huan@ntu.edu.tw

Synonyms

Chemiphoresis

Definition

Diffusiophoresis is defined as the migration of a colloidal particle in a solution in response to the macroscopic concentration gradient of a molecular solute that interacts with the surface of the particle; the solute can be either ionic or nonionic. Diffusiophoresis, which is due to the formation of a diffuse and mobile layer of neutral molecules or ions at the surface of the particle in an imposed solute concentration field, is different from *osmophoresis*, in which the particle is a vesicle composed of a body of fluid surrounded by a semipermeable membrane and the driving force for the migration is the osmotic pressure gradient along the particle surface caused by the solute concentration gradient prescribed in the ambient solution. In contrast to the diffusiophoresis of colloidal particles in prescribed solute concentration gradients, *diffusioosmosis* refers to the flow of a fluid solution in a micropore involving tangential concentration gradients of a solute that interacts with the pore wall.

Chemical and Physical Principles

A colloidal particle can be driven to move in a solution by the application of a nonuniform solute concentration field. The particle migrates toward or away from regions of higher solute concentration, depending on long-range interactions between the solute molecules and the particle. In a solution of uncharged solute, the solute molecules interact with the particle through the van der Waals and/or dipole forces, and thus, diffusiophoresis proceeds in the direction of increasing solute concentration. For a charged particle in an electrolyte solution, the particle-solute interaction is electrostatic in nature and its range is the Debye screening length κ^{-1}. In principle, diffusiophoresis of a charged particle in an electrolyte solution can be considered as a combination of two effects:

- chemiphoresis due to the nonuniform adsorption of counter-ions and depletion of co-ions over the surface of the particle, which is analogous to diffusiophoresis in nonionic media, and
- electrophoresis due to the macroscopic electric field generated by the concentration gradient of the electrolyte whose anion and cation have unequal diffusion coefficients.

A charged particle with a zeta potential of order kT/e ($\sim$25 mV; e is the elementary electric charge, k is Boltzmann's constant, and T is the absolute temperature) in electrolyte gradients of order 100 kmol/m^4(1 M/cm) will move by diffusiophoresis at speeds of several micrometers per second. The typical diffusiophoretic velocity of a particle in a solution of uncharged solute is of the same order of magnitude.

Key Research Findings

Diffusiophoresis of a Particle with a Very Thin Diffuse Layer

In an unbounded solution with a linear solute concentration distribution n^∞ or a constant macroscopic concentration gradient ∇n^∞, the diffusiophoretic velocity of a par-

ticle is [1–3]

$$\mathbf{U}^{(0)} = \frac{kT}{\eta} LK \nabla n^{\infty} \quad (1)$$

for the case of a nonionic solute, and

$$\mathbf{U}^{(0)} = \frac{\varepsilon\zeta}{\eta}\left(\alpha + \bar{\zeta}^{-1}\ln\cosh\bar{\zeta}\right)\frac{kT}{Ze}\nabla\ln n^{\infty} \quad (2)$$

for the case of a symmetric electrolyte solute with valence Z (which is positive). Here, L is a characteristic length for the particle-solute interaction (of order 1–10 nm), K is the Gibbs adsorption length characterizing the strength of the adsorption of the molecular solute [K and L are defined later by Eqs. (8) and (9)], η is the fluid viscosity, the dimensionless parameters

$$\alpha = \frac{D_2 - D_1}{D_2 + D_1}, \quad (3)$$

$$\bar{\zeta} = \frac{Ze\zeta}{4kT}, \quad (4)$$

D_1 and D_2 are the diffusion coefficients of the anion and cation, respectively, ζ is the zeta potential of the particle surface, and ε is the fluid permittivity. For the special case of $D_2 = D_1$ or $\alpha = 0$, Eq. (2) predicts that the particle movement (due to chemiphoresis only) is in the direction of increasing solute concentration, same as that predicted by Eq. (1) for a nonionic solution, regardless of the sign of ζ and the particle velocity is a monotonic increasing function of the magnitude of ζ.

Equations (1) and (2) indicate that the diffusiophoretic velocities of a particle are independent of the particle size and shape (and there is no rotational motion of the particle). However, their validity is based on the assumptions that the local radii of curvature of the particle are much larger than the thickness of the particle-solute interaction layer (diffuse layer) at the particle surface and that the effect of polarization (relaxation effect) of the diffuse solute species in the interfacial layer due to nonuniform "osmotic" flow is negligible. Important advances have been made in the past in the evaluation of the diffusiophoretic velocities of colloidal particles relaxing these assumptions and will be discussed below.

Diffusiophoresis of a Particle with a Thin but Polarized Diffuse Layer

For the case of diffusiophoretic motion of a colloidal sphere of radius a with a thin but polarized particle-solute interaction layer in a gradient of nonelectrolyte solute, the formula for the particle velocity was analytically derived by Anderson and Prieve [1],

$$\mathbf{U} = \frac{kT}{\eta} LK \left(1 + \frac{\beta}{a}\right)^{-1} \nabla n^{\infty}. \quad (5)$$

In the above equation, β is a relaxation coefficient defined by

$$\beta = (1 + \nu \mathrm{Pe}) K, \quad (6)$$

where

$$\mathrm{Pe} = \frac{kT}{\eta D} LK n^{\infty}, \quad (7)$$

$$K = \int_0^{\infty} \left[\exp(-\Phi(y)/kT) - 1\right] \mathrm{d}y, \quad (8)$$

$$L = K^{-1} \int_0^{\infty} y \left[\exp(-\Phi(y)/kT) - 1\right] \mathrm{d}y, \quad (9)$$

and

$$\nu = \left(LK^2\right)^{-1} \int_0^{\infty} \left\{ \int_0^{\infty} \left[\exp(-\Phi(y)/kT) - 1\right] \mathrm{d}y \right\}^2 \mathrm{d}y. \quad (10)$$

In Eqs. (7)–(10), Φ represents the potential energy resulting from the interaction between a single solute molecule and the particle surface (Φ is positive if the interaction force is repulsive and negative if it is attractive), D is the solute diffusion coefficient, and y is the normal distance measured from the particle surface into the fluid phase. The dimensionless parameter ν depends primarily on the shape of the function Φ rather than on its magnitude, and a typical value for it is 1/2. The adsorption length K equals the ratio of the Gibbs excess concentration of the solute in the adsorption layer to the solute concentration in the bulk solution at equilibrium, and it can be measured independently. There does not seem to be any means of quantitatively determining the length L, other than to say that it is positive and comparable to the size of the solute molecule. The relaxation coefficient β represents the ratio of apparent surface-to-bulk diffusion coefficients.

To obtain Eqs. (5)–(10), it was assumed that the concentration of solute within the adsorption boundary layer is related to the solute-surface interaction energy by a Boltzmann distribution. The essence of the thin-layer polarization approach is that a thin diffuse layer can still transport a significant amount of solute molecules so as to affect the solute transport outside the diffuse layer. For a strongly adsorbing solute (e. g., a surfactant), the dimensionless relaxation parameter β/a (or K/a) can be much

greater than unity. If all the adsorbed solute were "stuck" to the surface of the particle (the diffuseness of the adsorption layer disappears), then $L = 0$ and there would be no diffusiophoretic migration of the particle. In the limit of $\beta/a \to 0$ (very weak adsorption), the polarization of the diffuse solute in the interfacial layer vanishes and Eq. (5) reduces to Eq. (1).

Taking the double-layer distortion from equilibrium as a perturbation, Prieve and Roman [2] obtained a numerical calculation for the diffusiophoretic velocity of a dielectric sphere of radius a in concentration gradients of 1 : 1 electrolytes (KCl or NaCl) which was applicable to arbitrary values of ζ and κa, where κ^{-1} is the Debye screening length equal to $(2Z^2e^2n^\infty/\varepsilon kT)^{1/2}$. On the other hand, Keh and Chen [3] obtained an analytical expression for the diffusiophoretic velocity of a dielectric sphere surrounded by a thin but polarized electric double layer in the solution of a symmetric electrolyte,

$$\mathbf{U} = \frac{\varepsilon\zeta}{3\eta}\left\{c_1' - c_2' + \alpha(2 + c_1 + c_2) + \left[2 + c_1' + c_2' + \alpha(c_1 - c_2)\right]\bar{\zeta}^{-1}\ln\cosh\bar{\zeta}\right\}\frac{kT}{Ze}\nabla\ln n^\infty\,, \quad (11)$$

where

$$c_1 = \frac{1}{2a^2\Delta_1}\left(a^2 - 2a\beta_{11} + 3a\beta_{12} + a\beta_{22} + 2\beta_{12}\beta_{21} - 2\beta_{11}\beta_{22}\right)\,, \quad (12a)$$

$$c_2 = \frac{1}{2a^2\Delta_1}\left(a^2 - 2a\beta_{22} + 3a\beta_{21} + a\beta_{11} + 2\beta_{12}\beta_{21} - 2\beta_{11}\beta_{22}\right)\,, \quad (12b)$$

$$c_1' = c_1 - 3\frac{\beta_{12}}{a\Delta_1}\,, \quad (12c)$$

$$c_2' = c_2 - 3\frac{\beta_{21}}{a\Delta_1}\,, \quad (12d)$$

$$\Delta_1 = \frac{1}{a^2}\left(a^2 + a\beta_{11} + a\beta_{22} - \beta_{12}\beta_{21} + \beta_{11}\beta_{22}\right)\,, \quad (13)$$

and the relaxation coefficients

$$\beta_{11} = \frac{1}{\kappa}\left[4\left(1 + \frac{3f_1}{Z^2}\right)\exp\left(\bar{\zeta}\right)\sinh\bar{\zeta} - \frac{12f_1}{Z^2}\left(\bar{\zeta} + \ln\cosh\bar{\zeta}\right)\right]\,, \quad (14a)$$

$$\beta_{12} = -\frac{1}{\kappa}\left(\frac{12f_1}{Z^2}\right)\ln\cosh\bar{\zeta}\,, \quad (14b)$$

$$\beta_{21} = -\frac{1}{\kappa}\left(\frac{12f_2}{Z^2}\right)\ln\cosh\bar{\zeta}\,, \quad (14c)$$

$$\beta_{22} = \frac{1}{\kappa}\left[-4\left(1 + \frac{3f_2}{Z^2}\right)\exp\left(-\bar{\zeta}\right)\sinh\bar{\zeta} + \frac{12f_2}{Z^2}\left(\bar{\zeta} - \ln\cosh\bar{\zeta}\right)\right]\,. \quad (14d)$$

In the above equations, $f_m = 2\varepsilon k^2T^2/3\eta e^2D_m$ and $\bar{\zeta}$ was defined by Eq. (4).

To obtain Eqs. (11)–(14), it was assumed that the concentration of each ionic species within the electric double layer is related to the electric potential energy by a Boltzmann distribution. A comparison of Eq. (11) with the numerical results obtained by Prieve and Roman [2] shows that the thin-layer polarization model is quite good over a wide range of zeta potentials when $\kappa a > 20$. If $|\zeta|$ is small and κa is large, the interaction between the diffuse counter-ions and the particle surface is weak and the polarization of the double layer is also weak. In the limit of

$$(\kappa a)^{-1}\exp\left(2\left|\bar{\zeta}\right|\right) \to 0\,, \quad (15)$$

the effect of double-layer polarization disappears, $\beta_{11} = \beta_{12} = \beta_{21} = \beta_{22} = 0$, $c_1 = c_2 = c_1' = c_2' = 1/2$, and Eq. (11) reduces to the Eq. (2). Numerical calculations of Eq. (11) show that, even when κa is as large as 300, the effect of ionic transport inside the diffuse layer cannot be ignored if $|\zeta|$ equals several kT/e. In the other limit of very large relaxation coefficients, Eq. (12) becomes $c_1 = c_2 = c_1' = c_2' = -1$. Even for the case of $D_2 = D_1$, the particle velocity given by Eq. (11) for a finite value of κa may not be a monotonic function of the magnitude of $\bar{\zeta}$ and its direction can reverse (toward lower electrolyte concentration) when $|\bar{\zeta}|$ becomes large.

It could be found from Eqs. (5) and (11) that the effect of polarization of the diffuse layer is to decrease the particle velocity. The reason for this outcome is that the transport of the solute within the particle-solute interaction layer reduces the local solute concentration gradient along the particle surface. Although Eq. (11) is derived for the solution of a symmetric electrolyte, it can also be applied to the solution containing an arbitrary electrolyte using the reasoning that only the most highly charged counter-ions play a dominant role in the ionic fluxes along the particle surface.

On the other hand, the extension of Eqs. (5) and (11) to the diffusiophoretic velocity of spheroidal [4] and cylindrical [3, 5] particles with thin but polarized particle-solute

interaction layers was also derived. A remarkable feature was found that the diffusiophoretic velocity of a long circular cylinder in a transversely applied solute gradient is exactly the same as that of a sphere with an equal radius, given by Eqs. (5) and (11).

Diffusiophoresis of a Charged Particle with Arbitrary Double-Layer Thickness

Recently, analytical formulas in closed forms for the diffusiophoretic mobility of a charged sphere [6] and circular cylinder [7] of radius a in symmetric electrolytes at low surface charge density σ (valid for ζ up to 50 mV) and arbitrary κa have been obtained. The diffusiophoretic velocity of the charged particle can be expressed as an expansion in powers of ζ,

$$\mathbf{U} = \frac{\varepsilon}{\eta}\left[\frac{kT}{Ze}\alpha\Theta_1(\kappa a)\zeta + \frac{1}{8}\Theta_2(\kappa a)\zeta^2 + O\left(\zeta^3\right)\right]\nabla \ln n^{\infty} . \quad (16)$$

In this equation, Θ_1 and Θ_2 are functions defined by

$$\Theta_1(x) = 1 - e^x\left[5E_7(x) - 2E_5(x)\right] , \quad (17a)$$

$$\begin{aligned}\Theta_2(x) = 1 &+ \tfrac{1}{3}e^{2x}\left[10E_6(2x) + 7E_8(2x)\right] \\ &- 40e^{2x}E_7(x)\left[E_3(x) - E_5(x)\right] \\ &+ \tfrac{4}{3}e^x\left[3E_3(x) + 9E_4(x) - 7E_5(x) - 15E_6(x)\right] ,\end{aligned} \quad (17b)$$

$$E_n(x) = \int_1^{\infty} t^{-n}e^{-xt}\,\mathrm{d}t \quad (18)$$

for a spherical particle, and

$$\Theta_1(x) = 1 + B_{(0,3,1,0)}(x) - 4B_{(0,5,1,0)}(x) , \quad (19a)$$

$$\begin{aligned}\Theta_2(x) = 2 &- 4B_{(0,3,1,0)}(x) + 2B_{(0,3,2,0)}(x) \\ &+ 4\frac{K_1(x)}{K_0(x)}\left[B_{(1,2,1,0)}(x) - 2B_{(1,4,1,0)}(x)\right] \\ &- x^2\left[B_{(1,-1,2,0)}(x) - B_{(1,1,2,0)}(x) + 2B_{(1,1,2,1)}(x)\right] ,\end{aligned} \quad (19b)$$

$$B_{(m,n,i,j)}(x) = \int_1^{\infty} t^{-n}(\ln t)^j\left[\frac{K_m(xt)}{K_0(x)}\right]^i \mathrm{d}t \quad (20)$$

for a long circular cylindrical particle in a transversely imposed electrolyte concentration gradient, where K_m is the modified Bessel functions of order m of the second kind. The values of the functions $\Theta_1(x)$ and $\Theta_2(x)$ calculated numerically using Eqs. (17) and (19) are given in Tables 1 and 2, respectively. The effect of the polarization (or relaxation) of the diffuse ions in the electric double layer surrounding the particle is not included in Eq. (16) up to the order ζ^2. Note that the results of $\Theta_1(\kappa a)$ given by Eqs. (17a) and (19a) are the same as those derived by Henry for the electrophoretic mobilities of a dielectric sphere (6) and circular cylinder in the direction normal to its axis [7], respectively. All results of the above investigations show that the diffusiophoretic mobility of a particle in general decreases with an increase in $(\kappa a)^{-1}$. Also, the particle can reverse the direction of its migration when the value of $|\zeta|$, $(\kappa a)^{-1}$, or the valence of the electrolyte increases.

Diffusiophoresis, Table 1 Values of Θ_1 and Θ_2 calculated from Eq. (17)

x	$\Theta_1(x)$	$\Theta_2(x)$
0	0.667	0.000
0.1	0.667	0.027
0.5	0.673	0.066
1	0.684	0.092
2	0.710	0.142
3	0.734	0.194
5	0.773	0.289
10	0.835	0.462
20	0.894	0.643
30	0.922	0.733
50	0.949	0.823
100	0.972	0.904
∞	1.000	1.000

Diffusiophoresis, Table 2 Values of Θ_1 and Θ_2 calculated from Eq. (19)

x	$\Theta_1(x)$	$\Theta_2(x)$
0	0.500	0.000
0.1	0.502	−0.043
0.5	0.525	−0.088
1	0.557	−0.086
2	0.614	−0.026
3	0.659	0.050
5	0.723	0.188
10	0.812	0.417
20	0.885	0.630
30	0.917	0.730
50	0.947	0.825
100	0.972	0.907
∞	1.000	1.000

Particle-Interaction and Boundary Effects on Diffusiophoresis

In practical applications of diffusiophoresis, colloidal particles are not isolated and the surrounding fluid is externally bounded by solid walls. Thus, it is important to determine if the presence of neighboring particles and/or boundaries significantly affects the movement of a particle. In the limiting case that Eqs. (1) and (2) are applicable, the normalized velocity field of the immense fluid that is dragged by a single particle during diffusiophoresis is the same as for electrophoresis of the particle; thus, the particle-interaction and boundary effects on electrophoresis under the situation of infinitesimally thin double layer (satisfying Eq. (15)), which have been studied extensively

in the past, can be taken to interpret those in diffusiophoresis [8–10]. An important result of these investigations is that the particle-interaction and boundary effects on electrophoresis/diffusiophoresis are much weaker than on sedimentation, because the disturbance to the fluid velocity field caused by a phoretic particle decays faster than that caused by a Stokeslet.

When the polarization effect of solute species in the diffuse layer surrounding the particle is considered, the particle-interaction and boundary effects on diffusiophoresis can be quite different from those on electrophoresis, due to the fact that the particle size and some other unique factors are involved in each transport mechanism. Through the use of a boundary collocation method, the quasi-steady axisymmetric diffusiophoresis of a chain of colloidal spheres with thin but polarized diffuse layers was examined and numerical results of the diffusiophoretic velocity of the particles were presented for various cases. The diffusiophoretic velocities of two spherical particles with thin polarized diffuse layers but with arbitrary surface properties, arbitrary sizes, and arbitrary orientation with respect to the imposed solute concentration gradient correct to $O(r_{12}^{-7})$ were obtained by using a method of reflections, where r_{12} is the particles' center-to-center spacing. Based on the concept of statistical mechanics, the reflection results of interaction effects between pairs of spheres were also used to calculate approximately the average diffusiophoretic velocity of particles with thin but polarized diffuse layers in a statistically homogeneous suspension subjected to a uniform solute concentration gradient to the first order of the volume fraction of the particles. Using a unit cell model, the steady-state diffusiophoresis of a swarm of identical colloidal spheres with thin but polarized diffuse layers or with an arbitrary value of κa suspended uniformly in a solution with a constant imposed solute concentration gradient has been analyzed with various boundary conditions at the virtual surface of the cell [8]. The particle velocity as functions of the volume fraction of the particles was obtained in closed-form expressions, and comparisons of the results among the cell models and between the statistical model for dilute suspensions and the cell models have also been provided.

On the other hand, through the use of the boundary collocation technique, the diffusiophoretic motion of a colloidal sphere with a thin but polarized diffuse layer in the direction perpendicular to a plane wall was examined [9]. The wall effect on diffusiophoresis was found to be a complicated function of the properties of the particle and ions. Recently, the motions parallel to two plane walls at an arbitrary position between them and along the axis of a circular cylindrical pore were also investigated by using the boundary collocation method [10]. Numerical results of the wall corrections to Eqs. (5) and (11) for the particle velocity were presented for various values of the relative separation distances and other relevant parameters.

Examples of Application

Analogous to electrophoresis, diffusiophoresis is of practical importance in some applications to particle characterization and separation. In the metal and rubber technologies concerning surface treatment, diffusiophoresis is a transport mechanism in certain latex-particle coating processes. On the other hand, diffusiophoresis may be responsible for the repulsion of small particles by living cells, because each cell generates around itself a concentration field with gradient diminishing away from the cell as a result of material exchange with the surrounding continuous medium; the range of such repulsive forces may reach several tens of micrometers. Diffusiophoresis also plays an important role in other biological systems, such as the transport of proteins (hemoglobin, insulin, etc.) in solute concentration gradients.

Cross References

► Electrophoresis
► Electrical Double Layers

References

1. Anderson JL, Prieve DC (1991) Diffusiophoresis caused by gradients of strongly adsorbing solutes. Langmuir 7:403–406
2. Prieve DC, Roman R (1987) Diffusiophoresis of a rigid sphere through a viscous electrolyte solution. J Chem Soc Faraday Transact 2 83:1287–1306
3. Keh HJ, Chen SB (1993) Diffusiophoresis and electrophoresis of colloidal cylinders. Langmuir 9:1142–1149
4. Keh HJ, Huang TY (1993) Diffusiophoresis and electrophoresis of colloidal spheroids. J Colloid Interface Sci 160:354–371
5. Keh HJ, Huang TY (1994) Diffusiophoresis and electrophoresis of elliptic cylindrical particles. Colloid Polymer Sci 272:855–871
6. Keh HJ, Wei YK (2000) Diffusiophoretic mobility of spherical particles at low potential and arbitrary double-layer thickness. Langmuir 16:5289–5294
7. Keh HJ, Wei YK (2002) Osmosis through a fibrous medium caused by transverse electrolyte concentration gradients. Langmuir 18:10475–10485
8. Wei YK, Keh HJ (2002) Diffusiophoresis in a suspension of spherical particles with arbitrary double-layer thickness. J Colloid Interface Sci 248:76–87
9. Keh HJ, Jan JS (1996) Boundary effects on diffusiophoresis and electrophoresis: motion of a colloidal sphere normal to a plane wall. J Colloid Interface Sci 183:458–475
10. Keh HJ, Hsu YS (2006) Diffusiophoresis of a colloidal sphere in nonelectrolyte gradients in a circular cylindrical pore. Chem Eng Sci 61:3550–3563

Digital Microfluidics

CHEUK-WING LI, MENGSU YANG
Department of Biology and Chemistry, City University of Hong Kong, Hong Kong, China
bhmyang@cityu.edu.hk

Synonyms

Electrowetting on dielectric (EWOD)

Definition

Digital microfluidics is based upon the micromanipulation of discontinuous fluid droplets within a reconfigurable network. Complex instructions can be programmed by combining the basic operations of droplet formation, translocation, splitting, and merging.

Overview

Digital microfluidics is a relatively new term in Lab-on-a-Chip technology and its definition is not very clear. In the literature, digital microfluidics is a name given to a second-generation Lab-on-a-Chip architecture based upon micromanipulation of discontinuous fluid droplets. The basic operations required in digital microfluidics include droplet formation, droplet translocation, droplet splitting, and merging [1]. Although some continuous-flow microfluidic devices can also generate and manipulate discrete droplets [2], this is not commonly referred to as digital microfluidics. This could be due to the permanently etched microchannels involved, which limit the control reconfigurability and design scalability. Digital microfluidic networks are usually controlled by electrowetting on dielectric (EWOD), where droplets are driven by changing the substrate hydrophobicity using electric fields. A recently published magnetic droplet formation device may also fall into this category [3]. In such a device, a water droplet with magnetic particles added is driven by a changeable magnetic field controlled by a multilayer set of coils on a printed circuit board.

Basic Methodology

Theory

Figure 1 illustrates the electrowetting effect, where a polarizable, conductive liquid droplet is initially at rest on a hydrophobic surface [4]. When an electrical potential is applied between the droplet and an insulated counter-electrode underneath the droplet, a reduction in the contact angle of the droplet will occur and result in improved wetting. This improved wetting is a consequence of the lowering of the effective solid–liquid interfacial energy through the electrostatic energy stored in the capacitor formed by the droplet–insulator–electrode system. The dependence of the effective solid–liquid interfacial tension γ_{SL} on the applied voltage V is given by Lippmann's equation,

$$\gamma_{SL} = \gamma_{SL}^0 - \frac{\varepsilon V^2}{2d} \qquad (1)$$

where γ_{SL}^0 is the interfacial tension at zero applied potential, and ε and d are the dielectric constant and thickness of the insulating film. The effect of the Debye layer in the liquid can be neglected since its capacitance is connected in series with the solid insulator, which typically has a much smaller capacitance. Consequently, the electrowetting effect is relatively independent of the concentration or type of ions in the solution. Furthermore, the use of a solid insulator rather than a spontaneous space-charge layer to serve as the capacitor dielectric permits larger surface energies to be achieved at lower electric fields, while greater control over the surface chemistry is possible [12].

Experimental

Our experimental setup is illustrated in Fig. 2. The electrowetting system comprised a photolithographically patterned control electrode array (made from chromium or indium tin oxide, ITO) on a glass substrate, and a continuous ground plane (ITO on glass) parallel to it. Both electrode surfaces were covered by a film of hydrophobic insulation (e. g. a Teflon AF 1600 film, with a contact angle of 104° with water) that was insufficient to electrically insulate the ground electrode from the droplet. The control electrodes were patterned on a glass substrate using standard microfabrication techniques, and the top plate consisted of a glass substrate coated with a conducting layer

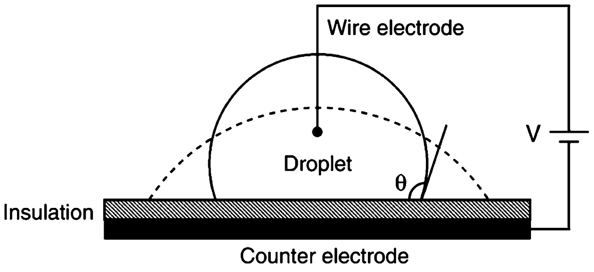

Digital Microfluidics, Figure 1 A droplet of conducting liquid forms a contact angle θ with a solid hydrophobic insulator (solid curve). Applying a voltage V between the droplet and a counterelectrode underneath the insulator reduces the solid–liquid interfacial energy, leading to a reduced θ and improved wetting of the solid by the droplet (dashed curve) [4]

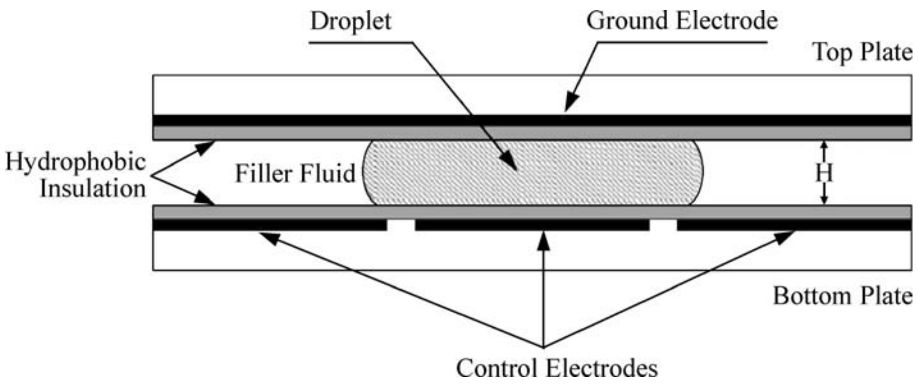

Digital Microfluidics, Figure 2 Schematic cross section of the electrowetting and optical-absorbance measurement setup

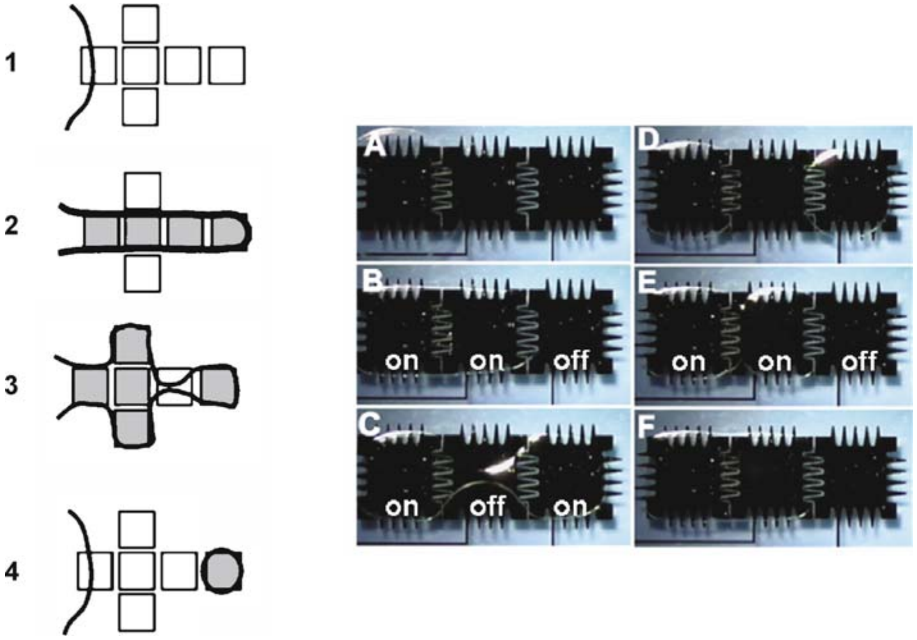

Digital Microfluidics, Figure 3 (**1**)–(**4**) Droplet formation sequence; gray squares depict energized electrodes. (**A**)–(**D**) Droplet splitting. (**E**) and (**F**) Droplet merging. See text for details

of optically transparent ITO to form the ground electrode. By clamping the two plates with a spacer between them, the electrode array and the ground plane were separated and a droplet was sandwiched between the two plates. Surrounding the droplet was a filler fluid (immiscible with the droplet, e. g. 1 cSt silicone oil) to prevent evaporation and facilitate transport. The electrode array was computer-controlled and was capable of independently switching each output between ground and the voltage output of a dc power supply [4, 5].

Key Research Findings

Basic Operations

Droplet Translocation

Translocation is achieved by sequentially energizing electrodes beneath the leading meniscus of a droplet. Pollack et al. [4] showed that the movement of a droplet was initiated at around 48 V, and thereafter the droplet was repeatedly transported. In the study of Cho et al. [6], movement of a droplet was achieved at a much lower applied poten-

tial, about 18 V. A combination of thin Teflon and oxide layers enabled this low-voltage operation.

Droplet Splitting and Merging

Sequentially captured images of the complete splitting process are shown in Figs. 3a–d. A neck shape is initially formed (Fig. 3c), and the droplet is then cut into two droplets (Fig. 3d). After the electric potential is turned off, the separated droplets relax into circular shapes. Droplet merging is essential for mixing in many microfluidic devices and is achieved by moving two droplets toward each other. This is the reverse process of splitting and is shown in Figs. 3e and 3f [4]. However, it has been reported that a design that can split droplets into two may not necessarily be able to merge two droplets back into one. This phenomenon is more likely to occur with a smaller channel gap and larger droplets, where the effect of contact angle hysteresis becomes more apparent [6].

Droplet Formation

To generate droplets from an on-chip reservoir, liquid needs first to be pulled out of the reservoir and separated from it. This process is strongly related to the droplet-splitting process, and a smaller channel gap (H in Fig. 2) makes droplet formation easier. The sequence of droplet formation is depicted in Fig. 3 (parts 1–4) [7], where gray squares represent energized electrodes and white squares represent electrodes that are not energized. Note that two side electrodes have been introduced beside the main fluid path. While this is not a prerequisite for droplet formation, side electrodes help to form a better-defined droplet and provide control of the location of the splitting. Without the side electrodes, it is reported that the liquid may continue to follow the leading meniscus to some extent, forming a long liquid column. The location of the splitting depends on the initial shape of the meniscus in the reservoir, on the surface condition, and on how the control electrodes are activated [4, 6].

Droplet Mixing

Droplet mixing is achieved by translocation of a droplet between several electrodes. For example, when three electrodes were used, the coalesced droplet had four possible configurations, as shown in Fig. 4a. Time-lapse images of three of the four configurations during three-electrode mixing at 8 Hz are shown in Fig. 4b. Flow reversibility is also demonstrated here. In the later frames, it can be observed that the interface between the fluorescent and nonfluorescent areas behaves as if it is more diffuse, even though flow reversibility can still be observed. A further increase in the number of electrodes can increase the number of possible mixing configurations. Since diffusion-based mixing depends on the total interfacial area generated within the coalesced droplet, increasing the number of possible configurations improves mixing by extending the interface. Moreover, increasing the frequency of oscillation will change this interface more quickly, since the switching time between different configurations is reduced. To achieve even faster mixing times, a greater number of electrodes can be used with operation at higher frequencies, at the cost of using a larger mixing area [8].

Applications

EWOD/Absorbance Detector for Glucose Detection

Figure 5 illustrates how optical absorbance measurements were made in a plane perpendicular to an EWOD device [13]. The setup consisted of a green LED (545 nm, RadioShack) and a photodiode (TSL257, Texas Advanced Optoelectronic Solutions), which functioned as a light-to-voltage converter. The voltage output of the photodiode $V(t)$ was directly proportional to the light intensity incident on it. A colorimetric enzyme-kinetic method was used for the determination of glucose concentration on the basis of Trinder's reaction. First, glucose was enzymatically oxidized to gluconic acid and hydrogen peroxide in the presence of a glucose oxidase. The hydrogen peroxide formed was reacted with 4-aminoantipyrine and *N*-ethyl-*N*-sulfopropyl-*m*-toluidine in the presence of a peroxidase to give violet-colored quinoneimine, which has an absorbance peak at 545 nm. Detection of glucose in a concentration range of 25 – 300 mg/dl was achieved [5].

EWOD/PCR

Figure 6 depicts an EWOD-based PCR biochip device, with operation details as follows. First, droplets containing a PCR reagent/primer and a cDNA sample were created from separate reservoirs. Then, both droplets were moved away from their respective reservoirs to reach the mixing region by means of basic droplet translocation operations. The droplets were merged and mixed using a 2×2 electrode array. By switching the voltages applied to the electrodes in specific cycles, the merged droplet could be completely mixed. When the mixed droplet reached the periphery of the PCR chamber, a surface tension gradient was induced by the hydrophobic/hydrophilic interface. Without power being applied, the mixed droplet was then moved to the micro-PCR chamber. Finally, the mixed droplet was completely transported inside the micro-PCR chamber.

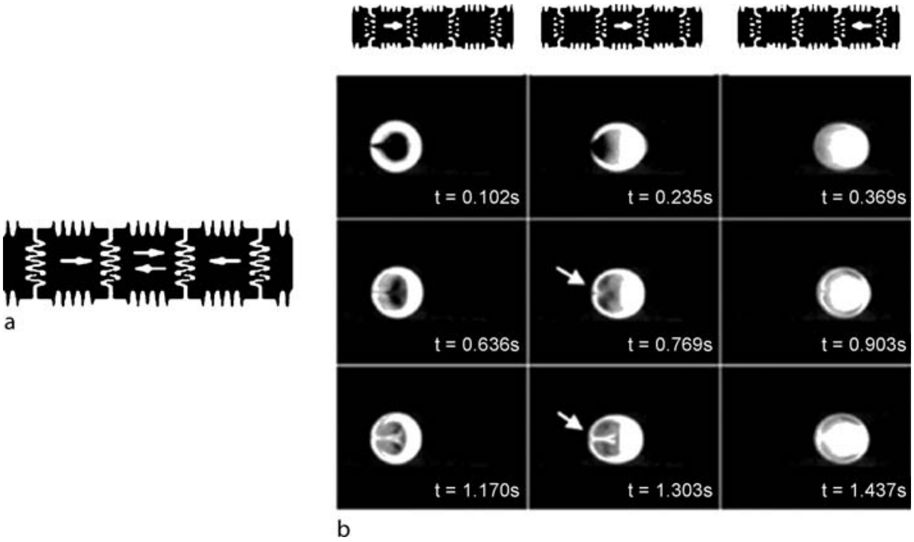

Digital Microfluidics, Figure 4 (**a**) Possible droplet positions and directions in three-electrode mixing. (**b**) Time-lapse images of three-electrode mixing at 8 Hz

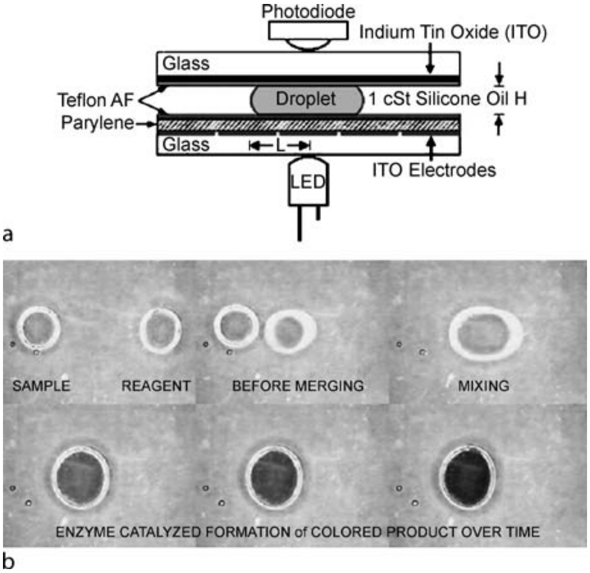

Digital Microfluidics, Figure 5 (**a**) Optical detection implemented by sandwiching an EWOD device between a green light-emitting diode and a photodiode. (**b**) A glucose assay was initiated by mixing a sample and reagent together. The change in absorbance was detected by the photodiode

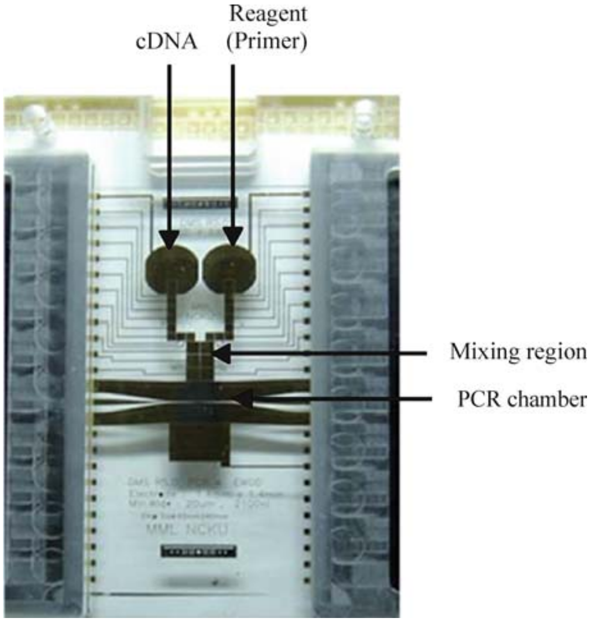

Digital Microfluidics, Figure 6 A digital EWOD/PCR biochip with integrated on-chip heater and temperature sensor. See text for details

Two microheaters and a temperature microsensor were integrated into the on-chip PCR chamber. A novel design of the hydrophobic (Teflon) and hydrophilic (SiO_2) layers was used to cover the microheaters. The different contact angles caused by the hydrophobic/hydrophilic structure generated a surface tension gradient that pulled mixed droplets into the PCR chamber with no power application. The whole pulling process took about 0.13 s. The PCR procedure was performed for 25 thermal cycles. The final PCR products were analyzed by using a gel electrophoresis technique in 1.5% agarose gel stained with ethidium bromide (Sigma Chemical, USA), and visualized

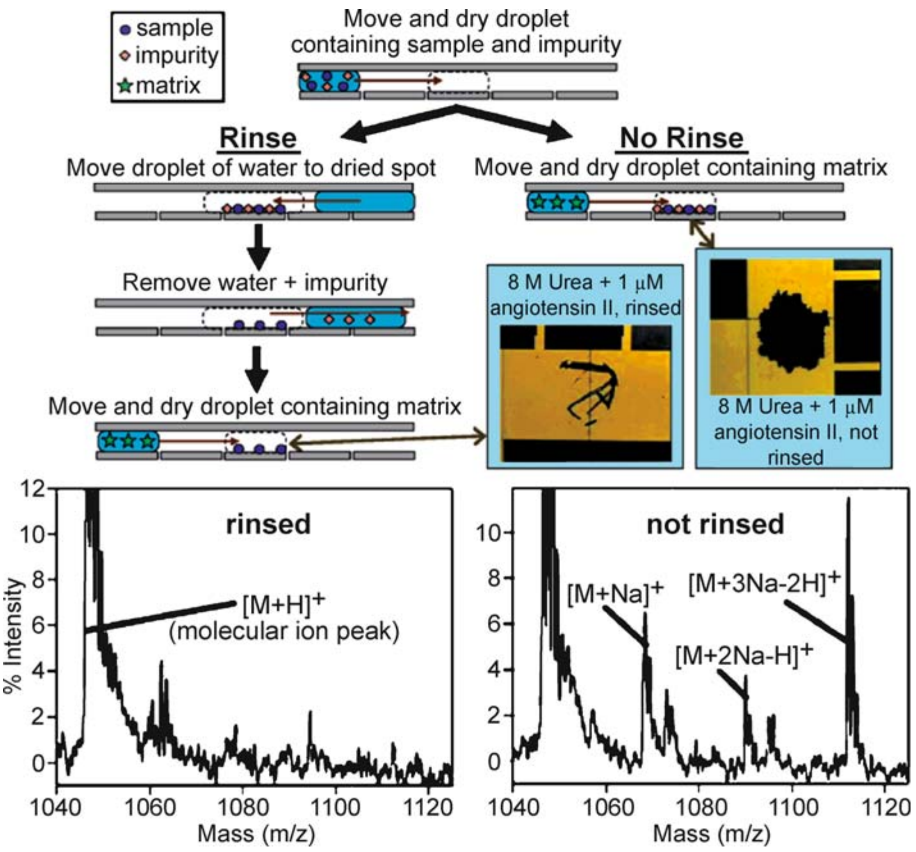

Digital Microfluidics, Figure 7 (**a**) EWOD-driven sample purification and micrographs of dried spots. Insets: the rinsed sample (left) appears to be primarily composed of DHB crystals, while the nonrinsed sample (right) is dominated by urea. MALDI-MS spectra of (**b**) rinsed and (**c**) control spots

with ultraviolet light. The total time for the on-chip PCR test was 55 min and the total sample volume consumed was 15 μL. In comparison with the total time of 110 min and total sample volume of 50 μL for a traditional PCR machine, the reductions of total time and sample consumption are 50% and 70%, respectively [9].

EWOD/MALDI-MS

Figure 7 illustrates an in-line sample purification method for MALDI-MS which relies on an EWOD-based technique. In this study, air was used as the filler medium instead of silicone oil because the oil hindered the droplet-drying process. A droplet containing peptides and impurities was moved by EWOD to a specific location on the array and then dried to form a spot. Subsequently, an EWOD-driven droplet of deionized water was moved onto the spot; after visual confirmation that the impurities had dissolved, the droplet was moved away from the spot. After this rinsing step, a droplet containing a MALDI matrix was moved by EWOD to the same spot and dried; finally, the spot was analyzed by MALDI-MS. Control experiments were performed without the water rinse. The purification method was originally evaluated using the same volume, 0.5 μL, for the sample and rinsing droplets. However, because the dried spot was protein-fouled and changed the surface properties, the size of the rinsing droplet was increased so as to touch the adjacent clean electrodes for droplet translocation. Rinsing droplets 1 μL in size were easily moved over spots formed from 0.5 μL sample droplets.

In MALDI-MS, impurities at low to intermediate concentrations form adducts with analyte molecules that can obscure the relevant data and reduce the overall signal intensity. Figures 7b and c contain representative EWOD-MALDI-MS spectra for rinsed and nonrinsed samples of angiotensin II prepared with 20 mM sodium phosphate. In the spectrum of the nonrinsed sample (Fig. 7b), peaks at $M + 23$, $M + 45$, and $M + 67$ corresponded to the monosodium, disodium, and trisodium adducts of the parent molecule. These adduct peaks are barely visible in the spectrum of the rinsed sample. The intensities of the molecular-ion peaks in the rinsed spectra were about twice as great as those observed in the control spectra [10].

Future Directions for Research

Since they feature permanently etched microchannels, continuous-flow microfluidic devices suffer from inherent difficulty in integrating and scaling them because the parameters that govern the flow field (e. g., pressure, fluid resistance, and electric field) vary along the flow path, making the fluid flow at any one location dependent on the properties of the entire system [11]. In other words, major redesign is often required just to integrate and scale up several functionalities. In contrast, increasing the complexity of digital microfluidic devices can be achieved through combining and reusing a finite set of basic instructions. Digital microfluidics seems to be an easier approach to achieving a high degree of functional integration and control to further advance microfluidic technology.

Cross References

- ► Electrowetting, Applications
- ► Electrowetting and Droplets
- ► Electrowetting
- ► Droplet Microreactors
- ► Droplet-Based Lab-on-Chip Systems

References

1. Zeng J (2006) Modeling and simulation of electrified droplets and its application to computer-aided design of digital microfluidics. IEEE Trans Comput Aided Design Integrated Circuits Syst 25:224–233
2. Adamson DN, Mustafi D, Zhang JXJ, Zheng B, Ismagilov RF (2006) Production of arrays of chemically distinct nanolitre plugs via repeated splitting in microfluidic devices. Lab Chip 6:1178–1186
3. Lehmann U, Vandevyver C, Parashar VK, Gijs MAM (2006) Droplet-based DNA purification in a magnetic lab-on-a-chip. Angew Chem Int Ed 45:3062–3067
4. Pollack MG, Fair RB (2000) Electrowetting-based actuation of liquid droplets for microfluidic applications. Appl Phys Lett 77:1725–1726
5. Srinivasan V, Pamula VK, Fair RB (2004) Droplet-based microfluidic lab-on-a-chip for glucose detection. Anal Chim Acta 507:145–150
6. Cho SK, Moon H, Kim CJ (2003) Creating, transporting, cutting, and merging liquid droplets by electrowetting-based actuation for digital microfluidic circuits. J Microelectromech 12:70–80
7. Fouillet Y, Achard J-L (2004) Microfluidique discrete et biotechnologie. C R Phys 5:577–588
8. Paik P, Pamula VK, Pollack MG, Fair RB (2003) Electrowetting-based droplet mixers for microfluidic systems. Lab Chip 3:28–33
9. Chang Y-H, Lee G-B, Huang F-C, Chen Y-Y, Lin J-L (2006) Integrated polymerase chain reaction chips utilizing digital microfluidics. Biomed Microdevices 8:215–225
10. Wheeler AR, Moon H, Bird CA, Rachel R, Loo O, Kim CJ, Loo JA, Garrell RL (2005) Digital microfluidics with in-line sample purification for proteomics analyses with MALDI-MS. Anal Chem 77:534–540
11. Su F, Chakrabarty K, Fair RB (2006) Microfluidics-based biochips: Technology issues, implementation platforms, and design-automation challenges. IEEE Trans Comput Aided Design Integrated Circuits Syst 25:211–223
12. Pollack MG, Shenderov AD, Fair RB (2002) Electrowetting-based actuation of droplets for integrated microfluidics. Lab Chip 2:96–101
13. Srinivasan V, Pamula VK, Fair RB (2004) An integrated digital microfluidic lab-on-a-chip for clinical diagnostics on human physiological fluids. Lab Chip 4:310–315

D

Dip-Pen Nanolithography

CLIFFORD L. HENDERSON
School of Chemical and Biomolecular Engineering, Georgia Institute of Technology, Atlanta, GA, USA
cliff.henderson@chbe.gatech.edu

Synonyms

DPN

Definition

Dip Pen Nanolithography (DPN) is a direct-write scanning-probe-based lithography method in which an atomic force microscope (AFM) tip or array of tips is used to deliver chemical reagents directly to specific regions of a substrate surface.

Overview

Dip Pen Nanolithography (DPN) is a direct-write scanning-probe-based lithography method in which an AFM tip is used to deliver chemical reagents directly to specific regions of a substrate surface as shown schematically in Fig. 1. It was originally developed and reported by Mirkin and coworkers in 1999 [1]. The early development of the technique involved use of the AFM tip to deliver alkanethiols to gold surfaces, allowing the formation of patterned self-assembled monolayers (SAMs). The patterns produced in this early work demonstrated the capability of the method to generate material patterns with high resolution and excellent spatial registration. Interestingly, it was also shown that the SAM monolayer patterns formed from the alkanethiol materials were of high quality, i. e. of high density. In fact, the early work with 1-octadecanethiol (ODT) and 16-mercaptohexadecanoic acid (MHA) showed that SAM patterns formed from these reagents on gold surfaces were crysystalline. This high quality nature of the SAM patterns allowed these features to be used as masking layers to resist etch processes such that metal and semiconductor nanostructures could be generated from the DPN pattern [2]. Such techniques have

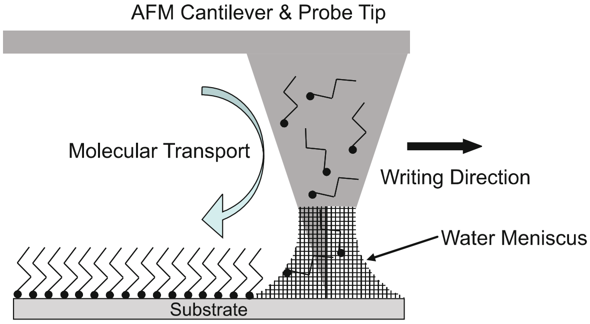

Dip-Pen Nanolithography, Figure 1 Schematic of the basic dip-pen nanolithography (DPN) process. In the example shown, molecules deposited onto the AFM probe tip are transferred to the substrate through the water meniscus formed at the probe tip-substrate contact point

subsequently been extended to produce a variety of high-resolution metal and semiconductor structures with controlled surface chemistry.

More recently, DPN techniques have been extended and developed to pattern a variety of ink-substrate combinations. DPN has been shown to be compatible with a wide array of ink types including small organic molecules, organic and biological polymers, colloidal particles, metal ions, and sols. DPN has also been demonstrated to work on a wide variety of substrates ranging from metals to insulators, but gold surfaces, silicon, and silicon oxide surfaces remain the most commonly used. DPN is perhaps the only lithography technique that offers a combination of extremely high resolution, precise registration, and the ability to directly print materials without need for other lithographic processing. Due to this combination of characteristics, DPN has become a particularly attractive tool for research related to the patterning of biological and soft organic surfaces. The main advantages for DPN in these applications are that biological and other sensitive molecules can be deposited in either ambient or inert environments without the need to expose them to either harsh radiation (e. g. UV or e-beam), the use of harsh solvents and chemicals required in most other lithography techniques is avoided, and cross-contamination of the surface is avoided since the materials are deposited only where they are wanted on the surface and no bulk chemical treatments of the surface are utilized.

Basic Methodology

In general, DPN is conceptually a very simple process. The major steps involved in the process are:

- the AFM tip is "inked" with the molecule of interest that is to be deposited,
- the AFM tip is aligned to a region where material is to be deposited,
- the tip is brought into contact with the surface and either allowed to dwell in a particular spot (i. e. to create a well defined dot) or scanned over the surface in some pattern-wise manner (to create features composed of lines), and
- the tip is disengaged from the surface to stop transfer of material from the tip to the substrate.

This procedure brings to light one of the limitations of conventional DPN using standard passive AFM probes, namely that material is being transferred from the tip to the substrate any time the tip is in contact with the substrate. Thus the tip must be engaged and disengaged from the surface to start and stop the writing process. Those who work with AFM systems know that this process of tip engagement is relatively slow which prevents the modulation of writing in conventional DPN at very high rates. As will be discussed later, a number of strategies that utilize active AFM cantilever probes have been developed to overcome this limitation and allow for faster modulation of writing in DPN.

Inking of the AFM tip with the molecules of interest can be accomplished using a variety of methods including:

- solution deposition,
- vapor deposition,
- solid precursor deposition directly onto the tip (generally followed by heating and melting of the material on the tip to allow the material to flow and better coat the tip), and
- direct wicking of the pure compound onto the tip.

The choice of method used to ink the tip depends on a variety of factors including the physiochemical properties of the molecule that is being coated, the amount of material that is desired on the tip, and the type of tip being used. In solution deposition, the molecule of interest is dissolved into an appropriate solvent at relatively low concentrations, the tip is placed in contact with the solution, molecules are allowed to adsorb to tip from solution, the tip is removed from contact with the solution and allowed to dry (which can result in further deposition of dissolved molecules depending on the method of drying the tip), and this process can be repeated if desired to attempt to build up a significant coating on the tip. The problem in general with this method is that it results in substantial coverage of all parts of the cantilever exposed to the solution, which can be problematic if the top of the AFM cantilever is coated to the extent that the coating interferes with laser reflection from the probe tip when and if the tip is used in a conventional AFM configuration. In vapor deposition, a quantity of the molecule of interest is heated to generate a significant vapor pressure and vapor stream of the

molecule and the tip to be coated is placed cold in contact with the vapor stream and material is allowed to condense on the surfaces of the AFM probe tip. Direct wicking involves placing the AFM probe tip in contact with a small quantity of the molecule of interest which may then require heating to melt the compound and provide sufficient molecular mobility to coat the tip.

Alignment of the tip to the substrate is accomplished using the various normal imaging modes available using an atomic force microscope. At this point, the problem mentioned earlier with DPN in which material is generally transferred from the tip to the surface any time the tip is in contact with the substrate can become problematic. When the coated tip is used to image the surface for the purposes of aligning the tip to the substrate, the accidental transfer of material and contamination of the surface can result. Since conventional DPN requires the tip to be in contact with the surface to transfer material, oscillatory modes of imaging (i. e. so-called "tapping-mode" imaging) can help to reduce accidental contamination of the surface under certain conditions. In other cases, control of the ambient environment around the tip can be used to dramatically affect the rate of deposition of material from the tip and can thus be used as a means to minimize contamination of the surface during imaging and alignment. For example, it has been shown in some cases that writing in a humid environment is needed for particular inks to be effectively deposited, in which cases it is believed that material transfer through a water meniscus formed at the tip-substrate interface is the important mode of material transfer. In such cases, imaging of the surface with the probe tip in a dry environment does not result in substantial material transfer and can be used to aid in tip alignment to features on the substrate surface.

Once the tip is aligned to a location on the surface where writing is to be performed, the tip is brought into contact with the surface and allowed to dwell in one spot (i. e. to deposit a spot) or is scanned over the surface to make extended features. The rate at which material is transferred to the surface and the shape and size of the deposited material region is affected by a number of factors including:

- the type of molecule being deposited and its physiochemical properties,
- the ambient environment in which the writing is being performed,
- the type of surface on which writing is being performed and the existence of any previous patterns on that surface, and
- the length of time the tip is allowed to dwell in one spot or equivalently the rate at which the tip is scanned over the surface and the total time it is scanned over the same spot [3, 4].

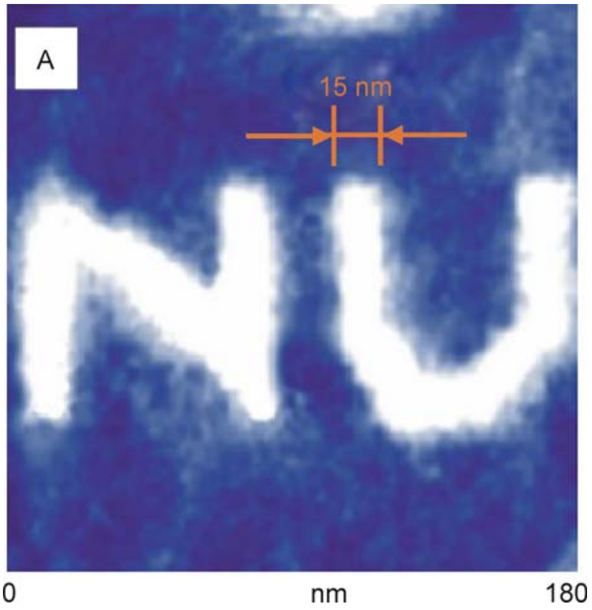

Dip-Pen Nanolithography, Figure 2 Example of high resolution pattern of mercaptohexadecanoic acid on atomically-flat gold surface formed using DPN (courtesy Mirkin group, Northwestern University)

The behavior observed in the transfer of material from the tip to the substrate surface is quite rich and the details of these phenomena are beyond the scope of the simple discussion presented here. Overall, transfer of material from the tip is accomplished via some combination of two basic mechanisms:

- thermal diffusion of molecules along the tip surface toward the point of tip-surface contact and ultimately onto the substrate and
- dissolution of the molecules into a solvent meniscus (commonly water under normal humid ambient conditions as mentioned earlier) and deposition of the molecules from the solvent onto the surface.

This first mode has been shown to be the principle mechanism involved in the transfer of hydrophobic, non-water soluble inks while the latter mechanism can be important in more hydrophilic, water soluble ink systems. Although both mechanisms have been shown to be active depending on the ink system used, in the case where a solvent meniscus is present the rates of material transfer are generally significantly enhanced.

Due to the difficulty in modulating writing using standard DPN due to the slow nature of engaging and disengaging a tip or tip array from the surface, a variety of strategies have been developed that allow for such modulation without requiring the crude removal of the cantilever or cantilever array from the surface. Such modulation strategies are of course also critical for applications where cantilever

arrays are used and it is desired that individual cantilevers in the array write independently of one another. One class of modulation techniques focuses on providing ways to locally mechanically actuate a cantilever tip and deflect it over a distance sufficient to remove it from contact with the surface and thus prevent material transfer without requiring gross removal of the AFM scanner head from proximity with the surface (i. e. like the process normally used in disengaging an AFM tip from the surface). Cantilevers and cantilever arrays have been designed that use a variety of local actuation methods including thermal deflection of the cantilever tip [5] and electrostatic deflection of the cantilever tip [6]. For example, in one example of the thermal deflection method, cantilevers were built in which the main cantilever arm consisted of a silicon nitride membrane coated with a gold layer (see Fig. 2). The gold was patterned into narrow lines at the base end of the cantilever to form a resistive heater element which could be heated by flowing a current through the gold lines. The difference in the thermal expansion coefficients of the gold metal and silicon nitride layers results in thermal stress build-up and bending of the cantilever when the temperature of the cantilever is raised. This provides a simple method for modulating contact of the cantilever with the surface by simply modulating current flow to the AFM cantilever probe. In fact, this basic design was used to fabricate a simple 10 element linear cantilever array and to demonstrate that each cantilever could be actuated independently to write different patterns as the array was scanned over a surface. A second method that has been employed to achieve active control of writing from the tip without requiring removal of the tip from the surface has been to use the DPN tip in an electrochemical mode whereby the tip not only delivers material to the surface, but in addition when current is also allowed to flow from the tip it causes an electrochemical reaction in the deposited molecules that forms the final desired product. In this case, the tip is not mechanically actuated to modulate the deposition process but is instead controlled by controlling current flow to the tip to modulate a chemical reaction involved in the deposition process. Thus, although precursor molecules may be deposited any time the tip is in contact with the surface, the desired material is only deposited when the electrochemical reaction is allowed to occur and thus the is modulating a bias between the tip and substrate to control current flow. Specifically, it has been demonstrated that such a combined DPN-electrochemical deposition technique can be used to deposit metal patterns using metal salt precursors [7]. Finally, a very interesting technique that utilizes heating of the cantilever probe tip to control when material is transferred from tip to the substrate has also been recently developed [8]. In this technique, which has been termed so-called "thermal dip-pen nanolithography" or tDPN, AFM cantilevers that contain an electrical resistance heater in the end of the cantilever platform above the base of the probe tip are used. The probe tip is inked with a molecule that is a solid and does not deposit at substantial rates at room temperature from the tip to the substrate. When current is allowed to flow to the heater on the cantilever, the probe tip temperature can be raised above the melting temperature of the ink and it can be transferred to the substrate at a significantly higher rate than in the case when the cantilever is operated at lower temperatures. Therefore, ink deposition can be controlled by modulating heating of the tip using control of current flow through the cantilever.

Key Research Findings

Dip Pen Nanolithography techniques provide the unique ability to directly deposit patterned material structures on surfaces with extremely high resolution, precise registration, and without the need for the multiple subsequent lithographic processing steps that are common to most lithographic processes. A wide variety of molecules and materials have been deposited using such techniques ranging from insulators to conductors and from inorganic materials to biological molecules. Therefore, DPN techniques are finding use in a wide variety of research fields ranging from microelectronics to genomics.

Future Directions for Research

As mentioned earlier, while DPN techniques present novel opportunities for the direct patterned deposition of materials at feature sizes that would either be difficult or significantly more expensive using other standard micro- and nanofabrication techniques, DPN is still limited to small scale research applications at this point. This limitation is due in large part to the fact that useful feature writing using passive cantilever probes is either

- not possible at speeds which are practical for many potential larger scale applications, or
- passive probe arrays do not offer the possibility to write the arbitrarily complex and heterogeneous layers of material that would be needed in such applications.

Therefore, as mentioned earlier, one active direction for future research is still in the development of methods for actively and independently controlling writing from large arrays of cantilever probes. In addition, as the name dip-pen nanolithography implies, standard probe tips must be re-inked at some point to continue to write features at a controlled rate and size. The development of more sophisticated approaches and tools for continuous delivery of ink to the cantilever probe tip to allow for uninter-

rupted continuous writing is still an active area of research. Finally, since DPN is a basic research tool and method, significant research will continue in terms of finding new applications for the technique.

Cross References

- ► Photolithography
- ► Microstereo Lithography
- ► Soft Photolithography
- ► Fabrication of 3D Microfluidic Structures

References

1. Piner RD, Zhu J, Xu F, Hong SH, Mirkin CA (1999) Dip-Pen Nanolithography. Science 283:661–663
2. Weinberger DA, Hong S, Mirkin CA, Wessels BW, Higgins TB (2000) Combinatorial generation and analysis of nanometer- and micrometer-scale silicon features via “dip-pen” nanolithography and wet chemical etching. Adv Mater 12:1600–1603
3. Peterson EJ, Weeks BL, De Yoreo JJ, Schwartz PV (2004) Effect of Environmental Conditions on Dip Pen Nanolithography of Mercaptohexadecanoic Acid. J Phys Chem B 108:15206–15210
4. Hampton JR, Dameron AA, Weiss PS (2006) Double-Ink Dip-Pen Nanolithography Studies Elucidate Molecular Transport. J Am Chem Soc 128:1648–1653
5. Bullen D, Wang X, Zou J, Chung SW, Mirkin CA, Liu C (2004) Design, fabrication, and characterization of thermally actuated probe arrays for Dip Pen Nanolithography. J Microelectromec Syst 13(4):594–602
6. Bullen D, Liu C (2006) Electrostatically actuated dip pen nanolithography probe arrays. Sens Actuators A 125(2):504–511
7. Li Y, Maynor BW, Liu J (2001) Electrochemical AFM “Dip-Pen” Nanolithography. J Am Chem Soc 123(9):2105–2106
8. Sheehan PE, Whitman LJ, King WP, Nelson BA (2004) Nanoscale deposition of solid inks via thermal dip pen nanolithography. Appl Phys Lett 85(9):1589–1591

Dirac Delta Function

Synonyms

Delta function; Unit impulse function

Definition

The Dirac delta function $\delta(x)$ is a function that has the value of unity at $x = 0$ while vanishes elsewhere. The integral of the Dirac delta from any negative limit to any positive limit is 1. The discrete analog of the Dirac delta function is the Kronecker delta.

Cross References

- ► Meshless Methods
- ► Volume and Finite Difference Method for Modeling and Simulation

Direct Bonding

► Wafer Bonding

Direct Current Dielectrophoresis (DC-DEP)

► DC Dielectrophoresis in Lab-on-a-Chip Devices

Discrete Element Analysis

► Lumped Analysis

Discrete Least Square

► Least Square

Discrete Method

► Non-Continuous Approaches

Discretization

Synonyms

Numerical discretization

Definition

Discretization refers the process of transforming continuous differential equations into discrete difference equations, suitable for numerical computing. The difference equations are usually algebraic equations expressed in terms of the problem unknowns.

The discretization also refers to the process of decomposing a computational domain into smaller sub-domains, frequently called cell or element, within which simple approximate functions can be used to define physical unknown variables. The discretized domain is frequently called a computational grid or mesh.

Cross References

- ► Meshless Methods
- ► Volume and Finite Difference Method for Modeling and Simulation

Disjoining Pressure

VICTOR M. STAROV
Department of Chemical Engineering, Loughborough University, Loughborough, Leicestershire, UK
V.M.Starov@lboro.ac.uk

Synonyms

Surface forces; Colloidal forces; DLVO theory

Definition

Pressure in thin liquid films (thickness usually less than 10^{-7} m) is different from the pressure in the bulk liquid. This difference is caused by the action of additional forces, which are referred to as surface or colloidal forces. This force over the area of the film is the disjoining pressure. The additional pressure can be either disjoining or conjoining. However, the term disjoining is used in the literature because of historical reasons.

Chemical and Physical Principles

For partial or complete wetting at non-equilibrium adsorption of vapor and flow from a droplet or a meniscus on the solid substrate occurs. As a result at equilibrium the solid surface is covered with a thin liquid layer of equilibrium thickness h_e. The presence of this layer changes the interfacial tension of the bare solid surface, γ_{sv}, to γ_{svh_e}, which is the surface tension of the solid substrate covered with a thin liquid layer of the equilibrium thickness h_e. Formation of this thin layer is caused by surface forces.

A sharp transition from the liquid droplet/meniscus to the liquid film is impossible (arrow in Fig. 1), otherwise the capillary pressure will be infinite. Hence, there is a smooth transition from the flat equilibrium liquid film on the solid surfaces to the spherical droplet, as shown in Fig. 1.

The presence of the transition zone shows that pure capillary forces cannot keep the liquid in this zone at equilibrium: to the right of the arrow in Fig. 1 the liquid profile is concave (hence, the capillary pressure under the liquid surface is higher than in the ambient air); to the left of the arrow in Fig. 1 the liquid profile is convex (hence, the capillary pressure under the liquid surface is lower than in the ambient air).

The surface phenomena are determined by the forces acting in thin liquid films or layers in the vicinity of the apparent three-phase contact line [1].

Surface forces are well known and are important in colloid science. They determine the stability and behaviour of colloidal suspensions and emulsions [2]. In the case of emulsions/suspensions their properties and behaviour (stability, instability, rheology, interactions, and so on) are governed by surface forces acting between colloidal particles or droplets [2]. The corresponding theory is widely referred to as DLVO theory [1] according to the names of four scientists who substantially contributed to the area: Derjaguin, Landau, Vervey and Overbeek.

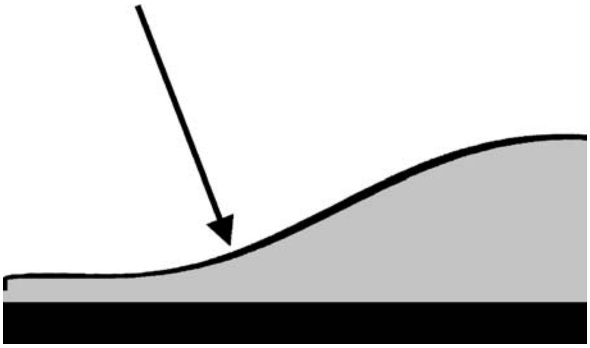

Disjoining Pressure, Figure 1 Transition zone from a flat equilibrium liquid film on a solid surface to a liquid droplet. The arrow shows the point where to the right the liquid profile is concave and to the left the profile is convex

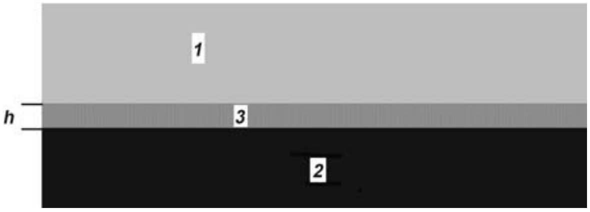

Disjoining Pressure, Figure 2 Interaction between two thick plates 1 and 2, possibly made of different materials, with a thin layer, 3, in between

The range of action of surface forces is usually of the order of 0.1 μm [1]. Note that in the vicinity of the three-phase contact line (Fig. 1), the liquid profile tends to zero thickness. The latter means that close to the three-phase contact line surface forces come into play and their influence cannot be ignored.

A manifestation of surface forces (either between particles, bubbles, emulsion droplets or in the vicinity of the three-phase contact line (Fig. 1)) is the disjoining pressure.

Let us consider the interaction of two thick plain parallel surfaces divided by a thin layer of liquid of thickness h (aqueous electrolyte solution, for example) in Fig. 2. The surfaces are not necessarily the same, as shown by two examples: (i) 1 is air, 3 is a liquid film, 2 is solid support; (ii) 1 and 2 are air or a liquid, 3 is a liquid film (of a different liquid). Example (i) is as a liquid film on a solid support and models a liquid layer in the vicinity of the

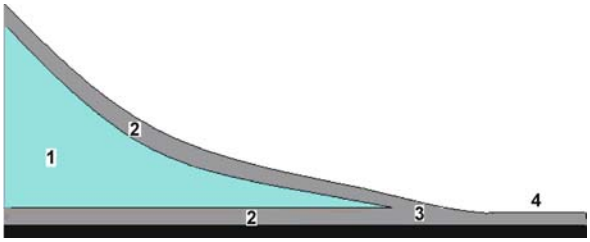

Disjoining Pressure, Figure 3 The liquid profile in the vicinity of the apparent three-phase contact line. 1, Bulk liquid, where boundary layers do not overlap; 2, boundary layer in the vicinity of liquid–air and liquid–solid interfaces; 3, a region where boundary layers overlap; 4, flat thin equilibrium film. The latter two are the regions where disjoining pressure acts

three-phase contact line; (ii) is a free liquid film and models the film between emulsion droplets/bubbles. There is a range of experimental methods to measure the interaction forces between these two surfaces as a function of the thickness h [1, 3, 4].

If h is bigger than 0.1 μm (Fig. 2), then the interaction force is equal to zero. However, if $h < 0.1$ μm, then an interaction force appears. This force can depend on the thickness h in a particular way. The interaction forces divided by the surface area of the plate has a dimension of pressure and is referred to as the disjoining pressure [1]. Note that the term *disjoining pressure* is misleading, because the force can be either disjoining (repulsion between surfaces) or conjoining (attraction between surfaces). However, disjoining is used because of historical reasons.

Let us consider a liquid–air interface as an example (Fig. 3). It is obvious that the physical properties of the very first layer on the interface are substantially different from the properties of the liquid in the bulk far from the interface. It is understandable that the physical properties do not change in an abrupt manner from the very first layer on the interface to the subsequent layers but the change proceeds in a continuous way. The latter results in the formation of a special layer, which we refer to as a boundary layer, where all properties differ from corresponding bulk properties.

Such boundary layers exist in proximity to any interface: solid–liquid, liquid–liquid, liquid–air. In the vicinity of the apparent three-phase contact line (Fig. 3) those boundary layers overlap. The overlapping of boundary layers is the physical phenomenon which results in the existence of surface forces. Let the thickness of the boundary layers be δ. In the vicinity of the three-phase contact line the thickness of a droplet/meniscus, h, is small enough, that is, $h \sim \delta$, and, hence, boundary layers overlap (Fig. 3), which results in the creation of disjoining pressure. A similar situation occurs at a contact of two particles in a liquid (Fig. 4). The above mentioned characteristic scale of boundary layer thickness, $\delta \sim 10^{-5}$ cm, determines the characteristic thickness where the disjoining pressure acts.

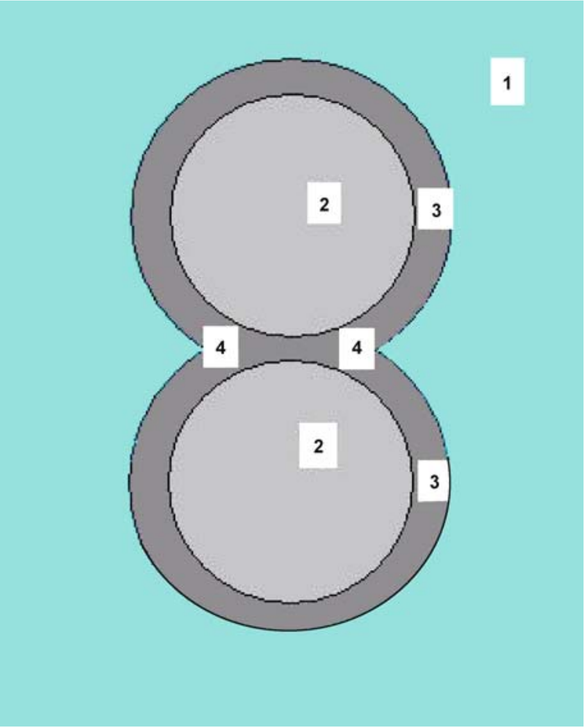

Disjoining Pressure, Figure 4 Colloidal interaction between two solid particles 2 in a liquid 1. 3, Boundary layers far from the contact; 4, overlapped boundary layers in the zone of contact, where the disjoining pressure acts

Components of the Disjoining Pressure

Molecular or Dispersion Component (van der Waals component)

Calculation of the molecular contribution to the disjoining pressure Π_m has been approached in two ways: from the approximation of interactions as pairwise additive, and from a field theory of many-body interactions in condensed matter. The simpler and historically earlier approach is a theory based on summing up of individual London–van der Waals interactions between molecules pair-by-pair undertaken by Hamaker [1].

The modern theory of Π_m was developed [1] based on a fluctuating electromagnetic field. The molecular component of the disjoining pressure, Π_m, for a film of uniform thickness h between two semi-infinite phases (1 and 2) in

vacuum (for simplicity) is [1] given by

$$\Pi_{\mathrm{m}} = \frac{kT}{\pi c^3} \sum_{N=0}^{\infty} \int_1^{\infty} p^2 \xi_N^3 \left\{ \left[\frac{(s_1+p)(s_2+p)}{(s_1-p)(s_2-p)} \exp\left(\frac{2p\xi_N h}{c}\right) - 1 \right]^{-1} + \left[\frac{(s_1+p\varepsilon_1)(s_2+p\varepsilon_2)}{(s_3-p\varepsilon_3)(s_2-p\varepsilon_2)} \exp\left(\frac{2p\xi_N h}{c}\right) - 1 \right]^{-1} \right\} \mathrm{d}p\,, \tag{1}$$

where c is the speed of light, $s_1 \equiv (\varepsilon_1 - 1 + p^2)^{1/2}$, $s_2 \equiv (\varepsilon_2 - 1 + p^2)^{1/2}$, subscripts 1 and 2 mark corresponding semi infinite phases, p is a dummy variable, $\xi_N = 2\pi kTN/\hbar$, $\hbar$ is the Plank constant, and the dielectric constants ε_1, ε_2 are functions of imaginary frequency $\omega \equiv \mathrm{i}\xi$ given by

$$\varepsilon(\mathrm{i}\xi) = 1 + \frac{2}{\pi} \int_0^{\infty} \frac{\omega \varepsilon''(\omega)}{\omega^2 + \xi^2} \mathrm{d}\omega\,, \tag{2}$$

where $\varepsilon''(\omega)$ is the imaginary component of the dielectric constant. In the limiting case of film thickness h small in comparison with the characteristic wavelength λ of the adsorption spectra of the bodies, the molecular component of disjoining pressure is inversely proportional to the cube of film thickness [1]:

$$\Pi_{\mathrm{m}} = \frac{\hbar}{8\pi^2 h^3} \int_0^{\infty} \frac{[\varepsilon_1(\mathrm{i}\xi) - 1][\varepsilon_2(\mathrm{i}\xi) - 1]}{[\varepsilon_1(\mathrm{i}\xi) + 1][\varepsilon_2(\mathrm{i}\xi) + 1]} \mathrm{d}\xi = \frac{A_{\mathrm{H}}}{h^3}\,, \tag{3}$$

where A_{H} is the Hamaker constant. Note that for historical reasons, instead of A in Eq. (3) $\Pi_{\mathrm{m}} = A/6\pi h^3$ is frequently used and the value A is also referred to as the Hamaker constant, i. e. $A_{\mathrm{H}} = A/6\pi$. In the limiting case of h large in comparison to λ, the disjoining pressure turns out to be inversely proportional to the fourth power of film thickness [1]:

$$\Pi_{\mathrm{m}} = \frac{\hbar c}{32\pi^2 h^4} \int_0^{\infty} \int_1^{\infty} \frac{x^3}{p^2} \left\{ \left[\frac{(s_{10}+p)(s_{20}+p)}{(s_{10}-p)(s_{20}-p)} e^x - 1 \right]^{-1} + \left[\frac{(s_{10}+p\varepsilon_{10})(s_{20}+p\varepsilon_{20})}{(s_{10}-p\varepsilon_{10})(s_{20}-p\varepsilon_{20})} e^x - 1 \right]^{-1} \right\} \mathrm{d}p\,\mathrm{d}x = \frac{B}{h^4} \tag{4}$$

where $s_{10} \equiv (\varepsilon_{10} - 1 + p^2)^{1/2}$, $s_{20} \equiv (\varepsilon_{20} - 1 + p^2)^{1/2}$ and ε_{10}, ε_{20} are the electrostatic values of the dielectric constants, i. e. the values of the dielectric constant at $\xi = 0$, $x = 2p\xi h/c$.

There are corresponding expressions for the molecular component of the disjoining pressure of films of non-polar liquids. Those expressions are presented in [1]. The functional dependency

$$\Pi_{\mathrm{m}}(h) = \begin{cases} \dfrac{A_{\mathrm{H}}}{h^3}\,, & h < \lambda \\ \dfrac{B}{h^4}\,, & h > \lambda \end{cases} \tag{5}$$

is approximately valid and frequently used.

A technique for calculating these properties to an adequate approximation from dielectric data has been suggested [1]. Precise measurements of Π_{m} in thin films of non-polar liquids are in good agreement with the theoretical predictions [1]. However, the latter theory does not apply to films so thin as to have dielectric properties that vary with thickness.

The Hamaker constant can be either positive (repulsion) or negative (attraction). Note that the precise value of the Hamaker constant according to direct summation can be wrong. This is a reason why a number of approximations have been developed to calculate the Hamaker constant using the exact theory [1].

The characteristic value of the Hamaker constant is $A_{\mathrm{H}} \sim 10^{-21}$ J (oil films on glass, quartz or mica surfaces).

Electrostatic Component of the Disjoining Pressure

Let us consider two charged surfaces (not necessarily of the same nature) in an aqueous electrolyte solution (Figs. 5a and b). The surfaces are assumed to be similarly or oppositely charged, i. e. there are electrical double layers near each of them. The sign of the charge of the diffusive part of each of electrical double layer is opposite to the sign of the charge of the corresponding surface. If the width of clearance between surfaces is $h \gg R_{\mathrm{d}}$, the electrical double layers of the surfaces do not overlap (Fig. 5a) and there is no electrostatic interaction of the surfaces. However, if the thickness of the clearance h is comparable with the thickness of the electrical double layer R_{d}, then electrical double layers overlap resulting in an interaction between the surfaces. If the surfaces are equally charged their diffusive layers are equally charged as well, i. e. the repulsion appears as a results of their overlapping (the electrostatic component of the disjoining pressure is positive in this case).

If surfaces are oppositely charged, then as a result of the overlapping of opposite charges an attraction appears, and the electrostatic component of the disjoining pressure is negative in this case.

There are a number of approximate expressions for the electrostatic component of the disjoining pressure [1]. For example, in the case of low potentials ζ of both surfaces the following relation is valid [1]:

$$\Pi_e(h) = \frac{\varepsilon\kappa^2}{8\pi}\,\frac{2\zeta_1\zeta_2\cosh\kappa h - \left(\zeta_1^2+\zeta_2^2\right)}{\sinh^2\kappa h}\,, \tag{6}$$

where ε is the dielectric constant of water and $1/\kappa = R_d$. The potential ζ is considered as low if the corresponding dimensionless potential $F\zeta/RT < 1$.

Note that in the case of oppositely charged surfaces and at relatively small distances the following expression for the electrostatic component of the disjoining pressure is valid [1]:

$$\Pi_e(h) = -\frac{\varepsilon}{8\pi}\,\frac{(\varsigma_1-\varsigma_2)^2}{h^2}\,, \tag{7}$$

which is always attraction. It is necessary to be very careful with this expression because in this case the attraction changes to repulsion at distances smaller than some critical distance [1].

Equations (6) and (7) show that the disjoining pressure does not vanish even in the case when only one of the two surfaces is charged (for example, $\zeta_1 = 0$). The physical reason for this phenomenon is the deformation of the electrical double layer if the distance between the surfaces is smaller than the Debye radius.

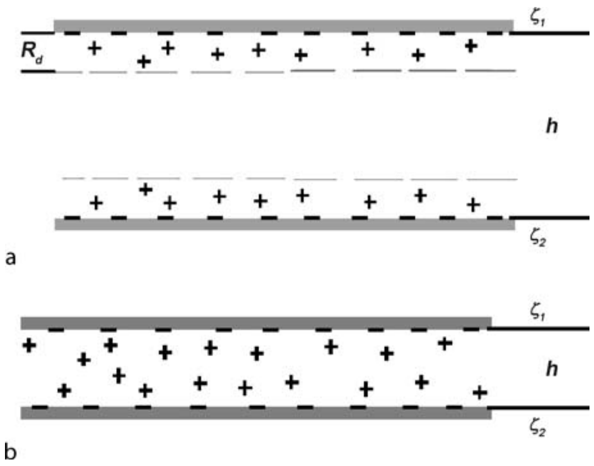

Disjoining Pressure, Figure 5 ζ_1 and ζ_2 are electrical potentials of charged surfaces. ζ_1 and ζ_2 are both negative. (**a**) The distance between two negatively charged surfaces, h, is bigger than the thickness of the Debye layers, R_d. Electrical double layers do not overlap and there is no electrostatic interaction between these surfaces. (**b**) The distance between two negatively charged surfaces, h, is smaller or comparable with the thickness of the electrical double layer, R_d. Electrical double layers of both surfaces overlap, which results in an interaction, which is repulsion in the case under consideration

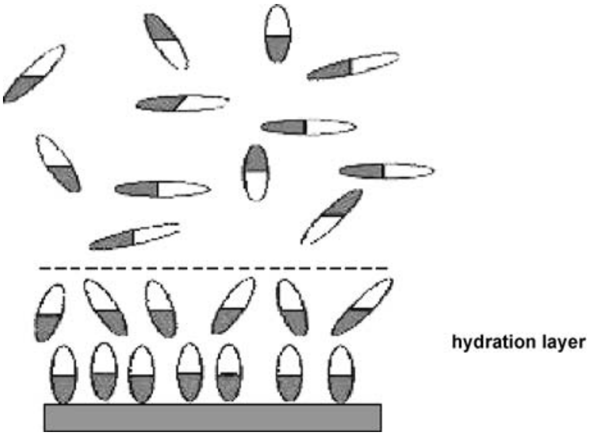

Disjoining Pressure, Figure 6 Formation of a hydration layer of water dipoles in the vicinity of a negatively charged interface. Darker parts of water dipoles are positively charged, lighter parts are negatively charged

The theory based on the calculation of the disjoining pressure involving the two components discussed above, i. e. dispersion $\Pi_m(h)$ and electrostatic $\Pi_e(h)$ components, is referred to as the DLVO theory. According to the DLVO theory the total disjoining pressure is the sum of the two components, i. e. $\Pi(h) = \Pi_m(h) + \Pi_e(h)$. The DLVO theory made possible an explanation of a range of experimental data on the stability of colloidal suspensions/emulsions [1, 2], as well as the static and the kinetics of wetting [5]. However, it has since been understood that these two components only are insufficient for explaining the phenomena in thin liquid films and layers as well as in colloidal dispersions.

Structural Component of the Disjoining Pressure

This component of the disjoining pressure is caused by orientation of water molecules in the vicinity of an aqueous solution–solid interface or aqueous solution–air interface. Water molecules can be modelled as an electric dipole.

In the vicinity of a negatively charged interface the positive part of water dipoles is attracted to the surface. That is, the negative part of dipoles are directed oppositely and the next water dipoles are facing a negatively charged part of dipoles, which in its turn results in the orientation of the next layer of dipoles, and so on.

The thermal fluctuations try to destroy this orientation (Fig. 6). As a result of these two opposite trends a finite layer forms where the structure of water dipoles differs

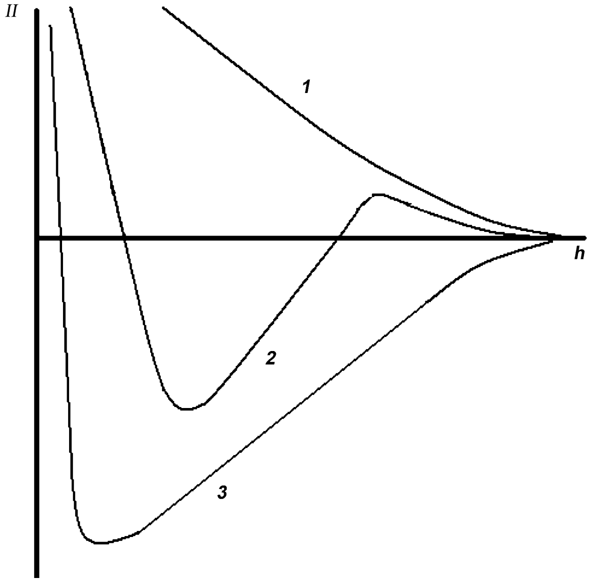

Disjoining Pressure, Figure 7 Types of isotherms of disjoining pressure: 1, complete wetting, observed for oil films on quartz, glass, metal surfaces [1]; 2, partial wetting, observed for aqueous films on quartz, glass, metal surfaces [1]; 3, non-wetting case

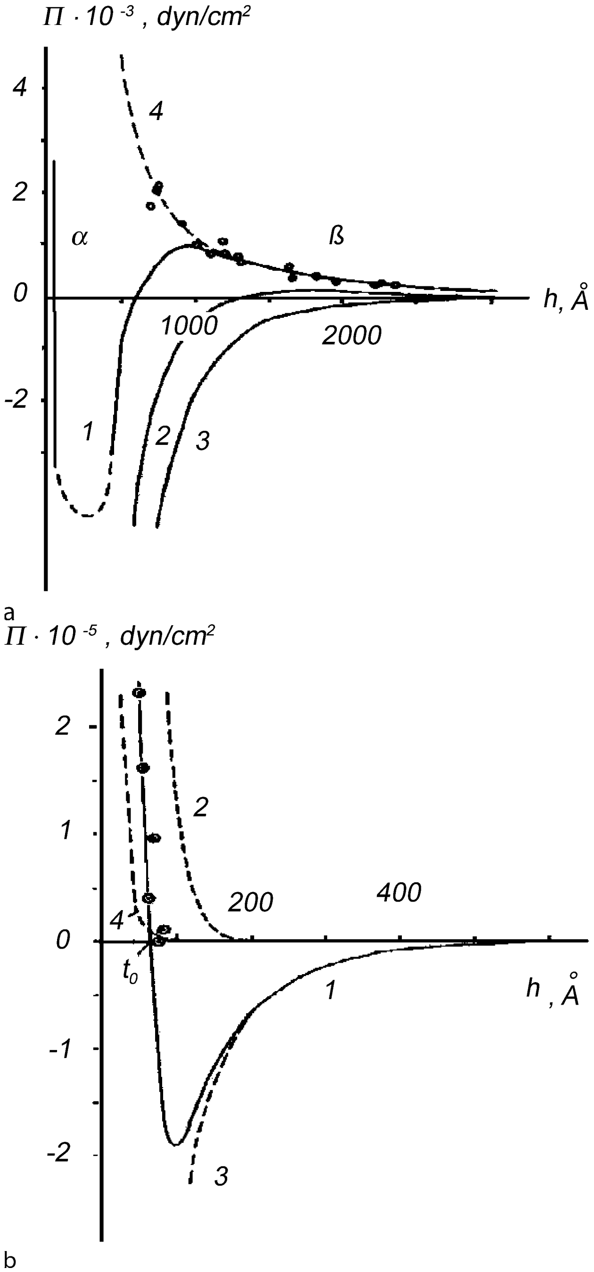

Disjoining Pressure, Figure 8 Calculated and experimentally measured isotherms of disjoining pressure, $\Pi(h)$, of films of water on a quartz surface at KCl concentration of $C = 10^{-5}$ mol/l, $pH = 7$, and dimensionless potential ζ of the quartz surface equal to -6 [1]. (**a**) Within the region of large thicknesses: dimensionless potential ζ of the film–air interface equals -2.2 (curve 1), -1 (curve 2) and 0 (curve 3); (**b**) within the region of small thicknesses: dimensionless potential ζ of the film–air interface equals -2.2 (curve 1). The structural component, $\Pi_S(h)$, of the disjoining pressure isotherm and electrostatic component, $\Pi_e(h)$, are shown by curves 2 and 3, respectively. Curves 4 in (**a**) and (**b**) are calculated according to Eq. (9)

from the random bulk structure. This layer is frequently referred to as a *hydration layer*. If now we have two interfaces with hydration layers close to each of them (or even one of them), then at a close separation, comparable with the thickness of the hydration layer, these surfaces "feel each other", that is, hydration layers overlap. This results either in attraction or repulsion of these two surfaces.

There is no firm theoretical background of the structural component of disjoining pressure and there is no reliable way to deduce theoretically in which case the structure formation results in an attraction and in which case in a repulsion. As a consequence only a semi-empirical equation exists, which gives the dependence of the structural component of disjoining pressure on the thickness of the liquid film [1]:

$$\Pi_S(h) = K e^{-\Lambda h} , \tag{8}$$

where K and Λ are constants. There is a clear physical meaning of the parameter $1/\Lambda$, which is the correlation length of water molecules in aqueous solutions. The latter gives $1/\Lambda \sim 10 - 15$ Å, which is the characteristic thickness of the hydration layer.

However, the pre-exponential factor K can be extracted on the current state of knowledge only from experimental measurements of the disjoining pressure.

Currently it is assumed [1] that the disjoining pressure of thin aqueous films is equal to the sum of the three components:

$$\Pi(h) = \Pi_m(h) + \Pi_e(h) + \Pi_s(h) \, . \quad (9)$$

In Fig. 7 a qualitative dependence of the disjoining pressure on the thickness of a flat liquid film is presented for the cases of complete wetting (curve 1, which corresponds to a dispersion or molecular component of disjoining pressure, $\Pi_m(h)$) and partial wetting (curve 2), which corresponds to a sum of all three components of the disjoining pressure, according to Eq. (9). The disjoining pressure shown by curve 1 in Fig. 7 corresponds to the case of complete wetting, for example, oil droplets on glass substrates, while curve 2 corresponds to the case of partial wetting, for example, aqueous electrolyte solutions on glass substrates. In [1–4] a number of experimental data on measurement of disjoining pressure are presented. The dependency of Eq. (5) has been firmly confirmed in the case of oil thin films on glass, quartz or metal surfaces, which corresponds to the case of complete wetting. In Fig. 8 experimental data and calculations according to Eq. (9) for aqueous thin films are presented.

All necessary details concerning experimental data presented in Fig. 8 are given in [1].

Examples of Application

The stability of colloidal suspensions, emulsions and foams as well as their transport properties are determined by the type of disjoining pressure, which acts between particles, droplets and bubbles. Equilibrium and kinetics of wetting is completely determined also by the shape of the disjoining pressure isotherm [5]. One of the most important applications is an expression of the equilibrium contact angles of either droplets on solid substrates or menisci in thin capillaries via the disjoining pressure isotherm [5]:

$$\cos\theta = 1 + \frac{1}{\gamma} \int_{h_e}^{\infty} \Pi(h) \, dh \, , \quad (10)$$

where the equilibrium thickness h_e is determined as a solution of the following equation [5]:

$$\Pi(h_e) = P \, . \quad (11)$$

Note that the excess pressure P is positive in the case of menisci and negative in the case of droplets and is determined by the vapor pressure in the ambient air. Note, according to Eq. (11) equilibrium film thicknesses differ for drops and menisci of identical liquids in contact with identical solids and so do the equilibrium contact angles according to Eq. (10).

Cross References

► Electrical Double Layer Interaction
► Electrical Double Layers
► Streaming Current and Electro-Viscosity
► Van der Waals Interaction Forces
► Wetting and Spreading

References

1. Deryaguin BV, Churaev NV, Muller VM (1987) Surface forces. Consultants Bureau, Plenum Press, New York
2. Russel WB, Saville DA, Schowalter WR (1999) Colloidal Dispersions. Cambridge University Press, Cambridge
3. Exerowa D, Kruglyakov P (1998) Foam and foam films: theory, experiment, application. Elsevier, New York
4. Israelashvili JN (1991) Intermolecular and surface forces. Academic, London
5. Starov V, Velarde M, Radke C (2007) Wetting and Spreading Dynamics. In: Surfactant Science Series, vol 138. Taylor and Francis, p 515

Dispensing

► Droplet Dispensing

Dispersed Magnetic Nanoparticles

► Ferrofluids in Microchannels

Dissipative Particle Dynamics

JOHN ABRAHAM
Department of Mechanical Engineering, Purdue University, West Lafayette, IN, USA
jabraham@ecn.purdue.edu

Synonyms

Mesoscopic method; Fluid particle model; Coarse-grained particle methods

Definition

Dissipative particle dynamics refers to a particle-based numerical method in which the dynamics of particles that interact through conservative, dissipative, and random forces are computed. The method is coarse-grained molecular dynamics, and has the ability to capture flow at mesoscopic scales, i. e. those scales that lie between microscopic and macroscopic ones.

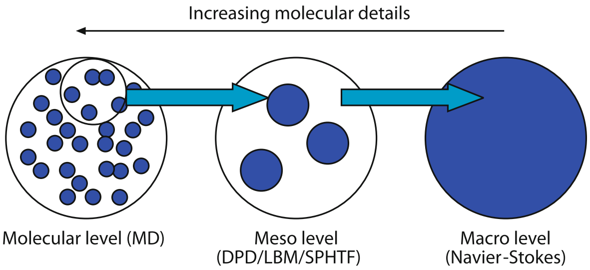

Dissipative Particle Dynamics, Figure 1 A schematic showing coarse-graining from molecular to macro level

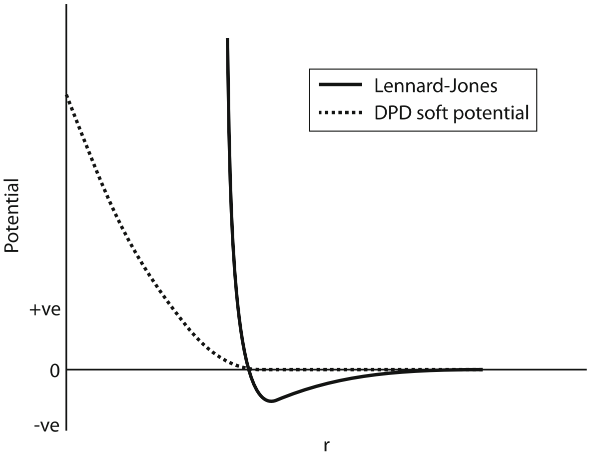

Dissipative Particle Dynamics, Figure 2 A schematic illustrating the hard-core nature of Lennard–Jones potential and the soft-core nature of DPD inter-particle potential

Overview

Dissipative particle dynamics (DPD) is a mesoscopic numerical method in which Newton's laws of motion are solved for interacting particles. The method may be conceptually visualized as coarse-grained molecular dynamics (MD), i. e. each DPD particle is a collection of many real molecules or atoms. This may be conceptually visualized as illustrated in Fig. 1. Coarse graining changes the force potential between atoms/molecules from one with a hard-core nature, like a Lennard–Jones (L–J) potential, to a soft-core one as illustrated in Fig. 2. This coarse-graining makes it possible to employ longer time steps in the numerical integration, but it also results in loss of some information accessible at the molecular level. Hence, models have to be introduced to compensate for the missing physics. This is achieved through addition of force terms to the conservative force $\boldsymbol{F}^{\mathrm{C}}$. A dissipative force $\boldsymbol{F}^{\mathrm{D}}$ is introduced to account for viscous effects. The randomness which exists at the molecular level, and manifests as Brownian motion, is modeled through a random force $\boldsymbol{F}^{\mathrm{R}}$. The $\boldsymbol{F}^{\mathrm{D}}$ and $\boldsymbol{F}^{\mathrm{R}}$ can be selected to maintain an isothermal system.

DPD belongs to the general class of mesoscopic numerical methods which includes lattice-gas automata (LGA), lattice-Boltzmann methods (LBM), smooth particle hydrodynamics with thermal fluctuations (SPHTF), Brownian dynamics, direct-simulation Monte Carlo (DSMC) methods, and stochastic rotation dynamics (SRD). In LGA, particles are constrained to move along the links of a lattice with prescribed velocities and respect specified collision rules. The collective properties of density and momentum at a given time and location are obtained by integrating the information carried by the particles over all particles at that time and location. In LBM, instead of solving the motion of particles, an equation for the transport of the single-particle distribution function of velocity is solved. This reduces the oscillations resulting from the Boolean nature of the LG calculations. In general, LG and LB methods have difficulties preserving Galilean invariance and isotropy. The lattice structure has to be appropriately selected to minimize this effect. DPD, on the other hand, preserves these properties. The DSMC method, a particle-based method for solving the Boltzmann equation, has been widely employed for the simulation of rarefied gas dynamics problems. The SRD method has features common to the DSMC method, but the treatment of the collision of particles differ. In many ways, DPD has the characteristics of the smooth-particle-hydrodynamics particle (SPH) method employed for fluid-flow simulations, and may be viewed as SPH with thermal fluctuations (SPHTF). Since the seminal work of Hoogerbrugge and Koelman [1, 2], there have been several contributions to clarify and strengthen the theoretical underpinnings of DPD. Espanol and Warren [3] showed that the DPD method is associated with a Fokker–Planck equation, and when the fluctuation-dissipation theorem is applied to derive an expression relating terms in the dissipative and random force components, the temperature of the system is related to the noise amplitude in the limit of vanishingly small numerical time steps in the updating algorithm. The system relaxes to the Gibbs–Boltzmann distribution under these conditions. The Langevin equation for Brownian motion is applicable to the system. Groot and Warren [4] further studied the model developed by Espanol and Warren and developed useful range of values for the parameters of the model from physical considerations. It has been shown that the equilibrium temperature of the system has a strong dependence on the integration time step, an important consideration if the method is employed to investigate equilibrium thermodynamic properties. An H-theorem for the free energy of the DPD system has

been proven, and the Fokker–Planck–Boltzmann equation for the single-particle distribution function derived and solved using Chapman–Enskog expansion to derive the hydrodynamic equations [5]. Extensions of the isothermal DPD model to include energy conservation have been presented [6, 7].

Basic Methodology

The governing equations of DPD are Newton's laws of motion given for particle i by

$$\frac{\mathrm{d}\boldsymbol{r}_i}{\mathrm{d}t} = \boldsymbol{v}_i\,, \tag{1}$$

$$\frac{\mathrm{d}\boldsymbol{v}_i}{\mathrm{d}t} = \boldsymbol{f}_i\,, \tag{2}$$

where $\boldsymbol{r}_i$, $\boldsymbol{v}_i$, and $\boldsymbol{f}_i$ are position, velocity, and force vectors, respectively. The force vector $\boldsymbol{f}_i$ is the sum of the internal, $\boldsymbol{f}_i^{\text{int}}$, and external, $\boldsymbol{f}_i^{\text{ext}}$, force components, i. e.

$$\boldsymbol{f}_i = \boldsymbol{f}_i^{\text{int}} + \boldsymbol{f}_i^{\text{ext}}\,, \tag{3}$$

where $\boldsymbol{f}_i^{\text{ext}}$ represents contributions from external sources, such as gravitational and electromagnetic forces, and

$$\boldsymbol{f}_i^{\text{int}} = \sum_{j \neq i} \left(\boldsymbol{F}_{ij}^{\text{C}} + \boldsymbol{F}_{ij}^{\text{D}} + \boldsymbol{F}_{ij}^{\text{R}} \right) \tag{4}$$

where $\boldsymbol{F}_{ij}^{\text{C}}$, $\boldsymbol{F}_{ij}^{\text{D}}$, $\boldsymbol{F}_{ij}^{\text{R}}$ are the conservative, dissipative, and random force components, respectively. While in principle all other particles interact with particle i, only interactions with those that are close to it, i. e. within a sphere of influence with a radius r_c, the cut-off radius, are important. This cut-off radius fixes the length scale of the system. The general form of $\boldsymbol{F}^{\text{C}}$ is given by

$$\boldsymbol{F}^{\text{C}} = -\frac{\partial \psi\left(\boldsymbol{r}_{ij}\right)}{\partial \boldsymbol{r}_{ij}} \boldsymbol{e}_{ij} \tag{5}$$

where ψ is the inter-particle interaction potential, and $\boldsymbol{e}_{ij} = \boldsymbol{r}_{ij}/\left|\boldsymbol{r}_{ij}\right|$. The form of conservative force which has been chosen by many researchers for single-phase and binary-fluid simulations is a linear function of the interparticle separation. This form of $\boldsymbol{F}_{ij}^{\text{C}}$ is given by

$$\boldsymbol{F}_{ij}^{\text{C}} = a_{ij} w^{\text{C}}\left(\boldsymbol{r}_{ij}\right) \boldsymbol{e}_{ij}\,, \tag{6}$$

where a_{ij} is a repulsion parameter between particles i and j. It is the maximum value of the conservative force and is related to the compressibility of the fluid [4]. The variable w^{C} is a weight function that has a form which reproduces the thermodynamic state of the system. It is usually taken to have the form

$$w^{\text{C}}(r) = \begin{cases} \left(1 - \dfrac{\boldsymbol{r}_{ij}}{r_c}\right) & \boldsymbol{r}_{ij} < r_c \\ 0 & \boldsymbol{r}_{ij} \geq r_c \end{cases} \tag{7}$$

In Eqs. (5–6), $\boldsymbol{r}_{ij} = \boldsymbol{r}_i - \boldsymbol{r}_j$, $\boldsymbol{r}_{ij} = \left|\boldsymbol{r}_{ij}\right|$. The dissipative force is given by

$$\boldsymbol{F}_{ij}^{\text{D}} = -\gamma w^{\text{D}}\left(\boldsymbol{r}_{ij}\right)\left(\boldsymbol{e}_{ij} \cdot \boldsymbol{v}_{ij}\right) \boldsymbol{r}_{ij}\,, \tag{8}$$

with the negative sign indicating that the particles are decelerated, and the random force is given by

$$\boldsymbol{F}_{ij}^{\text{R}} = \sigma w^{\text{R}}\left(\boldsymbol{r}_{ij}\right) \theta_{ij} \boldsymbol{e}_{ij}\,, \tag{9}$$

where w^{D} and w^{R} are weight functions which are dependent on the distance between particles and vanish for $|\boldsymbol{r}_{ij}| > r_c$, γ and σ are constant coefficients, $v_{ij} = v_i - v_j$, and θ_{ij} is a randomly fluctuating variable with Gaussian statistics, i. e. $\langle \theta_{ij}(t) \rangle = 0$ and $\langle \theta_{ij}(t)\theta_{k\ell}(t') \rangle = (\delta_{ik}\delta_{j\ell} + \delta_{i\ell}\delta_{jk})\delta(t - t')$. The random variable is independently selected for each pair of particles. The dissipative force reduces the system temperature by reducing the particle velocities, whereas the random forces increases the temperature. The two forces can be selected so that an isothermal system is described. In this case, it can be shown by employing the fluctuation dissipation theorem that the relation

$$w^{\text{D}}(r) = \left[w^{\text{R}}(r)\right]^2\,, \tag{10}$$

between the weight functions, and

$$\sigma^2 = 2\gamma k_B T\,, \tag{11}$$

between the coefficients, holds. Groot and Warren, and others, have suggested

$$w^{\text{D}}(r) = \left[w^{\text{R}}(r)\right]^2 = \begin{cases} \left(1 - \dfrac{r_{ij}}{r_c}\right)^2 & \boldsymbol{r}_{ij} < r_c \\ 0 & \boldsymbol{r}_{ij} \geq r_c \end{cases} \tag{12}$$

for the weight functions. Since the dissipative and random forces act to balance the temperature, DPD can be viewed as thermostated molecular dynamics if the appropriate potential is selected for the fluid.

DPD has been extended to two-phase flows [8–11]. The essential ideas employed to do this will now be briefly described. The general form of the conservative force that

gives rise to phase segregation and surface tension may be written as

$$\boldsymbol{F}_{ij}^{\mathrm{C}} = -\nabla\psi_{\text{non-ideal}} + \boldsymbol{F}_s\,, \tag{13}$$

$$\boldsymbol{F}_s = \kappa\nabla\nabla^2\rho\,, \tag{14}$$

where $\psi_{\text{non-ideal}}$ is the non-ideal part of the interaction potential and $\boldsymbol{F}_s$ is responsible for the surface tension effects in the two-phase system. The variable κ is a parameter that is dependent on the long-range attractive forces leading to surface tension. The first term in Eq. (13) can be derived once an equation of state (EOS) is selected. The EOS selected must be one which has a Maxwell loop. The determination of the non-ideal part of the free energy is dependent on the density of particles. The density in the vicinity of a particle i is calculated as the weighted average of contributions from its neighbors within the cut-off radius, i. e.

$$\rho_i = \sum_{j=1}^{N} w(r_{ij})\,,$$

where N is the number of particles and w is a weight function. The weight function has to be appropriately selected to have the desired properties. For example, Tiwari and Abraham [11] selected the Lucy weight function commonly used in smooth particle hydrodynamics. This weight function is given by

$$w(r, r_c) = \begin{cases} \dfrac{5}{\pi r_c^2}\left(1+\dfrac{3r}{r_c}\right)\left(1-\dfrac{r}{r_c}\right)^3 & r < r_c \\ 0 & r \geq r_c \end{cases}\,. \tag{15}$$

As an example, if the van der Waals EOS

$$p = \frac{\rho k_B T}{1-b\rho} - a\rho^2\,, \tag{16}$$

is adopted, then the non-ideal part of the free energy can be shown to be

$$\psi_{\text{non-ideal}} = -k_B T\ln(1-b\rho) - a\rho\,, \tag{17}$$

by employing the relation

$$\psi = -\frac{\partial p}{\partial v}\,, \tag{18}$$

$$\boldsymbol{F}^{\mathrm{C}} = -\nabla\psi_{\text{non-ideal}}\,, \tag{19}$$

where v is the specific volume.

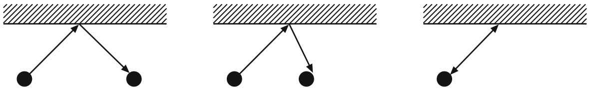

Dissipative Particle Dynamics, Figure 3 Three rules for reintroducing the DPD particle that penetrate the boundary

With substitutions, the overall expression, Eq. (13), for the inter-particle conservative force becomes [11]

$$\boldsymbol{F}_{ij}^{C} = \left[-\left\{\left(\frac{bk_BT}{1-b\rho_i}-a\right)+\left(\frac{bk_BT}{1-b\rho_j}-a\right)\right\} \times\frac{w'_{ij}}{[w]} + \kappa\frac{\partial^3 w(r_{ij})}{\partial r_{ij}^3}\right]\boldsymbol{e}_{ij}\,. \tag{20}$$

The approach to two-phase modeling described above is based on mean-field theory, and it breaks down in the vicinity of the critical point.

Boundary Conditions

Periodic boundary conditions may be implemented in DPD just as in MD. There are different approaches taken to implement wall boundary conditions in the solution of the DPD equations. Some of these will now be discussed. Two common methods are adopted to implement no-slip boundary conditions. In the first one, a layer of frozen particles is placed at the boundary and interaction of fluid particles with this layer obeys certain rules. In the second one, an extra layer of particles reflected from the DPD particles in the fluid are used for achieving no-slip.

In the frozen-layer scheme, a continuum limit is applied to the group of frozen layer particles to analytically obtain the effective form of the dissipative and random forces of interactions between the wall particles and the DPD fluid particle. An explicit rule is employed to maintain the impermeability of solid walls. Three possible rules for achieving this are illustrated in Fig. 3. For free-slip, specular reflection instead of bounce-back reflection for particles that cross the free-slip boundaries are employed.

In the extra-layer approach, all particles that lie within the cut-off radius r_c from the boundary are mapped into an extra layer that extends beyond the simulation domain. Figure 4 illustrates the concept. The velocities of the particles in the extra layer are chosen such that the mean of the velocity of the mirrored particle and the velocity of the original DPD particle gives the velocity at the wall. This algorithm has been reported to work well when used for calculating the dissipative force and the random force between the particles. But, if the conservative force

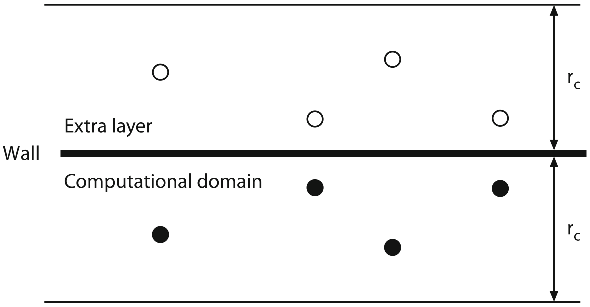

Dissipative Particle Dynamics, Figure 4 The extra-layer scheme

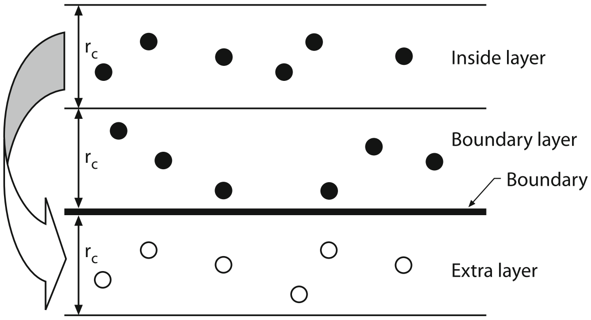

Dissipative Particle Dynamics, Figure 5 Extra layer scheme for conservative component

is calculated using this method, oscillations are observed in the density near the wall. This problem arises because of the lack of spatial correlation between the particles in the boundary layer and the mirror layer. To overcome this problem, an additional layer for calculating the conservative component alone can be employed, as illustrated in Fig. 5.

The density fluctuations arising near the boundary from the implementation of the conservative force at the wall is a cause of concern when implementing the no-slip boundary condition. To address this, a no-slip scheme based on the equivalent force between the wall and fluid particles may be introduced. In this method, layers of frozen particles are chosen as in the frozen-layer scheme, but a key difference is that the coefficient for the conservative force is adjusted in a manner so as to incorporate wall and fluid particle interactions. This leads to a correct no-slip implementation without fluctuations in density. Another proposal to reduce density fluctuations near the walls represents the boundary with two layers of frozen particles. The particles that penetrate the boundary are made to bounce back into the computational domain. No-slip at the wall is produced by using a twin image of the system being simulated. The second image has the same configurations and dynamics as the first, but operates with a different set of random numbers. Smooth particle and velocity distributions across the wall boundary are generated in this approach. Bounce-back reflection is used for particles that cross the system boundary. An extension of the approach for curved geometries has also been presented.

Numerical Integration

A suitable time-stepping algorithm may be employed to solve the governing equations. The pioneering work of Hoogerbrugge and Koelman [1] employed an Euler algorithm. However, this is first-order accurate in time and the cumulative effect of truncation errors can lead to a drift in the energy of the system. Since then, more robust schemes have been proposed. A popular integration scheme is the modified-Verlet scheme of Groot and Warren [4]. This scheme is given by

$$\begin{aligned}
\boldsymbol{r}_i(t+\delta t) &= \boldsymbol{r}_i(t) + \delta t \boldsymbol{v}_i(t) + \frac{1}{2}(\delta t)^2 \boldsymbol{f}_i(t)\,,\\
\tilde{\boldsymbol{v}}_i(t+\delta t) &= \boldsymbol{v}_i(t) + \lambda \delta t \boldsymbol{f}_i(t)\,,\\
\boldsymbol{f}_i(t+\delta t) &= \boldsymbol{f}_i(r(t+\delta t), \tilde{\boldsymbol{v}}(t+\delta t))\,,\\
\boldsymbol{v}_i(t+\delta t) &= \boldsymbol{v}_i(t) + \frac{1}{2}\delta t(\boldsymbol{f}_i(t) + \boldsymbol{f}_i(t+\delta t))\,,
\end{aligned} \tag{21}$$

where all symbols have the meaning as in the previous equations and λ is a variable parameter. A choice of $\lambda = 0.5$ would give the standard velocity-Verlet algorithm. In the above algorithm, the intermediate velocity $\tilde{\boldsymbol{v}}$ is chosen to give an estimate of velocities required in the calculation of forces. These velocities are finally corrected in the last step of the algorithm. Properties such as the system temperature are calculated after the last step. Vattulainen et al [12] have carried out a study in which they critically examined different integration schemes and concluded that the best schemes are those in which the velocity-dependence of the dissipative force is taken into account during the integration.

Parallelization Methods

A DPD simulation may involve as few as 1000 particles for simple equilibrium simulations to several million particles for simulations of complex fluids. Hence, it is important to run DPD codes in a parallel environment. There are several parallelization strategies, such as domain decomposition and force decomposition methods. One method that is appealing because of the particle-based nature of the method is the atom decomposition algorithm in which the computations for the N particles are split among P processors. Further advantage can be taken from the fact that DPD is a short-range method, i. e. each particle does

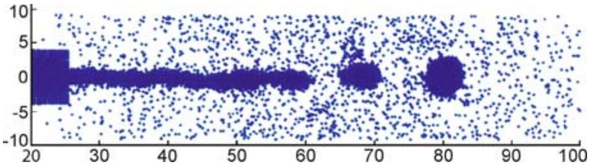

Dissipative Particle Dynamics, Figure 6 Simulations of nanojet breakup

not interact with all particles in the domain. This fact is exploited by creating neighbor lists for each particle. The neighbor lists are refreshed at specified intervals. Examples of neighbor lists include the Verlet neighbor list and the cell-based neighbor list.

Examples of Applications

Many applications of the DPD method exist in the literature. The following is not an exhaustive list. The DPD method is attractive for simulating systems where there is the motion of a chain of molecules, as in polymer solutions. The chain can be treated as a string of DPD particles interacting through force potentials. Obviously, not all the detail can be predicted with this approach. In many problems, however, information on picosecond time scales and Angstrom length scales may not be required to justify the use of full molecular simulations. Koelman and Hoogerbrugge [3] employed the method they developed to simulate hard-sphere suspensions subjected to a shear flow. DPD has been applied to study the flow of DNA molecules through microfluidic devices [13], simulate polymer solutions and colloidal suspensions [14], DNA chains in dilute suspensions [15], multiphase systems [8–11] including the simulation of pendant drops and drops in shear field [16], and liquid nanodrops, nanocylinders, and nanojets [17], biological membranes including cell damage [18], and domain growth and phase separation in binary immiscible fluids [19]. Figure 6 shows an illustration of a liquid nanojet breakup [17]. DPD has been shown to be capable of reproducing the influence of thermal fluctuations. The method has been employed in combination with MD to study colloidal systems, whereby the colloid itself is simulated using MD but the solvent using DPD [20]. DPD also has the flexibility to be combined with other models to capture multiple scales and this is an area of research that needs to be exploited.

Future Directions for Research

Since the DPD method is fairly new, there are areas for research in theoretical formulations especially as applied to multiscale problems and energy conserving schemes, formulation of adaptable boundary condition to minimize density fluctuations, numerical integration schemes which improve accuracy and efficiency, and a wide range of applications as illustrated by the examples above.

Cross References

► Mesoscopic Methods

References

1. Hoogerbrugge PJ, Koelman JMVA (1992) Simulating microscopic hydrodynamic phenomena with dissipative particle dynamics. Europhys Lett 19:155–160
2. Koelman JMVA, Hoogerbrugge PJ (1993) Dynamic simulation of hard sphere suspensions under steady shear. Europhys Lett 21:363–368
3. Espanol P, Warren P (1995) Statistical mechanics of dissipative particle dynamics. Europhys Lett 30:191–196
4. Groot RD, Warren PB (1997) Dissipative particle dynamics: bridging the gap between atomistic and mesoscopic simulation. J Chem Phys 107:4423–4435
5. Marsh CA, Backx G, Ernst MH (1997) Fokker–Planck–Boltzmann equation for dissipative particle dynamics. Europhys Lett 38:411–415
6. Avalos JB, Mackie AD (1999) Dynamic and transport properties of dissipative particle dynamics with energy conservation. J Chem Phys 111(11):5267–5276
7. Espanol P (1997) Dissipative particle dynamics with energy conservation. Europhys Lett 40:631–636
8. Pagonabarraga I, Frenkel D (2001) Dissipative particle dynamics for interacting systems. J Chem Phys 115:5015–5026
9. Warren PB (2003) Vapor-liquid coexistence in many-body dissipative particle dynamics. Phys Rev E 68:066702
10. Liu M, Meakin P, Huang H (2006) Dissipative particle dynamics with attractive and repulsive particle-particle interactions. Phys Fluids 18:01701
11. Tiwari A, Abraham J (2006) Dissipative-particle-dynamics model for two-phase flows. Phys Rev E 74:056701
12. Vattulainen I, Karttunen M, Besold G, Polson JM (2002) Integration schemes for dissipative particle dynamics simulations: from softly interacting systems towards hybrid models. J Chem Phys 116:3967–3979
13. Fan X, Phan-Thien N, Yong NT, Wu X, Xu D (2003) Microchannel flow of a macromolecular suspension. Phys Fluids 15(1):11–21
14. Kong Y, Manke CW, Madden WG, Schlijper AG (1997) Effect of solvent quality on the conformation and relaxation of polymers via dissipative particle dynamics. J Chem Phys 107:592–602
15. Symenoidis V, Karniadakis GE, Caswell B (2005) Dissipative particle dynamics simulations of polymer chains: scaling laws and shearing response compared to DNA experiments. Phys Rev Lett 95:076001
16. Clark AT, Lal M, Ruddock JN, Warren PB (2000) Mesoscopic simulation of drops in gravitational and shear fields. Langmuir 16:6342–6350
17. Tiwari A (2006) Dissipative Particle Dynamics Model for Two-Phase Flows. Ph.D. Thesis, Purdue University, West Lafayette, IN
18. Groot RD, Rabone KL (2001) Mesoscopic simulation of cell membrane damage, morphology change and rupture by nonionic surfactants. Biophys J 81:725–736

19. Coveney PV, Novik KE (1996) Computer simulations of domain growth and phase separation in two-dimensional binary immiscible fluids using dissipative particle dynamics. Phys Rev E 54(5):5134–5141
20. Dzwinel W, Yuen DA, Boryczko K (2002) Mesoscopic dynamics of colloids simulated with dissipative particle dynamics and fluid particle model. J Molecular Model 8:33–43

Distributed Parameter Model

► Transmission-Line Model

DLVO Theory

► Disjoining Pressure

DNA Array

► Biochip
► Bioprinting on Chip
► Microarray

DNA Chip

► DNA Microarrays

DNA Extraction

► Lab-on-a-Chip Devices for Sample Extractions

DNA Fragmentation

► Microfluidics for Studies of Apoptosis

DNA Hybridization

Definition

Hybridization is the process where two complementary, single-stranded nucleic acids are combined into a single molecule. Nucleotides will bind to their complement, so two perfectly complementary strands will bind or hybridized to each other. The hybridization process may be reversed by heating the double stranded molecule of DNA to break the hydrogen bonds between the nucleotides and separate the two strands. This is called melting or denaturation.

Cross References

► Electroosmotic Flow (DC)
► AC Electro-Osmotic Flow
► DNA-Microarrays
► Pressure-Driven Flow
► Reactive Ion Etching (RIE)
► SNP on Chip – Micro- and Nanofluidics for Single Nucleotide Polymorphism Discrimination

DNA Ladders

► Microfluidics for Studies of Apoptosis

DNA Microarrays

Bao Nguyen, Samuel K. Kassegne
MEMS Research Laboratory
Department of Mechanical Engineering
College of Engineering, San Diego State University, San Diego, CA, USA
mntnguyen@ntu.edu.sg, kassegne@mail.sdsu.edu

Synonyms

DNA chip; Gene chip

Definition

Microarrays are plastic, glass or silicon chips often used for gene expression and DNA sequencing and contain an array of single-stranded DNA segments known as probes attached to their surface to which a complementary DNA or RNA specifically binds.

Overview

Microarrays are devices made using processes such as photolithography, ink-jet printing, etc. and consist of many single-stranded DNA probes attached to the surface to which a complementary DNA or RNA of interest specifically binds as shown in Fig. 1 [1–4]. This binding or hybridization is then detected through various means such as through fluorescence tagging of the probes or mass spectroscopy. Microarrays allow DNA and RNA hybridization analysis in a parallel fashion on miniaturized platforms. The number of test sites in microarrays

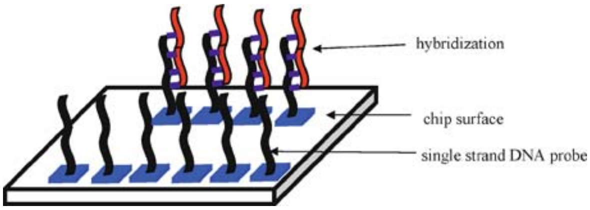

DNA Microarrays, Figure 1 DNA microarray with capture probes. The microarray is made using photolithography or ink-jet printing process and consist of many single-stranded DNA probes attached to the surface to which a complementary DNA or RNA of interest specifically binds

varies from a few hundred to several hundreds of thousands. Depending on the type of attached probes, DNA microarray could determine genetic sequence (DNA) or gene expression level (mRNA). Since the first application of microarrays was in DNA sequencing, microarrays are often called DNA microarrays. However, with the extension of the microarray technology to proteomics, cell and tissue biology, a distinction is necessary between DNA, cell, protein and tissue microarrays. Here DNA microarrays are discussed.

DNA microarrays work by exploiting the ability of a given mRNA sequence to bind specifically to, or hybridize to, its cDNA template from which it originated. By using an array containing many cDNA samples, it is possible to determine the expression levels of the numerous genes within a cell by measuring the amount of mRNA bound to each site on the array. With the aid of software, the amount of mRNA bound to the spots on the microarray could be determined, generating a profile of gene expression in the cell.

Basic Methodology

There are three major steps involved in DNA microarray analysis. The first is creating a single strand DNA with fluorescence tag from either genomic DNA or mRNA sequences. The fluorescently tagged sample is then hybridized against targeted probes that have been previously printed or micromachined on the DNA chip. An imaging system that usually consists of lasers or camera is then used to detect the level of fluorescence intensity emitted by the attached probes. The array reader is very similar to confocal microscopy technology.

DNA hybridization microarrays are generally fabricated on glass, silicon, or plastic substrates. Oligonucleotide DNA are the most common probes used in DNA microarrays. Amine or thiol linkers are added to these oligonucleotide probes to enable attachment to the glass, plastic or silicon surface of the chip. The attachment of these probes to the surface can be done mechanically through automated means. In a laboratory set-up, manual array spotters could be used.

Several methods exist for fabricating these microarrays. Photolithography techniques using masks have been used successfully such as in Affymetrix's (Santa Clara, CA) GeneChip® and Nanogen's (San Diego, CA) NanoChip®. Ink-jet printing technology where a precise amount of liquid is expelled onto the surface has also been used by companies like Agilent (Santa Clara, CA). Different printing techniques such as fine-pointed pins can also be used along with mechanical spotting where the sample is loaded to a pin by capillary action. As an overview, we will look at two prominent and technologically interesting technologies, namely that of GeneChip® by Affymetrix and NanoChip® by Nanogen.

The Affymetrix process consists of a light-directed synthesis of oligonucleotides on a substrate [5]. As shown in Fig. 2, the first step is exposing a surface to a UV light through a mask that contains the desired pattern. The surface consists of hydroxyls. In the illuminated regions, free hydroxyl groups are generated which then couple to a deoxynucleoside phosphoramidite which has the 5′-hydroxyl protected by a photolabile group. This is followed by capping and oxidation. The substrate is then rinsed and the surface subsequently exposed to UV light through a second mask to expose additional hydroxyl groups for coupling. Then, a second 5′-protected 3′-O-phosphoramidite-activated deoxynucleoside is brought to the surface. This process of selective photodeprotection and coupling cycles is repeated until the probes reach their desired full length, usually 25 nucleotides. As a rule, in this parallel process, $4n$-mers chemical synthesis steps (and hence a maximum of $4n$ photo masks) are required to synthesize a complete set of all probe sequences of length n-mers. For example, 20 process cycles are needed to synthesize 5-mer probes. The Affymetrix parallel fabrication process for microarrays is particularly suitable for making high-density microarrays. Commercially available arrays are typically manufactured at a density of over 1.3 million unique features per array. Densities as high as 10^6 unique sequences/cm^2, which correspond to feature sizes of less than 100 μm, have been reported [6]. The reported average stepwise efficiency of oligonucleaotide synthesis – which is affected by the average yield of the photochemical deprotection step after photolysis – is in the range of 90%–95% [7]. In terms of hybridization enabling process, the Affymetrix microarray depends on diffusion of target DNA to the array sites [8]. However, diffusion dependent transport scales with the square root of time and often takes several hours to achieve efficient hybridization of DNA molecules to capture probes. Further, this passive hybridization is known to exhibit some cross-hybridization

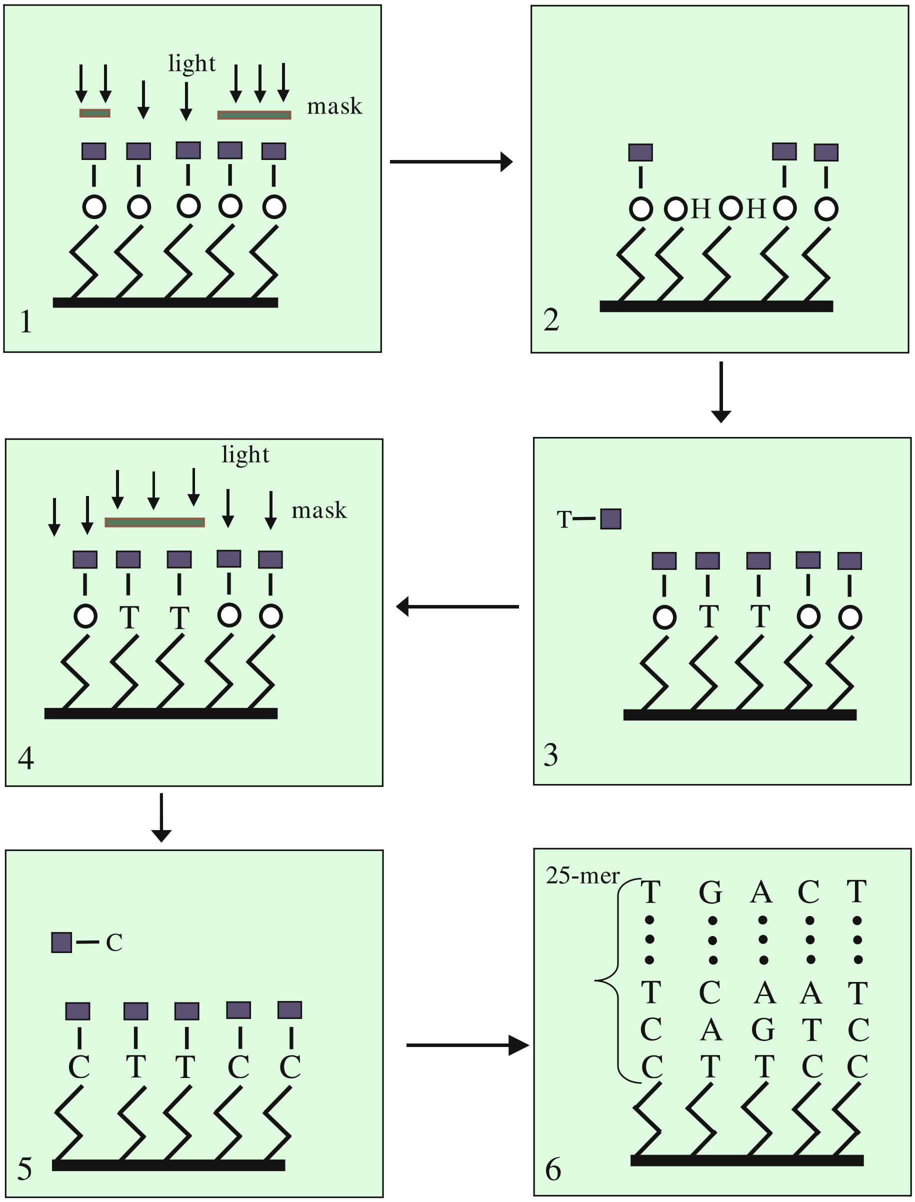

DNA Microarrays, Figure 2 Light-directed parallel chemical synthesis of peptides and oligonucleotides on solid supports of Affymetrix's DNA microarray [5, 6]. A photo-protected glass substrate is selectively exposed to UV light through a mask that contains the desired pattern (1). The deprotected areas are activated in step (2) followed by nucleoside incubation where chemical coupling occurs at activated positions (3). In step (4), a new mask pattern is applied. The coupling step is repeated in step (5). The deprotection and coupling process is repeated until the desired set of probes is obtained as shown in step (6)

between mismatched probes and targets [9]. Efforts are continuing to minimize this nonspecific binding [10].

The Nanogen electronic microarray consists of an array of electrodes fabricated on silicon using standard photolithography and deposition processes [11–13]. As shown in Fig. 3, the base structure of the array consists of silicon substrate over which an insulation layer of silicon dioxide is grown. A 20 nm Cr adhesion layer and 500 nm platinum are deposited and patterned to form electrodes and the electrical traces. The traces form electrical contact pads at their ends. Additional 2 μm of silicon dioxide and low-stress silicon nitride are deposited to provide electrical insulation for the platinum electrodes and traces. Finally, a 1–10 μm thick coating of hydrogel (agarose or polyacrylamide) is spin-coated over the chip surface to provide a permeation layer which allows the

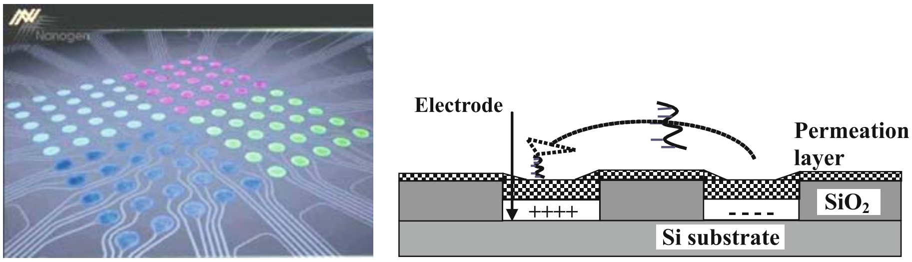

DNA Microarrays, Figure 3 Nanogen's DNA microarray with capture probes. 100-site electronically active NanoChip® is shown in **a** [14]. A cross-section of the chip is shown in **b**. An insulation layer of silicon dioxide is grown over a silicon substrate over which Cr adhesion layer and platinum are deposited and patterned to form electrodes. A coating of hydrogel is spin-coated over the chip surface to provide a permeation layer. Shown also is the electrophoretic transport of charged molecules (DNA, RNA, etc) on an active microelectronic array [12]

arrays to be run at current levels (> 100 nA) and voltages (> 1.2 V) by protecting the sensitive DNA hybridization reactions from adverse electrochemical effects at the electrodes. The permeation layer which contains linked streptavidin also acts as a matrix for the attachment of DNA capture probes and target DNA sequences. It further elevates the anchored probes above the electrodes [11, 12]. The chips are then flip-bonded to a ceramic substrate which is subsequently mounted in a plastic cartridge housing that contains a flow cell for liquid sample handling and an optical window for fluorescence measurements. The Nanogen technology uses electronically active DNA microarrays and involves electronically addressing biotinylated DNA samples, hybridizing complementary DNA reporter probes and applying stringency to remove unbound and nonspecifically-bound DNA after hybridization. An important feature of the recent generation of Nanogen's chip is the presence of on-board circuitry that permits the current or potential of each electrode to be individually controlled and measured. Electrophoresis, which has the advantage of speed which scales linearly with time and electric field, is used as a transport mechanism for the DNA samples. Consequently, typical transport times are two minutes or less [14]. The maximum number of array size reported so far in Nanogen's technology is 10,000 [1].

DNA Microarray Applications

The use of microarrays has expanded into several areas outside traditional genetic sequencing and gene profiling. The most important areas where microarrays are increasingly being used for are pharmacogenomics research, infectious and genetic disease and cancer diagnostics, and forensic and genetic identification applications [1]. Four important application areas are discussed here with some details.

Drug Discovery/Pharmacogenomics

Pharmacogenomics is the study of the genetic basis of the therapeutic responses of patients to drugs. Microarrays can be used in this area by predicting drug efficacy and toxicity through the monitoring of gene expressions in response to drug treatment. Microarrays enable querying expressions of thousands or tens of thousands of genes simultaneously. For example, gene expression changes in cells exposed to the anticancer chemotherapeutic agent doxorubicin has been studied using DNA microarrays [15].

Disease Diagnosis

Microarray technology finds application in disease diagnosis by providing information on the genetic basis to diseases. For such diseases as diabetes, heart diseases, cancer, and mental illnesses, research has shown that certain genetic sequences are associated with susceptibility to the expression of these diseases. Specifically, tiny variations in nucleotides (called SNPs for single nucleotide polymorphisms) which occur in about 0.1% of the sequence that comprises human DNA are responsible for the traits that distinguish one individual from another – including differences in disease susceptibility. Some of these SNPs are shared by large sections of the population, which make them highly attractive targets for disease research. Researchers have used microarrays to genotype hundreds of thousands of SNPs enabling whole-genome association studies of disease genetics [16, 17]. High-density microarrays for disease mapping studies have already enabled the identification of genes linked to sudden infant death syndrome, neonatal diabetes, bipolar disorder, age-related macular degeneration and other inherited diseases [18].

Gene Discovery

One of the interesting applications of microarrays is in the identification of new genes together with their func-

tions and expression levels under different conditions. For example, microarrays have been used to identify new genes that can contribute to vaccine initiatives or as targets for development of new drugs [19] and in protozoan parasites such as plasmodium falciparum, the causative agent of human malaria [20].

Toxicological Research

Microarrays can be used in toxicogenomics where a correlation between responses to toxicants and the changes in the genetic profiles of the cells exposed to such toxicants is studied. The measurements of gene expression levels upon exposure to a chemical can be used both to provide information about the mechanism of action of the toxicant and to form a sort of "genetic signature" for the identification of toxic products. A comprehensive review of the application of microarrays to compare the effects of chemicals such as arsenic and nickel in human bronchial cells as well as sodium arsenite on the expression of genes involved in transcription factors, inflammatory cytokines, kinases, and DNA repair, etc., is given in [21].

Major DNA Microarrays in the Market

An increasing number of companies have entered the DNA microarray market. Some of the most prominent players are: ACLARA Bio Sciences (Mountain View, CA) which specializes in microfluidics chips for biochemical processes, Affymetrix (Santa Clara, CA) which is the developer of the GeneChip™ microarray that is fabricated using lithographic techniques to directly synthesize targeted probes onto quartz wafer [5], Caliper Technologies (Mountain View, CA) the maker of LabChip, a microfluidics array used in high-speed DNA separation, Gamera Bioscience (Medford, MA) which is the maker of LabCD system, a centrifugal-based compact-disk (CD) platform, Genetix Ltd., a UK-based company specializing in microarrays with 16-pin microarraying head for spotting slides, Agilent (Santa Clara, CA) with its thermal jet probe-attachment system for cDNA microarrays, Illumina (San Diego, CA) a maker of self-assembled arrays of beads, Incyte Microarray Systems (Fremont, CA), a maker of gene expression microarrays, Nanogen (San Diego, CA) which develops electronically active microarray spots, Sequenom (San Diego, CA) which develops a high-throughput array used for genotyping, and Vysis Inc. (Downers Grove, IL) which markets GenoSensor used in genotyping.

The most commonly used application for microarray is gene expression analysis. Affymetrix is the leader in this market with its GeneChip®. As explained in detail before, Affymetrix utilizes lithographic techniques to directly synthesize targeted probes onto quartz wafer. Starting with a 5 inch quartz wafer, masks are used to initiate coupling of nucleotides. For 25 bases chip, a maximum of 100 masks are required. Agilent Technologies (Palo Alto, California USA), one of the other competitors, uses inkjet printing technology for probe attachment. Whole oligos or cDNA are first synthesized and printed onto a glass substrate. To increase hybridization efficiency, Nanogen (San Diego, California USA) developed an active hybridization method for sample analysis rather than using traditional passive hybridization as Agilent and Affymetrix [1].

Key Findings and Future Directions for Research

A significant amount of research and product development efforts are being carried out in three key areas in DNA microarrays, namely, (1.) preparing oligos and DNA probes, (2.) immobilization on attachment surface, and (3.) detection of hybridization on surfaces.

1. preparing oligos and DNA probes – One of the promising techniques is what is called "FAST slides" where a glass slide with a polymeric surface that binds DNA and proteins in a noncovalent but irreversible manner [22]. FAST slides have a much higher binding capacity for DNA. Automated liquid handling system for reagent-jet nanoliter dispensing [23] and ink-jet oligo synthesizers [24] are some of the methods being explored in new microarray techniques.
2. immobilization on attachment surface – Work on the use of polyacrylamide gel-immobilized microarrays for nucleic acids have been reported by Zlatanova and Mirzabekov [25]. The use of unmodified oligos to fabricate DNA microarrays where acid-washed slides are coated with epoxy-silane before probe deposition has also been reported [26].
3. detection of hybridization on surfaces – Improvement in fluorescent detections is a focus of many development efforts. Improvements in confocal scanning devices [27], high-resolution near-infrared imaging techniques [28], the use of surface plasmon resonance imaging for DNA and RNA hybridization adsorption with smaller hardware [29] are some of the efforts. Use of radioactive probes [30], the technique of primer elongation reaction [31] and direct electrical detection system through impedance or other electrical properties change is ongoing.

Cross References

- ► Protein Microarrays
- ► DNA Microarray
- ► Lab-on-a-Chip (General Philosophy)

References

1. Heller MJ (2002) DNA Microarray Technology: Devices, Systems, and Applications. Annu Rev Biomed Eng 4:129–153
2. Sobek J, Bartscherer K, Jacob A, Hoheisel JD, Angenendt P (2006) Microarray Technology as a Universal Tool for High-Throughput Analysis of Biological Systems. Comb Chem High Throughput Screen 9:365–380
3. Brewster JL, Beason KB, Eckdahl TT, Evans IM (2004) The Microarray Revolution. Biochem Mol Biol Educ 32:217–227
4. Ekins R, Chu FW (1999) Microarrays: Their origins and Applications. Trends Biotechnol 17:217–218
5. Pease AC, Solas D, Sullivan EJ, Cronin MT, Holmes CP, Fodor SPA (1994) Lightgenerated oligonucleotide arrays for rapid DNA sequence analysis. Proc Natl Acad Sci USA 91:5022–5026
6. Fodor SPA, Read JL, Pirrung MC, Stryer LT, Lu A, Solas D (1991) Light-directed, spatially addressable parallel chemical synthesis. Science 251:767–773
7. McGall GH, Barone D, Diggelmann M, Fodor SPA, Gentalen E, Ngo N (1997) The efficiency of light-directed synthesis of DNA arrays on glass substrates. J Am Chem Soc 119:5081–90
8. Chee M, Yang R, Hubbell E, Berno A, Huang X, Stern D, Winkler J, Lockhart D, Morris M, Fodor S (1996) Accessing genetic information with high-density DNA arrays. Science 274:610–614
9. Wu C, Carta R, Zhang L (2005) Sequence dependence of cross-hybridization on short oligo microarrays. Nucleic Acids Res 33:e84
10. Eklund AC, Turner LR, Chen P, Jensen RV, de Feo G, Kopf-Sill AR, Szallasi Z (2006) Replacing cRNA targets with cDNA reduces microarray cross-hybridization. Nature Biotechnol 24:1071–1073
11. Sosnowski R, Tu E, Butler WF, O'Connell JP, Heller MJ (1997) Rapid determination of single base mismatch mutations in DNA hybrids by direct electric field control. Proc Natl Acad Sci 94:1119–1123
12. Heller MJ, Forster AH, Tu E (2000) Active microelectronic chip devices which utilize controlled electrophoretic fields for multiplex DNA hybridization and other genomic applications. J Electrophor 21:157–164
13. Heller MJ, Tu E, Martinsons RR et al (2002) Active Microelectronic Array Systems for DNA Hybridization, genotyping, Pharmacogenomics and Nanofabrication Applications. In: Heller MJ, Guttmann A (eds) Integrated Microfabricated Beiodevices. Dekker, New York, pp 223–270
14. Kassegne SK, Reese H, Hodko D, Yang JM, Sarkar K, Smolko S, Swanson P, Raymond D, Heller MJ, Madou MJ (2003) Numerical Modeling of Transport and Accumulation of DNA on Electronically Active Biochips. J Sens Actuators B: Chem 94:81–98
15. Kudoh K, Ramanna M, Ravatn R, Elkahloun AG, Bittner ML, Meltzer PS et al (2000) Monitoring the expression profiles of doxorubicin-induced and doxorubicin-resistant cancer cells by cDNA microarray. Cancer Res 60:4161–4166
16. Kennedy GC et al (2003) Large-scale genotyping of complex DNA. Nat Biotechnol 21:1233–7
17. Matsuzaki H et al (2004) Parallel genotyping of over 10,000 SNPs using a one-primer assay on a high-density oligonucleotide array. Genome Res 14:414–25
18. Lipshutz R (2005) Using microarrays to detect disease and tailor therapy. Pharm Discov Dev 5:28–37
19. Duncan RC, Salotra P, Goyal N, Akopyants NS, Beverley SM, Nakhasi HL (2004) The Application of Gene Expression Microarray Technology to Kinetoplastid Research. Curr Mol Med 4:611–621
20. Hayward RE, Derisi JL, Alfahdi S, Kaslow DC, Brown PO, Rathod PK (2000) Shotgun DNA microarrays and stage-specific gene expression in Plasmodium falciparum malaria. Mol Microbiol 35(1):6–14
21. Lettieri T (2006) Recent Applications of DNA Microarray Technology to Toxicology and Ecotoxicology. Environ Health Persp 114(1):4–9
22. Stillman BA, Tonkinson JL (2000) FAST slides: a novel surface for microarrays. Biotech 29:630–635
23. Hicks JS, Harker BW, Beattie KL, Doktycz MJ (2001) Modification of an automated liquid-handling system for reagent-jet, nanoliter-level dispensing. Biotech 30(4):878–85
24. Hughes TR, Mao M, Jones AR, Burchard J, Marton MJ et al (2001) Expression profiling using microarrays fabricated by an ink-jet oligonucleotide synthesizer. Nat Biotechnol 19(4):342–47
25. Zlatanova J, Mirzabekov A (2000) Gel-Immobilized microarrays of nucleic acids and proteins: Production and application for macromolecular research. In: Rampal JB (ed) DNA Arrays. Method and Protocols. Humana Press, Totowa, NJ, pp 17–38
26. Call DR, Chandler D, Brockman F (2001) Fabrication of DNA microarrays using unmodified oligonucleotide probes. Biotech 30:368–379
27. Dixon AE, Damasinkos S (2001) Confocal scanning of genetic microarrays. Methods Mol Biol 170:237–46
28. Waddell E, Wang Y, Stryjewski W, McWhorter S, Henry AC, Evans D, McCarley RL, Soper SA (2000) High-resolution near-infrared imaging of DNA microarrays with time-resolved acquisition of fluorescence lifetimes. Anal Chem 72(24):5907–17
29. Nelson BP, Grimsrud TE, Lies MR, Goodman RM, Corn R (2001) Surface plasmon resonance imaging measurements of DNA and RNA hybridization adsorption on DNA microarrays. Anal Chem 73:1–7
30. Whitney LW, Becker KG (2001) Radioactive 33-P probes in hybridization to glass cDNA microarrays using neural tissues. J Neurosci Methods 10691:9–13
31. Erdogan F, Kirchner R, Mann W, Ropers HH, Nuber UA (2001) Detection of mitochondrial single nucleotide polymorphisms using a primer elongation reaction on oligonucleotide microarrays. Nucleic Acids Res 29(7):E36

Doppler OCT

► Optical Coherence Tomography and Optical Doppler Tomography

DPN

► Dip-Pen Nanolithography

DRIE (Deep Reactive Ion Etching)

► ICP Etching
► Plasma Etching

Drop

► Droplet Dispensing

Drop on Demand

► Droplet on Demand
► Transport of Droplets by Acoustics

Droplet

► Droplet Dispensing

Droplet Based Lab-on-Chip Devices

JAMES D. STERLING, ALI NADIM
Keck Graduate Institute, Claremont, CA, USA
jim_sterling@kgi.edu

Synonyms

Droplet microfluidics; Micro total analysis system (μTAS); μTAS; Bio-MicroElectroMechanical systems (BioMEMS); Micro fluorescently-activated cell sorting (μFACS)

Definition

Droplet based Lab-on-Chip devices represent a class of microfluidic systems that have been developed to miniaturize chemical, biochemical or cellular analysis. These devices utilize various droplet dispensing and manipulation mechanisms to isolate and control liquid-phase droplets of samples and/or reagents surrounded by a gas or an immiscible liquid. The droplets may be completely surrounded by the medium or may be placed onto a solid surface whose material properties are chosen to provide droplet confinement, chemical functionalization, or control of droplet motion. The devices also have some type of assay read-out method with associated hardware, software and data display.

Overview

Several reasons are routinely cited for developing Lab-on-a-Chip devices including reagent savings, use of smaller samples, ease of automation, and reduction of analysis time. Other reasons include the potential for reduction in the size of instrumentation, compatibility with laboratory automation equipment, the ability to provide portable instruments, and the ability to provide point-of-care clinical diagnostics.

The choice of using droplets is a natural progression associated with miniaturization of traditional laboratory methods of manipulating distinct chemical or biochemical reagents and samples to be analyzed. The traditional methods include the use of pipettes, glass beakers, tubes, pneumatic and piezoelectric automated dispensers, as well as standard (as defined by Society for Biomolecular Screening (SBS)) wells and plates. As the size of a liquid sample is reduced, the effect of surface tension increasingly dominates other physical effects and free surfaces tend to take on highly curved shapes. Thus, surface tension acts to confine the liquid in the form of discrete droplets that can be contained and manipulated without requiring the same degree of confinement by solid structures as is traditionally used.

A benefit associated with droplet based systems is the ability to automate dispensing, aliquoting, mixing, and movement of the droplets ranging from sub-nanoliter to several microliters in volume. Channel-based microfluidic systems using a single fluid medium have been developed for electrophoretic molecular analysis, molecular reaction rate determination using surface plasmon resonance, high pressure liquid chromatography and many other applications. These systems typically require that samples be prepared external to the instrument. Thus, there are often aliquoting, dilution, mixing, purification, centrifugation, and other steps that require multiple pipetting steps to be performed off-chip. With a goal of integrating many of these steps, a primary benefit of droplet based Lab-on-Chip devices is that they offer the potential for useful new sample-to-answer capabilities that are difficult to perform in single-fluid channel-based systems.

Most of the research and development for droplet based Lab-on-a-Chip technology has focused on methods of manipulating the droplets that also enable steps of sample preparation to be performed before the bio/chemical analysis. There are, however, examples of droplet based analysis systems for high-throughput biochemical analysis that use automated pipette-based or other dispensing systems which are completed without requiring any further droplet manipulation after spotting. These include gene-expression microarrays, protein arrays, and MALDI mass spectrometry plates. This article will not address these array-based systems further but will focus on droplet manipulation methods and several integrated droplet based labchip systems.

Basic Methodology

Automated droplet based manipulation methods described in this article include electrowetting, dielectrophoretic, thermocapillary, surface acoustic wave (SAW), and

pressure-driven channel-based droplet systems. Fabrication of arrays of elements to control these droplet manipulation methods typically involves the use of photolithography. The methods of addressing of the elements have become increasingly sophisticated with several efforts to utilize passive- and active-matrix control strategies. Trends and issues associated with each method are described.

Electrowetting

Perhaps the most well-developed droplet manipulation method is that of electrowetting. Electrowetting involves an electrostatic reduction of the contact angle of a sessile droplet or a droplet sandwiched between plates. If electrowetting is applied to one side of the droplet, translational motion can be induced. As shown in Fig. 1, the droplet will move to the activated electrode. Additionally, for droplets covering several electrodes, under appropriate conditions, if opposite sides of the droplet are electrowet, it can be split into two. A photograph of an electrowetting labchip droplet manipulation system using dedicated home-run wiring to each electrode is shown in Fig. 2. In this particular chip, a transparent array of three 2×8 Indium Tin Oxide (ITO) electrodes, plus 2 electrodes connecting these arrays, are coated with a Parylene dielectric layer and then thin gold lines are formed to surround the underlying ITO electrodes. Thus, no top plate is required to ground the droplet since the gold lines provide electrical grounding to sessile droplets residing on the surface.

A design of an active-matrix driving of an electrowetting chip with optical detection of the droplets is shown in Fig. 3. This so-called *Active Matrix Microfluidic* (AMM) design offers the use of TFT manufacturing processes that are commercially well-developed as well as use of active matrix addressing standards that are also well-developed for use in flat panel displays. Numerous researchers have fabricated arrays of electrodes and demonstrated droplet manipulation by electrowetting [2, 5, 9, 10]. Recent efforts have also made use of *optoelectrowetting* which holds promise as a method of using sequences of light images projected onto a photoconductive substrate to activate electrowetting [4].

Dielectrophoresis

Generation of non-uniform electric fields, either DC or AC, can impart forces on droplets or particles having a different dielectric constant from the surroundings. Gascoyne's research group [7] have developed arrays of electrodes for manipulating droplets by this method. In their system, aqueous droplets are suspended in 1-bromododecane and motion is induced without requiring any droplet spreading on a surface. The distinction between dielectrophoresis and electrowetting is subtle and the electromechanical fundamentals are described by Jones [8].

Thermocapillary

Thermocapillary droplet control is based on the principle that surface tension is a function of temperature. By using an array of sub-surface heaters or other means of controlling the temperature distribution around the periphery of a droplet, an imbalance of forces can be imposed on the droplet resulting in motion towards the cold regions [6]. Temperature increases of less than approximately 6 K were used by Darhuber et al. to move droplets of several different liquids. Their fabrication of metal electrodes involved photolithographic patterning and metal evaporation followed by coating with silicon dioxide.

Surface Acoustic Waves (SAW)

Generation of traveling surface acoustic waves across the surface supporting a droplet can result in the transfer of energy into translational motion of the droplet. Wixforth and coworkers [12] have studied the use of SAW systems combined with surface patterns of varying hydrophobicity to generate the desired droplet motion. Lithium Niobate $LiNbO_3$ piezoelectric with gold interdigitated transducers were used to generate SAWs using RF excitation of 100–800 MHz with resulting wavelengths from about 5 μm to 35 μm. They have shown the ability to dispense small droplets from a larger one and to control the movement of the droplets.

Droplets in Channels

There has been a spate of recent activity associated with the formation and flow of aqueous droplets in channels surrounded by immiscible oil [1]. The typical configuration is similar to that used for flow cytometry in which a sample flow is injected into a co-flowing sheath flow. In this chip-based manifestation, however, photolithography is used to fabricate a four-way intersection of channels and the sheath fluid is immiscible. Therefore the water-oil interfacial tension results in the formation of droplets. Typically, the aqueous sample flow enters the intersection head-on and the two side channels provide the flow of immiscible oil. These three flows then exit the single remaining channel. The flow rates are controlled such that droplets pinch-off within the oil to provide a series of droplets whose spacing can be controlled.

Clearly, there has been substantial research into droplet formation and control methods. Although these droplet manipulation methods are critical to the development of Lab-on-Chip systems, integration issues associated with

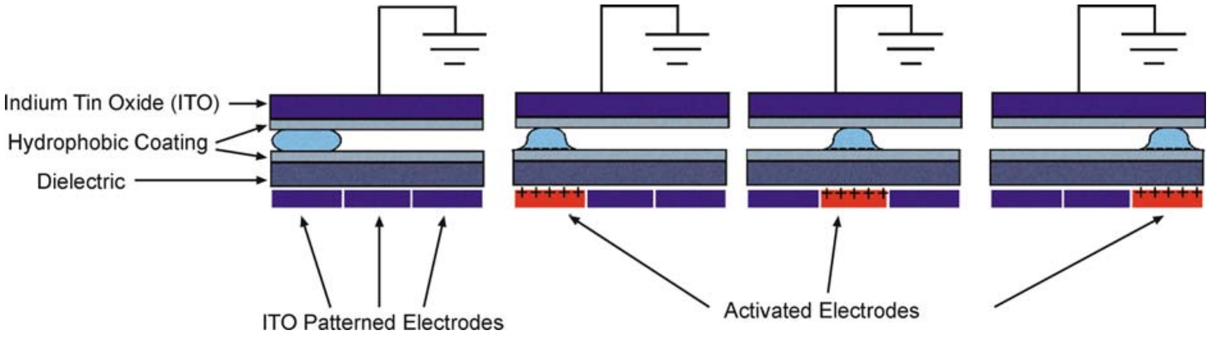

Droplet Based Lab-on-Chip Devices, Figure 1 Layout of electrowetting chip with droplet translation onto actuated electrodes

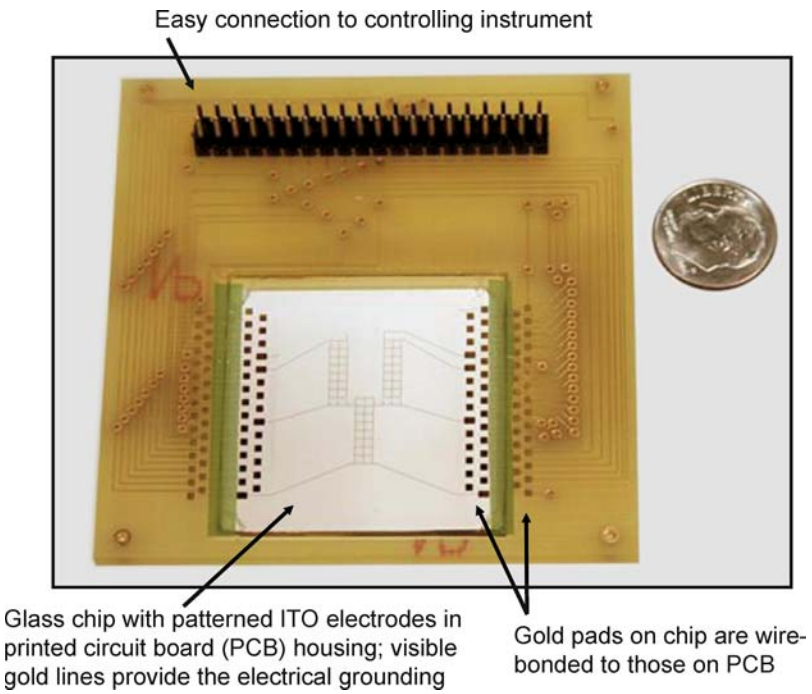

Droplet Based Lab-on-Chip Devices, Figure 2 Typical electrowetting droplet Lab-on-Chip design using *home-run* wiring with switching electronics off-chip. Chips of this type have been used to initiate DNA amplification reactions shown below

the read-out method for particular analytical techniques also represent significant challenges. Thus, in the following section we describe the research findings associated with droplet Lab-on-Chip systems that implement real analytical methods.

Key Research Findings

Several research efforts have been reported that utilize droplet Lab-on-Chip systems to perform chemical or biochemical assays with a high degree of automated control. The use of physiological fluids in electrowetting droplet systems has been demonstrated by Fair's group at Duke University [11], who also performed glucose assays and manipulated solutions used in polymerase chain reaction (PCR). Integrated steps of mixing reagents and samples as well as performing on-chip heating have been performed for PCR-based DNA amplification [3]. The company Advanced Liquid Logic, Inc. (www.liquid-logic.com) is currently commercializing this type of digital microfluidic system for applications such as neonatal blood diagnostics and protein crystallization. Systems that are based on droplets in channels driven by pumps are being commercialized by the company RainDance Technologies, Inc. (www.raindancetechnologies.com) with applications anticipated in various fields such as enzyme development,

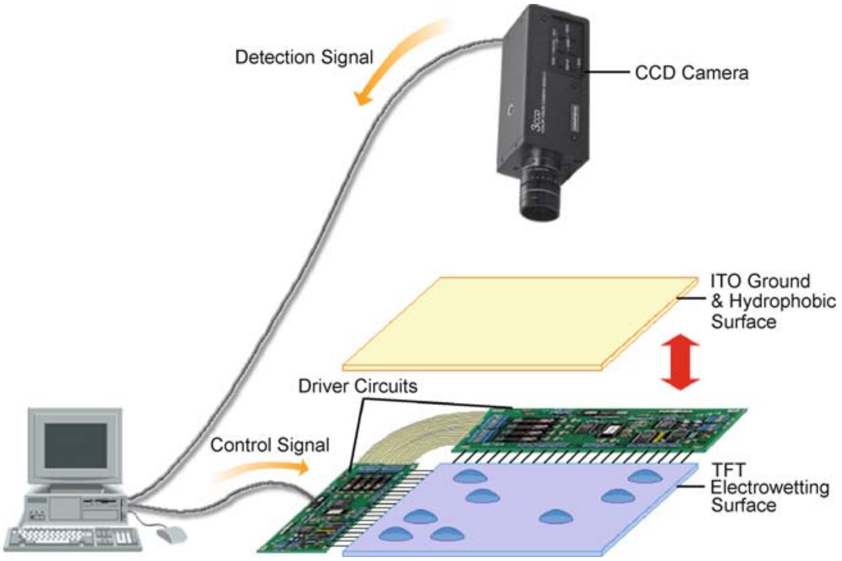

Droplet Based Lab-on-Chip Devices, Figure 3 Design of an electrowetting Lab-on-Chip utilizing active-matrix addressing of a high-density array of thin-film transistors (TFTs) similar to those used in Active Matrix Liquid Crystal Displays (AMLCDs) for Flat Panel Displays (FPDs). There is promise for these Active Matrix Microfluidic (AMM) designs to be used to perform complex protocols by generating row-column addressing with video signals in standard formats (e. g. SVGA, UXGA, QSXGA, ...)

proteomic assays, cancer diagnostics, and on-chip chemical synthesis.

Microcalorimetry has been performed on several sample biochemical reactions using electrowetting to initiate the reactions that are then monitored by on-chip embedded thermistors [13]. The differential temperature rise between adjacent sample-control pairs was used and 96 of these pairs were microfabricated on 9 mm spacing consistent with SBS 96-well format for compatibility with laboratory automation. Examples of reactions that were used to validate this platform were the binding of 2′-CMP to RNase A and the binding of biotin to streptavidin. Phosphorylation of glucose by hexokinase and the power output of mitochondrial respiration were also monitored.

In a similar effort involving real-time monitoring of a biochemical reaction, the amplification of DNA using an isothermal amplification method has been performed by our group at KGI. Electrowetting is used to initiate the coalescence of droplets and the fluorescence associated with DNA amplification is monitored. This isothermal DNA amplification method is called *EXPAR* and is described by Van Ness et al. [14]. Initiation of the reaction occurs upon coalescence and heating of (1) a master mix droplet containing the essential enzymes, dNTPs, and a single-stranded DNA template with (2) a sample droplet containing a short ssDNA sequence *trigger* that is unique to the organism or gene of interest.

The ssDNA template in the master mix is designed to include two identical sequences complementary to the trigger. These two identical sequences are separated by a short region complementary to an enzyme recognition sequence. The trigger ssDNA sequence is short enough that it only transiently binds to one end of the template at the temperature of the reaction (in our case 53°C). If, however, during the transient binding, the polymerase extends the double stranded portion several bases to form the enzyme recognition sequence, the duplex gains stability and the polymerase continues to extend the duplex to the end of the template. At this point, the N.BstNb$_1$ nicking-enzyme binds to the recognition site on the newly-formed dsDNA and nicks (cleaves a phosphodiester bond on) the newly-formed strand of the DNA to create an oligonucleotide that is below the threshold of stability leading to the release of a new trigger that is identical to the first. The polymerase can then re-extend the template-duplex such that new triggers are generated by these partial-duplex *trigger-generator* molecules at a rate of about 1 trigger/2.5 s for the conditions used in this study. As the ssDNA triggers are released into solution, they can bind to other ssDNA templates to create new trigger-generators. This process can be shown to provide an exponential increase in the number of trigger-generators in time leading to the name *Exponential Amplification Reaction*, or EXPAR. The progress of the reaction can be monitored using an intercalating dye, Sybr Green II, that binds to the duplex region of the trigger-generators.

The master mix was prepared with the following constituents:

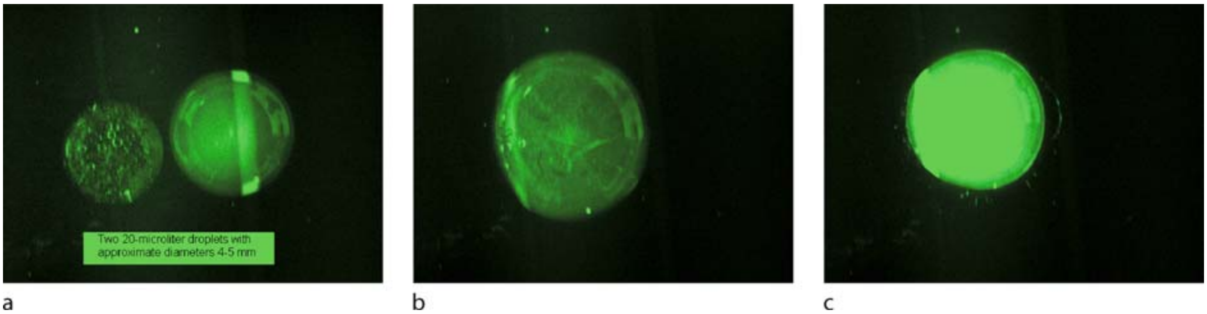

Droplet Based Lab-on-Chip Devices, Figure 4 Fluorescence images of DNA exponential amplification reaction in a heated droplet using Sybr Green II to indicate formation of double-stranded DNA templates. (**a**) Image of two 20 μL droplets before coalescence. The droplet on the left is a trigger/sample droplet containing a single-stranded DNA 12-mer and the droplet on the right contains a ssDNA 33-mer template with the enzymes and dNTPs required for exponential amplification. Note the gold ground line underneath the right droplet that reflects incident excitation light. (**b**) Image of droplet, 1 s after coalescence. (**c**) Image of droplet after 42 s of isothermal amplification. (Experiment performed by Mr. Peter Qu)

- 274 μL nuclease free water
- 100 μL Thermopol buffer
- 50 μL N.BstNb1 buffer
- 25 μL dNTP mix
- 40 μL N.BstNb1 enzyme
- 10 μL Bst polymerase
- 1 μL Sybr Green II dye
- 0.75% by weight of PEG 8000

In the reaction shown in Fig. 4, two 20 μL droplets are shown before and after coalescence and DNA amplification is evident by the clear increase in fluorescence. The concentration of template DNA in the amplification master mix was 0.4 μM and the template sequence was 5′–CCT CAT CGC GGG CTT CGA CTC CCT CAT CGC GGG–3′. The trigger DNA droplet had 0.2 μM of the sequence 5′–CCC GCG ATG AGG–3′. The chip was heated to 53°C and 50 V was applied to initiate motion of the trigger-containing droplet. The microscope was a Nikon Eclipse E800 with an excitation wavelength of 488 nm with long-pass filtered emission beyond 560 nm. The three images in Fig. 4 are taken from a movie of the amplification reaction. The droplet coalescence event takes less than 0.5 s from the initial droplet contact to the time that motion apparently ceases. The reaction is maintained at 53°C throughout the reaction and there is a dramatic increase in fluorescence indicating DNA amplification. The reaction is nearly complete at the time the final image was taken 42 s after droplet coalescence.

We note that the coalescence was a result of the motion of the trigger/sample droplet moving to join the master mix/template droplet. The contact lines of the latter droplet remained pinned, a phenomenon that is observed for droplets containing proteins of sufficiently high concentration. One method of avoiding this line pinning effect is to immerse the aqueous droplets in oil, allowing droplet motion even for high protein concentrations.

Future Directions for Research

There are several systems-level issues that must be addressed in the development of integrated Lab-on-Chip systems. Ultimately, every step of an assay, including sample preparation, reagent mixing, biochemical reaction, signal transduction, and readout technology should be integrated into such biosensors or diagnostic systems in order for them to prove useful and reliable to the end-users. This is expected to involve requirements-driven engineering for particular applications including immuno-assays, nucleic acid diagnostics, and cell-based systems. Trade-offs for particular applications require design decisions to be made regarding flexible/reprogrammable arrays vs. pre-determined droplet pathways, inexpensive disposable systems vs. reusable chips with cleaning protocols, and integration of all processes or modular or decoupled functional units. The high risk areas of these technologies are primarily associated with the integration issues and the degree to which the systems can be reused and cleaned between uses.

Cross References

- ▶ Biosample Preparation Lab-on-a-Chip Devices
- ▶ Digital Microfluidics
- ▶ Droplet Microreactors
- ▶ Electrowetting
- ▶ Electrowetting and Droplets
- ▶ PCR Lab-on-Chip Devices
- ▶ Thermocapillary Pumping
- ▶ Transport of Droplets by Acoustics

References

1. Ahn K, Kerbage C, Hunt TP, Westervelt RM, Link DR, Weitz DA (2006) Dielectrophoretic manipulation of drops for high-speed microfluidic sorting devices. Appl Phys Lett 88:024104

2. Berthier J, Clementz P, Raccurt O, Jary D, Claustre P, Peponnet C, Fouillet Y (2006) Computer aided design of an EWOD microdevice. Sens Actuators A 127:283–294
3. Chang YH, Lee GB, Huang FC, Chen YY, Lin JL (2006) Integrated polymerase chain reaction chips utilizing digital microfluidics. Biomed Microdev 8:215–225
4. Chiou PY, Moon H, Toshiyoshi H, Kim CJ, Wu MC (2003) Light actuation of liquid by optoelectrowetting. Sens Actuators A 104:222–228
5. Cooney C, Chen CY, Emerling MR, Nadim A, Sterling JD (2006) Electrowetting droplet microfluidics on a single planar surface. Microfluid Nanofluid 2:435–446
6. Darhuber AA, Valentino JP, Troian SM, Wagner S (2003) Thermocapillary actuation of droplets on chemically patterned surfaces by programmable microheater arrays. J Microelectromech Syst 12:873–879
7. Gascoyne PRC, Vykoukal JV, Schwartz JA, Anderson TJ, Vykoukal DM, Current KW, McConaghy C, Becker FF, Andrews C (2004) Dielectrophoresis-based programmable fluidic processors. Lab Chip 4:299–309
8. Jones TB (2002) On the relationship of dielectrophoresis and electrowetting. Langmuir 18:4437–4443
9. Lee J, Moon H, Fowler J, Schoellhammer T, Kim CJ (2002) Electrowetting and electrowetting-on-dielectric for microscale liquid handling. Sens Actuators A 95:259–268
10. Pollack MG, Shenderov AD, Fair RB (2002) Electrowetting-based actuation of droplets for integrated microfluidics. Lab Chip 2:96–101
11. Srinivasan V, Pamula VK, Fair RB (2004) An integrated digital microfluidic lab-on-a-chip for clinical diagnostics on human physiological fluids. Lab Chip 4:310–315
12. Strobl CJ, von Guttenberg Z, Wixforth A (2004) Nano- and pico-dispensing of fluids on planar substrates using SAW. Ieee Trans Ultrason Ferroelectr Freq Control 51:1432–1436
13. Torres FE, Kuhnt P, De Bruyker D, Bell AG, Wolkin MV, Peeters E, Williamson JR, Anderson GB, Schmitz GP, Recht MI, Schweizer S, Scott LG, Ho JH, Elrod SA, Schultz PG, Lerner RA, Bruce RH (2004) Enthalpy arrays. Proc Nat Acad Sci USA 101:9517–9522
14. Van Ness J, Van Ness LK, Galas DJ (2003) Isothermal reactions for the amplification of oligonucleotides. Proc Nat Acad Sci USA 100:4504–4509

Droplet-Based Microreactor

► Droplet Microreactor

Droplet Break Up

► Droplet Dispensing
► Droplet Dynamics in Microchannels

Droplet on Demand

Synonyms

Drop on Demand

Definition

A method for forming and delivering single droplets from a source fluid of larger volume as commanded. Typically droplets delivered on demand may be provided one at a time over long intervals or quickly in succession.

Cross References

► Piezoelectric Microdispenser

Droplet Dispensing

TIMO LINDEMANN, ROLAND ZENGERLE
Laboratory for MEMS Applications
Department of Microsystems Engineering,
University of Freiburg, Freiburg, Germany
zengerle@imtek.uni-freiburg.de

Synonyms

Drop; Droplet; Dispensing; Droplet ejection; Droplet injection; Droplet generation; Droplet formation; Droplet release; Droplet break up; Droplet tear-off

Definition

Droplet dispensing is the procedure of ejecting single droplets or small jets out of a nozzle of a dispensing apparatus. Here we only consider liquid droplet dispensing into a gaseous environment. Dimensionless numbers like the Reynolds, the ►Weber and the ►Ohnesorge numbers are well suited to describe the droplet formation qualitatively.

Overview

Liquid droplets of different volumes are used in many applications in various areas of interest. This is the reason why much research work has been dedicated to understand and to describe the numerous existing droplet generation mechanisms. There are many applications exploiting droplet generating devices and applications with increasing market potential. Due to the huge amount of available techniques, only some of them are selected as example and are presented in the following. Distinction is made between printing and coating, life sciences, electronics manufacture, optics and other main applications.

Printing and Coating

Printing and coating certainly is the biggest industrial market using single droplets or sprays, starting with the huge market of well-known home and office printers

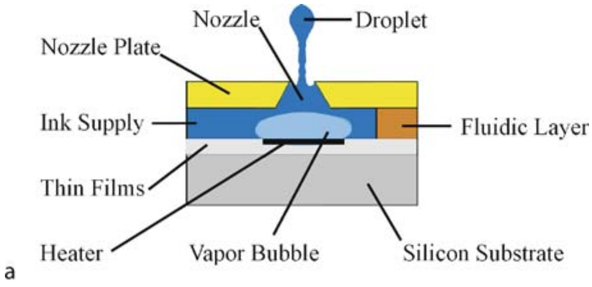

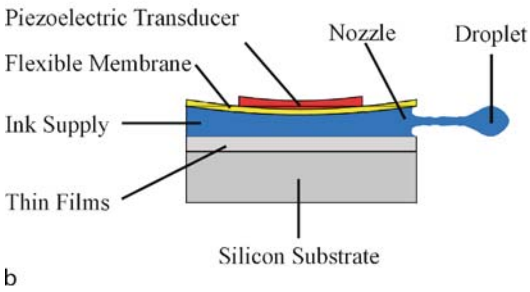

Droplet Dispensing, Figure 1 Principle of (**a**) a thermal bubble jet printhead and (**b**) a piezo-actuated inkjet printhead

based either on the ▶bubble jet or the piezo principle, and followed by many industrial large-format printers for the packaging of materials and direct labeling. High-quality color images, low machine cost and low printing noise are basically the main advantages of such ▶inkjet printers producing droplets in the 1 – 100 pl range. The two competing technologies in this field are the thermally actuated ▶bubble jet commercially available from Hewlett Packard, Canon, Olivetti I-Jet and others; and the piezoelectric-driven printheads commercially available from Epson, Xaar, Spectra and others. Both methods have made remarkable progress in the last two decades. Furthermore, there are thousands of applications of spray units used for spraying of colors, adhesives, oils and many more.
The functional principle of a thermal ▶bubble jet printhead is displayed in Fig. 1a. A current pulse applied to a microheater leads to a very short heating pulse at the solid–liquid interface. This heating pulse leads to a small vapor bubble which expands explosively. The increasing vapor bubble leads to a volume displacement of the ink towards the nozzle and finally to a droplet ejection. The detaching of the vapor bubble from the hot surface results in a concurrent cooling down of the bubble which results in condensation and collapse of the bubble. The suction of the collapsing bubble and the capillary forces inside the printhead lead to refilling of the nozzle chamber that is finished before the next shot within approximately 10 μs. The fast explosion of the bubble leads to a characteristic pressure behavior inside the liquid. Starting instantaneously with a very high pressure of about 7 to 9 MPa right at the beginning of the vaporization, the pressure decreases exponentially during a few microseconds.
The functional principle of a piezoelectric printhead is displayed in Fig. 1b. A bending of a piezoelectric transducer attached on a flexible membrane or similar leads to a volume displacement of the ink and a subsequent droplet ejection.

Life Sciences

Various examples of the use of droplet dispensing within the life sciences [1] are droplet-based Lab-on-a-Chip systems, fabrication of microarrays, combinatorial chemistry and high-throughput screening in drug discovery, inhalers in medical therapeutics, and many more.
The principal idea behind the use of droplet-based Lab-on-a-Chip implementations is the use of single droplets as reaction confinements for biological assays or chemical reactions. Dominant interfacial and surface tensional forces at the microscale enable the precise generation and spatial stabilization of these droplets. Since the droplets are kept isolated within an immiscible surrounding fluid like air or oil, lateral dispersion (Taylor dispersion) can be avoided while moving the droplets to different locations.
Droplets as reaction confinements can be regarded as nanoliter-sized batch reactors for mixing and reacting in contrast to the merely flow-through concept of the other platforms described so far. A multitude of parallel screening reactions, each consuming only a minute amount of reagents, are enabled inside the small-sized droplets. The reproducibility of the reaction conditions is very high, since the droplet volume as well as the reaction conditions within the droplet, i. e. temperature and mixing conditions, can be controlled precisely.
The droplet-based microfluidic platforms for Lab-on-a-Chip applications can be fundamentally divided into two basic setups, the channel-based and the planar surface approach [2]. The channel-based systems are mostly pressure driven with droplet generation and manipulation relying on actuation via liquid flows within closed microchannels. For the planar surface-based platforms, droplets can be arbitrarily moved in two dimensions representing planar programmable Lab-on-Chips. They are actuated by electrowetting (EWOD) or surface acoustic waves (SAW).
Furthermore, droplet generators are a key technology for fabricating so-called microarrays. A microarray is a two-dimensional arrangement of hundreds or even thousands of different DNA fragments or proteins immobilized on a surface. Microarrays are used as a highly parallel ana-

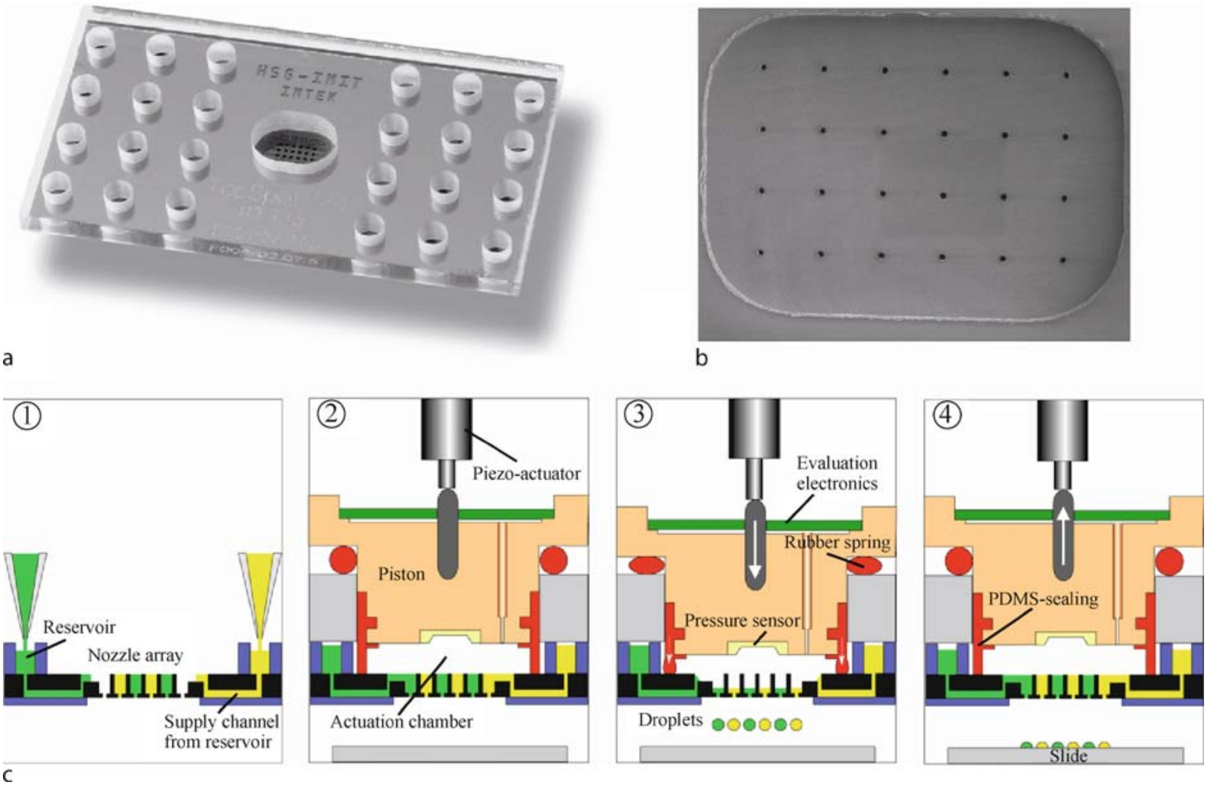

Droplet Dispensing, Figure 2 (**a**) A 24-channel TopSpot® printhead. (**b**) SEM image of the 24 nozzles at a pitch of 500 µm on the bottom side of the printhead. (**c**) Working principle of TopSpot: 1, filling of the printhead reservoirs; 2, placing a piston into the printhead; 3, actuation by moving of the piston; 4, retraction of the piston with capillary refill of the nozzles

lytic detection method to rapidly detect genetic patterns or the rapid identification of microorganisms. The microarray technology has revolutionized the fields of biotechnology and the life sciences. It has opened new perspectives for decoding the human genome, for molecular gene and DNA diagnostics, proteomics as well as for new ways in pharmacogenetics. Due to the high complexity and diversity of proteins, production of protein microarrays is a major technological challenge and requires very flexible printer systems.

For example, the TopSpot® technology [3, 4] has been developed for the fast mass production of low- and medium-density microarrays. The system enables highly parallel non-contact printing of different media like oligonucleotides, DNA or protein solutions. It is based on a micromachined printhead which is driven by a separate actuation unit. The printhead formats allow the simultaneous application of 24, 96 and even 384 different reagents in one step. A 24-channel TopSpot® printhead and the corresponding working principle are displayed in Fig. 2.

In modern drug discovery, potential drug candidates have to be identified from a huge number of different chemical compounds. This process is called high-throughput screening (HTS). It allows the testing of several hundred thousand chemicals per day. In HTS, biochemical assays are performed in standardized containments termed microwell plates. Due to the ongoing miniaturization smaller amounts of liquid have to be handled. Therefore, non-contact dispensing becomes increasingly important because of the increasing surface tension effects of small liquid droplets. Thus microdroplet generators are an appropriate solution for non-contact liquid handling. They can decrease the necessary amount of liquid and the processing time for drug discovery experiments where typically thousands to hundreds of thousands of tests involving novel biologically active reagents are required.

The Dispensing Well Plate (DWP™), as shown in Fig. 3, for example, is a dispensing system of up to 1536 dispensing units for the massive parallel delivery of liquid volumes in the volume range of 50 nl [5, 6]. One key application for the DWP system within HTS is the rapid compound reformatting by direct addition of nanoliter volumes to an assay in microwell plates. In that case the dispensing volume is defined by the geometrical volume of the micro-

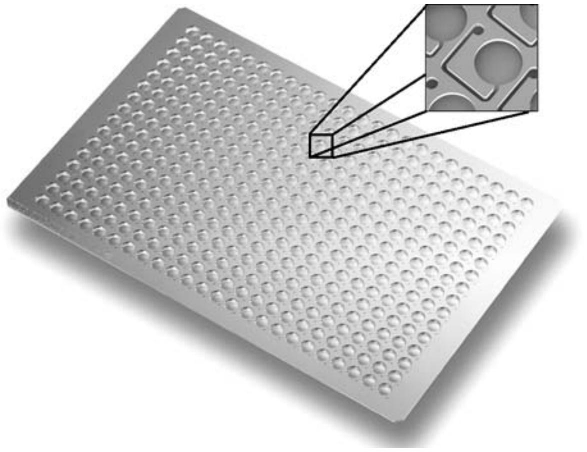

Droplet Dispensing, Figure 3 Dispensing Well Plate offering 384 dispensing units in parallel made by silicon bulk micromachining (pitch of 4.5 mm)

machined nozzle, leading to a very high reproducibility of dispensing volume with a CV of 2 – 5% and a homogeneity within individual droplet arrays of 1 – 2%. Advantages of the DWP system are the small dispensing volumes which can be handled accurately and in a highly parallel way and the possibility of an extremely high integration density up to a 1536-well plate format.

Another interesting field of research is cell sorting. Cell sorting can be used either to deposit single cells (cloning mode) or to collect large numbers of cells with similar properties (enrichment mode). A small droplet of several micrometers in diameter can contain a single cell. Due to this, such small droplets can be used to handle and sort cells. Cell sorting is a technique that typically includes a droplet generator, a droplet charging and deflecting system and sensors for measuring cell properties by fluorescence and light scattering.

A large application field in medicine is aerosol atomizers for drug delivery. Aerosolized droplets in the range of a few micrometers in diameter containing therapeutic reagents can be used to administer drugs to the lungs to treat various diseases.

In Fig. 4 the droplet ejecting technologies mentioned above are arranged in a graph indicating the suitable volume range of the different technologies and the number of *different reagents* that can be dispensed simultaneously and in parallel.

Electronics Manufacture

The main application using droplets in electronics manufacture is the deposition of molten solder on circuit boards. This technology can be used to make direct solder connections of components, vertical and horizontal conductive lines and solder bumps for flip chip bonding. Due to this, manufacturing technologies can be driven toward further automation, miniaturization and reductions in costs and cycle times. As a non-contact deposition method, this technology may also be applied to print on nonplanar and curved surfaces. A further application is the printing of adhesives for sealing and bonding of devices. This can be accomplished quite efficiently by drop-on-demand as well as continuous droplet generators.

D

Optics

Small droplets can be used to fabricate lenses and lens arrays suitable for use in fiber optics, laser diodes, imaging arrays, displays and optical switches. Cured optical plastics are used instead of glass to produce lenses where the curvature of the lens can be adjusted by control of surface tension and contact angle of droplets deposited on flat substrates.

Large-area displays like LCDs or TFTs usually are fabricated by screen printing or lithographic techniques. However, with increasing display resolution at reduced fabrication costs, non-contact droplet deposition of the colors could be a promising alternative.

Moreover polymer-based displays can also be manufactured using droplet dispensing systems. Organic polymers are usually used due to their potential low costs. They are typically deposited by spin coating or evaporation. The patterning of the necessary multiple organic layers for red, green and blue is difficult. A direct deposition of patterned luminescent doped polymers by droplet generators like ► inkjets provides a more simple manufacturing method. A further advantage using droplet generators is the reduction of the amount of material used. The polymer solutions of the three colors are printed directly in the required positions without any losses as is the case for spin coating.

Others

Another important application using droplet generators is in fuel injection systems which are the heart of modern combustion engines. The fuel is atomized into a spray of small droplets provided by a fuel injector. The droplet size distribution as well as the fuel–air ratio are crucial for optimum combustion.

A further application using microdroplets is the rapid prototyping of three-dimensional industrial objects making use of the ejection of high-temperature liquid metals, ceramic suspensions or hardenable polymers.

Besides these high-throughput applications, droplet generators can also be used in the drop-on-demand mode. They can be used to deposit lubricants where needed

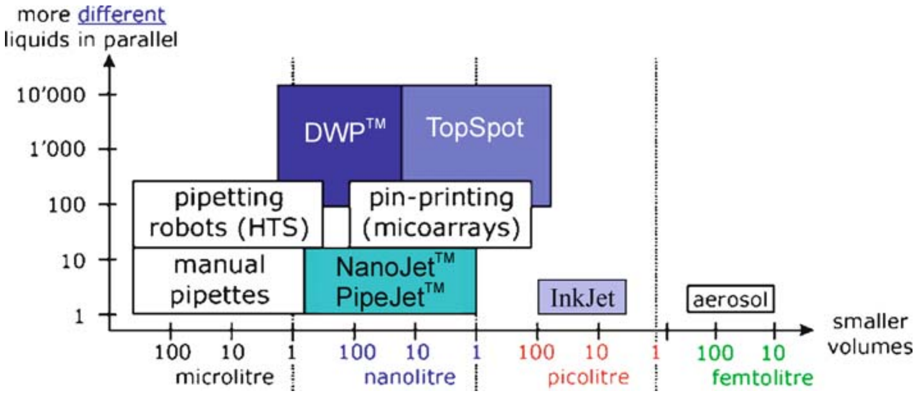

Droplet Dispensing, Figure 4 Classification of droplet ejectors depending on the ejected volume and the amount of liquids which can be handled in parallel

during manufacture, assembling or operating. For example special oils can serve as lubricants in small spindle motors without ball bearings. Therefore, the lubricant has to be provided with precise control of quantity and position.

Basic Methodology

Understanding and Describing Droplet Formation Processes

The state of the art in understanding and describing droplet formation processes is divided into two different perspectives: the continuum mechanics or fluid dynamics approach and the particle-based approach. Whilst the continuum mechanics approach is based usually on the Navier–Stokes equation, the continuum equation and the energy equation, the particle-based approach is based on the interconnecting forces between neighboring particles like molecules or pseudo particles.

Lord Rayleigh was the first who derived an analytical description of droplet generation caused by jet instabilities as early as the late 19th century [7]. After that at the beginning of the 20th century, the experimental study of droplet generation became increasingly important. However, even today analytical descriptions for the droplet formation process are still being refined and improved. These studies mostly use simplifications of the Navier–Stokes equations like axisymmetric, steady flows with a free surface to describe simple examples of droplet formation [8, 9]. A general analytical description of droplet generation, however, is inhibited by the complexity of the underlying differential equations like the Navier–Stokes equation and others. Therefore numerical techniques such as network descriptions, based on lumped elements or compact models, computational fluid dynamic (CFD) simulation or particle-based approaches like molecular dynamics (MD) or dissipative particle dynamics (DPD) are used to describe the droplet dispensing process.

Droplet Breakup Regimes

The breakup of droplets released from a nozzle into the air mainly can be categorized according the following different regimes.

Drop-on-Demand Breakup

This droplet breakup regime is characterized by an ejection of a single droplet with a diameter equal to or slightly bigger than the nozzle diameter. The ejected droplet can be followed by smaller satellite droplets or a tail which could also disperse into single satellite droplets after a while. In such a system the droplet can be ejected on demand which means that every actuation pulse produces one single droplet. The required actuation for such a droplet breakup should provide a fast actuation, if possible with a counter movement to enforce droplet breakup. The actuation force should be strong enough to overcome substantially the capillary forces.

Jet-on-Demand Breakup

The jet-on-demand regime is similar to the drop-on-demand regime with the main difference being that a jet is ejected rather than a single droplet. However, this jet could possibly also disperse into single droplets after jet tear-off. Nevertheless, the ejected volume is much bigger compared to single droplets produced in drop-on-demand mode. But the ejected jet is still on demand which means that also in this case every actuation pulse produces one single jet. Compared to drop-on-demand breakup the actuation takes longer which leads to the jet.

Rayleigh Breakup

Rayleigh breakup is a continuous mode rather than an on-demand mode which means that a liquid jet is ejected out of a nozzle continuously. This jet disperses into single droplets due to the so-called Rayleigh instability after a certain distance from the nozzle. This Rayleigh instability is either caused by naturally occurring disturbances on the jet or by additionally applied external disturbances. In this case the droplet volume almost only depends on the nozzle diameter. The actuation has to be applied for much longer compared to the on-demand modes and can be relatively small.

Atomization Breakup

Atomization breakup is mainly characterized by a liquid high-speed jet which disperses into a fine spray of many single droplets directly behind the nozzle exit. A further characteristic is the arising spray cone so that the droplet trajectory is not inevitably in line with the nozzle. The ejected droplets usually exhibit a droplet size distribution rather than a constant droplet volume. The actuation is continuous and very strong which leads to very high velocities inside the nozzle.

Classification of Droplet Generators

The aim of this section is to derive a clear classification of droplet generating devices releasing droplets from a nozzle into the air based on the applied actuation boundary condition. This is different from the majority of publications which consider the obvious construction elements of droplet generators (e. g. *piezo-dispenser*) or provide classifications based on historical reasons that are often misleading for understanding the real physical principle behind the individual dispensers.

Grounded on the concept applied in CFD simulations where either a *pressure boundary condition* or a *flow boundary condition* is used, real droplet generators can be distinguished using the type of boundary condition resulting from the actuation mechanism. However, there exist also droplet generators where a combination of pressure and flow represents the correct boundary condition. In this case neither an ideal pressure source nor an ideal flow source is the correct assumption. The pressure inside the system is influenced by the flow and vice versa. Due to this also a third group of droplet generators with a *combined pressure and flow boundary condition* has to be established. Finally, a fourth group is listed involving *acoustic actuation* which is a special kind of pressure boundary condition. The reason for the distinction is that the acoustic boundary condition has a totally different physical background compared to the other boundary conditions.

The presented classification, however, is not absolutely fixed by the fluidic setup because single-droplet generators can even change categories when being operated in different modes. For example, a device of the pressure or flow boundary condition class can convert to the combined pressure and flow boundary condition class or vice versa.

Pressure Boundary Condition

A pressure boundary condition exists when the nozzle chamber is pressurized by some kind of actuation producing a constant or transient pressure gradient. This results – according to the Navier–Stokes equation – in a volume flow depending on the geometry and the liquid properties. A feedback from the volume flow to the actuation pressure is neglected. In real devices the way the pressure is produced depends on the system under investigation. This group especially includes all droplet generators using a constant pressure with subsequent Rayleigh breakup or a constant pressure switched by a fast valve. In these cases the pressure can be considered to be provided from a large pressure reservoir which is not influenced by the small volume change caused by the droplet ejection.

Flow Boundary Condition

In the class of flow boundary condition-based devices predominantly the flow is generated by a fixed volume displacement within a certain period of time which leads to a preset volume flow. The pressure inside the system follows from the Navier–Stokes equation and depends on the geometry and the liquid properties. Feedback from the pressure gradient that builds up to the volume flow is neglected in this case. Such a volume displacement can be achieved by displacing a membrane or a piston or by squeezing a tube or a capillary by a very powerful actuator that is not affected by the pressure that is built up internally in the dispensing system.

Combined Pressure and Flow

Some droplet generators do fit in any of the above mentioned classes because neither the pressure nor the flow can be controlled independently. In these devices only a combination of quantities can be influenced. Either the actuator is not strong enough to impose a predefined boundary condition or the device is designed in a way to support coupling between liquid flow and pressure. The best example for this class is the thermal ▶ bubble jet printhead where the actuation is created by a heating pulse and

the resulting vapor bubble. This bubble represents a pressure as well as a flow boundary condition. In the first actuation period of the bubble creation a very high pressure is generated due to the explosive vaporization of the ink. In this period a pressure boundary condition dominates the actuation. After that the growing bubble generates a volume displacement due to its increasing size. In this period a flow boundary condition dominates the actuation. However, the vapor bubble is compressible and due to this the size of the bubble depends on the pressure inside the nozzle chamber as well as on the volume flow. Hence, the ► bubble jet principle involves definitely a combined pressure and flow boundary condition.

Acoustic Actuation

Acoustic actuation is a special kind of pressure boundary condition. There is a pressure involved for actuation, but in contrast to a pure pressure boundary condition creating a convective flow, acoustic actuation does not lead to a substantial liquid flow inside the device during droplet ejection. The spreading velocity of the induced density fluctuations is approximately the speed of sound in the liquid which is much faster than the liquid flow in the case of a pure pressure boundary condition. In practice the acoustic pressure is mostly generated with a piezoelectric transducer. The created shock wave travels through the liquid where it can be influenced by reflections from the channel walls. In some cases such reflections are intended to make use of constructive interferences by establishing a standing wave for a short period of time. When the shock wave hits the meniscus at the nozzle the pressure is transformed into kinetic energy and a droplet is ejected. This principle is very reproducible if all parameters are kept constant; however, it is very sensitive to the liquid properties and especially sensitive to trapped gas bubbles.

Key Research Findings

Droplet Generation Fundamentals

"The process of drop ejection is not as simple as taking a fluid chamber with a small hole and pressurizing it enough for fluid to start emerging from the ejection nozzle hole" [10]. To accomplish monodisperse droplets ejected out of a nozzle, one needs the ability to produce high-speed fluid jets of approximately the diameter of the desired droplets. Additionally, the behavior of the jets has to be controlled precisely enough to cause them to consistently disperse into uniformly sized droplets.

In general there are two different methods to eject monodisperse droplets. The first method, the continuous jet method, is to break up a continuously flowing fluid jet. This is done either by driving the fluid with a source of acoustic energy in order to form standing wave nodes along its length, or by disturbances that occur naturally. The ejected jet finally disperses into discrete droplets. The second method, the drop-on-demand method, is to generate single droplets instead of breaking up a continuous jet. This is mainly done by short pressure pulses, small volume displacements or acoustic actuation of single or multiple nozzles to eject a droplet on demand. These actuation principles are capable of producing droplets in the kilohertz range with random accessibility.

The main differences of the two methods are the maximum frequencies that can be achieved, the amount of liquid which is necessary, the random accessibility of droplets and the complexity of the system setup. While the continuous jet dispenser is capable of producing droplets in the megahertz range, the drop-on-demand method produces droplets with a frequency of several kilohertz. The advantage in terms of throughput of the continuous jet method is balanced by the disadvantages of the minimum amount of liquid which is needed and the relatively high complexity of the system setup compared to the drop-on-demand technique. However, the random accessibility of droplets, the smaller amount of liquid that is required and the simpler system setup are reasons why the drop-on-demand method is the more common method nowadays in most printing as well as in medical or biological dispensing applications. But nevertheless the continuous jet method is still used for some applications.

Critical Weber number

The creation of spherical droplets has been the focus of numerous studies over the years [11–14]. These show conclusively that for both steady and transient flows the onset and mechanisms of droplet breakup can be correlated with the non-dimensional ► Weber number. It is the most important dimensionless number characterizing droplet formation and can be applied to determine the threshold of droplet formation. However, the critical Weber number is only a sufficient condition for droplet breakup and not a necessary condition. This means that if the critical Weber number is surpassed in a process certainly droplet breakup will occur. But droplet ejection is also possible at lower Weber numbers. The only necessary condition for droplet formation is that the supplied energy is sufficient to overcome friction losses and the surface energy of an ejected droplet.

The dimensionless Weber number is considered as the ratio of kinetic energy E_{kinetic} and surface energy E_{surface}

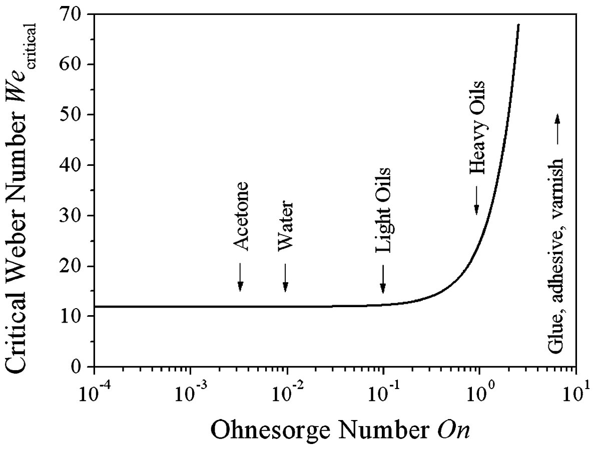

Droplet Dispensing, Figure 5 Critical Weber number $We_{critical}$ depending on the Ohnesorge number On and typical Ohnesorge regimes for different media

of a droplet ejected out of a nozzle:

$$\mathrm{We} \sim \frac{E_{\text{kinetic}}}{E_{\text{surface}}} = \frac{\frac{1}{2} \cdot m \cdot v^2}{A_{\text{droplet}} \cdot \sigma} = \frac{\frac{1}{12} \cdot \rho \cdot D^3 \cdot \pi \cdot v^2}{D^2 \cdot \pi \cdot \sigma} = \frac{1}{12} \cdot \frac{\rho \cdot D \cdot v^2}{\sigma} \quad (1)$$

$$\Rightarrow \mathrm{We} = \frac{\rho \cdot D \cdot v^2}{\sigma} \quad (2)$$

where v is a characteristic velocity of the liquid and D is a characteristic length. For droplet ejection out of a nozzle, these correspond to the velocity of the liquid inside the nozzle and the nozzle diameter, respectively.

The Weber number can be used for two different descriptions. On the one hand it describes whether a droplet can leave a nozzle at all due to higher kinetic energy compared to surface energy. On the other hand it can describe whether a droplet has a tendency for splashing when the kinetic energy is released at the impact on a surface. The higher the Weber number the more dominant is the kinetic energy. This means that most of the inserted energy converts into kinetic energy, i. e. an ejected droplet is faster with higher Weber number. The lower the Weber number the more dominant is the surface tension energy. This means that most of the inserted energy converts into surface tension energy, i. e. droplet formation is critical or even impossible.

The shortcoming of the Weber number is that it does not consider the effects from the viscosity of the fluid. Therefore the Weber number is not adequate to describe the release of droplets from highly viscous liquids which are known to be challenging to dispense. To account for the liquid viscosity in droplet formation, the appropriate nondimensional number is the ▶ Ohnesorge number which represents the ratio of internal viscosity dissipation to the surface tension energy [15]. The Ohnesorge number may be written in terms of the Reynolds and Weber numbers:

$$\mathrm{On} = \frac{\sqrt{\mathrm{We}}}{\mathrm{Re}} = \frac{\eta}{\sqrt{\rho \cdot D \cdot \sigma}} \quad (3)$$

The Ohnesorge number is sometimes also referred to as the stability number, viscosity number, Laplace number or Z number. It is independent of the velocity and therefore only adequate to describe droplet ejection in conjunction with the Weber number. The lower the Ohnesorge number the weaker are the friction losses due to viscous forces. This means that most of the inserted energy converts into surface tension energy, i. e. a droplet can be formed. The higher the Ohnesorge number the more dominant is the internal viscous dissipation. This means that most of the inserted energy converts into internal viscous dissipation, i. e. that droplet formation is critical or even impossible.

According to Eq. (2), a Weber number larger than 12 signifies that the disruptive hydrodynamic forces are larger than the stabilizing surface tension forces. Additionally this crucial Weber number, at which a droplet breakup first can occur, can also be determined empirically. This empirical crucial Weber number is also around $\mathrm{We} = 12$. However, a constant crucial Weber number is only valid for liquids with low viscosity such that the Ohnesorge number is small, $\mathrm{On} < 0.1$. This is the case for viscosities $\eta < 10\,\mathrm{mPa\,s}$ for appropriate spatial dimensions in the microscale. For higher viscosity fluids a viscosity-dependent expression has to be added to this crucial Weber number known as the critical Weber number $\mathrm{We}_{\text{critical}}$. A useful empirical expression for the critical Weber number with increasing viscosity is [13, 14]

$$\mathrm{We}_{\text{critical}} = 12 \cdot \left(1 + 1.077\,\mathrm{On}^{1.6}\right) \quad (4)$$

The dependency of the critical Weber number on the Ohnesorge number is displayed in Fig. 5.

In addition to the critical Weber number for a drop-on-demand breakup, the criterion of $\mathrm{We} > 8$ for a Rayleigh breakup has also been reported [16]. This limit can also be motivated by the lower limit of jet formation in the case of dripping out of a vertical capillary with diameter D_{nozzle} under the action of gravity. The static pressure p_{stat} inside a hanging droplet is

$$p_{\text{stat}} = \frac{4 \cdot \sigma}{D_{\text{droplet}}} \quad (5)$$

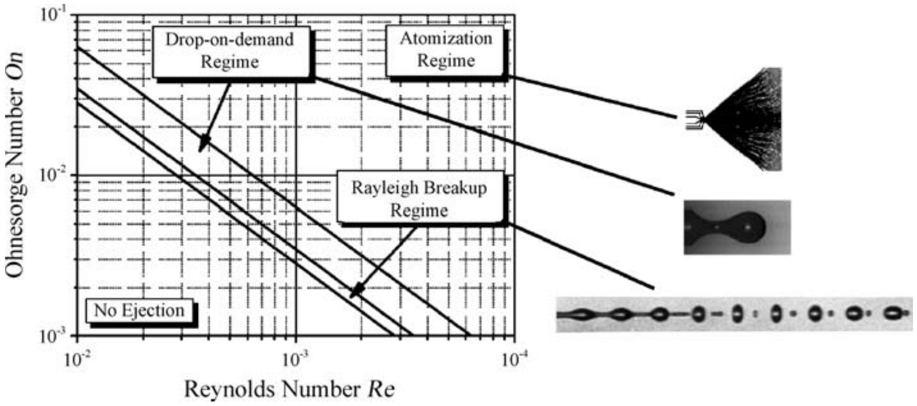

Droplet Dispensing, Figure 6 Different breakup regimes represented by the relationship of the Ohnesorge number versus the Reynolds number

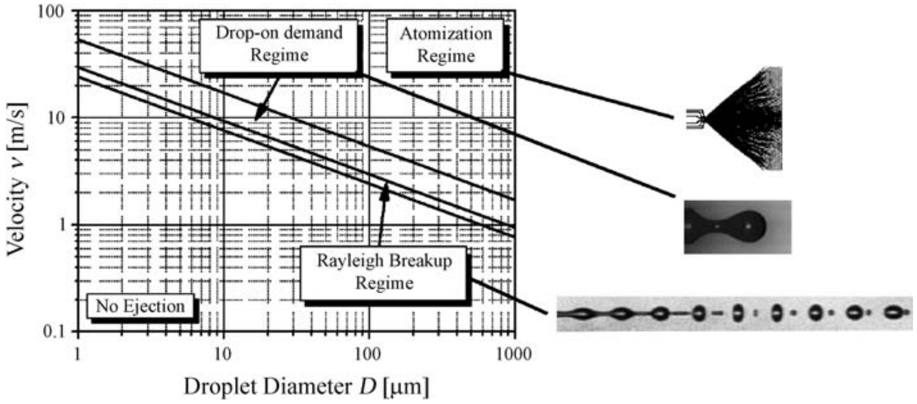

Droplet Dispensing, Figure 7 Different breakup regimes represented by the relationship of the velocity v versus the droplet diameter D for water as ejected liquid

The dynamic pressure p_{dyn} due to a velocity v yields

$$p_{\mathrm{dyn}} = \frac{\rho}{2} \cdot v^2 \tag{6}$$

Considering both pressures to be equal also leads to a correlation with the Weber number:

$$\frac{p_{\mathrm{dyn}}}{p_{\mathrm{stat}}} = \frac{1}{8} \cdot \frac{\rho \cdot D_{\mathrm{droplet}} \cdot v^2}{\sigma} = \frac{1}{8} \cdot \mathrm{We} \tag{7}$$

Hence, a Weber number of 8 arises from the equilibrium of dynamic and static pressure.

Furthermore, an additional criterion $\mathrm{We} > 40$ to predict the onset of the atomization regime has been suggested [16]. In contrast to the Rayleigh breakup regime and the drop-on-demand regime, during atomization the ejected jet breaks up completely within a short distance from the discharge nozzle exit in a chaotic and irregular manner forming a conical spray. The aerodynamic interaction, i. e. the very fast relative motion combined with air friction, causes irregularities in the originally smooth liquid jet surface. This leads to unstable wave growth on the jet surface producing unstable ligaments. The average droplet diameter generated by atomization is much smaller than the jet diameter.

In conclusion it is possible to distinguish between different mechanisms of droplet breakup. These breakup mechanisms are [16]:

$8 < \mathrm{We} \leq 12$ Rayleigh breakup regime

$12 < \mathrm{We} \leq 40$ Drop-on-demand regime

$40 < \mathrm{We}$ Atomization regime

However, this classification originally was introduced for jet breakups and not for drop-on-demand breakups with short pressure pulses. Since the Weber number can be written using the Reynolds number and the Ohnesorge number the different breakup regimes can be illustrated in a diagram of Ohnesorge number versus Reynolds number, as

displayed in Fig. 6. Due to the hyperbolic dependency of the Ohnesorge number on the Reynolds number, the critical values are represented by lines in the logarithmic plot. Furthermore, in Fig. 7 the different breakup regimes are displayed depending on the velocity v and the droplet diameter D for water as ejected liquid ($\rho = 1\,\mathrm{g/cm^3}$, $\sigma = 72.5\,\mathrm{mN/m}$ and $\eta = 1\,\mathrm{mPa\,s}$).

Using an energetic approach, two necessary conditions for a given system can be deduced which are sufficient for droplet ejection of one single droplet with the diameter of the nozzle D_{nozzle} to take place. The critical pressure p_{critical} has to be exceeded during at least the critical time t_{critical} to enforce single-droplet formation. If the critical time is exceeded by far a jet rather than a single droplet is ejected. Both these criteria can also be expressed in the form that the critical power has to be surpassed to enforce single-droplet formation.

Future Directions for Research

The general aim of future research is the further optimization of droplet generation concerning minimum droplet volume, maximum print frequency, maximum throughput, maximum accuracy and precision, minimum pitches and maximum droplet quality. Due to this, it is essential to understand the basics of droplet generation mechanisms in detail and in three dimensions. Furthermore the development of new applications using different kinds of droplet dispensers is also part of current research work.

Cross References

- ► Bioprinting on Chip
- ► Digital Microfluidics
- ► DNA Micro-arrays
- ► Droplet and Bubble Formation in Microchannels
- ► Droplet Based Lab-on-Chip Devices
- ► Droplet Dynamics in Microchannel
- ► Droplet Evaporation
- ► Droplet Microreactors
- ► Electrokinetic Dispensing
- ► Electrowetting and Droplets
- ► Interface Capturing Schemes for Free-Surface Flows
- ► Interface Tracking Schemes for Free-Surface Flows
- ► Piezoelectric Microdispenser
- ► Thermal Bubble

References

1. Jensen K, Lee A (2004) The Science and Applications of Droplets in Microfluidic Devices, Special Issue Foreword. Lab Chip 4:31N–32N. DOI:10.1039/b409797c
2. Haeberle S, Zengerle R (2007) Microfluidic Platforms For Lab-On-A-Chip Applications. Lab Chip 7:1094–1110
3. de Heij B, Daub M, Gutmann O, Niekrawietz R, Sandmaier H, Zengerle R (2004) Highly parallel dispensing of chemical and biological reagents. Anal Bioanal Chem 378(1):119–122
4. Gutmann O, Niekrawietz R, Kuehlewein R, Steinert CP, de Heij B, Zengerle R, Daub M (2004) Impact of medium properties on droplet release in a highly parallel nanoliter dispenser. Sens Actuators A 116(2):187–194
5. Koltay P, Steger R, Bohl B, Zengerle R (2004) The Dispensing Well Plate: A novel nanodispenser for the multi parallel delivery of liquids (DWP Part I). Sens Actuators A 116(3):483–491
6. Koltay P, Kalix J, Zengerle R (2004) Theoretical Evaluation of the Dispensing Well Plate method (DWP Part II). Sens Actuators A 116(3):472–483
7. Lord Rayleigh FRS (1878) On the Instability of Jets. Proc London Math Soc 10(4):4–13
8. Middleman S (1995) Modeling Axisymmetric Flows. Academic Press, San Diego
9. Eggers J (1995) Theory of Drop Formation. Phys Fluid 7(5):941–953
10. Lee ER (2002) Microdrop Generation. CRC Press, Boca Raton
11. Weber C (1931) Zum Zerfall eines Flüssigkeitsstrahles. Z angew Math Mech 11(2):136–154
12. Haenlein A (1931) Über den Zerfall eines Flüssigkeitsstrahles. Forsch Geb Ing 2(4):139–149
13. Pilch M, Erdman CA (1987) Use of Breakup Time Data and Velocity History Data to Predict the Maximum Size of Stable Fragments for Acceleration-Induced Breakup of A Liquid-Drop. Int J Multiph Flow 13(6):741–757
14. Thomas GO (2003) The aerodynamic breakup of ligaments. At Spray 13(1):117–129
15. von Ohnesorge W (1936) Die Bildung von Tropfen an Düsen und die Auflösung flüssiger Strahlen. Z angew Math Mech 16(6):355–358
16. Lin SP, Reitz RD (1998) Drop and Spray Formation from a Liquid Jet. Ann Rev Fluid Mech 30:85–105

Droplet Dynamics in Microchannels

SUMAN CHAKRABORTY
Department of Mechanical Engineering, Indian Institute of Technology, Kharagpur, India
suman@mech.iitkgp.ernet.in

Synonyms

Droplet motion in microchannels; Motion of a deformable drop in microchannels; Droplet generation; Droplet break up

Definition

Droplet dynamics in microchannels refer to the description of motion and deformation of droplets in capillaries or conduits of hydraulic diameters of the orders of microns.

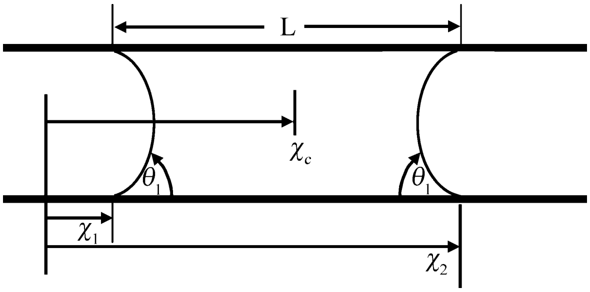

Droplet Dynamics in Microchannels, Figure 1 A deformable slug (droplet) in a micro-tube

Overview

Microscopic droplet formation and manipulation are key processes in many biomedical and biotechnological applications, involving the analysis of DNA, proteins and living biological cells. Droplets are also used to enhance the mixing efficiency in small volumes of fluids. In many of these applications, it is critical to understand the fundamentals of droplet dynamics through microchannels in a detailed manner, so as to impose stringent controls and optimization strategies for advanced bio-microfluidic arrangements.

Basic Methodology

To analyze the basics of droplet motion through microchannels, one may first consider a liquid slug of mass m and volume $\forall$ in a capillary tube of radius R, with the contact angles at its receding and advancing ends as θ_1 and θ_2, respectively. Let x_c be the centre of mass of the slug (refer to Fig. 1) and V_{r1} and V_{r2} be the contact line velocities of the two end caps. Neglecting inertial effects, the equation of motion of the slug can be written as

$$m\ddot{x}_c = (\cos\theta_2 - \cos\theta_1)\, 2\pi R - c\frac{V_{r1} + V_{r2}}{2} \tag{1}$$

where c is an equivalent frictional coefficient for the slug ($c = 8\pi\eta L$, for a fully developed flow with viscosity η). The volume, $\forall_{\text{sph}}$, enclosed by the spherical end caps and the plane that includes the contact line is determined by the contact angle, as

$$\forall_{\text{sph}}(\theta) = \frac{\pi R^3}{3}\frac{\cos\theta\,(2+\sin\theta)}{(1+\sin\theta)^2} \tag{2}$$

The centroid of the volume of the end cap, as measured from the plane of the contact line, can be obtained as

$$h(\theta) = \frac{3 - 2\sin\theta - \sin^2\theta}{4\cos\theta\,(2+\sin\theta)}R \tag{3}$$

To maintain the total volume of the slug as constant, the instantaneous slug length, i.e. $L(\theta_1, \theta_2)$, is determined by the initial slug length L_s and the static contact angle θ_s as

$$\begin{aligned}\forall &= \pi R^2 L_s - 2\forall_{\text{sph}}(\theta_s)\\ &= \pi R^2 L(\theta_1,\theta_2) - \forall_{\text{sph}}(\theta_1) - \forall_{\text{sph}}(\theta_2)\end{aligned} \tag{4}$$

$$\Rightarrow L(\theta_1,\theta_2) = L_s + \frac{1}{\pi R^2} \times \left[\forall_{\text{sph}}(\theta_1) + \forall_{\text{sph}}(\theta_2) - 2\forall_{\text{sph}}(\theta_s)\right] \tag{4a}$$

Position of the centre of mass of the slug can be obtained as

$$x_c = x_1 + \frac{\frac{\pi R^2 L(\theta_1,\theta_2)^2}{2} - \forall_{\text{sph}}(\theta_1)\, h(\theta_1)}{\forall} - \frac{\forall_{\text{sph}}(\theta_2)\,[L(\theta_1,\theta_2) - h(\theta_2)]}{\forall} \tag{5a}$$

and

$$x_c = x_2 - \frac{\frac{\pi R^2 L(\theta_1,\theta_2)^2}{2} - \forall_{\text{sph}}(\theta_2)\, h(\theta_2)}{\forall} - \frac{\forall_{\text{sph}}(\theta_1)\,[L(\theta_1,\theta_2) - h(\theta_1)]}{\forall} \tag{5b}$$

The contact line velocities at the two end caps (V_{r1} and V_{r2}) are related to the corresponding instantaneous positions as

$$V_{r1} = \frac{dx_1}{dt} \tag{6a}$$

and

$$V_{r2} = \frac{dx_2}{dt} \tag{6b}$$

Also, $\dot{x}_c$ is related to x_c as

$$\dot{x}_c = \frac{dx_c}{dt} \tag{7}$$

Equations (1), (4), (5a), (5b), (6a), (6b), (7) represent seven independent equations with nine unknowns, namely, $\theta_1, \theta_2, x_c, \dot{x}_c, V_{r1}, V_{r2}, x_1, x_2$ and L. To match the number of independent equations with the number of unknowns, two

additional independent constraining equations are necessary. These additional equations are available from the considerations of contact line slip, which can be generally described in the form of

$$\theta_{1,2} = f\,(V_r, \mathrm{Ca})_{1,2} \tag{8}$$

where Ca is the Capillary number ($\mathrm{Ca} = \eta V/\gamma_{lv}$). Detailed expressions for Eq. (8) depend on the particular slip models chosen. For a comprehensive physical description of the physical basis of 'contact line slip', the article on 'Electrocapillary' can be referred to.

The one-dimensional droplet transport model, presented as above, is somewhat generic in nature, and can take special forms depending on the specific modes of droplet motion actuation. For example, one may consider the thermocapillary driven droplet motion in a cylindrical capillary, in which the surface tension varies as a function of the local temperature. For small temperature variations, this dependence is approximately linear, and can be described as

$$\gamma_{lv} = \gamma_{lv,0} - a\,(T - T_0) \tag{9}$$

where $\gamma_{lv,0}$ and a are constants, depending on the specific fluid being transported. Under these conditions, a simple analytical solution of Eq. (1) can be obtained, by neglecting the droplet deformation and contact line slip, as

$$\dot{x}_c = \frac{R}{4\eta L}\left(1 - \exp\left(-\frac{8\eta t}{\rho R^2}\right)\right)\left[\{\gamma_{lv,0} - a\,(T - T_0)\cos\theta\}_2 - \{\gamma_{lv,0} - a\,(T - T_0)\cos\theta\}_1\right] \tag{10}$$

Identical equations can also be derived in case the droplet motion is actuated electrically (voltage modulated contact angle variation). For the derivation of a fundamental model on electrocapillary dynamics of liquid droplets, one may refer to the work of Chakraborty and Mittal [1]. In their work, a novel theoretical approach was devised to analyze the droplet dynamics in a microchannel subjected to electrocapillary actuation mechanisms. For mathematical modeling, a droplet of polarizable and conductive liquid was taken to be sandwitched between two parallel plates constituting a microfluidic channel. The upper plate contained a single continuous ground electrode and the lower plate contained an array of independently addressable controlling electrodes. The electrode surfaces were covered with a thin layer of hydrophobic insulation. The physical situation pertaining to this arrangement is depicted in Fig. 2. The contact angles at the rear and the front ends of

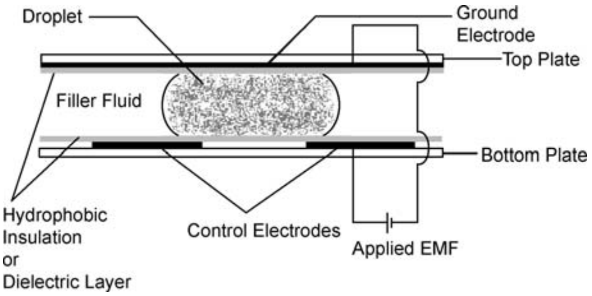

Droplet Dynamics in Microchannels, Figure 2 A schematic layout of the analyzed microfluidic apparatus, showing the droplet of a liquid sandwiched between the electrodes and insulators

the advancing droplet, along with the other pertinent geometrical features are depicted in Fig. 3. From their analysis, it was revealed that there exists a threshold limit on the value of the inter-electrode pitch, beyond which the overall microfluidic transport rates are substantially lowered. On the other hand, with inter-electrode spacings below the threshold limit, unnecessarily large number of electrodes might be necessary to achieve a desired droplet transport rate.

Key Research Findings

Mathematical models for describing the droplet dynamics in microchannels can turn out to be substantially more involved in case the multi-dimensionalities in the flow patterns need to be adequately resolved. One can demonstrate such a situation by describing the two-dimensional motion of a deformable droplet in a microchannel. The initial position and shape of the droplet are geometrically specified. Viscosity of the droplet is taken to be η_b and that of the continuous phase is taken to be η_c. For simplicity, the density of the two phases is taken to be the same ($= \rho$). The equations governing the flow-field in the microchannel, in this case, can be described as

$$\nabla \cdot \boldsymbol{V} = 0 \tag{11a}$$

$$\frac{\partial \boldsymbol{V}}{\partial t} + (\boldsymbol{V} \cdot \nabla)\,\boldsymbol{V} = \frac{1}{\rho}\left[-\nabla p + \nabla \cdot \left(2\eta \underline{\underline{\mathrm{D}}}\right) + \underbrace{\gamma \kappa \delta\,(d)\,\boldsymbol{n}}_{\text{surface tension force}}\right] \tag{11b}$$

where $\boldsymbol{V} = (u, v)$ is a two-dimensional velocity field, γ is the surface tension coefficient, κ is the curvature of the interface, $\underline{\underline{\mathrm{D}}}$ is the rate of deformation tensor, d is the normal distance to the interace, δ is the Dirac-delta function and $\boldsymbol{n}$ is the unit outward normal vector to the

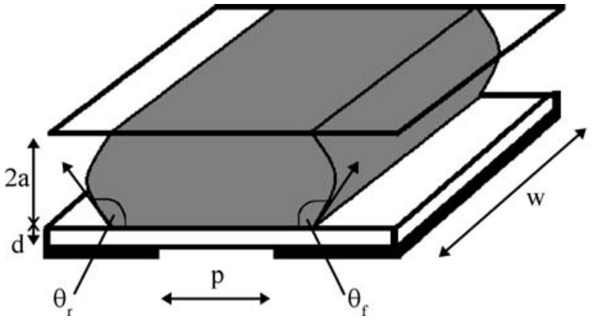

Droplet Dynamics in Microchannels, Figure 3 A schematic diagram specifying the contact angles at the rear and the front ends of the advancing droplet, along with the other pertinent geometrical features

interface. For an accurate prescription of the surface tension force term in Eq. (11b), an appropriate interface coupling method needs to be employed, such as the volume of fluid (VOF) method [2], or the level set method [3–5]. Here, we briefly describe the later one, in context of the present problem under concern. In the level set method, a level set function, ϕ, is defined at each point in the flow-field such that at each point P, the absolute value of ϕ equals the distance from the same to the droplet interface. If P is inside the droplet, ϕ is assigned a negative value, whereas if it is outside the droplet, ϕ is assigned a positive value. The droplet interface corresponds to the points for which $\phi = 0$. The evolution of ϕ satisfies the condition $D\phi/Dt = 0$, or equivalently

$$\frac{\partial \phi}{\partial t} + (\boldsymbol{V} \cdot \nabla)\,\phi = 0 \tag{12}$$

It is important to note here that while ϕ is initially defined as a distance function from the droplet interface, it needs to be reinitialized at the end of each time step to preserve the same physical meaning. If ϕ_0 be the solution of Eq. (12) at the beginning of each time step under concern, the re-initialization can be achieved by solving the following problem to the steady state:

$$\frac{\partial \phi}{\partial t} = S\,(\phi_0)\left(1 - \sqrt{\left(\frac{\partial \phi}{\partial x}\right)^2 + \left(\frac{\partial \phi}{\partial y}\right)^2}\right) \tag{13}$$

where $S\,(\phi_0)$ is the sign function. Equation (13) is coupled with the following initial condition:

$$\phi\,(\boldsymbol{x}, 0) = \phi_0\,(\boldsymbol{x}) \tag{13a}$$

For numerical computations, $S\,(\phi_0)$ can be smoothened as

$$S\,(\phi_0) = \frac{\phi_0^2}{\sqrt{\phi_0^2 + \varepsilon^2}} \tag{13b}$$

Eq. (13) has the property that ϕ remains unchanged at the interface, which implies that zero level sets of ϕ and ϕ_0 are identical. Away from the interface, ϕ will converge to a value consistent with the condition $\nabla\phi = \sqrt{(\partial\phi/\partial x)^2 + (\partial\phi/\partial y)^2} = 1$, thereby replicating the true distance function. It is also important to note here that there is expected to occur a sharp discontinuity in the fluid viscosity across the droplet interface, for which special numerical considerations need to be invoked. In order to accommodate this feature, the interface is usually smeared out over a finite thickness of $2a$, so that a smooth variation of the viscosity can be represented as

$$\eta\,(\phi) = \begin{cases} \eta_c & \text{if } \phi > a \\ \eta_b & \text{if } \phi < -a \\ \bar{\eta} - \Delta\eta \sin\left(\dfrac{\pi\phi}{2a}\right) & \text{otherwise} \end{cases} \tag{14}$$

where $\bar{\eta} = (\eta_b + \eta_c)/2$, $\Delta\eta = (\eta_b - \eta_c)/2$. The delta function appearing in Eq. (11b) can also be smoothened accordingly, as

$$\delta\,(\phi) = \begin{cases} \dfrac{1}{2a}\left(1 + \cos\left(\dfrac{\pi\phi}{a}\right)\right) & \text{if } |\phi| < a \\ 0 & \text{otherwise} \end{cases} \tag{15}$$

where a is a small number related to the grid spacings, as mentioned earlier. Once the value of ϕ is numerically obtained, the surface tension force term in Eq. (11b) can be evaluated in a straight forward manner, with $\kappa = \nabla \cdot \boldsymbol{n}$, where $\boldsymbol{n} = \nabla\phi / |\nabla\phi|$ and δ is defined in accordance with Eq. (15).

The physical situation represented by the above description can get substantially more complicated in case the droplets are formed as a consequence of the instabilities associated with the evolution of a phase-separated binary fluid AB, which flows past the chemically patterned walls of a microchannel. The microchannel walls are assumed to be decorated with a checkerboard pattern [5]; each checkerboard being composed of two A(B)-like patches. These patches are preferentially wetted by the A(B) fluid. Two separate fluid streams (A and B streams) are introduced into the microchannel such that the A stream first encounters a B surface patch whereas the B stream first encounters a A surface patch. The binary fluid, in general, can be characterized by an order parameter $\psi\,(\boldsymbol{r}, t) = n_A\,(\boldsymbol{r}, t) - n_B\,(\boldsymbol{r}, t)$, where $n_i\,(\boldsymbol{r}, t)$ represents the local thermodynamic behaviour of the component i (often expressed in terms of the corresponding number density). For such

a syste, the free energy functional can be described as

$$F = \underbrace{\int \left[-\frac{a}{2}\psi^2 + \frac{b}{4}\psi^4 + \frac{k}{2}|\nabla\psi|^2 \right] \mathrm{d}\boldsymbol{r}}_{\text{Ginzburg–Landau free energy for a binary mixture}}$$
$$+ \underbrace{\int \mathrm{d}\boldsymbol{r} \int \mathrm{d}\boldsymbol{s} \left[\frac{1}{2}\xi(\boldsymbol{s}) \exp\left(-\frac{|\boldsymbol{r}-\boldsymbol{s}|}{r_0} \right) \right] [\psi(\boldsymbol{r}) - \psi(\boldsymbol{s})]^2}_{\text{interaction of a fluid element at a point } \boldsymbol{r} \text{ within the patterned substrate}} \quad (16)$$

In Eq. (16), a and b are positive constants. The fluid may considered to be in the two-phase coexistence regime, where the equilibrium order parameter is given by $\psi_{A(B)} = \pm\psi_{\text{eq}} = \pm\sqrt{a/b}$. The term $k/2|\nabla\psi|^2$represents the cost of order parameter gradients. The parameter $\xi(\boldsymbol{s})$ represents the strength of interaction at each point on the checkerboard pattern. On the patterns, one may introduce a noise in these interactions as $\xi(\boldsymbol{s}) = \xi(1 + \alpha\chi(\boldsymbol{s}))$, where $\chi(\boldsymbol{s})$ are independently distributed random numbers in the range $[-1, 1]$. The parameter ξ is a constant on the patterns and is zero, otherwise. In Eq. (16) the parameter r_0 represents the range of the substrate pattern. Some typical values of the above-mentioned parameters are as follows [5]: $r_0 = 5$, $\xi = 0.003$, $\alpha = 0.03$. Physically, the free energy functional is reduced when the fluid is A(B) rich near A(B)-like patterns. The evolution of the order parameter, as appearing in Eq. (16), is described by the Cahn–Hillard equation, in which the flux of ψ is proportional to the gradient of the chemical potential, μ, such that

$$J_\psi = -M\nabla\mu \quad (17)$$

where $\mu = \partial F/\partial\psi$ and M is the mobility of the order parameter. In dimensionless units, the evolution of ψ satisfies the following equation:

$$\frac{\partial\psi^*}{\partial t} + \boldsymbol{V}^* \cdot \nabla\psi^* = \nabla^2\mu^* \quad (18)$$

where the normalizing length scale is taken as the thickness of the interface between A and B, i. e. $l_{\text{ref}} = \sqrt{k/a}$, and the time scale is taken as $t_{\text{ref}} = l_{\text{ref}}^2/aM$. The governing equation for fluid flow, with negligible inertia effects, can be described in the following non-dimensional form:

$$0 = -\nabla\Pi^* + \nabla^2\boldsymbol{V}^* + \boldsymbol{H} + C\frac{\partial F^*}{\partial\psi^*}\nabla\psi^* \quad (19)$$

where $\boldsymbol{H} = H_x\hat{i}(x$ being the axial direction of microchannel flow), with $H_x = (P_{\text{in}} - P_{\text{out}})(l_{\text{ref}}t_{\text{ref}}/\eta L)$ and L is the length of the microchannel. The last term in Eq. (19) is the non-dissipative part of the stress tensor, representing the hydrodynamic interactions. The parameter C is estimated as $\gamma l_{\text{ref}}/aM\eta$, where the interfacial tension $\gamma \approx k\psi_{\text{eq}}^2/l_{\text{ref}}$, and aM is the diffusivity. For a fluid with high viscosity, one has $C \ll 1$, which implies that the hydrodynamic interactions can be neglected. The parameter Π^* (non-dimensional pressure) mathematically acts like a Lagrange multiplier, which generates the incompressibility condition $\nabla \cdot \boldsymbol{V} = 0$. The boundary conditions on μ andψ are as follows (where $\boldsymbol{n}$ represents a normal direction to the boundary surface):

$$\left.\frac{\partial\mu}{\partial n}\right|_{\text{wall}} = 0 \quad (20a)$$

$$\frac{\partial\psi}{\partial n} = 0\,, \text{ for unpatterned surfaces} \quad (20b)$$

$$\frac{\partial\psi(\boldsymbol{s})}{\partial n} = \int \mathrm{d}\boldsymbol{s}_i \left\{ \xi(\boldsymbol{s}_i) [\psi(\boldsymbol{r}) - \psi(\boldsymbol{s}_i)] \right\}\Big|_{\boldsymbol{r}\to\boldsymbol{s}}\,,$$
$$\text{for patterned surfaces} \quad (20c)$$

Equation. (20c) arises explicitly from the minimization of free energy in presence of the substrate patterning. At the microchannel entry and exit, one may write

$$\frac{\partial\psi}{\partial n} = 0 \quad (20d)$$

The dynamic evolution of the droplet, in such systems, strongly depends on the parametr H. For more details, one may refer to the work of Kuksenok et al. [5].

So far we have discussed the droplet dynamics in single straight microchannels only. Droplet dynamics in other microchannel geometries, on the other hand, may be associated with certain distinctive features that are not usually apparent with flows in single straight microchannels. As an example, one may cite the case of droplet motion in a microchannel geometry that is characterized with a sudden contraction in the cross sectional area. Rosengarten et al. [6] have recently presented an interesting study on this aspect, especially dealing with the cases in which the droplet size is larger than the contraction but is smaller than the original microchannel section. The droplet transport can be of a filament type or a slug type, depending on the contraction Capillary number (Ca_{con}) and the Reynolds number (Re) of flow. The average extensional strain rate due to a contraction can be approximated as $(\bar{u}_2 - \bar{u}_1)/L$, where $\bar{u}_2 - \bar{u}_1$ is the difference in mean velocity between the upstream and the downstream channels and L is the distance over which this change takes place. If $\beta = d_1/d_2$ be the contraction ratio of the two capillaries then it can be inferred that the entry length and the upstream vortex attachment length for the flow through the contraction are $0.25d_2$ and $0.17d_1$, respectively [6].

Assuming $L \approx 0.25d_2 + 0.17d_1$, accordingly, the extensional strain rate becomes

$$\dot{\varepsilon} = \frac{\bar{u}_2 - \bar{u}_1}{0.25d_2 + 0.17d_1} \tag{21}$$

For an axisymmetric contraction, $\bar{u}_2 = \beta^2 \bar{u}_1$ (from continuity), which implies

$$\dot{\varepsilon} = \frac{\bar{u}_1 \left(\beta^2 - 1\right)}{0.25d_2 + 0.17d_1} \tag{21a}$$

Hence, the contraction Capillary number can be described as

$$\mathrm{Ca}_{\mathrm{con}} = \frac{\eta_c \dot{\varepsilon} R_0}{\gamma} \tag{22}$$

where R_0 is the original radius of the initially-spherical droplet and $\dot{\varepsilon}$ is given by Eq. (21). Beyond a threshold value of $\mathrm{Ca}_{\mathrm{con}}$, there occurs a transition of the droplet morphology in the contraction, from the slug shape to the filament shape. The transitional value of $\mathrm{Ca}_{\mathrm{con}}$ decreases as the flow Reynolds number is increases. For details of the droplet shape and contact angle evolution under these circumstances, one may refer to the work of Rosengarten et al. [6].

Another interesting feature of droplet dynamics in microchannels can be observed in the T-junctions, across which the droplets can be sheared, extended and split. In order to elucidate the underlying dynamics from a fundamental perspective, one may consider an underformed droplet (with viscosity η_b) of radius R in a matrix fluid of viscosity η_c, with a local velocity gradient of magnitude G and surface tension γ. The stresses scale as $\eta_c G$ and the drop extension time-scale is as $(1 + \eta_b/\eta_c)/G$. The surface tension, on the other hand, tends to relax a deformed droplet back to its spherical shape. Scaling analysis reveals that the capillary velocity scale is as γ/η_c, the drop relaxation time-scale is as $(1 + \eta_b/\eta_c)\eta_c R/\gamma$, and the capillary stresses scale as γ/R. The corresponding extensional flow Capillary number is as $\mathrm{Ca}_{\mathrm{ext}} = \eta_c GR/\gamma$, which physically represents the ratio of the viscous to the capillary stresses, or equivalently, inverse of the ratio of the corresponding time-scales. For the onset of droplet break-up, $\mathrm{Ca} = \mathrm{O}(1)$. Since $G \sim Q_0/R_i^3$, where R_i is the hydraulic radius of the microchannel and Q_0 is the volumetric flow rate, the above condition implies

$$R \sim \frac{\gamma R_i^3}{\eta_c Q_0} \tag{23}$$

Expression (23) reveals that larger the flow rate, smaller is the droplet size. It is important to mention here that this expression is applicable only when $R < R_i$, i.e., when the droplets are small enough so that the hydrodynamic forces exerted by the channel walls are rather inconsequential and the breakup solely relies on the straining of the imposed flow. Identical considerations can be corroborated by the trends of the droplet breakup phenomena that can be observed across the microchannel T-junctions [7]. For an extensional flow in the neighbourhood of a T-junction, $G \sim u/w_0$, where w_0 is the channel width. One may note here that $\mathrm{Ca}_{\mathrm{ext}} = \eta_c GR/\gamma = \mathrm{Ca}R/w_0$, where $\mathrm{Ca} = \eta_c u/\gamma$ is the standard deformation Capillary number. Extensional stress at the stagnation point, being much larger than the shear stresses upstream of the junction, change the droplet length from l_0 to l_e. For the critical condition at which the droplet just breaks, one may write

$$(l_e - l_0) \propto (G - G_0)^{1/2} \tag{24}$$

where G_0 is the upstream shear rate. When $G_0 \ll G$,

$$\mathrm{Ca}_{\mathrm{ext}} \propto \left(\frac{l_e - l_0}{R}\right)^2 \tag{24a}$$

At the stability limit of the droplet,

$$\frac{l_e}{\pi w_w} \sim 1 \tag{24b}$$

where w_e is the width of the stretched droplet. This criterion is consistent with the classical Rayleigh–Plateu instability, in which a cylindrical liquid thread can reduce its total surface area by breaking when its length (l_e) exceeds its circumference (πw_e). Further, from the considerations of volume conservation of the incompressible droplet, one may write

$$l_0 w_0^2 = l_e w_e^2 \tag{24c}$$

Using (24b) and (24c) in (24a) and denoting the initial extension as $\varepsilon_0 = l_0/\pi w_0$, a critical capillary number of droplet breakage at the T-junction can be estimated as

$$\mathrm{Ca}_{\mathrm{cr}} = \alpha \varepsilon_0 \left(\frac{1}{\varepsilon_0^{\frac{2}{3}}} - 1\right)^2 \tag{25}$$

where α is a dimensionless constant, which is a function of η_b/η_c and the geometry of the channel. For symmetrical T-junctions, $\alpha \sim 1$ has been found to excellently match with the experimental observations corresponding to the critical conditions for the breaking of droplets [7]. It is also important to note here that with $\varepsilon_0 > 1$, droplets are always found to break in the T-junction, even for the lowest achievable values of Ca (see Fig. 4). On the other hand,

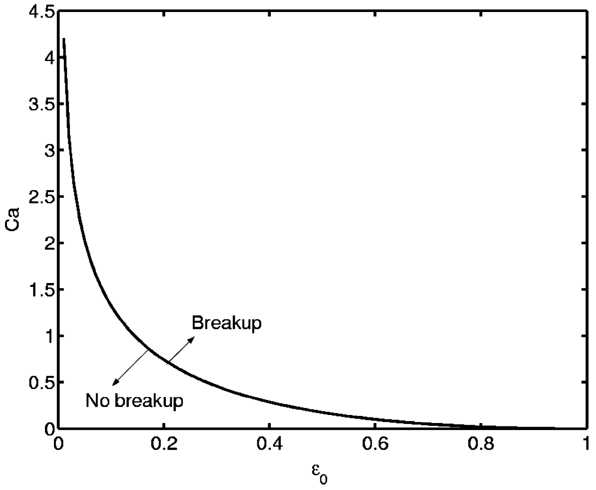

Droplet Dynamics in Microchannels, Figure 4 Critical conditions for droplet breaking at T-junctions

they never break up upstream in the straight portion of the channel preceeding the T-junction, despite satisfying the breaking criterion mathematically. This can be attributed to the fact that before the onset of breaking, the droplet may be perturbed with associated crests and troughs. The portions of the greatest lateral extensions (i. e., the crests) are characterized with pressures that are higher than the pressures at the regions of greatest lateral contractions (troughs). To restore the equlibrium, liquid would flow from higher pressure to lower pressure, thereby stabilizing the droplet. Physically, the confinement of the channel walls imparts the stabilizing effect to the droplet at the upstream locations, preventing the droplet breakup. At the T-junction, however, the droplet is offered with a provision of being free of any confinement over at least one portion of its lateral faces, allowing the perturbations to grow and the droplet to break up.

The development of fundamental models on droplet dynamics through microchannels has lead to a number of analytical and numerical studies reported in the literature in the recent past. Scheeizer and Bonnecaze [8] employed the boundary-integral method to numerically simulate the displacement of a two-dimensional droplet attached to a solid surface when the inertial and gravitational forces are negligible. These authors showed that as the capillary number was increased, the deformation of the droplet increased until a critical value was reached. Beyond this limit, no steady droplet shapes were observed. Increasing the droplet size resulted in an increase in the deformation of the interface at a given capillary number. The deformation of the droplet was found to be more severe with higher viscosity ratios. Both shear and pressure-driven flow regimes were examined and were shown to have similar values of the critical capillary number. Further, addition of surfactants was shown to reduce the deformation of the pinned droplets, as the surface Péclet number was increased.

Future Directions for Research

A comprehensive review on theoretical modeling and simulation of droplet dynamics in microchannels has been presented by Cristini and Tan [9]. In their paper, theoretical considerations relevant to controlled droplet generation, breakup and coalescence in micro channels were discussed. In particular, theoretical and numerical investigations of droplet breakup and coalescence in imposed flows were reviewed, including the methodologies commonly employed for simulating droplet generation, dynamics, breakup and coalescence in micro channels. From their review, following major conclusions could be drawn:

1. The magnitude and type of flow are both important in determining generation, breakup and coalescence times and droplet sizes. Detailed quantitative estimates in this regard are yet to be made.
2. The local velocity gradient imposed on a droplet is a function of position in the micro channel, and is a strong function of the channel geometry. This also needs to be studied from a more rigorous theoretical perspective.
3. The microchannel geometry and flow conditions can be optimised using adaptive simulations. More extensive research can be directed towards this aspect.
4. One open area on droplet based microfluidics research is the issue of droplet–wall interactions. For droplets of size comparable to the microchannel width, the hydrodynamic forces exerted by the wall on the droplet may exceed those exerted by the imposed channel flow. Under these situations, the droplet deformation, breakup and coalescence criteria and rates may be strongly affected, which are yet to be theoretically well-resolved.

Cross References

► Applications Based on Electrowetting
► Boundary Slip of Liquids
► Bubble Dynamics in Microchannel
► Capillary Filling
► Chaotic Flow
► Compute Mixing Efficiency
► Digital Microfluidics
► Droplet and Bubble Formation in Microchannels
► Droplet Based Lab-on-Chip Devices

- ► Droplet Despensing
- ► Droplet Evaporation
- ► Droplet Microreactors
- ► Electrocapillary
- ► Electrowetting and Droplets
- ► Surface Tension Driven Flow
- ► Transport of Droplets by Acoustics
- ► Transport of Droplets by Thermal Capillarity
- ► Wetting and Spreading

References

1. Chakraborty S, Mittal R (2007) Droplet dynamics in a microchannel subjected to electrocapillary actuation. J Appl Phys 101:104901
2. Hirt CW, Nichols BD (1981) Volume of fluid (VOF) method for the dynamics of free boundaries. J Comput Phys 39:201–225
3. Sussman M, Smereka P, Osher S (1994) A level set approach for computing solutions to incompressible two-phase flow. J Comput Phys 114:146–159
4. Majumder S, Chakraborty S (2005) A new physically-based approach of mass conservation correction in level set formulation for incompressible two-phase flows. Trans. ASME, J Fluid Eng 127:554–563
5. Kuksenok O, Jasnow D, Yeomans J, Balazs AC (2003) Periodic droplet formation in chemically patterned microchannels. Phys Rev Lett 91:108303-1–108303-4
6. Rosengarten G, Harrie D, Cooper-White J (2005) Using computational fluid dynamics to study the effect of contact angle on microdroplet deformation. ANZIAM J 46:C304–C319
7. Link DR, Anna SL, Weitz DA, Stone HA (2004) Geometrically mediated breakup of drps in microfluidic devices. Phys Rev Lett 92:054503-1–054503-4
8. Schleizer A, Bonnecaze RT (1999) Dispacement of a two-dimensional immiscible droplet adhering to the wall in shear and pressure-driven flows. J Fluid Mech 383:29–54
9. Cristini V, Tan Y-C (2004) Theory and numerical simulation of droplet dynamics in complex flows-a review. Lab Chip 4:257–264

Droplet Ejection

► Droplet Dispensing

Droplet Evaporation

Friedhelm Schönfeld
Institut für Mikrotechnik Mainz GmbH, Mainz, Germany
Schoenfeld@imm-mainz.de

Synonyms

Liquid–vapor phase change; Vaporization

Definition

The difference in the vapor pressure immediately above a droplet surface and the ambient (partial) pressure of the vapor far away from the drop, drives a diffusive flux leading to a gradual decrease of the liquid volume, which is termed droplet evaporation. Within a molecular picture, the probability of highly energetic liquid molecules going over into the gas phase is higher than that of them being re-adsorbed (condensating) in the course of the subsequent random walk (Brownian motion). Thus, there is a net-flow of molecules from the liquid to the gaseous phase. The associated transferred energy is termed the latent heat or enthalpy of vaporization.

Overview

Droplet evaporation plays a vital role in various fields of natural science and engineering such as: cloud physics, burning liquid-fuels, air/fuel-premixing, (biological) crystal growth, and painting. Moreover, the high heat transfer rates associated with evaporation suggests its use in contexts with a variety of thermal applications, such as spray-cooling or in the electronics industry for cooling of integrated circuits with high heat dissipation rates. Probably the most common application involving droplet handling and evaporation is ink-jet printing. Using piezo or thermally actuated print heads droplet sizes down to a few picoliters are generated. While home and common office applications rely on aqueous inks containing dyes or pigments, versatile printers suitable for polymer substrates use solvent inks with volatile organic liquids. Yet, ink-jet technology has a potential far beyond these applications, for instance in (bio-)chemistry or electronics, where circuit boards can be inexpensively manufactured by printing the electronic components.

Generally, phase change is governed by two counteracting aspects. On the one hand attractive intermolecular interactions which give rise to interfacial tension keep the liquid molecules together. Due to this surface tension small liquid volumes attain a minimum surface, i. e., a spherical shape for a free-floating drop. On the other hand the liquid molecules obey an energy distribution. A fraction of the molecules have energies above a certain threshold allowing them to overcome the cohesive forces within the liquid. These molecules give rise to the vapor pressure above the liquid surface. Moreover, when the *highly* energetic molecules go from the liquid to the vapor phase thermal energy (latent heat) is removed from the bulk liquid.

Besides these applications, droplet evaporation reveals several intriguing phenomena and is a prime example of a microfluidic *multiphysics* system, which is noticeably complex due to the interplay of mass and heat transfer, hydrodynamics of multiphase flow, interface energy effects as contact angle hysteresis, volumetric forces as gravity, and Marangoni flows.

In the present essay we focus on a commonly encountered case of slow evaporation of sessile drops, with an initial volume ranging from a few pL to some μL, typical evaporation times between 10^{-1} s and 10^{2} s, and we assume a stagnant ambient gaseous phase. Within the chosen model approach the restriction to sessile drops does not impose any major limitations since the dynamics of evaporating levitated spherical drops are recovered for the special case of a 90° contact angle. Moreover, slow evaporation of minute drops on a relatively *thermally heavy* substrate implies that typical temperature changes are small and may be neglected within qualitative modeling approaches.

Furthermore, we neglect forced or natural (buoyancy-driven) convection, surface oscillations and spreading phenomena; not to mention more sophisticated aspects such as Leidenfrost effects, i. e., retardation of evaporation on a hot substrate due to droplet levitation by the vapor, or aspects of thin film evaporation in the microregion, where the material properties deviate considerably from the bulk properties.

Basic Methodology

The experimental methods used to observe droplet evaporation which have been reported in the literature, may rely on the monitoring of successive silhouettes of sessile drops by video-microscope imaging, or on ultraprecision weighing with electronic microbalances and with quartz crystal microbalances, or on the use of atomic force cantilevers. What all these methods typically have in common is that data are provided which allow, among other possibilities, monitoring the decrease in the droplet volume over time. From this, material properties such as the vapor diffusion coefficient (D), the saturation pressure (p_{sat}), or likewise the saturation vapor concentration (c_{sat}), or for instance the solid–liquid contact angle (θ), may be deduced. But, the physical interpretation of the data requires some mathematical considerations. We will therefore outline the basic governing equation revealing the dependence of the volume change on the above-mentioned properties.

A comprehensive overview of the mathematical description has been given in [1] and in the original work cited therein. Here, we just present a brief outline along with the basic considerations. Small droplets with dimensions well below 1 mm take the shape of a spherical cap which in the present case is assumed to rest on a planar surface. The droplet volume V_{cap} can be expressed in terms of the contact angle θ and the contact line radius R, i. e., the radius of the circular three-phase contact line (cf. Fig. 1a):

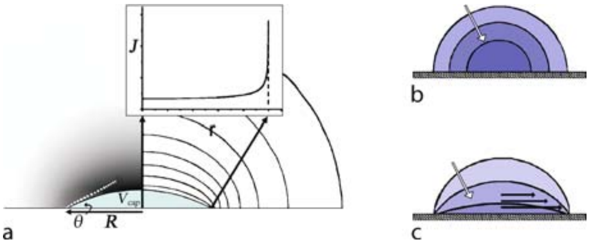

Droplet Evaporation, Figure 1 (**a**) Left side: simulated vapor concentration (gray-scale encoded) above a spherical-cap shaped droplet. Right side: iso-lines of vapor concentration. The inset shows the local evaporation rate (J) as function of the radial coordinate. The large concentration gradient (narrow iso-lines) leads to a diverging flux close to the three-phase contact line. (**b**) Sketch of an evaporating droplet in the constant contact angle mode. The arrow denotes the shrinkage of the droplet in the course of the evaporation. (**c**) Sketch of the pinned-contact line evaporation mode. Black arrows indicate the internal convective flow caused by the large evaporation rate at the rim

$$V_{\text{cap}} = \pi R^3 \frac{\beta(\theta)}{3\sin^3\theta}\,, \text{ with } \beta(\theta) = 2 - 3\cos\theta + \cos^3\theta \tag{1}$$

Examining the various timescales involved shows that droplet evaporation is commonly diffusion limited. Since the characteristic vapor diffusion times are well below the typical droplet evaporation times [2] the vapor concentration is assumed to adapt *instantaneously* to a droplet deformation, and within the so-called quasisteady approach the dynamics of the evaporation is controlled solely by the diffusional mass transport from the droplet surface into the ambient gas phase. A characteristic vapor distribution above the droplet, obtained by finite-element simulations, is shown in Fig. 1a. The local evaporation rate (with dimensions of mass per area and time), which is proportional to the gradient of the concentration at the droplet surface, is a function of the radial coordinate and the contact angle. But for the time being we leave these details aside. To determine the volume decrease of the droplet we need the total evaporation rate (mass per time), which is obtained by integrating the local evaporation rate over the droplet surface. Without going through the few intermediate steps we will simply discuss some consequences of the resulting equation which governs the decrease in droplet volume

$$-\left(\frac{\mathrm{d}V_{\text{cap}}(\theta,R)}{\mathrm{d}t}\right) = \frac{4\pi}{\rho_{\text{L}}}\left(\frac{3V_{\text{cap}}(\theta,R)}{\pi\beta(\theta)}\right)^{\frac{1}{3}} D\Delta c f(\theta) \tag{2}$$

where ρ_{L} denotes the liquid density, D is the diffusivity of vapor molecules in the gas phase, and Δc is the difference

between the saturation concentration c_{sat} and the ambient vapor concentration far away from the droplet. The function $f(\theta)$ contains the dependence of the total evaporation flux on the contact angle. A simple expression which approximates the exact dependence to within a few percent over almost the entire contact angle range is [1]

$$f(\theta) \approx -\frac{\cos\theta}{2\ln(1-\cos\theta)} \tag{3}$$

The temperature dependence of the evaporation is basically governed by two effects: the strong increase in the vapor pressure (and saturation pressure) with temperature (Antoine correlation) and the relatively weak temperature dependence of the diffusivity ($D \sim T^{1.75}$).

To recap, the evolution of the droplet volume in the course of evaporation obeys Eq. (2). However, the volume depends on the parameters θ and R, which may vary independently as function of time. Hence, the evaporation dynamics is not fully determined by a single equation. There are, however, two important limiting cases which are often encountered in experiments where Eq. (2) is sufficient.

Case (I): fixed contact angle $\theta(t) = \theta_0 = \text{const}$, $R(t)$ variable. On smooth, ideal surfaces in the absence of any contact angle hysteresis and dynamic effects the contact angle remains constant independent of the contact line radius, i. e., independent of the contact line position, and the radius of curvature of the interface (Fig. 1b). In this case Eq. (2) can readily be integrated, thus yielding the explicit volume decrease

$$V_{\mathrm{cap}}^{\frac{2}{3}} = V_{\mathrm{cap;init}}^{\frac{2}{3}} - \frac{2}{3} K f(\theta_0) \cdot t \tag{4}$$

where $V_{\mathrm{cap;init}}$ denotes the initial droplet volume and remaining constants have been lumped together into K ($\approx 12.37 \cdot D\Delta c/\rho_L \cdot \beta^{1/3}$). Note that Eq. (4) also covers the case of a floating evaporating droplet for the particular case $\theta_0 = \pi (f = 0.5)$ and $V_{\mathrm{drop}} = 2V_{\mathrm{cap}}$.

Case (II): pinned contact line $\theta(t)$ variable, $R(t) = \text{constant}$. On the other hand for inhomogeneous surfaces or under other nonideal conditions the contact line can be perfectly pinned. The contact line radius and thus the wetted area stay constant and the contact angle decreases over time, as sketched in Fig. 1c. In this case Eq. (2) has to be numerically integrated.

In both cases the complete evaporation dynamics is governed by Eq. (2) since the droplet volume only depends on one variable. In the case of slip-stick behavior, i. e., alternating behavior alternating between cases I and II, the data analysis can also be performed based on the above equation.

Key Research Findings

In this section we focus on some of the most important features of evaporating sessile drops: the scaling resulting from the above model and the consequences of the spatial nonuniform evaporation current commonly known as the *coffee stain* or *donut effect*.

For case I, Eq. (4) facilitates the determination of any of the involved quantities from experimental data of the droplet volume provided that all remaining parameters are known. Specifically, the predicted linear dependence of $V_{\mathrm{cap}}^{2/3}$ on time is commonly observed and allows for a reliable determination of parameters. As an example, the evaporation data of toluene, butanol and two alkanes are shown in Fig. 2. The factors $K \cdot f(\theta)$ are readily determined by linear fitting, cf. Eq. (4). But, in order to increase the quality of the parameter fits, a more accurate correlation than Eq. (3) is recommended [1]. Such a data analysis can be used to estimate the cooling of droplets during evaporation.

Furthermore, Eq. (4) implies the scaling of the total evaporation time (T_{evap}), the time it takes until the droplet has vanished, with the initial droplet volume, namely

$$T_{\mathrm{evap}} \propto V_{\mathrm{cap;init}}^{\frac{2}{3}} \tag{5}$$

This may also be exploited to determine the material constants. Eq. (5) also holds in the pinned (constant-radius) mode. In this case a faster evaporation is to be expected, due to the larger specific evaporation area. However, the precise value of the model-predicted proportionality constant is beyond analytical means and has to be computed numerically.

Further interesting physics is revealed by considering the evaporation rate in more detail. Exploiting the analogy between the concentration field outside an evaporating drop and the electrostatic potential of a similar-shaped charged body, as proposed by Maxwell more than a century ago, one can show that the evaporation current (J) is not constant all over the drop surface (cf. Fig 1a, right-hand side). In particular a diverging evaporation current is found at the outer edge near the contact line. This can be qualitatively explained within the molecular picture of the diffusion process, i. e., Brownian motion. Molecules which diffuse into the vapor phase leaving the drop at the center perform a random walk and thus have a high probability of being re-adsorbed at the liquid surface. Yet, for contact angles less than 90° the probability of re-adsorption at the liquid surface is lower for molecules which escape at the edge leading to a higher net evaporation flux near the contact line [3]. Moreover, as mentioned above, the contact lines are likely to be pinned on nonideal

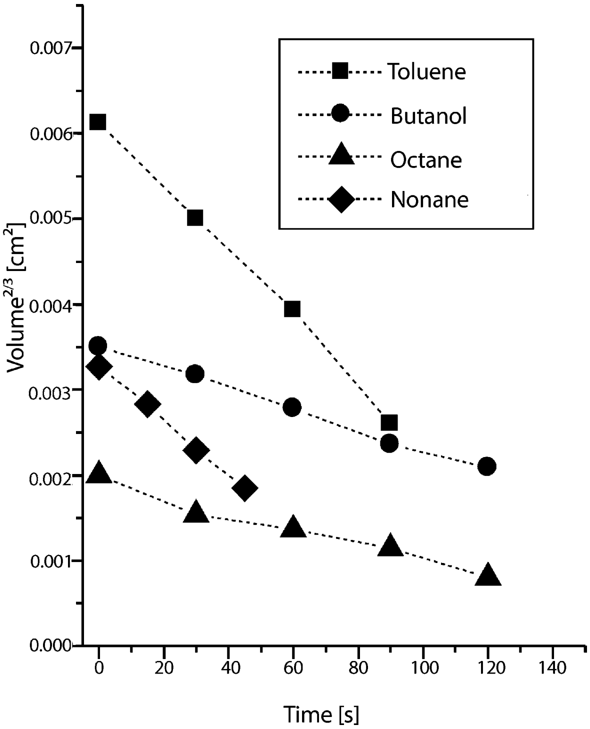

Droplet Evaporation, Figure 2 Time dependence of the two-thirds power of the drop volumes, data taken from [1]. Symbols denote data for toluene, butanol and two alkanes. The lines are provided as a guide to the eye

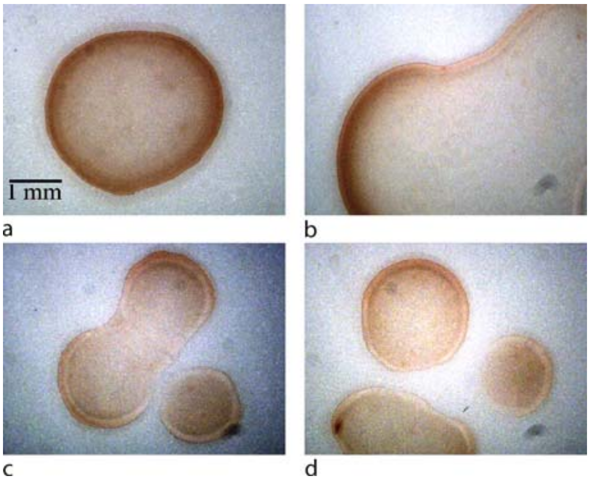

Droplet Evaporation, Figure 3 (**a**) Coffee stain arising from a nearly spherical cap droplet. (**b**) Ring stain after deposition of a larger drop showing a more (less) pronounced perimeter ring of deposited particles for a convex (concave) curvature of the contact line. (**c**) and (**d**) coffee stains showing less accentuated perimeter rings in regions where vapor concentration fields interfere

surfaces. Due to the large evaporation at the pinned contact line fluid has to be replenished from the drop interior leading to a radial outward flow within the drop as shown in Fig. 1c. This flow can be directly observed in experiments if, for instance, fluorescence particles are suspended in the drop. However, its consequence for the deposition of dispersed material after complete droplet evaporation is more obvious. Due to the outward flow material is constantly transported to the outer rim where the fluid evaporates most rapidly and the suspended material is deposited. This leads to the well-known *coffee stain* phenomenon: an evaporating droplet leaves a deeply colored outer rim of the initially suspended material whereas the interior of the wetted area is observed to stay almost coffee-free [3]. Corresponding experimental images of coffee stains are shown in Fig. 3. Fig. 3a shows a typical stain arising from a nearly spherical-cap droplet. Fig. 3b shows the influence of the contact line curvature for noncircular drops and Figs. 3c and 3d indicate that the stains of evaporated drops are altered due to the influence of droplets in the near vicinity [3]. As discussed above, the accumulation of suspended material during evaporation is driven by an internal convective flow within the drop which, in turn, is caused by the large evaporation near the contact line. Consequently, if evaporation at the contact line is decreased by locally increasing the ambient vapor concentration, e. g. by placing a second drop in the near vicinity, the tendency toward ring formation is suppressed (cf. Figs. 3c and 3d). The same arguments hold in the context with more (less) pronounced material accumulation near convex (concave) contact lines, as shown in Fig. 3b.

Coffee stains are a very clear example of surface patterning by means of evaporation. Since the patterns are predominantly created in the vicinity of the contact line, high-resolution patterns are achievable by surprisingly simple means. However, what has been discussed so far is just one particular scenario, generally various mechanisms are involved in pattern formation. A list of the most important ones is given below [4].

- High (diverging) evaporation rate of liquid near the contact line for contact angles less than 90°, which induces a radial outward flow toward the drop periphery, as discussed above.
- Pinning and depinning phenomena: the prerequisite for pronounced ring formation to occur is the pinning of the contact line. In many experiments pinning is observed right at the beginning of the evaporation, whereas the contact line may be released in the later stages and evaporation proceeds in the constant contact angle mode. The formation of ring stains, i. e., the deposition of solute at the three-phase contact line, strength-

ens an initial pinning or it may even initiate it. This so-called self-pinning mechanism can lead to various deposition patterns from cellular to almost fractal structures [3].

- Evaporation-induced higher solute concentration and lower temperature near the contact line cause the so-called Marangoni flows. These flows occur since the surface tension depends on various parameters such as the concentration of dissolved species and the temperature. Any gradient in these quantities induces a spatial variation of the surface tension and a corresponding pressure variation within the liquid which manifests itself in a convective flow.
- The temperature gradient within the droplet perpendicular to the substrate can induce Rayleigh–Bénard convection cells. The corresponding convective cells grow stronger near the drop periphery due to smaller thickness and a corresponding higher temperature gradient there.
- Interactions within the suspended material, such as colloidal nanoparticles [5, 6] and interactions between the suspended material and the susbstrate (see below).

The presence of surfactants, which adsorb at the liquid–vapor interface and reduce the surface tension, can also have a large impact on the evaporation-driven pattern formation. Inhomogeneities in the surfactant distribution create a surface tension gradient and a corresponding (additional) Marangoni flow. With respect to the Rayleigh–Bénard convection it has been shown that the surfactant-driven flow can favor the formation of convection cells and considerably alter the deposition patterns [7].

In the context of particle–particle interaction (the final point in the above list) it has been reported that subsequently to the accumulation of material at the outer rim capillarity mediated interaction can drive the particles into regular assemblies [5]. These self-organized patterns vary from the previously discussed *coffee* rings built up from particle monolayers for relatively low initial particle concentrations to plane crystal multilayers for higher particle volume fractions. Large, highly regular arrays of complex aggregates of nanoparticles are obtained by means of template-assisted methods, where patterned arrays of hydrophilic spots are used for regular arrangements of droplets and self-organization occurs within the droplets. Generally any kind of particle can be arranged by this technique provided that it has been well wetted by the evaporating carrier fluid [5, 6]. In this sense droplet evaporation provides additional features for evaporation-based colloidal crystallization. Furthermore, even the self-assembly of DNA in the so-called starburst pattern by deposition from evaporating drops has been observed [8, 9].

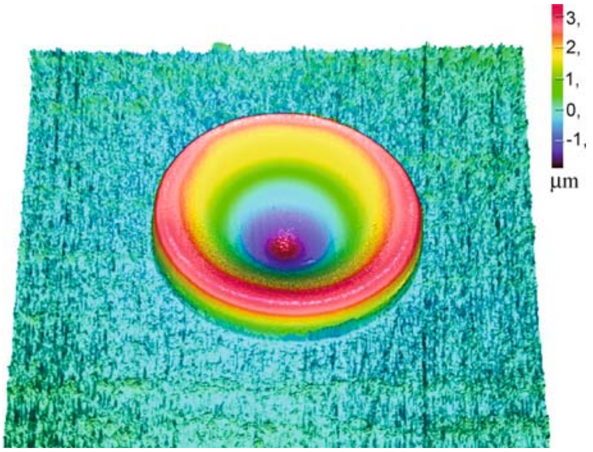

Droplet Evaporation, Figure 4 False-color surface plot of a microcrater caused by a toluene drop on polystyrene (molar mass 210 kDa, PDI = 1.07) after evaporation. The drop was deposited on the polymer substrate with a syringe, and the resulting microstructure was imaged with a confocal white-light microscope. (Figure provided by K Graf, Max-Planck-Institute for Polymer Research, Mainz, Germany)

Future Directions for Research

The patterning methods mentioned so far all involve nondissolving substrates. But, using dissolving substrates instead opens up a new field of research. For a solvent drop on a polymer surface, the substrate is locally softened and dissolved. Similar to the above-mentioned case of liquid suspensions, molecules from the substrate are transported to the rim. Close to the contact line the solute concentrations increases and piles up due to precipitation. Thus, by means of evaporation-driven internal convection, the topography of the substrate is changed. Within the given scenario the above list of mechanisms has to be expanded by dissolving/precipitation and phenomena resulting from the interaction with other effects. A typical microcrater formed by the deposition and subsequent evaporation of toluene on a polystyrene substrate is shown in Fig. 4. Similarly, microcraters of optical quality which can be utilized as concave lenses have been realized by Bonaccurso et al. [10] using ink-jet deposition of solvent droplets. Lenses with diameters between 20 µm and 200 µm and depths ranging from 100 nm to 8 µm could be realized, depending on the choice of droplet volumes and the number of deposited drops. This method provides a simple and inexpensive way of fabricating microvessels and microlenses, whose properties can be tailored by an appropriate choice of substrate materials, pure solvents or mixtures with different volatilities, number of droplets and dimensions.

Cross References

- ► Boiling and Evaporation in Microchannels
- ► Diffusion
- ► Droplet Based Lab-on-Chip Devices
- ► Evaporation for Film Deposition

References

1. Erbil HY, McHale G, Newton MI (2002) Drop evaporation on solid surfaces: constant contact angle mode. Langmuir 18:2636–2641
2. Hu H, Larson RG (2002) Evaporation of a sessile droplet on a substrate. J Phys Chem B 106:1334–1344
3. Deagan R, Bakajin O, Dupont TF, Huber G, Nagel SR, Witten TA (2000) Contact line deposits in an evaporating drop. Phys Rev E 62(1):756–765
4. Gonuguntla M, Sharma A (2004) Polymer patterns in evaporating droplets on dissolving substrates. Langmuir 20:3456–3463
5. Fan F, Stebe K (2004) Assembly of colloidal particles by evaporation on surfaces with patterned hydrophobicity. Langmuir 20:3062–3067
6. Dutta J, Hofmann H (2004) Self organization of colloidal nanoparticles. In: Nalwa HS (ed) Encyclopedia of Nanoscience and Nanotechnology. American Scientific Publishers, California, pp 617–640
7. Nguyen VX, Stebe K (2002) Patterning of small particles by a surfactant-enhanced Marangoni–Bénard instability. Phys Rev Lett 88(16):164501-1–164501-4
8. Jing J, Reed J, Huang J, Hu X, Clarke V, Edington J, Houseman D, Anantharaman TS, Huff EJ, Mishra B, Porter B, Shenker A, Wolfson E, Hiort C, Kantor R, Aston C (1998) Automated high resolution optical mapping using arrayed, fluid fixed, DNA molecules. Proc National Acad Sci, USA 95:8046–8051
9. Sukhanova A, Baranov AV, Perova TS, Cohen JHM, Nabiev I (2006) Controlled self-assembly of nanocrystals into polycrystalline fluorescent dendrites with energy-transfer properties. Angewandte Chemie (International Edition) 118(13):2102–2106
10. Bonaccurso E, Butt HJ, Hankeln B, Niesenhaus B, Graf K (2005) Fabrication of microvessels and microlenses from polymers by solvent droplets. App Phys Lett 86:124101-1–124101-3
11. Deagan R. (2000) Pattern formation in drying drops, Phys Rev E 61(1):475–485

Droplet Flow

► Microsegmented Flow

Droplet Formation

► Droplet Dispensing

Droplet Generation

► Droplet Dispensing
► Droplet Dynamics in Microchannels

Droplet Generator

► Piezoelectric Microdispenser

Droplet Injection

► Droplet Dispensing

Droplet Manipulation

► Transport of Droplets by Acoustics

Droplet Microfluidics

► Droplet Based Lab-on-Chip Devices
► Electrowetting and Droplets

Droplet Micromixer

► Droplet Microreactor

Droplet Microreactor

NGUYEN NAM-TRUNG
School of Mechanical and Aerospace Engineering,
Nanyang Technological University, Singapore, Singapore
mntnguyen@ntu.edu.sg

Synonyms

Droplet micromixer; Droplet-based microreactor; Capillary reactor

Definition

A droplet microreactor is a reaction platform that enables chemical reactions to be carried out inside a microdroplet with a volume on the order of a few microliters or less. The droplets are formed and suspended in an immiscible phase such as an oil. Mixing is achieved inside the droplet on the basis of chaotic advection, which is induced by either droplet motion or the channel shape.

Overview

The main advantages of droplet microreactors are the small amount of reagents, the enclosed reaction environment, and rapid mixing. Droplet microreactors are often

protected by an immiscible phase such an oil which prevents evaporation of the droplets. Thus, besides fast reactions, long processes such as protein crystallization can also be carried out in droplet microreactors.

There are two basic platforms for droplet microreactors: the planar platform and the in-channel continuous platform. In a planar platform, the droplet can move freely on a planar surface, while the motion of the droplet in an in-channel continuous platform is restricted by microchannels. The actuation of droplets in a planar platform is based on nonmechanical concepts such as electrowetting, thermocapillary forces, and magnetic forces. Most in-channel continuous platforms rely on pressure to move the droplets.

Both platforms for droplet microreactors require the following key functions for manipulating droplets: droplet formation, droplet transport, mixing inside droplets, droplet merging, and droplet splitting. In the following, the basic methods for obtaining these functions are discussed.

Basic Methodology

Planar Platform

Electrowetting

Direct electrowetting and electrowetting on dielectric are best suited for planar droplet microreactors. Electrowetting can be used for dispensing and transporting a liquid droplet [1]. Figure 1a depicts the general concept of electrowetting on dielectric. The aqueous-droplet microreactor is surrounded by an immiscible phase. For actuation, the droplet should be aligned with the control electrodes on the bottom surface. Applying a voltage to the electrode changes the hydrophobicity of the solid/liquid/liquid contact line. The difference in interfacial stress across the droplet causes its motion. An insulating layer and a hydrophobic layer function as the dielectric. The hydrophobic layer is made of a polymer with a low surface energy such as Teflon. The top electrode is made of transparent indium tin oxide (ITO) for optical access to the droplet reactor. Figures 1b–e show the various handling operations of a droplet microreactor: dispensing, merging, cutting, and transport. These basic operations allow merging and fast mixing of liquid droplets. The concept also works with liquid droplets surrounded by air. However, the liquid/air system may have the disadvantage of evaporation. A droplet microreactor based on electrowetting needs an electrolyte as a working fluid.

Thermocapillarity

Thermocapillary forces can be used to manipulate a droplet microreactor in the same way as electrowetting does [2]. However, the elevated temperature required may cause evaporation and, in the worst case, boiling of the droplet. Thermocapillary stresses caused by spatial variations of the surface tension at a gas/liquid interface can induce spontaneous flow of a liquid film to a cooler position. The surface tension at the cooler position is higher and induces a tangential force that moves the liquid droplet to the cooler place. Figure 2 depicts the device concept for a droplet microreactor based on thermocapillarity. The droplet is positioned on a homogeneous, partially wetting surface. The wetting surface also functions as an electrical insulator from the underlying heater. A heater array controls the temperature gradient at the surface and consequently the motion of the droplet. Compared with electrowetting, thermocapillarity is much slower owing to the relatively large heat capacity of the surface.

Magnetism

Magnetic forces can also be used for manipulating droplet microreactors [3]. Magnetic beads or a ferrofluid are needed for this actuation concept. Instead of electrodes or heaters, microcoils are integrated on the surface. Figure 3 shows the basic configuration of a magnetically actuated droplet microreactor. A pair of permanent magnets polarizes the magnetic particles in the droplet. A coil array induces a magnetic gradient, which moves the droplet.

In-Channel Continuous Platform

Droplets are formed by shear stress or a pressure drop in an in-channel continuous platform. The two basic configurations for droplet formation are shown in Fig. 4. The cross-junction configuration is similar to that for hydrodynamic focusing. The carrier fluid enters the channel from the middle inlet, while the droplet liquids join from both sides (Fig. 4a). The T-junction configuration lets the droplet liquids join perpendicular to the carrier flow (Fig. 4b). The formation behavior of droplets depends on the Capillary number, which represents the ratio between the friction force and the surface tension in a two-phase system,

$$\mathrm{Ca} = \frac{u\mu}{\sigma}, \tag{1}$$

where u is the mean velocity, μ is the dynamic viscosity, and σ is the interfacial tension between the two liquid phases, and on the sample fraction, which is defined as the ratio between the volumetric flow rate of the aqueous droplet liquid and the total volumetric flow rate of both phases,

$$r = \frac{\dot{Q}_{\mathrm{solution}}}{\dot{Q}_{\mathrm{solution}} + \dot{Q}_{\mathrm{Carrier}}}, \tag{2}$$

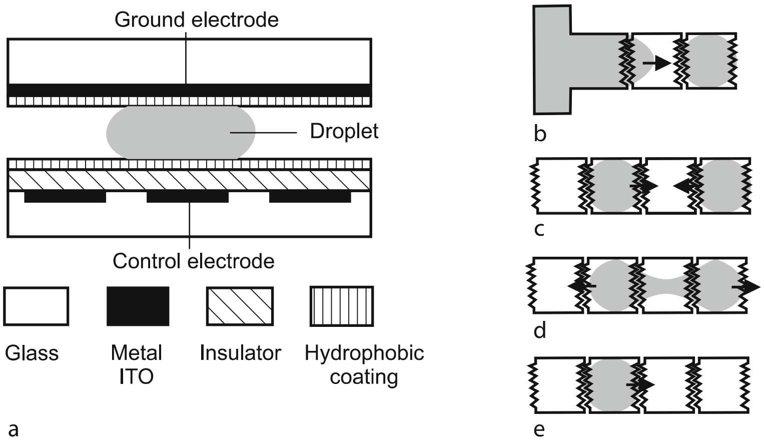

Droplet Microreactor, Figure 1 Droplet microreactor based on actuation by electrowetting. (**a**) Device concept. (**b**) The liquid is pulled in by activating the two electrodes on the right. When the middle electrode is turned off, surface tension breaks up the droplet, allowing precise dispensing. (**c**) Turning on the second electrode from the right lets the two droplets merge. (**d**) Turning on the first and the third electrode from the right causes the droplet to split. (**e**) Subsequent activation of the electrodes allows droplet transport

where $\dot{Q}_{\text{solution}}$ and $\dot{Q}_{\text{Carrier}}$ are the flow rates of the reactant solution and the carrier fluid, respectively.

Key Research Findings

Mixing in Droplet Microreactors

Planar Platforms

Mixing in planar platforms can generally be obtained by use of three actuation modes: merging, splitting and moving (Fig. 1c–e). Because of the small size of the droplets, coalescence alone allows mixing based on molecular diffusion within the droplet. Paik et al. reported a mixing time of 90 s for an approximately 2 μl droplet [1]. Moving the droplet around induces internal flow inside the droplet, which allows folding and stretching of the fluid, with short, chaotic advection. Chaotic advection created by a periodic split-and-merge action as shown in Fig. 1c, d reduces the mixing time to approximately 2 s at a 16 Hz switching frequency. Chaotic advection inside the droplet can also be induced by moving the merged droplet around (Fig. 1e). The droplet can be moved along a line with a $1 \times N$ electrode array or in a loop with a $2 \times N$ electrode array. The best mixing time, of 3 s, with this merge-and-move concept was achieved with a 2×4 electrode array [4].

In-Channel Continuous Platforms

Because the droplets are formed directly in the microchannel, very small droplet microreactors with sizes in the range 1 pl to 100 nl can be formed in an in-channel continuous platform. The confined environment removes the residence time distribution due to the nonuniform velocity profile that occurs in continuous-flow platforms, also known as dispersion. When a droplet moves in a microchannel, the shear stress on the droplet wall induces an internal flow pattern, which can be used to produce chaotic advection to improve mixing. However, if the microchannel is straight, as depicted in Fig. 5a, the flow pattern inside the droplet is symmetric and steady. The two vortices containing the reactants A and B exist in separate halves of the droplet and mixing is not improved significantly. If the microchannel has bends as depicted in Fig. 5b, the droplet has different velocities at the walls on the two sides owing to the different radii of curvature. Thus, the internal flow pattern is asymmetric and periodic. While moving through this repeating channel pattern, each side of the droplet takes its turn to have the faster vortex. Chaotic advection and, consequently, faster mixing can be achieved. In this concept, the larger vortex is dominant over the smaller vortex for each bend; this resembles the reorientation, stretching, and folding needed for micromixers based on chaotic advection. Since the number of cycles depends on the number of bends n, the improvement of mixing time compared with the case of a straight channel is 4^{n-1}. Compared with diffusive mixing with parallel lamination, the improvement of the mixing time can be described as follows:

$$\frac{t_{\text{chaotic}}}{t_{\text{diffusive}}} = \frac{\text{Pe}}{L^* \log \text{Pe}} \qquad (3)$$

where

$$\text{Pe} = \frac{uW}{D} \qquad (4)$$

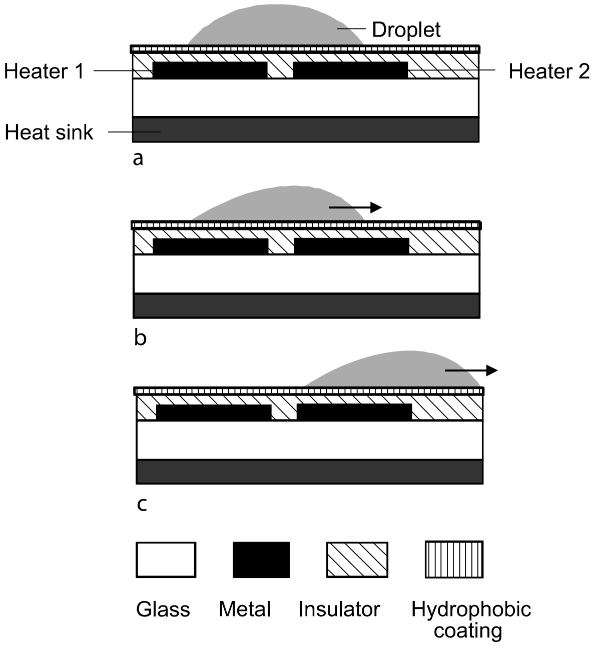

Droplet Microreactor, Figure 2 Droplet microreactor based on thermocapillary actuation. (**a**) Without a temperature gradient, the droplet is at equilibrium and does not move, (**b**) If heater 1 is on, the induced temperature gradient propels the droplet owing to the difference in surface stress between the sides of the droplet. (**c**) If the droplet moves out of the temperature field of heater 1, heater 2 is activated to propel the droplet further

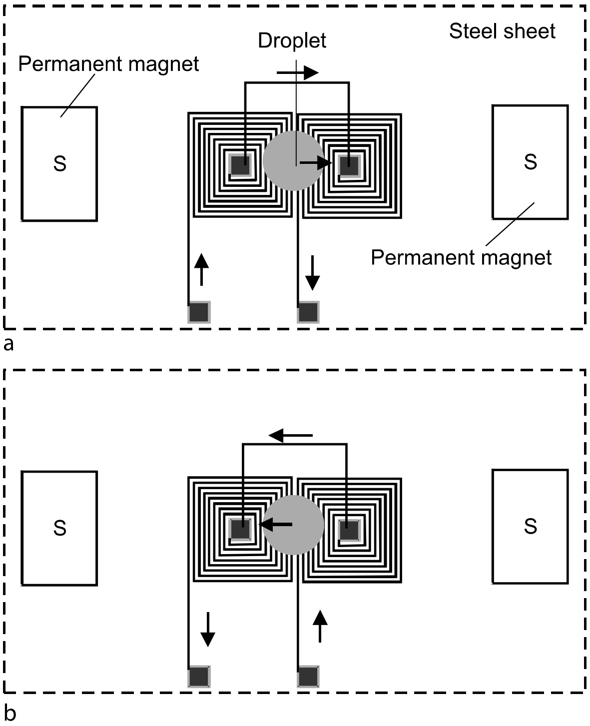

Droplet Microreactor, Figure 3 Experimental setup for controlling ferrofluid droplets. The permanent magnet and the soft magnetic steel sheet create a permanent magnetic field that polarizes the magnetic particles in the ferrofluid droplet. The coils are wired in such a way that their generated magnetic fields have opposite signs. The magnetic gradient generated by the two coils drives the ferrofluid. The direction of motion is determined by the direction of the current: (**a**) motion to the right, (**b**) motion to the left

is the Péclet number, and

$$L^* = \frac{L}{W} \tag{5}$$

is the dimensionless droplet length normalized by the channel width W.

Applications of Droplet Microreactors

Droplet microreactors find their main applications in analytical chemistry and chemical synthesis.

Chaotic advection inside droplet microreactors on a planar platform allows efficient mixing of large molecules such as DNA. A planar platform can accommodate both a droplet mixer and a reaction chamber for the polymerase chain reaction [6]. Droplets containing DNA samples and primer are merged and moved in a loop. Chaotic advection inside a droplet leads to fast mixing. The merged droplet is subsequently transported to a temperature-controlled region and undergoes thermal cycles. Both sample consumption and analysis time can be reduced significantly with droplet microreactors. In combination with an optical detection system, droplet microreactors can be used for biomedical diagnosis. Srinivasan et al. have demonstrated the detection of glucose in a planar platform based on merging and mixing with electrowetting [7].

Owing to their high throughput, in-channel continuous-flow platforms are more suitable for chemical synthesis. One popular application is the synthesis of colloidal nanoparticles such as CdS and CdS/CdSe particles [8]. Transporting the nanoparticles as reaction products in microdroplets prevents them from aggregating on the channel wall. Furthermore, a double emulsion could form an encapsulating layer around the droplet. Pills containing nanoscale drug particles can be synthesized with this reaction platform. Continuous-flow platforms allow one to form an array of alternate droplets in a capillary. This configuration allows diffusion of water from a droplet to a neighboring droplet containing a concentrated salt solution, owing to osmotic pressure. Protein crystallization can be achieved with this concentration method [9].

The droplets formed have the shape of a sphere to minimize their surface energy. Thus, polymerization reactions in droplets can be used for the synthesis of functional poly-

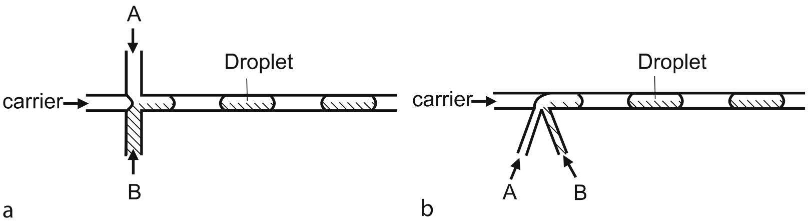

Droplet Microreactor, Figure 4 Droplet formation in an in-channel continuous platform: (**a**) cross junction, (**b**) T-junction

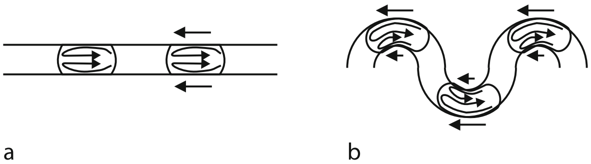

Droplet Microreactor, Figure 5 Flow patterns in a droplet microreactor: (**a**) straight channel, (**b**) curved channel

mer beads. In this application, droplets of monomers are formed by use of a shear stress. The polymerization reaction is subsequently activated by UV radiation or by an elevated temperature. The droplets harden and become spherical polymer beads [10].

Droplets formed in a in-channel continuous-flow platform provide an attractive solution for analysis of single cells [11]. First, cells are captured and encapsulated in droplets. Subsequently, a droplet containing a cell can be transported and trapped with optical tweezers. Photolysis can be used to release the organelles. Finally, an enzymatic assay can be carried out within the aqueous droplet.

Future Directions for Research

Droplet reactors are basic components of digital microfluidics. There are still a number of opportunities in droplet reactor research. The future directions can be categorized into fundamentals and applications. Fundamental research could result in other platforms for droplet reactors. While electrowetting has been widely reported in the past, microfluidic platforms based on thermocapillary and other forces are still underrepresented. More research on the systematic design of droplet-based reactors is needed to secure industrial adaptation and commercial success. The applications of droplet reactors have still not been fully exploited. The use of droplets as a reaction platform for cells and biomimetic applications is an interesting topic for future research.

Cross References

- ► Digital Microfluidics
- ► Electrowetting
- ► Thermocapillarity
- ► Transport of Droplets by Thermal Capillarity
- ► Thermocapillary Pumping
- ► Ferrofluid in Microchannel

References

1. Paik P, Pamula VK, Pollack MG, Fair RB (2003) Electrowetting-based droplet mixers for microfluidic systems. Lab Chip 3:28–33
2. Darhuber AA, Valentino JP, Troian SM, Wagner S (2003) Thermocapillary actuation of droplets on chemically patterned surfaces by programmable microheater arrays. J MicroElectromech Syst 12:873–879
3. Nguyen NT, Ng KM, Huang XY (2006) Manipulation of ferro fluid droplets using planar coils. Appl Phys Lett 89(5):052509
4. Paik P, Pamula VK, Fair RB (2003) Rapid droplet mixers for digital microfluidic systems. Lab Chip 3:253–259
5. Bringer MR, Gerdts CJ, Song H, Tice JD, Ismagilov RF (2004) Microfluidic systems for chemical kinetics that rely on chaotic mixing in droplets. Phil Trans R Soc Lond A 362:1087–1104
6. Chang YH, Le GB, Huang FC, Chen YY, Lin JL (2006) Integrated polymeric chain reaction polymerchip utilizing digital microfluidics. Biomed Microdevices 8:215–225
7. Srinivasan V, Pamula VK, Fair RB (2004) Droplet-based microfluidic lab-on-a-chip for glucose detection. Analyt Chim Acta 507:145–150
8. Shestopalov I, Tice JD, Ismagilov RF (2004) Multi-step synthesis of nanoparticles performed on millisecond time scale in a microfluidic droplet-based system. Lab Chip 4:316–321
9. Zheng B, Tice JD, Ismagilov RF (2004) Formation of arrayed droplets by soft lithography and two-phase fluid flow, and application in protein crystallization. Adv Mater 16:1365–1368
10. Nisisako T, Torii T, Higuchi T (2004) Novel microreactors for functional polymer beads. Chem Eng J 101:23–29
11. He M, Edgar JS, Jeffries GDM, Lorentz RM, Shelby JP, Chiu DT (2004) Selective encapsulation of single cells and subcellular organelles into picoliter- and femtoliter-volume droplets. Anal Chem 77:1539–1544

Droplet Motion in Microchannels

► Droplet Dynamics in Microchannels

Droplet Release

► Droplet Dispensing

Droplet Tear-Off

► Droplet Dispensing

Droplet Transport by Surface Acoustic Waves

► Transport of Droplets by Acoustics

Drug Delivery

► Integrated Microdevices for Medical Diagnostics

Dry Chemical Etch

Synonyms

Dry etch

Definition

Dry etching is the process of using reactive gases or lights to remove away unwanted material. The process is typically achieved by exposing the material to a bombardment of ions that dislodge portions of the material from the exposed surface.

Cross References

► Bulk Micromachining
► Plasma Etching
► Photo Etching
► Anisotropic Etching

Dry Etch

► Dry Chemical Etch

Duty Cycle

Definition

Nominal burn time or firing time of a thruster.

Dynamic Density Functional Theory (DDFT)

Markus Rauscher[1,2]
[1] Max-Planck-Institut für Metallforschung, Stuttgart, Germany
[2] Institut für Theoretische und Angewandte Physik, Universität Stuttgart, Stuttgart, Germany
rauscher@mf.mpg.de

Synonyms

Time-dependent Density Functional Theory (TDFT)

Definition

Dynamic Density Functional Theory (DDFT) is, on the one hand a time-dependent (dynamic) extension of the static Density Functional Theory (DFT), and on the other hand, the generalization of Fick's law to the diffusion of interacting particles. The time evolution of the ensemble-averaged density of Brownian particles is given as an integro-differential equation in terms of the equilibrium Helmholtz free energy functional (or the grand canonical functional). DDFT resolves density variations on length scales down to the particle size but only works for slow relaxing dynamics close to equilibrium.

Overview

One can prove that in thermal equilibrium, in a grand canonical ensemble (i. e., volume, chemical potential, and temperature are fixed), the grand canonical free energy $\Omega(\rho(\boldsymbol{r}))$ of a system can be written as a functional of the one-body density $\rho(\boldsymbol{r})$ alone, which will depend on the position $\boldsymbol{r}$ in inhomogeneous systems. The density distribution $\rho_{\text{eq}}(\boldsymbol{r})$ which minimizes the grand potential functional is the equilibrium density distribution. This statement is the basis of the equilibrium density functional theory (DFT) for classical fluids which has been used with great success to describe a variety of inhomogeneous fluid phenomena, in particular the structure of confined liquids, wetting, anisotropic fluids, and fluid–fluid interfaces. For a historical overview and further references see [1, 2].
Out of equilibrium there is no such rigorous principle. However, macroscopically one can find a large variety of phenomenological equations for the time evolution which are based on macroscopic quantities alone, e. g., the diffusion equation, the heat transport equation, and the Navier–Stokes equations for hydrodynamics. A microscopic dynamical theory for the time evolution of slow variables such as the momentum density or the particle

density with molecular spatial resolution is highly desirable.

In perhaps one of the simplest microscopic cases, a system of interacting Brownian (i. e., diffusing) particles, and in a local equilibrium approximation, one can write the time evolution of the ensemble-averaged one-body density as a functional of the density [3]

$$\frac{\partial \rho(\boldsymbol{r};t)}{\partial t} = \nabla \cdot \left(\mathrm{D}\rho(\boldsymbol{r};t)\nabla \left.\frac{\delta F[\rho]}{\delta\rho}\right|_{\rho(\boldsymbol{r};t)} \right) \qquad (1)$$

where D is the diffusion constant, and the Helmholtz free energy functional, $F[\rho(\boldsymbol{r})] = \Omega[\rho(\boldsymbol{r})] + \mu\rho(\boldsymbol{r})$. The chemical potential μ is constant throughout the system and the free energy functional has the form

$$F[\rho(\boldsymbol{r})] = \int \rho(\boldsymbol{r}')\left(\left(k_{\mathrm{B}}T \ln \Lambda^3 \rho(\boldsymbol{r}') - 1\right) + V(\boldsymbol{r}')\right) \mathrm{d}^3\boldsymbol{r}' + F_{\mathrm{ex}}[\rho(\boldsymbol{r})] \qquad (2)$$

where Λ is the thermal wavelength, $k_{\mathrm{B}}T$ is the thermal energy, and $V(\boldsymbol{r})$ is an external potential. The excess part of the free energy $F_{\mathrm{ex}}[\rho(\boldsymbol{r})]$ depends on the interactions among the particles and, apart from the trivial case of noninteracting (ideal) particles for which $F_{\mathrm{ex}}[\rho(\boldsymbol{r})] = 0$, it is only known exactly for a one-dimensional system of hard rods [3]. The key to the success of the equilibrium DFT as well as the nonequilibrium DDFT is to develop "good"functionals which can be tested against experiments and various simulations. Fundamental measurement theory has been very successfully used to construct functionals for hard sphere systems (a model for colloids in suspensions) [4]. Soft interactions, e. g., between polymer coils in a solution, can be treated in a nonlocal mean field (random phase) approximation as used by Penna et al. [5]. Their $F_{\mathrm{ex}}[\rho(\boldsymbol{r})]$ is written in a quadratic form in $\rho(\boldsymbol{r})$. For particles with a relatively hard core and an additional long-range interaction one can combine both concepts and write $F_{\mathrm{ex}}[\rho(\boldsymbol{r})]$ as the sum of a functional for hard spheres and a quadratic functional containing only the soft long-range part of the interaction [6].

Various extensions to DDFT have been proposed (see below). The generalization to mixtures of different particle types is straightforward. A background flow and a position-dependent diffusion constant can also be included.

To date, there has only been one attempt to develop a dynamic density functional theory for systems in which inertia plays a role [7]. However, it has been shown that the formal proof for the existence of a quantum mechanical dynamical density functional theory by Runge and Gross can be applied to classical systems [8]by starting from the Liouville equation for Hamiltonian systems (instead of the time-dependent Schrödinger equation), which therefore includes inertia terms. However, the proof is not of practical use (see below).

Dynamical density functional theories for the spatially coarse-grained density (to be distinguished from the ensemble-averaged density $\rho(\boldsymbol{r};t)$ discussed here) based on Zwanzig–Mori projection techniques have been suggested by many authors, but they are only valid on length scales that are large compared to the particle size. Their functional form is similar to Eq. (1) but with a conservative multiplicative noise term added. But in general, one is interested in ensemble-averaged quantities, i. e., quantities averaged over many realizations of the noise or the numerical experiment, such that a theory for ensemble-averaged quantities is of more practical use. For a discussion of the role of noise in DDFT see [9].

Basic Methodology

We now derive the DDFT (Eq. (1)) for the simplest case, i. e., a system of N pairwise interacting indistinguishable Brownian particles, following the derivation given in [9], before giving the DDFT equations (corresponding to Eq. (1)) for mixtures and for particles in a flowing solvent.

DDFT for Interacting Brownian Particles

A starting point for developing a DDFT for N interacting Brownian particles is the Fokker–Planck (or Smoluchowsky) equation for the probability density $W(\{\boldsymbol{r}_i\}_{i=1\ldots N})$ for finding particle 1 at position $\boldsymbol{r}_1$, particle 2 at position $\boldsymbol{r}_2, \ldots$, particle i at position $\boldsymbol{r}_i$, and finally particle N at position $\boldsymbol{r}_N$. For pairwise interactions among the particles we have

$$\frac{\partial W(\{\boldsymbol{r}_i\};t)}{\partial t} = \sum_{i=1}^{N} \nabla_i \cdot \left(\sum_{j=1}^{N} \mathbf{F}(\boldsymbol{r}_i - \boldsymbol{r}_j) + \mathbf{G}(\boldsymbol{r}_i) - k_{\mathrm{B}}T\nabla_i \right) W(\{\boldsymbol{r}_i\};t) \qquad (3)$$

where the interaction force $\mathbf{F}(\boldsymbol{r}) = -\nabla\Phi(\boldsymbol{r})$, the interaction potential is $\Phi(\boldsymbol{r})$, and the force due to the external potential $\mathbf{G}(\boldsymbol{r}) = -\nabla V(\boldsymbol{r})$. The generalization to many-particle interactions and to time-dependent external potentials is straightforward. The time evolution of the

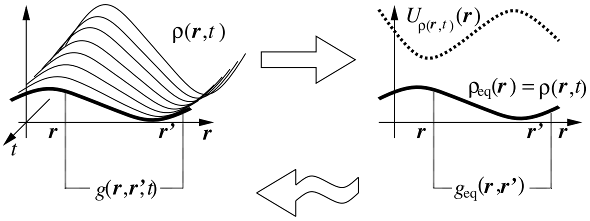

Dynamic Density Functional Theory (DDFT), Figure 1 Illustration of the local equilibrium approximation involved in the development of the DDFT. The left-hand side illustrates the nonequilibrium evolution of the density $\rho(\boldsymbol{r};t)$ (thin lines) up to time t (thick line). For the time evolution the equal-time correlation function $g(\boldsymbol{r},\boldsymbol{r};t)$ is needed. It is approximated by the equilibrium correlations $g_{\text{eq}}(\boldsymbol{r},\boldsymbol{r}')$ in an equilibrium system (right-hand side) with the same density $\rho_{\text{eq}}(\boldsymbol{r})$ (thick line) as in the nonequilibrium system. For given particle interactions and density such an equilibrium system can be obtained by applying an external potential $U_{\rho(\boldsymbol{r};t)}(\boldsymbol{r})$

ensemble-averaged density, i. e., the density averaged over many realizations of the thermal noise and initial conditions samples from the initial $W(\{\boldsymbol{r}_i\};t=0)$, can be calculated by integrating out $N-1$ degrees of freedom in Eq. (3) to obtain

$$\frac{\partial\rho(\boldsymbol{r};t)}{\partial t} = -\nabla\cdot\Big((\mathbf{G}(\boldsymbol{r})-k_{\text{B}}T\nabla)\,\rho(\boldsymbol{r};t) + \int g(\boldsymbol{r},\boldsymbol{r}';t)\mathbf{F}(\boldsymbol{r}-\boldsymbol{r}')\,\mathrm{d}^3\boldsymbol{r}'\Big) \tag{4}$$

with the nonequilibrium two-point correlation function $g(\boldsymbol{r},\boldsymbol{r}';t)$. Equation (4) is only the starting point of a hierarchy of N time evolution equations for correlation functions of increasing order.

The key to DDFT is to truncate this hierarchy and to express $g(\boldsymbol{r},\boldsymbol{r}';t)$ in terms of the density. In order to arrive at Eq. (1) one assumes that $g(\boldsymbol{r},\boldsymbol{r}';t)$ can be approximated by the two-point correlation function of an equilibrium system with the equilibrium density distribution $\rho_{\text{eq}}(\boldsymbol{r}) = \rho(\boldsymbol{r};t)$, as illustrated in Fig. 1. This is possible because for every given interaction potential $V(\boldsymbol{r})$ and density $\rho(\boldsymbol{r};t)$ one can find an external potential $U_{\rho(\boldsymbol{r};t)}(\boldsymbol{r})$ such that the equilibrium density distribution $\rho_{\text{eq}}(\boldsymbol{r})$ of the system with $U_{\rho(\boldsymbol{r};t)}(\boldsymbol{r})$ is equal to $\rho(\boldsymbol{r};t)$. Moreover, the excess parts of the free energy functionals of both systems, with and without $U_{\rho(\boldsymbol{r};t)}(\boldsymbol{r})$, are identical. One can therefore use a sum rule relating the integral in Eq. (4) (with $g(\boldsymbol{r},\boldsymbol{r}';t)$ replaced by $g_{\text{eq}}(\boldsymbol{r},\boldsymbol{r}')$) via the first direct correlation function $c^1(\boldsymbol{r})$ to the functional derivative of the excess part of the free energy.

$$\int g_{\text{eq}}(\boldsymbol{r},\boldsymbol{r}')\mathbf{F}(\boldsymbol{r}-\boldsymbol{r}')\,\mathrm{d}^3\boldsymbol{r}' = k_{\text{B}}T\rho(\boldsymbol{r};t)\nabla c^{(1)}(\boldsymbol{r}) = -\rho(\boldsymbol{r};t)\nabla\left.\frac{\delta F_{\text{ex}}[\rho]}{\delta\rho}\right|_{\rho(\boldsymbol{r};t)} \tag{5}$$

Writing the first term on the right-hand side of Eq. (4) as a variational derivative one arrives directly at Eq. (1).

For clarity we only derive Eq. (1) for the simplest case. However, Eq. (1) is also valid for arbitrary many-body interactions [6] as well as time-dependent external potentials $V(\boldsymbol{r};t)$. The latter simply leads to a time-dependent free energy functional $F[\rho;t]$ which is of the same form as the functional in Eq. (2).

DDFT for Particle Mixtures

The generalization to mixtures of M different particle types is straightforward and for the density $\rho_X(\boldsymbol{r};t)$ of component $1 \le X \le M$one obtains

$$\frac{\partial\rho_X(\boldsymbol{r};t)}{\partial t} = \nabla\cdot\left(D_X\rho_X(\boldsymbol{r};t)\nabla\left.\frac{\delta F\left[\{\rho_Y\}_{Y=1\ldots M}\right]}{\delta\rho_X}\right|_{\{\rho_Y(\boldsymbol{r};t)\}}\right) \tag{6}$$

where the diffusivity D_X of component X and the joint free energy functional depend on the density distribution of all M components.

DDFT in a Flowing Solvent

Flow in the medium in which the Brownian particles are embedded (e. g., the solvent for colloids) can also be included, as long as the back-reaction of the Brownian particles on the flow field $\mathbf{u}(\boldsymbol{r};t)$ is not taken into account. This results in a coupling of the density field to the Navier–Stokes equations. In the case most relevant for microfluidics, i. e., for vanishing Reynolds numbers and incompressible flows, one obtains

$$\frac{\partial\rho(\boldsymbol{r};t)}{\partial t} + \mathbf{u}(\boldsymbol{r};t)\cdot\nabla\rho(\boldsymbol{r};t) = \nabla\cdot D\rho(\boldsymbol{r};t)\nabla\left.\frac{\delta F[\rho]}{\delta\rho}\right|_{\rho(\boldsymbol{r};t)} \tag{7}$$

$$0 = -\nabla p + \eta\nabla^2\mathbf{u}(\boldsymbol{r};t) \tag{8}$$

$$\nabla\cdot\mathbf{u}(\boldsymbol{r};t) = 0 \tag{9}$$

where p is the pressure and η is the viscosity. Here we neglect the displacement of the solvent by the Brownian particles. A more complete theory would also include the osmotic pressure of the particles in terms of a density dependent pressure tensor in Eq. (8), similar to the coupled Cahn–Hilliard/Navier–Stokes systems used in phase field modeling of multiphase fluid systems.

DDFT in Inhomogeneous Media

A spatially varying diffusivity can model not only inhomogeneities in the medium but also hydrodynamic interactions between the Brownian particles and channel walls. The diffusivity is then replaced by a diffusion tensor $\mathbf{D}(\boldsymbol{r})$ and instead of Eq. (1) one obtains

$$\frac{\partial \rho(\boldsymbol{r};t)}{\partial t} = \nabla \cdot \mathbf{D}(\boldsymbol{r}) \rho(\boldsymbol{r};t) \cdot \nabla \left. \frac{\delta F[\rho]}{\delta \rho} \right|_{\rho(\boldsymbol{r};t)} \tag{10}$$

Eqs. (6)–(10) only give the simplest forms of the generalization of Eq. (1) discussed in the corresponding section. All the generalizations can be combined with each other.

The local equilibrium approximation for the two-point correlation function involved in the development of the DDFT has two issues. First, it is not a priori clear when it is justifiable to approximate the nonequilibrium correlations by equilibrium correlations. It has been shown that there are cases in which this approximation breaks down, in particular in driven steady-state systems. Second, the equilibrium sum-rule in Eq. (5) gives the two-point correlations in a grand canonical ensemble. But the locally conserved dynamics underlying Eq. (1) requires a canonical ensemble. In a grand canonical ensemble each point in space is connected to a reservoir fixing the chemical potential by adding or removing particles, while in a canonical ensemble the number of particles is fixed.

Key Research Findings

As DDFT is a relatively young technique only a few results are available. The remaining part of this section is organized in terms of the particle system under consideration, i. e., in terms of the excess free energy functional $F_{\text{ex}}[\rho(\boldsymbol{r})]$ used.

One-Dimensional Systems

The difference between the correlation functions in a canonical and a grand canonical ensemble is largest for one-dimensional systems with hard core interactions. This occurs because in such a system the particles cannot pass each other. This also leads to a significantly different diffusion behavior (single file diffusion). In a grand canonical setting, however, particles can pass each other via the

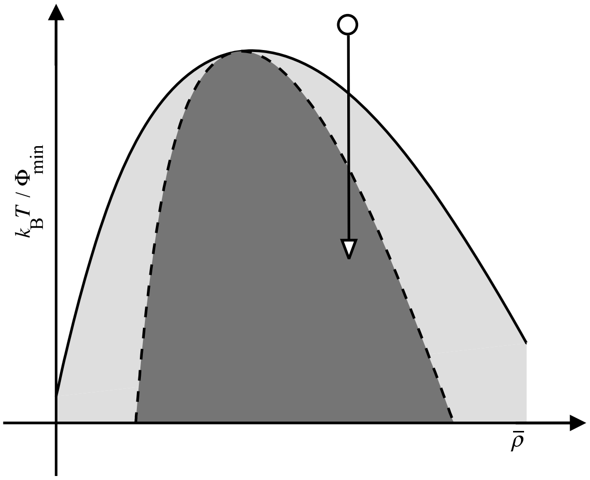

Dynamic Density Functional Theory (DDFT), Figure 2 Schematic phase diagram of a system of Brownian particles with an attractive interaction. Φ_{min} is the depth of the attractive minimum of the interaction potential and $\bar{\rho}$ is the particle density (averaged of the system volume). Only states above the full line, the bimodal, are stable. States between the full and the dashed lines, the spinodal, are metastable, and states below the spinodal are linearly unstable. The system considered in [6] is quenched from a stable state (circle) into the unstable region as indicated by the vertical arrow

reservoir which keeps the chemical potential fixed. Therefore, an ensemble of hard rods was the first test system used for DDFT, also because the free energy functional for hard rods is the only nontrivial functional for interacting systems which is known exactly. Some discrepancies between DDFT and Brownian dynamics simulations of the same system were observed, mainly for extreme heterogeneities, i. e., very far from equilibrium [3]. However, the intermediate and long-term behavior was captured correctly by DDFT, at least for large enough systems. The same system has been considered as a model for the diffusion of colloids in a narrow channel with an obstacle inside the channel [10]. The goal of this study was to investigate the interplay between the external driving forces, the interparticle interactions, and the potential barriers in nanochannels.

Soft Particles

Polymer chains in solution form a loose coil such that two coils can interpenetrate. The resulting effective interaction potential $\Phi(|\boldsymbol{r}|)$ is repulsive and is well approximated by a Gaussian potential of strength Φ_0 and with a range r_0 which is proportional to the radius of gyration R_g. The excess free energy functional for such soft systems can be

approximated by a quadratic form

$$F_{\mathrm{ex}}\left[\rho(\boldsymbol{r})\right] = \frac{1}{2}\iint \rho(\boldsymbol{r})\Phi\left(|\boldsymbol{r}-\boldsymbol{r}'|\right)\rho(\boldsymbol{r}')\,\mathrm{d}^3\boldsymbol{r}\,\mathrm{d}^3\boldsymbol{r}' \quad (11)$$

where $\Phi(r) = \Phi_0 \exp(-r^2/r_0^2)$. This has been used in order to describe the dynamics of polymer solutions in the vicinity of colloidal particles driven through the solution [10]. The main finding is that the layering of polymer coils around the colloid can be broken up, leading to a strongly inhomogeneous polymer density in the vicinity of particles. The influence of this inhomogeneity on the depletion interaction between particles has been studied [11]. A tendency for the particles to align, a result most relevant for sedimentation processes and in line with the simulations, was found.

This type of model potential has been also used to study the phase separation dynamics of binary mixtures in cavities [12]. An excellent agreement between DDFT and Brownian dynamics simulations was found. In this particular example the fact that DDFT is a theory for the ensemble-averaged density becomes most evident, i. e., the density shows the same symmetry as the underlying system, even though the actual realizations may have a broken symmetry. In this example this means that since the probability of having one phase on the left-hand side of the cavity and the other phase on the right-hand side is equal to the probability of the mirrored situation the ensemble-averaged densities are symmetric even if every realization of the system is asymmetric.

Hard Particles

Hard particles with an additional soft attractive interaction have been used in a study of spinodal decomposition [6]. Such a system can be realized in a colloidal suspension and exhibits a fluid–fluid phase separation between a colloid-rich and a colloid-poor phase (see the phase diagram in Fig. 2). Quenched below the spinodal, the system undergoes spinodal decomposition which leads finally to the formation of dense and less dense clusters. The main progress, as compared to nonlinear Cahn–Hilliard theories, is the more accurate description of the short wavelength correlations, a property which will become most relevant in confined systems.

Future Directions for Research

Applications of DDFT

DDFT is a relatively new technique and therefore much effort will be needed toapply DDFT to microfluidic and biological systems. In particular, the transport of colloidal suspensions and polymer solutions in channels that are a few times larger than the typical particle diameter is a problem for which the DDFT method is well suited. Mixing of suspended interacting particles and polymers in such channels is also well modeled by DDFT.

The internal dynamics of complex fluids, e. g., the diffusion of colloids in polymer solutions, is another problem for which DDFT could be useful. It has been shown recently that the structure of the polymer solution in the vicinity of a diffusing colloidal particle strongly influences its diffusivity [13]. DDFT could be used to determine this structure.

Further Development of DDFT

The greatest challenges for DDFT are hydrodynamic interactions and inertia. Either one, or both of these, are needed for most systems of interest. The following paragraphs briefly outline the status of the development and the obstacles to further progress.

Hydrodynamic Interactions

Currently, hydrodynamic interactions between suspended particles cannot be included in a DDFT. However, it is well known, that, e. g., the rheology of suspensions cannot be explained without taking these into account. Hydrodynamic interactions in a simple approximation based on Oseen-tensors have been included in the Fokker–Planck equation (Eq. (3)) and the equivalent of Eq. (4) has been derived and discussed [14, 15]. However, this equation contains three-point and two-point correlations in a form such that the sum rule in Eq. (5) cannot be used.

Simple Fluids

The DDFTs discussed in this article describe the time evolution of the density of Brownian particles. Although there are formal arguments for the existence of a DDFT for a system of particles which follow a Newtonian dynamics [8], in other words a system of particles for which inertia is important, to date, only one effort has been made to extend the concept of DDFT in this direction [7]. However, hydrodynamic modes were still excluded in that work.

The greatest obstacle for developing a hydrodynamic DDFT is that, the viscosity of a liquid is determined by the deviation of the two-point correlation function $g(\boldsymbol{r},\boldsymbol{r}';t)$ from the equilibrium value $g_{\mathrm{eq}}(\boldsymbol{r};\boldsymbol{r}')$. Approximating the first with the latter, as in the derivation of the DDFT for Brownian particles discussed above, would therefore result in a theory almost without viscosity.

Cross References

► Active Mixer
► Brownian Motion

- ► Brownian Motion and Diffusion
- ► Compute Mixing Efficiency
- ► Concentration Gradient Generation and Control
- ► Demixing
- ► Diffusion

References

1. Evans R (1992) Density Functionals in the Theory of Nonuniform Fluids. In: Henderson D (ed) Fundamentals of Inhomogeneous Fluids. Marcel Dekker, New York
2. Löwen H (2002) Density functional theory of inhomogeneous classical fluids: recent perspectives and new perspectives. J Phys Condens Matter 14:11897–11905
3. Marconi UMB, Tarazona P (2000) Dynamic density functional theory of fluids. J Chem Phys 110:8032–8044 (1999); J Phys Condens Matter 12:A413–A418
4. Roth R, Evans R, Lang A, Kahl G (2002) Fundamental measure theory for hard-sphere mixtures revisited: the White Bear version. J Phys Condens Matter 14:12063–12078
5. Penna F, Dzubiella J, Tarazona P (2003) Dynamic density functional study of a driven colloidal particle in polymer solutions. Phys Rev E 68:061407
6. Archer AJ, Evans R (2004) Dynamical density functional theory and its application to spinodal decomposition. J Chem Phys 121:4246–4245
7. Archer AJ (2006) Dynamical density functional theory for dense atomic liquids. J Phys Condens Matter 18:5617–5628
8. Chan GK-L, Finken R (2005) Time-dependent density functional theory of classical fluids. Phys Rev Lett 94:183001
9. Archer AJ, Rauscher M (2004) Dynamical density functional theory for interacting Brownian particles: stochastic or deterministic? J Phys A Math Gen 37:9325–9333
10. Penna F, Tarazona P (2003) Dynamic density functional theory for steady currents: Application to colloidal particles in narrow channels. J Chem Phys 119:1766–1776
11. Dzubiella J, Löwen H, Likos CN (2003) Depletion forces in nonequilibrium. Phys Rev Lett 91:248301
12. Archer AJ (2005) Dynamical density functional theory: phase separation in a cavity and the influence of symmetry. J Phys Condens Matter 17:3253–3258
13. Tuinier R, Dhont JKG, Fan T-H (2006) How depletion affects sphere motion through solutions containing macromolecules. Europhys Lett 75:929–935
14. Harris S (1976) Diffusion effects in solutions of Brownian particles. J Phys A Math Gen 9:1895–1898
15. Felderhof BU (1978) Diffusion of interacting Brownian particles. J Phys A Math Gen 11:929–937

Dynamic Mixing

► Active Mixer

EDL Potential

► Measuring Zeta Potential, Methods

Effective Coupling Coefficient

Definition

A coupling coefficient describes the efficiency of energy transfer from one form to another in a material or physical mechanism. The effective coupling coefficient is determined based on measurement of a mechanism's characteristics rather than relying on a derivation of the coefficient from underlying principles. The effective coupling coefficient often combines several disparate phenomena in these cases.

Cross References

► Piezoelectric Microdispenser

Einstein Relation

Definition

A relation that gives the mobility of an ion in terms of its diffusion coefficient and the surrounding temperature.

Cross References

► Electrokinetic Flow and Ion Transport in Nanochannels

Elastomeric Valve

► Pneumatic Valves

Electrets

► Piezoelectric Materials for Microfluidics

Electrical Current Monitoring Methods

CAROLYN REN
Department of Mechanical and Mechatronics Engineering, University of Waterloo,
Waterloo, ON, Canada
c3ren@mecheng1.uwaterloo.ca

Synonyms

Slope method; Current monitoring method; Current monitoring technique

Definition

Electrical current monitoring methods are the methods to measure the average velocity of electro-osmotic flow by monitoring the electrical current change for a replacement process, where one electrolyte solution is replacing another slightly less concentrated one (or slightly concentrated one) via electro-osmotic flow. For the purpose of measuring the specific surface conductivity, the replacement is not necessary.

Overview

When an external electrical field is applied to the liquid in a microchannel tangentially, the bulk liquid motion can be generated, which is commonly referred to as electroosmotic flow (EOF), due to the presence of a thin layer with net charges near the solid–liquid interface. This thin layer is called the electrical double layer (EDL) and the net charges in the EDL are the result of charge separation in the bulk liquid induced by the surface charge, which originates from several mechanisms [1], such as the ionization of surface groups and the electrolyte ion adsorption

to solid surfaces. The EDL generally consists of two layers: one is the inner compact layer where ions are strongly attracted to the charged surface and the other is the diffuse layer where ions are free to move. The electrical potential in the liquid generally decays dramatically from the surface and almost reaches zero at some distance slightly beyond the EDL region. The potential at the shear plane, which separates the compact layer and the diffuse layer, is referred to as the zeta potential, ζ, and can be experimentally measured [2].

When an EOF is generated by applying an external electrical field, an electrical current is also introduced, which commonly consists of three components:

- a conduction current, $I_{\text{cond,bulk}}$, resulting form the bulk conductivity of the electrolyte solution;
- a secondary conduction current, $I_{\text{cond,surf}}$, resulting from the surface conductivity; and,
- a convection current, I_{conv}, resulting from the electro-osmotic flow.

Generally, the convection current is evaluated by

$$I_{\text{conv}} = \int_{A_c} u\rho_e dA_c \ ,$$

which is several orders of magnitude smaller than the other two components of the current. Neglecting the contribution of I_{conv} results in the following equation for the total current, I_{total}:

$$I_{\text{total}} = I_{\text{cond,bulk}} + I_{\text{cond,surf}} = \lambda_b A_c \boldsymbol{E} + P\lambda_s \boldsymbol{E} \ , \qquad (1)$$

where $\boldsymbol{E}$ is the applied electrical field strength, λ_b is the bulk liquid conductivity measured in ohm^{-1}m^{-1}, λ_s is the surface conductivity measured along the length of the square sheet material of unit area and constant thickness (although negligible) and is measured in ohm^{-1}, P is the perimeter of the channel cross section, and A_c is the cross-sectional area of the channel. In many studies, the surface conductivity, λ_s, is neglected. This is a reasonable treatment for most high concentration solutions with a low net charge density in the EDL region; however, it may bring a significant error for low concentration solutions.

The zeta potential and surface conductance are functions of both interface and liquid properties and have significant influences on liquid flow. Lab-on-a-Chip devices have a wide range of applications in biomedical, chemical, environmental and biology areas, where a variety of liquid solutions and chip materials are involved. Each pair of solid–liquid interface has its unique zeta potential, specific surface conductivity, and electro-osmotic mobility, which makes the design and operational control of such devices very difficult and case specific. This requires the development of experimental methods for relatively easy and accurate measurements of the zeta potential, electro-osmotic mobility and surface conductivity.

There are three commonly used methods to measure the zeta potential, which involves pressure driven flow, electrophoresis, and electro-osmotic driven flow, respectively. For the measurement of the specific surface conductivity, there are primarily two methods involving pressure driven flow and electro-osmotic driven flow. In this entry, we will focus on the electrical current monitoring methods which can be used to measure the zeta potential, specific surface conductivity, volumetric flow rate, and electro-osmotic mobility, by employing electro-osmotic flow with a solution displacement process.

The traditional electrical current monitoring method was originally proposed by Huang et al. [3] to measure the average flow velocity in capillary zone electrophoresis. Since then, this method has been further developed for the measurements of the zeta potential, flow rate, and specific surface conductivity [4–6] for a given solid–liquid interface, which has been found more accurate, simpler and easier to operate as compared to the traditional streaming potential method involving pressure driven flow [7] and the electrophoresis method [8] involving the use of microscope techniques. The principles of the electrical current monitoring methods for measuring the zeta potential, electro-osmotic flow rate, and specific surface conductivity will be given in detail later. Briefly, when one solution is introduced into a channel to replace a slightly less concentrated one (vice versa) via electro-osmotic flow, the total resistance changes while the replacement is going due to their different conductivity values. Under a constant electrical potential difference applied to the ends of the microchannel, the electrical current will increase from a constant value at the beginning of the replacement when the channel is filled with the less concentrated solution and reach a plateau when the replacement ends and the channel is filled with the concentrated one. The electrical current can be monitored with respect to time for the replacement process and the current-time relationship in combination with numerical and analytical analysis allow the electro-osmotic flow rate, electro-osmotic mobility, zeta potential, and specific surface conductivity of a certain solid–liquid interface, to be determined.

Basic Methodology

Evaluation of the Electro-osmotic Flow Rate

Due to small dimensions and flow velocities in most microfluidic devices, microchannel flows are in the laminar flow regime with a typical Reynolds number below 0.1 and have a very small volumetric flow rate. For

instance, for a $1\times$TAE buffer solution in a 10 cm length of 100 μm i. d. capillary, under an applied electrical field of 7.5 kV/m, the velocity is around 0.4 mm/s, which yields a volumetric flow rate of approximate 0.2 μl/min. It is extremely difficult to measure such a small volumetric flow rate accurately using the traditional methods such as observing the movement of a meniscus in an adjoining capillary [1]. The current-monitoring method, however, is able to measure small volumetric flow rates in a much easier and more accurate manner by monitoring the current-time relationship while one solution is replacing another less concentrated one via electro-osmotic flow.

In the electrical current monitoring methods, a microchannel filled with one electrolyte solution is brought into contact with two reservoirs, one of which has the same concentration as that in the microchannel and the other has a higher concentrated one. The electrical field is set up simultaneously so that the higher concentrated one will gradually replace the less concentrated one in the channel via electro-osmotic flow. At the beginning of the replacement process, the microchannel is filled with one uniform solution and thus the current is constant. When the higher concentrated solution is pumped into the channel and the less concentrated one gradually flows out of the channel, the total resistance changes because of their different conductivity values, which are approximately proportional to their concentrations. Under a constant potential difference applied at the two ends of the microchannel, the current will increase and reach a plateau when the channel is completely filled with the high concentrated one. The current change can be monitored with respect to time for the replacement process. A typical current-time relationship measured for a $1\times$TAE buffer solution in a 10 cm length of 100 μm i. d. capillary under an applied electrical field of 7.5 kV/m, is shown in Fig. 1. The time between the two plateaus, Δt, is the time required for the solution to travel through the microchannel length, L. Therefore, from the current-time relationship, the average electro-osmotic velocity can be evaluated by

$$u_{\text{ave}} = \frac{L}{\Delta t} \,. \tag{2}$$

The electro-osmotic flow rate can then be calculated by $Q = u_{\text{ave}} A_{\text{c}}$. Although it is possible to directly measure the electro-osmotic mobility using the ultramicroscope technique [1], however, it is common to measure it by means of measuring the average electro-osmotic velocity. Once the average velocity is obtained, the electro-osmotic mobility can be easily determined by $\mu_{\text{eo}} = u_{\text{ave}}/E$.

In the current monitoring methods, the chemical species of the two solutions are the same, but the concentration is slightly different, i. e. 5% difference. For the purpose of measuring the average electro-osmotic velocity for one certain solution, it is important to maintain a small difference in concentration for the following two reasons. First, if there is a big difference in the concentration of the two solutions, the once sharp front surface between the two solutions becomes progressively blurred. The determined average velocity just indicates how fast for one solution to replace another solution under certain conditions. It can not, however, represent the average electro-osmotic velocity for any of the two solutions. Therefore, the measured average velocity can not be used to determine the electro-osmotic mobility, zeta potential or specific surface conductivity for a certain solution. Second, a big variation in concentration of the two solutions will cause a dramatic change in the electrical current at a certain point and very slow change at the beginning and the end of the replacement process. A typical current-time relationship for a 10 mM KCl solution replacing deionized ultrafiltered (DIUF) water (considered as a 1 μM KCl solution) in a 10 cm length of 100 μm i. d. capillary is shown in Fig. 2. This is because the total resistance is primarily determined by one of the two solutions for the majority time of the replacement process. For this particular case, the conductivity ratio between the two solutions can be assumed to be proportional to that of the concentration, which is around 10,000 times here. This means that as long as a very small portion of the channel (i. e. 1/10,000 of the channel length) is filled with 1 μM KCl solution, the total resistance and thus the current are dominated by this low concentration solution. When the channel is almost completely filled with the 10 mM KCl solution, the current will suddenly jump to a high value corresponding to this higher concentration solution and gradually reaches a maximum value. As shown in Fig. 2, it is very difficult to

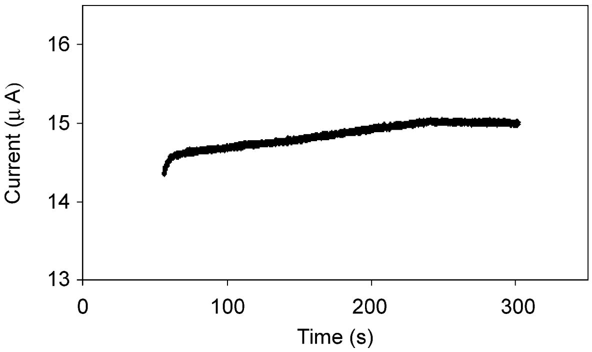

Electrical Current Monitoring Methods, Figure 1 A typical current–time relationship measured for a $1\times$TAE buffer solution replacing a 95% $1\times$TAE buffer solution in a 10 cm length of 100 μm i. d. capillary, under an applied electrical field of 7.5 kV/m

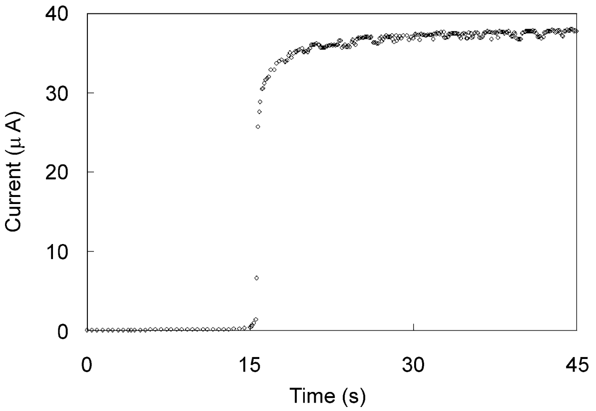

Electrical Current Monitoring Methods, Figure 2 A typical current-time relationship measured for a 1×10 mM KCl solution replacing DIUF Water in a 10 cm length of 100 μm i. d. capillary, under an electrical field of 3.5 kV/m

identify the beginning or the end point for such a replacement process, which will bring errors when determining the time required for one solution to replace another solution and thus the average velocity. Therefore, it is necessary to maintain a small difference in concentration when using the current monitoring methods.

Once the average velocity and the electro-osmotic mobility are obtained from the current-time relationship, the zeta potential, and specific conductivity can be evaluated in combination with numerical and analytical analysis as summarized below.

Evaluation of the Zeta Potential

There have been many methods developed for the zeta potential measurements as mentioned above. Here we will focus on the methods using the current monitoring technique. The zeta potential can not be directly measured using this method; however, it can be determined numerically and analytically through the measured average electro-osmotic velocity, which will be summarized below.

Consider an electro-osmotic flow of an aqueous solution in a microchannel, the flow field generally can be described by the continuity equation and the momentum equation:

$$\nabla \cdot \boldsymbol{V} = 0 \tag{3}$$

$$\rho \left[\frac{\partial \boldsymbol{V}}{\partial t} + (\boldsymbol{V} \cdot \nabla)\, \boldsymbol{V} \right] = -\nabla p + \eta \nabla^2 \boldsymbol{V} + \rho_e \boldsymbol{E} \,, \tag{4}$$

where $\boldsymbol{V}$ is the mass average velocity vector, ρ is the density of the liquid, η is the viscosity of the liquid, p is the pressure, and ρ_e is the local net charge density. For most microfluidic applications, the viscous force is dominant and the time for the flow to reach steady state is very small, which is on the order of ms ($t \approx \rho D_h^2/\eta = 10^{-2}$ s where $\rho = 1.0 \times 10^3\ \text{kg m}^{-3}$, $\eta = 1.0 \times 10^{-3}\ \text{kg m}^{-1}$, and D_h is the characteristic length chosen as $D_h = 100\ \mu\text{m}$). Therefore the transient term in the momentum equation can be neglected. Because of small channel dimensions and flow velocities (the typical velocity in microfluidic devices is on the order of mm/s), the Reynolds number, $\text{Re} = \rho u D_h/\eta$, which represents the ratio between the inertial force and the viscous force, ranges approximately from 0.001 to 0.1. Therefore, the flow in microfluidic devices is laminar flow and the convection term on the left hand side of the momentum equation can be ignored. For most microfluidic applications, no pressure difference is applied and the pressure gradient term is dropped off. It should be pointed out that induced pressure gradients do exist in most applications, where a complex channel layout is designed, primarily due to the Laplace pressure originating from the presence of different meniscus curvatures in the reservoirs. It is difficult to quantify the induced pressure effects because meniscus curvatures vary from experiments to experiments. The possible solutions to minimize the Laplace pressure are to increase the reservoir sizes and/or increase the flow resistance which can be realized by reducing the channel cross section and increasing the length of the flow path without increasing the channel length in one direction. This is because increasing the channel length in one direction will increase the chip size, which mitigates the key advantages that microfluidic chips can provide. Considering the above simplifications, Eq. (4) can be reduced to a very simple format:

$$\eta \nabla^2 \boldsymbol{V} = -\rho_e \boldsymbol{E} \,. \tag{5}$$

In order to solve the above equation, the net charge density must be known. According to the theory of electrostatics, the relationship between the net charge density and the electrostatic potential, ψ, is described by the Poisson equation:

$$\varepsilon_r \varepsilon_0 \nabla^2 \psi = -\rho_e \,, \tag{6}$$

where ε_r is the dielectric constant of the liquid, and ε_0 is the permittivity of vacuum ($\varepsilon_0 = 8.854 \times 10^{-12}\ \text{C/Vm}$). Consider a symmetric electrolyte solution, such as KCl solution, the local net charge density, ρ_e, is described by the Boltzmann equation:

$$\rho_e(r) = ze\big(n_+ - n_-\big) = -2zen_0 \sinh\left(\frac{ze\psi}{k_b T}\right) \,, \tag{7}$$

where z is the valence of the ion which is the same for the ions in a symmetric electrolyte solution, e is the electrical charge of an electron, n_0 is the initial concentration of the bulk solution, k_b is the Boltzmann constant and T is the absolute temperature. The well-known Poisson–Boltzmann equation is obtained by replacing the net charge density in Eq. (6) using Eq. (7):

$$\nabla^2\psi = \frac{2zen_0}{\varepsilon_r\varepsilon_0}\sinh\left(\frac{ze\psi}{k_bT}\right) . \tag{8}$$

The relationship between the velocity and the electrical potential can be derived by substituting Eq. (6) into Eq. (5)

$$\nabla^2\boldsymbol{V} = \frac{\varepsilon_r\varepsilon_0}{\eta}\boldsymbol{E}\nabla^2\psi . \tag{9}$$

Considering a fully developed flow in a parallel plate microchannel with a channel height of $2H$, the velocity and the electrical potential only vary in the height direction (y-direction). If the electrolyte solution or the channel surface is not uniform, the electrical field strength varies along the channel length; however, we only consider a constant electrical field here for the purpose of analysis. Equation (9) can then be simplified as

$$\frac{d^2u}{dy^2} = \frac{\varepsilon_r\varepsilon_0}{\eta}E_x\frac{d^2\psi}{dy^2} . \tag{10}$$

Eq. (10) is subject to the following boundary conditions:

$y = 0$ (the center of the channel) :

$$\frac{d\psi}{dy} = 0, \frac{du}{dy} = 0 \tag{11a}$$

$y = H$ (the wall of the channel) :

$$\psi = \zeta, u = 0 \tag{11b}$$

Integrating Eq. (10) with the boundary conditions specified in Eq. (11), we get

$$u = -\frac{\varepsilon_r\varepsilon_0}{\eta}E_x(\zeta\text{-}\psi) . \tag{12}$$

The average velocity can be calculated by integrating Eq. (12), such as

$$u_{ave} = -\frac{\varepsilon_r\varepsilon_0}{\eta H}E_x\int_0^H(\zeta\text{-}\psi)\,dy . \tag{13}$$

Once the zeta potential is known, the electrical potential can be obtained by solving the Poisson–Boltzmann equation. In other words, the electrical potential is a function of the zeta potential. Equation (13) shows that the average electro-osmotic velocity is also a function of the zeta potential. If the zeta potential is known, the electrical potential distribution can be determined and thus the average electro-osmotic velocity can be determined. The average velocity determined by this approach should be the same as that experimentally measured. However, in most situations, the zeta potential is unknown, which can be determined using the approach explained below. A guess value of the zeta potential can be made to solve the Poisson–Boltzmann equation for the electrical potential and then the average velocity is calculated using Eq. (13). The discrepancy between the numerically (or analytically) and experimentally determined average velocity suggests a new guess value for the zeta potential, which is used to repeat the above procedure until the two average velocity values converge. Therefore, the key here is to solve the Poisson–Boltzmann equation to get the electrical potential distribution.

E

Simplified Solution

As discussed above, the electrical potential drop dramatically from the zeta potential at the shear plane to zero at some distance slightly beyond the EDL. The detailed derivation of the electrical potential distribution can be found elsewhere [4]. Equation (12) indicates that the electro-osmotic velocity increases rapidly from zero at the shear plane to a maximum value at the edge of the EDL and keeps constant for the rest of the channel cross section. For most buffer solutions used in microfluidic chip applications, the concentration is on the order of mM, which gives a very thin EDL of around 10 nm. The EDL is around 0.01% of the channel height for a 100 μm high microchannel. Therefore, it is reasonable to neglect the variation of the electrical potential over the EDL region and assume zero potential cross the channel height. Considering this assumption, the zeta potential can be derived as a function of the average velocity from Eq. (13):

$$\zeta = -\frac{\eta}{\varepsilon_r\varepsilon_0}\frac{u_{ave}}{E_x} . \tag{14}$$

The above equation is a different form of the Helmholtz–Smoluchowski equation. Equation (14) shows that if the average electro-osmotic velocity is determined from the experimentally measured current-time relationship, the zeta potential can be calculated. Introducing the electro-osmotic mobility concept, $\mu_{eo} = u_{ave}/E_x$, Eq. (14) can be further simplified in the following format:

$$\zeta = -\frac{\eta}{\varepsilon_r\varepsilon_0}\mu_{eo} . \tag{15}$$

Equation (15) can be used to determine the zeta potential if the electro-osmotic mobility is known, vice versa.

Full Solution

It is true for many microfluidic applications, the EDL is very small compared to the channel dimensions and it is reasonable to assume zero electrical potential and a plug-like velocity profile cross the channel height. However, for dilute solutions such as water, the EDL is relatively big. For example, for a 1×10^{-6} M KCl solution in a 10 μm high parallel plate microchannel, the double layer thickness is around 300 nm, which is characterized by the inverse of the Debye–Huckle parameter, $1/\kappa = (2z^2e^2n_0/\varepsilon_r\varepsilon_0 k_b T)^{-1/2}$. The electrical potential variation occurs over a distance about $3/\kappa$, which is around 1 μm and is 10% of the channel height for this particular case. The assumption of zero electrical potential cross the channel height and thus a plug-like electro-osmotic velocity profile are not appropriate. The electrical potential distribution and the velocity profile must be obtained through numerical or analytical methods.

Numerical method Consider a symmetric electrolyte solution such as KCl solution in a parallel plate microchannel with a height of $2H$, the electrical potential distribution is described by the one-dimensional Poisson–Boltzmann equation:

$$\frac{d^2\psi}{dy^2} = \frac{2zn_0e}{\varepsilon_r\varepsilon_0}\sinh\left(\frac{ze\psi}{k_b T}\right) \tag{16}$$

with the following boundary conditions:

$$y = 0 \text{ (the center of the channel)}: \quad \frac{d\psi}{dy} = 0 \tag{17a}$$

$$y = H \text{ (the wall of the channel)}: \quad \psi = \zeta\,. \tag{17b}$$

Equation (16) can be easily solved using numerical techniques with the boundary conditions specified in Eq. (17). A typical potential distribution in a parallel plate microchannel obtained through numerical methods is shown in Fig. 3. Once the EDL potential, $\psi(y)$, is known, the average velocity can be calculated through Eq. (13). From the above procedure, it should be realized that the average velocity, u_{ave}, is an implicit function of the zeta potential, ζ (in the boundary condition, Eq. (17b)). If the average velocity can be measured directly using the current monitoring methods, the zeta potential can be determined by solving Eq. (13) and Eqs. (16,17) using an iterative procedure. First, Eqs. (16,17) are solved with an initial guess value of the zeta potential; second, Eq. (13) is used to determine the average velocity, and third, this numerically predicted average velocity will be compared to the experimentally measured one. If they are not the same, a new value of the zeta potential is assumed to repeat the above procedure until the two average velocity values converge. The zeta potential used for the last step calculation is the real zeta potential. In this process, an initial guessing value of the zeta potential, ζ_{guess}, may be obtained by invoking the Debye–Huckel approximation, as described below.

Analytical method Equation (16) can also be solved analytically with the boundary conditions specified in Eq. (17). In order to solve this equation easily using analytical methods, Eq. (16) should be nondimensionalized by the following parameters, $\Psi = ze\psi/k_bT$, and $Y = y/H$. The nondimensionalized Poisson–Boltzmann equation takes the form of

$$\frac{d^2\Psi}{dY^2} = \kappa^2H^2\sinh(\Psi)\,. \tag{18}$$

Introducing a relation

$$\frac{d}{dY}\left(\frac{d\Psi}{dY}\right)^2 = 2\frac{d\Psi}{dY}\frac{d^2\Psi}{dY^2} \tag{19}$$

and multiplying the both sides of Eq. (18) by $2(d\Psi/dY)$, yields

$$\frac{d}{dY}\left(\frac{d\Psi}{dY}\right)^2 = 2(\kappa H)^2\sinh(\Psi)\frac{d\Psi}{dY}\,. \tag{20}$$

Integrating the above equation gives:

$$\left(\frac{d\Psi}{dY}\right)^2 = 2(\kappa H)^2\cosh(\Psi) + C_1\,. \tag{21}$$

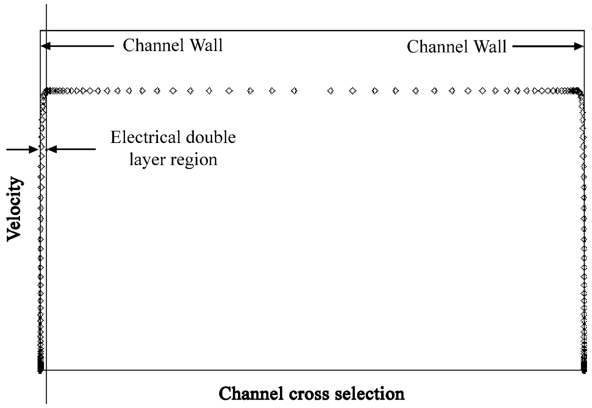

Electrical Current Monitoring Methods, Figure 3 Illustration of the velocity variation in a parallel plate microchannel

As explained above, for most microfluidic applications, the electrical potential is zero at some distance slightly beyond the EDL region. This is not true for the case where the EDL overlaps, which is not considered in this review. Interested readers are suggested consult with some of the recent publications [9] for more details. Therefore, the boundary conditions specified in Eq. (17a) can be extended to $Y = 0$, $\Psi = 0$, $\mathrm{d}\Psi/\mathrm{d}Y = 0$, which gives rise to $C_1 = -2(\kappa H)^2$ and Eq. (21) becomes:

$$\left(\frac{\mathrm{d}\Psi}{\mathrm{d}Y}\right)^2 = 2(\kappa H)^2(\cosh(\Psi) - 1) \tag{22a}$$

or

$$\frac{\mathrm{d}\Psi}{\mathrm{d}Y} = -\sqrt{2(\kappa H)^2(\cosh(\Psi) - 1)} = -2\kappa H \sinh\left(\frac{\Psi}{2}\right) . \tag{22b}$$

The negative sign in Eq. (22b) indicates that if the electrical potential is negative, the potential will increase from the zeta potential at the shear plane to zero in the bulk solution. Integrating Eq. (22b) yields $\tanh(\Psi/4) = -C_2\,\mathrm{e}^{-\kappa HY}$. Applying the boundary condition specified in Eq. (17b), C_2 is determined as $C_2 = -\tanh(\bar{\zeta}/4)$ where $\bar{\zeta}$ is the nondimensionalized zeta potential, $\bar{\zeta} = ze\zeta/k_\mathrm{b}T$. The final dimensional format of the solution to Eq. (16) is

$$\tanh\left(\frac{ze\psi}{4k_\mathrm{b}T}\right) = \tanh\left(\frac{ze\zeta}{4k_\mathrm{b}T}\right)\mathrm{e}^{-\kappa y} . \tag{23}$$

The electrical potential distribution can be determined using Eq. (23) with a guessed zeta potential value. The average velocity can then be calculated using Eq. (13). The comparison between the analytical solution and the experimentally determined average velocity will allow the zeta potential to be determined through iterative procedures as described above.

Debye–Huckle Approximation In some situations where the zeta potential is small (i.e. $< 25\,\mathrm{mV}$), the hyperbolic function in Eq. (16) can be approximated as $\sinh(ze\psi/k_\mathrm{b}T) \approx ze\psi/k_\mathrm{b}T$, which is called the Debye–Huckle approximation. Equation (16) then becomes

$$\frac{\mathrm{d}^2\psi}{\mathrm{d}y^2} = \kappa^2\psi . \tag{24}$$

With the boundary conditions specified in Eq. (17), the potential distribution can be obtained by solving Eq. (24), such as:

$$\psi = \zeta\,\mathrm{e}^{-\kappa(H-y)} \tag{25}$$

Using Eq. (13), the average velocity is determined by:

$$u_\mathrm{ave} = -\frac{\varepsilon_\mathrm{r}\varepsilon_0\zeta}{\eta}E_\mathrm{x}\left[\frac{\kappa H - 1 + \mathrm{e}^{-\kappa H}}{\kappa H}\right] \tag{26}$$

Thus, with the Debye–Huckel assumption, ζ_DH can be expressed as an explicit function of the channel height through the average velocity equation, such that if the average velocity is known, then the initial guess for the zeta potential can be determined as

$$\zeta_\mathrm{DH} = -\frac{\eta u_\mathrm{ave}}{\varepsilon_\mathrm{r}\varepsilon_0 E_\mathrm{x}}\left[\frac{\kappa H}{\kappa H - 1 + \mathrm{e}^{-\kappa H}}\right] \tag{27}$$

Using this ζ_DH value as the initial guess for ζ_guess in Eq. (16) to calculate u_ave, and comparing the result to the experimentally measured u_ave, a new ζ_guess is obtained. This procedure can be repeated until the calculated and the experimentally measured values of u_ave converge.

Evaluation of the Specific Surface Conductivity

As discussed above, the electrical current of an electro-osmotic flow can be described as:

$$I_\mathrm{total} = I_\mathrm{cond,bulk} + I_\mathrm{cond,surf} = \lambda_\mathrm{b}A_\mathrm{c}\boldsymbol{E} + P\lambda_\mathrm{s}\boldsymbol{E} . \tag{1}$$

For the case of a parallel plate microchannel with a channel height of $2H$ and a channel width of $2W$, and an electrical field, E_x, applied in the length direction only, I_total is given by:

$$I_\mathrm{total} = 4HW\lambda_\mathrm{b}E_\mathrm{x} + 2(H+W)\lambda_\mathrm{s}E_\mathrm{x} . \tag{28}$$

For a parallel plate microchannel, the channel width, $2W$, is considered to be much larger than the channel height. In general, the surface conductivity, λ_s, is unknown. The channel dimensions can be measured using a microscope and the bulk liquid conductivity can be measured using an electroconductivity meter, which can be treated known. E_x is the applied electrical field strength and is known. The total electrical current, I_total, can be obtained using a data acquisition system. Therefore, the surface conductivity, λ_s, is the only unknown value in Eq. (28) and can be solved such that:

$$\lambda_\mathrm{s} = \frac{I_\mathrm{total} - 4HW\lambda_\mathrm{b}E_\mathrm{x}}{2(H+W)E_\mathrm{x}} . \tag{29}$$

As seen from Eq. (29), by measuring the total current during a steady electro-osmotic flow, the bulk conductivity, the applied electrical field and the channel dimensions, the surface conductivity can be determined. Generally, this is a relatively simple method with a reasonable accuracy. It should be noted that for the measurement of the specific

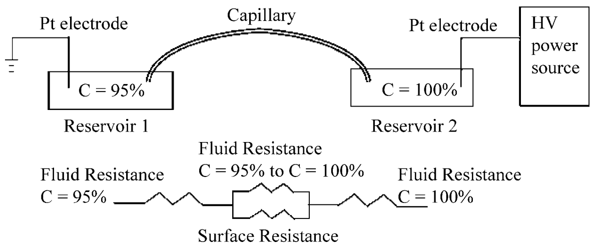

Electrical Current Monitoring Methods, Figure 4 Schematic diagram illustrating the experimental set-up for measuring the current variation and the complete displacement time of a two-concentration system

surface conductivity, the replacement between two similar solutions is not necessary.

Experimental

Traditional Electrical Current Monitoring Method

The experimental set-up commonly used for the current monitoring methods is shown in Fig. 4a [5]. In an experiment, reservoir 2 is filled with an electrolyte solution at a desired concentration. The microchannel and reservoir 1 are filled with the same electrolyte solution at a slightly lower concentration as compared with that in reservoir 2, for example, a 5% difference in concentration of the two solutions is often used. Immediately after the channel is brought contact with reservoir 2, a voltage difference between the two reservoirs is applied by setting reservoir 1 at ground potential and reservoir 2 to a high voltage power supply unit via Platinum electrodes.

The applied electrical field results in an electro-osmotic flow in the microchannel. During electro-osmosis, the higher-concentration electrolyte solution from reservoir 2 is gradually pumped into the microchannel and the same amount of the lower-concentration electrolyte solution is pumped out of the channel. As a result, the overall electrical resistance of the liquid and hence the current in the microchannel changes, as illustrated in Fig. 4b. A data acquisition chip and associated software are used to record the voltage (kV) and current (μA) as a function of time (seconds). Once the lower-concentration solution in the microchannel is completely replaced by the higher-concentration solution from reservoir 2, the current will reach a plateau. The measured time for the current to reach such a plateau value is the time required for the solution from reservoir 2 to travel through the entire channel length. The average velocity of the liquid flow can then be calculated by using Eq. (2),

$$u_{\text{ave,exp}} = \frac{L}{\Delta t} \tag{2}$$

where L is the length of the channel and Δt is the time required for the higher-concentration electrolyte solution to displace the lower-concentration electrolyte solution from the channel.

For the purpose of evaluating the specific surface conductivity, the solution replacement process is not necessary. In these cases, reservoir 1, reservoir 2 and the capillary tube will be filled with an electrolyte solution of the same concentration.

An Improved Method – Slope Method

The traditional current monitoring method as described above requires the determination of the time period for the current change during a replacement process via electro-osmotic flow. Experimentally it is very difficult to determine the exact required time for one solution completely replacing another solution because the gradual changing of the current with time and the small current fluctuations exist at both the beginning and the end of the replacement process. As shown in Fig. 1, it is very difficult to determine the exact beginning and ending time of the current change from the experimental results. In addition, for low concentration solutions, the average electro-osmotic velocity is very low, which requires a longer time to complete the replacement process. Two concerns arise from this situation. First, Joule heating is dependent on the running time of the replacement process, therefore, it may become an issue especially when the channel is made of polymer material such as poly (dimethylsiloxane) (PDMS) which has a low thermal conductivity. Second, the once sharp concentration front between the two solutions becomes progressively blurred. This mixing causes the sloped and plateau region of the current-time relationship to be smoothed together, which makes it difficult to determine the beginning and the end point for the replacement process. Consequently, significant errors could be introduced in the average velocity determined in this way.

It has been observed that, despite the curved beginning and ending sections, the measured current–time relationship is linear in most part of the process when the concentration difference is small. Therefore, a new method was developed [6] to determine the average electro-osmotic velocity by using the slope of the current–time relationship, which is often referred to as the slope method. To examine the reliability of this method, a numerical model is also developed in this study to calculate the average velocity in a microchannel with one solution displacing another similar solution.

When the concentration difference between the two solutions is small, a linear relationship between the current and time is observed. This may be understood in the follow-

ing way. In such a process, the concentration difference between these two solutions is very small, e. g., one is 1×10^{-4} M and another one is 0.95×10^{-4} M, and therefore the zeta potential, which determines the net charge density and hence the liquid flow, can be considered constant along the microchannel. Consequently, the average velocity can be considered as a constant during the replacing process. As one solution flows into the microchannel, the same amount of the other flows out of the microchannel at essentially the same speed. The two solutions have different electrical conductivity values, therefore, the overall electrical resistance of the liquid changes linearly, and hence the slope of the current–time relationship is constant during this process. In other words, there is a linear relationship between the current and time during the process of one solution replacing another similar solution via electro-osmotic flow. The slope of the linear current–time relationship can be described as

$$\text{slope} = \frac{\Delta I}{\Delta t} = \frac{\Delta\left(EA_c\lambda_b\right)}{\Delta t} \cdot \frac{L_{\text{total}}}{L_{\text{total}}} = u_{\text{ave}} \frac{EA\left(\lambda_{b2} - \lambda_{b1}\right)}{L_{\text{total}}}\,, \tag{30}$$

where L_{total} is the total length of the microchannel and u_{ave} is the average electro-osmotic velocity, E is the applied electrical field strength, and $(\lambda_{b2} - \lambda_{b1})$ is the difference in the bulk conductivity between the two solutions. In Eq. (30), all the parameters are known and constant during the replacing process. If we group all the known parameters and denote $\Gamma = EA\left(\lambda_{b2} - \lambda_{b1}\right)/L_{\text{total}}$, Eq. (30) can be rewritten as

$$\text{slope} = \Gamma u_{\text{ave}} \tag{31}$$

Equation (31) shows that the average electro-osmotic flow velocity can be determined by measuring the slope of the current–time relationship.

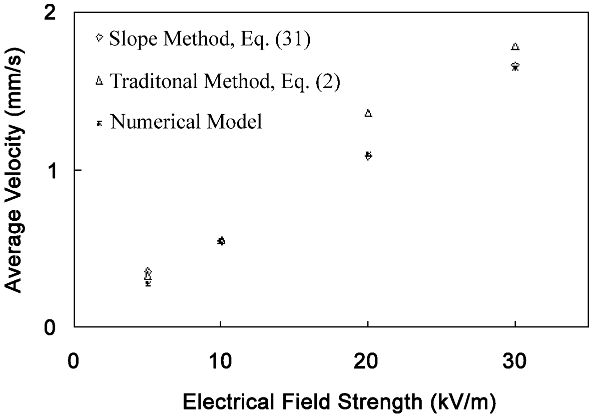

Electrical Current Monitoring Methods, Figure 5 Comparison of the model-predicted average velocity with the experimentally determined average velocity by Eq. (2) and by Eq. (30) for a 1×10^{-3} M KCl solution in a 10 cm length of 100 μm i. d. capillary

Key Research Findings

Electro-osmotic flow has been used as a major pumping mechanism for microfluidic devices. The current monitoring methods, which uses electro-osmotic flow as a transport mechanism for solution replacement processes, has been used for the measurements of the zeta potential, electro-osmotic mobility, and surface conductivity. The development of the slope method allows the accuracy of the average velocity measurement to be improved. Figure 5 shows the comparison of the determined average velocity between the traditional current monitoring method which uses Eq. (29) to determine the average velocity, a numerical method, and the slope method which uses Eq. (31) to determine the average velocity. One can see that the slope method agrees better with the numerical predictions than the traditional current monitoring method. The current monitoring methods are relatively easy and accurate for measuring electro-osmotic mobility, which becomes more apparent for the average flow velocity measurement in nanofluidic devices. Pennathur and Santiago [10] experimentally measured the average velocity in a nanochannel using the traditional current monitoring method and found that the electro-osmotic mobility decreased nonlinearly when the channel dimensions approached the double layer thickness. The electro-osmotic mobility is normally independent on the channel size for most microfluidic applications. Their experimental data agreed with their numerical predictions where finite but non-overlapped double layer was assumed and thus Poisson–Boltzmann equation was used to describe the applied electrical potential field.

Future Directions for Research

Microfluidic and Nanofluidic chips have a wide range of applications in the chemical, biomedical, environmental and biology areas, where a variety of chemical solutions are used. With the development of microfabrication technology, many new materials such as PDMS and Poly(methyl methacrylate) (PMMA) are also employed for chip fabrication. Since each pair of solid–liquid interface has its unique zeta potential and electro-osmotic mobility, which have significant influences on flow control in such small scale devices, it is very important to experimentally determine these two parameters using the current

monitoring technique in order to develop microfluidic and nanofluidic devices for various applications.

Although the electrical current monitoring methods can make accurate and easy measurements for the zeta potential and electro-osmotic mobility, other methods such as microPIV and scalar-based image velocimetry have also been used to measure the velocity profile, from which the zeta potential and electro-osmotic mobility can be determined. However, with the ever-increasing interests in microfluidic and nanofluidic devices, the current monitoring methods will have very compelling features for measuring the zeta potential and electro-osmotic mobility. First, microPIV involves the use of micro sized particles, which may block or adhere to the channel surfaces when the channel size is scaled down to nanometer. Second, scalar based velocity measurement methods often require the injection of caged dye and the visualization of fluorescent dye, which becomes very challenging when the channel size is in the nano scale. The current monitoring methods, however, requires a very simple experimental system. It is true that when the channel size is small, the resistance is large. As a result, the electrical current is small, which may bring difficulty in measuring the current–time relationship accurately. Therefore, more improvements in acquiring accurate measurements for small currents for a replacement process via electro-osmotic flow must be made in the future study.

Cross References

- ► Electroosmotic Flow (DC)
- ► AC Electro-Osmotic Flow
- ► Specific Surface Conductivity
- ► Electrical Double Layers
- ► Streaming Current and Electroviscosity

References

1. Hunter RJ (1981) Zeta potential in colloid science: principles and applications. Academic Press, London
2. Lyklema J (1995) Electric Double layers. In: Lyklema J (ed) Fundamentals of Interface and Colloid Science, vol II, Solid–Liquid Interfaces. Academic Press, London
3. Huang X, Gordon MJ, Zare RN (1988) Current-Monitoring Method for Measuring the Electro-osmotic Flow Rate in Capillary Zone Electrophoresis. Anal Chem 60:1837–1838
4. Li D (2004) Electrokinetics in Microfluidics. Academic Press, London
5. Arulanandam S, Li D (2000) Determining ζ Potential and Surface Conductance by Monitoring the Current in Electro-osmotic Flow. J Colloid Interface Sci 225:421–428
6. Ren L, Escobedo-Canseco C, Li D (2002) A New Method of Evaluating the Average Electro-osmotic Velocity in Microchannels. J Colloid Interface Sci 250:238–242
7. Gu Y, Li D (2000) The Zeta Potential of Glass Surface in Contact with Aqueous Solutions. J Colloid Interface Sci 226:328–339
8. Evans DF, Wennerström H (1999) The Colloidal Domain: Where Physics, Chemistry, Biology, and Technology Meet. Wiley–VCH, New York
9. Ren C, Li D (2005) Improved understanding of the effect of electrical double layer on pressure-driven flow in microchannels. Anal Chim Acta 531:15–23
10. Pennathur S, Santiago JG (2004) Transport mechanisms in electrokinetic nanoscale channels. Proceedings IMECE04, paper number IMECE2004–61356

Electrical Double Layer Potential

► Electrical Double Layers Interaction

Electrical Double Layers

SUMAN CHAKRABORTY
Department of Mechanical Engineering,
Indian Institute of Technology, Kharagpur, India
suman@mech.iitkgp.ernet.in

Synonyms

Diffuse double layer

Definition

When a solid is in contact with an electrolyte, the chemical state of the surface is generally altered, either by ionization of covalently bound surface groups or by ion adsorption. As a result, the surface inherits a charge while counterions are released into the liquid. For example, common glass, SiOH, in the presence of H_2O, ionizes to produce charged surface groups SiO^- and release of a proton. At equilibrium, a balance between electrostatic interactions and thermal agitation generates a charge density profile. The liquid is electrically neutral, but for a charged layer adjacent to the boundary, which bears a charge locally equal in amplitude and opposite in sign to the bound charge on the surface. This charged layer is commonly known as the electric double layer (EDL).

Chemical and Physical Principles

It is well known that in contact with an aqueous solution, most solid surfaces tend to acquire a net positive or negative charge. The surface charging can occur by several mechanisms [1]. In one such mechanism, the surface groups can dissociate into ions, in contact with the liquid molecules. For example, protons can dissociate from the carboxylic groups of the surface ($-COOH \rightarrow -COO^- + H^+$), leaving behind a negatively

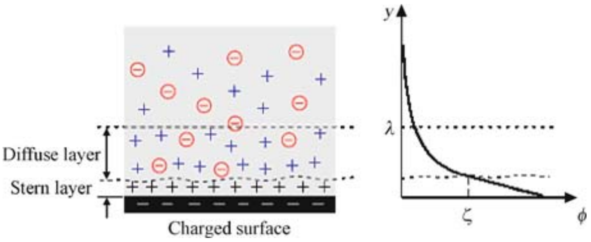

Electrical Double Layers, Figure 1 A schematic illustration of the ionic concentration and the potential field in an EDL in vicinity of a flat surface in contact with an aqueous solution. Zeta potential (ζ) is the potential at the shear plane. Debye length (λ) is the characteristic thickness of the EDL

charged solid substrate. On the other hand, if the surface contains basic groups such as OH, a dissociation of the basic groups (for example, release of OH^- ions to the aqueous solution, leaving behind positive charges on the surface) may generate a positively charged surface. Irrespective of the fact whether the surface is positively or negatively charged, the magnitude of the surface charge depends on the acidic or basic strengths of the surface groups and on the pH of the solution. A reduction in pH reduces the surface charge for a surface containing acidic groups, whereas an increase in pH reduces the surface charge for a surface containing basic groups. Another mechanism of surface charging can occur by means of preferential adsorption (binding) of ions from the solution. For example, Ca^{2+} ions can bind onto the zwitterionic headgroups of lipid bilayer surfaces to make the surface positively charged. The adsorption of ions from the solution can also occur onto oppositely charged surface sites. For instance, the adsorption of cationic Ca^{2+} to anionic COO^- sites (vacated by H^+ or Na^+ or K^+, as example) can occur by means of ion-exchange mechanisms. There may also occur a distribution of anions and cations between two immiscible phases such as water and oil. A similar situation may occur when a preferential dissolution of certain ionic species takes place. For example, when an AgI crystal is placed in water, dissolution takes place till the product of ionic concentrations of Ag^+ and I^- ions equals the solubility product ($= 10^{-16}$ mol/l^2). If equal amounts of Ag^+ and I^- ions were to dissolve, then the surface would be uncharged. However, in practice, the Ag^+ ions dissolve preferentially, leaving behind a negatively charged surface. In general, although the liquid solution is electrically neutral, an electrostatic force of attraction develops between the surface charges and the oppositely charged ions (counterions) in the liquid. Thus, a counterion concentration gradient establishes within the liquid, with a higher concentration near the solid surface and a lower concentration in the far-stream. On the other hand, the coion concentration near the surface is lower than that in the bulk liquid far away from the same, due to electrostatic repulsion. As a consequence, there is a net abundance of counterions close to the surface, which effectively balances the total charge of surface coions.

A schematic diagram depicting the charge and the potential distribution within an EDL is depicted in Fig. 1. Immediately next to the charged surface, a layer of immobilized counterions is present, which is known as the compact layer or the Stern layer or the Helmholtz layer. This layer is about a few Angstroms in thickness, and hence the potential distribution within the same can be taken as almost linear. The charge and the potential distributions within this layer are strong functions of the geometrical characteristics of the ions and the short-range interaction forces between the ions, wall and the adjacent dipoles. From the compact layer to the electrically neutral bulk liquid, the net charge density gradually reduces to zero. Since the Stern layer, featured with steep potential gradients (and hence steep velocity gradients), is extremely thin (of the order of the ion hydration radius, typically ~ 0.1 nm) as compared to the typical microchannel dimensions, the shear effects are virtually confined within this thin layer. This is extremely attractive in separation science, since it minimizes the hydrodynamic dispersion effects that are commonly associated with pressure-driven Poiseuille flows having parabolic velocity profiles. The layer of mobile ions beyond the Stern layer is called the Guoy-Chapman layer, or the diffused layer of the EDL. These two layers are separated by a shear plane. The potential at this shear plane is known as the zeta potential (ζ). The thickness of the EDL is known as the Debye length (λ), which is the length from the shear plane over which the EDL potential reduces to $(1/e)$ of ζ.

For a preliminary mathematical analysis, let us consider a single plate or surface in an infinite liquid phase. For the system to be in equilibrium, the electrochemical potential of the ions need to be constant everywhere, which implies that

$$\frac{d\bar{\mu}_i}{dy} = 0 \tag{1}$$

where the subscript i indicates type i ions and the electrochemical potential, μ_i, is defined as

$$\bar{\mu}_i = \mu_i + z_i e \psi \tag{2}$$

Here μ_i and z_i are the chemical potential and valence of type i ions and e is the charge of a proton. Further, from

thermodynamic considerations, one can write

$$\mu_i = \mu_i^0 + k_B T \ln n_i \tag{3}$$

where μ_i^0 is a constant for type i ions, k_B is the Boltzmann constant, T is the absolute temperature of the solution and n_i is the number concentration of the type i ions. Differentiating Eq. (3) with respect to y, one obtains

$$\frac{d\mu_i}{dy} = k_B T \frac{1}{n_i} \frac{dn_i}{dy} \tag{4}$$

Combining Eq. (4) with Eqs. (1) and (2), one gets

$$\frac{dn_i}{n_i} = -\frac{z_i e}{k_B T} d\psi \tag{5}$$

Equation (5) can be solved with the imposition of appropriate boundary conditions, based on the prevailing physical situation. Here we discuss two different boundary conditions (case 1 and case 2).

Case 1: At $y = h$, $\psi = \psi_h$, $n_i = n_i^h$. For this case, the solution of Eq. (5) is as follows:

$$n_i = n_i^h \exp\left(-\frac{z_i e}{k_B T}(\psi - \psi_h)\right) \tag{6}$$

Case 2: At $y \to \infty$, $\psi = 0$, $n_i = n_i^\infty$. The solution for this case is

$$n_i = n_i^\infty \exp\left(-\frac{z_i e \psi}{k_B T}\right) \tag{7}$$

Equation (7) gives the so-called Boltzmann distribution of ions near a charged surface [2]. The major assumptions implicit with the derivation of this distribution are as follows:

- The system is in equilibrium, with no macroscopic advection/diffusion of ions
- The solid surface is microscopically homogeneous
- The charged surface is in contact with an infinitely large liquid medium
- The strength (intensity) of the EDL field significantly overweighs the strength of any imposed electric field, close to the interface. As an example, for an EDL thickness of 10 nm and a surface potential of 100 mV, the EDL field strength is of the order of 10^7 V/m, which is significantly higher than the typical electric field strengths ($\sim$ kV/m) that are commonly employed to actuate fluid dynamic transport through microchannels.
- The far-stream boundary condition is applicable. This, however, loses its validity when the EDLs formed in vicinity of two narrowly-separated solid surfaces effectively protrude into the central plane that is located midway between the two surfaces and overlap with each other.

In practice, the validity of some of these assumptions may indeed be questionable, in a strict sense. For instance, one may cite the case of ionic charge distribution in presence of fluid flows, for which the system is not in thermodynamic equilibrium. However, for low flow velocities (Re < 10), the Boltzmann distribution can offer with a reasonably good approximation of ionic charge distribution. In order to prove this proposition, one may refer to the ionic species conservation equation, which describes the flux of the ith ionic species as

$$\nabla \cdot \boldsymbol{j}_i = 0 \tag{8}$$

In Eq. (8), $\boldsymbol{j}_i$ can be described by the Nernst–Planck equation as

$$\boldsymbol{j}_i = n_i \boldsymbol{u} - D_i \nabla n_i - \left(\frac{z_i e D_i n_i}{k_B T}\right) \nabla \psi \tag{8a}$$

Substituting Eq. (8a) in Eq. (8) and rearranging, one may write

$$\nabla \cdot (n_i \boldsymbol{u}) = \nabla \cdot (D_i \nabla n_i) + \nabla \cdot \left[\left(\frac{z_i e D_i n_i}{k_B T}\right) \nabla \psi\right] \tag{9}$$

In case the advection term in Eq. (9) can be neglected (which is true for low velocities), one can write, for a constant D_i

$$\nabla^2 n_i + \nabla \cdot \left[\left(\frac{z_i e n_i}{k_B T}\right) \nabla \psi\right] = 0 \tag{10}$$

For a one-dimensional situation (with gradients along y-direction only), Eq. (10) can be integrated to yield

$$\frac{dn_i}{dy} + \left(\frac{z_i e n_i}{k_B T}\right) \frac{d\psi}{dy} = 0 \tag{11}$$

which is same as Eq. (5), from which the Boltzmann equation can be derived by imposing the pertinent boundary conditions.

It is important to note here that the situations depicted by cases 1 and 2 are rather generic in nature, and can be judiciously extended to analyze the EDL formation

in between two parallel plates separated by a distance of $2h$, for example. When the characteristic EDL thickness (λ_D) is much less than h, the location of the midplane (centerline) can mathematically be treated as a far-field one, since the charge density gradients are only confined within the EDLs adjacent to the solid surfaces, beyond which the effects of near-wall potential distribution cannot effectively penetrate. In such situations, the mathematical description introduced by case 2 readily applies. On the other hand, case 1 is the representative of a more general situation, in which the EDLs formed in the vicinity of the two plates can penetrate into the mid-plane and in fact, may interfere with each other. We shall discuss about this situation more carefully, later in this article.

For analyzing the distinctive implications of the cases 1 and 2, let us first solve for the potential distribution consistent with case 1, with the consideration that the liquid phase is an aqueous solution with simple symmetric (1 : 1) electrolyte. In such situations, $z_1 = +1$, $z_2 = -1$, and accordingly, one may write

$$n_+ = n_+^h \exp\left(-\frac{e}{k_B T}(\psi - \psi_h)\right) \tag{12a}$$

$$n_- = n_-^h \exp\left(\frac{e}{k_B T}(\psi - \psi_h)\right) \tag{12b}$$

The net charge density per unit volume, ρ_e, can be described as

$$\rho_e = e\,(n_+ - n_-) \tag{13}$$

For further simplifications, one may note that for small values of the argument, it is possible to neglect higher order terms in an exponential series and approximate $\exp(x)$ as $1 + x$. This consideration, when applied to the potential distributions depicted by Eqs. (12a), (12b), forms the basis of the Debye–Hückel linearization principle [2], which effectively linearizes the pertinent exponential variation of ionic charge distribution for small values of $e\phi/k_B T$. Under such approximations, Eq. (13) can be simplified as

$$\rho_e = e\left[n_+^h\left(1 - \frac{e}{k_B T}\left(\psi - \psi_h\right)\right) - n_-^h\left(1 + \frac{e}{k_B T}\left(\psi - \psi_h\right)\right)\right] \tag{14}$$

The fundamental equation for electrostatic potential distribution within the system is nothing but the Poisson's equation, which states

$$\frac{d^2\psi}{dy^2} = -\frac{\rho_e}{\varepsilon} \tag{15}$$

where ε is the permittivity of the medium. Substituting Eq. (14) in Eq. (15), one gets

$$\frac{d^2\psi}{dy^2} - \frac{e^2}{\varepsilon k_B T}\left(n_+^h + n_-^h\right)\psi = \frac{e}{\varepsilon}\left[\left(n_-^h - n_+^h\right) - \frac{e}{k_B T}\left(n_-^h + n_+^h\right)\psi_h\right] \tag{16}$$

With the boundary conditions of $\psi = \psi_0$ at $y = 0$ (where ψ_0 is approximated as ζ, the zeta potential, in most electrokinetic models, although there is a minor difference between these two, in a strict sense) and $\psi = \psi_h$ at $y = h$, one gets

$$\psi = \psi_h + A_1 \exp\left(\sqrt{K_1}y\right) + A_2 \exp\left(-\sqrt{K_1}y\right) - K_2 \tag{17}$$

where

$$K_1 = \frac{e^2}{\varepsilon k_B T}\left(n_+^h + n_-^h\right)$$

$$K_2 = \frac{k_B T}{e}\frac{\left(n_-^h - n_+^h\right)}{\left(n_-^h + n_+^h\right)}$$

$$A_1 = \frac{\psi_0 - \psi_h}{1 - \exp\left(2\sqrt{K_1}h\right)} + \frac{K_2}{1 + \exp\left(\sqrt{K_1}h\right)}$$

$$A_2 = \frac{\psi_0 - \psi_h}{\exp\left(2\sqrt{K_1}h\right) - 1}\exp\left(2\sqrt{K_1}h\right) + \frac{K_2 \exp\left(2\sqrt{K_1}h\right)}{1 + \exp\left(\sqrt{K_1}h\right)}$$

The concentrations of cations and anions can be obtained by substituting Eq. (17) into Eqs. (12a) and (12b) to yield

$$n_+(y) = n_+^h\left[-\frac{K_3}{2}\exp\left(\sqrt{K_1}(y - h)\right) - \frac{K_3}{2}\exp\left(\sqrt{K_1}(h - y)\right) + K_3 + 1\right] \tag{18a}$$

$$n_{-}(y) = n_{-}^{h}\left[\frac{K_3}{2}\exp\left(\sqrt{K_1}(y-h)\right) + \frac{K_3}{2}\exp\left(\sqrt{K_1}(h-y)\right) - K_3 + 1\right] \tag{18b}$$

where $K_3 = \left(n_{-}^{h} - n_{+}^{h}\right)/\left(n_{-}^{h} + n_{+}^{h}\right)$.

It is important to mention here that the case of constant zeta potential boundary condition, as considered for the above analysis, may not be a very common feature for strongly interacting EDLs. Rather, the concerned boundary condition may be posed more appropriately by simultaneously invoking the pertinent equations for chemical equilibrium and surface charge density–surface potential relationship. For example, one may use [6]

$$\zeta(\sigma) = \frac{k_B T}{e}\ln\left(\frac{-\sigma}{e\Gamma + \sigma}\right) + \frac{\ln 10}{e/k_B T}(pK - pH) - \frac{\sigma}{C} \tag{18c}$$

where Γ is the surface density of chargeable sites, pH corresponds to that of the buffer solution, C is the Stern layer capacitance, pK is the equilibrium constant of the surface reaction. The surface charge density, σ, may be approximated using the Grahame equation for non-overlapped EDL conditions, as [6]

$$\sigma(\zeta) = \frac{2\varepsilon k_B T\kappa}{ze}\sinh\left(\frac{ze\zeta}{2k_B T}\right) \tag{18d}$$

In case of strong EDL overlap, Eq. (18d) ceases to hold valid. In that case, the variation of σ versus ζ is obtained by solving the potential distribution from the Poisson equation for different choices of the value of σ. The point of intersection of this characteristic with Eq. (18b) defines self consistent boundary values of σ and ζ.

Case 2 can be recovered as a special limiting form of case 1, with the following restrictions: as $h \to \infty$, $\psi_h \to 0$, $n_{-}^{h} = n_{+}^{h} = n^{\infty}$. This implies that for case 2 one can write $K_1 = 2e^2 n^{\infty}/\varepsilon k_B T$, $K_2 = 0$, $A_1 = 0$, $A_2 = \psi_0$. Thus, for case 2, the potential distribution takes the following form:

$$\psi(y) = \psi_0 \exp\left(-\sqrt{\frac{2e^2 n^{\infty}}{\varepsilon k_B T}}\,y\right) \tag{19}$$

The term $2e^2 n^{\infty}/\varepsilon k_B T$ appearing in Eq. (19) can be symbolized as κ^2, where $1/\kappa$ is commonly referred to as the characteristic thickness of the EDL, i.e., $1/\kappa \equiv \lambda$. This characteristic thickness solely depends on the properties of the liquid and not on any properties of the surface [1]. For example, for a 1:1 electrolyte of concentration C, $1/\kappa = 0.304/\sqrt{C}$ nm (where C is in molar units). This is estimated by taking $T = 298$ K, $\varepsilon = 78.5 \times 8.85 \times 10^{-12} C^2/\mathrm{N\,m}^2$, $e = 1.602 \times 10^{-19} C$, $k_B = 1.38 \times 10^{-23}$ J/K and $n^{\infty} = 1000N$, where N is the Avogadro number. Thus, for a 10^{-4} M NaCl solution, $1/\kappa \approx 30$ nm and for 1 M of the same solution $1/\kappa \approx 0.3$ nm. Physically, as the bulk ionic concentration increases, more counterions are attracted to the region close to the charged surface to neutralize the surface charge. As a result, the EDL thickness is reduced and the EDL appears to be somewhat *compressed*.

Out of the two cases described above, clearly the case 1 represents a more general situation in which the parameters n_{-}^{h}, n_{+}^{h} and ψ_0 are not independent constants, but are rather dependent on certain additional constraints. To appreciate the implications of these additional constraints, let us consider that the solid surface is composed of inorganic oxides (such as silica, zirconia, titania etc.). Either H_3O^+ or OH^- ions (formed as a consequence of dissociation of the aqueous medium carrying the electrolyte) can be adsorbed to the solid surface. The solid surface, accordingly, can become either positively or negatively charged, depending on the pH of the solution. The resultant surface charge density can then be described as [3]

$$\sigma_0 = \frac{eN_s\delta\sinh\left(\psi_N^* - \psi_0^*\right)}{1 + \delta\cosh\left(\psi_N^* - \psi_0^*\right)} \tag{20}$$

where $\psi_0^* = ze\psi_0/k_B T$, N_s is the site density on the oxide surface (a typical value may be of the order of 10^{14} to 10^{15} sites/cm^2, as an example), and ψ_N^* is the non-dimensional Nernst potential, given by

$$\psi_N^* = 2.303\left(\mathrm{pH_z} - \mathrm{pH}\right) \tag{21}$$

In Eq. (21), $\mathrm{pH_z}$ is the pH value when the solid surface reaches the point of zero charge (for most oxide surfaces, this value is between 5 and 6). For a pH value of the aqueous solution assumed as 7, the oxide surfaces would therefore be negatively charged due to an attachment of OH^- ions. This in turn implies that the concentration of OH^- ions in the bulk would decrease. As a consequence, to restore local equilibrium, certain number of H_2O molecules would further dissociate into H_3O^+ and OH^- ions. This consideration can be utilized to describe the mass conservation of H_3O^+ and OH^- ions in the charged EDL. The parameter δ in Eq. (20) can be described as

$$\delta = 2 \times 10^{-\Delta\mathrm{pK}/2} \tag{22}$$

where ΔpK is the dissociation constant difference (typically $\Delta\mathrm{pK} \sim 10$). For a given combination of the solid

surface and the solution, ψ_N^*, N_s and δ are uniquely prescribed, which implies that the parameter σ_0 varies with ψ_0^* only. Further, from the mass conservation of individual ionic types, one can write [3]

$$\int_0^h n_{H_3O^+}\,dy = n_{H_3O^+}^h + N_d \tag{23a}$$

$$\int_0^h n_{OH^-}\,dy = n_{OH^-}^h - \frac{\sigma_0}{e} + N_d \tag{23b}$$

where N_d is the number of H_2O molecules dissociated into H_3O^+ and OH^- ions. Defining the average concentration as $\bar{n}_i = \frac{1}{h}\int_0^h n_i\,dy$, Eqs. (23a) and (23b) can be re-written as

$$\bar{n}_{H_3O^+}h = n_{H_3O^+}^h + N_d \tag{24a}$$

$$\bar{n}_{OH^-}h = n_{OH^-}^h - \frac{\sigma_0}{e} + N_d \tag{24b}$$

Also, from the reaction equilibrium for dissociation of H_2O ($2H_2O \Leftrightarrow H_3O^+ + OH^-$), one can write

$$K_w = [H_3O^+] \times [OH^-] \tag{25}$$

where K_w is the dissociation constant depending on the prevailing temperature (for example, $K_w = 10^{-14}$ at 25 °C, provided that the ionic concentrations are taken in the units of M (mol/l)). The parameters $n_{H_3O^+}^h$ and $n_{OH^-}^h$, as appearing in Eqs. (24a) and (24b), can be obtained as

$$n_{H_3O^+}^h = N \times 10^3 \times [H_3O^+] \tag{25a}$$

$$n_{OH^-}^h = N \times 10^3 \times [OH^-] \tag{25b}$$

where N is the Avogadro number and the ionic concentrations are expressed in M (mol/l) units. Further, $[H_3O^+]$ and $[OH^-]$ can be described as

$$[H_3O^+] = 10^{-pH} \tag{25c}$$

$$[OH^-] = 10^{pH-14} \tag{25d}$$

With these considerations, the values of $n_{H_3O^+}^h$ and $n_{OH^-}^h$ can be estimated in consistency with the characteristics of the buffer solution under consideration. Furthermore, it can be assumed that the average concentrations of H_3O^+ and OH^- ions also obey equilibrium conditions, for which one can write, from Eqs. (25), (26a) and (26b)

$$\bar{n}_{H_3O^+} \times \bar{n}_{OH^-} = N^2 \times 10^6 \times K_w \tag{25e}$$

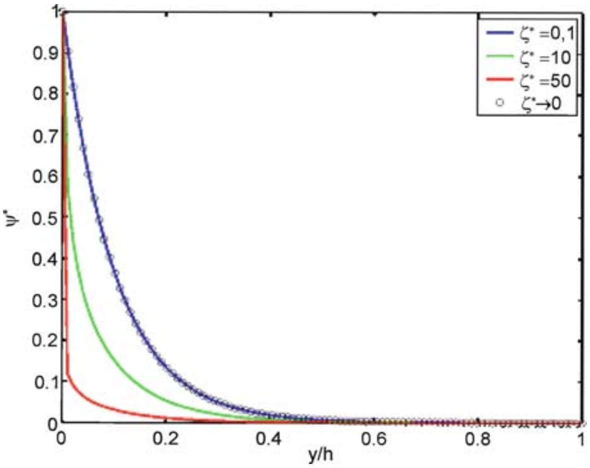

Electrical Double Layers, Figure 2 Variation of normalized electrical potential from the wall to the channel centerline

To obtain a correct description of the overall ionic charge distribution, one also needs to apply the charge conservation principle for all the positive and negative ions in the solution. Based on that, one may write (taking the example of a KCl solution as an electrolyte)

$$\int_0^h n_+\,dy = \int_0^h n_{K^+}\,dy + \int_0^h n_{H_3O^+}\,dy \tag{26a}$$

$$\int_0^h n_-\,dy = \int_0^h n_{Cl^-}\,dy + \int_0^h n_{OH^-}\,dy \tag{26b}$$

With the aid of Eqs. (18a) and (18b) and noting that $\int_0^h n_{K^+}\,dy = n^\infty \alpha h$, $\int_0^h n_{Cl^-}\,dy = n^\infty \beta h$ (where n^∞ is the original bulk ionic concentration of the electrolyte sample, $\alpha = \left(\int_0^h n_{K^+}\,dy\right)/\left(n^\infty h\right)$, $\beta = \left(\int_0^h n_{Cl^-}\,dy\right)/\left(n^\infty h\right)$),

$$\int_0^h n_{H_3O^+}\,dy = \bar{n}_{H_3O^+}h \quad \text{and} \quad \int_0^h n_{OH^-}\,dy = \bar{n}_{OH^-}h\,,$$

one can express Eqs. (26a) and (26b) in terms of the parameters n_+^h, n_-^h, $\bar{n}_{H_3O^+}$, and $\bar{n}_{OH^-}$. Finally, one may employ the asymptotic condition that as $\kappa h \to \infty$, and $n_+^h = n_-^h = n^\infty$. This hypothetical condition is practically satisfied when the value of κh is at least 10 or more, i. e., the location of the central plane of symmetry between the two plates is at a minimum distance of at least 10 times the EDL thickness from the solid surfaces. This consideration closes the system of Eqs. (20)–(26), and enables one to determine the parameters n_+^h, n_-^h and ψ_0, necessary for evaluation of the EDL potential for case 1 through Eq. (17).

Key Research Findings

From the analysis presented as above, it is apparent that the surface potential (or, equivalently, the ζ potential, in an approximate sense) plays a key role in determining the potential distribution within the EDL. The ζ potential, in turn, depends on the bulk ionic concentration and the pH [1]. The influence of ionic concentration can be quantitatively assessed by rewriting the Boltzmann distribution of ionic charges as

$$\frac{\mathrm{d}\,(\ln n_i)}{\mathrm{d}y} = \frac{-z_i e}{k_\mathrm{B} T}\,\frac{\mathrm{d}\psi}{\mathrm{d}y}\,,$$

or equivalently,

$$\frac{\mathrm{d}\psi}{\mathrm{d}\,(\ln n_i)} = \frac{-k_\mathrm{B} T}{z_i e}\,.$$

With $z_i = 1$, $T = 298\,\mathrm{K}$, the above implies $\mathrm{d}\psi/\mathrm{d}\ln n_i = -0.025689$. The above equation implies that a two-fold increase in n_i would result in only a small change in the value of ψ. On the other hand, the dependence of ψ on pH is much more dramatic. In fact, for a given electrolyte solution, the surface charge and ζ can be changed from positive to negative by varying the pH of the solution.

The mathematical descriptions outlined so far for analyzing cases 1 and 2 implicitly assume the validity of the celebrated Debye–Hückel linearization principle, as described earlier. However, for higher pH values (such as pH > 8), the surface potential may be such that the value of $e\psi/k_\mathrm{B}T$ cannot be taken to be small at all locations. A limiting condition that constraints the applicability of the Debye–Hückel approximation occurs for $e\psi/k_\mathrm{B}T \sim 1$, which for standard temperatures, corresponds to a value of approximately 25 mV for the surface potential. For values of ζ beyond this limit, the Debye–Hückel linearization might lose its validity and more general considerations need to be invoked. Such considerations are outlined in the following discussions.

In order to obtain a general solution of the Poisson equation (Eq. (15)) consistent with the Boltzmann distribution of ionic charges (Eq. (7)), one may first combine these two equations together to form the Poisson–Boltzmann equation, as

$$\frac{\mathrm{d}^2\psi^*}{\mathrm{d}y^2} = \kappa^2 \sinh\psi^* \tag{27}$$

It can be noted that in practice, the Poisson–Boltzmann equation can be used to a good effect even in the presence of *thick* EDLs, provided that the Peclet number based on the EDL thickness (i. e., $\mathrm{Pe}_{\kappa_D} = u_\mathrm{ref}\lambda/D$, where u_ref is the characteristic velocity scale along the axial direction and D is the diffusion coefficient of the solute) is small [4]. In such cases, a closed-form analytical expression for ψ can be obtained from Eq. (27) as

$$\psi(y) = \frac{8k_\mathrm{B}T}{ze}\sum_{i=0}^{\infty}\frac{q^{2i+1}}{\left(1-q^{4i+2}\right)}\,\frac{\cosh\left[(2i+1)\,\frac{y}{h}\chi\right]}{(2i+1)} \tag{28}$$

where

$$q = \exp\left(\frac{-\pi K}{K'}\right), \qquad K = F\left(\frac{\pi}{2}, k_0\right),$$

$$K' = F\left(\frac{\pi}{2}, \left(1-k_0^2\right)^{1/2}\right), \quad k_0 = \exp\frac{-ze\psi_h}{k_\mathrm{B}T},$$

$$\chi = \frac{\pi\kappa h}{2k_0^{1/2}K'},$$

ψ_h being the potential at the channel centerline. Here, the function F is an elliptic integral, defined as

$$F(\phi, k) = \int_0^{\phi}\frac{\mathrm{d}\theta}{\left(1-k^2\sin^2\theta\right)^{1/2}}\,.$$

An approximate solution of Eq. (28) can be obtained with a simplified consideration that $\psi_h^* \to 0$. In that situation, one may first multiply both sides of the Eq. (27) by $2\,\mathrm{d}\psi^*/\mathrm{d}y$ and integrate the same to obtain (noting that $\cosh\psi^* - 1 = 2\sinh^2\psi^*/2$)

$$\frac{\mathrm{d}\psi^*}{\mathrm{d}y} = -2\kappa\sinh\frac{\psi^*}{2} \tag{29}$$

Equation (29) can be integrated once more (noting that $\mathrm{d}/\mathrm{d}\psi^*\left(\ln\tanh\psi^*/4\right) = \frac{1}{2}\,\mathrm{cosech}\,\psi^*/2$), to obtain

$$\psi^*(y) = 4\left[\tanh^{-1}\left(\tanh\left\{\frac{\zeta^*}{4}\right\}\exp(-\kappa y)\right)\right] \tag{30}$$

Equation (30) is plotted in Fig. 2, for different values of ζ^*, by taking $\kappa h = 10$. It can easily be observed from the figure that for low values of ζ^*, the solution is virtually the same that is obtained with a Debye–Hückel approximation (as depicted by Eq. (19)).

It is also important to note here that the first integral of the Poisson–Boltzmann equation leads to an important relationship, known as the Grahame equation, and also as the Contact theorem [5]. This, fundamentally, is a relationship between the surface charge density, σ_0 (which is defined as $\sigma_0 = -\int\rho_\mathrm{e}\,\mathrm{d}y$, with a SI unit of $\mathrm{C/m^2}$) and the limiting value of the ionic density profile at the substrate-fluid interface. For a single flat surface with an infinite extent of

the adjacent liquid, an expression for σ_0 can be obtained from the Poisson–Boltzmann equation as

$$\sigma_0 = \frac{4n^{\infty}ze}{k}\sinh\left(\frac{ze\psi_0}{k_B T}\right) \quad (31)$$

Analogous to the case of flat surfaces, one can derive simple analytical expressions for the EDL field for cylindrical and spherical surfaces as well. A summary of the outcome of that analysis, under the Debye–Hückel approximation, is presented in Table 1.

A number of research investigations have recently been reported to elucidate several interesting aspects of EDL overlap. For example, Chakraborty and Padhy [6] reported the consequences of induced pressure gradients due to entrance and exit effects in electroosmotically driven flows through nanopores in presence of EDL overlap. Effects of EDL overlap in the context of AC electroosmosis have also been recently analyzed in a comprehensive manner [7, 8]. Other than using the traditional approaches of investigating the EDL effects, researchers have also employed order parameter based models (postulated on free energy formulation) for analyzing complicated physico-chemical effects within the EDL, including several issues of charge inversion [9]. Those aspects are not detailed here any further, within the scope of this introductory discussion.

Experimental Determination of Zeta Potential

From the discussions outlined so far, it is apparent that the zeta potential happens to one of the key parameters that dictates the overall potential distribution within the EDL. Several experimental techniques have been reported in the literature for an accurate measurement of this important parameter. In the subsequent discussions, the general principle behind these techniques is briefly outlined. The existing methodologies for the measurement of ζ primarily rely on the measurement of electroosmotic flow velocities through microfluidic conduits. When an electric field is applied tangentially to a solid-liquid interface, an electrical body force is exerted on the excess counterions in the diffuse EDL. These ions move under the action of the applied electric field, pulling the liquid with them. For thin EDLs (relative to the half channel width), the average electroosmotic flow velocity can be expressed as

$$\bar{u} = \frac{-\varepsilon\zeta E_x}{\eta} \quad (32)$$

where E_x is the applied axial electric field strength and η is the fluid viscosity. Under these conditions, the measured slope of the current (I)-time (t) relationship in electrosmotic flow can be utilized to measure zeta potential of flat surfaces [1], which can give more simple and accurate measurements in comparison to traditional streaming potential and electrophoresis based techniques [1]. If a capillary tube is connectedwith two different reservoirs containing different concentrations of an electrolyte at its two ends then during electroosmosis, the higher concentration electrolyte solution migrates from one reservoir into the capillary tube (which is initially filled with the electrolyte with a concentration same as that of the electrolyte in the lower-concentration reservoir) and displaces an equal volume of lower concentration electrolyte solution. As a result, the total resistance of liquid in the capillary tube changes and the current increases. The current reaches its maximum when the entire volume of lower concentration electrolyte is replaced with the higher concentration one. If a time of Δt is required to attain this state, then one can write

$$\bar{u} = \frac{L}{\Delta t} \quad (33)$$

where L is the length of the capillary. Based on this estimate of $\bar{u}$, one can obtain the values of ζ from Eq. (33). Although simple in principle, a major problem associated with this technique is the difficulty in the precise determination of Δt, due to small current fluctuations and gradual transitions in the current at the beginning and at the end of the replacement process. To avoid this problem, one might work with the linear portion of the $I-t$ characteristics experimentally observed (a major part of the $I-t$ characteristics is indeed linear, provided that the concentration differences are small) and calculate its slope (m) as

$$m = \frac{\Delta I}{\Delta t} \quad (34)$$

where ΔI and Δt are the changes in current and time, respectively, over the linear range. The total current, I, is the sum of the bulk conduction current, surface conduction current and the convection current. In practice, the first two contributions are significantly predominant over the third one, which means

$$\begin{aligned} I &\approx I_{\text{conduction,bulk}} + I_{\text{conduction,surface}} \\ &= \sigma_b A_c E_x + \sigma_s L E_x \end{aligned} \quad (35)$$

where σ_b is the bulk conductivity, σ_s is the surface conductivity and A_c is the area of cross section of the channel. Noting that $\Delta\sigma_s = 0$, one can write from Eqs. (33), (34) and (35)

$$m = \frac{\Delta\left(\sigma_b A_c E_x\right)}{\Delta t} = \frac{\Delta\left(\sigma_b A_c E_x\right)}{\Delta t} = \frac{\Delta\sigma_b A_c E_x \bar{u}}{L} \quad (36)$$

Electrical Double Layers, Table 1 A summary of EDL field adjacent to spherical and cylindrical surfaces (K_0 and K_1 are the 0th and 1st order modified Bessel function of 2nd kind, respectively)

	Governing equation	Boundary conditions	Surface charge balance equation	Charge on particle surface	EDL potential
Sphere	$\frac{1}{r^2}\frac{d}{dr}\left(r^2\frac{d\psi^*}{dr}\right) = \kappa^2 \sinh\psi^*$ where $\psi^* = \frac{ze\psi}{k_B T}$	$r = a$, $\psi^* = \frac{ze\psi_0}{k_B T}$, $r \to \infty$, $\psi^* \to 0$	$Q = -\int_a^\infty 4\pi r^2 \rho_e \, dr$	$Q = 4\pi\varepsilon a(1+\kappa a)\psi_0$	$\psi = \frac{1}{4\pi\varepsilon} \times \frac{Q}{1+\kappa a} \times \exp\left[-\frac{\kappa(r-a)}{r}\right]$
Cylinder	$\frac{1}{r}\frac{d}{dr}\left(r\frac{d\psi^*}{dr}\right) = \kappa^2 \sinh\psi^*$ where $\psi^* = \frac{ze\psi}{k_B T}$	$r = a$, $\psi^* = \frac{ze\psi_0}{k_B T}$, $r \to \infty$, $\psi^* \to 0$	$Q = -\int_a^\infty 2\pi r L \rho_e \, dr$	$Q = 4\pi\varepsilon a(2a+L)\psi_0 \times \frac{K_1(\kappa a)}{2K_0(\kappa a)}$	$\psi = \frac{\sigma_0 K_0(\kappa r)}{\varepsilon\kappa K_1(\kappa a)}$ where $\sigma_0 = \frac{Q}{2\pi aL + 4\pi a^2}$

Combining Eqs. (32) and (36), one gets

$$\zeta = \frac{\eta m L}{\varepsilon E_x^2 A_c \Delta\sigma_b} \tag{37}$$

Eq. (37) gives an expression for the determination of the value of ζ from the experimentally obtained I–t characteristics.

Restrictions on the Applicability of the Poisson–Boltzmann Equation

It is important to reiterate here that in most of the discussions presented in this article, the celebrated Poisson–Boltzmann equation has been utilized to describe the EDL potential distribution in simple analytical forms. However, as mentioned earlier, the Poisson–Boltzmann equation has its own limited applicability, especially when the surfaces under consideration constitute too narrow a fluid passage within which distinctive intermolecular and surface interactions take place. In brief, for such small separation distances, following effects are likely to occur, which are not considered while deriving the Poisson–Boltzmann equation [10]:

- Mobile counterions in the diffused EDL constitute a highly polarizable layer at each interface. These two opposing *conducting* layers experience an attractive van der Waals force (known as the ion correlation force), which becomes significant at small distances ($<$ 4 nm, typically).
- Effects of finite sizes of the ions (steric effects) tend to enhance the repulsion between two surfaces. This is analogous to the increased osmotic pressure of a van der Waals gas due to finite sizes of gas molecules. In a very similar manner, finite sizes of coions and counterions contribute to enhanced repulsion. In case of coions adsorbed on the surface, the repulsion is nothing but the steric repulsion between the overlapping Stern layers.
- Ionic charges interact with a surface because of the field reflected by the surface on being polarized. This reflected field is the same as if there were an image charge on the other side of the surface at the same distance. If ε be the permittivity of the aqueous medium and ε' be the permittivity of the surfaces, then an additional repulsive force due to this image charge interaction will occur if $\varepsilon' < \varepsilon$.
- Surface charges are discrete and are not *smeared out*, as has been implicitly assumed in the EDL theory. Discrete ions generally contribute to an additional attractive force, especially if the surface charges are mobile.
- Certain short range forces come into play when two surfaces approach closer than a few nanometers. Short-range oscillatory solvation forces of geometric origin arise whenever liquid molecules are induced to order into quasi-discrete layers between two surfaces or within highly restricted spaces. Additionally, surface-solvent interactions can induce orientational reordering in the adjacent liquid and can give rise to a monotonic solvation force that usually decays exponentially with the surface separation. Such forces are dependent on the physical and chemical properties of the surface and are not considered while describing the continuum-level EDL theories.

However, it is important to recognize here that interesting non-continuum effects (in many cases triggered by confinement induced hydrodynamic interactions) have recently been identified to alter the effective zeta potential [11] as a strong function of the slip coefficient. Such slip effects, in turn, may be prevalent in nanofluidic channels because of several reasons, including the formation of nanobubbles adhering to the wall on account of hydrophobic interactions. For more details, one may refer to [12–14].

Examples of Application

Some of the major applications of the EDL theory, in perspective of microfluidics research, are based on

the electrokinetics-based micro-flow actuation mechanisms. Based on these considerations, several Lab-on-a-Chip microdevices have been successfully constructed, which contain integrated microfluidic components such as pumps, mixers, reactors, dispensers, separators, along with the integrated circuitry, as embedded on thin glass or plastic plates (typically of a credit card size). Advantages of these devices include dramatic reduction in the amount of samples and reagents, very short reaction and analysis time, high throughput, automation and portability. Currently, technological improvements and requirements of economization of healthcare protocols are the major driving influences for electrokinetics-based microfluidic research. Some of the demanding applications are related to genomics and proteomics research, high-throughput screening, drug discovery and point-of-care clinical diagnostic devices. There are many specific applications of electrokinetics-based microfluidic actuation processes [1], including micro-total analysis systems (μTAS), capillary electrophoresis, electrochromatography, plymerised chain reaction (PCR) amplification, mixing, flow cytometry, DNA hybridization and analysis, protein analysis, cell manipulation, cell separation, cell patterning, immunoassay, enzymatic reactions, and molecular detection. An outline on these applications of microfluidics in biology and biomedical engineering are presented in the review papers of Beebe et al. [15] and Toner and Irimia [16].

Cross References

- ► Debye Layer
- ► Electrical Double Layer Interaction
- ► Electrical Pumps
- ► Electrochemical Techniques
- ► Electrokinetic Dispensing
- ► Electrokinetic Flow and Ion Transport in Nanochannels
- ► Electrokinetic Flow in Porous Media
- ► Electrokinetic Focusing
- ► Electrokinetic Motion of Cells and Nonpolarizable Particles
- ► Electrokinetic Motion of Polarizable Particles
- ► Electrokinetic Sample Injection
- ► Electrokinetic Transport in Nanofluidic Sensing Devices
- ► Electrokinetic Transport with Biochemical Reactions
- ► Electroosmotic Flow (DC)
- ► AC Electro-Osmotic Flow
- ► Electroosmotic Flow in Heterogeneous Microchannels
- ► Electroviscosity
- ► Zeta-Potential

References

1. Li D (2004) Electrokinetics in microfluidics. Elsevier, Amsterdam
2. Lyklema J (1991) Fundamentals of Interface and Colloid Science. Academic, London
3. Bockris J O, Reddy A K N, Gamboa-Aldeco M (1998) Modern Electrochemistry. Kluwer, New York
4. Atkins PW (1998) Physical Chemistry. Oxford University Press, Oxford
5. Hunter RJ (1981) Zeta potential in colloidal science. Academic, New York
6. Chakraborty S, Padhy S (2008) Induced pressure gradients due to entrance and exit effects in electroosmotically driven flows through nanopores within the continuum regime. J Phys D 41:065502(1–10)
7. Talapatra S, Chakraborty S (2008) Double layer overlap in AC-electroosmosis. Eur J Mech B Fluids. doi:10.1016/j.physletb.2003.10.071
8. Chakraborty S, Srivastava AK (2007) A Generalized Model for Time Periodic Electroosmotic Flows with Overlapping Electrical Double Layers. Langmuir 23:12421–12428
9. Besteman K, Zevenbergen MAG, Lemay SG (2005) Charge inversion by multivalent ions: Dependence on dielectric constant and surface-charge density. Phys Rev E 72:061501(1–9)
10. Israelachvili J (1992) Intermolecular & Surface Forces. Academic, London
11. Chakraborty S (2008) Generalization of Interfacial Electrohydrodynamics in the Presence of Hydrophobic Interactions in Narrow Fluidic Confinements. Phys Rev Lett 100:097801(1–4)
12. Chakraborty S (2007) Order parameter modeling of fluid dynamics in narrow confinements subjected to hydrophobic interactions. Phys Rev Lett 99:094504(1–4)
13. Chakraborty S, Das T, Chattoraj S (2007) A generalized model for probing frictional characteristics of pressure-driven liquid microflows. J Appl Phys 102:104907(1–11)
14. Chakraborty S (2007) Towards a generalized representation of surface effects on pressure-driven liquid flow in microchannels. Appl Phys Lett 90:034108(1–3)
15. Beebe DJ, Mensing GA, Walker GM (2002) Physics and applications of microfluidics in biology. Annu Rev Biomed Eng 4:261–286
16. Toner M, Irimia D (2005) Blood-on-a-Chip. Annu Rev Biomed Eng 7:77–103

Electrical Double Layers Interaction

SUMAN CHAKRABORTY
Department of Mechanical Engineering,
Indian Institute of Technology, Kharagpur, India
suman@mech.iitkgp.ernet.in

Synonyms

Electrical double layer potential

Definition

The interaction forces and potentials between two charged surfaces in an electrolyte are fundamental to the analy-

sis of colloidal systems, and are associated with the formation of electric double layers (EDLs) in vicinity of the solid surfaces. The charged surfaces typically interact across a solution that contains a reservoir of ions, as a consequence of the dissociation of the electrolyte that is already present. In colloid and interfacial sciences, the EDL interaction potential, coupled with the van der Waals interaction potential, lead to the fundamental understanding of inter-surface interaction mechanisms, based on the Derjaguin–Landau–Verwey–Overbeek (DLVO) theory [1]. In practice, the considerable variations in the EDL interaction, brought about by the variations in electrolytic concentration of the dispersing medium, pH of the medium and the surface chemistry, lead to a diverse nature of the colloidal behavior. A fundamental understanding of the physics of EDL interactions, therefore, is of prime importance in understanding the colloidal interactions in various microfluidic applications.

Chemical and Physical Principles

To begin with the fundamental analysis of EDL interactions, let us first consider the distribution of potential between two charged infinite parallel plates at a distance of $2H$ apart and subjected to constant surface potentials (refer to Fig. 1). Assuming a Boltzmann distribution of the respective ionic concentrations, one can write, for a symmetric 1 : 1 electrolyte (see essay ►electrical double layers)

$$\nabla^2\psi = \frac{2n_0 e z}{\varepsilon}\sinh\frac{z e\psi}{k_B T} \tag{1}$$

where ε is the permittivity of the fluid medium, z is the valence of the ionic species in the solution, n_0 is the concentration of the same species in the bulk solution, e is the charge of an electron, k_B is the Boltzmann constant and T is the absolute temperature. For small surface potentials, the Debye–Hückel linearization principle can be employed, so that one can write

$$\nabla^2\psi = \kappa^2\psi \tag{2}$$

where $\kappa^2 = \frac{2n_0 e^2 z^2}{\varepsilon k_B T}$. A one-dimensional solution of Eq. (2) can be obtained as

$$\psi = A_1\cosh\kappa y + A_2\sinh\kappa y \tag{3}$$

where A_1 and A_2 are constants of integration. With the boundary conditions of $\psi = \psi_1$ at $y = 0$ and $\psi = \psi_2$ at $y = 2H$, one gets

$$A_1 = \psi_1 \quad \text{and} \quad A_2 = \frac{\psi_2 - \psi_1\cosh 2\kappa H}{\sinh 2\kappa H}\,. \tag{4}$$

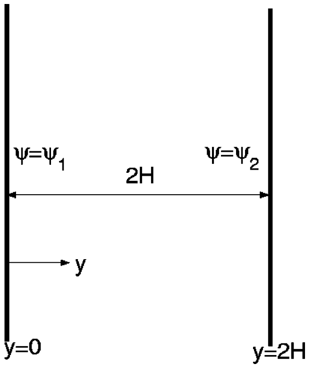

Electrical Double Layers Interaction, Figure 1 Two parallel plates with constant surface potentials

Potential energy of interaction (V) per unit area between the two EDLs equals the change in free energy (G) of the system when the plates are brought from infinity to a distance of $2H$ apart. Thus,

$$V = \Delta G = G_{2H} - G_\infty \tag{5}$$

where

$$G_{2H} = -\frac{1}{2}(\sigma_1\psi_1 + \sigma_2\psi_2) \tag{5a}$$

with σ as the surface charge density (i. e., charge per unit area). Fundamentally, an expression for the surface charge density can be derived by assuming two parallel plates of the same charge density, σ, to be located at a distance $2H$ apart. Under these conditions, one may note that the total charge of counterions in the gap must be equal and opposite to the total charge on the surface. This implies (applying the above principle over the half space between the two plates)

$$\sigma = -\int_0^H \rho_e\,\mathrm{d}y \tag{6}$$

where ρ_e is the charge density in the fluid medium. Using the Poisson's equation $\left(\mathrm{d}^2\psi/\mathrm{d}y^2 = -\rho_e/\varepsilon\right)$ for electrical potential distribution, Eq. (6) can be rewritten as (assuming a homogeneous permittivity of the fluid)

$$\sigma = \varepsilon\int_0^H \frac{d^2\psi}{\mathrm{d}y^2}\,\mathrm{d}y \tag{6a}$$

which, on simplification (noting that $\mathrm{d}\psi/\mathrm{d}y = 0$ at $y = H$) yields

$$\sigma = -\varepsilon\left.\frac{\mathrm{d}\psi}{\mathrm{d}y}\right|_{y=0}\,. \tag{6b}$$

Equation (6b) can be generalized to read

$$\sigma = -\varepsilon \left.\frac{d\psi}{dn}\right|_{\text{surface}} . \tag{6c}$$

where n represents a direction normal to the surface that is oriented towards the intervening fluid. Thus, for the physical problem depicted in Fig. 1, one can write

$$\sigma_1 = -\varepsilon \left.\frac{d\psi}{dy}\right|_{y=0} , \quad \text{and} \quad \sigma_2 = \varepsilon \left.\frac{d\psi}{dy}\right|_{y=2H} . \tag{6d}$$

Using the above definition in Eq. (3), one gets

$$\sigma_1 = -\varepsilon\kappa \left(\psi_2 \operatorname{cosech} 2\kappa H - \psi_1 \coth 2\kappa H\right) . \tag{7a}$$

Similarly,

$$\sigma_2 = \varepsilon\kappa \left(\psi_2 \coth 2\kappa H - \psi_1 \operatorname{cosech} 2\kappa H\right) . \tag{7b}$$

Using Eqs. (7a) and (7b) in Eq. (5a), one gets

$$G_{2H} = \frac{\varepsilon\kappa}{2}\left(2\psi_1\psi_2 \operatorname{cosech} 2\kappa H - \left(\psi_1^2 + \psi_2^2\right)\coth 2\kappa H\right) \tag{8a}$$

When $H \to \infty$, it follows from Eq. (8a) that

$$G_\infty = -\frac{\varepsilon\kappa}{2}\left(\psi_1^2 + \psi_2^2\right) . \tag{8b}$$

Using Eqs. (8a) and (8b) in Eq. (5), one gets

$$V = \frac{\varepsilon\kappa}{2}\left(\left(\psi_1^2 + \psi_2^2\right)(1 - \coth 2\kappa H) + 2\psi_1\psi_2 \operatorname{cosech} 2\kappa H\right) . \tag{9}$$

The corresponding EDL interaction force per unit area, F_{2H}, can be calculated as

$$\begin{aligned} F_{2H} &= -\frac{dV}{d(2H)} \\ &= -\frac{\varepsilon\kappa}{2}\left(\left\{(\psi_1 - \psi_2)^2 \operatorname{cosech}^2 2\kappa H\right\}\right. \\ &\quad \left. + \left\{2\psi_1\psi_2 \operatorname{cosech}^2 2\kappa H\,(1 - \cosh 2\kappa H)\right\}\right) . \end{aligned} \tag{10}$$

It is clear from Eq. (10) that F_{2H} can either be positive or negative if ψ_1 and ψ_2 are of the same sign, since, in that case the terms within the two curly brackets in Eq. (10) are of opposite sign, the resultant of which can be either positive or negative. However, if ψ_1 and ψ_2 are of the opposite sign then both the terms are of the same sign and the resultant F_{2H} becomes negative. This, in turn, implies that with surface potentials of opposite signs, the EDL interaction force is always attractive.

Equation (9) can be conveniently utilized to derive the interaction potential between two spherical EDLs, following the Derjaguni's method [2]. This is done by utilizing the fact that the EDL interactions between two thin parallel slices of the spherical surfaces are essentially governed by Eq. (9). For the sake of analysis, let us consider two spherical surfaces at a minimum distance of separation of H_0, as depicted in Fig. 2. From Fig. 2, the total potential energy of interaction between two infinitesimally small parallel rings of width dx and radius x can be described as

$$U(H_0) = \int_{H=H_0}^{H\to\infty} V\,(2\pi x\,dx) \tag{11}$$

where V is given by Eq. (9) and x is a function of H. Further, from the geometry of Fig. 2, one may note that

$$H - H_0 = a_1 + a_2 - \sqrt{a_1^2 - x^2} - \sqrt{a_2^2 - x^2} \tag{12}$$

which implies

$$dH = \left[\frac{1}{a_1\sqrt{1 - \frac{x^2}{a_1^2}}} + \frac{1}{a_2\sqrt{1 - \frac{x^2}{a_2^2}}}\right] x\,dx . \tag{13}$$

For $x \ll a_1$ and $x \ll a_2$, Eq. (13) gives

$$x\,dx \approx \frac{a_1 a_2}{a_1 + a_2}\,dH . \tag{14}$$

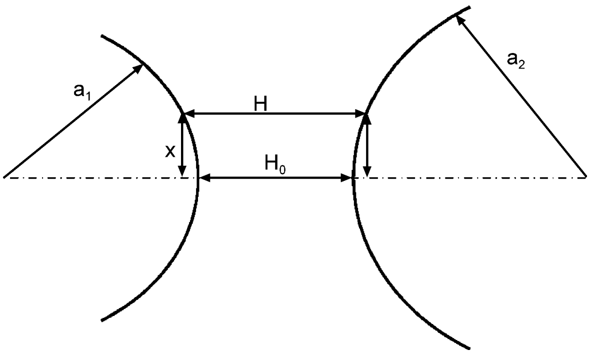

Electrical Double Layers Interaction, Figure 2 Geometrical features used for calculation of the EDL interaction potential between two spherical surfaces of radii a_1 and a_2

Using Eq. (9) and Eq. (14) in Eq. (11) and utilizing the facts that

$$\int_{H_0}^{\infty} (1 - \coth \kappa H)\, \mathrm{d}H = \frac{1}{\kappa} \ln\left[1 - \exp(-2\kappa H_0)\right] ,$$

$$\int_{H_0}^{\infty} \operatorname{cosech} \kappa H\, \mathrm{d}H = \frac{1}{\kappa} \ln\left[\frac{1+\exp(-\kappa H_0)}{1-\exp(-\kappa H_0)}\right] ,$$

one can obtain the following expression for the net EDL potential as

$$U(H_0) = \frac{\pi \varepsilon a_1 a_2}{a_1 + a_2}\Bigg(\left(\psi_1^2 + \psi_2^2\right) \ln\left[1 - \exp(-2\kappa H_0)\right] + 2\psi_1\psi_2 \ln\left[\frac{1+\exp(-\kappa H_0)}{1-\exp(-\kappa H_0)}\right]\Bigg) . \quad (15)$$

Equation (15) can be utilized to derive the EDL interaction potential between a sphere of radius a and a flat plate by setting $a_1 = a$, $a_2 \to \infty$, to obtain

$$U(H_0) = \pi \varepsilon a\Bigg(\left(\psi_1^2 + \psi_2^2\right) \ln\left[1 - \exp(-2\kappa H_0)\right] + 2\psi_1\psi_2 \ln\left[\frac{1+\exp(-\kappa H_0)}{1-\exp(-\kappa H_0)}\right]\Bigg) \quad (15a)$$

The corresponding EDL interaction force can be derived as

$$F(H_0) = -\frac{\partial U(H_0)}{\partial H_0} = 2\pi \varepsilon a \kappa \left(\psi_1^2 + \psi_2^2\right) \cdot \left(\frac{2\psi_1\psi_2}{\psi_1^2 + \psi_2^2} \frac{\exp(-\kappa H_0)}{1 - \exp(-2\kappa H_0)} - \frac{\exp(-2\kappa H_0)}{1 - \exp(-2\kappa H_0)}\right) . \quad (16)$$

Figure 3 depicts the EDL interaction force between a plane surface and a sphere. The non-dimensional parameters considered for plotting this figure are as follows: $DI = 4\pi \varepsilon a \psi_1 \psi_2 / k_B T$ and $Da = (\psi_1 - \psi_2)^2 / 2\psi_1\psi_2$, and ψ_1 and ψ_2 are taken to be of the same sign. Thus, a value of Da different from zero implies that ψ_1 and ψ_2 have different polarity and magnitude. In Fig. 3, however, only positive values of Da are represented. As evident from Fig. 3, the EDL interaction force becomes attractive at a small separation distance, despite the fact that the surface potentials have the same polarity. At larger separation distances, on the other hand, this force becomes repulsive in nature, analogous to the case with $Da = 0$. Further, larger the value of Da, stronger is the attractive potential at small distances of separation. It can also be observed that an asymmetry in the EDL interaction always reduces the repulsive force and moves the location of occurrence of the maximum repulsive force to a greater distance from the wall.

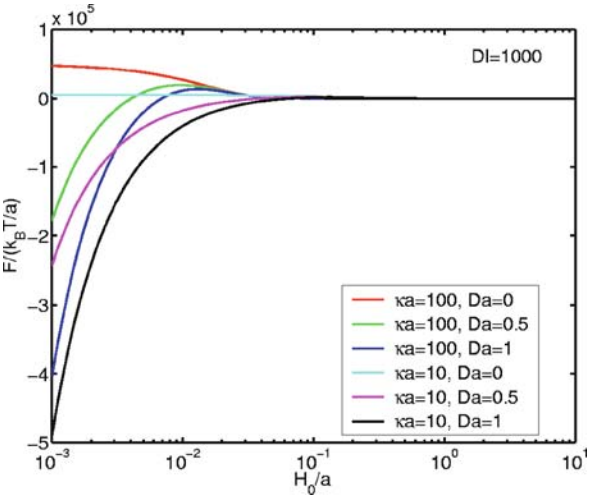

Electrical Double Layers Interaction, Figure 3 EDL interaction force (non-dimensional) as a function of the separation distance between the plane surface and the sphere

It is important to mention here that the EDL interaction potentials described by Eqs. (15) and (15a) are only applicable under the following restricted conditions:

1. $|e\psi/k_B T| < 1$ (consistent with the Debye–Hückel approximation), i. e., $|\psi_1|, |\psi_2| < 25$ mV. However, as shown by Hogg et al. [3], Eqs. (15) and (15a) are good approximations even for the values of ψ_1 and ψ_2 upto 50 to 60 mV.
2. $\kappa a_1 \gg 1$ and $\kappa a_2 \gg 1$, i. e., the EDL thicknesses are small relative to the particle sizes. However, Verwey and Overbeek [1] have showed that Eqs. (15) and (15a) are quite accurate if the values of κa_1 and κa_2 exceed 10.

The methodology described as above has recently been extended [4] to estimate the EDL interaction between a spherical particle (of radius a) and a cylinder (of radius R). The details of the derivations are presented elsewhere [4], and only the final results are summarized below.

$$U(H_0) = 4\varepsilon a^2 \psi_1 \psi_2 \kappa \int_0^{\frac{\pi}{2}} \left[\int_0^1 p\left(\bar{H}_0, \bar{x}, \theta\right) \bar{x}\, \mathrm{d}\bar{x}\right] \mathrm{d}\theta \quad (17)$$

where

$$p\left(\bar{H}_0, \bar{x}, \theta\right) = \operatorname{cosech} \kappa a \bar{H} + \left[\frac{(\psi_1 - \psi_2)^2}{2\psi_1\psi_2} + 1\right]\left(1 - \coth \kappa a \bar{H}\right) \quad (17a)$$

and

$$\bar{H} = \bar{H}_0 + 1 - \sqrt{1 - \bar{x}^2} + \frac{R}{a} - \sqrt{\frac{R^2}{a^2} - \bar{x}^2 \sin^2\theta} \,. \quad (17b)$$

Similarly,

$$F(H_0) = 4\varepsilon a \psi_1 \psi_2 \kappa \int_0^{\frac{\pi}{2}} \left[\int_0^1 f\left(\bar{H}_0, \bar{x}, \theta\right) \bar{x}\, \mathrm{d}\bar{x}\right] \mathrm{d}\theta \quad (18)$$

where

$$f\left(\bar{H}_0, \bar{x}, \theta\right) = -\frac{\partial p}{\partial \bar{H}_0} = \kappa a \left[\coth \kappa a \bar{H} \operatorname{cosech} \kappa a \bar{H} - \left[\frac{(\psi_1 - \psi_2)^2}{2\psi_1\psi_2} + 1\right] \operatorname{cosech}^2 \kappa a \bar{H}\right]. \quad (19)$$

The theoretical developments outlined so far pertain to a situation in which both the surfaces are kept at constant potentials. Another interesting situation may occur when both the surfaces posses constant charges. The analysis for this case is very much analogous to what has been presented here for the case of constant surface potentials. For illustration, one may consider the case of EDL interactions between two parallel plates with constant surface charge densities. For this case, employing the Debye–Hückel linearization principle, the potential distribution can be obtained in the same form as Eq. (3), although the constants of integration, A_1 and A_2, will differ from the earlier case of constant surface potential. To evaluate these constants for the constant surface charge case, one may utilize Eq. (6d) and obtain

$$A_1 = \frac{\sigma_2 + \sigma_1 \cosh 2\kappa H}{\varepsilon\kappa \sinh 2\kappa H}, \quad A_2 = -\frac{\sigma_1}{\varepsilon\kappa}. \quad (20)$$

For the case of constant surface charges, the free energy can be described as

$$G_{2H} = \frac{1}{2}(\sigma_1\psi_1 + \sigma_2\psi_2)\,. \quad (21)$$

Substituting the appropriate expressions in Eq. (21), a simplified expression of the free energy can be obtained as

$$G_{2H} = \frac{1}{2\varepsilon\kappa}\left[2\sigma_1\sigma_2 \operatorname{cosech} 2\kappa H + \left(\sigma_1^2 + \sigma_2^2\right)\coth 2\kappa H\right] \quad (22a)$$

Thus,

$$G_\infty = \frac{1}{2\varepsilon\kappa}\left(\sigma_1^2 + \sigma_2^2\right). \quad (22b)$$

Using Eqs. (22a) and (22b) in Eq. (5), one gets

$$V(2H) = \frac{1}{2\varepsilon\kappa}\left[2\sigma_1\sigma_2 \operatorname{cosech} 2\kappa H - \left(\sigma_1^2 + \sigma_2^2\right)(1 - \coth 2\kappa H)\right]. \quad (23)$$

The EDL interaction force per unit area can be evaluated from Eq. (23) as

$$F(2H) = -\frac{\partial V(2H)}{\partial (2H)} = \frac{1}{2\varepsilon}\left[\frac{\sigma_1^2 + \sigma_2^2 + 2\sigma_1\sigma_2 \cosh(2\kappa H)}{\sinh^2(2\kappa H)}\right]. \quad (24)$$

Eq. (24) can also be recast as

$$F(2H) = \frac{1}{2\varepsilon}\left[\left\{(\sigma_1 - \sigma_2)^2 \operatorname{cosech}^2 \kappa H\right\} + \left\{2\sigma_1\sigma_2 \operatorname{cosech}^2(\kappa H)(1 + \cosh \kappa H)\right\}\right]. \quad (24a)$$

Clearly, if σ_1 and σ_2 are of the same sign then Eq. (24a) predicts a positive (repulsive) interaction force. On the other hand, if they are of opposite polarity, the two expressions in the curly brackets of Eq. (24a) are essentially of opposite sign, which means that the resultant interaction can either be attractive or repulsive. It is important to note here that contrary to common intuitions, the origin of a net repulsive force between two identically charged surfaces in a polar solvent containing electrolyte ions is entropic (osmotic) and not electrostatic. It is true that the electrostatic contribution to the net force is attractive in nature, which is nothing but the Coulombic interaction between the coions and the counterions. Despite this attraction, the counterions remain away from the surface and maintain the diffuse EDL because of the repulsive osmotic pressure between themselves. This is also called an entropic interaction, since it tends to increase the

configurational entropy of the counterions. Bringing the two surfaces closer to each other forces the counterions to move towards the surface against their equilibrium state (i. e., against their osmotic repulsion), but favored by the electrostatic interactions. For identically charged surfaces, the former one dominates in reality, resulting the net force to be a repulsive one.

The two standard cases presented so far are by no means comprehensive and in reality, other types of boundary conditions could be operative as well. For example, out of the two parallel plates, plate 1 might be of constant surface potential and plate 2 might be of constant surface charge. The EDL free energy of formation, in that case, can be described as

$$G_{2H} = \frac{-\sigma_1\psi_1 + \sigma_2\psi_2}{2} . \tag{25}$$

The pertinent expressions for EDL potential energy and the interaction force are as follows:

$$V(2H) = \frac{\sigma_2^2 - \kappa^2\varepsilon^2\psi_1^2}{2\kappa\varepsilon}\left(\tanh 2\kappa H - 1\right) + \sigma_2\psi_1 \operatorname{sech} 2\kappa H \tag{26}$$

$$F(2H) = \operatorname{sech} h2\kappa H\left[-\frac{\sigma_2^2 - \kappa^2\varepsilon^2\psi_1^2}{2\varepsilon}\operatorname{sech} 2\kappa H + \kappa\sigma_2\psi_1 \tanh 2\kappa H\right] \tag{27}$$

Key Research Findings

The fundamental theories on EDL interactions have been substantially advanced by several researchers in the recent past, in order to incorporate the effects of other pertinent physico-chemical phenomena in the mathematical model and to generalize the underlying postulates. Kjellander and Mitchell [5] employed the dressed ion theory for EDL structure and interactions, which is nothing but an exact statistical mechanical formalism for electrolyte systems. In their theory, the *dressed ions* took equivalent roles as the bare ions in the Poisson–Boltzmann approximation. A practical method was also derived for evaluating the effective surface charge densities of the particles. Behrens and Borkovec [6] proposed a quantitative criterion to evaluate the degree of charge regulation for surfaces with arbitrary electrostatic potential. Their approach represented a generalization of the linearized regulation model that had been proposed earlier for the framework of the Debye–Hückel theory only. Their results suggested a new way of using the limiting conditions of constant charge and constant potential to approximate the interaction free energy of charge regulating surfaces. Based on the well-known Debye–Hückel approximation and the Derjaguin's integration method, Gu [4] obtained an integral solution for the EDL interaction between a spherical particle and a cylinder. The effects of the relative dimensions of the cylinder to the sphere on the EDL interaction were studied numerically. These numerical calculations indicated that, in general, the curvature effect on the EDL interaction cannot be neglected at small separation distances. The widely used sphere–flat plate approximation was found to considerably overestimate the actual EDL interaction between a spherical particle and a cylinder, under these circumstances. It was also revealed that the ratio of the radius of the particle to the EDL thickness also plays an important role in determining the EDL interaction at small dimensionless separation distances. Moreover, it was found that at small distances of separation, the EDL interaction can become attractive between two asymmetric EDLs, irrespective of their potentials having the same polarity. Briscoe and Attard [7] developed a counterion-only EDL theory, by adopting a constrained entropy maximization approach, based on an isothermal thermodynamic system. The free energy per unit area between two charged planar surfaces was obtained for the boundary conditions of constant surface charge density and charge regulation. Once applied to a non-polar medium, it was revealed that the electrical double-layer repulsion is weak and long-ranged. Asymptotically, the interaction was found to decay as a power law, in contrast with that in the presence of an ion reservoir which decays exponentially at large surface separations. Huang and Ruckenstein [8] developed a model for EDL interactions that accounts for the difference in dielectric constants because of the influences of hairy surfaces. The ion specificity was also taken into account by using Born's expression for the free energy of hydration of ions. The repulsive forces calculated via the Gouy–Chapman theory and via their new model were compared. It was revealed that the hairy regions can have a long range effect on the repulsive double-layer interactions, which cannot be captured if the short-range steric effects are only taken into account to model the hairy surfaces. Yu et al. [9] proposed a density-functional theory to describe the density profiles of small ions around an isolated colloidal particle. The excess Helmholtz energy functional was derived from a modified fundamental theory for the hard-sphere repulsion and a quadratic functional Taylor expansion for the electrostatic interactions. Their theoretical predictions were in good agreement with the results from Monte Carlo simulations and results from the previous investigations using integral-equation theory for the ionic density profiles and the zeta potentials of spherical particles. Their density-functional theory predicted the formation of a second

counterion layer near the surface of highly charged spherical particle. On the other hand, the nonlinear Poisson–Boltzmann theory and its variants were unable to capture the oscillatory behavior of small ion distributions and charge inversion. In fact, the density-functional theory predicted charge inversion even in a 1 : 1 electrolyte solution, so long as the salt concentration is sufficiently high. Das and Bhattacharjee [10] developed a finite element model of the EDL interaction between an approaching colloidal particle and a small region of a charged planar surface containing four previously deposited particles. The interaction forces obtained from their detailed three-dimensional finite element simulations suggest that with previously deposited spherical particles, the EDL repulsion experienced by the approaching particle is less than the corresponding sphere–plate interaction due to the presence of the previously deposited particles. The reduction in force is quite significant when the screening length of the electric double layer becomes comparable to the particle radius.

Examples of Application

In a very recent study, Zypman [11] outlined some exact expressions for colloidal plane–particle interaction forces and energies with applications to atomic force microscopy (AFM). A general formalism was employed in this study to assess the particle–plane interactions within the Derjaguin–Landau–Verwey–Overbeek (DLVO) framework. The main results of this work were employed to generate an analytical force-separation expression based on AFM experiments for a tip and surface immersed in an aqueous solution. The Derjaguin approximation was subsequently generalized by calculating the next order of approximation, thereby obtaining a useful formula for colloidal interaction estimations.

Cross References

► Electrical Double Layers
► Electrical Pumps
► Electrochemical Techniques
► Electrokinetic Dispensing
► Electrokinetic Flow and Ion Transport in Nanochannels
► Electrokinetic Flow in Porous Media
► Electrokinetic Focusing
► Electrokinetic Motion of Polarizable Particles
► Electrokinetic Motion of Cells and Nonpolarizable Particles
► Electrokinetic Sample Injection
► Electrokinetic Transport with Biochemical Reactions
► Electroosmotic Flow (DC)
► AC Electro-Osmotic Flow
► Electroosmotic Flow in Heterogeneous Microchannels
► Electroviscosity
► Zeta Potential Measurement

References

1. Verwey EJW, Overbeek JTG (1948) theory of the stability of lyphobic colloids. Elsevier, Amsterdam
2. Israelachvili J (1992) Intermolecular & Surface Forces. Academic, London
3. Hogg R, Healy TW, Fuerstenau DW (1966) Mutual coagulation of colloidal dispersions. Trans Farday Soc 62:1638–1650
4. Gu Y (2000) The electrical double-layer interaction between a spherical particle and a cylinder. J Coll Inter Sci 231:199–203
5. Kjellander R, Mitchell DJ (1997) Dressed ion theory for electric double layer structure and interactions; an exact analysis. Mol Phys 91:173–188
6. Behrens SH, Borkovec M (1999) Electric double layer interaction of ionizable surfaces: charge regulation for arbitrary potentials. J Chem Phys 111:382–385
7. Briscoe WH, Attard P (2002) Counterion-only electric double layer: a constrained entropy approach. J Chem Phys 117:5452–5464
8. Huang H, Ruckenstein E (2004) Double layer interaction between two plates with hairy surfaces. J Colloid Interface Sci 273:181–190
9. Yu Y-X, Wu J, Gao GH (2004) Density functional theory of spherical electric double layers and ζ potential of colloidal particles in restricted-primitive-model electrolyte solutions. J Chem Phys 120:7223–7233
10. Das PK, Bhattacharjee S (2005) Electrostatic double layer force between a sphere and a planar substrate in the presence of previously deposited spherical particles. Langmuir 21:4755–4764
11. Zypman FR (2006) Exact expressions for colloidal plane-particle interactions forces and energies with applications to atomic force microscopy. J Phys Condens Matter 18:2795–2803

Electrical/Electrochemical Impedance

Definition

Impedance is a measure of the ability of a circuit to resist the flow of an alternating current. It is usually measured by applying an AC potential to an electrochemical cell and measuring the current through the cell. The current response to a sinusoidal potential will be a sinusoid at the same frequency but shifted in phase. The impedance of the system can be calculated as an expression analogous to Ohm's Law as:

$$Z = \frac{E(t)}{I(t)} = \frac{E_0 \cos(\omega t)}{I_0 \cos(\omega t - \phi)} = Z_0 \frac{\cos(\omega t)}{\cos(\omega t - \phi)} \qquad (1)$$

The impedance is therefore expressed in terms of a magnitude, Z_0, and a phase shift, f. It is also possibly represented

as a complex number,

$$Z = \frac{E}{I} = Z_0 \exp(\mathrm{j}\phi) = Z_0(\cos\phi + \mathrm{j}\sin\phi) \tag{2}$$

The total impedance of a system is the sum of the impedance of the electrical elements in the circuit such as resistors, capacitors, and inductors. For linear impedance elements in series, the equivalent impedance can be calculated from:

$$Z_{eq} = Z_1 + Z_2 + Z_3 \tag{3}$$

For linear impedance elements in parallel, the equivalent impedance can be calculated from:

$$\frac{1}{Z_{eq}} = \frac{1}{Z_1} + \frac{1}{Z_2} + \frac{1}{Z_3} \tag{4}$$

Cross References

► Impedimetric Biosensors for Micro and Nano Fluidics

Electric Debye Layer

Definition

The thin layer of predominantly ions of the opposite sign that form near charged interfaces due to a balance between electrostatic attraction and random thermal fluctuations.

Cross References

► Electrokinetic Flow and Ion Transport in Nanochannels

Electric Heating

► Joule Heating in Electrokinetic Flow: Theoretical Models

Electric Paper-Like Display

► Electronic Paper

Electroactive Materials

► Piezoelectric Materials for Microfluidics

Electrocapillarity

► Electrocapillary

Electrocapillary

SUMAN CHAKRABORTY
Department of Mechanical Engineering,
Indian Institute of Technology, Kharagpur, India
suman@mech.iitkgp.ernet.in

Synonyms

Electrocapillarity

Definition

Electrocapillary phenomenon refers to the modification of the interfacial tension by the presence of electrical charges. The first comprehensive investigations on electrocapillary phenomena were performed by Lippman, way back in 1875 [1]. In Lippman's experimental apparatus, the interfacial tension modulation due to electrical effects was observed through a capillary rise phenomenon, and hence, was later termed as electrocapillarity. A decisive advantage of electrocapillary actuation, in comparison to its thermal counterpart (i. e., the thermocapillary effect, in which surface tension differentials are created by imposed temperature gradients) is the speed with which electrical potentials can be applied and regulated, with possible characteristic timescales of even less than a few milliseconds. Further, electrocapillary based microacatuators consume much less power, as compared to the typical thermocapillary microdevices.

Chemical and Physical Principles

General Theory of Electrocapillarity

The electrocapillary principles are all based on the fact that the surface tension occurs to be a strong function of the electric potential acting across an interface. For illustration, let us consider a discrete liquid droplet in a microchannel, as depicted in Fig. 1. On application of a voltage across the two ends, a motion of the droplet can be actuated, because of the establishment of a pressure differential on account of an asymmetric change in the interfacial tension and a consequent asymmetric deformation of the two menisci. This principle of actuation of fluid motion, commonly known as continuous electrowetting (CEW), happens to be a fundamental principle of

operation of different types of optical switches, micromotors and micropumps. However, such metal/electrode systems might not always be well-suited for microchannel networks, because of the high electrical conductance of the fluid system that can cause high currents and cross-links between neighbouring channels and cells. Moreover, because of large density differences, metal-electrolyte systems are often very sensitive to gravitational forces.

Unlike the CEW, two other types of electrocapillary principles can be employed in practice, which can be utilized to manipulate liquid droplets without necessitating another liquid medium. One such technique is known as electrowetting (EW), which refers to the control of wetting properties of a liquid (commonly, an electrolyte) on a solid (typically, electrode surface), by the modification electric charges present at the solid–liquid interface. Because of a spontaneous ionic charge distribution, an electric double layer (EDL) of a few nm in thickness is formed between the electrode and the aqueous solution. On application of a voltage between the liquid and the electrode, the effective solid–liquid interfacial energy is lowered, on account of the fact that the EDL essentially acts like a parallel plate capacitor that stores electrostatic energy within the same. This leads to an alteration in the apparent contact angle (θ) with the applied voltage, resulting in a net change in the driving force that acts on the liquid meniscus, and a consequent advancing or retracting motion of the same (refer to Fig. 2). A large capacitance of the EDL ($c \sim \varepsilon/\lambda_D$, λ_D being the Debye screening length, typically of the order of a few nm and ε being the permittivity of the ionic medium) effectively allows large changes in the contact angle for relatively small applied voltages.

A third type of electrocapillary principle is known as electrowetting on dielectrics (EWOD), in which the liquid and the electrodes are separated by a thin dielectric layer (refer to Fig. 3). Major advantages of such an arrangement lie in the fact that higher potentials can be applied without causing undesired electrochemical reactions between the electrode and the aqueous medium. Moreover, highly non-wetting surfaces can be designed, which can respond more prominently to the electrowetting actuation mechanisms.

A fundamental postulate that is common to the three basic electrocapillary actuation principles, mentioned as above, is the change in surface energy with the application of electrical potentials, as governed by the Lippman equation:

$$\gamma = \gamma_0 - \frac{1}{2} c V^2 \tag{1}$$

where γ_0 is the surface tension when there is no voltage applied across the interface and c is the capacitance per unit area of the EDL (for CEW and EW) or the dielectric layer (for EWOD). However, these three actuation principles have their own characteristic distinctive features, which are summarized in Table 1.

In order to appreciate the fundamental physical postulates associated with the principles of electrowetting, one may first consider the total free energy of a liquid droplet, in the absence of an electric field, as

$$E = \sum_{i \neq j} A_{ij} \gamma_{ij} - \lambda \forall \tag{2}$$

where $\forall$ is the droplet volume and λ is a Lagrange multiplier to enforce a constant volume constraint (physically, λ is equal to the pressure drop across the liquid-vapour interface, thermodynamically consistent with the definition of free energy of a system). Here A_{ij} is the interfacial area that demarcates the phases i and j, with the corresponding surface energy being designated as γ_{ij}. In this article, the subscripts l, s and v will be employed to represent the liquid, solid and vapour phases, respectively. It can also be noted that if A_{ls} is increased by some amount, A_{sv} is decreased by the same amount.

The free energy evaluation can be best illustrated through the example of a spherical droplet with an equilibrium contact angle θ (refer to Fig. 4), for which case one can write: $A_{sl} = \pi R^2 \sin^2\theta$, $A_{lv} = 2\pi R^2 (1 - \cos\theta)$,

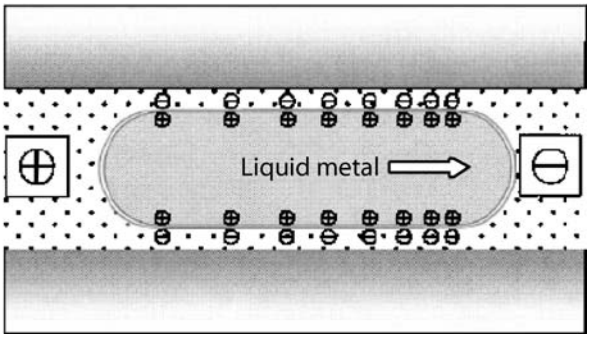

Electrocapillary, Figure 1 An electrically actuated liquid droplet in a microchannel

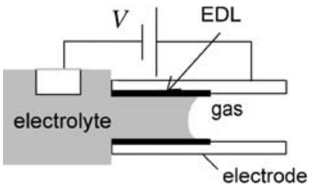

Electrocapillary, Figure 2 An advancing liquid meniscus actuated by electrowetting

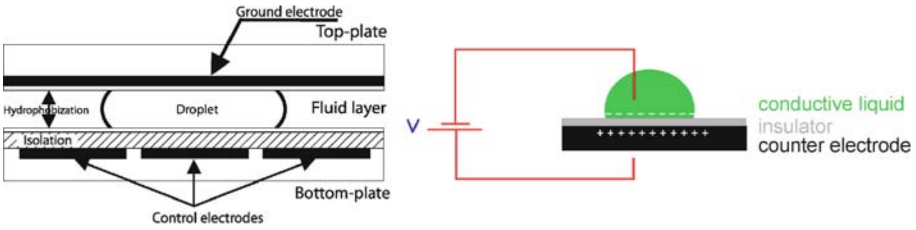

Electrocapillary, Figure 3 The arrangement for electrowetting on dielectrics of a liquid droplet. The right hand diagram is a simpler schematic illustration

Electrocapillary, Table 1 A comparison of different electrocapillary actuating mechanisms

	CEW	EW	EWOD
Capacitor	EDL	EDL	Dielectric layer
Modulated surface tension, γ	Liquid–liquid interfacial tension	Solid–liquid interfacial tension	Solid–liquid interfacial tension
Contact angle	Always 180°, as the droplet does not directly contact the solid surfaces	Variable	Variable

$\forall = \pi R^3(2/3 - 3/4\cos\theta + \cos 3\theta/12)$. Thus, for a spherical droplet

$$E = \underbrace{\pi R^2 \sin^2\theta\,(\gamma_{\mathrm{ls}} - \gamma_{\mathrm{sv}}) + \gamma_{\mathrm{lv}} 2\pi R^2\,(1 - \cos\theta)}_{f} - \lambda \left\{ \underbrace{\pi R^3 \left(\frac{2}{3} - \frac{3}{4}\cos\theta + \frac{\cos 3\theta}{12} \right)}_{g} \right\} \quad (3)$$

For minimization of E, one must have $\partial E/\partial\theta = 0$ and $\partial E/\partial R = 0$, which implies

$$\frac{\partial f}{\partial\theta}\frac{\partial g}{\partial R} = \frac{\partial f}{\partial R}\frac{\partial g}{\partial\theta} \quad (4)$$

Performing the necessary algebra and simplifying, it follows from Eqs. (3) and (4) that

$$\cos\theta = \frac{\gamma_{\mathrm{sv}} - \gamma_{\mathrm{sl}}}{\gamma_{\mathrm{lv}}} \quad (5)$$

Eq. (5) can also be interpreted as a balance between the horizontal components of all the forces that act on the 3-phase contact line (refer to Fig. 4). The vertical component of of this resultant force, on the other hand, is balanced by the normal stress in the rigid solid substrate. Further, substituting the value of cosθ from Eq. (5), one may calculate a value of the parameter λ (= Δp), as

$$\Delta p = \frac{\partial f/\partial\theta}{\partial g/\partial\theta} = \frac{2\gamma_{\mathrm{lv}}}{R} \quad (6)$$

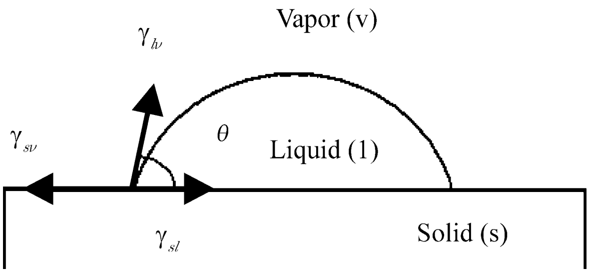

Electrocapillary, Figure 4 Equlibrium of a droplet

For a droplet of a more general shape, Eq. (6) can be generalized as

$$\Delta p = \gamma_{\mathrm{lv}} \left(\frac{1}{r_1} + \frac{1}{r_2} \right) \quad (7)$$

where r_1 and r_2 are the two principal radii of the curvature of the droplet surface. It is important to note here that the Eqs. (5) and (7) are two necessary conditions for equilibrium but not sufficient, since in addition, the second variation of E must also be positive for a minimization of the same. In fact, in presence of complex surfaces, certain morphologies may, indeed, result in unstable droplets, even though both of the necessary conditions are satisfied.

With the above perspective in view, let us take the example of a EWOD actuating mechanism, in which there is an additional electrostatic contribution (E_{el}) to the free energy, so that the net free energy (E_{net}) becomes an algebraic sum of E_{el} and E (as given by Eq. (5)). For that purpose, the following fundamental expression for E_{el} can be

utilized:

$$E_{\mathrm{el}} = -\frac{1}{2}\int \boldsymbol{E}(\boldsymbol{r}) \cdot \boldsymbol{D}(\boldsymbol{r})\, \mathrm{d}\forall \tag{8a}$$

where $\boldsymbol{E}(\boldsymbol{r})$ and $\boldsymbol{D}(\boldsymbol{r})$ are the electric field and the electrical displacement at a position vector $\boldsymbol{r}$ and $\mathrm{d}\forall$ is an elemental volume. In Eq. (8a), $\boldsymbol{D}(\boldsymbol{r})$ is given as

$$\boldsymbol{D}(\boldsymbol{r}) = \varepsilon(\boldsymbol{r})\boldsymbol{E}(\boldsymbol{r}) \tag{8b}$$

where $\varepsilon(\boldsymbol{r})$ is the permittivity of the medium at $\boldsymbol{r}$. In evaluating the integral in Eq. (8a), the liquid is considered to be a perfect conductor, which implies that the surface charges screen the electric fields completely from the interior of the liquid and consequently, the integral vanishes inside the droplet. Further, the electrostatic energy can be split into two parts. One part arises from a parallel plate capacitor formed by the droplet and the electrode, with $C = cA_{\mathrm{sl}}$, where $c = \varepsilon_d/d$, d being the thickness of the dielectric layer and ε_d being the corresponding permittivity. The second part arises from the stray capacitance along the edge of the droplet. However, since the fringe fields are mainly localised within a small range around the contact line, their contribution to the total energy can be neglected. The assumption that the insulator is a major contributor to the overall capacitance seems to be reasonable, since the insulator is much thicker than the EDL and a major part of the voltage drops across the insulator only. Thus, Eq. (8a) yields

$$E_{\mathrm{el}} = -\frac{1}{2}\frac{\varepsilon_d}{d}V^2 A_{\mathrm{sl}} \tag{9}$$

A physical interpretation to the E_{el} term can be provided as follows. Upon connecting the initially uncharged droplet to the power source (battery), a charge δQ flows from the battery to the droplet and to the electrode. The resultant work done on the droplet-electrode capacitor is given by $\delta W_{\mathrm{droplet}} = V_Q \delta Q$, where V_Q is the potential of the capacitor on being energized with an instantaneous charge of Q. Since V_Q = Q/C, the total work done is given by $\int \delta W_{\mathrm{droplet}} = 1/2CV_B^2$, where V_B is the potential of the power supply (battery). The incremental work done on the battery, on the other hand, is given by $\delta W_B = V_B \delta Q_B = V_B(-\delta Q)$. Since the battery voltage is a constant, we have, $\int \delta W_B = -V_B \int \delta Q_B = -CV_B^2$. Thus, the net work done on the battery-electrode system is given by $\int \delta W_{\mathrm{droplet}} + \int \delta W_B = -1/2CV_B^2$.
Substituting Eq. (9) in the expression for total free energy of the droplet (including the electrical energy), one obtains

$$E_{\mathrm{net}} = A_{\mathrm{sl}}\left(\gamma_{\mathrm{sl}} - \frac{1}{2}cV^2\right) + A_{\mathrm{sv}}\gamma_{\mathrm{sv}} + A_{\mathrm{lv}}\gamma_{\mathrm{lv}} - \forall \Delta p \tag{10}$$

Comparing Eq. (10) with Eq. (2), it can easily be observed that EWOD results in a lowering of the effective solid–liquid interfacial energy to a modified value, given by

$$\gamma'_{\mathrm{sl}} = \gamma_{\mathrm{sl}} - \frac{1}{2}cV^2 \tag{11}$$

Eq. (5) can now be utilized to describe the new equilibrium contact angle (θ') as

$$\cos\theta' = \frac{\gamma_{\mathrm{sv}} - \gamma'_{\mathrm{sl}}}{\gamma_{\mathrm{lv}}} \tag{12}$$

Combining Eqs. (5), (11) and (12), one gets

$$\cos\theta' = \cos\theta + \frac{1}{2}\frac{cV^2}{\gamma_{\mathrm{lv}}} \tag{13}$$

which is the well-known Young–Lippman equation [2] that relates a modification of the apparent contact angle with the applied voltage. In a physical sense, electrowetting decreases the effective contact angle, which is driven by the energy gain upon redistributing the charge from the battery to the droplet. This reduction of apparent contact angle is fundamentally related to the fact that a minimization of the free energy requires a maximization of the capacitance. Applying a potential between the droplet and the electrode, therefore, would tend to spread the droplet as much as possible, in an effort to increase the capacitance, which is proportional to A_{sl}. In even more simple terms, because of the applied electric field, opposite charge densities are induced at the fluid-solid interface and in the substrate electrode. The electrostatic attraction between the aqueous solution and the electrode enhances the coverage of the surface by the aqueous solution, thereby inducing an enhanced wetting effect. It can also be noted here that in general, there can be additional contributors to the capacitance per unit area, c, over and above the insulating material. Fundamentally, the solid–liquid interface consists of two layers: one electrically insulating coating in which the potential drops linearly with the thickness, the diffuse EDL being the other. However, when the EDL capacitance becomes much greater than that of the coating, the total capacitance is approximately same as the capacitance of the coating. Such conditions practically apply when the capacitance per unit area of the coating is typically less than $1\ \mu\mathrm{F/cm^2}$, which, for common dielectric materials, is equivalent to the capacitance of an insulator with a thickness greater than $0.1\ \mu\mathrm{m}$.

Electromechanical Viewpoint and Concept of Electrocapillary Pressure

The phenomenon of electrocapillarity, explained as above, can be looked from an electromechanical viewpoint as well, by noting that the net electrical body force per unit volume can be written as

$$f_i = \frac{\partial (\varepsilon E_j)}{\partial x_j} E_i - \frac{1}{2} E_k E_k \frac{\partial \varepsilon}{\partial x_i} + \frac{\partial}{\partial x_i} \left(\frac{1}{2} E_k E_k \frac{\partial \varepsilon}{\partial \rho} \rho \right) \quad (14)$$

Utilizing that $\nabla \times \boldsymbol{E} = 0$ (i. e., $\partial E_i/\partial x_j = \partial E_j/\partial x_i$), and noting that $f_i = \partial \tau_{ij}/\partial x_j$ (where τ_{ij} is the Maxwell stress tensor), one can write, for $\partial \varepsilon/\partial \rho = 0$,

$$\tau_{ij} = \varepsilon \left(E_i E_j - \frac{1}{2} \delta_{ij} E_k E_k \right) \quad (15)$$

To evaluate the resultant electromechanical force, one needs to utilize the fact that the tangential component of the electrical field at the surface of the liquid droplet vanishes, and accordingly, one may express the components of $\boldsymbol{E}$ on a plane with direction cosines n_i as $E_i = E n_i$. Utilizing the Cauchy's theorem relating the traction vector with the stress tensor components, one can write

$$F_i = \int \tau_{ij} n_j \mathrm{d}A \quad (16)$$

Assuming a uniform distribution of $\boldsymbol{E}$ over the droplet surface, Eq. (16) may be recast as (with the help of Eq. 15)

$$\frac{F_i}{A} = \frac{1}{2} \varepsilon E^2 n_i \quad (17)$$

The term $1/2\varepsilon E^2$, as appearing in Eq. (17), is a measure of the electrocapillary force per unit area, and therefore, can be termed as an equivalent electrocapillary pressure (p_{ec}). Since the local charge density (ρ_{e}) is given as $\rho_{\mathrm{e}} = \varepsilon E_i n_i = \varepsilon E$, Eq. (17) can be rewritten as

$$p_{\mathrm{ec}} = \frac{1}{2} \rho_{\mathrm{e}} E \quad (18)$$

Further, with the aid of Gauss' law, one can write $\rho_{\mathrm{e}} = \varepsilon_d V/d$. Moreover, $E = Vl/A_{\mathrm{c}}$, where l is the inner circumference of the conduit handling the liquid droplet and A_{c} is the cross sectional area (for a cylindrical capillary, $A_{\mathrm{c}}/l = R/2$. Thus, $p_{\mathrm{ec}} = 1/2\varepsilon_d V^2/dl/A_c$. Also, from Eq. (11), one can get an equivalent charge induced interfacial tension as $\Delta\gamma = 1/2\varepsilon_d V^2/d$. Hence, one can write

$$p_{\mathrm{ec}} = \frac{l \Delta\gamma}{A_{\mathrm{c}}} = \frac{l}{A_{\mathrm{c}}} \frac{1}{2} \varepsilon_d \frac{V^2}{d} \quad (19)$$

In a qualitative sense, the above represents the pressure generated in a microchannel by electrocapillary effects [3]. There is a subtle difference, however, between this concept and a general description of the electrowetting phenomenon, in a sense that this refers to a voltage dependent droplet meniscus pressure rather than the associated modifications in the apparent contact angles. Thus, material systems with a zero contact angle (complete wetting) or a contact angle of 180° (complete non-wetting) do not electrowet (i. e., do not exhibit a voltage dependence of the apparent contact angle), but do exhibit an electrocapillary pressure (i. e., a voltage dependent pressure in a capillary).

Fluid Dynamics in Presence of Electrocapillary Effects

The dynamics of droplets under electrocapillary actuation has probably been one of the key areas of research investigation over the past few decades, primarily dictated by the pertinent practical applications. In general, the motion of the centre of mass of a droplet (actuated by electrocapillary effects) is opposed by the dissipations originating out of the contact line friction, as well as the viscous resistances in the bulk. For the case in which the contact line friction is the dominating resistive mechanism, pressure within the droplet equilibrates quickly, retaining its spherical shape. However, the contact angle might still vary in a time-evolving manner. On the other hand, when the bulk viscous effects dominate, the contact angle assumes its local equilibrium value everywhere along the contact line. The resultant shape of the droplet becomes non-spherical, and a hydrodynamic pressure gradient prevailing within the same drives a local fluid flow.

To analyze the fundamentals of a droplet motion actuated by continuous electrowetting principles, for illustration, one may consider two infinite parallel plates separated by a distance H, with an intervening liquid. For a steady, fully developed incompressible flow along the x-direction, the Navier–Stokes equation assumes the following simplified form:

$$\mu \frac{\mathrm{d}^2 u}{\mathrm{d}y^2} = \frac{\mathrm{d}p}{\mathrm{d}x} \quad (20)$$

where y represents the transverse direction. The difference in inside and outside pressure across a meniscus of the liquid slug can be described by Eq. (7), with $r_1 = H/2$ and $r_2 \to \infty$. Thus, the difference in pressure between the advancing and receding ends of an hypothetical liquid slug of length Δx can be described as $\Delta p = 2\Delta\gamma/H$, where $\Delta\gamma$ is the surface energy differential across the two ends. Dividing the above expression by Δx and taking the limit as the same tends to zero, one obtains: $\mathrm{d}p/\mathrm{d}x = (2/H)\mathrm{d}\gamma/\mathrm{d}x$. In practice, however, the liquid slug is of

a finite length, and hence $d\gamma/dx$ can be replaced by its corresponding x-averaged value over the entire droplet length, i. e., $\langle d\gamma/dx\rangle$. With this understanding and the employment of the boundary conditions $u = 0$ at $y = 0$ (channel surface) and $du/dy = 0$ at $y = H/2$ (channel centreline), the following velocity profile can be obtained:

$$u = \frac{1}{\mu H}\left\langle\frac{d\gamma}{dx}\right\rangle(y^2 - Hy) \quad (21)$$

Averaging the above velocity profile over the channel cross section, one may obtain

$$\bar{u} = -\frac{H}{6\mu}\left\langle\frac{d\gamma}{dx}\right\rangle. \quad (22)$$

Physically, Eq. (22) implies that the liquid slug flows towards regions of lower surface energy, since it *attempts* to wet more the areas of lower surface tension. In electrowetting, the electrical voltage differentials are responsible for creating these gradients. For assessing the same, one may first differentiate Eq. (1) with respect to x and obtain $d\gamma/dx = -cVdV/dx$. The potential V, for this purpose, can be approximated as

$$V = \bar{\phi} - \langle\phi\rangle - \phi_Q \quad (23)$$

where $\bar{\phi}$ is the arithmetic mean of the potentials at the two ends of the slug of length L (i. e., $\bar{\phi} = (\phi_0 + \phi_L)/2$, the subscript 0 being an indicator of the receding meniscus and the subscript L being an indicator of the advancing meniscus of the slug), $\langle\phi\rangle = 1/L\int\phi dx$, and $\phi_Q = Q/c$, Q being the charge (per unit area) present at the interface in absence of the applied potential, ϕ (Q includes both externally applied charges and charges due to ion adsorption from the electrolyte). Further, $dV/dx \approx (\phi_L - \phi_0)/L$. Thus, Eq. (22) assumes the following form:

$$\bar{u} = \frac{cH}{6\mu L}\left(\bar{\phi} - \langle\phi\rangle - \phi_Q\right)(\phi_L - \phi_0) \quad (24)$$

It is important to observe from Eq. (24) that there is no dynamic effect if there is no interfacial charge and no axial gradient of electrical potential. Eq. (24) predicts $\bar{u}$ to be of the order of 1 cm/s, for $\bar{\phi} \approx \langle\phi\rangle$, $Q \approx 5\,\mu C/cm^2$ (typical to mercury in common aqueous electrolytes), $\mu = 0.001$ Pas, $\phi_L - \phi_0 \approx 1$ V and $H/L \approx 0.1$. Despite being a very crude estimate, the prediction is quite agreeable with the order of magnitude of the corresponding experimentally observed mean velocities (≈ 5 cm/s).

The droplet dynamics can also be analyzed in the perspective of the evolving contact angles at its advancing and receding ends, θ_A and θ_R, respectively. To analyze the situation, one may first note that for typical micro-capillaries, the Reynolds number is typically very small (~ 1 for a 10 µm diameter capillary handling water at a mean speed of 1 cm/s, as an example), which also implies that the hydrodynamic relaxation time of the fluid system is small enough to treat the interfacial regions to be in local electromechanical equilibrium. For the case of a cylindrical capillary, one can write the Newton's second law of motion of the advancing droplet (neglecting the inertial effects and assuming a fully developed velocity profile) as

$$\rho\pi R^2 L\ddot{x}_c = \underbrace{2\pi R\left[(\gamma_{lv}\cos\theta)_R - (\gamma_{lv}\cos\theta)_A\right]}_{\text{driving force due to surface tension}} - \underbrace{8\pi\mu L\dot{x}_c}_{\text{viscous resistance}} \quad (25)$$

where x_c is the position of the centre of mass of the droplet. Initial differences between the values of the apparent contact angles θ_A and θ_R can be created by electrocapillary actuation, resulting in a net driving force for initiation of the droplet motion. Subsequently, these initial contact angles can get further modulated during the droplet motion itself, because of complicated fluid dynamic phenomena such as contact line slip. On a microscopic scale, a possible mechanism in which such slip phenomena might occur on rough solid surfaces could be explained from the perspective that the contact line *jumps* across indentations while moving along the solid boundary (4). Moreover, in reality, the microscopic contact angle can itself be dependent on the capillary flow velocity. This can give rise to an additional velocity dependent frictional force in Eq. (25). The source of this frictional force is the excitation of damped capillary waves at the liquid–vapour interface due the contact line motions over the wall roughness elements. From experimentally obtained data, this can be modeled approximately in the following form:

$$F = 2\pi R\gamma_{lv}B\mathrm{Ca}^x \quad (26)$$

where Ca is the capillary number ($\mathrm{Ca} = \mu\bar{u}/\gamma_{lv}$), B and x are experimentally fitted constants [4]. A physical basis of the introduction of the Ca-dependent and slip-modulated frictional force, F, can be provided as follows. As mentioned earlier, the contact line jumps across the indentations on the solid boundaries, as the contact line moves forward. During the jump, the liquid–vapour interface is pulled forward by the interfacial tension and is retarded by the liquid viscosity. The jump speed is therefore of the order of γ_{lv}/μ, i. e., $\mathrm{Ca} \sim 1$. Because of the restoring effects, the liquid-vapour interface actually executes

a time-periodic motion on a local scale. Further, the contact line actually slips during the jump process, and the corresponding dissipative effects associated with this jump are responsible for the additional frictional force, which gives rise to a velocity dependent contact angle. One potential slip scenario is that the contact line actually leaves the solid surface on one side of the indentation and reattaches itself on the other side of the indentation, since, without that detachment, the large viscous stress near the contact line would retard the movement the same significantly, so that local jump speeds with Ca $\sim$ 1 would not be realizable.

During the droplet motion, it is also very much likely that the contact angle reaches its maximum value for the advancing meniscus and its minimum value for the receding meniscus. The difference between these two limiting values is known as contact angle hysteresis, which is related to certain non-idealities such as inhomogeneity and surface roughness. The physical mechanism associated with this phenomenon is far from being well understood at this stage.

Key Research Findings

EW Under AC Fields

The basic EW theory elucidated here has been directly extended to analyze electrocapillary effects under AC electric fields as well. For instance, if the AC frequency corresponds to a time scale that is less than the hydrodynamic response time of the droplet (typically ~ 0.01 s for mm-sized droplets), the droplet shape and contact angle evolution can be described by employing instantaneous quasiequilibrium considerations in accordance with Eq. (13). On the other hand, for higher frequencies, the droplet response depends only on the r.m.s value of the applied voltage, so long as the liquid can be treated as a perfect conductor. However, beyond a critical frequency (ω_c), the dissolved ions cannot follow the applied field and therefore, cannot screen the electric field from the interior of the liquid [2]). Far beyond ω_c, the droplet behaves like a dielectric, and is effectively actuated by dielectrophoresis mechanisms. For homogeneous bulk liquids, $\omega_c \sim \sigma_l/\varepsilon_l$, where σ_l and ε_l are the conductivity and permittivity of the liquid, respectively. For a typical aqueous solution (such as NaCl, with $\sigma_l \sim 0.1\ \mathrm{Sm}^{-1}$), $\omega_c \sim 10^8\ \mathrm{s}^{-1}$. However, for demineralised water ($\sigma_l \sim 10^{-6}\ \mathrm{Sm}^{-1}$), ω_c can be as low as $\sim 10^3\ \mathrm{s}^{-1}$.

Parametric Dependences of EWOD

EWOD has been found to be only weakly related to the liquid properties. On the contrary, the properties of the insulating layer are somewhat critical for controlling the EWOD phenomenon. The insulating material ideally needs to be such that the contact angle at zero voltage should be as large as possible, so as to achieve a large enough tuning range. This can be achieved by using either hydrophobic insulators (such as polymer materials) or by covering hydrophilic insulators with a thin hydrophobic coating (such as self-assembled monolayers or amorphous fluoropolymer layers). Further, thinner the dielectric material coating, higher is the effective capacitance and lower is the voltage necessary to achieve the same amount of contact angle modification. However, ultra-thin dielectric layers can lead to dielectric breakdown effects [5].

Optoelectrowetting

An optical actuation of the EW mechanism (termed as optoelectrowetting) has recently been experimentally demonstrated, by integrating a photoconductive material underneath a 2D array of electrowetting electrodes [6]. Contact angle changes as large as 30° have been achieved, when illuminated by a light source with an intensity in the tune of 50 to 100 $\mathrm{mW/cm^2}$. Electrode activation, in such situations, can be achieved by directing a laser beam onto the desired electrode, without necessitating electrical connections to all the electrodes.

Contact Angle Saturation in EW

The Young–Lippman equation has been experimentally found to hold only at relatively lower voltages. In fact, before a probable voltage induced transition to a complete wetting state ($\theta' = 0$) becomes possible, the contact angle tends to get saturated within a certain operating regime. The mechanisms that have been proposed by various researchers to explain this phenomenon are as follows:

- The immobilized charge carriers that get injected into the insulators partially screen the applied electrical field. With the assumptions that the immobilized charges are located at a fixed depth within the insulating layer and their densities are homogeneous within a distance of d (dielectric thickness) on both sides of the contact line, Eq. (13) gets modified as [7]

$$\cos\theta' = \cos\theta + \frac{1}{2}\frac{\varepsilon_d\,(V - V_\mathrm{T})^2}{d\gamma_\mathrm{lv}} \tag{27}$$

  where V_T is the potential of the trapped charge layer outside the droplet.
- For low conducting liquids (such as deionised water), the contact line itself is found to become unstable at

higher voltages, leading to the ejection of small satellite droplets from the edge of the main droplet. Such an instability is due to a mutual repulsion of like charges at the contact line. Beyond a critical voltage, surface tension cannot overcome the electrostatic repulsion, and emission of satellite droplets sets in [8].

- Contact angle saturation might also occur when either or both the assumptions of perfectly conductive liquid or perfectly insulating dielectric (as considered for deriving the Young–Lippman equation) are violated. Such situations can be encountered when the voltage partially drops within the bulk of the droplet, as an example. The potential drop within the droplet, in practice, increases with a decreasing contact angle, eventually causing a saturation.

It can easily be inferred from the diverse and case-specific explanations to contact angle saturation that the underlying physics is yet to be well understood, and still remains to be an open research issue.

Modulation of EW Through Surface Patterning

EW phenomena can be modulated to a significant extent by employing patterned substrates, which may alter the topology of the liquid by altering long range electrostatic attraction or repulsion at the contact line. Surface patterning of the electrodes has also been shown to have a profound effect on the droplet morphology. Topographical patterning of the surfaces, originated out of surface roughness elements, can also have profound influences on electrowetting. Due to small-scale surface undulations, the actual solid–liquid interfacial area ($A_{\mathrm{sl,act}}$) is always more than the apparent or projected solid–liquid interfacial area ($A_{\mathrm{sl,app}}$). This alters the apparent contact angle, as per Wenzel's law [2], as $\cos\theta_{\mathrm{mod}} = A_{\mathrm{sl,act}}/A_{\mathrm{sl,app}} \cos\theta$ (with $\theta_{\mathrm{c}} < \theta < 90°$, θ_{c} being a critical value of the contact angle, depending on the surface roughness). Beyond $\theta = 90°$, $A_{\mathrm{sl,act}}$ is dramatically reduced because of entrapped vapour layers underneath the droplet. With a reduced frictional contact, this can give rise to a higher mobility of the droplet.

EW on Hydrophobic Surfaces

If EW of an aqueous medium is done in another liquid environment (say, oil), then both the liquids can compete in wetting the solid surface [9]. With typical hydrophobic EW surfaces, complete wetting of the oil phase at zero voltage is quite common, resulting in the establishment of a thick layer of oil that separates the substrate and the aqueous phase. With higher voltages, however, the electrostatic pressures reduce the oil film thickness and tend to *push* the aqueous phase towards the substrate, leading to complicated micro-scale interactions, which are yet to be extensively investigated.

EW on Super-Hydrophobic Surfaces

EW on super-hydrophobic surfaces has received significant research attention for its engineering implications. Due to large contact angles, the liquid–vapour interfacial area of the droplet becomes quite large in these cases (however, since this area does not contribute to a differential in the surface energy, it does not result in a modification in the apparent contact angle). Not only that, the droplet-substrate interface is not equal to the solid–liquid interface, but is composed of a large number of tiny liquid–air and liquid–solid interfaces, which may be irregularly shaped. This can lead to a modification in the effective contact angle prediction of Eq. (13), through the incorporation of the fraction of solid of the solid–vapour heterogeneous super-hydrophobic surface as an additional parameter.

Examples of Application

Lab-on-a-Chip Applications

Lab-on-a-Chip applications [10] of EW have been primarily directed towards moving, merging, mixing and splitting of droplets. A sandwich design consisting of a droplet confined between two parallel substrates (typically, separated by a distance of $\sim$100 μm) has become a standard practice in this respect. For typical droplet volumes in the micro-litre range (dictated by the constraints that the droplet edges should preferably overlap two adjacent electrodes (with a characteristic electrode size of $\sim$1 nm), the droplet motion sets in with a typical threshold voltage in the tune of 10 V. Beyond this voltage, the droplet speed increases rapidly, reaching limiting values $\sim 10^{-2}$ m/s, within a relatively short interval of time.

One big challenge for all Lab-on-a-Chip devices is the tendency of biological macromolecules to be unspecifically adsorbed onto hydrophobic surfaces. This might alter the contact angles permanently. Such undesirable effects can be suppressed by using an oil phase as the ambient medium, instead of air. The oil phase may wet the hydrophobic surface and can act as a shield against a direct contact between the droplet and the polymer substrate.

EW has also been successfully employed for handling tiny amounts of liquid in biotechnological applications (see Fig. 5). For instance, using the EW-based dip-pin nanolithography technique, droplets in femtolitre to picolitre range have been successfully spotted onto surfaces, to form DNA and protein fluorescence-labelled arrays.

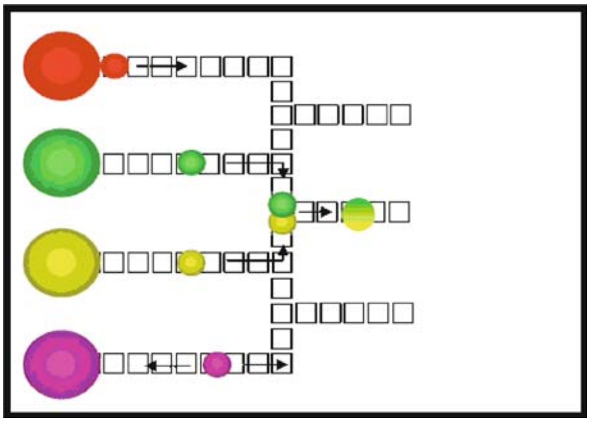

Electrocapillary, Figure 5 Electrowetting-based handling of tiny liquid droplets for Lab-on-a-Chip applications

Liquid Lenses

EW has been successfully used to tune the curvature of liquid lenses (by changing the contact angles of photopolymerizable conductive sessile droplets), so that they can be designed with variable focal lengths [11]. Once the desired refractive strength has been achieved through voltage modulation, the droplets can be cured by UV illumination. Subsequently, the solidified droplets can retain their shapes after removal of the applied voltage.

Fiber Optics Applications

More than two decades back, EW was identified as a possible mechanism for switching light in fibre-optic applications, in which Hg droplets can be moved inside channels to provide either a reflective surface or to allow for the transmission of light in an optical multiplexer. Subsequent applications of EW in fibre-optics have been based on surrounding the active (stripped off) part the optical fibres with liquids of suitably chosen refractive indices, in order to control the transmission of light waves through the fibre [12]. In this way, low power consuming ($\sim$1 mW) optical noise attenuators have been effectively designed, with a response time of as low as $\sim$100 ms.

Self-Excited Oscillations

Very recently, EW has been employed to trigger self-excited oscillations of millimetre-sized sessile droplets of water-glycerol mixtures [13]. During these oscillations, contact angles of the droplets have been found to vary periodically between 130° and 80°, with a frequency between 10 and 125 s^{-1}. The resultant mixing of fluids within the droplets has been found to be two orders of magnitudes faster than the conventional chaotic micromixing processes.

Reflective Fast Display on an Electronic Paper

EW has also been used to form the basis of a reflective fast display on an electronic paper (which combines the desirable viewing characteristics of a conventional printed paper with the ability to manipulate the displayed information electronically), so that the video contents can even be conveniently displayed [14]. This display principle utilizes the voltage-controlled movement of a coloured oil film adjacent to a white substrate. The reflectivity of the resultant colour displays has been found to be substantially stronger than the liquid crystal displays.

Radiation Absorption

EW-based optical absorbers have been designed to exploit EW-induced capillary rise for absorbing undesirable radiations (for example, X-rays), thereby minimizing unnecessary exposures of patients to radiations in medical diagnostics. Such absorbers can be formed by dissolving heavy salts in the liquid solution that can rise through a capillary or get depressed, on application of suitable actuation voltages [15].

Micromotors

EW based micromotors have been successfully designed, based on the motion of Hg droplets in electrolyte filled channels. By applying a small voltage along the channel, a charge density and interfacial energy gradient has been effectively established along the Hg droplet, leading to a continuous motion of the same [16].

Cross References

- ► Capillary Filling
- ► Dielectrophoresis
- ► Digital Microfluidics
- ► Droplet and Bubble Formation in Microchannels
- ► Droplet Based Lab-on-Chip Devices
- ► Droplet Despensing
- ► Droplet Dynamics in Microchannel
- ► Electrical Double Layers
- ► Electronic Papers
- ► Electrowetting
- ► Electrowetting, Applications
- ► Electrowetting and Droplets
- ► Integrated Micro Devices for Biological Applications
- ► Integrated Microfluidic Systems for Medical Diagnostics
- ► Interface Capturing Schemes for Free-Surface Flows

► Interface Tracking Schemes for Free-Surface Flows
► Lab-on-a-chip (General Philosophy)
► Lab-on-chip Devices for Protein Analysis
► Surface Tension Driven Flow
► Capillarity and Contact Angle
► Thermal Capillary
► Transport of Droplets by Thermal Capillarity
► Wetting and Spreading

References

1. Lippmann G (1875) Relations entre les phénomènes électriques et capillaries. Ann Chim Phys 5:494–549
2. Mugele F, Baret JC (2005) Electrowetting: from basics to applications. J Phys Condens Matter 17:R705–R774
3. Jones TB (2005) An electromechanical interpretation of electrowetting. J Micromech Microeng 15:1184–1187
4. Sheng P, Zhou M (1992) Immiscible-fluid displacement: Contact line dynamics and the velocity-dependent capillary pressure. Phys Rev A 45:5694–5708
5. Seyrat E, Hayes RA (2001) Amorphous fluoropolymers as insulators for reversible low-voltage electrowetting. J Appl Phys 90:1383–1386
6. Chiou PY, Moon H, Toshiyoshi H, Kim CJ, Wu MC (2003) Light actuation of liquid by optoelectrowetting. Sens Actuators A: Phys 104:222–228
7. Verheijen HJJ, Prins MWJ (1999) Reversible electrowetting and trapping of charge: model and experiments. Langmuir 15:6616–6620
8. Vallet M, Vallade M, Berge B (1999) Limiting phenomena for the spreading of water on polymer films by electrowetting. Eur Phys J B 11:583–591
9. Quilliet C, Berge B (2002) Investigation of effective interface potentials by electrowetting. Europhys Lett 60:99–105
10. Cho SK, Moon HJ, Kim CJ (2003) Creating, transporting, cutting, and merging liquid droplets by electrowetting-based actuation for digital microfluidic circuits. J Microelectromech Syst 12:70–80
11. Kuiper S, Hendriks BH (2004) Variable-focus liquid lens for miniature cameras. Appl Phys Lett 85:1128–1130
12. Mach P, Krupenkin T, Yang S, Rogers JA (2002) Dynamic tuning of optical waveguides with electrowetting pumps and recirculating fluid channels. Appl Phys Lett 81:202–204
13. Mugele F, Baret JC, Steinhauser D (2006) Microfluidic mixing through electrowetting-induced droplet oscillations. Appl Phys Lett 88(1–3):204106
14. Hayes RA, Feenstra BJ (2003) Video-speed electronic paper based on electrowetting. Nature 425:383–384
15. Prins MWJ, Welters WJJ, Weekamp JW (2001) Fluid control inmultichannel structures by electrocapillary pressure. Science 291:277–280
16. Lee J, Kim CJ (2000) Surface-tension-driven microactuation based on continuous electrowetting. J Microelectromech Syst 9:171–180

Electrocapillary Effect

► Electrowetting

Electrochemical Detection

► Amperometric Techniques

Electrochemical Etching

► Silicon Micromachining

Electrochemical Techniques

Gang Chen[1], Yuehe Lin[2]
[1] School of Pharmacy, Fudan University, Shanghai, China
[2] Pacific Northwest National Laboratory, Richland, WA, USA
gangchen@fudan.edu.cn, yuehe.lin@pnl.gov

Synonyms

Amperometric detection; Conductivity detection; Microfluidic chip

Definition

Sensitive, selective detection techniques are of crucial importance for capillary electrophoresis (CE), microfluidic chips, and other microfluidic systems. Electrochemical detectors for microfluidic systems have attracted considerable interest, with features that include high sensitivity, inherent miniaturization of both detection and control instrumentation, low cost, low power demand, and high compatibility with microfabrication technology. The electrochemical detectors commonly used can be classified into three general modes: conductimetry, potentiometry, and amperometry.

Overview

CE in its modern form was first described by Jorgenson and Lukacs in 1981 [1] and has been used to separate and determine a variety of samples because of its minimal sample volume requirements, short analysis time, and high separation efficiency. Since the pioneering work of Harrison et al. [2], microfluidic devices, particularly CE microchip systems, have generated considerable interest because of their high degree of integration, portability, minimal solvent/reagent consumption, high performance, and speed. CE microchips have received special attention because of their high degree of integration, portability, minimal solvent/reagent consumption, high performance, and speed. These microchip analysis systems hold

considerable promise for biomedical and pharmaceutical analysis, clinical diagnostics, environmental monitoring, forensic investigations, etc. As with other analysis systems, sensitive detection techniques are also necessary for conventional CE, microchip CE, and other microfluidic systems.

Ultraviolet (UV) detectors have commonly been employed to provide detection in microfluidic systems. Because the absorbance path length of the microchannels is very short, the low sensitivity of the UV detector results in a low detection limit (typically 10 μM). Usually, the content of the target analyte in a real sample is very low. Therefore, highly sensitive detection methods are in great demand. To meet this need, laser-induced fluorescence (LIF) and mass spectrometry (MS) have been employed. Currently, LIF has dominated detection in microchip CE. However, both LIF and MS need rather sophisticated and expensive instrumentation. LIF is limited to fluorescent analytes and analyte derivatives. Recently, electrochemical detection (ECD) has been coupled with microfluidic systems to obtain highly sensitive detection. ECD offers great promise for such systems, with features that include remarkable sensitivity, inherent miniaturization of both detector and control instrumentation, independence of sample turbidity and optical path length, low cost, minimal power demand, and high compatibility with microfluidic systems. Various techniques for ECD in microfluidic systems have been reported in the past decade.

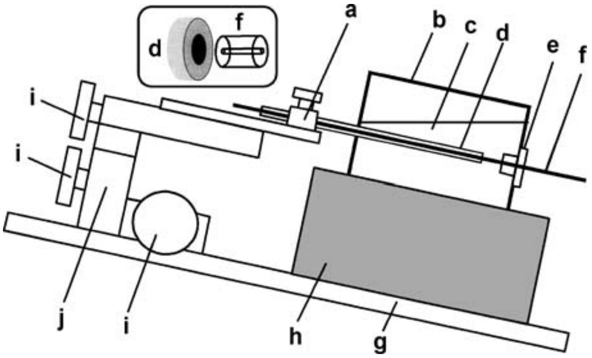

Electrochemical Techniques, Figure 1 Schematic of a three-dimensionally adjustable electrochemical detection system for capillary electrophoresis. (**a**) Screw for immobilizing the detection electrode; (**b**) electrochemical detection reservoir; (**c**) BEG; (**d**) detection electrode; (**e**) rubber stopper; (**f**) fused silica capillary; (**g**) plastic plate; (**h**) supporting block; (**i**) knobs for three-dimensional adjusting; (**j**) three-dimension manipulator

Basic Methodology

ECD can be classified into three general modes: conductimetry, potentiometry, and amperometry. Amperometry is the most widely reported ECD method for microfluidic analysis systems. It is accomplished by applying a constant potential to a working electrode and measuring the resulting current, which is proportional to the concentration of analyte oxidized or reduced at the electrode surface. In the conventional three-electrode system, a reference and an auxiliary electrode are also present. Sometimes, only a working electrode and a counterelectrode may be employed, in a two-electrode configuration. In CE, amperometric detection (AD) is usually performed in either an off-column or an end-column mode. In the case of off-column AD, a decoupling junction between the separation and detection capillaries is employed to minimize the effect of the separation voltage on the AD system. In the case of end-column AD, a microdisk detection electrode is placed directly opposite the outlet of the separation capillary, without a conductive joint. However, a gap is left between the capillary outlet and the detection capillary to reduce the interference of the high separation voltage. A major limitation that has prevented routine application of AD in CE is the precise alignment between the separation channel and the detection electrode. If the working electrode needs to be polished or changed, the whole system has to be refabricated. This is time-consuming and requires skilled personnel to operate the system. In the case of end-column detection in conventional and microchip CE, the development of a simple, convenient device to simplify the alignment procedures would be of great interest. A typical schematic diagram of a device for three-dimensional (3D) alignment between the detection electrode and the detection electrode is illustrated in Fig. 1. Before use, the disk detection electrode (Fig. 1d) is carefully positioned opposite the outlet of the capillary (Fig. 1f) with the aid of a 3D micromanipulator (Fig. 1j), and arranged in a wall–jet configuration. The interface between the capillary outlet and the surface of the detection electrode is illustrated in the inset of Fig. 1. The gap between the outlet and the detection electrode is usually adjusted to $25-50\,\mu$m using a micrometer caliper on the micromanipulator. A high voltage is applied between the anode in the anode reservoir and the grounded platinum electrode in the detection reservoir.

Conductivity detection (CD) is particularly promising for detecting small inorganic and organic ions in microfluidic systems. Conductimetry measures the conductance of a solution in a microchannel, and the response is proportional to the concentration of the analyte ions. CD can be classified into contact and contactless modes. Contact CD is carried out by galvanic contact between the measurement electrodes and the solution, while contactless CD is

carried out with external electrodes that are coupled capacitatively to the electrolyte. Comparatively, contact CD is more sensitive. However, the galvanic contact with the solution is a potential source of problems for microchip CE. The generation of bubbles by electrolysis, and electrode fouling may disturb the analysis. Furthermore, special protection of the detector circuit and electronics is required to prevent damage resulting from the high electric field. Contactless CD for microchip CE avoids the problems associated with direct solution contact by insulating the measurement electrodes electrically from the electrolyte.

Potentiometric detection in microfluidic systems is based on a detection electrode bearing sensing membranes, which allow the buildup of a measurable potential, which follows the Nernst equation. Such electrodes are known as ion-selective electrodes. For useful detection in electroseparation methods, the selectivity should extend to a range of ions so that universal potential sensors can be formed.

Key Research Findings

As the most commonly used ECD mode, AD has been employed in conventional CE, microchip CE, and other microfluidic analysis systems. The alignment between the channel outlet and the detection electrode is of high importance because it affects not only the sensitivity but also the separation efficiency. The distance between the channel outlet and the working electrode affects the post-capillary band broadening. Two approaches have been employed in the capillary/working-electrode arrangements for AD. One is to fabricate the working electrode in or just outside the exit of a microchannel. Woolley et al. were the first to report a CE chip with an integrated amperometric detector [3]. They fabricated a band-shaped platinum detection electrode just outside the exit of the separation channel using a photolithographic process. In this flow-by design, the surface of the platinum electrode was parallel to the flow direction. In view of the easy contamination of amperometric detectors, another approach has been developed, where the detection electrode is aligned with the channel outlet with the aid of a self-positioning electrode system. The separation channel and the detector are divided, because such placement of the working electrode results in self-isolation from the high separation potential because of the dramatic drop in potential across the capillary. Such a detector allows fast replacement of passivated electrodes, comparison and use of different electrode materials, and convenient surface modification. Wang et al. described a planar screen-printed carbon line electrode for a microchip CE system [4]. The electrode was mounted permanently, perpendicular to the channel outlet, allowing

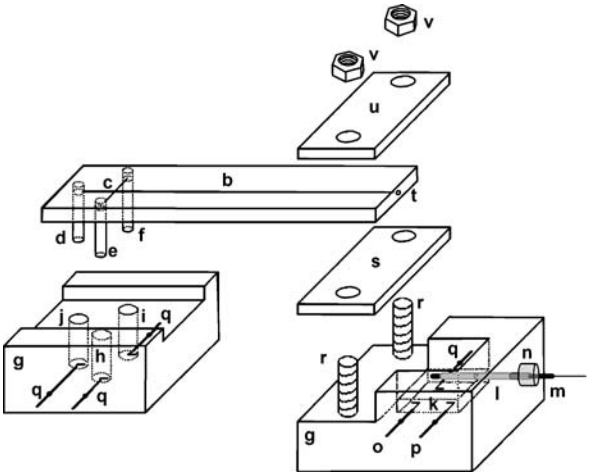

Electrochemical Techniques, Figure 2 Schematic diagram of a 3D adjustable device for AD in microchip CE: (a) glass microchip, (b) separation channel, (c) injection channel, (d) pipette tip for buffer reservoir, (e) pipette tip for reservoir (not used), (f) pipette tip for sample reservoir, (g) Plexiglas holders, (h) buffer reservoir (not used), (i) sample reservoir, (j) buffer reservoir, (k) detection cell, (l) stainless-steel guide tube, (m) capillary-based disk detection electrode, (n) silicone rubber holder, (o) auxiliary electrode, (p) reference electrode, (q) high-voltage power electrodes, (r) bolts, (s) silicone rubber sheet, (t) channel outlet, (u) Plexiglas cover plate, and (v) nuts. Reprinted with permission from John Wiley & Sons [5]

easy and fast replacement. Unfortunately, neither design allows 3D adjustment. If the carbon line electrodes are not printed in the middle of the support, or the position of the guiding tube moves after the epoxy has cured, the alignment between the channel outlet and the detection electrode will deteriorate. For end-column AD in microchip CE, it is still highly desirable to develop a simple and convenient device to simplify the microchannel–electrode alignment procedures.

Recently, Chen et al. have fabricated a novel 3D AD setup for microchip CE [5]. This facilitates precise 3D alignment between the channel outlet and the detection electrode without a complicated 3D manipulator. The performance of this unique system was demonstrated by separating five aromatic amines. Details of the microchip CE-AD system are illustrated in Fig. 2. Plexiglas holders (g) were fabricated for housing the separation chip (a) and the detection reservoir (k), allowing their convenient replacement and reproducible positioning, with silicone grease providing sealing. A three-electrode AD system fabricated in the detection reservoir consisted of a platinum wire auxiliary electrode (o), an Ag/AgCl wire reference electrode (p), and a 320 μm-diameter carbon disk detection electrode (m). The detection electrode was placed opposite the channel outlet (t) through a stainless-steel guide

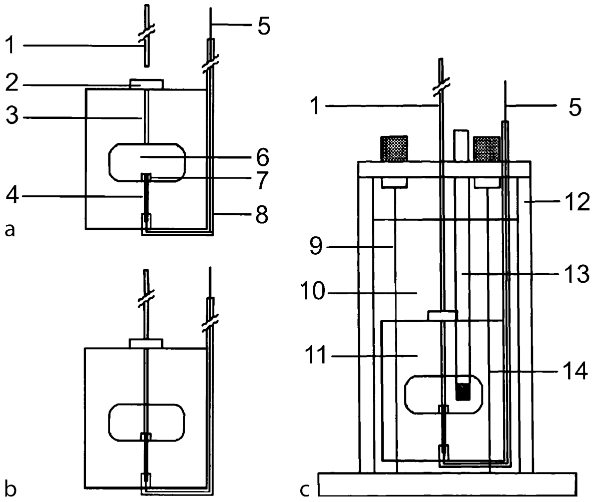

Electrochemical Techniques, Figure 3 Schematic diagrams of the self-positioning disk working-electrode system, (**a**) without and (**b**) with the capillary inserted; (**c**) elevation view of electrochemical cell. (1) Separation capillary, (2) rubber chip, (3) 400 μm-diameter bore, (4) 300 μm-diameter carbon rod, (5) copper magnet wire, (6) hole, (7) epoxy, (8) PVC tube, (9) platinum auxiliary electrode, (10) electrolyte solution, (11) self-positioning working-electrode system, (12) electrolyte reservoir, (13) reference electrode, and (14) grounded platinum electrode. Reprinted with permission from Elsevier [7]

tube (1500 μm I.D. × 800 μm O.D.). Short pipette tips (d–f) were inserted into each of the three holes in the glass chip for solution contact between the channel on the chip and the corresponding reservoir (h–j) on the left chip holder in Fig. 2. Platinum wires (q), inserted into the individual reservoirs (h–k), served as contacts to the high-voltage power supply. The end of the guide tube (l) outside the detection solution reservoirs on chips (k) was sealed by a small silicone rubber holder (n, 3 mm diameter, 2.5 mm thick), with the capillary-based detection electrode (m) inserted inside. The silicone rubber holder could not only prevent the solution in the detection reservoir from leaking out, but could also hold the detection electrode while allowing that electrode to move back and forth to define a desired gap distance from the channel outlet (t). The distance (20 mm) between the two bolts (r) on the right Plexiglas holder in Fig. 2 was wider than the width of the microchip (a, 6 mm), allowing the microchip to move right and left slightly to accomplish good alignment with the detection electrode. A piece of 2.5 mm-thick high-elasticity silicon-rubber sheet (s) was attached to the bottom of the microchip and subsequently sandwiched between a Plexiglas cover plate (u) and the Plexiglas holder (g) with the aid of the bolts (r) and nuts (v), allowing the microchip to be adjusted up and down within a range of approximately 1 mm to align the channel outlet with the detection electrode. With the aid of the 2D adjustable CE microchip (a) and the 1D adjustable disk detection electrode (m), the microchip CE-AD system shown in Fig. 2 facilitates 3D alignment between the channel outlet and the detection electrode without the need for a complicated 3D manipulator. This novel AD device has also been employed in conventional CE [6].

In addition, we have fabricated a novel self-positioning detection electrode system that facilitates the alignment of the working electrode with the capillary outlet [7]. The details of the device are illustrated in Fig. 3. Figure 3a shows an elevation of the novel self-positioning carbon disk detection electrode. A rectangular hole (10 mm × 5 mm) was machined through the center of a Plexiglas block (20 mm × 20 mm × 50 mm). The hole not only allows the diffusion of solution away from the detection point, but also makes polishing the surface of the working electrode more convenient. Two 400 μm-diameter holes were drilled carefully through the block in a line to locate the working electrode and the capillary. A disk-type carbon working electrode was used in this experiment. To fabricate the disk electrode, a piece of carbon rod (300 μm diameter, 9 mm length) with one end linked conductively to a piece of copper magnet wire (100 μm diameter, 10 cm length) and with the sides covered by an insulating coating was inserted into one hole in the block. A poly(methylmethacrylate) solution in chloroform (5%, w/w) was then applied to both ends of the hole to secure and seal the carbon rod in place and isolate the connection between the carbon rod and the copper lead. The carbon rod (ca.1 mm long) protruding from the hole was coated with epoxy. After the epoxy had cured, the sealed end of the carbon rod in the hole was filed to form a disk electrode. Another hole in the block guided the outlet of the capillary to the surface of the carbon disk electrode. The self-positioning working electrode makes it possible to align the detection electrode with the capillary outlet without a 3D micro-manipulator. A rubber chip with a self-sealing bore was glued to the top of the block to immobilize the capillary. In addition, a Plexiglas cell with inner dimensions of 2.2 cm width, 2.4 cm length, and 5 cm height was fabricated to accommodate a platinum ground electrode for CE, a platinum wire auxiliary electrode, a saturated calomel electrode, and the self-positioning working electrode, which were all immersed in the electrolyte solution contained in the cell. Figure 3c shows an elevation of the configuration in the electrochemical cell. It has been demonstrated that our self-positioning detection electrode facilitates the alignment of the working electrode with the capillary outlet without the need for a micromanipulator. The primary advantage of the capillary-electrode holder

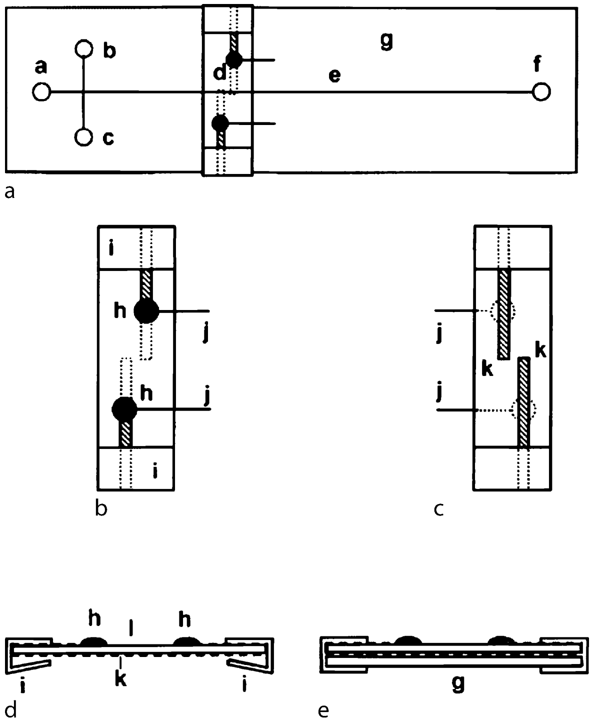

Electrochemical Techniques, Figure 4 (**a**) Schematic diagram of a microchip electrophoretic system with a movable, contactless conductivity detector. (**b–e**) Detailed design of the movable electrode system: top (**b**) and bottom (**c**) views, and cross-sectional views without (**d**) and with (**e**) the PMMA separation chip. (a) Run-buffer reservoir, (b) sample reservoir, (c) unused reservoir, (d) movable electrodes, (e) separation channel, (f) sample waste reservoir, (g) PMMA chip, (h) conductive silver epoxy, (i) PVC clamps, (j) copper wires, (k) aluminum foil electrodes, and (l) Plexiglas plate. Reprinted with permission from American Chemical Society [9]

is its simple design and construction, which makes the present setup very attractive for the routine analysis of electroactive species by CE with ED. A self-positioning carbon electrode has been successfully coupled with CE to determine bases in real DNA samples. This design has also been employed in AD for microchip CE [8].

In principle, conductivity detection is a universal detection method for most modes of capillary electrophoresis because all ions give a measurable response. It is carried out by applying an AC voltage to a pair of detection electrodes to eliminate faradic reactions. In an early arrangement, a pair of 25 μm Pt wires was inserted into a capillary through laser-drilled holes. In addition, a simpler wall–jet arrangement has been used in a commercial instrument for capillary zone electrophoresis. Conductivity detection is increasingly being used in chip-based CE microsystems. Such a detection scheme monitors differences between the conductivity of analyte zones and the background electrolyte and, hence, can sense all ionic species. Conductivity detection can be accomplished either by direct contact of the run buffer with the sensing electrodes or by a contactless mode in which the electrodes do not contact the solution. The contactless detection mode offers several distinct advantages, such as the elimination of surface fouling and bubble formation, simplified construction and alignment of the detector, and effective isolation from high separation voltages. We have developed a novel, movable contactless conductivity detection system for microchip CE [9]. A schematic diagram of a microchip electrophoretic system with a movable contactless conductivity detector is shown in Fig. 4. The movable detector is based on changing the detector position along the separation channel by *sliding* the sensing electrodes along the length of the microchip (Fig. 4). This mobile detector system consists of aluminum-film sensing electrodes (Fig. 4c, k) mounted on a thin polymer plate that is clipped onto both sides of a polymethylmethacrylate (PMMA) separation chip (Fig. 4e). Movement of the conductivity detector to different locations along the separation channel has been shown to offer several important advantages over fixed-detector formats. These include convenient visualization of the progress of separation, improved optimization of the separation process, a shorter analysis time (higher sample throughput), convenient switching between *total* and *individual* (fingerprint) assay modes in the same channel, and faster detection of late-eluting compounds (in connection with repositioning the detector during the run). We have given [9] a detailed characterization and reported the attractive analytical performance of the new moving CCD microchip detection system in connection with the detection of low-ionic explosives and nerve-agent degradation products.

Compared with separation-based techniques, potentiometry is a difficult technique to use to detect multiple analytes because of the selectivity of the ion-selective electrode. Because of the influence of the separation voltage, it is difficult to measure the response of the electrode potential, which is correlated logarithmically to the concentration of analyte; it has not yet been employed with microchip CE. Potentiometric detection has found application in conventional CE. Kappes and Hauser have fabricated a universal potentiometric sensor for CE by coating wire electrodes with a solid PVC membrane [10]. The sensor was of approximately the same diameter as the outside of the capillary and located at a distance of about 50 μm from the capillary outlet. A reference electrode was located beside the detection electrode. These coated-wire electrodes with PVC membranes have been employed to determine alkali and alkaline earth metals, small inorganic anions, and lipophilic organic ions such

as quaternary amines, aliphatic sulfonates, and carboxylates.

Future Directions for Research

Electrochemical techniques play a key role in conventional CE, microchip CE, and other microfluidic systems. Future directions in these techniques will focus on minimizing the size of the ECD device and integrating the electronic circuit and the detection electrodes on microfluidic chips. With the rapid development of microfluidic chips, it is highly desirable to develop new theoretical models, experimental methods, and new experimental devices for ECD in microfluidic analysis systems.

Cross References

► Amperometric Techniques
► Capillary electrophoresis
► Nanoscale Biosensors
► Photometer Lab-on-Chip Devices for Sample Extraction
► Resistance Temperature Detectors

References

1. Jorgenson JW, Lukacs KD (1981) Zone electrophoresis in open tubular glass capillaries. Anal Chem 53:1298–1302
2. Harrison DJ, Manz A, Fan Z, Lüdi H, Widmer HM (1992) Capillary electrophoresis and sample injection systems integrated on a planar glass chip. Anal Chem 64:1926–1932
3. Woolley T, Lao K, Glazer AN, Mathies RA (1998) Capillary electrophoresis chips with integrated electrochemical detection. Anal Chem 70:684–688
4. Wang J, Tian B, Sahlin E (1999) Micromachined electrophoresis chips with thick-film electrochemical detectors. Anal Chem 71:5436–5440
5. Chen G, Bao HM, Yang PY (2005) Fabrication and performance of a three-dimensionally adjustable device for the amperometric detection of microchip capillary electrophoresis. Electrophoresis 26:4632–4640
6. Yao X, Xu XJ, Yang PY, Chen G (2006) Carbon nanotube/PMMA composite electrode for capillary electrophoretic measurement of honokiol and magnolol in cortex magnoliae officinalis. Electrophoresis 27:3233–3242
7. Chen G, Han XH, Zhang LY, Ye JN (2002) Determination of purine and pyrimidine bases in DNA by micellar electrokinetic capillary chromatography with electrochemical detection. J Chromatogr 954:267–276
8. Chen G, Zhang LY, Wang J (2004) Miniaturized capillary electrophoresis system with a carbon nanotube microelectrode for rapid separation and detection of thiols. Talanta 64:1018–1023
9. Wang J, Chen G, Muck A (2003) Movable contactless-conductivity detector for microchip capillary electrophoresis. Anal Chem 75:4475–4479
10. Kappes T, Hauser PC (1998) Potentiometric detection of alkali and alkaline earth metal cations in capillary electrophoresis with simplified electrode alignment and enhanced separation and sensitivity. Anal Chem 70:2487–2492

Electrochemiluminescence

► Electro Chemo Luminescence (ECL)

Electro Chemo Luminescence (ECL)

MENGSU YANG, RONGSHENG CHEN, CHANGQING YI
Department of Biology and Chemistry,
City University of Hong Kong, Kowloon, Hong Kong
bhmyang@cityu.edu.hk

Synonyms

Electrochemiluminescence; Electrogenerated chemiluminescence

Definition

ECL is a type of chemiluminescence (CL) in which the light-emitting reaction is triggered by an electrochemical reaction. The electrochemically generated reactants undergo electron transfer from the excited state to generate excited molecules which emit light.

Overview

ECL involves the production of reactive intermediates from stable precursors at the surface of an electrode, which converts electrical energy into radiative energy. These intermediates then react under a variety of conditions to form excited states that emit light. Besides the advantages of CL such as extraordinary sensitivity, a wide dynamic range and inexpensive instrumentation, electrochemical reaction allows the time and position of the light emission to be controlled. The phenomenon of luminescence upon electrolysis has been known for a long time. Reports can be found as far back as 1927 for the light emission of Grignard compounds in anhydrous ether and 1928 for the ECL of luminol. However, this phenomenon was not studied in detail until the 1960s. Over 1000 papers have been published on ECL since the 1960s, ranging from mechanism investigations to analytical applications. Several comprehensive reviews and book chapters covering various aspects of ECL have been published [1–5].

ECL, which can be coupled with various separation techniques such as HPLC and capillary electrophoresis (CE), has been proved to be a powerful tool for analytical applications and investigations with high sensitivity ($< 10^{-11}$ M), high selectivity and wide linear range. Excellent chemical and ECL properties make $Ru(bpy)_3^{2+}$ (bpy = bipyridine) and its derivatives the most important

ECL systems for analytical applications. Interest in ECL immunoassay is rapidly growing. By employing ECL-active species as labels on biological molecules, ECL has found applications in immunoassays, enzymatic biosensors and DNA analysis [1, 4, 5]. Commercial ECL systems are also available for clinical diagnostics, environmental assays and food safety tests (examples can be found at http://www.igen.com/). Recently, ECL has shown great promise in the rapidly developing micro total analysis systems (also called Lab-on-a-Chip or μTAS), with the aim of realizing the whole analytical process of sampling, reaction, separation and detection on a several square centimeter-sized chip [6].

Basic Methodology

ECL Luminophores

ECL luminophores are the compounds that undergo electron transfer reactions to generate excited states which emit light. ECL luminophores involve a large number of compounds which can be generally divided into inorganic systems and organic systems.

Inorganic Systems

Many inorganic compounds and complexes have been observed to be electrochemiluminescent. The mostly investigated metals include Ru, Os, Cr, Cd, Pd, Re, Pt, Mo, Tb, Ir, Eu and Cu, but much attention has been paid to $Ru(bpy)_3^{2+}$ and its derivatives. $Ru(bpy)_3^{2+}$ can undergo ECL both in aqueous solutions and non-aqueous solutions, with or without co-reactants at room temperature, which make $Ru(bpy)_3^{2+}$ the most valuable luminophore for analytical applications. Other advantages of $Ru(bpy)_3^{2+}$ include easily attainable potentials with reversible one-electron transfer reactions and high quantum efficiency.

ECL from $Ru(bpy)_3^{2+}$ in acetonitrile using tetrabutylammonium tetrafluoroborate as the electrolyte is a classic example. ECL is generated by alternate pulsing of a potential on an electrode to form oxidized $Ru(bpy)_3^{3+}$ and reduced $Ru(bpy)_3^{+}$:

$$Ru(bpy)_3^{3+} - e^- \rightarrow Ru(bpy)_3^{3+} \quad (1)$$

$$Ru(bpy)_3^{3+} + e^- \rightarrow Ru(bpy)_3^{+} \quad (2)$$

$$Ru(bpy)_3^{3+} + Ru(bpy)_3^{+} \rightarrow Ru(bpy)_3^{3+} + Ru(bpy)_3^{3+} \quad (3)$$

$$Ru(bpy)_3^{3+} \rightarrow Ru(bpy)_3^{3+} + h\nu(610\,\text{nm}) \quad (4)$$

$Ru(bpy)_3^{2+}$ is the excited-state molecule that emits light (the emission maximum is ∼610 nm). The formation of an excited state as a result of electron transfer involves a kinetic manifestation of the Franck–Condon principle. The reactions are very energetic (typically 2–4 eV) and very fast. Since it is difficult for the molecular structure to absorb such a large amount of released energy in a mechanical form on such a short time scale, there is a significant probability that an excited product will be produced (Eq. (3)), with consequent light emission to return to the ground state (Eq. (4)).

By attaching suitable chemical groups to the bipyridine moieties, $Ru(bpy)_3^{2+}$ can be linked to biological molecules such as antibodies, where it serves as a label for analysis in a manner similar to that of radiative or fluorescent labels. This property results in a wide range of ECL applications in clinical diagnostic assays. It was reported that heterogeneous ECL immunoassays for carcinoembryonic antigen and α-fetoprotein as well as competitive ECL immunoassays for digoxin and thyrotropin could be realized by using $Ru(bpy)_3^{2+}$ NHS ester. Also, $Ru(bpy)_3^{2+}$ ECL was demonstrated to be applicable for the determination of the HIV-1 gag gene by detecting polymerase chain reaction (PCR) products.

Researches on the surfactant effect of $Ru(bpy)_3^{2+}$ ECL have attracted extensive interest. Soluble $Ru(bpy)_3^{2+}$ in aqueous nonionic surfactant solutions leads to significant and potentially useful changes in the ECL properties. For example, up to 8-fold increases in ECL efficiency were observed in surfactant media upon oxidation of $Ru(bpy)_3^{2+}$ and TPrA (TPrA = tri-*n*-propylamine). The precise mechanism of the surfactant effect is still under study, but it appears that the adsorption of surfactant on the electrode surface should be responsible for these surfactant effects. The dramatic increases in ECL intensity, coupled with work on more efficient ECL labels and co-reactants, may have profound impacts on the sensitivity of ECL for a variety of applications.

The properties of electrode surfaces greatly affect the ECL efficiency. For example, significant increases in TPrA oxidation rate and in $Ru(bpy)_3^{2+}$/TPrA ECL intensity were observed at alkanethiol-modified electrodes, whereas the influence of the thiol layer with a hydrophobic terminal group on both TPrA oxidation and ECL was much less.

Organic Systems

Organic ECL luminophores includes luminol (2,3-aminophthalhydrazide), ABEI (*N*-(4-aminobutyl)-*N*-ethylisoluminol), lucigenin (*N,N′*-dimethyl-9,9-bisacridinium), 9,10-diphenylanthracene (DPA), RUB (rubrene), diimides and various other organic compounds.

Luminol is a classic organic species that continues to generate interest. Light emission from luminol at electrodes

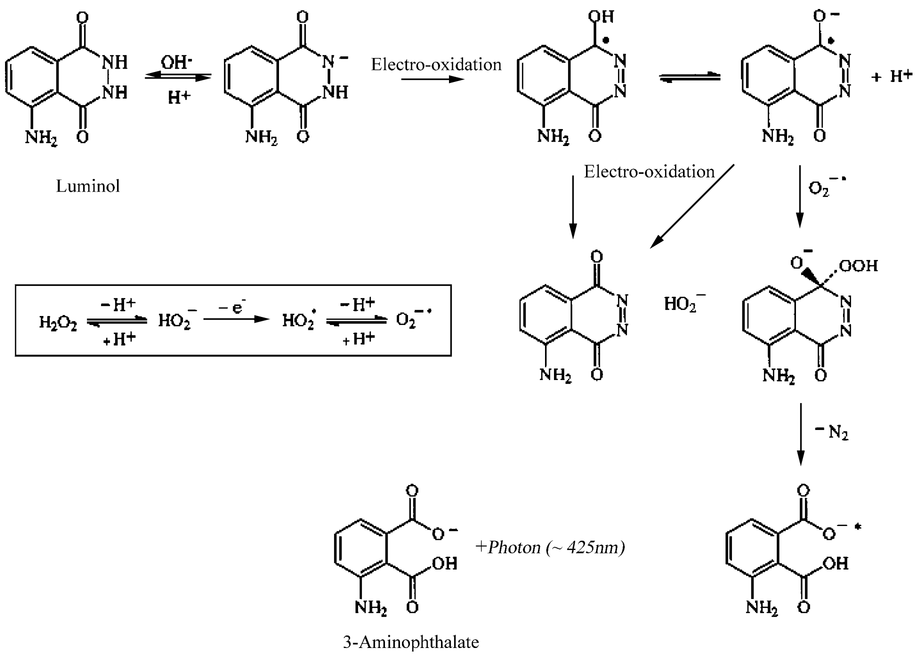

Electro Chemo Luminescence (ECL), Figure 1 Proposed mechanism for ECL reactions of luminol with hydrogen peroxide

was first reported in 1929 upon application of +2.8 V in aqueous alkaline solution. The proposed ECL mechanism for luminol is shown in Fig. 1. The ECL reaction of luminol with hydrogen peroxide in alkaline medium is similar to the chemiluminescence (CL) that is generated upon chemical oxidation. Luminol deprotonates in basic solution to form an anion that can undergo electrochemical oxidation. This intermediate species undergoes further electro-oxidation in the presence of hydrogen peroxide to produce 3-aminophthalate in an excited state. 3-Aminophthalate then produces the characteristic luminol emission at 425 nm. Different mechanistic pathways have been proposed depending on the applied potential. However, all result in the irreversible oxidation of luminol to non-recyclable species. The high nonspecific background ECL possibly due to the formation of oxygen at the anode in aqueous solution, followed by chemiluminescent reactions involving oxygen and the extremely basic conditions ($pH > 11$) that are needed to generate sufficient light emission have resulted in fewer practical applications for the luminol/H_2O_2 system compared to $Ru(bpy)_3^{2+}$.

An interesting area of luminol ECL is the study of electrogenerated catalysts that promote both the conventional CL reaction and the luminol/H_2O_2 ECL reaction. This allows the detection of analytes directly or by the enhancement of luminol ECL for the detection of analytes. A recent example is the enhancing effect of hydrazine on luminol ECL based on hydrazine's in situ electrochemical modification at a preanodized Pt electrode. A method for the determination of phloroglucinol was also reported with a detection limit of 1.2×10^{-4} g/l. The proposed mechanism involves the sensitization of the weak luminol anodic ECL signal in basic (0.1 M $NaHCO_3$) medium. Hydrogen peroxide is an integral part of most luminol studies. Its role in the ECL mechanism appears to involve the peroxide anion, HO_2^-, and the electrochemically formed superoxide radical, $O_2^{\bullet-}$. Because many enzymes produce hydrogen peroxide during their substrate-specific enzymatic activity, sensitive and selective detection in the presence of luminol may be possible. However, in order to fully exploit this chemistry, a compromise has to be found between the basic conditions required for luminol/H_2O_2 ECL and the destruction of enzymes in alkaline solution.

ABEI produces ECL when oxidized at ~1.0 V vs. Ag/AgCl in alkaline aqueous solution. In contrast to luminol, ABEI labels do not markedly lose their CL efficiency when conjugated with proteins. ECL immunoassays with a flow injection analysis (FIA) system using ABEI-isothiocyanate as a label were proposed, which have a better performance than either single-radial immunodiffusion or nephelometric immunoassays. ABEI can also be used as an oligonucleotide marker to label a DNA probe. The intensity of the ABEI ECL was linearly related to the concentration of the complementary sequence in the range 96 pM to 96 nM, and the detection limit was down to 30 pM.

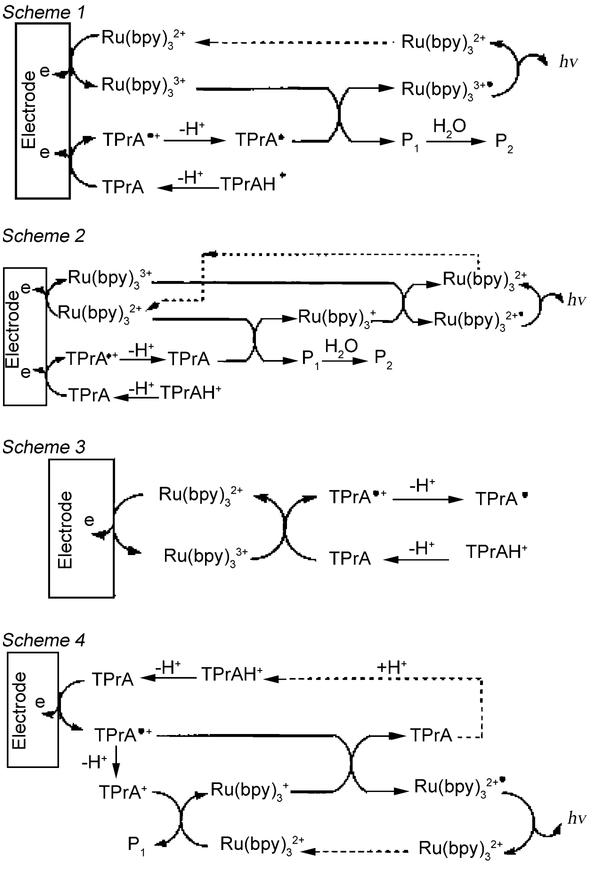

Electro Chemo Luminescence (ECL), Figure 2 Proposed ECL mechanisms for the $Ru(bpy)_3^{2+}$/TPrA system

General Mechanisms of ECL

Annihilation ECL

Annihilation ECL involves electron transfer reactions between an oxidized and a reduced species, both of which are generated at an electrode by alternate pulsing of the electrode potential. This approach is typically called annihilation. Radical ions are produced by anodic oxidation and cathodic reduction:

$$R_1 - e^- \rightarrow R_1^{\bullet+} \tag{5}$$

$$R_2 + e^- \rightarrow R_2^{\bullet-} \tag{6}$$

The excited singlet state $^1R_1^*$ is formed in an ion annihilation reaction involving the ion radicals $R_1^{\bullet+}$ and $R_2^{\bullet-}$, where R_1 and R_2 can be either the same or two different precursors. In energy sufficient systems the formation of the excited state is energetically accessible to the redox process and the ion annihilation occurs via the S-route:

$$R_1^{\bullet+} + R_2^{\bullet-} \rightarrow {}^1R_1^* + R_2 \tag{7}$$

$$^1R_1^* \rightarrow R_1 + h\nu \tag{8}$$

An energy sufficient system is one in which ΔH^0 of the electron-transfer reaction in Eq. (7) is larger than the energy required to produce the excited singlet state from the ground state (Eq. (8)). In contrast, in energy deficient systems, where the excited singlet state $^1R_1^*$ is inaccessible to the redox process, the emitting species are formed via a triplet–triplet annihilation (T-route) involving triplet intermediates:

$$R_1^{\bullet+} + R_2^{\bullet-} \rightarrow {}^3R_1^* + R_2 \tag{9}$$

$$^3R_1^* + {}^3R_1^* \rightarrow {}^1R_1^* + R_1 \tag{10}$$

$$^1R_1^* \rightarrow R_1 + h\nu \tag{11}$$

In both cases, S-route and T-route, the excited species can be either $^1R_1^*$ or $^1R_2^*$, depending on their relative energies. In energy sufficient systems light might be produced by both routes, but the S-route will usually dominate.

ECL of rubrene (RUB) is a classical example of an energy sufficient system. ECL is generated when a double-potential step is applied to an electrode to produce the radical cation ($RUB^{\bullet+}$) via anodic oxidation and the radical anion ($RUB^{\bullet-}$) via cathodic reduction. The resulting electrogenerated products can then react and undergo annihilation (Eq. (14)) to produce an excited state ($RUB^{\bullet}$) that is then able to emit light.

$$RUB - e^- \rightarrow RUB^{\bullet+} \tag{12}$$

$$RUB + e^- \rightarrow RUB^{\bullet-} \tag{13}$$

$$RUB^{\bullet+} + RUB^{\bullet-} \rightarrow RUB + RUB^{\bullet} \tag{14}$$

$$RUB^{\bullet} \rightarrow RUB + h \tag{15}$$

In RUB, one of the products of the reaction is therefore produced with excess energy that can be emitted as light. The ΔH^0 in Eq. (17) is 2.32 eV and the energy required in Eq. (18) is 2.30 eV ($\lambda_{max} \approx 540$ nm).

An example of an energy deficient system is the 9,10-diphenylanthracene (DPA) and N,N,N',N'-tetramethyl-p-phenylenediamine (TMPD) ECL system:

$$TMPD - e^- \rightarrow TMPD^{\bullet+} \tag{16}$$

$$DPA + e^- \rightarrow DPA^{\bullet-} \tag{17}$$

$$TMPD^{\bullet+} + DPA^{\bullet-} \rightarrow TMPD + DPA^{\bullet} \tag{18}$$

$$DPA^{\bullet} \rightarrow DPA + h\nu \tag{19}$$

$DPA^{\bullet}$ is the excited molecular radical that emits light. In theory, light may be emitted from either $DPA^{\bullet}$ or $TMPD^{\bullet}$.

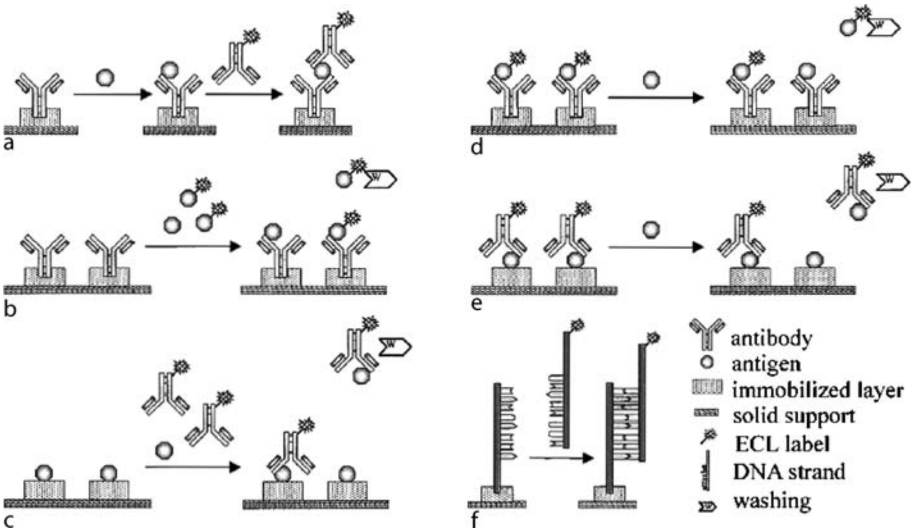

Electro Chemo Luminescence (ECL), Figure 3 Systems for ECL bioassays: (**a**) sandwich assay; (**b**) competition assay with immobilized antibody; (**c**) competition assay with immobilized antigen; (**d**) displacement assay with immobilized antibody; (**e**) displacement assay with immobilized antigen; (**f**) DNA-probe assay

However, the emitted light generated via ECL is identical to DPA photoluminescence, indicating that $DPA^{\bullet}$ is the ultimate product of charge transfer. However, the enthalpy for the electron-transfer reaction is 2.03 eV, much less than that required to reach the emitting singlet excited state for DPA of 3.00 eV. The proposed mechanism involves triplet intermediates, the so-called triplet or T-route:

$$TMPD^{\bullet+} + DPA^{\bullet-} \rightarrow TMPD + {}^{3}DPA^{\bullet} \quad (20)$$

$$^{3}DPA^{\bullet} + {}^{3}DPA^{\bullet} \rightarrow DPA + {}^{1}DPA^{\bullet} \quad (21)$$

Reaction (21) is generally called triplet–triplet annihilation, where the energy from two electron transfer reactions is pooled to provide sufficient energy to form the singlet excited state. Many ECL reactions with different precursors follow this route, and the T-route may also operate in energy sufficient systems.

The ECL quantum efficiency, Φ_{ecl}, is the ratio of the emitted photon number ($N_{h\nu}$) to the molecular number (N_r) of reactant which generates excited states. For example, for the RUB ECL system, this would involve annihilations between $RUB^{\bullet+}$ and $RUB^{\bullet-}$ (Eq. (14)) and the photons emitted (Eq. (15)). Values of Φ_{ecl} can be expressed by the following formula:

$$\Phi_{ecl} = \frac{N_{h\nu}}{N_r} = \frac{\int_t^0 Idt}{Q} \quad (22)$$

where I represents the total ECL intensity integrated over a period of time t, and Q represents the total charge transferred during the same time period. Relative ECL efficiency, which is often found in the literature, can be defined as the Φ_{ecl} ratio of an ECL system to a reference ECL system. For example, with $Ru(bpy)_3^{2+}$ as a reference system, the relative Φ_{ecl} of $Ru(dp-bpy)_3^{2+}$ and $Ru(dp-phen)_3^{2+}$ (dp-bpy = 4,4′-diphenyl-2, 2′-bipyridine; dp-phen = 4,7-diphenyl-1,10-phenanthroline) system is calculated to be 0.05 or 5%.

Experiments on ECL are often carried out in fairly conventional electrochemical apparatus. In annihilation ECL, however, ECL cells, electrodes and experimental procedures must be modified to allow electrogeneration of two reactants, rather than one, with considerations given to constraints imposed by optical measurement equipment and the need for light exclusion. Much attention should be paid to the purity of the solvent/supporting electrolyte system, especially with organic systems. Water and oxygen have been proved to be particularly harmful to annihilation ECL because they can quench this kind of ECL. Therefore, many apparatus are constructed to allow the distillation of solvents directly to the cell and de-gassing on a high-vacuum line, or the apparatus incorporates a nitrogen purging system.

Co-Reactant ECL

A co-reactant is a compound that can produce an intermediate via oxidation or reduction to react with an ECL luminophore to produce excited states. The

$Ru(bpy)_3^{2+}$/TPrA ECL system, a good example of an oxidative–reductive system, has been extensively studied [7]. The general ECL mechanism (Fig. 2) of this system indicates that oxidation of TPrA generates a strongly reducing species. This oxidation can be via a catalytic route where electrogenerated $Ru(bpy)_3^{3+}$ reacts with TPrA as well as by direct reaction of TPrA at the electrode described by both Scheme 1 and Scheme 2. The catalytic route involving homogeneous oxidation of TPrA with $Ru(bpy)_3^{3+}$ is shown in Scheme 3. The contribution of this process to the overall ECL intensity depends on the $Ru(bpy)_3^{2+}$ concentration and is small with relatively low concentrations of $Ru(bpy)_3^{2+}$. Scheme 4 summarizes an additional route for the generation of ECL within the potential range before direct oxidation of $Ru(bpy)_3^{2+}$ at the electrode, involving formation of excited state on reaction of $TPrA^{\bullet +}$ with $Ru(bpy)_3^{+}$ (formed by reaction of $Ru(bpy)_3^{2+}$ with $TPrA^{\bullet}$). If the maximum distance at which light is observed, $\sim 6\,\mu m$, represents the distance that $TPrA^{\bullet +}$ can diffuse before deprotonation, the half-life of the cation radical would be $\sim$ 0.2 ms.

Most of the ECL reactions of $Ru(bpy)_3^{2+}$/co-reactant are of oxidative–reductive type. It can undergo the reductive–oxidative pathway to generate ECL, with a strong oxidant as co-reactant. For example, the reduction of peroxysulfate ($S_2O_8^{2-}$) generates a strong oxidant sulfate radical ($SO_4^{\bullet -}$) to oxidize the ECL luminophore to generate light:

$$Ru(bpy)_3^{3+} + e^- \rightarrow Ru(bpy)_3^{+} \quad (23)$$

$$S_2O_8^{2-} + e^- \rightarrow SO_4^{\bullet -} + SO_4^{2-} \quad (24)$$

$$SO_4^{\bullet -} + Ru(bpy)_3^{+} \rightarrow Ru(bpy)_3^{3+} + SO_4^{2-} \quad (25)$$

$$Ru(bpy)_3^{3+} \rightarrow Ru(bpy)_3^{3+} + h\nu(610\,nm) \quad (26)$$

The electrochemical instruments for co-reactant ECL and annihilation ECL are usually the same. In co-reactant ECL the electrode typically only oxidizes or reduces the reagents in a single potential step, while in annihilation ECL a double-potential step is required to generate the highly energetic precursors. Also, co-reactant ECL can be generated in both nonaqueous and aqueous solutions. In contrast, annihilation ECL requires water and oxygen to be excluded. Co-reactant ECL is widely used in analytical applications, such as ECL immunoassays, flow injections, HPLC and CE.

Cathodic Luminescence

A different type of ECL can be observed at certain oxide-covered metal electrodes such as aluminum, tantalum, magnesium, gallium or indium, during the reduction of persulfate, oxygen or hydrogen peroxide. However, the mechanism is distinctly different from the other types of ECL reactions. Analytical applications of cathodic ECL for species such as copper, thallium and terbium chelates and salicylic acid and their use as labels in immunoassays have been reviewed, and the mechanism has been discussed in detail [5].

Key Research Findings

The use of ECL immunoassay is rapidly growing. ECL immunoassay with ECL detection has several advantages over existing immunoassay techniques. No radiative isotopes are used, thus reducing the problems of sample storage, handling and disposal. The ECL labels are extremely stable, having shelf lives in excess of 1 year at room temperature. The detection levels are extremely low at sub-picomole levels, since each label can emit several photons per measurement cycle, and the linear dynamic range extends over 6 or more orders of magnitude. Also their small size allows multiple labeling of the same molecule without affecting the immunoreactivity or hybridization of the probes. Assays have been developed for a wide range of applications, such as the diagnosis of thyroid diseases, pregnancy and sex function, tumors, anemia, cardiological function and infectious diseases. The scheme of ECL immunoassay methods is summarized in Fig. 3.

In immunoassays, the antigen or antibody can be modified with biotin and bound to streptavidin-modified magnetic beads. The immunoassay is then carried out with either a Ru complex-labeled antibody or antigen, depending on the chosen immunoassay format (sandwich, competition or displacement). Commercial instrumentation, available for the detection of DNA or messenger RNA by reverse transcription PCR based on $Ru(bpy)_3^{2+}$ ECL, includes the QPCR System 5000® from Perkin-Elmer and the Origen® Analyzer from Igen. The PCR product is immobilized on a solid support (magnetic beads) using biotin–streptavidin chemistry. The DNA (RNA) is then detected with a $Ru(bpy)_3^{2+}$ label down to attomolar levels. The systems use biotin labeled primers and labeled probes. In a recent publication, both instruments were used and mRNA isolated from 10 melanoma cells in a background of 107 cells could be detected.

IGEN International Inc. holds many patents related to $Ru(bpy)_3^{2+}$-based luminophores for diagnostic testing in markets such as immunoassay clinical diagnostics, life sciences and biodefense. Roche Diagnostics offer ECL instruments and commercial ECL kits based on IGEN's technology. In both commercially available models, Elec-

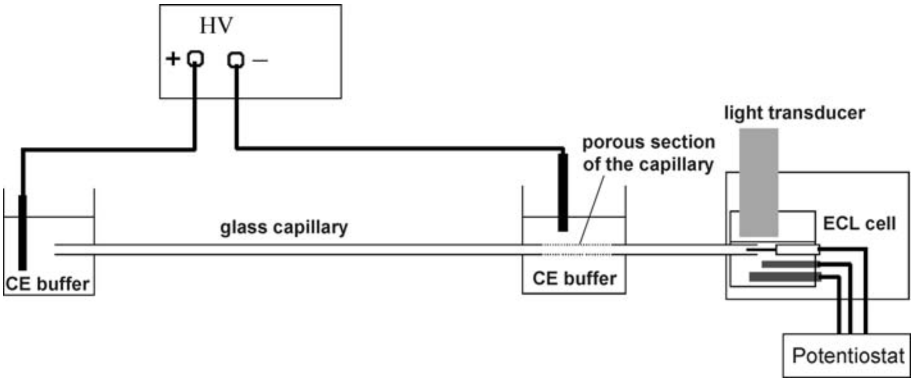

Electro Chemo Luminescence (ECL), Figure 4 Scheme of a typical instrument for ECL coupled with CE

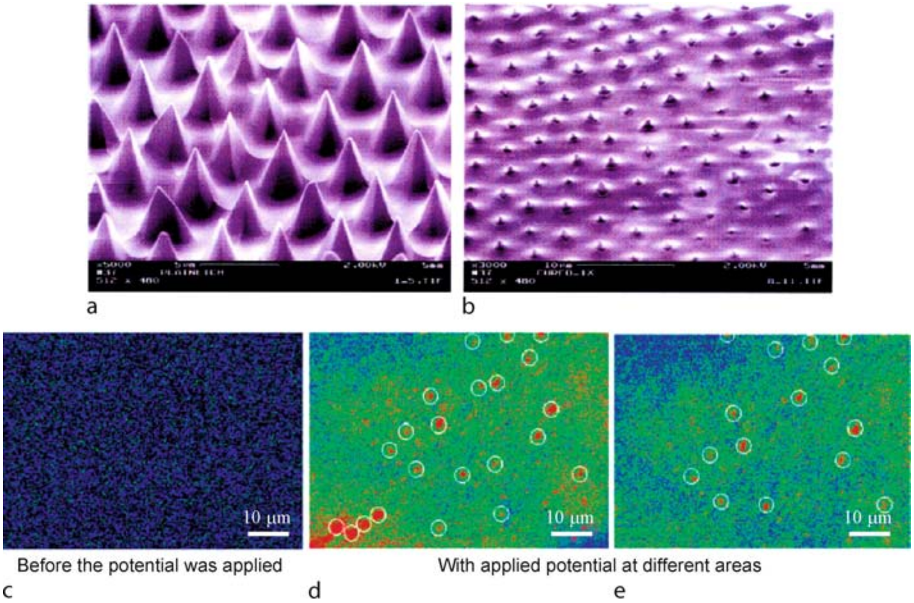

Electro Chemo Luminescence (ECL), Figure 5 (**a**) SEM image of an etched and gold-coated fiber array (array 1). (**b**) SEM image of an etched, gold-coated, and resin-insulated electrode array (array 2). (**c**)–(**e**) ECL images monitored at an etched, gold-deposited and partially polymer-insulated electrode array (array 2). White circles indicate identified ECL spots. $E = 1.2\,V/Ag/AgCl$ for 60 s; acquisition time, 2 s; 2 mM $Ru(bpy)_3^{2+}$/100 mM TPrA/phosphate buffer at pH = 7. The red color corresponds to the most intense ECL signal; green and blue correspond to little or no ECL signal

sys 1010 and 2010, the whole ECLIA procedure is fully automated. Various immunoassays have been developed for Elecsys 2010 since 1999, and lots of comparisons between different assay formats have been made. Generally, ECLIA has always had at least an equal analytical performance in these comparisons to other competing technologies.

ECL has been coupled with separation techniques such as HPLC and capillary electrophoresis to offer outstanding sensitivity and selectivity. And ECL has been reported with precolumn, on-column or postcolumn detection mode. The scheme of a typical instrument of ECL with postcolumn detection is shown in Fig. 4. The detection limit can be as low as that of LIF, but with simpler and much less costly instrumentation. The linear range is wide and the reactions typically have fast kinetics, making ECL well suitable to low-volume on-line detection. With the increasing interest in microfabricated devices, microchip-based CE has become popular recently. A wireless ECL detector for electrophoresis on a microfabricated glass device was reported [8]. The results show that a micellar electrokinetic separation and direct ECL detection of 10^{-16} mol of $Ru(phen)_3^{2+}$ and 4.5×10^{-16} mol of $Ru(bpy)_3^{2+}$ and the indirect detec-

tion of three amino acids were achieved. A solid-state ECL detector coupled with microchip-based CE was fabricated by immobilizing $Ru(bpy)_3^{2+}$ into an Eastman AQ55D-silica-carbon nanotube composite thin film on an indium tin oxide (ITO) electrode [9]. The results show that the solid-state ECL detector displays good durability and stability in the microchip CE–ECL system. Proline was selected to test the microchip device with a limit of detection of 2 μM (S/N = 3) and a linear range from 25 to 1000 μM. Compared with the CE–ECL of $Ru(bpy)_3^{2+}$ in aqueous solution, the microchip-based CE with solid-state ECL detector system gave the same sensitivity of analysis, a much lower $Ru(bpy)_3^{2+}$ consumption and a high integration of the whole system.

Spatially resolved ECL on an array of electrode tips has been reported [10]. An array of electrode tips with 6 μm center-to-center spacing, fabricated through chemical etching of an optical fiber bundle, and coated with gold (Fig. 5), was used for initiating ECL in an aqueous solution of $Ru(bpy)_3^{2+}$ and TPrA. ECL generated at the tips of the electrodes in the array was detected with a CCD camera and exhibited both high sensitivity and high resolution. In the case in which the ECL signal could not be distinguished from the background, ECL signals could be obtained by pulsing the array and summing multiple CCD images. Gold nanopariticle-enhanced ECL detection has been reported recently [11]. 4-(Dimethylamino)butyric acid (DMBA) labeling combined with gold nanoparticle amplification for ECL determination of bovine serum albumin (BSA) and immunoglobulin G (IgG) was demonstrated. ECL signals were generated from the electrodes immobilized with BSA or IgG. With gold nanoparticle amplification, the ECL peak intensity was proportional to the concentration over the range 1 – 80 and 5 – 100 μg/mL for BSA and IgG consuming 50 μL of sample, respectively. A 10- and 6-fold sensitivity enhancement was obtained for BSA and IgG over their direct immobilization on an electrode using DMBA labeling.

Future Directions for Research

Having been an important analytical technique since the first detailed studies in the mid-1960s, ECL will continue to have a promising future in analytical and bioanalytical science. The ECL of $Ru(bpy)_3^{2+}$ and its derivatives will be further investigated to expand the range of its applications, especially in the area of diagnostic testing and immunoassay. ECL coupled with separation techniques should still be attractive for analysts. The need for low-cost, portable analytical instruments in the areas of environmental analysis and food safety will be a great opportunity for ECL, which does not require a light source and results in simple instrumentation. There are also favorable prospects for ECL to be used in micro total analysis systems. ECL detectors have been used in micro total analysis systems successfully. And further miniaturization and integration and solid-state ECL techniques will mean a promising future for ECL on chips.

Cross References

▶ DNA Micro-arrays
▶ Electrophoresis
▶ Fluorescent Labeling
▶ Integrated Micro Devices for Biological Applications
▶ Integrated Microfluidic Systems for Medical Diagnostics
▶ Lab-on-Chip Devices for Immunoassay

References

1. Richter MM (2004) Electrochemiluminescence (ECL). Chem Rev 104:3003
2. Bard AJ, Faulkner LR (2001) Photoelectrochemistry and Electrogenerated Chemiluminescence. In: Bard AJ, Faulkner LR (eds) Electrochemical Methods Fundamentals and Applications. 2nd edn. Wiley, New York, pp 736–745
3. Dini D (2005) Electrochemiluminescence from Organic Emitters. Chem Mater 17:1933
4. Knight AW (1999) A review of recent trends in analytical applications of electrogenerated chemiluminescence. Trends Anal Chem 18:47
5. Fahnrich KA, Pravda M, Guilbault GG (2001) Recent applications of electrogenerated chemiluminescence in chemical analysis. Talanta 54:531
6. Auroux PA, Iossifidis D, Reyes DR, Manz A (2002) Micro total analysis systems. 2. Analytical standard operations and applications. Anal Chem 74:2637
7. Miao WJ, Choi JP, Bard AJ (2002) Electrogenerated Chemiluminescence 69: The Tris(2,2′-bipyridine)ruthenium(II), ($Ru(bpy)_3^{2+}$)/Tri-*n*-propylamine (TPrA) System Revisited—A New Route Involving TPrA Cation Radicals. J Am Chem Soc 124:14478
8. Arora A, Eijkel JCT, Morf WE, Manz A (2001) A Wireless Electrochemiluminescence Detector Applied to Direct and Indirect Detection for Electrophoresis on a Microfabricated Glass Device. Anal Chem 73:3282
9. Du Y, Wei H, Kang JZ, Yan JL, Yin XB, Yang XR, Wang EK (2005) Microchip Capillary Electrophoresis with Solid-State Electrochemiluminescence Detector. Anal Chem 77:7993
10. Szunerits S, Tam JM, Thouin L, Amatore C, Walt DR (2003) Spatially Resolved Electrochemiluminescence on an Array of Electrode Tips. Anal Chem 75:4382
11. Yin XB, Qi B, Sun XP, Yang XR, Wang EK (2005) 4-(Dimethylamino)butyric Acid Labeling for Electrochemiluminescence Detection of Biological Substances by Increasing Sensitivity with Gold Nanoparticle Amplification. Anal Chem 77: 3525

Electrodeless Dielectrophoresis

► DC Dielectrophoresis in Lab-on-a-Chip Devices

3D Electrodes

► Three-Dimensional Electrodes

Electroendosmosis

► Electroosmotic Flow (DC)

Electrogenerated Chemiluminescence

► Electro Chemo Luminescence (ECL)

Electrohydrodynamic Dispensing

► Electrokinetic Dispensing

Electrohydrodynamic Focusing

► Electrokinetic Focusing

Electrohydrodynamic Instability

► Interfacial Instability

Electrohydrodynamic Mixing

► Electrokinetic/ElectroHydrodynamic Flow Instability

Electrokinetic Dispensing

CAROLYN REN
Department of Mechanical and Mechatronics Engineering, University of Waterloo, Waterloo, ON, Canada
c3ren@mecheng1.uwaterloo.ca

Synonyms

Electrokinetic injection; Electroosmotic dispensing; Electrohydrodynamic dispensing

Definition

Electrokinetic dispensing is a method using electroosmotic pumping to inject a small quantity of samples, the size and concentration of which can be controlled by manipulating applied electrical potential fields, modifying channel surfaces and changing channel dimensions. A simple cross-linked microchannel is commonly employed for electrokinetic dispensing.

Overview

There has been tremendous interest in developing Lab-on-a-Chip (LOC) devices, which have a wide range of applications in life sciences, biotechnology, and biomedical engineering fields. A typical LOC device includes a microfluidic chip platform with a network of microchannels, electrodes, electrical circuits and detectors integrated on it to perform a series of sample processes such as cell separation, cell lysis, biomolecular separation, polymerase chain reaction and final detection. Although LOC devices hold great promise to revolutionize the current level of biomedical and chemical analysis and treatment, the development of LOC devices has been largely hindered due to the lack of the capability for precise on-chip sample manipulations, among which dispensing a sample volume on the order of nanoliter to picoliter is key. To this end, many researches have been done in developing miniaturized dispensing systems using different pumping mechanisms such as piezoelectric pumping, pneumatic (thermal and pressure) pumping, electrowetting pumping, surface acoustic wave pumping, ultrasonically driven pumping, and electroosmotic (EOF) pumping. We will focus on the introduction of electrokinetic dispensing using EOF pumping in this entry. Interested readers are referred to a thorough review of micropumps [1].

EOF is generated when an external electrical field is applied to the liquid in a microchannel tangentially, due to the presence of net charges within a thin layer near the solid-liquid interface. This thin layer is called the electrical double layer (EDL) and the net charges in the EDL are the result of charge separation in the bulk liquid induced by the surface charge, which originates from several mechanisms, such as ionization of surface groups and electrolyte ion adsorption to solid surfaces. The EDL generally consists of two layers: one is the inner compact layer where ions are strongly attracted to the charged surface and the other is the diffuse layer where ions are free to move. The

electrical potential in the liquid generally decays dramatically from the surface and almost reaches zero at some distance slightly beyond the EDL region. The potential at the shear plane, which separates the compact layer and the diffuse layer, is referred to as the zeta potential, ζ. The zeta potential is a function of both solid-liquid interface and liquid properties and is located at the fluid flow boundary, where zero velocity (no slip boundary) is assumed for an electroosmotic flow. The velocity then increases as a result of the force balance between the electrostatic force exerted on the net charges in the EDL and the viscous force in the liquid, and reaches a maximum value at the edge of the EDL. Because no forces exist in the bulk liquid, the velocity then keeps constant across the bulk liquid region. Considering a 10 mM electrolyte solution, which is the concentration commonly used in chemical and biomedical analysis, in a 100 μm-i.d. cylindrical capillary with a uniform surface property, the EDL is around 10 nm (0.01% of the channel diameter). The velocity variation over such a thin EDL is negligible and thus the liquid appears to slip on the surface exhibiting a plug-like velocity profile. This allows the assumption of a slip velocity boundary condition, which has been applied in many numerical and analytical studies of EOF flow.

EOF pumping is preferred in developing LOC devices because of its plug-like velocity profile eliminating sample dispersion due to cross-stream velocity gradients, the rate of flow rate control it allows, no moving parts involved eliminating maintenance working loads and its potential for integration. Therefore, it has also been used for dispensing applications, which is often referred to as electrokinetic dispensing. Early studies about on-chip sample dispensing using EOF were driven by capillary electrophoresis (CE) applications where sample separation requires a clear-cut initial sample plug to be generated. Harrison et al. [2] first integrated CE and sample handling (loading and dispensing) on a planar glass chip. Since then, many experimental and numerical studies involving on-chip sample dispensing have followed [3–5]. Although several channel layouts have been proposed for electrokinetic dispensing such as single cross, double-T and triple-T configurations, a straight cross-linked microchannel was mostly employed as shown in Fig. 1. In this layout, the separation channel (i. e., the channel between the intersection and the buffer waste reservoir) is normally designed much longer than the other three channels allowing sufficient time for samples to be separated. Generally, electrokinetic dispensing in such a configuration includes two steps which are the loading and dispensing step.

During the loading step, a small amount of sample is loaded from the sample reservoir to the intersection by applying potentials to the four reservoirs connected by microchannels. Once the loading process reaches steady state, the applied potentials are switched so that the sample in the intersection can be dispensed into the separation channel which is in the perpendicular direction to the loading direction as shown in Fig. 2. In order to dispense a desired sample size and volume, both the loading and dispensing processes must be understood and well controlled, which requires a better understanding of fluid flow and mass transport in microchannels. In this entry, we focus on the introduction to the numerical simulation of fluid flow and mass transport in a cross-linked microchannel for electrokinetic dispensing applications. A brief description of the experimental procedures for electrokinetic loading and dispensing is also provided.

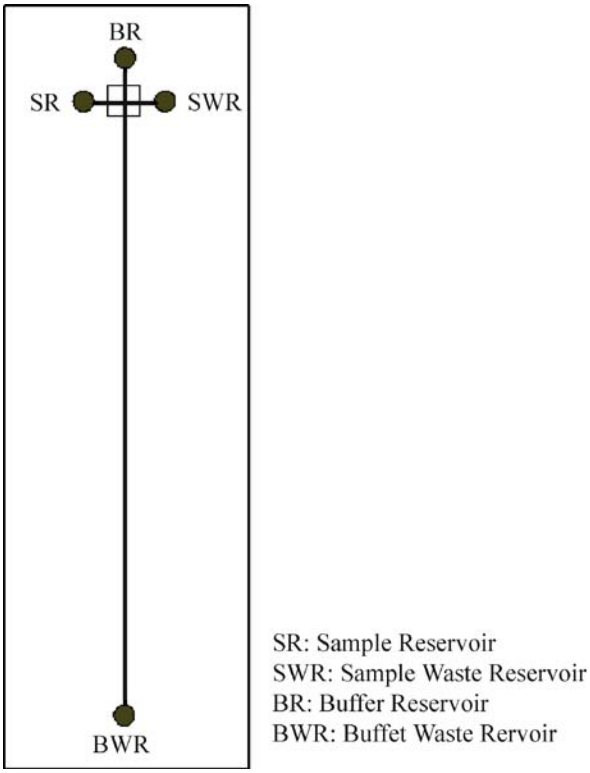

Electrokinetic Dispensing, Figure 1 Schematic diagram of a commonly used cross-linked microchannel for electrokinetic dispensing

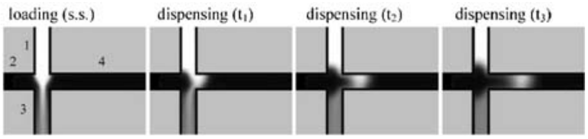

Electrokinetic Dispensing, Figure 2 A typical loading and dispensing of a sample

Basic Methodology

Governing Equations

In order to understand the physics of sample dispensing in a microfluidic chip and develop analysis tools for the design and control of microfluidic dispensers, a numerical model consisting of a set of governing equations must be developed. First, for precisely dispensing a small amount of sample, the sample concentration distributions for both the loading and dispensing step must be known. This requires the solution of the flow field, which influences the concentration through the convection effects, and the solutions of the EDL potential field and applied potential field which affect the flow field through the electrical driving force. The governing equations for the loading and dispensing should be the same, the boundary conditions, however, are different. Considering a simple cross-linked microchannel shown in Fig. 1, the equations describing the loading and dispensing processes and the boundary conditions are discussed below.

The Concentration Field

The concentration equations for a buffer solution which is electrically neutral in its bulk region and the ith sample species in the buffer solution are:

$$\frac{\partial C_\mathrm{b}}{\partial t} + \boldsymbol{u} \cdot \nabla C_\mathrm{b} = D_\mathrm{b} \nabla^2 C_\mathrm{b} + R_\mathrm{b} \quad (1)$$

$$\frac{\partial C_i}{\partial t} + \boldsymbol{u} \cdot \nabla C_i = D_i \nabla^2 C_i + \frac{D_i z_i e}{k_\mathrm{b} T} \nabla (C_i \nabla \Phi) + R_i \quad (2)$$

where subscripts b and i represents the buffer solution and ith sample species, C stands for concentration, D is diffusion coefficient, e is the element charge, k_b is the Boltzmann constant, R represents the reaction occurring during dispensing processes, which is neglected for most electrokinetic dispensing applications, T is absolute temperature, $\boldsymbol{u}$ is the vector of the mass-average flow velocity, z_i is the valence of the ith sample species, and Φ is the total electrical potential which is often split into two components: the electrical double layer potential, ψ, and the applied electrical potential, ϕ such as $\Phi = \psi + \phi$. The decoupling of the above two terms is often practiced in microfluidic chip applications because the relatively high concentration buffers commonly used in such applications yield a very thin double layer (i. e., 10 nm as discussed above). On one hand, the double layer potential only varies over the EDL region and has a very high electrical field strength on the order of 1×10^7 V/m, which is not likely affected by the applied electrical potential field which is generally on the order of 1×10^4 V/m and in a perpendicular direction to the EDL field. On the other hand, the net charges within such a thin double layer has negligible effects on the bulk liquid resistance and thus on the applied potential field. As shown above, the buffer concentration equation, Eq. (1), does not have the electromigration term, which is the second term on the right hand side of Eq. (2). This is because the electromigration term results from the electrical forces exerted on charged species, which generally do not exit in the bulk liquid region for buffer solutions. However, it must be considered for charged sample species. Neglecting the gravitational forces, only two forces exist for a charged particle in a stationary liquid under an applied electrical field: the drag force and the electromigration force. The balance between the drag force and the electrical migration force allows the electromigration term in Eq. (2) to be expressed as a velocity format such as

$$\boldsymbol{u}_{\mathrm{ep}_i} = -\frac{D_i z_i e}{k_\mathrm{b} T} \nabla \phi \quad (3)$$

where $\boldsymbol{u}_{\mathrm{ep}_i}$ is the electrophoretic velocity vector of the ith species and the negative sign indicates that a negatively charged species will migrate towards the anode under an applied electrical field. Based on the above assumptions, the species concentration equation, Eq. (2), is reduced to:

$$\frac{\partial C_i}{\partial t} + \left(\boldsymbol{u} + \boldsymbol{u}_{\mathrm{ep}_i}\right) \cdot \nabla C_i = D_i \nabla^2 C_i \quad (4)$$

It should be noted that for most electrokinetic dispensing applications, the buffer concentration is uniform across the chip and thus Eq. (1) is ignored in the problem. However, for the applications of sample pumping (multiple sample species are transported together without separation by utilizing a higher-conductivity buffer to carry samples) and sample stacking (sample species are separated more efficiently and sample concentrations are increased on-chip by using a lower-conductivity buffer to carry samples) [6], the driving buffer conductivity is different from the sample-carrying buffer. In such a scenario, the buffer concentration must be solved [7] to determine the electrical conductivity distribution, which will affect the applied electrical potential field and thus the flow field. Considering the similarity of the boundary and initial conditions for Eq. (1) and Eq. (4), only the boundary and initial conditions for Eq. (4) are introduced below.

For the loading step, Eq. (4) is subject to the following boundary conditions: $C_i = C_{i0}$ at the sample reservoir and zero flux boundary conditions, $\boldsymbol{n} \cdot \nabla C_i = 0$, at all the other boundaries across the chip, where $\boldsymbol{n}$ is the unit normal to the surface and C_{i0} is an initially applied concentration for the ith species. The initial conditions for Eq. (4) are $C_i = C_{i0}$ at the sample reservoir and $C_i = 0$ at all the

other places across the chip. For the dispensing step, the boundary conditions are similar to that for the loading step, however, the initial conditions are the concentration distribution of the loading step when it reaches steady state, $C_i = C_{i_\text{loading}}$.

The Flow Field

For an incompressible, Newtonian liquid flow, which is common for most electrokinetic dispensing applications, the flow field is described by the continuity equation,

$$\nabla \cdot \boldsymbol{u} = 0 \tag{5}$$

and the Navier–Stokes (N–S) equation,

$$\rho \left[\frac{\partial \boldsymbol{u}}{\partial t} + (\boldsymbol{u} \cdot \nabla)\, \boldsymbol{u} \right] = -\nabla P + \eta \nabla^2 \boldsymbol{u} + \rho_\text{e} \boldsymbol{E} \tag{6}$$

where ρ is the density of the liquid, P is pressure, η is the viscosity of the liquid, $\boldsymbol{E} = -\nabla\phi$ is the local electrical field strength which can be determined by solving the applied potential equation, and ρ_e is the net charge density in the liquid, which can be determined by solving the EDL potential equation. For most microfluidic applications, the viscous force is dominant and the time for the flow to reach steady state is very small, which is on the order of ms ($t \approx \rho D_\text{h}^2/\eta = 10^{-2}$ s where $\rho = 1.0 \times 10^3\,\text{kgm}^{-3}$, $\eta = 1.0 \times 10^{-3}\,\text{kgm}^{-1}$, and D_h is the characteristic length chosen as $D_h = 100\,\mu\text{m}$). Therefore the transient term in the N–S equation can be neglected. Because of small channel dimensions and flow velocities (the typical velocity in microfluidic devices is on the order of mm/s), the Reynolds number, $\text{Re} = \rho u D_\text{h}/\eta$, which represents the ratio between the inertial force and the viscous force, ranges approximately from 0.001 to 0.1. Therefore, the flow in microfluidic devices is in the laminar flow regime and the convection term on the left hand side of the N–S equation can be ignored. For most microfluidic applications, no pressure difference is applied; however, the induced pressure gradients do exist due to the presence of two-dimensional flow in the intersection of the microchannel. Even for a straight channel, the induced pressure gradient most likely exists because of the Laplace pressure originating from the presence of different meniscus curvatures in the reservoirs. It is difficult to quantify the induced pressure effects because meniscus curvatures vary from experiments to experiments. The possible solutions to minimize the Laplace pressure are to increase the reservoir sizes and/or increase the flow resistance which can be realized by reducing the channel cross section and increasing the length of the flow path without increasing the channel length in one direction. This is because increasing the channel length in one direction will increase the chip size, which mitigates the key advantages that microfluidic chips can offer. Considering the above assumptions, Eq. (6) can be simplified as:

$$-\nabla P + \eta \nabla^2 \boldsymbol{u} + \rho_\text{e} \boldsymbol{E} = 0 \tag{7}$$

When no external pressure gradients are applied, Eq. (7) is subject to the following boundary conditions: zero pressure gradient, $\boldsymbol{n} \cdot \nabla P = 0$, at solid walls, atmospheric pressure, $P = P_\text{a}$, at all the reservoirs, no slip velocity, $\boldsymbol{u} = 0$, at solid walls (no slip boundary) and fully-developed flow velocity, $\boldsymbol{n} \cdot \nabla u = 0$, at all the reservoirs. No tangential velocity is applied to the inlets and outlets (reservoirs). In fact, the velocities at the reservoirs are not known at the beginning. However, for a pure EOF flow, the body force is the electrical driving force, which generates a velocity in the reservoirs. This velocity is part of the solution; therefore, it is reasonable to assume the fully-developed flow boundary conditions at the reservoirs. If external pressure gradients are applied, the velocity boundary conditions are the same, but the pressures at the reservoirs will be changed to the applied pressures.

The EDL Potential Field

In order to solve the flow field, the net charge density must be known. According to the theory of electrostatics, the relationship between the net charge density and the electrostatic potential, ψ, is described by the Poisson equation:

$$\varepsilon_\text{r} \varepsilon_0 \nabla^2 \psi = -\rho_\text{e} \tag{8}$$

where ε_r is the dielectric constant of the liquid, and ε_0 is the permittivity of vacuum ($\varepsilon_0 = 8.854 \times 10^{-12}$ C/Vm). The corresponding boundary conditions for the above equation are, zeta potential, $\psi = \zeta$, at solid walls and zero potential gradient, $\boldsymbol{n} \cdot \nabla \psi = 0$, at the reservoirs. The above boundary conditions are valid for most LOC applications where uniform surface properties are assumed, however, for some applications where heterogeneous surface properties exist, the boundary conditions must be modified to account for the variation of the solid-liquid interface properties. The net charge density in Eq. (8) is given by, $\rho_\text{e} = \sum_i z_i e n_i$, where n_i is the ionic concentration of the ith species within the EDL and given by the Nernst–Planck conservation equation,

$$\nabla \cdot \left(\boldsymbol{u} n_j - D_j \nabla n_j - \frac{D_j z_j e \nabla \phi}{k_\text{b} T} n_j \right) = 0 \tag{9}$$

The above equation is subject to the zero flux boundary conditions, $\boldsymbol{n} \cdot \nabla n_j = 0$ at both solid walls and reservoirs.

E

As one can see that the Nernst-Planck equation is coupled with the Poisson equation and the N–S equation, which is very difficult to solve simultaneously. Another difficulty arises when all the species of a multi-species buffer must be considered for determining the net charge density. Two alternative solutions are commonly used for simplifying this problem. In the first method, the EDL potential equation is neglected and thus the electrical driving force term in the modified N–S equation (Eq. (7)) is ignored, which will be considered by applying the slip velocity boundary condition to solve the flow field. This treatment is reasonable for most LOC applications because of the presence of thin double layers as discussed above. The slip velocity boundary condition can be determined by the Helmholtz–Smoulchowski equation such as

$$u_{\mathrm{eo}} = \mu_{\mathrm{eo}} E_{\mathrm{x}} = -\frac{\varepsilon_{\mathrm{r}}\varepsilon_0\zeta}{\eta} E_{\mathrm{x}} \tag{10}$$

where u_{eo} is the electroosmotic velocity which is uniform in the cross-stream direction, and $\mu_{\mathrm{eo}} = -\varepsilon_{\mathrm{r}}\varepsilon_0\zeta/\eta$ is the electroosmotic mobility.

The second method is to neglect the convection term in Eq. (9) considering that the flow velocity is small for both EOF flow and electrophoretic flow, which decouples the flow field and the EDL potential field. In the second approach, the assumption of a two-species buffer and the application of the Boltzmann distribution are commonly made in order to solve the potential field easily, which yields the well-known Poisson–Boltzmann Equation:

$$\nabla^2\psi = \frac{2zen_0}{\varepsilon_{\mathrm{r}}\varepsilon_0}\sinh\left(\frac{ze\psi}{k_{\mathrm{b}}T}\right) \tag{11}$$

By solving Eq. (11), the EDL potential and net charge density can be determined, which can be used to determine the electrical driving force in the modified N–S equation for the flow field.

The Applied Potential Field

EOF is generated by applying external electrical potentials to the liquid in a microchannel. Therefore, the applied electrical potential field must be known in order to solve the flow field. When an electric field is applied along a microchannel, the current is setup along the channel. For most microfluidic applications where electrically neutral dilute solutions are often used, the local electric current vector is given by,

$$\boldsymbol{i} = \lambda\nabla\phi \tag{12}$$

where λ is the electric conductivity of the electrolyte solution and takes the form of

$$\lambda = \frac{e^2N_a}{kT}\Sigma\, z_j^2 D_j C_j \tag{13}$$

Eq. (13) is an expression of the Ohm's law for electrically neutral dilute solutions or solutions in a microchannel having a thin double layer, where C_j can be determined by a set of concentration equations. The charge conservation in the liquid, $\nabla\cdot\boldsymbol{i} = 0$, must be satisfied, which yields the equation of the applied electrical potential field:

$$\nabla\cdot(\lambda\nabla\phi) = 0 \tag{14}$$

The boundary conditions for the above equation are specified potentials at the reservoirs, $\phi_i = \phi_{\mathrm{applied}}$, and zero potential gradient at solid channel walls, $\boldsymbol{n}\cdot\nabla\phi = 0$. It should be pointed out that if there is no spatial conductivity gradient (λ is a constant), Eq. (14) takes a simpler format,

$$\nabla^2\phi = 0 \tag{15}$$

Depending on the problem of interest, a numerical model can be developed and numerically solved with appropriate boundary conditions to obtain the concentration distribution of the loaded and dispensed sample. The solution to the model can also be used to investigate the effects of the controlling parameters on the sample size, which may potentially provide an optimized configuration for particular dispensing applications.

Numerical Methods

The above governing equations can be numerically solved with the corresponding boundary conditions. Although many commercially available softwares such as FEMLAB have been widely applied in microfluidic studies benefiting from their capability of coupling different fundamental equations and user-friendly interfaces, most of them focuses primarily on simulation of fluid flow. The species transport, which is one of the most important phenomena in electrokinetic dispensing applications, has been paid less attention. Therefore, developing special codes is often practiced in numerically solving the above governing equations towards the design and control of electrokinetic dispensers.

The goal of numerical simulation is to obtain the distribution of a set of dependent variable at a set of discrete locations (often referred to as grid or node) in the domain of interest by solving a set of differential equations. In order to do so, the derivatives of the differential equations must be interpreted using the values at a certain point and its neighboring points. This process is called discretiza-

tion. Different discretization techniques lead to different numerical methods. Three commonly used numerical methods for microfluidic chip applications are the finite difference method, finite control volume method and finite element method. The finite difference method uses the Taylor series formulation to get the derivatives of interest where higher order derivatives are neglected assuming they are less important. The result is the discretized equation at each grid point which relates the values of a dependent variable at this grid and its neighboring points. This method is relatively simple; however, it lacks flexibility in dealing with complex geometry. The finite element method divides the domain of interest into subdomains (i. e., triangles) and approximates a solution to the equation on each subdomain. By using the method of weighted residual, the discretized equation can be constructed over each domain and then assembled for the entire domain. In this method, the selection of the weighting function is very important. The advantage of this method lies in its capability in dealing with complex geometries, such as structural analysis. The disadvantage of this method arises from the difficulty in choosing a successful weighting function for particular applications. The finite control volume method divides the domain of interest into many small and non-overlapping control volumes (grid points). The differential equation is integrated over each control volume which requires the value at each point and the assumption of the variation of a dependent variable between different neighboring control volumes. The result is the discretized equation for a dependent variable at each grid point. The solution obtained using the finite control volume method fully satisfies the integral conservation of quantities over each control volume and the entire domain. Therefore it is well suited for fluid dynamics problems. The disadvantage of this method is its difficulty in dealing with complex geometries as compared to the finite element method. Some techniques have been developed such as orthogonal curvilinear coordinates to overcome this difficulty. More recently, a control-volume based finite element method has been developed to combine the advantages of the both methods [7].

Singularity in Modeling Electrokinetic Dispensing

Most microfluidic chips for electrokinetic dispensing applications have a channel layout containing 90-degree corners, which will cause singularity problems at the corners in the applied electrical potential field and the EDL potential field. This is because the direction of the applied potential field (the direction of the potential gradient) at that corner changes dramatically (90 degree from x-direction to y-direction) and the potential is not differentiable at the corners. The possible solution to reduce the singularity effects on the numerical solutions is to choose fine grids near the corners, which will reduce the error caused by singularity. However, the potentials near the corners will not be very accurate. The more detailed mathematical derivation and discussion about singularity problems can be found elsewhere [8].

Experimental Approaches

As mentioned above, electrokinetic dispensing normally employs a straight cross-linked microchannel to dispense a small amount of sample. In this approach, EOF flow is used as a pumping method, which requires electrical potentials to be applied to the liquid in the microchannel through electrodes (i. e., platinum electrodes) plugged into the four reservoirs as shown in Fig. 1. Generally, an electrokinetic dispensing process includes two steps which are the loading step and dispensing step.

During the loading step, the sample solution is electrokinetically pumped from the sample reservoir into the intersection of the microchannel. The sample size in the intersection has significant influences on the dispensed sample size. Therefore, it is very important to control the loaded sample size, which can be achieved by manipulating applied potentials, changing channel dimensions, and modifying channel surfaces. For example, considering the fixed potentials applied in the reservoir 1 and 3 as shown in Fig. 2, the higher the applied potentials in the reservoir 2 and 4, the more focused sample plug can be obtained in the intersection.

After the loading step reaches steady state, the loaded sample can be dispensed in the perpendicular direction to the loading direction (i. e., towards the reservoir 4) by switching the applied potentials, as shown in Fig. 2. Many on-chip processes such as sample separation and mixing start from a small and well-controlled sample plug. Take sample separation as an example, the resolution of sample separation is highly dependent on the dispensed sample size and volume. Generally, a thin, highly concentrated sample plug gives a higher separation resolution. However, it should be noted that if the dispensed sample plug is too thin, it is very difficult to detect the sample peaks because the sample concentrations decrease quickly due to diffusion before they can reach the detector. Since there are many parameters (i. e., channel dimensions, applied potentials, buffer solutions, channel surface properties, etc.) which affect the dispensed sample size and volume, it is essential to perform parametric studies on electrokinetic dispensing using numerical simulation tools before proposing any design for expensive experimental tests.

Key Research Findings

Electrokinetic dispensing using EOF pumping has major applications in chemical, biological and biomedical analysis where a desired amount of sample must be dispensed in a controllable manner. There are too many studies about electrokinetic dispensing using EOF pumping to be listed here. A few numerical studies where relatively special numerical techniques were used for the purpose of electrokinetic dispensing are discussed here.

The earliest numerical study of EOF pumping in a cross-linked microchannel as shown in Fig. 1 was conducted by Patankar and Hu [8] in 1998. By justifying that the sample diffusion is much less important than the convection transport in such a small chip, this study focused on the investigation of the electroosmotic flow field. A three-dimensional numerical model was presented and numerically solved using the finite control volume method where the semi implicit method was used to deal with the pressure term [7]. It is found that the sample plug at the intersection during the loading step can be controlled by manipulating the potentials at the side reservoirs (the buffer reservoir and buffer waste reservoir). The higher potentials in these side reservoirs are applied, the more focused sample can be obtained. The loaded sample plug can also be controlled by applying pressures at the side reservoirs, which can be easily understood that more buffer solutions are driven into the intersection from the side reservoirs to focus the sample stream.

Almost at the same time, Ermakov et al. [3] presented a numerical model for electrokinetic transport in a simple cross-linked microchannel and a T-intersection microchannel. This model considered two sample species and was numerically solved using the finite difference method, where an intermediate velocity was introduced to generate an equation for the pressure and the continuity equation was used as a condition to ensure the mass conservation is satisfied. Sample focusing in the cross microchannel and sample mixing in the T-intersection channel were studied and the effects of the electroosmotic mobility, electrophoretic mobility and applied potentials on the sample plug in the intersection were investigated using the developed model. Their numerical results agreed well with their experimental results. Later, this model was applied to study more electrokinetic dispensing applications such as pinched and gated injection techniques by the same group.

Fu et al. [4] presented a numerical model for electrokinetic dispensing in microfluidic chips where simple cross, double-T and triple-T configurations were considered. In this model, the Nernst–Planck equation was employed to describe the ionic concentration instead of the Boltzmann distribution, which is a more general approach. The model was numerically solved using the finite difference method where the artificial compressibility method was employed to deal with the pressure term in the N–S equation. It is found that the applied potentials play an important role in controlling the loaded and dispensed sample shape. The unique feature of this study is the concept of the multi-T injection system which can function as a simple cross, double-T, or triple-T injection unit. Their numerical results agreed well with their experimental results. More injection techniques were also developed by the same group later.

Ren and Li [5] also presented a numerical model of sample transport in a microfluidic chip containing a simple cross microchannel aiming to provide an optimized configuration in terms of a set of controlling parameters for electrokinetic dispensing. This model was numerically solved using the finite control volume method where the pressure term was dealt with using the SIMPLE method. In addition to the applied potentials, the electroosmotic mobility of the buffer solution, and the electrophoretic mobility of the sample, the effects of the diffusion coefficient of the sample and the channel aspect ratio (the ratio between the horizontal channel and the vertical channel) on the sample dispensing were also studied. It is found that under the same applied potentials, a more focused sample can be achieved by utilizing a channel with an aspect ratio of $1/2$ (the horizontal channel has a half width of the vertical channel). This provides an opportunity to lower down the required voltages for achieving a certain focused sample plug, which is very helpful for integration. Later, by realizing that the flow and mass transport is one dimensional in the long separation channel and the places far away from the intersection, the same group presented another numerical model. In this new model, artificial boundaries were used to truncate the physical domain into a small computational domain containing the intersection and the information outside this domain was brought into consideration through the carefully designed boundary conditions. This approach allows the computation power to be concentrated on the two-dimensional phenomena near the intersection [9] and found that this method took 97.3% less computation time than a full domain simulation for particular cases. This model was further improved by the same group to consider conductivity gradients in the buffer solution, which has major applications in sample pumping and sample stacking [10].

Future Directions for Research

The ultimate goal of LOC devices is to integrate all the sample processes such as sample preparation, mixing, reaction and detection onto a single microfluidic chip.

Among all the processes, the sample preparation is the most challenging one to be integrated because it has to deal with original samples (i. e., a blood drop) which are often non-newtonia fluids. The study of electrokinetic dispensing for non-newtonia fluids will be very important for realizing the concept of the LOC device.

Nanofluidic chips have attracted increasing attention recently; however, the fluid flow in such a small scale might not be well described by the traditional Navier–Stokes equation, which has been used for most numerical models for electrokinetic dispensing. Therefore, the development of numerical models for electrokinetic dispensing in nanofluidic chips will be of great importance for the design and control of such small scale chips. In these models, other theories such as molecular dynamics might be used to describe the flow field.

Numerical simulation has been proven to be a very useful tool for microfluidics and nanofluidics research. The goal of numerical simulation is to make a set of analysis tools available for precise design and operational control of LOC devices. To this end, the traditional study of electrokinetic dispensing will continue to be attractive. The development of numerical models studying the effects of the complex channel layout, channel surface heterogeneities, buffer conductivity gradient, and multiple sample species on electrokinetic dispensing will be a promising direction.

Cross References

- ► Electrokinetic Sample Injection
- ► Electroosmotic Flow (DC)
- ► AC Electro-Osmotic Flow
- ► On-Chip Sample Separation

References

1. Laser DJ, Santiago JG (2004) A review of micropumps. J Micromech Microeng 14:R35–R64
2. Harrison DJ, Manz A, Fan Z, Leidi H, Widmer HM (1992) Capillary electrophoresis and sample injection systems integrated on a planar glass chip. Anal Chem 64:1926–1932
3. Ermakov SV, Jacobson SC, Ramsey JM (2000) Computer simulations of electrokinetic injection techniques in microfluidic devices. Anal Chem 72:3512–3517
4. Fu LM, Yang RJ, Lee GB, Liu HH (2002) Electrokinetic injection techniques in microfluidic chips. Anal Chem 74:5084–5091
5. Ren L, Li D (2002) Theoretical studies of microfluidic dispensing processes. J Colloid Interface Sci 254:384–395
6. Chien RL (2003) Sample stacking revisited: a personal perspective. Electrophoresis 24:486–497
7. Patankar SV (1980) Numerical Heat Transfer and Fluid Flow. Hemisphere Publishing Corp, New York
8. Patankar NA, Hu HH (1998) Numerical simulation of electroosmotic flow. Anal Chem 70:1870–1881
9. Ren L, Sinton D, Li D (2003) Numerical simulation of microfluidic injection processes in crossing microchannels. J Micromech Microeng 13:739–747
10. Ren CL, Li D (2004) Effects of spatial gradients of electrical conductivity on chip-based injection processes. Analytica Chimica Acta 518:59–68

Electrokinetic/ElectroHydrodynamic Flow Instability

JEFFREY D. ZAHN
Department of Biomedical Engineering, Rutgers,
The State University of New Jersey, Piscataway, NJ, USA
jdzahn@rci.rutgers.edu

Synonyms

Electrohydrodynamic mixing; Electrokinetic instability

Definition

Electrokinetic and electrohydrodynamic flow instabilities develop at a fluid-fluid interface due to the unstable growth of interfacial perturbations when electrical stresses are applied. The electrical stresses develop at the interface primarily due to a conductivity or permittivity gradient between two fluid phases. Electrokinetic and electrohydrodynamic instabilities have been demonstrated in both single phase aqueous systems with conductivity gradients as well as in two phase organic aqueous microflows and are modeled using classical linear stability analysis considering momentum transport equations and both kinematic and interfacial stress boundary conditions. These models test the stability of the fluid flow to infinitesimal disturbances. These instabilities have been applied primarily to enhancing mixing processes in microfluidic devices.

Overview

In most microfluidic devices, mixing occurs between two inlet streams of the same fluid where the two streams must be dispersed to remove any concentration gradients of dissolved components between the two streams. One category of active mixing has been reported using electrokinetic or electrohydrodynamic instabilities in microflows. Research on electrokinetic and electrohydrodynamic instabilities has been conducted either to promote mixing or to understand how the instabilities develop in order to design devices which avoid them. A full understanding of how the instability develops is especially important when dealing with samples and buffers in lab on a chip applications such as capillary electrophoresis or isoelectric focus-

ing whose conductivity and/or conductivity gradients are either unknown, poorly controlled or both.

The early work on modeling electrohydrodynamic instabilities performed a linear stability analysis of the electrical and fluid interfacial boundary conditions using the transfer relations developed by Melcher [1]. Melcher developed a dielectric model which describes liquids as being both polarizable and having free charge in an imposed electric field. Electrohydrodynamic instabilities have been demonstrated in macroscale systems [2, 3] by Hoburg and Melcher at an oil-oil interface with a discrete conductivity change at the interface under the influence of an applied electric field. Here, the instability is modeled as charge accumulation at a perturbed interface where the electrical force on the interface is balanced by the fluid interfacial stress tensor. The instability model is applied to determine the interfacial stability as to whether the perturbations will grow or decay exponentially. Melcher determined that a natural velocity scale for this instability is the electroviscous velocity which represents a balance between the electrical and viscous stresses at the fluid-fluid interface. This instability is analogous to many instabilities such as the Rayleigh–Taylor instability of a two fluid system when a denser fluid is placed on top of a lower density fluid in a vertical gravitational field.

Basic Methodology

Several different types of instability mixing have been reported: electrokinetic instability mixing in a single phase solution without conductivity gradients [4], electrokinetic [5, 6] and electrohydrodynamic [7] instability mixing with conductivity gradients, and multiphase electrohydrodynamic instability mixing [8]. In order to understand how electrohydroyanmic mixing will proceed, it is important to understand the stability criteria at the organic-aqueous interfaces. The instability can be modeled for single phase systems with a conductivity gradient along a fluid-fluid interface where all other physical properties (e. g., viscosity, permittivity) are constant across the interface [5–7]. A model for multiphase systems consists of a non-conducting fluid sandwiched between two perfectly conducting layers maintaining an initially flat interface, with a DC potential, V_0, applied across two parallel plate electrodes [8]. These models very closely resemble the physical flow profile of reported experimentally stratified flows.

For each of these models, a linearized perturbation analysis is performed by linearizing the flow and electrical field equations of the system. This process is modeled using stability analyzes applying the kinematic and stress conditions at the interface. Stability analysis is based upon superimposing a perturbation flow profile over the base flow and determining whether the perturbations will grow or decay in time. These analysis can predict the conditions for incipience of instability and initial instability growth rates. As the system is driven beyond the small signal linear range, computational methods may be employed to further characterize instability progression into mixing.

Governing Equations

The flow profiles of the two fluids are determined by conservation of mass assuming incompressible fluids and the Navier–Stokes equation which includes the imposed electrical forces

$$\nabla \cdot \boldsymbol{u} = 0 \tag{1}$$

$$\rho \left[\frac{\partial \boldsymbol{u}}{\partial t} + (\boldsymbol{u} \cdot \nabla)\, \boldsymbol{u} \right] = -\nabla p + \rho \boldsymbol{g} + \mu \nabla^2 \boldsymbol{u} + \boldsymbol{F}_\mathrm{e} \tag{2}$$

where $\boldsymbol{u}$ is the velocity vector, ρ is the fluid density, p is the pressure, μ is the fluid viscosity and $\boldsymbol{F}_\mathrm{e}$ is the electrical volume force density. The volume force density is related to the divergence of the electrical stress tensor and is

$$\begin{aligned} \boldsymbol{F}_\mathrm{e} &= \nabla \cdot \bar{\bar{\mathbf{T}}}^\mathrm{e} \\ &= \rho_f \boldsymbol{E} - \frac{1}{2} |\boldsymbol{E}|^2 \nabla \varepsilon + \nabla \left(\frac{1}{2} \rho \, |\boldsymbol{E}|^2 \left(\frac{\partial \varepsilon}{\partial \rho} \right)_T \right) \end{aligned} \tag{3}$$

where $\bar{\bar{\mathbf{T}}}^\mathrm{e}$ is the electrical stress tensor, ρ_f is the free charge density, $\boldsymbol{E}$ is the electric field and ε is the space varying dielectric permittivity. The first term on the right side of Eq. (3) represents the electrophoretic component of the force which is the electrical force exerted on the free charges in the electric field. In a perfectly conducting solution, the free volume charge in each fluid layer is zero ($\rho_\mathrm{f} = 0$), but there can be a surface charge on the fluid-fluid interface. The second term is the dielectrophoretic term and is the force density term exerted on a dielectric fluid. The third term is an electrostrictive force density and can be ignored for incompressible fluids as it can be lumped with the pressure term in Eq. (2). For multiphase systems using two incompressible liquids which are assumed to be completely immiscible [8], the dielectric permittivity and conductivity are modeled as a step function across each interface so that the permittivity and conductivity gradients are Dirac delta functions right on the interface. Since the dielectric permittivity and conductivity are constant in each layer, the total electric force density in each layer is zero except along the interface where the step change in permittivity and conductivity contributes to an interfacial surface force density. In addition, in systems where there is

a conductivity gradient within a single fluid, there will be a free charge density which results in a coulombic (electrophoretic) force density.

In electrostatic systems the electric field has zero curl so the electric field may be expressed in terms of a scalar electric potential

$$\nabla \times \boldsymbol{E} = 0 \Rightarrow \boldsymbol{E} = -\nabla \phi \tag{4}$$

Gauss's law may be written as

$$\nabla \cdot (\varepsilon \boldsymbol{E}) = \rho_{\mathrm{f}} \tag{5}$$

and for ohmic media with convection current

$$\boldsymbol{J} = \sigma \boldsymbol{E} + \rho_{\mathrm{f}} \boldsymbol{u} \tag{6}$$

where $\boldsymbol{J}$ is the current density and σ is the solution conductivity. Charge conservation requires that

$$\nabla \cdot \boldsymbol{J} + \frac{\partial \rho_{\mathrm{f}}}{\partial t} = 0 \tag{7}$$

Assuming the permittivity and conductivity are space varying Eqs. (5–7) reduce to

$$\begin{aligned} \frac{\varepsilon}{\sigma}\left(\frac{\partial \rho_{\mathrm{f}}}{\partial t} + \boldsymbol{u} \cdot \nabla \rho_{\mathrm{f}}\right) + \rho_{\mathrm{f}} &= \sigma \boldsymbol{E} \cdot \nabla\left(\frac{\varepsilon}{\sigma}\right) \\ &= -\varepsilon \boldsymbol{E} \cdot \frac{\nabla \sigma}{\sigma} + \boldsymbol{E} \cdot \nabla \varepsilon \end{aligned} \tag{8}$$

In the presence of a conductivity gradient in which ion transport is considered, the solution conductivity can be described by a convective-diffusion equation as

$$\frac{\partial \sigma}{\partial t} + \boldsymbol{u} \cdot \nabla \sigma = D_{\mathrm{eff}} \nabla^2 \sigma \tag{9}$$

where σ is the solution conductivity and D_{eff} is the effective diffusivity of the ions. It was also shown by Hoburg and Melcher that the velocity may be rescaled in terms of an electroviscous velocity, U_{ev}, which represents the balance between the viscous force and electric body force as

$$U_{\mathrm{ev}} = \frac{\varepsilon E_0^2 H}{\mu} \tag{10}$$

where E_0 is the applied electric field and H is the characteristic length scale of the system (e. g., the half width of a microfluidic channel for a two layer stratified system).

Kinematic and Stress Conditions

In the presence of an electric field the surface charge density and polarization force density at the interface influences the interfacial force balance boundary condition and the electric field can affect fluid flow. The interfacial stress balance boundary condition in the i direction on a surface whose normal, $\boldsymbol{n}$, is in the j direction is

$$\left\| \mathbf{T}_{ij}^{\mathrm{f}} n_{\mathrm{j}} \right\| + \left\| \mathbf{T}_{ij}^{\mathrm{e}} \right\| - \gamma \left(n_{j,j}\right) n_i = 0 \tag{11}$$

where $\mathbf{T}_{ij}$ is the stress tensor, the vertical bars represent the difference in stress across the interface, γ is the interfacial tension between the phases (if applicable), and the superscript refers to either the fluid (f) or electrical (e) contributions. For two dimensional problems with a planar interface with no variation in the y direction, with an equilibrium normal in the x direction and an interfacial displacement, $\xi(z)$, the small signal normal to first order terms is

$$\boldsymbol{n} = \boldsymbol{i}_x - \frac{\partial \xi}{\partial z} \boldsymbol{i}_z \tag{12}$$

The fluid and electrical stress tensor components are

$$\mathbf{T}_{ij}^{\mathrm{f}} = -p \boldsymbol{\delta}_{ij} + \mu \left(\frac{\partial u_i}{\partial x_j} + \frac{\partial u_j}{\partial x_i}\right) \tag{13}$$

and

$$\mathbf{T}_{ij}^{\mathrm{e}} = \varepsilon E_i E_j - \frac{1}{2} \boldsymbol{\delta}_{ij} \varepsilon E_k E_k \tag{14}$$

where $\boldsymbol{\delta}_{ij}$ is the Kronecker delta. The electrical stress tensor in Eq. (14) is derived from the volume force density in Eq. (3) due to the coulombic and polarization force densities.

Perturbation Variables

The primary objective of stability analysis is to test the stability of the fluid flow to infinitesimal disturbances. Here the perturbations are superimposed over the base flow so that interfacial displacements are represented as

$$\xi(z, t) = \xi_{\mathrm{equil}} + \mathrm{Re}\left[\hat{\xi} e^{j(\omega t - kz)}\right] \tag{15}$$

where ξ_{equil} is the equilibrium displacement, ω is the natural frequency of interfacial displacement, $\hat{\xi}$ is the complex amplitude of the interfacial displacement, k is the wavenumber component in the z direction and $j = \sqrt{-1}$. The wavenumbers are related to the wavelengths (λ) of the interfacial displacements as

$$k = \frac{2\pi}{\lambda} \tag{16}$$

Electric scalar potential perturbations may be described as

$$\phi(z,t) = \phi_{\text{equil}} + \text{Re}\left[\hat{\phi}e^{j(\omega t - kz)}\right] \quad (17)$$

Similarly, pressure and velocity perturbations may be described as

$$p(z,t) = p_{\text{equil}} + \text{Re}\left[\widehat{p}e^{j(\omega t - kz)}\right] \quad (18)$$

$$U_x(z,t) = U_{\text{xequil}} + \text{Re}\left[\hat{U}_x e^{j(\omega t - kz)}\right] \quad (19)$$

$$U_z(z,t) = U_{\text{zequil}} + \text{Re}\left[\hat{U}_z e^{j(\omega t - kz)}\right] \quad (20)$$

where the subscripted equil refers to the equilibrium base flow. The stability of the system may be modeled by linearizing the electrical and flow equations and applying the interfacial boundary conditions to test whether the interfacial perturbation will grow. The generalized analysis in [10] has proved that the incipience of instability occurs when $\omega = 0$. If the system is stable, ω is complex with a positive or zero imaginary part and if unstable the real part of ω is zero while the imaginary part is negative. When ω is negative imaginary it can be seen that the perturbation modeled by Eq. (15) will grow exponentially in time.

Key Research Findings

Some of the early work on electrokinetic (EK) instability mixing was done by Santiago and colleagues [4]. Here, mixing was produced using AC electrical excitation at a frequency of 10 Hz. With increasing applied voltage the flow became unstable and material line stretching and folding was observed (Fig. 1). Due to the fully three dimensional flow profile which developed at higher field strengths the observed phenomena was attributed to a flow instability. The instability was observed using a variety of channel materials and buffer solutions. However, a mechanism for the instability was not fully explored and it was unclear whether the instability was due to the electrical excitation or due to the flow oscillations as the authors note "At this time, we do not know if this instability is particular to electrokinetic flows in this regime or if the instability would also be observed in viscous channel flows with oscillating walls." However, more recent analysis using a multispecies electrokinetic instability model has demonstrated that the flow instability may be promoted when the conductivity ratio between two fluid streams is as low as 1.01 [5]. Thus, the instability seen in [4] may be due to a slight conductivity difference due to the fluorescent dye used for flow visualization.

Further mixing experiments were conducted using a two layer stratified aqueous electrokinetic flow with a conductivity gradient where one layer of fluid was at least 10 times more conductive than the other [6, 7]. Even though the instability originates in the bulk electrolyte, the terminology *electrokinetic instability* was chosen due to the relevance of the work to electrokinetic microdevices. Here, with the application of a critical electric field, the electrokinetic instability is seen to grow with characteristic instability waves as shown in Fig. 2. It was noted that the disturbance originates where the two fluids meet, increases in magnitude with increasing electric field and is convected downstream within the microchannel. Santiago and colleagues adapted the electrohydrodynamic model proposed by Melcher to electrokinetic flows to consider interfacial electrokinetic effects. Their model expanded upon the work done by Melcher and Hoburg to include "advective effects due to electroosmotic flows, an initial conductivity profile consistent with our experiments, and a diffusive component of the conductivity conservation equation critical in modeling EK instabilities." This diffusive component may stabilize the flow, so modeling the diffusive component is critical for determining the critical electric field for instability. In addition to this expansion of the instability model, a full three dimensional model was proposed and many of the salient experimental features observed were captured by computational simulation.

An example of an electrohydrodynamic mixer was demonstrated by El Moctar et al. [8]. Here, an oil–oil two layer system was chosen where one oil phase was doped with an oil miscible charge carrier to increase its conductivity and permittivity. Here a dimensionless timescale for interface charging was considered for AC excitation

$$T = \frac{\tau}{1/f} = \tau f \quad (21)$$

where $\tau = \varepsilon/\sigma$ is the charge relaxation time and f is the applied AC frequency. The authors consider the influence of using a DC applied electric field (Fig. 3), AC sinusoidal electric field and square-wave excitation. The electric field needed for efficient mixing was seen to decrease as AC and then square wave excitation was used. However, lower frequencies were preferred as it was noted that if T is much greater than 1 then the charges do not have time to accumulate along the fluid–fluid interface when higher frequencies are used. Thus, at higher frequencies the coulombic component of the interfacial force tensor is negligible and the polarization force due to the permittivity gradient dominates. However, it was also noted, that the permittivity difference between the two fluids also becomes very small

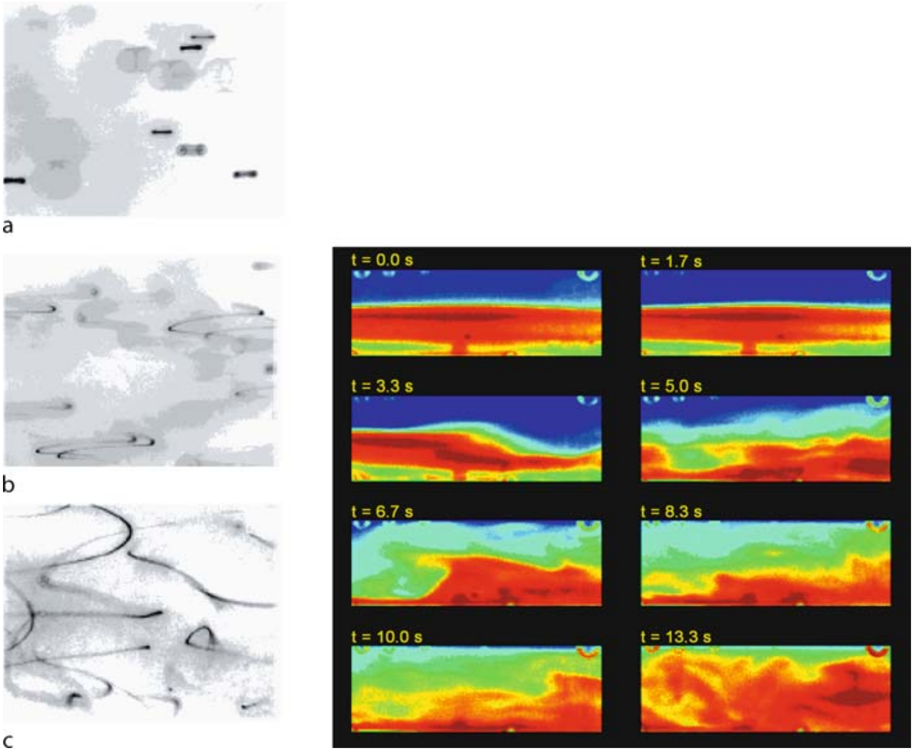

Electrokinetic/ElectroHydrodynamic Flow Instability, Figure 1 (*Left*) Imaged particle paths for 0.49 μm-diameter fluorescent particles. The image intensity scale is inverted to better visualize the particle paths. (**a**) Stable oscillations at 1 kV. (**b**) Particles oscillate in plane with a transverse component at a larger applied voltage of 4 kV. (**c**) Particle trajectories in the unstable state at 8 kV. Here the flow field is three-dimensional, as particles traverse the depth of field of the microscope moving in and out of focus. (*Right*) Images obtained from the electrokinetic instability micromixer during the mixing process with an initially stable interface and transition into instability mixing [4]

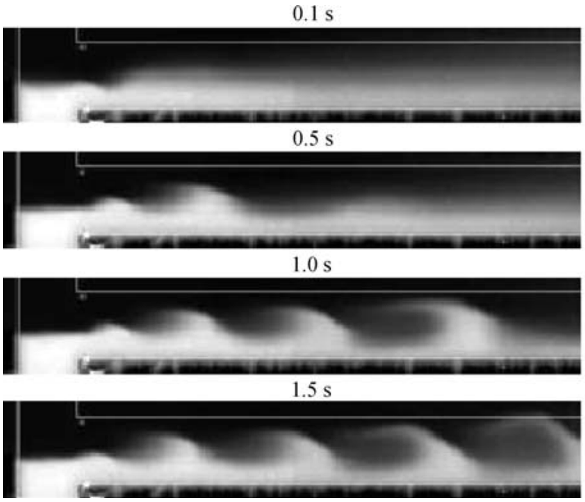

Electrokinetic/ElectroHydrodynamic Flow Instability, Figure 2 Time series images of instability waves due to an electrokinetic instability in a conductivity gradient at an applied field of 1.25 kV/cm. The two solutions are Borate buffers of 1 mM and 10 mM which are introduced into the device at a stable electric field of 0.25 kV/cm. The high-conductivity stream is seeded with a neutral fluorescent dye [6]

at high frequency excitation so that the polarization force also becomes small.

Zahn and Reddy recently demonstrated multiphase mixing using a three layer stratified system [9] consisting of a low conductivity organic layer sandwiched between two high conductivity aqueous layers. Here, the two fluid layers were immiscible so mixing in this context was not defined as molecular dispersion to remove concentration gradients but rather as an increase in interfacial area between the two phases from droplet formation to reversible dispersion of the two phases. The process was modeled using linear stability analysis and an analytical stability criteria for any two phase system consisting of an insulating fluid layers sandwiched between two conductive fluid layers was determined as the product of two terms, each of which may be zero

$$\left(((c_\mathrm{a}-c_\mathrm{b})+d_\mathrm{b})^2+\left(\left(a_\mathrm{a}+a_\mathrm{b}-\frac{\varepsilon_\mathrm{b}E_0^2k}{j\omega}\coth kb+\frac{\gamma k^2}{j\omega}\right)\right.\right.$$
$$\left.\left.+\left(b_\mathrm{b}+\frac{\varepsilon_\mathrm{b}E_0^2k}{j\omega\sinh kb}\right)\right)((e_\mathrm{a}+e_\mathrm{b})-f_\mathrm{b})\right)$$

Electrokinetic/ElectroHydrodynamic Flow Instability, Figure 3 Electrohydrodynamic mixing in a DC electric field. The images show the outlet branch of the microchannel after the device has been loaded with two fluids. (**a**) The initial condition showing a dark green fluid which corresponds to a doped and dyed oil while the clear fluid represents the pure oil. (**b**) The mixture after the application of an electric field $E = 4 \times 10^5$ V/m. (**c**) Electric field intensity of $E = 6 \times 10^5$ V/m. Images taken from [8]

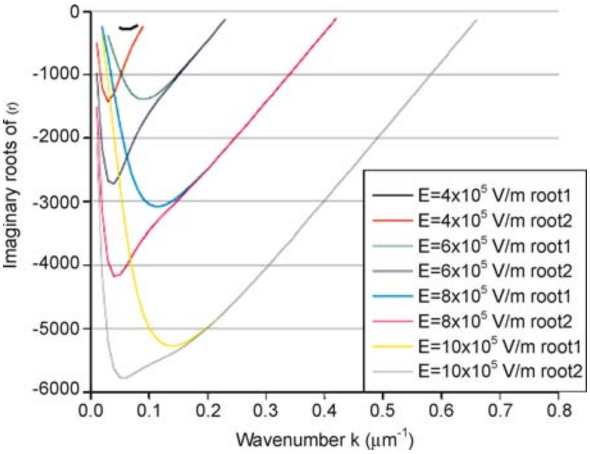

Electrokinetic/ElectroHydrodynamic Flow Instability, Figure 4 Plot of the negative imaginary (unstable) roots of ω versus wavenumber using the viscous analysis for a variety of applied fields. The flow is unstable as long as the root is negative imaginary [9]

$$\times\left(((c_a-c_b)-d_b)^2+\left(\left(a_a+a_b-\frac{\varepsilon_b E_0^2 k}{j\omega}\coth kb+\frac{\gamma k^2}{j\omega}\right)\right.\right.$$
$$\left.\left.-\left(b_b+\frac{\varepsilon_b E_0^2 k}{j\omega \sinh kb}\right)\right)((e_a+e_b)+f_b)\right)=0 \tag{22}$$

where b is the thickness of the organic layer, E_0 is the applied electric field, a through f are the elements defined in Eq. (23) and the subscript a or b relates to which layer, the aqueous (a) or organic (b), is used to evaluate the components. It was previously shown [1] that the perturbation x and z directed first order complex amplitude stresses may be described for a generic fluid layer of thickness Δ, density ρ and viscosity μ, to define the components a through f

$$a=\frac{-\mu\left(\delta^2-k^2\right)}{kD}\left(\frac{k}{\delta}\coth\delta\Delta-\coth k\Delta\right)$$

$$b=\frac{\mu\left(\delta^2-k^2\right)}{kD}\left(\frac{k}{\delta}\operatorname{csch}\delta\Delta-\operatorname{csch}k\Delta\right)$$

$$c=\frac{j\mu}{D}\left[\delta\left(1+\frac{3k^2}{\delta^2}\right)(\operatorname{csch}k\Delta\operatorname{csch}\delta\Delta\right.$$
$$\left.-\coth k\Delta\coth\delta\Delta)+k\left(3+\frac{k^2}{\delta^2}\right)\right]$$

$$d=\frac{-j\mu\left(\delta^2-k^2\right)}{\delta D}(\coth\delta\Delta\operatorname{csch}k\Delta-\coth k\Delta\operatorname{csch}\delta\Delta)$$

$$e=\frac{-\mu\left(\delta^2-k^2\right)}{\delta D}\left(\frac{k}{\delta}\coth k\Delta-\coth\delta\Delta\right)$$

$$f=\frac{-\mu\left(\delta^2-k^2\right)}{\delta D}\left(\operatorname{csch}\delta\Delta-\frac{k}{\delta}\operatorname{csch}k\Delta\right)$$

$$D=1+\frac{k^2}{\delta^2}+\frac{2k}{\delta}(\operatorname{csch}k\Delta\operatorname{csch}\delta\Delta-\coth k\Delta\coth\delta\Delta)$$

$$\delta=\left[k^2+(j\omega\rho/\mu)\right]^{\frac{1}{2}} \tag{23}$$

Using the physical values for the fluids used and layer thicknesses $a = b = 50$ μm, negative imaginary roots of ω were found as a function of wavenumber and increasing applied field when the applied field was beyond the incipience of instability as shown in Fig. 4. The fastest growth wavenumber is the minimum of the negative imaginary roots.

Experimentally, the instability was demonstrated by labeling the organic phase with a fluorescent dye and applying electrical excitation through patterned electrodes. A schematic of the experimental system is shown in Fig. 5a. Here, high frequency AC excitation was used to avoid electrolysis of the aqueous phase. Due to the large permittivity difference between the organic and aqueous phases a large polarization force density can be applied to the interface at high frequencies as compared to the single phase system where only a conductivity gradient exists limiting the interfacial force to the coulombic

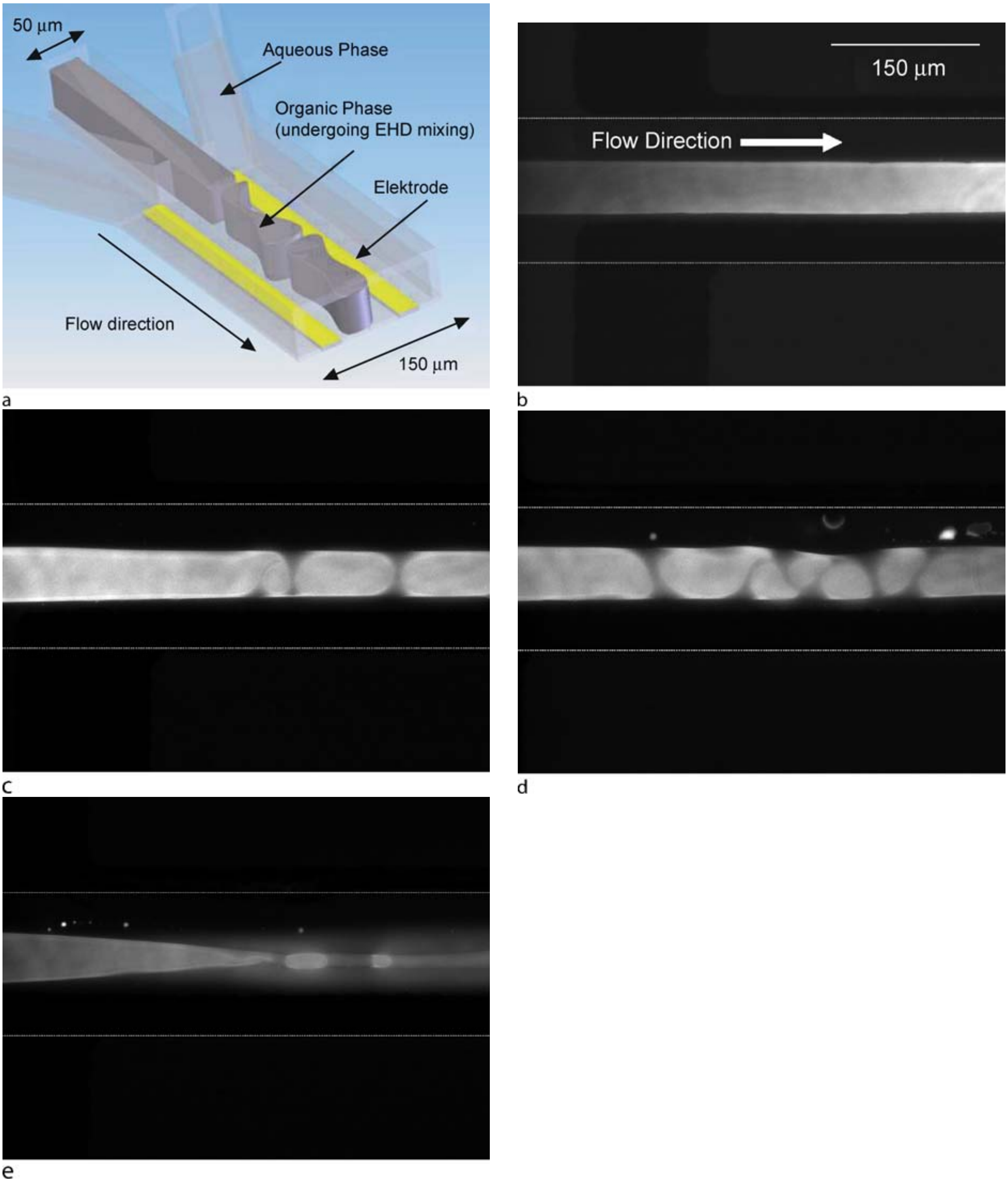

Electrokinetic/ElectroHydrodynamic Flow Instability, Figure 5 (**a**) Schematic of the three inlet geometry with electrodes and instability mixing. The channel height is 30 μm and the electrode to electrode spacing is 75 μm. (**b**) A stable flow in the absence of an electric field. (**c**) The disruption of flow after a 41 V_{RMS} potential (initial applied field $E_0 = 8.2 \times 10^5$ V/m) is applied at 250 kHz to the electrodes. (**d**) EHD instability at 44 V_{RMS} (initial applied field $E_0 = 8.8 \times 10^5$ V/m), 700 KHz. (**e**) Dispersion of the two phases at 45 V_{RMS} (initial applied field $E_0 = 9 \times 10^5$ V/m) and 10 MHz. The electrodes are spaced 75 μm apart in the aqueous phase above and below the organic phase but appear dark in the epifluorescent images. All images were taken using a 20× microscope objective and each image window size is 340 × 461 μm^2. The horizontal white lines delineate the channel boundaries [9]

force density. Increasing the electric field increases the instability growth rate and results in an increase in the level of mixing. The results show an increase in conductive aqueous fluid entrainment into the nonconducting organic fluid core (Fig. 5b to e) measured as a percentage of area of entrainment into the fluorescently labeled organic phase. The entrainment area increased from 1.9% to 28.6% as the applied field was increased from 8.0×10^5 to 9.0×10^5 V/m.

Future Directions for Research

Electrokinetic and electrohydrodynamic instability mixing in microsystems is a complex phenomenon which researchers are only beginning to exploit and understand. Future work requires a further development of experimental models and expansion of computational simulations to better understand how the instabilities form and grow. Specific applications of electrokinetic and electrohydrodynamic instabilities are still limited. The application of these instabilities to improve mixing between components should be explored. One example is through the use of multiphase systems where electrohydrodynamic instabilities are utilized to improve component partitioning for liquid extraction devices.

Cross References

- ► Active Mixer
- ► Droplet and Bubble Formation in Microchannels
- ► Electrokinetic Two Phase Flows
- ► Electroosmotic Flow (DC)
- ► AC Electro-Osmotic Flow
- ► Interfacial Instability
- ► Interfacial Electrokinetic Flow
- ► Lab-on-Chip Devices for Sample Extraction
- ► Microfluidic Mixing
- ► Pressure-Driven Two Phase Flows

References

1. Melcher JR (1981) Continuum Electromechanics. MIT Press, Cambridge
2. Hoburg JF, Melcher JR (1976) Internal electrohydrodynamic instability and mixing of fluids with orthogonal field and conductivity gradients. J Fluid Mech 73:333–351
3. Hoburg JF, Melcher JR (1977) Electrohydrodynamic mixing and instability induced by co-linear fields and conductivity gradients. Phys Fluid 20(3):903–911
4. Oddy MH, Santiago JG, Mikkelsen JC (2001) Electrokinetic Instability Micromixing. Anal Chem 73:5822–5832
5. Oddy MH, Santiago JG (2005) A Multiple-Species Model for Electrokinetic Instability. Phys Fluid 17:064108–1:064108-17
6. Chen CH, Lin H, Lele SK, Santiago JG (2005) Convective and Absolute Electrokinetic Instability with Conductivity Gradients. J Fluid Mech 524:263–303
7. Lin H, Storey BD, Oddy MH, Chen CH, Santiago JG (2004) Instability of electrokinetic microchannel flows with conductivity gradients. Phys Fluid 16(3):1922–1935
8. El Moctar AO, Aubry N, Batton J (2003) Electrohydrodynamic microfluidic mixer. Lab Chip 3(4):273–280
9. Zahn JD, Reddy V (2006) Electrohydrodynamic instability mixing: Two phase linear stability analysis and micromixing for a miniaturized DNA extraction module. Microfluid Nanofluid 2(2):399–415
10. Turnbull RJ, Melcher JR (1969) Electrohydrodynamic Rayleigh–Taylor Bulk Instability. Phys Fluid 12(3):1160–1166

Electrokinetic Flow

Synonyms

Electrokinetic transport; Electrokinetic motion

Definition

Electrokinetic flow covers in principle the transport of liquids (electroosmosis) and samples (electrophoresis) in response to an electric field. Both motions are associated with the electric double layer that is formed spontaneously at the solid–liquid interface in which there is a net charge density. Compared to the traditional pressure-driven flow, electrokinetic flow is more suited to miniaturization due to its nearly plug-like velocity profile and much lower flow resistance. However, Joule heating is a ubiquitous phenomenon in electrokinetic flow that will affect the transport of both liquids and samples via temperature sensitive material properties.

Cross References

- ► Electrical Double Layers
- ► Electroosmotic Flow (DC)
- ► AC Electro-Osmotic Flow
- ► Electrophoresis
- ► Streaming Current and Electroviscosity

Electrokinetic Flow and Ion Transport in Nanochannels

Sandip Ghosal
Department of Mechanical Engineering,
Northwestern University, Evanston, IL, USA
s-ghosal@northwestern.edu

Synonyms

Electroosmotic flow; Ion conductance in nanochannels; Ion transport in nanopores; Nanopore conductance

Definition

A nano-channel is a conduit between two reservoirs of fluid with a characteristic internal diameter of roughly one to several tens of nanometers. A nanometer is a billionth of a meter (10^{-9} m). The fluid is assumed to be an electrolyte, that is, water with some dissolved salts that dissociate into positive and negative ions. Electrokinetic flow refers to fluid flow generated in such a channel when an externally applied electric field is the primary motive force. Ion transport refers to the average drift of the ions along the channel due to the electric field superimposed on the random molecular motion and collisions with the surrounding water molecules and channel walls.

Overview

Nano vs. Micro-Fluidics

The phrase *one to several tens of nanometers* in the above definition may seem both arbitrary and vague and therefore needs further elucidation. Since the subject of discussion is the flow of water through narrow channels, they must be wide enough to allow the passage of a molecule of water, which is about 0.1 nm. On the other hand, if they are much wider than this size, let us say more than a 100 nm or 0.1 micron we are in the domain of microfluidics, where water can safely be regarded as a continuous material as we do in everyday engineering practice. Thus, the specification of *one to several tens* derives from the scale provided by the water molecule, the subject of discussion is channels that are neither too narrow nor too wide in comparison to the size of a water molecule. These definitions however are based on common usage and are necessarily imprecise; there is no exact boundary as to where nanofluidics ends and microfluidics begins. Nanochannels can be long, that is the length may be many times the characteristic width or short, that is, the length can be of the order of the width. The terms nanopore and nanochannel are usually used interchangably and we will do so here.

Nanochannels in Nature

Nanochannels and ion transport across nanochannels is a very common feature in living cells [1]. Cells contain various internal and external membranes made out of lipid molecules. These are called lipid bilayers. The nanochannels are made of proteins which form a pore on the lipid bilayer. Various kinds of such channels are known with different biological functions. For example, nerve cells contains channels that are permeable to Sodium, Pottasium or Calcium ions. Channels open or close in response to various factors. For example, voltage gated channels open in response to a change in the electrical potential across it. A ligand gated channel opens if a specific chemical (a ligand) binds to it. Proton pumps in the cell membrane cause the interior of the cell to be maintained at a small negative electric potential relative to the outside. The opening of the ion channels cause an equilibration of the ionic concentrations on either side of the membrane causing a collapse of the potential. Neighboring channels sense this drop in the potential and being voltage gated they respond by opening up and collapsing the potential in their own neighborhood. The effect propagates by the domino effect causing a zone of collapsed potential to propagate outward along the membrane. This is a nerve impulse and it is the mechanism behind all neuronal activity in living things. Another nanochannel in living systems help regulate the water content of cells; these are called aquaporins. They play an important role for example in the functioning of the kidney. The genetic material of a cell is stored in its nucleus. However, the proteins that are coded by the genes are actually manufactured outside the nucleus in the cytoplasm by organelles known as ribosomes. Some of these proteins are actually needed inside the cell nucleus itself or in the mitochondria. How do they cross the mitochondrial or the nuclear membrane? For this, the membranes of these bodies contain nanopores. The proteins are actually unfolded and they translocate across the membrane as a linear polypeptide chain through these nanopores. The details of the mechanism by which this happens is a subject of current research in cell biology.

Nanochannels in Technology

A number of applications of nanochannels have emerged recently in biotechnology partly inspired by their respective biological counterpart. One such application could lead to novel technologies for sequencing DNA that is orders of magnitude faster than what is currently possible. The idea had its origins in the Coulter counter for counting and sorting cells. The Coulter counter consists of a single micron size pore in an impervious membrane that separates two chambers both filled with an electrolyte. When a voltage is applied, a small current flows due to ion movement through the pore. If one of the chambers contain objects such as cells, occasionally a cell will enter the pore. When this happens, the volume of electrolyte in the pore, and therefore the conductance of the pore is reduced and this can be detected as a drop in the current. Thus, the device can be used to count cells and make estimates of their size. In a 1996 paper it was shown by Kasianowicz et al. [2] that if the microchannel in the membrane is replaced by a nanochannel the device is able to detect the passage of single molecules of DNA and RNA. The nanopore was a recon-

structed version of a natural ion channel from the bacteria Staphylococcus aureus. It is formed by a protein called α-hemolysin which self assembles under the right conditions on a lipid bilayer membrane and remains open and stable for extended time periods. Recently, techniques involving a combination of micro lithography followed by treatment using the beam from an electron microscope has been used to create artificial nanopores in the 1 to 10 nm range. These tend to be more stable and are easier to work with than the protein nanopores from living cells. It has been shown that the current signal from the nanopore can be used to determine the lengths of biopolymers and to tell apart homopolymers of identical length. However, the goal of actually reading off the sequence of bases as the polymer threads through the pore (in a manner similar to how the magnetic head in a tape recorder reads the signal encoded in a magnetic tape) still remains elusive. Recently the idea of the *Thousand Dollar Genome*: the goal of reducing the cost of a complete sequence of the three billion base pairs in a human genome to one thousand US dollars or less, has received much attention. This cost level is considered a threshold below which one may expect to see a large scale impact of this technology on the practice of medicine and on the national economy. For the sake of comparison, the Human Genome Project cost 3 billion dollars over a thirteen year period (about $1 per base). The latest advancement in automation has reduced this to 5 cents per base. It is believed that a revolutionary rather than evolutionary change in sequencing technology is needed to reach the 3 cents per 100,000 bases envisioned by the goal of a thousand dollar genome. The concept of sequencing using nanopores could be just the required revolutionary sequencing technology and is discussed in more detail later in this article (see [6] and [8]).

Nanochannels have been used to make an analogue of semiconductor transistors [3]. Charged surfaces in contact with electrolytes attract a layer of ions of the opposite sign (counter-ions) that neutralize the electric field. If the electrolyte is *ordinary* water (that is, water that has not been de-ionized through special treatment) the electric field near most charged surfaces drops to essentially zero over a distance of several nanometers. Because of this shielding effect, any electric field applied externally across the channel has essentially no effect on the conductance of the channel because the bulk of the electrolyte within the channel simply does not "see" the applied electric field. In nanochannels, the situation changes because now the penetration depth of the external voltage, which is of the same order as the thickness of the layer of counterions is comparable to the channel thickness. As a result, the electric conductance of the nanochannel can be controlled by applying a gate voltage across the channel, just as in a MOSFET transistor. If controlling the current with a gate voltage was the sole application of this technology, it would be of little interest, since semiconductor transistors achieve the same effect far more efficiently and it is a mature technology. Of much greater importance is the fact that the permeability to charged macromolecules can also be selectively controlled with a gate voltage. This is because, a negatively charged macromolecule would naturally be excluded from a nanochannel with negatively charged walls until the potential barrier is lowered through the application of a gate voltage. Thus, a pore that is selectively permeable to specific molecules can be created and the selectivity can be tuned. This is analogous to the gated pores in biological systems, though the gating is achieved in perhaps a different manner. Large scale practical uses of the technology is likely, but is still in the future.

Basic Methodology

There are primarily two approaches to modeling flow and transport in nanochannels: continuum models and molecular models.

In the first approach, the fluid and the various charged species in the electrolyte are considered to be continuous and are described by quantities such as $c(\boldsymbol{x}, t)$ (the concentration of a given species) which are continuous functions of space and time. The continuum model is an approximation to reality because an electrolyte really consists of discrete particles: the individual molecules of the solute, solvent and dissociated ions. The continuum model has a high degree of accuracy as long as the relevant length scales in the problem (such as width of the channel) are much larger than the typical distance between molecules. For liquids, such as water, the molecules are closely packed together. Therefore, the distance between molecules is about the same as the size of the molecules themselves which is on the order of 0.1 nm. For this reason, one can expect the continuum approach to give reasonably accurate results in the case of liquid flow through channels that are tens of nanometers wide. The distance between molecules in gases at atmospheric pressure is about ten times larger so it is easier to detect deviations from classical continuum models in the case of flow of gases in nanochannels. In high vacuum these intermolecular distances are even larger and the continuum approximation can break down even on macroscopic scales. The degree of validity of the continuum approximation is often characterized by the ►Knudsen number defined as $\mathrm{Kn} = \lambda/L$, where λ is the ►mean free path (the average distance a molecule travels before bumping into a neighbor) and L is a characteristic length of the problem of interest. Then, the regime of validity

of continuum models may be characterized by a Knudsen number that is much smaller than one ($\mathrm{Kn} \ll 1$).

In many cases, such as in most of the nanochannels found in biological systems, the channel diameter is so small that the continuum model would be clearly inappropriate. There are even nanochannels that are too small to permit the passage of even a single molecule of water. In such cases, one is forced to recognize the underlying molecular structure of matter and perform what is called a ▶ molecular dynamics (MD) simulation. It is important to recognize, just like the continuum approximation, the MD approach is also an approximation to reality but at a different level. In the MD approach one ignores the fact that the water molecule for example contains protons, neutrons and electrons which interact with the protons, neutrons and electrons of every other water molecule via quantum mechanical laws. Such a description would be enormously complicated! Instead, each molecule is treated as a discrete indivisible object and the interaction between them is described by empirically supplied pair interaction potentials. For example, the simplest MD model is the hard sphere model where each molecule is modeled by a sphere, and the molecules do not interact except when they touch in which case they rebound elastically like billiard balls.

There also exists a range of possibilities that fall between the continuum and molecular models. These are approaches that combine some features of both. For example, in the description of Brownian motion of macromolecules or latex beads in the 10 – 100 micron size range, one uses classical hydrodynamic results such as the Stokes law for drag on a sphere while at the same time modeling fluctuating forces from molecular collisions that arise at the level of the molecular description. In the theory of ionic solutions, the individual ions are considered to be discrete particles but the surrounding water is treated as if it was a continuous dielectric medium with a constant dielectric permittivity.

Continuum Models

The Basic Equations of Electrokinetics

In the continuum model, electrokinetic flows are described by the incompressible Navier-Stokes equations with a volume density of electrical forces $-\rho_e \nabla\phi$ where ρ_e is the electric charge density and ϕ is the electric potential:

$$\rho_0(\partial_t \boldsymbol{u} + \boldsymbol{u} \cdot \nabla \boldsymbol{u}) = -\nabla p + \mu \nabla^2 \boldsymbol{u} - \rho_e \nabla\phi \,. \qquad (1)$$

This is supplemented by the continuity equation which takes into account the fact that in a liquid the density changes almost not at all even for large changes in pressure :

$$\nabla \cdot \boldsymbol{u} = 0. \qquad (2)$$

In the above, ρ_0 is the (constant) density of the water, p is the pressure, $\boldsymbol{u}$ is the flow velocity. The relative size of the term on the left of Eq. (1) (due to fluid inertia) and the second term on the right (due to viscosity) is characterized by the ▶ Reynolds number

$$\mathrm{Re} = \frac{UL\rho_0}{\mu} \qquad (3)$$

where U and L denote a characteristic velocity and length for the flow. In most applications of nanoscale flows, $\mathrm{Re} \ll 1$ so that the left hand side of Eq. (1) is neglected (the ▶ Stokes approximation). The potential ϕ is related to the charge density through the Poisson equation of electrostatics (in CGS units):

$$\varepsilon \nabla^2 \phi = -4\pi \rho_e \,, \qquad (4)$$

ε being the permittivity of the liquid. If the electrolyte contains N species of ions with charges ez_k and concentration $n_k (k = 1, \ldots, N)$, e is the magnitude of the charge on an electron then $\rho_e = \sum_{k=1}^{N} ez_k n_k$. Each ion species obeys a conservation equation

$$\frac{\partial n_k}{\partial t} + \nabla \cdot \boldsymbol{j}_k = 0 \,. \qquad (5)$$

Here $\boldsymbol{j}_k$, the flux vector for the species k, can be modeled by the Nernst-Planck equation for ion transport

$$\boldsymbol{j}_k = -\nu_k z_k e n_k \nabla\phi - D_k \nabla n_k + n_k \boldsymbol{u} \,. \qquad (6)$$

In Eq. (6) ν_k is the ▶ ion mobility: the velocity acquired by the ion when acted upon by unit force. It is obviously related to the ▶ electrophoretic mobility: the velocity per unit of electric field as $\mu_k^{(ep)} = ez_k \nu_k$. The diffusivity of the kth species is D_k and $\boldsymbol{u}$ is the fluid velocity.

Boundary Conditions. The boundary conditions are those of no slip (see [9] for a discussion on the applicability of this condition to small scale systems) for the velocity at rigid boundaries,

$$\boldsymbol{u} = 0 \qquad (7)$$

and no ion flux normal to the wall

$$\boldsymbol{j}_k \cdot \hat{\boldsymbol{n}} = 0 \qquad (8)$$

where $\hat{\boldsymbol{n}}$ is the unit normal directed into the fluid. In the absence of external electric fields, the chemistry at the electrolyte substrate interface leads to the establishment

of a potential, $\phi = \zeta$. This so called ▶zeta-potential at an interface depends on a number of factors including the nature of the substrate and ionic composition of the electrolyte, the presence of impurities, the temperature and the buffer pH. The ion distribution near a planar wall at $z = 0$ with potential $\phi(z)$ is known from statistical thermodynamics: $n_k = n_k(\infty)\exp(-z_k e\phi/k_B T)$ where k_B is the Boltzmann constant and T is the absolute temperature of the solution. In order that this expression be a steady solution of Eq. (5) we must have the ▶Einstein relation

$$D_k/\nu_k = k_B T\,. \tag{9}$$

Therefore Eq. (6) can also be written as

$$\boldsymbol{j}_k = -n_k \nu_k \nabla\psi_k + n_k \boldsymbol{u} \tag{10}$$

where $\psi_k = ez_k\phi + k_B T \ln n_k$ is called the chemical potential for the species k.

The Equilibrium Debye Layer

Suppose that the system is in the steady state and that there is no fluid flow or imposed electric fields. Further suppose that the geometry is such that the electrolyte-substrate interface is an iso-surface of ψ_k. Then it readily follows from Eqs. (5) and (10) and the boundary condition of no flux into the wall that $\nabla\psi_k = 0$ everywhere. Therefore, $n_k = n_k^{(\infty)}\exp(-z_k e\phi/k_B T)$ where $n_k^{(\infty)}$ is the ion concentration where the potential $\phi = 0$; usually chosen as a point very far from the wall. Using the solution for n_k in the charge density ρ_e and substituting in Eq. (4), we get the non-linear Poisson-Boltzmann equation for determining the potential

$$\nabla^2\phi = -\frac{4\pi e}{\varepsilon}\sum_{k=1}^{N} n_k^{(\infty)} z_k \exp(-z_k e\phi/k_B T)\,. \tag{11}$$

with the boundary condition $\phi = \zeta$ on walls. Equation (11) was the starting point of a detailed investigation of the structure of the ▶electric Debye layer (EDL) by Gouy and Chapman. The description in terms of Eq. (11) is therefore known as the Gouy-Chapman model of the EDL.

Equation (11) is a nonlinear equation. It can be linearized by expanding the exponential terms on the right hand side in Taylor series and discarding all terms that are quadratic or of higher order in ϕ, which gives

$$\nabla^2\phi - \kappa^2\phi = 0 \tag{12}$$

where

$$\kappa = \left[\sum_{k=1}^{N}\frac{4\pi z_k^2 e^2 n_k^{(\infty)}}{\varepsilon k_B T}\right]^{1/2} \tag{13}$$

is a constant determined by the ionic composition of the electrolyte. In arriving at Eq. (12) we used the condition $\sum_{k=1}^{N} n_k^{(\infty)} z_k = 0$ which expresses the fact that the bulk solution ($\phi = 0$) is free of net charge. It is easily verified that κ has units such that $\lambda_D = \kappa^{-1}$ defines a length scale that is called the Debye-Length, and the linearization of Eq. (11) that lead to Eq. (12) is known as the Debye–Hückel approximation. The solution to Eq. (12) near a charged plate of potential ζ may be written as $\phi = \zeta\exp(-\kappa z) = \zeta\exp(-z/\lambda_D)$ where z is distance normal to the plate. Thus, the potential due to the charged plate is shielded by the free charges in solution and the effect of the charge penetrates a distance of the order of the ▶Debye-length λ_D; which gives a physical meaning to this very important quantity. For *ordinary* water the Debye length is typically $1-10$ nm. The linearization proposed by Debye–Hückel is justified provided that $|z_k\phi| \ll k_B T/e$ uniformly in all space and for all k. At room temperature $k_B T/e \approx 30$ mV. However, for silica substrates $|\zeta| \sim 50-100$ mV in typical applications. Thus, the ▶Debye–Hückel approximation is often not strictly valid. Nevertheless, it is a very useful approximation because it enormously simplifies mathematical investigations related to the Debye layer.

Equation (12) is linear and can be solved analytically under fairly general conditions. If appears in several other contexts such as in the solution of the diffusion equation and in wave propagation problems with evanescent waves. If κ^2 were negative Eq. (12) would be identical to the Helmholtz equation.

Exact solutions to Eq. (11) are known only for symmetric electrolytes (that is, $N = 2$, $z_1 = -z_2 = Z$ where Z is positive) in certain special geometries.

Half Plane. In front of an infinite charged flat plate (defined as $z = 0$) charged to a fixed ζ potential, the solution to Eq. (11) is

$$\tanh\left[\frac{Ze\phi}{4k_B T}\right] = \tanh\left[\frac{Ze\zeta}{4k_B T}\right]\exp(-\kappa z) \tag{14}$$

where $z > 0$. This solution can also be used to describe the Debye layers at the walls of a planar channel provided that the channel walls are sufficiently far apart that their Debye layers do not overlap. Clearly, if ϕ and ζ are both sufficiently small that the hyperbolic tangent terms can be approximated by their respective one term Taylor

expansion, $\tanh x = x + \ldots$, then the Debye–Hückel theory $\phi(z) = \zeta \exp(-\kappa z)$ is recovered.

Between Parallel Plates. An exact solution of Eq. (11) can be written [4] for a pair of plates separated by a distance $2H$ and each held at a potential ζ. The origin $z = 0$ is chosen on one of the plates so that the second plate is located at $z = 2H$. It is convenient to introduce the intermediate variables $k = \exp(-Ze\zeta/k_B T)$ and Φ defined by $\sin\Phi = k^{-1/2}\exp[-Ze\phi/(2k_B T)]$. Then the solution may be expressed in terms of the elliptic integral $F(\Phi, k)$ defined as

$$F(\Phi, k) = \int_0^{\Phi} \frac{d\theta}{(1 - k^2 \sin^2\theta)^{1/2}} \,. \tag{15}$$

This solution (originally due to Langmuir) is

$$\kappa z = 2k^{1/2}[F(\pi/2, k) - F(\Phi, k)] \,. \tag{16}$$

For small potentials (in the Debye–Hückel limit) this can be shown to reduce to

$$\phi(z) = \zeta \frac{\cosh[\kappa(H - z)]}{\cosh(\kappa H)} \tag{17}$$

Circular Cylinders. An analytical solution for the region inside infinitely long circular cylinders is available only for Eq. (12). The potential is

$$\phi(r) = \zeta \frac{I_0(\kappa r)}{I_0(\kappa a)} \tag{18}$$

where r is the radial distance and a is the radius of the cylinder.

Electro-Osmotic Flow

In the presence of fluid flow exact analytical solutions of the full electrokinetic equations are rare. An exceptional situation arises when the applied electric field and streamlines of the flow are both in a direction of homogeneity along which there is no variation of any physical quantity. In such cases, the effect of the external influence (such as the applied field) is to produce motion such that all movement of charges are along surfaces of constant charge density and therefore the equilibrium charge density is not altered by the flow. Examples of such a situation are

1. An electric field is applied parallel to a flat plate driving an electro-osmotic flow with streamlines that are also parallel to the plate.
2. An electric field is applied between a pair of parallel plates driving an electro-osmotic flow with streamlines that are also parallel to the plate.
3. An electric field is applied along the cylinder axis resulting in a flow along the axis of the cylinder.

The component of Eq. (1) in the flow direction then reduces to

$$\mu\nabla^2 \boldsymbol{u} - \rho_e^{(eq)} \nabla\phi^{(ext)} = \mu\nabla^2 \boldsymbol{u} + \frac{\varepsilon}{4\pi}\nabla^2\phi^{(eq)}\nabla\phi^{(ext)} = 0 \,, \tag{19}$$

where $\phi^{(eq)}$ is the potential distribution in the equilibrium EDL and $\nabla\phi^{(ext)}$ is the constant applied field in the homogeneous direction. This may be integrated to give the flow velocity at any location

$$\boldsymbol{u} = \frac{\varepsilon\nabla\phi^{(ext)}}{4\pi\mu}[\zeta - \phi^{(eq)}] \,. \tag{20}$$

If the solution to the problem of the equilibrium double layer $\phi^{(eq)}$ is known, then the velocity is determined by the above formula. Thus, the solutions to the respective flow problems for the equilibrium situations considered in the previous subsection are readily written down. Solution to the electrokinetic equations is facilitated if the Debye layer thickness λ_D may be assumed small compared to the characteristic channel width w_0. This however is not usually the case in nanochannels since w_0 and λ_D are both on the order of nanometers. Exact analytical solutions are therefore rare except in situations with a high degree of symmetry such as noted above.

Molecular Models

At scales approaching a nanometer or less, the continuum equations are entirely inappropriate. In such situations the fluid must be described as a collection of interacting atoms. The equations of motion of these atoms can be evolved in time by computer simulation, a procedure known as Molecular Dynamics. A very brief overview of Molecular Dynamics is provided here, for further details see the entry on that topic in this volume.

Dynamical Equations

The equations of motion of the individual atoms are given by the second law of Newton:

$$m_i \frac{d^2\boldsymbol{r}_i}{dt^2} = -\nabla_i V \,. \tag{21}$$

Here m_i is the mass of the ith atom and $\boldsymbol{r}_i$ is the position vector at time t. The symbol ∇_i indicates the gradient operator with differentiation with respect to the co-ordinates of the ith atom only, that is, in cartesian co-ordinates the right hand side has components $-\partial V/\partial x_i$, $-\partial V/\partial y_i$ and $-\partial V/\partial z_i$. The potential V which depends on the instantaneous location of every atom contains all the information

about how the atoms are held together within individual molecules as well as how two different molecules interact. A full determination of the potential V from first principles will require the solution of the quantum mechanical problem involving interactions of all of the nuclei and electrons. Such a computation is not practical in general but approximations that involve neglecting effects that are not dominant allow approximate interaction potentials to be obtained.

Interaction Potentials

First, the potential V is split into two parts, the *bonded* and *non-bonded* ones

$$V = V_{\text{bonded}} + V_{\text{non-bonded}}\,. \tag{22}$$

The first, V_{bonded} takes into account all of the forces that keep the atoms bound together into a molecule, the second, $V_{\text{non-bonded}}$ describe the interactions between the atoms within a molecule with those within another molecule.

The Bonded Potential As a simple example one might consider a diatomic molecule. Here one may write

$$V_{\text{bonded}} = \frac{1}{2}k_r(r - r_{\text{e}})^2 \tag{23}$$

where r_{e} is the equilibrium bond length, r is the instantaneous distance between the atoms and k_r is a positive constant (like a *spring constant*) that determines the frequency of oscillation of the dumbell shaped molecule about its equilibrium shape.

If there are three atoms 1, 2 and 3 connected by two bonds I and II then there will be two terms like Eq. (23), one for bond I and one for bond II with possibly different values of k. In addition, there would be a contribution

$$V_{\text{bonded}} = \frac{1}{2}k_\theta(\theta - \theta_{\text{e}})^2 \tag{24}$$

due to the fact that the bond can flex so that the bond angle undergoes small oscillations about the equilibrium value $\theta = \theta_{\text{e}}$.

If there are four atoms then there is an additional mode of distortion of the molecule. Atoms 1, 2 and 3 always lie on a plane, call this the plane 123. This plane however may not coincide with the plane 234 on which atoms 2, 3 and 4 lie. If it does, then we have a coplanar molecule, otherwise there is a non-zero angle ϕ between the two planes which could change as the molecule moves around and interacts with neighboring ones (see Fig. 1). In general there is a contribution to the potential that determines changes in ϕ. This piece of the bonded potential is usually written as

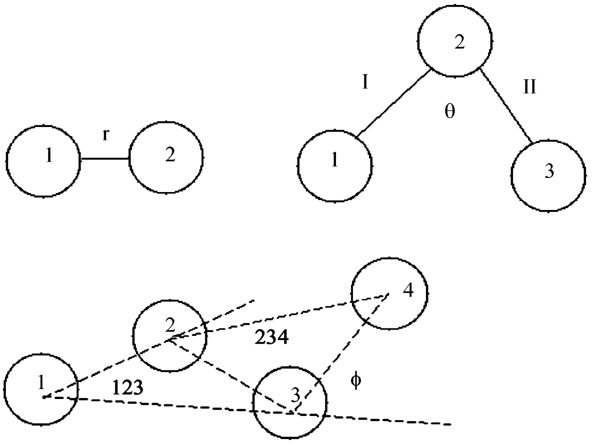

Electrokinetic Flow and Ion Transport in Nanochannels, Figure 1 Sketch showing the bonded interactions in the case of two, three and four atom molecules in an MD simulation

$$V_{\text{bonded}} = \frac{1}{2}\sum_{m=1}^{\infty} k_\phi^{(m)}\left[1 + \cos(m\phi - \phi_m)\right]. \tag{25}$$

The right hand side is nothing but one way of writing a Fourier series expansion of the potential in ϕ. Since the potential has to be periodic with period 2π it can always be written in this way for some values of the constants $k_\phi^{(m)}$ and ϕ_m. For $m = 1$, the ϕ dependence is given by $[1 + \cos(\phi - \phi_1)]$. This is identical to the potential that describes the motion of a simple pendulum where ϕ is the angular displacement and $\phi = \phi_1$ the position of stable equilibrium. It is useful to recall that the pendulum has two kinds of motion, oscillations about the position of stable equilibrium and rotation about its point of support. Similarly, Eq. (25) allows both small oscillations about equilibrium as well as full 360° rotations. For example, the ethane molecule C_2H_6 rotates very easily around the C–C bond. For longer molecules V_{bonded} is constructed by first identifying all bonds between atom pairs and adding up the contributions of the form of Eq. (23). Then all the bond angles are identified and each contributes a term like Eq. (24). Finally, all of the angles between planes of atoms are identified and each such angle will result in a contribution of type Eq. (25). This procedure describes the simplest kind of bonded interactions possible. The forms of Eqs. (23), (24) and (25) are not the only possible description of these interactions, different cross terms (such as *stretch-bend*) may be included for greater accuracy.

The Non-Bonded Potential It is convenient to decompose the non-bonded potential into 1-body, 2-body, 3-body, ... interactions:

$$V_{\text{non-bonded}} = \sum_{i} U_i + \sum_{i<j} U_{ij} + \cdots \tag{26}$$

Here U_i is the potential of atom i due to some external field (such as an applied electric field or due to confinement in a finite domain such as within the walls of a nanotube). The i–j pair interactions describe the force between atoms i and j in the absence of all other atoms. This however is only an approximation to the true force, because the presence of a third atom in the vicinity would generally cause some distortion in the electron cloud around atoms 1 and 2 and therefore change the interaction force. Such three and higher body interactions are however relatively small and are usually neglected. That is, the series Eq. (26) is usually truncated at the second term. We now discuss the most common types of pair interactions.

If a pair of atoms i–j on two different molecules carry a net charge of Q_i and Q_j then there is a Coulomb contribution to the non-bonded potential that arises out of this pair interaction

$$V_{\text{non-bonded}} = \frac{Q_i Q_j}{r_{ij}} \tag{27}$$

(in CGS units) where r_{ij} is the distance between the pair. There is an analogous contribution for each distinct pair of atoms and the total potential is given by the sum of all such terms. For example, in an ionic solution the ions will interact via such Coulomb interactions. In addition, every pair of atoms (charged or not) that sit on different molecules interact via an intermolecular potential for which most often the Lennard-Jones form is used:

$$V_{\text{non-bonded}} = 4\varepsilon \left[\left(\frac{\sigma}{r_{ij}}\right)^{12} - \left(\frac{\sigma}{r_{ij}}\right)^{6} \right]. \tag{28}$$

The parameters ε and σ depends on the kinds of atoms in the i–j pair. The important thing about the ▶Lennard-Jones potential is that it is repulsive at short range (characterized by a length scale σ) and attractive at long range with the attractive interaction inversely proportional to the sixth power of the distance. The short range repulsion is caused by the mutual repulsion of the electron clouds of the atoms that keep the atoms apart. The attractive interaction at long range is known as the ▶Van-der Waals attractions. For an explanation of its origin the reader is referred to the contribution on that subject in this volume. In addition particular classes of applications require the addition of special kinds of interaction potentials (e. g. hydrogen bonds, hydrophobic effects etc.) and these are described in more specialized books and papers.

Numerical Integration

Computer simulation of the molecular motion calls for the numerical integration of Eq. (21) for each atom starting from some random initial conditions. Various algorithms for doing this are known with their advantages and drawbacks. The simplest most robust and almost universally used technique is the Velocity-Verlet algorithm also known as the *Leap Frog Method*. To apply this algorithm, we first write Eq. (21) as a pair of first order equations:

$$\frac{\mathrm{d}\boldsymbol{r}_i}{\mathrm{d}t} = \frac{\boldsymbol{p}_i}{m_i} \tag{29}$$

$$\frac{\mathrm{d}\boldsymbol{p}_i}{\mathrm{d}t} = \boldsymbol{f}_i = -\nabla_i V\,. \tag{30}$$

Here $\boldsymbol{p}_i$ is the momentum of atom i and $\boldsymbol{f}_i$ is the force on it. The velocity Verlet algorithm with step size δt is:

$$\boldsymbol{p}_i(t + \frac{1}{2}\delta t) = \boldsymbol{p}_i(t) + \frac{\delta t}{2}\boldsymbol{f}_i(t) \tag{31}$$

$$\boldsymbol{r}_i(t + \delta t) = \boldsymbol{r}_i(t) + \boldsymbol{p}_i(t + \frac{1}{2}\delta t)\frac{\delta t}{m_i} \tag{32}$$

$$\boldsymbol{p}_i(t + \delta t) = \boldsymbol{p}_i(t + \frac{\delta t}{2}) + \frac{\delta t}{2}\boldsymbol{f}_i(t + \delta t). \tag{33}$$

Key Research Findings

The research literature on nanopores or nano-channels of biological origin is vast and spans more than half a century. These channels are a fraction of a nanometer to a few nanometer wide and are made of proteins embedded in lipid bi-layer membranes. The main scientific questions here relate to the physical mechanism of selectivity and gating, that is, questions such as what makes a sodium channel permeable to only sodium ions but not to potassium or calcium ions which are very similar. Further, by what physical mechanism do these channels open and close in response to voltage changes, ligand binding and other events? Electrokinetic flows is usually not the focus in this area of study and hence this is an area that we do not touch upon. The reader whose primary interest is in nanopores in the biological context could use [1] as an introduction to that subject.

In the realm of artificial nano-channels in the biotechnology context, a key issue concerns the electrical conductance of such channels. Artificial nano-channels are

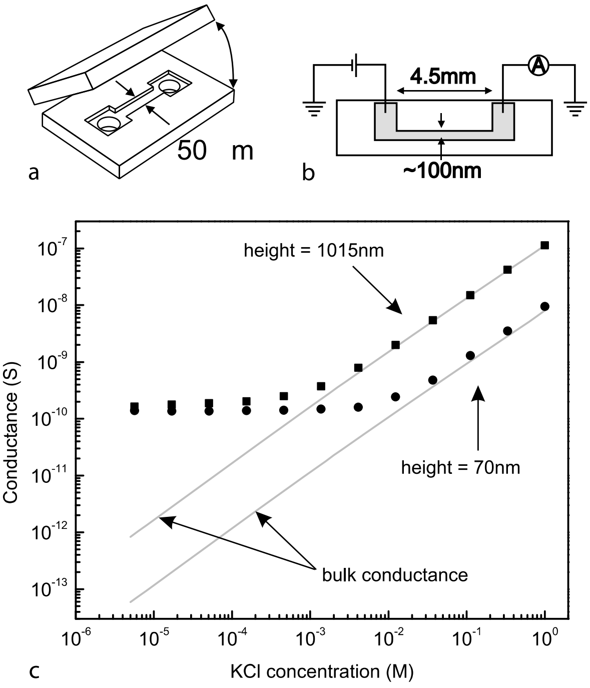

Electrokinetic Flow and Ion Transport in Nanochannels, Figure 2 The measured conductance of a nanochannel as a function of electrolyte concentration showing the transition from the expected behavior (lines) to a conductance determined by the surface charge. Panels (**a**) and (**b**) show the set up of the experiment [11]

tens of nanometers wide, so a length of the channel equal to its diameter contains of the order of a million water molecules. The interface between the channel wall and the water that it contains typically has an electrostatic charge which is characterized by its zeta-potential typically in the range of tens of millivolts. In an ionic solution the wall charge results in the formation of a Debye Layer of counter-ions next to it. Nano-channels differ from micro-channels with respect to the thickness of this Debye layer relative to the channel diameter: whereas in microchannels this fraction is extremely small, in a nanochannel it is typically of order unity. As a result, the conductance of nano-channels differ from the bulk conductance (conductance per unit volume of the electrolyte in the absence of confining walls multiplied by the volume of the channel). The channel conductance is found to depend on the electrolyte concentration as well as on the surface charge density of the channel. The dependence is shown in Fig. 2 and may be summarized as follows: at sufficiently high concentrations of the electrolyte the measured conductance approaches the bulk conductance which is proportional to the electrolyte concentration. As the concentration is lowered, the conductance deviates from the proportionality relation and approaches a value independent of the concentration. This constant value is higher the higher the surface charge density is in the nano-channel. Further, the transition from constant to proportionate behavior with respect to the electrolyte concentration shifts upwards with higher surface charge. This is because at high electrolyte concentrations, the Debye Layer is very thin so that most of the current is carried by the ions in the core of the channel. Thus, the conductance approaches the bulk conductance. At low concentrations, there are very few co-ions and the nano-channel attracts a sufficient number of counter-ions so that the channel as a whole is charge neutral. The conductance is determined by the number of such counter-ions present and this is determined by the surface charge not on the ion density in the bulk electrolyte. Thus, the conductance becomes independent of the electrolyte concentration and increases with the surface charge. A quantitative calculation based on the above physical picture gives reasonably good agreement with the measured data as seen in Fig. 2. In view of the fact that the conductance is controlled by the surface charge, it has been suggested that it may be possible to control the conductance of a channel by controlling the surface charge by an externally applied voltage. In fact, not just the electrical conductance but the flux of macro-ions can be controlled this way creating a *nano-transistor* that can be tuned to be selectively permeable to specific biomolecules much like the "gated" nanopores in biological systems.

Just as a voltage can drive charged macro-ions through nanopores, long chains of such ions or ▶polyelectrolytes (charged polymers) can also be driven through nanopores (see Fig. 3 and Fig. 4). Research in this area is driven by the possibility of developing a new technology for super

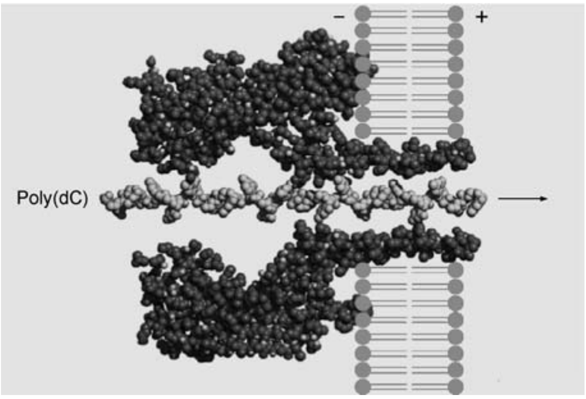

Electrokinetic Flow and Ion Transport in Nanochannels, Figure 3 Molecular model showing a single strand of poly(dC) DNA passing through an α-hemolysin protein pore in a lipid bi-layer membrane. The surrounding water molecules have not been shown [12]

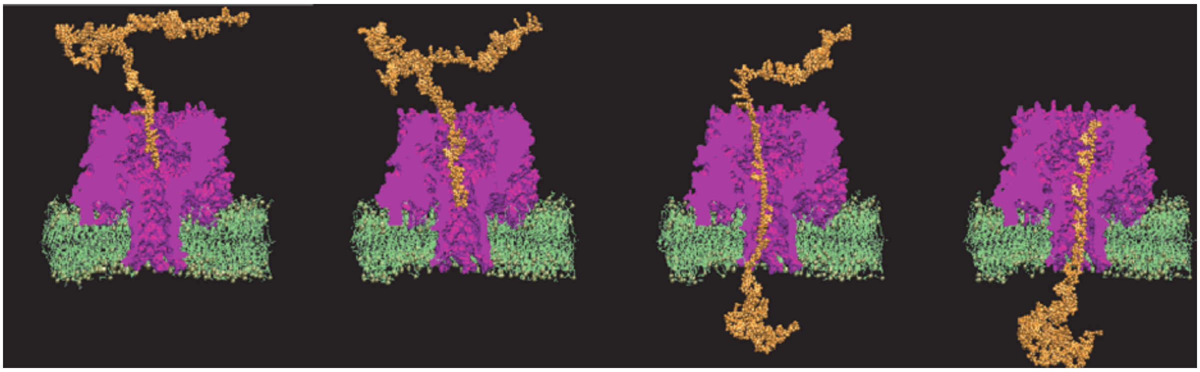

Electrokinetic Flow and Ion Transport in Nanochannels, Figure 4 A sequence of four frames (movie available on the online version of this volume) from a MD simulation movie showing a single stranded DNA molecule being pulled through an alpha Hemolysin nanopore by the application of an electric field [13]

fast DNA sequencing. The central fact is that the passage of a polyelectrolyte through a nanopore produces a measurable change in the pore conductance. It has been shown that using this effect DNA in solution can be detected and counted at the single molecule level. Further, based on the duration of the blockage the length of the DNA can be characterized with a margin of error of the order of a few tens of bases. Using a combination of translocation time and intensity of the current blockage, homopolymers of DNA and RNA made of pyridine bases can be distinguished from pyrimidines. Furthermore, block co-polymers such as AAAAAA.....CCCCC..... containing more than about 30 or so repeating units can be distinguished from other similar structures. A fundamental theoretical question in this area related to electrokinetic flows is: what determines the translocation time of a single polyelectrolyte across a nanopore? It has been shown that the shape of the distribution function for translocation times can be explained by means of a probabilistic *drift diffusion process*. A calculation of the average speed of translocation of polyelectrolytes of moderate size based on the continuum electrokinetic equations yields values consistent with the measured ones for solid state nanopores (diameter ~ 10 nm). The majority of theoretical papers in this area have focussed on the issue of how the mean translocation time scales with the length of the polymer and there appears to be different scaling regimes for short vs. long polymers (see [5] and references within).

Another key question relates to electroosmotic flow of water in nanochannels where the focus is on the question on whether or not any deviations from the predictions of the classical continuum electrokinetic equations is observable. Computer simulations by MD has shown that the flow profile shows considerable deviation from the classical regime in certain parameter ranges that can be attributed to a variety of effects (hydrogen bonding of water to negatively charged surfaces, the effect of charge oscillations due to correlations etc.) A fundamental question which is broader than the subject of electrokinetic flows concerns the applicability of the no-slip boundary condition to micro/nanoscale flows. It appears that the so called *Navier slip boundary conditions* $b\,\partial_z U + U = 0$ better describes the flow at small scales where U is the velocity along the impermeable surface and z is the direction perpendicular to it. The value of b depends on the wetting properties of the surface among other things and is closer to *no-slip* ($b = 0$) for hydrophyllic surfaces. Further discussion on this issue may be found in the contribution *Boundary Slip of Liquids* in this volume.

Future Directions for Research

The subject of flow and transport in nanochannels is a very young one and there are many avenues for theoretical as well as experimental investigations and the potential for many novel devices that might be developed as a result of these investigations. The idea of a *Nano Transistor* that can be tuned to be selectively permeable to certain macromolecules while blocking others is an area that may see some rapid development on the practical side. The same can be said about the idea of sequencing biopolymers using nanopore translocation. There are deep theoretical questions surrounding the issue of how fluid and ions flow through nanochannels and in what ways such transport differs from expectations based on classical hydrodynamics and the Poisson-Boltzmann equation [10]. The effect of correlations, finite size of molecules, hydrogen bonding and other short range interactions, wettability are all

expected to play a role and it is in extending our understanding of fluid flow and ion transport to account for these effects that the future challenge lies.

Cross References

- ► Boundary Slip of Liquids
- ► Electric Double Layer Interaction
- ► Electric Double Layers
- ► Electroosmotic Flow (DC)
- ► AC Electro-Osmotic Flow
- ► Gas Flow in Nanochannels
- ► Interfacial Electrokinetic Flow
- ► Ion Channel
- ► Micro- and Nanoscale Gas Dynamics
- ► Molecular Dynamics Simulation Method
- ► Nanochannel Fabrication
- ► Nanofluidic Systems for Single Molecule Detection
- ► Nanofluidics in Carbon Nanotubes
- ► Van der Waals Attraction Forces

References

1. Hille B (2001) Ion Channels of Excitable Membranes. Sinauer Associates Inc., Sunderland
2. Kasianowicz JJ, Brandin E, Branton D, Deamer DW (1996) Characterization of individual polynucleotide molecules using a membrane channel. Proc Natl Acad Sci USA 93:13770–13773
3. Karnik R, Fan R, Yue M, Yang P, Majumdar A (2005) Electrostatic control of ions and molecules in nanofluidic transistors. Nano Lett 5(5):953–948
4. Levine S, Marriott JR and Robinson K (1975) Theory of electrokinetic flow in a narrow parallel-plate channel. J Chem Soc Faraday Trans 71:1–11
5. Ghosal S (2006) Electrophoresis of a polyelectrolyte through a nanopore. Phys Rev E 74:041901
6. Deamer DW, Akeson M (2000) Nanopores and nucleic acids: prospects for ultrarapid sequencing. Trend Biotech 18:147–151
7. Luo K, Huopaniemi I, Ala-Nissila T, Ying S (2006) Polymer translocation across a nanopore under an applied external field. J Chem Phys 124:114704-1–114704-7
8. Heng JB, Aksimentiev A, Ho C, Dimitrov V, Sorsch T, Miner J, Mansfield W, Schulten K, Timp G (2005) Beyond the gene chip. Bell Labs Tech J, 10(3):5–22
9. Lauga E, Brenner MP and Stone HA (2005) Chapter 15 Microfluidics: The No-Slip Boundary Condition. In: Foss J, Tropea C, Yarin A (eds) Handbook of Experimental Fluid Dynamics. Springer, New York
10. Qiao R, Aluru NR (2005) Atomistic simulation of KCl transport in charged silicon nanochannels: Interfacial effects. Colloid Surf 267:103–109
11. Stein D, Kruithof M, Dekker C (2004) Surface-Charge-Governed Ion Transport in Nanofluidic Channels. Phys Rev Lett 93(3):035901-1–035901-4
12. Deamer DW, Akeson M (2000) Nanopores and nucleic acids: prospects for ultrarapid sequencing. Trends Biotechnol 18:147–151
13. Aksimentiev A (2006) private communication

Electrokinetic Flow in Porous Media

Chun Yang[1], Yuejun Kang[2], Xiaoyang Huang[1]

[1] School of Mechanical and Aerospace Engineering, Nanyang Technological University, Singapore, Singapore

[2] Department of Mechanical Engineering, Vanderbilt University, Nashville, TN, USA

mcyang@ntu.edu.sg

Synonyms

Electroosmotic flow in porous media; Electroosmosis in porous media

Definition

A porous medium is referred to as a solid frame or matrix permeated by an interconnected network of pores (voids) filled with a fluid (liquid or gas). In the field of micro- and nanofluidics, the term electroosmotic flow (usually interchangeable with electroosmosis or electrokinetic flow) is defined as the migration of bulk ionic liquid due to the interaction between an applied electric field tangentially along a charged surface and the excess net charge density in the electric double layer of such a charged surface. Therefore, electrokinetic flow in porous media is referred to as the motion of bulk ionic liquid flowing through a porous medium as a result of the interplay of an applied electric field and the excess charge density in the electric double layer of the charged porous structure.

Overview

Fluid flow through porous media is a subject of much interest and has a wide spectrum of applications in applied science and engineering. The discovery of electrokinetic flow in porous media can be traced back to the early 1800s when Reuss observed water migration through porous clay diaphragms under an applied electric field. Applications of electrokinetic flow in porous media can be found in many technological processes, such as dewatering of waste sludge and removing poisonous heavy metal ions from contaminated soils for environmental remediation [1].

The charging mechanisms of the porous solid–liquid interface are complex, possibly including the asymmetric dipoles of water molecules residing at the solid–liquid interface, adsorption of ions, disassociation of ionic groups, charge separation, etc. The presence of surface charges will influence the distribution of nearby ions in the solution. Counter-ions (i. e., ions of opposite charge)

are attracted towards the surface, while co-ions (i. e., ions of like charge) are repelled from the surface. This electrostatic interaction, together with the random thermal motion of the ions, leads to the formation of the so-called *electric double layer* (EDL). The model of EDL was developed by Gouy and Chapman in 1906, and then improved by Stern in 1924 [1]. According to Stern's model, the EDL consists of two layers: a compact layer and a diffuse layer. The compact layer, usually less than 1 nm, exists immediately next to the solid surface, where counter-ions are strongly attracted to the solid surface and are thus immobile. The diffuse layer of the EDL is the layer from the compact layer to the bulk liquid, and its thickness ranges from several nanometers to micrometers, depending on liquid properties. Compared to the ions in the Stern layer, the ions in the diffuse layer are less influenced by the charged surface and hence are mobile.

Within the diffuse layer of the EDL, there is an excess of counter-ions over co-ions, and thus the net charge density is not zero so as to neutralize the surface charge. If an electric field is applied tangentially along a charged surface, the electric field will exert a Coulombic force on the ions in the diffuse layer, resulting in a net migration of the liquid in the EDL region. This is called *electroosmosis* (EO). In a charged microcapillary, due to viscous forces the flow can be developed beyond the EDL region to the rest of the liquid in the microcapillary, leading to a bulk *electroosmotic flow* (EOF).

With the rapid development of micro- and nanofluidics in the past decade, electroosmosis has attracted wide attention due to its pumping capability. Compared to conventional mechanical pumping, EO pumping has numerous advantages including ease of fabrication and control, no need for moving parts, high reliability, no noise, etc. Extensive theoretical and experimental studies on EOF have been reported to further physical understanding and realize more advanced applications of this electrokinetic phenomenon.

Since electroosmosis is an interfacial phenomenon, use of capillaries packed with solid porous structures can greatly enlarge the interfacial area, and thus significantly enhance the pressure-building capacity of EOF. Taking advantage of such high pressure-building capacity of the EOF in packed capillaries, two technologies have been developed, namely capillary electrochromatography [2] for chemical analyses and molecular detection, and high-performance electrokinetic micropumps [3]. The first effort made to design electrokinetic micropumps may be attributed to Paul et al. who reported the ability to generate high pressures using electrokinetic pumping of liquid through porous media. Pressures in excess of 8000 psi have been achieved using silica capillaries packed with micrometer-size silica beads. Since then, a variety of electroosmotic micropumps have been developed [4].

Of the numerous methods developed to pack stationary porous medium/column in a microcapillary, two widely used approaches involve the packed beads column and the in situ polymerized monolithic column [5]. The preparation of the packed beads column includes the fabrication of retaining frits within a microcapillary as well as subsequent packing of micro-sized silica particles into the capillary. To avoid the problems associated with frit formation and bead packing, an alternative method is to prepare the monolithic column by performing in situ silicate- or photo-polymerization within a capillary using either thermal or UV initialization of polymer mixture solutions.

E

Basic Methodology

Method of Volume Averaging

In a natural porous medium, the distribution of pores with respect to shape and size is irregular. On the pore scale (microscopic scale) the flow quantities such as velocity, pressure, etc., are also irregular. But in typical experiments the quantities of interest are measured over areas that cross many pores and such space-averaged (macroscopic) quantities change in a regular manner with respect to space and time and hence are amenable to theoretical treatment. A macroscopic variable is defined as an appropriate mean over a sufficiently large *representative elementary volume* (REV). It is assumed that the result is independent of the scale of the REV. As illustrated in Fig. 1a, the length scale of the REV is much larger than the pore scale, but considerably smaller than the length scale of the macroscopic flow domain.

Under the volume averaging method, two major geometric constraint factors to characterize a porous medium are called porosity and tortuosity. The porosity is defined as $\phi = V_f/V$, where V_f and V are the void and total volumes of the porous medium, respectively, as illustrated in Fig. 1b. The other factor, as illustrated in Fig. 1c, tortuosity includes the non-alignment of most flow channels with the electric field, which is applied along the capillary axis. The fluid flow in a capillary packed with solid spherical particles will occur only within the interparticulate spaces. The individual flow channels comprise a highly complex, directionally non-uniform network, of which only a fraction will be aligned axially with the electric field. Most flow channels will be off-axis with respect to the field resulting in a lower effective field strength (decreased by a factor of $\cos\theta$). In addition, the fluid flowing in an off-axis channel must travel a greater distance (increased by a factor of $1/\cos\theta$) for a given displacement along the capillary axis. The tortuosity is defined

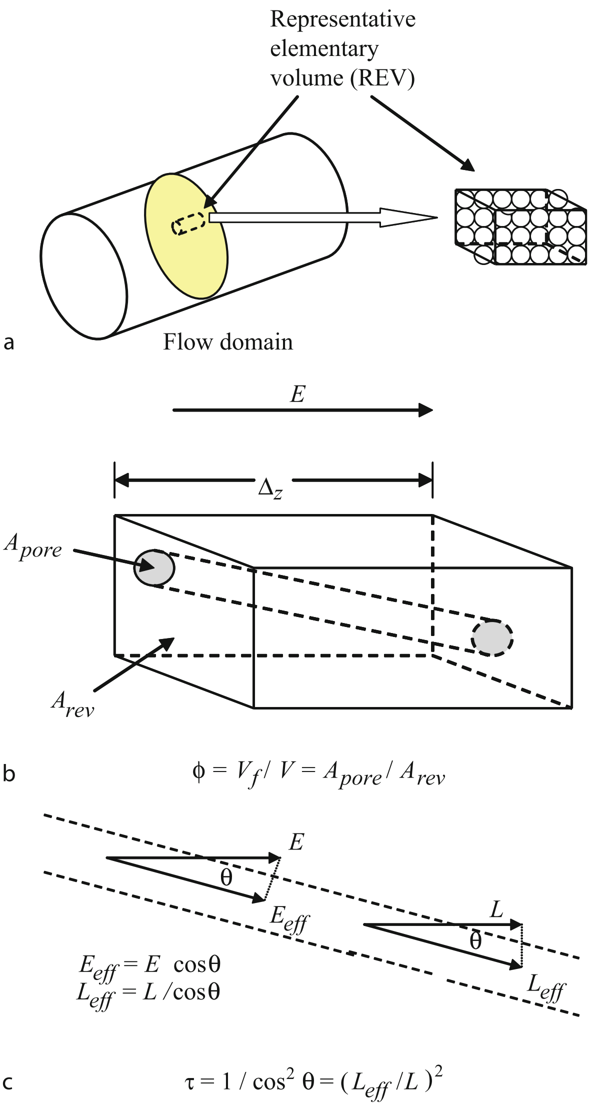

Electrokinetic Flow in Porous Media, Figure 1 Schematic illustration of (**a**) representative elementary volume (REV), (**b**) porosity, and (**c**) tortuosity. The length scale of the REV is much larger than the pore scale, but considerably smaller than the length scale of the macroscopic flow domain

as $\tau = 1/\cos^2\theta = (L_{\rm eff}/L)^2$, where $L_{\rm eff}$ is the effective length of travel for flow along the pore path and L is the physical length of the porous structure [6]. Combination of above factors results in the reduction of the velocity component along the axis by a factor of ϕ/τ.

For simplicity, we consider a charged cylindrical microcapillary of radius $R_{\rm w}$ packed with charged mono-sized microparticles of diameter $d_{\rm p}$. The liquid in the microcapillary is assumed to be an incompressible, Newtonian, mono-valence electrolyte of density ρ and viscosity μ. The zeta potentials of the inner wall surface and the particle

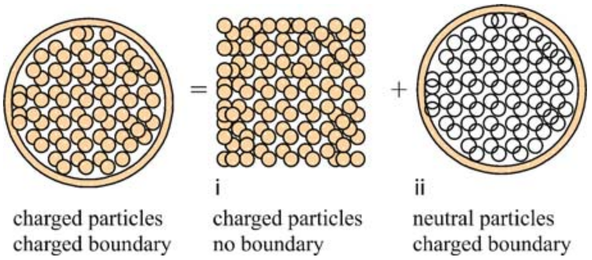

Electrokinetic Flow in Porous Media, Figure 2 Schematic illustration of decomposition of the overall macroscopic EOF velocity in a packed capillary into two separate components due to: (i) the contributions from homogeneous densely packed with charged microparticles, and (ii) the contributions from the charged capillary wall with neutral packing

surface are $\zeta_{\rm w}$ and $\zeta_{\rm p}$, respectively. When an external electric field, E_0, is applied along the axis of the microchannel, the electrolyte in the microcapillary will move due to the electroosmosis resulting from the interaction of the EDL (close to the interface of the particles as well as the channel wall) and the applied electric field. Joule heating effect due to axially imposed electric field is ignored in our model development. The overall macroscopic EOF velocity in the packed capillary is decomposed into two separate components due to the contribution from homogeneous densely packed charged microparticles and the contribution from the charged capillary wall with neutral packing, as illustrated in Fig. 2.

Macroscopic EOF in Homogeneous Charged Microspheres

Interstitial EOF Velocity

The present model development is based on a semi-heuristic model of flow through solid matrices using the concept of hydraulic diameter, which is also known as the *Carman–Kozeny theory* [7]. The theory assumes the porous medium to be equivalent to a series of parallel tortuous tubules. The characteristic diameter of the tubules is taken to be a hydraulic diameter or effective pore diameter; this diameter is conventionally defined as [6]

$$d_{\rm pore} = \frac{4 \times \text{Void Volume}}{\text{Surface Area}} = \frac{4\,\phi_\infty}{A_{\rm o}(1-\phi_\infty)} \qquad (1)$$

where ϕ_∞ is the average porosity of the porous medium. $A_{\rm o}$ is the volumetric or specific area based on the solid volume, i. e., $A_{\rm fs}/V_{\rm s}$, where $A_{\rm fs}$ is the interfacial area between the fluid and the solid phase and $V_{\rm s}$ is the solid volume. For spherical particles considered in this work $A_{\rm o} = 6/d_{\rm p}$, where $d_{\rm p}$ is the diameter of spherical particles. So the

hydraulic diameter can be expressed as

$$d_{\text{pore}} = \frac{2\,\phi_\infty}{3\,(1-\phi_\infty)} d_{\text{p}} \tag{2}$$

The interstitial tubules are cylindrical with an effective diameter (pore size) $d_{\text{pore}} = 2R_{\text{pore}}$. The inner wall of the cylindrical tubules is charged with zeta potential ζ_{p}. Because of the low Reynolds number flow, the interstitial EOF velocity $u_{\text{i}}(r)$ in each tubule is governed by the Stokes equation [7]

$$\mu \frac{1}{r}\frac{\text{d}}{\text{d}r}\left[r\frac{\text{d}u_{\text{i}}(r)}{\text{d}r}\right] + E_0\rho_{\text{e}}(r) + P_{\text{z}} = 0 \quad (0 \leqslant r \leqslant R_{\text{pore}}) \tag{3}$$

where $P_{\text{z}} = \Delta P/L$ is the global pressure gradient along the flow direction (L is the physical length of the flow domain). In the present discussion, no global pressure gradient is applied, i. e., $P_{\text{z}} = 0$. It should be pointed out here that from a microscopic point of view, a local backpressure gradient may be induced where the EOF becomes non-uniform due to the complicated geometry and packing conditions. For instance, at narrow constrictions the local electric field strength becomes higher if the porous packing has a lower permittivity than the working fluid. As we know, the EOF velocity is proportional to the electric field strength. Thus the local EOF tends to be strengthened to increase local velocity. When the EOF is non-uniform, local pressure-driven backflow must be induced to maintain the local mass conservation [8]. However, the geometrical non-uniformity and the induced local pressure are highly random within the bulk packing except at the end of the packed capillary – the interface of the retaining frits, where the flow path may subject to drastic decrease in cross-sectional area, depending on the quality of the frits. In the present discussion the end frit effect is ignored and we focus on the electroosmosis-driven flow through the porous packing. Under the space averaging method, the overall effect of the random local pressure gradient vanishes. Therefore the porous media is assumed as equivalent parallel tubules of uniform cross-sectional area without global pressure gradient.

Parameter $\rho_{\text{e}}(r)$ in Eq. (3) is the local volumetric charge density due to the presence of the EDL inside each interstitial tubule, and it is governed by the Poisson equation [1]:

$$\frac{1}{r}\frac{\text{d}}{\text{d}r}\left[r\frac{\text{d}\psi_{\text{i}}(r)}{\text{d}r}\right] = -\frac{\rho_{\text{e}}(r)}{\varepsilon_{\text{r}}\varepsilon_0} \quad (0 \leqslant r \leqslant R_{\text{pore}}) \tag{4}$$

where ε_{r} is the dielectric constant of the electrolyte and ε_0 is the permittivity of vacuum. Substituting Eq. (4) into Eq. (3), and using the following boundary conditions

$$\left.\frac{\text{d}u_{\text{i}}}{\text{d}r}\right|_{r=0} = 0 \quad \left.\frac{\text{d}\psi_{\text{i}}}{\text{d}r}\right|_{r=0} = 0 \tag{5a}$$

$$u_{\text{i}}|_{r=R_{\text{pore}}} = 0 \quad \psi_{\text{i}}|_{r=R_{\text{pore}}} = \zeta_p \tag{5b}$$

we can obtain an analytical expression for the velocity distribution, which takes the form

$$u_{\text{i}}(r) = -\frac{\varepsilon_{\text{r}}\varepsilon_0}{\mu}E_0\zeta_{\text{p}}\left[1 - \frac{\psi_{\text{i}}(r)}{\zeta_{\text{p}}}\right] \tag{6}$$

Under the volume averaging method, the macroscopic superficial velocity (also called the Darcy velocity) of the fluid over the representative elementary volume can be expressed by taking into account the tortuosity τ and the porosity ϕ, as

$$\begin{aligned} u_{\text{Di}} &= \frac{\phi}{\tau}\langle u_{\text{i}}\rangle = \frac{\phi}{\tau}\frac{2}{R_{\text{pore}}^2}\int_0^{R_{\text{pore}}} r u_{\text{i}}(r)\text{d}r \\ &= -\frac{\varepsilon_{\text{r}}\varepsilon_0}{\mu}E_0\zeta_{\text{p}}\frac{\phi}{\tau}(1-G) \end{aligned} \tag{7}$$

where

$$G = \frac{2}{\zeta_{\text{p}}R_{\text{pore}}^2}\int_0^{R_{\text{pore}}} r\psi_{\text{i}}(r)\text{d}r$$

and $\phi = \phi(r)$ is the local porosity distribution of the porous medium. In the literature, $\phi(r)$ is assumed to take a form of [7]

$$\phi(r) = \phi_\infty\left[1 + C_0\exp\left(-N\frac{R_{\text{w}}-r}{d_{\text{p}}}\right)\right] \quad (0 \leqslant r \leqslant R_{\text{w}}) \tag{8}$$

where $C_0 = 1.4$ and $N = 5$ are empirical constants.

Interstitial EDL Potential Field

The interstitial EDL potential distribution ψ_{i} in each tubule is governed by the Poisson–Boltzmann (P–B) equation, which is expressed as [1]

$$\frac{1}{r}\frac{\text{d}}{\text{d}r}\left[r\frac{\text{d}\Psi_{\text{i}}(r)}{\text{d}r}\right] = \kappa^2\sinh\Psi_{\text{i}}(r) \quad (0 \leqslant r \leqslant R_{\text{pore}}) \tag{9}$$

where $\kappa = (2n_0e_0^2/\varepsilon_{\text{r}}\varepsilon_0k_{\text{b}}T)^{1/2}$, dimensionless EDL potentials $\Psi_{\text{i}} = e_0\psi_{\text{i}}/k_{\text{b}}T$ and $\Psi_{\text{ip}} = e_0\zeta_{\text{p}}/k_{\text{b}}T$, e_0 is the elementary charge, n_0 is the ionic concentration in the bulk phase (i. e., far from the charged tubular wall), k_{b} is the Boltzmann constant, and T is the absolute temperature.

The boundary conditions given by Eq. (5a,5b) can be rewritten as

$$\left.\frac{\mathrm{d}}{\mathrm{d}r}\Psi_\mathrm{i}\right|_{r=0} = 0 \qquad \Psi_\mathrm{i}|_{r=R_\mathrm{pore}} = \Psi_\mathrm{ip} \tag{10}$$

Because of nonlinearity, the Poisson–Boltzmann equation (i. e., Eq. (9)) can be solved numerically. Using the Debye–Hückel approximation, an analytical solution of Eq. (9) for the EDL potential can be obtained as

$$\Psi_\mathrm{i}(r) = \Psi_\mathrm{ip}\frac{I_0(\kappa r)}{I_1(\kappa R_\mathrm{pore})} \quad \text{or} \quad \psi_\mathrm{i}(r) = \zeta_\mathrm{p}\frac{I_0(\kappa r)}{I_1(\kappa R_\mathrm{pore})} \tag{11}$$

where I_0 and I_1 are the zero-order and first-order modified Bessel functions, respectively.

Macroscopic EOF in a Charged Microcapillary Packed with Neutrally Charged Microspheres

EOF Velocity Field

Now we consider a charged cylindrical microcapillary of radius R_w, with the inner surface charged with zeta potential ζ_w. Inside the microchannel there are densely packed, neutrally charged spherical microparticles of diameter d_p. The Brinkman momentum equation, which originally was derived for a pressure-driven Darcy flow in porous media, then has been generalized by Brinkman to account for the inertial forces, pressure gradient, body forces, and shear stresses [6]. In the present situation, no pressure is exerted and hence no pressure gradient is present. Further, due to low Reynolds number flow in micro-sized pores, the macroscopic inertial force is ignored. The body force is the columbic force due to the interaction of the EDL and the external electric field. Thus the modified Brinkman momentum equation used for describing the macroscopic EOF of an incompressible, Newtonian electrolyte solution in a packed microcapillary under a steady state can be expressed as

$$\mu_\mathrm{eff}\frac{1}{r}\frac{\mathrm{d}}{\mathrm{d}r}\left[r\frac{\mathrm{d}u_\mathrm{Dw}}{\mathrm{d}r}\right] + E_0\phi\rho_\mathrm{ef}(r) - \left[\frac{\mu\phi u_\mathrm{Dw}}{K} + \rho\frac{F\phi u_\mathrm{Dw}^2}{\sqrt{K}}\right] = 0 \quad (0 \leqslant r \leqslant R_\mathrm{w}) \tag{12}$$

Here $u_\mathrm{Dw}(r)$ is the macroscopic EOF velocity (Darcy velocity) field through the neutrally charged porous medium inside the microcapillary. $\phi = \phi(r)$ is the local porosity distribution of the porous medium, determined by Eq. (8). The Darcy permeability K is defined by the *Carman–Kozeny* equation [7], $K = \phi^3 d_\mathrm{p}^2/a(1-\phi)^2$, and the inertial coefficient $F = b/\sqrt{a}\phi^{3/2}$, with $a = 150$ and $b = 1.75$ being the Ergun constants [6]. Parameter μ_eff is the effective fluid viscosity, a function of the fluid viscosity and the geometry of the permeable medium. For an isotropic porous medium, $\mu_\mathrm{eff}/\mu = 1/\phi\tau$ [6]. Parameter $\rho_\mathrm{ef}(r)$ is the average volumetric charge density due to the presence of the EDL, and it is assumed to satisfy the Boltzmann distribution:

$$\rho_\mathrm{ef}(r) = -2n_0e_0\sinh\left[\frac{e_0\psi_\mathrm{w}(r)}{k_\mathrm{b}T}\right] \quad (0 \leqslant r \leqslant R_\mathrm{w}) \tag{13}$$

Equation (12) is subject to the boundary conditions

$$\left.\frac{\mathrm{d}u_\mathrm{Dw}}{\mathrm{d}r}\right|_{r=0} = 0 \qquad \left.\frac{d\psi_\mathrm{w}}{\mathrm{d}r}\right|_{r=0} = 0 \tag{14a}$$

$$u_\mathrm{Dw}|_{r=R_\mathrm{w}} = 0 \qquad \psi_\mathrm{w}|_{r=R_\mathrm{w}} = \zeta_\mathrm{w} \tag{14b}$$

EDL Potential Field

The EDL potential distribution is governed by the Poisson–Boltzmann equation

$$\frac{1}{r}\frac{\mathrm{d}}{\mathrm{d}r}\left[r\frac{\mathrm{d}\Psi_\mathrm{w}(r)}{\mathrm{d}r}\right] = \kappa^2\sinh\Psi_\mathrm{w}(r) \quad (0 \leqslant r \leqslant R_\mathrm{w}) \tag{15}$$

which is subject to the boundary conditions

$$\left.\frac{\mathrm{d}\Psi_\mathrm{w}}{\mathrm{d}r}\right|_{r=0} = 0 \qquad \Psi_\mathrm{w}|_{r=R_\mathrm{w}} = \frac{e_0\zeta_\mathrm{w}}{k_\mathrm{b}T} \tag{16}$$

In the same fashion as for solving Eq. (9), the numerical method has to be used to solve Eq. (15). Of course, with the Debye–Hückel approximation, an analytical solution of the same format as Eq. (11) can also be sought, and is given by

$$\psi_\mathrm{w}(r) = \zeta_\mathrm{w}\frac{I_0(\kappa r)}{I_0(\kappa R_\mathrm{w})} \tag{17}$$

Analytical Solution of the Modified Brinkman Momentum Equation

No analytical solution is available for the modified Brinkman momentum equation (Eq. (12)), which can only be solved numerically. However, due to the low Reynolds number flow in the microcapillaries, we can safely ignore the high Reynolds number term, i. e., $\rho F\phi u_\mathrm{Dw}^2/\sqrt{K} \approx 0$. To emphasize only the electrokinetic wall effect, we can further assume that the porosity is uniform in the porous medium, i. e., $\phi = \phi_\infty$. Under these assumptions, we can

exclude the geometrical wall effect, and thus Eq. (12) can be simplified to

$$\frac{1}{r}\frac{\mathrm{d}}{\mathrm{d}r}\left(r\frac{\mathrm{d}u_{\mathrm{Dw}}}{\mathrm{d}r}\right)-\frac{a\tau(1-\phi_\infty)^2}{\phi_\infty d_\mathrm{p}^2}u_{\mathrm{Dw}} = -\frac{\phi_\infty^2\tau E_0}{\mu}\rho_\mathrm{e}(r) \quad (0\leqslant r\leqslant R_\mathrm{w}) \tag{18}$$

According to Poisson's equation

$$-\frac{\rho_\mathrm{e}(r)}{\varepsilon_\mathrm{r}\varepsilon_0}=\frac{1}{r}\frac{\mathrm{d}}{\mathrm{d}r}\left[r\frac{\mathrm{d}\psi_\mathrm{w}(r)}{\mathrm{d}r}\right] \tag{19}$$

Substituting Eq. (19) into Eq. (18) gives

$$\frac{1}{r}\frac{\mathrm{d}}{\mathrm{d}r}\left[r\frac{\mathrm{d}(u_{\mathrm{Dw}}-\eta\psi_\mathrm{w})}{\mathrm{d}r}\right]-\beta^2u_{\mathrm{Dw}}=0 \tag{20}$$

where

$$\eta=\frac{\phi_\infty^2\tau\varepsilon_\mathrm{r}\varepsilon_0E_0}{\mu} \quad \text{and} \quad \beta=\sqrt{\frac{a\tau(1-\phi_\infty)^2}{\phi_\infty d_\mathrm{p}^2}}$$

Introducing

$$v=u_{\mathrm{Dw}}-\eta\psi_\mathrm{w} \tag{21}$$

Eq. (20) becomes

$$\frac{1}{r}\frac{\mathrm{d}}{\mathrm{d}r}\left(r\frac{\mathrm{d}v}{\mathrm{d}r}\right)-\beta^2v=\beta^2\eta\psi_\mathrm{w} \tag{22}$$

In combination with Eq. (17), Eq. (22) can be rewritten as

$$\frac{1}{r}\frac{\mathrm{d}}{\mathrm{d}r}\left(r\frac{\mathrm{d}v}{\mathrm{d}r}\right)-\beta^2v=\beta^2\eta\zeta_\mathrm{w}\frac{I_0(\kappa r)}{I_0(\kappa R_\mathrm{w})} \tag{23}$$

This is a non-homogeneous zero-order modified Bessel equation, subject to the boundary conditions

$$\left.\frac{\mathrm{d}v}{\mathrm{d}r}\right|_{r=0}=0 \qquad v|_{r=R_\mathrm{w}}=-\eta\zeta_\mathrm{w} \tag{24}$$

A homogeneous solution and a particular solution to Eq. (23) are given respectively by

$$v_0(r)=-\frac{\kappa^2}{\kappa^2-\beta^2}\eta\zeta_\mathrm{w}\frac{I_0(\beta r)}{I_0(\beta R_\mathrm{w})} \tag{25a}$$

$$v_\mathrm{p}(r)=\frac{\beta^2}{\kappa^2-\beta^2}\eta\zeta_\mathrm{w}\frac{I_0(\kappa r)}{I_0(\kappa R_\mathrm{w})} \tag{25b}$$

The general solution to Eq. (23) can be constructed as

$$v(r)=v_0(r)+v_\mathrm{p}(r)=-\frac{\kappa^2}{\kappa^2-\beta^2}\eta\zeta_\mathrm{w}\frac{I_0(\beta r)}{I_0(\beta R_\mathrm{w})} + \frac{\beta^2}{\kappa^2-\beta^2}\eta\zeta_\mathrm{w}\frac{I_0(\kappa r)}{I_0(\kappa R_\mathrm{w})} \tag{26}$$

Making use of Eq. (17) and Eq. (21), we can obtain an analytical solution for the EOF velocity distribution in a charged microcapillary packed with neutrally charged microspheres:

$$u_{\mathrm{Dw}}(r)=v(r)+\eta\psi_\mathrm{w}(r) = -\frac{\varepsilon_\mathrm{r}\varepsilon_0}{\mu}E_0\zeta_\mathrm{w}\phi_\infty^2\tau\frac{\kappa^2}{\kappa^2-\beta^2} \times\left[\frac{I_0(\beta r)}{I_0(\beta R_\mathrm{w})}-\frac{I_0(\kappa r)}{I_0(\kappa R_\mathrm{w})}\right] \tag{27}$$

Overall Macroscopic EOF Velocity

We re-couple the two velocity components from the charged wall and the charged packing particles, and obtain the overall macroscopic EOF velocity in a charged cylindrical microcapillary with charged microsphere packing. The excess zeta potential is taken into account by such a treatment that the zeta potential of the capillary wall is replaced by $(\zeta_\mathrm{w}-\zeta_\mathrm{p})$, which is responsible for the electrokinetic wall effect:

$$u_\mathrm{D}=u_{\mathrm{Dw}}\left(1-\frac{\zeta_\mathrm{p}}{\zeta_\mathrm{w}}\right)+u_{\mathrm{Di}} \tag{28}$$

Specifically, in the case when $\zeta_\mathrm{w}=\zeta_\mathrm{p}$, Eq. (28) is reduced to $u_\mathrm{D}=u_{\mathrm{Di}}$, indicating no electrokinetic wall effect.

Key Research Findings

The mathematical models governing the EOF in a capillary packed with microspheres have been developed. In this section we will study how the EOF in a packed microcapillary is affected by the geometrical and electrokinetic parameters. In the calculations, the following parameters are bounded: ionic strength $=7.5\,\mu\mathrm{M}$, fluid viscosity $=1.0\times10^{-3}\,\mathrm{kg\,m^{-1}s^{-1}}$, density $=998\,\mathrm{kg\,m^{-3}}$, dielectric constant $=6.9\times10^{-10}\,\mathrm{C\,V^{-1}m^{-1}}$, and corresponding Debye length $\lambda_\mathrm{D}=0.11\,\mu\mathrm{m}$, which is the characteristic thickness of the EDL regime. Other fixed parameters are: zeta potential $=-100\,\mathrm{mV}$, porosity $=0.37$, and tortuosity $=1.5$. For all of the case studies, the reference velocity is $u_0=-\varepsilon_\mathrm{r}\varepsilon_0E_0\zeta_0/\mu$, where $E_0=300\,\mathrm{V\,cm^{-1}}$ and $\zeta_0=-100\,\mathrm{mV}$.

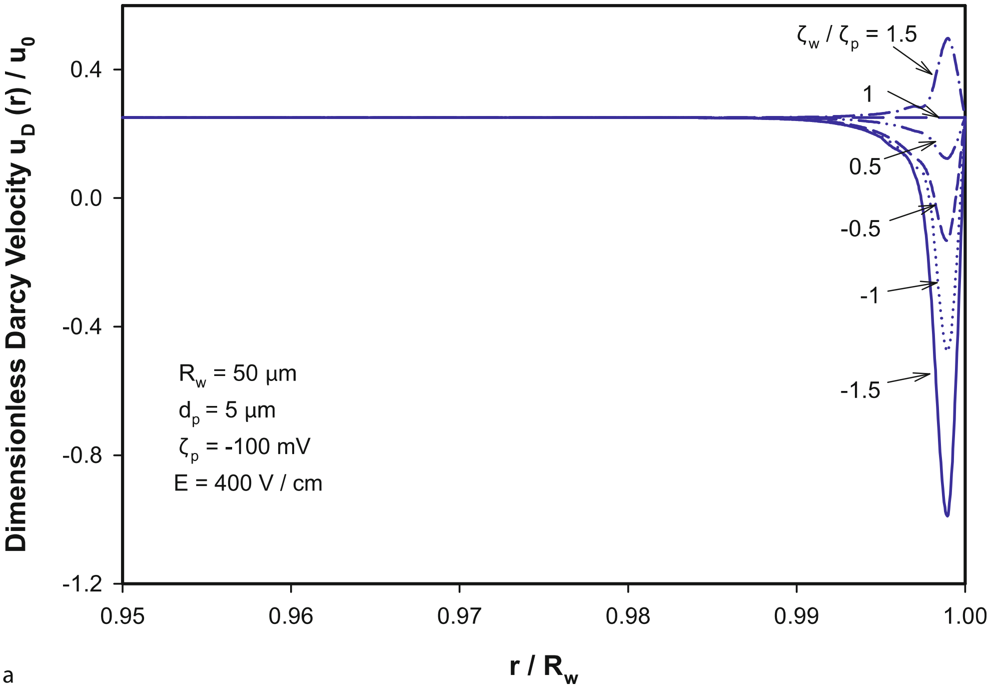

a

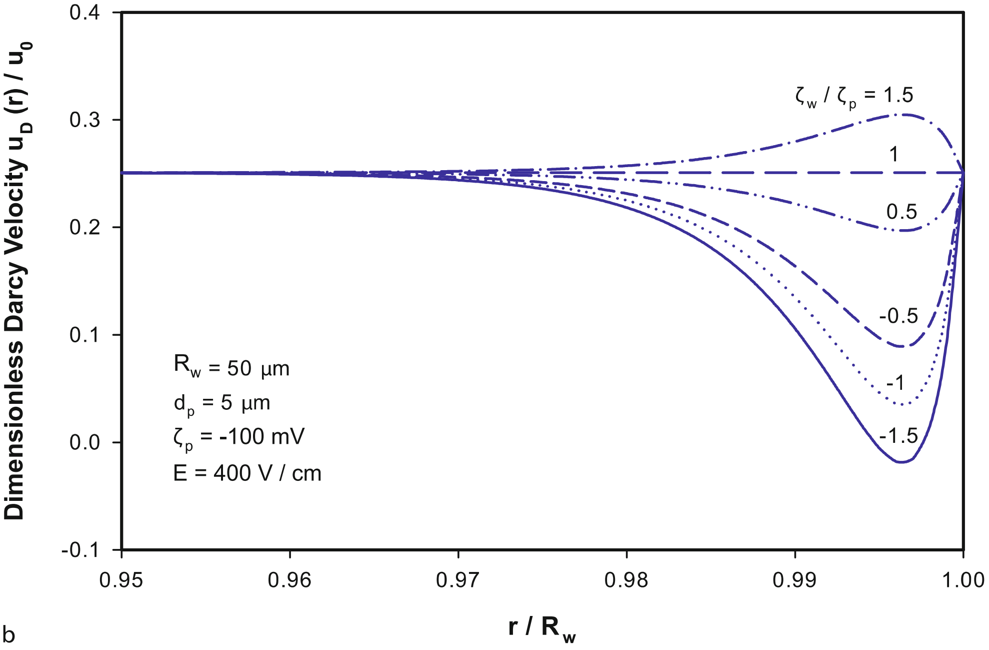

b

Electrokinetic Flow in Porous Media, Figure 3 Electroosmotic flow velocity distributions in a charged microcapillary packed with charged microspheres, for different values of zeta potential ratio ζ_w/ζ_p. The results are obtained on the basis of (**a**) the numerical solution of Eq. (12) and (**b**) the analytical solution based on Eq. (27)

In the following, the results under two different approaches, the complete numerical solution of Eq. (12) and the analytical solution based on Eq. (27), will be compared. Figures 3a and b show the electrokinetic wall effects for a given particle size $d_p = 5\,\mu m$ under different charge conditions of the capillary wall. The wall zeta potentials

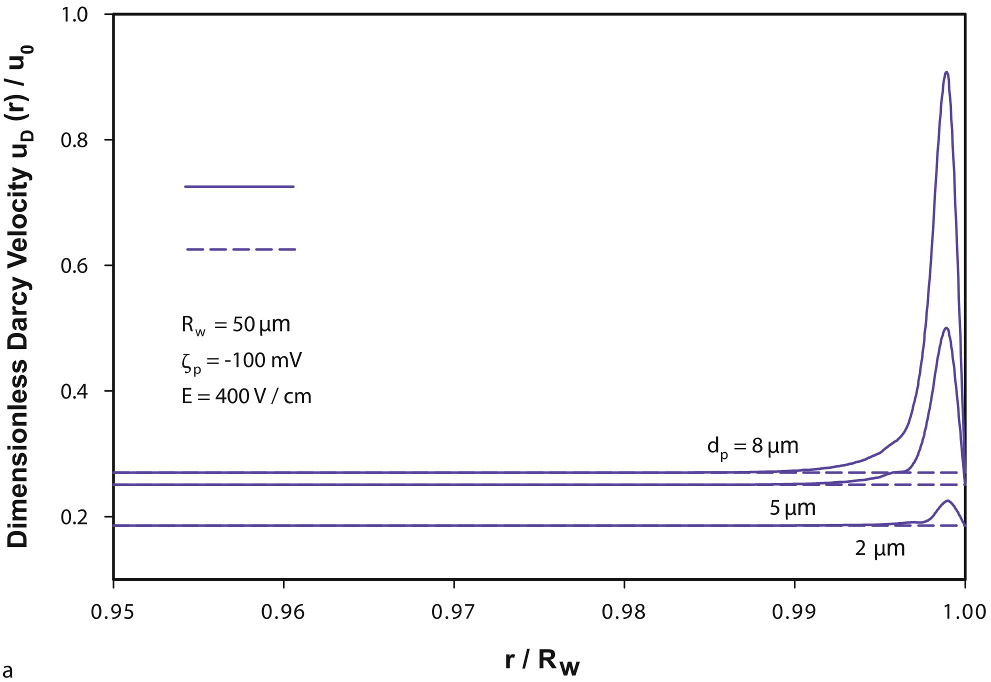

a

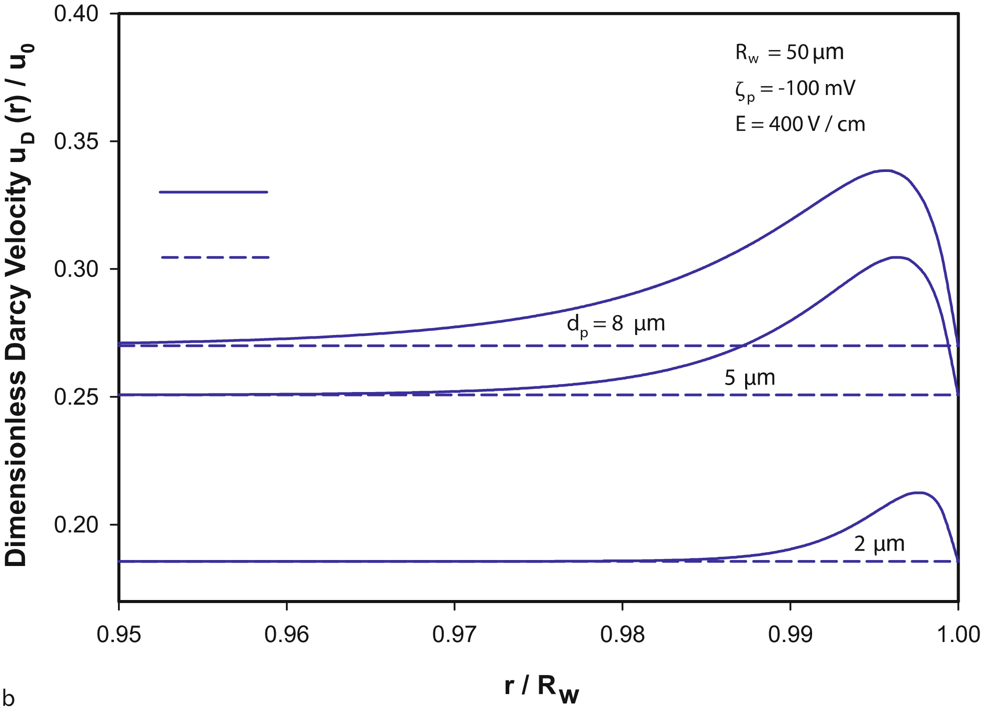

b

Electrokinetic Flow in Porous Media, Figure 4 Electroosmotic flow velocity distributions in a charged microcapillary packed with charged microspheres, for different sizes of packing particles, d_p. The results are obtained on the basis of (**a**) the numerical solution of Eq. (12) and (**b**) the analytical solution based on Eq. (27)

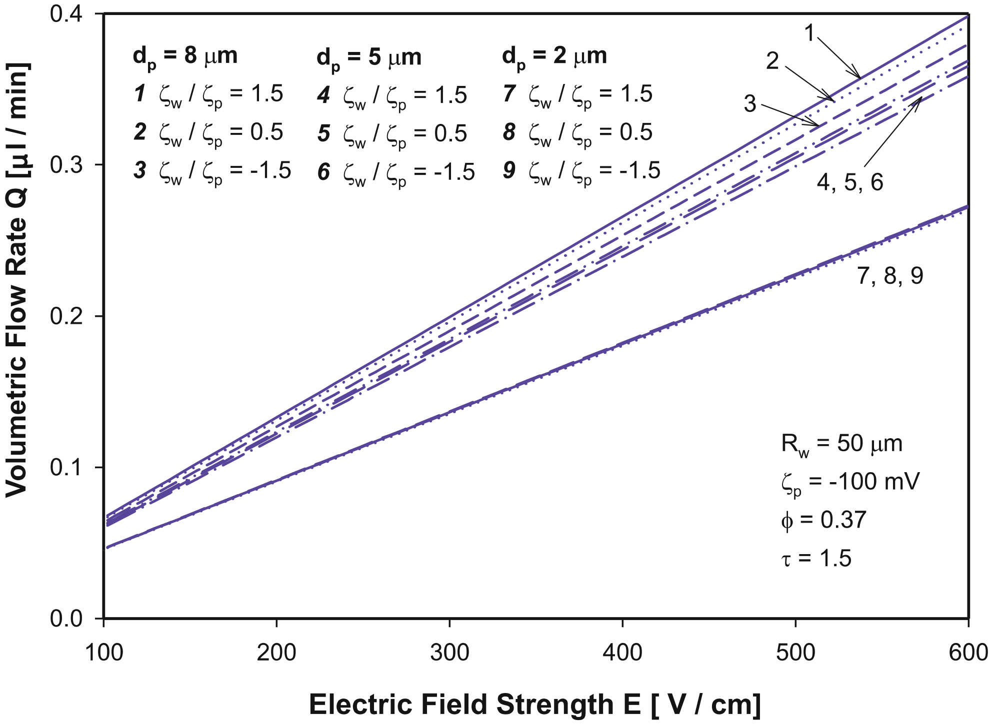

Electrokinetic Flow in Porous Media, Figure 5 Electroosmotic flow rate versus applied electric field for different values of particle diameter, d_p, and zeta potential ratio, $\zeta_\mathrm{w}/\zeta_\mathrm{p}$

are chosen to vary from positive to negative, relative to the polarity of the particle zeta potential. According to Eq. (28), it can be readily understood that when the zeta potential ratio $\zeta_\mathrm{w}/\zeta_\mathrm{p} = 1$ there is no electrokinetic wall effect. The velocity distributions exhibit a uniform profile along the cross-sectional area (i. e., a straight horizontal line), and this homogeneous velocity is equal to u_Di. The prediction results in Figs. 3a and b show that when the capillary wall is more negatively charged than the particles, i. e., $\zeta_\mathrm{w}/\zeta_\mathrm{p} > 1$, the EOF close to the wall is enhanced. In these cases, the EOF velocity starts to increase from u_Di on the wall to a maximum velocity, and then decreases to u_Di at the location around $0.98\,R_\mathrm{w}$. The local enhancement is due to the interaction between the applied electric field and the excessive EDL potential, which is limited within a region of several Debye lengths from the wall. In our calculation, the portion where the enhanced EOF occurs is limited in an annular region with thickness of around 0.75 μm, i. e., about 7 Debye lengths. Beyond this regime, the fluid remains uniform. This velocity enhancement by the channel wall cannot extend to the rest portion of the channel because the presence of packing particles causes a frictional force between the fluid and the surface of packing particles. This trend was experimentally verified by Tallarek et al. [8]. They used the pulsed field gradient nuclear magnetic resonance (PFG-NMR) and NMR imaging techniques to study the electroosmotic flow in packed capillaries. It was reported that higher EOF close to the capillary wall is detected when the channel wall is more negatively charged than the particles. Furthermore, the model predictions show that when the capillary wall is less negatively charged than the particles ($0 < \zeta_\mathrm{w}/\zeta_\mathrm{p} < 1$), neutral ($\zeta_\mathrm{w} = 0$), or positively charged ($\zeta_\mathrm{w} > 0$), the EOF close to the capillary wall becomes weakened, even leading to change of flow direction.

Comparison of Figs. 3a and b shows that at the center region of the capillary, the two methods give nearly the same results for velocity distributions, while adjacent to the charged channel wall the discrepancy is observed. It is shown that the enhanced regime under the analytical solution (i. e., Eq. (27)) is wider than that under the numerical solution of Eq. (12). This is due to the Debye–Hückel approximation used in the derivation of the analytical solutions. It is well known that use of the Debye–Hückel approximation usually overestimates the EDL region, and thus the area affected by the excessive zeta potential becomes larger. Nonetheless, evaluation of Figs. 3a and b indicates that compared to the numerical solution, the analytical solution underestimates the electrokinetic wall effect.

Figures 4a and b show the size effect of the packing particles on the EOF in a packed capillary. Three different sizes of spherical particles with diameters of 2, 5, and 8 μm are considered here. Two typical conditions are presented: with wall effect ($\zeta_w/\zeta_p = 1.5$) and no wall effect ($\zeta_w/\zeta_p = 1$). As discussed earlier, if there is no wall effect, the velocity exhibits a uniform profile along the channel radius. In this situation, use of larger packing particles can generate a higher uniform velocity u_{Di}. This is because, according to Eq. (2), the intraparticle pore size increases with increasing packing particle size. Moreover, the value of G in Eq. (7), which denotes the average EDL potential inside the intraparticle pore, decreases with increasing pore size. Thus the EOF velocity inside larger packing particles is higher. In terms of the wall effect, larger packing particles can generate stronger enhancement of local EOF velocity in the vicinity of the capillary wall. This can be explained by the fact that the void space between the particles is larger for larger particle sizes. Thus the drag force of the packing particles should be smaller.

Of practical interest for micropumps, we also study the effect of the channel wall and packing particles on the overall electroosmotic flow rate in a microcapillary. Flow rate versus applied external electric field, for different packing particle size and the zeta potential ratio ζ_w/ζ_p, is plotted in Fig. 5. It is noted that the flow rate increases linearly with increasing applied voltage. For larger packing particles, the flow rate is always higher. This is for the same reason that larger packing particles can generate higher velocity as shown in Fig. 4. For a given packing structure, the flow rate slightly increases when $\zeta_w/\zeta_p > 1$, and decreases when $\zeta_w/\zeta_p < 1$, due to the electrokinetic wall effect.

In addition to the aforementioned research findings, an analytical model for AC EOF in both open-end and closed-end cylindrical microcapillaries packed with uniform spherical particles was reported by Kang et al. [9]. It is shown that in a microcapillary with its two ends connected to reservoir and subject to ambient pressure, the oscillating Darcy velocity profile depends on both the pore size and the excitation frequency; such effects are coupled through an important aspect ratio of the tubule radius to the Stokes penetration depth. In a microcapillary with closed ends, a backpressure is induced to ensure a zero net flow rate. For a fixed excitation frequency, use of smaller packing particles can generate higher backpressure. When an AC electric field is used, the induced backpressure can be converted to forces for actuation if the sealed ends are made of movable or deformable components. This offers a potential application for the development of novel electrokinetic microactuators. Furthermore, Kang et al. [10] developed a numerical model to examine the transient Joule heating-induced temperature field and its effect on the electroosmotic flow in a capillary packed with microspheres. It is shown that the occurrence of Joule heating causes a noticeable axial temperature gradient in the thermal entrance region and causes a significant temperature increment inside the microcapillary. The temperature changes in turn greatly affect the electroosmotic velocity by means of the temperature-dependent fluid viscosity, dielectric constant, and local electric field strength. Also, the model predicts an induced pressure gradient to counterbalance the axial variation of the electroosmotic velocity so as to maintain the fluid mass continuity.

Future Directions for Research

It should be pointed out that the present model is based on the space averaging method which is commonly utilized in classic pressure-driven transport phenomena in porous media. This averaging method focuses on the equivalent macroscopic physics without considering the local complexity in the microscale. However, the EOF in porous media originates from the interaction of the external electric field and the EDL at internal surfaces of the porous structure. In reality from a microscopic viewpoint, the driving force is dependent on the local configuration of the interface and local pressure gradient is usually induced because of the complicated geometric structure and overlapped EDLs, which makes the real scenario very complex. Therefore, more accurate three-dimensional pore-size level modeling instead of the space averaging modeling should be developed to include such effects. In addition, the model presented in this study is based on the classic electroosmosis of the first kind resulting from the usual quasi-equilibrium EDL. As the complex porous sub-microstructure containing ion-exclusion regions can lead to concentration polarization under high electric field strengths, non-equilibrium EDL can be formed. Accordingly the electroosmosis of the second kind will be developed, giving rise to nonlinear electrokinetic flow in porous media that has not been studied yet.

Cross References

► Electrical Double Layers
► Electroosmotic Flow (DC)
► AC Electro-Osmotic Flow
► Electroosmotic Flow in Heterogeneous Microchannels
► Liquid Chromatography

References

1. Hunter RJ (1981) Zeta Potential in Colloid Science: Principles and Applications. Academic Press, London

2. Rathore AS, Horvath CS (1997) Capillary Electrochromatography: Theories on Electroosmotic Flow in Porous Media. J Chromatogr A 781:185–195
3. Paul PH, Arnold DW, Rakestraw DJ (1998) Electrokinetic generation of high pressures using porous microstructures. In: Proceedings of the 3rd international symposium on micro total analysis systems (μTAS'98). Banff, Alberta, Canada
4. Laser DJ, Santiago JG (2004) A review of Micropumps. J Micromech Microeng 14:R35–64
5. Allen D, Rassi ZE (2003) Silica-based Monoliths for Capillary Electrochromatography: Methods of Fabrication and Their Applications in Analytical Separations. Electrophoresis 24:3962–3976
6. Kaviany M (1995) Principles of Heat Transfer in Porous Media. Springer, New York
7. Probstein RF (1994) Physicochemical Hydrodynamics. Wiley, New York
8. Tallarek U, Scheenen TWJ, Van As H (2001) Macroscopic Heterogeneities in Electroosmotic and Pressure-driven Flow through Fixed Beds at Low Column-to-Particle Diameter Ratio. J Phys Chem B 105:8591–8599
9. Kang Y, Yang C, Huang XY (2004) AC Electroosmosis in Microchannels Packed with a Porous Medium. J Micromech Microeng 14:1249–1257
10. Kang Y, Yang C, Huang XY (2005) Joule Heating Induced Transient Temperature Field and Its Effects on Electroosmotic Flow in a Microcapillary Packed with Microspheres. Langmuir 21:7598–7607

Electrokinetic Focusing

TOM GLAWDEL, CAROLYN REN
Department of Mechanical and Mechatronics Engineering, University of Waterloo, Waterloo, ON, Canada
tglawdel@engmail.uwaterloo.ca, c3ren@mecheng1.uwaterloo.ca

Synonyms

Electrohydrodynamic focusing

Definition

Electrokinetic focusing refers to the application of electrokinetic sheath flows to confine a sample flow into a thin stream for dispensing. The most common configuration is a simple cross-linked microchannel.

Overview

Electrokinetic focusing is one of the major techniques used in many biological and biomedical applications. As an example, on-chip electrophoresis separation utilizes electrokinetic focusing to create a very thin sample stream before dispensing a small plug for separation [1]. Electrokinetic focusing is also applied in cell cytometry and cell sorting to dispense cells one at a time before they are transported to the detection region [2]. The most common geometry for on-chip electrokinetic focusing is a cross-channel where two sheath flows originating from the side channels constrict the sample flow into a thin stream at the outlet channel [3]. In the case of electrokinetic focusing, fluids are transported using electroosmotic flow as opposed to hydrodynamic focusing where pressure driven flow is used [4]. The amount of focusing is characterized by the width of the focused stream which is defined by the two streamlines that separate the sheath and sample flows. The width depends on the relative flow rates of the sample and sheath flows; thus the performance is related to the electroosmotic flow parameters including the applied electric potentials, solid–liquid properties of the channel walls and channel width ratio of the sample and sheath channels [5]. The width of the sample focusing stream can be experimentally determined through fluorescence-based visualization techniques. However, due to dye diffusion across the streamlines the cross-stream intensity profile does not exactly indicate streamline locations. The stream line location is estimated by evaluating the intensity profile using the full width at half maximum intensity (FWHM) method [6] by applying a Gaussian model. The advantage of the Gaussian fitting model is that it estimates the streamline locations independent of the physical properties of the dye sample employed in the experiments [5]. The reliability of electrokinetic focusing is coupled to the stability of the electroosmotic flow and the suppression of undesired pressure driven flow caused by small head differences and Laplace pressure differences at the reservoirs.

References

1. Harrison DJ, Manz A, Fan Z, Leidi H, Widmer HM (1992) Capillary Electrophoresis and Sample Injection Systems Integrated on a Planar Glass Chip. Anal Chem 64:1926–1932
2. McClain MA, Culbertson CT, Jacobson SC, Ramsey JM (2001) Flow Cytometry of Escherichia coli on Microfluidic Devices. Anal Chem 73:5334–5338
3. Jacobson S, Hergenroder R, Koutny LB, Warmack RJ, Ramsey JM (1994) Effects of Injection Schemes and Column Geometry on the Performance of Microchip Electrophoresis Devices. Anal Chem 66:1107–1113
4. Lee GB, Lin CH, Chang GL (2003) Micro Flow Cytometers with Buried SU-8/SOG Optical Waveguides. Sens Actuators A 103:165–167
5. Taylor J (2006) MASc thesis. University of Waterloo, Canada
6. Jacobson SC, Ramsey JM (1997) Electrokinetic Focusing in Microfabricated Channel Structures. Anal Chem 69:3212–3217

Electrokinetic Injection

► Electrokinetic Dispensing
► Electrokinetic Sample Injection

Electrokinetic Instability

► Electrokinetic/ElectroHydrodynamic Flow Instability

Electrokinetic Mobility

Definition

The movement of ions in solution due to potential applied across the media in which the ions exist.

Cross References

► Lab-on-a-Chip Devices for Chemical Analysis
► Electrokinetic Flow and Ion Transport in Nanochannels
► Electroosmotic Flow (DC)
► AC Electro-Osmotic Flow
► Electrophoresis

Electrokinetic Motion

► Electrokinetic Flow

Electrokinetic Motion of Cells and Nonpolarizable Particles

YUEJUN KANG, DONGQING LI
Department of Mechanical Engineering,
Vanderbilt University, Nashville, TN, USA
yuejun.kang@vanderbilt.edu

Synonyms

Electromigration; Cataphoresis

Definition

The migration of electrically charged cells or particles in liquid solution or suspension in an applied electric field.

Overview

Most substances acquire a surface charge when brought into contact with a polar medium because of chemical reaction at the interface. The charging mechanisms include ionization, ion adsorption, and ion dissolution [1]. Charge separation occurs at the solid/liquid interface when a particle is suspended in a liquid solution. As shown in Fig. 1, a negatively charged particle is surrounded by a diffuse layer

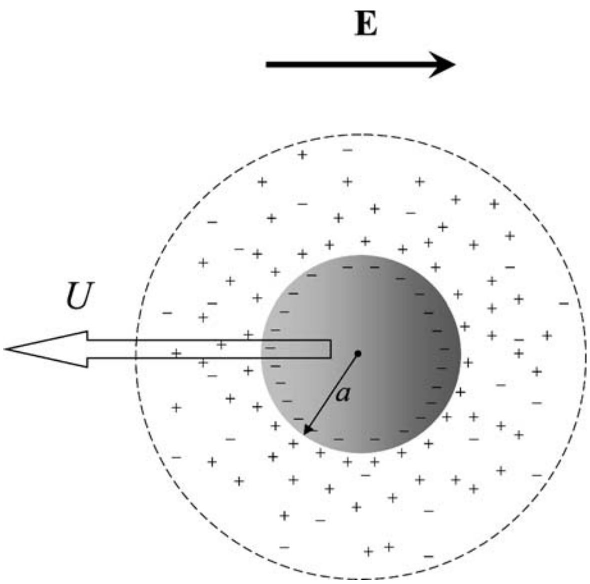

Electrokinetic Motion of Cells and Nonpolarizable Particles, Figure 1
Electrophoretic motion of a spherical particle

which contains an excess number of mobile ions of opposite charge relative to ions of like charge. Charged particles move toward electrodes of opposite electrical polarity under an external electric field. This movement is due to the Coulomb force, generated by the interaction between the net charge on the particle and the applied electric field. The electrophoretic velocity with which the particle moves with respect to its suspending medium is proportional to the strength of the applied electric field, the proportionality factor being called the *electrophoretic mobility*. The electrophoretic mobility μ_e is proportional to the magnitude of the net charge on the particle, and is inversely proportional to the size of the particle:

$$\mu_e = \frac{U}{E} = \frac{q}{f} , \tag{1}$$

where U is the electrophoretic velocity, E is the external electric field strength, q is the net charge carried by the particle, and f is the frictional coefficient. If the diffuse layer is thick, the particle may be treated as a point charge in an unperturbed electric field E_x, and the electrophoretic velocity of the particle can be expressed by the *Hückel equation*,

$$U = \frac{2}{3}\frac{\varepsilon\zeta E_x}{\mu} , \tag{2}$$

where ε is the permittivity of the particle, μ is the viscosity of the suspending medium, and ζ is the zeta potential of the particle, which is a measure of the surface

charge density. If the diffuse layer is thin, which is true for high ionic strengths or large particles of micron size, the electrophoretic velocity is given by the *Helmholtz–Smoluchowski equation*,

$$U = \frac{\varepsilon \zeta E_x}{\mu}\,, \tag{3}$$

Since electrophoresis can differentiate charged particles with great selectivity on the basis of their electrophoretic mobility, it has found extensive application in separation systems used in the biomedical industry, such as capillary electrophoresis [2], gel electrophoresis, and electrochromatography [3]. With the rapid development of modern microfluidic technology, electrophoresis has been successfully applied in the manipulation of microparticles and biological cells, by techniques such as isoelectric focusing [4] and electrokinetic dispensing [5].

Cross References

- ► Dielectrophoresis
- ► Dielectrophoretic Motion of Particles and Cells
- ► Electrokinetic Dispensing
- ► Electrophoresis
- ► Lab-on-Chip Devices for Particle and Cell Separation

References

1. Probstein RF (1994) Physicochemical Hydrodynamics: An Introduction. 2nd edn Wiley, New York
2. Chiem N, Harrison DJ (1997) Microchip-based capillary electrophoresis for immunoassays: analysis of monoclonal antibodies and theophylline. Anal Chem 69(3):373–378
3. Regnier FE, He B, Lin S, Busse J (1999) Chromatography and electrophoresis on chips: critical elements of future integrated, microfluidic analytical systems for life science. Tibtech 17:101–106
4. Cabrera CR, Yager P (2001) Continuous concentration of bacteria in a microfluidic flow cell using electrokinetic techniques. Electrophoresis 22(2):355–362
5. Xuan X, Li D (2005) Focused electrophoretic motion and selected electrokinetic dispensing of particles and cells in cross-microchannels. Electrophoresis 26(18):3552–3560

Electrokinetic Motion of Heterogeneous Particles

MARTIN Z. BAZANT[1,2]

[1] Department of Mathematics and Institute of Soldier Nanotechnologies, Massachusetts Institute of Technology, Cambridge, MA, USA

[2] Ecole Superieure de Physique et Chimie Industrielles, Paris, France

bazant@math.mit.edu

Synonyms

Transverse electrophoresis

Definition

The electrokinetic motion of heterogeneous particles, having non-uniform composition and/or irregular shape, involves translation, rotation, and deformation due to the combined effects of ► electrophoresis, ► induced-charge electrophoresis, and ► dielectrophoresis.

Overview

The electrokinetic motion of colloidal particles and molecules in solution in response to applied electric fields can be rather complicated, so many approximations have been made in theoretical treatments. The classical theory of ► electrophoresis, dating back over a century to Smoluchowski, considers homogeneous particles, which are

1. non-polarizable,
2. spherical,
3. uniformly charged,
4. rigid,
5. much larger than the thickness of the electrical double layer,
6. in an unbounded fluid, very far from any walls or other particles, and subjected to
7. uniform and
8. weak fields, applying not much more than the thermal voltage ($kT/e = 25$ mV) across the particle in
9. dilute electrolytes.

Under these assumptions, the particle's velocity is linear in the applied electric field, $U = bE$, where the electrophoretic mobility $b = \varepsilon\zeta/\eta$ is given by the permittivity ε and viscosity η of the fluid and the zeta potential ζ of the surface. In Smoluchowski's theory, the latter is equal to the voltage across the double layer, which is proportional to the surface charge at low voltage.

Much less attention has been paid to the electrokinetic motion of heterogeneous particles, which have non-spherical shape and/or non-uniform physical properties. By far the most theoretical work has addressed the case linear electrophoresis of non-polarizable particles with a fixed, equilibrium distribution of surface charge [1]. In that case, relaxing only assumption 2 leads to the classical prediction that the mobility of a particle of uniform composition (uniform zeta) is independent of the shape and size of the particle. Perhaps it was this insensitivity to geometry that led to the common belief that the electrophoretic mobility measures some kind of *average* surface charge, until the Anderson was the first to clearly point out that this is generally not the case [2]. By care-

fully relaxing only assumption 3, he predicted that a sphere of non-uniform zeta potential can move in a different direction from the field and that its mobility is not simply related to its total charge. Generalizing work of Fair and Anderson on doublet particles [3], Long and Ajdari showed that relaxing *both* 2 and 3 leads to even more complicated behaviour, including particles that rotate continuously or translate perpendicular to a uniform DC field [4]. Relaxing assumption 4, the electrophoresis of flexible heterogeneous particles has also been studied, such as DNA molecules connected to beads [5] and interacting with obstacles [6].

► Nonlinear electrokinetic phenomena, such as the ► electrokinetic motion of polarizable particles, have only been studied for a few decades, and attention is just beginning to be paid to the nonlinear motion of heterogeneous particles due to ► induced-charge electrophoresis [7–9]. Recent theoretical work has relaxed assumptions 1–3, but much remains to be done. Surprising new possibilities include particles that rotate continuously or translate perpendicular to a uniform AC field [9].

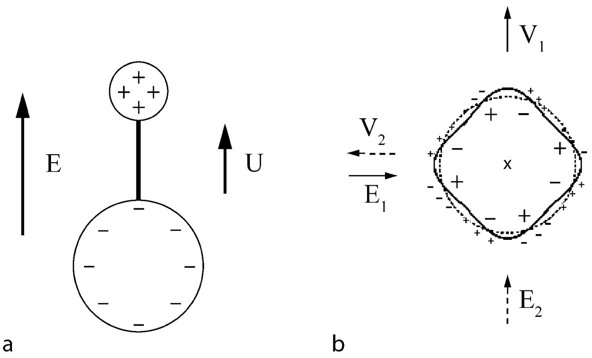

Electrokinetic Motion of Heterogeneous Particles, Figure 1 Examples of unusual linear electrophoretic motion of heterogeneous particles. (**a**) A dumbbell consisting of two oppositely charged spheres of connected by a rigid rod rotates to align as shown and moves in the direction of the electric field (positive mobility), even though the total charge is negative, if the positive sphere is smaller. (**b**) A particle of zero total charge with four-fold and eight-fold perturbations in shape and surface charge, respectively, moves perpendicular to the electric field, regardless of its orientation, from [4]

Basic Methodology

The underlying physical mechanisms for the electrokinetic motion of particles are described in other articles on ► electro-osmotic flow, electrophoresis, ► dielectrophoresis, nonlinear electrokinetic phenomena and electrokinetic motion of polarizable particles, along with various mathematical models. The effects of relaxing the assumptions above in these models, however, are often unexpected and have not yet been fully explored, either theoretically or experimentally. Here, we simply give a few examples of how heterogeneous particles can move in electric fields.

Key Research Findings

Linear Electrophoresis

It is tempting to think of the electrophoretic mobility of a heterogeneous particle as a measure of its *average charge*, when in fact it has a nontrivial dependence on the spatial distribution of surface charge [1–5]. This is clearly demonstrated by a counter-example of Long and Ajdari, motivated by chain-like polyelectrolytes, such as DNA molecules [5]. Consider a dumbbell-shaped particle consisting of two uniformly charged spheres with electrophoretic mobilities b_1 and b_2 and hydrodynamic drag coefficients ξ_1 and ξ_2, held together by an uncharged, rigid rod. As a first approximation, the rod has negligible drag and is long enough that hydrodynamic and electrostatic interactions between the spheres can be neglected. In a uniform electric field, the dumbbell rotates to a stable configuration aligned with the field axis, as shown in Fig. 1a and moves a velocity, $U = bE$, where b is the overall mobility. In order for each particle ($i = 1, 2$) to move at the same velocity, the rod must exert a force $F_i = \xi_i (U - b_i E)$. Force balance on the rod, $F_1 = -F_2$, then yields the mobility

$$b = \frac{\xi_1 b_1 + \xi_2 b_2}{\xi_1 + \xi_2} \propto \frac{Q_1}{R_1} + \frac{Q_2}{R_2} \tag{1}$$

which is the drag-weighted average of the two mobilities. In the last step, we have used Stokes formula, $\xi_i = 6\pi\eta R_i$ (where η is the fluid viscosity), and assumed that the *local* mobility (slip coefficient) is proportional to the surface charge density, $b_i \propto Q_i/4\pi R_i^2$, where Q_i is the total charge of each sphere. We see that, depending on the geometry, the mobility can have either sign, regardless of the sign the total charge $Q_1 + Q_2$. For example, as shown in Fig. 1a, a small sphere of charge $Q > 0$ connected to a larger sphere of charge $-2Q$ can have a positive mobility, even though its total charge is negative, as long as $R_2 > 2R_1$.

Variations in charge density and shape can lead to even more surprising *transverse* electrophoretic motion, which departs from the field axis. In linear electrophoresis, a spherical particle of non-uniform surface charge (or zeta potential) can move perpendicular to the field, but only for certain orientations; it can also rotate, but only transiently to align its dipole with the field axis [1]. If both the surface charge and the shape are perturbed, however, then these restrictions do not apply [4]: Figure 1b shows a cylindrical

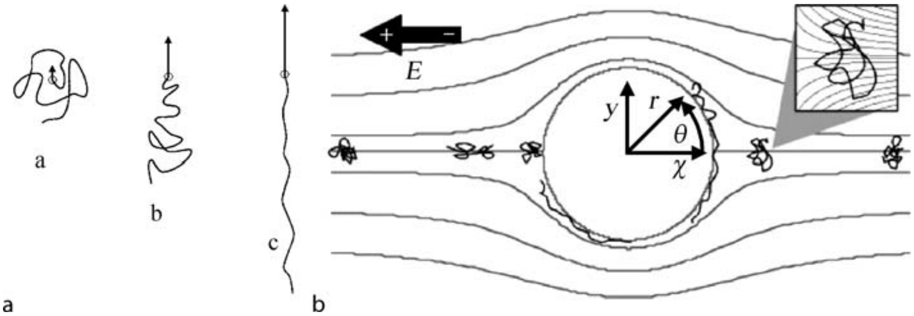

Electrokinetic Motion of Heterogeneous Particles, Figure 2 (**a**) Linear electrophoresis of a flexible, charged chain connected to a neutral bead in regimes of small, moderate, and large velocity as a model of end-labeled free-solution DNA electrophoresis, from [5]. (**b**) Centerline trajectories of DNA electrophoresis around a cylindrical obstacle in a microchannel, showing compression and extension of the molecule, from [6]

particle of zero total charge, which always moves perpendicular to the electric field, regardless of its orientation. It has four-fold shape perturbation and eight-fold surface charge perturbation, such that each bump on the surface has positive surface charge to the left and negative to the right. By constructing appropriate chiral perturbations of the shape and surface charge, it is also possible to design heterogeneous particles, which rotate continuously around a particular axis without translating, for a particular direction of the electric field.

Flexible objects undergoing electrophoresis also display complicated dynamics. Motivated end-labeled free-solution DNA electrophoresis, Long and Ajdari also considered the electrophoresis of flexible charged chains connected to larger beads [5]. As shown in Fig. 2, there are three different dynamical regimes for small, intermediate and large velocities, where the chain goes from its equilibrium configurations to a completely elongated state. The same motions would result if the chain were pulled at the end by an effective force. Similar phenomena occur in the electrophoresis of block co-polymers, which consist of two different chains connected at the ends.

Recently, Randall and Doyle have studied the electrophoretic collision of DNA with an obstacle in a microfluidic channel, both experimentally and theoretically [6]. In that case, large deformations due to field gradients and hydrodynamic strain near the obstacle quickly stretch and compress the molecule and cause configuration-dependent hooking interactions, as shown in Fig. 2b. (See also ►dielectrophoretic motion of particles and cells.)

Induced-Charge Electrophoresis

The preceding examples involve non-polarizable objects with fixed surface charge distributions, which do not respond to the electric field. The resulting electrophoretic motion is linear in the field amplitude and vanishes for AC fields. The electrokinetic motion of polarizable particles, however, has nonlinear field dependence due to the phenomenon of induced-charge electro-osmosis (ICEO), where the field acts on induced diffuse charge in the ►electrical double layer. At frequencies low enough for capacitive charging of the double layer (typically $< 10\,\text{kHz}$), the time-averaged motion in an AC field is resembles that in a DC field. In the canonical example of an uncharged metal sphere in a uniform field, the ICEO flow is quadrupolar, drawing in fluid along the field axis and expelling it radially, but there is no net motion.

Motivated by the examples from linear electrophoresis above, Bazant and Squires pointed out that broken symmetry in ICEO flow generally causes particle motion, which they called ►induced-charge electrophoresis (ICEP) [1]. Examples of broken symmetries include particles with irregular shapes and/or non-uniform physical characteristics, as well as non-uniform applied fields. In the latter case, ICEP occurs at the same time as dielectrophoresis (DEP), although the combined effects of ICEP and DEP on heterogeneous particles remain to be explored. Besides persisting in AC fields, ICEP also depends much more sensitively on particle shape and surface properties than does linear DC electrophoresis. Cases of non-spherical particles with uniform polarizability are discussed in the article on electrokinetic motion of polarizable particles, so here we focus on ICEP due to heterogenous surface polarizability.

The canonical example is that of a ►Janus particle with one metallic and one insulating hemisphere [9], using the standard low-voltage model for electrokinetic motion of polarizable particles. In response to an applied electric field, the Janus particle rotates to align the interface between the two hemispheres with the field axis, due to both ICEP (electrohydrodynamics) and DEP (electrostatics). At the same time, for any orientation, the particle

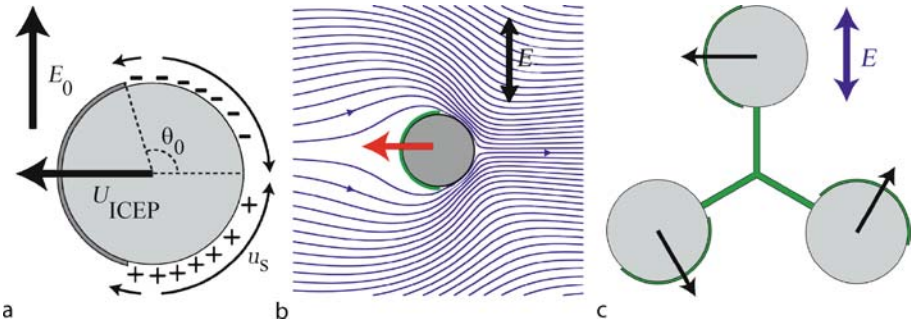

Electrokinetic Motion of Heterogeneous Particles, Figure 3 Induced-charge electrophoresis of Janus particles, illustrated for the case of metal partially coated with insulating thin films, from [9]. (**a**) Stable orientation in a uniform field, showing induced charge and slip velocities on the metallic side, resulting in motion toward the insulating end, perpendicular to the field. (**b**) Streamlines of ICEO flow. (**c**) An ICEP pinwheel, consisting of three Janus particles connected by rigid rods, which tilts to align and then spins continuous around the field axis

translates in the direction of its insulating end, propelled by ICEO flow on the metallic end, with a velocity

$$U = \frac{9\varepsilon RE^2}{64\eta\,(1+\delta)} \tag{2}$$

where ε is the permittivity, R is the particle radius, and δ is a dimensionless measure of the compact-layer capacitance. In particular, once the particle aligns in the field, it continues to move perpendicular to the electric field, with an azimuthal angle set by its initial orientation.

All the generic features of the dynamics still hold if the particle's insulating end is smaller or larger than the metallic end, since it is determined by the broken symmetry. Motion transverse to a uniform AC field cannot have any contribution from DEP, but it is easily understood by considering the ICEO flow in Fig. 3a. After alignment in the field, part of the usual quadrupolar ICEO flow is suppressed on the insulating end. The remaining ICEO flow over the metallic end sucks in fluid along the field axis and pushes it outward from the metallic pole, as shown in Fig. 3b, which propels the particle toward the insulating pole.

This example suggests how to design particles that spin continuously in a uniform field, as noted by Squires and Bazant [9]. Since a Janus particle always translates towards its less polarizable end, a set of three Janus particles connected by rigid rods can be set into continuous motion like a pinwheel, if connected as shown in Fig. 3c. This "ICEP pinwheel" responds to any DC or AC electric field (of sufficiently low frequency) by tilting to align the particle plane perpendicular to the field and then spinning around the field axis until the field is turned off. Perhaps such particles could be used to sense electric fields or to apply torques to attached molecules or cells.

Transverse ICEP motion of metallo-dielectric Janus particles in a uniform AC field has recently been observed by Gangwal et al. [10]. Consistent with theoretical predictions in Fig. 3, the particles align and translate perpendicular to the field in the direction of the less polarizable (light) end, as shown in Fig. 4. Larger particles move faster than smaller ones, as expected from Eq. (2), and the velocity scales like the field squared in dilute NaCl solutions. The ICEP velocity decays at higher concentrations, extrapolating to zero around 10 mM. The same concentration dependence is also observed in ►AC electro-osmotic flow and other nonlinear electrokinetic phenomena, which, although poorly understood, further reinforces that the motion is indeed due to ICEP.

Current research is focusing on how heterogeneous particles undergoing electrokinetic motion due to ICEP and DEP interact with walls and other particles. An interesting feature of the experiments in Fig. 3 is that the Janus particles are attracted to nearby glass walls, and the transverse motion is also observed close to the walls, where the theory of [9] does not strictly apply. The attraction can be understood as a consequence of ICEP torque, which redirects the Janus particle toward a nearby wall and causes it to tilt while translating transverse to the field.

Future Directions for Research

As illustrated by the examples above, the electrokinetic motion of heterogeneous particles is quite complicated and relatively unexplored. From a theoretical point of view, there are many opportunities to discover new phenomena by further relaxing the nine assumptions listed at the beginning of this article. From an experimental point of view, much remains to be done to characterize the motion of heterogenous particles in electric fields, especially by ICEP and DEP at low frequency.

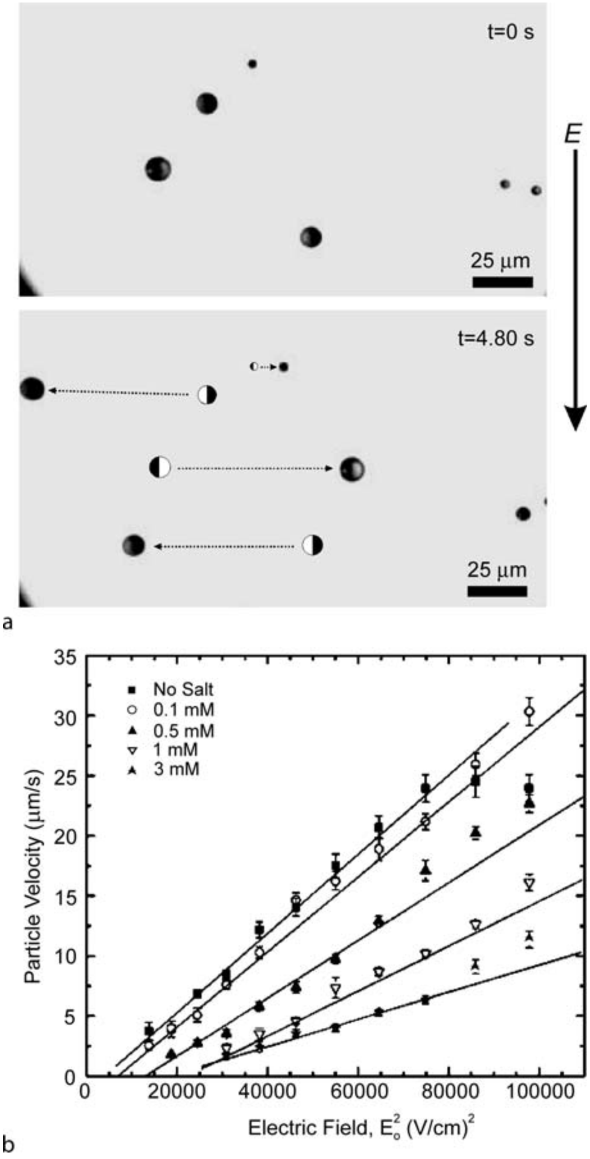

Electrokinetic Motion of Heterogeneous Particles, Figure 4 Experimental observation of ICEP of metallo-dielectric Janus particles in a uniform 10 kHz AC field, from [10]. (**a**) Sequence of micrographs demonstrating motion transverse to the field in the direction of the dielectric (light) end propelled by the metallic (dark) end, where the velocity increases with the particle size as in Eq. (2) (**b**) Velocity versus field amplitude squared at different bulk concentrations of NaCl

A major motivation to develop this subject is the possibility of new applications, opened by advances in microfluidics and nanotechnology. In principle, heterogenous particles of specific irregular shapes and non-uniform electrical and/or chemical properties can be designed and fabricated for specific applications. The complex electrokinetic motion of these particles could potentially be used for separation or sample concentration in chemical or biological assays, self-assembly in the fabrication of anisotropic materials, directional transport of attached *cargo*, electric-field sensing and applying forces and torques to molecules or cells.

Cross References

- ► AC Electro-Osmotic Flow
- ► Dielectrophoresis
- ► Dielectrophoretic Motion of Particles and Cells
- ► Electrical Double Layers
- ► Electrokinetic Motion of Polarizable Particles
- ► Electroosmotic Flow (DC)
- ► Electrophoresis
- ► Induced-Charge Electrophoresis
- ► Janus Particle
- ► Nonlinear Electrokinetic Phenomena

References

1. Anderson JL (1989) Colloid transport by interfacial forces. Ann Rev Fluid Mech 21:61–99.
2. Anderson JL (1984) Effect of nonuniform zeta potential on particle movement in electric fields. J Colloid Interface Sci 105:45–54
3. Fair MC, Anderson JL (1992) Electrophoresis of heterogeneous colloids – doublets of dissimilar particles. Langmuir 8:2850–2854
4. Long D, Ajdari A (1998) Symmetry properties of the electrophoretic motion of patterned colloidal particles. Phys Rev Lett 81:1529–1532
5. Long D, Ajdari A (1996) Electrophoretic mobility of composite objects in fee solution: Application to DNA separation. Electrophoresis 17:1161–1166
6. Randall GC, Doyle PS (2005) DNA deformation in electric fields:DNA driven past a cylindrical obstruction. Macromolecules 38:2410–2418
7. Bazant MZ, Squires TM (2004) Induced-charge electrokinetic phenomena:theory and microfluidic applications. Phys Rev Lett 92:066010
8. Yariv E (2005) Induced-charge electrophoresis of nonspherical particles. Phys Fluid 17:051702
9. Squires TM, Bazant MZ (2006) Breaking symmetries in induced-charge electro-osmosis. J Fluid Mech 560:65-101
10. Gangwal S, Cayre OJ, Bazant MZ, Velev OD (2007) Induced-charge electrophoresis of metallo-dielectric particles. http://arxiv.org/abs/0708.2417 (preprint)

Electrokinetic Motion of Polarizable Particles

Martin Z. Bazant[1]

[1] Department of Mathematics and Institute of Soldier Nanotechnologies, Massachusetts Institute of Technology, Cambridge, MA, USA

[2] Ecole Superieure de Physique et Chimie Industrielles, Paris, France
bazant@math.mit.edu

Definition

The electrokinetic motion of polarizable particles results from electro-osmotic flow (▶ induced-charge electrophoresis) of the first of ▶ second kind, in addition to electrostatic forces (▶ dielectrophoresis).

Overview

The classical theory of ▶ electrophoresis (particle motion due to ▶ electro-osmotic flow) assumes that surface charge remains fixed at its equilibrium value, when electric fields (or other perturbations) are applied [1]. For thin ▶ electrical double layers, the assumption of fixed charge implies that particles of uniform composition all have the same electrophoretic mobility b (velocity/field)

$$b = \frac{U}{E} = \frac{\varepsilon\zeta}{\eta} \tag{1}$$

regardless of their sizes and shapes. This naturally poses problems for electrophoretic separation and has led to the use of capillaries or gels to exploit additional effects.

In Eq. (1), the zeta potential ζ can be viewed as simply expressing the mobility in units of voltage, after factoring out the permittivity ε and viscosity η of the bulk solution. In Smoluchowski's original theory, still widely used a century later, the zeta potential is equal to the voltage ψ of the slip plane (atomically close to the surface) relative to the nearby bulk solution (just outside the diffuse part of the double layer), and, through the double-layer capacitance, it also measures the surface charge. The assumption of fixed charge thus becomes equivalent to that of constant zeta potential, and the mobility (1) reduces to a coefficient of linear response, $U \propto E$.

Since all materials are polarizable to some degree, the surface charge is generally not fixed. This leads to a broad class of ▶ nonlinear electrokinetic phenomena, where bulk electric fields interact with *induced* diffuse charge in solution to produce nonlinear electrophoretic motion, $\boldsymbol{U} = \boldsymbol{f}(\boldsymbol{E})$. In electrolytes, such effects of ▶ induced-charge electrophoresis (ICEP) occur in addition to the purely electrostatic effect of ▶ dielectrophoresis (DEP) in low-frequency AC fields (< 100 kHz), where there is enough time for diffuse-charge relaxation around the particle within each period. ICEP is a complex phenomenon, which can lead not only to nonlinear mobility (in the field direction) but also to rotation and motion in arbitrary directions, even in uniform fields.

At still lower frequencies (< 1 kHz), the passage of current through a particle, either by Faradaic reactions, surface conduction, or selective ionic conduction, can produce bulk salt concentration gradients and coupled effects of ▶ diffusiophoresis. If a ▶ superlimiting current is reached (typically in the DC limit), then ▶ electrophoresis of the second kind can occur, driven by extended ▶ space charge. Understanding all of these effects and exploiting them in microfluidic devices is an active field of research.

Basic Methodology

The theoretical description of nonlinear electrokinetic phenomena is challenging and not yet fully developed. In most of our examples below, we focus on the motion of an ideally polarizable particle, which maintains uniform potential $\varphi_0(t)$ and constant total charge Q without passing any direct current; we also neglect surface conduction and specific adsorption of ions. Under these conditions, ▶ induced-charge electro-osmotic flows are strongest, and a general mathematical framework has been developed [2–5] for the *weakly nonlinear* limit of thin double layers where the bulk salt concentration (and conductivity σ_b) remains nearly constant.

The calculation goes as follows for the motion of an isolated particle of arbitrary shape, subjected to a non-uniform, time-dependent electric field at infinity for $t > 0$. The bulk electrostatic potential satisfies Laplace's equation, $\nabla^2\varphi = 0$, subject to the far-field boundary condition,

$$\varphi \sim -\boldsymbol{E}_b \cdot \boldsymbol{r} - \frac{1}{2}\boldsymbol{r} \cdot \mathbf{G}_b \cdot \boldsymbol{r} - \ldots \quad \text{as} \quad r \to \infty \tag{2}$$

where $\boldsymbol{E}_b$ is the uniform component of the background field, $\mathbf{G}_b$ is the field-gradient tensor, etc. (Note that the constant background voltage has been set to zero.) The RC boundary condition is applied on the particle, just outside the double layer,

$$C(\psi)\frac{d\psi}{dt} = n \cdot (\sigma_b \nabla\phi) \tag{3}$$

where $C(\psi)$ is the differential capacitance of the diffuse part of the double layer, as a function of its voltage drop

$$\psi(\boldsymbol{r}, t) = \frac{\varphi_0(t) - \varphi(\boldsymbol{r}, t)}{1 + \delta} \tag{4}$$

where δ is a parameter controlling how much of the total double-layer voltage ends up across the compact layer (the ratio of the diffuse-layer and compact-layer capacitances at the point of zero charge). The particle's potential $\varphi_0(t)$

relative to the background is set by the constraint of constant total charge [2, 4],

$$Q = \oint \left(\int_0^{\psi_0} C(\psi')\mathrm{d}\psi' \right) \mathrm{d}A = \oint \left(\int_0^{\psi(\boldsymbol{r},t)} C(\psi')\mathrm{d}\psi' \right) \mathrm{d}A \quad (5)$$

This condition simplifies considerably if $C \approx$ constant, e. g. for small voltages $|\psi| \ll kT/e$ around the point of zero charge: The diffuse-layer voltage (and zeta potential) then redistributes without changing its surface average [3, 5]

$$\frac{\oint \psi(\boldsymbol{r},t)\mathrm{d}A}{\oint \mathrm{d}A} \approx \psi_0 \quad (6)$$

but it is important to remember that this assumption breaks down for large induced voltages and/or highly charged particles, since generally $\mathrm{d}C/d\psi \neq 0$. (See below.)

In the weakly nonlinear regime, the electrochemical and fluid mechanical problems decouple, except that the former provides the slip velocity driving the latter. The bulk fluid velocity satisfies the Stokes equations of viscous flow,

$$\frac{\partial \boldsymbol{u}}{\partial t} = -\nabla p + \eta \nabla^2 \boldsymbol{u} \quad \text{and} \quad \nabla \cdot \boldsymbol{u} = 0 \quad (7)$$

(keeping the unsteady term for time-dependent applied fields) subject to vanishing velocity at infinity. The boundary condition on the particle surface (just outside the double layer)

$$\boldsymbol{u} = \boldsymbol{u}_\mathrm{s} + \boldsymbol{U} + \boldsymbol{r} \times \Omega \quad (8)$$

describes electro-osmotic slip in the moving frame translating and rotating with the particle. Assuming constant permittivity and viscosity, the slip velocity is given by Smoluchowski's formula,

$$\boldsymbol{u}_\mathrm{s} = \frac{\varepsilon \psi}{\eta} \nabla_{||} \varphi \quad (9)$$

where $\psi(\boldsymbol{r},t)$ acts as the local zeta potential. Finally, as in classical ▶ electrophoresis and ▶ dielectrophoresis (effects which are both included here, along with ICEP), the translational and rotational velocities, $\boldsymbol{U}$ and Ω, are determined by the conditions of vanishing total force and torque, respectively,

$$\oint (\hat{n} \cdot \sigma)\mathrm{d}A = \oint r \times (\hat{n} \cdot \sigma)\mathrm{d}A = 0 \quad (10)$$

since viscous dissipation suppresses acceleration. In (10), the stress tensor includes viscous and electrostatic contributions

$$\sigma_{ij} = -p\delta_{ij} + \eta(\partial_i u_j + \partial_j u_i) + \varepsilon \left(E_i E_j - \frac{1}{2} E^2 \delta_{ij} \right) \quad (11)$$

and the integrals are over any surface containing the particle because the fluid is in mechanical quasi-equilibrium.

This basic methodology can be extended to more complicated situations, as outlined in the article on ▶ nonlinear electrokinetic phenomena. For example, if the particle is not ideally polarizable or has a dielectric coating, then Laplace's equation must also be solved for the electrostatic potential inside the particle, with appropriate matching conditions [3]. Channel walls can be described by replacing the conditions at infinity with appropriate electrostatic boundary conditions, including possible double-layer relaxation (3) and ICEO slip (9) on fixed metal structures or electrodes; multiple particles can also be described, usually with numerical methods. A greater complication is to allow the particle to selectively conduct ions or pass a Faradaic current and/or to adsorb significant salt from the bulk in its double layers. The resulting gradients in bulk salt concentration require solving the full Poisson–Nernst–Planck equations for the electrochemical relaxation [6] and allowing for bulk electroconvection in the fluid equations [7]. Concentration gradients also lead to ▶ diffusiophoresis, which adds a term proportional to $\nabla_{||} \log c$ to the *first kind* slip formula (9), and, if strong enough to produce bulk ▶ space charge, also to ▶ electrophoresis of the second kind [8, 18].

Key Research Findings

Field-Dependent Mobility

A well-known prediction of the classical theory of ▶ electrophoresis is that the mobility (1) only depends on the total charge (or average zeta potential), in the limits of thin double layers, small charge, and weak fields [1]. This remarkable result holds for any size or shape, even if the particle is polarizable and acquires a non-uniform charge (or zeta) profile in response to the applied field. It is not widely appreciated, however, that this follows from the assumption of constant double-layer capacitance, which reduces (5) to (6).

In the 1970s, S.S. Dukhin's group was perhaps the first to recognize that the electrophoretic mobility of polarizable particles must generally depend on the electric field [9]. In a series of Russian papers, which have yet to gain widespread attention, they predicted perturbations of the mobility as $\Delta b \propto E^2$ and thus nonlinear electrokinetic motion $\Delta U \propto E^3$, which they have come to call the

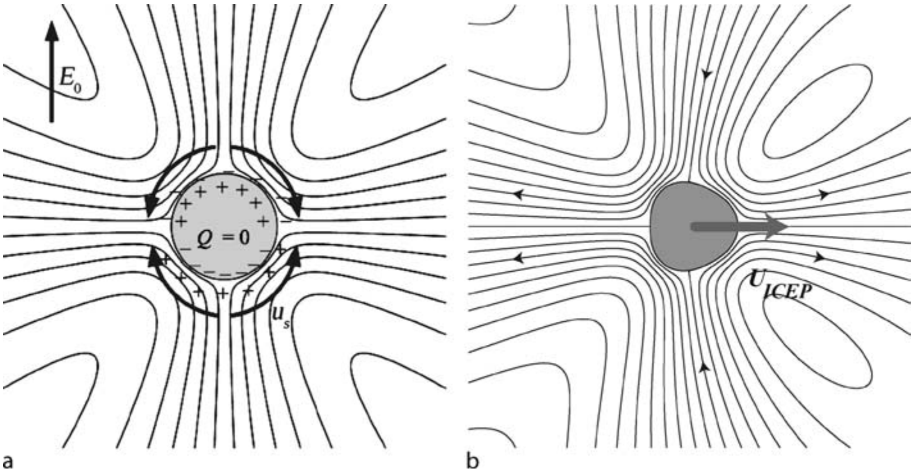

Electrokinetic Motion of Polarizable Particles, Figure 1 (**a**) Induced-charge electro-osmotic (ICEO) flow around a symmetric, uncharged, ideally polarizable particle [3]; (**b**) An example of ICEO flow and the resulting induced-charge electrophoretic (ICEP) velocity for an asymmetric shape [4]

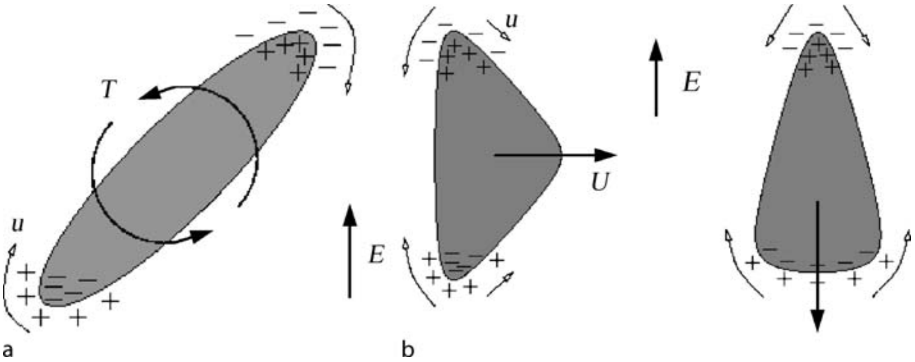

Electrokinetic Motion of Polarizable Particles, Figure 2 (**a**) Mechanism for ICEP torque on a rod-like, polarizable particle in a uniform electric field, which enhances dielectrophoretic (DEP) torque. (**b**) Possible ICEP velocities for asymmetric shapes, once their long axes have aligned with the field

► Stotz–Wien effect. For the case of a steady weak field applied to an ideally polarizable sphere of radius a, A.S. Dukhin derived an expansion for the mobility,

$$b \sim \frac{\varepsilon}{\eta}\left[\zeta - \frac{3}{8}\left(\frac{d}{d\psi}\log C\right)_{\psi=\zeta}(Ea)^2 + \dots\right] \quad (12)$$

which holds for any model of the ► electrical double layer [10]. The same result can be derived from the general formalism above by expanding (5) for $\psi \approx \psi_0 = \zeta$ and keeping corrections to (6), and large fields, non-spherical shapes, and AC forcing could also be considered. In principle, any field dependence of the mobility, regardless of its true cause, can be exploited to separate particles using an ► unbalanced AC field, which cancels the linear response (since $\langle E \rangle = 0$) while amplifying mobility corrections (since $\langle E^3 \rangle \neq 0$) [9, 11].

Induced-Charge Electrophoresis

Mobility perturbations for spherical particles, however, only hint at the rich phenomena that can arise in the electrokinetic motion of polarizable particles. Murtsovkin and co-workers were the first (and until recently the only ones) to experimentally observe nonlinear electrokinetic motion in a uniform AC field in directions *oblique to the field axis* [12]. They studied irregular quartz particles moving in water near the wall of a cuvette in surprising directions apparently set only by the particle shape. If a particle rotated enough by Brownian motion when the field was off, it could be seen to reverse direction when the field was turned back on. The velocity scaled with the square of the field amplitude and increased with the particle size. No theory was proposed for this phenomenon, in part since it was only observed near the wall and not in the bulk solution.

Bazant and Squires recently predicted that polarizable particles in the bulk can undergo essentially arbitrary translation and/or rotation by ICEP in a uniform electric field, as long as they possess appropriate *broken symmetries* [2, 4], such as non-spherical shapes and/or non-uniform surface properties (e. g. due to coatings of different polarizability or compact-layer capacitance). The former cases begin to explain Murtsovkin's early observations and beg for new experiments to test a variety of specific theoretical predictions, discussed below. The latter cases, which had not previously been observed, are described in a companion article on ▶ electrokinetic motion of heterogeneous particles. For homogeneous particles, the canonical example is that of an uncharged, ideally polarizable particle of irregular shape in a weak, uniform DC field. In that case, the basic velocity scale for ICEP is

$$U_{\mathrm{ICEP}} = \frac{\varepsilon a E^2}{\eta(1+\delta)} \quad \text{(uniform field)} \tag{13}$$

where a is a characteristic radius [2]. Using the low-voltage model (6 – 11) (with $C = \text{constant}$), Yariv derived general expressions for the translational and rotational velocities, respectively,

$$U_i = U_{\mathrm{ICEP}} \sum_{jk} \mathbf{C}_{ijk} E_j E_k \quad \text{and}$$
$$\Omega_i = \frac{U_{\mathrm{ICEP}}}{a} \sum_{jk} \mathbf{D}_{ijk} E_j E_k \tag{14}$$

where $\mathbf{C}$ is a dimensionless tensor and $\mathbf{D}$ a pseudo-tensor, each expressible as surface integrals involving the bulk potential, just outside the double layer. Squires and Bazant treated a number of specific examples by solving (6–11) directly using perturbation methods for nearly symmetric objects and discovered some simple principles to predict the motion of a particular shape [4].

The basic mechanism of ICEP for irregular particles is shown in Fig. 1. As shown in Fig. a and described in the article on ▶ nonlinear electrokinetic phenomena, the ICEO flow around a symmetric particle is quadrupolar [2, 3, 13], drawing fluid in along the field axis and ejecting it radially. If the particle has broken left/right symmetry as shown in Fig. b, then the radial flow is stronger on one side than the other, leading to ICEP motion perpendicular to the field. Similarly, breaking only fore/aft symmetry produces ICEP motion along the field axis, and combinations of these asymmetries can cause motion in an arbitrary direction.

ICEP can also contribute to the rotation of polarizable particles with elongated shapes [2, 4, 5, 15], as illustrated in Fig. 2a. It is well known that ▶ DEP causes such particles to align with the axis of a uniform field, due to electrostatic torque on the induced dipole. At low AC frequency (or in the DC limit), if the field persists in one direction long enough for ICEO flow to occur, then ICEP causes a rotational velocity with a basic scale that is independent of the particle size but sensitive to its shape,

$$\Omega_{\mathrm{ICEP}} = \frac{U_{\mathrm{ICEP}}}{a} = \frac{\varepsilon E^2}{\eta(1+\delta)} \tag{15}$$

This scale happens to be the same as that of the DEP rotational velocity, so ICEP rotation is easily overlooked and mistakenly interpreted as DEP. It is possible, however, to clearly distinguish the two effects, as recently demonstrated by experiments [14] and simulations [15] involving rod-like, metal particles in uniform AC fields (see Fig. 3.).

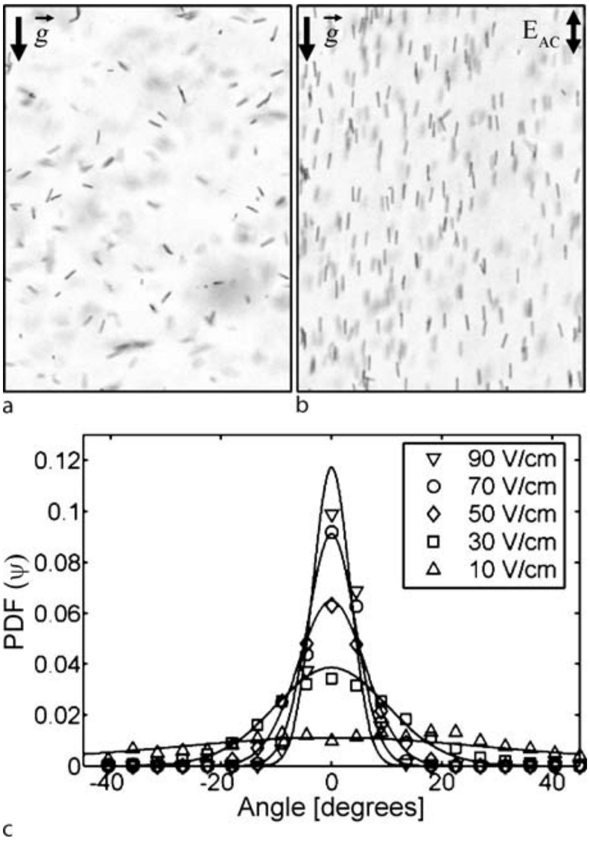

Electrokinetic Motion of Polarizable Particles, Figure 3 Experiments on cylindrical silver particles (0.318 μm diameter, 6 μm length) sedimenting in de-ionized water by gravity alone (**a**) and in a 100 Hz, 100 V/cm AC field aligned with gravity (**b**). The experimental distribution of angles in different fields (**c**) agrees well with theoretical curves (solid) which take into account both ICEP rotation and electrostatic torque [14]

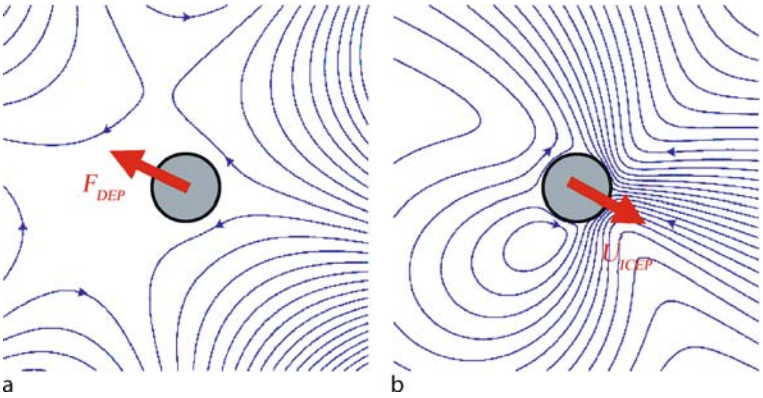

Electrokinetic Motion of Polarizable Particles, Figure 4 An ideally polarizable cylinder subjected to a non-uniform DC electric field in an electrolyte with thin double layers: (**a**) Field lines and the DEP force, typically directed down the field gradient. (**b**) Streamlines of ICEO flow and the ICEP velocity, which always directed opposite to the DEP force [4]

More complicated asymmetric particles can undergo essentially arbitrary ICEP motion, even in a uniform field. Even in the context of the simple model above, these effects have not yet been fully analyzed, but some general principles have been identified [4]. A striking example is shown in Fig. 2b, which illustrates how arrow-like particles of slightly different shapes can move in perpendicular directions in a uniform field, depending on their broken symmetries: On the left, a short, fat arrow rotates to align its long axis with the field and then moves perpendicular to the field, toward its pointed end; on the right, a long, thin arrow also rotates to align its long axis, but then moves parallel to the field, toward its blunt end. Such predictions are quite recent, however, and remain to be tested experimentally.

A telltale sign of ICEP is the presence of non-uniform ICEO flow around the particle, which leads to complex hydrodynamic interactions with other particles and walls. For example, the basic quadrupolar flow in Fig. 1a causes two symmetric particles to move toward each other along the field axis and then push apart in the normal direction [13, 15]. A finite cloud of such particles would thus become squashed into a disk-like "spreading pancake" perpendicular to the field axis [3]. The same flow field can also cause particles to be repelled from insulating walls (perpendicular to the field) [16] or attracted toward electrodes (normal to the field), but these are only guiding principles. Broken symmetries in particle shape or wall geometry, however, can cause different motion due to combined effects of DEP and ICEP, even opposite to these principles, and the interactions of multiple particles can also be influenced strongly by walls. Such effects have not yet been fully explored in experiments or simulations.

Low-Frequency Dielectrophoresis

In the 1970s, Shilov and Estrella-Lopis first recognized that electrohydrodynamics (what we now call ICEO) can contribute to the motion of particles in low-frequency, non-uniform electric fields [17], in addition to DEP, although the effect has not been studied much in theory or experiment. Shilov and Simonova analyzed the problem of an ideally polarizable sphere in a uniform field gradient and made the remarkable prediction that the particle does not move. Due to equal and opposite motions by DEP and ICEP, the sphere levitates in the field while driving a steady ICEO flow, but this is a unique case.

Squires and Bazant recently showed that broken symmetries in the field gradient and/or the particle shape generally cause a particle to move, due to subtle imbalances between ICEP and DEP [4]. Both effects have the same basic scaling,

$$U_{\text{ICEP}} = \frac{\varepsilon a^2 \nabla |E|^2}{\eta(1+\delta)} \quad \text{(non-uniform field)} \qquad (16)$$

Moreover, as illustrated in Fig. 3, the DEP force and ICEP velocity tend to act in opposite directions, at least for the case of an ideally polarizable particle with thin double layers in a non-uniform electric field (of arbitrary complexity). Similar to the case of rotational motion discussed above, ICEP can be easily overlooked and the observed translational motion attributed solely to DEP, if it is along the field gradient. Experiments clearly separating ICEP and DEP effects are still lacking, and an opportunity exists to exploit these combined effects for manipulating polarizable colloids, once the effects are better understood.

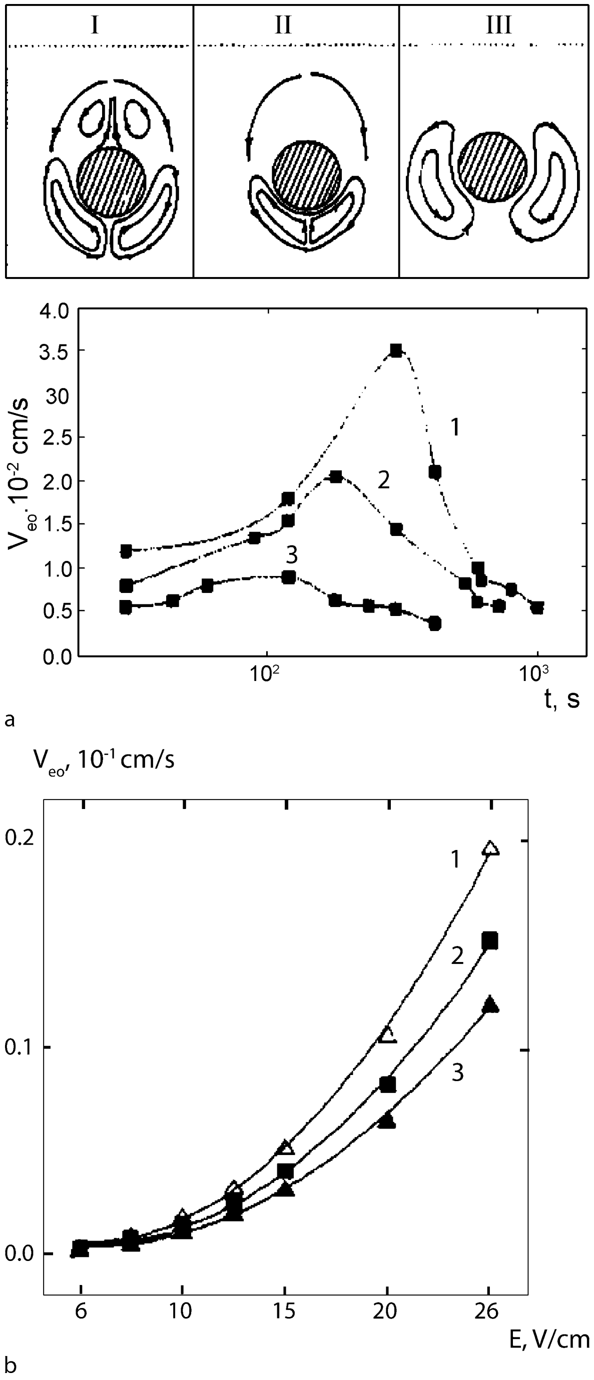

Electrokinetic Motion of Polarizable Particles, Figure 5 Experiments on electrophoresis of the second kind for cationite KU-2-8 particles in 10^{-4} MNaCl. (**a**) Velocity versus time for particles diameters 0.42 mm (1), 0.33 mm (2), and 0.21 mm (3) with sketches of the observed flow fields. (**b**) Scaling of velocity with applied field for diameters 0.31 mm (1), 0.28 mm (2), and 0.26 mm (3) [8]

Electrophoresis of the Second Kind

As described in the article on ►nonlinear electrokinetic phenomena, electro-osmosis of the second arises when the bulk salt concentration goes to zero at a surface passing a diffusion-limited current. Under conditions of ►super-limiting current, the density of counterions in the ►electrical double layer loses its classical quasi-equilibrium profile and a region of dilute ►space charge extends into the solution to the point where the bulk salt concentration becomes appreciable. In spite of the small counter-ion concentration, the expulsion of co-ions from the space charge layer leads to significant charge density and, in the presence of a tangential electric field, ►electroosmosis of the second kind [7].

If a particle is able to sustain a super-limiting current, then such flows can cause it to move by ►electrophoresis of the second kind, as first noted by S.S. Dukhin in the 1980s. As shown in Fig. 5, second-kind electrophoresis has been observed experimentally for large (> 10 μm) particles composed of cation-selective porous materials, and the flow structure has been studied in detail [8]. Due to the complexity of the phenomenon, however, the theory has mainly been limited to scaling arguments and heuristic boundary-layer approximations [18], but there is hope that the rigorous mathematical study of second-kind flows [7] could soon be extended to second-kind electrophoresis. Effects of walls, multiple particles, and broken symmetries should also eventually be studied.

Future Directions for Research

Compared to the vast literature on linear ►electrophoresis, the study of nonlinear electrokinetic motion is still its early stages. As indicated above, much remains to be done, both in making theoretical predictions and systematically testing them (or discovering new effects) in experiments. Modern mathematical methods and computational power now allow more sophisticated analysis, going beyond linear and weakly nonlinear approximations, as well as large scale simulations of interacting colloidal particles. Similarly, the advent of microfluidics provides new opportunities to observe and exploit nonlinear electrokinetic phenomena, since polarizable particles can now be fabricated with complicated shapes and material properties and electric fields controlled with submicron precision.

Applications of nonlinear electrokinetic motion are still largely unexplored. Aperiodic electrophoresis and other ICEP phenomena could be used to separate polarizable particles based on shape, size, and/or surface properties, in ways that cannot be accomplished using linear electrophoresis. Sorting, trapping, and assembling particles interacting via ICEP and DEP in microfluidic devices

could be used to engineer new materials with anisotropic electrical, mechanical, or optical properties. Polarizable particles can also be attached to biological molecules or cells and manipulated by ICEP and DEP for separation, characterization, or labeling.

Cross References

▶ AC Electro-Osmotic Flow
▶ Aperiodic Electrophoresis
▶ Dielectrophoresis
▶ Dielectrophoretic Motion of Particles and Cells
▶ Diffusiophoresis
▶ Electrical Double Layers
▶ Electrokinetic Motion of Heterogeneous Particles
▶ Electroosmotic Flow (DC)
▶ Electrophoresis of the Second Kind
▶ Electrophoresis
▶ Induced-Charge Electrophoresis
▶ Nonlinear Electrokinetic Phenomena
▶ Space Charge
▶ Stotz–Wien Effect
▶ Super-Limiting Current
▶ Unbalanced AC Field

References

1. Anderson JL (1989) Colloid transport by interfacial forces. Annu Rev Fluid Mech 21:61–99
2. Bazant MZ, Squires TM (2004) Induced-charge electrokinetic phenomena: theory and microfluidic applications. Phys Rev Lett 92:066010
3. Squires TM, Bazant MZ (2004) Induced-charge electro-osmosis. J Fluid Mech 509:217–252
4. Squires TM, Bazant MZ (2006) Breaking symmetries in induced-charge electro-osmosis. J Fluid Mech 560:65–101
5. Yariv E (2005) Induced-charge electrophoresis of nonspherical particles. Phys Fluids 17:051702
6. Chu KT, Bazant MZ (2006) Nonlinear electrochemical relaxation around conductors. Phys Rev E 74:011501
7. Zaltzman B, Rubinstein I (2007) Electro-osmotic slip and electroconvective instability. J Fluid Mech 579:173–226
8. Mishchuk NA, Takhistov PV (1995) Electroosmosis of the second kind. Colloid Surf A: Physicochem Eng Asp 95:119–131
9. Dukhin AS, Dukhin SS (2005) Aperiodic capillary electrophoresis method using an alternating current electric field for separation of macromolecules. Electrophor 26:2149–2153
10. Dukhin AS (1993) Biospecific mechanism of double layer formation and peculiarities of cell electrophoresis. Colloid Surf A: Physicochem Eng Asp 73:29–48
11. Chimenti RJL (1992) Electrophoretic separation. US Patent 5,106,468, 20 Dec 1985
12. Murtsovkin VA, Mantrov GI (1990) Study of the motion of anisometric particles in a uniform variable electric field. Colloid J USSR 52:933–936
13. Gamayunov NL, Mursovkin VA, Dukhin AS (1986) Pair interactions of particles in electric field. 1. Features of hydrodynamic interaction of polarized particles. Colloid J USSR 48:197–203
14. Rose K, Santiago JG (2007) Rotational electrophoresis of striped metallic microrods. Phys Rev E 75:011503
15. Saintillan D, Darve E, Shaqfeh ESG (2006) Hydrodynamic interactions in the induced-charge electrophoresis of colloidal rod suspensions. J Fluid Mech 563:223–259
16. Zhao H, Bau HH (2007) On the effect of induced-charge electroosmosis on a cylindrical particle next to a surface. Langmuir 23:4053–4063
17. Simonova TS, Shilov VN, Shramko OA (2001) Low-frequency dielectrophoresis and the polarization interaction of uncharged spherical particles with an induced debye atmosphere of arbitrary thickness. Colloid J 63:108–115
18. Ben Y, Demekhin EA, Chang H–C (2004) Nonlinear electrokinetics and superfast electrophoresis. J Colloid Interface Sci 276:483–497

Electrokinetic Potential

▶ Zeta Potential Measurement

Electrokinetic Sample Dispensing

▶ Electrokinetic Sample Injection

Electrokinetic Sample Injection

LUNG-MING FU[1], CHIEN-HSIUNG TSAI[2]
[1] Department of Materials Engineering, Pingtung, Taiwan
[2] Department of Vehicle Engineering, National Pingtung University of Science and Technology, Pingtung, Taiwan
loudyfu@mail.npust.edu.tw, chtsai@mail.npust.edu.tw

Synonyms

Electrokinetic injection; Electrokinetic sample dispensing

Definition

Kinetic sample injection is a method which employs electroosmotic flow to load and separate the samples for chemical and biomedical analysis in many bio- or chemical labchips. It is one of the injection techniques used for the microfluidic injector within microfluidic devices. The typical volume delivered by kinetic injection is about hundreds of picoliters.

Overview

Microfluidic devices have attracted considerable attention recently due to the development of an ever-increasing

number of applications in the fields of chemical and biological analysis. A typical application of such devices is the separation of DNA in genetic engineering processes. A fundamental feature common to all of these devices is that the mobility of charged particles can be controlled when they move under the influence of an applied electric field. This induced flow motion is generally referred to as electroosmotic flow (EOF) or capillary electrophoresis (CE) [1]. Micromachining technology now permits the fabrication of a network of microchannels on a single quartz, glass or plastic (poly(dimethylsiloxane) (PDMS), polycarbonate (PC), poly(methylmethacrylate) (PMMA)) substrate to form an integrated microfluidic chip capable of performing a variety of procedures, including sample handling, mixing, chemical reaction, pretreatment, separation etc. These devices are frequently employed to separate samples using a technique which is similar to that used in conventional CE analysis, but which is more efficient and faster.

An important component of many bio- or chemical Lab-on-a-Chip devices is the microfluidic injection system, the precise control of the size and concentration of the dispensed sample in the microfluidic injection system determines the performance of these Lab-on-a-Chip devices. Two methods are commonly adopted in microfluidic injection systems: electrokinetic injection and pressure injection. Pressure driven injections have the advantage that precise voltage control is not necessary and sample injections of uniform composition can be obtained. However, pressure injections require a means to transport or pump the sample that is dissolved in a liquid. Switchable valves which direct the flow into a desired direction can achieve flow control. These valves are difficult to integrate into microfluidic devices, so the kinetic injection system prevails within the microchip [2].

Traditionally, electrokinetic injection is the most common method for sample injection and separation into the microchannel utilizing some form of electroosmotic pumping. However, depending on the sample, due to the different mobility in an electric field, a bias to anionic, neutral, or cationic analytes is possible. Careful adjustment of pH and ionic strength can reduce this effect [2]. A broad injection band and sample leakage phenomena are also important defects of the electrokinetic injection method. Both are known to reduce the separation efficiency of a device since they result in a wide sample distribution within the microchannel and an increasing signal baseline as the number of injection runs increases [3–6], respectively. Other injection methods, like pressure injection, do not show this method-dependent effect.

A variety of valves capable of providing discrete injections configurations have been presented, including the T-form, the cross-form, and the double-T form. Improved reproducibility has been obtained by the double-T and cross-form injections. Jacobson et al. [7] and Slentz et al. [8] have described the injection techniques for floating injection, gated injection, and pinched injection. Fu and Lin [5] have proposed the double-L injection to reduce the sample leakage. When the EOF is the only force to transport a sample in a capillary, an electrophoretic bias [9] and the sample leakage has to be considered during injection.

Both the theoretical studies and the experimental studies have demonstrated that the loading and dispensing of sub-nanoliter samples using a microfluidic-crossing microchannel chip can be well controlled electrokinetically. The ability to inject and transport large axial extent, concentration-dense samples has been demonstrated in the literature. Both experimental and numerical results indicate that the shape, cross-stream uniformity, and axial extent of the samples are very sensitive to changes in the electric fields applied in the loading channel. In the dispensing process, larger samples are shown to disperse less than focused samples, maintaining more solution with the original sample concentration. Li [1] has outlined the effects of: buffer electroosmotic mobility, sample diffusion coefficient, sample electrophoretic mobility, the difference in conductivity of the solutions, the applied electrical field strength, the channel size, and channel configurations on the injection and the separation process. By understanding the complicated electrokinetic processes involved in the sample dispensing processes, we can find the optimal applied voltages and improved methods to control the size, shape and concentration of the dispensed samples. Tsai et al. [6] have employed a numerical simulation technique to investigate the leakage behavior in various microfluidic devices using different control voltage strategies. Five different injection systems are considered: cross-form, T-junction, double-T junction, focused flow cross-form, and triple-T form. For each injection system, various injection techniques are proposed with the intention of reducing sample leakage. The relative performance of each injection arrangement is assessed in terms of its effectiveness in reducing the sample leakage ratio, and hence by implication, its suitability for high detection resolution applications, and by considering the degree of complexity of its electric potential control system.

Many studies have demonstrated that the injection system on a CE microchip is one of the most fundamental components of the sample handling process, and that its characteristics determine the quality of the separation. Practical applications, such as separation or detection, require that the dispensed sample volume be precisely controlled and that sample leakage to the separation channel be prevented. Hence, developing viable low-leakage injection

techniques with the ability to dispense samples of variable volume is fundamental in improving the performance of microfluidic devices designed for biomedical applications. More sophisticated injection system configurations capable of providing variable-volume sample plugs have also been proposed [3, 4], including the multi-T form and the double-cross form. Implementing increasingly complex and integrated functions in a single chip demands an investigation into appropriate microchannel network designs and electric potential control strategies. Additionally, the electrokinetic transport phenomena in microfluidic devices must be fully understood if the design and control of biochips are to be optimized. Accordingly, many studies, both experimental and numerical, have been performed to investigate various aspects of microfluidic devices. These studies have confirmed the power of numerical methods for modeling the flow structures associated with various operating modes in different microchannel network configurations.

Basic Methodology

Reproducible injection for capillary electrophoresis on a microdevice/Lab-on-Chip is not easy to achieve. Different injection designs (e. g., T-type, double-T type, and cross-type) and different injection techniques have been applied (pinched injection, gated injection, double-L injection) within microfluidic devices. The volume and the concentration of the dispensed sample are the key parameters of this dispensing process, and they depend on the applied electrical field, the flow field, and the concentration field during the injection and separation processes. The problems and properties of the different modes are described below.

Cross-Form Injection Method

Figure 1a presents a schematic illustration of the cross-form injection system. There are four reservoirs connected to the four ends of the microchannels. Electrodes are inserted into these reservoirs to set up the electrical field across the channels. Initially, a sample solution (a buffer solution with sample analytes) is filled in the reservoir of the inlet Channel 1, the other reservoirs and the microchannels are filled with the pure buffer solution. Figure 1b shows the flow of the sample from the inlet Channel 1 to the waste Channel 2 caused by the application of a chosen injection voltage. This is the so-called injection step. When the sample has completely filled the cross-channel intersection, the electric potential distribution is switched immediately to the separation step, in which Channels 1 and 2 are maintained in an open condition and a separation voltage is applied to Channels 3 and 4. Under these conditions, the sample is forced out of the intersection into the separation channel, as shown in Fig. 1c. This is the so-called separation step. Injection of the sample involves discrete injection and separation steps, during which the controlling electrical fields are established in accordance with Kirchhoff's law. The volume and the concentration of the dispensed sample are the key parameters of this dispensing process, and they depend on the applied electrical field, the flow field, and the concentration field during the injecting and the separating processes.

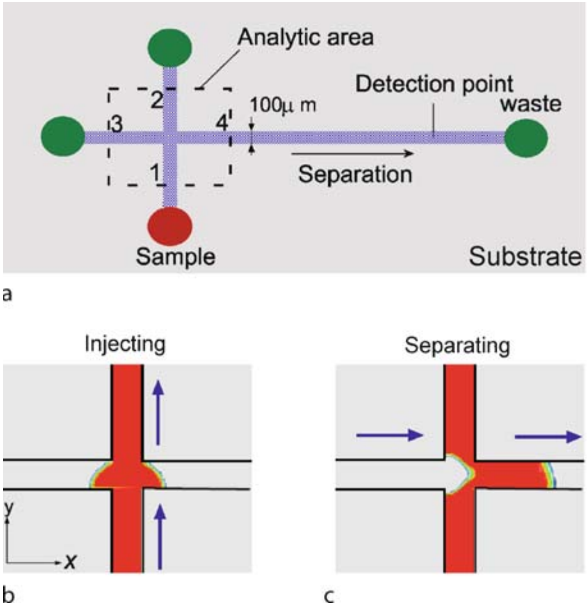

Electrokinetic Sample Injection, Figure 1 Cross-form injection method, (**a**) schematic diagram of injection system; (**b**) injection step; (**c**) separation step

T-Junction Injection Method

Figure 2a provides a schematic diagram of the T-junction injection system. Figure 2b shows the flow of the sample from the inlet channel (Channel 1) to the waste channel (Channel 3) under the influence of an injection voltage. When the sample has completely filled the junction area, the electric potential distribution is switched immediately to the separation step, in which Channel 1 is maintained in an open condition while a separation voltage is applied to Channels 2 and 3. Under these conditions, the sample is forced out of the intersection region into the separation channel, as shown in Fig. 2c. At this magnitude of separation voltage, a noticeable leakage of the sample occurs from Channel 1 as the plug is injected into the separation channel.

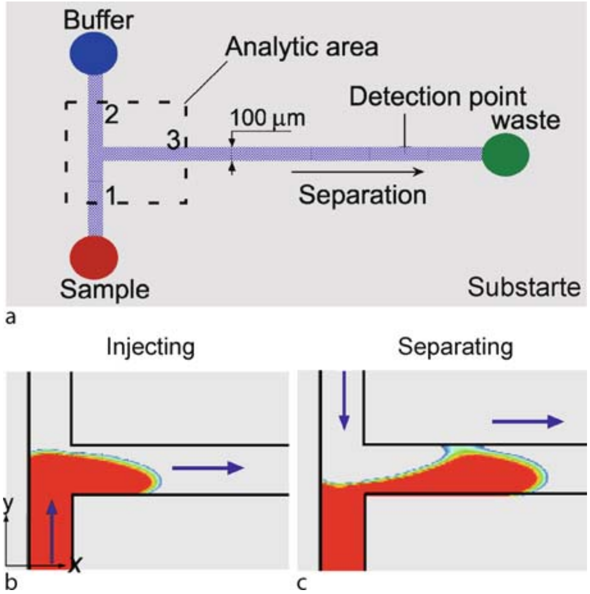

Electrokinetic Sample Injection, Figure 2 T-form injection method, (**a**) schematic diagram of injection system; (**b**) injection step; (**c**) separation step

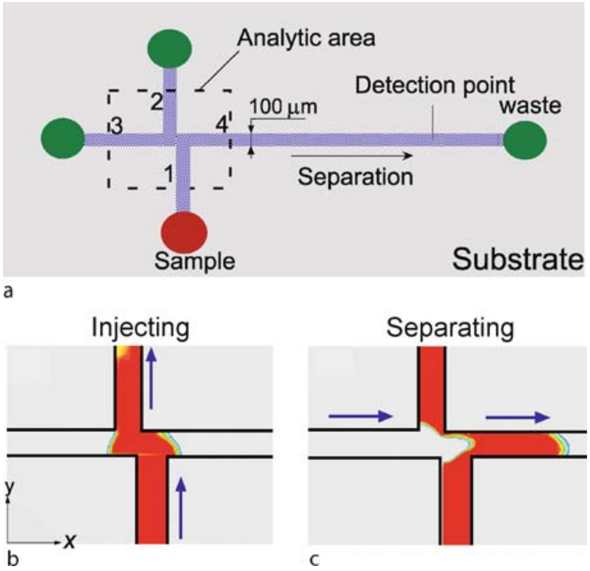

Electrokinetic Sample Injection, Figure 3 Double-T injection method, (**a**) schematic diagram of injection system; (**b**) injection step; (**c**) separation step

Double-T Injection Method

In the cross-form configuration, the volume of the sample plug is determined by the geometry of the cross-sectional area of the injection channel. Hence, the sample volume delivered by such a system is always constant. This arrangement is clearly unsuitable for applications requiring the supply of variable-volume sample plugs to the separation process. A more appropriate solution is to employ the double-T injection system shown schematically in Fig. 3a. This configuration serves as a basic component in a more sophisticated injection system such as multi-T injection system. Fig. 3b shows the flow of the sample from the inlet channel to the waste channel under the influence of an injection voltage. When the sample has completely filled the cross-channel intersection, the electric potential distribution is switched immediately to the separation step, in which Channels 1 and 2 are maintained in an open condition while a separation voltage is applied to Channels 3 and 4. This forces the sample out of the intersection region into the separation channel, as shown in Fig. 3c.

Double-L Injection Method

To overcome the problem of flow leakage in the cross-form microchip (Fig. 4a) without resorting to the complex potential control required by the other injection method, a novel double-L injection method has been proposed by Fu et al. [5]. In the injection step, the sample is loaded from Channel 1 to Channel 3 under an applied injection voltage and is diffused into the intersection of Channels 2 and 4 (Fig. 4b). In the separation step, the sample in the intersection region is driven into the separation channel (Channel 4) by a separation voltage applied to Channels 2 and 4 (Fig. 4c). The research demonstrates a clear reduction in the sample leakage into Channel 4 when this double-L injection method is applied. The electric potential control system for the double-L injection method is more straightforward and requires the use of just two control points.

Pinched Injection Method

A pinched injection can be described as an injection technique during which the voltage controls both the injection and the separation [7]. Fig. 5 illustrates the simulated sample plug distributions for the injection and separation procedures in the cross-form microchip (Fig. 5a). Fig. 5b shows the flow of the sample from the inlet channel to the waste channel under the influence of an injection voltage applied to Channels 1 and 2. Meanwhile the chosen electrical field strengths are also applied to Channels 3 and 4 to pinch the sample streams along the waste channel. When the flow reaches the stationary state, the electric potential distribution is switched immediately to the separation step, in which Channels 1 and 2 are maintained in an open con-

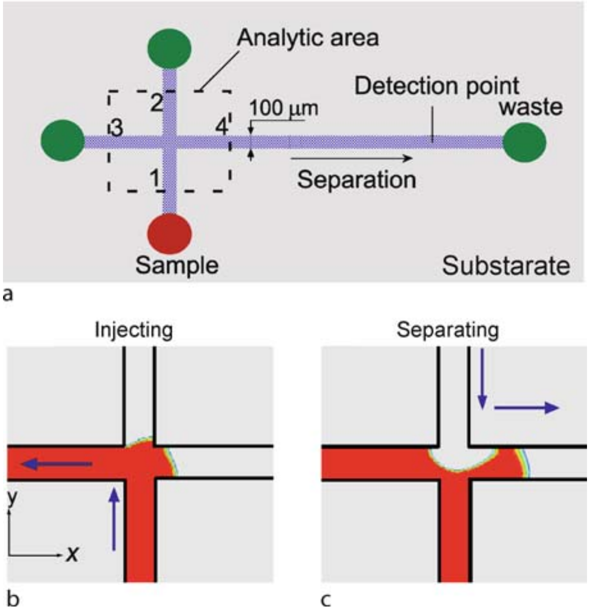

Electrokinetic Sample Injection, Figure 4 Double-L injection method in cross-form system, (**a**) schematic diagram of injection system; (**b**) injection step; (**c**) separation step

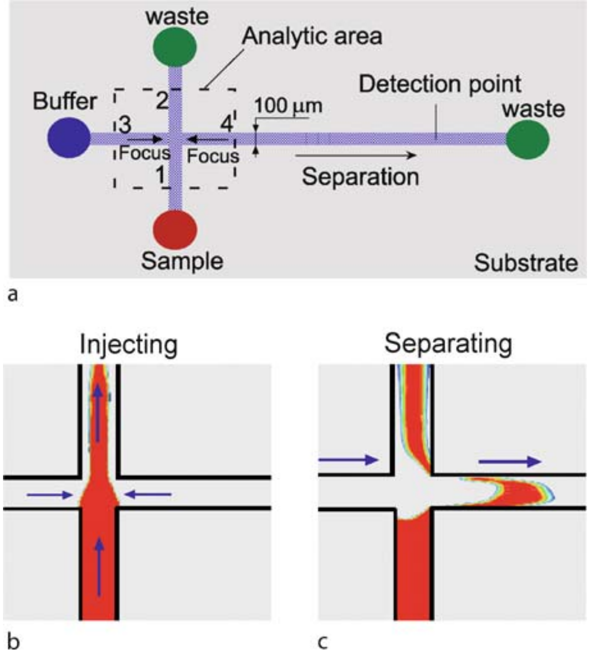

Electrokinetic Sample Injection, Figure 5 Pinched injection method in cross-form system, (**a**) schematic diagram of injection system; (**b**) injection step; (**c**) separation step

dition while a separation voltage is applied to Channels 3 and 4. This forces the sample out of the intersection region into the separation channel, as shown in Fig. 5c.

For homogeneous buffer and channel properties, material transport into and out of the microchip valve in Fig. 5a can be described as a simple circuit with the following constraint:

$$E_{\mathrm{w}} = E_{\mathrm{b}} + E_{\mathrm{a}} + E_{\mathrm{s}}$$

where E_{x} is the absolute value of the electric field strength in the buffer (b) Channel 3, sample (s) Channel 1, analysis (a) Channel 4, and sample waste (w) Channel 2.

By adjusting E_{s} relative to E_{b} and E_{a}, the degree of sample confinement in the cross-intersection can be controlled. The electrical field strengths in the buffer and analysis channels should be approximately equal ($E_{\mathrm{b}} \sim E_{\mathrm{a}}$) to achieve a symmetrical sample confinement. The pinching effect can be qualitatively described as weak pinch, medium pinch or strong, depending on the relative magnitude of electrical field strengths $E_{\mathrm{s}} > E_{\mathrm{b}}$, $E_{\mathrm{s}} \sim E_{\mathrm{b}}$ or $E_{\mathrm{s}} < E_{\mathrm{b}}$ respectively.

Gated Injection Method

Initial gated injections [8] also used a T-type configuration. The cross-injection is now widespread. Figure 6 shows the operating sequence of this gated valve. Figure 6a shows a schematic of the microchip used for the gated injection

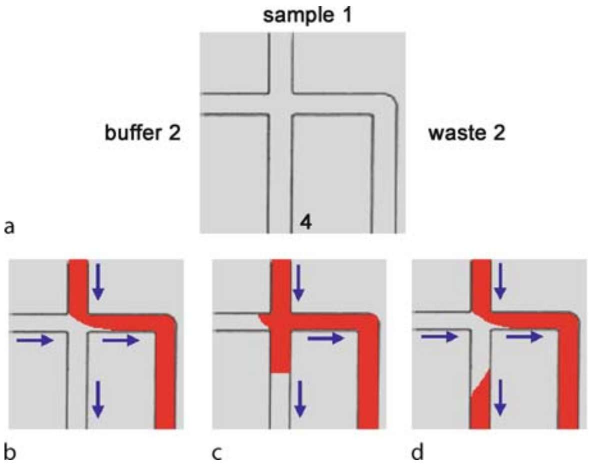

Electrokinetic Sample Injection, Figure 6 Gated injection method, (**a**) schematic diagram of injection system; (**b**) loading step; (**c**) injection step; (**d**) separation step

method. The sample is transported down the sample Channel 1 through the injection valve into the waste Channel (3) (Fig. 6b). The electric potential applied to the buffer reservoir through the high-voltage relay prevents sample leaking into the analysis channel (4). To load a sample from the sample channel into the analysis channel, the electric potential at the buffer reservoir is removed by opening the high voltage relay for a brief period of time, e. g., 0.4 s in

Fig. 6c. The sample is electrokinetically transported into the analysis channel. To terminate sample flow into the analysis channel, the electric potential at the buffer reservoir is reapplied (Fig. 6d). A small quantity of sample is dispensed into the analysis channel as shown in Fig. 6d. Due to the directionality of the buffer flow, i. e., traveling from left to right as pictured, the rear of the sample plug is triangular in shape but disappears in about one second due to the transverse diffusion within the analysis channel. The asymmetric shape observed at the rear of the sample plug does not hinder high-performance chromatographic separations which employ the gated valve.

For homogeneous buffer and channel properties, material transport in and out of the microchip valve shown in Fig. 6a can be described as a simple circuit with the following constraint:

$$E_\mathrm{b} + E_\mathrm{s} = E_\mathrm{a} + E_\mathrm{w}$$

where E_x is the absolute value of the electric field strength in the buffer (b) Channel 2, sample (s) Channel 1, analysis (a) Channel 4, and waste (w) Channel 3. To prevent the sample from electrokinetically transporting from the cross-intersection into the analysis channel during the sample loading mode

$$E_\mathrm{s} \leqq E_\mathrm{w1} \quad \text{or} \quad E_\mathrm{b} \geqq E_\mathrm{a} \,.$$

The ratio of the sample to waste electric field strength needed to prevent the sample from diffusing into the analysis channel depends on both the transit time of the sample through the cross-intersection and the diffusion coefficient of the sample. Sample to waste electric field strength ratios from 0.4 to 0.75 are obtained empirically for a neutral marker, e. g., rhodamine B. This range allows the sample to pass through the valve from the sample channel to the waste channel without diffusing into the analysis channel.

Key Research Findings

In general, the injections configurations and techniques (including the T-form, the cross-form, the double-T form, gated injection, pinched injection, and double-L injection) described in the above sections are used to load and dispense the sample for bio-analysis. The innate defects of kinetic injection systems are: electrophoretic bias and sample leakage. These effects have to be considered during injection to obtain the higher-resolution detection. Physically, the parameters that affect the quality of the injection are: buffer electroosmotic mobility, sample diffusion coefficient, sample electrophoretic mobility, the difference in conductivity of the solutions, the applied electrical field strength, the channel size, and channel configurations (injector geometry) [1, 10].

Cross-injection suffers from controlling the sample size and preventing sample leakage, but it is valuable for repeated injections with uninterrupted buffer flow. Jacobson has proposed a pinched injection technique to reduce the sample leakage. A modified pinched injection method with three steps, that minimizes the sample leakage more than the original method has also been proposed [2]. The steps in a three-step pinched injection are: pinched flow from sample reservoir to sample waste reservoir, short flow reversal (retraction into sample reservoir), and dispense sample with buffer from sample channel into analysis channel. The amount that is injected in pinched injection is time independent. Pinched injection does not suffer from controlling the sample size, but it is very limited in the variation of the sample size. The double-L injection technique has been studied in great detail by Fu and his co-workers utilizing experimental and numerical analysis [5]. For this method, sample flow direction is not as in a standard injection across the channel but *around the corner* of the channel cross. The double-L injection is claimed to be very suitable for high-resolution, high-throughput biochemical analytical applications, high precision analysis on a chip, and in many other applications throughout the micrototal analysis systems field.

The gated injector is time dependent and has an electrophoretical sample bias [9]. The performance of this valve is measured by recording temporal profiles at 1 mm downstream of the valve for injection times of 0.2, 0.4, and 0.8 s. The peak maximum does not increase at longer injection times. The peak area reproducibility is better than 0.5% relative standard deviation for 20 injections for each injection time. As with conventional electrokinetic injection schemes, this injection is also biased by the relative electrokinetic mobility of the sample ions. This valve dispenses sample volumes that are linearly proportional to the electrophoretic mobility for which this bias is easily compensated.

The majority of injection systems are only capable of delivering a fixed-volume sample plug into the analysis channel and are limited in function by their configuration. Fu and his co-workers have proposed the multifunction injection system and a variable-volume-injection system within the microfluidic chip as described below.

Multifunction Injection System

Traditionally, the design of the injection channel has always been in the form of a cross. A limitation of this configuration is that it is only capable of providing discrete, fixed-volume samples. However, some applications require the delivery of different sample volumes to the detection and separation processes. The unique multi-T

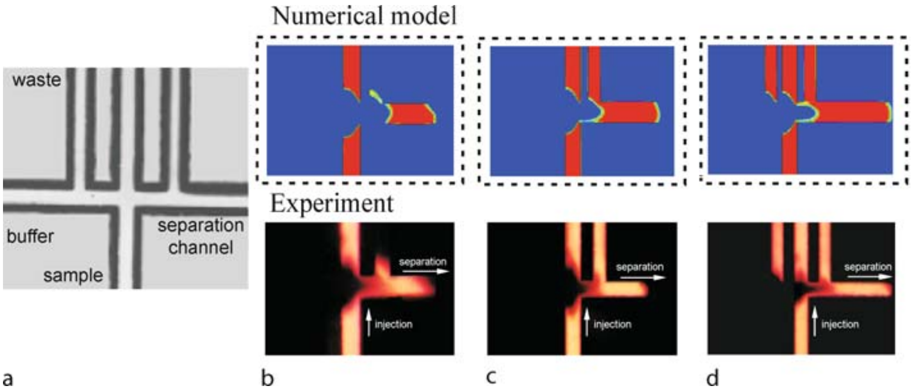

Electrokinetic Sample Injection, Figure 7 Multifunction injection system (**a**) schematic diagram of injection system; (**b**) cross form injection method, (**c**) double-T injection method, and (**d**) triple-T injection method

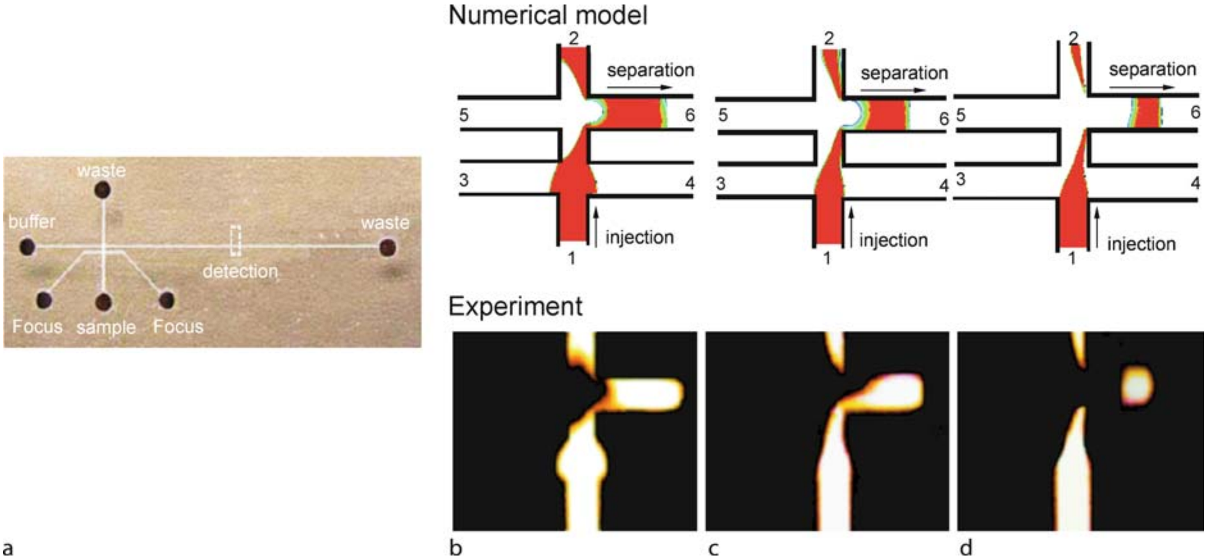

Electrokinetic Sample Injection, Figure 8 Variable-volume-injection system (**a**) microfluidic chip, (**b**) focusing ratios $F/\phi = 1$, (**c**) $F/\phi = 1.4$, and (**d**) $F/\phi = 1.8$

configuration injection system [3] has the ability to simulate the functions of the cross, double-T and triple-T systems through appropriate manipulations of the electric field within its various channels. Figure 7 shows the experimental and numerical simulation results of the proposed multi-T-form injection system.

Variable-Volume-Injection System

A double-cross-injection system, which combines conventional cross-injection systems and the electrokinetic focusing technique on a single microfluidic chip, has been designed and its performance analyzed. Through the appropriate specification of the electric focusing ratio, it has been shown that the proposed system is not only capable of performing the same function as the traditional cross-injection system, but that it is also able to generate sample plugs of different volumes. Finally, the results indicate that the proposed design improves the sample plug distribution in the analysis channel, and thus results in a superior separation detection performance. Figure 8 shows the experimental and simulated results for the double-cross-injection system [4] at focusing ratios of 1, 1.4, and 1.8, respectively.

Future Directions for Research

Quality assurance in micro-CE has yet to be studied in detail. Research focuses on practical applications and the transfer of separation problems to a microdevice. One

problem is the chip-to-chip variation from manufacturing, another the run-to-run performance due to reloading, the cleaning of the channel surfaces, the not perfect electrokinetic injection mode, or that instrumental setups are usually still in the trial state and have only been optimized for one purpose [2].

A problem for all microdevices is the introduction of a sample into the microreservoir or onto the microdevice. Usually the samples are loaded manually onto the device by means of a micropipette or similar tool. This process is not very compatible with an analytical device intended to be ultrafast, with a high sampling rate, and easily applicable in different areas. Methods in which injection and sample loading is done in one step should be developed more intensively in future.

Cross References

- ► Electrical Double Layers
- ► Zeta-Potential
- ► Electroosmotic Flow (DC)
- ► Electrokinetic Dispensing
- ► Proteomics in Microfluidic Devices
- ► Materials Used in Microfluidic Devices
- ► Microfluidic Devices in Tissue Engineering
- ► Single Cell Analysis in Microfluidic Devices

References

1. Li D (2004) Electrokinetics in Microfluidics. Academic Press, London
2. Wenclawiak BW, Puschl RJ (2006) Sample injection for capillary electrophoresis on a micro fabricated device/on chip CE injection. Anal Lett 39:3–16
3. Fu LM, Yang RJ, Lee GB, Liu HH (2002) Electrokinetic injection techniques in microfluidic chips. Anal Chem 74:5084–5091
4. Fu LM, Yang RJ, Lee GB (2003) Electrokinetic focusing injection methods on microfluidic devices. Anal Chem 75:1905–1910
5. Fu LM, Lin CH (2003) Numerical analysis and experimental estimation of a low-leakage injection technique for capillary electrophoresis. Anal Chem 75:5790–5796
6. Tsai CH, Yang RJ, Tai CH, Fu LM (2005) Numerical simulation of electrokinetic injection techniques in capillary electrophoresis microchips. Electrophoresis 26:674–686
7. Alarie JP, Jacobson SC, Culbertson CT, Ramsey JM (2000) Effects of the electric field distribution on microchip valving performance. Electrophoresis 21:100–106
8. Jacobson SC, Ermakov SV, Ramsey JM (1999) Minimizing the number of voltage sources and fluid reservoirs for electrokinetic valving in microfluidic devices. Anal Chem 71:3273–3276
9. Slentz BE, Penner NA, Regnier F (2002) Sampling bias at channel junctions in gated flow injection on chips. Anal Chem 74:4835–4840
10. Shultz-Lockyear LL, Colyer CL, Fan ZH, Roy KI, Harrison DJ (1999) Effects of injector geometry and sample matrix on injection and sample loading in integrated capillary electrophoresis devices. Electrophoresis 20:529–538

Electrokinetic Sample Introduction

Definition

Electrokinetic sample introduction is performed by using the electroosmotic flow (EOF) in the microchannel as a pump and can be easily controlled by outside high voltages.

Cross References

► Techniques for Transferring Samples to Chips

Electrokinetic Transport

► Electrokinetic Flow

Electrokinetic Transport with Biochemical Reactions

SUMAN CHAKRABORTY
Department of Mechanical Engineering,
Indian Institute of Technology, Kharagpur, India
suman@mech.iitkgp.ernet.in

Synonyms

Biomicrofluidics; Reacting electrokinetic flow

Definition

Biological macromolecules are often handled through microfluidic systems, in which these molecules can transport and react. A common driving force behind such microfluidic transport processes is the electrokinetic force, which originates as a consequence of interaction between the electrical double layer potential distribution and the applied electric field. This article discusses some of the important features of the biochemical reactions in such microfluidic systems.

Overview

The development of microfluidic systems enables the integration of miniaturized components for accomplishing biochemical processes or biomedical diagnostics. Performing these procedures in microfluidic systems allows a rapid biochemical analysis to be carried out at a volumetric scale that is several orders of magnitudes below that of conventional practice. Overall, bio-microfluidics provide great promise in improving the sensitivity, specificity and

processing time required, which are the key requirements for advanced biomedical analysis. It needs to be noted in this regard that most of the biological objects of interest, such as DNA, proteins and cells, have characteristic length scales from a few nanometers to micrometers. Electrokinetics are especially effective in such small domains, by taking advantage of the favorable scaling laws. From the implementation point of view as well, the integration of micro- or nanoscale electrodes in fluidic devices is a relatively simple procedure, with the advancement of MEMS fabrication technologies. As a consequence, electrokinetic forces turn out to be ideal for manipulating biological objects and performing fluidic operations in reactive biochemical systems.

Active and Passive Microarrays

In order to appreciate the significance of biochemical reactions in micro total analysis systems, it needs to be appreciated first that different methods, in principle, can be employed to detect eventual abnormalities or illnesses in patients. For viral infections or blood-related pathologies, for example, immunoassays can be performed to determine the nature of organisms that are responsible for disturbing the inherent immunological defensive systems in the living beings. One way of performing this is to use homogeneous systems in which the sample and detection molecules are both in a liquid system. Another way is to employ a heterogeneous system, in which one type of molecule involved is bound to the solid substrate. For genetic ailments, DNA analysis can be performed to figure out whether a patient possesses a mutation in a specific gene. One of the methods to analyze this condition is to perform a gel-phase electrophoretic separation of fragments formed from the DNA under question. Differences in fragment lengths from the patient's DNA and a healthy reference indicate the possibilities of certain genetic ailments. Another method for accomplishing this purpose is to introduce many different known single stranded (ss) DNA sequences, bound together with particles or gels in a reactive microsystem. The DNA sample under investigation can be "hybridized" with these different sequences. By figuring out the specific DNA sequence with which this sample reacts (there is only one complementary sequence with which such selective reaction becomes possible), one can determine the DNA sequence of the unknown sample. A general principle of operation of the heterogeneous assays is to probe molecules that are bound to the solid substrates, in order to detect the target molecules in a given sample. When a liquid sample is brought into contact with the surface-bound probe molecules, target molecules migrate towards the walls by diffusion, and react with the probe (capturing) molecules. A majority of DNA microarray technologies are based on such passive nucleic acid hybridization, i. e., the binding event depends upon diffusion of target DNA molecules to the capture probe DNAs. Unfortunately, the passive DNA hybridization approach may take several hours. This is because of the fact that the target DNAs, with a typical diffusion coefficient of the order of $10^{-7}\,\mathrm{cm^2/s}$ (for oligonucleotides that are 18 base pairs in length, for example), only reach the capture probes via Brownian (random) motion in order to hybridize. Because of this dependency on diffusion transport of target DNA, large amounts of target DNA and long hybridization times are often required to achieve detectable hybridization signals and repeatable results. Accordingly, many researchers have explored alternative methods to make the DNA sensing faster and more sensitive in solutions with low concentrations of target DNAs. One of the earlier alternative methods was to utilize electric fields to accelerate the rate of interaction between capture probes and target DNA molecules, since the DNA strand has multiple negatively charged groups. In diffusion-based transport of DNA, the time (τ) it takes a DNA molecule to travel over a distance x is given as

$$\tau = \frac{x^2}{2D} \tag{1}$$

where D is the diffusion coefficient. In the case of electrophoresis, the time it takes to move a molecule in the electric field (electrophorese) over a distance x is given by

$$\tau = \frac{x}{\mu E} \tag{2}$$

In this case, μ is the electrophoretic mobility and E is the electric field strength. Using typical values for D ($9.943 \times 10^{-7}\,\mathrm{cm^2/s}$) and μ ($15{,}000\,\mathrm{\mu m^2/V-s}$), and under an electric field of $0.004\,\mathrm{V/\mu m}$, it appears that electrophoretic transport may be 150 times faster over a $500\,\mathrm{\mu m}$ distance. Even though the electrophoretic transport method presents a clear hybridization speed advantage, one critical disadvantage is that the sample solution containing the target DNA must be desalted before hybridization in order to establish an appropriate electric field. In a high-salt solution, including most biological buffers, the electric field depth exists only in close proximity to the electrodes because the high concentration of ions nullifies the electric field in the area away from the electrodes. To facilitate rapid movement of DNA by an electric field, a low conductive buffer solution needs to be used. In contrast, in molecular biology, to achieve efficient hybridization, one always works in high-conductivity solutions. Therefore, desalting is not only counterintu-

itive, but also cumbersome. Rather, a more convenient approach can be to combine a DNA microarray with an electrokinetically driven microfluidic platform, in an effort to enhance the mass transport of target DNA to make detection faster and obtain a lower detection limit (LDL) for DNA hybridization. There are several advantages associated with such microfluidic DNA arrays: they enable detection at the lowest possible DNA concentrations, allow for shorter times to achieve this detection because of enhanced mass transport, offer the ability to monitor several samples in parallel by using a multichannel approach, reduce the potential for contamination by relying on an enclosed apparatus, and they hold the overall promise for integration of several functions in one apparatus (μ-TAS). While the case of biochemical reactions involving DNA samples represents a generic example, similar instances do exist for biochemical reactions involving other types of macromolecules as well.

Basic Reaction Kinetics

In order to appreciate the intricacies associated with biochemical reactions in electrohydrodynamic microsystems, it may be instructive to revisit certain basic definitions associated with the chemical kinetics of reactive systems. These basic concepts are briefly elucidated below.

1. Rate of reaction. For a chemical reaction of the form $A + nB \rightarrow mC + D$, the rate of reaction is defined as

$$r = r_D \left(= \frac{\mathrm{d}[D]}{\mathrm{d}t} \right) = \frac{1}{m} r_C \left(= \frac{1}{m} \frac{\mathrm{d}[C]}{\mathrm{d}t} \right)$$
$$= r_A \left(= -\frac{\mathrm{d}[A]}{\mathrm{d}t} \right) = \frac{1}{n} r_B \left(= -\frac{1}{n} \frac{\mathrm{d}[B]}{\mathrm{d}t} \right) .$$

   As such,r is a function of the concentration of individual species, i. e., $r = r([A], [B], [C], [D])$. For most substances, this relationship is empirical in nature and needs to fitted experimentally. The most common form of this functional relationship is $r = k[A]^a [B]^b$, where k, a and b are time-independent coefficients. The parameter k is called the "rate constant", which should not be confused with the thermodynamic definition of "equilibrium constant" of a specified reaction.

2. Order of reaction. If the rate of reaction is described by the above mentioned functional form, the order of reaction is defined as $o = a + b$. It is important to note here that the unit of k depends on the order of the reaction. For example, for a zero-order reaction k is expressed in units of mol/m^3/s, for a first-order reaction k is expressed in units of 1/s and for a second-order reaction k is expressed in units of m^3/mol/s. The rate constant is usually taken to vary with the activation energy (E_a) and temperature (T) by the Arrhenius law, as $k = k_0 \exp(-E_\mathrm{a}/RT)$. From molecular interpretations, the rate constant is the rate of successful collisions between the reacting molecules, the activation energy represents the minimum kinetic energy of the reactant molecules in order to form the products and k_0 corresponds to the rate at which these collisions occur.

3. Adsorption and the Langmuir model. In the case of adsorption of molecules on a solid functionalized surface, there are basically three components in the reaction. There is a free substrate in the buffer fluid (often called the target or analyte), with a concentration of $[S]$. Second, there is a surface concentration of the ligands or capturing sites immobilized on a functionalized surface, with a concentration of $[\Gamma]_0$. Finally, there is a surface concentration of the adsorbed targets (products of the reaction), with a concentration of $[\Gamma]$. The units of $[\Gamma]$ and $[\Gamma]_0$ are in mol/m^2, whereas $[S]$ is expressed in units of mol/m^3. In case of adsorption, the definitions of the reaction rates are somewhat modified from the usual rate constant definitions mentioned above, primarily because of the fact that the immobilization of the substrate S not only depends on the volume concentration at the wall, but also depends on the available sites for adsorption. Accordingly, one can write $-\mathrm{d}[S]/\mathrm{d}t = k_\mathrm{a}([\Gamma]_0 - [\Gamma])[S]_\mathrm{w}$ and $-\mathrm{d}[\Gamma]/\mathrm{d}t = k_\mathrm{d}[\Gamma]$, where k_a and k_d are the adsorption and dissociation rates, respectively. The concentration of Γ is increased by the former and is decreased by the latter, and the net rate of change is given by their balance, i. e.,

$$\frac{\mathrm{d}[\Gamma]}{\mathrm{d}t} = k_\mathrm{a}([\Gamma]_0 - [\Gamma])[S]_\mathrm{w} - k_\mathrm{d}[\Gamma] \tag{3}$$

Equation (3) can be integrated to obtain

$$\frac{[\Gamma]}{[\Gamma]_0} = \frac{k_\mathrm{a}[S]_\mathrm{w}}{k_\mathrm{a}[S]_\mathrm{w} + k_\mathrm{d}} \left[1 - \exp\left(-\left(k_\mathrm{a}[S]_\mathrm{w} + k_\mathrm{d}\right)t\right)\right] \tag{4}$$

Equation (4) represents an exponential growth of $[\Gamma]$ with time, until a saturation (asymptotic) value is reached ($[\Gamma]_\mathrm{a}/[\Gamma]_0 = k_\mathrm{a}[S]_\mathrm{w}/(k_\mathrm{a}[S]_\mathrm{w} + k_\mathrm{d})$ at $t = t_\mathrm{a}$, say). After this occurs, the remaining targets or analytes may be suddenly washed out. In that case, desorption becomes the driving mechanism. With the asymptotic condition as an initial condition for the desorption reaction, the kinetics of desorption is now governed by $-\mathrm{d}[\Gamma]/\mathrm{d}t = k_\mathrm{d}[\Gamma]$, leading to the following time variation of surface concentration:

$$\frac{[\Gamma]}{[\Gamma]_\mathrm{a}} = 1 - k_\mathrm{d}(t - t_\mathrm{a}) \tag{5}$$

Basic Methodology

The physicochemical processes associated with the biochemical reactions in the presence of electrokinetic transport are often mathematically described by invoking the governing equations for electric potential distribution and mass, momentum, energy and the species conservation equations. In this article, we shall describe these basic equations by referring to the example of DNA hybridization in electrokinetically driven microchannel flows, which is a problem of immense interest from bio-technological and biomedical perspectives. In fact, hybridization of nucleic acids to their complementary sequences is a fundamental process in molecular biology. It plays a major role in replication, transcription and translation, where specific recognition of nucleic acid sequences by complementary strands is essential for propagation of information content. In practice, microchip-based nucleic acid arrays presently permit the rapid analysis of genetic information by hybridization. Since their introduction, DNA chips have gained wide usage in bioanalytical chemistry, with applications in important areas such as gene identification, genetic expression analysis, DNA sequencing and clinical diagnostics. Many of these devices have been classically based on "passive" microarrays, which suffer from several limitations. First, since all nucleic acids are exposed to the same conditions simultaneously, capture probes must have similar melting temperatures to achieve similar levels of hybridization stringency. This places limitations on the length, GC content and secondary structure of the capture probes. Further, since the rate of hybridization is proportional to the initial concentration of the interrogated solution, high concentrations are required to achieve rapid hybridization. Moreover, due to difficulties associated with control of hybridization conditions, single base discrimination is generally restricted to oligomers of 20 bases or less with centrally placed differences. Overall, the entire phenomenon relies solely on diffusion of probe molecules to the DNA target surface, requiring several hours to achieve efficient hybridization of DNA molecules to capture probes. In an attempt to circumvent the above limitations, "active" microelectronic devices constituted of microchip-based hybridization arrays have recently been proposed, which utilize electric field as an independent parameter to control DNA transport, enhance hybridization and improve stringency of nucleic acid interactions. In typical arrangements utilizing such electrokinetic effects, electrode arrays are covered with a permeation layer with embedded DNA capture probes, in an effort to control the transport of biomolecules and achieve their accumulation and hybridization at desired sites. Such arrays primarily consist of patterned metal electrodes on an insulating substrate, and are contained in a plastic housing equipped with fluidic conduits to manipulate charged biomolecules as well as ions in the fluid sample. It has been effectively realized that electroosmosis, which refers to liquid flow by an applied electric field along electroosmotically charged surfaces, may turn out to be a very suitable method for manipulating liquid flows in such cases in order to transport the biological targets suspended in controlled liquid samples of nanovolumes. Although a number of reports have appeared in the literature to model electrokinetically driven microchannel flows, attempts have rarely been made towards a comprehensive mathematical modeling of transport and accumulation of DNA in a microfluidic channel. Paces et al. [1] were amongst the early groups of researchers to numerically model DNA accumulation and hybridization in the presence of electroosmotic transport of charged species in an electrolyte. Ozkan [2] in a similar study based on finite element methods, investigated the effects of charged species concentration, size, position, type of buffer solution and patterned electrode configuration on the electric field distribution, and hence electrokinetic transport of charged molecules. Kassegne et al. [3], in a more recent study, investigated the transport and accumulation of DNA in active electronic chips, through experimental and numerical modeling. Kinetics of DNA hybridization, however, was not considered in their model. In fact, compared to numerous experimental investigations, relatively few attempts have been made in the literature to develop fundamental models of DNA hybridization. Chan et al. [4] developed one of the more frequently cited solid-phase hybridization kinetics models, based on the receptor–ligand model developed by Axelrod and Wang [5], with a proposition that hybridization can occur either by direct hybridization from the bulk phase or hybridization after an initial nonspecific adsorption step followed by subsequent surface diffusion to the probe. Based on this approach, Zeng et al. [6] proposed a dynamic model combining these two basic mechanisms. Following an alternative approach, Sadana and Ramakrishnan [7] used fractal kinetics for pertinent hybridization data analysis. Erickson et al. [8] came up with a comprehensive model of dynamic solid-phase oligonucleotide hybridization kinetics, based on an approach which accounted for both the direct hybridization from the bulk phase and hybridization after an initial nonspecific adsorption stage. However, investigations regarding influences of electrosmotic flow mechanisms on DNA hybridization characteristics were beyond the scope of their study. Das et al. [9] have recently extended the DNA hybridization model developed by Erickson et al. [8] to include combined effects of electrokinetic and pressure-driven transport. In their study, a comprehensive mathe-

matical model was developed, quantifying the pertinent momentum, heat and species transfer rates. Influences of bulk and surface properties on the velocity field were critically examined, which in turn dictate the nature of thermosolutal transport, and hence the DNA concentration fields, in accordance with specific and nonspecific hybridization mechanisms. Joule heating and viscous dissipation effects were also incorporated, which can cause a perceptible temperature rise, and accordingly affect various flow parameters as well as the rate constants for the hybridization.

The fundamental analysis executed by Das et al. [9] deals with the microfluidic transport through a parallel plate microchannel of height $2a$ and width w, with $w \gg 2a$ (see Fig. 1a). The length of the channel is taken to be L0. Two capturing DNA probes are assumed to be attached to the bottom wall, each spanning over a length of LP (see Fig. 1b). A potential gradient is applied along the axis of the channel, which provides the necessary driving force for electroosmotic flow. Under these conditions, an electric double layer (EDL) forms near the liquid–wall interface. This EDL interacts with the externally applied electrical field. For example, positively charged ions of EDL are attracted towards the cathode and repelled by the anode, resulting in a net body force that tends to induce bulk motion of ionized fluid in the direction of the electric field. When this voltage is applied to a buffer solution with a finite thermal conductivity, the resulting current also induces an internal heat generation, often referred to as Joule heating. The thermal and fluid flow field, thus established within the channel, is responsible for the macromolecular transport, which has to be understood thoroughly to get a complete picture of the hybridization model. For mathematical modeling of the problem mentioned as above, the following major assumptions are made:

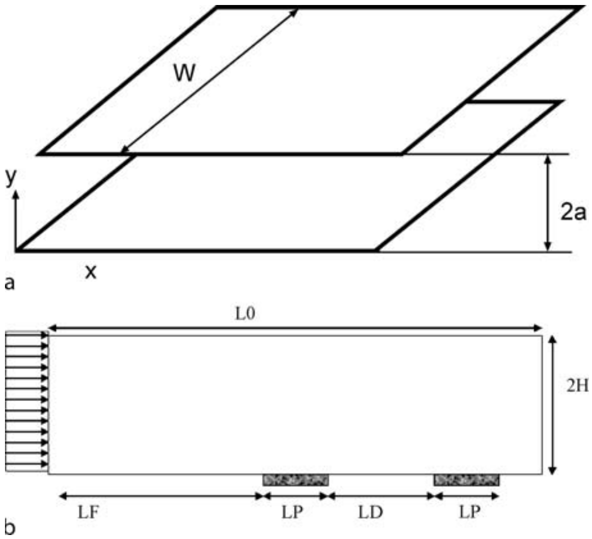

Electrokinetic Transport with Biochemical Reactions, Figure 1 (**a**) schematic diagram depicting the problem domain. (**b**) A schematic diagram depicting the probe arrangements at channel walls

1. The temperature, velocity and concentration fields are unsteady and two-dimensional.
2. The effect of pH change on the ensuing chemical reactions due to hydrogen and hydroxyl ions is neglected.
3. The effect of charges carried by the DNA species on the electric field is neglected.
4. The effect of permeation layer on the DNA transport and accumulation and electric field distribution is neglected.

The governing transport equations, under these circumstances, can be described as follows.

Continuity equation:

$$\frac{\partial \rho}{\partial t} + \nabla \cdot (\rho \boldsymbol{V}) = 0 \tag{6}$$

X-momentum equation:

$$\frac{\partial}{\partial t}(\rho u) + \nabla \cdot (\rho \boldsymbol{V} u) = -\frac{\partial p}{\partial x} + \nabla \cdot (\mu \nabla u) + b_{\mathrm{x}} \tag{7}$$

where b_{x} is the body force term per unit volume in the x-direction, given as: $b_{\mathrm{x}} = -\rho_{\mathrm{e}}(\partial\phi/\partial x)$, where ρ_{e} is the net electric charge density and ϕ is the potential distribution due to an externally imposed electric field.

Y-momentum equation:

$$\frac{\partial}{\partial t}(\rho v) + \nabla \cdot (\rho \boldsymbol{V} v) = -\frac{\partial p}{\partial y} + \nabla \cdot (\mu \nabla v) + b_{\mathrm{y}} \tag{8}$$

where b_{y} is the body force term per unit volume in the y-direction, given as: $b_{\mathrm{y}} = -\rho_{\mathrm{e}}(\partial\phi/\partial y)$. In both Eq. (7) and (8), the dynamic viscosity, μ, is a function of temperature, given as

$$\mu = 2.761 \times 10^{-6} \exp\left(\frac{1713}{T}\right) \tag{9}$$

where T is in K and μ is in Pa s. It can be noted here that the distribution of ϕ needs to be solved from the Laplace equation, as a consequence of an externally imposed electrical potential gradient. The corresponding governing differential equation is

$$\nabla \cdot (\sigma \nabla \phi) = 0 \tag{10}$$

where σ is the electrical conductivity of the solution. Further, distribution of the net electric charge density, ρ_{e}, appearing in the momentum conservation equations is to

be ascertained by solving the Poisson–Boltzmann equation for surface potential distribution as

$$\nabla \cdot (\varepsilon \nabla \psi) = -\frac{\rho_e}{\varepsilon_0} \tag{11}$$

where ψ denotes the EDL potential, ε_0 is the permittivity of free space and ε is the dielectric constant of the electrolyte which is a function of temperature, given as

$$\varepsilon = 305.7 \exp\left(-\frac{T}{219}\right) \tag{12}$$

where T is in Kelvin. In Eq. (11), ρ_e is described as

$$\rho_e = -2 n_0 e z \sinh\left(\frac{e z \psi}{k_B T}\right) \tag{13}$$

where n_0 is the ion number density, e is the electronic charge, z is the valence, k_B is the Boltzmann constant and T is the absolute temperature. To depict the relationship between the net electric charge density and Debye length, we express n_0 as a function of the Debye length, λ, given as

$$n_0 = \frac{\varepsilon k_B T}{8\pi e^2 z^2 \lambda^2} \tag{14}$$

Energy conservation equation:

$$\frac{\partial}{\partial t}(\rho C_P T) + \nabla \cdot (\rho C_P \boldsymbol{V} T) = \nabla.(k \nabla T) + \varphi + \dot{q} \tag{15}$$

where k is the thermal conductivity of the electrolyte solution, which is a function of temperature, given as

$$k = 0.6 + 2.5 \times 10^{-5} T \tag{16}$$

where T is in K and k is in $\mathrm{W/(m^2K)}$. In Eq. (15), φ is the heat generation due to viscous dissipation, given as

$$\varphi = 2\mu \left[\left(\frac{\partial u}{\partial x}\right)^2 + \left(\frac{\partial v}{\partial y}\right)^2\right] + \mu \left(\frac{\partial u}{\partial y} + \frac{\partial v}{\partial x}\right)^2 \tag{17}$$

Further, $\dot{q}$ is the heat generation due to Joule heating, which, according to Ohm's law, can be given as

$$\dot{q} = \frac{I^2}{\sigma} \tag{18}$$

It can be noted here that the electrical current density includes two parts: one is due to the applied electric field imposed on the conducting solution ($\sigma \boldsymbol{E}$), and the other is due to the net charge density moving with the fluid flow ($\rho_e \boldsymbol{V}$). Therefore, the electrical current density, I, can expressed as

$$\boldsymbol{I} = \rho_e \boldsymbol{V} + \sigma \boldsymbol{E} \tag{19}$$

Using Eq. (18) and (19) one can obtain the heat generation due to Joule heating as

$$\dot{q} = \frac{(\rho_e \boldsymbol{V} + \sigma \boldsymbol{E}) \cdot (\rho_e \boldsymbol{V} + \sigma \boldsymbol{E})}{\sigma} \tag{20}$$

Species conservation equation:

$$\frac{\partial (\rho c_i)}{\partial t} + \nabla \cdot (\rho \boldsymbol{V} c_i) = \nabla \cdot (\rho D_n \nabla c_i) + \mu_{os} z_i F \nabla \cdot (\rho c_i \nabla \phi) + \rho R_i \tag{21}$$

where c_i is the concentration of the ith species in the solution, μ_{os} is the electroosmotic mobility of the concerned species, z_i is the valence of the ith species and F is Faraday's constant. In Eq. (21), D_n is a generalized diffusion coefficient, which is the liquid-phase diffusion coefficient (D_3) in the bulk fluid and surface-phase diffusion coefficient (D_2) at the nonspecific adsorption sites. The term R_i is a generation/source term, details of which will be described subsequently.

The above model of species (DNA) transport is coupled with two basic mechanisms of hybridization (see Fig. 2), namely direct (specific) hybridization from the bulk phase

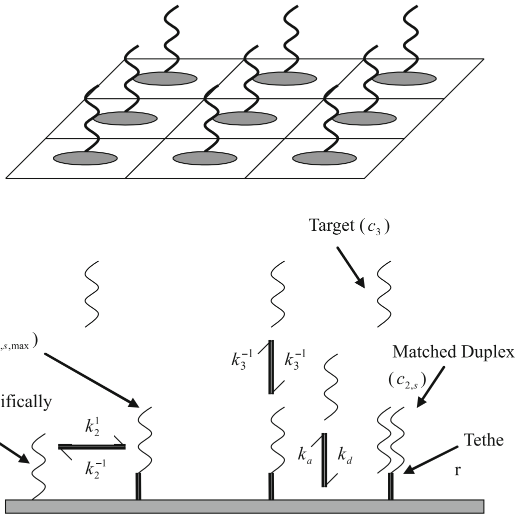

Electrokinetic Transport with Biochemical Reactions, Figure 2
A schematic diagram depicting the dual mechanism of DNA hybridization

to the surface-bound probes or by indirect (nonspecific) hybridization in which the target is initially nonspecifically adsorbed on the surface and then diffuses along the surface before reaching an available target probe molecule. In recent times, much research has been dedicated to demonstrate how the above reduction of dimensionality (RD) enhances the overall capture rate. In general, when a partner in a biomolecular reaction is immobilized on a surface, the rate of capture would depend on events in the bulk (3D) as well as on the surface (2D), and on the relative ratio of solute diffusion to the intrinsic reaction rate. However, hybridization that occurs in the interphase between a solid and solution is anticipated to demonstrate kinetics that is different from that observed in the bulk solution. It has been suggested in the literature [4] that nonselective adsorption of single-stranded oligonucleotide, followed by surface diffusion (2D diffusion coefficients) to immobilized probes can enhance hybridization rates in contrast to direct hybridization in the solution. This suggestion is based on a reduction of dimensionality of diffusion from a 3D to a 2D phenomenon. A generally accepted mechanistic description of the hybridization reaction between a homogeneously suspended probe DNA and an immobilized target DNA strand postulates that [5] in the first phase, the probe DNA strand diffuses towards the target strand. During the subsequent collision, a so-called nucleation site, involving the formation of the first short stretch of base pairing containing at least three contiguous bases, is formed. In the following phase, either a stable base pair is formed during a rapid "zippering" reaction, or, in case of a mismatch, the nucleation site loses its stability, and the probe strand detaches and prepares for another attempt, either with the same, or with a different target strand. With the basic binding step occurring very rapidly, the overall slowness of hybridization has either to be attributed to a large number of successive attempts which are needed before a successful collision occurs and/or the fact that the supply of unbound probe DNA strand occurs too slowly. Exact theories in this regard, however, are yet to be well established.

Regarding the interactions between bulk- and surface-phase kinetics mentioned above, Eq. (21) needs to be coupled with appropriate boundary conditions depicting specific and nonspecific hybridization, as applied to all reacting surfaces. In the present formulation, incorporation of these boundary conditions is effected by formulating the source term R_i in Eq. (21) such that $R_i = 0$ for the bulk phase. However, for the reactive bottom wall (where the capturing probes are attached):

$$R_i = -\left(\frac{\partial c_{2,\mathrm{s}}}{\partial t} + \frac{\partial c_{2,\mathrm{ns}}}{\partial t}\right) \tag{22}$$

where $c_{2,\mathrm{s}}$ and $c_{2,\mathrm{ns}}$ are the surface-phase concentration of specifically and nonspecifically adsorbed target molecules, respectively. Along the non-reacting surface, the above term reduces to a zero flux boundary condition, in effect. The terms involved in Eq. (22) can further be expressed as a set of coupled 2D kinetic equations as

$$\begin{aligned}\frac{\partial c_{2,\mathrm{s}}}{\partial t} &= \left[k_3^1 c_{3,\mathrm{m}}(c_{2,\mathrm{s,max}} - c_{2,\mathrm{s}}) - k_3^{-1} c_{2,\mathrm{s}}\right] \\ &\quad + \left[k_2^1 c_{2,\mathrm{ns}}(c_{2,\mathrm{s,max}} - c_{2,\mathrm{s}}) - k_2^{-1} c_{2,\mathrm{s}}\right]\end{aligned} \tag{23}$$

and

$$\begin{aligned}\frac{\partial c_{2,\mathrm{ns}}}{\partial t} &= \left[k_\mathrm{a} c_{3,\mathrm{m}}(c_{2,\mathrm{ns,max}} - c_{2,\mathrm{ns}}) - k_\mathrm{d} c_{2,\mathrm{ns}}\right] \\ &\quad - \left[k_2^1 c_{2,\mathrm{ns}}(c_{2,\mathrm{s,max}} - c_{2,\mathrm{s}}) - k_2^{-1} c_{2,\mathrm{s}}\right]\end{aligned} \tag{24}$$

where $c_{2,\mathrm{s,max}}$ is the maximum concentration of the hybridized targets (equivalent to the local concentration of the surface-bound probes available for hybridization), $c_{2,\mathrm{ns,max}}$ is the maximum concentration of the nonspecifically adsorbed molecules, $c_{3,\mathrm{m}}$ is the bulk-phase concentration of the targets in surface film, k_3^1 is the kinetic association constant for direct hybridization (from solution phase), k_3^{-1} is the kinetic dissociation constant for direct hybridization (from solution phase), k_2^1 is the kinetic association constant for indirect hybridization of the nonspecifically adsorbed targets (from surface phase), $k_2^{-1}$is the kinetic dissociation constant for indirect hybridization of the nonspecifically adsorbed targets (from surface phase), k_a is the kinetic association constant for nonspecific adsorption of the targets to the surface and k_d is the kinetic dissociation constant for nonspecific adsorption of the targets to the surface. Physically, Eq. (23) describes that the rate of change in surface concentration of hybridized species is a combination of the rate of change of targets getting hybridized directly from the bulk phase and the rate of targets getting hybridized after an initial nonspecific adsorption. Equation (24) implies that the rate of change in surface concentration of nonspecifically adsorbed targets is increased by the rate of adsorption from the bulk phase, but is decreased by the rate at which the nonspecifically adsorbed targets become hybridized.

Determination of the kinetic constants appearing in Eq. (23) and (24) needs microscopic and statistical theories of collision to be essentially invoked. A physical basis of this lies in the fact that pure diffusion, with its fractal-like path, necessarily leads to an infinitely high collision rate for the situation represented here, manifested by a non-zero average solute concentration immediately

in contact with each target. To account for finite reaction rates with non-zero local concentration in a diffusion-based framework, one must assume that the reaction probability per collision is diminishingly small, which may be a major deviation from the reality. The other approach, which is described here, recognizes that the molecules follow a Brownian motion path rather than a pure diffusion one, which yields a finite number of collisions from a finite solute concentration near the target probe. In Brownian motion, molecular velocity has a finite persistence length, since the instantaneous momentum of the molecule can be transferred to the solvent only at a finite rate of solvent velocity. Hence, the Brownian motion persistence length plays a central role in determining both reaction kinetic rates and reduction of dimensionality enhancement. Following fundamental postulates of statistical physics and the work of Axlerod and Wang [5], it can be postulated that the reaction rate of direct hybridization (R_3) can be obtained as a product of bulk-phase flux of target molecules colliding with the surface (F_3), probability of collision location being a probe site (P_p), probability that the probe is available for hybridization (P_a) and probability that the collision will result in successful hybridization (P_r). All these effects can be combined to obtain the following equation for rate of reaction [8]:

$$R_3 = k_3^1 C_{3,\mathrm{m}} \left(C_{2,\mathrm{ns,max}} - C_{2,\mathrm{s}}\right) \tag{25}$$

where $k_3^1 = 3D_3 N_\mathrm{v} \pi R_\mathrm{p}^2 \chi_3 / 2S_3$. In Eq. (20), N_v is the Avogadro number, R_p is the radius of probe site, χ_3 is the probability that 3D collision will result in a successful hybridization and S_3 is the frequency of collision in 3D. A similar approach can be followed to determine the rate of reaction for nonspecifically adsorbed target as

$$R_2 = k_2^1 C_{2,\mathrm{ns}} \left(C_{2,\mathrm{s,max}} - C_{2,\mathrm{s}}\right) \tag{26}$$

where $k_2^1 = 8D_2 N_\mathrm{v} R_\mathrm{p} \chi_2 / S_2$. In Eq. (21), D_2, χ_2 and S_2 are similar to D_3, χ_3 and S_3, except for the fact that the earlier group represents a 2D collision behavior.

Although Eq. (25) and (26) are fundamental in nature, the reaction probability, χ_n, is rather uncertain. Instead, a classical Wetmur–Davidson relationship [9] may be used to estimate the rate of hybridization for bulk-phase targets in the surface film as

$$k_3^1 = 3.5 \times 10^5 \frac{l^{0.5}}{N} \tag{27}$$

where N is the complexity of the target sequence and l is the number of nucleotide units. In general, complexity of the sequence is taken as the total number of non-repeating sequences in a DNA strand. In the absence of any steric interference, in which the bulk molecules are able to move freely within the surface film, the above is likely to be valid in an approximate sense. In cases of denser probe spacings or a large quantity of nonspecifically adsorbed targets, Eq. (27), however, is likely to overestimate the pertinent kinetic constant.

With the above estimation of k_3^1, k_2^1 can be obtained by dividing Eq. (25) by (26), and assuming that $\chi_2 = \chi_3$, $S_2 = S_3$, as

$$k_2^1 = k_3^1 \left(\frac{16}{3\pi}\right)\left(\frac{D_2}{D_3}\right)\left(\frac{1}{R_\mathrm{p}}\right) \tag{28}$$

The reverse kinetic constant may be obtained by appealing to thermodynamic stability requirements of the dissociation kinetics representing the solid-phase hybridization reaction. Thermodynamic stability of the target probe complex is governed by Gibbs free energy of binding as

$$\frac{k^1}{k^{-1}} = \exp\left(\frac{-\Delta G}{RT}\right) \tag{29}$$

where $\Delta G = \Delta H - T\Delta S$, ΔH being the binding enthalpy and ΔS being the binding entropy. For bulk-phase hybridization, a nearest-neighbor model [9] can be used to calculate ΔG for any complementary or single-base-pair mismatched duplex. For heterogeneous hybridization, however, the thermodynamic stability condition deviates from the above classical result, as the probe density is increased. Consequently, the above approximation is somewhat accurate in the limit of low probe density, with an underlying assumption that other surface effects are not thermodynamically important. Although some other thermodynamic models have been proposed in this respect [9], these are not comprehensive in terms of a complete theoretical development. Hence, one may utilize Eq. (29), with incorporation of an Arrhenius type of formulation for k^1 and k^{-1} as

$$k^1(T) = k_0^1 \exp\left[-\frac{E_\mathrm{a}}{R}\left(\frac{1}{T} - \frac{1}{T_0}\right)\right] \tag{30a}$$

$$k^{-1}(T) = k_0^{-1} \exp\left[-\frac{E_\mathrm{d}}{R}\left(\frac{1}{T} - \frac{1}{T_0}\right)\right] \tag{30b}$$

where k_0^1 and k_0^{-1} are values of k^1 and k^{-1} at T_0 (T_0 is 25°C below melting temperature of DNA). Further, using $E_\mathrm{a} - E_\mathrm{d} = \Delta H$, k^{-1} can be estimated from the above, on estimation of either E_a or E_d (both of which are situation specific). Now, since

$$k^{-1} = k_2^{-1} + k_3^{-1} \tag{31}$$

separate equations are required to estimate individual rate constants k_2^{-1} and k_3^{-1}. To achieve this goal, we assume that at steady state an independent equilibrium exists between directly hybridized probes and targets of bulk solution, as well as between indirectly hybridized probes and nonspecifically adsorbed target molecules. With incorporation of these into Eq. (23), it follows that

$$\left[k_3^1 c_{3,\mathrm{m}}(c_{2,\mathrm{s,max}} - c_{2,\mathrm{s,eq}}) - k_3^{-1} c_{2,\mathrm{s,eq}}\right] = 0 \qquad (32)$$

$$\left[k_2^1 c_{2,\mathrm{ns}}(c_{2,\mathrm{s,max}} - c_{2,\mathrm{s,eq}}) - k_2^{-1} c_{2,\mathrm{s,eq}}\right] = 0 \qquad (33)$$

where the subscript "eq" represents an equilibrium state. Equations (31)–(33) can be simultaneously solved to yield k_2^{-1}, k_3^{-1} and $C_{2\mathrm{s,eq}}$, to be used for the numerical simulations.

Regarding nonspecific adsorption kinetics, one may note that

$$\frac{k_\mathrm{a}}{k_\mathrm{d}} = \frac{C_{2,\mathrm{n,eq}}}{C_{3,\mathrm{m,eq}}\left(C_{2,\mathrm{ns,max}} - C_{2,\mathrm{ns,eq}}\right)} \qquad (34)$$

The unknown terms appearing on the right-hand side of Eq. (34), however, are yet to be theoretically determined. Therefore, one may use the experimental outcomes of Chan et al. [10, 14] to estimate $C_{2,\mathrm{ns,eq}}$, $C_{3,\mathrm{m,eq}}$ and k_d for various types of glass substrates. The term $C_{2,\mathrm{ns,max}}$ can be estimated by noting that because of a prior presence of surface probes (captured by specific hybridization) on the target area, a full monolayer of targets cannot be adsorbed there, leading to an effective radius of adsorbed target, R_t. Accordingly

$$C_{2,\mathrm{ns,max}} = \frac{1 - \pi R_\mathrm{p}^2 N_\mathrm{v} C_{2,\mathrm{s,max}}}{N_\mathrm{v} \pi R_\mathrm{t}^2} \qquad (35)$$

With the estimates mentioned above, k_a can be obtained from Eq. (34), leading to a complete determination of kinetic constants appearing in the source term of Eq. (21).

The governing conservation equations developed here lead to a well-posed system of partial differential equations, on specification of the appropriate boundary conditions. It can be noted here that boundary conditions corresponding to DNA hybridization are already incorporated through specification of the source term R_i (Eq. (21)) for control volumes adjacent to the channel–fluid interface, and need not be duplicated in prescription of boundary conditions. Other pertinent boundary conditions are summarized in Tab. 1.

Key Research Findings

In order to obtain significant insights regarding temporal variations of DNA concentration (hybridized targets, $c_{2,\mathrm{s}}$) at the probes as a function of prevailing flow conditions, one may refer to Fig. 3. Figure 3, in essence, shows an initial slow rate of increase of $c_{2,\mathrm{s}}$, followed by a comparatively higher hybridization rate that eventually approaches a saturation state with respect to time. It is observed that during initial transients, the concentrations of hybridized targets, for each of the cases investigated, remain somewhat close to each other. However, at later instants of time, as the system approaches a meta-stable state, concentration values corresponding to different situations investigated here start differing widely from each other. For a pure electroosmotic flow, the steady value of $c_{2,\mathrm{s}}$ is found to be somewhat less than that corresponding to a mixed flow occurring under a favorable pressure gradient, but turns out to be significantly greater than that observed for a mixed flow occurring under an adverse pressure gradient. This variation can be explained by arguing that for pure electroosmotic flows, the bulk concentration, and hence the film concentration ($c_{3,\mathrm{m}}$), is less as compared to that established in the presence of a favorable pressure gradient, but more than that established in the presence of an adverse pressure gradient. This, in turn, ensures the corresponding variations in $c_{2,\mathrm{s}}$ values, in an

Electrokinetic Transport with Biochemical Reactions, Table 1 Table of boundary conditions

	Boundary conditions			
Governing Equation	**Inlet (x=0)**	**Outlet (x=L0)**	**Bottom wall (y=0)**	**Top wall (y=2H)**
Laplace equation (Eq. 5)	$\phi = \phi_0$	$\phi = 0$	$\frac{\partial \phi}{\partial y} = 0$	$\frac{\partial \phi}{\partial y} = 0$
Poisson–Boltzmann equation (Eq. 6)	$\psi = 0$	$\frac{\partial \psi}{\partial x} = 0$	$\psi = \xi$ (zeta potential)	$\psi = \xi$ (zeta potential)
Continuity and momentum conservation (Eq. 1–3)	$u = u_\mathrm{in}$ or $\frac{\partial p}{\partial x} = K_0$ (K_0 is a constant) $v = 0$	$\frac{\partial u}{\partial x} = 0$ $v = 0$	$u = 0$ $v = 0$	$u = 0$ $v = 0$
Energy conservation (Eq. 10)	$T = T_\infty$	$\frac{\partial T}{\partial x} = 0$	$T = T_\mathrm{w}$	$T = T_\mathrm{w}$
Species conservation equation (Eq. 16)	$c_i = c_\infty$	$\frac{\partial c_i}{\partial x} = 0$	$\frac{\partial c_i}{\partial y} = 0$	$\frac{\partial c_i}{\partial y} = 0$

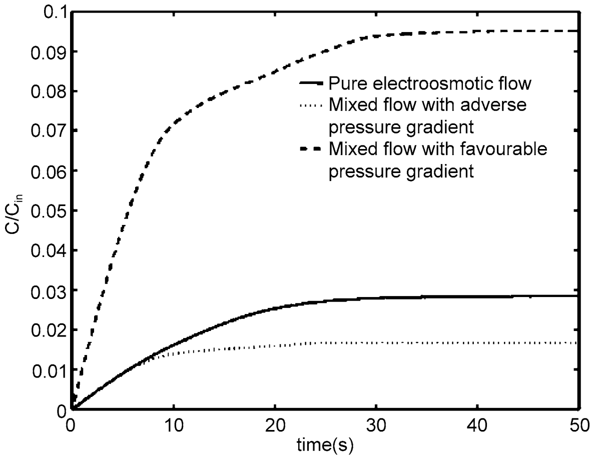

Electrokinetic Transport with Biochemical Reactions, Figure 3 Variation of concentration of hybridized targets with time, at probe location 1, for all cases. The pressure gradients taken for the computations are as follows: $\partial p/\partial x = -10^5\,Pa/m$ (favorable) and $\partial p/\partial x = 10^5\,Pa/m$ (adverse)

analogous fashion. It has also been earlier demonstrated that the rate of the hybridization reaction can be significantly increased due to a nonspecific adsorption of the single-stranded DNA on the surface, and a subsequent two-dimensional diffusion towards surface-bound complementary probe molecules, as compared to the sole effect of three-dimensional hybridization from the bulk [5]. Hence, the initial slowness of hybridization can be explained considering the "lag time" between nonspecific adsorption and consequent hybridization to the probe, mediated by two-dimensional diffusion. During this time, three-dimensional hybridization reaction predominates. However, once the lag phase is over, the rate of hybridization reaction increases at a faster pace, due to a coupled effect of the two types of mechanisms, and saturation reaction kinetics are eventually achieved when all the single-stranded probe molecules become hybridized with target complementary oligonucleotides. Regarding the specific impact of pressure gradients on DNA hybridization, it is revealed that steeper temporal gradients in concentration can be achieved with favorable pressure gradients, especially during early stages of hybridization. On the other hand, imposition of an adverse pressure gradient of similar magnitude may not be consequential enough to retard the hybridization rates drastically. This may be attributed to the fact that although such an adverse pressure gradient decelerates the flow locally, it also ensures that the target DNAs have a greater exposure time with the complementary capture probes, with an enhanced probability of hybridization. For the adverse pressure gradients reported here, these two counteracting effects almost nullify each other, leading to relatively insignificant impacts on the resultant hybridization behavior.

It is important to note here that the numerical computations necessary to come up with the theoretical predictions mentioned above are somewhat involved in nature, primarily because of the strongly interconnected and complicated features of mass, momentum and species transport characterizing the entire sequence of events. Under certain restricted conditions, however, approximate analytical solutions can also be obtained, depicting the interactions between an imposed electroosmotic flow field and the transient DNA hybridization occurring in a microchannel. Such models can turn out to be of immense scientific appeal, in terms of having a quantitative capability of directly capturing the influences of various consequential parameters (such as fluid flow) on DNA hybridization rates, through development of close-formed expressions, without demanding more involved numerical simulations, in many cases (for details, see the analytical solutions of Das et al. [11]).

Other than the DNA hybridization systems mentioned above, mass-transfer systems based on electrokinetic phenomena have shown practical potential for becoming powerful separation methods in other biotechnological and pharmaceutical applications as well. Grimes and Liapis [12] obtained the concentration profiles of charged species in packed chromatographic columns, as the adsorbate adsorbs onto negatively charged fixed sites on the surface of the nonporous particles. Their studies revealed that highly resolved adsorption fronts and large amounts of adsorbate in the adsorbed phase, for a given column length, can be obtained if (1) the ratio of the electroosmotic velocity of the mobile liquid phase at the column entrance to the electrophoretic velocity of the anion is nearly -1, (2) the ratio of the mobility of the cation to the mobility of the analyte is not very large and (3) the concentration of the analyte relative to that of the cation is increased.

Future Directions for Research

Some of the recent findings on reactive systems with electrokinetic transport have revealed certain interesting propositions, which can be potentially exploited to obtain enhanced rates of biomacromolecular transport and hybridization in microfluidic arrangements. For example, Das and Chakraborty [13], in a recent study, have theoretically established a novel proposition that the rate of macromolecular adsorption can be augmented with application of transverse electric fields across patterned walls of a microfluidic channel. In their study, an approximate fully developed velocity profile was derived, which was subse-

quently utilized to solve the species conservation equation pertaining to a combined advection–diffusion transport. Closed-form solutions for the concentration field were subsequently obtained, consistent with the typical second-order kinetics of macromolecular adsorption. It was suggested that the transverse electric field and pattern angles can be regulated as independent parameters to maximize the rate of macromolecular adsorption, under the prevailing conditions. The following major conclusions could be drawn from their study:

1. Benefits of transverse electric fields cannot be effectively realized if the channel surfaces are not patterned, which is primarily attributable to the excess equivalent pressure gradient that cannot be exploited without surface patterning.
2. For moderate values of axial potential gradient, increase in orders of magnitude of transverse potential gradients can augment the rate of macromolecular adsorption significantly. However, a large value of the axial potential gradient may virtually suppress any contributions from an enhanced transverse electric field, and can dictate the adsorption rate by itself alone. Nevertheless, such extreme situations might be rather undesirable, because of adverse effects of Joule heating and subsequent macromolecular degradation on account of high electrical field strength. Hence, in place of a strong axial electric field, a combination of moderate values of axial and transverse electric fields can turn out to be a better proposition for the practical purpose of enhancement of macromolecular transport and adsorption rates.
3. The beneficial effects of transverse electric fields in terms of augmenting the rate of macromolecular adsorption can be best exploited for pattern angles to the tune of 45°. While acute angles turn out to be advantageous in this respect, in general, obtuse angles effectively slow down the rate of macromolecular transport by inducing an equivalent "adverse" pressure gradient that retards the rate of macromolecular transport.
4. In practice, a judicious combination of transverse electric fields and surface patterning effects can be employed, to augment the rate of macromolecular adsorption, without incurring any adverse implications of Joule heating and consequent macromolecular degradation on account of axial electric fields of too high a strength.

Based on the above-mentioned theoretical findings, future efforts, indeed, can be directed to design and fabricate biomicrofluidic devices that can achieve much faster rates of reaction and hybridization, as compared to the maximum limit currently being permitted by the state-of-the-art electrokinetic arrangements.

Cross References

- ▶ Active Mixer
- ▶ Bioprinting on Chip
- ▶ Biosample Preparation Lab-on-a-Chip Devices
- ▶ Biosensors Using Atomic Force Microscopes
- ▶ Infrared Imaging and Mapping for Biosensors
- ▶ Biosensors Using Laser
- ▶ Cell Adhesion and Detachment
- ▶ Cell Culture (2D and 3D) on Chip
- ▶ Cell Patterning on Chip
- ▶ Chromatographic Chip Devices
- ▶ DNA Micro-arrays
- ▶ Electrical Double Layers
- ▶ Electrokinetic Motion of Cells and Nonpolarizable Particles
- ▶ Electrokinetic Sample Injection
- ▶ Electroosmotic Flow (DC)
- ▶ AC Electro-Osmotic Flow
- ▶ Electroosmotic Flow in Heterogeneous Microchannels
- ▶ Lab-on-Chip Devices for Biodefense Applications
- ▶ Lab-on-Chip Devices for Chemical Analysis
- ▶ Lab-on-Chip Devices for Particle and Cell Separation
- ▶ Lab-on-Chip Devices for Protein Analysis
- ▶ Lab-on-a-Chip Devices for Chemical Analysis
- ▶ Microfluidic Devices in Tissue Engineering
- ▶ Microfluidic Sample Manipulation
- ▶ Microfluidic Systems for Combinatorial Chemistry
- ▶ Droplet Microreactors
- ▶ On-Chip Cell Lysis
- ▶ Techniques of Manipulating Cells

References

1. Paces M, Lindner J, Havlica J, Kosek J, Snita D, Marek M (2000) Mathematical modeling of complex chemical microsystems in electric field. Proceedings of the Fourth International Conference on Microreaction Technology (IMRET 4), Atlanta, GA
2. Ozkan M, Ozkan CS, Kibar O, Wang MM, Bhatia SN, Esener S (2001) Heterogeneous integration through electrokinetic migration. IEEE J EMB 20:144–151
3. Kassegne SK, Resse H, Hodko D, Yang JM, Sarkar K, Smolko D, Swanson P, Raymond DE, Heller MJ, Madou MJ (2003) Numerical modeling of transport and accumulation of DNA on electronically active biochips. Sens Actuators B 94:81–98
4. Chan V, Graves DJ, McKenzie SE (1995) The biophysics of DNA hybridization with immobilized oligonucleotide probes. Biophys J 69:2243–2255
5. Axelrod D, Wang MD (1994) Reduction-of-dimensionality kinetics at reaction-limited cell surface receptors. Biophys J 66:588–600
6. Zeng J, Almadidy A, Watterson J, Krull UJ (2002) Interfacial hybridization kinetics of oligonucleotides immobilized onto fused silica surfaces. Sens Actuators B 90:68–75
7. Sadana A, Ramakrishnan A (2001) A fractal analysis approach for the evaluation of hybridization kinetics in biosensors. J Colloid Interface Sci 234:9–18

8. Erickson D, Li D, Krull UJ (2003) Dynamic modeling of DNA hybridization kinetics for spatially resolved biochips. Anal Biochem 317:186-200
9. Das S, Das T, Chakraborty S (2006) Modeling of coupled momentum, heat and solute Transport during DNA hybridization in a microchannel in presence of electro-osmotic effects and axial pressure gradients. Microfluid Nanofluid 2:37–49
10. Chan V, Graves D, Fortina P, McKenzie SE (1997) Adsorption and surface diffusion of DNA oligonucleotides at liquid/solid interfaces. Langmuir 13:320–329
11. Das S, Das T, Chakraborty S (2006) Analytical solutions for rate of DNA hybridization in a microchannel in presence of pressure-driven and electroosmotic flows. Sens Actuators B 114:957–963
12. Grimes BA, Liapis AI (2001) Modeling and analysis of the electrokinetic mass transport and adsorption mechanisms of a charged adsorbate in capillary electrochromatography systems employing charged nonporous adsorbent particles. J Colloid Interface Sci 234:223–243
13. Das S, Chakraborty S (2006) Augmentation of macromolecular adsorption rates through transverse electric fields generated across patterned walls of a microfluidic channel. J Appl Phys 100:014908(1–8)
14. Chan V, McKenzie SE, Surrey S, Fortina P, Graves DJ (1998) Effect of hydrophobicity and electrostatics on adsorption and surface diffusion of DNA oligonucleotides at liquid/solid interfaces. J Colloid Int Sci 203:197–207

Electrokinetic Two-Phase Flows

Teck Neng Wong, John C. Chai, Y. F. Yap, Gao Yandong, Yang Chun, Kim Tiow Ooi
School of Mechanical and Aerospace Engineering, Nanyang Technological University, Singapore, Singapore
mtnwong@ntu.edu.sg, mckchai@ntu.edu.sg

Synonyms

Liquid–liquid electroosmotic flow; Liquid–solid electrophoretic flow; Electroosmosis

Definition

In this article, two-phase flow refers to two immiscible fluids or liquid–solid flow. When two immiscible fluids or liquid–solid (particle) co-flow in a microchannel under an applied electric field, an interface forms separating the two phases. This is known as electrokinetic two-phase flow.

Overview

Most surfaces acquire a finite charge density when in contact with an aqueous solution. The effect of any charged surface in an aqueous (electrolyte) solution will be to influence the distribution of nearby ions in the solution and lead to the formation of a region close to the charged surface in which there is an excess of counter-ions over co-ions to neutralize the surface charge. This high capacitance charged region of ions close to the liquid–solid interface is known as an electric double layer (EDL) [1]. An obvious difference between the two-phase interface and the liquid–wall interface is that the interface between the two phases is not stationary. The external electric intensity interacts with the free charge at the interface (liquid–liquid, liquid–particle) to generate a surface force. This surface force is important and has to be taken into account in two-phase electroosmotic flow. In this article, the fundamental aspects of liquid–liquid electroosmotic flow and liquid–particle electrophoretic flow considering the free charge at the interface are studied to investigate the characteristics of such two-phase flow systems.

Basic Methodology

Liquid–Liquid Electroosmotic Flow

One major drawback of conventional electroosmosis is the requirement of aqueous solutions as the working fluid. Non-aqueous liquids such as organic solvents do not form an EDL layer at channel walls due to the very low conductivity. As such, non-aqueous liquids cannot be pumped by the conventional electroosmotic pumps. In order to drive non-conducting liquids, Brask et al. [2] and Gao et al. [3, 4] proposed the use of a conducting liquid as the driving mechanism to drag another non-conducting liquid. Figure 1 shows a schematic of two immiscible liquids, a conducting liquid and a non-conducting liquid, co-flowing in a rectangular microchannel. When an electric field is applied across the conducting liquid, an electroosmotic force will be generated in the conducting liquid. The flow of the two liquids depends on the viscosity ratio, the strength of the applied electric field, the electroosmotic characteristics of the conducting liquid and the interfacial phenomena between the two liquids. In this way, the non-conducting liquid is delivered by electroosmosis.

Theoretical Flow Models

Consider a two-liquid system, in which one is a conducting liquid containing ionic charges in contact with a charged

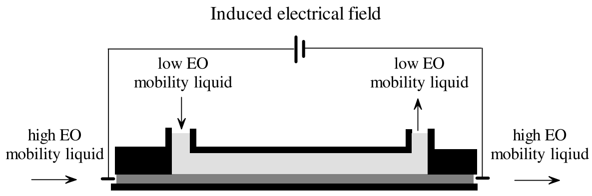

Electrokinetic Two-Phase Flows, Figure 1 Schematic of two-liquid electroosmotic flow

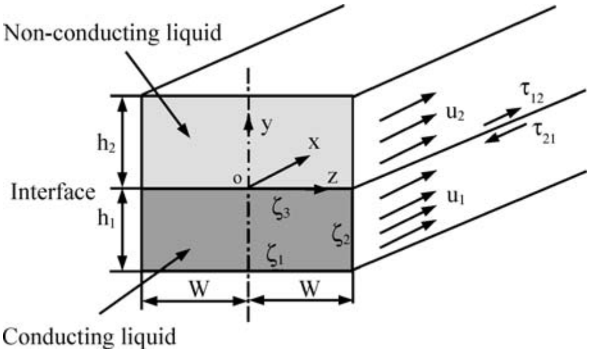

Electrokinetic Two-Phase Flows, Figure 2 Schematic of the coordinate system

smooth solid wall and the other is a non-conducting liquid. It is assumed that the two liquids are immiscible. A planar interface is assumed. To analyze this system, a Cartesian orthogonal coordinate system (x, y, z) is used where the origin point, O, is the intersection of the interface and the symmetric line as shown in Fig. 2. The heights of the conducting liquid and the non-conducting liquid are denoted as h_1 and h_2, respectively. Half of the width of the channel is denoted by w. When the flow is fully developed, at position $\boldsymbol{r}$, the velocities of two liquids, u_1 or u_2, along the channel are independent of the x-coordinate. The subscripts 1 and 2 denote the conducting liquid and the non-conducting liquid, respectively.

As a result of surface phenomena, electric double layers (EDLs) form at the liquid–liquid interface and the wall surfaces that are in contacted with the conducting liquid. For a more general situation, the bottom wall and the side walls may be made of different materials. We specify that the zeta potential at the bottom wall is ζ_1 and at the side walls is ζ_2; the zeta potential at the liquid–liquid interface is ζ_3. The electric potential in the conducting liquid due to a charged channel wall is taken as ψ and the net volume charge density in the conducting liquid as ρ_q. The length scale and velocity scale of the flow are taken as L and V, respectively. The independent variable $\boldsymbol{r}$ and dependent variables u, ψ and ρ_q are expressed in terms of the corresponding dimensionless quantities (shown with an overbar) by

$$\begin{aligned} \boldsymbol{r} &= L\bar{\boldsymbol{r}} \\ u &= V\bar{u} \\ \psi &= k_B T\bar{\psi}/(z_0 e) \\ \rho_q &= 2n_0 z_0 e\bar{\rho}_q \end{aligned} \tag{1}$$

where k_B is Boltzmann's constant, T is the absolute temperature, z_0 is the valence of the ions, e is the elementary charge and n_0 is the reference value of the ion concentration. Due to symmetry, only half of the cross-section of the rectangular channel is considered. At the mid-plane $z = 0$, a symmetric condition, $\partial\psi/\partial z = 0$ is held.

Electrical Double Layer Potential in the Conducting Liquid

It is assumed that the electric charge density is not affected by the external electric field due to the thin EDLs and small fluid velocity; therefore the charge convection can be ignored and the electric field equation and the fluid flow equation are decoupled. Based on the assumption of local thermodynamic equilibrium, for small zeta potential, the electric potential due to the charged wall is described by the linear Poisson–Boltzmann equation which can be written in terms of dimensionless variables as

$$\frac{\partial^2\bar{\psi}}{\partial\bar{z}^2} + \frac{\partial^2\bar{\psi}}{\partial\bar{y}^2} = K^2\bar{\psi} \tag{2}$$

where $K = L\kappa$ is the ratio of the length scale L to the characteristic double layer thickness $1/\kappa$. Here κ is the Debye–Hückel parameter, $\kappa = \left(2z_0^2 e^2 n_0/\varepsilon k_B T\right)^{1/2}$, which is referred to the characteristic thickness of the EDL. ε is the relative permittivity of the conducting liquid. The solution to the Poisson–Boltzmann equation is obtained as

$$\begin{aligned} &\bar{\psi}(\bar{y},\bar{z}) = \\ &\sum_{j=1}^{\infty} \frac{4(-1)^{j+1}[\bar{\zeta}_1 \sinh(B_j\bar{y}) + \bar{\zeta}_3 \sinh(B_j\overline{h_1} - B_j\bar{y})]\cos(\lambda_j\bar{z})}{(2j-1)\pi \sinh(B_j\bar{h}_1)} \\ &+ \sum_{p=1}^{\infty} \frac{2\bar{\zeta}_2\left[1+(-1)^{p+1}\right]\cosh(A_p\bar{z})}{p\pi\cosh(A_p\bar{w})} \sin\left(\frac{p\pi}{\bar{h}_1}\bar{y}\right) \end{aligned} \tag{3}$$

where

$$B_j = \sqrt{K^2 + \frac{(2j-1)^2\pi^2}{4\bar{w}^2}}$$

$$\lambda_j = \frac{(2j-1)\pi}{2\bar{w}}$$

$$A_p = \sqrt{K^2 + \frac{p^2\pi^2}{\bar{h}_1^2}}$$

From electrostatics, the normal component of the gradient of the electric potential, ψ, jumps by an amount propor-

tional to the surface charge density, ρ_q^s, that is

$$\rho_q^s = -\varepsilon \frac{\partial \psi}{\partial y} \tag{4}$$

It is assumed that the gradient of electric potential in the non-conducting liquid vanishes. Using the reference surface charge density as $(\varepsilon k_B T)/(z_0 eL)$, one obtains the dimensionless surface charge density at the liquid–liquid interface as

$$\overline{\rho_q^s} = \sum_{j=0}^{\infty} \frac{4(-1)^{j+1} B_j}{(2j-1)\pi} \left[\frac{\bar{\zeta}_3}{\tanh(B_j \bar{h}_1)} - \frac{\bar{\zeta}_1}{\sinh(B_j \bar{h}_1)} \right] \cdot \cos(\lambda_j \bar{z}) - \sum_{p=1}^{\infty} \frac{2\bar{\zeta}_2 \left[(-1)^{p+1} - 1 \right] \cosh(A_p \bar{z})}{\bar{h}_1 \cosh(A_p \bar{w})} \tag{5}$$

It should be mentioned that the surface charge at the interface, ρ_q^s, is opposite in sign to the volumetric net charge in the EDL region at the vicinity of the interface. Once the electric potential distribution is known, the volumetric net charge density can be obtained through the relationship

$$\bar{\rho}_q = -\bar{\psi} \tag{6}$$

This volumetric net charge density, Eq. (6), and the interface surface charge density, Eq. (5), are required to determine the electrostatic force caused by the presence of zeta potential. The bulk electrostatic force is considered as an additional body force acting on the conducting liquid to modify the conventional Navier–Stokes equation. The non-conducting liquid is dragged by the viscous forces from the conducting liquid and the external electrostatic force due to the surface charge density at the liquid–liquid interface.

Momentum Equation of Liquid–Liquid Flow

We now consider a transient, fully developed, laminar, liquid–liquid stratified electroosmotic flow through a rectangular channel as illustrated in Fig. 2. For electroosmotic flow in an open-ended channel, it is assumed that there is no pressure gradient along the microchannel.

EDLs form in the conducting liquid, and the momentum equations of the two liquids reduce to

$$\frac{\partial \bar{u}_1}{\partial \bar{t}} = \frac{1}{\text{Re}} \left(\frac{\partial^2 \bar{u}_1}{\partial \bar{z}^2} + \frac{\partial^2 \bar{u}_1}{\partial \bar{y}^2} \right) + G_x \bar{\rho}_q \quad \text{(for the conducting liquid)} \tag{7}$$

and

$$\bar{\rho}_2 \frac{\partial \bar{u}_2}{\partial \bar{t}} = \beta \frac{1}{\text{Re}} \left(\frac{\partial^2 \bar{u}_2}{\partial \bar{z}^2} + \frac{\partial^2 \bar{u}_2}{\partial \bar{y}^2} \right) \quad \text{(for the non-conducting liquid)} \tag{8}$$

where G_x is a parameter given as $G_x = (2z_0 e n_0 L E_x)/(\rho V^2)$, in which ρ is the liquid density and E_x the external electric field along the x-direction. The second term of the right-hand side of Eq. (7) represents the electric body force term, which is caused by the action of the applied electrical field on the volumetric net charge density in the EDLs of the conducting liquid, where $\beta = \mu_2/\mu_1$ is the dynamic viscosity ratio.

At the liquid–liquid interface ($y = 0$), due to the presence of the surface charge, shear stress is not continuous at the interface. The matching conditions are the continuities of velocity and the shear stress balance, which jumps abruptly at the interface.

$$\begin{cases} \bar{u}_1 = \bar{u}_2 \\ \frac{\partial \bar{u}_1}{\partial \bar{y}} = \beta \frac{\partial \bar{u}_2}{\partial \bar{y}} - \bar{M} \bar{\rho}_q^s \end{cases} \tag{9}$$

where $M = (\varepsilon k_B T E x) / (z_0 e V \mu)$.

The term $\bar{M} \bar{\rho}_q^s$ accounts for the surface force exerted on the interface due to the interface surface charge. Laplace transform method is applied to solve Eqs. (7) and (8) with the boundary conditions. The analytical solution is presented in [4].

Key Research Findings

Liquid–Liquid Electroosmotic Flow

In the analysis, an aqueous binary electrolyte, KCl, with univalent charge is used as the conducting liquid. The dimensions of the microchannel are 40 μm in width and 40 μm in height. We choose $h_1 = h_2 = 20$ μm and $\zeta_1 = \zeta_2 = -25$ mV. The concentration of the conducting liquid is 10^{-6} M, and hence $K = 130$ ($1/\kappa = 307$ nm). The kinematic and dynamic viscosity ratios are $\alpha = 1.5$ and $\beta = 1$, respectively.

Figure 3 shows the 3D time evolutions of the velocity profiles for the liquid–liquid electroosmotic flow. EDLs form at the liquid–liquid interface and the wall surfaces that are in contacted with the conducting liquid. The interface zeta potential $\zeta_3 = 0.5\zeta_1$ is assumed. It can be seen that upon the application of the electric field, the flow is activated within the EDLs of the conducting liquid and at the liquid–liquid interface. In the conducting liquid, EDLs at the liquid–wall and liquid–liquid interfaces drive the flow

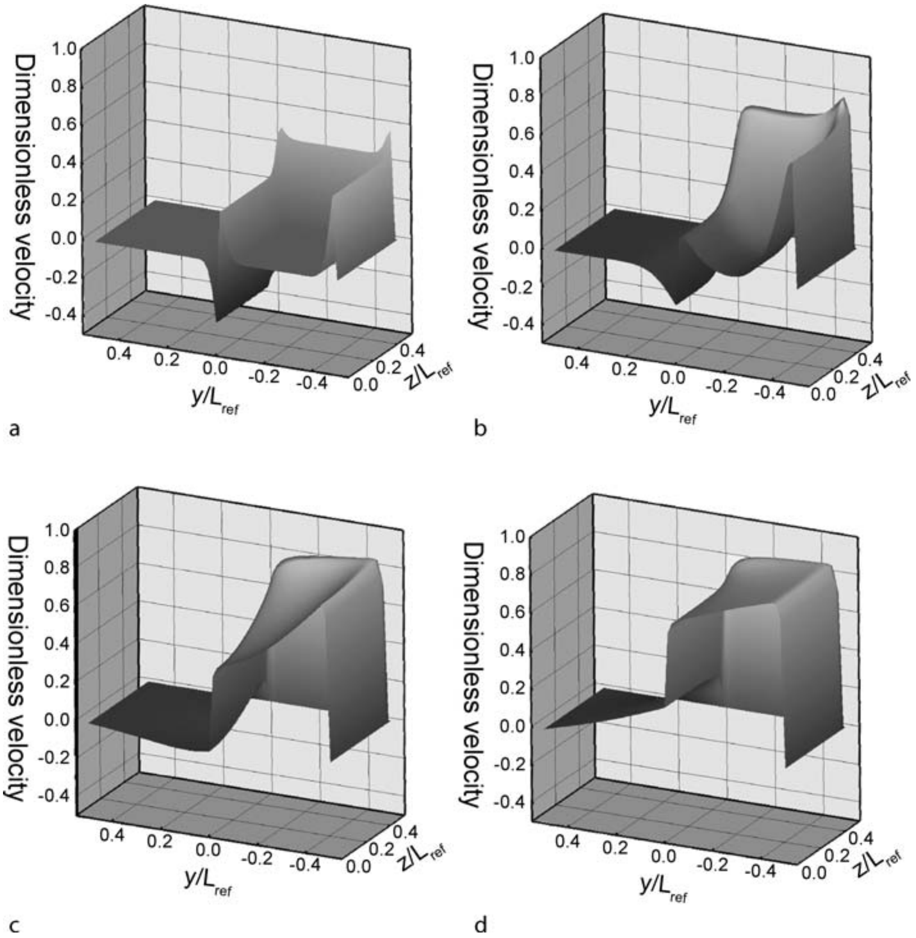

Electrokinetic Two-Phase Flows, Figure 3 Developing process for two-liquid electroosmotic flow: (**a**) $\bar{t} = 0.0005$, (**b**) $\bar{t} = 0.005$, (**c**) $\bar{t} = 0.05$, (**d**) $\bar{t} = 0.5$ ($K = 130$, $\alpha = 1.5$, $\beta = 1$, $\bar{\zeta}_1 = \bar{\zeta}_2 = 2\bar{\zeta}_3 = 0.97$)

in the positive x-direction. As the interface zeta potential ζ_3 is negative, the surface force at the interface drives the interface in the negative x-direction. The surface charge density at the liquid–liquid interface is directly related to ζ_3 as shown by Eq. (5). A surface force is generated due to the interaction between the surface charge density and the externally applied electric field as shown by the matching condition Eq. (9). During the transient period, the flow field near the interface region is significantly influenced by the surface force. As time elapses, the negative velocity reduces as the EDLs exert hydrodynamic shear stress on the adjacent liquid; the liquid flow outside the EDLs may be considered as 'passive' flow caused by the shear viscous forces. The flow characteristics of liquid–liquid electroosmotic flow depend on the coupling effects between the two liquids, which involve the electrokinetic driving forces in the conducting liquid and the interface phenomena. The interface phenomena include the interface surface force and the interfacial shear stress between the two liquids.

To investigate the effect of viscosity ratio between the two liquids, different values of β are chosen. Figure 4a and b show the dimensionless velocity profiles at the symmetric line when $\beta = 1$ and 10, respectively. The velocity profile of the non-conducting fluid is very much like Couette flow as the non-conducting liquid is dragged by the conducting liquid through the interfacial shear stress. As $\beta = \mu_2/\mu_1$, a smaller value of β corresponds to a lower flow resistance of the non-conducting fluid. The results show that when $\beta = 1$ the non-conducting fluid can be dragged relatively easily by the conducting liquid as compared to when $\beta = 10$. Figure 5 shows the dimensionless velocity profiles in the absence of the interface zeta potential ($\zeta_3 = 0$). Upon the application of the electric field, the flow is activated within the EDL at the liquid–wall interface in the conducting liquid. As there is no opposite sur-

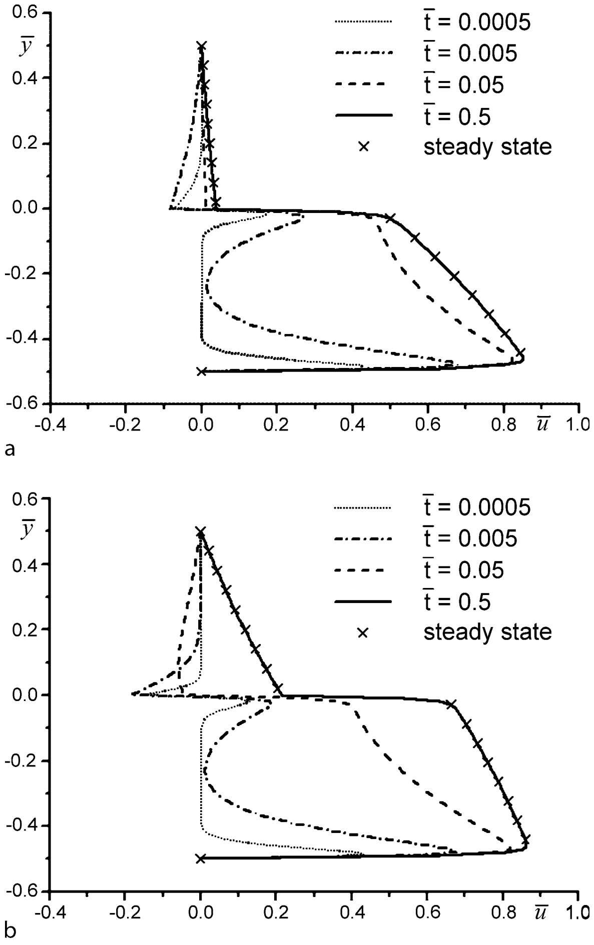

Electrokinetic Two-Phase Flows, Figure 4 Dimensionless transient two-liquid velocity at the symmetric line: (**a**) $K = 130$, $\alpha = 1.5$, $\beta = 1$, $\zeta_3 = 0.5\zeta_1$; (**b**) $K = 130$, $\alpha = 0.15$, $\beta = 10$, $\zeta_3 = 0.5\zeta_1$

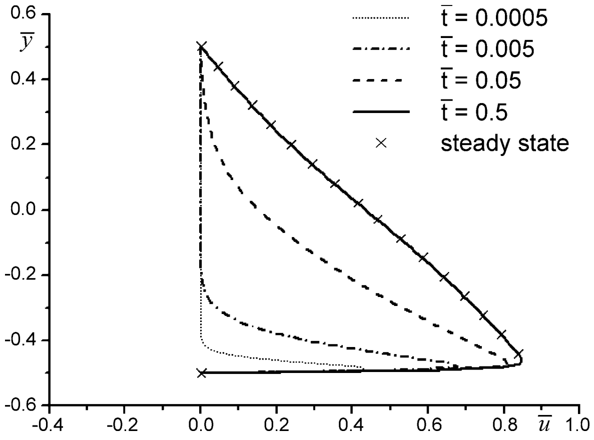

Electrokinetic Two-Phase Flows, Figure 5 Dimensionless transient two-liquid velocity at the symmetric line ($K = 130$, $\alpha = 1.5$, $\beta = 1$, $\zeta_3 = 0$)

face force exerted on the interface, the non-conducting liquid is delivered by electroosmosis of the conducting liquid, through the hydrodynamic viscous forces at the interface.

Liquid–Particle Electrophoretic Flow

Electrophoresis is the motion of a charged particle relative to the surrounding liquid due to an imposed external electric field [5]. Its applications include but are not limited to characterization and manipulation of organic and inorganic particles. In particular, electrophoresis has been applied to a variety of analytical separation problems involving nucleic acids, proteins and drugs.

For electrophoresis on various Lab-on-a-Chip platforms, the particles are of sizes comparable to the microchannel in which they flow. As such, particle–particle and particle–wall interactions are no longer negligible. Therefore, the electric field, the flow field and the particle motion are strongly coupled together.

Analytical solutions for some simplified situations have been obtained [6, 7]. For more complicated problems, numerical models have to be employed. For this purpose, a fixed-grid finite volume method is presented for electrophoresis of a particle. It is based on a previously developed fluid–particle flow model [8].

Figure 6 shows a rigid particle suspended in a fluid in a microchannel. The fluid is an aqueous electrolyte solution. Both the particle and the walls of the microchannel are non-conducting and uniformly charged with zeta potentials of ζ_P and ζ_W, respectively. When an electric field is applied along the microchannel, the fluid is electroosmotically driven into motion. At the same time, the particle undergoes electrophoresis. The particle is sufficiently large such that momentum is exchanged between the particle and the flowing fluid. As a result, the particle affects the fluid flow significantly and vice versa resulting

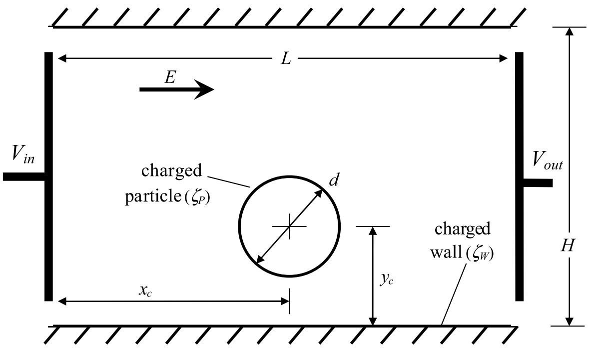

Electrokinetic Two-Phase Flows, Figure 6 Schematic of the electrophoresis of a charged particle in a microchannel

in a transient process where the motion of the particle, the flow field and the electric field are strongly coupled.

Particle Motion The particle location and orientation are determined from the motion of the particle. For a two-dimensional situation, the motion of the particle is characterized by its centroid location $\boldsymbol{x}_{\mathrm{P}}$ and orientation θ_{P}. The translational and rotational motions of the particle are governed respectively by

$$m\frac{\mathrm{d}^2\boldsymbol{x}_{\mathrm{P}}}{\mathrm{d}t^2} = \boldsymbol{F} + \boldsymbol{G} \tag{10}$$

and

$$I\frac{\mathrm{d}^2\theta_{\mathrm{P}}}{\mathrm{d}t^2}\hat{k} = \boldsymbol{T} \tag{11}$$

with $\boldsymbol{x}_{\mathrm{P}}$, $\mathrm{d}\boldsymbol{x}_{\mathrm{P}}/\mathrm{d}t$, θ_{P} and $\mathrm{d}\theta_{\mathrm{P}}/\mathrm{d}t$ known at $t = 0$. Parameters m, I, $\boldsymbol{F}$, $\boldsymbol{G}$ and $\boldsymbol{T}$ are the mass, moment inertia, resultant surface force, body forces and the induced torque on the particle, respectively.

Fluid Motion In this article, an unsteady incompressible laminar flow is considered. The continuity and the momentum equations are given by

$$\nabla \cdot \boldsymbol{u} = 0 \tag{12}$$

$$\frac{\partial(\rho\boldsymbol{u})}{\partial t} + \nabla\cdot(\rho\boldsymbol{u}\boldsymbol{u}) = -\nabla p + \nabla\cdot\left[\mu\left(\nabla\boldsymbol{u} + \nabla\boldsymbol{u}^T\right)\right] + \boldsymbol{g} \tag{13}$$

where $\boldsymbol{u}$, $\boldsymbol{g}$, p, ρ and μ are the velocity vector, body force per unit mass, pressure, density and viscosity, respectively. For a thin EDL with the electric field developing instantly, the electrical potential φ is governed by the Gauss law

$$\nabla\cdot(\varepsilon_{\mathrm{e}}\nabla\varphi) = 0 \tag{14}$$

where ε_{e} is the electrical permittivity. The ionic concentration is uniform and therefore the local volume charge density is zero.

Boundary Conditions For a thin EDL at the walls, the Helmholtz–Smoluchowski slip velocity is imposed:

$$\boldsymbol{u} = \frac{\varepsilon_{\mathrm{e}}\zeta_{\mathrm{W}}}{\mu}\left(\bar{\bar{I}} - \hat{N}_{\mathrm{W}}\hat{N}_{\mathrm{W}}\right)\cdot\nabla\varphi \tag{15}$$

where ζ_{W} and $\hat{N}_{\mathrm{W}}$ are the zeta potential and unit normal of the charged walls.

The velocity at the particle surface is set to

$$\boldsymbol{u} = \frac{\mathrm{d}\boldsymbol{x}_{\mathrm{P}}}{\mathrm{d}t} + \frac{\mathrm{d}\theta_{\mathrm{P}}}{\mathrm{d}t}\hat{k}\times(\boldsymbol{x} - \boldsymbol{x}_{\mathrm{P}}) + \frac{\varepsilon_{\mathrm{e}}\zeta_{\mathrm{P}}}{\mu}\left(\bar{\bar{I}} - \hat{N}_{\mathrm{S}}\hat{N}_{\mathrm{S}}\right)\cdot\nabla\varphi \tag{16}$$

where $\boldsymbol{x}$ and $\hat{N}_{\mathrm{S}}$ are the position vectors of the surface of the particle and the unit outer normal of the particle, respectively. The first and second terms on the right-hand side represent the translational and the rotational motions, respectively. The third term represents the Helmholtz–Smoluchowski slip velocity due to the presence of an EDL around the particle.

Liquid–Solid Electrophoretic Flow

Electrophoretic Motion of a Particle

In Fig. 6, the particle is subjected to an electrical field parallel to the x-axis. The length and height of the microchannel are set to $L = 400\,\mu\mathrm{m}$ and $H = 200\,\mu\mathrm{m}$, respectively. A circular particle of density $\rho_{\mathrm{P}} = 8960\,\mathrm{kgm}^{-3}$ and diameter $d = 80\,\mu\mathrm{m}$ is initially suspended at $(x_{\mathrm{c}}, y_{\mathrm{c}}) = (200, 100)$. Solutions are obtained for neutral ($\zeta_{\mathrm{P}} = 0$), positively charged ($\zeta_{\mathrm{P}} = +51\times10^{-3}\,\mathrm{V}$) and negatively charged ($\zeta_{\mathrm{P}} = -204\times10^{-3}\,\mathrm{V}$) particles. The zeta potential of the wall is set to $\zeta_{\mathrm{W}} = -102\times10^{-3}\,\mathrm{V}$.

Thin EDLs form at both the particle and the wall surfaces. The formation of EDLs at the surfaces sets the fluid in motion and consequently drives the particle. As the particle is located at the center of the microchannel, it experiences neither vertical translation nor rotation. Fig. 7 shows the instantaneous location of the particles with different zeta potentials. The translational velocity U of the particle is given by the gradient of the graph. For all cases, the gra-

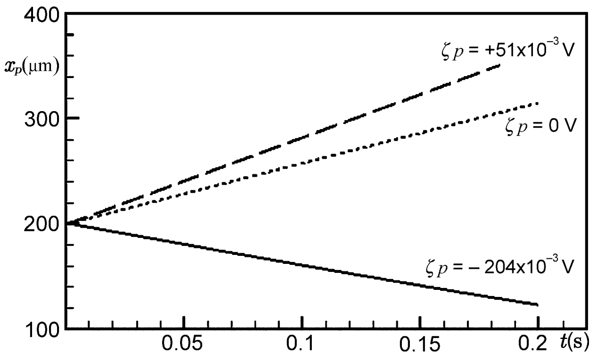

Electrokinetic Two-Phase Flows, Figure 7 Instantaneous location of particles with different zeta potentials

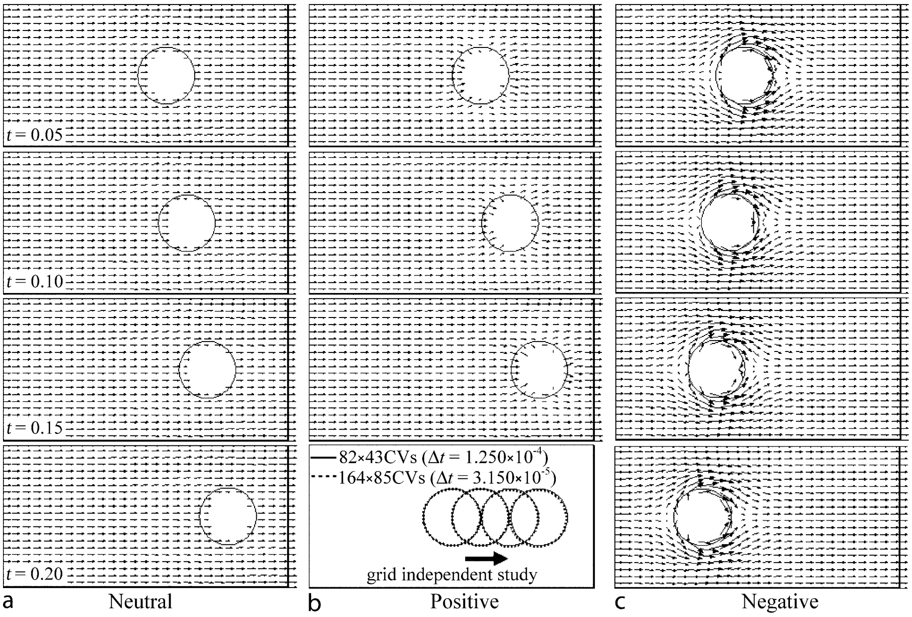

Electrokinetic Two-Phase Flows, Figure 8 Flow field around neutral, positively and negatively charged particles

dient is constant. This implies that the particles accelerate in a very short time to a constant velocity and move with that constant velocity thereafter. This is not unexpected as the inertia force is negligible in such a small-scale channel. The induced electroosmotic flow is in the positive x-direction. A neutral particle thus flows in the positive x-direction. Figure 8a shows the velocity field around the neutral particle at $t = 0.05$, 0.10, 0.15 and 0.20 s. No distortion of the velocity field is observed. This indicates that the particle flows with the same velocity as the fluid.

When the particle is charged, an additional electrophoretic flow field is induced around the particle. It pushes a positively charged particle to flow in the positive x-direction. With both electroosmotic and electrophoretic effects acting in the same direction, the particle flows with a higher velocity as implied by a larger gradient in Fig. 7. The velocity field around the positively charged particle is shown in Fig. 8b. Since the particle is flowing faster than the fluid, a low-pressure region is created at the trailing edge. Fluid is drawn into this region. On the other hand, a high-pressure region is created at the leading edge, pushing the fluid to move forward.

For the negatively charged particle, the electrophoretic effect tends to drive it in the negative x-direction. As the particle is highly negatively charged, the electrophoretic effect is strong enough to overcome the electroosmotic effect. As a result, the particle is driven to move in the negative x-direction creating regions of high velocity between the particle and the walls (Fig. 8c).

Future Directions for Research

The computational results demonstrate that the liquid–liquid electroosmotic pumping concept is feasible for relatively low interface zeta potentials and viscosity ratios. The time evolution of the velocity profile provides a detailed insight of the flow characteristic. It is recommended that detailed experiments to be carried to validate the model.

Modeling of electrophoresis of a particle in microchannel is presented. It is of interest to extend the model to a three-dimensional flow and to the case with a conducting particle.

Cross References

► Electroosmotic Flow (DC)
► Electrophoresis

References

1. Hunter RJ (1981) Zeta Potential in Colloid Science, Principle and Applications. Academic, New York
2. Brask A et al (2003) Electroosmotic pumping of non-conduction liquids by viscous drag from a secondary conducting liquid. In NanoTech 2003, proc, San Francisco, USA, February 2003, Vol. 1, pp 190–193
3. Gao Y, Wong TN, Yang C, Ooi KT (2005) Two-fluid electroosmotic flow in microchannel. J Colloid Interfacial Sci 284:306–314
4. Gao Y, Wong TN, Yang C, Ooi KT (2005) Transient two-liquid electroosmotic flow with electric charges at the interface. Colloids Surf A: Physicochem Eng Asp 266(1–3):117–128

5. Ghosal S (2006) Electrokinetic flow and dispersion in capillary electrophoresis, Annual Rev Fluid Mech 38:309–338
6. Keh HJ, Horng KD, Kuo J (1991) Boundary effects on electrophoresis of colloidal cylinders. J Fluid Mech 231:211–228
7. Liu H, Bau HH, Hu HH (2004) Electrophoresis of concentrically and eccentrically positioned cylindrical particles in a long tube. Langmuir 20:2628–2639
8. Yap YF (2007) Numerical modeling of multiphase flows in microchannels. PhD thesis, Nanyang Technological University, Nanyang, Singapore

Electromagnetically Actuated Pumps

► Magnetic Pumps

Electromagnetophoresis

► Magnetophoresis

Electromechanical Coupling

Definition

A quantity that describes the amount of energy transferred from electrical to mechanical forms, or vice versa, in a mechanism capable of making the energy transformation, namely, piezoelectric materials or electromagnetic solenoids. Often refers to a specific value between 0 and 1, where 1 represents a complete transformation of all energy from one form to the other via the mechanism.

Cross References

► Piezoelectric Microdispenser

Electromechanically Coupled Materials

► Piezoelectric Materials for Microfluidics

Electromigration

► Electrokinetic Motion of Cells and Nonpolarizable Particles

Electronic Packaging

► Packaging (and Wire Bonding)

Electronic Paper

JAESUNG LEE[1], KWAN HYOUNG KANG[2]
[1] LG Material & Parts R&D Center, LG Micron, Korea
[2] Department of Mechanical Engineering, Pohang University of Science and Technology, Pohang, South Korea
jaesung@lgmicron.com, khkang@postech.edu

Synonyms

Electric paper-like display

Definition

Conventional paper is a sheet made of cellulose pulp bearing writing or printing. It is characterized by it being thin, lightweight, flexible, shatterproof, sunlight readable. Electronic paper can be defined as a digital media with paper-like attributes and can alter its display properties when a voltage is applied on and off. That is why it has been called a paper-like electronic display.

Overview of Electronic Paper

A television using a cathode ray tube (CRT) installed in homes for almost a century has been rapidly replaced by flat panel displays such as the liquid crystal display (LCD) panel and plasma display panel (PDP). Along with the development of the telecommunications technology, a small flat panel display of portable electronic devices especially supplies a convenient interface to its user.

Since an LCD needs a backlight and a PDP uses a plasma source, power consumption is usually high. To increase power saving without a backlight, new reflective displays with bi-stability have been introduced into electronic paper, because bi-stable displays can keep an image for some period of time even if the power is turned off. Bi-stability enables the displays to have a long battery life when rapid updates of the image are not necessary. Flexibility is another important attribute to electronic paper. The glass used in conventional displays is substituted for a plastic film that is much thinner and more lightweight. These two remarkable characteristics cause the electronic paper to have a feature of paper [1]. Another outstanding advantage is sunlight viewability. This is an important characteristic for electronic paper to compete with LCDs. Examples of electronic paper suggested by industrial companies, as shown in Fig. 1, are (a) a weather forecast, (b) a flag or cloth, (c) a credit card, (d) a cell phone, and so on.

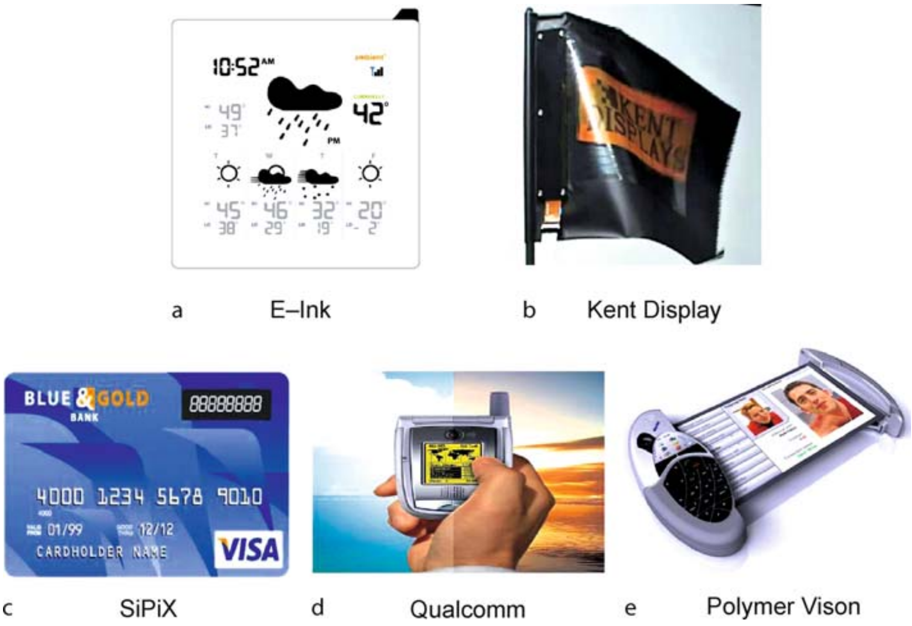

Electronic Paper, Figure 1 Various E-paper applications

Electronic Paper, Table 1 Comparison of various electronic papers

Core technology	Display type (company)	Driving voltage (V)	Contrast ratio	Response time (ms)	Reflectivity (%)
	Paper	–	15	–	70
Particle	Microcapsule (E-ink)	15 – 90	10	100	40
	Microcup (SiPix)	30	∼ 10	200	40
	Gyricon (Xerox)	50 – 150	∼ 8	80 – 100	20
	QR-LPD (Bridgestone)	100	∼ 9	0.2	40
Liquid crystal	ChLCD (Kent Display)	40	20 – 30	30 – 100	40
	STN (ZBD)	5	5	20	< 5
Fluid	Electrowetting (Philips)	20 – 30	15	< 10	60
MEMS	iMoD (Qualcomm)	5	10	10	50

The goal of electronic paper is to make a display that works like paper under various viewing conditions [1]. The interesting point is that there is no typical driving mechanism in electronic paper unlike in LCDs and PDPs. Many investigators have done remarkable work with diverse approaches: electrophoresis [2], liquid crystals [3], fluids [4], and micro-electro-mechanical systems (MEMS) [5]. The development status of several approaches up to the present, mainly from industry, are shown in Table 1, where the key factors compared are driving voltage, contrast ratio, response time and reflectivity.

Electronic paper based on particle technology has the longest history and has four distinct driving methods, as shown in Table 1. The common main principle is to use electrophoresis to display black or white when a voltage is applied on and off. Electrically charged particles suspended in oil can be included in a tiny capsule (E-ink), microcup (SiPiX) and a twisting ball (Xerox). Air is used as a fluid medium in the QR-LPD type by Bridgestone. This driving mechanism has advantages of mass production and bi-stability. However, the response time is long and high voltage is required. Therefore, it cannot be usefully applied to video-speed electronic paper. Color filters are also necessary to display color.

Kent Display is a pioneer of cholesteric liquid crystal displays (ChLCDs) in which the director of the liquid crystal twists around a helical axis [3]. The remarkable property is that the cholesteric material reflects light of certain

wavelengths depending on the pitch over which the director rotates. When an electric field is applied, the material can be switched into either one of two stable states, planar or focal conic. The planar and focal conic states are reflective mode and transparent mode, respectively. In order to display color, it does not require color filters; however, a stacking process is necessary and results in a thick module. Like particle-based electronic paper, it is also difficult to play video-rate displays due to a long switching speed.

Electrowetting-driven electronic paper was first introduced by Philips research laboratories [4], where colored oils act as a switcher under the influence of an electric field. This type is focused on increasing the response time for a video-speed electronic paper. The attractive points are low driving voltage and high reflectivity. Recently, the Steckl group at the University of Cincinnati has developed a light-wave coupled display using light emitting diodes [6].

The iMod type based on biomimetics reflects light using the principle of a photonic crystal, imitating butterfly wings or peacock feathers [5]. The periodic microstructure inside wings or feathers causes light to interfere with itself. The driving cell fabricated by MEMS is composed of a glass substrate with thin films and a reflective membrane, where an air gap between the thin-film stack and the membrane is controlled by a voltage. This approach has a strong advantage of power saving and response time, while the disadvantage is inflexibility due to the glass substrate.

Issues of fluid dynamics in electronic paper are in switching mechanisms and in fabrication processes such as coating, encapsulation and dispersion. For example, charged particles' switching time depends on electrophoretic mobility, given electric fields and cell gap. The contact line motion of oils is also a dominant process for electrowetting-based electronic paper. From the viewpoint of process, encapsulation is required for electrophoretic imaging film of E-ink and for cholesteric liquid crystals of Kent Display. The significant process to give flexibility to electronic paper is the process to coat or print display materials (such as encapsulated particles or cholesteric liquid crystals) or cells on a flexible substrate. In this article, these problems are discussed in the following section from the point of view of driving principles and fabrication processes for electronic paper.

Key Research Findings

Electrophoresis-Based Electronic Paper

Electrophoretic displays based on particles suspended in oil have been investigated for commercial use since the 1970s. E-ink Corporation has used the principle of electrophoresis to develop a microencapsulated electrophoretic imaging film, where charged pigment particles are contained in a colored or transparent fluid and switched under an electric field [2]. The main advantages of microcapsules are to prevent particles from migrating in a lateral direction and to give a tight packing between microcapsules. The former and the latter contribute to block a failure mode and to increase high optical contrast, respectively. The well-known cross-sectional view of the microencapsulated electrophoretic imaging film is presented in Fig. 2 [7]. To achieve the display image of white or black, white or black pigments are shifted by applied voltages on the back plane that can be flexible or solid.

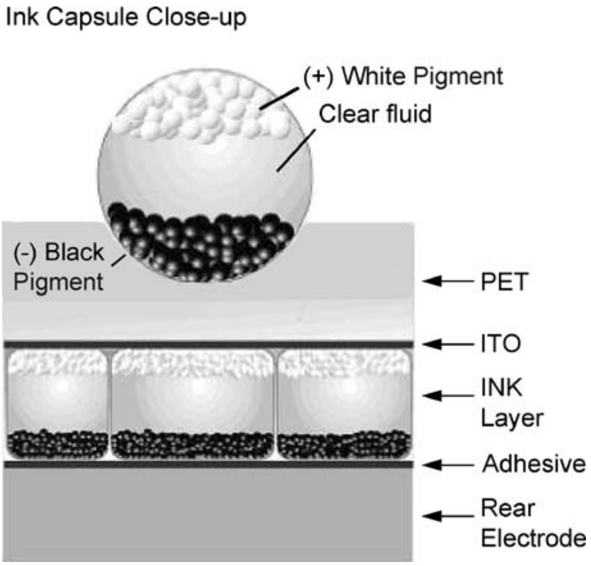

Electronic Paper, Figure 2 Physical configuration of a microencapsulated electrophoretic imaging film of E-ink. Figure from [7]

The transport of particles in electrophoretic image displays was simulated with an assumption of a normal distribution of particles, where charged pigments and charged inverse micelles through flocculation of surfactant molecules are assumed to have the same distribution [8]. Simulation results can be used to optimize the electrical and optical properties through physical parameters. For example, the switching time, t_{switch}, can be simply estimated as the ratio of the cell gap, h, to the average velocity, $v_{average}$:

$$t_{switch} \approx \frac{h}{v_{average}} = \frac{h^2}{\mu V_2 (1-\psi)}, \tag{1}$$

where

$$\psi = \frac{hN}{V_2 \varepsilon} \sqrt{\frac{4\pi Q V_1}{cst}}. \tag{2}$$

Here, V_2 is the applied voltage, V_1 is the voltage applied in the previous half period, μ is the mobility, N is the total amount of particles, ε is the dielectric constant, Q is the charge of the particles and cst is an unknown constant which has units of meters. When ψ is negligible, the main contributions of the switching time are the cell gap and the electrophoretic mobility of particles, because the applied voltage has a restriction corresponding to available electronics. Since the electrophoretic mobility is inversely proportional to viscosity of the surrounding fluid and proportional to the charge of the particles, a fast switching time can be obtained by small cell gap, a high particle charge and low fluid viscosity. ψ is the parameter to explain the effect of internal field screening due to diffusion of particles [8]. When the charge of particles increases or high V_1 is applied, the internal field screening becomes stronger in a way that the switching time increases. The internal field screening is also an important factor to obtain a fast switching speed.

Recently, the theory of dielectrophoresis was applied to explain the microscopic physics of the movement of pigments in electrophoretic image displays and to prove the discrepancies between theory and measurement [9]. Dielectrophoresis is induced by the interaction of the electric field and the induced dipole, and is used to describe the behavior of polarizable particles in a locally non-uniform electric field. For example, the phenomenon of the delay time can be explained by the principle of dielectrophoresis. In electrophoresis, when the backplane voltage is switched, the particles on the electrode have to move instantaneously under a given electric field. However, the particles need a removal time which results in a delay time in the switching process. The time constant to obtain an induced dipole from a particle at rest is derived by Schwarz's formula [10] and used to compute the dielectrophoretic force at its steady-state value. The force and the velocity fields under a non-uniform electric field due to the presence of pigments also help to estimate realistic values for physical properties.

Electrowetting-Based Electronic Paper

The technology using the principle of electrowetting enables one to manipulate rapid motion of a liquid on a micrometer scale and results in many applications such as liquid lenses for miniature cameras [10], an actuator on lap-on-a-chip and reflective displays [4]. The dynamics of droplet transport and wetting have been studied by many researchers [11] and a detailed explanation can be found in the literature. Reflective displays using the principle of electrowetting were first shown by Hayes and Feenstra [4], where a fast response time is a strong advantage to realize a video-speed electronic paper. Colored oils switched by the applied voltage are utilized as a color filter in LCD displays and give high brightness. The motion of liquid inside a pixel was studied as a function of oil film thickness, pixel size and oil viscosity to determine the electro-optical performance, where the white area percentage defined by the ratio of the area uncovered by oil is compared as a function of the above parameters [12].

Recently, the emissive display of electrowetting-driven electronic paper has been developed by Heikenfeld and Steckl [6], where a non-polar oil acts as a switcher of a light valve under the influence of a given electric field. The pixel luminance for LCD displays depends on the backlight, while this novel fluorescent display has $\sim 10-40$ times higher theoretical luminous efficiency than conventional LCD displays and the maximum luminance values for red, green and blue emission are 950, 5530 and 530 $\mathrm{cd/m^2}$, respectively. The core device is driven by light wave coupling and is composed of three components: a UV light storage plate (refractive index of ~ 1.5), a light wave coupling region and oils including lumophores for colors, as shown in Fig. 3. Violet light using LEDs is used as a light source to reduce optical absorption losses and not to decrease photo-degraded organic fluorescent oils. The lumophores in the oils are organic materials that emit visible light when violet light is excited. In the 'ON' state in Fig. 3a, the oil covers over the hydrophobic layer and visible light is emitted through lumophores, where the cladding layer reflects the violet light back into the UV storage plate due to a refractive index less than 1.3. In the 'OFF' state, the polar water repels the oil film due to the applied electric field and the

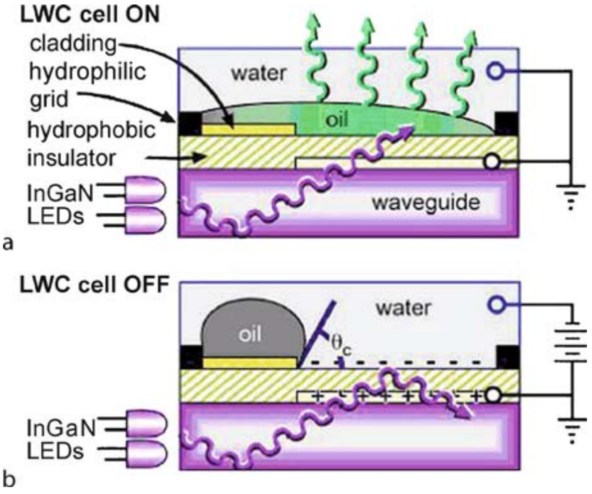

Electronic Paper, Figure 3 Light wave coupling display based on electrowetting. Figure from [6]

oils move on the hydrophobic cladding layer, where the violet light reflects over all the surface of the water (refractive index ~ 1.3) and the cladding layer due to low refractive index.

Cholesteric Liquid Crystal-Based Electronic Paper

Cholesteric liquid crystal (ChLC)-driven electronic paper has been investigated mainly by Kent Display [2]. Since ChLCs are chiral molecules, the particular color of light depends on the pitch denoted as P, where the pitch is the distance along the helical axis for ChLC to twist 360° and is determined by the amount and type of chiral additive within the liquid crystal mixture. ChLCDs are driven by switching the different textures of the ChLC electrically [1, 3], as shown in Fig. 4.

The ChLC has two stable states of planar and focal conic at zero field condition. In the planar state in Fig. 4a, the helical axis is arranged perpendicular to the cell substrate, and incident light is reflected backward due to the Bragg reflection. The reflection band is a narrow range of wavelengths and its bandwidth is defined as $\lambda_0 = (n_e - n_0)P$, where n_e and n_0 are the ordinary and extraordinary refractive index, respectively. In the focal conic state in Fig. 4b, the direction of the helical axis is randomly distributed within the cell in a way that Bragg reflection does not happen. Then, incident light is diffracted or scattered depending on the size of the helical pitch; the focal conic state is transparent to all wavelengths. When the absorption layer is coated on the bottom, the light in the focal conic state is absorbed. The ChLC in the homeotropic state, as show in Fig. 4c, relaxes to either the planar state or the focal conic state, depending on the magnitude of applied voltage. The ChLC can achieve the focal conic state when a low-voltage pulse is applied to the electrode on the substrate, and the planar state can be achieved when the power is removed from the homeotropic state. There exists a critical voltage, V_C, over which the focal conic state is transformed to the homeotropic state:

$$V_C = \frac{\pi^2 d}{P}\sqrt{\frac{K_{22}}{\varepsilon_0 \Delta\varepsilon}}, \tag{3}$$

where d is the thickness of cell gap, K_{22} is the twist elastic constant and $\Delta\varepsilon$ is the dielectric anisotropy of the ChLC [13].

When liquid crystals are encapsulated in a polymer-dispersed matrix, many different configurations of the droplets occur, depending on droplet morphology, surface anchoring, and applied fields [13]. In the case of spherical liquid crystals, when long helical axes of the droplets are perpendicular to the droplet wall, the radial and axial configurations occur, where the axial configuration has weak surface anchoring and results in a line defect along the equator of the droplet, while the radial configuration has strong surface anchoring and has a point defect in the center of the droplet. When tangential anchoring of the liquid crystal molecules is applied on the droplet wall, the bipolar configuration is obtained and two point defects at the poles are created.

Since liquid crystals have long thin molecules, the dynamics of liquid crystals is affected by the elastic and viscous response to an external stress induced by an electric field. One of the significant non-Newtonian flow behaviors is caused by coupling between the director field of liquid crystal and the imposed velocity field. Recently, the Lattice–Boltzmann method was used to investigate permeative flows in ChLCs [14], where the Beris–Edwards equations of motion for a cholesteric liquid crystal were considered. The viscosity of a ChLC can be changed enormously according as to whether the helical axis is pinned at the wall or not. In the case of free boundary condition, liquid crystal molecules can drift freely along the flow direction and viscosity increase is small. However, if the helical axis is anchored, viscosity increases greatly due to energy dissipation that is caused by anchoring effects at the wall. The computation result showed that a double twisted director pattern is observed when the strong flow field is imposed.

Fabrication Process

The method to manufacture cost-effective displays is to use proper processes for mass production or on a large scale. One example is a roll-to-roll process which needs a flexible substrate to be coated or printed display materials. Here, an important issue is to provide a monolayer of display materials. In order to supply this monolayer, a variety of methods have been tried for encapsulated cholesteric liquid crystals by Kent Display, microencapsulated electrophoretic display films by E-ink Corporation, and microcup shapes by SiPiX. In the case of the first and second types, encapsulation processes are a significant step.

The encapsulation process for ChLC is mainly attributed to its transport and optical properties [15]. Firstly, since viscosity of pure ChLC is close to that of water, its fluidity prevents ChLC from being coated on flexible substrates. Secondly, when a cholesteric liquid crystal is pressed, the flow generated inside makes the displayed image erase. Therefore, droplet dispersions by encapsulation act as a protector for its bi-stability and optical properties. The additional advantage is that encapsulated cholesteric liquid crystals are self-sealing; the materials confined to the droplets cannot flow through an interface of the droplets.

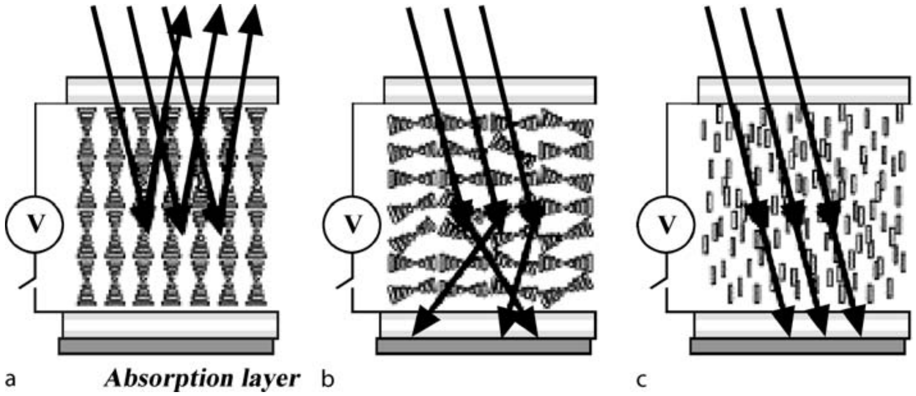

Electronic Paper, Figure 4 Different textures of the cholesteric liquid crystal: (**a**) planar state, (**b**) focal conic state and (**c**) homeotropic state. Figure from [15]

Encapsulating materials that have better adhesion to flexible substrates are used to maintain the cell thickness. The droplet morphology after encapsulation is also important. When droplets smaller than about 2 – 3 μm are used, different refractive indices between the droplets or the droplet and the encapsulating material result in light scattering; by using a smaller size of droplets, more light can be scattered. Then, a droplets size of as large as 30 – 50 μm is normally used. As the size of droplets decreases, the droplet shape tends to spherical due to surface tension. However, the spherical shape makes the planar texture unstable and decreases reflective brightness and contrast. A flattened or ellipsoidal droplet morphology is preferred to achieve the desired domain texture [16].

There are two classic approaches for encapsulation: emulsification [17] and phase separation [18]. The main difference between the two methods depends on how to make and process encapsulated droplets. In the emulsification method, water is used as a solvent to dissolve a polymer and to form a viscous solution, and cholesteric liquid crystals are mixed with the aqueous solution. By a shearing device like a propeller blade, small droplets of micrometer scale are formed and finally emulsified. The resulting emulsion is then printed on a plastic film and dried by evaporation of water. The disadvantage of this method is the broad size distribution of the droplets. In the phase separation method, cholesteric liquid crystals are homogeneously mixed with a prepolymer solution such as monomers or oligomers. Similarly, the mixture is then coated on a flexible substrate and phase separation to form droplets occurs by polymerization, cooling or solvent evaporation. This approach gives a narrow size distribution; however manufacture on a large scale is difficult. Recently, Stephenson [19] has proposed the limited coalescence process, where inorganic colloidal particles are used to stabilize dispersed droplets. This method makes it possible to investigate the effect of droplet size on optical performance. The novel approach by colloidal self-assembly has been demonstrated for a cost-effective single substrate approach [20], where a close-packed monolayer is formed by drying-assisted self-assembly.

Encapsulated liquid crystal droplets of non-spherical shapes show better electro-optical properties than those of spherical shapes [16]. The flattened droplets can be obtained by stretching a composite thermoplastic film in a solvent-induced or thermally induced phase separation method, where the mean aspect ratio is enhanced by local heat stress. In the photopolymerization-induced phase separation, droplets are elongated by a shear force during curing of the polymer binder and the final shape is reached by a cured polymer, if the plastic film thickness is larger than the initial size of the droplets. Electric field can be also applied to droplet deformation during phase separation in the direction either parallel or perpendicular to the field. At the negative dielectric permittivity of liquid crystals, the droplets are elongated in the main cell plane.

Future Directions for Research

The main advantages of electronic paper are lower fabrication costs and low power consumption compared to conventional displays. Thus, plastic printed electronics have been mainly investigated for low cost as well as flexibility. For instance, Plastic Logic Corporation has created flexible active matrix backplanes for rollable electronic paper. New battery technology like printable batteries is also required to give the attribute of flexibility to electronic paper. However, most of all, the stability of driving modes on electronic paper is significant to realize sufficient electrical and optical properties.

Cross References

- ▶ Applications Based on Electrowetting
- ▶ Electrowetting and Droplets
- ▶ Dielectrophoresis
- ▶ Electrophoresis
- ▶ Optofluidics: Optics Enabling Fluidics

References

1. Drzaic P (2006) Reflective displays: the guest for electronic paper. J Soc Inf Disp Seminar M-8
2. Comiskey B, Albert JD, Yoshizawa H, Jacobson J (1998) An electrophoretic ink for all-printed reflective electronic displays. Nature 394:253–255
3. Yang DK, Doane JW (1992) Cholesteric liquid crystal/polymer gel dispersion: Reflective display application. SID Symp Dig Technic Pap 23:759–761
4. Hayes RA, Feenstra BJ (2003) Video-speed electronic paper based on electrowetting. Nature 425:383–385
5. Gally BJ (2004) Wide-Gamut Color Reflective Displays Using iMoDTM Interference Technology. SID Symp Dig Technic Pap 35:654–657
6. Heikenfeld J, Steckl AJ (2005) Intense switchable fluorescence in light wave coupled electrowetting devices. Appl Phys Lett 86:011105
7. Amundson K, Sjodin T (2006) Achieving graytone images in a microencapsulated electrophoretic display. SID Dig Technic Pap 37:1918–1921
8. Bert T, Smet HD, Beunis F, Neyts K (2006) Complete electrical and optical simulation of electronic paper. Displays 27:50–55
9. Hu Y, Chen M (1998) Computer simulation of polarization of mobile charges on the surface of a dielectric sphere in transient electric fields. J Electrostatics 43:19–38
10. Kuiper S, Hendriks HW (2004) Variable-focus liquid lens for miniature cameras. Appl Phys Lett 85:1128–1130
11. Ren H, Fair RB, Pollack MG, Shaughnessy EJ (2002) Dynamics of electro-wetting droplet transport. Sensors and Actuators B 87:201–206
12. Roques-Carmes T, Hayes RA, Feenstra BJ, Schlangen LJM (2004) Liquid behavior inside a reflective display pixel based on electrowetting. J Appl Phys 95:4389–4396
13. Gennes PGD, Prost J (1993) The physics of liquid crystals. Oxford Univ. Press, New York
14. Marenduzzo D, Orlandini E, Yeomans JM (2004) Permeative flows in cholesteric liquid crystals. Phys Rev Lett 92:188301
15. Yang DK (2005) Flexible bistable cholesteric reflective displays. J Display Technol 2:32–37
16. Kloscowicz SJ, Aleksander M (2004) Effect of polymer-dispersed liquid crystal morphology on its optical performance. Opto-electronics Rev 12:305–312
17. Sage I (1991) Thermochromic liquid crystals in devices. In: Liquid Crystals: Applications and Uses. Bahadur B, World Scientific, Singapore
18. Penterman R, Klink SI, Koning HD, Nisato G, Broer DJ (2002) Single-substrate liquid-crystal displays by photo-enforced stratification. Nature 417:55–58
19. Stephenson S, Boettcher JW, Giacherio DJ (2002) Method for making materials having uniform limited coalescence domains. U.S. Patent No. 6,423,368
20. Chari K, Rankin M, Johnson DM, Blanton TN, Capurso RG (2006) Single-substrate cholesteric liquid crystal displays by colloidal self-assembly. Appl Phys Lett 88:043502

Electroosmosis

- ▶ Electrokinetic Two-Phase Flows
- ▶ Electroosmotic Flow (DC)
- ▶ Lattice Poisson–Boltzmann Method, Analysis of Electroosmotic Microfludics

Electro-Osmosis with Patterned Surface Charge

- ▶ Surface-Charge Patterning Techniques

Electroosmosis in Porous Media

- ▶ Electrokinetic Flow in Porous Media

Electroosmotic Dispensing

- ▶ Electrokinetic Dispensing

Electroosmotic Flow

- ▶ Electrokinetic Flow and Ion Transport in Nanochannels
- ▶ Electroosmotic Flow (DC)

Electroosmotic Flow (DC)

DAVID ERICKSON
Sibley School of Mechanical and Aerospace Engineering, Cornell University, Ithaca, NY, USA
de54@cornell.edu

Synonyms

Electroosmosis; Electro-osmotic flow; Electroendosmosis

Definition

Electroosmotic flow is the bulk liquid motion that results when an externally applied electric field interacts with the

net surplus of charged ions in the diffuse part of an electrical double layer. The term electroosmotic flow and electroosmosis are generally used interchangeably in the context of micro- and nanofluidics. Alternating current electroosmosis in which bulk flow is generated using creative application of AC electric fields is covered under a separate title.

Overview

The discovery that externally applied electric fields could be used to generate bulk liquid motion is generally credited to Reuss who, in 1809, reported the observation of water migration through porous clay under such an influence. Since then a number of prominent scientists and engineers have left their mark on the field (see the text by Dukhin and Deryaguin [1] for a complete historical perspective) and it has become a critical technology in a variety of fields ranging from integrated micro- and nanofluidic systems to environmental decontamination and remediation. In this article we will begin by providing a brief conceptual overview of direct current electroosmotic flow focusing on the former of these applications. This will be followed by a detailed review of the relevant fluid mechanics and electrostatics culminating in a brief review of some of current research directions and a few key recent technological advancements. For more detailed information on electroosmotic flow and electrokinetics in general it is suggested that readers consult one of a variety texts on the subject, each of which approaches the topic from a slightly different point of view: transport and hydrodynamics [2], colloidal systems [3], and surface and interfacial phenomena [4].

An electrical double layer (EDL) is a very thin region of non-zero net charge density near a two phase interface (for the cases of interest here, typically a solid-liquid interface). It is generally the result of adsorption or desorption of charged species from the surface and the resulting rearrangement of the local free ions in solution so as to maintain overall electro-neutrality. As shown in Fig. 1, the diffuse region of the EDL (indicated by the grey shading) decays roughly exponentially into the bulk solution with a depth characterized by the inverse of the Debye–Hückel parameter ($1/\kappa$). The penetration depth of the diffuse EDL can vary from a few 10 s of nanometers to over a micrometer, depending on the ionic strength of the bulk phase solution.

When an electric field is applied perpendicular to the decay of the EDL (or equivalently parallel with the surface), the surplus of either positive or negative ions results in a net body force on the fluid proportional to the local net charge density. The resulting velocity profile consist of a region

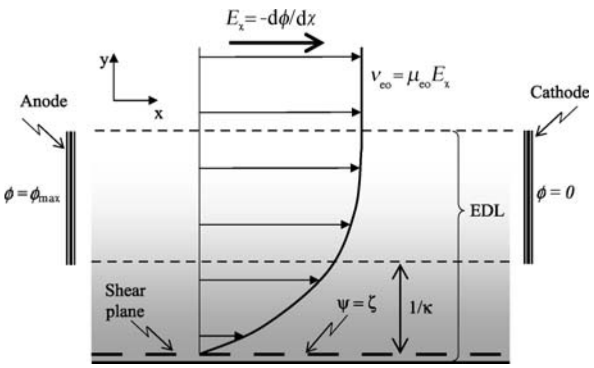

Electroosmotic Flow (DC), Figure 1

of very high shear rate near the surface where the velocity increases from zero at the shear plane to its bulk phase velocity (v_{eo} in Fig. 1) at the edge of the EDL. The proportionality between v_{eo} and the strength of the electric field, E_x, is given by the electroosmotic mobility, μ_{eo}, which is a function of both surface and solution phase properties. Unlike pressure driven flow, uniform electroosmotic flow exhibits a flat or "plug flow" velocity profile outside the double layer region.

The popularity of electroosmotic flow as a primary transport mechanism in microfluidic devices is largely the result of the simplicity of its implementation and the uniqueness of this velocity profile. In the classic example, the near flat velocity profile serves to minimize sample dispersion in capillary electrophoresis systems thereby facilitating highly efficient analytical separations. As will be discussed in further detail in the "Key Research Findings" section, since electroosmotic flow is a surface driven phenomena, v_{eo} is largely independent of channel size (outside the limit of double layer overlap). Thus it tends to be more suitable for operation of nanofluidic devices than traditional transport mechanisms. Additionally, the ability to perform precise, picoliter scale fluidic handling simply through the manipulation of externally applied voltages significantly simplifies device operation. The development and growing acceptance of new pressure driven architectures, such as multilayer soft-lithography, however has reduced the prominence of this final advantage.

The most significant disadvantages associated with the use of electroosmotic flow tend to be related to the relatively high applied potentials that are required to generate significant flow velocities. Generally μ_{eo} tends to be on the order of 10^{-8} m^2/Vs (though significant variability exists). As a consequence a potential of 1000 V applied over a 10 cm channel is required to reach the relatively meager flow rate of 100 μm/s. While the technical difficulties in generating potentials of this scale in portable and autonomous

devices are relatively minor (given the availability of relatively low cost, high efficiency DC to HVDC converters) this does tend to place an upper limit on the speed at which many manipulations can be performed. The use of these relatively high potentials also results in conditions of significant ohmic energy conversion generally referred to as joule heating. This effect can result in temperature variations within a channel network leading to: significant variations in local viscosity, uneven thermal conditions for chemical reactions, and potentially culminating in localized in-channel boiling. These high electric fields also cause difficulty when transporting living organisms since internal elements tend to exhibit different mobilities (and thus they migrate at different speeds) which can lead to significant damage to the target. Perhaps the most significant disadvantages associated with electroosmotic flow are that: it is only compatible with a limited class of fluids (specifically low ionic concentration, aqueous solutions), it exhibits extreme sensitivity to surface conditions (reflected in the electroosmotic mobility) and it cannot be used with semiconductive substrates such as silicon (as it requires a highly insulating substrate to confine the electric field to the fluidic channel).

Basic Methodology

Flow Field

Incompressible fluid flow is governed by the Navier–Stokes (momentum), Eq. (1), and continuity equations, Eq. (2), shown below,

$$\rho\left(\frac{\partial \boldsymbol{v}}{\partial t} + \boldsymbol{v}\cdot\nabla\boldsymbol{v}\right) = -\nabla p + \eta\nabla^2\boldsymbol{v} - \rho_e\nabla\Phi \tag{1}$$

$$\nabla\cdot\boldsymbol{v} = 0 \tag{2}$$

where $\boldsymbol{v}$, t, p, η and ρ are velocity, time, pressure, viscosity and density respectively. The assumption of incompressibility is not globally applicable to all microfluidic systems however most electroosmotic flows of interest tend to involve a single phase liquid and thus we can make this assumption without loss of generality. For the purposes of this discussion we also assume a constant viscosity solution, which is significantly more restrictive due to the importance of joule heating as mentioned above. This limits us to systems comprising of either high thermal conductivity substrates (which can reject internally generated heat from the flow system rapidly) or low applied electric field strengths (where joule heating is minimal). The final term in Eq. (1) represents the electroosmotic body force and is equivalent to the product of the net charge density in the double layer, ρ_e, multiplied by the gradient of the total potential, Φ.

The relatively small channel dimensions and flow velocities in micro and nanofluidics limits the flow to the strongly laminar, low Reynolds number, Re, regime ($\mathrm{Re} = \rho L v_{eo}/\eta$ where L is the hydraulic diameter). In the systems of interest here the Re tends to vary from negligibly small to a practical maximum of approximately Re $= 0.1$. As a result the transient and convective terms (those on the left-hand side of Eq. (1)) tend to be negligibly small and thus are typically ignored in order to further simplify the formulation. Removing the transient term from the formulation implies that the system reaches a steady state instantaneously. This tends also to be broadly applicable so long as the other quantities of interest (e. g. species transport) and variations in applied potential occur on longer timescales, which they typically do.

As is apparent from Eq. (1) evaluation of the momentum equation requires a description of the net charge density, ρ_e, and the total electrical potential, Φ. The latter of these comprises of the summation of the electrical double layer, ψ, and the applied electric potential, ϕ, as per Eq. (3),

$$\Phi = \phi + \psi \tag{3}$$

The decoupling of these two terms is contingent on a number of assumptions as detailed in [5]. The relatively high ionic strength buffers used in most Lab-on-Chip applications typically yield very thin double layers and thus this decoupling is very often valid within a reasonable degree of error.

Electrical Double Layer – General Formulation

The EDL potential and the net charge density are related via the Poisson equation,

$$\nabla\cdot(\varepsilon_w\varepsilon_0\nabla\psi) + \rho_e = 0 \tag{4}$$

where ε_0 and ε_w are the dielectric permittivity of a vacuum ($\varepsilon_0 = 8.854\times10^{-12}$ C/Vm) and the local relative dielectric permittivity (or dielectric constant) of the liquid respectively. The ionic species concentration field within the double layer is given in its most general form by the Nernst-Planck conservation equation,

$$\nabla\cdot\left(-D_i\nabla n_i - \frac{D_i z_i e}{k_b T} n_i\nabla\psi + n_i\boldsymbol{v}\right) = 0 \tag{5}$$

where D_i, z_i and n_i are the diffusion coefficient, valence and number density of the ith species and e (e $= 1.602\times10^{-19}$ C), k_B ($k_B = 1.380\times10^{-23}$ J/K) and T are the elemental charge, Boltzmann constant and temperature

respectively. These two equations (Eq. (4) and Eq. (5)) are coupled by the definition of the net charge density given by,

$$\rho_e = \sum_i z_i e n_i \tag{6}$$

Equations (4) and (6) are coupled to the flow field by the convective (3rd) term in Eq. (5) and as such they must, in principal, all be solved simultaneously. As with many of the cases mentioned above this tends to significantly complicate the mathematical system without adding significantly to the model at this stage. An additional complication results from the fact that according to Eq. (6), all charged species must be accounted for in order to accurately determine the net charge density. This tends to be exceedingly difficult particularly when one wishes to examine the multispecies buffers which are commonly used in most actual Lab-on-Chip devices. Thus it is common to implement a two species model based on the most highly concentrated ions (dominant) in the buffer solution and to ignore the rest.

Electrical Double Layer – Simplified Formulation

By making the above simplifications and assuming that the EDL only varies strongly in the direction normal to the surface, we can simplify Eq. (5) by imposing a no flux condition into the surface yielding,

$$\frac{1}{n_i}\frac{\mathrm{d}n_i}{\mathrm{d}y} + \frac{z_i e}{k_B T}\frac{\mathrm{d}\psi}{\mathrm{d}y} = 0 \tag{7}$$

Integrating Eq. (7) assuming a point exists where the bulk concentration of the electrolyte is equal to n_0 and $\psi = 0$ yields the Boltzmann distribution given by Eq. (8),

$$n_i = n_0 \exp\left(\frac{-z_i e\psi}{k_B T}\right) \tag{8}$$

Assuming a two species, symmetric electrolyte (as described above) we can combine the 1D version of Eq. (4) with the definition of net charge density, Eq. (6) and the above Boltzmann distribution to obtain,

$$\varepsilon_w \varepsilon_0 \frac{\mathrm{d}^2\psi}{\mathrm{d}y^2} - \left(\frac{2\,|z|\,en_0}{k_B T}\right)\sinh\left(\frac{|z|\,e\psi}{k_B T}\right) = 0, \tag{9}$$

which is commonly referred to as the Poisson–Boltzmann distribution for a symmetric electrolyte. While analytical solutions do exist to Eq. (9) (see [3]) it is common to perform one further simplification and linearize the second term in the equation to obtain the Debye–Hückel approximation,

$$\frac{\mathrm{d}^2\psi}{\mathrm{d}y^2} - \kappa^2\psi = 0 \tag{10}$$

where κ is the Debye–Hückel parameter and is given by $\kappa = (2z^2e^2n_0/\varepsilon_w\varepsilon_0 k_B T)^{1/2}$. As shown in Fig. 1, $1/\kappa$ is characteristic of the double layer thickness. Depending on the value of n_0 this thickness can vary from close to 1 μm down to a few 10 s of nanometers at high ionic concentration consistent with the buffers used in most Lab-on-Chip applications.

Though subject to the limitations discussed above one can capture the majority of the influence of the double layer on the flow field in uniform systems by solving Eq. (10), subject to a $\psi = \zeta$ boundary condition at the shear plane (as shown in Fig. 1) and an assumption that $\psi \to 0$ as $y \to \infty$. For the 1D case this yields,

$$\psi(y) = \zeta e^{-\kappa y} \tag{11}$$

which can then be substituted into Eqs. (6) and (8) to compute the net charge density field. Though this linearization of the Poisson–Boltzmann equations does introduce some error at higher ζ-potentials, in most microfluidic systems this tends to be reasonably minor. This formulation also ignores convective and electrical effects on the EDL distribution as well as the potential for overlap between opposing double layers. While not commonly encountered in microscale fluidics, these effects can be very significant in many nanofluidic systems.

The major drawback of using such a formulation is that information regarding the convective and electrical effects on the double layer field and the resulting influence on the flow structure are lost and thus there is an inherent assumption that ρ_e varies on spatial scales much smaller than that of the flow system (see comments on nanofluidics below).

Applied Electrical Potential

The electric potential is most generally governed by the conservation of current condition as below,

$$\nabla \cdot j = 0 \tag{12}$$

where j is the current flux. The current flux can be obtained by summation of the flux of each individual species multiplied by the valence and elemental charge yielding,

$$\nabla \cdot \left(\sum_i z_i e\left[-D_i\nabla n_i - \frac{D_i z_i e}{k_B T} n_i \nabla\phi + n_i \boldsymbol{v}\right]\right) = 0 \tag{13}$$

which is derived by combining Eq. (5) and (6) above (here we consider the conservation or charge as opposed to the conservation of individual species and the conditions of zero flux at the boundaries do not apply at the anode and cathode). For electroosmotic flow in Lab-on-Chip systems, the conduction current (2nd term) tends to be much larger than the other terms and thus the 1st and 3rd terms in Eq. (13) can be ignored.

$$\nabla \cdot (\lambda \nabla \phi) = 0 \tag{14}$$

where λ is the bulk solution conductivity. Note that Eq. (14) also assumes that any additional conduction through the double layer region (due to the higher ionic concentration) is negligible. In practice the bulk conductivity is usually measured directly however it can in principal be calculated from a summation of the constituent ionic species,

$$\lambda = \sum_i \frac{D_i z_i^2 e^2 n_{i,0}}{k_B T} \tag{15}$$

where $n_{i,o}$ is the bulk concentration of the ith species. While there are many examples of non-uniform conductivity solutions in on-chip processes in most cases it is assumed to be constant everywhere. In that case λ can be removed from the above formulation leaving a simple Laplacian to describe the applied potential,

$$\nabla^2 \phi = 0 \tag{16}$$

In most cases it is proper to assume that the channel walls are perfectly insulating, thus a zero gradient (insulation) boundary condition is applied at those points.

Simplifications and Analytical Solutions

Helmholtz–Smoluchowski Equation

The most common simplification encountered in electroosmotic flow analysis is the “Helmholtz–Smoluchowski” approximation. To derive this we begin by eliminating the non-linear and transient terms in Eq. (1) as described above and assume that the pressure gradient, ∇p, is zero everywhere. The latter of these assumptions is generally valid for pure electroosmotic flow (no applied pressure) with uniform surface (ζ-potential) and solution (viscosity and conductivity) properties. We also replace $-\nabla\Phi$ with the local applied electric field strength E_x, and use Poisson’s Equation (Eq. (4)) to express the net charge density in terms of the double layer potential, ψ. This yields,

$$\eta \frac{d^2 v_x}{dy^2} - \varepsilon_w \varepsilon_0 \frac{d^2 \psi}{dy^2} E_x = 0 \tag{17}$$

We integrate this equation with respect to y twice and apply the condition that as $y \to \infty$, both $dv_x/dy = 0$ and $d\psi/dy = 0$, and that at $y = 0$ (i. e. the shear plane), $\psi = \zeta$. Following this procedure and considering the region outside the double layer $\psi = 0$) yields,

$$v_x = v_{eo} = -\frac{\varepsilon_w \varepsilon_0 \zeta}{\eta} E_x \tag{18}$$

which is commonly referred to as the Helmholtz–Smoluchowski equation and is descriptive of a plug flow velocity profile. Commonly the terms which precede E_x in Eq. (18) are expressed as single linear proportionality coefficient between v_{eo} and E_x referred to as the electroosmotic mobility, $\mu_{eo} = (-\varepsilon_w \varepsilon_0 \zeta/\eta)$.

The essential criticism of Eq. (18) is that it provides us with absolutely no information regarding the flow field within the double layer. We can capture this information by incorporating the Debye–Hückel solution, Eq. (11), into Eq. (17) above which yields,

$$v_x(y) = \mu_{eo} E_x \left(1 - e^{-\kappa y}\right) \tag{19}$$

After application of a no slip boundary condition at $y = 0$ and $dv_x/dy \to 0$ as $y \to \infty$. As can be seen from Eq. (19), v_x varies exponentially from zero at the shear plane eventually reaching its steady state value of v_{eo} at the edge of the double layer. In situations where the linear approximation are not accurate (typically when the ζ-potential is very high) Eq. (19) can be further generalized by incorporating a non-linear Poisson–Boltzmann distribution. This however typically involves the use of a numerical technique to find a solution.

Extension to 2D and 3D Systems

In the majority of microfluidic cases where $1/\kappa$ is much smaller than the channel height the Helmholtz–Smoluchowski equation provides a reasonable estimate of the flow velocity at the edge of the double layer field. As such when modelling two and three dimensional flow systems it is common to apply this equation as a “slip” boundary condition on the bulk flow field. Since beyond the double layer by definition $\rho_e = 0$, the flow equation reduces to (assuming pure electroosmotic flow) to a simple Laplacian,

$$\nabla^2 v = 0 \tag{20}$$

which can be very easily solved numerically for complex geometries. Once of the great advantages of this formulation is that exhibits the same mathematical properties as the electric potential equation and thus good qualitative information on flow rates in complex channel networks

can be described analytically with relatively simple circuit models.

If we relax the condition of uniform surface properties (which occurs quite commonly in microsystems either by design or as a result of system fouling) local pressures are induced in order to maintain continuity. In such a case Eqs. (1) and (2) reduce to the Stokes flow equations as shown below,

$$\eta \nabla^2 v - \nabla p = 0 \quad (21)$$

$$\nabla \cdot v = 0 \quad (22)$$

In this case the variation in the surface properties is also expressed through the slip boundary condition. A numerical technique is typically required to capture a solution however nearly all commercial CFD packages provide this functionality. The advantage of the above system is of course that it allows one to describe 2D and 3D velocity fields in microfluidic devices which commonly have channel lengths on the order of several centimetres without having to worry about resolving the solution on the spatial scale of the double layer (which can be seven orders of magnitude smaller).

Nanofluidic Systems with Overlapped Double Layers

Nearly all the analytical derivations above have explicitly assumed that the system is sufficiently large that there exists a region far away from the surface where the double layer vanishes and both ρ_e and ψ go to zero. In nanofluidic systems however the channel height, h, is commonly on the same spatial order as the double layer thickness (i. e. $1/\kappa$) and as such the above approximation is no longer valid and the accuracy of these models are compromised. Fortunately this situation also occurs in problems of colloid stability and thus the theory for such problems has also been well developed [4].

Put simply the extension to overlapped double layer models involves the replacement of the vanishing double layer condition with that of either symmetry at the channel midplane (for a half domain solution) or the additional specification of the ζ-potential at the opposite surface. For the former of these it can be shown that the solution to Eq. (10) becomes,

$$\psi(y) = \zeta \frac{\cosh(\kappa |h/2 - y|)}{\cosh(\kappa h/2)} \quad (23)$$

Under conditions of double layer overlap the Helmholtz–Smoluchowski approximation looses meaning since the velocity profile never reaches a constant velocity "plug flow" velocity. We can however still compute a reasonable approximation to the average velocity through the channel, $v_{eo,odl}$, via Eq. (24),

$$v_{eo,odl} = v_{eo}\left(1 - \frac{\tanh(\kappa h/2)}{\kappa h/2}\right) \quad (24)$$

where v_{eo} is the Helmholtz–Smoluchowski velocity (for details on the derivation see Hunter [3]). In the limit of not large double layer overlap (typically cited as $\kappa h/2 > 3$) the correction term in Eq. (24) reduces to $\approx 1 - 2/\kappa h$.

E

Key Research Findings

The major application of DC electroosmotic flow in micro- and nano-fluidics continues to be as a general transport mechanism in Lab-on-Chip type devices. Specific applications along these lines are too numerous to mention here and thus interested readers should consult any one of a number of recent review articles (e. g. Erickson et al. [6]) for more details. Rather we provide a brief overview of a select number of key research findings with regards to "non-traditional" emerging technologies involving electroosmotic effects for micro- and nanosystems.

High Pressure Electroosmotic Pumps

A number of groups have recently developed high pressure electroosmotic pumps which, briefly speaking, operate on the principal that impeding or stopping the flow upstream of an electroosmotic cell induces a backpressure on the system. It can be relatively easily shown that the maximum obtainable pressure in such a system (occurring at no net flow rate) is given by,

$$\Delta P_{max} = \left|\frac{8\varepsilon_w \varepsilon_0 \zeta}{a^2}\right| \Delta\phi \quad (25)$$

where a is the pore or channel radius (in the limit of no double layer overlap). Using such systems very high pressures have been demonstrated (on the order of a 100 kPa per applied Volt) and work continues in developing cell materials and fluid systems which tend to increase the value of the proportionality term in Eq. (25) while avoiding overlapped double layer effects. Such devices are expected to find application in on-chip chromatography and electronics cooling (See Reichmuth et al. [7] for system examples).

Electroosmotic Control over Surface Phase Binding Stability

One of the well known but not well exploited characteristics of electroosmotic flow are the exceptionally high rates of shear at the surface. While a series of models exist for

electroosmotic transport in the presence "hairy" double layers, little is known about how these high rates of shear will affect probe orientation and the subsequent kinetics in surface phase binding reactions. Recently Erickson et al. [8] demonstrated the ability to discriminate single nucleotide polymorphisms in microfluidic architectures using a combination of these shear rates with electrophoretic and joule heating effects.

Electroosmotic/Electrokinetic Energy Conversion

Though more commonly associated with an analogous electrokinetic effect referred to as the streaming potential (whereby an externally induced flow is used to convect ions from the double layer to a downstream reservoir where they collect and form a steady state electric potential difference across the channel), electroosmotic effects are of critical importance in some of the recent work in electrokinetic energy conversion. The concepts behind using electroosmotic flow for mechanical energy (as in the electrokinetic pumps discussed above) and the analogous use of mechanically pumped flow for direct electrical energy conversion (via the streaming potential discussed above) have been developed for years. The emergence of new electroosmotic cell materials (similar to those described for the high pressure pumps above) along with the more global interest in developing new energy conversion devices has lead to some renewed interest in this field (see Yang et al. [9] and Daiguji et al. [10] for some recent works). Eventual application of such devices is likely to be relatively limited as predicted optimal efficiencies tend to be less than 1%.

Future Directions for Research

Although the basic fluid dynamics and transport issues in microscale systems are reasonably well described there have been a number of significant recent theoretical and experimental advancements in the study of electroosmotic flow. The majority of the models described generally assume uniformity of surface and solution properties and thus much of the recent work has involved investigating systems where uniform ζ-potential, solution conductivity and/or viscosity can no longer be assumed. This has led to the discovery of a number of new effects such as electrokinetic instabilities. Non-linear "induced charge" electroosmotic flows, though originally described years ago in the colloidal literature, have also been of interest in microscale systems.

Electroosmotic flow (and more broadly electrokinetics) is uniquely positioned to become the primary transport mechanism in nanofluidic devices and other confined nanosystems. As is well known the average velocity of a traditional pressure driven flow scales with the square of the channel height whereas an electroosmotic flow velocity varies much more weakly (as indicated by Eq. (24)) and then only in the limit of double layer overlap. At the same time the greater surface area to volume ratio of the systems leads to better rejection of joule heat from the flow enabling the application of much higher potentials. While much of the continuum based theory applicable to electroosmotic flows in nanochannels is reasonably well developed, greater availability of computing power has enabled the development of MD type simulation which enable more precise probing of the flow field. Modifications to existing theories which capture other relevant effects, such as ion size excluded volume effects, are also likely to be of increasing importance. From an experimental point of view the broader availability of nanofabrication facilities has enabled a much more systematic experimental study of electroosmotic flow in nanoscale systems.

Cross References

► Electrical Double Layers
► Electrophoresis
► Electrokinetic Flow
► Separations
► AC Electro-Osmotic Flow
► Dielectrophoresis
► Streaming Current and Electroviscosity
► Temperature Effects on the Zeta Potential
► Combined Pressure-Driven Flow and Electroosmotic Flow

References

1. Dukhin SS, Deryaguin BV (1974) Electro-kinetic phenomena In: Matijevic E (ed) Surface and Colloid Science. Wiley, New York
2. Probstein RF (1994) Physiochemical Hydrodynamics, An Introduction. Wiley, New York
3. Hunter RJ (1981) Zeta Potential in Colloid Science: Principles and Applications. Academic, London
4. Lyklema J (1991) Fundamentals of Interface and Colloid Science, Vol. 1: Fundamentals. Academic, London
5. Erickson D, Li D (2006) Microscale Flow and Transport Simulation for Electrokinetic and Lab-on-Chip Applications. In: Bashir R, Wereley S (ed) Biomems and Biomedical Nanotechnology, Vol IV: Biomolecular Sensing, Processing, and Analysis. Kluwer, New York
6. Erickson D, Li DQ (2004) Integrated microfluidic devices. Anal Chimica Acta 507(1):11–26
7. Reichmuth DS, Chirica GS, Kirby BJ (2003) Increasing the performance of high-pressure, high-efficiency electrokinetic micropumps using zwitterionic solute additives. Sens Actuators B 92(1–2):37–43
8. Erickson D, Liu XZ, Venditti R, Li DQ, Krull UJ (2005) Electrokinetically based approach for single-nucleotide polymor-

phism discrimination using a microfluidic device. Anal Chem 77(13):4000–4007
9. Yang J, Lu FZ, Kostiuk LW, Kwok DY (2003) Electrokinetic microchannel battery by means of electrokinetic and microfluidic phenomena. J Micromech Microeng 13(6):963–970
10. Daiguji H, Yang PD, Szeri AJ, Majumdar A (2004) Electrochemomechanical energy conversion in nanofluidic channels. Nano Lett 4(12):2315–2321

Electroosmotic Flow (EOF)

► Electroosmotic Pump

Electroosmotic Flow over Heterogeneous Surfaces

David Erickson
Sibley School of Mechanical and Aerospace Engineering, Cornell University, Ithaca, NY, USA
de54@cornell.edu

Synonyms

Electroosmotic flow over non-uniform surfaces

Definition

Electroosmotic flow is the bulk liquid motion that results when an externally applied electric field interacts with the net surplus of charged ions in the diffuse part of an electrical double layer (EDL). In the presence of non-uniform or heterogeneous ζ-potential, the net charge density in the EDL changes locally resulting in an irregular body force applied to the flow field and ultimately in a non-uniform flow field. Better understanding of this effect can lead to enhanced binding rates for surface phase reactions (through enhanced transport to the surface) and better mixing in microfluidic systems.

Overview

Transport over heterogeneous surfaces arises in a variety of electrokinetic characterization and micro-/nanofluidics based applications. With respect to the former of these the streaming potential technique has been used to monitor the dynamic or static adsorption of proteins (e. g. Norde and Rouwendal [1]) and colloidal particles (e. g. Zembala and Adamczyk [2]) onto a vast array of surfaces. In these systems the surface's electrokinetic properties are altered by introducing a heterogeneous region which has a different ζ-potential than the original surface. The introduction of this heterogeneous region induces a change in the surface's average ζ-potential, which is monitored via a streaming potential measurement, and dynamically related back to the degree of surface coverage. The presence of this streaming potential necessarily induces an electroosmotic flow in the direction opposite to the main pressure driven flow and thus it becomes important to understand the coupling of these two flow effects and how their presences affects the spatial distribution of counter ions in the double layer field in order to better relate global streaming potential measurements to local adsorption phenomena.

For the latter of these, electroosmotic flow has evolved into likely the most popular transport mechanism for integrated microfluidic devices, largely the result of the simplicity of its implementation and the uniqueness of its flat *plug-flow* like velocity profile (for more details see ► electroosmotic flow). While the majority of modeling and transport studies are done assuming uniformity of the surface ζ-potential, there exists a large number of applications where such an assumption become invalid. As an example, microfluidics based biosensors often involve selective capture of a solution phase target onto a surface phase probe (see Erickson et al. [3]). Probe patches are typically arranged in a periodic fashion and in general do not have the same electrokinetic properties of the homogeneous surface. Such systems are particularly interesting since the spatial scale of the non-uniformity exists both on the patch size (which affects the global velocity field) and the probe size (which affects the local flow and transport fields around the probe). Active and passive manipulation of the surface ζ-potential field has also proven successful at addressing mixing problems in microscale systems (as will be further demonstrated below) and for providing local control over ion and molecular transport in nanoscale systems (see Karnik et al. [4]).

Pioneering analytical studies examining these effects were conducted by Ajdari (e. g. [5]), Anderson (e. g. [6]) and Ghosal [7]). Anderson's work (which precedes the other two) was one of the first to look at the effects of surface non-uniformity on the electrophoretic motion of particles. In Ajdari's works it was predicted that the presence of surface heterogeneity could result in regions of electroosmotically induced bulk flow circulation, referred to as *tumbling* regions which was later observed experimentally. Ghosal presented an elegant lubrication theory approach to the solution of electroosmotic flow accounting for changes in both channel size and surface charge.

The mechanism for inducing electroosmotic flow is well described in the article on that subject within this encyclopedia, so here we only provide a brief qualitative explanation. As mentioned in that article, an electrical double layer (EDL) is a very thin region of non-zero net charge density near a two phase interface. The diffuse region of the EDL

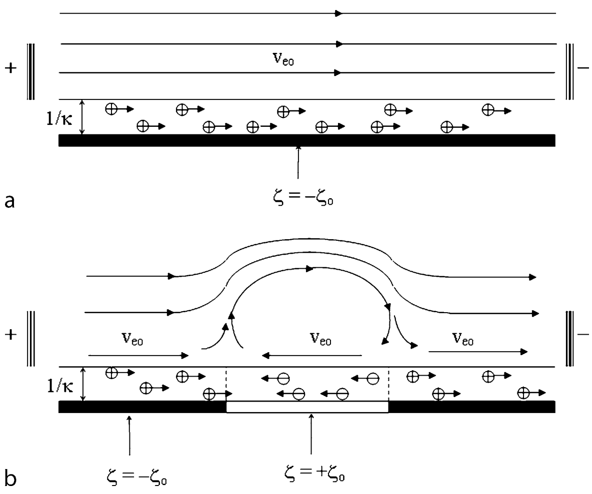

Electroosmotic Flow over Heterogeneous Surfaces, Figure 1 Electroosmotic flow near the double layer region for (**a**) a homogeneous surface ($\zeta = -|\zeta_0|$) and (**b**) a homogeneous surface with a heterogeneous patch ($\zeta = +|\zeta_0|$). Over the heterogeneous patch, the excess cations are attracted to the positive electrode resulting in an electroosmotic flow in the opposite direction to that over the homogeneous regions with an excess anion concentration. Arrows represent streamlines and $1/\kappa$ refers to the characteristic thickness of the electrical double layer

decays roughly exponentially into the bulk solution over a distance of 10 nm to as much as a few 100 nm and comprises bulk charge density of opposite polarity to that of the surface charge to maintain overall electrical neutrality. When an electric field is applied perpendicular to the surface, the surplus of either positive or negative ions results in a net body force on the fluid proportional to the local net charge density. For the homogeneous case (Fig. 1a) the electroosmotic body force applied to the liquid continua within the double layer is equivalent at each point along the flow axis and results in a constant bulk liquid velocity at the edge of the diffuse double layer, v_{eo}, which can be described by,

$$v_{eo} = -\frac{\varepsilon_w \varepsilon_o \zeta}{\eta} \boldsymbol{E} = \mu_{eo} \boldsymbol{E} \tag{1}$$

where μ_{eo} is the electroosmotic mobility, ε_w is the electrical permittivity of the solution, η is the viscosity and $\boldsymbol{E}$ is the applied electric field strength.

The same relation holds true for the heterogeneous surface except the ζ-potential (and by extension therefore μ_{eo}) is no longer constant across the domain of interest. As will be detailed below, when the change in ζ from the mean value is relatively small the result is a local slowing or quickening of the velocity near the surface which in turn results in an induced pressure driven flow to maintain overall continuity. The major consequence of this induced flow is that the superimposed parabolic velocity profile can lead to anomalous transport affects (namely sample dispersion) which tend to negate many of the advantages associated with electroosmotic plug flow. In the extreme case where the local ζ-potential is opposite sign to that of the mean surface, the electroosmotic body force now acts in the opposite direction to that in the homogeneous regions. This results in the formation of circulation zones which, as shown in Fig. 1b, extend into the bulk flow field.

A variety of analytical and numerical models have been proposed recently to investigate electrokinetic effects over heterogeneous surfaces. In general however these models can be separated into either slip flow approaches, whereby the electroosmotic contribution to the flow field is accounted for through the application of a slip velocity condition at the edge of the double layer, and the more comprehensive Nernst–Planck–Poisson–Navier–Stokes simulations in which the effects of the flow and electrical fields on the double layer distribution are also captured. In the following section we will introduce both of these approaches and some of our experimental work demonstrating surface heterogeneity enhanced mixing in electrokinetic systems. As mentioned above, the theory of electroosmotic flow has already been described in detail in the article by that name and thus here we focus on extensions to that theory as applicable to flow over heterogeneous surfaces. Some of the experimental aspects of our work will also be discussed.

Basic Methodology

Enhanced Species Mixing in Electroosmotic Flow due to the Presence of Non-Uniform Electrokinetic Surface Properties

Most microfluidic systems, particularly electroosmotically driven ones, are limited to the low Reynolds number regime and thus species mixing is largely diffusion dominated (as opposed to convection dominated at higher Reynolds numbers). Consequently, mixing tends to be slow and occur over relatively long distances and times. In the first section of this article we will describe how surface heterogeneity can enhance species mixing. The work described here is based on articles by Erickson and Li [8] and Biddiss, Erickson and Li [9].

Numerical Simulations

As our model system, we consider the mixing of equal portions of two buffer solutions, one of which contains a concentration, c_0, of a species of interest in a T-mixer type channel geometry (see Fig. 2a), 200 μm in width and 8 μm in depth. In general the introduction of surface heterogeneity induces flow in all three coordinate directions, thus necessitating the use of a full 3D numerical simulation. The length of the mixing channel used in our simulations

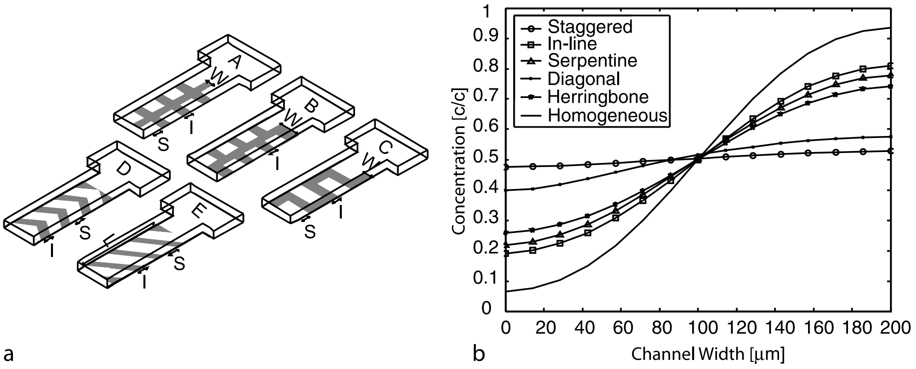

Electroosmotic Flow over Heterogeneous Surfaces, Figure 2 (**a**) Surface charge patterning configurations with a mixing region length *L* consistent for all configurations, a patch length *l*, a patch width *w*, and patch spacing *s* for (A) In-line pattern (B) Staggered pattern (C) Serpentine pattern (D) Herringbone pattern and (E) Diagonal pattern. (**b**) Numerically simulated concentration profiles across the channel width for the staggered pattern subsequent to the mixing region for an applied potential of 280 V/cm

was dictated by that required to obtain a uniform concentration (i. e. a fully mixed state) at the outflow boundary. Depending on the simulation conditions this required L_{mix} to be on the order of 200 times the channel width. This is an example of a case where we are primarily interested in steady state, bulk phase fluid flow and species transport. As such we have no specific interest the double layer field and thus the electroosmotic slip condition approach to model the flow field (see the "Simplifications and Analytical Solutions" section of the ▶electroosmotic flow). In systems such as that of interest here, species transport is accomplished by 3 mechanisms: diffusion, electrophoresis, and convection. In the most general case the superposition of these three mechanisms results in the following conservation equation

$$\frac{\partial c_i}{\partial t} = \nabla \cdot \left(D_i \nabla c_i + \mu_{\text{ep},i} c_i E - c_i v \right) + R_i \,, \tag{2a}$$

where c_i and D_i is the local concentration and diffusion coefficient of the ith species, μ_{ep} is the electrophoretic mobility ($\mu_{\text{ep}} = D_i z_i e / k_b T$) and R_i is a bulk phase reaction term. In this case we are primarily concerned with the steady state mixing profile and will not consider any bulk or surface phase reactions. Additionally here we only track a single species and drop the i notation. As such Eq. (2a) reduces to,

$$D \nabla^2 c + \mu_{\text{ep}} E \nabla c - v \nabla c = 0 \,. \tag{2b}$$

Details of the solution algorithm used here are available in Erickson and Li [8].

In general the strength of the relatively simple technique outlined above is that it allows one to relatively rapidly numerically prototype the system and perform a broad range of simulations in order to optimize the system.

In this article we focus on characterizing the pattern of surface charge heterogeneity and its effect on mixing enhancement. For the purposes of this article we define mixing efficiency as,

$$\varepsilon(y) = \left(1 - \frac{\int_0^W |c_i - c_\infty| \, \mathrm{d}x}{\int_0^W |c_0 - c_\infty| \, \mathrm{d}x} \right) \times 100\% \,, \tag{3}$$

where c_0 and c_∞ are the concentration profiles at the inlet to the mixer and after an infinitively long mixing profile respectively.

Figure 2 shows the results of these simulations for five different heterogeneous surface patterns (shown in Fig. 2a) expressed at the concentration profile downstream from the mixing region. For each configuration, the patch length and spacing parameters were selected to maintain a constant ratio of heterogeneous to homogeneous surface areas over a channel length of 1.8 mm. As can be seen in Fig. 2b, which shows the concentration profile downstream of the surface patterns, the non-symmetrical patterns, namely the staggered and the diagonal, generated better mixing distributions in comparison to the symmetrical herringbone and in-line arrangements. With a theoretical mixing efficiency of 96%, the staggered configuration provided the greatest degree of mixing, out-performing the diagonal, the herringbone and the serpentine configurations by 8%, 31% and 36% respectively. In comparison with the homogenous case, the staggered configuration provided a 61% increase in mixing efficiency.

Heterogeneous Surface Modification and Characterization

As mentioned above heterogeneous surface occur in a number of different micro- and nanofluidic applications,

here we describe a simple technique, developed as part of the Biddiss et al. [9] study, to create arbitrary surface charge patterns similar to those shown in Fig. 2a. Using rapid prototyping/soft lithography techniques [10] a PDMS master featuring a channel configuration corresponding with the pattern of heterogeneities to be examined, was created and was reversibly sealed to a glass slide. A negative pressure was applied to the downstream end of the system such and the PDMS master was flushed sequentially with 0.1 M sodium hydroxide for 2 min, deionized water for 4 min, and 5% Polybrene solution for 2 min, resulting in selective regions of positive surface charge while leaving the majority of the glass slide with its native negative charge. All fluid was then removed from the channel and the system was left exposed to air for 40 min before a second flush was done with water for 20 min. Following this second flush the channel was again evacuated and the system left exposed to air for 24 h prior to use. Following this the location of the surface pattern was land-marked and the PDMS master was removed from the glass slide. Figure 3 below shows an optical image of the surface after patterning.

To characterize the electroosmotic mobility of the Polybrene surfaces we performed a series of experiments using the well established current monitoring technique. In all our experiments a 25 mM sodium carbonate/bicarbonate run buffer with pH 9.0 was used. Details of the experimental technique can be found in Sze et al. [11]. Briefly however, to begin the buffer solution was diluted to 95% of its original concentration and introduced into a PDMS channel sealed to a glass surface which had undergone the polybrene surface treatment described above. After infusing the channel, the solution in the upstream reservoir was replaced with a second buffer concentrated at 105% of the final 25 mM solutions. An electric field was then applied across the channel and the current load monitored as a function of time. As the high conductivity buffer replaced the low conductivity buffer in the solution the current was observed to rise, eventually reaching a stable plateau once the original solution had been completely replaced. Given the applied voltage, the length of the channel and the time required for complete displacement the electroosmotic mobility, μ_{eo}, of the surface could be extracted using Eq. (4) below,

$$\mu_{\text{eo}} = \frac{\Delta V L^2}{\Delta t}\,, \tag{4}$$

where ΔV, Δt and L are the applied voltage, recorded time and channel length respectively. Given that the mobility of the untreated (in this case PDMS) surfaces is known the average μ_{eo} from Eq. (4) can be related to the local μ_{eo} of the polybrene treated surface through a surface area weighted averaging technique. Using this method the mobility of the polybrene surface was measured as $2.3 \times 10^{-4}\ \text{cm}^2/\text{Vs}$ (corresponding to a ζ-potential of $+33$ mV).

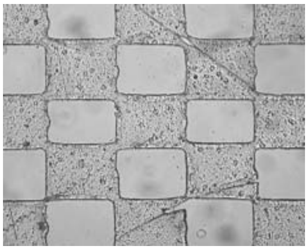

Electroosmotic Flow over Heterogeneous Surfaces, Figure 3 Optical image of polybrene patches on a surface

Experimental Validation and Characterization

To experimentally validate our system, a T-shaped microchannel with the same geometry as that used in our numerical simulations was fabricated in PDMS (also using soft lithography) and then permanently sealed to the glass slide such that the patterned surface heterogeneities were appropriately positioned within the mixing channel. For our experiments we used the optimized micromixer consisting of 6 offset staggered patches (Fig. 2a, pattern B) spanning 1.8 mm downstream and offset 10 μm from the channel centerline with a width of 90 μm and a length of 300 μm. Mixing experiments were conducted at applied voltage potentials ranging between 70 V/cm and 555 V/cm as corresponded to Reynolds numbers of 0.08 and 0.7 and Péclet numbers of 190 and 1500. As can be seen in Fig. 4, experimental results compared well with numerical simulations with images of the steady state flow for the homogenous and heterogeneous cases exhibiting near identical flow characteristics and circulation at 280 V/cm. Qualitatively, experimental visualization of a staggered configuration of heterogeneities exhibited the formation of highly unsymmetrical concentration gradients indicative of flow constriction and localized circulation in the patterned region. Bulk flow was forced to follow a significantly narrower and more intricate route thereby increasing the rate of diffusion by means of local concentration gradients. Convective mechanisms were also introduced by local flow circulation which transported a portion of the mixed downstream flow upstream. Additionally, sharp, lengthwise gradients absent in the homogeneous case resulted in an additional diffusive direction and enhanced mixing.

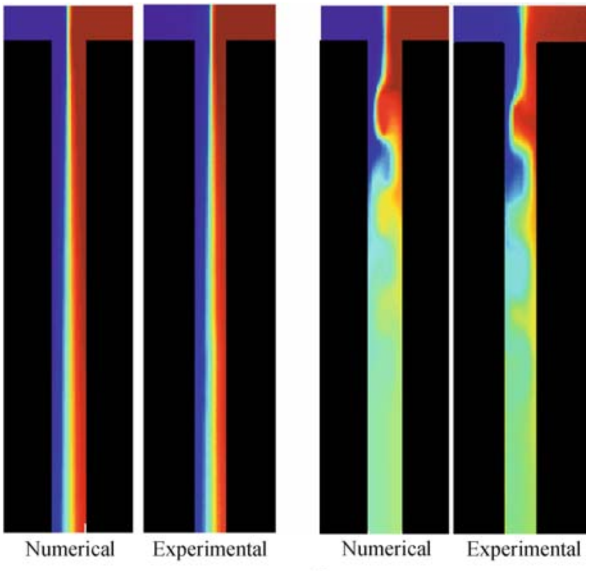

Electroosmotic Flow over Heterogeneous Surfaces, Figure 4 Images of steady state species transport for an applied potential of 280 V/cm for (**a**) the homogeneous microchannel and (**b**) the heterogeneous microchannel with 6 offset staggered patches as derived through numerical and experimental analysis

Comprehensive Nernst–Planck–Poisson–Navier–Stokes Simulation of Flows over Heterogeneous Surfaces

The modelling technique discussed above represent a relatively simple formulation which enables us to very rapidly (i. e. requiring minimal computational resources) simulate complex 2D and 3D electrokinetic flows and subsequent species transport. The ultimate limitation is that while the influence of the double layer on the bulk flow field can be reasonably well determined, the coupled effect of the flow and applied electrical fields on the double layer structure is ignored. As outlined in our recent review article [12] in many cases this represents a reasonable simplification given the ultimate goals of the simulation (which may simply be device numerical prototyping). Perhaps the most important reason for developing models which go beyond this level of understanding relate to the extreme conditions which exist within the double layer (for electroosmosis surface shear rates can be as high as 10^5 1/s) and how these conditions effect surface bound molecules. As an example we have recently demonstrated that by controlling the coupling of the shear, electrical and thermal energies within the double layer, sufficiently precise energy can be applied to specifically bound DNA so as to denature targets which contain single base pair mismatches, while those which are fully complementary remain bound [13].

Towards this end we have begun to investigate the flow in such systems using a variant of our finite element code. The numerical model used here is based on a simultaneous solution to the Nernst–Planck, Poisson and Navier–Stokes equations, which also allows us to shed the Poisson–Boltzmann double layer distribution assumption and to adopt a more general approach. The details of the analytical model and numerical solution method are described in detail in Erickson and Li [14]. Rather than focus on the technique here will present results for electroosmotically driven flow through a slit microchannel (i. e. a channel formed between two parallel plates) exhibiting the periodically repeating heterogeneous surface pattern shown in Fig. 5. To minimize the size of the solution domain it has been assumed that the heterogeneous surface pattern is symmetric about the channel mid-plane, resulting in the computational domain also shown in Fig. 5. As a result of these two simplifications, the inflow and outflow boundaries surfaces 2 and 4 represent periodic boundaries on the computational domain, while surface 3 at the channel mid-plane represents a symmetry boundary. From Fig. 5 it can be seen that in all cases the surface pattern is symmetric about surfaces 5 and 6 and thus these surfaces also represent symmetry boundaries.

For our simulations we will consider $l_x = 50\,\mu$m, $l_y = l_z = 25\,\mu$m computational domain (see Fig. 5) containing a 10^{-5} M KCl solution, an applied driving voltage of 500 V/cm and a surface charge density of $\sigma_{\text{homo}} = -4\times10^{-4}$ C/m^2. This represents a slightly different computational approach to that above in that now we enforce a Neumann boundary condition to the Poisson equation ($\sigma = \varepsilon_w \varepsilon_o \partial\psi/\partial n$, where n is the surface normal) The simulations revealed three distinct flow patterns, depending on the degree of surface heterogeneity, each of which is shown in Fig. 6. The contours in these figures represent the magnitude of the velocity perpendicular to the direction of the applied electric field ($v^2 = v_y^2 + v_z^2$) scaled by the maximum velocity in a homogeneous channel, which in this case is 1.7 mm/s.

At low degrees of surface heterogeneity ($\sigma_{\text{hetero}} \leqslant -2\times 10^{-4}$ C/m^2) the streamline pattern shown in Fig. 6a was obtained. As can be seen a net counter-clockwise flow perpendicular to the applied electric field is present at the first transition plane (i. e. at the initial discontinuity in the heterogeneous surface pattern) and a clockwise flow at the second transition plane. This flow circulation is a pressure induced effect that arises as a result of the transition from the higher local fluid velocity (particularly in the double layer) over the homogeneous surface on the right hand side at the entrance, to the left hand side after the first transition plane (and vice versa at the second transition plane). To satisfy continuity then there must be a net flow from

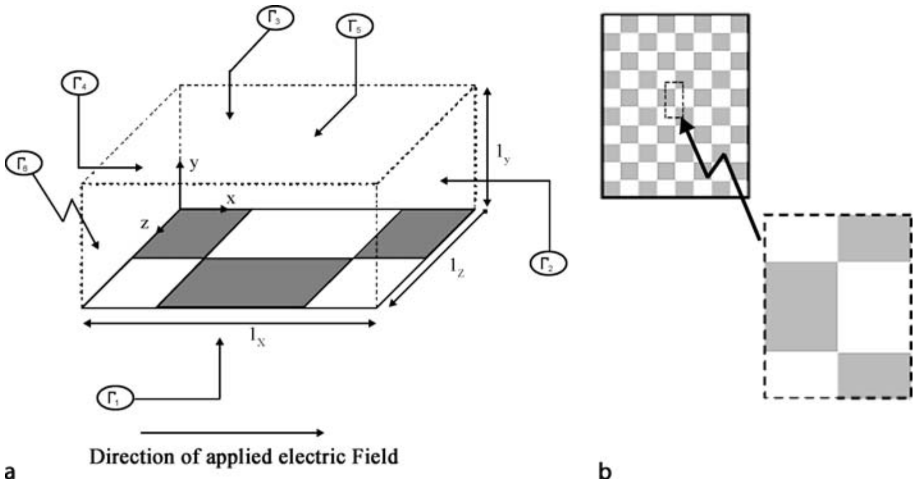

Electroosmotic Flow over Heterogeneous Surfaces, Figure 5 (**a**) Domain for periodically repeating computational cell (**b**) Patchwise surface periodicity pattern

right to left at this point, which in this case takes the form of the circulation discussed above. The relatively straight streamlines parallel with the applied electric field indicate that at this level the heterogeneity is too weak to significantly disrupt the main flow.

While a similar circulation pattern at the transition planes was observed as the degree of surface heterogeneity was increased into the intermediate range (-2×10^{-4} C/m$^2 \leqslant \sigma_{\text{hetero}} \leqslant +2\times10^{-4}$ C/m^2) it is apparent from the darker contours shown in Fig. 6b that the strength of the flow perpendicular to the applied electric field is significantly stronger reaching nearly 50% of the velocity in the homogeneous channel. Unlike in the previous case it is now apparent that the streamlines parallel with the applied electric field are significantly distorted due to the much slower or even oppositely directed velocity over the heterogeneous patch. At even higher degrees of heterogeneity ($+2\times10^{-4}$ C/m$^2 \leqslant \sigma_{\text{hetero}} \leqslant +4\times10^{-4}$ C/m^2) a third flow structure is observed in which a dominant circulatory flow pattern exists along all three coordinate axes, as shown in Fig. 6c. This results in a negligible, or even nonexistent, bulk flow in the direction of the applied electric field (which is to be expected since the average surface charge density for these cases is very near zero). As indicated by the contour plots, the velocity perpendicular to the flow axis has again increased in magnitude, reaching a maximum at the edge of the double layer near the symmetry planes at the location where a step change in the surface charge density has been imposed.

Key Research Findings

The above article (and cited works within) have focused on the modeling electroosmotic flow and transport over surfaces with non-homogeneous electrokinetic properties. The presence of periodically repeating heterogeneous patches is shown to induce distinct flow structures depending on the relative difference between the surface charge density of the homogeneous and heterogeneous regions. Small differences in the charge density are shown to induce fluid motion perpendicular to the applied electric field however the bulk flow remains largely unaffected. As the degree of heterogeneity is increased the streamlines in the direction of the applied electric field become significantly distorted. When oppositely charged surfaces are encountered a strong circulatory flow regime is observed which we have demonstrated both numerically and experimentally can be used to enhance mixing in electrokinetic systems.

Although we have focused here on periodic variations in surface charge patters, analogous works exists for non-uniform topographies intended to mimic electroosmotic flow over rough surfaces (see [15]). In the latter of these cases the general result is that the influence of the roughness extends into the bulk flow roughly on the same height scale as that of the roughness itself and thus tends not to have as dramatic of an effect as an irregular ζ-potential does.

Future Directions for Research

Electroosmotic flows over irregular surfaces can be modeled extremely well using the continuum based approaches described above, down to length scales of a few 10 s of nanometers. As such these models are likely to be very efficient at predicting both average and local flow structure down to scales of this order. In the above we mentioned that the initial motivation for investigating these

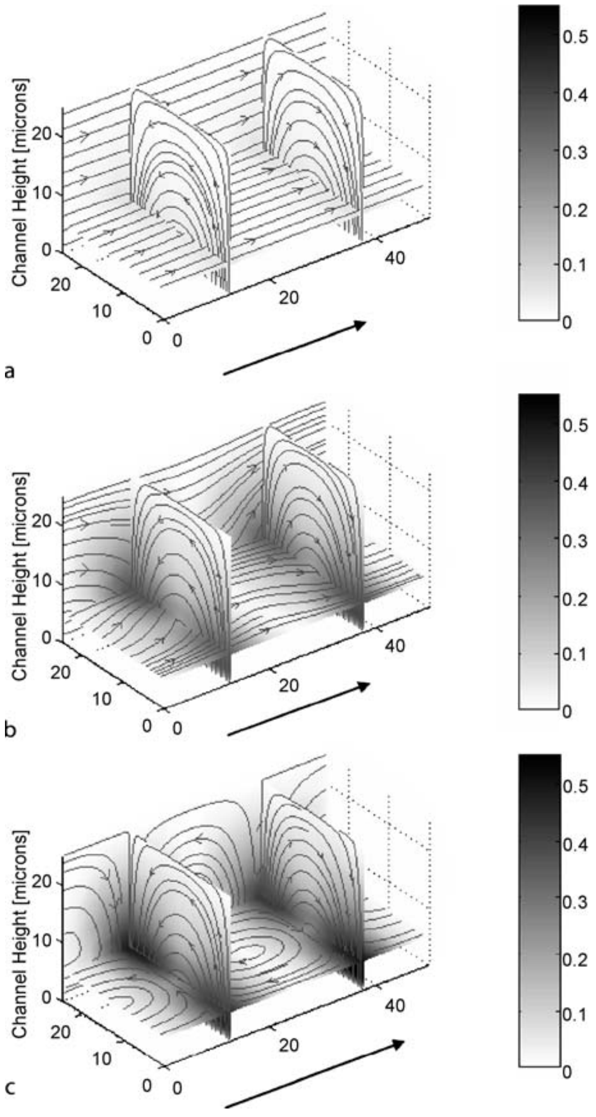

Electroosmotic Flow over Heterogeneous Surfaces, Figure 6 Electroosmotic flow streamlines over a patchwise heterogeneous surface pattern with $\sigma_{homo} = -4 \times 10^{-4}$ C/m^2 and (**a**) $\sigma_{hetero} = -2 \times 10^{-4}$ C/m^2 (**b**) $\sigma_{hetero} = +2 \times 10^{-4}$ C/m^2 (**c**) $\sigma_{hetero} = +4 \times 10^{-4}$ C/m^2. Contours represent magnitude of velocity perpendicular to the applied potential field, scaled by the maximum velocity in a homogeneous channel. Arrow represents direction of applied electric field

systems was our interest in electroosmotic flow and transport over DNA microarrays. In such systems the heterogeneity exists on two lengths scales, namely the patch (or spot) size and the probe size. Modeling the interaction of the flow, electrical and transport fields and their interaction with compliant structures such as immobilized DNA represents a significantly more challenging problem than those addressed here. It is not clear if simple continuum based modeling may be able to provide a reasonable approximation to such a system (whereby the DNA is treated as a compliant beam for example) or if more advanced atomistic simulation may be required.

Cross References

► Electroosmotic Flow (DC)
► AC Electro-Osmotic Flow

References

1. Norde W, Rouwendal E (1990) Streaming Potential Measurements as a Tool to Study Protein Adsorption-Kinetics. J Colloid Interface Sci 139(1):169–176
2. Zembala M, Adamczyk Z (2000) Measurements of streaming potential for mica covered by colloid particles. Langmuir 16(4):1593–1601
3. Erickson D, Li DQ, Krull UJ (2003) Modeling of DNA hybridization kinetics for spatially resolved biochips. Anal Biochem 317(2):186–200
4. Karnik R, Fan R, Yue M, Li DY, Yang PD, Majumdar A (2005) Electrostatic control of ions and molecules in nanofluidic transistors. Nano Lett 5(5)943–948
5. Ajdari A (1995) Electroosmosis on Inhomogeneously charged surfaces. Phys Rev Lett 75(4)755–758
6. Anderson JL (1985) Effect of nonuniform zeta potential on particle movement in electric fields. J Colloid Interface Sci 105(1)45–54
7. Ghosal S (2002) Lubrication theory for electro-osmotic flow in a microfluidic channel of slowly varying cross-section and wall charge. J Fluid Mech 459:103–128
8. Erickson D, Li DQ (2002) Influence of surface heterogeneity on electrokinetically driven microfluidic mixing. Langmuir 18(5)1883–1892
9. Biddiss E, Erickson D, Li DQ (2004) Heterogeneous surface charge enhanced micromixing for electrokinetic flows. Anal Chem 76(11):3208–3213
10. McDonald JC, Duffy DC, Anderson JR, Chiu DT, Wu HK, Schueller OJA, Whitesides GM (2000) Fabrication of microfluidic systems in poly(dimethylsiloxane). Electrophoresis 21(1)27–40
11. Sze A, Erickson D, Ren LQ, Li DQ (2003) Zeta-potential measurement using the Smoluchowski equation and the slope of the current-time relationship in electroosmotic flow. J Colloid Interface Sci 261(2):402–410
12. Erickson D (2005) Towards numerical prototyping of labs-on-chip: modeling for integrated microfluidic devices. Microfluid Nanofluid 1(4)301–318
13. Erickson D, Liu XZ, Venditti R, Li DQ, Krull UJ (2005) Electrokinetically based approach for single-nucleotide polymorphism discrimination using a microfluidic device. Anal Chem 77(13)4000–4007
14. Erickson D, Li DQ (2003) Three-dimensional structure of electroosmotic flow over heterogeneous surfaces. J Phys Chem B 107(44):12212–12220
15. Hu YD, Werner C, Li DQ (2003) Electrokinetic transport through rough microchannels. Anal Chem 75(21):5747–5758

Electroosmotic Flow Over Non-Uniform Surfaces

► Electroosmotic Flow over Heterogeneous Surfaces

Electroosmotic Flow in Porous Media

► Electrokinetic Flow in Porous Media

Electroosmotic Pump

YONG KWEON SUH, SANGMO KANG
Dong-A University, Busan, Korea
yksuh@dau.ac.kr

Synonyms

EO pump; EOP; Electroosmotic flow (EOF)

Definition

A pump whose working principle is electroosmosis.

Chemical and Physical Principles

Electroosmotic Pump Through a Single Channel

We consider a micro- or nanochannel having a uniform cross-section as shown in Fig. 1a. When the channel is in contact with an electrolyte, its surface is charged with usually negative ions. The counter-ions in the liquid are then attracted onto the surface while the co-ions are repelled away from the wall. The thin layer near the surface where the counter-ions are thus highly concentrated is called the electric double layer (EDL). The amount of accumulation of the counter-ions in the EDL is determined in such a way that the electric potential difference induced between the wall surface and the bulk equals the zeta potential, which is an intrinsic property of the interface. When an external electric field is applied along the channel, it exerts the Coulomb force to the ions thereby driving the fluid flow. This kind of fluid motion is called electroosmosis (e. g. [1]), the working principle of the electroosmotic pump.
The electric potential ϕ within the channel induced by the unbalanced distribution of the ions in the EDL is determined from the Poisson equation:

$$\nabla^2\phi = -\frac{\rho_e}{\varepsilon\varepsilon_0} \tag{1}$$

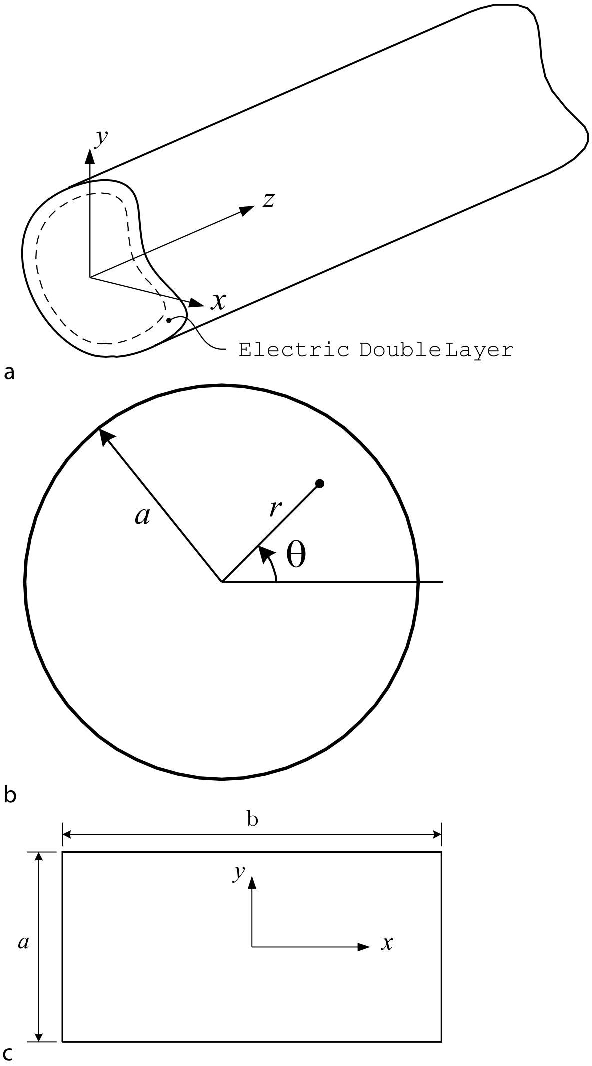

Electroosmotic Pump, Figure 1 Coordinates for analysis of the electroosmotic flow inside a single capillary with a uniform cross-sectional shape. (**a**) Perspective view of an arbitrary shape of cross-section; (**b**) circular section; (**c**) rectangular section

where $\nabla^2 = \partial^2/\partial x^2 + \partial^2/\partial y^2$ is the 2D Laplacian, (x, y) denotes the coordinates on the cross-sectional plane of the channel (Fig. 1a), ρ_e the net charge density (net charge per unit volume), ε the dielectric constant of the solution and ε_0 the permittivity of the vacuum. For symmetric ions, the charge density is given by

$$\rho_e = ze(n_+ - n_-) \tag{2}$$

Here z is the valence of the ions, e the proton charge and $n_\pm$ the number concentration (ion number per unit volume) of the cations and anions, respectively. Assuming the equilibrium Boltzmann distribution for the ion concentra-

tion, we can relate the number concentration to the potential as follows:

$$n_{\pm} = n_{\infty} \exp(\mp ze\phi / k_{\mathrm{b}}T)$$

where n_{∞} is the concentration of each ion in the bulk region, k_{b} the Boltzmann constant and T the temperature. Then Eq. (1) becomes

$$\nabla^2 \phi = \frac{2zen_{\infty}}{\varepsilon\varepsilon_0} \sinh(ze\phi / k_{\mathrm{b}}T) \tag{3}$$

Analytic solutions to this equation can be obtained under the assumption of small magnitude of $ze\phi / k_{\mathrm{b}}T$. Then Eq. (3) leads to

$$\nabla^2 \phi = \frac{\phi}{\lambda^2} \tag{4}$$

where

$$\lambda = \sqrt{\frac{\varepsilon\varepsilon_0 k_{\mathrm{b}} T}{(2z^2 e^2 n_{\infty})}} \tag{5}$$

denotes the Debye–Huckel parameter (or Debye length) representative of the EDL thickness. Such simplification is called the Debye–Huckel approximation [1].

The velocity vector $\boldsymbol{u}$ of the fluid flow caused by the nonzero charge density in the EDL is governed by

$$\mu \nabla^2 \boldsymbol{u} = \nabla p - \rho_{\mathrm{e}} \boldsymbol{E} \tag{6}$$

where $\boldsymbol{E}$ is the external electric field vector and μ the dynamic viscosity of the fluid. When the applied pressure gradient ∇p and the applied external electric field $\boldsymbol{E}$ are along the axial direction with uniform magnitudes, $\Delta p / L$ and E, respectively, we can assume a fully developed flow, and the only nonzero velocity component w, i. e. the axial component, can be decomposed into the pressure-driven and the electroosmosis-driven parts: $w(x, y) = w_{\mathrm{p}}(x, y) + w_{\mathrm{eo}}(x, y)$. Here the length of the pump unit is denoted as L and the applied pressure increase as Δp. This pressure increase is considered as the initially given one in solving Eq. (6), but in the actual application of the pump, it plays a role as a source of power like a voltage difference built across an electric battery. We then have

$$w_{\mathrm{p}} = \frac{-a^2}{\mu} \frac{\Delta p}{L} W_{\mathrm{p}}(x, y) \tag{7a}$$

$$w_{\mathrm{eo}} = \frac{-\varepsilon\varepsilon_0 \varsigma E}{\mu} \left(1 - \frac{\phi}{\varsigma}\right) \tag{7b}$$

where $W_{\mathrm{p}}(x, y)$ satisfies the Poisson equation,

$$\nabla^2 W_{\mathrm{p}} = \frac{-1}{a^2} \ . \tag{8}$$

a denotes a suitable length scale, such as radius of a capillary for the circular section (Fig. 1b) and the channel depth for the rectangular section (Fig. 1c) and ς is the zeta potential. Note that the Helmholtz–Smoluchowski formula for the electroosmotic velocity is recovered from Eq. (7b) for the thin EDL limit.

We obtain the flow rate from integration of the axial velocity over the whole cross-sectional area A as follows:

$$Q = -\frac{f_1 A a^2}{8\mu} \frac{\Delta p}{L} - \frac{g_1 A \varepsilon\varepsilon_0 \varsigma E}{\mu} \tag{9}$$

where dimensionless constants f_1 and g_1 are defined as

$$f_1 = \frac{8}{A} \int_A W_{\mathrm{p}}(x, y)\, \mathrm{d}A \tag{10a}$$

$$g_1 = \frac{1}{A} \int_A \left(1 - \frac{\phi}{\varsigma}\right) \mathrm{d}A \tag{10b}$$

The constant f_1 becomes unity for the circular capillary of Fig. 1b, and the constant g_1 approaches unity for any geometry if the EDL thickness λ tends to zero. Maximum flow rate is defined as the one attained when the pressure gradient vanishes or

$$Q_{\max} = \frac{-g_1 A \varepsilon\varepsilon_0 \varsigma E}{\mu} \ . \tag{11}$$

We can see that the maximum flow rate increases with the area of the cross-section as well as the electric field. The maximum pressure difference built between both ends of the pump unit is provided for the case when the flow rate becomes zero, or

$$\Delta p_{\max} = \frac{-8 g_1 \varepsilon\varepsilon_0 \varsigma V}{f_1 a^2} \tag{12}$$

where V is the external potential difference applied across the channel length; $V = EL$. It is seen that the maximum pressure difference increases as the external potential difference increases and also as the capillary size decreases. In terms of $Q_{\max}$ and $\Delta p_{\max}$, the formula for the flow rate can be expressed as follows:

$$Q = Q_{\max} \left[1 - \frac{\Delta p}{\Delta p_{\max}}\right] . \tag{13}$$

The thermal efficiency of the pump is determined from the following equation:

$$\eta = \frac{Q\Delta p}{IV} \tag{14}$$

where I indicates the total current through the electrolyte. The current flux is given as

$$j = \sigma E + \rho_e w \ . \tag{15}$$

Here σ is the conductivity. The first term corresponds to the electromigration (or conduction) effect and the second to the ion advection. We neglect the diffusion effect. The conductivity is related to the mobility β by

$$\sigma = \beta ze(n_+ + n_-) \tag{16a}$$

$$\beta = \frac{Dez}{k_b T} \tag{16b}$$

where D is the ion diffusivity [2]. Then the total current I is obtained by integrating j over the whole cross-section. The result is

$$I = g_2 A\sigma_\infty E + \frac{g_3 a^2 \varepsilon\varepsilon_0 \varsigma}{\mu L}\Delta p + \frac{g_4 a(\varepsilon\varepsilon_0)^2\varsigma^2}{\mu\lambda}E \tag{17}$$

where

$$\sigma_\infty = 2\beta zen_\infty \tag{18a}$$

$$g_2 = \frac{1}{A}\int_A \cosh\phi^* \, \mathrm{d}A \tag{18b}$$

$$g_3 = \frac{1}{\lambda^2\varsigma^*}\int_A W_p \sinh\phi^* \, \mathrm{d}A \tag{18c}$$

$$g_4 = \frac{1}{a\lambda\varsigma^*}\int_A \left(1 - \frac{\phi^*}{\varsigma^*}\right)\sinh\phi^* \, \mathrm{d}A \tag{18d}$$

$$\varsigma^* = \frac{ze\varsigma}{k_b T} \tag{18e}$$

The dimensionless potential ϕ^* has been scaled by the reference potential $k_b T/ze$ like Eq. (18e). Note that the factor $1/\lambda^2\varsigma^*$ in Eq. (18c) and $1/a\lambda\varsigma^*$ in Eq. (18d) are different from $a^2/A\lambda^2\varsigma^*$ used by Min et al. [2]. This factor is chosen in such way that, even for the limit of a thin EDL, the coefficients g_2 and g_3 take an $O(1)$ value. Then the efficiency Eq. (14) becomes

$$\eta = \frac{Q_{\max}\left(1 - \frac{\Delta p}{\Delta p_{\max}}\right)\Delta p}{E\left[g_2 A\sigma_\infty V + \left(\frac{g_3 a^2\varepsilon\varepsilon_0\varsigma}{\mu}\right)\Delta p + \frac{g_4 a(\varepsilon\varepsilon_0)^2\varsigma^2 V}{\mu\lambda}\right]} \tag{19}$$

We can see from this that when the effect of Δp in the denominator is negligible compared with other two terms, the maximum efficiency occurs at $\Delta p = \Delta p_{\max}/2$. Min et al. [2] provided further analysis for the case when Δp in the numerator is considered for a circular capillary. It was shown that the efficiency is increased with decreasing a, but it reaches maximum at around $\lambda = (0.3 \sim 0.4)a$ under the practical range of the zeta potential. For deionized water (10^{-6} M ion concentration), this corresponds to $a = (0.7 \sim 1)\,\mu$m, whereas for 10^{-4} M concentration $a = (0.07 \sim 0.1)\,\mu$m. The efficiency generally depends on ς; for the practical range of ς, it can reach as much as 15%.

For a circular cross-section, Eq. (4) can be written as

$$\frac{\partial}{r\partial r}\left(r\frac{\partial\phi}{\partial r}\right) = \frac{\phi}{\lambda^2} \tag{20}$$

under the assumption of axisymmetric profile for ϕ, where r denotes the radial coordinate (Fig. 1b). Then the solution becomes

$$\phi = \frac{\varsigma I_0(r/\lambda)}{I_0(a/\lambda)} \tag{21}$$

$$\rho_e = -\frac{\varepsilon\varepsilon_0\varsigma I_0(r/\lambda)}{\lambda^2 I_0(a/\lambda)} \tag{22}$$

where I_0 denotes the first kind of the modified Bessel function of zero-order and a the radius of the circle. The normalized axial velocity $W_p(r)$ is determined from Eq. (8) as follows:

$$W_p = \frac{1}{4}\left[1 - \left(\frac{r}{a}\right)^2\right] \ . \tag{23}$$

Further, the constants f_1 and g_1 are evaluated to be

$$f_1 = 1\,, \quad g_1 = 1 - \frac{2\lambda I_1\left(\frac{a}{\lambda}\right)}{aI_0\left(\frac{a}{\lambda}\right)} \ . \tag{24}$$

We assure that g_1 approaches unity in the thin EDL limit as addressed above. No closed-form solutions have been reported as for the constants g_2, g_3 and g_4. Most results reported so far have been given from the numerical integration of Eqs. (18b)–(18d).

For a rectangular cross-section, as shown in Fig. 1c, the solution to Eq. (4) and the subsequently given velocity component were provided in a double-series form by, for example, Li [1], and later in a single series form by Wang et al. [3]. The Helmholtz–Smoluchowski formula for the electroosmosis-driven flow velocity can be given of course

for the thin EDL limit. The series solution for the pressure-driven flow velocity is presented, for example, by Min et al. [2] as follows:

$$W_p = \frac{16}{\pi^3}\sum_{n=1}^{\infty}\frac{(-1)^{n-1}}{(2n-1)^3}\left\{1-\frac{\cosh\left[(2n-1)\frac{\pi x}{a}\right]}{\cosh\left[(2n-1)\frac{\pi b}{2a}\right]}\right\} \times \cos(2n-1)\frac{\pi y}{a} \quad (25)$$

As we can see from this formula, fortunately the series shows a very fast convergence property, and therefore only the leading-order term has been considered by several researchers.

Packed Column Electroosmotic Pump

In many microfluidic applications, e. g. microseparation techniques with chromatographic columns, the required pumping pressure is enormous. A packed-column electroosmotic pump is one of the most favorable alternatives replacing the membrane-displacement pump because it does not require moving parts such as valves and flow control is very easy.

It was shown from Eq. (12) that the maximum pressure difference Δp_{max} can be increased by decreasing the channel size a. However the maximum flow rate decreases when the channel size decreases as seen from Eq. (11). Therefore it is natural to consider using a parallel assembly of narrow capillaries or channels to achieve the high pressure difference as well as the high flow rate. The packed-column electroosmotic pump developed due to this reason is composed of a column packed with solid particles as shown in Fig. 2. The electrolyte completely fills the porous space. So, when the external electric potential difference is applied between both ends of the column (Fig. 2) the counter-ions accumulated in the EDL developed near the surface of particles drive the bulk fluid.

In this case the porous media can be modeled by an array of N capillaries with the inner radius a and an effective length L_e that differs from L_c, the actual length of the column. The effective length L_e can be understood as the averaged path length of the fluid particles traveling from the entrance to the exit of the column as shown in Fig. 2. Then it is required that the volume $A_e L_e$ should be the same as the total volume of the porous space, where $A_e = N\pi a^2$ is the total cross-sectional area of the collection of the capillaries. Then the porosity ψ, defined as the ratio of the volume of the porous space to the total volume of the column, can be given as

$$\psi = \frac{A_e L_e}{A_c L_c} \quad (26)$$

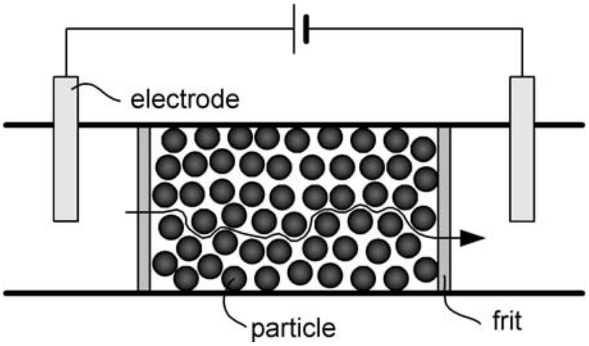

Electroosmotic Pump, Figure 2 Sectional view of a packed-column electroosmotic pump unit. The frit is also composed of a porous medium

where A_c stands for the cross-sectional area of the empty column. The tortuosity τ is defined as

$$\tau = \left(\frac{L_e}{L_c}\right)^2 . \quad (27)$$

Then we can write

$$A_e = \frac{\psi A_c}{\sqrt{\tau}} . \quad (28)$$

Therefore we can derive the formula for the flow rate from Eq. (9) as follows:

$$Q = -\frac{\psi A_c a^2}{8\tau\mu L_c}\Delta p - \frac{\psi g_1 A_c \varepsilon\varepsilon_0\varsigma}{\tau\mu L_c}V \quad (29)$$

where $f_1 = 1$ is applied as shown in Eq. (24). From Eq. (29) we can derive the following:

$$Q_{max} = -\frac{\psi g_1 A_c \varepsilon\varepsilon_0\varsigma V}{\tau\mu L_c} \quad (30a)$$

$$\Delta p_{max} = \frac{-8 g_1 \varepsilon\varepsilon_0\varsigma V}{a^2} . \quad (30b)$$

From the second equation, we can see that the maximum pressure difference is independent of the specific structure of the porous medium, i. e. ψ or τ.

The formula for the efficiency takes the same form as Eq. (19), in which A should be taken as the area of the individual capillary, i. e. $A = \pi a^2$. This implies that the efficiency is independent of the number of capillaries used in modeling the packed column.

The porosity ψ is usually measured from the dry and wet weight of the packed column, the calculation formula being

$$\psi = \frac{\mathrm{wt_{wet}} - \mathrm{wt_{dry}}}{\gamma A_c L_c} \quad (31)$$

where γ denotes the specific weight of the liquid. In order to determine the tortuosity τ we need to measure the resistance of the empty column, $R_{em} = \omega L_c / A_c$, and that of the packed one, $R_{pack} = \omega L_e / A_e$, where ω is the resistivity of the liquid [4]. It can be shown that the ratio of these two quantities becomes

$$\frac{R_{em}}{R_{pack}} = \frac{\psi}{\tau} \ . \quad (32)$$

Since ψ is predetermined from Eq. (31), this can offer τ. Now coupling Eqs (30a) and (30b) we get the formula that gives a as follows:

$$a = \left[\frac{8\tau\mu L_c}{\psi A_c} \frac{Q_{max}}{\Delta p_{max}} \right] \ . \quad (33)$$

This equation implies that to obtain a we need to know the ratio $Q_{max}/\Delta p_{max}$ from a separate experiment.
To demonstrate the calculation procedure, we use the data given by Zeng et al. [4]:

$$L_c = 5.4\,\text{cm}\,,\ D_c = 530\,\mu\text{m (diameter of the column)}\,,$$

$$\mu = 10^{-3}\,\text{Pa s}\,,\ \varepsilon = 80\,,\ \ \varepsilon_0 = 8.854 \times 10^{-12}\,\frac{\text{C}^2}{\text{Nm}^2}\,,$$

$$n_\infty = 7.5\,\mu\text{M}\,,\ z = 1\,,\ V = 2\,\text{kV}\,.$$

From the measurement of the dry and wet weight of the packed column, the porosity is calculated to be $\psi = 0.37$. They further provided the measurement results of R_{em}/R_{pack}, Q_{max} and Δp_{max} as follows:

$$\frac{R_{em}}{R_{pack}} = 0.24\,,\ Q_{max} = 4.8\,\mu\text{l/min}\,,\ \Delta p_{max} = 23.5\,\text{atm}$$

from which we can get $\tau = 1.54$ by using Eq. (32). Then Eq. (33) gives $a = 523$ nm. The zeta potential ς can be determined from either Eq. (30a) or (30b). However we need to evaluate g_1 from Eq. (24) for this. First λ is calculated from Eq. (5) as $\lambda = 112$ nm, where $T = 298$ K was assumed. Then we can get $a/\lambda = 4.67$, and from Eq. (24) we obtain $g_1 = 0.621$. Now we use either Eq. (30a) or (30b) to predict the zeta potential, the result being $\varsigma = -94.1$ mV; Zeng et al. [4] predicted this as $\varsigma = -95$ mV.
The validity of the formula for the flow rate, i. e. Eq. (29), can be checked from the plot Q versus V (Fig. 8 in [4] given from the experiment at a constant pressure difference, $\Delta p = 35$ atm. We first compute the slope

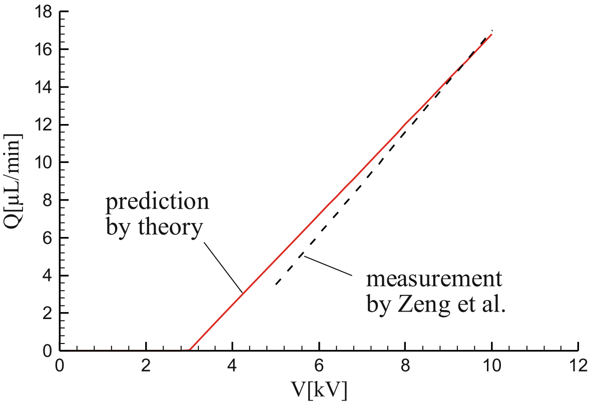

Electroosmotic Pump, Figure 3 Comparison of the linear relationship between the external potential V and the flow rate Q from the experiment of Zeng et al. [4] and from the theory (Eq. (34))

$(\partial Q/\partial V)_{\Delta p} = 4.00 \times 10^{-14}\,\text{m}^3/\text{sV}$ from Eq. (29). Then the linear dependence of Q on V is expressed by

$$Q = Q_0 + \left(\frac{\partial Q}{\partial V}\right)_{\Delta p} V \quad (34)$$

where $Q_0 = -1.19 \times 10^{-10}\,\text{m}^3/\text{s}$ is calculated from the first term on the right-hand side of Eq. (29) at $\Delta p = 35$ atm. Figure 3 shows a comparison between the experimental result given by Zeng et al. [4] and the theoretical one of Eq. (34). It reveals a fairly good agreement between the two predictions.

Key Research Findings

The effect of various parameters on Q_{max}, Δp_{max} and η will be important in the design of an electroosmotic pump. The effect of the parameters ζ, V, A_c, L_c, ψ, μ and τ on Q_{max} and Δp_{max} can be explicitly understood from the followings:

$$\frac{Q_{max}}{\frac{-\psi\varepsilon_w\varepsilon_0 A_c \varsigma V}{\tau\mu L_c}} = g_1\left(\frac{\varepsilon}{\varepsilon_w}\right) \equiv C_q \quad (35a)$$

$$\frac{\Delta p_{max}}{\frac{-8\varsigma V \varepsilon_w \varepsilon_0}{a_0^2}} = \frac{g_1\left(\frac{\varepsilon}{\varepsilon_w}\right)}{\left(\frac{a}{a_0}\right)^2} \equiv C_p = \frac{C_q}{\left(\frac{a}{a_0}\right)^2} \quad (35b)$$

where ε_w denotes the dielectric constant of the water and a_0 is a reference size of the capillary. Note that the right-hand side terms of the above formula are dimensionless. It is seen that Δp_{max} increases linearly with ζ and V, while Q_{max} increases linearly with ζ, V, A_c, ψ, $1/\mu$, $1/\tau$ and $1/L_c$.

The effect of the other parameters, a, ε and n_∞, should be implicitly understood from Eqs. (35a) and (35b) through λ of Eq. (5) and the constant g_1 of Eq. (24). The effect of the capillary size a is first investigated. It can be shown that $g_1 \sim a^2/8\lambda^2$ for small a/λ and $g_1 \to 1$ under the limit $a/\lambda \to \infty$. Therefore the coefficient C_p approaches a constant value for the limit $a/\lambda \to 0$ and tends to be proportional to $1/a^2$ for $a \to \infty$ (thin EDL limit). This implies that packing the column with smaller particles induces a higher pumping force, but use of particles that are too small leads to overlap of the EDL and thus results in a saturated value of $\Delta p_{\max}$ as shown in Fig. 4a, where $a_0 = 523\,\mathrm{nm}$ is chosen. On the other hand, the coefficient C_q shows the same behavior as g_1 as can be seen from Eq. (35a). Thus C_q approaches a constant value for $a \to \infty$ but it is proportional to a^2 for $a \to 0$ because of the EDL overlap effect. Shown in Fig. 4a is the effect of a on C_q. The asymptotic behavior of both coefficients for the high range of a/a_0 is not shown in this plot because such a range is not practically relevant. We can predict from this figure that selecting a particle size slightly larger than the present one, that corresponds to a_0, would result in a significantly higher flow rate but a slightly smaller maximum pressure difference.

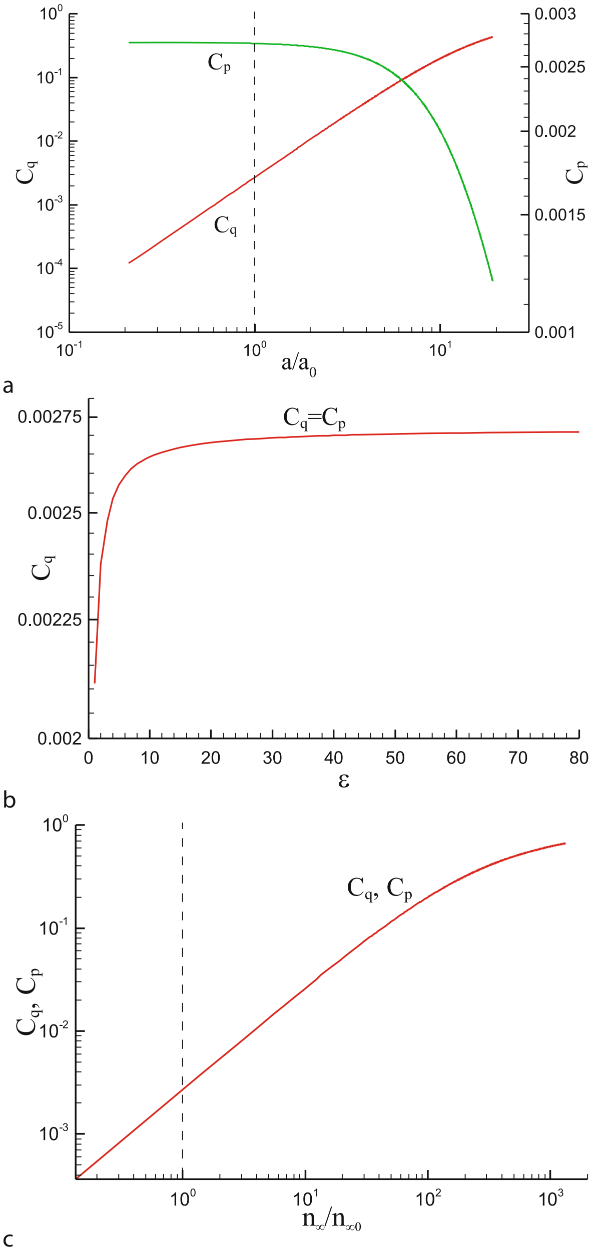

Electroosmotic Pump, Figure 4 Effect of the dimensionless capillary radius a/a_0 (**a**), the dielectric constant of the liquid ε (**b**) and the dimensionless bulk concentration $n_\infty/n_{\infty 0}$ (**c**) on the coefficient C_q for the maximum flow rate and C_p for the maximum pressure difference

The effect of the parameter ε on C_q and C_p is shown in Fig. 4b. Since the capillary radius a is selected as $a = a_0$, both C_q and C_p show identical behavior. It is seen that the coefficients approach a constant value for $\varepsilon \to \infty$ and show a linear increase with ε for small ε, both of which can be proved from Eqs (35a) and (35b). The reason that change of ε in the practical range does not significantly affect the coefficients arises from the fact that the pore size a is taken very small. When a larger a is selected, the coefficient curves become flatter over the whole range of ε.

The effect of n_∞ is shown in Fig. 4c. It also shows the same behavior for both coefficients for the reason explained above. In a similar manner to the case for the effect of ε, the coefficients tend to a constant value for large n_∞ and increase linearly with n_∞ for small n_∞. It can be predicted from this plot that a much greater increase of the concentration would produce much higher capacity.

Understanding the effect of the various parameters on the efficiency is not so simple. Min et al. [2] converted Eq. (19) to a dimensionless form for both numerators and denominators as follows:

$$\eta = \frac{(1 - \Delta p^*)\,\Delta p^*}{\alpha_0 + \alpha_1 \Delta p^*} \tag{36}$$

where $\Delta p^* = \Delta p/\Delta p_{\max}$ and

$$\alpha_0 = \left(\frac{g_2}{8g_1^2}\right)\left(\frac{\mu D}{\varepsilon\varepsilon_0 \varsigma^2}\right)\left(\frac{a}{\lambda}\right)^2 + \left(\frac{g_4}{8\pi g_1^2}\right)\left(\frac{a}{\lambda}\right)$$

$$\alpha_1 = -\left(\frac{g_3}{\pi g_1}\right)$$

When the effect of the second term on the denominator is small, the maximum efficiency $\eta_{\max}$ occurs at $\Delta p^* = 1/2$

as addressed previously. Min et al. [2] have thoroughly investigated the effect of the three dimensionless parameters on η_{max} based on Eq. (36). They have demonstrated that η_{max} can be increased by decreasing the viscosity or by increasing the dielectric constant of the liquid. They have also proposed the possibility that efficiencies as high as 15% are possible with careful attention to the channel size and the solution composition.

Examples of Application

It has been shown that the thermal efficiency of the electroosmotic pump is very low. Most of the electric energy put into the electrolyte liquid is dissipated into heat, so called Joule heating. In many cases, the mismatch between the theory and the measurement for the pressure is attributed to the Joule heating [5].

The maximum efficiency achievable through a careful selection of packed materials and electrolyte has been reported by Min et al. [2] to be at most 15%. In contrast, Griffiths and Nilson [6] reported that the likely maximum efficiency for any electroosmotic pump would be about 10% for operation at the condition of maximum work.

Hu and Chao [7] performed two-dimensional numerical simulation on the performance of an electroosmotic pump for planar channels. The model is able to handle the case with the dimensions comparable to the EDL thickness. Also no Debye–Huckle approximation and symmetric conditions are required. But the results show considerable deviation from the experimentally measured ones.

Yao and Santiago [8] provided useful review on the historical background of the development of EO pumps. They considered different molar conductivities for cations (Λ_+) and anions (Λ_-) in calculating the electric current caused by electromigration. They predicted that Λ_+ is almost twice Λ_- for sodium ions.

Kang et al. [9] considered the wall effect surrounding the packed materials. Zeta potentials on the inner surface may not be the same as those of packed spheres, and the porosity is a function of the distance from the wall. The wall effect is more enhanced for larger packed particles.

Yao et al. [10] studied an electroosmotic pump made from porous silicon membranes having straight circular pores. Tortuosity is unity and ψ was measured directly from SEM images of the cross-section. Zeta potential is calculated by using the formula for the ratio Q_{max}/I_{max} and the measured data of Q_{max} and I_{max}. Comparison between theory and experiment is good for the plots Q_{max} versus V and I_{max} versus V. There was considerable deviation for the prediction of Δp_{max} and Yao et al. attributed this discrepancy to the problem in the zeta potential measurement and non-uniform distribution of the pore size. At a lower flow rate, the buffer electrolyte shows variation of PH leading to unstable results.

Cross References

- ▶ Electroosmotic Flow (DC)
- ▶ Electroosmosis Flow in Heterogeneous Microchannels
- ▶ AC Electroosmotic Flow
- ▶ Analysis of Electroosmotic Flow by Lattice–Poisson–Boltzmann Method
- ▶ Combined Pressure-Driven Flow and Electroosmotic Flow
- ▶ Electrokinetic Flow in Porous Media
- ▶ Electrokinetic Sample Injection

References

1. Li D (2004) Electrokinetics in Microfluidics. Elsevier Academic Press
2. Min JY, Hasselbrink EF, Kim SJ (2004) On the efficiency of electrokinetic pumping of liquids through nanoscale channels. Sens Actuators B 98:368–377
3. Wang C, Wong TN, Yang C, Ooi KT (2007) Characterization of electroosmotic flow in rectangular microchannels. Int J Heat Mass Transfer 50:3115–3121
4. Zeng S, Chen C-H, Mikkelsen Jr. JC, Santiago JG (2001) Fabrication and characterization of electroosmotic micropump. Sens Actuators B 79:107–114
5. Morf WE, Guenat OT, de Rooij NF (2001) Partial electroosmotic pumping in complex capillary systems Part 1: principles and general theoretical approach. Sens Actuators B 72:266–272
6. Griffiths SK, Nilson RH (2005) The efficiency of electrokinetic pumping at a condition of maximum work. Electrophoresis 26:351–361
7. Hu JS, Chao CYH (2007) A study of the performance of microfabricated electroosmotic pump. Sens Actuators A 135:273–282
8. Yao S, Santiago JG (2003) Porous glass electroosmotic pumps: theory. J Colloid Interface Sci 268:133–142
9. Kang Y, Yang C, Huang X (2004) Analysis of the electroosmotic flow in a microchannel packed with homogeneous microspheres under electrokinetic wall effect. Int J Eng Sci 42:2011–2027
10. Yao S, Myers AM, Posner JD, Rose KA, Santiago JG (2006) Electroosmotic pumps fabricated from porous silicon membranes. J MEMS 15(3):717–728

Electropermeabilization

▶ Electroporation

Electrophoresis

KEVIN D. DORFMAN
Department of Chemical Engineering
and Materials Science, University of Minnesota,
Minneapolis, MN, USA
dorfman@umn.edu

Definition

Electrophoresis is the motion of charged particles in a fluid under the influence of an electric field.

Chemical and Physical Principles

Electrophoresis provides an important method of actuation in microfluidics. Many of the different types of species that need to be transported on a microfluidic device are charged, and electrophoresis thus provides a convenient method for moving them to different locations on a chip. Amongst the most important examples are colloidal particles, such as latex spheres, and biomolecules, such as proteins and DNA. Under certain circumstances, electrophoresis can also be used to separate these particles by zeta potential or size, which is an important part of biological analyses.

Electrophoresis also requires that the fluid entraining these particles be able to conduct electricity. Often, salts are added, yielding an electrolytic solution. The salts disassociate into positively charged ions (▶ cations) and negatively charge ions (▶ anions). The cations are attracted towards the negative electrode (the ▶ cathode) and anions are attracted towards the positive electrode (the ▶ anode). When dealing with biomolecules, the salts are usually weak acids and weak bases. The resulting solution is a buffer, which keeps the solution within a narrow pH range. As the charge and conformation of the biomolecules depend on the solution pH, the buffer composition plays an important role in biological applications of electrophoresis.

Consider first the simple case an isolated, charged ion moving in a uniform electric field, as illustrated in Fig. 1. While this is an overly simplistic picture of electrophoretic motion in solution, it serves to illustrate the general principle. We will consider a more realistic model of electrophoresis in free solution in the following section.

The ion possesses a charge Q, with $Q > 0$ for a cation and $Q < 0$ for an anion. The charge of the ion is given by the number of unpaired electrons or protons, with the elementary electric charge $e = 1.60219 \times 10^{-19}$ C per proton or electron. In this example, the ions in solution are assumed to be so dilute that they do not interact electrostatically. The ion is placed in a uniform electric field of strength E. The field strength is often reported in V/cm, although the proper SI units are V/m. In applications, one would typically apply a potential V between the two electrodes separated by a distance L. In this case, the electric field between them is simply

$$E = \frac{V}{L} \,. \tag{1}$$

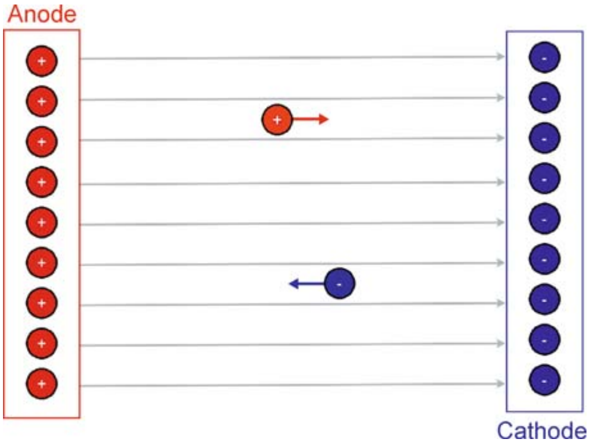

Electrophoresis, Figure 1 Electrophoresis of a cation and an anion in a uniform electric field. The anode and cathode are assumed to extend infinitely in the vertical direction to avoid end effects. The positively charged cations move towards the negatively charged cathode, whereas the negatively charged anions move towards the positively charged anode

The electrical force acting on the ion is the product of its charge and the electric field,

$$F_e = QE = \frac{QV}{L} \,. \tag{2}$$

For a nominal electric field of 10 V/cm acting on a monovalent ion (like Na^+), the electrical force would be 1.6×10^{-16} N – very small indeed! However, this force is sufficient to animate the ion because it is balanced by a very small drag force. If the ion is approximated as a spherical particle of radius a moving through a fluid of viscosity η, then the drag coefficient ξ is given by the Stokes drag

$$\xi = 6\pi\eta a \,, \tag{3}$$

and the drag force resisting the motion is

$$F_d = -\xi v \,. \tag{4}$$

By Newton's second law, the sum of the electrical force and the drag force equals zero. As a result, the ion has an electrophoretic velocity

$$v = \frac{QE}{\xi} \,. \tag{5}$$

Keeping the example of Na^+, the ionic radius is $a = 116$ pm. If the electrophoresis is performed in a fluid with a viscosity similar to that of water (which is typically the case), then $\eta = 1\,\text{cP} = 0.001\,\text{Pa s}$, and the resulting drag coefficient is $\xi = 2.18 \times 10^{-12}$ Ns/m. With an electric force of 1.6×10^{-16} N, the sodium ion would thus

move at a speed of 73 μm/s. Albeit a very slow speed on macroscopic length scales, the ion moves over its own radius over 500,000 times per second.

In general, data are not reported as electrophoretic velocities, but rather as electrophoretic mobilities. The electrophoretic mobility is defined as

$$\mu \equiv \frac{v}{E}\,. \tag{6}$$

If the velocity is a linear response to the electric field, as is the case here, then the electrophoretic mobility is independent of the field. This scaling breaks down in the case of ▶polyelectrolytes [1].

Determining the electrophoretic mobility of polyelectrolytes, such as colloidal particles and flexible polyelectrolyte chains such as DNA, is considerably more complicated because their electrostatics and hydrodynamics differ from the simple charged, spherical ion considered above. Polyelectrolytes are intrinsically uncharged, but contain ionizable groups (for example –OH and –H groups) that will dissociate from the particle when it is placed in solution. As indicated in Fig. 2, these ionizable groups, known as ▶counterions, dissociate from the macroion. The dissociation is not limited by mass action,

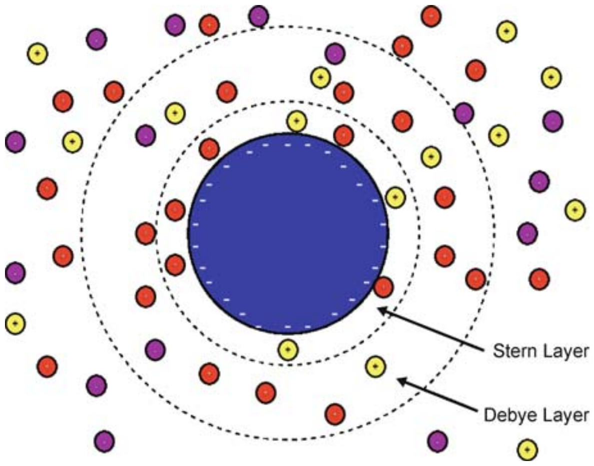

Electrophoresis, Figure 2 Polyelectrolytes contain ionizable groups that dissociate from the particle when it is placed in solution. In the figure, the red cations were originally associated with the colloidal particle. The yellow cations and purple anions represent the dissociated salts contained in the buffer solution. Nearby the particle, the counterions are strongly bound by electrostatics and chemical affinity for the colloid, leading to the formation of the Stern layer. The Stern layer is surrounded by a more diffuse layer of charges, known as the Debye layer, where the local density of counterions is governed by a balance between attraction towards the oppositely charged colloid, the repulsion from other counterions, and diffusion

although flexible polyelectrolyte chains do not necessarily completely dissociate due to Manning condensation [2]. Note that the solution can also contain counterions and ▶co-ions of its own (with co-ions having the same charge as the particle), which will normally be the case during electrophoresis in buffers. The overall system is electrically neutral – the number of counterions (red) equals the number of charges on the particle surface, and the number of counterions already in the solution (yellow) equals the number of solution co-ions (purple).

When the counterions dissociate from the particle, diffusion attempts to randomize their locations. However, the counterions are attracted to the particle by electrostatic interactions, which act over long distances. Immediately proximate to the particle is a molecular-sized layer of counterions, called the Stern layer. The counterions in the Stern layer are immobile as a result of their chemical affinity for the particle surface, as well as the very strong electrical attraction at short distances from the charged particle. The Stern layer also includes polar water molecules that are oriented to the surface. A second, larger layer of charges, called the ▶Debye layer, surrounds the Stern layer. These charges are mobile and their location is affected by electrostatic attraction to the sphere, which wants to pull them towards the inner edge of the Debye layer, and diffusion, which tries to randomize their locations. To further complicate the issue, the counterions repel one another, since they have the same charge. Exactly computing the structure of the Debye layer is a challenging task, requiring the solution of the nonlinear Poisson–Boltzmann equation (see ▶Lattice Poisson-Boltzmann Method, Analysis of Electroosmotic Microfluidics), but the characteristic thickness can be obtained from scaling, yielding

$$\kappa^{-1} = \sqrt{\frac{\varepsilon_0 \varepsilon_{\mathrm{b}} k_{\mathrm{B}} T}{2e^2 I}}\,. \tag{7}$$

In the latter, ε_0 is the permittivity of vacuum (8.854×10^{-12} F/m) and ε_{b} is the permittivity of the bulk solution (or the dielectric medium), k_{B} is Boltzmann's constant (1.38×10^{-23} J/K), and T is the temperature in Kelvin. The parameter I is the ionic strength of the medium,

$$I = \frac{1}{2}\sum_i z_i^2 c_i\,, \tag{8}$$

where z_i is the valence of ion i and c_i is its concentration. The ▶Debye length is historically written as an inverse length (i. e. κ has units of m^{-1}). In typical biological buffers, the Debye length is between 1 – 10 nm.

Key Research Findings

Free Solution Electrophoresis

The first key physical phenomenon to consider is the electrophoresis of colloidal particles and polyelectrolytes in free solution. The use of the term free solution here implies two assumptions: the particles are very far from any boundaries and the particles are sufficiently dilute so that they do not interact with one another. Free solution results are generally applicable for electrophoresis in an empty microchannel, provided that the particles are not too large relative to the smallest dimension of the channel. As a rule of thumb, the particle radius (or the radius of gyration, in the case of polyelectrolytes) should be at least one order of magnitude less than the smallest channel dimension. As systems move towards the nanoscale, the interactions with the walls (and other effects of confinement) will become increasingly important.

Consider first the electrophoresis of the colloidal particle of charge Q and radius a depicted in Fig. 3. As mentioned above, the particle dissociates into a single large, charged species (the macroion) and a number of small counterions. Since these species have different charges, they will move in opposite directions with respect to the electric field. Determining the electrophoretic mobility of a charged colloidal particle for an arbitrary Debye layer thickness is a daunting task. However, two simple limits can be computed relatively easily. The following two derivations follow very closely from Ref. [3].

In the case where the Debye layer is very large relative to the particle size, i. e. when $\kappa a \to 0$, then the counterions are distributed uniformly throughout space. As a result,

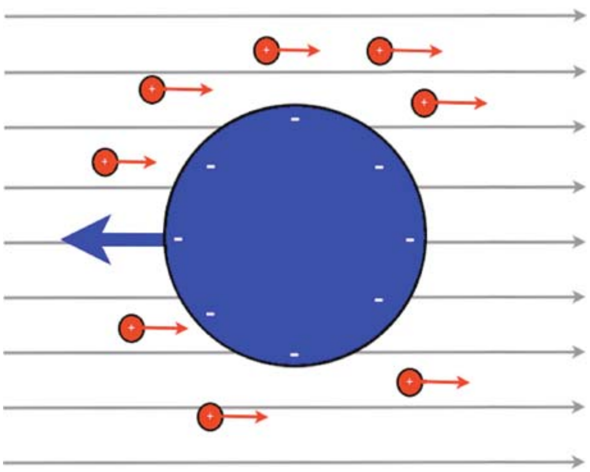

Electrophoresis, Figure 3 Schematic of the electrophoresis of a rigid colloidal particle. The electric field acts on both the counterions and the macroion, resulting in relative motion in opposite directions

their motion does not affect the motion of the colloidal particle and the electrophoretic mobility is given by Eqs. (5) and (6). We can further simplify this by noting that, for a spherical particle of total charge Q, Gauss's law requires that the particle's charge create an electric field

$$E = \frac{Q}{4\pi\varepsilon\varepsilon_0 r^2} \tag{9}$$

that decays like $1/r^2$ as we move away from a Gauss surface centered on and enclosing the particle. The potential ψ is related to the electric field by

$$E = -\nabla\psi\,. \tag{10}$$

In spherical coordinates, the potential at the surface of the particle is thus given by

$$\psi_\mathrm{s} = \int_a^\infty E\,\mathrm{d}r\,, \tag{11}$$

where we have set the potential at infinity to be zero. Integrating, we find the potential to be

$$\psi_\mathrm{s} = \frac{Q}{4\pi\varepsilon\varepsilon_0 a}\,. \tag{12}$$

If we assume that the drag on the sphere is given by Stokes Law,

$$\xi = 6\pi\eta a\,, \tag{13}$$

then substituting Eqs. (12)–(13) into Eq. (6) furnishes the mobility

$$\mu = \frac{2\varepsilon\varepsilon_0\psi_\mathrm{s}}{3\eta}\,. \tag{14}$$

While Eq. (14) is aesthetically pleasing, it is not particularly useful in practice for two reasons. First, although we can define a surface potential ψ_s for our calculation, in general it is not possible to measure the surface potential directly. Second, the presence of adsorbed counterions and oriented water in the Stern layer leads to an immobile layer immediately proximate to the sphere. To circumvent these problems, we define a zeta-potential, ζ. The zeta potential is a phenomenological parameter, which is often associated with the electrical potential at the edge of the Debye layer closest to the particle surface. Alternatively, the zeta-potential can be defined as the potential at the so-called "shear plane," i. e. the point at which the fluid begins to move at a different velocity than the sphere. In

principle, the zeta potential could be measured by electrophoresis through Eqs. (17) or (22), although it is normally determined by static methods (see ▶ zeta potential measurements).

As the Stern layer is quite thin, we can take the zeta-potential to be

$$\zeta = \psi(\delta + a)\,, \tag{15}$$

i. e. the potential ψ at some distance $a + \delta$ from the sphere center, where $\delta \ll a$. Returning to Eq. (11), we now have

$$\zeta = \int_{a+\delta}^{\infty} E\,\mathrm{d}r\,, \tag{16}$$

where the electric field E is still given by Eq. (9). Noting the thinness of the Stern layer relative to the particle size, the zeta potential is given approximately by Eq. (12), where upon the mobility in the infinite Debye layer limit is

$$\mu = \frac{2\varepsilon\varepsilon_0\zeta}{3\eta}\,. \tag{17}$$

The other simple result occurs in the opposite limit, $\kappa a \to \infty$, where the thickness of the Debye layer is very small relative to the size of the particle. This is particularly relevant for microfluidic applications in ionic buffers, which is the usual situation for bioanalyses. As the typical Debye layer thickness is several nanometers, the electrophoresis of any micron-sized particle will be governed by this limit.

Outside of the Debye layer, the fluid is electrically neutral. Inside the Debye layer, the fluid obeys the Navier-Stokes equation with an electrical body force

$$\eta\frac{\mathrm{d}^2 u}{\mathrm{d}z^2} + \rho^{(e)}E = 0\,, \tag{18}$$

where $\rho^{(e)}$ is the space charge inside the Debye layer. The latter is related to the electrical potential via Poisson's equation,

$$\varepsilon\varepsilon_0\frac{\mathrm{d}^2\psi}{\mathrm{d}z^2} = -\rho^{(e)}\,. \tag{19}$$

Working in a reference frame that moves with the particle, we require that the fluid velocity at the edge of the Stern layer (where $\psi = \zeta$) vanish due to the no-slip condition. As a result, Eq. (18) and the no-slip condition are satisfied by the fluid velocity

$$u(z) = -\frac{\varepsilon\varepsilon_0}{\eta}[\zeta - \psi(z)]E\,. \tag{20}$$

At the edge of the Debye layer, the potential drops to zero. As a result the bulk fluid is moving at a velocity

$$u = -\frac{\varepsilon\varepsilon_0\zeta}{\eta}E\,, \tag{21}$$

since the body force appearing in Eq. (18) is zero outside of the Debye layer. If we switch our frame of reference and consider a particle moving in an otherwise quiescent fluid, then the particle moves in the opposite direction to the fluid with a mobility

$$\mu = \frac{\varepsilon_0\varepsilon_\mathrm{b}\zeta}{\eta}\,. \tag{22}$$

Equation (22) reveals an important feature of electrophoresis in the small Debye layer limit: the electrophoretic mobility is independent of the size of the particle. As a result, particles of any size will move at the same speed in free solution. This is a desirable feature when the goal is to move the particles to different locations on a chip. On the other hand, Eq. (22) implies that the common task of sorting colloidal particles by size cannot be accomplished by free-solution electrophoresis.

Now consider the case of flexible polyelectrolytes such as DNA. There are two dominant hydrodynamic models for polymer motion, the Rouse model and the Zimm model [4]. In the Rouse model, the different parts of the chain are assumed to be hydrodynamically independent, so that the total friction of the chain is simply the sum of the friction of each segment. The Rouse model is also referred to as freely draining, since the polymer chain appears to be hollow to the fluid. The Zimm model includes both the Rouse friction of the individual segments with the fluid and the hydrodynamic interactions between different segments. The Zimm model is not freely draining; the polymer appears as a solid object to the surrounding fluid.

During electrophoresis in free solution, polyelectrolytes are freely draining and exhibit Rouse-like behavior. The reason for the absence of hydrodynamic interactions during electrophoresis is the exponential decay of electrostatic effects; the very thin Debye layer surrounding the polyelectrolyte screens the hydrodynamic interactions and allows each segment to act individually [2]. Thus, if the chain consists of N segments with charge q per segment, the total electrical force acting on the chain is

$$F_\mathrm{e} = qNE\,. \tag{23}$$

Likewise, if the friction on each segment is given by ξ, then the total frictional force on the chain will be given by

$$F_\mathrm{f} = -N\xi v\,. \tag{24}$$

Noting that these two forces balance one another, and making use of the definition in Eq. (6), the electrophoretic mobility of long polyelectrolytes is thereby independent of molecular weight,

$$\mu = \frac{v}{E} = \frac{qN}{N\xi} \sim N^0 \,. \tag{25}$$

The free solution electrophoresis of long polyelectrolytes is thus qualitatively the same as colloidal particles; all chains will move at the same speed, independent of molecular weight. Note that the latter scaling for the mobility does not hold for the diffusion coefficient. Polyelectrolyte chains still diffuse with a molecular weight-dependent Zimm diffusivity [4].

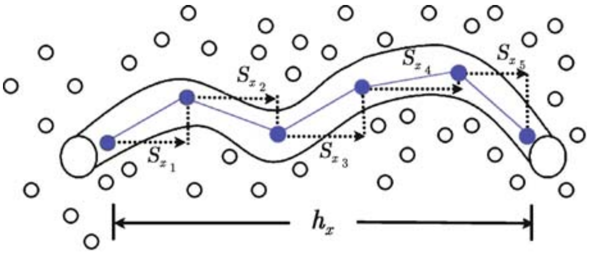

Electrophoresis, Figure 4 When a long polyelectrolyte like DNA is electrophoresed through a gel, the fibers of the gel confine the DNA to a reptation tube. The force acting on each segment of the tube depends on the orientation vector s_x of that segment in the electric field. The total projection of the chain, h_x, is the sum of the orientation vectors (Eq. (16)). The net velocity of the chain is computed from the average motion of the chain through many tubes, each of which has a different projection h_x

Gel Electrophoresis: Separating Polyelectrolytes by Size

The above discussion makes clear that colloidal particles and polyelectrolytes cannot be separated by size during free solution electrophoresis. As a result, many electrophoretic size separations for chemistry and biology are performed in gels. The precision afforded by microfabrication has led to miniaturized version of these classic protocols, as well as a number of novel separation techniques that differ distinctly from the separation principles prevailing in gels [5]. In order to best understand the current research in microfluidic separations of colloids and polyelectrolytes, in particular the important applications to protein and DNA separations, it is important to first understand the physics of gel electrophoresis.

For small particles, such as colloids and collapsed proteins, the dominant separation mechanism is Ogston sieving [1]. The underlying hypothesis behind the Ogston model is that the electrophoretic mobility is equal to the free volume available to that particle. In principle, this free volume argument should account for both the reduction in entropy due to excluded volume effects as well as the fact that large particles will run into "dead ends" in the gel. Although the Ogston hypothesis does not explicitly account for these effects, it nonetheless provides a useful model for the electrophoresis of globular particles in gels. The result of the model is that the mobility of a particle of size a in a gel of concentration c is given by

$$\frac{\mu(a, c)}{\mu(a, 0)} = \exp[-K(a)c] \,, \tag{26}$$

where $K(a) \sim a + R_{\text{fiber}}$ is the retardation factor, with R_{fiber} the size of the gel fibers.

The precision of micro- and nanofabrication should allow this model to be tested in well-controlled systems. Indeed, theoretical work by Slater and coworkers has questioned the validity of the Ogston model through a number of studies of electrophoresis in regular arrays of obstacles (see [6] and subsequent papers in this series).

Although their free-solution behaviors are similar, flexible molecules (like DNA and denatured proteins) exhibit dramatically different behavior in a sieving matrix. Once the size of the pores in the gel becomes small relative to the radius of gyration of the polyelectrolyte chain, the polyelectrolyte chain must uncoil in order to move through the gel. Although the uncoiling process is entropically unfavorable (since it reduces the number of available conformations for the chain), the entropy loss is offset by the reduction in the electrical potential energy as the chain moves in the field.

The mobility of flexible chains in gels is well described by the biased reptation model [1], which is indicated schematically in Fig. 4. In the model, the fibers of the gel are coarse-grained into a ►reptation tube that confines the chain. The chain thus slithers along the tube contour (the reptation part) under the influence of the electric field, which provides a tendency for the slithering motion to be in the direction of the electric field (the biased part).

The electrophoretic mobility can be computed from the picture presented in Fig. 4. The electric field exerts a force $\hat{q}Es_x$ on each segment of the chain, which depends on the orientation s_x of the segment in the direction of the electric field and its charge per unit length, $\hat{q}$. The total electric force acting on the chain is the sum of the force acting on each segment,

$$F_e = \sum (\hat{q}E)s_x \,. \tag{27}$$

As indicated in Fig. 4, the total projection of the chain is given by

$$h_x = \sum s_x \,, \tag{28}$$

whereupon the total electric force is given by summing the forces over the whole chain,

$$F_{\mathrm{e}} = QE\frac{h_{\mathrm{x}}}{L} \,. \tag{29}$$

In the latter, Q is the total charge of the chain and L is its contour length. The curvilinear friction counters the electrical force,

$$F_{\mathrm{f}} = -\xi_{\mathrm{c}} v_{\mathrm{c}} \,, \tag{30}$$

where ξ_{c} is the friction coefficient for motion along the contour at a velocity v_{c}. Balancing the friction against the electrical force, the velocity along the tube contour is thus

$$v_{\mathrm{c}} = \frac{F}{\xi_{\mathrm{c}}} = \frac{QEh_{\mathrm{x}}}{\xi_{\mathrm{c}} L} = \frac{\mu_0 E h_{\mathrm{x}}}{L} \,, \tag{31}$$

where the free solution mobility μ_0 is defined to be $\mu_0 = Q/\xi_{\mathrm{c}}$, analogous to Eq. (6). The time required to move through the tube is

$$t = \frac{L}{v_{\mathrm{c}}} \,, \tag{32}$$

during which time the chain has moved a distance h_{x} in the direction of the field. As a result, the velocity in the x-direction through a tube with an extension h_{x} is

$$v_{\mathrm{x}} = \mu_0 E \left(\frac{h_{\mathrm{x}}}{L}\right)^2 \,. \tag{33}$$

After the motion through many such tubes, the electrophoretic mobility is given by the average of the velocity in each tube divided by the field,

$$\frac{\mu}{\mu_0} = \frac{\langle h_x^2 \rangle}{L^2} \,, \tag{34}$$

where $\langle \cdots \rangle$ represents the average over many tubes. Albeit overly simplistic [1], the analysis leading to Eq. (34) qualitatively captures much of the key phenomena observed experimentally. As indicated in Fig. 5, when the field acting on the chain is weak, then the chain is not strongly deformed and retains its Gaussian conformation (with a size proportional to $L^{1/2}$). The average conformation is thus a random walk. The reptation tubes have the average extension

$$\langle h_{\mathrm{x}}^2 \rangle \sim L \,, \tag{35}$$

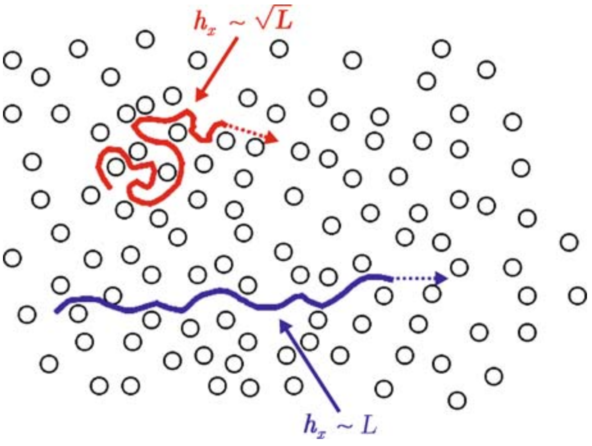

Electrophoresis, Figure 5 Illustration of biased reptation with and without orientation. For weak fields and small chains (as indicated in the upper red figure), the electric field does not strongly perturb the conformation of the chain and it remains in a Gaussian coil. The projection of the coil in the direction of the field thus scales like $L^{1/2}$ for a chain of length L. For long DNA or strong fields (as indicated in the lower blue figure), the chain tends to be come oriented in the direction of the electric field. The projection of the chain then scales like its total length L

and the mobility depends on molecular weight. If the field is strong, then the chain is strongly extended and the tubes are almost fully extended and

$$\langle h_{\mathrm{x}}^2 \rangle \sim L^2 \,. \tag{36}$$

As a result, the separation is lost and all chains will move at the same speed. These scaling results agree well with experiments, and the so-called compression band, where all of the long chains co-migrate, is a major limitation of gel electrophoresis. As a result, a great deal of effort in microfluidics and nanofluidics research has focused on designing systems which permit the separation of long DNA and other polyelectrolyte chains by methods other than biased reptation.

The Joule Heating Problem and Applying Microscale Electric Fields

In addition to the difficulties in electrophoretically separating particles by size, a second challenge in electrophoresis is Joule heating. The heat generated by a conducting solution is given by Joule's law,

$$W_{\mathrm{Joule}} = \sigma E^2 \tag{37}$$

where σ is the conductivity of the fluid. Heating can be catastrophic for electrophoretic processes; non-uniform changes of temperature lead to viscosity gradients, which

in turn result in strong convective currents that can overwhelm the electrophoretic motion. In practice, Joule heating leads to a smearing of the separation bands (or a single plug of solute) and limits the maximum electric field that can be applied.

Microfluidics and nanofluidics offer an excellent solution to the Joule heating problem. The Joule heat must be removed from the system by thermal diffusion. The diffusive heat flux for a temperature drop ΔT across a channel of size w is given by

$$W_{\text{diff}} \sim k\frac{\Delta T}{w^2}\,, \tag{38}$$

where k is the thermal conductivity of the solution. If these two heat fluxes [Eqs. (37) and (38)] are balanced, then the maximum permissible electric field scales like the inverse of the channel width. As a result, much higher electric fields (and thus faster electrophoretic velocities) are possible as the channel sizes are reduced. As microfluidic and nanofluidic systems also require transporting the solute over small distances, the total gain in process speed can be significant.

Joule heating is not the only problem associated with applying strong electric fields. In typical microsystem applications, the electric field is applied via platinum electrodes inserted into the various reservoirs on the chip. The application of the field leads to electrolysis of the water (i. e., the dissociation of water into oxygen and hydrogen) and bubble formation. When large reservoirs are used, the bubbles are generally not troublesome because they will rise to the top of the reservoir and exit the system. Indeed, electrolysis and Joule heating have long been recognized as problems in conventional gel electrophoresis, but the large size of the system and buffer recirculation can relieve the problem to some extent. These are not options for microsystems. When small reservoirs are used or the electrodes are located inside a channel system, the resultant bubble formation can be catastrophic. The bubbles are very difficult to remove from the system, clogging the channels and causing sharp changes in the channel current.

Examples of Application

Electrophoretic separation of small charged species was one of the earliest applications of Lab-on-a-Chip and microfluidics. Indeed, the paper [7] that introduced the term µTAS (micro-total analysis system) dealt primarily with the electric field limits imposed by Joule heating. Microfluidic electrophoresis leads to tremendous gains in the separation time and strongly reduces the amount of sample consumed on chip.

Microfluidics and nanofluidics have also lead to a number of new separation techniques for long DNA that circumvent the limits of gel separations [5]. One of the simplest approaches is to make an artificial gel by microfabricating an array of posts [8]. In this strategy, the post diameters are commensurate with the radius of gyration of the long DNA ($\sim 1\ \mu$m), whereas the posts are spaced by several microns. As a result, the DNA no longer needs to unwind and reptate through the artificial gel. Rather, the motion is governed by a cyclic process of collisions with the posts, unraveling and unhooking of the chain in a rope-over-pulley process, and then motion towards the next post. These dynamics are referred to as geometration, because they resemble the motion of an inchworm, and the motion can be analyzed by continuous time random walk theory [9]. Post arrays are but one example of the different electrophoretic separation techniques that have been proposed [5].

Cross References

- ▶ Lattice Poisson-Boltzmann Method, Analysis of Electroosmotic Microfluidics
- ▶ Dielectrophoresis
- ▶ Electrokinetic Motion of Cells and Nonpolarizable Particles
- ▶ Electrokinetic Motion of Heterogeneous Particles
- ▶ Electroosmotic Flow (DC)
- ▶ AC Electro-Osmotic Flow
- ▶ Electrophoretic Transport in Nanofluidic Channels
- ▶ Two-Dimensional Electrophoresis
- ▶ Zeta Potential Measurement

References

1. Viovy JL (2000) Electrophoresis of DNA and other polyelectrolytes: Physical mechanisms. Rev Mod Phys 72:813–872
2. Manning GS (1978) The molecular theory of polyelectrolyte solutions with applications to the electrostatic properties of polynucleotides. Quart Rev Biophys 11:179–246
3. Russel WB, Saville DA, Schowalter WR (1989) Colloidal Dispersions. Cambridge University Press, Cambridge
4. Doi M, Edwards SF (1986) The Theory of Polymer Dynamics. Oxford University Press, Oxford
5. Slater GW, Guillouzic S, Gauthier MG, Mercier JF, Kenward M, McCormick LC, Tessier F (2002) Theory of DNA electrophoresis ($\sim$ 1999–2002$^1/_2$). Electrophoresis 23:3791–3816
6. Slater GW, Guo HL (1996) An exactly solvable Ogston model of gel electrophoresis: I. The role of symmetry and randomness of the gel structure. Electrophoresis 17:977–988
7. Manz A, Graber N, Widmer HM (1990) Miniaturized total chemical analysis systems: a novel concept for chemical sensing. Sensors and Actuators B 1:244–248
8. Volkmuth WD, Austin RH (1992) DNA electrophoresis in microlithographic arrays. Nature 358:600–602

9. Minc N, Viovy JL, Dorfman KD (2005) Non-Markovian transport of DNA in microfluidic post arrays. Phys Rev Lett 94:198105

Electrophoresis of the Second Kind

Synonyms

Nonlinear electrophoresis; Superfast electrophoresis

Definition

Electrophoresis of the second kind refers to the nonlinear electrokinetic motion of a conducting particle passing a superlimiting current, due to electro-osmotic flow of the second kind.

Cross References

► Electrical Double Layers
► Electrokinetic Motion of Polarizable Particles
► Electroosmotic Flow (DC)
► AC Electro-Osmotic Flow
► Electrophoresis
► Electroosmosis of the Second Kind
► Induced-Charge Electro-Osmosis
► Induced-Charge Electrophoresis
► Nonlinear Electrokinetic Phenomena
► Super-Limiting Current

Electrophoretic Flow

► Electrophoretic Transport in Nanofluidic Channels

Electrophoretic Mobility

Definition

Velocity acquired by an ion per unit applied electric field.

Cross References

► Electrokinetic Flow and Ion Transport in Nanochannels

Electrophoretic Transport in Nanofluidic Channels

SUBRATA ROY[1], HARIBALAN KUMAR[2], RAMESH AGARWAL[3]

[1] Department of Mechanical and Aerospace Engineering, University of Florida, Gainesville, IA, USA
[2] Seamans Center for the Engineering Arts and Sciences, University of Iowa, Iowa City, IA, USA
[3] Aerospace Research and Education Center (AeREC) and Aerospace Engineering Program, Washington University, St. Louis, MO, USA
roy@ufl.edu, haribalan-kumar@uiowa.edu, rka@me.wustl.edu

Synonyms

Ion transport; Electrophoretic flow

Definition

The motion of electrically charged particles or molecules in a stationary medium under the influence of an electric field is called electrophoresis. In such transport the electric force is applied through a potential difference between electrodes. Selective use of the Lorentz force by applying a magnetic field can also induce such movement. Electrophoresis and electroosmosis are two key modalities of electrokinetic transport which are very useful in micro- and nanofluidics for a variety of applications including biomedical (bio-NEMS, etc.), fuel cell and micro total analysis systems (μ-TASs). In electroosmosis the bulk fluid moves due to the existence of a charged double layer at the solid–liquid interface. While one-dimensional electrophoresis is more commonly used, two-dimensional electrophoresis may also become a useful tool for the separation of gel proteins based on isoelectric property.

Overview

Let us consider an aqueous solution of a salt. A fraction of the salt dissociates into ions. Negatively charged ions are called anions, while positive ions are called cations. Such an ionic solution is called an electrolyte. If two electrodes are kept at a potential gap in such an electrolyte, the dissociated ions migrate towards oppositely charged electrodes at their characteristic speeds. Anions move towards the positive electrode, while cations are attracted by the negative electrode. The velocity and the number density of ions directly influence the electric current which increases with the strength of the electric field. Similar transport can also occur in a protein mixture that contains several charged species based on its degree of acidity. Chemical and electrical interactions may also occur during such transport. The electrons move across the electrochemical interface between the electrode and the electrolyte. The study of such migration of charged particles with or without the

movement of carrier fluid under an applied electromotive force is of great interest to biological systems, fuel cells and microelectronics [1, 2].

The history of electrokinetic transport is over 200 years old [1]. In 1771 Italian physician and physicist Luigi Galvani reported twitching of frog legs due to an electric arc. Twenty years later Allessandro Volta introduced a relationship between the potential difference and the electric force, and explained the twitching of frog legs using the concept of electrolytes. In 1884 Swedish chemist Svante Arrhenius wrote a thesis on galvanic conductivity of electrolytes which concluded that in water electrolytes dissociate into electrically positive (cation) and negative (anion) ions. His theory was inadequate for strong electrolytes. About 40 years later the Debye–Hückel theory was formulated for dilute ionic solutions. From then on, theoretical studies focused more on concentrated solutions involving large numbers of ions. Such problems include ion transport in the Stern layer, where finding a description for angstrom-scale models and related transport properties remains a challenge. Proper understanding of electrokinetic processes at this scale requires numerical modeling. Hjert'en [3] introduced electrophoresis through small capillaries. This was developed later over the next three decades by various groups.

The electrokinetic process in a small capillary is strongly influenced by the charge–surface interaction. For example, a selective surface ('gate') biasing in electrophoresis can influence directed charge transport resulting in specific charge depletion. Recently, Daiguji et al. [4] considered such electrophoretic transport in a nanochannel as a possible control device similar to a metal-oxide-semiconductor field effect transistor (MOSFET). Formation of the electric double layer is an important characteristic of a type of electrokinetic process, namely electroosmosis [5]. When negatively charged walls of a nanochannel come in contact with an electrolyte, the positive ions of the solution are attracted towards the surface as negative ions are repelled. Such redistribution creates a selective gradient of ions forming double layers called Stern or diffuse layers.

The ratio of electroosmotic to electrophoretic current increases as the surface charge density increases. Experimental study of Qiao and Aluru demonstrated that the amount of current flowing through a single-wall carbon nanoube channel can be modulated by five orders of magnitude by changing the voltage applied to a gate [6]. Our objective is to identify the effect of gate potential in selective electrokinetic transport of ions and to realize its potential for filtration of biological fluids. Similar but more extensive work for diffusion-limited patterning has been done recently by Karnik et al. [7].

Basic Methodology

The study of fluid behavior in nano-confinement is a relatively new research arena. The ratio of surface area to volume becomes extremely large at such small scales in which the non-dimensional Reynolds number Re is also typically low (< 1) and the flow remains laminar. Diaguji et al. [4] mention that, except for steric interactions, intermolecular interactions like van der Waals force and electrostatic force can be modeled as continua. Specifically, the continuum dynamics is an adequate description of liquid transport for length scales higher than 5 nm. In that context we aim to employ a hydrodynamic model to simulate ionic species transport through a 30 nm high nanofluidic channel with a reservoir upstream and a sink downstream.

This arrangement is similar to the field effect transistors in electronics where current flows along a semiconductor channel from the source electrode at one end to the drain electrode at the other end. A small voltage perturbation to a control electrode (gate) along the channel can cause large current change in the channel. Here we maintain the walls of the channel at negative bias. The distribution of ionic densities of aqueous solution and the resulting electric potential in the channel will be calculated using draft diffusion formulation. The product of the charge density and the electric field is incorporated into the fluid dynamic Navier–Stokes equation as the electrostatic body force to study the flow velocity change inside the channel. The channel height is orders of magnitude higher than the Stern layer thickness and thus neglected from detailed calculation.

We use a 5 μm long channel filled with KCl aqueous solution. Two reservoirs, $1\,\mu\text{m} \times 1\,\mu\text{m}$, are attached to either side of the channel. The channel is 30 nm in height. The problem of charge transport through the nanochannel is modeled using hydrodynamic equations for the ionic species. A 10^{-4} M ($\sim 6.022 \times 10^{22}\ \text{m}^{-3}$) aqueous solution of KCl is in contact with the walls of a silicon tube. The Debye length of ions is in the range of $500-40$ nm for ion density of $10^{-4}-10^{-2}$ M within the channel. When the height of the channel is smaller than the Debye length, the ionic current due to electrophoresis is dominant. For a given channel, as the charge density of wall surface increases, ionic current due to electroosmosis also becomes dominant and hence cannot be neglected [6]. The drift-diffusion-based Nernst–Planck approximation is utilized to represent the current (J) due to ionic species:

$$J_K = -eD_{\text{K}}\left(\nabla n_{\text{K}} + \frac{n_{\text{K}}}{kT}\nabla\phi\right), \quad (1)$$

$$J_{\text{Cl}} = -eD_{\text{Cl}}\left(\nabla n_{\text{Cl}} - \frac{n_{\text{Cl}}}{kT}\nabla\phi\right). \quad (2)$$

Here, n is the number density, ϕ is the potential, e is the electronic charge, D is diffusion coefficient of the ionic species and T is temperature in K. The Poisson equation represents charge difference as a function of potential in the system as

$$\nabla^2\phi = -\frac{e}{\varepsilon}(n_K - n_{Cl}) \ . \tag{3}$$

The system of Eqs. (1)–(3) is closed using the continuity equation

$$\nabla . J_K = 0 \quad \text{and} \quad \nabla . J_{Cl} = 0 \, . \tag{4}$$

Temperature of the ionic species (T) is 298 K. The permittivity of KCl aqueous solution (ε) is 7×10^{-10} $C^2/(N\,m^2)$. For steady, low Reynolds number incompressible flow in the absence of external pressure gradient, the Navier–Stokes equation gets modified into

$$\nabla . \ (\mu \nabla u) + e\,(n_K - n_{Cl})\,E = 0 \tag{5}$$

where u is the velocity and μ is the dynamic viscosity.

The boundary conditions on various edges of the model are summarized in Table 1. In the reservoir all edges are fixed as Dirichlet boundaries based on the bulk density and fixed reservoir potential. Along the walls of the nanochannel, insulation current condition is ensured. This requires that the gradient of the ionic charge density be a function of potential gradient based on Eqs. (1) and (2). For the potential Eq. (3), the flux is specified based on the charge density σ on the surface of the nanochannel wall. For the velocity Eq. (5), a no-slip condition is imposed at the channel wall.

Figure 1 shows the schematic of the channel. The nature of the domain involving abrupt changes in aspect ratio of the geometry from a micrometer-size reservoir to nanometer-size channel introduces considerable numerical complexity into the problem. We used a maximum aspect ratio of about 248 in this case, which occurs near the center of the channel. This may be acceptable as the center does not create adverse concentration or potential gradients due to the symmetric nature of the geometry. We used a Galerkin *weak* formulation-based finite element method for solving Eqs. (1)–(5) in a self-consistent fashion. The details of the numerical procedures are given in our earlier work [8].

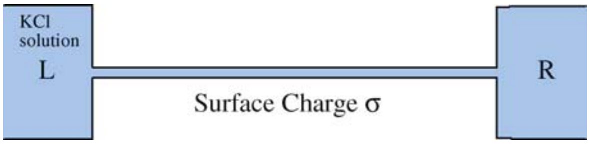

Electrophoretic Transport in Nanofluidic Channels, Figure 1
Schematic of a nanochannel for electrophoretic transport

Figures 2 and 3 show the distribution of normalized positive (K^+) and negative (Cl^-) ion number densities at steady state for surface charge of $\sigma = -10^{-3}$and -2×10^{-3} C/m^2 respectively on the channel wall. The distribution is plotted along the channel centerline (left) and across the mid-section of the channel (right). The left reservoir is at 0 V while the right reservoir is maintained at 1 V. As is evident from Fig. 2, the K^+ ion density is nine times more than that of Cl^- for $-1\,mC/m^2$ surface charge. Thus, the channel becomes a net unipolar (positively biased) solution of ions to neutralize the negative surface charge. A similar characteristic is also true for $\sigma = -2\,mC/m^2$, although in this case the ratio of positive to negative ions has nearly doubled. Interestingly, this trend continues for even higher negative wall bias.

Figure 4 plots the numerical results for $\sigma = -5\,mC/m^2$. Here the concentration of cations is about 40 times higher than that of the (negligible) anions making the channel essentially unipolar. The crosswise distribution of potential at the mid-section shows a sheath structure near the surface for all three cases (Figs. 2, 3 and 4). As expected the wall region is nearly devoid of anions for increasing surface charges. A sharp rise in the cation number density near the wall is also noticeable especially for $\sigma = -5\,mC/m^2$ (Fig. 4). Interesting effects in controlling the transport may be observed as one applies a gate charge σ_g along with the surface charge σ. The charge gradient due to net charge difference of $(\sigma - \sigma_g)$ over the surface affects the transport. For example, in Fig. 5 application of $\sigma_g = 0\,mC/m^2$ for $\sigma = -1\,mC/m^2$ leads to the Cl^- transport nearly tripling while the K^+ is quenched to only a third of its original density. This is uniquely suitable for separation of ions in a bio-transistor.

Electrophoretic Transport in Nanofluidic Channels, Table 1 Boundary conditions

Edge	Positive ion density	Negative ion density	Potential (V)
Boundary edges of left reservoir (L)	Bulk concentration	Bulk concentration	0
Boundary edges of right reservoir (R)	Bulk concentration	Bulk concentration	1
Nanochannel wall (σ = surface charge density)	$\nabla n_K = -\frac{en_K}{kT}\nabla\phi$	$\nabla n_{Cl} = \frac{en_{Cl}}{kT}\nabla\phi$	$\nabla\phi = -\frac{\sigma}{\varepsilon_0}$

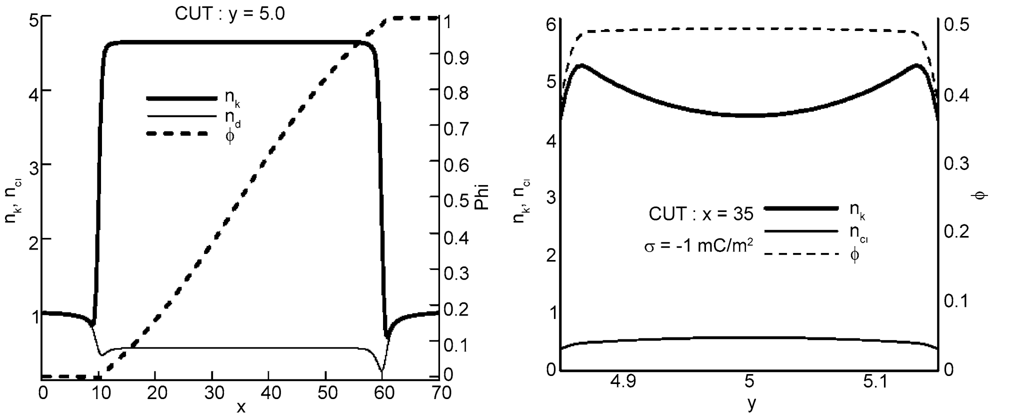

Electrophoretic Transport in Nanofluidic Channels, Figure 2 Results of simulation along the line of symmetry for surface charge density of $-1\ \mathrm{mC/m^2}$

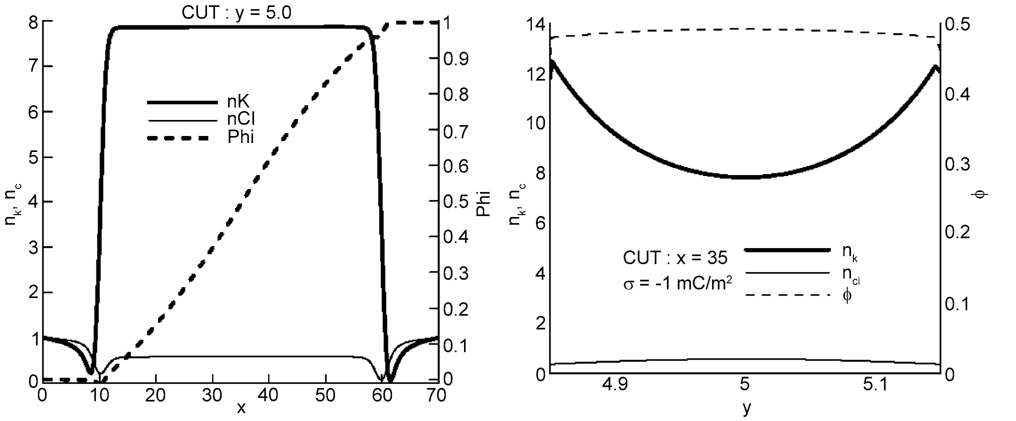

Electrophoretic Transport in Nanofluidic Channels, Figure 3 Results of simulation along the line of symmetry for surface charge density of $-2\ \mathrm{mC/m^2}$

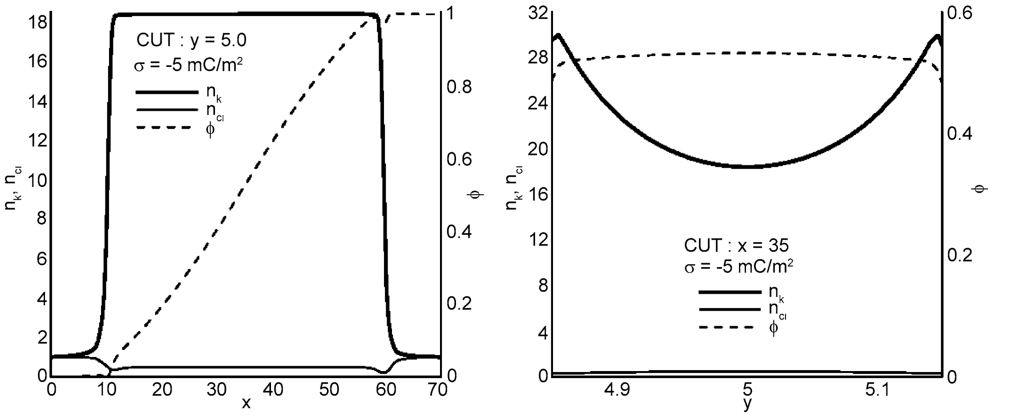

Electrophoretic Transport in Nanofluidic Channels, Figure 4 Results of simulation along the line of symmetry for surface charge density of $-5\ \mathrm{mC/m^2}$

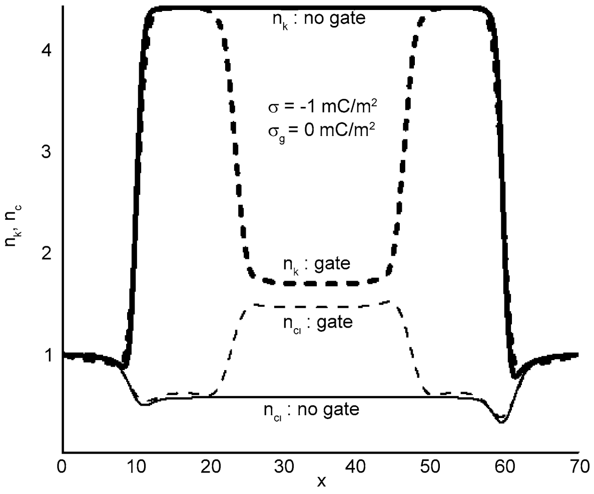

Electrophoretic Transport in Nanofluidic Channels, Figure 5 Application of gate charge significantly affects ion transport

Key Research Findings

We investigated the influence of surface charge in ion transport – a subject yet to be fully explored despite extensive recent research. We found the application of a surface charge gradient can significantly influence the local distribution of ion concentration in a nano-confinement. The accumulation of unipolar ions in the channel tries to neutralize the surface bias. A two-dimensional simulation demonstrated that selected ions can be attracted towards the wall region based on the charge density and polarity. The fluidic motion of the ions is also considered using an electrostatic force augmented Navier–Stokes formulation. The velocity distributions in streamwise and crosswise directions show a two-dimensional nature for high surface charge. Such charge separation is useful in many biomolecular applications.

Future Directions for Research

While significant experimental and theoretical studies have been done on the subject, consideration of the wall region (Stern double layer) will be required for capturing the physical processes governing such electrokinetic transport. For complicated tortuous nanochannels with realistic scales this is a modeling challenge. Similarly, detailed analysis is needed for understanding the two-dimensional electrophoresis specifically for a practical gel. A recent study [9] identified the design optimum of gate potential applied through a biased surface of a nanochannel for the most effective transport. Such sensitivity of the control mechanism needs to be carefully optimized.

Cross References

- ► AC Dielectrophoresis Lab-on-Chip Devices
- ► AC Electro-Osmotic Flow
- ► Dielectrophoresis
- ► Electrokinetic Flow
- ► Electrokinetic Flow and Ion Transport in Nanochannels
- ► Electrokinetic Flow in Porous Media
- ► Electroosmotic Flow (DC)
- ► Electrophoresis
- ► Nonlinear Electrokinetic Phenomena

References

1. Gouaux E, MacKinnon R (2005) Science 310:1461
2. Kagan CR, Mitzi DB, Dimitrakopoulos CD (1999) Science 286:945
3. Hjert'en S (1967) Free zone electrophoresis. Chromatogr Rev 9:122
4. Daiguji H, Yang P, Majumdar A (2004) Nano Lett 4:137
5. Ghosal S (2006) Annu Rev Fluid Mech 38:309
6. Conlisk AT, McFerran J, Zheng Z, Hansford D (2002) Anal Chem 74:2139
7. Qiao R, Aluru NR (2003) J Chem Phys 118:4692
8. Martel R, Schmidt T, Shea HR, Hertel T, Avouris P (1998) Appl Phys Lett 73:2447
9. Karnik R, Castelino K, Duan C, Majumdar A (2006) Nano Lett 6(8):1735
10. Roy S, Raju R, Chuang H, Kruden B, Meyyappan M (2003) J Appl Phys 93(8):4870–4879
11. Cooper SM, Cruden B, Meyyappan M, Raju R, Roy S (2004) Nano Lett 4(2):377–381
12. Roy S, Kumar H Electro-kinetic Control of Ions in Biological Fluids. Appl Phys Lett (in review)

Electroporation

Synonyms

Electropermeabilization

Definition

Electroporation is a technique in which an external electric field is applied to biological cells, causing an increase in cellular membrane permeability. Electroporation is often used as a means to transfect cells with extracellular material (e. g., with DNA in solution); it can also be used to permanently disrupt the cell membrane and effectively lyse the cell.

Cross References

- ► On-chip Cell Lysis
- ► Single Cell Analysis in Microfluidics

Electrospray Emitter on-Chip

► On-Chip Electrospray

Electrospray Ionization

Synonyms

ESI

Definition

Electrospray ionization (ESI) is one of two “soft” ionization techniques used to introduce biological samples into a mass spectrometer. In ESI, an electric field is applied to a solution of analyte to form a spray of charged droplets. Subsequent solvent evaporation and ion release enables analysis by MS. The developer of ESI (along with the developers of MALDI) was awarded the 2002 Nobel Prize in Chemistry.

Cross References

► Interfaces Between Microfluidics and Mass Spectrometry
► Mass Spectrometry
► Mass Spectrometry on Chip Devices

Electrospray Ionization-Mass Spectrometry (ESI-MS)

► On-Chip Electrospray

Electrospray Mass Spectrometry

► On-Chip Electrospray

Electrostatic Bonding

► Anodic Bonding

Electrostatic Quadrupole

► Quadrupole Filter

Electrostatic Valves

Markus Arnold, Heinz Kück
HSG-IMAT, Hahn-Schickard-Gesellschaft, Institute for Microassembly Technology, Stuttgart, Germany
arnold@hsg-imat.de, kueck@hsg-imat.de

E

Synonyms

Microvalve

Definition

Electrostatic valves are microvalves that utilize the electrostatic force that is generated in the electric field of the actuator, for switching the valve.

Overview

Electrostatic valves are microvalves that are driven by utilizing electrostatic forces. These valves can be suitable in industrial automation and medical engineering. The use of an electrostatic force as a valve drive is limited to a volume smaller than a few cm^3 due to scaling effects between electrostatic force and weight. The electrostatic valves are produced from silicon or in a new approach from metal-coated polymer materials using technologies for Moulded Interconnect Devices. The electrostatic drive is designed as a comb drive, where the actuator and housing are designed with electrodes, which are immersed into each other without an electrical contact. An electric field is formed by applying an electric voltage between the actuator and the housing and generates an attracting force always. The magnitude of the force can be estimated as the gradient of the stored energy. The energy in the electric field W_{el} is calculated in accordance with Eq. (1).

$$W_{el} = \frac{1}{2}CU^2 , \quad (1)$$

where C defines the capacitor and U is the voltage between the electrodes. The capacitance C is calculated from the electrode surface area A and the distance d between the electrodes (see Fig. 1). Not taking into account the stray fields and using the dielectric permittivity ε_0 of air the capacitance can be calculated in accordance with Eq. (2) as:

$$C = \frac{\varepsilon_0 A}{d} \quad (2)$$

The acting force F is calculated from the gradient of the energy W_{el} corresponding to the direction of motion in

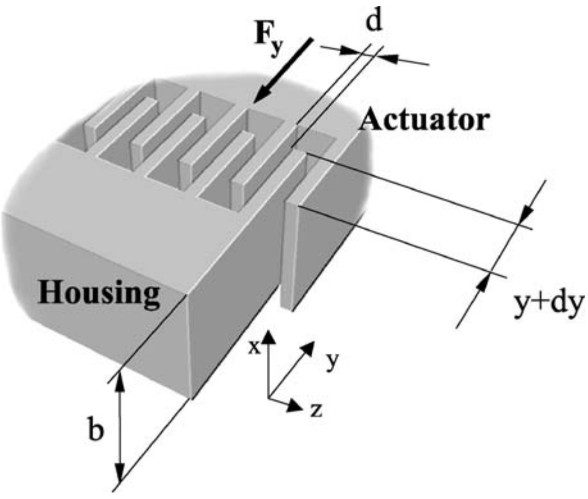

Electrostatic Valves, Figure 1 Comb drive structure

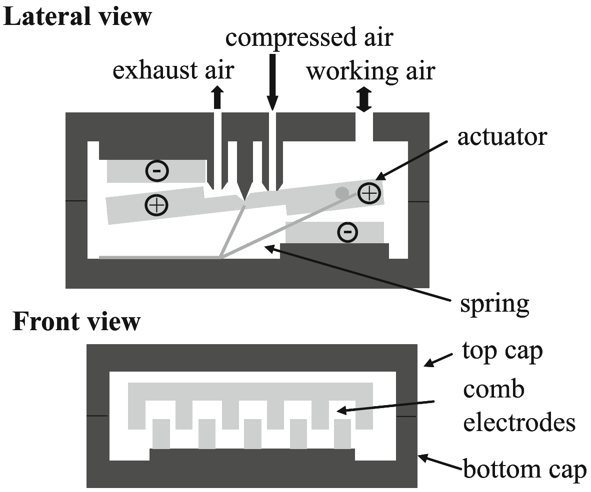

Electrostatic Valves, Figure 2 Schematic view of an electrostatic valve

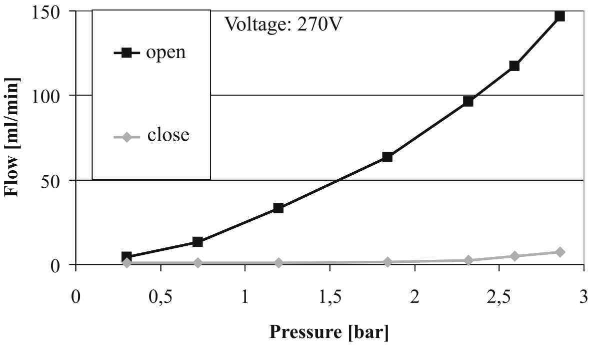

Electrostatic Valves, Figure 3 Flow vs. pressure at compressed air supply

accordance with Eq. (3) as:

$$F = \left| \frac{dW_{el}}{dy} \right| = \left| \frac{1}{2} U^2 \frac{\varepsilon_0}{d} b \right| \quad (3)$$

where b is the width of the electrodes [1].

Figure 2 shows a schematic of one type of an electrostatic valve. The top and bottom form the housing of the valve in which an actuator is disposed in such a manner that it will be rotated. Both the actuator and the housing comprise comb drive electrodes. In the initial position, the actuator is rotated by the pretensioned restoring spring in such a way that the compressed air supply is closed. A torque is generated by applying an electric voltage between the comb electrodes of the actuator and the housing, and moves the actuator into its second position. This rotary motion of the actuator opens the compressed air supply and simultaneously closes the exhaust air connection and deflects the restoring spring. After switching off and grounding the electric voltage, the electrostatic force completely drops and the potential energy of the restoring spring moves the actuator into its initial position. The compressed air supply is thereby closed and the exhaust air connection is simultaneously opened such that the working air can escape through the exhaust air connection [2].

A remarkable feature of electrostatically driven valves is the comparatively low electric power consumption of a few µW. The small construction size also results in a small dead volume during switching. It must be noted that the maximum electric operating voltage is limited by the breakdown voltage of the insulating layer between the electrodes, which depends on the fluid, the operating pressure and the distance between the electrodes [3].

The valve described in [1] is made from metal plated plastic and has a volume of 1.7 cm^3. Figure 3 shows the flow characteristics versus the pressure of the compressed air supply. In the initial position the valve is leak tight up to a pressure of 2 bar. The cycle time of the valve was found to be in the range of a few ms.

Cross References

- ► Electrochemical Valves
- ► Electromagnetic Valves
- ► Microactuators
- ► Piezoelectric Valves
- ► Pneumatic Valves
- ► Thermomechanical Valves
- ► Thermopneumatic Valves

References

1. Arnold M et al (2007) Elektrostatisch angetriebenes Mikroventil in MID-Technik. Innovative Klein- und Mikroantriebstechnik, Augsburg, 12–13 June 2007
2. Arnold M et al (2003) Fabrication of an Electrostatic Miniature Valve from Metallized Microinjection Molded Polymers. MICRO.tec, Munich, 13–15 Oct 2003
3. von Münch W (1993) Werkstoffe der Elektrotechnik, 7th edn. Teubner, Stuttgart

Electrostrictive

Definition

Strain-electric field coupling induced by the formation of dipoles within the material either via applied strain or electric field which are then used to generate a further strain or electric field within the material based on a change in the applied electric field or strain, respectively. Generally, the electric fields as a quadratic function of the applied strain in electrostrictive materials. Many non-conducting materials are electrostrictive, though usually weak. The buzzing sound in the ballast of fluorescent lights is due to this phenomenon. Relaxor ferroelectrics like the especially important, single-crystal PMN-PT have especially large electrostrictive coupling coefficients and actually provide larger responses than the best piezoelectric materials.

Cross References

► Relaxor ferroelectrics

Electrothermal Effects

Suman Chakraborty
Department of Mechanical Engineering,
Indian Institute of Technology, Kharagpur, India
suman@mech.iitkgp.ernet.in

Synonyms

Electrothermal flow

Definition

Electrothermal flows originate from the temperature gradient in a medium, which is generated as a consequence of the Joule heating effects. This temperature gradient induces local gradients in conductivity, permittivity, density and viscosity, which in turn, give rise to net forces which act on the liquid. For instance, conductivity gradients produce free volumetric charges and Coulombic forces, whereas permittivity gradients produce dielectric forces.

Overview

One can express the electrical force per unit volume in the following general form [1]:

$$f_e = \rho_e \boldsymbol{E} - \frac{1}{2}\boldsymbol{E}^2 \nabla\varepsilon + \frac{1}{2}\nabla\left(\rho \frac{\partial\varepsilon}{\partial\rho}\boldsymbol{E}^2\right) \tag{1}$$

where ρ_e is the volumetric charge density, $\boldsymbol{E}$ is the electric field strength, ε is the permittivity and ρ is the density of the medium. The first and second terms on the right-hand side of Eq. (1) are the Coulombic and dielectric forces, respectively. The last term is the electrostriction. As it is the gradient of a scalar, it can be combined with the pressure gradient term in the Navier–Stokes equation. For an incompressible fluid, this has no additional effect on the fluid dynamics, and accordingly, this term will be neglected in the subsequent analysis. The relative contributions of the first two terms in Eq. (1) can be assessed by adding a small perturbation field, $\boldsymbol{E}_1$, over and above the applied electric field, $\boldsymbol{E}_0$, such that $\boldsymbol{E} = \boldsymbol{E}_0 + \boldsymbol{E}_1$, with $|\boldsymbol{E}_1| \ll |\boldsymbol{E}_0|$. Noting that the charge density is given by the Poisson equation

$$\nabla\cdot(\varepsilon\boldsymbol{E}) = \rho_e \tag{2}$$

one can write

$$\nabla\cdot\left(\varepsilon\left(\boldsymbol{E}_0 + \boldsymbol{E}_1\right)\right) = \rho_e\,,$$

or equivalently

$$\nabla\varepsilon\cdot\boldsymbol{E}_0 + \nabla\varepsilon\cdot\boldsymbol{E}_1 + \varepsilon\nabla\cdot\boldsymbol{E}_0 + \varepsilon\nabla\cdot\boldsymbol{E}_1 = \rho_e\,. \tag{3a}$$

Since $\nabla\cdot\boldsymbol{E}_0 = 0$ and $|\boldsymbol{E}_1| \ll |\boldsymbol{E}_0|$, Eq. (3a) reduces to the following approximate form:

$$\nabla\varepsilon\cdot\boldsymbol{E}_0 + \varepsilon\nabla\cdot\boldsymbol{E}_1 = \rho_e\,. \tag{3b}$$

Using Eq. (3b) in Eq. (1) one obtains

$$f_e = \left(\nabla\varepsilon\cdot\boldsymbol{E}_0 + \varepsilon\nabla\cdot\boldsymbol{E}_1\right)\boldsymbol{E}_0 - \frac{1}{2}\boldsymbol{E}_0^2\nabla\varepsilon\,. \tag{4}$$

The charge conservation equation can be written in the following form:

$$\nabla\cdot\boldsymbol{J} + \frac{\partial\rho_e}{\partial t} = 0 \tag{5a}$$

where

$$\boldsymbol{J} = \underbrace{\sigma \boldsymbol{E}}_{\text{conduction current}} + \underbrace{\rho_e \boldsymbol{v}}_{\text{convection current}} \tag{5b}$$

where σ is the electrical conductivity. The relative contributions of conduction and convection currents in Eq. (5a) can be assessed by comparing the divergence of the convection charge with the divergence of the ohmic current

$$\frac{|\nabla \cdot (\rho_e \boldsymbol{v})|}{|\nabla \cdot (\sigma \boldsymbol{E})|} \approx \frac{|\rho_e \boldsymbol{v}|}{|\sigma \boldsymbol{E}|} = \frac{|\nabla \cdot (\varepsilon \boldsymbol{E})\, \boldsymbol{v}|}{|\sigma \boldsymbol{E}|} \approx \frac{\varepsilon v}{\sigma l}. \tag{6}$$

In Eq. (6), l and $\boldsymbol{v}$ are the length and velocity scales for the physical problem under consideration. Equation (6) can also be interpreted as the ratio of two timescales, namely, $t_{\text{relax}} = \varepsilon/\sigma$ and $t_{\text{advection}} = l/v$, where t_{relax} is the charge relaxation timescale and $t_{\text{advection}}$ is the advection timescale. With a typical value of $l \sim 10\,\mu\text{m}$ and $v \sim 200\,\mu\text{m s}^{-1}$, $t_{\text{advection}}$ is of the order of 0.1 s, which is several orders of magnitude higher than the typical values of t_{relax} in an aqueous solution. Thus, $\nabla \cdot (\rho_e \boldsymbol{v})$ can be neglected in comparison to $\nabla \cdot (\sigma \boldsymbol{E})$ in Eq. (5a). Accordingly, with the help of Eq. (3b), Eq. (5a) can be rewritten as (noting that $|\boldsymbol{E}_1| \ll |\boldsymbol{E}_0|$)

$$\nabla \sigma \bullet \boldsymbol{E}_0 + \sigma \nabla \bullet \boldsymbol{E}_1 + \frac{\partial \left(\nabla \varepsilon \bullet \boldsymbol{E}_0 + \varepsilon \nabla \bullet \boldsymbol{E}_1 \right)}{\partial t} = 0 \tag{7}$$

Assuming a time-varying electric field of the form

$$\boldsymbol{E}_0\,(t) = \text{Re}\big(\boldsymbol{E}_0 \exp\,(j\omega t)\big) \tag{8}$$

where $\boldsymbol{E}_0$ is the time-independent component (amplitude) of the unperturbed electric field, one obtains, from Eq. (7)

$$\nabla \sigma \cdot \boldsymbol{E}_0 + j\omega \nabla \varepsilon \cdot \boldsymbol{E}_0 + \sigma \nabla \cdot \boldsymbol{E}_1 + j\omega \varepsilon \nabla \cdot \boldsymbol{E}_1 = 0 \tag{9}$$

The divergence of the perturbation field can be obtained from Eq. (9) as

$$\nabla \cdot \boldsymbol{E}_1 = \frac{-\left(\nabla \sigma + j\omega \nabla \varepsilon\right) \cdot \boldsymbol{E}_0}{\sigma + j\omega \varepsilon} \tag{10}$$

Assuming that the liquid does not respond to the instantaneous value of the force at the frequency of the electric field, one can obtain the time-average of Eq. (4) and thus obtain

$$\langle f_e \rangle = \frac{1}{2}\text{Re}\left(\left(\nabla \varepsilon \cdot \boldsymbol{E}_0 + \varepsilon \nabla \cdot \boldsymbol{E}_1 \right) \boldsymbol{E}_0^* - \frac{1}{2} \boldsymbol{E}_0^2 \nabla \varepsilon \right) \tag{11}$$

where $\boldsymbol{E}_0^*$ is the complex conjugate of $\boldsymbol{E}_0$. Substituting Eq. (10) into Eq. (11), one obtains

$$\langle f_e \rangle = \frac{1}{2}\text{Re}\left[\left\{ \frac{(\sigma \nabla \varepsilon - \varepsilon \nabla \sigma) \cdot \boldsymbol{E}_0}{\sigma + j\omega \varepsilon} \right\} \boldsymbol{E}_0^* - \frac{1}{2} |\boldsymbol{E}_0|^2 \nabla \varepsilon \right] \tag{12}$$

For real $\boldsymbol{E}_0$, Eq. (12) can be simplified as [2]

$$\langle f_e \rangle = -\frac{1}{2} \left(\underbrace{\left(\frac{\nabla \sigma}{\sigma} - \frac{\nabla \varepsilon}{\varepsilon} \right) \cdot \boldsymbol{E}_0 \frac{\varepsilon \boldsymbol{E}_0}{1 + (\omega \tau)^2}}_{\text{Coulomb force}} + \underbrace{\frac{1}{2} |\boldsymbol{E}_0|^2 \nabla \varepsilon}_{\text{Dielectric force}} \right) \tag{13}$$

where $\tau = \varepsilon/\sigma$ is the charge relaxation time ($= t_{\text{relax}}$). The Coulombic force dominates in certain frequency ranges, but in other ranges the dielectric force dominates. At a certain frequency, say f_c, these two forces are of equal strength. This frequency can be estimated from Eq. (13) (noting that $\nabla \sigma = (\partial \sigma)/(\partial T) \nabla T$, $\nabla \varepsilon = (\partial \varepsilon)/(\partial T) \nabla T$), to yield

$$\omega_c = 2\pi f_c \approx \frac{1}{\tau} \left(\frac{2 \left| \frac{1}{\sigma} \frac{\partial \sigma}{\partial T} \right|}{\left| \frac{1}{\varepsilon} \frac{\partial \varepsilon}{\partial T} \right|} \right)^{\frac{1}{2}} \tag{14}$$

For water, $(1/\sigma)(\partial \sigma/\partial T) = 2\%$ per K and $(1/\varepsilon)(\partial \varepsilon/\partial T) = -0.4\%$ per K [2], for which $2\pi f_c \tau \approx \sqrt{10}$. In an order of magnitude sense, thus, $f_c \sim 1/\tau$, or $f_c = \sigma/\varepsilon$. For $f \gg \sigma/\varepsilon$ (typically high frequencies), the dielectric force dominates, whereas for $f \ll \sigma/\varepsilon$ (low frequencies) the Coulombic force dominates.

A detailed derivation of a comprehensive mathematical model of electrothermal effects has been presented in the review by Ramos et al. [2]. A brief description of the mathematical model is outlined here, for the sake of completeness. Following the analysis by Ramos et al. [2], simple analytical estimates of the electrothermal forces on a liquid can be obtained by considering two thin parallel metallic plates, with a very small interelectrode gap. The plates are covered in a dielectric liquid and are subjected to a potential difference of V across the gap, which sets up an electric field $\boldsymbol{E}\,(r, \theta)$ (see Fig. 1). Neglecting end effects, this electric field can be expressed as

$$\boldsymbol{E} = \frac{V}{\pi r} \boldsymbol{n}_\theta \tag{15}$$

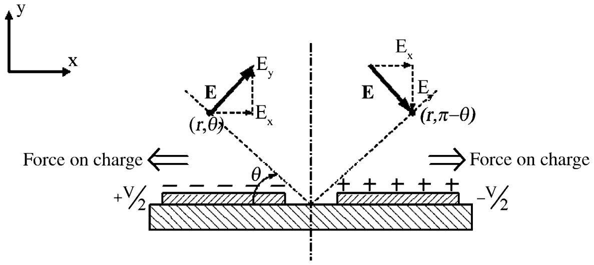

Electrothermal Effects, Figure 1 Two parallel plates with a small inter-electrode gapwhich is covered by a dielectric. A potential V is applied across the gap in the direction as shown

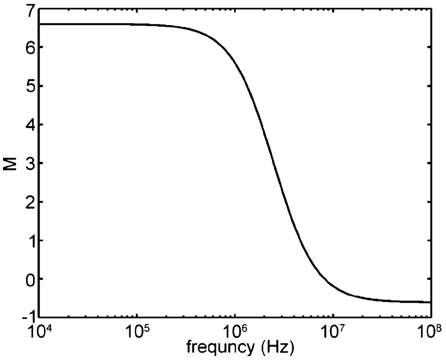

Electrothermal Effects, Figure 2 Magnitude of the factor $M(\omega, t)$ as a function of frequency

The corresponding energy dissipation per unit volume (σE^2) can be introduced into the governing equation of energy conservation as a volumetric source term, to yield

$$\frac{k}{r}\frac{\partial}{\partial r}\left(r\frac{\partial T}{\partial r}\right)+\frac{k}{r^2}\frac{\partial^2 T}{\partial\theta^2}+\frac{\sigma V^2}{\pi^2 r^2}=0 \tag{16a}$$

where k is the thermal conductivity of the liquid. Writing $T^* = T + (\sigma V^2\theta^2/2\pi^2 k)$, one can express Eq. (16a) in the form

$$\frac{k}{r}\frac{\partial}{\partial r}\left(r\frac{\partial T^*}{\partial r}\right)+\frac{k}{r^2}\frac{\partial^2 T^*}{\partial\theta^2}=0 \tag{16b}$$

Assuming that the electrodes act as thermal baths, i. e., $T = 0$ (a suitably chosen reference temperature) for $\theta = 0, \pi$, one can conclude that T^* is independent of r, which implies that

$$\frac{\partial^2 T^*}{\partial\theta^2}=0 \tag{16b}$$

A general solution Eq. (16b) can be obtained in the form

$$T^* = a_0\theta + b_0 \tag{17}$$

where a_0 and b_0 are obtained from the boundary conditions at $\theta = 0, \pi$, as $a_0 = (\sigma V^2/2\pi k)$ and $b_0 = 0$. Thus

$$T=\frac{\sigma V^2\theta}{2\pi k}-\frac{\sigma V^2\theta^2}{2\pi^2 k} \tag{18}$$

The maximum temperature occurs at $\theta = \frac{\pi}{2}$, as $T_{\max} = (\sigma V^2/8k)$. It is important to note that for the calculation of electrothermal forces, the most critical factor is not merely the temperature itself but also its gradient. The latter can be estimated from Eq. (18) as

$$\nabla T=\frac{\sigma V^2}{2\pi k}\left(1-\frac{2\theta}{\pi}\right)\frac{1}{r}\boldsymbol{n}_\theta \tag{19}$$

Equation (19) can be substituted in Eq. (13), with $\nabla\sigma = (\partial\sigma/\partial T)\nabla T$, $\nabla\varepsilon = (\partial\varepsilon/\partial T)\nabla T$, to yield

$$\langle f_e\rangle = -M(\omega, T)\frac{\sigma\varepsilon V_{\mathrm{rms}}^4}{2k\pi^3 r^3 T}\left(1-\frac{2\theta}{\pi}\right)\boldsymbol{n}_\theta \tag{20}$$

Here

$$M(\omega, T)=\left[\frac{\frac{T}{\sigma}\frac{\partial\sigma}{\partial T}-\frac{T}{\varepsilon}\frac{\partial\varepsilon}{\partial T}}{1+(\omega\tau)^2}+\frac{1}{2}\frac{T}{\varepsilon}\frac{\partial\varepsilon}{\partial T}\right] \tag{21}$$

is a dimensionless factor describing the variation of the time-averaged electrothermal force as a function of the applied frequency and the prevailing temperature. A plot of $M(\omega, T)$ as a function of frequency is shown in Fig. 2, with $T = 300$ K. The parameters considered for plotting this figure are as follows: $(1/\sigma)(\partial\sigma/\partial T) = 2\%$ per K, $(1/\varepsilon)(\partial\varepsilon/\partial T) = -0.4\%$ per K, $\sigma = 0.01\ \mathrm{Sm}^{-1}$, $\varepsilon = 640 \times 10^{-12}\ \mathrm{C^2/N{\cdot}m^2}$. It can be observed from the figure that M is positive for low frequencies, whereas it is negative for higher frequencies. For low frequencies, the force is dominated by the space charge and the flow occurs in the manner which is represented schematically in Fig. 3. At frequencies greater than the critical frequency, on the other hand, the flow direction is reversed and the liquid streams up in the center of the gap between the two electrodes. However, these conclusions are only valid if the interelectrode gap is infinitesimally narrow. For finite interelectrode spacings, a numerical solution of the fluid flow equations may be necessary to reveal the underlying flow picture.

In order to obtain analytical expressions for the velocity field of the physical problem described above, one can begin with the equation of motion (Navier–Stokes equation) in the steady state

$$-\nabla p+\eta\nabla^2\boldsymbol{v}+\langle f_e\rangle=0 \tag{22}$$

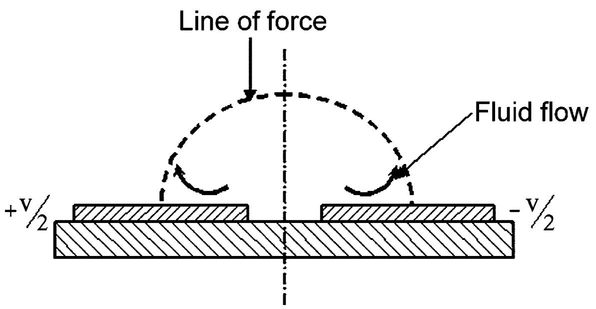

Electrothermal Effects, Figure 3 Flow patterns for frequencies below the charge relaxation frequency of the liquid

where η is the fluid viscosity and $\langle f_e \rangle$ is given by Eq. (20). One can eliminate the pressure gradient term from Eq. (22) by partially differentiating the r- and θ-components of that equation with respect to θ and r, respectively, and subtracting the two resultant equations, to obtain

$$-\eta \nabla^4 \psi + (\nabla \times \langle \boldsymbol{f}_e \rangle) \cdot \boldsymbol{n}_z = 0 \tag{23}$$

where $\boldsymbol{n}_z$ is a unit vector in the z-direction and $\boldsymbol{v} = \nabla \times (\psi \boldsymbol{n}_z)$. Incorporating the expression for $\langle f_e \rangle$ from Eq. (20) in Eq. (23), one can write

$$\left(\frac{1}{r} \frac{\partial}{\partial r} \left(r \frac{\partial}{\partial r} \right) + \frac{1}{r^2} \frac{\partial^2}{\partial \theta^2} \right)^2 \psi = \frac{2C}{r^4} \left(1 - \frac{2\theta}{\pi} \right) \tag{24}$$

where

$$C = M(\omega, T) \frac{\sigma \varepsilon V_{rms}^4}{2k\pi^3 T \eta}$$

Similarly to the considerations for the solution of the energy equation, one can also note that $\psi = \psi(\theta)$.This leads to the following general solution of Eq. (24):

$$\psi = -\frac{C}{2} \left(\frac{\theta^2}{2} - \frac{\theta^3}{3\pi} \right) + A_1 \sin 2\theta + A_2 \cos 2\theta + A_3 \theta + A_4 \tag{25}$$

where A_i are arbitrary independent constants of integration. Their values can be obtained by imposing the following boundary conditions:

$$\begin{aligned} &\psi = 0 \quad \text{at } \theta = 0, \pi \\ &\frac{\partial^2 \psi}{\partial \theta^2} = 0 \quad \text{at } \theta = 0, \pi/2 \quad \text{(from symmetry)} \end{aligned} \tag{26}$$

This gives the final solution of ψ as

$$\psi = -\frac{C}{2} \left(\frac{\theta^2}{2} - \frac{\theta^3}{3\pi} \right) - \frac{C\pi}{24} (\sin 2\theta - 2\theta) \tag{27}$$

The velocity distribution can be obtained from the above expression, as follows:

$$v_r = \frac{1}{r} \frac{\partial \psi}{\partial \theta} = \frac{C}{r} \left(-\frac{1}{2} \left(\theta - \frac{\theta^2}{\pi} \right) - \frac{\pi}{12} (\cos 2\theta - 1) \right) \tag{28}$$

It can be observed from Eq. (28) that $v_r = v_r|_{max} = (\pi C/24r)$ at $\theta = \frac{\pi}{2}$. Also, $v_r = 0$ at $\theta = 0.286\pi$ and $\theta = 0.714\pi$.

Key Research Findings

It is interesting to compare the electrothermal flow velocity (v_{fluid}) with the dielectrophoretic velocity (v_{DEP}) of submicron-size charged particles suspended in the aqueous medium. It should be noted that the time-averaged dielectrophoretic force on a particle of radius R can be described as $\langle \boldsymbol{F}_{DEP}(t) \rangle = 2\pi \varepsilon_m R^3 Re[K(\omega)] \nabla |\boldsymbol{E}_{rms}|^2$, where ε_m is the permittivity of the dielectric medium, $K(\omega)$ is the Clausius–Mossotti factor, given by $K(\omega) = (\tilde{\varepsilon}_p - \tilde{\varepsilon}_m)/(\tilde{\varepsilon}_p + 2\tilde{\varepsilon}_m)$. $\tilde{\varepsilon}_p$ and $\tilde{\varepsilon}_m$ are the complex permittivities of the particle and the medium, respectively ($\tilde{\varepsilon} = \varepsilon - j(\sigma/\omega)$), and $\nabla |\boldsymbol{E}_{rms}|^2$is the gradient of the square of the r.m.s electric field. Thus, one can compare the electrothermal and dieleletrophoretic flow velocities as

$$\frac{v_{fluid}}{v_{DEP}} \propto \frac{M(\omega, T)}{\mathrm{Re}[K(\omega)]} \frac{\sigma V_{rms}^2 r^2}{kTR^2} \tag{29}$$

This implies that the electrothermal flow velocity increases in proportion to the electrical conductivity of the medium. Not only that, the dielectrophoretic force also dominates near the electrode edges ($r \to 0$). On the other hand, the influence of the electrothermal forces becomes progressively stronger for larger particles.

The electrothermal effects in microflows can also be modulated by illuminating the electrodes with fluorescent light, as has been observed by Green et al. [3]. They described the importance of the illumination in generating the fluid flow, and found that the flow was dependent on both the intensity of illumination and the applied electric field. They also compared the theoretical estimates of the electrothermally induced flow velocities with their experimental observations. A reasonable agreement was found between the experiments and the theory, with the light

generating temperature gradients, and therefore gradients in the fluid permittivity and conductivity, and the electric field being responsible for the motive force. Although there may be several mechanisms through which the light could produce heat in the system, some of these mechanisms could be excluded by the experimental conditions that were used. For example, because an infrared filter was used the possibility of infrared heating was eliminated. Further, although the fluorescent particles could gain energy through the absorption/re-emission process and could generate heat, no global temperature gradients could be generated in this process, since the particles were uniformly distributed. One of the major reasons for the electrothermal flow could be the heating of the electrodes by the light, since a percentage of the light was absorbed by the metal during reflection. As the thin electrodes are more thermally resistant than water, the heat could easily be radiated away through the electrolyte, thereby creating temperature, conductivity and permittivity gradients. The electrothermal fluid flow, could therefore be attributed to the interaction between the electric field and these gradients.

Sinton et al. [4] have demonstrated that an axially nonuniform temperature distribution can induce a pressure disturbance, which in turn, can give rise to velocity gradients. This can lead to velocity profiles that are significantly different from the ideal plug-like electroosmotic flow velocity profiles in microchannels. In their experiments, the axial thermal gradients were induced passively by increased dissipation of Joule heat through the optical infrastructure of a viewing window surrounding a capillary. When large fields were applied, their temperature measurements indicated that the temperature of the fluid in the viewed region was as much as 30 °C lower than that elsewhere in the capillary. Despite an increase in viscosity because of this local cooling effect, this also resulted in a locally increased electroosmotic wall velocity, which induced a concave velocity profile in the viewed portion and a convex velocity profile elsewhere.

The electrothermal effects can also be exploited to design efficient microactuators, as has been demonstrated by Li and Uttamchandani [5] who presented a modified design to generate a large deflection and to control the peak temperature of the hot beam of a two-beam asymmetric thermal microactuator. Their analysis revealed that by changing the dimensions of a section of the hot beam, it was possible to achieve a higher average temperature but a lower peak temperature within the beam. Their analysis also demonstrated the effect of the geometry of the hot beam on the temperature distribution, and possible methods of optimization so as to avoid local hot spots which lead to thermal failure.

Future Directions for Research

Although electrothermal flows have been extensively studied in the literature, significant work is yet to be done to examine the interactions between AC electroosmosis and electrothermal flows. Significant research effort also needs to be devoted to investigate the electrothermal flows from a stochastic viewpoint, primarily because of the uncertainties in the various factors that eventually dictate the magnitude and direction of the net body force that acts on the fluid under these conditions.

Cross References

- ► AC Dielectrophoresis Lab-on-Chip Devices
- ► AC Electro-Osmotic Flow
- ► DC-Dielectrophoresis Lab-on-Chip Devices
- ► Dielectrophoresis
- ► Dielectrophoretic Motion of Particles and Cells
- ► Joule Heating in Electrokinetic Flow: Theoretical Methods

References

1. Stratton JA (1941) Electromagnetic Theory. McGraw-Hill, New York
2. Ramos A, Morgan H, Green NG, Castellanos A (1998) AC electrokinetics: a review of forces in microelectrode structures. J Phys D 31:2338–2353
3. Green NG, Ramos A, González A, Castellanos A, Morgan H (2000) Electric field induced fluid flow on microelectrodes: the effect of illumination. J Phys D 33:L13–L17
4. Sinton D, Xuan X, Li D (2004) Thermally induced velocity gradients in electroosmotic microchannel flows: the cooling influence of optical infrastructure. Exp Fluid 37:872–882
5. Li L, Uttamchandani D (2004) Modified asymmetric microelectrothermal actuator: analysis and experimentation. J Micromech Microeng 14:1734–741

Electrothermal Flow

► Electrothermal Effects

Electroviscosity

Definition

For pressure-driven flow of a dilute electrolyte solution in a small microchannel, due to the presence of electric double layer near the channel wall, the flow-induced streaming potential drives the counterions to move in the direction opposite to the pressure drop. These moving counterions drag the surrounding liquid molecules with them. This generates an opposite flow to the pressure-driven flow

and hence a reduced flow rate in the pressure-drop direction. This reduced flow rate seems to suggest that the liquid have an apparent higher viscosity. The apparent viscosity is called the electro-viscosity.

Cross References

► Streaming Current and Electroviscosity

Electrowetting

Leslie Yeo[1], Hsueh-Chia Chang[2]
[1] Micro/Nanophysics Research Laboratory
Department of Mechanical Engineering, Monash University, Clayton, VIC, Australia
[2] Center for Microfluidics and Medical Diagnostics
Department of Chemical & Biomolecular Engineering, University of Notre Dame, Notre Dame, IN, USA
leslie.yeo@eng.monash.edu.au

Synonyms

Electrocapillary effect; Electrowetting on dielectric (EWOD); Electrowetting on insulator coated electrodes (EICE); Electrowetting on line electrodes (ELE)

Definition

Electrowetting concerns the use of an externally applied electric field to actuate or manipulate small volumes of liquid by altering its interfacial tension and hence the macroscopic contact angle or by inducing bulk liquid motion through an interfacial electric stress.

Chemical and Physical Principles

Electrowetting derives its roots from early observations of electrocapillary phenomena by Gabriel Lippmann in 1875, who noted variations in interfacial tension as an electric potential is applied between an electrolyte solution in direct contact with a metal, in this case, mercury. This culminated in the classical Lippmann equation:

$$\left.\frac{\partial\gamma}{\partial V}\right|_{T,p,\mu} = -\frac{CV}{A}\,, \tag{1}$$

where γ is the interfacial tension (between the metal and electrolyte), V the applied potential, T the temperature, p the pressure and μ the chemical potential. The right hand side of Eq. (1) is the surface charge density, where C is the capacitance with cross sectional area A and separation d. Since $C = \varepsilon_0\varepsilon_l A/d$, where ε_0 is the permittivity of free space and ε_l the liquid dielectric constant, Eq. (1) can be written as

$$\Delta\gamma = -\frac{\varepsilon_0\varepsilon_l}{2d}V^2\,. \tag{2}$$

The term on the right hand side of Eq. (2) is hence the electrocapillary force per unit length (linear force density) in the solid plane along the contact line.

Strictly, the term *electrocapillarity* therefore refers to the change in the solid or liquid metal–electrolyte interfacial tension, as shown in Fig. 1a. For the principle to be practical, however, it was necessary to avoid electrolysis of the aqueous solution. This was later overcome by coating the electrode surface with a thin dielectric layer (e. g., polymer substrate) several microns to millimeters in thickness, from which the term *electrowetting-on-dielectric* (EWOD) or *electrowetting on insulator coated electrodes* (EICE) arises [1], as shown in Figs. 1b and 1c. In cases where the insulating layer is not hydrophobic (e. g., parylene), a very thin hydrophobic layer such as a fluoropolymer of order nanometers in thickness, is coated onto the insulator.

In general, the term *electrowetting*, at least for EWOD or EICE configurations in which spontaneous spreading does not occur and hence the contact angles are *static* (we shall deal with the case of *spontaneous electrowetting* below), has traditionally been associated with the change in the macroscopic liquid–solid wetting angle θ subtended at the three-phase contact line where the vapor, liquid and solid phases converge [2]. Henceforth, we shall delineate the distinction between *static* and *spontaneous electrowetting*. A force balance at the contact line (Fig. 2) yields Young's equation,

$$\gamma_{LV}\cos\theta = \gamma_{SV} - \gamma_{SL}\,, \tag{3}$$

where γ_{LV}, γ_{SV} and γ_{SL} are the vapor–liquid, vapor–solid and liquid–solid interfacial tensions, respectively. Substituting Eq. (3) into Eq. (1) with $\gamma = \gamma_{SL}$ gives

$$\frac{\mathrm{d}\cos\theta}{V\,\mathrm{d}V} = \frac{C}{\gamma_{LV}}\,, \tag{4}$$

which then leads to the equivalent Lippmann condition for electrowetting:

$$\cos\theta = \cos\theta_0 + \frac{\varepsilon_0\varepsilon_l V^2}{2d\gamma_{LV}}\,, \tag{5}$$

where θ_0 is the contact angle in the absence of an electric field. The electric field has changed the vapor–liquid surface force and hence altered the static contact angle when all three surface forces balance.

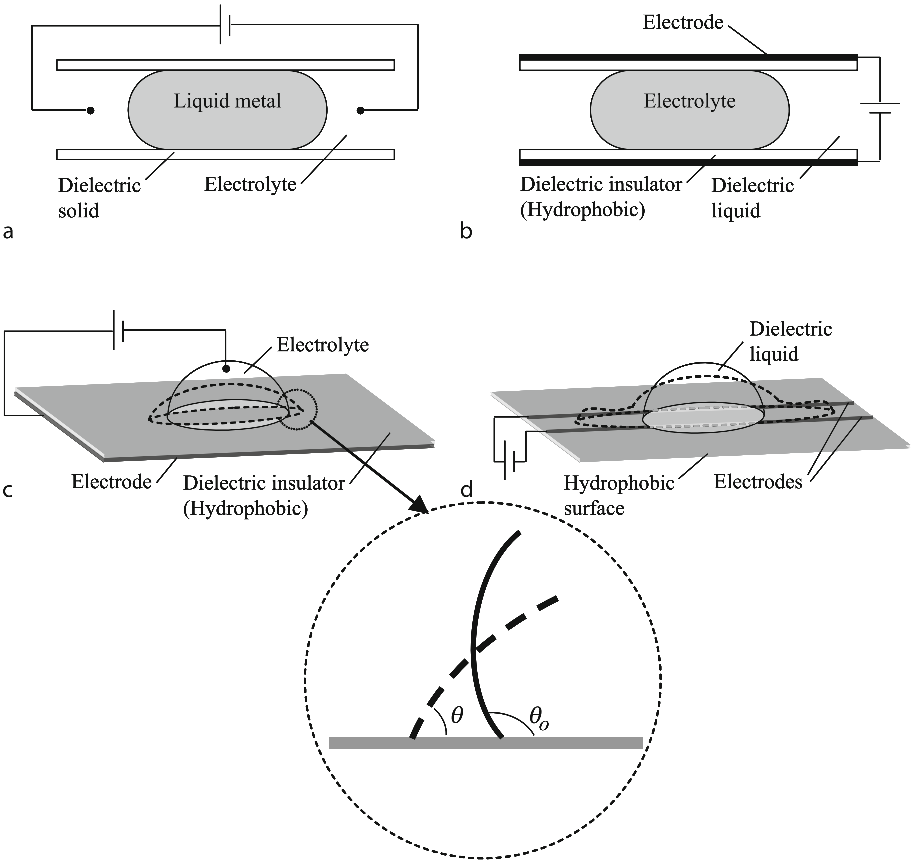

Electrowetting, Figure 1 Schematic illustration of the various electrode configurations used to demonstrate electrocapillary and electrowetting phenomena. (**a**) Electrocapillary phenomena involving a static change in the liquid metal–electrolyte contact angle. (**b**) Dielectric film coated top and bottom plate electrodes giving rise to static changes in the liquid–solid contact angle. (**c**) Dielectric film coated planar plate electrode giving rise to static changes in the liquid–solid contact angle. (**d**) Planar parallel line electrode configuration giving rise to spontaneous and dynamically advancing thin electrowetting films [2]. The inset shows an enlargement of the contact line region for case (**c**) wherein the macroscopic drop contact angle is altered from its equilibrium value θ_0 given by the Young equation to a new equilibrium value θ upon application of an electric field

The incorporation of a dielectric layer would result in a larger potential drop and a corresponding reduction in the capacitance. As most of the potential drop now occurs across the dielectric layer, the Lippmann condition in Eq. (5) can be written as

$$\cos\theta = \cos\theta_0 + \frac{\varepsilon_0\varepsilon_\mathrm{d} V^2}{2d\gamma_\mathrm{LV}}\,, \qquad (6)$$

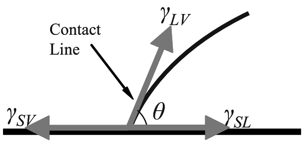

Electrowetting, Figure 2 Surface forces acting at the contact line

where ε_d is the permittivity of the dielectric layer, which is much smaller than ε_l. The above assumes the double layer capacitance, which is in series with the dielectric layer capacitance, to be negligible; this is not unreasonable given that the thickness of the double layer is typically much smaller than the dielectric layer thickness d, at least for conducting liquids. In any case, the reduction in the electric field intensity for electrowetting due to the presence of the dielectric layer requires a larger applied voltage to achieve the same electrowetting effect obtained in the absence of the dielectric layer. However, any increases in the applied voltage is restricted by a threshold voltage above which dielectric breakdown of the material occurs. Dielectric breakdown at these increased applied voltages can however be avoided by employing an AC field with a forcing frequency that is above the inverse of the RC time scale (R being the resistance of the bulk electrolyte

and C the dielectric layer capacitance) such that the potential drop across the dielectric layer is minimized.

Spontaneous electrowetting, in contrast, can arise using the parallel line electrode configuration shown in Fig. 1d, in what we shall term as *electrowetting on line electrodes* (ELE). This was first observed by Jones et al. [3], who noticed that a thin liquid film, several microns thick, is pulled out ahead of the macroscopic spreading drop when an electric potential is applied across the line electrodes, and advances much faster than the macroscopic spreading drop itself. This spontaneous and dynamically advancing film arises due to a bulk electric pressure gradient in the contact line region, which produces a negative capillary pressure that induces bulk liquid to flow into the contact line region, thus spontaneously pushing out a thin electrowetting film ahead of the macroscopic drop [2, 4].

Key Research Findings

Figure 3 shows a typical contact angle response to the applied voltage when the EWOD/EICE configuration is adopted. The observed change in the contact angle is *static* and proportional to the square of the voltage, and thus universally described by the Lippmann condition in Eq. (6) up to a limiting value in the voltage before complete wetting is achieved when deviation begins to occur. This is attributed to contact line saturation. In addition, near the saturation point, contact angle hysteresis is observed: The receding contact angle upon decreasing the voltage is observed to be smaller than the advancing contact angle at increasing voltage. It should be noted that this hysteresis effect is distinct from the usual contact angle hysteresis that occurs in drops on inclined planes, where the receding contact angle is always greater than the advancing contact angle.

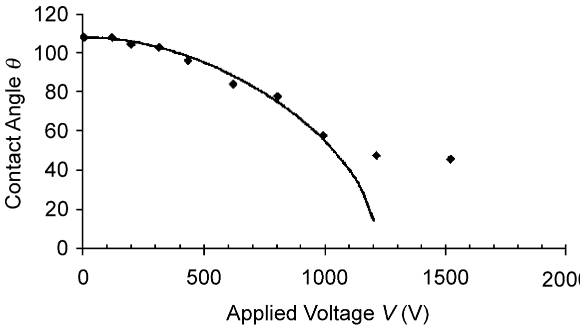

Electrowetting, Figure 3 Typical contact angle/voltage response in electrowetting-on-dielectric (EWOD) experiments. This particular set of experimental data corresponds to a 75 % aqueous glycerol drop sitting above a 100 μm poly(tetrafluoroethylene) dielectric layer under an applied AC field [5]

Contact line saturation has been attributed to several factors, although these are not well understood and it may be possible that these different factors could each give rise to saturation independent of the other [6]. One possible factor is the dielectric breakdown of the atmosphere in the contact line region. When the atmosphere ionizes, the ambient phase no longer acts as an insulator wherein the charges that accumulate at the contact line exert an outwardly directed electric force which gives rise to the spreading. As a result, the leakage of charges into the ambient phase weakens this force, thus suppressing the electrowetting effect [7]. When the ambient medium is water surrounding a dielectric liquid drop, contact line saturation has been suggested to arise due to charge leakage from the aqueous phase into the insulating polymer layer at high field intensities [8]. It has also been suggested that contact angle hysteresis occurs because of the delayed release of these leaked charges from the polymer surface back into the aqueous phase when the voltage is decreased. Several theoretical descriptions have been proposed to describe the electric field induced change in the macroscopic liquid–solid contact angle in *static electrowetting*. These are based on thermodynamic, molecular kinetic, electromechanic and static approaches [2]. Vallet et al. [7] and Kang [9] considered an infinite planar wedge analysis in the three-phase contact line region, as shown in Fig. 4. As the top electrode is in contact with the drop phase, represented by the wedge, it is assumed to be at constant potential, surrounded by a perfectly insulating ambient phase whose permittivity is assumed to be equal to that of the dielectric layer of thickness d. In the absence of free charges, the electrostatic potential in the ambient phase ϕ

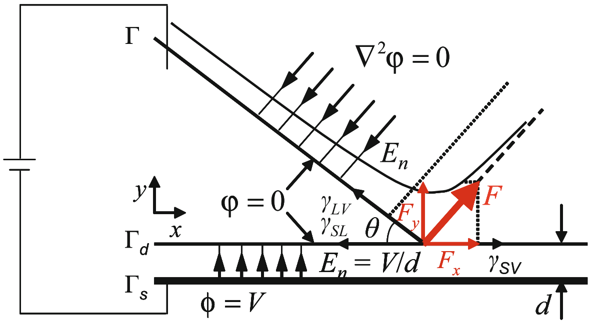

Electrowetting, Figure 4 Schematic illustration of the wedge representing the drop geometry in the contact line region in the *static electrowetting* analysis of [7] and [9]. The black arrows indicate the direction of the field and the light bold arrows indicate the resultant point force and its components at the contact line. The curve depicts the charge density or the normal field intensity along the drop interface which is singular at the tip or the three-phase contact line for all $\theta < \pi$ [2]

then obeys the Laplace equation:

$$\nabla^2\varphi = 0\,. \tag{7}$$

The boundary conditions are stipulated by the constant potential interfaces

$$\varphi = 0 \text{ on } \Gamma \text{ and } \Gamma_\mathrm{d} \qquad \text{and} \qquad \varphi = V \text{ on } \Gamma_\mathrm{s}\,, \tag{8}$$

where Γ, Γ_d and Γ_s denote the interfaces between the drop and the ambient phase, the drop and the dielectric layer and the dielectric layer and solid interfaces, respectively. Solving Eqs. (7) and (8) for small contact angles $\theta \to 0$ then yields a normal interfacial electric field that scales as

$$E_\mathrm{n}|_\Gamma \sim \frac{1}{|r|^{\frac{1}{2}}}\,, \tag{9}$$

where r is the distance along the drop interface away from the wedge tip where the contact line is located.

We note from Eq. (9) that E_n is weakly singular for $\theta < \pi$ and diverges only in a small region with length scale of order d away from the wedge tip. Since the electric pressure scales as $p_\mathrm{e} \sim E_\mathrm{n}^2$, the pressure gradient that arises as a result is localized in this small confined region at the contact line and cannot give rise to any bulk flow below the advancing contact angle. Yeo and Chang [2] also show that the solution of the biharmonic equation for the hydrodynamics within the wedge gives rise to an expression for the hydrodynamic pressure near the wedge tip as $r \to 0$ that is incompatible with the interfacial normal stress jump condition involving a singular electric stress given by Eq. (9), again suggesting the absence of any bulk flow in the contact line region. Moreover, the confined region in which the electric pressure gradient is significant is too small to be resolved in the continuum limit. As such, it is necessary to average out the electric stress, which results in a point electric force at the contact line [9]:

$$F = \frac{\varepsilon_0\varepsilon_\mathrm{d}}{2}\int_\Gamma E_\mathrm{n}^2\,\mathrm{d}r = \frac{\varepsilon_0\varepsilon_\mathrm{d}V^2}{2d}\operatorname{cosec}\theta\,. \tag{10}$$

Decomposing Eq. (10) into its horizontal and vertical components yields

$$F_x = \frac{\varepsilon_0\varepsilon_\mathrm{d}V^2}{2d}\,, \quad \text{and}\,, \quad F_y = \frac{\varepsilon_0\varepsilon_\mathrm{d}V^2}{2d}\cot\theta\,, \tag{11}$$

which, upon balancing the surface forces at the contact line, leads to the recovery of the Lippmann condition in Eq. (6). The electric pressure correction in Eq. (11) therefore accounts for the static change in the macroscopic contact angle. Since the point electric force balances the surface forces exactly, there is no net force and hence no bulk liquid flow into the contact line region. Thus, only a static change in the macroscopic contact angle results; no spontaneous electrowetting film is produced in the absence of any bulk fluid motion, therefore demonstrating why spontaneous electrowetting films cannot be produced when the EWOD/EICE configurations are adopted [2].

Yeo and Chang [4], on the other hand, have derived a lubrication model which couples the electrodynamic and hydrodynamic interactions in order to capture the formation and propagation of a spontaneous electrowetting film. Assuming a liquid with large dielectric constant, the electric field is largely confined to the liquid drop and film sitting on top of the line electrodes, as shown in Fig. 5. At the interface Γ the electric field is therefore predominantly tangential, and any normal field leakage into the ambient phase can be neglected:

$$E_\mathrm{n}|_\Gamma = -\left.\frac{\partial\varphi}{\partial z}\right|_\Gamma = 0\,. \tag{12}$$

At the line electrodes, constant potential conditions apply:

$$\varphi|_{\Gamma_\mathrm{s}} = \pm\frac{V}{2} \quad \text{at} \quad y = \mp\frac{R_\mathrm{e}}{2}\,. \tag{13}$$

In the above, x, y and z are the streamwise, transverse and vertical coordinates, respectively, and, R_e is the electrode separation.

The solution of the Laplace equation in Eq. (7) describing the potential in the liquid phase subject to the boundary conditions given by Eqs. (12) and (13) then yields the following tangential interfacial electric field near the wedge

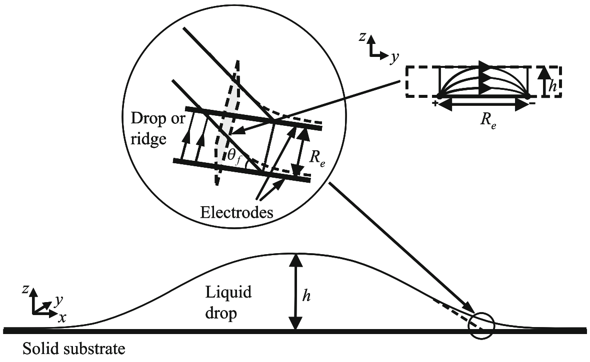

Electrowetting, Figure 5 Schematic depiction of the drop and film geometry for *spontaneous electrowetting* on parallel line electrodes. The inset shows a magnification of the contact line region in which the drop or the capillary ridge of the electrowetting film resembles a wedge-like geometry. A cross-section of this wedge and the transverse field lines arising due to the line electrodes, which resemble two point charges in this plane, is also shown [4]

tip as $h/R_e \to 0$, h being the film thickness:

$$E_t|_\Gamma = \frac{4V}{\pi R_e}\left(1 - \frac{8h^2}{R_e^2}\right) . \quad (14)$$

Given that $p_e \sim E_t^2$ and $h \sim (x_f - x)\tan\theta_f$, where x_f and θ_f are the position and contact angle of the advancing film front, the hydrodynamic pressure in the lubrication limit then reads

$$p = \gamma\frac{\partial^2 h}{\partial x^2} - \frac{8\varepsilon_0\varepsilon_1 V^2}{\pi^2 R_e^2}\left[1 - \frac{16\tan^2\theta_f}{R_e^2}(x_f - x)^2\right] , \quad (15)$$

from which we note that the hydrodynamics is enslaved to the electric field via the film thickness.

We therefore observe from Eq. (14) that the tangential field is maximum at the three-phase contact line where $h = 0$, and decays linearly along the interface away from the contact line at $x = x_f$. Unlike the *static electrowetting* case above, however, the field is non-singular in the contact line region and thus a macroscopic electric pressure gradient arises from the linearly decaying interfacial electric stress. It is this macroscopic electric pressure gradient that is responsible for a negative capillary pressure that forces liquid from the bulk into the contact line region, thus pushing out a thin spontaneous electrowetting film ahead of the macroscopic spreading drop. This is observed in the numerical results shown in Fig. 6a; we note the existence of a critical electric Bond number

$$B = \frac{8\varepsilon_0\varepsilon_1 V^2 L\tilde{L}}{\pi^2\gamma R_e^2 H} , \quad (16)$$

of approximately 10 for the formation of the electrowetting film. In Eq. (16), H and L are the characteristic height and length scales of the drop whereas $\tilde{H}$ and $\tilde{L}$ are those for the advancing film.

A dominant force balance between viscous and electric stresses at the contact line gives

$$\frac{\eta\tilde{U}}{\tilde{H}^2} \sim \frac{p_e}{\tilde{L}} , \quad (17)$$

where η is the viscosity, $\tilde{U} \sim \tilde{L}/T \equiv \gamma/\eta$ is the characteristic velocity of the film and T the time scale. It is possible to assume, consistent with the numerical results in Yeo and Chang [4] that the slope of the capillary ridge at the advancing front of the electrowetting film θ_f and the volume per unit width of the electrowetting film $V_f \sim \tilde{H}\tilde{L}$ are constant. From Eq. (15), the electric pressure gradient in Eq. (16) for constant θ_f then scales as

$$\frac{\partial p_e}{\partial x} \sim \frac{p_e}{\tilde{L}} \sim \frac{\gamma H B\tan^2\theta_f}{LR_e^2} , \quad (18)$$

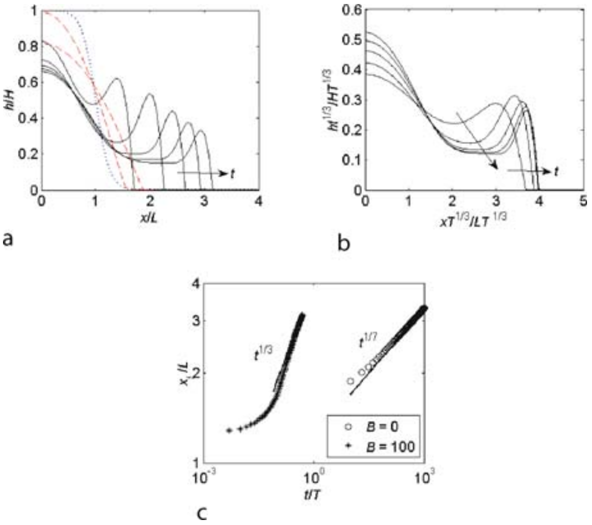

Electrowetting, Figure 6 (**a**) Transient drop and film evolution profiles for electric Bond number $B = 100$ for five equal time steps up to $t/T = 0.5$, where $T = \tilde{L}/U$ is the characteristic time scale with $U = H^3\gamma/\eta L^3$ being the characteristic system velocity. The dotted line shows the initial profile and the dashed lines indicate the spreading drop due to pure capillary motion when no electric field is applied ($B = 0$) at $t/T = 1$ and 10. (**b**) Similarity behavior of the advancing electrowetting film with the collapse of the interface profiles in time by replotting the data in (**a**) using a similarity transform. (**c**) Time dependent position of the advancing front of the drop radius or the electrowetting film x_f/L [2, 4]

which, together with Eq. (17), leads to

$$\tilde{L} \sim \left(\frac{\gamma H B\tan^2\theta_f V_0^2 T}{\eta L R_e^2}\right)^{1/3} . \quad (19)$$

Since θ_f is constant, the electric pressure gradient in Eq. (18) is also constant for a specific electrode separation R_e and hence Eq. (19) rendered dimensionless has the following similarity scaling for constant V_0:

$$x \sim t^{\frac{1}{3}} , \quad (20)$$

t being the time. Equation (20) suggests that the electrowetting film advances in a self-similar manner for electric field induced spreading. This is shown in Fig. 6b in which the film height profiles in Fig. 6a are rescaled using the similarity scaling in Eq. (20). The dynamics of the film is also shown in Fig. 6c showing that the electrowetting film advances as $t^{1/3}$, much faster than the $t^{1/7}$ behavior at which the drop spreads by pure capillary action in the absence of any electrical stresses [4]. It should be noted that the $t^{1/3}$ self-similar spreading is analogous to the self-similar gravity-driven fronts first observed by Huppert in 1982. This is because the electric pressure gradient,

given by Eq. (18) for constant θ_f acts as a constant body force term similar to gravity.

A detailed similarity analysis of the constant volume electrowetting film gives a prediction for the position of the advancing film as a function of time:

$$x_f = 0.4\left[\frac{\varepsilon_0\varepsilon_1 V^2 R_e t}{\eta}\right]^{\frac{1}{3}} . \tag{21}$$

We note therefore that the film advances independent of the dimensions and dynamics of the bulk macroscopic drop. Equation (21) can also be expressed as

$$x_f = 0.43 R_e\left[\frac{t}{T_{cap}}\right]^{\frac{1}{3}} , \tag{22}$$

where

$$T_{cap} \equiv \frac{\eta L_{cap}}{\gamma} \equiv \frac{\pi^2 \eta R_e}{8\varepsilon_0\varepsilon_1 V^2} , \tag{23}$$

and

$$L_{cap} \equiv \frac{\pi^2 \gamma R_e^2}{8\varepsilon_0\varepsilon_1 V^2} , \tag{24}$$

are the electrocapillary time and length scales, respectively. Fig. 7 shows a comparison between the prediction given by Eq. (22) with data from the *spontaneous electrowetting* experiments of Ahmed et al. [11] for deionized water in which parallel line electrodes were employed, indicating close agreement without the need for any empirical fitting parameters.

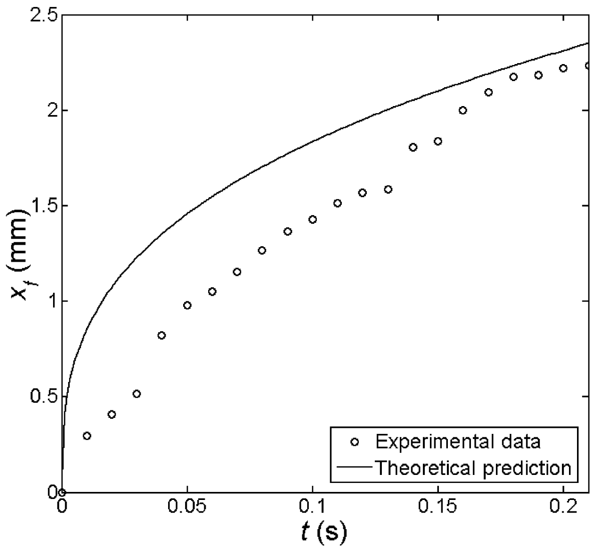

Electrowetting, Figure 7 Position of the advancing electrowetting film front x_f as a function of time t showing the close agreement between the model prediction (solid line) and the experimental data of Ahmed et al. [11] without the need for empirical fitting parameters. The experiments were carried out for deionized water ($\eta = 1$ cp , $\varepsilon_1 = 78$, $V = 200$ V and $R_e = 40$ µm); these same values were utilized for the parameters in the theoretical model [2, 4]

Examples of Application

The ability to control the wettability of a liquid, ideally without mechanically moving parts, is paramount in the handling and actuation of fluids in microfluidic devices. This has prompted a recent resurgence in electrowetting studies, which allows a rapid, reversible, and precise means for delivering and manipulating very small volumes of liquid with relatively low power consumption [10]. The success in generating fluid velocities in excess of several cm/s has also attracted significant interest in electrowetting for other applications such as electrostatic-assist coating and miniature optical focusing devices.

Cross References

- ► Applications Based on Electrowetting
- ► Digital Microfluidics
- ► Droplet Dispensing
- ► Electrocapillary
- ► Electrowetting and Droplets
- ► Interfacial Electrokinetic Flow
- ► Surface Tension, Capillarity and Contact Angle
- ► Wetting and Spreading

References

1. Quillet C, Berge B (2001) Electrowetting: A recent outbreak. Current Opinion Colloid Interface Sci 6:34–39
2. Yeo LY, Chang HC (2005) Static and spontaneous electrowetting. Modern Phys Lett B 19:549–569
3. Jones TB, Gunji M, Washizu M, Feldman MJ (2001) Dielectrophoretic liquid actuation and nanodroplet formation. J Appl Phys 89:1441–1448
4. Yeo LY, Chang HC (2006) Electrowetting films on parallel line electrodes. Phys Rev E 73:011605
5. Decamps C, De Coninck J (2000) Dynamics of spontaneous spreading under electrowetting conditions. Langmuir 16:10150–10153
6. Mugele F, Baret JC (2005) Electrowetting: From basics to applications. J Phys: Condensed Matter 17:R705–R774
7. Vallet M, Vallede M, Berge B (1999) Limiting phenomena for the spreading of water on polymer films by electrowetting. Euro Phys J B 11:583–591
8. Janocha B, Bauser H, Oehr C, Brunner H, Göpel W (2000) Competitive electrowetting of polymer surfaces by water and decane. Langmuir 16:3349–3354
9. Kang KH (2002) How electrostatic fields can change contact angle in electrowetting. Langmuir 18:10318–10322

10. Prins MWJ, Welters WJJ, Weekamp JW (2001) Fluid control in multichannel structures by electrocapillary pressure. Science 291:277–280
11. Ahmed et al. (2003) Proc. Int. Conf. Microchannels and Minichannels, ICMM2003-1110. ASME, Rochester, New York

Electrowetting, Applications

LESLIE YEO , JAMES FRIEND
Department of Mechanical Engineering,
Monash University, Clayton, VIC, Australia
leslie.yeo@eng.monash.edu.au

Synonyms

Electrowetting on dielectric (EWOD); Electrowetting on insulator coated electrodes (EICE); Electrowetting on line electrodes (ELE); Static electrowetting; Spontaneous electrowetting

Definition

Electrowetting employs an externally applied electric field to actuate or manipulate small volumes of liquid by altering its interfacial tension and hence the macroscopic contact angle or by inducing bulk liquid motion through an interfacial electric stress. Due to the low power consumption, electrowetting therefore affords an efficient, rapid, reversible, and precise means for actuating and manipulating very small volumes of liquid in microfluidic devices without the need for mechanical components.

Overview

At microscale dimensions, the surface area to volume ratio, which scales as the inverse of the characteristic length scale of the system L, becomes increasingly large, thus stipulating the dominance of surface forces over body forces. This makes it extremely difficult to move and manipulate small volumes of fluid in miniaturized fluidic devices. Several schemes that exploit Marangoni (surface tension gradient) and thermocapillary (temperature gradient) stresses to control the interfacial energy and hence drop motion have been proposed. Nevertheless, these suffer from several limitations in terms of reliability, controllability, response times and compatibility.

In contrast, the use of electrokinetics has generally been heralded as the preferred method for microfluidic manipulation due to the ease/low costs of electrode fabrication given the recent advances in micro/nano-fabrication technology, the precision and controllability afforded by electric fields, and, the reliability in the absence of mechanically moving parts. Electric field driven actuation is also rapid since the limitation is usually imposed by the hydrodynamic time scale $\mu_l L/\gamma \sim 10^{-4}$ s, which is typically larger than the time scale for charge separation $\varepsilon_0\varepsilon_l/\kappa_l \sim 10^{-6}$ s; μ_l, $\varepsilon_0\varepsilon_l$ and κ_l denote the liquid viscosity, permittivity and conductivity, respectively, and γ is the interfacial tension. As such, the use of electrowetting, in which an external electric field is exploited to modify the wettability of the drop through a change in its interfacial tension or by inducing bulk motion through an interfacial stress, has become increasingly attractive as a means for microfluidic actuation and manipulation.

Yeo and Chang [1, 2] proposed that electrowetting phenomena can, in general, be classified into *static electrowetting* and *spontaneous electrowetting*, depending on the electrode configuration adopted. Static electrowetting, in which the drop sits above a planar dielectric coated plate electrode (synonymous to the configurations employed in electrowetting-on-dielectric (EWOD) or electrowetting on insulator coated electrodes (EICE); see, for example, Fig. 1a), involves the alteration of the macroscopic contact angle of the drop due to the applied electric field. It was shown in [1] through an analysis of a conducting drop that the dominant gas-phase electric field endows the drop interface with an interfacial charge and hence normal interfacial electric stress that is weakly singular towards the three-phase contact line. Nevertheless, due to the confinement of this singularity in a very small region, of the order of the dielectric coating thickness (typically microns), the interfacial stress is insufficient to result in a bulk pressure gradient in the liquid; an electric force, which can be obtained by coarse graining, simply arises at the contact line that balances the surface forces. This is shown to give rise to a modification of the macroscopic contact angle of the drop θ which obeys the Lippmann condition:

$$\cos\theta = \cos\theta_0 + \frac{\varepsilon_0\varepsilon_l V^2}{2d\gamma_{LV}}, \tag{1}$$

where θ_0 is the equilibrium contact angle in the absence of the electric field, V the applied voltage, d the dielectric coating thickness and γ_{LV} the liquid–vapor interfacial tension.

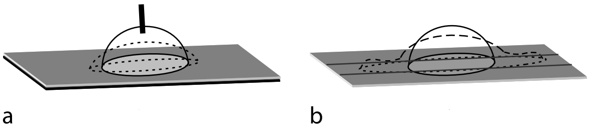

Electrowetting, Applications, Figure 1 Schematic illustration of (**a**) static electrowetting in which the applied electric field induces a macroscopic change in the contact angle, and, (**b**) spontaneous electrowetting in which a thin front-running electrowetting film is pulled out and advances ahead of the macroscopic spreading drop. The film thickness in (**b**) is not drawn to scale

Spontaneous electrowetting, on the other hand, arises when a thin front-running electrowetting film is pulled out and advances ahead of the macroscopic drop when parallel line electrodes are employed [2, 3], as shown in Fig. 1b. This has been termed electrowetting on line electrodes (ELE). In [2], the electric field in the liquid phase is dominant and gives rise to a non-singular tangential interfacial electric stress that decays away from the contact line with increasing interfacial height. This electric stress gradient consequently gives rise to a negative macroscopic pressure gradient that induces liquid flow from the bulk of the drop towards the contact line region, therefore pushing out a thin spontaneous electrowetting film ahead of the macroscopic drop, which advances with a constant contact angle self-similarly in time t as

$$x_f = 0.43 R_e \left(\frac{t}{T_{cap}} \right)^{1/3} , \tag{2}$$

independent of drop dimension, interfacial tension or wettability; x_f is the position of the advancing front, R_e the electrode separation and

$$T_{cap} = \frac{\pi^2 \mu_1 R_e}{8 \varepsilon_0 \varepsilon_1 V^2} , \tag{3}$$

is the electrocapillary time scale.

Basic Methodology

The majority of effort in developing applications based on electrowetting has largely centered on static electrowetting processes. As a result, the motion is essentially in the form of discrete steps rather than a single continuous process as in spontaneous electrowetting. In general, these static electrowetting schemes for moving and manipulating individual drops in open systems have collectively been described by the term *digital microfluidics* in order to provide a distinction to microfluidics systems involving continuous flow within closed microchannels. Less common is the use of the synonymous term *flatland microfluidics*. Although digital microfluidics is perhaps not particularly useful for continuous flow analysis, and particularly that involving larger liquid volumes, discrete drop microfluidics allows the possibility of scalability and reconfiguration such that analyses can be carried out in similar fashion to traditional benchtop protocols [4]. Besides, drops are often useful as carriers for biological entities and hence different biological agents can be transported separately in different drops without coming into contact with the other providing the drops never meet. Digital microfluidics also has the advantage of minimizing the amount of liquid required as well as

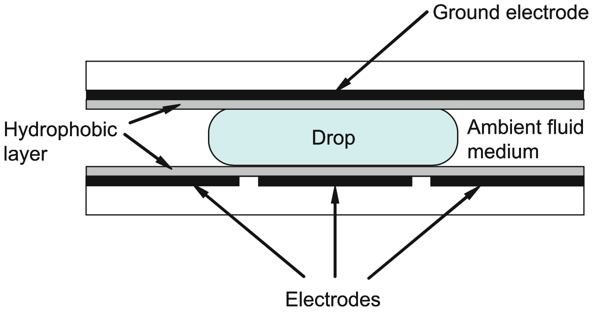

Electrowetting, Applications, Figure 2 Schematic depiction of a typical static electrowetting setup for drop actuation in a microfluidic device

the contact between the liquid and solid surface. The latter is crucial in applications, most commonly those that involve biomolecules, in which surface adsorption is undesirable [5]. Protein adsorption is commonly due to electrostatic interactions and the degree to which it occurs is dependent on the charge, polarity on the protein as well as the applied voltage [6]. The open system also eliminates the attenuation of detection signals through channel walls although it is prone to contamination and evaporation. A possibility to circumvent the problem due to evaporation is to house the system within an oil medium, which has been found to also suppress adsorption.

Practical static electrowetting schemes typically involve the use of a patterned array of multiple electrodes, each of which can be individually controlled, as shown in Fig. 2; note that the use of a wire electrode in contact with the drop in the usual EWOD/EICE setup in Fig. 1a is impractical due to the moving drop. The drop should also span across two electrodes at any one time to facilitate continual discrete motion [7]; the smallest liquid volume that can be manipulated is therefore constrained by the electrode size. The activation and subsequent deactivation of an applied potential across one electrode in the array and the ground electrode (top electrode plate in Fig. 1), then allows the drop to march forward discretely towards the next electrode in the array sequence which is then subsequently activated (and then deactivated again) to translate it forward to yet the next electrode. The programming of a sequential logic scheme for the activation/deactivation of individual electrodes then allows the drop to be translated in a desired direction. Increasingly complex control schemes have since been proposed to perform more complicated and sophisticated tasks such as drop splitting, recombination and mixing. This therefore allows applications in widespread areas, although efforts have largely concentrated around two major areas, i. e. microfluidic Lab-on-a-Chip devices as micro total analysis systems (μTAS) and electro-optic devices.

Key Research Findings

Microfluidic Components for Lab-on-a-Chip Devices

Electrowetting is most commonly used in Lab-on-a-Chip devices for microfluidic actuation and manipulation. In a typical system, very small amounts of analytes are metered into drops which are then transported, for example, to a reaction chamber where they are merged for the reaction to occur. Successive reactions can also be performed by merging drops containing intermediate reaction products. Parallel manipulation or detection can also be carried out by splitting the drop into smaller droplets [4]. All of these drop operations, namely, metering, translation, merging and splitting, can be carried out using static electrowetting schemes.

Early work on static electrowetting for these microfluidic applications focused on these individual tasks separately. These initial efforts were concentrated on driving a conductive drop through an open channel using electrowetting. The setup is similar to that shown in Fig. 2. The channel however is required to be open for positioning of the drop within, which required a fair amount of precision, and the filling of the medium around the drop; the channel could later be closed by employing a cover slip. Lee and Kim [8] employed a liquid metal drop surrounded by a liquid electrolyte medium. In this case, however, the electrodes were positioned at the end of channel instead of comprising the top and bottom plates. Although they termed their setup *continuous electrowetting*, the use of electric fields to change the macroscopic liquid metal–electrolyte contact angle is more akin to the classical electrocapillary experiments [1]. In any case, however, their work culminated in one of the first demonstrations of drop transport in a miniaturized fabricated device. An extension of this work is the fabrication of a 2 mm circular loop track along the periphery of which several electrodes are embedded in order to drive the drop around the track at rotation speeds up to 420 rpm with an operating voltage of 2.8 V. A similar demonstration is reported in Pollack et al. [7] with electrolyte drops within an air or oil medium. Drop translation with speeds over several cm/s were obtained with applied voltages of 1 – 100 V.

Elegant protocols for drop metering, splitting and merging were later proposed by Cho et al. [9]. The drop splitting process is illustrated in the image sequences given by Figs. 3a–3c. Of vital importance in order for the drop to split is the necking (negative radius of curvature at the neck position R_n) and rupture (when the drop radius of curvature at its ends, which is proportional to the drop size and roughly commensurate with the electrode width R_t, become equal, i. e. $R_n = -R_t$) processes, which, can be caused by removal of the voltage on the middle elec-

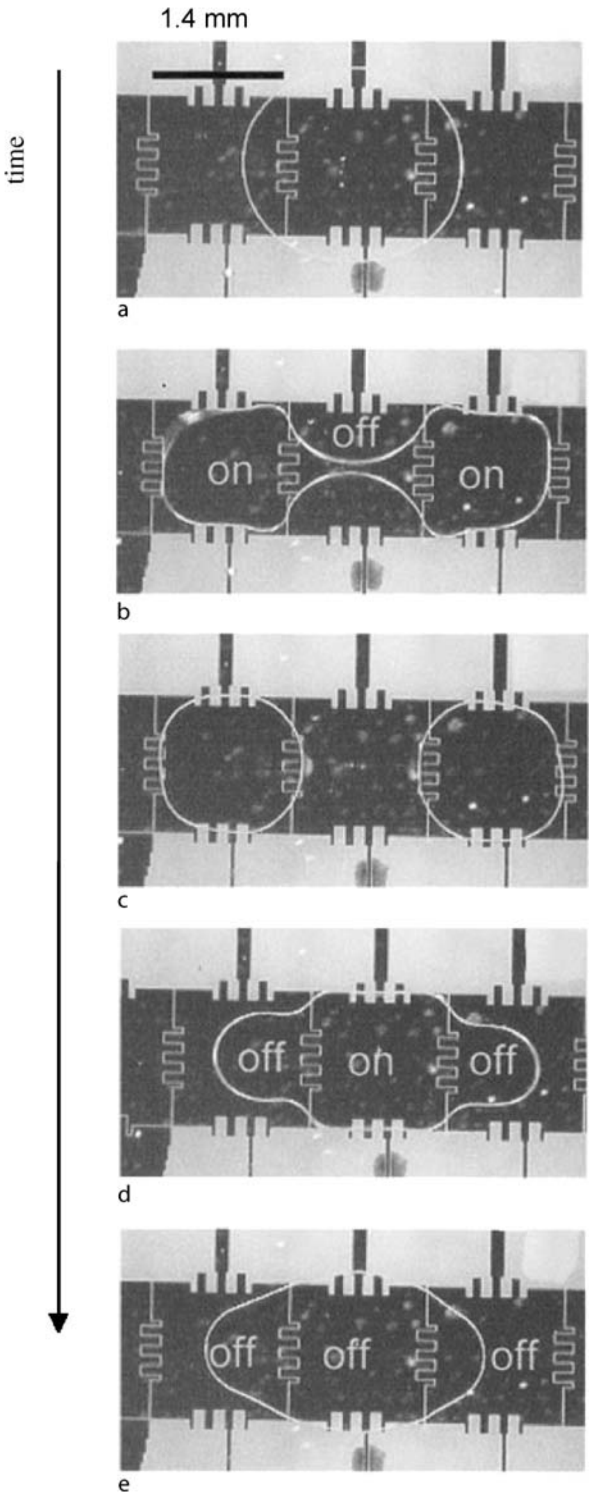

Electrowetting, Applications, Figure 3 Drop surgery by programmable static electrowetting protocols. The voltage on and voltage off states of individual electrodes are indicated. Images (**a**), (**b**) and (**c**) depict drop splitting whereas images (**c**), (**d**) and (**e**) show drop merging (from [9])

trodes. For necking to occur, however, the ratio of the channel height to the drop radius of curvature at its ends h/R_t needs to be below a critical value; this critical value itself increases as the ratio $|R_n|/R_t$ increases [9].

The procedure for drop metering from a reservoir is related to the drop splitting process. Again, this is facilitated by smaller channel heights and smaller drop reservoirs. Figure 4 shows the drop metering process; lateral electrode arrays are required to hold the drop reservoir in position whilst the electrodes ahead of the reservoir are activated in order to pull a drop out from the reservoir. By turning off the electrodes in the middle, necking occurs to split the drop from the reservoir. For the entire reservoir to be drained, however, the surface of the reservoir must be rendered hydrophobic [9]. The merging of drops, on the other hand, can be carried out by translating the drops together such that coalescence occurs by removing the voltage on the electrodes beneath the drops and activating the electrode between the drops [9]. This is shown in Figs. 3d and 3e.

Other microfluidic components have also been developed using static electrowetting. An electrowetting-actuated valve was proposed by Cheng & Hsiung [10]. A hydrophobic layer comprising plasma-modified poly(tetrafluoroethylene) was coated onto the channel to prevent through-flow; the plasma modification served to reduce the hydrophobicity of the poly(tetrafluoroethylene) slightly so that upon modification of the advancing liquid meniscus contact angle via an electric field, through-flow can be obtained.

Electrowetting-based platforms have also been proposed as a convenient means for driving micro-mixing of discrete drops of different chemicals. The simplest form of such mixing is to adopt a passive scheme in which two drops are translated together and merged by electrowetting using the procedures described above. However, it is also possible to induce active mixing after the coalescence event in order to reduce the mixing time. A straightforward way is to oscillate the merged drop between two or more electrodes in a linear arrangement at a fixed frequency. Paik et al. [11] observed that the mixing times decreased with increasing number of electrodes and the switching frequency (inverse of the time that the drop is present on one electrode), both of which increases the complexity of the flow recirculation within the drop. Electrowetting-driven mixing of ionic liquids containing different reagents was investigated by Dubois et al. [12]. These ionic liquids which have negligible vapor pressure are environmentally-friendly alternatives to the volatile organic solvents commonly used in chemical synthesis which are subject to evaporation problems in open microfluidic systems and problems due to oil/solvent miscibility and cross-contamination when the

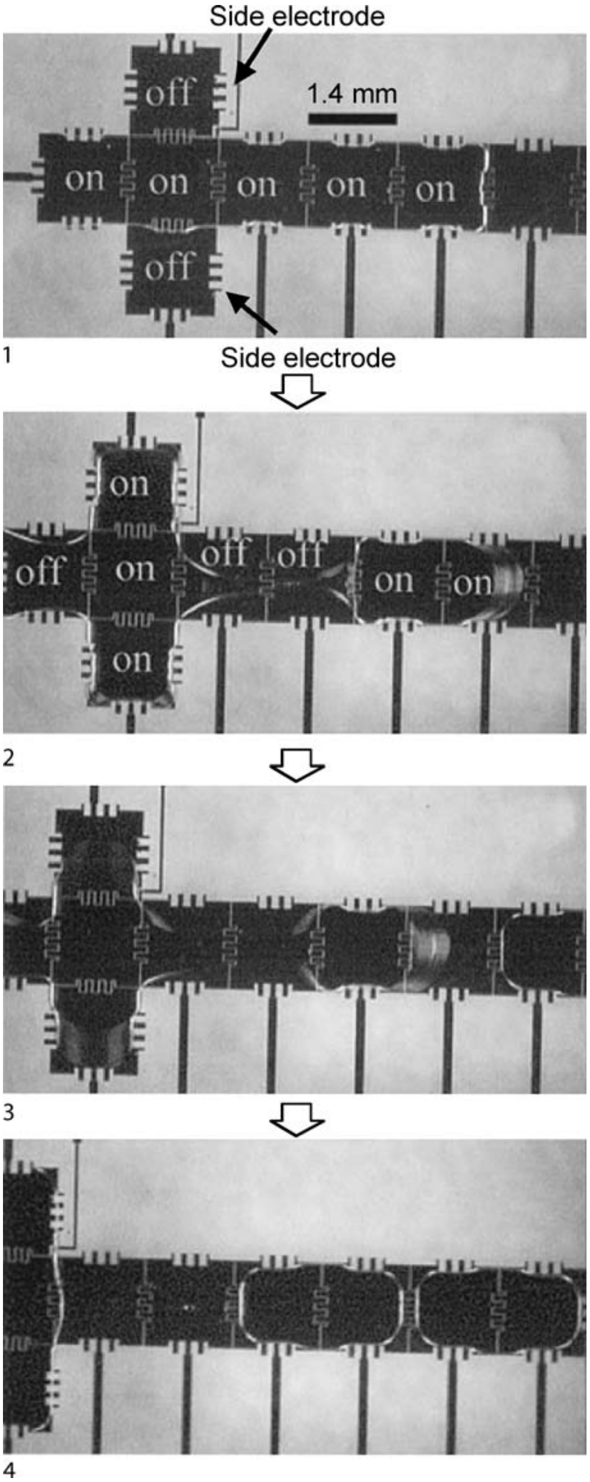

Electrowetting, Applications, Figure 4 Drop dispensing or metering from a reservoir using static electrowetting schemes (from [9])

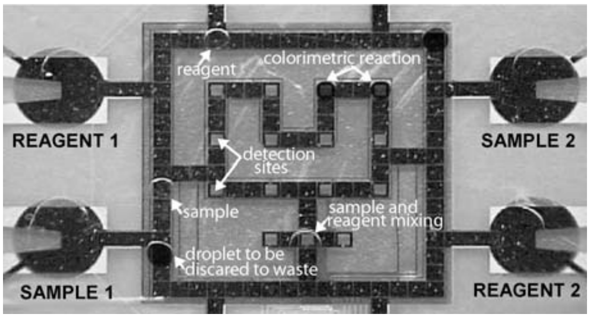

Electrowetting, Applications, Figure 5 Electrowetting based integrated microfluidic device for glucose assays (from [15])

drop analysis carried out under an oil layer to minimize evaporation.

These various drop actuation and manipulation schemes and microfluidic components have been integrated into more complex devices to perform multiple chip based tasks. Pollack et al. [13] employed a combination of electrowetting-driven microfluidic components for drop dispensing, actuation and merging/splitting to discriminate alleles with single base pair variations on an integrated polymerase chain reaction (PCR) microchip. Srinivasan et al. [14] developed an electrowetting-based microfluidic chip platform to perform glucose detection via colorimetric enzyme kinetics. The glucose assay consisted of three steps, namely, dispensing, mixing and detection; dispensing was carried out by manual pipetting, drop translation leading up to mixing by electrowetting and detection by measuring the absorbance signal corresponding to the color change in the system subsequent to an enzymatic reaction.

A more complex and integrated prototype miniaturized medical diagnostic platform based on electrowetting, as shown in Fig. 5, was engineered by Srinivasan et al. [15], in which it was confirmed that electrowetting actuation can be carried out, at least in principle, reliably and with a high degree of reproducibility on physiological liquid samples such as a whole blood, saliva, sweat, plasma, serum and urine. Biocompatibility issues, and, in particular, the problem of protein adsorption was discussed, in which it was found that a thin oil film wetting the hydrophobic substrate to avoid direct drop/surface contact led to suppression of the undesirable adsorption effects.

The highly programmable and controllable handling of individual drops using electrowetting lends itself conveniently to various microarray technologies. One example is the possibility of microfluidic chip multistep synthesis or multiplex reactions for high throughput combinatorial drug screening [16]. Another example is the preparation of drop arrays for matrix assisted laser desorption/ionization (MALDI) mass spectrometry proteomic analysis [17].

A way of spotting these microarray patterns onto a substrate is proposed by Yi and Kim [18] who drew out a drop from a liquid reservoir, transported it through a hydrophobic channel by electrowetting to a location where it can be deposited by capillarity onto the desired hydrophilic substrate, as shown in Fig. 6. They termed this as *soft printing* because biological materials contained within a liquid drop acting as a carrier can be spotted on a substrate without requiring solid to solid contact or drop ejection, for example, mechanical spotting or ink-jet printing, which are associated with problems such as splashing and spreading that lead to non-uniformities in the spot shape and size. Multiple spots can be achieved with multiple orifices at

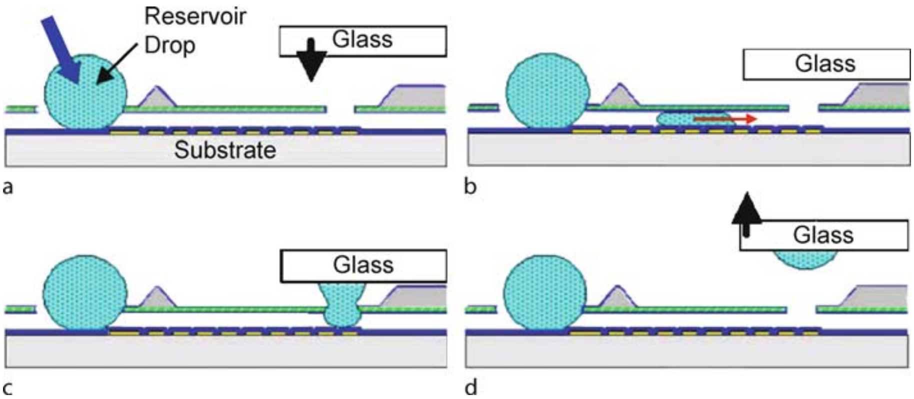

Electrowetting, Applications, Figure 6 Illustration of the *soft printing* process. (**a**) Loading of the sample and approach of the glass plate on which the drop is desired to be spotted. (**b**) Drop dispensing and drop translation to the orifice by electrowetting. (**c**) Drop contact with the glass plate through the orifice. (**d**) Glass plate lift off and adhesion of the drop due to capillarity (from [18])

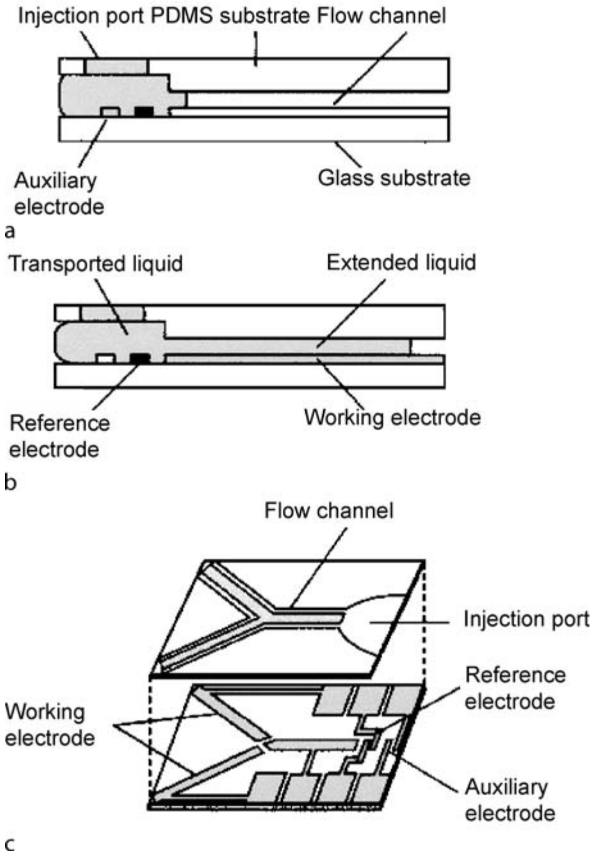

Electrowetting, Applications, Figure 7 Experimental setup of the *microchannel-like* flow type electrowetting device of Satoh et al. [19]. Panels (**a**) and (**b**) are cross-sectional views of the electrode and flow channel geometry, and, panel (**c**) shows the architecture of the device (from [19])

predetermined locations, the size of the spots being controlled by the metered drop volume.

We briefly mention an attempt to employ electrowetting to drive *microchannel-like* flow as opposed to individual drop translation by using arrays of elongated electrodes (Fig. 7) instead of the short electrode array shown in Fig. 2 [19]. Their setup consisted of a large reservoir, from which a liquid meniscus advances, much like the electrocapillary-driven height-of-rise experiments between two vertically oriented electrode plates [20]. However, by adopting horizontal channels, gravity is eliminated allowing the meniscus to advance much easier. The advancement of the meniscus front, however, remains discrete unlike true continuous microchannel flow, for example driven by electroosmosis. This is due to the need to sequentially activate successive electrodes, as in all static electrowetting schemes. The setup was subsequently extended to allow for two converging flow channels such that mixing could occur [21]. An additional electrode was employed where the two flows converged, as shown in Fig. 8. Upon activation, this mixing electrode causes both fluids to wet the area above it in order to drive the mixing. An ammonium detection component was also integrated into the device by introducing a third channel that drove an electrolyte solution towards the mixing area (Fig. 8c), which is separated from the electrolyte by an air gap. Ammonia gas released due to the mixing then diffuses across this air gap and into the electrolyte solution, thus increasing its pH, which is subsequently detected by a pH indicator electrode.

Electrowetting has also been proposed for inducing rapid reversible switching of the lateral position of a liquid stream flanked by two side gas streams in a microfluidic channel, as depicted in Fig. 9 [22]. By careful alignment of the electrodes housed under the microchannel substrate, fluid streams can be merged or split using this method. This is potentially useful in the control and sorting of two-phase microfluidic flows. Another potential application for this flow switching technique is for generating parallel and sequential lamination between streams for micro-mixing without requiring complex fabricated geometries.

Electro-Optical Applications

Static electrowetting techniques are also extremely attractive for many electro-optical devices. Electrowetting was first employed in these applications for the dynamic and latchable tuning of optical waveguides [23, 24]. In these fiber optic applications, electrowetting is employed to alter the amount by which a conducting fluid (the choice of which is contingent on its viscosity being sufficiently low and its refractive index being greater than that of the fiber) housed in an insulating lubricant medium surrounds a section of an optical fiber stripped of its coating which runs through the fluidic channel loop; the loop allows fluid recirculation to eliminate back pressure. This voltage adjustable overlapping then modifies the transmission characteristics of the fiber due to electromagnetic field leakage of the cladding resonance modes, obtained with the aid of in-fiber gratings, into the fluid. Mach et al. [22] reported attenuation beyond 45 dB across both narrow and broad bands at 10^{-3} s order switching speeds; the insertion losses, attributed to mechanical coupling between the fiber and the light source and spectrum analyzer with the use of a fusion splice, were observed to be approximately $2-3$ dB.

The ability to alter the interfacial shape of the drop via the application of an external electric field thus allows it to be used as an adaptive liquid lens whose focal length can be flexibly, reversibly and accurately adjusted via manipulation of the drop shape. The optical microcell consisted of two density-matched immiscible liquids (low conduc-

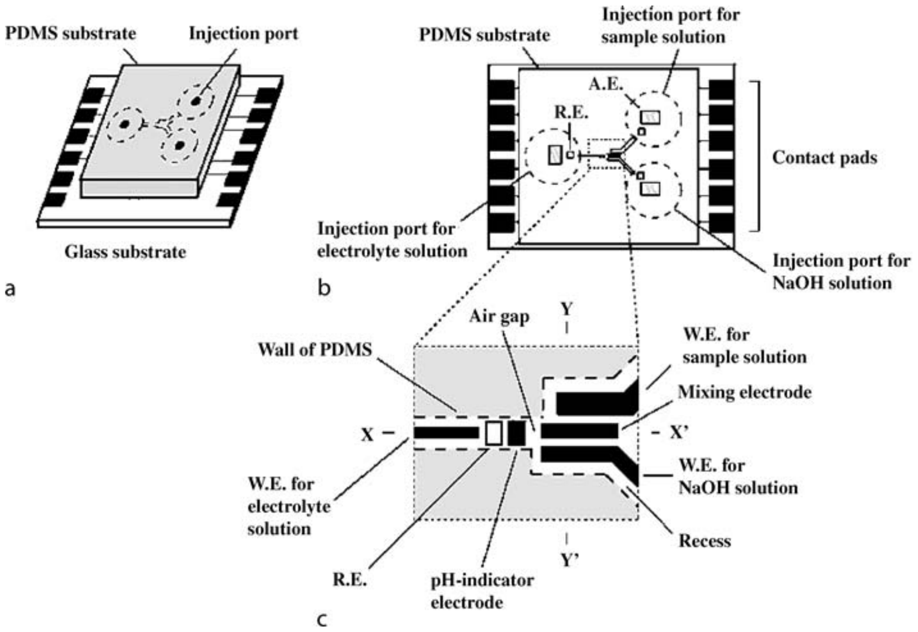

Electrowetting, Applications, Figure 8 Experimental setup of a miniaturized device which incorporates microfluidic actuation, mixing and sensing by electrowetting. Panel (**a**) shows the geometry of the channels and electrodes. Panel (**b**) shows the plan view of the device. Panel (**c**) is a magnification of the mixing and sensing chambers in which ammonia is detected (from [16])

tivity non-polar organic liquid drop under a conducting aqueous solution) to eliminate gravitational effects on the interfacial shape. As a consequence of the contact angle dependence on the applied voltage, the focal length and refractive power is also a function of the voltage. Berge and Peseux [25] observed very short response times which thus allowed the lens to be switched rapidly at typical frequencies of order $10^2 – 10^3$ Hz. This switching frequency is dependent on the liquid viscosity; liquids with low viscosity resulted in excessive oscillation prior to obtaining an equilibrium shape whereas extremely viscous liquids led to overdamping and hence slow response times. This variable focusing technology was later developed for specific applications such as mobile phone cameras [26] although other applications such as optical modulators and amplifiers are also envisaged [27]. Photopolymeric conductive liquid drops can also be used in order to solidify the drop and hence retain its drop interfacial shape in a fixed position through exposure to ultraviolet irradiation [28].

Another interesting electro-optical application that has been developed using static electrowetting is in display technology. This idea was initially proposed in the 1980s by Beni and Hackwood [29] although a demonstrable prototype concept was only produced in 2003 by Hayes and Feenstra [30]. The principle is illustrated in Fig. 10a. A dyed oil drop under a transparent aqueous solution is confined within a cell that represents a single pixel in the reflective display; the cell is placed atop a white substrate. A hydrophobic layer is coated at the bottom of the cell such that in the absence of an applied potential, the oil forms a thin equilibrium layer covering the entire cell area. Upon application of the electric field, however, the contact angle increases and the oil film retracts to form a drop in the corner of the cell. The extent to which the drop retracts is thus dependent on the applied voltage. The 250 μm^2 pixels are also believed to be sufficiently small such that an area average is only apparent to the observer; the retracted spot should therefore go unnoticed. The pixel can thus be switched between the colored (voltage on) and transparent (voltage off) states rapidly, the switching speed, typically milliseconds, depending on pixel size and the thickness and physical properties of the oil film [31], being sufficiently fast for current display applications, such as video graphics and electronic paper.

An electrowetting colored display was also demonstrated by subdividing the pixel cell into three subcells, as shown in Fig. 10b, above each of which a different color filter is placed. An additional oil layer/drop is included in each pixel, this time on the top of the cell, the interfacial shape of which can be altered independently of the bottom layer through the application of a potential between the aqueous phase and the top electrode. Hayes and Feenstra [30] reported that the brightness (in terms of intrinsic reflec-

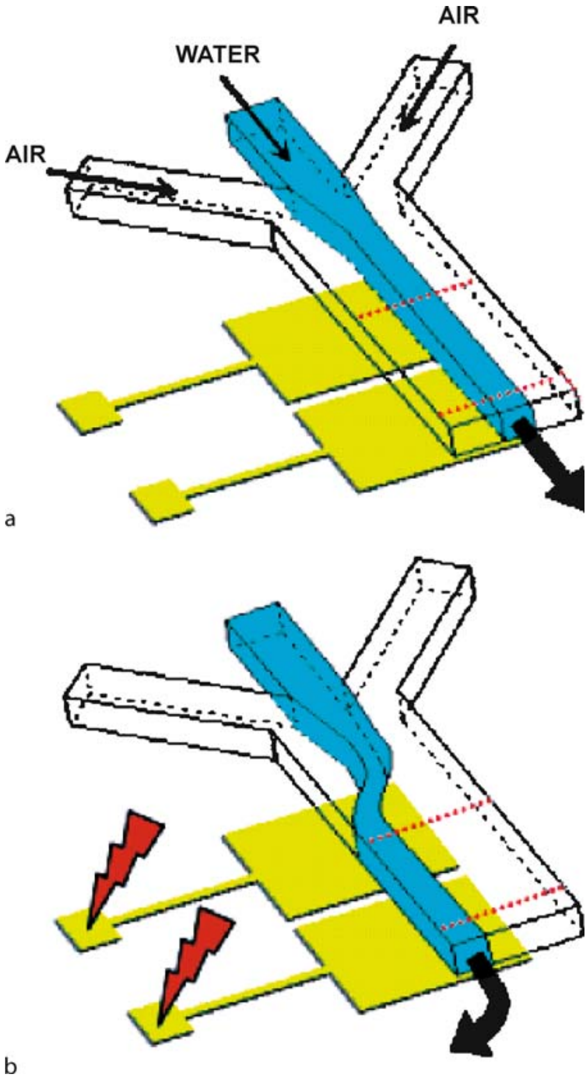

Electrowetting, Applications, Figure 9 Electrowetting activated liquid stream switching in two-phase microflows. (**a**) No applied voltage. (**b**) Voltage applied (from [22])

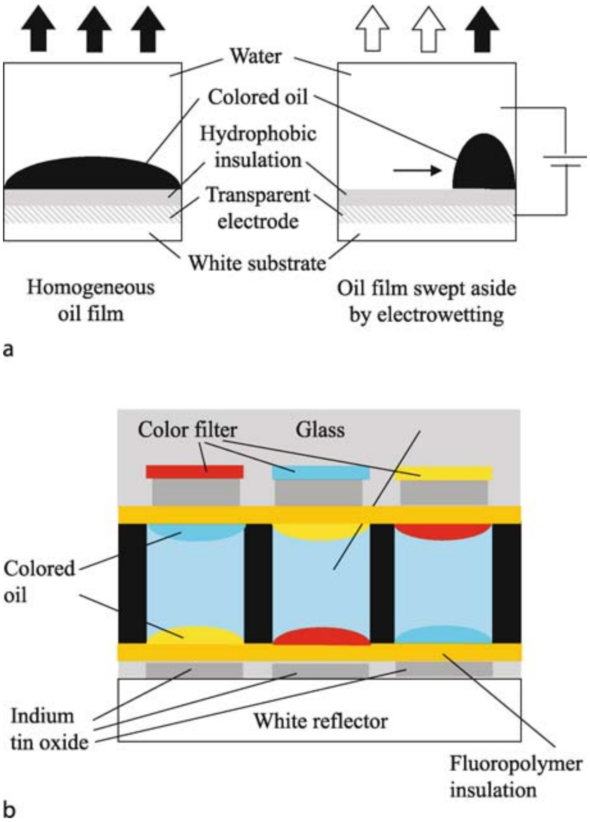

Electrowetting, Applications, Figure 10 (**a**) Principle of electrowetting display technology. The left images show the spreading of the homogeneous colored oil film across the entire pixel cell when no voltage is applied. The right images show the retraction of the oil drop to the corner of the pixel cell upon application of a voltage. (**b**) Principle of a color electrowetting display showing the division of the pixel cell into three subcompartments, each with two active layers. Different color filters are placed above each subcompartment (from [30])

tivity) of their full color display was approximately four times that of liquid crystal displays.

Other Applications

Various other applications based on static electrowetting have also been suggested. For example, Welters and Fokkink [32] propose that the spreading of drops due to static electrowetting is useful for temporary adhesion enhancement (e. g. in the drying of paint) or as a fast capillary switch. Prins et al. [20] demonstrated the use of electrically-induced capillary height-of-rise for the individual filling and draining of an array of vertical capillary channels. They demonstrated this by adding CsCl into the aqueous solution, which has the capability of absorbing X-rays, therefore presenting the capability of the device as a tunable optical filter, which can be exploited for X-ray shielding.

Applications Based on Spontaneous Electrowetting

Compared to static electrowetting, spontaneous electrowetting research is still in its infancy stages. Nevertheless, the technology holds substantial promise to be exploited in various microfluidic applications. The premise of generating a thin spontaneous front-running electrowetting film ahead of a macroscopic spreading drop using parallel line electrodes fabricated onto a hydrophobic substrate was first reported by Jones et al. [3] as a possible mechanism for microfluidic actuation. With slight

modification of the electrodes at predetermined locations downstream, Jones et al. showed the possibility of creating nanodrops at these locations upon removal of the electric field, upon which the film ruptures and dewets due to capillary instabilities [3].

Future Directions for Research

Given that electrowetting is now moderately well understood, the main thrust in this area of research has been in the development of microfluidic and electro-optical devices based on the technology. There are one or two electrowetting driven electro-optical devices now within reach of commercial product development stage. Nevertheless, there are several technical challenges that have to be addressed before most electrowetting based devices can be translated from laboratory bench type devices to that close to commercial realization. An important limitation is contact angle saturation at high voltages; at present there is no general consensus on why this arises. Joule heating is a problem that needs to be overcome, in particular, for microdevices. In addition, a reduction in typical magnitudes in the applied voltage to obtain the desired response will make electrowetting more attractive for integration into real microfluidic devices.

Cross References

► Digital Microfluidics
► Droplet Dispensing
► Electrocapillary
► Electrowetting
► Electrowetting and Droplets
► Interfacial Electrokinetic Flow
► Surface Tension, Capillarity and Contact Angle
► Wetting and Spreading

References

1. Yeo LY, Chang H-C (2005) Static and spontaneous electrowetting. Modern Phys Lett B 19:549–569
2. Yeo LY, Chang H-C (2006) Electrowetting films on parallel line electrodes. Phys Rev E 73:011605
3. Jones TB, Gunji M, Washizu M, Feldman MJ (2001) Dielectrophoretic liquid actuation and nanodroplet formation. J Appl Phys 89:1441–1448
4. Zeng J, Korsmeyer T (2004) Principles of droplet electrohydrodynamics for Lab-on-a-Chip. Lab Chip 4:265–277
5. Berthier J, Silberzan P (2006) Microfluidics for Biotechnology. Artech House, Norwood
6. Yoon J-Y, Garrell RL (2003) Preventing biomolecular adsorption in electrowetting-based biofluidic chips. Anal Chem 75:5097–5102
7. Pollack MG, Fair RB, Shenderov AD (2000) Electrowetting-based actuation of liquid droplets for microfluidic applications. Appl Phys Lett 77:1725–1726
8. Lee J, Kim C-J (2000) Surface-tension driven microactuation based on continuous electrowetting. J Microelectromech Syst 9:171–180
9. Cho SK, Moon H, Kim C-J (2003) Creating, transporting, cutting and merging liquid droplets by electrowetting-based actuation for digital microfluidic circuits. J Microelectromech Sys 12:70–80
10. Cheng J-Y, Hsiung L-C (2004) Electrowetting(EW)-based valve combined with hydrophilic Teflon microfluidic guidance in controlling continuous fluid flow. Biomed Microdev 6:341–347
11. Paik P, Pamula VK, Pollack MG, Fair RB (2003) Electrowetting-based droplet mixers for microfluidic systems. Lab Chip 3:28–33
12. Dubois P, Marchand G, Fouillet Y, Berthier J, Douki T, Hassine F, Gmouh S, Vaultier M (2006) Ionic liquid droplet as e-microreactor. Anal Chem 78:4909–4917
13. Pollack MG, Paik PY, Shenderov AD, Pamula VK, Dietrich VS, Fair RB (2003) Investigation of electrowetting-based microfluidics for real-time PCR applications. In: Northrup, et al (eds) Proceedings of the 7th International Conference on Micro Total Analysis Systems µTAS 2003, pp 619–622
14. Srinivasan V, Pamula VK, Fair RB (2004) Droplet-based microfluidic Lab-on-a-Chip for glucose detection. Anal Chim Acta 507:145–150
15. Srinivasan V, Pamula VK, Fair RB (2004) An integrated digital microfluidic Lab-on-a-Chip for clinical diagnostics on human physiological fluids. Lab Chip 4:310–315
16. Taniguchi T, Torii T, Higuchi T (2002) Chemical reactions in microdroplets by electrostatic manipulation of droplets in liquid media. Lab Chip 2:19–23
17. Wheeler AR, Moon H, Kim C-J, Loo JA, Garell RL (2004) Electrowetting-based microfluidics for analysis of peptides and proteins by matrix-assisted laser desorption/ionization mass spectrometry. Anal Chem 76:4833–4838
18. Yi U-C, Kim C-J (2004) Soft printing of droplets pre-metered by electrowetting. Sens Actuators A 114:347–354
19. Satoh W, Loughran M, Suzuki H (2004) Microfluidic transport based on direct electrowetting. J Appl Phys 96:835–841
20. Prins MWJ, Welters WJJ, Weekamp JW (2001) Fluid control in multichannel structures by electrocapillary pressure. Science 291:277–280
21. Satoh W, Hosono H, Suzuki H (2005) On-chip microfluidic transport and mixing using electrowetting and incorporation of sensing functions. Anal Chem 77:6857–6863
22. Huh D, Tkaczyk AH, Bahng JH, Chang Y, Wei H-H, Grotberg JB, Kim C-J, Kurabayashi K, Takayama S (2003) Reversible switching of high-speed air-liquid two-phase flows using electrowetting-assisted flow-pattern change. J Am Chem Soc 125:14678–14679
23. Mach P, Krupenkin T, Yang S, Rogers JA (2002) Dynamic tuning of optical waveguides with electrowetting pumps and recirculating fluid channels. Appl Phys Lett 81:202–204
24. Acharya BR, Krupenkin T, Ramachandran S, Wang Z, Huang CC, Rogers JA (2003) Tunable optical fiber devices based on broadband long-period gratings and pumped microfluidics. Appl Phys Lett 83:4912–4914
25. Berge B, Peseux J (2000) Variable focal lens controlled by an external voltage: An application of electrowetting. Eur Phys J E 3:159–163
26. Kuiper S, Hendriks BHW (2004) Variable-focus liquid lens for miniature cameras. Appl Phys Lett 85:1128–1130
27. Krupenkin T, Yang S, Mach P (2003) Tunable liquid microlens. Appl Phys Lett 82:316–318

28. Yang S, Krupenkin TP, Mach P, Chandross EA (2003) Tunable and latchable liquid microlens with photopolymerizable components. Adv Mater 15:940–943
29. Beni G, Hackwood S (1981) Electro-wetting displays. Appl Phys Lett 38:207–209
30. Hayes RA, Feenstra BJ (2003) Video-speed electronic paper based on electrowetting. Nature 425:383–385
31. Roques-Carmes T, Hayes RA, Schlangen LJM (2004) A physical model describing the electro-optic behavior of switchable optical elements based on electrowetting. J Appl Phys 96:6267–6271
32. Welters WJJ, Fokkink LGJ (1998) Fast electrically switchable capillary effects. Langmuir 14:1535–1538

Electrowetting on Dielectric (EWOD)

► Digital Microfluidics
► Electrowetting
► Electrowetting, Applications
► Electrowetting and Droplets

Electrowetting and Droplets

James D. Sterling, Reza Miraghaie, Ali Nadim
Keck Graduate Institute, Claremont, CA, USA
jim_sterling@kgi.edu, reza_miraghaie@kgi.edu,
ali_nadim@kgi.edu

Synonyms

Droplet microfluidics; Electrowetting on dielectric (EWOD); Electrowetting on insulator coated electrodes (EICE)

Definition

Electrowetting is the electrostatically-induced decrease of the liquid contact angle at a contact line formed at the intersection of a liquid, solid, and a third fluid that can be a gas or immiscible liquid. The contact angle is measured within the droplet between the solid surface and the fluid–fluid interface. It ranges from 0 for complete wetting to 180 degrees for non-wetting. As applied to droplets, electrowetting can be used to spread droplets, change the shape of droplets, induce shape-mode oscillations, split droplets, move droplets across the surface, and merge and mix droplets.

Overview

Electrostatic manipulation of droplets has been utilized for ink-jet printing, ESI mass-spectrometry and flow cytometry applications. In contrast to these droplet-in-air applications, electrowetting involves the electrostatic manipulation of droplets attached to solid surfaces. Applications that utilize this method include micro-optofluidic manipulations of droplets to serve as electrically-controlled zoom lenses [1, 5] and as shutters or color filters for flat panel displays [4]. Another application is in performing biological and chemical assays by manipulating sample and reagent droplets using electrowetting [9, 10]. Thus, electrowetting of droplets on surfaces is viewed as a method that may provide a Lab-on-a-Chip (LOC) platform to replace the use of pipettes, glass beakers, tubes, pneumatic and piezoelectric automated dispensers, as well as standard (as defined by Society for Biomolecular Screening (SBS)) wells and plates in the laboratory.

The focus of this entry is on some unique physical characteristics of electrowetting applied to droplets. In particular, electrowetting-induced droplet shape changes, mixing, and droplet translation are discussed and some novel results involving shape-mode oscillations with and without simultaneous droplet translation are presented.

Basic Methodology

Shape Changes

Electrowetting can be used to manipulate the curvature of a droplet immersed in an immiscible fluid. As described by researchers from Varioptic [1] and Philips [5], this change in curvature can provide a lens with a variable focal length. Varioptic (www.varioptic.com) reports that zoom lenses and autofocus lenses for cameras and video cameras used in cell phones, scanners, printers, barcode readers and other applications are being developed using electrowetting to adjust the curvature of the meniscus between two fluids. The engineering of a system of this type, an example of which is shown in Fig. 1, requires that fluids be selected with appropriate optical properties, appropriate temperature dependence of the refractive indices and viscosities appropriate to provide rapid response and stability of the meniscus shape. If the viscosity is too low, a change in the contact angle will cause a time-decaying oscillation of the shape corresponding to underdamped motion. However, if the viscosities are too large, the system may respond in an overdamped manner that relaxes too slowly to be acceptable for use as an adjustable lens.

Another application of electrowetting control of droplet shapes is within a pixel of a flat panel display. As described by researchers from Liquavista, a VC-backed spin-out company from Philips, electrowetting can be used to spread water over a pixel to displace colored oil into a corner of the pixel [4]. With an array of pixels of this type, a flat panel video display can be generated as shown in Fig. 2. This approach is well-suited to monochrome displays and triplet sub-pixelation can be used to gener-

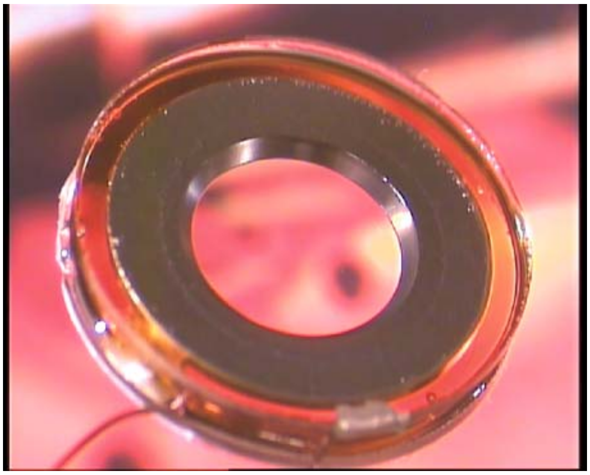

Electrowetting and Droplets, Figure 1 Electrowetting Liquid Lens (courtesy of Varioptic)

Electrowetting and Droplets, Figure 2 Electrowetting-based cyan display with 160 pixels/inch (courtesy of LiquaVista)

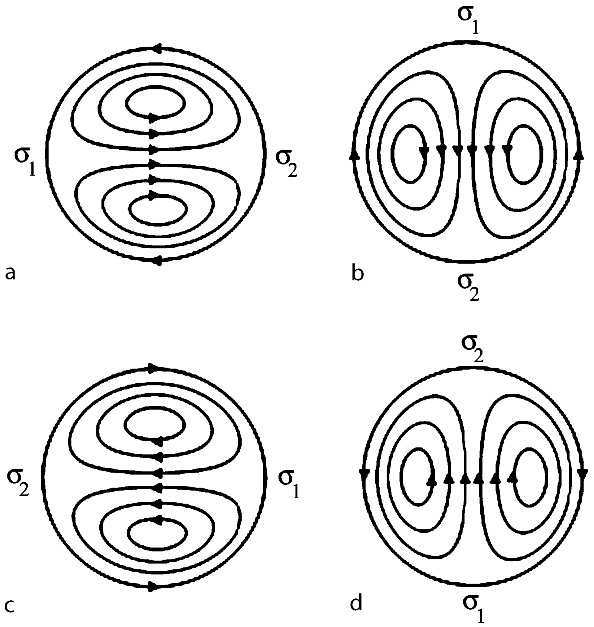

Electrowetting and Droplets, Figure 3 Flow field model for droplet motion in a square pattern. The actual three-dimensional electrowetting flow will be substantially different than this model but is expected to display similar chaotic advection with dependence on the period of the cycle. The flow model here is a time-dependent, high Peclet-number (low diffusion), two-dimensional Marangoni flow where the surface tension around the droplet periphery is varied in four phases: (**a**) for the first quarter of cycle $\sigma = (\sigma_1 + \sigma_2)/2 - (\sigma_1 - \sigma_2)\cos(\theta)/2$; (**b**) for the second quarter $\sigma = (\sigma_1 + \sigma_2)/2 + (\sigma_1 - \sigma_2)\sin(\theta)/2$; (**c**) for the third quarter the expression in (a) is used with σ_1 and σ_2 swapped; and (**d**) same as (b) with σ_1 and σ_2 swapped

ate a palette of apparent colors as used in current RGB schemes. An improved design allows the use of 3-layers of Cyan, Magenta, and Yellow oil dyes that can each be displaced to provide a broad range of colors without requiring any sub-pixelation.

Fluid Mixing

Upon coalescence of two droplets, the fluids from each droplet remain unmixed unless flows are generated within the newly-formed droplet in some manner. Internal flows and mixing can be induced through evaporation [3] which may also lead to thermal gradients and natural thermocapillary flows, but here we consider two electrowetting-induced mixing strategies that have been developed to accelerate the mixing process.

The first involves using an array of electrodes to move a droplet across a surface to generate fluid motion within the droplet. Using this approach there are two droplet movement patterns that have been considered: the droplet can be moved back-and-forth many times [7] or it can be moved in a square pattern on the array. The results of Paik et al. indicate that approximately 50 to 100 cycles of back-and-forth motion over a distance of 2–4 droplet diameters are required to obtain complete mixing. The type of flow generated by droplet movement through a square pattern can be modeled by the flow field shown in Fig. 3, which is a model flow within a two-dimensional, circular, viscous drop with non-uniform surface tension along its boundary generating the internal flow. The driving is switched periodically in time to generate the sequence of flows shown in the figure. This sequence of flows can result in chaotic advection of particles to provide thorough mixing. If the position of a single tracer particle is plotted after each complete cycle, a Poincaré map showing the basin of attraction of the particle can be generated.

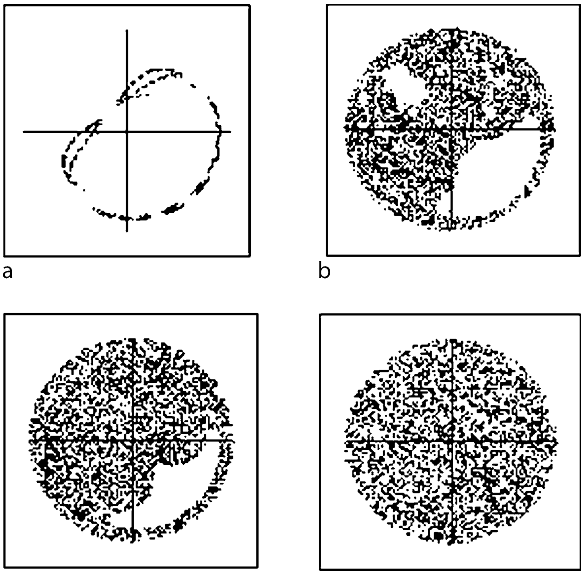

Electrowetting and Droplets, Figure 4 Poincaré maps of a single tracer particle location after each of 6400 periods of square pattern motion. The period of a complete cycle of the 4 flows from Fig. 1 is called T. Since we consider the droplet translation speed to be fixed, T can also be considered to be the size of the square pattern. The figures represent the Poincaré maps for four different periods of switching (**a**) $T = 4$, (**b**) $T = 8$, (**c**) $T = 9$, (**d**) $T = 10$

The maps shown in Fig. 4 demonstrate that, with convective flows alone (no diffusion), a particle can be made to visit any location within the droplet if the switching period is long enough. Mixing is quantified by tracking an initial swarm of particles whose population moments are observed to approach the completely-mixed values over time. The main result found using this model flow is that as the period increases, the number of cycles required for complete mixing decreases. However, as the period becomes long, corresponding to droplet motion over many droplet diameters, we find that no further reduction in the number of cycles for complete mixing can be obtained. The result is that further increases in the period proportionally increase the time for mixing.

The second method of mixing is through the generation of internal flows by the excitation of surface capillary waves. Mugele's research group has identified a condition of droplet oscillation in which a sessile droplet periodically attaches and detaches from a ground electrode wire whose axis is perpendicular to the surface of an EWOD chip. Through visualization of a fluorescent dye in the droplet, vertical mixing structures have been observed and mixing has been characterized [6]. We have generated similar oscillations of droplets using a unique *grounding-from-below* design for which a sessile droplet on an EWOD chip is grounded by a grid of microfabricated gold lines deposited after the dielectric so that good electrical contact with the droplet is maintained [2]. Application of an alternating current to the drive electrodes at an appropriate frequency is observed to generate large amplitude droplet motion. Improvements in mixing over a sandwiched-droplet configuration are described. The research results in the following section describe the details of the droplet shape-modes that are excited by application of an alternating potential.

E

Key Research Findings

The frequencies of the various Legendre modes of oscillating spherical droplets of liquid were first described by Lord Rayleigh [8] as

$$\omega_n = \sqrt{n(n-1)(n+2)\left(\frac{\gamma_{SV}}{\rho R^3}\right)}, \quad n = 2, 3, \ldots$$

where γ_{SV} is the liquid–vapor surface tension, ρ is the density of the liquid, and R is the radius of the droplet. He noted the interesting result that the oscillation of a droplet of water at 1 Hz requires a droplet radius of almost exactly 1 inch. This result is directly analogous to a mass-spring mechanical system in which the restoring force is surface tension which tends to force the droplet towards the unperturbed spherical shape. For a droplet attached to a surface, modes associated with even values of n in the above equation can be excited with the surface representing a plane of symmetry. This is a good approximation to the actual droplet shape if the contact angle remains close to $\pi/2$ and viscous boundary layers (i. e., the oscillatory Stokes layers) are thin.

In order to study the shape oscillations of a sessile drop, the experimental setup shown in Fig. 5 was designed and

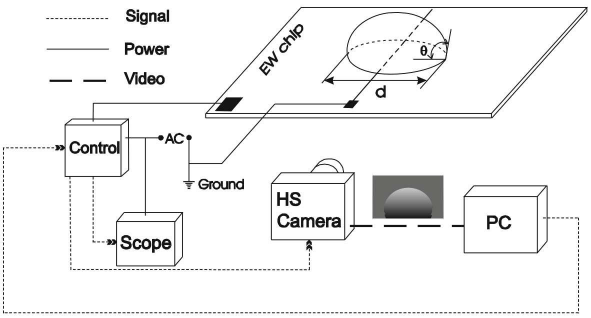

Electrowetting and Droplets, Figure 5 Experimental layout for electrowetting-induced droplet shape-mode oscillation experiments showing electrowetting chip, high-speed camera, and driving signal-generation system

assembled. The setup consists of an electrowetting chip, high-speed imaging unit and electronic timing devices. Forcing by AC signals was provided by a power-supply (California Instruments model 351-TL) with an output voltage of 60 V RMS and frequencies ranging from 1 to 4000 Hz. Imaging was performed using a Photron Inc. FASTCAM-X 512 PCI 10-bit high-speed camera. Typical imaging speeds were 2000 and 4000 frames per second depending on frequency of oscillation. Imaging was performed within a 512×256 pixel window corresponding to a 3.8 by 1.9 mm field of view. The field of view was illuminated using two 150 W fiber optic lamps illuminating a white screen behind the droplet resulting in high contrast between the droplet and the background screen. To avoid excessive heating of the droplet and light scattering from the surface of the drop, a tent-shaped shield made from regular paper was positioned over the droplet (not shown in Figure). To synchronize the excitation voltage, signal measurement and high-speed imaging during the oscillation of the droplet, triggering software was developed using LabVIEW™. The diameter, contact angle and maximum height were obtained using image processing techniques and were correlated for the entire duration of the oscillations. Typical activation time of the electrodes was 0.1 – 0.2 ms corresponding to 400 – 500 acquired frames.

The electrowetting chip used for excitation of the droplet was made of a 2.5 cm long by 2.5 cm wide glass slide covered by 120 nm of Indium Tin Oxide (CG-51IN-3084 from Delta Technologies). A 1 μm layer of Paralyne C (Cookson Electronics) was deposited using chemical vapor deposition to create the dielectric layer. Chromium/gold electrical grounding lines were patterned with a photolithographic lift-off technique on the dielectric. The entire surface of the chip was coated with 120 nm Teflon-AF (601, 6%, Dupont) diluted in a perfluoro-compound (FC75, Acros) creating a hydrophobic surface. The entire surface of the ITO-coated glass was considered one single electrode on which droplets were positioned. Grounding was performed via *grounding-from-below* as described in [2] through the ground line shown schematically in Fig. 5.

As seen in Fig. 6, excitations of the mode for $n = 6$ are shown for four phases during a cycle of oscillation of a 7 μL sessile droplet. Although the alternating current is applied at 180 Hz, the effective forcing is at 360 Hz in accordance with the Young–Lippman equation which describes that the electrowetting-induced changes are driven by the *square* of the applied voltage. Rayleigh's equation for $n = 6$, a 14 μL droplet (to include the reflection across the surface plane of symmetry of the 7 μL droplet) and surface tension equal to 73 mN/m indicates an oscillation frequency of 364.4 Hz. Thus we were forcing the droplet very close to this natural mode frequency.

The boundary of the droplet at any time (i. e., from an image frame) was determined through an automated image processing script. Fig. 7 demonstrates different stages of

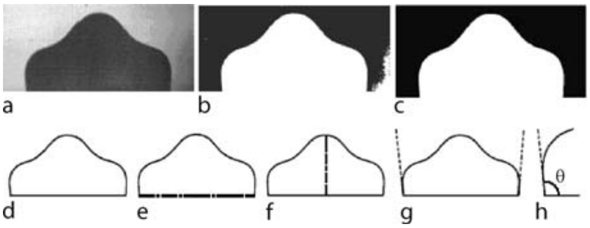

Electrowetting and Droplets, Figure 7 Boundary detection scheme applied to the acquired images. Raw images (**a**) are converted to gray-scale (**b**) and threshold filtering to get rid of noise (**c**). Subsequent to detection of the droplet boundary (**d**), diameter, maximum height and contact angles are estimated (**e**) to (**h**)

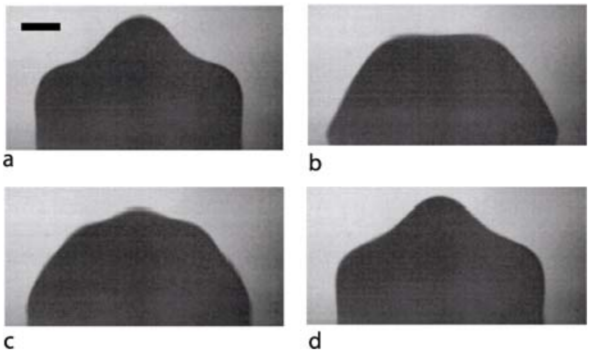

Electrowetting and Droplets, Figure 6 Snapshots of a 7 μl KCl droplet oscillating with a 60 V AC forcing at 180 Hz. Snapshots are 1 ms apart. Snapshots show $n = 6$ mode at several phases during oscillation. Scale bar corresponds to 0.5 mm

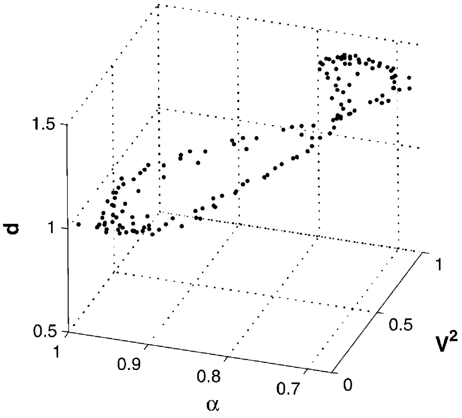

Electrowetting and Droplets, Figure 8 Phase portrait of droplet diameter and contact angle during AC excitation of voltage, V

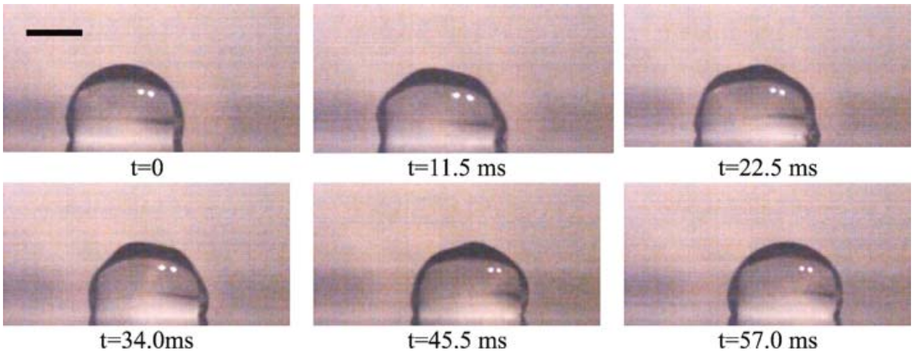

Electrowetting and Droplets, Figure 9 Snapshots of a 3 mL water droplet translating from over two neighboring 1 mm^2 electrodes. Forcing applied to the droplet was 60 V AC at 400 Hz. Two bright dots on the droplet are reflections of illumination sources. Scale bar corresponds to 1 mm

the image processing technique for individual frames. First, the frame was converted to a gray-scale image. Using a threshold value, the image was then converted to black-and-white based on a comparison of each pixel to the threshold. The border of the largest, contiguous, white region within this image was determined to be the boundary of the drop. To determine the width of the drop, a pixel sweep was performed for the left-most and right-most points on the boundary at the bottom of the drop. The difference in the resulting values represented the width of the drop. The height of the drop was determined to be equivalent to the value of upper-most point of the boundary which intersects the center of the width of the droplet. Contact angles were found by selecting all the left-most points and all the right-most points on the boundary of the drop between the bottom of the drop and 25 pixels (~ 0.2 mm) above the contact line. A linear fit was performed on both sets. The slope of each line represented the left and right side contact angles. Spectral analysis of the time series of these droplet height, radius and contact angles show the dominant response of the droplet at the forcing frequency with minor superharmonic components. A phase-portrait of the reconstructed time series is shown in Fig. 8.

Translation: Translation and oscillation of the droplet are caused by contact angle variations at the three-phase contact line resulting from the application of an electrical potential between the droplet and an electrode that underlies only a portion of the droplet. The platform used to experimentally study these phenomena consists of a grounded-from-below electrowetting chip patterned with arrays of 1 mm^2 electrodes, together with the high-speed imaging signal analysis. As seen in Fig. 9, AC excitation results in the formation of shape mode oscillations that occur while the droplet translates across the surface. Here, we see a droplet translation speed of approximately 1.5 cm/sec. A general observation of using AC excitation for sessile droplet translation is that a lower threshold voltage is required to initiate droplet motion than either a 2-plate sandwiched configuration or when DC electrowetting is performed. The lower required threshold voltage is attributed to the excitation of shape modes that apparently assist in breaking pinned contact-lines.

Future Directions for Research

There is substantial interest in the application of electrowetting to optofluidics and to the control of biological and chemical protocols for assays and biomedical diagnostics. Research efforts to control droplet shapes for lenses and displays are ongoing and are likely to lead to increased efforts to place electrowetting within chip-based optofluidic networks. Multi-step protocols remain a challenge for electrowetting-based systems because of the need to perform filtration and biomolecular separations as well as to handle multiple types of fluids that may contain surfactants, whole cells, lysates, proteins, nucleic acids, and other multi-component fluids. Thus, Lab-on-a-Chip applications will continue to be developed to address this multitude of challenges and to improve protocols, assays or diagnostics through miniaturization or acceleration of existing laboratory automation methods.

Cross References

▶ Applications Based on Electrowetting
▶ Droplet Dispensing
▶ Droplet-Based Lab-on-Chip Devices
▶ Digital Microfluidics
▶ Droplet Microreactors
▶ Electrowetting
▶ Microfluidic Mixing

References

1. Berge B, Peseux J (2000) Variable focal lens controlled by an external voltage: An application of electrowetting. Eur Phys J E 3:159–163
2. Cooney C, Chen CY, Emerling MR, Nadim A, Sterling JD (2006) Electrowetting droplet microfluidics on a single planar surface. Microfluid Nanofluid 2:435–446
3. Deegan RD (2000) Pattern formation in drying drops. Phys Rev E 61:475–485
4. Hayes RA, Feenstra BJ (2003) Video-speed electronic paper based on electrowetting. Nature 425:383–385
5. Kuiper S, Hendriks BHW (2004) Variable-focus liquid lens for miniature cameras. Appl Phys Lett 85:1128–1130
6. Mugele F, Baret JC, Steinhauser D (2006) Microfluidic mixing through electrowetting-induced droplet oscillations. Appl Phys Lett 88:204106
7. Paik P, Pamula VK, Fair RB (2003) Rapid droplet mixers for digital microfluidic systems. Lab Chip 3:253–259
8. Rayleigh L (1879) On the Capillary Phenomena of Jets. Proc R Soc London 29:71–97
9. Srinivasan V, Pamula VK, Fair RB (2004) An integrated digital microfluidic lab-on-a-chip for clinical diagnostics on human physiological fluids. Lab Chip 4:310–315
10. Wheeler AR, Moon H, Bird CA, Loo RRO, Kim CJ, Loo JA, Garrell RL (2005) Digital microfluidics with in-line sample purification for proteomics analyses with MALDI-MS. Anal Chem 77:534–540

Electrowetting on Insulator Coated Electrodes (EICE)

► Electrowetting
► Electrowetting, Applications
► Electrowetting and Droplets

Electrowetting on Line Electrodes (ELE)

► Electrowetting
► Electrowetting, Applications

Element Connectivity

Synonyms

Element connectivity matrix

Definition

The element connectivity is a set of data associated to an element that determines which nodes (or vertexes) form the element. This is frequently formed by moving about the element counter-clockwise and registering the node numbers as they are met. The number of entities in the connectivity of an element is equal to its number of nodes. When all element connectivities belonging to a computational grid are stored in a matrix, the so-called connectivity matrix is formed.

Cross References

► Meshless Methods
► Volume and Finite Difference Method for Modeling and Simulation

Element Connectivity Matrix

► Element Connectivity

Element-Free Methods

► Meshless Methods

Element Model

► Primitive Model

Elongated Bubble Flow

► Taylor Flow in Microchannels

Encapsulation

► Micro-Encapsulation

Endergonic

► Endothermic

Endothermic

Synonyms

Heat absorption; Endergonic

Definition

An endothermic process is one in which heat has to be supplied to the system from the surroundings.

Cross References

► Chemical Vapor Deposition for Film Deposition
► Plasma-Treatment Physics

Entrance Flows

► Developing Flows

Entrance Region

Gian Luca Morini
DIENCA, Università di Bologna, Bologna, Italy
gianluca.morini@mail.ing.unibo.it

Synonyms

Developing region; Establishing region

Definition

The entrance region of a microchannel corresponds to the part of the channel in which the velocity and/or the temperature fields are not completely developed.

Overview

The *hydrodynamic entrance region* of a microchannel is that region where the velocity boundary layer is developing from zero thickness at the entrance up to cover the whole cross-section far downstream. Usually, this region coincides with the part of the channel near the inlet section. The flow in this region is designated as hydrodynamically developing (Fig. 1).
For microchannels in which the flow is originated by means of electro-osmosis the hydrodynamic entrance region can start from an internal point of the channel where the zeta potential at the wall differs from zero.

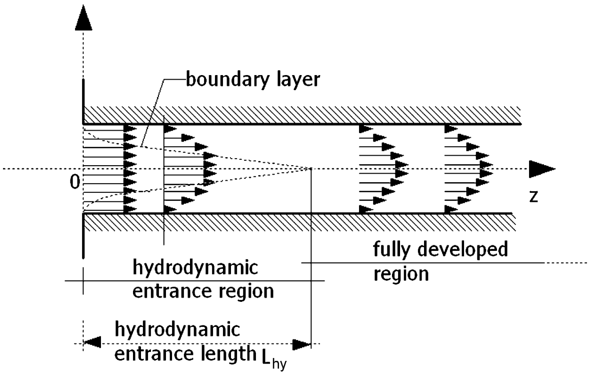

Entrance Region, Figure 1 The hydrodynamic entrance region

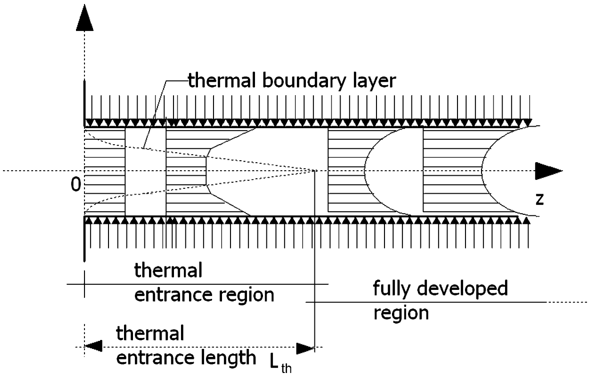

Entrance Region, Figure 2 The thermal entrance region

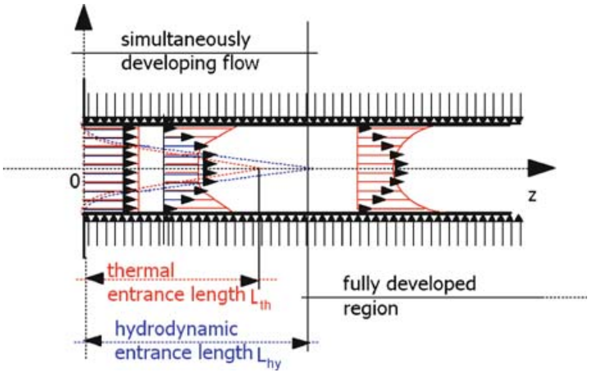

Entrance Region, Figure 3 Hydrodynamically laminar fully developed and thermally developing flow

In analogy, the *thermal entrance region* of a microchannel is defined as that region where the temperature boundary layer is developing (Fig. 2). The thermal entrance region can or cannot correspond with the inlet region of the microchannel; for example, if the heating begins only at some point after the inlet section the thermal entrance region can be uncoupled from the hydrodynamic entrance region. For this reason, in the thermal entrance region the velocity profile can be either developed or developing. In general, it is possible to individuate the following three categories of thermal entrance problems:

- The velocity profile is fully developed in the thermal entrance region and it remains fixed while the temperature profile develops. In this case the flow is designated as *hydrodynamically fully developed* and *thermally developing* flow; this situation can be obtained in a microchannel with adiabatic walls in the region near the entrance (*adiabatic preparation*) (see Fig. 3).

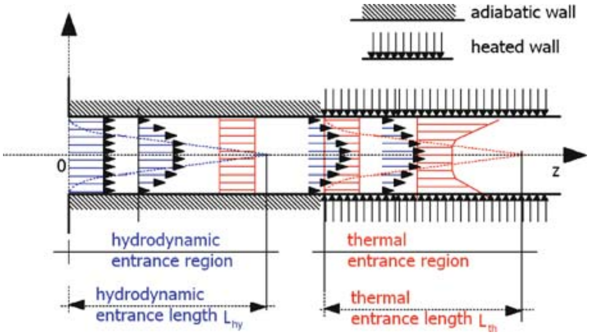

Entrance Region, Figure 4 Simultaneously developing flow

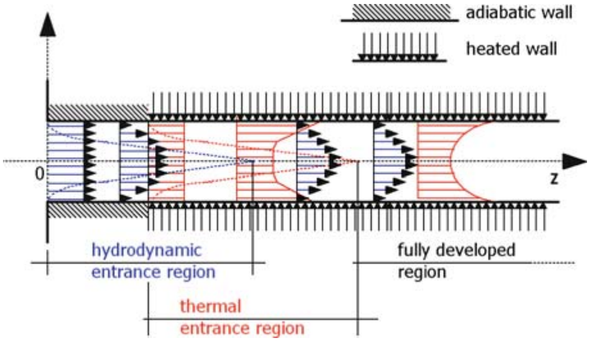

Entrance Region, Figure 5 Partially simultaneous developing flow

- The velocity and the temperature profiles develop simultaneously. In this case the flow is designated as *simultaneously developing flow*; this situation is obtained in the region near the entrance in a uniformly heated microchannel (see Fig. 4).
- The temperature profile starts developing at some point in the hydrodynamic entrance region (see Fig. 5). This situation can be obtained if the heating starts at some point within the hydrodynamic entrance region.

Basic Methodology

The rate of developments of velocity and temperature profiles in the entrance region depends on the Prandtl number defined as the ratio of fluid momentum diffusivity ν (kinetic viscosity) to fluid thermal diffusivity α:

$$\mathrm{Pr} = \frac{\nu}{\alpha} = \frac{\nu}{\frac{k}{\rho c_p}} = \frac{\mu c_p}{k} \tag{1}$$

where k is the fluid thermal conductivity, ρ is the fluid density, μ is the dynamic viscosity and c_p is the fluid specific heat.

The Prandtl number depends on the thermophysical properties of the fluid only. Typical values of the Prandtl number are 0.001 – 0.03 for liquid metals, 0.2 – 1 for gases, 1 – 10 for water, 5 – 50 for organic liquids and 50 – 2000 for oils. The Prandlt number depends on the bulk temperature of the fluid since the viscosity is a strong function of temperature; for this reason, especially in very narrow microchannels in which the viscous heating effects are not negligible (see ►viscous heating and ►viscous dissipation), the Prandlt number cannot be considered as a constant along the channel.

For $\mathrm{Pr} = 1$, the velocity and temperature profiles develop at the same rate, if both are uniform at the entrance; this situation is typical for gases. For $\mathrm{Pr} > 1$ (e. g. water), the velocity profile develops more rapidly than the temperature profile; for large values of the Prandtl number, such as for oils, the analysis of the thermal development in the entrance region can be conducted by considering the velocity as fully developed (see Fig. 3). For the limiting case of $\mathrm{Pr} = \infty$ the velocity profile is developed before the temperature profile starts developing; this case can be considered as a good approximation for highly viscous fluids. For $\mathrm{Pr} < 1$, the temperature profile develops more rapidly than the velocity one. For the limiting case of $\mathrm{Pr} = 0$ the velocity profile remains uniform over the cross-section (*slug flow*) while the temperature profile is developing; this case is generally used in order to model the entrance region for liquid metals or for electro-osmotic flows.

The velocity and temperature profiles in the entrance region have to be determined by solving the complete set of Navier–Stokes equations and the energy balance:

$$\begin{aligned} -\frac{1}{\rho}\frac{\mathrm{d}\rho}{\mathrm{d}t} &= \nabla\cdot\boldsymbol{v} \\ \rho(\boldsymbol{v}\cdot\nabla\boldsymbol{v}) &= -\nabla p + \rho\boldsymbol{g} - \nabla\cdot\tau \\ \rho c_p(\boldsymbol{v}\cdot\nabla T) &= -\nabla\cdot\boldsymbol{q} + \beta T\boldsymbol{v}\cdot\nabla p) - \tau : \nabla\boldsymbol{v} \end{aligned} \tag{2}$$

in which $\boldsymbol{v}$ is the velocity vector, ρ is the fluid density, t is the time, p is the pressure, D/Dt is the total derivative, τ is the viscous tensor, T is the temperature, β is the thermal expansion coefficient and $\boldsymbol{q}$ the heat flux (see ►viscous dissipation and ►convective heat transfer in microchannels).

For steady-state incompressible Newtonian flows the governing equations can be simplified as follows:

$$\begin{aligned} \nabla\cdot\boldsymbol{v} &= 0 \\ \rho(\boldsymbol{v}\cdot\nabla\boldsymbol{v}) &= -\nabla p + \rho\boldsymbol{g} + \mu\nabla^2\boldsymbol{v} \\ \rho c_p(\boldsymbol{v}\cdot\nabla T) &= -\nabla\cdot\boldsymbol{q} + \mu\Phi_{\mathrm{inc}} \end{aligned} \tag{3}$$

in which Φ_{inc} is the rate of viscous dissipation for an incompressible fluid (its expression can be found in ▶ viscous dissipation) and $\boldsymbol{v} = (v_x, v_y, v_z)$ where z is the axial coordinate.

The boundary conditions that have to be used together with Eq. (3) can be found in ▶ pressure-driven single phase liquid flow and in ▶ pressure-driven single phase gas flows for the momentum equation and in ▶ convective heat transfer in microchannel for the energy balance equation.

The hydrodynamic and thermal entry length problem can be solved either by employing the boundary layer-type idealizations or by considering the complete set of equations [1].

It may now be added here that rounded entrances or square-edged entrances can influence the values assumed by the convective heat transfer coefficient but especially by the friction factor in the entrance region.

All the numerical results obtained by solving numerically Eq. (3) for developing flows are obtained by considering the following entrance conditions:

- A uniform velocity profile (equal to the mean velocity W) at the entrance with negligible transversal components ($v_z = W$; $v_x = v_y = 0$). In this case the vorticity defined as $\varpi = (\partial v_z/\partial y - \partial v_y/\partial z; \partial v_x/\partial z - \partial v_z/\partial x; \partial v_y/\partial x - \partial v_x/\partial y)$ is not zero at the entrance. This situation can be obtained experimentally only by using a screen at the channel inlet. This is the entrance boundary condition that is most frequently used for hydrodynamic entrance problems.
- A uniform velocity profile with zero vorticity ($\varpi = 0$) at the entrance. This entrance condition is referred to as *irrotational flow entry*.
- Since an entrance condition of a uniform velocity profile cannot exist when axial diffusion of momentum or vorticity is included in the analysis, a mathematically more appropriate entrance condition imposes the velocity profile as uniform and parallel at the virtual section $z = -\infty$ by considering an impermeable frictionless wall between $z = -\infty$ and $z = 0$.

Since data cover only a few simple entrance geometries, the designer must exercise judgment in the application of the correlations proposed to calculate the friction factor and the convective heat transfer coefficient in the entrance region of a microchannel.

Hydrodynamic Entrance Length

The *hydrodynamic entrance length* (L_{hy}) is defined as the channel length required to achieve a maximum value of the velocity of 99% of the corresponding fully developed magnitude when the entering flow is uniform.

The hydrodynamic entrance length L_{hy} can be written in dimensionless form as follows:

$$L^+_{hy} = \frac{L_{hy}}{D_h \mathrm{Re}} \tag{4}$$

For conventional channels the hydrodynamic entrance length can be estimated for laminar flows by means of the following approximated equation:

$$L^+_{hy} = \frac{L_{hy}}{D_h \mathrm{Re}} = 0.05 \tag{5}$$

Let us consider a microtube with a fixed internal diameter D; the length of the microtube (L) is equal to 2000 times the internal diameter. Water flows through the microtube by means of an imposed pressure difference between the ends of the microtube. The water flow rate through the microtube increases with the imposed pressure difference. If the maximum value of the imposed pressure difference is fixed to 200 bar one can calculate the maximum value of the Reynolds number that it is possible to reach in the microtube (see ▶ pressure-driven single-phase liquid flow entry). In correspondence of the maximum value of the Reynolds number one can estimate the entrance length by using Eq. (5).

In Table 1 are quoted the maximum Reynolds number, the corresponding hydrodynamic entrance length and the length to entrance length ratio (L/L_{hy}) as a function of the internal diameter of the microtube for water as working fluid. The results quoted in Table 1 allow one to highlight the following main aspects:

- The typical Reynolds numbers that characterize liquid laminar flows in microchannels are in general lower than those obtained by working with conventional channels under the same pressure difference at the ends.

Entrance Region, Table 1 Maximum Reynolds number, hydrodynamic entrance length and total axial length to entrance length ratio for circular microchannels with a fixed L/D value ($L/D = 2000$) and pressure drop ($\Delta p = 200$ bar) as a function of the microtube internal diameter

D [μm]	L [m]	Re_{max}	L_{hy} [μm]	L/L_{hy}
5	0.01	10.4	2.6	3864
10	0.02	41.4	20.7	966
15	0.03	93.2	69.9	429
20	0.04	165.6	165.6	242
25	0.05	258.8	323.5	155
35	0.07	507.2	887.7	79
50	0.1	1035.2	2587.9	39
75	0.15	2329.1	8734.2	17

- The entrance length becomes very low for low internal diameters; for $D < 10\,\mu\text{m}$ the hydrodynamic entrance region is comparable to the diameter of the microtube.
- For a fixed value of the ratio L/D equal to 2000, the entrance region holds a larger part of the microchannel length if the internal diameter is increased.

From the data quoted in Table 1 it is evident that for microtubes having a diameter less than 20 μm the flow is usually characterized by very low Reynolds number (Re < 100 for a maximum Δp of 200 bar). It is easy to demonstrate that for nanotubes ($D < 1\,\mu\text{m}$) the maximum Reynolds number that corresponds to the maximum pressure drop of 200 bar approaches rapidly to 0. This fact highlights that for water laminar flows through microchannels with $D < 20\,\mu\text{m}$ viscous forces completely dominate inertial forces; this kind of flow is named in the literature *creeping flow*. This kind of flow becomes predominant for the smaller microchannels.

It has been numerically demonstrated that Eq. (5) no longer holds for creeping flows where the dimensionless hydrodynamic entrance length seems to be a function of the Reynolds number. It has been demonstrated that for very low Reynolds numbers the hydrodynamic entrance length has to be calculated by means of the following equation:

$$L_{\text{hy}}^{+} = \frac{L_{\text{hy}}}{D_{\text{h}}\text{Re}} = 0.056 + \frac{0.6}{\text{Re}(0.035\text{Re} + 1)} \qquad (6)$$

Equation (6) is useful in order to calculate the hydrodynamic entrance length for liquid flows characterized by very low Reynolds numbers (Re < 10) through small microchannels.

Another conclusion that can be highlighted by the data of Table 1 is that for the microchannels with a low value of the inner diameter the ratio L/L_{hy} tends to increase; this fact underlines that the entrance region of the smaller microchannels plays a negligible role with respect to the more extended fully developed region. On the contrary, when the inner diameter increases the entrance region tends to take place in a large part of the axial length of the microchannels and the role played by the entrance region on the pressure drop and on the convective heat transfer coefficients becomes more important.

On the other hand, it is important to underline that for gas flows in microchannels, for the same maximum pressure difference (200 bar) between the ends of a microtube, larger Reynolds numbers can be obtained (up to 2800 with nitrogen for $D = 5\,\mu\text{m}$). The entrance length obtained for gas flows is larger than that obtained for liquids if the same internal diameter (D), length (L) and Δp are considered. For a large pressure difference through the microtube the gas density variation in the axial direction becomes important and the gas flow tends to accelerate axially (gas compressibility effect). The conventional theory underlines that compressibility effects become important for a gaseous flow through a channel when at least one of the following inequalities is satisfied:

$$\begin{cases} Ma_{\text{avg}} > 0.3 \\ \frac{\Delta p}{p_{\text{in}}} > 0.05 \end{cases} \qquad (7)$$

where Ma_{avg} is the average value of the Mach number along the microtube and p_{in} is the value of the pressure at the inlet of the microtube. When the first inequality is satisfied, the gas flow cannot be considered as locally incompressible and the momentum and energy equation have to be solved as coupled. When the second inequality is satisfied, even if the gas flow can be locally modeled as incompressible, the density variation along the tube cannot be ignored. In this case, the effects due to the gas acceleration along the tube become important, even if the Mach number is low: this is usually the case for microchannels. In fact, since in microchannels the pressure drop along the tube length is much larger than for conventional-size tubes, the effects of the gas acceleration cannot in general be neglected, even for very low values of the Mach numbers. The gas acceleration leads to changes in the velocity profile not only in magnitude but also in shape. The magnitude increments produce additional pressure drop while the shape changes alter the friction factor at the walls. The continuous variation in shape of the velocity profile means that no fully developed and no locally fully developed flow occur. In this case the entrance region holds entirely the microchannel length. This fact influences also the convective heat transfer coefficient since no fully developed temperature profiles can occur if the flow is developing.

The hydrodynamic entrance length is also influenced by the cross-sectional geometry of the microchannel. In order to take into account the role played by the geometry of the microchannel cross-section on the hydrodynamic entrance length, Eq. (5) can be replaced by the following approximate equation:

$$L_{\text{hy}}^{+} = \frac{V_{\max}^{2} - 1 - K(\infty)}{4f\text{Re}_{\text{fd}}} \qquad (8)$$

This equation allows the evaluation of the hydrodynamic length if one knows, for the considered cross-section, the value of the fully developed Poiseuille number ($f\text{Re}_{\text{fd}}$), the fully developed ratio between the maximum and the mean value of the velocity and $K(\infty)$, the asymptotic incremen-

tal pressure drop number:

$$V_{\max} = \frac{v_{z,\max}}{W} \qquad K(\infty) = 2(K_e - K_d) \tag{9}$$

The fully developed values of $V_{\max}$, K_d, K_e and $f\mathrm{Re}_{fd}$ can be found in ►pressure-driven single phase liquid flow for the most common microchannel cross-sections.

Sometimes, the rarefaction effects for gas flows through microchannels cannot be ignored (especially for $D_h <$ 40 μm). For rarefied gases through microchannels (for which the Knudsen number (Kn) is larger than 10^{-3}) the gas rarefaction tends to increase L_{hy} in the slip flow regime, due to slip at the walls (see ►pressure–driven single phase gas flows for the definition of slip flow regime and Knudsen number). Barber and Emerson [3] used a two-dimensional finite-volume Navier–Stokes solver to simulate the flow of a gas entering a parallel-plate microchannel in the slip-flow regime, with first-order boundary conditions. Their simulated data for $\mathrm{Kn} \in [0; 0.1]$ and $\mathrm{Re} \in [0; 400]$ were fitted by a least-squares technique and led to the following expression for the hydrodynamic development length:

$$\frac{L_{hy}}{D_h} = \frac{0.332}{0.0271\mathrm{Re} + 1} + 0.011\mathrm{Re}\frac{1 + 14.78\mathrm{Kn}}{1 + 9.78\mathrm{Kn}} \tag{10}$$

where D_h is the hydraulic diameter equal to $2h$ with h defined as the distance between the parallel plates.

Pressure Drop

The ratio between the local wall shear stress τ_z to the flow kinetic energy per unit volume is defined as the local Fanning friction factor:

$$f_z = \frac{\tau_z}{\left(\frac{\rho W^2}{2}\right)} \tag{11}$$

where W is the value of the average fluid velocity and z is the axial coordinate. For very small microchannels and for nanochannels this way to normalize the local wall shear stress can be difficult to follow.

The mean Fanning friction factor in the hydrodynamic entrance region is defined as follows:

$$\bar{f} = \frac{1}{z}\int_0^z f_z \, \mathrm{d}z \tag{12}$$

In the hydrodynamic entrance region, the pressure drop can be considered as due to the wall shear and to the change in momentum flow. The total pressure drop for constant density flow between the entrance ($z = 0$) and z can be written by introducing the *apparent friction factor*:

$$\frac{\Delta p}{\frac{\rho W^2}{2}} = 4 f_{app} \frac{z}{D_h} \tag{13}$$

The value of the apparent friction factor can be calculated by means of Eq. (13) if the total pressure drop from $z = 0$ to z is known. The apparent value of the friction factor takes into account both the skin friction and the change in momentum rate due to change in the shape of the velocity profile in the hydrodynamic entrance region (see Fig. 1).

Sometimes, the pressure drop in the hydrodynamic entrance region is calculated by introducing the incremental pressure drop number $K(z)$; this term takes into account the additional pressure drop due to momentum change and the accumulated increment in wall shear between developing flow and developed flow. By introducing $K(z)$ the total pressure drop is calculated as follows:

$$\frac{\Delta p}{\frac{\rho W^2}{2}} = 4 f\mathrm{Re}_{fd}\left(\frac{z}{D_h \mathrm{Re}}\right) + K(z) \tag{14}$$

where $f\mathrm{Re}_{fd}$ is the Poiseuille number for the fully developed flow; the values of $f\mathrm{Re}_{fd}$ for the most common cross-sectional geometries for microchannels can be found in ►pressure-driven single phase liquid flow.

By combining Eqs. (13) and (14) the relation between the apparent Fanning friction factor and the incremental pressure drop number can be written as follows:

$$K(z) = 4(f\mathrm{Re}_{app} - f\mathrm{Re}_{fd}) z^{+} \tag{15}$$

where $z^{+} = z/(D_h \mathrm{Re})$.

Circular Cross-Section

The following correlation, proposed originally by Shah [2], can be used in order to calculate the apparent Poiseuille number for microtubes as a function of the dimensionless axial coordinate z^{+} for laminar flows:

$$f\mathrm{Re}_{app} = \frac{3.44}{(z^{+})^{0.5}} + \frac{1.25/(4z^{+}) + 16 - 3.44/(z^{+})^{0.5}}{1 + 0.00021(z^{+})^{-2}} \tag{16}$$

Parallel Plate Cross-Section

The following correlation gives the apparent Poiseuille number for parallel plate microchannels as a function of the dimensionless axial coordinate z^{+} for laminar flows:

$$f\mathrm{Re}_{app} = \frac{3.44}{(z^{+})^{0.5}} + \frac{0.674/(4z^{+}) + 24 - 3.44/(z^{+})^{0.5}}{1 + 0.00029(z^{+})^{-2}} \tag{17}$$

Entrance Region, Table 2 Apparent Poiseuille number for rectangular channels as a function of the axial dimensionless coordinate z^+ and of the aspect ratio β

	$f\mathrm{Re}_{\mathrm{app}}$		
z^+	$\beta = 1$	$\beta = 0.5$	$\beta = 0.2$
0.001	111.0	111.0	111.0
0.002	80.2	80.2	80.2
0.003	66.0	66.0	66.1
0.004	57.6	57.6	57.9
0.005	51.8	51.8	52.5
0.006	47.6	47.6	48.4
0.007	44.6	44.6	45.3
0.008	41.8	41.8	42.7
0.009	39.9	40.0	40.6
0.01	38.0	38.2	38.9
0.015	32.1	32.5	33.3
0.02	28.6	29.1	30.2
0.03	24.6	25.3	26.7
0.04	22.4	23.2	24.9
0.05	21.0	21.8	23.7
0.06	20.0	20.8	22.9
0.07	19.3	20.1	22.4
0.08	18.7	19.6	22.0
0.09	18.2	19.1	21.7
0.1	17.8	18.8	21.4

Rectangular Cross-Section

The values of the apparent Poiseuille number for rectangular channels as a function of the dimensionless axial coordinate z^+ and of the rectangular aspect ratio β (defined as the ratio between the height and the width of the channel) are quoted in Table 2.

Developing Nusselt Number

If one knows the temperature distribution in the entrance region the local value of the Nusselt number in a point on the heated perimeter can be calculated from its operational definition:

$$\mathrm{Nu}_z = \frac{h_z D_\mathrm{h}}{k} = \frac{D_\mathrm{h} \left.\frac{\partial T}{\partial n}\right|_\Gamma}{T_\mathrm{wm} - T_\mathrm{b}} \tag{18}$$

in which the peripheral mean wall temperature T_wm and the bulk temperature T_b have been defined as

$$T_\mathrm{wm} = \frac{\int_{\Gamma_\mathrm{h}} T|_\Gamma \,\mathrm{d}\Gamma}{\Gamma_\mathrm{h}} \qquad T_\mathrm{b} = \frac{1}{\dot{m} c_p} \int_\Omega \rho v_z c_p T d\Omega \tag{19}$$

where Γ_h is the heated perimeter, Ω is the microchannel cross-sectional area, and $\dot{m}$ is the mass flow rate.
The mean Nusselt number in the thermal entrance region is calculated as follows:

$$\mathrm{Nu}_\mathrm{m} = \frac{1}{z} \int_0^z \mathrm{Nu}_z \,\mathrm{d}z \tag{20}$$

For laminar flows, the value of the mean Nusselt number depends on the thermal boundary condition considered; a description of the most common thermal boundary conditions for microchannels can be found in ►convective heat transfer in microchannels (i. e. T, H1, H2 boundary conditions).

Circular Cross-Section

For laminar flows under the T boundary condition (see ►convective heat transfer in microchannels) with a fully developed velocity profile (*hydrodynamically fully developed* and *thermally developing* flow; Fig. 3), the following correlation, proposed originally by Shah [2] for conventional channels, can be used in order to calculate the mean Nusselt number in the entrance region for circular microtubes as a function of the dimensionless axial coordinate z^*:

$$\mathrm{Nu}_{\mathrm{m},T} = \begin{cases} \frac{1.615}{(z^*)^{1/3}} - 0.7 & \text{for } z^* \le 0.005 \\ \frac{1.615}{(z^*)^{1/3}} - 0.2 & \text{for } 0.005 < z^* < 0.03 \\ 3.657 + \frac{0.0499}{z^*} & \text{for } z^* \ge 0.03 \end{cases} \tag{21}$$

where z^* is defined as follows:

$$z^* = \frac{z}{D_\mathrm{h} \mathrm{Re}\,\mathrm{Pr}} \tag{22}$$

On the contrary, under the H boundary condition (see ►convective heat transfer in microchannels) with a fully developed velocity profile (*hydrodynamically fully developed* and *thermally developing* flow; Fig. 3) the mean Nusselt number for circular microtubes as a function of the dimensionless axial coordinate z^* for laminar flows can be calculated as follows:

$$\mathrm{Nu}_{\mathrm{m},H} = \begin{cases} \frac{1.953}{(z^*)^{1/3}} & \text{for } z^* \le 0.03 \\ 4.364 + \frac{0.0722}{z^*} & \text{for } z^* > 0.03 \end{cases} \tag{23}$$

Theoretically, the mean and the local Nusselt number along a channel having a length equal to L can be predicted

Entrance Region, Table 3 Coefficients of the generalized Hausen correlation (Eq. (22)) for hydrodynamically fully developed and thermally developing flow and for simultaneously developing flow in microtubes

Boundary condition	Velocity	Pr	Nu	$\overline{\text{Nu}}$	K_1	K_2	b
T	Developed	Any	mean	3.66	0.0668	0.04	2/3
T	Developing	0.7	mean	3.66	0.104	0.016	0.8
H	Developed	Any	local	4.36	0.023	0.0012	1
H	Developing	0.7	local	4.36	0.036	0.0011	1

by means of the following generalized *Hausen correlation*, valid for $\text{Re} < 3000$:

$$\text{Nu} = \overline{\text{Nu}} + K_1 \frac{\left(\frac{\text{Re}\,\text{Pr}\,D_\text{h}}{L}\right)}{\left(1 + K_2\left(\frac{\text{Re}\,\text{Pr}\,D_\text{h}}{L}\right)^b\right)} \tag{24}$$

In the *Hausen correlation* the Nusselt number is calculated as a sum of two terms: the first term ($\overline{\text{Nu}}$) is the fully developed value of the Nusselt number; its value can be found in ►convective heat transfer in microchannels for the most common microchannel cross-sections. The second term takes into account the effects of the thermal entrance region. The values of the coefficients K_1, K_2 and b for circular microchannels are quoted in Table 3.

Parallel Plate Cross-Section

For laminar flows under the T boundary condition (see ►convective heat transfer in microchannels) with a fully developed velocity profile (*hydrodynamically fully developed* and *thermally developing* flow; Fig. 3), the following correlation, proposed originally by Shah for conventional channels, can be useful to calculate the mean Nusselt number in the entrance region of parallel plate microchannels as a function of the dimensionless axial coordinate z^* :

$$\text{Nu}_{\text{m},T} = \begin{cases} \frac{1.849}{(z^*)^{1/3}} & \text{for } z^* \le 0.0005 \\ \frac{1.849}{(z^*)^{1/3}} + 0.6 & \text{for } 0.0005 < z^* \le 0.006 \\ 7.541 + \frac{0.0235}{z^*} & \text{for } z^* > 0.006 \end{cases} \tag{25}$$

On the contrary, under the H boundary condition (see ►convective heat transfer in microchannels) with a fully developed velocity profile (*hydrodynamically fully developed* and *thermally developing* flow; Fig. 3) the following correlation can be used in order to calculate the mean Nusselt number for parallel plate microchannels as a function of the dimensionless axial coordinate z^* for laminar flows:

$$\text{Nu}_{\text{m},H} = \begin{cases} \frac{2.236}{(z^*)^{1/3}} & \text{for } z^* \le 0.001 \\ \frac{2.236}{(z^*)^{1/3}} + 0.9 & \text{for } 0.001 < z^* < 0.01 \\ 8.235 + \frac{0.0364}{z^*} & \text{for } z^* \ge 0.01 \end{cases} \tag{26}$$

Rectangular Cross-Section

In Tables 4 and 5 the mean Nusselt numbers for *hydrodynamically fully developed* and *thermally developing* flow in rectangular microchannels are reported as a function of the dimensionless axial coordinate z^* and of the aspect ratio β for T and H1 boundary conditions (with four heated sides) respectively.

For *simultaneously developing flows* in rectangular microchannels the values of the mean Nusselt number are reported in Tables 6 and 7 for T and H1 boundary conditions respectively for a fluid having a Prandtl number equal to 0.72. By observing the mean Nusselt numbers quoted in Tables 4, 5, 6 and 7 it is evident that the Nusselt numbers for H1 boundary condition are larger than those obtained for T boundary condition. In addition, the mean Nusselt numbers for simultaneously developing flows are larger that those for *hydrodynamically fully developed* and *thermally developing* flows. The Nusselt number increases if the aspect ratio decreases.

Thermal Entrance Length

The *thermal entrance length* (L_th) is defined as the microchannel length required to achieve a value of the local Nusselt number Nu_z equal to 1.05 times the value of the Nusselt number for fully developed flow.

The thermal entrance length L^+_th can be written in dimensionless form as follows:

$$L^+_\text{th} = \frac{L_\text{th}}{D_\text{h}\text{Re}\,\text{Pr}} \tag{27}$$

In order to calculate the thermal entrance length one can investigate where the temperature at the channel centerline deviates from the inlet fluid temperature; in fact, at this point the thermal boundary layers merge. However, since the radial heat conduction becomes important near the region where the boundary layers merge the real centerline temperature at the end of the thermal entrance region may be significantly higher than the inlet fluid temperature.

When the effect of the fluid axial heat conduction is considered the thermal entrance length increases for decreasing Péclet number ($\text{Pe} = \text{Re}\,\text{Pr}$).

Entrance Region, Table 4 Mean Nusselt numbers for hydrodynamically fully developed and thermally developing flow in rectangular microchannels as a function of the dimensionless axial coordinate z^* and of the aspect ratio β for T boundary condition

	$Nu_{m,T}$					
$1/z^*$	$\beta = 1$	$\beta = 0.5$	$\beta = 1/3$	$\beta = 0.25$	$\beta = 0.2$	$\beta = 1/6$
0	2.65	3.39	3.96	4.51	4.92	5.22
10	3.50	3.95	4.54	5.00	5.36	5.66
20	4.03	4.46	5.00	5.44	5.77	6.04
30	4.47	4.86	5.39	5.81	6.13	6.37
40	4.85	5.24	5.74	6.16	6.45	6.70
60	5.50	5.85	6.35	6.73	7.03	7.26
80	6.03	6.37	6.89	7.24	7.53	7.77
100	6.46	6.84	7.33	7.71	7.99	8.17
120	6.86	7.24	7.74	8.13	8.39	8.63
140	7.22	7.62	8.11	8.50	8.77	9.00
160	7.56	7.97	8.45	8.86	9.14	9.35
180	7.87	8.29	8.77	9.17	9.46	9.67
200	8.15	8.58	9.07	9.47	9.79	10.01

Entrance Region, Table 5 Mean Nusselt numbers for hydrodynamically fully developed and thermally developing flow in rectangular microchannels as a function of the dimensionless axial coordinate z^* and of the aspect ratio β for H1 boundary condition

	$Nu_{m,H1}$			
$1/z^*$	$\beta = 1$	$\beta = 0.5$	$\beta = 1/3$	$\beta = 0.25$
0	3.60	4.11	4.77	5.35
10	4.48	4.94	5.45	6.03
20	5.19	5.60	6.06	6.57
30	5.76	6.16	6.60	7.07
40	6.24	6.64	7.09	7.51
60	7.02	7.45	7.85	8.25
80	7.66	8.10	8.48	8.87
100	8.22	8.66	9.02	9.39
120	8.69	9.13	9.52	9.83
140	9.09	9.57	9.93	10.24
160	9.50	9.96	10.31	10.61
180	9.85	10.31	10.67	10.92
200	10.18	10.64	10.97	11.23

Entrance Region, Table 6 Mean Nusselt numbers for simultaneously developing flow in rectangular microchannels as a function of the dimensionless axial coordinate z^* and of the aspect ratio β for T boundary condition

	$Nu_{m,T}$				
$1/z^*$	$\beta = 1$	$\beta = 0.5$	$\beta = 1/3$	$\beta = 0.25$	$\beta = 1/6$
10	3.75	4.20	4.67	5.11	5.72
20	4.39	4.79	5.17	5.56	6.13
30	4.88	5.23	5.60	5.93	6.47
40	5.27	5.61	5.96	6.27	6.78
50	5.63	5.95	6.28	6.61	7.07
60	5.95	6.27	6.60	6.90	7.35
80	6.57	6.88	7.17	7.47	7.90
100	7.10	7.42	7.70	7.98	8.38
120	7.61	7.91	8.18	8.48	8.85
140	8.06	8.37	8.66	8.93	9.28
160	8.50	8.80	9.10	9.36	9.72
180	8.91	9.20	9.50	9.77	10.12
200	9.30	9.60	9.91	10.18	10.51
220	9.70	10.00	10.30	10.58	10.90

The thermal entrance length required for the *simultaneously developing flows* (Fig. 4) is in general larger than that obtained by considering a fully developed velocity profile (Fig. 3).

Especially for laminar flows, the thermal entrance length depends on the thermal boundary conditions considered. For example, for a *hydrodynamically laminar fully developed* and *thermally developing* flow through circular microtubes the dimensionless thermal entrance length (L_{th}^{+}) is equal to 0.03347 for a T boundary condition (*constant wall temperature*) and equal to 0.04305 for an H boundary condition (*constant wall heat flux*). For a parallel plate channel the dimensionless thermal entrance length (L_{th}^{+}) is equal to 0.00797 for T boundary condition (*constant wall temperature*) and equal to 0.01154 for H boundary condition (*constant wall heat flux*).

In Table 8 the values of the dimensionless thermal entrance length for rectangular channels, parallel plates ($\beta = 0$) and for circular tubes are quoted as a function of the aspect

Entrance Region, Table 7 Mean Nusselt numbers for simultaneously developing flow in rectangular microchannels as a function of the dimensionless axial coordinate z^* and of the aspect ratio β for H1 boundary condition

	$Nu_{m,H1}$			
$1/z^*$	$\beta = 1$	$\beta = 0.5$	$\beta = 1/3$	$\beta = 0.25$
5	4.60	5.00	5.57	6.06
10	5.43	5.77	6.27	6.65
20	6.60	6.94	7.31	7.58
30	7.52	7.83	8.13	8.37
40	8.25	8.54	8.85	9.07
50	8.90	9.17	9.48	9.70
60	9.49	9.77	10.07	10.32
80	10.53	10.83	11.13	11.35
100	11.43	11.70	12.00	12.23
120	12.19	12.48	12.78	13.03
140	12.87	13.15	13.47	13.73
160	13.50	13.79	14.10	14.48
180	14.05	14.35	14.70	14.95
200	14.55	14.88	15.21	15.49
220	15.03	15.36	15.83	16.02

Entrance Region, Table 8 Dimensionless thermal entrance length for rectangular and circular channels

	L^+_{th}			
	Fully developed velocity profile		Simultaneously developing flow	
β	T	H1	T	H1
0	0.0080	0.0115	-	0.017
0.25	0.054	0.042	-	0.136
1/3	-	0.048	-	0.17
0.5	0.049	0.057	-	0.23
1	0.041	0.066	-	0.34
Circular	0.0335	0.0431	0.037	0.053

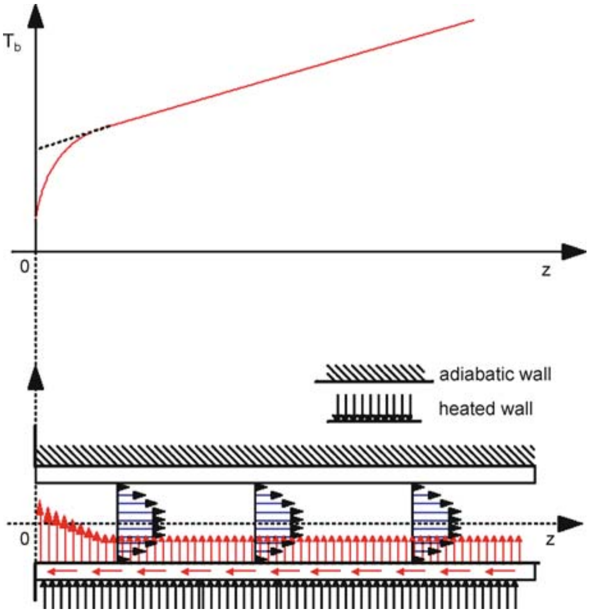

Entrance Region, Figure 6 Qualitative axial fluid temperature variation along a microchannel with conjugate wall–fluid heat transfer

ratio for T and H1 boundary conditions and for *simultaneously developing flows* and for *hydrodynamically laminar fully developed* and *thermally developing* flow.

It is evident that the thermal entrance length is larger for H1 boundary condition and for simultaneously developing flows.

Future Directions for Research

Most experimental data obtained by testing microchannels have been obtained in situations for which the entrance effects are not negligible. However, sometimes the experimental conditions are not suitable for comparison with the analytical results presented for laminar flows for the following reasons. Firstly, the numerical results of Tables 3–8 have been obtained by considering fluids with constant thermophysical properties. Some authors [4] have numerically demonstrated that in the entrance region of straight microchannels both temperature dependence of viscosity and viscous dissipation effects cannot be neglected in a wide range of operative conditions (see ► convective heat transfer in microchannels, ► viscous dissipation and ► viscous heating). For example, they demonstrated that, by taking into account a temperature-dependent viscosity and non-negligible viscous dissipation, the dimensionless hydrodynamic entrance length in microchannels can become about one order of magnitude larger than that in the corresponding constant property flow.

Secondly, the effect of the wall–fluid conjugate heat transfer tends to be very strong for moderate Reynolds numbers especially in the entrance region of a microchannel where the wall heat flux distribution becomes non-uniform (see Fig. 6) even for a uniformly heated microchannel (H boundary condition). For these reasons, further investigations on the combined effect of the conjugate heat transfer and of the temperature-dependent fluid properties (i. e. viscosity) on the mean value of the Nusselt number in the entrance region for the most common microchannel cross-sectional geometries can be considered mandatory.

Cross References

► Viscous Dissipation
► Pressure-Driven Single Phase Liquid Flow

► Pressure-Driven Single Phase Gas Flows
► Developing Flows
► Convective Heat Transfer in Microchannels

References

1. Bird RB, Stewart WE, Lightfoot EN (1960) Transport Phenomena. Wiley, NY
2. Shah RK, London AL (1978) Laminar Flow Forced Convection in Ducts. Adv Heat Transfer 14:196
3. Barber RW, Emerson DR (2002) The influence of Knudsen number on the hydrodynamic development length within parallel plate micro-channels. In: Rahman M, Verhoeven R, Brebbia CA (eds) Advances in Fluid Mechanics IV. WIT Press, Southampton, pp 207–216
4. Nonino C, Del Giudice S, Savino S (2007) Temperature Dependent Viscosity and Viscous Dissipation Effects in Simultaneously Developing Flows in Microchannels with Convective Boundary Conditions. J Heat Transfer ASME 129:1187–1194

Enzymatic Bioreactor

► Microfluidic Bioreactors

Enzymatic or Chemical Digestion

► Proteolysis

Enzymatic Fuel Cell

► Biofuel Cell

Enzymatic Nanolithography

► Enzyme Nanolithography

Enzyme Assay

Definition

An enzyme assay is a procedure used to evaluate the properties of an enzyme. Such assays are used to determine the kinetic characteristics of the enzyme, as well as its interactions with various substrates and inhibitors. In a homogeneous enzyme assay, enzymes, substrates, and inhibitors are mixed in the solution phase, while in a heterogeneous assay, one constituent (typically the enzyme) is immobilized on a solid surface while the other constituents are delivered via the solution phase.

Cross References

► Lab-on-Chip Devices for Protein Analysis
► Microfluidic Bioreactors
► Protein Microarrays
► Proteomics in Microfluidic Devices

Enzyme-Assisted Nanolithography

► Enzyme Nanolithography

Enzyme Based Nanolithography

► Enzyme Nanolithography

Enzyme Nanolithography

Levi A. Gheber
Department of Biotechnology Engineering
Ben-Gurion, University of the Negev, Beer-Sheva, Israel
glevi@bgu.ac.il

Synonyms

Enzyme-assisted nanolithography; Enzyme based nanolithography; Enzymatic nanolithography

Definition

The process of lithography with sub-micrometer resolution, with the aid of ►enzymes.

Overview

The importance of nanolithography cannot be overemphasized, in the context of Nano-Fluidics. It is the process by which nano-channels, nano-wells, and other components are fabricated in the material that serves as the support, or substrate, of the nano-fluidic devices.

Bio-lithography differs from the lithography employed in micro and nano electronics in the fact that it aims at producing the same kind of features *with* biomolecules, *on* biomolecules or *in* biomolecules. Since biomolecules are much more sensitive to their environment than inorganic materials (such as semiconductors and noble metals), most of the lithography technologies used in micro and nano electronics are unsuitable for bio-lithography. High or ultra high vacuum is unacceptable, evaporation/sputtering is inapplicable, etching with strong acids would damage biomolecules, irradiation with UV light would destroy DNA and proteins. Bio-lithography techniques, therefore,

must operate in close to ambient atmosphere and/or in liquid, close to room temperature and moderate pH. *Nano-biolithography* techniques have to comply with all the above *and* provide nanometer precision of positioning and nanometer-sized features. This is the reason that the most natural candidate for nano-bio-lithography is the Scanning Probe Microscope (SPM), which enjoys all these abilities. Since many (micro- and/or nano-) fluidic applications are targeted at biological molecules (DNA separation, protein purification, etc.), bio-lithography is of great importance to these areas. Although it is perfectly conceivable to have the fluidic platform manufactured in non-biological materials (silicon, polymers, elastomers, etc.), using conventional methods, and later using these platforms with biological molecules, this approach usually requires additional steps, such as surface functionalization (usually a multi-step process). Moreover, aided by evolution over a very long period, biology has come up with *specificity*, the ability to specifically recognize target molecules.

Enzymes, in particular, are proteins that act as chemical catalysts of specific biochemical reactions. An enzyme typically speeds up, or makes possible at all, a reaction between a set of reactants, which converts them into specific products.

The main difference between using enzymes and non-biological materials for purposes of lithography is that enzymes possess very high specificity for their substrate (the reactants), unlike their non-biological counterparts. Such ability to specifically recognize the substrate can lead to very sophisticated lithography schemes, based on biological recognition.

To summarize: enzymes possess biological specificity, an advantage over non-biological materials, in what concerns lithography. Since enzymes are biological molecules, and their catalytic action is performed on biological molecules, nano-lithography using enzymes needs to fulfill the demands presented by biological molecules (bio-nanolithography). For this purpose, the scanning probe microscopy (SPM) family of instruments is best suited, since it is able to operate in ambient conditions and in liquid.

Enzyme nanolithography has been introduced in 2003 and has gradually advanced since, using several SPM-based and non-SPM-based techniques.

Basic Methodology

Lithography in general and nano-lithography in particular can be subdivided into several categories, according to how it is done and what the resulting features are.

One classification is into *positive* and *negative* lithography, corresponding to whether the end-result is addition (positive) of material or removal (negative) of material. Positive lithography results in protrusions from the surface (mounds, ridges, etc.) while negative lithography results in depressions in the surface (holes, trenches, etc.)

Another classification is into *direct* and *indirect* lithography. The difference is that in indirect lithography – a multi-step procedure – the pattern is first inscribed in some way on the surface and in subsequent steps the features are fabricated according to this original *blue-print*, while in direct-write lithography the features are directly fabricated onto the surface.

By no means does the nomenclature imply advantages or disadvantages of the approaches. *Direct* is not necessarily better than *indirect* (or vice-versa) and *negative* is not necessarily worse than *positive* (or vice-versa). The various approaches have their advantages and should be carefully chosen in the context of the desired patterns, the substrates, reactants and deposition materials involved.

One more term that needs to be elucidated, is nanolithography using Scanning Probe Microscopy (SPM) techniques. SPM is a name describing a family of instruments, with the most widely known one being the Atomic Force Microscope (AFM), also known as Scanning Force Microscope (SFM). Very briefly, a soft cantilever (typical dimensions $\sim 100\ \mu m$) with a very sharp probe is scanned across a surface, while making contact (or intermittent contact) with the surface. An auxiliary system (typically a laser beam reflected from the back of the cantilever) is used to monitor the motion of the cantilever (up and down) as it follows the topography of the scanned surface. This leads to formation of a three dimensional image of the surface with extremely high resolution (in some cases, atomic resolution, and in most other cases a resolution of ~ 1 nm).

This family of *microscopes* can in fact be used also for surface modification and not only for surface imaging. The

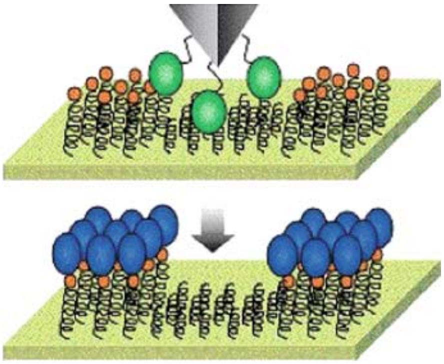

Enzyme Nanolithography, Figure 1 V8 protease is immobilized to the apex of an AFM probe, to create a depression in the peptide film (Fig. 2 from [1])

system controlling the probe-sample position with very high accuracy is used to position the probe in selected positions and modify the surfaces using many various mechanisms (a few examples include: mechanical indentation, scraping, electric field oxidation, deposition of various *inks*, etc.).

SPM-based lithography is a very advantageous methodology in what regards enzyme nanolithography (and bionanolithography in general) because SPMs can operate in ambient conditions (no vacuum) and in liquid, while applying very gentle forces that do not damage the biomolecules.

Key Research Findings

Negative, Direct, Enzyme Nanolithography

This type of nanolithography has been demonstrated so far using two SPM-based methods, and two different enzyme-substrate systems.

- The substrate was composed of synthetic peptides, immobilized to a mica surface. The *etching* enzyme was *Staphylococcal* serine V8 protease, an enzyme that recognizes either glutamic or aspartic acid residues in the peptide and digests the peptides carboxyl acid terminus [1]. The enzyme was immobilized to the apex of an AFM probe and the enzyme functionalized tip was scanned across the surface, in solution (phosphate buffer). This process created a rectangle shaped depression with a depth of a few nanometers.
- The substrate was composed of a dried film of bovine serum albumin (BSA) deposited on glass. The *etching* enzyme was trypsin, a proteolytic enzyme that cleaves on the carboxyl side of lysine and arginine residues. The enzyme was loaded in solution into a *nano-fountain pen* (NFP) probe (a capillary, heat-drawn into a sharp tip with an aperture of ~ 100 nm) [2] mounted as the probe of an AFM, and delivered in solution (phosphate buffer) to the BSA surface. Using this approach, it was possible to carve nano-wells with diameters as small as 600 nm and volumes of 0.2×10^{15} l, depending on the time spent by the probe in the specific position [3]. Also, trenches, or nano-channels with controlled dimensions have been fabricated by dragging the probe along the sample. It was also shown that crossing nano-channels (and networks of nano-channels) can be fabricated using this approach, and solutions may be flown along them [4].

Negative, Indirect, Enzyme Nanolithography

SPM-Based

- The first ever demonstration of negative enzyme lithography was reported in 1998 [5]. The study was not targeted to lithography per-se, however the authors showed a possible application and predicted *enzyme-controlled nanolithography in molecular thin films*. Subsequently, the same group showed a study dedicated to enzyme lithography on the same enzyme-substrate system [6].

  The substrate was a supported phospholipid bilayer made of dipalmitoylphosphatidylcholine (DPPC). DPPC is known to separate phases into solid-phase (or gel) domains and liquid-phase domains.

  The studied enzyme was Phospholipase A_2 (PLA_2) which is an interfacially activated enzyme that catalyzes regio- and stereospecific hydrolysis of the sn-2 acyl ester linkage of sn-3-glycero-phospholipids, producing fatty acid and lysophospholipid as reaction products.

  The enzyme was applied in solution on the DPPC bilayer and allowed to hydrolyze it. With the aid of an AFM tip, a uniform region of solid (gel) phase was perturbed, by applying some pressure with the tip, along a line. PLA_2 hydrolizes preferentially at phase inter-

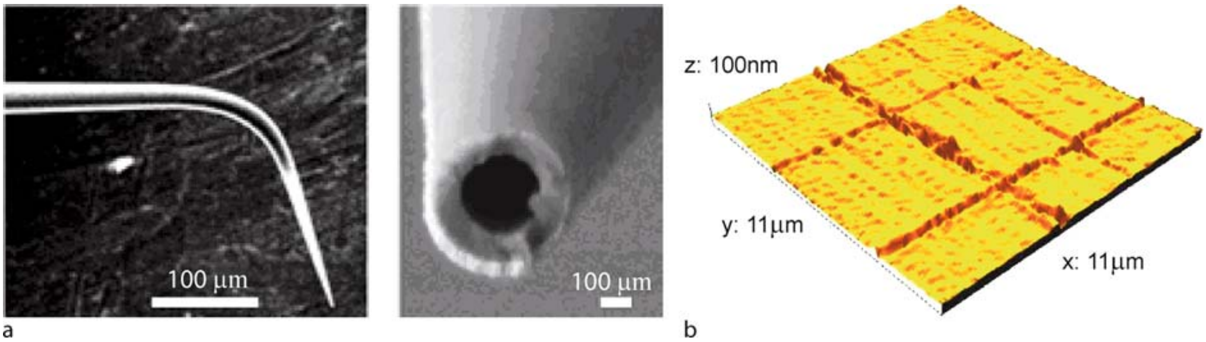

Enzyme Nanolithography, Figure 2 (**a**) SEM image of a nanopipette (**b**) Nano-channels etched in BSA by Trypsin deposited with NFP

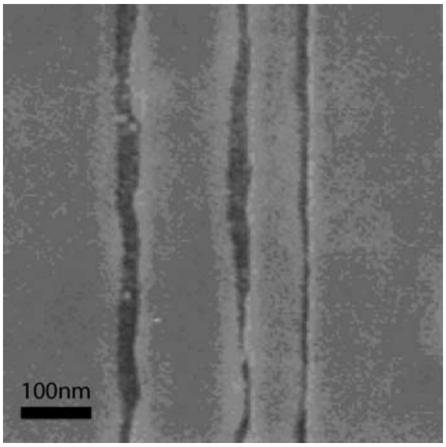

Enzyme Nanolithography, Figure 3 A gel-phase supported DPPC bilayer with lines which were etched into the bilayer by (PLA_2), after packing defects in the lipid bilayer were induced with the AFM tip (Fig. 2 in [6])

faces (or packing defects), and therefore *etched* the lipid bilayer along this line, creating a channel with a depth of 1.5 nm.

The two-stage process employed here, leading to the *indirect* classification is described as follows: *first stage* – creation of a pattern on the substrate (various phases with interfaces, or inducing the interfaces with the AFM tip) and *second stage* – etching along this previously introduced pattern.

- The substrate was composed of an oligonucleotide-terminated self-assembled monolayer of alkanethiols, tethered to the surface of gold by chemical self-assembly. The *etching* enzyme was DNase I, a non-specific endonuclease that digests double-stranded and single-stranded DNA into nucleotide fragments [7].

  In the *first stage* the enzyme was deposited onto the oligonucleotide SAM, using dip-pen nanolithography (DPN) – a method whereby an AFM probe is dipped into an *ink*, and subsequently used to *write* this ink onto a substrate [8]. The enzyme was not active at this stage, but was adsorbed on the surface in the precise positions where it has been written with DPN. In the *second stage*, the pre-patterned substrate was immersed in a solution containing Mg^{2+}, which activates DNase I. The activated enzyme produced nano-channels with depth of ~ 3 nm.

Non-SPM-Based

The substrate was composed of phospholipid bilayers consisting of condensed or solid-like DPPC stripes in a fluid DLPC matrix, onto a mica substrate [9]. The stripe pattern results from the superposition of the condensed DPPC stripe domains and fluid DLPC phases present in the layers.

The enzyme was phospholipase A_2 (PLA_2), which, in addition to its characteristics described above, is known to have stereoselectivity, i. e. it hydrolyzes the (natural) L lipid form, while it only binds, but does not cleave, the physicochemically identical D form.

It is shown that using various combinations of DPPC/DLPC (to create the stripes pattern), the enzyme cleaves the L stripes wile leaving untouched the D stripes. For example, D-DPPC stripes are left intact, while L-DLPC bilayer between the D-DPPC stripes is removed. This is an excellent demonstration of the specificity of enzymes and how it can be used in the context of nano-lithography.

The process is considered indirect due to the two stage approach: *first stage* consists of imprinting the pattern into the substrate, by creating the phase-separated stripe pattern. In the *second stage*, the enzyme etches along these patterns.

Positive, Direct, Enzyme Nanolithography

In the example described here [10], the enzyme used was alkaline phosphatase that dephosphorylates the substrate BCIP and forms in the presence of the cofactor NBT an insoluble precipitate. The enzyme was immobilized to the apex of an AFM tip and the substrate and cofactor were present in the buffer solution. Upon approaching the AFM tip to the mica surface, the authors were able to fabricate nano-mounds of reaction product. This shows how an enzyme can be used to deposit the reaction product of an enzyme in precise positions, and create nanostructures of a size depending on the enzyme activity.

Positive, Indirect, Enzyme Nanolithography

SPM-Based

In this example [11], several enzymes were studied and shown to catalyze the enlargement of metal seeds into fully developed metal nanowires. The enzymes were glucose oxidase (GOx), galactose oxidase (GalOx), and alkaline phosphatase (AlkPh). The enzymes were first modified with gold nanoparticles (NP). The NP-enzyme complexes served as the *biocatalytic ink*, which was patterned in the *first stage* on a silicon-oxide/silicon surface, using dip pen nanolithography (DPN) [8]. Following this stage, the patterns were exposed to a *developing* solution in the *second stage* that caused the deposition of additional metal (Au or Ag) on top of the patterned line. This enlargement process was catalyzed by the respective enzyme, and could not have occurred in the absence of the enzyme. The selectivity and specificity of enzyme lithography is very ele-

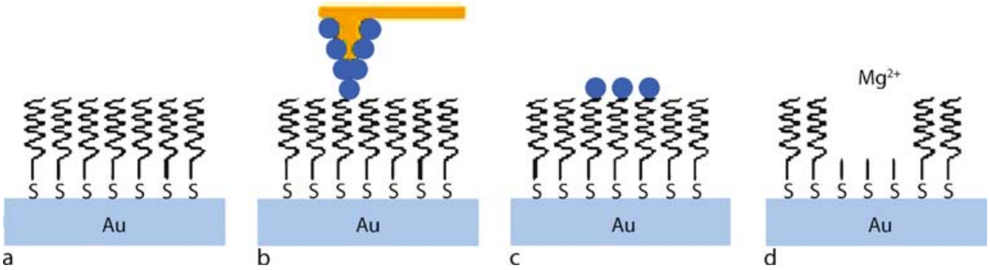

Enzyme Nanolithography, Figure 4 (**a**) Oligonucleotide SAM (**b**) Deposition of DNase I with DPN (**c**) inactive DNase I patterned on SAM (**d**) Mg^{2+} ions activate the enzyme, which digests the oligonucleotide layer (Scheme 1 from [7])

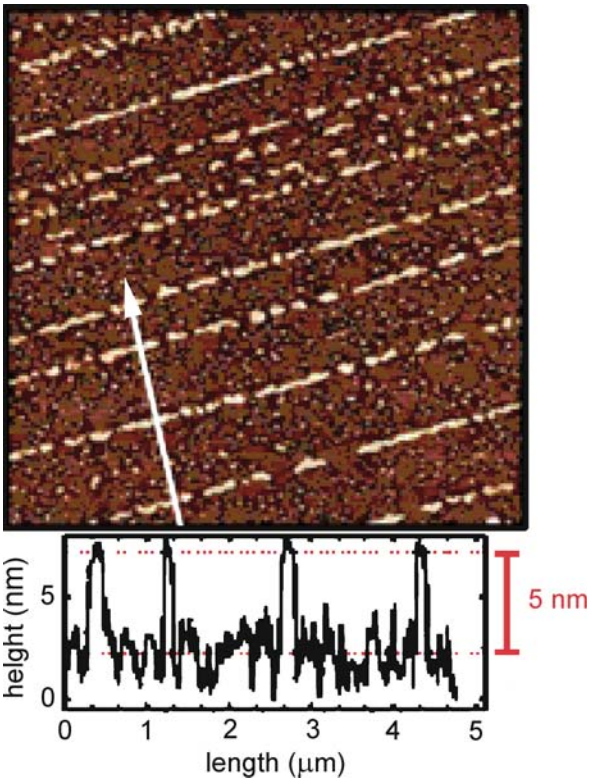

Enzyme Nanolithography, Figure 5 A D-DPPC/L-DLPC layer selectively etched by PLA_2 (Fig. 2B in [9])

gantly demonstrated in this case, by showing the ability to deposit metal nanowires of *different* metals on the same substrate, using a single first stage: Au – NP – GOx and Au – NP – AlkPh lines are patterned using DPN. The final *identity* of the fully developed nanowires is established in the second stage, where the GOx catalyzes the enlargement with Au of the wire on which it is presents, while AlkPh catalyzes the enlargement with Ag of the wire on which it is present. Although both reactions are not performed simultaneously (due to some *cross-talk*, leading to deposition of both Au and Ag on the same wires), this is still a very impressive demonstration of how the enzymes can serve for *addressing* of chemical reactions, due to their high selectivity and specificity.

Non-SPM-based

The enzyme terminal deoxynucleotidyl transferase (TdTase) repetitively adds mononucleotides to the 3′ end of single- or double-stranded DNA, thus extending an existing oligonucleotide. TdTase can directly catalyze the 5′ to 3′ extension of a short oligonucleotide template without the need for a separate DNA primer, unlike DNA polymerases. The authors of this manuscript [12] immobilized an oligonucleotide self assembled monolayer (SAM) onto gold pads. The gold pads (100 nm × 100 nm to 4 µm × 4 µm) were fabricated using conventional (nano-) lithography methods (e-beam lift-off), constituting the *first stage* of the process. The gold features were coated with a SAM of oligonucleotides (a 25-mer poly-T). These DNA fragments served as the *initiator* of the polymerization catalyzed by TdTase, and this constitutes a *second stage* of the process. In the *third stage*, a solution containing TdTase and a mononucleotide (dTTP proved to be the most efficient among those studied) was applied to the sample. The enzyme caused the addition of more T bases to the initial 25-T oligonucleotides, thus increasing the height of the features considerably.

Future Directions of Research

Enzyme nanolithography is a young research area, a technology being born. It is nowadays in its proof of concept stage and development of tools. The basic idea, of harnessing biological specificity, selectivity and finely tuned chemical catalysis – a result of a very long evolution – to creating nano-structures at will, is exciting and imaginative. The examples described above show that all approaches to lithography are attainable using enzymes, including direct and indirect methods of positive and neg-

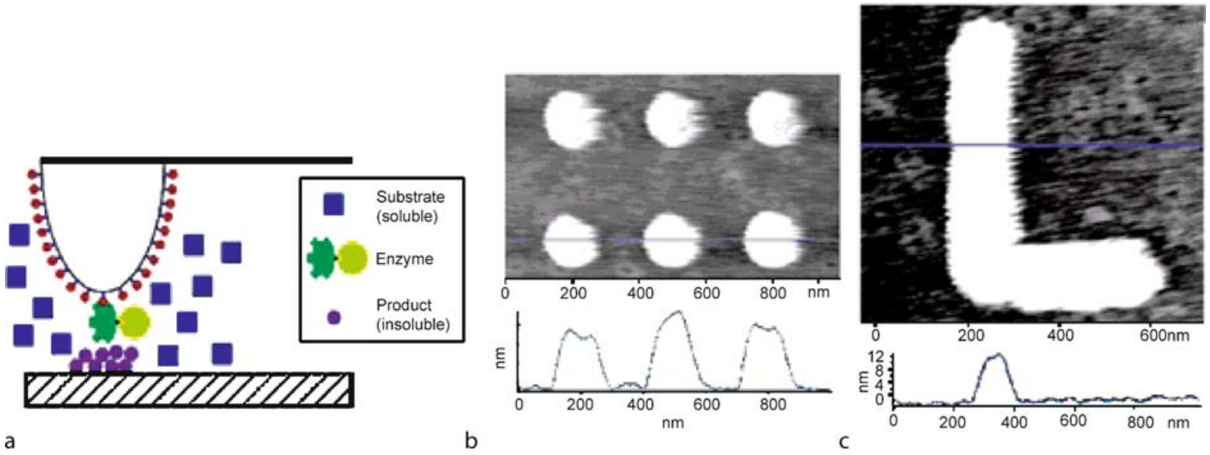

Enzyme Nanolithography, Figure 6 (**a**) Alkaline phosphatase immobilized to the AFM tip produces an insoluble product in the presence of the substrate BCIP and NBT, which precipitates on the surface. (**b**) dots and (**c**) lines written with this method (Fig. 3 in [10])

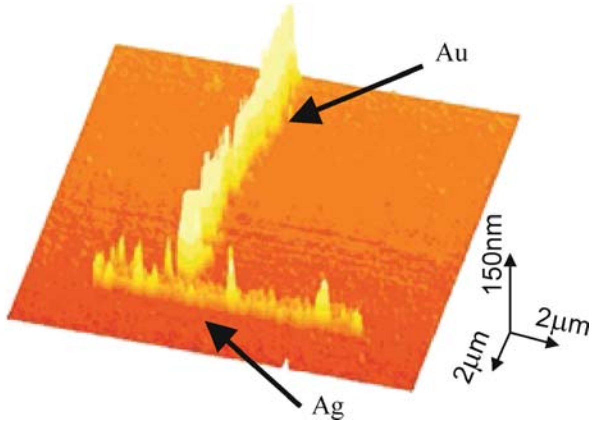

Enzyme Nanolithography, Figure 7 Two different metals (Au and Ag) deposited along DPN-patterned templates of enzymes as described above (Fig. 4D from [11])

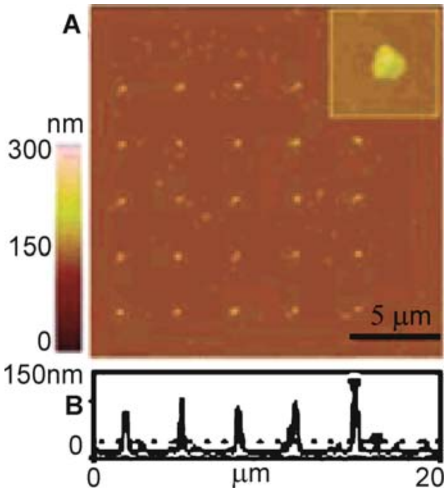

Enzyme Nanolithography, Figure 8 Poly-T nanostructures grown by TdTase activity on gold pads functionalized with a 25-mer poly-T (Fig. 2 from [12])

ative lithography, using SPM based methods or others. It is envisioned that future research will concentrate on two main tracks:

- Creation of complex patterns, making use of the selectivity of enzymes. Note that most works published to date (with a few exceptions) create one type of feature using one enzyme and its matching substrate. The big promise in enzyme lithography, though, is the enzymes' ability to distinguish between their substrate and something else. Thus, they should be able to act on some parts of the surface, while leaving others intact, such as demonstrated in [9] and [11]. This will most probably require a mixture between direct and indirect approaches, whereby the *road-signs* are imprinted in some way into the substrate, such that various enzymes will recognize some of them and disregard others. Use of SPM based methods in combination with such an approach should allow an even more precise control over the x,y dimensions and position of the created features.
- Studying the quantitative aspects of enzyme lithography. Parameters such as concentrations, time of reaction, etc. and their quantitative influence on the dimensions of the resulting features will allow a good control over the processes and enable the transformation of enzyme nanolithography into a true technology.

References

1. Takeda S, Nakamura C, Miyamoto C, Nakamura N, Kageshima M, Tokumoto H, Miyake J (2003) Lithographing of biomolecules on a substrate surface using an enzyme-immobilized AFM tip. Nano Lett 3:1471–1474
2. Lewis A, Kheifetz Y, Shambrodt E, Radko A, Khatchatryan E, Sukenik C (1999) Fountain pen nanochemistry: Atomic force control of chrome etching. Appl Phys Lett 75:2689–2691
3. Ionescu RE, Marks RS, Gheber LA (2003) Nanolithography using protease etching of protein surfaces. Nano Lett 3:1639–1642
4. Ionescu RE, Marks RS, Gheber LA (2005) Manufacturing of nanochannels with controlled dimensions using protease nanolithography. Nano Lett 5:821–827
5. Grandbois M, Clausen-Schaumann H, Gaub H (1998) Atomic force microscope imaging of phospholipid bilayer degradation by phospholipase A(2). Biophys J 74:2398–2404
6. Clausen-Schaumann H, Grandbois M, Gaub HE (1998) Enzyme-assisted nanoscale lithography in lipid membranes. Adv Mater 10:949–952
7. Hyun J, Kim J, Craig SL, Chilkoti A (2004) Enzymatic nanolithography of a self-assembled oligonucleotide monolayer on gold. J Am Chem Soc 126:4770–4771
8. Piner RD, Zhu J, Xu F, Hong SH, Mirkin CA (1999) "Dip-pen" nanolithography. Science 283:661–663
9. Moraille P, Badia A (2005) Enzymatic lithography of phospholipid bilayer films by stereoselective hydrolysis. J Am Chem Soc 127:6546–6547
10. Riemenschneider L, Blank S, Radmacher M (2005) Enzyme-assisted nanolithography. Nano Lett 5:1643–1646
11. Basnar B, Weizmann Y, Cheglakov Z, Willner I (2006) Synthesis of nanowires using dip-pen nanolithography and biocatalytic inks. Adv Mater 18:713–718
12. Chow DC, Lee WK, Zauscher S, Chilkoti A (2005) Enzymatic fabrication of DNA nanostructures: extension of a self-assembled oligonucleotide monolayer on gold arrays. J Am Chem Soc 127:14122–14123

Enzymes

Definition

Enzymes are proteins that accelerate, or catalyze, chemical reactions.

Cross References

► Enzyme Nanolithography

EOP

► Electroosmotic Pump

EO Pump

► Electroosmotic Pump

Epitaxial

Synonyms

Epitaxy

Definition

Epitaxy is a kind of interface between a thin film and a substrate. Epitaxial growth refers to the formation of crystals of one material on the crystal face of another or the same material. The lattice structure and orientation or lattice symmetry of the thin film material is identical to that of the substrate on which it is deposited.

Cross References

► Chemical Vapor Deposition for Film Deposition
► Plasma-Treatment Physics

Epitaxial Growth

Definition

Thin-film growth from a surface in one crystallographic orientation.

Cross References

► Fabrication of Self-Assembled Catalytic Nanostructures

Epitaxy

► Epitaxial

Equivalent Mean Free Path

Definition

Equivalent mean free path ℓ has the order of the mean free path and related to the shear viscosity μ, most probable molecular speed v_0 and pressure P as $\ell = \mu v_0 / P$.

Cross References

► Gas Flow in Nanochannels
► Heat Transfer in Microchannel Flows
► Supersonic Micro-Nozzles
► Micro- and Nanoscale Gas Dynamics
► Lattice Poisson-Boltzmann Method, Analysis of Electroosmotic Microfluidics

ESI

► Electrospray Ionization

Establishing Flows

► Developing Flows

Establishing Region

► Entrance Region

Etch Directionality

Synonyms

Etch profile

Definition

The etch directionality is due to directed energy input an etching reaction at a surface and can be accomplished by radical atoms, electrons, photons or ion bombardment of a surface exposed to a chemical etchant. It can be obtained by controlling the interaction between the plasma physical and chemical mechanisms to achieve the required etching profiles using the suitable reactor and adjusting the plasma parameters. Three types of plasma etched profiles are isotropic etching, sloped wall via etch and vertical wall (anisotropic etching).

Cross References

► Anisotropic Etching
► Isotropic Etching
► Reactive Ion Etching (RIE)
► Plasma etching

Etching Rate Ratio

► Etch Selectivity

Etching Single Crystalline Materials

► Anisotropic Etching

Etch Profile

► Etch Directionality

Etch Selectivity

Synonyms

Etching rate ratio

Definition

Etch selectivity between two materials is defined as the ratio between their etching rates at identical plasma conditions. High selectivity is usually referred in etching and related to a high etching rate ratio between chemically different materials or between the etched and the underlying layer.

Cross References

► Anisotropic Etching
► Isotropic Etching
► Reactive Ion Etching (RIE)
► Plasma Etching

Eulerian Streaming

► Acoustic Streaming

Evanescent Field

► Evanescent Wave

Evanescent Wave

Synonyms

Evanescent field

Definition

When an electromagnetic wave (light) in a dielectric medium is incident upon an interface of a different dielectric material of a lower optical density at an angle greater than the critical angle total internal reflection (TIR) occurs as predicted by Snell's Law. Although all of the incident energy is reflected, an electromagnetic field with exponentially decreasing intensity normal to the interface propagates in the less dense medium tangent to the interface.

This field is known as an evanescent wave and has a decay length or penetration depth on the order of the wavelength of the incident light.

Cross References

- ► Evanescent Wave Microscopy

Evanescent Wave Illumination

Synonyms

Total Internal Reflection Fluorescence (Microscopy); TIRM; TIRFM

Definition

Evanescent wave microscopy uses the evanescent wave produced by the total internal reflection of light at a dielectric interface to illuminate a layer of material within the penetration depth of the evanescent field. The material of interest is imaged using a microscope objective typically within 100 to 200 nm of the interface.

Cross References

- ► Evanescent Wave Microscopy
- ► Fluorescence Measurements
- ► Fluorescence Labeling
- ► Quantum Dots
- ► TIRF

Evanescent Wave Microscopy

JEFFREY S. GUASTO[1], PETER HUANG[2], KENNETH S. BREUER[1]
[1] Division of Engineering, Brown University, Providence, RI, USA
[2] Department of Biomedical Engineering, Tufts University, Medford, MA, USA
jguasto@brown.edu, kbreuer@brown.edu

Synonyms

Total Internal Reflection Fluorescence (Microscopy); TIRM; TIRFM

Definition

When an electromagnetic wave (light) in a dielectric medium of index n_1 is incident upon an interface of a different dielectric material of a lower optical density, n_2 at an angle θ_1 greater than the critical angle, $\theta_c = sin^{-1}(n_2/n_1)$, total internal reflection (TIR) occurs. Although all of the incident energy is reflected, an electromagnetic field with exponentially decreasing intensity propagates in the less dense medium. This field is known as an ►evanescent wave and has a decay length or penetration depth, d, on the order of the wavelength of the incident light, λ_0. The confined nature of the evanescent wave close to the interface is ideal for studying surface and near-surface phenomena pertaining to fluid mechanics and mass transport typically by fluorescence microscopy, which is known as total internal reflection fluorescence microscopy (TIRFM) or simply ►TIRF.

Overview

As fluid mechanics reaches into the micro- and nano-scale, interfacial phenomena become increasingly important, and several diagnostic techniques have been adapted from other fields to quantify fluid phenomena at these scales. In addition to general and fluorescence microscopy, an important technique for fluid-surface studies is the use of ►evanescent wave microscopy.

Origins

Evanescent wave microscopy or total internal reflection microscopy (TIRM) has been employed in the fields of biology and chemistry since the 1970s. The TIRM technique has long been used in cell biology studies and more recently cell-substrate contacts, vesicle fusion, and single-molecule observation. Here, cells on a microscope cover glass are illuminated by an evanescent field, which is produced through a total internal reflection (TIR) created at the cell/cover glass interface and imaged by a microscope. The technique has been used to measure chemical kinetics and surface diffusion, molecular conformation of adsorbates, cell development during culturing, visualization of cell structures and dynamics, and single molecule visualization and spectroscopy [1].

Applications to Fluid Mechanics

In micro- and nano-scale fluid mechanics, measurements of diffusion and velocity are used to probe fundamental physical phenomena and evaluate the performance of devices. ►Evanescent wave illumination has been combined with several other diagnostic techniques to make such measurements within the order of the penetration depth (about 100 – 200 nm) of fluid-solid interfaces with resolution sometimes as small as several nanometers. Laser–Doppler velocimetry has been applied to measure single point tracer particle velocities in the boundary layer

of a fluid within 1 µm of a wall. By seeding fluid with fluorescent dye, total internal reflection fluorescence recovery after photobleaching (FRAP) has been used to measure near-wall diffusion coefficients and velocity (for a summary of initial applications see Zettner and Yoda [2]).

A critical contribution of ▶ evanescent wave microscopy to micro- and nano-fluidics is the application of micro/nano-particle velocimetry techniques to measure velocity fields. Particle image velocimetry (PIV) and particle tracking velocimetry (PTV) have been viable macro-scale diagnostic techniques for measuring two-dimensional velocity fields since the 1980s. These techniques were later adapted to the micro-scale [3] (known as micro-PIV and micro-PTV), which made use of fluorescence microscopy. More recently, Zettner and Yoda [2] used the micro-PIV technique combined with evanescent wave illumination to measure the near-wall velocity field in a rotating Couette flow within about the penetration depth of the evanescent field from the wall. Micro-PTV has also demonstrated great success in measuring the near-wall velocity fields in an evanescent wave as well as the diffusion of tracer particles and even three-dimensional tracer displacements/velocities [4–6].

Advantages

The small length scales involved in micro- and nano-fluidics do not allow for the convenient production of a light sheet to visualize distinct planes of fluid. Instead, imaging was typically limited to volumetric flood illumination as the only visualization technique, which used the depth of focus (DOF) of the microscope objective to designate distinct fluid planes [3]. The DOF is generally described by

$$\mathrm{DOF} = \frac{\lambda_0 n_1}{\mathrm{NA}^2} + \frac{n_1}{M \cdot \mathrm{NA}} e. \tag{1}$$

where λ_0 is the illumination wavelength, n_1 is the index of the immersion medium, M is the magnification and e is the smallest distance that can be resolved by the detector. The DOF can be quite large for low magnification or low numerical aperture (NA) objectives, and even for high magnification, large NA objectives the DOF is on the order of several hundreds of nanometers. More importantly, flood illumination excites out-of-plane fluorophores outside of the DOF, which are imaged as background noise and significantly lower the signal-to-noise-ratio SNR).

Evanescent wave illumination provides an illuminated fluid layer of smaller dimension than by using the DOF alone, allowing for measurements closer to liquid–solid interfaces. The exponential decay of the light intensity away from the interface is well known, and studies have shown that the intensities of fluorescent tracer particles excited by the evanescent field closely follow the local field intensity [5]. Thus, through careful calibration, tracer particle intensity can be mapped to relative distance from the interface allowing for three-dimensional tracking. Finally, since only a thin layer of fluid is illuminated, there is virtually no background noise from out-of-plane excitation resulting in a very high SNR (Fig. 1).

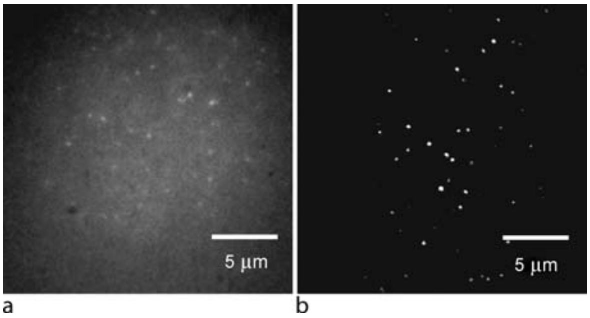

Evanescent Wave Microscopy, Figure 1 A comparison of (**a**) direct flood illumination versus (**b**) TIRF illumination of 200 nm diameter fluorescence polystyrene particles in water with a single 5 ns pulse from a Nd : YAG laser through a 100X objective with a NA = 1.45

Basic Methodology

Evanescent Field Theory

When an electromagnetic wave (light) in a dielectric medium of index n_1 is incident upon an interface of a different dielectric material with a lower optical density, n_2, at an angle θ_1 Snell's law predicts the refracted angle, θ_2, by:

$$n_1 \sin(\theta_1) = n_2 \sin(\theta_2) . \tag{2}$$

For incident angles greater than the critical angle,

$$\theta_c = \sin^{-1}\left(\frac{n_2}{n_1}\right) , \tag{3}$$

total internal reflection occurs as illustrated in Fig. 2. Although all of the incident energy is reflected, the solution of Maxwell's equations predict the existence of an electromagnetic field in the less dense medium with intensity decaying exponentially away from the interface. This evanescent wave propagates parallel to the interface and has a decay length, d, on the order of the wavelength of the illuminating light, λ_0. However, photons are not actually reflected at the interface, but rather tunnel into the low index material by optical tunneling. As a result, the reflected beam of light is shifted along the interface by a small amount ($\Delta x = 2d \tan\theta_1$), which is known as the

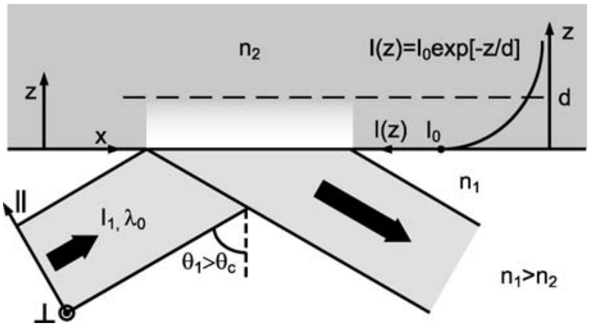

Evanescent Wave Microscopy, Figure 2 Illustration of geometry and parameters for an evanescent wave produced by the total internal reflection of plane waves incident on a dielectric interface

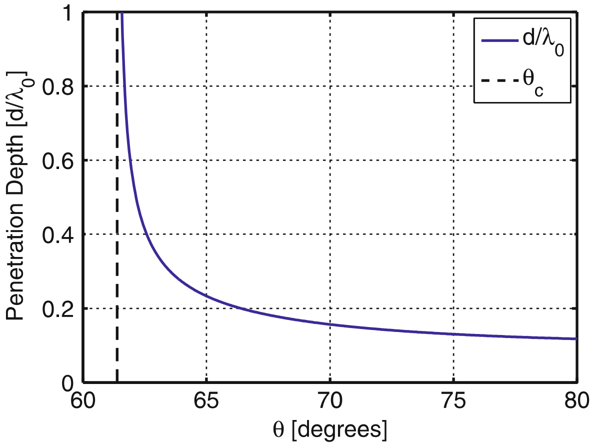

Evanescent Wave Microscopy, Figure 3 Behavior of the penetration depth d normalized by the incident wavelength λ_0 as a function of the incident angle θ_1 for a typical glass–water interface with $n = 0.878$

Goos–Haenchen shift. This shift is typically small for fluid diagnostic applications ($\Delta x < 1\,\mu$m) as compared to the field of view, which is on the order of 100 μm.

The full details to the solution of Maxwell's equations are outlined in several other resources [1]. Here, only the results relevant to ►evanescent wave microscopy are presented, specifically the functionality of the intensity field in the low density material, which is used for imaging. It should be noted that these solutions assume infinite plane waves incident on the interface. In practice, however, one typically uses a finite, Gaussian laser beam, which is well approximated using these assumptions. The intensity field has the exponential form

$$I(z) = I_0 e^{-z/d} , \tag{4}$$

where the decay length, d, is given by

$$d = \frac{\lambda_0}{4\pi n_1}[\sin^2\theta_1 - n^2]^{-1/2} , \tag{5}$$

and $n = n_2/n_1 < 1$. In a typical system, the substrate is a glass slide ($n_1 = 1.515$) and the interrogation medium is water ($n_2 = 1.33$), which gives $n = 0.878$. The behavior of d with respect to incident angle is shown in Fig. 3 for these conditions. For $\lambda_0 = 514$ nm (Argon Ion), the penetration depth is about $d = 140$ nm assuming an incident angle of $\theta_1 = 64.0°$. The polarization of the incident beam does not affect the penetration depth, but it does affect the amplitude of the evanescent field. For plane waves incident on the interface with intensity I_1 in the dense medium, the amplitude of the field in the less dense medium I_0 is given by

$$I_0^{\|} = I_1^{\|}\frac{4\cos^2\theta_1\left(2\sin^2\theta_1 - n^2\right)}{n^4\cos^2\theta_1 + \sin^2\theta_1 - n^2}, \tag{6}$$

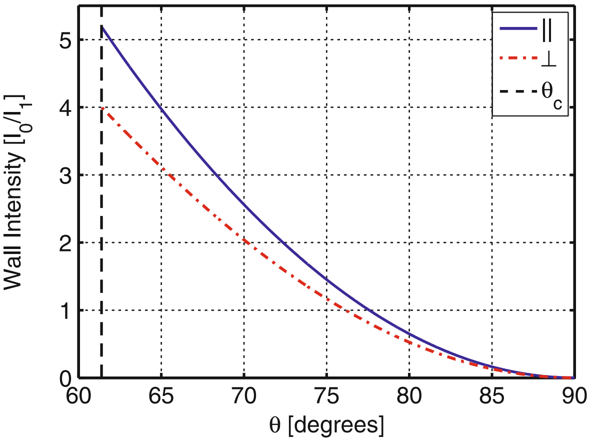

Evanescent Wave Microscopy, Figure 4 Amplitude of the evanescent field intensity at the interface in the low index material n_2 for both parallel and perpendicular polarization of the incident electromagnetic field

$$I_0^{\perp} = I_1^{\perp}\frac{4\cos^2\theta_1}{1 - n^2}, \tag{7}$$

for incident waves parallel and perpendicular to the plane of incidence, respectively, as shown in Fig. 4 [1].

Experimental Implementation

Due to the length scales involved, most interesting phenomena probed by the evanescent wave require microscope optics for imaging. In the past, several TIRM studies have been conducted using only scattering from objects in the evanescent field for imaging. More recently, fluorescence microscopy systems have become the standard imaging technique for evanescent wave microscopy

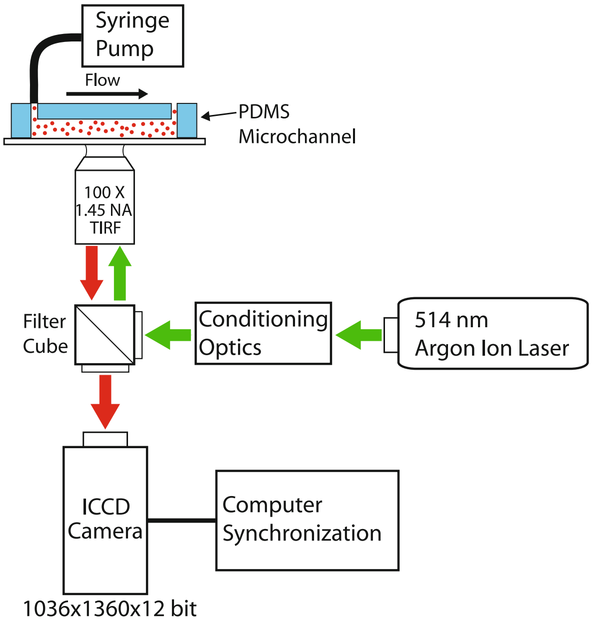

Evanescent Wave Microscopy, Figure 5 Schematic diagram of a possible TIRF system for micro- and nano-scale velocimetry using objective-base TIR illumination

(TIRF) due to superior SNR and the availability and variety of fluorescent probes. The basic components of a TIRF imaging system include: light source, illumination optics, specimen or flow cell, emission imaging optics and a camera (usually accompanied by a PC). An example of such a system is shown in Fig. 5.

Light sources are typically continuous-wave (CW) lasers (argon-ion, helium-neon, etc.) or pulsed lasers (Nd : YAG, etc.) for their collimation and single-wavelength characteristics. Non-coherent sources (arc-lamps) are not as common in typical homemade systems, but commercial versions are available. Conditioning optics are used to create the angle of incidence necessary for TIR and are of two types, which will be discussed below. The illumination optics must be held in contact with sample substrate, which can be glass, quartz or plastics as long as the surface is reasonably smooth (standard glass slides and cover slips are adequate). Finally, flow channels are available in a wide variety of forms (both commercial and homemade), which include PDMS channels bonded to glass slide substrates, etched glass channels and commercial glass or quartz flow chambers.

Fluorescence microscopy uses fluorescent molecules (fluorophores), which absorb light energy from the evanescent field created by the light source at wavelength λ_0 and re-radiate photons at a longer wavelength λ_1. Optical filters isolate the excitation light from the emitted light, which is then collected and imaged by a camera. High magnification microscope objectives (30X to 100X) serve as the collection optics and CCD cameras are used for capturing images. Depending on the level of light emitted from the probes, cooled or intensified CCD cameras may be necessary for better sensitivity. Fluorescent probes are commercially available in several forms with varying sizes: single fluorophores (fluorescein, rhodamine laser dye), polymer micro-spheres (50 nm to several μm diameter), ►quantum dots (5 – 25 nm diameter), etc. Most dyes and particles are soluble in water for ease of use and application to biological systems. However, investigations of some interesting flow physics are possible with other materials (polymers, organics, etc.). In the case of imaging single particles, most tracers are sub-wavelength, and thus, typically limited to imaging the diffraction limited spot. However, sub-wavelength and sub-pixel resolution is possible through post-processing procedures.

The two common types of illumination systems for creating evanescent wave illumination are prism-based systems and objective-based systems. There are several configurations for each, both of which have their own specific shortcomings, which are outlined elsewhere [1]. Two popular configurations for TIRM systems are presented below.

Prism-Based Systems Prism-based TIR illumination systems are typically home-build and low cost. A prism (triangular, square, hemispherical, etc.) is placed in contact with the sample substrate or flow channel (usually coupled to the substrate using an immersion medium). The laser beam is focused into the prism to illuminate the area of interest, then the angle is adjusted to create TIR at the interface of the sample. If the evanescent field is created on the surface of the flow channel opposite of the objective, then air, water or oil immersion objectives may be used provided they have the required working distance. Otherwise, if TIR is created on the same side as the objective, then oil immersion may not be used, since the beam will decouple from the system and fail to create an evanescent field. An example of a prism-based TIRM system is shown in Fig. 6.

Objective-Based Systems Objectives suitable for TIR are common (although expensive). They are typically limited to 60X to 100X magnification immersion objectives, and require very high numerical apertures (NA $>$ 1.4). In this method, the collimated light source is focused down onto the back focal plane of the objective to illuminate the sample. Light rays off of the optical axis are projected onto the sample interface at increasing incident angle. If the rays are localized and far enough off of the optical axis, then the full NA of the objective will be utilized and TIR

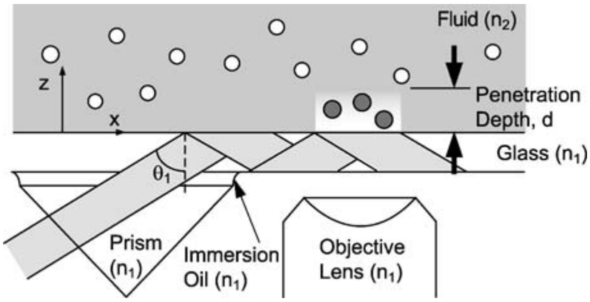

Evanescent Wave Microscopy, Figure 6 Schematic diagram illustrating the general experimental set-up for prism-based TIRM, where the beam of light is coupled into a glass slide using a prism

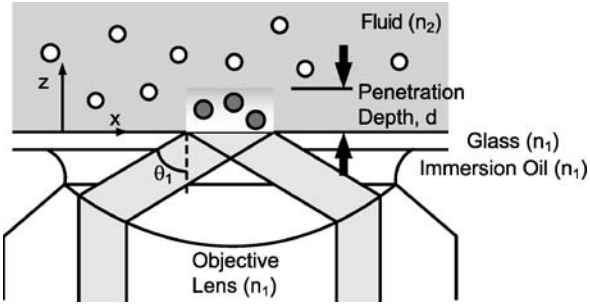

Evanescent Wave Microscopy, Figure 7 Schematic diagram illustrating the general experimental set-up for objective-based TIRM, where the beam of light is coupled directly into an objective. A large NA is necessary to achieve incident angles greater than the critical angle $\theta_1 > \theta_C$

will occur at the sample interface creating an evanescent wave in the sample medium as shown in Fig. 7.

Velocimetry and Tracking Techniques

With a TIRFM system in place, quantitative measurements can be made within 200 nm of the substrate surface. Typically, in fluid mechanics, a wealth of information about any given flow system can be found from the velocity field. As mentioned above, micro-PIV and micro-PTV are both well-established tools for extracting quantitative information from micro-scale fluid systems [3]. However, special care must be taken in applying these techniques to very near-wall flows with evanescent wave illumination. Both techniques require imaging the instantaneous positions of tracer particles seeded in the flow at two different instances in time to infer fluid velocities. Once a series of tracer particle images is obtained, PIV uses cross-correlations of segments from each image to determine the highest correlation for the movement of a group of particles from one image to the next and thus, the velocity of that group. PTV on the other hand, attempts to match individual tracer particles between the two images. This is performed through identification and center detection of all particles then, matching particles usually through nearest-neighbor algorithms to find the displacement and subsequently the velocity. Since there is little to no slip at the wall, two-dimensional velocimetry within the evanescent field measures the average velocity in the evanescent field weighted by the concentration profile and detectability of the tracer particles. Three-dimensional measurements are typically made by tracking algorithms and rely on the characterization of the evanescent field intensity to map tracer particle intensity to distance from the wall [5, 6].

Particle tracking algorithms have also been used successfully in two- and three-dimensional diffusion measurements and simultaneous diffusion/velocity measurements. The random, thermal motion exemplified by small particles in a surrounding fluid, (Brownian motion), is typically characterized by a diffusion coefficient. By utilizing particle tracking, diffusion coefficients can be measured by observing many thousands of individual particle motions to build an ensemble of displacement statistics. Measurements of diffusion are even more interesting near liquid–solid interfaces, accessible by TIRF, where diffusion coefficients can be anisotropic [6, 7]. In addition to the implications for interface science, these effects should be used in velocimetry algorithms by correcting observed particle displacements to account for anisotropic particle diffusion characteristics.

Near-Wall Effects

With the high resolution of the TIRM technique, one should be aware of several physical phenomena that are active on length scales comparable to the penetration depth. When an isolated particle is in the vicinity of a solid boundary, its Brownian motion is hindered due to an increase in hydrodynamic drag. The presence of the solid wall decreases the diffusion coefficient, resulting in hindered, anisotropic Brownian motion [7].

In many TIRM applications, it is important to know the concentration profile of tracer particles in the near-wall region. This is important for calculating average velocities in the evanescent field and mapping intensities to distances from the wall. Three physical phenomena may play a role of varying importance: (1) gravitational settling, (2) shear-induced lift (the Saffman effect) and (3) electrostatic attraction/repulsion. In all three cases, these effects compete with Brownian diffusion, which tends to mix the tracers into a uniform distribution throughout the fluid. The effect of gravitational settling is greatest for large particles ($2a \sim 1\,\mu$m) with density mismatch. Shear-induced migration or the Saffman effect is the migration of particles away from solid boundaries in the presence of

high shear. This becomes important for $\mathrm{Re} = 2a\rho U/\mu > 1$, where U is the mean velocity [3]. Electrostatic attraction or repulsion between tracers and the wall can also have a substantial effect on the concentration profile, depending on the relative charges of the particle and substrate. This can be suppressed by the addition of electrolytes to the fluid medium to provide charge screening.

Key Research Findings

Velocimetry with Evanescent Wave Illumination

Until recently, there were no direct experimental measurements of near-wall nano-scale flows. The development of evanescent wave velocimetry has enabled contributions in several areas. If one applies an electric field along the length of a microchannel, ions near the charged surface move, dragging the bulk fluid along and thus creating a plug-type Electro-Osmotic Flow. TIRV has been applied to characterize the two wall-parallel velocity components in EOF within 100 nm of the wall, which includes the electric double layer (EDL). Analytical and numerical studies suggesting uniform flow near the wall were verified using a nano-PIV technique with an evanescent wave, demonstrating that the EDL is much smaller than 100 nm as predicted [8].

Another research focus has been the investigation of the no-slip boundary condition between a liquid and a solid - an assumption that has been challenged by recent experimental results and molecular dynamic simulations and the subject of many recent investigations. Experimental studies have reported a wide range of slip lengths, ranging from micrometers to tens of nanometers or smaller (including no-slip). Molecular dynamics simulations, on the other hand, suggest small slip lengths, mostly less than 100 nm. The experiments have been conducted under various direct and indirect measurement techniques with varying accuracy and uncertainty Huang et al. (2006) [5] used 3D ► Total Internal Reflection Velocimetry (3D-TIRV) to make direct measurements of slip length within 150 nm of the surface. Particle tracking in the wall-normal direction was approximately 10% of the evanescent field penetration depth (about 20 nm), and they were able to show that there appears to be minimal slip over hydrophilic surfaces, while hydrophobic surfaces do appear to introduce a discernable, but small boundary slip, with a slip length of the order of 10 – 50 nm.

Given the small size of the observation region generated using evanescent wave illumination, it is desirable to minimize the size of the tracer particles for better resolution, and the use of semiconductor nanocrystals or quantum dots (QDs) has been demonstrated. QDs are single fluorophores with fluorescence lifetimes similar to traditional fluorophores. They exhibit several qualities beneficial to nano-scale velocimetry including small diameter (5 – 25 nm), narrow emission spectra and controllable surface chemistry. Although they are much brighter than traditional fluorophores, QDs have significantly lower intensity than larger, more common tracer particles measuring several hundred nanometers. Velocimetry with QDs in aqueous solutions is made possible by TIRV because of the extremely high SNR. QD tracking and velocimetry has been successfully demonstrated by several groups using nano-PTV techniques [9, 10].

Diffusion and Hindered Diffusion Measurements

When the distance h between a spherical particle of radius a and a solid boundary becomes sufficiently small ($h/a \sim 1$), hydrodynamic interactions between the particle and wall hinder the Brownian motion (diffusion) of the particle. Such effects are critical to fundamental near-wall measurements and the accuracy of micro-velocimetry techniques, which rely on the accurate measurement of micro/nano particle displacements to infer fluid velocity. By applying the 3D TIRV technique to freely suspended fluorescent particles, simultaneous observation of three-dimensional anisotropic hindered diffusion has been measured for particle gap sizes $h/a \sim 1$ with 200 nm diameter particles [6] and $h/a \ll 1$ with 3 μm diameter particles [7]. The latter results confirm the increase of hydrodynamic drag when a particle approaches a solid boundary, and such correction shall be applied to not only diffusion but also other translational motion of particles where the drag force is of concern.

Future Directions for Research

Evanescent wave microscopy has already yielded a number of contributions to the fields of micro- and nano-scale fluid and mass transport, including investigation of the no-slip boundary condition, applications to electrokinetic flows and verification of hindered diffusion. With more experimental data and improvements to TIRF techniques the accuracy and resolution these techniques are certain to improve. Improvements that will assist include the continued development of uniform, bright tracer particles (such as quantum dots), the improvement of high NA imaging optics and high sensitivity camera systems, and further development of variable index materials for better control of the penetration depth characteristics.

Cross References

► Brownian Motion and Diffusion
► Brownian Motion

- ► Evanescent Wave Illumination
- ► Fluorescence Measurements
- ► Fluorescence Labeling
- ► Micro-PIV-Based Diffusometry
- ► Quantum Dots
- ► TIRF

References

1. Axelrod D, Burghardt TP, Thompson NL (1984) Total internal reflection fluorescence (in biophysics). Annual Review Biophys Bioeng 13:247–268
2. Zettner CM, Yoda M (2003) Particle velocity field measurements in a near-wall flow using evanescent wave illumination. Exp Fluid 34:115–121
3. Wereley ST, Meinhart CD (2005) Chapter 2: Micron resolution particle image velocimetry. In: Breuer K (ed) Microscale Diagnostic Techniques Springer, Berlin
4. Jin S, Huang P, Park J, Yoo JY, Breuer KS (2004) Near-surface velocimetry using evanescence wave illumination. Exp Fluid 37:825–833
5. Huang P, Guasto JS, Breuer KS (2006) Direct measurement of slip velocities using three-dimensional total internal reflection velocimetry. J Fluid Mechan 566:447–464
6. Kihm KD, Banerjee A, Choi CK, Takagi T (2004) Near-wall hindered Brownian diffusion of nanoparticles examined by three-dimensional ratiometric total internal reflection fluorescence microscopy (3-D R-TIRFM). Exp Fluid 37:811–824
7. Huang P, Breuer KS (2006) Direct measurement of anisotropic, near-wall hindered diffusion using total internal reflection velocimetry. Submitted to Phys Rev E
8. Sadr R, Yoda M, Zheng Z, Conlisk AT (2004) An experimental study of electro-osmotic flow in a rectangular microchannel. J Fluid Mechan 506:357–367
9. Pouya S, Koochesfahani M, Snee P, Bawendi M, Nocera D (2005) Single quantum dot (QD) imaging of fluid flow near surfaces. Exp Fluid 39:784–786
10. Guasto JS, Huang P, Breuer KS (2006) Statistical particle tracking velocimetry using molecular and quantum dot tracer particles. Exp Fluid 41:869–880

Evaporation Deposition

Definition

A vacuum deposition technique where the material to be deposited is heated until it vaporises. This condenses on the substrate and forms a thin film

Cross References

- ► Sputtering for Film Deposition

Explosive Boiling in Microchannels

- ► Bubble Dynamics in Microchannels

Extensional

- ► Viscoelasticity

External Actuators

Definition

A micropump or active microvalve is said to use external actuators when the component responsible for opening or closing the valve, or moving the fluid, is added to the device after fabrication. Examples would be a separate miniature solenoid valve used to pressurize or depressurize air chambers in a pneumatic actuator, or piezoelectric patches glued to a micromachined silicon or glass membrane.

Cross References

- ► Electromagnetic Valves
- ► Electrostatic Valves
- ► Integrated Actuators
- ► Magnetic Pumps
- ► Membrane Actuation for Micropumps
- ► Microactuators
- ► Peristaltic Pumps
- ► Piezoelectric Valves
- ► Piezo/PZT in Microfluidics
- ► Pneumatic Valves
- ► Thermomechanical Valves
- ► Thermopneumatic Valves

Externalization of Phosphatidylserine

- ► Microfluidics for Studies of Apoptosis

Fabrication of 3D Microfluidic Channels

► Fabrication of 3D Microfluidic Structures

Fabrication of 3D Microfluidic Structures

Ji Fang[1], Weisong Wang[2], Shihuai Zhao[3]
[1] Institute for Micromanufacturing, Louisiana Tech University, Ruston, LA, USA
[2] Department of Astronomy, University of Texas at Austin, Austin, TX, USA
[3] Center for Microfibrous Materials Manufacturing Chemical Engineering, Auburn University, Auburn, AL, USA
jfang@latech.edu, weisong@astro.as.utexas.edu, szhao@auburn.edu

Synonyms

3D microfabrication; 3D micromachining; Microfabrication of three-dimensional microstructures; Three-dimensional patterning; Fabrication of 3D microfluidic channels

Definition

The fabrication of 3D microfluidic structures is related to the microfabrication or Micro-Electro-Mechanical Systems (MEMS) processes, which produce the micro-scale structures (or microchannels) involving or relating to three dimensions (*x*, *y* and *z*) or aspects and giving the illusion of depth, for the handling of fluids in biomedical, chemical, biological devices, etc. It is specifically referred to in the fabrication of microstructures with complex lateral contours using a 2D mask layout. These 3D microstructures may be sculpted in a bulk-substrate or created on the surface of a substrate.

Overview

3D microstructures have been highlighted in microfluidic devices and systems, and typically used to improve the properties of fluidic handling, such as micro-mixers, valves, pumps, micro total analysis systems (μ-TAS), etc. For instance, the microchannel geometry in a micromixer plays an important role in mixing, because only laminar flow is present in the straight microchannels. Well-defined three dimensional microchannels or microstructures can generate a heterogeneous mixture with a finely dispersed structure, and the diffusion of the fluid molecules in the adjacent domains produce a homogenous mixture at the molecular level. As one of the key microfluidic devices, the conventional micropump has been designed and fabricated using two dimensional or planar structures due to crystallographic orientation of the substrate. These pumps have intrinsic limitations such as dead volume, impedance mismatch in interconnects and low back pressure. The 3D fabrication technology provides a new design concept for the micropump and improves its performance. Over the last two decades, microfluidic handling and analysis have been emerging in the interdisciplinary research field of fluidics. The applications have also expanded to microarray, sample preparation, cell cultivation and detection, DNA sequencing, and environmental monitoring. Using 3D microfabrication technologies could potentially enhance the efficiency, reliability, and overall performance of various microfluidic devices. With the continually high demands of microfluidics applications, 3D microstructure fabrication technology becomes more interesting to researchers and industries.

Lithography, as a traditional pattern transfer technology, is normally the first step in top-down microfabrication. Several lithographic techniques offer intrinsic 3D structuring capabilities. For example, Electron beam lithography (EBL) can generate gray-scale profiles by controlling the exposure dose. Gray scale lithography can transfer 3D structure from a 2D gray scale mask. X-ray lithography (XRL) is capable to replicate multilevel masks by amplifying the thickness profile, and can generate complex 3D

structures with multiple exposures at tilted angles. Moreover, focused ion beam (FIB) lithography has shown the capability for direct milling and growth of hard materials. Holographic lithography can generate large volume periodic 3D structures with submicrometer resolution. However, lithographic techniques have their own peculiarities and potentialities that in many cases cannot be exploited to completely cover the entire spectrum of fabrication needs for 3D microstructures. The main disadvantages of these technologies include low speed processes and difficulty moving into mass production. On the other hand, these technologies can be used to fabricate reverse 3D microstructures in the form of molds to produce the final devices by casting, hot embossing, imprinting and soft lithography at low cost.

Most micromachined structures applied in MEMS are fabricated on silicon substrate. Silicon patterning with chemical and/or plasma etching has been extensively studied in the last two decades. Using wet chemical etching, one can define the 3D geometry profile into the silicon substrate by choice of mask geometry, etchant and crystallographic cutting of the substrate. Isotropic silicon etching can generate rounded sidewall profiles and anisotropic etching can produce more complicated profiles like V shape channel, square and rectangular hole, frustum of a pyramid, and other shapes. Plasma dry silicon etching makes it possible to etch controllable profiles without limitations due to crystal orientation. It also provides high etch rate and selectivity between substrate and masking material. Dry plasma etching is becoming a standard tool in microfabrication.

Recently, patterning of polymers, proteins and cells has been intensively studied for 3D polymer structure. In contrast to silicon, polymers show several major advantages that are currently not available in silicon or glass, including a wide range of material characteristics, biochemical compatibility, ease of fabrication and prototyping, and low cost. These benefits make polymers the most promising substrate materials for biomedical and biological applications. Poly(dimethylsiloxane) (PDMS), poly(methylmethacrylate) (PMMA) and SU-8 have been broadly used in microfluidic devices and systems. New technologies for polymer 3D micro/nano structure fabrication such as soft-lithography, hot embossing and different replica moldings are also developed as low-cost approaches to fabricate microfluidic devices.

Basic Methodology

Wet Chemical Etching

Wet chemical etching has its genesis in the semiconductor industry. In this process, the feature structures are sculpted

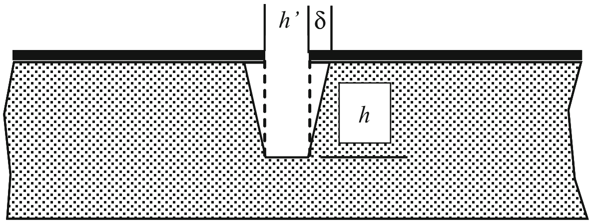

Fabrication of 3D Microfluidic Structures, Figure 1 Example of an etching profile

in bulk substrates such as silicon, quartz, SiC, GaAs, Ge and glass by orientation dependent (anisotropic) or orientation independent (isotropic) wet etchants. The first use of silicon as a substrate can be traced back to mid-1950s and early 1960s. Although this process has a long history, it is still a main conventional microfabrication technology. It is not only low cost and suitable for mass production, but also provides the ability of controlling the etching profile and the well-defined geometries of etched features.

Wet chemical etching can be considered as a sequence of three steps: transport of the reactant to the surface of substrate, reaction with the surface, and movement of reaction product into the etchant solution. Therefore, it includes three components: mask, etchant and substrate. Two important figures for the etching process are selectivity and directionality. Selectivity is the degree to which the etchant can differentiate between the masking layer and the layer to be etched. Directionality has to do with the etch profile under the mask. In isotropic etching, the etchant removes the substrate materials in all directions at the same etch rate and creates a semicircular profile under the mask. In anisotropic etching, the etch rate depends on the substrate's crystallographic orientation by which one can obtain straight sidewalls or other noncircular profiles. To describe the etching processes including wet and dry etching, the following terms are defined (Fig. 1).

Etch Rate (ER) It is the ratio of etch depth (h) and actual etching time (t).

$$ER = \frac{h}{t}$$

Selectivity (S) During the etching process, the mask layer and the substrate are both immersed in the etching media which can be a wet chemical etching bath or plasma. Although the etchant mainly reacts with the substrate, the mask layer is also attacked. The relationship between the etching of the substrate and the mask layer is the selectivity S which is given as the ratio of the etch rate of the

substrate (r) to the etch rate of the mask (r'):

$$S = \frac{r}{r'}$$

It is a critical parameter where deep etching is required.

Aspect Ratio (*AR*) It is defined as the ratio of the etch depth (h) with the channel opening width (h').

$$AR = \frac{h}{h'}$$

Undercut Rate (*UR*) Undercut rate is defined as the ratio of the undercut (δ) to the etch depth (h).

$$UR = \frac{\delta}{h}$$

Since the etch rate in isotropic etching is the same in all directions, its undercut rate is ~ 1. For orientation-dependent anisotropic ►wet etching, the undercut rate is basically < 1. If the undercut rate can be controlled in the etching process, the lateral contours along the z direction will be changed and a special 3D structure can be created with a 2D mask pattern.

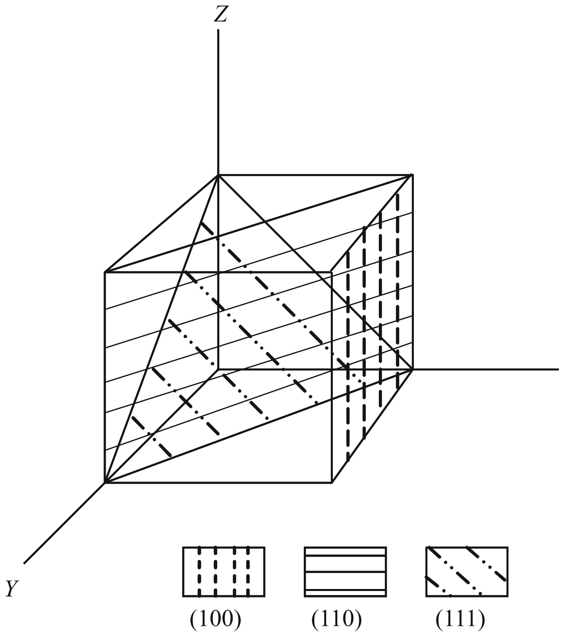

Fabrication of 3D Microfluidic Structures, Figure 2 Three main planes in a cubic lattice

Theory

The majority of substrate used for MEMS and microfluidic devices or systems is silicon. Crystalline silicon forms a covalently bonded structure and has the same atomic arrangement as carbon in diamond. The crystallographic orientation in crystals of the cubic class is described in terms of Miller notation [1]. Any plane in the space satisfies the equation

$$\frac{x}{a} + \frac{y}{b} + \frac{z}{c} = 1$$

Where a, b, and c are the intercepts made by the plane at the x, y, and z axes, respectively. A set of integers of h, k and l can be used and then the equation can be written as

$$hx + ky + lz = 1$$

The integer h, k, and l are called Miller indices. To identify a plane or direction, a series of three numbers are used. Figure 2 shows three planes in a cubic lattice nestled into the origin of the x, y, z coordinate system which illustrate the important planes (100), (110) and (111) in the conventional microfabrication process. Each plane is unique, differing in atom count and binding energy between the atoms. Each plane also has different mechanical, chemical and electrical properties. The etch rate is strongly affected by the crystallographic orientation of silicon. For example, the etch rate of the (100) plane is $\sim 0.6\,\mu m/min$ in 40% KOH at 70 °C while the etch rate is 1.3 $\mu m/min$ for the (110) plane and 0.009 $\mu m/min$ for the (111) plane. The (110) plane is the fastest etching primary surface. The ideal (110) surface has a more corrugated atomic structure than the (100) and (111) primary surfaces. The (111) plane is an extremely slow etching plane that is tightly packed, has a singling-bond per atom and is overall atomically flat. Table 1 lists the etch rates for some crystallographic orientations of silicon in KOH etchant with different concentrations. By understanding and using these orientation-dependent properties, 3D microstructures in a silicon substrate can be well defined.

Experimental

For wet isotropic etching of silicon, the commonly used etchant is a mixture of nitric acid (HNO_3), hydrofluoric acids (HF) and water or acetic acid (CH_3COOH). The reaction of silicon with acids suggests that chemical etching in aqueous solution occurs via the oxidation of the silicon surface by HNO_3 oxidation agent, followed by the dissolution of the silicon oxidation products in HF. The overall reaction mechanism for silicon etching in HF/HNO_3

Fabrication of 3D Microfluidic Structures, Table 1 Silicon etch rate at different crystal orientations in KOH

Crystallographic orientation	Etch rate at different KOH concentrations (μm/min) 30%	40%	50%
(100)	0.797	0.599	0.539
(110)	1.455	1.294	0.870
(210)	1.561	1.233	0.959
(211)	1.319	0.950	0.621
(221)	0.714	0.544	0.322
(310)	1.456	1.088	0.757
(311)	1.436	1.067	0.746
(320)	1.543	1.287	1.013
(331)	1.160	0.800	0.489
(530)	1.556	1.280	1.033
(540)	1.512	1.287	0.914
(111)	0.005	0.009	0.009

mixture is [2]:

$$Si + HNO_3 + 6HF$$
$$\longrightarrow H_2SiF_6 + HNO_2 + 2H_2O + H_2$$

The mixing weight ratio of HF to HNO_3 greatly affects the silicon etch rate. The highest etch rate is observed at the weight ratio of 2 : 1. Figure 3a shows the etching profile for this wet isotropic etching process. The etch rate is the same in all directions.

Anisotropic etchants are alkaline solutions and the etching process is characterized by a high etch rate and an excellent selectivity dominated by the substrate's crystal orientation. There are a wide variety of etchants available for anisotropic etching including KOH, NaOH, LiOH, CsOH, and RbOH. The most commonly used ones are KOH and EDP (ethylene-diamine/pyrocatechol with water). The normal etching temperature for KOH etchant is in the range of 20 – 80 °C, and it strongly influences the etch rate. Raising the etching temperature will increase the etch rate, but decrease the anisotropic degree (etching selectivity in different crystallographic directions). After several hours of the etching process at such temperatures, the concentration of the alkali solution will be changed. Therefore, closed vessels are recommended and the safety issue must be a concern. Since the photoresist will be quickly dissolved in an alkaline etching media, SiO_2 and Si_3N_4 are the common materials for mask layer. The etching selectivity ratio of silicon is ~100 to SiO_2 and > 500 to Si_3N_4. Si_3N_4 as a mask layer is necessary if an etch depth of over 200 μm is required. A SiO_2 film may be deposited on the Si_3N_4 film as a mask to pattern the Si_3N_4 film. Figure 3b illustrates the etching result for a V-groove in a (100) silicon wafer. The etching bonder at (111) planes is generally at 54.74° to the (100) surface of silicon. Figure 3c shows a straight sidewall feature using a properly aligned mask on a (110) silicon wafer.

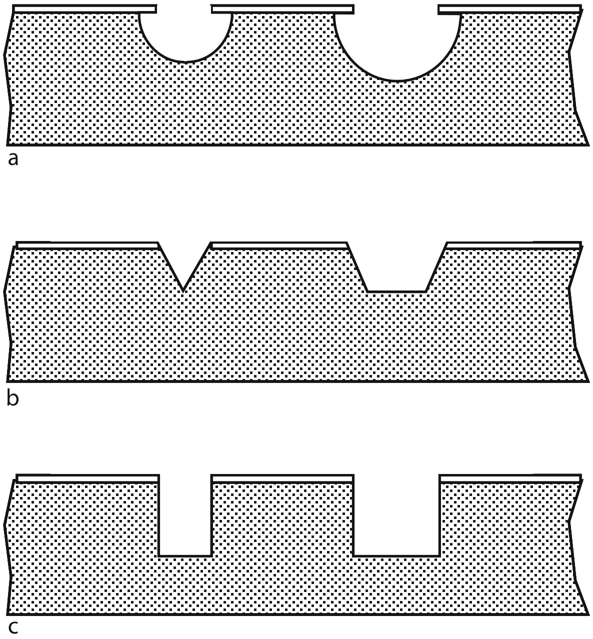

Fabrication of 3D Microfluidic Structures, Figure 3 Etching profiles in wet chemical etching

Dry Plasma Etching

Dry etching is referred to as plasma processing, which was first introduced in the 1960s. During the past forty years, a number of plasma sources have been developed for dry etching, including reactive ion etching (RIE), sputter etching, magnetically enhanced RIE (MERIE), electron

cyclotron resonance (ECR), inductively coupled plasma (ICP), etc. It has been shown that ICP etching is the most suitable and efficient plasma source for deep anisotropic silicon etching with high etch rate and provides the capability of creating 3D microstructures.

Plasma Physics and Chemistry of ICP Etching

In general, the plasma for dry etching is produced by the dissipation of electrical power in a gaseous medium at radio frequency (RF). Electrons gain sufficient energy during oscillation in the RF field to initiate collisions with atoms and molecules to generate the etching species, and to initiate processes such as excitation, ionization and dissociation. The inductively coupled plasma can be generated by using a time-varying axial magnetic field to induce an azimuthal electrical field which effectively confines the plasma current. The current path minimizes contaminants or particles resulting from direct ICP etching and chamber wall sputtering. The highest plasma intensity region is located close to the etching chamber sidewalls and ambipolar diffusion results in a highly uniform plasma inside the chamber.

Figure 4 is a schematic diagram of a typical ICP etching system. The sample is loaded into the etching chamber via a load chamber and either mechanically or electrostatically clamped to the lower electrode. Helium or nitrogen backside cooling provides good thermal conductance between the electrode and the sample. Process gases are admitted to the etching chamber and controlled to a pressure usually in the range of 2.5 – 13 Pa. The 13.56 MHz RF power is applied to the ICP coil to generate the high-density etching plasma. The RF power is also applied to the lower electrode for independent control of substrate bias power. Unused feed gases and volatile etch products are pumped away by a backed turbo pump.

The chemistries of ICP etching mainly include fluorinated, chlorinated, or bromine-based gases. When silicon substrates are dry-processed with fluorinated chemistry, the etch rate is a combination of contributions from spontaneous or thermal reactions between fluorine and silicon, ion bombardments, and a small effect of physical sputtering. A chlorinated chemistry allows easier control of the etching profiles as compared to fluorinated chemistry due to the lack of spontaneous etching of silicon. In general, a higher silicon etch rate as well as a higher etch selectivity of substrate to masking material is expected when using fluorinated chemistry. Moreover, fluorine-based compounds cause fewer health hazards and corrosion concerns than their chlorinated and brominated counterparts.

Among the available anisotropic process schemes and recipes, the Bosch process which is named after the German company that developed and patented the technique is recognized as a standard process for ICP system. The Bosch approach is based on a variation of the teflon-film sidewall passivation technique which avoids the recombination of active species in the gas phase. The deposition and etching steps are performed subsequently to control the sidewall profile of the 3D structures. In the deposition step, the precursor gas (CF_4, C_4F_8, CHF_3, C_2F_6 or higher molecular gas) is dissociated by the plasma. The ion and radical species undergo polymerization reactions. A passivation layer of n CF_2 is deposited on the etched pattern surface. A possible reaction scheme using CF_4 as an example is

$$CF_4 + e^- \longrightarrow CF_x^+ + CF_x^- + F^- + e^-$$

$$nCF_x^- \longrightarrow nCF_{2\ \text{adsorbed}} \longrightarrow nCF_{2\ \text{film}}$$

The deposited polymer film can be removed by ion bombardment with low energy. In the etching step, the etching gas (for instance SF_6) is dissociated by the plasma, liberating high amounts of etching species. These species are necessary to remove the polymer film at the bottom of the pattern and to effectively react with the silicon. The etching reactions involve the removal of the passivation layer

$$nCF_{2\,\text{film}} + F^-(+\text{ion energy})$$
$$\longrightarrow CF_{x\,\text{adsorbed}} \longrightarrow CF_{x\,\text{gas}}$$

and silicon etching

$$Si + F^- \longrightarrow Si - nF + (\text{ion energy})$$
$$\longrightarrow SiF_{x\,\text{adsorbed}} \longrightarrow SiF_{x\,\text{gas}}$$

Since the bombardment and etching reaction with the passivation film on the bottom of pattern are faster than on the sidewall, the silicon surface on the sidewall can be protected by the passivation layer during the etching step. Hence a straight sidewall for the etched feature can be obtained. The kinetics of etching silicon, based on the Langmuir type surface kinetics model, in fluorocarbon discharges using ICP reactors has been developed successfully, and can be found in [3].

Time-Multiplexed Deep Etching (TMDE)

Various 3D microstructures can be created by ICP etching utilizing two gas-feeding methods, continuous etching and time multiplexing. For the continuous etching technique,

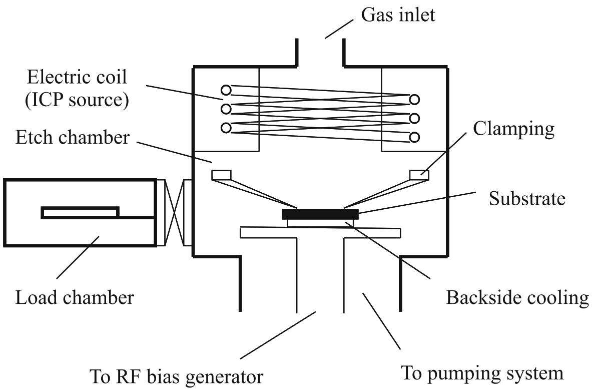

Fabrication of 3D Microfluidic Structures, Figure 4 Schematic of a typical ICP etching system

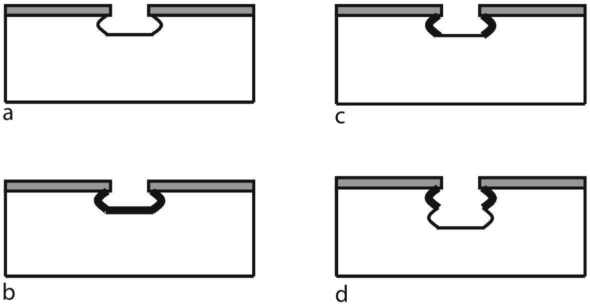

Fabrication of 3D Microfluidic Structures, Figure 5 Four process steps for time-multiplexed deep etching: (**a**) isotropic etching of silicon; (**b**) polymer passivation; (**c**) removal of formed polymer film on the horizontal surfaces; (**d**) further isotropic etching of silicon

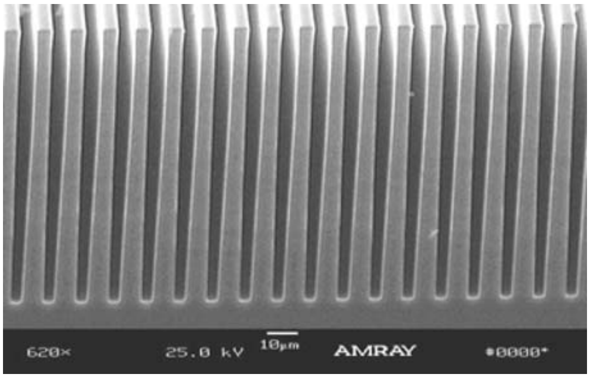

Fabrication of 3D Microfluidic Structures, Figure 6 SEM image of microfluidic channels with high aspect ratio of 20:1 (5 μm width and 100 μm depth) fabricated using TMDE process

all gas species (passivation and etching) are flowed into the etching chamber simultaneously. The etching results depend on the presence of radicals in the glow discharge to proceed with the etching and on other radicals for protecting the sidewalls during operation.

In ►time-multiplexed deep etching (TMDE), the etching and passivation gas monomers are flowed independently one at a time during operation. First, the etch step (normally ≤ 12 s) forms a shallow isotropic trench in the silicon substrate. Second, the passivation cycle (normally ≤ 10 s) forms a protective film on all the surfaces. In the subsequent etching step, ion bombardment promotes the preferential removal of the film on the horizontal surface and further isotropic etching of silicon, allowing the profile to evolve in a highly anisotropic structure (Fig. 5).

In a typical configuration, SF_6 is the etching gas and C_4F_8 is the deposition gas for the sidewall protection. By adjusting etch parameters (such as gas flow rates and durations, plasma source power, substrate bias power, chamber pressure and substrate temperature) in each process step, etch rate, surface roughness, sidewall profile, and etch selectivity can be controlled and optimized to achieve designed 3D microfluidic structures. Figure 6 shows a scanning electron microscopy (SEM) image of microfluidic channels fabricated using TMDE process and Alcatel 601E ICP system. The feature size of the microchannels is a 5 μm width with 100 μm depth. The process recipe is source power 1800 W, bias power 50 W, SF_6 flow rate 300 sccm and pulse duration 4 s, C_4F_8 flow rate 180 sccm and pulse duration 2 s, chamber pressure 5 Pa, substrate temperature 20 °C, and process time 20 minutes.

Besides the continuous and the TMDE process, single feeding gas (such as SF_6) has been utilized in fabrication of 3D microfluidic structures with isotropic features for special applications. At the present time, commercial ICP etchers are available from Alcatel, San Jose, CA; Surface Technology Systems, Ltd. (STS), Redwood City, CA; and Plasma-Therm, Inc., St. Petersburg, FL.

Polymer-Based 3D Microstructure Fabrication

Polymer materials are widely used in the current research involving microfluidic devices because they are chemically and biologically compatible, easy to handle, and low material and manufacturing cost. The devices made by polymer materials are also disposable.

The concept of polymer-based 3D microstructure utilizes replica molding. Therefore, the key fabrication processes include 3D mold fabrication and pattern transfer. The material property is a very important factor when choosing the polymer and mold materials for special applications. For easy handling and accurate shape transfer, the mold requires smooth surface and relatively low thermal expansion coefficient since the curing of the polymer often involves heat. Nowadays, several polymer materials such as PDMS, PMMA and SU-8 are popular choices for microfluidic applications.

Replica molding is a method to reproduce the desired structures by filling the mold with the particular material. It is used to create structures on the materials that are not easy to have patterns created. It has the advantages of low cost and the capability of mass production. Replica molding involves two steps: 3D mold fabrication and mold transfer.

3D Mold Fabrication

In recent decades, a number of technologies have been developed to fabricate 3D molds. These include ► photoresist reflow, ► inkjet printing, unconventional lithography and hybrids of those methods with conventional lithography.

Photoresist Reflow Photoresist reflow is a method to generate 3D hemispheric structures for microfluidic applications. First, a photoresist will be patterned by conventional lithography to generate cylindering or rectangular bars on a substrate. Then, the photoresist pattern is thermally treated for reflowing to form the hemispheric 3D shape. When temperature is higher than the glass transition temperature of the photoresist, it begins to melt and reflows around the pattern. Due to the surface tension of the liquid resist on the substrate and the surface property of the substrate, the liquid resist always tends to form a convex shape. This method was first suggested by Popovic in 1988. Figure 7a shows the photoresist reflow result of a mold for well or cell array. A well with smooth edge is shown in Fig. 7b.

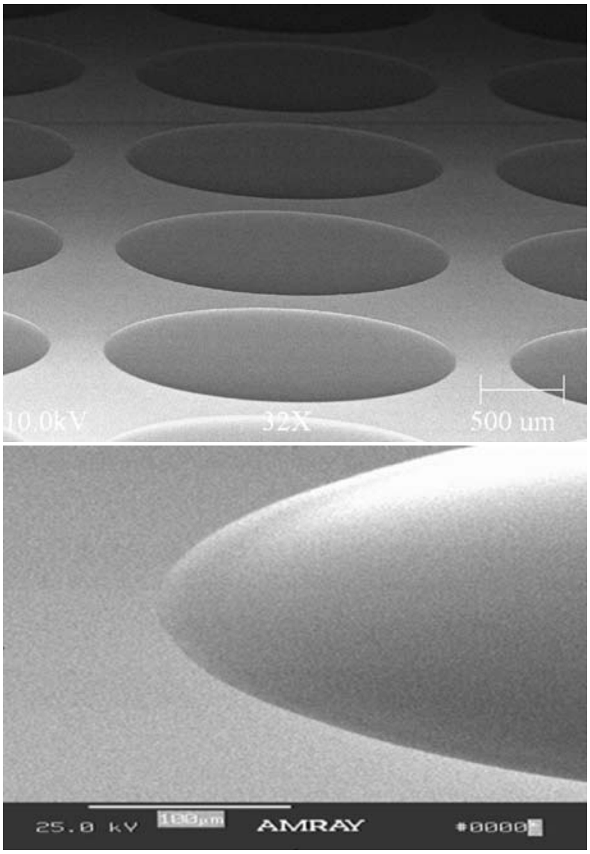

Fabrication of 3D Microfluidic Structures, Figure 7 SEM images of 3D structure of a mold fabricated by photoresist reflow: (**a**) well or cell array; (**b**) the enlarged edge of a single well mold

Inkjet Printing Inkjet printing technology is familiar to most people in the form of desktop printers. Repeatable generation of small droplets of a fluid (polymers) can be used to make 3D structures directly on a substrate for MEMS manufacturing applications.

In a drop-on-demand inkjet printer, the fluid is maintained at ambient pressure and a transducer is used to create a drop only when needed. The transducer creates a volumetric change in the fluid which creates pressure waves. The pressure waves travel to an orifice, and are converted to fluid velocity, which results in a drop being ejected from the orifice. Figure 8 shows a schematic of a drop-on-demand type inkjet system which can generate 60 μm diameter drops of butyl carbitol (an organic solvent) from a device with a 50 μm orifice at 4000 drops per second. Therefore, various molds for microfluidic applications could be created by this method.

Unconventional Lithography Methods Sometimes a mold can be generated directly by unconventional lithography methods such as e-beam, grey scale and stereo laser lithography. Electron-beam direct-write lithography (EBL) has been widely used for creating masks with sub-100 nm resolution. To generate 3D structures, controlling the exposure dose during beam scanning is very important in e-beam lithography. E-beam lithography creates patterns by serially exposing the resist beam spot by the beam spot. The differential levels of exposure dose determine the pattern depth of the exposed area after developing. By adjusting the dose of each exposed spot, lateral contours can be controlled and 3D structures can be created.

► Gray-scale lithography utilizes locally modulated exposure doses to develop 3D structures in photoresist. Differentially exposed doses lead to multiple depths of exposed photoresist across the surface. This is due to the ultraviolet (UV) light energy being absorbed by the photoactive compound as it travels in the depth of the photoresist. From the differentially exposed doses, a gradient height photoresist structure corresponding to the designed silicon structure will remain once the resist is developed.

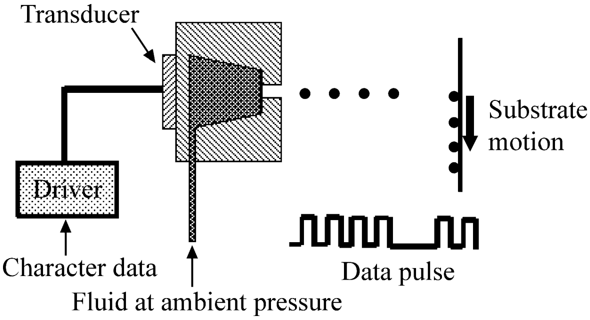

Fabrication of 3D Microfluidic Structures, Figure 8 Schematic of a drop-on-demand type inkjet system

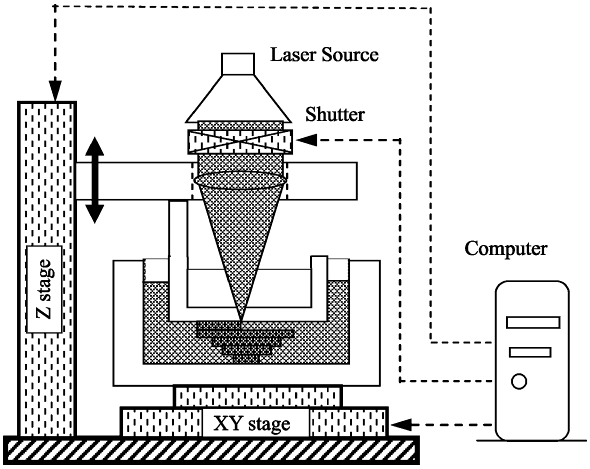

Fabrication of 3D Microfluidic Structures, Figure 9 Schematic of a micro stereo lithography system

There are two primary techniques to generate an optical mask capable of modulating the UV intensity passing through to the photoresist surface. One such method uses a high-energy-beam sensitive glass as an optical mask, in which the UV light transmission of the glass is changed by an e-beam direct write system. Thus, when using this mask to expose the photoresist, the exposed pattern will form 3D structures due to the different exposure levels. The second method utilizes projection lithography to induce diffraction by using a conventional chrome-on-glass (COG) mask.

Micro stereo lithography is a rapid prototyping method to generate 3D molds. It is a maskless process with layer-by-layer fabrication of microstructures via the projection of sliced images of 3D objects, as shown in Fig. 9. A laser beam directs to the photocurable resin which can be classified as an epoxy, vinylether, or acrylate. The 3D structure or mold is built on a platform which can be controlled by an XYZ positioner. When one layer is complete, the platform drops lower into the vat of resin, fresh resin washes over the part, and the laser proceeds to build the next layer. The 3D microstructure is built up in this additive process. When all layers are complete, the part is cleaned and post-cured. The major drawback of this technique is the considerable capital investment. Also, only photocurable resins can be used which can be a limitation if a special material is required.

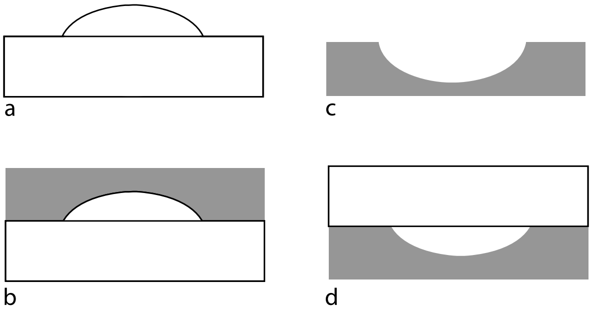

Fabrication of 3D Microfluidic Structures, Figure 10 Direct casting process: (**a**) making a 3D mold; (**b**) casting a polymer structure; (**c**) peeling off the 3D polymer structure; (**d**) bonding to form sealed microfluidic structure

Mold Transfer

After generating a mold, the next step is to transfer the 3D structure from the mold into the polymer. There are several technologies available.

Direct Casting The direct method is to cast the polymer material onto the mold and then peel off the 3D structure after the material is polymerized. Figure 10 illuminates this simple process. The reverse 3D structure is first prepared by microfabrication techniques as a mold. Then, a prepolymer with crosslink is cast onto the mold. After the polymer is well cured by heat or UV, the 3D polymer structure is produced by peeling off the polymer structure from the mold. To construct a microfluidic device, bonding the 3D polymer structure with a substrate is the next step to seal the fluidic channels and reservoirs.

Soft Lithography Soft lithography represents a non-photolithographic strategy based on self-assembly and replica molding for carrying out micro and nanofabrication [4]. It has been mostly developed in recent years. It is a favorable process for researchers to build nanometer scale structures. It includes the following techniques:

Replica Molding (REM) A PDMS stamp is cast against a conventionally patterned master. Polyurethane is then molded against the secondary PDMS master. In this way,

multiple copies can be made without damaging the original master. The technique can replicate features as small as 30 nm.

Micromolding in Capillaries (MIMIC) Continuous channels are formed when a PDMS stamp is brought into conformal contact with a solid substrate. Capillary action fills the channels with a polymer precursor. The polymer is cured and the stamp is removed. MIMIC is able to generate feature sizes as small as 1 μm.

Microtransfer Molding (μTM) A PDMS stamp is filled with a prepolymer or ceramic precursor and placed on a substrate. The material is cured and the stamp is removed. The technique is able to create multilayer systems and features as small as 250 nm.

Solvent-Assisted Microcontact Molding (SAMIM) A small amount of solvent (e.g., methanol, ethanol, or acetone) is spread on a patterned PDMS stamp which is placed on a polymer, such as photoresist. The solvent swells the polymer and causes it to expand to fill the surface relief of the stamp. Feature size as small as 60 nm can be reached.

Microcontact Printing (μCP) An ink of alkanethiols is spread on a patterned PDMS stamp. The stamp is then brought into contact with a substrate, which can range from coinage metals to oxide layers. The thiol ink is transferred to the substrate where it forms a self-assembled monolayer that can act as a resist against etching. Features can be made as small as 300 nm in this method.

Hot Embossing Hot embossing is essentially the stamping of a pattern into a polymer that is softened by raising the polymer's temperature just above its glass transition temperature. Some parameters such as loading pressure, demolding force and temperature play important roles in quality of the molded parts. Hot embossing often requires high loading pressure to stamp the polymer material in a vacuum chamber. However, the pressure should be controlled within a limit to avoid damaging the mold. And at the end of hot embossing, the demolding process requires fast release without damaging the stamped pattern. The surface roughness of the mold affects the demolding and the roughness of the stamped pattern as well. The stamp used to define the pattern in the polymer can be made in a variety of ways including micromachining from silicon, LIGA, and the methods that have been discussed above. A wide variety of polymers have been successfully hot embossed including polycarbonate and PMMA. The feature size can be in micro- or submicro-scale. This

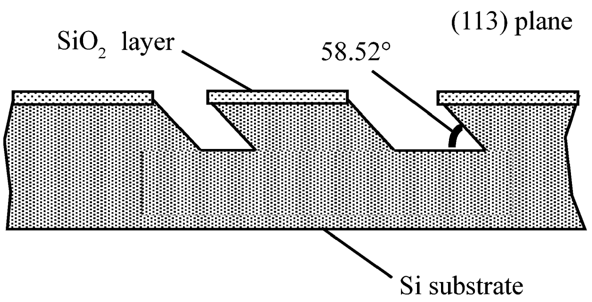

Fabrication of 3D Microfluidic Structures, Figure 11 Wet etch profile in a (113) silicon wafer

technique is used primarily for defining microchannels and wells for microfluidic devices. The benefits of this approach are the ability to take advantage of the wide range of the properties of polymers, as well as the potential to economically mass produce parts with micron-scale features.

Key Research Findings

Figure 11 shows the possible wet etching profile with (113) crystallographic orientation of a silicon wafer. The mask pattern is parallel stripes and aligned at an angle φ, relative to the substrate crystallographic orientation. The angle φ was estimated from the geometrical relationship including the inclination of the $(h\,k\,l)$ plane in relation to the (110) plane, equal to $(90° - \alpha)$. The angle of α represents the angle of inclination of $(h\,k\,l)$ planes toward the (100) plane.

$$\varphi = \arctan\left[0.707 \cos\left(90° - \alpha\right)\right]$$

The substrate used in this experiment was (113) silicon wafer with 1 μm SiO_2 layer. The SiO_2 was used to be the mask material for silicon wet etching. The first step was to use optical lithography and buffered HF wet etching to pattern the SiO_2 layer with a mask and an align angle $\varphi = 16.78°$. Then the silicon etching was carried out in 10 M KOH solution at 75 °C to create an anisotropic 3D structure [5].

The complex 3D structures with desired cross-section for special microfluidic applications can be realized by modifying three classes of ICP etching processes [6]. Figure 12 shows the resulting profiles of the 3D structures. The first patterning was carried out using an anisotropic continuous etching process (SF_6+ polymer-forming gas, high density plasma, and intensive ion bombardment). Afterwards, a polymer layer was deposited under the same conditions of the deposition step in a TMDE process. The deposition rate is $\sim$ 85 nm/min, and the uniformity of the thickness is $\sim$ 4%. After deposition of the polymer, isotropic silicon

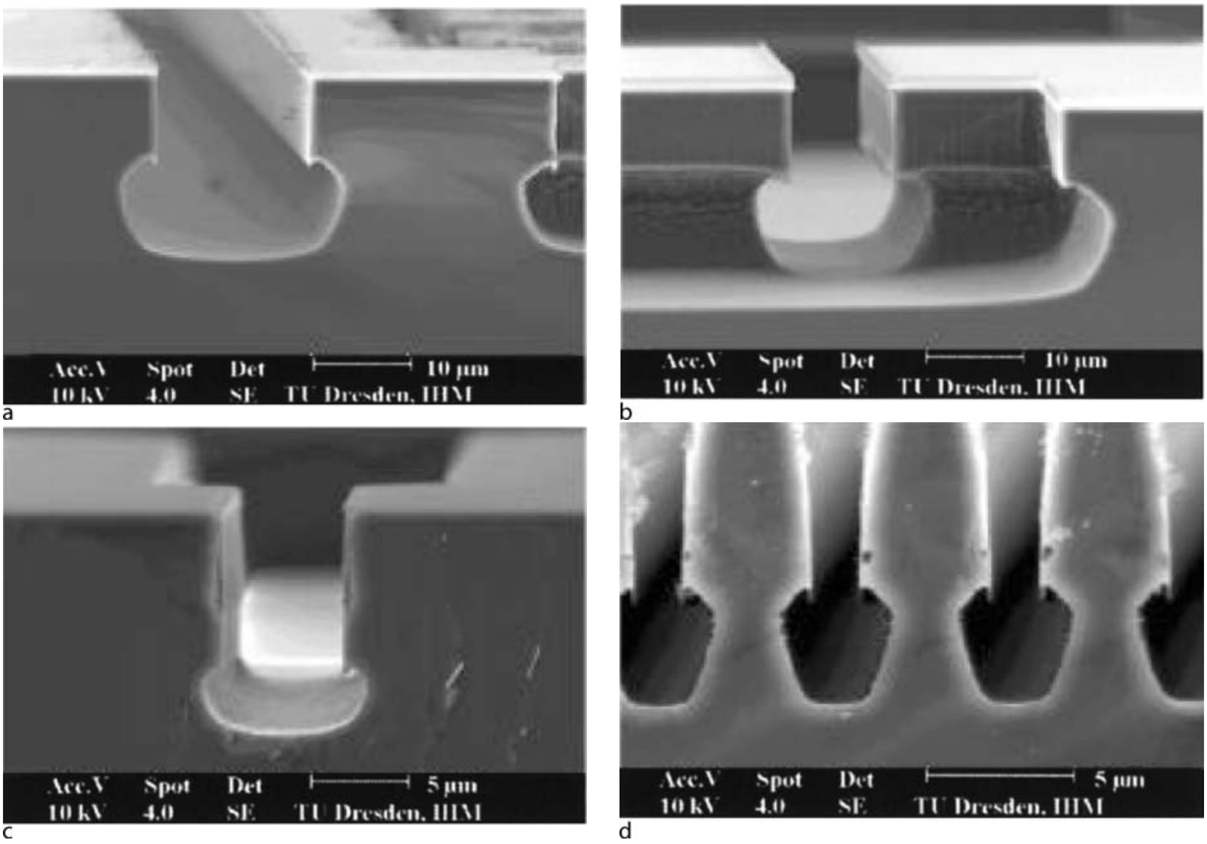

Fabrication of 3D Microfluidic Structures, Figure 12 SEM images of the composed etching profiles: (**a**), (**b**) patterns realized by anisotropic silicon etching, deposition of passivation polymer layer and isotropic silicon etching; (**c**), (**d**) patterns etched like (**a**) and (**b**), passivation with polymer and additional Si_3N_4 layer (5). (With permission from Elsevier)

etching using SF_6 plasma was carried out. The minimum pattern created in this way has a lateral width of 11 µm (Figs. 12a, b).

In addition to realize smaller patterns with the same cross-sectional area, a silicon nitride layer was deposited on the surface after anisotropic etching of the deep trenches. The polymer was then deposited and the silicon was etched by the isotropic process (only SF_6). The results are shown in Figs. 12c, d. In this case, the patterns with a minimum lateral width of 5 µm are realized.

The combination of conventional photolithography and photoresist reflow is an effective method to smoothly integrate microfluidic chambers with microchannels. To fabricate a PDMS 3D microstructure joined with the microchannel by mold transfer, a master mold is needed. The photoresist reflow method was adopted to make the master mold for the 3D chambers and a negative photoresist SU-8 was used to generate the microstructure master mold for the microchannels. Since SU-8 is an epoxy-based photoresist and has good chemical stability with stands temperatures up to 200 °C, the channel pattern can not be damaged during the whole processing. The processing schematic is shown in Fig. 13. First, negative photoresist SU-8 was used to form high bars for the microchannels' mold. Photoresist cylinders were then separately built by conventional lithography. In order to achieve large fluidic volume, thick photoresist AZ100XT was chosen and its patterned cylinders on the substrate were thermally treated on a hot plate. The reflow occurred at 120 °C in a period of 60 s. Sometimes, the organic solvent vapor surrounding the photoresist pattern can promote the reflow process. Figure 14a shows the SEM image for the photoresist mold, which smoothly joins hemispherical structure 2200 µm in diameter and 167 µm in depth with the microchannel.

After completing the mold, the next step was to transfer from the photoresist microstructure to PDMS by casting. The PDMS, Dow Corning Sylgard 184 silicone, was chosen as the casting material because of its high-dimensional accuracy and easy fabrication. After the PDMS substrate was cured in a vacuum oven for 2 h at 5 mTorr of pres-

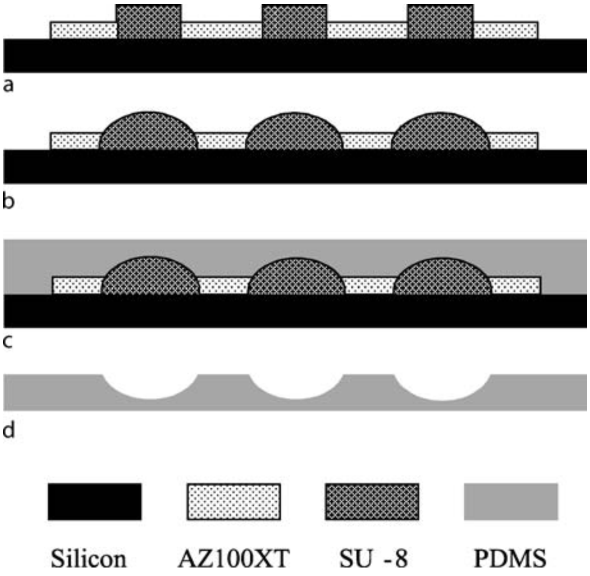

Fabrication of 3D Microfluidic Structures, Figure 13 Schematic of fabrication process of 3D polymer microstructures by combination of conventional photolithography and photoresist reflow: (**a**) photoresist patterned on the silicon wafer; (**b**) photoresist mold after thermal treatment; (**c**) PDMS casting on the photoresist mold; (**d**) PDMS with desired structures

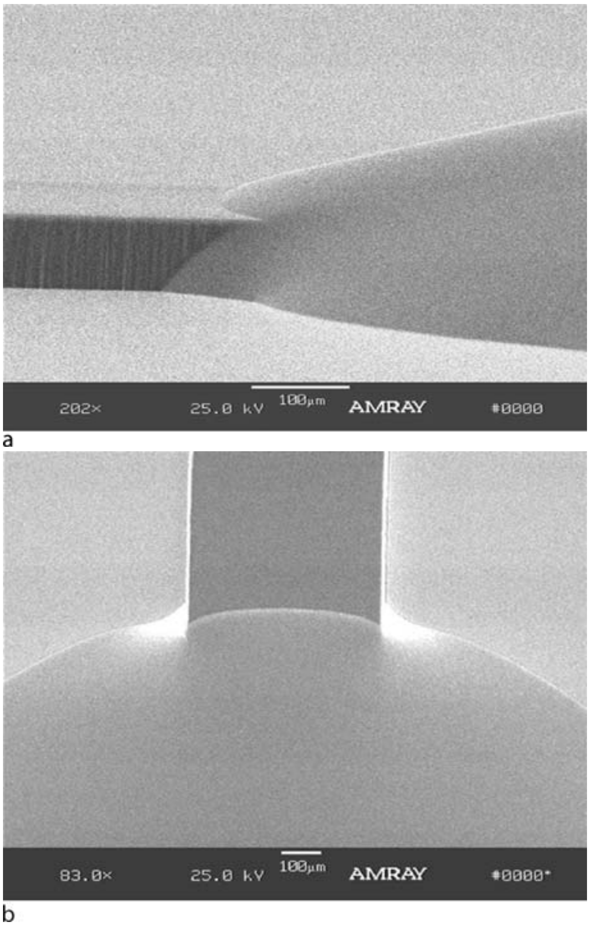

Fabrication of 3D Microfluidic Structures, Figure 14 SEM images of 3D microstructures fabricated by combination of conventional photolithography and photoresist reflow: (**a**) the photoresist mold; (**b**) the PDMS 3D microstructure of the hemispherical chamber joined smoothly with the microchannel

sure at 75 °C, it was then peeled off from the photoresist mold. The PDMS substrate consists of 3D structure joined smoothly together with the microchannel as shown in Fig. 14b.

Future Directions for Research

3D microfabrication being one of the most promising areas of microfabrication technologies has been extensively studied and developed over the last two decades. New technologies have been discovered and developed to design and fabricate a variety of microfluidic devices and systems [7, 8]. The demand for high-precision 3D microfluidic devices and efficient manufacturing technologies is rapidly growing in recent years, particularly in the application areas of drug discovery and delivery, diagnostics, biotelemetry, and genomics. It creates an obvious need for modular, non-silicon approaches to build inexpensive, disposable and biocompatible sensors and systems. To continually explore 3D fabrication methods using the extremely developed lithography technologies, new materials are expected, which are photosensitive, wet or dry etchable and biocompatible. To precisely control 3D microstructures, it is highly desirable to develop the analog 3D fabrication technologies or tools which can produce complex 3D structures without masks. Most microfluidic devices need to be sealed in order to perform certain liquid handling functions. Packaging for sealing a device with a lid or bonding with an additional layer is always a challenging issue in the fabrication of polymer-based microfluidic devices. New technologies and materials which are suitable to integrate 3D fabrication and sealing or bonding will promote rapid prototyping and commercialization for microfluidic devices and systems.

Cross References

- ► Methods for Simulating Migration of Polymer Chains
- ► Microfabrication Techniques
- ► Photolithography
- ► Photoresist SU-8
- ► Photoresist Reflow
- ► Plasma Etching
- ► Reactive Ion Etching (RIE)

► Soft Photolithography
► Thick Resist Lithography

References

1. Ghandhi SK (1994) VLSI Fabrication Principles (second version). Wiley, New York
2. Madou M (2004) Fundamentals of microfabrication. RCA Press LLC., Boca Raton
3. Kim MT (2004) Kinetics of etching in inductively coupled plasmas. Appl Surf Sci 228:245–256
4. Xia Y, Whitesides G (1998) Soft lithography. Annu Rev Mater Sci 28:153–184
5. Zubel I, Kramkowska M (2005) Possibility of extension of 3-D shapes by bulk micromachining of different Si (hkl) substrates. J Micromech Microeng 15:485–493
6. Richter K, Orfert M, Schührer H (2001) Variation of etch profile and surface properties during patterning of silicon substrates. Surf Coat Tech 142–144:797–802
7. Shaikh K, Ryu KS, Goluch E, Nam JM, Liu J, Thaxton CS, Chiesl T, Barron A, Lu Y, Mirkin C, Liu C (2005) A modular microfluidic architecture for integrated biochemical analysis. PNAS 102:9745–9750
8. Thorsen T, Maerkl S, Quake S (2002) Microfluidic large-scale integration. Science 298:580–584

Fabrication of Self-Assembled Catalytic Nanostructures

Michael Cross[1], W.J. Varhue[1], Darren L. Hitt[2]
[1] Electrical & Computer Engineering Program, School of Engineering, The University of Vermont, Burlington, VT, USA
[2] Mechanical Engineering Program, School of Engineering, The University of Vermont, Burlington, VT, USA
mcross@cems.uvm.edu, darren.hitt@uvm.edu

Synonyms

Nanorods; Nanocatalyst; Nanostructures

Definition

A nanocatalyst is a material which performs the role of chemical catalysis while confined to a physical size of 10 to 1000 nm. More important, the nanometer size of the catalyst material affords these materials access to unique physical and chemical properties which makes them capable of delivering enhanced catalytic performance. Most nanostructures are obtained as a result of self-assembly, governed by the physical and chemical nature of the material systems.

Overview

A catalyst is a material entity which participates in a chemical reaction in such a way as to reduce the activation energy required to change one chemical species, *reactants*, into a second chemical species, *products*. Ideally the catalyst material can emerge at the end of the desired chemical reaction unaltered after performing this function. If the catalyst material is in a different phase than the reactants (e. g. a gas-phase reaction occurring on a solid-state surface), the solid is characterized as a heterogeneous catalyst. From an economical point of view there is a desire to use catalyst materials that are not consumed in the planned chemical reaction. The performance of a catalytic material will improve when:

- The surface area exposed to the reacting species is large.
- The catalyst material is specifically suited to perform a desired chemical reaction.

The emergence of nanotechnology offers potential enhancement in both criteria. One of the fundamental advantages of a nanocatalyst is that it offers a large potential surface area of catalyst per mass of material. Prior to the advent of nanotechnology a large surface area could always be realized through the use of a finely divided powders or meshes. In a heterogeneous reactor environment the act of reclaiming the catalytic material would, however, impose certain difficulties. With regards to the specificity of a chemical catalyst, this ability relies on chemical and physical phenomena that can best be described as depending on the steric and/or quantum mechanical nature of the catalyst. Nanotechnology permits one to design physical structures endowed with specific geometric and electronic properties. There is currently great interest in growing nanostructured materials, attached to a substrate, into structures that are commonly referred to as nanorods, nanoribbons, quantum dots, etc. These intriguing structures occur as the result of processing conditions used to form these materials with a variety of physical and chemical processes. The act of formation of these material structures is referred to as self-assembly. As an example, in Fig. 1 GaSb crystalline droplets are formed on the surface of Si wafer, as a result of surface tensions produced because of lattice constant differences between the two materials. These dot-like structures have been given the name of quantum dots, because the physics which describes electronic behavior in these structures requires a quantum mechanical treatment. Self-assembly is also credited with building more complicated structures such as nanorods and ribbons; again the physics and chemistry of atomic assembly produce these structures governed by minimum energy.

Within the specific context of micro- and nanofluidics, the fabrication of self-assembled nanostrucures can represent an enabling technology for novel engineering applications. One such application – and the specific motivation for this article – lies in the creation of catalytic nanostructures for micro-/nanoscale reacting flow systems. A specific example is the catalyzed chemical decomposition of monopropellant fuels for the purposes of small satellite micropropulsion [1] (Fig. 2). Here, the size and density of nanorod formations naturally provide the high surface area-to-volume ratios desirable for efficient catalysis in microscale geometries. Certainly other important applications exist, including those that leverage nanotechnology to produce *clean* energy and/or reduce emission of greenhouse gases. Some specific, high-profile applications include: fuel cell electrode fabrication, pollution control, hydrogen production and chemical reagent production. For example, platinum (Pt) nanocrystalline layers are used in proton exchange membrane (PEM) fuel cells to catalyze the reduction of oxygen and oxidation of hydrogen on the cathodes and anodes, respectively. The current challenge is that the Pt nanostructured layer has been found to degrade through normal use owing to a number of factors such as fouling by fuel impurities, Pt dissolution, and nanoparticle coalescence and agglomeration [2]. Research efforts are targeted at identifying new alloy combinations with Pt that might overcome or mitigate these issues.

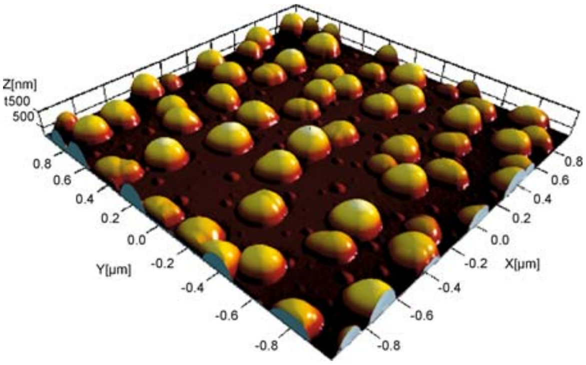

Fabrication of Self-Assembled Catalytic Nanostructures, Figure 1
Atomic force microscope image of GaSb quantum dots formed on a Si substrate. Dots formed as a result of self-assembly process

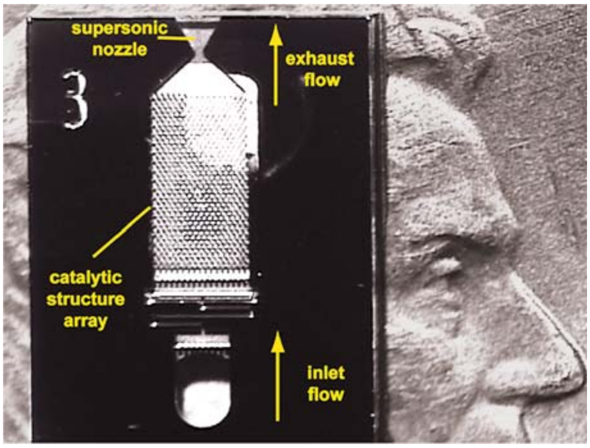

Fabrication of Self-Assembled Catalytic Nanostructures, Figure 2
A photograph of a prototype monopropellant-based microthruster developed for miniaturized satellite applications (*nanosats*) by NASA/Goddard Space Flight Center in collaboration with the University of Vermont [1]. This device utilizes the catalyzed decomposition of hydrogen peroxide as the energy source for propulsion. The catalytic structures in this device are not self-assembled, but rather consist of a three-dimensional array of MEMS-fabricated pillar-type structures coated with a silver catalyst. For reference of scale, the entire catalytic array is ~1 mm wide and 2 mm long

Basic Methodology

Scientist are developing an ability to use nanofabrication techniques to make artificially structured catalyst arrays that can drive a chemical reaction to products with dramatically improved energy efficiency and chemical specificity. In general, nanorod structures have been demonstrated in a growing number of solid-state materials; a non-exhaustive, but illustrative, list includes the following: Si, InP, SiC, ZnO, CdS, GaN, and RuO_2 [3–8]. Currently it is not possible to predict with certainty what will be the best catalyst material for a specific chemical reaction. Research is proceeding both experimentally and theoretically to develop a deeper understanding of these materials and processes that one day will make this possible.

Much of the initial work in the overall area of nanotechnology involved ZnO; this is a result of the fact that this material has a combination of physical and chemical properties which makes it ideal for the fabrication of complex nanostructures [4–9]. These properties have given ZnO a ubiquitous role in the nanotechnology world. Once nucleated, the growth of single-crystal ZnO nanostructures (nanorods) is possible. The epitaxial growth of single-crystal ZnO as a thin film is preferred in its *c*-axis along the (0001) direction. Further, from energetic considerations, crystal growth proceeds by maximizing the areas of its sidewall facets, oriented in the (2110) and (0110) directions. These growth mode constraints result in the formation of tall hexagonally shaped nanorod structures. It has been shown by Wang et al. [7] that the addition of elemental impurities can affect the final nanostructure of the grown material. Another interesting concept for the purposes of this application and nanotechnology in general is the continued growth of additional materials onto the sidewalls of existing ZnO or other nanorods. Norton et al. [4] reported on the epitaxial growth of a Mg-doped ZnO layer on the

sidewall of an existing ZnO nanorod. The process used to grow the additional layer on the ZnO nanorod structure in that study was molecular beam epitaxy (MBE).

There are a number of experimental techniques used to fabricate self-assembled nanostructures from ZnO and other materials. These techniques include the following: vapor–liquid–solid; metalorganic chemical vapor deposition; template-assisted; chemical reaction; molecular beam epitaxy; and reactive sputtering. In this section we provide a brief overview of these techniques.

Vapor–Liquid–Solid (VLS) Technique

In the VLS method, a thin layer (70 Å) of metal such as Au, Ag, Pt, Pd, Cu, or Ni is deposited on the substrate surface. The substrate is then annealed at high temperature (500 °C for Au) to form nanodots of the metal catalyst, which provide the preferential site for the adsorption of gas-phase reactants. For the case of ZnO nanorods, the substrate is placed in a furnace containing ZnO powder and a source of carbon. When heated to 700 °C, the ZnO and carbon react to produce CO_2 and Zn. The gaseous Zn is dissolved to supersaturation in the metal dot and crystal growth occurs from the substrate side of the metal dot. The growth continues as long as the conditions for growth remain sufficient, such as reactant concentration and the proper temperature for growth. The method has been used to form a variety of nanowires such as InP, GaN, CdS, and Si [6]. Several groups have repeated the process with variations such as the substrate used for growth and the reactor design.

Metalorganic Chemical Vapor Deposition (MOCVD)

To date the greatest success in growing straight, tall, and well-aligned rod-shaped structures has been with an MOCVD growth process. This approach relies typically on the use of chemical precursors (e. g. diethylzinc and oxygen in the case of ZnO growth). It appears that the chemical nature of this process technique encourages the growth of exceptionally straight nanorods. Different metalorganic precursors are used as the starting materials for different inorganic nanorod materials [8].

Template-Assisted Growth

This technique can use several different variations to achieve the growth of nanostructured materials. In one version, a metal catalyst is deposited and/or patterned into a desired layout. From these metal catalyst locations the nanorods materials are assembled to the finished length or size. Another approach can involve the actual growth of a different material inside or on an existing nanostructed material such a carbon nanotube. This technique can be used to grow nanostructured materials with chemical compositions that have not been fabricated into nanostructures [10].

Solution-Based Approaches

These methods are, in theory, the least technically challenging procedures for the fabrication of nanometer-sized structures of a given composition. The techniques of hydrothermal and solvothermal production are included under this general heading of solution-based approaches. These methods all involve the dissolution of a targeted nanorod material (e. g. TiO_2) in a basic solution (e. g. NaOH in water). This solution is raised to a temperature and pressure above standard temperature and pressure and held for several hours. The resulting nanostructure precipitates are freestanding and need to be collected from a liquid solution by filtration. The precipitate in this example would be $Ti(OH)_x$, and would require further processing called calcination. Calcination is performed at a temperature of about 700 °C removing the H species from the nanorod material.

Modifications of this process have resulted from the use of different basic solutions that have reduced the required process temperatures or pressures. An example would be the formation of Eu_2O_3 nanorods [11]. These are formed by dissolving $Eu(NO_3)_3$ in a cyclohexamine base solution. The resulting precipitate is calcinated at 700 °C for one hour and nanorods with a length of 300 nm and diameter of 20 – 30 nm are obtained.

These solution-based approaches have the benefit of producing a large volume of material with an inexpensive process. A downside is that the catalyst material is freestanding, and to be used in a heterogeneous reactor will require additional process complications.

Molecular Beam Epitaxy (MBE)

This technique is prized for the high level of control that is possible, in terms of both the control of desired (the materials which constitute the nanorods) and undesired species fluxes (contaminants, e. g. water and oxygen) at the growth surface. This technique has been successfully used to grow a wide variety of semiconductor nanostructures. Due to high capital cost and cost of operation, it is not expected that this technique will prove capable of producing catalyst materials on a large scale.

Reactive Sputtering

Deposition of metal oxide nanorods has been achieved by reactive sputtering. As an example of this deposition

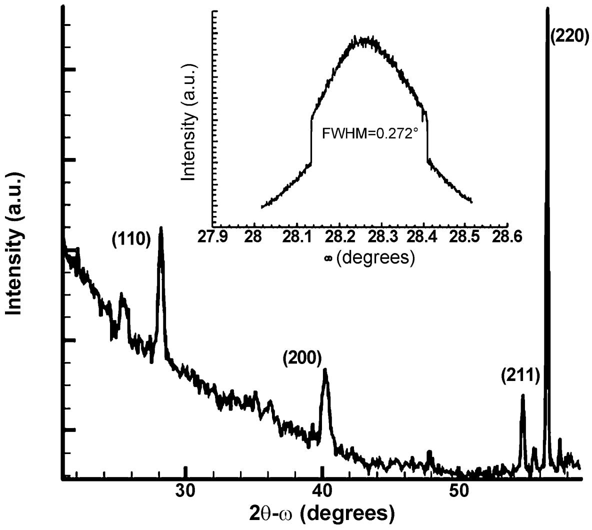

Fabrication of Self-Assembled Catalytic Nanostructures, Figure 3
The X-ray diffraction pattern of RuO_2 nanorods grown on a Si substrate for 10 min at 600 °C. The inset is an omega scan of (220) peak. Major peaks indicate particular crystal orientation of the atoms in the nanorods

approach, RuO_2 nanorods have been obtained by sputtering on a Si/SiO_2 surface [12]. In this particular case, these structures were used as the starting substrate for the further growth of TiO_2. Sputtering is a process that has been used in large-volume manufacturing such as the automotive industry; therefore it is possible to envision its use in the manufacture of heterogeneous catalyst layers.

Key Research Findings

The scientific literature has shown that self-assembled nanorod structures have been grown from a large number of materials and for a wide variety of engineering applications. For illustrative purposes, in this article we focus on the fabrication and growth characteristics of ruthenium oxide nanorods; the target application lies in the catalyzed decomposition of hydrogen peroxide for small satellite micropropulsion (e. g. Fig. 2). The findings reported here, while case specific, are nonetheless reflective of broader phenomena and considerations associated with the growth of self-assembled nanostructures.

Our laboratory at the University of Vermont has successfully grown RuO_2 nanorods by reactive sputtering on Si wafer substrates with a variety of pre-existing surface conditions. Proof of a crystalline structure has been obtained by X-ray diffraction. A sample X-ray diffraction spectrum of the deposited nanorods is shown in Fig. 3. Each of the major peaks in Fig. 3 corresponds to a single crystal orientation of the nanorods. Although each nanorod is single crystal, each nanorod is randomly oriented relative to another, thus displaying the random pattern observed under scanning electron microscopy (SEM) imaging (Fig. 4).

Experimental Apparatus

The reactor used in this investigation is shown in Fig. 5. The samples were prepared by sputtering from a 1.5 inch diameter Ru metal target, operated at 13.56 MHz and a power level of 50 W. The reactor ambient was obtained by flowing 100 sccm of a 5/95% O_2/Ar gas mixture, throttled to a pressure of 15 mtorr. The samples were heated radiatively from behind with a resistive boron nitride-coated pyrolitic graphite heater. Silicon wafer substrates with three different surface preparations were used: Si with a native oxide layer; Si with the oxide layer removed by hydrofluoric acid (HF) treatment leaving a hydrogen passivated surface; and Si with Au dots nucleated on the sur-

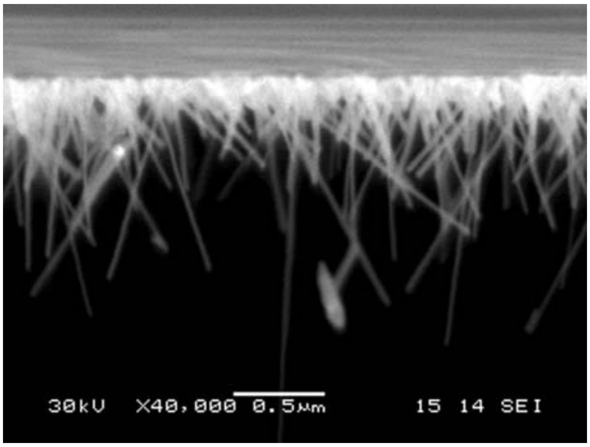

Fabrication of Self-Assembled Catalytic Nanostructures, Figure 4
Scanning electron microscope image of RuO_2 nanorods grown on (100) Si at 600 °C for 10 min

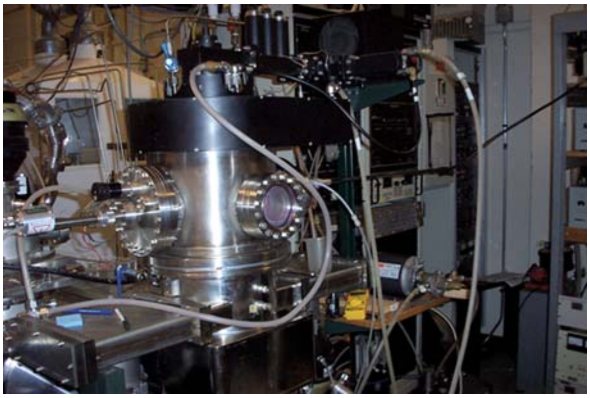

Fabrication of Self-Assembled Catalytic Nanostructures, Figure 5
Sputtering system used in the growth of RuO_2 nanorods in our laboratory

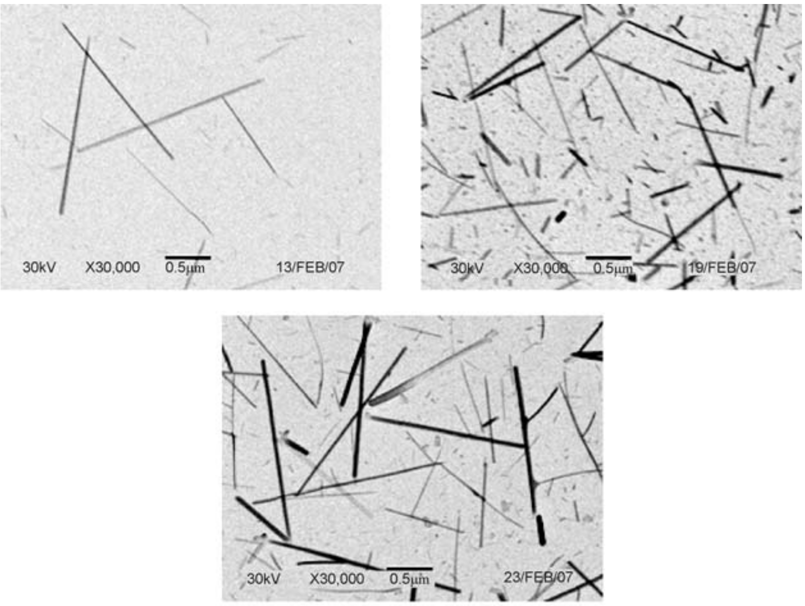

Fabrication of Self-Assembled Catalytic Nanostructures, Figure 6 SEM images (shown in negative tone) of RuO_2 nanorods grown at 600 °C. Shown clockwise from top left are nanorods deposited on HF-dipped Si, Au dots, and native oxide

face. Nanorod growth was obtained to varying degrees on all surface preparations, as can be observed in Fig. 6.

Temperature Dependence of Growth

Ruthenium oxide nanorods were found to form on all samples independent of pre-existing surface preparation, yet not at all substrate temperatures. Initially the effect of substrate temperature on the growth of RuO_2 nanorods was investigated. SEM images of samples prepared at varying substrate temperatures are shown in Fig. 7 for the case of RuO_2 grown on Si covered with Au nucleation sites. The RuO_2 layer was prepared by exposing the Si surface to the sputtered Ru flux at substrate temperatures of 400, 500, 600, and 700 °C for a period of 5 minutes. At a substrate temperature of 400 °C, short, sparse RuO_2 nanorods formed. There is also the appearance of randomly scattered dots on the surface, assumed to be composed of RuO_2 deposited on a continuous island-like thin-film structure. Increasing the substrate temperature to 500 °C resulted in conditions that caused these nucleation sites to develop into nanorods again rising above a continuous cauliflower-like film. From a plan view SEM image such as seen in Fig. 7, the nanorods appear to be randomly oriented. Measuring the average length of the nanorods from this vantage point is not possible because of the nanorod's angular projection from the Si surface. It is more significant to simply measure the length of the longest nanorods for a given set of process conditions and compare these to those obtained for different growth conditions. Considering that the number of rods sampled in a field of view is large (approximately 6 μm^{-2}), the measured rod length is an accurate representation of the maximum rod length. At a substrate temperature of 400 °C, 0.18 μm tall nanrods were observed. The conditions of a 500 °C substrate temperature produced nanorods with a maximum length of 0.6 μm. When the temperature was increased further to 600 °C, the maximum length of the nanorods has grown to 1.3 μm. Finally when a substrate temperature of 700 °C is used, growth of the nanorods is not obtained past the formation of RuO_2 dots.

Axial Growth Rate

To further understand the mechanism which governs the growth of RuO_2 nanorods in a radiofrequency sputtering process, a series of runs were made under identical process conditions and were terminated after increasingly longer periods of time, following which characterization was carried out. The process conditions used in this sequence of runs were similar to those in the temperature investigation, but in this case a substrate temperature of 600 °C was used. The periods of growth were 2, 3, 6.5, 10 and 13 min. From the plot in Fig. 8, one can observe that the density of nanorods increases with time. The maximum nanorod length for these depositions is approximately 1.3 μm and this value does not change with time.

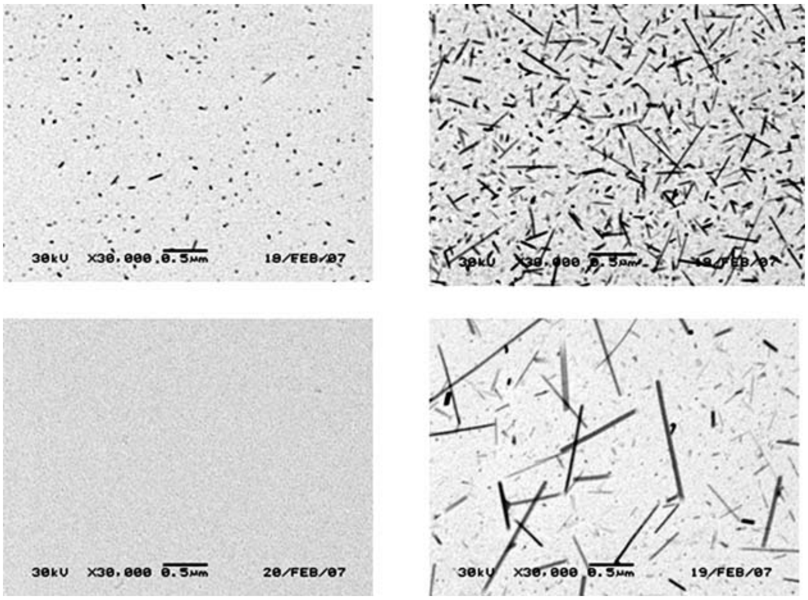

Fabrication of Self-Assembled Catalytic Nanostructures, Figure 7 SEM images (shown in negative tone) of RuO_2 nanorods. Nanorods were deposited on Au dots for 5 min. Shown clockwise from top left are substrate temperatures of 400, 500, 600, and 700 °C

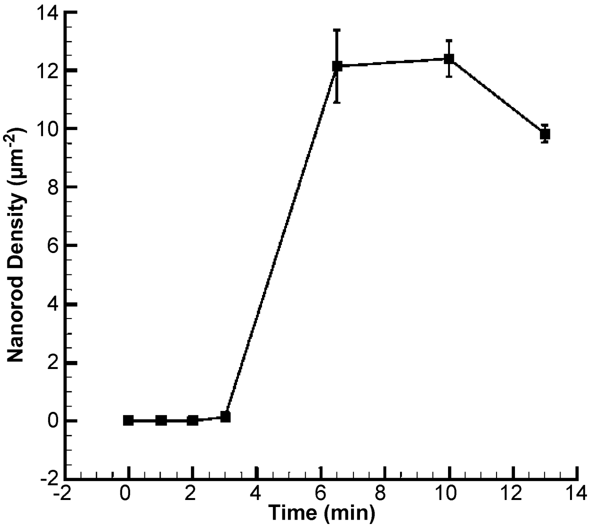

Fabrication of Self-Assembled Catalytic Nanostructures, Figure 8 Plot of a RuO_2 nanorod density at varying deposition times. Nanorods were deposited at 600 °C

Relative to the growth rate of nanorods presented in the literature, using different processing techniques, the rate of growth observed herein is relatively fast. In the time evolution study described above, the nucleation of nanorods is very fast, and short relative to the time increments investigated. In the time period from 3 to 6.5 min, the density of nanorods increases at a rate of 5.41×10^6 cm^{-2} s^{-1}. The Rutherford backscattering spectrometry (RBS) analysis of a film deposited at room temperature can be used to calculate a measured flux of Ru atoms to be 7.08×10^{-10} mol cm^{-2} s^{-1}. The diameter of the nanorods grown after a time of 10 min was observed by SEM to be approximately 100 nm. Assuming a final rod diameter of 100 nm and that all of the sputtered flux of Ru adatoms are successfully incorporated into the nanorods structure, a simple mass balance can be performed to estimate the average length of the nanorods. Using this assumption and the measured Ru flux and density of nanorods formed, a nanorod length of 0.32 µm is estimated. This value is comparable with the values obtained from the cross-sectional SEM view shown in Fig. 4.

Radial Growth Rate

The growth of nanorods in the vertical direction is very fast once nucleated. After viewing all SEM images it is interesting to note that for varying periods of growth, the nanorods grew to a maximum length and then virtually stopped. There seems to be no apparent explanation for the cessation of vertical growth. Under closer examination, the SEM images of RuO_2 nanorods grown under identical conditions, but after different periods of growth (5, 15, 25, and 60 min), were examined (Fig. 9). It is first observed that the nanorods actually have a square profile. It is further observed that the square profile of the nanorods is also increasing with time. The nanorod radial growth rate is

estimated to be 1.9 nm min^{-1}. It is proposed that the further axial growth is halted as a result of the consumption of Ru adatoms used in the radial growth process. The axial reaction rate constant is assumed to be large relative to the radial growth constant, and the axial growth dominates initially. As the cross-section of the square rod increases, the density of surface states dominates the consumption of Ru adatoms and axial growth is halted.

In this article, a brief overview of fabrication techniques and issues associated with the growth of nanostructures made of catalytic materials has been given. Illustrative research findings were also presented for the specific case of RuO_2 nanostructures.

Future Directions for Research

To date, much of the research in this area can best be categorized as phenomenological. As such, there are many important areas for future research. We close this article by identifying three key areas for immediate research:

- *Growth mechanisms.* Observations on the growth mechanisms of RuO_2 nanorods have been reviewed. In particular, the dependence of the length of nanorods on substrate temperature and the width of nanorods on deposition time has been described. Further studies are required to fully develop a theoretical model for the growth mechanism of these structures and to gain a better understanding of the limiting factors of growth.
- *Mechanical characterization.* For the application of catalytic nanostructures, these nanorods may experience significant forces due to the flow of liquid and gas around them. The mechanical robustness of the nanorod structures as well as the connection to the substrate must be evaluated. Techniques such as manipulation via an atomic force microscope may be used to determine the strength of these structures. Theoretical modeling will also contribute to this effort.
- *Device application and integration.* It is clear that self-assembled nanostructures hold great promise for future applications. Nanorod structures have been studied for nearly a decade now; however, very little progress has been made in the implementation of these structures into/as devices. Further work is required in order to integrate these structures into devices. Future work in our laboratory will study the catalytic efficiency of RuO_2 nanorods in a microthuster device.

Acknowledgements

This work was supported, in part, by the US Air Force Office of Sponsored Research (AFOSR) under Grant #FA9550-06-1-0364.

Cross References

► Chemical Vapor Deposition for Film Deposition
► Droplet Dynamics in Microchannel
► Fabrication of 3D Microfluidic Structures
► Flow in Channels with 3D Elements
► Microfluidic Systems in Space Science
► Supersonic Micro-Nozzles
► Microrockets
► Microscale Energy Conversion Devices
► Quantum Dots
► Self-Assembly
► Self-Assembly Fabrication
► Sputtering for Film Deposition

References

1. Hitt DL, Zakrzwski CM, Thomas MK (2001) MEMS-Based Satellite Micropropulsion Via Catalyzed Hydrogen Peroxide Decomposition. Smart Mater Struct 10:1163–1175
2. Ferreira PJ, la O' GJ, Shao-Horn Y, Morgan D, Makharia R, Kocha S, Gasteiger HA (2005) Instability of Pt/C Electrocatalysts in Proton Exchange Membrane Fuel Cells. J Electrochem Soc 152(11):A2256–A2271
3. Duan X, Huang Y, Agarwal R, Lieber C (2003) Single-nanowire electrically driven lasers. Nature 421:241–245
4. Norton DP, Heo YW, Ivill MP, Ip K, Pearton SJ, Chisholm MF, Steiner T (2004) ZnO: growth, doping and processing. Mater Today 7(6):34–40
5. Han W, Fan S, Li Q, Hu Y (1997) Synthesis of GaN nanorods through a carbon nanotube confined reaction. Science 277(5330):1287
6. Gudiksen MS, Lieber CM (2000) Diameter-selective synthesis of semiconductor nanowires. J Am Chem Soc 122:188
7. Wang G, Hisieh CS, Tsai DS, Chen RS, Huang YS (2004) Area-selective growth of ruthenium dioxide nanorods on $LiNbO_3$ (100) and Zn/Si substrates. J Mater Chem 14:3503–3508
8. Si J, Desu B (1996) RuO_2 Films by Metal-Organic Chemical Vapor Deposition. J Mater Res 8(10):2644
9. Wang ZL (2004) Nanostructures of ZnO. Mater Today 7(6):26–34
10. Quinn BM, Lemay SG (2006) Single-walled carbon nanotubes as templates and interconnects for nanoelectrodes. Adv Mater 18:855–859
11. Du N, Zhang H, Chen B, Wu J, Li D, Yang D (2007) Low temperature chemical reaction synthesis of single-crystalline $Eu(OH)_3$ nanorods and their thermal conversion to Eu_2O_3. Nanotechnol 18:065605
12. Cheng KW, Lin YT, Chen CY, Hsiung CO, Gan JY, Yeh JW, Hsieh CH, Chou LJ (2006) In situ epitaxial growth of TiO_2 on RuO_2 nanorods with reactive sputtering. Appl Phys Lett 88:43115

Fabry-Perot Optical Filter

Synonyms

Optical narrow passband filter

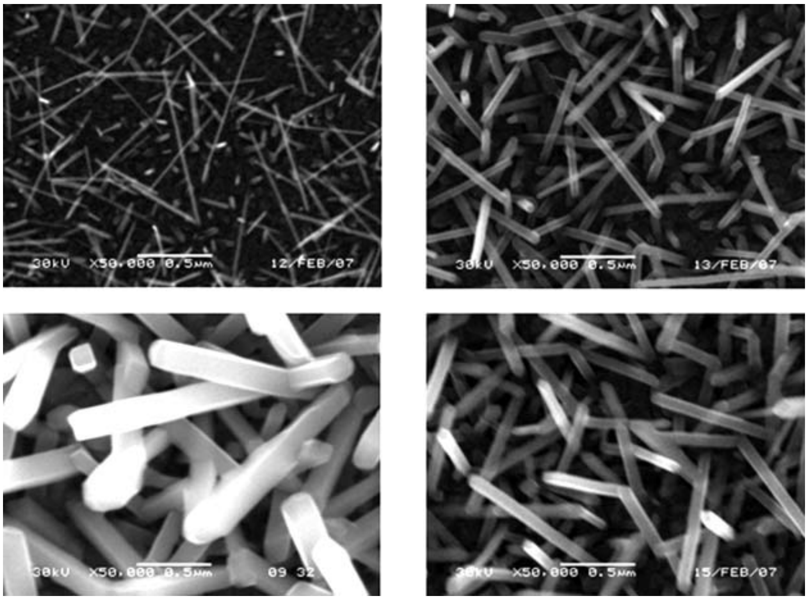

Fabrication of Self-Assembled Catalytic Nanostructures, Figure 9 SEM images of RuO_2 nanorods. Nanorods were deposited on HF-dipped Si at 460 °C. Shown clockwise from top left are deposition times of 5, 15, 25, and 60 min

Definition

A Fabry-Perot optical filter consists of two flat highly-reflective and parallel mirrors spaced a well-defined distance apart, with the reflecting part facing each other. The space in between the mirror surfaces is essentially a resonance cavity. The incident light suffers multiple reflections between the coated surfaces that define the cavity. When the cavity width is equal to an odd multiple of a half wavelength of the incident light, the reflected beams interfere constructively and the optical transmission is maxim. At other cavity widths, the reflected beams interfere destructively and the optical transmission can be reduced toward to zero. Therefore, this device acts as a passband filter that transmits certain wavelengths. To perform high reflectivity and high transmittance, dielectric mirrors are used instead of metallic mirrors.

Cross References

- ► Lab-on-a-Chip Device for Chemical Analysis
- ► Optofluidics: Optics Enabling Fluidics
- ► Sputtering for Film Deposition

Feature Size Dependent Etching

► RIE Lag

Feedback

Definition

The cycle of observing a dynamic system (sensing), making a decision (control computation), implementing that decision by actuators (actuation), and then observing the new dynamics at the next time instant. This cycle of sensing → computation → actuation is what is meant by the term feedback. Feedback is routinely used in complex systems ranging from electronic systems, to airplanes and cars, chemical plants, and is ubiquitous in biological systems (living cells use feedback to control all aspects of their operation).

Cross References

► Control of Micro-Fluidics

Ferroelectric

Definition

The characteristic of an insulating material that exhibits non-centrosymmetric crystal organization. In the strictest sense, a distinct characteristic of ferroelectric materials is the presence of hysteresis. All ferroelectric materials are both piezoelectric and pyroelectric. PZT is a common ferroelectric material.

Cross References

- ► Electrostrictive
- ► Hysteresis
- ► Pyroelectricity
- ► Pyroelectric Flow Sensors
- ► Spontaneous Polarization

Ferrofluids in Microchannels

NGUYEN NAM-TRUNG
School of Mechanical and Aerospace Engineering,
Nanyang Technological University, Singapore, Singapore
mntnguyen@ntu.edu.sg

Synonyms

Magnetic fluid; Liquid magnet; Dispersed magnetic nanoparticles

Definition

A ferrofluid is a liquid consisting of ferromagnetic nanoparticles suspended in a nonmagnetic carrier fluid, typically water or oil. The ferromagnetic nanoparticles are coated with a surfactant such as oleic acid to prevent their agglomeration. The magnetic particles have typical diameters on the order of 5 – 15 nm and a volume fraction of about 5 – 10%.

Chemical and Physical Principles

Although certain pure substances such as liquid oxygen also behave as magnetic liquids, ferrofluids are commonly understood as colloidal ferrofluids (Fig. 1). The fluid is composed of a carrier fluid and ferromagnetic nanoparticles, usually magnetite, hematite, or some other compound containing iron in the 2+ or 3+ state. These nanoparticles are solid, single-domain magnetic particles. The particles are coated with a monolayer of surfactant molecules to prevent them sticking to each other. Because these particles are so small, Brownian motion is able to disperse them homogeneously in the carrier fluid. The dispersion is sufficiently strong that the solid particles do not agglomerate or separate even under strong magnetic fields. A typical ferrofluid is opaque to visible light. It should be noted that the term *magnetorheological fluid* (MRF) refers to liquids similar in structure to ferrofluids but different in behavior. The particle sizes of MRFs are on the order of micrometers and are 1 – 3 orders of magnitude larger than those of ferrofluids. MRFs also have a higher volume fraction of particles, on the order of 20 – 40%. Exposing an MRF to a magnetic field can transform it from a light viscous fluid into a thick solid-like material.

The ferromagnetic nanoparticles can be fabricated using size reduction through ball milling, chemical precipitation, or thermophilic iron-reducing bacteria. In ball milling, a magnetic material with a particle size of several micrometers such as magnetite powder is mixed with the carrier liquid and the surfactant. The ball-milling process takes approximately 1000 h. Subsequently, the product mixture undergoes centrifuge separation to filter out oversized particles. The purified mixture can be concentrated or diluted to obtain the final ferrofluid.

Synthesis by chemical precipitation is a more common approach, in which the particles precipitate out of solution during chemical processes. A typical reaction for magnetite precipitation is

$$5NaOH + 2FeCl_3 + FeCl_2 \rightarrow Fe_3O_4 + 5NaCl + 4H_2O \quad (1)$$

The reaction product is subsequently coprecipitated with concentrated ammonium hydroxide. Next, a peptization process transfers the particles from the water-based phase to an organic phase such as kerosene with a surfactant such as oleic acid. The oil-based ferrofluid can then be separated by use of a magnetic field.

Another approach to the fabrication of ferrofluids is based upon thermophilic bacteria that reduce amorphous iron oxyhydroxides to nanometer-sized iron oxide particles. Thermophilic bacteria are able to reduce a number of different metal ions. Thus, this approach allows other compounds, such as Mn(II), Co(II), Ni(III), and Cr(III) compounds, to be incorporated into magnetite. Varying the composition of the nanoparticles can adjust the magnetic, electrical, and physical properties of the substituted magnetite and, consequently, of the ferrofluid. Ferromagnetic particles with an extremely low Curie temperature can be designed with this method. For instance, $Mn_xFe_{1-x}Fe_2O_4$ nanoparticles may have Curie temperatures between 75 °C and 325 °C. Most of the particle materials commonly used in ferrofluids have much higher Curie temperatures. The temperature dependence of the magnetic properties depicted in Fig. 2 can be used in microfluidic applications.

Key Research Findings

At the typical channel size of microfluidics (about 100 μm), ferrofluid flow in a microchannel can be described as a continuum flow. The governing equations are based on conservation of mass and conservation of momentum. In case of temperature-dependent magnetic

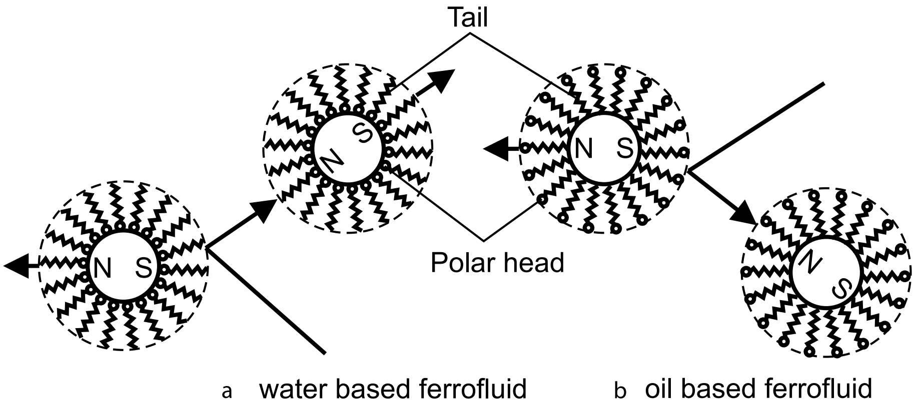

Ferrofluids in Microchannels, Figure 1 Colloidal model of magnetic nanoparticles and schematic representation of an elastic collision between particles: (**a**) water-based ferrofluid, (**b**) oil-based ferrofluid

properties, conservation of energy may be needed for calculating the temperature field.

The continuity equation has the general form

$$\frac{\mathrm{D}\rho}{\mathrm{D}t} + \delta \operatorname{div} \nabla = 0 \,, \tag{2}$$

where ∇ is the nabla operator and $\mathrm{D}\rho/\mathrm{D}t$ is the substantial (or total) derivative operator:

$$\frac{\mathrm{D}}{\mathrm{D}t} = \frac{\partial}{\partial t} + u\frac{\partial}{\partial x} + v\frac{\partial}{\partial y} + w\frac{\partial}{\partial z} = \frac{\partial}{\partial t} + (\boldsymbol{v} \cdot \nabla) \,. \tag{3}$$

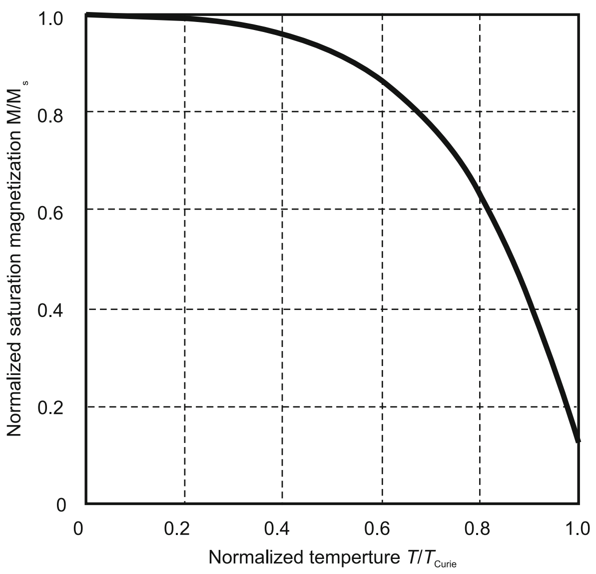

Ferrofluids in Microchannels, Figure 2 Temperature dependence of magnetization

Newton's second law formulates the conservation of momentum:

$$\begin{aligned} \rho\frac{\mathrm{D}\boldsymbol{v}}{\mathrm{D}t} &= \sum \boldsymbol{f}_i = \boldsymbol{f}_{\text{pressure}} + \boldsymbol{f}_{\text{viscous}} + \boldsymbol{f}_{\text{gravity}} + \boldsymbol{f}_{\text{magnetic}} \\ \rho\frac{\mathrm{D}\boldsymbol{v}}{\mathrm{D}t} &= -\nabla p + \eta\nabla^2\boldsymbol{v} + \rho\boldsymbol{g} + \boldsymbol{f}_{\text{magnetic}} \end{aligned} \tag{4}$$

Compared with a nonmagnetic fluid, the Navier–Stokes equation (4) for ferrofluid flow in a microchannel has an additional term for the magnetic force [1]:

$$\mathbf{f}_{\text{magnetic}} = -\nabla \left[\mu_0 \int_0^H \left(\frac{\partial M\upsilon}{\partial \upsilon} \right)_{H,T} \mathrm{d}H \right] + \mu_0 M \nabla H \tag{5}$$

where $\mu_0 = 4\pi \times 10^{-7}\,\mathrm{H\,m^{-1}}$ is the permeability of free space, M is the intensity of magnetization, υ is the specific volume, and H is the magnetic field strength in A/m. The magnetic pressure can be grouped together with the static pressure to form an apparent pressure. Thus the conservation of momentum can be reduced to the conventional Navier–Stokes equation. Since the magnetic force is a body force, the flow of a ferrofluid in a microchannel should have the same velocity distribution as a pressure-driven flow. The first term in Eq. (5) shows that the magnetic force is a body force, which is proportional to the volume. According to the scaling law, or the so-called *cube–square law*, the magnetic force will be dominated by the viscous force on the microscale. However, the second term in Eq. (5) may have advantages on the microscale owing to the high magnetic-field gradient ∇H that is achievable

with integrated microcoils. As mentioned above, ferrofluids with a low Curie temperature are readily available. Using the temperature dependence of the magnetization shown in Fig. 2, the magnetization can be adjusted by varying the temperature from room temperature to an acceptably low Curie temperature. The temperature dependence of the magnetization can be implemented in the first term of Eq. (5); the magnetic force then has the form [2]

$$\mathbf{f}_{\text{magnetic}} = \frac{1}{2}\mu_0 \left(H \frac{\partial M}{\partial T} \right) \nabla T + \mu_0 M \nabla H \qquad (6)$$

It is clear from Eq. (6) that the high temperature gradient ∇T that can be achieved on the microscale can be another advantage when one wishes to drive a ferrofluid in a microchannel.

Examples of Applications

The following examples present the utilization of the high magnetic gradient and temperature gradient on the microscale for pumping ferrofluids.

Manipulation of Ferrofluid Microdroplets

The magnetic force is proportional to both the magnetic moment and the gradient of the magnetic field. At a constant temperature below the Curie point, the magnetic moment is proportional to the volume. The disadvantage of volume-based actuation on the microscale can be compensated by the high magnetic-field gradient achievable with microcoils. Since the magnetic nanoparticles in a ferrofluid have a diameter on the order of a few nanometers, the random movement of the particles is larger than the effects of magnetic and gravitational forces. Thus the dispersion of these particles is stable even under a strong magnetic field. Nanoparticles polarized by an external magnetic field cause a ferrofluid droplet to act as a liquid magnet. This unique feature allows a ferrofluid droplet to be controlled by an external magnetic field. A controlled ferrofluid microdroplet can potentially be used as a reaction platform for handling samples in Lab-on-a-Chip applications.

Figure 3 shows the basic setup for controlling a ferrofluid microdroplet [3]. The main part of the setup is a double-sided printed circuit board (PCB). Two planar coils are etched on each side of the PCB, as depicted. The black and gray lines represent coils on the front and the back, respectively, of the PCB. Two permanent magnets (NdFeB) are placed on a soft magnetic steel sheet, which carries the PCB device. The permanent magnets induce a large uniform magnetic field perpendicular to the

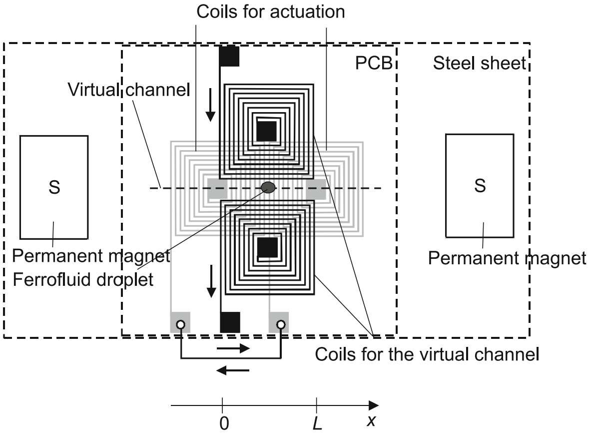

Ferrofluids in Microchannels, Figure 3 Experimental setup for controlling ferrofluid droplets. The coils are etched on a double-sided printed circuit board. The gray coils are on the back of the PCB. The PCB is placed on a soft magnetic steel sheet with two permanent magnets at either side. The magnetic field of the two permanent magnets polarizes the magnetic particles in the ferrofluid droplet

direction of motion x of the ferrofluid droplet, and consequently polarize the magnetic particles in the ferrofluid. The fields generated by the two front coils (black in Fig. 3) are permanent and have the same sign. These fields form a potential valley between the coils, where the gradient in the y-direction is zero. Thus, these fields work as a *virtual channel* for the ferrofluid droplet. The ferrofluid droplet is confined in this *virtual channel* and can move only in the x-direction. This *virtual channel* can be replaced by a real microchannel in the x-direction. In this case, only two driving coils are needed. The two coils on the back of the PCB are connected in series, so that their fields always have opposite signs. The field gradients between the two coils have the same sign, allowing the droplet to move in a prescribed direction. The direction of motion can be changed if the current in the coils is reversed. The switching circuit for changing the current direction is shown in Fig. 4.

The carrier liquid of the ferrofluid used in the experiment (APG S10n, Ferrotec) was a synthetic ester oil which was immiscible in silicone oil. The viscosity η, density ρ, and surface tension σ of the ferrofluid at 25 °C were 0.406 kg/ms, 1330 kg/s, and 32×10^{-3} N/m, respectively. The saturation magnetization and the initial susceptibility χ of this ferrofluid were 44 mT and 1.6, respectively. Two silicone oils with different viscosities were used to investigate the effect of viscous friction: $[-\mathrm{Si(CH_3)_2O}-]_n$, with a kinematic viscosity of $\nu = 50$ cSt, and $[-\mathrm{C_7H_8OSi}-]$, with a kinematic viscosity of 100 cSt. Both oils had approximately the same surface tension of 2.03×10^{-7} N/m and a density of 960 kg/m^3. In the experiments, the ferrofluid droplet was surrounded

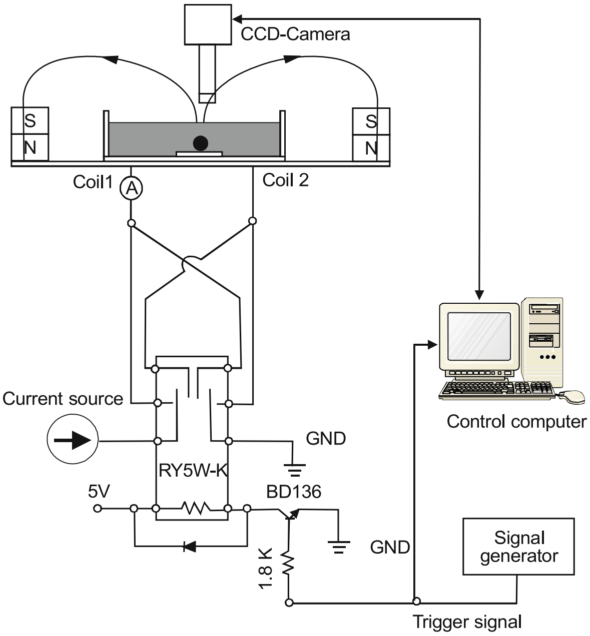

Ferrofluids in Microchannels, Figure 4 Switching circuit and optical setup

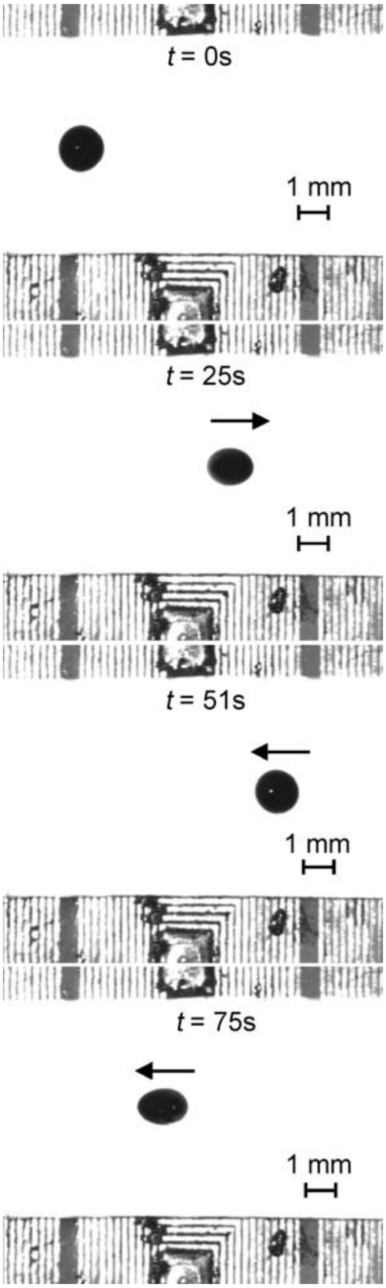

Ferrofluids in Microchannels, Figure 5 Recorded motion of a ferrofluid microdroplet

by the silicone oil. The higher density of the ferrofluid ensured that the droplet remained on the bottom surface of a 0.5 mm thick Teflon sheet. The hydrophobic surface of the Teflon sheet allowed the droplet to keep its spherical shape. The two virtual-channel coils were supplied with a constant current of 750 mA. The direction of the current in the driving coils was switched using the control circuit shown in Fig. 4. The periodic motion of the ferrofluid droplet was captured with a CCD camera. The camera was synchronized with the switching signal to record the position of the droplet at given time instants. Figure 5 shows an example of a recorded image sequence from this experiment. It is apparent that the droplet elongates under the induced magnetic force. Since the driving magnetic force is a body force, a larger droplet will have a better volume-to-surface ratio, or a larger ratio between the magnetic force and the drag force. A larger droplet can accelerate faster and reach its final position in a shorter time.

This actuation concept can be used for transport and sorting applications in droplet-based microfluidics. The results show the potential use of ferrofluid droplets as both a vehicle and a microreaction platform for droplet-based Lab-on-a-Chip applications.

Ferrofluid as an Actuator

The above example shows that a ferrofluid droplet or plug in a microchannel can function as an actuator. The actuating force is induced by an external magnetic field. The external magnetic field can be generated either by a microcoil, as demonstrated in the previous example, or by a moving magnet. In this concept, a ferrofluid plug is suspended in the channel. An external permanent magnet controls the position of the ferrofluid plug. Moving the permanent magnet pushes the ferrofluid plug in the

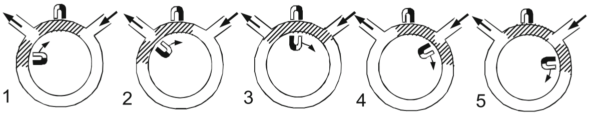

Ferrofluids in Microchannels, Figure 6 Concept of a ferrofluidic micropump

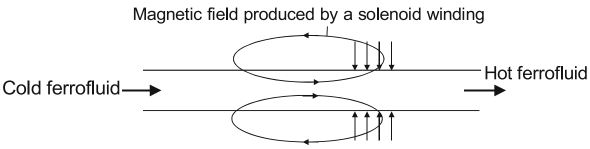

Ferrofluids in Microchannels, Figure 7 Concept of magnetocaloric pumping

desired direction. While moving in the microchannel, the ferrofluid plug pushes the surrounding liquid on one side and pulls it on the other side. The effect causes a pumping effect. If the magnet stops, the magnetic field holds the plug at its current location and prevents the pumped liquid from moving back. This sealing property means that a ferrofluid plug can also work as an active valve. The pumping power depends on the gradient of the external magnetic field and the magnetization of the ferrofluid. The field strength can be adjusted by the external permanent magnet, and so the pump design becomes independent of the type of liquid pumped.

Magnetic pumping using a ferrofluid has been implemented on a microscale by Hatch et al. [4]. The pump was fabricated in silicon and glass. The channel structure was etched in silicon and bonded anodically to a borosilicate glass plate. Two permanent magnets were used, as a valve actuator and a plug actuator. The working principle of this rotary concept is explained in Fig. 6. A fixed permanent magnet creates a stationary ferrofluid plug between the inlet and the outlet (1). First, a moving permanent magnet merges a second plug with the stationary plug (2). After complete merging has occurred, the large plug blocks both the inlet and the outlet (3). When the large plug is separated into one stationary and one moving plug, the fluid is sucked into the inlet and pushed out of the outlet (4). The design of the pump is similar to the concepts of a rotary pump and a check valve pump. However, this design is a pure magnetic micropump because no mechanical moving parts are involved. This micropump is able to deliver a maximum flow rate of 70 mL/min and a maximum back pressure of 1.3 kPa.

Ferrofluids in Microchannels, Table 1 Curie Temperature and saturation magnetization of various ferromagnetic solids

Substance	Curie temperature (°C)	$\mu_0 M_S$ (T)
Cobalt	1120	1.82
Dysprosium	−185	3.67
Gadolinium	19	2.59
Iron	770	2.18
Magnetite	585	0.56
Nickel	358	0.64

Continuous Pumping of Ferrofluid in a Microchannel Using a Temperature Gradient

According to Eq. (6), a temperature gradient can cause a magnetic force. This actuation concept has been termed magnetocaloric pumping by Love et al. [2]. Figure 7 shows a simple configuration for this. A magnetic field is induced by a coil or a permanent magnet. A temperature gradient along the flow direction causes a gradient in the magnetization, which in turn results in a net force that pumps the ferrofluid. The relationship between magnetization and temperature shown in Fig. 2 indicates that the closer the heating temperature is to the Curie temperature of the magnetic nanoparticles, the larger the force and the higher the flow rate. The ideal particle would have a Curie temperature close to the maximum expected thermal-cycling temperature. Table 1 lists the Curie temperatures of a number of ferrous materials. Most commercial-grade ferrofluids are based on magnetite particles and have a relatively high Curie temperature of 585 °C. Thus, almost all liquids will evaporate before this pumping concept works. The solution to this problem is the use of magnetic materials with Curie temperatures below the boiling point or any other critical temperature of the liquids used in the microfluidic system.

Cross References

► Digital Microfluidics
► Droplet and Bubble Formation in Microchannels
► Droplet-based Lab-on-Chip Devices
► Magnetic Pumps
► Temperature Gradient Generation and Control

References

1. Rosenzweig RE (1985) Ferrohydrodynamics. Cambridge University Press, Cambridge
2. Love LJ, Jansen JF, McKnight TE, Roh Y, Phelps TJ (2004) A magnetocaloric pump for microfluidic applications. IEEE Trans Nanobiosci 3:101–110
3. Nguyen NT, Ng KM, Huang XY (2006) Manipulation of ferro fluid droplets using planar coils. Appl Phys Lett 89:052509
4. Hatch A, Kamholz AE, Holman G, Yager P, Böhringer KF (2001) A ferrofluidic magnetic micropump. J Microelectromech Syst 10:215–221

Fiber Optic Cables

Definition

Fiber optic cables are flexible tubes which allow user-friendly transportation of light; thus positioning and handling of a light beam or spot is possible without using a complex system of mirrors and lenses. Fiber optic cables consist of a bundle of tiny glass fibers or they are filled with a transparent liquid. A clever exploitation of total reflectance and interference at the inner surface of the fiber leads to lossless channeling of the light.

Fiber Optics

► On-Chip Detection Using Optical Fibers

Field Assisted Bonding

► Anodic Bonding

Field Asymmetric Ion Mobility Spectrometry

► Miniaturized Ion Mobility Spectrometry

Field-Dependent Electrophoretic Mobility

► Aperiodic Electrophoresis
► Stotz–Wien Effect

Field-Effect Flow Control

► Microfluidic Circuits

Film Coating

► Chemical Vapor Deposition for Film Deposition

Filters

► Microfilters

Finite Volume and Finite Difference Methods for Modeling and Simulation

SUMAN CHAKRABORTY
Department of Mechanical Engineering, Indian Institute of Technology, Kharagpur, India
suman@mech.iitkgp.ernet.in

Synonyms

Control volume method; Control volume based finite difference method; Computational fluid dynamics (CFD)

Definition

The present article briefly discusses two of the basic discretization techniques commonly used for computational fluid dynamics (CFD) analysis of systems involving fluid flow, heat transfer and associated phenomena such as chemical reactions. These mathematical tools, however, are generalized enough to address other transport processes occurring in electrical, magnetic or electromagnetic systems as well.

Overview

In order to simulate fluid flow, heat transfer, and other related physical phenomena over various length scales, it is necessary to describe the associated physics in mathematical terms. Nearly all the physical phenomena of interest to the fluid dynamics research community are governed by the principles of continuum conservation, and are expressed in terms of first or second order partial differential equations that mathematically represent these principles (within the restrictions of a continuum-based framework). However, in case the requirements of continuum hypothesis are violated altogether for certain physical problems (for instance, in case of high Knudsen number rarefied gas flows), alternative formulations in terms of the particle-based statistical tools or the atomistic simulation techniques need to be resorted to. In this article, we shall only focus our attention to situations in which the governing differential equations physically originate out of continuum conservation requirements, and can be expressed in the form of a general differential equation that incorporates the unsteady term, the advection term, the diffusion term and the source term, to be elucidated as follows.

Finite Volume and Finite Difference Methods for Modeling and Simulation, Table 1 Conservation equations in the general form

Equation	Φ	Γ	S
Continuity	1	0	0
Momentum	$\boldsymbol{V}$	μ	$-\nabla p + \boldsymbol{F}$
Energy	T	k/c_p	$\dot{Q}/C_p$

A generic form of the general conservation principle for any dependent variable, ϕ, can be expressed as

$$\underbrace{\frac{\partial}{\partial t}(\rho\phi)}_{\text{transient term}} + \underbrace{\nabla\cdot(\rho \boldsymbol{V}\phi)}_{\text{advection term}} = \underbrace{\nabla\cdot(\Gamma\nabla\phi)}_{\text{diffusion term}} + \underbrace{S}_{\text{source term}}. \quad (1)$$

The well known equations of mass, momentum and energy conservation can all be cast in the above general form, with the expressions for ϕ, Γ (general diffusion coefficient) and S (general source term) being the sole distinctive features of one equation from another. This issue is summarized in Table 1, for convenience. In Table 1, μ denotes the viscosity, p denotes the pressure, $\boldsymbol{F}$ denotes the body force per unit volume, T denotes the temperature, k denotes the thermal conductivity, c_p denotes the specific heat, and $\dot{Q}$ denotes the rate of heat generation per unit volume.
In many situations, the complicated and/or coupled nature of the governing differential equations makes it difficult, if not impossible, to solve them analytically. Keeping that in view, it has always been a challenging task to the research community to develop efficient numerical techniques for solving the general transport equations. Fundamental to the development of a numerical method for solving these differential equations is the idea of discretization. Although an analytical solution to a partial differential equation gives us the value of the variable ϕ as a continuous function (in the absence of any continuum-level discontinuities in the problem domain) of the independent variables (namely, the spatial and temporal variables), the numerical solution aims to provide us with values of ϕ at a *discrete* number of points in the domain. These points are typically called as *grid points*, or equivalently, as the *nodes* or the *cell centroids*, depending on the specific numerical method being employed. The process of converting the governing transport equation into a set of equations for the discrete values of ϕ is called the *discretization process* and happens to be one of the key aspects of the numerical solution strategy. The specific methods employed to bring about this conversion are called as the *discretization methods*. The finite different and the finite volume methods are two of the common discretization methods often employed for fluid flow analysis, and will be briefly discussed here. The other commonly used methods, such as the finite element method, the boundary element method, the meshless method, etc. fall beyond the scope of this article and will not be discussed here. It however, needs to be kept in mind that all these discretization methods share one common philosophy: their only goal is to convert the governing differential equation into a system of discretized algebraic equations (the number of algebraic equations being same as the number of scalar unknowns considering the discrete grid points (or the nodal points) at which these variables are to be solved). It is the methodology and philosophy of this discreization technique in which one numerical method differs from the other.

Basic Methodology

Finite Difference Method

The finite difference methods approximate the derivatives in the governing differential equation using the truncated Taylor series expansions, for the purpose of discretization [1]. The starting point of formulating a finite difference scheme is to discretize the domain into a number of grid points and to express the derivatives at those grid points in terms of the nodal values of the function itself. The grid points can be numbered by a number of free indices (depending on the dimensionality of the problem), provided that the grid-system is a structured one. For illustration, let us express the value of a variable in the vicinity of the grid point i, in the form of Taylor series, as

$$\begin{aligned}\phi(x) = \phi(x_i) + (x-x_i)\left(\frac{\partial\phi}{\partial x}\right)_i \\ + \frac{(x-x_i)^2}{2!}\left(\frac{\partial^2\phi}{\partial x^2}\right)_i \\ + \frac{(x-x_i)^3}{3!}\left(\frac{\partial^3\phi}{\partial x^3}\right)_i \\ + \dots \\ + \frac{(x-x_i)^n}{n!}\left(\frac{\partial^n\phi}{\partial x^n}\right)_i + H\end{aligned} \quad (2)$$

where H means the *higher order terms*. By replacing x by x_{i+1} or x_{i-1} in Eq. (1), one may obtain the expressions for the values of the variable ϕ at these points, in terms of the values and derivatives at the point x_i. Executing this exercise, the first order derivative of at the point x_i can be

written in any of the following ways (Eq. (3a), (3) or (3c)):

$$\left(\frac{\partial\phi}{\partial x}\right)_i = \frac{\phi_{i+1}-\phi_i}{x_{i+1}-x_i} - \frac{x_{i+1}-x_i}{2}\left(\frac{\partial^2\phi}{\partial x^2}\right)_i - \frac{\left(x_{i+1}-x_i\right)^2}{6}\left(\frac{\partial^3\phi}{\partial x^3}\right)_i + H \tag{3a}$$

where $\phi_i \equiv \phi\,(x = x_i)$.

$$\left(\frac{\partial\phi}{\partial x}\right)_i = \frac{\phi_i-\phi_{i-1}}{x_i-x_{i-1}} - \frac{x_i-x_{i-1}}{2}\left(\frac{\partial^2\phi}{\partial x^2}\right)_i - \frac{\left(x_i-x_{i-1}\right)^2}{6}\left(\frac{\partial^3\phi}{\partial x^3}\right)_i + H \tag{3b}$$

$$\left(\frac{\partial\phi}{\partial x}\right)_i = \frac{\phi_{i+1}-\phi_{i-1}}{x_{i+1}-x_{i-1}} - \frac{\left(x_{i+1}-x_i\right)^2-\left(x_i-x_{i-1}\right)^2}{2\left(x_{i+1}-x_{i-1}\right)}\left(\frac{\partial^2\phi}{\partial x^2}\right)_i - \frac{\left(x_{i+1}-x_i\right)^3+\left(x_i-x_{i-1}\right)^3}{6\left(x_{i+1}-x_{i-1}\right)}\left(\frac{\partial^3\phi}{\partial x^3}\right)_i + H \tag{3c}$$

All three of the above expressions are exact if all terms in the right hand side are retained. However, the terms involving the higher derivatives can be neglected in case the distance between the successive grid points is small enough, except for the typical situations in which the magnitudes of the higher order derivatives are locally very large. The truncation of the Taylor series upto the first term in the right hand side of the Eqs. (3a), (3), (3c) leads to the following approximations of the first order derivative:

$$\left(\frac{\partial\phi}{\partial x}\right)_i \approx \frac{\phi_{i+1}-\phi_i}{x_{i+1}-x_i} \tag{4a}$$

$$\left(\frac{\partial\phi}{\partial x}\right)_i \approx \frac{\phi_i-\phi_{i-1}}{x_i-x_{i-1}} \tag{4b}$$

$$\left(\frac{\partial\phi}{\partial x}\right)_i \approx \frac{\phi_{i+1}-\phi_{i-1}}{x_{i+1}-x_{i-1}}\,. \tag{4c}$$

Expressions (4a), (4b) and (4c) correspond to the so-called *forward difference scheme*, *backward difference scheme* and *central difference scheme*, respectively. The error incurred in truncating the infinite Taylor series upto a finite number of terms for the calculation of the derivatives is known as the *truncation error*. Since the higher order terms are expected to be smaller (as they vary with higher powers of the small grid spacing), the first truncated term is usually the principle source of truncation error. The order of the truncation error, therefore, is usually estimated by the order of this term. For an equally spaced grid arrangement (such that $x_{i+1} - x_i = x_i - x_{i-1} = \Delta x$ (say)), the forward difference and the backward difference schemes for evaluating the first order derivatives are $O\,(\Delta x)$, whereas the central difference scheme for the same is $O\left(\Delta x^2\right)$. It is, however, possible to derive higher order versions of these schemes, by using higher order polynomial interpolations as approximations for evaluating the functional derivatives, instead of going through the direct route of Taylor series approximations.

Analogous to the first derivative, the second order derivatives can also be approximated by going through the route of Taylor series expansions. For example, one can approximate the second order derivative in terms of a central difference of the first order derivatives, as

$$\left(\frac{\partial^2\phi}{\partial x^2}\right)_i \approx \frac{\left(\frac{\partial\phi}{\partial x}\right)_{i+1} - \left(\frac{\partial\phi}{\partial x}\right)_i}{x_{i+1}-x_i}\,. \tag{5}$$

Good choices of points for evaluation of the first order derivatives appearing in the above expression may be the points that are located midway between x_i and x_{i+1} and x_{i-1} and x_i. Central difference approximations for these derivatives are as follows:

$$\left(\frac{\partial\phi}{\partial x}\right)_{i+\frac{1}{2}} \approx \frac{\phi_{i+1}-\phi_i}{x_{i+1}-x_i}\,, \quad \left(\frac{\partial\phi}{\partial x}\right)_{i-\frac{1}{2}} \approx \frac{\phi_i-\phi_{i-1}}{x_i-x_{i-1}} \tag{6}$$

The above leads to a simplified expression of Eq. (5), for equidistant grid spacings, as

$$\left(\frac{\partial^2\phi}{\partial x^2}\right)_i \approx \frac{\phi_{i+1}-2\phi_i+\phi_{i-1}}{(\Delta x)^2} \tag{7}$$

Equation (7) is a well-known expression for a second order accurate estimation of the second order derivatives using the central difference scheme.

One of the disadvantages associated with the finite difference method is that the physical principle of conservation is not automatically enforced in the scheme, unless special care is taken. Moreover, the implementation of this method is often restricted to simple geometries, since this method

cannot be implemented with convenience on unstructured grids.

Finite Volume Method

Starting point of the finite volume method is the integral form of the governing conservation equations [2]. This is achieved by first sub-dividing the problem domain into a number of contiguous control volumes of finite dimensions, and then integrating the governing differential equation over each of these elemental control volumes. The representative value of the variable to be solved for each control volume may be taken as the value of the variable at the geometric centre of the control volume. For evaluating the integrals, suitable profile assumptions for the dependent variable can be taken (giving rise to approximating quadrature formulae for the surface and the volume integrals), without violating the constraints of physical consistency and overall balance. However, once the integrals have been evaluated, the history of the profile assumption is essentially lost. This gives the analyst a freedom to adopt different profile assumptions for the same variables appearing in different terms of a governing equation. Integrations with respect to time can be carried out with the following linear interpolation formula:

$$\int_{t}^{t+\Delta t} \phi \, \mathrm{d}t = \left[f\phi^{t+\Delta t} + (1-f)\,\phi^{t} \right] \Delta t\,, \quad 0 \leqslant f \leqslant 1 \tag{8}$$

The special cases of $f = 0$, $f = 0.5$ and $f = 1$ give rise to the *explicit scheme*, *Crank Nicholson scheme* and the *implicit scheme*, respectively. The integration with respect to the temporal and the spatial variables eventually results in a system of algebraic equations (one for each control volume), which can be solved by standard numerical techniques.

For a simple illustration of the finite volume discretization methodology, one may consider a two-dimensional rectangular control volume with the grid point P at its geometric centre, as depicted in Fig. 1. The neighboring grid points for the point P are the points E, W, N and S (symbolizing the 'east', 'west', 'north' and 'south' neighbors). The locations of the four faces of the control volume containing the point P are denoted by the corresponding lowercase alphabets. If we take the two-dimensional transient heat conduction equation as a prototype example, in the form

$$\rho c_{\mathrm{P}} \frac{\partial T}{\partial t} = \frac{\partial}{\partial x}\left(k\frac{\partial T}{\partial x}\right) + \frac{\partial}{\partial y}\left(k\frac{\partial T}{\partial y}\right) + S \tag{9}$$

then an implicit time-discretization, piecewise linear temperature profile assumption between consecutive grid

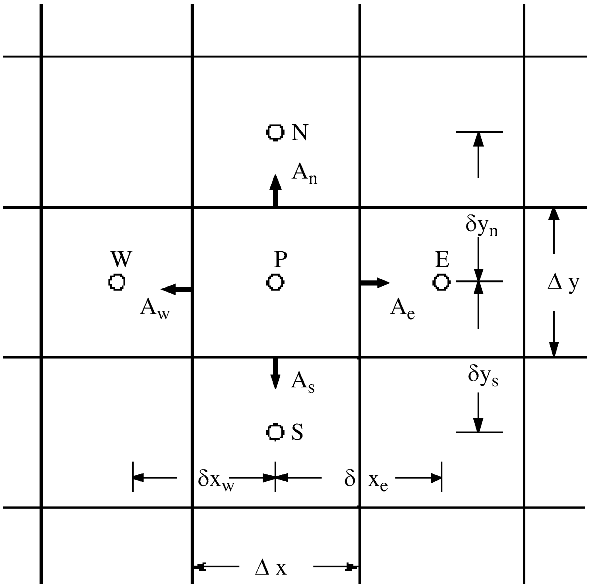

Finite Volume and Finite Difference Methods for Modeling and Simulation, Figure 1 A generic finite volume discretization stencil in two dimensions

points for the diffusion terms, and a piecewise constant temperature profile within each control volume for the source term give rise to a discretized version of the control volume-integral of Eq. (9) in the following form:

$$a_{\mathrm{P}} T_{\mathrm{P}} = a_{\mathrm{E}} T_{\mathrm{E}} + a_{\mathrm{W}} T_{\mathrm{W}} + a_{\mathrm{N}} a T_{\mathrm{N}} + a_{\mathrm{S}} T_{\mathrm{S}} + a_{\mathrm{P}}^{0} T_{\mathrm{P}}^{0} + b \tag{10}$$

where $a_{\mathrm{E}} = k_{\mathrm{E}} \Delta y/\delta x_{\mathrm{e}}$, $a_{\mathrm{W}} = k_{\mathrm{w}} \Delta y/\delta x_{\mathrm{w}}$, $a_{\mathrm{N}} = k_{\mathrm{n}} \Delta x/\delta y_{\mathrm{n}}$, $a_{\mathrm{S}} = k_{\mathrm{s}} \Delta x/\delta y_{\mathrm{s}}$, $a_{\mathrm{P}}^{0} = \rho c_{\mathrm{p}} \Delta x \Delta y/\Delta t$, $b = S_{\mathrm{c}} \Delta x \Delta y + a_{\mathrm{P}}^{0} T_{\mathrm{P}}^{0}$, $a_{\mathrm{P}} = a_{\mathrm{E}} + a_{\mathrm{W}} + a_{\mathrm{N}} + a_{\mathrm{S}} + a_{\mathrm{P}}^{0} - S_{\mathrm{P}} \Delta x \Delta y$. Here the superscript '0' symbolizes the value at a time instant of t and the superscript is omitted to symbolize the value at a time instant of $t + \Delta t$. Further, the source term is linearized in the form $S = S_{\mathrm{c}} + S_{\mathrm{P}} T_{\mathrm{P}}$, to arrive at the above discretization. In general, for executing the finite volume discretization of heat conduction problems, the following important points may be taken into account [2]:

- The profile assumption should be consistent with the requirements of the continuity of fluxes at the control volume faces.
- All coefficients in the discretized algebraic equation should be of the same sign.
- The interfacial value of thermal conductivity can be best interpolated by invoking a harmonic mean approximation, based on values of the same at the adjacent grid points.

- The explicit scheme gives rise to a system of discretized algebraic equations that are not mathematically coupled. However, the cost that one might have to pay against this simplification is that the scheme is conditionally stable. On the other hand, the implicit scheme requires a coupled system of linear algebraic equations to be solved, but is unconditionally stable (the issues of 'stability' in the context of discretized equations will be elaborated later).

Key Research Findings

Convection–Diffusion Problems

The finite volume formulation for diffusion type problems can be extended for solving the convection–diffusion types of problems, in which additional advection terms appear in the governing differential equations. Assuming that the velocity field is already obtained from a separate solution module, various discretization strategies can be formulated for solving the convection–diffusion problem, based on the 'cell Peclet number' (P), which is nothing but the ratio of the advection to diffusion strengths, based on control volume specific length scales. Considering the following generic form of a two-dimensional unsteady state convection–diffusion equation as an illustrative example:

$$\frac{\partial}{\partial t}(\rho\phi) + \frac{\partial}{\partial x}(\rho u\phi) + \frac{\partial}{\partial y}(\rho v\phi) = \frac{\partial}{\partial x}\left(\Gamma\frac{\partial \phi}{\partial x}\right) + \frac{\partial}{\partial y}\left(\Gamma\frac{\partial \phi}{\partial y}\right) + S \quad (11)$$

one can arrive at a discretization equation as

$$a_P\phi_P = a_E\phi_E + a_W\phi_W + a_N\phi_N + a_S\phi_S + a_P^0\phi_P^0 + b \quad (12)$$

where $a_E = D_eA(|P_e|) + \max(-F_e, 0)$, $a_W = D_wA(|P_w|) + \max(F_w, 0)$, $a_N = D_nA(|P_n|) + \max(-F_n, 0)$, $a_S = D_sA(|P_s|) + \max(F_s, 0)$, $a_P^0 = \rho_P^0\Delta x\Delta y/\Delta t$, $b = S_c\Delta x\Delta y + a_P^0\phi_P^0$, $a_P = a_E + a_W + a_N + a_S + a_P^0 - S_P\Delta x\Delta y$. Here, $D_e = \Gamma_e\Delta y/\delta x_e$, $D_w = \Gamma_w\Delta y/\delta x_w$, $D_n = \Gamma_n\Delta x/\delta y_n$, $D_s = \Gamma_s\Delta x/\delta y_s$, $F_e = (\rho u)_e\,\Delta y$, $F_w = (\rho u)_w\,\Delta y$, $F_n = (\rho v)_n\,\Delta x$, $F_s = (\rho v)_s\,\Delta x$, $P_e = F_e/D_e$, $P_w = F_w/D_w$, $P_n = F_n/D_n$, $P_s = F_s/D_s$.

The function $A(|P|)$, as appearing in the above equation, depends on the specific interpolation scheme chosen to discretize the convection–diffusion terms. Appropriate expressions of the same, for different schemes, are given in Table 2. Regarding the choice of a suitable scheme, certain important considerations can be noted [2]:

- The central difference scheme can give rise to physically inconsistent solutions, in case $|P| > 2$.
- The upwind scheme does not suffer from the above limitation, but tends to overpredict diffusion.
- Although the exponential scheme gives a reasonably accurate estimation of the profile variation of ϕ, it involves costly computation of exponential terms.
- The hybrid scheme is a piecewise linearlization of the exponential scheme, and therefore, retains a correct physical behaviour. However, it tends to set the diffusion effects to zero as soon as $|P| > 2$.
- The Power law scheme is essentially a curve-fitting of the exponential scheme that attempts to eliminate the above-mentioned discrepancy.
- The upwind scheme had been identified by many researchers as a common source of 'numerical diffusion' or 'false diffusion', which means an 'overprediction' of the diffusion strength as a numerical artifact. However, a different (and possibly, more logical) viewpoint is that the false diffusion is not so much attributable to the specific convection–diffusion scheme chosen (since, the best portrayed scheme for overcoming false diffusion, namely the central difference scheme, itself ceases to work at high values of cell Peclet number), but can be associated with the obliquity of the flow directions with respect to the grid lines that form the discretized space. Higher order upwind schemes, for example, the QUICK (quadratic upstream interpolation scheme for convective kinetics) differencing scheme [3], have been suggested as alternative remedies to overcome false diffusion effects. Such alternative schemes, however, also suffer from certain shortcomings in the sense that these are conditionally stable.

Discretization of Fluid Flow Equations

So far, we have discussed the solution of general transport equations, by assuming the velocity field to be known. In principle, the equations governing the velocity field (namely, the continuity and the momentum conservation equations) are also of a general conservative nature (see

Finite Volume and Finite Difference Methods for Modeling and Simulation, Table 2 convection–diffusion discretization schemes

Scheme	$A(\|P\|)$
Central difference	$1-0.5\|P\|$
Upwind	1
Exponential	$\|P\|/(\exp\|P\|-1)$
Hybrid	$\max(0, 1-0.5\|P\|)$
Power law	$\max(0, (1-0.5\|P\|)^5)$

Table 1), and ideally, should have been solvable by the standard convection–diffusion discretization methodologies discussed as earlier. In reality, however, the strategy does not work in that way and additional considerations need to be invoked. This is because of the fact that the momentum equation source terms contain pressure as an additional scalar variable, although there is no separate explicit governing differential equation for pressure. Early efforts in solving the fluid flow equations were mainly based on the stream function-vorticity approach, in which the pressure gradient terms from the momentum conservation equations are eliminated by cross-differentiating the two components of the momentum conservation equation (in case of a two-dimensional flow-field) and subtracting one from the other, giving rise to the following two coupled equations:

$$\frac{\partial \zeta}{\partial t} + u\frac{\partial \zeta}{\partial x} + v\frac{\partial \zeta}{\partial y} = \frac{\mu}{\rho}\left(\frac{\partial^2 \zeta}{\partial x^2} + \frac{\partial^2 \zeta}{\partial y^2}\right) \tag{13}$$

$$\frac{\partial^2 \psi}{\partial x^2} + \frac{\partial^2 \psi}{\partial y^2} = -\zeta \tag{14}$$

where $\boldsymbol{\zeta}$ is the vorticity vector ($\boldsymbol{\zeta} = \nabla \times \boldsymbol{V}$) and ψ is the stream function ($u = \partial\psi/\partial y,\ v = -\partial\psi/\partial x$). These two coupled equations can be discretized in the same manner outlined as above, and the pressure field can subsequently be computed by solving for the following Poisson equation:

$$\frac{\partial^2 p}{\partial x^2} + \frac{\partial^2 p}{\partial y^2} = 2\rho\left[\frac{\partial^2 \psi}{\partial x^2}\frac{\partial^2 \psi}{\partial y^2} - \left(\frac{\partial^2 \psi}{\partial x \partial y}\right)^2\right] \tag{15}$$

The apparently-elegant stream function vorticity approach, however, suffers from certain shortcomings, as follows [2]:

- The vorticity at the wall may be difficult to specify for many practical problems.
- The pressure can be required as an intermediate outcome for updating the density values through the equation of state, so that a complete elimination of pressure might not always be desirable.
- Most importantly, the method cannot be extended to three dimensions in which the stream function is not defined.

In order to overcome such shortcomings, the primitive variable based methods have been suggested as better alternatives in the literature. The challenges associated with the primitive variable methods are not to elimininate the pressure, but to convert the indirect information in the continuity equation into a direct algorithm for the calculation of pressure. However, a straight forward discretization of the pressure gradient terms in the momentum conservation equation, based on the linearly-interpolated values of pressure from the adjacent grid points may give rise to certain anomalies, leading to a condition in which a zigzag pressure field could be numerically interpreted as a uniform one. As a remedy, the concept of 'staggered' (displaced) grids has been introduced, according to which the velocity components are calculated for the points that lie on the faces of the control volumes (see Fig. 2). Advantages of such kinds of grid arrangement are mainly twofold [2]:

- The discretized continuity equation would contain the differences of the adjacent velocity components, so that wavy velocity fields are not wrongly predicted as outcomes of the continuity equation for cases in which a uniform velocity field is expected to physically exist.
- The pressure difference between two adjacent grid points becomes the natural driving force for the velocity variations between these grid points, so that unrealistic predictions of the pressure field are ruled out.

It is important to mention here that the use of staggered grids is not always a compulsion. In case special pressure interpolation schemes are employed to overcome the difficulties associated with the non-staggered grids mentioned as earlier, the staggered grid arrangement might not be necessary. In such cases, the same grid arrangement can be employed for solution of the velocity field and the other scalar variables, which is commonly referred to as a 'co-located grid'.

Several algorithms do exist in the literature for numerical computation of fluid flow problems on the basis of primitive variables, in a finite volume framework. One of the most commonly used algorithms of this kind is the SIMPLE (semi implicit method for pressure linked equations) algorithm [2]. With reference to a generic staggered control volume for solution of the momentum equation for u (see Fig. 3) and with similar considerations for the other velocity components, major steps of the SIMPLE algorithm can be summarized as follows:

(i) Guess the pressure field, p^*.

(ii) Solve the discretized momentum conservation equations, to be cast in the following forms:

$$a_e u_e^* = \sum a_{nb} u_{nb}^* + b + (p_P^* - p_E^*)A_e\ ;$$

$$a_n v_n^* = \sum a_{nb} v_{nb}^* + b + (p_P^* - p_N^*)A_n\ ;$$

$$a_t u_t^* = \sum a_{nb} w_{nb}^* + b + (p_P^* - p_T^*)A_t\ ,$$

where the subscript 'nb' refers to the neighbouring grid points.

(iii) Substitute a 'velocity correction' formula, expressed in terms of 'pressure corrections' at the main grid points in the discretized continuity equation (discretized over the main control volume, not the staggered one), to get the pressure correction equation in the following form (with 'T' and 'B' denoting the 'top' and 'bottom' grid points relative to the point P in a three-dimensional space):

$$a_P p'_P = a_E p'_E + a_W p'_W + a_N p'_N + a_S p'_S + a_T p'_T + a_B p'_B + b \quad (16)$$

where $a_E = \rho_e d_e \Delta y \Delta z$ (where $a_E = A_e / a_e$), $a_W = \rho_w d_w \Delta y \Delta z$, $a_N = \rho_n d_n \Delta x \Delta z$, $a_S = \rho_s d_s \Delta x \Delta z$, $a_T = \rho_t d_t \Delta x \Delta y$, $a_B = \rho_b d_b \Delta x \Delta y$, $a_P = a_E + a_W + a_N + a_S + a_T + a_B$, and

$$b = \frac{(\rho_P^0 - \rho_P)\Delta x \Delta y \Delta z}{\Delta t} + \left[(\rho u^*)_w - (\rho u^*)_e\right]\Delta y \Delta z + \left[(\rho v^*)_s - (\rho v^*)_n\right]\Delta x \Delta z + \left[(\rho w^*)_b - (\rho w^*)_t\right]\Delta x \Delta y$$

(iv) Correct the pressure field as $p = p^* + p'$.
(v) Correct the velocity field as $u_e = u_e^* + d_e\left(p'_P - p'_E\right)$, and similarly for the other velocity components.
(vi) GOTO step (ii) with the corrected value of p obtained from step (iv) ad the new p^*.
(vii) Repeat the loop until convergence.

With regard to the SIMPLE algorithm outlined as above, certain important points can be carefully noted:

- No attempt is made for the direct solution of momentum equations. In the velocity correction expression, i. e., $u'_e = \sum a'_{nb} u'_{nb} + b + \left(p'_P - p'_E\right) A_e$, the first term in the right hand side is essentially dropped, which enables one to cast the pressure correction equation in a general conservative form.
- The algorithm is called as *semi implicit* to acknowledge the dropping of the term $\sum a'_{nb} u'_{nb}$. This term essentially represents an indirect or implicit influence of the pressure correction on velocity. Although pressure corrections at nearby locations can alter the neighbouring velocities and thus can cause a velocity correction at the point under consideration. This influence is not considered in the SIMPLE algorithm. However, it needs to be noted here that this semi-implicit nature has nothing to do with any possible implicit or explicit nature of the time-discretization scheme.
- On convergence, all the velocity and pressure corrections tend to zero. This implies that no error is incurred on dropping the $\sum a'_{nb} u'_{nb}$ term, once the convergenced solution has been obtained, with an understanding that the term 'b' in Eq. 15, which is essentially a mass source term for the discretized continuity equation, should tend to zero once the mass conservation is satisfied. The sole emphasis here is to obtain a pressure

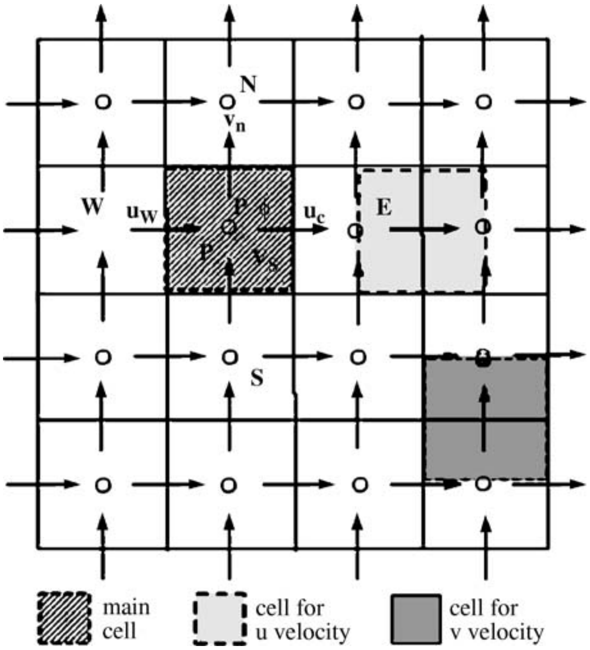

Finite Volume and Finite Difference Methods for Modeling and Simulation, Figure 2 Staggered grid arrangement for the solution of momentum equations

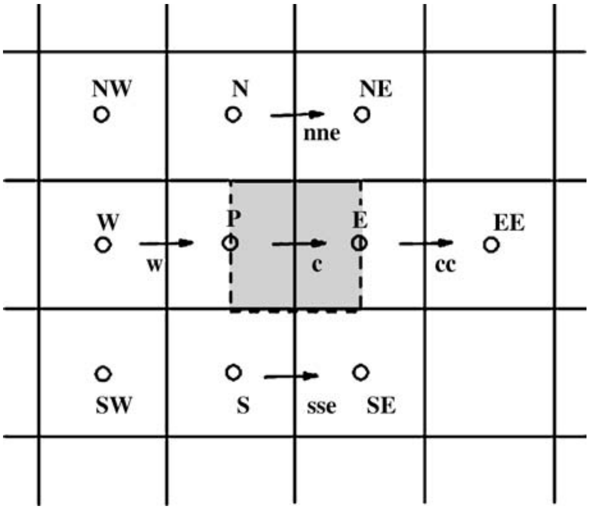

Finite Volume and Finite Difference Methods for Modeling and Simulation, Figure 3 A generic staggered control volume for discretization of the x-momentum equation

field that satisfies the continuity equation. The dropping of the $\sum a'_{\text{nb}} u'_{\text{nb}}$ term, however, is related to the rate at which the convergence is obtained.

- For highly compressible flows, the pressure correction formula should also accommodate the provision of a density correction term.
- The pressure is a relative variable, as an outcome of this algorithm, and not an absolute quantity.
- The approximation introduced in the derivation of the pressure correction equation by dropping the term $\sum a'_{\text{nb}} u'_{\text{nb}}$ leads to a rather exaggerated pressure correction. Because of the omission of the neighbouring velocity corrections, the pressure correction carries the entire burden of correcting the velocities, which results in a rather severe pressure correction field. Thus, although the pressure correction equation does a fairly good job in correcting the velocities, it does a poorer job in correcting the pressure. Taking this into consideration, a revised version of the SIMPLE algorithm, namely, the SIMPLER algorithm [2] has later been proposed, in which a separate pressure equation is formulated (by discretizing the continuity equation) to solve for the pressure field, and the pressure correction is solely employed to correct the velocity field but not the pressure field. This leads to a faster convergence, although a slightly increased overhead of solving another scalar equation (namely, the pressure equation).
- Other variants of the SIMPLE algorithm have also been proposed in the literature. For example, Van Doormal and Raithby [4] developed the SIMPLEC (SIMPLE-Consistent) algorithm, which follows similar steps as that of the SIMPLE algorithm, with the sole difference that the momentum equations are manipulated so that the modified velocity correction formulae omit terms that are less significant than those omitted in the SIMPLE algorithm. Issa [5] introduced the PISO (Pressure Implicit with Splitting of Operators) algorithm for the non-iterative computation of unsteady compressible flows. This algorithm involves one predictor step and two corrector steps, as an extension of the SIMPLE algorithm. The SIMPLEC and the PISO algorithms have been found to work as efficiently as the SIMPLER algorithm in many cases, although it cannot be convincingly concluded their relative superiorities, which strongly depend on the extent of coupling between the velocity field and the other scalar fields, and often on the strategy of solving the system of discretized algebraic equations.

Issues of Consistency, Stability and Convergence

Irrespective of the discretization method chosen, the success of the numerical scheme depends heavily on certain factors, associated with the terminologies such as consistency, stability and convergence. A numerical scheme is said to be consistent if it produces systems of algebraic equations that can be demonstrated as equivalent to the original governing differential equation, in the limit as the grid spacings tend to zero. In more technical terms, the truncation error must tend to zero with limitingly thin grid spacings. In general, the truncation error can be numerically assessed by obtaining the numerical solutions over two different grid spacings (h and $2h$, say). Let the corresponding numerical solutions be $\phi_h$and ϕ_{2h}, respectively. It can also be noted that for sufficiently fine grids, the truncation error is proportional to the leading order term in the Taylor series, i. e., $T.E \approx \alpha h^p + H$, where α depends on the derivatives at a given point but is independent of h, and H stands for the higher order terms. Thus, one can write

$$\phi_{\text{exact}} = \phi_h + \alpha h^p + H = \phi_{2h} + \alpha\,(2h)^p + H \tag{17}$$

so that the truncation error for the grid size of h can be estimated as

$$(T.E)_h \approx \frac{\phi_h - \phi_{2h}}{2^p - 1} \tag{18}$$

Equation (16) forms the basis of the Richardson extrapolation formula [6] commonly used in Numerical analysis, for improving the accuracy of the numerical solutions by accommodating for the truncation error estimates.

Another important factor for the successful performance of a discretization scheme is its stability. In simple terms, a numerical solution method is said to be stable if it does not magnify the errors that appear in the course of a numerical solution process. For unsteady problems, stability guarantees that the numerical method yields a bounded solution provided that the solution of the original governing differential equation is also bounded. For iterative methods, the iterations act as *virtual* time steps, and the meaning of stability has analogous physical implications. Classically, the stability of a discretization scheme is assessed by employing the von Neumann analysis. For non-linear problems, stability might be rather difficult to investigate by adopting this method. Here, we outline the stability analysis of a linear problem in which explicit method of time discretization is used, for the sake of illustration. For simplicity, let us consider a one-dimensional diffusion problem with constant thermophysical properties and no source terms, numerically solved by employing uniform grids and an explicit time-discterization scheme. In this special case, the discretization equation takes the form of

$$a_{\text{P}}\phi_{\text{P}} = a_{\text{E}}\phi^0_{\text{E}} + a_{\text{W}}\phi^0_{\text{W}} + \left(a^0_{\text{P}} - a_{\text{E}} - a_{\text{W}}\right) x\phi^0_{\text{P}} \tag{19}$$

where $a_E = \Gamma_e/\delta x_e$, $a_W = \Gamma_w/\delta x_w$, $a_P^0 = \rho \Delta x/\Delta t$ and $a_P = a_P^0$. Let Φ represent a solution of the discretized equations (not the original governing differential equation) using infinite computational precision. With practical computing systems, however, there would definitely be some round-off error, given as $\varepsilon = \phi - \Phi$. Using this definition in Eq. (19) and noting that Φ satisfies this equation exactly, one obtains

$$a_P \varepsilon_P = a_E \varepsilon_E^0 + a_W \varepsilon_W^0 + \left(a_P^0 - a_E - a_W\right) \varepsilon_P^0 \qquad (20)$$

In order to assess whether the round-off error gets amplified with time, one may expand the error in an infinite series as

$$\varepsilon(x,t) = \sum_m e^{\sigma_m t} e^{i\lambda_m x}, \quad m = 0, 1, 2, \ldots, M \qquad (21)$$

where σ_m is either real or complex, and $\lambda_m = m\pi/L$, $m = 0, 1, 2, \ldots, M$; L being the width of the problem domain. If σ_m is real and greater than zero, then the error grows with time, wheres if σ_m is real and less than zero then the error is damped out with time. If σ_m is complex, the solution is oscillatory. In particular, the nature of evolution of the error can be estimated from the amplification factor, $a = \varepsilon(x, t + \Delta t)/\varepsilon(x,t)$. If the magnitude of a is greater than unity then the error grows with the time-step, whereas if a is less than unity then the error is damped out with the time-step so that the scheme can be predicted as stable. In order to assess this factor for the special case under consideration, one may exploit the linearity of the equation and just examine the stability consequences of a single error term in Eq. (21), rather than the summation. Substituting a single term from Eq. (21) in Eq. (20), one can obtain an expression for a as

$$a = e^{\sigma_m \Delta t} = 1 - \frac{4\Gamma \Delta t}{\rho (\Delta x)^2} \qquad (22)$$

The above gives rise to the conditional stability criterion of the explicit scheme, as

$$\Delta t \leqslant \frac{\rho (\Delta x)^2}{2\Gamma} \qquad (23)$$

Analogous stability analyses can be executed for the other time-discretization schemes as well. It is important to note here that although the von Neumann stability analysis yields a limiting time-step estimate to keep the round-off errors bounded, it does not preclude the occurrence of an *bounded* but *unphysical* solutions. A classical example is the Crank-Nicholson scheme, which from the von Neumann viewpoint is unconditionally stable, but can give rise to bounded unphysical solutions in case all the coefficients of the discretization equation do not happen to be of the same sign [2].

Closely associated with the concepts of consistency and stability is the idea of convergence. A numerical scheme is said to be convergent if the solution of the discretized equations tends to the exact solution of the governing differential equation as the grid spacing tends to zero. For linear initial value problems, both consistency and stability are the necessary and sufficient conditions of convergence as per the Lax equivalence theorem [6], which states "given a properly posed linear initial value problem and a finite difference approximation to it that satisfies the consistency condition, stability is the necessary and sufficient condition for convergence". For non-linear problems, however, consistency and stability are only the necessary conditions for convergence but not sufficient.

F

Concepts of Discretization in Unstructured Meshes

The use of unstructured meshes [7] for solving fluid flow and other transport problems has become increasingly popular over the past few decades, because of its elegant capability of discretizing complicated and irregular-shaped geometries. Although the finite volume method was originally developed for structured grids (as outlined in the preceding discussions), it has been subsequently adapated to accommodate the features of unstructured meshes. A conceptual distinguishing feature between the structured and the unstructured meshes is that an unstructured mesh has the provision of having a variable number of neighboring cell vertices (although it might not exploit this feature always), whereas in a structured mesh each cell vertex has a fixed number of neighbouring cell ver-

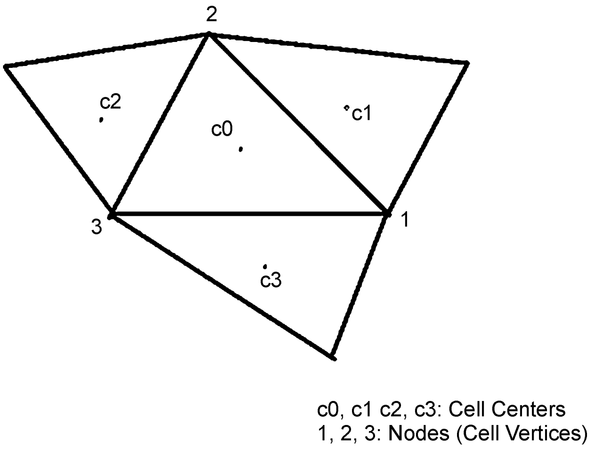

Finite Volume and Finite Difference Methods for Modeling and Simulation, Figure 4 A triangular shaped control volume (with cell centre at c0) and three of its neighbouring control volumes

tices (except for the boundary cells). Since the fluxes calculated at the cell faces in unstructured meshes need not necessarily be aligned with the direction joining the neigbouring grid points, special considerations are necessary to formulate the discretization equations. In this context, it needs to be recognized that in case of unstructured grids, it is possible to have a hybrid mesh composed of polygons with different shapes. Although the discretization policy, in principle, is similar for all polygonal shapes, precise forms of the discretization equations strongly depend on the specific shape of the control volume under consideration. Here, for the sake of illustration, we only outline the discretization methodology for unstructured triangular meshes. A typical triangular control volume with three neighbouring triangular cells is depicted in Fig. 4. Here, we illustrate a prototype discretization of the steady version of the x-momentum equation. The first step is to integrate the governing differential equation over the triangular control volume, to yield

$$\underbrace{\int_{CV} \nabla\cdot(\rho \boldsymbol{V} u)\,\mathrm{d}\forall}_{\text{term 1}} = \underbrace{-\int_{CV} \frac{\partial p}{\partial x}\,\mathrm{d}\forall}_{\text{term 2}} + \underbrace{\int_{CV} \nabla\cdot(\mu\nabla u)\,\mathrm{d}\forall}_{\text{term 3}} \quad (24)$$

The various terms appearing in Eq. (24) can be simplified by applying the divergence theorem, so as to convert the volume integrals into equivalent surface integrals, to obtain

$$\text{term 1} = \int_{CV} \nabla\cdot(\rho \boldsymbol{V} u)\,\mathrm{d}\forall = \int_{CS} (\rho \boldsymbol{V} u)\cdot \mathrm{d}\boldsymbol{A}$$

$$= \sum_{i=1}^{\substack{\text{number}\\ \text{of edges (3)}}} (\rho u_{\mathrm{f}})_i\,(\boldsymbol{V}\cdot \mathrm{d}\boldsymbol{A})_i\,,$$

or equivalently,

$$\text{term 1} = \sum_{i=1}^{3} (\rho u_{\mathrm{f}})_i\, U_{\mathrm{f},i} = \sum_{i=1}^{3} F_i U_{\mathrm{f},i}\,,$$

say, where

$$\boldsymbol{U} = \boldsymbol{V}\cdot \mathrm{d}\boldsymbol{A} = u\,\mathrm{d}A_{\mathrm{x}} + v\,\mathrm{d}A_{\mathrm{y}}$$

is the contravariant velocity vector, the subscript ‘f’ refers to a cell face and F symbolizes the advection strength.

$$\text{term 2} = \int_{CV} -\frac{\partial p}{\partial x}\,\mathrm{d}\forall = \int_{CS} -\left(p\hat{i}\right)\cdot \mathrm{d}\boldsymbol{A}$$

$$= -\sum_{i=1}^{3} (p\,\mathrm{d}A_{\mathrm{x}})_i\,,$$

or equivalently,

$$\text{term 2} = -\sum_{i=1}^{3} p_i \Delta y_i$$

$$= -\big[(p_{c1} - p_{c0})\,\Delta y_1 + (p_{c2} - p_{c0})\,\Delta y_2 + (p_{c3} - p_{c0})\,\Delta y_3\big]\,.$$

Here, Δy_i represents the difference of the y-coordinates of the two vertices of the edge ‘i’, the vertices being taken in a specific (positive oriented, as a convention) order for the evaluation of this parameter, for all edges.

$$\text{term 3} = \int_{CV} \nabla\cdot(\mu\nabla u)\,\mathrm{d}\forall = \int_{CS} (\mu\nabla u)\cdot \mathrm{d}\boldsymbol{A}$$

$$= \sum_{i=1}^{3} \mu_i \left[\frac{\partial u}{\partial x}\Delta y - \frac{\partial u}{\partial y}\Delta x\right]_i\,.$$

The partial derivatives appearing in this expression can be evaluated by choosing auxiliary control volumes surrounding an edge ‘i’, for the evaluation of integrals associated with that edge. For example, for evaluation of the integrals over the edge $1-2$, one can construct an auxiliary control volume with the bounding edges as $1 - c1 - 2 - c0 - 1$. As an illustration, the term $(\partial u/\partial x)_i$ can be evaluated as follows:

$$\left(\frac{\partial u}{\partial x}\right)_i = \frac{\int_{A_i} \frac{\partial u}{\partial x}\,\mathrm{d}A}{A_i} = \frac{\int_{C} u\,\mathrm{d}y}{A_i}\,,$$

where C is a closed contour that forms the surface of the auxiliary control volume. This contour integral can be numerically approximated by employing the Trapezoidal rule, so that one can write

$$\left(\frac{\partial u}{\partial x}\right)_1 = \frac{\big[(u_{c1} - u_{c0})\,\Delta y_1 + (u_1 - u_2)\,\Delta y_{c1-c0}\big]}{A_1}\,,$$

where $\Delta y_1 = y_2 - y_1$ and $\Delta y_{c1-c0} = y_{c1} - y_{c0}$. Analogous considerations can be made for the other integrals to be

evaluated for term 3, as well. The discretized form of term 3, therefore, becomes

$$\text{term } 3 = \underbrace{\sum_{i=1}^{3} D_i \left(u_{ci} - u_{c0}\right)}_{\text{orthogonal diffusion flux}} + \underbrace{D_{n1}\left(u_1 - u_2\right) + D_{n2}\left(u_2 - u_3\right) + D_{n3}\left(u_3 - u_1\right)}_{\text{non-orthogonal diffusion flux}},$$

where

$$D_i = \frac{\mu_i}{2A_i}\left[(\Delta x)^2 + (\Delta y)^2\right]_i,$$

$$D_{ni} = \frac{\mu_i}{2A_i}\left[(\Delta x)_i (\Delta x)_{ci-c0} + (\Delta y)_i (\Delta y)_{ci-c0}\right].$$

For numerical implementation, the orthogonal diffusion flux may be treated implicitly, whereas the non-orthogonal diffusion flux may be treated explicitly by clubbing the same together with the source term. The discretized forms of the three terms can finally be assembled together to obtain the discretized x-momentum equation for the triangular control volume in the following form:

$$a_P u_{c0} = A_1 u_{c1} + A_2 u_{c2} + A_3 u_{c3} + S \qquad (25)$$

where $A_i = \left[D_i A(|Pe|_i) + \max(\pm F_i, 0)\right]$ (F_i is taken to be positive if the cell is to the left of edge i, otherwise it is taken as negative), $A_P = A_1 + A_2 + A_3$, and $A(|Pe|_i)$ depends on the chosen interpolation scheme for representing the convection–diffusion phenomenon (see Table 2). Similar considerations can be made for discretization of other equations as well.

Future Directions of Research

CFD has now become a somewhat mature field, in which the basics of algorithm development associated with the finite difference and finite volume methodologies have been relatively well established. However, there are certain issues yet to be well resolved, on which future directions of research related to these topics can be based:

- Efficient parallelization of the solution strategies
- Embedding the aspects of multi-scale physics in the discretization techniques
- Establishing hybrid simulation strategies with coupled molecular and continuum based discretizations.

Cross References

► Boundary Element Method and its Application to the Modelling of MEMS Devices
► Volume and Finite Difference Method for Modeling and Simulation
► Lattice Boltzmann Method (LBM)
► Molecular Dynamics Simulation Method
► Monte Carlo Method
► Multiscale Methods
► Multiscale Modeling and Numerical Simulations

References

1. Anderson DA, Tannehill JC, Pletcher RH (1984) Computational fluid mechanics and heat transfer. Hemisphere, New York
2. Patankar SV (1980) Numerical heat transfer and fluid flow. Hemisphere, New York
3. Leonard BP (1979) A stable and accurate convective modeling procedure based on quadratic upstream interpolation. Comput Method Appl Mech Eng 19:59–98
4. Van Doormal JP, Raithby GD (1984) Enhancements of the SIMPLE method for predicting incompressible fluid flows. Numer Heat Transf 7:147–163
5. Issa RI (1986) Solution of the implicitly discretized fluid flow equations by operator splitting. J Comput Phys 62:40–65
6. Ferziger JH, Peric M (1996) Computational methods for fluid dynamics. Springer, New York
7. Mathur SR, Murthy, JY (1997) A Pressure-based Method for Unstructured Meshes. Numer Heat Transf Part B 31:195–215

Flexible Member Pump

► Peristaltic Pumps
► Positive Displacement Pump

Flexible Shear Stress Sensor

Synonyms

Smart skin

Definition

Fluid shear stress information is of great interest for many fluidic dynamic monitoring/diagnostics applications. For example, oscillatory shear stress plays an important role in the biological activities of vascular endothelial cells, which may lead to atherosclerosis. The emergence of Micro-Electro-Mechanical Systems (MEMS) technology provides us with the miniaturization of shear stress sensors with perfect spatial and temporal resolutions. The conventional MEMS sensors are based on the fabrication with the rigid silicon substrate, which limits the application to

only on the flat surface. In vivo biomedical applications demand the deployment of the sensors on the curved and non-planar surface, which will maximize the measurement precision and minimize the disturbance due to intruding the sensor. Scientists have combined the silicon technology with the polymer process to fabricate the sensor skin, which can conformally coat the non-flat surface and precisely measure the microfluidic parameters, such as shear stress, temperature and pressure.

Cross References

► Micro- and Nano-Scale Anemometry: Implication for Biomedical Applications

Flip of Phosphatidylserine

► Microfluidics for Studies of Apoptosis

Flow Bifurcation in Microchannel

Y. F. Yap, Yali Zhang, Teck Neng Wong, Nam-Trung Nguyen, John C. Chai
School of Mechanical & Aerospace Engineering, Nanyang Technological University, Singapore, Singapore
mtnwong@ntu.edu.sg, mntnguyen@ntu.edu.sg

Synonyms

T-junction; Bifurcating microchannel

Definition

Flow bifurcation in microchannels is discussed in this article. In this article, flow bifurcation refers to geometrical bifurcation. Specifically, the transport of droplets in microchannel where a mother branch bifurcates into two daughter branches with thermocapillary effects is examined.

Overview

Microchannel bifurcations have been employed in manipulating droplets. These manipulations include but are not limited to droplet fusion and splitting. Fusing of droplets has been demonstrated using a microchannel with three bifurcating branches [1]. A bifurcating T-junction can be employed to split a droplet into two daughter droplets of smaller size [2]. The relative size of the two daughter droplets is determined by the length of the branches. A longer branch creates larger resistance to flow and therefore creating smaller daughter droplet. In the extreme case where one of the branches is sufficiently long, the droplet does not break but is switched into the other branch. Such a passive geometrical control is limited in terms of its versatility. A more versatile active control utilizing thermocapillary effects [3] is presented in this study. The focus is on unequal splitting and switching the droplet into a desired branch at a T-junction.

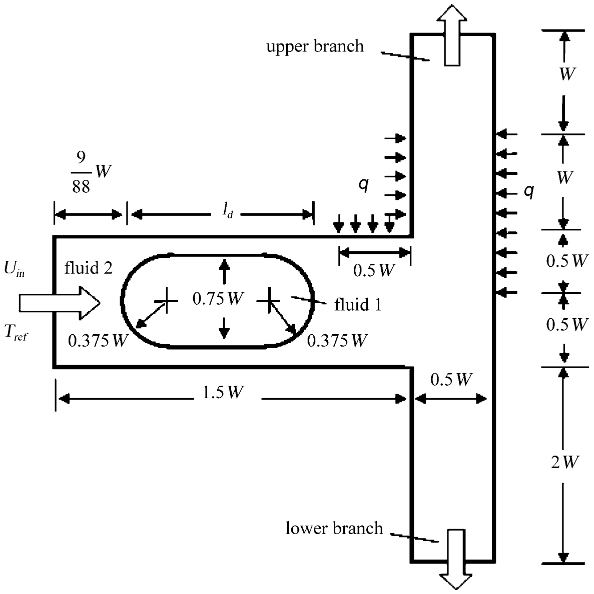

Flow Bifurcation in Microchannel, Figure 1 Schematic of a droplet in a micro T-junction

Basic Methodology

Problem Description

Figure 1 shows a fluid 1 droplet of length in a micro T-junction. Fluid 2 at temperature T_{ref} flows into the micro T-junction with a fully developed velocity profile of u_{in} at the inlet. This corresponds to a mean velocity of u_{m}. As fluid 2 flows, it carries the droplet.

An asymmetric temperature field is induced in the T-junction by applying a heat flux q at the selected locations. The remaining walls of the channel are properly insulated. As a result, the temperature dependent surface tension $\sigma(T)$ varies along the droplet interface. σ is assumed to vary linearly with temperature, i. e.

$$\sigma = \sigma_o + \frac{\mathrm{d}\sigma}{\mathrm{d}T}(T - T_{\mathrm{ref}}) \qquad (1)$$

where σ_o is the surface tension at temperature T_{ref}. The variation of σ induces an additional interfacial (thermocapillary) force on the droplet at the interface. This suggests that the net force on the droplet, and thus its motion,

can be controlled by adjusting the heater power.
Driven by the pressure gradient and the thermocapillary force, fluid 2 together with the droplet flows out of the domain via either the upper or the lower branch. It is possible that the droplet splits at the T-junction. The two outlets are maintained at the same pressure with a fully developed temperature profile.

Governing Equations

The level-set method [4] is used to capture the droplet interface. The level-set function ξ is defined as the signed distance function from the interface. Obviously, the value of ξ at the interface is zero. In the present study, the value of ξ for fluid 2 (the carrier fluid) is assigned negative. The distance function ξ for fluid 1 (the droplet) is positive. As a result, ξ can be expressed as

$$\xi(\boldsymbol{x}, t) = \begin{cases} < 0\,, & \text{if } \boldsymbol{x} \in \text{fluid 2} \\ = 0\,, & \text{if } \boldsymbol{x} \in \text{interface} \\ > 0\,, & \text{if } \boldsymbol{x} \in \text{fluid 1} \end{cases} \tag{2}$$

With the knowledge of ξ, any property of the fluid α (e. g. the density, viscosity, thermal conductivity or other properties of interest) in the domain at any given time t can be calculated conveniently as

$$\alpha = (1 - H)\,\alpha_1 + H\alpha_2 \tag{3a}$$

where subscripts 1 and 2 refer to fluid 1 and 2 respectively. The smoothed Heaviside function H is given by [6]

$$H(\xi) = \begin{cases} 0\,, & \xi < -\varepsilon \\ \frac{\xi+\varepsilon}{2\varepsilon} + \frac{1}{2\pi}\sin\left(\frac{\pi\xi}{\varepsilon}\right)\,, & |\xi| \leqslant \varepsilon \\ 1\,, & \xi > \varepsilon \end{cases} \tag{3b}$$

The Heaviside function is smoothed over a finite thickness of 2ε. The parameter ε is related to the grid size and is usually taken as a factor of the grid spacing. In this article, ε is set to one control volume thickness.
The conservation equations, i. e. continuity, incompressible Navier-Stokes, energy equations, can now be written for the whole domain. These are expressed as

$$\nabla \bullet \boldsymbol{u} = 0 \tag{4}$$

$$\frac{\partial(\rho\boldsymbol{u})}{\partial t} + \nabla \bullet (\rho\boldsymbol{u}\boldsymbol{u}) = -\nabla p + \nabla \bullet \left[\mu\left(\nabla\boldsymbol{u} + \nabla\boldsymbol{u}^T\right)\right] + \boldsymbol{f}_F \tag{5}$$

$$\frac{\partial(\rho cT)}{\partial t} + \nabla \bullet (\rho c\boldsymbol{u}T) = \nabla \bullet (k\nabla T) \tag{6}$$

where $\boldsymbol{u}$, p, ρ, μ, T, c and k are the velocity vector, pressure, density, viscosity, temperature, specific heat and thermal conductivity respectively. Viscous dissipation is neglected in the energy equation.
In the Eq. (5), the surface tension force $\boldsymbol{f}_F$ is modeled using the Continuum Surface Force model [7]. It is reformulated as an equivalent body force acting within a band of 2ε at the interface using a smeared-out Dirac delta function $D(\xi)$. The surface tension force can be expressed as

$$\boldsymbol{f}_F = -\kappa\sigma\boldsymbol{N}_F D(\xi) + (\boldsymbol{N}_F \times \nabla\sigma) \times \boldsymbol{N}_F D(\xi) \tag{7a}$$

where $D(\xi)$, $\boldsymbol{N}_F$ and κ are defined respectively as

$$D(\xi) \equiv \begin{cases} \frac{1+\cos(\pi\xi/\varepsilon)}{2\varepsilon} & |\xi| < \varepsilon \\ 0 & \text{otherwise} \end{cases} \tag{7b}$$

$$\boldsymbol{N}_F \equiv \frac{\nabla\xi}{|\nabla\xi|} \tag{7c}$$

$$\kappa \equiv \nabla \bullet \boldsymbol{N}_F \tag{7d}$$

The first and the second terms on the right side of Eq. (7a) represent the capillary and the Marangoni effects respectively. The capillary force is induced by the curvature of the interface and acts perpendicular to the interface. However, the Marangoni force is generated by a variation of surface tension along the interface and acts tangentially along the interface. For the present situation, since the variation of surface tension is caused by temperature gradient, the Marangoni force is referred to as thermocapillary force.
The interface is convected by the velocity field. The evolution of the interface is governed by

$$\frac{\partial\xi}{\partial t} + \boldsymbol{u} \bullet \nabla\xi = 0 \tag{8}$$

To ensure that ξ remains a distance function, i. e. satisfying $|\nabla\xi| = 1$, redistancing is performed. This is achieved by solving for the "steady-state" solution of a second distance function ψ given by

$$\frac{\partial\psi}{\partial\bar{t}} = \text{sign}(\xi)\,(1 - |\nabla\psi|) \tag{9}$$

where $\bar{t}$ is a pseudo time for the variable ψ. The "initial" condition for Eq. (13) is $\psi(\boldsymbol{x}, 0) = \xi(\boldsymbol{x})$. Even with proper redistancing, mass might not be conserved. To overcome this, a global mass correction [5] is employed. The "steady-state" solution to a third distance function ψ' that

F

ensures proper mass conservation is solved. This is written as

$$\frac{\partial \psi'}{\partial t'} = \text{sign}\,(\xi_{\text{ref}})\,\frac{M_{\text{d}} - M_{\text{c}}}{M_{\text{d}}} \tag{10a}$$

where M_{d} and M_{c} are the desired mass and the most current mass of the reference phase respectively. The mass of the reference phase can be calculated as

$$M = \begin{cases} \sum \rho_{\text{ref}} H \Delta V & H_{\text{ref}} = 1 \\ \sum \rho_{\text{ref}}\,(1 - H)\,\Delta V & H_{\text{ref}} = 0 \end{cases} \tag{10b}$$

The summation is performed over the whole solution domain. The desired mass of the reference phase is calculated as the initial mass of the reference phase. In Eq. (10a), t' is a pseudo time. The term sign (ξ_{ref}) refers to the sign of ξ for the reference phase. The droplet is chosen as the reference phase in this article. The "steady-state" values of ψ gre used as the "initial" condition for Eq. (10a).

Boundary Conditions

In this article, the normal and tangential velocities at the inlet are specified as u_{in} and zero respectively. No slip condition is used at all walls. The two outlets are set to the same pressure. For the energy equation, the temperature at the inlet is specified and zero-gradient is applied at both outlets. All walls are insulated except the locations where the heat fluxes are applied. For the level-set functions, $|\nabla \xi| = 1$ is imposed at all boundaries.

Solution Procedure

The solution procedure can be summarized as:

1. Specify the locations of the interface at time $t = 0$ and construct ξ for all nodes.
2. Set $t = t + \Delta t$.
3. Specify the properties for all nodes using Eqs. (3).
4. Solve the continuity and momentum equations (Eqs. (4) and (5)) for $\boldsymbol{u}$ and p at $t + \Delta t$.
5. Solve the energy equation (Eq. (6)) for T at $t + \Delta t$.
6. Solve for ξ (Eq. (8)), perform redistancing (Eq. (9)) and mass correction (Eq. (10)).
7. Repeat Steps 3 to 6 until the solution converges.
8. Repeat Steps 2 through 7 for all time steps.

Numerical Method

The continuity (Eq. (4)), Navier–Stokes (Eq. (5)), energy (Eq. (6)), level-set (Eqs. (8), (9) and (10a)) equations are special cases of a general transport equation

$$\rho \frac{\partial \phi}{\partial t} + \rho u_j \frac{\partial \phi}{\partial x_j} = \frac{\partial}{\partial x_j}\left(\Gamma \frac{\partial \phi}{\partial x_j}\right) + S \tag{11}$$

where ϕ, ρ, Γ, and S are the dependent variable, density, diffusion coefficient and source term respectively. The finite-volume method of Patankar [8] is used to solve the transport equation given in Eq. (11). A staggered grid with the scalar variables stored at the centers of the control volumes (CVs) and the velocities located at the CVs is employed. In this article, the power-law of Patankar [8] is used to model the combined convection-diffusion effect in the momentum equations. The CLAM scheme [9] is used to model the convection of the level-set equations. The SIMPLER algorithm is used to resolve the velocity-pressure coupling. The fully implicit scheme is used to discretize the transient term. The resulting algebraic equations are solved using the TriDiagonal Matrix Algorithm.

Key Research Findings

The present problem is governed by a total of 8 dimensionless numbers: droplet length to channel width ratio (l_{d}/W), density ratio (ρ_1/ρ_2), viscosity ratio (μ_1/μ_2), thermal diffusivity ratio (α_1/α_2), Prandtl number (Pr), Reynolds number (Re), Capillary number (Ca) and Marangoni number (Ma). Pr, Re, Ca and Ma are defined respectively as

$$\text{Pr} = \frac{\mu_2}{\rho_2 \alpha_2} \tag{12}$$

$$\text{Re} = \frac{\rho_2 u_m W}{\mu_2} \tag{13}$$

$$\text{Ca} = \frac{u_m \mu_2}{\sigma_o} \tag{14}$$

$$\text{Ma} = \frac{|d\sigma/dT|\,\Delta T}{\mu_2 u_m} \tag{15a}$$

The Marangoni number represents the ratio of the thermocapillary force to the viscous force. The driving temperature difference ΔT is created by the applied heat flux q. For the purpose of non-dimensionalization, the applied heat flux q is assumed to increase the fluid 2 temperature flowing out at the upper outlet by ΔT. With this, ΔT can be expressed in terms of q as

$$\Delta T = \frac{6q}{\rho_2 u_m c_{p2}} \tag{15b}$$

The dimensionless time t^* and temperature T^* are given by

$$t^* = \frac{t u_m}{W} \tag{16}$$

$$T^* = \frac{T - T_{\text{ref}}}{\Delta T} \tag{17}$$

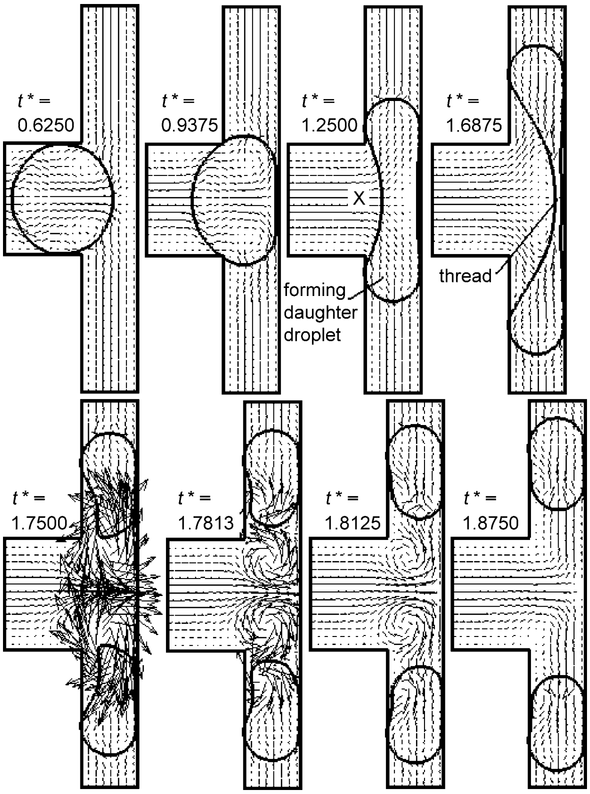

Flow Bifurcation in Microchannel, Figure 2 Evolution of a droplet in a T-junction for Ma = 0

Computations were made for a micro T-junction of $W = 400\,\mu$m. The dimensionless numbers are set to $l_d/W = 1.1$, $\rho_1/\rho_2 = 1.0961$, $\mu_1/\mu_2 = 0.0192$, $\alpha_1/\alpha_2 = 1.1078$, $Pr = 441.9882$, $Re = 0.0175$ and $Ca = 0.00625$. Of the 8 dimensionless numbers, only variation of Ma is considered as the effect of the thermocapillary force on the droplet motion is of interest. Results for the case of Ma = 0, 40 and 80 are presented. Validations of the solution procedure were presented in [5] and will not be repeated here.

The Case of Ma = 0

Figure 2 shows the evolution of a droplet in the T-junction for the case where the heater is switched off, i. e. Ma = 0. Only the portion of the T-junction containing the droplet is depicted. To avoid over-crowding the figure, only one in every two velocity vectors is shown. Although not shown, a mesh of 63 × 150 CVs with a time step of $\Delta t^* = 1.5625 \times 10^{-4}$ is sufficient to achieve grid independent solution. Therefore, all subsequent computations were made with this mesh and time step size.

The droplet is much larger than either of the branches. When it arrives at the T-junction ($t^* = 0.9375$), it blocks

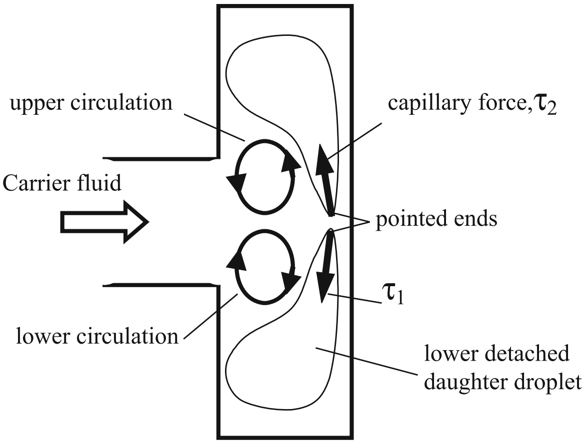

Flow Bifurcation in Microchannel, Figure 3 Formation of vortices as the two daughter droplets detach

the T-junction and consequently creates an upstream pressure build-up. The pressure build-up squeezes the droplet into the shape of a dumbbell. The two forming daughter droplets at the two ends of the mother droplet are joined by a fluid 1 thread ($t^* = 1.2500$). These two forming daughter droplets further block the flow of carrier fluid into the branches. With the increase in the pressure build-up, the forming daughter droplets are pushed further into the branches and results in a thinning of the thread ($t^* = 1.6875$). The fluid 1 thread breaks eventually. The two forming daughter droplets detach from each other and become two smaller daughter droplets.

The velocity field just after the breaking off of the fluid 1 thread is highly complicated with vortices forming adjacent of the daughter droplets. For the ease of explanation, a schematic of the two daughter droplets just after the thread breaks is shown in Fig. 3.

Upon detachment, a pointed tail forms at the rear of each daughter droplet from the broken fluid 1 thread. Such a sudden creation of pointed interfaces with large curvature generates strong capillary forces instantly. The sudden availability of these strong capillary forces has a profound effect on the flow field. Given the symmetric of the flow field, the effect of the capillary forces on the lower forming daughter droplet only is discussed. τ_1 is the capillary force acting on lower daughter droplet at the pointed tail. It acts to pull the pointed tail towards the center of lower daughter droplet, effectively shortening the tail in the process. τ_1 is so large that the tail is able to drag along the particles of the carrier fluid adjacent to it and simultaneously increases the carrier fluid velocity dramatically. This can be seen from the suddenly increase in the carrier fluid velocity around the detached daughter droplets. However, the lower daughter droplet is still blocking branch B. This

drives the fluid particles of the carrier fluid to circulate at the T-junction, generating the lower circulation. As the tail of the droplet is shortened, it becomes more rounded off, thus possesses a smaller curvature. The decrease in curvature is accompanied by decreasing capillary force. It follows that the circulation dies down as the capillary force at the tail is no longer strong enough to sustain it. Similar phenomenon occurs to the upper daughter droplet resulting in the formation and decay of the upper circulation.

The daughter droplets become more and more circular as they travel downstream under the influence of surface tension ($t^* = 1.8750$). The two daughter droplets are of equal size. This is expected given the symmetry of the flow field. Each of these daughter droplets leaves the T-junction via one of the branches.

From the above observation, a mother droplet of size smaller than the branch does not break for it fails to create the required pressure build-up for splitting. It can only flow into one of the channel at the T-junction depends on the flow conditions in these branches.

The Case of Ma = 40

The heater is now switched on. A non-zero heat flux q, corresponding to $\mathrm{Ma} = 40$, is generated. The induced asymmetric dimensionless temperature field is shown in Fig. 4. A strong temperature gradient is induced in the upper branch. This gives a larger variation of surface tension and results in a larger thermocapillary force. However, given the location of the applied heat flux, the temperature gradient along branch B is minimal. As a result, the variation of surface tension and the thermocapillary force are both smaller. The evolution of the droplet is shown in Fig. 5.

The droplet is asymmetrically split with a larger daughter droplet formed in the upper branch. The detachment of the daughter droplets occurs earlier ($t^* = 1.6563$) than that in the case of $\mathrm{Ma} = 0$ ($t^* = 1.7500$). To explain these, Fig. 6, illustrating the flow induced by the thermocapillary forces, is constructed.

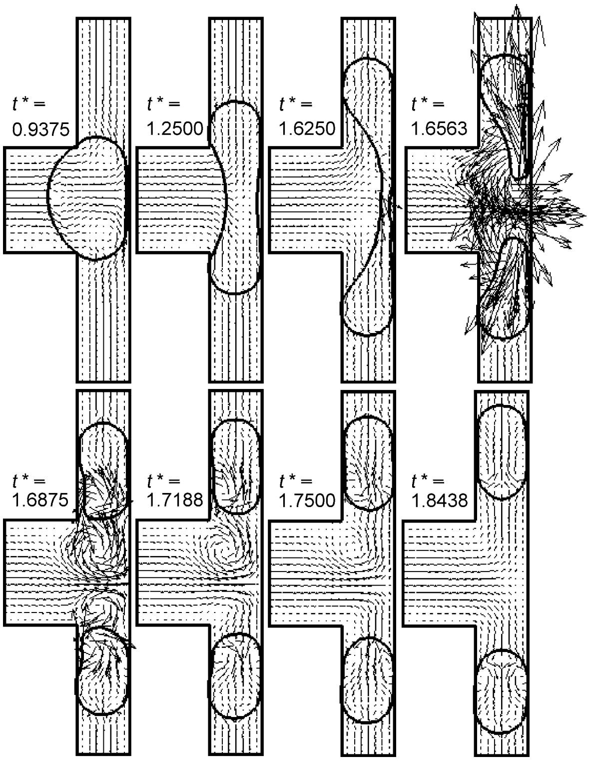

Flow Bifurcation in Microchannel, Figure 5 Unequal splitting of a droplet in a T-junction for Ma = 40

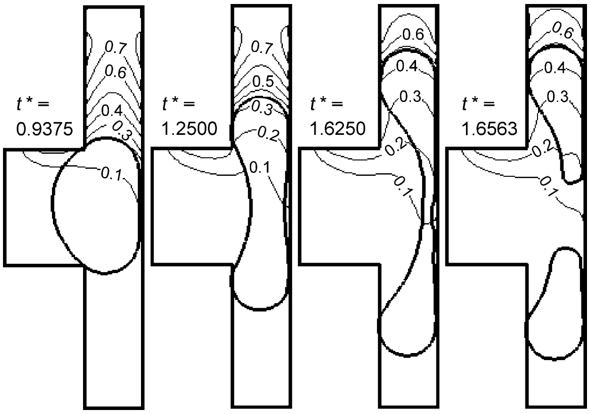

Flow Bifurcation in Microchannel, Figure 4 Dimensionless temperature field in a T-junction for Ma = 40

Figure 6 shows the thermocapillary forces, τ_1, τ_2, τ_3 and τ_4, acting at different locations of the droplet interface. These forces, downwardly directed, induce a secondary flow within the droplet of the following nature. The thermocapillary forces drive the fluid 1 particles adjacent to the interface downwards into the lower forming daughter droplet. This has the effect of depleting the fluid 1 thread and accelerates its thinning. The accumulation of the fluid 1 particles in the lower forming daughter droplet tends to inflate it. It should be noted that the magnitude of the surface tension in lower branch is larger than that of the upper branch given the lower temperature in the lower branch. Creating larger interfacial area at the tip of the lower forming daughter droplet to accommodate additional fluid 1 is not favorable as more energy is required. The fluid 1 particles then turn and flow upwards into the upper forming daughter droplet via the center of the fluid 1 thread. When these particles reach the tip of the upper forming daughter droplet, larger interface can be favorably created as the surface tension is smaller and thus less

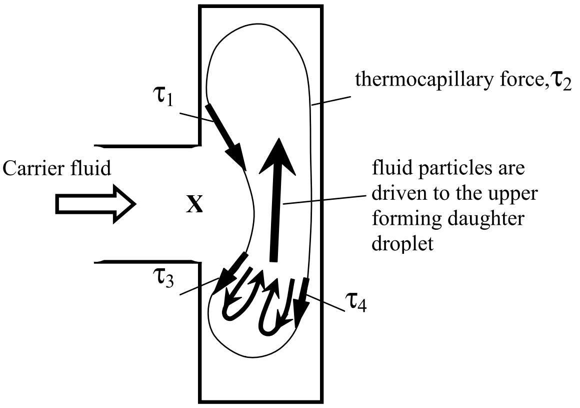

Flow Bifurcation in Microchannel, Figure 6 Thermocapillary forces acting on a droplet at a T-junction

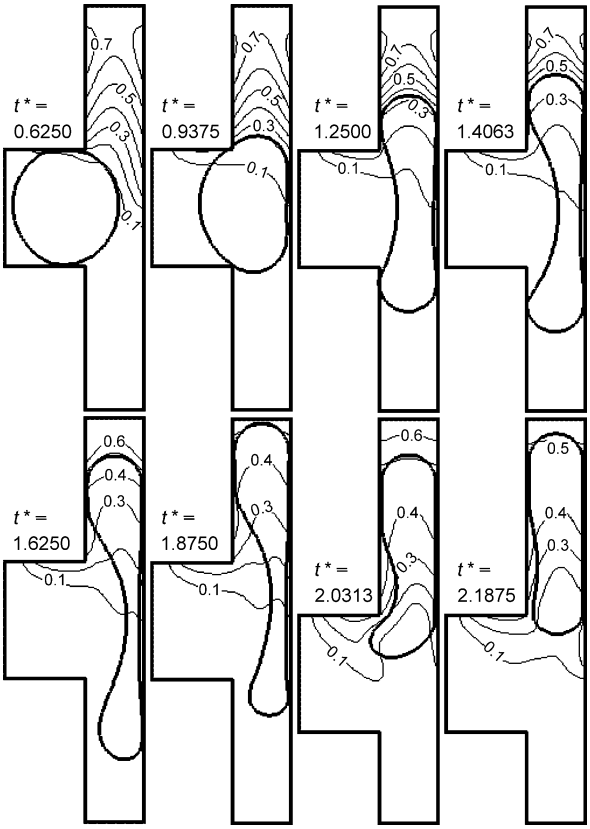

Flow Bifurcation in Microchannel, Figure 7 Dimensionless temperature field in a T-junction for Ma = 80

energy is required. As a result, more fluid 1 particles accumulate in the upper forming droplet. Upon the detachment of the two daughter droplets, the upper daughter droplet is naturally larger.

The mechanism in generating the circulations is similar to the case of Ma = 0. However, since now the interfacial forces (the resultant of capillary and thermocapillary forces) at the pointed tails of the detached daughter droplets are no longer of the same magnitude, the strength of the induced circulations is different. Although the capillary force at the tip of the upper detached droplet is smaller, it is compensated by a much stronger thermocapillary force. With this, the upper circulation is stronger and dies down slower.

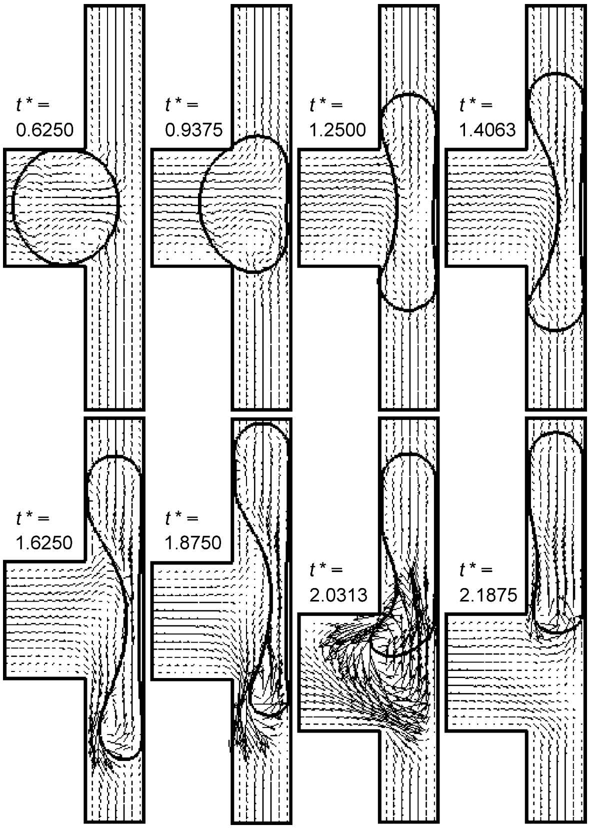

Flow Bifurcation in Microchannel, Figure 8 Switching of a droplet in a T-junction for Ma = 80

The Case of Ma = 80

The heat flux is further increased to achieve Ma = 80. Figure. 7 shows the induced dimensionless temperature field. The dimensionless temperature field exhibits a similar trend to that of the case Ma = 40. It should be noted that the actual temperature and its gradient are twice of the case with Ma = 40 as a larger q is used in obtaining the dimensionless temperature. The thermocapillary effect should therefore be twice as strong. The thermocapillary force is so strong that the droplet becomes asymmetric as early as $t^* = 0.9375$. The corresponding velocity field during the evolution of the droplet is given in Fig. 8. In this

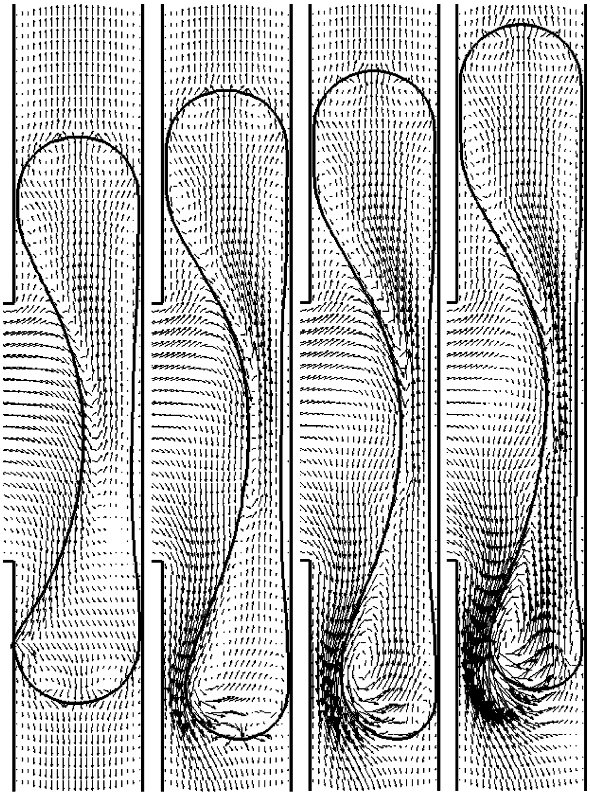

Flow Bifurcation in Microchannel, Figure 9 Circulations in the lower forming daughter droplet

case, the droplet no longer splits but switches entirely into the upper branch.

To obtain a clearer picture of the switching mechanism, a more detailed flow field is required. Figure 9 shows the evolution of the droplet from $t^* = 1.4063$ to $t^* = 1.7813$ with all the velocity vectors plotted. For the present case, the secondary flow induced by the thermocapillary forces is much stronger. The induced secondary flow of a circulatory nature (as in the case of Ma = 40) within the upper forming daughter droplet is obvious ($t^* = 1.4063$). It increases significantly the flow of fluid 1 particles into the upper forming daughter droplet. The asymmetrical shape of the droplet is obvious with a larger upper forming daughter droplet. Since temperature gradient induced in the lower branch is minimal, no obvious circulatory motion is observed.

Although the lower forming droplet is smaller, it is still sufficient to block the lower branch at $t^* = 1.4063$. Pressure does build up. The pressure build-up pushes the two forming daughter droplets into the respective branch. This is accompanied by a thinning of the fluid 1 thread. However, given the different size in the forming daughter droplet, the ability to withstand the pressure build-up is different. The smaller lower forming droplet fails to withstand further pressure build-up eventually and the pressure forces the creation of a small gap between the lower forming droplet and the wall ($t^* = 1.5625$). The sudden release of pressure accelerates the carrier fluid into the lower branch via the gap ($t^* = 1.5625$). This generates a large shear stress, downwardly directed, on the interface of the lower forming daughter droplet, creating two circulations within it. The stronger circulation accelerates the fluid particles in the lower forming daughter droplet upwards into the upper forming daughter droplet. The lower forming daughter droplet becomes smaller ($t^* = 1.7813$). The fluid 1 thread does not break for (1) there is no further pressure build up thinning it and (2) the flow of the fluid 1 particles from the lower daughter droplet to the upper daughter droplet replenishes it. As a result, the lower forming daughter droplet does not detach but merges with the upper forming daughter droplet instead. In the process, the whole mother droplet is switched into the branch A.

The two cases of non-zero Ma suggest that a temperature gradient can be used to (1) split a droplet or droplet into two daughter droplets of controllable sizes and (2) switch a droplet into a desired branch in a bifurcating microchannel.

Future Directions for Research

Controllable splitting and switching of a droplet into a desired branch at a bifurcating T-junction with thermocapillary effects has been demonstrated numerical. The relative size of the two daughter droplets, strongly dictated by the Marangoni number, is a parameter of interest and requires further investigation. Occasionally, the droplet carries non-fluid particles, e. g. cells or bioparticles, in the form of encapsulation. These particles may break out from the encapsulation during splitting or switching. Therefore, effect of having these encapsulated particles needs to be examined.

Cross References

► Droplet Dynamics in Microchannel
► Thermocapillarity
► Surface Tension Driven Flow
► Two-Phase Flow

References

1. Tan YC, Fisher JS, Lee AI, Cristini V, Phillip A (2004) Design of microfluid channel geometries for the control of droplet volume, chem concentration sorting. Lab Chip 4:292–298

2. Link DR, Anna SL, Weitz DA, Stone HA (2004) Geometrically Mediated Breakup of Drops in Microfluid Devices. Phys Rev Lett 92(5):054503/1–4
3. Ting TH, Yap YF, Nguyen NT, Wong TN, John JC, Yobas L (2006) Thermally mediated breakup of drops in microchannels. Appl Phys Lett 89(23):234101/1–3
4. Osher S, Sethian JA (1988) Fronts Propagating with Curvature-Dependent Speed: Algorithms Based on Hamilton–Jacobi Formulations. J Comp Phys 79:12–49
5. Yap YF, Chai JC, Wong TN, Toh KC, Zhang HY (2006) A global mass correction scheme for the level-set method. Num Heat Transf B 50:455–472
6. Chang YC, Hou TY, Merriman B, Osher S (1996) A Level Set Formulation of Eulerian Interface Capturing Methods for Incompressible Fluid Flows. J Comp Phys 124:449–464
7. Brackbill JU, Kothe DB, Zemach C (1992) A continuum method for modelling surface tension. J Comp Phys 100:335–354
8. Patankar SV (1980) Numerical Heat Transfer and Fluid Flow. Hemisphere, New York
9. Van Leer B (1974) Towards the ultimate conservative difference scheme. II. Monotonicity and conservation combined in a second-order scheme. J Comp Phys 14:361–370

Flow Boiling Instability

DAVID BRUTIN
Poytech Marseille, IUSTI Laboratory, Marseille, France
david.brutin@polytech.univ-mrs.fr

Synonym

Two-phase flow instability; Liquid–vapor instability

Definition

When two-phase flow phase change occurs in a channel with a small hydraulic diameter compared with the capillary length, *flow boiling instabilities* may arise. As in classical-sized channels, the instabilities can be static or dynamic; however their intensity is higher in microchannels due to the higher rate of volumic generation of vapor which induces considerable pressure drops.

Overview

Between 1985 and 2006, 1247 papers were published on Sciencedirect® on the subject of boiling, of which only 49, i. e., about 4%, deal with mini or microchannels. Four of these 49 papers report flow instabilities. Even if flow boiling is a well-developed research subject, flow boiling in microchannels, not to mention instabilities which occur in these microchannels, have not been discussed or reported to any considerable extent in the literature. In Table 1 a few studies dealing with *flow boiling instabilities* in microchannels are listed. We will discuss some of these studies below.

Wu and Cheng [1] conducted experiments using 8 parallel silicon microchannels heated from the bottom. They observed water flows with large-amplitude or long-period oscillating boiling modes as a function of heat flux and mass flux depending on whether the water outlet is at saturation temperature or superheated.

Qu et al. [2] found evidence of two kinds of unsteady flow boiling for 21 parallel microchannels measuring 231 × 713 µm. They observed in their parallel microchannel array either a global fluctuation of the whole two-phase zone for all the microchannels (Fig. 1) or chaotic fluctuations of the two-phase zone (Fig. 2): over-pressure in one microchannel and under-pressure in another. The individual microchannel mass flow rate was not controlled.

Hetsroni et al. [3] created an experimental setup to study liquid–gas and liquid–vapor flow in parallel triangular microchannels with diameters of 103 to 161 µm. They used a fast video camera coupled with a microscope through a Pyrex plate to record the flow patterns. They showed the influence of the injection method (plenum shape) and found evidence for the same inlet conditions,

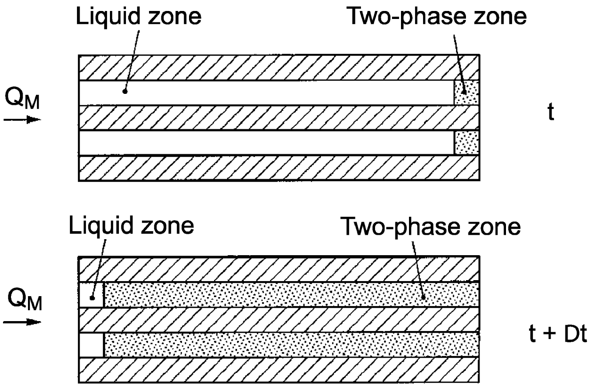

Flow Boiling Instability, Figure 1 Top view of a severe pressure drop oscillation [2]

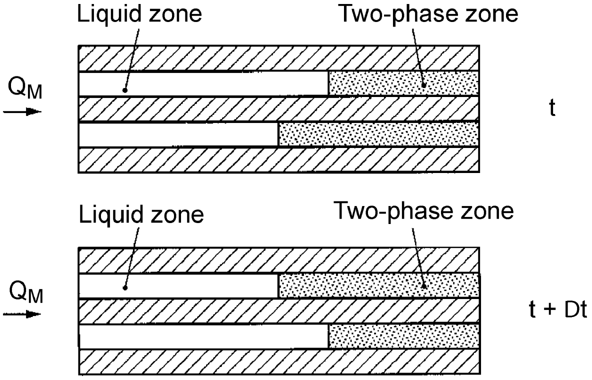

Flow Boiling Instability, Figure 2 Top view of a mild parallel channel instability [2]

Flow Boiling Instability, Table 1 Studies on boiling flow instabilities in microchannels

Authors, Year [Reference]	Size	Shape	Aim of the study
Brutin, 2003 [7]	889 µm	Rect.	evidence of confinement flow instabilities
Wu, 2003 [1]	186 µm	Tri.	surface temperature fluctuations
Peles, 2003 [4]	50 – 200 µm	Tri.	observation of flow regimes
Bergles, 2003 [10]	-	-	CHF and flow instabilities
Qu, 2003 [2]	349 µm	Rect.	coupling instabilities in parallel microchannels
Li, 2003 [11]	51.7 µm	Tri.	unsteady flows observed in two parallel microchannels

Rect.: rectangular / Tri.: triangular

i. e., mass flow rate and heat flux, different flow patterns (annular flow, bubbly flow, etc.). The random nature of this flow in the parallel microchannels results from the inlet mass flow rate, which is not constant but depends on the pressure drop in each microchannel.

Peles [4] made a micro heat exchanger using photolithography processes on a silicon substrate. The micro heat exchanger was based on multiple parallel triangular microchannels. The results obtained using pressure measurements and fast video recording of flow boiling evidence various flow regimes such as *rapid bubble growth*, *complete bubble flow*, *bubbly flow* and *annular flow*. The first two regimes described by the author are presented as specific at the microscale. Flow instabilities are observed such as temperature and pressure fluctuations at a frequency which decreases with increasing mass flow rates (high peristaltic pump frequency).

As for flow boiling instabilities in classical channels, several types of instabilities have been observed and reported by different authors. Table 2 summarizes these instabilities and their physical consequences on the fluid flow. We also show in the following table which publications reported these instabilities in microchannels. This classification is based on the one proposed for channels by Bergles in 1976 [5] and is divided into two categories:

- static instabilities induce a shift of the equilibrium point to a new steady-state point: Ledinegg instability, boiling crisis, bumping, geysering or chugging are all static instabilities since they can be analyzed using only stationary models;
- dynamic instabilities are driven by the inertia of the system; the stationary state is not sufficient to predict the destabilization threshold of theses instabilities such as acoustic waves, pressure drop oscillations or thermal oscillations.

Basic Methodology

Influence of Confinement on Flow Boiling

The confinement effect on boiling appears through the influence of the wall on the flow. In a large tube, boiling is not influenced by the wall of the duct and the flow is free to structure itself and evolve inside. In our minichannel, dimensions are such that the bubble growth from a nucleation site is modified by the proximity of the wall (Fig. 3). One criterion is to verify whether the theoretical diameter of the bubbles is larger than the diameter of the duct. We estimate the bubble detachment diameter using the correlation of Fritz [6] which takes into account nucleation surface orientation for *n*-pentane. Equation (1) is used where θ is the wetting angle expressed in degrees. This relation is based on the balance between surface tension and buoy-

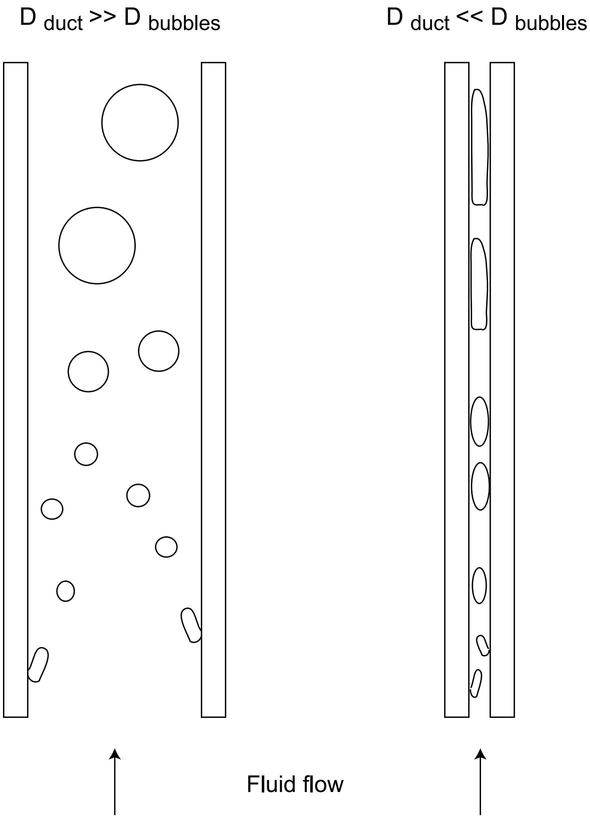

Flow Boiling Instability, Figure 3 Wall influence on flow boiling behavior

Flow Boiling Instability, Table 2 Classification of flow instabilities (based on [5])

Class	Type	Characteristics	Observed by
Static	Ledinegg instability	Flow undergoes sudden, large amplitude excursion to a new stable operating condition	[3, 7]
Static	Boiling crisis	Wall temperature excursion and flow oscillation	[3, 7]
Static	Flow pattern transition instability	Cyclic flow pattern transition and flow rate variations	[8]
Static	Bumping, geysering or chugging	Period process of super-heat and violent evaporation with possible expulsion and refilling	[7]
Dynamic	Acoustic oscillations	High frequencies related to time required for pressure wave propagation in system	-
Dynamic	Density wave oscillation	Low frequencies related to transmit time of a continuity wave	-
Dynamic	Thermal oscillations	Occur in film boiling	-
Dynamic	Coupling instabilities	Strong only for a small fuel time constant and under low pressures	[3, 7]
Dynamic	Pressure drop oscillations	Very low frequency periodic process	[2, 7]

ancy forces. We obtain a bubble detachment diameter of 600 μm, which means that inside our minichannel with a thickness of 500 μm the proximity of the wall influences the evolution of the bubble. Thus it is reasonable to think that wall confinement influences the vapor bubble behavior and coalescence in the minichannel.

$$D_{\text{bubbles}} = 0.0208\,\theta \sqrt{\frac{\sigma}{g(\varrho_L - \varrho_G)}} \qquad (1)$$

We can consider that one degree of freedom has been removed. The consequence is that bubbles grow along the other two axes (width and length). Whereas bubbles are supposed to be spherical without the influence of any wall, here they are compressed. This modification of shape induces an increase in wall friction. Confinement increases bubble coalescence by reducing the volume of the channel for a given heating surface; the volumic density of the bubbles grows quickly and thus bubbles group together to form slugs. Due to the proximity of the wall, wall friction for the evolution of bubbles and slugs is increased. When vapor slugs flow through the minichannel, this induces overheating of the wall due the reduction of heat transfer associated with the vapor phase (Fig. 4 and 5). These periodical slugs become more and more numerous as the heat flux increases or the liquid mass flow rate decreases.

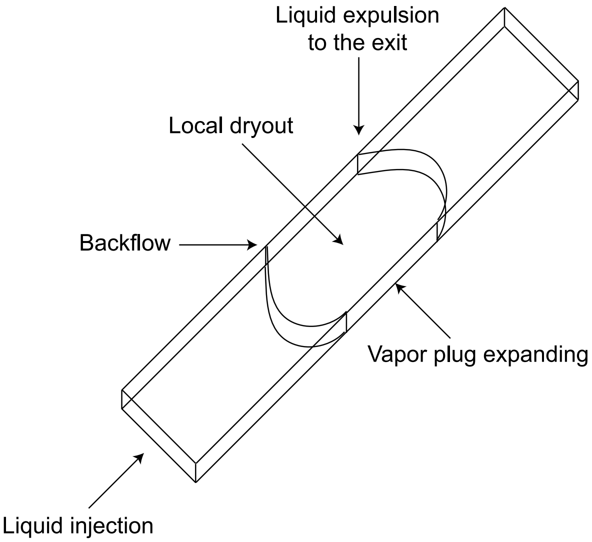

Flow Boiling Instability, Figure 4 Local dryout due to a vapor slug

Analysis of Instabilities

Pressure Drop and Visualization of Flow Patterns

To analyze flow boiling instabilities in a minichannel or a microchannel, pressure measurements recorded at a high frequency (e. g., 200 Hz) are usually performed. The analysis of the microchannel pressure drop is then related to flow patterns to understand destabilization mechanisms.

Brutin et al. [7] recorded the pressure signal of the unsteady flow simultaneously with video recording to compare both frequencies: pressure drop and flow pattern oscillation frequencies. In Fig. 6, they analyze the two-phase flow behavior which is partially presented with pictures in Fig. 7. The different steps observed during one period are the following:

- Liquid flows in the channel (point A). Bubbles are created at the beginning of the two-phase flow zone. Their size and generation rates are such that bubbles coalesce into vapor slugs which evolve in the channel. Vapor slugs generate over-pressure which reduces the upstream boiling flow rate.

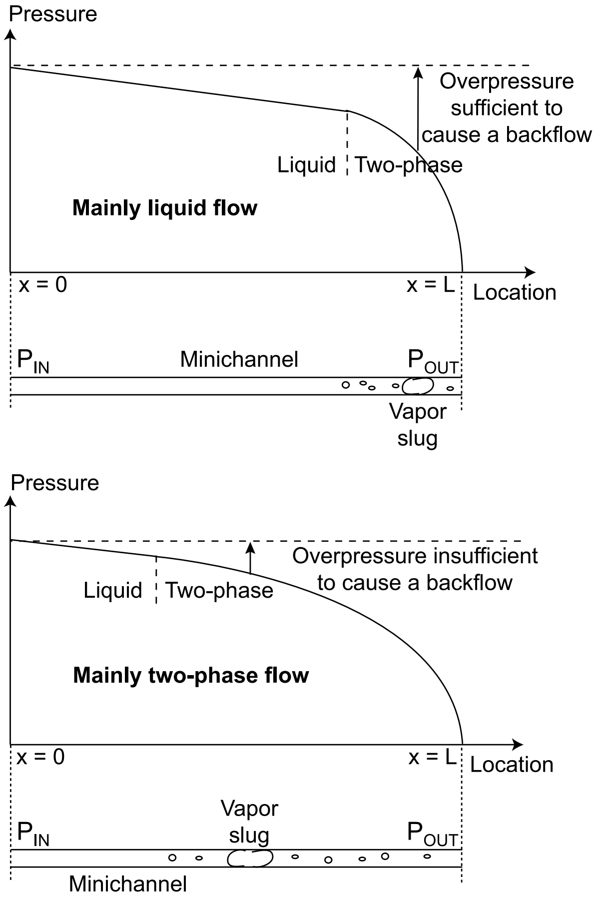

Flow Boiling Instability, Figure 5 Local pressure in a minichannel for two situations: a mainly liquid flow and a mainly two-phase flow

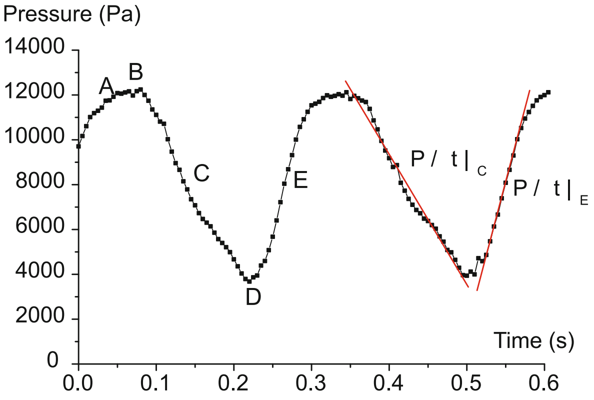

Flow Boiling Instability, Figure 6 Typical outlet pressure signal during unsteady boiling shown over 2 periods. ($D_H = 888.9\,\mu$m, $L = 200$ mm, $Re_L = 955$, $Q_W = 9.6\,W\,cm^{-2}$)

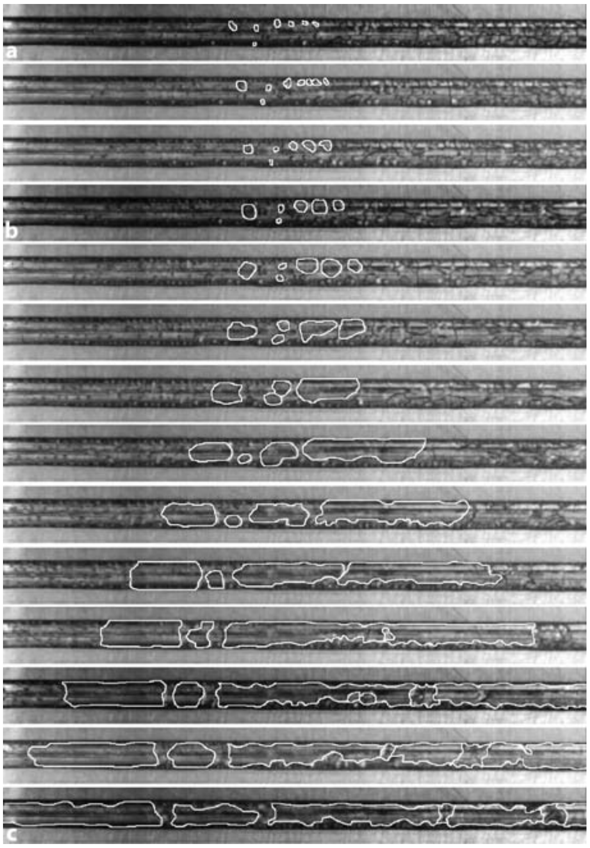

Flow Boiling Instability, Figure 7 Vapor slug formation during flow boiling: example of backflow (5 ms between 2 pictures) (some bubble outlines were evidenced in order to follow their evolution)

- Bubbles growing before the vapor slug slow down, stop (point B) and then quickly reach the entire channel cross-section. Vapor created by bubble expansion must be evacuated, but downstream in the channel vapor slugs block the flow.
- Expanding vapor pushes the inflow back to the entrance using the buffer tank as a mass flow storage (point C).
- Eventually the channel is full of vapor (point D). The surface temperature rises due to the fact that the heat flux is permanently supplied to the fluid and not removed by boiling.
- When the channel is empty and upstream pressure before the channel entrance is sufficient, the entire vapor slug which occupies the channel is expelled. The channel is refilled with liquid (point E).
- Due to the high surface temperature, bubbles are formed rapidly (point A) and the phenomenon is repeated.

If we look at the evolution of pressure in Fig. 6, we observe three distinct parts in one period (about 275 ms). The first consists of the decrease in pressure for approximately 150 ms from B to D. The average pressure decrease in C is 62 kPa/s, whereas in the second part the refilling of the liquid, with a duration of about 65 ms, corresponds to

the D to A part on the curve. The average pressure increase in E is about 136 kPa/s. The third part between A and B flowing in the channel and slowing down accounts for only 60 ms of one period.

Qu et al. [2] observed in their experiment that hydrodynamic instabilities influence inlet and outlet pressures and can induce a degree an uncertainty in the measurement of pressure drop. They recorded temporal pressure signals and made the following observations: even with a small heat flux supplied to the parallel channels, the case of pressure drop oscillations presents pressure fluctuations with quite constant frequency, whereas in the case of instability in the parallel channels the fluctuations are small and random.

Hetsroni et al. [3] also found evidence of a coupling phenomenon for an array of 17 parallel microchannels. In Fig. 7 from [3], they found evidence of two-phase flow oscillations. Only one channel is followed as a function of time. The water-steam flow is from the left to the right. Steam appears in the 5th picture. The liquid–vapor interface then moves to the exit or to the entrance. This interface movement is representative of a non-constant mass flow provided to the microchannel. The inlet condition before the plenum is a constant inlet pressure; however, due to the plenum, the flow can come back and induce such coupling. The frequency of the interface oscillation can usually be related to the total pressure drop oscillation frequency.

Scaling Laws Analysis

Scaling laws help to understand the flow patterns and heat transfer phenomenon without any constraint of geometry, fluid type or operation conditions. The terms used to determine these scaling laws are dimensionless and usually balance the physical processes involved. In the present case of flow boiling, the pressure drop is considered without dimension usually using the dynamic pressure.

Figure 8 from [8] presents the total minichannel pressure loss as a function of the inlet Reynolds number. The total pressure loss includes liquid, two-phase and vapor depending on the boiling stage in the minichannel. The curve behavior is a classical N-shape observed for all the heat fluxes studied. The total minichannel pressure loss is the sum of fluid pressure loss for each zone and arises when the friction term in the two-phase zone reaches a maximum then decreases when the flow is mainly vapor. With increasing heat fluxes, the pressure loss shifts to higher values and the N-shape is more and more pronounced. Using the experimental results of the visualization, it is possible to propose a global behavior of the fluid flow in the channel with the non-dimensioned pressure loss vari-

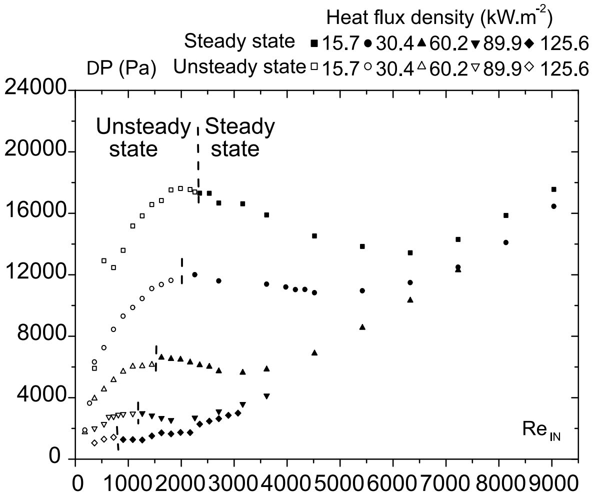

Flow Boiling Instability, Figure 8 Average pressure loss versus inlet Reynolds number when the buffer is not connected to the loop for 5 heat fluxes

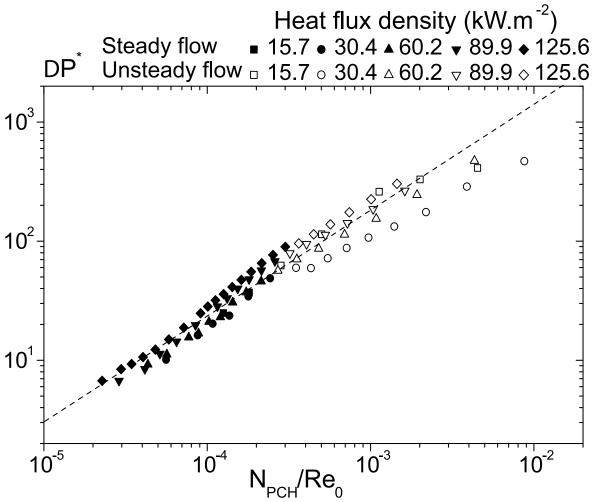

Flow Boiling Instability, Figure 9 Pressure loss scaling law for all heat flux densities provided: non-dimensioned pressure loss function of the ratio between the phase change number and the Reynolds number for only exit vapor qualities strictly between 0 and 1

ation. If we remove all points which present liquid flow operating conditions and those for mainly vapor flow, we obtain in Fig. 9 [9] only the operating conditions which satisfy the exit vapor quality strictly between 0 and 1.

The case studied is characterized by a constant mass flow rate supplied to the channel entrance. All the results concerning pressure loss are on one line, which means the same variation law. Equation (2) gives the pressure loss scaling law numerically. It is also possible from Fig. 9 to extract the criterion for the transition from steady to

unsteady. This law provides an equivalent friction factor for the two-phase flow.

$$\Delta P^*_{\text{comp}} = 4.46 \times 10^4 \left(\frac{N_{\text{pch}}}{\text{Re}_0}\right)^{0.818} \tag{2}$$

Figure 9 evidences a possible generalization of the steady and unsteady results. The stability transition appears for a given abscissa and thus a given ordinate. These coordinates are summarized by the ratio K_2/K_1 previously detailed with Eq. (21). The experimental value of K_2/K_1 is $4.94 \times 10^{-6} \pm 30\%$ with a comparison with the theoretical value which is $3.92 \times 10^{-6} \pm 7.5\%$. We obtain a good agreement between experimental and theoretical thresholds. The gap of 26% for the confinement case should be compared with the total uncertainty of 37.5%. The uncertainty of the experimental and theoretical destabilization thresholds (Eqs. (3), (4)) is 4 times the liquid inlet velocity uncertainty, 4 times the hydraulic diameter uncertainty plus the total pressure drop and the heat flux uncertainties.

$$\Delta P^* = \frac{\Delta P}{\frac{1}{2}\varrho_0 U_0^2} \tag{3}$$

$$\frac{N_{\text{pch}}}{\text{Re}_0} = \frac{Q_W}{U_0^2}\frac{4L\nu_0}{\varrho_0 D_H^2} \tag{4}$$

The two-phase flow oscillation frequencies observed can also be analyzed using a non-dimensional approach. Their experimental values are obtained on the basis of the fast Fourier transformation of the pressure drop which evidences frequencies of high energy. The fundamental frequency is the one we deal with here. The oscillation mechanism is based on the two-phase transport along the minichannel; the pressure oscillations are mainly driven by a convective phenomenon. Thus the convective time (τ) defined in Eq. (5) is used:

$$\tau = \frac{L}{U_0} \tag{5}$$

The non-dimensional two-phase flow frequency ($F.\tau$) is plotted as a function of ($N_{\text{pch}}/\text{Re}_0$). A single curve is found for all the operating conditions. This behavior confirms that the oscillation frequency is mainly driven by the phase change phenomenon and inertia effects (Fig. 10). The dispersion is probably due to the uncertainty associated with the measurement of the frequency.

Scaling laws of flow boiling instabilities can also be applied to heat transfer. In Brutin et al. [9] the heat transfer coefficient calculated is based on the average surface and fluid temperature. A total heat flux is provided ($\overline{Q}_W$) whereas locally the heat flux is redistributed inside the aluminum rod. Thus the local surface and fluid temperatures cannot be used to calculate a local heat transfer coefficient but can only provide a global heat transfer coefficient. Using the average temperature difference between surface and fluid ($\overline{T}_S - \overline{T}_F$) and the total heat flux transferred to the fluid, we calculate a global heat transfer coefficient (Eq. (6)). Figure 12 of [8] presents only operating conditions which correspond to a two-phase zone in the minichannel. The objective is to analyze how the two-phase flow contributes to heat transfer.

For increasing heat fluxes, the N-shape is more and more pronounced. Dark points in Fig. 12 of [8] represent a steady flow whereas the white points are for an unsteady flow. A mean heat transfer coefficient is deduced. Introducing the Stanton number, we compare the heat flux transferred to the fluid with the heat transported with the fluid. If we only consider the operating conditions which satisfy a two-phase zone mainly in the minichannel (Fig. 8 of [9]), a heat transfer scaling law appears (Eq. (8)). Thus it is possible to predict a mean heat transfer coefficient when a two-phase zone is mainly inside the minichannel.

$$\overline{h} = \frac{\overline{Q}_W}{\overline{T}_S - \overline{T}_F} \tag{6}$$

$$\text{St} = \frac{\overline{h}}{\varrho_0 Cp_0 U_0} \tag{7}$$

$$\text{St} = 0.776 \left(\frac{N_{\text{pch}}}{\text{Re}_0}\right)^{0.589} \tag{8}$$

Destabilization Mechanism

To use or predict flow boiling instabilities, it is essential to understand the mechanisms which lead to the instabilities. These mechanisms can usually be found by analyzing the flow patterns. For flow boiling in a microchannel, the previous section evidenced that flow boiling instabilities appear and lead to periodical pressure oscillations. The flow even returns to the entrance (Fig. 7). To determine the destabilization mechanism which occurs in such a situation, we quantified the phenomena involved in the instability, such as vapor generation rate, total channel pressure drop, etc.

Brutin et al. [9] studied the transition from steady to unsteady flow boiling and developed a transition criterion. This study was performed experimentally in minichannels but the theory also applies to confined geometries such as microchannels. This criterion is based on observations of the unsteady two-phase flow: the two-phase flow stops at a location in the microchannel; then all the fluid after this location is expelled towards the exit whereas all the fluid

before this location is sent back to the entrance. This two-phase backflow has been evidenced previously [7]; however, the location of this split remained unexplained.

On the basis of Fig. 5 from [9], L_c was defined as the location in the channel where the flow stops and the slug expands and then purges all the fluid out of the minichannel. U_0 is the injection liquid velocity at the bottom of the minichannel and $\overline{U}$ the average two-phase flow evacuation velocity. Two terms were quantified: the over-pressure induced by the expansion of the vapor slug, and the injection pressure minus the minichannel outlet pressure.

The pressure necessary to evacuate all the fluid from the minichannel is the minichannel pressure loss because the outlet pressure is higher than atmospheric pressure. To estimate the friction pressure loss in the minichannel, acceleration and gravity terms were ignored. The physical properties of two-phase flow were considered to be the average between the inlet and the outlet. When unsteady states appear, the fluid was considered as entering in a saturated condition. Thus the expression was established of the over-pressure (ΔP_{slug}) required to evacuate the entire two-phase flow from the minichannel (Eq. (9)). The flow regime considered just after the flow stops is laminar as this minimizes the energy used for the evacuation; a turbulent regime would necessitate much more enthalpy and thus the over-pressure would be much higher. In the expression $\overline{\lambda} = \alpha/\overline{\text{Re}}$, $\alpha = 82.36$ was taken for their geometry aspect ratio. The minichannel pressure loss is $\Delta P_{\text{minichannel}}$. The over-pressure created by the vapor slug is scaled by the dynamic pressure $(1/2)\,\varrho_0 U_0^2$.

$$\Delta P_{\text{slug}} = \overline{\lambda}\frac{L}{D_{\text{H}}}\frac{\varrho_{\text{m}} U_{\text{m}}^2}{2} = \frac{\alpha L \overline{\nu} \varrho_{\text{m}} U_{\text{m}}}{2 D_{\text{H}}^2} \tag{9}$$

$$\frac{\Delta P_{\text{slug}}}{\frac{1}{2}\varrho_0 U_0^2} = \overline{\lambda}\frac{L}{D_{\text{H}}}\frac{\overline{\varrho} U_{\text{m}}^2}{\varrho_0 U_0^2} = \frac{\alpha L \overline{\nu} \varrho_{\text{m}} U_{\text{m}}}{\varrho_0 U_0^2 D_{\text{H}}^2} \tag{10}$$

If the over-pressure created by the vapor slug is higher than the minichannel pressure loss, the slug can grow and purge the minichannel. This condition can be written as Eq. (11) and in non-dimensioned form as Eq. (12).

$$\Delta P_{\text{slug}} > \Delta P_{\text{channel}} \tag{11}$$

$$\frac{\Delta P_{\text{slug}}}{\frac{1}{2}\varrho_0 U_0^2} > K_1 \tag{12}$$

Thus K_1 is the critical threshold to be reached. Viscosity, density and average velocity of the two-phase flow to be purged must be determined. With the average vapor quality it is possible to estimate the product between the density and average velocity of the two-phase flow. Thus if

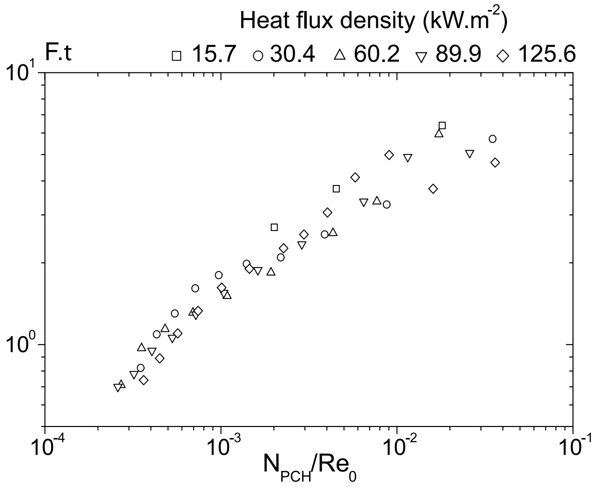

Flow Boiling Instability, Figure 10 Non-dimensioned oscillation frequency as a function of $N_{\text{pch}}/\text{Re}_0$

we consider Eq. (13), the solution of the enthalpy equation gives Eq. (14). The heated perimeter for a rectangular microchannel $(d + 2e)$ will henceforth be referred to as δ for the purpose of mathematical simplification.

$$\varrho_0 U_0 L_{\text{V}} \frac{\text{d}\chi_{\text{V}}}{\text{d}z} = \frac{Q_{\text{W}}(d + 2e)}{A_{\text{H}}} \tag{13}$$

$$\chi_{\text{V}}(z) = \frac{Q_{\text{W}}\delta z}{A_{\text{H}} L_{\text{V}} \varrho_{\text{L}} U_{\text{L}}} \tag{14}$$

The average vapor quality $(\overline{\chi}_{\text{V}})$ is obtained by the continuous averaging of the vapor quality along the minichannel. It can also be defined as the ratio between the average vapor mass flow rate and the total liquid flow injected (Eq. (16)).

$$\overline{\chi}_{\text{V}} = \frac{1}{L}\int_{z=0}^{z=L} \chi_{\text{V}}(z)\,\text{d}z = \frac{Q_{\text{W}}\delta L}{2 A_{\text{H}} L_{\text{V}} \varrho_0 U_0} \tag{15}$$

$$\overline{\chi}_{\text{V}} = \frac{\overline{\dot{m}}_{\text{V}}}{\dot{m}_0} = \frac{\varrho_{\text{m}} U_{\text{m}}}{\varrho_0 U_0} \tag{16}$$

$$\varrho_{\text{m}} U_{\text{m}} = \frac{Q_{\text{W}}\delta L}{2 A_{\text{H}} L_{\text{V}}} \tag{17}$$

The average viscosity $\overline{\nu}$ is estimated from the Dukler correlation (Eq. (18)) for a homogeneous medium. Using the average vapor quality, it is deduced that the average two-phase flow viscosity is $\nu_0/2$.

$$\begin{aligned} \overline{\nu}(z) &= \nu_{\text{V}}\chi_{\text{V}}(z) + \nu_{\text{L}}\left[1 - \chi_{\text{V}}(z)\right] \\ &= \nu_{\text{L}} - \chi_{\text{V}}(z)\left[\nu_{\text{L}} - \nu_{\text{V}}\right] \end{aligned} \tag{18}$$

F

The criterion which must be satisfied in order to allow vapor slug expansion is given by Eq. (19). When it is expressed using the inlet control parameters (heat flux: Q_W; liquid inlet velocity: U_0), we obtain

$$\frac{\alpha L \nu_0 \varrho_m U_m}{2\varrho_0 U_0^2 D_H^2} > K_1 \tag{19}$$

$$\frac{Q_W}{U_0^2} > K_1 \frac{4\varrho_0 A_H L_V D_H^2}{\alpha \nu_0 \delta L^2} \tag{20}$$

The threshold of Eq. (20) will be referred as K_2 in further calculations. The relation between K_1 and K_2 is given by Eq. (21) which only depends on physical and geometric parameters. The uncertainty of the threshold is only due to the uncertainty of the hydraulic diameter of the minichannel.

$$\frac{K_2}{K_1} = \frac{\alpha \nu_0 \delta L^2}{4\varrho_0 A_H L_V D_H^2} \tag{21}$$

Using this theoretical threshold it is possible to link the critical pressure loss to a critical heat flux through Eq. (22). There exists a critical pressure loss for a given heat flux, fluid and geometry which destabilizes the two-phase flow.

$$\frac{\Delta P^c_{\text{channel}}}{Q^c_W} = \frac{\varrho_0}{2}\frac{K_2}{K_1} = \frac{\alpha \nu_0 \delta L^2}{8 A_H L_V D_H^2} \tag{22}$$

Key Research Findings

Research over the last decade has provided a huge amount of data on flow boiling instabilities in microchannels. As far as we know today, the instabilities which occur in microchannels appear in the same way as in classical channels (see Table 2). Scaling laws have been evidenced for the stability transition criteria, such as the oscillation frequency of the instabilities, as has been shown in the previous sections. This enables us to conclude that all flow boiling instabilities in microchannels have at least one origin, which is space confinement. However, other phenomena, such as coupling with the experimental loop or the injection device, can lead to other supplementary instabilities.

Future Directions for Research

The literature provides studies on flow boiling in single and parallel microchannels. Both configurations lead to flow instabilities which are clearly identified. The specificity of flow instabilities in microchannels is the appearance of intermittent dryout which can lead to vapor recoil. New experiments on a smaller scale need to be performed to investigate the phenomena which occur at the scale of a bubble. In such confinements where the bubble size is close to or bigger than the hydraulic diameter, the physics involved does not seems to be the classical physics used to model or study pool boiling or flow boiling in ducts. The physical description required to build the theory and the models needs to be close to the triple line.

Such instabilities also appear for different gravity levels, which is also a research subject investigated over the last decade. The ESA (European Space Agency) and CNES (French Space Agency) currently fund research programs on boiling on a microscale either in pool boiling at the scale of a bubble or for flow boiling. The objective is to enable the industrial development of compact heat exchangers working in microgravity. Experiments must be performed in microgravity, using for example parabolic flights (Novespace®) during which it is possible to create microgravity conditions (± 0.05 g) lasting about 20 s.

Cross References

▶ Boiling and Evaporation in Microchannels
▶ Bubble Dynamics in Microchannels
▶ Droplet and Bubble Formation in Microchannels
▶ Pressure-Driven Two Phase Flows

References

1. Wu HY, Cheng P (2003) Two large-amplitude/long-period oscillating boiling modes in silicon microchannels. 1st International Conference on Microchannels and Minichannels. ASME, Rochester, pp 629–633
2. Qu W, Mudawar I (2003) Measurement and prediction of pressure drop in two-phase micro- channels heat sinks. Int J Heat Mass Transf 46:2737–2753
3. Hetsroni G, Mosyak A, Segal Z, Pogrebnyak E (2003) Two-phase flow patterns in parallel micro-channels. Int J Multiphase Flow 29:341–360
4. Peles YP (2003) Two-phase boiling flow in microchannels – instabilities issues and flow regime mapping. In: 1st International Conference on Microchannels and Minichannels, Rochester
5. Bergles AE (1976) Review of instabilities in two-phase systems. In: Two-phase flows & heat transfer. NATO advanced study institute, Istanbul, pp 383–423
6. Fritz W (1935) Maximum volume of vapor bubbles. Phys Z 36:379
7. Brutin D, Topin F, Tadrist L (2003) Experimental study of unsteady convective boiling in heated minichannels. Int J Heat Mass Transf 46(16):2957–2965
8. Brutin D, Tadrist L (2004) Pressure drop and heat transfer analysis on flow boiling in a minichannel: influence of the inlet condition on two-phase flow stability. Int J Heat Mass Transf 47(10–11):2365–2377
9. Brutin D, Tadrist L (2006) Destabilization mechanisms and scaling laws of convective boiling in a minichannel. J Thermophys Heat Transf Underpress 20(4):850–855
10. Bergles AE (2003) Critical heat flux in microchannels: Experimental issues and guidelines for measurements. In: 1st Inter-

national Conference on Microchannels and Minichannels, Rochester
11. Li HY, Lee PC, Tseng FG, Pan C (2003) Two-phase flow instability of boiling in a double microchannel system at high heating powers. 1st International Conference on Microchannels and Minichannels. ASME, Rochester, pp 615–621

Flow Boiling in Microchannels

► Boiling and Evaporation in Microchannels

Flow Boiling in Narrow Channels

► Boiling and Evaporation in Microchannels

Flow in Channels with 3D Elements

ZHEMIN WU, DONGQING LI
Department of Mechanical Engineering,
Vanderbilt University, Nashville, TN, USA
zhemin.wu@vanderbilt.edu

Synonyms

Flow in microchannels with 3D roughness; Flow and mass transport through rough microchannels

Definition

Electrokinetic or pressure-driven liquid flow in microchannels with three-dimensional (3D) surface roughness generated by manufacturing techniques or by adhesion of biological particles from the liquid.

Overview

Fundamental understanding of liquid flow through microchannels is important to the design and operation of Lab-on-a-Chip devices. The microchannel surfaces may exhibit certain degrees of roughness generated by the manufacturing techniques or by adhesion of biological particles from the liquids. The reported surface roughness elements range from 0.1 to 2 μm [1–3]. Microfabrication techniques such as photolithography can also make 3D elements inside microchannels (see Fig. 1). The surface roughness of microchannels not only increases the reaction-sensing surface area but also plays an important role in determining the flow characteristics. In early experimental investigations of flow and heat transfer in microtubes and trapezoidal microchannels, the increase in flow friction and decrease in heat transfer attributed to surface roughness effects were observed [1–3].

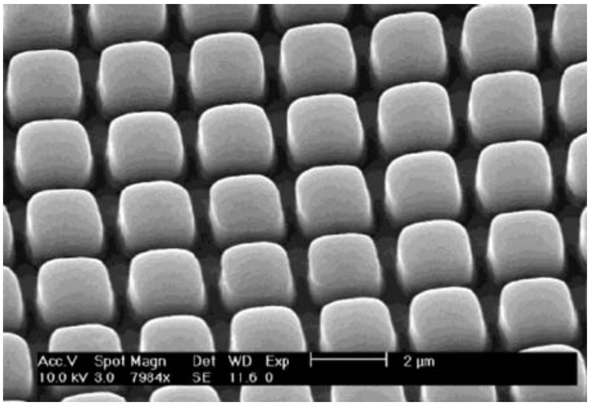

Flow in Channels with 3D Elements, Figure 1 An example of a silicon surface with microfabricated, symmetrically arranged prism elements

For low Reynolds number pressure-driven flow through microchannels, the pressure drop over the microchannels is greatly increased by the existence of the 3D surface roughness elements, and periodical fluid expansions and compressions between rough elements are generated. These were clearly predicted by the 3D numerical simulations developed by Hu et al. [4]. The roughness elements act on the flow in two ways: causing the expansion and compressions of the streamlines, and obstructing the flow directly, both giving energy losses of the fluids.
The roughness on channel walls also significantly influences the electrokinetic flows [5]. The electrical field is distorted by the presence of the nonconducting surface roughness elements, which makes the electroosmotic slip velocity of the liquid nonuniform [5]. The electroosmotic flow in a rough microchannel induces a periodic pressure field between rough elements that makes the central flow velocity smaller than that in the near-wall region, and hence reduces the overall flow rate. The induced pressure field causes an exchange of liquid between the rough element gaps and the central flow, causing an even-out effect [5]. The flow congestion and flow circulation can be obtained in microchannels with heterogeneously charged 3D elements (i. e., with different zeta potentials) and a tidal wave-like concentration field is found in heterogeneous channels with oppositely charged rough elements [6]. The electrokinetic flow behaviors in rough microchannels were verified by using the current monitoring technique and particle tracking technique [7].
As an application, the flow in rough microchannels was applied theoretically in the nucleic acids extraction process [8], which is the first critical step for many nucleic acid probe assays. Using a microchannel with 3D prismatic elements on the channel wall can dramatically increase the surface area-to-volume ratio and hence

enhance the nuclei acid adsorption on the wall. The opportunity for molecule adsorption is also increased due to the induced pressure resisting the central bulk electroosmotic flow. It is found that decreasing the electroosmotic flow velocity or the channel height enhances nuclei adsorption.

Cross References

- ► Electroosmotic Flow (DC)
- ► AC Electro-Osmotic Flow
- ► Combined Pressure-Drive Flow and Electroosmotic Flow
- ► Electrokinetic Flow in Porous Media
- ► Electroosmotic Flow in Heterogeneous Microchannels

References

1. Mala GM, Li D (1999) Flow characteristics of water through microtubes. Int J Heat Fluid Flow 20:142
2. Qu W, Mala GM, Li D (2000) Pressure-driven water flows in trapezoidal silicon microchannels. Int J Heat Mass Transf 43:353
3. Qu W, Mala GM, Li D (2000) Heat transfer for water flow in trapezoidal silicon microchannels. Int J Heat Mass Transf 43:3925
4. Hu Y, Werner C, Li D (2003) Influence of 3D surface roughness on low-Reynolds pressure-driven flow through microchannels. Fluid Eng 125:871
5. Hu Y, Werner C, Li D (2003) Electrokinetic transport through rough microchannels. Anal Chem 75:5747
6. Hu Y, Werner C, Li D (2004) Influence of the 3D heterogeneous roughness on electrokinetic transport in microchannels. J Colloid Interface Sci 280:527
7. Hu Y, Xuan X, Werner C, Li D (2007) Electroosmotic flow in microchannels with prismatic elements. Microfluid Nanofluid 3:151
8. Hu Y, Li D (2007) Modeling of nucleic acid adsorption on 3D prisms in microchannels. Anal Chem Acta 581:42

Flow Control

- ► Microflaps
- ► Turbulence Control (Microflap, Microballoon, Microsynthetic Jet)

Flow of Coolants in Micro-Conduits

- ► Microscale Cooling Devices

Flow Cytometer Lab-on-Chip Devices

Jongin Hong, Jennifer R. Lukes
Department of Chemistry, Imperial College London, South Kensington Campus, London, UK
hong.jongin@gmail.com, jrlukes@seas.upenn.edu

Synonyms

Micromachined flow cytometer; Microfabricated flow cytometer; Micromachined Coulter counter; Microfabricated Coulter counter; Miniaturized fluorescence-activated cell sorting devices

Definition

Flow cytometry is a popular technique for counting and sorting individual cells or particles. Also, it is used for measurement of various physicochemical characteristics and distribution of cell populations. A flow cytometer Lab-on-a-Chip is a microfluidic tool for flow cytometry that is made using microfabrication techniques. It incorporates many components and functionalities of a typical room-sized laboratory onto a small chip.

Overview

Reynolds' late 19th century principles of laminar flow and 20th century advances in flow microscopy, cell counting techniques and ink jet technology form the intellectual foundations of flow cytometry [1]. Moldvan (1934) was the first to suggest an instrument for identifying single cells using a microscope with a photodetector. Before Coons (1941) directly labeled antibodies with fluorescent dyes, there was no technique for visualizing cells and identifying their physical structure and orientation. Microscopes equipped with cameras or photodetectors enabled the precise quantitative analysis of fluorescence intensity patterns within the field of view [1]. Kamentsky and Melamed (1965) developed a microscope spectrometer that measured and recorded ultraviolet absorption and the scatter of blue light arising from the flow of cells. Then, in 1967, they modified the spectrometer to create a spectrophotometric cell sorter with electronic actuation, which separated cells of predetermined optical properties from a large population of cells in suspension. In particular, the monoclonal antibody technique, which was invented by Georges Köhler and Cesar Milstein in 1975, also led to a vast increase in the number of cellular constituents that could be specifically stained and used to classify cells.

Wallace Coulter invented a non-optical means of counting and measuring the size of particles suspended in a conducting fluid (1953). In this approach, cells displaced conducting solution while flowing through an orifice, resulting in increases of electrical resistance measured across the orifice. Crosland-Taylor (1953) was the first to introduce the principle of hydrodynamic focusing, in which particles injected into a faster stream of fluid flowing in the same direction could be spatially confined. Fulwyler (1965)

developed an electronic cell sorting device that combined Coulter methodology with ink jet technology. The device added a charge to the droplets containing cells differently according to the cell volume measured in a Coulter aperture, thereby allowing deflection of the droplets under an electrostatic field. Dilla and coworkers (1969) developed the first fluorescence-detection cytometer with the principle of hydrodynamic focusing. The cytometer, which included a photomultiplier and an argon ion laser, was configured with the axes of flow, illumination and detection all orthogonal to each other.

Improvements on the above pioneering works in flow cytometry and related fields have led to the development of modern flow cytometers for various applications. Currently, there are a number of commercial flow cytometers that can sort up 10,000 cells per second without affecting cell viability. Through different staining techniques and minor modifications of conventional flow cytometry, analytical capabilities have been extended from single molecules to large biological particles, including carbohydrates, lipids, cholesterol, proteins, ions, chromosomes, DNA/RNA, islet cells and embryonic stem cells. Although conventional flow cytometers provide rapid and reliable analytical cell sampling capabilities, complex optical components like focused laser beams, various optical filters/photodetectors, and complicated electronics make the conventional flow cytometer bulky and expensive. Moreover, its operation still relies on specialized personnel, complex preparation procedures and a relatively high volume of cells or particles to be analyzed.

Over the past decade, the drawbacks of conventional flow cytometers coupled with the increased need for miniaturization and sophisticated analysis have motivated the development of the micromachined flow cytometer. It has many potential benefits including disposability, smaller size, lower consumption of sample, reagents and power, enhanced performance and inexpensive instrumentation. Also, the integration of the microfluidic and detection systems on a single chip can enhance the reliability and functionality of the flow cytometer. For example, Miyake et al. (1991) was the first to report a multilayered flow chamber that could generate a hydrodynamically focused narrow stream of fluorescent dyes and particles within a water sheath. Similarly, Sobek et al. (1993) demonstrated a micromachined flow cytometer fabricated on quartz wafers and consisting of two symmetric parts bonded together to define the geometry of a sheath flow chamber and a detection channel. Later, Larsen et al. (1997) and Koch et al. (1999) presented designs for micromachined Coulter counters that could count individual particles; however, electrical testing of these designs was not performed. Alternatively, Aletendorf et al. (1996) demonstrated a bench top optical flow cytometer utilizing silicon V-groove flow channels, in which a laser diode and a photodiode detector were used for cell counting. Nowadays, the goal of novel micromachined flow cytometers is to enable more precise and rapid manipulation of cells or particles and to take advantage of different driving forces for controlling fluid flows. Also required is the integration of optics and electronics to perform detection and sorting of cells or particles of interest. Herein, we present the basic principles of flow cytometer operation and discuss and recent progress in micromachined flow cytometers. We recommend that the audience read [1, 2] for understanding these fields.

F

Basic Methodology

Basic Principles

A flow cytometer is an instrument for counting and sorting suspended cells or particles in a stream of fluid and analyzing their physicochemical characteristics. A flow cytometer has several key components: (a) a flow cell that carries the suspended single cells through the instrument and past the light source, (b) a light or excitation source, typically a laser that emits light at a specific wavelength, (c) a detector that is capable of measuring the light signals from the cells, (d) data-analysis electronics that characterize the multiparametric properties of the cells, and (e) a sorter that is able to separate each cell according to the predetermined optical properties. The basic operation principles of a flow cytometer are shown in Fig. 1. Before suspension in a sample reservoir, cells or particles can be combined with various fluorescent probes that stain cellular components to elucidate functions of interest. The suspended cells or particles are aspirated into a flow cell through a nozzle by air pressure applied on top of the sample or a syringe controlled by a precise motor. A flow cell delivers the sample stream to the center of the sheath flow and then accelerates the flow to squeeze the central sample flow into a narrow stream and to maintain a cell spacing within the surrounding fluid sheath. This phenomenon, called hydrodynamic focusing, is the keystone of a flow cytometer (Fig. 1a).

Every single cell or particle is then intercepted as it flows by a fixed light source like a laser beam and then the light is either scattered or absorbed. Scattered light is either reflected or refracted. In most flow cytometers, there are two types of scatter; forward-angle scatter and right-angle scatter. Forward-angle scatter is the amount of light scattered at small angle ($< 10°$) in the forward direction with respect to the direction of the laser beam, and is known to be related to the size of the particle. Right-angle scatter consists of photons scattered at 90° with respect to the incident laser beam, and depends primarily on the cell

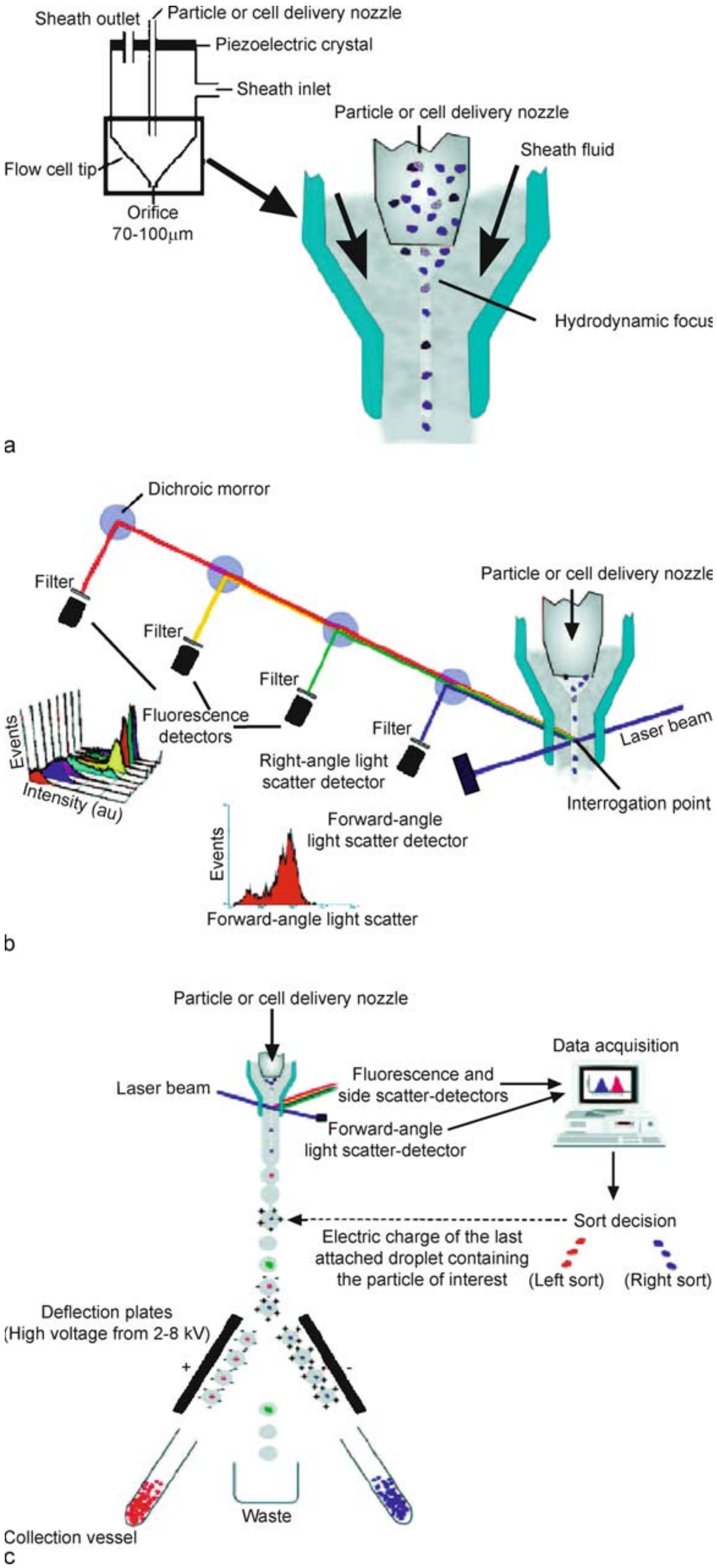
Sheath outlet
Particle or cell delivery nozzle
Piezoelectric crystal
Sheath inlet
Flow cell tip
Orifice
70-100μm
Particle or cell delivery nozzle
Sheath fluid
Hydrodynamic focus
a
Dichroic morror
Filter
Filter
Filter
Filter
Particle or cell delivery nozzle
Fluorescence
detectors
Events
Intensity (au)
Right-angle light
scatter detector
Laser beam
Interrogation point
Forward-angle
light scatter detector
Events
Forward-angle light scatter
b
Particle or cell delivery nozzle
Data acquisition
Laser beam
Fluorescence and
side scatter-detectors
Forward-angle
light scatter-detector
Sort decision
Electric charge of the last
attached droplet containing
the particle of interest
(Left sort)
(Right sort)
Deflection plates
(High voltage from 2-8 kV)
+
-
Waste
Collection vessel
c

structure and granularity. Absorbed light of the appropriate wavelength may be re-emitted as fluorescence if the cell contains a naturally fluorescent substance or fluorescent dyes are added to the sample. The fluorescent signal helps to identify cells of interest. The scattered or re-emitted light is collected by a number of detectors where the stream passes through the light beam: one photodetector in line with the light beam (a forward scatter detector) and other photodetectors perpendicular to it (side scatter and fluorescent detectors). A set of dichroic mirrors and filters split the optical signals in spectral wavelength ranges. The resulting electrical pulses are digitized and then the data is stored, analyzed and displayed through a computer system (Fig. 1b).

The amount of scattered or fluorescent light subsequently needs to be displayed for interpretation. These profiles are normally displayed as single dimension (histogram) or two dimensions (cytogram). A histogram displays a frequency distribution of the cell for any particular parameter, whereas a cytogram displays the data in two dimensions like a spatial map. Both histograms and cytograms can represent the population distribution of scattered and fluorescent signals received from a large number of cells or particles. Also, multiple fluorescent dyes can be used simultaneously in a flow cytometer. Therefore, this allows a multiparametric analysis at the single cell level and so it can be used to select and purify a specific subset of cells or particles within a population.

The most common method for sorting is the stream-in-air configuration in which a continuous stream of cells or particles emerging from a nozzle is converted into droplets containing single cells using mechanical vibration of the nozzle tip. If a stream of liquid is vibrated along its axis, the stream will break up into droplets. The characteristics of this droplet formation are governed by an equation: $v = f \cdot \lambda$, where v is the velocity of the stream, f is the frequency of the vibration applied, and λ is the distance between droplets [1]. After forming the droplets in a regular pattern, a charge is added the droplets. Then, the charged droplets are deflected by a strong electric field into different collecting chamber (Fig. 1c).

Coulter Counter

The Coulter counter is a resistive pulse technique of particle sizing invented in 1953. The measurement principle is as follows. A particle passes through a pore and displaces conducting fluid in that pore (Fig. 2). The resistance of a pore R_p increases by δR_p when a particle enters since the particle displaces conducting fluid. Assuming that the current density is uniform across the pore, δR_p can be estimated for a pore aligned along the z-axis by [3]

$$\delta R_p = \rho \int \frac{dz}{A(z)} - R_p \quad (1)$$

where $A(z)$ represents the cross sectional area occupied by fluid at a particular z-position of the pore containing a particle, and ρ is the resistivity of the fluid. The particle resistivity is assumed infinite in this analysis. For a spherical particle of diameter d in a pore of diameter D and length L, the relative change in resistance is expressed as [3]

$$\frac{\delta R_p}{R_p} = \frac{D}{L}\left[\frac{\arcsin(d/D)}{\sqrt{1-(d/D)^2}} - \frac{d}{D}\right] \quad (2)$$

where L is the pore length. For cases where cross section $A(z)$ varies quickly, i. e., when $d \ll D$, Debolis and Bean (1970) formulated an equation based on approximate solution to the Laplace equation:

$$\frac{\delta R_p}{R_p} = \frac{d^3}{LD^2}\left[\frac{D^2}{2L^2} + \frac{1}{\sqrt{1+(D/L)^2}}\right] F\left(\frac{d^3}{D^3}\right) \quad (3)$$

where $F(d^3/D^3)$ is a numerical factor that accounts for the bulging of the electric field lines into the pore wall. If R_p is the dominant component of measurement circuit, then relative changes in the current are equal in magnitude to those in the resistance.

Fabrication

We briefly describe the general methods to fabricate flow cytometers. Conventional flow cytometers contain flow chambers or cuvettes made from glass or quartz tubes, with an injector inserted into the middle of the tube. Recently, microfabricated flow cytometers have been developed using photolithography and micromachining techniques. The two kinds of micromachining techniques are surface micromachining, where thin layers of new materials are added to a substrate, and wet bulk micromachining, where a substrate is etched isotropically or anisotropically depending on etchants. Typical substrates are silicon, glass and quartz. In addition, soft microlithography can replicate microfluidic components by casting polymer against a master mold. The master mold is a positive relief structure that hollows out negative relief structures in the cured polymer cast against it. Poly(dimethylsioxane) (PDMS), which is an optically

Flow Cytometer Lab-on-Chip Devices, Figure 1 Basic principles of a flow cytometer: (**a**) flow cell and the principle of hydrodynamic focusing, (**b**) flow cytometer optics, (**c**) principle of electrostatic sorting based droplet formation [13] ◀

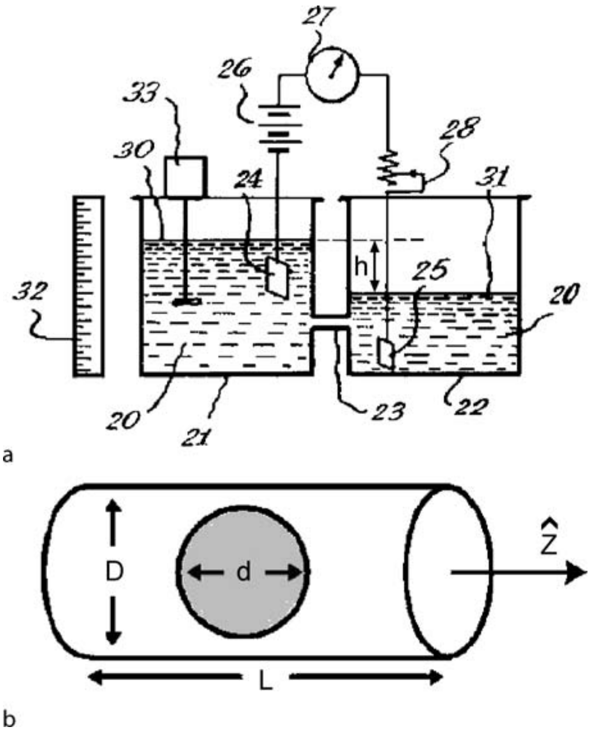

Flow Cytometer Lab-on-Chip Devices, Figure 2 Coulter counting: (**a**) Schematic overview of the Coulter counter from the original patent. A conductive liquid suspending the particles to be analyzed (20) is moved through a small aperture (23) from one vessel (21) into the other (22) by different levels of liquid (30,31). The impedance over the aperture is measured using two electrodes (24, 25) that are connected to a readout circuit, which consists of a battery (26), current meter (27) and a variable resistor (28). The instrument is equipped with an agitator (33) to keep the particles suspended and a graduated scale alongside the vessel (32) to measure the change of volume, [12] and (**b**) a schematic diagram of spherical particle of diameter d in a pore of diameter D and length L [3]

transparent and mechanically soft elastomer, is the most commonly used for fabricating ► microfluidic systems. The soft lithography is very suitable for demonstrating prototype devices at the early stages of development. Further information in this area can be found in ► microfabrication techniques.

Key Research Findings

Hydrodynamic Focusing

The microfluidic device design and the relative flow rate of sheath and sample play important roles in hydrodynamic focusing. Lee et al. (2001) proposed a theoretical model to predict the width of focused center flow inside a microfabricated flow cytometer [14]. Based on potential flow theory, they derived the equation for flow inside a planar microfabricated flow cytometer under the two dimensional situation shown in Fig. 3a. The flow is considered laminar, and the diffusion and mixing between focused stream and sheath flows is assumed negligible. With these assumptions, conservation of mass yields.

$$\dot{m}_{\text{in}} = \rho_1 \bar{v}_1 \cdot D_1 + \rho_2 \bar{v}_2 \cdot D_2 + \rho_3 \bar{v}_3 \cdot D_3 \tag{4}$$

$$\dot{m}_{\text{out}} = \rho_a \, \bar{v}_a \, \cdot D_a \tag{5}$$

$$\bar{v}_2 \cdot D_2 = \bar{v}_c \cdot d \tag{6}$$

where $\dot{m}_{\text{in}}$ and $\dot{m}_{\text{out}}$ are mass flow rates (per unit depth) of the inlet and outlet flows; D_1, D_2 and D_3 are the width of inlet channels 1, 2, and 3, respectively; $\bar{v}_1$,$\bar{v}_2$ and $\bar{v}_3$ are average velocities in sections 1, 2 and 3; $\bar{v}_a$ is the average velocity inside the outlet section; $\bar{v}_c$ and d are velocity and width of focused beam, respectively. If the sheath flow rate is much higher than the sample flow rate, the final output flow will be dominated by the sheath flow and then the velocity profile can be approximated as a parabolic flow of just the sheath fluid. It follows that

$$v_c = v_{\max} = 1.5\bar{v}_a \tag{7}$$

Therefore, the width of the focused center stream can be derived as

$$\begin{aligned} d &= \frac{\bar{v}_2}{v_c} \cdot D_2 \\ &= \frac{\rho_a D_a}{1.5\big(\rho_1(\bar{v}_1/\bar{v}_2)(D_1/D_2) + \rho_2 + \rho_3(\bar{v}_3/\bar{v}_2)(D_3/D_2)\big)} \end{aligned} \tag{8}$$

This expression indicates that the width of the focused stream is inversely proportional to the ratio of sheath flow rate to sample flow rate and proportional to volumetric flow rate of the sample flow. Lee et al. also performed experiments showing two-dimensional hydrodynamic focusing could achieve a focused stream with width less than 10 μm when the sample was injected at the middle of the outer nozzle and the ratio of sheath flow rate to sample flow rate was increased (Fig. 3b). Their experimental results agree well with theoretical predictions.

Chung et al. (2003) investigated the difference between two- and three-dimensional hydrodynamic focusing using numerical simulation based on Poiseuille flow, which is pressure driven flow between stationary parallel plates with no contribution from gravity, and experimental observations with scanning confocal microscopy. Two- and three-dimensionally focused streams were achieved by planar and two-level channel geometries using poly(dimethylsiloxane) (PDMS). They found that two dimensional focusing was not as successful as three

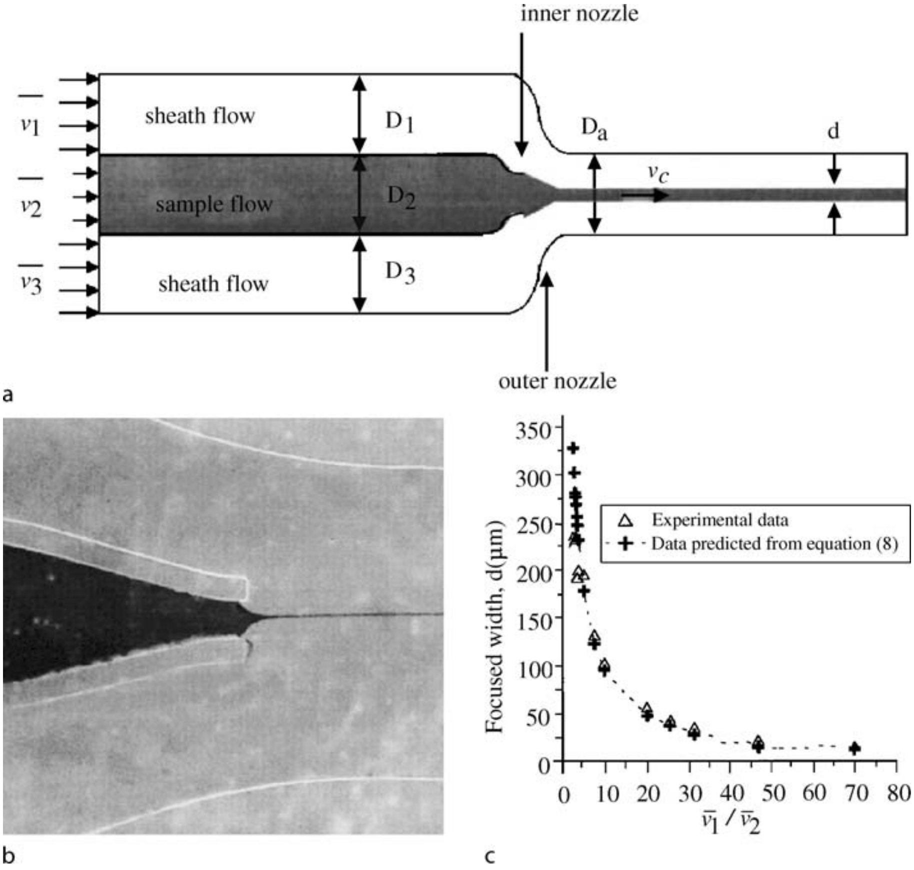

Flow Cytometer Lab-on-Chip Devices, Figure 3 Hydrodynamic focusing for mircofabricated flow cytometers: (**a**) schematic diagram of a 2-dimensional microfabricated flow cytometer for a theoretical approach, (**b**) photograph of focused sample stream inside a flow cytometer, and (**c**) variation of the width of the focused stream as a function of the relative flow rates of sample and sheath [14]

dimensional focusing. That is, three dimensional focusing better confined sample particles in the vertical direction and made detection signals more stable.

Although hydrodynamic focusing with sheath fluid serves as a standard technology in conventional and microfabricated flow cytometers, large amount of sheath fluid is requires to process a small amount of sample and continuous pumping of sheath fluid at high flow rates is needed to generate a narrow sample stream. Further reduction in the size and volume of the whole system is also limited. Alternative methods are electrokinetic focusing, which uses direct current (DC) at high voltages, and dielectrophoretic focusing, which uses alternating current (AC) to focus particles and liquids into a narrow stream. These topics are of significant research interest but are beyond the scope of this entry.

Optical Detection

Micromachined flow cytometers open new opportunities to integrate optical components and solid-state devices with the microfluidic platform. Tung et al. (2004) investigated the feasibility of silicon-based PIN photodiodes, which consisted of P–N junctions with an intrinsic region in the middle combined with self-aligned optical fibers for multi-color excitation and multi-angle fluorescence detection in PDMS-based flow cytometers [4]. Replacing photomultiplier tubes (PMTs) and avalanche photodiodes (APDs) with PIN photodiodes for fluorescence detection in flow cytometry presented significant technical challenges, since the fluorescent signals generated from biological cells only produce a few nA of current in the PIN photodiodes. Thus, Tung et al. applied a lock-in amplification technique to increase the signal-to-noise ratio (S/N). At a single interrogation point, multi-color laser excitation and multi-angle fluorescence detection were demonstrated to detect hydrodynamically focused fluorescent microspheres and biological particles (Fig. 4).

Lee et al. (2003) proposed a novel approach to integrate polymeric optical waveguides onto microfabricated flow cytometers. Instead of inserting optical fibers through

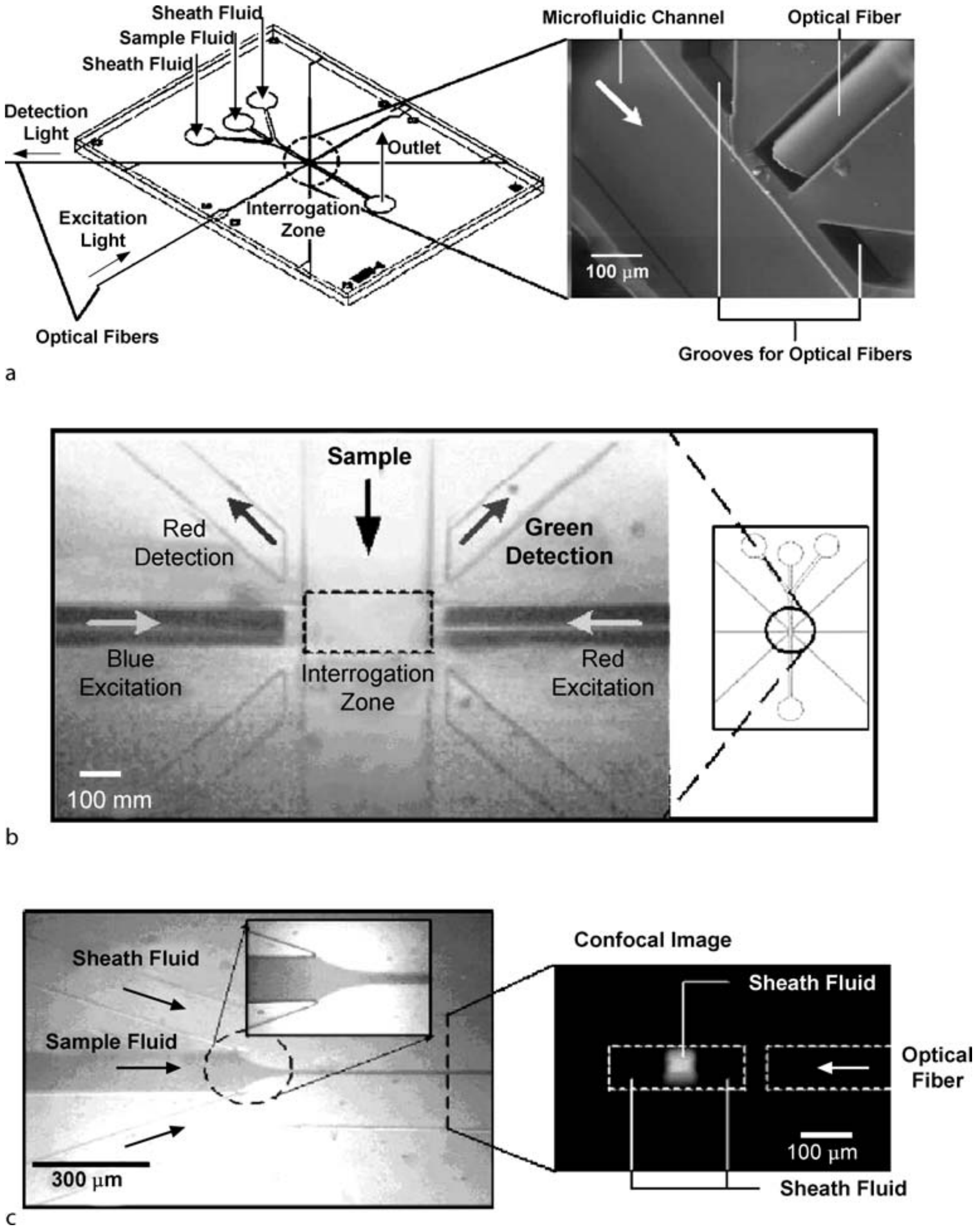

Flow Cytometer Lab-on-Chip Devices, Figure 4 Integrated optical components on a PDMS-based flow cytometer: (**a**) design of PDMS observation channel with embedded optical fibers (arrangement shown with 45° angle between excitation and detection optical fibers), (**b**) arrangement of optical fibers for two-color excitation/detection experiment, and (**c**) optical and confocal microscope photos demonstrating hydrodynamic focusing (the water containing fluorescein is excited using a blue ($\lambda = 440$ nm) laser) [4]

microfabricated grooves, they developed a new method to embed photoresist (SU-8)-based optical waveguides with a thin layer of spin-on-glass (SOG). The seamless configuration and large difference in refractive indices between SU-8 (1.80) and SOG (1.36) enhanced the efficiencies of light guiding and coupling. The working principle is that the detection light can propagate in the waveguide by total internal reflection. Light intensity, which changes when cells or particles pass through the interrogation point, is collected by the other waveguide buried on the other side of the microfluidic channel. The advantage of this method is that it permits counting and analysis of cells and particles without microscopes and delicate optical alignment.

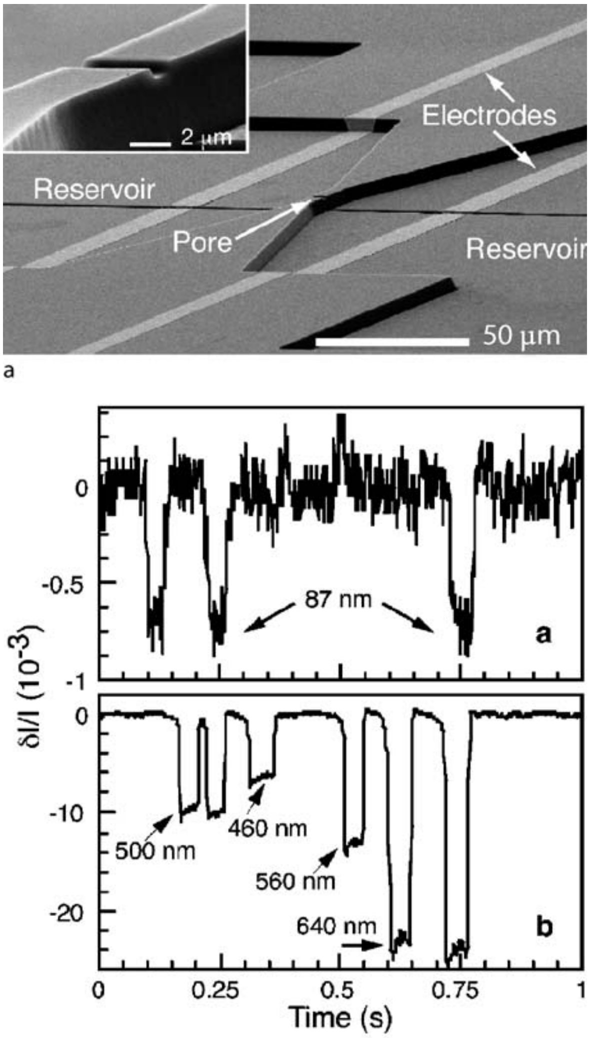

Flow Cytometer Lab-on-Chip Devices, Figure 5 Microfabricated Coulter counter: (**a**) scanning electron microscope image of the Coulter counter. The 3.5 μm deep reservoirs and the inner Ti/Pt electrodes, which control the voltage applied to the pore but pass no current, are only partially shown. The inset shows a magnified view of this devices' pore, which has dimensions $5.1\times1.5\times1.0 \mu m^3$ and (**b**) relative changes in baseline current versus time for a mono-disperse solution of 87 nm diameter latex colloids and a poly-disperse solution of latex colloids with diameters 460, 500, 560, 640 nm [3]

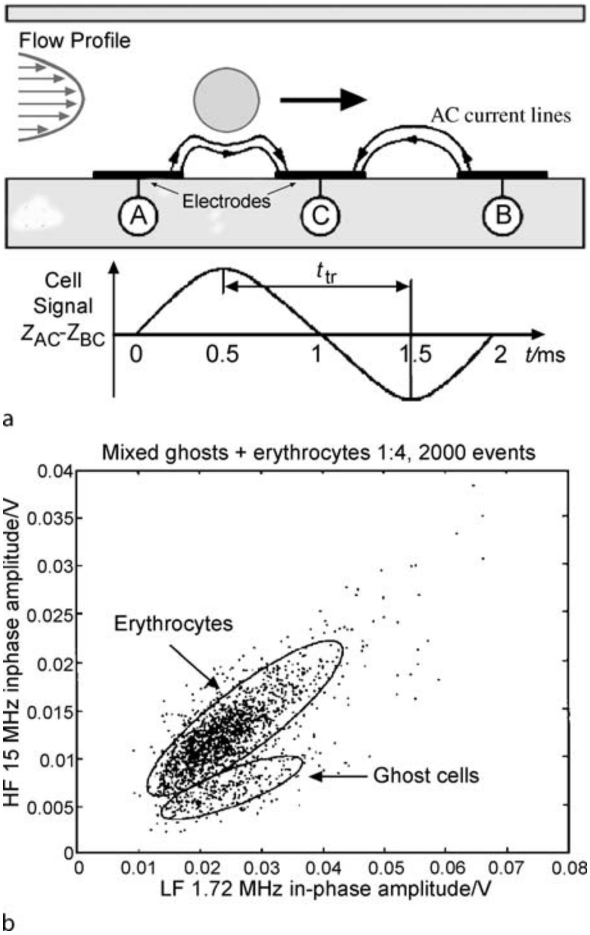

Flow Cytometer Lab-on-Chip Devices, Figure 6 Micromachined impedance flow cytometer: (**a**) side schematic view of the microchannel showing a particle passing over three electrodes (A, B, and C). The impedance signal is measured differently ($Z_{AC} - Z_{BC}$). As the distance between two measurement areas and time t_{tr} separating the signal spikes are known, the speed of the particle can be calculated, and (**b**) Signal inphase amplitude of 2000 erythrocytes and ghost cells recorded simultaneously for 2 frequencies [15]

Electrical Detection

In optics-based flow cytometry, molecular level detection individual cells or particles is enabled by tagging biomarkers with various fluorescent probes. These probes inherently alter the cells/particles: tagging requires an incubation step, antigenic exposure risks triggering cell differentiation, and non-surface probes require membrane permeabilization. Although some leukocytes can be separated without the use of probes by their forward scatter and side scatter signals, the efficiency is not as high as that of fluorescence-based optical detection. Thus, new label-free detection methods are emerging in the field of microfabricated flow cytometers. Saleh and Sohn (2001) were the first to present a microfabricated Coulter counter on quartz substrate utilizing a four-point measurement of the current through the pore (Fig. 5) [3]. The Coulter counter was able to detect latex colloidal particles as small as 87 nm in diameter and 500 nm-diameter colloids with a resolution of ±10 nm, although its sensitivity depends on the relative size of the pore and the particle to be measured. Also, Saleh and Sohn in 2003 corrected off-axis effects

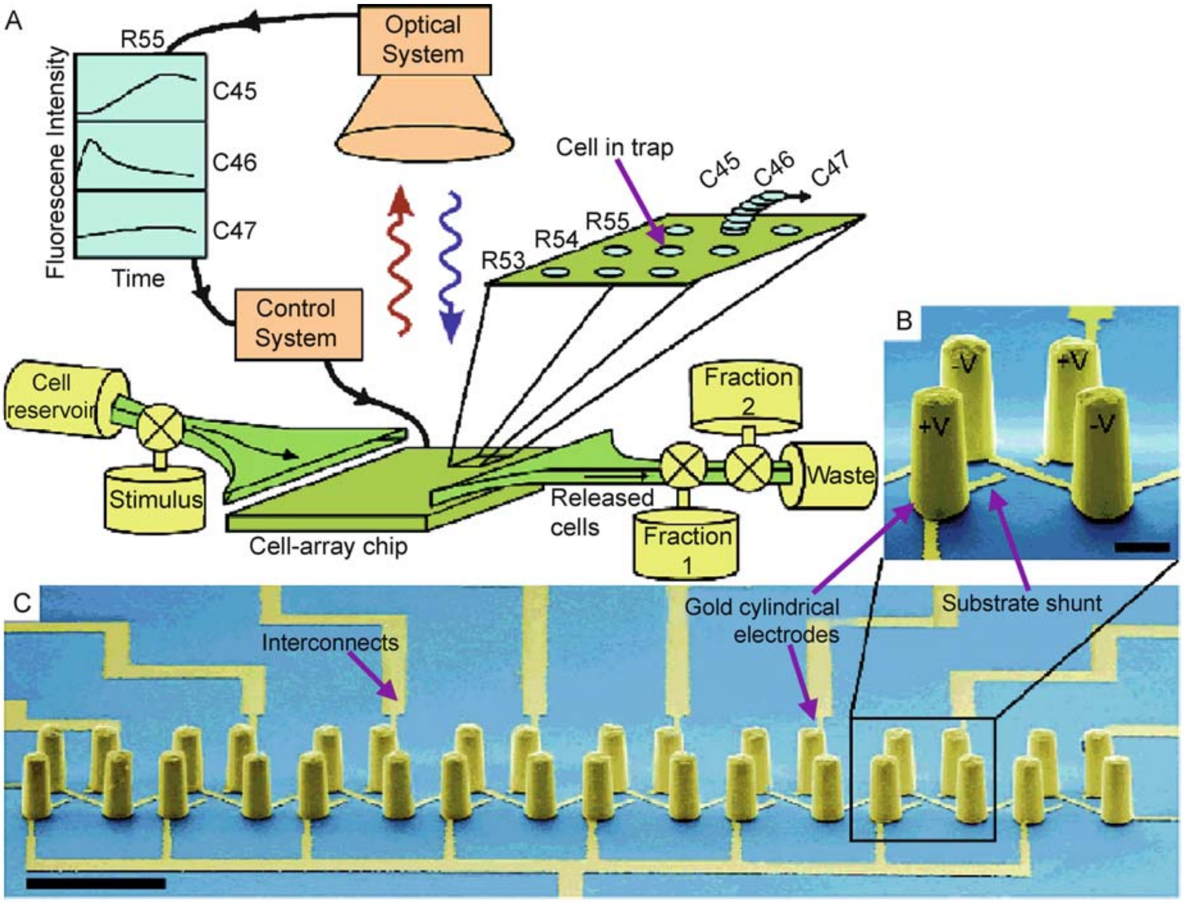
A
Optical System
R55
Fluorescene Intensity
C45
C46
C47
Time
Cell in trap
C45 C46 C47
R53 R54 R55
Control System
Cell reservoir
Stimulus
Cell-array chip
Fraction 2
Waste
Released cells
Fraction 1
B
-V
+V
+V
-V
C
Interconnects
Gold cylindrical electrodes
Substrate shunt

a

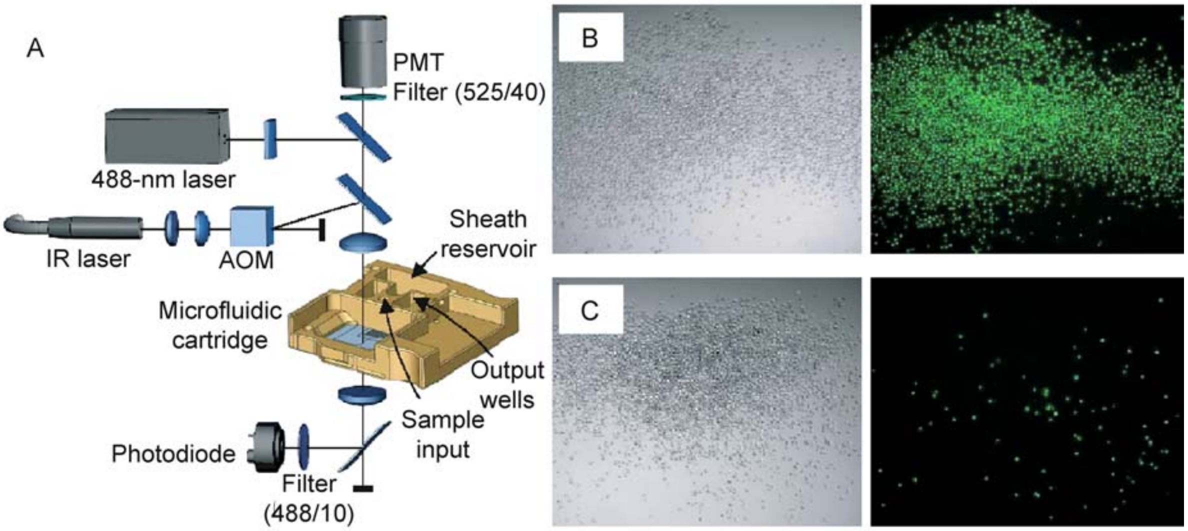
A
PMT
Filter (525/40)
488-nm laser
IR laser
AOM
Sheath reservoir
Microfluidic cartridge
Output wells
Sample input
Photodiode
Filter (488/10)
B
C

b

Flow Cytometer Lab-on-Chip Devices, Figure 7 Cell sorting: (**a**) a dielectrophoresis-based cell trapping and sorting system: A. Schematic representation of the system, showing single cells loaded onto the cell-array chip and one cell, in row 55 and column 46, being sorted by the control system into the fraction collectors after acquisition of dynamic luminescence information from the entire array, B. Pseudocolored scanning electron micrograph (SEM) showing a single trap consisting of four electroplated gold electrodes arranged trapezoidally along with the substrate interconnects, C. SEM of a completed 1×8 trap array. Scale bars: B. 20 μm, C. 100 μm [8] and (**b**) an optically switched microfluidic fluorescence-activated cell sorter: A. Schematic representation of the cell sorter instrument and the microfluidic cartridge. The near-infrared laser and 488 nm laser are focused through the same lens onto the microfluidic chip. The presence of a cell in the analysis region is detected by a photodiode and the fluorescence of that cell is measured by the PMT. Based on a gating of the fluorescence signal the AOM is triggered to optically switch the cell (GFP-positive cells are switched to the collection well). Sample is loaded directly onto and off the cartridge by pipette. Windows on the bottom of the collection wells permit viewing of the sorted populations. IR, infrared. (B,C) Brightfield (left) and fluorescence (right) images of the resulting cell populations in the collection well (B) and waste well (C) are shown for a typical sort of the GFP-expressing HeLa cells [9] ◀

due to particles traveling off the central axis of the pore. Off-axis particles take longer to transit the pore due to the parabolic distribution of fluid velocity within the pore, causing wider pulses and large changes in electrical resistance due to the nonuniform distribution of electric current density. They proposed that off-axis effects can be effectively removed in the data analysis of a given population by the nearly linear correlation between height ΔR and width τ in measured resistance pulses. Nieuwenhuis et al. (2004) presented the integrated Coulter counter that has a controllable liquid aperture, defined by a non-conductive sheath liquid surrounding the conductive sample stream, whereas microfabricated flow cytometers reported before had a fixed Coulter aperture [5]. The dynamic Coulter aperture to the particle size enables to achieve optimal sensitivity and to prevent clogging.

Impedance spectroscopy of living biological cells over a wide frequency range gives various information such as cell size, membrane capacitance, and cytoplasm conductivity as a function of frequency. At low frequencies, the cell membrane offers a significant barrier to current flow and so the cell size can be measured as in Coulter counting. At intermediate frequencies, the decrease in plasma membrane polarization reduces the capacitance of the cell. This effect is known as β-dispersion or dielectric relaxation. At high frequencies, the plasma membranes are minimally polarized and so, above the β-relaxation frequency, the signal contains information about the heterogeneous structure and dielectric properties of the cell interior. Renaud and co-workers (2001) demonstrated successfully that a microfabricated cell impedance analyzer could discriminate between cell types and particle sizes with the rate of over 100 samples per second [15]. Simultaneous impedance measurements at multiple frequencies enabled the differentiation of subpopulations in the mixture of normal erythrocytes and erythrocyte ghost cells, illustrating the capability of identifying different cell types (Fig. 6). Recently, they proposed a model to determine the influence of different cell properties including size, membrane, capacitance and cytoplasm conductivity on the impedance spectrum in their flow cytometers and showed the discrimination between unlabelled neutrophils (granular, 12–15 μm diameter, multi-lobed nucleus), lymphocytes (agranular, 5-10 μm, large nucleus), and monocytes (agranular, 12-18 μm diameter, U-shaped nucleus) [16].

Cell Sorting

The ability of high speed sorting based on the predetermined properties of cells or particles has been an important issue in the development of microfabricated flow cytometers. Quake and co-workers (1999) presented disposable fluorescence-activated cell sorting (FACS) of microbeads and bacterial cells in a microfluidic device based on electrokinetic switching of liquid streams [7]. When a fluorescently labeled cell was detected in the input channel, the sample stream flowing from an inlet to a waste port was quickly switched by reversing the electric field to deliver target particles selectively to a sample collector. This technique demonstrated sorting of fluorescent microbeads and E. coli at the rate of ~ 10 beads/s and 20 cells/s, respectively. Later, Fu et al. integrated pneumatically actuated components which enabled self-contained and automated cell trapping and sorting at a higher rate (26–44 cells/s)

Voldman et al. (2002) introduced an innovative dynamic array cytometer for single-cell assays and sorting based on the principle of dielectrophoresis, in which forces arise on particles in a nonuniform electric field due to induced polarization or charge dipoles (Fig. 546a) [8]. Their asymmetric extruded quadrupole geometry allowed noncontact trapping of multiple single cells, holding them against disrupting fluid flow and increasing the trapping efficiency. Also, the novel dielectrophoretic trap could be physically arrayed and electrically addressed. By controlling the potential of one electrode in each trap, selected subpopulations of cells could remain trapped or be released from the trap based on the fluorescence information.

Wang et al. (2005) described a high throughput cell sorter with all-optical control switch for live cells (Fig. 546b) [9]. The optical forces, which depend on the optical power and relative optical properties of the particle and its surrounding fluidic medium, were used to deviate the cell from the

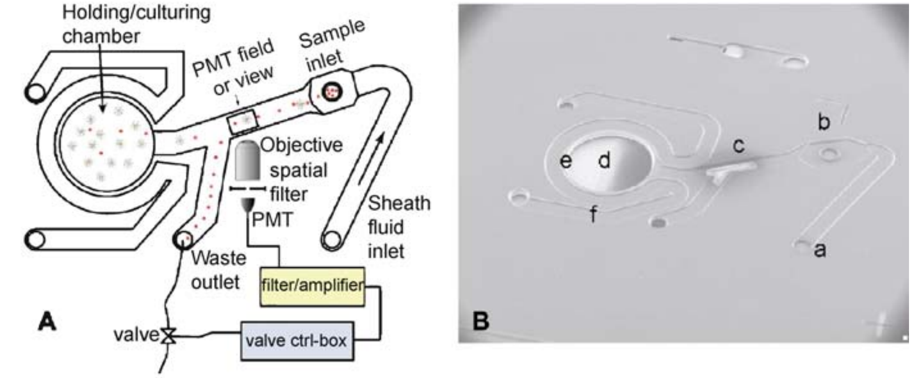

a

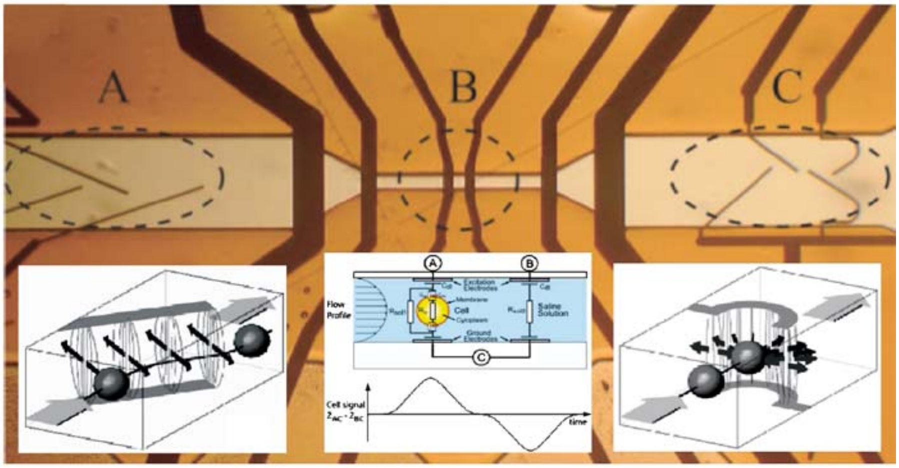

b

c

Flow Cytometer Lab-on-Chip Devices, Figure 8 Flow cytometer Lab-on-a-Chip: (**a**) Set-up and SEM image of the second-generation micro cell sorter chip with integrated holding/culturing chamber (a, sheathing buffer inlet, b, chimney sample inlet, c, detection zone, d, holding/culturing chamber, e, sieve to allow diffusion of nutrients and confinement of cells, f, channel for draining excess liquid during sorting and for feeding fresh media to the cells during cultivation, g, waste outlet) [10], (**b**) Integrated impedance flow cytometer (A, cell dipping electrodes, B, detection electrodes, C, sorting/trapping electrodes) [6, 16], and (**c**) a photograph of the cell counting/sorting system incorporated with a microfabricated flow cytometer chip [11]

flow stream to a sufficient degree to that it was directed toward the target output channel. They have shown that sorting runs of cell populations ranging from as few as 1,000 cells up to 280,000 cells can be completed in less than an hour.

Flow Cytometer Lab-on-a-Chip

A flow cytometer Lab-on-a-Chip should incorporate many components and functionalities of a typical room-sized laboratory onto a small chip. Although the perfect flow cytometer Lab-on-a-Chip has not yet emerged, we introduce novel examples for this issue. Recently, Wolff et al. (2003) designed and developed a new pressure-driven microfabricated FACS device with advanced functional components including a chamber for holding and culturing the sorted cells and monolithically integrated waveguides for cell analysis (Fig. 8a) [10]. They achieved a 100-fold enrichment of fluorescent beads at a throughput of 12,000 cells per second while sorting fluorescent latex beads from chicken red blood cells. In particular, a new structure for coaxial sample sheathing and hydrodynamic focusing was built on the principle of *the smoking chimney*, where the sample was sheathed and carried downstream from the inlet like a wisp of smoke from a chimney. Renaud and co-workers (2005) have developed a microfabricated impedance flow cytometer that incorporates deflective dielectrophoresis barriers and controlled pressure driven liquids flows (Fig. 8b) [6]. The integrated flow cytometer had the following capabilities;

- cells trapped in electric cages could be subjected to two or more different fluids for cell transfection
- cells could be brought into an adjacent liquid (reagent) stream and washed shortly afterwards
- cells could be characterized by the opacity, which is the ratio of the impedance magnitude at a high frequency to a low frequency.

Lee and co-workers (2006) presented a compact cell counting/sorting system with several essential components including a micromachined flow cytometer chip device, an optical detection system and a data analysis and control system to achieve the functions of cell sample injection, optical signal detection and cell collection. Its dimensions were 37 cm in length, 16 cm in width and 18 cm in height (Fig. 8c) [11].

Future Directions for Research

We can envision that the future ► flow cytometer Lab-on-a-Chip devices will miniaturize and integrate monolithically a variety of optical components like light sources, photodetectors, filters, waveguides and lenses that can detect multiple fluorescence colors simultaneously. Other potential approaches without optical components include integrated flow cytometers based on electrochemical impedance detection, electrokinetic focusing/switching/sorting, MEMS-based filtering/pumping/switching, and electromagnetic isolation. Also, future cytometers may combine optical components with non-optical components monolithically for high throughput multi-parametric analysis of cells or particles.

Cross References

► Electrokinetic Motion of Cells and Nonpolarizable Particles
► Cell Sorting
► Cell-Based Assays Using Microfluidics
► Control of Microfluidics
► Electrokinetic Focusing
► Fluorescence Measurements
► Fluorescent Labeling
► Lab-on-a-Chip Devices for Particle and Cell Separation
► Lab-on-a-Chip Devices for Sample Extraction
► Lab-on-a-Chip Devices for Separation-Based Detection
► Based Detection
► Microfabrication Techniques
► Microfluidic Systems for High-Troughput Screening

References

1. Givan AL (2001) Flow cytometry: first principles. Wiley, New York
2. Huh D, Gu W, Kamotani Y, Grotberg JB, Takayama S (2005) Microfluidics for flow cytometric analysis of cells and particles. Physiol Meas 26:R73–R98
3. Saleh OA, Sohn LL (2001) Quantitative sensing of nanoscale colloids using a microchip Coulter counter. Rev Sci Inst 72(12):4449–4451
4. Tung YC, Zhang M, Lin CT, Kurabayashi K, Skerlos SJ (2004) PDMS-based opto-fluidic micro flow cytometer with two-color multi-angle fluorescence detection capability using PIN photodiodes. Sens Actuators B 98:356–367
5. Nieuwenhuis JH, Kohl F, Bastemeijer J, Sarro PM, Vellekoop MJ (2004) Integrated Coulter counter based on 2-dimensional liquid aperture control. Sens Actuators B 102:44–50
6. Cheung K, Gawad S, Renaud P (2005) Impedance spectroscopy flow cytometry: on-chip label-free cell differentiation. Cytom Part A 65A:124–132
7. Fu AY, Spence C, Scherer A, Arnold FH, Quake SR (1999) A microfabricated fluorescence-activated cell sorter. Nat Biotechnol 17:1109–1111
8. Voldman J, Gray ML, Toner M, Schmidt MA (2002) A microfabrication-based dynamic array cytometer. Anal Chem 74:3984–3990
9. Wang MM, Tu E, Raymond DE, Yang JM, Zhang H, Hagen N, Dees B, Mercer EM, Forster AH, Kariv I, Marchand PJ, Butler WF (2005) Microfluidic sorting of mammalian cells by optical force switching. Nat Biotechnol 23(1):83–87
10. Wolff A, Perch-Nielsen IR, Larsen UD, Friis P, Goranovic G, Poulsen CR, Kutter JP, Telleman P (2003) Integrating advanced

functionality in a microfabricated high-throughput fluorescent-activated cell sorter. Lab Chip 3:22–27
11. Yang SY, Hsiung SK, Hung YC, Chang CM, Liao TL, Lee GB (2006) A cell counting/sorting system incorporated with microfabricated flow cytometric chip. Meas Sci Technol 7:2001–2009
12. Coulter WH (1953) Means for counting particles suspended in a fluid. US Patent 2,656,508
13. Bernas T, Grègori G, Asem EK, Robinson JP (2006) Integrating cytomics and proteomics. Mol Cell Proteomics 5(1):2–13
14. Lee GB, Hung CI, Ke BJ, Huang GR, Hwei BH, Lai HF (2001) Hydrodynamic focusing for a micromachined flow cytometer. J Fluids Eng 123:673–679
15. Gawad S, Schild L, Renaud P (2001) Micromachined impedance Spectroscopy flow cytometer for cell analysis and particlesizing. Lab Chip 1:76–82
16. Cheung KC, Renaud P (2006) BIOMEMS for medicine: On-chip cell characterization and implantable microelectrodes. Solid-State Electronics 50:551–557

Flow Field-Effect Transistor

► Microfluidic Circuits

Flow Instabilities

► Chaotic Mixing Based on Viscoelasticity

Flow and Mass Transport Through Rough Microchannels

► Flow in Channels with 3D Elements

Flow Measurement

► Flow Rate Measurements, Methods

Flow Meters

► Velocity Sensors

Flow in Microchannels with 3D Roughness

► Flow in Channels with 3D Elements

Flow Patterns

Definition

In single phase flow, flow pattern means whether the flow is laminar or turbulent, or whether flow separation or secondary flow exists. In multiphase flow, flow pattern refers to the internal geometry of the flow; i. e., the relative location of interfaces between the phases, such as stratified and dispersed.

Cross References

► Bubble Dynamics in Microchannels

Flow Profiling

► Velocimetry
► Visualization Based on Molecular Tagging Methods

Flow Rate

► Picoliter Flow Calibration

Flow Rate Measurements, Methods

John Collins[1], Abraham P. Lee[2]
[1] Maxwell Sensors Inc., Fullerton, CA, USA
[2] Department of Biomedical Engineering and Department of Mechanical Aerospace, University of California, Irvine, CA, USA
Collins.biomint@gmail.com, aplee@uci.edu

Synonyms

Flow sensors; Flow measurement; Fluidic pressure sensing

Definition

In microfluidics, the volumetric flow rate is the volume of fluid flowing per unit time in the cross section of a microfluidic channel. The mass flow rate is significant in multiphase flow, where different fluid phases have different densities. A fluidic pressure sensor measures the pressure drop due to the flow of fluid. Velocimetry is a technique for measuring the velocity profile of fluids by means of particles which are viscously dragged by the bulk of the fluid. Under laminar flow with no slip at the wall boundaries, a parabolic velocity distribution exists, and a good

flow sensor integrates the parabolic velocity profile over the cross section of the flow.

Overview

In microfluidics, control and manipulation of fluid flow can be accomplished by pressure-driven, electrokinetic, magnetohydrodynamic, centrifugal, and capillary forces. When forces such as electrokinetic and magnetohydrodynamic forces act on the walls of a microchannel, slip in the fluid flow occurs at the walls. On the other hand, when forces such as pressure-driven forces act on the inlet or outlet, a laminar flow of fluid experiences no slip at the walls. Thus the middle of the channel flows at a higher velocity than near the walls. Figure 1 shows a microfluidic device used in a biosensing application. Figure 1a shows the flow of particles under a constant pressure gradient. Figure 1b shows the parabolic velocity profile of a flow front of high-density particles. Note that the particles in the middle of the channel travel with a higher velocity, thereby showing a lower density, and the particles near the walls travel with a lower velocity, thereby showing a higher density. Observing a statistical distribution of particles in a flow is equivalent to discretizing the entire fluid volume with velocity elements. This velocity profile can be integrated mathematically at any cross section of the fluid flow in order to compute the flow rate. The flow of a fluid with a velocity u and pressure p at a time t is given by the Navier–Stokes partial differential Eq. (1)

$$\frac{\partial \boldsymbol{u}}{\partial t} + (\boldsymbol{u} \bullet \text{grad})\, \boldsymbol{u} + \text{grad}(p) = \frac{1}{\text{Re}} \Delta \boldsymbol{u} \tag{1}$$

where Re is the Reynolds number, given by the ratio of inertial to viscous forces, and is very small for the laminar-flow regime of microfluidics. Figure 2 shows the flow of a fluid under constant pressure. The bulk fluid is dispensed by drawing the flow out at the bottom outlet and venting air at the top inlet. Figure 3 shows the flow characteristics when a constant negative pressure is applied at the outlet. These calculations were based on computational fluid dynamic (CFD) simulations using the volume-of-fluid (VOF) model for the immiscible fluids air and water. A hydrophobic material with a contact angle of 109 °C was assumed in the CFD simulation, and fluidic properties of air and water were also assumed. The fluidic impedance caused by the geometry of the channel was evaluated from the pressure–flow-rate characteristics. In the case of a hydrophobic wall, there is a threshold pressure that drives the flow against a hydrophobic force. A steady-state flow is obtained, and the flow is proportional to the pressure. Integration of the flow rate at every element of the cross section of a flow channel is performed in an ideal flow sensor.

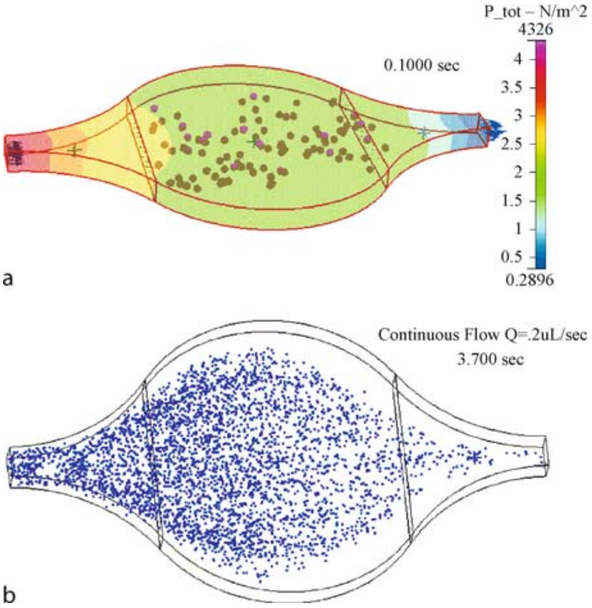

Flow Rate Measurements, Methods, Figure 1 A frame from a continuous flow of particles in a reaction chamber. (**a**) Flow of particles under a pressure gradient (the arrows at the inlet and outlet show the flow). (**b**) Flow front of high-density particles, showing a parabolic velocity profile. Note that the particles in the middle travel at a high velocity, thereby showing a low density, and the particles at the sides travel at a low velocity, thereby showing a high density

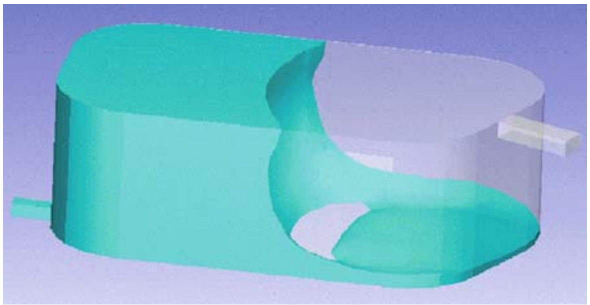

Flow Rate Measurements, Methods, Figure 2 Dispensing of fluid from a tank, where air is sent in at the inlet (top) and water is released at the outlet (bottom)

The measurement of flow rates and the performance of quantitative analysis on fluids in minute volumes is greatly advancing the development of multifunctional, high-throughput Lab-on-a-Chip devices. Traditionally, there have been many MEMS-based flow sensors for gaseous flows. In recent times, several advancements have taken place in measuring microflows of liquids. Some examples of sensing principles for the measurement of microflu-

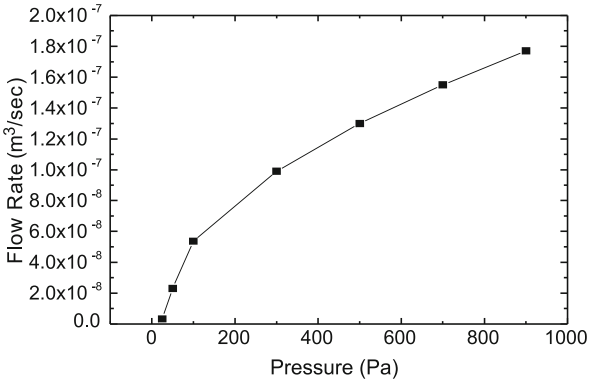

Flow Rate Measurements, Methods, Figure 3 Flow characteristics for a hydrophobic geometry of the kind shown in Fig. 2, showing the applied negative pressure and the flow rate at the outlet

idic flow include heat transfer detection [1], molecular sensing [2], noninvasive optical techniques [3], atomic-emission detection [4], streaming-potential measurements, electrical-impedance measurements [5, 6], electrochemical redox cycling [7], amperometric sensing [8], ion-selective field-effect transistors, micromechanical sensing [9], and detection of periodic flapping motion [10]. Flow sensors are critical for controlled, precision flow to enable active micrototal analysis systems.

Basic Methodology

Many of the well-established macroflow sensing methods such as the use of shear stress sensors, thermal anemometers, magnetohydrodynamic sensors, particle imaging, and fluorescent imaging have been adapted and scaled down for microfluidics. However, miniaturization and integration issues have opened up new opportunities for microflow sensing. Broadly, flow sensors can be classified as either obstructive or nonobstructive to the flow. Obstructive flow sensors add fluidic resistance to the flow, and so nonobstructive flow sensors are generally preferred. These nonobstructive flow sensors can themselves be classified into invasive and noninvasive flow sensors. In invasive flow sensors heat, electric current, or foreign substances such as fluorescent dyes or particles are added to the flow in order to perform the flow rate measurement. For example, fluorescence-correlation-spectroscopic and optical-Doppler-coherence tomographic measurements fall into this category. In noninvasive flow sensors, the sensing element does not physically make contact with the flow. Mostly, the flow sensing depends on optical parameters of the fluid, such as the refractive index, that depend on the flow rate. Sonic and radio-frequency signals can also be used for such measurements. In reality, there are no ideal noninvasive flow-sensing techniques. However, flow sensors that minimally modulate the flow optically, thermally, or electrically have been adapted for micrototal analysis applications. There is still research under way into high-sensitivity and very low-flow-rate measurements.

Time-of-flight (TOF) measurement is popular in microflow measurements. The time of flow of a pulse of temperature or of molecular tracers from one point in a microchannel to another point is characterized to measure the flow rate. An emitter and a collector are integrated into TOF sensors. Various optimizations of these sensors have been carried out, using temperature pulses or electrochemical production of molecular tracers. These sensors calculate the flow rate at one point in the cross section of the channel and are calibrated with a known flow rate. Flow measurement using microparticles captures the velocity profile at many such locations in the channel cross section and allows one to calculate the flow rate. Figure 4 shows the principle of a flow sensor using a CFD simulation of convective diffusion of heat or molecular tracers generated at an emitter. The collector in the flow sensor records a measure of the flow. The relation between the flow sensor reading and the actual flow rate is nonlinear, and the flow sensor is calibrated for a window of operation of flow measurements.

Experimental Techniques for Flow Sensing

Heat-Transfer-Detection-Based Flow Sensors

These thermal-anemometer-based flow sensors can sense very low flows in microchannels. The measurement principle is based on the thermal time of flight. The length of the heating pulse and the time of flight used in the measurement are measured in milliseconds. An example of the structure of a flow sensor is shown in Fig. 5 [1]. The structure consists of a heater in the middle, with an upstream and a downstream temperature sensor integrated into the wall of the channel. When there is no flow in the channel, heat diffuses into the two temperature sensor regions and no differential temperature is detected. An increase in the flow rate in the channel favors convection of heated fluid in the direction of the flow, and the differential temperature detected by the sensors increases.

The process flow for the fabrication of the microfluidic system includes a single or double metallization layer, a polymer layer for the fluidic system, and a glass sealing cap. There have been some efforts during fabrication to minimize the thermal-dissipation loss. The temperature difference between the two points where the sensors are located is measured with a differential current amplifier, and the flow rate is calibrated. At low flow rates, the tem-

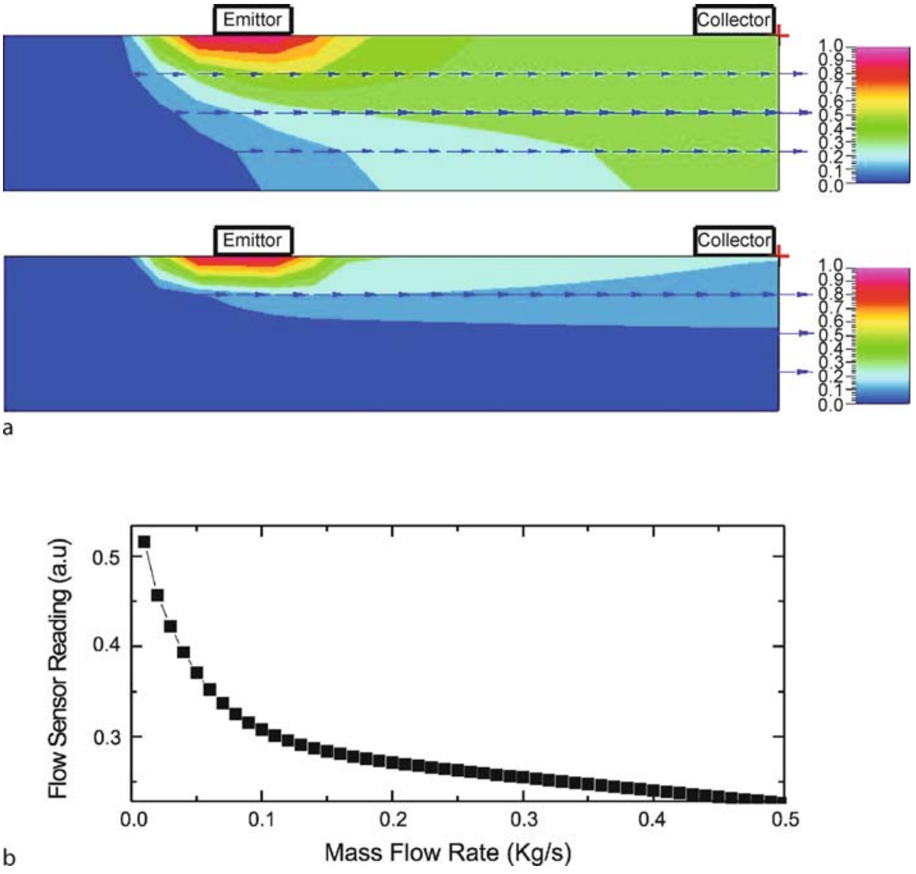

Flow Rate Measurements, Methods, Figure 4 Principle of a time-of-flight flow sensor using CFD simulation. (**a**) Convective diffusion of heat or of a molecular tracer originating from the emitter wall. (**b**) Flow sensor reading, in arbitrary units, measured at the collector

perature difference is a linear function of the flow rate as in Fig. 6. Measurements without heat insulation decrease the sensitivity of the flow sensor and increase the lower limit of flow rate detection. The distance between the heater and the sensors is optimized for the maximum differential temperature.

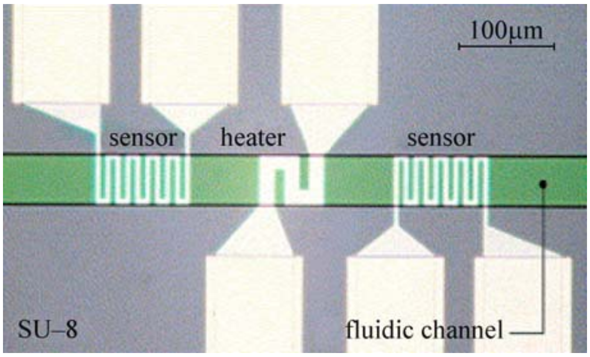

Flow Rate Measurements, Methods, Figure 5 Photomicrograph of a microfluidic mass flow sensor [1]

Micromechanical Flow Sensors

Micromechanical flow meters measure shear forces produced as a result of fluid flow. The deflection of a micromechanical plate due to the shear force can be measured optically using a system coupled to a laser deflection system. Figure 7 shows a schematic of such a plate, encapsulated in a channel. The major interaction between the fluid and the plate is through the stress field, which contains both normal (pressure) and shear stresses.

Assuming steady, unidirectional flow in the channel, the Navier–Stokes equation can be written as

$$\frac{\partial^2 u}{\partial y^2} + \frac{\partial^2 u}{\partial z^2} = \frac{1}{\mu}\frac{\mathrm{d}P}{\mathrm{d}x}$$

where u is the velocity of the fluid in the x-direction, μ is the dynamic viscosity of the fluid, and $\mathrm{d}P/\mathrm{d}x$ is the pres-

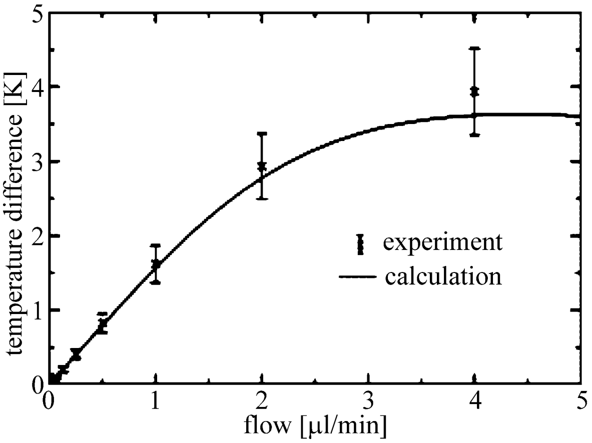

Flow Rate Measurements, Methods, Figure 6 Flow characteristics of a heat-transfer-based flow sensor. The lowest flow rate without heat insulation is on the order of 30 nL/min [1]

sure gradient along the direction of flow. The equation can be solved for the x-component of the fluid velocity to yield a relation between the volumetric flow rate and the pressure gradient, as below:

$$\frac{\mathrm{d}P}{\mathrm{d}x} = \frac{3\mu Q}{4ab^3}S$$

where Q is the volumetric flow rate, a and b are half of the height and half of the width of the channel, respectively, and S is a factor depending on the geometry of the channel. The shear stress acting on the top surface of the plate is given by

$$\tau = -z\frac{3\mu Q}{4ab^3}$$

Flow was established in the microfluidic channel shown in Fig. 7 by means of a syringe pump, and the angular deflection of the plate was monitored. The encapsulated plate provided local flow information along the length of the channel. Such plates operate independently of the absolute pressure, and sensors of this kind can provide local flow information along the length of a microfluidic system. The resolution of the angular-deflection measurement system was approximately 50 μrad, yielding a flow resolution of about 1 μL/min for the sensor. Figure 8 shows the response of the plate to a flow of ethanol [9]. The response of the flow meter was measured for flow rates ranging from 2.1 to 41.7 μL/min.

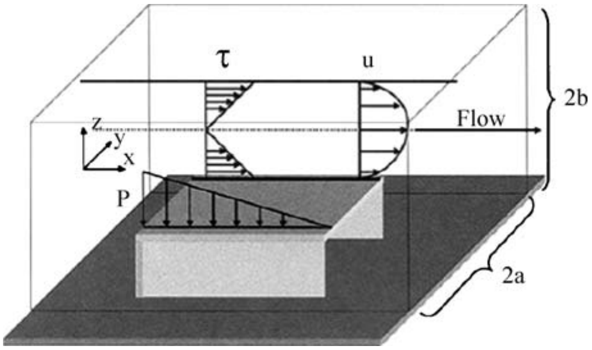

Flow Rate Measurements, Methods, Figure 7 Schematic of a plate encapsulated in a channel, showing the flow direction and the velocity profile for laminar flow above the device [9]

Molecular Sensing

This type of electrochemical flow sensor is similar to a thermal sensor; here, molecules such as oxygen are generated by applying an electric current. One such system is based on measuring dissolved oxygen in an aqueous solution using two closely spaced integrated oxygen sensors. Figure 9 shows the geometrical details of such a flow sensor [8].

Upon application of a negative potential to the working electrodes, oxygen is reduced and a current passes through:

$$O_2 + 4H^+ + 4e^- \rightarrow 2H_2O$$

During measurement, the upstream amperometric oxygen sensor consumes part of the dissolved oxygen and the response of the downstream amperometric sensor is reduced, since the two sensors are closely spaced. The velocities in the y and z directions and diffusion along the x direction can be neglected. The kinetics of the electrode reaction are fast enough to deplete the oxygen immediately, and the oxygen concentration at the surface of the working electrode is zero. The current passing through the working electrode, i, is calculated according to Faraday's law:

$$i = 4\mathrm{F}AD\frac{\mathrm{d}c}{\mathrm{d}y}$$

where F is the Faraday constant, c is the concentration of oxygen, D is the diffusion coefficient, and A is the area of the working electrode.

The difference between the responses of the two sensors is related to the convective transportation. By comparing the outputs of the two amperometric sensors, the flow rate can be obtained. Figure 10 shows the measured amperometric response of the upstream oxygen sensor at different flow rates. For curve a, a gas mixture of 10% oxygen and 90% nitrogen was bubbled into a Phosphate Buffered Saline (PBS) solution. For curve b, air was bubbled into

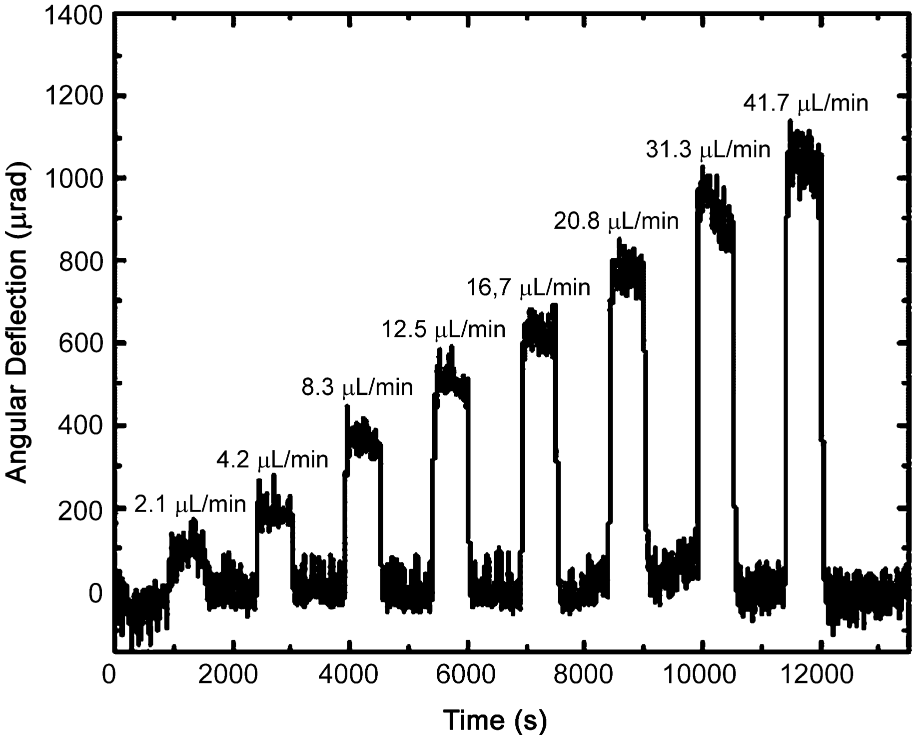

Flow Rate Measurements, Methods, Figure 8 Graph of the response of the plate to a flow of ethanol at eight different flow rates [9]

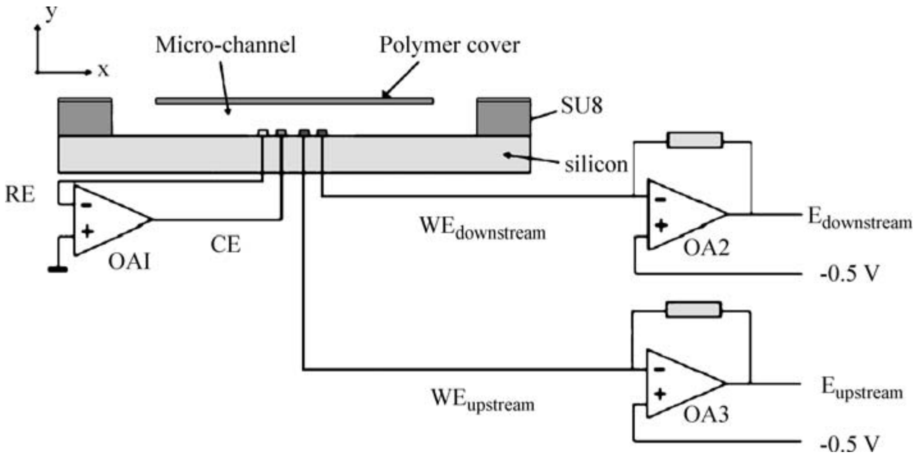

Flow Rate Measurements, Methods, Figure 9 Longitudinal cross section of a fabricated flow sensor and the related measurement setup. (The upstream and downstream oxygen sensors share a common counter and reference electrode) [8]. RE – reference electrode, CE – counter electrode, WE – working electrodes, OA – operational amplifier, SU8 – channel material

the solution. The figure shows that the current passing through the oxygen sensors is related to both the flow rate and the oxygen concentration in the solution. The ratio of the responses of the two sensors is related only to the flow rate and is not affected by the change of the dissolved oxygen concentration. This electrochemical flow sensor can detect flow rates in the region of several microliters per minute, and the advantage of this flow sensor is that no additional tracers have to be added or produced during the flow measurement.

Electrical-Impedance Sensing

Electrical-impedance-based flow sensing uses a pair of electrodes along the channel; this type of sensor is suitable for conducting solutions. An understanding of the

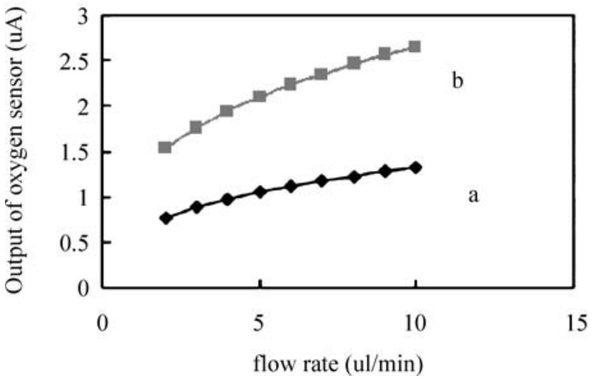

Flow Rate Measurements, Methods, Figure 10 Current passing through the upstream amperometric oxygen sensor at different flow rates for two solutions. Curve a: the solution was purged with a gas mixture of 10% oxygen and 90% nitrogen; curve b: the solution was purged with air [8]

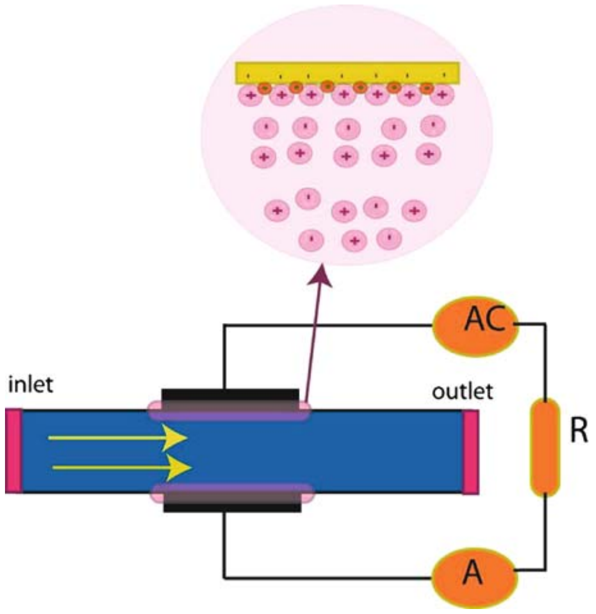

Flow Rate Measurements, Methods, Figure 11 Electrical-impedance-based flow-sensing device

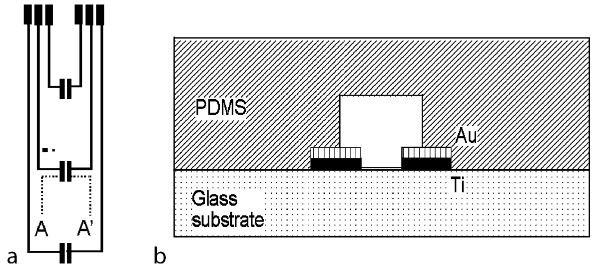

Flow Rate Measurements, Methods, Figure 12 (**a**) Layout of fabricated electrodes and wiring for measuring the current flow. (**b**) Cross section of the fabricated flow sensor through the electrodes at AA' in (**a**) [6]

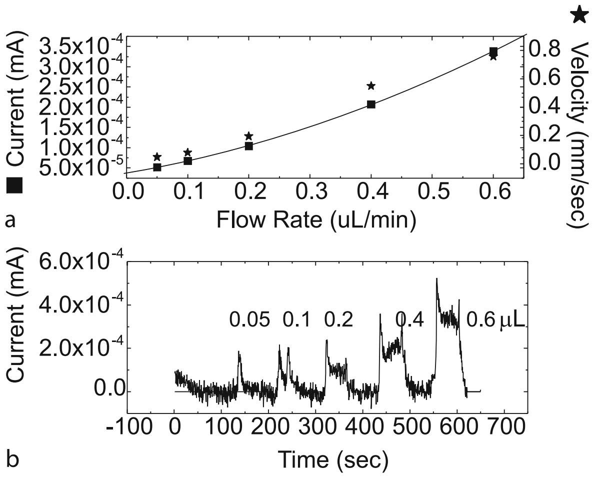

Flow Rate Measurements, Methods, Figure 13 Response of flow sensor at very low flow rates. (**a**) Instantaneous current values when the flow was varied and switched. The results in (**a**) are replotted in (**b**). The velocities of beads at different flow rates of the fluid are also shown on the right axis of (**a**). (The peaks in (**b**) correspond to the flow rate values labeled) [6]

electrical double layer is important for understanding the principle of operation of this flow sensor. When the flow rate is increased, the counterbalancing ions are replaced by the bulk solution, thereby lowering the average ionic concentration within the recording zone. This local concentration drop results in an increase in the real part of the impedance. Under hydrodynamic conditions, forced convection dominates the transport of ions to the electrodes within the flow channel. The electrical double layer formed across the channel, as shown in Fig. 11, is formed from two capacitances of the equivalent circuit, namely the diffusion layer capacitance (C_s) and the outer Helmholtz plane capacitance (C_e). The former is due to an excess or depletion of ions in the channel, and the latter is due to free electrons at the electrodes and is independent of the electrolyte concentration. The smaller of these capacitances dominates the admittance, since these capacitances are in series. The frequency of the applied ac voltage, the flow rate, and the conductivity of the fluid are the factors affecting the admittance of the fluidic system, and the flow-sensing principle is based on the optimization of these parameters.

For the electrochemical oxidation of a species A to A^{+} in a microchannel, the convective–diffusive equation for mass transport under steady-state conditions is given by

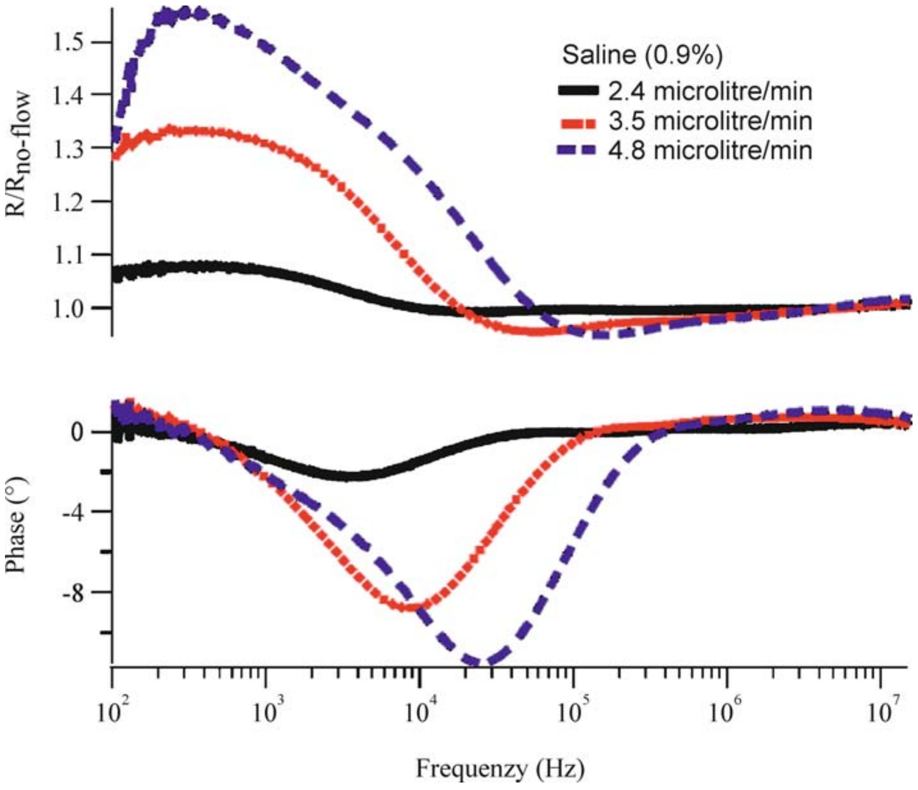

Flow Rate Measurements, Methods, Figure 14 Magnitude and phase data for the flow condition after the impedance spectra of the solution have been divided by the no-flow spectra [5]

Flow Rate Measurements, Methods, Table 1 Summary of the most popular flow sensors

Method	Flow rate limit	Sensitivity	Limitations
Heat transfer	0.01 μL/min	1.4 mV/(nL/min)	Heats the sampling fluid (~ 1 K/min/μL), complex fabrication
Mechanical	1.0 μL/min	50 μrad/(μL/min)	Moving parts, complex fabrication
Molecular sensing	2.5 μL/min	–	Aqueous fluids with dissolved oxygen
Optical	0.048 μL/min	–	No integration available
Flapping frequency	0.1 mm/s	–	Reported for gas flow, complex fabrication
Impedance sensing	0.05 μL/min	10^{-4} mA/(μL/min)	Limited to conducting fluids

Eq. (2) below:

$$D_A \frac{\partial^2 [A]}{\partial y^2} - v_x \frac{\partial [A]}{\partial x} = 0 \qquad (2)$$

$$\frac{\partial A}{\partial t} = 0 \qquad (3)$$

$$i_L = 0.925 n \mathrm{F} [A]_{\mathrm{bulk}} D_A^{2/3} Q^{1/3} w \cdot \sqrt[3]{\frac{x_\mathrm{e}^2}{h^2 d}} \qquad (4)$$

Here $[A]$ is the concentration of the species A, D_A is the diffusion coefficient, and v_x is the velocity in the direction of flow. The first term represents lateral diffusion in the microchannel, and the second term represents transport along the length of the channel. Under steady-state flow conditions, the boundary condition is given by Eq. (3). The solution of this equation predicts the mass-transport-limited current as a function of the flow rate Q as given by Eq. (4), where n is the number of electrons transferred, F is the Faraday constant, x_e is the electrode length, h is the cell half-height, d is the width of the cell, and w is the electrode width. Note that the current due to the flow of electrolyte is directly proportional to the cube root of the volume flow rate of the fluid. An ac voltage signal is considered rather than a dc voltage, since the application of an ac voltage to the flow sensor does not promote any electrode reactions. Optimization of electrical parameters such as the voltage

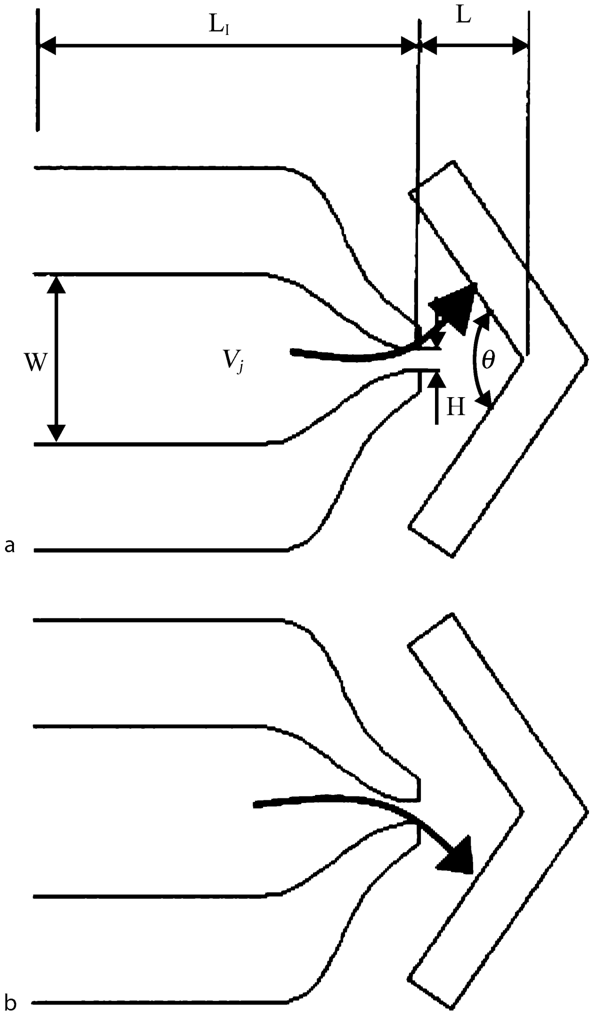

Flow Rate Measurements, Methods, Figure 15 Schematic representation of the flapping motion of the jet column for a microflow sensor with a convergent nozzle and a V-shaped plate. Periodic flapping motion occurs when the impinging jet reaches the V-shaped plate. (**a**) Jet column flaps upwards, and (**b**) jet column flaps downwards [10]

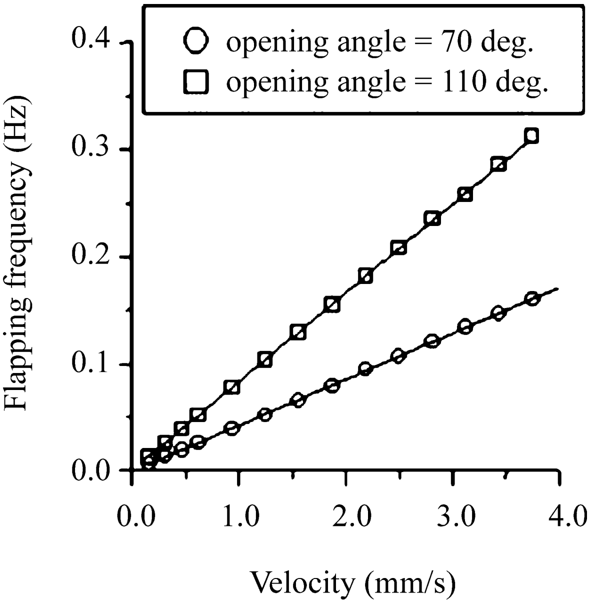

Flow Rate Measurements, Methods, Figure 16 The flow velocity is linearly proportional to the flapping frequency, and two sensors with different opening angles have similar behaviors [10]

and frequency of the ac signal is an essential condition for measuring low flow rates.

A flow sensor of this type was fabricated on a glass substrate with gold surface electrodes (Fig. 12a), and the microfluidic channel was made of PDMS. Gold of thickness 100 nm was deposited on an adhesion layer of titanium of thickness 20 nm using e-beam deposition. A spun layer of Shipley photoresist (1827) was used for patterning the metal (Fig. 12b). PDMS channels of width 500 μm were made from an SU8 mold. The glass and PDMS were bonded together after treatment with an oxygen plasma for 1 min. The fluidic channel was aligned with the parallel electrodes using a stereo microscope. The measuring instrumentation was similar to that used in strain gauge and thermocouple interfaces. The microfluidic flow was maintained at a constant flow rate using a Harvard Picoplus syringe pump. This flow sensor was capable of measuring very low values of flow rate, starting at 0.05 μL/min (< 1 nL/s). The response showed a cube root behavior even at very low flow rates, as shown in Fig. 13 [6]. The sensitivity after optimization was 5.2×10^{-4} mA/(μL/min). Fluorescent beads of diameter 2.5 μm were sent through the channel, and video microscopy of their flow profile was performed. The flow sensor results were compared with the velocity of the beads (shown by the asterisks in Fig. 13) and showed a similar response. Figure 14 shows the magnitude and phase data for the flow condition after the impedance spectra for the solution had been divided by the no-flow spectra [5].

Periodic-Flapping-Motion Detection

A flow sensor using this principle has been demonstrated [10] for gas flows; it works on the principle of detecting a periodic flapping motion of a planar jet impinging on a V-shaped plate downstream in the low-Reynolds-number regime. The Strouhal number St, which describes an oscillating flow by the ratio of the inertial forces due to unsteady flow to the inertial forces due to changes in velocity, was found to remain nearly constant if the open-

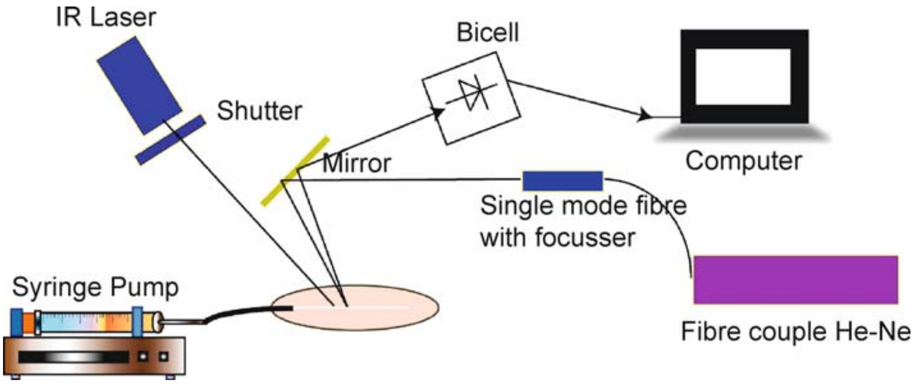

Flow Rate Measurements, Methods, Figure 17 Block diagram of the experimental setup for a backscatter interferometric flow-sensing system [3]

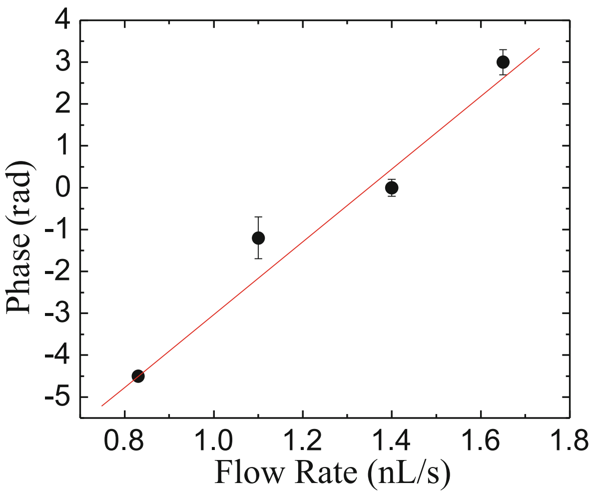

Flow Rate Measurements, Methods, Figure 18 Calibration curve of phase change vs. flow rate in a microfluidic channel [3]

ing angle of the V-shaped plate was appropriately chosen. The Strouhal number is defined as

$$\mathrm{St} = \frac{f_F L}{Vj}$$

where f_F, L, and V_j are the flapping frequency, the length of the impinging jet, and the jet exit velocity, respectively. Instead of sensing DC current or voltage signals induced by small volumes in the flow, this flow sensor detects the oscillation frequency of the periodic flapping jet, resulting in a higher sensitivity and a larger dynamic range than those of existing products. The sensor is composed of a planar convergent nozzle, a V-shaped plate downstream, and a pair of sensing resistors. A sample flow containing a dye allows the flapping motion of the impinging jet to be visualized under a microscope. The flapping motion has been confirmed experimentally even at a low flow velocity (0.15 mm/s). The flapping frequency is detected using built-in microsensing resistors driven by a constant-current circuit. Figure 15 shows a schematic of the flapping motion of the jet column for a microflow sensor with a convergent nozzle and a V-shaped plate. Even on the microscale, the flow velocity is linearly proportional to the frequency of the flapping motion, as shown in Fig. 16, and the velocity or volumetric flow rate of small amounts of flow can be measured by detecting the flapping frequency.

Optical-Sensing-Based Flow Sensors

Backscatter interferometry, optical coherent tomography, and particle-imaging velocimetry are some of the optical techniques for flow sensing. The backscatter interferometric flow-sensing system [3] may be considered to be in this category. This system is based on synchronous detection, and measurements of the phase difference with respect to fluid-heating events upstream produced by a focused IR source. The heating upstream is repeated for several cycles using a mechanical shutter inserted into the IR beam path. The frequencies of both the shutter and the detected signals are synchronous and time-varying. However, the detected signal downstream lags behind the shutter signal by the amount of time it takes for the fluid to warm up and propagate from the heating region to the detection region. The fluid flow velocity in the microchannel can be quantified by performing Fourier decomposition of the signals and calculating the phase change between the appropriate harmonics of those signals in the Fourier domain. A block diagram of the experiment is shown in Fig. 17. The interferometric backscatter detector is based on a fiber-coupled HeNe laser that illuminates a portion of an isotropically etched channel, and a position-sensitive transducer to measure fringe pattern shifts. An infrared laser with a mechan-

ical shutter is used to heat a section of the flowing volume, and the resulting refractive-index change is detected downstream as a time-dependent perturbation. The fluid velocity is quantified by changes in the phase difference with respect to the shutter signal, as in Fig. 18. This flow sensor has been established to be suitable for flow measurements in the range $3-6\,\mu L/h$ with a detection limits of $0.127\,nL/s$.

Key Research Findings

There have been reports on the theory of most types of flow sensor, and CFD simulations and experimental validations of them. Table 1 summarizes the most popular flow sensors, with the flow rate resolution or lower limit, and their limitations.

Future Directions for Research

There is a need for the development of flow sensors integrated into specific applications. Integrated micrototal analysis systems would require a feedback loop for reconfigurable and programmable assays, for controlling the dosage in the case of drug delivery, for reagent concentration control in bioassays, and for advanced on-chip micropumps that have flow regulation built in. Moreover, it is necessary to develop linear flow sensors which require no calibration and do not affect the fluid or the flow rate.

Cross References

► Bio-MicroElectroMechanical Systems (BioMEMS)
► Heat Transfer in Microchannel Flows
► Microflow Sensors
► Micromechanical Flow Sensors
► Nanoscale Biosensors
► Time-of-Flight Flow Sensors
► Velocimetry

References

1. Scholer L, Lange B, Seibel K, Schafer H, Walder M, Friedrich N, Ehrhardt D, Schonfeld F, Zech G, Bohm M (2005) Monolithically integrated micro flow sensor for Lab-on-Chip applications. Microelectron Eng 78–79:164–170
2. Wu JA, Sansen W (2002) Electrochemical time of flight flow sensor. Sens Actuators A 97–98:68–74
3. Markov DA, Dotson S, Wood S, Bornhop DJ (2004) Noninvasive fluid flow measurements in microfluidic channels with backscatter interferometry. Electrophoresis 25(21–22):3805–3809
4. Nakagama T, Maeda T, Uchiyama K, Hobo T (2003) Monitoring nano-flow rate of water by atomic emission detection using helium radio-frequency plasma. Analyst 128(6):543–546
5. Ayliffe HE, Rabbitt RD (2003) An electric impedance based microelectromechanical system flow sensor for ionic solutions. Meas Sci Technol 14(8):1321–1327
6. Collins J, Lee AP (2004) Microfluidic flow transducer based on the measurement of electrical admittance. Lab Chip 4(1):7–10
7. Amatore C, Belotti M, Chen Y, Roy E, Sella C, Thouin L (2004) Using electrochemical coupling between parallel microbands for in situ monitoring of flow rates in microfluidic channels. J Electroanal Chem 573(2):333–343
8. Wu J, Ye J (2005) Micro flow sensor based on two closely spaced amperometric sensors. Lab Chip 5(12):1344–1347
9. Czaplewski DA, Ilic BR, Zalalutdinov M, Olbricht WL, Zehnder AT, Craighead HG, Michalske TA (2004) A micromechanical flow sensor for microfluidic applications. J Microelectromech Syst 13(4):576–585
10. Lee GB, Kuo TY, Wu WY (2002) A novel micromachined flow sensor using periodic flapping motion of a planar jet impinging on a V-shaped plate. Exp Therm Fluid Sci 26(5):435–444

Flow Sensors

► Flow Rate Measurements, Methods
► Velocity Sensors

Flow Simulations in Transitional and Rarefied Regimes

► Numerical Solution of Boltzmann Equation

Flow by Surface Acoustic Waves

YANDONG GAO, DONGQING LI
Department of Mechanical Engineering, Vanderbilt University, Nashville, TN, USA
yandong.gao@vanderbilt.edu

Synonyms

Surface acoustic waves; Liquid handling; Micro-/nanofluidics

Definition

Surface acoustic wave (SAW) devices are widely used for frequency filtering in mobile communications [1]. Recently published works [2–10] have demonstrated the use of SAWs to manipulate liquid flow in microfluidic devices. A SAW is excited by the application of a radiofrequency (rf) signal to an interdigital transducer (IDT) on a piezoelectric substrate such as quartz or $LiNbO_3$. The wavelength of the SAW, having a typical value of a few micrometers, is determined by the geometry of the IDT. The amplitudes of the SAW are typically about a nanometer, depending on the applied rf power. As a SAW propagates on the surface of a piezoelectric solid, any viscous

materials such as liquids located at the solid surface will absorb most of its energy, which is indicated by an exponentially decaying amplitude. The interaction between the SAW and the liquid creates an acoustic radiation pressure (ARP) in the direction of propagation of the SAW in the liquid. This induces liquid currents or jets called acoustic streaming. This can lead to the flow of the liquid if the amplitudes of the SAWs are large enough [2].

Overview

The piezoelectric chip generating the SAW is coupled to microfluidic devices. The flow actuated by the SAWs is nonintrusive. There are no mechanical moving parts inside. It can comprise sealed containers without external plumbing. SAWs have been used to manipulate droplets [2–4] and to mix and pump liquids [5–10].
Wixforth et al. [3] have shown that droplets can be split, merged, mixed and actuated along predetermined trajectories using SAWs. Because of the nonlinear interaction between a SAW and a droplet, only droplets of certain size are agitated by a given SAW wavelength and power. This effect can be used to dispense droplets of a certain size out of others. When the SAW amplitude reaches a critical value, the pulse excitation even causes droplet ejection [4]. The ability of SAWs to stir and mix liquids is also used to eliminate non-uniformities in concentrations, as in a micro-mixer [5–8]. A higher applied rf power on the IDTs leads to a significant improvement in the mixing efficiency. However, the temperature also increases with the higher applied voltage [8]. Another feature of flow by SAWs is the rapid decay of the induced velocity field away from the IDTs. Guttenberg et al. [9] have shown that the velocity decreases with the inverse third power of the distance from the ultrasound generator.

Cross References

► Acoustic Streaming
► Transport of Droplets by Acoustics

References

1. White RM, Voltmer FW (1965) Direct piezoelectric coupling to surface elastic waves. Appl Phys Lett 7:314–316
2. Wixforth A (2003) Acoustically driven planar microfluidics. Superlattices Microstruc 33:389–396
3. Wixforth A et al (2004) Acoustic manipulation of small droplets. Anal Bioanal Chem 379:982–991
4. Bennes J et al (2005) Droplet ejector using surface acoustic waves. IEEE Ultrasonic Symp. Rotterdam, Netherland, pp 823–826
5. Zhu X, Kim ES (1998) Microfluidic motion generation with acoustic waves. Sens Actuators A 66:355–360
6. Yang Z et al (2001) Ultrasonic micromixer for microfluidic systems. Sens Actuators A, 93:266–272
7. Sritharan K et al (2006) Acoustic mixing at low Reynold's numbers. Appl Phys Lett 88:054102
8. Tseng W et al (2006) Active micro-mixers using surface acoustic waves on Y-cut 128° $LiNbO_3$. J Micromech Microeng 16:539–548
9. Guttenberg Z et al (2004) Flow profiling of a surface-acoustic-wave nanopump. Phys Rev E 70:056311
10. Renaudin A et al (2006) SAW nanopump for handling droplets in view of biological applications. Sens Actuators B 113:389–397

Flow Tagging

► Visualization Based on Molecular Tagging Methods

Flow-Through Electrodes

► Three-Dimensional Electrodes

Fluerics

► Microfluidic Circuits

Fluid Dispersion

► Hydrodynamic Dispersion

Fluidic Amplification and Oscillation

► Microfluidic Circuits

Fluidic Diodes

Definition

Fluidic devices exhibiting different hydrodynamic properties for the two different fluid flow directions.
In the *forward* direction, fluid passes through a fluidic diode easily, encountering very small hydraulic resistance (dissipance). In the other, *reverse* direction the resistance is high. When supplied with an alternating fluid flow, this difference in properties results in the fluidic rectification effect. The simplest way how to obtain the diode properties is to use a moving component blocking the available flowpath in one of the two directions. More robust, easier to make, and capable operating at a higher frequency are no-moving-part diodes.

Cross References

► Valve-Less Rectification Pumps
► Fluidic Rectification

Fluidic Logic

► Microfluidic Circuits

Fluidic Multiplexer

► Sampling Unit

Fluidic Pressure Sensing

► Flow Rate Measurements, Methods

Fluidic Pumping

Definition

A method of generating non-return (or nearly non-return) fluid flow by processing the supplied alternating flow.
Fluidic devices need a supply of the fluid with which they operate. Sometimes there is an available external fluid source and in other cases the fluid may be provided from a pressurized vessel. Most often, however, the fluidic circuits are supplied with fluid flow from a fluidic pump. This consists of two essential parts: an alternator producing an alternating flow, usually by motion of a reciprocating plunger, piston, or diaphragm, and a rectifier which changes the alternating flow into a one-way or non-return flow.

Cross References

► Fluidic Rectification
► Valve-Less Rectification Pumps

Fluidic Rectification

Definition

The process of converting an alternating fluid flow into a one-way flow.
Usually fluidic devices need for their operation a source of one-way fluid flow. Much easier to generate, however, is an alternating flow produced by reciprocating motion of a displacing component. The simples way how to rectify an alternating flow is using a non-return valve with a moving component blocking the available flowpath. In the so called *valve-less* pumps the rectification effect is obtained by using inertial effects in fluid on one of the three basic sorts of devices: fluidic diodes, fluidic jet-type rectifiers, and traveling-wave rectifiers.

Cross References

► Valve-Less Rectification Pumps
► Fluidic Diodes
► Jet-Type Rectifier
► Traveling-Wave Pump

Fluidic Sequencing Circuits

► Sampling Unit

Fluid Metering

CHENG-TSAIR YANG, CHUN-MIN SU
Flow Measurement Laboratory
Center for Measurement Standards, Industrial Technology Research Institute, Hsinchu, Taiwan
ctyang@itri.org.tw

Synonyms

Fluid metrology; Measurement standards; Weights and measures; Fluid quantification

Definition

Fluid metering concerns the measurement of fluids, liquids in particular, in the form of flow rate and/or fluid volume. Apart from accuracy and precision, the uncertainty and traceability of measurements are important factors to be considered. For micro- and nanofluidic applications, the fluid may flow in channels with dimensions of a few millimeters or below, with flow rates ranging typically from microliters to nanoliters per minute, and the fluid may be dispensed in volumes on the order of microliters to picoliters.

Overview

Microfluidics is bringing about innovations in biotechnology, medicine, energy, and many other industries, and is one of the major branches of nanobiotechnology research [1]. However, the lack of reliable and accurate flow metering or even flow monitoring is one of

the key challenges to related applications that are delaying the commercial success of many innovations, because microfluidic products, especially those for medical use, must pass certification processes to prove their capability, reliability, safety, etc. Therefore, for accurate and reliable measurement, all metering techniques and devices should be traceable to basic SI units and/or international measurement standards. In the case of microscale fluid metering, the accuracy still needs to be improved, and the traceability chain and measurement standards need to be well established.

Fluids in capillaries or microchannels which are millimeters to micrometers in diameter or width can flow in a continuous form. Sometimes, however, in many applications, the fluid is dispersed into discrete droplets, for example in the case of a liquid that is injected onto a microarray chip. Therefore, in this article, metering of fluids is categorized into continuous flow rate measurement and droplet volume measurement.

Metering of Continuous Fluid Flow

In the case of flow in microscale pathways, some important parameters in macroscale fluid mechanics remain important, but the features of the flow are very different. The influences of viscosity and surface effects are much more significant compared with fluid flow in traditional pipelines or channels. That is, the ratio of the inertial force to the viscous force (Reynolds number) is in general smaller than unity, and the ratio of the inertial force to surface tension (Weber number) is also small, so that accurate microfluidic metering is somewhat more difficult than metering for macroscopic flows. For gas flows, the effect of the Knudsen number, defined as the ratio of the molecular mean free path to the channel size, is high and cannot be ignored for microscale channels, and hence the fluid metering discussed here will be for liquids only. The Reynolds number Re, the Weber number We, and the Knudsen number Kn are expressed as follows:

$$\begin{aligned} \mathrm{Re} &= \frac{\text{inertial force}}{\text{viscous force}} = \frac{\rho U L}{\mu}\,, \\ \mathrm{We} &= \frac{\text{inertial force}}{\text{surface force}} = \frac{\rho U^2 L}{\sigma}\,, \\ \mathrm{Kn} &= \frac{\text{molecular mean free path}}{\text{channel size}} = \frac{\lambda}{L}\,, \end{aligned} \tag{1}$$

where ρ and μ are the density and dynamic viscosity, respectively, of the fluid, U is the mean fluid velocity in a channel with a characteristic length L, σ is the surface tension, and λ is the molecular mean free path.

The flow rate in microfluidics, which is a key parameter in microbioassays, drug delivery, biomedical microfluidic systems, etc., ranges from some milliliters per minute to nanoliters per minute or even less.

As shown in Fig. 1, the flow rate for medical uses ranges from about 1 nl/min to about 10 ml/min in the case of anesthesia, dialysis, and drug dosing. For analytical instruments for biomedical technology such as liquid chromatography and mass spectrometry, the flow rate is mainly in the range of nanoliters per minute to microliters per minute. For nanobiotechnology applications, such as microarrays for high-throughput diagnosis and labs-on-a-chip for biochemical analysis, the required flow rate reduces to less than 1 nl/min, a level typically referred to as *subnanoliter per minute*.

Many technologies have been developed to monitor or measure fluid flow in microdevices. The underlying mechanisms of these devices are based mainly on thermal or mechanical principles; examples of the variables to be measured are temperature, differential pressure, and drag force, which translate to thermal changes, deflection of cantilever beams, and shear strain, respectively. Most of these microflow sensors are manufactured by microelectromechanical systems (MEMS) processes without moving parts, and the flow rate measurements are mainly translated from velocity detection. For example, because flows in microchannels are in most cases laminar, the pressure drop Δp along a channel can be expressed as follows:

$$\Delta p = \mathrm{Re} \cdot f \frac{\mu L}{2 D_\mathrm{h}^2} U\,, \tag{2}$$

where f is the friction coefficient, L is the channel length, D_h is the hydraulic diameter, and U is the mean flow velocity. From Eq. (2), we can see that Δp is a linear function of U, and the flow rate, which is the product of the flow velocity and the channel cross section, can be determined by measuring the pressure difference.

Because direct measurement of flow rate by using microscale devices is difficult, most microflow sensors are designed to meter flow velocity. This is convenient and useful. For instance, a carbon nanotube (CNT) has been used as a flow sensor which generates a voltage when a polar liquid flows over it. The voltage produced shows a logarithmic dependence on the flow velocity, and the sensor exhibits a dynamic range of operation covering six orders of magnitude, from 100 nm/s to some cm/s [2]. This level of dynamic range is virtually impossible to achieve with traditional macroscale flow meters. Theoretically, multiplying the metered velocity by the cross-sectional area of the microchannel or capillary gives the flow rate. However, because of the uncertainty in the mea-

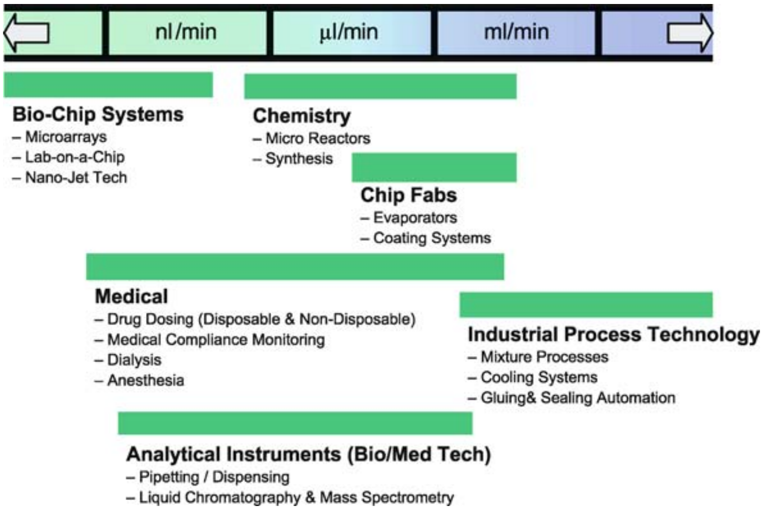

Fluid Metering, Figure 1 Flow rate ranges suitable for various industries

surement of areas in such small dimensions, the flow rate or fluid quantity is usually obtained by use of some built-in conversion after calibration.

Metering of Discrete Droplet Volumes

The measurement of discrete droplet volumes is now playing a more and more important role in various applications such as pipettes, drug dispensing systems, inkjet printer heads, and microarray biochip spotters. The purpose of dispensing is to deliver a certain amount of a liquid sample, buffer solution, or frequently used library compound from a storage vial or mother plate to a cultivation container, test tube, assay plate, or microarray chip for subsequent handling. Applications in this field today are showing a trend toward a decrease in the volume of liquid to be handled, a trend that is promoted by the common interests of reducing the cost and increasing the speed and is made possible by the advancement of micro- and nanofluidic technologies.

The instrument most often used to dispense a measured volume of liquid is a pipette (also called a pipet or pipettor). It is commonly used in research in chemistry and molecular biology, as well as in medical tests, and the typical range of liquid volume that pipettes can handle is from 0.1 μl to 20 μl. For applications in which dispensing speed and cost-effectiveness are of particular concern, such as microarray biochips, automated dispensing is a prerequisite, and the liquid volume delivered goes down to nanoliters or even picoliters. The technologies used to deliver such tiny amounts of liquid are many, and can in general be categorized into contact dispensing, noncontact dispensing, and true contactless dispensing [3].

The dispensed liquid volume is one of the key parameters that need to be properly controlled in order for experiments and tests to be well conducted. In fact, experiments may fail simply because an erroneous liquid volume has been introduced, resulting mainly from an operator's poor technique or the use of uncalibrated instrument. For applications such as high-throughput screening, making sure that the liquid volume delivered is well controlled becomes even more important, since a small difference leads to a relatively large deviation, and the accuracy of the dispensed volume can substantially affect the analysis results. Therefore, measurement of the dispensed liquid volume is indispensable for satisfactory quality control of related products.

The method of measuring macroscale liquid volumes is simple and straightforward. The mass of the dispensed liquid is measured by a balance with appropriate precision, and then divided by its density. When the performance of a dispensing tool such as a piston-operated volumetric apparatus is evaluated, water is typically adopted as the working fluid, and the temperature is, in general, the only variable that needs to be monitored and controlled. The procedure suggested by the international standard ISO 8655-6 [4] is generally followed to ensure that the measurement uncertainty is within the acceptable range. However, for micro- and nanoscale droplet dispensing, the traditional weighing method encounters difficulties in yielding accurate and consistent measurement results. Therefore, the International Organization for Standardization (ISO) published a new standard, ISO 8655-7 [5], in 2005, detailing the use of nongravimetric methods, in particular photometric and titrimetric methods, for the assessment of equipment performance. Many other methods for

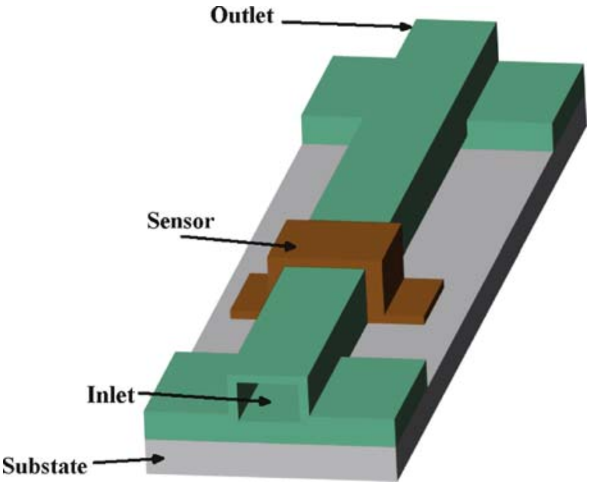

Fluid Metering, Figure 2 Example of a MEMS structure for metering the flow rate in a microchannel, based on the theory of constant-temperature anemometry

measuring or monitoring liquid volume have also been proposed, such as methods based on droplet images, fluorescent intensity, electric impedance, and interference fringes. These methods are somewhat specific and require further justification of their traceability when used in fluid metering; thus, they will not be discussed here.

Basic Methodology

Continuous Fluid Flow Measurement

Since thermal transfer accompanies the mass transfer of a fluid flow, microflow sensors based on thermal effects are the most common. An example of a MEMS thermal flow sensor is shown in Fig. 2.

When the sensor is heated and fluid flows through the sensor, heat will be taken away downstream. We can use this effect to measure the fluid flow. One application of the thermal effect is similar to the hot-wire anemometry used to measure wind velocity. Let us imagine that the sensor is made of tungsten wire, which will produce heat when electric power is supplied. If we try to keep the wire at a constant temperature, a higher current is needed for a faster fluid velocity. When thermal balance is reached, the heat generated by the electric power equals that dissipated owing to fluid flow. Therefore,

$$\begin{aligned} I^2 R_\mathrm{w} &= h \cdot A \cdot (T_\mathrm{w} - T_0) \\ &= \mathrm{Nu} \cdot (k_f/d) \cdot A \cdot (T_\mathrm{w} - T_0)\,, \end{aligned} \tag{3}$$

where I is the electric current, R_w is the resistance at the working temperature T_w, h is the heat transfer coefficient, A and d are the cross-sectional area and diameter, respectively, of the wire, Nu is the dimensionless heat transfer rate (Nusselt number), k_f is the coefficient of heat conduction, and T_0 is the fluid temperature. The dimensionless heat transfer rate can usually be expressed as

$$\mathrm{Nu} = A' + B'\,\mathrm{Re}^n\,, \tag{4}$$

where A', B', and n are empirical constants, usually determined by calibration. For a given working fluid and wire, the Nusselt number can then be expressed in terms of the mean fluid velocity U as follows:

$$\mathrm{Nu} = a + bU^n\,, \tag{5}$$

where a and b are constants to be determined. The resistance R_w at the working temperature T_w can be obtained from the following equation:

$$R_\mathrm{w} = R_0 \cdot \left[1 + \alpha\,(T_\mathrm{w} - T_0)\right]. \tag{6}$$

Thus, we have

$$\frac{(R_\mathrm{w} - R_0)}{R_0} = \alpha\,(T_\mathrm{w} - T_0)\,, \tag{7}$$

where R_0 is the resistance at a fluid temperature T_0, and α is the temperature coefficient of resistance. Equation (3) can be rewritten as the following equations:

$$I^2 R_\mathrm{w} = A \cdot (k_f/d) \cdot (T_\mathrm{w} - T_0) \cdot (a + bU^n)\,, \tag{8}$$

$$I^2 R_\mathrm{w}^2 = A \cdot R_\mathrm{w} \cdot (k_f/d) \cdot \frac{(R_\mathrm{w} - R_0)}{\alpha R_0} \cdot (a + bU^n)\,. \tag{9}$$

If the fluctuation in fluid temperature remains insignificant and the resistance R_w is made constant by keeping T_w constant with a feedback circuit, the relationship between the voltage drop in the wire V_w and the fluid velocity can be formulated as

$$V_\mathrm{w}^2 = I^2 R_\mathrm{w}^2 \propto \left(a + bU^n\right). \tag{10}$$

The coefficients can be determined by a calibration process, and the fluid velocity can then be obtained by measuring the voltage drop. When the fluid velocity has been obtained, the volumetric flow rate can be calculated by multiplying the velocity by the cross-sectional area.

A sensing line embedded in the wall of a microchannel is more complicated than a single tungsten wire, but the analysis is the same. In order to successfully integrate a suitable metering element, various sensing structures need to be designed and tested. Linearity, reliability, and sensitivity to velocity variation are key features to be concerned

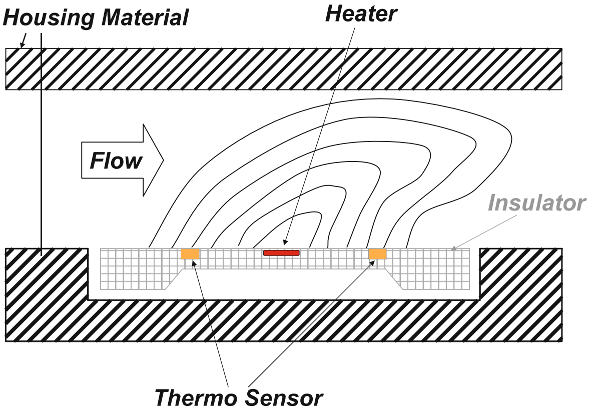

Fluid Metering, Figure 3 Illustration of the operational principle of a microflow sensor that uses a heating element to heat the fluid, and two thermosensors to measure the temperatures upstream and downstream of the element. The temperature difference is used to determine the flow rate

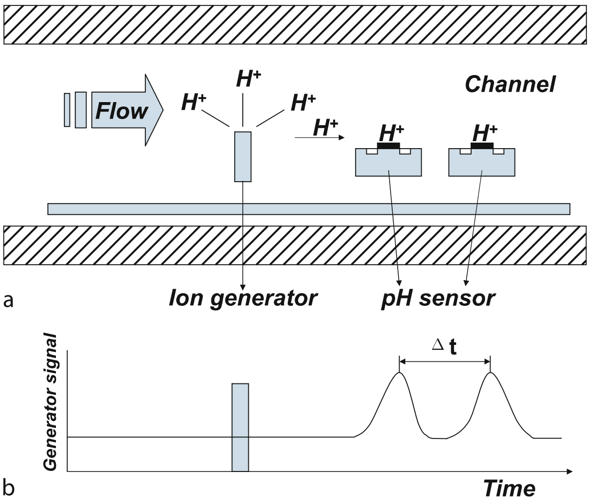

Fluid Metering, Figure 4 Illustration of the operational principle of a microflow sensor that uses an ion generator and two pH sensors to measure the flow rate. The ions follow the fluid flow, and the difference of the arrival times at the two sensors determines the flow velocity

with. Generally, a design with high temperature coefficient of resistance in Eq. (6) is preferred, since this should increase the sensitivity of the sensor.

Another approach to measuring fluid flow, which also applies thermal principles, is illustrated in Fig. 3.

A resistor providing a continuous heating power of a few milliwatts is placed in the flow channel. At both the left and right sides of the resistor, two thermosensors are embedded symmetrically to measure the temperature. If the fluid in the channel is still, the temperature field, represented by the isotherms, is symmetric and the two sensors will measure the same temperature. When the fluid flows at some velocity, the isotherms will be distorted and hence the thermosensors will measure different temperatures, which are then used to determine the fluid velocity. The temperature field affected by the fluid flow can be simulated numerically by using the Navier–Stokes equations with a boundary condition of constant flow velocity.

The concept of *time of flight* has also been adopted, similarly to its use in ultrasonic flowmeters for macroscale flows. A heat pulse is generated upstream by a laser or electric coil, and the heated fluid is detected downstream. The time difference is used to determine the velocity and then the volumetric flow rate. However, diffusion of heat in the fluid results in a broadened temperature distribution when the fluid reaches the sensors, and hence results in difficulty in determining the transit time accurately. An ion generator can be used to replace the heater for the purpose of determination of the time of flight [6].

As shown in Fig. 4, H^+ or OH^- ions are generated on demand by an upstream ion generator, and two pH-sensitive sensors located downstream are used to detect the time of flight of ions flowing from the upstream sensor to the downstream sensor.

Verification of Flow Rate Measurement

As mentioned earlier, most metering devices in fact measure the flow velocity. When a measurement is made with a microflow sensor, if the flow in the microchannel can be resolved simultaneously by using high-resolution velocimetry, such as by means of a microresolution particle image velocimetry (μ PIV) system that has been calibrated by use of a calibrated interferometer and timer, traceability can be achieved by comparing the results. For devices that indicate a flow rate or fluid quantity on a panel, however, direct tracing back to reference standards is faster and more reliable. For example, a flow sensor or flow controller such as a syringe pump can be calibrated by use of a standard flow rate system that has been certified and is traceable to basic physical standards such as standards of time, length, mass, and luminous intensity.

Some researchers have tried to set up calibration facilities to verify the metering performance of their microflow sensors. A simple way is to connect the sensor to a pipette with a scale [7]. As shown in Fig. 5, the liquid is pushed by compressed air, and the scale is read over a time interval to obtain a reference flow rate. The meter error E can be easily estimated by direct comparison:

$$E = Q_\mathrm{m} - Q_\mathrm{s} = Q_\mathrm{m} - \left(\frac{\Delta l \cdot \pi d_\mathrm{i}^2}{4 \Delta t} \right) , \qquad (11)$$

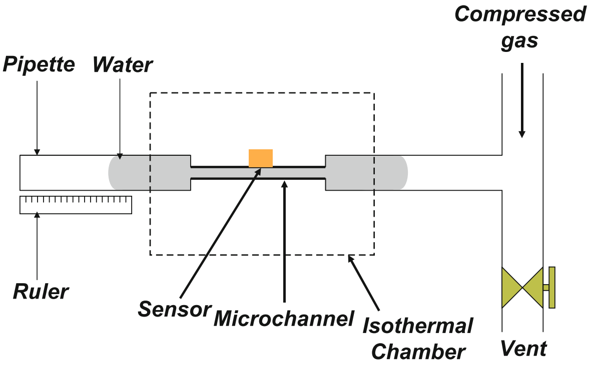

Fluid Metering, Figure 5 Schematic diagram of an experimental setup for the calibration of a microflow sensor. The liquid, driven by compressed air, flows through the sensor under test into a pipette with a scale. The liquid volume collected in the pipette within a certain time interval is used to determine the flow rate

where Q_m is the meter reading of the microflow sensor, and Q_s is the reference standard obtained from the distance of travel Δl of the liquid–air interface during a time interval Δt and the inner diameter d_i of the pipette.

In another approach, which is a little more complicated [8], a glass capillary is placed on a cooled metal plate to stabilize the temperature of the fluid and then an infrared laser pulse heats up a mass of liquid. Because the refractive index is a function of temperature, instruments that are sensitive to the change of refractive index are installed downstream to detect the heated liquid. However, thermal diffusion makes it complicated to accurately determine the arrival time of the heated mass of liquid.

For a standard of flow rate metering, traceability is the top priority; the measurement uncertainty should be sufficiently small, and a system that features simple operation, low measurement uncertainty, and high repeatability is desirable. Therefore, approaches based on weighing are, above all others, favorable candidates for such a purpose. As shown in Fig. 6, a gravimetric primary metering standard has been set up to achieve these requirements [9]. Liquid water is driven by a pneumatic pressure control mechanism to obtain flow rates down to less than a microliter per minute. The measurement capability depends on the weighing of the collection beaker, the stability of the pressure difference, the time interval, and the variation of the ambient temperature. Buoyancy variation and liquid evaporation are critical concerns for measurements associated with such a small quantity of liquid.

In this setup, a liquid in a reservoir tank is pushed into 1/8 inch connection pipes or microchannels by a preset air pressure. The air pressure must be well controlled, for example by using a two-stage valve system followed by a pressure modulator. The liquid flows through the microflow sensor to be verified and then into a collection tank installed on a high-precision balance. To eliminate buoyancy effects due to changes in the air density during calibration, a twin-balance arrangement has been adopted. This means that a similar collection tank is installed on another balance, and the difference between readings before and after the calibration period is used for buoyancy compensation. Both the balances are well covered with a glass shield to avoid any influence from the ambient air flow. In addition, the liquid in the collection tank is covered with low-volatility oil to eliminate evaporation. The oil should be full to the edge of the collection tank, which is placed inside a larger beaker. The oil will overflow into the larger beaker so as to maintain a constant outlet pressure and reduce possible weight variations.

After the fluid meter has been connected in series between the reservoir and the collection beaker, calibration can begin when the fluid flow reaches steady state. The recorded weights before and after a preset time interval are used to calculate the mass flow rate. The mass flow rate is expressed accurately as follows:

$$
\begin{aligned}
q_m &= \frac{m_1 - m_0}{t} \\
&= \frac{V_{cv} \times \rho_{l,1} + W_1 + (V_{tank} + \Delta V_{tank}) \times \rho_{a,1}}{t} \\
&\quad - \frac{(V_{cv} \times \rho_{l,0} + W_0 + V_{tank} \times \rho_{a,0})}{t} \\
&= \frac{V_{cv} \times (\rho_{l,1} - \rho_{l,0}) + (W_1 - W_0)}{t} \\
&\quad + \frac{V_{tank} \times (\rho_{a,1} - \rho_{a,0}) + \Delta V_{tank} \times \rho_{a,1}}{t} \\
&= \frac{V_{cv} \times (\rho_{l,1} - \rho_{l,0}) + (W_1 - W_0)}{t} \\
&\quad + \frac{(W_1 - W_0)/\rho_{l,1} \times \rho_{a,1} + V_{tank} \times (\rho_{a,1} - \rho_{a,0})}{t} \\
&= \frac{V_{cv} \times (\rho_{l,1} - \rho_{l,0}) + (W_1 - W_0)}{t} \\
&\quad + \frac{(W_1 - W_0)/\rho_{l,1} \times \rho_{a,1} + V_{tank,\,ref} \times (\rho_{a,1} - \rho_{a,0})}{t} \\
&= \frac{V_{cv} \times (\rho_{l,1} - \rho_{l,0}) + (W_1 - W_0)(1 + \rho_{a,1}/\rho_{l,1})}{t} \\
&\quad + \frac{(W_{ref,1} - W_{ref,0})}{t} \\
&= f(V_{cv}, \rho_{l,1}, \rho_{l,0}, W_1, W_0, \rho_{a,1}, W_{ref,1}, W_{ref,0}, t)\,, \qquad (12)
\end{aligned}
$$

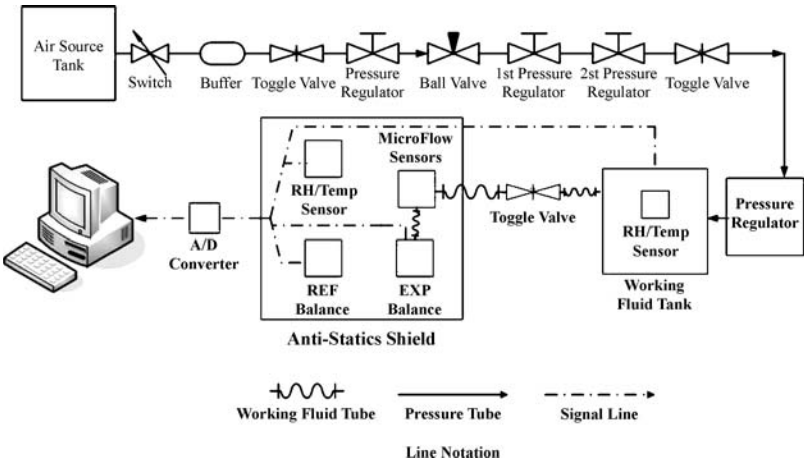

Fluid Metering, Figure 6 Diagram of a twin-balance weighing system serving as a primary standard for microflow sensor calibration

where q_m is the mass flow rate in g/min, m is the liquid mass in the collection beaker in g, W is the reading from the balance in g, V_{cv} is the control volume between the outlet of the fluid meter and the collection beaker in cm^3, ρ_l and ρ_a are the density of the liquid and air, respectively, in g/cm^3, and t is the collection time in minutes. The subscripts 0 and 1 represent the initial and final conditions, respectively, and ref denotes the reference balance. A total of nine variables are considered in the equation. The volume flow rate q_v can be obtained by dividing the mass flow rate by the liquid density:

$$q_v = \frac{q_m}{\rho_{l,1}} = g(V_{cv}, \rho_{l,1}, \rho_{l,0}, W_1, W_0, \rho_{a,1}, W_{ref,1}, W_{ref,0}, t) . \quad (13)$$

The density of liquid water is a function of its temperature T_l, and can be determined from the following formula:

$$\rho_l = 0.99985308 + 6.32693 \times 10^{-5} \times T_l - 8.523829 \times 10^{-6} \times T_l^2 + 6.943248 \times 10^{-8} \times T_l^3 - 3.821216 \times 10^{-10} \times T_l^4 . \quad (14)$$

A check standard, used to confirm the reliability of the calibration, is always necessary. For example, a circular capillary can be used, and the Hagen–Poiseuille formula can be applied to obtain the theoretical flow rate,

$$q_V = \frac{\pi}{8} \frac{r_0^4 \cdot \Delta p}{\nu \cdot \Delta l} , \quad (15)$$

where r_0 is the inner radius of the capillary tube, Δp is the pressure difference between two detection points a distance Δl apart, and ν is the dynamic viscosity. Periodically connecting this capillary to the calibration standard and measuring the flow rate simultaneously for comparison is important.

Volume Measurement of Discrete Droplets

The gravimetric method is suitable for measuring the volume of liquid dispensed by pipettes, and it is commonly adopted to assess the performance of such instruments. Trained personnel are required to carry out such tests. The balances used for this purpose may have a precision of four to seven decimal places, depending on the volume to be measured and the desired accuracy. It should be well

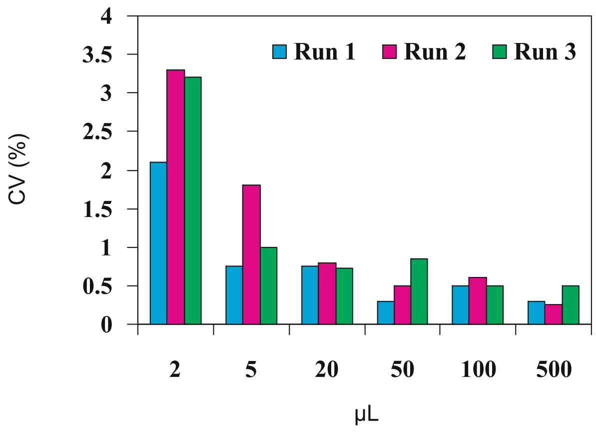

Fluid Metering, Figure 7 Performance verification results for measurements of dispensed liquid volumes conducted by the gravimetric method

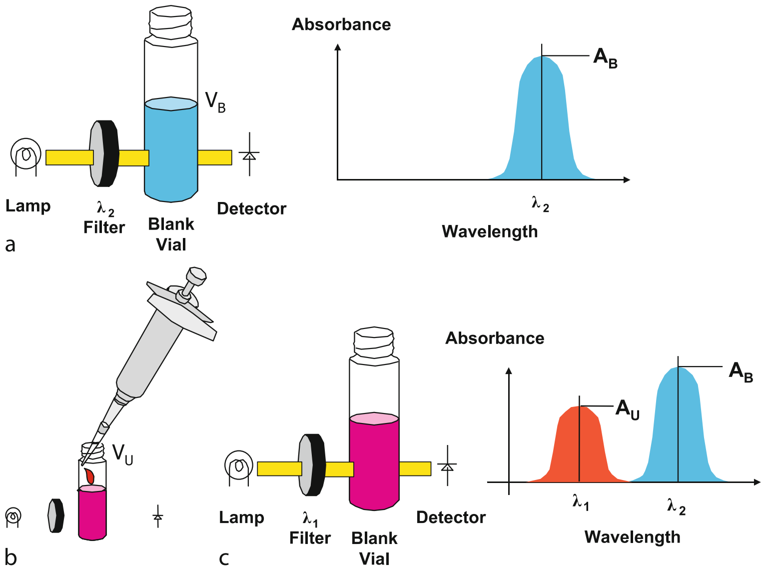

Fluid Metering, Figure 8 Measurement procedure using the dual-dye, dual-wavelength photometric method for the determination of dispensed liquid volume

established that the experimental setup is free from environmental disturbances such as vibration and air flow. Two points need to be addressed when the gravimetric method is used. The first one is the determination of the Z-factor, which is the transformation factor between the volume V and mass m of liquid. The volume dispensed is determined by the following equation:

$$V = m \cdot Z\,. \tag{16}$$

The Z-factor has units of microliters per milligram (μl/mg), and its value, dependent on barometric pressure and temperature, is tabulated in the literature [4]. For example, at one atmosphere, the value of the Z-factor for temperatures between 15 and 30 °C ranges from 1.0020 to 1.0054. The second point is the error due to evaporation, which inevitably takes place during the measuring process. Especially for small volumes below 50 μl, the evaporation rate should be calculated, and the design of the weighing vessel and the test cycle time are important. The mean volume $\bar{V}$ in the case of multiple dispensing can be calculated from the following equation:

$$\bar{V} = (\bar{w} + \bar{e} \cdot t) \cdot Z\,, \tag{17}$$

where $\bar{w}$ is the average weight, $\bar{e}$ is the average evaporation rate, and t is the test cycle time.

For the measurement of very small volumes of liquid, the gravimetric method becomes difficult to implement with accuracy.

As demonstrated in Fig. 7, which shows the results for a pipette checked using the gravimetric method, the coefficient of variation (CV, defined as the ratio of the standard deviation to the mean) for a run consisting of 10 measurements of a given volume increases considerably when the dispensed liquid volumes are less than 5 μl. Evaporation, buoyancy, vibration, and the effects of static electricity are the primary causes of these results. A possible alternative method to determine microscale droplet volumes is one based on measurement of the concentration of a liquid solution. Two practices, also recommended by the ISO standard [5], are commonly used, namely the photometric and titrimetric methods.

The theory of operation of the photometric method for determining dispensed liquid volumes is based on the Beer–Lambert law, which can be written as follows:

$$A(\lambda) = \log_{10}\left(\frac{I(0)}{I(l)}\right) = -\log_{10}(T(\lambda)) = \varepsilon(\lambda) l C\,, \tag{18}$$

where A is the absorbance, which is a function of the wavelength λ of the incident light; $I(0)$ and $I(l)$ are the intensities of the incident and transmitted light, respectively; l is the length of material that the light travels through; T is the transmittance; ε is the molar absorptivity; and C is the molar concentration of the material. Eq. (18) implies that for a given substance and a fixed wavelength of light, the absorbance of the sample has a linear relationship to its molar concentration and the path length. Although a setup with a single-dye, single-wavelength design is feasi-

ble for determining the volume of liquid delivered, a dual-dye, dual-wavelength ratiometric photometry technique is generally used since it enables the measurement to be independent of the path length.

The measurement procedure using the dual-dye, dual-wavelength photometric method is shown in Fig. 8. A test vial is loaded with a blank solution of known volume (V_B) and concentration (C_B), with a peak absorbance (A_B) at a wavelength λ_2. A drop of the sample solution, which has a peak absorbance at another wavelength λ_1 and nearly zero absorbance at λ_2, with a known concentration (C_S) and an unknown volume (V_U), is dispensed into the test vial, and it is mixed fully with the blank solution. The absorbance (A_U) of the mixture at the wavelength λ_1 is then measured. With a knowledge of the extinction coefficients of the blank and sample solutions ε_B and ε_S, respectively, the unknown droplet volume can be calculated using the following formula derived from the Beer–Lambert law:

$$V_U = V_B \left[\frac{\frac{A_U}{A_B}}{\frac{\varepsilon_S C_S}{\varepsilon_B C_B} - \frac{A_U}{A_B}} \right] . \tag{19}$$

The sources that need to be taken into consideration in the evaluation of the measurement uncertainty of the photometric method include instrument-related uncertainties, for example imprecision and drift in absorbance readings; reagent-related uncertainties, for example uncertainties in the volume and temperature of the reagents, incomplete mixing, pH dependence, and evaporation; and system-related uncertainties, for example system nonlinearity.

The principle of the titrimetric method is based on the chemical equivalence of two solutions. In general, any titration system can be used. A test solution with a known concentration C_D and an unknown volume V_U is dispensed into a titration vessel containing a receiver liquid, followed by a titration process with a titration solution of known concentration C_T. An auxiliary solution may be required to adjust the pH value before the titration starts. The equivalence point E_Q (in milliliters) is determined by potentiometric detection, for example with a silver electrode. The unknown volume can be calculated using the following formula:

$$V_U = E_Q \times \frac{C_T}{C_D} . \tag{20}$$

The titrimetric method described here is, according to ISO 8655-7 [5], suitable for measuring dispensed liquid volumes greater than 500 µl. This is not satisfactory, since our goal here is to measure liquid volumes of a few microliters or under. However, a technique based on the principle of titration of two liquids and measurement of the pH value of the resulting solution has been demonstrated to be feasible for the characterization of liquid volumes in the nanoliter range [10]. The long test cycle time and some issues in the evaluation of the uncertainty of this technique are, however, yet to be resolved.

Verification of measurements conducted by the photometric or titrimetric technique can be done easily by comparing the results with results from the gravimetric method if the volume dispensed is sufficiently large. However, for the measurement of small liquid volumes where the gravimetric method is no longer applicable, verification can be difficult. In that case, cross-validation between various measuring techniques and/or comparison with a calibrated dispenser is essential.

Key Research Findings

According to ISO GUM, which is a guide to the expression of uncertainty in measurements, the measurement uncertainty of the primary flow rate calibration system described above can be estimated as follows:

$$\begin{aligned} \left[\frac{u_c(q_\mathrm{m})}{q_\mathrm{m}}\right]^2 &= \left[\frac{\partial f}{\partial V_\mathrm{cv}}\frac{u(V_\mathrm{cv})}{q_\mathrm{m}}\right]^2 + \left[\frac{\partial f}{\partial \rho_{\mathrm{l},1}}\frac{u(\rho_{\mathrm{l},1})}{q_\mathrm{m}}\right]^2 \\ &+ \left[\frac{\partial f}{\partial \rho_{\mathrm{l},0}}\frac{u(\rho_{\mathrm{l},0})}{q_\mathrm{m}}\right]^2 + \left[\frac{\partial f}{\partial W_1}\frac{u(W_1)}{q_\mathrm{m}}\right]^2 \\ &+ \left[\frac{\partial f}{\partial W_0}\frac{u(W_0)}{q_\mathrm{m}}\right]^2 + \left[\frac{\partial f}{\partial \rho_{\mathrm{a},1}}\frac{u(\rho_{\mathrm{a},1})}{q_\mathrm{m}}\right]^2 \\ &+ \left[\frac{\partial f}{\partial W_{\mathrm{ref},1}}\frac{u(W_{\mathrm{ref},1})}{q_\mathrm{m}}\right]^2 + \left[\frac{\partial f}{\partial W_{\mathrm{ref},0}}\frac{u(W_{\mathrm{ref},0})}{q_\mathrm{m}}\right]^2 \\ &+ \left[\frac{\partial f}{\partial t}\frac{u(t)}{q_\mathrm{m}}\right]^2 . \end{aligned} \tag{21}$$

Similarly,

$$\begin{aligned} \left[\frac{u_c(q_\mathrm{v})}{q_\mathrm{v}}\right]^2 &= \left[\frac{\partial g}{\partial V_\mathrm{cv}}\frac{u(V_\mathrm{cv})}{q_\mathrm{v}}\right]^2 + \left[\frac{\partial g}{\partial \rho_{\mathrm{l},1}}\frac{u(\rho_{\mathrm{l},1})}{q_\mathrm{v}}\right]^2 \\ &+ \left[\frac{\partial g}{\partial \rho_{\mathrm{l},0}}\frac{u(\rho_{\mathrm{l},0})}{q_\mathrm{v}}\right]^2 + \left[\frac{\partial g}{\partial W_1}\frac{u(W_1)}{q_\mathrm{v}}\right]^2 \\ &+ \left[\frac{\partial g}{\partial W_0}\frac{u(W_0)}{q_\mathrm{v}}\right]^2 + \left[\frac{\partial g}{\partial \rho_{\mathrm{a},1}}\frac{u(\rho_{\mathrm{a},1})}{q_\mathrm{v}}\right]^2 \end{aligned} \tag{22}$$

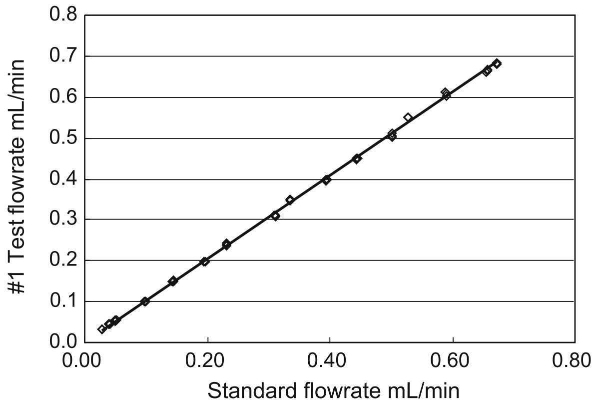

Fluid Metering, Figure 9 Example of calibration of a microfluid meter using the gravimetric method

$$+\left[\frac{\partial g}{\partial W_{\mathrm{ref},1}}\frac{u(W_{\mathrm{ref},1})}{q_{\mathrm{v}}}\right]^2+\left[\frac{\partial g}{\partial W_{\mathrm{ref},0}}\frac{u(W_{\mathrm{ref},0})}{q_{\mathrm{v}}}\right]^2$$
$$+\left[\frac{\partial g}{\partial t}\frac{u(t)}{q_{\mathrm{v}}}\right]^2 ,$$

where u denotes the standard uncertainty of the variable within the accompanying parentheses, and the partial differential of each variable is the sensitivity coefficient. Each variable could contribute its measurement uncertainty to the final combined standard uncertainty u_{c}, in the form of a Type A or Type B uncertainty, defined in ISO GUM. If we consider a gravimetric system, that system could be a measurement standard for flow rates of 0.1 mg/min to 10 g/min (0.1 μl/min to 10 ml/min) at temperatures of 15 to 26 °C and pressures of 1 kPa to 60 kPa, and the relative expanded uncertainty of the system is smaller than 1.1%.

An example of a calibration is shown in Fig. 9, where flow rates obtained from a meter under test, denoted by squares along with a linear fit, have been plotted against those of a calibration system. Because the instruments used to measure the nine variables can have their own calibration chains, the traceability of the microflow meter has therefore been established.

If flow rates down to 1 nl/min are required, the gravimetric method is no longer practical owing to the limits of balances, and evaporation or leakage during the long time required for calibration.

Therefore, a chip-based, time-of-flight-type microflow rate calibrator, as shown in Fig. 10, has been proposed [9]. When an interface formed by two fluids that have different dielectric constants and are insoluble in each other, for example a water/air or water/oil interface, passes through an electrode node, the potential changes owing to the change in equivalent capacitance. In contrast to other approaches of this kind, which generally suffer from the effects of diffusion, the determination of the time of flight in this calibrator can be more precise, since the interface follows the flow faithfully and does not change over time while moving in the microchannel. The volume between any two electrode nodes could be obtained from a calibrated flow rate determined by a primary system and the time interval between two detection signals. This calibrator can thus be traced back to the primary standard and be used to calibrate lower flow rates.

In principle, the capability to determine small dispensed liquid volumes using concentration measurement increases as the amount of diluent or receiver liquid in the test container is reduced, as long as taking measurements remains possible with the instruments used. This feature is a consequence of the scalability of these methods. However, the use of a large volume is essential in order to obtain measurements with low uncertainty, and it is virtually inevitable, to a certain degree, that the uncertainty becomes higher as the liquid volume handled becomes lower. This is a trade-off and requires elaborate consideration when these methods are to be used.

Future Directions for Research

Accurate micro- and nanoscale fluid metering is important since it serves as a basis for evaluating the performance of microfluidic devices, and thus is critical to the quality control of those devices and systems using them. Establishment of a traceability chain and evaluation of the measurement uncertainty for flow rate and droplet volume metering instruments are important, especially for levels of liquid quantity that cannot feasibly be dealt with by gravimetric methods. Moreover, reliable methods to mea-

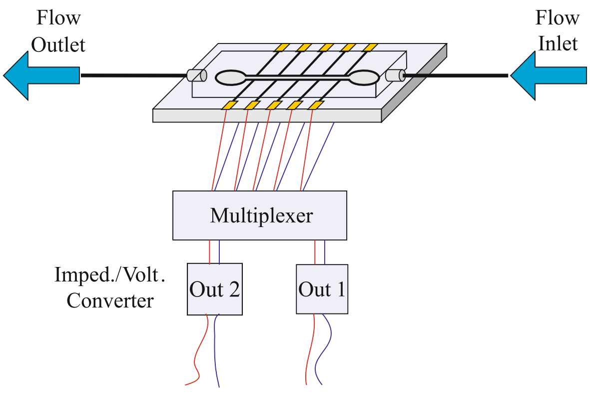

Fluid Metering, Figure 10 Schematic of a chip-based volumetric microflow rate calibrator. Electrode nodes are used to detect a liquid/air or liquid/liquid interface passing through the microchannel

F

sure extremely small liquid volumes, for example 10 nl or below, are yet to be developed.

Cross References

- ► Nanofluidics in Carbon Nanotubes
- ► Droplet Dispensing
- ► Methods for Flow Rate Measurement
- ► Picoliter Flow Calibration
- ► Pyroelectric Flow Sensors
- ► Thermocapacitive Flow Sensor
- ► Thermoelectric Flow Sensors

References

1. Whitesides G (2003) The right size in nanobiotechnology. Nat Biotechnol 21(10):1161–1165
2. Ghosh S, Sood AK (2003) Carbon nanotube flow sensors. Science 299:1042–1044
3. Comiey J (2002) Nanolitre dispensing – on the point of delivery. Drug Discovery World Summer 2002:33–44
4. ISO 8655-6:2002(E): Piston-operated volumetric apparatus – Part 6: Gravimetric methods for the determination of measurement error.
5. ISO 8655-7:2005(E): Piston-operated volumetric apparatus – Part 7: Non-gravimetric methods for the assessment of equipment performance.
6. Poghossian A, Yoshinobu T, Schoning MJ (2003) Flow-velocity microsensors based on semiconductor field-effect structures. Sensors 3:202–212
7. Wu S, Lin Q, Yuen Y, Tai YC (2001) MEMS flow sensors for nano-fluidic applications. Sens Actuators A 89(1–2):152–158
8. Markov DA, Bornhop DJ (2001) Nanoliter-scale non-invasive flow-rate quantification using micro-interferometric back-scatter and phase detection. J Anal Chem 371:234–237
9. Yang CT, Lin WT, Yang FR, Feng CC (2005) A metrological traceability system for microflowrate measurement. ASME IMECE2005-29443, Orlando, FL, USA
10. Cavallaro A, Saggere L (2005) Picoliter fluidic flow characterization using ion-selective measurement. ASME IMECE2005-82646, Orlando, FL, USA

Fluid Metrology

► Fluid Metering

Fluid Particle Model

► Dissipative Particle Dynamics

Fluid Quantification

► Fluid Metering

Fluorescence

Definition

Fluorescence is the property whereby some atoms and molecules absorb light at a particular wavelength and subsequently emit light of longer wavelength after a brief interval, termed the fluorescence life-time. Photons from an external source are absorbed by the fluorophore and this produces excited singlet state electrons. However, the time taken for these electrons to return to the lower energy level is known as the excited state lifetime. The emission of light occurs as fluorescence from an excited electron singlet state, where all the electrons in the molecule are spin-paired. The return to ground states occurs, with the emission of photons. Emission rates are fast being in the region of $10^8\ s^{-1}$ and fluorescence life-times are relatively short. Many fluorophores have sub-nanosecond life-times and, therefore, the fluorescence emitted by these dyes is short-lived.

Cross References

- ► Photometer
- ► Fluorescent Labeling
- ► Fluorescent Thermometry
- ► Photometer

Fluorescence Detection

► Time-Gated Fluorescence Detection

Fluorescence Efficiency

► Quantum Efficiency

Fluorescence Lifetime

Definition

The fluorescence lifetime of an excited dye molecule represents the average time a fluorophore remains in its excited state and is given by the inverse of the total rate at which radiative and non-radiative relaxation to the ground state occurs.

Cross References

► Fluorescent Thermometry

Fluorescence Measurements

GEA O. F. PARIKESIT
Quantitative Imaging Group, Delft University of Technology, Delft, The Netherlands
g.o.f.parikesit@tudelft.nl

Synonyms

Fluorescence microscopy; Fluorescent microscopy; Fluorescence visualization; Fluorescent visualization

Definition

Fluorescence is the phenomenon where a molecule absorbs energy from incoming light and instantaneously emits another light, in which the emitted light has a longer wavelength than the absorbed light. Fluorescence measurements are methods to quantitatively visualize and characterize a physical, biological, or chemical process, based on the characteristics of fluorescence that occurs during the process.

Overview

Fluorescence is a type of luminescence, which is light that is not generated by high temperature. In fluorescence, a molecule (usually called as a fluorochrome, a fluorophore, or a fluorescent dye) absorbs energy from incoming light and instantaneously emits another light, where the emitted light has a longer wavelength than the absorbed light [1]. The molecule stops emitting light immediately when there is no more incoming light. The fluorescence signals can be measured to quantitatively visualize and characterize a physical, biological, or chemical process. Fluorescence measurements are very useful because they are sensitive and specific to the studied process. Moreover, the fluorescently visualized process can be imaged in detail and analyzed further using various image processing and analysis techniques. This advantage, along with the high spatial measurement capabilities allowed by optical microscopy, is highly crucial for investigations in very small scale such as in microfluidics and nanofluidics. Several methods to measure fluorescence signals, in particular related to quantitative visualization and characterization of phenomena in microfluidic and nanofluidic channels, will be reviewed in this entry.

The fluorescence phenomenon occurs in three steps: excitation of the fluorochrome by the energy absorbed from incoming light (it occurs in 10^{-15} s); vibrational relaxation of the fluorochrome, where the energy of the fluorochrome is lowered from the original excited state to the lowest excited state (it occurs in 10^{-12} s); and emission of light with longer wavelength from the fluorochrome (it occurs in 10^{-9} s) [1]. The various energy levels involved in the fluorescence phenomenon are illustrated in the so-called Jablonski diagram, as shown in Fig. 1.

Both the energy absorbed from the incoming light and the energy contained in the emitted light occur in discrete amounts, which are termed quanta, and can be expressed by the equation:

$$E = \mathrm{h}f = \mathrm{h}\frac{\mathrm{c}}{\lambda}\,, \tag{1}$$

where E is the energy, h is Planck's constant ($6.626068 \times 10^{-34}\,\mathrm{m^2 kg\,s^{-1}}$), f is the light frequency, c is the speed of light in vacuum, and λ is the light wavelength. In general, fluorescence measurements are performed using lights with wavelengths ranging from ultraviolet to visible, which is between 250 and 750 nm. The difference of wavelengths between the excitation and emission light is caused by the second step in the fluorescence phenomenon, which is the vibrational relaxation of the fluorochrome. In this step, some of the absorbed energy is transformed into changes in structural arrangement of the fluorochome molecule. The shift of wavelength from the excitation light to the emission light is termed as the Stokes shift. Once a fluorochrome molecule reaches its original state, it can be excited again, and the fluorescence signal can be generated repeatedly using a continuous excitation light.

Fluorochrome molecules are usually characterized using their quantum yield and ►fluorescence lifetime. Quantum efficiency is a measure of the efficiency of the fluorochrome's fluorescence emission compared to all possible energy relaxation pathways. This dimensionless parameter is expressed as the ratio between the number of photons (that is the smallest discrete amount of light) emitted and

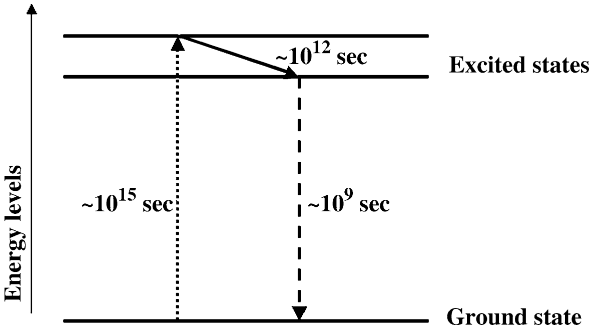

Fluorescence Measurements, Figure 1 The Jablonski energy diagram of the fluorescence phenomenon. The dotted line illustrates the excitation of the fluorochrome molecule, the solid line represents the vibrational relaxation of the excited fluorochrome molecule, and the dashed line shows the emission of light with longer wavelength

the number of photons absorbed. Hence, in general, fluorochromes with higher quantum efficiency are preferred. The fluorescence lifetime (τ) is the time that a fluorochrome molecule remains in the excited state before generating the emission light. The decaying of the fluorescence intensity coming from a fluorochrome molecule after a pulse excitation light is given by an exponential function:

$$I(t) = I_0 \mathrm{e}^{(-t/\tau)}\,, \tag{2}$$

where $I(t)$ is the fluorescence intensity at time t and I_0 is the initial fluorescence intensity immediately after the pulse excitation. Therefore the fluorescence lifetime can also be defined as the time in which the fluorescence intensity from the fluorochrome molecule decays to $1/\mathrm{e}$ of the initial intensity.

The fluorescence signal given by the emission light can be significantly reduced by two different phenomena: quenching and photobleaching. In quenching, the excited fluorochrome molecule loses its energy non-radiatively, for example through collisions with other molecules. Meanwhile photobleaching is the irreversible destruction of the fluorochrome molecules using very intense excitation light. For imaging purposes, both quenching and photobleaching should generally be avoided. However, for quantitative visualization of transport phenomena in microfluidics and nanofluidics, these phenomena can be useful, as we will discuss later.

Fluorescence signals are also influenced by characteristics of the environments surrounding the fluorochrome molecule. One of the most common environmental factors is the concentration of other molecules, which causes quenching as described above. Another factor is the pH of the aqueous medium containing the fluorochromes. In most imaging applications, the sensitivity of fluorochromes to different pH levels is unwanted. In biological and chemical measurements, however, the pH of the medium can provide extra information of the investigated process. To measure the pH level, two different types of fluorochromes are typically used; each is being sensitive to different pH levels. In this so-called ratio-metric measurement method, the emission light's intensity ratio between the two fluorochromes indicates the actual pH level of the medium.

Below we will describe the optical microscopy setups for performing fluorescence measurements. Afterwards we will discuss the application of the fluorescence measurements to quantitatively visualize and characterize transport of fluid and individual biological molecules in microfluidic and nanofluidic studies.

Basic Methodology

Fluorescence Microscopy Setup

In general, the fluorescence measurements can be done without using an optical microscope. Fluorescence signals given by bulk materials can readily be measured using standard macro-scale optical methods. For measurements in very small scales, such as the investigations performed in microfluidics and nanofluidics, however, an optical microscope is necessary. Here we start by describing the most common fluorescence microscopy setup. Figure 2 illustrates the basic anatomy of a fluorescence microscopy setup. The light that is used in the setup usually comes from a mercury (Hg) arc-discharge lamp, located at the back of the microscope. The emission light generated from the fluorescence measurements is then imaged to an optical detector, typically a digital CCD (charge-coupled devices) camera, for further processing and analysis.

Among the most important elements of the setup are the set of optical filters, which separate the excitation light from the emission light [1]. It comprises mainly the excitation filter, the emission filter, and a dichroic mirror (also known as a di-chromatic beam-splitter, which splits two lights with different wavelengths to two different paths). The excitation filter serves to ensure that only the light with a certain range of wavelengths illuminates, and eventually excites, the fluorochrome molecules. The filter absorbs all the light with wavelengths outside the desired range. After passing the excitation filter, the light is directed by the dichroic mirror onto the fluorochrome molecules. With the help of the lens near the molecules, the excitation light is focused toward the molecules. After excitation, the fluorochrome molecules eventually generate the emission light, which is then again collected by the same lens near the molecules. The collected emission light than pass through the dichroic mirror; a dichroic mirror is designed so that it reflects light with the same range of wavelengths as the excitation light, while it transmits light with the same wavelengths as the emission light. To ensure that only the emission light reaches the detector, the emission filter is used. This filter absorbs noises that have the same range of wavelengths as the excitation light, such as excitation light scattered by objects near the fluorochrome molecules.

A fluorescence microscope setup that uses such optical filter set, as depicted in Fig. 2, is known as an Epi-Fluorescence Microscope [1]. The word Epi-Fluorescence means that both the excitation light path and the emission light path use the same lens near the fluorochrome molecules. When excitation light illuminates the fluorochrome molecules, the lens serves as a condenser lens, which focuses the light into the object plane. Mean-

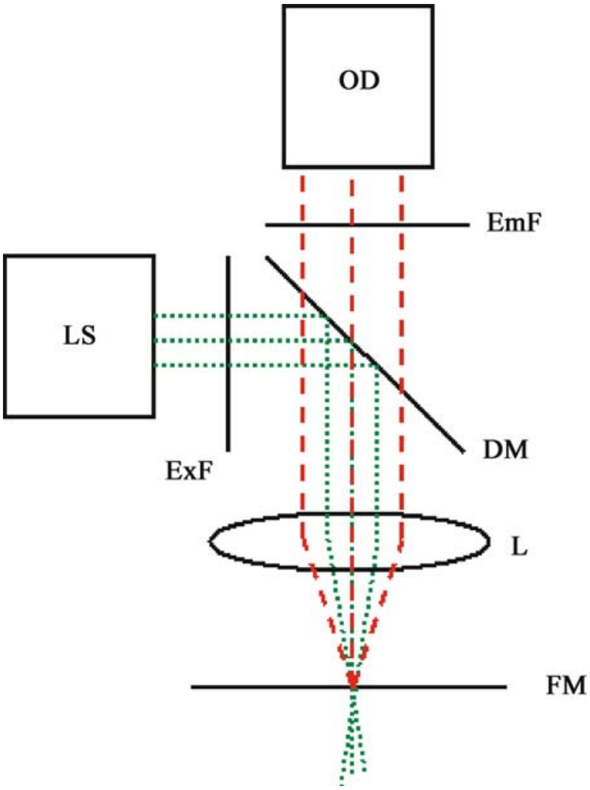

Fluorescence Measurements, Figure 2 The basic anatomy of a common fluorescence microscopy setup. LS = light source, OD = optical detector, ExF = excitation filter, EmF = emission filter, DM = dichroic mirror, L = lens, and FM = position of fluorochrome molecules

while, when the fluorochrome molecules generate emission light, the lens serves as an objective lens, which gathers light from the object plane into optical detectors. Therefore by using the Epi-Fluorescence Microscope setup, we can keep the fluorochrome molecules in the object plane always in focus, simultaneously for the excitation light path and the emission light path.

The fluorochrome molecules, which are exactly in the focal plane of the lens, can be imaged clearly in the optical detector. Other molecules, however, will be imaged poorly because they are out of focus. The transition between being in focus and out of focus occurs gradually, such that there is a range of space in which the molecules can still be imaged clearly even though they are not exactly in focus. This range of space, termed depth of focus [1], can be expressed as:

$$Z = n\lambda/(\mathrm{NA})^2 \,, \tag{3}$$

where Z is the depth of focus for a lens, n is the refractive index of the medium containing the fluorochrome molecules, λ is the wavelength of the emission light, and NA is the numerical aperture of the lens, which in turn is defined as $\mathrm{NA} = n(\sin\theta)$ with θ as the maximum angle that can be captured by the lens.

The notion of depth of focus is important in microfluidic and nanofluidic studies, because it influences the spatial resolution of the measurement. Let us consider a microfabricated channel with a channel depth of d, in which fluorochrome molecules are being contained and measured. If $Z > d$, then all the fluorochrome molecules are always in focus, and they all are imaged clearly in the optical detector. Consequently, in microfluidic channels, where the fluorochrome molecules are typically much smaller than the channel depth d, the position of the fluorochrome molecules along the channel depth cannot be resolved anymore. Hence, multiple molecules that are positioned near each other cannot be distinguished from each other, and three-dimensional measurements (for instance, to characterize the transport of fluid inside such channels) cannot be performed. In nanofluidic channels, however, where the fluorochrome sizes are more similar to the channel depth d, the measurements can be described as a quasi-2D problem, and it is not required anymore to resolve along the channel depth.

Meanwhile, if $Z < d$, then only fluorochrome molecules within the depth of field are imaged clearly n the optical detector. By scanning the position of the microfabricated channels relative to the lens, the positions of fluorochrome molecules along the channel depth can be resolved, and a 3D measurement can be performed.

If all the emission light, both from the fluorochrome molecules in focus and the fluorochrome molecules out of focus, is collected by the microscope setup, than the setup is termed as having a wide-field configuration. Emission light from molecules that are out of focus is typically not wanted in fluorescence measurements, because it serves as a background signal that reduces the measurement quality. To eliminate this background, another type of configuration, termed the confocal configuration [1, 2], is used. Figure 3 provides the schematic concept of a confocal configuration.

In a confocal configuration, a pair of pinholes is positioned near the optical filter set: one pinhole (called a light-source pinhole) is located prior to the excitation filter, while another pinhole (called a detector pinhole) is located after the emission filter. Their positions are arranged such that the lens images the light-source pinhole into a single point in the object plane, and this point in the object plane is imaged, again by the same lens, exactly into the detector pinhole. Using this configuration, the light-source pinhole ensures that a smaller volume in the object plane is illuminated by the excitation light; thus spatial resolution in exci-

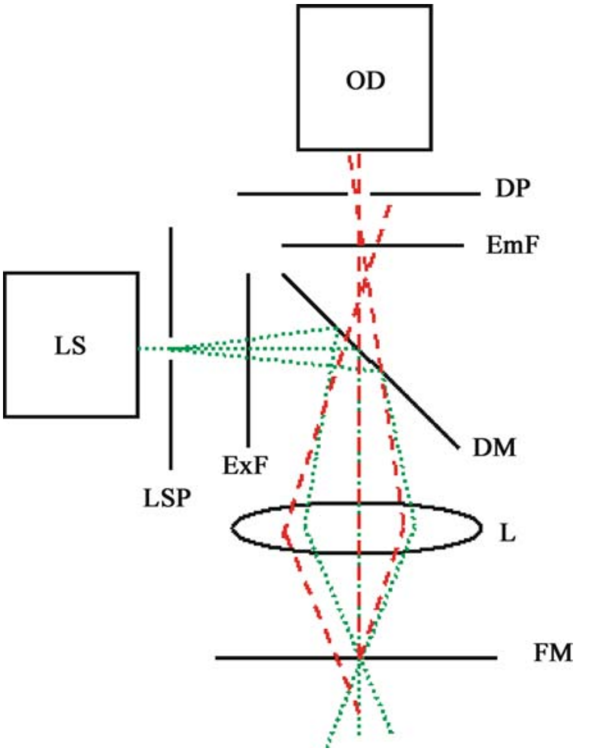

Fluorescence Measurements, Figure 3 The schematic concept of a confocal fluorescence microscope configuration. LS = light source, OD = optical detector, ExF = excitation filter, EmF = emission filter, DM = dichroic mirror, L = lens, FM = position of fluorochrome molecules, LSP = Light-source pinhole, and DP = detector pinhole. Note that the emission light coming from out-of-focus fluorochrome molecules is blocked away by the detector pinhole

tation is improved compared to the wide-field configuration. Moreover, the detector pinhole ensures that emission light generated by fluorochrome molecules that are out-of-focus is eliminated; hence background fluorescence signals are removed from the measurements. There is a trade-off, however, between the advantages described above and the longer time required in measurements with a confocal configuration [1, 2]. Because a smaller excitation volume is obtained in a confocal configuration, the excitation volume needs to be scanned through the whole object; in case of measurements in microfluidic and nanofluidic channels, this means scanning along the depth, length, and width of the channels. Multiple pinholes can then be used to reduce the scanning time, where the pinholes perform fluorescence measurements on several excitation volumes simultaneously.

Compared to macro-scale fluidic channels, the surface-to-volume ratio in microfluidic and nanofluidic channels is significantly larger, and consequently the physical effects caused by channel surfaces become more promi-

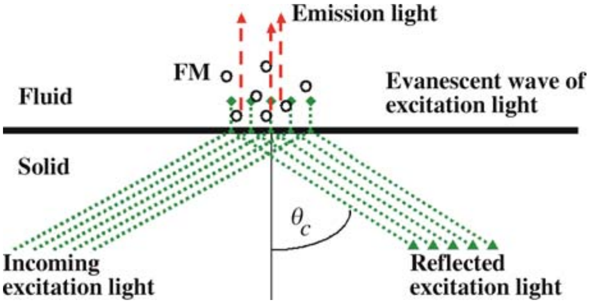

Fluorescence Measurements, Figure 4 The schematic concept of TIRF. FM = fluorochrome molecules. Note that only fluorochrome molecules that reside very close to the solid–fluid interface is illuminated by the excitation light and generates the emission light; the other fluorochrome molecules are not involved in the measurement

nent. Therefore it also becomes increasingly important to understand microfluidics and nanofluidics phenomena at these surfaces. A particular fluorescence microscope setup that is suitable for this kind of measurements is the so-called TIRF (total internal reflection fluorescence) setup. Figure 4 illustrates the concept of TIRF.

In a TIRF microscopy setup, the fluorochrome molecules reside near a solid–fluid interface. The excitation light is illuminating the fluorochrome molecules from a steep angle, coming from the solid side toward the fluid medium. When this angle is larger than a certain critical angle θ_c, then almost all of the excitation light is reflected back from the solid–fluid interface toward the solid side. This critical angle is expressed as:

$$\theta_c = \sin^{-1}(n_f/n_s)\,, \quad (4)$$

with n_f as the refractive index at the fluid medium and n_s the refractive index at the solid side. Hence only a very small amount of the excitation light goes through the solid–fluid interface. This small amount of excitation light, termed as evanescent wave, decays rapidly as it travels away from the solid–fluid interface toward the fluid medium. In effect, the excitation light only illuminates a very thin region in the fluid medium, with depth of only tens of nanometers, near the solid–fluid interface. Consequently, only fluorochrome molecules very near to the solid–fluid interface are excited and fluorescence measurements can be performed in detail on the surface.

Flow Visualization

To be able to design devices based on microfluidics and nanofluidics, it is crucial to quantitatively visualize the flow of fluids in the microfluidic and nanofluidic channels. There have been many flow visualization methods being

developed for macro-scale fluid flow (for example: hot-wire anemometry), but most of them are not suitable for micro- and nano-scale measurements because they are too intrusive for micro- and nano-scale fluid flows [3]. Fluorescence measurements are very suitable for quantitatively visualizing flow in micro- and nano-scales, because it is non-intrusive and it allows for measurements with a high spatial resolution.

Fluorescence-based flow visualization methods can be categorized into two types: particle-based methods and scalar-based methods [3]. In particle-based methods, the fluid motion is deducted from the observed motion of fluorescence particles embedded in the fluid. The fluorescence particles are typically formed as microspheres, where fluorochrome molecules coat each sphere (see for example: the FluoSpheres from Invirogen, CA, USA). To infer the fluid flow, the motion of the fluorescence particles must be processed and analyzed. When a CCD camera is used in the setup, the image sequence capturing the particles motion can be processed and analyzed digitally in a computer. Several analysis methods are available: the most popular is the so-called Micro-PIV (micro-scale particle image velocimetry). This method analyzes patterns of particles ensembles, and infer the fluid motion by performing correlation analysis between the recorded patterns. Micro-PIV is derived from its macro-scale counterpart, PIV. Another particle-based method that can be used is PTV (particle tracking velocimetry), in which individual particles are tracked and the pathlines of the individual particles are analyzed to infer the fluid flow.

In scalar-based methods, the velocity of a conserved scalar is being observed and analyzed to infer the fluid flow. The fluorescence signals themselves can be used as the scalar by preparing a fluid solution containing the fluorochrome molecules. Due to the typically short fluorescence lifetime of fluorochrome molecules, however, it is difficult to visualize the fluid motion using only fluorescence; as soon as the excitation light is terminated, no emission light is generated anymore. Therefore a modification to this method is needed.

The first type of modification is performed by inducing photobleaching on the fluorochrome molecules. Prior to the measurement, the whole fluidic channel is illuminated and all the fluorochrome molecules generate emission light. Exactly at the beginning of the measurement, another excitation light, with much higher intensity illuminates a certain region of the fluidic channel for a very short time. To shape this certain region, for example in a straight line across the channel width, a line-shaped aperture positioned before the excitation filter. This extra excitation induces photobleaching, but only to fluorochrome molecules that is located within the straight light. Hence the motion of the photobleached region can be analyzed to infer the fluid flow. The main disadvantage of this method is that it needs an extra light-source for inducing the photobleaching.

The second type of modification is done by using the so-called caged-fluorescence dyes. The caged-fluorescence dyes are fluorochrome molecules that have been modified chemically so that they become non-fluorescent. When a certain light (normally ultra-violet light) is exposed to the caged-fluorescent dyes, however, the chemical modification is reversed and the original fluorochrome molecules become fluorescent again. Prior to the measurement, the caged-fluorescence dyes fill the fluidic channels. Exactly when the measurement starts, the ultra-violet light illuminates a certain region of the fluidic channel (for example: in a shape of a line, as in the photobleaching method described above). Therefore only caged-fluorescence dyes located within that certain region is transformed back into the original fluorochrome molecules, and the molecules motion can be studied to deduce the fluid flow. As in the photobleaching method, this method also requires an extra light-source to perform measurements.

Single-Molecule Detection

As we go from microfluidics to nanofluidics, and the sizes of tracer-particles are more and more reduced to the limit of a single-molecule of fluorochromes, the distinction between the scalar-based and particle-based methods becomes obsolete [3, 4]. In turn, the small dimensions of the microfluidic and nanofluidic channels also allow for increased sensitivity in the fluorescence detections: the background signal (caused by sample impurities and scattered photons) scales linearly with the size of the detection volume, while the fluorescence signal of each fluorochrome single-molecules is independent of the detection volume.

One of the most important applications of the single-molecule fluorescence detection in microfluidics and nanofluidics is the investigation on individual DNA (deoxyribonucleic acid) molecules [4]. DNA molecules are usually tagged using the so-called intercalating cyanine dyes. These fluorochrome molecules, popularly known as TOTO and YOYO, are virtually non-fluorescent in solution, but form highly fluorescent complexes with DNA molecules, with $>$ 1000-fold fluorescence enhancement [5]. The fluorescence signal of the DNA-dye complexes has been shown as insensitive to DNA base composition, and the fluorescence intensity is linearly proportional to the DNA length, which allows for fluorescence-based sizing of the DNA molecules. When tagged using these dyes, the motion of DNA molecules inside microflu-

idic and nanofluidic channels can be imaged and studied in detail.

Key Research Findings

Fluorescence measurements are very useful in general because of its sensitivity and specificity to the investigated physical, biological, or chemical process. Moreover, the fluorescently visualized process can be imaged in detail and analyzed further using various image processing and analysis techniques. This advantage, along with the high spatial measurement capabilities allowed by optical microscopy, is highly crucial for investigations in very small scale such as in microfluidics and nanofluidics.

Fluorochrome molecules are usually characterized using their quantum yield and fluorescence lifetime. Quantum efficiency is a measure of the efficiency of the fluorochrome molecules, which is expressed as the ratio between the number of photons emitted and the number of photons absorbed. In general, fluorochrome molecules with higher quantum efficiency are preferred. Meanwhile, the fluorescence lifetime is defined as the time in which the fluorescence intensity from a fluorochrome molecule decays to 1/e of the initial intensity, after a pulse excitation is introduced. This parameter is related to the speed and the temporal resolution that can be achieved during fluorescence measurements.

For fluorescence measurements in very small scales, such as the investigations performed in microfluidics and nanofluidics, an optical microscope is necessary. Among the most important elements of the setup are the set of optical filters, which separate the excitation light from the emission light. When both the excitation light path and the emission light path use the same lens near the fluorochrome molecules, the setup is termed as an Epi-Fluorescence Microscopy setup.

Depth of focus is defined as a range of space in which the fluorochrome molecules can still be imaged clearly even though they are not exactly in focus. This parameter is important in microfluidics and nanofluidics, as it influences the spatial resolution of the measurement. Emission light from fluorochrome molecules that are out of focus is typically not wanted in fluorescence measurements, because it serves as a background signal that reduces the measurement quality. To eliminate this background, the confocal configuration can be used. Meanwhile, to perform detailed fluorescence measurements on surfaces, the so-called TIRF (total internal reflection fluorescence) microscopy setup is usually used.

The main application of fluorescence measurements in microfluidics and nanofluidics is for quantitatively visualizing fluid flow. Two particle-based methods are commonly used: PIV, which uses the pattern of particles motion to induce the fluid motion, and PTV, which tracks individual particles to achieve the same objective. Alternatively, scalar-based methods can also be used, where the fluorescence signal itself serves as the observed scalar. Due to the typically short fluorescence lifetime of fluorochrome molecules, however, it is difficult to visualize the fluid motion using only fluorescence. Hence modifications are required, for example by inducing photobleaching and by using caged-fluorescence dyes.

As we go from microfluidics to nanofluidics, the distinction between the scalar-based and particle-based methods becomes obsolete, and in turn, the small dimensions of the microfluidic and nanofluidic channels also allow for increased sensitivity in the fluorescence detections. This, along with the invention of intercalating cyanine dyes, spurs another major applications of fluorescence measurements in microfluidics and nanofluidics: the investigation on individual DNA molecules.

Future Directions for Research

Fluorescence measurements are very important in studies on microfluidics and nanofludiics, with main applications on flow visualization and single-molecule detection. To achieve measurements with higher spatial resolution, which becomes more significant with the rapid development of nanofluidics, research efforts should be focused on developing more advanced fluorescence microscopy setups. The particularly useful setups will be the ones that can break the classic optical diffraction limit.

Cross References

▶ Micro-PIV-Based Diffusometry
▶ Detection Using Confocal Microscopy
▶ Detection Using TIRF Microscopy
▶ Evanescent-Wave Sensing
▶ Fluorescent Labeling
▶ Fluorescent Thermometry
▶ Methods of Flow Rate Measurements
▶ Microscale Flow Visualization
▶ Nanoscale Flow Visualization Methods
▶ Surface Plasmon Resonance Sensors
▶ Visualization Based on Molecular Tagging Methods

References

1. Murphy DB (2001) Fundamentals of light microscopy and electronic imaging. Wiley-Liss, New York
2. Pawley JB (2006) Handbook of biological confocal microscopy. Springer, Berlin
3. Sinton D (2004) Microscale Flow Visualization. Microfluid Nanofluid 1(1):2–21

4. Dittrich PS, Manz A (2005) Single-molecule fluorescence detection in microfluidic channels—the Holy Grail in µTAS? Anal Bioanal Chem 382(8):1771–1782
5. Rye HS, Yue S, Wemmer DE, Quessada MA, Haugland RP, Mathies RA, Glazer AN (1992) Stable fluorescent complexes of double-stranded DNA with bis-intercalating asymmetric cyanine dyes: properties and applications. Nucleic Acids Research 20(11):2803–2812

Fluorescence Microscopy

► Fluorescence Measurements

Fluorescence Resonance Energy Transfer (FRET)

Definition

FRET is defined as the energy transfer mechanism between two fluorescent molecules. When a donor molecule is excited at its specific fluorescent excitation wavelength its energy can be nonradiatively transferred to an acceptor molecule. This occurs through a series of dipole-dipole coupling reactions and is dependent on the distance between the molecules, the orientation of the molecules and the spectral properties of both. FRET techniques are widely used in fluorescence-based detection of biomolecules, fluorescence microscopy and molecular biology applications.

Cross References

- ► Biosensors Using Laser
- ► Lab-on-a-Chip Devices for Immunoassay
- ► Fluorescent Labeling

Fluorescence Visualization

► Fluorescence Measurements

Fluorescence Yield

Definition

The ratio of the number of molecules that fluoresce to the total number of excited molecules.

Cross References

- ► Lab-on-a-Chip Devices for Chemical Analysis
- ► Fluorescence Measurements

Fluorescent Labeling

Elizabeth Tully, Richard O'Kennedy
Applied Biochemistry Group
School of Biotechnology and Biomedical Diagnostics Institute
National Centre for Sensor Research, Dublin City University, Dublin, Ireland
richard.okennedy@dcu.ie

Synonyms

Luminescent labels; Biomolecule detection

Definition

► Fluorescent probes are relatively small molecules that are used to label biomolecules such as proteins, antibodies and nucleic acids. They contain functional groups and specific physical and chemical characteristics that confer suitability for their use as detection moieties. To date, thousands of fluorescent probes are known each with varying spectral properties. Fluorophores may be intrinsic or extrinsic in nature. Intrinsic fluorophores are naturally occurring whereas extrinsic fluorophores are added to generate a fluorescence signal to facilitate measurement of a specific target molecule. Fluorescent labels have provided excellent sensitivity for a range of assay systems that can be applied to the determination of almost any analyte.

Overview

The use of fluorescence to facilitate measurements in biological systems has increased dramatically and includes applications in spectroscopy, flow cytometry, clinical chemistry, in situ hybridisation, immunoassays, immunocytochemistry, immunohistochemistry and microarrays. ► Luminescence is the emission of light from any substance occurring when an electron returns from an electronically excited state to ground state. There are two main categories of luminescence, fluorescence and phosphorescence and these are dependent on the nature of the excited state. ► Fluorescence is the property whereby some atoms and molecules absorb light at a particular wavelength and subsequently emit light of longer wavelength after a brief interval, termed the fluorescence lifetime [1]. Photons from an external source are absorbed by the fluorophore and this produces excited singlet state electrons. However, the time taken for these electrons to return to the lower energy level is known as the excited state lifetime. The emission of light occurs as fluorescence from an excited electron singlet state, where all the elec-

trons in the molecule are spin-paired. The return to ground states occurs, with the emission of photons. Emission rates are fast being in the region of $10^8\ s^{-1}$ and fluorescence life-times are relatively short. Many fluorophores have sub-nanosecond life-times and, therefore, the fluorescence emitted by these dyes is short-lived. ►Phosphorescence is the emission of light from triplet-excited states, whereby one set of electron spins is unpaired. This means that electrons in the excited orbital have the same spin as the ground state electrons. Therefore, transition to ground state is not possible and emission rates are slow (in the region of $10^3 - 10^1\ s^{-1}$). Phosphorescent life-times have durations in the millisecond range. Following exposure to light, phosphorescent substances glow for several minutes as the excited phosphors return to the ground state very slowly.

Fluorescence-based detection has a number of major advantages over other light-based investigative methods. Changes in concentration can be monitored very rapidly and samples are not affected or destroyed in the process. Fluorescence typically occurs from aromatic molecules e. g. naturally occurring fluorescent substances such as quinine, fluorescein, rhodamine B, acridine orange and 7-hydroxycoumarin. In contrast to aromatic organic molecules, atoms are generally non-fluorescent in the condensed phase. The lanthanides, however, a group of elements including terbium and europium do not follow this rule. Fluorescence occurs in these molecules as a result of electron transitions between orbitals. Lanthanides exhibit long decay-times due to the shielding effect of electron transitions between the orbitals and also low emission rates because of their low extinction co-efficients.

A fluorescence emission spectrum is a plot of fluorescence intensity versus wavelength (nm) or wavenumber (cm^{-1}). Emission spectra vary widely from fluor to fluor and are dependent on chemical structure and environmental conditions e. g. pH, buffer components, solvent polarity and dissolved oxygen. A number of processes are involved in fluorescence emission which can have an effect on the fluorescence characteristics of a fluorophore. These include collisions with quenchers, rotational and translational diffusion and complex formation with solvent/solute. Fluorescent molecules absorb photons of energy at one wavelength and subsequently emit energy at another wavelength. During the absorption process (excitation), the quantum energy levels of some flours increases with photon uptake. This absorption band is not isolated at a discrete (single) photon energy level but spread over a range of wavelengths, giving rise to a peak of maximal absorbance. The extinction coefficient (E) is the absorbance peak maximum and is specific for each fluorophore. The ratio of total photon emission over the entire range of fluorescence to the total photon absorption (range $0-1$) is known as the quantum yield (Q). The higher the quantum yield the brighter the luminescence (photon emission) will be. Another characteristic that is an important consideration for fluorophores is the size of its Stoke's shift. Stoke's Law states that the emission wavelength of a given fluorophore should be longer and of lower energy than the excitation wavelength, so that the emission spectrum should be separated sufficiently from its excitation spectrum.

The intensity of emitted fluorescence can be decreased by a number of processes and this is known as quenching. Collisional quenching occurs when the excited state fluorophore is de-activated upon contact with some other molecule in solution. Fluorophores can form non-fluorescent complexes with quenchers and static quenching can occur in the ground state since no diffusion or molecular collisions are occurring. Quenching can also happen by other non-molecular mechanisms such as attenuation of the incident light by the fluorophore itself or another absorbing species in the sample [2]. Another problem encountered with fluorescent labels is over labelling. As the level of probe attachment to biological molecule is increased, decreases in emission intensities can occur. This is because fluorophores self-quench at high label levels, due to the energy transfers from excited state molecules to ground state dimers.

In ►immunoassays, antibodies and antigens can be labeled directly with a fluorescent molecule. Fluorescence-based detection is a safe, rapid, non-invasive technique suitable for a wide range of biological applications. Fluorescence-based detection of antibody-antigen binding interactions was traditionally performed with organic fluorescent tags such as FITC, cyanine 3 & 5 and rhodamine [2]. Most organic fluorophores have narrow excitation spectra and broad emission bands. Therefore multiplexing of assays is difficult as spectral overlap can take place. Quenching, photobleaching and autofluorescence can also often occur, affecting the generated signal, giving rise to skewed or invalid results. Another problem associated with the use of organic fluorescent probes is that conjugation strategies must be tailored to both the target molecule for labeling and the fluorescent dye. Therefore, the efficiency of labeling is often compromised, whereby over or under labeling can occur. There are many techniques for the direct and indirect labeling of biomolecules with fluorescent tags for biological applications. The selection of an appropriate fluorescent tag is dependent on a number of parameters such as sample type, mode of action, immobilisation strategy, excitation and emission characteristics of the fluorophore and the type of analyte being detected.

The evolution of novel fluorophores that exhibit greater stability and brightness, has led to improved sensitivity and reproducibility in biological monitoring. The advent of inorganic fluorophores such as quantum dots, nanocrystals and functionalised nanoparticles has revolutionised fluorescence-based detection methods. Novel fluorescent probes have higher quantum yields and high resistance to photodegradation and the main advantages of such probes are their narrow predictable emissions, extreme photostability and brightness. Functionalisation of the polymer shell of such molecules is generally quite simple and allows direct coupling of the probe to biomolecules. For example, silica nanoparticles are easy to modify, either through NHS activation, silanisation or carboxyl modification facilitating conjugation to biomolecules. Recombinant proteins and antibody fragments can also be specifically engineered with fluorescent tags but these tags can often change the binding properties of the molecule due to changes in structure and conformation.

Basic Methodology

Detection of labels for use in biological applications can be performed by either spectrophotometric or radioactive methods. Labels can alternatively be indirectly detected through another labelled substance. The use of spectrophotometric probes includes both chromogenic (coloured) labels and fluorescent labels. Chromogenic labels are mainly used for the non-covalent staining of structural features within cells as the coloured pigments in the dye bind to specific areas in the cell. However, there are a number of problems associated with these tags. The sensitivity of visible wavelength dyes is generally not sufficiently sensitive for detection of low concentrations of antigen and, even if a biomolecule is covalently modified with the chromogen, a relatively large amount of dye is required. Biomolecules can also be labelled with radioactive probes. Radioactive probes are detected with highly specialised equipment and there are certain safety considerations that must be addressed when working with such materials.

However, with fluorescent labels sensitivity can be increased dramatically. Fluorescence-based detection is a simple safe and effective way of labeling molecules for biological applications. Fluorescent tags have a number of attributes including large quantum emission yield upon excitation and easy conjugation to biomolecules via reactive groups that make them highly suitable for biological detection. The availability of multiple tags directed to specific reactive groups on biomolecules allows multiplexing of assays, whereby different probes can be used to detect for multiple antigens on a biomolecule in tissue or cells.

Fluorescent Labels

The physical and chemical properties exhibited by an ideal fluorescent label are shown in Table 1. These include high quantum yield and a large Stoke's shift to ensure good separation of excitation and emission wavelengths. A large Stoke's shift will increase the fluorescent signal generated as interference from Rayleigh scattered excitation light is decreased. The aromatic ring system contained in most fluorophores generates the luminescence and, as the ring gets larger, the emission shifts to red and the quantum yield increases. Aromatic ring constituents affect the fluorescent behaviour of each dye. Ring activators i. e. electron donating groups increase the quantum yield of a fluorophore whereas electron withdrawing groups decrease it. The presence of heavy atoms can also diminish the quantum yield by enhancing the probability of the excited singlet state going into triplet transition. Energy decay from a triplet excited state causes phosphorescence instead of fluorescence. The phosphorescent band is located at longer wavelengths and hence at lower energies, relative to the fluorescence spectrum. The energy transition to the triplet state is an opposite reaction to that of fluorescence and so a decrease in potential luminescence is caused. Polycyclic structures in the aromatic ring system are important to maintain fluorescent properties. Co-planar structures, i. e. rings in the same dimensional plane, show the greatest fluorescence. Malachite green and rhodamine have very similar structures yet the oxygen bridges on upper phenyl rings of rhodamine confer a planar shape, thus enhancing its luminescent qualities [2].

Intrinsic fluorophores are naturally occurring whereby the intrinsic fluorescence originates within the aromatic amino acids such as tryptophan, tyrosine and phenylalanine. The indole groups of tryptophan residues are the dominant source of UV absorbance/emission in proteins. Fluorescence emission from phenylalanine is observed

Fluorescent Labeling, Table 1 List of ideal properties of fluorescent probes

Properties	Ideal fluorescent probe
Light emitted	Narrow band of emission
Stability	Emits brightly Photostable
Stokes shift	Large shift Good distance between excitation and emission wavelengths
Quantum yield	High quantum yield, approaching 1
Fluorescence lifetime	Long lifetime
Light source	Broad excitation range Inexpensive

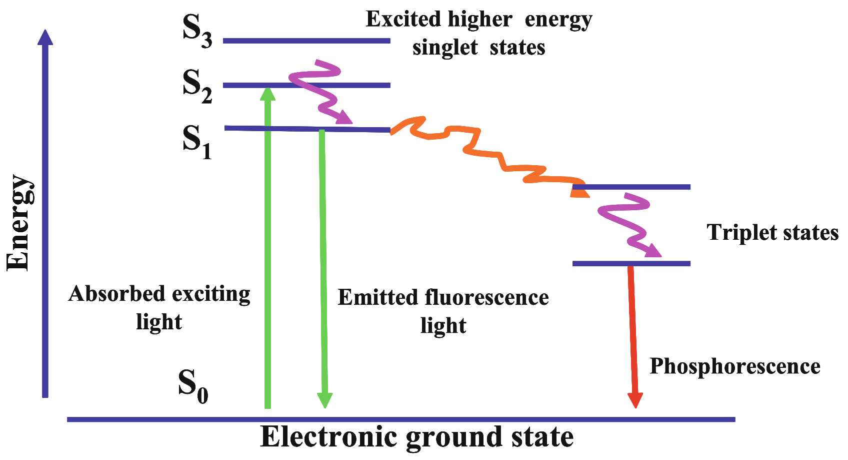

Fluorescent Labeling, Figure 1 Jablonski diagram (adapted from Lackowicz, 1983). When a photon provided by an external light source is absorbed by a fluorophore, it is excited from a vibrational level in the electronic ground state (S_0) to a higher electronically excited state. The electronic state of an organic molecule can be either a singlet state whereby all electrons in the molecule are spin-paired or a triplet state where one set of electrons is unpaired. The excited singlet states (S_{1-3}) are reached after initial absorption. A molecule in this energy level will quickly fall to the lowest vibrational level of this state by energy loss through collision. Fluorescence occurs as photon of light is emitted; returning the fluorophore to ground state. The Jablonski diagram shows the possible routes by which an excited molecule can return to ground state via unstable triplet states. A quick return to ground state results in fluorescence, whereas a delayed return is known as phosphorescence

only when the sample protein lacks both tyrosine and tryptophan residues and this is a very rare occurrence. Emission of tryptophan is very sensitive to local environmental changes and can be used as a reporter group for protein conformational changes. Spectral shifts are observed on binding of ligands and on protein-protein association. The emission maximum of proteins reflects the average exposure of tryptophan residues to the aqueous phase. Tryptophan fluorescence is subject to quenching by iodide, acrylamide and disulfide groups and also by nearby electron-deficient groups and protonated histidine residues. Extrinsic fluorophores are added to samples to provide fluorescence and change the spectral properties. In addition, the molecule of interest is often non-fluorescent or the intrinsic fluorescence is too weak. Proteins with weak intrinsic fluorescence can be labelled with fluorophores that have longer excitation and emission wavelengths than their constituent aromatic amino acids. There are huge numbers of such fluorophores available. Reagents are available that can be used for both the covalent and non-covalent labeling of proteins. In the case of covalently bound probes a variety or reactive groups are available for effective coupling with amine, sulfyhdryl and histidine side chains in proteins. Ideally, for labeling of biomolecules, each fluorophore should have several analog forms each with a different reactive group suitable for coupling to a different specific functional group on the target molecule. Popular organic labels include derivatives of fluorescein, rhodamine, coumarins and Texas red, as shown in Table 2.

Common Fluorophores

Fluorescein and rhodamine are common fluorophores used for the fluorescent labeling of proteins in biological applications. This is due to a number of advantageous properties such as long absorption maxima, insensitivity to solvent polarity, high molar extinction co-efficient and the availability of a wide variety of reactive derivatives. Fluorescein derivatives are characterised by a multi-ring aromatic structure, due to the planar nature of an upper, fused, three-ring system, (Fig. 2). Derivatives of the basic structure of fluorescein involve substitution of carbons number 5 or 6 of the lower ring, for modification and labeling of biomolecules. The effective excitation wavelength range is between 488 – 495 nm, while the emission spectrum lies between 518 – 525 nm, depending on the derivative. The quantum yield of fluorescein derivatives can be up to 0.75. However, quick photobleaching can be observed when the dye is dissolved in buffers, exposed to light or pH variations or subjected to long-term storage. Amine reactive fluorescein derivatives such as fluorescein isothiocyanate (FITC) react under slightly alkaline conditions with primary amines in biomolecules to form stable highly fluorescent derivatives. FITC is synthesised by modification of the lower ring at carbon positions 5 or 6. Isothiocyanates react with nucleophiles such as amines, sulfydryls and the phenolate ion of tyrosine side chains. They form a stable product on reaction with biomolecules at primary amines. FITC is almost entirely selective for modifying N-terminal amines in proteins. The reaction involves the attack of

Fluorescent Labeling, Table 2 List of common organic fluorophores

Fluorophore	Mr (Da)	λ_{ex}(nm)	λ_{em}(nm)	Fluorescent lifetime (ns)	Quantum Yield (Q)	Reacts with
Fluorescein Isothiocyanate	389	494	520	~ 4.1	0.75	Amines
NHS-Fluorescein	457	491	518	~ 4.0	0.75	Amines
Iodoacetamidofluorescein	515	491	520	~ 4.0	0.75	Sulfhydryls
Fluorescein-5-maleimide	427	490	515	~ 4.0	0.75	Sulfhydryls
Fluorescein-5 thiosemicarbazide	421	492	516	~ 4.0	0.75	Aldehyde/Ketone
5-(2-Carbohydrazino)methyl) thio)acetyl)-aminofluorescein	493	490	516	~ 4.0	0.75	Aldehyde/Ketone
Tetramethylrhodamine-5-(6)-isothiocyanate	444	544	570	~ 1.5	0.25	Amine
NHS-Rhodamine	528	546	579	~ 1.5	0.25	Amine
Lissamine Rhodamine Sulfonyl Chloride	577	556	576	~ 2.1	0.25	Amine
Texas Red Sulfonyl Chloride	577	556	576	~ 4.2	0.25	Amine
Tetramethylrhodamine-5-(6)-iodoacetaminde	569	540	567	~	0.25	Sulfhydryls
Lissamine Rhodamine B Sulfonyl Hydrazine	573	560	585	~	0.25	Sulfhydryls
Texas Red Hydrazine	621	580	604	~	0.25	Sulfhydryls
7-Amino-4-methyl-coumarin-3-acetic-acid	233	345	450	~	0.49	Amines (using EDC activation)
Succinimidyl-7-mino-4-methyl-coumarin-3-acetic-acid	330	345	450	~	0.49	Amines
Sulfosuccinmidyl-7-mino-4-methyl-coumarin-3-acetic-acid	431	345	450	~	0.49	Amines
4,4-difluoro-5,7-dimethyl-4-bora-3a,4a-diaza-S-indacene-3-proponic acid, succinimidyl ester (BODIPY FL C3-SE)	389	502	510	~	0.8	Amines
4,4-difluoro-5,7-diphenyl-4-bora-3a,4a-diaza-S-indacene-3-proponic acid (BODIPY 530/550 C3)	416	535	552	~	0.8	Amines
Cyanine 3	767	550	570	~ 0.2	~ 0.25	Amines
Cyanine 5	792	649	670	~ 0.3		Amines

a nucleophile on the central electrophilic carbon of the isothiocyanate group. The resulting electron shift creates a thiourea linkage between FITC and the biomolecule. FITC is water soluble above pH 6.0 and isothiocyanate reagents are reasonably stable in aqueous solution for short periods, but degrade over time.

The main applications of FITC are as follows:

- labelling of antibodies to detect antigens in cells, tissues, immunoassays, blots, chips, and microarrays;
- detecting proteins after electophoretic separations;
- microsequencing analysis of proteins/peptides;
- identification of molecules separated by capillary zone electrophoresis;
- labels in flow cytometry.

NHS-Fluorescein is an amine reactive carboxy-succinimidyl ester group at carbon position 5 or 6 of the lower ring and is more stable than FITC. The NHS-ester reaction proceeds rapidly at slightly alkaline pH values, resulting in stable amide-linked derivative. It has similar properties to FITC with the extinction coefficient dependent on environmental conditions such as pH or buffer. NHS-fluorescein is insoluble in aqueous solution; therefore all stock solutions should be made up in an organic solvent. The optimal pH for NHS ester functionality is 7 – 9. NHS-fluorescein is also available with a long chain spacer. This may be useful for reducing steric hindrances around the fluorescent molecule encountered during labeling, thus minimising quenching effects.

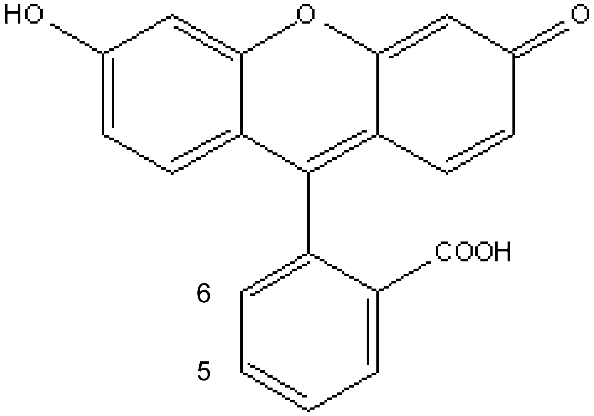

Fluorescent Labeling, Figure 2 Structure of Fluorescein

Sulfhydryl-reactive derivatives of FITC contain sulfyhdryl groups on the lower ring structure. These groups direct the labeling to more limited sites on target molecules. Coupling through sulfhydryl residues instead of amines can avoid active centres in proteins, preserving functional activity. Sulfhydryl reactive sites are naturally available through free cystine side chains generated by the reduction of disulfides or the use of thiolation reagents. Iodoacetamido-fluorescein is an intense fluorophore derived by modification of a sulfhydryl reactive iodacetyl group at carbon 5 or 6. Iodacetyl groups react with sulfhydryls under slightly alkaline conditions to yield stable thioether linkages. They do not react with unreduced disulfides in cystine residues. It is important to protect these reagents from light since the light catalyzed breakdown of iodaecetyl groups causes quenching. The molar extinction co-efficient is dependent on environmental factors such as pH. These reagents are soluble in organic solvent and aqueous solution above pH 6.0. Fluorescein-S-malemide has a sulfhydryl reactive malemide group on the lower ring structure. It forms stable thioether bonds that are pH controlled and has fluorescent properties close to fluorescein. If no −SH groups are available disulfides can be reduced with thiolation reagents. Fluorescein-S-malemide is soluble in aqueous solution above pH 6.0 at low concentrations.

Fluorescent derivatives of fluorescein with hydrazide groups on carbons 5 or 6 can be used to label aldehyde or ketone-containing molecules. Hydrazides react with aldehyde and ketone functional groups to form hydrazone linkages. Many biomolecules have no aldehyde or ketones groups in their native state, except for those with sugar residues such as carbohydrates, glycoproteins and RNA. These molecules can be oxidised with sodium periodate to produce reactive formyl groups. Modification reagents that generate aldehydes upon coupling to a molecule can also produce hydrazide reactive sites. DNA and RNA can be modified with hydrazide reactive probes by reacting cytosine residues with bisulfite to form sulfone intermediates Fluorescein-5-thiosemicarbazide is a hydrazide derivative of fluorescein and is involved in a spontaneous reaction with aldehyde/ketone-containing molecules to form covalent hydrazone linkages. It can also label cytosine residues in DNA/RNA by way of bisulfite activation. This derivative is soluble in organic solvents and aqueous solutions above pH 7.0. However, it is prone to photobleaching and so protection from light is essential. It is useful for the site-directed labeling of antibodies through carbohydrate side chains. 5-((((2-carbohydazino)-methyl)-thio)-acetyl)-aminofluorescein is another derivative of fluorescein that has a longer spacer arm on carbon 5. It is very similar to fluorescein-5-thiosemicarbazide and reacts with aldehydes/ketones in the same way. It can label cytosine residues and is soluble in organic solvents and aqueous solutions above pH 7.0.

Rhodamine derivatives obtain their fluorescent character from a planar multi-ring aromatic structure. They are very similar to fluorescein but with a nitrogen atom replacing oxygen on the outer ring as shown in Fig. 3. Activated rhodamine probes have reactive groups made through substitution on carbon 5 or 6 of the lower ring. Alterations to the basic rhodamine structure modulate its fluorescence characteristics, giving rise to an intense and stable fluorescence. There are a number of derivatives of the basic rhodamine structure.

These include the following:

Tetra methyl rhodamine derivative 2 methyl groups on each nitrogen on the outer ring

Rhodamine B 2 ethyl groups on each nitrogen on the outer ring plus a carboxylate at position 3

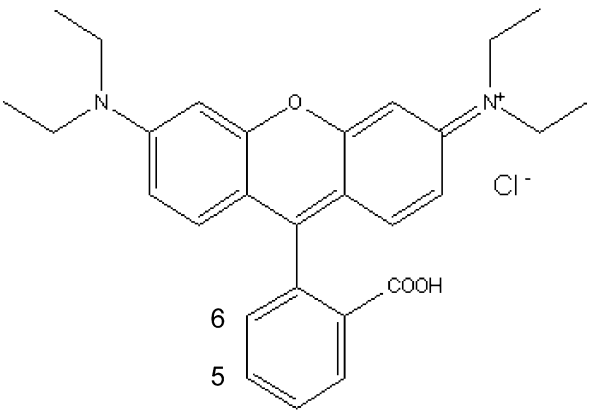

Fluorescent Labeling, Figure 3 Structure of Rhodamine

Rhodamine G6 2 methyl groups on each nitrogen on the outer ring plus an ethyl ester on a carboxylate at position 3

Sulforhodamine B 2 ethyl groups on each nitrogen on the outer ring plus a sulfonate at position 3 and 5 (Lissamine rhodamine B)

Sulforhodamine 101 (Texas red) intense luminescent properties in the far red region of spectrum

The basic characteristics of rhodamine probes are as follows. The effective excitation wavelength is in the visible light spectrum (500 – 590 nm) and associated emission wavelengths occur from high 500s to early 600s i. e. the orange to red portion of the visible spectrum. The quantum yield of rhodamine derivatives is generally lower than fluorescein, typically being 0.25. However, rhodamine probes exhibit slower bleaching in that the intensity fades slowly when dissolved in buffers or exposed to light. The red emission of rhodamine probes is in stark contrast to fluorescein so this makes it ideal for double staining when used in conjunction with FITC. A number of amine reactive derivatives are commonly used and these include tetramethylrhodamine (TMR)-isothiocyanate, NHS rhodamine, lissamine rhodamine sulfonyl chloride and Texas red sulfonyl chloride. Coupling through sulfhydryls instead of amines can help to avoid interference with active centres in biomolecules, thus minimising the effect on the biological activity. Reaction sites are available via free cystine side chains and the use of thiolation reagents. An example of a sulfhydryl reactive probe is TMR-iodoacetamide.

Finally, another group of derivatives are the aldehyde/ketone reactive probes. This group is based on the activation of a sulfonyl-hydrazine group of carbon number 5. They are based on Lissamine and Texas red structures and used to label aldehyde/ketone-containing molecules (with sugars). The most common aldehyde/ketone reactive probes are Lissamine rhodamine B hydrazine and Texas red hydrazine.

Coumarin Derivatives

Coumarins are naturally occurring substances found in Tonka beans, lavender oil and sweet clover and many are inherently fluorescent. The basic structure of a coumarin molecule is shown in Fig. 4. Some coumarin derivatives are also highly fluorescent e. g. 7-amino-4-methyl-coumarin-3-acetic acid (AMCA) has a carboxylate group that is easily functionalised for conjugation [4]. It gives rise to an intense fluorescence in the blue region of visible spectrum. Coumarins are also good donors for excited state energy transfer to fluorescein. Their emission spectra are in a region that does not overlap with other major probes and are therefore suitable for double staining applications. The main advantages of coumarin probes are a large Stoke's shift, a good quantum yield of ∼ 0.49 and activity over a wide pH range (3 – 10). Coumarin derivatives are easily coupled to biomolecules via a carbodiimide reaction with EDC. The most common probes are NHS-AMCA and sulfo-NHS-AMCA, which have similar properties. Coumarin labels are highly useful for double labeling techniques since their emission wavelengths are sufficiently distant from the more common organic fluorophores. Therefore, coumarins are highly appropriate for use in multiplexed immunostaining applications.

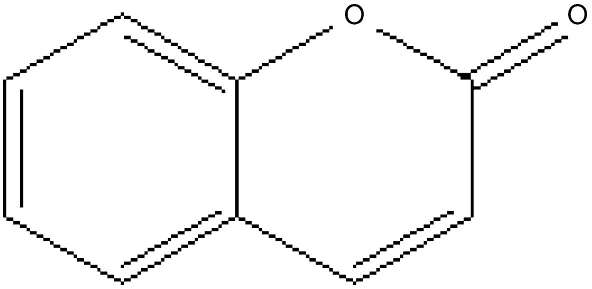

Fluorescent Labeling, Figure 4 Structure of Coumarin

BODIPY Derivatives

4,4-difluoro-4-bora-3a-4a-diaza-s-indacene (BODIPY) has a fused multi-ring structure. Modifications at 1, 3, 5, 7 and 8 carbon positions cause spectral shifts in excitation and emission wavelengths and functional sites for coupling. BODIPY derivatives have a high quantum yield (∼ 0.8) and are relatively insensitive to pH changes. One disadvantage of BODIPY probes is the relatively small Stoke's shift (20 nm maximum), which can cause problems since excitation at sub-optimal wavelengths is required to prevent interference and light scattering from the excitation source. BODIPY is suitable for use with molecules with only one free amine group, since the label is easily quenched by excess presence of dye.

DNA Labels

There are numerous probes available that spontaneously bind to DNA, displaying enhanced emission. Ethidium bromide weakly fluoresces in water but this intensity is greatly increased upon binding to DNA (Fig. 5). The mode of binding is due to the intercalation of the planar aromatic ring between base pairs of double helical DNA. Acridine orange also binds to DNA by intercalation and 4'6-diamidino-2-phenylindole (DAPI) binds into the minor groove of DNA. Fluorescence is most enhanced

when adjacent to *adenine-thymine-rich* regions of DNA. These labels are used to image DNA on agarose gels using a UV transilluminator for molecular biological applications.

Non-Covalent Fluorescent Probes

Some dyes are weakly fluorescent or non-fluorescent until the occurrence of a particular event, i. e. enzymatic cleavage. An example of this is 7-umbelliferyl phosphate, a coumarin derivative, and a non-fluorescence phosphate ester that becomes highly fluorescent upon hydrolysis. It can be used to measure the activity of alkaline phosphatase in ELISA and enzyme-amplified DNA assays. Some dyes become fluorescent upon reacting with amines. Fluorescamine is one such dye and can be used for protein labeling but more common applications of this dye are the determination of protein concentration and as a tracking dye in protein sequencing. Anionic dyes can be used to bind to residues of proteins, which carry positive charges. Upon binding the fluorescent intensity can be either enhanced or quenched. In the case of enhancement, changes in microenvironment can cause changes in hydrophobicity of a given biomolecule. Probes that are non-fluorescent in water may be highly fluorescent in apolar media. Non-covalent probes can also be used in a quenching capacity, for example at pH 3.1; Eoisin Y exhibits strong green fluorescence, whereas on binding to protein, the fluorescence is quenched. Another example is the non-covalent binding of the near-infrared anionic dye IR-125 to casein. This was investigated with the use of steady-state and picosecond laser fluorescence measurements. In an aqueous borate buffer minimal fluorescence emission from the dyes was observed. When casein was added to the solution, enhancements in the fluorescence emission were found. The reason for this is that the dye distributes between the hydrophobic core of the protein and the interstitial aqueous solution. The dye molecules residing in the interior of the protein exhibit enhancements in their fluorescence due to a more favorable microenvironment.

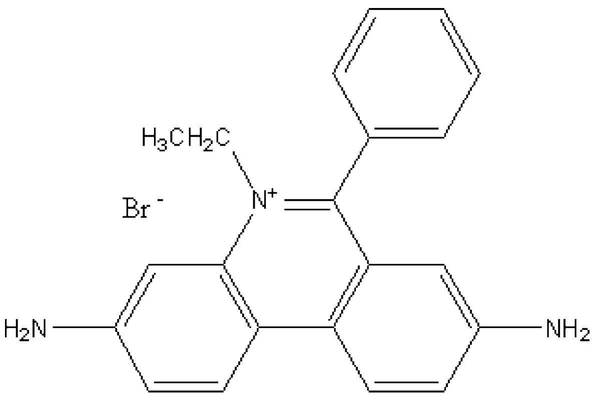

Fluorescent Labeling, Figure 5 Structure of Ethidium Bromide

Near-Infrared (NIR) Fluorescent Probes

NIR detection of biomolecules has a number of advantages including low fluorescence background, since very few naturally occurring molecules can undergo electronic transitions in this low energy region of the spectrum. Scatter is also reduced at higher wavelengths at this end of the spectrum and sample photodecomposition is reduced. Excitation is usually by a cheap, stable laser diode, which increases sensitivity. NIR probes have high quantum yields, large Stoke's shifts, photochemical stability and a high tolerance to quenching. Good examples of NIR probes are the group of cyanine dyes. These molecules have emission maximums between 600 – 800 nm. The quantum yields of these probes in aqueous solutions are very low. However, on binding to analytes changes in absorption and emission wavelengths are increased as the fluorescent life-time increases. Cyanine dyes can label proteins by covalent and non-covalent binding. The non-covalent attachment of cyanine is useful for the detection of large proteins, as the positive charge of dyes can be used for non-covalent labeling. Fig. 6 shows the basic structure of a cyanine dye.

Cyanine derivatives with alkyl SO_3^- groups and active groups such as isothiocyanate, iodoacetamide and N-succinimidyl can be used for covalent attachment to biomolecules. Di-carbocyanine dyes (adding a −CH = CH-entity to the polymethine chain of cyanine) cause a large red shift (up to 100 nm) in absorption maximum. Di-carbocyanine dyes with NHS-esters are suitable for the covalent labeling of molecules with primary/secondary amines, under slightly alkaline conditions. Cyanine dye fluorophores are bright fluorescent dyes that contain a −CH group linking two nitrogen-containing heterocyclic rings as shown in Fig. 6. They can be functionalised with NHS ester, maleimide, isothiocyanate and hydrazine chemistries for biomolecule attachment. They exhibit high molar extinction coefficients and favourable quantum yields. The small size of these dyes reduces steric hindrance, and therefore, loss of activity. Cyanine dyes can be used for standard fluorescence, fluorescence resonance energy transfer (FRET), time-resolved fluorescence (TRF) and fluorescence polarisation applications. The favourable properties of cyanine dyes include good aqueous stability, tolerance to organic solvents, pH insensitivity (range

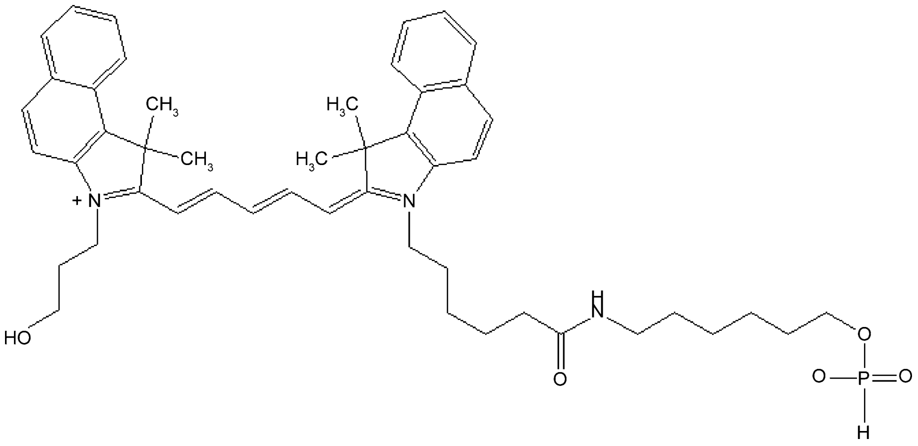

Fluorescent Labeling, Figure 6 Structure of Cyanine 5

pH 3 – 10), low non-specific binding and high photostability. They are suitable for labeling via a range of amine, thiol and aldehyde groups. The sensitivity of fluorescence detection is often limited by autofluorescence of biological samples. This is decreased as the excitation wavelength becomes longer and, therefore, detectability over background is increased. Longer wavelength probes can be excited with simple excitation sources such as LEDs. Cyanine dyes have absorption and emission wavelengths above 650 nm. They also have a small Stoke's shift with the absorption maximum shifted from the emission maximum. The charged side chains of cyanine dyes are used for improved water solubility and to prevent self-association, the main cause of self-quenching.

Lanthanides

Long life-time probes are those with fluorescent lifetimes greater than those of traditional organic probes (1 – 10 ns). Lanthanides are transition metals with fluorescent life-time decay times between 0.5 – 3 ms [5]. Transition metal ligand complexes are made up of metal and organic ligands. They contain mixed singlet-triplet states and have intermediate lifetimes of 400 ns to μs. Their absorption co-efficients are very low and emissive rates very slow, giving rise to long life-times. They are not directly excited but use chelated organic liquids as conduits. Lanthanides can substitute chemically for calcium in calcium-dependent proteins. They can be used with proteins that do not have intrinsic binding sites. They are particularly useful in immunoassay applications. Biological samples can exhibit autofluorescence, which can be limiting, since autofluorescence from the sample decays on a nanosecond timescale, as does the fluorescence of most probes. However, due to the long decay time of lanthanides, they continue to emit following the disappearance of autofluorescence. ►Time-gated detection can be used with lanthanides whereby steady state intensity measurements are taken over a period of time following pulsed excitation. This principle of time-gated detection of long life-time probes is illustrated in Fig. 7.

In Vivo Labeling

The green fluorescent protein (GFP) from the jellyfish, *Aequorea Victoria,* is a versatile reporter for monitoring gene expression and protein localization in a variety of cells and organisms [11]. GFP emits bright green light on excitation. The chromophore in GFP is intrinsic to the primary structure of the protein, and fluorescence from GFP does not require additional gene products, substrates or other factors. GFP fluorescence is stable, species-independent and can be monitored non-invasively using the techniques of fluorescence microscopy, fluorescence-activated cell sorting (FACS), flow cytometry and fluorescence resonance energy transfer (FRET). Since the first use of the green fluorescent protein (GFP) in living organisms, over ten years ago, live cell fluorescence microscopy has become an indispensable tool for cell biologists. In recent years many fluorescent reporters suitable for in vivo experiments have been developed, including a wide range of fluorescent proteins in various colours. The technique of in vivo labeling of genes and proteins for microarray purposes is a useful tool in the development of the field of gene and protein expression analysis. In vivo labeling methods give accurate pictures of what is happening in the natural dynamic environment and these techniques are becoming a vital tool for fluorescence-based detection, especially for microarray applications.

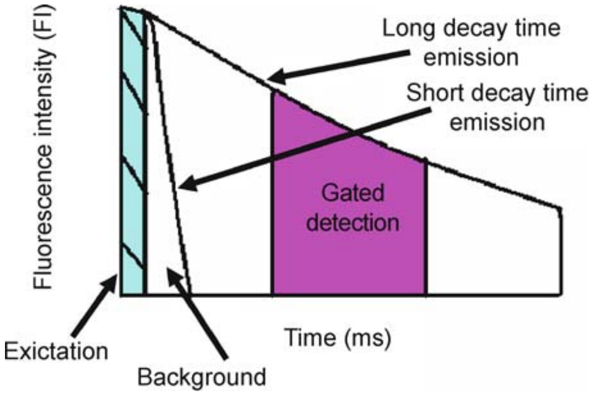

Fluorescent Labeling, Figure 7 Principle of time-gated fluorescence detection. Time-gated fluorescence detection is used to monitor the fluorescence of a sample as a function of time after excitation by a flash or pulse of light. This figure shows a schematic of the system used with the lanthanides whereby steady-state intensity measurements of emitted fluorescence are taken over a period of time following pulsed excitation. Time resolution is optically gated, whereby short laser pulse acts as a gate for the detection of emitted fluorescence and only fluorescence that arrives at the detector at the same time as the gate pulse is collected. In time-gated detection systems, the detector is turned on after excitation and the fluorescence intensity generated is integrated. This method is useful for long lifetime probes

Fluorescent Labeling of Biomolecules

A standard protocol for the fluorescent labeling of biomolecules is difficult to derive as optimisation of labeling condition such as buffer; pH and concentration is highly specific for each dye. Gel filtration can be used to remove azide, which interferes with the labeling process or for buffer exchange and is often found as a preservative in biological preparations. Typically, phosphate buffered saline comprising of 0.13 mM NaH_2PO_4, 0.528 mM Na_2HPO_4 and 0.51 mM NaCl, pH 7.4 or 0.5 M carbonate buffer, pH 9.6, are used for labeling reactions. The amount of fluorescent labeling reagent used for each reaction is dependent on the amount of protein to be labeled. By using the appropriate molar ratio of labeling reagent to protein, the extent of conjugation can be controlled. For protein concentrations in the range of 2 – 5 mg/ml, a 10 M excess is used, for concentrations < 2 mg/ml, a 15 M excess is used and for protein concentrations < 1 mg/ml, 20 M excess of dye is used. The fluorescent label is generally dissolved in an organic solvent, as most fluorescent dyes are insoluble in aqueous solution, at concentration of 10 mg/ml. Taking into account the molar ratio of dye and biomolecule, the correct volume of label can be determined and added to the protein stock. The tubes are incubated end on end and left to react overnight at 4 °C, in the dark to avoid any photobleaching. The following day the fluorescent conjugate is purified to remove unreacted dye, either by gel purification, spin column centrifugation or dialysis. The conjugate concentration and dye/protein ratio are then determined spectrophotometrically. The level of label incorporation can be measured by determining the absorbance at or near the characteristic extinction maximum of the label. It is also important to determine the dye/protein ratio for all derivatives prepared with tags. The equations below are used to calculate this information.

$$\frac{A_{280} - (A_{\max} \times CF) \times DF}{E_{\text{protein}}} \tag{1}$$

$$\frac{A_{\max}}{E_{\text{dye}} \times Prot.Conc} \times DF \tag{2}$$

$A_{\max}$ = Absorbance of the conjugate at the excitation maximum wavelength for the dye; A_{280} = Absorbance of the conjugate at 280 nm; CF = Correction factor, i. e., A_{280} dye/$A_{\max}$ dye; DF = Dilution factor; E_{protein} = protein molar extinction co-efficient; E_{dye} = dye protein molar extinction co-efficient.

Biotinylation

Another efficient method of labeling biomolecules for fluorescence applications is biotinylation. Biotin is a B vitamin, which binds with high affinity to avidin and streptavidin. It is the strongest non-covalent binding reaction with an affinity constant (K_a) of 10^{15} M^{-1}. It can be easily conjugated to proteins since many derivatives are available. Analogues of biotin are also available with an extended spacer arm that reduces steric hindrances thus improving binding capability. Biotin forms a stable amide bond with primary amines at pH 7 – 9. The optimal biomolecule concentration for successful biotinylation is approximately 1 – 2 mg/ml. However, for less concentrated solutions of biomolecule this can be adjusted once the molar excess of both dye and biomolecule is taken into account. Unreacted biotin is removed from the biomolecule post-conjugation by ultrafiltration, microcentrifugation or dialysis. Silica-encapsulated quantum dots or nanoparticles can be coupled directly to streptavidin through a carbodiimide-mediated coupling reaction. This theoretically yields a high number of streptavidin molecules, typically up to 20, binding to the inorganic label. Biotinylated biomolecules can then be coupled directly to streptavidin-labelled fluorescent tags.

Novel Fluorophores

The main advantages of novel inorganic fluorescent probes such as nanoparticles and quantum dots are their narrow

predictable emission, extreme photostability, multiple tunable colours, brightness, broad excitation, large Stoke's shift and high quantum yields [6]. Functionalisation of the polymer shell of such molecules is generally quite simple and allows direct coupling of the probe to biomolecules. Silica nanoparticles are easy to modify, either through NHS activation, silanisation or carboxyl modification. Quantum dots are nanocrystalline semi-conductors that exhibit unique light emitting properties that can be customised by changing the size or composition of the dots. Quantum dots are typically 2 – 8 nm in size and covered with a layer of organic material that allows functionalisation of the surface for biomolecule attachment. The colour is determined by the size of the particles and the composition of the material used, which in turn dictate the optical properties. One of the main advantages of nanocrystalline fluorophores is that they absorb light over a broad spectral range. By absorbing all wavelengths shorter than their emission wavelength (blue wavelengths), only a single light source is required for the excitation of multiple coloured dots. This simplifies instrumentation, lowering costs and enabling multiplexing of assays. The narrow emission spectra of nanocrystals give rise to sharper colours and high spectral resolution, which improves assay sensitivity since nanocrystals emit more light than their constituent dye. Quantum dots are not liable to photobleaching, exhibit excellent photostability and, relative to conventional fluorophores, are up to 100 times more stable [6]. It is this photostability that allows repeated interrogation of the materials over longer periods. Quantum dots have high excitation cross sections, whereby they absorb much of the light with which they are irradiated, and high quantum yields in that they re-emit more than 50% of the light they absorb [7]. This gives rise to strong fluorescence signals, thus increasing detection sensitivity. The potential uses of quantum dots in biological applications include drug delivery, diagnostics, drug discovery, genetic analysis and observation of biomolecular interactions. Multiple proteins or biomolecules can be identified by multiplexing different coloured quantum dots in microarray applications.

Organic fluorescent labels such as FITC, Cy5 and rhodamine can exhibit high optical background in immunoassay applications, which reduces sensitivity [3]. The use of long-decay fluorescent probes and time-resolved detection allows for a significant decrease in background and, therefore, an increase in sensitivity. The lanthanide chelates, such as europium and terbium have traditionally been used as probes for the time-resolved fluorescent detection of analytes. Functionalised deriviatives of these dyes are available commercially for both homogenous and heterogeneous assays. However, an enhancement step is often necessary such as dissociative enhancement (DELFIA) or addition of enzyme labels to improve performance, resulting in an enzyme-amplified lanthanide luminescence system. Another group of structures, the metalloporphyrins are particularly suitable for biological applications, due to their relatively long decay times and provide a realistic alternative to fluorescent lanthanide chelate labels. Phosphorescent metalloporphyrins, such as the water-soluble platinum and palladium complexes of coproporphyrin, have a number of advantages as labels for immunoassay development. These include high quantum yields of up to 40%, simple laser excitation at 532 nm, broad red emission (600 – 750 nm) and long phosphorescent life-times (10 – 1000 μs). The platinum and palladium porphyrins can have either isothiocynate reactive groups or malemide reactive groups, allowing conjugation to be tailored exactly to suit the substance being labeled. There are two main conjugation strategies for porphyrin attachment to proteins. The first involves the activation of the porphyrin by carbodiimide, followed by nucleophilic attack of the primary amino groups of the biomolecule to produce bioconjugates via the amide bond. The second method employs carbodiimide to preactivate the porphyrin in the presence of an active ester, which results in a porphyrin derivative with active functional groups that can react with the amino groups of a biomolecule. Novel derivatives of platinum and palladium coproporphyrin were used to make phosphorescent conjugates of antibodies, avidin, biotin and neutravidin. These labels and conjugates were evaluated in solid phase immunoassays using commercial phosphorescence-based detectors. Successful use of these probes was reported for a number of plate-based assay formats [8].

Ruthenium complexes are designed specifically to have long fluorescence life-times close to 500 nanoseconds. These labels are laser-excitable metal ligand complexes and can be used to label amines on biomolecules under mild conditions. The main advantages of these dyes as protein-labels include high photostability, good water solubility, a lack of dye-dye interactions and large Stoke's shifts. In addition, the fluorescence signal of such long-lived fluorophores can be gated to eliminate the emission from short-lifetime fluorophores, and autofluorescence from cells and biomolecules, to further improve sensitivity. Castellano et al. [9] described the development and characterisation of highly luminescent ruthenium complexes for covalent linkage to human serum albumin (HSA) and human immunoglobulin (hIgG). The conjugation reactions were performed at 4 °C in the dark using a thiol-reactive ruthenium complex, dissolved in an organic solvent. Unreacted dye was removed by gel filtration and dialysis and the conjugates were characterised spectro-

F

scopically. Ruthenium metal-ligand complexes were also used in ►fluorescence resonance energy transfer (FRET) immunoassays. The antigen, ruthenium-labeled HSA was reacted with an anti-HSA antibody, labeled with a non-fluorescent absorber, reactive blue 4. The conjugation of ruthenium dye to HSA employed a simple covalent linkage using a 10 M excess of dye. The association of Ru-labeled HSA to the anti-HSA antibody was detected by a change in the spectral parameters of Ru-HSA. The intensity and decay time of Ru-labeled antigen decreased upon binding to the acceptor-labelled antibody. Antibodies labelled with NHS-functionalised ruthenium complexes have also been used for the electrochemiluminescence detection of interferon alfa-2b in human serum. Labelled antibodies were prepared by incubating the antibody with the Ru-NHS ester at a molar excess of 10 for one hour at room temperature with agitation. Unreacted dye was removed by dialysis.

Fluorescent nanoparticles exhibit considerable advantages in detection over organic fluorescent dye molecules and quantum dots. The superiority of nanoparticles is apparent in their stability, brightness and ease of functionalisation for bioconjugation. Ow et. al. [10] described a class of highly fluorescent core-shell nanoparticles, up to 20 times brighter and photostable than their constituent fluorophore. The fabrication of such molecules employs a microemulsion technology. This method encapsulates fluorescent dye molecules into a silica matrix, giving rise to dye-doped nanoparticles with high intensity of fluorescent signal. The excellent photostability of doped nanoparticles is due to exclusion of oxygen by the silica encapsulation. Surface modification post-fabrication allows efficient conjugation to biomolecules. Silica is easy to modify, either through NHS activation, silanisation or carboxyl modification [11]. SEM, TEM and fluorescence spectroscopy were used to characterise the doped nanoparticles to determine size uniformity, quantum yield, fluorescent life-time and fluorescent intensity. Each nanoparticle encapsulates thousands of fluorescent dye molecules in the protective silica matrix, providing a highly amplified and reproducible signal for fluorescence-based bioanalysis. Traditional immunoassays employ the use of one or more fluorescent dye molecules linked to an antibody to trace the antibody-antigen binding interaction. Nanoparticles have been successfully conjugated to antibodies, proteins, streptavidin and avidin. The efficiency of the conjugation process can be monitored and the conjugation rate predicted, with respect to the initial ratio of biomolecule to nanoparticle (NP) by applying mathematical formulae which take into account the size of the nanoparticles, their capacity for binding (mg protein present per mm^2 of nanoparticle surface) and the mean diameter of the nanoparticles.

Key Research Findings

The use of fluorescence in immunoassay for the detection of medically and biologically important analytes has become an important tool in diagnostics. Sun [7] showed the use of quantum dots as novel fluorescent probes for a glass chip-based sandwich immunoassay. Carboxyl-coated quantum dots were linked to antibodies via EDC chemistry. Glass chips were silanised for the immobilsation of capture antibodies and a sandwich assay was successfully developed on the chip, with detection using laser confocal scanning microscopy and array software. Luminescent quantum dot bioconjugates were also prepared using engineered poly-histidine terminated proteins. A recombinant single chain antibody fragment (scFv) specific for trinitrotoluene (TNT) was conjugated to CdSe-ZnS quantum dots through a carboxy terminal histidine tail and the conjugated scFv were used to detect TNT in a competitive immunoassay.

The use of nanoparticles to improve the performance and sensitivity of immunoassays is an emerging technology. Seydack [6] reported on the use of nanoparticles in immunoassays with improved detection limits, multiplexing of assays, reduction in photobleaching, signal amplification and improved sensitivity. Both dye-doped and metallic-enhancement nanoparticles are easily fabricated for use as fluorescent tags in immunosensing technologies. The preparation and characterisation of tetramethylrhodamine (TMR), ruthenium and fluorescein-doped nanoparticles was reported by Lian et al. [11] and the application of such molecules in solid-phase and biochip applications was shown. The applications of nanoparticles in immunoassay formats include direct and indirect binding assays for the detection hIgG, using avidin nanoparticles in direct comparison with Texas red and quantum dots, [11]. DNA microarray technology was also explored, using genomic DNA from *Pseudomonas aeringosa*. Dilutions of DNA were printed on gamma amino propyl silane (GAPS) slides and post-hybridisation labeling with avidin-nanoparticles versus Streptavidin–Cy5 was investigated. Clusters of arrayed DNA were imaged and under the same conditions the nanoparticle spots were much brighter. Lian et al. also investigated the use of nanoparticles in a protein microarray application with high detection sensitivity reported. The use of europium (III) chelate-doped nanoparticles as donors in homogenous proximity assays has also been reported. Antibody fragment-coated nanoparticles are prepared by activa-

tion of the carboxyl groups on the nanoparticles with EDC/NHS chemistry. Covalent linkage occurs between the activated carboxyl groups on the nanoparticle surface and amino groups on the Fab. Lochner et al. [12] show the principle of nanoparticle-enhanced fluorescence. This phenomenon occurs when the surface of a metallic nanoparticle is illuminated, generating an electromagnetic field. The interaction of this field with nearby fluorophores results in a fluorescent enhancement effect. Silanised plates were used to couple silver nanoparticles on the surface and Fc-specific antibody fragments were used to immobilise antigen-specific antibodies. Fluorescein-labelled-antigen was detected in the sample only in the presence of the silver colloid.

Tully et al. [13] described a fluorescence-based immunoassay for the detection of a *Listeria monocytogenes*-derived protein, Internalin B, using quantum dots as fluorescent labels. A polyclonal antibody-based competitive assay with a limit of detection of 12 ng/ml was developed. The multicolor sensitivity and stability of quantum dots makes them ideal for the analysis of complex samples for histology, pathology and cytology in immunostaining applications. Quantum dots are similar in size to organic dyes so can be substituted for current fluorescence-based techniques [6]. The main advantage of quantum dots for the immunostaining of *L. monocytogenes* is the ability to multiplex without the need for multiple excitation sources, thus facilitating double or triple immunostaining of bacterial cells surface components.

Future Directions for Research

Fluorophores can be covalently attached to macromolecules and the emission of these fluorescent probes can be from UV to NIR. Probes are available with short (nanosecond) to long (micro to millisecond) life-times. Future trends in fluorescent labeling for biological applications lie with a number of emerging technologies. Labels with better spectral properties such as larger Stoke's shift, greater stability, solubility in aqueous solution and high brightness are constantly being developed. The evolution of these tags coupled with advances in functionalisation methods for inorganic probes are giving rise to a new generation of sophisticated probes suitable for high throughput screening in diagnostics. Metallic nanoparticles and inorganic probes are highly complex, spectroscopically tailored tags that improve assay sensitivity, reproducibility and multiplexing capabilities. Easily functionalised nanoparticles, quantum dots and nanocrystals are consistently brighter and more robust and will provide important reagents in the future for fluorescence-based detection. Another key group of fluorescent tags are those genetically engineered into biological molecules through in vivo labeling and the cloning of naturally fluorescing moieties. Further development of existing tags and generation of novel probes, as outlined, will have a very significant influence in the area of fluorescence-based analysis in the near future.

Acknowledgements

The financial support of Enterprise Ireland and Science Foundation Ireland is gratefully acknowledged.

F

References

1. Lakowicz JR (1999) Principles of Fluorescence spectroscopy (2nd edn). Kluwer Academic / Plenum Publishers, New York
2. Hermanson GT (1996) Bioconjugate Techniques. Academic Press, London
3. Wolfbeis OS (ed) (1993) Fluorescence Spectroscopy: New methods and applications. Springer-Verlag, Berlin, Heidelberg, New York
4. O'Kennedy R, Thornes RD (eds) (1997) Coumarins Biology, Applications and Mode of Action. John Wiley & Sons Ltd., Chichester
5. Handl HL, Gillies RJ (2005) Lanthanide-based luminescent assays for ligand-receptor interactions. Life Sci 77:361–371
6. Seydack M (2005) Nanoparticle labels in immunosensing using optical detection methods. Biosens Bioelectron 20:2454–2469
7. Sun C, Yang J, Li L, Wu X, Liu Y, Liu S (2004) Advances in the study of luminescence probes for protein. J Chromatog B 803:173–190
8. O'Riordan T, Soini A, Soini J, Papkovsky DB (2002) Performance Evaluation of the Phosphorescent Porphrin Label: Solid-Phase Immunoassay of α-Fetoprotein. Anal Chem 74(22):5845–5850
9. Castellano F, Dattelbaum JD, Lakowicz JR (1998) Long-lifetime Ru (II) complexes as labeling reagents for sulfyhdryl groups. Anal Biochem 255:165–170
10. Ow H, Larson DR, Srivastava M, Baird BA, Webb WW, Wiesner U (2005) Bright and stable core-shell silica fluorescent nanoparticles. Nanoletts 5(1):113–117
11. Lian W, Litherland S, Badrane H, Tan W, Wu D, Baker HV, Gulig PA, Lim DV, Jin S (2004) Ultrasensitive detection of biomolecules with fluorescent dye-doped nanoparticles. Anal Biochem 334:135–144
12. Lochner N, Lobmaier C, Writh M, Leitner A, Pittner F, Gabor F (2003) Silver nanoparticle enhanced immunoassay: one step 'real-time' kinetic assay for insulin in serum. Eur J Pharm Biopharm 56:469–477
13. Tully E, Hearty S, Leonard P, O'Kennedy R (2006) The development of rapid fluorescence-based immunoassays, using quantum dot-labelled antibodies for the detection of *Listeria monocytogenes* cell surface proteins. Int J Biol Macromol 39(1–3):127–134

Fluorescent Microscopy

► Fluorescence Measurements

Fluorescent Probes

Synonyms

Luminescent labels; Fluorophores

Definition

Fluorescent probes are relatively small molecules that are used to label biomolecules such as proteins, antibodies and nucleic acids. They contain functional groups and specific physical and chemical characteristics that confer suitability for their use as detection moieties. To date, thousands of fluorescent probes are known each with varying spectral properties. Fluorophores may be intrinsic or extrinsic in nature. Intrinsic fluorophores are naturally occurring whereas extrinsic fluorophores are added to generate a fluorescence signal to facilitate measurement of a specific target molecule. Fluorescent labels have provided excellent sensitivity for a range of assay systems that can be applied to the determination of almost any analyte.

Cross References

- ► DNA Micro-arrays
- ► Lab-on-a-Chip (General Philosophy)
- ► Quantum Dots
- ► Fluorescent Labeling

Fluorescent Thermometry

VINAY K. NATRAJAN, KENNETH T. CHRISTENSEN
Department of Mechanical Science and Engineering,
University of Illinois, Urbana, IL, USA
ktc@uiuc.edu

Synonyms

Photoluminescence; Temperature measurement using fluorescence

Definition

Fluorescent thermometry involves the use of a fluorescent dye, whose fluorescence intensity is a strong function of temperature, to infer the temperature of a fluid or surface. The dye is dissolved in a fluid of interest, or coated on a surface, and is excited to fluoresce by incident light. The fluoresced light is recorded with a ► CCD camera and variations in its intensity are proportional to variations in the local temperature.

Overview

There exists a growing demand for the development of advanced diagnostics for high-precision temperature measurements at the microscale. This demand is driven by the ever-increasing use of complex microfluidic devices such as micro-total analysis systems (μ-TAS) and μ-heat exchangers. Lab-on-a-Chip devices, which integrate multiple complex laboratory functions onto a single chip-sized substrate, often require precise temperature control to maximize the productivity of chemical operations like mixing, reactions and separations. Such control becomes especially critical when electrokinetic pumping is used for driving flow through these devices, as the current flowing through the buffer solution can result in significant internal heat generation, a phenomenon known as Joule heating. Since most microfluidic-based MEMS devices utilize very high heat and mass transfer rates, a thorough understanding of their thermal transport characteristics is paramount for optimizing their design for increased performance and reliability.

While several methods exist for measurement of fluid and/or surface temperature at the macroscale, the direct application of these methods to the microscale may not be possible. In particular, the accuracy of these techniques at the microscale can be compromised because dissipation of thermal gradients occurs over extremely short time scales due to high heat transfer rates and large surface area-to-volume ratios. Therefore, obtaining accurate measurements of fluid temperature at the microscale is still a challenge. Until recently, temperature measurements in microfluidic systems were limited to measurements of bulk fluid temperature at the inlet and outlet of microfluidic sections or measurements of the substrate's temperature itself. With regard to local temperature measurements, the use of high-precision thermocouple probes to measure fluid and/or substrate temperature is generally restrictive. In addition to being physically intrusive, these probes can suffer from poor spatial resolution since most probes have a characteristic size of a few microns. Alternatively, microfluidic devices can be fabricated with integrated microscale resistance temperature detectors (RTD's) embedded in the substrate with spatial extents on the order of a few microns (Wu et al. [11]). However, this fabrication procedure can be quite complex and, like thermocouple probes, RTD's suffer from poor spatial resolution which limits their ability to resolve local thermal gradients. Further, while these sensors are convenient for monitoring surface temperature, they do not provide a direct measure of local fluid temperature.

In contrast, fluorescent thermometry (a specific application of the more general ► laser-induced fluorescence

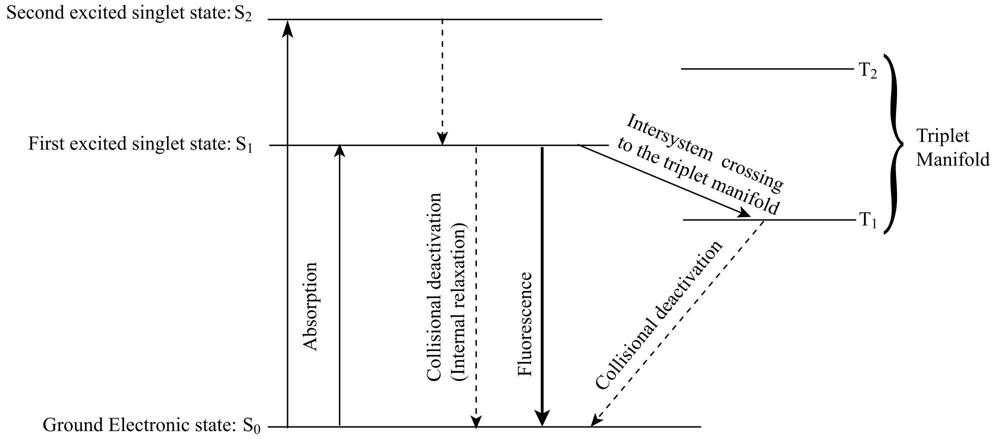

Fluorescent Thermometry, Figure 1 Schematic illustrating the energy levels of a diatomic molecule (adapted from Guilbault [3])

(LIF) technique) represents one of the most accurate temperature measurement techniques at the macroscale. In this technique, a fluorescent dye whose fluorescence intensity is a strong function of temperature is dissolved in a fluid of interest or is coated on a surface of interest. In the case of fluid temperature measurement, the fluid in a plane of interest is illuminated with incident light (typically a sheet of laser light) and the dye is excited to fluoresce. In the case of surface temperature measurement by fluorescence, the surface coated with the dye would be illuminated with incident light. In both cases, the fluoresced light is imaged with a CCD camera and the resulting image is converted to a temperature field using an a priori temperature calibration of the dye's fluorescence intensity. Unlike macroscale LIF where multiple directions of optical access are usually available, fluorescent thermometry at the microscale is often complicated by the fact that most microfluidic devices have only one principal direction of optical access, usually in a direction normal to the plane of the network. Therefore, illumination of the test section from this direction will inherently illuminate the entire depth dimension of the domain of interest. There is no adverse effect from volume illumination in the case of surface temperature measurement since presumably only the bottom surface of the device would be coated with the dye. However, in the case of fluid temperature measurement by fluorescence the dye is homogeneously dissolved in the solvent, meaning fluorescent molecules along the entire depth dimension are excited to fluoresce. As a result, fluid temperature measurements via fluorescence at the microscale often suffer from significantly more out-of-focus noise than similar measurements at the macroscale where sheets of laser light minimize the volume of fluid illuminated in the depth direction. Furthermore, the extremely small thermal transport time scales at the microscale render measurements of instantaneous and unsteady temperature fields much more difficult than similar measurements at the macroscale. Nevertheless, significant progress has been made in adapting fluorescent thermometry to the microscale and this contribution summarizes the state-of-the-art in this regard. Single- and two-dye techniques are discussed in detail and representative experimental results are summarized.

Basic Methodology

As illustrated in Fig. 1, when a photon of a given energy is absorbed by a fluorophore, the energy state of the molecule transitions from the ground state, S_0, to higher electronic states (S_1, S_2, etc.). Energy is subsequently dissipated at these excited states until the molecule reaches the lowest level of the first excited singlet state, S_1. Thereafter, the molecule at the first singlet state can return to the ground state in multiple ways. The process by which the excited molecule returns to the S_0 state by a radioactive decay process, wherein no further energy is dissipated by collisions and its return to the ground state occurs purely by the emission of energy, is referred to as ► fluorescence. In such a scenario, a portion of the remaining energy is lost by the molecule before the emission occurs, meaning that the emitted energy is of a longer wavelength than the energy it initially absorbed. The shift in wavelength of the fluoresced light relative to the absorption wavelength is known as ► Stokes shift.

While the emission of fluoresced light represents one possible path for the transition of a molecule from the first singlet state to the ground state, there exist other non-radiative processes, like internal conversions and intersystem crossings, by which an excited molecule can return to its ground state (Fig. 1). As such, the efficiency of the fluorescence

emission by a dye is often quantified by its ▶ quantum efficiency

$$\phi = \frac{k_r}{k_r + k_{nr}}, \tag{1}$$

where k_r is the rate of emission of photons via fluorescence and k_{nr} represents the rate at which non-radiative relaxation to the ground state occurs. Similarly, the efficiency of a dye can also characterized by the fluorescence lifetime of its excited species

$$\tau = \frac{1}{k_r + k_{nr}}, \tag{2}$$

which represents the average time the fluorophore remains in its excited state.

For a dye of concentration C (kg m^{-3}) illuminated with an incident light flux of intensity I_0 (Wm^{-3}), the fluorescence energy emitted per unit volume, I (Wm^{-3}), is

$$I = I_0 C \phi \epsilon, \tag{3}$$

where ϵ (m^{2}kg^{-1}) is the absorption coefficient of the dye. Variations in I with temperature are predominantly attributable to a dye's quantum efficiency, ϕ, which displays some degree of temperature dependence for most organic dyes. While this temperature sensitivity is small for most dyes (typically a fraction of a percent per K), there are some dyes that exhibit significantly more temperature dependence, like Rhodhamine B (2.3% K^{-1}). In contrast, ϵ has a very weak temperature dependence, usually of the order of 0.05% K^{-1} (Sakakibara and Adrian [9]). Therefore, by employing a dye whose quantum efficiency is highly-sensitive to temperature variations, the temperature distribution in a fluid or on a surface can be inferred from intensity variations in the light fluoresced by the dye.

Single-Dye Fluorescence

Temperature measurement using a single fluorescent dye is the simplest adaptation of fluorescent thermometry at the microscale. If the intensity of the illuminating light flux, I_0, is assumed constant in both space and time, then the ratio of the emitted fluorescence intensity measured at a temperature T to that measured at a reference temperature T_{ref} for a fixed dye concentration is given by the ratio of the quantum efficiencies of the fluorescent dye at these temperatures:

$$\frac{I}{I_{ref}} = \frac{\phi(T)}{\phi(T_{ref})} = f(T). \tag{4}$$

Therefore, assuming that the variation of the ratio of quantum efficiencies, or equivalently the ratio of the emitted fluorescence intensities, has been properly calibrated as a function of temperature, an estimate of the unknown temperature distribution is arrived at by comparing its fluorescence intensity to that given by the calibration. The spatial resolution of this measurement is defined by the imaging optics while the temporal resolution is defined either by the framing rate of the imaging camera or by the illumination time of the incident light (since the fluorescence lifetime, given by Eq. (2), is quite short for most dyes–typically a few ns to a few μs).

A schematic of the imaging configuration used for the measurement of temperature via single-dye fluorescence is presented in Fig. 2. Light from an illumination source, like an Nd:YAG laser, Argon-ion laser or a mercury arc lamp, is directed through an epi-fluorescent filter cube and through a microscope objective lens to excite the fluorescent dye molecules in the microfluidic device. The filter cube allows the relatively weak fluorescent signal to pass to a CCD camera while simultaneously blocking the intense illumination wavelength. Given the relatively weak fluorescent signal from the dye, the CCD camera employed must have very low noise levels and a high sensitivity to the emitted wavelength in order to maximize the signal-to-noise ratio of the measurement. A reference image is first acquired at a known, preferably uniform, temperature while a second image is acquired at an unknown, possibly non-uniform, temperature. A ratio of intensities is then obtained by dividing the intensity recorded at each pixel of the measurement image by the corresponding intensity at the same pixel of the reference image. This intensity ratio is then converted to temperature using an a priori calibration of the dye that tabulates the variation of the fluorescence intensity ratio with temperature (Eq. (4)).

Two-Dye Fluorescence

As outlined in Single-Dye Fluorescence, the fluorescence intensity measured by single-dye fluorescence depends solely on temperature only if the dye concentration and the incident light flux are constant. While maintaining a constant dye concentration is quite simple, sustaining a constant incident light flux is much more difficult since all illumination sources exhibit some degree of spatial and/or temporal variability in their intensity. As such, the measured fluorescence intensity not only embodies temperature variations through ϕ, but also variations in the illuminating intensity through I_0. Therefore, the accuracy of temperature measurements via single-dye fluorescence is strongly dependent on the stability and homogeneity of the illuminating light source. To alleviate such issues, a two-dye methodology was introduced

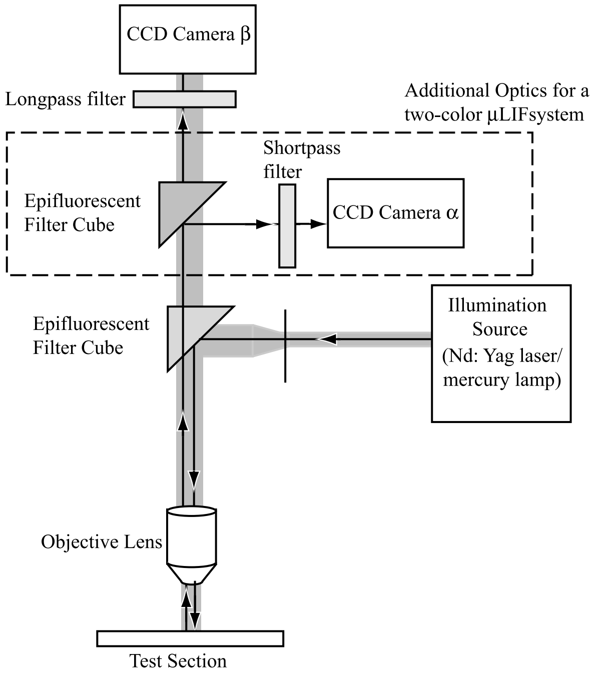

Fluorescent Thermometry, Figure 2 Representative schematic of the optical configuration for microscale fluorescence thermometry. The dashed box outlines the additional optics required for a two-dye fluorescence imaging

by Sakakibara and Adrian [9] to improve the accuracy of macroscale fluorescent thermometry. In this technique, spatial and/or temporal intensity variations within the illuminating light source are accounted for via a second fluorescent dye whose quantum efficiency exhibits little, or no, temperature dependence. Therefore, while the intensity of the fluoresced light from the temperature-dependent dye embodies both variations in temperature and illuminating intensity, any variations in the fluorescence intensity of the temperature-insensitive dye are directly attributable to variations in the illuminating intensity. Therefore, one can account for variable illumination intensity by simultaneously imaging the fluoresced light from each dye with separate CCD cameras and normalizing the fluorescence intensity of the emission from the temperature-sensitive dye by that of the temperature-insensitive dye.

Temperature measurement by two-dye fluorescence requires efficient separation of the two fluorescent emissions so that their emissions can be imaged separately over identical spatial domains at the same instant in time. Such separation is achieved by adding a second camera and additional spectral filters to the aforementioned single-dye optical arrangement (these additions are identified by the dashed bounding box in Fig. 2). In this optical arrangement, both dyes must have similar excitation wavelengths since the same illumination source is typically used to simultaneously excite both dyes. However, the dyes must have different emission spectra so that they can be effectively separated using low- and high-pass spectral filters just upstream of the cameras. If the emission from the two dyes, labeled A (temperature sensitive) and B (temperature insensitive), are separated perfectly into cameras α and β, the ratio of the fluorescence intensities recorded by both cameras is given by

$$\frac{V^{\alpha}}{V^{\beta}} = \frac{I_A}{I_B} = \frac{C_A \phi_A \varepsilon_A}{C_B \phi_B \varepsilon_B}\,, \tag{5}$$

where V^{α} and V^{β} are voltage outputs from the CCD's of cameras α and β, respectively. Note that this ratio depends on the temperature via ϕ_A/ϕ_B but is independent of the incident light flux, I_0. In practice, however, it is nearly impossible to obtain perfect separation of the two emissions, I_A and I_B, both because the emission spectra of most organic dyes are rather broad, meaning some overlap of their emissions is to be expected, and because spectral filters are inherently imperfect (filtering efficiencies of 90–95% are typical). Sakakibara and Adrian [9] considered the case of imperfect separation, wherein some fraction of the fluorescent intensity of the emission from dyes A and B are imaged by cameras β and α, respectively, and derived the expression

$$\frac{V^{\alpha}}{V^{\beta}} = \frac{I_A}{I_B} = \frac{C_A C'_B \phi_A \phi'_B V^{\alpha}_{C_B=0} + C_B C'_A \phi_B \phi'_A V^{\alpha}_{C_A=0}}{C_A C'_B \phi_A \phi'_B V^{\beta}_{C_B=0} + C_B C'_A \phi_B \phi'_A V^{\beta}_{C_A=0}}\,, \tag{6}$$

that accounts for this effect. Here, C'_A, ϕ'_A, $V^{\alpha}_{C_B=0}$ and $V^{\beta}_{C_B=0}$ are the measured parameters for fluorescent dye A with $C_B = 0$, and C'_B, ϕ'_B, $V^{\alpha}_{C_A=0}$ and $V^{\beta}_{C_A=0}$ are the measured parameters for fluorescent dye B with $C_A = 0$. In this context, $V^{\alpha}_{C_A=0}$, $V^{\beta}_{C_A=0}$, $V^{\alpha}_{C_B=0}$ and $V^{\beta}_{C_B=0}$ are constants for a given optical configuration. Therefore, the intensity ratio I_A/I_B is only a function of the concentration of the two dyes, C_A and C_B, and the temperature, T.

Apart from issues related to properly imaging the light fluoresced by the two dyes, accurate determination of the temperature distribution over the chosen spatial domain in the two-camera arrangement requires that both cameras have identical fields of view. Therefore, one must not only ensure that the magnifications of the two CCD cameras are identical but also that the cameras are aligned such that each pixel location in the two CCD arrays map back to the same physical coordinate in the measurement domain. This alignment is a crucial step in the two-dye methodology because one must divide the two intensity fields pixel-by-pixel, as outlined in Eq. (6), to determine the tempera-

ture distribution over the spatial domain of interest. Therefore, any misalignment of the two CCD cameras will prevent one from properly accounting for spatial variations in the illuminating intensity, thereby reducing the overall accuracy of the measurement.

Dye Selection

The fluorescent properties of an organic dye are governed by the chemical structure of the dye molecules and their interaction with the solvent molecules. In general, dyes whose molecules have rigid and planar structures display higher fluorescence efficiencies, meaning that their fluorescence can be imaged with very high signal-to-noise ratios. Unfortunately, such dyes seldom display a strong temperature sensitivity since the temperature dependence of a dye is often governed by the structural mobility of its functional groups. For instance, while Rhodamine 101 exhibits a temperature-insensitive quantum yield close to 100%, Rhodamine B (RhB), when dissolved in ethanol, has a quantum yield of roughly 40% at 25 °C that steadily decreases to only a few percent with increasing temperature. This RhB behavior is attributed to the increased mobility of its diethylamino groups with increasing temperature compared to the relatively rigidized diethylamino groups in Rhodamine 101. Therefore, one often must sacrifice some signal-to-noise ratio during imaging for strong temperature sensitivity. In addition, when measuring fluid temperature, the fluorescent properties of a dye can be highly dependent on the properties of the solvent itself. In most cases, solvents with higher viscosities increase the fluorescence efficiency of dyes since a higher viscosity not only restricts the mobility of the functional groups in the dye molecules, but also minimizes the energy transfer between these molecules by reducing the number of molecular collisions. Rhodamine B, for instance, exhibits a quantum yield of nearly 100% in viscous solvents like glycerol as compared to 40% in less-viscous ethanol. Further, the fluorescent efficiencies of most organic dyes also depend on other solvent properties in sometimes complicated fashions. For instance, although using water as a solvent can counteract inhomogeneities in the temperature distribution of the dye solution due to thermal energy released during the lasing process, water is known to enhance aggregation of dye molecules to form dimers and higher aggregates. These aggregates, which have different absorption spectra compared to the dye molecules themselves, can adversely affect the accuracy of the temperature measurement. Hence, the choice of fluorescent dyes and their solvents is highly dependent on the application under consideration (The reader is directed to Drexhage [1] and Guilbault [3] for a more detailed explanation of the structure and properties of fluorescent dyes).

For temperature measurement by single-dye fluorescence, the temperature sensitivity of a dye, specifically its quantum efficiency, effectively defines the temperature resolution of the measurement itself. Rhodamine B is the most-common temperature-dependent fluorescent dye used in both macro- and microscale liquid applications because of its relatively strong temperature sensitivity of 2.3% K^{-1} in water over a temperature range of 0 – 120 °C. This dye is also soluble in many other organic solvents, like ethanol, making it a practical choice in a variety of microfluidic applications. Moreover, its absorption spectrum is rather broad (470 – 600 nm with a peak at 554 nm), meaning it can be readily excited with conventional illumination sources like mercury arc lamps as well as Argon-ion (continuous) and Nd:YAG (pulsed) lasers. Further, its emission spectrum is also rather broad (centered at 575 nm) so a portion of its fluoresced light can be faithfully filtered from the illuminating wavelength. Pyrene is another fluorescent dye whose quantum efficiency exhibits relatively strong temperature dependence (0.9% K^{-1}) in the range 20 – 130 °C when dissolved in decane. This dye has an excitation peak at 330 nm and a broad emission spectrum centered at 475 nm. For a more comprehensive list of temperature-sensitive fluorescent dyes, the reader is referred to Lou et al. [5].

In the case of two-dye fluorescence, the ideal choice of dyes would include one dye that has strong temperature sensitivity and one that has strong temperature insensitivity. Such a combination will maximize the temperature sensitivity of the ratio of their quantum efficiencies as given by Eq. (6). However, one must also consider other constraints on the choice of dyes, particularly their absorption and emission spectra. As noted earlier, since the two dyes are typically excited by the same illumination source, both dyes should have similar absorption spectra. In addition, both dyes should exhibit strong Stokes shifts so that the relatively weak fluoresced light from both dyes can be efficiently separated from the more intense illuminating wavelength prior to imaging. However, it is also paramount that the dyes have as different emission spectra as possible so that they can be effectively separated from one-another prior to imaging. Finally, in the case of fluid temperature measurements both dyes must also exhibit good solubility characteristics in the chosen solvent, particularly homogeneity at the molecular scale.

As in the single-dye technique, RhB (absorption and emission peaks of 554 nm and 575 nm, respectively) is generally chosen as the temperature-sensitive dye in two-dye fluorescence because of its broad absorption and emission spectra as well as its solubility in a number

of commonly-used solvents. Rhodamine-110 (Rh110) is often chosen as the temperature-insensitive dye because it exhibits a weak temperature sensitivity of 0.13% K^{-1} in water and its emission peak of 520 nm is far enough from that of RhB to achieve efficient separation of the two emission signals. However, its absorption peak at 496 nm implies that its use is limited to cases where an Argon-ion laser, or an alternative illumination source of similar wavelength, is employed. In situations where an Nd:YAG laser is used for illumination (which emits at 532 nm), Nile Red (absorption and emission peaks of 553 nm and 620 nm, respectively) represents an alternative temperature-insensitive dye (0.1% K^{-1}), particularly since its emission spectrum can be effectively separated from that of RhB. Unfortunately, Nile Red is not soluble in water, although Nile Red and RhB are both soluble in ethanol. Rhodamine-101 (Rh101; absorption and emission peaks at 575 nm and 635 nm, respectively) and Rhodamine-6G (Rh6G; absorption and emission peaks at 520 nm and 566 nm, respectively), both of which are soluble in ethanol, can also be used as temperature-insensitive dyes. However, one must select a more compatible temperature-sensitive dye for use with Rh101 and Rh6G as the former has an absorption spectrum that overlaps the emission spectrum of RhB and the latter has an emission spectrum that significantly overlaps that of RhB. Finally, fluorescein, which is soluble in ethanol, represents another option as a temperature-insensitive dye because of its high quantum yield of 0.97 and its convenient absorption and emission peaks at 500 nm and 545 nm, respectively.

Temperature Calibration

The exact temperature dependence of the chosen dye(s) must be known before the measured intensity ratio fields, given by Eq. (4) for single-dye fluorescence and Eq. (6) for two-dye fluorescence, can be faithfully converted to temperature fields. In the context of single-dye fluorescence, this calibration is accomplished by isolating a fixed amount of the chosen dye at a known concentration in a well-insulated reservoir whose temperature is both known and precisely controlled. One then maintains the dye solution at a known temperature, begins illuminating the dye solution and acquires an ensemble of images of the light fluoresced by the dye using the same optical configuration outlined earlier (Fig. 2). The temperature of the dye is then varied slightly and a new ensemble of images is acquired at this new temperature. This procedure is repeated until image ensembles have been acquired at several known temperatures over the range expected in a given experiment. An average over each image ensemble and/or a spatial average over neighboring pixels is often performed at a fixed temperature to minimize variations in the intensity of the recorded fluorescence due to noise (attributable to variations in the intensity of the illuminating light as well as noise from the CCD array). This procedure yields a single, average intensity value associated with each temperature. These intensities are then normalized by the intensity of the fluoresced light at a reference temperature, yielding a calibration curve of intensity ratio (or equivalently quantum-efficiency ratio) versus temperature. A typical calibration curve of RhB dissolved in deionized water at a concentration of 1 mmol/l is shown in Fig. 3 (adapted from Ross et al. [8]). Note that the dependence of RhB's intensity ratio on temperature is quite non-linear.

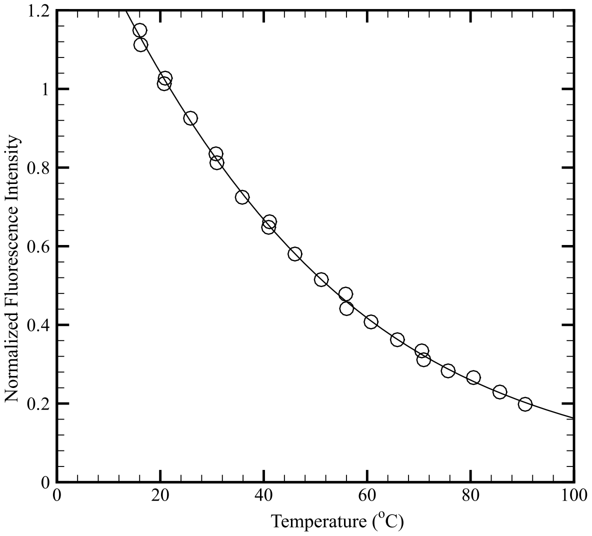

Fluorescent Thermometry, Figure 3 Representative calibration curve illustrating the dependence of Rhodamine B on temperature (adapted from Ross et al. [8])

In the context of two-dye fluorescence, the calibration methodology is identical except that one must now assess the temperature dependence of each dye. This calibration is accomplished by applying the procedure outlined above to the temperature-sensitive and temperature-insensitive dyes separately, yielding the temperature dependence of each dye's quantum efficiency as

$$\phi_{A(B)}(T) = \phi_{A(B)}(T = T_{\text{ref}}) \frac{I_{A(B)}(T)}{I_{A(B)}(T = T_{\text{ref}})} , \qquad (7)$$

where T_{ref} is a reference temperature at which the quantum efficiency of dye $A(B)$ is known.

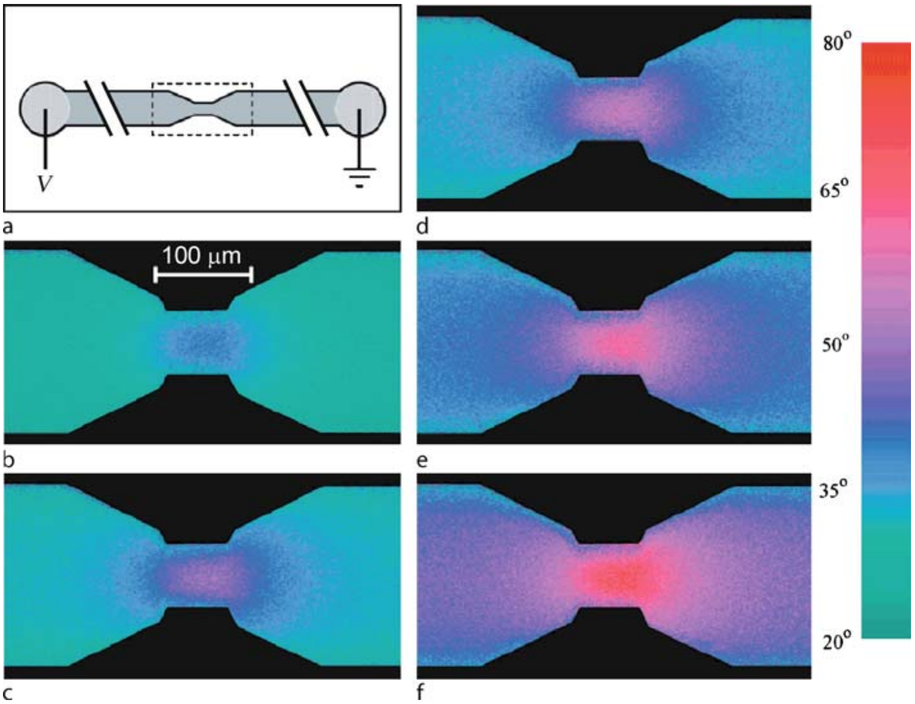

Fluorescent Thermometry, Figure 4 (**a**) Schematic of a microfluidic circuit through which flow is driven by electrokinetic pumping. (**b**)–(**f**) Temperature fields through a constriction in the microfluidic circuit acquired 0.2, 0.4, 0.6, 1.4 and 3.8 s after the driving voltage was switched on (adapted from Ross et al. [8])

Photobleaching

As illustrated in Fig. 1, a fluorophore that is excited to higher energy levels often dissipates a portion of its energy that is in excess of the first excited singlet state, S_1. Ideally, the highest fluorescent efficiencies are obtained when a reverse transition from the S_1 state to the S_0 state occurs by the spontaneous emission of photons in the form of fluoresced light. However, there are other non-radiative processes that can act to compete with the emission of fluoresced light, thereby decreasing the fluorescent efficiency of the dye. These non-radiative processes include internal conversions, wherein non-radiative relaxation brings the energy state back to the ground state, S_0, and intersystem crossings, where the energy state is converted to the triplet state. As a consequence, molecules in the triplet state, as well as those that are at singlet states higher than the S_1 state, are susceptible to an irreversible alteration of their chemical structures that can yield non-fluorescent compounds. This decrease in the emitted fluorescent intensity as a result of the decay of fluorescent molecules is termed ►photobleaching.

Prolonged exposure of the fluorescent molecules to high-intensity incident light can raise the energy level of these molecules to energy states that are higher than the S_1 excited singlet state, thereby increasing the probability of degradation via the mechanisms detailed above. As such, minimizing the number of exposures and/or the exposure time to the incident illumination in conjunction with the use of lower excitation intensities and higher exciting wavelengths can aid in delaying the effects of photobleaching. In most measurements of fluid temperature, photobleaching effects are of little concern because the fluid in which the fluorescent dye is dissolved is typically moving through the measurement domain. In cases where the average time required for a dye molecule to enter and leave the image domain, τ_d, is small compared to the time between exposures (defined by the framing rate of the imaging system), photobleaching losses are minimal since, on average, each dye molecule will only be exposed to a single exposure of incident light. If, however, τ_d is large compared to the time between exposures, or $\tau_d \to \infty$ (i. e., the limiting case of a stationary fluid or dye coated on a stationary surface), photobleaching effects are inevitable and can severely compromise the accuracy of the temperature measurement. One can attempt to account for these losses by performing an a priori photobleaching calibration that embodies such effects.

Key Research Findings

Single-Dye Fluorescence

Temperature measurement at the microscale by single-dye fluorescence was first accomplished by Ross et al. [8] using RhB as the temperature-dependent fluorescent dye and a mercury arc lamp for illumination. Ross et al. [8] conducted measurements of fluid temperature distributions resulting from Joule heating in a microfluidic circuit (Fig. 4a) due to electrokinetic pumping. Figures 4b–f present a time series of fluid temperature fields acquired by Ross et al. [8] through a constriction in the microfluidic circuit. These temperature fields clearly highlight the drastic rise in fluid temperature that can occur in the presence of electrokinetic pumping. A spatial resolution of 1 μm and a temporal resolution of 33 ms were reported, yielding temperature uncertainties in the range 2.4 – 3.5 °C with no spatial or temporal averaging. Improved measurement uncertainties (as low as 0.03 °C) were achieved but at a significant cost in spatial and/or temporal resolution. This single-dye methodology was also employed by Erickson et al. [2] to examine Joule heating and heat transfer in electrokinetically-driven flows at the junctions of PDMS and PDMS/glass microfluidic devices. The temperature fields obtained with RhB excited by a mercury illumination source were found to agree with complementary numerical simulations to within ±3 °C. They also reported a repeatability of approximately ±2 °C and a noise level of ±1 °C. Improved noise levels were achieved by applying a Wiener-type filter to their raw image data.

Sato et al. [10] used single-dye fluorescence to study the two-dimensional surface temperature distributions associated with convective mixing in a T-shaped microchannel bound by a cover glass. Water at different temperatures was injected into the opposite inlets of their test section as a means of simulating a Hele–Shaw flow condition. Tris(bipyridine)ruthenium(II), with a temperature sensitivity of $-3\%\,K^{-1}$, was spin-coated on the interior of the cover glass of their test section and excited with a mercury illumination source as a means of measuring the wall temperature distribution. Sato et al. [10] reported a temperature resolution of 0.26 °C with a measurement uncertainty of 1.2 °C. They also acquired velocity fields in the same measurement domain using microscopic particle-image velocimetry (μPIV) which, in concert with the measured temperature fields, allowed direct evaluation of the heat fluxes due to conduction and convection. This analysis revealed that conduction effects were an order-of-magnitude larger than convective effects.

Two-Dye Fluorescence

Kim et al. [4] implemented the two-dye methodology to measure steady fluid temperature fields associated with thermal buoyancy in the interior of a 1 mm-wide closed test section at low Grashof–Prandtl numbers. Instead of employing a two-camera imaging arrangement, which requires accurate alignment of their fields of view, Kim et al. [4] instead used a single-camera arrangement to image the fluorescence emissions of RhB and Rh110 excited by a continuous Ar-ion laser. Separate imaging of the two emissions was achieved by alternating two band-pass filters just upstream of the camera, meaning that the RhB and Rh110 images were not acquired simultaneously but rather were separated in time by 50 ms as defined by the framing rate of the CCD camera. As such, this imaging setup limited their measurements to steady-state temperature variations. The measured fluid temperature fields were found to agree well with complementary numerical simulations of the same thermal system. Kim et al. [4] cited measurement uncertainties from 1.967 °C with a spatial resolution of 150×100 μm to 0.412 °C with a spatial resolution of 1200×800 μm. They also observed root-mean-square deviations of the measured temperatures from their computational predictions of 2.3 °C and 0.92 °C for spatial resolutions of 19 μm and 76 μm, respectively.

Most recently, Natrajan and Christensen [7] considered the development of a two-dye fluorescence method for temperature measurement using a pulsed, Nd:YAG laser as the illumination source. In this context, the Nd : YAG laser provided narrow pulse widths (~ 5 ns), enabling the measurement of instantaneous temperature fields. The experimental setup employed was a true dual-camera arrangement (identical to that illustrated in Fig. 2) implemented with two 12-bit, cooled CCD cameras with an effective chip area of 1392×1040 pixels (Photometric, CoolSnap HQ2). Rhodamine B and Sulforhodamine-101 were selected as the temperature-sensitive and temperature-insensitive dyes, respectively, yielding a sensitivity of 1.5 %/K for the dye mixture dissolved in ethanol. Natrajan and Christensen [7] validated this methodology via measurements of steady-state temperature in a microfluidic device specifically designed to maintain a linear temperature gradient. This device, designed in the spirit of the protocol outlined by Mao et al. [6], consisted of an array of seven parallel microchannels (width = 100 μm, depth = 100 μm; made of PDMS) spaced 100 μm apart that were fabricated between two large reservoirs (width = 3.2 mm, depth = 3.2 mm) spaced 2 mm apart. As illustrated in Fig. 5a, one reservoir acted

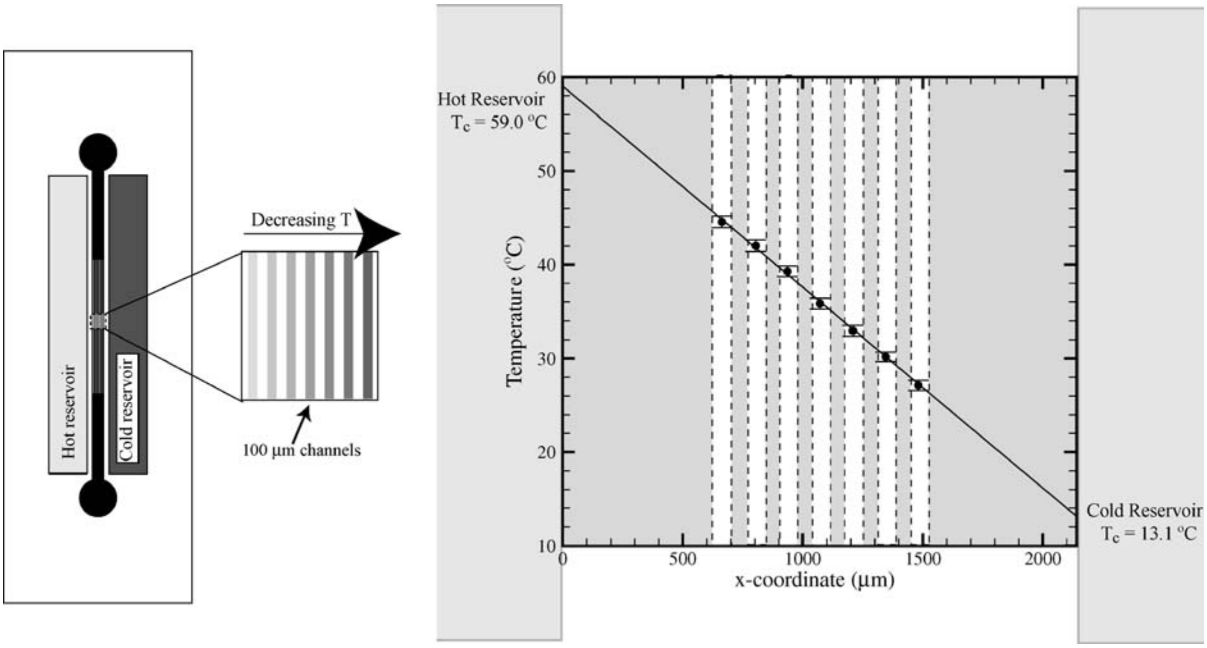

Fluorescent Thermometry, Figure 5 (**a**) Schematic of the microfluidic device used by Natrajan and Christensen [7] to obtain a one-dimensional, steady-state temperature gradient. (**b**) Variation of temperature across the microfluidic device shown in (**a**). The solid circles represent the mean temperatures obtained via two-dye LIF measurements while the solid line indicates the predicted linear temperature profile across the microchannel array. The span of the error bars represents twice the standard deviation for each mean temperature. Adapted from [7]

as a heat source and the other as a heat sink. Continuous circulation of heated and cooled water through the reservoirs ensured that they remained at constant temperatures. An independent measure of the temperature of the heated and cooled walls on either side of the channel array was obtained with two thermocouples inserted into the device through the hot and cold reservoirs. As reported by Mao et al. [6], such an arrangement generates a linear temperature gradient across the channel array which is filled with the dye mixture. When illuminated with the Nd : YAG laser, a measure of the temperature of the dye mixture in each channel was obtained by imaging the fluorescence emission from the dyes.

Figure 5b presents the measured variation of the steady-state temperature distribution across the microchannel array imposed by the hot and cold reservoirs computed from an ensemble of sixty instantaneous snapshots of the temperature field across the array as reported in [7]. Note that variations of fluid temperature *within* each microchannel were not resolved, so the spatial resolution of these measurements is 100 µm (i. e., the size of the microchannels). In this figure, the filled circles represent the mean temperatures of the dye mixture in the microchannel array obtained by averaging over the sixty samples, while the predicted linear temperature variation across the device (solid line in Fig. 5b) is obtained by fitting a line through the independently-measured wall temperatures of the hot and cold reservoirs. An estimate of the uncertainty in the measurements was obtained by computing the standard deviation of the data sets comprising the ensemble. Figure 5b illustrates that the mean temperature of the dye mixture in each of the seven microchannels of the microfluidics device is in very good agreement with the predicted temperature distribution (span of error bars represent two standard deviations). The maximum deviation of the LIF-measured mean temperatures from the linear prediction is 0.4 °C while the computed standard deviation lies in the range 0.5 – 0.63 °C. This range of standard deviations yields relative uncertainties (standard deviations normalized by measured temperatures) of 1.4 – 2.0%, with the relative uncertainty increasing with decreasing temperature. Natrajan and Christensen (2008) noted that these uncertainties are 2 – 3 times larger than those normally achieved in macroscale implementations of two-dye fluorescent thermometry, indicating that volume illumination can be a non-trivial source of error in LIF implementations at the microscale.

Future Research Directions

While significant progress has been made in adapting fluorescent thermometry to microfluidic applications, the

accuracy of the technique is still nearly an order of magnitude lower than similar implementations at the macroscale. This stark difference is attributable not only to the volume-illumination effect at the microscale but also to the relatively weak fluorescent signals that must be imaged with high signal-to-noise ratio. In the case of a stationary fluid (or equivalently a dye-coated stationary surface), the accuracy of the technique is further compromised by photobleaching effects. Therefore, significant effort must be put forth to solve such issues before fluorescent thermometry becomes a standard technique employed in a wide variety of practical applications. One promising path toward resolving the aforementioned issues involves the use of ► quantum dots as thermal markers, although researchers are just beginning to explore this intriguing possibility. Quantum dots are nanometer-scale semiconductors that are formed by confining the motion of electrons and/or holes (the absence of electrons) in all directions and can range in size from a few to a few hundred nanometers depending upon how they are fabricated (typically by molecular beam epitaxy or self assembly). Quantum dots behave similarly to fluorescent dyes in that they can be excited with an illumination source to fluoresce light with rather large Stokes shifts and their fluorescence intensity is strongly dependent upon temperature. However, quantum dots are superior to fluorescent dyes in several respects. First, they have extremely broad absorption spectra, meaning a wider variety of illumination sources can be employed (like diode lasers). In addition, the wavelength of the light fluoresced by a quantum dot is a function of its size, so one can tailor the spectral characteristics of the thermal marker by simply altering its size. In this regard, smaller dots fluoresce toward the blue end of the spectrum while larger dots fluoresce toward the red. This spectral behavior is attributable to the fact that larger dots are more efficient at absorbing weaker photons which tend to reside in the red portion of the spectrum. Finally, of critical importance is the fact that quantum dots display significantly higher quantum yields compared to fluorescent dyes and yet do not suffer from photobleaching effects. Therefore, not only is the signal-to-noise ratio of the fluorescence imaging greatly enhanced by using quantum dots as thermal markers but their viability is not compromised by continued exposure to illuminating light as is unfortunately the case with fluorescent dyes. All of these characteristics make quantum-dot-based fluorescent thermometry an intriguing possibility for applications ranging from meso-scale surface-temperature monitoring in electronics cooling, whereby the surface would be coated with a single layer of quantum dots, to temperature monitoring of microscale biological processes wherein precise temperature control is of critical importance.

Cross References

► Fluorescence Measurements
► Fluorescent Labeling
► Laser-Induced Fluorescence (LIF)
► Liquid Crystal Technique for Measuring Temperature
► Methods for Temperature Measurements
► Quantum Dots
► Resistance Temperature Detectors
► Thermocouples

References

1. Drexhage KH (1990) Structure and properties of laser dyes. In: Schaefer FP (ed) Dye Lasers. Springer, New York, pp 154–200
2. Erickson D, Sinton D, Li D (2003) Joule heating and heat transfer in poly(dimethylsiloxane) microfluidic systems. Lab Chip 2:141–149
3. Guilbault GG (1990) General aspects of luminescence spectroscopy. In: Guilbault GG (ed) Practical Fluorescence. Dekker, New York, pp 1–40
4. Kim HJ, Kihm KD, Allen JS (2003) Examination of ratiometric laser induced fluorescence thermometry for microscale spatial measurement resolution. Int J Heat Mass Transf 46:3967–3974
5. Lou J, Finegan TM, Mohsen P, Hatton TA, Laibinis PE (1999) Fluorescence-based thermometry: Principles and applications. Rev Anal Chem 18:235–283
6. Mao H, Yang T, Cremer PS (2002) A Microfluidic Device with a Linear Temperature Gradient for Parallel and Combinatorial Measurements. J Am Chem Soc 124:4432–4435
7. Natrajan VK, Christensen KT (2008) A Two-Color Fluorescent Thermometry Technique for Microfluidic Devices. AIAA Paper 2008-0689, pp 1–10
8. Ross D, Gaitan M, Locascio LE (2001) Temperature measurement in microfluidic systems using a temperature-dependent fluorescent dye. Anal Chem 73:4117–4123
9. Sakakibara J, Adrian RJ (1999) Whole field measurement of temperature in water using two-color laser induced fluorescence. Exp Fluids 26:7–15
10. Sato Y, Irisawa G, Ishizuka M, Hishida K, Maeda M (2003) Visualization of convective mixing in microchannel by fluorescence imaging. Meas Sci Technol 14:114–121
11. Wu S, Mui J, Tai YC, Ho CM (1999) Micro heat exchanger by using MEMS impinging jets. In: Proc IEEE Micro Electro Mech Syst

Fluorescent Visualization

► Fluorescence Measurements

Fluorophores

► Fluorescent Probes

Focused Ion Beam Milling (FIB)

Definition

This is a fabrication procedure used to machine or modify materials on the micro-scale. A focused beam of high-energy ions is targeted at a material and the impacting ions sputter atoms from the surface; a prescribed scanning of the ion beam thus has the effect of a milling procedure.

Cross References

► Supersonic Micro-Nozzles

Force-Based Biosensors

► Biosensors Using Atomic Force Microscopes

Force Biosensors

► Biosensors Using Atomic Force Microscopes

FOV – Field of View

Definition

Describes the extend of an image which is captured with the camera. The bigger the magnification of the optics the smaller is the field of view.

Free Boundary Reflection

Definition

A virtual boundary (interface) exists between a gas jet exhausting from a nozzle and the surrounding quiescent medium. Compression and/ or expansion pressure waves propagating within the jet will undergo a reflection at the virtual boundary in such a way as to maintain a continuity in pressure across the interface.

Cross References

► Supersonic Micro-Nozzles

Free-Flow Magnetophoresis

► Magnetophoresis

Free Molecular Regime

► Gas Flow in Nanochannels

Free-Surface Atomization

Definition

Formation of droplets from a fluid-fluid interface of a scale at least an order of magnitude smaller than the characteristic scale of the interface. Acoustic atomizers are typical examples of free-surface atomization.

Cross References

► Piezoelectric Microdispenser

Free Surface Electrohydrodynamics

► Interfacial Electrokinetic Flow

Free Surface Electrokinetics

► Interfacial Electrokinetic Flow

Free Surface Flow

► Interface Capturing Schemes for Free-Surface Flows

Frequency Response

Definition

The frequency response (although called transfer function) is a common function in signal analysis and control engineering when the dynamic behavior of a system must be analyzed. Therefore the input and output parameter of the system will be compared as a function of frequency. For example when the system is stimulated with a harmonic input signal of a certain frequency the system will answer with the same frequency, but with attenuated amplitude and a shifted phase. Since the amplitude attenuation and the phase shift are both functions of the stimulation frequency, it is common to plot them in Bode-diagrams, where the amplitude response and the phase response are displayed separately over the frequency.

Friction Factor in Microchannels

► Turbulence in Microchannels

Front Capturing

► Interface Capturing Schemes for Free-Surface Flows

Front Tracking

► Interface Capturing Schemes for Free-Surface Flows

Fuel Cell

Definition

Conceptually similar to a battery, a fuel cell is an electrochemical device that converts chemical energy stored in a fuel and an oxidant into electrical energy. The fundamental difference between a fuel cell and a battery is that fuel and oxidant are supplied from outside the reaction chamber and waste products are removed. The heart of the fuel cell contains an anode and a cathode, separated by an ion-conducting electrolyte. Its operation is conceptually straightforward. The fuel is oxidized at the anode, releasing protons (H^+ ions) and electrons. The protons travel through the electrolyte, which conducts ions but is electrically insulating, and recombine with the oxidant at the cathode. The electrons, that are required for the cathodic reaction, are conducted from the anode to the cathode through external wiring, thereby generating an electrical current used to drive a load. Most fuel cells operate at low temperatures and therefore require an electrochemical catalyst such as platinum to reduce the activation energy of the chemical reactions and generate useful electrical power.

Cross References

► Microfluidic Fuel Cells
► Micro-structured Hydrogen Fuel Cells
► Microscale Energy Conversion Devices

Full-Width Half-Maximum (FWHM)

Definition

The FWHM is the width of the narrow transmitted peaks, by an optical filter, at half-height.

Cross References

► Lab-on-a-Chip Device for Chemical Analysis
► Optofluidics: Optics Enabling Fluidics
► Sputtering for Film Deposition

Fundamentals of Diffusion in Microfluidic Systems

PRAMOD CHAMARTHY, ALOKE KUMAR, JINHUA CAO, STEVEN T. WERELEY
Department of Mechanical Engineering,
Purdue University, West Lafayette, IN, USA
pramodc@purdue.edu, wereley@purdue.edu

Synonyms

Self-diffusion

Definition

Brownian motion is defined as the irregular motion of microscopic particles suspended in a fluid due to collisions with the surrounding fluid molecules. The mean square displacement of a particle executing Brownian motion is directly proportional to the temperature of the fluid and inversely proportional to the viscosity of the fluid and the diameter of the particle.

Chemical and Physical Principles

In the latter half of the nineteenth century and the beginning of the twentieth century, Brownian motion played an important role in the debate about the molecular reality of nature. The random movement of microscopic particles suspended in a liquid is named after the botanist Robert Brown, who discovered this phenomenon while observing pollen grain suspended in water. Though Brown himself states that this motion was observed by other researchers before him such as Leeuwenhoek (1632–1723), Buffon (1800s), Spallanzani (1800s), and Bywater (1819), he is credited with conducting the first systematic experiments to study the nature of this motion. He observed that both organic and inorganic particles exhibited this motion and that it was not caused by local currents in the fluid or any other such disturbances; he concluded that the motion originated in the particles themselves and called them *active molecules*.

Several investigations [1] were carried out to study this motion between 1860 and 1900 and it was established that external factors such as vibration, temperature, surface

tension, and incident light were not the cause of Brownian motion. It was proposed that the random movement of these particles was caused due to the bombardment by the molecules of the fluid, as predicted by kinetic theory. This hypothesis was open to a simple test. On the basis of the law of equipartition of energy, it was known that the mean kinetic energy of the molecules in a fluid in any one direction was

$$\frac{1}{2}m\left\langle v_x^2\right\rangle = \frac{1}{2}kT\,, \tag{1}$$

where m is the mass of a molecule, v_x is the velocity of a molecule in the x-direction, k is Boltzmann's constant, and T is the temperature of the fluid. On the basis of statistical mechanics, it was proposed that a particle suspended in a fluid should have the same kinetic energy. Several experiments were attempted to verify this theory, but the values of the kinetic energy differed by a factor of up to 100,000 [2].

The theoretical explanation of Brownian motion was derived independently by Einstein [3] and Smoluchowski around the same year. Later, Paul Langevin [4] derived the same expression through a completely different approach. Einstein's derivation will be discussed in the following section.

Einstein's Derivation

In the first part of the argument, Einstein derived a relationship between the diffusion coefficient and other physical quantities. On the basis of the molecular kinetic theory of heat, he asserted that particles suspended in a liquid will experience the same osmotic pressure that molecules do. If an external force K acts on a suspension of Brownian particles, then in equilibrium this force will be balanced by osmotic-pressure forces given by the relation

$$K = kT\frac{\nabla \cdot c}{c}\,, \tag{2}$$

where c is the number of particles per unit volume. Here, the force K can be any external force, such as gravity. The Brownian particles moving in the fluid because of this force will experience a resistance from the fluid of the form

$$\frac{K}{m\beta}\,, \tag{3}$$

where β is a constant with dimensions of frequency, and m is the mass of the particle. Therefore the number of particles that pass through a unit area per unit time owing to the action of the force K is given by

$$\frac{cK}{m\beta}\,. \tag{4}$$

The number of particles that pass through a unit area per unit time t owing to diffusion is given by the diffusion equation

$$\frac{\partial c}{\partial t} = D(\nabla \cdot c)\,. \tag{5}$$

Since the system is in dynamic equilibrium, the number of particles displaced owing to K will be restored by diffusion, giving the relation

$$\frac{cK}{m\beta} = D(\nabla \cdot c)\,. \tag{6}$$

Using (2) and (6), K and c can be eliminated, giving the relation

$$D = \frac{kT}{m\beta}\,. \tag{7}$$

If the Brownian particles are spheres of radius a, then the frictional resistance is given by Stokes's theory as

$$m\beta = 6\pi\eta a\,, \tag{8}$$

where η is the dynamic viscosity of the fluid. Combining (7) and (8), we obtain Einstein's equation for the diffusion coefficient,

$$D = \frac{kT}{6\pi\eta a}\,. \tag{9}$$

In the second part of his argument, Einstein relates the diffusion coefficient to a measurable property of Brownian motion such as the mean displacement of the particles. Let $c(x, t)$ denote the probability for a Brownian particle to be at position x at time t. By following a probabilistic argument, the spatial and temporal changes in the concentration of the particles were shown to be related to the diffusion coefficient by

$$\frac{\partial c}{\partial t} = D\frac{\partial^2 c}{\partial x^2}\,. \tag{10}$$

This equation was established by Adolf Fick, but was reinterpreted and applied to the problem of Brownian motion by Einstein. Integrating (10), we obtain

$$c(x, t) = \frac{n}{\sqrt{4\pi D}}\frac{e^{-\frac{x^2}{4Dt}}}{\sqrt{t}}\,, \tag{11}$$

where n is the total number of particles suspended in the fluid. The mean square of the displacement $\langle x^2 \rangle$ of the particles along the x-axis in a time Δt can be obtained by solving the integral equation

$$\left\langle x^2 \right\rangle = \left(\frac{1}{n}\right) \int_{-\infty}^{+\infty} x^2 c(x,t)\mathrm{d}x\,, \tag{12}$$

which gives the final result,

$$\left\langle x^2 \right\rangle = 2D\Delta t\,. \tag{13}$$

If the displacements along all three dimensions are considered,

$$\left\langle r^2 \right\rangle = \left\langle x^2 + y^2 + z^2 \right\rangle = 6D\Delta t\,. \tag{14}$$

Mathematical Foundation

The theory of Brownian motion has grown far beyond the domain of its initial application and has benefited enormously from the contributions made by mathematicians. An interesting aspect of Brownian motion is its interpretation as a particular limiting case of a random walk, which is the motion generated by taking successive steps, of a fixed length, in a random direction. Hence Brownian motion is often stated to be the random-walk motion of small particles suspended in a fluid due to bombardment by molecules obeying a Maxwellian velocity distribution. Such a motion can be easily demonstrated experimentally by taking a sequence of images of a Brownian particle. Figure 1 shows a simulated random walk of a particle undergoing Brownian motion in two dimensions. Figure 1a shows the motion of a particle on a large timescale and Fig. 1b shows the same motion recorded on a smaller timescale. It can be seen that the path of the Brownian motion contains fine details. More and more details emerge as smaller timescales are chosen to sample the data. The assumption that the mean square displacement of the particles is proportional to the time interval becomes invalid at very small timescales [5]. As soon as a particle receives momentum from the fluid molecules, the fluid in the immediate vicinity of the particle is disturbed. Owing to the inertial effect of the surrounding fluid, there is a time delay in the transition from ballistic motion to a purely diffusive motion. This effect is called the hydrodynamic memory effect and becomes important at timescales much less than 1 μs [6, 7].

In a strict mathematical sense, Brownian motion can be classified as a Weiner process. A Weiner process is a class of stochastic processes which satisfies the following conditions [8]:

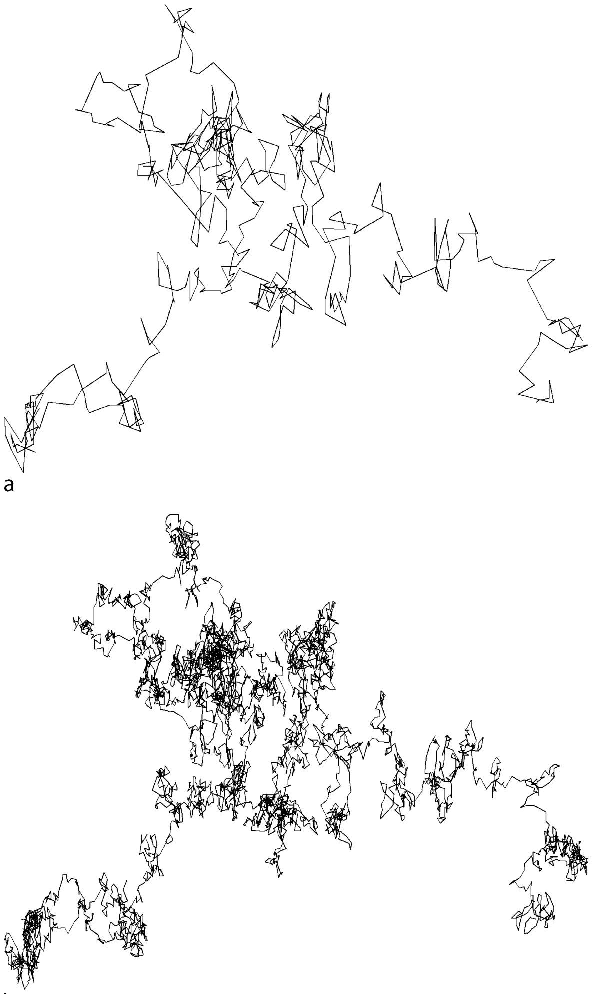

Fundamentals of Diffusion in Microfluidic Systems, Figure 1 Simulated paths of a Brownian particle. (**a**) Path recorded on a large timescale and (**b**) same path recorded on a smaller timescale. More details emerge as we use smaller time scales

1. $X(0) = 0$;
2. $\{X(t),\, t \geq 0\}$ has stationary and independent increments;
3. For every $t > 0$, $X(t)$ is normally distributed with mean 0 and variance $\sigma^2 t$.

This definition shows that Brownian motion is closely linked to the Gaussian/normal distribution. The formalism of Weiner processes opens stochastic processes to rigorous mathematical analysis and has enabled the use of Weiner processes in the field of stochastic differential equations. Stochastic differential equations are analogs of classical differential equations where the coefficients are stochastic variables rather than constants or deterministic variables. The field of stochastic differential equations finds wide application in many practical situations where mod-

eling using stochastic models becomes a necessity. Examples of such situations include population growth models where *noise* is present, and electrical circuits with noise. The non-differentiability of the Weiner process requires the introduction of concepts of white noise; an appropriate text may be referred to for a deeper understanding [9].

Key Research Findings

Influence of Brownian Motion on Particulate Flows

In the past two decades, the biological and medical fields have seen great advances in the development of biochips capable of characterizing and quantifying biomolecules. Biochips, also known as labs on a chip or μTAS (micro-total analysis systems), are microscale systems that interact with biological components on their characteristic length scale. Many biochips work with *particles* (cells, bacteria, DNA, etc.) suspended in fluids.

Generally, two major phenomena act on suspended neutrally buoyant particles to determine their spatial distribution: particle migration due to hydrodynamic forces, and Brownian motion. Bulk migration of particles has been shown in non-Brownian suspension flows both theoretically and experimentally in many studies since Segré and Silberberg's pioneering reports [10, 11] on the inertial migration of particles in tube flow and Leighton and Acrivos's report [12] on particle–particle interaction in concentrated suspensions. Considering the characteristic length scale (several microns or less) of biological components and their typical speed in both biomedical devices, Brownian motion cannot be neglected.

Concentrated Suspensions

Frank et al. [13] investigated particle migration in concentrated Brownian suspensions both by experiment and by modeling of flow in a mixer. The flow rate was quantified by the dimensionless Péclet number, which, conceptually, is the ratio of the time required for Brownian diffusion to move a particle by its own size, $a^2/D = a^2/(kT/6\pi\eta a)$, to the time required for shear flow to move it by the same distance, γ^{-1} (where γ is the shear rate of the surrounding flow field), yielding

$$\mathrm{Pe} = \frac{6\pi\eta\gamma a^3}{\kappa T} . \qquad (15)$$

Confocal microscopy was used to study the flow of Brownian particles experimentally by directly imaging the particle motion and concentration. The experimental setup was a long, rectangular glass channel of cross section $50 \times 500\,\mu\mathrm{m}^2$, connected on each side to a Teflon tube. Concentration profiles were measured across the narrow dimension of the glass channel as shown in Fig. 2. The results are shown in Fig. 3. It can be seen that there is an increase in concentration in the center, which shows that at high volume fractions particles migrate toward the centerline, with the migration becoming progressively stronger as Pe increases. Comparisons of the experimental data with the modeling indicate that the dependence of the extent of migration on Pe is captured well but that discrepancies arise, at least in part because the assumption of fully developed flow is not valid for these experiments.

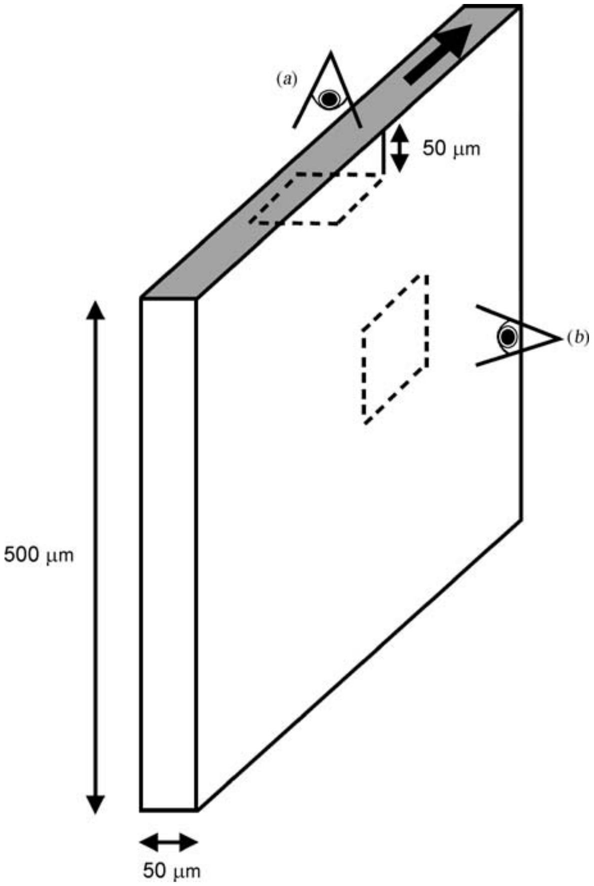

Fundamentals of Diffusion in Microfluidic Systems, Figure 2 Sketch of an experimental flow chamber; the bold arrow indicates the flow direction. Concentration profiles were obtained by looking through the top (**a**) at a fixed distance (50 μm) from the top wall. Velocity profiles were taken by scanning a horizontal plane through the side (**b**) of the chamber, across the 50 μm width of the channel

Dilute Suspensions

In Poiseuille flow, rigid, spherical, non-Brownian particles are subjected to lateral forces that result in migration to an equilibrium radial region located at approximately 60% of the distance from the tube axis to the tube wall, which

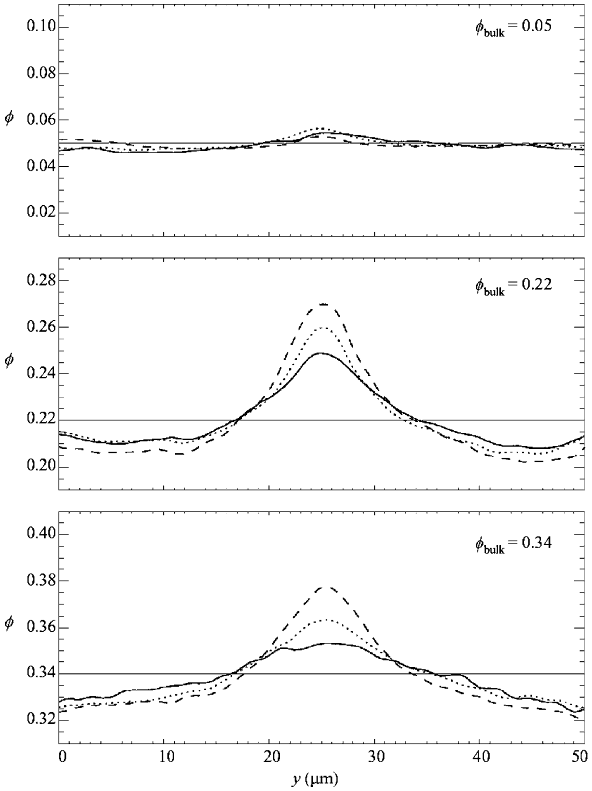

Fundamentals of Diffusion in Microfluidic Systems, Figure 3 Plots of the local volume fraction ϕ as a function of the distance across the channel for an average volume fraction $\phi_{bulk} = 0.05$, 0.22, and 0.34 at flow rates of 0.125 μl min^{-1} (solid line, Pe = 69), 1.0 μl min^{-1} (dotted line, Pe = 550), and 8.0 μl min^{-1} (dashed line, Pe = 4400) [13]

is called the *Segré and Silberberg effect* [10, 11]. The migration of Brownian particles in a Poiseuille flow for a range of particle volume fractions ϕ much less than 0.01 has been investigated using epifluorescent microscopy and microparticle image velocimetry [14]. When Pe is smaller than 1000, particles migrate away from the channel wall, with a nearly uniform particle concentration everywhere else in the channel, as shown in Fig. 4. When Pe is greater than 1000, the Segré and Silberberg effect is observed: particles move toward a preferred position, with the migration effect becoming progressively stronger as Pe increases, which results in an increase in the concentration profile between the channel center and channel wall.

Influence of Brownian Motion on Velocity Measurements

In typical particle image velocimetry (PIV) analysis, the correlation of an image with itself is called an autocorrelation, and the correlation of an image with another image is called a cross-correlation. The location of the correlation peak gives the average displacement of the particles, and the shape of the correlation peak depends on the particle size and on the imaging optics. It has been observed that for low velocities (< 10 μm/s), the submicron-sized particles used to seed the flow undergo enough Brownian motion to introduce significant errors in velocity measurements made by microparticle image velocimetry (μPIV) [15]. This uncertainty in locating the peak center was, however, substantially minimized through ensemble averaging over multiple images. This had the effect of causing a widthwise spreading of the correlation function. The effect of Brownian motion on the cross-correlation function is illustrated in Fig. 5. Figure 5a shows a typical autocorrelation peak, Fig. 5b shows a typical cross-correlation peak without any Brownian motion, and Fig. 5c shows a typical cross-correlation peak in the presence of Brownian motion. It can be seen that the peak width of the correlation function in the presence of Brownian motion is broader and the peak is lower than for the correlation function without any Brownian motion.

Olsen and Adrian [16] performed a theoretical study of the effect of Brownian motion on the μPIV correlation signal peak and derived a function quantifying the broadening of the correlation function. They postulated that this widthwise broadening of the correlation function could be used to calculate the temperature of the fluid, since Brownian motion has a direct dependence on temperature. This method would utilize the same data as that obtained for making μPIV measurements, eliminating the need to set up an entirely different experiment for measuring the temperature [15]. This idea was further developed by Hohreiter et al. [17], where the measurement technique was demonstrated with an experimental uncertainty of ±3 °C.

Measurement of Brownian Motion

Several attempts have been made to experimentally verify the theory of Brownian motion proposed by Einstein. Svedberg's results [18] were close to the expected values, but several researchers remained skeptical. Henri [19] used the recently invented film camera, attached to a microscope, to record the trajectories of latex particles suspended in water, but could not find quantitative agreement with Einstein's formula. The theory was finally verified by Perrin [20] by a series of experiments. In these experiments, the data was obtained using a microscope and a camera, while the displacements and the number of particles were measured manually.

At present, several different methods can be used to measure diffusion. The commonly used techniques to measure Brownian motion are briefly discussed below.

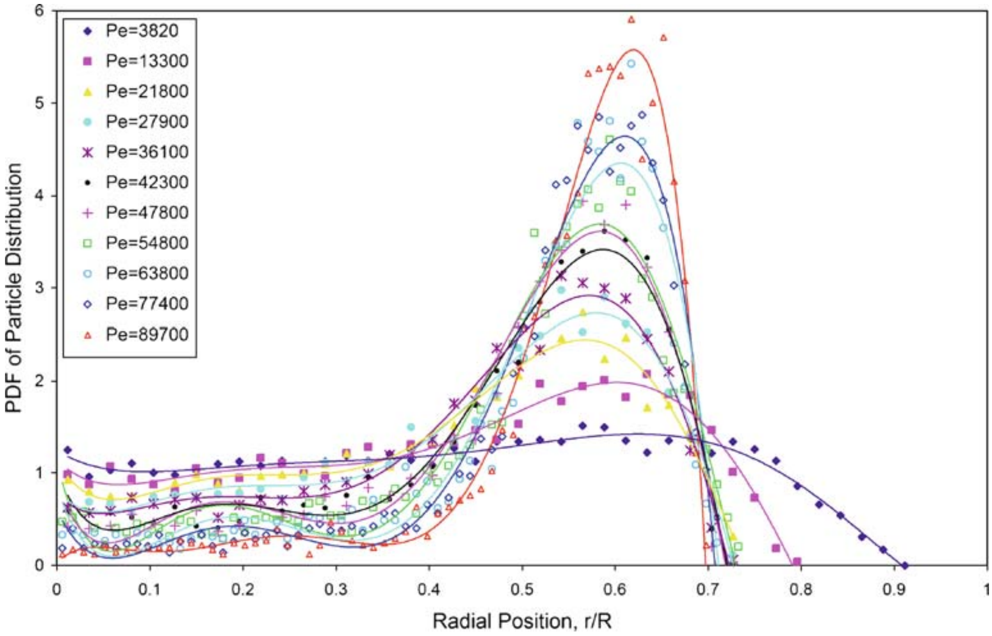

Fundamentals of Diffusion in Microfluidic Systems, Figure 4 Plot of the relative concentration (probability density function of the particle distribution) as a function of the radial position in a round capillary tube

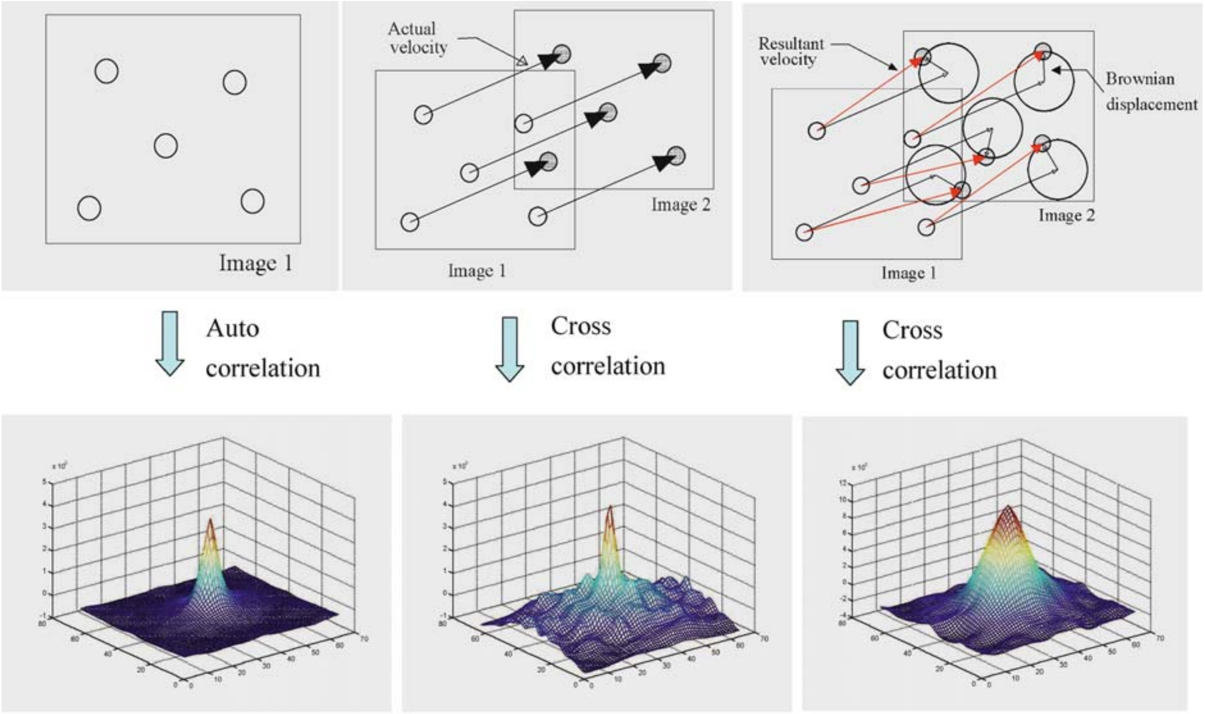

a $\Delta s_{o,a} = \sqrt{2d_e^2/\beta^2}$ b $\Delta s_{o,c} = \sqrt{2d_e^2/\beta^2}$ c $\Delta s_{o,c} = \sqrt{2(d_e^2 + 8M^2\beta^2 D\Delta t)}$

Fundamentals of Diffusion in Microfluidic Systems, Figure 5 Broadening of cross-correlation function in the presence of Brownian motion. (**a**) Auto-correlation function. (**b**) Cross-correlation function. (**c**) Cross-correlation function with Brownian motion

Light Scattering

When a beam of light is incident on a particle, it is partially reflected, refracted, and transmitted, depending on the size and properties of the particle. Light scattering can be broadly classified into classical light scattering and dynamic light scattering. In classical light scattering, if the particle size is of the order of or smaller than the wavelength of light, the light is scattered in all directions (Rayleigh scattering) and is a function of the molar mass and of the size of the particle. If the particle size is much greater than the wavelength of light, the intensity of the scattered light is dependent on the angle (Mie scattering). Classical light-scattering techniques are commonly used to study the size, shape, and structure of biological molecules in cells.

Dynamic light scattering involves the study of time-dependent fluctuations in the intensity of scattered light which are the result of the Brownian motion of the particles. The random movement of the particles causes the distances between the particles to fluctuate, causing constantly varying constructive and destructive interference patterns. This time-dependent fluctuation in the intensity can be correlated with itself to obtain the diffusion coefficient of the particles. This method is also called photon correlation spectroscopy (PCS) and quasi-elastic light scattering (QELS) [21, 22].

Fluorescence Correlation Spectroscopy

In fluorescence correlation spectroscopy (FCS), the fluorescence intensity of molecules within a small volume is statistically correlated to measure the concentration and the particle size. Typically, the sample is illuminated with a laser beam and the intensity, which is dependent on the number of fluorescent molecules, is measured. Since these fluorescent molecules exhibit Brownian motion, the number of particles present in the region will be constantly changing, resulting in a fluctuating intensity signal. If the time series of the intensity is correlated with itself, the resulting plot gives a measure of the number of fluorescent molecules present in that volume, as well as the diffusion coefficient of the molecules. By using a ▶confocal microscope, the background noise can be eliminated and the fluorescence intensity of a single molecule can be measured [23].

Fluorescence Recovery After Photobleaching (FRAP)

If a fluorescent molecule is irradiated with a high-intensity laser, the molecule undergoes a permanent chemical reaction, as a result of which it loses its fluorescent capability. This phenomenon is called photobleaching. In this method, high-intensity laser light is used to photobleach a small volume of the sample and low-intensity laser light is used to image the sample. Immediately after photobleaching, there is a dark region, where the fluorescent molecules have been inactivated, surrounded by a bright region containing unaffected fluorescent molecules. But, as time progresses, the fluorescent molecules from the bright region diffuse into the dark region. By measuring this fluorescence recovery after photobleaching, the mobile fraction and the rate of motion of the molecules in a region can be measured. The rate of motion can be used to calculate the diffusion coefficient.

The spatial resolution in FRAP (also known as fluorescence photobleaching recovery, FPR) measurements is limited by the minimum diffraction-limited size of the laser beam [24, 25].

Single-Particle Tracking

The most straightforward method of measuring diffusion is by tracking the movement of individual particles. Particles executing Brownian motion are imaged at fixed time intervals with the help of a video camera or CCD camera attached to a microscope. The images are then processed to locate the centers of the particles and to measure the distance that each particle travels within each time interval. The diffusion coefficient is obtained directly by plotting the mean square of the displacement as a function of time, as given by (14).

Several researchers have studied the Brownian motion of submicron-sized particles suspended in a fluid using digital video microscopy. Crocker and Grier [26] made use of optical tweezers to study the hydrodynamic correction to Brownian motion in the case of two spheres in close proximity. They argued that with careful experiments, diffusion coefficients can be experimentally measured to an accuracy of $\pm 1\%$. Nakrohis et al. [27] measured Boltzmann's constant, and Salmon et al. measured Avogadro's number by studying the Brownian motion of submicron-sized particles. Park et al. used optical serial-sectioning microscopy (OSSM) to measure Brownian particle displacements in all three dimensions and deduced temperature information with uncertainty differentials of 5.54%, 4.26%, and 3.19% for the 1D, 2D, and 3D cases. Kihm et al. used 3D ratiometric total internal reflection fluorescence microscopy (3D R-TIRFM) to measure Brownian displacements near a wall and calculated the hindered diffusion constant of 200 nm particles in the lateral and normal directions relative to the wall.

Examples of Application

Brownian motion is a rich field in terms of the attention it has received from both physicists and mathematicians,

and various models exist which incorporate other physical features. The study of Brownian motion is now being applied in fields as varied as financial modeling, protein–DNA interactions, fractal analysis in medical imaging, and estimation of floods.

Cross References

- ► Optical traps
- ► Microparticle Image Velocimetry

References

1. Haw MD (2002) Colloidal suspensions, Brownian motion, molecular reality: A short history. J Phys – Condens Matter 14(33):7769–7779
2. Nelson E (1967) Dynamical Theories of Brownian Motion. Princeton University Press, Princeton, NJ, USA, p 142
3. Einstein A (1905) The motion of elements suspended in static liquids as claimed in the molecular kinetic theory of heat. Ann Phys 17(8):549–560
4. Langevin P (1908) The theory of brownian movement. C r Hebd Seances Acad Sci 146:530–533
5. Hinch EJ (1975) Application of Langevin equation to fluid suspensions. J Fluid Mech 72(DEC9):499–511
6. Lukic B, Jeney S, Tischer C, Kulik AJ, Forro L, Florin EL (2005) Direct observation of nondiffusive motion of a Brownian particle. Phys Rev Lett 95(16):160601-1–160601-4
7. Kao MH, Yodh AG, Pine DJ (1993) Observation of Brownian-motion on the time scale of hydrodynamic interactions. Phys Rev Lett 70(2):242–245
8. Ross SM (2003) Introduction to Probability Models, 8th edn. Academic Press, San Diego
9. Øksendal BK (1998) Stochastic Differential Equations: An Introduction with Applications, 5th edn. Springer, Berlin
10. Segré G, Silberberg A (1962) Behaviour of macroscopic rigid spheres in Poiseuille flow. 1. Determination of local concentration by statistical analysis of particle passages through crossed light beams. J Fluid Mech 14(1):115–135
11. Segré G, Silberberg A (1962) Behaviour of macroscopic rigid spheres in Poiseuille flow. 2. Experimental results and interpretation. J Fluid Mech 14(1):136–157
12. Leighton D, Acrivos A (1987) The shear-induced migration of particles in concentrated suspensions. J Fluid Mech 181:415–439
13. Frank M, Anderson D, Weeks ER, Morris JF (2003) Particle migration in pressure-driven flow of a Brownian suspension. J Fluid Mech 493:363–378
14. Cao J, Wereley ST (2004) Brownian particle distribution in tube flows. In: Proceedings of the ASME International Mechanical Engineering Congress and Exposition. Anaheim, CA
15. Santiago JG, Wereley ST, Meinhart CD, Beebe DJ, Adrian RJ (1998) A particle image velocimetry system for microfluidics. Exp Fluid 25(4):316–319
16. Olsen MG, Adrian RJ (2000) Brownian motion and correlation in particle image velocimetry. Opt Laser Technol 32(7–8):621–627
17. Hohreiter V, Wereley ST, Olsen MG, Chung JN (2002) Cross-correlation analysis for temperature measurement. Meas Sci Technol 13(7):1072–1078
18. Svedberg T (1906) Concerning the proper motion of particles in colloidal solutions. Z Angew Elektrochem Angew Phys Chem 12:853–860
19. Henri V (1908) Cinematographic study of brownian movements. C r Hebd Seances Acad Sci 146:1024–1026
20. Perrin J (1910) Brownian movement and molecular science. Phys Z 11:461–470
21. Berne BJ, Pecora R (2000) Dynamic Light Scattering: With Applications to Chemistry, Biology, and Physics. Dover Publications, Mineola, NY
22. Schmitz KS (1990) An Introduction to Dynamic Light Scattering by Macromolecules. Academic Press, Boston
23. Rigler R, Elson E (2001) Fluorescence Correlation Spectroscopy: Theory and Applications. Springer, New York
24. Klonis N, Rug M, Harper I, Wickham M, Cowman A, Tilley L (2002) Fluorescence photobleaching analysis for the study of cellular dynamics. Eur Biophys J Biophys Lett 31(1):36–51
25. Elson EL (1985) Fluorescence correlation spectroscopy and photobleaching recovery. Annu Rev Phys Chem 36:379–406
26. Crocker JC, Grier DG (1996) Methods of digital video microscopy for colloidal studies. J Colloid Interface Sci 179(1):298–310
27. Nakroshis P, Amoroso M, Lagere J, Smith C (2003) Measuring Boltzmann's constant using video microscopy of Brownian motion. Am J Phys 71(6):568–573

Fusion Bonding

- ► Thermal Fusion Bonding
- ► Wafer Bonding

Gage Pressure

► Pressure

Gas Chromatography

Olgica Bakajin
Chemistry, Materials, Earth and Life Sciences Directorate, Lawrence Livermore National Laboratory, Livermore, CA, USA
bakajin1@llnl.gov

Synonyms

GC; Micro gas chromatography; Micro gas analyzers; μGC; MGA

Definition

Gas chromatography (GC) is a chemical analysis technique for separating chemicals in a complex sample. In a gas chromatography setup, the sample is passed through a narrow tube known as the *column*, through which different chemical constituents of a sample pass in a gas stream (carrier gas, *mobile phase*) at different rates depending on their various chemical and physical properties and on their interaction with a specific column filling, referred to as the *stationary phase*. Interaction of the analytes with the stationary phase causes each one to exit the column at a different time (*retention time*). Separated chemicals are detected and identified at the end of the column. Miniaturization of GC systems can lead to small size and extremely low power consumption.

Overview

In the 50 years since its introduction, the use of GC by the petroleum industry has helped foster many breakthroughs in GC instrumentation. Open-tubular GC columns and the theory that describes them were first introduced by Golay and Ettre in the mid-1950s. The further development of open-tubular capillary columns was done by Desty of British Petroleum, and with subsequent refinement, this technique is now the standard method for most GC applications. The use of GC for sample analysis was also quickly adopted by the pharmaceutical and food industries and is used for fundamental studies of reaction kinetics and physiochemical measurements. Today the use of GC for the analysis of complex samples such as serum proteins, natural products, essential oils, and environmental samples has become routine with multidimensional separation techniques and multivariate *chemometric* analysis providing identification and quantification of trace analytes from complex samples in the sub-ppb range. A GC system usually consists of the following elements (Fig. 1):

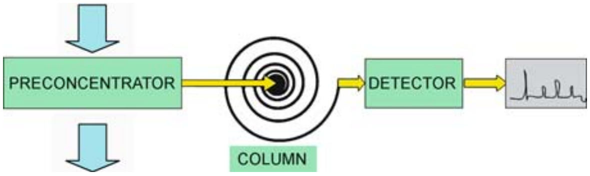

Gas Chromatography, Figure 1 Schematic of a GC system

Injector/Preconcentrator

Most common injectors are microsyringes, solid-phase microextraction fibers, or a gas source switching system.

Column

Two types of columns are used in GC:

Capillary Columns

Conventional capillary columns have a very small internal diameter, of the order of a few tenths of millimeters, and lengths between 25 and 60 m. The inner column walls are coated with a thin layer of stationary phase material. Most capillary columns are made of fused silica with a poly-

imide outer coating. These columns are flexible, so a very long column can be wound into a small coil.

Packed Columns

Conventional macroscale packed columns are 1.5–10 m in length and have an internal diameter of 2–4 mm. The tubing is usually made of stainless steel or glass and contains a *packing* of finely divided, inert, solid support material (e. g. diatomaceous earth) that is coated with a liquid or solid stationary phase.

Detector(s)

A detector is used to monitor the outlet stream from the column; thus, the time at which each component reaches the outlet and the amount of that component can be determined. Generally, substances are identified by the order in which they emerge (elute) from the column and by the retention time of the analyte in the column.

The most common are the flame ionization detector (FID) and the thermal conductivity detector (TCD). Both detectors are sensitive to a wide range of components, and both work over a wide range of concentrations. While TCDs are essentially universal and can be used to detect any component other than the carrier gas, FIDs are sensitive primarily to hydrocarbons, and are more sensitive to them than TCDs.

Gas chromatographs are often connected to a *mass spectrometer* (MS) which acts as the detector. The setup, known as *GC/MS*, is powerful because the MS can identify compounds by mass giving another dimension to the separation.

Additional Parameters

Because molecular adsorption and the rate of progression along the column depend on temperature, the column temperature is carefully controlled during the separations. Temperature can also be ramped during the separation to obtain faster and more efficient separations. This is referred to as temperature programming.

Typical carrier gases include helium, nitrogen, argon, hydrogen, and air. Which gas to use is usually determined by the detector being used, the sample's matrix, or based on safety and availability.

Basic Methodology

Conditions in which the gas separations are done need to be optimized for a desired analysis. During the analysis, the following conditions can be varied: inlet temperature, detector temperature, column temperature, temperature program, carrier gas and carrier gas flow rates, the column's stationary phase, diameter and length, inlet type and flow rates, sample size, and injection technique.

The column temperature is selected as a compromise between the length of the analysis and the level of separation. Separations that are done at the same temperature for the entire analysis are called *isothermal*. Most of the time, to obtain a better separation, temperature is increased during the analysis. The initial temperature, rate of temperature increase (the temperature *ramp*), and final temperature are referred to as the *temperature program*. A temperature program shortens the time it takes for late-eluting analytes to pass through the column while allowing analytes that elute early in the analysis to separate well.

Key Research Findings

In the past few years there has been a considerable development in microscale gas chromatography. Several portable instruments are commercially available (by Varian, Agilent, Electronic Sensor Technology). These are not fully microfabricated instruments so as not to be confused with chip-based GC instruments often referred to as μGC instruments. The first microfabricated GC device was reported by Terry et al. [1]. The only commercially available fully integrated μGC system is being advertised by SLS Micro Technology (http://www.slsmt.de/). It consists of a gas chromatography module of the size of a credit card integrated on multilayer printed circuit board with standard gas connectors, a micro-injection system, a micromachined separation column, and μTCD for detection. The column is only 0.86 m in length and can use temperature programming, maximum temperature of 250 °C, for analysis times that are typically less than 60 s. The instrument is capable of high sensitivity of measurement, fully automated operation as well as stand-alone interpretation and rapid transmission of results.

In recent years several advances in μGC technology have been made in the following areas.

Column Channel Design and Fabrication

Typical materials used for μGC include silicon, metal, and a variety of polymers etched for column configuration. Typically, rectangular channels are etched using deep reactive ion etching, wet chemical etching, and high-energy laser etching. Recent work by Spangler [2, 3] has updated the model for chromatographic theory from that used for traditional round column GC to the rectangular channel dimensions of μGC systems. Some of the examples of published μGC systems include the packed-bed μGC system incorporated as part of the μChemLab project at Sandia [4] and work by Lambertus et al. [5] where they used

a square spiral design and commercial dimethylpolysiloxane stationary phase.

Novel Stationary Phases

New efficient and robust stationary phases for μGC are essential because traditional polymer GC stationary phases in the angular cornered channels of the μGC do not result in a uniformly thick stationary phase, i. e. the polymer phase tends to be significantly thicker in the corners of the channel, introducing unwanted band broadening. Nanostructured materials are being explored for this purpose such as monolayer protected gold nanoparticles [6], carbon nanotubes [7], and others.

Thus, research on ways to refine the use of polymer stationary phases within the μGC channel design also continues. Examples include using UV photopolymerization of gas-phase monomers for thin-film deposition [8] and plasma polymerization [9].

Interconnects/Interfaces

With the desire for high-speed separations on short columns, μGC systems must be carefully designed in order to minimize sources of extra-column band broadening such as dead volumes at connection points and within detectors, large injection pulses, and non-uniform flow patterns. The interface of the chip with instrumental components is extremely important and integration of all of the components directly with the column is preferred.

Future Directions for Research

One of the most active areas in the development of true microscale gas analyzers (chip based) has been motivated by the desire to build extremely small and fast gas analyzers for military use. DARPA is currently funding a micro gas analyzers (MGA) program. The goal of the MGA program is to attain tiny separation analyzer-based chemical warfare agent (CWA) sensors capable of orders of magnitude reductions in analysis time, detection limit, and power consumption, over equivalent bench top systems, while maintaining the true to false alarm ratios on a par with benchtop GC/MS systems. By harnessing the advantages of microscale miniaturization, the MGA program is expected to yield chip-scale gas analyzers with the following performance characteristics:

- An ability to identify all relevant CWAs against plausible background mixtures of more than 30 different species, including fuels with true to false alarm ratios on par with GC/MS systems, which are the gold standard of gas analysis.
- Overall size less than 2 cm^3 not including the power source, but including control electronics and any fluid transport, pre-concentration, and detection mechanisms, whichever used.
- Detection limit better than 1 ppt.
- Total analysis time less than 4 s, to include the time needed for any pre-concentration, separation, and detection steps.
- Energy per analysis less than 0.5 J (less than 1 J for full GC/MS).

Research topics and activities relevant to the implementation of MGA include:

- fast microscale pre-concentration;
- strategies for suppression of unwanted species;
- micro- or nanoengineered separation methods, such as ultrathin chromatographic columns;
- nanoengineered stationary phases;
- methods for fluid transport, including pumpless strategies;
- microscale thermal isolation for low power operation; and
- micro- or nanoengineered detectors with unprecedented sensitivity.

MGA-enabled devices with characteristics similar to those listed above and fabricated via low-cost, batch fabrication methods are expected to enable a myriad of strategic capabilities. In particular, the sheer portability of the CWA sensors sought by the MGA program should introduce a host of new applications and deployment scenarios, including wearable sensors for dismounted warriors, projectile-delivered sensors for remote detection applications, and unattended ground sensors for perimeter protection and advanced warning purposes. Although the small size and power consumption sought by MGA are obvious enablers for wearable CWA sensors, it is actually the MGA program's pursuit of false alarm rates on a par with tabletop GC/MS systems that makes possible this sort of *per soldier* deployment strategy. Presently that kind of deployment is hindered by the unacceptably high incidence of false positives exhibited by current fielded portable CWA sensors. In addition, the fast analysis speed and tiny size (for resilience against high g forces) targeted by the MGA program, together with miniature wireless technologies targeted by other DARPA programs (e. g. NMASP), will enable projectile-deployed MGAs for remote detection of distant CWAs, effectively allowing miniature point detectors to operate in a stand-off-like fashion. Furthermore, MGA-enabled low power and low false alarm rates should greatly facilitate the deployment of unattended sensor networks for first warning perimeter applications, as well as environmental monitoring applications in both military and civilian sectors. By enabling an expansion of applica-

tions, as illustrated above, miniaturization via MGA technology is expected to generate a need for high-volume manufacturing that, together with wafer-level batch fabrication methods enabled by MEMS technology, should substantially lower the cost of GC/MS-equivalent systems, and thus further fuel expansion of the application suite for MGA technology.

Cross References

- ► Chromatographic Chip Devices
- ► Mass Spectroscopy
- ► Lab-on-Chip (General Philosophy)
- ► Mass Spectrometry on Chip Devices
- ► Stationary Phases in Microchannels

References

1. Terry SC, Jerman JH, Angell JB (1979) Gas-Chromatographic Air Analyzer Fabricated On A Silicon-Wafer. IEEE Trans Electron Devices 26(12):1880–1886
2. Spangler GE (1998) Height equivalent to a theoretical plate theory for rectangular GC columns. Anal Chem 70(22):4805–4816
3. Spangler GE (2001) Relationships for modeling the performance of rectangular gas chromatographic columns. J Microcolumn Separations 13(7):285–292
4. Frye-Mason G, et al (2001) Micro Total Analysis Systems, Proceedings of the 5th microTAS Symposium 658–660
5. Lambertus GR, et al (2005) Silicon microfabricated column with microfabricated differential mobility spectrometer for GC analysis of volatile organic compounds. Anal Chem 77(23):7563–7571
6. Gross GM, et al (2003) Monolayer-protected gold nanoparticles as a stationary phase for open tubular gas chromatography. Anal Chem 75(17):4558–4564
7. Stadermann M, et al (2006) Ultrafast gas chromatography on single-wall carbon nanotube stationary phases in microfabricated channels. Anal Chem 78(16):5639–5644
8. Hsieh MD, Zellers ET (2002) In situ UV-photopolymerization of gas-phase monomers for microanalytical system applications. Sens Actuators B 82(2–3):287–296
9. Lehmann U, Krusemark O, Muller J (2000) Micro Total Analysis Systems, 4th Proceedings of the microTAS Symposium 167–170

Further Reading

- Eiceman GA, Gardea-Torresdey J, Dorman F, Overton E, Bhushan A, Dharmasena HP (2006) Anal Chem 78(12):3985
- Gross GM, Reid VR, Synovec RE (2005) Current Anal Chem 1(2):135
- Eiceman GA, Gardea-Torresdey J, Overton E, Carney K, Dorman F (2004) Anal Chem 76:3387
- Eiceman GA, Gardea-Torresdey J, Overton E, Carney K, Dorman F (2002) Anal Chem 74:2771
- Frye-Mason G, Kottenstette R, Mowry C, Morgan C, Manginell R, Lewis P, Matzke C, Dulleck G, Anderson L, Adkins D, (2001) In: Ramsey JM, van den Berg A (eds) Micro Total Analysis Systems, Proceedings of the microTAS Symposium, 5th, Kluwer Academic Publishers, Dordrecht, Neth.: Monterey, CA, USA, 658–660
- Lehmann U, Krusemark O, Muller J (2000) In: van den Berg A, Olthuis W, Bergveld P (eds) Micro Total Analysis Systems 2000, Proceedings of the 4th microTAS Symposium, Enschede, Netherlands, Kluwer Academic, Dordrecht, pp. 167–170

Gaseous Flow

► Single-Phase Gaseous Flow

Gaseous Samples

Definition

Gaseous samples need to be extracted or dissolved in liquid before being transferred to chips.

Cross References

► Techniques for Transferring Samples to Chips

Gas Flow

► Micro- and Nanoscale Gas Fluidics

Gas Flow in Nanochannels

FELIX SHARIPOV
Departamento de Física, Universidade Federal do Paraná, Curitiba, Brazil
sharipov@fisica.ufpr.br

Synonyms

Internal rarefied gas flows; Slip flow regime; Transitional regime; Free molecular regime

Definition

Gas flow in nanochannels is distinguished by the regime when a characteristic size of a channel is comparable with the mean free path of gaseous molecules.

Mean free path is the average distance traveled by a gaseous molecule between two successive collisions.

Knudsen number is the ratio of mean free path of gaseous molecules to a typical dimension of gas flow.

Mass flow rate is the mass quantity of gas flowing through a cross-section of channel per unit time.

Overview

A typical magnitude of the mean free path ℓ in equilibrium air under standard conditions is about 5×10^{-8} m. Thus, if a channel has a cross-section size a in the range from 10^{-9} m to 10^{-7} m, then the *Knudsen number* $\mathrm{Kn}=\ell/a$ is not so small in order to use the approach based on continuum mechanics. In this case, gas flows must be considered on the kinetic level, i. e. the methods of ▶ rarefied gas dynamics based on the ▶ Boltzmann equation must be used. The advantage of the kinetic approach is that it is applicable for any value of the *Knudsen number*, namely for very small values ($\mathrm{Kn}\ll1$) corresponding to the channel size larger than 10^{-6} m (microchannels), for transitional values ($\mathrm{Kn}\sim1$) when the size a is about 10^{-8} m, and for large values ($\mathrm{Kn}\gg1$) if the channel size is close to 10^{-9} m (nanochannels). Thus, the kinetic equation is a tool allowing us to have a unique approach to micro- and nanochannels.

As is known, Poiseuille flow, i. e. gas motion due to a pressure gradient, is a typical phenomenon in all kinds of channels. However, a new phenomenon arises in nanochannels, namely ▶ thermal creep, i. e. gas flow due to a temperature gradient from a cold region to a hot one. In the transitional regime, i. e. when $\mathrm{Kn}\sim1$, this phenomenon is significant and should be taken into account together with the Poiseuille flow. Note that under the standard conditions the transitional regime is realized if the cross-section of channel a is about 10^{-8} m. Thus, if a nanochannel is non-isothermal then the two driving forces, such as pressure and temperature gradients, must be considered.

A numerical solution of the exact ▶ Boltzmann equation requires great computational effort that is not justified in practical and engineering calculations. That is why the so-called ▶ model equations allowing one to reduce the effort are widely used in practice.

In the open literature one can find reliable results on gas flows through long tubes, long rectangular channels and thin orifices over the whole range of the *Knudsen number*. Such flows were calculated for both driving forces, i. e. for pressure and temperature gradients. Numerical calculations were carried out on the basis of the model equations and also applying the exact Boltzmann equation itself. A consequence of the non-complete accommodation of the gaseous molecules on nanochannel walls was also intensively studied. Most of the published results can be applied directly to numerical simulations of microfluidics.

Basic Methodology

Here, long channels with two types of cross-section are considered: rectangular with a height a and width b and cylindrical with a radius a as is shown in Fig. 1. Further, the rectangular channel will be referred to as just *channel*, while the channel with the cylindrical cross-section will be called *tube*. It is assumed the channel/tube length L to be significantly larger than its cross-section size. i. e. $L\gg a$ and $L\gg b$. A rarefied gas moves along the channel/tube due to small longitudinal gradients of pressure P and temperature T denoted as

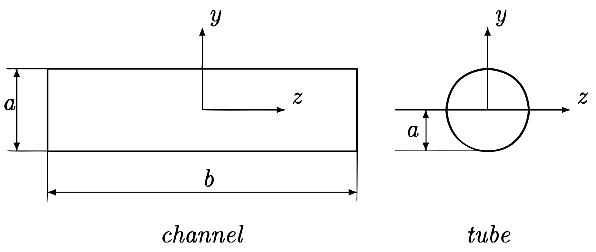

Gas Flow in Nanochannels, Figure 1 Cross-sections and coordinates

$$\xi_{\mathrm{P}}=\frac{a}{P}\frac{\mathrm{d}P}{\mathrm{d}x},\qquad \xi_{\mathrm{T}}=\frac{a}{T}\frac{\mathrm{d}T}{\mathrm{d}x},\tag{1}$$

respectively. Here, x is the longitudinal coordinate. In practice, one is interested in the mass flow rate $\dot{M}$ defined as

$$\dot{M}^{\mathrm{ch}}=\int_{\frac{-b}{2}}^{\frac{b}{2}}\int_{\frac{-a}{2}}^{\frac{a}{2}}\rho u_x(y,z)\,\mathrm{d}y\,\mathrm{d}z\tag{2}$$

for channel and

$$\dot{M}^{\mathrm{tb}}=2\pi\int_0^a\rho u_x(r)r\,\mathrm{d}r,\qquad r=\sqrt{y^2+z^2}\tag{3}$$

for tube, where ρ is the mass density and u_x is the bulk velocity of the gas. Since the gradients ξ_{P} and ξ_{T} are small the mass flow rate depends linearly on them, i. e.

$$\dot{M}^{\mathrm{ch}}=\frac{abP}{v_0}\left(-G_{\mathrm{P}}^{\mathrm{ch}}\,\xi_{\mathrm{P}}+G_{\mathrm{T}}^{\mathrm{ch}}\,\xi_{\mathrm{T}}\right)\tag{4}$$

for channel, and

$$\dot{M}^{\mathrm{tb}}=\frac{\pi a^2P}{v_0}\left(-G_{\mathrm{P}}^{\mathrm{tb}}\,\xi_{\mathrm{P}}+G_{\mathrm{T}}^{\mathrm{tb}}\,\xi_{\mathrm{T}}\right)\tag{5}$$

for tube. Here, v_0 is the most probable molecular speed

$$v_0=\left(\frac{2k_{\mathrm{B}}T}{m}\right)^{\frac{1}{2}},\tag{6}$$

$k_{\mathrm{B}}=1.380662\times10^{-23}$ J/K is the Boltzmann constant and m is the molecular mass of the gas in kg. The coefficient G_{P} corresponds to the gas flow induced by a pressure gradient and it is called the ▶ Poiseuille coefficient.

Note that if the super-index ch or tb is omitted the quantity is referred to both channel and tube. The coefficient G_T describes a gas flow due to a temperature gradient and it is called the ▶ thermal creep coefficient. The coefficients G_P and G_T are introduced so that they are always positive. They are calculated from the kinetic equation and determined by the ▶ rarefaction parameter

$$\delta = \frac{Pa}{\mu v_0}, \tag{7}$$

where μ is the gaseous viscosity in Pa s. Moreover, the coefficients G_P and G_T are affected by the gas-surface interaction law.

A moderate gas rarefaction, say $5 \leq \delta \leq 100$, can be taken into account applying the Navier–Stokes equation with the velocity slip boundary conditions. This is the so-called *slip flow regime*. In practice, the slip boundary conditions mean that the bulk velocity is not equal to zero on the wall, but its tangential component u_t is proportional to its normal gradient

$$u_t = \sigma_P \, \ell \, \frac{\partial u_t}{\partial x_n}, \quad \text{at} \quad x_n = 0, \tag{8}$$

where σ_P is the ▶ viscous slip coefficient, x_n is the coordinate normal to the surface directed toward the gas, and $\ell = \mu v_0 / P$ is the ▶ equivalent mean free path. Since a rarefied gas flow is induced by a temperature gradient too, then the tangential velocity is proportional to the longitudinal temperature gradient, i. e.

$$u_t = \sigma_T \frac{\mu}{\rho} \frac{\partial \ln T}{\partial x_t}, \quad \text{at} \quad x_n = 0, \tag{9}$$

where σ_T is the ▶ thermal slip coefficient and x_t is the tangential coordinate. The detailed technique of calculations of the slip coefficients σ_P and σ_T on the basis of the kinetic equation and their numerical values can be found in many papers (e. g. [5, 8, 13]).

The values recommended in practical calculations are as follows:

$$\sigma_P = 1.018, \qquad \sigma_T = 1.175, \tag{10}$$

which were obtained under an assumption of the diffuse scattering of gaseous particles on the surface. In most practical situations this assumption is fulfilled. Only in some special situations, the deviation from the diffuse scattering can be significant (e. g. [9]). If one deals with such a situation, then the expression

$$\sigma_P(\alpha_t) = \frac{1}{\alpha_t} \left[1.016(2 - \alpha_t) - 0.2640(1 - \alpha_t) \right] \tag{11}$$

should be used, which was obtained as an interpolation of the numerical data [13] based on the kinetic equation and ▶ gas–surface scattering kernel obtained by Cercignani and Lampis. Here, α_t is the tangential momentum accommodation coefficient. Numerical data of the slip coefficients σ_P and σ_T for gaseous mixtures can be found in [16, 17], respectively.

However, in the transitional regime, i. e. when the rarefaction parameter is intermediate ($\delta \sim 1$), the slip solution is not valid. Such a situation is realized when the channel/tube size a is less than 2×10^{-7} m. In this case the kinetic ▶ Boltzmann equation is applied to calculate the coefficients G_P and G_T. In the free-molecular regime, i. e. when the rarefaction parameter is very small ($\delta \ll 1$), the intermolecular collisions can be neglected and the ▶ Boltzmann equation is significantly simplified. This happens if the channel/tube size a is smaller than 10^{-9} m.

For brief information about the calculations of G_P and G_T see in ▶ micro- and nanoscale gas dynamics. The details of such calculations and recommended data on the coefficients G_P and G_T can be found in [18]. Below, some of these data and examples of their applications are given.

Key Research Findings

Free-Molecular Regime

In the free-molecular regime ($\delta = 0$) assuming the diffuse gas–surface interaction on the channel/tube wall, the coefficients G_P and G_T can be calculated directly without numerical solution of the kinetic equation. In the case of the channel the ▶ Poiseuille coefficient G_P^{ch} is given by the following double integral:

$$G_P^{ch} = \frac{1}{\sqrt{\pi}} \frac{a}{b} \int_0^{b/a} \int_0^1 \left[\zeta \ln \frac{C + \eta}{C - \eta} + \eta \ln \frac{C + \zeta}{C - \zeta} \right] d\eta \, d\zeta,$$
$$C = \sqrt{\eta^2 + \zeta^2}. \tag{12}$$

The numerical values of G_P^{ch} for some aspect ratios are given in Table 1. If the channel is sufficiently wide, i. e. $b \gg a$, then the expression given above is simplified as

$$\lim_{b/a \to \infty} G_P^{ch} = \frac{1}{\sqrt{\pi}} \left(\ln \frac{2b}{a} + \frac{1}{2} \right). \tag{13}$$

In the case of a tube the expression of the ▶ Poiseuille coefficient G_P^{tb} is quite simple:

$$G_P^{tb} = \frac{8}{3\sqrt{\pi}}. \tag{14}$$

Gas Flow in Nanochannels, Table 1 Coefficients $G_P^{ch}(\delta = 0)$, H, and S vs. aspect ratio b/a

b/a	G_P^{ch} $(\delta = 0)$	H	S
1	0.839	0.422	0.562
10	1.99	0.937	0.949
20	2.37	0.968	0.975
∞	∞	1.0	1.0

The ▶ thermal creep coefficient G_T in both channel and tube is given by

$$G_T = \frac{G_P}{2}. \tag{15}$$

Slip Flow Regime

To calculate the ▶ Poiseuille coefficient G_P in the slip flow regime ($5 \leq \delta \leq 100$) the Navier–Stokes equation is solved with the velocity slip boundary conditions (8). Then for the channel the flow rate reads

$$G_P^{ch} = \frac{\delta}{6} H + \sigma_P S,$$
$$H = 1 - \frac{192}{\pi^5} \frac{a}{b} \sum_{i=0}^{\infty} \frac{\tanh\left(\pi\left(i+\frac{1}{2}\right)\frac{b}{a}\right)}{(2i+1)^5} \tag{16}$$

The coefficients H and S are calculated numerically (see [12]). They depend only on the aspect ratio and can be used with any ▶ viscous slip coefficient σ_P including that obtained for the non-diffuse gas–surface interaction (11) and for gaseous mixtures [16]. The numerical values of H and S are given in Table 1. If the channel is wide, i. e. $b \gg a$, then the expression (16) is reduced to

$$\lim_{b/a \to \infty} G_P^{ch} = \frac{\delta}{6} + \sigma_P. \tag{17}$$

For tube the expression of the ▶ Poiseuille coefficient G_P reads

$$G_P^{tb} = \frac{\delta}{4} + \sigma_P. \tag{18}$$

The ▶ thermal creep coefficient G_T is also obtained from the Navier–Stokes equation, but applying the thermal slip boundary condition (9). It is verified that this coefficient does not depend on the type of the cross-section in the slip flow regime, but in any case considered here it takes the form

$$G_T = \frac{\sigma_T}{\delta}. \tag{19}$$

Transitional Regime

To calculate the coefficients G_P and G_T in the transitional regime ($\delta \sim 1$) the kinetic equation is applied. The coefficients G_P^{ch} and G_T^{ch} for the channel flow obtained in [11] assuming the diffuse scattering are presented in Figs. 2 and 3, respectively. For all values of the aspect ratio b/a the ▶ Poiseuille coefficient G_P^{ch} has the Knudsen minimum near the point $\delta \approx 1$. For the square channel ($b/a = 1$) the minimum is rather shallow. Since the variation of G_P^{ch} near the free molecular regime is small its free molecular value can be used for practical calculations in the range $0 \leq \delta \leq 5$. Then for $\delta > 5$ the hydrodynamic solution (16) with the slip boundary condition can be used. Such an approximation works with a precision of 10%. However,

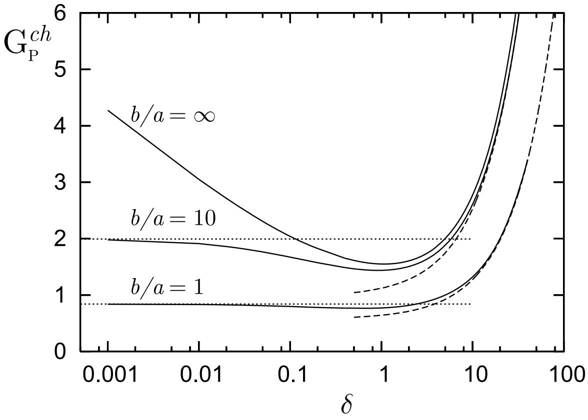

Gas Flow in Nanochannels, Figure 2 Poiseuille coefficient G_P^{ch} vs rarefaction parameter δ: solid lines – kinetic equation solution [11], pointed line – free molecular value based on Eq. (12), dashed line – Navier–Stokes solution Eq. (16)

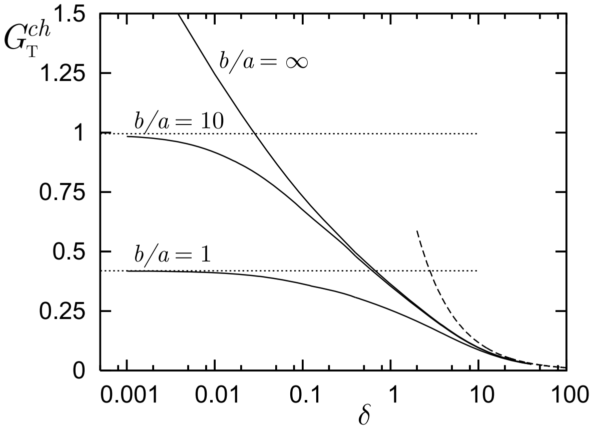

Gas Flow in Nanochannels, Figure 3 Thermal creep coefficient G_T^{ch} vs rarefaction parameter δ: solid lines – kinetic equation solution [11], pointed line – free molecular value based on Eqs. (12) and (15), dashed line – Navier–Stokes solution Eq. (19)

for large values of the aspect ratio, i. e. at $b/a \geq 10$, the Knudsen minimum is deep and reliable results can be obtained only by solving the kinetic equation. The ▶ thermal creep coefficient G_T^{ch} vanishes in the hydrodynamic regime ($\delta \to \infty$) in accordance with Eq. (19) and in the free-molecular regime it tends to a constant value given by Eqs. (12) and (15). Note that both coefficients G_P^{ch} and G_T^{ch} have a singularity, i. e. they tend to infinity, at $\delta \to 0$ and $b/a \to \infty$, which is related to the degenerated geometry. However, in practice the aspect ratio b/a is always finite, so the flow rate is never infinite.

The coefficients G_P^{tb} and G_T^{tb} for the tube flow reported in [18] are presented in Figs. 4 and 5, respectively. Like for the channel, the ▶ Poiseuille coefficient G_P^{tb} also has a small minimum in the transition regime ($\delta \sim 1$). Its variation near the free molecular regime is very small. For large values of the ▶ rarefaction parameter δ the numerical solution tends to the analytical expression (18). The ▶ thermal creep coefficient G_T^{tb} vanishes in the hydrodynamic limit ($\delta \to \infty$) according to Eq. (19) and it tends to the constant value given by Eqs. (14) and (15) in the free molecular regime.

To show how the gas–surface interaction affects the flow rates, some values of G_P^{tb} and G_T^{tb} for the Cercignani–Lampis ▶ gas–surface scattering kernel obtained in [14] are given in Tables 2 and 3 (reprinted from [14] with permission from Elsevier), respectively. In all regimes the influence of the energy accommodation coefficient α_n on the ▶ Poiseuille coefficient G_P^{tb} is weak, while the momentum accommodation coefficient α_t affects significantly this coefficient in the transition ($\delta = 1$) and near the free molecular ($\delta = 0.01$) regimes. Both accommodation coefficients α_n and α_t moderately affect the ▶ thermal creep coefficient G_T^{tb} in all regimes of the flow. Since both transitional and free molecular regimes usually occur in nanochannels, a correct consideration of the gas–surface interaction and reliable data on the accommodation coefficients are very important.

To illustrate the application of the results given above let us consider helium flowing through a channel with height $a = 2.17 \times 10^{-8}$ m and width $b = 2.17 \times 10^{-7}$ m, i. e. the aspect ratio b/a is equal to 10. Let us assume the pressure to be $P = 10^5$ Pa and the temperature to be $T = 293.15$ K,

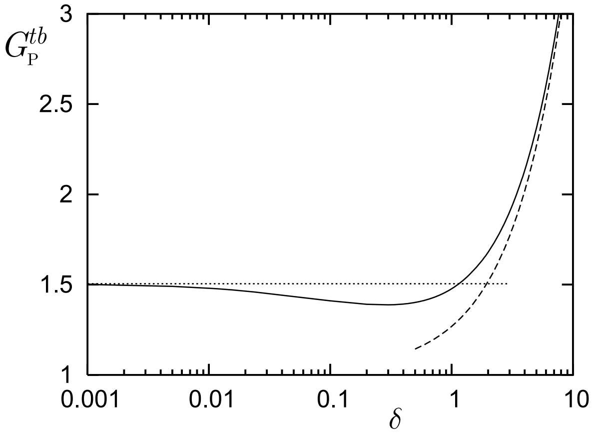

Gas Flow in Nanochannels, Figure 4 Poiseuille coefficient G_P^{tb} vs rarefaction parameter δ: solid lines – kinetic equation solution [18], pointed line – free molecular value based on Eq. (14), dashed line – Navier–Stokes solution Eq. (18)

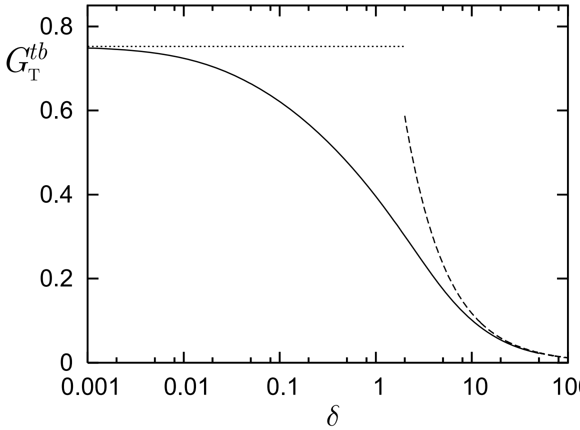

Gas Flow in Nanochannels, Figure 5 Thermal creep coefficient G_T^{ch} vs rarefaction parameter δ: solid lines – kinetic equation solution [18], pointed line – free molecular value based on Eqs. (14) and (15), dashed line – Navier–Stokes solution Eq. (19)

Gas Flow in Nanochannels, Table 2 Poiseuille coefficient G_P^{tb} vs. accommodation coefficients α_t and α_n [14]

		G_P^{tb}		
δ	α_t	$\alpha_n = 0.5$	0.75	1
0.01	0.5	3.328	3.302	3.284
	0.75	2.089	2.079	2.071
	1.	1.477	1.477	1.477
	1.25	1.105	1.112	1.119
	1.5	0.8296	0.8445	0.8594
1.	0.5	3.265	3.264	3.263
	0.75	2.070	2.070	2.069
	1.	1.477	1.477	1.477
	1.25	1.120	1.121	1.121
	1.5	0.8726	0.8736	0.8742
10.	0.5	5.372	5.360	5.350
	0.75	4.179	4.173	4.168
	1.	3.577	3.577	3.577
	1.25	3.212	3.217	3.222
	1.5	2.964	2.975	2.986

Gas Flow in Nanochannels, Table 3 Thermal creep coefficient G_T^{tb} vs. accommodation coefficients α_t and α_n [14]

δ	α_t	G_T^{tb} $\alpha_n = 0.5$	0.75	1
0.01	0.5	0.8769	0.8054	0.7550
	0.75	0.7755	0.7473	0.7245
	1.	0.7210	0.7210	0.7210
	1.25	1.1047	1.1121	1.1190
	1.5	0.8296	0.8445	0.8594
1.	0.25	0.4856	0.4787	0.4725
	0.5	0.4232	0.4186	0.4144
	0.75	0.4029	0.4008	0.3988
	1.	0.3968	0.3968	0.3968
	1.25	0.3911	0.3928	0.3948
	1.5	0.3740	0.3775	0.3815
10.	0.25	0.0930	0.0986	0.1040
	0.5	0.0954	0.0990	0.1026
	0.75	0.0986	0.1003	0.1021
	1.	0.1020	0.1020	0.1020
	1.25	0.1054	0.1037	0.1019
	1.5	0.1082	0.1049	0.1014

i. e. 20 °C. Under such conditions the gas viscosity is $\mu = 19.73 \times 10^{-6}$ Pa s and the most probable speed is $v_0 = 1.10 \times 10^3$ m/s. Substituting these values into Eq. (7) the ► rarefaction parameter is obtained as $\delta = 0.1$. According to Figs. 2 and 3 the coefficients G_P^{ch} and G_T^{ch} are equal to 1.67 and 0.68, respectively. If the gas flow is induced by the pressure gradient $\xi_P = 0.01$ and by the temperature gradient $\xi_T = 0.01$, then from Eq. (4) the mass flow rate is obtained as $\dot{M}^{ch} = 4.24 \times 10^{-15}$ kg/s. Considering a gas flow under the same conditions through a tube of radius $a = 2.17 \times 10^{-8}$ m with the help of Figs. 4 and 5 we obtain $G_P = 1.41$ and $G_T = 0.62$ at $\delta = 0.1$. Then the mass flow rate is calculated from Eq. (5) as $\dot{M}^{tb} = 1.06 \times 10^{-15}$ kg/s. If the drops of pressure and temperature are large then the technique elaborated in [10, 18] must be used. In the case of isothermal flow, i. e. $\xi_T = 0$, the following simple formulas are obtained for the mass flow rate:

$$\dot{M}^{ch} = \frac{ab\mu}{L} \int_{\delta_1}^{\delta_2} G_P^{ch}(\delta)\, d\delta, \tag{20}$$

$$\dot{M}^{tb} = \frac{\pi a^2 \mu}{L} \int_{\delta_1}^{\delta_2} G_P^{tb}(\delta)\, d\delta, \tag{21}$$

where δ_1 and δ_2 are ► rarefaction parameters on the channel/tube ends.

Numerical results on the capillary flow of polyatomic gases can be found in [4]. Comparing these results with the data presented here it is concluded that the ► Poiseuille coefficient G_P is slightly affected by the internal structure of molecules. The ► thermal creep coefficient G_T for polyatomic gases differs from that for monatomic gases.

A methodology of calculation of gaseous mixtures flowing through long nanochannels is described in [6, 7, 15]. From these data it is concluded that if the molecular masses of species are close to each other then the results for a single gas are applicable to this mixture. If the masses are quite different then calculations based on the kinetic equation should carried out for every specific mixture.

Future Directions for Research

Calculations of mass flow rate through a short channel, i. e. when the length L, width b and height a are arbitrary, would be useful in practice. In many applications, e. g. micropumps, the channels/tubes have a spiral form. Thus, calculations of gas flow through curve channels is needed. Until now, only some simple flows of polyatomic gas and gaseous mixtures were calculated. A further investigation in this direction would be interesting.

Cross References

- ► Control of Microfluidics
- ► Curved Microchannel Flows
- ► Developing Flows
- ► Flow in Channels with 3D Elements
- ► Heat Transfer in Microchannel Flows
- ► Methods for Flow Rate Measurements
- ► Micro- and Nanoscale Gas Dynamics
- ► Supersonic Micro-Nozzles
- ► Rarefied Gas Dynamics
- ► Roughness Effect on Microscale Transport
- ► Single-Phase Gaseous Flow

References

1. Cercignani C (1988) The Boltzmann Equation and its Application. Springer, New York
2. Ferziger JH, Kaper HG (1972) Mathematical Theory of Transport Processes in Gases. North-Holland Publishing Company, Amsterdam
3. Kogan MN (1969) Rarefied Gas Dynamics. Plenum, New York
4. Lo SS, Loyalka SK (1989) Flow of a rarefied polyatomic gas between parallel plates. J Vac Sci Technol A7 4:2766–2773
5. Loyalka SK (1989) Temperature jump and thermal creep slip: Rigid sphere gas. Phys Fluid A 1:403–408
6. Naris S, Valougeorgis D, Kalempa D, Sharipov F (2005) Flow of gaseous mixtures through rectangular microchannels driven by pressure, temperature and concentration gradients. Phys Fluid 17(10):100607
7. Naris S, Valougeorgis D, Sharipov F, Kalempa D (2004) Discrete velocity modelling of gaseous mixture flows in MEMS. Superlattices Microstruct 35:629–643

8. Ohwada T, Sone Y, Aoki K (1989) Numerical analysis of the shear and thermal creep flows of a rarefied gas over a plane wall an the basis of the linearized Boltzmann equation for hard-sphere molecules. Phys Fluid A 1(9):1588–1599
9. Sazhin OV, Borisov SF, Sharipov F (2001) Accommodation coefficient of tangential momentum on atomically clean and contaminated surfaces. J Vac Sci Technol A 19(5):2499–2503. Erratum: 20(3), 957 (2002)
10. Sharipov F (1997) Rarefied gas flow through a long tube at arbitrary pressure and temperature drops. J Vac Sci Technol A 15(4):2434–2436
11. Sharipov F (1999) Non-isothermal gas flow through rectangular microchannels. J Micromech Microeng 9(4):394–401
12. Sharipov F (1999) Rarefied gas flow through a long rectangular channel. J Vac Sci Technol A 17(5):3062–3066
13. Sharipov F (2003) Application of the Cercignani-Lampis scattering kernel to calculations of rarefied gas flows. II. Slip and jump coefficients. Eur J Mech B / Fluid 22:133–143
14. Sharipov F (2003) Application of the Cercignani-Lampis scattering kernel to calculations of rarefied gas flows. III. Poiseuille flow and thermal creep through a long tube. Eur J Mech B / Fluid 22:145–154
15. Sharipov F, Kalempa D (2002) Gaseous mixture flow through a long tube at arbitrary *Knudsen number*. J Vac Sci Technol A 20(3):814–822
16. Sharipov F, Kalempa D (2003) Velocity slip and temperature jump coefficients for gaseous mixtures. I. Viscous slip coefficient. Phys Fluid 15(6):1800–1806
17. Sharipov F, Kalempa D (2004) Velocity slip and temperature jump coefficients for gaseous mixtures. II. Thermal slip coefficient. Phys Fluid 16(3):759–764
18. Sharipov F, Seleznev V (1998) Data on internal rarefied gas flows. J Phys Chem Ref Data 27(3):657–706
19. Sharipov FM, Subbotin EA (1993) On optimization of the discrete velocity method used in rarefied gas dynamics. Z Angew Math Phys (ZAMP) 44:572–577
20. Sone Y (2002) Kinetic Theory and Fluid Mechanics. Birkhäuser, Boston

Gas–Surface Scattering Kernel

Definition

Gas-surface scattering kernel $R(\boldsymbol{v}', \boldsymbol{v})$ relates the velocity distribution function of reflected particles $f^+(\boldsymbol{v})$ to that of incident ones $f^-(\boldsymbol{v})$

$$v_n f^+(\boldsymbol{v}) = -\int_{v_n' \leq 0} v_n' f^-(\boldsymbol{v}') R(\boldsymbol{v}', \boldsymbol{v})\, \mathrm{d}\boldsymbol{v}', \quad v_n \geq 0,$$

Cross References

- ► Gas Flow in Nanochannels
- ► Heat Transfer in Microchannel Flows
- ► Supersonic Micro-Nozzles
- ► Micro- and Nanoscale Gas Dynamics
- ► Roughness Effect on Microscale Transport

Gate in the Cell Wall

► Ion Channel

Gaussian Filter

Definition

The Gaussian Filter belongs to ►local filters. Based on image processing, this means that neighbor pixels which take part on the filtering operation are not considered equally. They are weighted by a two dimensional Gaussian function (normal probability curve).

GC

► Gas Chromatography

Gene Chip

► DNA Microarrays

Generalized Boltzmann Equation

► Numerical Solution of Boltzmann Equation

Generalized Formulation

► Weak Formulation

Genosensors

Definition

Biosensors are bioanalytical systems defined by the integration of the four key components of: sample presentation, biotransduction, instrumentation and data output. Central to the biosensor system is the biotransducer that converts the activity (concentration) of the targeted analyte into a proportionate signal via an intimate combination of a biological recognition membrane layer and a physico-chemical transducer. The biological recognition membrane is to provide its specificity by the use of biomolecules such as DNA, RNA, PNA, enzymes, antibodies, enzyme-linked antibodies and receptors, and may

be sub-cellular fragments such as mitochondria, cell membranes components (receptors), or whole cells (bacteria or mammalian cells), and/or tissue slices (liver, brain, etc.). An impedimetric biosensor is constructed by immobilizing biological recognition elements onto an electrode surface. It reports, through measurement and/or monitoring, the targeted analyte through the output of an electrical impedance signal made proportional to analyte activity.

Cross References

► Impedimetric Biosensors for Micro and Nano Fluidics

Glass

► Non-Metallic Inorganic Materials

Glass-Polymer Bonding

Janko Auerswald[1], Philippe Niedermann[1],
Henri Haquette[2], Francisco Dias[2],
Herbert Keppner[2], Helmut F. Knapp[1]
[1] Division Microrobotics, Centre Suisse d'Electronique et de Microtechnique (CSEM S.A.), Alpnach, Switzerland
[2] HE-Arc, Institut des Microtechnologies, La Chaux-de-Fonds, Switzerland
janko.auerswald@csem.ch

Synonyms

Bonding of non-metallic inorganic surfaces and polymers

Definition

A ►polymer is a material composed of large macromolecules. These macromolecules are formed by chains of hundreds or thousands of connected (polymerized) monomer molecules. The three main classes of polymers are thermoplastics, elastomers and thermosets. They differ in the degree of cross-linking of their macromolecules – from no cross-linking (thermoplastics) to moderate cross-linking (elastomers, rubbers) to high cross-linking (thermosets).
A non-metallic inorganic material can be a bulk material (e. g., a glass chip, a quartz chip or a silicon chip which possesses a natural silicon oxide layer similar to glass) or a coating (e. g., a dielectric transition metal oxide coating on a chip).
The gage ►pressure is the pressure difference between the measured absolute pressure and the normal atmospheric pressure (101,325 Pa).

Overview

Polymers have become established materials in microfluidics. They offer a good potential for cost-efficient mass fabrication of microfluidic systems. For pure polymer microfluidic systems, the sealing of the microchannels can be accomplished using well-known techniques. For example, the most established sealing techniques for thermoplastic-thermoplastic bonding include lamination, ultrasonic welding or thermo-compression bonding (diffusion bonding). Thermo-compression bonding can be enhanced by solvent or plasma treatment.
However, there are applications when polymer microfluidic channels have to be bonded to a glass chip, a quartz chip, a silicon chip or a chip coated with a dielectric oxide ceramic layer. This is the main focus of the present article. One example is a glass or silicon chip with photolithographically defined electrodes for electrochemical detection. Other examples include a variety of microfluidic sensor chips for label-free detection, e. g., evanescent light based wavelength interrogated optical systems (WIOS) or surface plasmon resonance (SPR) chips. WIOS chips usually consist of a glass substrate coated with an amorphous transition metal oxide layer, e. g., tantalum oxide or titanium oxide. SPR chips can be glass chips coated with a gold layer (or silver, depending on the light source) and additionally also with a dielectric layer like the oxides mentioned before or hafnium oxide. There is a trend to combine SPR or WIOS sensors with mass spectroscopy for a more complete analysis of proteins. This can be done either by eluting the captured proteins from the SPR sensor chip surface, or by transferring the sensor chip with the captured and precipitated proteins to a mass spectrometer. In the latter case, the glass-thermoplastic bonding has to be reversible.
Another application includes glass or silicon chips for DNA or protein detection where the biochemical immobilization of capture (probe) molecules on the chip surface is based on a particular surface chemistry. The most common surface chemistries on biochips are thiol and silane chemistries. With silane chemistry the probe molecules are immobilized directly on the silicon or glass substrate. With thiol chemistry the probe molecules are immobilized on metal spots or electrodes (e. g., gold) which are fabricated by photolithography on glass or silicon chips. There are also surface chemistries for silicon or glass chips based on very reactive organic double (alkene) and triple (alkyne) bonds.

Further applications comprise glass chips with photolithographic electrodes for dielectrophoresis or for flow cytometry based on impedance spectroscopy, which are bonded to polymer fluidic scaffolds.

Chemically, a glass surface, a quartz surface, a silicon surface with a natural silicon oxide layer and an oxide ceramic coating surface are similar. Hence the methods for bonding polymer microfluidic scaffolds to them are similar. For simplicity, in the following subchapters the term *glass* stands for all these ► non-metallic inorganic materials.

In the following subchapters of the overview, glass-polymer bonding strategies are sketched for all three polymer classes. Glass-thermoplastic bonding strategies, which are particularly interesting from the market perspective because of the potential of low-cost mass fabrication of thermoplastic microfluidic scaffolds, are discussed in more detail in the chapter *Key Research Findings*.

Glass–Thermoset Bonding

In a thermoset, the cross-linking degree of the macromolecules is very high resulting in a stiff material which cannot "melt". Thermosets include e. g., negative-tone photoresists where the high degree of cross-linking is achieved by curing with heat or ultraviolet (UV) light. Therefore, thermosets are materials well-known and widely used in clean-room microfabrication. A good overview on the bonding of silicon with thermosets like BCB (benzocyclobutene) or photoresists used in clean-room microfabrication is given in [1]. For microfluidic channel fabrication, negative photoresists like SU-8 and photosensitive polyimide (PI) are used. Before structuring the microchannels, electrodes can be integrated on the glass substrate using a lift-off process. The adhesion bond of the SU-8 and polyimide channels on the glass substrate is good.

The advantage of this bonding strategy is the precise alignment of the microchannels with respect to the glass chip and the electrode or sensor structures on which they are made by photolithography. After curing of the photoresist on the glass substrate, the channels can be sealed with PDMS or a photoresist laminate. For some applications, the microfluidic channels have to be sealed with a glass cover which may also contain metal electrodes, e. g., for impedance spectroscopy or dielectrophoretic separation. In the case of SU-8, two glass chips with electrodes and soft baked microfluidic channels can be bonded in a final curing process under pressure. Sealing of SU-8 channels has also been demonstrated by lamination with a glass chip carrying a layer of uncured SU-8 [2], or a glass substrate laminated with uncured PMMA [3]. In the case of PI channels, the laminate can be a glass substrate coated with soft-baked PI. The final cure of the laminate for sealing is done under contact pressure [4]. The disadvantage of fabricating microfluidic channels in photoresist is the cost of the photolithography step. Further, the high temperatures involved in the final curing step do not allow the pre-deposition of bio-molecules in the microfluidic channels before bonding.

Another approach to form sealed microfluidic channels on glass substrates is derived form stereolithography. Photocurable thermoset is built up layer by layer between two plates. After curing, due to the surface properties of the plates, the adhesion to one plate is strong and weak to the other plate, allowing for separation there to build up the next layer. The integration of metallic electrodes is also possible. The thermoset properties can be adapted by mixing additives to it [5].

Glass–Elastomer Bonding

In an elastomer (rubber), the macromolecules are cross-linked. The cross-linking degree is moderate so that elastomers can be stretched easily. A transparent elastomer widely used in microfluidics is the silicone rubber polydimethylsiloxane (PDMS).

Glass-PDMS bonding is one of the most common methods in microfluidics research. Usually, the PDMS contains microfluidic channel structures replicated by polymerizing and cross-linking the PDMS on a master, e. g., a deep reactive ion etched (DRIE) master wafer or a master with SU-8 structures. The PDMS can be bonded to the glass reversibly by simply placing it onto the glass chip after some simple cleaning and pre-treatment steps (self-sealing), or irreversibly after an oxygen (or air) plasma treatment. The plasma treatment results in a replacement of the methyl ($\equiv \mathrm{Si}-\mathrm{CH_3}$) groups on the PDMS surface with hydroxyl ($\equiv \mathrm{Si}-\mathrm{OH}$) groups [6]. The hydroxyl groups on the PDMS and on the glass surface interact forming a strong bond ($\equiv \mathrm{Si}-\mathrm{O}-\mathrm{Si}\equiv$) and a water molecule ($H_2O$, condensation).

PDMS as a channel material has the disadvantage that bio-molecules tend to be adsorbed on it and to diffuse into it.

Glass–Thermoplastic Bonding

In a thermoplastic, the macromolecules are not cross-linked so that the material can "melt", i. e. above the glass transition temperature the material begins to soften. Thermoplastics can be amorphous or semi-crystalline. In microfluidics, amorphous polymers are often preferred because of their optical transparency. Amorphous polymers include polymethylmethacrylate (PMMA), polycar-

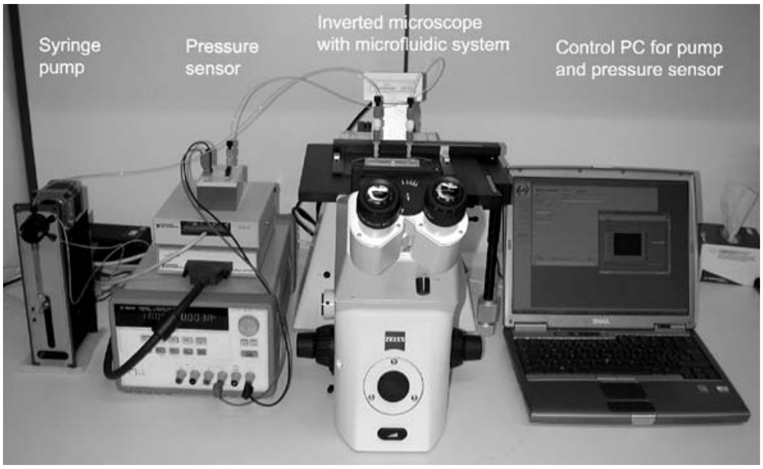

Glass-Polymer Bonding, Figure 1 Experimental setup for leak tests. The bonded chip is mounted on top of an inverted light microscope for optical leak detection. The pressure is generated with a syringe pump at the chip inlet side and measured at the outlet side with a MEMS gage pressure sensor

bonate (PC), polystyrene (PS), and cyclic olefin polymers (COP) and copolymers (COC). COP and COC, unlike most other polymers, are also transparent for UV light.
Thermoplastics are a particularly attractive material class because they have the potential for cost-efficient mass fabrication of microfluidic scaffolds, e. g., by injection molding. Therefore, the chapters *Basic Methodology* and *Key Research Findings* are devoted entirely to discussing glass-thermoplastics bonding strategies in detail.

Basic Methodology

Glass-thermoplastics bonding can be accomplished reversibly or irreversibly. Reversible approaches include clamping using microfabricated gasket membranes. Irreversible approaches include microstructured double-sided adhesive tape gaskets and gluing. These bonding strategies will be described and evaluated in more detail in the chapter *Key Research Findings*.

Typical Pump Pressures in Microfluidic Systems

For the evaluation of the bonding quality, it is important to know which pump pressures are typically involved in microfluidics. Table 1 gives a brief overview.

Leak Test Setup for Bond Quality Evaluation

For evaluation of the bonding quality obtained with the different bonding strategies, each approach was subjected to a series of leak tests. The following setup was used for this purpose. The bonded test system consisting of a glass chip bonded to a PMMA microfluidic scaffold was mounted onto an inverted microscope. In an inverted microscope, the objectives are below the observed object allowing easy access for fluidic connections to the microfluidic system from above. The microscope was used to observe possible leaks in the system. For this purpose, it was operated in the bright field mode and DIC (differential interference contrast) mode. The fluorescence mode was not used because of the auto-fluorescence of the PMMA.
On the inlet side, the microfluidic system was connected to a syringe pump with a 100 µl syringe. The pump generated a gage pressure of about 33,000 Pa covering the pressure range generated by typical microfluidic pumps (Table 1). On the *dead-end* outlet side, a MEMS gage pressure sensor measured the pressure in the system both to obtain quantitative data and to have a second means for possible leak detection. The experimental setup is shown in Fig. 1.

Glass-Polymer Bonding, Table 1 Typical pump pressures in microfluidic systems [7]

Pump type/actuation	Typical maximum pump pressure Δp_{max}/Pa
Piezoelectric	6000 – 17,000
Electrostatic	29,000
Thermopneumatic	3000 – 16,000
Pneumatic	2000 – 35,000
Shape memory alloy	530
Electromagnetic	5000 – 10,000
Electrowetting	700
Electrohydrodynamic	250 – 780
Electroosmotic (micromachined channels)	5000 – 33,000
Magnetohydrodynamic	170

Biocompatibility Issues

Another important issue for many hybrid glass-polymer bonding applications is biocompatibility. This includes both the materials involved in the bonding process and the bonding process parameters. Material biocompatibility means that the bio-molecules are not degraded or do not become dysfunctional after contact with the chip or bonding materials. On the other hand, the bonding process itself may have to be biocompatible. For example, capture (probe) bio-molecules are sometimes already attached to the chip surface before the chip is bonded and sealed with the microfluidic scaffold. That requires the bonding process to be compatible with the bio-molecules, e. g., in terms of bonding temperature, exposure to radiation or chemical environment. All used adhesive tapes and the glue where medical grade, i. e. biocompatible. No UV or thermal curing step was required for the glue. PDMS gaskets are also compatible with many bio-molecules. In addition, the contact area with the PDMS gasket channel side walls is very small. If necessary, the PDMS gasket channel walls can be passivated prior to a bioassay.

Key Research Findings

The following glass-thermoplastic bonding strategies will be discussed in this chapter:

- Clamping with microfabricated rubber gaskets (reversible bond)
- Bonding with microstructured double-sided adhesive tapes (not a truly reversible bond, but also not strictly irreversible)
- Gluing (irreversible bond)
- Bonding with heat and pressure (irreversible bond)

Glass–Thermoplastic Bonding by Clamping With Microfabricated Gaskets

Clamping is a reversible bonding method. The glass chip and the thermoplastic microfluidic scaffold are pressed together by a mechanical clamping system. Reversible sealing is interesting if the sensor chip or the microfluidic scaffold are used more than once, e. g., if a complex fluidic system with valves or actuators has to be re-used after cleaning. It is also of interest if bio-molecules are captured and precipitated or crystallized on certain sensor or detection sites on a glass chip and in a next step analyzed by mass spectroscopy. In this case, the glass chip with the captured bio-molecules can be separated from the microfluidic scaffold after the capturing the bio-molecules and transferred to a mass spectrometer.

To achieve a good sealing between glass chip and thermoplastic microfluidic scaffold, an elastic membrane, e. g., a silicone rubber, should be used as a gasket. The gasket membrane usually contains the microfluidic channel leading to the sensor. In the scaffold, the channel can go up a level to connect to a manifold of microfluidic inlet and outlet channels, mixers or other microfluidic elements. In microfluidics, the membrane gaskets forming the channels are usually only 30 – 100 μm high. The channel width is typically smaller than a millimeter. Therefore, the manufacturing of gasket membranes forming these miniature channels requires microfabrication.

Gasket Microfabrication

Two approaches are described here for gasket microfabrication: casting and laser cutting. The gasket material is a silicone rubber, PDMS.

Casting of PDMS gaskets The PDMS is cast on DRIE silicon masters. The DRIE masters ensure very accurate lateral channel dimensions of the gaskets. For a better cutout and demolding, rims are recommended on the DRIE master around each individual gasket. The rims should have the same height as the microchannels on the master. The silicon masters are silane treated to facilitate demolding.

The DRIE masters are placed into a casting setup as shown in Fig. 2. The casting setup is a stack of the following components: aluminum holder with internal threads, 0.1 mm PE foil so that the masters are not glued to the aluminum, DRIE masters on which the PDMS monomer solution is cast after degassing, a 0.05 mm PE foil on which the PDMS sticks after curing allowing for an easy demolding, a 1 mm PMMA sheet, a 2 mm cured PDMS stress homogenizer and a PMMA clamp with screws. The setup is transparent and allows optical observation from above. The setup is clamped together using the screws. The DRIE master channel structures and the rims of the same height act as spacers ensuring the accurate thickness of the PDMS gaskets.

The PDMS is cured in the casting setup at 65 °C for 4 h. Since the PDMS shrinks during the curing in the mold but adheres to the DRIE master structures, the gaskets will have the defined height at the channel walls and the rims and will be somewhat lower in between. That is no disadvantage because the sealing is accomplished at the highest thickness, the channel wall. The effect can be avoided by an intelligent mold design. In a multi-channel gasket, channel separation walls have been demonstrated as thin as 200 μm for an eight channel system with 1 mm wide channels. After curing, the demolding of the gaskets and further handling should be done in alcohol, e. g., methanol,

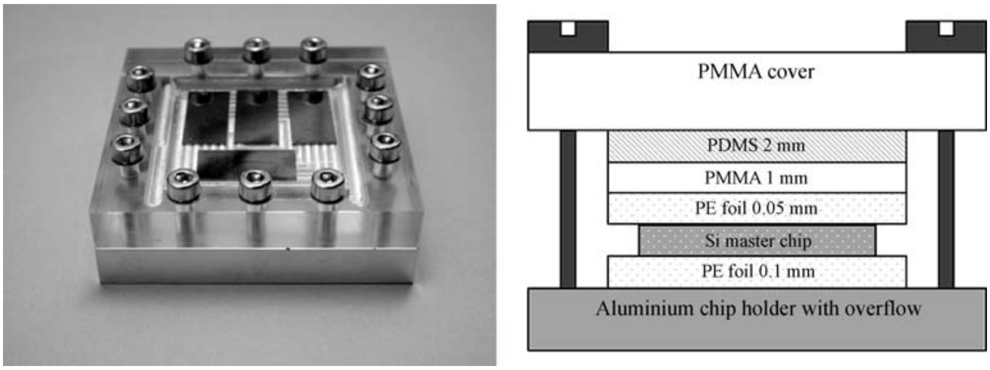

Glass-Polymer Bonding, Figure 2 Setup for the casting of PDMS membrane gaskets. The PDMS monomer solution is applied and compressed between the DRIE silicon master and the 0.05 mm PE foil. Gaskets down to 50 μm thickness were fabricated using this method

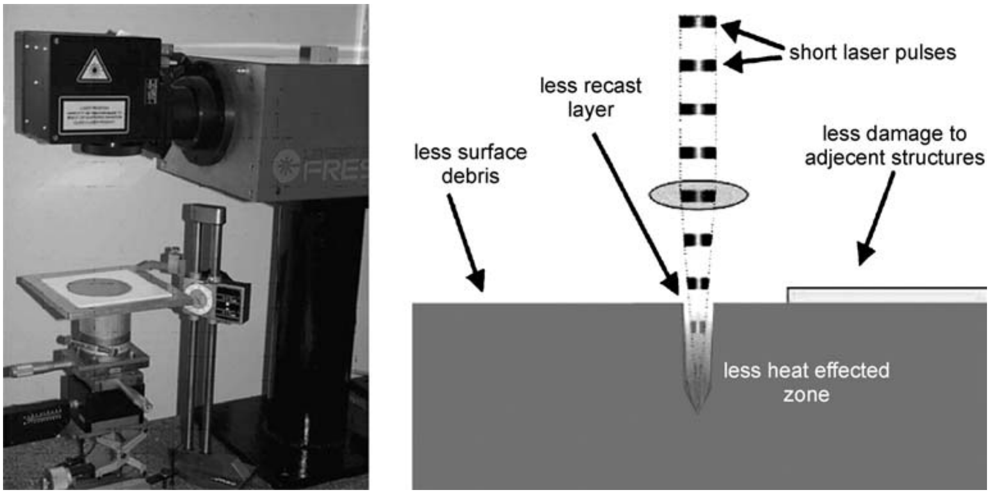

Glass-Polymer Bonding, Figure 3 Nd.YAG 355 nm (frequency tripler) UV laser for cutting PDMS membrane gaskets and adhesive tape gaskets. The spot size is 20 μm. The laser burns less material in thermoplastics than IR lasers resulting in a cleaner cut and runs more stable than UV excimer lasers

ethanol or isopropanol. This helps to avoid curling or damaging the delicate gaskets.

Laser cutting of PDMS gaskets Before laser cutting, the degassed PDMS monomer is spin-coated or knife-coated with the desired thickness on a substrate. Glass, for example, is a recommended substrate. The PDMS is cured at 65 °C for 4 h. For laser cutting, a Nd : YAG 355 nm laser was used (Fig. 3). The laser is a UV (ultraviolet light) laser. Compared to conventional IR (infrared light) lasers for material cutting, it causes less material damage in a polymer, i. e. it burns less material (smaller melt zone). That allows fabricating channel widths down to 20 – 40 μm as compared to typical IR laser channel widths of 250 μm [8]. In addition, the laser can be operated in short pulses. Therefore, the formation of the usual recast layer (bulges) at the cutting edges is reduced or even avoided [9]. Of particular interest is the beam diameter of 20 μm. This is the line width of the removed material. The Nd : YAG 355 nm laser is more stable in its operation than excimer UV lasers.

Laser cut gaskets possess a homogeneous thickness from the spin-coating or knife-coating process. Again, the peeling of the cut gaskets from the substrate and their handling should be done in alcohol, e. g., methanol, ethanol or isopropanol to avoid curling or damage.

Results: Clamping with Gaskets

The laser-cut or cast microchannel gaskets can be wetted with alcohol and placed and aligned on the glass chip or, alternatively, on the thermoplastic fluidic scaffold. For an optimal alignment, corresponding alignment marks should be provided. After the alcohol has dried, the glass chip and

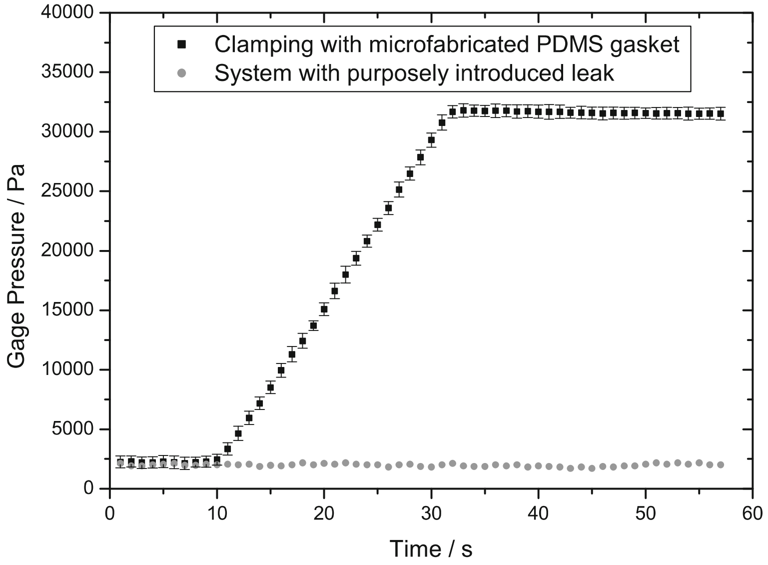

Glass-Polymer Bonding, Figure 4 Gage pressure curve of a series of 15 leak tests performed with glass-PMMA systems clamped together using a PDMS membrane gasket. After full compression of the syringe pump (after about 32 s), a gage pressure of about 32,500 Pa is generated in the systems. This pressure is equal or higher than the maximum pressure generated by typical microfluidic pumps (see Table 1). No leaks were observed under the microscope and in the gage pressure curve. For comparison, a test curve of a system with a purposely introduced leak is shown. The pressure curves of the leak tests with systems bonded by adhesive tape bonding and gluing look similar

Glass-Polymer Bonding, Table 2 Surface roughness and waviness of glass chips and PMMA microfluidic scaffolds measured at the contact area of clamping

	R_a/nm	R_t/nm	R_z/nm	W_a/nm	W_t/nm
PMMA	29 ± 15	161 ± 86	230 ± 120	5 ± 4	117 ± 87
Glass	5.0 ± 2.8	28 ± 14	44 ± 29	0.48 ± 0.40	7.1 ± 2.7

the thermoplastic microfluidic scaffold with the gasket in between can be clamped together.

A series of leak tests was performed with glass chips clamped to PMMA microfluidic scaffolds using PDMS microfabricated gaskets. Both the optical observations under the inverted microscope and the quantitative pressure measurements with a gage pressure sensor indicated a perfect sealing in all tests. Figure 4 shows the gage pressure curve of a series of 15 leak tests. The pressure was generated with a 100 µl syringe pump. The gage pressure of about 32,500 Pa in the systems at the end of the leak test is as high or higher than typical maximum pump pressures generated by microfluidic pumps (see Table 1).

Another interesting result is that clamping with 50 µm thin PDMS gaskets did even seal systems where the glass chip had 300 nm thick electrodes on the surface. Planar electrodes microfabricated on glass chips are widely used in microfluidic systems, e. g., for electrochemical detection, ECL (electrochemoluminescence) detection, dielectrophoresis, AC electroosmotic flow and electrohydrodynamic pumping. As discussed earlier, glass-thermoplastic sealing with clamped PDMS gaskets are also suitable for multichannel systems.

Results: Clamping Without Gaskets

Another series of leak tests with clamped glass-thermoplastic systems was performed without the PDMS sealing gaskets. The microfluidic channels where micromilled into a PMMA fluidic scaffold. The surface roughness and the waviness values of glass and PMMA at the contact area are given in Table 2. Roughness is defined as the short range surface unevenness. R_a is the arithmetic average deviation of all roughness measurement points from the center line, R_t the difference between the highest and lowest roughness deviation from center line, and R_z the difference between the average of the five maximum positive and the average of the five maximum negative roughness deviations from the center line. Waviness is defined as the long range surface unevenness and

serves as the center line for the roughness. W_a is the average waviness and W_t the peak/valley waviness. The total surface unevenness comprises the sum of waviness and roughness.

The leaks between the relatively even PMMA surface and the glass chip were of capillary nature. The capillary leaks were filled immediately upon filling of the system and did not disturb the flow characteristics of the channel. They could only be observed under the microscope and were not detected by the gage pressure sensor in the measurement range up to about 33,000 Pa, which is above typical microfluidic pump pressures. The outside end of the PMMA-glass interface very likely marked the end of the leak, since the end of the interface acted as a capillary flow stop. No water was detected outside the system. This could perhaps be good enough for a disposable one-channel device, especially if the outside finish of PMMA-glass interface is additionally sealed with viscous glue or a rubber material after clamping. However, it would not be adequate for a multi-channel system because of possible cross-talk of substances/fluids through the capillary leaks between the different parallel channels.

Alternative to Gaskets: PDMS Polymerized on the Sealing Surface of Thermoplastic Fluidic Scaffolds

The PDMS can also be applied to the sealing surface of the thermoplastic fluidic scaffold by stamping or as the second step in a two-component injection molding process. In the stamping approach, there is a risk of blocking the microfluidic channels with excess PDMS. In the two-component injection molding approach, the fabrication of channels with dimensions smaller than 1 mm becomes difficult because of the mechanical machining restrictions for the injection molding tool. Both risks are eliminated when microfabricated PDMS gaskets are used for clamping, as described above. The bond between PDMS surface and glass sensor chip can be made, e. g., by clamping or plasma bond.

In another approach, a flat cured PDMS sheet is adhesively laminated to a polycarbonate (PC) substrate. The microfluidic channels are hot embossed into the composite, with all three resulting channel walls and the sealing interface consisting of PDMS [10]. This composite fluidic scaffold can be clamped or plasma-bonded to the glass sensor chip. Controlling the shape of the microfluidic channels seems to be a problem because PDMS as an elastomer, even if glued to a thermoplastic like PC, is not an optimal hot embossing material.

Bonding of pre-baked (more viscous PDMS) spin-coated on a substrate chip to a thermoplastic fluidic scaffold without blocking the channels is also an interesting approach [11]. But if the substrate is a glass chip with a sensor, the sensor surface will be blocked by the PDMS. Photostructurable polysiloxane could provide an interesting alternative here in the future.

Glass–Thermoplastic Bonding With Microstructured Adhesive Tape Gaskets

In this approach, the glass chip and the thermoplastic microfluidic scaffold are bonded together by a double-sided adhesive tape. The bonding is done at room temperature allowing deposition of bio-molecules on the sensor chip before sealing the system. The tape had to meet certain criteria to qualify as a sealing tape.

G

Tape Choice

Many commercially available office or packaging tapes and commercial blue tapes made double-sided sticky with adhesive transfer tape on the non-sticky side are not suitable. The adhesive on these tapes is usually not homogeneous, i. e. it forms islands resulting in leaks when the glass chip and the thermoplastic fluidic scaffold are bonded together. Further, these tapes tend to make poor contact with low-energy surfaces (thermoplastics).

An ideal tape is composed of a polyester substrate with polyester liners to protect the adhesive on both sides. Polyester is well-suited for laser cutting (see below). The adhesive film should cover the tape as a homogeneous layer (no islands). It should make good contact to low-energy thermoplastic surfaces. Finally, for microfluidic systems targeted at life sciences or diagnostic applications (protein assay, DNA chips, cell handling etc.) the adhesive should be biocompatible. Medical grade, pressure sensitive acrylic adhesives meet these stringent requirements.

For completeness it should be mentioned that there are adhesive transfer tapes. The adhesive layer is protected by two removable liners. This transfer adhesive may be a choice if very thin channels are required not allowing for accommodation of a double-sided adhesive tape with a stabilizing polymer substrate between the two adhesive layers. Transfer adhesive tapes can also be used for self-made double-sided adhesive tapes with a non-standard substrate material.

Structuring of Microfluidic Channels into the Tape

Bonding with adhesive tapes is an attractive low cost and low temperature method for polymer and glass-polymer bonding. First tests for microfluidic applications were reported with unstructured tapes [12]. If the glass chip carries a sensor or electrodes, it is necessary to cut microflu-

idic channels into the tape in order not to block the sensor or electrode surface. There are two methods to accomplish that.

Die cutting (punching) Die cutting of double-sided adhesive tapes becomes tricky for channel dimensions below 1 mm. The dimensional limitations are caused by the fabrication and wear of the cutting tools. There are, however, reports of punching tools made by wire electric discharge machining with lateral feature dimensions as small as 300 μm [13]. This lateral resolution is almost as good as for IR lasers. UV lasers are still better by one order of magnitude which makes laser cut tapes for microfluidic glass-polymer sealing very interesting.
During the punching, the tape should be protected and stabilized on both sides by supporting material, e. g., thermoplastic foils or sheets, to avoid tape deformation during die cutting.

Laser cutting The same UV laser system as for cutting the PDMS gaskets was used to structure the microfluidic channels into the double-sided adhesive tape. The use of IR lasers has been reported for cutting coarse structures into transfer adhesive tapes (one transfer adhesive layer with two liners for protection) for sealing gaskets of micropumps [14]. But for cutting of microchannels, a UV laser is recommended to achieve the required finer lateral resolution, particularly for cutting through a real double-sided adhesive tape (one substrate with two adhesive layers and two liners on each side).
Laser cutting allows for almost free design of the microfluidic channels in the tape gasket. The design limitations are the laser spot size (20 μm in our system) and the step size of the laser (3 μm in our system). For a multitude of microfluidic applications, this is good enough. Figure 5 shows laser-cut double sided adhesive tapes with microfluidic channels. The tape adhesive is still protected by its liners.

Results

The to-be-bonded surfaces should be clean (e. g., ultrasonic bath and/or rinsing with isopropanol, blow drying). The tape can be aligned with respect to the glass chip and thermoplastic fluidic scaffold using alignment marks. During tape application and bonding, air bubble trapping should be avoided, e. g., through a rolling application or a slow application of the tape and by applying a contact pressure.
The leak tests showed that the glass-thermoplastic sealing using the microstructured adhesive tapes was good. No leaks were observed both under the microscope and in the

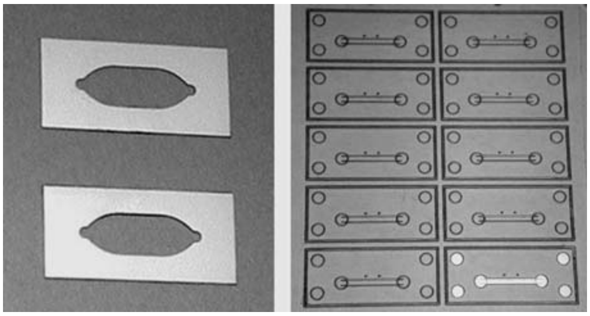

Glass-Polymer Bonding, Figure 5 Laser-cut double sided adhesive tapes. The adhesive is still protected by the liners. Polyester is the preferred tape substrate and liner material for UV laser cutting

pressure measurements up to the gage pressure of about 32,500 Pa generated by the syringe pump. The sealing is therefore strong enough for typical microfluidic pump pressures (Table 1).

Glass–Thermoplastic Bonding by Gluing

Gluing is an irreversible bonding method. When a glass chip with a sensor is bonded to a thermoplastic microfluidic scaffold, the microchannels are often in the thermoplastic material. The main risk with this bonding strategy is that the glue may go into and thus block the channels. To avoid that and to achieve a good bond quality by gluing, the process parameters need to be controlled. On the other hand, voids can form between the bonded parts due to solvent out-gassing, inhomogeneous wetting or too little amount of glue.

Important Process Parameters

Glue deposition The glue can be deposited by different methods, such as dispensing or another kind of transfer, e. g., stamping with a spin-coated substrate or a dedicated intermediate stamp.

Glue viscosity For dispensing or transfer by stamping, glues with low viscosities of about 50 mPas are favorable. They wet the thermoplastic surface very well (homogeneous layer), can be deposited as an only a few microns thin layer or thinner and tend to have no trapped bubbles. The microfluidic channel itself can act as a capillary flow stop for the glue, i. e. the glue stops at the channel wall and does not go into the channel if the other parameters are chosen correctly (e. g., amount and position of glue, contact pressure, possible pre-curing etc.).

Amount of deposited glue Too much glue will result in blocking of the microfluidic channels. On the other hand,

if the amount of applied glue is not large enough, the glue may not advance to channel wall leaving some capillary leaks between the thermoplastic and the glass open.

Location of deposited glue and design of bonded parts Besides the amount of glue, the position of the glue, i. e. its distance form the microfluidic channels, is important. Another issue is the design of the bonded parts, e. g., providing overflow cavities to absorb excess glue. To reduce the risk of glue being pressed into the microfluidic channel during bonding, the channel walls should have sharp edges at the contact surface and an orientation perpendicular to the contact surface (not trapezoidal) [15]. With a sharp perpendicular edge, the channel walls form a capillary flow stop for the glue in the bonding process.

Glue pre-curing: An interesting approach to avoid blocking of the microfluidic channels with glue is a pre-curing step after glue application and before the actual bonding. The glue is applied while it still has its original low viscosity, thus wetting the thermoplastic surface well. Then a pre-curing is done, increasing the glue viscosity. As a result, the contact pressure during bonding is less likely to press the glue into the microfluidic channels.

Contact pressure during curing As mentioned above, the channel walls acts as a capillary flow stops for the glue. If the contact pressure is too high, the capillary flow stop is overcome, and glue flows into the channel. If on the other hand the contact pressure is too low, the glue may not advance to the channel wall (if it was deposited in some distance from it) leaving capillary leaks between the thermoplastic and the glass open.

Surface cleaning/pre-treatment In order to achieve a constant wettability for the glue, the to-be-bonded surfaces of the thermoplastic fluidic scaffold and the glass chip can be pre-treated in an isopropanol bath, rinsed and blow dried, or exposed to UV radiation or plasma. The latter can not be done with the sensor chip if bio-molecules are deposited on it before bonding.

Glue biocompatibility For life science or diagnostic applications, the biocompatibility of the glue is important. If probe molecules (capture molecules) are already deposited on the glass sensor chip prior to bonding, the curing regime of the glue is also an important parameter. UV curing and thermal glues should be avoided in that case.

There are no universal recommendations for glue choice and gluing process parameters. This set of parameters needs to be developed and optimized for a particular application. This development process may require considerable effort.

Results

A fast-curing (non-UV, non-thermal) acrylic low-viscosity medical glue was chosen for a series of bonding experiments. This allows for the presence of bio-molecules on the sensor chip when the microfluidic system is being sealed. With the right choice of process parameters, glass chips could be bonded to PMMA fluidic scaffolds without clogging the microfluidic channels. However, to achieve this for a certain chip geometry and glue, some process development was necessary. It also proved to be difficult to keep the process stable, probably because a critical parameter is the wettability of the bonded surfaces. This is a disadvantage compared to the clamping or adhesive tape approach. Once a good bonding was achieved, the sealing of the microfluidic channels was good. No leaks were observed both under the microscope and in the pressure measurements. The bond sealed up to the tested gage pressure of about 32,500 Pa which is high enough to seal against the pump pressures of typical microfluidic pumps (see Table 1).

Glass–Thermoplastic Bonding Based on Heating

For this bonding strategy, the thermoplastic material is heated up to around its glass transition temperature. The major disadvantage of this strategy is that no bio-molecules can be deposited on the sensor chip before the bonding process because typical glass transition temperatures of thermoplastics are well above 40 °C, the limit to which most bio-molecules can be heated without degradation or damage.

Bonding with Laminated Thermoplastic Films

Two glass or silicon chips or a combination of both are used for this approach. One glass or silicon chip has microfluidic channels. A thin film (thickness below one micrometer) of thermoplastic polymer, e. g., polypropylene, fluorocarbon polymer or parylene, is deposited on both to-be-bonded parts, e. g., by plasma polymerization. The microfluidic channels are not blocked because they are considerably deeper than the thickness of the thermoplastic coating. The lamination bonding is performed under heat close to the glass transition temperature of the thermoplastic and pressure. A problem of this approach is that no bio-molecules can be deposited on the sensor chip prior to sealing due to the high temperatures involved in the process. Also, sensor integration into the microfluidic channel

can be difficult if both chips have to be coated with a thermoplastic layer for a good lamination bond.

Another lamination approach is the bonding of a film of thermoplastic liquid crystal polymer (LCP) to glass. The LCP layer can be structured with microchannels dry etched in oxygen plasma using an aluminum mask. After removal of the aluminum mask, the LCP can be laminated onto glass, silicon or a metal under pressures at temperatures around 260 – 270 °C [16]. Again, the temperature is too high for bio-molecule pre-deposition.

Localized Heat Glass-Thermoplastic Bonding

For this approach, the microfluidic channel is micromachined into glass or silicon. On the bonding surface of the chip, close to the channel rim, metallic (aluminum) heater elements are patterned. The thermoplastic counterpart is a Mylar (polyethylene) foil laminated with a PVDC (polyvinylidene chloride) contact layer. The two parts are pressed together while maintaining a temperature of 150 – 200 °C at the aluminum-PVDC interface to locally melt the PVDC [17].

The advantage of this localized heating method compared to heating with thermal rollers for lamination, microwaves, ultrasound, laser or electromagnetic fields is the very local heat generation due to the microfabricated heaters. This interesting bonding method has two disadvantages. Firstly, it has been demonstrated only with thin Mylar-PVDC laminates. Therefore, the integration of a sensor on the glass or silicon substrate is problematic because it also contains the microfluidic channels. Secondly, the heating elements require an additional photolithographic step. Thirdly, if bio-molecules are present on the chip during the bonding process, the microfluidic channels have to be filled with water or a buffer during the bonding in order not to heat the bio-molecules above 40 °C.

Future Directions for Research

Several interesting research activities can be observed in the field of glass-polymer and particularly glass-thermoplastic bonding. One approach is direct bonding of glass and thermoplastic materials using plasma or UV radiation and special (e. g., softer) grades of thermoplastic materials or solvent-treated thermoplastic surfaces.

Another direction is the development of photostructurable polysiloxane grades (PDMS like materials structured by photolithography like photoresists). These materials could be used instead of gaskets with much better and easier alignment for clamping or perhaps for direct plasma bonding to glass chips.

The laser cutting process for silicone gasket membranes and double sided adhesive tape gaskets will be developed further. Die cutting (punching) tools might also improve due to advances in mechanical machining and microfabrication.

Clever designs and processes for glue dispensing or glue transfer could lead to advances in gluing glass chips to thermoplastic microfluidic scaffolds.

Another interesting approach in glass-polymer bonding technologies is the direct bonding of photolithographically structured *soft* SU-8 microchannels to glass or thermoplastic materials without another laminate SU-8 or PMMA layer.

Both for fluidic issues (e. g., hydrophilic/hydrophobic) and bonding issues (e. g., for glue deposition), it is desirable to have better control of the surface properties of thermoplastic materials. This can be achieved by progress in thermoplastic surface modeling and physical or chemical surface treatment, and by better control of material and process parameters in thermoplastics fabrication.

Cross References

- ► AC Dielectrophoresis Lab-on-Chip Devices
- ► Evanescent Wave Sensing
- ► Flow Cytometer Lab-on-Chip Devices
- ► Hybrid Bonding
- ► Laser Ablation
- ► Laser Based Micromachining
- ► Microfluidic Assembly
- ► Micromolding (Injection and Compression Molding)
- ► On-Chip Waveguide
- ► Packaging (Including Wire Bonding)
- ► Photolithography
- ► Plasma Treatment Physics
- ► Surface Plasmon Resonance Sensors

References

1. Niklaus F, Enoksson P, Kälvesten E, Stemme G (2001) Low-temperature full wafer adhesive bonding. J Micromech Microeng 11:100–107
2. Carlier J, Arscott S, Thomy V, Fourrier JC, Caron F, Camart JC, Druon C, Tabourier P (2004) Integrated microfluidics based on multi-layered SU-8 for mass spectometry analysis. J Micromech Microeng 14:619–624
3. Bilenberg B, Nielsen T, Clausen B, Kristensen A (2004) PMMA to SU-8 bonding for polymer based lab-on-a-chip systems with integrated optics. J Micromech Microeng 14:814–818
4. Gawad S, Schild L, Renaud P (2001) Micromachined impedance spectroscopy flow cytometer for cell analysis and particle sizing. Lab Chip 1:76–82
5. Götzen R (1994) German Patent DE 4420996. http://www.microtec-d.com
6. McDonald JC, Duffy DC, Anderson JR, Chiu DT, Wu H, Schueller OJA, Whitesides GM (2000) Fabrication of microfluidic systems in poly(dimethylsiloxane). Electrophoresis 21:27–40

7. Laser DJ, Santiago JG (2004) A review of micropumps. J Micromech Microeng 14:35–64
8. Klank H, Kutter JP, Geschke O (2002) CO_2-Laser micromachining and back-end processing for rapid production of pmma-based microfluidic systems. Lab Chip 2:242–246
9. Gomez D, Goenaga I, Lizuian I, Ozaita M (2005) Femtosecond laser ablation for microfluidics. Opt Eng 44:1–8
10. Miller P, Schuenemann M, Sbarski I, Gengenbach T, Spurling T (2005) Proc 55th Electron Compon Technol Conf 1:597–602
11. Chow WWY, Lei KF, Shi G, Li WJ, Huang Q (2006) Microfluidic channel fabrication by PDMS-interface bonding. Smart Mat Struct 15:112–116
12. Lai S, Hudiono Y, Lee LJ, Daunert S, Madou MJ (2001) Proc SPIE 4557:280–287
13. Fu C, Rummler Z, Schomburg W (2003) Magnetically driven micro ball valves fabricated by multilayer adhesive film bonding J Micromech Microeng 13:96–102
14. Truong TQ, Nguyen NT (2004) A polymeric piezoelectric micropump based on lamination technology J Micromech Microeng 14:632–638
15. Flachsbart BR, Wong K, Iannacone JM, Abante EN, Vlach RL, Rauchfuss PA, Bohn PW, Sweedler JV, Shannon MA (2006) Design and fabrication of a multilayered polymer microfluidic chip with nanofluidic interconnects via adhesive contact printing. Lab Chip 6:667–674
16. Wang X, Engel J, Liu C (2003) Liquid crystal polymer (LCP) for MEMS: processes and applications. J Micromech Microeng 13:628–633
17. Su YC, Lin L (2005) Localized bonding processes for assembly and packaging of polymeric MEMS. IEEE Trans Adv Packag 28:635–642

Glycosidase

Synonyms

Glycoside hydrolase

Definition

Glycosidases catalyze the hydrolysis of the glycosidic linkage to generate two smaller sugars.

Cross References

- ► Biomolecular Synthesis in Microfluidics
- ► Microfluidic Bioreactor
- ► Lab-on-a-Chip Devices for Chemical Analysis
- ► Microfluidics for Bio- and Chemical Reactions

Glycoside Hydrolase

► Glycosidase

Gravity Wave

Definition

A wave generated at the interface between two fluids with different densities under the influence of gravity, such as ocean waves.

Cross References

► Piezoelectric Microdispenser

Gray-Scale Lithography

Synonyms

Gray-tone lithography

Definition

Gray-scale lithography is an inexpensive one-step lithography technology to create 3-D microstructures in a photoresist layer using an optical gray-scale mask. The ultraviolet (UV) light through the gray-scale mask during lithography process produces local intensity modulation and the 3-D profile on the surface of photoresist remains on the substrate once the exposed photoresist is stripped off by developing. This is due to various light energies absorbed by the photoactive compound as the light travels in the depth of the photoresist.

The gray-scale mask is a key component in this process. It can be generated by either using the sub-resolution, two-dimensional binary patterns (or cells) as the pixels on a conventional chrome-on-glass mask, or exposing special high energy beam sensitive (HEBS) glass with electron beam, which achieves high resolution at the gray-scale level.

The 3-D profile also can be transferred from the photoresist to a substrate such as silicon by plasma dry etching for MEMS and microfluidic applications.

Cross References

- ► Fabrication of 3-D Microfluidic Structures
- ► Photolithography
- ► Photoresist SU-8
- ► Photoresist Reflow
- ► Soft Photolithography

Gray-Tone Lithography

► Gray-Scale Lithography

Guard Flows

Definition

Small fluid flows used in the no-moving-part fluidic and microfluidic valves to ensure no cross-contamination takes place between various fluids leaving the valves into a common vent space. Guard flows are used especially in the valvesof a sampling unit. Since the guard flow enters the vent outlet of the valve and dictates the direction of the flow away from the valve into the vent, it prevents the indiscriminate mixture existing in the common downstream space to move upstream into the valve. The amount of fluid forming the guard flow is sacrificed, being subtracted from the fluid the flow of which is controlled in the valve. This requires the guard flows to be as small as possible.

Cross References

► Sampling Unit

HARMST (High Aspect Ratio Micro-Structure Technology)

► LIGA

Head Pressure

► Pump Head

Heat Absorption

► Endothermic

Heat Capacity

Definition

Heat capacity *c* is a measurable physical quantity that characterizes the ability of a body to store heat as it changes in temperature.

Heating Foil

Definition

Heating foils are thin plates consisting of pure metals, metal alloys (e. g. Cr/Ni) or insulating materials like Capton with metal wires interlaced. Applying an electric current through these foils an almost homogeneous heat flux density normal to the surface will be produced following ohm's law. Heating foils are flexible, in principle available in any size and have wide applications prospects wherever homogeneous heating of a surface is required.

Heat Transfer in Microchannel Flow

► Convective Heat Transfer in Microchannels

Helical Microchannel Flow

► Curved Microchannel Flow

Helmholtz Cavity

Definition

A chamber with one or more relatively small orifices that permit the passage of fluid to and from the chamber. If the fluid is caused to pass into and from the chamber in a harmonic manner, the fluid motion may resonate at specific frequencies which are proportional to the orifice area, square root of the static pressure, and inversely proportional to the mass of air and volume in the cavity.

Cross References

► Piezo/PZT for Microfluidics
► Piezoelectric Valves

Hemholtz Resonance

Synonyms

Cavity resonance; Port resonance

Definition

A resonance arising from the transfer of an entity to and from a volume through an area. The area is typically

small in scale in comparison to the volume, and examples include acoustic Hemholtz resonances which pass a fluid.

Cross References

► Piezoelectric Microdispenser

Hermann–Mauguin Notation

Synonyms

International notation

Definition

This notation defines the symmetries of a crystalline material in terms of point, plane, and space groups, and is closely tied to the crystal systems (triclinic, monoclinic, tetragonal, etc.), and crystal class. It is also related to Schöenflies and orbifold notations and offers a definition of the relevant symmetry axes.

Cross References

► Inversion Symmetry
► Non-Centrosymmetric

Heterogeneous Membrane

Definition

An ion-exchange membrane structure which has charged functionalities mixed into the membrane support structure. This structure gives the membrane an ionic character throughout the membrane backbone as opposed to being on the surface of the membrane only.

Cross References

► Ion Exchange Membranes

High Aspect Ratio Si Etching

► Plasma Etching

High Performance Liquid Chromatography (HPLC)

Definition

A form of column chromatography used frequently in biochemistry and analytical chemistry. HPLC is used to separate components of a mixture by using a variety of chemical interactions between the substance being analyzed (analyte) and the chromatography column.

Cross References

► Liquid Chromatography

High Pressure Liquid Chromatography (HPLC)

► Liquid Chromatography

High-Throughput Chemical Testing

► Microfluidic Systems for Combinatorial Chemistry

High-Throughput Screening (HTS)

Definition

High-throughput screening is a class of analytical techniques in which many different assays are performed in parallel, or very rapidly in succession.

Cross References

► Microfluidic Systems for High-Throughput Screening

Homogenization

► Microfluidic Mixing

Hot Embossing

► Micromolding

Hot Film

► Temperature Sensitive Resistor
► Thermoresistive Flow Sensors

Hot Press Bonding

► Thermal Fusion Bonding

Hot Press Molding

► Micromolding

Hot Wire

► Micro- and Nanoscale Anemometry: Implication for Biomedical Applications
► Temperature Sensitive Resistor
► Thermoresistive Flow Sensors

Hot Wire Anemometer

► Micro- and Nanoscale Anemometry: Implication for Biomedical Applications

HSV

► HSV Color Space

HSV Color Space

Definition

The HSV (Hue, Saturation, Value) model, also known as HSB (Hue, Saturation, Brightness), defines a color space in terms of three constituent components:

- Hue, the color type (such as red, blue, or yellow) ranges from 0 – 360° (but normalized to 0 – 100%)
- Saturation, the "vibrancy"of the color ranges from 0 – 100%. The lower the saturation of a color, the more "grayness"is present and the more faded the color will appear
- Value, the brightness of the color ranges from 0 – 100%.

The HSV model was created in 1978 by Alvy Ray Smith. It is a nonlinear transformation of the RGB color space, and may be used in color progressions.

HSV / Intensity Images

► HSV Color Space

Hybrid Bonding

Definition

Bonding of different material classes, e. g., polymers and non-metallic inorganic materials like glass. The bonding partners have substantially different physical and chemical properties. For example, non-metallic inorganic materials like glass are rather hydrophilic (wetted well by water) because both the material and the water molecules have strong dipoles. Polymers are usually more or less hydrophobic (not very well wetted by water) depending on the number of physical (e. g., van der Waals bonds) and chemical (e. g., oxygen-containing acrylic or epoxy groups) dipoles in the polymer.

Cross References

► Glass-Polymer-Bonding

Hybrid Simulation

► Multiscale Modeling and Numerical Simulations

Hydrodynamic Dispersion

DEBASHIS DUTTA
Department of Chemistry, University of Wyoming,
Laramie, WY, USA
ddutta@uwyo.edu

Synonyms

Band broadening; Convective dispersion; Fluid dispersion; Taylor dispersion; Taylor–Aris dispersion

Definition

Hydrodynamic dispersion refers to the stretching of a solute band in the flow direction during its transport by a convecting fluid. Variation in the fluid velocity across the channel cross-section leads to such band broadening which is often quantified in terms of the Taylor–Aris dispersion coefficient.

H

Overview

Dispersion of solute samples in a convective fluid (gas or liquid) is an area of significant interest to many branches in science and engineering. This phenomenon governs a wide range of processes from the spreading of contaminants in streams and rivers to the productivity of commercial scale reactors used in chemical industries. On miniaturized analytical devices, the broadening of analyte bands during their transport through the analysis channel also affects the speed and efficiency of assays performed on these systems [1]. While hydrodynamic dispersion in microchannels tends to reduce the resolution of pressure-driven separations, it diminishes the throughput of the device in other applications by decreasing the frequency with which samples can be analyzed.

Hydrodynamic dispersion of solute slugs in a straight conduit occurs due to non-uniformities in the fluid velocity across the channel cross-section. On microfluidic devices, such solutal spreading is commonly encountered during the pressure-driven transport of analyte samples. The slowing down of the fluid by the channel walls in this case introduces differences in the streamline velocity that stretches out a solute band as it travels through the duct. Although such dispersion is usually negligible under electroosmotic flow conditions due to a nearly uniform fluid velocity profile, unwanted pressure-driven flows in these devices can introduce significant band broadening [2]. Pressure gradients in electrokinetically-driven systems can arise due to differences in the hydrostatic head of end-channel reservoirs, gradients in channel wall surface charges (i. e., gradients in zeta potential at the channel wall) or gradients in fluid conductivity (as in sample stacking). Moreover, the Joule heating of the liquid in these devices can lead to a spatial variation in the fluid viscosity yielding a non-uniform flow profile. In the limit of small temperature differentials however, the resulting solutal spreading is quite similar to that in pressure-driven flows. In this entry, we present a review of the hydrodynamic dispersion phenomenon for unidirectional pressure-driven flow through microchannels. To quantify such solutal spreading the method of moment formulation that was proposed by Aris has been outlined here. We further discuss how changing the shape of the channel cross section affects this dispersion process and suggest ways for tailoring the channel geometry to control such band broadening.

The process of solutal spreading in pressure-driven flows was first analyzed by Sir Geoffrey Taylor in 1953. He showed that the variation in the fluid velocity over the channel cross-section in these systems spreads out an analyte band as convection proceeds in the flow direction. This convective spreading is ultimately limited by molecular

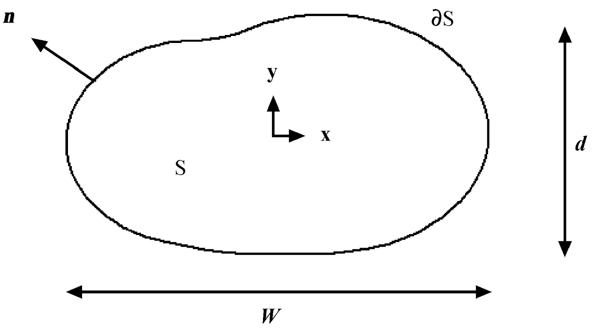

Hydrodynamic Dispersion, Figure 1 A conduit of arbitrary cross-section defined by the surface S and bounded by the closed curve ∂S. Here *d* and *W* are the characteristic depth and width of the channel respectively, while ***n*** is the vector normal to its boundary ∂S

diffusion across streamlines and may be described in terms of an effective dispersivity [3], often referred to as the Taylor–Aris dispersivity (K). The Taylor–Aris dispersivity determines the rate at which the spatial variance of the solute slug grows in the axial direction (σ^2) with time (t) i. e., $\mathrm{d}\sigma^2/\mathrm{d}t = 2\mathrm{K}$ and depends critically on the flow conditions in the channel. In pressure-driven flow between two parallel plates for example, the quantity K is given by

$$K = D\left[\underbrace{1}_{\text{axial diffusion component}} + \underbrace{\frac{1}{210}\left(\frac{Ud}{D}\right)^2}_{\text{conevtive disperson component}}\right] \qquad (1)$$

where U is the average fluid velocity, d is the separation distance between the plates and D is the molecular diffusion coefficient of the solute species. The dimensionless group in Eq. (1) denotes the characteristic Peclet number which quantifies the relative magnitude of convective to diffusive transport for the analyte molecules in the system. Eq. (1) shows that the overall dispersivity in simple pressure-driven flow between two parallel plates may be decomposed into two additive contributions. While the first term given by the molecular diffusion coefficient of the solute species, quantifies the effect of axial diffusion in the system, the second term determines the effect of fluid shear in the channel and scales with the square of the Peclet number (Ud/D) times the diffusivity of the solute molecules. The proportionality constant for the convective dispersion component in the expression, i. e., $1/210$, depends on the flow conditions and the exact geometry of the analysis channel. Note that in pressure-driven systems the axial diffusional limit of slug dispersion between two parallel plates is only realized for a Peclet number $\ll \sqrt{210}$. Such conditions are typically encountered during gas phase transport when analyte diffusion is often significant compared to solute convection due to fluid flow. In

liquid phase systems however, the convective dispersion component is usually more dominant and tends to determine the spreading of solute slugs in the microchannel.

While Eq. (1) quantifies the broadening of analyte bands between two parallel plates, this result can be significantly affected by the exact cross-section of the conduit. Mathematically, one can evaluate this effect by introducing a function f in Eq. (1) to yield

$$K = D\left[1 + \frac{1}{210}\left(\frac{Ud}{D}\right)^2 f\right] \quad (2)$$

where d here denotes the characteristic narrower transverse dimension of the channel (see Fig. 1). The constant $1/210$ in the above expression could, of course, be absorbed into f. However, its value is chosen such that this function is equal to unity for the parallel-plate device. In this situation, f essentially quantifies the dispersion due to the slowing down of the fluid by the channel sidewalls, and is, therefore, expected to assume values greater than 1 for most closed channel profiles. For example, the reduced velocity in the side-regions of a rectangular duct causes a substantial increase in the magnitude of f which grows with its aspect ratio (ratio of the channel width W to its depth d) approaching a value of about 7.95 in the limit $d/W \to 0$ [4, 5].

It is important to note that the Taylor–Aris dispersion limit for band broadening described above is reached only after solute molecules have a chance to diffuse across the wider channel dimension (W), i.e., $t \gg \left(1/4\pi^2\right)\left(W^2/D\right)$. The numerical prefactor $1/4\pi^2$ for this time scale arises from the decay of the corresponding eigenvalue problem determining the higher moments of the solute concentration in the system. While the exact magnitude of this prefactor depends on the precise geometry of the conduit, numerical simulations have shown [6] that the slug dispersivity approaches 95% of its Taylor–Aris dispersion limit for $t \sim W^2/(20D)$. Because we focus on this asymptotic limit for solutal spreading in this entry, the analysis presented here strictly holds for microchannels with lengths on the order of $UW^2/(20D)$ or greater. For a fluid velocity of 1 mm/s and a solute diffusivity of $10^{-6}\,\mathrm{cm^2/s}$, this corresponds to a length of 0.5 cm for a 100 μm wide channel. In shorter conduits, the broadening of the analyte bands is usually smaller than that predicted by the results based on the Taylor–Aris dispersion limit discussed here.

Basic Methodology

Method of Moments Formulation

The mathematical formulation that is commonly used to quantify the hydrodynamic dispersion of sample slugs is based on the work that was presented by Aris in 1956. In his article, Aris described a general procedure to frame and solve the equations governing the integral moments of the solute concentration in a flow stream [7]. We outline this mathematical formulation in this section for calculating the dispersivity of analyte bands in a pressure-driven flow though a straight conduit.

Using the method of moments formulation proposed by Aris, it is possible to show that the solutal spreading in a unidirectional pressure-driven flow can be calculated by solving two 2-dimensional problems. First, the velocity field $u(x, y)$ for the analyte molecules is determined under steady-state condition based on the fluid flow in the system. For a straight channel whose axis is aligned along the z-direction, this quantity is governed by the 2-dimensional Poisson equation

$$\begin{aligned} &\text{Dimensional form:} && \nabla^2 u = -\frac{\Delta P}{\eta L} \\ &\text{Boundary condition:} && u|_{\partial S} = 0 \\ &\text{Dimensionless form:} && \nabla^{*2} u^* = -1 \\ &\text{Boundary condition:} && u^*|_{\partial S} = 0 \end{aligned} \quad (3)$$

In the above expression, all length scales have been rendered dimensionless with respect to the narrower channel dimension d while u has been normalized by the characteristic velocity $U_c = \left(\Delta P d^2\right)/(\eta L)$. Here $\Delta P/L$ denotes the pressure drop per unit length in the flow direction and η denotes the viscosity of the fluid. Note that the operator ∇^2 is the two-dimensional Laplacian because there is no variability in the z-direction. Its dimensionless form $\left(\nabla^{*2}\right)$ in Eq. (3) has been obtained upon normalization with respect to d^2. Once we obtain u^* by solving Eq. (3), the average fluid velocity in the channel, $\overline{U}$, may be determined using the integral

$$\overline{U} = \frac{U_c}{A^*}\int_S u^*\,\mathrm{d}A^* \quad (4)$$

where $A^* = A/d^2$ is the dimensionless cross-sectional area of the conduit normalized with respect to d^2. This velocity may then be used to renormalize u as $\hat{u} = u/\overline{U}$.

The concentration profile $c(x, y, z, t)$ of a passive tracer under these flow conditions can be determined using the diffusion-convection equation given below

$$\begin{aligned} &\frac{\partial c}{\partial t} + u(x, y)\frac{\partial c}{\partial z} = D\left(\nabla^2 c + \frac{\partial^2 c}{\partial z^2}\right) \\ &\text{Boundary Condition:} \quad (D\nabla c)\,.\,\boldsymbol{n}|_{\partial S} = 0 \end{aligned} \quad (5)$$

Here D is the diffusion coefficient of the solute molecule and ∇ denotes the two-dimensional gradient operator. The quantity $\boldsymbol{n}$ appearing in the boundary condition here refers to the unit vector pointing outward normal to the channel surface (see Fig. 1). It is important to note that Eq. (5) assumes that the analyte molecules moves with the local fluid velocity u and diffuses uniformly throughout the channel. The description presented here therefore, is only valid for systems in which the size of the solute particles is negligible compared to the channel dimensions. While the effect of a finite particle size may be taken into account using a vectorial, position-dependent form for the parameter D and appropriate modifications to the velocity field u [8], this analysis focuses on the simpler situation.

For systems with solute molecules much smaller than the channel size, we proceed further by expressing Eq. (5) in a dimensionless form after normalizing t with respect to the diffusion time scale d^2/D,

$$\frac{\partial c}{\partial t^*} + \mathrm{Pe}\,\hat{u}\frac{\partial c}{\partial z^*} = \nabla^{*2}c + \frac{\partial^2 c}{\partial z^{*2}} \qquad \text{Boundary Condition:} \quad \nabla^* c\,.\,\boldsymbol{n}|_{\partial S} = 0 \tag{6}$$

where $\mathrm{Pe} = \overline{U}d/D$. Following the method of moments, Eq. (6) may be rewritten as

$$\begin{aligned} &\frac{\partial \phi_p}{\partial t^*} - p\,\mathrm{Pe}\,\hat{u}\phi_{p-1} = \nabla^{*2}\phi_p + p\,(p-1)\,\phi_{p-2} \\ &\quad\text{where} \quad \phi_p = \int_{-\infty}^{\infty} z^{*p} c\,\mathrm{d}z^* \\ &\frac{\mathrm{d}m_p}{\mathrm{d}t^*} = p\,\mathrm{Pe}\int_S \hat{u}\phi_{p-1}\,\mathrm{d}A^* + p\,(p-1)\int_S \phi_{p-2}\,\mathrm{d}A^* \\ &\quad\text{where} \quad m_p = \int_S \phi_p\,\mathrm{d}A^* \end{aligned} \tag{7}$$

If the total amount of solute in the channel is normalized to unity (i. e., $m_0 = 1$), it may be shown that the asymptotic solutions $\phi_0 = 1/A^*$ and $m_1 = \mathrm{Pe}\,t^*$ satisfy Eq. (7).

Under these steady-state conditions, the solute slug acquires a constant velocity in the channel and hence ϕ_1 grows linearly in time yielding the following expression for the Taylor–Aris dispersivity

$$\begin{aligned} &\phi_1 = \frac{\mathrm{Pe}\,t^*}{A^*} + \frac{\mathrm{Pe}}{A^*}g\,(x,y) \qquad \text{and} \\ &\frac{K}{D} = \frac{\mathrm{d}\left(m_2 - m_1^2\right)}{\mathrm{d}t^*} = 1 + \mathrm{Pe}^2\frac{1}{A^*}\int_S \hat{u}\,g\,\mathrm{d}A^* \end{aligned} \tag{8}$$

where g is the solution to the differential equation

$$\nabla^{*2}g = 1 - \hat{u} \qquad \text{satisfying the conditions}$$
$$\nabla^* g.\boldsymbol{n}\big|_{\partial S} = 0 \qquad \text{and} \qquad \int_S g\,\mathrm{d}A^* = 0 \tag{9}$$

In the absence of any spatial variation in u, as in electroosmotic flow, the function g is identically equal to zero. It is the interaction of g with the velocity field that results in dispersion of the solute slugs under pressure-driven flow conditions. The dispersivity function f defined in Eq. (2) in this situation can be simply obtained from the area integral

$$f = \frac{210}{A^*}\int_S \hat{u}\,g\,\mathrm{d}A^* \tag{10}$$

The above equations can be solved analytically to yield f for simple geometries such as a tube, an ellipse and a rectangular channel with no sidewalls. For more complicated geometries such as a trapezoidal channel or one arising from isotropic etching fabrication methods, one has to resort to numerical solutions. In these cases, commercially available solvers such as FEMLAB and PDE Toolbox in MATLAB may be used to rapidly determine the dispersivity function f via numerical techniques.

Key Research Findings

In this section, we analyze the hydrodynamic dispersion of solute slugs using the dispersivity function f defined above for unidirectional pressure-driven flow through microchannels. We also discuss how changing the shape of the cross section affects this band broadening as we move from one channel geometry to another. Based on this understanding, this section further suggests ways to control such solutal spreading by tailoring the cross-section of the analysis channel.

Rectangular Channels

Microchannels created using dry etching techniques on silicon-based substrates often have a cross section that is close to a rectangle. This geometry is also common in polymer based microchips e. g., created using PDMS (polydimethylsiloxane) material, which are popularly used in the research community due to their simpler fabrication procedure. The effect of the rectangular geometry on the hydrodynamic dispersion of solute slugs has been well investigated in the past by several researchers [4, 5]. These studies have shown that the function f for this profile increases monotonically with an increase in the

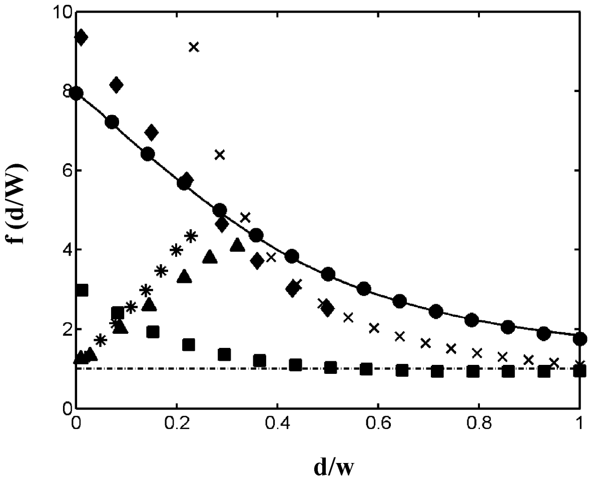

Hydrodynamic Dispersion, Figure 2 Effect of aspect ratio on solute dispersivity in pressure-driven flow systems for a fixed channel depth. (•) rectangular channels; (♦) single-etched isotropic channels; (×) elliptical channels; (∗) optimum double-etched isotropic channels; (▲) optimum double-etched rectangular channels; (■) optimum channels with bowing; (— · —·) parallel plate limit

aspect ratio of the conduit (see Fig. 2). While $f \approx 1.76$ for a square cross section ($d/W = 1$), this function approaches a value of 7.95 in the opposite limit when $d/W \to 0$. The greater dispersion in a rectangular channel over that in a parallel plate design occurs due to the slowing down of the fluid around its vertical sidewalls. This results in an increase in the average fluid shear and also produces velocity variations in the transverse direction which usually, on account of its greater length scale, is subject to greater diffusional limitation. It is important to note that these two effects dominate the dispersion process in a rectangular channel in two different scenarios. For small aspect ratio profiles ($d/W \approx 1$), the characteristic length scale for diffusion along the vertical and horizontal directions of the rectangle are similar. In this case, the larger dispersion in a rectangular conduit over that between two parallel plates occurs due to a greater fluid shear introduced by the channel side-walls. With a decrease in the value of d/W however, this contribution to band broadening diminishes. This occurs as the channel sidewalls in a rectangular conduit slow down the fluid only over a length scale of order d around them. In designs with $d/W \ll 1$, because these slow moving regions are widely separated the diffusional resistance across them has a larger effect on the overall band broadening. Although the Taylor–Aris dispersivity still scales with d^2 in the limit $d/W \to 0$, the coefficient multiplying Pe^2 is nearly 8 times greater than that resulting from diffusion in the narrower direction.

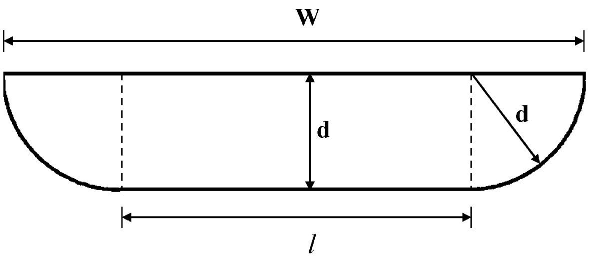

Hydrodynamic Dispersion, Figure 3 Cross-section of an isotropically etched channel

Isotropically Etched Channels

On glass substrates, microfluidic ducts are commonly fabricated using isotropic wet etching techniques originally developed in the semiconductor industry. Such techniques often yield channels that are not rectangular but rather have cross-sections close to the profile depicted in Fig 3. These conduits referred to as isotropically etched channels consist of a rectangular central section of depth d and width l, with quarter disk shaped side regions of radius d (see Fig. 3). In this situation their overall width is given by $W = l + 2d$ restricting their aspect ratio W/d to values greater than 2. The quarter circular sidewalls in the isotropically etched channel significantly modify the pressure-driven flow field and hence affect the dispersivity in the system. This is shown in Fig. 2 where we have quantified the effect of the aspect ratio on solute dispersion in this geometry. As may be seen, the function f for this profile assumes values somewhat greater than that for a rectangular design in the limit of small d/W. This occurs as the quarter circular sidewalls slow down the fluid to a greater extent than the vertical walls in the rectangular geometry. This yields an asymptotic value of 9.42 for f in the limit of $d/W \to 0$, about 18% greater than that in a rectangular channel. It is interesting to note that the isotropically etched profile causes lower band broadening in the opposite limit when d/W approaches its minimum value of 0.5. This is simply a consequence of a smaller average channel depth, which in turn reduces the diffusional resistance in the vertical direction. Overall, the two channel cross-sections exhibit a similar dispersivity for all values of d/W. This similarity in the behavior of rectangular and isotropically etched channels also suggests a similar performance of glass and polymer (e. g., PDMS) based microdevices. In this situation, polymer microchips can be a better commercial choice compared to their glass counterparts in view of the lesser fabrication effort required to produce them. The elasticity of polymers however, may significantly increase analyte dispersion in these devices under high pressure conditions due to bowing of microchannels as will be discussed later in this entry.

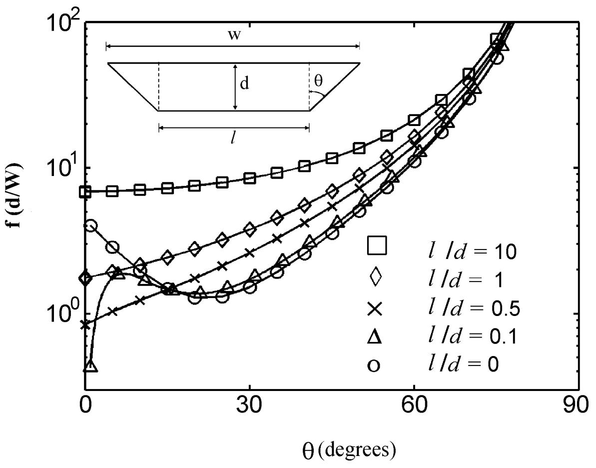

Hydrodynamic Dispersion, Figure 4 Effect of the different geometric parameters on solute dispersion in a trapezoidal channel for a fixed depth in its central section

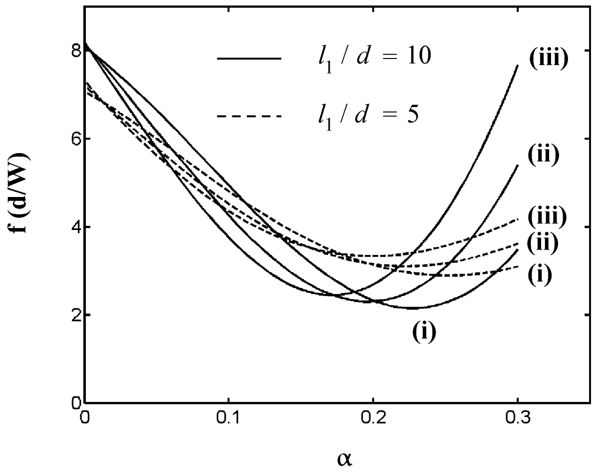

Hydrodynamic Dispersion, Figure 5 Effect of the second etch on solute dispersion in the double-etched isotropic profiles (i) $l_2/d = 0$ (ii) $l_2/d = 0.2$ (iii) $l_2/d = 0.4$

Trapezoidal Channels

A channel profile also commonly employed in microchip based analytical devices is the trapezoidal geometry. Such cross sections result from techniques in which the substrate material is etched away at different rates along different directions (e. g., anisotropic etching). Microchannels created on crystalline silicon wafers, for example, tend to have geometries close to the idealization depicted in Fig. 4. The trapezoidal profile essentially comprises of a rectangular central section of depth d and width l in between two triangular side-regions having a wedge angle θ. The key difference between the trapezoidal and isotropically etched designs is that the width of the side-regions in the former case can be much greater than the channel depth. Note that this width determines the length scale over which the fluid is slowed down by the side-walls and, therefore, the scaling for the additional dispersivity introduced as a result of this effect. In Fig. 4, we have presented the effect of the dimensionless geometric parameters l/d and θ on the dispersivity function f for a trapezoidal channel. As may be seen, the band broadening in this profile diverges in the limit of large wedge angles as $\theta \to \pi/2$, for all values of l/d. This occurs due to an unbounded increase in the width of its triangular side-regions, which grow as $d \tan\theta$. In this situation, the dispersion in these sections dominate the overall solutal spreading in the channel yielding a function f that scales as $\tan^2\theta$ and has a weak dependence on the parameter l/d (see Fig. 4). The ratio l/d, however, becomes more significant for designs with smaller wedge angles in which $\tan\theta$ assumes a value on the order of 1 or less. Figure 4 shows that while the dispersivity in a trapezoidal conduit increases monotonically with θ for moderate and large values of l/d, it actually goes through a minimum for geometries with $l/d \ll 1$. In a triangular channel, this occurs for a value $\theta \approx 22°$ when the width of the upper wall is about 80% of the channel depth. Moreover, for this optimum wedge angle the convective dispersion component in this geometry is reduced by about a factor of 4 over its value at $\theta = 0$.

It is important to note that while the dispersivity function f in a triangular profile assumes a value of about 4 for $\theta = 0$, this quantity decays off as $(l/d)^2$ for trapezoidal channels with $l/d \ll 1$. In this situation, f rises sharply with θ for small wedge angles ($\theta \ll l/d$) as the contribution to dispersion from its side-regions starts dominating the overall solutal spreading. The combination of this effect with the behavior discussed in the previous paragraph means that the dispersivity function shows an inflection point (a maxima followed by a minima) for small but non zero l/d (see Fig. 4). The maxima in the curve occurs for these designs when $\theta \approx l/d$ while the minima is observed when $\theta \approx 22°$. In this situation, the inflection point in f is observed only for trapezoidal designs with $l/d \ll \tan 22°$. For profiles with the central rectangular section having an aspect ratio greater than this value, a monotonic increase in the dispersivity is observed with θ. The dispersivity for the case $\theta = 0$ in these designs is equal to that in a rectangular channel of identical depth and width.

Double-Etched Isotropic Profiles

The analyses presented in the previous sections show that the overall dispersion in large aspect ratio channel geome-

tries is often dominated by the contribution arising due to their slow moving side-regions. It may, therefore, be possible to reduce such band broadening by simply speeding up the fluid in the vicinity of the sidewalls. One way to realize this effect is to modify the cross section of the microchannel, which in turn alters the pressure-driven flow field in it. In particular, a greater depth in the side-regions of the conduit can lead to a local increase in the solute average velocity around these corners, yielding a lower dispersion in the system [9]. Such channel geometries created using standard isotropic etching techniques have been proposed recently [6, 10]. In this design, the side-regions are first etched out (shallow etch) to a depth $\Delta d = \alpha d$, followed by subjecting the whole channel to a second etch (deep etch) process excavating an additional distance d (see Fig. 5b). The resulting cross section can be completely specified using three dimensionless parameters l_1/d, l_2/d and α. Note that the value of l_2 in this geometry is determined by the line thickness that is photolithographically patterned onto the substrate for the shallow etching process. In Fig. 5a, we have presented the effect of the extra depth in the double etched profiles on the hydrodynamic dispersion of solute slugs. As may be seen, the function f for these geometries is minimized for an optimum choice of α when the average fluid velocity in the side-regions equals that in the center. The performance of these optimum designs, however, deteriorates with an increase in the value of l_2/d for a given aspect ratio due to an increase in the average depth of the channel. Increasing l_2/d also shifts the optimum value of α downward for these designs. Note that these effects are more prominent for larger values of d/W when the solute fraction in the side-regions of the microfluidic channel is significant.

In Fig. 2, we have compared the performance of the optimized profiles to that of the single-etched geometries, which shows a dramatically different effect of the aspect ratio on the function f. Instead of increasing for small values of d/W as in the case of the single-etched designs, it actually approaches an asymptotic value of unity as $d/W \to 0$ in the double-etched channels. This occurs as the variation in the average solute velocity across the wider direction of this modified cross section is almost completely eliminated. Although the greater depth in their side-regions introduces some additional dispersion, this contribution diminishes in the limit of large aspect ratios. The choice of α_{opt} for these designs is not a strong function of d/W and only varies between 0.1 and 0.3 for the case $l_2/d = 0$ (see Fig. 5b). The optimum double etched profiles yield a dispersion that increases with a reduction in their widths, eventually offering no benefits over the single-etched geometries for designs with $d/W > 0.25$. However, for a value of $d/W = 0.1$ the dispersivity in this cross section is the same as the minimum possible for a single-etched isotropic profile ($d/W = 0.5$), even though its area is more than five times greater. This results in a significant benefit for applications requiring some fixed solute throughput in the system.

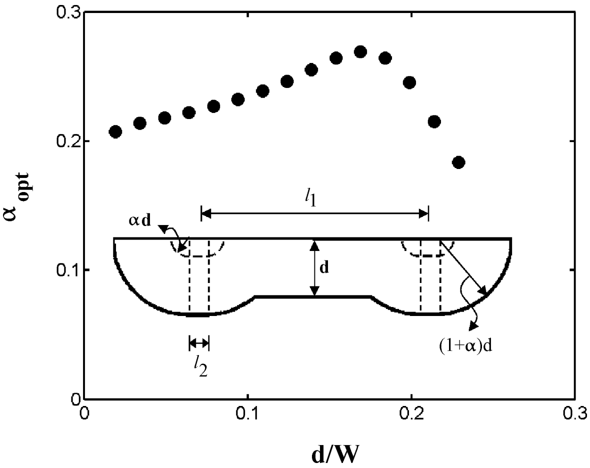

Hydrodynamic Dispersion, Figure 6 Optimum choice of α that minimizes hydrodynamic dispersion for the design $l_2/d = 0$

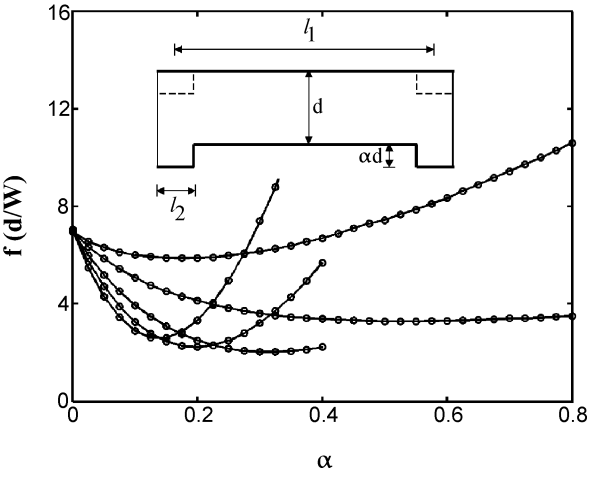

Hydrodynamic Dispersion, Figure 7 Effect of the second etch on solute dispersion in the double-etched rectangular channels

Double-Etched Rectangular Channels

While the fabrication of the optimum profiles described above requires the use of isotropic wet etching techniques, dry etching methods may also be used to produce geometries that minimize band broadening in pressure-driven flow systems. In this case, a shallow etch in the side-regions by an amount $\Delta d = \alpha d$ followed by a deep etch of the entire channel by a distance d yields a cross sec-

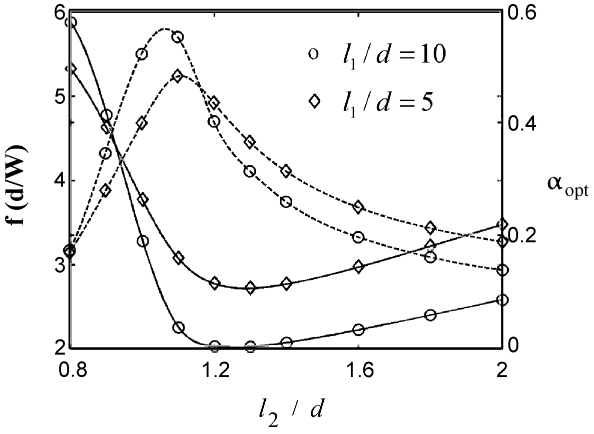

Hydrodynamic Dispersion, Figure 8 The solid lines depict the effect of the feature width in the double-etched side-regions on the performance of the optimized designs and the dashed lines here denote the optimum choice for α in these profiles

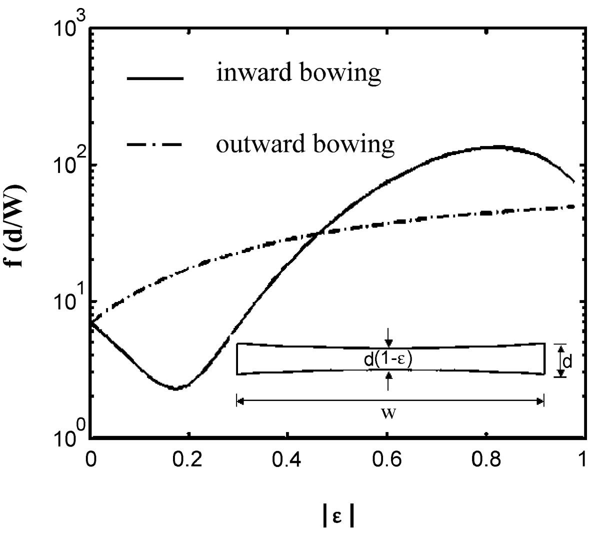

Hydrodynamic Dispersion, Figure 9 Effect of bowing on the dispersion of solute slugs in rectangular channels

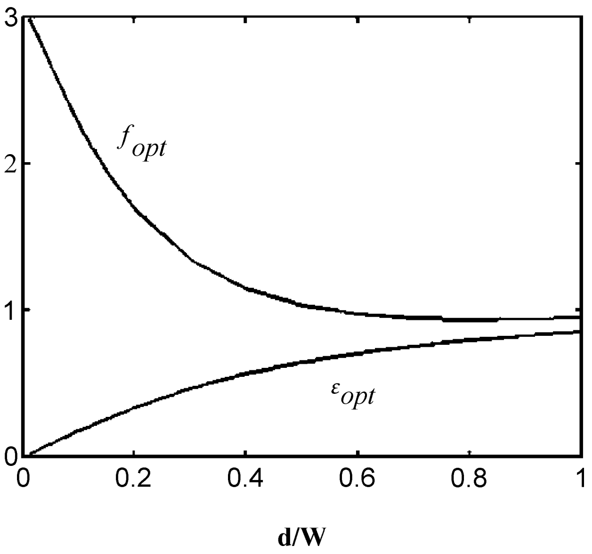

Hydrodynamic Dispersion, Figure 10 Optimum choice of ε that minimizes band broadening in positively bowed rectangular profiles

tion close to the idealization depicted in Fig. 6a. Note that the lack of any undercutting beneath the photo-patterned mask provides a better control over the geometry around the sidewalls in the dry etched designs. In Fig. 6a, we have presented the effect of α on the dispersion of solute slugs in the double-etched rectangular channels. As expected, the extra etch around the sidewalls of this profile again leads to a minima in the function f for a given value of l_2/d and l_1/d. Moreover, the width of these deeper regions may be further optimized with respect to the parameter l_2/d in the system (see Fig. 6b). The optimum choice of α and l_2/d, however, depends weakly on the aspect ratio of the channel (see Fig. 6b). As in the case of the double-etched isotropic profiles, the performance of the optimum dry etched designs improves with an increase in their widths, approaching the parallel plate limit as $d/W \to 0$. For a given value of d/W, the optimum double-etched rectangular channels also yield a slightly lower dispersion compared to their wet etched counterparts, again due to a greater control over the feature width in their side-regions.

Channels with Bowing

The analyses presented above describe hydrodynamic dispersion in idealized geometries that closely approximate the actual channel cross sections commonly used in microfluidic devices. However, fabrication constraints and flow conditions can lead to significant deviations from these idealized forms, particularly for large aspect ratio designs. For example, during the anodic bonding of a silicon substrate to a glass plate, the strong electrical force exerted on the device can lead to inward bending and even collapse of the surfaces. A similar inward bowing near the channel center is also observed during the thermal annealing of conduits milled out on a plastic footprint. Moreover, the elasticity of the polymers often used for creating microchannels (e. g., PDMS) renders them susceptible to outward bulging under sufficiently high flow pressures. In this section, we consider the effect of such bowing of microchannels on the Taylor–Aris dispersion of solute slugs during their pressure-driven transport.

Consider the bowed microchannel cross-section depicted in Fig. 7a with a depth d and width W. The easiest way of

capturing the effect of bowing for this geometry is to introduce a quadratic variation in the channel depth across the width of the conduit i. e., $h = W\left[1 - \varepsilon + 4\varepsilon\,(x/W)^2\right]$. In this design, the dimensionless parameter ε represents the degree of bowing into the channel whose effect on the dispersivity function $f\,(d/W, \varepsilon)$ has been shown in Fig. 7a for an channel aspect ratio of $d/W = 0.1$. As may be seen from the figure, for rectangular channels with an outward bowing $(\varepsilon < 0)$, f increases monotonically with an increase in the magnitude of ε. This occurs as the greater depth around the channel center in these geometries further speeds-up the faster moving streamlines increasing the disparity in the depth-averaged fluid velocity across the channel width. In the case of inward bowing however, an increase in the parameter ε actually slows down the fluid near the channel center. This results in a decrease in the value of f which reaches a minimum when the average flow speed in the side-regions equals that in the channel center. If ε is increased beyond this optimum value of 0.17, the fluid around the channel side-walls now starts traveling faster than the average flow velocity in the system leading to an increase in the function f. Note that beyond a critical bowing of $\varepsilon = 0.3$, the dispersion coefficient is actually greater than that for a plain rectangular channel with the same aspect ratio. For even larger values of ε, the dispersion coefficient shows a maximum and then decreases. This final decrease is due to a reduction in the area of the slow moving central region as the channel pinches off at $\varepsilon = 1$. Finally in Fig. 7b we have depicted the variation in the optimum bowing and the minimum dispersion in the positively bowed rectangular conduits as a function of the channel aspect ratio. These results show that for moderate aspect ratios, the optimally bowed channels yield a lower dispersion than the optimized double-etch profiles discussed earlier. But unlike the double-etch optimization strategy where the increase in channel depth is provided exactly where it is required, i. e., near the channel sidewalls, bowing alters the channel depth throughout the width of the conduit. This limits the performance of the bowing strategy compared to the double-etch strategy at large aspect ratios.

Future Directions for Research

In large aspect ratio channels as typically used in microfluidic devices, diffusion limitations across the slow moving side-regions tend to dominate slug dispersion under pressure-driven flow conditions. The theoretical analysis presented here show that this contribution however, can be substantially reduced by increasing the channel depth around these corners. Such a modification in the channel geometry leads to a higher fluid velocity near the sidewalls yielding lower dispersion in the system. Although the low-dispersion designs proposed in this work can be realized using standard photolithographic techniques, experimental data supporting their better performance is lacking in the literature. In the future, experimental work in this area needs to be performed and the results need to be compared with the theoretical predictions presented here.

Cross References

► Curved Microchannel Flow
► Electroosmotic Flow in Heterogeneous Microchannels
► Microfluidic Mixing
► Joule Heating in Electrokinetic Flow: Theoretical Methods

H

References

1. Stone HA, Stroock AD, Adjari A (2004) Engineering flow in small devices: Microfluidics toward a Lab-on-a-Chip. Ann Rev Fluid Mech 36:381–411
2. Li D (2004) Electrokinetics in Microfluidics. Academic Press, London
3. Taylor GI (1953) Dispersion of soluble matter in solvent flowing slowly through a tube. Proc R Soc A 219:186–203
4. Doshi MR, Daiya PM, Gill WN (1978) 3-dimensional laminar dispersion in open and closed rectangular conduits. Chem Eng Sci 33:795–804
5. Chatwin PC, Sullivan PJ (1982) The effect of aspect ratio on longitudinal diffusivity in rectangular channels. J Fluid Mech 120:347–358
6. Dutta D, Leighton DT (2001) Dispersion reduction in pressure-driven flow through microetched channels. Anal Chem 73:504–513
7. Aris R (1956) On the dispersion of a solute in a fluid flowing through a tube. Proc R Soc A 235:67–77
8. Brenner H, Edwards DA (1993) Macrotransport Processes. Butterworth-Heinemann, Boston
9. Golay MJE (1981) The height equivalent to a theoretical plate of retentionless rectangular tubes. J Chromatogr 216:1–8
10. Dutta D, Ramachandran A, Leighton DT (2006) Effect of channel geometry on solute dispersion in pressure-driven microfluidic systems. Microfluid Nanofluid 2(4):275–290

Hydrogels

► Stationary Phases in Microchannels

Hydrogen Bond

Definition

A *hydrogen bond* is a special type of attractive interaction that exists between certain chemical groups of oppo-

site polarity. Although stronger than Van der Waals forces, the typical hydrogen bond is much weaker than both the ionic bond and the covalent bond. Within macromolecules such as proteins and nucleic acids, it can exist between two parts of the same molecule, and figures as an important constraint on such molecules' overall shape. As the name "hydrogen bond"implies, one part of the bond involves a hydrogen atom. The hydrogen atom must be attached to a relatively electronegative element.

Cross References

- ► Biosensor
- ► Chemical bonds

Hydrogen Passivation

Definition

Process where dangling bonds in the crystal lattice become bonded to hydrogen atoms, thus rendering them non-reactive and shifting their electronic bandgap to higher levels.

Cross References

- ► Fabrication of Self-Assembled Catalytic Nanostructures

Hydrophilic/Hydrophobic Patterning

TETSU TATSUMA
Institute of Industrial Science, University of Tokyo, Tokyo, Japan
tatsuma@iis.u-tokyo.ac.jp

Synonyms

Hydrophobic/hydrophilic patterning; Wettability patterning

Definition

Hydrophilic/hydrophobic patterning is to prepare two-dimensional patterns consisting of hydrophilic and hydrophobic regions on a solid surface.

Overview

Hydrophobic/hydrophilic patterning is a useful technique for preparing microfluidic channels. The technique is also used for the preparation of sensor arrays, biochips and electronic circuits because a solution of a functional molecule or a suspension of conducting nanoparticles can be trapped in the hydrophilic regions. There are several different ways for the pattering.

A hydrophilic surface is modified with an organic hydrophobic layer. The layer may be a self-assembled monolayer of a hydrophobic silane coupling agent such as a fluoroalkylsilane or an alkylsilane in the case of glass substrates or other surfaces with hydroxyl groups. In the case of a gold surface, the hydrophobic layer may be formed by treatment with a fluoroalkylthiol or an alkylthiol. The organic hydrophorbic layer is partially removed by irradiation with deep-UV light through a photomask [1, 2], near UV-light through a photomask coated with a TiO_2 photocatalyst (photocatalytic lithography) [3, 4] or scanned electron or ion beam [5, 6].

An elastomeric stamp [7, 8] and a normal photolithographic technique with a lift-off process can also be used for preparing hydrophobic patterns on a hydrophilic surface.

Introduction of nano- or micro-roughness onto the substrate surface enhances both hydrophilicity and hydrophobicity so that super-hydrophobic/super-hydrophilic patterns could be obtained.

Cross References

- ► Photolighography
- ► Self-Assembled Monolayers
- ► Surface Modification
- ► Wetting and Spreading

References

1. Dulcey CS, Georger JH Jr, Krauthamer V, Stenger DA, Fare TL, and Calvert JM (1991) Deep UV photochemistry of chemisorbed monolayers: patterned coplanar molecular assemblies. Science 252:551–554
2. Dressick WJ, Calvert JM (1993) Patterning of self-assembled films using lithographic exposure tools. Jpn J Appl Phys 32:5829–5839
3. Tatsuma T, Kubo W, Fujishima A (2002) Patterning of solid surfaces by photocatalytic lithography based on the remote oxidation effect of TiO_2. Langmuir 18:9632–9634
4. Kubo W, Tatsuma T, Fujishima A, Kobayashi H (2004) Mechanisms and resolution of photocatalytic lithography. J Phys Chem B 108:3005–3009
5. Rieke PC, Tarasevich BJ, Wood LL, Engelhard MH, Baer DR, Fryxell GE (1994) Spatially resolved mineral deposition on patterned self-assembled monolayers. Langmuir 10:619–622
6. Mino N, Ozaki S, Ogawa K, Hatada M (1994) Fabrication of self-assembled monolayer patterns by selective electron beam irradiation and a chemical adsorption technique. Thin Solid Films 243:374–377

7. Kumar A, Whitesides GM (1993) Features of gold having micrometer to centimeter dimensions can be formed through a combination of stamping with an elastomeric stamp and an alkanethiol "ink" followed by chemical etching. Appl Phys Lett 63:2002–2004
8. Kumar A, Biebuyck HA, Whitesides GM (1994) Patterning self-assembled monolayers: applications in materials science. Langmuir 10:1498–1511

Hydrophobic/Hydrophilic Microfluidics

► Surface-Directed Capillary Flow Systems

Hydrophobic/Hydrophilic Patterning

► Hydrophilic/Hydrophobic Patterning

Hysteresis

Synonyms

Memory; Memory-effect

Definition

Hysteresis is a property of systems (usually physical systems) that do not instantly follow the forces applied to them, but react slowly, or do not return completely to their original state: that is, systems whose states depend on their immediate history. For instance, if you push on a piece of putty it will assume a new shape, and when you remove your hand it will not return to its original shape, or at least not immediately and not entirely. The term derives from an ancient Greek word υστέρησις, meaning *deficiency*. The term was coined by Sir James Alfred Ewing.

H

ICEO

► Induced-Charge Electro-Osmosis

ICEP

► Induced-Charge Electrophoresis

IC Packaging

► Packaging (and Wire Bonding)

ICP Etching

Synonyms

DRIE (Deep reactive ion etching); Advanced silicon etching (ASE™); Bosch process; Switching etching; Multiplexed time etching

Definition

Inductively coupled plasma (ICP) etching is considered as the etching process using a high density plasma generated by the inductive coupling of RF power through an antenna, which is widely used in Si micromachining for high aspect ratio and deep microstructure fabrication.

Cross References

► Anisotropic Etching
► Reactive Ion Etching (RIE)
► Plasma Etching
► Silicon Micromachining

Illuminance

► Photometer

Imaging for Biosensors/Biochips/Microchips

► Infrared Imaging and Mapping for Biosensors

Immersed Boundary Method

HAOXIANG LUO
Department of Mechanical Engineering,
Vanderbilt University, Nashville, TN, USA
haoxiang.luo@vanderbilt.edu

Synonyms

Immersed interface method

Definition

The immersed boundary method is a numerical method in computational fluid dynamics where the flow boundary is immersed in the grid that does not conform with the boundary. In the immersed boundary method, special treatment has to be taken at the boundary to incorporate the boundary conditions.

Overview

The immersed boundary method was first introduced by Peskin [5] to simulate the blood flow in the heart. Since then a few variants have emerged and the method has been used to compute many flows with complex and/or moving geometries (Mittal and Iaccarino [4]). The distinguishing feature of this method is that the computations are done on either a Cartesian grid or a curvilinear grid which do not necessarily conform to the flow boundary.
When simulating flow in an irregular domain, the conventional method is to employ a structured or unstructured grid that conforms to the domain boundary. In either case, the grid usually has to be generated numerically, which may significantly increase the computational cost. Especially, if the flow boundary is moving, the grid has to be

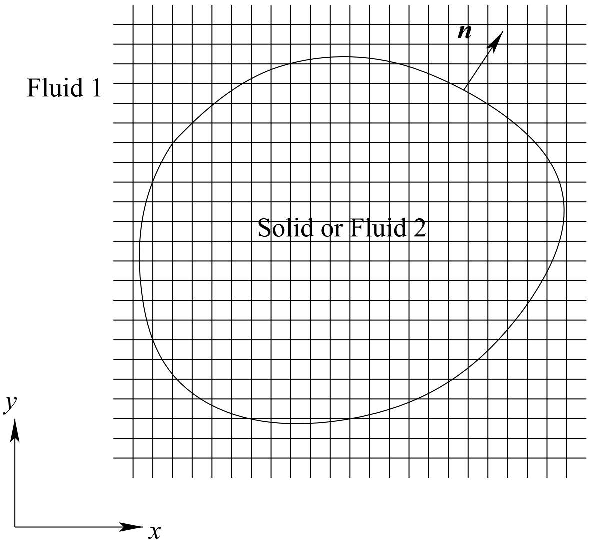

Immersed Boundary Method, Figure 1 Schematic the fluid–fluid or fluid–solid interface and the Cartesian grid used for the immersed boundary method

re-computed correspondingly, and the associated calculations may become very expensive. In contrast, the grid generation in the immersed boundary method is easy, and once generated, the grid may remain fixed even if the flow boundary moves. Furthermore, in the immersed boundary method, the calculations can be done efficiently on the structured grid. This is particularly attractive when compared to an unstructured grid based method.

The downside of the immersed boundary method is that implementation of the boundary conditions is not straightforward since the boundary does not coincide with any grid line. In addition, the immersed boundary method has less flexibility of distributing the grid in the vicinity of the boundary compared to the boundary-conforming methods. Figure 1 shows an example where a Cartesian grid is used to discretize the domain including both sides of the boundary. The fluid–fluid boundary or fluid–solid boundary intersects with the grid lines. The governing equations are discretized on the grid using a finite-difference method. Near the boundary, special treatment has to be taken in order to incorporate the boundary conditions. Different boundary treatments lead to different variants of the immersed boundary method.

In this article, we consider incompressible Newtonian flows and briefly describe the underlying numerical methodology of the immersed boundary method. We will use the Cartesian grids for the purpose of illustration. The same methodology can be applied to the compressible flows (e. g., Ghias et al. [2]) and on the curvilinear grids (e. g., Luo et al. [3]).

Basic Methodology

Fluid–Fluid Interface

Consider a two-fluid flow governed by the incompressible Navier–Stokes equations:

$$\rho\left(\frac{\partial \boldsymbol{u}}{\partial t}+\boldsymbol{u}\cdot\nabla\boldsymbol{u}\right)=-\nabla p+\mu\nabla^2\boldsymbol{u} \tag{1}$$

$$\nabla\boldsymbol{u}=0\,, \tag{2}$$

where $\boldsymbol{u}$, t, p are velocity, time, and pressure respectively, and $\mu=\mu_j$, $\rho=\rho_j$, $j=1$ or 2, are the viscosities and densities of the two fluids. The flow is subject to the kinematic condition requiring continuity of the velocity at the interface, and a dynamic condition expressing a balance between the hydrodynamic traction exerted on either side of the interface,

$$\Delta\mathbf{f}\equiv\left(\boldsymbol{\sigma}^{(1)}-\boldsymbol{\sigma}^{(2)}\right)\cdot\boldsymbol{n}=\gamma 2\kappa_m\boldsymbol{n}\,, \tag{3}$$

where $\boldsymbol{\sigma}^{(j)}$ is the Newtonian stress tensor in the jth fluid, $\boldsymbol{n}$ is the unit normal vector, and $\kappa_m=(1/2)\nabla\cdot\boldsymbol{n}$ is the mean curvature of the interface, as illustrated in Fig. 1. The interface is assumed to be clean. When a surfactant is present, Marangoni traction has to be added to the right-hand side of Eq. (3).

The momentum equation for both fluids can be combined into a generalized equation incorporating viscosity and density differences as well as the jump in the traction across the singular interface,

$$\rho\left(\frac{\partial \boldsymbol{u}}{\partial t}+\boldsymbol{u}\cdot\nabla\boldsymbol{u}\right)=-\nabla p+2\nabla\cdot(\mu\mathbf{E}) - \int_{\mathrm{I}} D_2(\boldsymbol{x}-\boldsymbol{x}')\Delta\mathbf{f}(\boldsymbol{x}')\,\mathrm{d}s(\boldsymbol{x}')\,, \tag{4}$$

where $\mathbf{E}=1/2\left(\nabla\boldsymbol{u}+\nabla\boldsymbol{u}^T\right)$ is the rate-of-deformation tensor, D_2 is Dirac's delta function, the jump in the interfacial traction, $\Delta\mathbf{f}$, is defined in Eq. (3), and $\boldsymbol{x}'$ is a point on the interface denoted by I. The surface integral in the equation is defined on the interface. It is reckoned that the physical properties of the fluid undergo a step discontinuity across the interface.

The basic idea of Peskin's immersed boundary method is to choose an approximate delta function to smear the interface, and therefore, the physical properties of the fluid and the interfacial traction undergo a smooth transition across the interface. One example of such approximation in the two-dimensional space is

$$D_2(\boldsymbol{x}-\boldsymbol{x}_{\mathrm{I}})\simeq\frac{1}{16\Delta x\Delta y}(1+\cos\hat{x})(1+\cos\hat{y})\,, \tag{5}$$

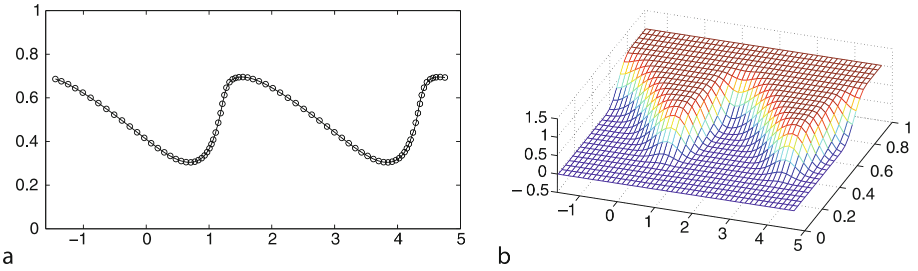

Immersed Boundary Method, Figure 2 (**a**) A snapshot of an evolving interface between two fluids, computed using the immersed boundary method, and (**b**) the corresponding mollifying function, $c(\boldsymbol{x})$ (simulation done by the author)

for $|x - x_\mathrm{I}| < 2\Delta x$ and $|y - y_\mathrm{I}| < 2\Delta y$, where $\boldsymbol{x}_\mathrm{I} = (x_\mathrm{I}, y_\mathrm{I})$ is a point on the interface, Δx and Δy are spatial discretization intervals associated with the finite difference method, and

$$\hat{x} \equiv \frac{\pi(x - x_\mathrm{I})}{2\Delta x}\,, \qquad \hat{y} \equiv \frac{\pi(y - y_\mathrm{I})}{2\Delta y}\,. \tag{6}$$

Next, a mollifying function, $c(\boldsymbol{x})$, can be defined such that its gradient is aligned with the surface normal $\boldsymbol{n}$,

$$\nabla c(\boldsymbol{x}) = -\int_\mathrm{I} D_2(\boldsymbol{x} - \boldsymbol{x}')\,\boldsymbol{n}(\boldsymbol{x}')\,\mathrm{d}l(\boldsymbol{x}')\,, \tag{7}$$

where l is the arc length along the interface. The mollified fluid properties are then described as $\mu(\boldsymbol{x}) = \mu_1 + (\mu_2 - \mu_1)c(\boldsymbol{x})$, and $\rho(\boldsymbol{x}) = \rho_1 + (\rho_2 - \rho_1)c(\boldsymbol{x})$. The mollifying function can be obtained by taking the divergence of Eq. (7) and solving the result-in Poisson equation for c. An example of the mollifying function for a two-layer flow is illustrated in Fig. 2, where the function takes the value of of zero in Fluid 1 and unity in Fluid 2, and undergoes a quick but smooth transition across the curved interface.

Using the approximate delta function, the integral term on the right-hand side of Eq. (4) can be evaluated for any collocation points, $\boldsymbol{x}$, on the Cartesian grid using a surface integration scheme. As a result, the surface force, $\Delta\mathbf{f}$, is smeared and distributed into the flow near the interface, acting as a body force. When marching the flow field in time, the interface is updated at each step using a Lagrangian method

$$\frac{\mathrm{d}\boldsymbol{x}_\mathrm{I}}{\mathrm{d}t} = \boldsymbol{u}(\boldsymbol{x}_\mathrm{I}, t)\,, \tag{8}$$

where the velocity at the interface, $\boldsymbol{u}(\boldsymbol{x}_\mathrm{I}, t)$, is interpolated from the flow field. The mollified fluid properties and distributed interfacial force are computed for the updated interface, and the generalized Navies–Stokes equations can be solved using a standard finite-difference method as if there were no interface. For further details, readers are referred to Blyth et al. [1].

When the fluid–fluid interface has a massless elastic membrane, the jump in the traction across the membrane, $\Delta\mathbf{f}$ in Eq. (4), is computed using the physical law that describes the constitutive relationship between the stress in the membrane and the membrane deformation. The generalized Navies–Stokes equations can be solved in the same way as for the pure fluid–fluid interface (e. g., Peskin [5]).

Fluid–Solid Interface

In some variants of the immersed boundary method dealing with the boundary between a fluid and a solid body, the fictitious fluid is introduced inside the solid body, and a boundary force, $\boldsymbol{F}$, in place of $\Delta\mathbf{f}$ in Eq. (4), is distributed into the augmented flow field in the same way as described for the fluid–fluid interface (e. g., Goldstein et al. [6]). To impose the no-slip and no-penetration boundary conditions at the interface, $\boldsymbol{F}$ is modeled as

$$\boldsymbol{F} = \alpha \int_0^t \boldsymbol{u}(\boldsymbol{x}_\mathrm{I}, \tau)\,\mathrm{d}\tau + \beta\boldsymbol{u}(\boldsymbol{x}_\mathrm{I}, t)\,. \tag{9}$$

where $\boldsymbol{u}(\boldsymbol{x}_\mathrm{I}, \tau)$ is the velocity at the boundary and α, β are the coefficients. The force has to be computed iteratively such that the boundary velocity is brought to the specified condition.

In some other immersed boundary methods for a fluid–solid interface, the no-slip/no-penetration conditions are enforced via an interpolation scheme (e. g., Mittal [4]). To carry out the interpolation, the variables on the grid points near the interface are used, and the interpolation may involve the "ghost nodes" defined outside the flow domain. In these methods, the boundary conditions are satisfied at the exact location of the interface. There is no need to compute the boundary force, and the interface may remain sharp.

I

Cross References

► Finite Volume and Finite Difference Methods for Modeling and Simulation
► Interface Tracking Schemes for Free-Surface Flows

References

1. Blyth MG, Luo H, Pozrikidis C (2006) Stability of axisymmetric core–annular flow in the presence of an insoluble surfactant. J Fluid Mech 548:207–235
2. Ghias R, Mittal R, Dong H (2007) A sharp interface immersed boundary method for compressible viscous flows. J Comput Phys 225(1):528–553
3. Luo H, Blyth MG, Pozrikidis C (2007) Two-layer flow in a corrugated channel. J Eng Math (in press)
4. Mittal R, Iaccarino G (2005) Immersed boundary methods. Annu Rev Fluid Mech 37:239–261
5. Peskin CS (1977) Numerical Analysis of Blood Flow in the Heart. J Comput Phys 25:220–252
6. Goldstein D, Handler R, Sirovich L (1993) Modeling a no-slip flow boundary with an external force field. J Comp Phys 105:354–366

Immersed Interface Method

► Immersed Boundary Method

Immobilized Enzyme Biosensor

► Microfluidic Bioreactors

Immobilized Enzyme Reactor

► Microfluidic Bioreactors

Immobilized Microfluidic Enzyme Reactor (IMER)

► Microfluidic Bioreactors

Immunoassay

Definition

An immunoassay is an analytical procedure that takes advantage of the very specific binding between antibodies and antigens to evaluate the characteristics of a system. Immunoassays can be classified as competitive or non-competitive. Competitive assays introduce a known amount of antibody-antigen complex to the sample and the amount of antigen displaced from the complex is used to infer the amount of antigen present (i. e., by *competing* with the antigen already bound) in the sample. Non-competitive assays measure the amount of antigen present in a sample by quantifying the amount of antibody-antigen complex formed when the sample is exposed to an antibody.

Immunoassays can also be classified as homogeneous or heterogeneous. In a homogeneous immunoassay, antigen, antibody, and sample are mixed in the solution phase, while in a heterogeneous assay, one constituent (typically the antibody) is immobilized on a solid surface while the other constituents are delivered via the solution phase.

Cross References

► Biosensors Using Lasers
► DNA Array
► Fluorescent Labeling
► Lab-on-Chip Devices for Immunoassay
► Lab-on-Chip Devices for Protein Analysis
► Protein Array
► Protein Microarrays
► Proteomics in Microfluidic Devices

Immunochemistry

► Lab-on-Chip Devices for Immunoassays

Immunodiffusion

► Lab-on-Chip Devices for Immunoassays

Impact Evaporation

► Sputtering for Film Deposition

Impedance

Definition

The effective resistance of a system to an alternating current signal.

Cross References

► Sputtering for Film Deposition

Impedance Biosensors

► Impedimetric Biosensors for Nano- and Microfluidics

Impedance Measurements of Cells

TAO SUN, HYWEL MORGAN
Nanoscale Systems Integration Group
School of Electronics and Computer Science,
University of Southampton, Highfield, Southampton, UK
ts5@ecs.soton.ac.uk

Synonyms

Dielectric spectroscopy; Single cell impedance spectroscopy

Definition

Impedance measurements are performed by applying an AC excitation voltage to an unknown system whilst measuring the current. The ratio of the excitation voltage to the current gives the complex impedance of the system. Impedance measurements of cells provide data on the intrinsic dielectric properties of the cells.

Overview

A biological cell is the basic structural and functional unit of all living organisms; often called the *building block of life*. Working at the cellular level is of fundamental importance for biomedical and clinical applications.

Cellular analysis requires a combination of biophysical and technological approaches, including counting, manipulation (trapping/focusing/sorting/rotating) and identification (staining/labeling) of cells. Traditional analysis is performed with bulk techniques, which are well established. However, measurements on large populations of cells only provide population averaged information. Individual cells, which may look identical, have different characteristics and behaviour. High throughput single cell analysis platforms offer the unique ability to characterize large numbers of individual cells at high speed. Microscale devices can be used for single cell analysis. Standard laboratory processes, including sample preparation, chemical reaction and synthesis can all be integrated on a single Lab-on-a-Chip (LOC).

Fluorescence spectroscopy is performed by binding antibody conjugated fluorescent probes to the cells and then performing analysis in a flow cytometer. Electrical measurement of cells are performed using high speed dielectric/impedance spectroscopy, a technique which is non-invasive and label-free.

The dielectric properties of biological cells and tissues have been of interest for nearly a hundred years. The early work of Maxwell [1] and Wagner [2], Fricke [3], Cole [4] and Schwan [5], amongst others laid the foundations for this field of research; see [6] for a review. In dielectric/impedance spectroscopy, the dielectric properties of a system are determined by applying a frequency-dependent excitation signal and measuring the response. Conventionally, a small AC voltage, $\tilde{U}(j\omega)$, over a range of frequencies is used as the excitation signal. The electrical current response, $\tilde{I}(j\omega)$, is measured and the complex impedance of the system, $\tilde{Z}(j\omega)$, is given by:

$$\tilde{Z}(j\omega) = \frac{\tilde{U}(j\omega)}{\tilde{I}(j\omega)} = \tilde{Z}_{\mathrm{re}}(\omega) + j\tilde{Z}_{\mathrm{im}}(\omega)\,,$$

where $\tilde{Z}_{\mathrm{re}}(\omega)$ and $\tilde{Z}_{\mathrm{im}}(\omega)$ are the real and imaginary parts of the complex impedance, respectively. The real part is called resistance while the imaginary part is called reactance.

The magnitude and phase angle of the complex impedance are:

$$\left|\tilde{Z}(j\omega)\right| = \sqrt{\left[\tilde{Z}_{\mathrm{re}}(\omega)\right]^2 + \left[\tilde{Z}_{\mathrm{im}}(\omega)\right]^2}$$

and

$$\angle\tilde{Z}(j\omega) = \arctan\left(\frac{\tilde{Z}_{\mathrm{im}}(\omega)}{\tilde{Z}_{\mathrm{re}}(\omega)}\right)\,.$$

In impedance-based microfluidic cytometers, microelectrodes are fabricated inside a microchannel and the impedance signals of large numbers of cells are measured at high speed, one cell at a time (Fig. 1). The first cytometer capable of measuring the electrical properties of single cells, was developed by Coulter [7]. The device measures the DC resistance between two electrically isolated fluid-filled chambers as cells pass through a small connecting orifice. For a fixed sized orifice, the change in electrical current can be used to count and size the cells. Recent micro-chip designs now use AC signals at high frequencies to give information on cell dielectric properties as well as cell volume [8–10].

A typical example of on-chip single cell impedance measurement is shown in Fig. 1. Two pairs of microelectrodes are fabricated in a microchannel which is typically 20 to 40 μm high and wide. The two electrodes allow a differential impedance measurement to be made. One pair is used for sensing the electrical signal fluctu-

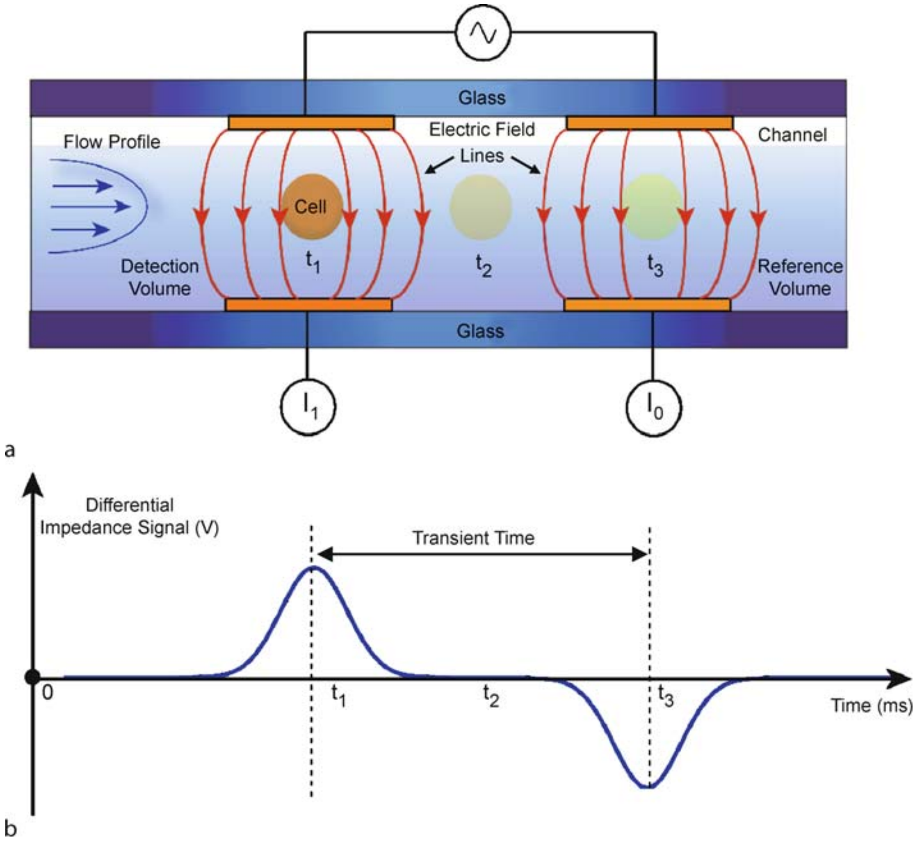

Impedance Measurements of Cells, Figure 1 (**a**) Diagram showing the impedance analysis chip and a single cell flowing through the microfluidic channel. In the differential measurement scheme, the difference between the currents passing through the detection and reference volume is measured. The electrodes are typically 20 to 40 μm wide and long. (**b**) Diagram showing the variation of the differential signal as the particle passes through the channel

ation induced by the cell, the other measures the electrical signal passing through the unperturbed medium as an electrical reference. As the cell passes through the AC electric field in the channel (under pressure-driven flow), there is a change in the impedance which is indicative of the size, shape and dielectric properties of the cell. This impedance signal is sensed as a changing current signal by the bottom microelectrodes. A positive and negative peak is observed, as the cell passes though the channel (Fig. 1b).

For small cells (low volume fraction), the complex permittivity of a cell in suspension is determined by Maxwell's mixture theory [1]. This approach works well for volume fractions less than 10%; the analysis was extended for higher volume fraction by Bruggeman [11] and Hanai [12]. The characteristics of the impedance spectrum of the suspending system can vary over different frequency ranges. A cell has a thin insulating membrane, and the measured permittivity of a suspension of cells has a high value at low frequencies due to charging of this membrane. As the frequency increases, the value of the permittivity decreases, approaching that of the suspending medium. Using a differential measurement scheme, and for a cell suspended in physiological medium, the cell size is determined at low frequencies (< 1 MHz). The cell membrane capacitance can be measured in a frequency window between 1 – 10 MHz and at even higher frequencies, the properties of the cell cytoplasm are probed. The technique can be used to discriminate between different cell types (e. g. sub-populations of leukocytes), measure the effects of chemical agents on cells, or probe changes in cell structure.

In summary, impedance measurements of single cells gives information on cell size, membrane capacitance and cytoplasm conductivity. It allows the identification and differentiation of cells sub-populations at high speed. It is non-invasive and label-free, and has a wide range of biotechnological and biomedical applications.

Cross References

- ► Capacitance Method
- ► Electrokinetic Motion of Cells and Nonpolarizable Particles
- ► Cell Assays

References

1. Maxwell JC (1954) A treatise on Electricity and Magnetism. Dover, New York
2. Wagner KW (1914) Electricity of the dielectric behaviour on the basis of the Maxwell theory. Arch J Elektrotech 2:371–387
3. Fricke H (1925) The electric capacity of suspensions with special reference to blood. J Gen Physiol 9:137–152
4. Cole KS (1928) Electric impedance of suspensions of spheres. J Gen Physiol 12:29–36
5. Schwan HP (1957) Electrical properties of tissues and cell suspensions. Adv Biol Med Phys 5:147–209
6. Morgan H, Sun T, Homes D, Gawad S, Green NG (2007) Single cell dielectric spectroscopy. J Phys D: Appl Phys 40:61–70
7. Coulter WH (1956) High speed automatic blood cell counter and cell analyzer. Proc Natl Electron Conf 12:1034–1040
8. Gawad S, Cheung K, Seger U, Bertsch A, Renaud P (2004) Dielectric spectroscopy in a micromachined flow cytometer: theoretical and practical considerations. Lab Chip 4:241–251
9. Cheung K, Gawad S, Renaud P (2005) Impedance spectroscopy flow cytometer: on-chip label-free cell differentiation. Cytom Part A 65A:124–132
10. Morgan H, Holmes D, Green NG (2006) High speed simultaneous single particle impedance and fluorescence analysis on a chip. Curr Appl Phys 6:367–370
11. Bruggeman DAG (1935) Berechnung verschiedener physikalischer Konstanten von heterogene Substanzen; I Dielektrizitätskonstanten und Leitfähigkeiten der Mischkörper aus isotropen Substanzen. Ann Phys Leipz 24:636–664
12. Hanai T, Koizumi N, Irimajiri A (1975) A method for determining the dielectric constant and the conductivity of membrane-bounded particles of biological relevance. Biophys Struct Mech 1:285–294

Impedimetric Biosensors for Nano- and Microfluidics

Liju Yang[1], Anthony Guiseppi-Elie[2]

[1] Biomanufacturing Research Institute & Technology Enterprise, and Department of Pharmaceutical Sciences, North Carolina Central University, Durham, NC, USA

[2] Center for Bioelectronics, Biosensors, and Biochips (C3B)
Department of Chemical and Biomolecular Engineering, and Department of Bioengineering, Clemson University, Clemson, SC, USA

lyang@nccu.edu, guiseppi@clemson.edu

Synonyms

NEMS-based biosensors; Impedance biosensors; Nanobiosensors for nano- and microfluidics; Biological sensors; Lab-on-a-Chip; Diagnostic biochip; MEMS biosensor

Definition

► Biosensors are bioanalytical systems defined by the integration of four key components: sample presentation, biotransduction, instrumentation, and data output. Central to the biosensor system is the ► biotransducer that converts the activity (concentration) of the targeted analyte into a proportional signal via an intimate combination of a biological recognition membrane layer and a physicochemical transducer. The biological recognition membrane provides its specificity by the use of biomolecules such as DNA, RNA, PNA, enzymes, antibodies, enzyme-linked antibodies, and receptors, and may use subcellular fragments such as mitochondria and cell membrane components (receptors), whole cells (bacteria or mammalian cells), and/or tissue slices (liver, brain, etc.). An impedimetric biosensor is constructed by immobilizing biological recognition elements onto an electrode surface. It reports, through measurement and/or monitoring, the targeted analyte through the output of an ► electrical impedance signal made proportional to analyte activity.

Overview

Biosensors have gained in popularity over the last two decades because of the growing need to offer an analytical footprint considerably smaller than laboratory-based instruments. This growing need is nowhere more pressing than in clinical molecular diagnostics, home health care, "theranostics" (the molecular linkage of diagnostics with therapeutics, particularly with regard to personalized patient dosing), and global security from chemical and biological threats and potential terror attacks. In the areas of most promising growth it is the need for rapid, point-of-concern decision making that motivates attention to biosensors. In these cases, the biosensor system may serve as a screening test for further confirmatory tests performed at a remote site or molecular diagnostics laboratory, thereby eliminating the cost burden associated with running large numbers of costly confirmatory tests when they are not warranted, or it may itself be a confirmatory test intended to elicit actionable decisions at the point of concern.

The advent of micro- and nanofluidics has led to a resurgence of interest in biosensors; in part because the purposeful manipulation of small volumes of liquids within a single device platform allows the streamlined integration

of many sample preparation operations with the biosensor detection and monitoring system. Two major criticisms of biosensor systems, reflecting their poor commercial success to date, have been their continued reliance on traditional, operator–intensive sample preparation and manipulation prior to bioanalytical measurement and the need for relatively large amounts of sample. By successfully integrating micro- and nanofluidics with biosensors, many of the unit operations associated with sample preparation and presentation, such as separation (cell or biomolecule), mixing, incubation, and concentration, may be performed directly in a Lab-on-a-Chip format. Also, the use of microliter and nanoliter volumes implies the use of smaller sample volumes, smaller quantities of usually costly reagents, and greater analytical sensitivity.

Impedance, as a transduction principle, has been applied to biosensor systems and so-called impedimetric biosensors. It has been regarded as an effective way for sensing the formation of antigen–antibody, biotin–avidin complex, oligonucleotide–DNA interactions, etc., on electrode surfaces by probing the features of the interfacial properties (capacitance, electrode transfer resistance, etc.) of the electrode. The advances in microfabrication technologies have launched the use of microfabricated ▶ interdigitated microelectrodes (IMEs) in impedimetric biosensors. An IME consists of a pair of microband arrays of digit electrodes that mesh with each other. The width of digit electrodes and the interdigit space is in the micrometer to nanometer range. The dimensional compatibility of the IME with biological entities makes it an obvious choice for its ability to detect sensitively the biological reactions on the electrode surface without any amplification step, achieving label-free biosensing. Besides, microelectrodes in general have great advantages over conventional electrodes for analytical measurements, such as low ohmic drop of potential, applied high potential scanning, high signal-to-noise ratio, rapid attainment of steady state, and the use of small volumes of solutions. Attractively, the integration of IMEs with micro- and nanofluidics would allow the biosensor to perform in a Lab-on-a-Chip format. The basic methodology for impedance measurements, the use of IMEs, and the immobilization of biological elements onto microelectrodes are illustrated below.

Basic Methodology

Electrical and Electrochemical Impedance

Generally, there are two categories in impedance measurement: electrical and electrochemical impedance. Electrical impedance (EI) is a two-electrode measurement performed using a lock-in amplifier and function generator or frequency response analyzer (FRA) with a pair of electrodes, the working electrode (WE) and counter electrode (CE), which may be of equal or different areas. Electrochemical impedance (ECI) is a three-electrode measurement performed using similar instruments along with a front-end potentiostat. The electrode arrangement includes an additional electrode, the reference electrode (RE), which contributes a half-cell potential, to which the potentiostat references its interrogating voltage. Figure 1 shows the schematic setup for the measurement of EI and ECI. In both cases the instrumentation delivers a sinusoidally varying and interrogating potential of specified frequency to the CE and the ensuing AC current is measured at the WE. The transfer function, the ratio of V/I in the complex plane, allows a measure of the impedance of the device under test (DUT). The applied excitation voltage is sinusoidal and given by

$$V = V_{\mathrm{m}} \sin \omega t \tag{1}$$

in which ω is the radial frequency, V_{m} is the maximum voltage at the peak, and V is the voltage at any given instant. The AC response (i) is characterized by both its amplitude (i_{m}) and its phase shift (θ) with respect to the applied AC voltage, as follows:

$$i = i_{\mathrm{m}} \sin(\omega t + \theta) \tag{2}$$

The ratio of the amplitudes of the applied and the response signal ($V_{\mathrm{m}}/i_{\mathrm{m}}$) and the phase shift between these signals (θ) is used to determine the impedance of the DUT, which can be represented as a complex number. The real component of impedance is known as the resistance, R, and the imaginary component, X, is known as the reactance:

$$Z = R + jX \tag{3}$$

The reactance, X, describes that part of the DUT that behaves as a capacitor or inductor while the resistance term, R, describes that part of the DUT that behaves as a resistor; reactance indicates charge storage aspects of the DUT and resistance indicates dissipative aspects. The magnitude of the impedance, determined by the square root of the sum of the squares of the resistance and reactance [1], and the phase angle are determined by

$$|Z| = \sqrt{R^2 + X^2} \qquad \text{and } \theta = \arctan X/R \tag{4}$$

When a range of frequencies is applied to the DUT, both EI and ECI techniques are called spectroscopies, i. e., electrical impedance spectroscopy and electrochemical impedance spectroscopy. Electrochemical impedance spectroscopy (EIS) profiles, measured as a function of the

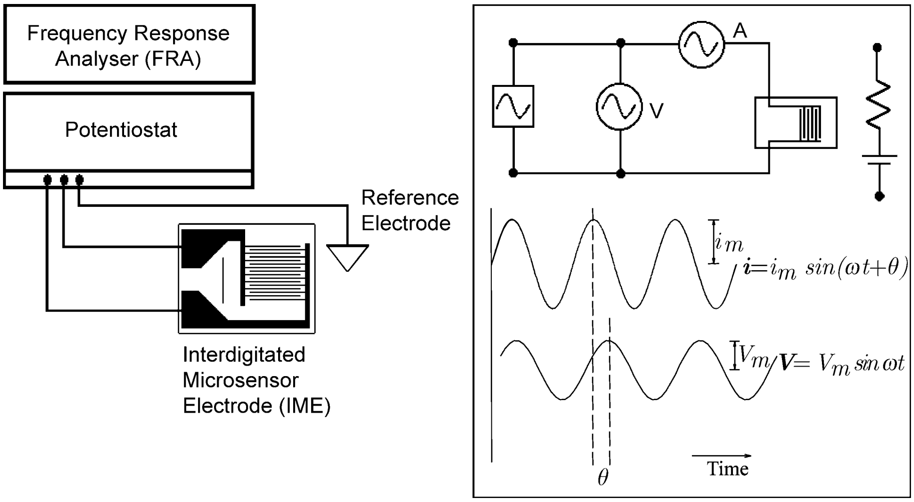

Impedimetric Biosensors for Nano- and Microfluidics, Figure 1 The basic instrumental setup for the measurement of electrical impedance and/or electrochemical impedance spectroscopies and impedimetry

interrogating frequency, can be presented by two popular plots: Complex plane impedance diagrams, sometimes called Nyquist or Cole–Cole plots, and Bode ($|Z|$ and θ) plots (Fig. 2). As the impedance, Z, is composed of a real and an imaginary part, the Nyquist plot shows the relationship of the imaginary component of impedance, Z'' (on the Y-axis), to the real component of the impedance, Z' (on the X-axis), at each frequency. A diagonal line with a slope of 45° on a Nyquist plot represents the Warburg impedance which would be equivalent to a phase shift of 45° on a Bode plot. The semicircle is characteristic of a single *time constant*. Electrochemical impedance plots often contain several time constants, but often only a portion of one or more of the semicircles can be seen. However, the major shortcoming of a Nyquist plot is that the plot does not explicitly show the frequency data. The two-component Bode plot is a comprehensive and detailed representation of the frequency dependence of the impedance and presents the magnitude of the impedance, $|Z|$, and the phase shift, θ, in relation to the interrogating frequency. Specific regions of the spectrum can be linked to characteristic frequency ranges [1].

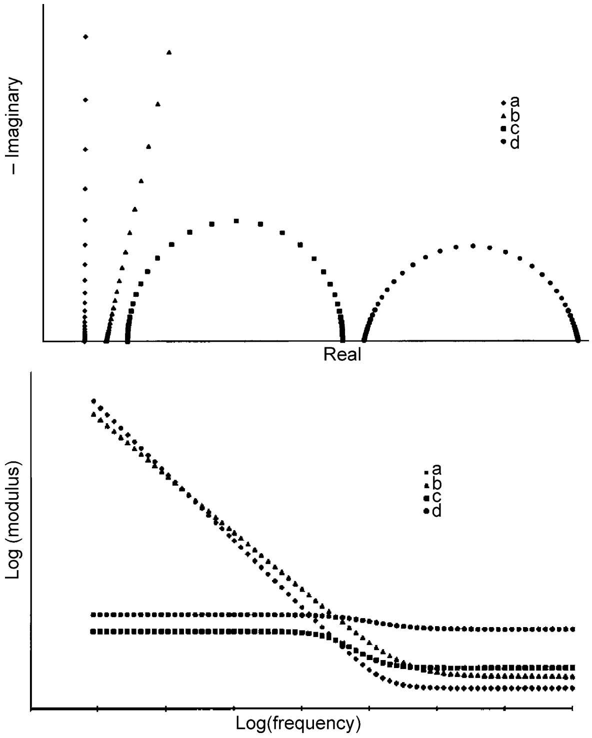

Impedimetric Biosensors for Nano- and Microfluidics, Figure 2 Representative (**a**) Complex plane diagrams (Nyquist or Cole–Cole plots) and (**b**) Bode plots from electrochemical impedance spectroscopy measurements

EIS data are generally interpreted based on defining an appropriate equivalent circuit model that best fits the acquired frequency-dependent real and imaginary data. An equivalent electrical circuit usually consists of a specific arrangement of resistors, capacitors, and inductors in series or parallel (or both) combinations. Table 1 lists the common circuit elements and their impedances and phase shifts. The impedance of a resistor is independent of frequency and has only a real component. The current through a resistor is always in phase with the voltage. The impedance of a capacitor decreases as frequency increases and has only an imaginary impedance component. The current through a capacitor is phase shifted by −90° with

Impedimetric Biosensors for Nano- and Microfluidics, Table 1 Impedance properties of common electrical elements

Element	Impedance	Phase shifted*
Resistor	$Z = R$	0
Capacitor	$Z = 1/j\omega C$	−90
Inductor	$Z = j\omega L$	90

Z, R, C, and L stand for impedance, resistance, capacitance, and inductance; $\omega = 2\pi f$, where f is frequency (Hz); $j = \sqrt{-1}$.
* Indicates phase shift with respect to voltage.

respect to the voltage. An inductor's impedance increases as frequency increases and has only an imaginary component. The current through an inductor is phase shifted by 90° with respect to the voltage. However, the inductance is usually negligible in electrochemical measurements.

To be useful, the elements in an equivalent circuit should always have physicochemical significance in the physical electrochemistry of the tested system. For example, in most equivalent circuits, a resistor is used to represent the solution resistance, and the double-layer capacitance is represented by a capacitor since it closely resembles a pure capacitance. Considering a system that is treated as a series combination of a resistor and a capacitor, the impedance of the system (Z) is a function of its resistance (R), capacitance (C), and applied frequency (f):

$$Z = R_s + \frac{1}{j2\pi fC} \tag{5}$$

Microfabricated IME Devices for Impedimetry

For integration with micro- and nanofluidics, a suitable format for the two- and three-electrode arrangements used in impedimetry is that based on the microlithographically fabricated, co-planer, interdigitated microsensor electrode array (IME or IDA). Each sensor element of the array consists of a pair of opposing platinum, gold, or indium tin oxide (ITO) electrodes of 1 – 5 mm digit length and of digit width and separation that may be equal or unequal in the range 100 nm to 10 µm. These dimensions serve to define the serpentine length (width of the channel), the interdigit space (length of the channel), and the overall area of interdigitation. The metallization is typically 10 nm of magnetron sputter-deposited titanium/tungsten (Ti/W), which serves as an adhesion-promoting layer for the metals (chromium is entirely inappropriate for the electrolytic environment), followed by 100 nm of electron-gun-deposited platinum, magnetron sputter-deposited gold, or is entirely of ITO (ITO has good adhesion to most substrates). The substrate may be oxidized silicon with a minimum 100 nm of thermally grown oxide or may be a highly polished, electronics-grade borosilicate glass such as Schott D262. These independently addressable interdigitated elements are sufficient for two-electrode impedimetry or electrical impedance spectroscopy. However, they may be accompanied by a large-area counter electrode of area 100 to 1000 times that of the area of each region of interdigitation. Such a counter electrode would serve to support the electrochemical oxidation or reduction of electroconductive layers (e. g., conductive, electroactive polymers) that may be deposited or grown on each region of interdigitation. Finally, a reference electrode of silver/silver chloride may also be included to allow for electrochemical impedance spectroscopy. This reference electrode provides the reference potential for the electrochemical impedance determination of each multiplexed element of the array. This reference electrode, one on each chip or associated with each sensing element of the chip, may be fabricated of platinum and subsequently electroplated with silver. This process of silverization introduces an additive step that essentially creates a new metal surface on the device. Similar electroless and electroplating options may be explored in creating arrays of different metals, e. g., gold and palladium. The subtractive steps in the microlithography that serve to define the conductor pattern may be via ion bean milling or lift-off techniques. Figure 3 summarizes the several steps in the microlithographic preparation of IME devices.

EIS of Microfabricated IME Devices

In the case of the impedimetric IME sensor, the two sets of electrodes of the IME can be two poles in a two-electrode configuration for electrical impedance measurements. Figure 4 shows 4a a picture, 4b a schematic, 4c the equivalent circuit model for the IME device, and 4d the Bode plot of the electrochemical impedance spectrum obtained in aqueous 0.01 M phosphate-buffered saline containing 10 mM ferricyanide at room temperature. The equivalent circuit for the IME device in Fig. 4c consists of an ohmic resistance (R_s) of the electrolyte between two sets of electrodes and the double-layer capacitance (C_{dl}), an electron transfer resistance (R_{et}), and Warburg impedance (Z_W) around each set of electrodes [2]. R_s and the two branch circuits are connected in series, since all the current must pass through the uncompensated resistance of the electrolyte and each set of the array electrodes. Each of the two identical branch circuits represents the behavior of each set of electrodes. Considering the total current through the electrode surface is the sum of faradic current (i_f) and double-layer charging current (i_c), the Warburg impedance is considered to be in series with the electron transfer resistance and both of them

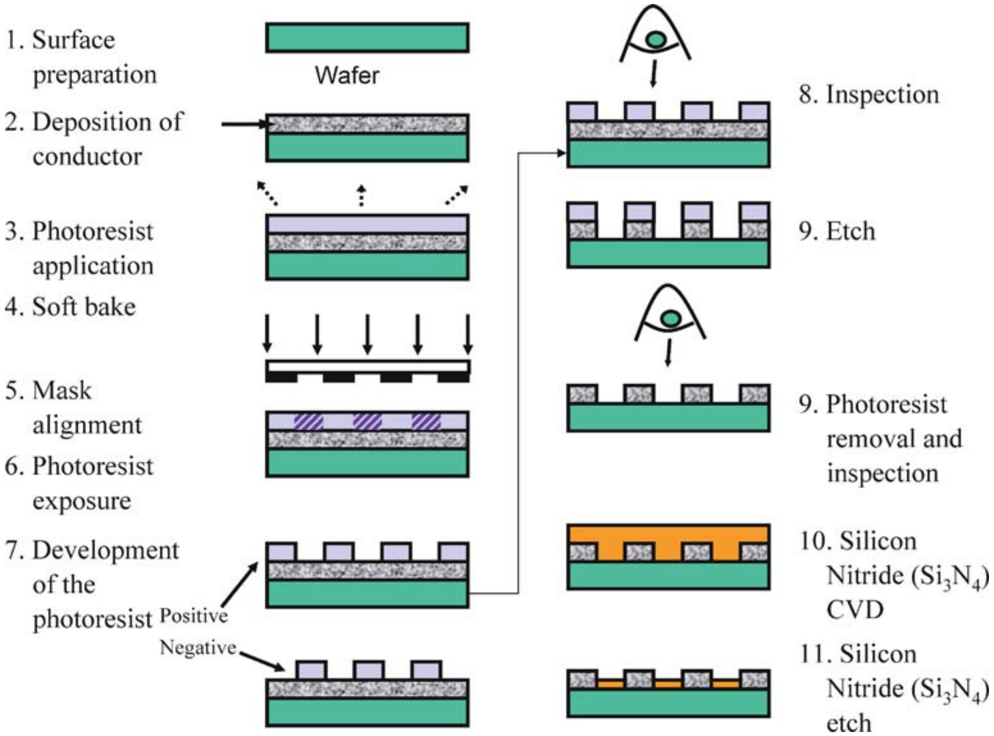

Impedimetric Biosensors for Nano- and Microfluidics, Figure 3 Schematic illustration of the several steps involved in the preparation of microlithographically fabricated interdigitated microsensor electrode (IME) arrays

are connected in parallel with the double-layer capacitance. Among these electrical elements, R_s and Z_W represent the properties of the bulk solution and the diffusion of the redox probe, respectively, whereas C_{dl} and R_{et} depend on the dielectric and insulating features at the electrode/electrolyte interface, respectively. The electrochemical impedance spectrum in Fig. 4d shows a typical Bode plot for the IME system with mixed kinetic and charge transfer control. The agreement between the measured data (solid line) and the fitting spectrum (broken line) indicates that this equivalent circuit provides a feasible, if not unique, model to describe the performance of the IME electrode system.

Conferring Biospecificity to IME Devices

Biospecificity is the property of the ►biorecognition membrane of the biotransducer that is conferred by the purposeful use of a bioactive receptor. There exists a wide range of possible approaches to the conferment of biospecificity to impedimetric array biosensors. These methods vary somewhat depending upon the bioactive receptor to be immobilized (molecule, subcellular fragment, cell, or tissue). However, these methods have one major purpose: to confer the molecular recognition and specificity inherent to the bioactive receptor to the biotransducer in a manner that maximizes the sensitivity of the physicochemical transducer that lies beneath. Amongst the various ►bioimmobilization approaches are:

- adsorption (physical, chemical, and electrostatic),
- adsorption followed by covalent cross-linking,
- covalent tethering, and
- entrapment (physical or covalent) within host matrices (e. g., polymers, polymeric hydrogels, and sol–gels).

Regardless of the specific linking chemistry and substrate employed, the key goals in all biomolecule immobilization strategies are:

- reproducible, high-density coverage of the biomolecule on the substrate,
- the orientation of the biomolecule for efficient kinetics of the biological reaction,
- minimal background and nonspecific adsorption to the support or substrate,
- improved sensitivity, and
- long-term stability (retained bioactivity) of the immobilized biomolecule.

These, of course, also apply to the biomolecule immobilization in impedimetric IME devices.

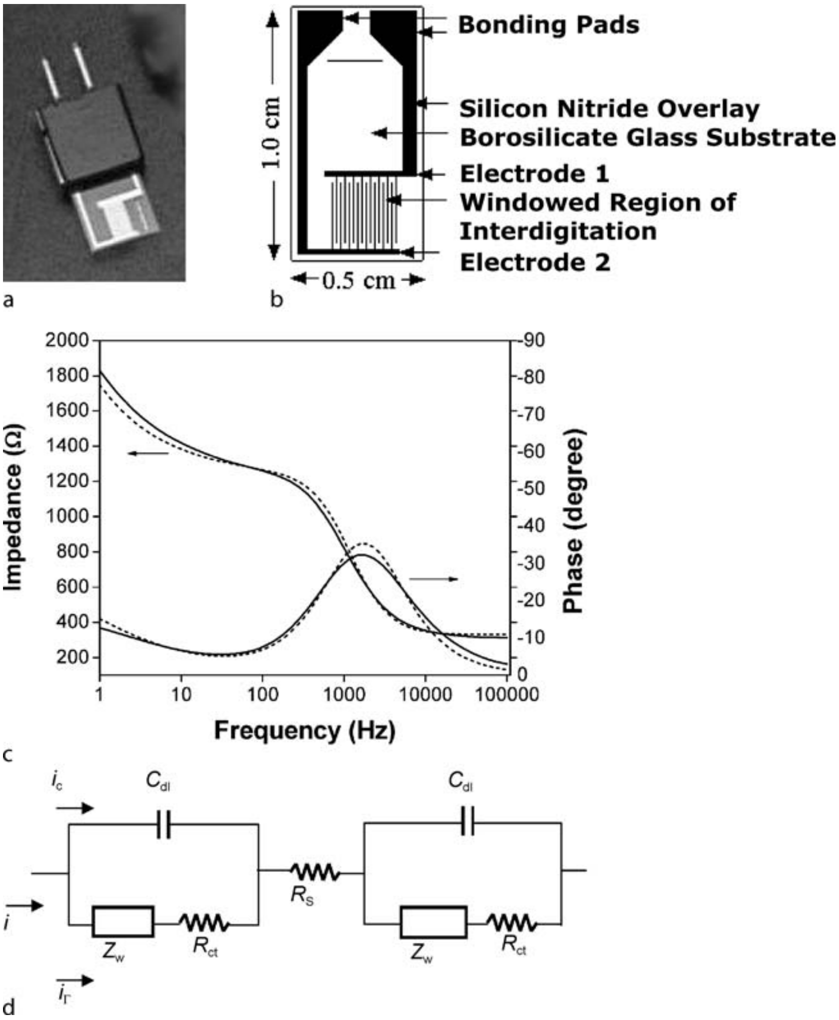

Impedimetric Biosensors for Nano- and Microfluidics, Figure 4 (**a**) A picture of a microfabricated interdigitated microsensor electrode, (**b**) a schematic illustration of the IME, (**c**) the Bode plot of $|Z|$ and θ obtained from the frequency dependent interrogation of an IME 1525.3 ITO device in 0.01 M PBS containing 10 mM $[Fe(CN)_6]^{3-/4-}$ (solid line, 10 mV p-t-p, offset = 0) and the corresponding fitting data (dotted line), and (**d**) the equivalent circuit model derived from the NLLS fitting of the impedance data

The most common immobilization of biomolecules onto an IME device for impedimetric detection is the covalent linkage by the use of organosilane chemistries on the exposed glass of the interdigit space and alkanethiol chemistries on the gold digits. However, immobilization of the biological elements to the interdigit space between the electrodes or to the digit electrode surface affects the final signal in impedance detection through different response mechanisms. The impedimetric response of an IME device with biological molecules immobilized on the digit electrodes arises principally from the change in dielectric constant at the interface as water and ions become excluded following biological binding reactions. Such responses are manifest largely in the capacitative term of the complex impedance and are generally not very sensitive to the biological reactions because the alkanethiol layer has already contributed appreciably to the capacitative character of the electrified interface. The impedimetric response of an IME device with biomolecules immobilized within the interdigit space arises principally from the change in ion density within the electric field formed between the electrodes. Such responses are manifest in the solution resistance term of the complex impedance and are generally sensitive to biological reactions occurring on the device.

Here we describe examples of the immobilization of DNA, enzymes, and antibodies to IME devices at the interdigit space for impedimetic biosensing. In general this proceeds by the cleaning (activation) and subse-

quent surface modification of the IME device using organosilane chemistry on the exposed glass. A commonly used covalent coupling protocol uses 1-(3-dimethylamino-propyl)-3-ethylcarbodiamide hydrochloride (EDC) and *N*-hydroxysulfosuccinimide (sulfo-NHS) to activate carboxylic acid groups followed by coupling to primary amines of the biomolecules. An additional requirement is that the silanol that is condensed on the gold digits must be removed to expose the interrogating metallic electrodes. This may be achieved by repeatedly electrochemically scanning the IME device in 0.1 M H_2SO_4 until a stable gold oxidation/reduction cyclic voltammogram is obtained.

Impedimetric Genosensors Using Immobilization of Oligomeric DNA

Figure 5 illustrates 5a the immobilization chemistry and 5b the hybridization scheme for DNA at the IME device using organosilane chemistry. Synthetic 5′-amine-terminated single-stranded oligonucleotides (ssDNA) were immobilized on the glass surface between the metallic digits of microlithographically fabricated microsensor electrodes (IMEs) using 3-glycidoxypropyltrimethoxysilane. Nonspecifically adsorbed probes onto the metallic digits were removed by a cathodic cleaning step [3]. Such a sensor provides a useful means to directly detect the hybridization of DNA strands using electrical impedance measurements. The ensemble of single-stranded DNA chains immobilized between the opposing electrodes is associated with counter cations that support ionic conductivity. The hybridization reaction occurs on the IME genosensor when the complementary strand DNA molecule present in the sample solution makes sufficient use of hydrogen bonding between the nucleic acid bases to expel water from between the double helix. Therefore, the density of water molecules, and thus solvated ions, associated with the double helix is correspondingly reduced when compared with the single strand. Consequently, an increase in the overall impedance of the IME is anticipated upon the DNA hybridization reaction.

In DNA immobilization, several factors, such as the line and space dimensions of the IME (cell constant), immobilization strategy, the nature of the immobilized DNA molecules, and the length of the DNA probe, may affect the final signal in impedimetric detection. For example, oligonucleotide probes that are oriented parallel to the electrode result in decreased conductance compared to oligonucleotides that are oriented perpendicular to the electrode. The increase in conductance is associated with increased current and hence lowered detection limits. In general, upon immobilization the Brownian motion and translational degrees of freedom of the immobilized DNA are reduced, which affects the final performance of the IME biosensor through the hybridization kinetics. However, immobilized DNA can result in a rate of reaction that is comparable to the reaction rate of complementary strands free in solution. The length of the immobilized DNA strand has also been shown to have a much greater effect than the effect of immobilization on a two- or three-dimensional surface for DNA strands with lengths greater than 100 bases. The hybridization rate was shown to decrease with linker lengths greater than 712 bases.

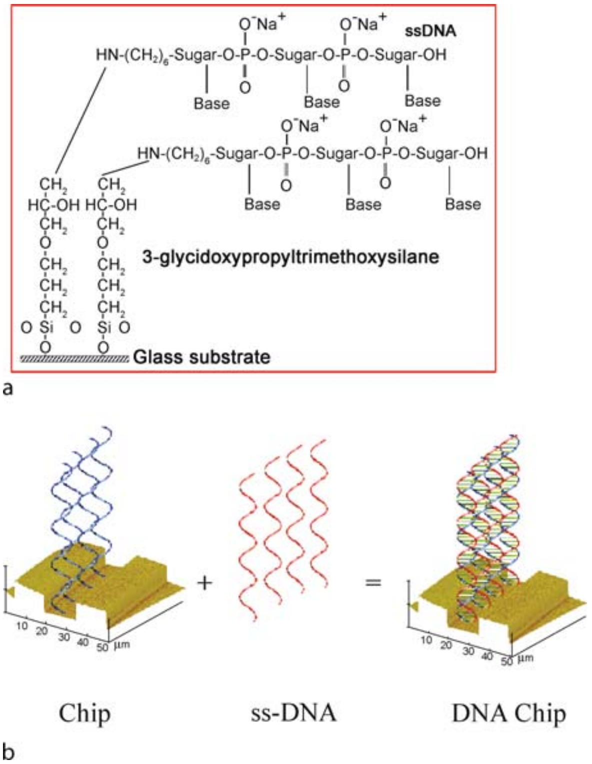

Impedimetric Biosensors for Nano- and Microfluidics, Figure 5 (**a**) The immobilization of DNA on the glass surface between the metallic digits of microlithographically fabricated microsensor electrodes (IMEs) using 3-glycidoxypropyl-trimethoxysilane. (**b**) A schematic illustration of the cross-sectional representation of DNA hybridization reaction occurring between a pair of electrode digits (Dimensions are not to scale)

Impedimetric Enzyme Biosensor using Immobilization of Enzyme

Immobilization of urease onto an IME device can produce an impedimetric enzyme biosensor for determination of urea [4]. The enzyme urease can be immobilized by a similar covalent tethering strategy to the interdigit surface via 3-aminopropyltrimethoxysilane monolayer and sulfo-NHS and EDC as crosslinkers. This creates an enzyme

layer which is very thin relative to the electrode dimensions. The immobilized urease catalyzes the hydrolysis of neutral urea, leading to the formation of ammonium, bicarbonate, and hydroxide ions:

$$\text{Urea} + 3H_2O \xrightarrow{\text{urease}} 2NH_4^+ + HCO_3^- + OH^-$$

The charged products of the above reaction increase the solution conductivity in the vicinity of the IME surface, which results in a change in impedance signal detected by the IME. The conductivity change, measured in a low-conductance environment such as tris buffer or deionized water, may be made directly proportional to the urea concentration.

Impedimetric Immunosensors using Immobilization of Antibody

An impedimetric immunobiosensor may be fabricated by the covalent immobilization of primary or secondary IgG (immunoglobulin G) to the IME device on the exposed glass or on the exposed gold. To immobilize IgG to the gold digits, a self-assembled monolayer (SAM) of 11-mercaptoundecanoic acid (MUDA) or 11-amino-1-undecanethiol hydrochloride (AUT) is first formed on the gold surface. Following SAM formation, the surface–COOH groups of MUDA-modified electrodes are activated by EDC/sulfo-NHS, and then incubated in primary or secondary IgG solutions. To immobilize the IgG to the interdigit glass space, similar protocols are used, except an organosilane, such as 3-aminopropyltrimethoxysilane, replaces the alkanethiol in the surface modification step. The silanol that is condensed on the gold digits is removed by repeatedly electrochemically scanning the device in 0.1 M H_2SO_4.

The two foregoing modification approaches produce devices in response to impedance in two different ways: capacitive and resistive, as described above. Both are label-free approaches with the potential directly to detect antigens and haptens in sandwich or competitive immunoassay formats. However, they are both somewhat limiting in their overall sensitivity. Non-label-free impedimetric approaches that offer enhancements in sensitivity are the use of electroactive polymer layers and the use of redox-active and/or nanoparticle labels.

Electropolymerizable monomers that give rise to conductive electroactive polymers (CEPs) provide a convenient approach for the immobilization of antibodies and other biomolecules for the creation of biosensors [5]. Polypyrrole has been explored for the immobilization of antibodies in immunosensors. Pyrrole monomer may be electrochemically oxidized (aqueous solution; +0.75 V vs. Ag/AgCl) to produce a highly conjugated and electronically conductive polymer film in which dopant anions can be incorporated to maintain charge neutrality. The thickness of the film and its morphology may be controlled by the amount of charge passed and by the conditions of the electropolymerization. Because of the overall negative charge on IgG molecules, direct incorporation within electroactive polymer films is achievable in which the IgG acts as a single macromolecular counter anion dopant. Retained immunoactivity may, however, be compromised. A companion approach is to form copolymers using pyrrole and pyrrolebutyric acid. The copolymer presents available carboxylic acid groups at the surface that may serve to covalently immobilize the IgG. Figure 6 illustrates the covalent tethering of amine-functionalized biotin following EDC/sulfo-NHS activation of the pendant carboxylic acid groups of poly(pyrrole-*co*-pyrrolylbutyric acid). Subsequent incubation in streptavidin or neutravidin followed by incubation in biotinylated IgG immobilizes the primary antibody to the device surface. This format has been used to build sandwich immunoassays for antigens that are detected by the indirect action of the oxidoreductase enzyme-linked antibodies on the conductivity of the polymer film.

A further alternative is to implement these approaches with the use of redox and/or nanoparticle labels. The redox and nanoparticle labels replace the familiar enzyme labels in enzyme-linked immunosorbent assays (ELISAs) and offer the advantages of simplified protocol, wider linear dynamic range, higher stability compared to enzymes, and higher separation efficiency. Redox labels such as ferrocene, viologen, and (η^5-cyclopentadienyl)tricarbonyl manganese (cymantrenyl) may be directly conjugated to primary or secondary antibodies to serve as amperometric, voltammetric, and impedimetric reporters of immunobound conjugates. Since they invoke the faradic component of the impedance, they may be made quite sensitive.

Colloidal gold nanoparticles and carbon nanotubes may be used as reporting labels in immunobinding reactions on IME chips [6, 7]. These highly conductive particles make a contribution to a conductive network upon the immunobonding reaction. More appropriate when implemented in a threshold sensitivity switch in a YES/NO vs. a quantitative bioassay, these conductive labels once assembled on the surface provide a very sensitive electrical means for reporting the equilibrium binding condition.

Impedimetric Biosensors for Whole Cells

An impedance biosensor for whole cell detection is constructed by immobilizing antibodies or receptors that are specific to the target cells on an electrode surface. The sen-

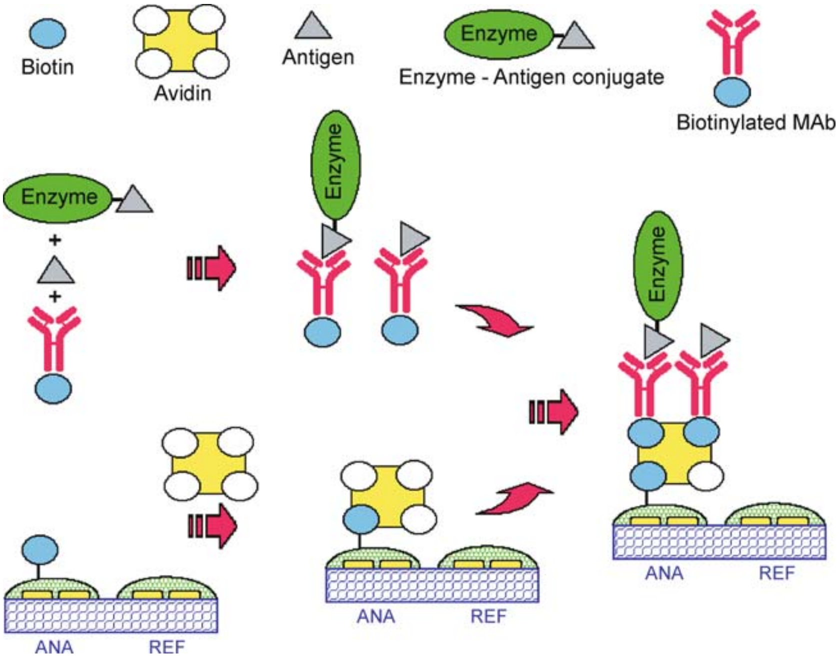

Impedimetric Biosensors for Nano- and Microfluidics, Figure 6 Illustration of the immobilization biotinylated IgG to the IME device surface, through the covalent tethering of amine–functionalized biotin following EDC/sulfo-NHS activation of the pendant carboxylic acid groups of poly(pyrrole-co-pyrrolylbutyric acid), with subsequent incubation in streptavidin or neutravidin following by incubation in biotinylated IgG

sor probes the attachment of cells by measuring the change in electrical properties of the sensor due to the insulating property of the cell membrane. The presence of intact cell membranes on the electrodes determines the current flow and thus the sensor signal. The overall impedance of a biological cell includes the resistance and the capacitance of the cell membrane. Natural cell membranes (thickness 5 – 10 nm) show a membrane capacitance of $0.5 – 1.3\ \mu F/cm^2$ and a membrane resistance of $10 \times 10^2 – 10 \times 10^5\ \Omega\, cm^2$. The structure and size of an IME have made it the best choice to realize a label-free biosensor for cell detection that is amenable to impedance measurement. Compared with the size of a bacterial cell, 1 – 2 μm long and ~ 0.5 μm in diameter, or a mammalian cell of 5 – 10 μm in diameter, the dimensional compatibility of the IME makes it an obvious choice for its ability sensitively to detect cells on the electrode surface without any amplification step.

Impedimetric Biosensors for Bacteria Detection

Figure 7 shows the detection principle of an impedimetric IME biosensor for bacterial detection [8]. It is based on measurements of electrochemical faradic impedance in the presence of $[Fe(CN)_6]^{3-/4-}$ as a redox probe. When a bare interdigitated microelectrode is immersed into an electrolyte solution containing the redox couple and a small-amplitude AC potential (5 mV) is applied to the electrode, the faradic process of oxidation and reduction of the redox couple occurs, and then electrons are transferred between the two sets of array electrodes through the redox couple (Fig. 7a). When antibodies are immobilized onto the electrode surface (Fig. 7b) they form a layer that can inhibit the electron transfer between the electrodes, and thus an increase in the electron transfer resistance can be expected. If bacterial cells attach to the antibody-modified electrode surface (Fig. 7c), the intact cells can create a further barrier for the electrochemical process, thereby hindering the access of the redox probe to the electrode surface, resulting in a further increase in the electron transfer resistance.

Capture of Bacteria Cells in Microfluidic Devices

Taking advantage of the IME, the capture of bacterial cells in a micro-/nanofluidic device could be realized using ▶dielectrophoresis (DEP). DEP is the electrokinetic motion of dielectrically polarized particles in non-uniform electric fields [9]. Combining the advantages of DEP concentration and antibody capture, target cells may be captured from a flow field achieved in a microfluidic biochip [8]. With the assistance of DEP to capture cells within the microfluidic device, IME impedi-

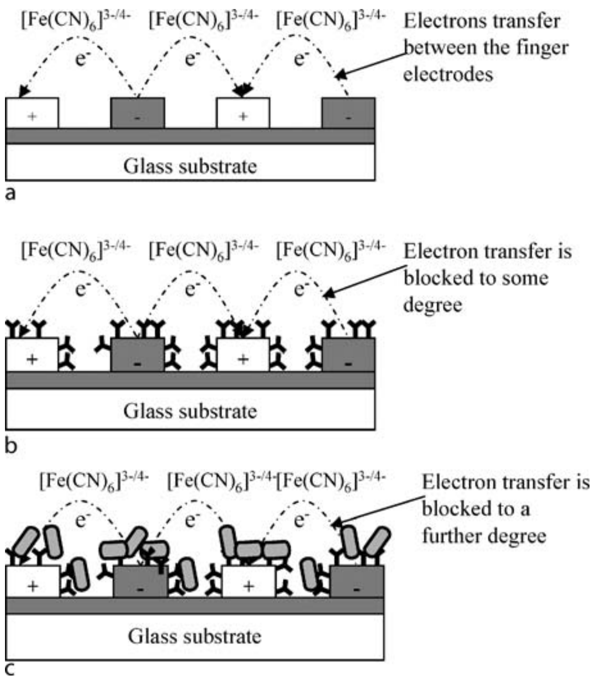

Impedimetric Biosensors for Nano- and Microfluidics, Figure 7 The detection principle of impedimetric IME biosensor for bacterial detection

metric biosensors have shown great potential in bacterial detection. Suehiro et al. [10] reported a detection technique called dielectrophoretic impedance measurement (DEPIM), which utilizes positive DEP to trap suspended biological cells onto an interdigitated microelectrode array to form pearl-chains. Cell population can be quantitatively evaluated by monitoring the change in the electrode impedance or admittance. Later, this DEPIM method was combined with antigen–antibody reaction to realize selective detection of *E. coli*. To further increase the sensitivity of this technique, the same group reported an improved DEPIM method for detection of *E. coli* by combining this technique with electropermeabilization, in which a high AC electric field was applied to the trapped bacterial cells, leading to intracellular ion release through damaged cell membranes, which causes an effective conductance increase.

Immobilization of Mammalian Cells for Toxicity Biosensors

Mammalian cell immobilization to electrode surfaces is vitally important for the construction of cell-based biosensors which hold out the promise for the development of practical methods for the screening of drugs for possible toxic side effects and for the monitoring of the effects of biochemical warfare agents. Surface modification of the substrate could effectively enhance the attachment of mammalian cells on the substrate. For example, pheochromocytoma cells (PC-12) are inherently poorly adherent cells that proliferate on substrates. Covalent immobilization of the extracellular matrix (ECM) protein laminin to the surface of gold electrodes can yield conditions that allow for tighter neuron-to-electrode contract [11]. The gold electrode is first modified with SAMs of ω-amine alkanethiols, cysteamine (CA), or 11-amino-1-undecanethiol (11-AUT). These amine-terminated SAMs then serve to irreversibly couple laminin to the electrode surface and give rise to a strong covalent linkage between the electrode and laminin. Laminin is able to establish the strong attachment of PC-12 cells to a gold IME, because the immobilized laminin induces secretion of neuron adherence molecules that act as receptors in the neuron cell membrane and offer a wide range of potential adhesive interactions. An excellent area of application is that of microfluidic cell-based sensors with well-positioned recording sites for cell adhesion.

Key Research Findings

In impedimetric biosensor systems, biological reactions such as DNA hybridizations, enzymatic reactions, and immunoreactions usually involve the production or consumption of ions, which results in electrical impedance changes at the interface of the IME electrodes. We present here some representative results from an impedimetric biosensor for urea. The impedance response of this urease biosensor is contributed by charged products of the enzymatic reaction, which increases the solution conductivity in the vicinity of the IME surface and is detected by the change in IME impedance. Figure 8 shows typical experimental plots (points) and numerical simulations (solid lines) of the apparent solution conductivity with time when the immobilized urease biosensor is immersed in urea samples at concentrations ranging from 0.01 to 5.0 mM. At any given concentration, the conductivity increases most rapidly upon first immersion in the urea solution and increases less rapidly as time evolves establishing a kinetic assay. The final conductivity is also directly proportional to the urea concentration, as it increases most rapidly and to the highest level at the highest urea concentration.

It was found that the geometry of the IME used to construct the biosensor influences the magnitude of the response, but not the kinetics, which is solely determined by the reaction rate and mass transport. In the urease biosensor, a change only in the lateral extent of the array, affected by modifying the length of the digits or the number of digits, will not affect the response. A more interesting case to consider is miniaturization of the sensor, by reducing the digit width and/or interdigit spacing. If

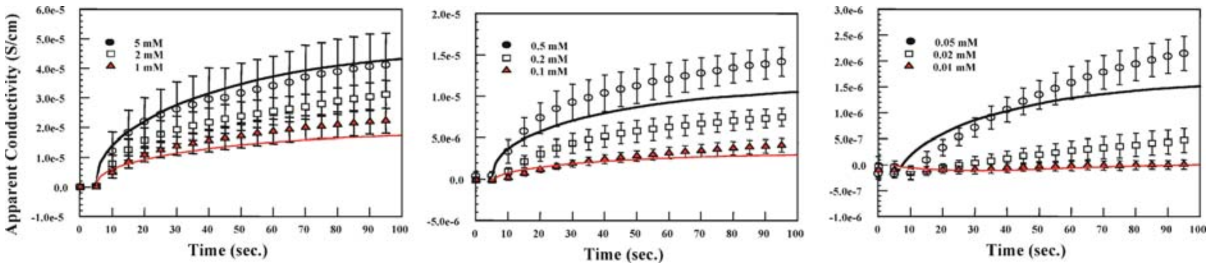

Impedimetric Biosensors for Nano- and Microfluidics, Figure 8 Typical experimental plots (points) and simulations (lines) of the apparent solution conductivity with the time when the immobilized urease biosensor is immersed in urea samples at concentrations ranging from 0.01 to 5.0 mM

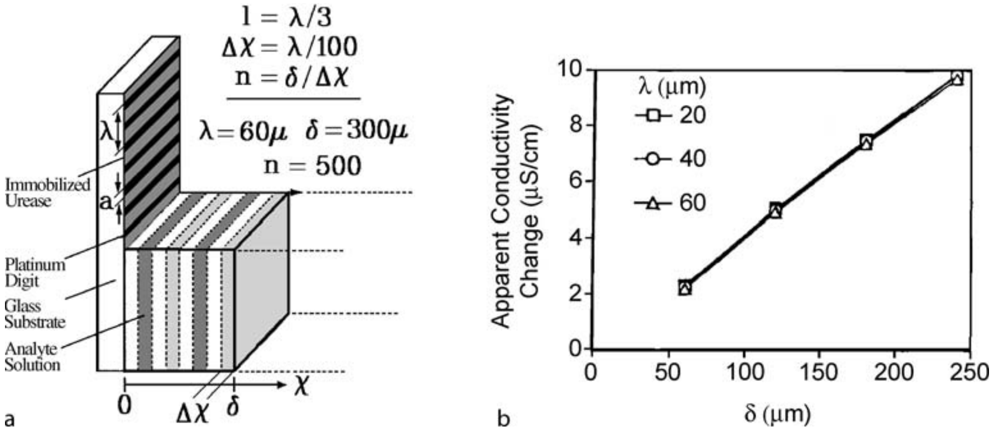

Impedimetric Biosensors for Nano- and Microfluidics, Figure 9 The effect of decreasing the spatial wavelength, λ, of the interdigitated microsensor electrode array. (**a**) Schematic illustration of λ and δ. (**b**) A plot of the steady-state, apparent conductivity change versus boundary layer thickness for devices having λ's of 20, 40 and 60 μ immersed in a 1 mM urea solution

these are reduced proportionately, while maintaining the original length of the digits, then the cell constant will remain unchanged [4]. Figure 9 illustrates the definition of the spatial wavelength, λ and the effect of decreasing the spatial wavelength of the interdigitated electrode array on the response. The figure is a plot of the steady-state, apparent conductivity change vs. boundary layer thickness for devices having values of λ of 20, 40, and 60 (used in the experiments) μ, and immersed in a 1 mM urea solution. Decreasing λ increases the magnitude of the response; the progressively smaller volume of electrolyte sampled by the miniaturized sensor has a higher average conductivity, since the conductivity decreases with distance away from the sensor surface. However, for the boundary layer thicknesses of 100 μm or more expected in practice, Fig. 9 demonstrates that the steady-state conductivity changes differ by less than 5% for the three different devices. It is believed that this geometry influence also occurs in impedimetric DNA sensors, immunosensors, and cell-based biosensors. Therefore, optimization of geometry/dimension of the IME is very important in construction of the biosensor.

Impedimetric biosensors for whole cells have demonstrated two mechanisms in response. Considering the overall impedance of a biological cell as including the resistance and the capacitance of the cell membrane, the presence of intact cell membranes on the electrodes would contribute to the sensor's capacitance and/or resistance, and would determine the current flow and thus the sensor signal. However, when cells are attached to the electrode surface, they are usually separated by a gap of 10–20 nm (up to several hundred nanometers). This aqueous gap between the cell membrane and the electrode surface prevents a direct influence of the cell membrane capacitance on the impedance of the electrode. Therefore, the cell membrane resistances of these attached cells act as resistors on the IME surface and affect the interfacial resistance. The interfacial resistance is best represented as electron transfer resistance in the presence of a redox probe (e. g., $[Fe(CN)_6]^{3-/4-}$) and can be sensitively monitored. Figure 10a presents a representative group of Nyquist plots of the impedance spectroscopic responses of an IME-based biosensor to different cell numbers of *E. coli* O157 : H7 at 10a antibodies, 10b 4.36×10^5 CFU/ml,

10c 4.36 × 10^6 CFU/ml, 10d 4.36 × 10^7 CFU/ml, and 10e 4.36 × 10^8 CFU/ml. Each of the impedance spectra includes a semicircle portion and a linear portion, which correspond to the electron transfer process and diffusion process, respectively. The electron transfer resistances (the diameters of the semicircles at the x-axis) of the sensor increase with increasing cell concentration. The analyzes of cell concentration can be realized on the basis of the linear relationship between the electron transfer resistance and logarithmic value of *E. coli* concentrations (Fig. 10b). As shown in Fig. 10, when the electron transfer resistance of the antibody immobilized IDA microelectrode was taken as the threshold of the signal, the detection limit of this immunosensor was 10 × 10^6 CFU/ml, which is comparable with other label-free immunosensors for detection of pathogenic bacteria using different transducer techniques.

Mammalian cells present the same impedance biophysics as bacterial cells at electrodes. Fig. 11a shows the normalized temporal impedance change (average and standard deviation) of PC-12 cells cultured on laminin-modified gold electrodes. Figure 11b shows similar PC-12 cells cultured on laminin-modified gold electrodes and dosed with 5 mM nifedipine. There is a clear immediate reduction in network impedance upon dosing with nifedipine.

Nifedipine (3,5-pyridinedicarboxylic acid-1,4-dihydro-2,6-dimethyl-4-(2-nitrophenyl)-dimethyl ester, $C_{17}H_{18}N_2O_6$; $MW = 346.3$ g/mol) is a calcium channel antagonist L-type Ca^{2+} channel blocker that inhibits depolarization-induced Ca^{2+} uptake into the cells. Statistically significant differences in the temporal response to different dosing levels of the same drug and differences arising from different drug classes are the bases for the development of a neurotoxicitiy biosensor. The PC-12 cells are progenitor cells capable of chemically induced differentiation. The impedance responses of chromafin-like PC-12 cells vs. neuronal-like PC-12 cells establish the basis for a neurotoxicitiy biosensor that informs on likely tissue-specific responses to candidate drugs. In vitro temporal impedance output from the whole cell neurotoxicity biosensor will allow determination of toxicity of chemical agents on cellular health and serve as an alternative to the use of whole animals in toxicity screening.

Future Directions for Research

Microfabricated IME-based impedimetric biosensors are ready to be integrated with micro- and nanofluidic systems. Many of the operations (surface modification, derivatization, bioimmobilization, incubation, washing, etc.) needed to achieve reproducible, high-density covalent immobilization of biomolecules or whole cells

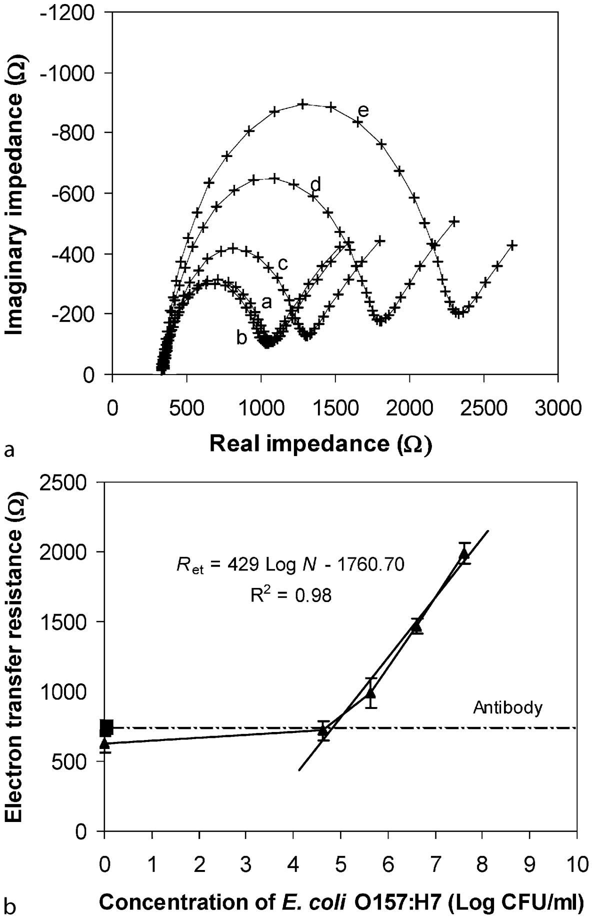

Impedimetric Biosensors for Nano- and Microfluidics, Figure 10 The principle of IME impedimetric detection of the antibody immobilization and the bacterial attachment. (**a**) Nyquist impedance spectra of the IME-based biosensor upon antibody immobilization and bacterial attachment with different number of *E. coli* O157:H7 cells on their surface. a = antibodies only, $b = 4.36 \times 10^5$ CFU/ml, $c = 4.36 \times 10^6$ CFU/ml, $d = 4.36 \times 10^7$ CFU/ml, and $e = 4.36 \times 10^8$ CFU/ml. Data points from left to right correspond to decreasing frequency. Amplitude voltage: 5 mV; Electrolyte: 10 mM $[Fe(CN)_6]^{3-/4-}$ (1 : 1) in 0.01 M PBS, pH 7.4. (**b**) The linear relationship between the electron transfer resistance and logarithmic value of *E. coli* concentrations derived from Fig. 10a

on the IME device may be performed directly within the microfluidic environment of a fully integrated Lab-on-a-Chip. However, within a micro-/nanofluidic device, biological reactions often occur in a dynamic fluid which is quite different from the usual static environment. Because of the flow within a micro-/nanofluidic device, biological molecules would have much less opportunity to come into contact with the biosensor surface that is embedded in a microfluidic channel and to interact with the immobilized biomolecules, which would lead to a low probability of biological reaction. Therefore, integration of other techniques to manipulate biological entities in microflu-

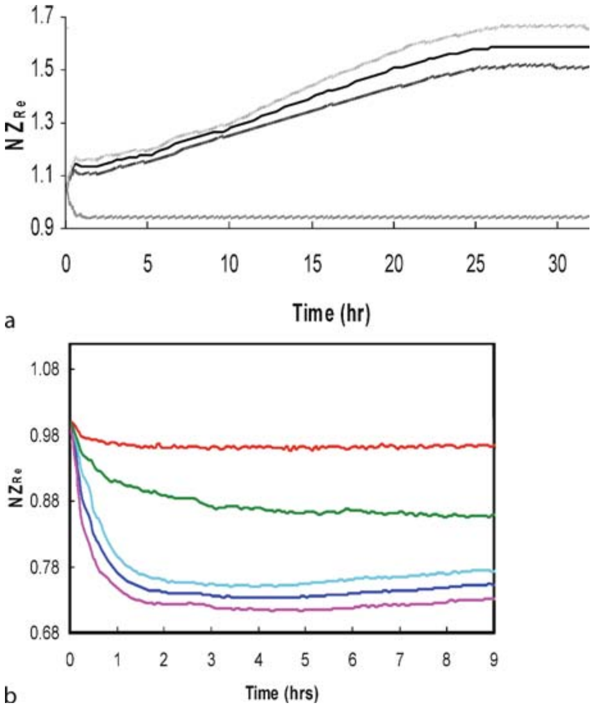

Impedimetric Biosensors for Nano- and Microfluidics, Figure 11 The time-dependent profile (mean and standard deviation) of the normalized impedance response of the self-assembled monolayers (SAMs) of ω-amine alkanethiols, cysteamine (CA)-laminin modified IME chip (**a**) cultured with PC-12 cells ($n = 6$) and (**b**) PC-12 cells exposed to 5 mM nifedipine

idic environments is needed. Thus, dielectrophoresis to contain cells and nanoparticles, electrophoresis to drive biomolecular targets to the reactive surfaces, and pre-concentration techniques that enhance driving fluxes are expected to improve the efficiency and kinetics of biological reactions within microfluidic systems. This integration is highly desirable in order to drive micro-/nanofluidic detection systems towards the practical applications in point-of-concern molecular diagnostics. Efficient and reliable sample preparation, including cell sorting, lysis, DNA isolation, and protein separation, and methods to reduce the large volume of samples to microliters are necessary as the volumes required to perform analyzes in microfluidic devices usually range from a few to hundreds of microliters. Successful integration of impedimetric biosensors with micro-/nanofluidic systems presents one opportunity to approach the desirable result of the *tissue in–information out* paradigm of modern molecular diagnostics.

Cross References

► Biosensor
► Capacitance Methods
► Conductivity Measurement
► Dielectrophoresis
► Pyroelectric Flow Sensors
► Electrochemical Techniques
► MEMS-Based Biosensor
► Nanoscale Biosensors
► Self-Assembled Monolayers

References

1. Kell DB (1987) The principles and potential of electrical admittance spectroscopy: an introduction. In: Turner A, Karube I, Wilson GS (eds) Biosensors: Fundamentals and Applications, Oxford University Press, Oxford
2. Yang L, Li Y, Erf GF (2004) Interdigitated array microelectrode-based electrodechemical impedance immunosensor for detection of *Escherichia coli* O157:H7. Anal Chem 76:1107–1113
3. Hang TC, Guiseppi-Elie A (2003) Frequency dependent and surface characterization of DNA immobilization and hybridization. Biosens Bioelectron 19:1537–1548
4. Sheppard Jr NF, Mears D, Guiseppi-Elie A (1996) Model of an immobilized enzyme conductimetric urea biosensor. Biosens Bioelectron 11:967–979
5. Guiseppi-Elie A, Brahim S, Wilson A (2006) Biosensors Based on Electrically Conducting Polymers. In: Skotheim T, Reynolds JR (eds) Handbook of Conducting Polymers: Conjugated Polymer Processing and Applications, 3rd edn. Dekker, New York
6. Cullen K, Guiseppi-Elie A (2000) DNA detection using colloidal gold nanoparticles: towards near patient DNA diagnostics. In: Proc Spring 2000 MRS Meeting, San Francisco
7. Park SJ, Taton TA, Mirkin CA (2002) Array-based electrical detection of DNA using nanoparticle probes. Science 295(5559):1503–1506
8. Yang L, Banada PP, Chatni MR, Lim KS, Bhunia AK, Ladisch M, Bashir R (2006) A multifunctional micro-fluidic system for dielectrophorectic concentration coupled with immuno-capture of low number of *Listeria monocytogenes*. Lab Chip 6:896–905
9. Pohl HA (1978) Dielectrophoresis. Cambridge University Press, Cambridge
10. Suehiro R, Yatsunami R, Hamada R, Hara M (1999) Quantitative estimation of biological cell concentration suspended in aqueous medium by using dielectrophoretic impedance measurement method. J Phys D Appl Phys 32:2814–2820
11. Slaughter GE, Bieberich E, Wnek GE, Wynne KJ, Guiseppi-Elie A (2004) Improving neuron-to-electrode surface attachment via alkanethiol self-assembly: an alternating current impedance study. Langmuir 20:7189–7200

Impulse Bit

Definition

The impulse imparted to a spacecraft by a single firing of a thruster; the minimum impulse bit reflects the level of precision associated with the propulsion system.

Induced-Charge Electro-Osmosis

Synonyms

ICEO; Nonlinear electro-osmosis

Definition

Induced-charge electro-osmosis refers to nonlinear electro-osmotic flow of a liquid electrolyte, when an electric field acts on its own induced diffuse charge near a polarizable surface.

Cross References

- ► Aperiodic Electrophoresis
- ► AC Electro-Osmotic Flow
- ► Electrical Double Layers
- ► Electrokinetic Motion of Heterogeneous Particles
- ► Electrokinetic Motion of Polarizable Particles
- ► Electroosmosis of the Second Kind
- ► Electroosmotic Flow (DC)
- ► Electrophoresis
- ► Electrophoresis of the Second Kind
- ► Induced-Charge Electrophoresis
- ► Nonlinear Electrokinetic Phenomena
- ► Stotz–Wien Effect

Induced-Charge Electrophoresis

Synonyms

ICEP; Nonlinear electrophoresis

Definition

Induced-charge electrophoresis refers to the translational and rotational motion of a polarizable particle due to induced-charge electro-osmotic flow.

Cross References

- ► Aperiodic Electrophoresis
- ► Electrical Double Layers
- ► Electrokinetic Motion of Heterogeneous Particles
- ► Electrokinetic Motion of Polarizable Particles
- ► Electrophoresis of the Second Kind
- ► Electroosmotic Flow (DC)
- ► AC Electro-Osmotic Flow
- ► Electrophoresis
- ► Electrophoresis of the Second Kind
- ► Induced-Charge Electro-Osmosis
- ► Nonlinear Electrokinetic Phenomena
- ► Stotz–Wien Effect

Infrared Imaging and Mapping for Biosensors

KARSTEN HINRICHS
ISAS - Institute for Analytical Sciences, Berlin, Germany
hinrichs@isas.de

Synonyms

Infrared (IR) mapping; Imaging for biosensors/biochips/microchips; Biosensors Using Infrared Imaging

Definition

Infrared imaging or mapping techniques are meant here as those that potentially can be used for biosensors and their characterization. The mid-infrared (MIR) spectral range is defined from 2.5 to 16 μm (IR in [1]). For the production of laterally resolved images typically a two-dimensional sample movement stage is employed for defined lateral movements of the sample, whereby for every position a measurement with a single detector is performed or alternatively the image is obtained in one shot involving a detector array (e. g. focal plane array in [2]). Typical spectrometers used for the MIR range are Fourier transform infrared (FTIR) spectrometers; however, for specific purposes also infrared grating spectrometers are used.

Overview

Many optical techniques could potentially be used for biosensors and their characterization [1]. Among the label-free optical vibrational spectroscopies are Raman spectroscopy (RS) and infrared spectroscopy, which are frequently used as fingerprinting methods for characterization of thin films of biological compounds and biosensors. In comparison to the visible, for the IR spectral range absorption bands of molecular vibrations deliver often a higher spectral contrast. The interpretation of absorption bands can deliver, for example, thickness, molecular identification, molecular orientation, and composition. For the IR spectral range standard methods are transmission spectroscopy, IR microscopy [2], external reflection spectroscopy (e. g. reflection absorption IR spectroscopy (RAIRS) and IR spectroscopic ellipsometry (IRSE) [3]), and IR internal reflection spectroscopy (e. g. attenuated total reflection (ATR) [1, 4]). All of them are typically noninvasive, contactless, and could potentially be used for biosensors. Additionally they offer the possibility to be coupled with imaging techniques. Even though there

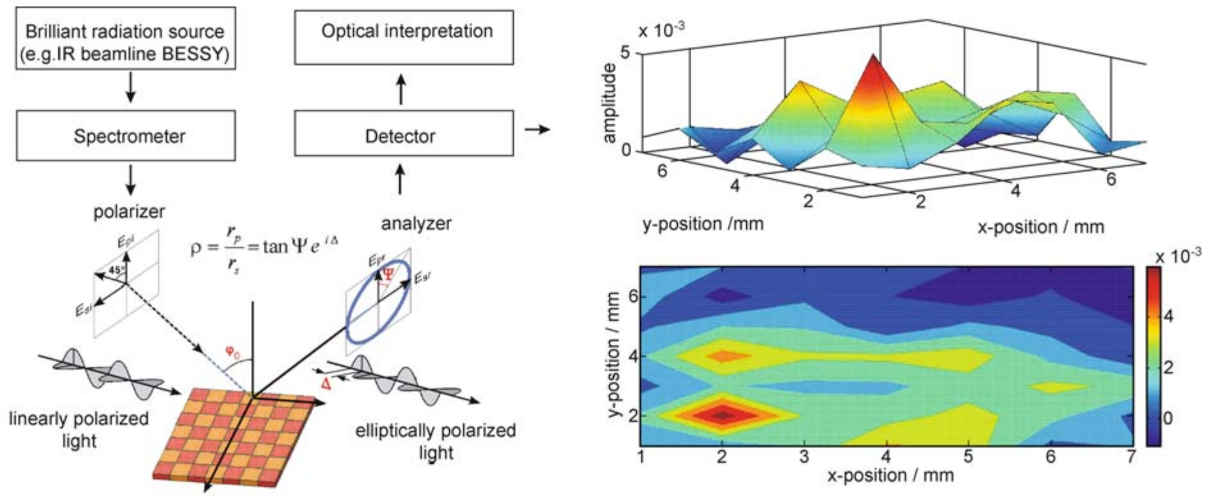

a principle of synchrotron mapping ellipsometry

b map of band amplitudes: peptide adsorption on biosensor

Infrared Imaging and Mapping for Biosensors, Figure 1 (**a**) Principle of ellipsometric mapping measurement. Due to reflection at the sample, the polarization of the radiation is changed. For example, the incident linearly polarized radiation becomes elliptically polarized. The sample is moved by a two-dimensional mapping table and a spectrum is taken for every probed spot. The ellipsometric parameters defined by the quantity ρ, which is the ratio of the complex reflection coefficients r_p and r_s, are measured for every spot. Δ is the phase shift and tan Ψ the amplitude ratio of p- and s-polarized reflection coefficients. (**b**) Three-dimensional presentation and contour plots of 7 mm $\times$ 7 mm map of ellipsometric (tan Ψ) band amplitudes of a peptide band at 1547 cm^{-1} (adapted from [5]). The peptide Cys-GCN4 was immobilized on a linker-covered silicon wafer. In principle electronic recognition of the specific adsorption site could serve for fast analysis of the samples under investigation [5]

is an emerging potential for IR spectroscopy for studying biosensors [5, 6] and IR imaging of biomedical samples [7–9], only a few studies with respect to the IR imaging of biosensors have been published up to now [5]. Figure 1b shows an experimental example of biosensor characterization by IR synchrotron mapping ellipsometry (Fig. 1a). Important key properties of the imaging techniques in the MIR range are:

- *Lateral resolution.* When brilliant light sources like lasers or synchrotron radiation are used the lateral resolution typically is diffraction limited in the range of a few micrometers for IR microscopy [2, 10]. This can be improved by orders of magnitude with scanning near-field IR microscopy (SNIM) [11], which enables resolution down to a few tens of nanometers. However, for broad-band sources such SNIM studies have not been performed so far. IRSE biochip characterization with lateral resolution down to approximately 200 µm $\times$ 400 µm is possible.
- *Sensitivity.* For SNIM, RAIRS, ATR, and IRSE the high sensitivity allows detection of nanometer thick biomolecular films.
- *Quantification of experimental results.* Reliable quantification of optical spectra and signals can be performed by involvement of optical modeling of RAIRS, ATR, and IRSE spectra. Here, IRSE has some advantages because it delivers up to three method-independent parameters (phase shift and amplitude ratio of s- and p-polarized reflection coefficients and the polarization degree). For SNIM quantitative evaluation is more difficult than for the other methods and is dependent on the geometry of SNIM.

Cross References

► Biosensors Using Atomic Force Microscopes
► Biosensors Using Lasers
► Biosensors Using Surface-Enhanced Raman Scattering
► Oxidation (of Silicon)
► Protein Microarrays
► Spectral Methods
► Wafer Bonding

References

1. Eggins BR (2002) Chemical Sensors and Biosensors. Wiley, Chichester
2. Garidel P, Boese M (2007) Mid Infrared Micro spectroscopic Mapping and Imaging: A Bio-Analytical tool for spatially and chemically resolved tissue characterization and evaluation of drug permeation within tissues. Microsc Res Tech 70:336–349
3. Clayborn M, Umemura J, Merklin GT, Kattner J, Hoffmann H, Mendelsohn R, Flach CR, Frey BL, Corn RM, Weibel SC, Röseler A, Korte E-H (2002) Mid-Infrared external reflection

spectroscopy. In: Griffiths PR, Chalmers J (eds) Handbook of Vibrational Spectroscopy, vol 2. Wiley, Chichester, pp 969–1090
4. Mirabella FM, Fitzpatrick J, Reffner JA, Chabal YJ (2002) Mid-Infrared internal reflection spectroscopy. In: Griffiths PR,Chalmers J (eds) Handbook of Vibrational Spectroscopy, vol 2. Wiley, Chichester, pp 1091–1123
5. Hinrichs K, Gensch M, Esser N, Schade U, Rappich J, Kröning S, Portwich M, Volkmer R (2007) Analysis of biosensors by chemically specific optical techniques: Chemiluminescence-imaging and infrared spectroscopic mapping ellipsometry. Anal Bioanal Chem 387:1823–1829
6. Lucas P, Solis MA, Le Coq D, Juncker C, Riley MR, Collier J, Boesewetter DE, Boussard-Pledel C, Bureau B (2006) Infrared biosensors using hydrophobic chalcogenide fibers sensitized with live cells. Sens Actuators B 119:355–362
7. Kidder LH, Haka AS, Lewies EN (2002) Instrumentation of FT-IR imaging. In: Griffiths PR, Chalmers J (eds) Handbook of Vibrational Spectroscopy, vol 2. Wiley, Chichester, pp 1386–1404
8. Attas M (2002) Functional Infrared Imaging for biomedical applications. In: Griffiths PR, Chalmers J (eds) Handbook of Vibrational Spectroscopy, vol V. Wiley, Chichester, pp 3388–3398
9. Fabian H, Mäntele W (2002) Infrared spectroscopy of proteins. In: Griffiths PR, Chalmers J (eds) Handbook of Vibrational Spectroscopy, vol V. Wiley, Chichester, pp 3399–3425
10. Chan KLA, Kazarian SG (2003) New opportunities in micro- and macro-attenuated total reflection infrared spectroscopic imaging: Spatial resolution and sampling versatility. Appl Spectrosc 57:381–389
11. Raschke MB, Molina L, Elsaesser T, Kim DH, Knoll W, Hinrichs K (2005) Aperture less near-field vibrational imaging of block-copolymer nanostructures with ultra high spectral resolution. Chem Phys Chem 6:2197–2203

Infrared (IR) Mapping

► Infrared Imaging and Mapping for Biosensors

Infrared Radiation

► Infrared Thermography

Infrared Thermography

Definition

Since all bodies with a temperature above 0 Kelvin emits heat radiation it is possible to determine the body temperature by analyzing the emitted radiation. While the spectra of the visible light are between 380 to 750 nm, infrared (IR) radiation lies between 0.7 and 1000 microns. Usual IR cameras have a sensitivity range between 3.5 and 14 microns because the atmosphere is transparent in this range. IR Thermography means displaying the infrared light intensity in images which are visible for the human eye. IR Thermography is a contact less technique; thus very fast processes like explosions can be visualized in sequence of frames.

Injection Molding

► Micromolding
► Micromolding (Injection and Compression Molding)

Injection Slit

Definition

This etched structure is used to optimize and automate the injection procedure for shear-driven systems. Instead of injecting the sample by introducing it in front of the channel, an etched structure (injection slit) stands perpendicular towards the flow direction and the injection becomes more repeatable and an automated can be performed.

Inkjet

Definition

Inkjet printing certainly is the biggest industrial market using single droplets. Nearly all existing home and office inkjet printers are based either on the ►bubble jet or the piezo principle. High quality color image, low machine cost and low printing noise are basically the main advantages of such *inkjet* printers producing droplets in the 1 – 100 pl range. The two competing technologies in this field are the thermally actuated *bubble jet* commercially available from Hewlett Packard, Canon, Olivetti I-Jet and others and the piezoelectric driven printheads commercially available from Epson, Xaar, Spectra and others. Both methods made remarkable progress in the last two decades.

Cross References

► Bioprinting on Chip
► Bubble Jet
► DNA Micro-arrays
► Droplet and Bubble Formation in Microchannels
► Droplet Based Lab-on-Chip Devices
► Electrowetting and Droplets
► Piezoelectric Microdispenser
► Thermal Bubble

Inkjet Print

► Inkjet Printing
► Inkjet Printing in Microfabrication

Inkjet Printing

Synonyms

Inkjet print

Definition

Inkjet printing is a microfabrication technology to print the designed polymer patterns on a substrate by using an inkjet printing system (similar to the desktop printer) for MEMS and microelectronics applications. It is a bottom-up fabrication method. 3-D microstructures are sprayed directly on the substrate by the repeatable generations of small fluid droplets. The 3-D profile is precisely controlled by layer-by-layer printing associated with the computer program.
The printing fluids are often UV-curable, heat-sensitive or conductive polymers for various applications. The resolution of 3-D structure is limited by the size of droplet or nozzle, usually with diameters of $25 \sim 125\,\mu$m. The quality of the printing system determines the speed and precision of the spray and stage control. This technology is adapted in various applications of optical interconnect, electrical devices, microfluidic structures and assembly.

Cross References

► Fabrication of 3-D Microfluidic Structures
► Photolithography
► Photoresist SU-8
► Photoresist Reflow
► Soft Photolithography

Inkjet Printing in Microfabrication

Synonyms

Inkjet print

Definition

Inkjet printing is a microfabrication technology to print the designed polymer patterns on a substrate by using an inkjet printing system (similar to the desktop printer) for MEMS and microelectronics applications. It is a bottom-up fabrication method. 3D microstructures are sprayed directly on the substrate by the repeatable generation of small fluid droplets. The 3D profile is precisely controlled by layer-by-layer printing associated with the computer program.
The printing fluids are often UV-curable, heat-sensitive or conductive polymers for various applications. The resolution of 3D structure is limited by the size of droplet or nozzle, usually with diameters of $25 \sim 125\,\mu$m. The quality of the printing system determines the speed and precision of the spray and stage control. This technology is adapted in various applications of optical interconnect, electrical devices, microfluidic structures and assembly.

Cross References

► Fabrication of 3D Microfluidic Structures
► Inkjet printing
► Photolithography
► Photoresist Reflow
► Soft Photolithography

In situ Polymerized Materials

► Stationary Phases in Microchannels

Insulating Post Dielectrophoresis

► DC Dielectrophoresis in Lab-on-a-Chip Devices

Insulator-Based Dielectrophoresis (iDEP)

► DC Dielectrophoresis in Lab-on-a-Chip Devices

Integrated Actuators

Definition

A micropump or active microvalve is said to use integrated actuators when the component responsible for opening or closing the valve, or moving the fluid, is fabricated as an integral part of the device. An example would be an integrated movable flap or membrane that is electrostatically attracted to an integrated electrode when a voltage is applied.

Cross References

► Electromagnetic Valves
► Electrostatic Valves
► External Actuators
► Magnetic Pumps

- ▶ Membrane Actuation for Micropumps
- ▶ Microactuators
- ▶ Peristaltic Pumps
- ▶ Piezoelectric Valves
- ▶ Piezo/PZT in Microfluidics
- ▶ Pneumatic Valves
- ▶ Thermomechanical Valves
- ▶ Thermopneumatic Valves

Integrated Biochips

- ▶ Integrated Microdevices for Biological Applications
- ▶ Integrated Microdevices for Medical Diagnostics

Integrated Light Confiners

- ▶ On Chip Waveguides

Integrated Light Guiding

- ▶ On Chip Waveguides

Integrated Light Propagator

- ▶ On Chip Waveguides

Integrated Microdevices for Biological Applications

SUNG YANG[1], JEFFREY D. ZAHN[2]
[1] Department of Mechatronics, School of Information and Mechatronics, Gwangju Institute of Science and Technology (GIST), Gwangju, Republic of Korea
[2] Department of Biomedical Engineering,Rutgers, State University of New Jersey, Piscataway, NJ, USA
syang@gist.ac.kr, jdzahn@rci.rutgers.edu

Synonyms

Integrated biochips; Micro chemlab

Definition

Integrated microdevices for biological applications seek to create autonomous microfluidic devices capable of processing biological material from whole cell sample introduction to component extraction, biological sample manipulation and analysis. Although, there has been considerable research in creating devices for cell handling and analysis and proteomics, the major research thrust in creating integrated microdevices for biological applications has been towards genomic research and DNA analysis. Here, integrated devices for DNA purification, and DNA analysis for both plasmid and genomic DNA and a wide variety of biochips performing many different laboratory functions have been produced with varying levels of integrated functionality. Specific modules which have been demonstrated are fluidic cell concentration chambers, a DNA extraction chamber for DNA preparation, molecular biology reaction chambers for PCR amplification, and capillary electrophoresis separation arrays. These techniques are fundamental components of highly integrated biological analysis systems by allowing efficient DNA purification and analysis.

Overview

In biological studies, biological organisms can be studied on many levels. The whole organism can be directly investigated to study its behavior. In order to study a single cell, tissues or organs can be further broken down by either mechanical lysis or chemical (enzymatic) digestions. In order to study subcellular components of cells, cells are further broken down (disrupted) to extract subcelluar components of interest. After obtaining either subcellular or molecular components, a sample is further processed with techniques that may include sample purification, DNA amplification, and analysis. There are several essential techniques that are commonly used in subcellular levels studies. In this section, cell lysis, polymerase chain reaction (PCR), and electrophoresis (EP), are briefly reviewed as foundations of integrated microdevices for biological applications, although there are many other techniques commonly used in cellular or molecular biology studies as found in [1].

Integrated microfluidic devices have many advantages over conventional methods such as fast analysis time, small reagent and sample consumption, and less waste generation. In addition, they have the capability of integration, coupling sample preparation and analysis processes such as cell lysis, capillary electrophoresis (CE) and PCR. Therefore, integrated microfluidic devices enable hundreds of assays to be performed in parallel and in an automated manner.

Basic Methodology

Cell Lysis

Individual cells may be studied either by examining the cell morphology using a wide variety of specific cell stain-

ing procedures and microscopy or by isolating individual cells and culturing them for further molecular studies. In order to examine cells on a subcellular or molecular level, it is necessary to extract and purify subcellular components such as DNA, RNA, proteins and individual organelles from the cells of interest. However, it is well known that all cells contain a plasma membrane, which acts as a barrier between the extracellular and intracellular environment. Thus, in order to purify subcellular components the plasma membrane must be disrupted (lysed). Cell lysis may be achieved by either mechanical, chemical methods or a combination of both. Mechanical cell lysis may be accomplished by mechanical grinding of the sample by a mortar and pestle or rotating blade (blender) to process a large amount of biological samples. However, this method may also induce damage of the subcellular component of interest. A second method is through the use of sonication. Ultrasonic vibration produced by sonication can break the plasma membrane. However, heating produced by sonication may vesiculate the membrane and subcellular components. The most widely used method for cell lysis is to use detergents and simple agitation. Detergents can disrupt the lipid bilayer of the membrane causing the release of subcellular components [1]. However, many detergents can also denature proteins and are difficult to remove, once cell lysis process is finished. Therefore, the method used strongly depends on the cell type and the ultimate application of the research because the cell lysis may destroy the targeted sample of interest.

Polymerase Chain Reaction (PCR)

Since PCR was invented by Kary Mullis in 1983, it is widely used in molecular biology. PCR can selectively amplify DNA segments in a test tube by multiple cycles of DNA denaturation, specific primer hybridization and DNA polymerization [2]. The targeted DNA segments amplified by PCR may represent a small part of a large and complex mixture of DNAs such as from a genomic DNA lysate. In PCR, reactants are mixed together with an initial DNA sample. This mixture contains the DNA which is to be amplified, the enzyme DNA Taq polymerase, small primer sequences of DNA specific to and flanking the DNA sequence to be amplified and a large supply of the four nucleotide bases A, T, C, and G. Since the primers are specific to a single DNA sequence the primers gives PCR its specificity. The reaction mixture is heated to 90 – 95 °C for about thirty seconds. At this temperature the DNA strands separate as the hydrogen bonds holding them together break down. The mixture is cooled down to 55 – 60 °C. At this temperature the primers bind (or anneal) to the single DNA strands. The primers are short sequences of nucleotide bases which must join to the beginning of the separated DNA strands for the full copying process to begin. In the final step the mixture is heated up again to ∼ 72 °C for at least a minute. This is the optimum temperature for the DNA polymerase enzyme. The polymerase attaches nucleotide bases to the ends of the primers using the original DNA sequence as a template to build up complementary strands of DNA identical to the original molecule. The PCR cycle may be repeated up to thirty times to produce around 1 billion copies (2^{30}) of the original DNA. The whole process takes about 3 – 5 hours in a standard PCR reactor. The reasons for such a long processing time for PCR is mainly due to the large thermal mass of typical PCR systems, leading to slower heating and cooling rates.

Electrophoresis (EP)

Electrophoresis describes the migration of a charged molecule in a separation medium under the influence of an electric field. An accelerating force (F) acing on the molecule with charge q by an electric field E can be expressed by the Newton's law ($F = qE$). A terminal speed (u_E) of the molecule under the electric field can be achieved when the acceleration force equals to the frictional force (fu_E) generated by the separation medium [3],

$$u_E = \frac{qE}{f} \tag{1}$$

where f is a friction coefficient and u_E is the electrophoretic terminal speed. Also, the friction coefficient for a spherical particle of radius r moving through a fluid of viscosity η is given by $6\pi\eta r$. Thus, the terminal speed of a spherical molecule under influence of an electric field E can be written as,

$$u_E = \frac{qE}{6\pi\eta r} \tag{2}$$

where μ_E ($= q/6\pi\eta r$) is the molecule's mobility. Therefore, the difference in mobility (through either number of charges or size) produces a separation of molecules. Typically, electrophoresis is carried out in a sieving media made from either agar or polyacrylamide gels. Double-strand DNA is most commonly separated by gel electrophoresis. The sieving matrix slows down the migration rate of large molecules so that for a molecule of constant charge to mass ratio (such as DNA) there is a logarithmic dependence on the migration distance in the sieving matrix with respect to molecular weight. Electrophoretic separation is also used on other biological entities such as proteins, which are usually separated by sodium dodecyl sulfate polyacrylamide gel electrophoresis (SDS-PAGE)

where the SDS binds to the protein to create a constant charge to mass ratio on the protein surfaces.

Key Research Findings

In order to develop a fully integrated microfluidic device for biological applications, it is desirable to integrate essential biological processing functions such as cell lysis, sample purification, and genetic analysis. In addition, since integrated microfluidic devices are often made by connecting individual processing components which have to be individually controlled, the connection and control of a microfluidic network must also be developed. In this section, several examples demonstrating not only integrated microfluidic devices for biological applications but also unique control mechanisms of the network are discussed.

Belgrader et al. [4] reported the development of a personal PCR instrument by Cepheid Corporation. They demonstrated a battery-powered notebook thermal cycler for rapid multiplex real-time PCR analysis of nucleic acids in an inexpensive, portable format (Fig. 1). The instrument consists of a notebook computer, a reaction module, and integrated optics for four-color fluorescence detection. In the reaction module, several subcomponents such as heater elements and reaction chambers for PCR are included. In the optical module, an excitation block of 4 LEDs (470, 510, 540, and 574 nm) and a detection block of 4 photodiodes (520, 550, 585, and 628 nm) flanked the two bottom edges of the reaction tube. These edges served as optical windows for a series of focusing objectives, mirrors, and band-pass filters. They designed modules which could be operated together or independently. Using this system, they successfully demonstrated the detection and identification of that *Bacillus subtilis* and *Bacillus thuringensis* spores which have been used as safe biowarfare (anthrax) simulants. In addition, they characterized a single nucleotide polymorphism (SNP) for the hereditary hemochromatosis gene which is implicated in the hereditary disease hemochromatosis where a patient loses the ability to properly regulate the uptake of iron in the body. This system demonstrated how merging microelectronics with microbiology and genomics applications may result in smaller, less expensive bioinstrumentation with more flexibility, portability and functionality.

Woolley et al. [5] have successfully integrated silicon PCR reactors with glass capillary electrophoresis (CE) chips (Fig. 2). They directly connected the PCR chamber and the CE chip through a micropatterned channel filled with a hydroxyethylcelluose sieving matrix. They have shown that the PCR amplification of a β-globin target cloned in M13 took only a 15 min as well as the CE separation was completed within 120 sec, providing a total PCR-CE analysis time under 20 min. In addition, they also demonstrated that a rapid assay for genomic *Salmonella* DNA was able to be completed within 45 min, implying that challenging amplifications of diagnostically interesting targets can also be performed.

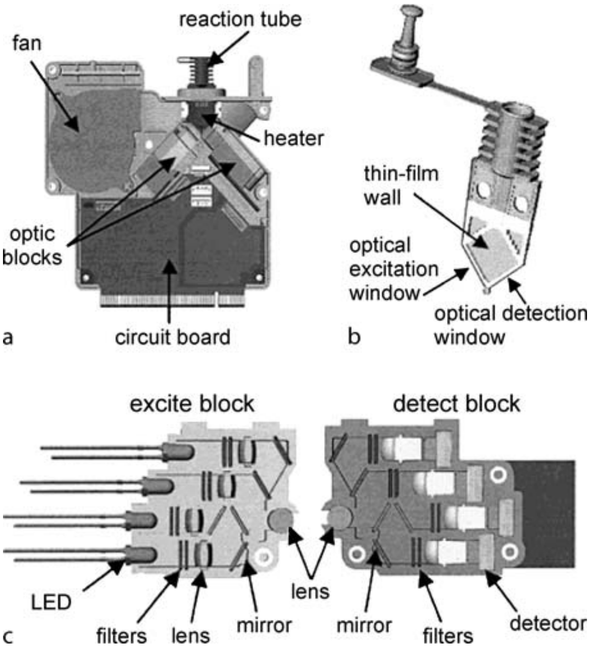

Integrated Microdevices for Biological Applications, Figure 1 The system consists of two reaction modules and one optical module for detection. (**a**) the complete reaction module, (**b**) the disposable 100 μl reaction tube, and (**c**) the four-color LED optical detection system. Reprinted with permission from Belgrader et al. A battery powered notebook thermal cycler for rapid multiplex real-time PCR analysis. Reprinted with permission from [4]

Easley et al. [6] reported a microfluidic genetic analysis system capable of accepting whole blood as a crude biological sample with the endpoint generation of a genetic profile (Fig. 3). Upon loading the sample, the glass microfluidic genetic analysis system device carries out on-chip DNA purification, PCR-based amplification, separation and detection in a sequential manner with a total process time of less than 30 min. The performance (genetic profiling) of the system was demonstrated using *Bacillus anthracis* (anthrax) presented in 750 nl of whole blood from living asymptomatic infected mice and *Bordetella pertussis* presented in 1 μl of nasal aspirate from a patient suspected of having whooping cough.

Blazej et al. [7] also reported a microfabricated bioprocessor for integrated nanoliter-scale Sanger DNA sequencing (Fig. 4). The bioprocessor is able to conduct all three Sanger sequencing steps, thermal cycling, sample purification, and capillary electrophoresis. They were able to

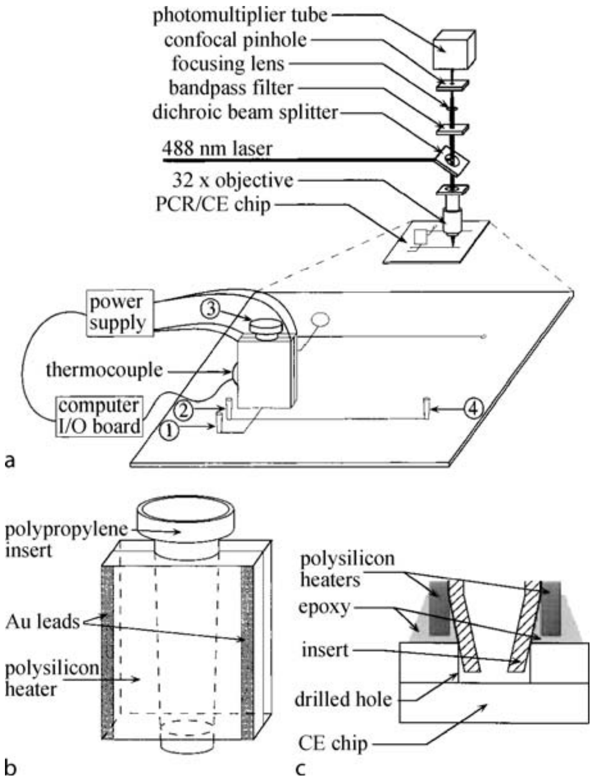

Integrated Microdevices for Biological Applications, Figure 2 Schematic drawing of the integrated PCR-CE microdevice (**a**) Laser-excited confocal fluorescence detection apparatus and an integrated PCR-CE microdevice. (**b**) Expanded view of the microfabricated PCR chamber. (**c**) Expanded cross-sectional view of the junction between the PCR and CE devices. The size of the epoxy filled gaps is exaggerated for viewing clarity. Reprinted with permission from Woolley et al. Functional Integration of PCR Amplification and Capillary Electrophoresis in a Microfabricated DNA Analysis Device. Reprinted with permission from [5]

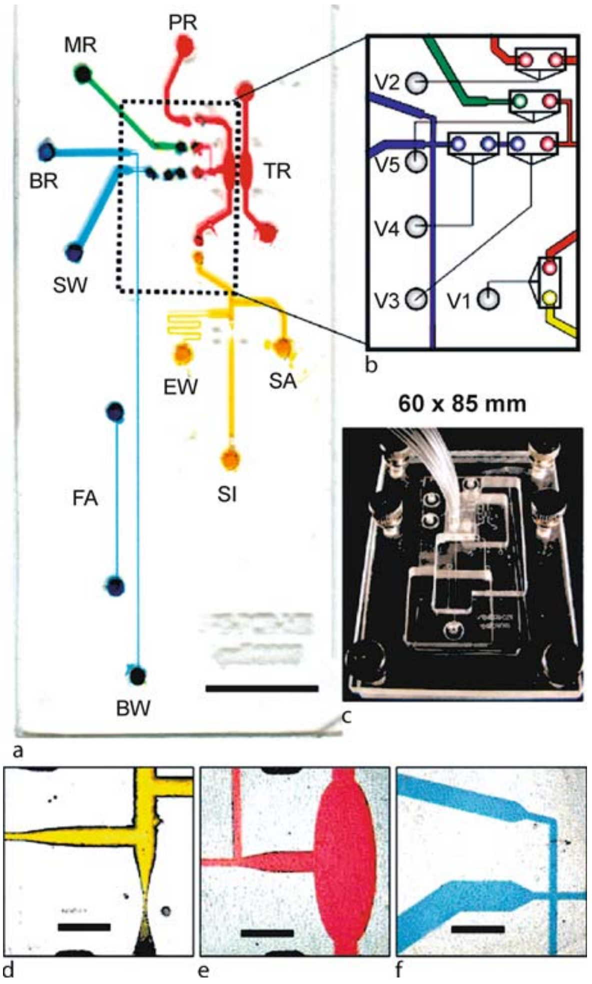

Integrated Microdevices for Biological Applications, Figure 3 Images of the microfluidic genetic analysis device. Domains for DNA extraction (**d**), PCR amplification (**e**), injection, and separation (**f**) are connected through a network of channels and vias. Easley et al. A fully integrated microfluidic genetic analysis system with sample-in-answer-out capability. Reprinted with permission from [6]

conduct complete Sanger sequencing from only 1 fmol of DNA template. In addition, they demonstrated that 556 continuous bases could be sequenced with 99% accuracy.

Lee et al. [8] reported a fully integrated microfluidic system for the DNA amplification and processing. This system integrated all essential cell processing functions from cell lysis, solution mixing, microfluidic transport (micropumping), and DNA amplification in a single system. In order to actively control each function, they integrated an electroosmotic pump, an active micromixer and an on-chip temperature control system (Fig. 5). In order to amplify the DNA of interest, the cell lysis is initially performed in a micro cell lysis reactor. The DNA samples are extracted from the cell lysis reactor, and the DNA samples, primers and reagents are driven by an electroosmotic pump into an active mixing chamber. Once a completely homogenized mixture is achieved, thermal cycling in a micro-PCR chamber to amplify the DNA fragments of interest is conducted. They demonstrated the functionality of the device using a 273 bp fragment obtained from *Streptococcus pneumoniae*, the most common cause of bacterial meningitis in adults.

Lagally et al. [9] also reported a fully integrated PCR-capillary electrophoresis microsystem for DNA analysis. The system consists of microfabricated heaters, resistance temperature detectors (RTDs), 8 parallel polymerase chain reaction (PCR) chambers, and a capillary electrophoretic (CE) DNA separation channel (Fig. 6).

In order to provide controlled and sensorless sample positioning and immobilization of the sample into the PCR chambers, valves and hydrophobic vents were used. In addition, by using microfabricated heaters and tempera-

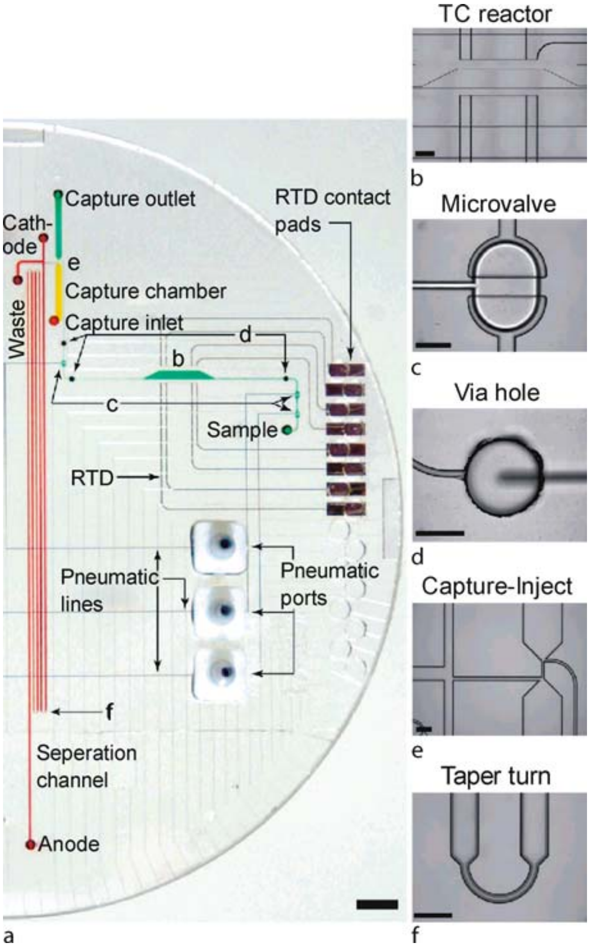

Integrated Microdevices for Biological Applications, Figure 4 Photograph of bioprocessor components including sequencing reagents, capture gel, separation gel, and pneumatic channels. Blazej et al. Microfabricated bioprocessor for integrated nanoliter-scale Sanger DNA sequencing. Reprinted with permission from [7]

ture sensing systems, they were able to achieve a rapid heating and cooling rate ($20\,^{\circ}\mathrm{C\,s^{-1}}$) in the PCR chamber. Once the amplified PCR product was obtained, the sample was labeled with a fluorescent dye. Finally, the sample was injected into the gel-filled capillary to conduct capillary electrophoretic analysis. Throughout their demonstration, they have used human genomic DNAs as a template for multiplex PCR amplification and obtained successful multiplex amplification of sex markers from human genomic DNA in less than 15 min. This device is promising because it demonstrated an integrated analysis microprocessor for use not only in point-of-care diagnostics and sample analysis but also in forensics, where only an extremely low sample volume may be available.

One issue which affects the integration of many biologically functional components on a single chip is to control

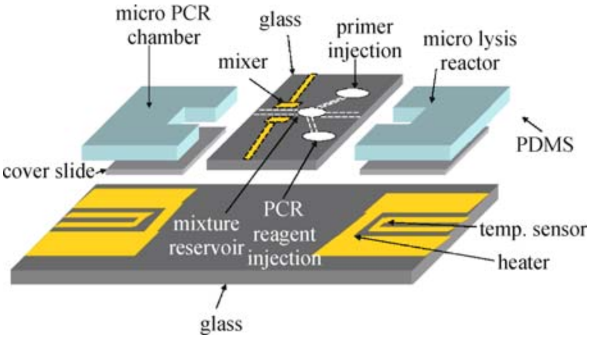

Integrated Microdevices for Biological Applications, Figure 5 (**a**) Schematic drawing of a fully integrated microfluidic system for cell lysis, mixing/pumping and DNA amplification. Lee et al. Integrated microfluidic systems for cell lysis, mixing/pumping and DNA amplification. Reprinted with permission from [8]

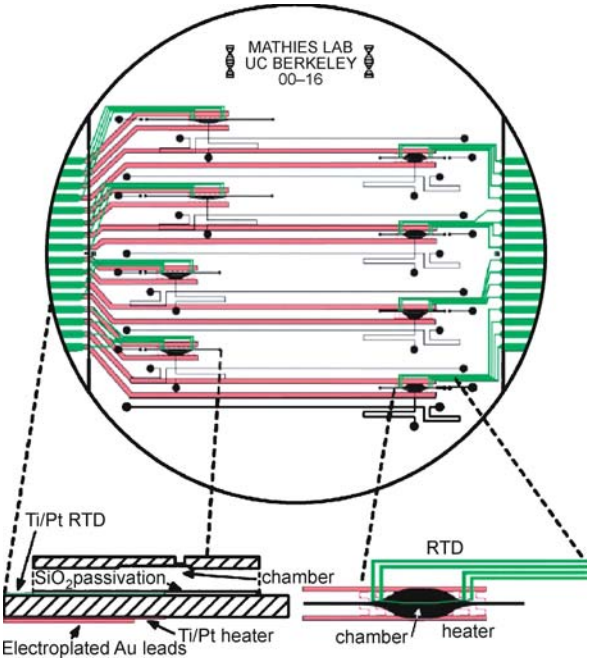

Integrated Microdevices for Biological Applications, Figure 6 Schematic of a fully integrated PCR-CE microdevice. The device consists of microfabricated heaters, RTDs, 8 parallel PCR chambers, and a CE device. Lagally et al. Fully integrated PCR-capillary electrophoresis microsystem for DNA analysis. Reprinted with permission from [9]

many fluidic components in an autonomous fashion. For instance, media or sample solutions often have to be transported into a designated area to allow appropriate reactions to occur. Thus, many research groups have attempted to develop methods for microfluidic network control.

Thorsen et al. [10] reported a novel method to control a complex microfluidic network. Their microfluidic network is analogous to large-scale integration (LSI) of electronic circuits on a semiconductor wafer. The microflu-

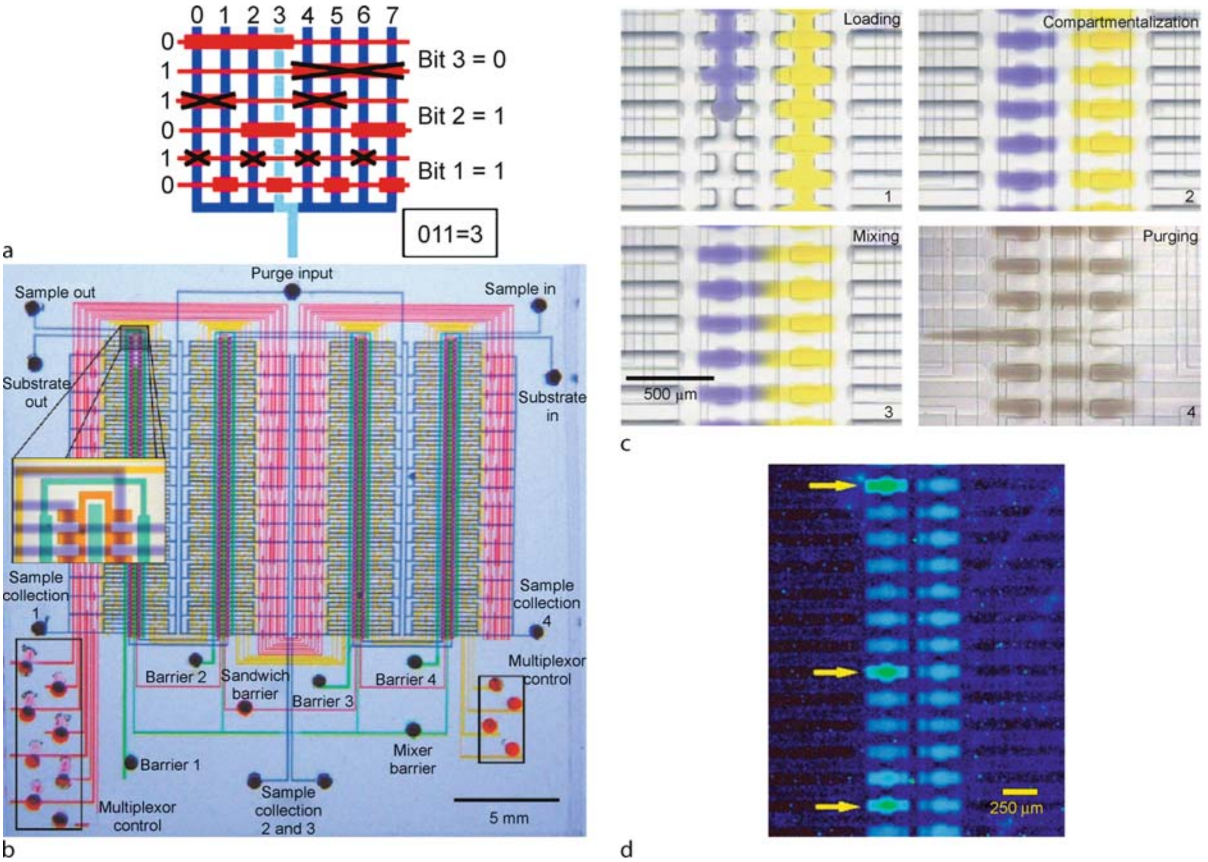

Integrated Microdevices for Biological Applications, Figure 7 (**a**) Operating principle of a multiplexor. (**b**) Optical micrograph of the microfluidic comparator chip. In order to visualize each element, food dyes have been loaded. (**c**) Set of optical micrographs showing the comparator in action. 1. Loading, 2. Compartmentalization. 3. Mixing. 4. Purging. (**d**) A fluorescence image showing cells (arrows) at comparator regions. Due to the enzyme reaction between CCP-expressing E. Coli in reagent and Amplex Red, cells produce fluorescence (resorufin), while other chambers remain low fluorescence due to the absence of CCP-expressing E. Coli. Thorsen et al. Microfluidic large-scale integration. Reprinted with permission from [10]

idic network consists of microfluidic channels with thousands of pneumatically actuated microvalves and hundreds of individually addressable sample processing chambers. An essential component of this fluidic network is the microfluidic multiplexor. The microfluidic multiplexors are combinatorial arrays of binary valve patterns that increase the processing power of the network by allowing complex fluid manipulations with a minimal number of controlled inputs. Figure 7a shows an operating principle of the multiplexor. Fluidic valves were placed at the intersection of the wide part of a control channel with a flow channel. By precisely controlling actuation pressure of control lines, the wide membranes placed at the intersection of control channels and fluid channels can be fully deflected and act as valves. Thus, the processing power of the fluidic network can be exponentially increased by placing hundreds of binary valve patterns. For instance, n fluidic channels can be individually addressed with only $2 \log_2 n$ control channels. In order to demonstrate this algorithm, they designed a device containing 2056 microvalves. This device can perform distinct assays in 256 subnanoliter reaction chambers and then recover the sample of interest with only 18 required external connections. In order to demonstrate complex fluid manipulation, they filled the fluid input lines with two dyes to demonstrate the process of loading, compartmentalization, mixing, and purging of the reagents of single chamber within a column of interest (Fig. 7c). Also, they have used this device as a microfluidic comparator to test for the expression of a particular enzyme. In their test, *Escherichia coli* expressing recombinant cytochrome c peroxidase (CCP), was used as a signal. In the presence of CCP, a fluorogenic substrate can be converted into a fluorescent product. In order to compare the signal generated by the enzymatic

reaction, the nonfluorescent resorufin derivative Amplex Red was used as a fluorogenic substrate. When an input signal chamber contains cells expressing the enzyme CCP, the nonfluorescent resorufin Amplex Red is converted to the fluorescent product, resorufin. Thus, the output fluorescent signal remains low in the absence of CCP. Figure 7d shows a fluorescence image of the comparator region of the chip after opening the mixing barrier located between the cell input and fluorogenic substrate input channels. Due to the enzyme reaction between the CCP-expressing *E. Coli* and Amplex Red, cells produce a fluorescence (resorufin) signal, while other chambers remain at a low fluorescence state due to the absence of CCP-expressing *E. Coli*. This result is very promising in many respects because it demonstrates how many different assays could be conducted in parallel on a single chip without contamination between samples.

Future Directions for Research

Although a variety of technologies related with microfluidic devices for biological applications are introduced here, there are still many challenges in producing these microdevices. For instance, many of these devices are still in the research phase of development and require significant personnel training for proper operation. Thus, there are significant challenges in improving the user input and operation for less stringent training requirements to make the systems available to a wide variety of researchers. They also have to be proven to be superior over conventional biological laboratory technology before they will be adopted in a wide number of biology laboratories.

Cross References

- ► Biosample Preparation Lab-on-a-Chip Devices
- ► Microfluidic Systems for High-Throughput Screening
- ► Lab-on-Chip Devices for Separation Based Detection
- ► Lab-on-a-Chip Devices for Sample Extraction
- ► Chromatographic Chip Devices

References

1. Sambrook J, Fritsch EF, Maniatis T (1989) Molecular Cloning: A Laboratory Manual. Cold Spring Harbor Laboratory Press, New York
2. Alberts B, Bray D, Lewis J, Raff M, Roberts K, Watson J (1994) Molecular Biology of The Cell. Garland Publishing, New York
3. Madou MJ (2002) Fundamentals of Microfabrication: The Science of Miniaturization. CRC Press, New York
4. Belgrader P, Young S, Yuan B, Primeau M, Christel LA, Pourahmadi F, Northrup MA (2001) A battery powered notebook thermal cycler for rapid multiplex real-time PCR analysis. Anal Chem 73:286–289
5. Woolley AT, Hadley D, Landre P, deMello JA, Mathies RA, Northrup MA (1996) Functional Integration of PCR Amplification and Capillary Electrophoresis in a Microfabricated DNA Analysis Device. Anal Chem 68:4081–4086
6. Easley CJ, Karlinsey JM, Bienvenue JM, Legendre LA, Roper GM, Feldman SH, Hughes MA, Hewlett EL, Merkel TJ, Ferrance JP, Landers JP (2006) A fully integrated microfluidic genetic analysis system with sample-in-answer-out capability. PNAS 103(51):19272–19277
7. Blazej RG, Kumaresan P, Mathies RA (2006) Microfabricated bioprocessor for integrated nanoliter-scale Sanger DNA sequencing. PNAS 103(19):7240–7245
8. Lee CY , Lee GB, Lin JL, Huang FC, Liao CS (2005) Integrated microfluidic systems for cell lysis, mixing/pumping and DNA amplification. J Micromech Microeng 15:1215–1223
9. Lagally ET, Emrich CA, Mathies RA (2001) Fully integrated PCR-capillary electrophoresis microsystem for DNA analysis. Lab Chip 1(2):102–107
10. Thorsen T, Maerki SJ, Quake SR (2002) Microfluidic large-scale integration. Science 298:580–584

Integrated Microdevices for Medical Diagnostics

Jeffrey D. Zahn
Department of Biomedical Engineering, Rutgers, The State University of New Jersey, Piscataway, NJ, USA
jdzahn@rci.rutgers.edu

Synonyms

Integrated biochips; i-STAT; Blood analysis; Drug delivery; Biomedical microdevices

Definition

Integrated microdevices for medical diagnostics seek to create autonomous microfluidic devices capable of performing laboratory grade analyses in a rapid, portable fashion where rapid results may mean the difference between life or death such as in an ambulatory or emergency room situation, or in harsh environments where there are no proper refrigeration or storage facilities such as in the third world or developing nations without access to these facilities. Another application of such technology is in personalized medicine allowing continuous patient monitoring during surgery or continuous feedback controlled drug delivery such as insulin, analgesics for chronic pain management or chemotherapy for cancer treatment. In these examples, integrated devices for blood analyses, blood typing, vaccine, antibiotic, or insulin delivery are presented, although a wide variety of biochips performing many different laboratory functions have been produced with varying levels of integrated functionality. These techniques are fundamental components of highly integrated

Integrated Microdevices for Medical Diagnostics, Figure 1 The i-STAT Portable Clinical Analyzer [1]

medical devices allowing personalized medicine or efficient point of care medical diagnostic systems.

Overview

The development of integrated microdevices for medical diagnostics allows rapid, reproducible laboratory grade tests for applications in point of care diagnostics, continuous patient monitoring and feedback controlled drug delivery and technologies to provide medical diagnostics and treatment especially to the developing world. Since these devices are very sophisticated, they must be designed for easy operation without technical training, improve patient compliance, provide advantages in time to analysis over conventional laboratory procedures. Furthermore, these integrated diagnostic modules must be inexpensive to produce and operate and be able to withstand harsh environments without the need for refrigeration, especially when used in the developing world. Most integrated microdevices for medical diagnostics fall into one of three categories described in this article; Specimen (blood, urine, saliva, etc.) analysis devices, continuous patient monitor, or controlled drug delivery devices although some integrated devices fall into more than one of these categories.

Basic Methodology

Most medical diagnostics are performed in a centralized laboratory within a hospital. A patient's specimen is collected and sent to this facility for analysis. Blood is usually collected via venipuncture with the blood drawn into color coded tubes. Urine is collected by patient excretion. Finally some specimens are collected on a cotton swab (cheek swab, cervical swab, etc.). After the specimen is collected it is analyzed in the lab facility. Blood is usually analyzed for a complete blood count (CBC) which determines the concentration of red blood cells, all types of white blood cells and platelets. A plasma chemistry panel may also be used to determine the relative amounts of different medically relevant components in the blood (i. e., sodium, potassium, chloride, magnesium, calcium, cholesterol, creatinine, urea, total protein, glucose, etc.). Urine is usually analyzed for glucose, protein, ketones and any blood within the urine, nitrite and leukocyte esterase. Urinalysis may provide clues to kidney disorders or infection. Cheek swabs are usually used for DNA genotyping of patients, while swabs from other areas such as vaginal or cervical swabs may be used to look for infection or sexually transmitted diseases.

Key Research Findings

Current Research on Integrated Microdevices for Medical Diagnostics

One of the first point of care devices developed was the i-STAT Portable Clinical Analyzer [1, 2]. This device is designed to perform laboratory grade blood analysis in an ambulatory or emergency department setting with a faster turnaround than drawing blood and waiting for laboratory results which may take up to several hours. The i-STAT uses a disposable cartridge which is inserted into an analysis unit that performs simultaneous assays of whole blood for sodium, potassium, chloride, glucose, urea nitrogen and hematocrit concentrations in less than 2 min (Fig. 1). The disposable cartridge is loaded with $\sim 65\,\mu$l of blood obtained from the patient which is transported to a parallel sensor array which performs the required tests. Sodium, Potassium, and Chloride are determined by direct ion-selective electrode potentiometry. Urea is hydrolyzed to ammonium by the enzyme urease and subsequently measured on another ion-selective electrode. Glucose is measured using standard enzyme based amperometry. The glucose is oxidized to gluconic acid and hydrogen peroxide by the enzyme glucose oxidase and the hydrogen peroxide is oxidized at a working electrode where the current generated is measured by amperometry. Finally, the blood hematocrit is determined by the blood conductivity. In correlating the results from the i-STAT device taken by non-laboratory personnel at a patient's bedside with the results from a standard centralized hospital blood analysis laboratory, the coefficient of variance between the i-STAT and central laboratory facility was less than 6.2% for all tests [1].

Another blood analysis device has recently been described by Ahn and colleagues [3]. Since blood typing is a critical procedure required for blood transfusions, the researchers fabricated an inexpensive disposable microdevice to rapidly determine blood type. This system is com-

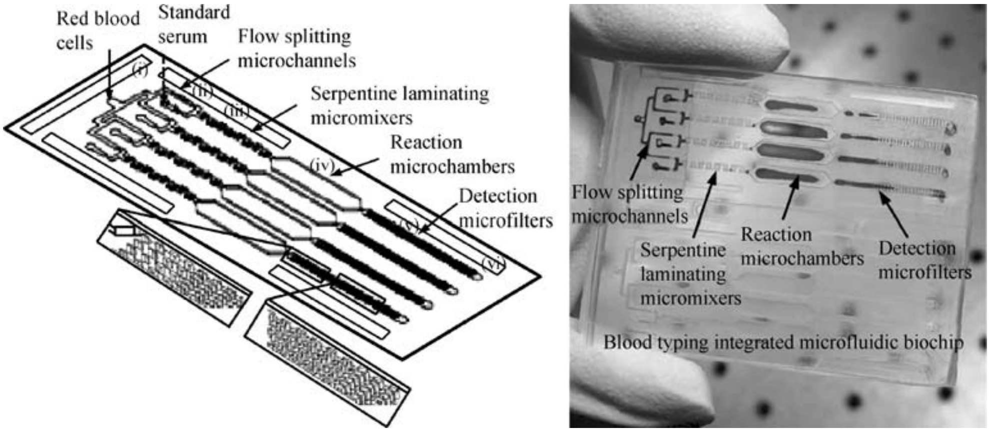

Integrated Microdevices for Medical Diagnostics, Figure 2 (Left) Schematic diagram of a blood typing biochip. The device contains flow splitting microchannels, a serpentine micromixer, reaction microchambers and detection microfilters. The reaction chamber holds $\sim 3\,\mu$l of blood. The agglutinated RBCs formed by antibody-antigen reaction between the blood cells and test solution are observed in the microfilter region. (Right) A photograph of the blood typing biochip [3]

posed of integrated sample entry channels, micromixers for mixing the blood with the reaction sera, reaction microchambers and detection microfilters (Fig. 2). The blood sample is introduced and mixed with the reaction blood typing serum which contains either anti-A, anti-B or anti-AB antibodies. If the red blood cells (RBCs) express either the A or B surface antigen they will agglutinate (clump together) in the appropriate serum containing either the anti-A or anti-B antibodies. Each of these antibody/RBC reactions is performed in parallel in different microchannels/microreactors to detect whether the RBCs agglutinate to determine if they express the A, B, neither or both surface antigens. The researchers demonstrated the functionality of the device by typing blood samples which were A+, B+ and AB+ blood types by detecting RBC agglutination in two parallel microreactors with one containing an anti-A serum and the other containing the anti-B serum (Fig. 3).

There are also major research efforts to create microfluidic devices to affect global healthcare in the developing world [4]. These devices must be able to function in a wide variety of environments considering the fact that many healthcare facilities in the developing world do not have access to refrigerated storage of perishables, calibration standards and reagents, trained personnel and in some cases even stable electrical power or sterile medical supplies. Thus, the challenges for using point of care microfluidic devices for delivering healthcare to the developing world are considerable. As highlighted in [4] immunochromatographic strip tests for diphtheria toxin, or sexually transmitted diseases like HIV, gonorrhea or syphilis among others are one of the few diagnostic technologies which have been successfully used in the developing world and should be the format which microfluidic platforms should aspire to supplant. These tests are formatted for the detection of a wide variety of antigens or antibodies, are stable at ambient temperature and can be shipped and stored without refrigeration. It would also be preferable to used body fluids other than blood (which requires a sterile syringe to obtain) such as urine or saliva. An example of an integrated microfluidic diagnostic card for analyzing saliva is shown in Fig. 4. The authors highlight the use of an H-filter for sample preconditioning to separate small molecules from other contaminating components followed by a micromixer for combining the saliva with an antibody solution. An H-Filter is comprised of two converging microchannels into a single daughter channel at the inlet and a diverging channel at the filter outlet. When two fluid streams are brought together with different solution composition, material will transfer from one stream into the other by diffusion. Since small molecules (e. g., ions) have higher diffusivity than larger molecules or particles (e. g., proteins or cells) these differences in diffusivity can be used to separate molecules or particles by tailoring the residence time of the fluid streams within the H-filter. Therefore, the H-filter is seen as a way of continuously extracting molecules from one fluid stream without the need for membrane filtration. After preconditioning, the solution is then transported to a gold surface for analysis by surface plasmon resonance (SPR) based detection. SPR is an optical method which measures the refractive index of a solution within ~ 300 nm of a gold film surface. The surface plasmon is an optical wave which propagates along the metal/solution boundary. When used for biosens-

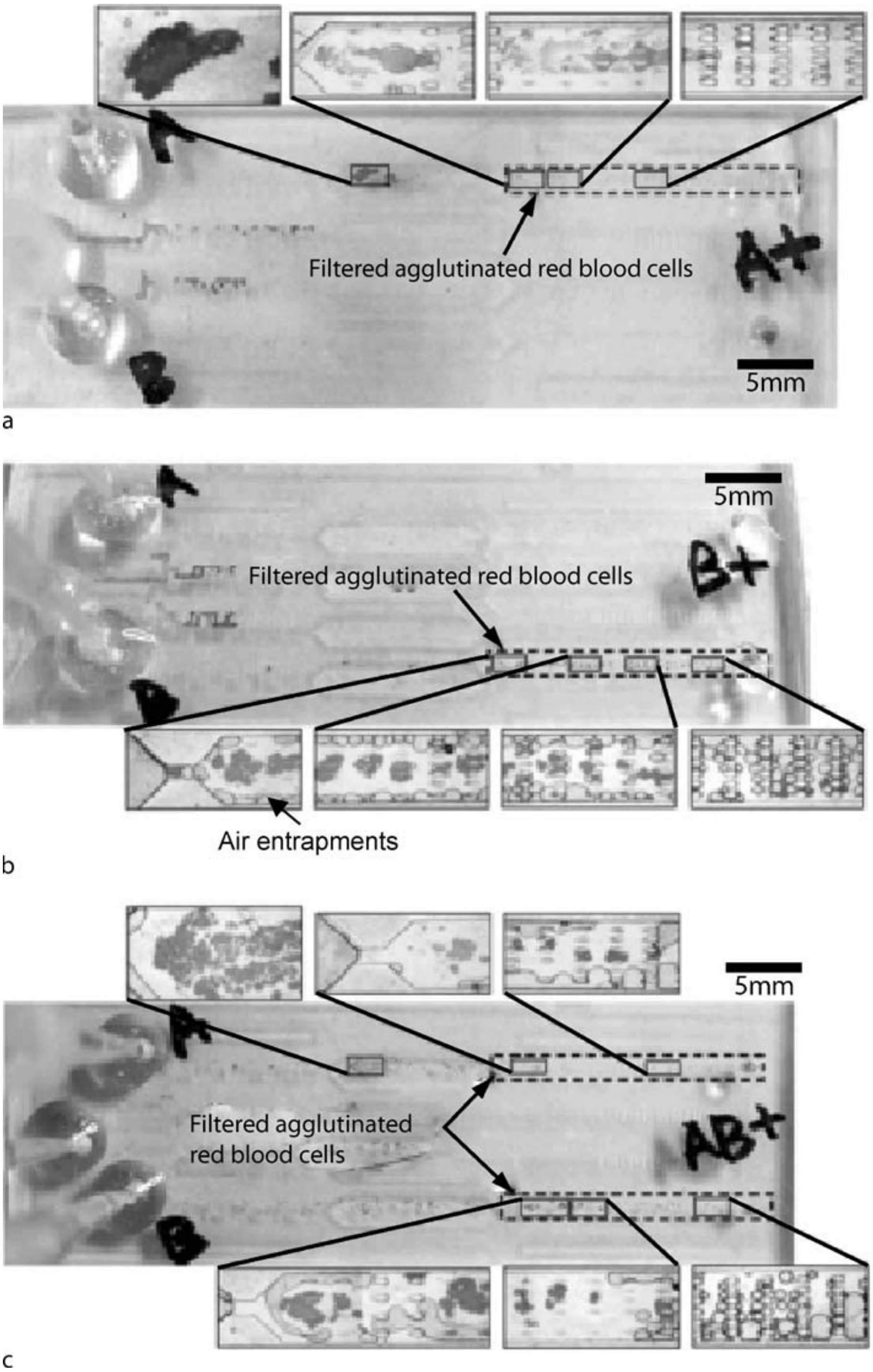

Integrated Microdevices for Medical Diagnostics, Figure 3 ABO typing results of (**a**) blood group A sample (**b**) blood group B sample and (**c**) blood group AB sample. The insets show the agglutinated RBCs [3]

ing, SPR is sensitive to molecular adsorption to the metal surface determined by the change in refractive index at the surface. This change in refractive index can be correlated to the analyte of interest in a concentration dependant manner since the higher the analyte concentration in solution, the larger the surface adsorption and therefore the larger

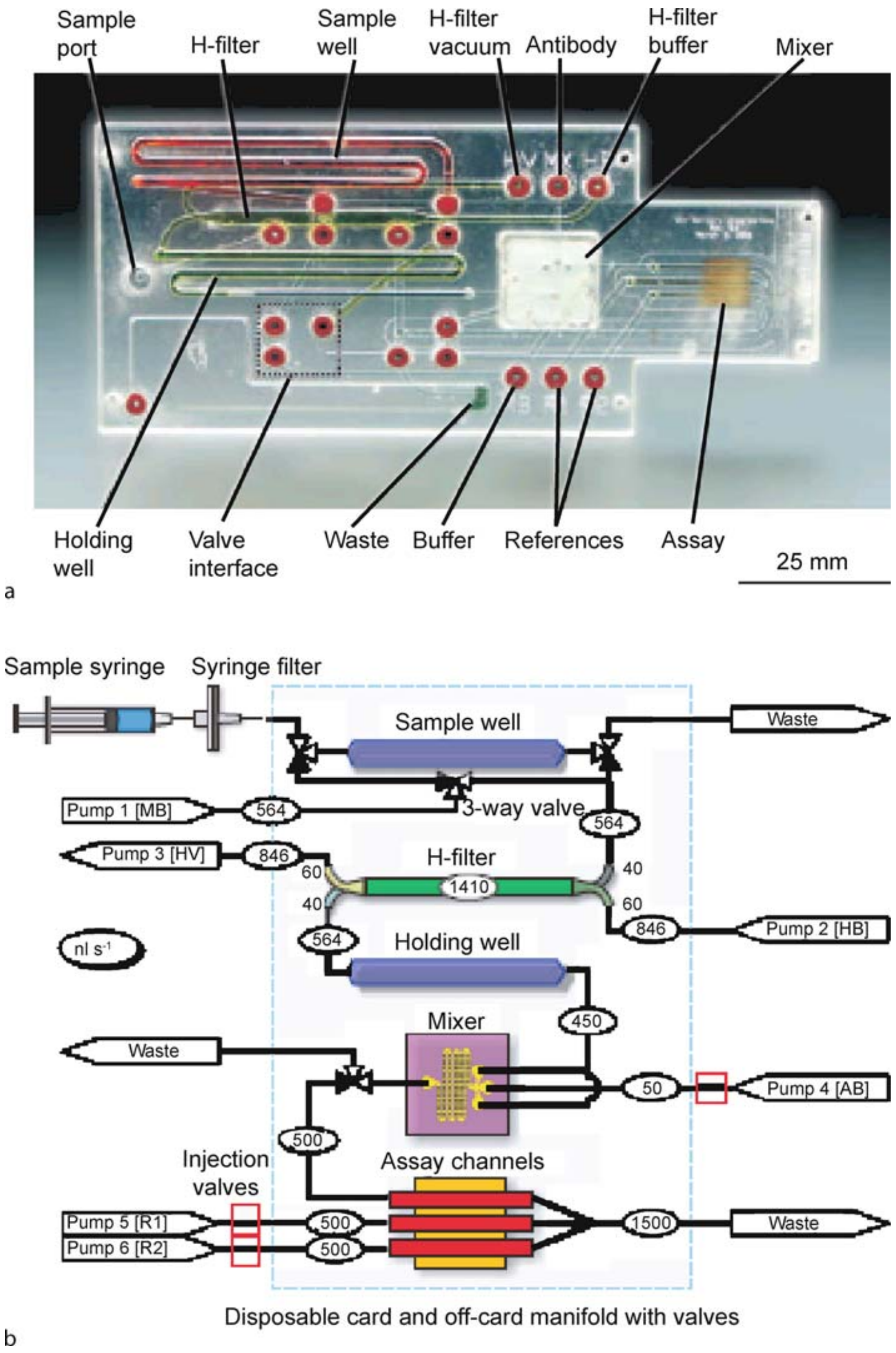

Integrated Microdevices for Medical Diagnostics, Figure 4 (**a**) Image of a POC diagnostic card for saliva analysis. (**b**) Schematic of a card showing an H-filter for sample preconditioning, micromixer for introducing antibodies to the sample and gold coated surfaces for SPR immunoassay based detection [4]

the change in refractive index. Selectivity to a single analyte can be improved by preadsorbing antibodies or ligands which bind the analyte of interest.

Another approach for creating integrated microfluidic devices for medical diagnostics is to create a device for the reconstitution (hydration) of a lyophilized (freeze dried) drug solution, followed by dilution, and delivery into a patient at a constant rate. Such a system could utilize freeze dried antibiotics, analgesics, or insulin for treating a diabetic patient as described in [5]. This system,

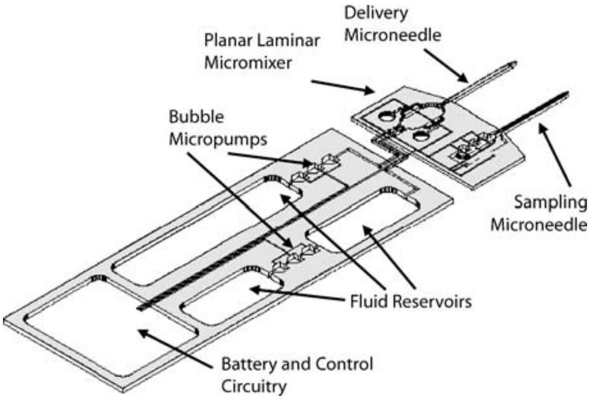

Integrated Microdevices for Medical Diagnostics, Figure 5 Schematic of a drug reconstitution and delivery system [5]

shown schematically in Fig. 5, consists of several fluid reservoirs, micropumps for moving fluid within the device, a micromixer for sample dilution and microneedles for drug delivery. Since, diabetes accounts for a large percentage of healthcare expenses in the United States and around the world and is growing in prevalence, many of these integrated technologies are being developed to treat this disease. The individual components in development for a feedback controlled insulin delivery system for diabetes treatment is also described in [6]. This system describes the use of miniaturized microdialysis systems and insulin delivery through microneedles which are particularly well suited to allow feedback controlled insulin delivery. In particular, the use of microneedles for insulin delivery has been demonstrated [7] as well as the development of microdialysis systems for continuous glucose sensing [8]. The real advantage of using such miniaturized systems lies in the ability to obtain greater patient compliance by having miniaturized sensing systems with faster response times and greater patient sampling frequencies along with less invasive (and less painful) drug delivery. These systems will allow truly personalized medicine for closed loop patient monitoring with feedback controlled drug delivery. These devices, first designed for diabetes treatment, are expected to impact the treatment of many diseases by allowing truly continuous patient monitoring for continuous personalized medical treatment.

Another example of an integrated microfluidic device for medical diagnostics is a device under development for the continuous monitoring of a patient undergoing heart surgery, especially when cardiopulmonary bypass (CPB) is used. The systemic inflammatory response in patients undergoing CPB is significantly affected by the artificial cardiopulmonary bypass pump and associated equipment (tubing, blood oxygenator, arterial filter, etc.). This inflammation may lead to significant postoperative complications including vital organ dysfunction while the symptoms may not present until several hours or days post surgery. Currently, there is no effective medical intervention for preventing or even studying this inflammatory response in real time. Real time monitoring of inflammation markers will help surgeons understand how CPB and surgical procedures may be modified to prevent the inflammatory response. Furthermore, it would allow surgeons and clinicians to take appropriate clinical action to the inflammatory responses earlier to avoid some of the severe postoperative complications. The system described in [9] presents a integrated microdevice designed to effectively separate blood cells from plasma and to analyze the inflammation markers (cytokines, complements, etc.) in the blood plasma in real time, while the surgery is proceeding, so that medical intervention can be taken to severe inflammation. The system described combines a continuous flow plasma separation module with an immunoassay module. The plasma separation module is driven by the pressure generated by CPB pumphead which drives the circulation during the surgery, while the device is connected to an arterial port off of the membrane oxygenator. The device is able to continuously skim plasma off from the blood sample by having a well defined flow structure which does not allow cells to enter the plasma channels. Next, the immunosensing function is accomplished by creating a well defined flow structure which uses a fluorescent activated cell sorting (FACS) mechanism for processing cytometric immunosensing beads. The microdevice is designed to allow individual serial bead processing steps to occur. In the case demonstrated in [9], a strepavidin coated bead is introduced into the device, and transported into a biotin-FITC fluorescent solution. The strepavidin on the bead binds the biotin in solution. The flow structure is designed in such a way to allow the bead to cross over from the bead carrier solution into the biotin solution without mixing and dilution of the biotin concentration. Next, the bead is ejected from the biotin solution into a washing solution where the background florescence is removed. The bead then moves into a detection window where the fluorescence intensity of the bead is detected. Since the fluorescence intensity on the bead is proportional to the biotin concentration in solution and the beads are continuously injected into the solution, this system is able to track changes in the biotin concentration over time. Further research is being conducted to allow real time immunosensing using a similar mechanism.

A final concern in the creation of integrated devices for medical diagnostics is the ability to integrate light sources for fluorescence based detection techniques. One popular area of research to miniaturize detection methods for

point of care devices is through the integration of organic light emitting diodes (OLEDs) with microfluidics. This is an attractive approach to integrated detection due to the small footprint of OLEDs, ability to multiplex and parallelize detectors, lower cost compared to solid state LEDs and ease of integration with microfluidic channels. Yao et al. [10] describe the integration of a green OLED as a fluorescence excitation source with microfluidic channels and the ability to detect 35 fmol (50 μM) of Rhodamine 6G and 1.4 fmol (2 μM) of Alexa 532 dyes in a volume of 0.7 nl. The OLED was fabricated as a p-n diode from layers of 40 nm thick α-napthylphenylbiphenyl (NPB) and 60 nm thick tris(8-hydroxyquinoline) aluminum (Alq_3) sandwiched between anode and cathode conductive layers. On top of the OLED an interference filter pinhole layer and microfluidic channel were layered. The pinhole layer was used to aligning the green light with the microfluidic structure. The emission light was collected by a fiberoptic detector coupled to a photomultiplier tube. This device was also used to detect bovine serum albumin conjugates labeled with the Alexa 532 dye during a capillary electrophoresis experiment.

Future Directions for Research

Although a variety of technologies related with microfluidic devices for medical diagnostics are introduced here, there are still many challenges to producing microdevices for medical diagnostics. For instance, with the exception of the i-STAT system many of these devices are still in the research phase of development and will require significant clinical trials and Food and Drug Administration approval before they can be used in a clinical environment. In addition, there are still many challenges in integrating fluorescence detectors into point of care diagnostics. They also have to be proven to be superior over conventional laboratory diagnostics. These challenges implies that there still needs to be substantial improvement in the further development of these medical diagnostic microsystems for truly realizing the promise of personalized medical platforms for patient point of care diagnostics.

Cross References

- ▶ Bead Based Microfluidic Platforms
- ▶ Microneedles – Application & Devices
- ▶ Microdialysis
- ▶ Integrated Microdevices for Biological Applications

References

1. Erickson KA, Wilding P (1993) Evaluation of a novel point of care system, the i-STAT portable clinical analyzer. Clin Chem 39(2):283–287
2. Jacobs E, Vadasdi E, Sarkozi L, Coman N (1993) Analytical evaluation of i-STAT portable clinical analyzer by nonlaboratory healthcare professionals. Clin Chem 39(6):1069–1074
3. Kim DS, Lee SH, Ahn CH, Lee JY, Kwon TH (2006) Disposable integrated microfludic biochip for blood typing by plastic microinjection molding. Lab Chip 6:794–802
4. Yager P, Edwards T, Fu E, Helton K, Nelson K, Tam MR, Weigl BH (2006) Microfluidic diagnostic technologies for global public health. Nature 442(27):412–418
5. Liepmann D, Pisano AP, Sage B (1999) Microelectromechanical systems technology to deliver insulin. Diabetes Technol Ther 1(4):469–476
6. Zahn JD, Hsieh YC, Yang M (2005) Components of an integrated microfluidic device for continuous glucose monitoring with responsive insulin delivery. Diabetes Technol Ther 7(3):536–545
7. McAllister DV, Wang PM, Davis SP, Park JH, Canatella PJ, Allen MG, Prausnitz MR (2003) Microfabricated needles for transdermal delivery of macromolecules and nanoparticles; Fabrication methods and transport studies. Proc Natl Acad Sci 100:13755–13760
8. Hsieh YC, Zahn JD (2007) On-chip microdialysis system with flow-through glucose sensing capabilities. J Diabetes Sci Technol (submitted)
9. Yang S, Ji B, Ündar A, Zahn JD (2006) Microfluidic devices for continuous blood plasma separation and analysis during pediatric cardiopulmonary bypass procedures. ASAIO J 52(6):698–704
10. Yao B, Lou G, Wang L, Gao Y, Lei G, Ren K, Chen L, Wang Y, Hu Y, Qui Y (2005) A microfluidic device using a grenn organic light emitting diode as an integrated excitation source. Lab Chip 5:1041–1047

Integrated Microfluidic Devices

▶ Microfluidic Systems

Integrated Nanoliter System

▶ Microfluidic Systems for High-Throughput Screening

Integrated Temperature Control in Microfluidic Systems

▶ Temperature Control in Microfluidic Systems

Integrated Waveguides

▶ On Chip Waveguides

Intelligent Gels

▶ Temperature-Sensitive Hydrogels

Inter-Atomic Potential

Definition

Chemical energy associated with the interaction between any two atoms. The potential gives rise to a force that can be repulsive or attractive and is usually dependent on the distance between the two atoms.

Interdigitated Microelectrode

Definition

Interdigitated microelectrodes (IME) or Interdigitated microelectrode array (IDA) are microelectrodes that each sensor element consists of a pair of opposing metal electrodes of digit width and separation that may be equal or unequal in the range 100 nm to 10 μ. These electrodes are usually microlithographically fabricated on silicon or glass substrates. They may be accompanied by a large area counter electrode of area 100 to 1000 times that of the area of each region of interdigitation. A reference electrode of silver/silver chloride may also be included to provide the reference potential for the electrochemical measurement. Such microelectrodes are well suited for electrical/electrochemical impedance spectroscopy, and have been widely used in impedimetric biosensing for DNA, enzymes, proteins, and cells.

Cross References

► Impedimetric Biosensors for Micro and Nano Fluidics

Interface Capturing Schemes for Free-Surface Flows

ALI NADIM
School of Mathematical Sciences, Claremont Graduate University, Claremont, CA, USA
ali.nadim@cgu.edu

Synonyms

Volume of fluid (VOF) method; Level set method; Phase field method; Diffuse interface model; Interfacial flow; Free surface flow; Interface tracking; Front tracking; Front capturing

Definition

Free-surface and interfacial flows refer to two-phase or multi-phase fluid flow problems that involve two or more immiscible fluids (e. g., liquid–liquid or liquid–gas systems) separated by sharp interfaces which evolve in time. Typically, when the fluid on one side of the interface is a gas that exerts negligible shear (tangential) stress upon the interface, the latter is referred to as a *free* surface. Interface capturing schemes are methods that are able to locate the interface, not by *tracking* the interface in a Largrangian sense (e. g., by following marker points that reside on the interface), but by *capturing* the interface by keeping track, in an Eulerian sense, of the evolution of an appropriate field such as a level-set function, a volume-fraction field, a phase-indicator field or a so-called color function.

Overview

Broadly speaking, there are two computational approaches to solving fluid flow problems that include an evolving interface between two fluid phases. These can be categorized as *interface tracking* and *interface capturing*. The former refers to methods that explicitly parameterize the interface and follow the points on the surface precisely in time. Examples include boundary-integral methods for Stokes or potential flows in which, in the case of two-dimensional or axisymmetric geometries, the interface is simply a curve and is often parameterized via arclength and followed in time. Another example is the use of *markers* on an interface which are tracked in a Lagrangian sense as the interface evolves, although the underlying flow field may be solved on a fixed Eulerian grid. The other approach, which is the subject of the present contribution, treats such problems by *capturing* the interface via an implicit representation. Examples include the level-set method, in which the interface is considered to be a level surface of a function that is defined over all space, and the volume-of-fluid method, in which the location of the interface is captured by keeping track of the volume fraction of each computational cell in the grid with respect to one of the fluid phases: cells that have a volume fraction of zero or unity do not contain an interface, whereas those that have a fractional value do.

In this contribution, first a number of fundamental concepts that are central to interface capturing are presented, including definitions of level-set functions and unit normal and curvature at an interface. This is followed by consideration of kinematic and dynamic boundary conditions at a sharp interface separating two immiscible fluids and various ways of incorporating those conditions into a continuum, whole-domain formulation of the equations of motion. Next, the volume-of-fluid (VOF) and level-set methods are presented, followed by a brief outlook on future directions of research and other interface capturing/tracking methods such as the diffuse interface model and front tracking.

Basic Methodology

In this section, we begin by reviewing the implicit representation of an interface as the level surface of a function defined over all space, together with appropriate definitions of the unit normal vector and the curvature at that interface. We then present a key result from vector calculus that is needed in deriving the proper boundary conditions at an interface. This sets the stage for the formulation of two-phase flow problems including the governing equations and boundary conditions, as well as a whole-domain formulation that combines the two.

Level-Set Functions

The set of points that reside on a two-dimensional interface in three-dimensional space can, at times, be given explicitly in a certain convenient coordinate system, e. g., $z = z(x, y)$ in a Cartesian system or $r = r(\theta, \phi)$ in spherical coordinates. However, such a description is not always practical. For instance, describing a spherical surface of radius a in a Cartesian system would require a multi-valued function: $z = \pm(a^2 - x^2 - y^2)^{1/2}$. The more general way of describing such an interface is as the set of points on which a function $\phi(x, y, z)$ is a constant, that is, as the constant-level set of the function. This function is not unique; for instance, the above sphere can be represented by $x^2 + y^2 + z^2 = a^2$, or by $(x^2 + y^2 + z^2)^{1/2} - a = 0$, among others. When the interface evolves in time, we can simply add the time variable t to the argument of the function. Also, without loss of generality, one can take the constant to be zero. Thus, an evolving two-dimensional interface in three-dimensional space can be considered as the set of points which satisfy the constraint

$$\phi(\boldsymbol{x}, t) = 0 \tag{1}$$

in which $\boldsymbol{x}$ is the position vector and t is time. It is often convenient to choose functions ϕ that change sign across the interface, being negative on one side and positive on the other.

One particular such function that has been found convenient in level set applications [10, 12] is the so-called signed distance function (SDF) which is the simply the minimum distance (or the negative thereof) from any point in space to the interface, usually taken with a positive sign in the region outside a closed surface and negative inside. For a circle of radius a in 2D, the SDF would be given by $\phi(x, y) = r - a$ where $r = (x^2 + y^2)^{1/2}$. This conical surface is plotted on the left side in Fig. 1 for a circle of radius $a = 0.2$ centered at $(0.5, 0.5)$ in the (x, y)-plane. Alternatively, the same circle can also be represented in a different form as the level-curve of a phase-field function [9, 13] such as $\phi = 0.5\left[1 - \tanh((r - a)/W)\right]$, with the boundary of the circle corresponding to $\phi = 0.5$ and with the property that $\phi \to 0$ far away from the circle and $\phi \approx 1$ well inside. The parameter W controls the steepness of the hyperbolic tangent profile in the vicinity of the interface. The right panel in Fig. 1 is a plot of such a representation of the above circle.

Normal and Curvature

From elementary vector calculus, it is known that the vector $\nabla\phi$ is normal to surfaces of constant ϕ. Therefore, the unit normal to the interface, which points in the direction of increasing ϕ, can be written in the form

$$\hat{\boldsymbol{n}} = \frac{\nabla\phi}{|\nabla\phi|} \quad \text{on } \phi = 0\,. \tag{2}$$

Along the interface, one can define the surface gradient operator ∇_s (cf. [8]) by projecting the usual gradient operator onto the surface using the operation $\nabla_s = (\mathbf{I} - \hat{\boldsymbol{n}}\hat{\boldsymbol{n}}) \cdot \nabla$, which removes any component parallel to $\hat{\boldsymbol{n}}$ from the gradient. Here, $\mathbf{I}$ is the unit isotropic tensor in three-dimensional space and the combination $\mathbf{I} - \hat{\boldsymbol{n}}\hat{\boldsymbol{n}} \equiv \mathbf{I}_s$, which is a surface-projection operator, can be thought of as the unit tensor in the two-dimensional surface. Strictly speaking, the unit normal $\hat{\boldsymbol{n}}$ given by (2) is only defined on the interface $\phi = 0$; therefore, one may only 'differentiate' it with respect to surface coordinates. If one adopts a locally orthogonal coordinate system on the surface with s_1 and s_2 denoting the arclengths along the two coordinate curves and with $\boldsymbol{i}_1$ and $\boldsymbol{i}_2$ unit vectors along the two directions, the surface gradient of $\hat{\boldsymbol{n}}$ (referred to as the curvature tensor) can be written as

$$\nabla_s\hat{\boldsymbol{n}} = \left(\boldsymbol{i}_1\frac{\partial}{\partial s_1} + \boldsymbol{i}_2\frac{\partial}{\partial s_2}\right)\hat{\boldsymbol{n}} = \frac{\boldsymbol{i}_1\boldsymbol{i}_1}{R_1} + \frac{\boldsymbol{i}_2\boldsymbol{i}_2}{R_2}\,, \tag{3}$$

in which it is recognized that $\partial\hat{\boldsymbol{n}}/\partial s_k = \boldsymbol{i}_k/R_k$ $(k = 1, 2)$, with R_k the radius of curvature of the coordinate curve. Upon taking the trace of the above tensor one finds that the surface divergence of the normal is exactly equal to twice the mean curvature of the interface:

$$\kappa = \nabla_s \cdot \hat{\boldsymbol{n}} = \mathbf{I}_s : \nabla_s\hat{\boldsymbol{n}} = \frac{1}{R_1} + \frac{1}{R_2}\,, \tag{4}$$

providing a convenient starting point for computing the mean curvature of any curved surface. More generally, if one defines an *extension* of $\hat{\boldsymbol{n}}$ which is identical to $\hat{\boldsymbol{n}}$ on the interface itself, is well-defined in the immediate neighborhood of the surface, and is a *unit*-vector throughout that

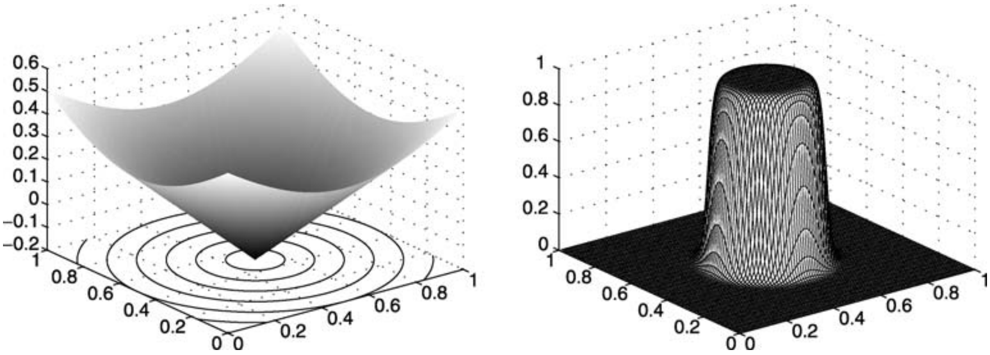

Interface Capturing Schemes for Free-Surface Flows, Figure 1 A circle represented by a signed distance function (left panel) and with a phase field function (right panel)

region, the mean curvature can also be calculated by taking the regular divergence of the extended vector field $\hat{\boldsymbol{n}}$ and evaluating the result at the surface. Namely,

$$\nabla_{\mathrm{S}} \cdot \hat{\boldsymbol{n}} = (\nabla - \hat{\boldsymbol{n}}\hat{\boldsymbol{n}} \cdot \nabla) \cdot \hat{\boldsymbol{n}} = \nabla \cdot \hat{\boldsymbol{n}}\,, \tag{5}$$

as long as $\hat{\boldsymbol{n}} \cdot \hat{\boldsymbol{n}} = 1$ everywhere for the extended field. Generally, the function $\phi(\boldsymbol{x}, t)$ is well-defined away from the interface as well, being negative on one side and positive on the other, and exactly zero on the surface. Thus, expression (2) (prior to evaluation on $\phi = 0$) defines a vector field which coincides with the normal on the surface and is normalized throughout the domain. Hence, the curvature of the surface can be calculated using the convenient formula

$$\kappa = \nabla \cdot \left(\frac{\nabla \phi}{|\nabla \phi|} \right) = \frac{\nabla^2 \phi - \hat{\boldsymbol{n}}\hat{\boldsymbol{n}} : \nabla\nabla\phi}{|\nabla \phi|}\,, \tag{6}$$

provided that the final result is evaluated on $\phi = 0$.

Surface Divergence Theorem

An important vector identity which is useful in deriving the dynamic boundary condition at a fluid–fluid interface is the two-dimensional generalization of the three-dimensional Gauss divergence theorem. The equivalent result for a curved two-dimensional surface S (see Fig. 2) must have the integral over the bounding curve C on its right-hand side, with the unit normal *to the curve* tangent to the surface (i.e., $\hat{\boldsymbol{\nu}}$ in Fig. 2) appearing therein. This surface divergence theorem can be obtained starting from the well-known Stokes curl theorem [8]. It is given in the form:

$$\int_S \left[-\hat{\boldsymbol{n}}(\nabla_{\mathrm{S}} \cdot \hat{\boldsymbol{n}}) + \nabla_{\mathrm{S}} \right] \square\, \Psi \,\mathrm{d}S = \oint_C \hat{\boldsymbol{\nu}} \square\, \Psi \,\mathrm{d}\ell\,. \tag{7}$$

Here, Ψ is an arbitrary scalar, vector or tensor field and the operation $\square$ can be a dot or cross product or a simple polyadic (tensor) multiplication. Upon noting that $\nabla_{\mathrm{S}} \cdot \mathbf{I}_{\mathrm{S}} = -(\nabla_{\mathrm{S}} \cdot \hat{\boldsymbol{n}})\hat{\boldsymbol{n}}$, the surface divergence theorem can also be written in the more compact form

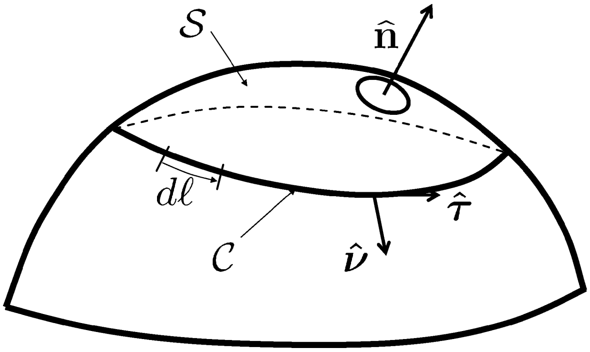

Interface Capturing Schemes for Free-Surface Flows, Figure 2 Schematic of surface patch S bounded by directed curve C

$$\int_S \nabla_{\mathrm{S}} \cdot (\mathbf{I}_{\mathrm{S}} \square \Psi)\,\mathrm{d}S = \oint_C \hat{\boldsymbol{\nu}} \square\, \Psi\,\mathrm{d}\ell\,. \tag{8}$$

As an example, suppose Ψ is simply the surface tension σ which is a scalar field defined at every point of the surface. This yields

$$\oint_C \hat{\boldsymbol{\nu}}\,\sigma\,\mathrm{d}\ell = \int_S \left[\nabla_{\mathrm{S}}\sigma - \hat{\boldsymbol{n}}(\nabla_{\mathrm{S}} \cdot \hat{\boldsymbol{n}})\sigma \right] \mathrm{d}S\,, \tag{9}$$

which is used in the derivation of the normal and tangential stress balances at an interface.

Boundary Conditions at a Fluid–Fluid Interface

The kinematic boundary condition on the evolving interface described by $\phi(\boldsymbol{x}, t) = 0$ is simply that

$$\frac{\mathrm{D}\phi}{\mathrm{D}t} = \frac{\partial \phi}{\partial t} + \boldsymbol{v} \cdot \nabla \phi = 0 \tag{10}$$

with $\boldsymbol{v}$ the interface velocity field. That is, the value of ϕ remains constant (equal to zero) as seen by an observer that moves with the interface.

To derive the corresponding dynamic boundary condition, suppose that the surface patch S depicted in Fig. 2 separates two fluids (called fluid 1 and fluid 2) at some instant of time, with the unit vector $\hat{\boldsymbol{n}}$ pointing into fluid 2. The balance of forces on the surface patch S thus takes the form:

$$\int_S \hat{\boldsymbol{n}} \cdot \Pi_2 \, \mathrm{d}S + \int_S (-\hat{\boldsymbol{n}}) \cdot \Pi_1 \, \mathrm{d}S + \oint_C \hat{\boldsymbol{\nu}}\sigma \, \mathrm{d}\ell = 0 \,. \quad (11)$$

The first term is the force on the interface by bulk fluid 2, with Π_2 referring to the total stress tensor in that fluid; the second term is the force on the interface by bulk fluid 1 on the other side of interface; and the third term is the force due to surface tension σ acting along the closed contour C that bounds the surface patch. Ordinarily, the sum of such forces must be equated to the *mass* of the surface patch multiplied by its acceleration, according to Newton's second law of motion. However, since the interface S is massless, the sum of the forces is zero not just under static conditions, but also in dynamic conditions when the surface is evolving. Using Eq. (9) to convert the contour integral to a surface integral, combining all three terms in Eq. (11) under a single integral sign, and recognizing that the combined integral is zero regardless of the choice of the surface patch S, one obtains the differential form of the surface force balance:

$$\hat{\boldsymbol{n}} \cdot (\Pi_2 - \Pi_1) = -\nabla_\mathrm{s} \cdot (\mathbf{I}_\mathrm{s}\sigma) = \hat{\boldsymbol{n}}(\nabla_\mathrm{s} \cdot \hat{\boldsymbol{n}})\sigma - \nabla_\mathrm{s}\sigma \,. \quad (12)$$

If the surface tension is uniform along the interface, its surface gradient (which is responsible for Marangoni flows) vanishes and the stress balance takes the simplified form:

$$\hat{\boldsymbol{n}} \cdot (\Pi_2 - \Pi_1) = \sigma\kappa\hat{\boldsymbol{n}} \,, \quad (13)$$

with $\kappa = \nabla_\mathrm{s} \cdot \hat{\boldsymbol{n}}$ as defined earlier.

Governing Equations

The equations of motion governing the flow of a single incompressible Newtonian fluid, known as the Navier–Stokes equations, consist of the conservation of mass:

$$\nabla \cdot \boldsymbol{v} = 0 \,, \quad (14)$$

and conservation of momentum equation:

$$\rho\frac{\mathrm{D}\boldsymbol{v}}{\mathrm{D}t} = \rho\boldsymbol{g} + \nabla \cdot \Pi = \rho\boldsymbol{g} - \nabla p + \nabla \cdot \left[\mu(\nabla\boldsymbol{v} + \nabla\boldsymbol{v}^T)\right] , \quad (15)$$

in which $p(\boldsymbol{x}, t)$ and $\boldsymbol{v}(\boldsymbol{x}, t)$ are the pressure and velocity fields, respectively, and ρ and μ are the fluid density and viscosity, and $\boldsymbol{g}$ is the gravitational acceleration. The stress tensor Π includes contributions from pressure and viscous stresses in the form:

$$\Pi = -p\mathbf{I} + \mu(\nabla\boldsymbol{v} + \nabla\boldsymbol{v}^T) \,, \quad (16)$$

with superscript T referring to the transpose. For the case of two immiscible fluid phases separated by an interface, Eqs. (14) and (15) are written for each fluid phase with its respective density and viscosity, and kinematic and dynamic boundary conditions (10) and (11) are applied at the interface where, in addition, continuity of velocity between the two phases is assumed.

In contrast, in interface capturing methods, it has been found convenient to formulate a *whole-domain* [11] or *one-fluid* [6] model that automatically captures the appropriate conditions at the interface between the fluids. The momentum equation is this formulation can be written as

$$\rho\frac{\mathrm{D}\boldsymbol{v}}{\mathrm{D}t} = \rho\boldsymbol{g} + \nabla \cdot \Pi + \delta_S\nabla_\mathrm{s} \cdot \Pi_\mathrm{s} \,, \quad (17)$$

in which $\Pi_\mathrm{s} = \sigma\mathbf{I}_\mathrm{s} = \sigma(\mathbf{I} - \hat{\boldsymbol{n}}\hat{\boldsymbol{n}})$ is the surface stress tensor and δ_S is the Dirac delta function centered on the surface (more precisely, the Dirac delta function of the signed distance from the interface). The last term on the right-hand side of Eq. (17) captures surface tension effects as an effective body-force term in the momentum equation. It can be written in several equivalent forms:

$$\delta_S\,(\nabla_\mathrm{s} \cdot \Pi_\mathrm{s}) = \nabla_\mathrm{s} \cdot (\delta_S\Pi_\mathrm{s}) = \nabla \cdot (\delta_S\Pi_\mathrm{s}) = -\delta_S\sigma\hat{\boldsymbol{n}}\kappa \,, \quad (18)$$

with the last two forms yielding the continuum surface stress [11] and continuum surface force [2] models, respectively. To see that the whole-domain formulation captures the correct boundary conditions at the fluid–fluid interface, one can simply integrate Eq. (17) over the volume occupied by a so-called *pillbox* that might straddle the surface patch S in Fig. 2 (not drawn). In the limit as the thickness of the pillbox tends to zero, the contributions from the first and second term in (16) to the volume integral tend to zero, whereas the third and fourth terms in (17) reproduce the dynamic stress boundary condition (12).

The fluid density and viscosity in the whole-domain formulation are expressed as functions of a phase-indicator function χ. For instance, with $\chi = 1$ in fluid 1 and $\chi = 0$ in fluid 2, the fluid properties can be written in the forms:

$$\rho = \rho_1\,\chi + \rho_2\,(1 - \chi) \quad \text{and}$$
$$\mu = \mu_1\,\chi + \mu_2\,(1 - \chi) \,. \quad (19)$$

The phase-indicator or color function χ can be related to a level set function ϕ which changes sign across the interface. For instance, if ϕ is negative in fluid 1 and positive in fluid 2, the appropriate relation is $\chi = 1 - H(\phi)$ where H is the Heaviside step function. Note that with the help of the phase-indicator function χ, the combination $\delta_S \hat{\boldsymbol{n}}$ that appears in the continuum surface force model is given by $\delta_S \hat{\boldsymbol{n}} = -\nabla \chi$.

The phase indicator function χ satisfies the simple advection equation

$$\frac{\mathrm{D}\chi}{\mathrm{D}t} = \frac{\partial \chi}{\partial t} + \boldsymbol{v} \cdot \nabla \chi = 0\,, \tag{20}$$

as do, in consequence, the fluid density and viscosity fields.

Key Research Findings

Numerical interface capturing methods consist of various techniques for integrating the above system of conservation of mass and momentum equations, together with advection of an appropriate level set or phase-indicator function, to enable an approximate localization of the interface and proper assignation of fluid properties. We now describe two widely used methods to accomplish this: volume-of-fluid and level-set methods.

Volume-of-Fluid Method

In the volume-of-fluid (VOF) method [3, 4, 11], a discretized analog of the phase-indicator function χ is used to track or capture the location of the interface. This analog is the volume-fraction field, defined as the fraction of each computational cell that is occupied by fluid 1, say, at any given instant. For instance, in a three-dimensional grid with cell $\{i, j, k\}$ having volume V_{ijk}, the volume fraction C_{ijk} is defined by

$$C_{ijk} = \frac{1}{V_{ijk}} \int_{V_{ijk}} \chi(\boldsymbol{x}, t)\, \mathrm{d}V\,. \tag{21}$$

Thus, cells in which $C_{ijk} = 1$ are fully within fluid 1, those where $C_{ijk} = 0$ are entirely in fluid 2, whereas those having $0 < C_{ijk} < 1$ contain a portion of the interface.

The evolution of the interface and advection of the phase-indicator function is accomplished by reconstructing the interface within each computational cell and computing the volume flux that occurs from each cell to its immediate neighbors under the prevailing flow. The surface reconstruction problem [11] is one of finding an interface with the correct unit normal vector which divides the computational cell into two regions, each occupied by the respective fluid phase. One popular way to accomplish this is using the Piecewise Linear Interface Calculation or Construction (PLIC) in which a linear interface with a given normal is found in each of the cells with a fractional value of C_{ijk}.

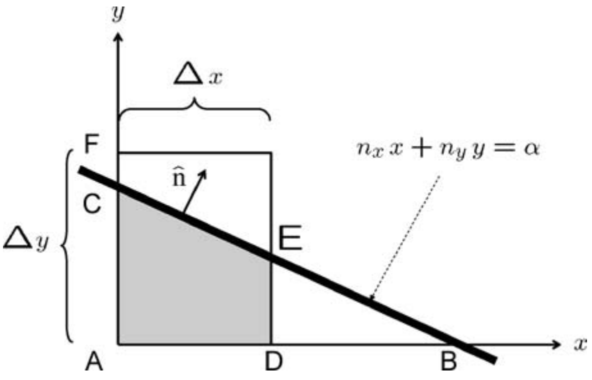

Interface Capturing Schemes for Free-Surface Flows, Figure 3
Piecewise Linear Interface Calculation (PLIC) in two dimensions.

The two-dimensional version of this calculation (cf. [11]) can be understood by referring to Fig. 3. Suppose that the unit normal to the interface in computational cell $\{i, j\}$ in 2D has been calculated by numerical differentiation of the volume fraction field: $\hat{\boldsymbol{n}}_{ij} = -\nabla C_{ij}/|\nabla C_{ij}|$, pointing away from fluid 1. Dropping the subscript ij for convenience, with a local origin chosen at the lower left corner of the computational cell (of width Δx and height Δy, as shown in Fig. 3), the equation for the straight line representing the interface would be given by $n_x x + n_y y = \alpha$, where parameter α represents the distance from the origin (lower left corner of the computational cell) to the line. As α varies for a fixed $\hat{\boldsymbol{n}}$, a family of parallel straight lines are generated, each cutting the cell at different places and thus representing a different volume fraction value. The relation between α and the volume fraction is obtained by finding the area of the shaded region *ADEC* in Fig. 3 as a function of α. For the particular case shown in the figure, this area is the difference between the area of the triangle *ABC*, which is given by $\frac{1}{2}|AB||AC| = \frac{1}{2}(\alpha/n_x)(\alpha/n_y)$, and the area of the smaller triangle *DBE* which is 'similar' to the original triangle with area ratio $|DB|^2/|AB|^2 = (\alpha/n_x - \Delta x)^2/(\alpha/n_x)^2$. However, the smaller triangle *DBE* only exists if point B falls to the right of point D, i. e., if $\alpha/n_x > \Delta x$. The area of the shaded region is thus given by:

$$\frac{1}{2}\frac{\alpha}{n_x}\frac{\alpha}{n_y}\left[1 - H\left(\frac{\alpha}{n_x} - \Delta x\right)\left(\frac{\alpha - n_x \Delta x}{\alpha}\right)^2 - H\left(\frac{\alpha}{n_y} - \Delta y\right)\left(\frac{\alpha - n_y \Delta y}{\alpha}\right)^2\right]. \tag{22}$$

The leading term in the square brackets provides the area of the triangle ABC and the next two terms subtract the area of triangle DBE (only if point B is to the right of D) and a similar triangle that might form above the computational cell if point C happened to be above point F. The Heaviside step functions H in Eq. (22) properly account for these conditions. We thus have the expression relating parameter α to the volume fraction C_{ij}, which is the ratio of the above shaded area to the cell area $\Delta x\, \Delta y$. In practice, we need the inverse of this result. That is, given the volume fraction C_{ij} and the normal $\hat{\boldsymbol{n}}_{ij}$, we must find the parameter α_{ij} which uniquely determines the straight line. The piecewise-quadratic expression in α is relatively easy to invert. However, some logic needs to be incorporated into such calculations to account for cases when the normal vector is directed such that the shaded region surrounds one of the other cell corners. Also, in situations when one component of the normal is nearly zero and the line is nearly vertical or horizontal, care must be taken to avoid subtraction of two large numbers (triangle areas) to calculate the relatively small remainder (shaded region). Similar calculations are required in three dimensions when the interface is represented by a plane that intersects a cube.

Advection of the volume fraction field (i. e., the discretized phase-indicator or color function) is usually effected in separate steps in x and y (and z, if three-dimensional) directions [11]. In each step, one-dimensional velocities defined on cell faces or edges are used to calculate the velocity throughout the cell by linear interpolation. Translation of the points on the interface by their local velocities for one time-step leads to affine transformation of the straight line, leaving it straight but with a new unit normal vector that is easily calculated. One then calculates the fluid volumes (of fluid 1, say) that have been transported to the neighboring cells in that dimension, as well as the volume that has stayed within the current cell. By summing the appropriate volumes, updated volume fraction fields can be computed. Upon repeating this for the remaining space dimensions, provided that the overall velocity field had been divergence free, excellent volume conservation is achieved and the volume of the final deformed fluid body is in good agreement with its starting volume. Upon coupling such a volume advection scheme with standard approaches to solving the fluid flow equations, the combined VOF-PLIC method is capable of simulating complex flows in multiphase systems.

Level Set Method

The level set method [10, 12] is an interface capturing scheme in which the evolution of an interface is tracked by evolving a level set function $\phi(\boldsymbol{x}, t)$ throughout space but focusing on the location of a specific level surface (or curve in 2D) of ϕ to capture the position of the desired interface. In contexts other than two-phase fluid flow, the evolution equation for the level set function can account for advection by a specified external velocity field $\boldsymbol{v}(\boldsymbol{x}, t)$, as well as propagation of the interface in the direction of the local normal vector at a constant speed a, and the motion of the interface in the normal direction at a speed proportional to the local curvature κ with proportionality constant $-b$. The resulting evolution equation for ϕ then takes the form:

$$\frac{\partial \phi}{\partial t} + \boldsymbol{v} \cdot \nabla \phi + a\ |\nabla \phi| = b\kappa\ |\nabla \phi|\ , \tag{23}$$

where curvature κ is given by Eq. (6). This equation is usually solved numerically by treating the advection terms using various upwind Essentially Non-Oscillatory (ENO) methods or Weighted versions thereof (WENO) [10] and by discretizing the curvature term on the right-hand side with central differences, using 5-point or 9-point stencils for the Laplacian operator.

If the level set function ϕ happens to be a signed distance function (SDF), one can show that (away from possible *kinks* that occur at points that are equidistant to two or more points on the interface), ϕ satisfies the nice conditions that:

$$|\nabla \phi| = 1 \text{ and } \kappa = \nabla^2 \phi \quad (\text{if } \phi \text{ is an SDF})\,. \tag{24}$$

This simplifies Eq. (23) into the much simpler convection-diffusion form

$$\frac{\partial \phi}{\partial t} + \boldsymbol{v} \cdot \nabla \phi + a = b\nabla^2 \phi\,. \tag{25}$$

However, even if one starts with an SDF for ϕ, after each time-step of Eq. (25), the resulting level set function will not remain a signed distance function. Thus, to take advantage of the simpler form provided by Eq. (25), after every time step, one also needs to *reinitialize* the resulting level set function into an SDF. An efficient procedure for doing so is based on the Fast Marching Method [12] in which, starting with the grid points in the immediate neighborhood of the interface, the level set function in a narrow band of cells near the interface is updated to become a signed distance and this is propagated out until an SDF is established throughout the desired computational domain. Another popular method is to solve a so-called re-initialization equation in pseudotime τ to relax the given level set function into an SDF. The re-initialization equation has the form:

$$\frac{\partial \phi}{\partial \tau} = S(\phi)\big(1 - |\nabla \phi|\big)\,, \tag{26}$$

where $S(\phi)$ is the sign function or an approximate or smeared version thereof [10].

In the context of fluid flow, the Navier–Stokes Eqs. (14) and (17) are integrated numerically, together with the advection equation $\mathrm{D}\phi/\mathrm{D}t = 0$ for the level set function (i. e., Eq. (24) or (25) with $a = 0$ and $b = 0$) and the re-initialization Eq. (26) is applied periodically or at every time step to keep the level set function well behaved. While this is more straightforward that the procedures involved in the volume-of-fluid method, it has been found that the VOF method has better mass conservation properties that the simple level set method.

Recent work has therefore focused on modifying the level set method appropriately in order to improve its mass (or volume) conservation properties when applied to two-phase flow. For general interface capturing using a level set function, one promising approach has been to replace the SDF function with a phase-field function ϕ that is forced to maintain a hyperbolic tangent profile near the interface [13]. This is called *sharp interface tracking* and is achieved by changing the evolution equation for ϕ to the form [13]:

$$\frac{\partial\phi}{\partial t} + \boldsymbol{v}\cdot\nabla\phi + a\,|\nabla\phi| = b\left[\nabla^2\phi + \frac{\phi(1-\phi^2)}{W^2}\right] . \quad (27)$$

The right-hand side of this equation approximates the curvature-drive motion for the case when the function ϕ is approximately possesses a hyperbolic tangent profile near the interface in the form

$$\phi = -\tanh\left(\frac{n}{\sqrt{2}\,W}\right) ,$$

with W a measure of the width or steepness of the profile and n the signed distance from the interface. Note that in this case, the interface is still a zero-level surface of ϕ but ϕ tends to ± 1 as one moves away from the interface into the two bulk regions.

For cases when one does not desire the interface to have any curvature-driven motion, the term on the right-hand side is still maintained in order to keep the sharp, hyperbolic tangent profile near the interface; however a so-called *counter term* is subtracted from the right-hand side in order to cancel the main curvature-driven flow. The resulting equation then becomes [13]:

$$\frac{\partial\phi}{\partial t} + \boldsymbol{v}\cdot\nabla\phi + a\,|\nabla\phi| = b\left[\nabla^2\phi + \frac{\phi\left(1-\phi^2\right)}{W^2} - \kappa\,|\nabla\phi|\right] , \quad (28)$$

in which the very last term in the square brackets on the right-hand side cancels a main portion of the curvature-driven flow generated by the first two terms in the bracket. In this context, interface speed a is set to zero to avoid constant-speed normal propagation of the surface and coefficient b is taken to be rather small in order to provide some numerical diffusion. Optimal values of b and W are explored in [13] and are found to be approximately $b \approx \Delta x$ and $W \approx 2\Delta x$, where Δx is the grid-size in a Cartesian grid. Good volume conservation properties have been achieved by this approach.

Another promising approach for the case of two-phase fluid flow, with some similarities to the above, has been to work with a level set function ϕ that varies from zero to unity, with the interface of interest being the constant surface of level 0.5 [9]. This level set function is updated in two steps during the flow. The first step is simple advection by the underlying incompressible flow, which is numerically implemented in its conservation form:

$$\frac{\mathrm{D}\phi}{\mathrm{D}t} = \frac{\partial\phi}{\partial t} + \boldsymbol{v}\cdot\nabla\phi = \frac{\partial\phi}{\partial t} + \nabla\cdot(\boldsymbol{v}\phi) = 0 , \quad (29)$$

with the final form integrated on a staggered grid with velocities defined on cell surfaces (or edges) used to calculate the flux of function ϕ from one cell to the neighboring cell, thus keeping the overall 'amount' conserved. This is followed by a second step in which the level set function is evolved in pseudotime τ to achieve an interface of constant profile and thickness. In contrast with [13], this step is also formulated in the form of a conservation equation [9]:

$$\frac{\partial\phi}{\partial\tau} + \nabla\cdot\boldsymbol{F} = 0 , \quad (30)$$

where vector flux $\boldsymbol{F}$ is given by

$$\boldsymbol{F} = \phi(1-\phi)\hat{\boldsymbol{n}} - \varepsilon\nabla\phi . \quad (31)$$

The first term in the flux expression provides an *artificial compression* that keeps the interface profile sharp; the second term provides a small amount of viscosity that controls the final thickness of the interface. The combined equation is thus of the form:

$$\frac{\partial\phi}{\partial\tau} + \nabla\cdot\left[\phi\,(1-\phi)\,\frac{\nabla\phi}{|\nabla\phi|}\right] = \varepsilon\nabla^2\phi . \quad (32)$$

Parameter ε which characterizes the diffusion (or viscosity) is chosen in accordance with the grid size in the form $\varepsilon = 0.5(\Delta x)^{1-d}$ with $d \geq 0$ (e. g., $d = 0$ or $d = 0.1$) to obtain good convergence and conservation properties [9].

Applications

Level set and VOF methods are often applied to a number of test problems such as propagation of a curve (e. g., a cosine function) in the normal direction at a given speed, advection of a circle in a translating or rotating flow, rotation of a *slotted disk,* or curvature-driven motion of a dumbbell-shaped region [9, 13]. Actual two-phase flow problems such as rising bubbles [9], settling droplets [3, 9], drops and bubbles passing through an interface, break-up of liquid jets [11], liquid sloshing in a container, and pinch-off of drops from a nozzle [3] have also been studied. Recently, applications of interface capturing methods to microfluidic problems have also begun to appear in much of the literature on nanotechnology, micro- and nano-fluidics, sensors and actuators, emphasizing problems of micro-droplet or bubble movement in micro-channels and Lab-on-a-Chip devices.

Future Directions for Research

The aforementioned interface capturing methods are finding use in fundamental studies and numerical simulations of microfluidic devices that involve two or more fluid phases separated by sharp interfaces in which capillary effects are important. Additionally, such problems often involve movement of contact lines that occur when a fluid-fluid interface meets a solid boundary. Models are being devised to incorporate contact line dynamics in the simulations though this is a challenging issue since the usual no-slip boundary condition at a solid interface is not compatible with contact line motion (resulting in infinite stresses at the contact line) and therefore some degree of slip in the neighborhood of the contact line needs to be allowed.

There are a number of limitations in interface capturing schemes that continue to be addressed by researchers. One is the problem of so-called parasitic or spurious currents [11] which can be attributed to the interfacial regions being under-resolved. These currents can be reduced via formulations that strictly enforce energy conservation and account for exchanges of kinetic and surface energies [5]. There are also difficulties in computations at small values of surface tension when the computed objects (drops, filaments, bubbles) become very small and cannot be properly resolved on the mesh [11]. The major short-coming of the level-set method has been its difficulty in conserving mass, though recent conservative formulations [9] appear to have overcome this issue to a reasonable extent.

Other approaches that combine concepts from the volume-of-fluid and level set methods [14] are also likely to be developed further. In parallel, interface tracking methods which follow the sharp interface in a Lagrangian sense through an Eulerian grid (e. g., [15]) or use adaptive grids that fit the instantaneous shape of the interface and provide grid refinement in regions of flow that require better resolutions [7] will also be highly competitive techniques for modeling interfacial and free-surface flow problems. Finally, approaches based on diffuse interface models (both single-component and binary) [1] appear to be equally promising for simulations of multiphase flows in microfluidics.

Cross References

- ▶ Boundary Element Method and its Application to the Modelling of MEMS Devices
- ▶ Boundary Slip of Liquids
- ▶ Bubble Dynamics in Microchannels
- ▶ Capillary Filling
- ▶ Capillary Force Valves
- ▶ Cavitation in Microdomains
- ▶ Digital Microfluidics
- ▶ Droplet Based Lab-on-Chip Devices
- ▶ Droplet Dispensing
- ▶ Droplet Dynamics in Microchannels
- ▶ Droplet Evaporation
- ▶ Electrocapillary
- ▶ Electrokinetic Two Phase Flow
- ▶ Electrowetting
- ▶ Electrowetting and Droplets
- ▶ Finite Volume and Finite Difference Methods for Modeling and Simulation
- ▶ Immersed Boundary Method
- ▶ Interface Tracking Schemes for Free-Surface Flows
- ▶ Interfacial Electrokinetic Flow
- ▶ Interfacial Instability
- ▶ Liquid–Liquid Stratified Flow in Microchannels
- ▶ Marangoni Convection
- ▶ Pressure-Driven Two Phase Flows
- ▶ Surface Directed Capillary Flow Systems
- ▶ Surface Tension Driven Flow
- ▶ Surface Tension, Capillarity and Contact Angle
- ▶ Thermocapillarity
- ▶ Thermocapillary Pumping
- ▶ Transport of Droplets by Acoustics
- ▶ Transport of Droplets by Thermal Capillarity

References

1. Anderson DM, McFadden GB, Wheeler AA (1998) Diffuse-Interface Methods in Fluid Mechanics. Annu Rev Fluid Mech 30:139–165
2. Brackbill JU, Kothe DB, Zemach C (1992) A Continuum Model for Modeling Surface Tension. J Comput Phys 100:335–354
3. Gueyffiera D, Lie J, Nadim A, Scardovelli R, Zaleski S (1998) Volume-of-Fluid Interface Tracking with Smoothed Surface

Stress Methods for Three-Dimensional Flows. J Comput Phys 152:423–456
4. Hirt CW, Nichols BD (1981) Volume of Fluid (VOF) Method for the Dynamics of Free Boundaries. J Comput Phys 39:201–225
5. Jamet D, Torres D, Brackbill JU (2002) On the theory and computation of surface tension: The elimination of parasitic currents through energy conservation in the second-gradient method. J Comput Phys 182:262–276
6. Lakehal D, Meier M, Fulgosi M (2002) Interface Tracking Towards the Direct Simulation of Heat and Mass Transfer in Multiphase Flows. Int J Heat and Fluid Flow 23:242–257
7. Zheng XM, Lowengrub J, Anderson A, Cristini V (2005) Adaptive Unstructured Volume Remeshing, II: Application to Two- and Three-dimensional Level-Set Simulations of Multiphase Flow. J Comput Phys 208:626–650
8. Nadim A (1996) A Concise Introduction to Surface Rheology with Application to Dilute Emulsions of Viscous Drops. Chem Eng Comm 148–150:391–407
9. Olsson E, Kreiss G (2005) A Conservative Level Set Method for Two Phase Flow. J Comput Phys 210:225–246
10. Osher S, Fedkiw R (2003) Level Set Methods and Dynamic Implicit Surfaces. Springer, Berlin
11. Scardovelli R, Zaleski S (1999) Direct Numerical Simulation of Free-Surface and Interfacial Flow. Annu Rev Fluid Mech 31:567–603
12. Sethian J (1999) Level Set Method and Fast Marching Methods. Cambridge University Press, Cambridge
13. Sun Y, Beckermann C (2007) Sharp Interface Tracking Using the Phase-Field Equation. J Comput Phys 220:626–653
14. Sussman M, Puckett EC (2000) A Coupled Level Set and Volume of Fluid Method for Computing 3D and Axisymmetric Incompressible Two-Phase Flows. J Comput Phys 162:301–337
15. Unverdi SO, Tryggvason G (1992) A Front-Tracking Method for Viscous, Incompressible, Multi-Fluid Flows. J Comput Phys 100:25–37

Interfaces between Microfluidics and Mass Spectrometry

Sergio Freire, Aaron R. Wheeler
Department of Chemistry, University of Toronto, Toronto, ON, Canada
awheeler@chem.utoronto.ca

Synonyms

Coupling microfluidic devices to mass spectrometers; Interfacing Lab-on-a-Chip platforms with mass spectrometers using MALDI and ESI

Definition

The ▶ mass spectrometer (MS) is an analytical tool that provides information about sample composition based on the mass-to-charge ratio (m/z). In order to analyze biological samples by MS, the relevant analytes must be driven into the gas phase, and ionized (charged). Two techniques are currently the most popular for the ionization of biological analytes are ESI (▶ Electrospray Ionization) and MALDI (Matrix-Assisted Laser Desorption/Ionization). In ESI, an electric field is applied to a solution of analyte to form a spray of charged droplets. Subsequent solvent evaporation and ion release enables analysis by MS. In MALDI, the analyte is co-crystallized with a solid matrix to form a dry spot on a surface. Under vacuum, the sample is then irradiated with a laser, which desorbs the sample from the surface and ionizes it. The developers of these so-called *soft* ionization techniques, which enabled, for the first time, the capacity to analyze large biomolecules such as proteins, were awarded the 2002 Nobel Prize in Chemistry.

I

Overview

In the last decade, mass spectrometry has emerged as one of the most powerful tools in bioanalysis. MS is commonly integrated with high performance liquid chromatography (HPLC) and other separation tools; as separations has been the most popular application for microfluidics, it is perhaps natural that interest has grown in interfacing mass spectrometry with microfluidics. While the focus of this chapter is on the microfluidics-MS interface, we note that one of the most popular applications for mass spectrometry is in the field of proteomics (the study of the complement of proteins expressed in a system), which has emerged as the next great scientific challenge in the post-genome era. Thus, many of the descriptions in this essay are viewed through the lens of proteomics; for more comprehensive information on this topic we refer the reader to other chapters of the Encyclopedia (▶ proteomics in microfluidic devices, ▶ integrated micro devices for biological applications).

Basic Methodology

Mass Spectrometers

The principle of operation of mass spectrometers is that electric and/or magnetic fields can be used to manipulate ions in space, and that their trajectory is a function of mass and charge. Ions of interest can be manipulated as a beam or trapped by confining electrodes, leading to different mass resolution and accuracy depending on the type of MS used. Although mass spectrometers have been used for approximately a century, the analysis of high molecular weight compounds has only become possible with advances in electronic instrumentation and the development of soft ionization techniques. Currently, it is possible to characterize analytes with molecular weight over 500 kDa [1].

Of special importance is the technique of tandem mass spectrometry (MS/MS), which integrates two stages of mass analysis. A particular ion of interest (called the parent or precursor ion) is selected in the first MS stage, allowed to fragment, and then analyzed further by the second MS stage. This technique has become important in proteomics, as protein sequences can be elucidated from the pattern of fragmentation. The ultimate identification of proteins requires complex database searching algorithms (e. g., SEQUEST [2]), and presents big challenges for data analysis (► mass spectrometry).

Ionization Methods

Several methods can be used to ionize samples, enabling the analysis by mass spectrometry. Two *soft* ionization methods are currently the most popular, ESI and MALDI. In ESI [3], an electric field is used to generate an aerosol of charged droplets from the end, or *tip*, of a fluid-filled tube. A schematic depicting the ESI process [4] is shown in Fig. 1a. The applied field leads to accumulation of charge close to the edge of the ESI tip. When the forces generated by charge repulsion overcome those associated with surface tension, the meniscus of the liquid assumes a conical shape, called a Taylor cone. When working properly, the shape of the cone is well defined, and results in a spray of droplets leading to the spectrometer.

After spraying, each charged droplet shrinks due to solvent evaporation. As the forces driven by coulombic repulsion and surface tension become similar, the surface-charged liquid droplet becomes unstable and disintegrates. This phenomenon is called coulombic fission, and can be predicted by the Rayleigh stability limit [3] As the droplets reduce to nanoliter volumes after successive bursts of fission, charged analytes are released into the gas phase. Two mechanisms have been proposed to explain this process: solvent evaporation from droplets containing just one ion; and direct release of ionized samples from droplets. As microfluidic devices handle volumes of liquids in the order of nanoliters, integrating microchannels with ESI requires dedicated nozzles (called nanoelectrospray, or nanospray, tips) capable of spraying minute volumes. The principles that apply for the stability of nanospray tips are the same as for conventional ESI.

A second popular soft ionization method is MALDI. In this technique, analytes are co-crystallized with a matrix (typically a small, acidic, organic molecule), with an absorption maximum close to the wavelength of a laser used to irradiate the substrate. This process is typically performed in vacuum (although it has been shown to be feasible at atmospheric pressure); after the analytes have been desorbed and ionized (in MALDI, fast heating caused by the laser pulse desorbs analytes into gas phase; however, the process by which proteins become charged is still a topic of study), they are guided to the MS for analysis [5] (Fig. 1b).

ESI and MALDI have distinct advantages and disadvantages, such that they are complementary for many applications. Of the two techniques, ESI is the softer one, allowing for ionization of intact multi-molecule complexes; however, in the presence of high concentrations of salts or other unwanted constituents, the formation of ions can be suppressed (making analysis impossible). This effect is less pronounced in MALDI, which can produce ionized products even in the presence of salts; but MALDI spectra

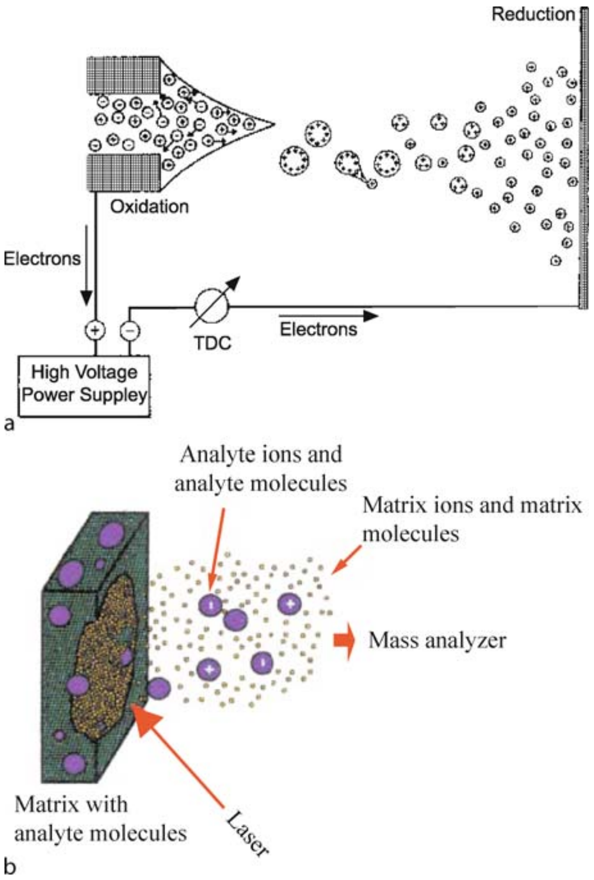

Interfaces between Microfluidics and Mass Spectrometry, Figure 1 Schematic depictions of (**a**) ESI and (**b**) MALDI mass spectrometry. In (**a**), the electric field causes an accumulation of positive charges at the liquid meniscus. When coulombic repulsion forces overcome the forces associated with surface tension, a spray is formed. Additional mechanisms (see text) lead to the release of analytes from the droplets. Reprinted with permission from Kebarle et al. [4]. In (**b**), analytes are co-crystallized with a matrix which has an absorption maximum near the wavelength of the laser used to desorb the analytes for analysis by MS. Reproduced by permission of Annual Reviews [5]

tend to be very noisy in the mass range below 500 daltons (Da), due to the presence of matrix ions. MALDI usually generates singly charged analytes, making data analysis trivial; ESI generates many differently charged species for each analyte, which makes interpretation of spectra more challenging, as complex mixtures lead to spectra with hundreds of peaks. Finally, in MALDI, the intensity of the signal associated with a particular analyte is not easily related to the amount of sample; this contrasts with ESI, where the intensity of the signal increases linearly with the analyte concentration over a wide range.

ESI and MALDI are considered to be the most appropriate candidates for coupling microfluidic devices to mass spectrometry. In what follows, we present a survey of the different kinds of microfluidic-MS interfaces reported in the literature and discuss the most promising geometries.

Key Research Findings

Electrospray Ionization

A variety of strategies for integrating microfluidic devices with nanoelectrospray ionization have been reported. Proteomic sample solutions are pumped through microchannels pneumatically or by electroosmotic flow (EOF) at $\sim 100 - 300\,\mathrm{nL/min}$; samples are typically dissolved in low-pH buffers modified with organic solvents suitable for positive mode mass spectrometry, with detection limits in the fmol-amol range. These methods can be broadly classified by how the electrospray is generated, including: direct spray from channels [6]; spray from mated, conventional tips [7]; and (3) spray from microfabricated tips [8–12].

The simplest approach for interfacing microchannels with mass spectrometry is to electrospray directly from a channel (i. e., the unmodified edge of a device). As reported by Xue et al. [6] the first microchannel-ESI interface exhibited limited performance due to eluent spreading at the edge of the chip resulting from the non-tapered geometry and the hydrophilicity of the substrate. Others improved the method by mechanically tapering the edge of substrates and by integrating hydrophobic coatings on the edges of the devices. However, these methods do not match the performance of conventional nanospray tips, and the strategy of spraying directly from channels has been largely abandoned.

A second strategy for interfacing microchannels with mass spectrometry is the coupling of microfluidic devices to conventional pulled glass capillary tips. These devices are capable of efficiently sampling analytes into the spectrometer, generating mass spectra with sensitivities similar to those of conventional techniques. For example, Lazar et al. [7] reported sub-attomole detection of peptides using a glass microfluidic device mated to a conventional electrospray tip. A major drawback for this strategy, however, is in separation resolution: bands of analytes mix as they pass through dead volumes in the interface between chip and capillary. As a result, this device geometry is not likely to be useful for most applications.

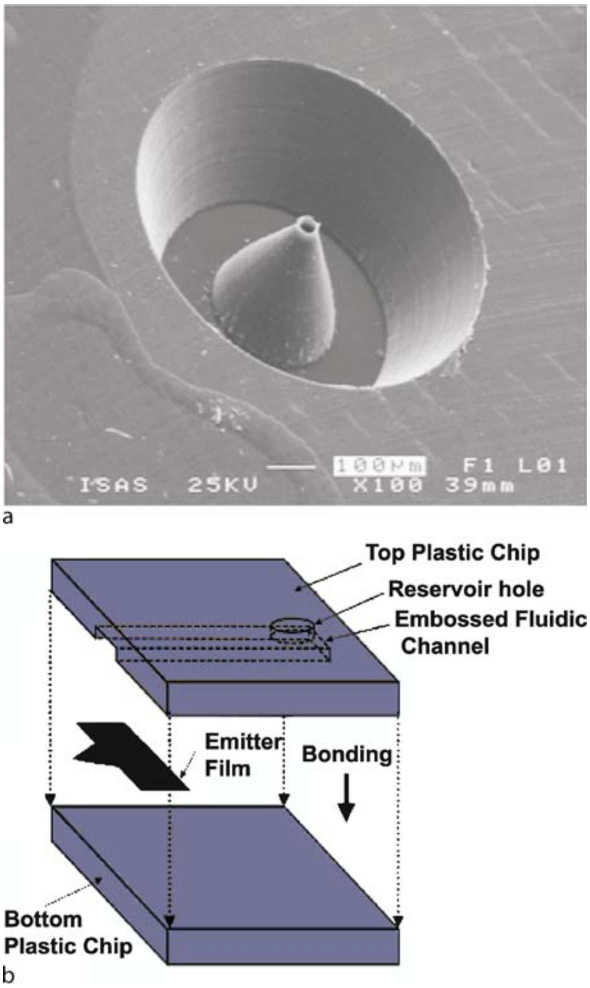

Interfaces between Microfluidics and Mass Spectrometry, Figure 2 Two nanospray sources: (**a**) nozzle fabricated by micro milling of PMMA, reproduced by permission of [8]; (**b**) nozzle formed by sandwiching a 2D parylene tip between cover plates. Reprinted with permission from Kameoka et al. [10]

A third strategy for microfluidic-nanospray interfaces, microfabricated, tapered electrospray tips [8–12] is the most promising that has been reported. In fact, several devices with this configuration are now available commercially (for example, from Advion Biosciences and Agilent Laboratories). Several authors have fabricated devices capable of sustaining a stable spray with no dead volume between the channel and tip. For example, Fig. 2a shows a micro-milled electrospray nozzle in poly(methyl

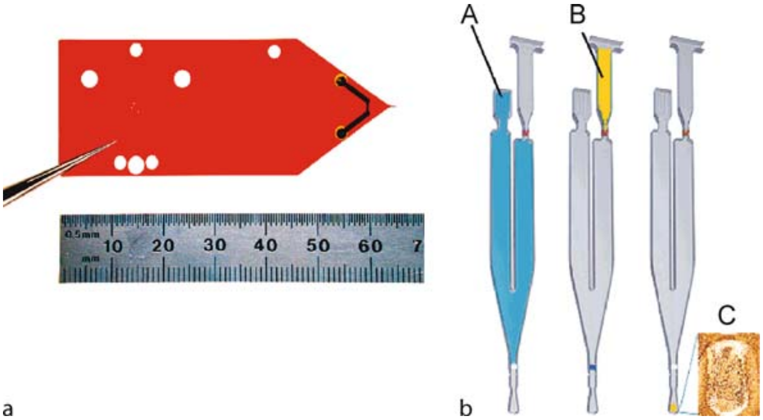

Interfaces between Microfluidics and Mass Spectrometry, Figure 3 Two commercial microfluidics-MS interfaces: (**a**) a polyimide microchannel device with integrated ESI tip formed by laser ablation. Reprinted with permission from Yin et al. [11] and (**b**) schematic of MALDI CD device (see text for details). Reprinted with permission from Gustafsson et al. [15]

methacrylate) (PMMA) fabricated by Schilling et al. [8] The performance of the spray is dependent on the nozzle diameter and apex angle. Large diameter nozzles (100 μm) have to be coated with fluorinated polymer to prevent liquid spreading, and performance depends on the state of the coating. The best performing tip geometry had a 30 μm wide nozzle with a 60° angle, with no coating; this device was capable of generating a stable spray for several hours. Xie et al. [9] used vapor-deposited parylene-C to fabricate ESI tips on silicon microfluidic devices, enabling integrated liquid chromatography with mass spectrometry detection with comparable performance to conventional techniques. The drawback for these devices is the complexity involved in their fabrication, requiring many sequential photolithography steps in a cleanroom. However, parylene is a material with high chemical resistance, and may be a useful choice for the construction of nanospray tips in future work. For example, Kameoka et al. [10] constructed a nanospray tip comprising a parylene film sandwiched between two plastic plates (Fig. 2b). This device is relatively easy to fabricate, and demonstrates that a 3D hydrophobic nozzle is not required; a stable spray of bioanalytes can be obtained by using a planar, triangular parylene tip.

The most promising microfabricated ESI interface may be the one developed by Yin et al. [11], which features a nanospray tip formed by laser ablation (355 nm) of a polyimide substrate (Fig. 3a). The fabrication required to form these tips is relatively simple, and the devices integrate separation and sample enrichment modules which lead to mass spectrometry analysis with peak resolution, limits of detection and signal-to-noise ratio (S/N) similar to those obtained by conventional macro-scale methods. Complex protein mixtures from blood plasma were characterized using this platform [12], with a detection limit in the low femtomole range; this device is now commercially available (Agilent Laboratories).

MALDI

MALDI is an alternative to ESI for an interface between microfluidic platforms and MS. The geometry of MALDI detection targets features arrays of crystallized sample spots on an open surface, and the process is (in general) performed under vacuum. Thus, MALDI is not an obvious match for interfacing with microfluidics; despite this, several interfaces with microfluidics have recently been developed.

Enclosed microchannels are by definition not accessible to laser desorption/ionization, which requires an open surface from which analytes can be sampled into the spectrometer. Several strategies have been adopted to circumvent this challenge, including the elution of bands of analytes from microfluidic devices onto an open substrate, where they are dried and analyzed. Alternatively, Brivio et al. [13] developed means to desorb analytes directly from enclosed channels through sub-micron pores in the device cover. Musyimi et al. [14] employed a rotating ball to transfer analytes from polymer microchannels to a MALDI-MS system without compromising the vacuum required for mass spectrometry.

In one of the most complete microfluidic systems developed for mass spectrometry applications to-date, Gustafsson et al. [15] developed a MALDI interface for compact disk (CD)-based microfluidics, a technology in which reactions and separations are powered by centrifugal forces on a spinning device (CD Lab-on-a-Chip). Fig. 3b demonstrates the operation of an individual analysis region (each CD contains 96 such regions). The sample

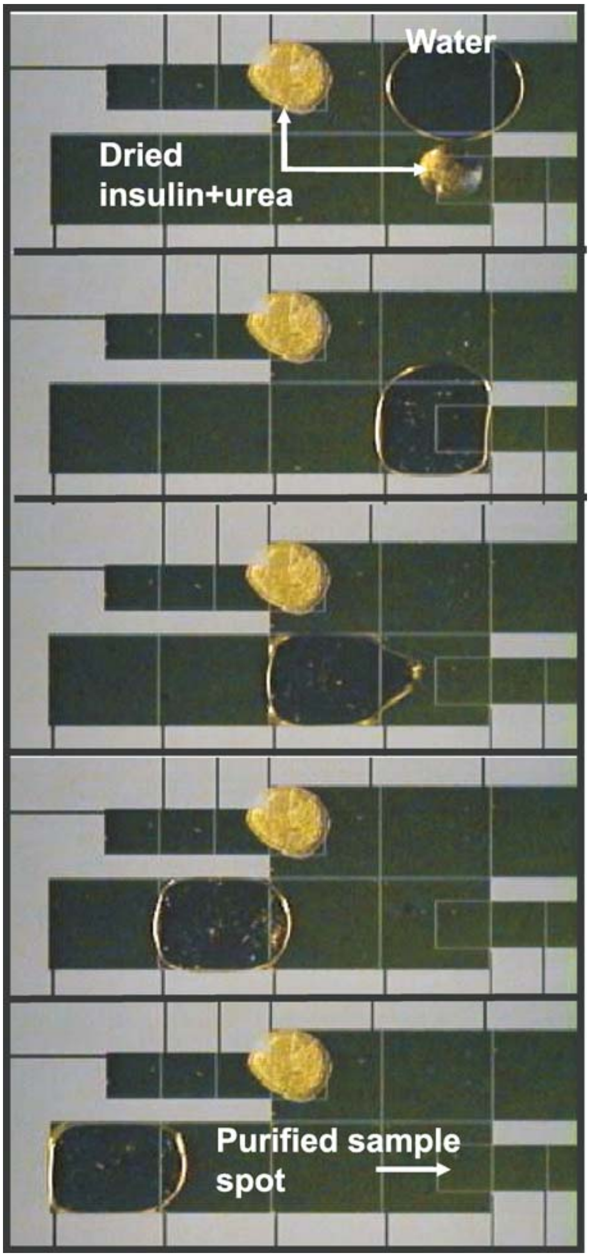

Interfaces between Microfluidics and Mass Spectrometry, Figure 4 Video sequence (top-to-bottom) depicting digital microfluidics-based analysis of a sample containing insulin and urea. The large electrodes are used to move a water droplet to the dried spot, where it selectively dissolves the urea. Because the rinsing droplet primarily touches clean surfaces on the surrounding electrodes, it is easily moved away, leaving behind an (invisible) insulin film, ready for analysis by MALDI-MS. Reproduced by permission of [20]

is loaded (A), and then washed and eluted from a reversed-phase column (B). Finally, the sample is co-crystallized with a MALDI matrix (C) for analysis by mass spectrometry. In proof-of-principle experiments, the CD technology enabled the identification of tryptic digests with higher certainty than in identical analyses using conventional techniques (i. e., steel MALDI target), with better sequence coverage, and the same resolution and mass accuracy. This platform is now commercially available.

Future Directions for Research

Two factors favor the use of nanoelectrospray ionization for coupling microfluidic devices to mass spectrometers. The first is the similarity between the conventional pulled-glass capillary tips and the nanospray nozzles developed for microdevices discussed in the previous section; the second springs from the linear geometry of microfluidic channels. Thus, we believe that nanospray ionization techniques are the most likely to be used for the construction of robust interfaces between microfluidics and mass spectrometry for most applications in the future [16].

Despite the assessment above, we can't help but imagine that MALDI will continue to be an important tool used with Lab-on-a-Chip devices, given how amenable it is to high-throughput analysis (i. e., probing densely packed arrays of sample spots). The solutions that have been developed for interfacing MALDI-MS with enclosed microchannels (described above) are ingenious; however, such solutions are probably not practical for widespread use. Several alternative solutions have recently emerged that are not *microfluidics* per se, but may be a better match for MALDI-MS. For example, some authors have demonstrated the construction of arrays of patterned hydrophobic regions [17] or the use of piezoelectric pipets to dispense nanoliter amounts of liquid in silicon etched wells [18] Others have used electrospray to deposit homogeneous protein spots directly on MALDI targets; using this approach, Wang et al. [19] characterized 3.5 fmol of Angiotensin by mass spectrometry.

Digital microfluidics (DMF) is a related technique in which droplets are moved on a substrate by means of electrowetting and/or dielectrophoretic forces (► digital microfluidics, ► applications based on electrowetting). DMF been used to process proteomic samples and form arrays of spots for analysis by MALDI-MS [20]. As shown in Fig. 4, the technique has been used to perform in situ sample cleanup on an open substrate, after which, samples were interrogated by MALDI-MS, with similar detection efficiencies, resolution, and S/N as conventional techniques. DMF may enable the processing of several analytes at the same time, and is thus a promising tool for implementing high-throughput profiling proteomics using MALDI-MS.

The trend towards laboratory miniaturization is leading to the necessity of robust and reliable interfaces between MS and microfluidics. Although general tools for wide-

spread use are not yet available, it is clear that technologies are becoming more effective and reproducible. (see Freire and Wheeler [16] for a review). Of paramount importance in future work will be functional characterization of the devices when in contact with complex proteomic samples, evaluating, among other things, undesirable non-specific adhesion, long term operation, and the capacity to deliver the analytes of interest to the MS for analysis. In particular, the latter requires an efficient release of sample from MALDI targets or ionization when sprayed from a liquid containing salts, impurities and large abundance proteins that may conceal the desired signal.

Cross References

- ► Proteomics in Microfluidic Devices
- ► Integrated Micro Devices for Biological Applications
- ► Mass Spectrometry
- ► Digital Microfluidics
- ► Lab-on-a-Chip (General Philosophy)
- ► Applications Based on Electrowetting

References

1. Loo JA, Berhane B, Kaddis CS, Wooding KM, Xie Y, Kaufman SL, Chernushevich IV (2005) Electrospray ionization mass spectrometry and ion mobility analysis of the 20S proteasome complex. J Am Soc Mass Spectrom 16:998–1008
2. Eng JK, Mccormack AL, Yates JR (1994) An Approach to Correlate Tandem Mass-Spectral Data of Peptides with Amino-Acid-Sequences in a Protein Database. J Am Soc Mass Spectrom 5:976–989
3. Birendra N, Pramanik A, Ganguly K, Gross ML (eds) (2002) Applied electrospray mass spectrometry. Marcel Dekker, Inc., New York
4. Kebarle P, Peschke M (2000) On the mechanisms by which the charged droplets produced by electrospray lead to gas phase ions. Anal Chim Acta 406:11–35
5. Mann M, Hendrickson RC, Pandey A (2001) Analysis of proteins and proteomes by mass spectrometry. Annu Rev Biochem 70:437–473
6. Xue QF, Foret F, Dunayevskiy YM, Zavracky PM, McGruer NE, Karger BL (1997) Multichannel microchip electrospray mass spectrometry. Anal Chem 69:426–430
7. Lazar IM, Ramsey RS, Sundberg S, Ramsey JM (1999) Subattomole-sensitivity microchip nanoelectrospray source with time-of-flight mass spectrometry detection. Anal Chem 71:3627–3631
8. Schilling M, Nigge W, Rudzinski A, Neyer A, Hergenroder R (2004) A new on-chip ESI nozzle for coupling of MS with microfluidic devices. Lab Chip 4:220–224
9. Xie J, Miao Y, Shih J, Tai YC, Lee TD (2005) Microfluidic platform for liquid chromatography-tandem mass spectrometry analyses of complex peptide mixtures. Anal Chem 77:6947–6953
10. Kameoka J, Orth R, Ilic B, Czaplewski D, Wachs T, Craighead HC (2002) An Electrospray Ionization Source for Integration with Microfluidics. Anal Chem 74:5897–5901
11. Yin NF, Killeen K, Brennen R, Sobek D, Werlich M, van de Goor TV (2005) Microfluidic chip for peptide analysis with an integrated HPLC column, sample enrichment column, and nanoelectrospray tip. Anal Chem 77:527–533
12. Fortier MH, Bonneil E, Goodley P, Thibault P (2005) Integrated microfluidic device for mass spectrometry-based proteomics and its application to biomarker discovery programs. Anal Chem 77:1631–1640
13. Brivio M, Tas NR, Goedbloed MH, Gardeniers HJGE, Verboom W, Van Den Berg A, Reinhoudt DN (2005) A MALDI-chip integrated system with a monitoring window. Lab Chip 5:378–381
14. Musyimi HK, Guy J, Narcisse DA, Soper SA, Murray KK (2005) Direct coupling of polymer-based microchip electrophoresis to online MALDI-MS using a rotating ball inlet. Electrophoresis 26:4703–4710
15. Gustafsson M, Hirschberg D, Palmberg C, Jornvall H, Bergman T (2004) Integrated Sample Preparation and MALDI Mass Spectrometry on a Microfluidic Compact Disk. Anal Chem 76:345–350
16. Freire SLS, Wheeler AR (2006) Proteome-on-a-chip: Mirage, or on the horizon? Lab Chip 6:1415–1423
17. Gundry RL, Edward R, Kole TP, Sutton C, Cotter RJ (2005) Disposable hydrophobic surface on MALDI targets for enhancing MS and MS/MS data of peptides. Anal Chem 77:6609–6617
18. Little DP, Cornish TJ, O'Donnell MJ, Braun A, Cotter RJ, Köstet H (1997) MALDI on a Chip: Analysis of Arrays of Low-Femtomole to Subfemtomole Quantities of Synthetic Oligonucleotides and DNA Diagnostic Products Dispensed by a Piezoelectric Pipet. Anal Chem 69:4540–4546
19. Wang YX, Zhou Y, Balgley BM, Cooper JW, Lee CS, DeVoe DL (2005) Electrospray interfacing of polymer microfluids to MALDI-MS. Electrophoresis 26:3631–3640
20. Moon H, Wheeler AR, Garrell RL, Loo JA, Kim CJ (2006) An integrated digital microfluidic chip for multiplexed proteomic sample preparation and analysis by MALDI-MS. Lab Chip 6:1213–1219

Interface Tracking

► Interface Capturing Schemes for Free-Surface Flows

Interfacial Electrohydrodynamics

► Interfacial Electrokinetic Flow

Interfacial Electrokinetic Flow

Leslie Yeo
Micro/Nanophysics Research Laboratory
Department of Mechanical Engineering, Monash University, Clayton Campus, Clayton, VIC, Australia
leslie.yeo@eng.monash.edu.au

Synonyms

Free surface electrokinetics; Interfacial electrohydrodynamics; Free surface electrohydrodynamics

Definition

The term interfacial electrokinetic flow here encompasses all electrokinetically driven flows involving free-surfaces or freely deforming boundaries, i. e., gas–liquid interfaces or immiscible liquid–liquid interfaces.

Overview

Free surfaces are commonly encountered in many microfluidic applications. One class of free surface microfluidic applications involves individual or discrete drops and sprays, the former being termed *digital microfluidics*. Another class of free surface microfluidic applications is that which involves two-phase microchannel flows wherein either a gas bubble or stream flows within or adjacent to a liquid stream, or, a liquid phase flows within an immiscible liquid continuum (i. e., a *microemulsion*), or, a liquid stream stratifies another immiscible liquid stream. These classifications are, however, not mutually exclusive. For example, discrete drops or sprays are not just limited to open microfluidic systems, where they are exposed to an ambient environment. Often, to prevent evaporation, for example, the discrete drops are housed within an oil layer. Alternatively, a liquid spray can be encased within an immiscible liquid medium as a means for generating microemulsions.

In addition to the usual mathematical difficulties associated with free surface problems, the consideration of free surfaces becomes extremely important in microfluidics, especially given the increasing dominance of surface forces over body forces as the surface area to volume ratio increases with miniaturization. In addition, the curvature of the free surface becomes commensurate with the characteristic length scale of the system at these small scales. For example, the bubbles generated due to electrode reactions in electrokinetic microdevices can have dimensions which are on the same order as the microchannel width or height.

Electrokinetics is currently the preferred method for moving and transporting fluids in microchannels due to the ease of electrode fabrication and since electrokinetic mechanisms involve no moving mechanical parts which are prone to reliability concerns. Whilst significant progress has been achieved in understanding electrokinetic phenomena in the context of microfluidic technology, there is still a significant need to increase our fundamental understanding concerning the underlying complex hydrodynamic and physicochemical behavior associated with

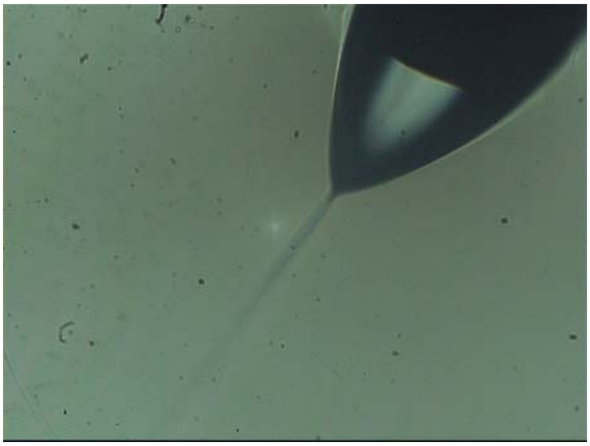

Interfacial Electrokinetic Flow, Figure 1 Liquid meniscus issuing from a 100 μm capillary in DC electrospraying showing its conical shape and a thin jet that emanates from the meniscus tip. The jet subsequently breaks up due to hydrodynamic or Coulombic instabilities to generate very small aerosol drops

interfacial electrokinetic systems such as electrospraying or electrohydrodynamic atomization, electrospinning, electrocapillarity, electrowetting, electrokinetically-driven bubble transport and electrohydrodynamically-induced surface and bulk recirculation.

Basic Methodology

Governing Equations

For a Newtonian, incompressible fluid, the governing hydrodynamic equations are stipulated by the conservation of mass and momentum:

$$\nabla \cdot \boldsymbol{u} = 0 \,, \tag{1}$$

$$\rho \left(\boldsymbol{u}_t + \boldsymbol{u} \cdot \nabla \boldsymbol{u} \right) = \nabla \cdot \mathbf{T} \,, \tag{2}$$

where $\boldsymbol{u}$ is the velocity vector, ρ the fluid density and the subscript t denotes a time derivative. In Eq. (2),

$$\mathbf{T} = -p\mathbf{I} + \mu \left[\boldsymbol{n} \cdot \left(\nabla \boldsymbol{u} + \nabla \boldsymbol{u}^{\mathrm{T}} \right) \cdot \boldsymbol{t} \right] + \mathbf{T}_{\mathrm{M}} \,, \tag{3}$$

is the total stress tensor, comprising of the hydrostatic stress component, in which p is the fluid pressure and $\mathbf{I}$ the identity tensor, the viscous stress component, in which μ is the fluid viscosity, and, $\boldsymbol{n}$ and $\boldsymbol{t}$ the unit outward normal and tangential vectors, respectively, and, a electric (Maxwell) stress component $\mathbf{T}_{\mathrm{M}}$. In the above, the superscript T denotes the transpose of the tensor $\nabla \boldsymbol{u}$.

The coupling between the hydrodynamics and the electric field therefore arises through the Maxwell stress tensor. The total electric force density comprises the sum of the

Coulombic force arising from the presence of free charges and the dipole force arising due to the existence of bound charges:

$$f = \rho_e E + P \cdot \nabla E \,, \tag{4}$$

where ρ_e is the free space charge density, $E = -\nabla\phi$ the electric field vector and P the polarizability vector; ϕ is the electric potential. It can then be shown that for an electrically linear and isotropic medium, Eq. (4) can be expressed as [1]

$$f = \rho_e E - \frac{\varepsilon_0}{2} \nabla \left(\varepsilon - \rho \left. \frac{\partial \varepsilon}{\partial \rho} \right|_T \right) E \cdot E \,, \tag{5}$$

in which ε is the dielectric constant and ε_0 is the permittivity of free space. The second term in the parenthesis comprises a ponderomotive force term arising due to the inhomogeneity of the dielectric permeability, represented by a jump in ε, and an electrostrictive term at constant temperature T which accounts for the compressibility of the media. For incompressible fluids, electrostriction effects are negligible and hence this term can be omitted. Equation (5) can be expressed in terms of a divergence of a tensor $f = \nabla \cdot \mathbf{T}_M$, from which we obtain an expression for the Maxwell stress tensor:

$$\mathbf{T}_M = \varepsilon\varepsilon_0 EE - \frac{\varepsilon\varepsilon_0}{2} (E \cdot E) \mathbf{I} \,. \tag{6}$$

The net Maxwell stress at an interface then has the following normal and tangential components:

$$\mathbf{T}_{M_n} = n \cdot \mathbf{T}_M \cdot n \tag{7}$$

$$= \frac{1}{2} \left[\varepsilon (E \cdot n)^2 - \varepsilon (E \cdot t_1)^2 - \varepsilon (E \cdot t_2)^2 \right]_i^o \,,$$

$$\mathbf{T}_{M_t} = n \cdot \mathbf{T}_M \cdot t_i = \varepsilon \left[E \cdot n \right]_i^o (E \cdot t_i) \,, \tag{8}$$

respectively, where t_1 and t_2 are the unit vectors orthogonally tangent to the interface. The square parenthesis $[\cdot]_i^o$ denotes a jump in the inner quantity across the interface, obtained by subtracting the quantity of the inner phase i from that of the outer phase o.

In both phases, the electrostatic behavior can be described by Gauss' law:

$$\nabla \cdot E = \nabla \cdot (-\nabla\varphi) = -\nabla^2\varphi = \frac{\rho_e}{\varepsilon\varepsilon_0} \,. \tag{9}$$

In addition, the condition of electric field irrotationality also holds:

$$\nabla \times E = 0 \,. \tag{10}$$

Charge conservation also requires

$$\nabla \cdot i = \frac{\partial \rho_e}{\partial t} \,. \tag{11}$$

in which

$$i = -\sigma E - D\nabla\rho_e + \rho_e u \,, \tag{12}$$

is the current density. In Eq. (12), σ is the electrical conductivity and D is the ion diffusivity.

Boundary Conditions

A free surface or a deformable interface between two fluid phases requires that fluid particles move only tangentially along the interface. As such, if the position of the interface Γ in a Cartesian coordinate system (x, y, z) is geometrically defined by $z = h(x, y, t)$, then, given that the interface itself is a streamline, a Lagrangian description of a fluid particle as it follows the streamline can be geometrically described by the implicit function

$$F(x, y, z, t) = z - h(x, y, t) = 0 \,. \tag{13}$$

In the Eulerian reference frame, the material derivative of F, i. e., $DF/Dt = (\partial F/\partial t) + u \cdot \nabla F$ must be equal to zero, which then leads to the kinematic boundary condition [2]:

$$\frac{\partial h}{\partial t} + u_n n \cdot \nabla h = 0 \,, \tag{14}$$

where u_n is the normal velocity and $n = \nabla h / |\nabla h|$ is the outward unit vector normal to the interface.

The hydrodynamic boundary condition at the interface Γ is given by

$$n \cdot [u]_i^o = 0 \,. \tag{15}$$

In addition, we also require continuity of shear stresses and the jump in the normal stress across the interface at Γ:

$$[n \cdot \mathbf{T} \cdot t]_i^o = 0 \,, \tag{16}$$

and

$$[n \cdot \mathbf{T} \cdot n]_i^o = \gamma\kappa \,, \tag{17}$$

where γ is the interfacial tension and $\kappa = \nabla_s \cdot n$ is twice the mean curvature of the interface in which $\nabla_s \equiv \nabla \cdot (\mathbf{I} - nn)$ is the surface gradient operator.

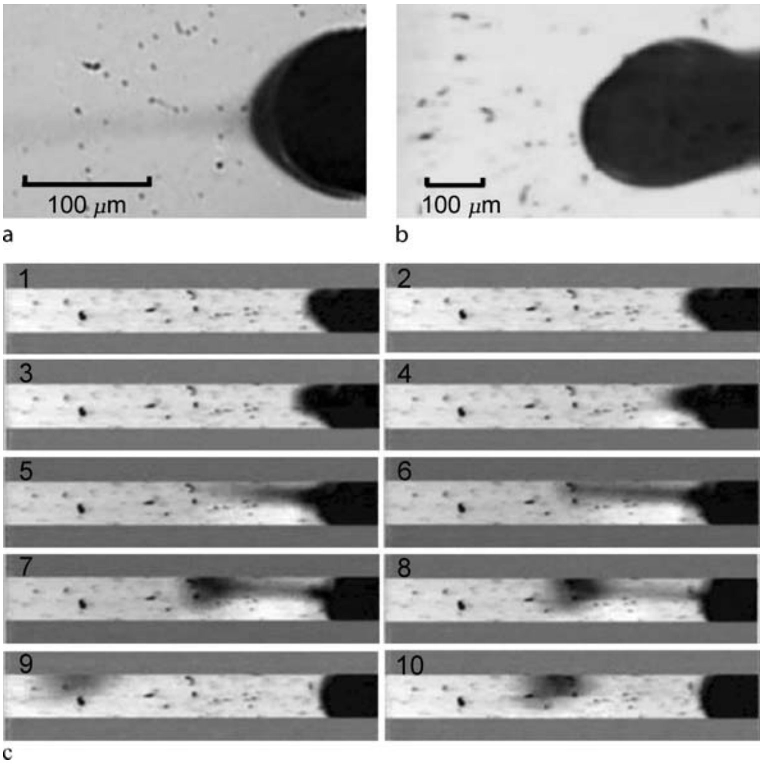

Interfacial Electrokinetic Flow, Figure 2 AC electrospray modes [11, 12]. (**a**) Tip streaming mechanism by which aerosol drops are periodically ejected from a resonating meniscus due to viscous-capillary forces. (**b**) Electrowetting phenomenon at high voltages which causes liquid to recede up the capillary thus suppressing drop ejection. (**c**) Sequence of images at 6000 fps showing the formation of a long slender microjet due to viscous-inertia forcing from which a drop is ejected

The remaining boundary conditions are given by the continuity of electric potential and electric stresses at the interface at Γ:

$$[\varphi]_i^o = 0\,, \tag{18}$$

$$[\boldsymbol{E} \cdot t]_i^o = 0\,, \tag{19}$$

$$[\varepsilon \boldsymbol{E} \cdot n]_i^o = q\,, \tag{20}$$

in which q is the surface charge density at the interface Γ, which from Eq. (11), obeys

$$q_t + \boldsymbol{u} \cdot \nabla_s q = q\boldsymbol{n} \cdot (\boldsymbol{n} \cdot \nabla)\,\boldsymbol{u} - [\sigma \boldsymbol{E}]_i^o \cdot \boldsymbol{n}\,. \tag{21}$$

In the above, the subscripts i and o refer to the inner and outer phases respectively. The terms on the right of Eq. (21) represent the changes in the interfacial charge density due to surface dilation and electromigration, respectively. Also, the diffusion term has been neglected in Eq. (21), which is justifiable for sufficiently high field strengths typical in electrokinetic applications where the dimensionless field intensity $eV/k_\mathrm{B}T \gg 1$, in which e is the electron charge, V the applied potential, k_B the Boltzmann constant and T the absolute temperature [3].

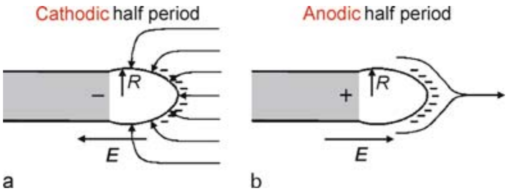

Interfacial Electrokinetic Flow, Figure 3 Plasma polarization mechanism in AC electrospraying [11]. (**a**) In the cathodic half period of the AC forcing cycle, the negative plasma generated forms a thin conducting layer surrounding the meniscus. As a result, the external electric field coincides with the interface in a normal orientation. (**b**) In the anodic half period, no plasma is generated. However, because there is insufficient time for the plasma to disperse due to diffusion, the plasma layer remains, thereby screening the external electric field. Consequently, the electric field is predominantly tangential to the interface

Key Research Findings

In this section, we discuss recent developments on various interfacial electrokinetic flow phenomenon that have

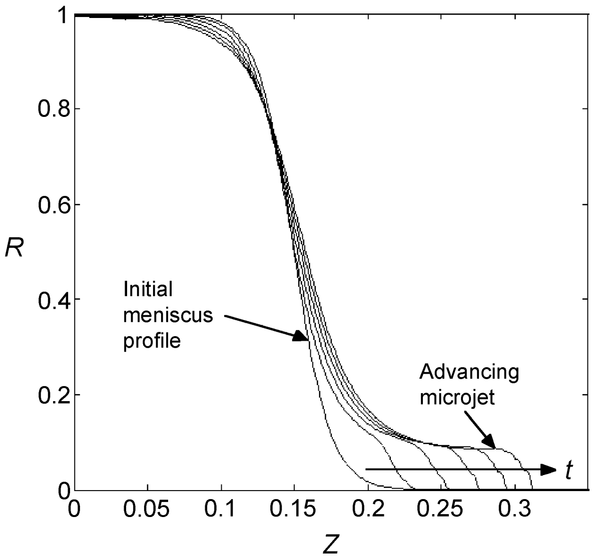

Interfacial Electrokinetic Flow, Figure 4 Spatio-temporal evolution profiles of the electrospray meniscus height R showing the initial stages of microjet formation obtained through an axisymmetric longwave model [11]

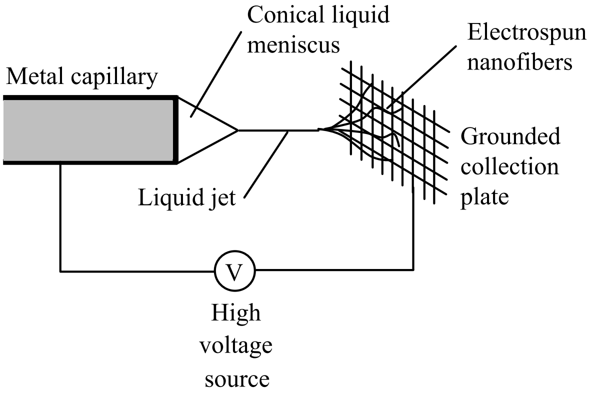

Interfacial Electrokinetic Flow, Figure 5 Schematic illustration of the electrospinning setup for the generation of nanometer and micron sized fibers

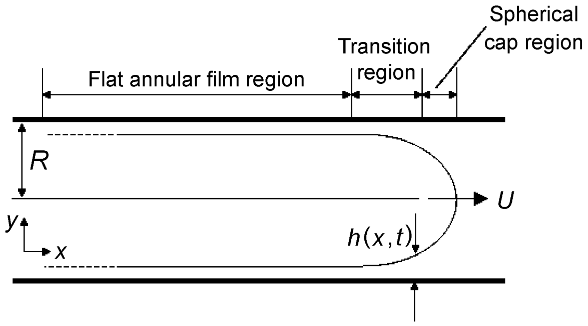

Interfacial Electrokinetic Flow, Figure 6 Schematic illustration of the front cap of a bubble translating in a long capillary tube. After Chang [16]

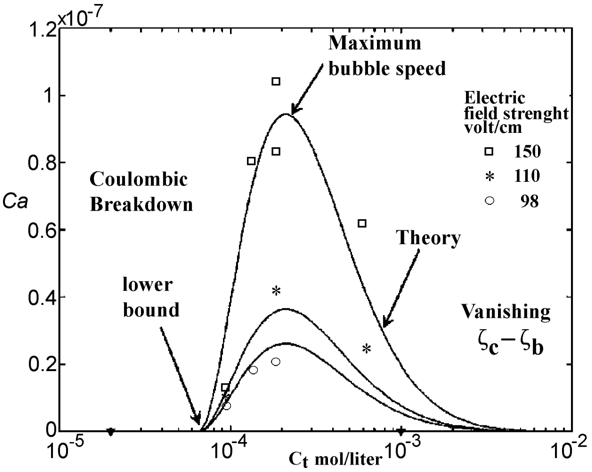

Interfacial Electrokinetic Flow, Figure 7 Electrokinetic bubble transport in a capillary. Dimensionless bubble speed represented by the capillary number Ca as a function of the total concentration of ionic surfactant C_t [17]

potential applications in microfluidic devices. In particular, we focus on electrohydrodynamic atomization (or more commonly known as electrospraying) and electrospinning, electrokinetic bubble transport, and, electrohydrodynamically driven surface and bulk microflows. Electrocapillarity and electrowetting which are other examples of interfacial electrokinetic flows will not be discussed here; the reader is referred to the more detailed entries on electrocapillarity and electrowetting, as well as that on electrowetting applications. The reader should also consult the reviews on electrowetting by Mugele and Baret [4] and Yeo and Chang [5].

Electrospraying/Electrohydrodynamic Atomization

Electrospraying or electrohydrodynamic atomization is a mechanism for the generation of micron or nanometer dimension aerosols with the use of an applied electric stress [3]. DC electrospraying has been the subject of intense investigation over the past decade, in particular, due to its use as a soft ionization technique for the characterization of large complex and non-volatile biomolecules such as proteins and DNA in mass spectrometry. This technique is now known widely as electrospray ionization mass spectrometry or ESI-MS [6]. A balance between the Maxwell stress in Eq. (6) and the capillary stress gives an estimate of the critical voltage V_c required for electrospraying:

$$V_c \sim \sqrt{\frac{\gamma d^2}{\varepsilon \varepsilon_0 R}}\,, \qquad (22)$$

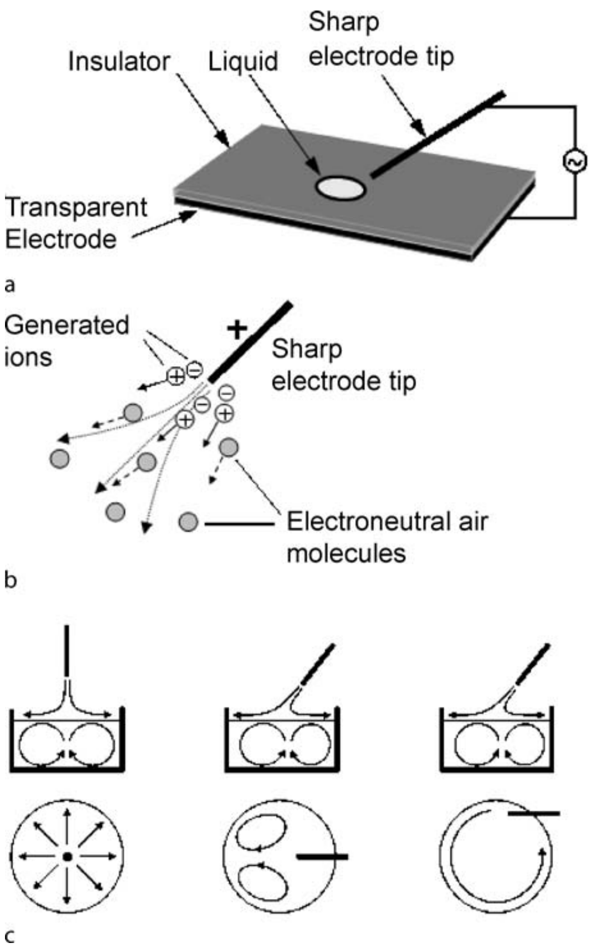

Interfacial Electrokinetic Flow, Figure 8 Electrohydrodynamically induced surface recirculation. (**a**) Schematic depiction of the experimental setup. (**b**) Schematic illustration of the corona wind mechanism by which bulk electrohydrodynamic air thrust is generated. (**c**) Liquid recirculation patterns are generated depending on the orientation of the sharp electrode tip. After Yeo et al. [18, 19]

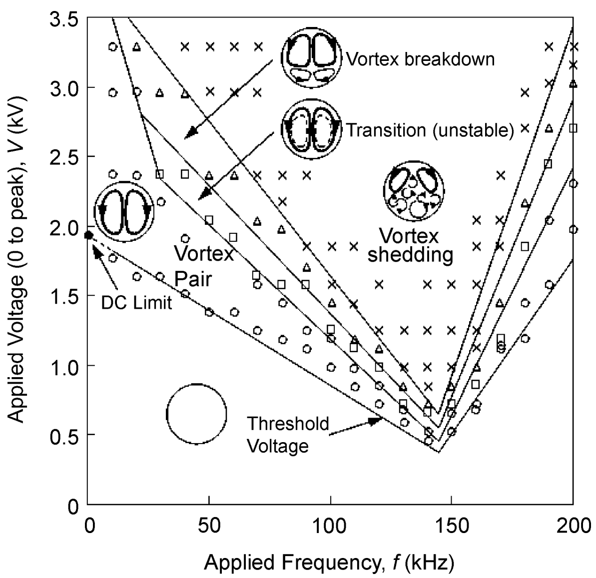

Interfacial Electrokinetic Flow, Figure 9 Liquid recirculation patterns as a function of the applied frequency and voltage. After Yeo et al. [18]

where d is the separation between nozzle and the ground electrode, and, R is the radius of curvature of the meniscus. Typically, $\gamma \sim 10^{-2}\,\mathrm{kg/s^2}$, $d \sim 10^{-2}\,\mathrm{m}$, $\varepsilon\varepsilon_0 \sim 10^{-10}\,\mathrm{C^2/Jm}$ and $R \sim 10^{-4}\,\mathrm{m}$, thus suggesting that extremely large voltages of order 10 kV are required for the onset of electrospraying.

In DC electrospraying, the absence of any external periodic forcing permits sufficient time for charge separation to occur within the liquid meniscus emanating from the nozzle orifice. Tangential ion conduction along a thin electric double layer at the meniscus interface is then responsible for co-ion accumulation, the repulsion of which then results in Coulombic fission wherein a thin liquid jet emanates from the tip once the Rayleigh limit is reached where the charge repulsion exceeds the surface force. This charged jet then undergoes various hydrodynamic or Coulombic instabilities leading to its breakup and hence the generation of charged drops. These drops suffer from further disintegration when the drop evaporates leading to higher charge densities and hence the possibility of successive break up when the Rayleigh limit for Coulombic fission is exceeded. This disintegration cascade therefore gives rise to very small drops of nanometer order.

For perfectly conducting liquids, Taylor [7] showed that a conical meniscus with a half angle of 49.3° is produced by considering the static equilibrium balance between the capillary and Maxwell stresses in Eqs. (3), (6) and (17). In the perfect conducting limit, the drop is held at constant potential and hence the gas-phase electric field at the meniscus interface is predominantly in the normal direction. It can then be shown that the normal gas phase electric field $E_{\mathrm{n,g}}$ scales as $1/R^{1/2}$ in which R is the meniscus radius which then stipulates from Eq. (7) that the Maxwell pressure $p_{\mathrm{M}} \sim E_{\mathrm{n,g}}^2$ scales as $1/R$, therefore exactly balancing the azimuthal capillary pressure $p_{\mathrm{C}} \sim \gamma/R$ for all values of R. This exact balance, and absence of a length scale selection, is responsible for the formation of a static Taylor cone (Fig. 1) in the dominant cone-jet mode in DC electrosprays [8].

Li et al. [9] and Stone et al. [10] later extended Taylor's perfectly conducting limit to allow for the effect of finite liquid conductivities, showing in these cases that the tangential electric field within the slender conical liquid meniscus dominates. However, the tangential liquid phase electric field $E_{\mathrm{t,l}}$ also scales as $1/R$ and thus an exact bal-

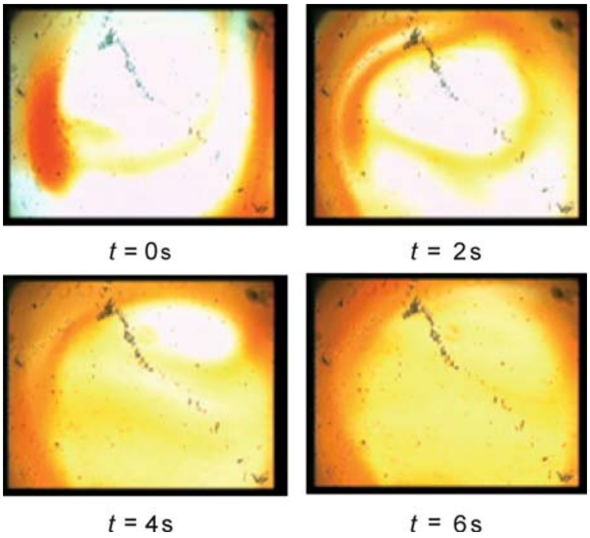

Interfacial Electrokinetic Flow, Figure 10 Demonstration of rapid micro-mixing via the electrohydrodynamically induced surface microvortices in a microfluidic chamber 8 mm in diameter and 4 mm in height. After Yeo et al. [18]

ance between the Maxwell stress $p_M \sim E_{t,1}^2$ and the capillary stress p_C is again obtained, giving rise to a cone-like structure [11]. The cone angle, however, depends critically on the liquid to gas permittivity ratio $\beta \equiv \varepsilon_1/\varepsilon_g$; the Taylor angle is then recovered in the perfectly conducting limit as $\beta \to \infty$.

High frequency ($10\,\text{kHz} \leq \omega \leq 200\,\text{kHz}$) AC electrosprays [11–13], on the other hand, behave very differently from DC electrosprays. The drops generated are larger (of order microns) than the nanometer dimension DC electrospray drops. In addition, the Taylor cone characteristic of DC electrosprays is not observed. Instead, the drops are ejected from a curved meniscus or from a peculiar microjet that protrudes intermittently from the meniscus, as shown in Fig. 2. The high frequency periodic forcing does not permit sufficient time for charge separation to occur and hence co-ions accumulate at the meniscus tip, thereby rendering the ejected drops electroneutral. This explains the absence of Coulombic fission and hence the observation of larger drops since the Coulombic fission disintegration cascade does not occur. The drop electroneutrality allows the AC electrospray to be used for drug delivery applications in which charged aerosols that could possibly lead to surface adsorption and compound ionization are undesirable [13]. Moreover, the absence of drop charge also stipulates that the current and hence power requirement is negligible, allowing the technology to be miniaturized for portable consumer use [11–13].

The absence of tangential ion conduction also results in a weaker liquid phase tangential electric field. As such, the AC electrospray behavior was found to be insensitive to liquid conductivity [12]. This passivity of the liquid phase is compounded by the formation of a thin, highly-conducting, permanent negatively charged plasma polarization layer that envelopes the liquid meniscus, giving rise to a dominant normal gas phase electric field in one AC half period [11]. This negative charge does not originate within the drop due to the insufficient time for charge separation within the liquid phase. In addition, the drop ejection time, roughly 10^{-3} s, is much larger than the period associated with the AC forcing frequency thus allowing any charge within the drop to essentially equilibriate during the ejection event [12].

Given that the AC electrospray requires a working liquid of sufficiently high volatility (e.g., alcohols), the negatively charged plasma cloud could possibly arise due to evaporation and subsequent ionization of the liquid from the meniscus when the applied voltage exceeds a threshold voltage associated with the ionization potential. In the cathodic half period, when the meniscus and capillary have the same polarity as the plasma cloud forming a thin highly conducting layer enveloping the meniscus, the local gas phase normal electric field at the interface is significantly enhanced, as illustrated in Fig. 3a, since the meniscus and the plasma layer both resemble constant potential bodies in which the interfacial field is predominantly normal. On the contrary, plasma is not generated in the anodic half period. Nevertheless, a plasma layer still surrounds the meniscus unless there is sufficient time for it to be dispersed. The plasma layer is now oppositely charged to the meniscus and capillary, effectively screening the external field such that a weak tangential gas phase field arises, as shown in Fig. 3b. However, the enhanced normal gas phase field in the cathodic half period dominates and hence, averaged over many cycles, produces a net Maxwell stress that is responsible for the meniscus dynamics observed [11].

This plasma polarization mechanism also explains the appearance of a minimum in the frequency dependent critical voltage of approximately 165 kHz for spraying to occur. Below this optimum frequency, as $\omega \to 0$, there is adequate time for the dispersion of the plasma generated away from the meniscus. Above this optimum frequency, as $\omega \to \infty$, there is insufficient time for the dispersion to occur. Maximum interfacial plasma polarization therefore occurs at the optimum frequency, therefore producing the largest enhancement of the local normal Maxwell field at the meniscus interface [11].

Since both meniscus and plasma layer resemble constant potential bodies, the solution of the Eq. (9) governing the gas phase electrostatics in the weak polarization limit

where ρ_e is negligible gives rise to a specific scaling for the normal interfacial gas phase electric field $E_{n,g}$. Assuming an arbitrary axisymmetric meniscus shape but not precluding the existence of a conical geometry, it can be shown from spheroidal harmonics that $E_{n,g} \sim 1/R^{1/2}$ for a sharp conical meniscus. On the other hand, $E_{n,g} \sim 1/R$ is obtained for more slender bodies such as an elongated ellipsoid or cylinder. Nevertheless, given that the more singular $1/R$ scaling for a slender geometry dominates at the meniscus tip, as $R \to 0$, the Maxwell pressure $p_M \sim E_{n,g}^2$ scales as $1/R^2$ and hence an exact balance with the azimuthal capillary pressure $p_C \sim \gamma/R$ is only possible for one specific value of R [11]. This length scale selection therefore excludes the possibility of a cone-like meniscus and instead suggests that the meniscus is stretched to a more elongated cylinder-like geometry such as that of the microjet shown in Fig. 2, thus suggesting why a non-steady microjet is produced in AC electrosprays instead of a steady Taylor cone [11].

The role of the Maxwell pressure resulting from a normal gas phase interfacial electric field that scales as $1/R$ in elongating the liquid meniscus into a cylindrical microjet structure can also be verified through a dynamic simulation in which the equations governing the coupled interactions between the hydrodynamics (Eqs. (1)–(3)) and electrodynamics (Eq. (9)) are solved simultaneously for a constant potential liquid meniscus in the longwave limit in axisymmetric polar coordinates $(r, 0, z)$, subject to the boundary conditions given by Eqs. (14)–(20). The polarization in the bulk gas phase is assumed to be weak, i. e., $\rho_e \sim 0$, such that Eq. (9) reduces to the Laplace equation. Further details of the model are given in [11]. A typical spatio-temporal evolution profile is illustrated in Fig. 4 in which an axial pressure gradient resulting from the interfacial distribution of the normal Maxwell stress with a $1/R^2$ scaling along the meniscus is observed to stretch the initially curved meniscus and pull out a slender microjet resembling that in Fig. 2. After a short transient, the microjet is observed to propagate forward at roughly constant velocity whilst maintaining an approximately constant radius [11].

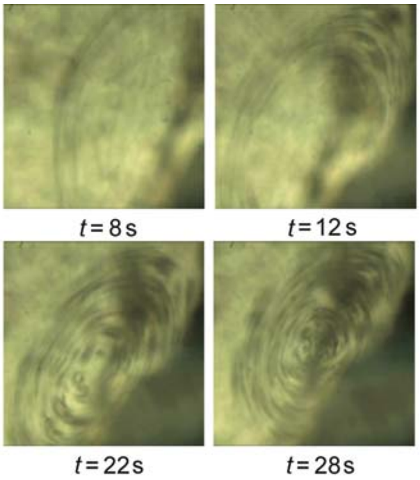

a

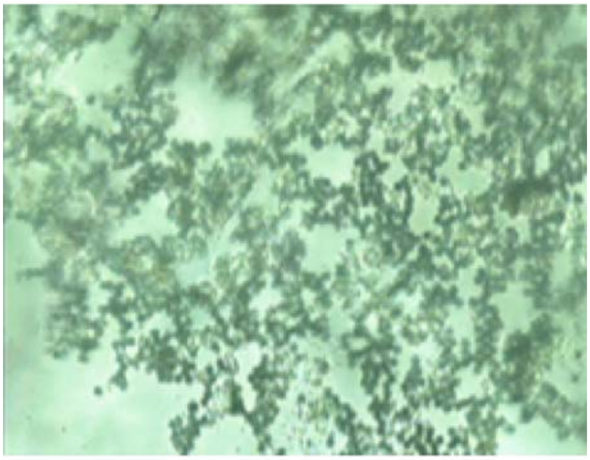

b

Interfacial Electrokinetic Flow, Figure 11 (**a**) Demonstration of microparticle (10 μm latex particles) trapping and concentration within the electrohydrodynamically induced surface microvortices. (**b**) The particle aggregate remains intact as a planar interfacial colloidal crystal structure even after cessation of the flow upon removal of the applied electric field. After Yeo et al. [18]

Electrospinning

The electrospinning of micron and nanometer dimension fibers is a hybrid technology that arose out of electrospraying. In the past decade, fiber electrospinning has observed exponential growth in interest. However, the concept and technique has not evolved much from the original setup, shown in Fig. 5, which is very similar to that for electrospraying. A wide variety of polymer and polymer composite fibers with different morphologies (e. g., beaded, pored, hollow, core-shell, etc.) have since been electrospun, examples of which are summarized in [14]. The AC electrospray setup has also been modified to synthesize fibers of micron order thickness from biodegradable polymeric excipients [13], although it should be mentioned that the mechanism by which the fibers are generated, predominantly due to extensional stresses that lead to the stretching of the microjet in Fig. 2 and subsequent solvent evaporation and hence jet solidification into a fiber, differs from that in DC electrospinning where the mechanism is largely due to evaporative solidification of the solvent from the thin jet that emanates from the Taylor cone as a result of Coulombic fission.

Electrospinning has been modeled through an analysis of electrically forced axisymmetric liquid jets [15], in which the asymptotic limit requirement of either assuming the liquid as a perfect conductor or a perfect dielectric is relaxed such that the existence of interfacial charge can be accounted through Eq. (21). This is because whilst bulk conduction can be neglected in the small free space charge density ρ_e limit, interfacial charge and hence conduction is not usually negligible. The existence of such charge also gives rise to a finite tangential Maxwell stress given by Eq. (8) which can only be balanced by the viscous stress.
A similar axisymmetric model to that described above, assuming the jet to be slender such that the longwave approximation holds ($R_0 \ll L$, in which R_0 is the initial meniscus height and L the characteristic length scale of the jet), is then derived. In this limit, the external electric field can be simplified such that a slender dielectric meniscus can essentially be described as an effective axial line distribution of free and interfacially bound charges λ. An electric field flux balance on Gaussian surfaces S_1 and S_2 around and encompassing the meniscus interface then leads to [15]

$$\oint_{S_1} \boldsymbol{E}\cdot\boldsymbol{n}\,\mathrm{d}A = \left[\left(\pi R^2 E_{\mathrm{t},1}\right)_z + 2\pi R E_{\mathrm{n},1}\right]\mathrm{d}z = 0\,, \quad (23)$$

and

$$\oint_{S_2} \boldsymbol{E}\cdot\boldsymbol{n}\,\mathrm{d}A = \left[\left(\pi R^2 E_{\mathrm{t},1}\right)_z + 2\pi R E_{\mathrm{n,g}}\right]\mathrm{d}z = 4\pi\lambda\,\mathrm{d}z\,, \quad (24)$$

in which A denotes the area and the subscript z denotes derivatives in the axial direction. Equations (23) and (24) can be substituted into Coulomb's Law describing the gas phase electric potential in the region far from the interface [15]:

$$\Phi_g = \Phi_\infty + \int \frac{\lambda\left(z', t\right)}{\sqrt{r^2 + (z - z')^2}}\,\mathrm{d}z'\,, \quad (25)$$

where Φ_∞ is the applied potential, to yield a second order ordinary differential equation for the tangential electric field in the liquid phase [15]:

$$E_{\mathrm{t},1} - \ln\frac{R_0}{L}\left[\frac{1}{2}\left(\frac{\varepsilon_1}{\varepsilon_g} - 1\right)\left(R^2 E_{\mathrm{t},1}\right)_{zz} - 4\pi\,(qR)_z\right] - E_\infty = 0\,, \quad (26)$$

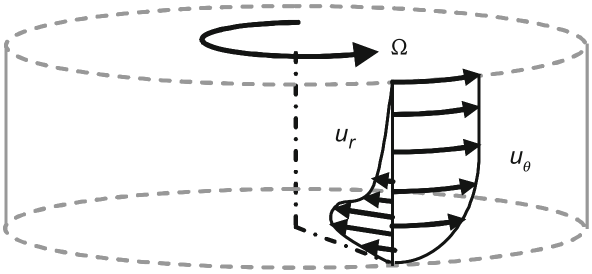

Interfacial Electrokinetic Flow, Figure 12 Schematic depiction of the azimuthal and radial velocity profiles, u_θ and u_r, respectively, in Batchelor flows (liquid flow between rotating and stationary circular disks; the angular rotation is Ω). After Yeo et al. [19]

in which E_∞ denotes the applied electric field. The choice of boundary conditions at the nozzle orifice is also critical to the stability of the numerical solutions. A detailed discussion can be found in [15] and is also summarized in [14].

Electrokinetic Bubble Transport in Microchannels

Chang [16] showed that the pressure drop across a bubble translating in a microcapillary with speed U, as illustrated in Fig. 6, scales as $(\gamma/R)\mathrm{Ca}^{2/3}$, which is essentially the difference in the capillary pressures between the cap pressures at the front and rear of the bubble; R is the capillary radius and $\mathrm{Ca} \equiv \mu U/\gamma$ is the capillary number. Given that the pressure drop required to drive a liquid slug of length L at speed U is $\mu UL/R^2$, then the pressure drop across a bubble corresponds to an equivalent slug length of $R\mathrm{Ca}^{-1/3}$, obtained by balancing the pressure drop in both cases. Since Ca is typically between $10^{-8} - 10^{-4}$ in microcapillaries, this means that the pressure drop required to drive a bubble is extremely large to overcome the viscous dissipation associated with the bubble, and is equivalent to driving a liquid slug with a length that is several orders of magnitude of the capillary radius [16].
As the usual parabolic velocity profile of pressure-driven Poiseuille flow leads to the flowrate scaling as R^4 whereas the flat velocity profile obtained in pure electroosmotic flow gives rise to a flowrate that scales as R^2, it can be seen that it is more efficient to drive microchannel flows where R becomes very small using electrokinetic flows as opposed to pressure-driven flow. However, there are some design issues to be considered in electrokinetic bubble transport.
From Ohm's law,

$$i = \frac{I}{A_c L} = \sigma E\,, \quad (27)$$

where i is the current density, E the local electric field, I the corresponding current, and, A_c and L are the cross-sectional area and length of the capillary, respectively, we observe that $E \sim 1/A_c$. The electroosmotic slip velocity is given by

$$u_s = \frac{\varepsilon\varepsilon_0 \zeta E}{\mu}\,, \tag{28}$$

where ζ is the electrokinetic (or zeta-) potential, which stipulates that $u_s \sim 1/A_c$. It then follows from Eqs. (27) and (28) that the volumetric flowrate is

$$Q = u_s A_c = \frac{\varepsilon\varepsilon_0 \zeta I}{\mu \sigma L}\,, \tag{29}$$

which suggests that the flowrate due to electrokinetic flow is independent of the capillary cross-sectional area. This, and the fact that the electrokinetic flow velocity profile is virtually flat across the channel, is quite unfortunate because it requires the flow in the thin annular film around the bubble to be equal to the flow behind it. As a result, it is impossible to build up a back pressure driving force behind the bubble. The electrolyte simply flows around the bubble, rendering it stationary [16].

Thus, in order to drive bubble transport using electrokinetic flow, the flow invariance to the cross-section must be eliminated such that the flow in the annular film is less than the flow behind the bubble. Chang [16] proposes several ways to reduce the annular film flow by introducing drag at the bubble interface to retard the annular film (however, this only works if the bubble is essentially a viscous liquid drop) or by adding surfactants that reduce the local interfacial tension and hence generate Marangoni stresses (stresses arising due to interfacial tension gradients). Alternatively, it is also possible to introduce an ionic surfactant that resides at the bubble interface such that the double layer at the interface has an opposite charge to that of the capillary tube surface. Thus, the ζ-potential at the interface would have an opposite sign to that at the capillary surface. From the Smoluchowski slip in Eq. (28), we then note that the velocity at the bubble interface is in the opposite direction to that at the capillary surface. Careful control of the amount of ionic surfactants could also give rise to equal but opposite velocities, thus eliminating the flow in the annular film completely.

Figure 7 shows the dimensionless bubble translation speed Ca as a function of the surfactant (anionic surfactant since the glass capillary used has positive surface charge) ionic concentration for various electric field strengths [17]. At low concentrations, given that the Debye screening length scales as the inverse of the square root of the concentration, the electric double layer thickness becomes comparable to the thickness of the annular film. The overlapping double layers of different polarities then leads to Coulombic attraction which causes the annular film to collapse. As such, there is a critical value for the ion concentration of approximately 10^{-5} mol/l before which bubble motion is observed. At high concentrations, however, the bubble speed again diminishes due to the vanishing electric double layer.

Electrohydrodynamically-Induced Interfacial Recirculation

Very recently, a novel way of driving liquid recirculation has been developed by exploiting a bulk electrohydrodynamic air thrust generated from a nearly singular electric field at a sharp electrode tip mounted a small height (~4 mm) above the liquid surface [18], as depicted in Fig. 8a. This air propulsion, also known as *corona wind* or *ionic wind*, arises when the voltage at the electrode tip exceeds the threshold ionization voltage leading to the breakdown of the air surrounding the electrode tip. Counter-ions are then repelled away from the electrode, colliding into the electroneutral air molecules along the way, as illustrated in Fig. 8b. The momentum transfer arising from these collisions then gives rise to the bulk air flow. By inclining the electrode such that the air flow is directed towards the liquid surface, interfacial shear then results in recirculation at the surface. Depending on the positioning of the needle, a clockwise or anti-clockwise motion or a pair of surface vortices can be generated (Fig. 8c). Figure 8c also shows the secondary bulk recirculation generated due to the primary surface flow; this will be discussed subsequently.

The voltage-frequency behavior is depicted in Fig. 9. We observe that the critical voltage to obtain liquid recirculation decreases with increasing applied frequency until approximately 145 kHz before increasing again. This optimum frequency is associated with the inverse RC time scale of the plasma charging mechanism [18], where R is the resistance and C the capacitance. At low frequencies as $\omega \to 0$, there is sufficient time for any plasma generate to diffuse away. At high frequencies as $\omega \to \infty$, on the other hand, there is insufficient time for plasma to be generated in each half AC period.

Moving diagonally across the voltage-frequency characteristic of Fig. 9 in the direction of increasing voltage and frequency also yields interesting behaviour in which the vortices become increasingly unstable, breaking down to spawn off additional vortex pairs. At yet higher voltages and frequencies, the vortex breakdown continues to produce a cascade of vortices with a continuum of length scales, similar to that observed in vortex shedding [18]. The stability of the original vortices can however be recovered by reducing the voltage at a fixed frequency.

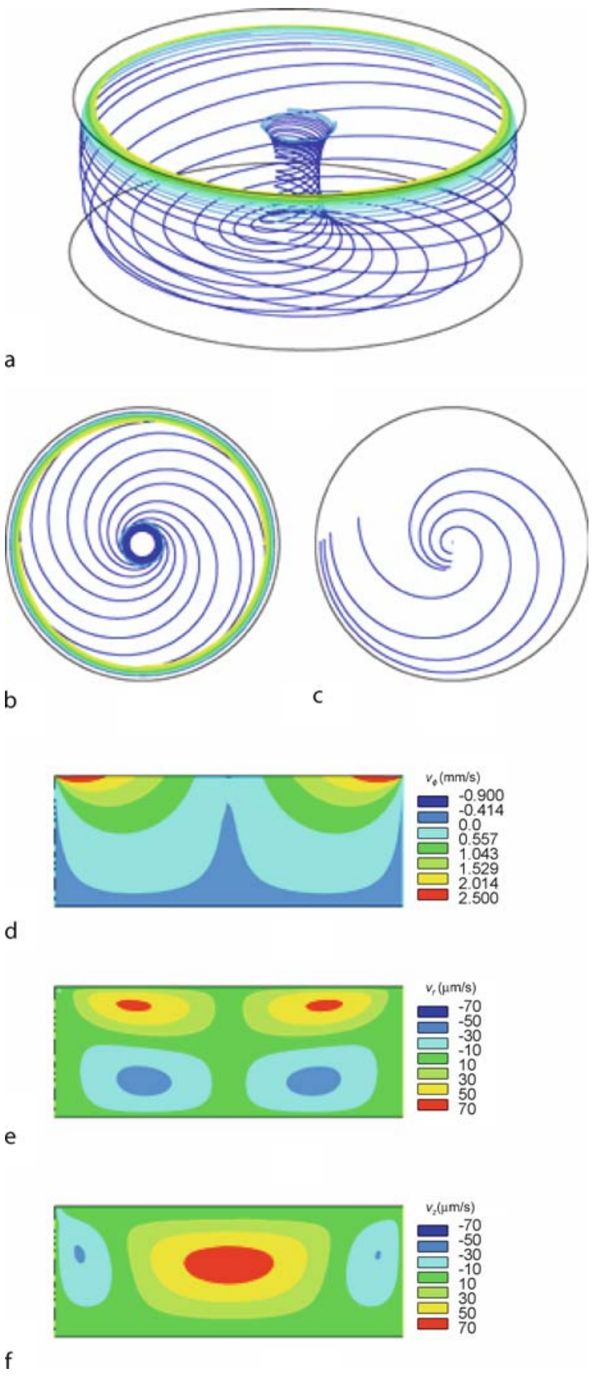

Interfacial Electrokinetic Flow, Figure 13 Numerical flow simulation results of the secondary meridional flow arising from primary surface recirculation of the liquid. (**a**), (**b**) and (**c**) are flow field traces; (**b**) is a cross-sectional plan view of the flow field at the top surface and (**c**) is a cross-sectional plan view at a small distance just above the base. (**d**), (**e**) and (**f**) are circumferential θ, radial r and vertical z velocity profiles, respectively. Bright shades indicate motion along the respective axis directions and dark shades indicate motion against the axis direction. After Yeo et al. [19]

These surface vortices provide an efficient means for microfluidic mixing, as shown in Fig. 10 where a dye is rapidly mixed within several seconds. The mixing can be enhanced by inducing the vortex instabilities wherein turbulent-like mixing efficiencies are observed [18]. In addition, particles dispersed in the flow are also observed to be drawn into the vortices due to positive dielectrophoresis towards a point on the interface closest to the needle where the field is most intense. Once a sufficient particle concentration is achieved within the vortex, shear-induced migration leads to cross-streamline transport such that the interior of the vortex is populated [18], as shown in Fig. 11a. Upon relaxation of the electric field and hence termination of the flow, we observe the particle aggregate to remain intact, possibly due to van der Waals attraction (Fig. 11b). This therefore provides a mechanism for particle trapping and concentration.

The induced surface flow also gives rise to secondary bulk fluid motion, in the same way that bulk meridional vortices are generated in a fluid trapped between rotating and stationary disks in Batchelor flows [19], as depicted in Fig. 12. In this flow recirculation mode, particles dispersed in the flow are convected to the bottom by the bulk meridional recirculation. However, due to the inward radial velocity in the Ekman boundary layer (see Fig. 13), the particles begin to swirl in a helical-like manner towards the center of the base [19]. Although the flow recirculates back up a central spinal column, the gravitational force on the particle is sufficient to trap the particles at a pseudo-stagnation point at the base. This was demonstrated to be another mechanism for particle trapping and concentration. Figure 14 shows the efficient trapping of red blood cells for microfluidic blood plasma separation in several minutes [19].

These surface and bulk electrohydrodynamic recirculation, whilst having the usual advantages of electrokinetic devices wherein mechanically moving parts are absent, also benefit from low field penetration into the liquid given that the field is predominantly in the gas phase, thus posing little threat in lysing biological cells. In addition, the absence of electrode-sample contact also minimizes sample contamination through electrolytic reactions, non-specific adsorption of biological compounds or Joule heating [19].

Future Directions for Research

Electrokinetic flows in microchannels has been extensively studied over the past decade. However, there is still a need for a greater understanding of electrokinetic flows involving freely deforming surfaces such as electrospraying, electrospinning, electrowetting and electrohy-

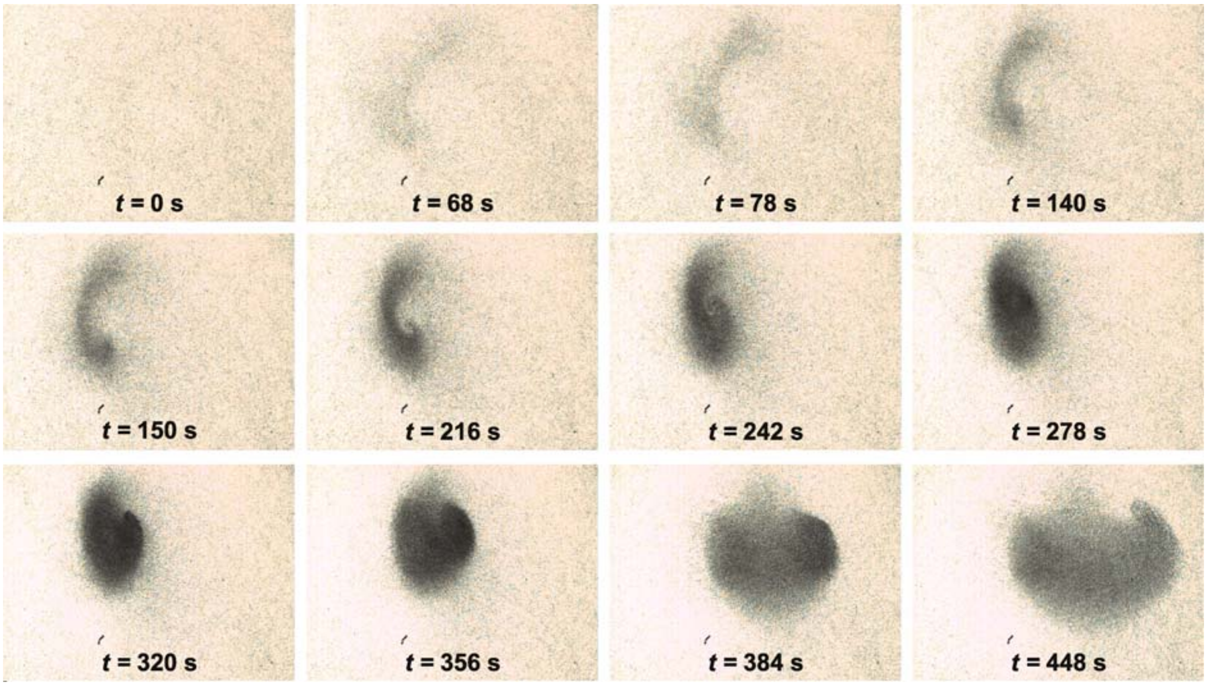

Interfacial Electrokinetic Flow, Figure 14 Sequence of images showing the separation of red blood cells from blood plasma via the secondary meridional bulk liquid recirculation. The final plasma effluent above contains a hematocrit less than 0.003%. After Yeo et al. [19]

drodynamically induced surface flows. In particular, the complex physicochemical behavior at the interface and its coupling to the bulk flow is still not well understood. One example is how surface polarization and tangential ion conduction affects the flow behavior. There is also a further need for accurate theoretical models that are underpinned by a correct fundamental physical understanding of such systems. For example, free surface models developed for investigating the behavior of interfacial flows driven by Marangoni and thermocapillary stresses have been extended to study the effects of electrical stresses (see, for example, [20]). It is anticipated that these models will form the basis of other more complex free-surface electrohydrodynamic models to investigate interfacial flow behavior and stability.

Cross References

- ► Applications Based on Electrowetting
- ► Bubble Dynamics in Microchannel
- ► Centrifugal Microfluidics
- ► Dielectrophoresis
- ► Digital Microfluidics
- ► Droplet and Bubble Formation in Microchannels
- ► Droplet Based Lab-on-a-Chip Devices
- ► Droplet Dispensing
- ► Droplet Dynamics in Microchannel
- ► Droplet Microreactors
- ► Electrocapillary
- ► Electrokinetic Two-Phase Flows
- ► Electrowetting
- ► Electrowetting and Droplets
- ► Interface Capturing Schemes for Free-Surface Flows
- ► Interface Tracking Schemes for Free-Surface Flows
- ► On-Chip Electrospray
- ► Surface Tension, Capillarity and Contact Angle

References

1. Landau SC, Lifshitz EM (1960) Electrodynamics of Continuous Media. Pergamon, Oxford
2. Castellanos A, González A (1998) Nonlinear electrohydrodynamics of free surfaces. IEEE Trans Diel Elec Insul 5:334–343
3. Saville DA (1997) Electrohydrodynamics: The Taylor–Melcher leaky dielectric model. Ann Rev Fluid Mech 29:27–64
4. Mugele F, Baret J-C (2005) Electrowetting: From basics to applications. J Phys Cond Mat 17:R705–R774
5. Yeo LY, Chang H-C (2005) Static and spontaneous electrowetting. Mod Phys Lett B 19:549–569
6. Fenn JB, Mann M, Meng CK, Wong SF, Whitehouse CM (1989) Electrospray ionization for mass spectrometry of large biomolecules. Science 246:64–71
7. Taylor G (1964) Disintegration of water drops in an electric field. Proc Royal Soc London A 280:383–397
8. Grace JM, Marijnissen JCM (1994) A review of liquid atomization by electrical means. J Aero Sci 25:1005–1019

9. Li H, Halsey TC, Lobkovsky A (1994) Singular shape of a fluid drop in an electric or magnetic field. Europhys Lett 27:575–580
10. Stone HA, Lister JR, Brenner MP (1999) Drops with conical ends in electric and magnetic fields. Proc Royal Soc London A 455:329–347
11. Yeo LY, Chang HC (2006) High frequency AC electrosprays: Mechanisms and applications. In: Rahman M, Brebbia CA (eds) Advances in Fluid Mechanics VI. WIT, Southampton, pp 223–231
12. Yeo LY, Lastochkin D, Wang S-C, Chang H-C (2004) A new ac electrospray mechanism by Maxwell-Wagner polarization and capillary resonance. Phys Rev Lett 92:133902
13. Yeo LY, Gagnon Z, Chang H-C (2005) AC electrospray biomaterials synthesis. Biomaterials 26:6122–6128
14. Yeo LY, Friend JR (2006) Electrospinning carbon nanotube polymer composite nanofibers. J Exp Nanosic 1:177–209
15. Hohman MM, Shin M, Rutledge G, Brenner MP (2001) Electrospinning and electrically forced jets I. Stability theory, Phys Fluid 13:2201–2220
16. Chang H-C (2002) Bubble/Drop transport in microchannels. In: Gad-el-Hak M (ed) The MEMS Handbook. CRC, Boca Raton
17. Takhistov P, Indeikina A, Chang H-C (2002) Electrokinetic displacement of air bubbles in microchannels. Phys Fluid 14:1–14
18. Yeo LY, Hou D, Maheshswari S, Chang HC (2006) Electrohydrodynamic surface microvortices for mixing and particle trapping. Appl Phys Lett 88:233512
19. Yeo LY, Friend JR, Arifin DR (2006) Electric tempest in a teacup – The tea leaf analogy to microfluidic blood plasma separation. Appl Phys Lett 89:103516
20. Yeo LY, Chang HC (2006) Electrowetting films on parallel line electrodes. Phys Rev E 73:011605

Interfacial Flow

► Interface Capturing Schemes for Free-Surface Flows

Interfacial Flow Modelling

► Numerical Techniques for Free Surface Flows: Interface Capturing and Interface Tracking

Interfacial Instability

Jeffrey D. Zahn
Department of Biomedical Engineering, Rutgers, The State University of New Jersey, Piscataway, NJ, USA
jdzahn@rci.rutgers.edu

Synonyms

Rayleigh instability; Bridging instability; Electrohydrodynamic instability; Rosensweig instability

Definition

Interfacial instabilities develop at an fluid–fluid or fluid–gas interface due to the unstable growth of interfacial perturbations. These instabilities may be surface tension driven (Rayleigh, liquid bridge instability), electrically driven (electrohydrodynamic instability) or magnetically driven (Rosensweig instability). These instabilities have been used in applications as diverse as inkjet printing to surface tension measurements. Interfacial instabilities are modeled using classical linear stability analysis considering momentum transport equations and both kinematic and interfacial stress boundary conditions. These models test the stability of the interfacial perturbations to infinitesimal disturbances.

Overview

The Rayleigh instability [1] is an example of a capillary driven instability which causes droplet breakup and has been used extensively for inkjet printing. Other interfacial instabilities such as a liquid bridge instability [2] have been studied to explore the stability criteria of coalescing two droplets from binary capillaries and determining whether the droplet will form a stable liquid bridge between the two capillary ends or if the bridge will rupture to have a droplet suspended on a single capillary end. Electrohydrodynamic instabilities occur when electrical stresses are applied at an interface. The electrical stresses develop at the interface primarily due to a conductivity or permittivity gradient between two fluid phases. The early work on modeling electrohydrodynamic instabilities performed a linear stability analysis of the electrical and fluid interfacial boundary conditions using the transfer relations developed by Melcher [3]. Melcher developed a dielectric model which describes liquids as being both polarizable and having free charge in an imposed electric field. Finally instabilities have been demonstrated using ferrofluids [4] which are colloidal suspensions of magnetic nanoparticles with a high magnetic susceptibility. When a ferrofluid is exposed to a magnetic field which is strong enough to promote instability, the surface of the fluid will spontaneously form a regular pattern of vertical spikes (peaking instability) consisting of the ferrofluid protruding from the initially flat interface.

Basic Methodology

The Rayleigh instability is the basis for most inkjet printing applications. When fluid is forced through an orifice (such as an inkjet printer head) a cylindrical fluid jet is produced with a fluid–air interface. As the jet falls under the influence of gravity it accelerates and is stretched so

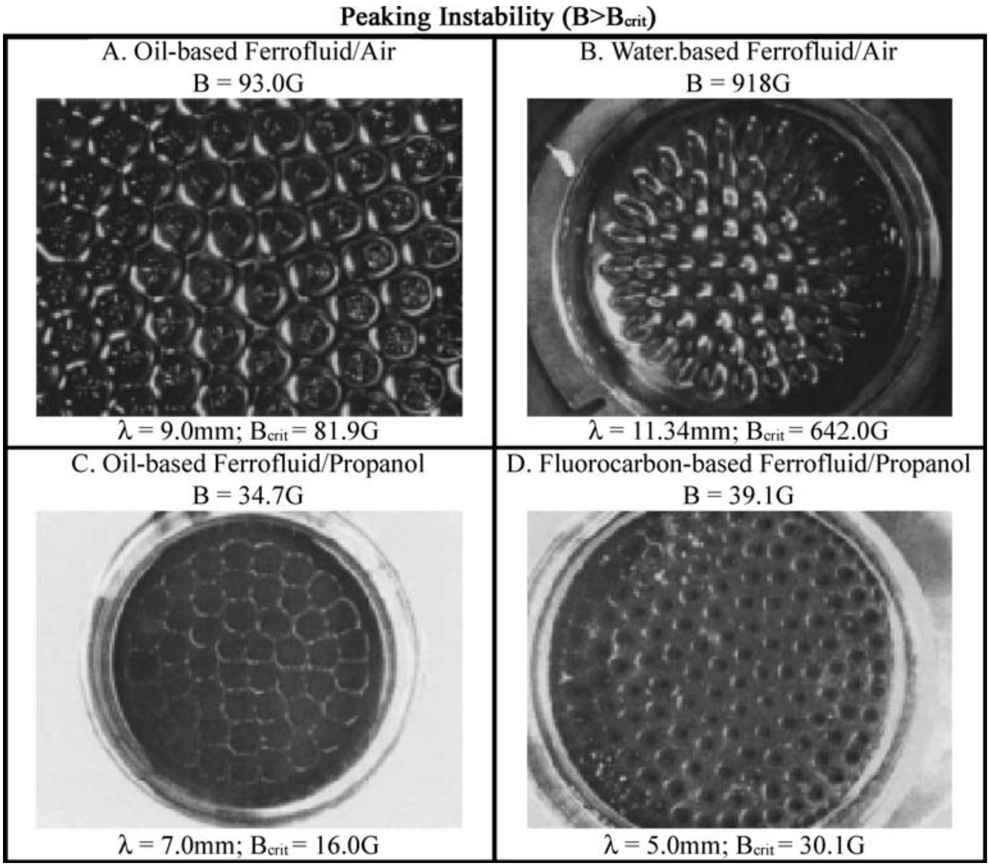

Interfacial Instability, Figure 1 Images of the peaking instability of different ferrofluids with applied magnetic fields above the critical values needed for instability. Images taken from [6]

that the jet radius decreases. At a critical radius the surface tension of the fluid causes spherical droplet breakup so that the volume of the droplet is the same as that of the cylindrical element protruding in the jet but minimizes surface area between the fluid and air. Inkjet printing uses this principle to create small ink droplets which are dispensed onto paper in a well defined pattern to produce printed characters and images made up of many droplets. A review of the evolution of inkjet printing technology is presented in [5]. Many different methods for actuating inkjet printer heads to dispense the proper amount of liquid, control drop size and maximize droplet dispensing (printing speed) have been investigated. Two of the most popular methods for dispensing droplets are using thermopneumatic actuation, where a portion of the fluid is heated to cause a gaseous phase change through liquid boiling to produce a pressurized gas bubble which forces a volume of ink through the printer head (bubble jet printers) or using piezoelectric actuation using a piezoelectric element to produce the appropriate pressure for droplet dispensing.

Hoburg and Melcher [7] demonstrated electrohydrodynamic instabilities in macroscale systems at an oil-oil interface with a discrete conductivity change at the interface under the influence of an applied electric field. In the presence of an applied electric field, charge accumulates at the fluid–fluid interface and the electrical force on the interface is balanced by the fluid interfacial stress tensor. At a critical field strength the electrical force exceeds the interfacial fluid forces and interfacial perturbations grow exponentially. Melcher determined a natural velocity scale for this instability, termed the electroviscous velocity which represents a balance between the electrical and viscous stresses at the fluid–fluid interface defined as

$$U_{\text{ev}} = \frac{\varepsilon E_0^2 H}{\mu} \quad (1)$$

where ε is the fluid dielectric constant, μ is the fluid viscosity, E_0 is the applied electric field and H is the characteristic length scale of the system (e. g., the half width of a microfluidic channel for a two layer stratified system).

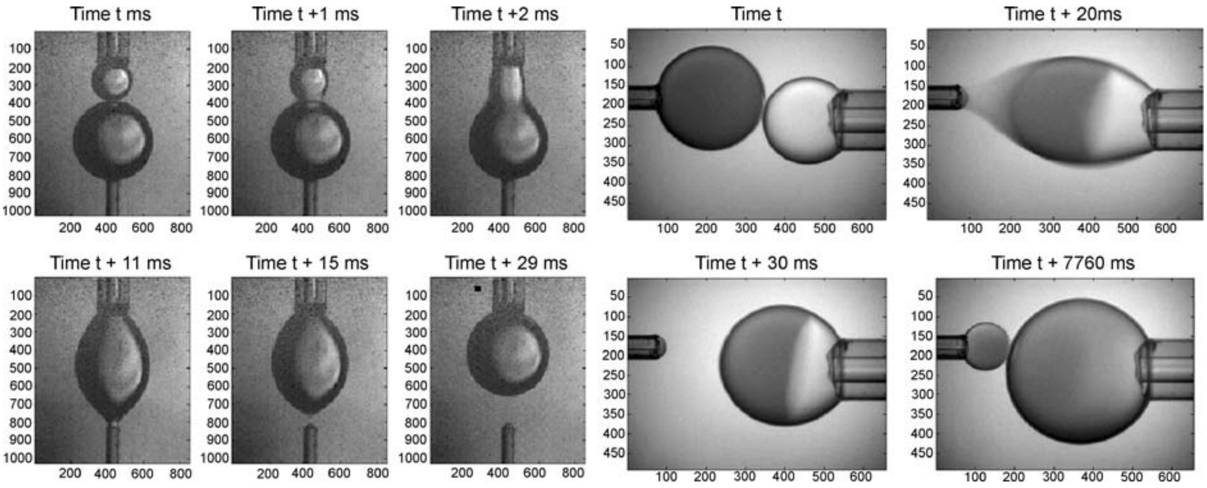

Interfacial Instability, Figure 2 *(Left)* High speed images of liquid bridge rupture after droplet coalescence. *(Right)* The mixing of a dye containing drop with an undyed droplet. The image at $t + 7760$ ms shows a mixed droplet after six instability injections of the dyed fluid. Images taken from [2]

Next, in macroscale systems the spiking phenomena of instabilities in magnetic fluids has been extensively studied [4, 6] (Fig. 1). These spikes will occur when the applied magnetic force promoting the instability is large enough to overcome the surface tension and gravitational force on the ferrofluid interface. Amin, et al. [6] studied the peaking instability of several ferrofluid configurations: an oil-based ferrofluid in air, a water-based ferrofluid in air, an oil-based ferrofluid, and fluorocarbon-based ferrofluid, both below a blend of 50% propanol and 50% deionized water. From the peaking instability and spacing between the peaks they were able to accurately determine the interfacial tension between the ferrofluid and air when compared to surface tension determined by tensiometry. They determined their surface tension as

$$\gamma = \frac{g\left(\rho_{\text{ferro}} - \rho_{\text{air}}\right)}{k_{\text{c}}^2} \quad (2)$$

where g is the gravitational constant, ρ is the fluid density where the subscript refers to either the ferrofluid or air and k_{c} is the critical wavenumber at the incipience of the instability defined as

$$k_{\text{c}} = \frac{2\pi}{\lambda} \quad (3)$$

where λ is the measured spacing between the spikes, the Taylor wavelength of the instability.

Key Research Findings

In microfluidic systems interfacial instabilities are promoted in immiscible multiphase flow systems. A review of many of the applications of multiphase flows in microfluidics is presented by Baround and Willaime [8]. They review many of the relevant challenges to integrating multiphase flows in microfluidic devices including how wetting and surface tension affects the multiphase flow regimes. One of the critical challenges is controlling droplet breakup and sizes due to the large surface tension forces between the liquid phases driving droplet formation. One critical area of investigation being pursued is understanding how to precisely control droplet size and patterns. There are many applications of droplet based devices in microfluidic systems.

Another area of investigation is coalescing droplets using liquid bridges [2]. Here the authors would combine two reagent containing aqueous droplets suspended from microcapillary tips under density matched silicone oil. When the droplets are brought in contact they coalesce into a single droplet. If different reactants are placed in each fluid then the merged droplets may be thought of as individual microreactors. They authors are exploring the use of droplets to dispense Polymerase Chain Reaction (PCR) reactants required for DNA amplification. The authors modeled the liquid breakup by considering surface energy minimization to predict the stability limits. Figure 2 shows both the coalescing of two droplets with liquid bridge breakup as well as mixing within the droplets due to their merging. They considered the stability of the liquid bridge as a function of the droplet slenderness (the ratio of the capillary tip separation to the mean diameter of the supporting capillary) and a volumetric ratio (ratio of actual droplet volume to the volume of a cylinder of liquid with the same radius as the supporting capillaries). The authors also investigated the effect of having different

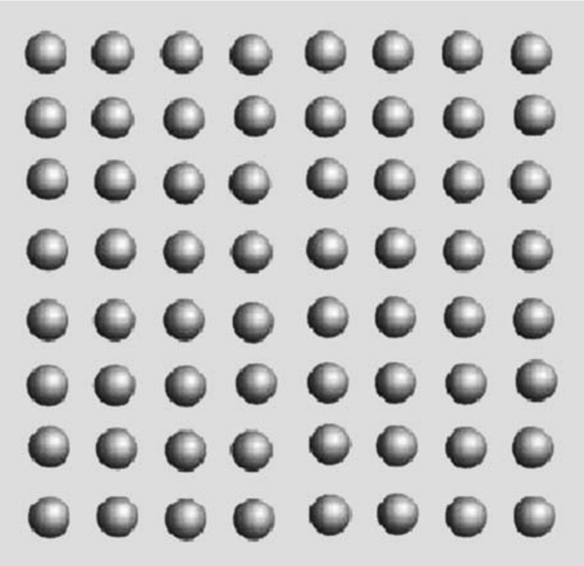

Interfacial Instability, Figure 3 A rectangular polymer array produced by inkjet printing. Image taken from [9]

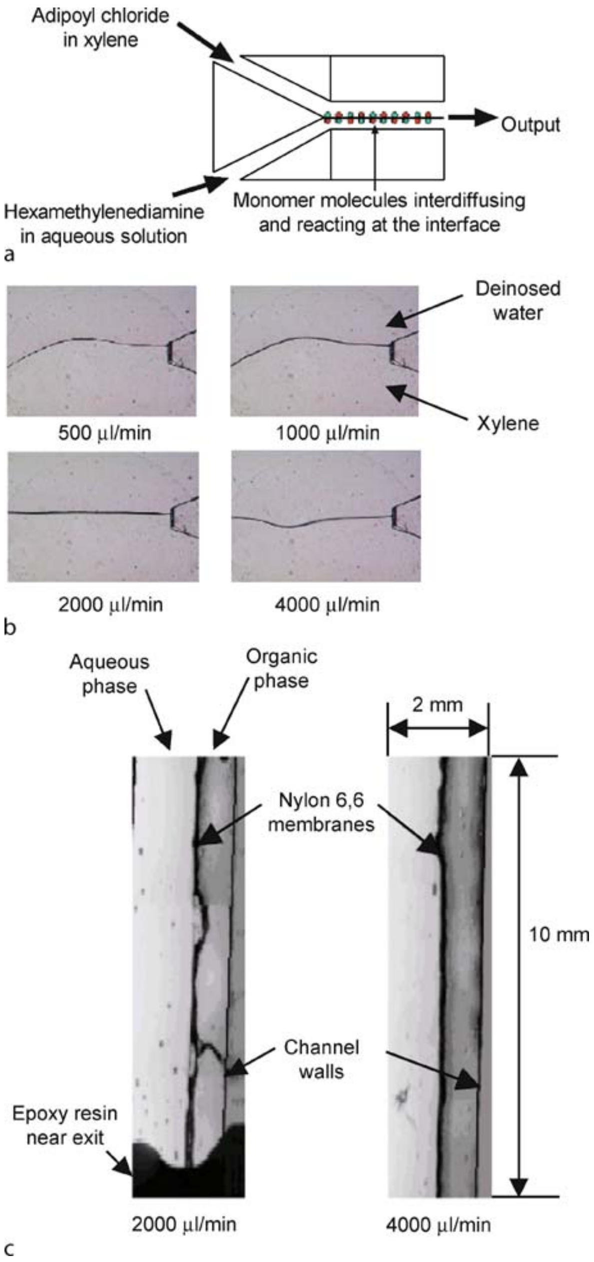

Interfacial Instability, Figure 4 (**a**) Schematic of a Y-channel for co infusion of an organic and aqueous solution containing reactants with interfacial membrane polymerization. (**b**) Stable two phase flow between xylene and water within the Y-channel structure. (**c**) Nylon 6,6 membranes formed along the Y-channel length. Images taken from [10]

supporting capillary radii (i. e. one capillary has a larger radius than the other). They found that the liquid bridges are stable at higher volumetric ratios and lower slenderness ratios (i. e., more fluid is dispensed and the capillaries are placed closer together). They also demonstrated that as the ratio of the capillary radii change, they needed an even higher volumetric ratio or lower slenderness to obtain stable bridges. However, using different radius capillaries, they could induce directional liquid bridge rupture, where the bridge would always rupture in the necking region closest to the smaller diameter capillary, so that a reactant containing fluid could be dispensed into a host droplet without the host fluid contaminating the dispensing capillary tip.

Other areas of interest are in using interfacial instabilities for materials production. Gans and Schubert describe the use of inkjet technology for the production of polymer microarrays [9]. They describe how droplet dispensing may be used in the fabrication of polymer microarrays (Fig. 3), polymer microoptical parts (microlenses), combinational polymeric materials production, polymer LED displays or polymer electronic devices. They also cite reports of inkjet printing technology applied to the production of microarrays of luminescent materials, catalyst combination for carbon nanotube (CNT) production, and patterning of DNA or other biological molecules. The polymers droplets are produced through a Rayleigh instability as previously described and dispensed onto a printing surface. Afterwards, the polymers are solidified either through solvent evaporation or UV curing of curable resins.

Another area which applied microfluidics to materials production is reported in [10]. Here the authors coinfused solutions of adipoyl chloride in xylene and hexamethylenediamine in 0.1 NaOH for laminar flow pattern-

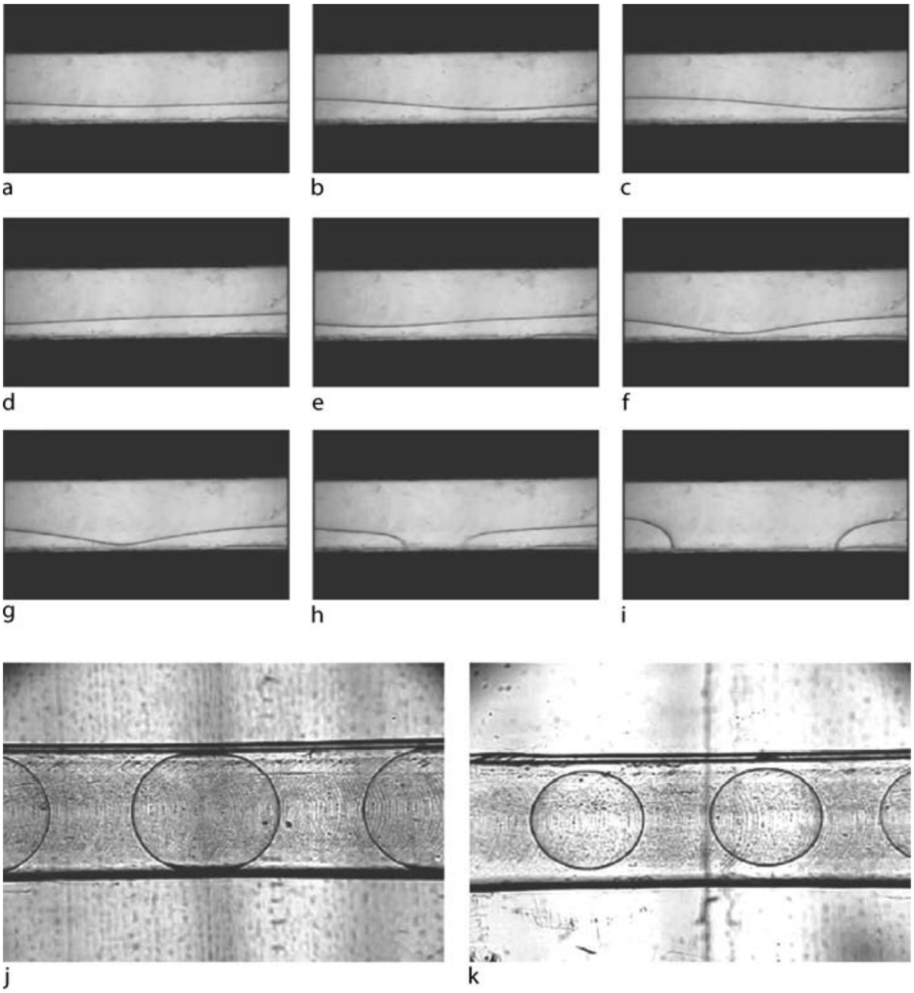

Interfacial Instability, Figure 5 (**a**)–(**i**) Droplets formed by an electrohydrodynamic instability due to the deflection of the interface in a two layer stratified flow. The top and bottom layers are corn oil and glycerine respectively. (**j**), (**k**) evolution of droplet shape downstream of the electric field region. Images taken from [12]

ing of nylon 6,6 membranes (Fig. 4). Using this method, the reactants in the different fluid phases would diffuse to the organic-aqueous interface where they would react in a polycondensation reaction to form nylon 6,6 (Fig. 4a). The authors also tested the stability of the interface with just the organic and aqueous solvents (Fig. 4b). Of particular interest to the authors was the stability of the flow due to the jump in viscosity and density across the interface which may destabilize the flow patterns. They were also concerned about how the polycondensation of the nylon membrane may cause time varying changes in the local density and viscosity close to the fluid–fluid interface. The authors tested a variety of device geometries in the production of nylon 6,6 membranes and found that in devices where the flow channels converge in ether a 90° angle in a 'T'-junction or at a smaller angle in a 'Y'-junction they were able to produce stable flows with well formed nylon membranes at the fluid–fluid interface. Thicker polymer films were reported at lower flow rates, and the authors suggest that at higher flow rates there is a higher shear force on the membrane leading to the removal of nascent polymer leaving only a more consolidated core film. Unstable flow patterns were also observed in other channel geometries. One geometry in particular was wider at the point of entry where the two fluids merged and the channel thinned along its length. Only uneven, fragmented and laterally displaced membranes were produced in this geometry. The authors suggest that the velocity gradient along the length of the channel contributed to the loss of flow stability.

Recently electrohydrodynamic instabilities have been demonstrated and analyzed in both two layer [11, 12] and

three layer stratified flows [13]. The two layer system consisted of glycerine and corn oil, while the three layer system consisted of a low conductivity organic layer (phenol:chloroform:isoamyl alcohol 25 : 24 : 1 mixture by volume) sandwiched between two high conductivity aqueous layers. In these two configurations the two fluid layers are immiscible. These two geometries have been modeled using linear stability analysis and an analytical stability criteria for the two configurations were determined [11, 13]. Experimentally, these instabilities were demonstrated within similar microfluidic configurations. Each system consisted of a converging channel geometry for introducing the respective fluids and electrodes for applying electrical excitation. For the two layer system shown in Fig. 5, once the electrodes are energized an electric field is generated which causes interfacial deflections (Fig. 5b–g). The authors report that for sufficiently high electric fields the interface ruptures when the top fluid (corn oil) periodically touches the opposite wall (Fig. 5h–i). Each time the interface contacts the wall glycerine droplets are formed and are convected downstream by the flow. It is noted that the droplets retain the deformed shape seen in Fig. 4h–i while they are in the region of the device with the applied electric field. Once the droplets enter a downstream portion of the device without electrodes their shape changes into spherical droplets under the action of surface tension as shown in Fig. 5j–k. The authors note that droplet size may be controlled by controlling both the applied voltage and the relative fluid flow rates. At higher applied field strengths the droplet sizes decrease due to the larger interfacial force causing the interface to contact the wall at a higher frequency, thus decreasing the volume in the droplets and hence their size.

Future Directions for Research

Interfacial instabilities in microsystems are complex phenomena and may be promoted by many different means. Future work requires a further development of experimental models and expansion of computational simulations to better understand the criteria under which instabilities develop. In addition, specific applications using interfacial instabilities for fluid manipulation, analysis and materials production should be continued to be explored.

Cross References

► Droplet Dispensing
► Droplet Dynamics in Microchannel
► Droplet and Bubble Formation in Microchannels
► Electrokinetic Two Phase Flows
► Interfacial Lab-on-Chip Devices for Sample Extraction
► Pressure-Driven Two Phase Flows

References

1. Rayleigh FRS (1878) On the instability of jets. Proc Lond Math Soc 10(4):4–13
2. Curran K, Colin S, Baldas L, Davies M (2005) Liquid bridge instability applied to microfluidics. Microfluid Nanofluid 1:336–345
3. Melcher JR (1981) Continuum Electromechanics. MIT Press, Cambridge
4. Cowley MD, Rosensweig RE (1967) The interfacial stability of a ferromagnetic fluid. J Fluid Mech 30:671–688
5. Le HP (1998) Progress and Trends in Ink-jet Printing Technology. J Imag Sci Technol 42(1):49–62
6. Amin MS, Elborai S, Lee SH, He X, Zahn M (2005) Surface tension measurement techniques of magnetic fluids at an interface between different fluids using perpendicular field instability. J Appl Phys 97:10R308
7. Hoburg JF, Melcher JR (1976) Internal electrohydrodynamic instability and mixing of fluids with orthogonal field and conductivity gradients. J Fluid Mech 73:333–351
8. Baroud CN, Willaime H (2004) Multiphase flows in microfluidics. CR Phys 5:547–555
9. Gans BJ, Schubert US (2003) Inkjet Printing of Polymer Microarrays and Libraries: Instrumentation, Requirements, and Perspectives. Macromol Rapid Commun 24:659–666
10. Gargiuli J, Shapiro E, Gulhane H, Nair G, Drikakis D, Vadgama P (2006) Microfluidic systems for in situ formation of nylon 6,6 membranes. J Membr Sci 282:257–265
11. Ozen O, Aubry N, Papageorgiou DT, Petropoulos PG (2006) Electrohydrodynamic linear stability of two immiscible fluids in channel flow. Electrochim Acta 51:5316–5323
12. Ozen O, Aubry N, Papageorgiou DT, Petropoulos PG (2006) Monodisperse drop formation in square microchannels. Phys Rev Lett 96:144501-1–144501-4
13. Zahn JD, Reddy V (2006) Electrohydrodynamic instability mixing: Two phase linear stability analysis and micromixing for a miniaturized DNA extraction module. Microfluid Nanofluid 2(5):399–415

Interfacing Lab-on-a-Chip Platforms with Mass Spectrometers Using MALDI and ESI

► Interfaces between Microfluidics and Mass Spectrometry

Intermittent Flow

► Taylor Flow in Microchannels

Internal Friction

► Viscous Dissipation
► Viscous Heating

Internal Rarefied Gas Flows

► Gas Flow in Nanochannels

International Notation

► Hermann–Mauguin Notation

Internucleosomal DNA Fragmentation

► Microfluidics for Studies of Apoptosis

Interrogation Area

Definition

The ► field of view of an image is divided into interrogation areas by a grid. This is done for further image processing algorithms in example for ► PIV algorithms or local averaging of the information.

Intracellular Ca2+ Concentration Changes

► Microfluidics for Studies of Apoptosis

Intracellular Ca2+ Fluxes

► Microfluidics for Studies of Apoptosis

Inversion Symmetry

Definition

Implies the appearance and organization of atoms in a crystalline solid would be identical if all atoms were moved such that vectors from a point within the material to each atom in their original location were to have their lengths *inverted*, that is, to have them pointing in the opposite direction and with the same length .

Cross References

► Hermann–Mauguin Notation
► Non-Centrosymmetric

Ion Channel

CHAN HEE CHON , DONGQING LI
Department of Mechanical Engineering, Vanderbilt University, Nashville, TN, USA
Chanhee.chon@vanderbilt.edu

Synonyms

Gate in the cell wall

Definition

Ion channels are passageways for ions to be transported across cell membranes. They are nanometer-sized channels.

Overview

Ions, charged particles, have a significant effect on many biological cell processes. Cells use inorganic ions for transmitting signals across the cell membranes or along the surfaces of the cells. However, it is difficult for ions to pass through the membranes by simple diffusion because cell membranes consist of hydrophobic phospholipids that oppose the passage of hydrophilic ions. Furthermore, the negatively charged phosphate head groups of the phospholipids tend to repel negatively charged anions and trap positively charged cations. Therefore, ions require a specific gate to pass through the membrane [1]. Such a gate constituted of a large and diverse group of pore-forming membrane proteins is called an ion channel (Fig. 1). Ion channels are present in the membranes that surround all biological cells. Ion channels govern the electrical properties of all living cells and help to establish and control the small voltage gradient across the plasma membrane of all living cells by allowing the flow of ions down their electrochemical gradient.

Each ion channel species is characterized by its ion selectivity sequence (K^+ channels, Na^+ channels, Ca^{2+} channels, Cl^- channels, and nonselective cation channels). Highly specific ion channels only allow passage of a single ion species and less specific ion channels allow passage of a few or several ion species. Functionally, ion channels are broadly divided into voltage- and ligand-gated channels, referring to the type of physiological stimulus that activates the channel [2, 3]. Voltage-gated ion channels are a class of transmembrane ion channels that are activated by changes in electrical potential difference near the channel (Fig. 1a). These are typical in neurons. Ligand-gated ion channels are a group of intrinsic transmembrane ion channels that are opened or closed in response to binding of a chemical messenger (Fig. 1b).

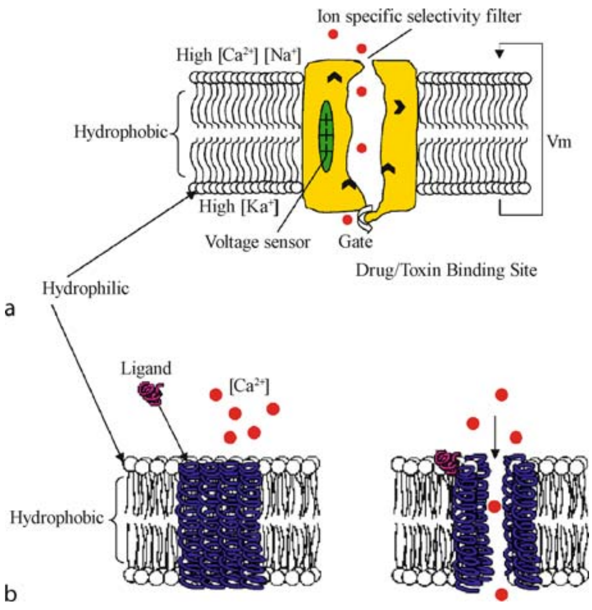

Ion Channel, Figure 1 Schematic of (**a**) voltage-gated ion channel [2] and (**b**) ligand-gated ion channel [3]

Dysfunction of ion channels causes many diseases. Some ion channel diseases are genetic. Channelopathies are caused directly by mutations in genes coding for ion channels [4–7]. Examples of channelopathies are cystic fibrosis, epilepsy, and arrhythmias such as the long QT syndrome. Some other ion channels may be involved in nongenetic diseases such as diarrhea, which is mediated by toxicological effects on ion channel function [8].
The human genome was sequenced with at least 400 ion channel structures. However, currently only about 100 have been identified. Because specific ion channels interact with selective drugs, it is important to identify new ion channels and validate these as novel drug targets.

Cross References

► Ion-Exchange Membranes

References

1. Krogh D (2000) Biology. Prentice Hall, New Jersey
2. Denyer J, Worley J, Cox B, Allenby G, Banks M (1998) HTS Approaches to Valtage-Gated Ion Channel Drug Discovery. Drug Discov Today 3:323–332
3. Bensaccount (2006) Ligand-gated ion channel. http://en.wikipedia.org/wiki/Image:LGIC.png. Accessed 26 Nov 2007
4. Kass RS (2005) The Channelopathies: Novel Insights into Molecular and Genetic Mechanisms of Human Disease. J Clin Invest 115:1986–1989
5. de Silva SM, Kuncl RW, Griffin JW, Cornblath DR, Chavoustie S (1990) Paramyotonia Congenita or Hyperkalemic Periodic Paralysis? Clinical and Electrophysiological Features of Each Entity in One Family. Muscle Nerve 13:21–26
6. Scheffer IE, Berkovic SF (1997) Generalized Epilepsy with Febrile Seizure Plus. A Genetic Disorder with Heterogeneous Clinical Phenotypes. Brain 120:479–490
7. Tristani-Firouzi M et al (2002) Functional and Clinical Characterization of KCNJ2 Mutations Associated with LQT7 (Andersen Syndrome). J Clin Invest 110:381–388
8. Waxman SG (2001) Acquired Channelopathies in Nerve Injury and MS. Neurology 56:1621–1627

Ion Conductance in Nanochannels

► Electrokinetic Flow and Ion Transport in Nanochannels

Ion Counter

► Ion Detector

Ion Detector

Synonyms

Ion counter

Definition

A device for detecting ions that operates by converting the ion back into a neutral molecule, the resulting electron motion generating a flow of current in a detection circuit. Examples include Faraday cups and electron multipliers. For singly charged ions, Faraday cups yield one electron per ion, whereas multipliers provide a typical amplification factor of $10^6 - 10^7$.

Cross References

► Detection Using Mass Spectrometry

Ion Exchange Membranes

Dominic S. Peterson
Chemistry Division, Los Alamos National Laboratory,
Los Alamos, NM, USA
DominicP@lanl.gov

Definition

Ion Exchange Membranes are semi-permeable membranes in which an ionic functionality is fixed to the backbone of the membrane. These ionic species enable the concentration, separation, or exclusion of ionic species from a fluid flow. The two types of ion exchange mem-

branes are cationic- and anionic-exchange membranes. Ion exchange membranes are used for a wide range of industrial processes.

Chemical and Physical Properties

Ion exchange membranes have been in use since their discovery over 100 years ago. Large ion-exchange membranes are widely used by industry and have many commercial uses including water purification (desalination, water softening, etc), separation and preconcentration of food products and pharmaceutical products and in the manufacture of basic chemical products [1]. Because of their diversity and high efficiency, their use has been investigated in microfluidic systems as a way to enable sample cleanup of small volumes of analytes and solvent streams.
There are two main types of ion-exchange membranes, they are classified into the type of ions that they interact with in solution. ► Anion exchange membranes interact with anions and typically consist of amine functionalities ($-NH_3^+$, $-NRH_2^+$, etc). ► Cation exchange membranes interact with cations and have a variety of anion functional groups affixed to the membrane ($-COO^-$, $-SO_3^-$, $-PO_3^{2-}$, $-C_6H_4O^-$, etc). The ion exchange allows the passage of the charges opposite to those on the membrane while preventing the passage of ions of the same charge. In addition, different ions of the opposite charge will be retained to different degrees depending on its ability to interact with the ionic functionalities on the membrane surface. This binding will be dependant to large extent on the pH of the solution and the ions of interest.
In addition to classifying ion exchange membranes according to their ionic functionalities, it is also useful to identify how the support membrane has been formed to understand how the ionic functionalities will interact with a solution. A homogenous membrane has ionic functionalities bound to the surface of the membrane, but the support structure is non-ionic. A ► heterogeneous membrane has the charged functionalities mixed into the membrane support structure, which gives the structure an ionic character throughout the membrane.
The preparation of a homogeneous membrane can follow one of several approaches. The first method involves using a monomer that contains an ionic functionality or is easily converted to an ionic functional group. This starting monomer is then copolymerized with other monomers to form the ion exchange membrane. Another method that can be used to make an ion exchange membrane is to use a polymer film and then to modify the polymer directly or by a grafting reaction in order to introduce the ionic functional groups to the membrane. The third method that can be used to make a homogeneous ion-exchange membrane is to dissolve an ionic moiety into a polymer and then casting the polymer into a film to form the membrane.
In making ion-exchange membranes it is also important to consider the materials that the support membrane is composed of. The most common materials that are used to produce ion-exchange membranes are organic polymers, such as poly(styrene-co-divinylbenzene), poly(propylene), poly(ethylene), etc. It is also possible to utilize organic–inorganic composite materials to form the membrane material. These are called hybrid ion exchange membranes. The organic constituent of these composite materials provide structural flexibility and simplified processing. The inorganic component of composite membranes provide mechanical rigidity, thermal stability, and the potential for various properties such as magnetic, and high carrier motilities. Hybrid materials can be made from a variety of methods including blending, in situ polymerization, self assembly, or by a sol-gel process, which is the most common technique.
It is also possible to mix multiple functionalities into a single ion exchange membrane. One of these types of membranes is called a ► bipolar membrane. This type of membrane is a composition membrane that consists of a layered ion –exchange structure composed of a cation exchange layer and an anion exchange layer. The use of these compositions enables a large number of functionalities, such as anti-fouling, water dissociation, and the separation of mono and divalent ions. In particular it is possible to separate acids and bases into their component salts. These types of membranes have shown utility primarily in electro dialysis and have application in chemical production and separation. However, bipolar membranes tend to be instable in high current conditions. The fabrication of bipolar membranes is most directly performed by the use of a commercially available cation exchange membrane and anion exchange membranes. It is also possible to prepare this type of membrane by casting a polyelectrolyte solution onto a commercial exchange membrane of the opposite charge (cation solution on an anion membrane, or vice versa).
There is also a type of ion-exchange membrane that includes both a weak anion exchange and a weak cation exchange functionalities into the same membrane. These types of membranes are called ► amphoteric ion exchange membranes since they contain both anion and cation functionalities. In these membranes the anion exchange and cation exchange portions are randomly distributed throughout the membrane matrix. Amphoteric ion exchange membranes have the advantage that they are capable of passing both cations and anions. The passage and the separation of these analytes is controlled simply by controlling the pH within a relatively narrow range. The

pH change can control precisely the surface charge that is exhibited by the ion exchange membrane. In addition, amphoteric membranes prevent the adsorption of organic compounds and biological macromolecules onto the surface of the membrane.

An alternative to an amphoteric membrane is a mosaic ion exchange membrane, which consists of both anion exchange and cation exchange functionalities in the same membrane. However, where amphoteric membranes involve randomly distributed anion exchange and cation exchange functionalities, a mosaic ion exchange membrane involves anion and cation exchange elements that are arranged in parallel to one another. Because the two different exchange elements are arranged in parallel it is possible for both anions and cations to flow through the membrane through the individual channels. Mosaic exchange membranes have several unique properties such as negative salt rejection and osmotic pressure which can be used for different separation approaches for waste streams or other high salt solutions. The synthesis of a mosaic exchange membrane is quite complex, and even large scale membranes are not yet commercially available. Several synthetic methods are available to produce mosaic exchange membranes, but they are not typically suited to industrial production techniques.

There are several parameters associated with the ion-exchange membrane and the solvent that analyze ions are dissolved in that affect the ability of the membrane to retain or pass the ions or to separate them in the case of ion-exchange chromatography operations. The structure of the membrane directly affects the introduction of the ions to the functional ion-exchange medium. The overall capacity of the membrane to retain analyte ions will affect how much can actually be retained. If the ion-exchange membrane becomes saturated with ions its effectiveness will be greatly diminished. The strength of the eluent refers to the ability to elute sample ions. For instance, carbonate (a bivalent anion) has a greater eluting strength than monovalent anions. The eluent concentration will also have an effect on the release of the sample ions, with higher concentrations resulting in shorter release times. Finally, it is possible to include a small percentage of organic solvent (10% to 20%) in elution solutions. The organic solvent ensures that samples remain in solution and do not precipitate out.

Key Research Findings

The key to using ion-exchange membranes in microfluidic systems is finding a way to simply, effectively, and reproducibly incorporate the membrane into the system. The simplest method that can be devised to integrate a membrane into a microfluidic system is to place it in line with the microchannels. This can be done by placing it at the entrance or exit of a microchannel [2]. This type of system has been used to desalt protein samples prior to their analysis by electrospray ionization mass spectrometry. Another method that can be used is to place the membrane between two chips that have the channels fabricated on them [3]. By sandwiching the membrane between the two plates makes the fabrication simple and allows a wide range of ion-exchange membranes to be used. These devices have been used previously to perform sample cleanup steps before a sample is introduced to the microfluidic system. This can be a simple pre-concentration of the analyte and removal of any interferences, or it can involve a minimal separation of analytes from one another on the membrane and their introduction into the device. Another approach that has been used when interconnecting microchannels via a membrane is to connect channels that are orthogonal to one another [4]. This approach allows more complex systems of channels to be constructed and the incorporation of the ion-exchange membrane enables sample clean up to be performed between steps or it allows only a particular analyte or reagent to be introduced into a microchannel.

An interesting and challenging way to incorporate a membrane into a microchannel is to fabricate the membrane directly within the channel. This can be accomplished by forming an aqueous/organic phase interfacial boundary within the channel [5]. A condensation reaction can then be performed to make the membrane. This approach was used to fabricate a nylon membrane, but it should be possible to extend the approach to ion-exchange membranes. Alternatively, a polymerization mixture can be placed in a microchannel and a thin membrane can be polymerized by using a focused laser [6]. These methods for fabricating a membrane within a channel are still in the process of being developed, and in the future it should be possible to use a wide range of chemistries to produce a diverse set of membranes. These membranes will enable microfluidic devices to be used with more complex solutions eventually including environmental samples.

Examples of Applications

While ion exchange membranes have been studied for many decades and have been applied to many areas, they are only beginning to be applied to microfluidic applications. The primary area that ion exchange membranes have been applied to in microfluidics has been for the pre-concentration of analytes in microfluidic systems. Pre-concentration is of critical importance in microfluidic systems because the analyte concentrations are typically too low for the detection methods used. This requires that the

analytes be concentrated prior to separation and/or detection in order to enhance the detection limits of the systems. In addition to pre-concentration applications, ion-exchange membranes have started to be demonstrated for other applications in microfluidic devices. One application is using ion-exchange membranes in conjunction with electrokinetic pumps [7], which are devices that pump liquid in a microdevice when an electric field is applied. In this device, the ion-exchange membrane served to electrically isolate the pump from the rest of the solution while still enabling the liquid flow that is generated by the device to flow through the system. This extends the utility of on-chip electokinetic pumps because the solvent requirements for the electrokinetic pump can be separate from the solvent needs for the rest of the device.

Another microfluidic application for ion-exchange membranes is ion suppression [8]. This approach involves allowing excess ions in one solvent to flow through ion-exchange into another waste solvent. This has the effect of suppression of the unwanted ions, and allows the conductivity of the solution to be measured and to measure the presence and concentrations of analytes of interest, such as heavy metals.

Cross References

► Electrokinetic Flow and Ion Transport in Nanochannels
► Fabrication of 3D Microfluidic Structures
► Ion Channel
► Ion Implantation
► Lab-on-Chip Devices for Separation Based Detection
► Microfluidic Sample Manipulation
► Stationary Phases in Microchannels

References

1. Xu T (2005) Ion exchange membranes: State of their development and perspective. J Membrane Sci 263:1–29
2. Lion N, Gellon JO, Jensen H, Girault HH (2003) On-chip protein sample desalting and preparation for direct coupling with electrospray ionization mass spectrometry. J Chromatogr A 1003:11–19
3. Xiang F, Lin YH, Wen J, Matson DW, Smith RD (1999) An integrated microfabricated device for dual microdialysis and on-line ESI-Ion trap mass spectrometry for analysis of complex biological samples. Anal Chem 71:1485–1490
4. Ismagilov RF, Ng JMK, Kenis PJA, Whitesides GM (2001) Microfluidic arrays of fluid–fluid diffusional contacts as detection elements and combinatorial tools. Anal Chem 73:5207–5213
5. Hisamoto H, Shimizu Y, Uchiyama K, Tokeshi M, Kikutani Y, Hibara A, Kitamori T (2003) Chemicofunctional membrane for integrated chemical processes on a microchip. Anal Chem 75:350–354
6. Song S, Singh AK, Shepodd TJ, Kirby BJ (2004) Microchip dialysis of proteins using in situ photopatterned nanoporous polymer membranes. Anal Chem 76:2367–2373
7. Pu Q, Liu S (2004) Microfabricated electroosmotic pump for capillary-based sequential injection analysis. Anal Chim Acta 511:105–112
8. Kuban P, Dasgupta PK, Morris KA (2002) Microscale continuous ion exchanger. Anal Chem 74:5667–5675

Ion Implantation

Definition

The bombardment with ions of sufficient energy that they become embedded beneath the surface of the target material.

Cross References

► Sputtering for Film Deposition

Ionization Source

► Ion Source

Ion Mobility

Definition

Velocity acquired by an ion per unit applied force.

Cross References

► Electrokinetic Flow and Ion Transport in Nanochannels

Ion Mobility Spectrometer

► Miniaturized Ion Mobility Spectrometry

Ion Source

Synonyms

Ionization source

Definition

A device for generating a flux of ionized molecules. Examples include hot- and cold-cathode electron impact ion sources, photoionization ion sources and electrospray ion sources.

Cross References

► Mass Spectrometry
► Interfaces between Microfluidics and Mass Spectrometry

Ion Transport

► Electrophoretic Transport in Nanofluidic Channels

Ion Transport in Nanopores

► Electrokinetic Flow and Ion Transport in Nanochannels

Ion Trap Mass Spectrometer

► Quadrupole Ion Trap

IPRT

► Resistance Temperature Detectors

Irradiance

► Photometer

Isentropic Flow

Definition

Formally, a flow which is both adiabatic and reversible, and hence entropy remains constant. In practice, this is a flow in which sources of irreversibility (e. g., friction, thermal diffusion, chemical non-equilibrium) are considered negligible. Shock-free compressible flows are typically modeled as isentropic.

Cross References

► Supersonic Micro-Nozzles

Isotropic Etching

MICHAEL KÖHLER
Institut für Physik, Technische Universität Ilmenau, Ilmenau, Germany
michael.koehler@tu-ilmenau.de

Synonyms

Non-directional etching

Definition

Isotropic etching includes all etching processes with equal etch rates for all spatial directions. Isotropic etch processes are rate controlled either by transport processes with direction-independent transport rate (most frequent case of isotropic etching) or by surface processes in the case of removing completely isotropic built materials. Isotropic etching includes wet chemical processes as well as dry etching processes.

Overview

Microlithographic etching represents a class of key processes of planar technology. Etching plays a very important role in microsystem technology and in the fabrication of integrated circuits. All etching processes are applied for removing material from solid films in order to generate small well-defined structures of functional material. Therefore, microlithographic etching is one of the so-called subtractive micropatterning techniques. In this process, firstly, a complete film of a certain material (functional material) is deposited at the surface of a substrate. Secondly, this film is covered by a light- or radiation-sensitive film *(resist)*, which is exposed and developed for patterning. And thirdly, the functional film is etched through the openings *(windows)* of the resist.

Etching processes can be applied for thin films, but also for ultrathin films, thick films and bulk materials. It is frequently applied for the generation of microstructures but can also be used for the preparation of features down to the nanometer range.

All etching processes are based on the conversion of a solid material in a movable form and the removal of the atoms of the material from the surface. Two general types of etching processes are distinguished. The first, micropatterning by liquids *(etching baths)*, is called *wet etching*. Sometimes the wet etching techniques are also summarized as *chemical etching*. This is not completely correct, because the dry etching processes are also frequently determined by specific chemical processes. The second process, etching by transfer of the released material into the gas phase, a plasma or vacuum, is called *dry etching*. Frequently, dry etching processes are classified as *physical etching* due to the predominance of physical effects in the etching process and in contrast to chemically dominated wet etching.

Basic Methodology

Modern microtechnology uses a wide variety of etching techniques (Fig. 1). There are two main classes of etching processes. Corrosive liquids are used in wet etching. Highly reactive corrosive gases, plasmas and ion beams are applied in dry etching processes. In addition, etching procedures are distinguished by selectivity of material removal and by the isotropic or anisotropic character of pattern transfer. Anisotropic etching can take place in wet and in dry etching processes. The principal difference between anisotropic and isotropic etching processes consists in the angle of the side walls and the distance of underetching under the resist mask. Crystallographic etching represents a special case of anisotropic processes (Fig. 2). A significant undercutting of mask edges always takes place in isotropic etching (Fig. 2a). Etch grooves are marked by rounded profiles. In contrast, particular crystal planes with high etch resistance are prepared during crystallographic etching. Different variants of trapezoid profiles are formed during time-controlled crystallographic etching if the crystal planes with low etch rate are inclined (Fig. 2b). V-grooves or pyramidal holes are obtained in such materials (for example Si(100)) after complete removal of material following crystal planes with higher etch rate. The depth of these V-shaped grooves or pyramidal holes is determined by the lateral width of the mask window (Fig. 2c). The shapes of grooves formed in isotropic etch processes are marked by considerable underetching (at least in the dimension of the etch depth) and – in most cases – by a smaller angle of the side walls (Fig. 3).

Wet etching processes use the conversion of solids into a state of solvated ions or molecules or into dissolved coordination compounds. In many cases metals or semiconductors have to be removed. Therefore, the formation of coordination compounds or ions must be accompanied by an electron transfer step. Wet etching of metals and semiconductors is an electrochemical process (Fig. 4). The removal of material is caused by the transition of metal atoms at the surface to metal ions and the formation of a soluble species (anodic partial process). The remaining electrons must be removed by a second electrochemical process, in which an oxidizing agent is reduced at the surface (cathodic partial process). Both electrochemical partial processes are coupled by a common electrode potential. So, an electric current flows from the cathodic to the anodic active surface sites. Oxidizing agents of sufficient high oxidation power (redox potential) are necessary for keeping the electrode potential high enough for the anodic process of metal dissolution.

Wet etching processes work isotropically, if the material is isotropic or the etching process is transport-controlled. Isotropic etching results in equal etch rates in all directions. An undercutting of the resist edges in the dimension of the film thickness is always observed. The isotropic character of etch processes makes it impossible to generate openings with high aspect ratios. But, it can be applied for the controlled release of cantilevers, air bridges and other movable structures for micromechanics by underetching. In contrast, anisotropic etching is observed if a single-crystalline material is etched with rate control of the anodic surface process. The alkaline etching of silicon single crystals is a typical example of an anisotropic wet etching process. It supplies characteristic features like V-grooves, trapezoid channel cross-sections, pyramidal grooves and rhomboid patterns, depending on the crystal cut and orientation of the lithographic pattern in relation to the crystal planes (see Fig. 2). The etching characteristics (isotropic or anisotropic) can be adapted by choosing a suitable etch bath.

Dry etching processes can be based on purely mechanical removal of material by ion impact (physical or sputter etching (PE) and ion beam etching (IBE)) or on the removal of material by very reactive gases or plasmas (plasma etching) or by combinations of both process types (reactive ion etching (RIE), reactive ion beam etching (RIBE) or chemical-assisted ion beam etching (CAIBE)). Plasma etching occurs in a moderate vacuum (typically around 1 torr). The active etching species are radicals in most cases. Therefore, this etching technique shows comparatively high selectivity, but only a low anisotropy. As a rule, considerable underetching is observed. A higher precision of pattern transfer from the resist into the functional layer is achieved by sputter or ion beam etching. In these processes, highly accelerated ions impact the material and evaporate clouds of atoms and clusters. The particle energies are in the range between several hundred and several million eV. Energies of several keV are typical for many processes. Therefore, the pressure has to be in the region of a millitorr or below. Sputtering and ion beam etching are not selective. RIE, RIBE and CAIBE combine the sputter effect of accelerated ions with the specificity of plasmochemical reaction. With optimized devices and protocols, comparatively high etching rates, high anisotropy and a certain material specificity can be achieved. The pressure is typically in the range between about 0.1 and 10 mtorr. The etch rates depend on the material, on the ion current density and on the reactivity and concentration of active radicals. For RIE, RIBE and CAIBE, reactive gases are fed into the etch equipment. Typical etching gases are chlorine (for aluminum), CF_4 or other fluorine-containing small molecules for etching of silicon and some other semiconductors and metals, and oxygen for etching of polymers. In contrast to these tech-

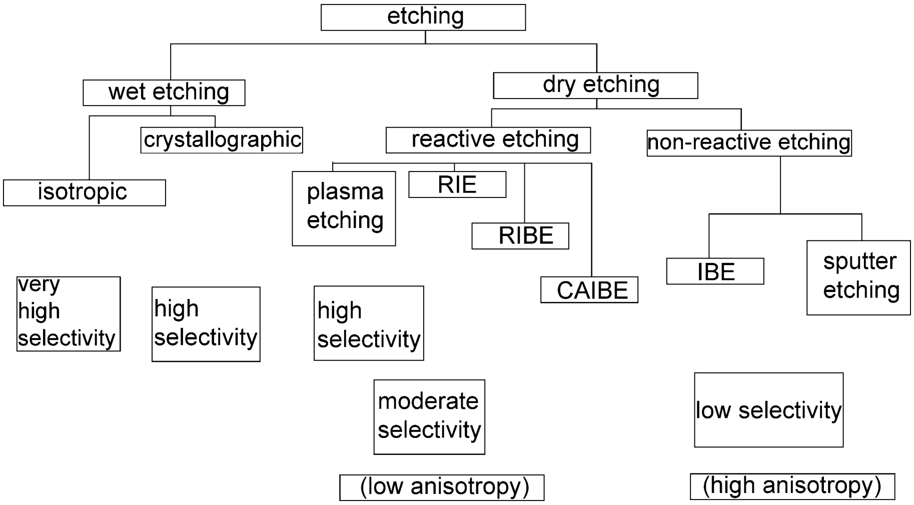

Isotropic Etching, Figure 1 Overview of microlithographic etching techniques

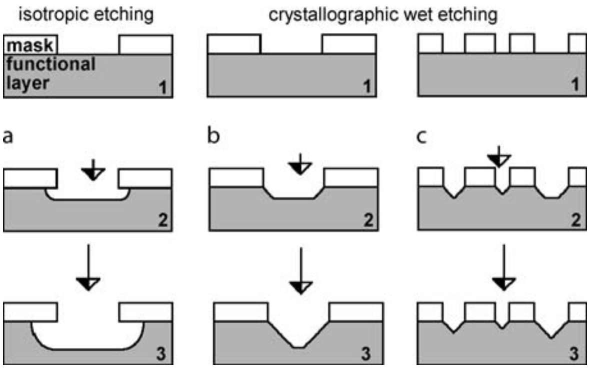

Isotropic Etching, Figure 2 Comparison between the formation of cross-section geometries in isotropic wet etching (**a**), crystallographic wet etching with time control (**b**) and crystallographic wet etching with geometry control (**c**)

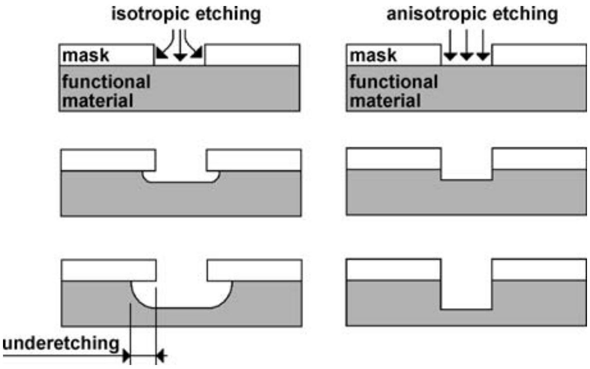

Isotropic Etching, Figure 3 Comparison of isotropic and ideal anisotropic etching: evolution of sidewall profiles

niques, the plasma technique is the only isotropic dry etch technique.

Key Research Findings

Wet Etching

Isotropic wet etching can be applied for nearly all materials, in principle. Wet etching consists in the transfer of solid material into the liquid phase by the formation of molecular dispersed species. A crucial precondition for this transfer is solvation. Therefore, all etch baths have to contain solvent molecules or other components with high solvation power in relation to the material to be etched. For oxides, hydroxides and similar materials, special coordinating ligands are necessary, in most cases, for dissolution in addition to the solvent. The ligands must form stable and soluble complexes with the metal atoms of the material. Stable oxides can be etched mostly only by substitution of oxygen from the coordination sphere by an element with a higher stiffness electron shell (low polarizability). Fluorine is the only element that meets this demand. That is the reason that many etch baths contain hydrofluoric acid or fluoride ions (see Spierings [6]). Fluoride ions are necessary as ligands in all baths for the etching of oxides of metals with higher oxidation number, which means ions with the character of a hard Lewis acid. The fluoride ion represents a very hard Lewis base and forms fluoro complexes which are completely solvated and can diffuse into solution. In particular, silicon dioxide as well as silicate compounds and inorganic glasses are etched isotropically by etch baths containing fluoride ions. Thereby, the hexafluorosilicate complex is formed from the stable oxidic material. In analogy to silicon oxide, other stable metal

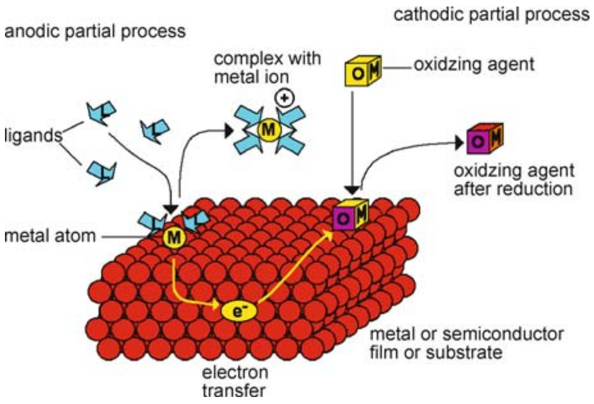

Isotropic Etching, Figure 4 Partial processes during the open-circuit wet etching of metals and semiconductors (schematic): M, metal; OM, oxidizing agent; L, ligand; e^-, electron

and semiconductor oxides of low polarizability ions can be etched by fluoride-containing solutions, for example titanium dioxide.

Frequently, the interface between oxidic materials and photo or electron beam resists is sensitive to etch baths containing fluoride ions. So, in these cases the resist mask cannot be used directly for patterning of oxidic materials like silicon dioxide and glass. This is also the case for the fabrication of fluidic microchannels in glass substrates. Therefore, an auxiliary metal or semiconductor film is applied for patterning. This film is first patterned lithographically. The resist is then stripped and the metal film is used as an etch mask for the oxide. Films of chromium, nickel–chromium, polysilicon or titanium are used frequently as masks for the isotropic etching of glass.

Softer Lewis bases have to be applied in etch baths for oxides and salts of metals or semiconductors with a softer Lewis acid character of their cations. Materials consisting of compounds of heavier metals frequently become dissolvable in the presence of higher halogenide ions like chloride or bromide. So, Cu(I) which is not well solvated in water as the unbound ion, becomes dissoluble in the presence of, for example, chloride ions by forming Cu(I) chlorocomplexes. The choice of suitable complex ligands depends on the particular coordination chemistry of the heavier metals or semiconductors inside the oxidic or salt-like functional materials. In some cases, ammonia or amines are suitable. So, the formation of a silver diamine complex can be used for the etching of Ag(I) compounds, for example. Also, sulfur-containing compounds (thiols, thiourea) are efficient additives for the dissolution of some soft Lewis acids because of their soft base character. In many cases, chelate ligands as diamines support dissolution efficiently.

Low molecular weight organic materials can be dissolved simply by application of suitable organic solvents. As a rule, the dissolution of linear polymers also succeeds by choosing suitable solvents. In contrast, covalently cross-linked polymer matrices cannot be dissolved by simple dissolution. In this case, etch baths must contain components that are able to break the chemical bonds inside the polymer chains or inside the molecular bridges. This breaking of bonds demands oxidizing agents of high redox potential. Such agents are not compatible with organic solvents by reason of their redox reactions with the solvent. So, they are applied in aqueous solution in most cases. However, this means that the organic matrix must be decomposed completely by the etching bath. Typical oxidizing agents for removal of polymer layers are the same as components of cleaning baths for the removal of organic contaminations. Therefore, strong oxidizing water-soluble agents like hydrogen peroxide, peroxosulfates or dichromate are applied. Organic resist masks cannot be used for the application of these etching baths, because they are damaged or destroyed. So, inorganic films like silicon dioxide, silicon itself or metals like titanium or chromium are used as the mask layer in these cases. Isotropic etching of polymers by these baths can also be applied for the removal of polymers as sacrificial layers below functional structures of inert materials.

Oxidation is also needed in addition to solvation in all etching processes of metals and semiconductors. In most cases, this process is performed without an outer current. This means that the anodic subprocess which corresponds to the formation of metal cations is completely compensated by a cathodic partial current, which must be realized by the electrochemical reduction of an oxidizing agent of suitable electrochemical potential. Open-circuit (electroless) wet etching processes lead to the formation of a mixed electrode potential, which depends on the involved materials, composition of the etching bath, temperature and transport conditions inside the liquid. The etch rate corresponds to the anodic partial current density and is, therefore, directly dependent on the electrochemical potential. The selectivity of wet etching of certain metallic materials can be very high. It can be controlled by choosing the redox potential of the oxidizing agent, the selection of suitable ligands, the pH value and the temperature. Additionally, electrochemical passivation can help in achieving selectivity.

The electrochemical character of metal and semiconductor wet etching is responsible for some special features in the etching processes. Electrochemical processes always include a characteristic series of process steps. So, ligands must first diffuse to the solid surface. Than the surface process with the electrochemical charge transition can occur.

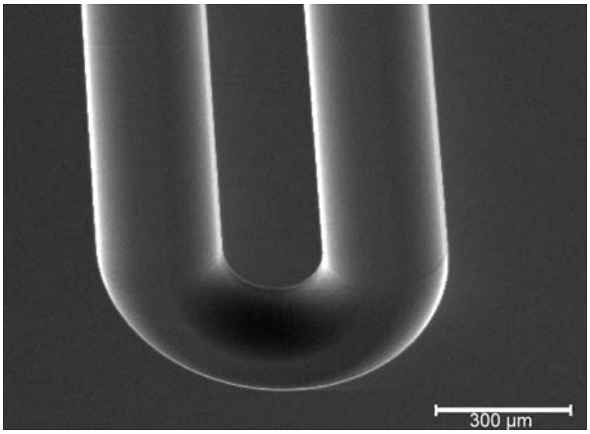

Isotropic Etching, Figure 5 Micro channel obtained after isotropic etching in glass (scanning electron micrograph, scale bar: 0.3 mm, IPHT Jena)

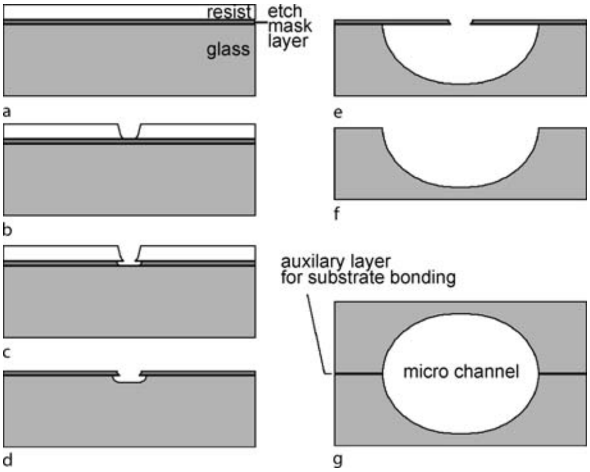

Isotropic Etching, Figure 6 Preparation of microchannels with nearly circle-shaped cross-section: (**a**) substrate covered by mask layer and photoresist, (**b**) resist structure after exposure and development, (**c**) etching of transfer layer (mask for isotropic glass etching), (**d**) starting glass etching after removal of photoresist, (**e**) finished near circle-like profile after isotropic glass etching, (**f**) half-shell with channel structure after removal of etch mask (transfer layer) and (**g**) completed microchannel after bonding of two complementary half-shells

Finally, the complexes formed have to desorb from the surface and diffuse into the solution. The slowest of these three steps determines the rate of the overall process. Ideal isotropic behavior is found if one of the diffusion steps is rate-determining. Diffusion is caused by the Brownian motion of particles and therefore is independent of direction. That is the reason that transport control in wet etching results in isotropic etch behavior.

Transport control is always associated with an enhancement of transport efficiency at the edges of etch windows. This effect is due to the additional space for diffusion near the edges of lithographic features. Transport control in the anodic subprocess is therefore always accompanied by edge effects in etching. The central parts of a feature are more slowly removed than peripheral parts. The same effect is responsible for an enhancement of the etch rate of small features in comparison with larger features. Size effects are typical for isotropic etch processes. If the distance between several structures is comparable to or smaller than the characteristic diffusion length (normally some tens up to some hundreds of micrometers), the size effect can lead to pattern-dependent etch rates because then the degree of coverage determines the total diffusion current to or from the surface.

The transition of metal or semiconductor atoms into cations or complexes is the anodic subprocess. The electrons delivered by this process must be consumed by an outer electrical current or by a cathodic subprocess in order to keep the electrode potential high enough for the etching. As well as transport control in the anodic subprocess, the cathodic process can also be transport-controlled. The convection and the concentration of oxidizing agent inside solution are responsible together for the intensity of the cathodic process. The cathodic process does not occur exactly at the same place on the surface as the anodic process. So, a local current also flows in the case of an outer currentless etching process. The local current can also flow to areas of metals which are not dissolving at a certain electrode potential in the case of the presence of two or more metals which are in electrical contact. In this case, the area ratios of different materials can effect additionally the etch rate.

Plasma Etching

Transport control under diffusional limitation is also the precondition for isotropic etching in dry etching processes. At low pressure (below about 0.1 torr), as is applied in all ion beam and ion etching procedures, the probability of collisions between particles is so low that the directed transport dominates. As a result, etching is always anisotropic.

Plasma etching takes place at pressures between about 0.1 and some tens of torr. The plasma contains only low concentrations of ions, but high concentrations of free radicals. These free radicals are the active species for etching. At comparatively high pressure, the radicals move by diffusion. The free path lengths are smaller than the typical dimensions of microfluidic channel structures. So, the diffusive character of radical transport is also given in the direct environment of the etch areas. The reaction rate of suitable radicals with the species at the solid surface is

normally very high due to the high reactivity of radical species. As a result, the transport of radicals to the surface or the transport of reaction products from the surface into the gas is slower than the surface reaction itself. So, the conditions for transport-controlled process rates are present.

Analogous to isotropic wet etching processes, plasma processes can be used for undercutting of etch masks and for the preparation of free-standing membranes and other free-standing structures. They can also be used for the preparation of microchannels inside different materials. Fluorine-containing plasmas are mainly applied for the patterning of glass or quartz glass substrates as well as for the patterning of silicon dioxide films. Instead of free fluorine, tetrafluoromethane, difluoroethane or sulfur hexafluoride are mainly applied. The electrical excitation of the plasma leads to the formation of fluorine radicals which are very reactive. They form silicon tetrafluoride by the reaction with glass and similar materials. Silicon tetrafluoride is gaseous, desorbs quickly from surfaces and can easily be removed from the etching vessel by pumping.

Isotropic Glass Etching for Micro- and Nanofluidic Applications

For micro- and nanofluidics, the wet etching of glass is of particular importance. Isotropic wet etching is applied for the generation of rounded channel structures and for preparation of channels with circular or nearly circular cross-sections. Cross-sections with a nearly circular shape demand etch windows that are much smaller than the resulting channel. The lithographic etch process is an underetch process for the most part. The isotropy of the wet etching process results in equal etch rates in all etching directions. The direction-independent etch rate causes the formation of circle-like geometries. Round structures are obtained in all three spatial directions. Rectangular corners in the windows of the resist mask become a quarter of a circle in the substrate plane. Long slits in the mask are transferred in half-cylindrical etch grooves. Small openings in the resist mask are transferred into a groove with the shape of a half sphere during the underetching.

Round, smooth structures are obtained if there are small openings in the mask layer. In this way, channels of different width and orientation can be prepared (Fig. 5). Circular cross-sections are formed by bonding of complementary half-shells after isotropic etching and removal of the etch mask (Fig. 6). Regular arrays of small openings can also be used for the generation of certain surface topographies. An example of a periodic surface pattern obtained after isotropic etching through an array of small windows with complete lifting of the mask layer is shown in Fig. 7.

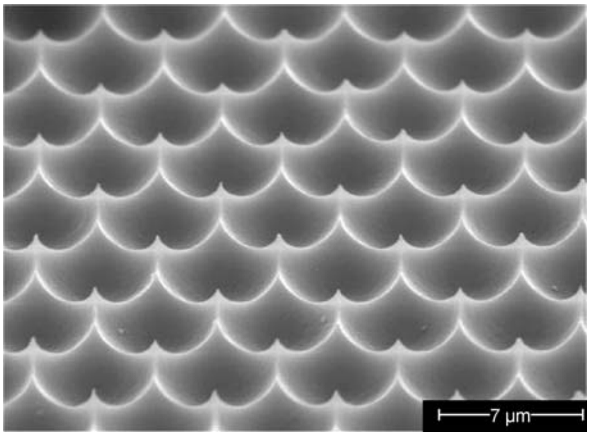

Isotropic Etching, Figure 7 Regular microtopography after isotropic etching of a plane substrate through a mask layer with a two-dimensional array of small openings (scanning electron microscopy image of the tilted substrate; scale bar, 7 μm; IPHT Jena)

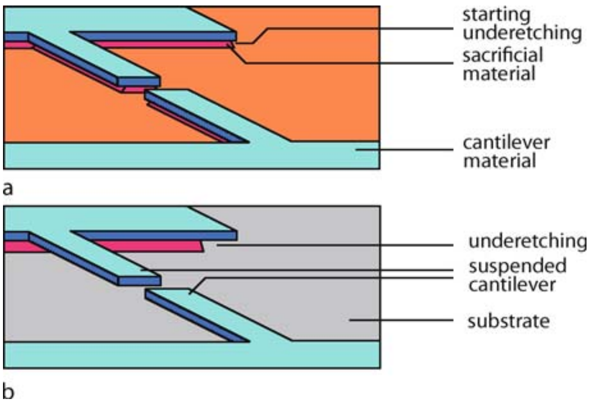

Isotropic Etching, Figure 8 Preparation of free-standing structures by isotropic etching of a sacrificial layer: (**a**) intermediate etching state after removal of the sacrificial material in the openings of the mask; (**b**) residual sacrificial material under the beam structures; (**c**) final state with free-standing cantilevers after complete removal of the sacrificial material under the beam structures

The selective isotropic etching of glass substrates can be applied in order to generate movable microstructures (bulk micromachining). These structures are of importance, for example for the preparation of valves and pumps in microfluidics. The complete removal of film material below small film elements by isotropic etching is also used for the preparation for free-standing bridges and cantilevers in surface micromachining (Fig. 8).

Future Directions of Research

Etching is an old and very well-established technology, in principle. But, several details of etching mechanisms are not completely known. New challenges arise from new

demands of geometries of microlithographically etched structures and from new types of materials.

New structural demands include

- further miniaturization,
- microstructures with freely defined three-dimensional structures and
- the use of self-organization principles in microstructuring.

Special challenges from new materials are related to

- the etching of very stable materials,
- the improvement of selectivity in the case of two or more materials exposed to etch baths or plasmas and
- the etching of anisotropic materials, nanoheterogeneous materials and nanocomposite materials.

There are several methods for preparing masks in the mid and lower nanometer range. Electron beam lithography (EBL) or focused ion beam lithography (FIBL) can be applied. In addition, scanning probe techniques can used for creating nanometer-sized mask patterns. Etching processes use the conversion of solids into small molecules or atoms which can be taken away by gaseous or liquid media. The only serious problem is that isotropic etching is mainly used for the generation of rounded geometries by matching the required time for material removal. So, the problem of miniaturization is less related to the etching itself but to the time control of etching and to the homogeneity of the materials. Transport-controlled processes are always fast in comparison with surface-controlled processes. Thus, exact rate control and very precise determination of the starting and ending of etching steps is required if ultrasmall structures are to be generated.

Technical micropatterns are mainly generated by the use of lithographic techniques. In contrast, nature uses molecular self-organization for the generation of a wide spectrum of different functional structures. It would be very helpful if patterning by self-organization could be used for the generation of mask structures or directly in etching of a certain micro- or nanopattern. In principle, there are several possibilities for spontaneous pattern generation, for example by relaxation structures in double or multilayer structures under mechanical stress or by formation during autooscillating chemical processes. In most cases, the spontaneous evolved structures are not controlled precisely enough for technical use and the reproducibility is too poor for technical applications. It is assumed that the further miniaturization of lithographic structures down to the mid and lower nanometer range will enforce the challenge for the application of self-organization principles in the generation of micropatterns by etching.

The lithographic etching of highly stable materials remained a serious problem over the whole long tradition of etching. Patterning always requires mask layers. The mask materials must be more stable than the material to be etched in the etch baths or plasmas. Hence, it is necessary to apply special auxiliary layers or special mask materials for highly stable materials. In isotropic etching, in which no highly accelerated ions are applied, the differentiation between stable mask material and patterned functional material must always be realized by chemical specificity. That demands special developments for etching of noble metals and alloys, for passivating metals and, in particular, for highly stable materials like carbides and nitrides.

In most devices a group of materials is involved in order to realize different functions. Isotropic etch processes are mainly marked by high selectivity. But, the majority of materials used in different technical applications now demand the adaptation of etch baths and plasma procedures for the realization of new selectivities. The protection of materials is of particular importance in the case of very thin films and small features. Selectivity also becomes important in the case of integration of a diversity of sensors and actuators consisting of different materials. This is the case, for example, in micro- and nanofluidic devices equipped with special micropatterned transducers. The homogenous etching of inhomogeneous material is the opposite demand to high selectivity and is a real challenge for etching innovations. It becomes more and more important with the increase in use of nanocomposite materials. The problem is related to the fact that the etching procedure must take away all material independently of the specific chemical properties, in particular for the generation of isotropic etch patterns. A general solution leading to a universal etch medium for all classes of materials seems to be excluded. So, the demand remains for developing etch procedures for certain selective material combinations. It is comparatively easy to realize approximately equal etch rates in dry etching processes. In RIE, IBE, RIBE and so on, the removal of substrate atoms by impact of accelerated ions is only slightly dependent on atomic masses and the etch rates of different materials are approximately of the same order of magnitude for a given ion energy and ion density. In contrast, the isotropic plasma etching and the isotropic wet etching are marked by high chemical specificity. So, it is necessary to find suitable complex compositions of etch gases for plasma etching or complex compositions of etch baths with ligands and oxidizing agents in order to obtain equal etch rates of different materials inside composite materials.

Cross References

► Anisotropic Etching
► Bulk Micromachining

► Chemical Etching
► Dry Etching
► Microstereo Lithography
► Nanochannel Fabrication
► Photolithography
► Plasma Etching
► Silicon Micromachining
► Wet Etching

References

1. Gardeniers H, VandenBerg A (2004) Micro- and nanofluidic devices for environmental and biomedical applications. Int J Environ Chem 84:809–819
2. Köhler M (1999) Etching in Microsystem Technology. Wiley-VCH, Weinheim
3. Lee KB, Lin LW (2004) Surface micromachined glass and polysilicon microchannels using MUMPs for BioMEMS applications. Sens Actuators A 111(1):44–50
4. Madou M (1997) Fundamentals of Microfabrication. CRC, Boca Raton
5. Manos DM, Flamm DL (1989) Plasma Etching. Academic, Elsevier Amsterdam
6. Spierings GACM (1993) Wet chemical etching of silicate glasses in hydrofluoric acid-based solutions. J Mater Sci 28:6261
7. Völklein F, Zetterer T (2006) Ätzen. In: Praxiswissen Mikrosystemtechnik, 2nd edn. Vieweg, Wiesbaden

Isotropic Silicon Etching

► Silicon Micromachining

I-STAT

► Integrated Microdevices for Medical Diagnostics

Janus Particle

Synonyms

Two-faced particle

Definition

A particle with two sides of different physical properties, such as half-coated sphere, is called a Janus particle, after the two-faced Roman god.

Cross References

- ► Electrokinetic Motion of Heterogeneous Particles
- ► Polymer Synthesis within Microfluidic Reactor

Jet Pumping

Definition

Generation of fluid flow by the suction action generated in its surroundings by a fluid jet.

This effect is caused by entrainment of the surrounding fluid into the jet, which carries away this fluid away. It ahs has to be replaced by the fluid pumped into the vicinity of the jet by the jet pumping. The effect is much stronger in turbulent jets, existing at higher values of Reynolds number. In fluidic sampling units built using no-moving-part fluidic valves, the jet pumping is employed to remove fluids from the downstream spaces and thus to ensure purity of the handled fluid samples.

Cross References

- ► Sampling Unit

Jetting

Definition

Process of throwing out fluid in a column from an orifice or region small with respect to the length of the column of fluid formed.

Cross References

- ► Piezoelectric Microdispenser

Jet-Type Rectifier

Definition

A device for fluidic rectification based on the inertial effects in a fluid jet formed by fluid flow issuing from a nozzle.

In fluidic pumps with the rectification performed without the action of any moving parts the conversion of an alternating flow into the desirable one-way flow is achieved by utilizing inertial effect if flowing fluids. To obtain these effects, the characteristic Reynolds number of the flow has to be sufficiently high. One way how such rectification is produced is based on the properties of a fluid jet accelerated in a nozzle and incapable of changing its flow direction while the return flow directed back into the nozzle may be easily turned by a quite large flow direction angle.

Cross References

- ► Valve-Less Rectification Pumps
- ► Fluidic Diodes
- ► Fluidic Pumping
- ► Traveling-Wave Pump
- ► Fluidic Rectification

Joule Heating and Chip Materials

HUI YAN, HONGKAI WU
Department of Chemistry, Hong Kong University of Science and Technology, Hong Kong, China
chhkwu@ust.hk

Synonyms

Joule heating effect; Ohmic heating

Definition

Joule heating is named for James Prescott Joule, the first to articulate what is now Joule's law, relating the amount of heat released from an electrical resistor to its resistance and the charge passed through it. Joule's law gives the amount of heat Q liberated by a current I flowing through a resistor with a resistance R for a time t,

$$Q = Pt = I^2Rt\,.$$

An electrokinetic flow in a chip is a flow of liquid in a channel driven by an electric field.

Overview

When experiments are carried in microfluidic channels, forces are needed to drive liquids to flow through the microchannels. Electrokinetics is now being studied in a variety of forms, such as electroosmosis, dielectrophoresis, and electrowetting, for the purpose of controlling microflows in chips. While electrokinetic methods can greatly simplify species transport in microfluidic systems, a significant characteristic is the internal generation of heat (i. e. Joule heating) caused by current flow through the buffer solution. The equation for calculation of the Joule heating is given below and discussed in detail. The common chip materials, the surface modifications used in microchip electrophoresis, *electro-evoked methods*, and techniques for temperature measurements on chips are summarized. As a typical example of a study of Joule heating and its relation to the chip material, Joule heating and heat transfer in poly(dimethylsiloxane) microfluidic systems is briefly described. Finally, the key research findings in this area are summarized and future directions for research are proposed.

The development of microfluidics-based Lab-on-Chip devices involves the incorporation of many of the necessary components and functionality of a typical laboratory onto a small chip-sized substrate. When experiments are carried out in a Lab-on-Chip, forces are needed to drive liquids to flow through microchannels. Microfluidic flows are readily manipulated using many kinds of external field (pressure, electric, magnetic, capillary, and so on). As the dimensions shrink, the importance of surface forces relative to volume forces increases. Such manipulations of the flow can either be achieved by forces applied macroscopically, for example at appropriate inlets and outlets, or be generated locally within the microchannel by integrated components. Table 1 summarizes the frequently mentioned driving forces for controlling microflows.

Electrokinetics has also been applied in a variety of forms for controlling microflows. Examples include

- electroosmosis, where the fluid moves relative to stationary charged boundaries;
- dielectrophoresis, where an interface (often a particle) moves in a gradient of electric field; and
- electrowetting, where an electric field modifies wetting properties.

Both AC and DC fields can be used, and the system response then depends on the frequency and amplitude of the field. Both capillary-driven and electrically driven flows offer advantages relative to the more familiar pressure-driven flows as the device scale is reduced, though both types of flow may be hindered, or potentially even eliminated, by significant surface contamination or heterogeneities.

However, in the great majority of microfluidic circuits, especially those that use electrophoretic separation, fluid flows are driven and directed using electroosmotic flow. Electroosmotic pumps offer a number of advantages over micromachined pressure-driven pumps, such as ease of fabrication and the absence of moving parts. Moreover, the sample plugs suffer little from dispersion because the fluid velocity is nearly constant across the channel diameter. These pumps are usually controlled by manipulating an externally applied electroosmotic-flow-generating voltage. While electrokinetic means can greatly simplify species transport in microfluidic systems, a significant drawback is the internal heat generation (commonly referred to as Joule heating) caused by current flow through the buffer solution.

Recently, microfluidic systems and biochips made from low-cost polymeric materials such as poly(dimethylsiloxane) (PDMS) and poly(methylmethacrylate) (PMMA), as opposed to traditional materials such as glass or silicon, have become more and more prevalent. The primary attractiveness of these materials is that they tend to involve simpler and significantly less expensive manufacturing techniques (for example casting, injection and replica molding, and hot embossing); however, they are also amenable to surface modification, and the wide variety of physiochemical properties allows the matching of specific polymers to particular applications. While the

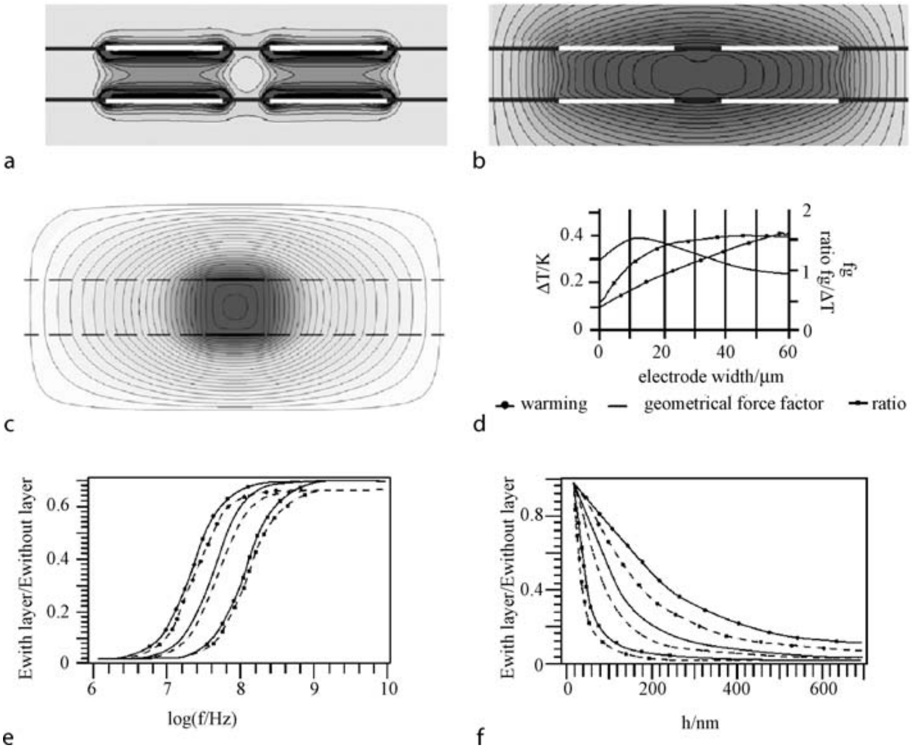

Joule Heating and Chip Materials, Figure 1 (**a**) E^2 in a vertical cross section through an octode cage with 40 μm electrode spacing driven with a ROT phase pattern. (**b**) Temperature distribution corresponding to the field distribution in (a). (**c**) Steady-state isotherms of a two-electrode system as derived by finite difference simulation on a 600×300 grid with a 0.5 μm mesh width. (**d**) Dependence of the warming and the attainable dielectrophoretic force on the electrode width. (**e**) Influence of covering the electrodes with a passivation layer of height h. (**f**) Normalized electric field strength as a function of the layer thickness

Joule Heating and Chip Materials, Table 1 Forces and external fields with which flows can be manipulated in microfluidic configurations. It is also possible to use external means to manipulate particles embedded in flows, as in electrophoresis or the use of magnetic forces

Driving force	Subcategorization	Remarks; representative references
Gradient of pressure p		A familiar case, as in pipe flow
Capillary effects	Surface tension γ Thermal Electrical (electrocapillarity) Surface tension gradients $\nabla\gamma$ Chemical Thermal Electrical Optical	Capillary pressure difference (e. g., Sammarco & Burns 1999) (e. g., Pollack et al. 2000; Prins et al. 2001) Typically involve thin films (e. g., Gallardo et al. 1999) (e. g., Kataoka & Troian 1999) Photoresponsive materials
Electric fields E	DC electroosmosis AC electroosmosis Dielectrophoresis	Uniform velocity field Rectified flows Response $\propto \nabla E^2$
Magnetic fields/Lorentz forces	Magnetohydrodynamic stirring	(e. g., Bau et al. 2001)
Rotation	Centrifugal forces	(e. g., R.D. Johnson et al. 2001)
Sound	Acoustic streaming	

development of these systems has reduced the time from idea to chip from weeks to days, and the per-unit cost by a similar ratio (particularly with the advent of rapid prototyping techniques), the low thermal conductivities inherent in these materials ($0.18\,\mathrm{W\,m^{-1}K^{-1}}$ for PDMS, which is an order of magnitude lower than that of glass) retards the rejection of internally generated heat during electroosmosis.

Basic Methodology

Calculation of Joule Heating

If a liquid in an electric field between electrodes has an electrical conductivity σ, then the heating power P per volume element V depends linearly on σ and on the square of the electric field strength E, with E being proportional to the voltage U applied to the electrodes:

$$q = \frac{P_{\mathrm{heat}}}{V} = \sigma \cdot E_{\mathrm{rms}}^2 \propto \sigma \cdot U_{\mathrm{rms}}^2 \,, \tag{1}$$

where *rms* denotes the root mean square value. In the steady state, P_{heat} equals the power P_{diss}which is dissipated through the surface S of the volume under consideration. If P_{diss} is regarded as being mainly determined by heat conduction, then Fourier's law,

$$P_{\mathrm{diss}} = \lambda \cdot \frac{S}{d} \cdot \Delta T \,, \tag{2}$$

applies, where λ denotes the thermal conductivity. At a distance d from the surface S, a temperature rise of ΔT relative to the environment occurs inside the heated volume. Consequently, $P_{\mathrm{heat}} = P_{\mathrm{diss}}$ can be solved for ΔT, which in the case of a cubic volume with side length a yields $\Delta T = k \cdot U^2$, where $k = d/(6 \cdot a \cdot \lambda)$. The center of a cube has a mean distance from its surface of $d = (a/36) \cdot \left(6 \cdot \left(\sqrt{3} + \ln(7 + 4 \cdot \sqrt{3})\right) - \pi\right) \approx 0.64 \cdot a$. However, σ itself varies with the temperature. Therefore, σ ought to be replaced by a linear dependence $\sigma = \sigma_0 \cdot (1 + \alpha \Delta T)$, where $\alpha = 0.022\,\mathrm{K}^{-1}$, which leads to

$$\Delta T = \frac{k \cdot \sigma_0 \cdot U^2}{1 - \alpha \cdot k \cdot \sigma_0 \cdot U^2} \,. \tag{3}$$

The temperature dependence of λ is one order of magnitude smaller than the effect of temperature on the electrical conductivity and, therefore, is neglected in the following. These considerations provide an estimate of ΔT. Only for simple electrode designs can the resulting temperature field be derived analytically. Usually, a numerical approach is required to calculate the distribution of the electric field E and of the T field.

In Jaeger's study [4], a finite difference method was used to iteratively solve the system of complex field equations (charge conservation law for temporal periodicity) $\nabla\left((\sigma + i \cdot \omega \cdot \varepsilon) \cdot \nabla\Psi\right) = 0$ with $\boldsymbol{E}(\boldsymbol{r}, t) = -\nabla \mathrm{Re}(\Psi \boldsymbol{r}) \cdot e^{i \cdot \omega \cdot t}$), coupled via the Joule heating to the temperature T, which was determined by $\nabla(\lambda \cdot \nabla T) = -q$. Here, r and t are the spatial and temporal coordinates, respectively, Ψ is the electric potential, Re denotes the real part, $i = \sqrt{-1}$, and $\omega = 2 \cdot \pi \cdot f$. A fixed temperature and no electric current were assumed at the outer boundaries. The T field thus evaluated describes how far the temperature increase extended along a microchannel. As Eq. (1) shows, the warming is proportional to the square of the electric field strength. Figures 1a and b show fields in a region of size $280\,\mu\mathrm{m} \times 200\,\mu\mathrm{m}$ that were obtained using a grid of size $90\,\mu\mathrm{m} \times 90\,\mu\mathrm{m} \times 50\,\mu\mathrm{m}$ with a $4\,\mu\mathrm{m}$ mesh width. In Fig. 1a, the red areas near the electrodes (white bars) are areas with a high electric field strength, and the thin black lines show equipotential lines. Therefore, as a consequence of Eq. (1), the heat production is maximal in the vicinity of the electrodes. This, however, does not coincide with the region of highest temperature, because in a stagnant liquid the thermal energy can be dissipated only through heat conduction, which in glass is about 1.5 times higher than in a buffer solution (Fig. 1b). As Fig. 1c shows additionally, the warming between two electrodes also depends on their size. The two horizontal solid lines represent electrodes ($U = 1\,\mathrm{V_{rms}}$) which extend infinitely normal to the plane of the paper. They have a width of $40\,\mu\mathrm{m}$ and a distance between them of $40\,\mu\mathrm{m}$. The dashed lines indicate the ceiling and floor of a channel formed in $55\,\mu\mathrm{m}$ thick glass and filled with aqueous buffer ($0.27\,\mathrm{S\,m^{-1}}$). In Fig. 1d, this relationship is quantified numerically. Obviously, ΔT scales almost linearly with the electrode width. In contrast, the dielectrophoretic force experienced by a particle in the vicinity of the two electrodes approaches a constant value. This is because the force F is a function of the gradient of the electric field. A particle of radius R showing negative dielectrophoretic behavior will be levitated to the central plane between the two electrodes. There, the maximum repulsive force can be simplified to $F = 2\pi\varepsilon_0\varepsilon_1(R/d)^3 \mathrm{Re}\,(f_{\mathrm{CM}}) U_{\mathrm{rms}}^2 f_{\mathrm{s}}(x/d)$, where the permittivity of the liquid is ε_1, the distance between the electrodes (channel height) is d, and the complex Clausius–Mossotti factor, which relates the polarizabilities of the particle and the surrounding medium, is $f_{\mathrm{CM}} \cdot f_{\mathrm{s}}$ is a geometric scaling factor for the force and depends on the ratio between the electrode width x and the distance between the electrodes d (Fig. 1d). With increasing electrode width x, the electric field in the central region between the electrodes becomes increasingly homogeneous, like that in an infinitely extended capaci-

Joule Heating and Chip Materials, Table 2 Material properties for chip fabrication

	PMMA	PC (polyethylene terephthalateglycol)	High-viscosity PETG	PE (polyethylene), branched homopolymer	Polyimide	Styrene copolymer	Silicone
Melt flow (g/10 min)	1.4 – 2.7	3 – 10		0.25 – 27.0	4.5 – 7.5	1.4	
Melting temperature (°C)	85 – 105	50	81	98 – 115	388	100 – 200	
Mold (linear) shrinkage	0.001 – 0.004	0.005 – 0.007	0.002 – 0.005	0.015 – 0.05	0.0083	0.003 – 0.005	0.0 – 0.006
Process injection temperature (°C)	163 – 260	294	249	149 – 232	390 – 393	182 – 288	
Molding pressure (10^7 Pa)	3.4 – 13.8	6.9 – 13.8	0.69 – 13.8	3.5 – 10.0	2.0 – 13.8	3.5 – 13.8	
Hardness, Rockwell	*M*68 – 105	*M*70 – *M*75	R106		E53 – 99, R129, M95	M80, R83, 75	
Coefficient of linear thermal expansion (10^{-6} °C)	50 – 90	68		100 – 220	45 – 56	65 – 68	10 – 19
Thermal conductivity (10^{-4} g cal cm s^{-1} cm^{-2}°C)	4.0 – 6.0	4.7		8	2.3 – 4.2	3.0	3.5 – 7.5
Dielectric strength, 0.003175 m specimen (MVm^{-1})	16 – 20	15 – 16		18 – 39	16 – 22	17	16 – 22

tor, and, consequently, does not contribute to the dielectrophoretic force. For a semi-infinite plate capacitor without heating, and not taking the liquid–glass interfaces into account, $\lim_{x\to\infty} f_s = (27\pi)/64$. As shown in Fig. 1d, normalization of the force exerted with the corresponding temperature increase suggests that an electrode width of approximately 15 μm is optimal for the configuration used. Figures 1e and f show the influence of covering the electrodes with a passivation layer, and the normalized electric field strength as a function of the layer thickness, respectively. In Fig. 1e, the electric field strength is normalized to the value that is reached in the absence of an insulating layer. The solid lines denote the results for a layer thickness of 600 nm, and the dashed lines the results for 700 nm ($\varepsilon_{\text{layer}} = 5$, $\varepsilon_{\text{liquid}} = 80$, $\sigma_{\text{layer}} = 10^{-6}\text{Sm}^{-1}$). The electrical conductivity of the liquid was 0.27, 0.546, and 1.5 Sm^{-1} for the red, green, and blue curves, respectively. The solid lines are for 9 MHz and the dashed lines are for 6.58 MHz in Fig. 1f.

Chip Materials

In microfluidic applications, the properties of the material that may be of fundamental importance include machinability, surface charge, molecular adsorption, electroosmotic flow mobility, optical properties, and many others. When a polymer-based substrate is chosen, the properties of the material are critical for both the fabrication process and the successful application of the device.

Material Properties and Fabrication

In many applications in the literature, plastics, rather than pure polymers, are used to fabricate microfluidic devices. Plastics can contain a number of additives that impact on their processing and shelf life, and these should be considered. These additives may include fillers (e. g. mica, talc, and calcium carbonate), plasticizers (e. g. dioctyl phthalate in PVC), heat stabilizers (e. g. organotin compounds in PVC), antioxidants (e. g. phenols and amines), and UV stabilizers (e. g. benzophenones and salicylates).

Different fabrication protocols have different and very specific constraints with regard to the properties of the material. For instance, with hot-embossing and injection-molding methods, the glass transition temperature, melt temperature, and thermal expansion coefficient are some of the most critical parameters for successful fabrication. Cross-linked polymers and thermoplastics that con-

tain very long polymer chains with strong intermolecular attractions do not melt and flow, but remain soft until they decompose. The thermal expansion coefficient is related to the change in length or volume resulting from a specified change in temperature. This parameter is important not only in several fabrication processes, but also in sealing processes, where different materials are thermally bonded.

Material Properties and Applications

Electroosmotic pumping is the most common method used to propagate flow in microfluidic systems. In electroosmotically driven systems, it is critical that the substrate material exhibits good electrical insulating properties so that the electric field will drop across the fluid-filled channel and not through the substrate. This effect may be evaluated in terms of several parameters, including the dielectric strength and electrical resistance. The dielectric strength is the voltage that can be applied across an insulator before breakdown occurs. The dielectric strengths of several common polymers are given in Table 2.

A second consideration when using electrically driven pumping is heating. It is well established that Joule heating can be substantial in systems employing electroosmotic flow. If heat is not effectively dissipated in a microchannel system, elevated local temperatures can dramatically impact on the efficiency of chemical separation, and induce solution degassing and eventually boiling. With plastics that have a low melting temperature, highly localized heating can also cause significant channel deformation. Therefore, heat dissipation in the substrate material is a very important consideration when electroosmotic pumping is utilized. The capacity for heat dissipation is characterized by the thermal conductivity of the material. The thermal conductivities of several polymers are given in Table 2. For comparison, fused quartz has a higher thermal conductivity $(33 \times 10^{-4}\ \mathrm{g\ cal\ cm\ s^{-1}\ cm^{-2}\ {}^{\circ}C})$ and a much higher melting point (1665 °C) than most plastics.

A third consideration when using electrically driven pumping is charge in the microchannel. Electroosmotic flow is generated by the surface charge on the microchannel walls in combination with an electric field along the microchannel. Because polymer materials exhibit a wide range of charge densities, the electroosmotic flow in microchannels made from different polymer materials is highly variable. Electroosmotic flow has been measured in various polymer microchannels fabricated by laser ablation and by imprinting, and in PMMA channels fabricated by LIGA methods. These measurements indicate that the fabrication method, as well as the material itself, can affect the surface charge density and therefore can have a profound effect on the electroosmotic flow. For instance, laser-ablated channels support higher electroosmotic flow than channels that have been hot-embossed in a similar material owing to the fact that reactive species are incorporated into the microchannel surface during the ablation process. The location of charged groups on PMMA substrates has also been determined to be dependent on the fabrication procedure; for example, room-temperature-imprinted channels can have highly charged walls, whereas hot-embossed channels fabricated in a similar material have a low surface charge density on the walls. Finally, the surface charge and electroosmotic flow can also be modulated in polyethyleneterephthalate (PETG) by alkaline hydrolysis and in PDMS by plasma treatment. Charge density, charge location, and electroosmotic flow can therefore be controlled by several parameters including the choice of polymer material, the fabrication protocol, and various surface treatments.

Other material parameters that are critical to the successful application of microfluidic devices include autofluorescence (when optical detection is used), permeability (when living cells are used), chemical resistance (when nonaqueous solutions are used), and analyte adsorption. Table 2 lists the chemical resistances of several common polymeric materials. Analyte adsorption is a parameter that is highly dependent on several material characteristics, including hydrophobicity and surface charge. The biocompatibility of many plastic materials is associated with both of these parameters and has been evaluated and characterized extensively in the biomedical engineering literature.

Surface Modification in Microchip Electrophoresis

Surface chemistry is also of great importance in chip-based microfluidic devices, especially in highly miniaturized and integrated systems, owing to the high surface-area-to-volume ratio. The motivations for performing surface manipulation are similar to those for classical *CE*.

Microchannel wall coatings can be separated into two major categories: permanent coatings and dynamic coatings (physically adsorbed coatings). In permanent coatings, chemical compounds (often polymers) are covalently bound to functional groups on the surface or immobilized (e. g., via cross-linking of a polymer) at the surface so as to become insoluble in the electrolyte. In dynamic coatings, dissolved surface-active compounds are utilized, which adsorb strongly at the surface. This can be accomplished by rinsing with a solution of the modifier prior to analysis or by addition of the modifier to the electrolyte. As the adsorption/desorption process is reversible, the adsorbed compounds will participate in an exchange process with the solution and significant amounts of the surface-active

compounds can be present in the electrolyte. This can be detrimental in the case of affinity studies, *MS*-coupling, and chemical reactions.

Some Electrokinetic Methods

Electrophoresis (see Fig. 2) is the migration of electrically charged particles in solution or suspension in the presence of an applied electric field. Each particle moves toward an electrode of opposite electrical polarity. An electrophoresis experiment may be either analytical, in which case the objective is to measure the magnitude of the electrophoretic mobility, or preparative, in which case the objective is to separate various species that differ in their electrophoretic mobilities under the experimental conditions of the solution. *Capillary zone electrophoresis* is the simplest and most widely used form of capillary velectrophoresis. The capillary is filled with a homogeneous buffer, and compounds are separated on the basis of their relative charge and size. Most often, fused silica capillaries are employed. In this case, an electrical double layer is produced at the capillary surface owing to the attraction of positively charged cations in the buffer to the ionized silanol groups on the capillary wall. In the presence of an electric field, the cations in the diffuse portion of this double layer move toward the cathode and drag the solvent with them, producing an *electroosmotic flow*. The electroosmotic flow is pH-dependent, and it is highest at alkaline pH values. *Dielectrophoresis* is a phenomenon in which a force is exerted on a dielectric particle when it is subjected to a nonuniform electric field. This has allowed, for example, the separation of cells and the orientation and manipulation of nanoparticles.

Some Techniques for Making Temperature Measurements on Chips

Reliable measurement and control of temperatures on the microscale are required to develop electrically driven microdevices such as microreactors and PCR and μTAS systems. There exist various techniques for temperature measurement in microdevices. These techniques can be largely classified into contact and noncontact ones. While resistance thermometers, thermocouples, thermodiodes, and thermotransistors measure the temperature at a specified point in contact with the sensor, techniques based on infrared thermography, thermochromic liquid crystals (TLCs), and temperature-sensitive fluorescent dyes such as rhodamine-B, whose emission intensity is sensitive to temperature, measure the temperature of the whole field.

Resistance Thermometry

Resistance thermometry, which is based on the variation of resistance with temperature, is one of the most traditional techniques used for temperature measurement on the microscale. It is stable and is applicable to a wide range of temperatures, but it is subject to inaccuracies from self-heating since it requires the use of an electric current to make measurements. Among the various types of resistance thermometry, resistance temperature detectors (RTDs) and thermistors are most frequently used for microscale temperature measurement. In general, RTDs are made from metals, whose temperature coefficients of resistivity are positive and linear, whereas thermistors (semiconducting thermoresistors) are made from ceramic materials whose temperature coefficients of resistivity are much higher than those of metal resistors and show negative and highly nonlinear behavior. The resistance material and the sensor geometry are determined by the temperature range, the accuracy required, the measurement target (i. e., the application, and the fabrication processes available, the latter being particularly important for microdevices), and other factors. Polysilicon with a dopant is frequently used to fabricate microtemperature sensors. This kind of thermometry requires carefully controlled fabrication, including the use of sensor material of high purity; it also requires precise control of dose rate, and calibration of sensors. In particular, it is recommended that calibration of sensors should be performed, since the resistances of the sensor, lead wires, and contact pads can all be dependent on temperature.

Thermocouples

The thermocouple is one of the most common temperature sensors because it is inexpensive, reliable, and interchangeable, and covers a wide range of temperature. The operating principle is based on the well-known Seebeck effect: if two junctions between two different metals (e. g., copper and iron) are held at different temperatures, then an electromotive force (EMF) is generated and an electrical current flows between them. As the temperature increases, the output EMF of the thermocouple rises, though not necessarily linearly. Specifications of typical metal/alloy thermocouples are presented in Gardner. A thermoelectric generator to be applied to low-power devices has been developed, exploiting a working principle based on the Seebeck effect. The application of commercial thermocouples to microscale measurement suffers from some limitations, such as their relatively large spatial resolution of several hundred microns and their physical intrusiveness, especially into the flow. Recently, a microfabricated thermocouple array has been applied to measure the sur-

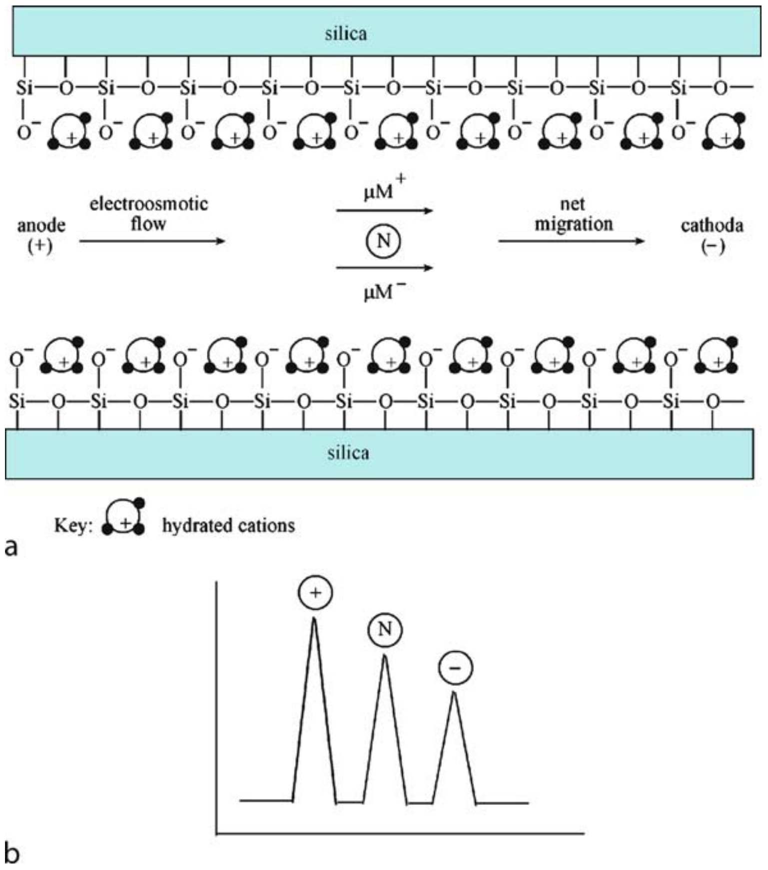

Joule Heating and Chip Materials, Figure 2 Electrophoresis. (**a**) Separation mechanism showing electrophoretic mobility of a positive ion (μM^{+}) and a negative ion (μM^{-}); N is a neutral molecule. (**b**) Migration order of the ions

face temperature distribution on a microchannel heat sink cooled by an impinging air jet, and served as a flow sensor to measure the velocity profile in the boundary layer very near the wall (about 65 μm from the surface).

Infrared Thermography

Infrared (IR) thermography is one of the most advanced nondestructive methods and is based on the fact that all bodies whose absolute temperature is above zero emit electromagnetic radiation, which ranges over a wide spectrum of wavelengths depending on the temperature of the object. The key element of an IR camera is the detector. IR detectors can be classified into two types: photon detectors, such as detectors based on indium antimonide (InSb) and mercury cadmium telluride (MCT), and thermal detectors, such as those based on deuterated triglycine sulfate (DTGS). There are two basic types of IR imaging system: mechanical scanning systems and focal-plane array (FPA) systems. The major advantages of FPA cameras are their lower price, simpler construction, quicker reading time, and high spatial and thermal resolution. But FPA cameras have some problems, such as the Narcissus effect, problems of cooling the semiconductor devices, and problems of image acquisition and processing. Further, there is no internal temperature reference for FPA cameras. This problem can be successfully overcome by calibrating frequently.

IR thermography has been applied to numerous engineering problems, such as turbulent heat transfer, temperature measurement of electronic systems, and defect diagnosis. Recently, several researchers have applied IR thermography to microscale temperature measurements. IR thermography has also used to confirm the formation of thermally isolated integral microhotplates, which is a key element in the development of arrays of micropellistors and conductivity-type gas sensors. The surface temperature of a heated capillary and the interfacial temperature during phase changes in capillary tubes have been measured using IR thermography. In particular, the

temperature profile generated by differential evaporation cooling along the meniscus interface was measured. The high spatial resolution and sensitivity of IR thermography allowed the strong evaporative cooling at the meniscus to be detected. IR techniques, however, have a critical problem when they are applied to temperature measurement of liquids. That is, the temperature is measured on the basis of the radiation emitted from an object, which means that it is necessary to know the emissivity accurately. However, the emissivity of a liquid is sensitive to the wavelength in the IR range. In addition, the transparent solid media used in windows and magnifying optics strongly absorb IR waves. Therefore, more careful consideration is needed when we use IR thermography.

Thermochromic Liquid Crystal

Thermochromic liquid crystals have the property that their dominant reflected wavelength is dependent on the temperature, and they have been employed for full-field mapping of temperature fields for over three decades. TLCs have been used in the form of a thin layer coated on a surface to visualize heat transfer from obliquely impinging jets on flat plate, to study heat transfer over film-cooled gas turbine nozzle guide vanes under transonic conditions, and to visualize artificially created turbulent spots in a laminar boundary layer over a heated surface under the influence of adverse pressure gradients. Here, special care was taken in relation to calibration and optical settings to obtain accurate temperature distributions. Although the TLC technique is a nonintrusive and cost-effective method for providing whole-field temperature information, there are some problems in applying it to temperature measurements on the microscale. The size of encapsulated TLCs is typically tens of micrometers, which is impractical for use in micron-sized structures. The time response of TLCs varies from a few milliseconds to several hundred milliseconds, according to the material and form of the TLC.

Laser-Induced Fluorescence

Fluorescence is the property that some dye molecules have of absorbing energy at a particular wavelength and emitting energy at another wavelength, longer than that of the absorption, in the wavelength range of visible light. The emitted fluorescence intensity depends on the concentration of the dye molecules, and some fluorescent molecules have the characteristic that their emission intensity is sensitive to temperature and/or pH. Many studies of temperature measurement using laser-induced fluorescence (LIF) have been carried out on the macroscale. However, there have been only a few studies devoted to the measurement of temperature fields on the microscale. In these studies, rhodamine B was used as a temperature-sensitive dye because it has a relatively high dependence of the emission on temperature and is commercially available. For rhodamine B dissolved in an aqueous liquid, the variation of the emission with temperature is reported to be -1.5 to $-3\%\,K^{-1}$. The LIF technique measures the temperature from the fluorescence intensity, rather than from the reflected light intensity as in the case of the TLC technique, so that the effect of illumination is less severe. However, there are several inherent problems affecting the accuracy of the measured temperature, such as variation of the dye concentration in the measurement area, fluctuation of the illumination light, photobleaching, and the shadowgraph effect. Recently, some improvements have been made in the accuracy of temperature measurement by the LIF technique. The most popular method is two-color LIF, which uses two different fluorescent dyes; one is sensitive to temperature and the other is insensitive. However, this technique also has several problems: the dye concentration ratio must be constant throughout the entire liquid, and the spectral bands of the absorption and emission of the two

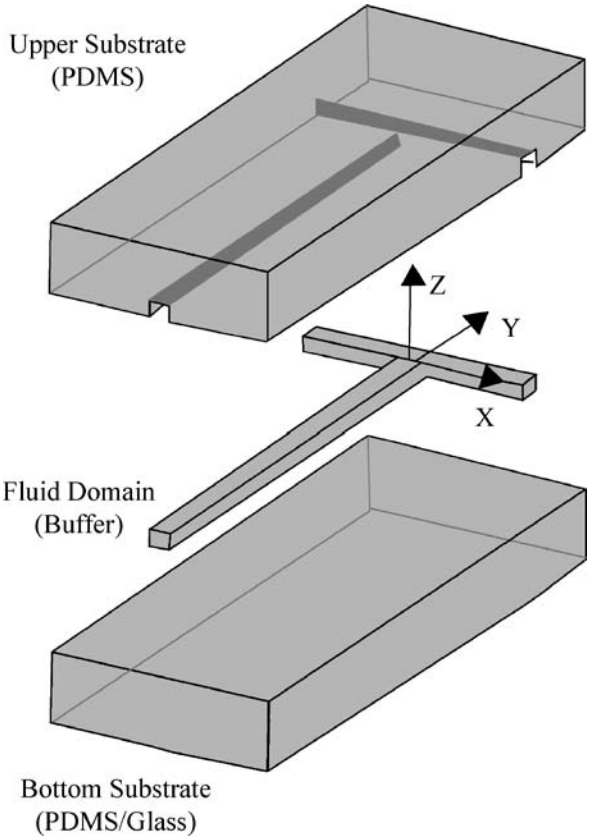

Joule Heating and Chip Materials, Figure 3 Computational geometry for a PDMS/PDMS or PDMS/glass hybrid microfluidic system

dyes must overlap. Very recently, a multicolor technique, which obtains the temperature from the ratio(s) of two or three intensities measured at different bands with a single fluorescent dye, has been proposed to circumvent the difficulties of using two dyes.

Examples of Studies on Joule Heating with Various Chip Materials

Joule Heating and Heat Transfer in Poly(dimethylsiloxane) Microfluidic Systems

Microchannel Fabrication The PDMS/PDMS and hybrid PDMS/glass microchannel systems (see Fig. 3) used in the study described here were manufactured using a soft lithography technique. An enclosed microchannel was then formed by bonding the PDMS cast to either another piece of PDMS or a glass slide (forming the lower substrate) by placing both sides in a plasma cleaner and oxidizing them. This was done immediately after removal of the PDMS cast from the master to minimize surface-aging effects. Following oxidation, the two halves were brought into contact and an irreversible seal was formed. After sealing, a carbonate buffer solution was introduced into the channels by applying a negative pressure at the downstream end.

Experimental Technique and Image Analysis Rhodamine B dye is one of a class of fluorescent dyes whose quantum yield is strongly dependent on temperature. Therefore, the in-channel temperature profile could be obtained by observing the relative spatial and temporal changes in the local intensity of the dye using a fluorescence imaging technique. Images were captured every 0.25 s for approximately 40 s. Prior to each experiment, the microchannel system was allowed to cool to room temperature and an isothermal *cold-field* intensity image of the system was taken. Following the acquisition of the cold-field image, an electric field was switched on (inducing electroosmotic flow and Joule heating in the microchannel) and full-speed image acquisition was initiated. In all cases, a uniform potential was applied at all upstream inlet reservoirs, while the downstream waste reservoir was grounded. Following the capture of 150 high-resolution images, the excitation light was blocked and the electric field was turned off, allowing the system to cool back down to room temperature. After cooling was complete, a second cold-field image was acquired. The second cold-field image was then compared with the initial image and, in general, it was found that the intensity values of the two images were identical, suggesting that any photobleaching of the dye during the experiment was not significant. To extract the in-channel temperature profiles from the captured intensity images, each image was first normalized by the cold-field image. The intensity values of the treated images were then converted to temperature using an intensity vs. temperature calibration of the kind discussed in the preceding section.

From the experimental results, we can say that electrokinetic pumping can greatly simplify species transport in microfluidic systems; however, Joule heating caused by the current flow through the buffer solution can lead to significant increases in the buffer temperature. The relatively low thermal conductivities associated with polymeric microfluidic substrates (such as PDMS) make the rejection of this heat more difficult. In general, it was found that PDMS/glass microfluidic systems maintained a much more uniform and lower buffer temperature than PDMS/PDMS systems. Also, in general, the analysis revealed that a thinner lower substrate can significantly improve heat rejection, whereas the thickness of the upper substrate had a much smaller effect. The increase in temperature was shown to significantly increase the current load and doubled the volume flow rate through the PDMS/PDMS system. The flow structure and velocity profile remained relatively constant, despite the large temperature gradients, owing to the counterbalancing effects of the decreased viscosity and decreased potential-field gradient in the hotter sections of the channel. In general, it was observed that (except in extreme cases) the channel aspect ratio had only a marginal effect on the temperature rise in the fluid system.

Key Research Findings

Joule heating results from current flow through an electrolyte solution when an electric field is applied to achieve electrokinetic flow. This internal heat generation is useful in some cases, such as in PCR on chip, but very deleterious in other cases, for example electrophoretic separation. So, chip materials should be selected carefully for the particular purpose intended, because of their different heat conductivities. There has been much research on the deleterious effects of Joule heating. The heat is taken away not only by the coolant surrounding the capillary (through convection in either air or a liquid, and by radiation as well), but also by the cold liquid inside the reservoirs connected to the two ends of the capillary (through conduction).

De Jesus et al. [11] found that the Joule-heating dissipation in a separation channel on glass chip was very efficient. The low thermal conductivities of typical polymers (shown in Table 2) used in capillaries result in a less efficient transfer of the heat generated by Joule heating of

the electrolyte to the outside of the channels. This phenomenon is an important consideration for all electrokinetic microfluidic devices, because temperature changes in the electrolyte result in decreases in the precision, accuracy, and robustness of the method. Accurately defined temperatures in microseparation devices are also important for achieving reproducible separation selectivity, since the electrophoretic mobilities of analytes are temperature-dependent. Joule heating and determination of temperatures in CE and *CEC* have been discussed in Rathore's 2004 [12] review article. Evenhuis et al. [13] studied the longer-term objective of studying the heating effects occurring in polymeric microfluidic devices. Also, Li [1] examined Joule heating and heat transfer in a T-shaped microchannel intersection in a PDMS microfluidic system, and experimentally observed dramatic temperature gradients as predicted by a *whole-chip* simulation.

If thermal end effects are neglected, Joule heating is known to cause an increase and a radial gradient in the fluid temperature. The Smoluchowski equation for the electroosmotic flow velocity, $U = [\varepsilon_0 \varepsilon_r \zeta / \mu] E_z$, has been used to accurately predict this velocity at elevated temperatures. Maynes and Webb [14] presented analytical solutions for thermally fully developed electroosmotic flow in circular and parallel-plate microchannels, considering the Joule heating effect, viscous dissipation, and convective heat transfer in thermally (and hydrodynamically) fully developed combined pressure–electroosmotically driven flows in circular microchannels. Li et al. [15] observed that at elevated temperatures, the experimentally measured velocities of electroosmotic flow in microchannels were sometimes considerably higher than those predicted analytically using the Smoluchowski equation, and they characterized the influence of temperature on the zeta potential for a number of commonly used buffers in both PDMS:glass and PDMS:PDMS microchannels. Li and his colleagues derived an analytical formula for the electroosmotic flow, considering only the radial temperature profile in a capillary.

The elevation of the buffer temperature and the induced temperature gradient would in turn affect the temperature-dependent properties of the buffer and sample, including the viscosity, dielectric constant, electrical conductivity, diffusivity, electromobilities, and pH value. Therefore, various cooling methods, such as the use of a liquid coolant in a well-thermostatted system and the use of air by natural or forced convection in a nonthermostatted system, have been developed to maintain the correct capillary temperature and thus minimize Joule heating effects. On the other hand, a potential use of Joule heating effects to precisely control the temperature in microfluidic devices was recently reported. Analyses based on simplified theories and/or empirical correlations have been reported by numerous researchers. Peterson et al. [5] took a closer look at Joule heating effects in microchip-based and capillary-based electrophoretic separation systems. These authors argued that the main influence of Joule heating on separation efficiency is via the radial temperature profile, not the overall temperature rise in the buffer solution. On the basis of the assumption of a parabolic temperature profile, Grushka et al. [16] examined the effect of radial temperature gradients on the efficiency of capillary electrophoretic separation and proposed certain conditions for operating a capillary electrophoretic system to minimize the undesirable effects of thermal gradients. Jones and Grushka derived a simplified 1D model to show that the temperature profile is parabolic for low power inputs but is distorted for high power inputs. An improved thermal model for estimating the Joule-heating-induced band broadening was formulated by Gobie and Ivory [17]. More recently, analytical solutions for the effects of Joule heating on sample band broadening were obtained by Xuan and Li [7] and by Tang et al. [18–20]. Some mathematical formulations of the effects of Joule heating on electrokinetic transportation in capillary electrophoresis have also been presented.

Future Directions for Research

More and more materials with various thermal conductivities can be used to prepare chips with the chip fabrication techniques that have been developed; these provide us with more opportunities to make use of electrokinetic flow. In the future, more methods and techniques should be developed to measure and control the temperatures generated by Joule heating more precisely. New materials should also be studied for with the aim of obtaining faster heat dissipation and easier chip fabrication.

Cross References

▶ AC Dielectrophoresis Lab-on-Chip Devices
▶ DC Dielectrophoresis Lab-on-Chip Devices
▶ AC Electro-Osmotic Flow
▶ Dielectrophoretic Motion of Particles and Cells
▶ Electrocapillary
▶ Electrokinetic Flow and Ion Transport in Nanochannels
▶ Electrokinetic Motion of Cells and Nonpolarizable Particles
▶ Electroosmotic Flow (DC)
▶ Electrophoresis
▶ Joule Heating in Electrokinetic Flow: Theoretical Methods

References

1. Erickson D, Sinton D, Li D (2003) Joule heating and heat transfer in poly(dimethylsiloxane) microfluidic systems. Lab Chip 3:141–149
2. Belder D, Ludwig M (2003) Surface modification in microchip electrophoresis. Electrophoresis 24:3595–3606
3. Yoo JY (2006) Recent studies on fluid flow and heat transfer in thermal microdevices. Nanoscale Microscale Thermophys Eng 10:67–81
4. Jaeger MS, Mueller T, Schnelle T (2007) Thermometry in dielectrophoresis chips for contact-free cell handling. J Phys D 40:95–105
5. Petersen NJ, Nikolajsen RPH, Mogensen KB et al (2004) Effect of Joule heating on efficiency and performance for microchip-based and capillary-based electrophoretic separation systems: A closer look. Electrophoresis 2:253–269
6. Tang GY, Yang C, Chai CJ (2003) Modeling of electroosmotic flow and capillary electrophoresis with the joule heating effect: The Nernst–Planck equation versus the Boltzmann distribution. Langmuir 19(26):10975–10984
7. Xuan XC, Li DQ (2005) Analytical study of Joule heating effects on electrokinetic transportation in capillary electrophoresis. J Chromatogr A 1064(2):227–237
8. Hu GQ, Xiang Q, Fu R (2006) Electrokinetically controlled real-time polymerase chain reaction in microchannel using Joule heating effect. Anal Chim Acta 557(1–2):146–151
9. Guijt RM, Baltussen E, van Dedem GWK (2002) Use of bioaffinity interactions in electrokinetically controlled assays on microfabricated devices. Electrophoresis 23(6):823–835
10. Bruin GJM (2000) Recent developments in electrokinetically driven analysis on microfabricated devices. Electrophoresis 21(18):3931–3951
11. de Jesus DP, Blanes L, do Lago CL (2006) Microchip free-flow electrophoresis on glass substrate using laser-printing toner as structural material. Electrophoresis 27:4935–4942
12. Rathore AS (2004) Joule heating and determination of temperature in capillary electrophoresis and capillary electrochromatography columns. J Chromatogr A 1037:431–443
13. Evenhuis CJ, Guijt RM, Macka M, Marriott PJ et al (2005) Internal electrolyte temperatures for polymer and fused-silica capillaries used in capillary electrophoresis. Electrophoresis 26:4333–4344
14. Maynes D, Web BW (2004) The effect of viscous dissipation in thermally fully-developed electro-osmotic heat transfer in microchannels. Int J Heat Mass Transf 47:987–999
15. Venditti R, Xuan XC, Li DQ (2006) Experimental characterization of the temperature dependence of zeta potential and its effect on electroosmotic flow velocity in microchannels. Microfluid Nanofluid 2:493–499
16. Grushka E, Mccormick RM, Kirkland JJ (1989) Hyperlink Effect of temperature-gradients on the efficiency of capillary zone electrophoresis seperations. Anal Chem 61:241–246
17. Gobie WA, Ivory CF (1990) Thermal-model of capillary electrophoresis and a method for counteracting thermal band broadening. J Chromatogr 516:191–210
18. Tang GY, Yang C, Gong HQ et al (2006) Numerical simulation of Joule heating effect on sample band transport in capillary electrophoresis. Anal Chim Acta 561:138–149
19. Tang GY, Yan DG, Yang C et al (2006) Assesment of Joule heating and its effects on electroosmotic flow and electrophoretic transport of solutes in microfluidic channels. Electrophoresis 27:628–639
20. Tang GY, Yan DG, Yang C et al (2007) Joule heating and its effects on electrokinetic transport of solutes in rectangular microchannels. Sens Actuators A Phys 139:221–232

Joule Heating Effect

► Joule Heating and Chip Materials

Joule Heating in Electrokinetic Flow: Theoretical Models

XIANGCHUN XUAN[1], DONGQING LI[2]

[1] Department of Mechanical Engineering, Clemson University, Clemson, SC, USA

[2] Department of Mechanical Engineering, Vanderbilt University, Nashville, TN, USA

xchxuan@mie.utoronto.ca, dongqing.li@vanderbilt.edu

Synonyms

Ohmic heating; Resistive heating; Electric heating

Definition

Joule heating in electrokinetic flow refers to the increase in temperature of a liquid as a result of its resistance to an electrical current. This current arises from the electrical voltage that is applied across a channel to generate liquid electroosmosis and species electrophoresis.

Overview

Joule heating is a ubiquitous phenomenon in electrokinetic flow. This internal heat source can lead to significant increase and non-uniformity in liquid temperature. The elevated liquid temperature may on one hand, denature live biological samples, while on the other, be exploited in heat related physico-chemical processes, for example, the thermal cycling in PCR. Meanwhile, as most liquid properties are temperature sensitive, the induced temperature gradients make the liquid properties non-uniform and thus draw disturbances to the electrokinetic flow of both liquids and species samples [1, 2]. Therefore, it is important to study Joule heating in electrokinetic flow in order for the optimal design and efficient operation of microfluidic devices. This assay is focused on the theoretical models that describe Joule heating and its effect on electrokinetic flow in microfluidic channels. We will begin with a summary of the basic methodology including general transport equations. This will be followed by a detailed review of the analytical modeling of Joule heating in electrokinetic

microchannel flows. After that a few key research findings are briefly presented. Finally we suggest some future directions for research on Joule heating in electrokinetic flow.

Basic Methodology

Provided in this section are the general equations that govern the transport of heat (temperature field), electricity (electric field), momentum (flow field) and mass species (concentration field) involved in electrokinetic flow. These equations form the basis of the theoretical modeling of Joule heating in electrokinetic flow.

Temperature Field Joule heating, the most right term in Eq. (1), takes effects in the liquid domain only (denoted by the subscript l) where the transient energy equation is written as

$$\rho_l C_{p,l}\left(\frac{\partial T}{\partial t}+\boldsymbol{u}\cdot\nabla T\right)=\nabla\cdot(k_l\nabla T)+\Phi+\lambda\nabla\phi\cdot\nabla\phi \quad (1)$$

where ρ is the mass density, C_p the specific heat, T the temperature, t the time coordinate, $\boldsymbol{u}$ the liquid velocity, k the thermal conductivity, Φ the viscous heating, λ the electrical conductivity, ϕ the externally applied electric potential. Generally Φ contributes little to energy equation in low-Reynolds flows and thus is often neglected in electrokinetic microfluidics. Joule heating in the liquid is dissipated in two ways: one is through the channel ends that is reflected in the boundary conditions of Eq. (1), and the other is through the solid substrate (denoted by the subscript s) wherein the energy equation takes the form

$$\rho_s C_{p,s}\frac{\partial T}{\partial t}=\nabla\cdot(k_s\nabla T)\,. \quad (2)$$

Electric Field The electric potential φ in electrokinetic flow can be split into two terms, i. e., $\varphi=\phi+\psi$, where ϕ, the electric potential externally applied along the axis of a channel, produces Joule heating in Eq. (1), and ψ, the double-layer potential internally induced over the channel cross-section, causes liquid electroosmosis via Eqs. (4) and (5). These two electric potentials satisfy, respectively, the Laplace equation and the Poisson equation

$$\nabla\cdot(\lambda\nabla\phi)=0 \quad (3)$$

$$\nabla\cdot(\varepsilon\nabla\psi)=-\rho_e \quad (4)$$

where ε is the liquid permittivity and ρ_e is the net charge density.

Flow Field The transient electroosmotic flow field is solved from Navier–Stokes equations and the continuity equation,

$$\rho_l\left[\frac{\partial \boldsymbol{u}}{\partial t}+(\boldsymbol{u}\cdot\nabla)\,\boldsymbol{u}\right]=-\nabla p+\nabla\cdot(\eta\nabla\boldsymbol{u})-\rho_e\nabla\phi \quad (5)$$

$$\frac{\partial\rho_l}{\partial t}+\nabla\cdot(\rho_l\boldsymbol{u})=0 \quad (6)$$

where p is the hydrodynamic pressure and η is the liquid viscosity.

Concentration Field The electrokinetic transport of sample species is described by the Nernst–Planck equation

$$\frac{\partial c}{\partial t}+\nabla\cdot\left(-D\nabla c-\mu_{ep}c\nabla\phi+c\boldsymbol{u}\right)=0 \quad (7)$$

where c is the species concentration, D the diffusion coefficient, and μ_{ep} the electrophoretic mobility of species.

Obviously the transport Eqs. (1) through (7) are coupled via temperature dependent liquid properties, of which the two most important ones are liquid conductivity λ and viscosity η [1]. Especially, the coupling among temperature field, electric field and flow field in the energy Eq. (1) necessarily forces the use of numerical simulation [3]. Only in few simple cases are analytical solutions available, which will be addressed in the next section. Numerical modeling of electrokinetic transport in microchannels is complicated by the simultaneous presence of three separate length scales: the channel length in millimeters, the channel cross-sectional dimension in micrometers, and the double-layer thickness in nanometers. A full solution on all the three length scales would require a prohibitive amount of memory and computational time. Therefore, either an artificial magnification or a complete elimination of the length scale of double-layer thickness (by imposing an electroosmotic slip condition on channel walls) has been frequently used to resolve the problem. As the conductivity within electrical double layer might be orders of magnitude larger than that in the bulk liquid due to the locally strong accumulation of counter-ions, the magnification of double-layer thickness is anticipated to have a noticeable influence on Joule heating. Hence, the application of electroosmotic slip condition is recommended to simplify the numerical modeling. In addition, thermal diffusion necessarily extends the computational domain for thermal modeling from the fluidic region to encompass the solid substrate (and thus the reservoirs in reality), which significantly complicates the simulation by introducing another length scale of chip dimension in centimeters. This difficulty can be partly alleviated through an

appropriate reduction of the lateral width of the computational domain [4]. However, an approach to the efficient simulation of Joule heating in an entire microfluidic chip is definitely in need.

Simplifications and Analytical Solutions

Analytical modeling of Joule heating in electrokinetic flow can basically be divided into two main categories. In the first category, liquid flow is assumed to have negligible effect on the temperature field that is assumed fully developed in the entire channel. Therefore, liquid temperature varies only in the cross-stream direction. In the second category, the flow effect on temperature field is considered while the transverse variation in liquid temperature is assumed small. Therefore, the local liquid temperature can be replaced by its cross-sectional average. This section reviews in detail the analytical solutions of Joule heating in electrokinetic microchannel flows with axially uniform or non-uniform cooling. These two cases correspond to the capillary electrophoretic separation with and without thermostating, respectively. The channel cross-section could be of either cylindrical or rectangular shape while only the former is discussed in this article. Hence, the axisymmetric structure and boundary condition reduces the energy Eq. (1) and thus Eqs. (2) through (7) to two-dimensional at most, which certainly facilitates the development of analytical solutions.

Joule Heating in Electrokinetic Flow with Uniform Cooling

In capillary electrophoresis without thermostating, the whole channel is uniformly cooled by the free air around its outer surface. In such a circumstance, the theoretical studies of Joule heating in electrokinetic flow are divided into two main groups: the first group concerns the electrophoretic separation in an infinitely long channel where only radial temperature non-uniformity exists [5]; the second group studies the electrokinetic transport in a relatively short channel (e. g., on-chip electrophoresis) where the reservoir-based cooling effects, i. e., thermal end effects, have to be considered that gives rise to axial temperature gradients [6].

Without Thermal End Effects Neglecting the flow effect and considering only the steady-state radial temperature variation reduce Eq. (1) to

$$\frac{1}{y}\frac{\mathrm{d}}{\mathrm{d}y}\left(y\frac{\mathrm{d}T}{\mathrm{d}y}\right) = -\frac{\lambda E_0^2 R_1^2}{k_1} \tag{8}$$

where $y = r/R_1$ is the non-dimensional radial coordinate with R_1 being the lumen radius, and E_0 is the strength of the applied electric field. Assuming a linear relationship of liquid conductivity λ to temperature

$$\lambda = \lambda_0\left[1 + \alpha\,(T - T_0)\right] \tag{9}$$

where λ_0 is the liquid conductivity at room temperature T_0 and α is the temperature coefficient, the radial temperature profile can be derived as

$$T = T_0 + \frac{1}{\alpha}\left[\frac{J_0(qy)}{J_0(q) - qJ_1(q)/\mathrm{Bi}} - 1\right] \tag{10}$$

where $q = \sqrt{\alpha\lambda_0 E_0^2 R_1^2/k_1}$ may be called *Joule number* (dimensionless), $\mathrm{Bi} = UR_1/k_1$ is the Biot number (dimensionless), and J_0 and J_1 are the Bessel functions of the first kind. In the definition of Biot number, U is the overall heat transfer coefficient between the liquid and the external coolant given by $1/R_1\left[\ln\left(R_w/R_1\right)/k_w + \ln\left(R_p/R_w\right)/k_p + 1/hR_p\right]$ where h is the convective heat transfer coefficient of the coolant. Note that the subscripts l, w and p indicate the liquid, capillary wall and polyimide coating, respectively. It is apparent that the applied electric field strength E_0 must not be too high. Otherwise, the term $J_0(q) - qJ_1(q)/\mathrm{Bi}$ would become zero or even negative, causing a physically unrealistic temperature (i. e., thermal runaway). It is also clear from the definition of q that the effect of capillary internal radius R_1 on Joule heating is similar to that of the electric field strength while stronger than the liquid conductivity. As the Joule number q is typically small, Eq. (10) can be approximated as

$$T = T_w + \Delta T(1 - y^2) \tag{11}$$

where $T_w = T_0 + qJ_1(q)/\alpha[J_0(q) - qJ_1(q)/\mathrm{Bi}]$ is the liquid temperature at the capillary wall and $\Delta T = q^2/4\alpha[J_0(q) - qJ_1(q)/\mathrm{Bi}]$ is the temperature difference between capillary center and wall. In other words, the radial temperature distribution in capillary electrophoresis follows an essentially parabolic profile.

The fully developed, steady-state electroosmotic velocity u_{eo} is now available from Eq. (5) in conjunction with Eq. (4),

$$\frac{\mathrm{d}}{\mathrm{d}y}\left(y\eta\frac{\mathrm{d}u_{eo}}{\mathrm{d}y}\right) = \varepsilon E\frac{\mathrm{d}}{\mathrm{d}y}\left(y\frac{\mathrm{d}\psi}{\mathrm{d}y}\right) \tag{12}$$

As liquid viscosity varies with temperature by $\eta = A\exp(B/T)$, its inverse can be approximated by a Taylor series around T_w, i. e., $1/\eta = [1 + \omega(1 - \eta^2)]/\eta_w$ where A and B are both empirical constants, $\omega = B\Delta T/T_w^2$, and

η_w is the viscosity at the temperature T_w. Therefore, integrating Eq. (12) gives rise to

$$u_{eo} = \mu_{eo,w} E_0 \times \left\{ 1 - \frac{\psi}{\zeta}\left[1+\omega(1-y^2)\right] - 2\omega \int_1^y \frac{\psi}{\zeta} y' dy' \right\} \quad (13)$$

where $\mu_{eo,w} = -\varepsilon\zeta/\eta_w$ is the electroosmotic mobility at the capillary wall. As ω is normally very small, Eq. (13) may be safely simplified to [5]

$$u_{eo} = \mu_{eo,w} E_0 (1 - \psi/\zeta) \quad (14)$$

which holds the same form as that in the absence of Joule heating. Following the distribution of double layer potential ψ that is also slightly affected by Joule heating, the electroosmotic flow profile is therefore still plug-like except very close to the capillary wall. It is, however, noted that $\mu_{eo,w}$ is enhanced by Joule heating because of the reduced liquid viscosity. Similarly, the electrophoretic velocity of species can be approximated to

$$u_{ep} = \mu_{ep,w} E_0 \left[1 + \omega(1-y^2)\right] \quad (15)$$

where $\mu_{ep,w} = z_v e / 6\pi\eta_w a$ is the electrophoretic mobility calculated at the wall temperature T_w, z_v the species valence, e the unit charge, and a the radius of ionic species. Transforming the concentration Eq. (7) by $z_1 = z - u_s t$ where z is the axial coordinate and $u_s = \mu_{eo,w} E_0 + \mu_{ep,w} E_0 (1+\omega)$ is the mean migration velocity of species, and then averaging the new equation over the cross-section lead to

$$\frac{\partial \bar{c}}{\partial t} = K \frac{\partial^2 \bar{c}}{\partial z_1^2} \quad (16)$$

where $\bar{c}$ is the mean species concentration, and K denotes the effective dispersion coefficient. In ideal circumstances, K is reduced to solely species diffusivity. However, the non-plug-like profiles of liquid electroosmosis and species electrophoresis both cause ▶hydrodynamic dispersion. If the contribution from liquid electroosmosis is neglected, the dispersion coefficient due to the parabolic profile of electrophoretic velocity and the radially non-uniform diffusion is given by

$$K = D_w(1+\gamma) + \frac{1}{48} \frac{\omega^2}{(1+\omega)^2} \frac{\left(1 - \frac{1}{5}\gamma\right)}{1+\gamma} \frac{R_1^2 u_s^2}{D_w} \quad (17)$$

where $D_w = k_B T_w / 6\pi\eta_w a$ is the diffusivity at the wall temperature T_w with k_B being the Boltzmann constant. Note that $\gamma = \omega/2 + \Delta T/2T_w$ characterizes the radial non-uniformity of diffusivity D. If a sample plug of uniform concentration c_0 and half width w_0 is initially injected to the capillary inlet, an analytical solution of $\bar{c}$ is available from Eq. (16),

$$\bar{c} = \frac{c_0}{2}\left[\operatorname{erf}\left(\frac{w_0 - z + u_s t}{2\sqrt{Kt}}\right) + \operatorname{erf}\left(\frac{w_0 + z - u_s t}{2\sqrt{Kt}}\right)\right] \quad (18)$$

where $\operatorname{erf}(x)$ denotes the error function and the true axial coordinate z has been recovered from z_1. Consequently, a larger value of K produces more dispersion in the species concentration field, indicating lower separation efficiency due to Joule heating effects.

With Thermal End Effects In practical electrokinetic flow, electroosmosis continuously pulls the cold liquid from the inlet reservoir while pushing the hot liquid into the outlet reservoir. Therefore, flow effect should be considered in the energy Eq. (1). Moreover, reservoir-based cooling effects, i. e., thermal end effects, produce a thermal developing region at each end of the capillary. Accordingly, there should also form a developing region for both electric field and flow field due to the temperature dependent liquid conductivity and viscosity [6].

Since the lateral temperature variation is typically very small in free air-cooled electrokinetic flow (while the temperature gradients may be very large), it is acceptable to replace the local liquid temperature T with its cross-sectional average, $\bar{T}$. Neglecting the effect of transverse liquid flow and averaging each term in Eq. (1) over the capillary cross-section yield

$$\frac{d^2\bar{T}}{dz^2} - \frac{\bar{u}}{\alpha_l}\frac{d\bar{T}}{dz} - \frac{2U}{k_l R_1}(\bar{T} - T_0) + \frac{\lambda_0[1 + \alpha(\bar{T} - T_0)]E^2}{k_l} = 0 \quad (19)$$

where $\alpha_l = k_l/\rho_l C_{p,l}$ is the thermal diffusivity of liquid, $E = -d\phi/dz$ the axial electric field strength, and $\bar{u}$ the mean liquid velocity that must be continuous through the capillary and will be specified later. Meanwhile, the electrical current density J should also be constant resulting in

$$\lambda_0\left[1 + \alpha(\bar{T} - T_0)\right]E = J. \quad (20)$$

Therefore, for small values of temperature rise, Eq. (19) may be rewritten as the following non-dimensional form (see [6] for the derivation)

$$\frac{\mathrm{d}^2\Theta}{\mathrm{d}Z^2} - \mathrm{Pe}\frac{\mathrm{d}\Theta}{\mathrm{d}Z} - \beta^2\Theta + 1 = 0 \tag{21}$$

where $\Theta = (\bar{T} - T_0)/q'$ is the non-dimensional temperature, $q' = J^2 R_1^2/\lambda_0 k_1$ the reference temperature, $Z = z/R_1$ the non-dimensional axial coordinate, $\mathrm{Pe} = \bar{u}R_1/\alpha_1$ the Péclet number (dimensionless), and $\beta = \sqrt{2\mathrm{Bi} + \alpha q'}$ (dimensionless). Considering the thermal end effects $\Theta(0) = \Theta(L) = 0$, one can derive from Eq. (21)

$$\Theta(Z) = \frac{1}{\beta^2}\left[1 - \frac{\left(\mathrm{e}^{A_1 L} - 1\right)\mathrm{e}^{A_2(L-Z)} + \left(\mathrm{e}^{A_2 L} - 1\right)\mathrm{e}^{A_1 Z}}{\mathrm{e}^{(A_2+A_2)L} - 1}\right] \tag{22a}$$

$$A_1 = \sqrt{\frac{\mathrm{Pe}^2}{4} + \beta^2} + \frac{\mathrm{Pe}}{2} \quad \text{and} \quad A_2 = \sqrt{\frac{\mathrm{Pe}^2}{4} + \beta^2} - \frac{\mathrm{Pe}}{2} \tag{22b}$$

where $L = L_0/R_1 \gg 1$ with L_0 being the capillary length. On assuming a positive $\bar{u}$ in Eq. (22), the thermal entrance length that corresponds to the temperature reaching 99% of the fully developed temperature is estimated as $4.605\,R_1/A_2$. Similarly, the length of thermal exit region, where the liquid temperature adjusts rapidly to that of the cold liquid in the outlet reservoir, is given by $4.605\,R_1/A_1$. Considering the fact $A_1 > A_2$, the axial temperature profile inclines to the direction of liquid flow. As to the fully developed liquid temperature, it has an approximate magnitude of $1/\beta^2$.

Turn to the unknown electrical current density J. For small values of temperature rise, Eq. (20) yields, to a good approximation,

$$E = \frac{-\mathrm{d}\phi}{\mathrm{d}z} \cong \frac{J\left[1 - \alpha(\bar{T} - T_0)\right]}{\lambda_0} \tag{23}$$

Incorporating the temperature distribution in Eq. (22) and then integrating Eq. (23) yields

$$\frac{\lambda_0 E_0 L_0}{J R_1} = L - \frac{\alpha q'}{\beta^2}\left[L - \frac{\left(\mathrm{e}^{A_1 L} - 1\right)\left(\mathrm{e}^{A_2 L} - 1\right)\left(\frac{1}{A_1} + \frac{1}{A_2}\right)}{\mathrm{e}^{(A_2+A_2)L} - 1}\right] \cong L\left(1 - \frac{\alpha q'}{\beta^2}\right) \tag{24}$$

where the approximation is valid only at $\exp(A_1 L) = \mathrm{O}\left[\exp(A_2 L)\right] \gg 1$. Thus, a compact formula for the electrical current density in the presence of Joule heating and thermal end effects is available from Eq. (24) after recovering q' and β,

$$J = \frac{U}{\alpha R_1 E_0}\left(1 - \sqrt{1 - 2J_0\frac{\alpha R_1 E_0}{U}}\right) \tag{25}$$

where $J_0 = \lambda_0 E_0$ is the electrical current density free of Joule heating. The terms within the square root imposes a limit to the applied electric field E_0, beyond which J becomes physically meaningless. This limit is mainly attributed to the linear approximation made in Eqs. (21) and (23), which differs from the limitation in Eq. (10) due to the aforementioned thermal runaway. Therefore, a new model with the linear approximation released is in need. In the range of $E_0 < \sqrt{U/2\alpha\lambda_0 R_1}$, J is always higher than J_0 and their difference grows larger at a higher E_0.

The mean liquid velocity $\bar{u}$ still remains unknown. Comparing the orders of magnitude in the flow equation tells that the pressure p only varies along the length direction and thus Eqs. (5) and (6) are reduced to

$$\frac{1}{y}\frac{\partial}{\partial y}\left(y\frac{\partial u_z}{\partial y}\right) = \frac{R_1}{\eta}\frac{\partial p}{\partial Z} \tag{26}$$

$$\frac{1}{y}\frac{\partial}{\partial y}(y u_r) + \frac{\partial u_z}{\partial Z} = 0\,. \tag{27}$$

As discussed previously, an electroosmotic slip condition $u_{\mathrm{slip}} = \mu_{\mathrm{eo}}E$, which varies along the length direction in the present circumstance, can be imposed on the capillary wall instead of the no-slip condition. Integrating Eq. (26) twice with respect to r gives

$$u_z(y, Z) = \mu_{\mathrm{eo}}E - \frac{R_1}{4\eta}\frac{\mathrm{d}p}{\mathrm{d}Z}(1 - y^2) \tag{28}$$

Referring back to Eq. (19), it is natural to average each term in Eq. (28) over the capillary cross-section,

$$\frac{\mathrm{d}p}{\mathrm{d}Z} = (\mu_{\mathrm{eo}}E - \bar{u})\frac{8\eta}{R_1}\,. \tag{29}$$

As the two reservoirs in ►capillary electrophoresis are both open to air, i. e., $p(0) = p(L) = 0$, integrating Eq. (29) along the capillary length yields

$$\bar{u} = \frac{-\int_0^L \varepsilon\zeta E \mathrm{d}Z}{\int_0^L \eta \mathrm{d}Z} \tag{30}$$

The final formula for the axial liquid velocity is written as

$$u_z(y,Z) = \mu_{eo}(z)E(z) - 2\left[\mu_{eo}(z)E(z) - \bar{u}\right]\left(1-y^2\right) \quad (31)$$

Therefore, Joule heating and thermal end effects not only alter the local electroosmotic velocity, but also induce axial-position dependent pressure-driven flows in electrokinetic flow.

It is certainly useful to have a compact formula for the mean liquid velocity $\bar{u}$ like that for the electrical current J in Eq. (25). Incorporating the temperature distribution in Eq. (22) and the electric field strength in Eq. (23), one can specify $\bar{u}$ in Eq. (30) as

$$\begin{aligned}\bar{u} &= \left\{1 - \frac{\omega'}{\beta^2}\right. \\ &\quad \times \left.\left[1 - \frac{1}{L}\frac{\left(e^{A_1 L}-1\right)\left(e^{A_2 L}-1\right)(1/A_1+1/A_2)}{e^{(A_2+A_2)L}-1}\right]\right\}^{-1} \\ &\quad \times \left[-\frac{\varepsilon\zeta E_0}{\eta_0}\right] \\ &\cong \frac{1}{1-\omega'/\beta^2}\left[-\frac{\varepsilon\zeta E_0}{\eta_0}\right]\end{aligned} \quad (32)$$

where $\omega' = Bq'/T_0^2$ has a similar definition to ω in Eq. (13). Obviously the square bracketed term on the most right side of Eq. (32) is the electroosmotic velocity without Joule heating effects, whose prefactor, always larger than 1, is reflective of the flow enhancement due to the rise of liquid temperature.

As the initially injected sample plug is normally a distance away from the capillary inlet in capillary electrophoresis, the entrance region should have negligible influence on the species transport. In the region of fully developed (denoted by the subscript fd) flow field, the thermally induced pressure-driven flow causes additional hydrodynamic dispersion to the species diffusion. Analogous to Eq. (17), the effective dispersion coefficient is given by

$$K = D_{fd} + \frac{\left(\bar{u}-u_{z,fd}\right)^2 R_1^2}{48 D_{fd}} \quad (33)$$

The electrokinetic transport of mean species concentration $\bar{c}$ is still described by Eq. (18).

Joule Heating in Electrokinetic Flow with Non-Uniform Cooling

In capillary electrophoresis with thermostating, a short length of the channel at each end must be left outside the thermostated cartridge for sample injection and detection. These two regions are exposed to free air (un-thermostated) so that the local liquid temperature is higher than that in the middle section subject to forced-air (or liquid) cooling. Therefore, axial temperature gradients are formed, which by analogy to thermal end effects will induce pressure-driven flows upon the electroosmotic flow field [7].

For simplicity, the transition regions in both temperature and flow fields near the channel entrance and at the junctions of un-thermostated and thermostated regions are assumed negligibly small and thus are not considered. This implies a discontinuity in the temperature and velocity at the above junctions. In each region itself, however, there are no axial variations. Given the fact that the radial profile of liquid temperature is essentially parabolic, one can obtain the cross-sectional average temperature $\bar{T}_i$ at each region of the capillary (denoted by the subscript index $i = 1, 2, 3$) from Eq. (11),

$$\bar{T}_i = T_{w,i} + \frac{\Delta T_i}{3} \quad (34)$$

Here, a new formula is derived for $T_{w,i}$ and ΔT_i in order to simplify the analytical modeling. Referring back to Eq. (8) and its boundary condition yields

$$E_i^2 \lambda_0 \left[1 + \alpha(\bar{T}_i - T_0)\right] R_1^2 = 4k_1 \Delta T_i \quad (35)$$

$$E_i^2 \lambda_0 \left[1 + \alpha(\bar{T}_i - T_0)\right] R_l = 2U_i(T_{w,i} - T_0) \quad (36)$$

where Eq. (35) is an approximate integration of Eq. (8). It is then straightforward to get

$$T_{w,i} = T_0 + \frac{1}{2U_i/E_i^2\lambda_0 R_1 - \alpha(1 + U_i R_1/4k_1)} \quad (37)$$

$$\Delta T_i = \frac{U_i(T_{w,i} - T_0)R_1}{2k_1} \quad (38)$$

Once again, Eq. (37) requires that the applied electric field strength E_0 be lower than $\sqrt{2U_i/\alpha\lambda_0 R_1(1 + U_i R_1/4k_1)}$ in order to avoid the thermal runaway.

Without loss of generality, the heat transfer conditions (reflected by U_i) in the injection ($i = 1$) and detection ($i = 3$) regions are assumed identical, resulting in $T_1 = T_3$ and thus $E_1 = E_3$. Then, the condition of current continuity gives rise to

$$\left[1 + \alpha\left(\bar{T}_1 - T_0\right)\right] E_1 = \left[1 + \alpha\left(\bar{T}_2 - T_0\right)\right] E_2 \quad (39)$$

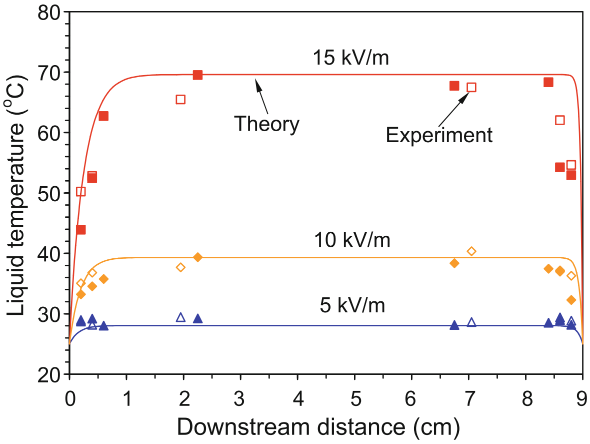

Joule Heating in Electrokinetic Flow: Theoretical Models, Figure 1 Comparison of liquid temperature along the axis of a capillary in electrokinetic flow between numerical calculations (lines) and experimental measurements (symbols). Reprinted from [8]

In addition, the electric voltage across the whole capillary column should satisfy

$$E_1\,(L_1 + L_3) + E_2 L_2 = E_0\,(L_1 + L_2 + L_3) = E_0 L_0 \quad (40)$$

where E_0 is the average strength of the applied electric field, L_1, L_2 and L_3 are the lengths of the injection, forced air-cooling ($i = 2$) and detection regions, respectively, and L_0 is the total channel length. Referring to Eq. (34) for the average liquid temperature at each section, it is sufficient to determine the electric field strengths E_i from Eqs. (39) and (40). These results are omitted here for compactness. As for the mass continuity, we first integrate Eq. (12) with consideration of the electroosmotic slip condition leading to

$$u_i\,(y) = \mu_{\mathrm{eo,w},i} E_i - \left(\frac{\partial P}{\partial z}\right)_i \frac{R_1^2}{4\eta_{\mathrm{w},i}} \times \left[1 + \frac{1}{2}\omega_i - \left(1 + \omega_i - \frac{1}{2}\omega_i y^2\right) y^2\right] \quad (41)$$

The first term on the right hand side is the plug-like electroosmotic velocity, and the second term is the pressure-driven flow that is slightly different from a parabola due to the small quartic term caused by radial temperature gradients. Therefore, the cross-sectional average liquid velocity in each region $\bar{u}_i$ is easily derived as

$$\bar{u}_i = \mu_{\mathrm{eo,w},i} E_i - M_i \frac{\Delta P_i}{L_i} \quad (42)$$

where $M_i = (1 + \omega_i/3) R_1^2 / 8\eta_{\mathrm{w},i}$ can be understood as the hydrodynamic conductivity in the presence of radial temperature gradients, and ΔP_i is the pressure difference in region i. Then, the mass continuity requires

$$\mu_{\mathrm{eo,w},1} E_1 - M_1 \frac{P_1}{L_1} = \mu_{\mathrm{eo,w},2} E_2 - \frac{M_2 (P_2 - P_1)}{L_2} = \mu_{\mathrm{eo,w},1} E_1 + \frac{M_1 P_2}{L_3} \quad (43)$$

where P_1 and P_2 indicate the induced pressures at the two ends of the forced cooling region. Note that $\mu_{\mathrm{eo,w},1} = \mu_{\mathrm{eo,w},3}$ and $M_1 = M_3$ have been invoked in Eq. (43). Hence, P_1 and P_2 are easily determined from Eq. (43) as

$$P_1 = \frac{\mu_{\mathrm{eo,w},2} E_2 - \mu_{\mathrm{eo,w},1} E_1}{\frac{M_1}{L_1} + \frac{M_2 (1 + L_3/L_1)}{L_2}} \quad (44)$$

$$P_2 = -P_1 \frac{L_3}{L_1} \quad (45)$$

These axial temperature gradients induced pressure-driven flows can cause hydrodynamic dispersion (see Eq. (33)) and thus reduce the separation efficiency. The latter is usually evaluated in terms of the theoretical plate height H

$$H = \frac{2Kt}{L_0} = H_{\mathrm{dif}} + H_{\mathrm{axT}} \quad (46a)$$

$$H_{\mathrm{dif}} = \frac{2}{L_0} \sum_{i=1}^{3} \frac{D_i L_i}{\bar{u}_i} \quad \text{and} \quad H_{\mathrm{axT}} = \frac{R_1^2}{24 L_0} \sum_{i=1}^{3} \frac{\bar{u}_{i,\mathrm{pd}}^2 L_i}{D_i \bar{u}_i} \quad (46b)$$

where H_{dif} and H_{axT} denote, respectively, the plate heights due to molecular diffusion and axial temperature gradients, and D_i is the diffusion coefficient at the average liquid temperature $\bar{T}_i$. Note that a higher value of H indicates lower separation efficiency.

Key Research Findings

As noted above, the direct consequence of Joule heating in electrokinetic flow lies in the variation of liquid temperature. The indirect consequences of Joule heating that originate from the temperature dependent liquid properties include the increased current load, enhanced flow rate, induced pressure-driven flows, and reduced separation efficiency. We provide here a brief overview of the key effects of Joule heating and as well the experimental verifications if available.

Fig. 1 shows the comparison of numerically calculated (lines) and experimentally measured (symbols) liquid temperatures in electroosmotic microchannel flow [8]. Overall, the numerical and experimental results are in good

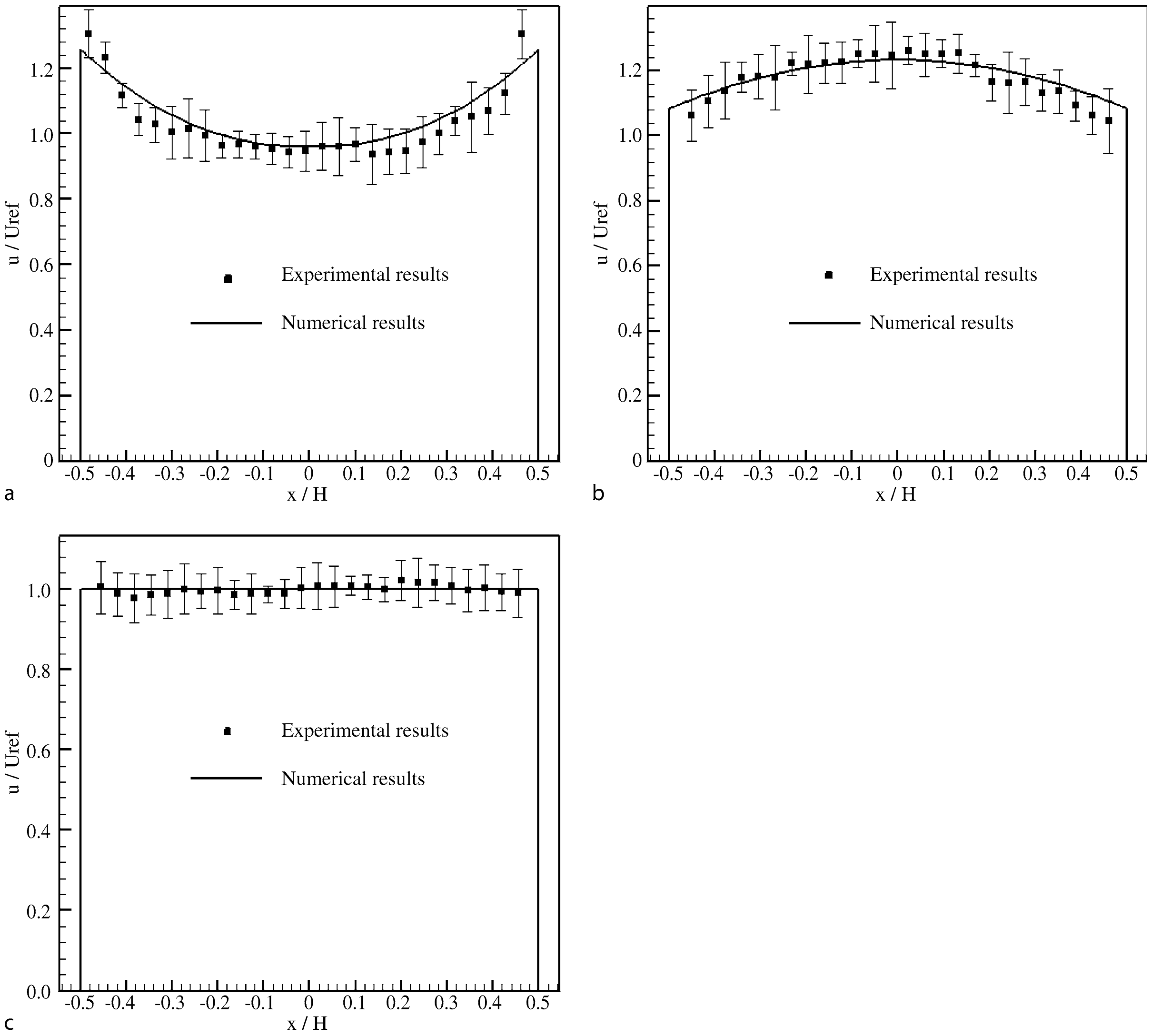

Joule Heating in Electrokinetic Flow: Theoretical Models, Figure 2 Comparison of transverse velocity profiles of electrokinetic flow in a poly(dimethylsiloxane) (PDMS) microchannel between the experiment (symbols with error bars) and simulation (lines): (**a**) entry region with significant Joule heating; (**b**) body region with significant Joule heating; (**c**) body region with negligible Joule heating. Reprinted from [9]

agreement. The numerical model was based on the finite element method, and the liquid temperature was extracted from the fluorescence images of rhodamine B dyes. Sharp temperature drops are observed close to the channel ends while in the middle there forms a high temperature plateau due to Joule heating and thermal end effects. In addition, the temperature profile is inclined to the downstream due to the advective effect of liquid electroosmosis. These phenomena are also predicted in the analytical solution, Eq. (22). Figure 2 compares the transverse velocity profiles of electrokinetic flow in a poly(dimethylsiloxane) (PDMS) microchannel between the microPIV (Particle Image Velocimetry) experiment (symbols with error bars) and 3D finite-volume simulation (lines) [9]. As a consequence of thermal end effects, the liquid velocity profile is concave in the entry region (Fig. 2a) while turns convex (Fig. 2b) in the body region if Joule heating is significant. This observation is consistent with the analytical solution, Eq. (31). In the circumstance of negligible Joule heating, however, the plug-like electroosmotic velocity profile (Fig. 2c) is resumed as expected [1].

Figure 3 plots the theoretical steady-state cross-stream velocity profiles (lines) with corresponding experimental results (symbols) for electrokinetic flow in a microchannel with non-uniform cooling [10]. The theoretical profiles were determined from Eq. (41) along with Eqs. (44) and (45). The experimental profiles were obtained from the images of uncaged fluorescent dye electrokinetic trans-

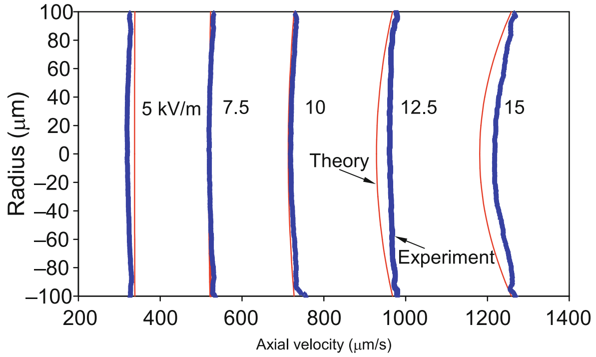

Joule Heating in Electrokinetic Flow: Theoretical Models, Figure 3 Comparison of steady-state cross-stream velocity profiles of electrokinetic flow within the cooled viewing window of a microchannel between experimental measurements (data points) and the analytical solution (line). Reprinted from [10]

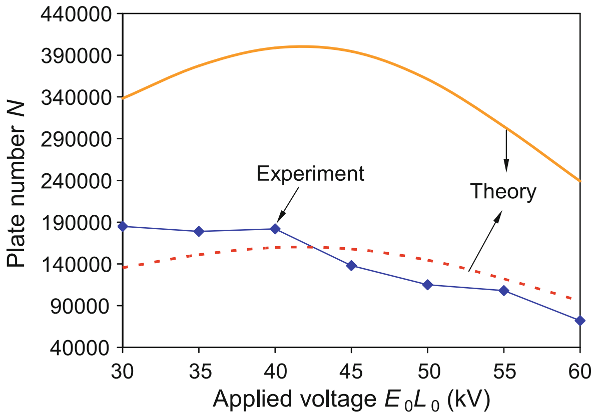

Joule Heating in Electrokinetic Flow: Theoretical Models, Figure 4 Comparison of the theoretical plate numbers, $N = L_0/H$, between the analytical solution (lines) and the previous experiment (symbols). The solid line is determined from Eq. (46) while the dashed line accounts for 40% of the plate numbers in the solid line. Reprinted from [7]

port within the viewing window that was locally cooled by a drop of immersion oil. Although agreement between theory and experiment is not exact, the concave curvature of velocity profile is similar and apparent in both sets of results. Figure 4 shows the comparison of theoretical and experimental plate numbers, $N = L_0/H$, in capillary electrophoresis with thermostating [7]. The experimental plate numbers (symbols connected by lines) were adapted from previous measurements. The solid line displays the plate numbers calculated from Eq. (46) while the dashed line accounts for 40% of the values in the solid line. In the latter, all other sources of dispersion, for example, injection, detection and adsorption etc., are considered. Apparently the analytical model predicts properly the trend of the plate numbers with respect to the applied voltage.

Future Directions for Research

Regarding the future directions for theoretical research on Joule heating in electrokinetic flow, it may be interesting and important to clarify the true expression of Joule heating within electrical double layer, to determine the appropriate thermal boundary condition at the outlet of microchannels, to examine the role of Joule heating in electrokinetic instability with conductivity gradients, and to develop a numerical model for an efficient simulation of Joule heating in chip-based electrokinetic microfluidic devices.

Cross References

► Electroosmotic Flow (DC)
► Electrophoresis
► Fluorescent Thermometry
► Temperature Control in Microfluidic Systems
► Hydrodynamic Dispersion
► Joule Heating and Chip Materials
► Methods for Temperature Measurements
► Temperature Effects on the Zeta Potential
► Temperature Gradient Focusing
► Viscous Heating

References

1. Knox JH (1988) Thermal effects and band spreading in capillary electro-separation. Chromatographia 26:329–337
2. Rathore AS (2004) Joule heating and determination of temperature in capillary electrophoresis and capillary electrochromatography columns. J Chromatogr A 1037:431–443
3. Tang G, Yang C, Chai CK, Gong HQ (2004) Joule heating effect on electroosmotic flow and mass species transport in a microcapillary. Int J Heat Mass Transfer 47:215–227
4. Erickson D, Sinton D, Li D (2003) Joule heating and heat transfer in poly(dimethylsiloxane) microfluidic systems. Lab Chip 3:141–149
5. Xuan XC, Li D (2004) Joule heating effects on peak broadening in capillary zone electrophoresis. J Micromech Microeng 14:1171–1180
6. Xuan XC, Li D (2005) Analytical study of Joule heating effects on electrokinetic transportation in capillary electrophoresis. J Chromatogr A 1064:227–237
7. Xuan XC, Li D (2005) Band broadening in capillary zone electrophoresis with axial temperature gradients. Electrophoresis 26:166–175
8. Xuan XC, Xu B, Sinton D, Li D (2004b) Electroosmotic flow with Joule heating effects. Lab Chip 4:230–236
9. Tang G, Yan D, Yang C, Gong HQ, Chai CK, Lam YC (2006) Assessment of Joule heating and its effects on electroosmotic flow and electrophoretic transport of solutes in microfluidic channels. Electrophoresis 27:628–639
10. Sinton D, Xuan XC, Li D (2004) Thermally-induced velocity gradients in electroosmotic microchannel flows: The cooling influence of optical infrastructure. Exp Fluid 37:872–882

Karhunen–Loève (K–L) Approach

► Proper Orthogonal Decomposition (POD) Based MOR

Karhunen–Loève (K–L) Decomposition

► Proper Orthogonal Decomposition (POD) Based MOR

Karhunen–Loève (K–L) Expansion

► Proper Orthogonal Decomposition (POD) Based MOR

Kelvin–Hemholtz Instability

Definition

Kelvin–Hemholtz instability arises because of shear along an interface between two different fluids. Related to turbulence and transition phenomena, it also describes the onset of ocean wave formation, jetting instabilities, and cloud formation. In microfluidics it is commonly seen in fluid-fluid interfaces. Not to be confused with Rayleigh–Taylor, or Rayleigh instabilities (► Rayleigh-Taylor instability).

Cross References

► Piezoelectric Microdispenser

Kernel Function

Synonyms

Nucleus; Smoothing function

Definition

The notion of kernel or smoothing function has its root in interpolation theory. In effect, the introduction of a localized kernel function works as a smoothing interpolation filter that generates a locally continuous field. In other words, kernels are used to localize the partial differential equations through a convoluted integration.
Considering a function A defined on a domain D, the integral representation of a this function can be written as

$$A(x) = \int_D A(\xi)\delta(x - \xi)\mathrm{d}\xi \,,$$

where x is a location vector and $\delta(x)$ is the Dirac delta function centred at the position x. Inspired by this form, the integral approximate of the function, $\langle A \rangle$, is written as

$$\langle A(x) \rangle = \int_D A(\xi) W(x - \xi, h)\mathrm{d}\xi$$

where W is a kernel function and h is a scaling variable with dimensions of length and is frequently known as the smoothing length of the kernel. The symbol $\langle \rangle$ denotes the approximated interpolation value.
In meshless methods, the choice of the interpolation kernel is the core of the method. Various types of kernel functions are used in the literature; the Gaussian kernel and spline-based kernels such as the cubic-spline, quartic or quintic kernels are among the most frequently used kernels.

Cross References

► Meshless Methods

Kinetic Boltzmann Equation

► Micro- and Nanoscale Gas Dynamics

Kinetics

Definition

The study of how fast a reaction takes place in a chemical reaction.

Cross References

► Lab-on-a-Chip Devices for Chemical Analysis

Kinetic Theory of Gases

► Micro- and Nanoscale Gas Dynamics

Knoevenagel Condensation

Definition

A Knoevenagel condensation is a nucleophilic addition of an active hydrogen compound such as malonates to a carbonyl group followed by an dehydration reaction in which a molecule of water is eliminated (hence condensation). The product is an alpha, beta conjugated enone.

Cross References

► Biomolecular Synthesis in Microfluidics
► Lab-on-a-Chip Devices for Chemical Analysis

Knudsen Number

Definition

Knudsen number is the ratio of the mean free path of fluid molecules to a typical dimension of gas flow.

Cross References

► Electrokinetic Flow and Ion Transport in Nanochannels
► Gas Flow in Nanochannels
► Heat Transfer in Microchannel Flows
► Supersonic Micro-Nozzles
► Micro- and Nanoscale Gas Dynamics
► Lattice Poisson-Boltzmann Method, Analysis of Electroosmotic Microfluidics

Lab-Cd

► Centrifugal Microfluidics

Lab-on-a-Chip

► Biomolecular Adsorption in Microfluidics
► On-Chip Detection Using Optical Fibers
► Impedimetric Biosensors for Nano- and Microfluidics
► Lab-on-Chip Devices for Separation-Based Detection
► Microfluidics for Studies of Apoptosis
► Microfluidic Systems

Lab-on-Chip Devices for Biodefense Applications

DHARMALINGAM SUGUMAR[1], LINGXUE KONG[2]
[1] Faculty of Manufacturing Engineering, Technical University Malaysia, Ayer Keroh, Malaysia
[2] Centre for Material and Fiber Innovation, Deakin University, Geelong, VIC, Australia
sugumar@utem.edu.my, lingxue.kong@deakin.edu.au

Synonyms

Biosafety; Bioterrorism; Biosecurity; Biothreat

Definition

Biodefense is a method to protect a country from potential attack by deliberate release of agents such as viruses, bacteria or other germs used to cause illness or death in people, animals, or plants. These agents are typically found in nature, but could also be changed to increase their ability to cause diseases, to make them resistant to current medicines or to increase their ability to be spread into the environment. Biological agents can be spread through the air, water or in food.

Overview

Microfluidic and micro Lab-on-Chip technologies, which move microscopic and nanoscale drops of fluid, have great potential to be applied in the lucrative military market. The growing concern and lingering threat of possible unconventional warfare in the near future have generated tremendous demands for high technology and innovative devices for detecting this type of threat. Field portable devices that are faster, simpler and more reliable for use on the battlefield are much sought after by the military. The threat is not only concentrated on the battlefield, but also in homeland security, such as terrorist attacks. Real-time monitoring devices are urgently required to protect the well-being of military personnel and civilians, to ensure food safety and to avoid water contamination. This is especially useful when the detection of chemical or biological warfare agents is done in a rapid and sensitive manner which could provide an early warning of their possible impending catastrophic effects, thus minimizing or even eliminating any casualties by enabling preventive measures to be taken to contain the threat. With these devices, those who are exposed to the threat can be handled promptly by the medical providers to give appropriate treatments and to assure unexposed persons of their health status. These devices can also be used to detect noncombat threats such as diseases or infections when operating in hostile environments such as jungles and deserts.

Highly accurate and fast analytical devices are also urgently required for supporting various military and homeland security operations such as the investigation of bombing sites. Therefore, the device should offer high sensitivity and selectivity in detecting a threat, providing a fast detection and a high level of accuracy. Portability, rather than transportability, requires these devices to be portable, energy efficient, easy to operate and maintain, of low weight, have low power consumption and of low cost

to be deployed for field use such as a war zone. For effective sampling of biological agents, the device must have a portable sensor technology, which should be extremely sensitive, universal, reliable, fast and able to detect multiple threats simultaneously. Furthermore, the device must use fewer consumables, be of low maintenance and have a long shelf life. It should also be highly specific and sensitive to detect threats at threshold levels, process and deliver results within minutes and also able to store the data for later use. Figure 1 summarizes the basic requirements of a biodefense Lab-on-Chip device [1].

The devices that are currently available are either too bulky or slow to respond in detecting threats. Designing and manufacturing an appropriate device which is portable and easy to use by retaining the high sensitivity and selectivity is a major challenge.

Basic Methodology

Biological Warfare Agent

A biological agent is an infectious disease that can be used in biological warfare. There are more than 1200 different kinds of biological agents. Biological agents include prions, microorganisms (i. e. viruses, bacteria and fungi) and some unicellular and multicellular eukaryotes (e. g., parasites) and their associated toxins. Examples of biological agents are ►anthrax, avian influenza, botulism, foodborne illness, hantavirus, legionnaires' disease, molds and fungi, pneumonic plague, smallpox, tularemia and viral hemorrhagic fevers (VHFs) [2].

Lab-on-Chip-Based Immunoassays

Recent developments in ►immunoassays enable the detection of biological warfare agents. The principal measurement technique in immunoassays is the shape recognition of an antigen by the antibody to form an antibody-antigen complex binding. This type of assay allows the measurement of minute or trace amount of bindings in samples. The conventional measuring methods of immunoassays are slow and involve multiple processes which involve liquids handling. Sato et al. [3] developed an immunoassay microchip to detect cancer cells. The device was made of glass that integrated polystyrene beads, pre-coated with anti-CEA (carcinoembryonic antigen) antibody, with a microfluidic system using thermal lens microscopy as the detection method. The reaction time of this device was reduced to about 1% of that required for a conventional ELISA (enzyme linked immunosorbant assay). A novel cell analysis system consisting of a scanning TLM detection system and a cell culture microchip was also developed [4]. A microflask ($1 \times 10 \times 0.1$ mm; 1 μl) was fabricated in a glass microchip. The system could detect nonfluorescent biological substances with an extremely high sensitivity without labeling any materials and had a high spatial resolution of 1 μm. The microchip system is good for liquid control and simplifies troublesome procedures. This system was applied to monitor cytochrome c distribution in a neuroblastoma–glioma hybrid cell cultured in the microflask.

Lab-on-Chip Based on DNA Analysis

Rapid and accurate identification of bioagents are crucial in biodefense strategy. DNA recognition offers unique possibilities for identification of biological warfare agents and holds great promise for on-site detection. One of the key methods in DNA-based detection systems is the polymerase chain reaction (PCR) method. The PCR method enables detection of specific organisms of even a very low concentration. The PCR method also requires minimal amount of reagents and samples for detection and identification of harmful pathogens. Figure 2 shows a simple PCR chip fabricated from glass.

Delehanty and Ligler [5] used an antibody microarray system with continuous fluid flow to detect microbial toxins and simultaneously detected both cholera toxin and staphylococcal enterotoxin at a detection level as low as 8 and 4 ng/ml, respectively, within 15 min. Yang et al. [6] developed a device for detecting and genotyping influenza A viruses. Construction of the device utilizes solid-state electronics microfabricated in silicon and glass, deposition of resistive heaters for thermal cycling, a reaction chamber for restriction digestion and a miniature gel separation column, with DNA driven by an electric field produced by miniature microfabricated electrodes. The possible uses of this type of device are the tracking of influenza variants, including H1, H3, H5, H9 and other subtypes.

Related Biodefense Strategy

A threat to military personnel does not only come through the use of chemical and biological warfare agents, but also from hostile natural environments and the existing health status of the personnel concerned. Diseases inflicted by nature can be malaria, cholera, dengue fever and yellow fever. Military personnel in the field need a portable device that can detect diseases or contamination when they are far away from their base stations or camps where fast medical attention and analysis can be provided.

Rapid and sensitive detection of the presence of harmful pathogens in water, air or food is important for ensuring health safety. Timmer et al. [7] developed a micro-device to measure low concentration of ammonia levels in water.

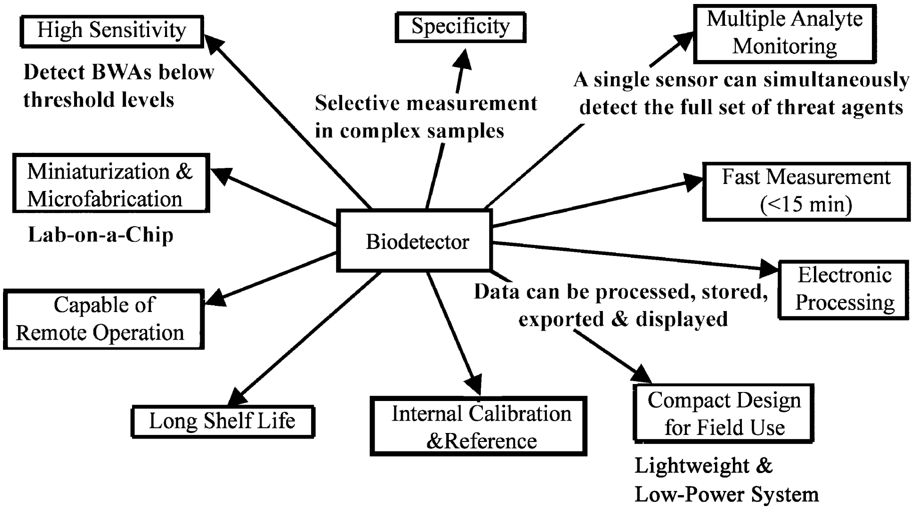

Lab-on-Chip Devices for Biodefense Applications, Figure 1 Requirements for biodefense Lab-on-Chip device [1]

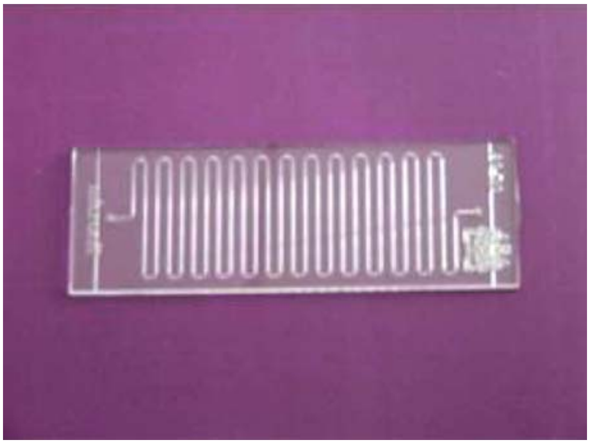

Lab-on-Chip Devices for Biodefense Applications, Figure 2 A simple PCR chip (Courtesy of Institute for Research in Molecular Medicine, Universiti Sains Malaysia)

The device can be used for fast diagnosis of patients with disturbed urea balance, either due to kidney disorder or *H. pylori* bacterial infection. From the experiments conducted, they showed that the system is sensitive to ammonia concentrations below 1 ppm.

A droplet-based microfluidic device for the measurement of glucose for clinical diagnostics was presented by Srinivasan et al. [8]. The device uses the electrowetting-based digital microfluidic platform for biochemical assay. The device is able to detect glucose concentrations in the range 25 – 300 mg/dl within 60 s for a dilution factor as low as 2 and 3. The device is also capable of detecting other human metabolites such as lactate, glutamate and pyruvate.

Key Research Findings

The success of Lab-on-Chip devices for biodefense is dependent on successful coupling of these devices with novel detection and diagnosis system. Lab-on-Chip devices must be able to provide fast, accurate, reliable and timely field identification and quantification of biothreat agents. Recent developments of Lab-on-Chip devices made possible integrated microfabricated devices for performing reagent and sample mixing, immunological reaction and affinity capillary reactions in a single chip. This chip is able to conduct the complete analysis within 60 s and is capable of nanomolar-scale detection accuracy. Several research organizations have started commercially developing rapid biodefense Lab-on-Chip devices. Cepheid (Sunnyvale, USA) has developed I-CORE® for performing fast PCR in large volumes. This device can perform PCR with a cycle time of less than 30 s for a sample volume as large as 100 µl. Other designs based on the I-CORE module are the MIDAS® (Microfluidic Integrated DNA Analysis System) and the Smart Cycler®.

The Lawrence Livermore National Laboratory (LLNL) has developed a handheld-type device named Handheld Advanced Nucleic Acid Analyzer (HANAA) (Fig. 3) which is capable of rapid detection of bioagents such as *B. anthracis* in the field. It uses the TaqMan-based PCR assay system. Due to its small footprint and low weight, it is ideal for field applications. Another development from them is the Nanowire Barcode System which speeds up detection of pathogens such as anthrax, small pox, ricin and botulinum. Antibodies of specific pathogens are attached to the nanowires which produce small, reliable and sensitive detection systems.

Lab-on-Chip Devices for Biodefense Applications, Figure 3 The Handheld Advanced Nucleic Acid Analyzer from Lawrence Livermore National Laboratory

Agilent's Bioanalyzer is another breakthrough system which enables real-time analysis of different bioagents. It combines a variety of approaches, including DNA microarrays, bioinformatics and Lab-on-Chip. This device integrates fluid handling, sample processing, separation and detection in miniature chip.

Future Directions for Research

The increasing threat of bioterrorism and continued emergence of new infectious diseases have driven a major resurgence in biomedical research efforts to develop improved treatments, diagnostics and vaccines, as well as to increase the fundamental understanding of the host immune response to infectious agents. As MEMS devices continue to merge sensing, actuation, control with computation, communication, power generation on microscale systems, so will Lab-on-Chip devices merge traditionally compartmentalized medical practices such as diagnostics (in vitro) and treatment (in vivo). For example, early detection of disease using transdermal sample acquisition devices can be integrated with drug synthesis and controlled drug delivery to monitor and control physiological parameters of choice. One of the challenges in applying Lab-on-Chip technology to biodefense screening is how to overcome the problem of low concentration of target pathogens. The US Biological Defense Research Program through Microfluidic Systems Inc. is creating microfluidic-based devices for a rapid detection system for pathogens that can concentrate and identify viruses, bacteria and other air- or waterborne toxins in less than 5 min. The system depends on the air or liquid flow across a series of deep etched pillars, 5 μm tall and 150 μm in diameter to capture DNA, proteins or cells and elute into 50 μl fractions.

Cross References

- ► Integrated Micro Devices for Biological Applications
- ► Integrated Microfluidic Systems for Medical Diagnostics
- ► PCR Lab-on-Chip Devices
- ► Proteomics in Microfluidic Devices

References

1. Ivnitski D, O'Neil DJ, Gattuso A, Schlicht R, Calidonna M, Fisher R (2003) Nucleic acid approaches for detection and identification of biological warfare and infectious disease agents. Biotech 35:862–869
2. Noji EK (2001) Bioterrorism: A 'New' Global Environmental Health Threat. Glob Chang Human Health 2(1):46–53
3. Sato K, Tokeshi M, Kimura H, Kitamori T (2001) Determination of carcinoembryonic antigen in human sera by integrated bead-bed immunoassay in a microchip for cancer diagnosis. Anal Chem 73(6):1213–1218
4. Sato K, Hibara A, Tokeshi M, Hisamoto H, Kitamori T (2003) Microchip-based chemical and biochemical analysis systems. Adv Drug Deliv Rev 55(3):379–391
5. Delehanty JB, Ligler FS (2002) A Microarray Immunoassay for Simultaneous Detection of Proteins and Bacteria. Anal Chem 74(21):5681–5687
6. Yang M, Srivastava N, Lin R, Burns M, Solomon M, Burke D, Fuller O, Herlocher L, Larson R (2004) The development of microfabricated devices for influenza A detection and genotyping. Int Congr Ser 1263:367–371
7. Timmer BH, van Delft KM, Otjes RP, Olthuis W, van den Berg A (2004) Miniaturized measurement system for ammonia in air. Anal Chim Acta 507(1):137–143
8. Srinivasan V, Pamula VK, Fair RB (2004) Droplet-based microfluidic Lab-on-a-Chip for glucose detection. Anal Chim Acta 507(1):145–150

Lab-on-a-Chip Devices for Chemical Analysis

GRACA MINAS
Department of Industrial Electronics, University of Minho, Guimaraes, Portugal
gminas@dei.uminho.pt

Synonyms

Laboratorial microsystem; Micro total analysis system (μTAS); μTAS; On-chip laboratory

Definition

A Lab-on-a-Chip for chemical analysis is a miniaturized device capable of analyzing chemical parameters in fluids. It comprises in a single chip the liquid-handling, the detection and the readout systems. Its reduced size and weight could improve the performance of an analysis and allow the device to be used in mobile chemical analysis equipment, such as medical diagnostics units.

Overview

The healthcare sector is nowadays one of the most dynamic and where novelty is a strategic and operational imperative. The possibility of increasing the quantity and quality of clinical analyses, performed with instantaneous results and outside clinical laboratories, contributes to a better quality in healthcare services and also a better efficiency in clinical and administrative processes. The healthcare sector is under pressure to provide better service at a lower price. Therefore, more cost-efficient practices are needed. One of the places to improve efficiency is at the physician's office.

When the physician is confronted with an ill patient he or she will start looking for symptoms. However, when these symptoms lead to a wrong diagnosis, there is a problem for the physician, the patient and society. A wrong diagnosis can lead to a wrong treatment that ultimately brings further harm to the patient and increases society expenses. The best way of increasing the quality of diagnosis is to give the physician more precise information about the state of the patient. Presently, this information is often based on the measurement of chemical parameters in biological fluids, such as blood and urine. Most diseases leave a molecular fingerprint in those fluids and by measuring that fingerprint in the right way, the precision of the diagnosis can be increased. Traditionally, this chemical parameter analysis is performed by mixing milliliters of samples and reagents in conventional test tubs or cuvettes and analyzing the product in an analytical instrument, e. g., a spectrophotometer. Moreover, the analysis is carried out in clinical laboratories and the results become available after several hours, sometimes days. As a consequence a reliable diagnosis cannot be performed within the consultation time. Mistakes in the logistics, such as lost samples and mislabeling, may further delay the diagnosis. The automated equipment used in a state-of-the-art laboratory reduces errors, but uses large sample and reagent volumes, making the analysis systems expensive and does not contribute to patient comfort. Outside the laboratory environment, reagent strips for colorimetric detection are commercially available. They provide a color when a fluid sample contacts the strip. However, such strips are intended for a limited set of compounds to be analyzed and provide a qualitative result in the form of a color readout (by visual inspection). The need for rapid and on-line measurements with low sample volumes has led to the development of miniaturized analyses devices with the fluidic, the detection and the readout (the data-processing) systems all integrated in a single chip. A system that encompasses those requirements is known as a "point-of-care" system, where "point-of-care" means that the analysis is performed where the physician meets the patient, or more generally, close to the place where the analysis needs to be performed. However, the physician is highly skilled in the art of medicine but has no routine or training in performing the advanced chemical analysis that is needed to decode the information of the biological fluids. Thus, to be of any value for the physician, the analysis system has to be highly automated, very robust, independent of a laboratory and laboratory personnel and the results must be processed so that it is easy for the physician or a regular user to interpret. A delicate combination of science and technology originating from microelectronic device fabrication, electrical engineering and analytical chemistry was essential in the development and optimization of these miniaturized analytical systems, which have been revolutionizing the field of chemical sensing. Moreover, microfabrication allows reproducing the same designed miniaturized analytical systems faithfully in very large numbers. The vision of those miniaturized devices was presented in 1990 [1] and has since then been the inspiration for an intense research effort geared towards miniaturization of macroscopic chemical analyses methods. Nowadays, they are called "Lab-on-a-Chip", which means an analytical laboratory of a microchip size. The great interest in Lab-on-a-Chip technology stems from the inherent performance gains that arise when most analytical systems are downsized to the micrometer scale. The advantages associated with shrinking clinical analyses systems include: reduced sample size, higher degree of integration and hence enhanced potential for automation, shortened response time, potential for improved analytical performance, reduced chemical storage and hence laboratory safety and a considerable reduction in samples handling, logistics and costs.

Chemical analysis systems, such as spectrophotometry, high-performance liquid chromatography, capillary electrophoresis and immunoassays, always consist of a combination of a reaction or separation and a detection system. In the following section, some generic features for chemical reactions and separations are addressed, and the major conventional detection techniques as well as the integration and miniaturization of optical components used in chemical analysis are briefly reviewed. In the "key

research findings" section, the latest Lab-on-a-Chip technologies for chemical analysis based on spectrophotometry are discussed.

Basic Methodology

Downscaling

Shrinking of clinical analysis systems is fundamentally limited by the amount of molecules available in the sample volume and thus by the concentration of the desired analyte. An analyte is the substance (element, ion, compound or molecule) being analyzed. The relation between the sample volume, V, and the analyte concentration, C_i, is given by [1]

$$V = \frac{1}{\eta_s N_A C_i}, \quad (1)$$

where η_s is the sensor efficiency ($0 \le \eta_s \le 1$) and $N_A = 6.02 \times 10^{23}$ is the Avogadro number. This equation demonstrates that the sample volume or the size of the microfluidic device is determined by the concentration of the desired analyte. Common clinical chemistry analyses of human biological fluids require the reproducible measurement of analyte concentrations between 10^5 and 10^{12} molecules per picoliter. Consequently, a picoliter sample volume is realistic only if the detection system can measure a detection limit of 10^5 molecules. For example, in human urine, albumin is the protein that has the lowest target molecules (on average 1 µmol in 1 l of urine) and also the lowest concentration (less than 15 mg/dl). For a low concentration of albumin in urine, for example 5 mg/dl, there are still 3.35×10^5 molecules per picoliter. Whether actual shrinking to the picoliter range is feasible depends not only on the sensitivity of the detection system, but also on practical aspects. For example, practical aspects for absorbance detection are the channel height (or optical pathlength) required to achieve measurable absorption (which depends on the analyte absorption coefficient (α), for example $\alpha = 0.27\,\mathrm{m}^{-1}$ for an albumin concentration of 5 mg/dl), as well as the minimum channel width and the photodetector area, which are both set by lithographic constraints. A typical minimum dimension for the optical pathlength in absorbance detection is 500 µm. The reduction of this optical pathlength makes solutes with poor absorption coefficients difficult to detect, even with a highly accurate optical detection system.

Chemical Analysis: Reaction and Separation

In a chemical analysis there needs to be a step that is specific for the analyte. For many applications the concentration of an analyte in a medium that contains mixtures of other compounds, often at much higher concentrations, must be detected. One way of obtaining specificity is to introduce a reagent with a chemical specificity and affinity for the analyte in the analysis (generally called affinity ►assay – assay means analysis). The term affinity in a chemical sense means a strong tendency for two entities to bind. Two molecules that bind with a high strength are said to have a high affinity for each other. For example, in colorimetric reactions, the shift produced in the spectrum of the mixture when the analyte is bound to the reagent is used; in immunoassays the high affinity between an antibody and its antigen is utilized; and in DNA hybridization one uses the high affinity of two single strands of DNA with complementary nucleotides. These techniques are well established with a multitude of reagents that are well characterized and commercially available.

It has been shown that a key component of a chemical analysis is the chemical reaction. Therefore, many analyte concentrations are measured by using a mixture of a reagent with a fluid sample. In addition, another essential requirement for any practical fully integrated Lab-on-a-Chip device in a single chip is the ability to mix two or more fluids thoroughly and efficiently, i. e., providing a homogeneous reaction in a reasonable amount of time. The microscale conditions have distinctive properties due to the small dimensions (of the order of 100 µm) and typically low volume flow rate. First, liquid flow is laminar (►laminar flow). Since velocities are of the order of 1 mm/s, the Reynolds number of microflows is usually less than 1. For these small Reynolds numbers the flow is dominated by viscous effects. Inertial effects are very small and turbulent mixing is impossible. Second, shrinking the dimensions of a Lab-on-a-Chip means that both molecular and thermal diffusion times are significantly reduced. As a result, ►diffusion can be used for mixing fluids, e. g., to bring reactants together across small channels. With a constant flux, the mass transport by diffusion is proportional to the contact surface of the two mixed species. The average diffusion time, t_D, over a relevant mixing path, d, is given by

$$t_D = \frac{d^2}{2D}, \quad (2)$$

where D is the diffusion coefficient of the analyte. This equation shows that the diffusion time changes with the square of the mixing path. Because of their small sizes, micromixers decrease the diffusion time significantly, so, while 17 min are required for diffusion across 1 mm, only 100 ms are required for a 10 µm distance. Therefore, fast mixing can be achieved with smaller mixing path and large contact surface. Furthermore, the small volumes involved

facilitate rapid dilution or injection of reactants into the system. Despite the fast mixing, some reactions need to wait for a reaction time determined by the ▶ kinetics inherent to the reaction.

This brief analysis shows that mixing only by diffusion is viable when small mixing paths are used. However, if the channel geometry is very small, the large fluid molecules must collide often with the channel wall and not with other molecules. Moreover, diffusion coefficients of solutions containing large molecules (e. g., enzymes and some proteins) are two orders of magnitude lower than those of most liquids. Therefore, if those large molecules with small diffusion coefficients must react, mixing only by diffusion may take long transit times (several minutes or even hours) and, consequently, long microchannels are necessary. This may be undesirable for some applications and alternative mixing methods must be developed.

The use of microelectromechanical systems (MEMS)-based devices as active mixers, such as microvalves and micropumps, is an alternative for accelerating the mixing, but their use increases the cost of the system, needs complex control systems and is difficult to integrate. To enable high-efficiency reactions overcoming the disadvantages of MEMS and the long transit times due to diffusion, acoustic waves are an interesting solution. They have been used both to promote mixing and to pump fluids [2]. Sound waves that propagate in the fluid generate pressure differences that induce so-called acoustic streaming. Two forms of acoustic streaming can be applied to microfluidic systems: quartz wind and Rayleigh flow. Quartz wind is generated when sound waves propagate along the fluid. Since some of the energy of the sound waves dissipates in the fluid due to viscous effects, a pressure drop is generated that induces fluid flow along the path of the sound waves. Rayleigh flow is generated by standing waves that create vortices. Secondary flows can be created in the plane perpendicular to the main flow in the channel [2]. These secondary flows promote mixing by convection between otherwise parallel currents. Therefore, acoustic microagitation could be a simple actuation source for mixing and promoting fluid reactions. In order to produce the ultrasounds, the fluidic die of the Lab-on-a-Chip must have an ultrasound transducer.

In applications where heating and cooling are necessary, such as the polymerase chain reaction (PCR), the miniaturization is an additional advantage. Conventional equipments need long cycles to perform PCR due to the large time constants associated with the heating and cooling. Once miniaturized systems allow the use of small volumes (nanoliters or even picoliters) as well as materials with high thermal conductivity, such as glass or silicon, the time needed for heating and cooling is drastically reduced.

In some chemical analyses it is necessary to separate the analytes present in a mixture, to identify the different analytes and to quantify their amount. Some of the common processes that perform this manipulation of analytes include extraction, precipitation, dialysis, ultrafiltration, distillation, centrifugation, chromatography and electrophoresis. The last two are the most frequently used separation techniques by those who do chemical analyses of biological fluids.

Chromatography performs separation according to the size, charge and affinity of the analyte, based on the different velocities that each compound is carried by a solvent in an appropriate porous medium. In electrophoresis, the separation is based on the ▶ electrokinetic mobility of particles under the influence of an electric field. More detailed information can be found in books such as [3].

A trend in Lab-on-a-Chip-based separations is to shorten the analysis time, increasing separation power and decreasing detection limits. The separation length is a crucial parameter in liquid chromatography (LC) and capillary electrophoresis (CE), determining analytical performance. These two techniques are highly suitable for implementation in a Lab-on-a-Chip format. Using CE as an example, the analysis time, t, is determined by the migration time of the slowest detectable analyte, i, and can be calculated from [4]

$$t = \frac{L^2}{\mu_i V_{\text{sep}}} \,, \tag{3}$$

where L denotes the distance between injection and detection, μ_i the vector sum of the electroosmotic and the electrophoretic mobility of the analyte i and V_{sep} the potential drop across L. Equation (3) shows that to shorten the analysis time, decreasing the separation length or increasing the applied voltage can be considered. Often, the voltage is limited by material restrictions (dielectric breakdown of chip materials) or increased Joule heating. The separation efficiency is only limited by diffusion and is proportional to the strength of the electric field, which means that it is relatively independent of the separation pathlength and is, therefore, compatible with miniaturization.

The dominance of electrophoresis over chromatography has been a trend in separations with Lab-on-a-Chip devices. The reason is that from an engineering point of view it is easier to apply a voltage across the terminals of microchannels than the application of a pressure difference. In CE, electrokinetic control of fluid transport eliminates the need for external components such as pumps and valves. Furthermore, miniaturization of chromatography systems involves technical challenges that are usually not necessary in CE. However, LC is the most used separa-

tion technique in conventional systems. Therefore, investigation for implementing this technique in Lab-on-a-Chip devices is an active trend.

Chemical Analysis Based on Spectrophotometry

In clinical diagnostics, one of the most commonly used analytical techniques for chemical analysis of body fluid samples is ▶spectrophotometric analysis (the study of the interaction of electromagnetic radiation with chemical compounds). Biological molecules interact in some way with many different parts of the electromagnetic spectrum. Spectrophotometry is a very popular technique and can be used to determine the concentration and/or amount of a particular analyte, determine the structure of a new compound, identify a specific compound and determine the activity of a specific enzyme, among others. The spectrophotometric detection methods are briefly reviewed in the following paragraphs. More detailed information can be found in books such as [3].

Chemical Analysis Based on UV/Visible Absorbance Detection

The UV/visible region of the electromagnetic spectrum is the most commonly used region for quantitative chemical measurements of biological fluids. In absorbance detection, the sample is excited by a light source of intensity I_0. The light intensity that passes through the sample is measured, I. The ratio of these two quantities is denominated as the absorbance, A, and is linked to the concentration of the analytes according to the Lambert–Beer law [3]

$$A = -\log \frac{I}{I_0} = \alpha c d\,, \tag{4}$$

where d is the pathlength, c is the concentration of the analyte in the sample and α its corresponding molar absorption coefficient. The Lambert–Beer law, as written above, is not directly applicable to circular microchannels. Diffraction and reflection effects strongly modify the pathlength, and therefore a correction factor must be applied.

In microchip format, the reduction of the optical pathlength has a severe impact on the detection sensitivity and it makes solutes with poor absorptivity difficult to detect. The shorter the optical pathlength, the fewer the molecules affected and the difference between I_0 and I is smaller. This reduces the I_0/I ratio and consequently the sensitivity of the measurement. Nevertheless, it has been shown that sensitivity can be improved by increasing the optical pathlength while detection volume is maintained small (further referred to in the "key research findings" section).

Chemical Analysis Based on Fluorescence Detection

Fluorescence detection is not only a very sensitive detection technique but also very selective and has been used most widely for detection using Lab-on-a-Chip devices. The detection is applied to compounds that contain fluorophores. An excitation source (of intensity I_0) is directed toward the sample and, consequently, fluorescent light is emitted. The intensity of the emitted light, F, is measured and is linked to the concentration of the analyte present in the sample [3]

$$F = I_0 \varphi \left(1 - 10^{-\alpha c d}\right)\,, \tag{5}$$

where φ is the ▶fluorescence yield. The wavelength of the excitation source and of the fluorescent emitted light differs. Therefore, one is no longer dependent on the ratio of two signals at a single wavelength, but is rather looking for one signal in the presence of light at other wavelengths, resulting in a very low measured background signal and consequently in a low detection limit. Because spectral filtering alone is not sufficient to guarantee this, fluorescence detection is generally carried out by placing the detector at some angle with respect to the incident light beam. Less excitation light collected by the detector improves the signal-to-noise ratio (SNR). In conventional fluorimeters, this angle is usually 90°.

Laser-induced fluorescence (LIF) detection uses a laser as the excitation light source, which increases the sensitivity because of its high intensity allowing detection limits reaching the attomolar range. A drawback of using a laser is that a continuous variation of the wavelength is not possible. Moreover, working at a fixed wavelength restrains one to only few analytes. The use of chemistry with some type of fluorophores allows the extension of fluorescence detection to many analytes. Furthermore, the use of a fluorescent carrier electrolyte combined with indirect detection also extends the type of detectable analytes with LIF. For indirect detection a fluorescent substance with a charge of the same sign as that of the analyte is added to the background buffer and its displacement (in order to maintain electroneutrality) is measured in the form of negative-going peaks. Nevertheless, in CE, indirect LIF should be considered as a last resort, because small changes in a background signal are monitored and the methods are thus limited by the noise on the baseline. Moreover, poor (when compared to direct LIF) detection limits have been reported (0.1 μmol). This is partly due to the fact that existing laser sources are unstable, yielding a noisy background signal. Conventional lasers are Ar^+, He – Ne and He – Cd lasers. Semiconductor or diode lasers are promising because they are more robust (longer life time), com-

pact and stable than the conventional lasers. This is important for indirect detection, which as such has a potential to become a useful on-chip technique. The miniaturization of the photodetector and the use of CMOS-compatible interference filters are also important. By making channels in silicon, the integration of photodetectors is possible, resulting in a very compact system.

Low-volume sample (less than a picoliter) fluorescence detection requires to date relatively bulky optical systems using lenses, mirrors and filters, and having excitation light directly to a tiny detector volume. Alignment of these optical elements is critical and the number of detector configurations limited. However, a number of research groups are investigating the miniaturization of these elements for integrating them into Lab-on-a-Chip devices, and consequently increasing both flexibility and performance of fluorescence detection.

Chemical Analysis Based on Chemiluminescence Detection

Chemiluminescence offers high sensitivity, low background noise, high specificity and reduced instrumental complexity due to the absence of an optical source for excitation, but it is limited in its applicability. This technique has a reduced spatial resolution when compared to fluorescence techniques. Since the light-emitting species are normally not surface-associated, they may diffuse across surfaces and cause emission from different parts.

Chemical Analysis Based on Electrochemistry

In electrochemical detection, changes in solution current, potential or conductivity as a function of the analyte concentration are measured. The chemical signal is directly converted into an electronic signal using simple electrodes. Since electrode deposition is a well-established process in microfabrication, the implementation of detection techniques using integrated electrodes has become an attractive approach for Lab-on-a-Chip devices. In electrochemical detection the output signal is dependent on electrode surface area. As a result, limits of detection (in concentration terms) do not degrade as rapidly as they would for optical techniques where the output signal is dependent on available detection volumes. Moreover, devices incorporating detection electrodes do not require a large amount of peripheral equipment for the acquisition of the detector signal. This makes the development of portable Lab-on-a-Chip devices a realistic possibility. However, electrochemical detection is not applicable to all situations where portable devices are required, and will never compete with fluorescence in terms of sensitivity. The electrochemical detection methods are briefly reviewed in the following paragraphs. More detailed information can be found in books such as [3].

Chemical Analysis Based on Amperometric Detection

Amperometric detection makes use of three electrodes: the auxiliary, the reference and the working electrode. The first two mentioned are used to monitor the potential in the solution, and the working electrode is the detection electrode. A constant potential is kept between the solution in the cell and the working electrode. Redox reactions of the analyte at the working electrode produce the detection signal. The generated current, I, is proportional to the amount of redox reactions, and thus to the concentration of the analytes [3]

$$I = z\mathrm{F}(c_i - c_0)\,, \qquad (6)$$

where z is the number of electrons transferred in the reaction, F is the Faraday constant, c_i is the concentration of the analytes that enter the detection cell and c_0 is the concentration of analytes that exit the detection cell. The coulombic efficiency is defined as the percentage of an electroactive analyte undergoing an electrode reaction inside the cell, and is linked to c_i and c_0. The detection sensitivity is strongly linked to the coulombic efficiency.

The reference electrode is in most applications a silver/silver chloride (Ag/AgCl) electrode. However, the material for the working electrode differs according to the analyte ions that have to be detected. The materials employed are gold, platinum, palladium, copper and carbon.

Amperometric detection is comparable to LIF detection: it is selective (only electroactive analytes are detected) and it has a low detection limit (femtomolar).

The electrochemical reactions that take place at the electrodes may result in a modification of their surface. These effects are prevented by pulse amperometric detection, where the polarization voltage is applied for only a short time and is followed by a reverse polarization in order to clean the electrodes.

Chemical Analysis Based on Potentiometric Detection

Potentiometric detection is similar to amperometric detection in the sense that both involve electrochemistry at the surface of a chemically active electrode. In the case of amperometry, a known electrode potential is applied, and the current resulting from redox activity is measured. This implies that the electrode has a low impedance in order to allow the flow of the redox current. The case of potentiometry is the opposite. A high electrode impedance keeps

the current negligible and the redox activity at the electrode leads to accumulation of charge at the surface. The resulting potential drop, denominated as the Nernst potential, is measured. In Lab-on-a-Chip devices ion-selective potentiometry has become a routine analytical technique for both in vivo and in vitro chemical analysis [5]. Special membranes have to be used for this purpose in order to achieve detection of a range of ions rather than the usually desired selectivity to just a single ion.

Chemical Analysis Based on Conductivity Detection

In conductivity detection, the concentration of an analyte is determined by measurement of the liquid conductivity. Two electrodes are placed in the channels. An alternating voltage, v_{in}, is applied between the electrodes and the resulting current, i_o, is measured. The value of the current is proportional to the liquid conductivity, κ (Sm^{-1})

$$i_o = \frac{v_{\text{in}}}{\text{K}}\kappa \,, \tag{7}$$

where K is the cell constant (m^{-1}).

Conductivity detection has also been investigated for chip-based separation and is a good technique in particular for small (inorganic) ions which are otherwise not readily detected [6].

The primary advantage of amperometric and potentiometric detection over conductivity detection is the high sensitivity induced by the electrochemical reactions that take place at the electrode surface. Only electrochemically active compounds can be detected using these methods, thereby eliminating interference from other compounds present in the sample. This selectivity can also turn into a disadvantage, since it strongly limits the applicability of the detection system. Additionally, the interference between the electrical separation field and the detection electrodes and associated electronics can be a problem.

Chemical Analysis Based on Mass Spectroscopy Detection

Mass spectroscopy offers a powerful tool for the detection and identification of compounds. The method is highly sensitive to small changes in mass, it needs minimal sample preparation and it allows structure elucidation and accurate molecular weight determination. It is the natural figure of merit when detecting single small entities such as bacteria, viruses, nanoparticles or individual molecules [7]. Furthermore, DNA-based assays are easy to perform [4]. Interfacing of microfluidic systems with mass spectrometers represents a special challenge. However, as miniaturization of this detection offers no meaningful advantages in terms of sensitivity or selectivity, mainly conventional-size detectors have been used in combination with chip-based separation systems.

Integration of Optical Detection Systems

If a Lab-on-a-Chip is defined to be a unit that should be able to perform all chemical functions and detection in a monolithic device that fits in the palm of one's hand (or smaller), then existing Lab-on-a-Chip units are generally still quite underdeveloped. This miniaturization will require increased integration not only of fluidic elements, but also of electrical, optical or other types of elements. The major criteria that lead the choice of a detection scheme are the properties of the analyte (optical, electrical, electrochemical and physical), the composition of the sample (do the analytes have similar properties and/or similar concentrations?) and the required detection limit. Other specific criteria can be the price, ease of use and implementation and, as far as Lab-on-a-Chip devices are concerned, the ease of fabrication and the possibility for miniaturization. In applications where the Lab-on-a-Chip is discarded after a single use, the cost of the device is very important and can even limit the choice of detection scheme.

As said before, a Lab-on-a-Chip device is composed basically of two elements: the fluidic and detection elements. These elements can be totally integrated in the same substrate, can be bonded and thus integrated or, when total integration is not possible, they can have a multi-chip-module (MCM) configuration. Figure 1 shows a schematic of a device using absorption spectrophotometry as the optical detection scheme. In a chip format device, distances between elements are reduced, resulting in better coupling of light from one element to the next. Moreover, the number of optical interfaces has also been reduced by directly contacting the various components one to the other, thereby reducing interfaces at which optical losses can take place.

Integrated Light Sources

Many semiconductors and their combinations form the basis of light-emitting diodes (LEDs) and laser diodes, a class of devices producing light in different wavelength regions from the blue to the near infrared. LEDs have been employed as external light sources for on-chip absorbance and fluorescence detection [8], and also as integrated arrays for sensing applications. Laser diodes have mainly been employed for LIF detection in on-chip CE. However, portable Lab-on-a-Chip units for in-field or point-of-care applications clearly should avoid external light sources.

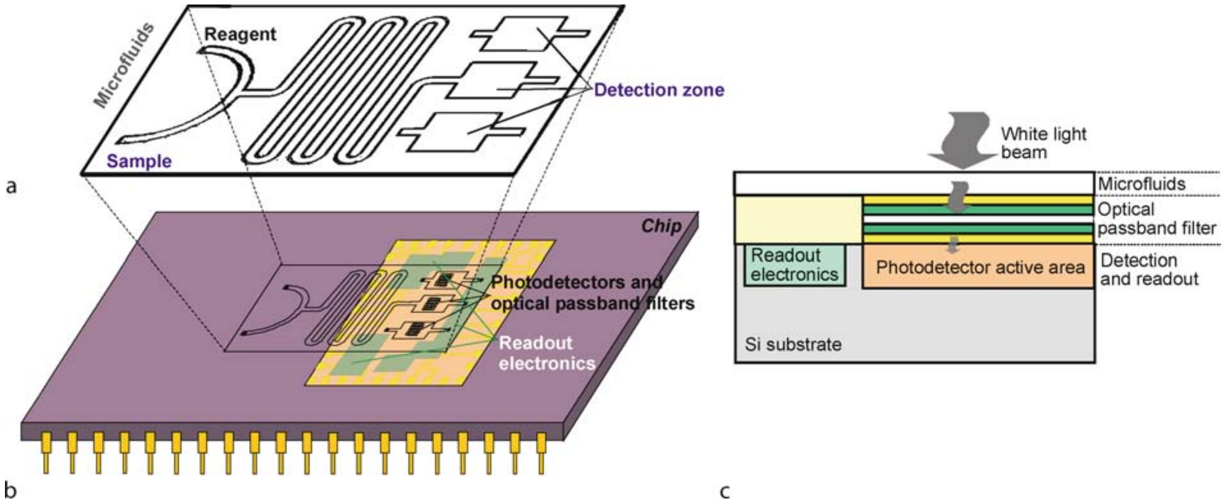

Lab-on-a-Chip Devices for Chemical Analysis, Figure 1 Schematic of a Lab-on-a-Chip structure: (**a**) microfluidic die; (**b**) optical detection die; (**c**) cross-section of the structure for a single optical channel

The integration of organic light-emitting diodes (OLEDs) as an excitation source is a promising alternative. The use of solution-processable semiconducting polymers or vacuum-deposited small-molecule organic semiconductors offers simple routes to device fabrication and tunable optical properties. These characteristics have been extensively demonstrated for thin-film polymer light-emitting diodes (pLED) which have entered the market place for simple display applications [9].

A typical OLED comprises one or more organic layers sandwiched between two electrodes, of which at least one must be transparent. The organic layer emits light under electrical excitation (via radioactive recombination of injected electrons and holes) and the devices may therefore be used as light sources. The emission color is determined by the chemical structure of the organic material and it may therefore be controlled using standard synthetic chemistry [10]. Therefore, an array of OLEDs producing light in the visible spectrum from blue to red may be fabricated. Many of the organic materials are soluble allowing for low-cost deposition from solution. Once OLEDs are fully compatible with polymeric substrates, and also the organic layers can be fabricated using simple layer-by-layer deposition procedures, they may be easily integrated into existing microchip structures at marginal additional cost. The tunable optical properties, simple fabrication, small size and low cost of OLEDs have already attracted considerable interest for employing them as integrated light sources for on-chip spectrophotometric measurements.

If the same device is needed to analyze more than one analyte an integrated light source such as a LED or semiconductor laser is not enough, since they cannot output a continuous variation of the wavelength. Macroscopic equipments for chemical analysis based on spectrophotometry include a wavelength-dependent light source illuminator, such as a monochromator, for illuminating the sample at the wavelength at which the analyte has its absorption or fluorescence maximum. However, Lab-on-a-Chip devices for portable point-of-care chemical analysis should avoid those external, complex and expensive macroscopic optical systems. This means that the monochromator must be integrated on-chip with the optical detector and the readout electronics devices. For that purpose, a regular white light source and an on-chip monochromator, as well as on-chip optical detectors with high spectral selectivity over a relatively wide wavelength range are required. However, on-chip integration of a monochromator, based on a grating as dispersive element, is expensive and difficult, due to the limited optical pathlength available.

Integrated Optical Filters

A Fabry–Perot (FP) interferometer can be used in an optical sensing system to pass a specific part of the spectrum, functioning like a monochromator. A FP structure is the most suitable for passband optical filters. A ►Fabry–Perot optical filter consists of two parallel mirrors with a resonance cavity in the middle (Fig. 2). The equation $\lambda q = 2nd$ shows its operation principle, where n is the refractive index of the cavity medium, d the cavity length, λ the incident wavelength and q the interference order ($q = 1, 2, 3, \ldots$). Therefore, in a FP optical filter the thickness of the resonance cavity, n, determines the tuned wave-

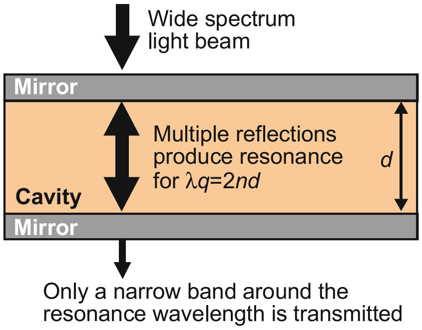

Lab-on-a-Chip Devices for Chemical Analysis, Figure 2 FP structure

length, λ [11]. The most important parts of the FP devices are the mirrors. Two types of highly reflective coatings are used for the mirrors: metallic and dielectric. Metallic mirrors have high absorption losses, but they can be attractive in certain applications due to the simplicity of their fabrication: only three layers are deposited and wavelength selection is performed by changing only the thickness of the cavity layer. The layout design for the etching/deposition process of the several cavities is crucial to minimize the number of masks and etching/deposition steps. Moreover, if the filters can be co-fabricated in a CMOS process and post-processed on top of the silicon optical detectors, the resulting Lab-on-a-Chip will be a low-cost disposable device and can be used for point-of-care diagnosis. A structure that comprises an array of 16 FP optical filters with metallic mirrors has been demonstrated [11]. It uses silver and aluminum as the top and bottom mirrors, respectively, and SiO_2 as the cavity layer. The aluminum bottom layer was evaporated on top of the photodetectors. Then a SiO_2 layer was deposited by chemical vapor deposition. In subsequent plasma etching steps, for which a mask is used, the 16 resonance cavities were realized in the SiO_2 layer. The evaporation of the silver layer on top of the resonance cavities ends the array fabrication. However, FP filters using metallic mirrors cannot provide both high ►transmittance and low ►full-width at half-maximum (FWHM) due to the optical absorption in the metal layers. The price of such simple a fabrication process was the 10% of transmittance for achieving a FWHM = 7 nm.

These drawbacks can be avoided using a FP structure with dielectric mirrors. Dielectric mirrors, when properly designed and fabricated, offer high-performance characteristics (high reflectivity with low absorption losses). When using dielectric layers, at least two different materials with high and low refractive index and alternately deposited are needed to obtain narrow passband optical filters. A structure that comprises an array of 16 FP optical filters with dielectric mirrors has been demonstrated [12] and is shown in Fig. 3. The fabrication process is similar to that described above. Each optical channel is sensitive in a single wavelength with a FWHM of 6 nm and with a peak intensity higher than 86%. The 16 optical channel array fabrication requires only four masks, used with different deposition times. It uses TiO_2 and SiO_2 (with refractive indexes of about 3.0 and 1.5 in the visible spectrum, respectively) for the fabrication of the dielectric mirrors. These films are hard materials, and thus it is extremely difficult, or even almost impossible, to remove them from the substrate. SiO_2 has been selected because the wavelength dependence of its refractive index for the spectral band between 480 and 700 nm is almost constant (1.465 and 1.457, respectively). TiO_2 has been selected due to fabrication constraints (the deposition process is well characterized).

Instead of an array of fixed sized FP optical filters, a tunable scheme would be an alternative. A conventional tunable filter comprises, usually, an air-gap cavity and one movable mirror using, for example, electrostatic actuation. Comparing both schemes, the array of fixed-sized FP optical filters has the following disadvantages:

- it requires a large area (proportional to the number of different sized cavities);
- several layers have to be deposited/etched for the several cavity widths; and
- the spectral range covered is smaller.

However, it is relatively simple to operate. The tunable approach has three disadvantages:

- fabrication requires complex micromachining, which is difficult to be merged with a standard process;
- large voltages are required for actuation; and
- operation is difficult, mainly for achieving parallelism between the mirrors during the tuning of the filter.

An alternative to solve the problem of maintaining parallel mirrors in tunable FP optical filters is using a polymer such as poly(vinylidene fluoride) (PVDF) in its β-phase as the resonance cavity, instead of an air-gap cavity. The filter is tuned through an electric voltage inducing dipolar orientation in the β-PVDF film. Since the thickness changes of the β-PVDF film are due to variations at a molecular level, the changes are rather homogeneous within the samples. This is reflected in the ability to maintain parallel mirrors. Furthermore, the fabrication process is simpler and of lower cost, when compared with the conventional tunable FP optical filter. This kind of filter can be fully integrated with the polymeric substrate of the microfluidic element, allowing a Lab-on-a-Chip suitable for low-cost disposable point-of-care diagnosis. This idea leads to integrated monolithic optical filters that can be attached to the substrate of the microfluidic chip or even to the photode-

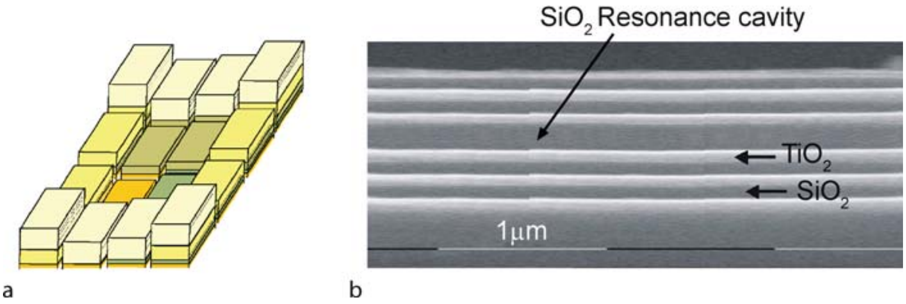

Lab-on-a-Chip Devices for Chemical Analysis, Figure 3 (**a**) Layout of the resonance cavity for an array of 16 FP optical filters; (**b**) scanning electron microscopy image showing the cross-section of one of the FP optical filters

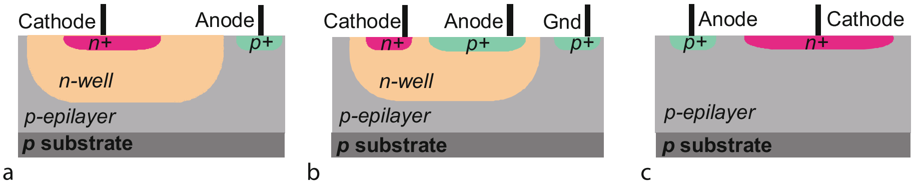

Lab-on-a-Chip Devices for Chemical Analysis, Figure 4 The three junction photodiodes in a standard *n-well* CMOS process: (**a**) *n-well/p-epilayer*; (**b**) *p+/n-well*; (**c**) *n+/p-epilayer*

L

tectors, when organic photodetectors are used. For example, a structured dye-doped polydimethylsiloxane (PDMS) layer can serve concurrently as a microfluidic network and optical filter.

Integrated Detectors

Generally, silicon and other semiconductor materials exhibit active optical properties, such as the ability to absorb and emit light. In a standard *n-well* CMOS process, three photosensitive structures are possible as vertical junction photodiodes: *n-well/p-epilayer*, *p+/n-well* and *n+/p-epilayer*, formed by doping the silicon substrate (see Fig. 4). These structures operate by converting absorbed photons directly into electronic carriers which are ultimately detected. At a particular wavelength, their ▶ quantum efficiency varies according to their junction depth. The quantum efficiency of a photodiode reveals how well it collects the incident light. In the visible spectrum, blue light (of about 450 nm) is more efficiently collected by a shallower junction (*p+/n-well* and *n+/p-epilayer*) and red light (of about 650 nm) by a deeper junction (*n-well/p-epilayer*). Moreover, despite the shallower junction of the *n+/p-epilayer* photodiode, it has the higher quantum efficiency at wavelengths of about 500 nm, due to the different doping concentration between the n- and the p-side, which extends the p-side depletion area more deeply. Since technology rules from the CMOS process should be met, the design of the optical path is restricted to combinations of the three dielectric layers available on top of the pn junction. The second oxide layer and the silicon nitride layer were removed (without affecting the CMOS process) to eliminate the wavelength dependence of the transmission through these layers. The first oxide layer should remain to protect the photodiode active area. In addition, removal of the first oxide layer would introduce random surface roughness, which introduces wavelength dependence that would adversely affect the optical performance. CMOS photodetectors have the advantage of being generic, favoring the integration of multiple electronics functions with a high yield and the CMOS process is, currently, the cheapest of the competing technologies.

An alternative approach to silicon photodiodes is the use of organic photodiodes [10]. They can be realized on different substrate materials, such as glass, plastic foil, ceramics silicon or even paper. However, plastic-based organic photodiodes are mechanically flexible, very thin, of low weight and may be fabricated at low temperature using simple layer-by-layer deposition procedures. Unlike silicon-based photodiodes, their size is not limited by the size of a silicon wafer. Organic photodiodes comprise one or more layer of organic semiconducting material sandwiched between two electrodes (the same structure as for OLEDs). They generate a measurable current under illumination. The photovoltaic effect in organic photodiodes is based on the formation of electron–hole pairs (excitation) and subsequent dissociation and charge collection at the electrodes. While photoinduced charge generation is enhanced by large interfaces between electron donor and acceptor materials, good connectivity to

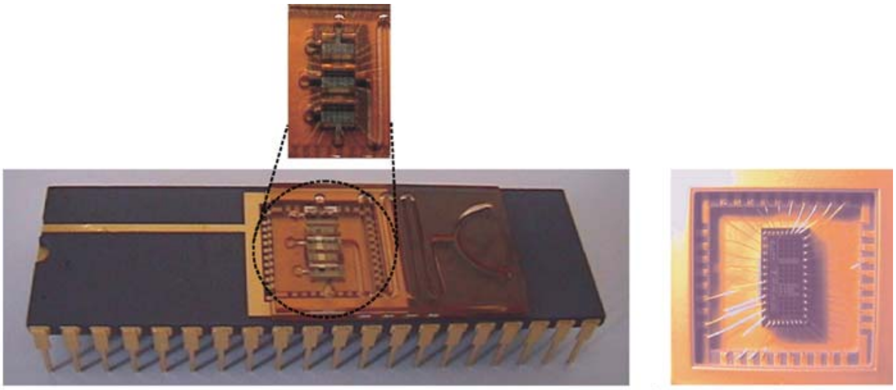

a b

Lab-on-a-Chip Devices for Chemical Analysis, Figure 5 Photograph of a Lab-on-a-Chip: (**a**) zoom of the detection chambers and (**b**) zoom of the CMOS chip. The CMOS chip includes FP optical filters, photodetectors and readout electronics. Each detection chambers is 2 mm wide, 3 mm long and 500 μm deep (this depth is crucial for optical absorption measurements). The main channel is 500 μm wide, 70 mm long and 500 μm deep, with a liquid volume quantity of 20 μl. This volume is fitted for any untrained person to inject with an appropriate syringe

the collection electrodes must also be ensured [10]. Once organic photodiodes are fully compatible with plastic substrates, they can be easily integrated on the microchannel substrate resulting in a fully integrated Lab-on-a-Chip device. Nowadays plastic-based fluidic microchannels are the most used. For example PDMS has good biocompatibility and optical transparency over the visible range and allows for rapid molding-based prototyping and scalable manufacturing at low cost and with high reliability. The combination of PDMS microfluidic chips with organic photodiodes offers an attractive route to fabricating low-cost diagnostic devices, which incorporate the fluidic channels, the detectors and even OLEDs into a single monolithic package. Such devices, when used in combination with integrated filters reported above, may offer a means of creating completely monolithic ultra-low-cost microfluidic devices suitable for use in disposable point-of-care diagnostics [13].

Waveguides

Fundamental premises for the use of fiber optic technology are the possibility of confining and propagating the light along specific pathways for transporting it from one location to another with as little loss as possible. The integration of waveguiding structures in planar chips has attracted interest for achieving optical components of greater robustness and minimal cost. Waveguiding structures have been previously fabricated in silicon substrates by oxide deposition, ion-exchange and anisotropic etching. However, their fabrication using polymers such as SU-8 and PDMS have grown in popularity, due to the low cost of these materials and the rapid fabrication processes based upon them. Combination of such structures with liquid guiding microchannels has been reported [14, 15]. For example, waveguiding channels can be integrated into the walls of a channel in order to launch light across it for being collected on the other side [14].

Key Research Findings

Lab-on-a-Chip Devices for Chemical Analysis Based on Absorbance Detection

A Lab-on-a-Chip for point-of-care routine analysis of urine is presented in Fig. 5. It measures the concentration of 16 different chemical parameters in urine by optical absorption. Usually, urine analyses in conventional clinical laboratories are performed by absorbance.

It includes an array of highly selective optical filters, based on FP thin-film optical resonators that are integrated on top of silicon CMOS photodetectors. Integrated CMOS readout electronics are also included for data acquisition. This scheme avoids the use of a dedicated light source allowing a regular white light illumination for the absorbance measurements. The microfluidic channels and detection chambers are fabricated using a layer of ►photoresist SU-8 deposited on a glass substrate. This epoxy-based material provides low sidewall roughness and a deep rectangular vertical profile of the microchannels, which is suitable for optical absorption measurements (the Lambert–Beer law can be directly applied). Moreover, it also provides a low-cost fabrication process, UV lithography semiconductor compatibility and does not require expensive masks. Therefore, the microfluidic die can be a disposable die avoiding contaminations between analyses, a requirement that should be fulfilled in point-of-care systems for

Lab-on-a-Chip Devices for Chemical Analysis, Table 1 Result of linear fit from absorbance measurements using white light as light source (a 200 W halogen lamp)

Analyte (measured conc. range (mg/dl))	$\lambda_{(abs\ max)}$ (nm)	Linear conc. range (mg/dl)	Slope (a.u.) (dl/mg)	Intercept (a.u.)	Correlation coefficient (R^2)	Reproducibility of 10 assays (%)
Uric acid (0 – 120)	495	0 – 30	$(1.9 \pm 0.4) \times 10^{-3}$	$(3 \pm 2) \times 10^{-3}$	0.9802	10
Total protein (0 – 100)	592	0 – 100	$(1.9 \pm 0.2) \times 10^{-4}$	$(-0.5 \pm 2) \times 10^{-4}$	0.9966	10
Glucose (0 – 400)	512	0 – 400	$(2.0 \pm 0.05) \times 10^{-4}$	$(1.5 \pm 0.8) \times 10^{-3}$	0.9957	10
Calcium (0.5 – 30)	575	0.5 – 15	$(2.5 \pm 0.1) \times 10^{-3}$	$(2.4 \pm 1.0) \times 10^{-3}$	0.9898	15
Chloride (1 – 400)	488	1 – 200	$(2.0 \pm 0.1) \times 10^{-4}$	$(2.3 \pm 1.5) \times 10^{-3}$	0.9902	10
Creatinine (0.25 – 4)	528	0.25 – 2	$(1.2 \pm 0.2) \times 10^{-2}$	$(7.3 \pm 2.1) \times 10^{-3}$	0.9742	20

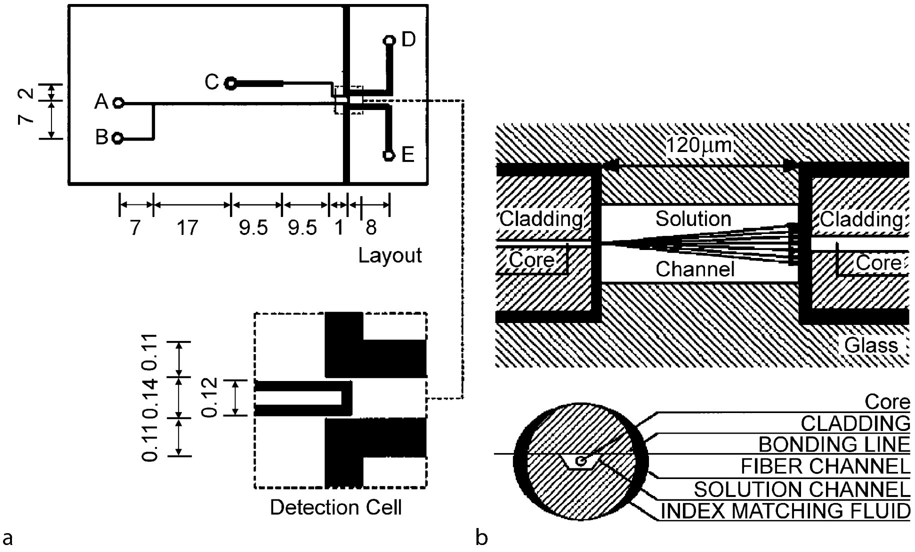

Lab-on-a-Chip Devices for Chemical Analysis, Figure 6 Geometric layout of channels etched with glass plate. (**a**) Reservoirs A, B and C are connected to the electrophoresis injector and the separation capillaries, which form the U-shaped cell with a 100 – 140 μm longitudinal pathlength. Reservoirs D and E are connected to channels into which optical fibers are inserted to launch and collect light. The dimensions are in millimeters. (**b**) Collection fibers around the U-cell of the flow channels. Flow channels are etched only into the bottom plate, and a top plate is thermally bonded. The center of the channel for the optical fiber is offset from the plane of the glass–glass bond, so that the light path is aligned with the center of the separation channel. (Reprinted with permission from [16])

use by any untrained person. The chosen structure of the channels, in conjunction with the sample and reagent fluid properties, allows a complete and homogeneous mixing of the reagent with the sample, driven only by diffusion (no external devices for pumping are needed). The combination of the integrated optical detection scheme and the low cost fabrication of the SU-8 microfluidic structure offers unique opportunities for spectrophotometric analysis in clinical diagnostics, in addition to the general advantages of Lab-on-a-Chip units concerning small sample volume. Moreover, the device can be broadly applicable and a powerful tool in hospitals, operating rooms, doctors' offices, clinical laboratories as well as in patient homes, e. g., a point-of-care device. The results obtained using this Lab-on-a-Chip (see Table 1) agree with macroscopic measurements performed with well-known standards and using state-of-the-art laboratory equipment. The features such as performance, precision, reliability and sensibility of the analysis were the same from the ones obtained in clinical analysis laboratories.

Increasing the Optical Pathlength

In applications where the liquid volume is very small, such as CE, absorbance detection is difficult because of the reduced optical pathlength. Using micromachining techniques, an easy route to small-volume, long-pathlength detector cells can be offered. Liang et al. [16] showed how to increase the optical pathlength without increasing the sample volume. They included optical fibers fit-

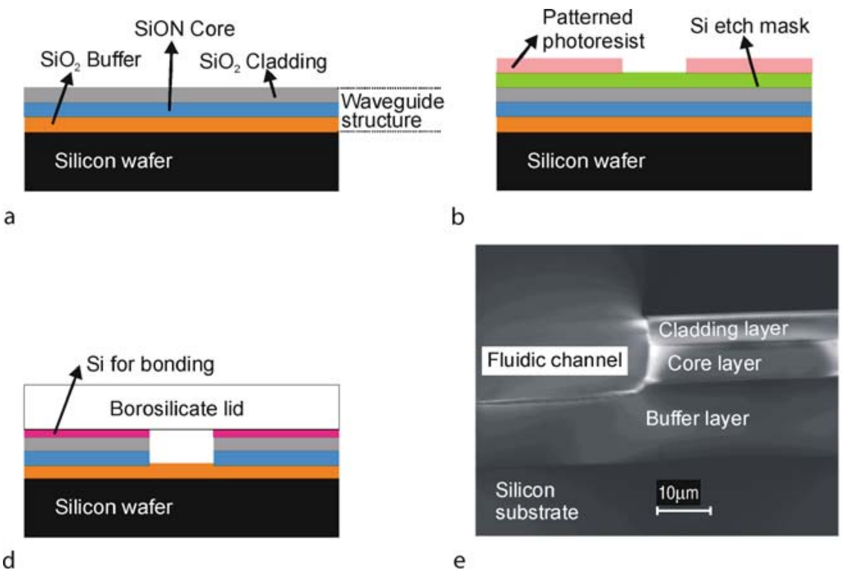

Lab-on-a-Chip Devices for Chemical Analysis, Figure 7 Process flow for the fabrication of integrated waveguides: (**a**) silicon substrate with a three-layered waveguiding structure; (**b**) mask for forming the (**c**) microfluidic channel in the waveguiding layer; (**d**) bonding of a glass lid; (**e**) photograph of the device before bonding of the lid. Reprinted with permission from [14]

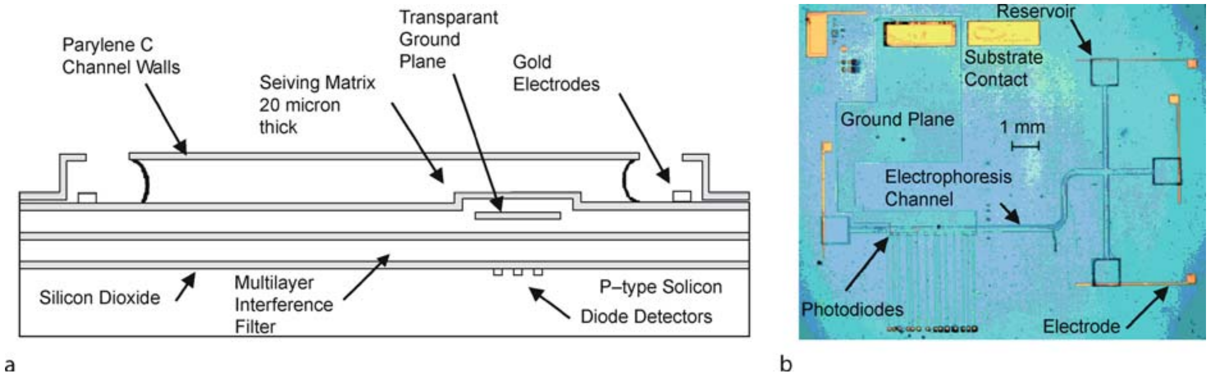

Lab-on-a-Chip Devices for Chemical Analysis, Figure 8 (**a**) Cross-sectional layout of an electrophoresis device; (**b**) photograph of the integrated electrophoresis device. (Reprinted with permission from [8])

ted into two etched channels and placed at the end of the detection channel (Fig. 6). However, the finite dimensions of the optical fibers (usually > 100 μm in diameter) limit their use for detection at multiple, closely spaced points along a channel. Additional freedom can be provided in many cases by the integration of waveguide structures directly into the microfluidic devices. For example, deep grooves can be fabricated in the microfluidic device into which fused silica capillary can be placed, forming buried waveguides. Light could be coupled to the waveguides via optical fibers, which were in turn fixed in the chip by connectors formed in its substrate. Mogensen et al. [14] extended this concept further to integration of waveguiding and microfluidic channels together in the same device (Fig. 7).

That example demonstrates the benefits of using MEMS technologies for absorbance detection in microfluidic devices, especially in terms of improving sensitivity by increasing the optical pathlength. However, Mogensen et al. [17] and Liang et al. [16] point out that this sensitivity is often achieved at the cost of lower transmitted optical power, which at some point will begin to reduce the SNR. Mogensen et al. [17] proposed the inclusion of focusing and reflecting elements in its device that could alleviate this problem somewhat. The use of the longitudinal direction of a flow channel, in which mirrors above and bellow of the channel have been patterned, is another possibility for increasing the optical pathlength. Light can be introduced in such a way that it will encounter the channel walls several times and will be reflected as it propagates

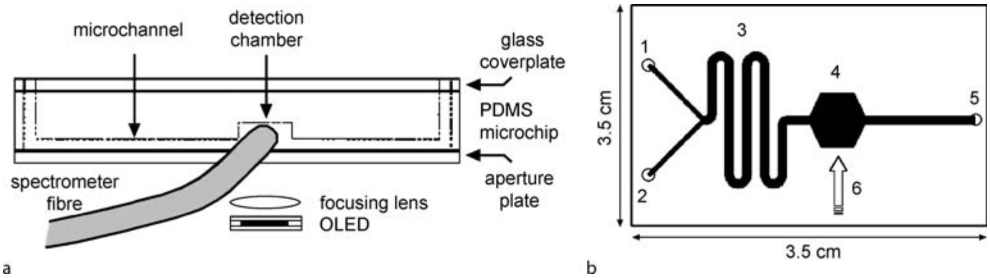

Lab-on-a-Chip Devices for Chemical Analysis, Figure 9 (**a**) Schematic of experimental setup and (**b**) microchip layout. The device comprises two inlets, a meandering mixing channel, a detection chamber and an outlet. The inlets are 400 μm wide, 800 μm deep and 10 mm long, while the mixing channel is 800 μm wide, 800 μm deep and 520 mm long. The extended detection chamber is 5 mm long, 5 mm wide and 1.6 mm deep, with a volume of 27 μl. (Reprinted with permission from [9])

down the channel. This can be still more advantageous, as the effective optical pathlength of the channel is increased beyond the actual length of the channel. In this scheme, source and detection will be positioned on opposite sides of the flow channel and absorbance can thus be measured in the direction of the flow.

Lab-on-a-Chip Devices for Chemical Analysis Based on Fluorescence Detection

LIF is, at present, the most widely used detection technique for fluorescence detection in CE Lab-on-a-Chip devices, because of its high sensitivity. Kamei et al. [18] proposed a hydrogenated amorphous silicon (a-Si : H) pin photodiode used as the fluorescence sensor for detecting fluorescein in a CE device for DNA analysis. The a-Si : H is a suitable material for fabricating integrated fluorescence sensors on glass and plastic because of its compatibility, low dark current and low manufacturing cost. More important, the enhanced optical absorption of a-Si : H in the visible range matches perfectly with the fluorescence bands of most practical labeling dyes used in molecular biochemistry (except green fluorescence). The hybrid integrated sensor comprises a fluorescence collecting lens, a multilayer optical interference filter with a pinhole and a ring-shaped a-Si:H pin photodiode. The fluorescence measurements are performed using vertical laser excitation. Using this integrated device, the limit of detection achieved for fluorescein in a 50 μm deep channel was 17 nM with a SNR = 3. From the viewpoint of laser integration, an important aspect of this device is vertical laser excitation through the detector. When combined with vertical cavity surface emitting laser diodes, this integrated a-Si:H sensor should facilitate the construction of a coaxial excitation–detection module for low-cost portable microfluidic bioanalyzers.

Another example of a monolithic CE device with integrated on-chip fluorescence detection has been reported by Webster et al. [8]. The device incorporates a silicon photodiode, an optical interference filter that prevents excitation light from inhibiting the fluorescence detection and a thin-film plastic (parylene) electrophoresis channel above (Fig. 8). Chemical isolation to prevent ions in the separation solution from reaching the ion-sensitive silicon detectors below is provided by a 5 μm thick lower wall of the electrophoresis channel. A transparent aluminum zinc oxide conducting ground plane is also used to prevent the high electric fields, needed for the separation, from interfering with the photodiode response. The performance of the device was demonstrated in the separations of DNA restriction fragments. The achieved detection limits were of the order of femtograms.

Waveguides have also been integrated into microchannel devices for fluorescence detection. Silica on silicon chip technology was commonly used to form the heart of a fiber for fluorescence measurements.

Human microalbuminuria typically relies on fluorescence detection due to the very low concentrations that must be detected. Hofmann et al. [9] reported the use of a thin-film OLED as an excitation source for microscale fluorescence detection. The OLED has a peak emission wavelength of 540 nm with a FWHM that overlaps with the absorbance spectrum of the microalbuminuria complex reagent assay. Fluorescent at 620 nm is emitted by the reaction when excited by the OLED. Concentrations down to 10 mg/l were measured with a linear range from 10 to 100 mg/l and without the need of a filter between the excitation light and the generated fluorescent light. Orthogonal detection geometry, implemented using a microfluidic layer with optical grade side surface, avoided the use of such a filter (Fig. 9). The concentration range measured and its sensitivity comprise the required range for human microalbuminuria detection.

In this approach the detection architecture was not fully integrated on-chip. However, recently the same group reported a monolithically integrated optical longpass filter for use in microchip fluorescence detection [13]. The inte-

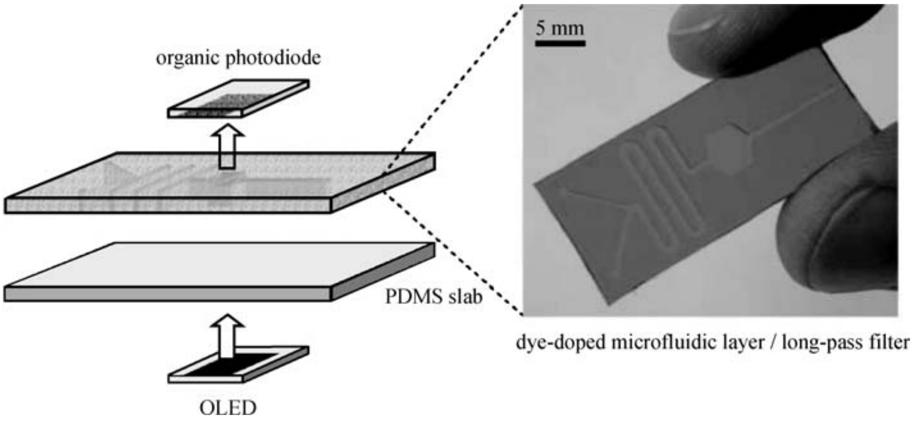

Lab-on-a-Chip Devices for Chemical Analysis, Figure 10 Schematic of a monolithically integrated optical longpass filter. The structured dye-doped PDMS layer is able to serve concurrently as the microchannel medium and optical filter, negating the need for an additional filter layer, and allowing for improved collection of the fluorescence signal, since the detector can be placed in closer proximity to the channel. The enclosed microchannels are obtained by sealing the doped layer against a second nondoped PDMS slab. For a collinear detection geometry the excitation source and detector are positioned below and above the assembled microchip. The photograph shows a Sudan II-doped PDMS filter with 800 μm wide and 800 μm deep microchannels. (Reprinted with permission from [13])

grated filters are monolithically attached to the substrate of the microfluidic chip. They were prepared by incorporating dye molecules into a PDMS microfluidic chip substrate, allowing for the fabrication of colored substrates that serve concurrently as channel medium and optical filter (see Fig. 10). The filter features 0.01% transmittance below 500 nm, more than 80% transmittance above 570 nm and negligible autofluorescence. These kinds of filters integrated with OLEDs and organic photodiodes offer a means of creating a completely integrated monolithic Lab-on-a-Chip fabricated at low cost, compared to fully integrated filters for silicon based devices, which is suitable for disposable point-of-care diagnosis.

Yin et al. [15] described a fully integrated SU-8 microfluidic chip for detection, manipulation and analysis of bioparticles (Fig. 11). It integrates liquid-core optical waveguides with fluidic reservoirs and solid-core antiresonant reflecting optical waveguides to define sub-picoliter excitation volumes and transport and collect light on the chip, resulting in fully planar beam geometries. The liquid-core optical waveguides guide both light and fluids in the same volume. The photograph of Fig. 11c visualizes the propagation of a light beam across a SU-8 microfluidic channel filled with solution containing a fluorescent die [15].

Lab-on-a-Chip Devices for Chemical Analysis Based on Chemiluminescence Detection

A fully integrated Lab-on-a-Chip device for chemiluminescence was proposed by Jorgensen et al. [19]. This device takes advantage of both semiconductor properties and the advanced micromachining possibilities of silicon. It integrates a backside silicon photodiode with a microfluidic channel network on the front side of the same silicon substrate wafer. The Lab-on-a-Chip has all fluidic and electrical connections on one side of the chip. The channel networks were sealed using anodic bonding (glass to silicon) on the front side of the silicon wafer. The chip size is 10 mm wide and 20 mm long. The sample and reagent channels have a meandering layout and they meet in a laminar mixer. The device performance was demonstrated in chemiluminescence-based detection of hydrogen peroxidase and luminol.

Thin-film organic photodiodes as integrated photodetectors for microscale chemiluminescence assays were reported by Hofmann et al. [10]. The organic photodiodes are based on vacuum-deposited bilayers of copper phthlocyanine (CuPc) and fullrene (C_{60}) to detect the emission signal from peroxyoxalate chemiluminescence reactions. The organic photodiodes have an external quantum efficiency of approximately 30%, an active area of 16 mm^2 (large when compared with the 2 mm^2 area of the detection zone) and a total thickness around 2 mm. For applied flow rates of 25 μl/min a chemiluminescence signal of 8.8 nA within 11 min was obtained as well as a background signal of 1 nA (high value due to the mismatch between the photodiode area and the detection zone area). Preliminary quantization of hydrogen yielded a detection limit of approximately 1 mM, which is high compared to the 10 μM reported by Jorgensen et al. with inorganic devices [19].

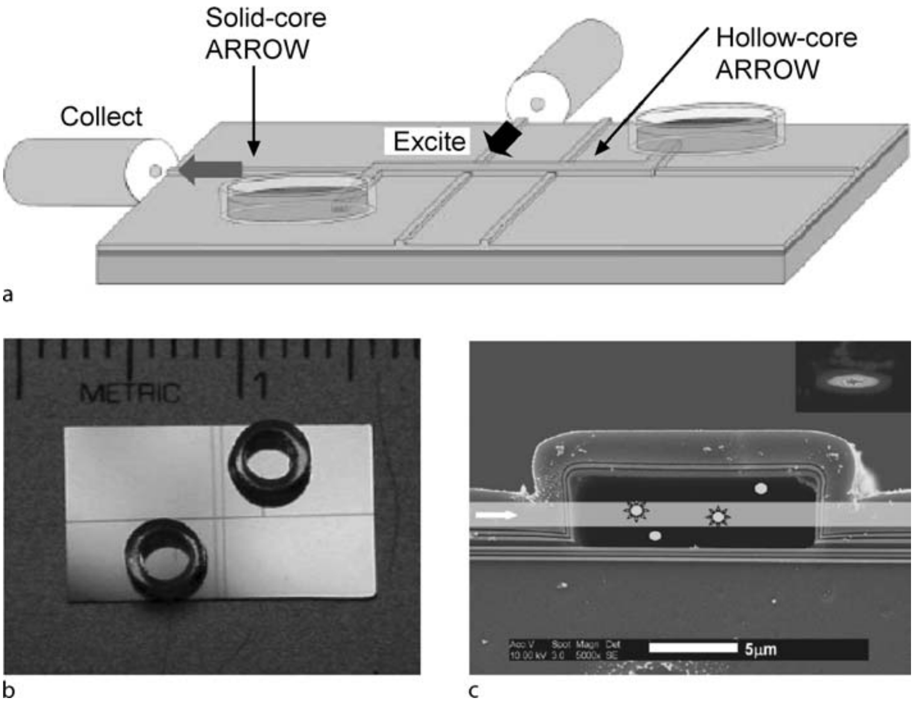

Lab-on-a-Chip Devices for Chemical Analysis, Figure 11 Planar optofluidic chip: (**a**) schematic of integrated optofluidic chip showing hollow- and solid-core waveguides; (**b**) photograph of the finished chip; (**c**) photograph showing schematically the excitation beam traversing the microchannel (as indicated by the arrow) and fluorescing particles that may diffuse in and out of the excitation volume. (Reprinted with permission from [15])

That detection limit was recently improved by Wang et al. [20]. The authors replaced the 16 mm^2 vacuum-deposited CuPc-C_{60} bilayer devices by 1 mm^2 solution-processed polymer devices based on a 1 : 1 blend by weight of the conjugated polymer poly(3-hexylthiophene) (P3HT) and 6,6-phenyl-C_{61}-butyric acid methyl ester (PCBM), a soluble derivative of C_{60}. The device has an active area of 1 mm^2 and an external quantum efficiency of more than 50% between 450 and 550 nm (Fig. 12). The device area is well matched with the detection zone area of the microfluidic chip, which results in a minimized background signal (225 pA). The achieved detection limit for detecting the emission signal from peroxyoxalate chemiluminescence reactions was 10 μM. The photodiodes have a simple layered structure that permits easy integration with planar chip-based systems. The authors are investigating the use of integrated electronics for readout and display of the photodiode current, in order to obtain a completely integrated Lab-on-a-Chip for disposable point-of-care diagnosis.

Future Directions for Research

Much of the investigation performed of Lab-on-a-Chip devices for chemical analysis is driven by the promise of cheap and disposable devices. The fact that many of the devices presented above require additional processing in a cleanroom makes them unattractive for applications requiring inexpensive solutions, once the cost reduction in silicon micromachining is not possible (no potential in downscaling of the footprint). That is why many Lab-on-a-Chip approaches have lost focus on the total analysis in favor of single operations, such as separation and detection. However, the growing knowledge based on the replication of devices in plastics will help to change this. Microfabrication technologies for polymers like injection molding or hot embossing are probably the most promising alternatives, as it becomes possible to form both microoptical and microfluidic elements in single devices by these processes. For more demanding applications in which the optical signal is weak, some increase in complexity is inevitable. The challenge for the next generation of cheap and disposable Lab-on-a-Chip devices for chemical analysis by spectrophotometry is improving the sensitivity, so that these devices can accomplish low-light tasks. This implies that there still needs to be substantial improvement in filter performance and in the efficiency of detectors in collecting the light for the promise of having truly implemented Lab-on-a-Chip platforms for chemical analysis by spectrophotometry that can outperform the

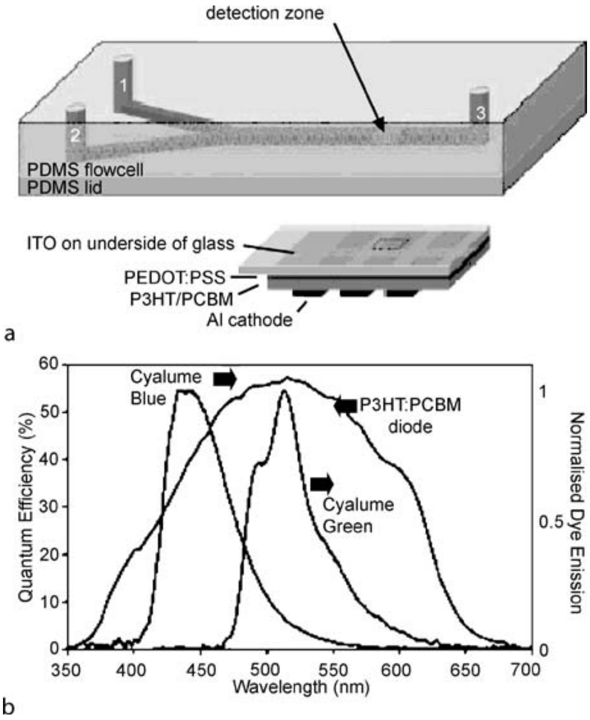

Lab-on-a-Chip Devices for Chemical Analysis, Figure 12 (**a**) Microchip layout. The inlets are 400 μm wide, 800 μm deep and 10 mm long. The mixing channel is 800 μm wide, 800 μm deep and 520 mm long. The active area of the photodiode used for chemiluminescence detection is 1×1 mm^2. The photodiode is located at a position 10 mm downstream from the point of confluence of the two inlet streams. (**b**) Quantum efficiency spectrum of the organic photodiode and the normalized emission spectra for the two chemiluminescent dyes used in the work (cyalume blue and cyalume green). The emission spectra of both dyes overlap the spectral response of the photodiode. (Reprinted with permission from [20])

standard macroscale technologies. Maybe it will not be too long until we will all be able to have our own Lab-on-a-Chip at home: you feel sick one day and maybe you can know what is wrong by simply loading urine or saliva into a Lab-on-a-Chip device.

Cross References

- ► Electrochemical Techniques
- ► Electrophoresis
- ► Finite Volume and Finite Difference Methods for Modeling and Simulation
- ► Fluorescence Measurements
- ► Lab-on-a-Chip (General Philosophy)
- ► Microfabrication Techniques
- ► Microfluidic Mixing
- ► Photolithography
- ► Photoresist Reflow
- ► Sputtering for Film Deposition
- ► Wafer Bonding

References

1. Manz A, Graber N, Widmer HM (1990) Miniaturized total chemical systems: a novel concept for chemical sensing. Sens Actuators B 1:244–248
2. Bengtsson M, Laurell T (2004) Ultrasonic agitation in microchannels. Anal Bioanal Chem 378(7):1716–1721
3. Skoog DA, West DM, Holler FJ (1996) Fundamentals of analytical chemistry. Saunders College Publishing, Orlando
4. Jakeway SC, de Mello AJ, Russel EL (2000) Miniaturized total analysis systems for biological analysis. Fresenius J Anal Chem 366:525–539
5. Hisamoto H, Yasuoka M, Terabe S (2006) Integration of multiple-ion-sensing on a capillary-assembled microchip. Anal Chim Acta 556:164–470
6. Belin GK, Krähenbühl S, Hauser PC (2007) Direct determination of valproic acid in biological fluids by capillary electrophoresis with contactless conductivity detection. J Chromatogr B 847:205–209
7. Wang L, Morris ME, (2005) Liquid chromatography–tandem mass spectroscopy assay for quercetin and conjugated quercetin metabolites in human plasma and urine. J Chromatogr B, 821:194–201
8. Webster JR, Burns MA, Burke DT, Mastrangelo CH (2001) Monolithic Capillary Electrophoresis Device with Integrated Fluorescence Detector. Anal Chem 73:1622–1626
9. Hofmann O et al (2005) Towards microalbuminuria determination on a disposable diagnostic microchip with integrated fluorescence detection based on thin-film organic light emitting diodes. Lab Chip 5:863–868
10. Hofman O et al (2005) Thin-film organic photodiodes as integrated detectors for microscale chemiluminescence assays. Sens Actuators B 106:878–884
11. Minas G, Ribeiro JC, Martins JS, Wolffenbuttel RF, Correia JH (2004) An array of Fabry-Perot optical-channels for biological fluids analysis. Sens Actuators A 115:362–367
12. Minas G, Wolffenbuttel RF, Correia JH (2006) An array of highly selective Fabry-Perot optical channels for biological fluid analysis by optical absorption using a white light source for illumination. J Opt A: Pure Appl Opt 8:272–278
13. Hofmann O et al (2006) Monolithically integrated dye-doped PDMS long-pass filters for disposable on-chip fluorescence detection. Lab Chip 6:981–987
14. Mogensen KB, Petersen NJ, Hübner J, Kutter JP (2001) Monolithic integration of optical waveguides for absorbance detection in microfabricated electrophoresis devices. Electrophoresis, 22:3930–3938
15. Yin D et al (2007) Planar optofluidic chip for single particle detection, manipulation, and analysis. Lab Chip 7:1171–1175
16. Liang Z et al (1996) Microfabrication of a planar absorbance and fluorescence cell for integrated capillary electrophoresis devices. Anal Chem 68:1040–1046
17. Mogensen KB, El-Ali J, Wolff A, Kutter JP (2003) Integration of polymer waveguides for optical detection in microfabricated chemical analysis systems. Appl Opt 42:4072–4079
18. Kamei T et al (2004) Fusion of a-Si : H sensor technology with microfluidic bioanalytical devices. J Non-Cryst Solid 338–340:715–719

19. Jorgensen AM, Mogensen KB, Kutter JP, Geschke O (2003) A biochemical microdevice with an integrated chemiluminescence detector. Sens Actuators B 90:15–21
20. Wang X et al (2007) Integrated thin-film polymer/fullerene photodetectors for on-chip microfluidic chemiluminescence detection. Lab Chip 7:58–63

Lab-on-Chip Devices for Immunoassays

Dharmalingam Sugumar[1], Lingxue Kong[2]
[1] Faculty of Manufacturing Engineering, Technical University Malaysia Malacca, Malacca, Malaysia
[2] Center for Material and Fiber Innovation, Deakin University, Geelong, VIC, Australia
sugumar@utem.edu.my, lingxue.kong@deakin.edu.au

Synonyms

Immunodiffusion; Immunochemistry

Definition

An immunoassay is a biochemical test that measures the level of a substance in a biological liquid, using the reaction of an ►antibody or antibodies to its ►antigen. The assay takes advantage of the specific binding of an antibody to its antigen. ►Monoclonal antibodies are often used as they only usually bind to one site of a particular molecule, and therefore provide a more specific and accurate test, which is less easily confused by the presence of other molecules. The antibodies picked must have a high affinity for the antigen.

Overview

Microfluidic devices have been one of the earliest success stories in the commercialization of microelectromechanical systems (MEMS). Efforts to dispense minute amounts of liquid at high precision date back to the early 1950s and constitute the basics of modern inkjet technology. When MEMS were still chiefly an academic topic in the 1980s, microfluidic research outside the inkjet world focused on the miniaturization of conventional components like pumps and valves. Later, design paradigms began to shift. Novel operating principles based on genuine microfluidic effects emerged which could not be realized by simply downscaling traditional solutions.

The heart of a microfluidic device is often a microchannel, in which reaction, separation or detection takes place. The flow of liquids in microchannels is laminar, and therefore mixing at the micrometer scale is difficult to achieve. The large surface to volume ratio of microchannels can make interfacial reactions efficient. Microfluidic devices sometimes comprise a complex mix of elements and functionalities, making them efficient for tasks as elementary as metering liquids as well as for processing and analyzing complex biological samples. It can be as simple as glass capillary tubes or as complex as microchips having micropumps, sensors and electronic circuitry to move liquids.

Immunoassays are analytical experiments in which identification and quantification of target molecules are done by using highly specific antibodies. Antibody-based immunoassays are the most commonly used technique to identify different types of analytes such as proteins, peptides and low molecular weight molecules. This technique has been used in hospitals, laboratories and industries for the last few decades to detect antibody–antigen in samples.

Basic Methodology

Immunoassays are analytical experiments in which antibodies are used for detection and quantification of target molecules. Immunoassays have been used in the medical field, life sciences, prognostics and diagnostics, environmental control and pharmaceutical and biotechnology industries for the past 40 years. The method has been reliable in detecting the presence and the amount of antibody and antigen in a sample. Conventional immunoassays are a time-consuming process which requires several steps such as reagent addition and washing. Some of the common immunoassay methods include radio immunoassays, enzyme linked immunosorbent assays (ELISA), enzyme immunoassays (EIA) and fluorescent immunoassays (FIA).

Antibodies are the key element in an immunoassay method. Typically, there are two types of antibodies: monoclonal and ►polyclonal. Monoclonal antibodies are completely homogeneous with respect to antigen while polyclonal antibodies are heterogeneous and always a mixture of various antibodies.

Antibodies are proteins developed by animals to counteract the invasion of foreign molecules (antigens) into the body. Antibodies can be found in body fluid such as blood and tissue. The main function of antibodies is to bind to antigens to render them harmless to the body function. There are five main classes of antibodies: IgM, IgG, IgA, IgD and IgE. All antibodies have at least two antigen binding sites. IgM has ten potential binding sites, IgA has four binding sites while IgG has only two binding sites. Even though all antibodies are antigen specific, they do, however, cross react with other antigens that look similar to the one to which they are specific.

The binding of antibodies to antigen assays can be classified into three different categories: direct, competitive

and sandwich [1]. Direct assays are a simple procedure whereby excessive antibody is incubated with antigens. The sensitivity of this method is proportional to the amount of antibody present in the assay. The antibody is fixed to a substrate and a fixed amount of labeled antigen and varying amount of unlabeled antigen are introduced to the sample. Then the amount of bindings or antibody–antigen is measured [2]. In a *competitive* immunoassay, the antigen in the sample competes with the labeled antigen for a limited number of antibody binding sites. The bound antigen is separated from the excess antigen not bound to the antibody. The amount of antigen in the unknown sample is inversely proportional to the amount of labeled antigen, as measured in a gamma counter or spectrophotometer. Examples of competitive immunoassays are double antibody radioimmunoassays (RIAs), coated tube RIAs and coated well enzyme immunoassays (EIAs).

In non-competitive immunoassays, the antigen is a *sandwich* between two antibodies, the capture antibody and the detection antibody. Typically, the capture antibody is coated to a solid phase, such as a tube or a well, and the detection antibodies are labeled with either an isotope or an enzyme. The amount of antigen in an unknown sample of these immunoassays is directly proportional to the amount of labeled detection antibody measured by the detection system. Examples of non-competitive assays are IRMA and ELISA. Figure 1 illustrates different types of binding.

A number of methods are used for the detection of antibody–antigen bindings. The most common methods used are radioisotopes, fluorophores, color changing enzymes and metallic and magnetic beads. The advanced detection methods make use of ► chemiluminescent chemicals, and immunoblotting and signal amplification.

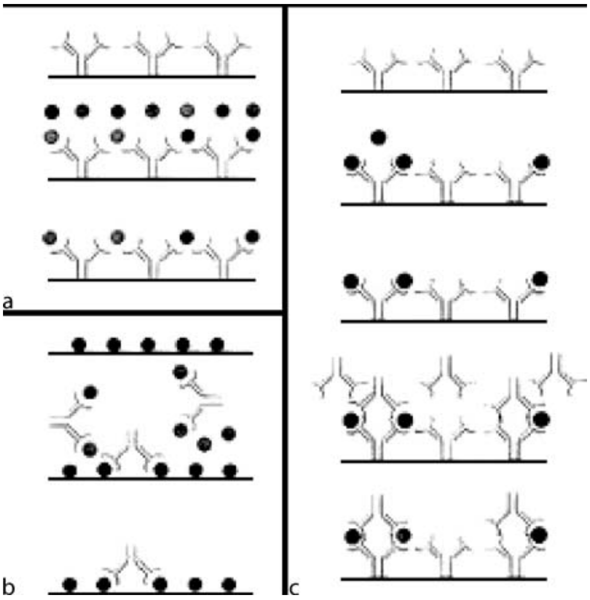

Lab-on-Chip Devices for Immunoassays, Figure 1 Different types of immunoassay binding: (**a**) direct; (**b**) competitive; (**c**) sandwich [2]

Key Research Findings

Fairly comprehensive research on immunoassays based on microfluidic technology has been made recently. Antibody microarrays are still in their infancy but rapidly growing. Microarrays are used in the detection of diseases, cancer research and drug discovery. Immunoassay microarrays consist of antibodies immobilized on a solid substrate. Immunoassay microarrays are fabricated by using antibody microspots on a solid substrate. Samples containing antigen are incubated on the microspots coated with capture antibodies. Unbound molecules are then washed away and labeled conjugate or detection antibodies are allowed to bind to the captured antigens on the microspots. The signals from the labeled conjugate antibodies which are bound to the captured antigens are then detected using scanners. Signal intensities are commensurate with the amount of captured analytes present in the sample. A significant amount of research has been conducted towards integrating microfluidic technologies with protein microarrays.

An important aspect of microarrays is the capability of detecting multiple analytes in a single sample for rapid analysis of sample fluids. A simultaneous detection of 24 cytokines with a very high sensitivity was reported by Huang et al. [3]. This method is comparable to the ELISA method in terms of specificity, detection limit and sensitivity using enhanced chemiluminescence (ECL). An improved fluorescence-based detection microarray system has also been developed using planar optical waveguide technology [4]. The capture antibodies are immobilized on the planar waveguide in a microarray format (Fig. 2). This method does not require the washing steps to remove the unbound antibodies. The antibody binding is detected using laser light to excite the surface-bound fluorophores.

Recent developments in bead-based immunoassays mean they have an edge over the normal fluidic systems. There are several main advantages of using microbeads [5]. The surface to volume ratio (SVR) is increased even in a microfluidic system. As a result, the sensitivity of the assays increases due to higher efficiency of interactions between the samples and reagents. Another advantage is that the beads can be easily transported in a fluidic system using pressure-driven or electric fields. The beads can also be modified by altering the surface properties which can provide multiple functionalities to a single microflu-

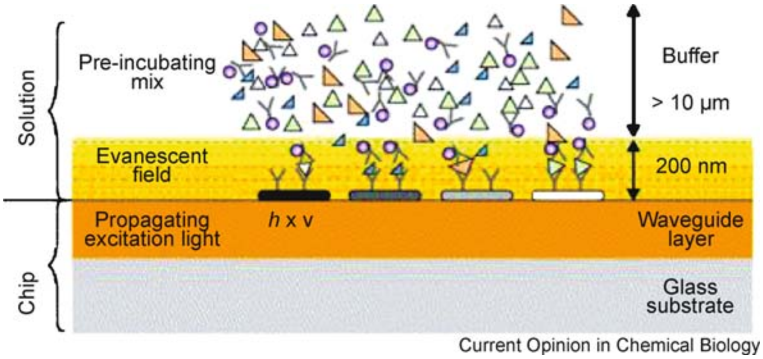

Lab-on-Chip Devices for Immunoassays, Figure 2 Immunoassay based on planar waveguide [4]

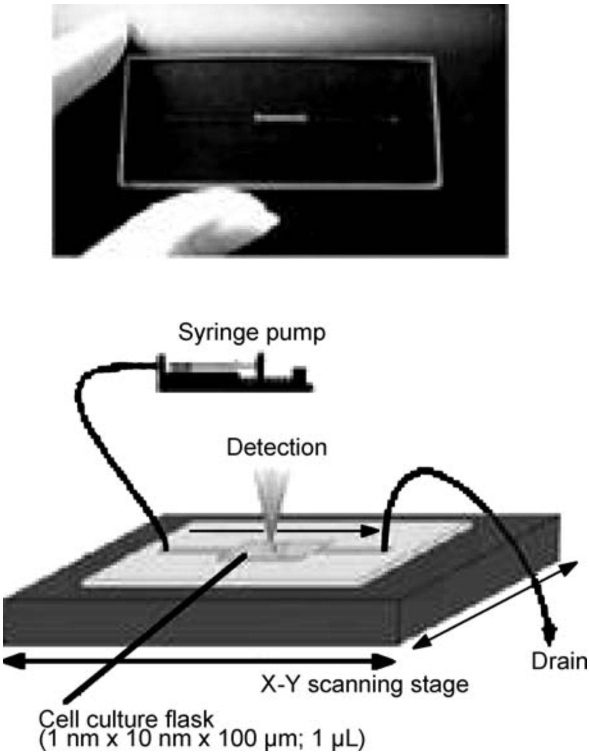

Lab-on-Chip Devices for Immunoassays, Figure 3 (**a**) Cell culture chip; (**b**) Single-cell imaging using thermal scanning lens [6]

idic device. A glass-based immunoassay microchip has been reported involving the integration of polystyrene beads with pre-coated anti-CEA antibody. This microfluidic system uses thermal lens microscopy as the detection method [6]. By using this device, reaction time was reduced to about 1% of that required for ELISA. The system has inlet holes and a reaction zone with a reservoir for the microbeads to be detected. A sensitivity of 1 ng/ml was achieved for the detection of peptide hormone concentration. Figure 3 shows the experimental setup for this method. The incorporation of luminescence-based tags into proteins as well as bead-based surface chemistries has resulted in new types of immunoassay systems. Bead-based detection systems use synthetic beads pre-coated with antibody to detect antigens in analytes. Bead-based immunoassays contain an immunosorptive area much larger than that of microarrays. Since the beads are exposed to the entire sample, reaction takes place in entire volume. Beads are easily manipulated, collected from the sample and immobilized for readout purposes. In multi-analyte-based reading, each bead is coated with a specific antibody or antigen. Colored beads are the most common method for this purpose. Choi et al. [7] reported a bead-based device consisting of an integrated bio-filter, an electrochemical immunosensor and a series of custom designed microvalves. The bio-filter is comprised of a planar electromagnet to capture magnetic beads carrying the target antigen.

More recently, multiple immunoassays in microfluidic chips have been developed. A compact disc-shaped microfluidic immunoassay device based on centrifugal force was explored [8]. The study examined the imprecision of assays carried out with 200 nl of samples. The study concluded that the day-to-day total imprecision of the immunoassays on the compact disc-shaped device is less than 20%. Another group successfully developed a method for a high-throughput multi-antigen microfluidic immunoassay system [9]. The system was able to perform up to five tests for each of ten samples with each sample consisting of 100 nl. A theoretical model was developed to understand the relative importance of various parameters affecting the immunoassay in a microfluidic device [10]. In this study, the effect of analyte transport, binding kinetics between analyte in a solution and a surface-immobilized antibody and the footprint of a capture antibody on the substrate for the assay was examined

theoretically. The model shows that assays can be greatly optimized by varying the flow velocity of the solution. The model also shows the degree of influence of the analyte–antibody binding constant and the surface density of the capture antibodies on the performance of the assay.

Future Directions for Research

The new Lab-on-Chip immunoassay devices form the basis of new and smaller analyzers and may ultimately be used in even smaller devices useful in decentralized testing. In contrast to previous analytical technologies, Lab-on-Chip devices offer an enlarged and unified menu of tests, which will have far-reaching effects on the future of central laboratories. The impact of Lab-on-Chip devices on life sciences could be significant via timely intervention and monitoring, combined with improved treatments. Empowerment of health consumers to perform self-testing is limited, but Lab-on-Chip devices could accelerate this process and so produce a level of self-awareness of biochemical and genetic information hitherto unimaginable. The next level of miniaturization is nanometer-sized features, and the technological foundation for these futuristic devices will be built on nanofluidics and self-assembled molecular structures.

Cross References

► Integrated Microdevices for Biological Applications
► Lab-on-Chip Devices for Protein Analysis

References

1. Vo-Dinh T, Sepaniak MJ, Griffin GD, Alarie JP (1993) Immunosensors: principles and applications. Immunomethods 3:85–92
2. Selvaganapathy PR, Carlen E, Mastrangelo C (2003) Recent Progress in Microfluidic Devices for Nucleic Acid and Antibody Assays. Proc IEEE 91(6):954–975
3. Huang RP, Huang R, Fan Y, Lin L (2001) Simultaneous Detection of Multiple Cytokines from Conditioned Media and Patient's Sera by an Antibody-Based Protein Array System. Anal Biochem 294(1):55–62
4. Joos TO, Stoll D, Templin MF (2002) Miniaturised multiplexed immunoassays. Curr Opin Chem Biol 6(1):76–80
5. Lim CT, Zhang Y (2007) Bead-based microfluidic immunoassays: The next generation. Biosens Bioelectron 22(7):1197–1204
6. Sato K, Tokeshi M, Odake T, Kimura H, Ooi T, Nakao M, Kitamori T (2000) Integration of an Immunosorbent Assay System: Analysis of Secretory Human Immunoglobulin A on Polystyrene Beads in a Microchip. Anal Chem 72(6):1144–1147
7. Jin-Woo Choi KWO, Thomas JH, Heineman WR, Halsall HB, Nevin JH, Helmicki AJ, Henderson HT, Ahn CH (2002) An integrated microfluidic biochemical detection system for protein analysis with magnetic bead-based sampling capabilities. Lab Chip 2:27–30
8. Honda N, Linberg U, Anderson P, Hoffman S, Takei H (2005) Simuttaneous multiple immunoassays in a compact disc shaped microfluidic device based on centrifugal force. Clin Chem 51(10):1955–1961
9. Kartalov EP, Zhong JF, Scherer A, Quake SR, Taylor CR, Anderson WF (2006) High throughput multi-antigen microfluidic fluorescence immunoassays. BioTechniques 40(1):85–90
10. Zimmerman M, Delamarche E, Wolf M, Hunziker P (2005) Modeling and optimization of high sentivity, low vol microfluidic based surface immunoassays. Biomed Microdevices 7(2):99–110

Lab-on-a-Chip Devices for Particle and Cell Separation

Sung Yang[1], Jeffrey D. Zahn[2]
[1] Department of Mechatronics, School of Information and Mechatronics, Gwangju Institute of Science and Technology (GIST), Gwangju, Republic of Korea
[2] Department of Biomedical Engineering, Rutgers University, Piscataway, NJ, USA
syang@gist.ac.kr, jdzahn@rci.rutgers.edu

Definition

Lab-on-a-Chip Devices for Particle and Cell Separation are used to either remove particles of interest, sort a mixed population of particles into subpopulations of like particles or concentrate (enrich) particles for downstream processing within microdevices. Methods for particle or cell separations exploit specific physical properties which include: fluorescence-based, magnetic-based, affinity-based, and cell density gradient-based separations depending on the properties of the particles of interest. Particle separation devices are often geared towards biomedical research and diagnostics particularly in blood cell separation and blood diagnostics.

Overview

The separation of a specific biological cell from an original mixed biological sample is an essential step for a variety of applications in biological research, biomedical diagnostics and treatment. In most cases, one specific cell type must be examined to quantify the population, obtain genetic material or assay for gene expression and protein synthesis. However, raw biological samples obtained from various sources, (e. g., blood, tissue, or primary cell culture), generally contain many different types of cells mixed together. To use these samples in diagnostics, a purified sample containing only the desired material must be separated before specific analysis assays can be conducted. Furthermore, the desired biological sample population must often be concentrated from the initial raw sample concentration to acquire a sufficient quantity of material for anal-

ysis. For instance, typically in clinical blood tests, several milliliters of whole blood are sampled from patients and then centrifuged in a density gradient in order to separate the appropriate blood components based on their density. Also, in order to conduct detailed investigations on blood related diseases, separation of a specific blood cell type is required such as the separation of lymphocytes from the mixture of erythrocytes, other leukocytes, and platelets in whole blood. In addition, rare cell separation from mixed cell populations is very important in biological research activities including stem cell biology studies. Currently, the conventional methods for particle or cell separations exploit specific cell properties and include fluorescence-based, magnetic-based, affinity-based, and cell density gradient-based separations depending on the properties of the cells of interest. In the *basic methodology* section, the conventional methods for particle or cell separation are briefly introduced. In the *key research findings* section, the latest Lab-on-a-Chip technologies for particle or cell separations are discussed.

Basic Methodology

Fluorescence-Based Cell Separation

Fluorescence-activated cell sorting (FACS) is a type of flow cytometer and one of the most common techniques used in investigation of cell populations because of its effective performance in discrimination and sorting of cells into their subpopulations. In general, a concentrated cell suspension is allowed to bind with a fluorescent antibody or fluorescent dye that reacts with a specific particle or molecule existing on or inside the target cells. The cell suspension is then mixed with a buffer (sheath) fluid and the cells are transported through the FACS system in a single-file format where they pass through the path of a laser and the fluorescent light emitted by each cell is measured. The light scattered by each cell is also measured at the same time which can be correlated with cell size and sphericity. Once properties of the cells are determined based on both fluorescence and light scattering, the fluid stream containing the cells is broken into single droplets containing only a single cell. During droplet formation, each droplet is given an electrical charge, which is proportional to the amount of fluorescence of the cell within the droplet. Each droplet is then separated in an electric field and collected. Ideally, after this separation step the dyed cells are collected in a single purified population. FACS scanners are also used to determine the relative population of different cells within a mixed population based upon multiple fluorescent labels with different emission spectra (e. g., green emission versus red emission) or scattering properties such as individual white blood cell populations (e. g., lymphocytes versus granulocytes versus monocytes) which can aid in the understanding of blood disorders such as leukemia.

Magnetic-Based Cell Separation

Magnetic-activated cell sorting (MACS) is an attractive method because the magnetic force can decouple the movement of the cell of interest from the rest of a cell population allowing them to be separated within a magnetic field. In many cases, micron or nanometer sized magnetic particles are used in MACS. These particles are usually conjugated with the appropriate antibodies to physically bind with antigens on the target cells. Once the magnetic particles bind with the target cells, they are attracted by a magnetic field gradient towards designated regions for downstream analysis, while the unwanted cells pass to a waste container. Magnetic separation is applicable to cells which can be separated by selective binding of the antibody bound magnetic particle to specific surface antigens.

Affinity-Based Cell Separation

The most conventionally used macroscale affinity-based cell separation system is cell affinity chromatography (CAC). These systems can provide relatively high purity ($> 95\%$) and high throughput ($10^8 - 10^9$ cells/h). CAC procedures can be divided into three consecutive steps: loading, washing, and elution. Affinity-based cell separation technologies are generally based on the immobilization of either antibodies or antigens on a substrate with selective binding and immobilization of the target cells, while unwanted cells pass through the device. After the target cells are captured, they are released and eluted by changing the buffer medium with the appropriate solutions.

Centrifugation-Based Cell Separation

The most common method for particle or cell separations is centrifugation-based separation. In biological or medical research labs, these particles are usually cells, organelles, or large molecules. When two particles in suspension differ in either mass or density, they will settle to the bottom of a centrifugation tube at different rates under centrifugation. There are two types of centrifugation: preparative and analytical centrifugation. In preparative centrifugation, the main purpose is to separate specific particles. In analytical centrifugation, the main purpose is to measure the physical properties of particles by measuring the sedimentation properties of the particles. In most cases, the centrifugation-based separation means the

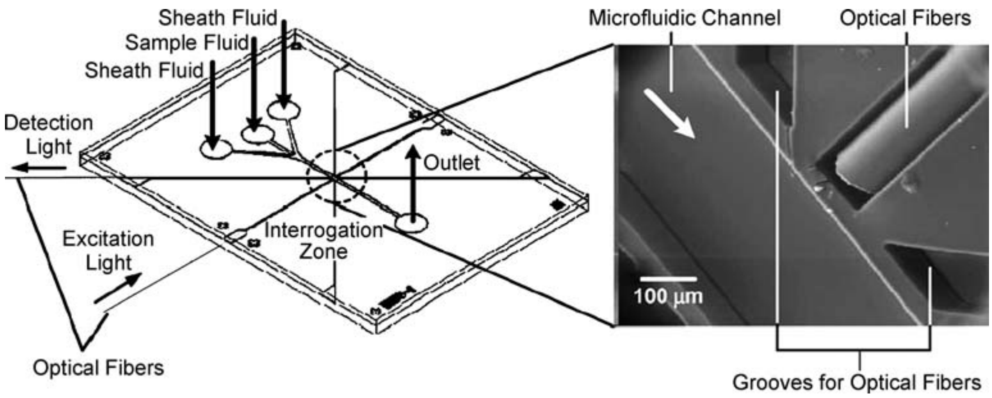

Lab-on-a-Chip Devices for Particle and Cell Separation, Figure 1 PDMS-based optofluidic micro flow cytometer with two-color, multi-angle fluorescence detection capability using PIN photodiodes. Optical fibers are manually embedded close to a microfluidic channel to excite particles and detect emitted light from particles. Reprinted from [1], with permission from Elsevier

preparative centrifugation. Cells of varying density may also be separated using density gradient centrifugation. In this case a density gradient may be developed either by layering sucrose solutions of decreasing density and centrifuging or using specialized media which naturally develops a density gradient under centrifugation. Again, density gradient centrifugation is often used for white cell separation as erythrocytes will collect at the bottom of a gradient and the individual white cell populations will migrate and collect in bands based on their density which can be removed using a micropipette.

Key Research Findings

Lab-on-a-Chip Devices for Particle or Cell Separations Based on FACS

Recently, there have been several Lab-on-a-Chip devices based on FACS reported. For instance, Tung et al. [1] reported a PDMS-based optofluidic micro flow cytometer with two-color, multiangle fluorescence detection capability using PIN photodiodes. They integrated laser excitation with silicon-based PIN photodiode detectors on a microchannel in conjunction with optical fiber waveguides (Fig. 1). By using multiple angles for the fluorescence excitation of particles and detection of emitted light through the optical fibers, they demonstrated multicolor excitation of single particles at a single interrogation point within the microfluidic channel and examined the ability of using lock-in amplification techniques to increase the signal-to-noise ratio of the PIN-based photodetector. Experimentally, they demonstrated the detection of weak fluorescence signals from fluorescently labeled nucleic acids in yeast (*S. cerevisiae*) at a counting rate of 500 particles/s.

Another example of a particle or cell separation device based on FACS was reported by Quake and colleagues [2]. In this system, the fluid flow is controlled by pneumatically actuated pumps and microvalves which can control fluid flow direction. The flow direction is changed as fluorescence from a target particle population is detected with a forward-sorting algorithm so that target particles are sent directly to the collection channel. The reverse-sorting algorithm allows rare-event capture at a rate independent of the switching speed of the device. A high fluid flow rate is established from the input well to the waste channel. After each fluorescence event detection, the fluid flow is halted and reversed until the bead is detected a second time. It is then directed at a slower speed to the collection channel (Fig. 2). A mixed population of *E. coli* bacteria with one strain expressing green fluorescence protein (GFP) and the other expressing p-nitrobenzyl (pNB) esterase were sorted using this reverse sorting algorithm based on the fluorescence of the GFP expressing cells. The recoveries from multiple devices, with varying input cell concentrations and input GFP fraction ranged from 16 to 50% and enrichment of the GFP population varied from 6.9 to 89 times over the input sample fraction. The authors noted several advantages of this system over conventional FACS systems including: minimal background fluorescence noise from the cell media and channel materials, higher detection sensitivity, being mass producible and having a self-contained cell sorting system on a chip.

Lab-on-a-Chip Devices for Particle or Cell Separations Based on MACS

Magnetic sorting of particles is of particular interest since it can be miniaturized easily and utilized in applications where a small sample volume is required. One of the chal-

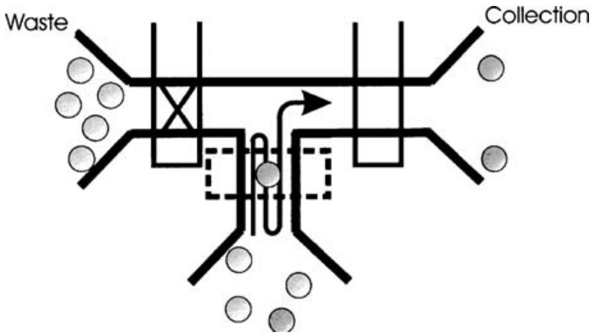

Lab-on-a-Chip Devices for Particle and Cell Separation, Figure 2 Schematic drawing of the cell trapping algorithm proposed by Quake's group. A cell can be trapped in the detection region (dashed box) by reversing the flow within the detection region. Reprinted with permission from [2]

lenges in designing MACS based Lab-on-a-Chip devices is to achieve an efficient separation in a continuous manner. Thus, it is essential to understand the fundamental physics underlying the behavior of the magnetic particles when they are exposed to various forces including an external magnetic field, hydrodynamic drag and gravity.

The behavior of magnetic particles within a magnetic field strongly depends on their magnetic properties and the magnetic force on the particles can be derived from Maxwell's equations. Magnetic micro- and nanoparticles used in most biotechnology applications are paramagnetic so the magnetic force exerted on magnetic particles vanishes once the external magnetic field is turned off. If ferromagnetic particles are used, then the particles could aggregate and may be difficult to disperse in a carrier fluid. For paramagnetic particles, the magnetic force exerted on a particle is

$$\boldsymbol{F} = \frac{1}{2}\mu_0 v_\mathrm{p}(\chi_\mathrm{p} - \chi_\mathrm{f})\nabla\,|\boldsymbol{H}|^2 \tag{1}$$

where $\mu_0 = 4\pi \times 10^{-7}$ H/m is the magnetic permeability of vacuum, v_p is the volume of a particle, χ_p and χ_f are the magnetic susceptibility of the particle (p) and the carrier fluid (f), and $\boldsymbol{H}$ is the applied magnetic field. For Lab-on-a-Chip systems using magnetic particles, three types of forces affect the trajectory of a magnetic particle: gravity, hydrodynamic drag, and magnetic forces. In this case, Newton's equation acting on a spherical particle can be written as

$$\begin{aligned}\frac{4\pi R_\mathrm{p}^3}{3}\left(\rho_\mathrm{p} + \frac{\rho_\mathrm{f}}{2}\right)\frac{d\boldsymbol{V}_\mathrm{p}}{dt} &= \frac{1}{2}\mu_0 v_\mathrm{p}(\chi_\mathrm{p} - \chi_\mathrm{f})\nabla\,|\boldsymbol{H}|^2 \\ &\quad - 6\pi\eta R_\mathrm{p}(\boldsymbol{V}_\mathrm{p} - \boldsymbol{V}_\mathrm{f}) \\ &\quad - g v_\mathrm{p}(\rho_\mathrm{p} - \rho_\mathrm{f})\hat{y}\end{aligned} \tag{2}$$

where $\boldsymbol{V}_\mathrm{p}$ and $\boldsymbol{V}_\mathrm{f}$ are the velocities of the particle (p) and fluid (f) respectively, η is the dynamic viscosity of the carrier fluid, R_p is the particle radius, ρ_p and ρ_f are densities of particle (p) and fluid (f), g is the gravitational acceleration, and $\hat{y}$ is the unit vector in the vertical direction. Therefore, the movement of the particle under the influence of magnetic forces, hydrodynamic drag, and gravity can be determined by solving Eq. 2. The left hand side of Eq. 2 accounts for both the particle and fluid inertial force. However, under most conditions, a creeping flow limit is assumed so the left hand side of Eq. 2 is set to zero and the right hand side determines the steady state velocity of the particles.

A simple demonstration of magnetic particle separation on-a-chip was demonstrated by Pamme and Manz [3]. They showed that on-chip free-flow magnetophoresis could continuously separate a heterogeneous particle population using a combination of flow and magnetic forces (Fig. 3). The particle separation was demonstrated by infusing two types of magnetic (2 and 4.5 μm in diameter, with magnetic mass susceptibilities of 1.12×10^{-4} and 1.6×10^{-4} $\mathrm{m^3/kg}$ respectively) and nonmagnetic (∼ 6 μm in diameter) particles into the device at the same time. A permanent magnet is placed along the flow path of the device. Since the magnetic particles are deflected under the external magnetic field and the nonmagnetic particles are not, a separation of the magnetic particles from the nonmagnetic particles was achieved. The deflected magnetic particles were further separated according to their size because the larger particles (∼ 4.5 μm) have larger magnetic susceptibility than the smaller particles (2 μm) and therefore a larger magnetic force is exerted on them causing a larger deflection than the smaller particles.

Magnetic cell separation was also be demonstrated in microfluidic structures, as described by Inglis et al. [4]. They demonstrated a continuous-flow microfluidic device that enables cell separation of leukocytes from erythrocytes in whole blood using a CD45 sensitive magnetic bead to selectively bind with the CD45 antigen expressed on the surface of the target leukocytes. In their demonstration, they allowed both unlabeled erythrocytes and the labeled leukocytes to flow over an array of microfabricated magnetic strips which are aligned at a constant angle of 9.6° from the flow direction. Since a series of large magnitude magnetic field gradients are created by the parallel magnetic strips, the magnetically labeled leukocytes are deflected along the direction of the strips while the erythrocytes flow straight through the device (Fig. 3b). After some time the leukocytes have been deflected by a large enough amount that they are separated from the rest of the blood cell population.

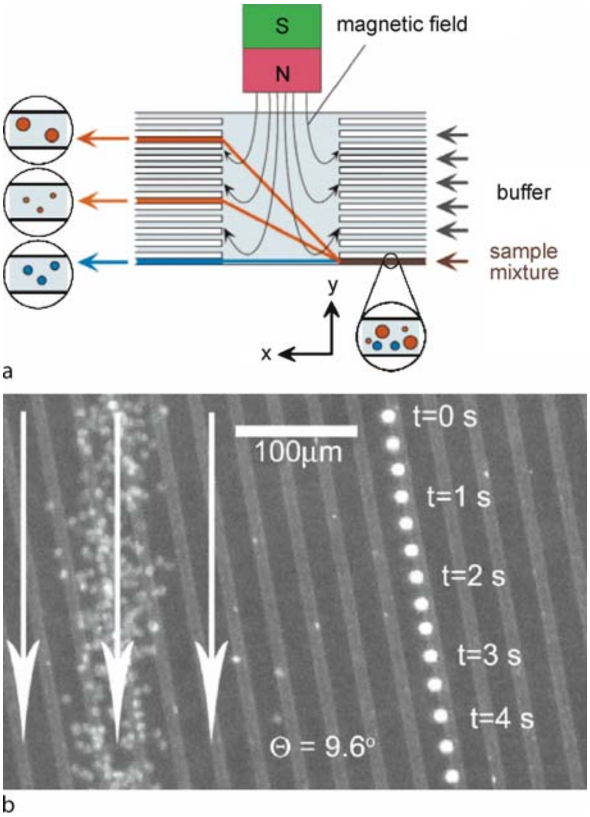

Lab-on-a-Chip Devices for Particle and Cell Separation, Figure 3 (**a**) Conceptual drawing of free-flow magnetophoresis. A mixture of magnetic and nonmagnetic particles are infused into a device. The magnetic particles are deflected into the upper microfluidic channel due to the presence of the magnetic field perpendicular to the flow direction. However, nonmagnetic particles are not affected by the magnetic field and continue to flow in the same direction. Magnetic particles can be further separated according to their size and magnetic susceptibility. Reprinted with permission from [3]. (**b**) Time lapse image showing a single tagged fluorescing leukocyte at different times moving along a magnetic stripe at an angle of 9.6° from the direction of the fluid flow represented by the white arrows. The red blood cells on the left are from a single image. All cells entered the chip at the same point approximately 1.5 mm above the field of view. Reprinted with permission from [4]

Lab-on-a-Chip Affinity Based Devices for Particle or Cell Separations

Affinity based systems typically rely on the immobilization of antibodies or antigens onto which a cell of interest will bind to. For example, Revzin et al. [5] have described a microfabricated cytometry platform for creating high-density leukocyte arrays and demonstrated the retrieval of single cells from the array. To create their devices they used a combination of surface patterning and immobilization of cell adhesive ligands. Briefly, in order to modify surfaces through avidin-biotin conjugation, a glass substrate with lithographically micropatterned poly(ethylene

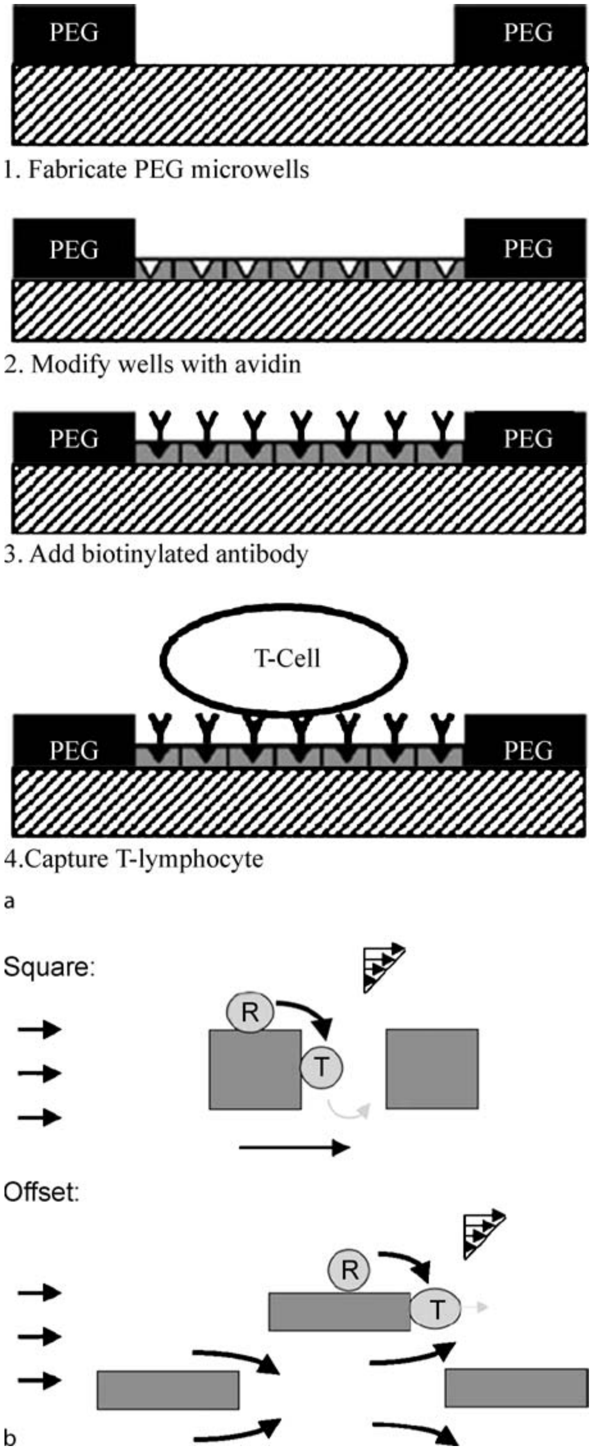

Lab-on-a-Chip Devices for Particle and Cell Separation, Figure 4 (**a**) Schematic procedure to obtain T-cell immobilization within micropatterned PEG wells. Reprinted with permission from [5]. (**b**) Schematic drawing cell dynamics around E-selectin coated micropillars. Depending on the shape of the micropillars, a cell can either escape from the micropillar array (offset array) or be recaptured by the next adjacent pillar (square array). Reprinted with permission from [6]

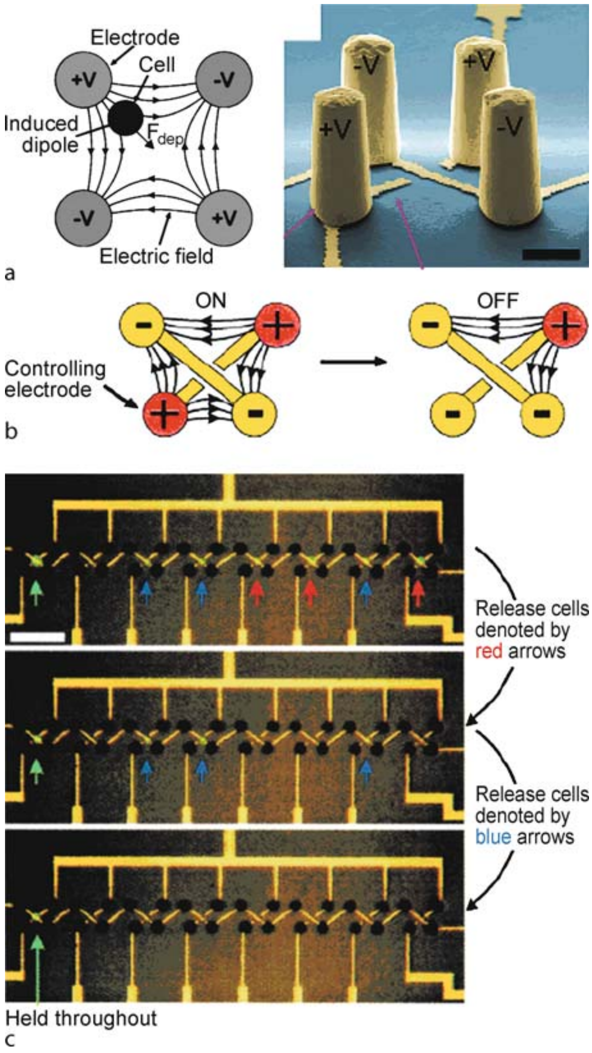

Lab-on-a-Chip Devices for Particle and Cell Separation, Figure 5 (**a**) Schematic representation of a quadrupole DEP trap, showing the four electrodes of the quadrupole and a cell trapped in the middle. A pseudo-colored SEM image showing a DEP trap consisting of four trapezoidally arranged gold electrodes. (**b**) Schematic representation of potential configuration to release a captured cell from the DEP trap. (**c**) A series of bright field and fluorescence images demonstrating selective and independent trap control. Reprinted with permission from [7]

glycol) (PEG) wells were placed in avidin solution for 1 h. After obtaining avidin adsorption at the bottom of the well, the substrate was rinsed with DI water to remove unbound avidin. Next, the substrate was placed in a solution of biotinylated antibody for 2 h to immobilize the antibody within the wells through an avidin-biotin conjugate followed by washing of unbound antibody with DI water. As a final step, they seeded leukocytes and incubated the cells for 30 min (Fig. 4a). By applying this principle using an anti CD5 antibody as a cell adhesive binding they found that 95% of the micropatterned PEG wells were occupied by CD5+ T-lymphocytes. They further described the removal of cells using laser capture microdissection (LCM) which involves capping the PEG wells with an adhesive thermoplastic which is selectively melted to envelop the cells of interest using an IR laser. The thermoplastic is then removed from the array with the captured cells of interest.

Chang et al. [6] have described a microfluidic device for separating leukocytes by mimicking the physiological process of leukocyte recruitment to blood vessel walls: adhesive cell rolling and transient tethering. To accomplish their separation, they first coated the surface of silicon pillars with E-selectin IgG chimera protein and investigated cell capture using HL-60 promyelocytic leukemia and U-937 histiocytic lymphoma myeloid cell lines, both of which produce ligands for the immobilized E-selectin. They studied two types of micropillar arrays: a square structure where the pillars are placed in a linear array and an offset structure where the pillars are staggered between each other (Fig. 4b). In the offset array device, the cells initially roll slowly tangential to the flow direction due to viscous shear on cells. Once the cells reach the trailing edge of the micropillars, the cells experience viscous shear loading which causes them to move perpendicularly away from the pillar. As a result, the cells are detached from the pillar surface and leave to the free stream and are not captured by the next post (Fig. 4b part a). However, in the square array device, the cells that move into the free stream are always recaptured by the next micropillar due to the sluggish flows behind the micropillars (Fig. 4b part b). Cell density enrichment up to 400 fold over the initial cell density was demonstrated with the HL-60 cells due to the accumulation of the cells on the surface of the pillar array. For the two different cell types tested in the square array device, transit velocities of 1.4 ± 0.8 mm/s and 2.7 ± 1.4 mm/s were obtained for the HL-60 and U-937 cell lines, respectively. This difference in transit velocities was suggested as a mechanism to separate the different cell populations from each other.

Lab-on-a-Chip Devices for Particle or Cell Separations Based on Dielectrophoresis

Dielectrophoresis (DEP) refers to the motion of polarizable particles or cells suspended in an electrolyte subjected to a nonuniform electric field. Dielectric particles, including cells, can be categorized into two types depending on their behavior within the nonuniform electric field, i. e., positive and negative DEP. Positive DEP occurs when the particle is more polarizable then the surrounding media so the particles or cells are attracted toward areas of high elec-

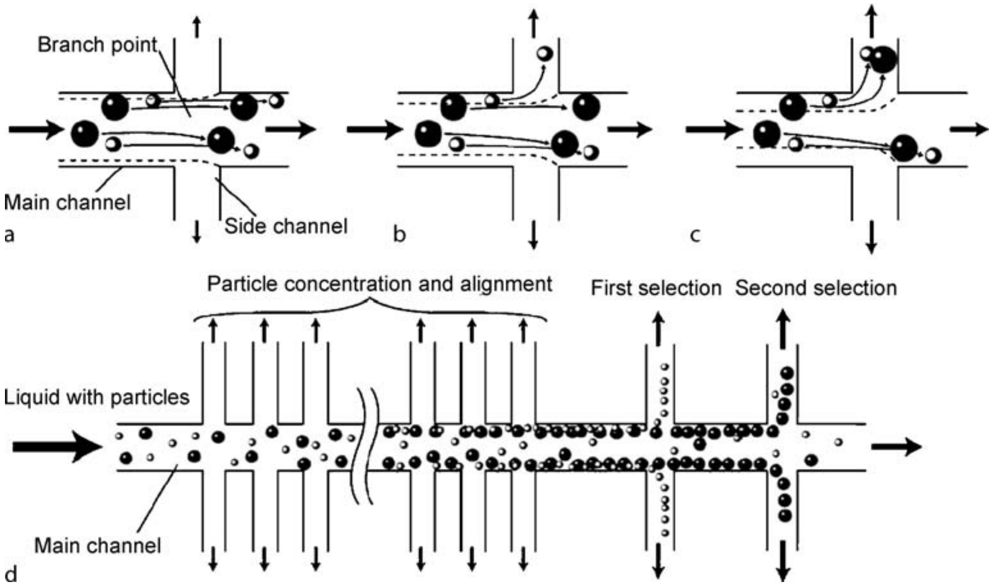

Lab-on-a-Chip Devices for Particle and Cell Separation, Figure 6 Principle of hydrodynamic filtration. (**a**) When the flow rate ratios between the side and main channels are low, (**b**) medium, and (**c**) high. Broken lines show the virtual boundaries (critical streamline) of the flows distributed into the side and main channels. (**d**) Schematic diagram showing particle concentration and classification in a microchannel having multiple branch points and side channels. Reprinted with permisiion from [8]

tric field strength. On the contrary, in negative DEP, the particles or cells are less polarizable than the surrounding media and move towards areas of low electric field strength.

Quantitatively, a force ($\boldsymbol{F}$) acting on a spherical particle, whose radius is a and polarization $\boldsymbol{P} = \alpha\boldsymbol{E}$ where α is the polarizability and $\boldsymbol{E}$ is the electric field, is given by

$$\boldsymbol{F} = \boldsymbol{P}v_{\mathrm{p}} \cdot \nabla\boldsymbol{E} = \frac{2}{3}\pi a^3 \alpha \nabla |\boldsymbol{E}|^2 \quad (3)$$

When a steady state sinusoidal electric field is applied, the polarizability of the particle and solvent becomes complex and the force in Eq. 3 can be generalized as

$$\langle\boldsymbol{F}\rangle = 2\pi a^3 \varepsilon_0 \varepsilon_{\mathrm{r,solvent}} \mathrm{Re}(f_{\mathrm{CM}}) \nabla |\boldsymbol{E}_{\mathrm{RMS}}|^2 \quad (4)$$

where $\varepsilon_0 \approx 8.854 \times 10^{-12}$ F/m is the vacuum permittivity, $\varepsilon_{\mathrm{r,solvent}}$ is the relative permittivity of the solvent, $\boldsymbol{E}_{\mathrm{RMS}}$ is the root mean squared applied electric field and $\mathrm{Re}(f_{\mathrm{CM}})$ is the real part of the Clausius–Mossoti factor. The Clausius–Mossoti factor depends on the complex permittivity of both the particle and medium. For a spherical particle surrounded by an infinite fluid

$$f_{\mathrm{CM}} = \frac{\varepsilon_{\mathrm{p}} - \varepsilon_{\mathrm{f}}}{\varepsilon_{\mathrm{p}} + 2\varepsilon_{\mathrm{f}}} \quad (5)$$

where ε_{p} and ε_{f} is the complex permittivity of the particle and fluid respectively. It should also be noted that the Clausius–Mossoti factor varies for different particle types and is also frequency dependent due to the dielectric relaxation of both the particle and surrounding media. The direction of the force directly depends on the sign of $\mathrm{Re}(f_{\mathrm{CM}})$. Thus it is possible to change from positive to negative DEP simply by changing the excitation frequency using AC excitation. If the $\mathrm{Re}(f_{\mathrm{CM}})$ is positive, then the particle will be attracted toward the electrode where the magnitude of the electric field is maximum. This is called positive DEP as mentioned above. In the opposite situation, if the $\mathrm{Re}(f_{\mathrm{CM}})$ is negative, then the particle will be repelled from where the electric field magnitude is largest, negative DEP. Another important consequence of DEP is that the force acting on the particle is proportional to the gradient of the external electric field intensity squared. Thus, the larger $\nabla|\boldsymbol{E}|^2$; the larger the force acting on the particle. The gradient of the electrical field intensity can be increased either by increasing voltage across electrodes, decreasing distance between electrodes, and/or by increasing the nonuniformity of the electric field. In macroscopic DEP devices, there is usually a technical limitation to how far the distance between electrodes can be decreased, and electrical breakdown limits the maximum voltage and smallest electrode spacing. In microscale DEP devices, these strategies can be applied to maximize the force acting on a particle. This is the main reason that Lab-on-a-Chip devices based on DEP are very efficient for particle separation. Since the force depends on the elec-

tric field gradient squared the external electric field used for DEP may be either a DC (as represented by Eq. 3) or AC (as represented by Eq. 4) field. However, it is usually undesirable to use a DC electric field because it can cause particle electrophoresis, which counteracts the DEP force in the motion of the particles. Thus, for most DEP based particle or cell separations, an AC electric field is applied. Voldman et al. [7] have developed a microfabrication-based dynamic array cytometer (μDAC) for use in a parallel luminescent single-cell assay that can separate small cell populations. They designed quadrupole DEP trap arrays to trap cells. Figure 5a shows a schematic representation of a quadrupole DEP trap. If a negative-DEP is used, then an effective dipole moment in the cell is antiparallel to the electric field. Thus the cell is repelled from each electrode and the cell is stably trapped at the quadrupole's field minimum, at the center of the quadrupole. Figure 5b shows how a cell can be ejected from the DEP trap. By switching the potential on one of the controlling electrodes from positive to negative, the symmetry of the electric fields within the quadrupole is disrupted so that the cell can be ejected. To demonstrate selective cell sorting, the cells (HL-60 cell line) were fed into the chip via a reservoir and then exposed to calcein to fluorescently stain each cell. Then they were individually loaded into each trap and optically interrogated over time for their fluorescence response to the calcein (Fig. 5c). First, three cells designated by red arrows were released by changing the potential of the controlling electrode from +3 V to −3 V. Next, three cells designated by blue arrows were released by following the same principle. Only one cell designated by the large green arrow in the bottom panel was left in a single activated trap.

Lab-on-a-Chip Devices for Particle or Cell Separations Based on Hydrodynamics

Hydrodynamic particle or cell separation is also an attractive and ideal way to separate particles or cells because it requires only well controlled flow structures. Usually, this method utilizes a cell's physical properties to distinguish them from other cell types. Cell size, density, and stiffness can be used as criteria for separating the cells of interest from the rest of a population.

Continuous particle separation in microfluidic channels based on particle size was extensively studied by Yamada et al. [8]. In their report, they proposed a concept called *hydrodynamic filtration*. Figure 6 shows the principle of hydrodynamic filtration. When side channels are designed to have sufficiently lower flow rate than the downstream of the main channel (Fig. 6a), only a small portion of fluid near the wall will be skimmed into a side channel, while the majority of fluid flow is through the main channel. The streamline which separates the fluid skimmed into the side channel and the fluid which remains in the main channel is known as the critical streamline. Thus, there is a lower probability that particles will flow into the side channel. On the contrary, as the flow rate in the side channel increases, there is a larger possibility that the particles will flow into the side channel because more fluid can flow into the side channel so a larger percentage of the main channel width is skimmed into the side channel capturing particles further from the walls beyond the critical streamline (Fig. 6a through Fig. 6c). This leads to a separation of particles based on size because the centroid of a particle cannot be within one particle radius from the channel wall so larger particles will not flow into the side channels until the critical streamline placement corresponds to the particle's centroid. Based on this principle, they have demonstrated leukocyte enrichment and/or removal of erythrocytes. The initial particle counts reported of erythrocytes and leukocytes were 27,400 and 35 respectively. After conducting the hydrodynamic filtration twice, they obtained particle counts of 3180 and 118. This result corresponds to a 29-fold increase in leukocyte concentration.

Based on a similar principle, Yang et al. [9] have developed a microfluidic device for continuous, real time blood plasma separation from whole blood. The device is composed of a blood inlet, a bifurcating region which leads to a purified plasma outlet, and a concentrated blood cell outlet. They have precisely designed flow rate ratios at each bifurcation so that no blood cells (erythrocytes, leukocytes, or platelets) flow into the side channels, while blood plasma is skimmed into the purified plasma collection channels. The experimentally determined plasma selectivity with respect to blood hematocrit level was almost 100% regardless of the inlet hematocrit (Fig. 7a). The total plasma separation volume percent varied from 15% to 25% with increasing inlet hematocrit (Fig. 7b).

Shevkoplyas et al. [10] reported a platform for the autoseparation of leukocytes within a microfluidic device. Their device is composed of a series of bifurcating rectangular microfluidic channels. They imitate leukocyte flow behavior in vivo to obtain a leukocyte rich sample at the device outlet. It is well known that blood exhibits unique flow characteristics within the microcirculation. Erythrocytes tend to flow in the center of blood vessels, leaving a plasma-rich zone near the vessel wall. The red blood cells also flow faster than leukocytes which causes mechanical collisions between leukocytes and erythrocytes within a vessel, yielding an uneven distribution of leukocytes across the blood vessel. Thus, leukocytes usually have a larger population near the blood vessel wall than the center of the vessel. Thus, by mimicking this

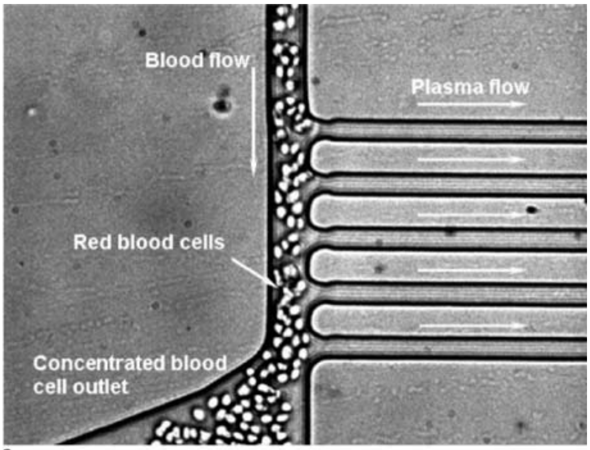

a

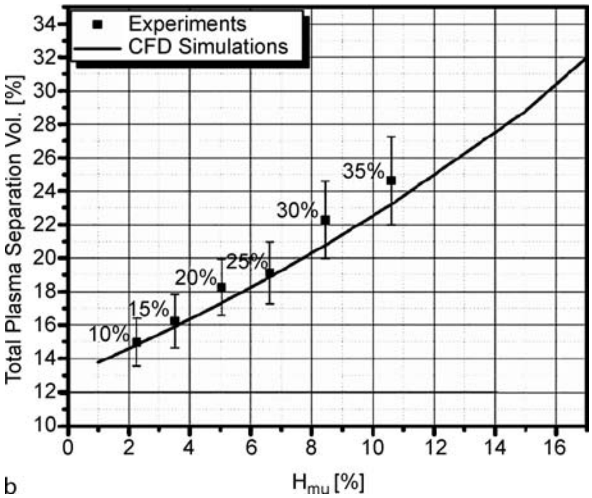

b

Lab-on-a-Chip Devices for Particle and Cell Separation, Figure 7 (**a**) A snapshot of the blood plasma separation region (40× magnification, 1376×1040 pixels) with a shutter open time of 20 μs (**b**) A comparison of the experimental and CFD simulation results of the total plasma separation volume percent with respect to the upstream microchannel hematocrit level; The digits shown above each data point represent the inlet hematocrit levels. Reprinted with permission from [9]

property, Shevkoplyas et al., designed a flow structure which diverted the leukocyte-rich plasma layer through several bifurcations (Fig. 8), to obtain a 34-fold increase in the leukocyte-to-erythrocyte concentration ratio compared with the inlet concentration. This device is particularly useful in applications where high concentrations of leukocytes are required.

Lab-on-a-Chip Devices for Particle or Cell Separations Based on Ultrasound

It is well known that the ultrasonic standing wave can exert forces on particles and have been used in many fields including chemical and materials engineering to separate or enrich suspended particles in a medium at well defined positions. The force produced by ultrasonic standing waves move particles to either the pressure node or antinodes of the standing wave depending on the density and compressibility of the particles and the medium.

The primary acoustic force ($F(z)$), which acts on a spherical particle in a one-dimensional standing wave propagation direction, is [11]

$$\langle F(z) \rangle = 4\pi\rho\Phi^2(ka)^3 K_s(\lambda,\sigma)\sin 2kz \quad (6)$$

where a is the particle radius, $k = \omega/c_f$, the wave number in the fluid, ρ is the density of the fluid, Φ is the amplitude of the velocity potential of a standing wave, and c_f is the speed of sound in the fluid. The acoustic contrast factor K_s is described by

$$K_s(\lambda,\sigma) = \frac{1}{3}\left(\frac{5\lambda - 2}{2\lambda + 1} - \frac{1}{\lambda\sigma^2}\right) \quad (7)$$

where $\lambda = \rho_P/\rho_F$ is the density ratio between the particle and fluid and $\sigma = c_p/c_f$ is the sound speed ratio between the particle and fluid. Aside from the primary acoustic force on the particle, there are also secondary forces which act on particles. These secondary forces are mainly caused by the interaction between two particles within the acoustic field. When these secondary forces are generated, the two particles are attracted to each other and move together. However, these secondary forces are negligibly small when compared with the primary acoustic force.

Recently, Petersson et al. [12] have developed a Lab-on-a-Chip device for particle separation based on this ultrasonic principle. In order to demonstrate the separation of particles with different physical properties in a continuous laminar flow, they have prepared a microfluidic device with a 750 μm wide and 250 μm deep channel. As a test material, a mixture of milk and blood was used. The ultrasound half standing wave at 2 MHz was produced by a piezoelectric ceramic, which was glued directly on the bottom of the microfluidic device. Milk was used as an initial test medium (Fig. 9a and 9b) to confirm that the lipid particles within the milkfat were attracted toward the pressure anti-nodes of the half standing wave, which exist along the microfluidic channel wall. In addition, when they infused a mixture of milk and blood, they found efficient separation of blood cells from the mixture (Fig. 9c). This demonstration showed that a mixture of heterogeneous components can be effectively separated by utilizing ultrasonic standing waves, combined with the laminar flow in microfluidic channels. The separation efficiency of erythrocytes from the mixture was about 70%, while more than 80% of the milkfat lipid particles were

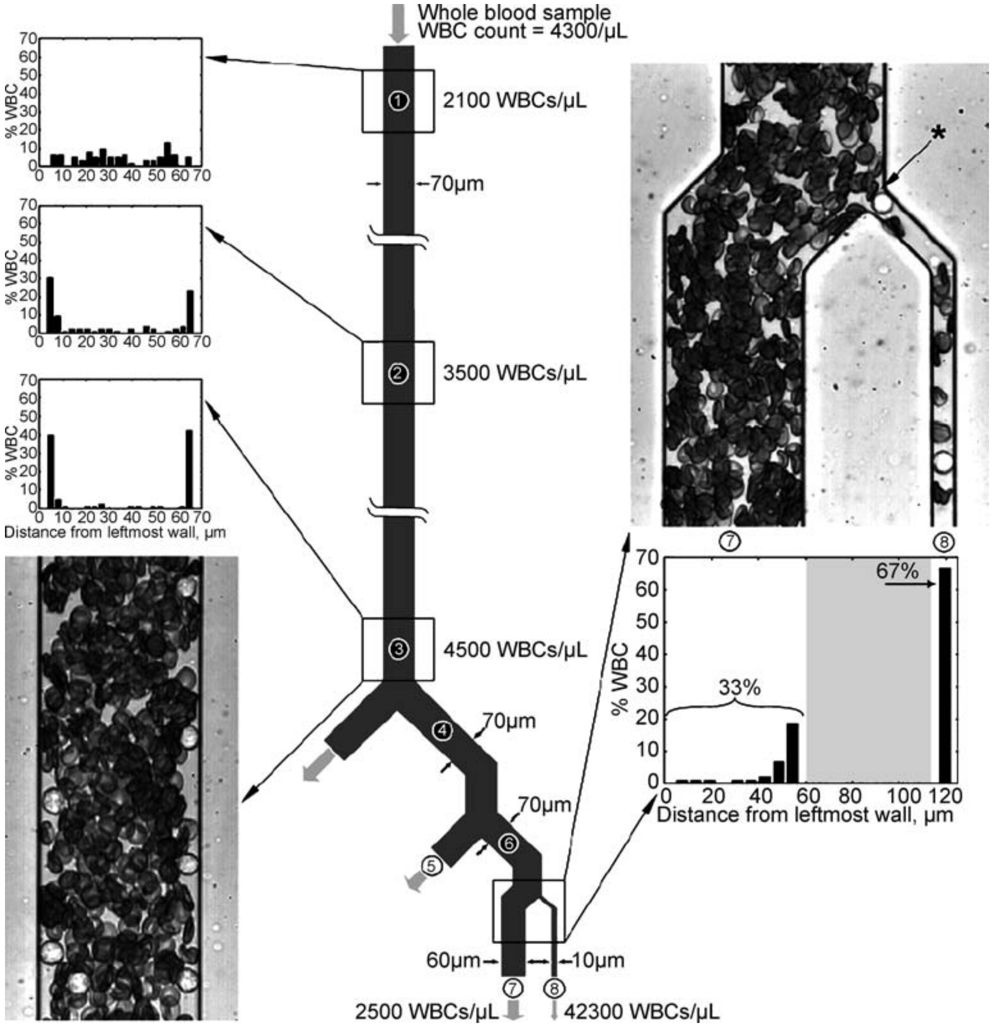

Lab-on-a-Chip Devices for Particle and Cell Separation, Figure 8 Leukocyte autoseparation device. By imitating leukocytes' behavior in vivo, the leukocyte-to-erythrocyte ratio is significantly increased (29-fold compared with the inlet ratio). Reprinted with permission from [10]

removed. Based on these demonstrations, they proposed that this technique might be useful for intraoperative blood wash applications, where shed blood can be collected and returned to the patient during or after surgery.

Future Directions for Research

Although a variety of technologies related with the Lab-on-a-Chip devices for particle or cell separations are introduced here, there are still many challenges to producing efficient Lab-on-a-Chip based particle separation technologies over the conventional particle separation methods. For instance, although they have relatively high separation efficiency some of the microsystem technologies such as FACS-based, DEP-based and affinity-based separations still have lower throughput when compared with the conventional macroscale method. In addition, MACS-based and hydrodynamics-based separation technologies show significantly lower separation efficiency. This implies that there still needs to be substantial improvement in the further development of these particle and cell based separation microsystems for truly realizing the promise of Lab-on-a-Chip separation platforms which can outperform the standard macroscale technologies.

Cross References

- ► AC Dielectrophoresis Lab-on-a-Chip Devices
- ► Acoustic Streaming
- ► Bead-Based Microfluidic Platform
- ► Biosample Preparation Lab-on-a-Chip Devices
- ► Cell Adhesion and Detachment

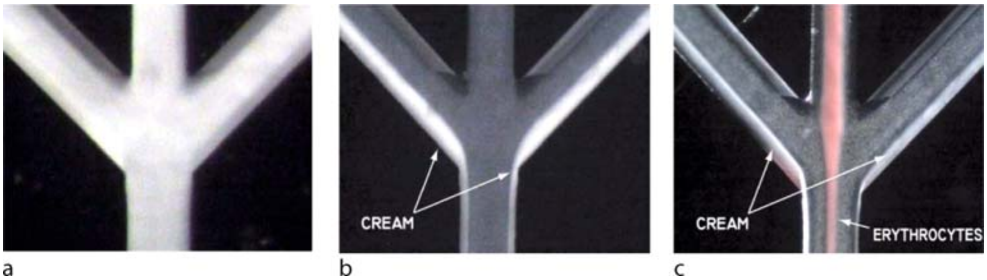

Lab-on-a-Chip Devices for Particle and Cell Separation, Figure 9 Demonstration of erythrocyte separation from a mixture of milk and blood using ultrasonic standing waves. Milk flowing through a microfluidic channel (**a**) without and (**b**) with ultrasound turned on. The milkfat particles are moved to the pressure antinodes with ultrasound application. (**c**) Blood separation from a mixture of milk and blood when ultrasound is turned on. Reprinted with permission from [12]

► Cell-Based Assays Using Microfluidics
► Cell Sorting
► Dielectrophoresis
► Dielectrophoretic Motion of Particles and Cells
► Sample Purification Using Magnetic Particles

References

1. Tung YC, Zhang M, Lin CT, Kurabayashi K, Skerlos SJ (2004) PDMS-based opto-fluidic micro flow cytometer with two-color, multi-angle fluorescence detection capability using PIN photodiodes. Sens Actuators B 98:356–367
2. Fu AY, Chou HP, Spence C, Arnold FH, Quake SR (2002) An integrated microfabricated cell sorter. Anal Chem 74:2451–2457
3. Pamme N, Manz A (2004) On-chip free-flow magnetophoresis: Continuous flow separation of magnetic particles and agglomerates. Anal Chem 76:7250–7256
4. Inglis DW, Riehn R, Austin RH, Sturm JC (2004) Continuous microfluidic immunomagnetic cell separation. Appl Phys Lett 85:5093–5095
5. Revzin A, Sekine K, Sin A, Tompkins RG, Toner M (2005) Development of a microfabricated cytometry platform for characterization and sorting of individual leukocytes. Lab Chip 5:30–37
6. Chang WC, Lee LP, Liepmann D (2005) Biomimetic technique for adhesion-based collection and separation of cells in a microfluidic channel. Lab Chip 5:64–73
7. Voldman J, Gray ML, Toner M, Schmidt MA (2002) A microfabrication-based dynamic array cytometer. Anal Chem 74(16):3984–3990
8. Yamada M, Seki M (2005) Hydrodynamic filtration for on-chip particle concentration and classification utilizing microfluidics. Lab Chip 5:1233–1239
9. Yang S, Ündar A, Zahn JD (2006) A microfluidic device for continuous, real time blood plasma separation. Lab Chip 6(7):871–880
10. Shevkoplyas SS, Yoshida T, Munn LL, Bitensky MW (2005) Biomimetic autoseparation of leukocytes from whole blood in a microfluidic device. Anal Chem 77:933–937
11. Haake A, Dual J (2002) Micro-manipulation of small particles by node position control of an ultrasonic standing wave. Ultrason 40:317–322
12. Petersson F, Nilsson A, Holm C, Jönsson H, Laurell T (2004) Separation of lipids from blood utilizing ultrasonic standing waves in microfluidic channels. Analyst 129:938–943

Lab-on-Chip Devices for Protein Analysis

Siddhartha Panda[1], Saiju Pyarajan[2]
[1] Department of Chemical Engineering, IIT Kanpur, Kanpur, India
[2] Department of Pathology and NYU Cancer Institute, New York University School of Medicine, New York, NY, USA
spanda@iitk.ac.in, Saiju.Pyarajan@med.nyu.edu

Synonyms

Miniaturized systems; Chip-based systems; Proteomics; Protein chip; Protein profiling

Definition

Devices that have the capability of performing one or more analytical laboratory functions on a single platform of a small area (a few square millimeters to a few square centimeters) and are capable of handling extremely small fluid volumes (down to less than pico liters), which (among other applications) can be used for protein analysis.

Overview

Proteins are encoded by DNA and translated from RNA in the cell and are the *effector molecules* that play essential roles in carrying out cellular function. In disease state, various molecular changes occur in an individual at the DNA, RNA and protein level. Disease, therapy and drugs alter the structure, metabolism and functions of proteins. Understanding the expression and function of proteins in normal and pathophysiological conditions is critical for developing effective therapeutic strategies.

Protein analysis in general refers to sequencing, identification, and characterization of the structure, metabolism and function of proteins. The new and developing field of proteomics focuses on protein profiling, which is the identifi-

cation and ideally the quantification of proteins on a large scale at the cell and tissue level.

Conventional Techniques for Protein Analysis

Conventional bench/lab methods of protein separation and identification include one dimensional (1D) and two dimensional (2D) gel-electrophoresis (GE), mass-spectrometry (MS), immuno assays and affinity chromatography. 1 and 2D electrophoresis techniques separate proteins based on their charge and/or mass in an electric field within a matrix, while MS is widely used to detect mass of biomolecules with very high accuracy. Immunoassays take advantage of specific binding of antibodies to peptide ligands or antigens making it highly specific in identifying proteins. X-ray diffraction (XRD) of protein crystals and nuclear magnetic resonance (NMR) are some of the techniques that have been traditionally used for the characterization and structural/functional analysis of proteins. These techniques offer the capability for detailed measurement of spatial arrangement of atoms within the protein molecules and thus provide insights on protein structure and function. Protein analysis methods for functional characterization include immuno–precipitation, confocal and electron microscopy of tagged/labeled proteins, which have been widely used to study protein–protein interaction and the spatial and temporal arrangement of proteins within the cell and cellular compartments. Functional assays that provide a snapshot of what the protein actually does in the living cell have been carried out using techniques like spectroscopy, colorimetric and chemical detection assays.

Limitations of Conventional Techniques

Limitations of conventional methods include poor detection limits, large sample volumes, long processing times, cumbersome sample preparation, complex instrumentation and requirement of specific expertise. For example, conventional gel-based methods require a great deal of expertise and hands-on time. The process is slow, difficult to automate leading to lack of reproducibility across different personnel, laboratories and samples. While methods like liquid chromatography (LC)/MS perform well when used by skilled operators, even these techniques are limited by their difficulty to set up. Also, protein analysis using conventional methods are largely confined to research/diagnostics laboratories, and still have many logistical hurdles for adoption in clinics or other point-of-care facilities. Thus, there is an urgent need for new portable technologies specifically designed for use in clinics, for example, in health diagnostics. Also, with the advent of systems biology and 'omics' approaches, there is a need for large-scale experimentation and analysis using small amount of reagents/samples, and the information needs to be available accurately, quickly and cheaply. These requirements are not met by the conventional methods which in turn spurred interest in other innovative technologies for protein analysis. Various studies including one by Bill and Melinda Gates foundation and NIH to identify the "Grand Challenges for Global Health", have highlighted the need for *modified molecular technologies* that allow assessment of individuals for multiple disease conditions or pathogens at the point-of-care as well as quantitative assessment of population health status.

Miniaturized Systems or Lab-on-Chips

Miniaturization enabled by micro- and nano-technologies have given a new thrust to the field by introducing rapid low cost analytical systems and methods with better sensitivity that can also be multiplexed to allow large-scale analysis of multiple proteins. Other advantages of these miniaturized systems or Lab-on-Chips (LOC) include lower sample volumes and thus lower potential sample loss, better reproducibility of experiments, reduction in possible contamination and carry-overs, simpler infrastructure requirements, automation allowing for unattended operation, portability enabling on-site analysis, reduced waste generation, more efficient reactions through enhanced heat and mass transfer and no reactor dead volumes, and lower operating costs.

Micro-Total Analysis Systems

Another advantage of LOC devices is the possibility of integration of different steps of the entire analytical procedure on to a single device, resulting in a micro-Total Analysis Systems (μ-TAS). Only a limited number of LOC device developments have reached the status of a complete laboratory, where all the stages of conventional laboratory systems are integrated on a chip. Most of the currently available systems are semi-integrated.

Classification of Lab-on-Chips for Protein Analysis

LOC systems can be broadly classified into

- microfluidic based and
- spotted microarray based systems.

LOC systems can also be variously classified based on sample preparation/separation methods (e. g. gelfilteration, chromatography), detection methods used (e. g. MS, optical systems, immuno-detection) and application (research vs. diagnostics, multiuse vs. single use).

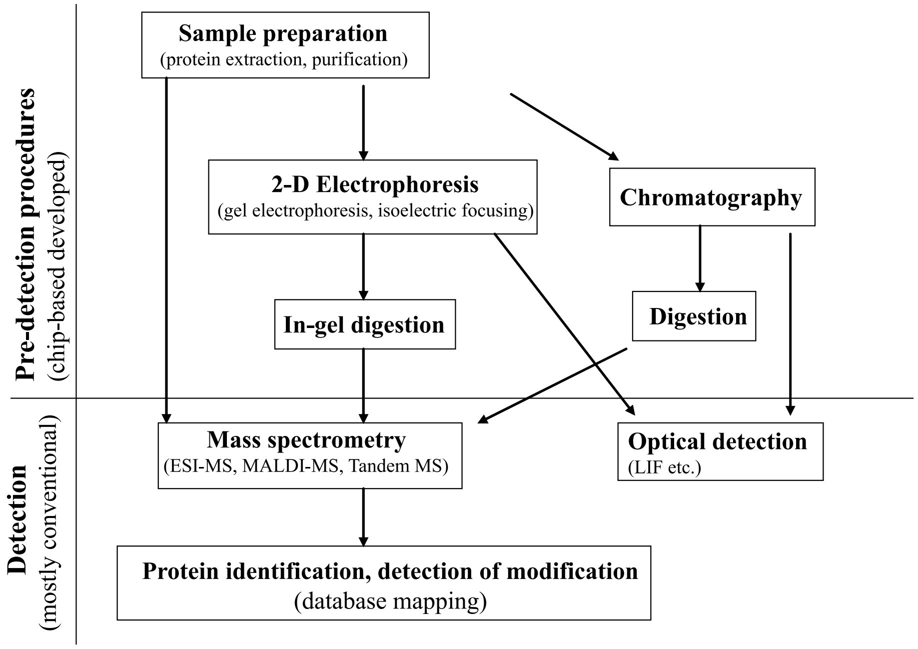

Lab-on-Chip Devices for Protein Analysis, Figure 1 Typical flow scheme of microfluidic protein separation and detection

Basic Methodology

Microfluidic Based Technologies

In microfluidic based systems, material is transported within microstructures (of typical dimensions of 10 – 500 μm) where separations, reactions and other processes occur. Focus has been on the realization of the traditional separation techniques (electrophoresis, chromatography, isoelectric focusing etc.) and reactions in the microchip format. The principles of separation, as in the conventional formats, are based on differences in mass and charge (thus mobility) and partitioning between phases. However, advantages associated with the small dimensions provide superior performance. For example, the higher surface to volume ratio arising from the smaller dimensions, results in lower heat and mass transfer resistances, and thus an improved performance.

A majority of the separation-based approaches in the microfluidic chip format for protein analysis have focused on single or multidimensional separations with detection by conventional MS or optical methods (e. g. laser induced fluorescence (LIF)). Microfluidic separation chips have also been adapted for use in immunoassays. They have also been utilized for the pre-MS sample preparation followed by conventional detection by MS. A typical flow scheme of microfluidic protein separation and detection is shown in Fig. 1.

Glass, and to some extent silicon, have been the main material for fabrication of the microfluidic devices. Microstructures for these systems are fabricated by traditional techniques employed in the microelectronics industry. For example, the structures are made by depositing photoresist on surfaces, applying lithographic techniques to expose the desired pattern followed by etching (wet or dry). Wafer pieces are then fused together to form enclosed systems by bonding. The schematic of a typical process flow is shown in Fig. 2. There has been recent interest in the use of polymeric materials for fabricating chips. These polymeric materials include polymethyldisiloxane (PDMS), polymethylmethacrylate (PMMA), polycarbonate (PC), etc. Some important advantages of polymeric materials include inert surface characteristics, low temperature fabrication methods, relative ease and lower cost of fabrication and disposability of devices. The microstructures on polymers fabricated using techniques of soft lithography, injection molding, hot embossing etc.

Microarray Based Technologies

DNA microarrays have been successfully used to measure mutations and/or gross changes in genomic DNA and levels of messenger RNA (mRNA). Measuring DNA or mRNA does not provide a direct measure of the levels, activation state or function of proteins. Hence, protein

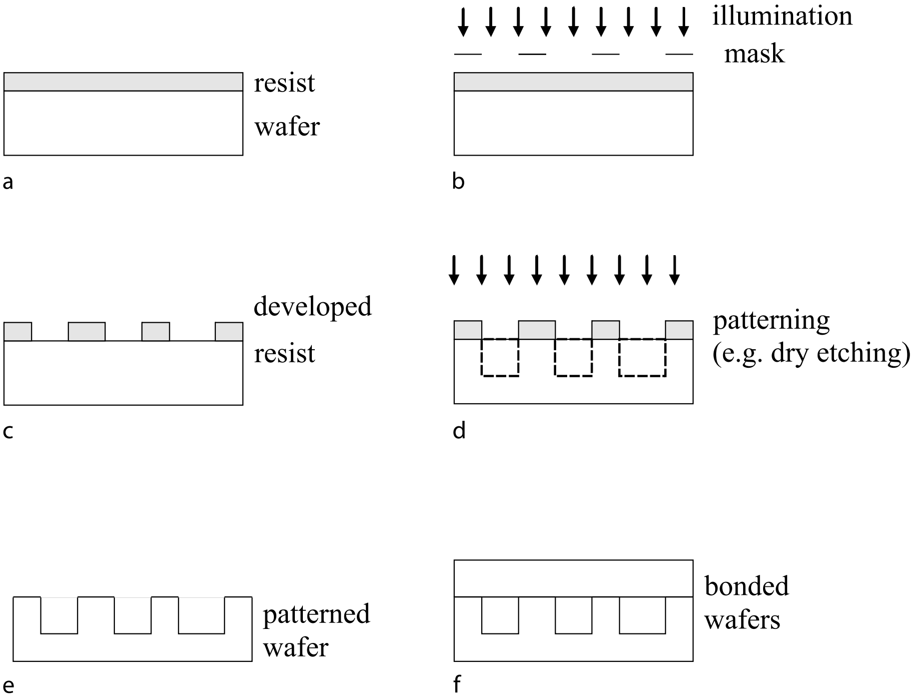

Lab-on-Chip Devices for Protein Analysis, Figure 2 Typical flow scheme for formation of microchannels in silicon or glass: (**a**) resist coated on wafer (**b**) resist exposure (**c**) resist development (**d**) patterning of exposed wafer (**e**) removal of remaining resist (**f**) bonding of wafers to form closed channels

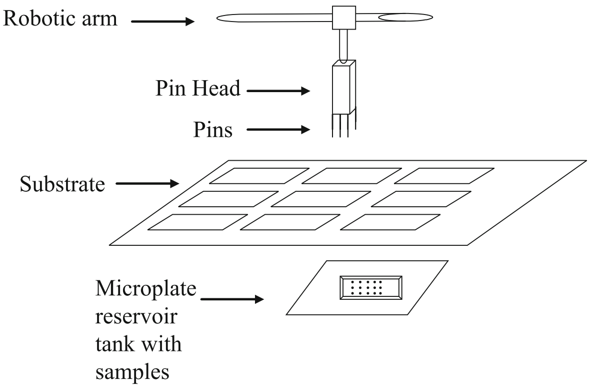

Lab-on-Chip Devices for Protein Analysis, Figure 3 A general schematic for microarray printing where the pin head carrying the printing device (pins) is mounted on a robot arm that carries the sample from the reservoir to the plate (substrate) where it is deposited in an array format (adapted from [2])

microarrays were developed to study the protein–protein, protein–ligand (like DNA, lipid, small molecule drugs etc.) interaction, and protein profiling. Though similar in concept and principles to DNA microarray, the physicochemical differences lack of amplification methods and the requirement to maintain native 3D molecular structure of proteins for function necessitates development of different handling procedures for protein microarrays. Apart from DNA and protein there are cell and tissue microarrays that have been developed [1].

Fabrication of microarrays involve deposition of nanoliter quantities of biological fluids (proteins) in a desirable arrangement of discrete spots on a substrate (e. g. glass or plastic) surface. All microarray techniques target efficient deposition of dense but uniform, homogeneous spots. There are two main types of spot formation techniques – contact printing and non-contact printing. The contact printing is a serial deposition method that forms array of spots by direct contact between the printing device (pin or tip) and substrate. Pin printing, microstamping and nanotip printing are some of the other technologies that have been developed. These methods are useful with reproducibility, but suffer from low-throughput fabrication. The non-contact printing involves techniques based on photochemistry, electro-printing, droplet dispensing and laser writing [2]. These later technologies have the advantage over the contact printing methods in being able to reduce contamination and having higher fabrication throughput. Figure 3 shows a general schematic for microarray printing where the pin head carrying the printing device (pins) is mounted on a robot arm that carries the sample from the reservoir to the plate (substrate) where it is deposited in an array format (adapted from [2]).

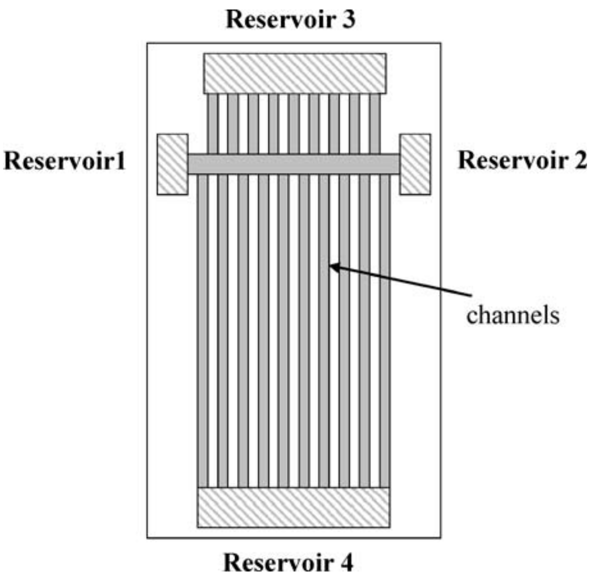

Lab-on-Chip Devices for Protein Analysis, Figure 4 Schematic of a microfluidic chip protein separation by 2D GE. The separation in the first dimension (by IEF) occurs in the channel between Reservoir 1 and Reservoir 2. Separation in the second dimension (by GE) occurs in the channels between Reservoir 3 and Reservoir 4. Appropriate voltages are applied across the reservoirs (adapted from [4])

Key Research Findings

Technology

Microfluidic Based Technologies

1D Separation of Proteins There has been considerable research devoted to the development of microfluidic platforms capable of performing small-scale protein separations. In addition to diffusion based methods [3], nearly every type of electrokinetically driven separation has been demonstrated in a chip-based platform, including free-flow electrophoresis, capillary electrophoresis, capillary gel electrophoresis, isoelectric focusing (IEF), micellar electrokinetic chromatography and capillary electrochemical chromatography.

2D Separation and Combination Methods 1D separation methods are frequently limited in providing the resolution required for the analysis of complex biological samples. 2D separations, where separation occurs in orthogonal directions, however, greatly increase resolving power. Several such 2D methods and combinations of 1D methods have been implemented on microchip format for protein separations, such as free-flow electrophoresis coupled with isoelectric focusing, gel electrophoresis coupled with isoelectric focusing, open channel electrophoresis with micellar electrokinetic chromatography, open channel electrochromatography and capillary electrophoresis, and parallel capillary zone electrophoresis and capillary electrochemical chromatography separations. A schematic of a microfluidic chip protein separation by 2D gel electrophoresis is shown in Fig. 4. The separation in the first dimension (by isoelectric focusing) occurs in the channel between reservoir 1 and reservoir 2, and separation in the second dimension (by gel electrophoresis) occurs in the channels between reservoir 1 and reservoir 2, with appropriate voltages applied across the reservoirs (adapted from [4]).

Interface with MS Systems for Detection MS is one of the most popular methods for peptide sequencing. However, the long (up to 24 h) incubation times and extensive manual sequences employed in conventional sample preparation procedures are bottlenecks for process improvement. A number of papers on coupling microfluidic chips, where the pre-MS sample preparation steps are performed, to mass spectrometers have been reported [5] and references 1–33 there in. Advantages of miniaturization of sample preparation steps include small sample volume, reduction in processing time and improved MS efficiency. For example, in an application of temperature-controlled silicon based microreactors, comprising microchannels and reaction chambers [6], the sample preparation time was reduced from the conventional time of about 24 h (chemical denaturation) and 3.5 h (thermal denaturation) to 11 min (thermal denaturation for 1 min and trypsin digestion for 10 min). This study also demonstrated that enhanced digestion efficiency was achieved by miniaturization of the reaction system. In another study, an integrated microfluidic chip of glass substrates with electrowetting-on-dielectric actuation for multiplexed proteomic sample preparation and analysis by MALDI-MS was described [7]. The integrated device was demonstrated for processing four angiotensin peptide/urea samples in parallel through a sequence of seven actuation steps. While a considerable amount of work has been done to realize protein separations on microfluidic platforms, interfacing with MS has been a bottleneck. An example of progress in this area has been the integration of a microfabricated IEF chip with an electrospray ionization (ESI) tip [8]. More recently, a microfluidic chip, that integrated all the fluidic components of a gradient liquid chromatography system and an electrospray nozzle has been reported [9]. The device was used to perform a liquid chromatography-tandem mass spectrometry (LC-MS/MS) analysis of a mixture of peptides from the trypsin digestion of bovine serum albumen (BSA). Compared to the analysis of the same sample using a commercial nanoflow LC system, the chromatographic resolution was nearly as

good, and the total cycle time was significantly reduced because of the minimal volume between the pumps and the column. Agilent (Santa Clara, CA) reported a polymeric microfluidic chip that integrated an enrichment column, separation column, and electrospray source on a single chip [10]. Overall system performance was demonstrated through reversed-phase gradient separations of tryptic protein digests at flow rates between 100 and 400 nL/min.

Integrated Optical Systems for Detection Detection of labeled proteins by means of laser-induced fluorescence (LIF) is a popular technique associated with separation based processes. The limitations (of mobility) due to the bulkiness of the conventional detection system spurred an interest in optical detection systems integrated to chip based separations of biomolecules For example, Viellard et al. [11], reported a glass/PDMS hybrid microfluidic chip for electrophoretic separations (capillary zone electrophoresis and capillary gel electrophoresis) of proteins with integrated optical waveguides for fluorimetric detection. Also, Mizukami et al. [12], fabricated an integrated micro-electrophoretic chip by implementing an acrylic microfluidic channel directly on top of a photosensor array. Capillary gel electrophoresis was performed for the separation of a mixture of two labeled proteins and the separation process was visualized as a sequence of two-dimensional images. Calliper Technologies (Mountain View, CA) has described a microfabricated analytical device on a glass chip that performed a protein-sizing assay, by integrating the required separation, staining/destaining, and detection steps.

Immunoassay Microfluidic networks have high resolution and contrast capabilities for simultaneously patterning lines of proteins onto a surface. This has been utilized, for example, by Bernard et al. [13], to create a miniaturized mosaic of imminoassays by patterning lines of antigens on PDMS surfaces by a microfluidic network and delivering the analytes by another set of microfluidic channels at right angles to the direction of the first set. Microfluidic separations have also been combined with immunoassay based detection. For example, Lonnberg et al. [14], reported fabrication and performance of a porous monolith chip where ion-exchange chromatographic separation of protein isoforms was integrated with immunoassay detection. Sensitivity was demonstrated with transferrin isoforms which differed only by a pH of 0.1 in their pI.

Microarray Based Technologies

Proteins can be identified by antibodies, enzymes, or aptamers. Microarray technology has proven successful in detection and quantitation of proteins and studying protein–protein interactions. The basic technique involves immobilization of a set of proteins on a solid surface preserving their native folded confirmations in an array format using high precision robotics and then allowing them to interact with another set of proteins [15]. Each spot on the array can contain a homogeneous or heterogeneous set of "bait" molecules. A spot on the array may display an immobilized antibody, a cell or phage lysate, a recombinant protein or peptide, a drug, or a nucleic acid. The array can then be queried with

1. a probe (labeled antibody or ligand), or
2. an unknown biological sample (e. g., cell/tissue lysates or serum sample) containing analytes of interest.

The querying molecules are tagged with a signal-generating moiety, such that for each spot, the intensity of signal is proportional to the quantity of applied query molecules bound to the bait molecules. An image of the generated positive and negative pattern of spots is captured using various detection methods, analyzed, and interpreted. Protein microarrays are broadly classified into

1. Forward Phase Arrays (FPA) that immobizes the bait and captures analyte from solution, allowing assay of multiple analytes from a single sample, and
2. Reverse Phase Arrays (RPA) where the test sample is immobilized and query molecule in applied in solution phase allowing for analysis of a single analyte across multiple samples.

Shown in Fig. 5 is a general scheme for the use of protein microarray to analyze patient tissue for various applications.

Applications

Unlike LOC technologies associated with DNA and RNA, the protein analysis platforms for these technologies are not fully mature. Nevertheless, useful implementation of protein analysis technologies in LOC formats are beginning to be developed and field tested.

Some of the successful applications have been in Antibody screening, drug discovery, drug target identification, patch-clamp assay for cell membrane ion channels function and electric signals in neuron. Besides these basic applications many diagnostic tools have also been developed to detect pathogens and disease agents like HIV/AIDS, malaria, tuberculosis, pertussis, meningitis, lymphatic filariasis, gonorrhea, leishmaniasis, trypanosomiasis, liver cirrhosis, osteoarthritis, rheumatoid arthritis, to name a few [16].

LOC devices are being demonstrated to be superior than conventional methods in many applications. LOC

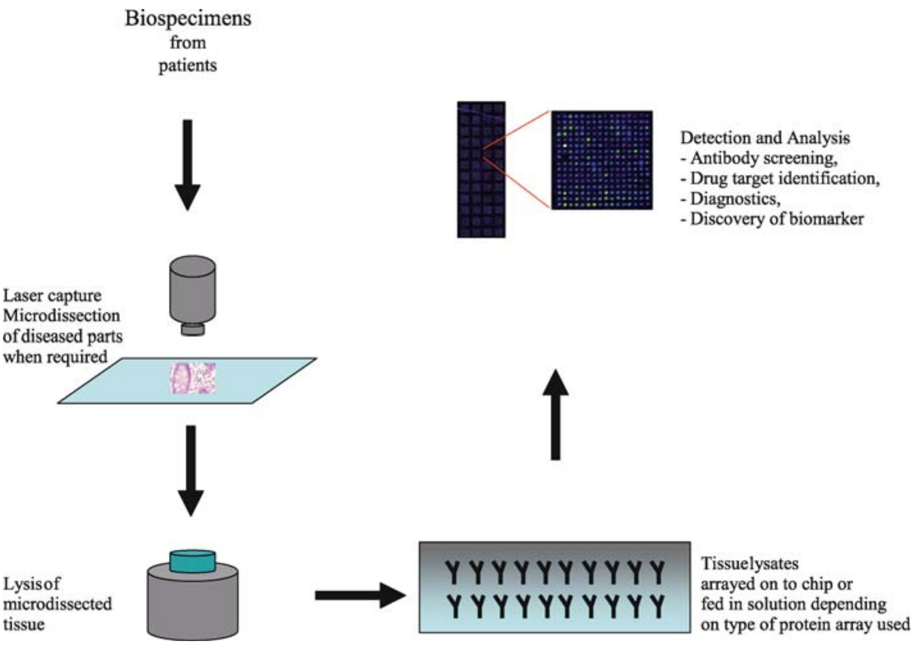

Lab-on-Chip Devices for Protein Analysis, Figure 5 Biomedical applications of Protein microarray. A general schema for analyzing disease tissue samples from patients using protein microarray technology

immunoassay to detect C-reactive protein in saliva using porous beads to capture probes on solid phase is 1000 fold more sensitive than traditional ELISA [17]. Use of micron scale paramagnetic beads and complimentary metal oxide conductor (CMOS) chip has been demonstrated to have application as an immunosensing devise [18]. A self-contained point-of-care device that can detect enterotoxin B in urine, milk etc. with considerable sensitivity has recently been developed [19].

Zyomyx (Hayward, CA) has developed the Zyomyx human cytokine Biochip that uses microfluidics to measure 30 different human cytokines simultaneously. Biosite (San Diego, CA) markets commercial microfluidics chip based immunoassay for clinical applications. Multiplexed assays using fluorescent microspheres/beads in Lab-on-Chip format manufactured by Becton-Dickinson (Franklin, NJ), Diasorin (Stillwater, MN) and Luminex Corp. (Austin, TX) are also available for use in clinics.

Protein arrays have been employed for studying biomolecular interactions including antibody specificity, mechanism of gene regulation and protein phosphorylation. Ciphergen Biosystems Inc. (Fremont, California) makes ProteinChip, the first commercial tool available for profiling serum biomarkers in disease – pancreatic cancer. For clinical diagnostics, Caliper Life Sciences (Hopkinton, MA) has developed LabChip – a capillary electrophoresis chip that can assay 500 different protein kinases and can analyze 12 different biomolecules per minute. Tecan Group Ltd. (Mannedorf, Switzerland) has developed LabCD, a CD format microfluidics and reaction chambers. These compact disc shaped microfluidic device can perform 48 drug screening assays simultaneously with centrifugation.

Future Directions for Research

The field of biology in general and biomedicine in particular is turning to a *systems approach* where all genes (DNA), translational products/messenger (RNA), and proteins and their relationship to each other in response to perturbations are studied in tandem. This current thrust will lead to more of a predictive science and as a result, to individualized preventative medicine. Advancement in technology that allows for sampling, manipulation and measurement of individual molecules with high spatial signal resolution has allowed the packaging of these technologies onto a Lab-on-Chip format with some success. DNA and RNA based technologies have made rapid strides in the last decade, while the protein technology has generally lagged behind. In the coming decades the field needs to bring to fruition the promises of LOC technologies in protein analysis to achieve success of the *systems approach*.

The general challenges of protein analysis (and thus applicable to LOC-based analysis) include those related to the composition of the proteome and the analytical meth-

ods. No ideal protocols exists, for example, to selectively, reproducibly and non-intrusively isolate the full complement of proteins from tissue samples. The vast diversity in protein expressions, charged states, molecular sizes and configurations etc. make sample preparation a challenging task. Also, extreme range of concentration of proteins in any given sample with a large number of proteins of interest for drug targets and biomarkers occurring in low abundances necessitates enrichment techniques which again have drawbacks [20]. These, in conjunction with lack of any amplification methods for proteins pose challenges for protein analysis. More specifically for microfluidic systems, the small analyte volumes put a high demand on the detection system. The requirement of high affinity antibodies/ligands and unique affinity constants for each antibody–ligand interactions etc. are some of the other challenges of microarray technology that needs to be addressed. Another challenge is to lower the manufacturing costs of the devices and increase their range of applications. The ultimate goal of the Lab-on-Chip technology would be the integration and automation of multiple diagnostic processes (and thus the total sequence of the laboratory processes) on the same miniaturized platform and research needs to focus in this direction.

The impact of rapid and reliable protein analysis technology using LOC devices will not be limited to the development of diagnostic tools like detection of pathogens, disease biomarkers or target identification. Rather, this technology in combination with other developing technologies will become essential tools in rational drug design and personalized medicine. Inexpensive LOC technology will also play a very critical part in global healthcare assessment and influence future healthcare policies.

Cross References

- ▶ Biochip
- ▶ Chromatographic Chip Devices
- ▶ DC-Dielectrophoresis Lab-on-Chip Devices
- ▶ Electrokinetic Flow and Ion Transport in Nanochannels
- ▶ Electrokinetic Transport with Biochemical Reactions
- ▶ Electrophoresis
- ▶ Fabrication of 3D Microfluidic Structures
- ▶ Lab-on-Chip (General Philosophy)
- ▶ Lab-on-Chip Devices for Immunoassay
- ▶ Lab-on-Chip Devices for Separation Based Detection
- ▶ Microfluidic Assembly
- ▶ On-Chip Electrospray
- ▶ Protein Microarrays
- ▶ Two-Dimensional Electrophoresis

References

1. Wu RZ, Bailey SN, Sabatini DM (2002) Cell-biological applications of transfected-cell microarrays. Trends Cell Biol 12(10):485–488
2. Barbulovic-Nad I et al (2006) Bio-microarray fabrication techniques–a review. Crit Rev Biotechnol 26(4):237–259
3. Schoch RB, Bertsch A, Renaud P (2006) pH-controlled diffusion of proteins with different pI values across a nanochannel on a chip. Nano Lett 6(3):543–547
4. Li Y et al (2004) Integration of isoelectric focusing with parallel sodium dodecyl sulfate gel electrophoresis for multidimensional protein separations in a plastic microfluidic [correction of microfludic] network. Anal Chem 76(3):742–748
5. Yang Y et al (2005) A polymeric microchip with integrated tips and in situ polymerized monolith for electrospray mass spectrometry. Lab Chip 5(8):869–876
6. Sim TS et al (2006) Application of a temperature-controllable microreactor to simple and rapid protein identification using MALDI-TOF MS. Lab Chip 6(8):1056–1061
7. Moon H et al (2006) An integrated digital microfluidic chip for multiplexed proteomic sample preparation and analysis by MALDI-MS. Lab Chip 6(9):1213–1219
8. Wen J et al (2000) Microfabricated isoelectric focusing device for direct electrospray ionization-mass spectrometry. Electrophoresis 21(1):191–197
9. Xie J et al (2005) Microfluidic platform for liquid chromatography-tandem mass spectrometry analyses of complex peptide mixtures. Anal Chem 77(21):6947–6953
10. Yin H et al (2005) Microfluidic chip for peptide analysis with an integrated HPLC column, sample enrichment column, and nanoelectrospray tip. Anal Chem 77(2):527–533
11. Vieillard J et al (2007) Application of microfluidics chip with integrated optics for electrophoretic separation of proteins. J Chromatogr B 845:218–225
12. Mizukami Y et al (2002) A novel microchip for capillary electrophoresis with acrylic microchannel fabricated on photosensor array. Sens Actuators B 81:202–209
13. Bernard A, Michel B, Delamarche E (2001) Micromosaic immunoassays. Anal Chem 73(1):8–12
14. Lonnberg M, Carlsson J (2006) Lab-on-a-chip technology for determination of protein isoform profiles. J Chromatogr A 1127(1–2):175–182
15. MacBeath G, Schreiber SL (2002) Printing proteins as microarrays for high-throughput function determination. Science 289(5485):1760–1763
16. Chin CD, Linder V, Sia SK (2007) Lab-on-a-chip devices for global health: past studies and future opportunities. Lab Chip 7(1):41–57
17. Christodoulides N et al (2005) Toward the development of a lab-on-a-chip dual-function leukocyte and C-reactive protein analysis method for the assessment of inflammation and cardiac risk. Clin Chem 51(12):2391–2395
18. Aytur T et al (2006) A novel magnetic bead bioassay platform using a microchip-based sensor for infectious disease diagnosis. J Immunol Methods 314(1–2):21–29
19. Naimushin AN et al (2002) Detection of Staphylococcus aureus enterotoxin B at femtomolar levels with a miniature integrated two-channel surface plasmon resonance (SPR) sensor. Biosens Bioelectron 17(6–7):573–584
20. Garbis S, Lubec G, Fountoulakis M (2005) Limitations of current proteomics technologies. J Chromatogr A 1077(1):1–18

L

Lab-on-a-Chip Devices for Sample Extractions

JEFFREY D. ZAHN[1], VARUN REDDY[2], XIAOLE MAO[2]
[1] Department of Biomedical Engineering, The State University of New Jersey, Piscataway, NJ, USA
[2] Department of Bioengineering, The Pennsylvania State University, University Park, PA, USA
jdzahn@rci.rutgers.edu

Synonyms

Sample purification; DNA extraction; Solid phase extraction; Liquid extraction; Phenol extraction

Definition

Sample extraction involves purifying a single component from a complex mixture. It usually is based on exploiting a unique property of the component of interest such as solubility or charge which allows it to be separated from other components in solution. Sample extraction is often referred to in the context of nucleic acid purification from a complex biological mixture such as a cell lysate.

Overview

A major research thrust in microfluidic science and technology is the development of autonomous platforms for the extraction and purification of biological material from cells. Batch fabricated diagnostic and medical treatment units hold great potential to enable both research and healthcare advances. This article presents research focused on sample extraction and purification with an emphasis on steps taken towards miniaturizing one of the fundamental preparative techniques used in molecular biology: DNA extraction and purification from a complex biological sample. After the extraction procedure, the DNA can be processed downstream for Polymerase Chain Reaction (PCR) amplification, restriction enzyme digest and capillary electrophoresis. Two approaches to sample extraction techniques will be discussed: solid phase extraction and liquid phase extraction techniques. The fabrication methods for creating the extraction modules should also be compatible with downstream sample analysis technologies. These approaches form some of the basic requirements towards the development of highly integrated biological and genomic analysis systems by allowing efficient DNA purification.

Basic Methodology

Standard Macroscale Extraction Techniques

Genomic or plasmid DNA purification from a cell sample using extraction techniques is one of many standard techniques routinely performed in biology laboratories [1]. These extraction techniques can be classified as either liquid phase extraction or solid phase extraction techniques and involve extracting DNA or RNA from a biological sample while removing other biological molecules such as lipids and proteins. Historically, liquid phase extraction techniques were developed first. However, solid phase DNA extraction preparative kits have recently become more popular because of their ease of use and the avoidance of organic solvents used in liquid extraction techniques. Briefly, the liquid extraction procedure termed 'phenol extraction' consists of lysing cells in a basic lysis buffer (10 mM Tris pH 8.0, 0.1 M EDTA, 20 μg/ml Pancreatic RNAase, 0.5% Sodium dodecyl sulphate (SDS), and 100 μg/ml proteinase K) and adding an equal volume of phenol:chloroform:isoamyl alcohol (25 : 24 : 1 parts by volume) mixture to the aqueous solution. The organic (phenol) phase is immiscible with the aqueous phase and so the two phases separate by gravity or centrifugation. A vortexing step 'mixes' the two phases and allows the different cellular components to partition into either the aqueous or organic phases. With effective mixing, the cell components naturally distribute themselves into the two phases in order to minimize interaction energies of the biological components with the surrounding solvents. The membrane components and protein will partition to the organic–aqueous interface while the DNA remains in solution within the aqueous phase. Thus, effective mixing maximizes the surface area over which this partitioning occurs. Therefore, the smaller the discrete phase domains, the more effective the DNA extraction procedure is. After the mixing step, the two immiscible phases are allowed to separate by centrifugation at 10,000 RPM for 10 min. The lower density aqueous phase which contains the DNA separates above the phenol phase and is carefully pipetted into a new tube. The centrifugation can be repeated up to three times to completely separate the aqueous phase from the organic phase. The DNA is then concentrated by precipitation in ethanol and resuspended in an aqueous Tris-EDTA pH 8.0 (TE) buffer. Two to two and a half times the aqueous sample volume of ice cold 100% ethanol is added to the aqueous solution and gently mixed. The mixture is then spun for 20 min in a fixed-angle microcentrifuge to precipitate the DNA and 'pellet' it at the bottom of the sample tube. After centrifugation the supernatant is removed leaving only the DNA pellet at the bottom of the tube. A 1 ml 70% ethanol wash is added to the tube, gently mixed and

spun at 10,000 RPM for 1 min in the centrifuge. The supernatant is again removed and the DNA pellet is resuspended in 20 – 50 μL of TE buffer.

Recently, the use of DNA extraction centrifugation compatible columns such as those offered by Qiagen Corporation has become more commonplace. These extraction procedures are based on the alkaline lysis of cells followed by a chaotropic salt induced adsorption of DNA onto a silica surface within a silica gel matrix in a high ionic strength salt solution which shields the coulombic interactions between the DNA and silica surface. Cells are lysed in an alkaline solution, and the lysate is neutralized and adjusted to a high-salt concentration for optimal DNA binding. Following the alkaline lysis of the cells, the crude lysate is loaded directly onto a filter where the denatured and precipitated cellular components are removed by filtration through an integrated filter membrane. The dissolved components flow through the filter directly into the silica matrix where selective adsorption of the DNA in the high salt buffer occurs. The column is centrifuged at 10,000 RPM for 10 min. The buffers in these preparative kits are optimized for the cell lysis procedure and the silica gel binding to ensure that only DNA remains in the gel matrix, while RNA, cellular proteins, and metabolites are not retained in the matrix but are found in the flow-through. Free trace nucleases are removed by a short wash-centrifugation step. The DNA is then eluted from the column with 50 – 100 μl of a low ionic strength salt elution buffer followed by 1 min of centrifugation. During this step, the DNA and silica negative charges are no longer shielded so the DNA elutes from the silica surface.

After extraction by either procedure, the purified DNA concentration is usually about 1 mg/ml and can be quantified either by using a spectrophotometer monitoring the solution absorbance at 260 and 280 nm or by gel electrophoresis against known concentration standards. The purified DNA is free of other cellular components such as free nucleases which can interfere with other DNA processing techniques required in biological research such as restriction endonuclease cutting, PCR amplification, or gel electrophoresis.

The ability to miniaturize DNA extraction and analysis devices will benefit many research areas which require portable and rapid analysis of biological samples. Some of these areas are those where only a small DNA sample such as samples from only a few cells must be efficiently detected such as is commonly encountered in forensic analysis at crime scenes or is necessary for biological warfare monitoring. Miniaturized DNA analysis can also be adapted to replace conventional DNA extraction techniques. There is a huge reduction in the quantity of reagents which are used and the small size naturally lends itself to mass production and automation that will reduce the cost per device and analysis time. Approaches toward miniaturizing both solid phase and liquid phase extraction techniques are discussed in the next section.

Key Research Findings

Current Research on Solid Phase Extraction Techniques

The basic approach towards developing devices allowing solid phase DNA extraction has been to try to miniaturize the basic components of the solid phase DNA preparative kits. Most microdevices for solid phase DNA extraction still depend on selective DNA binding to a silica surface followed by a DNA elution step. One of the first reports of DNA purification in a solid phase extraction technique was by Cepheid Corporation [2]. In their research, the extraction of DNA was accomplished by creating high aspect ratio silicon pillar microstructures through Deep Reactive Ion Etching (DRIE) which have a high binding surface area to fluid volume ratio. The device is housed within a cartridge with reagent containment reservoirs, areas for solution mixing and the DNA extraction module. A raw cell sample containing the DNA of interest is lysed and introduced into the cartridge. The cartridge with the crude lysate is then inserted into an instrument that drives the sample through the DNA extraction module containing the silicon pillars (Fig. 1a). The DNA binds to the native silicon dioxide (silica) surface which forms on the surface of the silicon pillars. The device is designed to ensure that the silicon pillars have a sufficient binding capacity and adequate capture rate to allow quick flowthrough of the sample volume with enough time for DNA binding. A DNA washing step is then performed by flowing a buffer through the extraction module to remove any PCR inhibitors such as heavy metals (iron in hemoglobin), enzymes, proteins and nucleases. At this point the DNA is still bound to the silicon pillars. The bound DNA is then eluted using a low salt elution buffer. The eluted DNA is then amplified by an on chip rapid multichannel PCR thermal cycling module that has been integrated into the device (Fig. 1b). The PCR amplification unit has resistive heaters in the form of thick-films that perform rapid thermal cycling. When fluorescent molecules are incorporated into the DNA, the DNA fluorescence increases with each amplification cycle and is detected by an optical module. The reaction is stopped when a fluorescence threshold is reached. DNA extraction using this technology has been demonstrated using both high and low concentration DNA test samples.

Landers and colleagues have demonstrated [3, 4] a microchip-based DNA purification technique where DNA from biological samples such as blood has been isolated. The approach taken here was to maximize the surface area of

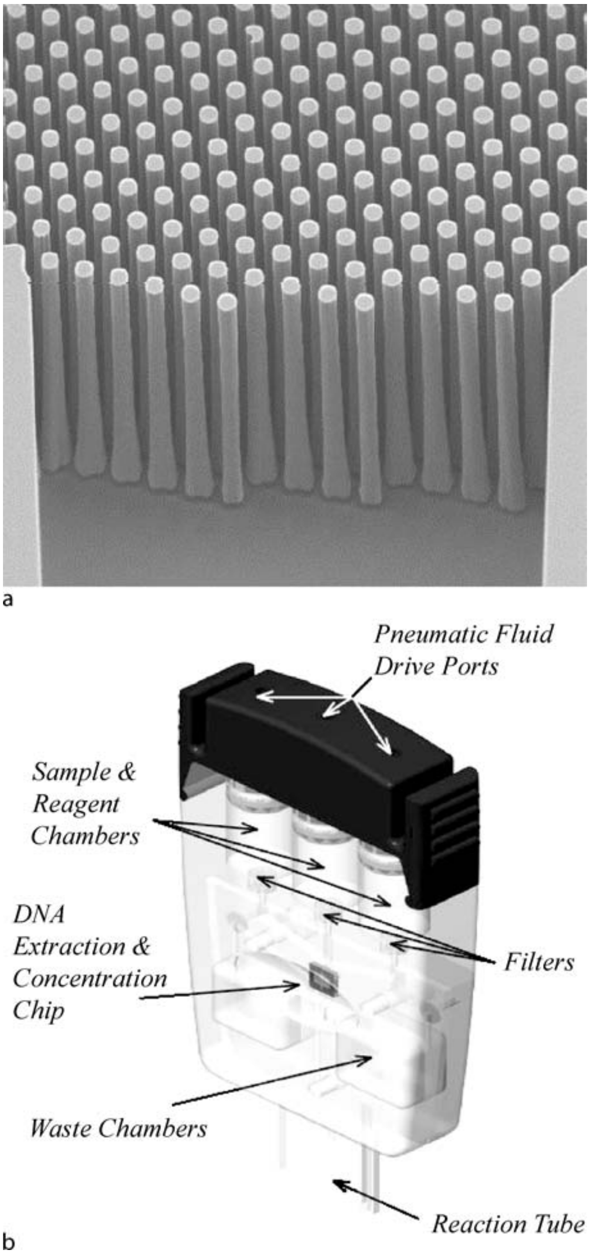

Lab-on-a-Chip Devices for Sample Extractions, Figure 1 (**a**) SEM image of a micromachined DNA extraction module consisting of 200 mm tall pillars with an 18 mm diameter. (**b**) Figure showing an integrated DNA extraction cartridge containing a DNA extraction chip, sample and reagent ports, filters, integrated waste, and PCR tube. Image copyright 1999, Cepheid Corporation. Used with permission

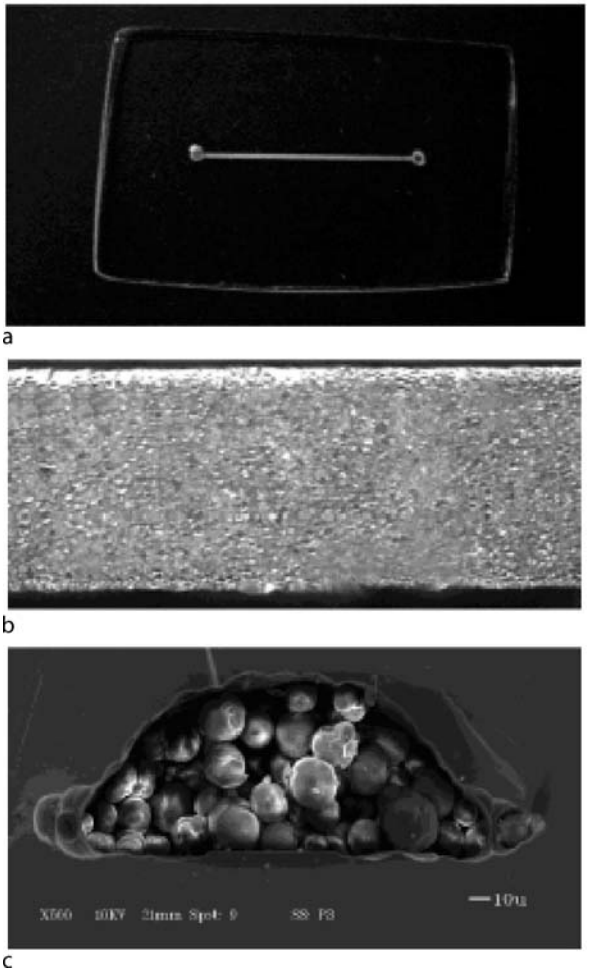

Lab-on-a-Chip Devices for Sample Extractions, Figure 2 Microchip packed with silica particles and immobilized within a sol–gel: (**a**) No magnification; (**b**) top view of a packed column at 10 times magnification; (**c**) cross-section of packed channel at 500 times magnification. (Reprinted with permission from [3])

interaction for DNA adsorption to the silica. Hence, silica beads of $\sim 10\,\mu m$ diameter were packed into a microfabricated channel (Fig. 2) as a means to increase the silica-DNA interaction surface area. To pack the column, the silica beads are first introduced into the microfluidic channel and then the beads are immobilized within a sol–gel. In the silica particle/sol–gel hybrid approach employed here, the sol–gel acts as filler material as well as an interparticle glue which immobilizes the silica particles. It was found that by immobilizing the silica particles within the sol–gel there was a significant improvement in both DNA extraction reproducibility and the number of times the devices could be used over simply using a column packed with the silica beads. The improved recovery rate using the sol–gel/silica particle hybrid as compared to just using silica particles is attributed to the presence of the sol–gel preventing tight and dynamic packing of the silica particles during column pressurization. In order to extract the DNA, the devices were first conditioned with methanol (MeOH) for 30 min and washed with TE elution buffer for

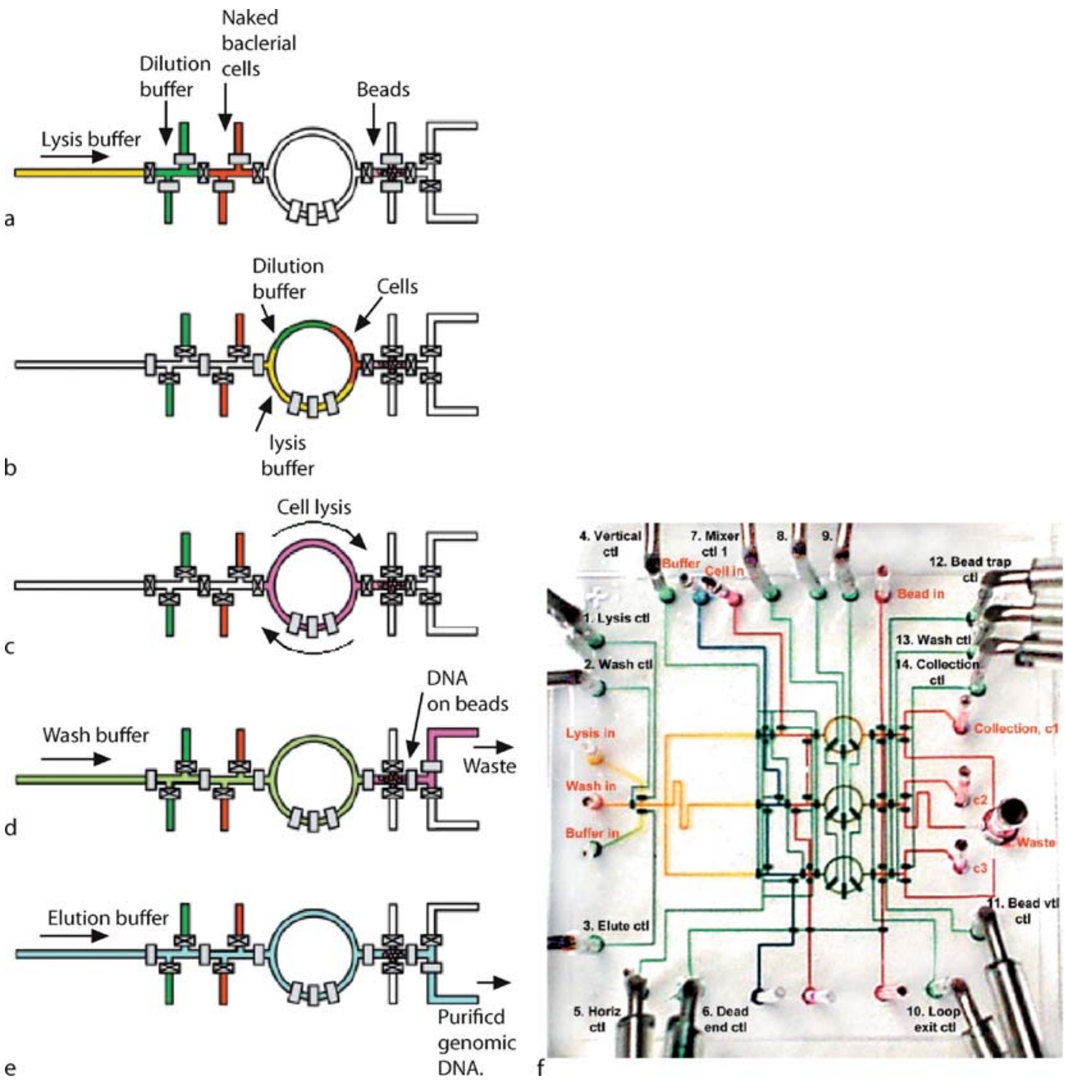

Lab-on-a-Chip Devices for Sample Extractions, Figure 3 An integrated cell lysis and DNA extraction device. Parts (**a**) to (**e**) show the sequence of steps involved in introducing the cell sample, lysis buffer and mixing to extract DNA. Part (**f**) shows the parallel architecture implementation of the DNA extraction system. (Reprinted by permission from [5])

30 min. The extraction procedure consisted of a sample loading, washing and elution step. In the load step 20 μl of load buffer (6 M guanidine hydrochloride, 1% Triton X-100 in TE buffer) containing the DNA is passed through the device. Trace proteins and other PCR inhibitors that may also be adsorbed onto the silica during this step are removed by flowing a wash buffer (2-propanol/water 80/20 (v/v)) through the device. The DNA is then eluted in a low ionic strength TE buffer. Ten DNA extractions per device have been demonstrated with a λ-phage DNA. An average recovery of 76% (10% Standard Deviation) with a chip to chip reproducibility average of 68% (6% Standard Deviation) has been demonstrated.

Finally, an integrated sample lysis and DNA extraction device has been demonstrated by Quake and colleagues [5]. The unique feature of this design is that all steps required for DNA extraction are carried out on the chip without any cell sample pretreatment. The device is fabricated using soft lithography techniques and consists of a series of chambers (Fig. 3) with integrated pumping and valving functions operated by external hydraulic activation (Fig. 3f). The integrated pumping and valving functions allows the sequential operation of the steps required for DNA isolation from a bacterial cell sample and the ability to pump the fluid through the different reaction chambers. Each reagent solution and silica

beads with DNA binding capacity are loaded into their appropriate chamber prior to device use. Each chamber allows the sequential introduction of the different reagents which are necessary for DNA extraction. The main chambers include the lysis buffer chamber, followed by a dilution buffer chamber and the cell chamber. These respective chambers are first filled with the lysis buffer, dilution buffer and bacterial cells. In device operation, the hydraulic valves that initially separated the chambers are opened (Fig. 3a) and the contents of the three chambers are pumped into a circular chamber (Fig. 3b). Here, the contents are mixed by pumping the solution around the circular chamber (Fig. 3c). During the mixing process, the cells are lysed by the lysis buffer in the solution. The mixture is then pumped further downstream into a chamber filled with the DNA adsorption beads (Fig. 3d). The DNA binds to the beads while the remaining solution flows through the chamber and is directed through a waste outlet. The DNA is then eluted off the beads through the introduction of a elution buffer (Fig. 3e) and collected at the device outlet. Extraction of DNA from single cells has been demonstrated using this device. The microfluidic structure has also been parallelized (Fig. 3f) to increase throughput and also to increase the level of automation in analyzing different cell populations simultaneously.

Current Research on Liquid Phase Extraction Techniques

Liquid phase extraction techniques, though less developed than solid phase extraction for biological sample preparation, have nonetheless seen an increase in interest in recent years. One of the reasons liquid phase extraction techniques have not developed as rapidly as solid phase techniques is due to the need for a fluid–fluid interface through which material may partition and therefore a need for a fuller understanding of multiphase microflows. Two-phase flow is the simultaneous flow of two immiscible fluid phases and is the simplest case of multiphase flow. Within the microfluidic device, the mass transfer rate is determined, to a large extent, by the fluid flow pattern. In previous studies, factors that affect the flow pattern of co-infused organic–aqueous flows were investigated. Two phase flow most often involves an interface between the two phases and this interface has various degrees of influence on the flow characteristics. The presence of the interfacial forces influences the microflow profiles which can be exploited to realize certain types of flows. The tendency of immiscible liquids to form dynamic droplet emulsion patterns as a function of capillary number and flow velocity ratios between a continuous and noncontinuous phase has been exploited from a T-section microfluidic channel [6] to obtain a tight control of the emulsion droplet size distribution. A number of techniques have been used to improve the interfacial stability or the overall stability of two phase flow in microfluidic systems. Some of the techniques include patterning the base of the micro-channel with ridges that guide the flow [7], and the incorporation of surfactant [8, 9]. Stable and unstable stratified flow profiles have been studied using immiscible organic/aqueous solvent mixtures [8, 9]. Kitomori and colleagues have demonstrated stable two phase systems for continuous liquid extraction techniques of molecules from one phase into another [7]. Here, a methyl red dye was extracted across a stratified three layer multiphase system where the dye was extracted from an aqueous donor phase across an organic cyclohexane membrane and finally into a acceptor aqueous phase. In this case, all of the dye transport is due to diffusion from the donor phase to the acceptor phase as the fluid moves through the microchannels.

Zahn and colleagues has begun to explore approaches towards developing a miniaturized phenol extraction module using a two or three inlet converging microchannel geometry. Here, two phases are coinfused through a microfluidic network where one of the components is Phenol : Chloroform : Isoamyl alcohol (25 : 24 : 1) and the other is a 0.5% SDS aqueous solution. Here, biological interactions at the organic aqueous interface were studied. A fluorescent rhodamine dye labeled Bovine Serum Albumin (BSA) protein was added to the aqueous phase containing surfactant and coinfused with the phenol phase through a microchannel in a stable stratified flow. As the protein solution flowed through the device, the BSA was seen precipitating at the organic–aqueous interface to create a line of protein precipitate which appeared bright under epifluorescent microscopy demonstrating the ability to remove protein from an aqueous solution at the organic–aqueous interface. Complete removal was not possible due to the limited surface area of the interface and because the protein transport to the interface was diffusion limited. More recently, an electrohydrodynamic approach for destabilizing the stratified phenol-aqueous flow to increase the interfacial area between the two phases to improve extraction efficiency has been investigated [10]. Additionally, it has been recognized that a droplet flow profile between the phenol and water phases improves extraction efficiency because of a convective enhancement to the mass transport due to internal fluid circulation within a droplet as it moves through the microchannel [11]. To demonstrate this effect, a sulphorhodamine dye is added to the aqueous phase. The rhodamine dye was observed to naturally partition from the aqueous phase into the organic phase so it was utilized as a fluorescent marker to visualize the component extraction from the aqueous phase into the organic phase. A large increase in dye extraction efficiency

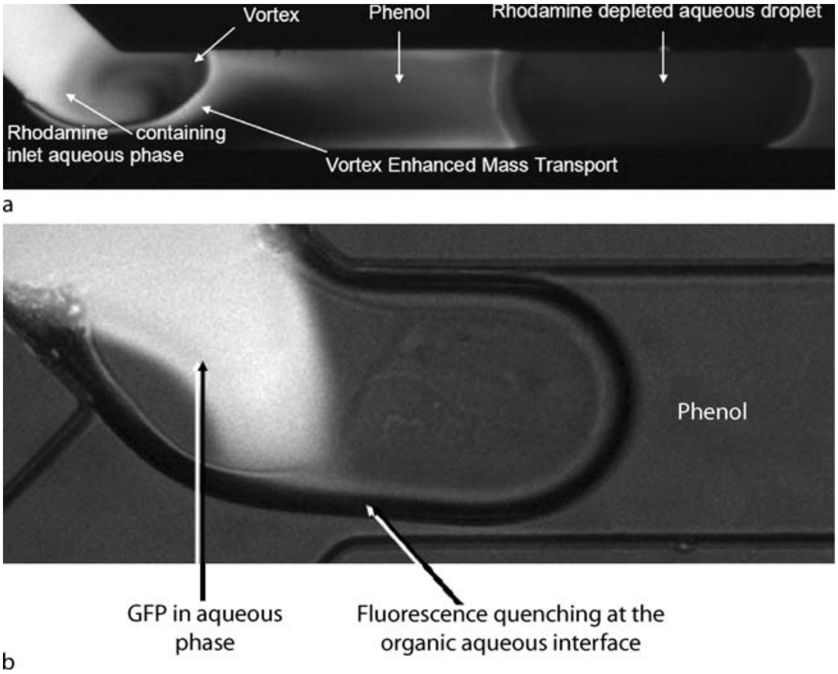

Lab-on-a-Chip Devices for Sample Extractions, Figure 4 (**a**) Experiment results of two phase extraction using rhodamine dye. Internal circulation of the fluorescent dye helps the mass transfer from the aqueous to the phenol phase. At the same time, the fluorescent dye in the previous aqueous droplet moving through the channel has almost been depleted. (**b**) Image of a cell lysate droplet containing Green Fluorescent Protein (GFP) near the inlet intersection. The GFP is quenched at the two phase interface due to protein denaturation at the organic-aqueous interface. (Reprinted with permission from [11])

has been shown when droplet flow is used as opposed to a stable stratified flow due to this convective enhancement. Figure 4a shows a fluorescent microscopy image of an aqueous droplet forming within the microchannel. By initially labeling the aqueous phase with rhodamine, the fluid–fluid interface as well as the extraction between two phases can be tracked. It is clearly shown that the circulating flow pattern is developing within the forming droplet. A significant amount of fluorescent dye has been transferred into the organic phase even before the droplet formation process is complete. The ‘flare’ of the fluorescent trace extending from the interface toward the organic phase indicates that the fluorescent dye is quickly being transported across the organic/aqueous interface. Downstream of the forming droplet, the previous droplet which has broken off has been almost completely depleted of fluorescent dye. In order to demonstrate the feasibility of using a droplet flow pattern to remove protein from a DNA containing biological sample, an aqueous cell lysate solution containing a green fluorescent protein (GFP), DNA, and other cell components was tested. The sample was co-infused into the channel with phenol and an epifluorescence image was obtained as shown in Fig. 4b. The image shows the lysate solution droplet is being generated near the inlet intersection. The GFP within the droplet emits fluorescence while it still maintains its folded 3 dimensional structure and biological function. However, when the GFP is transported to the organic/aqueous interface the fluorescence of GFP was rapidly quenched, due to protein denaturization at the organic aqueous interface. When the protein denatures, the GFP fluorochrome unfolds resulting in a loss of fluorescence. This result implies that the protein is rapidly transported to the organic aqueous interface and removed from the aqueous phase. This is similar to results seen in [9] where the rhodamine labeled BSA was visualized denaturing and precipitating along the organic aqueous interface in a stratified flow.

Future Directions for Research

The development of Lab-on-a-Chip devices for sample extraction is important to allow further advances in genomics, proteomics and bioinformatics. The further development and commercialization of both solid phase extraction and liquid phase extraction technologies will be fundamental to providing the next generation of integrated microfluidic systems for high throughput genomic analysis. In addition, the next generation devices should also be developed to allow protein extraction and purification for proteomic analysis.

Cross References

- ► Biosample Preparation Lab-on-a-Chip Devices
- ► Microfluidic Systems for High-Throughput Screening
- ► Lab-on-Chip Devices for Separation Based Detection
- ► Integrated Micro Devices for Biological Applications
- ► Chromatographic Chip Devices
- ► Interfacial Instability
- ► Electrokinetic/Hydrodynamic Flow Instability

References

1. Sambrook J, Fritsch EF, Maniatis T (1989) Molecular Cloning: A Laboratory Manual. Cold Spring Harbor Laboratory Press, NY
2. Christel LA, Petersen K, McMillan W, Northrup MA (1999) Rapid, Automated Nucleic Acid Probe Assays Using Silicon Microstructures for Nucleic Acid Concentration. J Biomech Eng 121:22–27
3. Breadmore M, Wolfe K, Arcibal I, Leung W, Dickson D, Giordano B, Power M, Ferrance J, Feldman S, Norris P, Landers J (2003) Microchip-based purification of DNA from biological samples. Anal Chem 75(8):1880–1886
4. Wolfe KA, Breadmore MC, Ferrance JP, Power ME, Conroy JF, Norris PM, Landers JP (2002) Toward a microchip-based solid-phase extraction method for isolation of nucleic acids. Electrophoresis 23:727–733
5. Hong J, Studer V, Hang G, Anderson W, Quake S (2004) A nanoliter scale nucleic acid processor with parallel architecture. Nat Biotechnol 22:435–439
6. Thoresen T, Roberts RW, Arnold FH, Quake SR (2001) Dynamic pattern formation in a vesicle generating microfluidic device. Phys Rev Lett 86(18):4163–4166
7. Suremeian M, Slyyadnev MN, Hisamoto H, Hibara A, Uchiyama K, Kitamori T (2002) Three-layer flow membrane system on a microchip for investigation of molecular transport. Anal Chem 74:2014–2020
8. Dreyfus R, Tabeling P, Willaime H (2003) Ordered and disordered patterns in two phase flows in microchannels. Phys Rev Lett 90(14):144505
9. Reddy V, Zahn JD (2005) Interfacial Stabilization of Organic Aqueous Two Phase Microflows for a Miniaturized DNA Extraction Module. J Colloid Interface Sci 286(1):158–165
10. Zahn JD, Reddy V (2006) Electrohydrodynamic instability mixing: Two phase linear stability analysis and micromixing for a miniaturized DNA extraction module. Microfluid Nanofluid 2(5):399–415
11. Mao X, Yang S, Ahn D (2006) Experimental Demonstration and Numerical Simulation of Organic-Aqueous Liquid Extraction Enhanced by Droplet Formation in a Microfluidic Channel. Proc IMECE 2006, Paper Number IMECE2006-16084

Lab-on-Chip Devices for Separation-Based Detection

John T.W. Yeow, Weijie Wan
Department of Systems Design Engineering, University of Waterloo, Waterloo, ON, Canada
jyeow@engmail.uwaterloo.ca,
wwan@engmail.uwaterloo.ca

Synonyms

Lab on chip; Lab-on-a-chip; Lab on a chip; Micro total analysis system (μTAS)

Definition

Lab-on-Chip devices refer to devices that integrate one or several biochemical analysis functions on a chip of small size using semiconductor manufacturing processes, and are capable of handling extremely small volume of fluid. They usually have the size of only square millimeters to a few square centimeters and are able to handle fluid volumes down to picoliter levels.

Lab-on-Chip devices for separation-based detection refer to Lab-on-Chip devices that are capable of performing detection based on the result of separation. Both separation and detection functionalities should be integrated in a single chip.

Overview

The history of Lab-on-Chip devices can be dated back to 1975, when the first Lab-on-Chip device, a gas chromatograph used to separate a mixture of various gases, was invented [1]. However, the real boost and serious growth in Lab-on-Chip devices were not seen until 1990 when the term "μ-TAS" was first proposed by Manz et al. [2] who demonstrated a microchip incorporating sample separation and detection. For the past few years, research activities and investment have been growing continuously in this rapidly emerging field. Microfabrication technology has allowed the realization of Lab-on-Chip devices. Miniaturizing a conventional biochemistry laboratory down to the size of a silicon microchip is the driving concept behind Lab-on-Chip technology. Ideally, each Lab-on-Chip device may have one or more sample injection reservoirs, sample mixing chambers, sample separation channels, chemical reaction chambers and a monitor and measuring system. Lab-on-Chip devices offer many benefits. Due to their small sizes, they consume very tiny amounts of biochemical reagents. This is very desirable since many reagents are very expensive. Moreover, using small amounts of chemicals will result in a reduction of analysis time and a faster response as chemicals can mix and react more quickly. Furthermore, since some reagents and reaction products can be very harmful to humans, Lab-on-Chip devices minimize human interaction with chemicals and reaction products by consuming and producing small amount of chemicals. High-throughput analysis is enabled by massive parallelization due to compactness of the system. Small size also enables portability of Lab-on-Chip devices. Because fabrication of Lab-on-Chip devices

is based on highly developed semiconductor processing techniques, it is fairly easy to manufacture Lab-on-Chip devices in large quantities, and thereby reducing cost per chip.

Detection in biochemical experiments refers to the extraction of information, such as concentration of ions in a solution, from a signal such as induced electric current. It plays an essential role in Lab-on-Chip devices. No biological experiments or chemical analysis is considered complete until the signals collected during the process have been detected. Separation is another routine task in biochemical experiments. It refers to the process of separating a type of substance from other types or separating different types of biochemical reagents from each other. Separation-based detection combines the two tasks. A very common example is the blood test performed in hospital. The process separates different cells from the blood plasma followed by a series of other steps including detection and characterization. Compared to conventional separation-based detection analysis, which requires long analysis time, expensive cumbersome equipments and provides limited throughput, Lab-on-Chip devices for separation-based detection offer shorter analysis time, low reagent consumption, low fabrication costs, small size and better fluidic control.

Basic Methodology

The working principle for separation-based detection can be divided into two parts: separation and detection. In this section, a variety of mainstream separation and detection techniques suitable for Lab-on-Chip devices including electrophoresis separation, dielectrophoresis separation, ultraviolet (UV)-visible absorbance detection, fluorescence detection and electrochemical detection will be discussed in detail.

Separation Techniques

Electrophoresis (EP)

Electrophoresis (EP) is the movement of an electrically charged particle within a solution medium under the influence of an applied electric field. The movement is due to the EP force acting on the particle. The EP force is a type of Coulomb force in its origin and is simply given by

$$F = qE \tag{1}$$

where q is the number of net charges on the particle and E is the applied electric field intensity. In fact, the viscous or frictional force experienced by the particle within the solution medium tends to balance the EP force such that the particle velocity of migration is constant in a constant and homogeneous electric field. The electrophoretic mobility

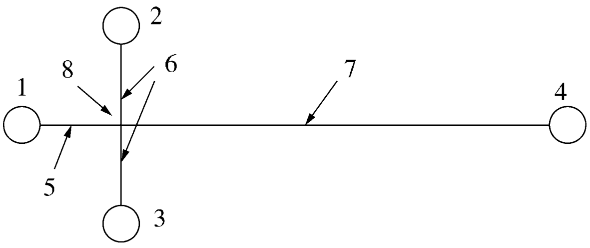

Lab-on-Chip Devices for Separation-Based Detection, Figure 1 A typical microcapillary electrophoresis system with straight capillary separation channel: (1) buffer reservoir, (2) sample reservoir, (3) sample waste reservoir, (4) end waste reservoir, (5) buffer injection channel, (6) sample injection channel, (7) capillary separation channel, (8) injection cross point

μ is a parameter used to describe the velocity of a particle or a group of particles under an applied electric field, and is defined as

$$\mu = \frac{v}{E} = \frac{\varepsilon_m \zeta}{\eta} \tag{2}$$

where v is the velocity of the particle, ε_m is the absolute permittivity of the solution medium, ζ is the zeta potential of the particle and η is the liquid viscosity. The ultimate goal of separation is to generate a position gradient for each type of paricles, in other words to move different types of particles to different locations. In Eq. (2), the only parameter that characterizes different types of particles is the zeta potential, since ε_m and η are constant once a solution medium is chosen. Therefore, separation based on EP force is dependent on different particles having different zeta potential. As a result, separation along the moving direction of the particles can be achieved.

Capillary electrophoresis (CE) is a widely used separation technique based on EP. Due to its ease of miniaturization and operation, CE is commonly used in Lab-on-Chip devices to perform separation tasks. Figure 1 shows a typical CE configuration in Lab-on-Chip devices. It consists of: (1) a buffer reservoir used to hold buffer solution; (2) a sample reservoir used to hold sample solution; (3) a sample waste reservoir used to collect unnecessary sample solution; (4) an end waste reservoir used to collect solution flowing through the separation capillary channel; (5) a buffer injection channel used to direct the buffer solution to the injection cross point; (6) a sample injection channel used to direct sample solution to the injection cross point; (7) a thin and relatively long separation capillary channel used to direct solution for separation; and (8) an injection cross point for mixing the sample solution and the buffer solution. The inner diameter of the capillary channel in Lab-on-Chip devices usually ranges from 25 μm to 100 μm while the length ranges from

L

10 mm to 100 mm depending on the applications. Buffer and sample injection can be achieved by several methods. One method is to apply a high voltage between the buffer reservoir (1) and the end waste reservoir (4) for buffer injection, and between the sample reservoir (2) and the sample waste reservoir (3) for sample injection, to generate an electroosmotic flow (EOF) that causes the bulk flow motion of the liquid solution to the injection cross point (8). Another method is to create a pressure gradient either between the buffer reservoir (1) and the end waste reservoir (4) for buffer injection, or between the sample reservoir (2) and the sample waste reservoir (3) for sample injection, to direct the solution to the injection cross point (8). After buffer and sample injection is completed, a high voltage is then applied between the buffer reservoir (1) and the end waste reservoir (4) for CE separation. The effective separation length is from the injection cross point (8) to the end waste reservoir (4). The migration speed of particles in CE is determined by their sizes and charges. Generally speaking, small, highly charged particles will migrate more quickly than large, less highly charged particles.

Dielectrophoresis (DEP)

Dielectrophoresis (DEP) is a phenomenon different from electrophoresis (EP). In fact, any non-polar material experiences a certain degree of polarization when exposed to an electric field. Depending on the material properties of the particle, electric dipoles are generated on opposing ends of the particle. The DEP force is due to the interaction between the dipole induced by an applied electric field and the spatial gradient of that electric field. The general expression of the DEP force exerted on a particle in an electric field is

$$\boldsymbol{F}_{\text{dep}} = \boldsymbol{p} \cdot \nabla \boldsymbol{E} \tag{3}$$

where $\boldsymbol{p}$ is the dipole moment of the particle and $\boldsymbol{E}$ is the electric field intensity. It has to be noted that in order for the DEP force to be nonzero, the gradient of the electric field ($\nabla \boldsymbol{E}$) has to be nonzero, which explains why the DEP force can be seen only when particles are in non-uniform electric fields. For a uniform sphere placed into an electric field, the induced dipole moment is given by

$$\begin{aligned} \boldsymbol{p} &= 4\pi \varepsilon_{\text{m}} R^3 \left(\frac{\varepsilon_{\text{p}}^* - \varepsilon_{\text{m}}^*}{\varepsilon_{\text{p}}^* + 2\varepsilon_{\text{m}}^*} \right) \cdot \boldsymbol{E} \\ &= 4\pi \varepsilon_{\text{m}} R^3 \cdot f_{\text{CM}}(\omega) \cdot \boldsymbol{E} \end{aligned} \tag{4}$$

where R is the radius of the particle and ε_{p} and ε_{m} denote the permittivities of the particle and the medium, respectively. The asterisk denotes the complex conjugate of the dielectric constant which is expressed by $\varepsilon^* = \varepsilon - \mathrm{i}\,(\sigma/\omega)$, where ε is the permittivity, σ is the electric conductivity, i is the imaginary number and ω is the angular frequency of the applied electric field. $f_{\text{CM}}(\omega)$ is known as the Clausius–Mossotti (CM) factor which describes frequency dependent characteristics of the particle relative to the medium. In a linearly polarized sinusoidal field, the time-average DEP force is usually used and is given by [3]

$$\langle \boldsymbol{F}_{\text{dep}} \rangle = \pi \varepsilon_{\text{m}} R^3 \,\text{Re}\left[f_{\text{CM}}(\omega) \right] \cdot \nabla \left| \boldsymbol{E} \right|^2 \tag{5}$$

where $\langle \ \rangle$ denotes the time average. Due to the spatial non-uniformity of the electric field, the particle experiences a force with orientation determined by the relative polarization of the particle with respect to the medium. If the polarization of the particle is greater than that of the suspending medium, $\text{Re}\left[f_{\text{CM}}(\omega)\right]$ will be positive and the dipole will align with the field and the particle will be drawn to the region of stronger electric field. This is known as positive DEP, or pDEP. However, if the polarization of the suspending medium is greater than that of the particle, $\text{Re}\left[f_{\text{CM}}(\omega)\right]$ will be negative and the dipole of the particle will align against the field and the particle will be attracted to the region of lower electric field strength, known as negative DEP, or nDEP. A translational force on particles can be generated in a field with spatially varying phase by assigning voltages with the same frequency but different phases to multi electrodes. The resulting DEP force is termed traveling-wave DEP (TWD) and is given by [3]

$$\langle \boldsymbol{F}_{\text{tw dep}} \rangle = 2\pi \varepsilon_{\text{m}} R^3 \,\text{Im}\left[f_{\text{CM}}(\omega) \right] \cdot \nabla \times \left(\text{Im}\left[\boldsymbol{E}\right] \times \text{Re}\left[\boldsymbol{E}\right] \right) \tag{6}$$

DEP-based separation can be achieved by the sign of $\text{Re}\left[f_{\text{CM}}(\omega)\right]$. For particles with different electrical properties, a frequency and solution conductivity can be chosen such that $\text{Re}\left[f_{\text{CM}}(\omega)\right]$ is negative for one group of particles (nDEP) and $\text{Re}\left[f_{\text{CM}}(\omega)\right]$ is positive for another group (pDEP). Therefore, the group subject to the pDEP force will be attracted to the electrodes and the one subject to the nDEP force will be repelled from the electrodes, resulting in separation. One can also make use of the magnitude of $\text{Re}\left[f_{\text{CM}}(\omega)\right]$ and $\text{Im}\left[f_{\text{CM}}(\omega)\right]$ to achieve DEP-based separation for particles with subtle difference. Subject to the nDEP force, particles with different electrical properties will be lifted up to specific corresponding heights. The height is determined by the nDEP force and the gravity of the particle. Thus, different types of particles will appear in different heights. TWD is also useful and can be used as a separation scheme. Particles subject to TWD force

tend to move in one direction continuously. The velocity of the particles is a balance of the TWD force and the fluid frictional force. Since different particles experience different frictional forces, separation along the moving direction can be achieved.

Detection Techniques

Ultraviolet (UV)-Visible Absorbance Detection

Most organic molecules and biological cells are partially or completely opaque under ultraviolet (UV) or visible light. UV-visible absorbance detectors make use of this by responding to substances that absorb light with wavelengths in the range of 200 to 400 nm for UV light absorbance and 400 to 800 nm for visible light absorbance. UV-visible light is directed to pass through the sample and fall on a photo-electric array. The output from the photo-electric array then enters an amplifier and finally translates to a recorder or an image acquisition system. The relationship between the intensity of the UV-visible light after interacting with a sample, P_t, and the analyte concentration, c, is given by Beer's law, which states that

$$P_t = P_0 \mathrm{e}^{-klc} \quad \text{or} \quad A = \ln(P_0/P_t) = klc \tag{7}$$

where P_0 is the intensity of the UV-visible light before entering the sample, k is the molar extinction coefficient of the analyte for the specific wavelength of the UV-visible light, l is the optical path length of the sample and A is absorbance. From Eq. (7) it is easy to see that the absorbance is linearly dependent on the concentration of the sample. This is quite convenient in terms of analyzing extracted data from measurements.

There are two possible modes for UV-visible absorbance detection. One is to detect a single type of substance at a specific UV-visible wavelength if all the other substances do not absorb the light at all. The other mode is to detect several substances at one time by measuring the spectrum over a wide range of UV-visible wavelengths. A UV-visible absorbance detection system usually contains a light source with high output power, a set of lenses that are properly aligned to focus light onto a small area with a high power density, several pieces of fibers used for concentration and transmission of light, a band-pass filter that can select an appropriate wavelength to detect a single type of substance or a monochromator that can sequentially detect several wavelengths within a wide range, and a light-sensitive detection device such as a charge-coupled device (CCD) camera that can receive and amplify the signal to achieve detection with high accuracy.

Fluorescence Detection

Fluorescence detection is quite useful in detecting particular components of complex biological samples such as living cells. Very precise and selective detection can be achieved by measuring the visible or nonvisible light emitted from fluorescent dyes or fluorophores attached to the specific target cells or molecules of interest. The first step in fluorescence detection is to attach fluorescent dyes or fluorophores to specific target cells or molecules of interest if necessary since most particles do not have fluorescent properties. Typical examples of fluorophores include ethidium bromide, Fluorescein-isothiocyanate (FITC) and Texas Red. The second step is to use a high-energy light source with an excitation wavelength of λ_1 to illuminate the sample. Both laser and light emitting diode (LED) can be used as the excitation light source. Upon absorbing light energy, a fluorophore can reach an excited energy state S_e of higher energy than the ground energy state S_0. The excited energy state exists only for a finite period of time called the excited-state lifetime, typically $1-10$ ns. During this time, the fluorophore is unstable and undergoes conformational changes. It dissipates a part of the energy and returns from a relaxed energy state S_r to the ground energy state S_0. During this process, visible or nonvisible light is emitted with a wavelength of λ_2. Due to energy dissipation during the excited-state lifetime, the energy of the emission light is lower than that of the excitation light, and therefore of longer emission wavelength than the excitation light. Typical values of the excitation and emission wavelengths of fluorophores are 545 and 605 nm for ethidium bromide, 490 and 520 nm for FITC, and 596 and 620 nm for Texas Red.

A fluorescence detection system is quite similar to a UV-visible absorbance detection system, except that a laser light source or a LED with high output power is used, a set of band-pass filters must be present to select appropriate wavelengths for the excitation and emission light to achieve precise measurements, and fluorescent tags must be attached to the target particles if necessary.

Electrochemical (EC) Detection

In fact, most compounds are not naturally fluorescent and must be pre-bound with a fluorophore before being detected through fluorescence. Electrochemical (EC) detection is a universal label-free technique that is cost-effective and easy for integration with other functionalities in Lab-on-Chip devices. EC detection can be further divided into three categories:

- conductimetry (conductivity detection);
- amperometry (amperometric detection); and
- potentiometry (potentiometric detection).

The principle of conductivity detection is the measurement of conductivity variation of the analyte solution with respect to the background solution. The basic configuration of conductivity detection involves two electrodes which can either be placed in direct contact with the analyte solution, namely contact mode, or can remain external and are capacitively coupled to the solution, namely contactless mode. Usually, An AC voltage is applied across the two electrodes, and the electrical conductivity signal is measured. When the analyte flows in and replaces the background electrolyte, a change in the conductivity of the solution is induced. The concentration of the analyte is directly related to the change in conductivity, which is given by [4]

$$C = \frac{A}{L}\sum_{i=1}^{N}\lambda_i c_i \tag{8}$$

where C is the conductivity of the analyte solution, A is the electrode surface area, L is the distance between two electrodes, N is the number of ions, c_i is the concentration of the ion i and λ_i is its molar conductivity.

Amperometric detection refers to a detection method in which the current is proportional to the concentration of the species generating the current. It consists of two electrodes, a working electrode and a reference electrode, across which a DC voltage is applied. A redox reaction is induced at the working electrode when analyte solution flows in between two electrodes and the current change is monitored. The current response is directly proportional to the number of moles of analyte oxidized or reduced at the working electrode surface as described by Faraday's law:

$$i(t) = \frac{\mathrm{d}Q}{\mathrm{d}t} = nF\frac{\mathrm{d}N}{\mathrm{d}t} \tag{9}$$

where $i(t)$ is the current generated at time t, Q is the charge induced at the electrode surface, n is the number of moles of electrons transferred per mole of analyte, F is the Faraday constant and N is the number of moles of analyte oxidized or reduced.

Potentiometric detection is based on the induced potential on a membrane which is semipermeable and ion-selective. When certain ions pass through the semipermeable membrane while others do not, different ion activities at both sides of the membrane result in the buildup of a potential difference which is measured and monitored against a fixed potential of a reference electrode. A unique feature of potentiometric detection is that the detection signal does not scale down when the size of the electrode decreases.

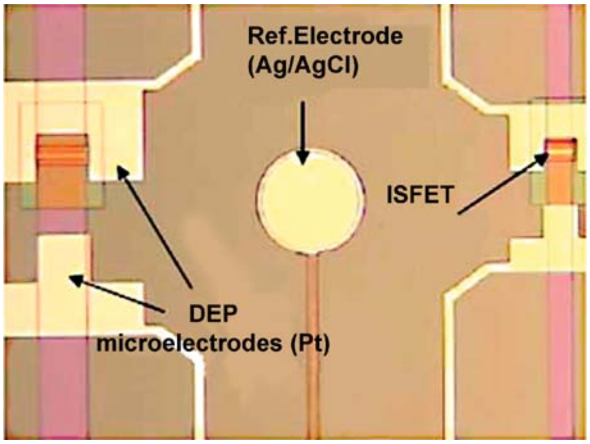

Lab-on-Chip Devices for Separation-Based Detection, Figure 2 Photomicrograph of the central part of a microchip incorporating DEP positioning and EC detection, showing the central Ag reference electrode and two sets of ISFET and DEP microelectrodes [7]

The potential response of the membrane electrode is given by the Nicolsky–Eisenman equation:

$$E = E^o + \frac{GT}{F}\ln\left(\sum_{i=1}^{N} K_i^{\mathrm{pot}} c_i^{1/z_i}\right) \tag{10}$$

where E is the electrode potential, E^o is a constant, G is the universal gas constant, T is the temperature, F is the Faraday constant, K_i^{pot} the selectivity coefficient of the species i, c_i is its concentration and z_i is its charge.

Key Research Findings

There are many good review papers discussing Lab-on-Chip devices for separation-based detection [5, 6]. Only four representative examples are selected to illustrate separation and detection principles, and to identify challenges in this rapidly emerging research area.

Integrated Microchip Incorporating DEP Positioning and Potentiometric Detection

Castellarnau et al. [7] demonstrated a miniaturized microsystem integrating DEP-based positioning and EC detection together. The chip included ion-sensitive field effect transistors (ISFETs), a single pair of castellated microelectrodes and a reference Ag/AgCl microelectrode. An ISFET is a type of EC sensor based on potentiometry, where the gate area is sensitive to ions and is open to contact with the liquid while the source and drain leads are carefully encapsulated. The current flowing through the transistor will change as the ion concentration of the solution changes. The ISFET sensing membrane was

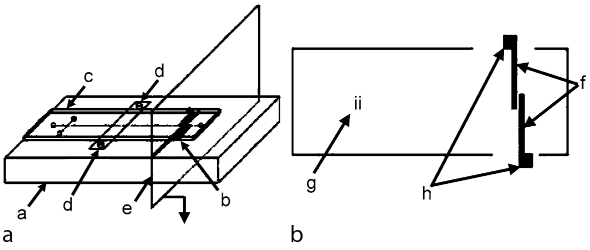

Lab-on-Chip Devices for Separation-Based Detection, Figure 3 Illustration of a microchip incorporating CE separation and contactless conductivity detection. (**a**) Schematic representation of the microchip including a: microchip holder, b: electrode plate, c: microchip, d: screws and clip and e: Faraday shield. (**b**) Anti-parallel detection electrode configuration including f: detection electrodes, g: basis laminate and h: electrode extensions used to connect the signal from the function generator and to the detector circuitry [8]

positioned at the minimum electric field region where cells were directed to by nDEP force. Figure 2 shows the central part of the chip. Cell position can be manipulated by adjusting the amplitude and frequency of the applied AC voltage across DEP microelectrodes. In their experiments, yeast cells were detected when a voltage of 8 V peak to peak at 20 kHz was applied and *E. coli* cells were detected when a voltage of 10 V peak to peak at 500 kHz was applied. The width and length of the ISFET sensing area are 60 and 10 μm respectively. The dimension of the internal U-shaped area of the positioning microelectrodes is 70 μm × 70 μm. Although the researchers only demonstrated the positioning and detection of one type of cells at one time, the microsystem has potential for the separation and detection of viable and non-viable cells based on pDEP and nDEP force experienced by the two types of cells.

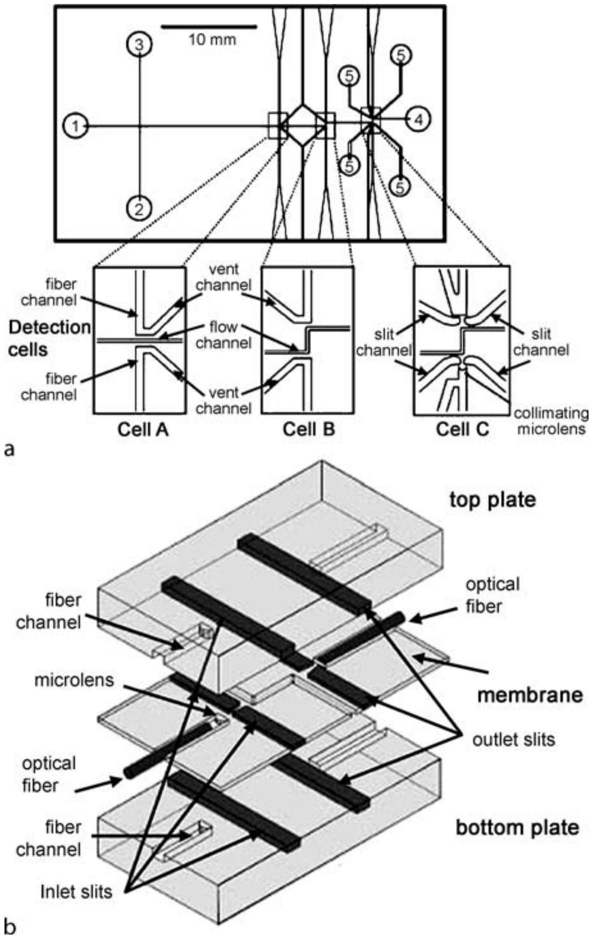

Lab-on-Chip Devices for Separation-Based Detection, Figure 4 (**a**) Layout of a microchip incorporating CE separation and UV-visible absorbance detection. The insets show the three types of detection units: unit A, unextended, on-column detection unit; unit B, uncollimated Z-shaped detection unit; unit C, collimated Z-shaped detection unit with a microlens and slits. (**b**) Detailed geometric description of unit C [9]

Integrated Microchip Incorporating CE Separation and Contactless Conductivity Detection

Kubáň et al. [8] provided a comprehensive report evaluating the effects of electrode geometry and operating parameters on the performance of capacitively coupled contactless conductivity detection (C^4D) for microchip CE. Unlike the contact conductivity EC detection, the sensing electrodes in C^4D were not in direct contact with the analyte solution but were placed on the surface of the separation device. A schematic representation of the assembly is shown in Fig. 3(a). The current reflecting the change of ion concentrations in the analyte was measured when a voltage was applied across the two sensing electrodes. The researchers fabricated several microchips to investigate the seven major factors that could affect the performance of C^4D. The seven factors are:

- the configuration of the electrodes;
- the electrode length;
- the electrode width;
- the size of the gap between the electrodes;
- the stray capacitance which resulted from direct capacitive coupling between two electrodes;
- the distance of the electrodes from the capillary channel; and
- the excitation voltage and feedback resistor which was used to convert the induced current to the output voltage.

The researchers successfully demonstrated the separation and detection of six ions (NH_4^+, K^+, Ca^{2+}, Na^+, Mg^{2+}, Li^+) in real water samples using a C^4D with optimized electrode geometry and operating parameters based on the

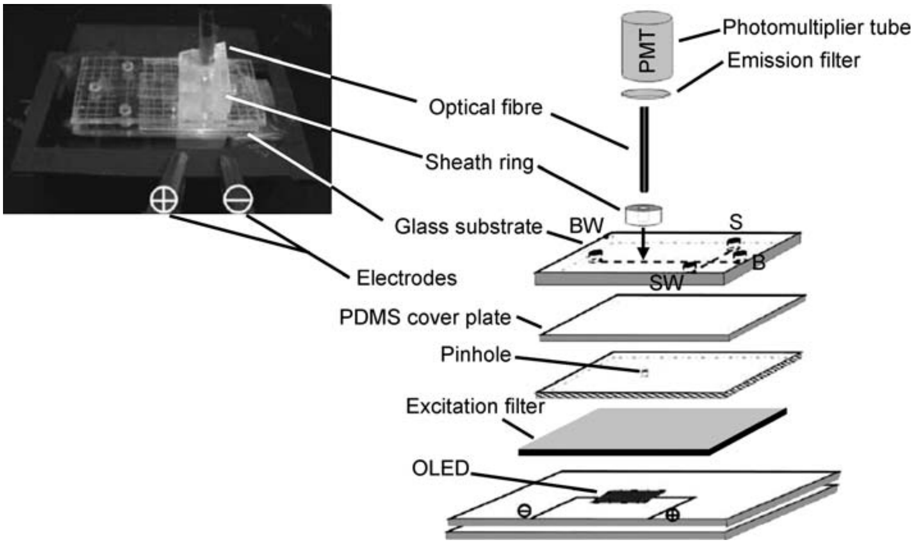

Lab-on-Chip Devices for Separation-Based Detection, Figure 5 Geometry overview and optical setup of a microchip incorporating CE separation and fluorescence detection [10]

understanding of the seven performance-affecting factors. The width, height and effective length of the CE separation channel were 50 µm, 50 µm and 75 mm respectively with a separation voltage of 3 kV. Anti-parallel detection electrode configuration shown in Fig. 3b was used for C^4D with the length, width and gap size being 1.4 cm, 1 mm and 0.5 mm respectively. The distance of the electrodes from the channel was 175 µm, being the thickness of the poly(methyl methacrylate) cover on the separation channel. The excitation voltage, frequency and feedback resistor were 20 V peak-to-peak, 500 kHz and 2.2 MΩ respectively.

Integrated Microchip Incorporating CE Separation and UV Absorbance Detection

Ro et al. [9] developed an integrated light collimating system incorporating a microlens, a pair of slits for extended optical path length and optical fibers for UV absorbance detection in a CE microchip. They fabricated three different detection units shown in Fig. 4a. Unit A was the simplest form with only two optical fibers on both sides of the separation channel, unit B was based on unit A and was incorporated with an extended optical path length and unit C was based on unit B but was equipped with an integrated light collimator consisting of a focusing microlens and a pair of slit channels. The microchip was fabricated by stacking three PDMS layers and Fig. 4b shows how unit C was arranged. Each unit had a pair of channels used for inserting optical fibers for the excitation and transmission light, whose size was 125 µm wide and 127 µm deep (50 µm from top plate, 27 µm in middle plate defining the depth of the separation channel, and 50 µm from bottom plate). A microlens with a radius of 50 µm was formed at the end of the excitation optical channel to collimate the divergent excitation light through an aperture. Another aperture was formed in front of the transmission optical channel. The 3D slit channels used to form two apertures were filled with black ink and sealed to serve as a barrier to prevent the vertically undesired divergent excitation light from entering the transmission optical fiber. The separation channel length from the injection point to unit C was 25 mm and a voltage of 1.5 kV was applied across the separation channel for CE. Separation detection of three reagents, fluorescein (10 µM), orange II (120 µM) and new coccine (60 µM), was completed after around 45 s for unit A and after around 63 s for unit C. An argon ion laser with a wavelength of 488 nm was used as the excitation light source. The researchers reported an approximately 10 times increase in sensitivity for unit C over that of unit A due to the 10 times longer optical path length of unit C [9]. The researchers also obtained 3.8% of stray radiation readout fractions for unit C compared with 31.6% for unit B, which was believed to be the significant reduction of the divergent and scattered light using the microconvex lens and slits of unit C.

Integrated Microchip Incorporating CE Separation and Organic Light Emitting Diode (OLED)

Yao et al. [10] presented a microfluidic device using a green organic light emitting diode (OLED) and a thin-

film interference filter as integrated excitation light source applied to fluorescence detection of proteins based on CE separation. Figure 5 shows the geometry overview and optical setup of the microchip. A p-n diode bottom emitting structure serving as the OLED was first fabricated on a 0.5 mm thick glass substrate. The OLED structure had an array of 250 μm × 250 μm illuminants which operated at 4.5 to 12 V and emitted green fluorescence with a peak excitation at 520 nm and approximately 60 nm bandwidth. The relatively wide excitation spectrum had an overlap with the emission spectrum, which increased the background noise and degraded the detection sensitivity. Thus, the researchers fabricated a thin-film interference filter of 300 μm in thickness consisting of 30 alternating layers of SiO_2 and TiO_2 to block nearly 80% of the unwanted light before entering the microchannel and the receiving optical fiber. A 12 μm thick silver foil with a pinhole used to confine the detection region was inserted between the excitation filter and a PDMS cover plate (100 μm in thickness). The microchip containing capillary microchannels was placed on top of the PDMS cover plate. The microchannels were 70 μm deep and 100 μm wide with a separation channel being 3 cm long and a sample channel being 1.5 cm long. An optical fiber of 500 μm in diameter was inserted into a 1 mm deep hole and was placed 0.7 mm above the separation channel to collect fluorescence signals. The researchers characterized the driving voltage for the OLED and found that high sensitivity and stable output were obtained at 12 V. The size of the pinhole also had an effect on the detection signal. The researchers found that a pinhole of 200 μm in diameter was the optimal dimension. In one of their experiments, CE separation was performed at 1.4 kV and two components, hydrolytes and photolytes of 140 μM Alexa 532, a fluorescent dye, were successfully separated and detected in less than 110 s. In another experiment, separation and detection of bovine serum albumin (BSA) conjugates labeled with Alexa 532 in less than 200 s was demonstrated. The researchers confirmed that the sensitivity of fluorescence detection was improved by using the thin-film excitation filter eliminating the undesired light.

Future Directions for Research

One important research trend in separation-based detection is to integrate more laboratory functionalities on the same chip to provide a complete device encompassing all that a macroscopic biochemistry laboratory has to offer. The second trend is to develop and explore biocompatible materials instead of traditional semiconductor materials to fabricate Lab-on-Chip devices. A typical example is cell manipulation where the materials that are in contact with the cells should maintain the natural states of the biological samples by not adversely affecting the cells. Another trend is to incorporate different separation techniques other than EP and DEP with the detection techniques for suitable applications.

Cross References

► Dielectrophoresis
► Electroosmotic Flow (DC)
► AC Electro-Osmotic Flow
► Electrophoresis
► Lab-on-Chip Devices for Particle and Cell Separation
► On-Chip Detection Using Optical Fibers
► On-Chip Micro-Optical Detection

L

References

1. Terry SC (1975) A gas chromatography system fabricated on a silicon wafer using integrated circuit technology. Ph.D dissertation, Department of Electrical Engineering, Stanford University, Stanford
2. Manz A, Graber N, Widmer HM (1990) Miniaturized total chemical analysis systems: A novel concept for chemical sensors. Sens Actuators B 1:244–248
3. Voldman J (2006) Electrical forces for microscale cell manipulation. Ann Rev Biomed Eng 8:425–454
4. Vandaveer IV WR, Pasas-Farmer SA, Fischer DJ, Frankenfeld CN, Lunte SM (2004) Recent developments in electrochemical detection for microchip capillary electrophoresis. Electrophoresis 25:3528–3549
5. Erickson D, Li D (2004) Integrated microfluidic devices. Anal Chim Acta 507:11–26
6. Radisic M, Lyer RK, Murthy SK (2006) Micro- and nanotechnology in cell separation. Int J Nanomedicine 1(1):3–14
7. Castellarnau M, Zine N, Bausells J, Madrid C, Juárez A, Samitier J, Errachid A (2006) Integrated microanalytical system based on electrochemical detection and cell positioning. Mater Sci Eng C 26:405–410
8. Kubáň P, Hauser PC (2005) Effects of the cell geometry and operating parameters on the performance of an external contactless conductivity detector for microchip electrophoresis. Lab Chip 5(4):407–415
9. Ro KW, Lim K, Shim BC, Hahn JH (2005) Integrated light collimating system for extended optical-path-length absorbance detection in microchip-based capillary electrophoresis. Anal Chem 77(16):5160–5166
10. Yao B, Luo G, Wang L, Gao Y, Lei G, Ren K, Chen L, Wang Y, Hu Y, Qiu Y (2005) A microfluidic device using a green organic light emitting diode as an integrated excitation source. Lab Chip 5(10):1041–1047

Lab-on-a-Chip (General Philosophy)

JOSE L. GARCIA-CORDERO, ANTONIO J. RICCO
Biomedical Diagnostics Institute
National Centre for Sensor Research, Dublin City University, Dublin, Ireland
ajricco@alum.mit.edu

Synonyms

Lab-on-a-chip; Micro total analysis system (μTAS); Miniaturized analysis systems

Definition

Lab-on-a-Chip is a field of research and technological development with the goal of integrating onto monolithic platforms the micro(nano)fluidic functionalities and components necessary to accomplish one or more biochemical or chemical processes – often analytical – in an autonomous, typically parallel fashion, using orders-of-magnitude less sample, reagent, power and manual manipulation than conventional laboratory methods and instruments. The most highly integrated Lab-on-a-Chip devices include all processes and devices on a single chip or card so that the introduction of an unprocessed sample leads to the output of an analytical result – an "answer" – from that same chip. This is the *sample-to-answer* philosophy of Lab-on-a-Chip devices.

Principles

Imagine standing in a chemistry, biology or clinical laboratory and observing the activity: a chemist deciphering the composition of a new substance, a biochemist developing a new drug to cure a disease, technicians analyzing patients' blood samples for pathogens or diagnostic markers. Now, imagine the possibility of devices, some as small as electronic microchips, none much larger than a human hand, that perform these and many other laboratory tasks without human intervention, providing a more efficient, rapid and reliable way to detect the composition of a substance, to develop not just a new but a more effective drug, or to provide more comprehensive information about a patient's state of health. This possibility is gradually becoming reality; this article examines how such devices are developed, what impedes widespread implementation of the Lab-on-a-Chip vision and how implementing this philosophy generates advances in basic science and applied technology.

In general, laboratory processes, including biochemical or chemical syntheses, analytical assays and in vitro experiments with microorganisms, involve manipulation of samples and reagents and, in many cases, the subsequent detection or quantification of analytes using detectors and instruments. Diverse labware, balances, dispensers, mixers, filters and incubators, together with instruments such as spectrometers and chromatographs, enable such processes. Volumes from tens of nanoliters to many milliliters of solutions are typical. Time-consuming manipulations are carried out by a variety of personnel; qualified technicians operate costly equipment and instruments. It is remarkable, with feats of modern engineering surrounding us – particularly the many examples of miniaturization and automation – that some procedures have changed very little in more than a century, still relying on skilled human labor. How is it possible that such procedures, particularly the most common, have not been integrated into automated systems?

Decades ago, the manufacturing industry began adopting automation systems in the form of robots, increasing productivity, reducing costs, minimizing human error and avoiding hazardous situations. Clearly, automatic systems could mechanize many of the human manipulations in assays; except for minimizing human labor and error, however, merely automating established, lengthy procedures in their human-executable form provides minimal benefit in terms of time, efficiency, operating cost or other measures of performance. Still, criticizing modern engineering for failing to address the needs of complex laboratory manipulations and measurements would be unjust: flow-injection analysis (FIA) systems automate liquid handling and analysis for tiny samples; the fluorescence-activated cell sorter (FACS) analyzes and sorts single cells at rates near 100,000 per second; laboratory automation is a thriving commercial endeavor, with robotic dispensers, multiwell plate conveyors, plate-reading spectrometers and incubators linked together for high-throughput automated assays. Mass spectrometers and DNA sequencers, along with their sample-introduction *front ends* and software, are impressive examples of engineering integration applied to difficult analytical challenges. Impressive indeed, but the sizes of these instruments dwarf the scale of the samples they analyze: µl or pg of biological cells, biopolymers or small molecules. Furthermore, while the human genome sequencing project owes its ahead-of-schedule finish to the automated DNA sequencer [1], as much as 75% of the cost of sequencing the genome was associated with sample preparation involving manual manipulations, with highly automated electrophoretic sequencing accounting for just 25%. Protein analysis (proteomics) and drug candidate screening also need new tools to process large numbers of samples in a specified time period, i. e. they have throughput requirements to attain economic viability [2].

Simply automating human-executed steps or applying conventional automation and instrumentation engineering to laboratory procedures are not in accord with the Lab-on-a-Chip philosophy. Rather, to realize the vision of major scale-down, comprehensive integration and massive parallelization of laboratory tasks, new paradigms and architectures must be developed to shrink and adapt sequences of laboratory processes to the components and methods of microfluidics. The newly integrated Lab-on-a-Chip tools often must provide better limits of detection or enhanced resolution at lower cost than the laboratory systems they replace in order to be adopted by practitioners of traditional laboratory methods.

Can modern science and technology lead to the attainment of such ambitious goals? Are miniaturization and integration invariably beneficial? Can complex manipulations in fact be replaced by on-chip operations? How is all this to be accomplished? The following sections address these questions.

Historical Perspective

The use of modern microfabrication technologies to construct and integrate the components of miniaturized analytical instrumentation was inaugurated some 30 years ago when researchers at Stanford described a microfabricated gas chromatograph (GC) constructed on a single silicon wafer [3]. Just a few years earlier, advances in glass capillary-based chromatography had shown that high-performance separations were possible using column cross-sections measured in µm, provided column lengths were measured in cm to m. Advances in conventional chromatography were made in both gas and liquid phase, with the improved performance of liquid chromatography (LC) giving rise to the term *high-performance liquid chromatography* (HPLC).

Comparable utilization of the tools of microfabrication for liquid-phase analyses came a decade later, when electrokinetic phenomena were proposed to separate dissolved species on chips: the application of a high electric field between the ends of a small-diameter column or channel can both transport and separate dissolved species in conductive solution without moving mechanical parts. The concept of *chip-CE* (capillary electrophoresis) was first described in the patent literature in 1990 [4], wherein CE separations are performed in microfabricated columns or microchannels on planar substrates. At the same time, publications appeared detailing the concept of integrating separations and other processing steps on a chip, extolling its potential to revolutionize chemical analysis [5].

Research and development of chemical and biological sensors preceded the first chip-integrated analytical separations systems by a decade or more, but the considerable enthusiasm for the elegant *immerse-and-read* sensor-based analytical method was damped by the realization that requirements for low limits of detection (LODs), high chemical specificity and rapid reversibility can be contradictory. This made the *ideal* sensor an elusive, often unattainable goal: rapid reversibility requires small interaction energies, while high specificity and low LODs imply strong binding. This potential Achilles' heel applies to some of the most important samples. Medical analytes, as well as many environmental, health-and-safety and industrial process-control samples, are often (bio)chemically complex mixtures, typically requiring one of three strategies to avoid errors due to interference with the target analyte: high selectivity, usually with accompanying irreversibility – making the sensor a dosimeter for all practical purposes; use of an array of sensors, wherein the pattern of responses from multiple partially selective sensors provides chemical discrimination without loss of reversibility; or coupling of the sensor – which in effect becomes a detector – with a chromatographic *front end* that separates complex mixtures into their components.

Many samples, both biological and chemical, require not only separation of interferences to provide meaningful sensor response, but may also require significant processing to cleanse the sample of debris, to add reagents, to change the concentration of background ions or change the solvent, to attach readily detectable *labels* to the target species, to carry out thermally stimulated reactions or to enhance LODs by pre-concentration or replication (termed *amplification* for nucleic acids) of the target species. Because of the success in miniaturizing LC, instead of employing traditional methods that use tubing to connect components and glassware for sample processing, scientists and engineers have embraced the Lab-on-a-Chip philosophy to miniaturize and integrate the purification, isolation, reaction, concentration and separation steps and, where applicable, the detectors or sensors, into one integrated chemical analytical system [5–7]. Because many such systems have analysis as the end goal, they are frequently referred to as micro-total analytical systems, or µTAS; the central role played by fluidics on the micrometer scale (detailed in the following sections) has resulted in these systems often being called simply *microfluidic devices*. Regardless of nomenclature, the Lab-on-a-Chip philosophy, even as it enables analyses not possible with discrete sensors alone, signals a paradigm shift in the way laboratory work is performed.

Miniaturization

The advantages of reducing the size of an integrated (bio)chemical processing/analysis system can be signif-

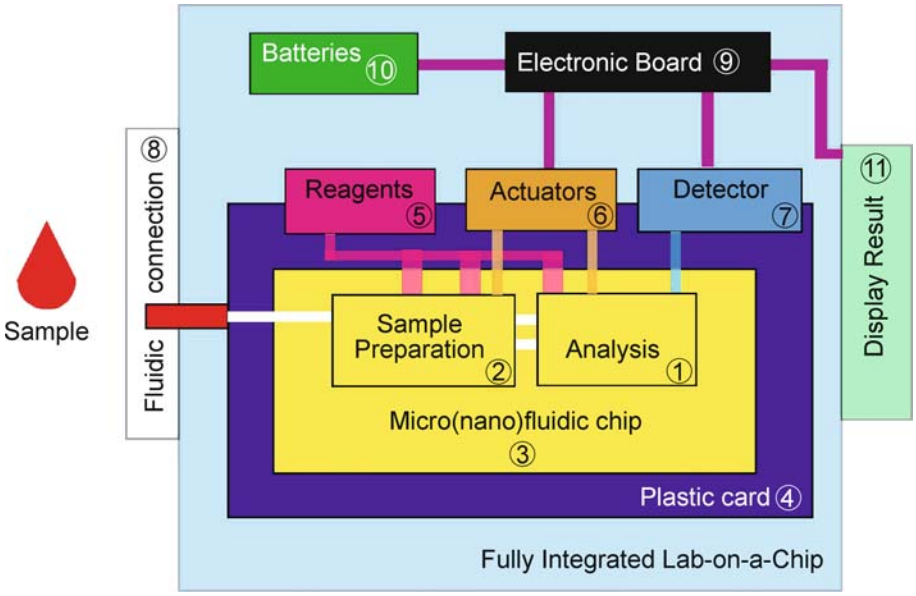

Lab-on-a-Chip (General Philosophy), Figure 1 Illustration of a fully integrated Lab-on-a-Chip (LOC) system, with components numbered according to their (approximate) historic integration with other LOC components, prevalence of research activities and publications that include that level of integration, and criticality of integration in order to accomplish an effective analysis. Historically, the analysis component (1) was first to be miniaturized and is indispensable to detect the analyte; it often includes a separation process. Sample preparation (2) is often required to make real-world samples amenable to analysis; the core microfluidic chip (3) thus consists of these two components connected by microchannels. For systems to be manufactured inexpensively in large volumes, the microfluidic chip might be fabricated on a plastic card (4) or other supporting substrate. Reagents (5) may be needed for sample preparation or analysis, for example to label the analyte with fluorescent molecules. Actuators (6) to motivate and regulate fluid movement through the various modules of the microfluidic chip can be integrated (or supported) on the same plastic card with the microfluidic device or remain external. The detector (7) is more often integrated in the case of electrical (electrochemical, impedance) detection approaches than for optical transduction. Sample is introduced to the chip through fluidic connections (8). An electronics board (9) controls the system and collects data; batteries (10) power the system. Following analysis with the aid of software, the answer is displayed (11)

icant, with overall enhancement of performance, measured in various ways, emerging as a common theme. Specific benefits can be deduced by assessing how some parameters, such as volume, reaction time and device density, change as the system is scaled down in size [2, 8]. Imagine a reaction of sample and reagent carried out in two different-sized cube-shaped flasks with edge length d. The first flask ($d = 1$ cm) is a macrosystem: it has a volume of 1 ml. The second flask ($d = 100\,\mu$m) is a microsystem: it has a volume of 1 nl. The 100-fold reduction in linear dimension results in a million-fold decrease in volume. Other factors being unchanged, the microscale system requires a million times less sample and reagent volume to perform an assay, so many times more analyses can be performed with the same amount of solution. Less chemical waste is produced; expensive reagents are consumed in smaller quantities. Also, chemical reactions including highly toxic or reactive species that are prone to cause accidents in laboratories are more easily controlled and safer using miniature systems because lower volumes mean less hazardous material and lower risk of thermal runaway.

Another relevant parameter is device density, which is well represented here by the number of reaction vessels per unit area. In the context of the two systems compared above, 100 vessels in the macrosystem would occupy 100 cm^2; in the microsystem, they occupy 1 mm^2, a 10,000-fold reduction in surface area. Further reducing the edge length of the vessels to 1 μm (assuming no space is required between adjacent reactions) would fit 10^{10} simultaneous reactions in the same area.

Now, for the same systems, consider a concentration of a certain *target* molecule of one nanomolar (nM). There will be almost 10^9 target molecules in the macrosystem and 1000 molecules in the microsystem. Further reduction of the edge length to 1 μm, easily attainable with current microfabrication techniques, provides just 1 molecule per μm^3. One must then consider the interplay between dimensions, numbers of molecules and detection: single-molecule detection is possible, but very challenging to implement on-chip, very limiting as to choice of detection

technologies and, at the single-molecule level, probability considerations mean that detection will only be successful some of the time.

Agitating and stirring (forcing convection) of a multicomponent solution or mixture of multiple solutions reduces the time for the solution to become homogeneous (completely mixed). Length, volume and concentration reductions in the microsystem require scale-specific assessment of the behavior of fluids and molecules in a restricted space. A localized group of molecules having a diffusion coefficient of 10^{-5} cm^2/s requires about one day to evenly diffuse, or spread, throughout the macrosystem in the absence of convection; in the microsystem, this process takes 10 s, and diffusion across 10 μm takes just 100 ms (diffusion time scales with the square of length). Such short diffusion times can allow reaction rates to be limited only by how fast the reaction takes place (reaction kinetics), rather than by forced movement of the substances involved.

In addition to performance enhancements related to volume, time and density of reactions, miniaturization also improves performance by other measures, for example, separations efficacy [5, 8]. Some components, however, are proving challenging or unsuitable for miniaturization or monolithic integration because of inherent complexities in their design [8], for example ultrahigh-sensitivity detectors. Attempts to miniaturize macrosystem components are often motivated primarily by gains in performance and time rather than a desire to minimize space [5], although some biomedical applications for which wearable or hand-held sensing systems are necessary, as well as remote military and aerospace applications, often place a high premium on size, mass and power.

Microfluidics: Fluid Movement and Handling

Fluid manipulation and transport of samples and reagents are often implemented in a network of microfluidic channels that interconnect the various components on a common substrate. These microchannels have dimensions ranging from hundreds of nm to hundreds of μm – comparable to, or in many cases much smaller than, a human hair. Flow in microchannels behaves very differently than in *macrochannels* such as laboratory tubing, water pipes or a river.

In microchannels, the viscosity and, in many situations, the surface tension of the fluid dominate inertial (mass-related) forces. Thus, fluid movement shows a smooth, predictable behavior known as laminar flow [9]. Turbulence in microchannels is always negligible, although in-channel convection (without turbulence) can be created in a number of often complex ways: rapid, effective mixing has proved to be one of the most interesting and well-studied fundamental challenges in microfluidics. In many cases, Fickian diffusion alone, without any deliberately created convection, is relied upon for mixing because of its rapidity on μm length scales, but the system must be carefully evaluated when taking this approach: two streams of liquid flowing parallel to one another in a 200 μm-wide channel at a velocity of 1 mm/s over a distance of 3 mm would have to be slowed by a factor of 3 to 30 (depending on the diffusing molecules) to mix to better than 95% homogeneity before exiting that short channel.

Because of the properties of microchannels, such as the material and coating of the surface, the high surface area-to-volume ratios can affect the behavior of the flow. Surface effects, many depending on interfacial tension (surface energy), can give rise to interesting applications such as the formation of droplet emulsions, the use of capillary forces to pump fluid and the modification of the surfaces to create hydrophobic-stop valves [9]. Also, high surface area-to-volume ratios facilitate rapid and controlled heating and cooling. Surface effects and topography (the route of the channel) define flow motion in the microchannel. The control and consequences of various microchannel characteristics make them useful as components in their own right. For example, by changing their geometry they can be used as mixers, filters, injectors, separators and the like [5, 9]. Other fluidics-relevant physical phenomena, including electrokinetic, acoustic and thermal effects, are described in a recent review [9].

Fabrication

The development of microfluidic devices has been both limited and spurred by limitations of and advances in the materials they are built from and how they are made. Without a doubt, the microelectronics industry gave a critical first impulse to the field by lending its microfabrication tools. Even today, the fabrication techniques used to make microfluidic devices are influenced by advances in the microelectronics industry.

Glass is ubiquitous in laboratory manipulations, while plastic dominates many modern molecular biology, biochemistry and drug development laboratories. Glass does not react with most substances and is optically transparent; certain plastics are biocompatible, readily moldable into complex structures and inexpensive enough to be discarded after a single use. The first microfluidic devices used glass or silicon as the substrate material, both substrates relying on microelectronics industry-type patterning methods. However, the time, cost and special (etching) facilities needed to fabricate devices with these methods and materials initially deterred some researchers

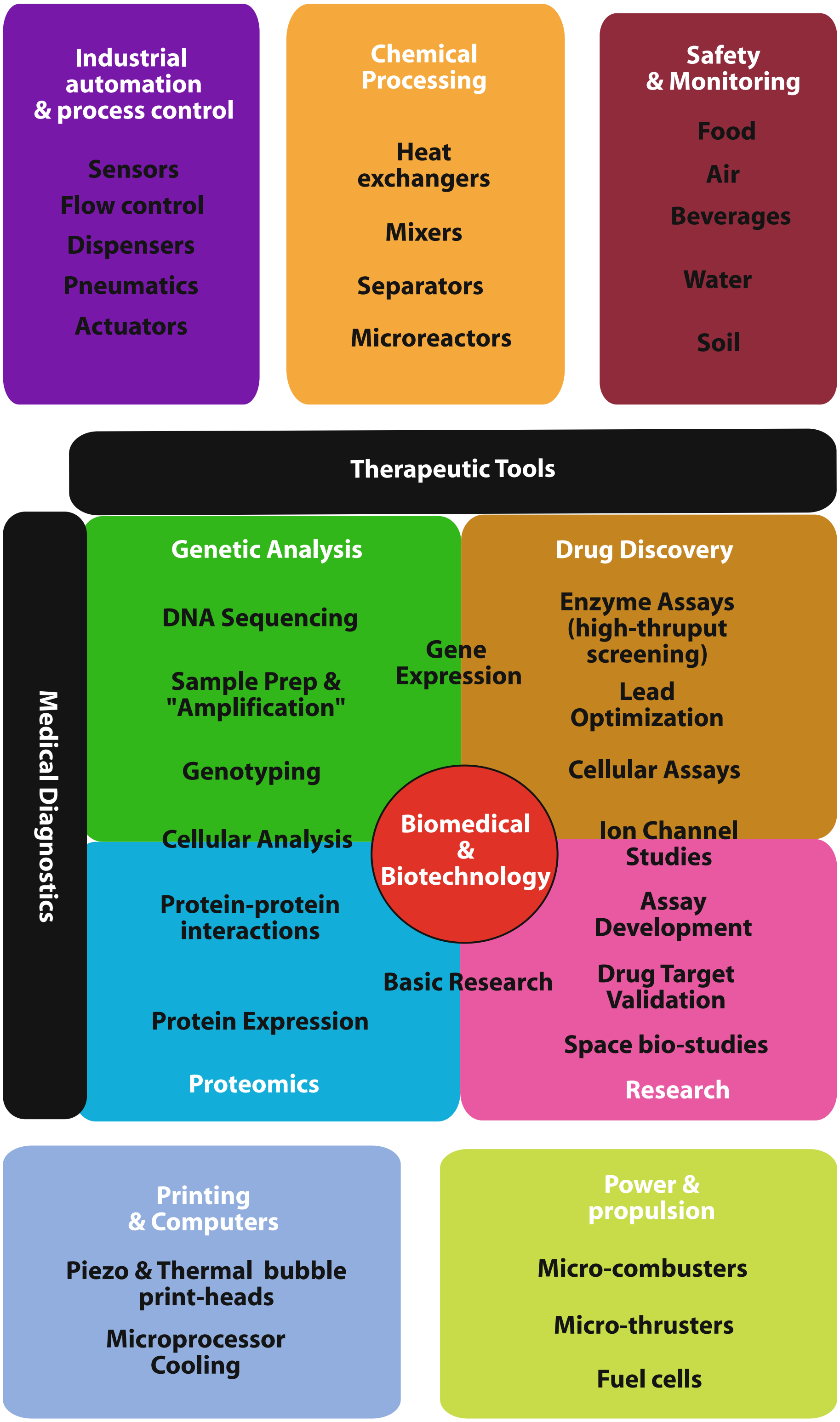

Lab-on-a-Chip (General Philosophy), Figure 2 Applications of Lab-on-a-Chip technologies

from entering the field. New fabrication techniques for microfluidics based on *soft polymers* as well as traditional thermoplastics began to be developed in 1991 [3], but not until the end of the 1990s were these approaches more widely described [10] and adopted for rapid prototyping of devices at minimum cost [6]. The *soft lithography* technique was quickly adopted as de facto for fabrication of biologically focused microfluidic devices in academic laboratories. Unfortunately, soft polymers are incompatible with many organic chemicals, including small molecules of interest in drug development; this approach has yet to be proven for mass fabrication of a commercial microfluidic device. Plastics are much "in vogue" nowadays, mainly because they are readily prototyped and suitable for manufacturing with long-standing techniques, such as hot embossing and injection molding, but also because they are inexpensive as a material and very familiar to the life sciences. To date, no single standard material has been adopted for the fabrication of microfluidic devices.

The Lab-on-a-Chip Concept

Scientists and engineers from diverse disciplines – physics, chemistry, biology and computer science, together with mechanical, chemical, electrical and materials engineering – have broadened the approaches and concepts of μTAS and microfluidics. Contributions from and interactions among these fields have created more complex, sophisticated and novel devices, which, together with the merging of the μTAS and microfluidics concepts, have led to the field of research and technology called Lab-on-a-Chip (LOC). The reader should note that these three terms, Lab-on-a-Chip, microfluidic devices and micro-total chemical analysis system, are often, and erroneously, used interchangeably.

The workhorse and core of a LOC is the microfluidic system. Built around it is some combination of detectors and sensors, actuators, electronic controls (microprocessors, field-programmable gate arrays, A-to-D converters, etc.), software and reagents [7]. The microfluidic device consists of microchannels and components that effect operations such as filtration, pre-concentration, washing, mixing, purification, isolation and separation. The configuration of the components of a microfluidic device should be dictated by whether the goal is to synthesize a compound, to grow an organism, to detect the presence of a target or to determine the concentration of an analyte.

Analysis requires appropriately sensitive and, if separations are not part of the fluidic system, selective detectors; these have varying degrees of sensitivity, accuracy, performance, ease of integration and cost. Common detector technologies include optical, electrochemical, magnetic, impedimetric (conductance and/or capacitance), mechanical and thermal. The specific type and configuration of detector depends on the details of the application. Non-optical detectors tend to be less sensitive and, in some cases, less selective (optical detectors can include wavelength-based selectivity), but are generally smaller than optical detectors and easier to integrate with the microfluidic device.

Optical detection, particularly laser-induced fluorescence, is widely used with microfluidic devices due to high sensitivity, but infrequently integrated on chip. For most optical detection approaches, *labels*, i. e. molecules that fluoresce or strongly absorb light of a selected wavelength, must be (bio)chemically attached to *tag* the analyte, adding an additional, sometimes challenging, process step. The more sensitive and readily implemented optical detectors also require an external optics system, which usually occupies significant physical space, often consumes more power than all the rest of the system and can be the most expensive part of a LOC system.

Unlike optical detection, integrated electrical detectors (impedimetric, electrochemical, most mechanical and thermal, certain magnetic) require electrode interconnections and on-chip electrical *traces* (conductive pathways) to connect to external electronics. Although this is an added complication, it is typically easier to implement than full monolithic integration of an optical excitation-and-detection system.

Actuators, such as valves or pumps, can be either integrated or external to the microfluidic device, and are needed to regulate the movement of fluids in the microchannels. Strict fluid regulation and control is important because the tasks executed by the fluidic components need to be completed in a systematic and timely fashion for the analysis to be successful.

Because vast amounts of information can potentially be generated in LOC systems, and because sophisticated analysis may be required to generate meaningful information from raw data, e. g. for protein analysis or drug discovery, data analysis requires appropriate computational power and speed. Thus, when data volume and analysis complexity are minor, appropriate microprocessors and affiliated components can be integrated in a hybrid fashion with the microfluidics or, more commonly, included on an external electronics board, eliminating the need for an external computer.

Reagents often must be mixed with the sample at one or more process steps to facilitate purification, separation, amplification or labeling (for detection). It is possible, and for many commercial applications desirable, to integrate the reagents in liquid or powder (often lyophilized)

form on the chip. Optimally, the sample will be the only assay component dispensed onto the microfluidic device for analysis or reaction, making the LOC system easier to use, more efficient in reagent and power consumption and more robust to errors in measurement or sequence.

Easily integrable, user-friendly and, ideally, standardized fluidic connections that facilitate microfluidic input/output (I/O) are vital. Because of the varying size of microfluidic devices – sub-mm^2 to the size of a multiwell plate ($> 100\ cm^2$) – a related key challenge is an easy-to-handle, standard user interface.

The term *Lab-on-a-Chip* has been used in a wide variety of contexts. Some of the best-studied applications are in chemical analysis, biological research and medical diagnosis, with many other exciting uses under development, such as chemical synthesis, space studies, industrial automation and process control, fuel cells and power generation, printing devices, and environmental and food-safety monitoring. LOC may refer to a chemical or biological microreactor, a micro-cytometer, a screening tool for drug discovery, a diagnostic device for clinical use or a sampling-and-analysis system for environmental monitoring. The ultimate goal of LOC is to integrate the microfluidic components with detectors, actuators, electronics, fluidic connections and reagents in a single (often single-use) device that enables a complete process, whether synthetic, analytic or life support, in an autonomous and automated fashion.

Key Research Findings

LOC is now an area of intense research and technological development, having grown exponentially in the past two decades. Initially, LOC began by proving its feasibility and justifying its existence: postulating and demonstrating that miniaturization and integration of the components of biochemical and chemical systems were not only possible, but would bring substantial improvement relative to traditional macroscale systems. A vast number of proof-of-concept components have been developed during the past few years and, when successfully integrated together, will form the basis of a range of functional LOC systems.

Simple LOC systems, lacking sophisticated integration and focusing on the detection of a small concentration of a certain molecule or measuring one parameter like pH, are already a reality and have found their way to market [1, 6]. The creation of a LOC that is capable of processing and analyzing high-volume, complex samples with low analyte concentrations, such as the sets of biological markers for cancer or other diseases, remains elusive, though there are a few commercial success stories (http://www.biosite.com; http://www.abbottpointofcare/isat/). Although many of the necessary components are already available or demonstrated, progress in monolithically integrating disparate technologies has been slower than expected.

There are two explanations for why realization of the LOC vision is proving difficult. First, challenges are many, development is gradual and many refinements are needed before the technology is accepted, reliable and robust. Frequently, components are built in vastly different ways, with different geometries or structures, different performance and fundamental incompatibilities. Often, the more effective or successful components require cumbersome fabrication procedures and/or exotic materials. Additional components that would ideally be integrated may require a completely different set of fabrication steps that render integration incompatible with low-cost, automated manufacturing. Clearly, adopting standard components that are robust, give reproducible results, perform well and are amenable to integration is essential for successful implementation of the LOC philosophy. Second, this field, like few others, requires synergistic expertise and multidisciplinary cooperation in engineering, physics, chemistry, biology, computer science. If LOCs are to be applied successfully to relevant and needy problems, engineers and physicists must more often liaise and communicate with biologists or chemists to understand their needs and questions. For success, those working in each of these fields must become knowledgeable in the basics and language of the disciplines with which they interact to make collaborations fruitful. The additional education and training for all the involved parties are essential, so more universities should establish undergraduate and graduate programs encouraging an interdisciplinary, *applications-aware* education [1]. This will expand the ranks of scientists and engineers with the skills necessary to make fundamental and unconventional advances in LOC science and technology [1].

LOC systems have the potential to enhance, perhaps transform, our understanding of cell biology and biochemistry. It is likely they will play a major role in the development of new drugs, and almost certainly in the earlier, more accurate diagnosis of disease. Nonetheless, much is still to be discovered and conceived: the promise of nanofluidics, ways to include optics directly on fluidic chips, the integration of multiple detector types, more efficient means to detect small numbers of molecules, etc. LOC technology is already finding special application niches in environmental monitoring and space exploration, with promise for everything from power generation to therapeutics to information technology. Most importantly, LOCs are poised to impact the world economy and society as a whole, in much the same way as microelectronics technology now shapes our world.

Examples of Applications

Figure 2 shows examples of applications developed and envisioned for LOC technologies. The largest number of applications is in biomedicine and biotechnology, but other fields are benefiting from the advantages of these technologies, including industrial automation and process control, chemical processing, safety and monitoring, power and propulsion, and printing and computing.

Refer to the following entries within this encyclopedia for examples of applications: Lab-on-a-Chip Devices for Drug Delivery, ►Lab-on-a-Chip Devices for Biodefense Applications, ►Lab-on-a-Chip Devices for Chemical Analysis, ►Lab-on-a-Chip Devices for Immunoassays, ►Lab-on-a-Chip Devices for Protein Analysis, ►PCR Lab-on-Chip Devices, ►Integrated Micro Devices for Biological Applications, ►Integrated Microfluidic Systems for Medical Diagnostics.

Cross References

► Lab-on-a-Chip Devices for Biodefense Applications
► Lab-on-a-Chip Devices for Chemical Analysis
► Lab-on-a-Chip Devices for Immunoassays
► Lab-on-a-Chip Devices for Protein Analysis
► SNP on Chip
► PCR Lab-on-Chip Devices
► Flow Cytometer Lab-on-Chip Devices
► Integrated Micro Devices for Biological Applications
► Integrated Microfluidic Systems for Medical Diagnostics
► Materials Used in Microfluidic Devices
► Microfabrication Techniques
► Soft Photolithography
► Microfluidic Systems in Space Science
► Microfluidic Systems for High-Throughput Screening

References

1. Fields S (2001) The interplay of biology and technology. Proc National Acad Sci USA 98(18):10051–10054
2. Dittrich PS, Manz A (2006) Lab-on-a-chip: microfluidics in drug discovery. Nature Reviews Drug Discovery 5(3):210–218
3. Reyes DR, Iossifidis D, Aurous P, Manz A (2002) Micro Total Analysis Systems. 1. Introduction, Theory, and Technology. Anal Chem 74(12):2623–2636
4. Pace SJ (1990) US Patent 4,908,112; Kovacs GTA, Holland KO (1990) EP 0376611A2; Eckström B, Jacobson G, Ohman O, Sjodin H (1991) PCT Application WO 91/16966; Soane DS, Soane ZM (1992) US Patent 5,216,022
5. Manz A, Graber N, Widmer HM (1990) Miniaturized Total Chemical Analysis Systems; a Novel Concept for Chemical Sensing. Sens Actuators, B1:244–248
6. Whitesides GM (2006) The origin and future of microfluidics. Nature 442(1701):368–373
7. Chow AW (2002) Lab-on-a-Chip: Opportunities for Chemical Engineering. AIChE J 48(8):1590–1595
8. Janasek D, Franzke J, Manz A (2006) Scaling and the design of miniaturized chemical-analysis systems. Nature 442(1701):374–380
9. Squires TM, Quake SR (2005) Microfluidics: Fluid Physics ad the nanoliter scale. Rev Mod Phys 77(3):977–1026
10. Boone TD, Fan ZH, Hooper HH, Ricco AJ, Tan H, Williams SJ (2002) Plastic Advances Microfluidic Devices. Anal Chem 74(3):78A–86A

Lab-on-a-Disk

► Centrifugal Microfluidics

Laboratorial Microsystem

► Lab-on-a-Chip Devices for Chemical Analysis

Laminar Flow

Definition

In laminar flow layers of liquid slide by one another in a direction that is parallel to the surface containing the liquid.

Cross References

► Lab-on-a-Chip Device for Chemical Analysis
► Microfluidic Mixing

Laminar Flow-Based Fuel Cells

► Microfluidic Fuel Cells

Laminar to Turbulent Flow Transition

► Transition to Turbulence in Microchannels

Laplace Pressure

Synonyms

Laplace pressure drop

Definition

The surface curvature associated driving force for capillary fluid transport.

Cross References

► Surface-Directed Capillary Flow Systems

Laplace Pressure Drop

► Laplace Pressure

Laser Ablation

ZHENG CUI
Rutherford Appleton Laboratory, Didcot, UK
z.cui@rl.ac.uk

Synonyms

Laser machining

Definition

Laser ablation is one of the laser machining processes in which materials are removed in vapor or plasma form directly from the solid state by irradiation of an intense pulsed laser beam.

Overview

Laser machining is a very mature technology. There is a long history of using lasers for cutting, slicing, drilling, marking, welding and surface modification in mechanical and electronic industries. Conventional laser machining is a thermally based process, i. e. a laser beam of high energy density generates highly localized heating on a work piece, causing material to melt and then to vaporise, so that material can be removed layer by layer, according to the depth of photon absorption. Laser ablation, on the other hand, is a non-thermally based process. Laser ablation of metallic materials, whether it is a thermal process or an ablation process, primarily depends on the duration of the laser pulse compared to heat diffusion time. This is not an abrupt but a gradual transition process, because different materials have different thermal conductivities, hence different heat diffusion times. When a laser pulse is longer than the material heat diffusion time, the heat generated by laser energy is accumulated, causing material melting and boiling. Evaporation occurs from the liquid state of the material. There are also other associated processes, such as ejecting blobs of molten material and surface shock waves causing microcracks in the heated zone. The machining quality using long laser pulses is generally poor. For laser pulses shorter than the heat diffusion time, the photon energy deposited in the material does not have time to leak away from the spot by thermal diffusion. So much energy is deposited in the material so fast that the material is forced into a state of plasma. This plasma then expands away from the material as a highly energetic gas (seen as a plume), taking almost all the heat away with it. Essentially, the material goes from a solid to a gas phase without first going through the liquid phase. Consequently, very little heat is left behind to damage the material. Figure 1 compares two holes drilled into a 100 μm thick steel foil, one with nanosecond pulse laser and the other with femtosecond pulse laser [1].

The physics behind laser ablation is much more complicated than as explained above. Three characteristic time scales are involved to define the nature of laser interaction with a metallic material [1]. They are the electron cooling time τ_e, lattice heating time τ_i and laser pulse duration τ_L. For a nanosecond pulse laser, $\tau_L \gg \tau_i$: the process is predominantly laser heating. For a picosecond pulse laser, $\tau_e \ll \tau_L \ll \tau_i$: the process is in between ablation and heating. For a femtosecond pulse laser, the process is exclusively a laser ablation process. Laser ablation of semiconductor and dielectric materials involves different mechanisms [2].

In contrast to the laser ablation of inorganic materials, such as metals, semiconductors and dielectrics, organic polymer materials interact with photons very differently. Laser ablation of polymers is dependent less on laser pulse duration and more on laser wavelength and energy. Ablation of polymers with an excimer laser at UV wavelengths was first reported in 1982. It was found that an ArF excimer laser (193 nm wavelength) irradiating a poly(ethylene terephthalate) film could cause etching of the film in air [3]. The polymer material simply sublimed under the excimer laser irradiation. Since the first report, extensive research and development in laser ablation of polymers have taken place. Although still not fully understood, the mechanism of laser ablation of polymers is broadly considered as a photochemical decomposition process. High-energy photons break up the polymer chain to oligomers of much lower molecular weight along with the production of gases such as C_2, CO and CO_2 and monomers. Gaseous products are ejected in the form of plumes from the surface at supersonic velocity carrying with them oligomer particles [4]. Figure 2 shows an array of ink jet printer nozzles drilled into a polyimide sheet by a KrF laser. The hole is 30 μm in diameter. It is very clean cut with a smooth edge. However, there are debris visible surrounding the holes, which are the ejected polymer particles landing on the surface.

The photochemical decomposition process occurs exclusively at UV wavelengths with excimer lasers, such as XeCl (308 nm), KrF (248 nm) and ArF (193 nm). The laser pulse duration has much less effect on ablation. Long pulses of laser irradiation of the order of microseconds can still cause polymer ablation. However, there is a thresh-

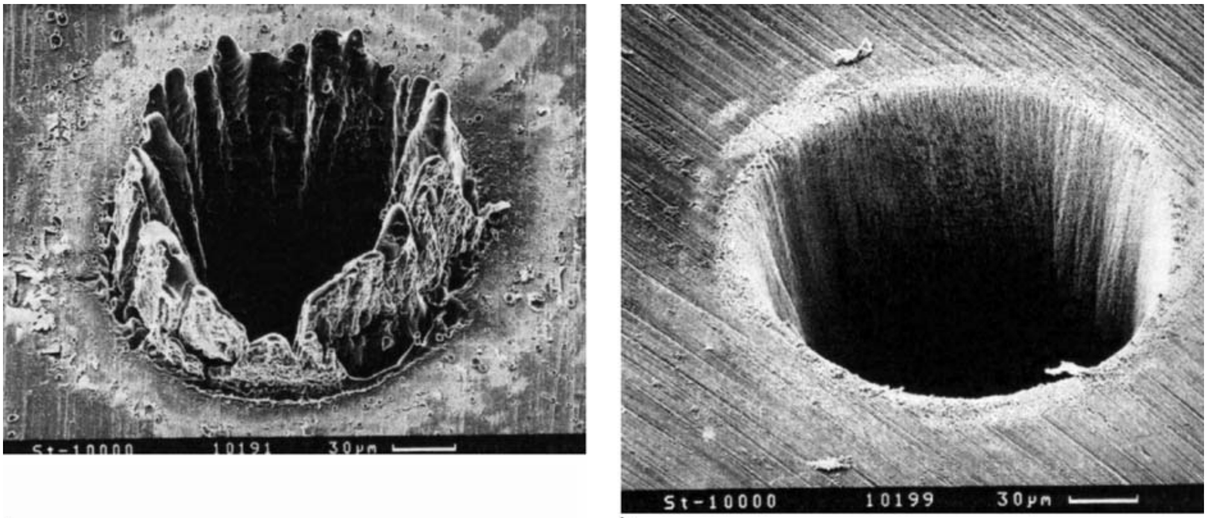

a b

Laser Ablation, Figure 1 (**a**) Nanosecond-pulse laser ablation of a hole in a 100 mm thick steel foil with a pulse width of 3.3 ns, fluence of 4.2 J/cm^2 at a laser wavelength of 780 nm. (**b**) Femtosecond laser ablation of a hole in a 100 mm thick steel foil with a pulse width of 200 fs, fluence of 0.5 J/cm^2 at a laser wavelength of 780 nm

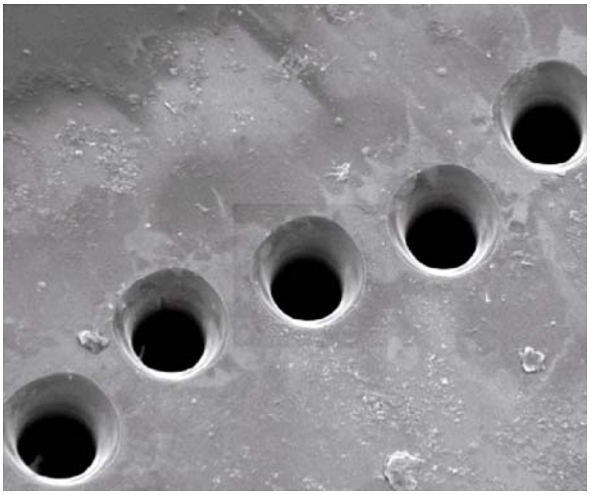

Laser Ablation, Figure 2 KrF laser-drilled ink jet printer nozzles (30 µm diameter) in polyimide

old fluence (mJ/cm^2) above which the ablation occurs. The threshold fluence is different for different polymers, for different photon wavelengths and for different pulse durations [5].

Laser ablation has become a versatile machining technique, particularly in machining of microstructures. Although there are other microfabrication techniques, such as lithography, wet chemical and reactive ion etching, laser ablation provides a direct and fast structuring method. For some materials, laser ablation seems to be the only means to achieve microstructures. Laser ablation of polymers is of particular importance in constructing microfluidic systems. Laser ablation can achieve deep trenches with near vertical side walls in polymer materials, which is often called a LIGA-like micromachining technique. This is ideal for polymer-based microfluidic devices, and polymers are low-cost materials compared with other materials such as silicon and glass.

Basic Methodology

Laser ablation requires an appropriate combination of laser and ablated materials. Many lasers have been used for machining of microstructures, including CO_2 lasers, solid-state lasers, copper vapour lasers and excimer lasers. Pulsed lasers are used because of their ability to deliver high peak power. For a continuous laser a shutter control can provide the necessary pulsation. The peak power, laser intensity and fluence are calculated by the following equations:

$$\text{Peak power (W)} = \frac{\text{pulse energy (J)}}{\text{pulse duration (s)}} \tag{1}$$

$$\text{Intensity (W/cm}^2) = \frac{\text{peak power (W)}}{\text{focal spot area (cm}^2)} \tag{2}$$

$$\text{Fluence (J/cm}^2) = \frac{\text{laser pulse energy (J)}}{\text{focal spot area (cm}^2)} \tag{3}$$

Excimer lasers usually have very low duty cycles or repetition rates (1 – 100 Hz). However, because the pulse can

be very short, the peak power can be very high even though the average power from an excimer laser is low. Each type of excimer laser has a fixed wavelength, e. g. XeCl laser ($\lambda = 308$ nm), KrF laser ($\lambda = 248$ nm) and ArF laser ($\lambda = 193$ nm). They are large in size and expensive to operate. Solid-state lasers offer many advantages. Solid-state lasers include Nd:YAG lasers ($\lambda = 1064$ nm) and Ti:sapphire lasers ($\lambda = 800$ nm). A frequency-tripled Nd:YAG laser can deliver photon wavelength at 355 nm. Solid-state lasers can offer [6]:

- Wide choice of wavelengths (either through direct tunability or via harmonic generation)
- Variety of temporal pulse widths (ranging from milliseconds to a few femtoseconds)
- High pulse repetition rates (from tens to hundreds of kilohertz)
- Large choice of output powers
- Excellent *wall-plug* efficiencies (especially with diode-pumped systems)
- Compact sizes
- Economically favorable running costs.

There are several parameters critical to laser ablation. The first is the wavelength of the laser, which should have a minimum absorption depth in the ablated material. This will ensure a high energy deposition in a small volume for rapid and complete ablation. The second is a short pulse duration to maximize peak power. The third is the pulse repetition rate. At high repetition rate the residual heat generated by laser irradiation can be retained, thus limiting the time for conduction, and the ablation will be more efficient. More of the incident energy will go toward ablation and less will be lost to the surrounding work material and the environment. The fourth is the beam quality. Beam quality is measured by the intensity, as shown above, and is related to a small and well-focused beam spot.

For laser ablation of polymers, the key parameter is the laser fluence. Each combination of polymer material, laser wavelength and pulse duration has a distinctive threshold fluence, below which no ablation takes place. The typical ablation depth vs. laser fluence is shown in Fig. 3. It plots the average ablation depth of poly(methyl methacrylate) at different fluences with a 193 nm excimer laser [4].

There is an empirical relation between ablation rate and the threshold fluence, as shown in Eq. (4) [7]:

$$R = \frac{1}{k} \ln \left(\frac{F}{F_t} \right) \tag{4}$$

where F is the laser fluence, F_t is the threshold fluence and k is the UV absorption coefficient of the polymeric material. The threshold fluence can be measured from experiment, as shown in Fig. 3. The formula is then useful

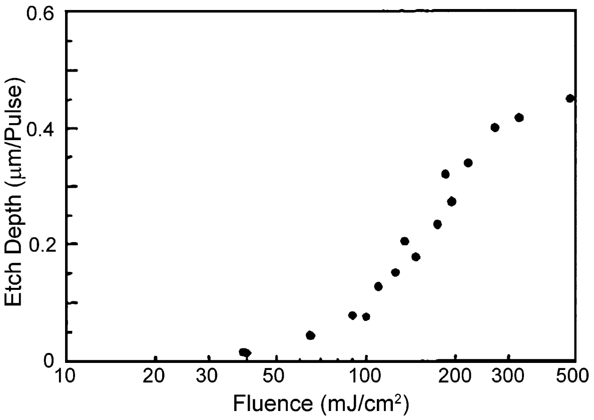

Laser Ablation, Figure 3 Etch depth vs. log fluence for laser ablation of poly(methyl methacrylate) at 193 nm wavelength

to determine the UV absorption coefficient k. Because the UV absorption is different for different polymers at different UV wavelengths, the threshold fluence is also different. High UV absorption results in low threshold fluence. Generally, a longer wavelength photon has a smaller absorption coefficient, therefore a larger threshold fluence. For example, the threshold fluence of polyimide (Kapton) ablation is 30 mJ/cm^2 for an ArF laser, 70 mJ/cm^2 for a KrF laser and 100 mJ/cm^2 for a XeCl laser.

Key Research Findings

Laser ablation is a simple and straightforward process. It has been used as a material processing technique for several decades. From the practical application point of view, R&D in laser ablation has been focused on improving efficiency and precision of machining, and on reducing the heating effect and debris-induced contamination. The most significant development in laser ablation has been the advent of femtosecond lasers and their application in micromachining processes. Femtosecond laser ablation can avoid all the problems associated with laser heating of materials. There are no thermal damages, unmatched machining accuracy down to 100 nm and no wavelength dependence, which means that any materials can be machined with the same laser.

Excimer lasers have been the primary tools for ablation of various polymeric materials, due to their strong absorption of UV photons. However, commercially available polymers often perform poorly in UV laser ablation, such as high ablation threshold, low ablation rate and redeposition of debris, and it becomes worse at longer UV wavelengths. An interesting development in recent years has been that of *designer* polymers, with properties tailored to improve ablation characteristics for specific applications [8]. New

polymers based on a triazene chromophore were specially designed. These polymers exhibit superior laser ablation properties (sharp ablation edges, no debris, low threshold fluence and high etch rates at low fluences) and a high absorption coefficient for the XeCl excimer laser wavelengths.

Future Directions for Research

Although laser ablation has been practiced since lasers were invented and is considered as a mature technology, the mechanism, particularly the mechanism of polymer ablation, is still not fully understood. For polymer ablation, there is the ablative photodecomposition model, the thermal ablation model and the thermal–photochemical ablation model [9]. Many time-resolved measurement techniques have been used to observe what exactly is happening at the laser ablation site and to measure the products generated from laser ablation [10]. These investigations are likely to go on. On the engineering side, there is growing interest in laser ablation of organic tissue materials for biological applications and organic light emitting polymers for photonic applications. The application for prototyping micro- and nanofluidic devices and systems will also expand in the near future.

Cross References

► Laser Based Micromachining

References

1. Chichkov BN, Momma C, Nolte S, von Alvensleben F, Tuennermann A (1996) Femtosecond, picosecond and nanosecond laser ablation of solids. Appl Phys A63:109–115
2. Miller JC, Haglund RF (eds) (1998) Laser Ablation and Desorption. Academic, London
3. Srinivasan R, Mayne-Banton V (1982) Self-developing photoetching of poly(ethylene terephthalate) films by far-ultraviolet excimer laser radiation. Appl Phys Lett 41(6):576–578
4. Srinivasan R, Braren B, Casey KG (1990) Ultraviolet laser ablation and decomposition of organic materials. Pure Appl Chem 62(8):1581–1584
5. Taylor RS, Singleton DS, Paraskevopoulos G (1987) Effect of optical pulse duration on the XeCl laser ablation of polymers and biological tissues. Appl Phys Lett 50(25):1779–1981
6. Gower MC, Rizvi NH (2000) Applications of laser ablation to microengineering. Proc SPIE 4065:452–460
7. Andrew JE, Dyer PE, Forster D, Key PH (1983) Direct etching of polymeric materials using a XeCl laser. Appl Phys Lett 43(8):717–719
8. Lippert T, Wei J, Wokaun A, Hoogen N, Nuyken O (2000) Polymers designed for laser microstructuring. Appl Surf Sci 168:270–272
9. Dyer PE (2003) Excimer laser polymer ablation: twenty years on. Appl Phys A77:167–173
10. Hauer M, Funk DJ, Lippert T, Wokaun A (2003) Laser induced decomposition of a designed and a commercial polymer studied by ns-interferometry and shadowgraphy. Appl Phys A77:297–301

Laser-Based Biosensors

► Biosensors Using Lasers

Laser Based Micromachining

KYOO DONG JO , SMITI BHATTACHARYA,
AARON T. TIMPERMAN
C. Eugene Bennett Department of Chemistry,
West Virginia University, Morgantown, WV, USA
atimperm@wvu.edu, atimperm@wvu.edu

Synonyms

Laser micromachining; Microfabrication

Definition

Laser Micromachining refers to a broad range of processes used to form materials through the use of intense light with high spatial resolution and feature sizes down to the submicron level. Laser micromachining typically involves the removal of material through ablation or thermal processes, but also includes formative processes where the light can be used to control deposition or molecular reactions.

Overview

Laser micromachining is one of many commonly used methods for the formation of microfluidic devices. Laser micromachining has direct write capabilities, can be used to form high aspect ratio channels and features, and can be used for the fabrication of 3D fluidic structures. These characteristics prove advantageous in many applications and differentiate it from other methods for the fabrication of microfluidic devices, including wet chemical etching, polymer casting, hot-embossing and deep reactive ion etching. Laser micromachining has been used with numerous microfluidic substrates, including silicon dioxide (glass) and numerous polymers.
Laser ablation refers to the removal of material from a substrate surface when the photon flux overcomes a threshold that causes breaking of covalent bonds and expulsion of material from the solid to the gas phase. To overcome the desorption threshold extremely high irradiances (power/area) must be achieved. Lasers are well suited for providing such high irradiances over small areas, because they are characterized by high irradiance (power/area),

low beam divergence, and high coherence. The low divergence and high coherence make it straightforward to further increase the intensity through optical focusing. In the direct write mode, the laser is focused onto the substrate, and either the optics or substrate is moved to mill out channels, holes, or other features. Static machining can also be used to mill multiple features within a small area in parallel by using an optical mask to define the areas that are ablated. During static machining a beam expander can be used, but the irradiance must be high enough to overcome the ablation threshold.

The phenomenon of laser ablation was first reported in 1973 by Emmony et al. where the group reported damage in a germanium mirror of a TEA CO_2 laser at a wavelength of 10.6 μm [1]. In 1982, Srinivasan and Mayne-Banton of IBM reported the laser ablation of polyethyleneterphthalm (PET) [2].

Two fundamental modes of laser micromachining can be differentiated based on the temporal width of the laser pulses used. Ultrashort pulses provide rapid bursts of photons that interact with a material in time frames that are shorter than time scales of thermal processes and are less than 10 ps in width. Therefore, in ultrashort laser pulses dissociative processes dominate and thermal conduction of heating to the surrounding areas is minimized, which nearly eliminates cracking and thermal damaging of the surrounding areas. The resulting plasma that forms is a highly energetic gas that expands away from the material taking most of the heat away with it [3]. In processes that use laser pulses greater than 10 ps, thermal heating and conduction are important processes that lead to increased heating and damage. In yet longer and continuous wave processes, thermal heating leads to melting of the material before it is evaporated. Long pulsed lasers may be used for additive processes such as welding.

Clearly, the precision and reproducibility of the laser micromachining process are largely dependent on the characteristics of the laser beam used. First and foremost, the wavelength of radiation used by the laser must be absorbed by the substrate that is being micromachining. The minimum spot size and depth of focus are critical in determining the minimum size of features that can be micromachined with a given system. For ablation to occur, the irradiance of the light must exceed the ablation threshold. Thus the laser intensity and intensity distribution must be carefully considered. The laser pulse helps define the peak power and the degree to which heat dissipation can occur.

Laser Wavelength

Laser micromachining is based on the absorbance of electromagnetic radiation in by the substrate material. Thus most basic requirement is that the substrate must be capable of absorbing the wavelength of the electromagnetic used for the micromachining to be successful. Absorption by the molecular or inorganic substrate relies on the electronic transitions from the ground to excited states. For short wavelengths, of less than ~ 200 nm, the photons have enough energy to cause $\sigma \rightarrow \sigma*$ and $n \rightarrow \sigma*$ transitions that cause electrons in bonding orbitals to be excited to antibonding orbitals and electrons in non-bonding orbitals to be excited to antibonding orbitals, respectively. The volatile fragments produced by bond cleavage are removed from the substrate surface during the machining process. At longer wavelengths above 300 nm for example, the energy of a single photon is not sufficient to break the bonds of the substrate and multiphoton process are required for laser micromachining of glass and polymers. Longer wavelength lasers are still used for micromachining, but rely on thermal processes that heat, melt, and evaporate the substrate. For longer wavelength lasers, it is still necessary that the substrate absorbs at the wavelength of the laser for the thermal processes to occur.

Most laser micromachining is achieved with single-photon absorption, in which a single photon whose energy matches an electronic transition of the substrate, is absorbed and causes an electronic transition. With single photon mechanisms, the absorption increases linearly as the intensity of the radiation or laser light is increased.

Two-photon absorption is a nonlinear optical phenomenon that occurs when two photons are absorbed simultaneously and the combined energy of two photons matches an electronic transition. Under normal conditions, the probability of two photons being absorbed simultaneously is extremely low, and therefore to utilize two-photon absorption processes for ablation very high irradiances much be achieved. An important part of the aspect of the optical instrument used for two-photon processes is the use of high numerical aperture optics that can provide very small focal spots with minimal depth of field. The probability of a two-photon absorption increases non-linearly, as a function the intensity squared [4]. Thus, when properly tuned the ablation by two-photon processes is constrained to a very small volume centered at the beam waist and limited by the depth of focus. The excitation wavelength is selected such that before the light is focused to the beam waist, the material is transparent to single photon absorption. This penetration of the excitation enables 3-dimensional micromachining with two-photon processes. Femtosecond lasers are used because the irradiance delivered by their short pulses is extremely high. In addition to ablation, two-photon processes can be used for photopolymerization of material within the focal spot in a similar manner.

Spot Size of Laser and Depth of Focus

For both one and two photon processes the irradiance is greatest at the beam waist. Consequently, precise control of the spot size is required for accurate micromachining. A poorly controlled spot size can result in larger features widths and increased sloping of the side walls. The smallest obtainable spot size determines the minimum feature size, which is limited to half the wavelength of the light used. Under the conditions where a perfect lens with no spherical aberration is used to focus a laser beam that is collimated, the minimum diameter of the focused laser beam d_{min} is given by:

$$d_{min} = \frac{4M^2 \lambda f}{\pi d_0} \tag{1}$$

Where λ = wavelength of radiation
M^2 = the beam mode parameter
d_0(mm)= diameter of the beam at the focusing lens
f = focal length of the lens.
Therefore improved spatial resolution can be achieved by reducing the wavelength, using a large diameter lenses, fully filling the lens, and using a short focal length. A large diameter lens with short focal length has low f-numbers, making the use of low f-number lenses advantageous.
The depth of focus is defined as the distance between the values where the beam diameter is $\sqrt{2}$ times greater than what it is at the beam waist as shown in Fig. 1. It may be expressed by the following equation [5]:

$$DOF = \pm \left(\frac{8\lambda M^2}{\pi}\right)\left(\frac{f}{d_0}\right)^2 \tag{2}$$

For surface micromachining, a short depth of focus requires a very flat substrate surface.

Laser Irradiance or Power Density

The irradiance has units of W/cm^2 and is defined as the power divided by the focal spot area, where the power is the pulse energy divided by the pulse duration in time. For a given number of photons, the intensity increases as the area the photons are focused on decreases and the time period during which the photons arrives decreases. The fluence describes the energy per unit area and has units of J/cm^2.

Laser Spot Intensity Profile for TEM_{00}

The spatial profile of a laser beam at the exit of the laser aperture is determined by the geometry of the laser cavity and the propagation of light within the cavity. The transverse electromagnetic modes are represented by TEM_{mn}

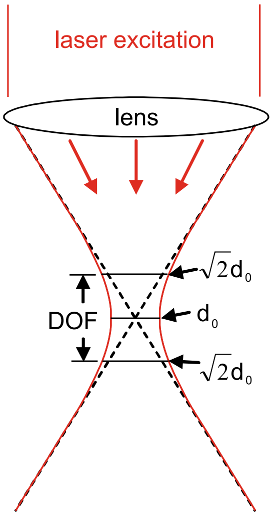

Laser Based Micromachining, Figure 1 The focal spot at the beam waist has a diameter of d_0. The depth of focus (DOF) is typically defined as the region bounded by above and below the beam waist. The beam waist, as shown by the red line (light grey in the print version), is normally greater than or equal to the diffraction limit. The irradiance is greatest in the volume contained in the region defined by the DOF, and consequently ablation will be centered about this volume

where m and n represent the number of nodes in the orthogonal directions. The TEM_{00} mode has no nodes in either orthogonal directions, and consequently has the greatest symmetry and is most often used for laser micromachining. The intensity of a TEM_{00} spot is cylindrically symmetrical, and the cross-section of the intensity profile is Gaussian. This intensity as a function of distance from the spot center (r) is given by the following equation:

$$I(r, t) = I_0(t) \exp\left[-\frac{r^2}{w^2}\right] \tag{3}$$

where I_0 = peak intensity at the spot center where $r = 0$, w =radius of the point where the intensity drops by a factor of 1/e with respect to I_0, and r = the radial coordinate that expresses distance from the spot center.

Laser Pulse Length

Pulsed lasers provide intermittent periods of photon emission. Averaged over time, the time off is usually much greater than the time on when photons are emitted. The laser pulse length is the length in time during which photons are emitted from the laser during each individual pulse. For laser micromachining, the major difference between a long pulse laser and a short pulse laser is nature of the heat diffusion into the material. In the

case of a long pulse laser, the material experiences considerable thermal diffusion which reduces the overall efficiency of the process. Energy that could have been used to remove material through ablation is lost into the surrounding material. In contrast, when a short pulse laser is used, the heat deposited by the light does not have the time to move away from the area ablated. This pulse creates a plasma on the surface, and the force from the plasma causes the material to expand outward and away from the surface. The zone around the machined area is referred as the heat affected zone (HAZ). The waves propagating through the HAZ may cause mechanical stress that may cause substrate cracking. This effect is more prominent in systems with long pulse lengths more than short pulse length systems, because the heating in the surrounding zone is diminished in short pulse systems. For a given number of photons the irradiance during the pulse decreases as the pulse length increases. Therefore, with longer pulse a higher fluence must be used to reach the ablation threshold.

Femtosecond laser machining, with pulses of femtosecond duration, has attracted much attention due to advantages such as small heat-affected zones (HAZ), and the ability of three-dimensional processing inside a transparent substrate. When femtosecond laser pulses are focused into a transparent medium, ultrahigh fluence in the neighborhood of the focus can result in nonlinear multiple photon absorption including optical breakdown and subsequent formation of localized three-dimensional features inside the medium. The most common applications of using femtosecond lasers are laser direct writing to create embedded three dimensional microfluidic structures in glass and polymer substrates, such as poly(dimethylsiloxane) (PDMS) and PMMA, and drilling microholes for the microfluidic devices [6–9]. The use of glass-based microfluidic channels in Lab-on-Chip devices has led to increasing attention being paid to glass micromachining. It is desirable to avoid damage and microcracks around the laser machined region and femtosecond lasers have proven to be excellent sources for such precise machining work [6, 10].

Typical Channel Profile

The morphology of an ablated microfluidic channel is determined by a number of parameters. These include the laser irradiance, spot size, speed of the x-y stage, repetition rate of the laser, properties and characteristics of the substrate being ablated, and the chemical environment under which the ablation occurs. It is also dependent on the temporal and spatial profile and wavelength of the laser pulse. Waddell et al. determined that as the fluence is increased above the ablation threshold for a particular substrate, the depth of the ablated channels increases and the roughness of the area surrounding the channel is increased [11]. In contrast, a lower fluence produces a shallower and smoother channel, but decreasing the power below the ablation threshold will result in the removal of no material. The nature of the substrate material and the external environment of the substrate during the ablation process play an important role in the morphology of the ablated channels. Waddell et al. studied these aspects of laser-ablated channel, and noted that ablated poly methyl methacrylate (PMMA) structures have a rougher surface and exhibits more cracking when compared with poly ethylene terephthalate glycol (PETG), polycarbonate (PC) and poly vinyl chloride (PVC) [11]. These differences are attributed to the light absorption properties of the respective materials at the laser wavelength and thermal conductivities of the materials.

When PMMA was ablated in an atmosphere of nitrogen and in methanol the channels were rectangular. On the other hand, when the ablation was under water, the profile was wedge shaped. This change in channel geometry was attributed to the change in the path of the laser beam through the water [11].

Commonly Used Lasers

A variety of lasers can be used for machining the microfluidic channels, from nanosecond lasers to femtosecond lasers or from IR lasers to UV lasers, depending on the materials to be fabricated and desired applications.

The most widely used lasers for fabricating microfluidic channels in polymer substrates are UV lasers, excimer, and Nd:YAG laser. UV lasers are typically operated in pulsed mode with pulses of nanosecond duration. Excimer lasers produce various wavelengths depending on the gas composition; 157 nm F_2, 193 nm ArF, 248 nm KrF, 351 nm XeF and 308 nm XeCl. The excimer laser- due to low coherence beam with high pulse energies- is generally used for fabrication by mask projection methods.

The solid state Nd:YAG lasers can be frequency converted from fundamental 1064 nm wavelength to 355 nm and 266 nm by using non linear crystals. The Nd:YAG lasers generally have highly coherent beam and are able to focus more tightly to enable more rapid material removal. Thus, these lasers are suited to direct writing dynamic mode.

Their applications of machining the microfluidic channels in polymers include a number of substrates: poly(ethylene terephtalate) (PET), polystyrene, poly carbonate, cellulose acetate, poly(methyl methacrylate) (PMMA), poly (vinyl chloride) (PVC), poly(ethylene terephthalate glycol) (PETG), polytetrafluoroethylene (PTFE) and poly-

imide [11–14].

In contrast to UV lasers, IR lasers ablate the substrates photothermally. When the focused laser beam hits the substrate surface, the temperature of the irradiated spot will rise rapidly that the material will first melt and then decompose, leaving a void in the substrate. The actual decomposition mechanism depends on the strength of the chemical bonds of the monomers that make up the polymer and the structure of the polymer itself.

The most widely used IR laser for machining microfluidic channels in polymers are CO_2 lasers, which are continuous wave lasers. The primary emission wavelengths of CO_2 lasers are in the IR region and centered at 9.4 and 10.6 μm produced. Poly(methyl methacrylate) (PMMA) is highly compatible with CO_2 laser machining due to its high absorbance in IR region, low heat capacity, low heat conductance, and good thermal decomposition into volatile byproducts [15, 16].

Basic Methodology

Micromachining System Instrumentation

The basic laser micromachining system is quite simple and requires a laser, focusing optics, and translation stages or masks. The minimal requirements vary somewhat depending on the mode of operation used. The two basic modes of operation are direct writing and parallel processing. In direct writing, as the name suggests, the laser beam is focused on the surface and is used to directly ablate the material where the laser is tightly focused. Each area to be machined is ablated sequentially in a serial fashion. In the parallel processing mode, the laser is not focused into a tight spot but is expanded to illuminate a mask. The transparent areas of the mask allow for the light to pass through, and ablate the exposed regions. One mask or several masks may be used to complete the machining process depending on the size of the patterns and the maximum area over which the intensity is sufficient for ablation.

In order to maintain the proper spatial orientation of the channels and other features, the translational stage must have the required resolution and reproducibility. Typically x-y stages are used for controlling the location along the surface of the substrate. The vertical or z-dimension is often controlled by translating the focusing optic in the vertical dimension. Off-axis optics can be used to form a circular scribing or trepanning head. For cutting microchannels of greater dimension than the laser spot, multiple parallel passes or trepanning with linear translation can be used. To trepan a linear channel the diameter of rotation of the spot on the substrate surface is equal to the channel width, and the linear translation increases the length.

The minimum feature size is largely dependent on spot size and accuracy and reproducibility of the positioning system. Commercial systems provide well developed control programs and platforms that allow for rapid production of prototype designs. Digital cameras can be used for real-time monitoring of the micromachining process and can aid in alignment of features. Masks can also be used with direct write systems to tailor the shape of the laser spot and provide different channel cross-sections. As the mask aperture is reduced the laser fluence and the rate of material removal is reduced. The local environment around the ablated area may be controlled to the benefit of the process in various ways. One such method flow a gas of the ablated site for removal of the particles produced during ablation and minimize the recast. Another approach is to immerse the material in a liquid that is transparent to the laser light.

The parallel mode for batch processing uses a mask imaging technique. A mask is placed between the laser and the substrate, and the collimated light from the laser is used to ablate an image of the mask on the substrate surface. Typically the optics are chosen to give a demagnified image (*10 times smaller*) to give high power densities on the surface and avoid damage to the mask [17] .

L

Laser Etching with Chemical Assistance

The process of micromachining may be assisted by either dry or wet chemical etchants for building high quality 3D micromachines. As an example, chlorine may be used as an etchant and is photodissociated to react with the substrate. If the ablation is performed in Cl_2 gas, the silicon vapour leaving the surface react with chlorine to form $SiCl_4$ gas and is removed from the surface. Reducing recast through chemical assistance produces significantly higher removal rates and produces cleaner and more sharply defined parts.

Key Research Findings

It was the groundbreaking paper published by Manz group in 1990 that established the field of miniaturized total chemical analysis systems (μTAS) and the area of μTAS, also called *Lab-on-a-Chip*, microfluidic system, is a rapidly developing field. A standard architecture consisted of a network of microchannels etched into the surface of a planar substrate using standard photolithography, and chemical wet-etching techniques. Laser micromachining provides an alternative and complimentary method to wet chemical etching. In terms of microfluidic devices, laser micromachining provides three main benefits: 1) it can be used to produce high aspect ratio channels, 2) it

can be used to create 3D channel structures, and 3) it is well suited for rapid prototyping.

The surface characteristics of a microfluidic channel are very important in determining the flow in electrokinetically driven systems. In electrokinetically driven systems, the bulk flow is created by movement of the mobile diffuse layer near the channel wall/solution interface that is termed electroosmotic flow (EOF). The EOF is dependent on the surface of the microchannel walls. Roberts et al. demonstrated the generation of EOF on laser ablated polymer substrates for the first time, using the parallel processing mode with a photomask an ArF excimer laser at 193 nm [17]. A variety of polymer substrates such as polystyrene, polycarbonate, cellulose acetate, and poly (ethylene terephthalate) (PET) were ablated to fabricate microfluidic channels. The laser ablation process alters the surface chemistry of the machined regions and produced negatively charged, functionalized polymer surfaces capable of generating EOF.

There are differences in the surface of the laser ablated polymer depending on the mode of operation, static and dynamic laser ablation mode. Rossier et al. investigated differences in surface states of polymer PET as a result of these two modes of ablation [18]. Their studies revealed that the static ablation mode produced a homogeneous and hydrophobic surface with poor wettability, whereas the dynamic ablation mode produced an inhomogeneous and hydrophilic surface with high wettability. These differences were attributed to the redeposition of fragments.

Alterations in the charge on the channel surface are important to consider because the surface charge density is important for electrokinetic microfluidic applications such as maintaining electro osmotic flow (EOF) in the micro channel. Pugmire et al. investigated changing the ablation atmosphere during the excimer laser ablation of polymer microchannels as well as controlling their surface properties and associated electro osmotic mobility in a single step process [12]. The ablation of polycarbonate under the different atmospheres, such as argon, nitrogen, and oxygen, results in channels with different EOF's [12]. The changes in the surface charge are thought to be because of altered chemical functionality of the surface of the polymer. This result is of significance in Microfluidic applications where the wall charge is used to alter the electroosmotic flow. Unlike the case where dynamic or permanent coatings are used to alter the EOF which requires additional fabrication, laser ablation allows the modification of the surface chemistry under different atmospheres.

Combining electrokinetically and hydrodynamically driven systems can be challenging. Razunguzwa et al used laser micromachining with a copper vapour laser to form hydrodynamic restrictors that allowed coupling an electrokinetically driven system with low EOF and hydrodynamic flow. The narrow width of the channels formed with laser micromachining provides increased frictional resistance to flow, while the increased depth and ability to fabricate many channels in parallel increases the cross-sectional area. Increasing the cross-sectional area is required to decrease the current density below levels where Joule heating causes bubble formation. Bubble formation causes current break-down that stops electrokinetically driven systems [19].

From a microfluidic system perspective, one of the most advantageous features of laser micromachining lies in its capability to construct three dimensional structures both in silicon materials and polymeric materials. The three dimensional processing of polymers and glasses is of significance to the development of advanced solutions for bonding process in fabricating microfluidic systems. In the following discussion, recent publications will be introduced that show development of three-dimensional processing of glasses and polymer toward the one-step processing for the fabrication of enclosed micro-nano fluidic devices.

Giridhar et al. used femtosecond direct laser writing technique at a wavelength of 1660 nm to ablate the glass substrate at or below the surface [10]. The well defined spot of the pulsed laser was focused into the bulk substrate, resulting in localized ablation below the surface. Though silicate glass is normally transparent at this wavelength, the extremely high intensity of the focused beam causes multiphoton absorption, resulting in subsurface ablation localized at the beam waist. This process relies on multiphoton excitation to drill a micro tunnel under the substrate surface connecting two adjacent pits machined by the same laser in a glass substrate. To prevent substrate fragments from depositing in the working area, dry nitrogen gas was used during the entire writing process. An important advantage of using pulsed laser micromachining is its ability to drill subsurface tunnels into glass substrates and form 3D channel networks.

Direct three dimensional laser machining of submicrometer subsurface fluidic channels in glass through optical breakdown near critical intensity using a femtosecond pulsed laser was demonstrated by Ke et al. [6]. Glass substrate was machined using laser systems with 800-fs pulses at 527 nm. In this technique, no postprocessing is required, such as etching and bonding. Extremely long, deep channels ($> 200\ \mu m$) of extremely small diameter (< 700 nm) were produced. Subsurface channels can be successfully fabricated with this method because microbubbles play a critical role by transporting the fluid-entertained debris away from the machining site. Salient advantages of this method include production of 3D nanochannels with arbi-

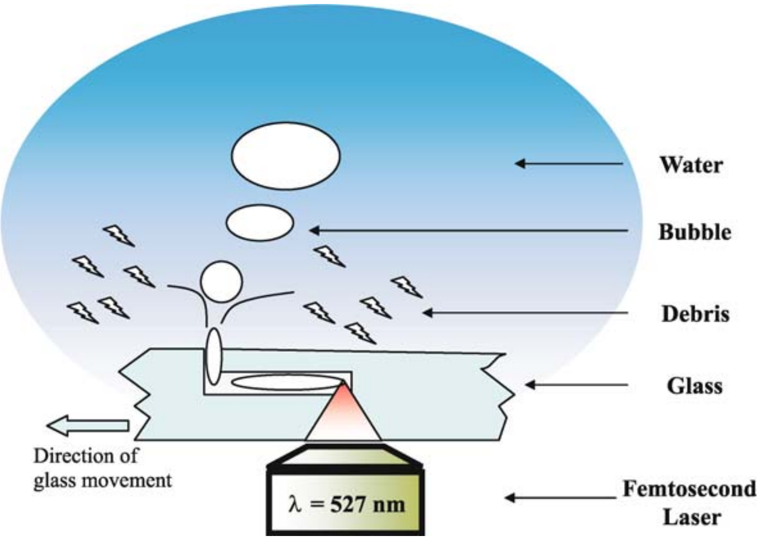

Laser Based Micromachining, Figure 2 Schematic of laser micromachining system for rapid prototyped three-dimensional channel networks using a femtosecond laser. The femtosecond laser provides intensities that overcome the ablation threshold at the tightly focused beam waist. The glass substrate is immersed in water and bubbles formed by heating remove debris from the channel. The substrate is articulated with a micro-positioning stage that is similar to other systems, but positioning along the vertical dimension controls channel depth

L

trary channel geometries, aspect ratios larger than 280 and roughness within the channel of the order of 10 nm as well as avoiding the need for bonding. The small feature sizes and the ability to machine in 3D enable integration of microfluidic channels for HPLC devices, micro-sensors, and integrated nanopores for patch-clamp studies of cell.

Fabrication of subsurface microchannels in polymer substrate is very challenging process because of clogging of channels by debris and rough fractured channel walls. However, Farson et al. successfully made subsurface microchannels in PMMA substrate [8]. They used $Ti:Al_2O_3$ chirp-pulse amplified laser producing 150 fs pulses at a repetition rate of 2 kHz. The maximum output power of the laser was 1.6 W, corresponding to an average pulse energy of 0.8 mJ. The laser beam was focused inside the material, resulting in the ablation of an internal channel. The debris was evacuated from the channel by blowing a stream of Ar gas through a vent channel, providing a vacuum for removal of the debris gas. The venting technique resulted in smooth channels without obvious cracking. The fabricated channel diameter ranged from 2 μm to 20 μm and the maximum length of smooth channel ranged from 5 mm to 10 mm.

Future Directions for Research

Research in laser micromachining will continue to new methods for the fabrication of microfluidic devices, particularly from polymers and glass. The development of 3D channel networks is important for numerous fluidic applications which will fuel future the demand for more research in this area. As these methods are refined the processes will be tailored to processing of many different types of polymers. Future work will continue to seek methods to decrease the roughness of microchannels. Analysis of complex mixtures of biomolecules requires surfaces that minimize non-specific adsorption. In order to minimize problems with surface adsorption, characterization of the ablated surface will continue.

Cross References

- ► Laser Ablation
- ► Bulk Micromachining
- ► Silicon Micromachining
- ► Laser Based Micromachining
- ► Ultrasonic Machining
- ► Nanochannel Fabrication
- ► Lab-on-a-Chip (General Philosophy)

References

1. Emmony DC, Howson RP, Willis LJ (1973) Laser mirror damage in germanium at 10.6 mm. Appl Phys Lett 23(11):598–600
2. Srinivasan R, Mayne-Banton V (1981) Self-developing photoetching of poly(ethylene terephthalate) films by far-ultraviolet excimer laser radiation. Appl Phys Lett 41(6):576–578
3. Liu X, Du D, Mourou G (1997) Laser ablation and micromachining with ultrashort laser pulses. IEEE J Quantum Electron 33(10):1706–1716

4. Andrews DL (1985) A simple statistical treatment of multiphoton absorption. Am J Phys 53(10):1001–1002
5. Madou MJ (2002) Comparison of miniaturization techniques: top –down and bottom-up manufacturing in fundamentals of microfabrication: the science of miniaturization. CRC:402–411
6. Ke K, Hasselbrink Jr EF, Hunt AJ (2005) Rapidly Prototyped Three-Dimensional Nanofluidic Channel Networks in Glass Substrates. Anal Chem 77(16):5083–5088
7. Wolfe DB, Ashcom JB, Hwang JC, Schaffer CB, Mazur E, Whitesides GM (2003) Customization of poly(dimethylsiloxane) stamps by micromachining using a femtosecond-pulsed laser. Adv Mater 15(1):62–65
8. Farson DF, Choi HW, Lu C, Lee LJ (2006) Femtosecond laser bulk micromachining of microfluid channels in poly(methylmethacrylate). J Laser Appl 18(3):210–215
9. Iga Y, Watanabe W, Ishizuka T, Li Y, Nishii J, Itoh K (2003) Fabrication of micro-holes in silica glass by femtosecond laser pulses. Proc SPIE - Int Soc Opt Eng 5063(Laser Precision Microfabrication) pp. 129–132
10. Giridhar Malalahalli S, Seong K, Schulzgen A, Khulbe P, Peyghambarian N, Mansuripur M (2004) Femtosecond pulsed laser micromachining of glass substrates with application to microfluidic devices. Appl Opt FIELD 43(23):4584–4589
11. Waddell EA, Locascio LE, Kramer GW (2002) UV laser micromachining of polymers for microfluidic applications. Jala 7(1):78–82
12. Pugmire DL, Waddell EA, Haasch R, Tarlov MJ, Locascio LE (2002) Surface Characterization of Laser-Ablated Polymers Used for Microfluidics. Anal Chem 74(4):871–878
13. Kim DY, Lee KC, Lee C (2003) Surface modification of silicon and PTFE by laser surface treatment: improvement of wettability. Proc SPIE – Int Soc Opt Eng 5063 (Laser Precision Microfabrication) pp 66–70
14. Stamm U, Fiebig M, Govorkov SV, Mayer EE, Osmanov R, Scaggs MJ, Slobodtchikov EV, Wiessner AO, Basting D (2000) Novel results of laser precision microfabrication with excimer lasers and solid state lasers. Proc SPIE – Int Soc Opt Eng 4088 (Laser Precision Microfabrication) pp 118–123
15. Cheng JY, Wei CW, Hsu KH, Young TH (2004) Direct-write laser micromachining and universal surface modification of PMMA for device development. Sens Act B 99(1):186–196
16. Yuan D, Das S (2007) Experimental and theoretical analysis of direct-write laser micromachining of poly(methyl methacrylate) by CO2 laser ablation. J Appl Phys 101(2):024901/1–024901/6
17. Roberts MA, Rossier JS, Bercier P, Girault H (1997) UV laser machined polymer substrates for the development of microdiagnostic systems. Anal Chem 69(11):2035–2042
18. Rossier JS, Bercier P, Schwarz A, Loridant S, Girault H (1999) Topography, crystallinity and wettability of photoablated pet surfaces. Langmuir 15(15):5173–5178
19. Razunguzwa TT, Lenke J, Timperman AT (2005) An electrokinetic/hydrodynamic flow microfluidic CE-ESI-MS interface utilizing a hydrodynamic flow restrictor for delivery of samples under low EOF conditions. Lab Chip 5(8):851–855

Laser Doppler Anemometry

► Micro Laser Doppler Velocimetry (μ-LDV)

Laser Doppler Sensor

► Micro Laser Doppler Velocimetry (μ-LDV)

Laser-Induced Fluorescence (LIF)

Synonyms

Planar laser-induced fluorescence

Definition

Laser-induced fluorescence (LIF) is a non-intrusive flow visualization technique that can provide instantaneous whole-field measurements of a variety of flow characteristics, including concentration, density, temperature and velocity with high spatial and temporal resolution. In a typical LIF experiment, a fluorescent dye is used to mark the fluid and a region of the flow is illuminated with incident light whose wavelength can excite electronic transition of the fluorophores. The light fluoresced by the dye is imaged using one or more CCD cameras after it is separated from the illuminating wavelength using optical filters. These intensity fields can then be related to a flow variable of interest following an a priori calibration of the dye's fluorescence intensity as a function of variations in the flow variable.

Cross References

► Fluorescent Thermometry
► Fluorescence Measurements
► Fluorescent Labeling

Laser-Induced Molecular Tagging

► Visualization Based on Molecular Tagging Methods

Laser-Induced Photochemical Anemometry

► Visualization Based on Molecular Tagging Methods

Laser Machining

► Laser Ablation

Laser Micromachining

► Laser Based Micromachining

Laser Scanning Confocal Microscopy (LSCM)

► Confocal Microscopy, Detection

Lattice Boltzmann Equation

► Lattice Boltzmann Method (LBM)

Lattice Boltzmann Method (LBM)

JUNFENG ZHANG[1], DANIEL Y. KWOK[2]
[1] School of Engineering, Laurentian Universtiy, Sudbury, ON, Canada
[2] Department of Mechanical Engineering
Schulich School of Engineering, University of Calgary, Calgary, AB, Canada
jzhang@laurentian.ca, daniel.kwok@ucalgary.ca

Synonyms

Lattice Boltzmann equation

Definition

The lattice Boltzmann method is a mesoscopic simulation method for complex fluid systems. The fluid is modeled as fictitious particles as they propagate and collide over a discrete lattice domain at discrete time steps. Macroscopic continuum equations can be obtained from this propagation–collision dynamics through a mathematical analysis. The nature of particulates and local dynamics also provide advantages for complex boundaries, multiphase/multicomponent flows, and parallel computation.

Overview

The lattice Boltzmann method (LBM) is a relatively new simulation technique for complex fluid systems which has attracted a great deal of interest from researchers in computational physics. Unlike the traditional computation fluid dynamics (CFD), which numerically solves the conservation equations of macroscopic properties (i. e., mass, momentum, and energy), LBM models the fluid consisting of fictitious particles, and such particles perform consecutive propagation and collision processes over a discrete lattice mesh. Due to its particulate nature and local dynamics, LBM has several advantages over conventional CFD methods, especially in dealing with complex boundaries, incorporation of microscopic interactions, and parallel computation [1].

Historically, LBM originated from the lattice gas automata (LGA), which can be considered as a simplified, fictitious molecular dynamics in which space, time, and particle velocities are all discrete. Each lattice node is connected to its neighbors by, for example, six lattice velocities from a hexagonal FHP (Frisch–Hasslacher–Pomeau) model. There can be either one or zero particle at a lattice node moving along a lattice direction. After a time interval, each particle then moves to the neighboring node in its direction, and this process is called the propagation. When there are more than one particles arriving at the same node from different directions, they collide and change their directions according to a set of collision rules. Good collision rules should conserve the particle number (mass), momentum, and energy before and after the collision. However, it was also found that LGA suffers from several native defects including the lack of Galilean invariance, presence of statistical noise, and absence of exponential complexity for three-dimensional lattices.

The main motivation for the transition from LGA to LBM was the desire to remove statistical noise by replacing the Boolean particle number in a lattice direction with its ensemble average, the so-called density distribution function. Accompanying this replacement, the discrete collision rules also have to be modified as a continuous function – the collision operator. In the LBM development, an important simplification is to approximate the collision operator with the Bhatnagar–Gross–Krook (BGK) relaxation term. This lattice BGK (LBGK) model makes simulations more efficient and allows flexibility of the transport coefficients. On the other hand, it has been shown that the LBM scheme can also be considered as a special discretized form of the continuous Boltzmann equation. Through a Chapman–Enskog analysis, one can recover the governing continuity and Navier–Stokes equations from the LBM algorithm [2]. In addition, the pressure field is also directly available from the density distributions and hence there is no additional Poisson equation to be solved as in the traditional CFD methods.

Simulating multiphase/multicomponent flows has always been a challenge to conventional CFD because of the moving and deformable interfaces. More fundamentally, the interfaces between two bulk phases (e. g., oil and

L

water) originate from the specific interactions among different molecules. Therefore it is difficult to implement such microscopic interactions into the macroscopic Navier–Stokes equation. However, in LBM, the particle kinetics allows a relatively easy and consistent avenue to incorporate the underlying microscopic interactions by modifying the collision operator. Several LBM multiphase/multicomponent models have been developed [3, 4]. Phase separations can be generated automatically from particle dynamics and no special treatment is needed to manipulate the interfaces as in traditional CFD methods. Successful applications of the multiphase/multicomponent LBM models can be found in various complex fluid systems, including interface instability, bubble/droplet dynamics, wetting on solid surfaces [4], interfacial slip [5], and droplet electrohydrodynamic deformations [6].

Despite the increasing popularity of LBM in simulating complex fluid systems, one should also be aware of the limitations of this novel approach. At present, high Mach number flows in aerodynamics are still difficult for LBM, and a consistent thermohydrodynamic scheme is absent. For multiphase/multicomponent models, the interfacial thickness is usually large and the density ratio across the interface can only be small when compared with real fluids. Nevertheless, applications and advancements of this method during the past 20 years have proven its potential in computational physics, including microfluidics.

Basic Methodology

LBM Algorithm

In LBM, a fluid is modeled as fictitious particles moving in a lattice domain at discrete time steps. The major variable in LBM is the density distribution $f_i(\boldsymbol{x}, t)$, indicating the number of particles moving along the i-th lattice direction at position $\boldsymbol{x}$ and time t. The time evolution of density distributions is governed by the so-called lattice Boltzmann equation with a BGK collision term [1, 2]:

$$f_i(\boldsymbol{x}+\boldsymbol{c}_i\Delta t, t+\Delta t) - f_i(\boldsymbol{x}, t) = -\frac{f_i(\boldsymbol{x}, t) - f_i^{\mathrm{eq}}(\boldsymbol{x}, t)}{\tau} \quad (1)$$

where $\boldsymbol{c}_i$ denotes the i-th lattice velocity, Δt is the time step, and τ is a relaxation parameter toward the equilibrium distribution f_i^{eq}, which can be expressed as [2]

$$f_i^{\mathrm{eq}} = \rho t_i\left[1 + \frac{\boldsymbol{u}\cdot\boldsymbol{c}_i}{c_{\mathrm{s}}^2} + \frac{1}{2}\left(\frac{\boldsymbol{u}\cdot\boldsymbol{c}_i}{c_{\mathrm{s}}^2}\right)^2 - \frac{u^2}{2c_{\mathrm{s}}^4}\right] \quad (2)$$

Here the fluid density ρ and velocity $\boldsymbol{u}$ can be obtained from local density distributions through

$$\rho = \sum_i f_i$$
$$\rho\boldsymbol{u} = \sum_i f_i\boldsymbol{c}_i \quad (3)$$

Other parameters, including the lattice sound speed c_{s} and weight factor t_i, are lattice structure dependent. For example, for a typical D2Q9 (two dimensions and nine lattice velocities; see Fig. 1) lattice structure, we have $t_0 = 4/9$, $t_{1-4} = 1/9$, $t_{5-8} = 1/36$, and $c_{\mathrm{s}}^2 = \Delta x^2/3\Delta t^2$, where Δx is the spatial distance between two nearest lattice nodes. Through the Chapman–Enskog expansion, one can recover the macroscopic continuity and momentum (Navier–Stokes) equations from the above-defined LBM dynamics:

$$\frac{\partial\rho}{\partial t} + \nabla\cdot(\rho\boldsymbol{u}) = 0$$
$$\frac{\partial\boldsymbol{u}}{\partial t} + (\boldsymbol{u}\cdot\nabla)\boldsymbol{u} = -\frac{1}{\rho}\nabla P + \nu\nabla^2\boldsymbol{u} \quad (4)$$

where ν is the kinematic shear viscosity given by

$$\nu = \frac{2\tau - 1}{2}c_{\mathrm{s}}^2\Delta t \quad (5)$$

and P is the pressure expressed as

$$P = c_{\mathrm{s}}^2\rho \quad (6)$$

An external force $\boldsymbol{F}$ can be included in the above LBM algorithm by adding an extra term to the collision operator (RHS of Eq. (1)) and the lattice Boltzmann equation becomes

$$f_i(\boldsymbol{x}+\boldsymbol{c}_i\Delta t, t+\Delta t) - f_i(\boldsymbol{x}, t) = -\frac{f_i(\boldsymbol{x}, t) - f_i^{eq}(\boldsymbol{x}, t)}{\tau} + \frac{t_i\Delta t}{c_{\mathrm{s}}^2}\boldsymbol{F}\cdot\boldsymbol{c}_i \quad (7)$$

or by redefining an equilibrium velocity

$$\boldsymbol{u}^{\mathrm{eq}} = \frac{1}{\rho}\left(\sum_i f_i\boldsymbol{c}_i + \tau\Delta t\boldsymbol{F}\right) \quad (8)$$

and utilizing it in the calculation of equilibrium distribution f_i^{eq} in Eq. (2) [3]. After such modifications, the

total fluid momentum increases an amount of $\Delta t\boldsymbol{F}$ during a time step, while the total fluid density remains unchanged.

As with other numerical approaches, appropriate boundary conditions (BCs) are necessary for meaningful simulations. Since the principal variables in LBM are the density distributions f_i, LBM BCs are implemented through specifying the unknown f_i entering the simulation domain across boundaries, instead of the macroscopic fluid properties such as velocity and pressure. This feature poses both conveniences and difficulties. For example, to model a no-slip boundary over a solid surface, one can simply reverse the particle directions toward the boundary back to their original locations, the so-called bounce-back scheme. Periodic boundaries are even easier to implement: all particles which leave the domain across a periodic boundary will re-enter the domain from the opposite side. However, for the general pressure and velocity boundary conditions, there are usually more unknown incoming density distributions than the number of constraint equations from the boundary conditions (see Eq. (3)), i. e., more unknowns to be determined from less constraints. To have a valid system of equations, assumptions are sometimes necessary and inappropriate choices could lead to unphysical boundary effects and also hamper simulation stability. Tremendous efforts have been devoted to develop accurate and efficient boundary schemes for different situations, and detailed descriptions can be found in the literature [7].

It can be seen from the above description that the LBM dynamics is local (i. e., only the very neighboring lattice nodes are involved in updating the density distributions), and hence LBM algorithm is advantageous for parallel computations.

Multiphase/Multicomponent LBM Models

It can be seen from the pressure–density relationship of Eq. (6) that the fluid in the general LBM is an ideal fluid. To simulate a multiphase/multicomponent system, the above method must be modified to incorporate any microscopic intermolecular interactions or the macroscopic equation of state. Such a modification can be carried out by applying an additional force term as in Eqs. (7) and (8), or by reformulating the equivalent density distribution given in Eq. (2). New sets of density distributions are also introduced in multicomponent models to represent the individual components. Different from those in traditional CFD methods, the LBM multiphase/multicomponent algorithm is uniform throughout the entire domain and phase separation as well as interface evolution can be obtained with ease without front-capturing and front-tracking treatments. So far, several models have been proposed. These models typically have been validated by means of stationary bubbles for the Laplace law of capillary and dynamic interfacial waves for the wavelength–frequency dispersion relations. Applications of these multiphase/multicomponent models in micro- and nanofluidics include bubble/droplet dynamics, sample mixing, interfacial slip, and dynamics of wetting.

A LBM-like Algorithm for Electrical Field

In addition, LBM-like algorithms have been proposed to solve problems with convection, diffusion, heat transfer, and electrical field. Such algorithms are designed so that the corresponding macroscopic equations can be recovered through a Chapman–Enskog analysis. However, such algorithms are purely differential equation solvers, the *density distributions* here have no physical meaning as in the original LBM for fluid mechanics. For the sake of clarity, an LBM-like algorithm for electrical field in the description of electroosmotic flow is illustrated below.

Generally, the electric potential ϕ in an electrolyte due to charged surfaces is governed by the Poisson equation

$$\nabla \cdot (\varepsilon \nabla \phi) = -\frac{\rho_\mathrm{e}}{\varepsilon_0} \tag{9}$$

where ε and ε_0 are, respectively, the dielectric constant of the electrolyte and the permittivity of the vacuum, and ρ_e is the net charge density, which can be related to the electric field through the Boltzmann distribution. To solve this equation in the framework of LBM, He and Li [8] proposed the following lattice equation for the potential distribution h_i:

$$h_i(\boldsymbol{x} + \boldsymbol{c}_i \Delta t, t + \Delta t) - h_i(\boldsymbol{x}, t) = -\frac{h_i(\boldsymbol{x}, t) - h_i^\mathrm{eq}(\boldsymbol{x}, t)}{\tau_\phi} + \frac{t_i \rho_\mathrm{e}}{\varepsilon_0} \tag{10}$$

where $h_i^\mathrm{eq} = t_i \phi$ and $\tau_\phi = 3\varepsilon + 0.5$. The interested electrical potential ϕ is just a sum of all potential distributions h_i, i. e., $\phi = \sum_i h_i$. Again the Chapman–Enskog analysis can be applied to Eq. (10) and the original Poisson Eq. (9). Other similar schemes exist for convection–diffusion and heat transfer equations.

Key Research Findings

In recent years, LBM has been applied to study many microscale and nanoscale transport phenomena and processes, including gas flows, electroosmotic flows, interfacial phenomena, and colloid suspensions. In the following, we briefly review major advances of LBM in the description of electrokinetics and interfacial phenomena.

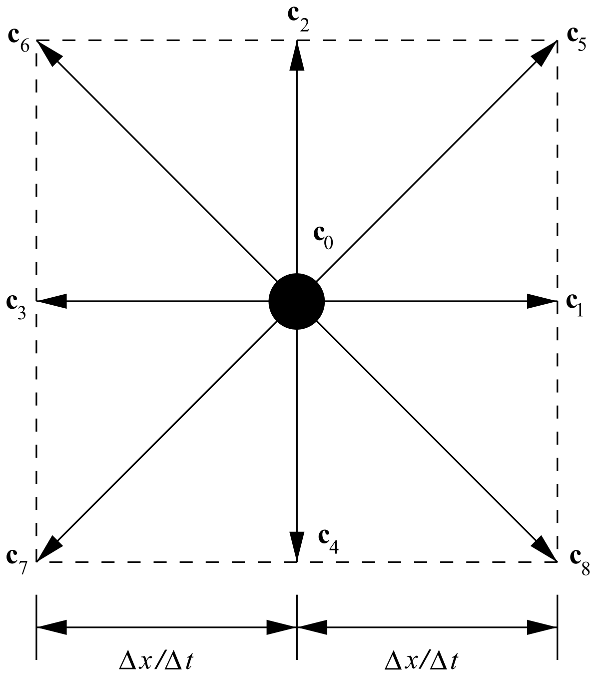

Lattice Boltzmann Method (LBM), Figure 1 The discrete lattice velocities of a D2Q9 lattice structure; $\boldsymbol{c}_0 = (0, 0)$ corresponds to the rest portion of the particles f_0

Electroosmotic Flows

Application of LBM to single-phase flows in microsystems is straightforward. To simulate electroosmotic flows, one needs to incorporate the electrical forces in the electrical double-layer region near the solid–liquid interface due to the net charge and external electrical field. Joule heating effect and sample mixing in microchannels have also been studied. In these studies, the general LBM is utilized for the fluid dynamics, and the electrical potential, temperature, and sample concentration fields were also solved by the appropriate LBM-like algorithms. For example, Tian et al. [9] investigated the electroosmotic flows in microchannels with heterogeneous surface potentials, and found that local circulations can be produced near the heterogeneous region. It was also noted that there is a clear tradeoff between mixing and transport in microfluidics with heterogeneous surfaces: A higher mixing efficiency is associated with a lower volumetric flow rate. These numerical studies could be useful for the design of microfluidic devices.

Solid–Liquid Interfacial Slip

In fluid mechanics, the no-slip boundary condition between a fluid and a solid surface has traditionally been an assumption in solving the Navier–Stokes equation. Despite macroscopic experimental supports, it still remains an assumption without physical principles. In fact, studies on fluid slip have long been an interesting subject since the pioneering work by Navier and Maxwell. Recent measurements indeed indicate significant slip on solid surfaces, and this fact has also been confirmed by molecular dynamics simulations. In general, both experimental and molecular dynamics simulation results show that there is a strong relationship between the magnitude of slip and the surface hydrophobicity: larger slip is usually observed on more hydrophobic surfaces and no slip on hydrophilic surfaces.

Recently, LBM has also been employed to study this interesting phenomenon (e. g., [5]). The fluid was modeled as a nonideal fluid and surface hydrophobicity was adjusted by tuning the specific solid–fluid interactions. For a liquid droplet sitting on a flat solid surface, the resulting contact angle is directly related to the solid–fluid attractions. High contact angles are observed on surfaces with week attractions (hydrophobic surfaces) and the liquid will completely wet the surface if the attraction is strong enough (hydrophilic surfaces). These are very similar to molecular dynamics results. Furthermore, the flow rate of the liquid in a channel with such surfaces also deviates from the theoretical prediction of a Poiseuille flow. A larger flow rate was found by using a more hydrophobic channel and, from a macroscopic viewpoint, this can be interpreted as an interfacial slip. The slip magnitude can be characterized by the apparent slip length which was found to increase with surface hydrophobicity (contact angles). For relatively hydrophilic surfaces, even negative slip lengths could result due to the strong solid–fluid interactions. These findings are in good agreement with other experimental and molecular dynamics studies. Since such an interfacial slip is generated by direct variation of the solid–fluid interactions instead of an applied slip boundary, these results demonstrate that the underlying microscopic interactions have been well represented and LBM could be useful in microfluidic and nanofluidic studies.

Dynamic Wetting

Since with LBM it is relatively easy to incorporate microscopic interactions, it certainly allows an attractive alternative to study wetting dynamics of a liquid on a surface. Dynamic contact angles from LBM simulations have been compared to a theoretical adsorption/desorption model with good agreement [4]. Furthermore, the LBM results also imply more adsorption sites and a higher displacement frequency on a hydrophilic surface when the solid–fluid attractions are strong. These suggest that the underlying physics in the LBM model has been reasonably repre-

sented. Wetting behaviors over chemically heterogeneous surfaces and capillary flows have also been examined.

Recently, superhydrophobic surfaces have attracted great interest for their potential in reducing flow resistance. Due to the geometrical and physical complexity of the system, traditional theoretical and numerical methods encounter severe challenges to study this phenomenon. Several LBM attempts have been performed (e. g., [10]) and the results are promising. For example, it has been found that the advancing contact angle increases and resistance to droplet sliding decreases with decreasing fractional solid area. Further LBM simulations could be valuable to improve our understanding of the phenomenon.

Future Directions for Research

We have noticed that most current LBM applications to microfluidics utilize LBM as a differential equation solver; and the true merit of this method – a good representation of the underlying microscopic interactions – has not been well exploited. Solid–fluid interfacial phenomena in microsystems could be particularly suitable for LBM, since it couples the fluid and interface dynamics in a natural way. Future directions for research may include utilizing non-uniform or unstructured lattice meshes for complex microstructures (e. g., surface roughness), combining LBM with molecular dynamics and CFD (hybrid algorithms), and applying LBM to bio-microfluidics.

Cross References

- ► Wetting and Spreading
- ► Surface Tension, Capillarity and Contact Angle
- ► Electrowetting and Droplets
- ► Boundary Slip of Liquids
- ► Droplet Dynamics in Microchannel
- ► Electrical Double Layers
- ► Electroosmotic Flow (DC)
- ► AC Electro-Osmotic Flow

References

1. Chen S, Doolen GD (1998) Lattice Boltzmann method for fluid flows. Annu Rev Fluid Mech 30:329–64
2. Qian YH, d'Humieres D, Lallemand P (1992) Lattice BGK models for Navier-Stokes equation. Europhys Lett 17:479–484
3. Shan X, Chen H (1994) Simulation of nonideal gases and liquid-gas phase-transitions by the lattice Boltzmann-equation. Phys Rev E 49(4):2941–2948
4. Zhang J, Kwok DY (2004) Lattice Boltzmann study on the contact angle and contact line dynamics of liquid-vapor interfaces. Langmuir 20(19):8137–8141
5. Zhang J, Kwok DY (2004) Apparent slip over a solid-liquid interface with a no-slip boundary condition. Phys Rev E 70(5):056701
6. Zhang J, Kwok DY (2005) A 2D lattice Boltzmann study on electrohydrodynamic drop deformation with the leaky dielectric theory. J Comput Phys 206(1):150–161
7. Zhang J, Kwok DY (2006) Pressure boundary condition of the lattice Boltzmann method for fully developed periodic flows. Phys Rev E 73(4):047702
8. He X, Li N (2000) Lattice Boltzmann simulation of electrochemical systems. Comput Phys Commun 129(1-3):158–166
9. Tian F, Li B, Kwok DY (2005) Tradeoff between mixing and transport for electroosmotic flow in heterogeneous microchannels with nonuniform surface potentials. Langmuir 21(3):1126–1131
10. Zhang J, Kwok DY (2006) Contact line and contact angle dynamics in superhydrophobic channels. Langmuir 22(11):4998–5004

Lattice Poisson–Boltzmann Method, Analysis of Electroosmotic Microfludics

MORAN WANG
Nanomaterials in the Environment, Agriculture and Technology (NEAT) Department of Biological and Agricultural Engineering, University of California Davis, Davis, CA, USA
mmwang@ucdavis.edu

L

Synonyms

Electroosmosis; Microfluidics; Numerical simulation

Definition

Electroosmotic microfluidics have many promising applications in microsystems. However, the simulation and analysis of electroosmotic flows have always been large challenges especially for complex geometries. By introducing a high-efficiency lattice Poisson–Boltzmann method, this contribution presents the latest progress in the simulation and analysis of electroosmotic flows in either homogeneously or heterogeneously charged channels, either straight or rough channels, either isotropic or anisotropic porous media. The results agree with some of the existing experimental data. The results will improve our understanding of the electroosmotic flow mechanism in micro- and nanoscale geometries and provide valuable information for the design and optimization of microsystems.

Overview

Micro- and nanofluidic devices have gained much recent attention due to their increasing applications in chemical analysis, biological and medical diagnostics and energy supply [1, 2]. The inherent advantages of miniaturization

lie in the integration of complex multifunctions while retaining precise control of objects. Actuating without any moving parts is a new and promising direction for microsystem designs despite the low efficiency [3]. Electrokinetic flow (EKF) is one of the most important nonmechanical techniques for micro- and nanofluidics, and has been widely applied for pumping, mixing, and separating [2–5]. Recently, charged porous media structures have been employed in microdevices to change the fluid behavior. A low flow rate together with a high pumping pressure is therefore obtained, which has been used in capillary electrochromatography (CE) and improved high-performance micropumps [3, 5].

Due to their many applications, electrokinetic microfluidics and nanofluidics have been much studied in the past decades, both theoretically and numerically. From the macroscopic point of view, the EOFs are governed by the Poisson–Boltzmann equation for electrical potential distributions and the Navier–Stokes equations for flows [1, 6]. Accurate and efficient solution of the nonlinear Poisson–Boltzmann equation is a challenge for both mathematicians and physicists. Hundreds of research papers related to this topic appear every year. Most previous research has employed conventional partial differential equation (PDE) solvers, such as the finite difference method (FDM) and the finite element method (FEM) to solve the nonlinear Poisson–Boltzmann equation in its linearized form. Good predictions have been obtained by solving the original nonlinear Poisson–Boltzmann equation using FDM or FEM [7, 8], however, they have suffered from the huge computational due to the strong nonlinearity. The fast Fourier transform (FFT) and the multigrid techniques greatly improve the efficiency of the numerical solution of the nonlinear Poisson–Boltzmann equation; however, it is a large challenge to extend them for complex geometries.

In recent years, a mesoscopic statistics-based method, the lattice Boltzmann method (LBM), has been developed for electrokinetic transports in microdevices. He and Li [9] have proposed a lattice Boltzmann scheme to analyze the electrochemical processes in an electrolyte based on a locally electrically neutral assumption. Li and Kwok [10] have simulated the electrokinetic flows in microchannels using a LBM with a one-dimensional linearized solution of the Poisson–Boltzmann equation. Melchionna and Succi [11] have solved the nonlinear Poisson–Boltzmann equation by an efficient multigrid technique and have predicted the flow behavior using a lattice Boltzmann scheme. The multigrid technique is very efficienct at solving the nonlinear Poisson–Boltzmann equation; however, it has rarely been extended to complex geometries. Guo et al. [12] have presented a finite-difference-based lattice Boltzmann algorithm for electroosmotic flows with the Joule heating effect. Wang et al. [13] have developed a lattice Poisson–Boltzmann method (LPBM) which combined a lattice Poisson method (LPM) for solving the nonlinear Poisson–Boltzmann equation for electric potential distribution with the LBM for solving the Boltzmann–BGK equation for fluid flow. The LPBM has been applied to study the electroosmotic flows in straight or rough microchannels [13–15] and in various charged microporous media [16–18]. This essay introduces the latest progress in the analysis of electroosmotic microfludics using the LPBM. The results will be compared with existing theoretical and experimental data and the fluid mechanisms will be analyzed and discussed.

Basic Methodology

Governing Equations

When the polarization and chemical absorption effects are negligible, consider an N-component Newtonian electrolyte flowing with velocity $\boldsymbol{u}(\boldsymbol{r}, t)$ in the interstices of a porous material. Let $\psi(\boldsymbol{r}, t)$ be the electric potential prevailing within the solution; the flux $\boldsymbol{j}_i$ of each ith ion species, composing the solute, is given by the following constitutive equation [19]:

$$\boldsymbol{j}_i = -D_i \nabla n_i - e z_i b_i n_i \nabla \psi + n_i \boldsymbol{u} \tag{1}$$

where n_i is the number density of the ith ion species, z_i is the ith ion algebraic valence, and e is the absolute charge of the electron. D_i and b_i are, respectively, the ion's diffusivity and electric mobility, related by the Stokes–Einstein equation

$$D_i = b_i kT \tag{2}$$

where k is the Boltzmann constant and T is the absolute temperature. The ionic flux $\boldsymbol{j}_i$ and the concentration n_i obey the continuity equation

$$\frac{\partial n_i}{\partial t} + \nabla \cdot \boldsymbol{j}_i = 0 \tag{3}$$

For an incompressible laminar flow, the movement of the electrolyte is governed by the continuity and momentum equations

$$\nabla \cdot \boldsymbol{u} = 0 \tag{4}$$

$$\rho \frac{\partial \boldsymbol{u}}{\partial t} + \rho \boldsymbol{u} \cdot \nabla \boldsymbol{u} = -\nabla p + \mu \nabla^2 \boldsymbol{u} + \boldsymbol{F}_{\mathrm{E}} \tag{5}$$

where ρ is the solution density, p is the pressure, μ is the dynamic fluid viscosity and $\boldsymbol{F}_{\mathrm{E}}$ is the electric force density vector. In general, the electrical force in electrokinetic fluids can be expressed as

$$\boldsymbol{F}_{\mathrm{E}} = \boldsymbol{F}_{\mathrm{ext}} + \rho_{\mathrm{e}}\left(\boldsymbol{E}_{\mathrm{int}} + \xi \times \boldsymbol{B}_{\mathrm{int}}\right) + \boldsymbol{F}_{\mathrm{V}} \tag{6}$$

where $\boldsymbol{F}_{\mathrm{ext}}$ represents the external field body forces, including the Lorentz force associated with any externally applied electric and magnetic field. For only an electrical field, $\boldsymbol{F}_{\mathrm{ext}} = \rho_{\mathrm{e}}\boldsymbol{E}$, where$\rho_{\mathrm{e}}$ is the net charge density and $\boldsymbol{E}$ is the electrical field strength. $\boldsymbol{E}_{\mathrm{int}}$ and $\boldsymbol{B}_{\mathrm{int}}$ are, respectively, the internally smoothed electrical and magnetic fields due to the motion of the charged particles inside the fluid. $\boldsymbol{F}_{\mathrm{V}}$ is a single equivalent force density due to the intermolecular attraction [10]. In the present contribution, we are concerned with steady-state electroosmosis so that the electromagnetic susceptibility is negligible. The net charge density ρ_{e} can be expressed as

$$\rho_{\mathrm{e}} = \sum_i e z_i n_i \tag{7}$$

The local electrical potential is governed by the Poisson equation

$$\nabla^2\psi = -\frac{\rho_{\mathrm{e}}}{\varepsilon_{\mathrm{r}}\varepsilon_0} = -\frac{1}{\varepsilon_{\mathrm{r}}\varepsilon_0}\sum_{i=1}^{N} e n_i z_i \tag{8}$$

where ε_{r} is the dimensionless fluid dielectric constant and ε_0 is the permittivity of a vacuum. Eqs. (3)–(8) are the governing equations for electroosmosis and can be solved subject to the following boundary conditions on the liquid–solid interface Ω:

$$(\boldsymbol{v} \cdot \boldsymbol{j}_i)_{\Omega} = 0 \tag{9}$$

$$\boldsymbol{u}_{\Omega} = 0 \tag{10}$$

$$\psi_{\Omega} = \zeta \tag{11}$$

where $\boldsymbol{v}$ is the outer normal to Ω, and ζ is the zeta potential. For the electroosmotic flow of dilute electrolyte, the macroscopic velocity is low so that the equilibrium is satisfied everywhere in the flow field base, so one can obtain the Boltzmann distribution for n_i

$$n_i = n_{i,\infty}\exp\left(-\frac{e z_i}{kT}\psi\right) \tag{12}$$

where $n_{i,\infty}$ is the bulk ionic number density. Substituting Eq. (12) into Eq. (8) yields the famous nonlinear Poisson–Boltzmann equation for electrokinetic flows [6]

$$\nabla^2\psi = -\frac{1}{\varepsilon_{\mathrm{r}}\varepsilon_0}\sum_i e z_i n_{i,\infty}\exp\left(-\frac{e z_i}{kT}\psi\right) \tag{13}$$

The present contribution actually solves the governing equations (Eqs. (4)–(7), (12), (13)) subject to the boundary conditions (Eqs. (9)–(11)) by the numerical methods described in the next section.

The LPBM

The continuity and momentum equations can be solved by tracking the movements of molecule ensembles through the evolution of the distribution function [20] using the popular LBM. The lattice Boltzmann equation (LBE) can be derived from the Boltzmann equation. For the flows with external forces, the continuous Boltzmann–BGK equation with an external force term, F, is

$$\frac{Df}{Dt} \equiv \partial_t f + (\xi \cdot \nabla)f = -\frac{f - f^{\mathrm{eq}}}{\tau_\nu} + F \tag{14}$$

where $f \equiv f(x, \xi, t)$ is the single particle distribution function in the phase space (x, ξ), ξ is the microscopic velocity, τ_ν is the relaxation time, and f^{eq} is the Maxwell–Boltzmann equilibrium distribution. For a steady fluid immersed in a conservative force field, the equilibrium distribution function is defined by adding a Boltzmann factor to the Maxwell–Boltzmann distribution

$$f^{\mathrm{eq}} = \frac{\rho_0}{(2\pi RT)^{D/2}}\exp\left(-\frac{U}{kT}\right)\exp\left(-\frac{(\xi - \boldsymbol{u})^2}{2RT}\right) \tag{15}$$

where U is the potential energy of the conservative force field, ρ_0 is the fluid density where U is lowest, R is the ideal gas common constant, D is the dimension of the calculation space, k is the Boltzmann constant, and $\boldsymbol{u}$ is the macroscopic velocity. The external force term, F, needs to be chosen carefully. Dimensional analysis leads to the following form of F:

$$F = \frac{\boldsymbol{G}\cdot(\xi - \boldsymbol{u})}{RT}f^{\mathrm{eq}} \tag{16}$$

where $\boldsymbol{G}$ is the external force per unit mass [20]. The Chapman–Enskog expansion can be used to transform the Boltzmann–BGK equation (Eq. (14)) into the correct continuum Navier–Stokes equations.

For the two-dimensional case, third-order Gauss–Hermite quadrature leads to the nine-speed LBE model with the

L

discrete velocities

$$\boldsymbol{e}_\alpha = \begin{cases} (0,0) & \alpha = 0 \\ (\cos\theta_\alpha, \sin\theta_\alpha)c, & \theta_\alpha = (\alpha-1)\pi/2 \\ & \alpha = 1,2,3,4 \\ \sqrt{2}(\cos\theta_\alpha, \sin\theta_\alpha)\,c, & \theta_\alpha = (\alpha-5)\pi/2 + \pi/4 \\ & \alpha = 5,6,7,8 \end{cases} \tag{17}$$

where c is the speed of sound and the density equilibrium distribution is

$$f_\alpha^{\mathrm{eq}} = \omega_\alpha \rho_0 \exp\left(-\frac{U}{kT}\right) \times \left[1 + 3\frac{\boldsymbol{e}_\alpha \cdot \boldsymbol{u}}{c^2} + \frac{9}{2}\frac{(\boldsymbol{e}_\alpha \cdot \boldsymbol{u})^2}{c^4} - \frac{3\boldsymbol{u}^2}{2c^2}\right] \tag{18}$$

with

$$\omega_\alpha = \begin{cases} 4/9 & \alpha = 0 \\ 1/9 & \alpha = 1,2,3,4 \\ 1/36 & \alpha = 5,6,7,8 \end{cases} \tag{19}$$

Thus, the discrete density distribution satisfies the evolution equation

$$f_\alpha(\boldsymbol{r} + \boldsymbol{e}_\alpha\delta_t, t+\delta_t) - f_\alpha(\boldsymbol{r}, t) = -\frac{1}{\tau_\nu}\left[f_\alpha(\boldsymbol{r}, t) - f_\alpha^{\mathrm{eq}}(\boldsymbol{r}, t)\right] + \delta_t F_\alpha\,, \tag{20}$$

where $\boldsymbol{r}$ is the position vector, δ_t is the time step, and τ_ν is the dimensionless relaxation time which is a function of the fluid viscosity

$$\tau_\nu = 3\nu\frac{\delta_t}{\delta_x^2} + 0.5 \tag{21}$$

where ν is the kinetic viscosity and δ_x is the lattice constant (or grid size).

For electrokinetic flows in dilute electrolyte solutions, the external electrical force in Eq. (5) can be simplified to

$$\boldsymbol{F}_{\mathrm{E}} = \rho_{\mathrm{e}}\boldsymbol{E} - \rho_{\mathrm{e}}\nabla\Phi \tag{22}$$

where Φ is the stream electrical potential caused by the ion movements in the solution based on the Nernst–Planck theory. Generally, the stream potential dominates the electroviscosity effect in pressure-driven flows, but its value is much less than the external potential and can be ignored in electrically driven flows. Therefore, the external force in the discrete LBE should include the pressure and electric force

$$F_\alpha = \frac{(-\nabla P + \rho_{\mathrm{e}}\boldsymbol{E} - \rho_{\mathrm{e}}\nabla\Phi)\cdot(\boldsymbol{e}_\alpha - \boldsymbol{u})}{\rho RT} f_\alpha^{\mathrm{eq}}\,. \tag{23}$$

The macroscopic density and velocity can be calculated using

$$\rho = \sum_\alpha f_\alpha \tag{24}$$

$$\rho\boldsymbol{u} = \sum_\alpha \boldsymbol{e}_\alpha f_\alpha \tag{25}$$

Borrowing from the LBM, one can rewrite Eq. (13) as a Boltzmann-like equation by expanding a time-dependent term

$$\frac{\partial\psi}{\partial t} = \nabla^2\psi + g_{\mathrm{rhs}}(\boldsymbol{r}, \psi, t) \tag{26}$$

where

$$g_{\mathrm{rhs}} = \frac{1}{\varepsilon\varepsilon_0}\sum_i z_i e n_{i,\infty}\exp\left(-\frac{z_i e}{k_{\mathrm{b}}T}\psi\right)$$

represents the negative right-hand side term of the original Poisson–Boltzmann equation. The solution of Eq. (13) is actually the steady-state solution of Eq. (26). The evolution equation for the electrical potential on the two-dimensional discrete lattices can then be written as

$$g_\alpha(\boldsymbol{r} + \Delta\boldsymbol{r}, t + \delta_{\mathrm{t,g}}) - g_\alpha(\boldsymbol{r}, t) = -\frac{1}{\tau_{\mathrm{g}}}\left[g_\alpha(\boldsymbol{r}, t) - g_\alpha^{\mathrm{eq}}(\boldsymbol{r}, t)\right] + \left(1 - \frac{0.5}{\tau_{\mathrm{g}}}\right)\delta_{\mathrm{t,g}}\omega_\alpha g_{\mathrm{rhs}} \tag{27}$$

where the equilibrium distribution of the electric potential evolution variable g is

$$g_\alpha^{\mathrm{eq}} = \varpi_\alpha\psi, \quad \text{with} \quad \varpi_\alpha = \begin{cases} 0 & \alpha = 0 \\ 1/6 & \alpha = 1,2,3,4 \\ 1/12 & \alpha = 5,6,7,8 \end{cases} \tag{28}$$

The time step in Eq. (27) is

$$\delta_{\mathrm{t,g}} = \frac{\delta_x}{c'}\,, \tag{29}$$

where c' is a pseudo-speed of sound in the potential field [13]. The dimensionless relaxation time for Eq. (27) is

$$\tau_g = \frac{3\chi\delta_{t,g}}{2\delta_x^2} + 0.5 \tag{30}$$

where χ is defined as the potential diffusivity which equals unity in these simulations.

The evolution equations (Eqs. (27)–(30)) were proved to be consistent with the macroscopic nonlinear Poisson–Boltzmann equation (Eq. (6)). After evolving on the discrete lattices, the macroscopic electrical potential can be calculated using

$$\psi = \sum_{\alpha}(g_\alpha + 0.5\delta_{t,g}g_{rhs}\omega_\alpha) \tag{31}$$

Though the electrical potential evolution equations are in an unsteady form, only the steady-state result is realistic, because the electromagnetic susceptibility has not been considered. Although the lattice evolution method for the nonlinear Poisson equation is not as efficient as the multigrid solutions due to its long wavelength limit, it has the advantage that it is suitable for complex geometries and parallel computing. Although this essay only presents two-dimensional cases, the algorithm can easily be extended to three-dimensional cases.

Boundary Treatments

The boundary condition implementations play a very critical role in the accuracy of the numerical simulations. The hydrodynamic boundary conditions for the LBM have been studied extensively. The conventional bounce-back rule is the most popular method used to treat the velocity boundary condition at the solid-fluid interface due to its easy implementation, where momentum from an incoming fluid particle is bounced back in the opposite direction as it hits the wall [20]. However, the conventional bounce-back rule has two main disadvantages. First, it requires the dimensionless relaxation time to be strictly within the range (0.5, 2), otherwise the prediction will deviate from the correct result. Second, the nonslip boundary implemented by the conventional bounce-back rule is not located exactly on the boundary nodes, as mentioned before, which will lead to inconsistence when coupling with other partial differential equation (PDE) solvers on a same grid set [17].

To overcome the inconsistence between the LBM and other PDE solvers on a same grid set, an alternative solution is to modify the boundary condition treatments of the PDE solver for the electric potential distribution to be consistent with the LBM bounded by the bounce-back rule.

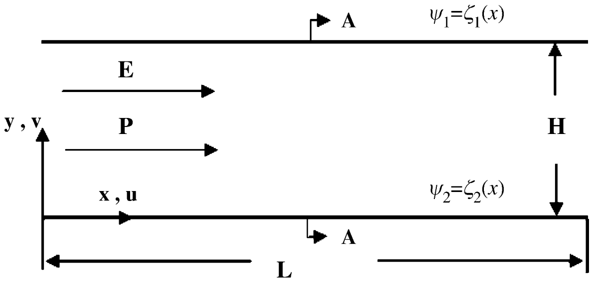

Lattice Poisson–Boltzmann Method, Analysis of Electroosmotic Microfludics, Figure 1 Boundary conditions for electroosmotic flow in a microchannel

In this contribution, the half-way bounce-back rule for nonequilibrium distribution proposed by Zou and He [21] is introduced and extended to both hydrodynamic and electrodynamic boundary implementations to deal with the complex geometries.

At the boundary the following hydrodynamic boundary condition holds:

$$f_\alpha^{neq} = f_\beta^{neq} \tag{32}$$

where the subscripts α and β represent opposite directions. Analogously, the nonequilibrium *bounce-back* rule for the electric potential distribution at the wall surfaces is suggested as

$$g_\alpha^{neq} = -g_\beta^{neq} \tag{33}$$

The *half-way* bounce-back scheme with interpolation is used to deal with the curved surfaces [22]. This boundary treatment has a superlinear accuracy when the wall surface varies between two adjacent nodes and approximately second-order accuracy if the wall surface is in the middle. This method is easy to implement for complicated boundary conditions without special considerations for the corners.

The LPBM simulates the EOF in two steps: first, the lattice method solves the nonlinear Poisson–Boltzmann equation for a stable electrical potential distribution; second, the LBM is used to simulate the steady electrically driven fluid flow in the microchannel.

Key Research Findings

After validation, the LPBM has been employed to simulate the electroosmotic flows in microgeometries. Besides the straight channel, complex geometries have also been considered, including a rough channel, porous arrays, and even random porous media. The simulation results are also compared with the existing experimental data.

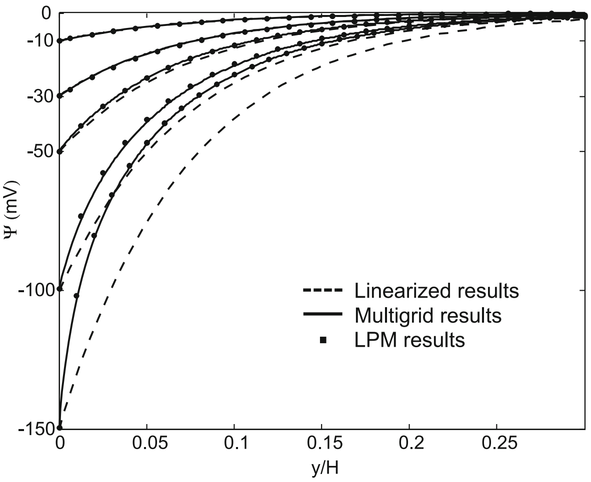

Lattice Poisson–Boltzmann Method, Analysis of Electroosmotic Microfludics, Figure 2 LPM results compared with the linearization results and multigrid solutions for various surface zeta potentials (−10 mV, −30 mV, −50 mV, −100 mV, −150 mV)

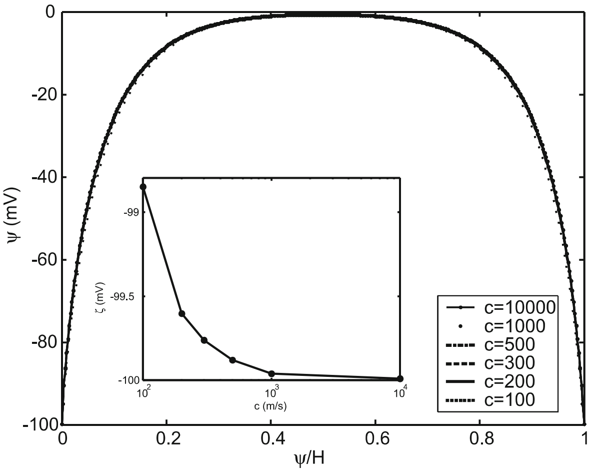

Lattice Poisson–Boltzmann Method, Analysis of Electroosmotic Microfludics, Figure 3 Effects of the pseudo speed of sound values on the potential distribution and the zeta potential (inset) for the Dirichlet boundary condition calculations at $\zeta_0 = -100$ mV

Numerical Issues

Figure 1 shows a two-dimensional straight microchannel which is charged homogeneously or heterogeneously on the walls. The zeta potential distributions on the upper and lower walls are $\zeta_1(x)$ and $\zeta_2(x)$. The channel is H wide and L long. The electrolyte solution in the channel is driven by an electrical field, a pressure field, or both of these.

For a 1 : 1 electrolyte solution flowing in a microchannel with periodic inlet/outlet boundaries and homogeneous walls, the Poisson–Boltzmann equation (Eq. (13)) can be simplified into the one-dimensional form

$$\frac{d^2\psi}{dy^2} = \frac{2n_\infty ze}{\varepsilon\varepsilon_0} \sinh\left(\frac{ze}{kT}\psi\right) \tag{34}$$

If $ze\psi/kT$ is small, $\sinh(ze\psi/kT) \approx ze\psi/kT$. Eq. (33) can be linearized as

$$\frac{d^2\psi}{dy^2} = \frac{2n_\infty z^2e^2}{\varepsilon\varepsilon_0 kT}\psi = \kappa^2\psi \tag{35}$$

where $\kappa = \sqrt{2n_\infty z^2e^2/\varepsilon\varepsilon_0 kT}$ is defined as the reciprocal of the Debye length in Debye–Huckel theory. The linear one-dimensional ordinary differential equation in Eq. (35) has a simple analytical solution for a specified set of boundary conditions.

Figure 2 compares the LPM results for the nonlinear Poisson–Boltzmann equation (Eq. (13)) and the analytical solutions of the linearized equation (Eq. (35)), together with a numerical solution using the multigrid method. The parameters are: the bulk ionic molar concentration $c_\infty = 10^{-4}$ M, $n_\infty = c_\infty N_A$ where N_A is Avogadro's number, $z = 1$ is the dielectric constant of the solution $\varepsilon\varepsilon_0 = 6.95 \times 10^{-10}\ C^2/J\,m$, the temperature $T = 273$ K, and $\psi_1 = \psi_2 = \psi_s$ with ψ_s as a constant.

In general, the linearization is accurate when ψ is small. Figure 2 shows that the LPM results agree perfectly with multigrid solutions at all zeta potentials and with the analytical solution of the linearized equation when the absolute value of the surface zeta potential ζ is small, less than about 30 mV. This validates the accuracy of the LPM. When the absolute value of the zeta potential is large (> 30 mV), the numerical results of the LPM depart from the linearized analytical solutions as expected.

The accuracy of the present LPBM relies on the size of the lattice relative to the width of the electric double layer (EDL). Previous study showed that the lattice should be smaller than the EDL width for an accurate numerical simulation [13]. In the simulations of this work, the size of the lattice is set much smaller than the width of the EDL, i. e., δ_x is usually between 1/10 and 1/3 for each EDL width. We can initialize a still system and judge the steady status of the electrical potential and velocity distributions by the relative errors every 100 steps with the middle point being smaller than 10^{-10}.

The computational efficiency also depends on the dimensionless relaxation times (τ_ν and τ_g) that are chosen. When the lattice size and the fluid properties are given, the relaxation time is determined by the lattice speed of sound (c and c'). Figure 3 shows the effects of c' on the LPM simulation results. The results show that the electric potential distribution is little influenced by c'. The inset in Fig. 3

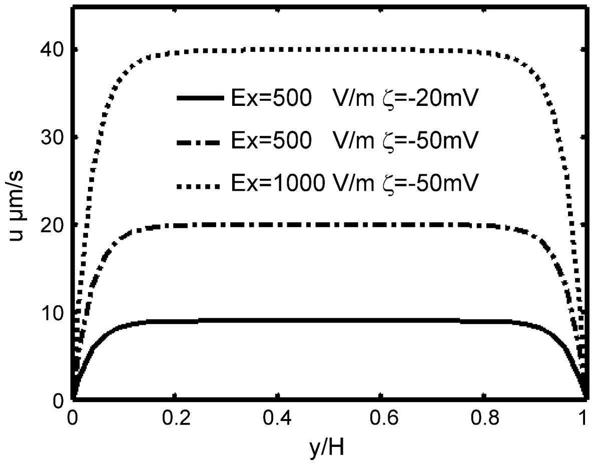

Lattice Poisson–Boltzmann Method, Analysis of Electroosmotic Microfludics, Figure 4 Velocity profiles for various external electrical fields and different zeta potentials

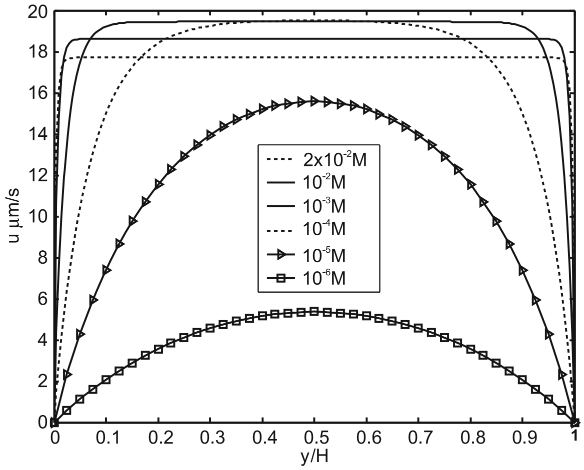

Lattice Poisson–Boltzmann Method, Analysis of Electroosmotic Microfludics, Figure 5 Velocity profiles for various ionic molar concentrations for electrically driven flow

shows that the c values affect the calculated zeta potential on the surface. A larger c' value leads to a value of the zeta potential which is closer to the prespecified value. However, when c' is larger than 300, the deviation may be below 0.3%. Calculations at a larger value of c' need more computational time to reach stable results. One can obtain a balance between efficiency and accuracy according to the level of detail required.

Straight Microchannel Flow

The first example considers a flow driven by only the electrical field in a homogeneous microchannel. The inlet and

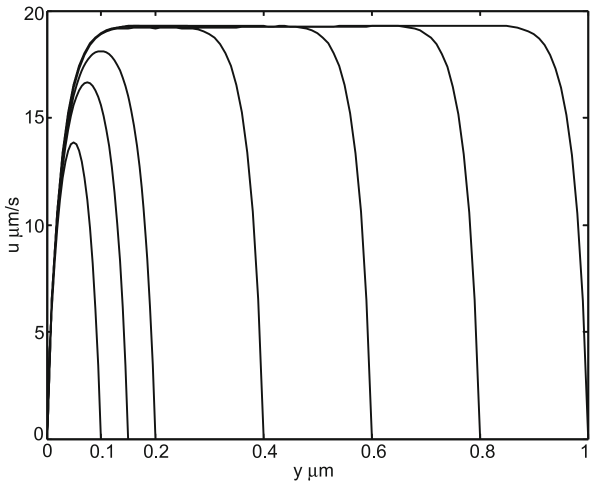

Lattice Poisson–Boltzmann Method, Analysis of Electroosmotic Microfludics, Figure 6 Velocity profiles for different channel widths: $c_\infty = 10^{-4}$ M, $E = 5 \times 10^2$ V/m, $\psi_s = -50$ mV

outlet boundaries are periodic. The channel is 0.8 μm wide and the ionic molar concentration far from the wall surface is 10^{-4} M for the results shown in Fig. 4. As has previously been observed in qualitative results both experimentally and numerically [1], the velocity in the electrically driven osmotic flow is nearly proportional to the external electrical field strength, as well as the surface zeta potential in a homogeneous channel. These results have also been observed in MD simulations in nanochannel flows [23].

Figure 5 shows the velocity profiles for the various bulk ionic concentrations c_∞. The channel width is 0.4 μm, the external electric field strength $E = 5 \times 10^2$ V/m, and the surface zeta potential $\psi_s = -50$ mV for both walls. The fluid properties are the same as those of water at the standard state which are the dielectric constant $\varepsilon\varepsilon_0 = 6.95 \times 10^{-10}\, C^2/J \cdot m$, the density $\rho = 1.0 \times 10^3\, kg/m^3$ and the viscosity $\mu = 0.89$ Pa s. The results show an optimal ionic concentration that maximizes the average velocity. As the ionic molar concentration decreases from a high value (2×10^{-2}), the EDL thickness increases so that although the force is slightly reduced, the electrical force domain increases and thus the average velocity increases. There is a concentration at which the effect of the electrical force can dominate the entire channel and make the velocity reach maximum (10^{-4} – 10^{-3} M for current simulations). As the ionic concentration decreases (e. g., from 10^{-4} to 10^{-6}), the reduction in the force becomes the most important factor and the average velocity decreases. The lower ionic concentrations also result in a more parabolic-like velocity profile.

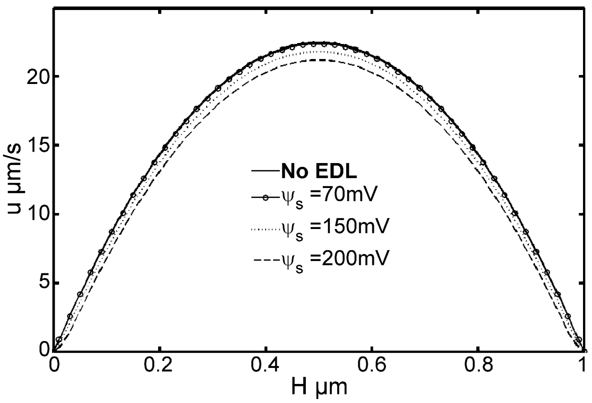

Lattice Poisson–Boltzmann Method, Analysis of Electroosmotic Microfludics, Figure 7 Velocity profiles for various surface zeta potentials in a homogeneous channel with pressure driven flow

Figure 6 shows the velocity profiles for various channel widths for $c_\infty = 10^{-4}$ M, $E = 5\times10^2$ V/m and $\psi_s = -50$ mV. The channel width varies from 0.1 µm to 1 µm. For channel widths larger than double the thickness of the EDLs, the maximum velocity seldom changes with the channel width. However, for channels widths less than double the size of the EDL thickness, a smaller channel width leads to a smaller velocity.

When an electrolyte solution flows in a microchannel driven only by the pressure gradient, the charged wall surface will increase the resistance, which is defined as the electroviscosity effect. This effect has been proven experimentally [1]. Dynamic models based on the Navier–Stokes equations have been built to model this effect [1]. The following example investigates this effect using the LPBM.

For a two-dimensional electrokinetic steady-state flow in microchannels, the streaming potential, Φ, in Eq. (22) can be defined by the constraint of current continuity [1, 10]

$$\Phi = -L\frac{\int_0^H u(x,y)\rho_e(x,y)\,dy}{(\lambda_b + \lambda_s\kappa)H} \tag{36}$$

where λ_b is the electrical conductivity of the bulk fluid and λ_s is the surface conductance. In the present simulations, λ_b is 1.42×10^{-3} S/m and λ_s is 1.64×10^{-9} S.

Velocity profiles for flow in a homogeneous channel are show in Fig. 7 for a channel having a width of 1×10^{-6} m, $c_\infty = 10^{-4}$ M, $dP/dx = 1\times10^6$ Pa/m, and the surface zeta potentials, ψ_s, range from 0 to −200 mV. When $|\psi_s|$ is very small (< 100 mV), the velocity profile is almost same as the non-EDL channel flow profile. When $|\psi_s|$ is larger than 100 mV, the electroviscosity effect becomes noticeable and the effect increases with $|\psi_s|$. Unlike the regular viscosity effect, the electroviscosity effect mainly affects the velocity distribution near the wall away from the parabolic shape.

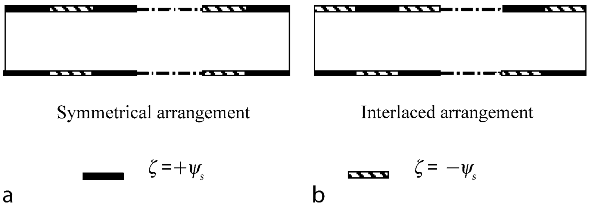

Lattice Poisson–Boltzmann Method, Analysis of Electroosmotic Microfludics, Figure 8 Two typical charge arrangements of the zeta potential

It is difficult to obtain a complete mixing in the microfluidic systems because the operations are always limited to low Reynolds number regimes characterized by laminar flow. Therefore a number of microfluidic mixing-enhancement devices [1, 4], which can be broadly classified as either passive or active mixers, have been develpoed. The electrokinetic flow can be used as an active mixer with no mechanically moving parts. It has many promising applications due to its easy control and suitability for integration with M/NEMS devices.

Figure 8 shows two typical zeta potential arrangements on the wall surfaces: the symmetrical arrangement (Fig. 8a) and the interlaced arrangement (Fig. 8b). Each wall is divided into N parts each of which is charged $+\psi_s$ or $-\psi_s$. Figure 9 shows the calculated velocity contours for these two arrangements when other conditions are same. The parameters are $H = 0.4$ µm, $c_\infty = 10^{-4}$ M, $dP/dx = 1\times10^6$ Pa/m, $\psi_s = -50$ mV, and $E = 5\times10^2$ V/m. The electrical force causes vortices to appear near the surface that act as small stirrers in the channel. If two kinds of fluids or a suspension flows in the channels, the vortices will enhance the mixing. The mixing strength can easily be controlled by changing the electrical field strength or the zeta potentials. A quantitative investigation has been carried out on the effects of the arrangement scheme, division part number (N), and external electric field strength on the mixing enhancements in a heterogeneously charged microchannel by adding another lattice evolution method for concentration propagation [14]. The results showed that the mixing enhancement effect for the interlaced arrangement was 35% higher than for the symmetrical arrangement for a certain condition [14].

Roughness and Cavitation Effects

Although the electroosmotic flow in smooth straight microchannels has been much studied, the results are some way from realistic applications because there is much roughness and cavitations on the wall surfaces instead of

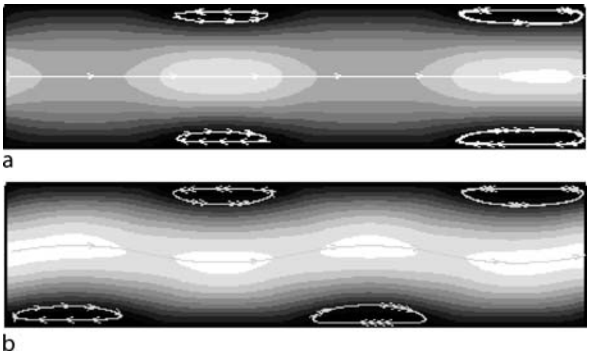

Lattice Poisson–Boltzmann Method, Analysis of Electroosmotic Microfludics, Figure 9 Velocity contours for different heterogeneous zeta potential distributions in electro-pressure driven flows. (**a**) Symmetrical arrangement of surface potential; (**b**) interlaced arrangement of surface potential.

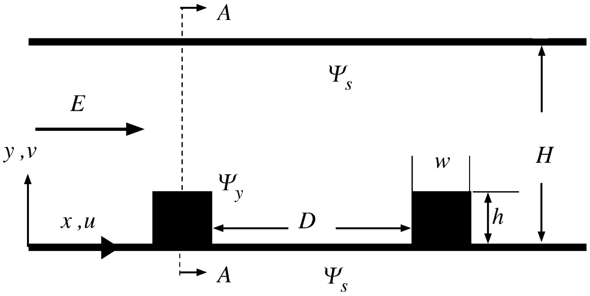

Lattice Poisson–Boltzmann Method, Analysis of Electroosmotic Microfludics, Figure 10 Geometries and boundary conditions for a microchannel with roughness

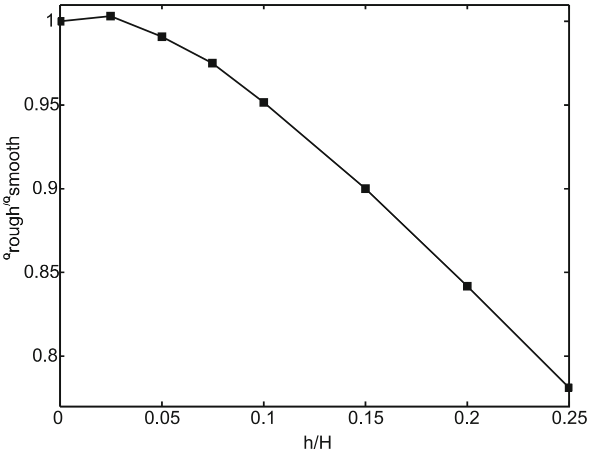

Lattice Poisson–Boltzmann Method, Analysis of Electroosmotic Microfludics, Figure 11 Variation of flow rate with height of roughness: $c_\infty = 10^{-4}$ M, $E = 5\times10^2$ V/m, $\psi_s = \psi_r = -50$ mV, $H = 0.4$ μm, $w = H/4$, $D = 3H/4$

ideal smoothness. Sometimes the roughness or cavitation could be used for some special function in microchannel flows. To the author's knowledge, there is only a small amount of published literature which presents an analysis of the EOF in rough channels [1]. This section will introduce some new results for the roughness and cavitation effects on EOF in microchannels using the LPBM.

The roughness is simplified as a group of rectangles on the lower channel wall here, as shown in Fig. 10. The channel is H in width, with both walls charged with a surface zeta potential ψ_s. The channel is periodic in the x-direction. The roughness is w in width and h in height. The roughness is uniformly arranged in the channel with an interval space D. The three surfaces of each roughness are charged at a surface zeta potential ψ_r. The A–A section is the middle cross-section for each roughness. The electrolyte solution is driven by an external electrical field E. The fluid parameters are the same as those used in Sect. Straight Microchannel Flow. We now consider various cases for different roughness heights (h), different arrangement interval spaces (D), and different surface zeta potentials (ψ_r).

Figure 11 shows the flow rate changing with the height of the roughness. The ionic concentration of the electrolyte solution is $c_\infty = 10^{-4}$ M. The external electrical field strength is $E = 5\times10^2$ V/m. Both the channel and roughness surfaces are homogeneously charged at $\psi_s = \psi_r = -50$ mV. The channel is 0.4 μm wide and is divided into 40 lattices. The roughness width is $w = H/4$ and the interval space $D = 3H/4$. The roughness height h changes from 0 (smooth case) to $H/4$. The results indicate that the electrically driven flow rate changes very slowly with the height of the roughness when the roughness is very small ($h/H < 0.05$). A very short roughness ($h/H < 0.025$) even seems to slightly enhance the flow rate. The charged roughness plays two roles: first it changes the electrical field distribution which may enhance the electric driving force, and second it increases the flow resistance. When the former factor dominates, the flow rate could increase; otherwise the flow rate will decrease. When the roughness height is larger than 1/10 of the channel width, the flow rate will decrease sharply with the height of the roughness. The interesting anomalous variation of flow rate with the height of the roughness has not been reported and validated. A further analysis and consideration on the flow mechanism will be performed in future work using our multiscale simulation tools by coupling atomistic and continuum methods.

Figure 12 shows the flow rates influenced by the roughness interval space when the width and height of the roughness are $H/4$. The other parameters are $c_\infty = 10^{-4}$ M, $E = 5\times10^2$ V/m, $\psi_s = \psi_r = -50$ mV, and $H = 0.4$ μm.

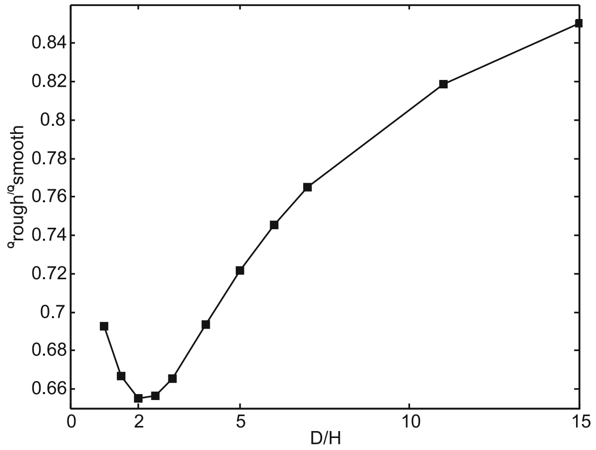

Lattice Poisson–Boltzmann Method, Analysis of Electroosmotic Microfludics, Figure 12 Variation of flow rate with roughness interval: $c_\infty = 10^{-4}$ M, $E = 5\times10^2$ V/m, $\psi_s = \psi_r = -50$ mV, $H = 0.4\,\mu$m, $w = H/4$, $h = H/4$

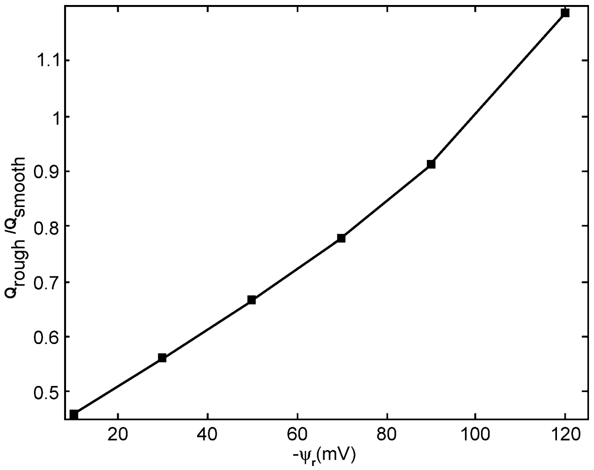

Lattice Poisson–Boltzmann Method, Analysis of Electroosmotic Microfludics, Figure 13 Variation of flow rate with roughness surface potential for heterogeneously charged roughness: $c_\infty = 10^{-4}$ M, $E = 5\times10^2$ V/m, $\psi_s = -50$ mV, $H = 0.4\,\mu$m, $w = H/4$, $D = 3H/4$, $h = H/4$

When the roughness interval is smaller than twice the width of the roughness, the flow rate decrease with the interval space. However, when the roughness interval is larger than twice the width of the roughness, a larger interval space leads to a larger flow rate. Even for very sparse roughness cases, such as $D = 15$ w, the flow rate is lower than 90% that of a smooth channel, which shows that the roughness effect is not negligible in the analysis of electroosmotic flows in microfluidics.

The heterogeneously charged rough channel is also simulated here. The channel surface zeta potential remains at $\psi_s = -50$ mV and the roughness surface zeta potential ψ_r is changed from -10 to -120 mV. The asymmetric potential boundaries destroy the symmetry of the flow. Larger values of the surface zeta potential induce larger velocities near the surface. The flow rate also increases superlinearly with the roughness surface zeta potential. as shown in Fig. 13. In the current case, when the roughness surface zeta potential is -120 mV, the flow rate of the rough channel is even higher than that of the homogeneously charged smooth channel. Such characteristics could be used to enhance the flow rate in microfluidics by inserting high-surface-potential objects into the microchannel.

Both roughness and cavitations are fundamental aspects of the surface of a rough channel. In macroscopic flow, no divisions have been made between them. However, in microchannel flow, some difference has been reported on the flow friction between roughness and cavitations. Here the electroosmotic flows in microchannels with cavitations are simulated and analyzed, which has been seldom studied before.

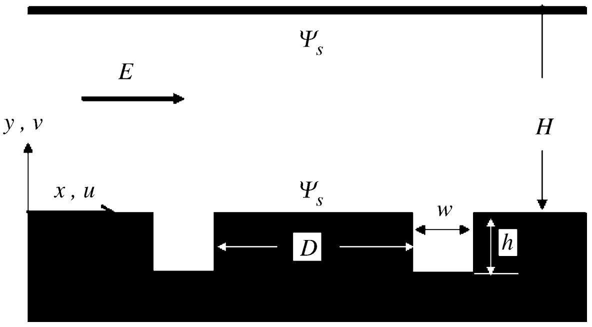

Lattice Poisson–Boltzmann Method, Analysis of Electroosmotic Microfludics, Figure 14 Geometries and boundary conditions for a microchannel with cavitations

A microchannel with cavitations is shown in Fig. 14. The geometry and boundaries are quite similar to those for the roughness. The cavitation is h in depth, w in width and there is an interval, D, between each of them. Here the homogeneously charged case is only considered at $\psi_s = -50$ mV.

Figure 15 shows the relationship between the flow rate and the depth of the cavitations when $w = H/4$ and $D = 7H/4$. The other parameters are $c_\infty = 10^{-4}$ M, and $E = 5\times10^2$ V/m. The relative depth h/H changes from 0 (smooth channel) to 0.3. When the cavitations are very shallow ($h < 3\%H$), the flow rate remains almost unchanged with the depth of the cavitations. As the depth of the cavitations increases, the electrically driven flow rate decreases sharply. If the cavitations are deep enough (e. g., $h > 10\%H$), the flow rate decrease becomes slow

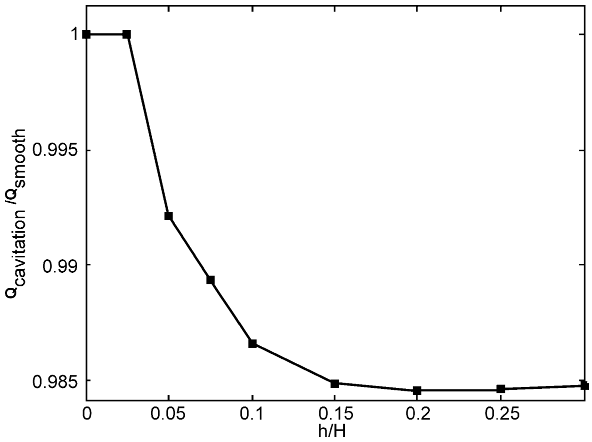

Lattice Poisson–Boltzmann Method, Analysis of Electroosmotic Microfludics, Figure 15 Variation of flow rate with depth of cavitations at $w = H/4$ and $D = 7H/4$ where $c_\infty = 10^{-4}$ M, $E = 5 \times 10^2$ V/m, $\psi_S = -50$ mV, $H = 0.4$ μm

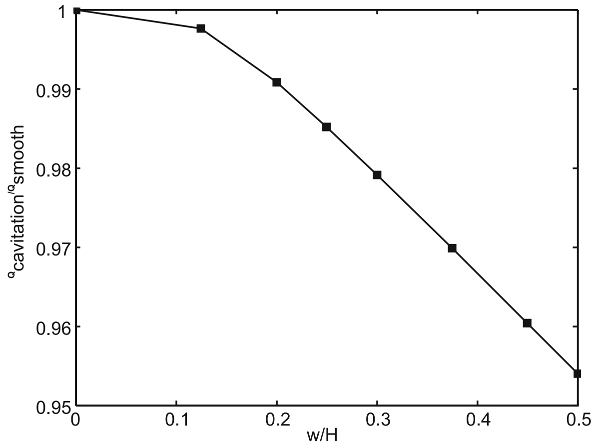

Lattice Poisson–Boltzmann Method, Analysis of Electroosmotic Microfludics, Figure 16 Variation of flow rate with width of cavitations: $c_\infty = 10^{-4}$ M, $E = 5 \times 10^2$ V/m, $\psi_S = -50$ mV, $H = 0.4$ μm

and the flow rate is asymptotically stable to a constant when the cavitations are very deep ($h \gg 20\%H$). Figure 9 indicates that the effect of the cavitations on the flow rate is not as significant as the roughness. The electrically driven flow rate difference in between a smooth channel and a cavitational channel is less than 3% for the current situations. The cavitations decrease the flow rate in the electroosmotic channel flows, which is different from the reported results in previous pressure driven flows, however, this is consistent with the atomistic simulation results [24]. The reason may be that the cavitations decrease the electric driving force more than they decrease the surface resistance to electroosmotic flows.

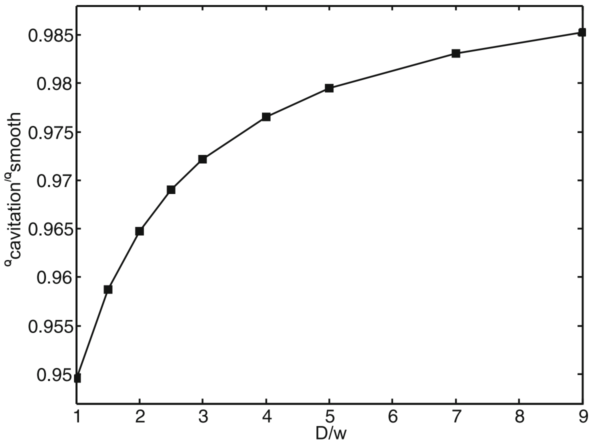

Lattice Poisson–Boltzmann Method, Analysis of Electroosmotic Microfludics, Figure 17 Variation of flow rate with the cavitation intervals: $c_\infty = 10^{-4}$ M, $E = 5 \times 10^2$ V/m, $\psi_S = -50$ mV, $H = 0.4$ μm

The width and interval effects of the cavitations on the flow rate are shown in Figs. 16 and 17. In Fig. 16, the cavitations are deep enough, $h = 0.3H$, to eliminate the depth effect on the flow rate and the cavitations interval $D = 7H/4$. The results in Fig. 16 indicate that the flow rate decreases with the width of the cavitations. In Fig. 17, both the width and depth of the cavitations are fixed at $H/4$, and the interval space changes from one width to nine widths. The results indicate that the sparser the cavitations are, the larger the flow rates are and closer the flow rate is to the value of a smooth channel. Comparing Fig. 17 with Fig. 6 shows that the effect of the cavitations on the flow rate is much smaller than that of the roughness.

Pumping Effects of Charged Porous Media

Electrokinetic transport phenomena in porous media have been studied much in the past decade both theoretically and numerically; however, most results were actually based on linearization approximations of the Poisson–Boltzmann equation [5] so that reliable applications were limited to cases where the EDL length was very thin or very thick compared to the channel size. To our knowledge, there are very few publications that present successful numerical simulations for the electrokinetic flows in charged porous media by solving the nonlinear Poisson–Boltzmann equation and the Navier–Stokes equations by the classical CFD techniques [3, 5]. Because of easy implementation and high efficiency for fluid-solid boundary conditions, the LPBM great advantage in simulations of such flows.

Figure 18 shows a typical illustration of electrokinetic flows in structured porous media packed in a microchan-

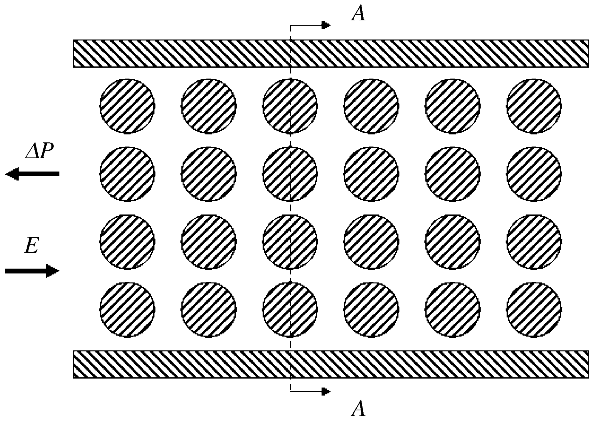

Lattice Poisson–Boltzmann Method, Analysis of Electroosmotic Microfludics, Figure 18 Schematic illustration of electrokinetic flow in a microchannel packed with charged porous media. The *A–A* section crosses the centers of the cycles in the same section

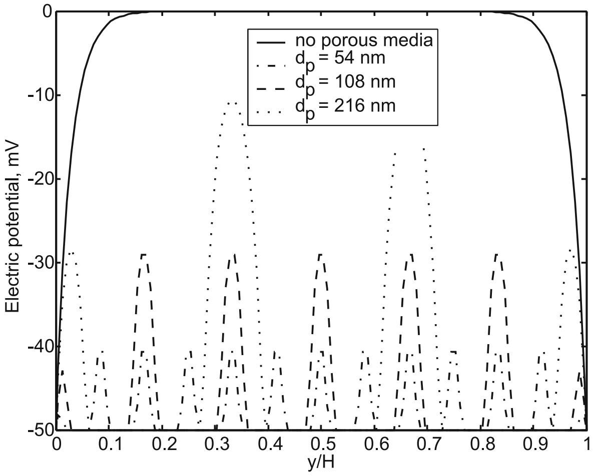

Lattice Poisson–Boltzmann Method, Analysis of Electroosmotic Microfludics, Figure 19 Electric potential and velocity profiles of *A–A* section for different particle sizes

nel. Both the channel walls and the particle surfaces are charged. The flow of the electrolyte solution is driven by an external electric field, a pressure drop or both effects. In this section, we will simulate the electrokinetic pumping effects in charged porous media using the mesoscopic evolution numerical methods. The effects of particle size, ionic concentration, external electric field strength, and particle surface zeta potential on the electrokinetic pump performance are analyzed.

In the following two-dimensional simulations, the channel walls are homogeneously charged with the zeta potential $\psi_w = -50$ mV. The channel width H is 1 μm. The charged microspheres are arranged as a structured array with equal spaces between the channels. The particle diameter d_p varies in the range 54 – 325 nm, with the porosity remaining constant at 0.33. The particle surfaces are homogeneously charged. Their potentials ψ_p vary from -10 mV to -90 mV. The electrolyte solution is driven through the porous media, whose properties are: the relative dielectric constant $\varepsilon = 81$, the density $\rho = 1000\,\text{kg/m}^3$, and the dynamic viscosity $\mu = 0.889$ mPa s. The bulk ionic concentration c_∞ changes from 10^{-6} to 10^{-3} M and the external electric field strength E changes from 1 to 5 kV/m.

The effects of particle size on the electric potential distribution are first considered. In most previous analytical or numerical modeling of electroosmosis in porous media, the EDL was mostly assumed to be small compared to the particle size so that the Debye–Huckle theory would lead to simplified expressions for the electric potential and velocity fields [5]. However, when the particle size is the same as or even smaller than the EDL thickness, the particle surface zeta potential will significantly affect the bulk electric potential distribution, not only on the boundary conditions. Figure 19 shows the electric potential profiles across the *A–A* section for different particle sizes. Because the particle diameter and the gap distance are both comparable to the EDL thickness, the electric potential distribution is significantly affected by the particle surface charge. The electric potential profile in a channel packed with charged porous media is quite different from that in a vacant channel. Smaller particles lead to smaller electric potential maxima across the channel.

Since the porous media additive has been reported to improve the performances of the electroosmotic micropump, the nanoscale particle size effects on the pumping performance are investigated here. Figure 20 shows the backpressure versus flow rate for different particle sizes when $E = 1$ kV/m, $\psi_p = -50$ mV, and $c_\infty = 10^{-4}$ M. Compared with the no porous media additivity case, the porous media additivity improves the pump performance significantly with much higher pumping pressures and lower flow rates. A smaller particle size leads to a higher backpressure maximum and a lower zero-pressure-drop flow rate. Under the current parameters and conditions the backpressure maximum reaches over 50 MPa/m for $d_p = 54$ nm. For each case, the pressure and flow rate are in a linear relationship, which agrees with the experimental data in [5].

The maximum pumping pressure for each case can be obtained from the intercept of the pressure-flow rate curve on the y-axis. The curves of the maximum pumping pressure versus particle diameters are plotted in Fig. 21. The results indicate that the smaller the particle diameter, the higher the maximum pumping pressure. The subplot in Fig. 21 shows that the maximum pumping pressure is almost inversely proportional to the particle diameter. This

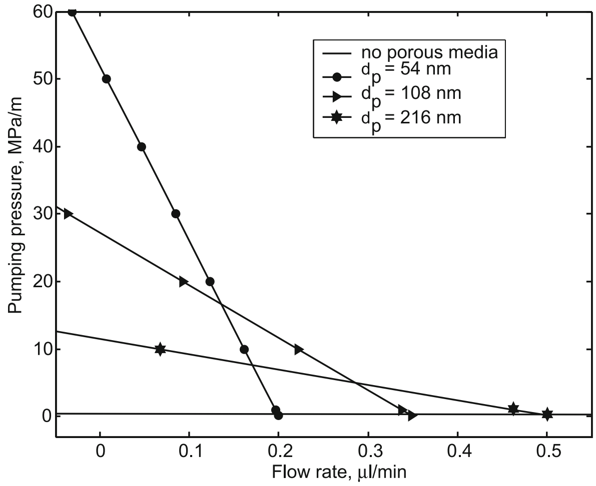

Lattice Poisson–Boltzmann Method, Analysis of Electroosmotic Microfludics, Figure 20 Backpressure versus flow rates for different particle sizes

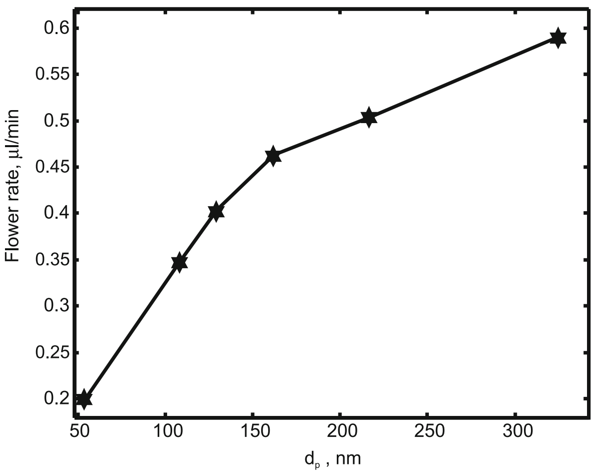

Lattice Poisson–Boltzmann Method, Analysis of Electroosmotic Microfludics, Figure 22 Flow rate versus particle diameter under zero pressure drop

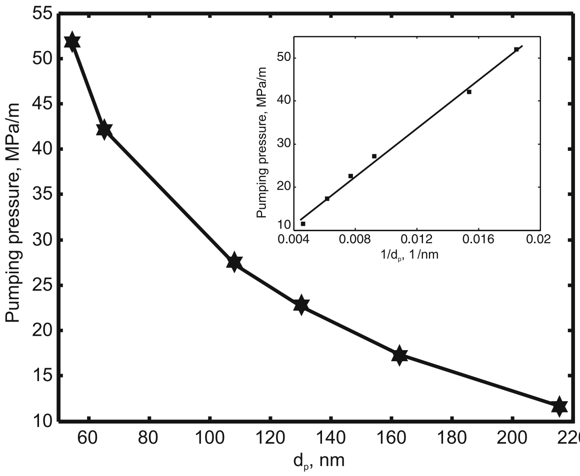

Lattice Poisson–Boltzmann Method, Analysis of Electroosmotic Microfludics, Figure 21 Maximum pumping pressure versus particle diameter

result disagrees with the macroscopic linearized analytical solution which results in a maximum pumping pressure which depends on the inverse square of the diameter of the particle [5]. The reason for this is that the surface electric potentials of nanoscale particles change the bulk potential distribution and the consequent driving force differently from those at macroscale.

In macroscale analysis, the flow rate is independent of the particle size for given structural parameters of porosity and tortuosity [5]. However, things change at nanoscale. Figure 22 shows the pumping flow rate versus particle size when $E = 1\,\text{kV/m}$, $\Delta P = 0\,\text{Pa/m}$, $\psi_\text{p} = -50\,\text{mV}$, and $c_\infty = 10^{-4}\,\text{M}$. The flow rate increases sharply with the particle size when the particle is smaller than 160 nm and a small plateau when the particle becomes larger. For macroscale cases, the variety of particle size only changes the locations of the boundaries but never changes the shape and maximum value of the electric potential profiles under the thin EDL assumption. However, for nanoscale, the particle size not only changes the maximum electric potential but also changes the profile shape, as shown in Fig. 19. This is why the current results disagree with the macroscale predictions. This result also suggests that fine porous media can be used to control electric fluids precisely.

Since the ionic concentration has a great effect on the electric potential distribution in microchannels [13], we can model the flow rate versus the ionic concentration in an electroosmotic micropump packed by nanoscale charged porous media when $E = 1\,\text{kV/m}$, $\Delta P = 0\,\text{Pa/m}$, $\psi_\text{p} = -50\,\text{mV}$, and $d_\text{p} = 108\,\text{nm}$. Figure 23 indicates that the flow rate increases monotonically with the ionic concentration.

Besides the isotropic porous media represented by an array of spheres, the anisotropic structure effects on EOF characteristics can also be studied by modeling the electrically driven flows through ellipse arrays packed in a microchannel whose shape and orientation angle are used to control the anisotropy of porous media [17]. The results show that flow rates increase with the axis length along the external electric field direction for a certain porosity and decrease with the angle between the semimajor axis and the bulk flow direction when the orientation angle is smaller than $\pi/2$. After introducing random fac-

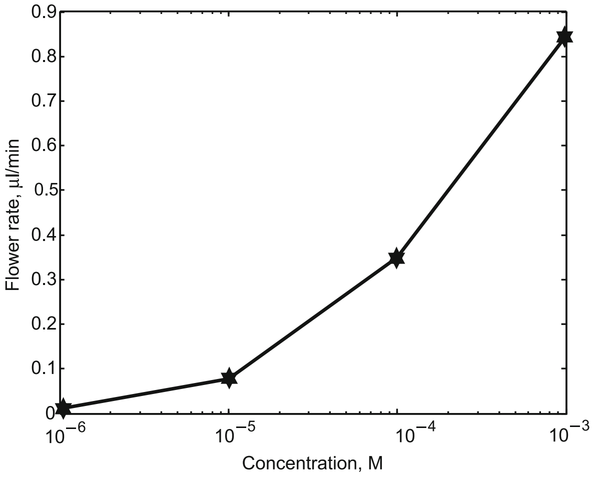

Lattice Poisson–Boltzmann Method, Analysis of Electroosmotic Microfludics, Figure 23 Flow rate versus ionic concentration

tors into the microstructures of porous media, the statistical results for the flow rate show that the anisotropy of the microstructure decreases the permeability of EOFs in porous media.

Future Directions for Research

Since a mesoscopic numerical tool for simulating electroosmotic microfludics has been established, it should be extended to other scientific and engineering applications. A few promising directions include:

- *Electroosmotic flows in random porous media.* A full simulation and analysis of electroosmosis in natural porous media has always been a big challenge due to the geometric complexity of porous media and the consequent computational cost though lots of applications exist in geophysics, the environment, and microdevices such as the microfuel cell. The LPBM has an inherent advantage when dealing with complex boundary conditions and provides a chance to work them out. Various methods have been developed to reproduce the microstructures of random porous media in computer data [25]. When the microstructures of the porous media have been correctly described, the governing equations can be solved by our high-efficiency LPBM. The flow characteristics and mechanism of electroosmosis in random porous media will therefore be analyzed.
- *Electroosmotic multiphase flows.* Multiphase flows driven by electric force have attracted increasing levels of interest and potential applications in biomedical techniques. Such flows include unchanging-interface suspension flows, such as blood cell or DNA molecules suspension, and multiphase interface flows, such droplet movement in a microchannel driven by an electric field. No good solutions by conventional CFD have been found for such flows. Since much progress has been made in solving the multiphase interface problems by LBM, the LPBM is very promising to provide full simulations and analysis of electroosmotic multiphase flows.
- *Multiphysical transports in electroosmotic flows.* Multiple physical transports may accompany the electroosmotic flow, such as heat transfer, oscillation spreading, etc. Some transports may be coupled. Probably the geometry is complex in the real world. The LPBM provides a method though it also faces challenges due to such complicated problems.

In most microfluidics and nanofluidics, the atomistic effects on electroosmotic flows are negligible. But when the characteristic length is comparable with the molecular size of fluid, it should be considered. Molecular dynamics methods have been used to simulate the particle effects in nanoscale electroosmotic flows [23, 24]. However, it is too time-consuming to simulate a real electroosmotic micro- and nanofluidics by molecular dynamics. The multiscale modeling and analysis would be a possible research direction.

Cross References

► Electrical Double Layers
► Cavitation in Microdomains
► Electrokinetic Flow in Porous Media
► Electroosmotic Flow in Heterogeneous Microchannels
► Electroosmotic Pump
► Lattice Boltzmann Method (LBM)

References

1. Li DQ (2004) Electrokinetics in Microfluidics. Academic Press, Oxford
2. Stone HA, Stroock AD, Ajdari A (2004) Engineering flows in small devices: Microfluidics toward a lab-on-a-chip. Ann Rev Fluid Mech 36:381–411
3. Laser DJ, Santiago JG (2004) A review of micropumps. J Micromech Microeng 14(6):R35–R64
4. Biddiss E, Erickson D, Li DQ (2004) Heterogeneous surface charge enhanced micromixing for electrokinetic flows. Anal Chem 76(11):3208–3213
5. Zeng SL, Chen CH, Mikkelsen JC, Santiago JG (2001) Fabrication and characterization of electroosmotic micropumps. Sens Actuators B 79(2-3):107–114
6. Honig B, Nicholls A (1995) Classical electrostatics in biology and chemistry. Science 268(5214):1144–1149
7. Li DQ (2001) Electro-viscous effects on pressure-driven liquid flow in microchannels. Colloids Surf A 195:35–57
8. Masliyah JH, Bhattacharjee S (2006) Electrokinetic and Colloid Transport Phenomena. Wiley, New York

9. He XY, Li N (2000) Lattice Boltzmann simulation of electrochemical systems. Comp Phys Commun 129:158–166
10. Li B, Kwok DY (2004) Electrokinetic microfluidic phenomena by a lattice Boltzmann model using a modified Poisson–Boltzmann equation with an excluded volume effect. J Chem Phys 120:947–953
11. Melchionna S, Succi S (2004) Electrorheology in nanoparticles via lattice Boltzmann simulation. J Chem Phys 120:4492–4497
12. Guo ZL, Zhao TS, Shi Y (2005) A lattice Boltzmann algorithm for electro-osmotic flows in microfluidic devices. J Chem Phys 112(14):144907
13. Wang JK, Wang M, Li ZX (2006) Lattice Poisson–Boltzmann simulations of electro-osmotic flows in microchannels. J Colloids Interface Sci 296(2):729–736
14. Wang JK, Wang M, Li ZX (2005) Lattice Boltzmann simulations of mixing enhancement by the electro-osmotic flow in microchannels. Mod Phys Lett B 19:1515–1518
15. Wang M, Wang JK, Chen SY (2007) Lattice Boltzmann simulations of electro-osmotic flows in microchannels with roughness and cavitations. J Comput Phys 226(1):836–851, and Commun Comput Phys 2(6):1055–1070
16. Wang M, Wang JK, Chen SY, Pan N (2006) Electrokinetic pumping effects of charged porous media in microchannels using the lattice Poisson–Boltzmann method. J Colloids Interface Sci 304(1):246–253
17. Wang M, Pan N, Wang JK, Chen SY (2007) Lattice Poisson–Boltzmann simulations of electroosmotic flows in charged anisotropic porous media. Commun Comput Phys 2(6):1055-1070
18. Wang M, Chen SY (2007) Electroosmosis in homogeneously charged micro- and nanoscale random micro porous media. J Colloids Interface Sci (under revision)
19. Levich VG (1962) Physico-Chemical Hydrodynamics. Prentice Hall, Englewood Cliffs
20. He XY, Chen SY, Doolen GD (1998) A novel thermal model for the lattice Boltzmann method in incompressible limit. J Comput Phys 42(146):282–300
21. Zou QS, He XY (1997) On pressure and velocity boundary conditions for the lattice Boltzmann BGK model. Phys Fluid 9(6):1591–1598
22. Yu D, Mei R, Shyy W, Luo LS (2002) Force evaluation in the lattice Boltzmann method involving curved geometry. Phys Rev E 65:041203
23. Cui ST, Cochran HD (2004) Electroosmotic flow in nanoscale parallel-plate channels: Molecular simulation study and comparison with classical Poisson–Boltzmann theory. Molec Simulat 30(5):259–266
24. Qiao R (2007) Effects of molecular level surface roughness on electroosmotic flow. Microfluid Nanofluid 3(1):33–38
25. Wang M, Wang JK, Pan N, Chen SY (2007). Mesoscopic predictions of the effective thermal conductivity of microscale random porous media. Phys Rev E 75:036702

LC-LIGA (Low-Cost LIGA)

► LIGA-Like Techniques

Lead Zirconate Titanate

► Piezoelectric Materials for Microfluidics

Least Square

Synonyms

Ordinary least square; Discrete least square; Regular least square; Weighted least square

Definition

Least square is a mathematical optimization method which attempts to find a function (a best fit) which closely approximates a set of given data. Assuming that the approximation function $g(x)$should approximate a function $f(x)$, for $x \in [a, b]$, the method attempts to minimize the sum of the squares of the ordinate differences (called residuals) between points generated by the function and corresponding points in the data. In other words, if there are n data points, then the residual is formed by

$$e = \sum_{i=1}^{n} \left[f(x_i) - g(x_i)\right]^2$$

for a discrete set of data and by

$$e = \int_a^b W(x). \left[f(x) - g(x)\right]^2 \mathrm{d}x$$

for continuous functions, where $W(x)$ is a weight function. When $W = 1$, the so-called regular least square method is recovered.

If the approximation function is described as a linear combination of shape functions $\varphi_j(x)$so that

$$g(x) = \sum_{j=1}^{m} c_j \varphi_j(x)\,,$$

then the least square method requires that

$$\frac{\partial e}{\partial c_j} = 0 \quad for \quad j = 1, \ldots, m$$

giving m linear equations to be solved simultaneously to find m unknowns c_j.

Cross References

► Meshless Methods
► Volume and Finite Difference Method for Modeling and Simulation

L

Lennard-Jones Potential

Definition

An approximate potential function describing interactions between molecules; it is weakly attractive at large distances and strongly repulsive at close (with respect to molecular size) range.

Cross References

► Electrokinetic Flow and Ion Transport in Nanochannels

Level Set Method

► Interface Capturing Schemes for Free-Surface Flows

LIGA

Zheng Cui
Rutherford Appleton Laboratory, Oxford, UK
z.cui@rl.ac.uk

Synonyms

Deep lithography; HARMST (High Aspect Ratio Micro-Structure Technology)

Definition

LIGA is the German acronym of *Lithographie (LI) Galvanoformung (G) Abformung (A)*. In English it is *lithography, electroforming, moulding*, a combination of three microfabrication techniques. As originally developed, the lithography was based on irradiation of highly parallel X-rays from a synchrotron radiation source (SRS), which was capable of producing very high aspect ratio polymer structures. The technology became synonymous with high aspect ratio micro-structure technology (HARMST). LIGA allows the fabrication of structures which have vertical dimensions from hundreds of microns to millimeters and horizontal dimensions which can be as small as microns.

Overview

Microfabrication techniques, developed from CMOS integrated circuit manufacturing, are primarily thin film based, i.e. the structures are less than a few micrometers in height (or thickness, depth). However, there are many applications which require microtructures to be deep or thick in Z direction, particularly for those MEMS devices for delivering high mechanical force/torque or for those microfluidic systems of deep flow channels. Conventional lithography is not able to penetrate deep in photoresist or to produce high aspect ratio microstructures. LIGA is a unique microfabrication technique in that microstructures with aspect ratio as high as over 100:1 can be made, with the help of hard X-ray irradiation. The so-called *hard* X-ray is the X-ray radiation of very short wavelength, generally around a few angstroms. Such hard X-ray can penetrate over 1mm thick PMMA resist.

LIGA technology was first developed at Karlsruhe Nuclear Research Institute (KFK) in Germany in early 1980s [1]. That's where the German acronym LIGA came from. The basic LIGA process is illustrated in Fig. 1. X-ray first exposes a thick layer of resist, normally PMMA resist, through a LIGA mask. The deep resist structure after development serves as a mould and is filled with metal, normally nickel, by electroplating. Metal microstructures are formed after removal of the resist mould. The metal microstructures can then be used as a mould for moulding or embossing of plastic. In this way, hundreds and thousands of plastic replications of the original resist structures can be made.

The original motivation to develop the LIGA technology was to make micronozzles for the refinement of uranium isotopes [1]. These micronozzles have minimum feature of micrometers, but the overall structure is of millimetres. Fig. 2a is one of such micronozzles in PMMA resist, Fig. 2b is the electroplated nickel structure from the resist mould and Fig. 2c is the plastic replication of the micronozzle.

Traditionally, mould insert for injection moulding and hot embossing of plastic microcomponents are made from metals by precision machining or wire electro discharge machining (EDM). LIGA technology offers a new route for making such mould inserts with much better accuracy and much higher aspect ratio. Though making mould inserts was the original motive to develop the LIGA technique, metal structures themselves made by LIGA have also been widely used as MEMS components and systems. There were plenty of examples reported that LIGA made metal structures were used as micromotors, microgrippers and microtwizers. LIGA has the unique capability to make precision metal components that no conventional precision machining tool can compete with.

It has to mention that the LIGA described here is specifically for LIGA using X-ray for the lithography. The X-ray has to be of very short wavelength which can only be produced in a synchrotron radiation source. The SRS is a very expensive large scale instrument not readily available to a wider community. Therefore, many low cost LIGA-like

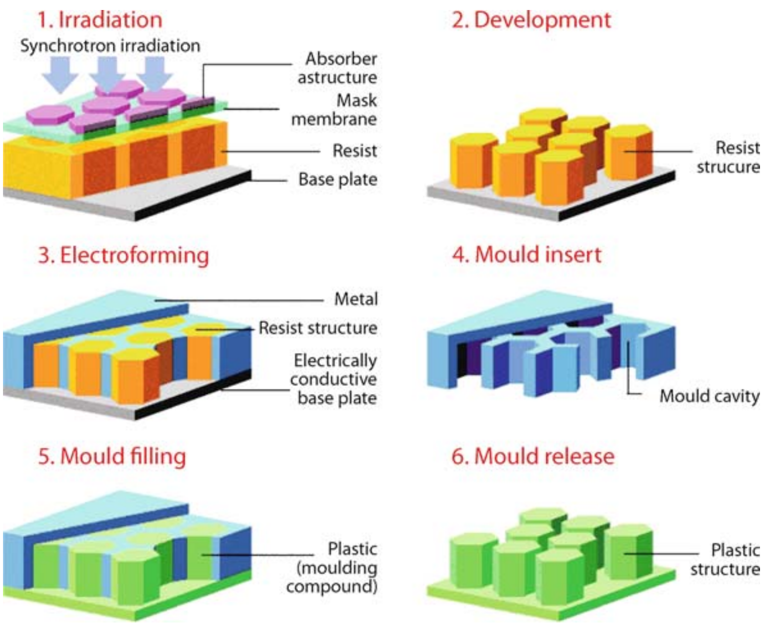

LIGA, Figure 1 Schematic of LIGA process steps

technologies have been developed after the advent of X-ray LIGA. Generally, LIGA-like technologies use non X-ray methods to make high aspect ratio microstructures, such as laser LIGA, UV LIGA. The LIGA-like micromachining technologies will be described in a separate entry in this Encyclopaedia.

Basic Methodology

The basic elements of X-ray based LIGA technology consist of X-ray source, LIGA mask and thick resist process [2].

X-ray Source

The synchrotron radiation source (SRS) is the only lithography light source for X-ray LIGA. The principle of synchrotron radiation is that high energy electrons travelling in a speed approaching speed of light on a circular orbit (storage ring) can radiate wide spectrum of electromagnetic wave along the tangential direction of the orbit. Because of the wide range of wavelengths of radiation coming out of SRS, special magnetic wiggler has to be fitted to the beam line in order to let out the very short wavelength of X-ray beam. The penetration depth of X-ray in PMMA resist is wavelength dependent. For example, if a X-ray source with 7 A wavelength is used to expose 400 μm thick PMMA, 4 repeated exposures are needed in order to fully expose thick resist layer. If 2 – 3 A wavelength X-ray is used one exposure can penetrate 500 μm thick PMMA layer [3]. X-ray with wavelength above 10 A is generally called soft X-ray. Soft X-ray has the photon energy normally at 1 – 2 keV, whereas the photon energy of hard X-ray is above 20 keV. Another important feature is that the X-ray beam from a SRS is highly parallel, with beam divergent angle less than 1 mrad. Such a parallel irradiation makes possible the exposure of high aspect ratio structures with very vertical sidewalls.

LIGA Mask

LIGA mask consists of supporting membrane which is a low density material and near transparent to the hard X-ray, and high density metal patterns which absorb most of the X-ray photon energy so that it becomes opaque to the X-ray. The requirements on the supporting membrane of a LIGA mask are:

- Low absorbance and high transparency to X-ray
- High resistance to X-ray irradiation. Material property does not change at long period of X-ray irradiation
- Good stability in lateral structure (low internal stress and bowing), which will be less likely to cause distortion of absorber patterns
- Compatible with photoresist process and electroplating process
- It would be desirable if the membrane is also optically transparent, which would facilitate alignment and overlay exposure

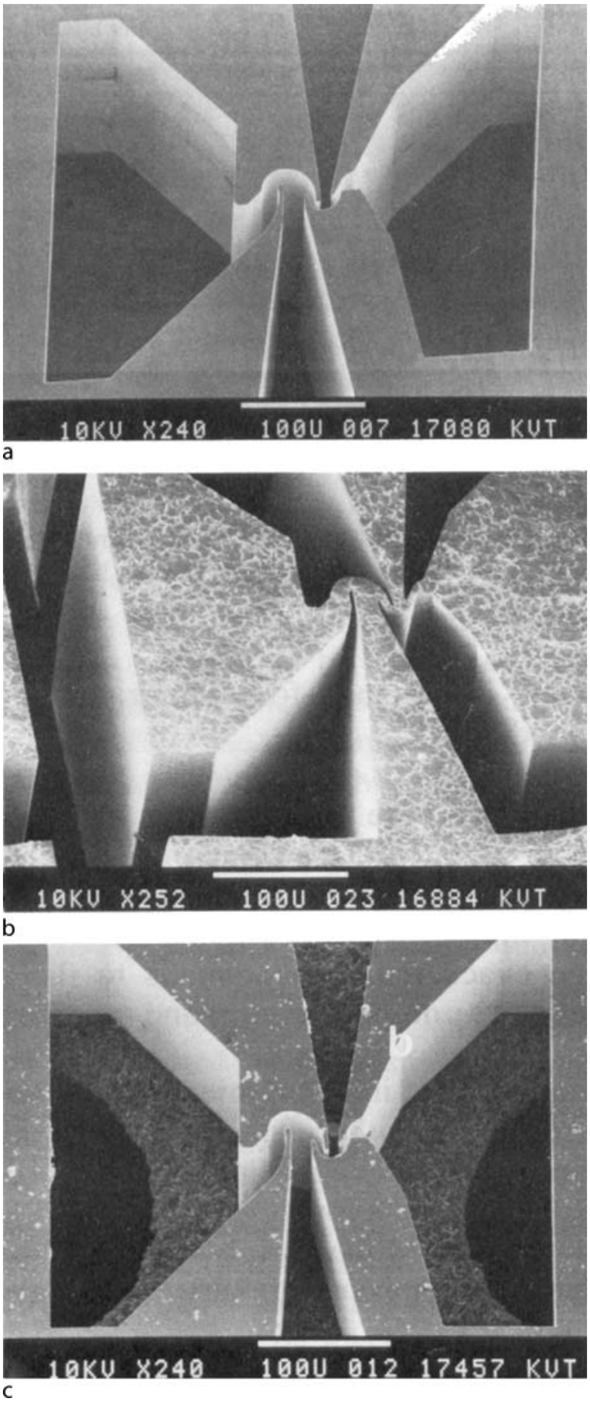

LIGA, Figure 2 Micronozzle fabrication by LIGA at different stages (**a**) PMMA resist mould by X-ray lithography (**b**) nickel structure after electroforming and removal of resist mould (**c**) Plastic replication by moulding from the nickel mould

Materials which can meet most of above requirements are silicon, silicide, beryllium, titanium, graphite, diamond and kapton. The thickness of the supporting membrane

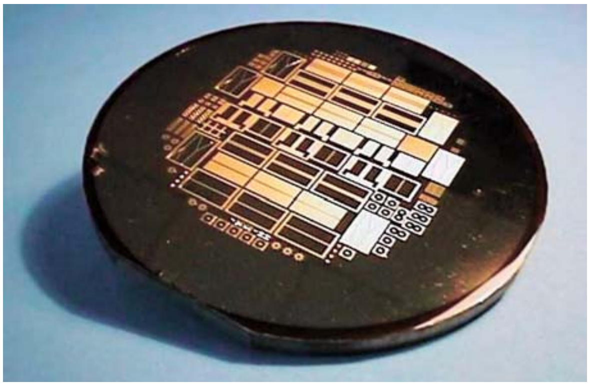

LIGA, Figure 3 A LIGA mask made from beryllium membrane with gold absorber patterns on the membrane

depends on the transmission of X-ray through the membrane. The better the transmission, the thicker the membrane is allowed. Beryllium is the best membrane material for LIGA masks. Gold is commonly used as the absorber material because of its high density and mature electroplating process to deposit the absorber layer. To absorb the hard X-ray the thickness of gold absorber is in the range of 10 – 20 µm thick. To expose 1mm thick PMMA, the gold absorber has to be 50 µm thick. Fig. 3 shows a typical LIGA mask. The beryllium membrane is supported by a steel frame. Gold absorber patterns are clearly visible on the membrane surface.

Thick Resist Process

LIGA structures are firstly made into a polymer resist by X-ray exposure. The commonly used polymer resist for LIGA is PMMA. Upon exposure to X-ray, the PMMA degrades from high molecule weight to low molecule weight, so the PMMA can be dissolved in a developer solution. There are many practical process issues when the PMMA layer becomes a few hundreds of micrometers thick. Spin coating such thick PMMA layer is difficult. Multi coating process has to be used, or the thick PMMA layer is formed by gluing a PMMA sheet (Perspex) onto the substrate. To expose thick layer of PMMA, high exposure dose is needed, which means very long exposure time under X-ray irradiation. X-ray decays in PMMA. The energy absorbed in PMMA produces heat. In order that the bottom part of a thick PMMA layer receives enough exposure dose, the top part of PMMA layer may get over exposed. Excessive heating may cause surface foaming at the top layer of PMMA. Shorter wavelength X-ray has less decay in PMMA, therefore, can achieve much uniform exposure over the thickness of PMMA.

Once the PMMA deep structures are made by X-ray lithography, the electroplating of metal and replication from the metal mould insert are all standard processes. The most commonly used metal for electroplating is nickel, because electroplating of nickel is a mature technique and nickel has the necessary hardness as a structure material for mould insert or functional microcomponents.

Key Research Findings

Although PMMA has been used for a long time as the only resist for LIGA, its biggest drawback is low sensitivity, which requires long exposure time. It becomes more serious at ultra thick resist exposure. For example, to expose 1mm thick PMMA will need nearly 24 hours exposure time. In recent years, a new type of chemical amplified resist, SU-8, found wide applications in MEMS. SU-8 is a photoresist and can be patterned by UV exposure. SU-8 can also be exposed by X-ray. The biggest advantage of SU-8 over PMMA is its high sensitivity to X-ray. The exposure, which may take more than 10 h with PMMA, only needs over 10 min with SU-8 [4]. In optical lithography, SU-8 has demonstrated very high contrast and high aspect ratio. It has become the key photoresist for the UV LIGA (see LIGA like micromachining). The contrast of SU-8 patterns obtained by X-ray lithography is even better, because of the high parallelism of X-ray from a SRS. Conventional UV lithography of SU-8 can achieve pattern aspect ratio of 20:1 to 30:1. With X-ray lithography, the SU-8 patterns can reach aspect ratio of 50:1 or even 100:1. The only problem with SU-8 as the resist is its removal after electroforming. With PMMA, the resist mould after electroforming of metal can be easily dissolved in acetone. However, acetone has little effect on SU-8. Other removal methods have been developed, though not as effective as removal of PMMA [5].

Although LIGA technology is able to make microstructures with very high aspect ratio and very vertical sidewalls, there are some factors which have limited further improvements in pattern accuracy, minimum feature size and sidewall verticality in LIGA. These factors include X-ray diffraction and photoelectron scattering, penumbra effect, non-vertical sidewall in absorber patterns, mask distortion and secondary electrons induced by X-ray in substrate material [6]. However, the detrimental effects to the accuracy of LIGA patterning is only relative. As LIGA technology is mainly for making microstructures used in MEMS and Microsystems, which are normally in the dimension of a few tens or few hundreds micrometers, these inaccuracies in the range of sub-micrometers are generally negligible compared with the overall dimension of microstructures.

Future Directions for Research

X-ray based LIGA technology has been developed for over two decades. It has become a mature manufacturing technique for making mould inserts or special metal microcomponents. There is less fundamental research being carried out but more development in practical applications. The main aim of application oriented research is to expand the scope of its application, particularly for making high value added microcomponents, so that the cost of using this technology can be offset.

References

1. Becker EW, Ehrfeld W, Münchmeyer D, Betz H, Heuberger A, Pongratz S, Glashauser W, Michel HJ, Siemens R v (1982) Production of separation nozzle systems for uranium enrichment by a combination of X-ray lithography and galvanoplastics. Naturwissenschaften, 69(11):520–523
2. Z Cui (2006) Micro-Nanofabrication Technologies and applications, Chapter 5: X-ray lithography. Springer-Verlag, Berlin
3. Becker EW Ehrfield W, Hagmann P, Maner A, Münchmeyer D (1986) Fabrication of microstructures with high aspect ratios and great structural heights by synchrotron radiation lithography, galvanoforming and plastic moudling (LIGA process). Microelectron Eng, 4(1):35–56
4. Cui Z, Jenkins DWK, Schneider A, Mcbride G (2001) Profile Control of Su-8 Photoresist Using Different Radiation Sources. SPIE 4407:119–125
5. Z Cui (2006) Micro-Nanofabrication Technologies and applications, Chapter 2: Optical lithography. Springer-Verlag, Berlin
6. Griffiths SK (2004) Fundamental limitations of LIGA X-ray lithography: sidewall offset, slope and minimum feature size. J Micromech Microeng 14:999–1011

LIGA-Like Techniques

CHE-HSIN LIN
Department of Mechanical and Electromechanical Engineering, National Sun Yat-sen University, Kaohsiung, Taiwan
chehsin@mail.nsysu.edu.tw

Synonyms

Poor man's LIGA; UV-LIGA; LC-LIGA (low-cost LIGA)

Definition

LIGA is a micromachining technique which utilizes X-ray lithography, electroforming and micromolding processes to produce precise and high-aspect-ratio microstructures. Like the LIGA process but without accessing a synchrotron radiation source, LIGA-like techniques use alternative micromachining technologies such as UV lithography, laser writing, focused ion beam, electron beam

and reactive ion etching to produce high-aspect-ratio microstructures for molding purposes. A series of fabrication processes including electroforming and molding is then used to reproduce the microstructures.

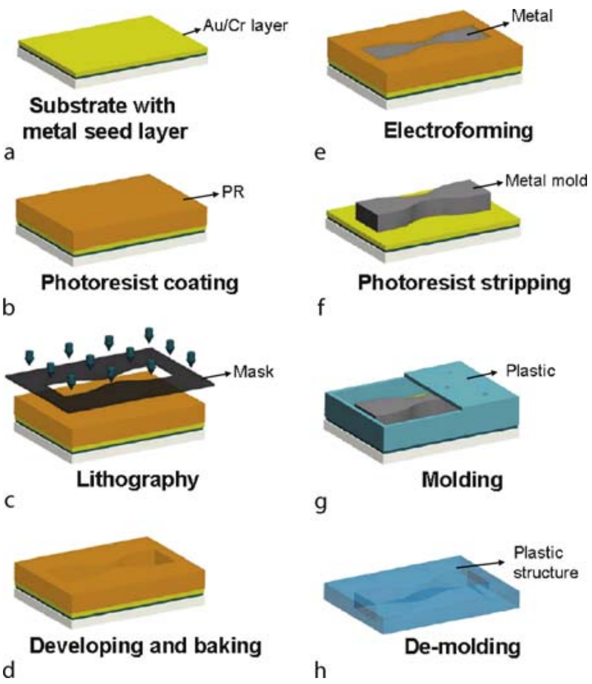

LIGA-Like Techniques, Figure 1 Schematic of a simplified fabrication process of a LIGA-like technique

Overview

LIGA is a micromachining technique including lithography, electroforming and micromolding processes, which usually uses X-ray lithography to generate ultra-thick microstructures with millimeter-sized thickness. This process was first developed at Karlshruhe and the Institute for Micromechanics (IMM) in Germany, such that the term *LIGA* is an acronym formed from the German words *Lithographie* (lithography), *Galvanoformung* (electroforming) and *Abformung* (molding). High-intensity and highly collimated X-rays generated from a synchrotron radiation source are used to provide high-resolution and ultra-deep lithographic capability. However, the need for a synchrotron radiation source limits its application for researchers and the process is inherently time consuming and expensive. In this regard, cheaper light sources and alternative micromachining technologies incorporating new photoresist materials to produce thick microstructures were soon reported. The LIGA-like process usually uses a UV aligner or laser writer as exposure energies and also includes electroplating and molding processes. Most LIGA-like techniques focus on the lithography method for generating the first micromold for molding purposes. Since EPON SU-8 epoxy resin, a negative-tone photoresist, was reported, LIGA-like techniques have become popular in the microelectromechanical systems (MEMS) community. Microstructures with a thickness of several hundred micrometers can be obtained by a single coating and a thickness of up to a millimeter can also be achieved by multiple coating [1]. Ultra-thick microstructures can be fabricated in a simple and low-cost way with this new technique. However, surface flatness of the coated photoresist layer and the long processing time are also critical issues for the multicoating process. Therefore, a modified process for fabricating ultra-thick microstructures in SU-8 photoresist was reported, which used a single coating technique, a modified backing process and a new mask design to overcome the problems that matter seriously during LIGA-like processes [2]. Micromolds with millimeter thickness and large area can be fabricated in a fast and simple method with this LIGA-like technique.

Figure 1 presents a simplified schematic for the fabrication process of the proposed LIGA-like technique in SU-8 epoxy resin. Briefly, a substrate is firstly coated with metal seed layers for the electroforming process (Fig. 1a). A chromium or titanium layer with a thickness of several hundred angstroms is usually used as the adhesion layer. A gold or copper seed layer of several micrometers in thickness is then deposited on the adhesion layer to be the bottom conductive layer for the electroplating process. A thick layer of SU-8 photoresist is applied on the substrate with a modified single-coating process as mentioned above (Fig.1b). The coated substrate is then soft-backed on a hot-plate and exposed with a standard UV lithography procedure (Fig.1c). SU-8 is a negative-tone photoresist which needs a postexposure bake process at 95 °C to enhance the further cross-linking of the exposed photoresist. Note that the exposed area of SU-8 photoresist and the stiffness of the substrate may cause undesired problems in an ultra-thick photoresist process because the residual stress in the cross-linked photoresist is considerable which may bend the substrate. In general, a small and discrete pattern design for the lithography mask is preferred. After the exposure and postexposure bake process, the substrate is developed using pure propylene glycol monomethyl ether acetate (PGMEA) with a gentle ultrasonic agitation and then baked at 90 °C for 10 min to remove the residual organic solvent. The patterned SU-8 structure is finally hardbaked to stabilize and further cross-link the polymer structures (Fig. 1d). The electroforming process is then carried out after the lithography process to produce

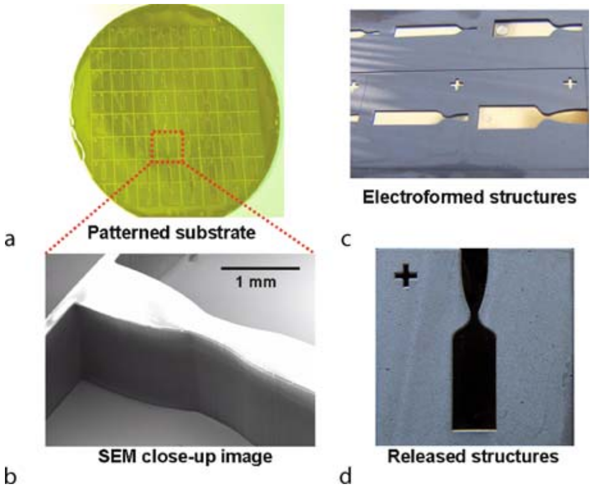

LIGA-Like Techniques, Figure 2 Images of (**a**) silicon substrate with ultra-thick photoresist, (**b**) the patterned photoresist, (**c**) electroformed nickel structure and (**d**) released nickel structure

metal-based microstructures (Fig. 1e). A nickel sulfamate bath is popular in the MEMS community due to the low residual stress in the electroformed nickel structures. Note that other materials including copper, cobalt, ferroalloy or even metal–ceramic composites can also be chosen for this plating process. The SU-8 photoresist is stripped after the electroforming process to release the fabricated metal mold (Fig. 1f). The metal mold is then used as the master for reproduction purposes (Fig. 1g) and the final plastic product is formed after the de-molding process (Fig. 1h). Hot embossing, injection molding and other polymer casting methods are usually adopted for reproducing plastic products.

Figure 2 presents images of a LIGA-like process at different stages. Figure 2a shows the patterned substrate after the UV lithography process (see Fig. 1d). The seed layer for this process is composed of 500 Å of chromium and 2 μm of gold. Figure 2b shows a scanning electron micrograph of the UV-patterned SU-8 structure. The height of the SU-8 microstructure is 1.5 mm and the minimum line width is 100 μm, resulting in an aspect ratio of 15. Figures 2c and 2d show images of a substrate after the electroforming process and a released nickel structure, respectively. The nickel structures are formed from a nickel sulfamate bath and have a thickness of around 1 mm. Although the cost and process complexity for fabricating microstructures using the LIGA-like process are significantly reduced, the X-ray LIGA process still provides the best linewidth precision, smallest sidewall roughness, deepest structure and largest aspect ratio compared with the reported LIGA-like techniques. However, LIGA-like technology is undoubted a valuable alternative to the original LIGA process especially for research institutes and small- to medium-sized companies.

Cross References

- ► LIGA
- ► Thick Resist Lithography

References

1. Lorenz H, Despont M, Fahrni M, Brugger J, Vettiger P, Renaud P (1998) High-aspect-ratio, ultrathick, negative-tone near-UV PR and its applications for MEMS. Sens Actuators A 64:33–39
2. Lin CH, Lee GB, Chang BW, Chang GL (2002) A new fabrication process for ultra-thick microfluidic microstructures utilizing SU-8 photoresist. J Micromech Microeng 12:590–597

Ligand

Definition

In the context of proteomics, a ligand is any molecule, atom, or ion that is capable of binding to a specific site on a protein via a chemical bond. Ligand binding is often essential for the protein to become fully functional, and often more than one type of ligand can compete for a particular binding site.

Cross References

- ► Lab-on-Chip Devices for Protein Analysis
- ► Protein Microarrays
- ► Proteomics in Microfluidic Devices

Light Sheet

Definition

A light sheet has a bigger width than thickness and is used to specially illuminate the part of the scene which is interesting for the photography. Compared to the volume illumination less background noise occurs. Light sheets are generated with cylindrical lenses for laser light and with slits for white light.

Linear Peristaltic Pump

Definition

Linear peristaltic pumps transport fluid through a flexible duct using traveling contraction waves. In a typical linear

peristaltic pump, discrete translational elements rhythmically compress a straight section of flexible tube, moving fluid volumes. In contrast to rotary peristaltic pumps, linear peristaltic pumps usually do not use rollers or sliding contact elements. Because a moving boundary displaces fluid and induces the flow, linear peristaltic pumps are an example of positive-displacement pumps.

Cross References

► Peristalsis
► Peristaltic Pumps
► Rotary Peristaltic Pumps

Liquid Chromatography

Aaron T. Timperman, Brent Reschke, Kathleen Kelly
C. Eugene Bennett Department of Chemistry, West Virginia University, Morgantown, WV, USA
atimperm@wvu.edu

Synonyms

High pressure liquid chromatography (HPLC)

Definition

Liquid chromatography is a method for separating molecules dissolved in a liquid mobile phase. A pressure gradient drives the mobile phase through the stationary solid phase. Thermodynamic partitioning of the analytes between the liquid phase and stationary phase causes differential transport and spatial separation of different molecular species.

Overview

Molecular separations are used to reduce the complexity of a mixture of compounds. While complete separation of two or more compounds is typically desired, complete separation is theoretically impossible. In practice, the separation of a purified sample can appear to be complete, if the contamination is below the limits of detection. While the concepts discussed pertain to chromatography in general, the terminology and details will specifically address bonded phase column chromatography.

Theory

A sample mixture is composed of different molecular components that have different chemical structures, and to be detectable each component must have a population of molecules. All of the molecules of a single component have the same chemical structure, and this population of molecules is referred to as the sample or analyte band as it moves through the column. The chemical structure of each component determines the strength and type(s) of intermolecular forces it has with the mobile phase and the stationary phase. These intermolecular forces govern the relative strength of analyte-mobile phase and analyte-stationary phase interactions, which determines the relative amounts of the analyte molecules in mobile and stationary phases. If the analyte interactions with the stationary phase are strong enough, the analyte molecules will bind or adsorb to the stationary phase. Stronger analyte interactions with the stationary phase increase the fraction of analyte adsorbed to the stationary phase and decrease the analyte velocity. The process of molecules leaving the stationary phase and becoming solvated in the mobile phase is referred to as desorption. This adsorption/desorption process or partitioning can be described by the reaction shown in Eq. (1), where $[A]_{mp}$ is equal to the concentration of the analyte A in the mobile phase and $[A]_{sp}$ is the concentration of the analyte A in the stationary phase.

$$[A]_{mp} \leftrightarrow [A]_{sp} \tag{1}$$

The equilibrium constant, termed the partition coefficient (K), is the ratio of the analyte concentration in the stationary phase to the concentration in the mobile phase, as shown in Eq. (2).

$$K = \frac{[A]_{sp}}{[A]_{mp}} \tag{2}$$

The tendency of any chemical system to approach equilibrium drives adsorption and desorption of the sample band as it migrates through the column. Equilibrium cannot be reached, because the mobile phase is constantly moving and forcing the analyte concentration profile in the mobile phase ahead of the solid phase profile. Thus, the leading edge of the sample band has a solute concentration in the mobile phase above the equilibrium position, increasing the rate of adsorption above the equilibrium level, while the trailing edge solute concentration in the mobile phase is lower than the equilibrium position, increasing the rate of desorption in this zone above equilibrium levels. Analytes with larger K values will spend more time adsorbed to the stationary phase and will elute later than those that have smaller K values.

The separation is usually monitored by a detector that records the intensity at one fixed point at or near the end of the column. The intensity values are related to the analyte concentration and are plotted against time, where the

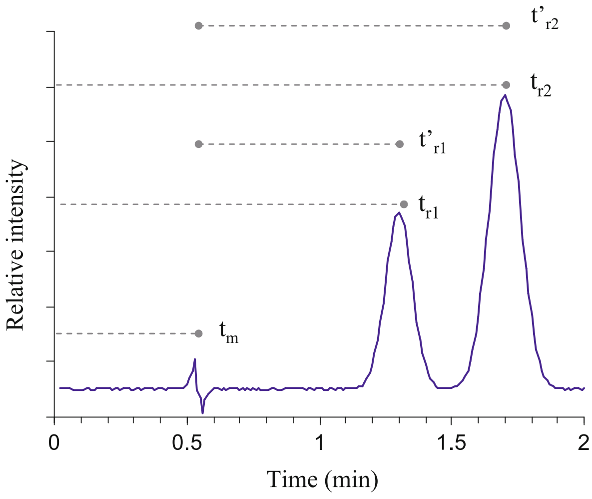

Liquid Chromatography, Figure 1 Measurement of the retention times (t_r), void time (t_m), and adjusted retention times (t_r') are shown. The void time is equal to the elution time of the un-retained substances, and it can be related by the flow-rate to the void volume, which is the volume of solution between the injector and detector. Two analyte peaks are shown with their corresponding retention times. The retention time of the first eluting analyte is t_{r1}, and the retention time of the second eluting analyte is t_{r2}. The void time is subtracted from the retention times to provide the corresponding adjusted retentions times (t_{r1}' and t_{r2}')

injection time is equal to zero. The time for the analyte to travel from the injector to the detector is referred to as the retention time, t_r, as shown in Fig. 1. The retention time is measured at the point of maximum intensity or peak maximum for the analyte band. The void time, t_m, describes the time required for a compound that does not interact with the stationary phase to travel from the injector to detector. By subtracting the dead time from the retention time, the adjusted retention time, t_r', is given as shown in Eq. (3).

$$t_r' = (t_r - t_m) \tag{3}$$

Another important parameter for characterizing the retention of a compound is the capacity factor, k', which is defined as the mass of solute in the stationary phase divided by the mass of solute in the mobile phase as shown in Eq. (4). In contrast with partition coefficient, k' is not a state function and is dependent on the column's characteristic phase ratio, which is equal to the volume of the stationary phase (V_s) divided by the volume of the mobile phase (V_m). A greater stationary phase volume increases interactions with the stationary phase, thereby increasing the retention time and k'. It is important to note that the capacity factor is also equivalent to the adjusted retention time divided by the void time, which are obtained directly from the chromatogram. This important parameter can be intuitively described as a measure of the strength of an analyte's interaction with the stationary phase in a particular chromatographic system.

$$k' = \frac{\text{mass}_{sp}}{\text{mass}_{mp}} = \frac{(t_r - t_m)}{t_m} \tag{4}$$

The main objective of liquid chromatography is separation, and the quality of the separation of two analyte bands or peaks is measured by the resolution, R. The resolution is calculated by dividing the difference in retention times by their average base widths (w_b) as shown in Eq. (5).

$$R = \frac{t_{r2} - t_{r1}}{\frac{1}{2}(w_{b1} - w_{b2})} \tag{5}$$

It should be noted from Eq. (5) that there are two fundamental approaches to improving the resolution: increasing the separation between the two peaks or decreasing the peak width. The difference in retention time is determined by the selectivity of the chromatographic system for the two analytes. Manipulating the difference in retention times to improve the resolution is usually achieved by adjusting the mobile phase or the stationary phase, but the effects of such adjustments are difficult to predict. In samples with many components, improving the resolution of a single pair often results in a scrambling of retention times and in poor resolution of other analyte pairs.

For complex samples, the peak capacity is best for evaluating the separation power of a particular system. Peak capacity is calculated in Eq. (6) where L is the separation length in time, w is the peak width in time, and R is the specified resolution.

$$n = \frac{L}{wR} \tag{6}$$

This equation reveals the number of ideally spaced peaks of set width and set resolution that can be separated in the characteristic separation time. Clearly, in a real sample containing components with unrelated properties, the peak spacing will be random and the number of well resolved peaks will be much less than the peak capacity. Although the calculated peak capacity is unobtainable in practice, it is well suited for comparing the effectiveness of different systems for separating complex mixtures.

The most direct and universal means of improving a separation is to decrease the peak width, which is typically described by separation efficiency. The separation efficiency is equal to the length of the separation squared divided by the peak variance (σ^2) and is dimensionless;

$$N = \frac{L^2}{\sigma^2} = \frac{t_r^2}{\sigma^2} = \frac{5.55 t_r^2}{{w_{1/2}}^2} = \frac{L}{H}, \tag{7}$$

L

where L represents the column length, $w_{1/2}$ is the peak width at half maximum, and σ the peak width measured as the standard deviation of a Gaussian peak. Therefore, the separation efficiency, N, can be thought of as the variance of peak width, normalized to the elution time. The quotient is inverted, so larger separation efficiencies represent better performance. The plate height, H, is also used to characterize the peak width and is inversely proportional to the separation efficiency as shown in Eq. (7).

A peak in a chromatogram represents the distribution of molecules in an analyte band. An analyte band is composed of many molecules that are identical in structure, but that experience different microenvironments as they travel through the column. As the analyte bands move through the column, band broadening increases the peak width and decreases the peak height. Therefore, the analyte band is both lengthened and the concentration is diluted as it moves through the column. Band broadening can be caused by many processes some of which are unavoidable and random in nature. Random processes give rise to analyte bands that have Gaussian concentration profiles, creating the symmetric peaks shown in good chromatograms. Other non-random processes can cause asymmetric peak shapes, but these can typically be eliminated with the proper mobile phase and stationary phase composition. Band broadening increases the peak width, and consequently it must be minimized for optimal performance.

Rate theory describes the contribution of different band broadening processes as a function of mobile phase flow rate, μ_x. The original rate theory developed by van Deemter in 1956 [1], relates the plate height to the three major band broadening terms. This theory is used to minimize peak width in terms of plate height (H), and was further refined to the Hawkes' equation, which is shown in Eq. (8).

$$H \approx \frac{B}{\mu_x} + C_s\mu_x + C_m\mu_x \tag{8}$$

This equation is defined by the parameters B, C_s, and C_m that are dependent on the column characteristics and mobile phase viscosity. These three band broadening components are: longitudinal diffusion, B, mass transfer in the stationary phase, C_s, and mass transfer in the mobile phase, C_m. The first term is longitudinal diffusion, which is the amount of band broadening along the length of the column that increases peak width directly. Higher flow rates μ_x minimize the B-term, by decreasing the time during which longitudinal diffusion can occur. For bonded phases, the stationary phase mass transfer is dependent on the capacity factor and the molecular adsorption and desorption kinetics. Increasing the homogeneity of the stationary phase functional groups and decreasing unwanted interactions with the solid support decreases band broadening.

To minimize band broadening in the mobile phase, the velocity distribution of the molecules in the sample band must be minimized. Contributing to the different mobile phase velocities are: the parabolic flow profile of pressure driven flow, variations in inter-particle flow path diameters, and stagnant mobile phase pools in pores. Thus band broadening is minimized by using smaller inner diameter columns that minimize the variation in flow paths. Additionally, performance increases as bead diameter, size distribution, and porosity decrease; performance also increases as the beads are packed in a more uniform manner. However, smaller bead sizes increase the backpressure requiring the use of higher pressures or shorter columns. While, decreasing the porosity decreases the capacity factor, which decreases resolution and sample loading capacity. Therefore, it is important to emphasize that miniaturization improves performance.

Basic Methodology

In liquid chromatography there are two primary methods of eluting analyte from a column, isocratic elution and gradient elution. Isocratic elution is characterized by using constant solvent composition. Gradient elution uses a mixture of two or more solvents that are mixed at different ratios during the run to change the solvent composition. Each of the two methods will be discussed in more detail below; in addition, the advantages and disadvantages of each method will be established.

Isocratic Elution

As mentioned above an isocratic elution is performed using a single solvent or a solvent mixture with a constant composition. Isocratic elution is best suited for separating analytes with similar capacity factors and provides the best resolution for these mixtures. Conversely, if the difference in capacity factors is large, the separation can be prohibitively long with no definite end. Additionally, as the retention time increases, band broadening can decrease the peak height and increase the peak width, making detection more difficult. Altering the column or mobile phase to decrease retention improves the detection of the latter eluting peaks and decreases the separation time, but worsens the separation of the early eluting peaks. On the other hand, increasing retention improves the separation of early eluting peaks, but makes the latter eluting peaks less detectable and increases the length of separation.

Gradient Elution

To improve separations of analytes with a wide range of capacity factors, gradient elution can be used to solve the general elution problem. Gradient elution is achieved by changing the solvent composition as a function of separation time. Typically, the solvent system is designed so that the initial k' values are very high, leading to complete adsorption of all of the analytes on the column. This initial adsorption process provides sample extraction and concentration, allowing the injection and cleaning of large sample volumes without an increase in peak width. After the separation is started, the solvent composition is changed to lower the k' values until the k' values of all of the analytes are low enough to allow their migration down the column. Because the solvent composition is continually being changed to lower the k' values, the analyte bands move quickly down the column after their desorption. The constant decrease in the k' values provide consistent peak widths throughout the separation, improving the detection of latter eluting compounds. With steeper gradients, the solvent strength at the trailing edge of the sample band is substantially greater than at the leading edge, causing the trailing edge to move faster than the leading edge. This difference in velocities provides focusing of the bands that can improve the detection limits up to a factor of 3. Gradient separations also have a well defined beginning and end, eliminating the indefinite end time encountered with isocratic separations. However, the same number of analyte peaks are compressed into a shorter separation time that is not compensated for by the reduction in peak width. This case leads to the only major drawback in performance encountered with gradient separations – a reduction in resolution and peak capacity.

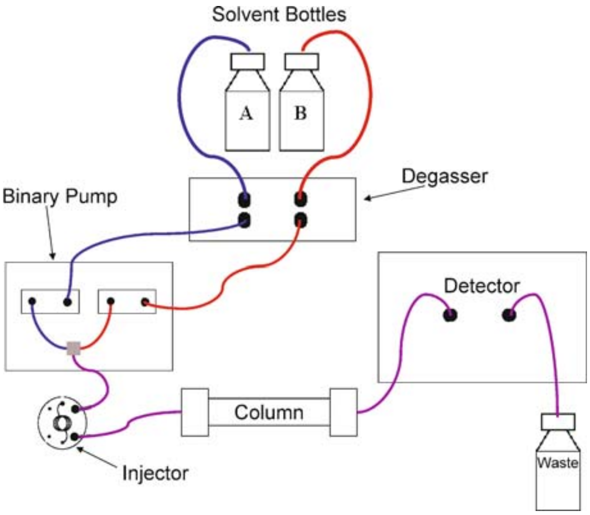

Liquid Chromatography, Figure 2 A schematic showing the components of a typical HPLC system. Here a binary pump is shown, which can be used for gradient separations by utilizing two different solvents (A and B). The degasser removes dissolved gases from the solvents before the pumps and the high pressure mixing tee to prevent air bubbles from forming in the system. The solvent then flows to the injector and through the column before reaching the detector

Instrumentation

Most HPLC systems have a modular design that provides flexibility and allows for many different combinations. In Fig. 2, the basic components of an HPLC are shown. In most microfluidic HPLC systems, the column is miniaturized while the other components are from a typical benchtop HPLC.

Injectors

HPLC injectors serve two basic functions: to load a precise volume and to enable the use of high pressure. The small particle and column diameters used in analytical and microfluidic HPLC can cause large backpressures, requiring high pressure for moving the sample solution and mobile phase through the column. However, a specific design of a chromatography column can greatly affect the pressure needed for injection, and low back pressure columns do not require the use of an injection valve. For typical HPLC columns, an injector that can withstand high pressure consists of a sample injection loop and a multiport valve. The sample loop is made from a tube whose interior defines a precise volume. A sample injection valve is used to switch the sample loop between different ports that alternate between the sample injection port and HPLC pump on the inlet side. On the outlet side, the excess sample waste line and the column are connected. In the sample loading position, the valve connects the inlet port and the sample waste line. This configuration allows the sample to be injected into the loop with low backpressure. Following sample loading, the sample loop is connected with the HPLC pump and the column, beginning the separation. In this manner, the sample is easily injected using a syringe at low pressure, and the HPLC pump is used to inject the sample plug onto the column.

Pumps

There are multiple types of pumps utilized for HPLC; however, this discussion will focus on reciprocating pumps since most commercial instrumentation is equipped with this type of pump. Reciprocating pumps are widely used, because they have many qualities desirable for HPLC, including the ability to generate high pressures and reproducible gradients. This type of pump uses a piston to

L

draw solution into a chamber as the piston retracts. On the forward stroke, the check valve closes and the piston pushes the solution out of the chamber through the injector and column. To reduce pulsations, a dual piston design is used in which one piston retracts while the other advances. When this pump design is used in combination with a pulse dampener, the net result is a constant virtually pulse free solvent flow.

For microfluidic systems, the flow rate range of the pump is an important consideration. Most pumps are designed to work effectively for the 5 ml/min to 0.1 ml/min range, while microfluidic systems typically require flow rates in the 1 μl/min to 50 nl/min range. The flow with such pumps can be reduced easily with a flow splitter. However, the flow splitter should be upstream of the injector to avoid sample loss. Downstream of the injector the volume of the connective tubing used for sample delivery must be kept to a minimum. Many conventional auto-samplers have connective tubing volumes that are too large for the flow rates used by microfluidic systems causing excessive delay times.

Columns

The column is the key component of an LC system, because it is used to effect the separation and holds the stationary phase. The choice of stationary phase is of critical importance, because the stationary phase largely determines what molecular properties the separation will be based on. An appropriate stationary phase should interact with all the analytes, but have a wide range of interaction strength.

While there are many types of stationary phases to choose from, most are bonded phases in which the functional moieties are covalently linked to the surface of a solid support. The functional coating is usually considerably less than a monolayer and must have batch to batch reproducibility to provide consistent retention times. Ideally there is no interaction between the uncoated surface of the solid support and the analytes, which would result in irreproducible retention times.

After the type of functionality is chosen, the next two most important considerations are the particle size and porosity. For high efficiency separations, smaller particles usually in the 0.5 to 10 μm range with a narrow size distribution are used. Increasing bead porosity increases the surface area and sample capacity of the beads; however, if the porosity is too high it will lead to band broadening. Smaller pores work better for smaller analytes, while large pores work better for larger analytes. Commercial HPLC columns are common in lengths ranging from 10 to 30 cm with inner diameters ranging from 2 to 10 mm. For isocratic separations, increasing the column length (L) increases the resolution by the $\sqrt{L}$, while the increase in backpressure is directly proportional to L. For gradient separations, the column must be long enough to provide sufficient sample loading capacity, but has a reduced effect on resolution.

Detectors

There are many different detection methods that can be coupled to an HPLC system; however, this section will only discuss three methods of detection, namely UV-visible absorbance, fluorescence, and mass spectrometry (MS).

The most commonly used detection methods are the optical detection methods, UV-visible absorbance and fluorescence. Both are methods of molecular spectroscopy, and therefore the spectra contain broad bands that can not be used for structural characterization of unknowns, but can be used for identification by matching with standard spectra. UV-visible absorbance has relatively high detection limits, but its wide use stems from it being the most universal detector. The signal/noise (S/N) is path length dependent for absorbance, so decreasing the column diameter raises the detection limits. Fluorescence detection limits are not path length dependent and are the best of the methods discussed. In addition, it is also more selective than UV-visible absorbance. However, this selectivity can be a disadvantage since few analytes fluoresce natively, although it is possible to fluorescently derivatize analytes with a label such as fluorescein isothiocyanate (FITC).

Mass spectrometry provides an unparalleled combination of structural information and sensitivity. However, coupling a liquid phase separation to an analytical instrument that operates at high vacuum was not straightforward. In 1985, Fenn's lab developed an electrospray ionization (ESI) interface that provided soft ionization of molecules in solution making it well suited for coupling HPLC and MS [2]. ESI is concentration sensitive, so decreasing the eluted band volume by decreasing the column diameter and flow rate improves the detection limits for mass-limited samples. MS separates ions in the gas phase and measures the mass to charge ratio (m/z). Further structural information can be obtained by isolating an ion in the MS, fragmenting the ion, and measuring the m/z of the fragment ions through a process called tandem MS. Typically ions are fragmented individually and the fragmentation process requires a finite amount of time, so the analysis of complex samples with dilute components is aided greatly by coupling with an HPLC. The HPLC injects concentrated sample bands at different times improving sample utilization and MS sensitivity.

Key Research Findings

The field of liquid chromatography is well established and reliable methods have been developed for analytical and preparative separations. Column miniaturization improves performance for analytical separations. Numerous stationary phases have been developed to separate analytes based on a wide variety of molecular properties including hydrophobicity, ionic interactions, and molecular size. Mobile phase modifiers can be used to aid in the minimization of unwanted interactions with the solid support. Although the field is well established, current research continues to improve separations for both microscale analytical and larger preparative separations. Recent publications will be highlighted that demonstrate the developments toward integrating HPLC components and separation techniques onto microfabricated devices.

A major problem associated with performing HPLC on chips is the difficulty of making a column using traditional solid support in a microfluidic channel. The difficulty with creating a column on chip lies in trapping and packing the support. However, Regnier et al. [3] showed using microfabrication methods that an HPLC column could be made on a microfluidic device without using traditional media. In this work, a $5 \times 5 \times 10\,\mu m$ collocated monolith support structure was created by etching $1.5\,\mu m$ wide $\times$ $10\,\mu m$ deep channels in a crossed diagonal pattern on a quartz wafer. This microfluidic device demonstrated a separation efficiency of approximately 35,000 theoretical plates from a 4.5 cm length column, compared to 40,000 to 60,000 theoretical plates from a conventional 10 – 30 cm column.

In another publication also by Regnier and coworkers, a highly integrated microfluidic device was created [4]. In the first section of the device, a tryptic digest of FITC labeled bovine serum albumin was performed. Next, immobilized metal affinity chromatography (IMAC) was performed on the tryptic digest to extract histidine containing peptides, which were finally separated using the monolith support design discussed above. This publication is an excellent example of the integration that is possible in a microchip format.

Another strategy to avoid packing beads in a microfluidic device is in-situ polymerization of a porous monolithic stationary phase. Svec et al. [5] have formed monolithic columns in microfluidic chips by using methacrylate chemistry to form reversed-phase or ion exchange stationary phases. Preconcentration was used to increase the concentration of GFP by a factor of 10^3. Another advantage to this technique lies in the ability to control the porosity of the monolith. The ability to control the porosity decreased the backpressure allowing for flow rates as high as $10\,\mu l/min$.

An additional example of integration on a chip format was demonstrated by Thibault [6] using an Agilent chip after they launched a product for performing on-chip liquid chromatography. The chip is made of polyimide and is coupled to a typical injector as described in the instrumental section. However, a clamp to ensure proper alignment and sealing between the components of the injector and the chip was necessary. The Agilent chip also included an enrichment column with a 40 nl volume. The separation column was 4.5 cm in length and utilized $5\,\mu m$ reversed phase beads. The reported peak capacity was 141 for a separation of peptides.

To further integrate on-chip LC, it is necessary to miniaturize LC components. Terry Lee's group has worked to utilize the gas produced from hydrolysis to act as the pumping mechanism for on-chip chromatography [7]. In order to effectively develop this pumping mechanism, high backpressure needed to be considered when delivering the solvent for on-chip LC. Backpressure causes the flow rate to be inadequate to practically perform a separation. Their electrochemical pump was able to deliver 70 nl/min at a backpressure of 80 psi.

Two of these pumps have been successfully coupled to generate gradients that were used to perform a separation with $3\,\mu m$ beads, a 1.2 cm column, and 80 nl/min flow rate. The sample consisted of 600 femtomols of digested BSA, which was also separated on a commercial nanoLC system for comparison. The resolution was superior for the commercial system. Although the commercial system demonstrated better resolution, it could be attributed to the 15 cm column.

Future Directions for Research

Future research will continue to improve the fabrication of liquid chromatography columns on microfluidic chips. The high porosity and high surface area of in-situ polymerized monolithic columns makes this approach most promising. Implementation of comprehensive analytical methods for characterization of biological systems in fields such as proteomics and metabolomics require large improvements allowing for more complex samples to be analyzed while reducing the amount of sample needed. Such developments should include integrated microfluidic devices capable of performing multidimensional separations that can analyze complex biological samples. Although miniaturization increases resolving power, it also decreases the loading capacity making it more difficult to detect components of low relative abundance. Therefore, many challenges remain in improving the detection limits, particularly for the analysis of

complex, mass limited samples. In addition, further developments need to include miniaturized integrated components, such as miniaturized pumps capable of higher pressures.

Cross References

- ▶ Chromatographic Chip Devices
- ▶ Diffusion
- ▶ Disjoining Pressure
- ▶ Fluorescence
- ▶ High Performance Liquid Chromatography (HPLC)
- ▶ Hydrodynamic Dispersion
- ▶ Mass Spectrometry
- ▶ Pressure Driven Flow
- ▶ Ultrasonic Machining

References

1. van Deemter JJ, Zuiderweg FJ, Klinkenberg A (1956) Longitudinal diffusion and resistance to mass transfer as causes of nonideality in chromatography. Chem Eng Sci 5:271–289
2. Whitehouse CM, Dreyer RN, Yamashita M, Fenn JB (1985) Electrospray interface for liquid chromatographs and mass spectrometers. Anal Chem 57:675–679
3. He B, Regnier F (1998) Microfabricated liquid chromatography columns based on collocated monolith support structures. J Pharmac Biomed Anal 17:925–932
4. Slentz BE, Penner NA, Regnier FE (2003) Protein proteolysis and the multi-dimensional electrochromatographic separation of histidine-containing peptide fragments on a chip. J Chromatogr A 984:97–107
5. Yu C, Davey MH, Svec F, Frechet JM (2001) Monolithic porous polymer for on-chip solid-phase extraction and preconcentration prepared by photoinitiated in situ polymerization within a microfluidic device. Anal Chem 73:5088–5096
6. Fortier MH, Bonneil E, Goodley P, Thibault P (2005) Integrated microfluidic device for mass spectrometry-based proteomics and its application to biomarker discovery programs. Anal Chem 77:1631–1640
7. Xie J, Miao Y, Shih J, He Q, Liu J, Tai YC, Lee TD (2004) An Electrochemical Pumping System for On-Chip Gradient Generation. Anal Chem 76:3756–3763
8. Xie J, Miao Y, Shih J, Tai YC, Lee TD (2005) Microfluidic Platform for Liquid Chromatography-Tandem Mass Spectrometry Analyses of Complex Peptide Mixtures. Anal Chem 77:6947–6953

Liquid Crystal Technique for Measuring Temperature

PETER STEPHAN, E. WAGNER, R. NASAREK
Technical Thermodynamics
Mechanical Engineering Faculty, Darmstadt University of Technology, Darmstadt, Germany
pstephan@ttd.tu-darmstadt.de,
nasarek@ttd.tu-darmstadt.de

Synonyms

Thermochromic liquid crystals; TLCs

Definition

Thermochromic liquid crystals (TLCs) are a mixture of organic chemicals which have an optical active twisted molecular structure. Within a certain range of temperature they react to changes in temperature by changing color, when illuminated with white light. These temperature-dependent reflections (of a narrow band of wavelengths) are often called *color play*. The color play is reversible and can be calibrated accurately enough for measuring temperature fields with high resolution.

Overview

In the course of the fast growing development of microfluidic devices like ▶ Lab-on-a-Chip, ▶ microreactors, and ▶ micro heat pipes it is essential to develop effective systems for measuring the temperature distribution in the microscale. For example, for observing the ▶ heat transfer in microchannel flows it is a matter of particular interest to know both the temperature distribution along the wall and the temperature distribution in the fluid flow. Conventional ▶ methods for temperature measurements are based on ▶ thermocouples and ▶ resistance thermometers which have a minimum size of about 10 μm and which always interfere with the system to be measured. Contactless methods for measuring temperature, e. g. ▶ infrared thermography, have many advantages. But, according to the fundamental laws of optics, there is a maximum possible limit for spatial resolution in thermal imaging, which lies in the micrometer range for thermal infrared radiation. But it is not possible with infrared thermography to measure the temperature profile of a fluid flow. ▶ Fluorescent thermometry might be a solution for this case. With a system based on thermochromic liquid crystals (TLCs) both options are possible: measuring temperature fields in flows and on solid surfaces. Furthermore the velocity field can be acquired with TLC ▶ tracers and ▶ particle image velocimetry (PIV).
When illuminated, the TLCs reflect the light in a special way: an opalescent color play occurs, strongly dependent on temperature. These light reflections, a narrow band of wavelengths, can be recorded with the usual ▶ color cameras and ▶ microscopic lenses. With a special calibration technique the *RGB* information of the color images is converted into the scalar *hue-value* and from that into a temperature value for each pixel of the frame. Thus, it is possible to determine entire temperature fields with high spatial resolution.

Liquid Crystal Technique for Measuring Temperature, Table 1 Abbreviations

CCD	Charged Coupled Devices
CMOS	Complementary Metal Oxide Semiconductor
FOV	Field of View
HSV	Hue-Saturation-Value
LCT	Liquid Crystal Thermography
PIT	Particle Image Thermometry
PIV	Particle Image Velocimetry
RGB	Red-Green-Blue
TLC	Thermochromic Liquid Crystals
Δt	Time interval
s	Pixel displacement
d_r	Length of a square pixel
a	Thermal diffusivity
L_0	Pitch length
λ_0	Wavelength
$\bar{n}$	Mean refraction index
φ	Angle of incident light

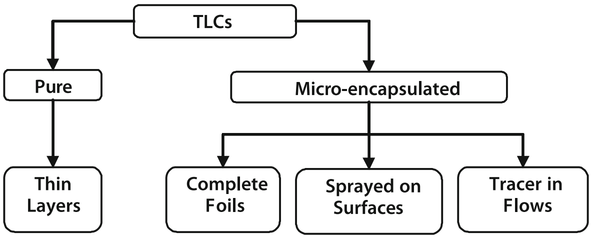

Liquid Crystal Technique for Measuring Temperature, Figure 1 Overview of different TLC packing forms and applications

Researchers operating with the TLC technique have some general options, shown in Fig. 1. The pure (unencapsulated) TLC substance applied in very thin films onto a flat surface offers temperature field measurements with a spatial resolution of about 800 nm. But, unencapsulated TLCs require sophisticated application techniques and the pure TLC substance is very sensitive to UV light and contaminations, particularly oxygen from the air. More common are ► micro-encapsulated TLCs which are stable and easier to handle. They are available as complete foils, in binder mixtures for spray applications and as *tracers*. With the latter it is possible to acquire the temperature distribution in liquid flows.

The activity range of the TLC color play is limited to a certain bandwidth of 0.5 to 30 K. The start temperature of the color play varies from −30 to 120 °C.

Basic Methodology

Temperature measurements using TLCs are based on certain physical properties of the liquid crystal molecules. The technique requires a general experimental setup with illumination and camera and particularly a sophisticated image processing procedure.

Physical Background of Thermochromic Liquid Crystals

Molecular Structure

TLCs are optically active mixtures of organic molecules. The correct name for TLCs used for temperature measurements is ► chiral nematic or ► cholesteric liquid crystals. TLCs are characterized by well-analyzed reflections of visible light (color play) within a definite bandwidth of temperature. A certain temperature leads to reflections of an explicit spectrum of wavelengths, with a local maximum and a narrow bandwidth. Below the start temperature of the color play, called red-start temperature, the TLCs are transparent, when applied in thin layers; the bulk looks milky and white. In this state the molecules, which are elongated like a cigar, have a typical size of about 2 – 5 nm [1], are well ordered and close to each other like in a solid crystal (see Fig. 2a). When the temperature increases the arrangement passes through the ► mesomorphic state, which characterizes the TLCs. The crystals are still optically inactive or transparent, but the molecules are separated in layers.

Above the red-start temperature the molecules are in the cholesteric phase: they are optically active and reflect light selectively and strongly depending on temperature. With increasing temperature the reflected light changes from red to orange, to yellow, green and blue. The molecules are now arranged in layers, within the alignment is identical. In between two layers the molecule orientation is twisted by a certain angle. Cumulatively, an overall helicoidal architecture is formed, whereas the molecular director traces out a helix in space [2]. The degree of twist is defined by the pitch length L_0, which is the height of the helical structure after one 360° rotation and which is proportional to the wavelength λ_0 of the selective reflected light. This relationship can be described by the ► Bragg diffraction equation:

$$\lambda_0 = L_0 \cdot \bar{n} \cdot \sin\varphi\,, \qquad (1)$$

where $\bar{n}$ is the mean refraction index and φ is the angle of the incident light beam normal to the surface [2].

If the temperature continues to increase, the molecular structure of the helix disbands and the molecules are uniformly distributed like in an isotropic liquid. Above this so-called clearing point the crystals are optical inactive

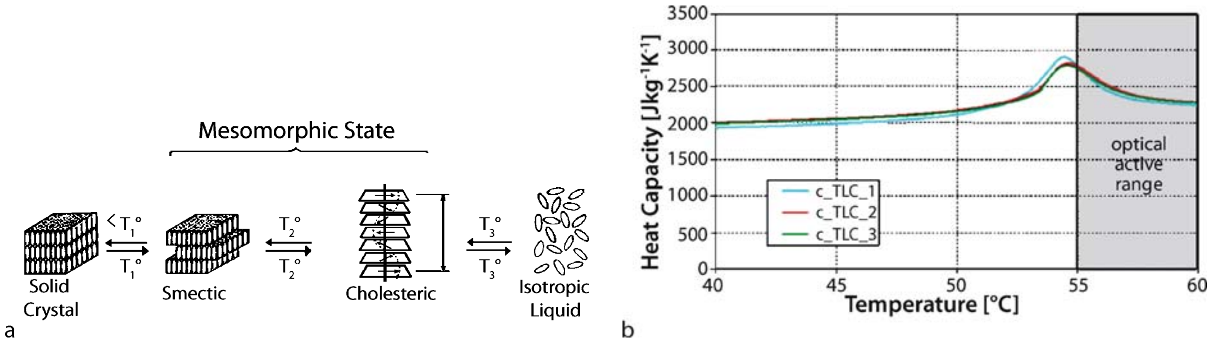

Liquid Crystal Technique for Measuring Temperature, Figure 2 (**a**) Different states of the TLC molecule structure with increasing temperature [2]. (**b**) Heat capacity of pure TLC substance R55C5W as a function of temperature (three different samples)

again. Exceeding this temperature might lead to a permanent damage of the TLCs, depending on time and extent of the overheating.

In Fig. 2b the ▶ heat capacity of a pure TLC substance is plotted as a function of temperature. There is a noticeable peak of the heat capacity just before the red-start temperature caused by the heat of fusion. When numerical modeling of the TLC layer is required, this dependency on temperature has to be taken into account.

Temperature Range and Bandwidth

Red-start temperature and bandwidth of TLCs are important criteria when designing a TLC application of temperature measurements. As a manufacturer of TLCs, the Hallcrest Company provides a large assortment of mixtures with red-start temperatures between 12 and 120 °C and with bandwidth between 1 and 20 K. The designation R50C10W, for example, classifies a TLC mixture with a red-start temperature of 50 °C and a bandwidth of 10 K.

Encapsulation and Application Techniques

According to the requirements of the experiment, different TLC applications can be chosen, depending on lateral or temporal resolution and suitability of the technique. High lateral resolution of about 800 nm can be achieved when the pure TLC substance is applied as a thin film directly onto the surface to be observed.

However, the pure TLC substance is very sensitive to UV light and contamination with air and other substances. Without protection the pure substance undergoes fast ▶ aging and will be unusable after some hours. Therefore, TLCs are most commonly used within ▶ micro-encapsulation. Mixed with a binder the TLC capsules can be applied onto a surface via an airbrush. Complete adhesive foils produced with micro-encapsulated TLCs are available for measuring the surface temperature with reduced lateral resolution. Another different technique is accessible when micro-encapsulated TLCs are dissolved in a liquid. Thus, it is possible to determine the temperature field within a fluid. In general the capsules reduce the lateral resolution; tracers in liquids for example have a minimum resolution of about 100 μm.

Hardware and Experimental Setup

When designing an experiment for measuring temperature fields with TLCs, a basic hardware setup is needed which is exemplarily shown in Fig. 3. In general two different setups are possible. On the left side of Fig. 3 a thin metallic ▶ heating foil is used for observing the heat transfer from a hot wall to cold liquid. On the back side of the heating foil a thin layer of TLCs is applied which displays a temperature-dependent color play. On the right side of Fig. 3 small TLC capsules are dissolved in the liquid. Here the TLCs respond to the temperature of the liquid. Every particle displays a certain color which is a function of the temperature at the particular position and time.

In both cases the TLCs require bright illumination of white light, while the system should be shielded from unwanted heat input. ▶ Cold light sources with ▶ fiber optic cables are a common possibility. To ensure high lateral resolution of the temperature field the color play can be recorded with modern color cameras through microscopic lenses. Thus, the lateral resolution of the surface temperature measurements depends on the magnification of the optics and on the capsule size of the TLCs. When TLCs are used for temperature measurement in liquids, the magnification and the density of the TLC capsule seeding determine the lateral resolution. The temporal resolution depends on the camera speed and on the thermal inertia of the TLC assembly.

Application Techniques of TLCs

The application techniques of TLC films and tracers are some of the most important criteria when designing an experiment. Often much experience is required, especially when using unencapsulated TLCs.

TLC Films

The left side of Fig. 3 shows a TLC layer composition for observing the temperature distribution from the back side of a thin heating foil. The thickness of the heating foil determines when microscale effects should be observed, due to lateral heat conduction. Since metal foils have a very high ► reflective index it is hard to filter out the light reflections from the TLCs – when no background is used. The Hallcrest Company provides a black lacquer which can be applied via an airbrush to avoid light reflections. Another very thin and absolute homogenous layer of black paint can be applied by rubbing of graphic stripes from the Alfac Company. The TLC layer itself can also be applied via an airbrush when micro-encapsulated TLCs are used in combination with a binder. The technique requires some experience since the capsules tend to form porous structures within relatively thick layers. The lateral resolution is therefore reduced. However, the TLC layer is stable, and the TLCs are protected against contamination from the environment. Complete TLC sheets with black background, protective foil and adhesive for binding onto surfaces are available from different distributors. These foils are the first choice, if high lateral resolution is not needed. If very high lateral resolution in the sub-micrometer range is required, accurate measurements are possible with a thin layer of unencapsulated TLCs. The technique is quite sophisticated and requires some experience.
In the following a special technique is described, which was developed in the authors' institute and was applied in [3] and [4]. For realizing a thin film, the surface is previously heated up above the red-start temperature of the TLC substance. Then a small droplet of the substance is placed and distributed with a paintbrush while controlling the homogeneity of the color play with the naked eye. After this, a 12 μm thin polyester sheet is placed to cover the TLCs and to ensure an almost homogenous thickness due to capillary forces. While doing so, the polyester sheet must be *rolled* over the TLCs to avoid any air bubbles inside the TLCs. The TLCs have to be applied and calibrated for every experiment due to effects of aging, contamination and flowing of the film.
The group of David Kenning also did extensive studies in the 1990s using a thin film of pure TLC substance applied with a paintbrush on the back side of a 100 μm thick stainless steel foil [5].

TLC Tracers

When used in encapsulated form, TLCs can be applied as tracer particles. By means of the reflected wavelength it is possible to obtain the temperature of the particles. This method is called *PIT* (► particle image thermometry) and was first implemented by Rhee et al. [6] in the form of expertise through the human eye. Quantitative temperature measurements with TLCs in liquids were first performed by Dabiri and Gharib [7].
There are several things which should be borne in mind before using encapsulated TLCs. It is important to choose a working liquid which has a density close to that of the TLCs (1.1 – 1.2 g/ml) and does not chemically attack the polymer shell of the TLCs. Water or a mixture of water and glycerin are often used as a working liquids. The ideal concentration of TLCs in a liquid depends on the kind of illumination, the measurement depth and other factors. When ► volume illumination is used as shown in Fig. 3, an excess concentration leads to a low signal-to-noise ratio due to disturbing reflections of TLCs which are out of the camera focus, while a concentration which is too low results in a decrease of the spatial resolution. The chosen particle diameter depends on the magnification, the optical resolution of the camera and the size of the ► FOV (field of view). Note that TLCs with small diameter offer better thermal response character while bigger TLCs reflect more light. The diameter of the TLC should be approximately 3 – 4 pixels of the investigated digital image.
In the main, flow visualization with TLCs offers some elementary advantages. It is a non-intrusive measurement technique, the TLCs are easy to handle, the measurement is nearly instantaneous and the TLCs can also be used as tracers for 2D and 3D micro PIV to determine the velocity profile.

Illumination

Most suitable for the illumination of the TLCs is white light, while infrared and ultraviolet radiation should be avoided. The effect of different light sources on the calibration curves was analyzed in [8]. Especially in micro applications with high temporal resolution a strong light source is needed which might lead to photon absorption through the background and thus to unwanted heat input. A pulsed light source without infrared and ultraviolet radiation minimizes this effect. It is well known that the angle between the camera and the illumination axis has an influence of the reflection properties (e. g. [9]). Furthermore it is important to avoid non-uniform illumination; otherwise the color play of the TLCs also depends on their location within the *FOV*.

L

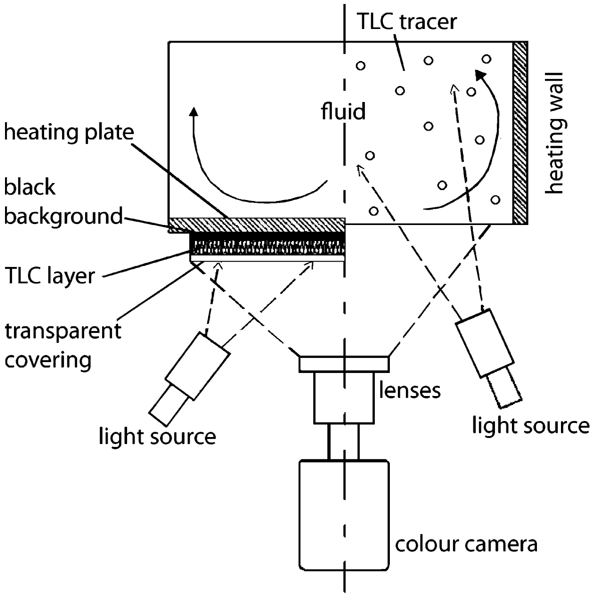

Liquid Crystal Technique for Measuring Temperature, Figure 3 Example of a heat transfer experiment between hot wall and cold fluid. Left: observing the wall temperature distribution with a thin layer of TLCs. Right: observing the temperature distribution in the fluid with TLC tracers

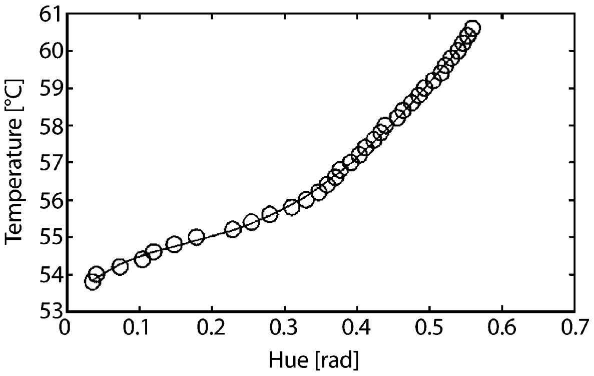

Liquid Crystal Technique for Measuring Temperature, Figure 4 Temperature-hue calibration curve for R55C5W, applied as a thin layer of pure TLC substance

Generally there are two possibilities for the illumination of flows whereby the most common is the illumination with a ▶ light sheet perpendicular to the camera axis. Especially in micro applications it is often not possible to generate a light sheet with a thickness of a few micrometers or there is no optical access. For that reason the whole volume is illuminated and the ▶ measurement depth is defined by the ▶ depth of field of the optical setup.

General Experimental Procedure

After setting up the experimental assembly a typical procedure has to be undertaken which leads to sequences of temperature fields.

Calibration

Qualitative observations of the TLC color play are possible with the naked eye. But for precise temperature field analysis an optical–electronic calibration process is required where the TLC color play has to be analyzed at a series of different temperatures. This procedure should be carried out by slow heating of the system, to ensure a homogeneous temperature distribution inside the *FOV*. At various temperature levels single pictures are recorded and saved in connection with the actual temperature recorded by thermocouples e. g.

It has to be noted that in situ calibration is absolutely necessary for every experimental setup. If pure TLC substance is used, it must be applied fresh by taking into account the purity of all substances and materials. The light source intensity, the angle of illumination and all camera parameters must be set before the calibration procedure. This is important, since small variations of these parameters can falsify the measurement results in a wide range.

Image Processing

Since all recorded frames from the color camera are saved to hard disk, the color information is available in ▶ RGB matrixes (red, green, blue). A common way of color analysis is available by the use of the ▶ HSV color space. For this, a color is given by the hue (H), the saturation (S) and the value of the brightness (V). The hue value can be interpreted as an angle in the HSV color space. The corresponding colors vary from red through yellow, green, cyan, blue, magenta, and back to red. The *RGB* information can be converted into hue with a certain formula in such a way that the color information is available in the form of a scalar:

$$hue = \arctan \frac{\sqrt{3}(G-B)}{2R-G-B} \qquad (2)$$

Other equations for transformation of the *RGB* values to the *HSV* values are available and their influences on the measurement accuracy are discussed by Hay et al. [10]. In Fig. 4 the hue values are plotted versus the corresponding temperatures for TLCs with an activity range from 55 to 60 °C. A polynomial is fitted through the measurement points and finally describes the dependence of the hue values on the temperature.

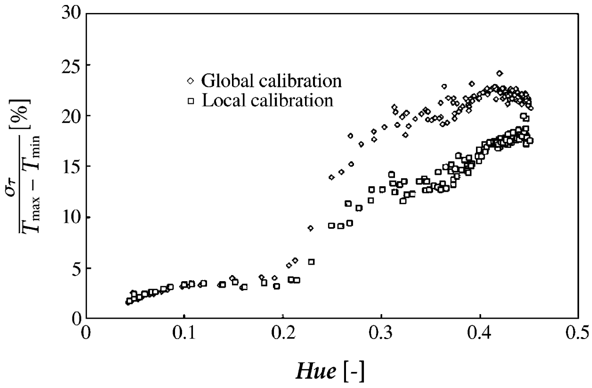

Liquid Crystal Technique for Measuring Temperature, Figure 5 Normalized standard deviation of temperatures calculated with local and global calibration curves under isothermal properties for encapsulated TLCs in liquid

A problem occurring is the deviation of the reflected hue values at isothermal conditions which is caused by several factors (see Sect. *measurement accuracy*). To decrease the position-dependent errors like illumination or image acquisition, a local calibration can be done. Hereby the *FOV* is divided in ►interrogation areas and a temperature–hue calibration curve is generated for every interrogation area. The improvement of the measurement signal for encapsulated TLCs suspended in water is shown in Fig. 5. The deviation of the indicated temperatures under isothermal conditions can be reduced.

Special Image Processing for Encapsulated TLC Tracers in Liquids

The potential of the simultaneous estimation of the temperature and the velocity distribution in a liquid is a big advantage of the TLC measurement technique. The procedure is shown in Fig. 6.

PIT – Particle Image Thermometry

The acquired *RGB* images are transformed into ►HSV images and the intensity information is taken for the detection of the particles. Before that, the intensity image is pre-processed by classic image operations such as ►background subtraction and ►low-pass filtering. Particle detection can be done by a ►threshold filter or by the estimation of local maxima. With the location of the particles and their corresponding hue values from the HSV image, a location-dependent temperature is calculated with the according (local) calibration polynomial(s). Generally the hue values of the TLCs and thus the calculated temperatures are afflicted with errors (see Sect. *measurement accuracy*). To enhance the measurement results, the hue values have to be post-processed. One possibility is ►temporal averaging where several pictures of the same area are taken at different times. Hence the investigated flow has to be time independent. Another possibility to decrease the deviation of the hue values is ►local filtering of the image. Common filters for this purpose are ►mean filter, ►Gaussian filter and ►median filters. Note that filtering always leads to loss of resolution.

PIV – Particle Image Velocimetry

To obtain the velocity field with the *PIV* method (see also ►Micro-PIV-Based Diffusometry) two images with a short time interval Δt are applied. It is possible to use the same images for the estimation of the temperature and the velocity fields (see Fig. 6). Therefore intensity images are created of the RGB images, which are pre-processed as described above and divided into interrogation areas. The two-dimensional cross correlation of related interrogation areas leads to the pixel displacement in the measurement plane direction s, and with the length of a square pixel d_r and time interval Δt the velocity vector can be calculated with the formula:

$$v = s \cdot \frac{d_r}{\Delta t} \tag{3}$$

Measurement Accuracy

In [3] the maximum occurring ►standard deviation of the hue values is estimated to 5% of the activity range. This has been conducted for a thin film of unencapsulated TLCs on a flat surface.

Park [11] found a standard deviation of up to 20% of the activity range for encapsulated suspended TLCs. This relatively high deviation can be minimized with the above mentioned image processing techniques to maximum of 10%.

The deviation of the reflected hue values of the TLCs at isothermal conditions and therefore the uncertainty of the temperature measurement is caused by several factors, as discussed below.

Non-Uniformity of the Manufactured Encapsulated TLC Particles

This occurs due to variations in the chemical composition, variation of the thickness of the polymer shell, and ►residual stress due to the encapsulation process and results in different reflective properties [11].

L

Illumination and Viewing Angles

The angle between the optical and the illumination axes affects the color response of the TLCs. This has been observed by several authors (e. g. [9]). Furthermore a non-uniform illumination results in position-dependent deviation of the hue values.

Thermochromic Liquid Film Thickness

When thin films of TLCs are used the thickness is a deciding factor for the quality of the color play. Layers greater than 100 μm appear misty due to reflections from deeper molecules, and very thin layers (less than 10 μm) display too low an intensity of the color information. Around 20 μm is an ideal thickness for unencapsulated TLCs and around 50 μm for encapsulated layers.

TLC Concentration in Liquids

If the concentration of the TLCs in the suspension is too low, a loss in spatial resolution occurs while a suspension with too many TLCs leads to a high noise.

Response Time

While the response of the TLCs themselves lies in the range of about a millisecond [12, 13] most of the signal attenuation and phase shift is caused by heat conduction and by the capacity of the TLC and capsule material. Kobayashi and Saga [14] performed numerical calculations of the dynamical heating of the TLCs.

Hysteresis and Aging

If the particles are heated above their maximum activity temperature, they are damaged and a ►hysteresis of the temperature–hue values of the heating and cooling gradient appears (e. g. [15, 16]). In [3] calibration curves were recorded for the same layer of unencapsulated TLCs after 1, 10, and 20 days, which led to a temperature uncertainty of around 40% of the activity range.

Digital Resolution

Since the R, B, and G values are digitized by the image acquisition, they have a restricted resolution of 8 bits (for most digital cameras). Therefore the hue value, which is a function of the R, B, G values (Eq. 2), has a definite uncertainty. Wiberg and Lior [16] and Behle et al. [9] stated a resulting temperature uncertainty of 1% of the activity range due to the digital resolution. Limitation of this uncertainty can be achieved through illumination with a wide color spectrum [8] and proper adjustments of the camera.

Key Research Findings

In this article applications with TLCs for high temporal and spatial resolution are presented for thin TLC films and for TLC tracers.

Surface Temperature Measurements with TLCs

Lateral Resolution

Very high lateral resolution is one of the most important criteria when using unencapsulated TLC films. To the authors' knowledge there is no other technique which provides higher lateral resolution in the sub-micrometer range.

Figure 7 shows the hue value frequency of an unencapsulated TLC layer in comparison to a more common layer with micro-encapsulated TLCs (►micro-encapsulation). While unencapsulated TLCs display a clear-cut signal for a homogenous temperature distribution, micro-encapsulated TLCs show a much more attenuated and blurred signal. This is due to the empty space between the capsules which displays no color information and due to the reflections on the capsule surface.

With unencapsulated TLCs in [3] the microscale cooling effect of an evaporating liquid meniscus could be visualized. Within a width of about 40 μm a distinctive temperature drop of about 0.2 K could be observed (see Fig. 8). The lateral resolution in this experiment was 800 nm.

Temporal Resolution

At present it is important to know if the TLC technique is also suitable for observing dynamic processes with high frequencies, e. g. nucleate boiling. In this case the thermal inertia of all substances and materials close to the nucleation site plays an important role. The composition of the heated wall consisting of a thin metallic foil, a black background color, the TLC layer and a transparent covering obviously has an influence on the time response of the entire system. Kenning did extensive studies of nucleate boiling on electrically heated thin metallic foils [5]. He used unencapsulated TLCs to observe the temperature field on the back side of these foils and found that the maximum bubble departure frequency, which can be followed by TLCs, lies between 0 and 20 Hz. Ireland and Jones determined a time delay of the TLC color play appearance during heating rates of 2000 K/s and more [12]. They used a blackened aluminum foil which was electrically heated and laminated with a mixture of 10 μm TLC capsules and PVA binder. They found that the measured time delay of about 3 ms must be a consequence of both conduction as well as an intrinsic physical lag. In [13] the ►frequency response of a pure TLC film was inves-

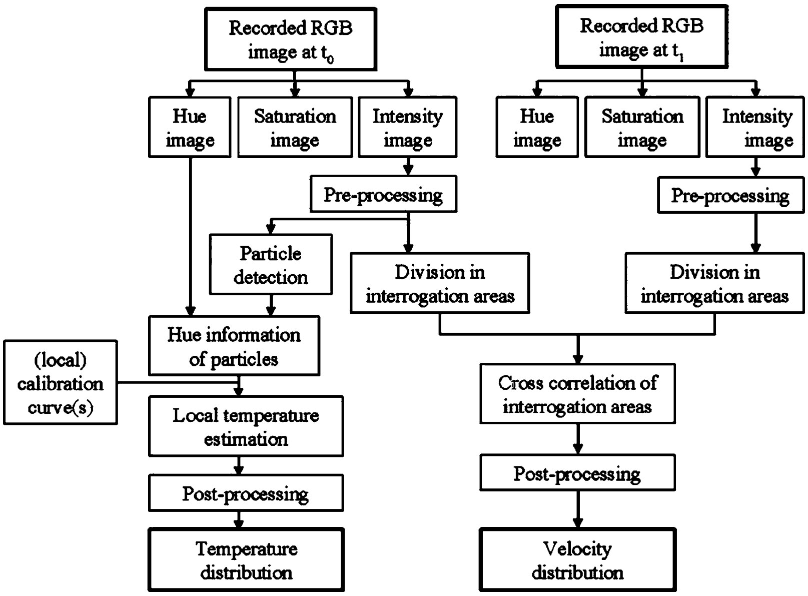

Liquid Crystal Technique for Measuring Temperature, Figure 6 Flow chart of simultaneous measuring of temperature and velocity

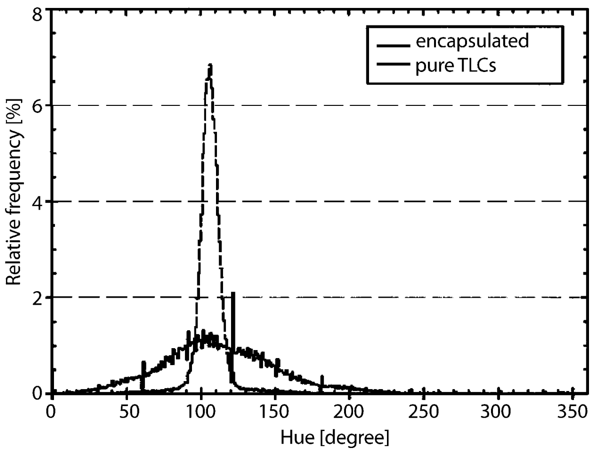

Liquid Crystal Technique for Measuring Temperature, Figure 7 Hue value–frequency distribution of two different TLC layers applied onto a flat surface with a homogeneous temperature [3]

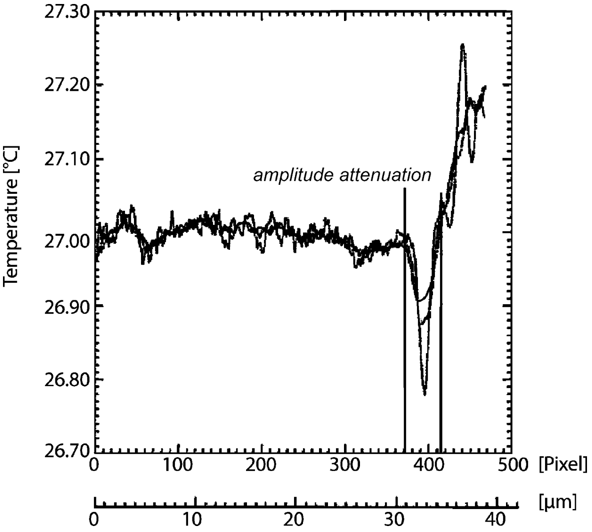

Liquid Crystal Technique for Measuring Temperature, Figure 8 Local cooling effect of an evaporating liquid meniscus [3]

tigated using an electric resistance heater with harmonic oscillations within a frequency band of 3 to 70 Hz. It was found that for frequencies above 1 Hz the TLCs do not display the actual heater temperature due to amplitude attenuation and phase shift; a maximum frequency of 70 Hz could be analyzed. In Fig. 9 the temperature time progression simulated with a numerical approach is displayed for different positions along the thickness of the layer assembly.

While the highest amplitude is computed in the centre of the heating foil (rectangle label), the amplitude decreases rapidly with increasing distance from the heater plate: in the centre of the TLC layer, where the measurement fits best with the numeric result, the amplitude is only about 60% of the heating foil amplitude.

Summarizing these results, it can be said that the dominating effect of amplitude attenuation and phase shift is a problem of heat conduction inside the TLC system. The

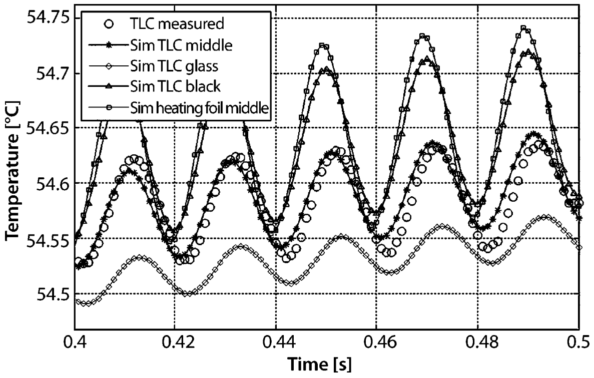

Liquid Crystal Technique for Measuring Temperature, Figure 9
Simulated temperature progression inside a 20 μm thick TLC [4]

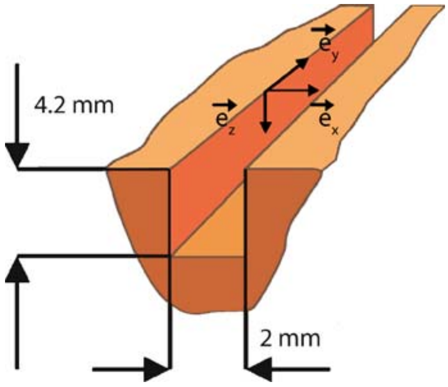

Liquid Crystal Technique for Measuring Temperature, Figure 10
Sketch of the mini channel

problem can be simulated by simple models of heat conduction. A residual time shift between the numeric and experimental results of about 1 ms might be caused by the averaging process over the TLC layer thickness or by an intrinsic physical lag of the TLC molecule orientation.

Flow Visualization with Encapsulated TLCs

The application of TLCs in liquids is well known for bigger fields of view and slower flow rates and was employed by Dabiri and Gharib [7]. Typical investigated processes are free convection in a tube or crystallization of water (e. g. [6]). Only a few experiments have taken place with a high lateral resolution. Richards and Richards [17] put TLCs in a water droplet which was cooled by an air flow. The diameter of the droplet was less than 1 mm and they investigated the temperature profile with a spatial resolution of 100 μm. They used volume illumination and a *CCD camera* with a depth of field of 100 μm.

The free convection of water with suspended TLCs in a small vertical gap with dimensions of $1.1\times 10\times 10\ \text{mm}^3$ $(b\times d\times h)$ is considered by Heiland et al. [18]. Heating of one side wall and cooling of the other led to a convective flow of the liquid. Heiland et al. [18] used a ► light sheet with a thickness of 1 mm for illumination and a ► CCD camera for image acquisition. The temperature and the velocity field were investigated with TLCs as tracer particles with a spatial resolution of approximately 150 μm for temperature and 80 μm for velocity field. The maximal measured velocity was 0.1 mm/s.

Liquid flows with higher velocities were investigated by Park [11]. He used two xenon flash lamps which were fired at 15 Hz each. The flash lamps were synchronized with a CCD RGB camera. Park was able to measure the temperature and the velocity field of a wake behind a cylinder with a spatial resolution of 280 μm and a measurement frequency of 30 Hz.

The group of Rudolf von Rohr [19, 20] used encapsulated TLCs to investigate a liquid flow over a wavy bottom wall. For the *PIV* measurements a Nd:YAG laser as pulsed light source and a 12 bit monochrome camera were used. Within the same *FOV* ($35\times 45\ \text{mm}^2$), a *CCD* color camera acquired the color distribution of the TLCs illuminated by a stroboscope. Both the laser light and the white light were focused with lenses to *light sheets* and triggered so that the *FOV* was illuminated alternately. The images were acquired with a frequency of 15 Hz [20].

In the laboratories of the authors simultaneous PIT/PIV measurements with TLCs are performed and a flow in a mini channel is investigated (Fig. 10). The illumination is done by two 250 W halogen ► cold light sources and the images are acquired by a high-speed color ► CMOS camera with a long-distance microscope. With this measurement setup, measurements with a frequency of 1000 Hz are possible. The camera can be moved perpendicular to the streaming direction in micrometer steps whereby it is possible to measure on different layers and 3D temperature fields can be obtained (Fig. 11a) under steady flow conditions. The velocity fields (Fig. 11b) are estimated simultaneously and a spatial resolution of 100 μm is achieved for both the velocity and the temperature fields.

Future Directions for Research

Particularly the temperature measurement with encapsulated TLCs shows extensive deviation in the reflected wave length. To minimize this, the illumination technique should be enhanced to receive a uniform illuminated ► FOV. Furthermore strong illumination is needed for applications with high lateral and temporal resolution. Another problem is the heat introduced by the illumination especially when continuous volume illumination is used. A pulsed illumination decreases this effect.

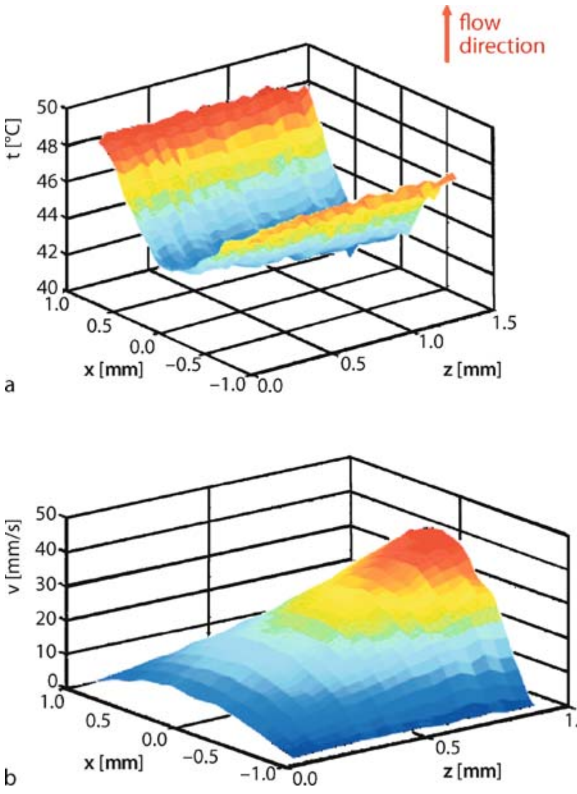

Liquid Crystal Technique for Measuring Temperature, Figure 11 (**a**) Temperature profiles on several *z*-positions. (**b**) Velocity profiles on several *z*-positions

When encapsulated TLCs are used in flows with high temperature gradients, a fast thermal response time is needed. To study the possible use of encapsulated TLCs, their thermal response time should be investigated.

The resolvable spatial resolution of temperature measurements in liquids mainly depends on the concentration of the TLCs in the suspension, the size of the averaging area (interrogation area) and the size of the TLC particles. To decrease the size of the averaging area, a better hue response of the temperature of the TLCs is needed. Since the concentration of the *encapsulated* TLCs in the suspension is restricted by the signal-to-noise ratio, only a smaller diameter of the particles can improve the resolvable spatial resolution.

Cross References

► Fluorescent Thermometry
► Heat Tansfer in Microchannel Flows
► Lab-on-a-Chip (General Philosophy)
► Methods for Temperature Measurements
► Micro Heat Pipes
► Microscale Flow Visualization
► Droplet Microreactors
► Micro-PIV-Based Diffusometry

References

1. Jakli A, Saupe A (2006) One- and Two-dimensional Fluids, Properties of Smectic, Lamellar and Columnar Liquid Crystals. Taylor & Francis, New York, London
2. Parsley M (1991) Hallcrest Handbook of Thermochromic Liquid Crystal Technology. Hallcrest, Glenview
3. Höhmann C (2004) Temperaturmessverfahren zur räumlich hochauflösenden Untersuchung des Wärmetransports an einem verdampfenden Flüssigkeitsmeniskus. Dissertation TU Darmstadt, D17, Shaker Verlag, Aachen
4. Wagner E, Sodtke C, Schweizer N, Stephan P (2006) Experimental study of nucleate boiling heat transfer under low gravity conditions using TLCs for high resolution temperature measurements. Heat Mass Transf 42:875–883
5. Kenning DBR (1992) Wall temperature patterns in nucleate boiling. Int J Heat Mass Transf 35:73–86
6. Rhee HS, Koseff JR, Street RL (1984) Flow visualization of a recirculating flow by rheoscopic liquid and crystal techniques. Exp Fluids 2:57–64
7. Dabiri D, Gharib M (1991) Digital particle image thermometry: The method and implementation. Exp Fluids 11:77–86
8. Anderson MR, Baughn JW (2005) Liquid-Crystal Thermography: Illumination Spectral Effects. Part 1-Experiments. J Heat Transf 127:581–587
9. Behle M, Schulz K, Leiner W, Fiebig M (1996) Color-Based Image Processing to Measure Local Temperature Distributions by wide-Band Liquid Crystal Thermography. Appl Sci Res 56:113–143
10. Hay JL, Hollingsworth DK (1996) A Comparison of Trichromic Systems for Use in the Calibration of Polymer-Dispersed Thermochromic Liquid Crystals. Exp Therm Fluid Sci 12:1–12
11. Park HG (1998) A Study of Heat Transport Processes in the Wake of a Stationary and Oscillating Circular Cylinder Using Digital Particle Image Velocimetry / Thermometry. PhD thesis, California Institute of Technology, Pasadena, California
12. Ireland PT, Jones TV (1987) The time response of a surface thermometer employing encapsulated thermochromic liquid crystal. J Phys E Sci Instrum 20:1195–1199
13. Wagner E, Stephan P (2007) Frequency response of a surface thermometer based on unencapsulated TLCs. Exp Fluid Therm Sci 31:687–699
14. Kobayashi T, Saga T (1998) Time Response of Microcapsulated Liquid-Crystal Particles. Heat Transf Jpn Res 27(5):390–398
15. Baughn JW, Anderson M R, Mayhew J E, Wolf J D (1999) Hysteresis of thermochromix liquid crystal temperature measurement based on hue. J Heat Trans 121:1067–1072
16. Wiberg R, Lior N (2004) Errors in thermochromic liquid crystal thermometry. Rev Sci Inst 75:2985–2994
17. Richards CD, Richards RF (1998) Transient temperature measurement in a convectively cooled droplet. Exp Fluids 25:392–400
18. Heiland HG, Wozinak G (2003) 3D Particle Tracking Thermometry for Thermo-Convective Flow Analysis. Proceedings in Applied Mathematics and Mechanics 3:386–387
19. Günther A, Rudolf von Rohr P (2002) Structure of the temperature field in a flow over heated waves. Exp Fluids 33:920–930

L

20. Kruse N, Rudolf von Rohr P (2005) Isothermal and Non-Isothermal Turbulent Flow over solid Waves: Transport and Structure, PhD Thesis, ETH Zürich, Switzerland, Diss. ETH 16031
21. Hiller WJ, Koch S, Kowalewski TA, Stella F (1993) Onset of Natural Convection in a Cube. J Heat Trans 13:3251–3263

Liquid Extraction

► Lab-on-a-Chip Devices for Sample Extractions

Liquid Handling

► Flow by Surface Acoustic Waves

Liquid–Liquid Electroosmotic Flow

► Electrokinetic Two-Phase Flows

Liquid–Liquid Stratified Flow in Microchannels

TECK NENG WONG, CHENG WANG, YANDONG GAO, NAM-TRUNG NGUYEN, CHUN YANG, KIM TIOW OOI
School of Mechanical and Aerospace Engineering, Nanyang Technological University, Singapore, Singapore
mtnwong@ntu.edu.sg, mntnguyen@ntu.edu.sg

Synonyms

Two-fluid stratified flow

Definition

When two liquids co-flow in a microchannel, an interface forms between them due to the low Reynolds number. This is known as liquid–liquid stratified flow.

Overview

Liquid–liquid stratified flow in microchannels is often used in biological analysis, such as during ion exchange or solvent extraction from one phase to another phase [1]. For liquid flow in microfluidics, the Reynolds number is small and the flows are always laminar. Laminar fluid diffusion interfaces (LFDIs) are generated when two or more streams flow in parallel within a single microstructure [2], as shown in Fig. 1a. For laminar streams flowing side by side, diffusion is the only mechanism by which molecules can pass from one phase to another. The diffusion through the phases is a function of diffusion coefficient and distance. The mixing time is proportional to the square of the distance traveled. The mixing time can be reduced effectively by decreasing the diffusion distance. Much research has studied ways to promote mixing at the small scale [3]. However, non-mixing in microchannels can be very useful as well. Because only diffusion occurs between different streams of flow, it is used for extraction or separation in biological analysis. Diffusion-based microfluidic devices, such as the T-sensor® and the H-filter®, have been developed for commercial use by Micronics, Inc.

In an extraction or separation of biological analysis, the two liquids used are biological liquid and aqueous reagent [4]. These two liquids are very different in properties such as density, surface tension and viscosity. The mismatch of the viscosity of the two liquids can be problematic in diffusion-based applications. The liquid with higher viscosity will spread more widely in the channel while having a smaller velocity; the liquid with lower viscosity flows at a larger velocity with a smaller fraction of the channel volume. Consequently, the resulting liquid–liquid interface deviates from the central position, shown in Fig. 1b. This applies when the two flows have the same volumetric flow rate. The unmatched viscosity also affects the diffusion in terms of the residence time. The average residence time of the more viscous liquid increases, while that of the less viscous liquid decreases. To overcome this problem, one method is to measure the viscosity of one liquid, then add viscosity-enhancing solute to the less viscous liquid so as to match the viscosity. Another method, the *flow-rate-ratio* method, is used to control the ratio of the volumetric flow rate of the two liquids. Hydrodynamic spreading and narrowing can be controlled by adjusting the flow rates of the two co-flowing liquids. However, the unmatched average residence time problem still remains unsolved, because the less viscous fluid flows faster and has a shorter average residence time within the channel.

As dimension shrinks, the surface area to volume ratio increases by orders of magnitude. Many forces or fields, which are not significant in macroscale fluid flow, become important in manipulating and controlling fluids in microfluidics. These effects include the thermal capillary effect, electroosmosis, surface tension and magnetohydrodynamics. These forces or fields provide us with alternative means to control the microfluidic flow behaviors. In this article, we propose a theoretical model to predict the interface position of two liquids flowing through a rectangular cross-section microchannel, as shown in Fig. 2. One liquid is a conducting liquid with high electroosmotic mobility and the other is a nonconducting liquid with low electroosmotic mobility. When an external

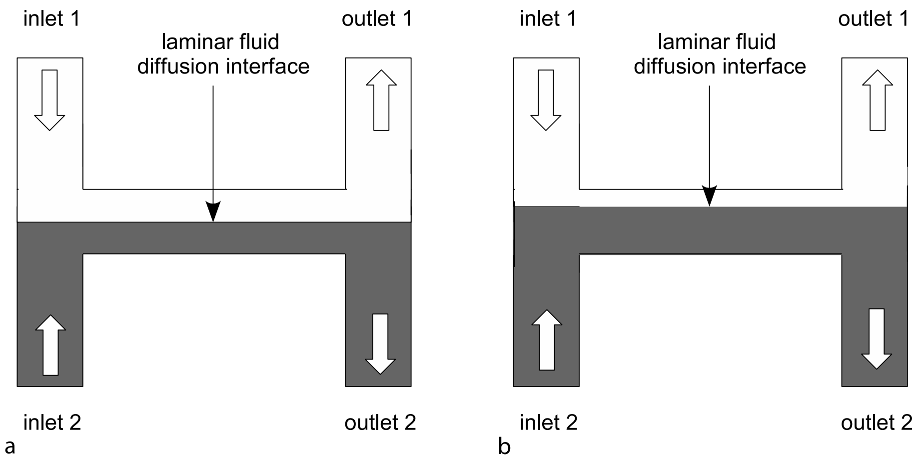

Liquid–Liquid Stratified Flow in Microchannels, Figure 1 Schematic of liquid–liquid interface in an H-shaped microchannel: (**a**) the laminar fluid diffusion interface (LFDI) at the center of the microchannel; (**b**) LFDI deviating from the center

electric field is applied across the conducting liquid, electroosmotic forces will be generated and the velocity of the conducting liquid can be regulated depending on the direction and strength of the applied electric field. We will show that by adjusting the applied electric field, the interface position can be precisely controlled. Analytical formulas are presented for the interface position as a function of the ratio of the input flow rates, the ratio of the shear viscosities, the aspect ratio of the channel, the applied electric field and concentration of the conducting liquid. Predictions from the mathematical model are validated by experimental results.

Basic Methodology

Theory

Consider a two-liquid system, in which one is a conducting liquid containing ionic charges in contact with a charged smooth solid wall and the other is a nonconducting liquid. It is assumed that the two liquids are immiscible. A planer interface shape is assumed. Due to the symmetry, only half of the cross-section of the rectangular channel is considered. The half-width of the channel is taken as w. The height is taken as h and the heights of the conducting and nonconducting liquids are denoted by h_1 and h_2, respectively. To analyze this system, a Cartesian coordinate system is used where the origin point is at the intersection of the interface and the symmetric line as shown in Fig. 2.

Electrical Double Layer in the Conducting Liquid

The two liquids move due to both pressure gradient and electroosmotic body force. When the flow is fully developed, at position r, the velocities of two liquids, u_1 or u_2, along the channel are independent of the x-coordinate. The subscripts 1 and 2 denote the conducting and nonconducting liquids, respectively. Provided that the aspect ratio $\chi = h/2w$ is large, the pressure gradient at the fully developed region is uniform across the channel. Symmetric electrolyte is considered as the conducting liquid. The electric potential in the conducting liquid due to a charged channel wall is taken as ψ and the net volume charge density in the conducting liquid as ρ_q. The length scale and velocity scale of the flow are taken as L and V, respectively. The independent variable r and dependent variables u, p, ψ and ρ_q are expressed in terms of the corresponding dimensionless quantities (shown with an overbar) by

$$\begin{cases} r = L\bar{r} & \\ u = V\bar{u} & p = \rho_1 V^2 \bar{p} \\ \psi = \dfrac{k_B T \bar{\psi}}{(z_0 e)} & \rho_q = 2 n_0 z_0 e \bar{\rho}_q \end{cases} \tag{1}$$

where ρ is the liquid density, k_B is Boltzmann's constant, T is the absolute temperature, z_0 is the valence of ions, e is the elementary charge and n_0 is the reference value of the ion concentration.

First we consider the electric potential in the conducting liquid. It is assumed that the electric charge density is not affected by the external electric field due to the thin electrical double layers (EDLs) and small fluid velocity; therefore the charge convection can be ignored and the electric field equation and the fluid flow equation are decoupled [5]. Based on the assumption of local thermodynamic equilibrium, for small zeta potential, the electric potential due to the charged wall is described by the lin-

ear Poisson–Boltzmann equation which can be written in terms of dimensionless variables as

$$\nabla^2 \bar{\psi} = K^2 \bar{\psi} \tag{2}$$

where $K = L\kappa$ is the ratio of the length scale L to the characteristic double-layer thickness $1/\kappa$. Here κ is the Debye–Hückel parameter:

$$\frac{1}{\kappa} = \left(\frac{\varepsilon \mathrm{k_B} T}{2 z_0^2 e^2 n_0} \right)^{1/2} \tag{3}$$

where ε is the relative permittivity of the conducting liquid.

As the channel walls are made of different materials, we specify the zeta potential at the bottom wall is ζ_1, at the sidewall is ζ_2 and at the interface is ζ_3. At the mid-plane $z = 0$, a symmetric condition, $\partial\psi/\partial z = 0$ holds. The solution to the Poisson–Boltzmann equation subjected to the above boundary conditions is obtained as

$$\begin{aligned} \bar{\psi}(\bar{y}, \bar{z}) = \sum_{j=1}^{\infty} \Bigg\{ & \left[\bar{\zeta}_1 \sinh\left(B_j \bar{y}\right) + \bar{\zeta}_3 \sinh\left(B_j \bar{h}_1 - B_j \bar{y}\right) \right] \\ & \times \frac{4(-1)^{j+1} \cos\left(\lambda_j \bar{z}\right)}{(2j-1)\pi \sinh\left(B_j \bar{h}_1\right)} \Bigg\} \\ & + \sum_{p=1}^{\infty} \Bigg\{ 2\bar{\zeta}_2 \left[1 + (-1)^{p+1} \right] \\ & \times \frac{\cosh\left(A_p \bar{z}\right)}{p\pi \cosh\left(A_p \bar{w}\right)} \sin\left(\frac{p\pi}{\bar{h}_1} \bar{y} \right) \Bigg\} \end{aligned} \tag{4}$$

where

$$\begin{cases} B_j = \sqrt{K^2 + \dfrac{(2j-1)^2 \pi^2}{4\bar{w}^2}} \\ \lambda_j = \dfrac{(2j-1)\pi}{2\bar{w}} \\ A_p = \sqrt{K^2 + \dfrac{p^2 \pi^2}{\bar{h}_1^2}} \end{cases}$$

From electrostatics, the normal component of the gradient of the electric potential, ψ, jumps by an amount proportional to the surface charge density, ρ_q^s, that is

$$\rho_q^s = -\varepsilon \frac{\partial \psi}{\partial y} \tag{5}$$

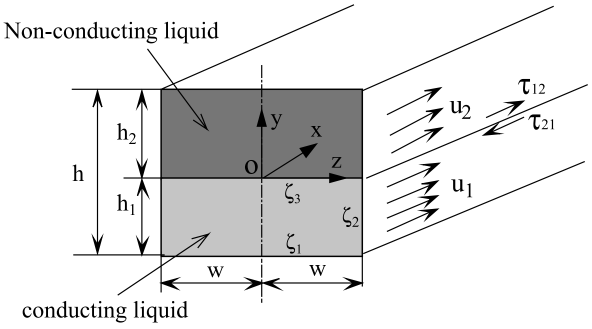

Liquid–Liquid Stratified Flow in Microchannels, Figure 2 Schematic representation of the coordinate system

It is assumed that the gradient of electric potential in the nonconducting liquid vanishes. Using the reference surface charge density as $(\varepsilon \mathrm{k_B} T)/(z_0 e L)$, one obtaines the dimensionless surface charge density at the two-liquid interface as

$$\begin{aligned} \bar{\rho}_q^s(\bar{z}) = & \sum_{j=0}^{\infty} \frac{4(-1)^{j+1} B_j}{(2j-1)\pi} \left[\frac{\bar{\zeta}_3}{\tanh\left(B_j \bar{h}_1\right)} - \frac{\bar{\zeta}_1}{\sinh\left(B_j \bar{h}_1\right)} \right] \\ & \times \cos\left(\lambda_j \bar{z}\right) - \sum_{p=1}^{\infty} \frac{2\bar{\zeta}_2 \left[(-1)^{p+1} + 1 \right] \cosh\left(A_p \bar{z}\right)}{\bar{h}_1 \cosh\left(A_p \bar{w}\right)} \end{aligned} \tag{6}$$

It should be mentioned that the surface charge at the interface, ρ_q^s, is opposite in sign to the volumetric net charge in the EDL region at the vicinity of the interface. From Eq. (6), it can be seen that the contribution of zeta potential at the bottom wall, ζ_1, is relatively small and the contribution of the sidewalls, ζ_2, is also relatively small except when z approaches w. Once the electric potential distribution is known, the volumetric net charge density can be obtained through the relationship

$$\bar{\rho}_q = -\bar{\psi}(\bar{y}, \bar{z}) \tag{7}$$

This volumetric net charge density, Eq. (7), and the interface charge density, Eq. (6), are required to determine the electrostatic force caused by the presence of zeta potential. The bulk electrostatic force is considered as an additional body force exerted on the conducting solution to modify the conventional Navier–Stokes equation. The nonconducting liquid is dragged by the viscous forces from the conducting liquid and the external electrostatic force (E_x) due to the electrokinetic charge density at the interface. If the external electric field varies, such applied electroosmotic body forces will be changed correspondingly. As a result, for a given inlet flow rate, the velocities of the

two liquid depend on the applied electroosmotic force; hence the interface position between the two liquids can be controlled.

Momentum Equation of Two-Liquid Flow

We assume that the two liquids are Newtonian and incompressible and that the Reynolds number ($\mathrm{Re} = \rho_1 LV/\mu_1$, where μ is the liquid viscosity) of the flow is much smaller than unity so that inertia effects on the liquid flow may be neglected. For a fully developed flow, the momentum equation for the conducting liquid becomes

$$\nabla^2 \bar{u}_1 = \mathrm{Re}\frac{\mathrm{d}\bar{p}}{\mathrm{d}\bar{x}} - \mathrm{Re} G_x \bar{\rho}_{\mathrm{q}} \tag{8}$$

where $\mathrm{d}\bar{p}/\mathrm{d}\bar{x}$ is a constant dimensionless pressure gradient. For a fully developed flow, the pressure gradients of the two liquids are equal and G_x is the parameter given as

$$G_x = \frac{2 z_0 e n_0 L E_x}{\rho V^2} \tag{9}$$

For the nonconducting liquid, the momentum equation gives

$$\nabla^2 \bar{u}_2 = \frac{\mathrm{Re}}{\beta}\frac{\mathrm{d}\bar{p}}{\mathrm{d}\bar{x}} \tag{10}$$

where $\beta = \mu_2/\mu_1$ is the dynamic viscosity ratio. The velocities of the two liquids vanish at the lower ($y = -h_1$), upper ($y = h_2$) and side ($z = w$) boundaries. Additionally, at the interface ($y = 0$), matching conditions have to be obeyed. These are the continuities of velocity and shear stress balance, which jump abruptly at the interface due to the presence of surface charge:

$$\begin{cases} \bar{u}_1 = \bar{u}_2 \\ \dfrac{\partial \bar{u}_1}{\partial \bar{y}} = \beta \dfrac{\partial \bar{u}_2}{\partial \bar{y}} - M \bar{\rho}_{\mathrm{q}}^{\mathrm{s}} \end{cases} \tag{11}$$

where

$$M = \frac{\varepsilon k_{\mathrm{B}} T E_x}{z_0 e V \mu}\,.$$

Because of linearity, the velocity of the conducting liquid in Eq. (8) can be decomposed into two parts:

$$\bar{u}_1 = \bar{u}_1^{\mathrm{E}} + \bar{u}_1^{\mathrm{P}} \tag{12a}$$

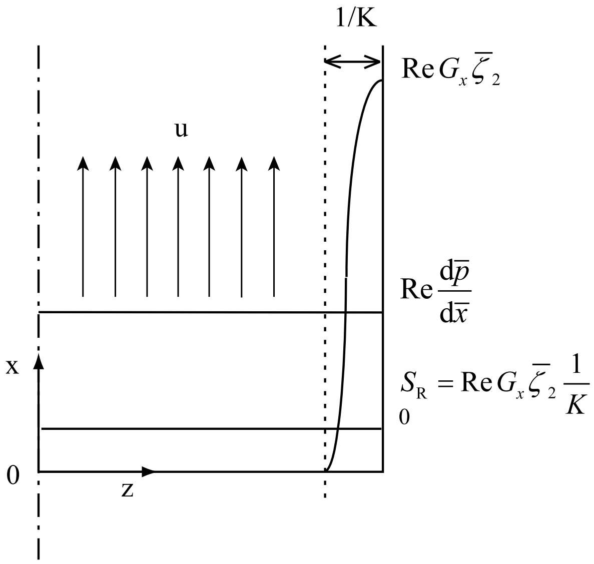

Liquid–Liquid Stratified Flow in Microchannels, Figure 3 Schematic of the meaning of S_{R}

where $\bar{u}_1^{\mathrm{E}}$ corresponds to the velocity component driven by the electroosmotic forces and $\bar{u}_1^{\mathrm{P}}$ corresponds to the velocity component driven by the pressure gradient. Consequently, the velocity of the nonconducting liquid is decomposed as

$$\bar{u}_2 = \bar{u}_2^{\mathrm{E}} + \bar{u}_2^{\mathrm{P}} \tag{12b}$$

where $\bar{u}_2^{\mathrm{E}}$ corresponds to the velocity component influenced by the electroosmotic flow in the conducting liquid and $\bar{u}_2^{\mathrm{P}}$ corresponds to the velocity component influenced by the pressure gradient.

Using the separation of variables method, the analytical velocity components corresponding to the electroosmotic force are obtained as

$$\begin{aligned} \bar{u}_1^{\mathrm{E}}(\bar{y},\bar{z}) = \sum_{j=1}^{\infty} \cos(\lambda_j \bar{z}) \Big\{ b1_j^{\mathrm{E}} \big[\sinh(\lambda_j \bar{y}) \\ - \tanh(\lambda_j \bar{h}_1)\cosh(\lambda_j \bar{y}) \big] \\ - \frac{\Phi_j(\bar{h}_1)\cosh(\lambda_j \bar{y})}{\cosh(\lambda_j \bar{h}_1)} + \Phi_j(\bar{y}) \Big\} \end{aligned} \tag{13a}$$

$$\begin{aligned} \bar{u}_2^{\mathrm{E}}(\bar{y},\bar{z}) = \sum_{j=1}^{\infty} \cos(\lambda_j \bar{z}) \Big\{ b2_j^{\mathrm{E}} \big[\sinh(\lambda_j \bar{y}) \\ - \tanh(\lambda_j \bar{h}_2)\cosh(\lambda_j \bar{y}) \big] \Big\} \end{aligned} \tag{13b}$$

$$\Phi_j(\bar{y}) = -\frac{4\mathrm{Re}G_x\bar{\zeta}_1(-1)^{j+1}\sinh(B_j\bar{y})}{(2j-1)\pi\left(\lambda_j^2-B_j^2\right)\sinh(B_j\bar{h}_1)} + \frac{4\mathrm{Re}G_x\bar{\zeta}_3(-1)^{j+1}\sinh\left(B_j\left(\bar{h}_1-\bar{y}\right)\right)}{(2j-1)\pi\left(\lambda_j^2-B_j^2\right)\sinh(B_j\bar{h}_1)} - \sum_{p=1}^{\infty}\left\{4\mathrm{Re}G_x\bar{\zeta}_2\left[1+(-1)^{p+1}\right] \times \frac{\lambda_j(-1)^{j+1}\sin(p\pi\bar{y}/\bar{h}_1)}{p\pi\bar{w}\left(\lambda_j^2+A_p^2\right)\left[(p\pi/\bar{h}_1)^2+\lambda_j^2\right]}\right\}$$

$$\Phi'_j(\bar{y}) = \frac{-4\mathrm{Re}G_x\bar{\zeta}_1(-1)^{j+1}B_j\cosh(B_j\bar{y})}{(2j-1)\pi\left(\lambda_j^2-B_j^2\right)\sinh(B_j\bar{h}_1)} + \frac{4\mathrm{Re}G_x\bar{\zeta}_3(-1)^{j+1}B_j\cosh\left[B_j\left(\bar{h}_1-\bar{y}\right)\right]}{(2j-1)\pi\left(\lambda_j^2-B_j^2\right)\sinh(B_j\bar{h}_1)} - \sum_{p=1}^{\infty}\left\{4\mathrm{Re}G_x\bar{\zeta}_2\left[1+(-1)^{p+1}\right] \times \frac{\lambda_j(-1)^{j+1}\cos(p\pi\bar{y}/\bar{h}_1)}{\bar{h}_1\bar{w}\left(\lambda_j^2+A_p^2\right)\left[(p\pi/\bar{h}_1)^2+\lambda_j^2\right]}\right\}$$

The velocity components corresponding to the pressure gradient are

$$\bar{u}_1^{\mathrm{P}}(\bar{y},\bar{z}) = \cos(\lambda_j\bar{z}) \sum_{j=1}^{\infty}\left\{\frac{4\mathrm{Re}(-1)^{j+1}}{(2j-1)\pi\lambda_j^2}\frac{\mathrm{d}\bar{p}}{\mathrm{d}\bar{x}}\left[\frac{\cosh(\lambda_j\bar{y})}{\cosh(\lambda_j\bar{h}_1)}-1\right] + b1_j^{\mathrm{P}}\left[\sinh(\lambda_j\bar{y}) - \tanh(\lambda_j\bar{h}_1)\cosh(\lambda_j\bar{y})\right]\right\} \tag{14a}$$

$$\bar{u}_2^{\mathrm{P}}(\bar{y},\bar{z}) = \cos(\lambda_j\bar{z}) \sum_{j=1}^{\infty}\left\{\frac{4\mathrm{Re}(-1)^{j+1}}{\beta(2j-1)\pi\lambda_j^2}\frac{\mathrm{d}\bar{p}}{\mathrm{d}\bar{x}}\left[\frac{\cosh(\lambda_j\bar{y})}{\cosh(\lambda_j\bar{h}_2)}-1\right] + b2_j^{\mathrm{P}}\left[\sinh(\lambda_j\bar{y}) - \tanh(\lambda_j\bar{h}_2)\cosh(\lambda_j\bar{y})\right]\right\} \tag{14b}$$

From the matching condition Eq. (11), the following constants can be obtained:

$$b1_j^{\mathrm{E}} = \beta b2_j^{\mathrm{E}} + \frac{M}{\lambda_j}\bar{\rho}_{\mathrm{q}j}^{\mathrm{s}} - \frac{\Phi'_j(0)}{\lambda_j} \tag{15a}$$

$$b2_j^{\mathrm{E}} = \frac{\frac{M}{\lambda_j}\bar{\rho}_{\mathrm{q}j}^{\mathrm{s}}\tanh(\lambda_j\bar{h}_1) + \frac{\Phi_j(\bar{h}_1)}{\cosh(\lambda_j\bar{h}_1)}}{\tanh(\lambda_j\bar{h}_2) - \beta\tanh(\lambda_j\bar{h}_1)} - \frac{\frac{\Phi'_j(0)}{\lambda_j}\tanh(\lambda_j\bar{h}_1) - \Phi_j(0)}{\tanh(\lambda_j\bar{h}_2) - \beta\tanh(\lambda_j\bar{h}_1)} \tag{15b}$$

$$b1_j^{\mathrm{P}} = \beta b2_j^{\mathrm{P}} \tag{15c}$$

$$b2_j^{\mathrm{P}} = \frac{\frac{4\mathrm{Re}(-1)^{j+1}}{(2j-1)\pi\lambda_j^2}\frac{\mathrm{d}\bar{p}}{\mathrm{d}\bar{x}}\left[\frac{1}{\cosh(\lambda_j\bar{h}_1)} - 1 - \frac{1}{\cosh(\lambda_j\bar{h}_2)\beta} + \frac{1}{\beta}\right]}{\beta\tanh(\lambda_j\bar{h}_1) - \tanh(\lambda_j\bar{h}_2)} \tag{15d}$$

The dimensionless volumetric flow rates through the rectangular channel can be defined by $\bar{q}_1 = \bar{q}_1^{\mathrm{E}} + \bar{q}_1^{\mathrm{P}} = q_1/\left(L^2V\right)$ and $\bar{q}_2 = \bar{q}_2^{\mathrm{E}} + \bar{q}_2^{\mathrm{P}} = q_2/\left(L^2V\right)$. The dimensionless flow rates are given by

$$\bar{q}_1^{\mathrm{E}} = 2\int_{-\bar{h}_1}^{0}\int_0^{\bar{w}}\bar{u}_1^{\mathrm{E}}(\bar{y},\bar{z})\,\mathrm{d}\bar{y}\,\mathrm{d}\bar{z} = 2\sum_{j=1}^{\infty}\left\{\left[1-\frac{1}{\cosh(\lambda_j\bar{h}_1)}\right]\frac{b1_j^{\mathrm{E}}}{\lambda_j} + \frac{\Phi_j(\bar{h}_1)}{\lambda_j}\tanh(\lambda_j\bar{h}_1) + \Phi_j^I(0) - \Phi_j^I(\bar{h}_1)\right\}\frac{\sin(\lambda_j\bar{w})}{\lambda_j} \tag{16a}$$

$$\bar{q}_2^{\mathrm{E}} = 2\int_0^{\bar{h}_2}\int_0^{\bar{w}}\bar{u}_2^{\mathrm{E}}(\bar{y},\bar{z})\,\mathrm{d}\bar{y}\,\mathrm{d}\bar{z} = 2\sum_{j=1}^{\infty}\left[\frac{1}{\cosh(\lambda_j\bar{h}_2)}-1\right]\frac{b2_j^{\mathrm{E}}}{\lambda_j^2}\sin(\lambda_j\bar{w}) \tag{16b}$$

$$\bar{q}_1^{\mathrm{P}} = 2\int_{-\bar{h}_1}^{0}\int_0^{\bar{w}}\bar{u}_1^{\mathrm{P}}(\bar{y},\bar{z})\,\mathrm{d}\bar{y}\,\mathrm{d}\bar{z} = 2\sum_{j=1}^{\infty}\left\{\left[1-\frac{1}{\cosh(\lambda_j\bar{h}_1)}\right]\frac{b1_j^{\mathrm{P}}}{\lambda_j} + \frac{4\mathrm{Re}(-1)^{j+1}}{(2j-1)\pi\lambda_j^2}\frac{\mathrm{d}\bar{p}}{\mathrm{d}\bar{x}}\left(\frac{1}{\lambda_j}-\bar{h}_1\right)\right\}\frac{\sin(\lambda_j\bar{w})}{\lambda_j} \tag{16c}$$

$$\bar{q}_2^{\mathrm{P}} = 2\int_0^{\bar{h}_2}\int_0^{\bar{w}}\bar{u}_2^{\mathrm{P}}(\bar{y},\bar{z})\,\mathrm{d}\bar{y}\,\mathrm{d}\bar{z} = 2\sum_{j=1}^{\infty}\left\{\left[1-\frac{1}{\cosh(\lambda_j\bar{h}_2)}\right]\frac{b2_j^{\mathrm{P}}}{\lambda_j} + \frac{4\mathrm{Re}(-1)^{j+1}}{(2j-1)\beta\pi\lambda_j^2}\frac{\mathrm{d}\bar{p}}{\mathrm{d}\bar{x}}\left(\frac{1}{\lambda_j}-\bar{h}_2\right)\right\}\frac{\sin(\lambda_j\bar{w})}{\lambda_j} \tag{16d}$$

where

$$
\begin{aligned}
\Phi_j^I(\bar{y}) = &\frac{-4\mathrm{Re}G_x\bar{\zeta}_1(-1)^{j+1}\cosh\left(B_j\bar{y}\right)}{(2j-1)\pi\left(\lambda_j^2-B_j^2\right)\sinh\left(B_j\bar{h}_1\right)B_j} \\
&+\frac{4\mathrm{Re}G_x\bar{\zeta}_3(-1)^{j+1}\cosh\left[B_j\left(\bar{h}_1-\bar{y}\right)\right]}{(2j-1)\pi\left(\lambda_j^2-B_j^2\right)\sinh\left(B_j\bar{h}_1\right)} \\
&+\sum_{p=1}^{\infty}\left\{4\mathrm{Re}G_x\bar{\zeta}_2\left[1+(-1)^{p+1}\right]\right. \\
&\left.\times\frac{\lambda_j\bar{h}_1(-1)^{j+1}\cos\left(p\pi\bar{y}/\bar{h}_1\right)}{p^2\pi^2\bar{w}\left(\lambda_j^2+A_p^2\right)\left[\left(p\pi/\bar{h}_1\right)^2+\lambda_j^2\right]}\right\}
\end{aligned}
$$

We define the holdup of the conducting fluid, α, as the ratio of the area occupied by the conducting fluid to the whole area of the cross-section of the channel. As a planar interface between the two liquids is assumed, the holdup is given by $\alpha = |h_1| / \left(|h_1| + |h_2|\right)$. Furthermore, if a reference length scale L is taken as the height of the channel, holdup α is the absolute value of h_1. From Eq. (16) the flow rates of the two liquids are a function of the holdup and the pressure gradient:

$$
\begin{cases}
\bar{q}_1 = q_1\left(\alpha, \dfrac{\mathrm{d}\bar{p}}{\mathrm{d}\bar{x}}\right) \\
\bar{q}_2 = q_2\left(\alpha, \dfrac{\mathrm{d}\bar{p}}{\mathrm{d}\bar{x}}\right) .
\end{cases}
\tag{17}
$$

If the flow rate conditions are specified, the system of equations can be solved. In this work, the holdup and pressure gradient are obtained by the Newton–Raphson method.

To investigate the relative importance of the electric force to the pressure gradient on the liquids, a new parameter S_R is defined as $S_\mathrm{R} = \mathrm{Re}G_x\bar{\zeta}_2/K$. Substituting Eq. (7) into Eq. (8) yields

$$
\nabla^2\bar{u}_1 = \mathrm{Re}\frac{\mathrm{d}\bar{p}}{\mathrm{d}\bar{x}} + \mathrm{Re}G_x\bar{\psi}\left(\bar{z},\bar{y}\right) \tag{18}
$$

In Eq. (18) the pressure gradient is uniform across the channel while the electroosmotic force is concentrated in the EDL regions close to the walls of the channel. $1/K$ is the dimensionless thickness of the EDL region. Figure 3 shows the meaning of S_R. The parameter S_R appears as apparent uniform forces acting on the liquid across the channel.

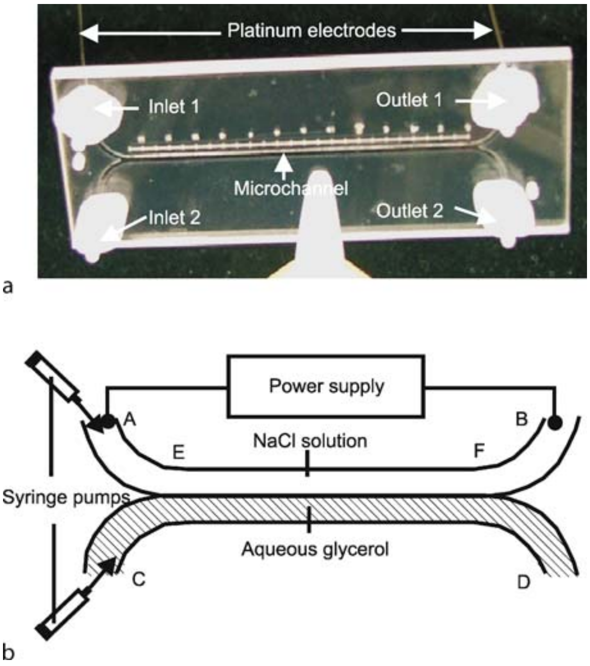

Liquid–Liquid Stratified Flow in Microchannels, Figure 4 The fabricated H-shaped microfluidic device used in the experiment

Experiment

The H-shaped microchannel used in the experiments is shown in Fig. 4. The fabrication is based on the adhesive lamination techniques. In this method, two polymethylmethacrylate (PMMA) plates ($75\,\mathrm{mm} \times 25\,\mathrm{mm}$) were bonded by a layer or layers of double-sided adhesive tapes to form a closed microfluidic channel with inlet and outlet holes. The channel structure was cut through the adhesive tape (Arclad 8102 transfer adhesive, Adhesives Research Inc.). Thus the adhesive tapes define the depth of the channel. The two liquids flow side by side in the straight microchannel in the direction from left to right from the syringe pump. The two liquids are introduced from inlet 1 and inlet 2; outlet 1 and outlet 2 are for collection of the products or wastes. Across the microchannel, platinum electrodes (Aldrich-Sigma, Singapore) were inserted for the application of the electric field.

The measurement setup can be used for both fluorescence imaging and microparticle image velocimetry (micro-PIV) measurements [6]. It consists of four main components: an illumination system, an optical system, a charge coupled device (CCD) camera and a control system. The control system, consisting of a peripheral component interface (PCI) card and its corresponding software, is implemented in a personal computer (PC). The PC can control and synchronize all actions related to illumination and

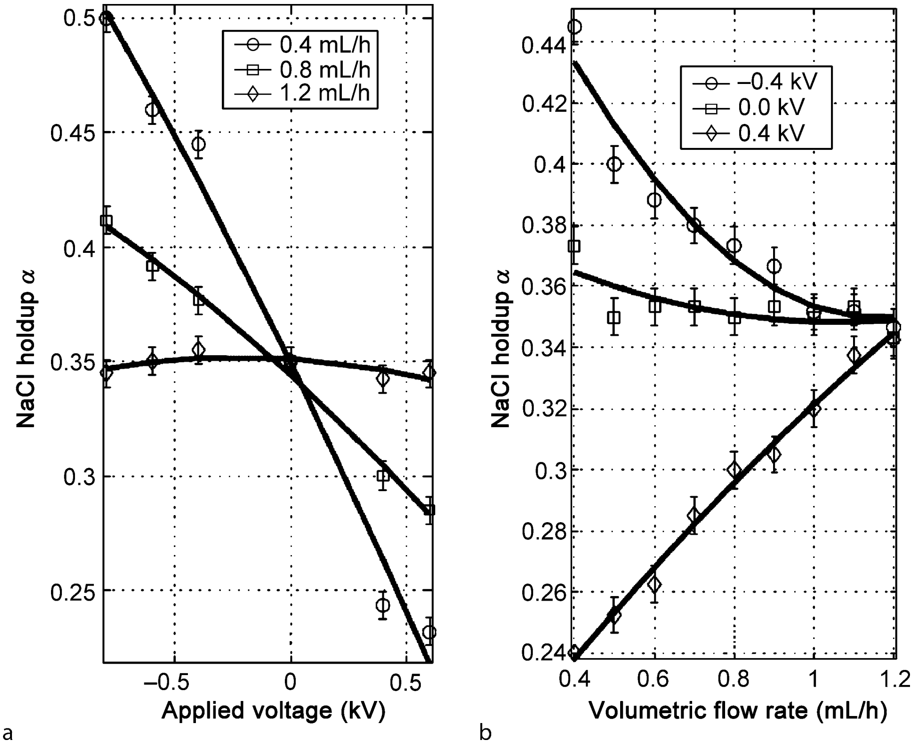

a b

Liquid–Liquid Stratified Flow in Microchannels, Figure 5 Relationship between NaCl solution holdup and (**a**) different applied voltage for the same volumetric flow rates of the two liquids or (**b**) volumetric flow rate under the same applied voltage

image recording. Two different light sources were used for the two measurements. For the fluorescence imaging measurements, a single mercury lamp was used for illumination. Because of the ability of precise timing and intensity control, a double-pulsed Q-switched (quality switched) Nd:YAG laser beam was used for the micro-PIV measurements. The optical system was a Nikon inverted microscope (model ECLIPSE TE2000-S) with a set of epifluorescent attachments. There are three optical elements in a filter cube: excitation filter, dichroic mirror and emission filter. Emission filters are used in both measurements to select more specifically the emission wavelength of the sample and to remove traces of excitation light. An interline transfer CCD camera (Sony ICX 084) was used for recording of the images.

Aqueous NaCl solution (concentration 7×10^{-4} M) and aqueous glycerol (volume concentration 14%) were introduced at inlets A and C through syringes (500 μl gastight, Hamilton) and syringe pump (Cole-Parmer, 74900-05, 0.2 to 500 μl/h, accuracy of 0.5%) system. The same volumetric flow rates of the two inlet flows were ensured by using two identical syringes driven by the syringe pump. Fluorescent dye (fluorescein disodium salt $C_{20}H_{10}Na_2O_5$, also called Acid Yellow 73) was added in the NaCl solution in the fluorescence imaging experiment to determine the interface location. In the micro-PIV measurement, the seeding particles used were Duke red particles (Duke Scientific Co.). The particles have a maximum excitation wavelength of 540 nm (green, very close to the characteristic wavelength of Nd:YAG laser) and a maximum emission wavelength of 610 nm (red). The diameter of the particles can be chosen from several hundreds of nanometers to several micrometers. The PIV measurement uses an epifluorescent attachment of type Nikon G-2E/C (excitation filter for 540 nm, dichroic mirror for 565 nm and an emission filter for 605 nm). Both filters in the attachment have a bandwidth of 25 nm.

Key Research Findings

Liquid–Liquid Interface Position

As shown in Fig. 5a, as the electric field changes in magnitude and direction, the holdup of NaCl solution changes accordingly. When no voltage is applied across the microchannel, the flow is simply a pressure-driven two-fluid flow. The aqueous glycerol used is more viscous than NaCl solution, by about 1.5 times. The less viscous NaCl solution occupies a smaller portion of the chan-

nel under pressure-driven condition. The holdup value is about 0.35 when no externally applied voltage is present, as shown in Fig. 5a. When a negative electric field is applied across the microchannel (A is negative, B is positive), the holdup of NaCl solution increases. The electroosmotic flow is against the pressure-driven flow under a negative electric field. More resistance force will be encountered to drive the NaCl solution. Apparently, the NaCl solution becomes more "viscous" due to the electroosmotic effect, thus occupying a larger channel width. The holdup of NaCl solution increases with the increase of negative electric field. Due to the same pressure drop across the microchannel, in order to achieve the same volumetric flow rates, the more viscous fluid has to spread to a larger width, i. e. a higher liquid holdup. In another case where the positive electric field is applied (A is positive, B is negative), the NaCl electrolyte solution apparently possesses a lower "viscosity", since the electroosmotic flow is in the same direction as the pressure-driven flow. In other words, the electroosmotic effect aids the flow of the NaCl solution.

Figure 5a also shows that, as the inlet volumetric flow rates of the two liquids increase, the electroosmotic flow effect on the pressure-driven flow becomes weaker. At a flow rate of 1.2 ml/h, it seems that the holdup, α, of NaCl remains constant, although the voltage varies from -0.8 to 0.6 kV. For a typical electroosmotic flow, in which an electric field of hundreds of volts per centimeter is applied, the resulting velocity is of the order of 0.1 to a few millimeters per second. But for the pressure-driven flow in microchannels, the velocity can be controlled in a wider range. In this experiment, when the flow rate is at 0.4 ml/h, the average velocity of NaCl through the channel is 3.48 mm/s with no external applied electric field, the magnitude of which is comparable with that from the electroosmotic flow. Figure 5a shows that, by adjusting the electric field, the interface position between the two liquids, i. e. variation of the NaCl holdup, α, from 0.25 to 0.50, has been successfully controlled.

The relationship between the NaCl holdup, α, at different flow rates under the fixed electric field is shown in Fig. 5b. The NaCl holdup remains the same (0.35) for different volumetric flow rates in the absence of an externally applied electric field. This is because the volumetric flow rate ratio between the two liquids is kept unchanged at 1 : 1. This agrees very well with the previous theoretical and numerical study reported in the literature. From Fig. 5b, it can be seen that, as the flow rate increases, holdup α converges to a constant value, 0.35; that is, the value without the externally applied electric field. The reason is that larger pressure-driven flow velocity makes the electroosmotic flow effect almost insignificant.

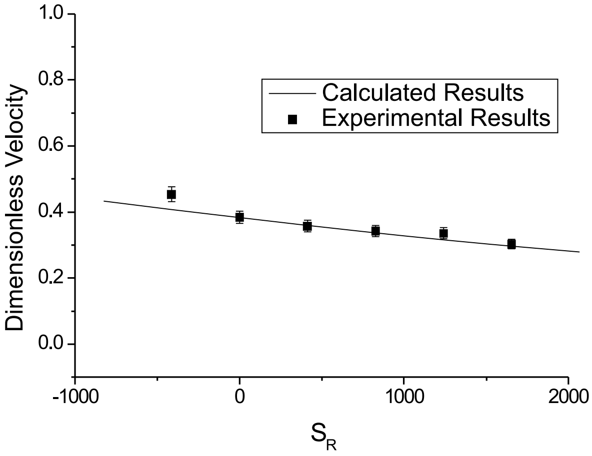

Liquid–Liquid Stratified Flow in Microchannels, Figure 6 Comparison of the holdup of the conducting liquid between calculated and experimental results; $q_1 = q_2 = 0.05$ ml/h

Figure 6 shows a comparison between the analytical results and the experimental results of the interface positions for different applied electric fields. In calculations, the reference velocity $V = 1.13 \times 10^{-3}$ m/s and the reference length $L = 910$ µm. The viscosity of NaCl solution and aqueous glycerol is 1.12 and 1.8 Ns/m^2, respectively. Under these conditions, the dimensionless flow rate is 0.0148 for 0.05 ml/h.

Velocity Profile

The micro-PIV measurement reported in this experiment was carried out with a ×4 objective lens. With a CCD sensor size of 6.3 mm × 4.8 mm, the size of an image pixel is 2.475 µm and the size of the measured area is 1584 µm × 1188 µm. Fluorescent particles with a diameter of 3 µm were used to trace the flow. A microchannel with cross-section of 910 µm × 50 µm and length of 5 mm was used. The liquids used in the experiment were aqueous NaCl solution (concentration 10^{-4} M) and aqueous glycerol (volume concentration 24%). The integration area was 32 px × 32 px. Previous studies show that the entry length of two-liquid flow in a microchannel is very short [7]. The measurement was taken at 1 mm downstream of the entrance; thus a stable velocity field was obtained.

The total measured velocity of the fluorescent tracing particles is a superposition of the electroosmotic, pressure-driven and electrophoretic and Brownian motion velocity components [8]. It can be expressed as

$$u_{\text{particle}} = u_{\text{eof}} + u_{\text{pressure}} + u_{\text{eph}} + u_{\text{b}} \tag{19}$$

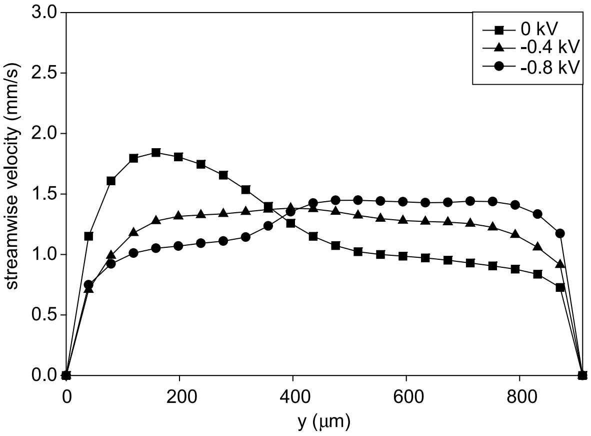

Liquid–Liquid Stratified Flow in Microchannels, Figure 7 Velocity profile under different applied voltage (flow rate = 0.1 ml/h; NaCl on left side, glycerol on right side)

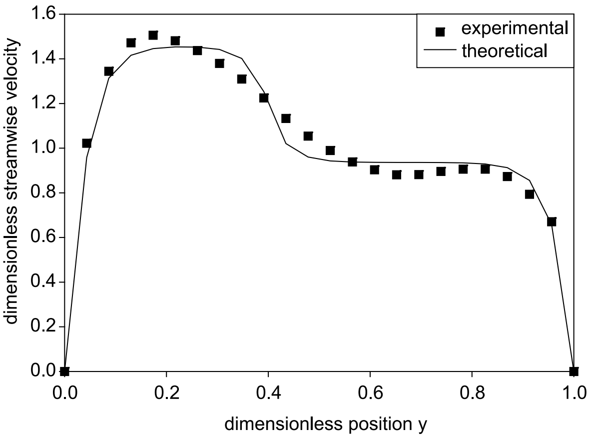

Liquid–Liquid Stratified Flow in Microchannels, Figure 8 Comparison between PIV measurement and theoretical analysis at flow rate of 0.1 ml/h, under applied electric voltage of − 0.2 kV

where u_{eph} is the electrophoresis velocity of the tracing particle and u_{b} is the velocity due to Brownian motion of the particle. The electrophoresis velocity is a function of the particle's surface zeta potential in the solution [5], expressed as

$$u_{\mathrm{eph}} = \frac{\varepsilon E_x \zeta_{\mathrm{p}}}{\mu} \tag{20}$$

where ζ_{p} is the particle's surface zeta potential, and ε and μ are the permittivity and the dynamic viscosity of the fluid. In this experiment, the particle's zeta potential was measured as $-25.2\,\mathrm{mV}$. From Einstein's Brownian movement equation, the average Brownian velocity during the time elapsed between two subsequent images can be estimated as

$$u_{\mathrm{b}} = \sqrt{\frac{2D}{\Delta t}} \tag{21}$$

where Δt is the elapsed time duration and D is the diffusivity of the particles. The diffusivity is given by

$$D = \frac{\mathrm{k_B} T}{3\pi \mu d_{\mathrm{p}}} \tag{22}$$

where T is the absolute temperature, $\mathrm{k_B}$ is Boltzmann's constant and d_{p} is the particle diameter.

The effect of the applied voltage on the velocity profile is shown in Fig. 7. Without the externally applied voltage, the NaCl (on the left side in Fig. 7) flows faster. When a negative electric field is present, the velocity of NaCl decreases whereas the velocity of aqueous glycerol increases. It is noted that as the applied voltage is set to $-0.4\,\mathrm{kV}$, both liquids achieve about the same velocity,

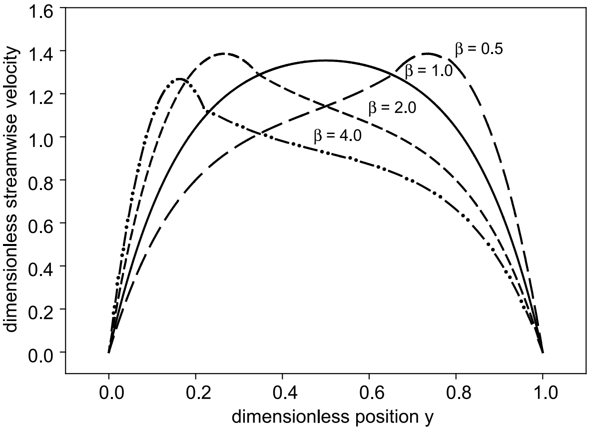

Liquid–Liquid Stratified Flow in Microchannels, Figure 9 Dimensionless velocity profile for different viscosity ratios

and hence the same average residence time. If the applied voltage continues to increase to $-0.8\,\mathrm{kV}$, the NaCl flows at smaller velocity and spreads more in the channel. As the magnitude of the applied voltage increases, the interface position shift increases. This is in agreement with the fluorescent experiment observation.

A comparison between experiment and theoretical analysis under an applied electric field of $-0.2\,\mathrm{kV}$ is shown in Fig 8. Reasonable agreement is obtained. In the theoretical prediction, a relatively sharp transverse velocity gradient occurs at the interface as the model assumes two immiscible liquids. In fact, glycerol is miscible in water; therefore, there exists an interfacial region in the measured velocity profiles.

Our theoretical model considers both the pressure gradient and electroosmosis. If there is no electroosmosis effect

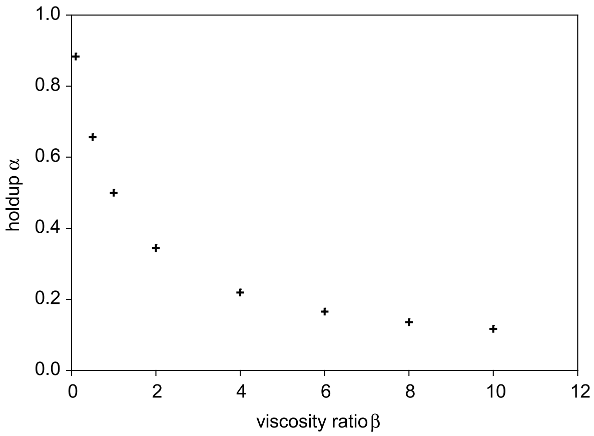

Liquid–Liquid Stratified Flow in Microchannels, Figure 10 Holdup for different viscosity ratios

involved, such as in the case where no external electric field is applied, the theoretical model reduces to a simple pressure-driven flow. In Fig. 9, the dimensionless velocity profile for different liquid viscosity ratios is shown. When the viscosity ratio equals 1, the two-liquid flow is in fact a pressure-driven flow of a single liquid, showing a parabolic velocity profile. The holdup for different viscosity ratios is shown in Fig. 10. The values of viscosity ratio in the figure are 0.1, 0.5, 1.0, 2.0, 4.0, 6.0, 8.0 and 10.0. We note that for two-liquid flow under only pressured gradient the holdup does not depend on the flow rate. It only depends on the viscosity ratio between the two liquids.

Future Directions for Research

The interface position and velocity profile of liquid–liquid stratified flow in microchannels can be controlled using the electroosmosis effect, which can retard or aid the flow of one liquid. The experiment demonstrated a new method to solve the unmatched viscosity problem of liquid–liquid flow in diffusion-based microfluidic applications. Other potential uses include development of flow switching or flow focusing for multi-liquid flow in microfluidics.

Cross References

► Electroosmotic Flow (DC)
► Flow Rate Measurements

References

1. Kuban P, Dasgupta PK, Morris KA (2002) Microscale continuous ion exchanger. Anal Chem 74:5667–5675
2. Weigl BH, Bardell RL, Kesler N, Morris CJ (2001) Lab-on-a-Chip sample preparation using laminar fluid diffusion interfaces – computational fluid dynamics model results and fluidic verification experiments. Fresenius J Anal Chem 371:97-105
3. Nguyen NT, Wu Z (2005) Micromixers—a review. J Micromech Microeng 15(2):R1–R16
4. Hatch A, Garcia E, Yager P (2004) Diffusion-based analysis of molecular interactions in microfluidic devices. Proc IEEE 92
5. Li D (2004) Electrokinetics in Microfluidics. Academic, London
6. Wang C, Gao Y, Nguyen NT, Wong TN, Yang C, Ooi KT (2005) Interface control of pressure-driven two-fluid flow in microchannels using electroosmosis. J Micromech Microeng 15:2289–2297
7. Wu Z, Nguyen NT, Huang X (2004) Nonlinear diffusive mixing in microchannels: theory and experiments. J Micromech Microeng 14:604–611
8. Devasenathipathy S, Santiago JG, Takehara K (2002) Particle tracking techniques for electrokinetic microchannel flows. Anal Chem 74:3704–3713

Liquid Magnet

► Ferrofluids in Microchannels

Liquid–Solid Electrophoretic Flow

► Electrokinetic Two-Phase Flows

Liquid–Vapor Phase Change

► Cavitation in Microdomains
► Droplet Evaporation

Lithography

► Photo Patterned

Local Filtering

Definition

In image processing local filtering is used to increase the quality of an image. As a wanted result the image is smoothed and noise is removed. Typical local filters are ►mean filter, ►low-pass filter, ►Gaussian filter, and ►median filter. Local averaging causes loss of spatial information.

Low-Frequency Capacitance

► Shunt Capacitance

Low-Pass Filtering

Definition

When a low-pass filter is used high frequencies are attenuated while low frequencies pass through. An image which is low-pass filtered appears smoothed.

Ludwig–Soret Effect

► Thermophoresis

Luminescence

Definition

Luminescence is the emission of light from any substance occurring when an electron returns from an electronically excited state to ground state. Luminescence can be caused by a number of factors, most commonly chemical or biochemical changes, electrical energy or subatomic motions. There are two main categories of luminescence, fluorescence and phosphorescence and these are dependent on the nature of the excited state.

Cross References

► Fluorescent Labeling

Luminescent Labels

► Fluorescent Labeling
► Fluorescent Probes

Lumped Analysis

Synonyms

Discrete element analysis

Definition

Technique using approximate and simplified representation of complex phenomena as a combination of elements, each of which are individually simple to represent and solve. Many models employ electrical circuit elements to form such representations.

Cross References

► Piezoelectric Microdispenser

Lumped Capacitance

Definition

A simplifying assumption for diffusive heat transport processes that is often invoked for materials with high thermal conductivities. Under this assumption, the transient temperature within a body subject to heating/cooling is assumed to be spatially uniform at any instant of time.

Cross References

► Supersonic Micro-Nozzles

Mach Number

Definition

A dimensionless number defined by the ratio of the local flow velocity to the local speed to sound. A flow with a Mach number exceeding unity is termed ’supersonic’; for Mach numbers less than unity the flow is ’subsonic’.

Cross References

► Supersonic Micro-Nozzles

Macromodel

Definition

Macromodels are constructed via assembly of primitive models or a set of Differential–Algebraic Equations (DAEs) in a system representation and describe the dynamic response of the system.

Cross References

► Primitive Model

Macromolecular Transport

► Simulating Migration of Polymer Chains, Methods

Magnetic-Based Biosensors

► Biosensors Using Magnetics

Magnetic Biosensors

► Biosensors Using Magnetics

Magnetic Coils

Definition

Magnetic coils or electromagnets produce a magnetic field in the core of a coil where an electric current is circulating.

Cross References

► Magnetic Field-Based Lab-on-Chip Devices

Magnetic Field-Based Lab-on-Chip Devices

NICOLAS MINC
Department of Microbiology, Columbia University,
NYC, NY, USA
nm2268@columbia.edu

Synonyms

Magnetic field-based microfluidic devices; Microfluidics and magnetism

Definition

Magnetic fields are used to manipulate or organize magnetic materials for Lab-on-Chip applications.

Overview

The use of ►magnetic fields for Lab-on-Chip applications has become very common over the past few years. Indeed, a great deal of research in microfluidics has been focused on developing not only magnetic-field based Lab-on-chips for biological or chemical applications, but also microfluidic actuators. The first class of these Lab-on-chips, as is often the case in microfluidics, consisted of a direct downscaling of existing methods for biological or chemical sample handling through the use of ►magnetic microbeads. More recently, the use of magnetic fields in microfluidics has been extended to devise mixers, sorters

or on-chip detection systems. Magnets and magnetic coils can now be fabricated on the micrometer scale and be directly integrated in the chip. Therefore, this makes magnetic-field based Lab-on-Chip an exciting topic that we will review in this entry.

Generalities on Magnetism

Magnetic fields can be created by permanent ▶magnets or ▶magnetic coils and be used to apply global forces or organize different materials. The magnetic properties of a material are characterized by its ▶magnetic susceptibility χ. It represents the degree of magnetization M of a material in response to an applied magnetic field $\boldsymbol{B}$:

$$\boldsymbol{M} = \chi \boldsymbol{B} \tag{1}$$

The magnetic susceptibility can be negative, in which case the field will repel the material; a positive χ stands for a material that is attracted by the field. As summarized in Table 1, among the values of χ, three main classes of magnetism are distinguished:

- Diamagnetic materials have a very weak susceptibility and are thus often simply considered as non-magnetic.
- Paramagnetic materials become magnetic under an external field and are then attracted by the field. This mechanism is reversible, meaning that when the external field is turned off, the material loses its magnetic properties.
- Finally, ferromagnetic materials become magnetic under an external field, identical to paramagnetic materials, but with a much higher susceptibility. Also, when the field is turned off, the material remains magnetic and produces a magnetic field called remanence.

Upon the application of an external magnetic field $\boldsymbol{B}$ a magnetic particle gets magnetized and is submitted to a force $\boldsymbol{F}$:

$$\boldsymbol{F} = \frac{V(\chi - \chi_{\mathrm{m}})}{\mu_0}(\boldsymbol{B}.\nabla)\boldsymbol{B} \tag{2}$$

In this equation, V represents the volume of the particle, χ its magnetic susceptibility, χ_{m} the susceptibility of the surrounding medium and μ_0 the magnetic permeability of the vacuum. Following formula (2), one may notice that in a homogeneous field the particle is magnetized, but the force is zero. Only a magnetic field gradient produces a force on the particle, and it results in a translational movement of the particle toward the maxima of the field.

Magnetic Beads

Magnetic particles are certainly the most useful tools of magnetic fields for Lab-on-Chip applications. They have embedded magnetic entities and thus can be manipulated at relatively long distances using permanent magnets or electromagnets. The effort that has been put into the development of these particles has turned them into a very strong tool for biomedical applications. Mainly any biological component (cell, DNA, proteins, antibody, etc…) or chemical can be very specifically attached to the particles. They can scale from 100 nm up to 100 μm and can be fabricated in a highly monodisperse manner. They are now used in numerous biomedical applications and provide a day-to-day tool for biologists.

As illustrated in Fig. 1b, these beads are suspensions of ferrofluids embedded in a polymer shell. The ferrofluid is made of nanometric particles of magnetic oxide (usually magnemite Fe_3O_4 or maghemite γ-Fe_2O_3) dispersed in organic oil. The concentration of magnetic entities in each bead is very high and thus they have magnetic susceptibilities typical of ferromagnetism [1–10]. Nevertheless, when the external field is turned off, the strong thermal agitation at the level of the nanoparticle redistributes the direction of the magnetic moments of these particles and the global magnetization of the bead returns to 0. Thus, the

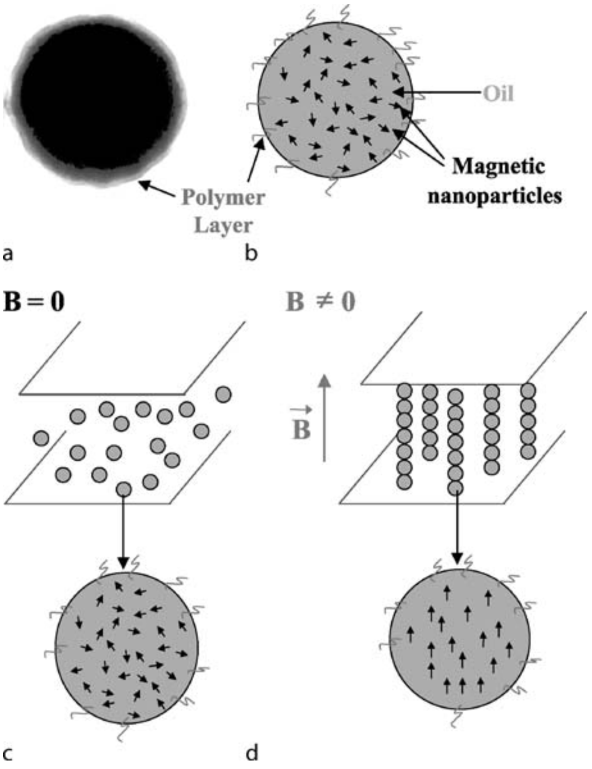

Magnetic Field-Based Lab-on-Chip Devices, Figure 1 Magnetic beads: (**a**) Electron micrograph of a magnetic bead. (**b**) Schematic representation of a magnetic bead. (**c**) and (**d**) Self-organization of magnetic beads in a confined space

Magnetic Field-Based Lab-on-Chip Devices, Table 1 Classification of the magnetism of matter

Type of Magnetism	Examples of materials	Sign of χ	Typical values of χ
Diamagnetism	Water, DNA, cells, plastic, gold	$-$	-10^{-6} to -10^{-4}
Paramagnetism	Aluminium, platinium, oxygen, calcium	+	10^{-5} to 10^{-3}
Ferromagnetism	Iron, Nickel, Magnetite (Fe_3O_4)	+	1 to 10^5

bead, whilst being strongly magnetic, conserves the property of reversibility of the paramagnetism. This particular and valuable property is called ► superparamagnetism.

Another remarkable property of magnetic particles is their ability to self-organize under an external magnetic field. As mentioned above, when a magnetic field is applied, each bead becomes magnetized and behaves as a magnetic dipole pointing in the direction of the field. The resulting dipole–dipole attraction between beads will lead to the formation of chains parallel to the field. Furthermore, when the suspension is confined in the direction of the field (in a microchannel, for example) the chains have a size equal to the height of the channel. Lateral dipolar isotropic repulsions between chains lead to the formation of a hexagonal array of these chains in the plane perpendicular to the field (see Figs. 2c and 2d). When the concentration of beads is too high, the order is lost and the array adopts a "labyrinth-like" structure. These structures are generally called supra-particle structures (SPS).

Basic Methodology

Applying a Magnetic Field in a Microfluidic Channel

Depending on the type of application, one may choose to use either permanent magnets or magnetic coils to apply the magnetic field. They can consist of conventional large-scale objects simply placed in the vicinity of the microchannels or be microfabricated and directly integrated in the chip.

Permanent magnets would preferably be used for creating strong local gradients (and thus apply a force) in order to attract and/or immobilize magnetic material to one side of a channel. Combinations of magnets placed in certain geometries can also create precise gradients across or along a microchannel. These magnets are usually made of rare-earth alloys, the most common being the Neodymium iron boron (NdFeB) magnets. They are relatively affordable and can be fabricated in a wide variety of shapes (down to sizes of a fraction of a millimeter) and produce fields ranging from 0.1 T to 1 T at their surfaces. The use of magnetic coils, less popular than permanent magnets, allows for the creation of very uniform fields at the scale of the channel. They can also be used for the creation of a local gradient when combined with tapered magnetic cores. The field can easily be switched on and off, tuned in strength or even alternated through the control of the current in the coil. Compared to permanent magnets, they are much more expensive and the magnitude of the field they produce is limited by Joule heating, hardly reaching 50 mT.

At the microscale level, permanent magnets can be fabricated using standard lithography methods. Briefly, layers of magnetic metals are first deposited on a substrate by either sputtering, electroplating or vapor deposition. Then, lithography followed by etching and lift-off techniques allow for the creation of the desired patterns [1]. This has, for example, been used to design magnetic posts (see Figs. 2a and 2b) [2] or stripes in a microfluidic channel [3]. As an innovative alternative, Psychari et al. stamped ferrofluid spots on the surface of a microchannel. When an external uniform field is applied they behave as micromagnets [4]. A more complex process allows for the creation of miniaturized electromagnets: Microwires made of a conductive metal such as copper or gold are first patterned in spiral-like shapes on the substrate. Then, one has to address both the proper insulation of the wires and connection to an external control of the current. This method has recently been used to devise an array of magnetic microcoils (see Fig. 2c) [5]. Each microcoil has a width of 10 μm, produces a field of 1.5 mT and can be independently manipulated using an integrated circuit. Finally, devising microcoils also allows for the conception of micro NMR spectroscopy systems that permit the elucidation of chemical molecular structures while consuming a small amount of the chemical.

Use of Magnetic Beads as Solid Phases in Heterogeneous Assays

The most straightforward application of magnetic fields for microfluidics is the use of magnetic beads as a solid phase in a heterogeneous assay. This method is in fact a direct downscaling of a technique used very commonly in biology laboratories. In the first step, chemicals or

M

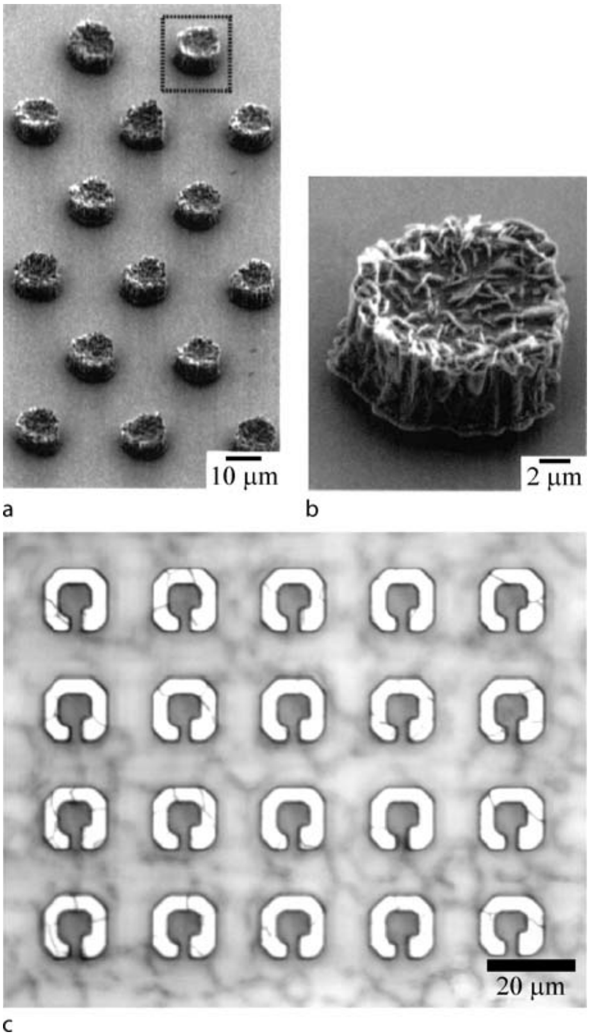

Magnetic Field-Based Lab-on-Chip Devices, Figure 2 Microfabricated magnets and magnetic coils: (**a**) Array of paramagnetic posts made in Ni in a microchannel. (**b**) Same post at a higher magnification [2]. (**c**) Array of micro-magnetic coils in a microchannel [5]

biomolecules are grafted onto magnetic beads. Then the beads are introduced into a microchannel and immobilized by one magnet, a pair of magnets or a magnetic coil placed in the vicinity of the channel [6]. The reactants (the mobile phase) are flowed through the immobilized plug of beads (the solid or stationary phase) and reaction occurs between the two phases. The high surface to volume ratio of the beads leads to a high density of binding sites and the compaction of the beads in the plug strongly decreases the diffusion time for the reactants to react with the solid phase. In addition to the reduction of the reaction time, this method keeps the two phases separated and thus avoids contamination from one phase to the other. Finally, by turning off the field, the beads can be washed out of the channel and stored for further use.

The high compaction of the beads in the plug gives rise to a pressure increase in the microchannel. This often leads to local breakage of the magnetic structure and opens large channels in the plug. In those apertures, the biological substance in the mobile phase can travel fast without having the time to diffuse to the surface of the beads. One idea to overcome this problem is to self-organize the beads in the plug [7]. To that aim, the authors used a longitudinal magnetic field created by two magnets pointing in the same direction and making a small angle (20°) with the channel (see Fig. 3a). At the beginning of the immobilization, magnetic particles self-organize in chain-like columns along the channel direction (Figs. 3b and 3c). When the concentration of beads increases, the plug becomes opaque, probably due to the formation of a "labyrinth-like" structure made of tortuous and ramified "walls" with one direction colinear to the field (Figs. 3d and 3e). The distance between the walls is maintained by dipole–dipole repulsion, keeping in the bulk of the plug channels colinear to the flow, with a thickness of a few micrometers. This structure has a low-hydrodynamic resistance and maintains an appropriate pore size well adapted for most biological molecules.

The use of magnetic beads as solid phases for bioassay has been widely used, and examples of biological applications include immunoassays, DNA or RNA hybridization, protein digestion or cell analysis [1]. As a typical example, Fig. 4 depicts a micro-immunoassay based on this method [8]. An immunoassay is a biochemical test that measures the level of a substance (virus, protein, etc...) in a biological liquid, using the reaction of an antibody to the substance also called antigen. In this example, a plug of beads coated with an antibody is immobilized on the side of a microchannel. A corresponding antigen is subsequently flowed through the channel and the small diffusion time allows for a fast and efficient binding of the antigen to the antibody attached on the bead. A second, fluorescently labeled antibody is then injected and binds to the antigen immobilized in the plug. A calibrated fluorescent detection finally allows for the precise measurement of very small concentrations of the antigen (down to 1 μg/l).

Application of Self-Organized Supraparticle Structures

The self-organization of magnetic beads introduced earlier has also been used for Lab-on-Chip application. The perhaps most well-known sets of experiments use an array of self-organized magnetic columns identical to the one represented in Fig. 2d as a matrix of obstacles for DNA electrophoresis [9]. DNA electrophoresis allows for separat-

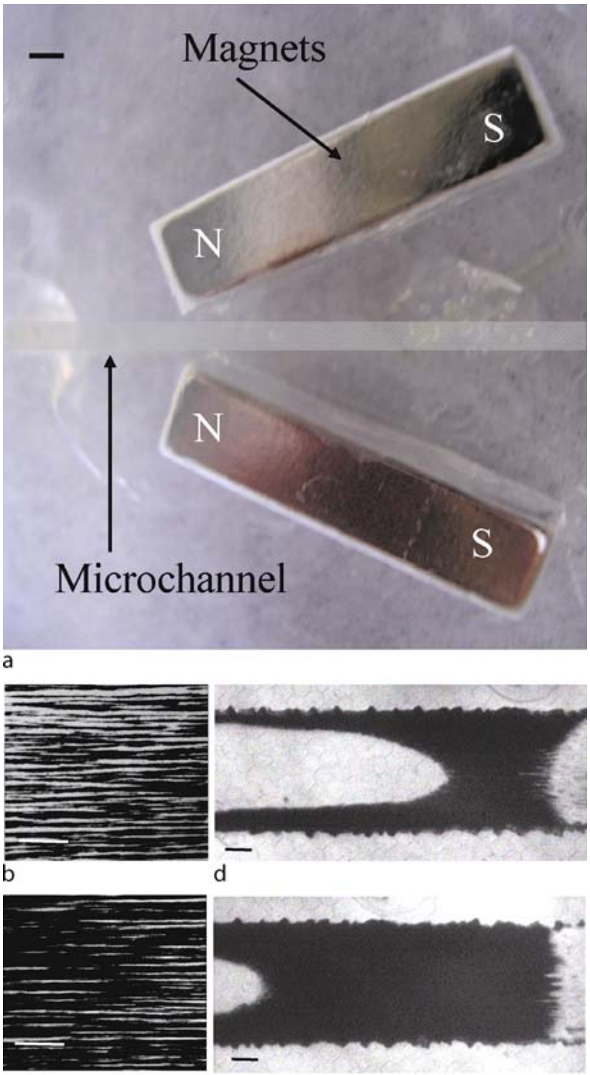

Magnetic Field-Based Lab-on-Chip Devices, Figure 3 Use of self-organization for a heterogeneous bioassay. (**a**) Microchannels with magnets on the side (the bar is 1mm long). (**b**)-(**e**) Resulting self-organization of magnetic chains parallel to the flow direction (bars are 100 μm long)

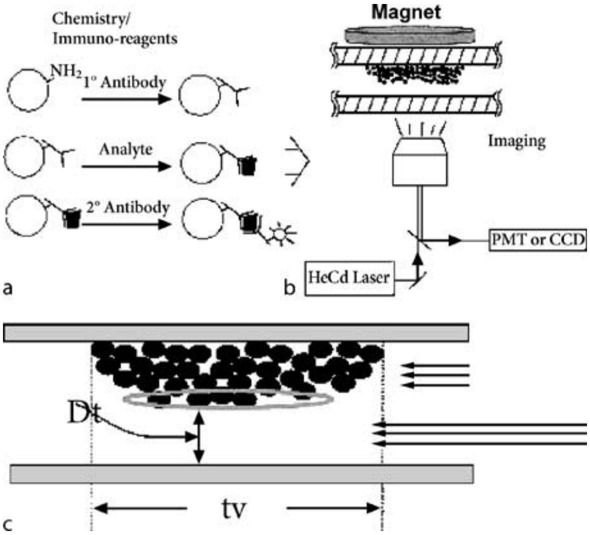

Magnetic Field-Based Lab-on-Chip Devices, Figure 4 Example of magnetic-field based micro immunoassay (Fig. based on [8]). (**a**) Molecules successively attached to the beads: Grafting of the first antibody; antigen attached to this antibody; second labeled antibody attached to the antigen. (**b**) Magnets on the side of the channel and complete set-up for observation. (**c**) At a relative slow flow-rate molecule can diffuse to the beads

ing DNA fragments by size. Its use is ubiquitous in many types of biological analysis. DNA (charged molecule) is mobilized by an applied electric field into a matrix of obstacles (most commonly an agarose gel). Basically, the bigger the DNA, the longer it takes for it to go through the maze of obstacles. This process gives rise to separation. In this example, the self-organized columns of magnetic beads serve as posts on which the DNA molecules will collide and remain stuck for a certain time that scales with the size of the fragment. Therefore, the array serves as the matrix to achieve the separation. The properties of the array can be tuned by changing the concentration of the beads allowing for optimization of the separation device. By stamping spots of ferrofluids on the channel surface, the same group recently demonstrated the possibility of guiding the self-organization of the matrix onto these spots [4]. This has been used to create a very dilute array of large columns strongly anchored to the magnetic spots and has been applied to the sorting of rare cells in a heterogeneous population. To that aim, antibodies specific to surface proteins of one cell kind are first grafted onto the beads. When a mixture of cells is then flowed through the array of columns, the specific cells remain stuck on the columns while the rest flow through the array.

Mixing Enhancement

Mixing (or lack thereof) is often crucial to the effective functioning of microfluidic devices and hence a lot of innovative systems have been developed for this technique. Magnetic fields can also be employed for these applications [1]. Most of the devices consist of a direct downscaling of the conventional bench magnetic stirrer. Some groups microfabricated magnetic rotors and directly integrated them in a microchannel. The rotors were simply actuated by a bench stirrer plate. Another group used assembled chains of magnetic beads as micro-stirrers in the channel. Finally, the alternated self-organization

and disorganization of magnetic supra-particle structures appeared to be a very efficient way of mixing in the microchannels [6].

Sorting with Magnetic Fields

As mentioned previously, when submitted to a field gradient, magnetic beads are submitted to a force (see Eq. (2)). They thus move in the direction of the field maxima and are submitted to the viscous drag:

$$\boldsymbol{F}_{\mathrm{d}} = 6\pi\eta r\boldsymbol{v} \tag{3}$$

In this expression, η represents the viscosity of water, r the radius of the particle and $\boldsymbol{v}$ its velocity. Combining Eqs. (2) and (3), we define and calculate the magnetophoretic mobility ξ as follows:

$$\xi = \frac{\|\boldsymbol{v}\|}{\|(\boldsymbol{B}.\nabla)\boldsymbol{B}\|} = \frac{2r^2\chi}{9\eta} \tag{4}$$

This quantity represents how easily the particle can be magnetically mobilized. According to this expression, at fixed susceptibility and field, bigger beads will move faster than smaller beads, and this allows for separating either magnetic beads or biological samples attached to beads. This phenomenon, called magnetophoresis, has for example been used in a microfluidic device for sorting cells among their size [10]. As represented in Fig. 5a, the device is composed of 2 series of 16 channels converging into a separation chamber. A magnet is placed on one side of this chamber and deflects the trajectory of the beads exiting one of the channels. The deflection of the trajectory relies on Eq. (4), and the biggest magnetic particles are strongly deflected, exiting in one of the top channels. Alternatively, cells of different sizes are attached onto the same beads and sorted by the same principle (see Figs. 5b and 5c). However, in this case, the viscous drag is imposed by the cell and the bigger cells will be less deflected than the smaller ones.

In a second example, Inglis and coworkers developed a magnetic cell sorter based on an array of microfabricated magnetic stripes [3]. In this device, non-labeled cells and cells labeled with magnetic beads are mixed together and injected into the channel. The direction of the flow makes an angle of about 10° with the array of parallel stripes thus deflecting the labeled cells and giving rise to separation (see Fig. 6).

Magnetic Beads for Detection

Magnetic beads can also be used as labels for detection. This method involves the use of precise magnetic field detectors such as Giant magnetic resistance (GMR) or spin-valve sensors. Basically, these sensors are made of alternating layers of magnetic and non-magnetic conductive materials. When an external magnetic field (produced by beads for example) is applied, it induces a change in the resistance of the conductive layer that can be detected. These sensors are commonly used as read-heads in hard-disk drives. For Lab-on-Chip application, this process can again be used to detect biomolecules grafted on the beads. Some examples including DNA hybridization detection have been developed, but the technique has a limited resolution and no one has yet reported the detection of a single bead.

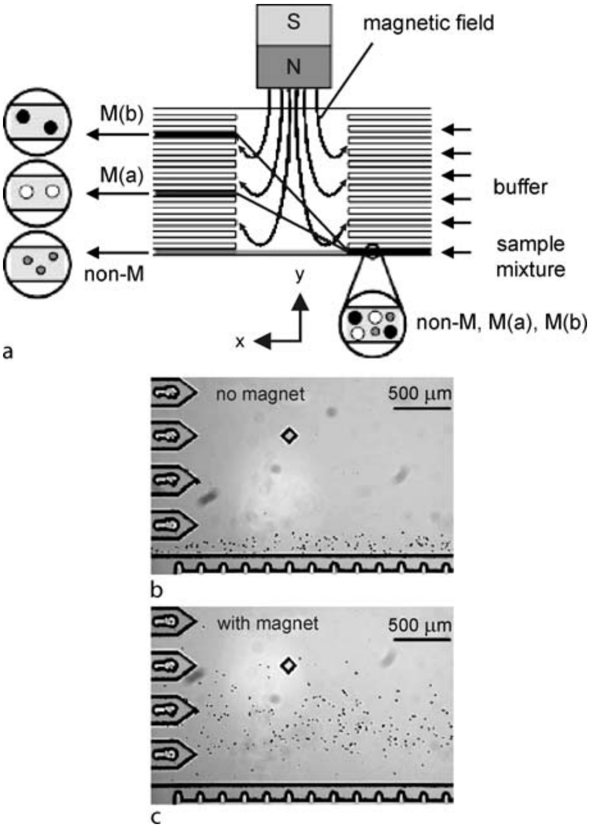

Magnetic Field-Based Lab-on-Chip Devices, Figure 5 Magnetic fields for applications in sorting (based on [10]) (**a**) Sorting of magnetic particles of different sizes. (**b**) and (**c**) Sorting of cells attached on beads

Key Research Findings

Interest in using magnetic fields for Lab-on-Chip applications has widely grown over the past decade. This has given rise to a large number of interesting devices that sometimes offer a lot of advantages as compared to their conventional counterparts.

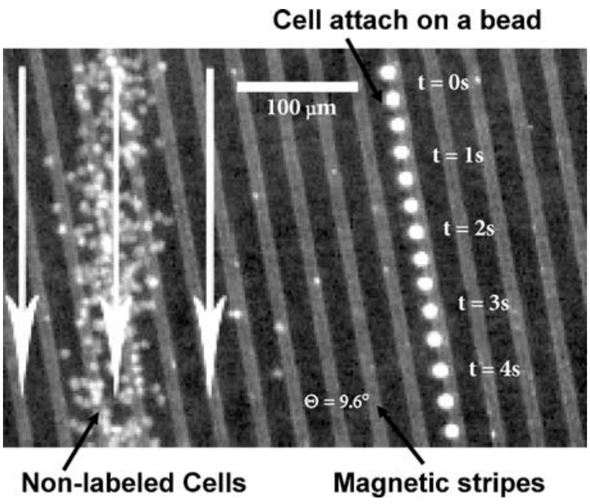

Magnetic Field-Based Lab-on-Chip Devices, Figure 6 Magnetic fields for applications in sorting (based on [3]): Continuous cell sorting using magnetic stripes

One typical example stands in the heterogeneous bioassays. Miniaturizing this method offers many advantages and thus the optimization of the technique is crucial for further commercialization. Prior to using magnetic beads, several groups used non-magnetic glass beads immobilized between weirs in microchannels to create the solid phase of the assay. The use of magnetic beads, even if quite straightforward, appeared later. This has perhaps been a consequence of the aforementioned inhomogeneities in the immobilized structure created by the pressure drop. However, recent work improved the method and showed that a good reproducibility was achievable [7]. The miniaturization of the magnets and their direct integration in the chip should also offer new possibilities for improving those types of applications. Also, some devices are now appearing where several plugs of beads would allow for realizing more complex biological analysis.

Even if the mixing devices afford a convenient and efficient alternative, there is little chance that they will replace their conventional counterpart in the future. One of the main reasons is that, to date, they all involve the presence of stirrers (magnetic chains, magnetic sheets or microfabricated rotors) in the channel. Also, for the moment, the use of magnetic beads as labels for detection will not replace the use of fluorescent labels. On the other hand, the magnetic-based sorting systems are very competitive and should become an important tool in this field. The self-organization of beads has offered a great advantage in numerous applications. The ability to tune the order of the structure makes them a strong tool and further improvement and new applications should soon appear.

Finally, the use of magnetic fields has also been integrated in more complex Lab-on-Chip system to fulfill one of the steps of a complete biological analysis. Beads are, for example, used to trap and immobilize cells at the beginning of a complete genetic analysis that requires several steps (polymerase chain reaction, electrophoresis, etc. . .).

Future Directions for Research

Magnetic fields will take a growing place in the future of microfluidics. The miniaturization of the magnets and magnetic coils will soon replace the use of their large-scale counterparts, and most of the devices should soon have them integrated in the chip. The specific grafting of biomolecules onto magnetic beads still suffers from a great variability depending on the molecule. An effort in research has to be made to provide new methods or new beads that will facilitate this process. Finally, most of the work presented in this entry is still at the level of proof of principle. The reproducibility and reliability of these devices must be addressed before we see them integrated in commercial Lab-on-Chip.

M

Cross References

- ▶ Magnetic Pumps
- ▶ Magnetophoresis
- ▶ Electromagnetic Valves
- ▶ Ferro Fluid in Microchannel
- ▶ Integrated Micro Devices for Biological Applications
- ▶ Lab-on-Chip Devices for Particle and Cell Separation

References

1. Pamme N (2005) Magnetism and microfluidics. Lab Chip 6:24–38
2. Deng T, Prentiss M, Whitesides GM (2002) Fabrication of magnetic microfiltration system using soft lithography. Appl Phys Lett 80(3):461-463
3. Inglis DW, Riehn R, Austin RH, Sturm JC (2004) Continuous microfluidic immunomagnetic cell separation. Appl Phys Lett 85:5093–5095
4. Psychari E, Saliba AE, Fütterer C, Slovakova M., Goubault C, Viovy JL (2005) Cell sorting in a microfluidic channel with magnetic nanoparticules. Proceedings of µTAS 2005 conference, Boston, p 355
5. Lee H, Liu Y, Westervelt RM, Ham D (2006) IC/Microfluidic hybrid system for magnetic manipulation of biological cells. IEEE 41:1471–1480
6. Gijs MAM (2004) Magnetic bead handling on-chip: new opportunities for analytical applications. Microfluid Nanofluid 1:22–40
7. Slovakova M, Minc N, Bilkova Z, Smadja C, Faigle W, Fütterer C, Taverna M, Viovy JL (2005) Use of self assembled magnetic beads for on-chip protein digestion. Lab Chip 5:935–942
8. Hayes MA, Polson NA, Phayre AN, Garcia AA (2001) Flow based microimmunoassay. Anal Chem 73:5896–5902

9. Doyle PS, Bibette J, Bancaud A, Viovy JL (2002) Self-assembled magnetic matrices for DNA separation chips. Science 295:2237
10. Pamme N, Wilhelm C (2006) Continuous sorting of magnetic cells via on-chip free-flow magnetophoresis. Lab Chip 6:974–980

Magnetic Field-Based Microfluidic Devices

► Magnetic Field-Based Lab-on-Chip Devices

Magnetic Fields

Definition

Magnetic fields are created by permanent magnets or magnetic coils and can be used to magnetize and/or apply forces on other magnetic materials.

Cross References

► Magnetic Field-Based Lab-on-Chip Devices

Magnetic Filter

Synonyms

Magnetic mass spectrometer

Definition

A mass filter that separates ions according to their trajectories in a magnetic field. A device with a fixed magnetic field normally acts as a mass spectrograph, whereas a device with a variable field acts as a mass spectrometer.

Cross References

► Mass Spectrometry

Magnetic Fluid

► Ferrofluids in Microchannels

Magnetic Mass Spectrometer

► Magnetic Filter

Magnetic Microbeads

Definition

Magnetic microbeads are micrometer spherical particles that have magnetic entities embedded in a latex shell.

Cross References

► Magnetic Field-Based Lab-on-Chip Devices

Magnetic Pumps

Barbaros Cetin, Dongqing Li
Department of Mechanical Engineering, Vanderbilt University, Nashville, TN, USA
barbaros.cetin@vanderbilt.edu

Synonyms

Electromagnetically actuated pumps; Magnetohydrodynamic pumps

Definition

Magnetic pumps are pumps using electromagnetic or magnetic fields to actuate or to control the fluid motion in microchannels. The application of electromagnetic or magnetic forces is a flexible way of manipulating fluids in lab-on-a-chip devices.

Overview

Micropumps can be classified into two general categories: mechanical and non-mechanical micropumps (an excellent review on micropumps can be found elsewhere [1]). In most mechanical pumps, a membrane is used to produce the pumping action. Non-mechanical micropumps on the other hand generally have no moving parts. Magnetic pumps can be found in both categories in the literature.

Khoo and Liu [2] presented results on the design, fabrication and testing of a novel, micromachined magnetic membrane microfluidic pump. Their pump was composed of a magnetic microactuator, which is based on a thin polydimethylsiloxane (PDMS) membrane, and two polymer-based one-way diffuser valves. Membrane displacement was achieved by the interaction of an external magnet (Fig. 1) with ferromagnetic materials which are embedded within the membrane. It was indicated that the flow rate of the micropump can be controlled by controlling the magnetic field strength and the actuation frequency of the membrane.

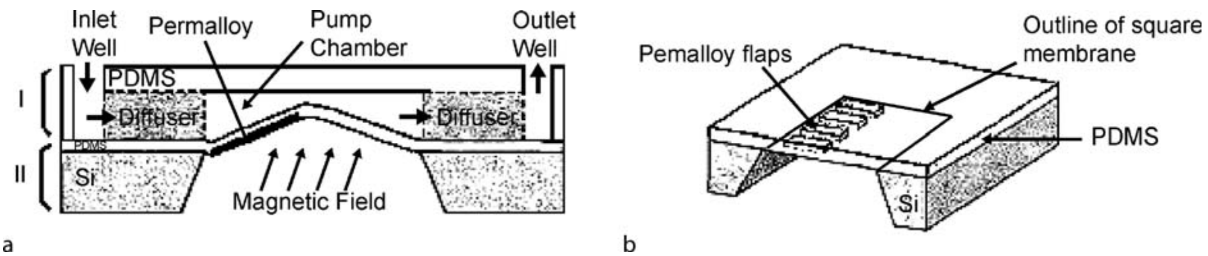

Magnetic Pumps, Figure 1 (**a**) Cross-section of assembled micropump and (**b**) schematic cut-out of membrane actuator. Reprinted from [2] with permission from Dr. Liu

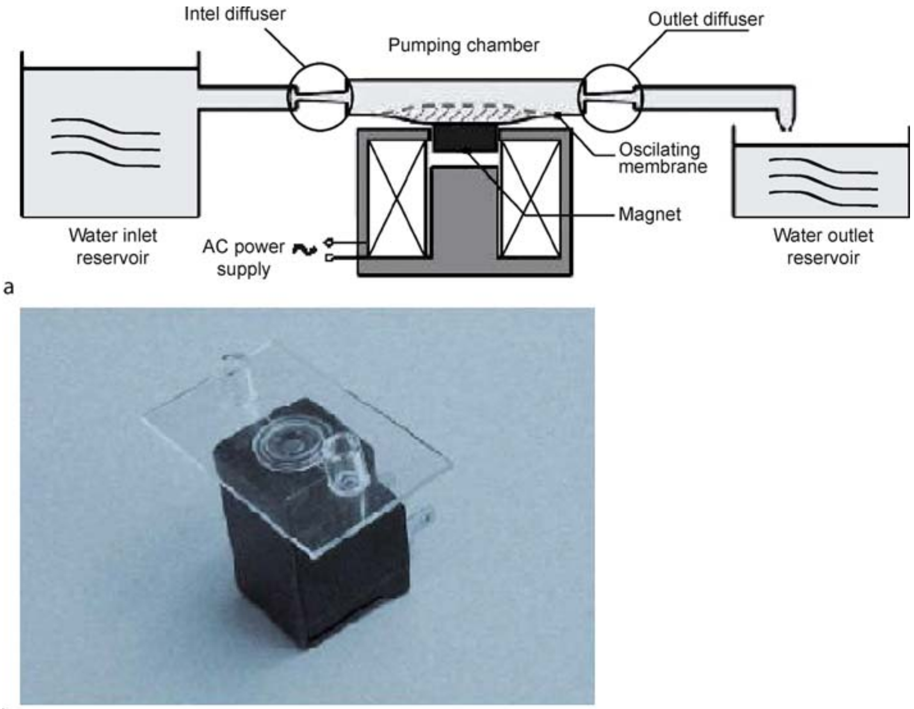

Magnetic Pumps, Figure 2 (**a**) Schematic and (**b**) photograph of micropump system of [4]. Reprinted from [4] with permission from Dr. Yamahata

Yamahata et al. [3] fabricated and characterized a poly(methyl methacrylate) (PMMA) valveless micropump which was actuated magnetically using an external electromagnet. The pump consisted of two diffuser elements and a PDMS membrane with an integrated composite magnet made of magnetic powder. They tested the setup with water and air. They relate the flow rate with the actuation frequency, and showed that frequency near to the natural frequency of the membrane generates higher flow rates due to the larger amplitude membrane vibrations. In their following study [4] (Fig. 2), they used glass instead of PMMA, and used a newly designed membrane, an improved actuation coil and a solid magnet rather than a polymer-bound powder magnet. They achieved four times larger pumping pressures compared to their PMMA-based pump.

Pan et al. [5] studied a magnetically driven PDMS membrane micropump with two ball check-valves (Fig. 3). Two driving mechanisms to generate the external magnetic force for the membrane were used: one used a permanent magnet with a small direct current (DC) motor and the other an integrated coil. They obtained higher flow rates with the latter mechanism but lower power consumption with the former mechanism.

Non-mechanical micropumps using the principle of magnetohydrodynamics (MHD) for fluid motion have also been studied in the literature. If an electrical field, $\boldsymbol{E}$, and

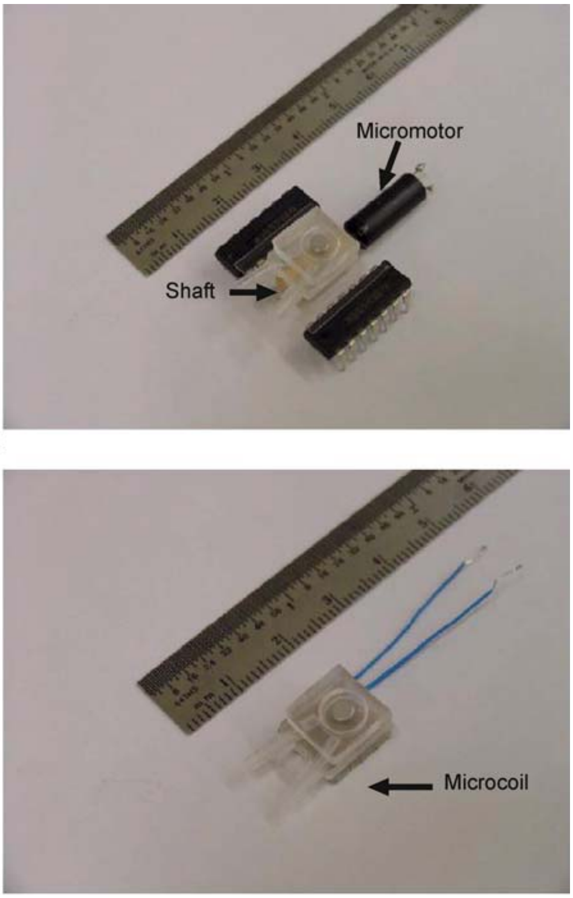

Magnetic Pumps, Figure 3 Test and measurement setup for two micropumps of different driving mechanisms: (**a**) permanent magnet with a small DC motor; (**b**) integrated coil. Reprinted from [5] with permission from Dr. Ziaie

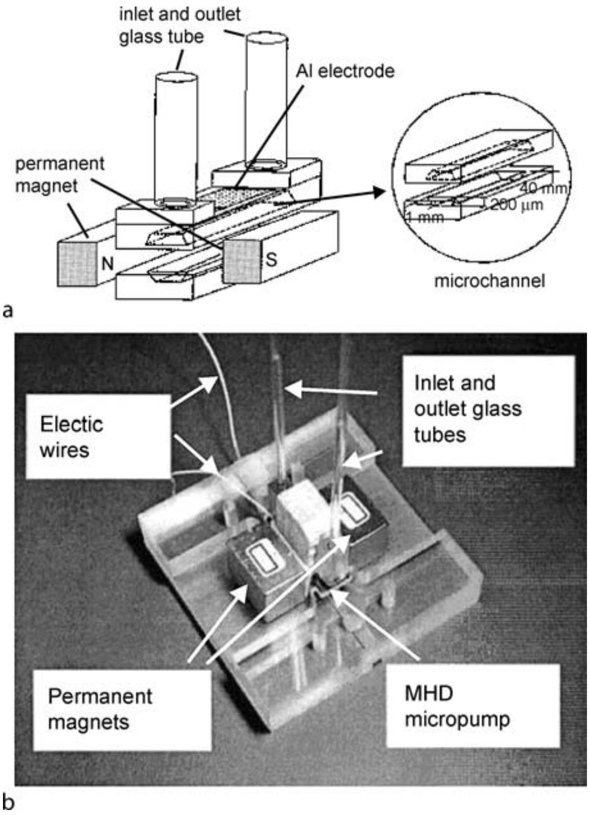

Magnetic Pumps, Figure 4 (**a**) Schematic and (**b**) photograph of micropump system of [6]. Reprinted from [6] with permission from Dr. Jang

a magnetic field, $\boldsymbol{B}$, are applied perpendicular each other they create a Lorenz force in the direction of $\boldsymbol{J} \times \boldsymbol{B}$, where $\boldsymbol{J}$ is the electrical current density. Since the mean free path of ions in a liquid is extremely small, momentum is transferred from the ions to the solvent molecules rapidly by collisions. Therefore, the sum of the Lorentz forces on all of the ions inside the liquid is just the net driving force causing the bulk liquid motion in MHD pumps. Jang and Lee [6] (Fig. 4), Huang et al. [7] and Zhong et al. [8] successfully applied the MHD principle for the development of micropumps using DC. The pressure head generated by MHD pumps can be controlled by adjusting the intensity of the magnetic field, the magnitude of the applied voltage across the electrodes and the length of the actuation section, which makes the usage of MHD pumps very flexible. However, all these micropumps suffer from bubble generation at certain voltage values at the electrodes that are used to generate the electrical field. Lemoff and Lee [9] used alternating current (AC) in their MHD micropump and eliminated bubble generation (Fig. 5). They used an electromagnet to generate the magnetic field. They showed that by using an electromagnet, multiple pumps can be driven independently by varying the amplitude and phase of the currents of electrodes and electromagnet.

Cross References

- ► Electrical Pumps
- ► Ultrasonic Pumps
- ► Thermocapillary Pumping

References

1. Laser DJ, Santiago JG (2004) A review of micropumps. J Micromech Microeng 14:35–64
2. Khoo M, Liu C (2000) A novel micromachined magnetic membrane microfluidic pump. Proceedings of the 22nd Annual EMBS International Conference, July 23–28, Chiago, IL, 2394–2397
3. Yamahata C, Lotto C, Al-Assaf E, Gijs MAM (2005) A PMMA valveless micropump using electromagnetic actuation. Microfluid Nanofluid 1:197–207

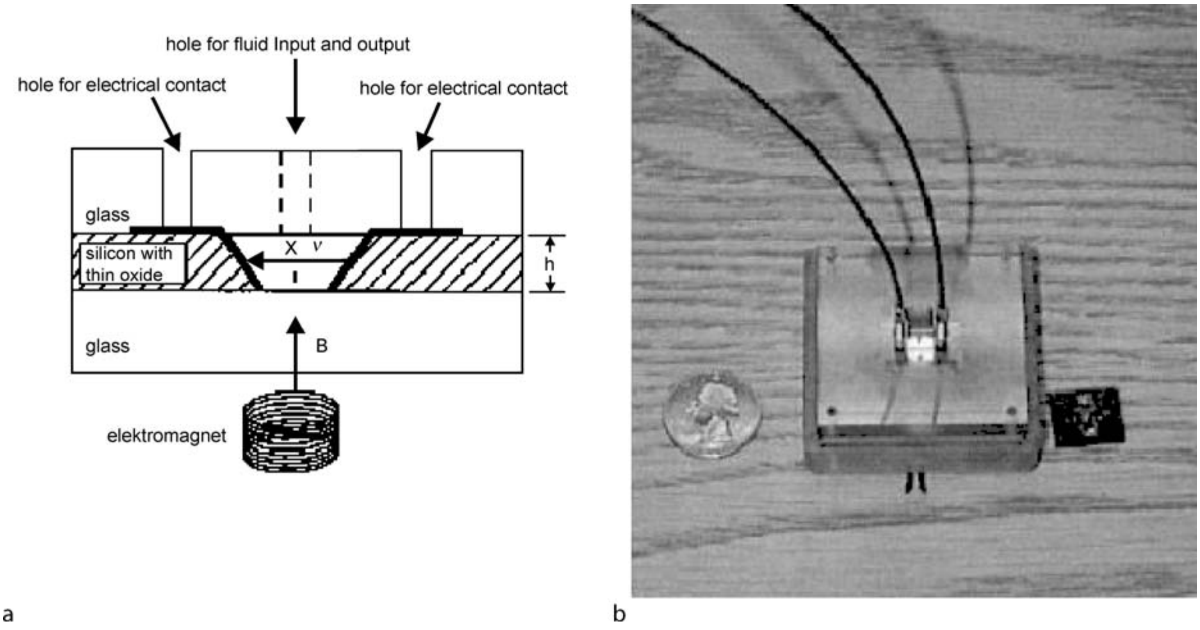

Magnetic Pumps, Figure 5 (**a**) Cross-section of AC MHD and (**b**) photograph of micropump system of [9]. Reprinted from [9] with permission from Dr. Lee

4. Yamahata C, Lacharme F, Gijs MAM (2005) Glass valveless micropump using electromagnetic actuation. Microelectron Eng 78–79, 132–137
5. Pan T, Mcdonald SJ, Kai EM, Ziaie B (2005) A magnetically driven PDMS micropump with ball check-valves. J Micromech Microeng 15:1021–1026
6. Jang J, Lee SS (2000) Theoretical and experimental study of MHD (magnetohydrodynamic) micropump. Sens Actuators 80:84–89
7. Huang L, Wang W, Murphy MC, Lian K, Gian ZG (2000) LIGA Fabrication and test of a DC type magnetohydrodynamic (MHD) micropump. Microsyst Technol 6:235–240
8. Zhong J, Yi M, Bau HH (2002) Magneto hydrodynamic (MHD) pump fabricated with ceramic tapes. Sens Actuators A 96:59–66
9. Lemoff AV, Lee AP (2000) An AC magnetohydrodynamic micropump. Sens Actuators B 63:178–185

Magnetic Split-Flow Thin Fractionation

► Magnetophoresis

Magnetic Susceptibility

Definition

The magnetic susceptibility represents the amount of magnetization of a material in response to an applied magnetic field.

Cross References

► Magnetic Field-Based Lab-on-Chip Devices

Magnetohydrodynamic Pumps

► Magnetic Pumps

Magnetophoresis

Hui Yan, Hongkai Wu
Department of Chemistry, Tsinghua University, Beijing, P. R. China
hkwu@mail.tsinghua.edu.cn

Synonyms

Free-flow magnetophoresis; On-chip free-flow magnetophoresis; Magnetic split-flow thin fractionation; Capillary magnetophoresis; Electromagnetophoresis

Definition

Magnetophoresis, a nondestructive method for selectively collecting or separating magnetic particles, is the process of magnetic particle motion in a viscous medium under the influence of the magnetic field; the viscous medium may

be a magnetic or immunomagnetic liquid and the magnetic field should be in a gradient format.

Chemical and Physical Principles

The operating principle of the magnetophoresis is that the direction and velocity of the particle movement in a gradient magnetic field are determined by magnetic ($\boldsymbol{F}_{\mathrm{m}}$), gravitational ($\boldsymbol{F}_{\mathrm{g}}$), and drag ($\boldsymbol{F}_{\mathrm{d}}$) forces. By selectively controlling these forces, it is possible to control the mobility of the different species and, therefore, magnetically fractionate mixtures of them into discrete groups. If the analysis is limited to the motion of small particles, the inertial force can be neglected and the force balance equation is written as

$$\boldsymbol{F}_{\mathrm{m}} + \boldsymbol{F}_{\mathrm{g}} + \boldsymbol{F}_{\mathrm{d}} = 0 \tag{1}$$

Where (1)

$$\boldsymbol{F}_{\mathrm{m}} = \frac{4}{3\mu_0}\pi r^3 \Delta x\, |B|\, \nabla\, |\boldsymbol{B}| \tag{2a}$$

$$\boldsymbol{F}_{\mathrm{g}} = \frac{4}{3}\pi r^3 \left(\rho_{\mathrm{P}} - \rho_{\mathrm{f}}\right) \boldsymbol{g} \tag{2b}$$

$$\boldsymbol{F}_{\mathrm{d}} = 6\pi \eta r \boldsymbol{U} \tag{2c}$$

In Eqs. (2a)–(2c), r is the particle radius (m); Δx is the difference between the volume magnetic susceptibility of the particle and separation fluid; B is magnetic induction (Tesla); μ_0 ($= 4\pi \times 10^{-7}$ H/m) is the permeability of free space; ρ_{p} and ρ_{f} are the density of the particle and separation fluid, respectively (kg/m^3); η is the dynamic viscosity of separation fluid (kg/ms); and $\boldsymbol{U}$ is the particle migration velocity (m/s).
Inserting Eqs. (2a)–(2c) into Eq. (1), the migration velocity can be obtained

$$\boldsymbol{U} = \frac{2r^2 \Delta x |B| \nabla |\boldsymbol{B}|}{9\eta\mu_0} + \frac{2r^2 \left(\rho_{\mathrm{P}} - \rho_{\mathrm{f}}\right) \boldsymbol{g}}{9\eta} \tag{3}$$

Equation (3) considers the magnetic field and field gradient generated by the magnet only, and the interactions between particles are not included. Equation (3) shows that the migration velocity is strongly dependent on particle size.

Key Research Findings

Free-Flow Magnetophoresis of Continuous Flow Separation of Magnetic Particles

In continuous flow, magnetic particles were deflected from the direction of laminar flow by a perpendicular magnetic field depending on their magnetic susceptibility and size and on the flow rate. The particles with the larger susceptibility were deflected further from the direction of laminar flow than the other magnetic particles. Nonmagnetic beads, however, were not deflected at all. Magnetic particles could thus be separated from each other and from nonmagnetic materials. The applied flow rate and the strength and gradient of the applied magnetic field were the key parameters in controlling the deflection.
The central component is a rectangular flat separation chamber over which a laminar flow is generated in the x-direction by a number of inlet and outlet channels (Fig. 1). Magnetophoretic separation is based on deflection of the particles into the y-direction. Perpendicular to the direction of laminar flow, i. e., in the y-direction, an inhomogeneous magnetic field is applied, which forms a magnetic field gradient over the separation chamber. A mixture of particles can be injected continuously into the system through the sample inlet channel. The nonmagnetic particles are not influenced by the magnetic field and leave the chamber at the exit opposite the sample inlet. Superparamagnetic particles, however, become magnetized and are hence dragged into the inhomogeneous magnetic field. The deflection of the magnetic particles, $\boldsymbol{U}_{\mathrm{defl}}(\mathrm{ms}^{-1})$ can be described as the sum of two vectors: the vector for the magnetically induced flow velocity on the particle, $\boldsymbol{U}_{\mathrm{mag}}(\mathrm{ms}^{-1})$, and the vector for the velocity of the hydrodynamic flow $\boldsymbol{U}_{\mathrm{hyd}}(\mathrm{ms}^{-1})$:

$$\boldsymbol{U}_{\mathrm{defl}} = \boldsymbol{U}_{\mathrm{mag}} + \boldsymbol{U}_{\mathrm{hyd}} \tag{4}$$

The magnetically induced flow, $\boldsymbol{U}_{\mathrm{mag}}$, is the ratio of the magnetic force, $\boldsymbol{F}_{\mathrm{mag}}(\boldsymbol{N})$, exerted on the particle by the magnetic field to the viscous drag force:

$$\boldsymbol{U}_{\mathrm{mag}} = \frac{\boldsymbol{F}_{\mathrm{mag}}}{\boldsymbol{F}_{\mathrm{drag}}} = \frac{\boldsymbol{F}_{\mathrm{mag}}}{6\pi\eta r} \tag{5}$$

where η is the viscosity of the medium ($\mathrm{kgm}^{-1}\mathrm{s}^{-1}$) and r the particle radius (m).
The magnetic force, $\boldsymbol{F}_{\mathrm{mag}}$, is:

$$\boldsymbol{F}_{\mathrm{mag}} = \frac{\Delta x \cdot V_{\mathrm{p}}}{\mu_0} \cdot (\nabla \cdot B) \cdot \boldsymbol{B} \tag{6}$$

When inserting Eq. (6) into Eq. (5), it can be seen that, for a given magnetic field and a given viscosity, the magnetic velocity, $\boldsymbol{U}_{\mathrm{mag}}$, is dependent on the size and the magnetic characteristics of the particle. It is proportional to the square of the particle radius and to the magnetic susceptibility of the particle:

$$\boldsymbol{U}_{\mathrm{mag}} \propto r^2 \Delta x \tag{7}$$

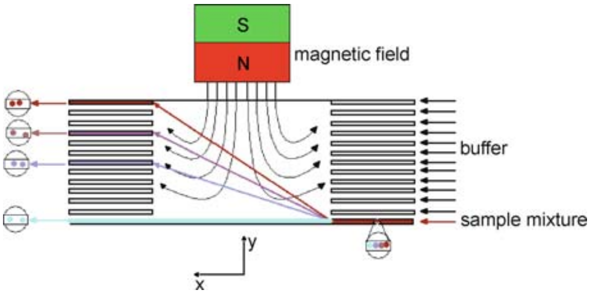

Magnetophoresis, Figure 1 Concept of free-flow magnetophoresis. Magnetic particles are pumped into a laminar flow chamber; a magnetic field is applied perpendicular to the direction of flow. Particles deviate from the direction of laminar flow according to their size and magnetic susceptibility and are thus separated from each other and from nonmagnetic material

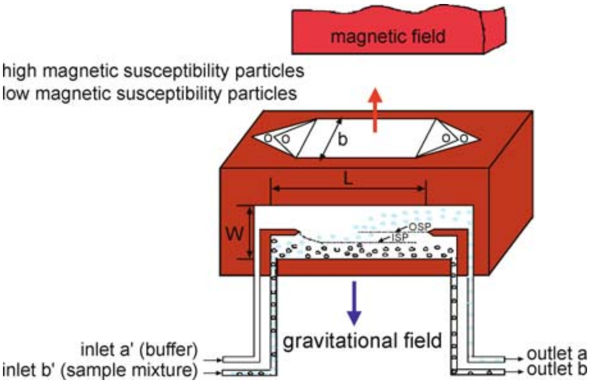

Magnetophoresis, Figure 2 Diagram of magnetic separator. Magnetic force is applied upward and gravitational force downward. The flow-rate conditions: $\boldsymbol{U}(a') > \boldsymbol{U}(b')$, $\boldsymbol{U}(a) = \boldsymbol{U}(b)$, $\boldsymbol{U}(b) > \boldsymbol{U}(b')$

Hence, particles that are either different in size, r, or different in their magnetic susceptibility, x_{p}, will be deflected from the direction of laminar flow to a different degree.

Free-flow magnetophoretic separations could be hyphenated with other microfluidic devices for reaction and analysis steps to form a micro total analysis system, i. e. on-chip free-flow magnetophoresis.

Magnetic Split-Flow Thin (SPLITT) Fractionation

A magnetic field was utilized as a driving force for split-flow thin (SPLITT) fractionation by Fuh and co-workers. This technique allowed the complete separation of paramagnetic ion-labeled particles from non-labeled particles. Zborowski et al. constructed a cylindrically-symmetric SPLITT fractionation channel that used a quadrupole magnetic field. In SPLITT fractionation the separation axis is the thin dimension of the channel.

The system set-up is shown in Fig. 2. The system had two inlets, two outlets, an inlet and an outlet splitter. The theory of operation of system is that magnetic force and gravitational force were applied in opposite direction on the channel to facilitate separation by the set-up. The sample mixture with carriers was introduced into inlet b' and the sample-free buffer (separation medium) was introduced into inlet a' to confine the samples into a small zone close to the bottom wall of the channel. Magnetic force drove the particles with high magnetic susceptibility upward toward the top wall, while particles with low magnetic susceptibility or nonmagnetic settled toward the bottom wall due to gravitational force. Particles with high magnetic susceptibility came out at outlet a, and particles with low magnetic susceptibility or nonmagnetic came out at outlet b.

For a species to be transported across a lamina of flow-rate $\boldsymbol{U}_i$, the field-induced flow-rate ($bL\boldsymbol{U}$) must be larger than or equal to $\boldsymbol{U}_i$, as shown in the following equation [8]:

$$bL\boldsymbol{U} \geq \boldsymbol{U}_i \tag{8}$$

where b is the channel breadth, L is the channel length, and $\boldsymbol{U}$ is the field-induced velocity. All particles with high magnetic susceptibility exit at outlet a when Eq. (8) is satisfied. This means that the net flow-rate resulting from subtracting the magnetically-induced flow-rate ($bL\boldsymbol{U}_{\mathrm{m}}$) from the gravitationally-induced flow-rate ($bL\boldsymbol{U}_{\mathrm{g}}$) was higher than the flow-rate at outlet b. Similarly all particles with low magnetic susceptibilities exit at outlet b when Eq. (9) is satisfied. The requirement that particles with very low magnetic susceptibility are fully retrieved at outlet b is quite straightforward from Eq. (9) when $\boldsymbol{U}(b) > \boldsymbol{U}(b')$ (i. e., the volumetric flow-rate at outlet b is higher than that at inlet b'). The gravitationally-induced flow-rate does not play an important role for particles with very low magnetic susceptibilities as shown in Eq. (9). The conditions of flow-rate used in this study keep $\boldsymbol{U}(b) > \boldsymbol{U}(b')$ valid. In order to achieve complete separation, Eqs. (8) and (9) must both be satisfied by particles with high and low magnetic susceptibilities

$$bL\boldsymbol{U}_{\mathrm{mh}} - bL\boldsymbol{U}_{\mathrm{g}} \geq \boldsymbol{U}(b) \tag{9}$$

$$bL\boldsymbol{U}_{\mathrm{ml}} - bL\boldsymbol{U}_{\mathrm{g}} < \boldsymbol{U}(b) - \boldsymbol{U}(b') \tag{10}$$

All particles with high magnetic susceptibilities exit at outlet a when Eq. (8) is satisfied. All particles with low magnetic susceptibilities exit at outlet b when Eq. (9) is satisfied.

Where $\boldsymbol{U}_{\mathrm{m}}$ is the magnetically-induced velocity ($\boldsymbol{U}_{\mathrm{mh}}$ and $\boldsymbol{U}_{\mathrm{ml}}$ are used for magnetically-induced velocities of particles with high and low magnetic susceptibilities, respectively), $\boldsymbol{U}_{\mathrm{g}}$ is the g gravitationally-induced velocity, $\boldsymbol{U}(b)$

is the volumetric flow-rate at outlet b, and $\boldsymbol{U}(b')$ is the volumetric flow-rate at inlet b'. Magnetically-induced velocity, $\boldsymbol{U}_{\mathrm{m}}$, can be calculated using

$$\boldsymbol{U}_{\mathrm{m}} = \frac{\Delta x \Delta H^2 d}{48\eta} \tag{11}$$

where $\Delta x = x_{\mathrm{p}} - x_{\mathrm{f}}$. x_{p} and x_{f} are the respective magnetic susceptibilities of particles and separation fluid, η is the fluid viscosity, d is the spherical particle diameter or the effective spherical diameter, and symbol ΔH is the drop in magnetic field strength. Gravitationally-induced velocity, U_{g}, can be calculated using

$$\boldsymbol{U}_{\mathrm{g}} = \frac{\Delta\rho d^2 g}{18\eta} \tag{12}$$

where η is the fluid viscosity, $\Delta\rho$ is the particle density minus the carrier fluid density, g is gravitational acceleration, and d is the spherical particle diameter or the effective spherical diameter. For particles with magnetically-induced velocity $\boldsymbol{U}_{\mathrm{m}}$ is between $\boldsymbol{U}_{\mathrm{mh}}$ and $\boldsymbol{U}_{\mathrm{ml}}$, the fraction of particles exiting at outlet a could be calculated using:

$$\frac{bL\boldsymbol{U}_{\mathrm{m}} - bL\boldsymbol{U}_{\mathrm{g}} - \boldsymbol{U}(b) + \boldsymbol{U}(b')}{\boldsymbol{U}(b')} \tag{13}$$

Capillary Magnetophoresis

The configuration of the magnets shown in Fig. 3 generated a large magnetic field gradient along the x-axis and enabled the magnetophoresis. The edge of the iron tips was defined as $x = 0$ and the direction toward the interior of the gap between the tips as $x > 0$.

In an inhomogeneous magnetic field, a particle in a solution experiences two types of forces. One is the magnetic force working on the particle itself, $\boldsymbol{F}_{\mathrm{p}}$, and the other is the magnetic buoyancy, $\boldsymbol{F}_{\mathrm{f}}$, exerted by the paramagnetic medium, with a direction opposite to $\boldsymbol{F}_{\mathrm{p}}$. The net force working on a particle, $\boldsymbol{F}_{\mathrm{m}}$, can be described as follows

$$\boldsymbol{F}_{\mathrm{m}} = \boldsymbol{F}_{\mathrm{p}} - \boldsymbol{F}_{\mathrm{f}} = \frac{V\left(x_{\mathrm{p}} - x_{\mathrm{f}}\right)}{\mu_0}\left(B\frac{\mathrm{d}B}{\mathrm{d}x}\right) \tag{14}$$

where V is the volume of the spherical particle (m^3), x_{p} and x_{f} are the respective magnetic susceptibilities per unit volume of the particle and the medium, m is the vacuum magnetic permeability (NA^{-2}) and $\mathrm{d}B/\mathrm{d}x$ the gradient of magnetic flux density ($\mathrm{NA}^{-1}\mathrm{m}^{-2}$). Acceleration and mass of the particle are so small in our system that the particles can migrate with a constant velocity, $\boldsymbol{U}$, keeping balance between the net magnetophoretic force, $\boldsymbol{F}_{\mathrm{m}}$, and the viscous or m frictional force, $\boldsymbol{F}_{\mathrm{U}}$, which is expressed by Stokes' law

$$\boldsymbol{F}_{\mathrm{v}} = 6\pi\eta r v \tag{15}$$

where η is the fluid viscosity (Pas) and r the radius of the spherical particle (m).

From Eqs. (14) and (15), we can obtain the migration velocity v of a spherical particle as

$$\boldsymbol{U} = \frac{2}{9}\frac{\left(x_{\mathrm{p}} - x_{\mathrm{f}}\right) r^2}{\mu_0 \eta}\left(B\frac{\mathrm{d}B}{\mathrm{d}x}\right) \tag{16}$$

This equation can be used for the determination of $B(\mathrm{d}B/\mathrm{d}x)$ on the micrometer scale from the measurement of the velocity of a microparticle as a function of x. Also, at the point of minimum $B(\mathrm{d}B/\mathrm{d}x)$, a microparticle can be trapped in the capillary with the force of $\boldsymbol{F}_{\mathrm{m}}$. In addition, by controlling the rate of counter-current flow against the magnetophoretic buoyancy, differently sized microparticles can be segregated. If the flow-rate is lower than the velocity represented by Eq. (16), the particle cannot go through the minimum point and is trapped. When the flow-rate is the same as the velocity v, the probability of the particle passing through the minimum point is 50%. A flow-rate higher than $\boldsymbol{U}$ will result in complete passing.

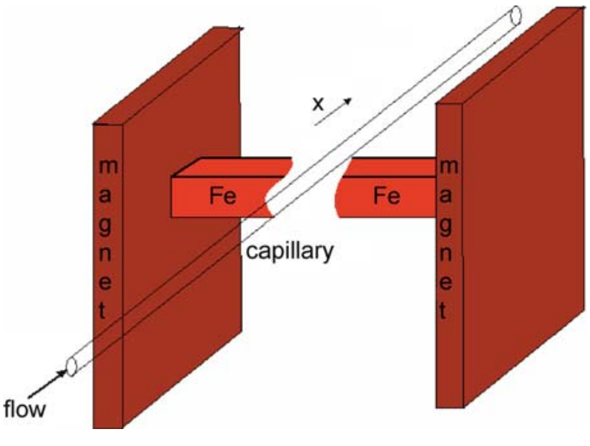

Magnetophoresis, Figure 3 Enhanced of the magnetic field gradient by the pair of iron pieces

Electromagnetophoresis

The general concept of electromagnetophoresis (EMP) is the application of Lorentz force to migration analysis. The basic theory of electromagnetophoresis was proposed by Kolin in 1953. Electromagnetophoresis is a phenomenon where particles in an electrolyte solution migrate in the direction perpendicular to both a magnetic field and an electric current when the electric current is applied through the conductive fluid and the homogeneous magnetic field

is perpendicular to the current. When an electric current of density j (Am^{-2}) passes through a conductive fluid of volume V (m^3) perpendicular to a magnetic field, the fluid invariably experiences a force, the Lorentz force, expressed as

$$\boldsymbol{F} = \mu_0 \mu H \boldsymbol{j} \boldsymbol{V} \tag{17}$$

where μ_0 is the vacuum magnetic permeability (Ns^2C^{-2}), μ is the magnetic permeability of the conductor, and H is the magnetic field strength (Am^{-1}). As the current passes through the conductive fluid under a magnetic field, all of the fluid experiences the force and so a pressure gradient is produced inside. Figure 4 shows a schematic drawing of forces exerted on a particle in the fluid in this situation. When a current is applied through the enclosed conductive fluid in the homogeneous magnetic field, the force is exerted on both the fluid and the particles. If the force exerted on the fluid is equal to the one acting upon the particles, the particles dispersed in the fluid will be at rest. However, if the two forces are different, migration of the particles will be caused. The two forces acting on a particle in Fig. 4 are called the electromagnetic weight (EMW), $\boldsymbol{F}_{\mathrm{EMW}}$, and the electromagnetic buoyancy (EMB), $\boldsymbol{F}_{\mathrm{EMB}}$, acting opposite to $\boldsymbol{F}_{\mathrm{EMW}}$. The strength of FEMB is equivalent to the force working on the fluid whose volume is equal to that of the particle (V). The electromagnetophoretic force, $\boldsymbol{F}_{\mathrm{EMP}}$, exerted on a particle in a closed

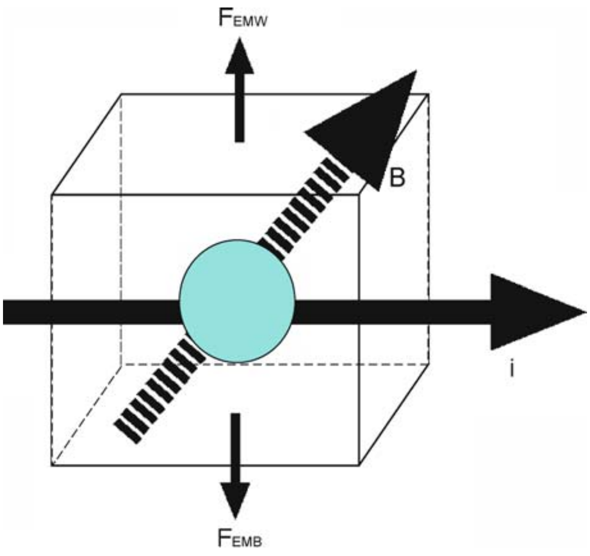

Magnetophoresis, Figure 4 Schematic drawing of the electromagnetic weight, FEMW, and the electromagnetic buoyancy, FEMB, exerted on a particle. They are perpendicular to a homogeneous magnetic field is maintained at right angles to the current enhanced of the magnetic field gradient by the pair of iron pieces

cell which has an inner section of S (m^2) is expressed as the sum of $\boldsymbol{F}_{\mathrm{EMW}}$ and $\boldsymbol{F}_{\mathrm{EMB}}$:

$$\boldsymbol{F}_{\mathrm{EMP}} = \boldsymbol{F}_{\mathrm{EMW}} + \boldsymbol{F}_{\mathrm{EMB}} = 2BV\left(\frac{\sigma_{\mathrm{P}} - \sigma_{\mathrm{f}}}{2\sigma_{\mathrm{f}} + \sigma_{\mathrm{P}}}\right)\frac{i}{S} \tag{18}$$

where B is the magnetic flux density ($NA^{-1}m^{-1}$), σ_{p} is the electrial conductivity (Sm^{-1}) of the particle, σ_{f} is the electrical conductivity (Sm^{-1}) of the medium, and i is the current (A). The electromagnetophoretic velocity $\boldsymbol{U}_{\mathrm{EMP}}$ of a spherical particle in the fluid is expressed as

$$\boldsymbol{U}_{\mathrm{EMP}} = \frac{4}{9}\left(\frac{\sigma_{\mathrm{P}} - \sigma_{\mathrm{f}}}{2\sigma_{\mathrm{f}} + \sigma_{\mathrm{P}}}\right)\frac{iBr^2}{S\eta C_{\mathrm{W}}} \tag{19}$$

where η is the fluid viscosity (Pa s), r is the radius of the spherical particle (m), and C_{W} is the viscous drag coefficient due to the surface of the wall.

Examples of Application

Analogous to electrophoresis, magnetophoresis is a nondestructive method for selectively collecting or separating magnetic particles. Magnetophoresis applications involving the controlled movement of magnetic micro/nanoparticles in microfluidic systems are diverse and growing rapidly. Some of the most interesting of these are in the fields of microbiology and biomedicine where magnetic particles are used to target, label, manipulate and separate biomaterials such as cells, enzymes, antigens and DNA. The intense research in these areas is due primarily to advances in microfluidic technology, and progress in the development of surface-functionalized magnetic particles that can selectively transport a target biomaterial. Separating magnetic particles from each other as well as from nonmagnetic material in continuous flow on a microfluidic chip (on-chip free-flow magnetophoresis) is also very interesting. The device features a separation chamber over which a laminar flow was generated by a number of inlet and outlet channels. A magnetic field was applied perpendicular to the direction of flow. Magnetic particles were dragged into this field and thus deflected from the direction of laminar flow, depending on their size and magnetic susceptibility.

Cross References

► Electrophoresis

References

1. Vickrey TM, Garciaramirez JA (1980) Magnetic field-flow fractionation – theoretical basis. Sep Sci Technol 15:1297–1304

2. Pamme N, Manz A (2004) On-Chip Free-Flow Magnetophoresis: continuous flow separation of magnetic particles and agglomerates. Anal Chem 76:7250–7256
3. Fuh CB, Chen SY (1998) Magnetic split-flow thin fractionation: new technique for separationof magnetically susceptible particles. J Chromatogr A 813:313–324
4. Chalmers JJ, Zborowski M, Sun L, Moore L (1998) Flow through, immunomagnetic cell separation. Biotechnol Prog 14:141–148
5. Watarai H, Namba M (2001) Magnetophoretic behavior of single polystyrene particles in aqueous manganese(II) chloride. Anal Sci 17:1233–1236
6. Watarai H, Namba H (2002) Capillary magnetophoresis of human blood cells and their magnetophoretic trapping in a flow system. J Chromatogr A 961:3–8
7. Kolin A (1953) An electromagnetokinetic phenomenon involving migration of neutral particles. Science 117:134–137
8. Kolin A (1967) Preparative electrophoresis in liquid columns stabilized by electromagnetic rotation: I. The apparatus. J Chromatogr A 26:164–179
9. Kolin A (1967) Preparative electrophoresis in liquid columns stabilized by electromagnetic rotation: II. Artifacts, stability and resolution. J Chromatogr A 26:180–193
10. Watarai H, Suwa M, Iiguni Y (2004) Magnetophoresis and electromagnetophoresis of microparticles in liquids. Anal Bioanal Chem 378:1693–1699

Magnetron

Definition

A device consisting of an evacuated chamber fitted with magnets for manipulated the paths electrons.

Cross References

► Sputtering for Film Deposition

Magnets

Definition

Magnets are pieces of ferromagnetic material; they produce a permanent magnetic field.

Cross References

► Magnetic Field-Based Lab-on-Chip Devices

MALDI

► Matrix Assisted Laser Desorption/Ionization

Manipulating Cells, Techniques

Daniel Irimia
Massachusetts General Hospital, Harvard Medical School, Boston, MA, USA
dirimia@partners.org

Synonyms

Cell handling

Definition

The collection of means for precise control of the static or dynamic position of individual biological cells with the purpose of observing, probing, and/or altering the cellular responses.

Overview

Different techniques for manipulating cells in microfluidic devices have been proposed for a wide variety of applications. The purpose of this essay is to systematize the techniques by the physical principles and forces used for controlling cell position. The reader is encouraged to follow the links to chapters describing in more detail how the interaction between cells and mechanical and biochemical entities, or with electrical, magnetic, or optical fields can be implemented at microscale for the handling of cells for various applications.

Several factors are usually considered for the choice of a cell manipulation method for a particular application. One important factor in the choice for a manipulation technique is the static or dynamic condition of the cell. In static conditions, cells are in a stationary phase and have to be actively moved to the desired location. In dynamic conditions, cells follow stream lines and the manipulation

Manipulating Cells, Techniques, Table 1 Classification of the techniques for manipulating cells by physical mechanisms employed

Physical Mechanism	Cell Condition	
	Static	Dynamic
Mechanical	Cell patterning	Sieves, posts, stagnation points
Biochemical	Chemical patterns	Antibody coated surfaces
Magnetic	Magnetic bead-mediated	Magnetic bead-mediated trapping
Electric	DEP traps	DEP barriers
Optical	Optical traps	Optical barriers

would either block cells in predetermined locations or only veer them into different stream lines. Some mechanisms are more appropriate for static conditions (e. g., cell patterning), while others benefit from the effects of the flow (e. g., sieves, light diffraction patterns). The choice of a manipulation mechanism is also related to the particular type of the cell to be manipulated. Bacteria cells are smaller (few microns) but more resistant to alterations of microenvironment around them, and thus are more difficult to manipulate mechanically and easier to handle using electric fields. Eukaryotic cells on the other hand are larger (10 – 20 μm diameter) but very sensitive to changes in the composition or temperature of their microenvironment, and thus mechanical methods are usually preferred. Finally, some of the manipulation mechanism can be made specific for a target cell type in a more complex sample, and differential handling and sorting of cells can be achieved by the use of particular manipulation mechanisms.

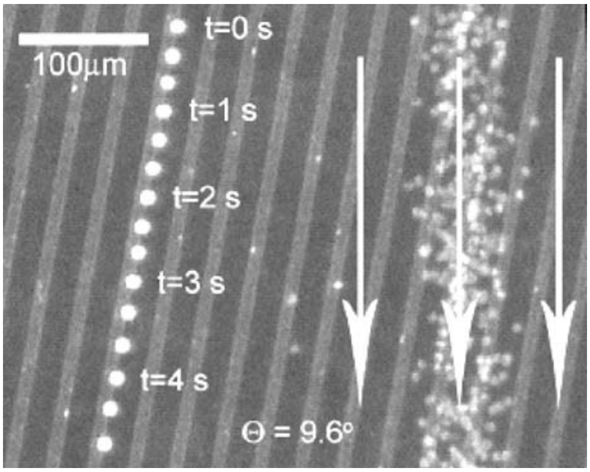

Manipulating Cells, Techniques, Figure 1 Dynamic handling of cells using magnetic beads. Time lapse image showing the separation of magnetically tagged leukocytes and non-tagged red blood cells using magnetic fields and recessed magnetic stripes [4]

Basic Methodology, Key Research Findings

The implementation of physical mechanisms at the microscale for cell manipulation takes advantage of the scaling laws at sizes comparable to cells sizes. Some of the techniques are widely used and very well developed (see the chapters on ► cell patterning, ► dielectrophoretic motion, ► optical tweezers). Other techniques are still emerging and our understanding of the practical aspects of these is still evolving.

By far the easiest to implement at microscale are the mechanical features for patterning and trapping cells in precise locations. Microwells and microchannels can be used to pattern cells and allow them to grow in precise configurations inside microfluidic chips (see also: ► cell culture 2D and 3D on chip). Eukaryotic cells can be mechanically trapped from flowing solutions by using arrays of posts, weir type structures, or channels of size too small for the cells to go through. For higher throughput applications, methods based on pinched flow and deterministic lateral displacement [1] are usually preferred.

Biochemical methods can be tuned to achieve the highest selectivity for the manipulation of cells from complex cell suspensions. Cell patterning (see ► cell patterning on chip) is now a well-established method and homogeneous as well as heterogeneous patterns, with various numbers of cells, and in various configurations have been described [2]. Selective capture of cells under flow conditions, on surfaces or posts is emerging as a reliable method for isolating specific cells from clinical samples that could be as complex as blood [3] (see also: ► integrated microfluidic systems for medical diagnostics).

The use of magnetic beads for manipulating cells has originally been developed for bulk assays. Magnetic beads coated with antibodies against proteins on the surface of cells are used as *a handle* to manipulate specific cells from complex suspensions. The integration of these assays in microfluidic format takes advantage of the capability of producing high magnetic field gradients at the microscale, in the close proximity of microscopic magnetic features. This approach has been demonstrated both for trapping cells in precise locations as well as for the deviation of tagged cells across streamlines and cell sorting [4] (see also magnetic particle labeling).

Dielectrophoresis methods for manipulation use electric fields to induce electrical polarization of cells and induce translational motion or reorientation of the cells. Dielectrophoresis is extremely attractive at the microscale because it can be fine tuned to be selective to different characteristics of the cells, and because low voltages are usually enough to produce intense electric fields [5, 6]. This technique is widely applied for bacteria handling in microfluidic devices, and applications for mammalian cells are emerging, including both trapping and dynamic perturbation in cell suspensions (see also ► dielectrophoretic motion of particles and cells).

Last but not least, optical methods for trapping and separating cells can achieve the highest precision and spatial resolution while having minimal secondary effects on the manipulated cells. Large scale arrays of optical traps are being used to manipulate multiple cells and particles at the microscale [7] and the integration of dynamically reconfigurable optical lattices have been demonstrated for

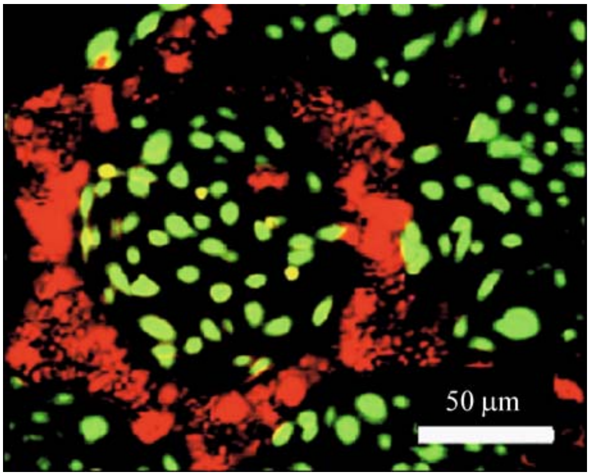

Manipulating Cells, Techniques, Figure 2 Static manipulation of cells. Micropatterning techniques were employed to precisely position hepatocytes (light gray, red in the online version) and fibroblasts (darker gray, green in the online version) in a configuration comparable to the regular liver functional unit [2]

the separation of particles based on size and refractive index (see also ► optical tweezers for manipulating cells and particles, and optophoresis for cell sorting). Despite their unmatched precision, optical methods have been so far confined to research applications only, mainly because of the requirements for expensive optical instruments that could not be integrated on the microfluidic chips.

Future Directions for Research

The interest in manipulating cells in microfluidic devices is growing because of increasing interest in the development of devices that use cells for basic research and clinical diagnostic purposes [8]. High throughput methods for manipulation of cells that could be applied to complex cell mixtures are expected to have a great impact in the development of point of care devices. New capabilities for manipulation and subsequent comprehensive analysis of single cells would become valuable discovery tools pushing the frontiers of biological research to new limits.

Cross References

- ► AC Dielectrophoresis Lab-on-Chip Devices
- ► Biomimetics
- ► Biosample Preparation Lab-on-a-Chip Devices
- ► Cell Adhesion and Detachment
- ► Cell Culture (2D and 3D) on Chip
- ► Electrokinetic Motion of Cells and Nonpolarizable Particles
- ► Cell Patterning on Chip
- ► Cell Sorting
- ► Cell-Based Assays Using Microfluidics
- ► Dielectrophoretic Motion of Particles and Cells
- ► Flow Cytometer Lab-on-Chip Devices
- ► Integrated Micro Devices for Biological Applications
- ► Integrated Microfluidic Systems for Medical Diagnostics
- ► Lab-on-a-Chip (General Philosophy)
- ► Lab-on-a-Chip Devices for Sample Extraction
- ► Lab-on-a-Chip Devices for Separation-Based Detection
- ► Lab-on-Chip Devices for Particle and Cell Separation
- ► Microfluidic Sample Manipulation
- ► Microfluidics for Stem Cell Therapy
- ► On-chip Cell Lysis
- ► Optical Tweezers for Manipulating Cells and Particles
- ► Single-Cell Analysis in Microfluidics

References

1. Davis JA, Inglis DW, Morton KJ, Lawrence DA, Huang LR, Chou SY, Sturm JC, Austin RH (2006) Deterministic hydrodynamics: Taking blood apart. Proc Natl Acad Sci USA 103(40):14779–14784
2. Folch A, Toner M (2000) Microengineering of cellular interactions. Annu Rev Biomed Eng 2:227–256
3. Cheng X, Irimia D, Dixon M, Sekine K, Demirci U, Zamir L, Tompkins RG, Rodriguez W, Toner M (2007) A microfluidic device for practical label-free CD4(+) T cell counting of HIV-infected subjects. Lab Chip 7(2):170–178
4. Inglis DW, Riehn R, Austin RH, Sturm JC (2004) Continuous microfluidic immunomagnetic cell separation. Appl Phys Lett 85(21):5093–5095
5. Voldman J (2006) Electrical forces for microscale cell manipulation. Annu Rev Biomed Eng 8:425–454
6. Gascoyne PR, Vykoukal J (2002) Particle separation by dielectrophoresis. Electrophoresis 23(13):1973–1983
7. Gluckstad J (2004) Microfluidics: Sorting particles with light. Nat Mater 3(1):9–10
8. Toner M, Irimia D (2005) Blood-on-a-chip. Annu Rev Biomed Eng 7:77–103

Marangoni Convection

Charles N. Baroud
LadHyX and Departement de Mécanique, Ecole Polytechnique, Palaiseau, France
baroud@ladhyx.polytechnique.fr

Synonyms

Thermocapillary convection; Solutal marangoni

Definition

The Marangoni effect refers to the variation of surface tension of a liquid with temperature (thermocapillarity) or

with the concentration of a surfactant (solutal Marangoni effect). The variation of surface tension in turn leads to convective motion of the fluid: Marangoni convection. This motion along the surface of the liquid layer in turn leads to flow in the bulk and may be used to transport fluids in microfluidic devices.

Overview

Solutal Marangoni convection is caused by variations in the concentration of a surfactant at the interface between two liquids or a liquid and a gas. The surface tension being a function of the local surface concentration of surfactant, a variation in the latter will affect the value of surface tension locally and therefore give rise to stresses along the interface. The relation between the surface concentration of surfactant and the surface tension is a complex one which will be addressed first. Furthermore, three important dynamical phenomena need to be accounted for in order to compute the Marangoni flow for a moving interface:

1. Adsorption of surfactant molecules to the surface
2. Transport of surfactant molecules in the bulk
3. Surface dilation or contraction

In the following, we start by describing the equilibrium relations that determine surface tension as a function of surfactant concentration. Then the mechanisms for dynamic variation are incorporated. Finally, the dynamic variations are related to the presence of Marangoni surface stresses and therefore Marangoni convection.

Surface Tension vs. Surface Concentration

Surfactants come in a very wide variety of sizes and compositions. What they have in common is their affinity for the surface of a liquid, which means that the free energy of the solvent/solute system is reduced when a surfactant molecule migrates to the surface, compared to when it is in the bulk of the fluid. As the concentration along the surface (Γ, in mol/m^2) increases, the original interface starts to give way to two new interfaces: solvent–surfactant and surfactant–air, with a lower global surface tension (γ, typically measured in mN/m or mJ/cm^2).

Surfactant molecules are typically composed of two parts: a hydrophilic head and a hydrophobic tail. Owing to this structure, a surfactant molecule will tend to adhere to the surface with a well determined orientation, for example with its hydrophobic part pointing out of the water phase. The final surface tension of the liquid–surfactant solution will therefore depend on the quality of the packing of surfactant molecules and their chemistry. They are termed 'soluble' if they can be dissolved in the bulk, even though they prefer to be on the interface. Common examples of soluble surfactants are soaps or other detergents.

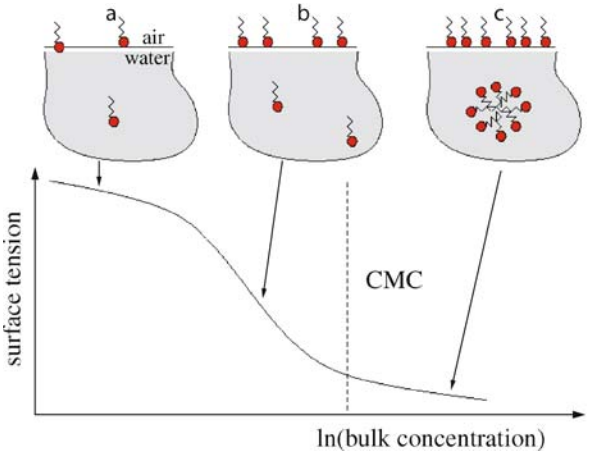

Marangoni Convection, Figure 1 Schematic of surfactant surface concentration and the corresponding surface tension, as a function of bulk concentration of surfactant on a logarithmic scale. The dashed line corresponds to the critical micellar concentration, discussed in the text

The relation between the surface tension of the interface and the surfactant concentration can be understood by thinking of the molecules as rigid objects covering the surface (Fig. 1). At very low concentrations (Fig. 1a), the molecules sit on the surface, far from each other, and do not affect the surface energy (and therefore surface tension) very significantly. As the concentration is increased however (Fig. 1b), the molecules start to cover a more significant part of the surface and the surface tension starts to decrease significantly. Beyond a critical concentration of surfactant (Fig. 1c), a new state becomes thermodynamically available to molecules, that of forming micelles, which are groupings of surfactants whose heads are exposed to the liquid and whose tails are enclosed within the ball. Beyond this critical micellar concentration (CMC), the surface tension remains approximately constant in spite of increasing the surfactant concentration in the solution.

Around 1920, I. Langmuir formalized the first nonlinear model to describe the surface tension dependence on surface concentration (see Ref. [1] for a detailed description). Langmuir's model is based on a lattice description of the adsorption sites, making three assumptions about the lattice which we quote from Ref. [1]:

1. every adsorption site on the lattice is equivalent;
2. the probability for adsorption at an empty site is independent of the occupancy of neighbouring sites; and
3. there are no interactions between the surfactant molecules in the lattice, and no intermolecular forces act between them.

By accepting that there is a maximum surface concentration (Γ_∞) and given an equilibrium constant K_L which

relates the rates of adsorption vs. desorption, we may write the equilibrium surface concentration as

$$\Gamma = \Gamma_\infty \left(\frac{K_L c}{1 + K_L c} \right) , \tag{1}$$

with c being the bulk concentration of surfactant molecules. Equation (1) contains two independent free parameters, K_L and Γ_∞ which must be measured from experiments, in practice.

By using this so-called Langmuir isotherm, one may write the surface tension, as derived by Frumkin, as

$$\gamma = \gamma_0 + RT\Gamma_\infty \ln (1 - \Gamma/\Gamma_\infty) . \tag{2}$$

Though it does not account for molecule–molecule interactions, this Frumkin–Langmuir model accounts for the trends of Fig. 1. It is currently the most widely used model for modelling surface tension dependence on bulk concentration.

Dynamic Situations

The above discussion accounts for the equilibrium state of a surface. However, when a new surface is formed (e. g. during drop formation), this equilibrium state will be reached after a transient time which ranges from milliseconds to hours, depending on the surfactant. The transient time is determined by the mobility of the molecules and their adsorption dynamics on the interface, which we discuss below.

Adsorption Dynamics

As stated above, the adsorption and desorption of molecules on an interface must be accounted for in understanding the dynamic variations of surface tension. Let us consider a newly formed interface of a liquid which contains a bulk concentration c of surfactant. At the initial moments, the interface is almost free of surfactant molecules and may resemble the situation of Fig. 1a. In this case, any surfactant molecules which happen to be in the neighbourhood of the interface will stick to it, and the rate at which the molecules arrive at the interface will limit their adsorption. In the absence of other driving mechanisms, this rate will depend only on the diffusion of molecules to the surface, and is typically very short.

At later times, the interface will start to look more like Fig. 1b, and now a molecule will adsorb to the surface only if it reaches an empty site. Furthermore, the high concentration of molecules at the interface means that they may also diffuse away, and then their desorption must also be modelled.

A classic model for accounting for adsorption/desorption dynamics is the Ward and Tordai equation [2]. This model predicts the presence of a subsurface layer, a few molecular diameters in size. Molecules present in the subsurface immediately adsorb to the surface at early times, while at later times they might linger there or possibly diffuse back into the bulk. Therefore, transport from the bulk to the subsurface is purely diffusive, while the mechanism between the subsurface and the surface depends on time in a more complex manner. The Ward–Tordai equation may be written as

$$\Gamma(t) = 2c_0\sqrt{\frac{Dt}{\pi}} - \sqrt{\frac{D}{\pi}} \int_0^{\sqrt{t}} c_s \, \mathrm{d}\left(\sqrt{t-\tau}\right) , \tag{3}$$

where c_0 is the bulk surfactant concentration far from the subsurface, D is the diffusion coefficient of the surfactant molecule, c_s is the concentration in the subsurface and τ is a dummy integration variable. Note that Eq. (3) constitutes an equilibrium relation between the diffusion of molecules from the bulk (first term) and the diffusion that takes place in the subsurface, both treated using Fick's law.

At short times ($t \to 0$), the second term may be neglected and $\Gamma(t)$ increases simply by diffusion from the bulk. The surface tension variation at those times can be written as

$$\gamma_{t\to 0} = \gamma_0 - 2RTc_0\sqrt{\frac{Dt}{\pi}} . \tag{4}$$

At long times ($t \to \infty$), the first term of Eq. (3) tends to its equilibrium value, while the second term approaches zero as $t^{1/2}$. The surface tension in this case can be modelled as

$$\gamma_{t\to\infty} = \gamma_{\mathrm{eq}} + \frac{RT\Gamma_{\mathrm{eq}}^2}{c}\sqrt{\frac{\pi}{4Dt}} . \tag{5}$$

However, there are no analytical solutions for Eq. (3) for intermediate times, although numerical solutions are easy to produce.

Transport in the Bulk

The model above assumed that the only transport mechanism in the bulk flow was through diffusion, which may not be true for many situations in microfluidics. For instance, Marangoni flows are of great importance in situations of bubble or drop formation when new interfaces are created. In microfluidics, droplets are often formed in a strong shear, which means that the fluid flow displays large velocity gradients present.

A classic situation of surfactant transport is the situation of a stationary drop in a moving fluid [3]. Indeed, this situation can be simply related to the situation of a moving drop

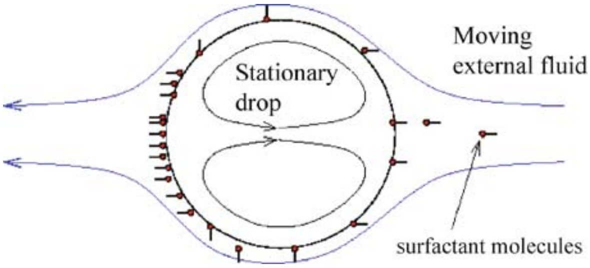

Marangoni Convection, Figure 2 Schematic of a stationary drop subjected to the flow of a surfactant-laden external fluid. The surfactant molecules which adsorb on the interface are transported by the flow on this surface towards the rear stagnation point. This leads to a strong concentration of surfactant molecules in the rear region

by a transformation of the reference frame. Let us consider the flow in the reference frame of the drop, as shown in Fig. 2. In this frame, the drop sees a surfactant-rich flow arriving from the right and this surfactant is adsorbed on the interface between the drop and the outer fluid. However, the outer flow also creates recirculation zones inside the drop which redistribute the surfactant molecules on the rear (left) end of the drop. This situation creates an imbalance in the surfactant concentration along the drop surface, which translates into a surface stress. This surface stress in turn creates a net force on the drop from the left side to the right side, which slows down the external flow.

The relative importance of the advective transport compared to diffusion is measured by calculating the Péclet number. This dimensionless number is defined as

$$\mathrm{Pe} = \frac{Ul}{D}\,, \tag{6}$$

where U is a typical flow velocity, l is a typical length scale over which molecules must diffuse and D is the diffusion constant of the surfactant molecule. For small Pe, the transport due to the mean flow is small and the diffusion dominates, while in the opposite case, transport by the mean flow is dominant and diffusion is not sufficiently fast to redistribute the surfactant molecules. While in large-scale industrial or geophysical flows the Péclet number is always large, the scale and velocities typical in microfluidics imply that one may observe both regimes of high and low Pe. This is especially true since different surfactants have widely varying diffusion coefficients, based for instance on the length of their hydrophobic chains.

Variations of Interface Surface Area

Marangoni effects may play a major role during the formation and detachment of a drop or bubble, since the formation of such a drop naturally involves the formation of a new surface which needs to be covered by surfactant. In this situation, surfactant coverage of the new interface occurs gradually as it is formed, and the rate at which the new surface is covered is limited by the transport mechanisms discussed above. In contrast, the rate at which the surface is created is independently determined by the dynamics of the fluid flow. For instance, the surface concentration Γ may decrease as the surface area is increased, even for a fixed number of surfactant molecules. The relative rates of surface dilation and surfactant transport give rise to several regimes, leading to drops which are subject to strong Marangoni stresses in the case of rapid surface variation, or drops with even distribution of surfactant in the slower cases.

However, drop formation is not the only situation during which a new surface is created. Indeed, while the volume of fluid inside a drop must be conserved, its shape may very well vary, leading to very different values of the surface area. For instance, a spherical drop (of minimal surface area) may be deformed by the external flow to form an oval or other shape. This creation of a new surface is coupled with the presence of Marangoni stresses: as we shall see below, the surface variation can create Marangoni stresses but it can also be caused by uneven distribution of surfactant.

M

Basic Methodology

Numerical simulations of Marangoni flows always have to deal with free interfaces and the associated difficulties. These difficulties are related to meshing, in order to account for large gradients (e. g. in surfactant concentration) near the interface, but also due to moving interfaces in the case of translating or deforming drops. Furthermore, the transport of surfactant in the bulk must also be modelled and coupled with the equations of state of the interface in order to obtain the surface stresses. The modelling of the transport depends strongly on the Péclet and Reynolds number regimes under consideration and will require different numerical techniques depending on the values of the dimensionless parameters.

Therefore the details of the numerical simulations will vary greatly depending on the regime under study. Typically, the flow field around the drop or bubble is computed, e. g. using finite volume methods. The flow field is then coupled with a transport equation for the surfactant which involves diffusion and/or advection. Similar techniques may be used for thermal Marangoni convection by replacing surfactant concentration with thermal energy. The computed surface tension, using for instance the Langmuir relation of Eq. (2), then provides the stress

boundary condition at the interface. This dynamic boundary condition is then used in the calculation of the next time step [4].

Boundary element methods are also used for the calculation of the flow field, since they automatically take into account the free surface. These methods are based on the reformulation of the flow as a potential field, which can be solved in terms of an integral equation on the field boundary, usually taken to be the free drop interface. This technique, which reduces the problem dimensionality by one, is well adapted for the solution of deformable drops since it does not require a mesh to be generated everywhere in the flow but only on the surface [5].

One model system has been at the centre of many studies on Marangoni effects, namely the flow in a gap of small thickness compared to the other typical scales. This system, known as a Hele–Shaw cell, significantly reduces the complexity of the problem, allowing a formulation as a two-dimensional potential flow which admits many elegant analytical solutions. Although the flow of a drop in a Hele–Shaw cell in the presence of surfactants does not have a single analytical solution, it does offer a simplified system which can be realized experimentally and numerically. Furthermore, the Hele–Shaw model is of great significance to microfluidic flows, where surface microfabrication techniques often lead to rectangular channels which may have a large width/height aspect ratio.

Key Research Findings

An initial and important result is that the accumulation of surfactant molecules at the rear stagnation point of a translating droplet imposes a surface stress which opposes the outer flow (see Fig. 2). A direct implication is that for a gas bubble rising in a quiescent liquid, the surface is immobilized and the rise velocity is more similar to the rise of a rigid disc than to an inviscid bubble.

Studies of bubble rise in Hele–Shaw cells demonstrated the production of an 'anomalous' wake structure which encircles the bubble completely and yields a larger effective size of the bubble. A systematic study found that the velocity of a bubble in the presence of surfactant could be almost an order of magnitude lower than the velocity expected in the case of a clean interface. More surprisingly, drops could take on complex shapes such as oval or dumbbell shapes, or even forming tails behind them [6]. Similar drop shapes may be obtained in microfluidic situations, as shown in Fig. 3 for the case of a droplet with a tail.

Further stresses on the liquid interface lead to the phenomenon of tip streaming. This phenomenon was first reported by G.I. Taylor in 1934 and involves the production of singular tips and tiny droplets from a larger drop. Tip streaming may be understood as a destabilization of drops with tails as follows [7]. A strong concentration of surfactant can build up at the tail of the drop, while the rest of the interface remains at low concentration. In this case, a very large difference of concentration occurs, giving rise to a pressure imbalance inside the drop. In order to balance the pressures, the drop shape must change locally and produce regions of high curvature where the surface tension is low, i. e. in the tail region. This process may cascade and lead to continually increased curvatures, which occur at the cost of elongating the tail. In turn, the elongated thin tail is destabilized by the Rayleigh Plateau instability and sheds droplets much smaller in size than the mother drop.

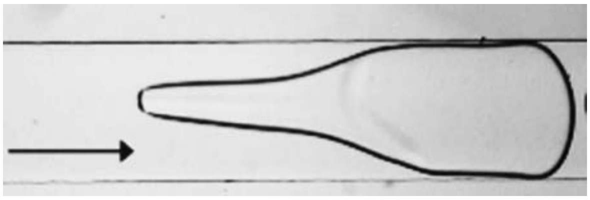

Marangoni Convection, Figure 3 A drop of water in oil, flowing in a microchannel in the presence of surfactant. The shear induced on the drop from the external flow produces the tail-shape discussed in [6]. (Photo: Charles Baroud, LadHyX, Ecole Polytechnique)

Microfluidic observations of this phenomenon were recently reported [8]. An external flow of oil and surfactant was used to focus a stream of water in a sheared geometry. The resulting concentration of surfactant on the tip of the water surface was shown, for sufficiently high shear rates, to produce drops that were much smaller than the typical length scale of the microchannels.

Marangoni convection has also been identified as a major driving mechanism in the spread of surfactant and other liquids lining the lung airways [9]. This layer lining the pulmonary airways is necessary for the proper inflation and deflation of the lung and for the transport of pollutants that may be inhaled. It may be damaged by disease or in premature births. Surfactant replacement therapy (SRT) is used in this case, and may consist of inducing the inhalation of a liquid plug, rich in surfactant, which must travel through the successive bifurcations in the airway tree. Although the transport of the surfactant in plug form is limited by the inhaled liquid volume, transport in the further reaches of the lung is enhanced by the presence of a surface tension gradient due to the variations in surfactant concentration. Therefore surfactant-rich liquid near the mouth is drawn deeper into the pulmonary tree by Marangoni convection, thus enhancing the success of SRT.

Future Directions for Research

Since surfactants are almost always present in droplet microfluidics, a further understanding of their dynamics and their effect on the formation and transport of drops is crucial. In particular, micro-droplet production is a mechanism which produces very large amounts of new surface area in a confined volume, i. e. with a limited amount of surfactant molecules. Although drops in microfluidics are typically produced in a periodic fashion, recent work has demonstrated that the number of drops produced per period varies as a function of forcing rates, up to several drops per period. This raises questions about the homogeneity of the surfactant coverage on the successive drops, which influences their later evolution.

Furthermore, the temporal evolution of a train of drops in the presence of surfactant will be influenced by Marangoni effects. Drops may catch up with their neighbours due to Marangoni retardation effects discussed above and this may lead to destabilization of a microemulsion, or variations of timing in situations where the droplets are used as microreactors in series.

The merging of drops in the presence of surfactants is also a major question. Surfactants have been demonstrated to retard droplet merging, thus stabilizing emulsions. However, drops offer great promise for use as microreactors since they may contain small volumes of reactants and transport them in a microfluidic lab-on-a-chip. Therefore, merging drops will be important in order to bring in contact the different chemical species and perform the desired reactions but the merging process will have to overcome the surfactant barrier. Moreover, the merging may produce Marangoni stresses on the resulting drop which may enhance or retard the mixing of the two reactants in the drop. Such questions have not yet been addressed.

More complex questions involving production or depletion of surfactant also will probably be important in the near future. Recent work has demonstrated complex Marangoni flows and tip streaming on a drop surface that underwent a chemical reaction which produced surfactant. The localized production of surfactant may therefore be considered in applications to microfluidic forcing. Furthermore, the depletion of surfactant through localized heating has been demonstrated to induce large forces on droplets which may be used as a forcing tool for droplet microfluidics. This combination of thermal and solutal Marangoni flows promises to be a rich field with a variety of phenomena and applications.

Cross References

► Thermal Capillary
► Interfacial Electrokinetic Flow
► Interface Capturing Schemes for Free-Surface Flows
► Interfacial Instability
► Surface Tension Driven Flow
► Capillarity and Contact Angle

References

1. Eastoe J, Dalton JS (2000) Dynamic surface tension and adsorption mechanisms of surfactants at the air-water interface. Adv Colloid Interf Sci 85:103–144
2. Ward AFH, Tordai L (1946) Time-dependence of boundary tensions of solutions. 1. the role of diffusion in time-effects. J Chem Phys 14(7):453–461
3. Levich VG (1962) Physicochemical Hydrodynamics. Prentice Hall, Englewood Clifs
4. Palaparthi R, Papageorgiou DT, Maldarelli C (2006) Theory and experiments on the stagnant cap regime in the motion of spherical surfactant-laden bubbles. J Fluid Mech 559:1–44
5. Pozrikidis C (1997) Introduction to Theoretical and Computational Fluid Dynamics. University Press, Oxford
6. Park CW, Maruvada SRK, Yoon DY (1994) The influence of surfactant on the bubble motion in hele-shaw cells. Phys Fluid 6:3267–3275
7. Eggleton CD, Tsai T-M, Stebe KJ (2001) Tip streaming from a drop in the presence of surfactants. Phys Rev Lett 87:048302–1–4
8. Anna SL, Bontoux N, Stone HA (2003) Formation of dispersions using ’flow-focusing’ in microchannels. Appl Phys Lett 82(3):364–366
9. Espinosa FF, Kamm RD (1999) Bolus dispersal through the lungs in surfactant replacement therapy. J Appl Physiol 86(1):391–410

Marangoni Effect

► Thermocapillarity

Mass Analyser

► Mass Filter
► Mass Spectrometry on a Chip

Mass Filter

Synonyms

Mass analyser

Definition

A device for separating ions based on their mass-to-charge ratio. Many different types of mass filter exist, exploiting different combinations of static and time varying electric and magnetic fields for ion separation.

Cross References

► Mass Spectrometry

Mass Spectrometer

Definition

A mass spectrometer is an analytical instrument that provides information about sample composition based on the mass-to-charge ratio (m/z).

Cross References

► Interfaces Between Microfluidics and Mass Spectrometry
► Mass Spectrometry
► Mass Spectrometry on Chip Devices

Mass Spectrometry

SRINIVAS IYER
Bioscience Division, Los Alamos National Laboratory, Los Alamos, NM, USA
siyer@lanl.gov

Synonyms

MS; MS/MS; Tandem MS

Definition

Mass spectrometry (MS) is a sizing technique that provides a mass to charge (m/z) ratio of target analyte ions.

Overview

MS has its origins in J.J. Thomson's vacuum tube where the existence of electrons and *positive rays* was demonstrated. Thomson observed that the new technique could be used by chemists to analyze chemicals. This was in the early part of the century, however it took decades for MS to be used as an effective analytical chemistry technique. Subsequently, advances in MS technology in concert with computational tools and separation methods, laid the foundation for the now extensive use of MS in biochemical research. MS is a powerful analytical technique that can identify and quantify compounds, and also elucidate the structure and chemical properties of molecules. Detection of compounds can be accomplished at extremely low concentrations and often very rapidly. The versatility of mass spectrometry is evident in the valuable information it provides to diverse applications such as detection of illegal drug use, composition of molecular species in a variety of samples, adulteration/contamination of food products etc. In the biological research setting, mass spectrometry is used to identify structures of biomolecules, sequence proteins and oligosaccharides and perform differential proteomic analysis. It may be argued that MS-based protein analysis has made the most significant impact on postgenomic science.

Working principle(s)

A mass spectrometer analyzes ions that are created from molecules. The overall working scheme can be viewed as a combination of three major processes: ionization, sorting and detection. **a)** The first step is introduction of sample into the instrument. Samples can be introduced as either a solid, liquid, or vapor into a vacuum chamber through an inlet. Depending on the type of inlet and ionization techniques used, the sample may already exist as preformed ions or it may be ionized in the ion source. Several ionization modes [1] are commercially available with electrospray ionization (ESI) [2] and Matrix Assisted Laser Desorption/Ionization (MALDI) [3, 4] being the most widely used nowadays. ESI uses an electric field to produce a droplet spray, the sample in this case is typically in a volatile solvent. Irrespective of the original sample source, the final sprayer is usually a fine metal needle that is maintained at high voltage. The solvent vaporizes as it leaves the spray needle and enters additional nebulizing chambers, resulting in positively (or negatively) charged ions that become smaller and more densely charged. This production of multiply charged ions makes ESI particularly useful to study molecules with larger masses, since the actual measurement in MS is the m/z. ESI is most typically used with liquid chromatography (LC) as the upstream separation but is also easily coupled with solution phase separation systems such as capillary electrophoresis (CE) [5]. MALDI differs in being able to desorb analyte ions from a solid phase. Here samples are mixed with an excess of a UV-absorbing matrix, typically small organic acids like sinapinic acid or 3-hydroxypicolinic acid. A small volume of this sample-matrix mixture is spotted on a probe and allowed to dry. Desorption-ionization is achieved by focusing a laser on the sample. **b)** Gas phase ions are sorted in a mass analyzer according to their mass-to-charge (m/z) ratios by one or more methods. Common sorting approaches are magnetic sector, drift tubes (**T**ime-**o**f-**F**light), electrical fields (quadrupole), used alone or often in combination, depending on the requirements of the experiment. MS/MS or tandem MS refers to multiple stages of mass analy-

sis interspersed by the fragmentation of parent ions into daughter ions. Such fragmentation, often induced by gas phase collisions, are critical to structural analysis by MS. **c)** Separated ions are detected by converting the sorted ion flux into a recordable (electrical) function of m/z. The output is displayed as a mass spectrum with relative intensity on the Y–axis and m/z on the X–axis. A typical MS data set can be rather large and complex, which explains the necessity of computers and sophisticated algorithms to analyze spectra.

Interfaces

Separation methods and MS analysis often go hand in hand. MS is a powerful downstream detection method for most separations. Conversely, good MS analysis of compounds depends on effective separation of the individual components. Separation is necessary for unambiguous identification because two compounds present in the source region simultaneously create an overlapping or mixed spectrum and even simple compounds can generate many fragment ions. Gas chromatography (GC) was the earliest separation technique coupled to mass spectrometry allowing compounds already in the vapor phase to enter the mass spectrometer separated in time. Presently, liquid chromatography and capillary electrophoresis are the primary separation systems interfaced to mass spectrometers and present a large opportunity to interface smaller scale separation devices. Effective interfacing of a separation system with MS analysis is critical and presents the biggest challenge to using MS with microfluidic separations. Thus, a significant level of effort is evident in the literature on developing suitable MS interfaces, some of which have already entered the market.

Cross References

► Mass Spectrometry on Chip Devices

References

1. Vestal ML (2001) Methods of Ion Generation. Chem Rev 101:361–376
2. Fenn J, Mann M, Meng C, Wong S, Whitehouse C (1989) Electrospray ionization for mass spectrometry of large biomolecules. Science 246:64–71
3. Karas M, Bachmann D, Bahr U, Hillenkamp F (1987) Matrix-assisted ultraviolet-laser desorption of nonvolatile compounds. Int J Mass Spectrom Ion Process 78:53–68
4. Tanaka K, Waki H, Ido Y, Akita S, Yoshida Y, Yoshida T (1988) Protein and Polymer Analyses up to m/z 100,000 by Laser Ionization Time-of-flight Mass Spectrometry. Rapid Commun Mass Spectrom 2:51–153
5. Olivares JA, Nguyen NT, Yonker CR, Smith RD (1987) On-line mass spectrometric detection for capillary zone electrophoresis. Anal Chem 59:1230–1232

Further Reading

The web page of the American Society for Mass Spectrometry provides excellent tutorials and links to further information. www.asms.org. Follow links to publications.

Mass Spectrometry on a Chip

Richard R. A. Syms
Electrical and Electronic Engineering Department,
Imperial College London, London, UK
r.syms@imperial.ac.uk

Synonyms

Mass analyser

Definition

A mass spectrometer is a vacuum analytical instrument that uses electric or magnetic fields or a mixture of the two to separate ions based on the ratio of their mass m to their charge q. A distinction is made between mass spectrometers, which produce a serially scanned output, and mass spectrographs, which produce a parallel (and sometimes graphical) output. The mass-to charge ratio is often written as m/z, where $q = ze$, $e = 1.6 \times 10^{-19}$ C is the electronic charge and z is the charge number. The ions are created from analyte molecules by processes that give rise to a characteristic pattern of fragments, in addition to the molecular ion itself, allowing a mass spectrometer to be used for chemical identification, compositional quantification and structural analysis. Performance is characterized in terms of the mass range (defined by the maximum mass $m_{\max}$ that can be measured), the mass resolution (defined as $m/\Delta m$, where Δm is the uncertainty in the mass being measured) and the sensitivity. Applications include analytical chemistry, process and pollution monitoring, forensic science, the detection of drugs, chemical and biochemical weapons, and space exploration. In some cases, high performance is essential, while in others, low cost, small size, and portability are more desirable. Increasingly, key components are being constructed on chip, to allow overall system miniaturization.

Overview

A complete mass spectrometer normally contains an ►ion source, a ►mass filter and one or more ►ion detectors. In addition, the system will require a vacuum chamber,

a method of sample introduction, vacuum pumps (usually a roughing pump and a main pump), a vacuum gauge, control electronics and a data acquisition, display and storage system.

A variety of different operating principles can be used for each component. The most common methods of ionization in miniaturised devices are:

- Electron impact ionization, for gaseous analytes
- Electrospray ionization, for liquid analytes

Similarly, the most common variants of miniaturised mass filter are:

- ►Time-of-flight filters
- ►Magnetic field and ►crossed-field filters
- Electrostatic ►quadrupole filters and quadrupole ion traps

Finally, ion detectors may be single elements or arrays of

- Faraday cup,
- Electron multiplier.

The main factor dominating the size, weight and the cost of the overall system is the pump set. Pumping requirements are largely determined by the size of the vacuum chamber, which is in turn controlled by the size of the components therein. Consequently, there is a drive to use planar processing or microelectromechanical systems (MEMS) technology to construct miniature ion sources, mass filters and detectors. Other drivers include the use of cold cathode field emission electron sources as low power ion sources (for example, for space applications), nanospray capillaries as low-flow-rate sources for liquid analytes (for example, in drug discovery) and arrayed detectors in high-resolution mass spectrographs.

Because of the reduced ion flight path, miniature mass spectrometers can operate at higher pressures than conventional systems. However, size-scaling laws and limitations on achievable features affect the performance of microfabricated devices. Although many MEMS mass spectrometers now exist, and are producing increasingly realistic data, their designs have not yet reached the sophistication of conventional systems, where cascaded or double-focusing analyzers are common.

Basic Methodology

The operation of all types of mass spectrometer is subject to simple size scaling laws, which become very significant as devices are miniaturized.

Mean Free Path

According to the kinetic theory of gases, the mean free path λ in a gas with a molecular collision diameter d at an absolute temperature T and pressure P is:

$$\lambda = \frac{kT}{(\sqrt{2}\pi d^2 P)} \tag{1}$$

Here, $k = 1.38 \times 10^{-23}$ J/K is Boltzmann's constant. Since the overall flight path L in a mass spectrometer must be smaller than the mean free path if the ions are to transit successfully, the operating pressure must be:

$$P < \frac{kT}{(\sqrt{2}\pi d^2 L)} \tag{2}$$

This result implies that operating pressures can vary inversely with the dimensions of the system. Assuming the typical value of $d = 3.7 \times 10^{-10}$ m for the collision diameter (for N_2), at $T = 300$ K we obtain $P = 6.8 \times 10^{-1}/L\,\mathrm{N/m^2}$, where L is in cm. Since the dimensions of microengineered mass spectrometers are typically one or two orders of magnitude smaller than conventional systems, operating pressures can in principle be up to two orders higher. However, the need to avoid discharges often tends to negate this advantage.

Electron Impact Ionisation

Electron impact ionization (EI) is primarily suitable for gaseous analytes. In an EI source, electrons are produced by either thermionic emission from a hot filament or by field-induced tunneling from a cold surface. They are accelerated into an ionization region, where they encounter the analyte. At low energies (<20 eV), there is insufficient energy for ionization. At higher energies (in a broad range near 70 eV), the de Broglie wavelength of the electrons matches the length of typical molecular bonds, and ionization and molecular fragmentation rates are both maximised. At higher energies, the electron wavelength reduces and the ionization efficiency decreases. Typical ionization efficiencies (i. e., the number of ions produced per electron) are extremely low, around 1 in a 1000.

In thermionic emission, the current density J obtained from the electrically heated filament in the presence of an electric field E obeys the modified Richardson–Dushman equation:

$$J = AT^2 \exp\left(-\frac{\phi - \Delta\phi}{kT}\right) \tag{3}$$

Here ϕ is the work function of the filament material, and A is Richardson's constant, given by $A = 4\pi m_e k^2 e/h^3$, where m_e is the electron mass and $h = 6.62 \times 10^{-34}$ Js is Planck's constant. The field-induced term is $\Delta\phi = (eE/4\pi\varepsilon_0)^{1/2}$, where $\varepsilon_0 = 8.85 \times 10^{-12}$ F/m is the vacuum permittivity. Because of the exponential variation above, materials such as tungsten that can survive operation at very high temperatures are required. Difficulties

in fabrication and thermal management have hindered the development of integrated hot filament sources.

This drawback has led to a focus on cold-cathode sources, which operate by tunelling from a surface in the presence of a strong electric field. The current density obtained is given in this case by the Fowler–Nordheim equation:

$$J = AE^2 \exp\left(-\frac{B\phi^{3/2}}{E}\right) \tag{4}$$

Here A and B are different constants. In this case, the dominant factor is the electric field. Suitable fields can be obtained at voltages of $\approx 100\,\mathrm{V}$ from tips with radii of $\approx 1\,\mathrm{nm}$, which can be made by microfabrication. Since $\log_e(J/AE^2) = -B\phi^{3/2}/E$, a plot of $\log_e(I/V^2)$ versus $1/V$ (where I is the emission current and V is the voltage) should be a straight line with a negative slope. The reduction in operating temperature and the elimination of a heater current makes cold-cathode sources a strong candidate for low-power portable systems.

Electrospray Ionization

Electrospray ionization (ESI) is primarily suitable for liquid analytes. In ESI, a voltage is applied between an electrode and a capillary containing the analyte. Liquid is extracted from the tip and drawn into a Taylor cone, from which large charged droplets are emitted. The droplets are accelerated to supersonic speed, evaporating as they travel. Coulomb repulsion of the charges in the shrinking droplet results in fragmentation to ions when the Rayleigh stability limit is reached. The resulting ions can be multiply charged. In a conventional electrospray system, with capillaries of $\approx 100\,\mu\mathrm{m}$ internal diameter, flow rates are of the order of $1\,\mu\mathrm{lmin}^{-1}$, and extraction voltages lie in the range $2.5-4\,\mathrm{kV}$. Flow rates and voltages are reduced in so-called "nanospray systems", based on capillaries having internal diameters down to $\approx 10\,\mu\mathrm{m}$. Decreasing the capillary diameter and lowering the flow rate also tends to create ions with higher mass-to-charge ratio, extending the applicability further towards biomolecules.

Forces

An ion of mass m and charge q travelling with a velocity $\boldsymbol{v}$ in an electric field with strength $\boldsymbol{E}$ and a magnetic field with flux density $\boldsymbol{B}$ experiences a force $\boldsymbol{F}$ defined by the Lorentz force law. This equation can be combined with Newton's laws to yield the acceleration $\boldsymbol{a}$ as:

$$\boldsymbol{F} = q(\boldsymbol{E} + \boldsymbol{v} \times \boldsymbol{B}) = m\boldsymbol{a} \tag{5}$$

Many combinations of electric and magnetic field are exploited in mass spectrometry.

Ion Velocity

For example, in an electric field E that acts only in the x-direction, we obtain:

$$F = qE = m\frac{\mathrm{d}^2x}{\mathrm{d}t^2} \tag{6}$$

Here t is time, and $E = \mathrm{d}V/\mathrm{d}x$, where $V(x)$ is the potential variation that gives rise to the field. Integrating from zero potential at the origin to V_a at x we obtain the ion velocity v as:

$$\frac{1}{2}mv^2 = qV_\mathrm{a} \quad \text{so that} \quad v = \sqrt{\frac{2qV_\mathrm{a}}{m}} \tag{7}$$

This result implies that ions accelerated through a common potential will acquire a velocity that varies as the inverse square root of their mass.

M

Filtering by Time-of-Flight

A simple method of constructing a mass spectrometer is based on time-of-flight (TOF), first described by Cameron in 1948. A pulse of ions of mass m entering an analyser of length L at zero time will exit at time τ , given by:

$$\tau = \frac{L}{v} \quad \text{so that} \quad \frac{m}{q} = \frac{2V_\mathrm{a}\tau^2}{L^2} \tag{8}$$

This result implies that the time-of-flight τ is a direct measure of the mass-to-charge ratio m/q. However, the time-scale is non-linear, and flight times reduce linearly with the characteristic dimension L of the system. Consequently, very short ion pulses and fast detector electronics are required in miniaturised TOF-MS.

Magnetic Filtering

An alternative method of filtering is based on the use of a magnetic field. Magnetic mass spectrometers were developed and improved by the fathers of mass spectrometry, Thompson, Aston and Bainbridge, in the early part of the 20th century. An ion with velocity v travelling in a perpendicular magnetic field of flux density B will follow a circular trajectory of radius r, found from a balance between the magnetic and centrifugal forces as:

$$qvB = \frac{mv^2}{r} \quad \text{so that} \quad r = \frac{m}{q}\frac{v}{B} \tag{9}$$

This result may be combined with the earlier expression for velocity to obtain:

$$\frac{m}{q} = \frac{B^2 r^2}{2V_a} \tag{10}$$

These two results imply that a magnetic field will disperse ions into trajectories of different radius, depending on their mass. Greater dispersion can be obtained by reducing the ion energy V_a; however, V_a cannot be reduced arbitrarily, and must typically be significantly larger than the thermal energy of the ion. A small radius (and hence a compact instrument) is only obtained with a powerful magnet. Consequently, magnetic filtering is difficult to scale into the MEMS size domain.

Crossed Field Filtering

Consider now the case when an additional electrostatic field E is introduced, perpendicular to both the ion velocity and the magnetic field. This field will generate an additional force, which can compensate for the magnetic force, partially straightenening the ion trajectories in a magnetic mass spectrograph. The two forces can balance exactly if:

$$qvB = qE \quad \text{so that} \quad v = \frac{E}{B} \tag{11}$$

In this case, the trajectory is exactly a straight line. An arrangement of crossed fields, with a pair of co-linear apertures allowing only line-of-sight path, will therefore act as a filter (first demonstrated in 1898 by Wien) for ions with the velocity given above. If the exit aperture in a Wien filter is replaced with a detector array, ions will be dispersed across the array so that the device acts as a mass spectrograph. In this case, the mass resolution is:

$$\frac{m}{\Delta m} = \frac{EL^2}{2V_a \Delta w} \tag{12}$$

Here L is the length of the filter and Δw is the spacing of the detector array.

Quadrupole Filtering

Filtering may be carried out in an entirely different way using a method invented by Paul and Steinwedel in 1953 and based on a time-varying hyperbolic electrostatic field. Four parallel electrodes with suitable cross-sections are used to establish the two-dimensional potential $\phi(x, y) = \phi_0 \left(x^2 - y^2\right)/2r_0^2$. Here r_0 is the radius of an inscribed circle that just touches the electrodes, where the potential $\phi = \pm\phi_0/2$. The field will exert forces in both the x- and y-directions on an ion moving in the z-direction. For a singly charged ion, the equations of motion are:

$$m\frac{d^2x}{dt^2} = -e\frac{\partial\phi}{\partial x} = -e\frac{\phi_0 x}{r_0^2} \qquad m\frac{d^2y}{dt^2} = +e\frac{\phi_0 y}{r_0^2} \tag{13}$$

When the time variation of the potential is $\phi_0(t) = U - V\cos\left[\omega\left(t - t_0\right)\right]$, where $\omega = 2\pi f$ is the angular frequency, ωt_0 is the starting phase and U and V are constant potentials, we obtain:

$$\frac{d^2u}{d\zeta^2} + \left\{a_u - 2q_u \cos\left[2\left(\zeta - \zeta_0\right)\right]\right\}u = 0 \tag{14}$$

Here, the normalised parameters used are $\zeta = \omega t/2$, $\zeta_0 = \omega t_0/2$, $a = 4eU/\left(m\omega^2 r_0^2\right)$ and $q = 2eV/\left(m\omega^2 r_0^2\right)$, u is x or y, and $a = a_x = -a_y$ and $q = q_x = -q_y$.
Solution of the equations shows that the nature of the trajectory depends almost entirely on a and q, varying little with the initial conditions ζ_0, $u(0)$ and $u'(0)$ of the ion. There are a several regions on the $q - a$ plane that give rise to stable solutions. The so-called "lower stability region", most commonly used for mass filtering, is an approximately triangular region, bounded by the loci:

$$\begin{aligned} a_0(q) &= \frac{q^2}{2} - \frac{7q^4}{128} + \frac{29q^6}{2304}\cdots \\ b_1(q) &= 1 - q - \frac{q^2}{8} + \frac{q^3}{64} - \frac{q^4}{1536}\cdots \end{aligned} \tag{15}$$

The locus a_0 defines the limit for trajectories that are stable in the y-direction, while b_1 is the limit for trajectories in the x-direction. Between the two, trajectories are stable in both directions. The apex of the stable region lies at $a = 0.237$, $q = 0.706$ so that $a/2q = U/V = 0.168$. In a quadrupole mass spectrometer, U and V are normally ramped together, following a line passing just below the apex of the lower stability region. Stable trajectories are only obtained for a narrow mass range, so that the device acts as a tuneable mass filter. An attractive feature of miniaturisation is that U and V scale with r_0^2, so that decreasing the linear dimension of an instrument by (say) 10 will reduce both potentials 100-fold.
The mass resolution varies as $m/\Delta m \approx n^2/20$, where n is the number of cycles of the RF field experienced by an ion. Ions are normally injected with a constant axial energy V_a. The number of cycles is $n \approx fL/v$, where L is the quadrupole length, so the uncertainty in mass is:

$$\Delta m \approx \frac{40eV_a}{f^2L^2} \tag{16}$$

Thus, the uncertainty in mass increases as the quadrupole is reduced in size. Compensation can be provided, by increasing the frequency, but this in turn requires an increase in voltage.

Quadrupoles are attractive candidates for miniaturisation, since they do not require either a magnetic field or very fast electronics. However, the challenge in miniaturising a quadrupole is generally to achieve a suitably high mechanical precision, since the accuracy of the hyperbolic field determines the ultimate resolution. One important aspect is electrode mounting, which requires precise assembly. Another is the shape of the electrodes. Hyperbolic electrode cross-sections are normally too complex to machine, and are replaced by cylinders, with the ratio of the cylinder radius r_e to r_0 being chosen to give the best approximation to a hyperbolic potential variation.

Ion Trap Filtering

The ion trap is a variant of the quadrupole mass spectrometer, which was first described by Paul and Steinwedel in 1960. It consists of a circular hyperbolic electrode, with spherical electrode caps at the top and bottom, and can be conceived as a quadrupole bent round in a circle. The three electrodes correspond to three of the rods of the bent quadrupole, while the fourth (inner) rod is reduced to a vanishingly small point.

As with the quadrupole spectrometer, a potential $+\phi_0$ consisting of both DC and radio frequency AC components is applied to the end caps, while a potential $-\phi_0$ is applied to the ring electrode. Ions of all masses are then trapped by the resulting three-dimensional, time-varying electrostatic field, and follow stable, closed trajectories, that are shaped approximately like the figure “eight”.

In a quadrupole, ions are injected continually, and the potentials are adjusted so that only ions of a particular mass can transit successfully. In the ion trap, however, the method of obtaining a mass spectrum is rather different. The different masses are held together inside the trap, and are expelled in sequence by applying a further voltage at a particular resonant frequency to obtain the spectrum. Consequently, the sensitivity of a miniaturized ion trap is limited by the amount of charge that can be stored inside a small volume in the face of charge repulsion effects. A general problem with miniaturisation is therefore loss of sensitivity, but this may be overcome to some extent by using a two-dimensional array of traps. Ion traps are also attractive candidates for miniaturisation. Once again, exactly shaped electrodes are generally too complex to machine, and structures with optimised combinations of cylindrical ring and planar end-cap electrodes are normally used.

Key Research Findings

We now give a few examples of miniaturised mass spectrometer systems, restricting the discussion to cases where planar technology has clearly been employed.

Ion Sources

Most of the results from microfabricated mass filters to date have been obtained from hybrid systems fitted with conventional ion sources, and only limited work appears to have been carried out on planar sources. Consequently, the ideal of a fully integrated chip-based mass spectrometer still appears some way off.

Yoon et al. of Ajou University have successfully fabricated a tungsten filament with an extraction grid and other electrodes formed in nickel on a silicon substrate, as shown in Fig. 1a [1]. To allow its very high operating temperature to be reached, the filament was suspended over a pit formed by anisotropic wet chemical etching. Emission currents up to 7 nA were obtained with an applied voltage of 35 V.

Considerably more attention has been paid to cold cathode sources, due to intensive industrial efforts to develop field emission displays. Emitters are constructed in the classical Spindt geometry, in which a sharp tip with a radius of 1 – 10 nm is fabricated by isotropic dry etching of silicon in a SF_6 plasma. Self-aligned anodes and focusing electrodes have been demonstrated, emission currents have been stabilised, and current densities and lifetimes have been improved using coatings of thin film diamond-like carbon. Figure 1b shows the cross-section and emission characteristic of a source fabricated by Huq of Rutherford Appleton Laboratory, which follows the Fowler–Nordheim relation given earlier [2]. Cold cathode sources have been used extensively with ion traps, because the geometry allows electrons to be injected directly into the trap as shown in Fig. 1c.

Müller of the Technische Universität Hamburg-Harburg has demonstrated an interesting plasma ion source [3]. The source is a small chamber operating at higher pressure than the mass analyser, within which a discharge is excited. Figure 1d shows the source, which uses a three-layer stack of etched Pyrex wafers containing a plasma chamber beneath a DC extraction grid. Ionisation is accomplished with electrons extracted from inert gas plasma. The plasma is ignited by a piezoelectric spark discharge and sustained by microwave excitation. Electron currents of 100’s of μA have been obtained using RF powers of 350 mW at pressures of 80 Pa, with accelerating voltages as low as 100 V.

Considerably more work has been carried out on chip-based electrospray ionisation sources. Ramsey et al. of Oak Ridge National Laboratory were the first to show that a spray could be drawn from the edge of a glass

M

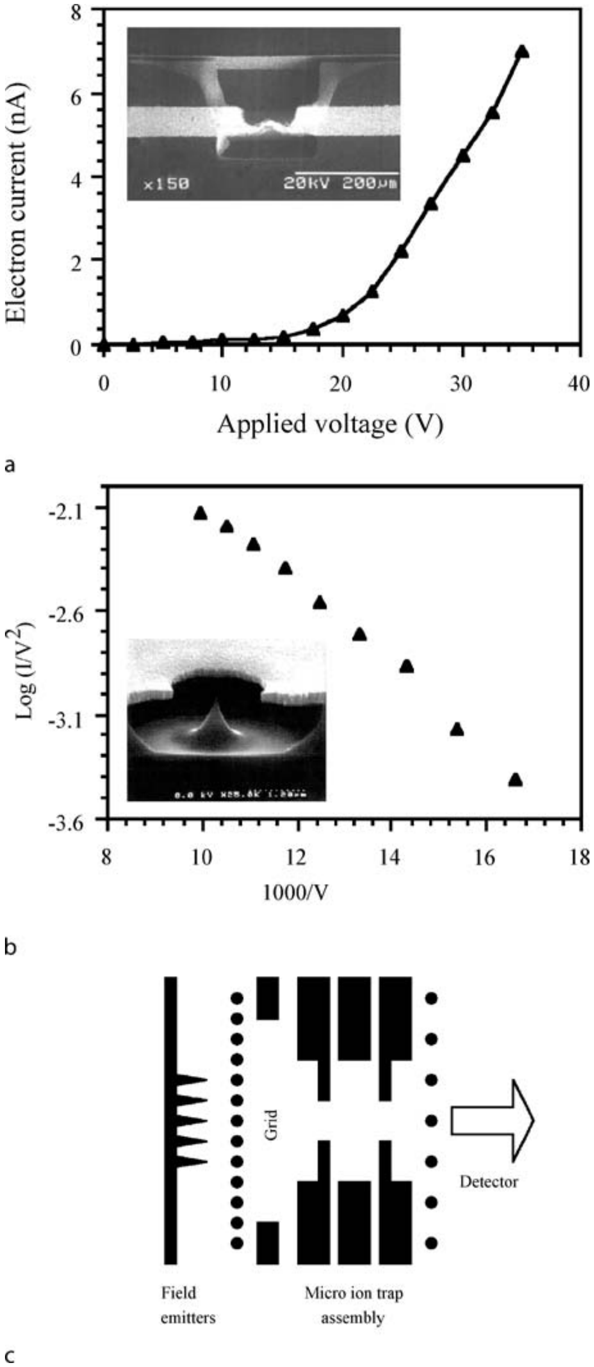

Mass Spectrometry on a Chip, Figure 1 (**a**) Emission characteristic of a microfabricated filament (courtesy Dr Hyeun Joong Yoon); (**b**) Emission characteristic of a silicon field emitter (courtesy Dr Ejaz Huq); (**c**) Field emission ionizer with an ion trap (courtesy Prof. Michael Ramsey)

chip containing an etched capillary [4]. Since then, integrated capillaries have been demonstrated in many materials and geometries. Nozzles have been combined with a sample and buffer reservoirs in glass substrates, and additional channels have been provided for sheath flow. More complicated devices combine sample inlet ports, preconcentration sample loops, separation channels and pneumatic nebilizers. One issue with all glass substrates is their hydrophilic nature, which allows the Taylor cone to spread laterally over the edge of the chip as the flow rate increases, reducing the separation of mass peaks. This problem has been overcome using plastics and a wide variety of coatings and substrate materials have been investigated. Other geometries suitable for planar integration, including open channels and nibs, have also been demonstrated.

Mass Filters

Many of the ‘classical’ variants of mass filter have been demonstrated using planar technology. A recent review by can be found in [5].

The best example of a chip-based time-of-flight filter is the previously mentioned example developed by Yoon [1], which uses electroplated metal electrodes for ion coupling and detection. Using a 1 cm^2 chip, the flight times were up to 5 μS for masses up to 100 atomic mass units (amu). Despite the small size of the chip, mass filtering has been convincingly demonstrated. Figure 2a shows the mass spectrum of acetone, which was however obtained using a Q-switched Nd-YAG laser for ionization rather than the hot-filament source.

A novel microengineered instrument with a rather different planar electrode layout has been proposed by Müller [3]. Figure 1d shows the device, which uses the microwave ion source described earlier and electrostatic filtering. This time, however, mass selection is based on the filtering action provided by the interaction between the ion beam and a three-phase travelling electrical field, which is created by a periodic electrode structure fed by suitably phased drive signals.

Syms of Imperial College London and Taylor of Liverpool University have demonstrated microfabricated quadrupole filters using a pair of etched silicon substrates separated by glass rods [6]. Each substrate carried two of the four cylindrical electrodes, and the glass rods spaced the assembly apart by the distance needed to achieve the quadrupole geometry. Mass spectra were demonstrated early on, but various aspects of performance (particularly, the mass range, which was restricted to 100 amu) were limited by RF heating caused by capacitative coupling through the substrates.

Geear et al. of Microsaic Systems [7] has demonstrated a more advanced MEMS quadrupole. The device is formed from two bonded silicon-on-insulator substrates, which

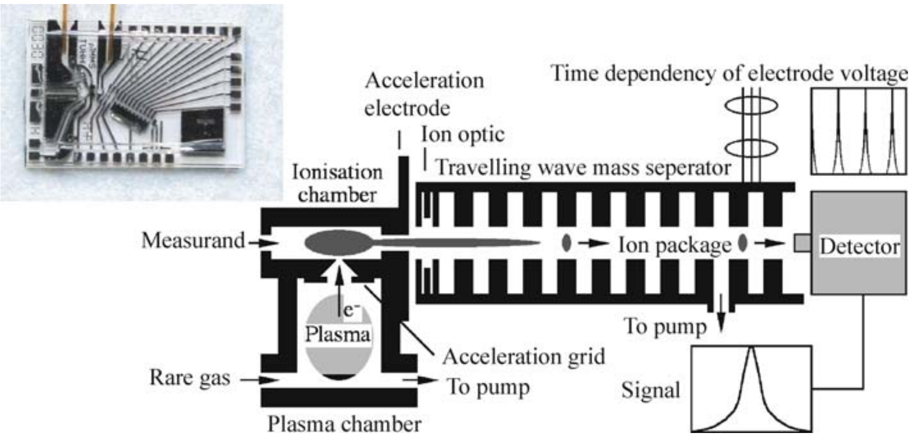

Mass Spectrometry on a Chip, Figure 1 (**d**) Microfabricated plasma ion source with a travelling-wave mass filter (courtesy Prof. Jörg Müller)

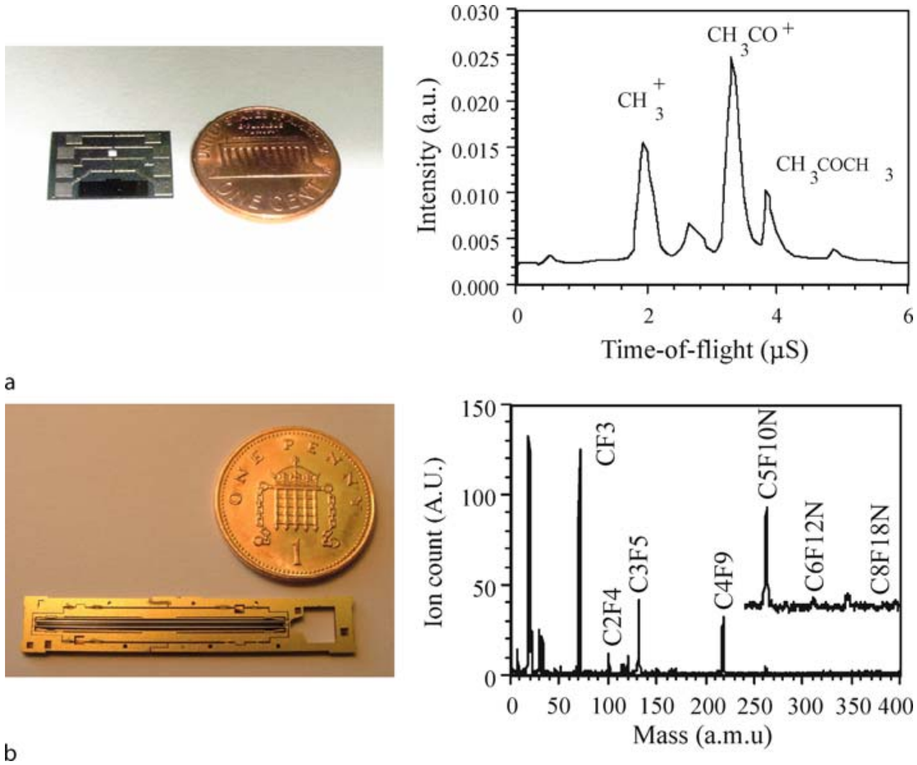

Mass Spectrometry on a Chip, Figure 2 (**a**) Microfabricated time-of-flight mass filter and a mass spectrum obtained for acetone (courtesy Dr. Hyeun Joong Yoon); (**b**) Microfabricated quadrupole mass filter and a mass spectrum obtained for PFTBA (courtesy Microsaic Systems Ltd.)

are attached together to form a monolithic block. Deep etched features and springs formed in the outer silicon layers are used to locate cylindrical metal electrode rods, while similar features formed in the inner silicon layers are used to define integrated ion entrance and exit optics. Mass filtering has been demonstrated, with a mass range of ≈ 400 amu and a resolution of 1 amu at a mass of 219 amu, using quadrupoles with rods of 500 μm diameter and 30 mm length, operating at 6 MHz RF frequency. Figure 2b shows the device itself and the mass spectrum of perfluorotributylamine (PFTBA).

Many groups have fabricated ion traps, using the cylindrical approximation to the ideal hyperbolic geometry shown earlier in Fig. 1c. Ramsey and Whitten at Oak Ridge

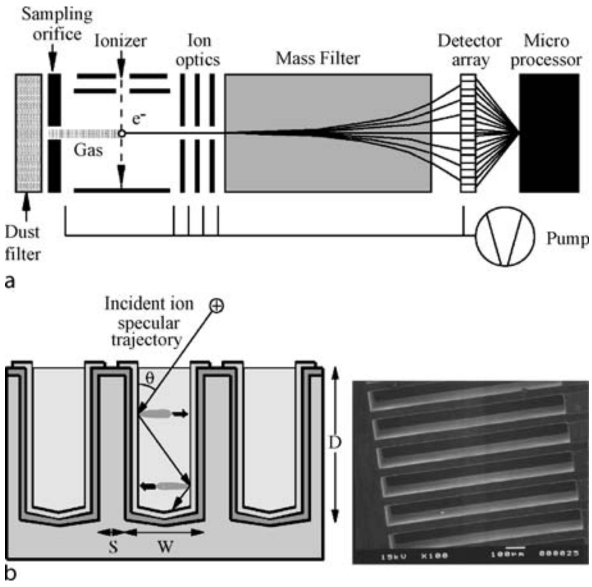

Mass Spectrometry on a Chip, Figure 3 (**a**) Microfabricated Wien mass filter by (courtesy Dr. Carl Freidhoff); (**b**) Microfabricated Faraday cup array (courtesy Prof. Bruce Darling)

National Laboratory have constructed traps, with 1/1000 of the volume of conventional devices [8]. A mass range from 40 to 400 amu has been demonstrated, with peak widths less than 0.2 amu for single scans. The device has been operated with a frequency quadrupled Nd-YAG laser photo-ionization source, and both hot cathode and cold-cathode electrode impact ionization sources.

Freidhoff et al. of Northrop Grumman has developed a microfabricated Wien filter mass spectrometer [9]. The device is a mass spectrograph based on a continuous ion source, fixed, crossed magnetic and electric fields, and an ion detector array, as shown in Fig. 3a. The whole analyser is formed in a shallow cavity etched into a single silicon substrate a few cm long. Because of the near-planar geometry of the cavity, it is difficult to establish a uniform, fixed electric field, and a discontinuous field approximating the desired field is derived from a set of parallel coplanar electrodes biassed by a resistor chain. Despite these difficulties, preliminary data has been obtained for a mass range of 40 – 200 amu with a peak width of 1 amu at 60 amu.

Ion Detectors

Most miniature mass spectrometers have used a single detector such as a channeltron, which allows spectra to be obtained in serial form by scanning the filter passband. For example, in a magnetic separator, the magnetic field can be ramped, and in a quadrupole, the two components of the electric field can be varied in a fixed ratio. This method has the disadvantage that ions of a given mass are only observed for a fraction of the time available. Improved sensitivity is obtained by parallel detection, which allows continual observation.

The most advanced chip-based ion detectors are the microfabricated Faraday cup arrays fabricated by Darling of Washington University [10], for use with a compact linear dispersion magnetic mass spectrograph. Deep reactive ion etching of silicon was used to form high aspect ratio trenches, which were then oxidised and metallised to form an array of independently addressable MOS capacitors as shown in Fig. 3c. Detector arrays were constructed with up to 256 elements and with pitches down to 150 μm, and the arrays have been combined with an electronic multiplexer to allow serial readout.

Future Directions for Research

The overall goal of miniaturizing mass spectrometers – to allow wider access to the most versatile method of chemical analysis yet developed – is an important one. Particularly, the availability of portable systems could allow the use of accurate identification methods outside the laboratory. The key goals of future work are to improve mass range and mass resolution of miniaturized mass filters, and the reliability and efficiency of compatible ion sources.

Cross References

► Mass Spectrometer
► Mass Spectrometry
► Detection Using Mass Spectrometry
► Interfaces Between Microfluidics and Mass Spectrometry
► Microfabrication Techniques
► Silicon Micromachining

References

1. Yoon HJ, Kim JH, Choi ES, Yang SS, Jung KW (2002) Fabrication of a novel micro time-of-flight mass spectrometer. Sens Actuators A 97(8):441–447
2. Huq SE, Kent BJ, Stevens R, Lawes RA, Xu NS, She JC (2001) Field emitters for space application. J Vac Sci Tech B 19:988–991
3. Siebert P, Petzold G, Hellenbart A, Müller J (1998) Surface microstructure/miniature mass spectrometer: processing and applications. Appl Phys A 67:155–160
4. Ramsey RS, Ramsey JM (1997) Generating electrospray from microchip devices using electroosmotic pumping. Anal Chem 69:1174–1178
5. Badman ER, Cooks RG (2000) Special feature: Perspective – miniature mass analysers. J Mass Spect 35:659–671

6. Syms RRA, Tate TJ, Ahmad MM, Taylor S (1998) Design of a microengineered quadrupole electrostatic lens. IEEE Trans Electron Dev TED 45:2304–2311
7. Geear M, Syms RRA, Wright S, Holmes AS (2005) Monolithic MEMS quadrupole mass spectrometers by deep silicon etching. IEEE/ASME J Microelectromech Syst 14:1156–1166
8. Kornienko O, Reilly PTA, Whitten WB, Ramsey JM (1999) Micro ion trap mass spectrometry. Rapid Comm in Mass Spect 13:50–53
9. Freidhoff CB, Young RM, Sriram S, Braggins TT, O'Keefe TW, Adam JD, Nathanson HC, Syms RRA, Tate TJ, Ahmad MM, Taylor S, Tunstall J (1999) Chemical sensing using non-optical microelectromechanical systems. J Vac Sci Tech A 17:2300–2307
10. Darling RB, Scheidemann AA, Bhat KN, Chen TC (2002) Micromachined Faraday cup array using deep reactive ion etching. Sens Actuators A 95:84–93

Materials Used in Microfluidic Devices

XIN LIU, BINGCHENG LIN
Dalian Institute of Chemical Physics, Chinese Academy of Sciences, Dalian, China
bclin@dicp.ac.cn

Synonyms

Bulk materials; Device substrates

Definition

The intensive interplay of engineering and materials science has always been an important driving force in the rapid evolution of microfluidic technologies and their strikingly wide range of applications [1]. To date, numerous materials, including silicon, quartz/fused silica, glass, ceramics, polymers, and metals, have been used in fabricating microfluidic devices bearing diverse functionalities. In general, a microfluidic device can be built by first fabricating (by dry or wet etching, mechanical machining, molding, or casting) open microchannels or features in a flat substrate, and then bonding this substrate to another flat plate with predrilled access holes, thereby forming an enclosed microchannel network with the desired configuration and dimensions. The materials used, which serve as the building blocks of various types of microfluidic devices, are also called the *bulk materials* or *substrates* of these devices.

Chemical and Physical Principles

More than simply serving as the mechanical support and defining the structures of the embedded microfluidic networks, materials also play a critical role in the determination of the specific properties, overall performance, and range of applicability of microdevices [2]. The bulk of the material can serve as a medium for heat transfer, electrical conduction, transmission of light, or transduction of mechanical force; the surfaces that form the channel walls will significantly interact with the fluid medium and, consequently, influence the constitution or physical behavior of the fluid. All these functions of materials are determined by their intrinsic physical and chemical properties, and various techniques for controlling these properties. Table 1 [3] lists some of the materials commonly used for fabrication of microfluidic devices, and typical properties of them that are relevant to the performance of microfluidic devices.

The success of a microfluidic device is significantly influenced by the properties of the substrate materials, and thus it is of crucial importance to choose the right materials for specific devices and, sometimes, it is also necessary to find techniques to modify the bulk or surface properties of these materials. These are very much dependent on the desired application and the required functionality of the microfluidic device. For instance, if one is building a microreactor for a chemical reaction that requires a wide range of controllable operating temperatures and pressures, silicon and stainless steel might be the materials of choice owing to their superior temperature and mechanical performance [4]. On occasions where imaging or optical detection of processes in the device is required, optical transparency within a suitable wavelength range is a prerequisite property of the material. Another example is single-molecule detection, where quartz is generally chosen to fabricate the chip because this material has an extremely low intrinsic fluorescence, thus significantly increasing the signal-to-noise ratio. Consideration should also be given to the processability of the material. For instance, silicon might be a better choice if high-aspect-ratio features are required, as these can be obtained through well-established dry or wet etching procedures; for glass or fused silica, only shallow channels or features with a low aspect ratio are obtainable if wet chemical etching is adopted. For microfluidic devices for cellular analysis, the material in which microchannels are embedded is generally required to be porous to maintain communication of the cells with the external environment (exchange of nutrients, CO_2, O_2, etc). In this case, hydrogels are suitable materials. Their porosity can be adjusted thermally or electrically.

One basic attribute of microchannels or microstructures is their substantially high surface-to-volume ratio, which is a direct consequence of miniaturization. Thus the surface properties of a material usually play a predominant role in realizing specific functionalities or influencing the performance of a microfluidic device. For instance, in a glass

M

Materials Used in Microfluidic Devices, Table 1 Properties of materials commonly used for fabrication of microfluidic devices [3]

Material property	Si (single-crystal)	Glass	SiO_2	PDMS[a]	PMMA[b]	Parylene C[c]	Polycarbonate
Coefficient of thermal expansion ($10^{-6}\,°C^{-1}$)	2.6	0.55	0.55	310	55	0.35	70.2
Thermal conductivity at 300 K ($W\,cm^{-1}\,K^{-1}$)	1.57	0.011	0.014	0.0018	0.002	0.00083	0.002
$>$ 70% optical transmittance (nm)	$>$ 700	$>$ 350	$>$ 350	400 – 700	400 – 700	400 – 700	400 – 700
Maximum processing temperature (°C)	1315	550 – 600	1700	~ 150	~ 100	~ 290	~ 100
Bulk resistivity (μΩ)	2.3×10^{11}	$> 10^{10}$	$> 10^{10}$	$> 10^{20}$	$> 10^{20}$	$> 10^{20}$	$> 10^{20}$
Dielectric strength ($10^6\,V\,cm^{-1}$)	3	5 – 10	2 – 3	2.1	0.17 – 0.19	2.67	0.39
Water contact angle, advancing (degrees)	110	20 – 35	~ 30	~ 110	60 – 75	87	78

[a]PDMS: poly(dimethylsiloxane), [b]PMMA: poly(methyl methacrylate), [c]Parylene C: polyparaxylylene.

microdevice, hydrolysis of the surface silicon dioxide leads to formation of a negative charge on the channel surface. This property of glass provides a basis for realizing electroosmotic pumping and electrophoretic separation. In addition, there are often occasions where techniques for modifying the surface properties are required. Many biochemical applications, for instance, require surfaces with substantially suppressed adsorption of biomolecules or cells. This can sometimes be achieved by physical or chemical modification of the channel surface with surfactants or polymers, such as polyacrylamide, poly(ethylene glycol), and poly(vinyl chloride) [5]. In this case, the amenability of the material to surface modification (generally determined by the chemical composition of the material) needs also to be considered.

Principally, the selection of an appropriate material for any particular type of microdevice is dependent on the microfluidic assay implemented in the device. In practice, there is often a compromise between the desired properties of the material and the availability of a technology for micromachining or tuning the properties of the material. For this reason, in the field of microfluidics, there has always been interest in testing and designing new materials and, at the same time, developing novel techniques for microfabrication of these materials.

Key Research Findings

Historically, silicon and, later on, glass were the materials mainly used in early microfluidic devices. As a result of the growing desire for new applications of microfluidic devices and the demand for more advanced and flexible functionalities in these devices, however, the range of materials applicable in microfluidic devices has been constantly expanding. At present, the most frequently used substrate materials include silicon, glass or quartz, and various types of polymers.

The early microfluidic devices were mostly fabricated in silicon, because it was a straightforward choice to adopt well-developed microfabrication methods and materials from the semiconductor industry. Well-established wet and dry etching procedures enable the fabrication of microstructures in silicon with controlled geometries and dimensions. The excellent mechanical strength and thermal performance of silicon make it a good material of choice for building microreactors [4]. In addition, the availability of technologies for modification of its surface, for silicon–silicon and silicon–glass bonding, and for fabrication of various chemical or physical sensors has also greatly extended its application in microfluidics. However, the semiconducting properties of silicon have limited its application in electric-field-driven processes such as electroosmotic pumping and electrophoresis. Its opacity to UV and visible light has also hindered applications that require optical detection or imaging.

Glass and fused silica are attractive as substrate materials for microfluidic devices owing to several advantages over silicon and many other materials. Their transparency in the UV and visible range facilitates their application in optical detection and imaging. Their chemical and thermal resistance makes them also applicable in chemical-reaction devices. The desired microchannel features can be easily constructed on glass or quartz substrates by use of photolithographic technology originating from the semiconductor industry [6]. The native surfaces of glass/quartz microchannels bear a negative charge in aqueous media, making them ideal substrates for electrophoresis devices. In addition, since there are many well-established meth-

ods for the physical and chemical modification of the surfaces of glass and fused silica, these materials have frequently become the first choice for building miniaturized bioanalytical devices. The usability of glass or fused silica is mainly limited by the difficulties of fabricating high-aspect-ratio microstructures in these materials. This has limited their application where complex microstructures are required.

Most of the polymeric materials used in microfluidic devices are transparent, and can generally be classified into elastomers (e. g. PDMS) and plastics (e. g. PMMA). The increasing interest in these polymeric materials is driven by the fact that they can be fabricated with desired microstructures with a high throughput and low cost. The microstructures can be fabricated by casting, injection molding, or thermal molding [7]. All of these methods involve repetitive usage of a mold that includes a prefabricated negative of the desired microstructure; a similar process is used widely for the mass production of polymeric products, and thus the costs of production of microfluidic devices from polymers can be substantially lower than from other materials. High-aspect-ratio and complex microstructures are easily obtainable in these materials, although this depends on the quality of the mold. The main concern in using polymeric materials lies in their comparatively poor surface properties and their incompatibility with most organic solvents. Efforts have been put into testing and designing new polymers with improved properties and developing new methods for surface modification [8].

One noteworthy trend in microfluidics is the introduction of novel materials that, conventionally, have rarely been considered as microdevice substrates. One recent example is the use of a biodegradable polymer as a base material to fabricate microdevices with embedded microfluidic networks that resembles microvascular systems [9], work that is helping to expand the range of applications of microfluidic devices into the field of tissue engineering.

Examples of Application

Poly(dimethylsiloxane) (PDMS) is probably the most popular material used in microfluidic devices at present. PDMS is a transparent elastomeric material that is made by heating a precursor mixture containing vinyl-terminated linear polymers of poly(dimethylsiloxane), a certain amount of a cross-linking agent, and a catalyst. The microfabrication of PDMS is rather straightforward and cost-effective: by casting a liquid precursor mixture over a mold and heating at 60 – 80 °C for several hours, an elastomeric solid with a faithfully replicated microstructure can be formed. This process is often referred to as replica molding. The fabricated PDMS slab can be easily bonded to another flat PDMS or glass slab by either conformal contact (reversible bonding) or covalent bonding. Whitesides et al. [10] were the first to propose the use of PDMS for microfabrication and for building microfluidic devices by use of these methods. The PDMS material was demonstrated to be a strikingly versatile material that enabled a wide range of new functions and applications of microfluidic devices. One of the fully explored properties of PDMS is its elasticity. A typical example of an application is the fabrication of multilayered fluidic structures in this material; by applying a force to cause deformation of a fluid channel and then releasing the force, active valves or pumps can be realized [11].

Cross References

► Electroosmotic Flow (DC)
► AC Electro-Osmotic Flow
► Electrophoresis
► Biomolecular Adsorption in Microfluidics
► Methods for Surface Modification
► Microfabrication Techniques
► Microfluidic Devices in Tissue Engineering
► Micromolding
► Droplet Microreactors
► Wafer Bonding

References

1. Whitesides GM (2006) The origins and the future of microfluidics. Nature 442:368–373
2. Zhang XL, Haswell SJ (2006) Materials matter in microfluidic devices. MRS Bulletin 31:95–99
3. Lagally ET, Mathies RA (2004) Integrated genetic analysis microsystems. J Phys D 37:R245–R261
4. Jensen KF (2006) Silicon-based microchemical systems: Characteristics and applications. MRS Bulletin 31:101–107
5. Dittrich PS, Tachikawa K, Manz A (2006) Micro total analysis systems. Latest advancements and trends. Anal Chem 78:3887–3907
6. Reyes DR, Iossifidis D, Auroux PA, Manz A (2002) Micro total analysis systems. 1. Introduction, theory, and technology. Anal Chem 74:2623–2636
7. Becker H, Locascio LE (2002) Polymer microfluidic devices. Talanta 56:267–287
8. Soper SA, Henry AC, Vaidya B, Galloway M, Wabuyele M, McCarley RL (2002) Surface modification of polymer-based microfluidic devices. Anal Chim Acta 470:87–99
9. King KR, Wang CCJ, Kaazempur-Mofrad MR, Vacanti JP, Borenstein JT (2004) Biodegradable microfluidics. Advanc Mat 16:2007
10. Whitesides GM, Ostuni E, Takayama S, Jiang XY, Ingber DE (2001) Soft lithography in biology and biochemistry. Ann Rev Biomed Eng 3:335–373
11. Thorsen T, Maerkl SJ, Quake SR (2002) Microfluidic large-scale integration. Science 298:580–584

Matrix Assisted Laser Desorption/Ionization

Synonyms

MALDI

Definition

Matrix Assisted Laser Desorption/Ionization (MALDI) is one of two "soft" ionization techniques used to introduce biological samples into a mass spectrometer. In MALDI, the analyte is co-crystallized with a solid matrix to form a dry spot on a surface. Under vacuum, the sample is then irradiated with a laser, which desorbs the sample from the surface and ionizes it. The developers of MALDI (along with the developer of ESI) were awarded the 2002 Nobel Prize in Chemistry.

Cross References

- ► Interfaces Between Microfluidics and Mass Spectrometry
- ► Mass Spectrometry
- ► Mass Spectrometry on Chip Devices

Mean Curvature

► Curvature

Mean Filter

Definition

Mean filters are also known as box filters. The value to be filtered is averaged with its neighbors.

Mean Free Path

Definition

Mean free path is the average distance travelled by gaseous particle between collisions.

Cross References

- ► Gas Flow in Nanochannels
- ► Heat Transfer in Microchannel Flows
- ► Supersonic Micro-Nozzles
- ► Micro- and Nanoscale Gas Dynamics
- ► Lattice Poisson-Boltzmann Method, Analysis of Electroosmotic Microfluidics

Measurement Depth

Definition

At visualization of flows the measurement depth and field of view define the measurement volume. The extension of the measurement volume in direction of the camera is the measurement depth. If ► volume illumination is used, the measurement depth is dependent on the ► depth of field of the camera optics. Otherwise, when illuminating with a ► light sheet, the measurement depth is defined by the thickness of the ► light sheet, since the ► depth of field is larger than the thickness of a ► light sheet in most applications.

Measurement Standards

► Fluid Metering

Measuring Zeta Potential, Methods

CHUN YANG
School of Mechanical and Aerospace Engineering,
Nanyang Technological University, Singapore, Singapore
mcyang@ntu.edu.sg

Synonyms

EDL potential; Surface potential

Definition

Zeta potential is defined as the electric double layer (EDL) potential located at the shear plane between the Stern layer and the diffuse layer of the EDL that is formed in the neighborhood of a charged solid–liquid interface. Zeta potential is an experimentally measurable electrical potential that characterizes the strength and polarity of the EDL of the charged solid–liquid interface. Depending on the solid surface and the solution, zeta potentials values are within a range of -100 mV to $+100$ mV for most solid–liquid interfaces in aqueous solutions.

Overview

Electric Double Layer and Zeta Potential

The necessary condition for development of zeta potential is the presence of electrostatic charges at solid–liquid interface. The charging mechanisms of the solid–liquid

interface are complex, possibly including the asymmetric dipoles of water molecules residing at the solid–liquid interface, adsorption of ions, disassociation of ionic groups, charge separation etc. Such surface charges influence the distribution of nearby ions in the solution. Counter-ions (i. e., ions of opposite charge) are attracted towards the solid surface, while co-ions (i. e., ions of like charge) are repelled from the surface. This electrostatic interaction together with the random thermal motion of the ions, leads to the formation of the so-called *electric double layer* (EDL). The model of EDL was first developed by Gouy and Chapman in 1906, and then improved by Stern in 1924 [1]. According to Stern's model, the EDL consists of a compact (or Stern) layer and a diffuse layer. The Stern layer, usually less than one nanometer, exists immediately next to the solid surface, where counter-ions are strongly attracted to the solid surface thus immobile. The diffuse layer of the EDL is the layer from the Stern layer to the bulk liquid, and its thickness ranges from several nanometers to sub-micrometers, depending on liquid solution properties. Compared to the ions in the Stern layer, the ions in the diffuse layer are less influenced by the charged surface and hence are mobile. A review of modern EDL theory including recent descriptions and formulations of the basic structure (and component regions) of the EDL is given by Dukhin et al. [2].

The zeta potential (ζ) is thought to be the same as the Stern potential which is defined at the plane dividing the Stern layer and the diffuse layer of the EDL. Zeta potential is an experimentally measurable electrical potential that characterizes the EDL, and it plays an important role in many applications such as stability of colloidal dispersion, characterization of biomedical polymers, electrokinetic transport of particles, and capillary electrophoresis, etc. In addition, zeta-potentials of the particles and the channel wall are crucial to the design and process control of microfluidic devices. A review on measuring the zeta potential of microfluidic substrates was provided by Kirby and Hasselbrink [3].

Methods for Measuring Zeta Potential

Several techniques have been developed to measure the zeta potential, based on the principle of electrokinetics. In this entry, the conventional methods of measuring the zeta potential using the mechanisms of electrophoresis, streaming potential, and electroosmotic flow will be outlined first. Then, a novel method will be presented for simultaneously determining the zeta potentials of both the microchannel surfaces and the tracer particles by using the microscale particle image velocimetry (micro-PIV) technique. This method combines the theories of electroosmosis and electrophoresis, and uses micro-PIV technique to measure the steady electrokinetic velocity distributions of tracer particles in open- and closed-end microchannels [4].

Electrophoresis Method

Electrophoresis refers to the motion of a charged particle in a solution in response to an applied electric field. The electrophoresis technique has been widely used to characterize the electrokinetic properties of charged particle–liquid interfaces. In the electrophoresis method, fine particles (usually of 1 µm in diameter) are dispersed in a solution. Under an applied electric field, the particle electrophoresis mobility, v_E, defined as the ratio of particle velocity to electric field strength, is measured using an appropriate microscopic technique. The particle ζ-potential is determined from the measured electrophoresis mobility, v_E by using the Smoluchowski equation expressed as

$$v_E = \frac{\varepsilon_0 \varepsilon_r \zeta}{\mu} \tag{1}$$

where ε_r is the dielectric constant of the solution, ε_0 is the permittivity of vacuum, μ is the dynamic viscosity of the solution.

This technique has been also applied to characterize flat solid surfaces by initially grinding the flat surfaces into fine powders. However, it is unclear if the surface electrostatic properties of these grinded particles are equivalent to the precrushed surfaces.

Streaming Potential Method

The streaming potential technique has been extensively used to characterize the electrokinetic properties of flat solid–liquid interfaces. The streaming potential is an induced electrokinetic potential in a pressure-driven flow through a charged capillary. In principle, when a liquid is forced to flow through a capillary under an applied hydrodynamic pressure, the non-zero net charge density in the diffuse layer of the capillary EDL is carried by the flow, giving rise to an electrical current in the pressure-driven flow direction, called the streaming current. Correspondingly, there is an induced electrokinetic potential called the streaming potential which is a potential difference that builds up along the capillary. Such induced streaming potential acts on ions in the electrolyte solution to generate a so-called conduction current in opposite direction of the flow. It is obvious that when ions move in a viscous liquid, they will pull the liquid molecules along

with them, resulting in a reduced flow rate in the pressure-driven flow. As such change in the flow characteristics is associated with the EDL of the capillary, the ζ-potential of the capillary–liquid interface is directly related to the streaming potential. For a steady, laminar liquid flow, the relationship between the streaming potential and the capillary ζ-potential without consideration of the surface conductance effect is given by

$$\frac{E_s}{\Delta P} = \frac{\varepsilon_0 \varepsilon_r \zeta}{\lambda_b \mu} \tag{2}$$

where E_s is the streaming potential, ΔP is the applied pressure difference along the capillary, λ_b is the bulk electrical conductivity. While this technique is inherently suitable for a fluid flow over charged surfaces, accurately measuring the streaming potential seems not a simple task.

Electroosmosis Method

Electroosmosis refers to the liquid motion related to a stationary charged solid–liquid interface due to the interaction between an external electric field applied tangential to the charged surface and the excess net charges in the EDL of the surface. It is known that within the diffuse layer of the EDL, there is an excessive of counter-ions over co-ions, and thus the net charge density is not zero so as to neutralize the surface charge. If an electric field is applied tangentially along a charged surface, the electric field will exert the Columbic force on the ions in the diffuse layer, resulting in a net migration of the liquid in the EDL region. This is called *electroosmosis* (EO). In a charged micro-capillary, due to viscous forces the flow can be developed beyond the EDL region to the rest of the liquid in the capillary, leading to a bulk *electroosmotic flow* (EOF). Certainly the induced EOF is affected by the capillary EDL, which in turns is related to the capillary ζ-potential. Under the slip velocity approximation, the Smoluchowski equation can be used to describe the relationship between the average velocity of the EOF and the capillary ζ-potential, expressed as:

$$u_{eo} = \frac{\varepsilon_0 \varepsilon_r \zeta E}{\mu} \tag{3}$$

where E is the applied electric field strength, and u_{eo} is the average velocity of the EOF.

In the literature, several methods such as the neutral marker method, the current monitoring method [5] etc have been introduced to indirectly determine the average liquid velocity of the EOF in a microcapillary so that the capillary ζ-potential can be determined using Eq. (3). However, in practice, there exist difficulties in identifying a real, electrically neutral marker and in locating the cut-off of the asymptotic current vs. time curve.

In following, a method will be introduced for simultaneously determining the zeta potentials of both the microchannel surfaces and the tracer particles by using the microscale particle image velocimetry (micro-PIV) technique.

Basic Methodology

Theory

Micro-PIV technique is used to measure the steady velocity of tracer particles in an electrolyte in both open- and closed-end microchannels. Under an applied DC electric field, the observed particle velocity, u_p evaluated from the micro-PIV measurement is the superposition of the electrophoresis velocity of the charged particle, u_{ep}, and the electroosmotic velocity of the electrolyte, u_{eo}:

$$u_p = u_{eo} + u_{ep} \tag{4}$$

In the following, we will provide the analytical expressions for u_{ep} and u_{eo} in an open- and closed-end rectangular microchannel.

Velocity Distribution of the Steady Electroosmotic Flow in Open and Closed-end Microchannels – Slip Velocity Approach

Consider a rectangular microchannel having a height, $2a$, a width, $2b$, and a length, l as shown in Fig. 1. The liquid filled in the microchannel is assumed to be an incompressible, Newtonian, symmetric electrolyte of constant density, ρ, viscosity, μ, and dielectric constant, ε_r. The channel wall is uniformly charged with a zeta potential, ζ_w. When an external electric field, E is applied along the axial direction of the channel, the liquid sets into motion as a result of the interaction between the net charge density in the EDL of the channel and the applied electric field. The driving force of electroosmotic flow is present only within the EDL. The typical thickness of an EDL is in the range of 1 to 100 nm; while the characteristic hydraulic diameter of microfluidic channels is of order 10

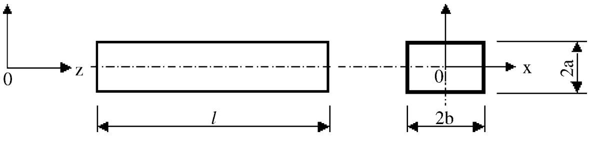

Measuring Zeta Potential, Methods, Figure 1 Geometry of the rectangular channel. The channel length is l and the size of the rectangular cross section $2a \times 2b$

to 100 μm. Because of such orders of the magnitude difference, the electroosmotic velocity profile inside the EDL region becomes insignificant, and thus the electroosmotic flow can be considered to be induced by a moving wall with velocity (slip velocity) given by the Smoluchowski equation,

$$u_s = \frac{\varepsilon_0 \varepsilon_r \zeta_w E}{\mu} \tag{5}$$

In the literature, the fluid flow actuated by moving boundary of the wall and driven by hydrodynamic shear stresses is referred to as the Stokes second problem, and is specifically referred to as the slip velocity approach in electroosmotic flows. More general discussions of the applicability of such slip velocity approach in electrokinetic flows were provided elsewhere [6]. Using the slip velocity approach, the steady velocity field of a fully-developed flow driven by an applied electric field, E and a pressure gradient, $\mathrm{d}p/\mathrm{d}z$ is governed by the Stokes equation, expressed as

$$\frac{\partial^2 u}{\partial x^2} + \frac{\partial^2 u}{\partial y^2} = \frac{1}{\mu}\frac{\mathrm{d}p}{\mathrm{d}z} \tag{6}$$

The appropriate boundary conditions applicable to Eq. (6) are

$$u|_{x=b} = u_s \qquad u|_{y=a} = u_s \tag{7a}$$

$$\left.\frac{\partial u}{\partial x}\right|_{x=0} = 0 \qquad \left.\frac{\partial u}{\partial y}\right|_{y=0} = 0 \tag{7b}$$

Equation (6) together with its boundary conditions specified by Eqs. (7a) and (7b) can be non-dimensionalized by using the following dimensionless parameters:

$$\bar{u} = \frac{u}{U} \qquad X = \frac{x}{D_h} \qquad Y = \frac{y}{D_h}$$

$$Z = \frac{z}{D_h \mathrm{Re}_0} \qquad \bar{P} = \frac{p}{\rho U^2}$$

where U is the reference velocity, $D_h = 4ab/(a+b)$ is the hydraulic diameter of the rectangular channel, and $\mathrm{Re}_0 = \rho D_h U/\mu$ is the reference Reynolds number. Further, we introduce a transform

$$\bar{v} = \bar{u} - \bar{u}_s \tag{8}$$

Then, the governing Stokes equation and its boundary conditions can be rewritten in dimensionless form as

$$\frac{\partial^2 \bar{v}}{\partial X^2} + \frac{\partial^2 \bar{v}}{\partial Y^2} = \frac{\mathrm{d}\bar{P}}{\mathrm{d}Z} \tag{9}$$

with the boundary conditions

$$\bar{v}|_{X=b/D_h} = 0 \qquad \bar{v}|_{Y=a/D_h} = 0 \tag{10a}$$

$$\left.\frac{\partial \bar{v}}{\partial X}\right|_{X=0} = 0 \qquad \left.\frac{\partial \bar{v}}{\partial Y}\right|_{Y=0} = 0 \tag{10b}$$

where $\bar{v} = v/U$ and $\bar{u}_s = u_s/U = -(\varepsilon_0 \varepsilon_r \zeta_w E)/(\mu U)$.
Using Green's function method, the solution of Eq. (9) subjected to boundary conditions given by Eqs. (10a) and (10b) can be explicitly expressed as [7]

$$\bar{v}(X, Y) = \lim_{\bar{t}\to\infty} \int_{\tau=0}^{\bar{t}} \mathrm{d}\tau \int_{X'=0}^{b/D_h} \int_{Y'=0}^{a/D_h} G\left(X, Y, \bar{t} \middle| X', Y', \tau\right) \left(-\frac{\mathrm{d}\bar{P}}{\mathrm{d}Z}\right) \mathrm{d}X'\mathrm{d}Y' \tag{11}$$

Here, the Green's function $G\left(X, Y, \bar{t} \middle| X', Y', \tau\right)$ can be obtained by using the separation of variables method. The expression for $G\left(X, Y, \bar{t} \middle| X', Y', \tau\right)$ is given by [7]

$$G\left(X, Y, \bar{t} \middle| X', Y', \tau\right) = \frac{4D_h^2}{ab} \sum_{m=1}^{\infty}\sum_{n=1}^{\infty} \cos(\alpha_m X) \cos\left(\alpha_m X'\right) \cos(\beta_n Y) \cos\left(\beta_n Y'\right) \mathrm{e}^{-T_{mn}(\bar{t}-\tau)} \tag{12}$$

where $\alpha_m = \left(\frac{2m-1}{2}\right)\frac{D_h}{b}\pi$, $\beta_n = \left(\frac{2n-1}{2}\right)\frac{D_h}{a}\pi$ and $T_{mn} = \alpha_m^2 + \beta_n^2$.
Substituting Eq. (12) to Eq. (11) and carrying out the integration, we obtain

$$\bar{v}(X, Y) = -\frac{\mathrm{d}\bar{P}}{\mathrm{d}Z}\frac{16}{\pi^2} \sum_{m=1}^{\infty}\sum_{n=1}^{\infty} \frac{(-1)^{m+n} \cos(\alpha_m X) \cos(\beta_n Y)}{(2m-1)(2n-1) T_{mn}} \tag{13}$$

Here, two cases are considered:
Case 1: Electroosmotic flow field in an open-end rectangular microchannel
In this situation, $\mathrm{d}\bar{P}/\mathrm{d}Z \equiv 0$, because no external pressure is applied (assuming that the microchannel is infinitely extended). Thus, Eq. (12) becomes

$$\bar{v}\left(X, Y, \bar{t}\right) = 0 \quad \text{or} \quad \bar{u}\left(X, Y, \bar{t}\right) = \bar{u}_s \tag{14}$$

Equation (14) shows that for steady, fully-developed electroosmotic flow in an open-end rectangular microchannel,

the slip velocity approach leads to a "plug-like" velocity profile, given by the Smoluchowski equation:

$$u_{\mathrm{eo-open}} = -\frac{\varepsilon_{\mathrm{r}}\varepsilon_0\zeta_{\mathrm{w}}E}{\mu} \tag{15}$$

Case 2: Electroosmotic flow field in a closed-end rectangular microchannel

Due to the closed-end structure, an inner backpressure gradient $\mathrm{d}\bar{P}/\mathrm{d}Z$ is induced to fulfill the condition of the zero net flow rates, which mathematically is expressed as

$$\int_{-b/D_{\mathrm{h}}}^{b/D_{\mathrm{h}}}\int_{-a/D_{\mathrm{h}}}^{a/D_{\mathrm{h}}} \bar{u}\left(X, Y, \bar{t}\right)\mathrm{d}X\mathrm{d}Y = 0 \tag{16}$$

For an infinitely extended channel, $\mathrm{d}\bar{P}/\mathrm{d}Z$ is constant along the axial flow direction. Substituting Eqs. (8) and (13) into Eq. (16), we can show that the dimensionless induced pressure gradient is given by

$$\frac{\mathrm{d}\bar{P}}{\mathrm{d}Z} = \frac{\pi^4}{64}\frac{\bar{u}_{\mathrm{s}}}{\sum_{m=1}^{\infty}\sum_{n=1}^{\infty}\frac{1}{(2m-1)^2(2n-1)^2T_{mn}}} \tag{17}$$

Further substituting Eq. (17) back to Eq. (13) and noticing $\bar{v} = \bar{u} - \bar{u}_{\mathrm{s}}$, we can obtain

$$\bar{u}\,(X, Y) = \bar{u}_{\mathrm{s}} - \frac{\pi^2\bar{u}_{\mathrm{s}}}{4}\frac{\sum_{m=1}^{\infty}\sum_{n=1}^{\infty}\frac{(-1)^{m+n}\cos(\alpha_m X)\cos(\beta_n Y)}{(2m-1)(2n-1)T_{mn}}}{\sum_{m=1}^{\infty}\sum_{n=1}^{\infty}\frac{1}{(2m-1)^2(2n-1)^2T_{mn}}} \tag{18}$$

Equation (18) gives the electroosmotic velocity distribution in a closed-end rectangular microchannel.

As the microscope objective is focused on the mid-plane of the channel (i. e., $Y = 0$) during the micro-PIV experiment, the dimensional electroosmotic velocity at the mid-plane is expressed as

$$\begin{aligned} u_{\mathrm{eo-closed}}\,(X, 0) &= \bar{u}_{\mathrm{eo-closed}}\,(X, 0)\,U \\ &= -\zeta_{\mathrm{w}}\frac{\varepsilon_0\varepsilon_{\mathrm{r}}E}{\mu}\left[1 - \frac{\pi^2}{4}\frac{\sum_{m=1}^{\infty}\sum_{n=1}^{\infty}\frac{(-1)^{m+n}\cos(\alpha_m X)}{(2m-1)(2n-1)T_{mn}}}{\sum_{m=1}^{\infty}\sum_{n=1}^{\infty}\frac{1}{(2m-1)^2(2n-1)^2T_{mn}}}\right] \end{aligned} \tag{19}$$

Electrophoresis Velocity of the Tracer Particles

Under assumptions of the undisturbed EDL structure of a charged particle and the Debye–Hückel approximation, the electrophoresis velocity of tracer particles, according to Henry [1] can be expressed as:

$$u_{\mathrm{ep}} = \frac{2}{3}f\,(\kappa a)\,\frac{\varepsilon_{\mathrm{r}}\varepsilon_0\zeta_{\mathrm{p}}E}{\mu} \tag{20}$$

A simple expression for Henry's function $f\,(\kappa a)$ can be expressed as:

$$f\,(\kappa a) = 1 + \frac{1}{2\left[1 + \frac{2.5}{\kappa a(1+2\mathrm{e}^{-\kappa a})}\right]^3} \tag{21}$$

Here a is the radium of the tracer particle, and κ is the Debye parameter defined as

$$\kappa = \sqrt{\frac{2e^2z_{\mathrm{v}}^2n_0}{\varepsilon_{\mathrm{r}}\varepsilon_0 kT}}$$

(where e is the fundamental charge, z_{v} is the valence of the symmetric electrolyte, n_0 is the ionic number concentration of the bulk electrolyte, k is the Boltzmann constant, and T is the absolute temperature). It should be pointed out here that the Henry's expression for the electrophoresis velocity of tracer particles is applicable to both open-end and closed-end channels.

Relationships Between the Micro-PIV Measured Particle Velocity and the Zeta Potentials of the Channel Surface and the Particles in Open- and Closed-end Channels

As indicated by Eq. (4), the particle velocity measured from the micro-PIV technique is a combination of the electrophoresis velocity of the tracer particles which is related to the particle zeta potential, ζ_{p} and the electroosmotic flow field which is associated with the zeta potential of the channel surface, ζ_{w}. If micro-PIV experiments are carried out in an electrolyte in open-end and closed-end microchannels, according to Eq. (4), we can write the expressions for the micro-PIV measured velocity of the tracer particles in open-end and closed-end rectangular microchannels as below:

$$u_{\mathrm{p-open}} = u_{\mathrm{eo-open}}\,(\zeta_{\mathrm{w}}, E_1) + u_{\mathrm{ep}}\left(\zeta_{\mathrm{p}}, E_1\right) \tag{22}$$

$$u_{\mathrm{p-closed}} = u_{\mathrm{eo-closed}}\,(\zeta_{\mathrm{w}}, E_2) + u_{\mathrm{ep}}\left(\zeta_{\mathrm{p}}, E_2\right) \tag{23}$$

where E_1 and E_2 are the electric field applied across the open-end and closed-end channel, respectively.

We define the particle mobility, μ_p measured by micro-PIV technique in an electric filed, E as

$$\mu_p = \frac{u_p}{E} \tag{24}$$

Making use of the results of Eqs. (15), (19), and (20), we can further rewrite Eqs. (22) and (23) in terms of the measured particle mobility as

$$\mu_{p-open} = \zeta_w F + \zeta_p G \tag{25}$$

$$\mu_{p-closed} = \zeta_w H(x) + \zeta_p G \tag{26}$$

where the expressions for F, H, and G are given by

$$F = -\frac{\varepsilon_r \varepsilon_0}{\mu} \qquad G = \frac{2}{3} f(\kappa a) \frac{\varepsilon}{\mu} \tag{27a}$$

$$H(x) = -\frac{\varepsilon_0 \varepsilon_r}{\mu}\left[1 - \frac{\pi^2}{4} \frac{\sum_{m=1}^{\infty}\sum_{n=1}^{\infty} \frac{(-1)^{m+n}\cos(\alpha_m x/D_h)}{(2m-1)(2n-1)T_{mn}}}{\sum_{m=1}^{\infty}\sum_{n=1}^{\infty} \frac{1}{(2m-1)^2(2n-1)^2 T_{mn}}}\right] \tag{27b}$$

In principle, Eqs. (25) and (26) show that if the distributions of the particle mobility measured by micro-PIV in the open-and closed-end channels are known, the zeta potentials of both the particles and the channel surface can be determined simultaneously.

Experimental

The measurement cell consists of a borosilicate glass microchannel (VitroCom), a polymer holder, and two reservoirs. Such microchannel has a rectangular 300 μm × 300 μm cross section and is 4 cm long. Prior to experiment, the channel was cleaned in an ultrasonic cleaner with a NaOH base solution and then flushed with deionized water. For the closed-end cell, epoxy glue was used for sealing the two ends of the channel.

Fluorescent polystyrene particles of radius $a = 465$ nm (Duke Scientific Co.) were used for tracking the flow. Such tracer particles have the excitation and emission wavelength of 540 nm and 610 nm, respectively. In all experiments, the number concentration of tracer particles was approximately about 2×10^9 particles per ml.

A DC electric field was applied using platinum wire electrodes inserted into the two reservoirs at the ends of the microchannel. A high-voltage power supply (PS350, Stanford Research) was used to apply 400-V potential difference on the two electrodes, giving rise to a 100 V/cm strength of the applied DC field.

Three types of working fluids were used including sodium chloride and boric acid with various concentrations (10^{-2} M, 10^{-3} M, 10^{-4} M and 10^{-5} M) as well as deionized water.

The micro-PIV setup consists of four main components: an illumination system, an optical system, a coupled charge device (CCD) camera and a control system. The control system consists of a peripheral component interface (PCI) card, and its corresponding software is implemented in a Personal Computer. The computer can control and synchronize all actions related to illumination and image recording. The schematic of the setup is illustrated in Fig. 2.

Particles were imaged using an epifluorescent microscope (Nikon TE2000-S) and a 20× objective lens with a numerical aperture (NA) of 0.45. An interline transfer CCD camera (Sony ICX 084) was used for recording the images. The resolution of the camera is 640 pixels × 480 pixels, with 12 bits grayscale. The active area of the CCD sensor is 6.3 mm × 4.8 mm. The minimum inter-frame transfer time, and thus the fastest time delay for the two PIV images, is $\Delta t_{PIV} = 500$ ns. To ensure that the CCD camera is working at its optimum temperature of −15 °C, a cooling system is integrated in the CCD camera. In the mode of double exposure in double frames, the camera records two frames of the flow fields and then digitizes them in the same image buffer.

Key Research Findings

Micro PIV Images and Particle Velocity Data

Focusing the objective lens on the mid-plane (i. e., $y = 0$) of the rectangular channel as shown in Fig. 1, we used the micro-PIV to measure the particle velocity distributions in both the open- and closed-end channels. The images acquired from micro-PIV measurements were then evaluated with PIVview software (PivTec GmbH) to obtain the particle velocity data. Extracting the velocity data and averaging the values along the flowing direction, we can obtain the averaged velocity values.

Least-Square Analysis

With the experimental data, we can use the least-square analysis to determine the values of the fitted zeta potentials of both the particels and the channel surface by minimizing the sum of the square of the errors between the meausured and predicted particle mobility.

Along the lateral (x-axis) direction of the channel, we assume the measured average particle's mobility at the ith position in the open-end channel as $\mu_{p-open,i}$ and the measured average particle's mobility at the$i$th position in

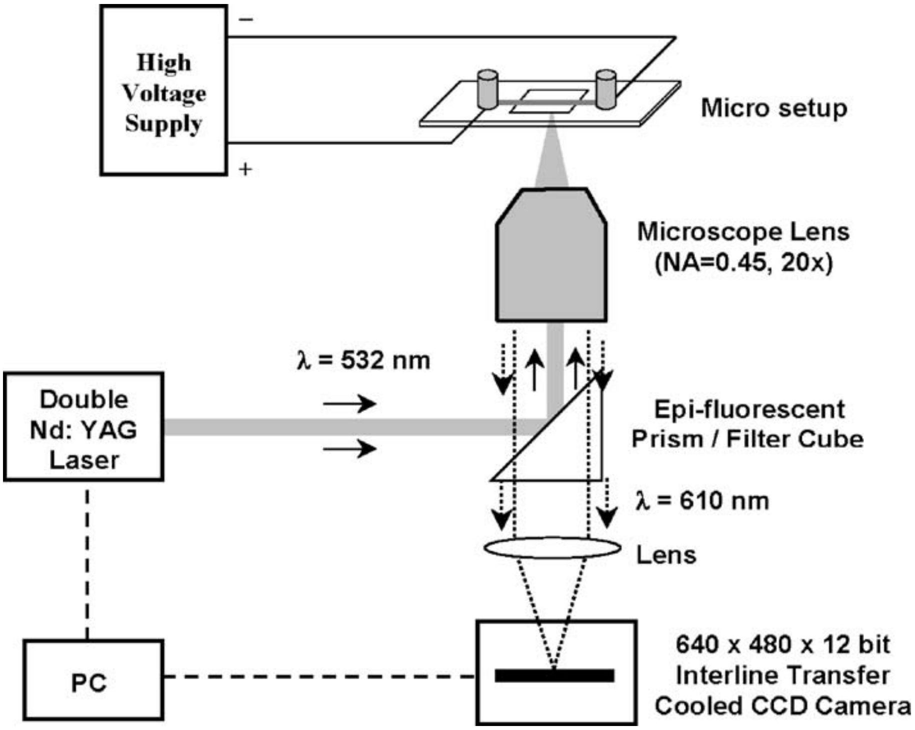

Measuring Zeta Potential, Methods, Figure 2 Schematic of the micro-PIV setup. The PC controls and synchronizes the lasers for illumination, CCD camera for image recording, and high voltage switch for turning on the high voltage supply

the closed-end channel as $\mu_{\text{p-closed},i}$. Applying the least-square method, we introduce the least-square function S as

$$S = \sum_{i=1}^{N} \left[\left(\mu_{\text{p-closed},i} - \mu_{\text{p-closed}}\right)^2 + \left(\mu_{\text{p-open},i} - \mu_{\text{p-open}}\right)^2 \right] \quad (28)$$

where N is the number of the measured points along the lateral direction of the mid-plane of the channel. Thus, the best-fitted values of the two zeta potentials, ζ_{w} and ζ_{p} can be obtained by minimizing the value of S. Substituting Eqs. (25) and (26) into Eq. (28), we know that the derivatives of function S with aspect to ζ_{w} and ζ_{p} should be equal to zero:

$$\frac{\partial S}{\partial \zeta_{\text{w}}} = \sum_{i=1}^{N} \left[2\left(\mu_{\text{p-closed},i} - \mu_{\text{p-closed}}\right)\left(-H\left(x_i\right)\right) + 2\left(\mu_{\text{p-open},i} - \mu_{\text{open}}\right)(-F) \right] = 0 \quad (29)$$

$$\frac{\partial S}{\partial \zeta_{\text{p}}} = \sum_{i=1}^{N} \left[2\left(\mu_{\text{p-closed},i} - \mu_{\text{p-closed}}\right)(-G) + 2\left(\mu_{\text{p-open},i} - \mu_{\text{open}}\right)(-G) \right] = 0 \quad (30)$$

Rearranging Eqs. (29) and (30) and making use of Eqs. (25) and (26), we obtain

$$\zeta_{\text{w}} \sum_{i=1}^{N} \left[F + H\left(x_i\right)\right] + \zeta_{\text{p}}\,(2NG) = \sum_{i=1}^{N} \left(\mu_{\text{p-open},i} + \mu_{\text{p-closed},i}\right) \quad (31)$$

$$\zeta_{\text{w}} \sum_{i=1}^{N} \left[F^2 + \left(H\left(x_i\right)\right)^2\right] + \zeta_{\text{p}} \sum_{i=1}^{N} \left[G\left(F + H\left(x_i\right)\right)\right] = \sum_{i=1}^{N} \left[F\mu_{\text{p-open},i} + H\left(x_i\right)\mu_{\text{p-closed},i}\right] \quad (32)$$

It is convenient to express Eqs. (31) and (32) in the matrix form

$$\begin{bmatrix} \sum_{i=1}^{N} \left[F + H\left(x_i\right)\right] & 2NG \\ \sum_{i=1}^{N} \left[F^2 + \left(H\left(x_i\right)\right)^2\right] & \sum_{i=1}^{N} \left[G\left(F + H\left(x_i\right)\right)\right] \end{bmatrix} \begin{bmatrix} \zeta_{\text{w}} \\ \zeta_{\text{p}} \end{bmatrix}$$

$$= \left[\begin{array}{c} \sum_{i=1}^{N} \left(\mu_{\mathrm{p-open},i} + \mu_{\mathrm{p-closed},i} \right) \\ \sum_{i=1}^{N} \left[F \mu_{\mathrm{p-open},i} + H(x_i)\, \mu_{\mathrm{p-closed},i} \right] \end{array} \right] \tag{33}$$

Introducing

$$A = \left[\begin{array}{cc} \sum_{i=1}^{N} [F + H(x_i)] & 2NG \\ \sum_{i=1}^{N} \left[F^2 + (H(x_i))^2 \right] & \sum_{i=1}^{N} [G(F + H(x_i))] \end{array} \right] \tag{34}$$

and

$$B = \left[\begin{array}{c} \sum_{i=1}^{N} \left(\mu_{\mathrm{p-open},i} + \mu_{\mathrm{p-closed},i} \right) \\ \sum_{i=1}^{N} \left[F \mu_{\mathrm{p-open},i} + H(x_i)\, \mu_{\mathrm{p-closed},i} \right] \end{array} \right] \tag{35}$$

we get

$$\begin{bmatrix} \zeta_{\mathrm{w}} \\ \zeta_{\mathrm{p}} \end{bmatrix} = A^{-1} B \tag{36}$$

With the measured data for $\mu_{\mathrm{p-open},i}$ and $\mu_{\mathrm{p-closed},i}$, A and B are known matrices. Using Eq. (36), we can simultaneously determine the two zeta potentials of the channel surface and the tracer particles in deionized water as $\zeta_{\mathrm{w}} = -62 \pm 6$ mV and $\zeta_{\mathrm{p}} = -37 \pm 4$ mV, respectively. Furthermore, we used the same method to determine the zeta potentials in the sodium chloride and boric acid solutions with various concentrations. We plot the zeta potential data versus the electrolyte concentration and present the results in Fig. 3. It is noted that all the zeta potentials are negative. It can also be observed that the higher the electrolyte concentration, the smaller the absolute value of zeta potentials will be. This tendency is common for the zeta potentials of glass or polymer surfaces in aqueous solutions such as NaCl. Using the streaming potential technique, Gu and Li [8] measured the zeta potential of glass surface in contact with different aqueous solutions of various concentrations. For NaCl solutions, they reported the zeta potential values, ranging from -20 mV to -60 mV, which are in good agreement with our data obtained in the present work.

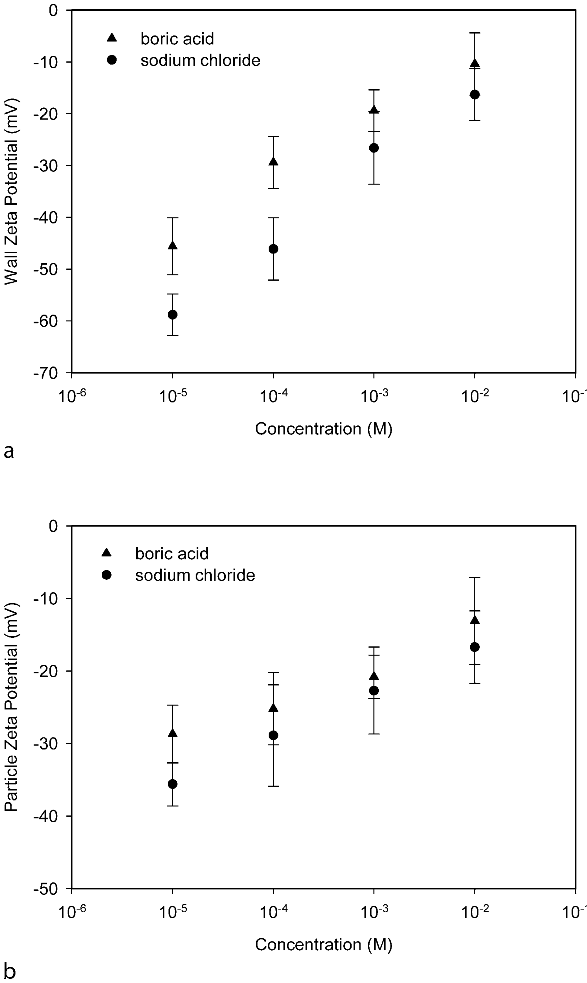

Measuring Zeta Potential, Methods, Figure 3 Measured zeta potentials versus solution concentration (mole/liter) of the sodium chloride and boric acid electrolytes for (**a**) the microchannel surface, and (**b**) the tracer particles

Measurement Errors Due to Brownian Motion

In micro-PIV measurement, the major uncertainty is due to the Brownian motion of tracer particles. In particular, the Brownian motion plays an important role when submicron tracer particles are used in PIV experiments with flow velocities of less than 1 mm/s. According to Einstein, the Brownian motion induced random velocity can be estimated from

$$u_{\mathrm{B}} = \sqrt{\frac{2D}{\Delta t_{\mathrm{PIV}}}} \tag{37}$$

The mass diffusivity of dilute tracer particles suspended in water is given by the Einstein-Stokes equation expressed as,

$$D = \frac{kT}{6\pi \mu a} \tag{38}$$

Given the tracer particles of $a = 465$ µm, room temperature $T = 298$ K and the PIV exposure time $\Delta t_{\mathrm{PIV}} = 500$ ns,

the Brownian velocity is estimated as 30 μm/s. As a result, the measurement error due to the Brownian motion, $\varepsilon_B \equiv u_B/u_f$ is about 3% when the characteristic fluid velocity u_f is chosen as 1 mm/s.

Future Directions for Research

Zeta potential plays an important role in micro- and nano-scale flow and transport processes. More experimental data regarding zeta potential are needed for various liquid-microchannel systems. As in nanofluidic channels, it is not clear whether the zeta potential will be maintained constant or the surface charge density will be kept constant, it is highly desirable to develop new theoretical models, experimental methods and the experimental data for determining zeta potential of nanochannels.

Cross References

- ► Electrical Double Layers
- ► Surface Conductivity Measurement
- ► Electroosmotic Flow (DC)
- ► Electrophoresis
- ► Streaming Current
- ► Zeta-Potential

References

1. Hunter RJ (1981) Zeta Potential in Colloid Science: Principle and Applications. Academic Press, London
2. Dukhin SS, Deryaguin BV (1974) Electrokinetic Phenomena. In: Matijevic E (ed) Surface and Colloid Science. John Wiley, New York
3. Kirby BJ, Hasselbrink Jr EF (2004) Zeta potential of microfluidic substrates. Electrophor 25:187–202
4. Yan DG, Yang C, Nguyen NT, Huang XY (2006) A method for simultaneously determining the zeta potentials of the channel surface and the tracer particles using microparticle image velocimetry technique. Electrophor 27:620–627
5. Arulanandam S, Li D (2000) Evaluation of Zeta Potential and Surface Conductance by Measuring Electro-Osmotic Current. J Colloid Interface Sci 225:421–428
6. Cummings EB, Griffiths SK, Nealson RH, Paul PH (2000) Conditions for Similitude between the Fluid Velocity and Electric Field in Electroosmotic Flow. Anal Chem 72:2526-2532
7. Ozisik MN (1993) Heat Conduction, 2nd edn. Wiley, New York
8. Gu Y, Li D (2000) The Zeta Potential of Glass Surface in Contact with Aqueous Solutions. J Colloid Interface Sci 226:328–339

Mechanical Nanodetectors

► Mechanical Nanosensors

Mechanical Nanosensors

TEIK-CHENG LIM
School of Science and Technology, SIM University, Singapore, Singapore
tclim@unisim.edu.sg

Synonyms

Mechanical nanodetectors

Definition

Mechanical nanosensors are devices that measure physical and chemical properties in a nano-scale region or detect the presence of (bio)molecules based on principles of mechanics.

Overview

Mechanical nanosensors possess comparative advantages over optical nanosensors and electromagnetic nanosensors for the measurement of nanoscale mechanical properties [1].

Elastic Modulus Measurement

The Young's modulus of a cell can be measured using an atomic force microscope (AFM) by indenting the cell with the AFM tip. Based on Hertz model, the Young's modulus, E, can be calculated as [2]

$$E = \frac{\pi}{2}\left(\frac{1-\nu^2}{\delta^2 \tan\alpha}\right)F\,, \tag{1}$$

where ν is the Poisson's ratio (taken as 0.5 assuming the cell to be incompressible), δ is the indentation depth, α is the opening angle of the AFM tip, and F is the applied indentation force.

The Young's modulus of a vertical nanowire or nanorod can be measured using an AFM through applied lateral force, as shown in Fig. 1.

The Young's modulus of a fixed fixed-free column undergoing such lateral deflection can be estimated by

$$E = 0.61584F\frac{\left[h^2 + (l - h\tan\theta)^2\right]^{\frac{3}{2}}}{r^4(l - h\tan\theta)}\,, \tag{2}$$

where F is the maximum lateral bending force, h is the vertical retraction of the AFM tip, l is the corresponding lateral displacement of the AFM tip from initial contact to the nanorod to the point where the nanorod and AFM tip disconnection, θ is the half apex angle of the AFM tip,

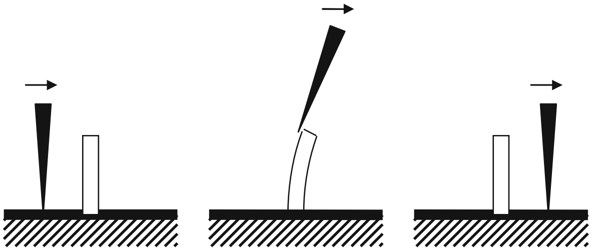

Mechanical Nanosensors, Figure 1 Measuring the Young's modulus of a nanowire using AFM tip [3]

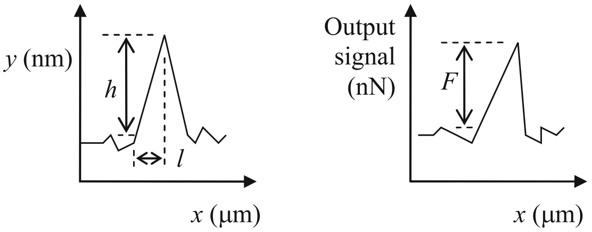

Mechanical Nanosensors, Figure 2 Typical profiles of AFM tip retraction and measured lateral force versus lateral displacement

and r is the nanorod radius [3]. The readings of F, h and l can be obtained from the typical profile of AFM output, as shown in Fig. 2.

Force Measurement

Identification of specific molecules can also be made through the measurement of unbinding (or adhesion) force between a pair of molecules with specific binding, such as ligand–receptor, ligand–protein, antigen–antibody, etc. This is because the force needed to separate a ligand from its binding site is significantly higher than the force required to remove a non-specifically bound ligand [4, 5]. The adhesion force can be inferred from the force-distance curves plotted from the AFM.

Cantilever Beam-Bending

The presence of specific molecules can be detected using a microscale cantilever beam functionalized on a single side. As a result of beam bending due to adsorption on one side of the cantilever, the beam curvature amplifies to nanoscale displacement at the free edge of the cantilever [6]. Assuming the cantilever length, L, to remain constant throughout the event of molecular adsorption, then the deflection, d, at the free edge is

$$d = \rho\left[1 - \cos\left(\frac{L}{\rho}\right)\right], \quad (3)$$

where the cantilever radius of curvature, ρ, is assumed to be inversely proportional to the amount of molecular adsorption and the type of molecules adsorped.

Nano-Scale Mass Measurement

The resonant frequency of a cantilever is inversely proportional to the square root of its mass. Hence attachment of mass to a cantilever results in a change to the cantilever's resonant frequency. The resonant frequency shift of a carbon nanotube (CNT) is [7]

$$\Delta f = f - f_0\,, \quad (4)$$

where f_0 is the original resonant frequency of the CNT, while f is the CNT's resonant frequency upon attachment of mass.

Strain, Pressure and Temperature Measurement

Although the use of cantilever, such as CNT, for measuring the resonant frequency shift is obvious in regard to the measurement of mass, Eq. (4) can also be applied for measurement of other mechanical conditions such as strain and the changes in pressure and temperature. As a result of prescribed strain, applied pressure and temperature change, the coordinates for carbon atoms in the CNT are altered. This coordinate change leads to a change in the CNT resonant frequency [8]. The decrease in

- CNT length,
- attached mass and
- relative distance from mass to CNT fixed-end

result in increase of resonant frequency.

Shorter and thinner CNT are associated with higher change in resonant frequency resulting from axial CNT strain, and temperature and pressure increment. Apart from CNT, the resonant frequency shift technique can also be applied on cantilever beam due to change in mass as a result of molecular adsorption [9].

Cross References

► Nanoscale Biosensors
► Methods for Pressure Measurements
► Methods for Temperature Measurements

References

1. Lim TC, Ramakrishna S (2006) Conceptual review of nanosensors. Z Naturforsch A 61:402–412
2. Radmacher M, Fritz M, Catcher CM, Cleveland JP, Hansma PK (1996) Measuring the viscoelastic properties of human platelets with atomic force microscope. Biophys J 70:556–567
3. Song JH, Wang XD, Riedo E, Wang ZL (2005) Elastic property of vertically aligned nanowires. Nano Lett 5:1954–1958

M

4. Lee C-K, Wang Y-M, Huang L-S, Lin SM (2007) Atomic force microscopy: determination of unbinding force, off rate and energy barrier for protein-ligand interaction. Micron 38:446–461
5. Dupres V, Verbelen C, Dufrene YF (2007) Probing molecular recognition sites on biosurfaces using AFM. Biomaterials 28:2393–2402
6. Cheng MM-C, Cuda G, Bunimovich YL, Gaspari M, Heath JR, Hill HD, Mirkin CA, Nijdam AJ, Terracciano R, Thundat T, Ferrari M (2006) Current Opinion in Chemical Biology. Nanotechnol Biomol Detect Med Diagn 10:11–19
7. Li CY, Chou TW (2004) Mass detection using carbon nanotube-based nanomechanical resonators. Appl Phys Lett 84:5246–5248
8. Li CY, Chou TW (2006) Atomistic modeling of carbon nanotube-based mechanical sensors. J Intel Mater Syst Struc 17:247–254
9. Lee JH, Hwang KS, Park J, Yoon DS, Kim TS (2005) Immunoassay of prostate-specific antigen (PSA) using resonant frequency shift of piezoelectric nanomechanical microcantilever. Biosens Bioelectron 20:2157–2162

Median Filters

Definition

A median filter is a non-linear filter. All values within the filter box are sorted according to their size. The value in the middle of the order is representative and replaces the value to be filtered. With this filter extreme values (outliners) can be removed.

Medical Imaging

► Acoustics Based Biosensors

Membrane Actuation for Micropumps

Laxman Saggere
University of Illinois at Chicago, Chicago, IL, USA
saggere@uic.edu

Synonyms

Diaphragm actuation; Thin-film actuation; Thick-film piezoelectric actuation

Definition

Membrane actuation for micropumps refers to the reciprocating periodic motion of a thin flexible layer–diaphragm or membrane made of silicon or other materials–bounding one side of a displacement micropump to create volume and pressure oscillations in a fluid (i. e., liquid or gas) stored in the chamber of the micropump that is rectified by other means to accomplish a net fluid flow through the micropump. The mechanical energy necessary for the membrane actuation in micropumps is generally derived from electrical, thermal, optical or other forms of energy.

Overview

Micropumps based on a variety of operating principles have been developed since early 1970s for pumping and/or precisely controlling fluid volumes on the order of a milliliter and below, which has enabled numerous emerging applications including dosing therapeutic drugs into the body, Lab-on-a-Chip diagnostic tools, microelectronics cooling, chemical and biological analysis, and micropropulsion. Micropumps have been classified in many different ways in the literature over the years. However, based on the manner in which energy is transmitted to fluid, micropumps are often classified broadly into two types:

1. *mechanical pumps* or *displacement pumps*, which exert pressure on the working fluid through one or more moving boundaries and
2. *non-mechanical pumps* or *dynamic pumps*, which continuously add energy to the working fluid in a manner that increases either its momentum or its pressure directly [1, 2].

Displacement micropumps generally operate by transmitting a periodic motion, which mostly is of reciprocating type, to the working fluid by means of a moving boundary surface using a principle similar to their macro-scale counterparts. The moving boundary surface in macro-scale reciprocating displacement pumps is generally realized by a piston sealed inside a cylinder; however, at micro-scale, owing to complexities of three-dimensional microfabrication and assembly, the piston-like reciprocating action is achieved by means of a thin deformable plate–the membrane or the diaphragm–that is micromachined integrally with the micropump structure such that it attaches to the sides of the micropump chamber bounding one side of the micropump. Generally, by itself, the membrane is passive and driven by an actuator–either integrated with the membrane or external to the membrane–that converts electrical or other forms of energy into mechanical energy of the membrane's reciprocating motion. The various principles of membrane actuation are discussed below in more detail. A schematic of a generic reciprocating displacement micropump including flow rectification components (either passive or active valves or simply two nozzles) on other side(s) of the micropump is shown in Fig. 1.

Membrane Geometry

Reciprocating displacement micropumps have been designed with a wide range of geometry and performance characteristics for various applications. Most reported

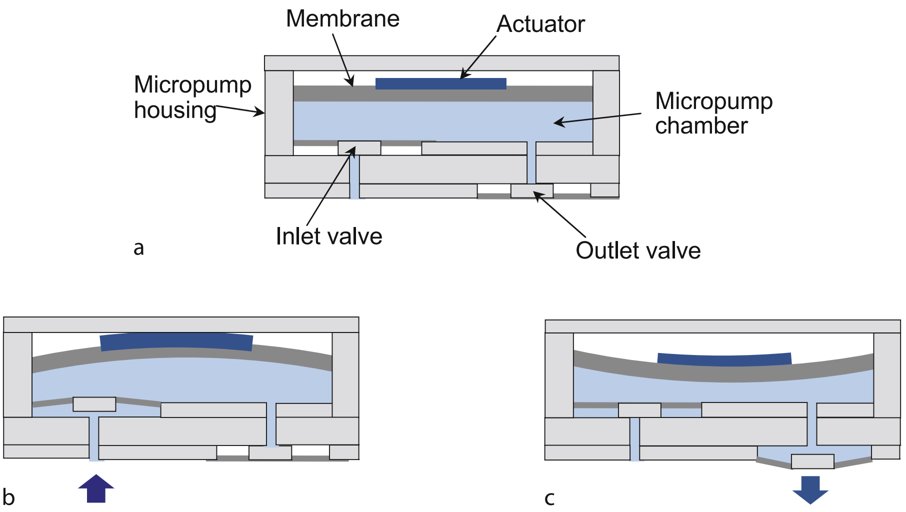

Membrane Actuation for Micropumps, Figure 1 Schematics of a generic reciprocating displacement micropump and its working principle. (**a**) Membrane in the initial flat configuration, (**b**) membrane bowing upwards during the suction stroke, (**c**) membrane bowing downwards during the discharge stroke

reciprocating displacement micropumps are roughly planar structures between 1 mm and 4 mm thick [2]. The membranes in these micropumps are also mostly planar with thickness values ranging from 5 μm to several hundreds of micrometers. Non-planar membrane geometries with bosses at their centers have also been applied to a limited extent in reciprocating displacement micropumps. Most membranes are circular in shape; however, square shaped membranes have also been used in few micropumps reported in the literature. The overall size of the membrane, which must be large enough to produce the required volume displacements, depends on the micropump capacity and the actuation driver force capacity. Even if the driver is capable of supplying effectively large force, the membrane displacement is limited by the diaphragm's failure criteria, which scale unfavorably with decreasing membrane diameter. Scaling down the membrane diameter presents a significant challenge for designers of reciprocating displacement micropumps.

Membrane Materials

The choice of the passive membrane material is critical to the performance of micropump and is often dictated by the type of actuator and the fabrication method selected. For micropumps driven by low frequency and/or low-force actuators, a low-modulus material generally allows the volume displaced by the membrane to be maximized, favorably impacting performance. Commonly used low modulus materials for membranes are elastomers, polyimide, pyrelene, and polydimethylsiloxane (PDMS), and silicone rubber. However, since the membranes act against with the working fluid in the micropump, soft polynmer membranes suffer from stability issues. For actuators capable of operating at a high frequency and adequate force, the fast mechanical response of a stiff membrane generally yields the best performance. For this reason, silicon, glass and plastic are the most commonly used materials for membranes driven by piezoelectric actuation, which is capable of operating at very high frequencies.

Membrane Fabrication

The most common method for fabricating passive silicon membranes for micropumps is micromachining combined with glass bonding layers. The micromachining techniques generally involve photolithography followed by either wet etching or deep reactive ion etching (DRIE) from one side of the wafer. Integration of actuators and electrodes with the passive membrane involves additional fabrication steps that are often complicated. For example, a composite of thin film piezoelectric material layer sandwiched between two electrode layers is formed on the membrane by a variety of techniques including: physical vapor deposition techniques (ion beam sputtering, RF planar magnetron sputtering, dc magnetron sputtering), chemical vapor deposition (CVD) techniques (metal-organic-chemical vapor deposition or MOCVD), chemical solution deposition (CSD) techniques (including sol-gel routes, metal-organic-decomposition), and pulsed laser deposition (PLD) [5]. A number of reciprocating displacement micropumps have been fabricated through means other than traditional silicon/glass micromachining such as precision machining of brass, stereolithography of an

ultraviolet-photocurable polymer. Improvements in techniques for fabricating precision components from plastic have led to increasing use of plastics in reciprocating displacement micropumps.

Purpose of the Membrane Actuation in Micropumps

The main purpose of the membrane actuation in a displacement micropump is to create volume, and therefore, pressure oscillations in the chamber of the micropump to enable displacement of the fluid stored in the micropump chamber. During its operation, an actuator drives the membrane displacing the membrane from its initial flat configuration in a transverse (up and down) motion in a periodic manner. The membrane actuation frequencies vary widely from DC to several kilohertz in the micropumps reported depending on the application. The working principle of a reciprocating displacement micropump can be described by a cyclic process, which is divided into a supply mode (the pump chamber volume increases) and a pump mode (the pump chamber volume decreases). The alternating stroke volume ΔV of the membrane causes increase and decrease in the dead (initial) volume V_0 of the micropump chamber cyclically leading to pressure oscillations of amplitude $|\Delta p|$ in the pump chamber. During the supply mode, low pressure is generated in the pump chamber, which causes fluid to be drawn into the pump chamber through the inlet valve, *as soon as* Δp *becomes larger than the inlet valves threshold pressure* Δp_{crit}. During the pump mode, overpressure occurs in the pump chamber, which transfers liquid from the pump chamber into the outlet *as soon as* Δp *becomes larger than the outlet valves threshold pressure* Δp_{crit} [3]. In this stage, the inlet valve is designed to prevent a reverse flow, and likewise the outlet valve does during the supply phase. Thus the membrane volume oscillations are rectified into a net flow through the micropump over a two-stroke pump cycle by means of valves at the inlet and outlet oriented to favor flow into and out of the micropump chamber during the chamber expansion stroke and contraction stroke respectively.

Basic Methodology

This section details the actuation techniques used to drive the membrane, the modeling techniques for designing a membrane actuator, and the fabrication techniques employed to realize membrane actuators.

Membrane Actuation Techniques

The periodic motion of the passive membrane structure in a micropump is achieved by means of an actuator that is either external to the membrane or integrated with the membrane. A wide range of actuation principles involving both external and integrated actuators have been applied to drive membranes in micropumps. The membrane actuator stroke, stiffness, frequency of operation, response time, and hence, the performance of the micropump, are directly impacted by the choice and design of the actuator principle. External actuation principles used for membranes in micropumps include: electromagnetic actuators with solenoid plunger and external magnetic field, disk type or cantilever type piezoelectric actuators, stack type piezoelectric actuators, pneumatic actuators, and shape memory actuators. While external actuators have the advantage of imparting relatively large forces and displacement to the membranes, their bulkiness restricts the packaged size of the micro-pumps. Integrated actuators are micromachined with the pumps. Most common integrated actuators are thin film type piezoelectric actuators, electrostatic actuators, thermopneumatic actuators, electromagnetic actuators, and thermomechanical (bimetallic) actuators [3, 4]. Other less commonly used actuation principles used for membrane actuation in micropumps include shape memory alloys, magnetostrictive materials, electrowetting, bimetallic drivers, and magnetoelastic drivers. The three most common integrated actuator principles are discussed in more detail below.

Piezoelectric Actuation

Piezoelectric actuation provides the advantages of a comparatively high stroke volume, a high actuation force combined with a fast mechanical response, and is, therefore, a very attractive and most commonly used actuation principle for micropumps. The disadvantages of the piezoelectric actuation are relatively high actuation voltage and quite involved fabrication process. Most membranes actuated by the piezoelectric principle are made of brass, silicon, glass and plastic, and the most commonly used piezoelectric materials are zinc oxide and PZT (lead zirconate titanate) family of ceramics due to their excellent dielectric properties and compatibility with micromachining in a thin film form [5]. Piezoelectric materials in their bulk or stack forms have also been manually integrated with the passive membrane and used to drive the membrane. In thick or thin film form, the piezoelectric material can drive a membrane in either predominantly lateral or predominantly axial configurations as illustrated in Fig. 2a respectively, whereas in a bulk or stack form, the piezoelectric material drives the membrane predominantly in its axial direction Fig. 2b. The maximum piezoelectric free strain that can be produced in the membrane, which directly relates to the stroke volume of the microp-

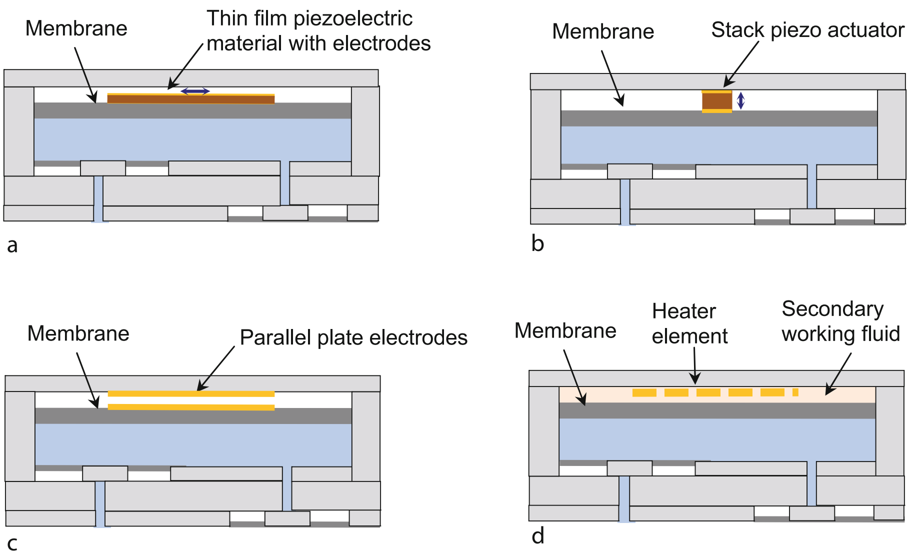

Membrane Actuation for Micropumps, Figure 2 Schematic illustration of the principal types of membrane actuations in micropump. (**a**) Thin film piezoelectric actuation, (**b**) Stack piezoelectric actuator, (**c**) Parallel plate electrodes for electrostatic actuation, (**d**) Thermopneumatic actuation using thermal expansion of a secondary working fluid

ump, is determined by the driving voltage and the piezoelectric characteristics of the piezo material such as the polarization limit and the strain coefficients in lateral and transverse directions and the fabrication process. Piezoelectrics can be driven at several hundreds of kHz frequencies by electric fields on the order of $10\,\text{kVcm}^{-1}$ or higher.

The physical basis for the design of piezoelectric membranes is based on simple combined electrical and mechanical relations (Gauss' law and Hooke's law). The relationship between the electrical and mechanical properties of piezoelectrics is governed by the following constitutive equations:

$$s_i = s_{ij}^E T_j + d_{ki} E_k$$

$$D_i = d_{lm} T_m + \varepsilon_{ln}^{\tau} E_n$$

where $i, j, m = 1, \ldots, 6$ and $k, l, n = 1, 2, 3$. Here, S, D, E, and T are the strain, dielectric displacement, electric field, and stress, respectively, and S_{ij}^E, d_{kl}, and $\varepsilon_{ln}^{\tau} E_n$ are the elastic compliances (at constant field), the piezoelectric constants, and dielectric permittivities (at constant stress) [5].

Electrostatic Actuation

The electrostatic actuation for membranes in micropumps provides several advantages: fast response time, compatibility with micromachining techniques, ability to operate at high frequencies and good reliability; however, electrostatic actuation produces relatively small stroke and small force, and as such, this principle is suitable for micropumps with very low power consumption. Due to geometric constraints, electrostatic actuator is realized mostly in parallel-plate configuration as shown in Fig. 2c by creating one of the plate electrodes on the membrane and the other plate electrode is fixed above the electrode on the membrane with the electric field applied across the air gap between the plates. In the parallel plate configuration, the bottom electrode mounted on the moving membrane typically bows during micropump operation and the actuation force becomes non-uniform across the width of the membrane and the force values are difficult to calculate, however, the electrostatic force at the very beginning of the pump stroke (when both electrodes are flat) can be easily calculated. The capacitance between a pump membrane of diameter d and a counterelectrode of equal size separated by a distance s is

$$C = \frac{\varepsilon \pi d^2}{4s}$$

The electrostatic force between the two plates is given by

$$F = \frac{1}{2}\frac{\partial C}{\partial s}V^2 = \frac{\varepsilon \pi d^2}{8s^2}V^2$$

where ε is the permittivity of the medium separating the plates and V is the potential difference between them.

Thermopneumatic Actuation

The thermopneumatic actuation has the ability to produce relatively large stroke and pressures, but needs a large amount of thermal energy, and consequently, such actuators consume considerable amount of electric power. The temporal response of thermopneumatic actuators is limited by the rate of heat transfer into and out of the secondary working fluid, and so thermopneumatically driven membranes typically operate at relatively low frequencies. Other drawbacks of thermopneumatic actuation include high temperatures and complicated thermal management. The thermopneumatic principle, illustrated in Fig. 2d, involves heating (usually with an integrated thin-film resistive heater) of a secondary working fluid causing it to expand, and thereby, actuate the membrane. In order to maximize the volume displaced by the membrane, low-modulus materials such as polyimide, pyrelene, elastomer and polydimethylsiloxane (PDMS) are often used for membranes driven by thermopneumatic principle.

Key Research Findings

Membrane actuation used in reciprocating micropumps has enabled numerous applications involving precise fluid handling very small volumes of the working fluid over the past two decades. The piezoelectrically driven micropumps, which can be traced to a class of ink jet printheads developed in the 1970s, have received considerable attention and such micropumps are now available commercially. Micropumps using membrane actuation have been developed for dispensing therapeutic agents into the body [6]. Among such micropumps, implantable insulin delivery systems for maintaining diabetics' blood sugar levels without frequent needle injections are currently available. Micropumps might also be used to dispense engineered macromolecules into tumors or the bloodstream. Micropumps are also found in a few current-generation micro total analysis systems (μTAS) employed in chemical and biological analysis.

Future Directions for Research

The membrane actuation is crucial for micropumps as researchers are working on developing new applications for micropumps and further miniaturization of micropumps for precise handling of even smaller amounts fluids on the order of nano- and picoliters. On the new applications side, micropumps are being developed for use in cryogenic spot cooling of microelectronic devices and micropropulsion for space exploration [2]. Control of smallest amounts of fluids is of increasing interest in modern bioanalytical and pharmaceutical research and industry. Micropumps including those utilizing membrane actuation will see a more widespread application especially in life sciences area as researchers are seeking to address issues related to their reliability, complexity of microfabrication, power consumption, cost and biocompatibility. Research is also ongoing to improve the performance of currently available membrane actuation technologies and active materials for membrane actuation.

Cross References

► Piezo/PZT in Microfluidics
► Piezoelectric Microdispenser

References

1. Nguyen NT, Huang X, Chuan TK (2002) MEMS-Micropumps: A Review. J Fluids Eng Trans ASME 124(2):384–392
2. Laser DJ, Santiago JG (2004) A review of micropumps. J Micromech Microeng 14:R35–R64
3. Woias P (2001) Micropumps – summarizing the first two decades, Microfluidics and BioMEMS. Proc SPIE 4560:39–52
4. Shoji S, Esashi M (1994) Microflow Devices and Systems. J Micromech Microeng 4:157–171
5. Polla DL, Francis LF (1998) Processing and Characterization of Piezoelectric Materials and Integration into Microelectromechanical Systems. Ann Rev Mater Sci 28:563–97
6. Polla DL, Erdman AG, Robbins WP, Markus DT, Diaz-Diaz J, Rizq R, Nam Y, Brickner TH (2000) Microdevices in medicine. Ann Rev Biomed Eng 2:551–576

Membraneless Fuel Cells

► Microfluidic Fuel Cells

Membrane Pump

► Peristaltic Pumps
► Positive Displacement Pump

Membrane Reactor

► Microfluidic Bioreactors

Memory

► Hysteresis

Memory Effect

► Hysteresis

MEMS Actuators

► Microactuators

MEMS-Based Biosensor

YONG-JUN KIM, EUN-SOO HWANG, YONG-HO KIM, SEUNG-IL YOON, SECHUL PARK
Microsystems Laboratory, School of Mechanical Engineering
Yonsei University, Seoul, Republic of Korea
yjk@yonsei.ac.kr

Synonyms

MEMS biosensor; Microbiosensor

Definition

A *MEMS-based biosensor* is a biosensor which is realized by microfabrication technology and takes advantage of the small size. It incorporates a biological component with a physiochemical transducer such as a microsystem. It is a special class of chemical sensor that takes advantage of the high selectivity and sensitivity of biologically active materials. It involves immuno, enzyme and microorganism sensors.

Overview

Since the first biosensor was described by Clark and Lyons in 1962, a vast number of biosensors have been proposed for detecting tissue, microorganisms, organelles, cell receptors, enzymes, antibodies, nucleic acids and so on. A biosensor consists of three parts as shown in Fig. 1: an analyte recognition element, a transducer whose mechanism may be electrochemical, optical, thermometric or magnetic and a read-out element. At the analyte recognition element, the analyte is specifically recognized by a biologically sensitive substance while other biological substances are not detected. The recognition leads to a specific change of the transducer which is subsequently converted into a measurable form, generally an electrical signal, in the read-out element. A biosensor can be classified by various standpoints such as its application field or its transducing mechanism. It is also called a medical

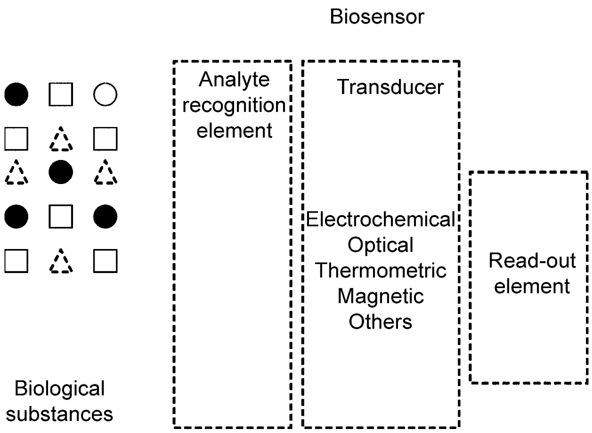

MEMS-Based Biosensor, Figure 1 Schematic of a conventional biosensor

or environmental sensor when it is applied in the corresponding field. The transducing mechanism may be electrical, chemical, mechanical, optical, magnetic or acoustic. In this entry, a biosensor will be classified by its transducing mechanism such as electrochemical, optical, etc.

In the case of conventional biosensors, each of the three components is realized separately, have different scientific background but their own function in the biosensor. For example, biology, physics, chemistry or medical science are the main scientific fields for the analyte recognition element, mechanical, electrical and electronic engineering for the transducer, and mechanical, electrical, electronic engineering and physics for the detection element. Even though the conventional biosensors are successful to an extent, they are expensive and their usage is limited to a specifically organized environment.

Due to well-established micromachining technology, the transducer and read-out elements are starting to be realized in a single device. Such a miniature device is called a MEMS biosensor generally. However, full function of the read-out element is not integrated yet. The current MEMS biosensor is a miniature device in which the transducer is miniaturized and a part of the function of the read-out element is also integrated. The MEMS biosensor has many advantages such as small size, low cost, sharply reduced power consumption and enhanced usability. A good example is a microcantilever biosensor [1]. This includes a read-out element as well as a physical transducer. When an analyte is reacted with a recognition element which is immobilized on the surface of the microcantilever, it induces chemical stresses and subsequently bending of the microcantilever. This results in a change of electrical resistance which is due to a piezoresistor integrated with the microcantilever.

M

Basic Methodology

Electrochemical Method

Introduction

MEMS biosensors based on electrochemical methods can measure quantitative concentrations of biochemicals in biological systems such as immunological systems and glucose metabolism. They convert biochemical reactions to electrical signals. Changes in potential, conductance and current between two electrodes are the main parameters that are measured. Electrochemical methods are a dominant biosensing methodology because of the simple structure and easy measurement compared with other MEMS biosensors such as optical biosensors, acoustic biosensors and so on. MEMS biosensors based on electrochemical methods can be classified into three types according to measured parameters [2].

Potentiometric MEMS biosensors (potentiometry) are based on potential measurement of an electrode in a solution. This potential is measured in an equilibrium state. In other words, current flow should not exist during the measurement. According to the Nernst equation, the potential is proportional to the logarithm of the concentration of the electroactive species.

Voltammetric MEMS biosensors (voltammetry) are based on measuring the current-voltage relationship in an electrochemical cell consisting of electrodes in a solution. After a potential is applied to the sensor, current, which is proportional to the concentration of the electroactive species of interest, is measured. Amperometry is a special case when potential is maintained so as to be constant with time.

Conductometric MEMS biosensors (conductometry) are based on measuring conductance between two electrodes in a solution. Conductance is measured by applying a small quantity of AC potential to block a polarization. The existence of ionic elements is measured as an increase in conductance.

Theory of Electrochemical MEMS Biosensors

Potentiometric MEMS Biosensors Potentiometric MEMS biosensors are a direct analytical application of the Nernst equation through measurement of the potential of non-polarized electrodes when current is zero. A reference electrode is necessary to investigate potential changes due to biochemical reactions. Without a stable reference electrode, reliability of the biosensor cannot be achieved [3].

Among MEMS biosensors based on potentiometric methods, a microcalorimeter is a good example. A microcalorimeter is a kind of a self-generation sensor in which the heat of a biochemical reaction is detected. Generally, an output voltage is a function of the concentration of the substance to be measured. It is based on thermocouples. Thermocouples are two-lead elements that measure the temperature difference between the ends of the wires. They are based on the thermoelectric Seebeck effect that a temperature difference ΔT in a biosensor creates an electrical voltage $\Delta V/\Delta V = \alpha_S \Delta T$, where α_S is the Seebeck coefficient expressed in V/K [4]. Figure 2 shows a schematic of the Seebeck effect and a simplified thermopile.

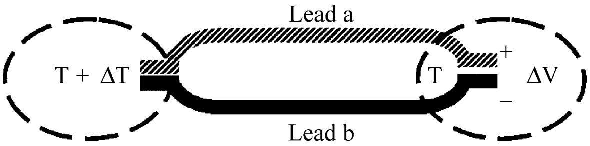

MEMS-Based Biosensor, Figure 2 The Seebeck effect: an electrical voltage ΔV is generated due to a temperature difference ΔT [4]

Microcalorimeters can be used for both gaseous and liquid media. In both cases, the substance to be measured is converted into another substance by means of a catalytic or enzymatic reaction that produces heat. The catalyst or enzyme is deposited on the sensing area of the thermal sensor. Figure 3 shows an example of a microcalorimeter [5].

Voltammetric MEMS Biosensors Voltammetric MEMS biosensors measure the current flow at an electrode which is a function of the potential applied to the electrode. Voltammetric measurement gives the current–potential curve or voltammogram. These curves can be used for qualitative, quantitative, thermodynamic and kinetic studies. In contrast to potentiometry, voltammetry gives a linear current response as a function of the concentration, which is a notable advantage [6].

Among voltammetric MEMS biosensors, a piezoresistive microcantilever is a good example. The general configuration of a piezoresistive microcantilever sensor is shown in Fig. 4. The stress caused by biochemical reactions is concentrated on the surface of the microcantilever. Piezoresistors are usually placed on the microcantilever to the rim, where the stress is maximal. When the microcantilever is bent due to biochemical reaction, the resistivity of the microcantilever is changed. And by measuring the change, the concentration of the biochemical is detected [7].

Conductometric MEMS Biosensors Electrolytic conductance is a non-faradaic process that can give useful chemical information. Electrolytic conductance originates from the transport of anions to the anode and cations to the cathode. In order to complete the current path,

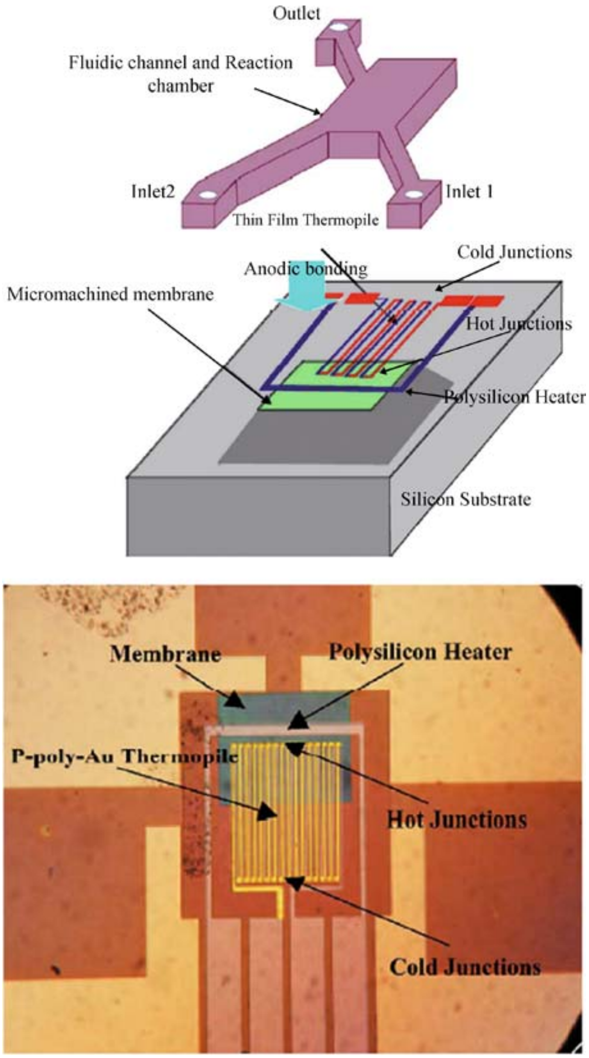

MEMS-Based Biosensor, Figure 3 Calorimetric biosensor with integrated microfluidic channels [5]

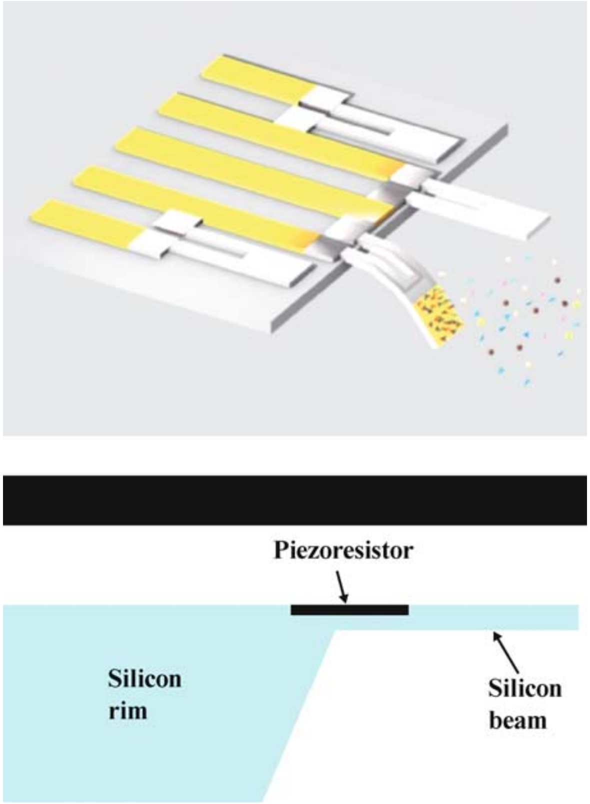

MEMS-Based Biosensor, Figure 4 Schematic and cross-sectional view of a piezoresistive microcantilever [7]

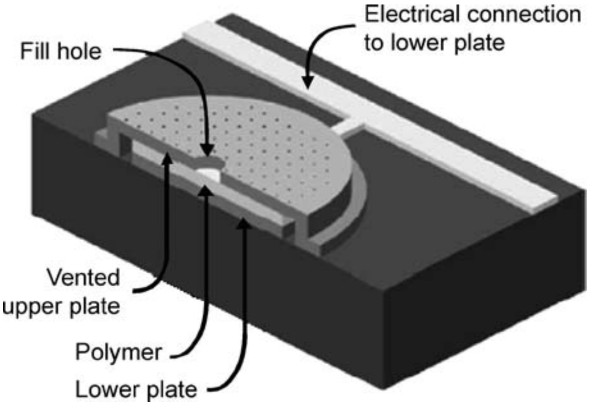

MEMS-Based Biosensor, Figure 5 A cross-sectional view of a conductometric sensor [9]

electrons are transferred at the electrode surface to and from the ions. The conductance of an electrolyte is measured in a conductance cell consisting of two identical non-polarizable electrodes. To prevent polarization, an AC potential is applied to these electrodes and the AC current is measured [8].

A chemicapacitive sensor is a capacitor that has a selectively absorbing material such as a polymer as a dielectric: As chemicals are absorbed into the dielectric, effective permittivity of the capacitive sensor is changed. This leads a change of the capacitance. A cross-sectional view of the basic structure of micromachined parallel plates is shown in Fig. 5 [9]. The conductance of the polymer depends on the types and quantities of biochemicals.

Optical Method

Introduction

The principle of optical biosensors is measuring the change in optical absorption or emission of a molecule or molecules at a particular region of the spectrum [10]. Inter-

action of the component being measured with the immobilized reagent phase causes a change in the optical properties of the reagent phase.

In traditional optical biosensors, the measurement setup consists of a light source, a detecting system, waveguiding equipment and chemical chambers where the interaction occurs. The use of optical fibers makes it possible to bring light from a source to a sample and back to the detecting system. And the use of immobilization makes it possible to do chemistry on the sample in situ [11].

In MEMS-based optical biosensor systems, similar configurations are used. Light propagates in free space or is guided by optical fibers or planar optical waveguides. In one setup, only the mechanical structure (mirror, cantilever or reaction chamber) is fabricated on wafers. After dicing, optical fibers are aligned and fixed on the structure to build the complete device. In another setup, all the elements are fabricated with collective techniques on the same substrate. Therefore, MEMS-based optical biosensors have the advantages of enhanced reliability and low cost. They also benefit from the advantages offered by mechanical structures [12–14].

Optical sensors offer some advantages over electrochemical methods [10, 11]. First, no reference electrode is required; however, reference intensity is necessary to minimize environmental effects on the system. Second, fiber-optic sensors are immune to electrical noise, but ambient light can be a problem. Finally optical sensors have the potential for higher information content than electrical sensors because there is a complete spectrum of information available. However, the linearity is usually limited to a very narrow range.

General Optical Detection Methods

Direct Method When the analyte binds to the receptor, a change in optical absorption or fluorescence occurs. The interaction of an indicator reagent with analyte may be represented as

$$A + R \leftrightarrow A \cdot R$$
$$K_R = \frac{[A \cdot R]}{[A][R]} \tag{1}$$

where R is a reagent and A is an analyte. Given that the total amount of reagent is fixed, then $[R]_{tot} = [R]_{eq} + [A \cdot R]_{eq}$. The equilibrium concentration of the bound analyte-reagent is given by

$$[A \cdot R]_{eq} = \left(\frac{[A]_{eq}}{(1/K_R) + [A]_{eq}} \right) [R]_{tot} \tag{2}$$

and the equilibrium free-reagent concentration is given by

$$[R]_{eq} = \left(\frac{1}{(1/K_R) + [A]_{eq}} \right) [R]_{tot} \tag{3}$$

- If the measured optical parameter is proportional to $[A \cdot R]_{eq}$, then response is proportional to $[A]_{eq}$ at low concentrations ($[A]_{eq} \ll 1/K_R$). The response shows saturation behavior reaching a limiting value as $[A]$ increases to values $\gg 1/K_R$ Eq. (2).
- If the measured optical parameter is proportional to $[R]_{eq}$, then the signal decreases with added analyte. In this case, a linear working curve is obtained based on Eq. (3).
- If one can measure both $[A \cdot R]_{eq}$ and $[R]_{eq}$, since the ratio of the two is directly proportional to analyte concentration, the dependence on $[R]_{tot}$ can be eliminated:

$$\frac{[A \cdot R]_{eq}}{[R]_{eq}} = K_R [A]_{eq}$$

Where feasible, this is the preferred situation. The measurement of $[R]_{eq}$ serves as the reference for the measurement of $[A \cdot R]_{eq}$, since the measured ratio is independent of instrumental fluctuations and any changes in reagent-phase optical properties.

Indirect (Competitive Binding) Method There are two competing reactions occurring, the analyte-receptor reaction and an analog-receptor reaction. The analog molecules are fluorescently labeled molecules that are similar in structure to the analyte molecules. Thus, the analog molecules will bind to the receptors, though not as strongly as the analyte molecules. The optical change, which is measured, is in the analog-receptor reaction.

Figure 6 shows the competitive-binding scheme. Since there are fixed concentrations of receptor and analog immobilized in the chamber, as the concentration of the analyte increases, the amount of analog bound to the receptors decreases, and thus the optical signal will change.

- Analyte-receptor reaction: Eq. (1).
- Analog-receptor reaction, which is described by

$$L + R \leftrightarrow L \cdot R$$
$$K_L = \frac{[L \cdot R]}{[L][R]} \tag{4}$$

where the analog molecules and the receptor molecules are represented by L and R, respectively.

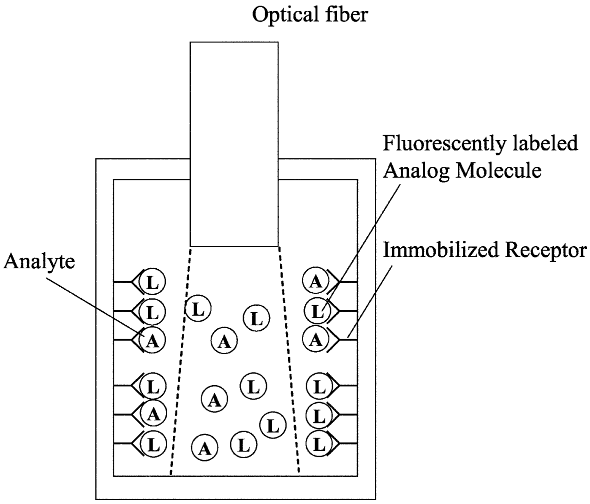

MEMS-Based Biosensor, Figure 6 The competitive-binding scheme for optical biosensors. The analyte molecules are indicated by A and the fluorescently labeled analog molecules are indicated by L [10]

The total number of receptors is fixed, and the total amount of analog is also fixed:

$$[R]_{\text{tot}} = [A \cdot R]_{\text{eq}} + [L \cdot R]_{\text{eq}} + [R]_{\text{eq}} \tag{5}$$

$$[L]_{\text{tot}} = [L \cdot R]_{\text{eq}} + [L]_{\text{eq}} \tag{6}$$

Thus, the concentration of analyte is

$$[A] = \frac{[A \cdot R][L]}{[L \cdot R]} \frac{K_{\text{L}}}{K_{\text{R}}} \tag{7}$$

If the equilibrium constants are large, $[R] \ll [L \cdot R], [A \cdot R]$, then

$$[A] = \frac{([R]_{\text{tot}} - [L \cdot R])\,[L]}{[L \cdot R]} \frac{K_{\text{L}}}{K_{\text{R}}} \tag{8}$$

Thus, the analyte concentration can be determined from the optical detection of either the analog, L, or the bound analog-reagent complex, $L \cdot R$.

Other Methods

Catalyst The immobilized reagent can catalyze transformation of an analyte to a product with different optical properties. For example, a sensor based on the use of immobilized alkaline phosphatase to catalyze the hydrolysis of *p*-nitrophenylphosphate to *p*-nitrophenoxide has been reported [15].

Bioluminescence- and Chemiluminescence-based Biosensors These reactions are the most sensitive chemical probes. The simplest accepted mechanism for the production of light from biological reactions is that of the crustacean *Cypridina hilgendorfi*:

$$\text{Luciferin} + \text{luciferase} \xrightarrow[H_2O]{O_2} \text{Oxyluciferin*}$$

$$\text{Oxyluciferin*} \longrightarrow \text{Oxyluciferin} + \textit{light}$$

where the luciferin is the molecule that emits light and the luciferase is the enzyme that oxidizes the luciferin to its excited state, which is denoted by the asterisk. Typical bioluminescence reactions are much more complicated [16].

Fluorophore- and Chromophore-based Biosensors Chromophore and fluorophore molecules show a change in absorbance or fluorescence at a particular wavelength due to a change in oxidation state of the molecule. Thus a chemical sensor can be constructed for the usual chemical parameters, such as pH, oxygen and ammonia, which then can be coupled to enzyme reactions.

M

Optical Sensor Configurations

- Bifurcated device in which separate fibers are used to transmit light to and from an immobilized reagent phase.
- Sensor in which the same (single) fiber carries light to and from the immobilized reagent.
- Sensor in which the reagent phase is coated on the outside of the fiber. This arrangement takes advantage of the fact that light transmitted through the optical fiber penetrates a small distance of cladding. Changes in the refractive index and/or the absorptive properties of the reagent phase will modify the intensity of light transmitted through the fiber.

Examples of Optical MEMS Biosensors

Integrated Mach–Zehner Interferometer

Principles These sensors make use of guided waves or modes in planar optical waveguides. The waveguide materials usually include high-refractivity silicon dioxide and silicon nitride films on oxidized silicon wafer substrates. Interaction of an analyte molecule with a recognition structure immobilized on the waveguide surface changes the effective refractive index near the evanescent field. These changes induce changes of guided wave modes

since the effective refractive index is the most important physical quantity of the guided modes [12–14, 17].

Configuration A waveguide is split into an open measurement path and a protected reference path and recombined after some distance. The phase difference introduced by analyte interaction (refractive index change) in the sensing path is detected by interference effects.

Typical Applications These include the detection of different organic solvents in liquid phase and biotin/streptavidin-meditated immuno-sensing involving antibody-antigen binding experiments.

Fabry–Pérot-based Microspectrometer

Principles A Fabry–Pérot interferometer (FPI) is an optical element consisting of two partially reflecting, low-loss, parallel mirrors separated by a gap. The optical transmission characteristics through the mirrors consist of a series of sharp resonant transmission peaks occurring when the gap is equal to multiples of half a wavelength of the incident light. These transmission peaks are caused by multiple reflections of the light in the cavity. Small changes in the gap (width, absorptivity) can produce large changes in the transmission response. The transmission is a function of both the gap spacing and the radiation wavelength [12, 13].

Configuration There are many kinds of FPI for biosensors. A typical FPI interferometer consists of an LED, a channel for bio reaction, a micro-FPI and a detector.

Typical Applications These include gas sensors to monitor carbon monoxide, carbon dioxide and hydrocarbons, and biosensors to measure the absorption spectrum of blood.

Other MEMS Biosensors

Besides MEMS-based electrochemical and optical biosensors, there are other types of MEMS biosensors: acoustic wave, nanomaterial-based and magnetic microbiosensors.

MEMS-Based Acoustic Wave Biosensors

Introduction A MEMS-based acoustic wave biosensor is a chemical sensor which detects changes in resonant frequency of a mechanical resonator when biomolecules are adsorbed on the surface of a biologically active membrane. Since frequency change can be measured very precisely, very small mass changes can be measured. This leads high sensitivity of the biosensors. Typical acoustic wave biosensors are bulk acoustic wave (BAW) and surface acoustic wave (SAW) sensors.

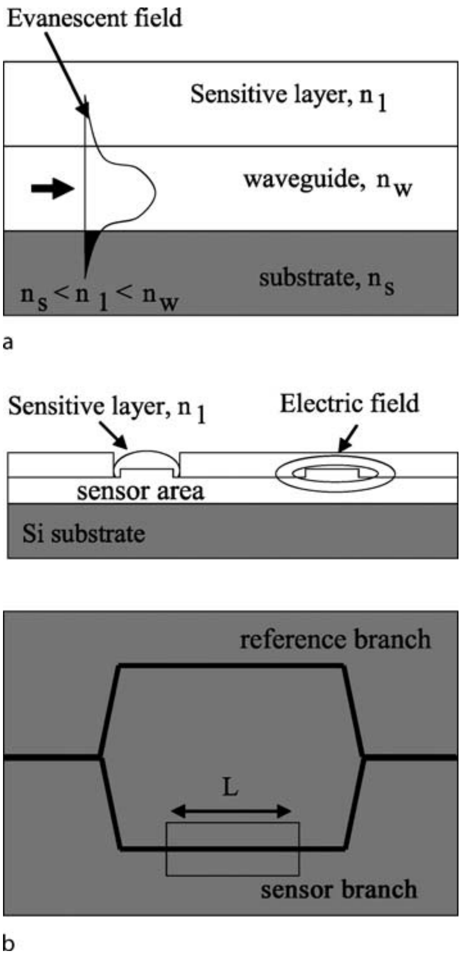

MEMS-Based Biosensor, Figure 7 (**a**) Schematic of an evanescent wave traveling in an optical waveguide. The traveling light in the waveguide is influenced by analyte-induced changes of the refraction index in the adjacent sensitive layer. (**b**) Schematic of a conventional Mach–Zehnder interferometer: The cross-section shows the separate sensor and reference branches [12]

Theory BAW sensors utilize quartz crystal as a substrate. Generally, the crystal is a thin disk where square or rectangular metal electrodes are deposited on the opposite faces. Frequency is changed according to mass change, which can be calculated by Eq. (9) under the assumption that the change in mass is negligible compared to the mass of the crystal ($\Delta m \ll m$):

$$\Delta f = -f_0 \frac{\Delta m}{m} \tag{9}$$

where m is the mass of the crystal and Δm is the mass change due to a biological substance.

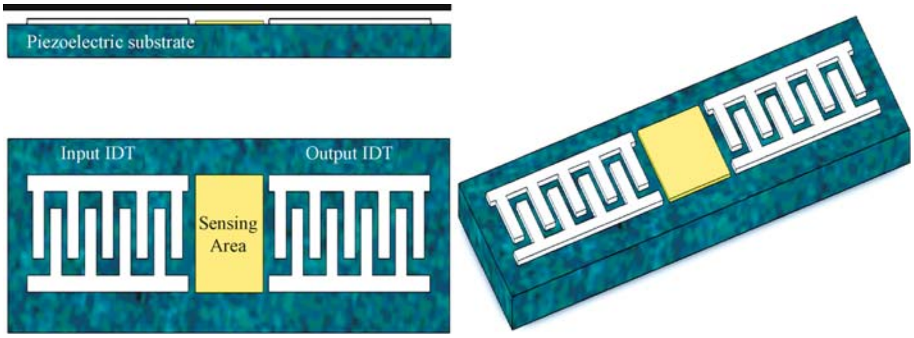

MEMS-Based Biosensor, Figure 8 Schematic of MEMS-based acoustic wave biosensor

In contrast, SAW transducers use Rayleigh waves that are excited from one pair of interdigital electrodes (IDT). The transit time of the wave packet from one set of electrodes to the other will be extended by adsorption of mass on the delay-line surface:

$$\Delta f = (k_1 + k_2) f_0^2 \frac{\Delta m}{A} \tag{10}$$

where k_1 and k_2 are material constants of the SAW substrate. Figure 8 shows the typical structure of a MEMS-based SAW biosensor.

When a biological substance reacts with a sensing layer which is coated on the piezoelectric substrate, the resonant frequency of the MEMS biosensor is changed. The frequency shift is related to the mass change of the biologically sensitive membrane.

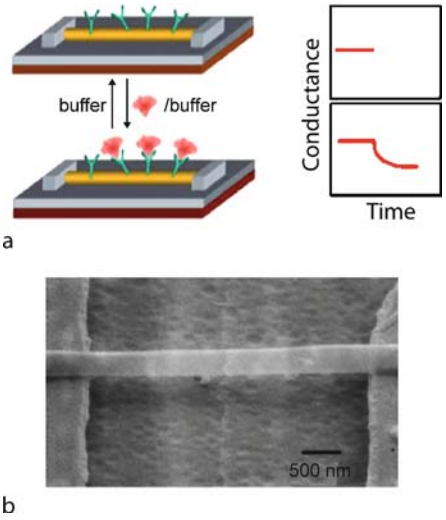

MEMS-Based Biosensor, Figure 9 (**a**) Schematic of MEMS-based nanowire biosensor [20]; (**b**) SEM image [21]

Nanomaterial-Based MEMS Biosensors

Introduction A nanomaterial-based MEMS biosensor utilizes nanostructured materials as sensing media as well as a transducer. This is a unique characteristic compared to the other types of MEMS biosensors mentioned up to now. The nanomaterials have good electrical properties and high sensitivity for biological substances. Furthermore, they are transducers as well as sensing media. This enables direct detection of biological substances without any labels. Nanomaterial-based MEMS biosensors are used for the detection of DNA, RNA, proteins, ions, small molecules, cells and even the pH values [19].

MEMS Biosensors Based on Nanowires A MEMS biosensor based on the unique properties of nanowire enables highly sensitive and selective detection because nanowire as an electrode has a high surface-to-volume ratio for adsorption. When a chemically functionalized nanowire is immersed in an analyte solution, analytes react to biological active materials. As results of the reaction, electrical properties of the nanowire such as resonant frequency, conductivity and resistance are changed [20, 21]. Schematic and SEM images of a MEMS-based nanowire biosensor are shown in Fig. 9.

MEMS Biosensors Based on Nanoparticles Nanoparticles are often utilized as an analyte recognition element in MEMS biosensors. Nanoparticles have a quite large sensing area mainly due to their extremely small size. This enhances the reaction possibility of biomolecules. Furthermore, sensitivity of the biosensor can be increased when metal nanoparticles are positioned between two metal electrodes. When the analyte conjugated with metal nanoparticle is captured between two electrodes, the electric field intensity is amplified. Gold, silver, metal oxide and magnetic nanoparticles are widely used for detection

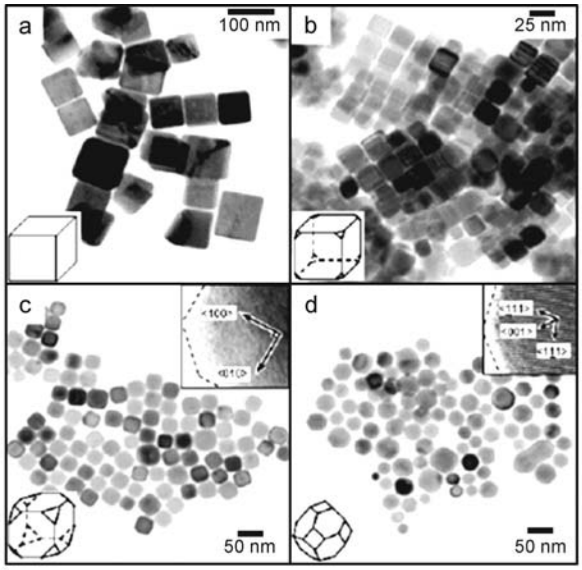

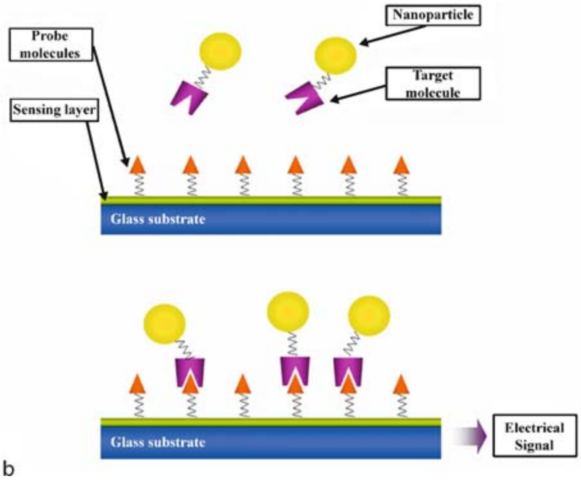

MEMS-Based Biosensor, Figure 10 (**a**) SEM image of nanoparticle [22]; (**b**) schematic of MEMS-based nanoparticle biosensor

of biomolecules in electrochemical biosensors. Figure 10a shows a SEM image of a semiconductor nanoparticle, PbS [22]. A general configuration of biosensing based on nanoparticles is shown in Fig. 10b. Probe molecules in a recognition layer are reacted with target biomolecules specifically. This reaction leads to changes in electrical signals.

MEMS-Based Magnetic Biosensors

Introduction Most MEMS-based magnetic biosensors manipulate a magnetic bead where biomolecules are conjugated. It is still a challenging problem to manipulate biomolecules directly. However, the manipulation of a magnetic bead is relatively easy because a magnet such as an inductor facilitates control of the biomolecules when they are conjugated with a magnetic bead. Thus, this section focuses on magnetic MEMS biosensors based on a magnetic bead.

Theory Typical MEMS-based magnetic biosensors are magnetoresistive (MR) sensors, anisotropic magnetoresistive (AMR) sensors and giant magnetoresistive (GMR) sensors. The MR effect is a change in the electrical resistivity when magnetic field changes. The AMR effect is the change of electrical resistivity when the magnetization changes from parallel to transverse with respect to the current flow. The GMR effect is based on resistivity change due to magnetic alignment of two magnetic layers which is a stacked structure of a ferromagnetic, nonmagnetic and ferromagnetic layer. When the magnetic direction of the two ferromagnetic layers is parallel, the electrical resistance of the structure is low. When the direction is perpendicular, the resistance is high [23]. In most MEMS-based magnetic biosensors, the analyte to be detected is magnetically labeled and passes over an array of specific probe molecules that is immobilized on magnetic field sensors. When the magnetic beads are captured on a magnetic component, unbound biomolecules are washed away. The magnetic property change of the magnetic component is then measured. Figure 11 shows schematically the sensing principle of a MEMS-based magnetic biosensor. MEMS-based magnetic biosensors have been used to detect various biomolecules including streptavidin, microorganisms and cells.

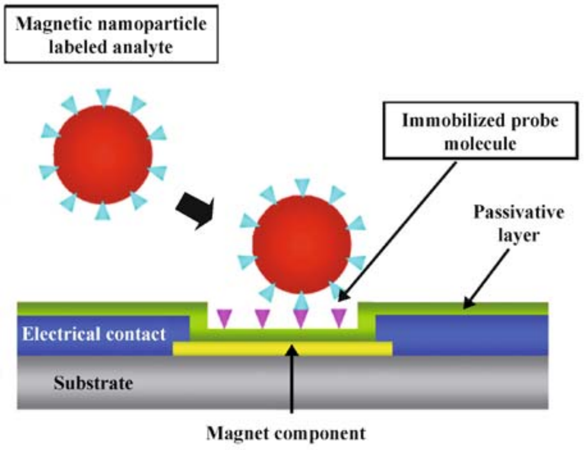

MEMS-Based Biosensor, Figure 11 Schematic of MEMS-based nanoparticle biosensor [23].

Future Directions for Research

MEMS-based biosensors offer uninterrupted analysis of biological substances potentially because detection and evaluation are carried out by a transducer and a read-out element simultaneously. Up to now, miniaturization of transducers has progressed successfully. However, integration of read-out elements is quite limited. So it is necessary for conventional measurement equipment to provide recognizable results. Thus, it is highly desirable to integrate a read-out element that is capable of offering recognizable detection results having its full function, so eliminating the need for conventional measurement equipment.

Cross References

► Acoustics Based Biosensors
► Conductivity Measurements
► Electrochemical Techniques
► Integrated Micro Devices for Biological Applications
► Lab-on-Chip Devices for Chemical Analysis
► Lab-on-Chip Devices for Immunoassay
► Nanoscale Biosensors

References

1. Fritz J, Baller MK, Lang HP, Rothuizen H, Vettiger P, Meyer E, Guntherodt HJ, Gerber C, Gimzewski JK (2000) Translating Biomolecular Recognition into Nanomechanics. Science 288:316–318
2. Eggins BR (1996) Transducer I – Electrochemistry. In: Biosensors: an Introduction. John Wiley & Sons and B. G. Teubner Publishers, Chichester, New York 51–79
3. Lambrechts M, Sansen W (1992) Basic electrochemical principles. In: Biosensors: Microelectrochemical Devices. Institute of Physics Publishing, Bristol, Philadelphia 32–39
4. Sze SM (1994) Thermal Sensors. In: Semiconductor Sensors. John Wiley & Sons Inc. 351–354, 369–370
5. Zhang Y, Tadigadapa S (2004) Calorimetric biosensors with integrated microfluidic channels. Biosens Bioelectron 19:1733–1743
6. Lambrechts M, Sansen W (1992) Basic electrochemical principles. In: Biosensors: Microelectrochemical Devices. Institute of Physics Publishing, Bristol, Philadelphia 39–66
7. Sze SM (1994) Mechanical Sensors. In: Semiconductor Sensors. John Wiley & Sons Inc. 176–181
8. Lambrechts M, Sansen W (1992) Basic electrochemical principles. In: Biosensors: Microelectrochemical Devices. Institute of Physics Publishing, Bristol, Philadelphia 67–69
9. Patel SV, Mlsna TE, Fruhberger B, Klaassen E, Cemalovic S, Baselt DR (2003) Chemicapacitive microsensors for volatile organic compound detection. Sens Actuators B 96:541–553
10. Sze SM (1994) Biosensors. In: Semiconductor Sensors. John Wiley & Sons Inc. 447–452
11. Turner APF, Karube I, Wilson GS (1989) Optical sensors based on immobilized reagent. In: Biosensors Fundamentals and Applications. Oxford University Press, New York 599–616
12. Hierlemann A, Brand O, Hagleitner C, Baltes H (2003) Microfabrication techniques for chemical/biosensors. Proc IEEE 91:839–863
13. Stievater TH, Rabinoich WS, Newman HS, Ebel JL, Mahon R, McGee DJ, Goetz PG (2003) Microcavity Interferometry for MEMS device characterization. J Microelectromech Syst 12:109–116
14. Ollier E (2002) Optical MEMS devices based on moving waveguides. IEEE J Sel Topics Quantum Electron 8:155–162
15. Arnold MA (1985) Enzyme-based fiber optic sensor. Anal Chem 57:565–566
16. Eggins BR (1996) Transducers optical methods. In: Biosensors: an Introduction. Wiley and Teubner 87–120
17. Lukosz W (1995) Integrated optical chemical and direct biochemical sensors. Sens Actuators B 29:37–50
18. Sze SM (1994) Biosensor. In: Semiconductor Sensors. John Wiley & Sons Inc. 452–456
19. Vaseashtaa A, Dimova-Malinovska D (2005) Nanostructured and nanoscale devices, sensors and detectors. Sci Technol Adv Mater 6:312–318
20. Patolsky F, Lieber CM (2005) Nanowire nanosensor. Mater Today 8:20–28
21. Evoy S, DiLello N, Deshpande V, Narayanan A, Liu H, Riegelman M, Martin BR, Hailer B, Bradley JC, Weiss W (2004) Dielectrophoretic assembly and integration of nanowire devices with functional CMOS operating circuitry. Microelectron Eng 75:31–42
22. Jun YW, Lee JH, Choi JS, Cheon J (2005) Symmetry-controlled colloidal nanocrystals: nonhydrolytic chemical synthesis and shape determining parameters. J Phys Chem B 109:14795–14806
23. Graham DL, Ferreira HA, Freitas PP (2004) Magnetoresistive-based biosensors and biochips. Trends Biotechnol 22:455–462

MEMS Biosensor

► Impedimetric Biosensors for Nano- and Microfluidics
► MEMS-Based Biosensor

MEMS-Nozzle

► Supersonic Micro-Nozzles

MEMS Packaging

► Packaging (and Wire Bonding)

MEMS-Thruster

► Supersonic Micro-Nozzles

Meniscus

Definition

Curved surface at an interface between immiscible fluids. With respect to microfluidics, the meniscus generally relates to a curved surface at a gas-liquid interface.

Cross References

► Surface-Directed Capillary Flow Systems

Meshfree Methods

► Meshless Methods

Meshless Methods

Mehrdad T. Manzari
Sharif University of Technology, Tehran, Iran
mtmanzari@sharif.edu

Synonyms

Meshfree methods; Element-free methods; Particle methods

Definition

Meshless methods belong to a class of techniques for solving boundary/initial value ►partial differential equations in which both geometry representation and numerical ►discretization are principally performed based on nodes or particles. In meshless methods, there is no inherent reliance on a particular mesh topology meaning that no ►element connectivity is required. In practice, however, in many meshless methods recourse must be taken to some kind of background meshes at least in one stage of the implementation.

Overview

Analysis of many practical processes in modern engineering requires modeling of problems with time dependent geometry or boundary conditions. Pulsating flow of blood in heart, metal forming processes and stretching of a polymer filament are only a few examples. Conventional mesh based methods such as the Finite Volume and Finite Element Methods face serious difficulties when dealing with large element deformations and/or element entanglement. This is particularly true in the case of problems involving discontinuities and moving boundaries. Examples of such problems are complex free surface flows, fluid-structure interactions, projectile impact and material break up during manufacturing processes. Standard mesh based techniques handle such problems using adaptive remeshing techniques. This means that the computational mesh (grid) is remeshed either globally or locally to correctly represent the deformed geometry. This technique however suffers from two drawbacks. Firstly, generating a new mesh may not only be troublesome but also consume considerable time. This is particularly true when complex three-dimensional geometries are to be meshed using automatic mesh generators. Secondly, the mapping of the state variables from the old mesh to the new mesh can introduce significant numerical errors into the computations. To alleviate this problem, special numerical techniques have been devised in which the material and the mesh move independently.

In recent years, interest in meshless methods has grown rapidly because such methods can circumvent the above mentioned difficulties in a more convenient fashion. The main advantages of meshless methods can be summarized as follows:

- Problems with large deformations can be handled since the connectivity among nodes is generated during the computation and can change in time.
- There are no constraints imposed from the system geometry and the system may evolve far from the initial conditions.
- The accuracy of the solution can be controlled easily, since nodes can be added in the regions where refinement is required.
- Complex geometries can be accurately represented by particles.
- The particles map onto the mass density of the fluid, leading automatically to higher resolution in the high-density regions.
- Fairly simple implementation procedure.

Abundance of meshless methods, as well as many variations in the terminology adopted in the literature makes a thorough review unfeasible for the purpose of this manuscript. Instead, this review attempts to give an overview of this class of methods by briefly describing some of their most important features.

Based on the physical principle, meshless (particle) methods can be classified as deterministic and probabilistic. Many of the meshless methods are based on probabilistic principles. The Molecular dynamics, Monte Carlo methods, the Lagrangian Probability Density Functions (PDF) methods, and the Lattice Boltzmann (LBM) method are among these methods. Methods such as the Smoothed Particle Hydrodynamics (SPH) and the Vortex method ini-

tially developed as probabilistic methods but nowadays they are most frequently used as deterministic.

The meshless methods can be also classified as strong and ▶ weak formulations of the associated partial differential equations. The strong formulation of a partial differential equation is usually obtained by a collocation technique. The Smoothed Particle Hydrodynamics method, the Vortex method and the Generalized Finite Difference method (GFD) are based on the strong form. On the other hand, weak forms are often based on Galerkin formulations. The Diffuse Element Method (DEM), the Element Free Galerkin Method (EFGM), the Reproducing Kernel Particle Method (RKPM) (▶ Kernel function), the hp cloud method, the Partition of Unity Method (PUM), and the Meshless Local Petrov–Galerkin Method (MLPG) are all among this category. Some particle methods like the Particle-in-Cell method can be used in both strong and weak formulations.

When studying phenomena such as dynamic interaction of molecules or the non-equilibrium movements of atoms in nano-scales, in which the object under consideration is a set of particles (i. e. molecules and atoms), particle methods are a natural choice. The current trend in computational methods is to use particle methods both as discretization tools as well as physical models for continuum physics simulation.

In reality many of meshless methods are not truly mesh free and belong to one of the following categories:

- Methods that require background grids for the computation of resulting integrals numerically. The creation of a background mesh is generally a trivial task and can be automated. Element Free Galerkin methods belong to this group.
- Methods that require background grids only locally for the integration process. Generally, creation of local mesh is a far easier task. Meshless Local Petrov–Galerkin method belongs to this category.
- Methods that do not require a mesh at all, but their stability and accuracy depend considerably on the selection of nodes. Collocation methods and the Generalized Finite Difference methods using irregular meshes belong to this group.
- Particle methods that require a predefinition of particles for their computations. Such methods require some kind of mesh to predefine the particles. Smoothed Particle Hydrodynamics method belongs to this category.

As the name *meshless methods* is used for a wide range of numerical techniques, it is difficult to specify a definite starting date for these methods. The earliest works, however, may be attributed to those reporting extension of the Finite Difference Methods to general irregular or unstructured grids in the early 60's. While the classical finite difference method uses regular grids, the GFD method can use even irregular sets of points. The GFD method is suitable for irregular geometries and the number of points in different regions of the solution domain can vary. This is achieved by adding or removing points anywhere required to increase the accuracy or decrease the computational expenses. This method has been used in studying many engineering problems involving heat transfer, flow in deformable channels and deformation of membranes. The GFD method is explained briefly in the sequel.

In 1977, Lucy [1] and Gingold and Monaghan [2] independently introduced the so-called Smoothed Particle Hydrodynamics method which is one of the oldest meshless methods. The method was originally developed for astrophysical studies such as formation of asteroids and the evolution of galaxies and has now become a standard tool in this field. In recent years, SPH has been extensively used for various fluid flow problems including both compressible and incompressible flow regimes. The method has been recently used for simulation of the generalized non-Newtonian and viscoelastic fluid flow problems. The SPH method has been also employed in the field of solid mechanics involving complex phenomena such as crack propagation and material fragmentation.

M

In 1996, a complete volume (Vol. 139) of the journal of Computer Methods in Applied Mechanics and Engineering was devoted to meshless methods and some of the pioneering works at the time were published. In the past ten years the meshless methods have constantly gained more popularity and been applied to a wider range of engineering applications.

Today, there are books written about meshless methods [3] and several excellent review articles are also available each emphasizing on a particular class of meshless methods [4–6]. There are also several specialist groups worldwide working on various types of meshless methods.

Basic Methodology

Meshless methods like all other computational methods for solving partial differential equations consist of the following general steps:

1. Specify a ▶ computational domain from the ▶ physical domain of the problem under consideration and define the proper boundary and initial conditions for it.
2. Generate an initial node (particle) distribution on the computational domain. In mesh-based methods, a mesh is generated at this stage.
3. Choose a proper approximation function so that every function can be constructed in the computational domain.

4. Construct the discretized form of the governing equations. This stage normally results in a system of linear equations.
5. Solve the system of equations to obtain the unknowns (e. g., velocity or temperature) at each computational node (particle).
6. Post-process the solution to obtain any additional required engineering data, e. g., drag or heat flux rate.

The main difference between the meshless methods and the mesh-based methods lies at the stage three. Below, this stage is described in more detail for a number of meshless methods. It should be kept in mind that the meshless techniques are by no means restricted to the following methods.

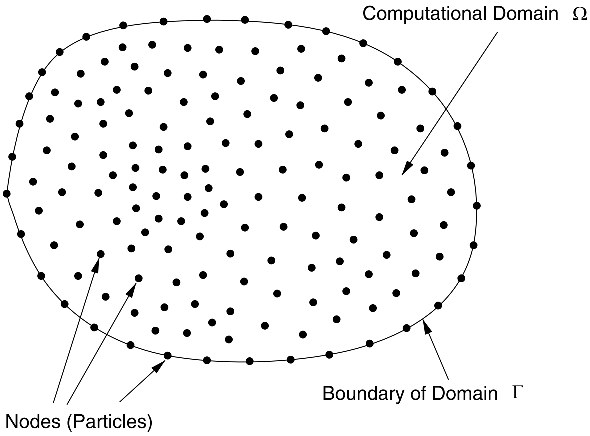

Meshless Methods, Figure 1 Computational domain and nodes

Meshless Approximation Functions

Consider a function $u(\boldsymbol{x})$ in a domain Ω. Within the domain, a set of nodes (particles) $\boldsymbol{x}_I$, $I = 1, ..., n$, is constructed and the value of u at I is denoted by u_I. Then, the approximated value of u, i. e. u^h, at any other point $\boldsymbol{x}$ is given by

$$u^h(\boldsymbol{x}) = \sum_I w(\boldsymbol{x} - \boldsymbol{x}_I)\; u_I\, \Delta V_I\,, \tag{1}$$

where w is the weight function of the approximation and ΔV_I is some measure of the domain surrounding node I. A weight function is defined to have ▶compact support. This means that the subdomain over which the weight function is nonzero is small relative to the rest of domain. Then, the summation is only over points I, where $w(\boldsymbol{x} - \boldsymbol{x}_I) > 0$. To each node I, a subdomain $\Delta\Omega_I$ is associated which is sometimes called the domain of influence of the node. These subdomains are usually in the form of either rectangles or circles in a two-dimensional domain. For three-dimensional problems, discs or balls are often used. Subdomains of different shapes may be used in a single model. Figure 1 shows a typical computational region, nodes and their associated support regions. Note that in practice there is a considerable overlay of support regions. Usually five to ten subdomains overlap each node.

Figure 2 presents distribution of the weighting function around a typical node I in a two-dimensional domain along with the approximated function $u(x, y)$. Below, the approximation functions for a number of meshless methods are briefly described. The presentation will be according to their historical appearance.

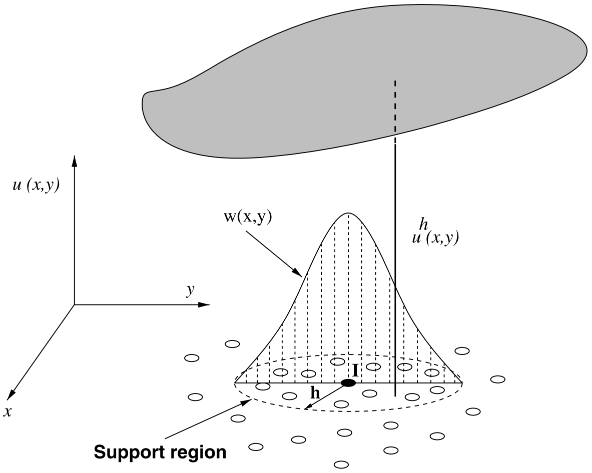

Meshless Methods, Figure 2 Weight function, support region and the approximated function

Generalized Finite Difference Methods

The extension of the classical Finite Difference Method to irregular grids and geometries led to the development of the Generalized Finite Difference Methods. The bases of GFD were published in early seventies. The method relies on the Taylor's series expansion and its accuracy depends on the number of terms kept in the series. The main disadvantage of this method is the possibility of becoming singular or ill-condition when improper set of nodes are used in the approximation formula. Removal of this singularity or ill-conditioning is the subject of current research in the field [7].

Like all other meshless methods, the first step in GFD is to scatter nodal points in the computational domain and along the boundary. To each node (point) a collection of neighboring nodes are associated which is called star. The number and the position of nodes in each star are decisive factors affecting the Finite Difference approximation. Par-

ticular node patterns can lead to ill-conditioned situations and ultimately degenerated solutions. Using the Taylor's series expansion the value of any sufficiently differentiable smooth function u at the central node of star, u_0, can be expressed in terms of the value of the same function at the rest of nodes, u_i, with $i = 1, \dots, N$ where N is the total number of neighboring nodes in the star and is one less than the total number of nodes in it. In two dimensions, a second-order accurate Taylor series expansion can be written as

$$u_i = u_0 + h_i \frac{\partial u_0}{\partial x} + k_i \frac{\partial u_0}{\partial y} + \frac{1}{2}\left(h_i^2 \frac{\partial^2 u_0}{\partial x^2} + k_i^2 \frac{\partial^2 u_0}{\partial y^2} + 2 h_i k_i \frac{\partial^2 u_0}{\partial x \partial y} \right), \tag{2}$$

where $h_i = x_i - x_0$, $k_i = y_i - y_0$, the coordinates of the central node are (x_0, y_0) and the coordinates of the i nodes are shown by (x_i, y_i). This expression is valid for all $i = 1, \dots, N$ and may be added to obtain:

$$\sum_{i=1}^{N} (u_i - u_0) = \sum_{i=1}^{N} h_i \frac{\partial u_0}{\partial x} + \sum_{i=1}^{N} k_i \frac{\partial u_0}{\partial y} + \frac{1}{2}\left(\sum_{i=1}^{N} h_i^2 \frac{\partial^2 u_0}{\partial x^2} + \sum_{i=1}^{N} k_i^2 \frac{\partial^2 u_0}{\partial y^2} + \sum_{i=1}^{N} 2 h_i k_i \frac{\partial^2 u_0}{\partial x \partial y} \right). \tag{3}$$

It is then possible to define the function $B(u)$ in the following form:

$$B = \sum_{i=1}^{N} \left[\left(u_0 - u_i + h_i \frac{\partial u_0}{\partial x} + k_i \frac{\partial u_0}{\partial y} + \frac{h_i^2}{2} \frac{\partial^2 u_0}{\partial x^2} + \frac{k_i^2}{2} \frac{\partial^2 u_0}{\partial y^2} + h_i k_i \frac{\partial^2 u_0}{\partial x \partial y} \right) w(h_i, k_i) \right]^2 \tag{4}$$

where $w(h_i, k_i)$ is the weight function. The ► least square method is then used and the function B is minimized with respect to $\partial u_0/\partial x$, $\partial u_0/\partial y$, $\partial^2 u_0/\partial x^2$, $\partial^2 u_0/\partial y^2$ and $\partial^2 u_0/\partial x \partial y$. This results in a set of five linear equations with the aforementioned partial derivatives as five unknowns. The solution to this system of equations gives explicit equations of the unknowns in terms of the nodal value of function u in the star. Note that in the present situation, the star must have at least five nodes. When solving a partial differential equation using GFD, one needs to substitute the relevant expressions for the partial derivatives in the differential equation so that an algebraic equation is obtained for every node in the computational domain. These equations are in the following form:

$$u_0 = \sum_{i=1}^{N} m_i u_i . \tag{5}$$

This is called the star equation. When the same process is carried out for each node of the domain, an equation is obtained for each unknown and the system can be solved to determine the nodal values of the unknown function u and all its partial derivatives.

Several factors affect the adequacy of the star equation. These are:

- Number of nodes of the star. The minimum number of nodes in star depends on the problem. For a second-order partial differential equation to be solved in two dimensions, the minimum number of nodes is five. The use of excessive number of nodes makes the computations more time consuming without any significant improvement in the accuracy.
- The shape of star or in other words the relative coordinates of the nodes of the star with regards to the central node is also important. The quality of the GFD is sensitive to grid smoothness. Thus, very sharp changes of mesh density should be avoided. Several criteria have been developed to appropriately select nodes for the star. A simple yet efficient method in two dimensions is the so called four quadrant criterion which uses the nearest nodes in each quadrant constructed around the central node.
- The importance of the weight function is obvious from the definition of $B(u)$. In fact, the value of the function in every node of the domain is the weighting sum of its values in the rest of the nodes of the star. Various weighting functions are used in practice. The exponential function $w(x, y) = \exp(-10(x^2 + y^2))$ and the cubic spline function are only two examples. Weight functions usually have a compact support.

Smoothed Particle Hydrodynamics

In the context of SPH methods, Monaghan [8] introduced an approximation in the form of

$$u^h(\boldsymbol{x}) = \int_{\Omega} w(\boldsymbol{x} - \boldsymbol{x}', h) u(\boldsymbol{x}') \mathrm{d}\Omega , \tag{6}$$

where $w(\boldsymbol{x} - \boldsymbol{x}', h)$ is a kernel, smoothing or weight function, and h refers to the size of the support region. Various requirements or properties for the smoothing function are applied in different literatures. Summarized below are the most general ones:

- The smoothing function must be normalized, $\int_{\Omega} w(\boldsymbol{x}-\boldsymbol{x}', h)\, \mathrm{d}\Omega = 1$.
- It should have a compact support. That is $w(\boldsymbol{x}-\boldsymbol{x}') = 0$ for $|\boldsymbol{x}-\boldsymbol{x}'| > \kappa h$ where κ is a constant parameter.
- $\lim_{h\to 0} W(\boldsymbol{x}-\boldsymbol{x}', h) = \delta(\boldsymbol{x}-\boldsymbol{x}')$ in the compact support region $|\boldsymbol{x}-\boldsymbol{x}'| \leqslant \kappa h$. Here, δ is the ► Dirac delta function.
- The function w should be monotonically decreasing.
- The smoothing function should be a sufficiently smooth even (symmetric) function.

Various weight functions have been proposed in the literature. Two of these are the exponential ($\alpha = 0.4$)

$$w(s) = \begin{cases} \exp\left[-(s/\alpha)^2\right] & \text{for } s \leqslant 1 \\ 0 & \text{for } s > 1\,, \end{cases} \tag{7}$$

and the cubic spline

$$w(s) = \begin{cases} \frac{2}{3} - 4s^2 + 4s^3 & \text{for } s \leqslant \frac{1}{2} \\ \frac{4}{3} - 4s + 4s^2 - 4\frac{s^3}{3} & \text{for } \frac{1}{2} < s \leqslant 1 \\ 0 & \text{for } s > 1\,, \end{cases} \tag{8}$$

weight functions. In these definitions, $s = S/S_{\max}$ where S is the length of vector $\boldsymbol{x}-\boldsymbol{x}'$ and $S_{\max}$ is the radius of the support region. These are isotropic or polar weight functions where the supports are circular. It is also possible to generate weight functions with rectangular supports using tensor products. For example in two dimensions, one can write $w(\boldsymbol{x}-\boldsymbol{x}') = w(x-x')\, w(y-y')$.

In the context of SPH, one needs a discrete form of Eq. (6) to devise practical approximations. In multi-dimensions, a formula similar to Eq. (1) is used. In this equation, $\varphi_I(\boldsymbol{x}) = w(\boldsymbol{x}-\boldsymbol{x}_I)\Delta V_I$ is the shape function of the SPH method. Note that in most cases $u_I \neq u^h(\boldsymbol{x}_I)$ and the shape functions do not pass through the data making imposition of Dirichlet boundary conditions difficult.

Moving Least Square

This type of approximation originates in data fitting. In the Moving Least Square method (MLS), the following approximation form is used [4]

$$u^h(\boldsymbol{x}) = \sum_{i=1}^{m} p_i(\boldsymbol{x})\ a_i(\boldsymbol{x}) \equiv \mathbf{p}^{\mathrm{T}}(\boldsymbol{x})\ \boldsymbol{a}(\boldsymbol{x})\,, \tag{9}$$

where m is the number of terms in the basis, $p_i(\boldsymbol{x})$ are monomial basis functions, and $a_i(\boldsymbol{x})$ are their coefficients. Examples of common basis functions in one and two dimension are

$$\begin{aligned} &\text{1D:} \begin{cases} \mathbf{p}^{\mathrm{T}}(\boldsymbol{x}) = (1,\ x) & \text{linear} \\ \mathbf{p}^{\mathrm{T}}(\boldsymbol{x}) = (1,\ x,\ x^2) & \text{quadratic} \end{cases} \\ &\text{2D:} \begin{cases} \mathbf{p}^{\mathrm{T}}(\boldsymbol{x}) = (1,\ x,\ y) & \text{linear} \\ \mathbf{p}^{\mathrm{T}}(\boldsymbol{x}) = (1,\ x,\ y,\ x^2,\ xy,\ y^2) & \text{quadratic} \end{cases} \end{aligned} \tag{10}$$

In MLS methods, although it is more common to use monomial functions, it is also possible to use other functions as basis. For example, in problems with singular solutions, singular functions can be used.

The coefficients $a_i(\boldsymbol{x})$ are obtained by performing a weighted least square fit for the local approximation $u^h(\boldsymbol{x})$. This is achieved by minimizing the following quadratic form

$$\begin{aligned} J &= \sum_I w(\boldsymbol{x}-\boldsymbol{x}_I)\left[u^h(\boldsymbol{x}, \boldsymbol{x}_I) - u(\boldsymbol{x}_I)\right]^2 \\ &= \sum_I w(\boldsymbol{x}-\boldsymbol{x}_I)\left[\sum_i p_i(\boldsymbol{x}_I)\ a_i(\boldsymbol{x}) - u_I\right]^2 \end{aligned} \tag{11}$$

where $w(\boldsymbol{x}-\boldsymbol{x}_I)$ is a weighting function with compact support. Usually the same weight functions as in the SPH method are used. It should be emphasized that in Eq. (11), index I refers to points while index i is used for the polynomial terms.

Therefore, coefficients $a_i(\boldsymbol{x})$ can be obtained by solving the following system of m equations

$$\frac{\partial J}{\partial \boldsymbol{a}} = \boldsymbol{A}(\boldsymbol{x})\boldsymbol{a}(\boldsymbol{x}) - \boldsymbol{B}(\boldsymbol{x})\boldsymbol{u} = 0 \tag{12}$$

where $\boldsymbol{u} = (u_1,\ u_2,\ ...,\ u_n)^{\mathrm{T}}$, $\boldsymbol{A} = \boldsymbol{P}^{\mathrm{T}}\boldsymbol{W}(\boldsymbol{x})\boldsymbol{P}$ is a $m\times m$ matrix, and $\boldsymbol{B} = \boldsymbol{P}^{\mathrm{T}}\,\boldsymbol{W}(\boldsymbol{x})$ is a $m\times n$ matrix. Note that $\boldsymbol{a}(\boldsymbol{x}) = \boldsymbol{A}^{-1}(\boldsymbol{x})\,\boldsymbol{B}(\boldsymbol{x})\,\boldsymbol{u}$. In these definitions, $\boldsymbol{P}$ is a $m\times n$ matrix whose (i,j)-th element is $p_j(x_i)$ and $\boldsymbol{W}(\boldsymbol{x})$ is a $n\times n$ diagonal matrix whose (i,i)-th element is $w(x-x_i)$.

By these definitions, the approximation for $u(\boldsymbol{x})$ can be written as

$$u^h(\boldsymbol{x}) = \sum_{I=1}^{n} \varphi_I^k(\boldsymbol{x})\, u_I\,, \tag{13}$$

where the shape functions are given by $\varphi^k = [\varphi_1^k(\boldsymbol{x})\ \ \varphi_2^k(\boldsymbol{x})\ \ ...\ \ \varphi_n^k(\boldsymbol{x})] = \boldsymbol{p}^{\mathrm{T}}(\boldsymbol{x})\boldsymbol{A}^{-1}(\boldsymbol{x})\boldsymbol{B}(\boldsymbol{x})$. Here, superscript k denotes the order of the polynomial basis. The lowest order form of the Moving Least Square, i. e. for $k = 0$, are called the Shepard function

$$\varphi_I^0(\boldsymbol{x}) = \frac{w(\boldsymbol{x}-\boldsymbol{x}_I)}{\sum_I w(\boldsymbol{x}-\boldsymbol{x}_I)}\,. \tag{14}$$

Equation (11) presents a discrete form of the MLS method. A continuous counterpart of this method can be obtained by defining $J(\boldsymbol{x})$ as

$$J(\boldsymbol{x}) = \int_{\Omega} w(\boldsymbol{x}-\boldsymbol{x}') \left[u^h(\boldsymbol{x},\boldsymbol{x}') - u(\boldsymbol{x}')\right]^2 \mathrm{d}\Omega \tag{15}$$

where $w(\boldsymbol{x}-\boldsymbol{x}')$ is a weight function as before and $u^h(\boldsymbol{x},\boldsymbol{x}') = \sum_i p_i(\boldsymbol{x}')a_i(\boldsymbol{x})$.

Applying the least square technique to (11) results in

$$u^h(\boldsymbol{x}) = \int_{\Omega} p_i(\boldsymbol{x})\, A_{ij}^{-1}(\boldsymbol{x})\, p_j(\boldsymbol{x}')\, w(\boldsymbol{x}-\boldsymbol{x}')\, u(\boldsymbol{x}')\, \mathrm{d}\Omega \tag{16}$$

where

$$A_{ij}(\boldsymbol{x}) = \int_{\Omega} w(\boldsymbol{x}-\boldsymbol{x}')\, p_i(\boldsymbol{x}')\, p_j(\boldsymbol{x}')\, \mathrm{d}\Omega \tag{17}$$

A comparison between Eq. (16) and Eq. (6) reveals that there is an interesting similarity between the SPH and MLS approximations and $p_i(\boldsymbol{x})\, A_{ij}^{-1}(\boldsymbol{x})\, p_j(\boldsymbol{x}')$ can be considered as a modification function. In fact, this similarity has been used to devise modified SPH methods.

Partition of Unity

This approximation technique is another base to construct meshless methods. In this method, the computational domain is covered by overlapping subdomains Ω_I associated with each point I. Within each subdomain I, a function $\varphi_I(\boldsymbol{x})$ is defined which is nonzero only in Ω_I and has the following property in Ω

$$\sum_I \varphi_I(\boldsymbol{x}) = 1\,. \tag{18}$$

Note that the shape functions φ^k for any k in the MLS are partitions of unity. The view point used in partition of unity inspired researchers to develop several meshless methods such as the hp-clouds method and the partition of unity finite element method.

Numerical Implementation

Meshless methods are normally based on two types of discretization:

- Collocation methods, which are used in SPH, Generalized Finite Difference and Moving Least Square methods.
- Galerkin methods, which are used in Element Free Galerkin method, Reproducing Kernel Particle method, etc.

Below, the implementation of both methods is briefly described for solving the Poisson equation in a domain Ω with boundary Γ. The problem is formulated as

$$\begin{cases} \nabla^2 u = f & \text{in } \Omega \\ u = u_D & \text{on } \Gamma_D \\ \frac{\partial u}{\partial n} = g & \text{on } \Gamma_N \end{cases} \tag{19}$$

where Γ_D and Γ_N ($\Gamma = \Gamma_D \cup \Gamma_N$) are segments of the boundary on which Dirichlet and Neumann boundary conditions are imposed, respectively. Also, $\boldsymbol{n} = (n_1, n_2, n_3)$ refers to the direction normal to the boundary, u_D is a prescribed value and g is the prescribed normal gradient of u on Γ_N.

To implement the collocation method, the computational domain including its boundaries is covered with a set of n nodes so that Eq. (12) holds. Then, the approximation is applied to the Poisson equation only for internal nodes (i. e. $\Omega - \Gamma$). The resulting discrete equations are

$$\begin{aligned} \sum_I \nabla^2 \varphi_I(\boldsymbol{x}_J)\, u_I &= f(\boldsymbol{x}_J)\,, \\ \sum_I \varphi_I(\boldsymbol{x}_J)\, u_I &= u_D(\boldsymbol{x}_J)\,, \\ \sum_I \nabla \varphi_I(\boldsymbol{x}_J)\,.\,\boldsymbol{n}\, u_I &= g(\boldsymbol{x}_J)\,, \end{aligned} \tag{20}$$

which must be solved for a set of unknowns u_J for $J = 1, \ldots, n$.

In the context of SPH methods, the procedure is frequently implemented by multiplying the governing equation (Poisson equation) by the weight function w. Then, the resulting equation is integrated over the domain followed by twice applying integration by parts on the left hand side. After dropping the boundary terms, the discretized form for internal nodes becomes

$$\sum_I \nabla^2 w_I(\boldsymbol{x}_J)\, \Delta V_I\, u_I = \sum_I w_J(\boldsymbol{x}_I)\, \Delta V_I\, f(\boldsymbol{x}_J) \tag{21}$$

The implementation of either of the above approaches is simple and straightforward. First, at any node J, one should determine the nodes which contain node J within their domain of influence. Then, the construction of Eq. (21) simply involves calculating the second derivative of the shape functions of all relevant nodes at $\boldsymbol{x} = \boldsymbol{x}_J$.

To implement the Galerkin method, one needs a weak form or a variational principle the same way as in the Finite Element Method. For the Poisson equation, this reads

$$\int_{\Omega} \nabla\delta u\, \nabla u\, \mathrm{d}\Omega = -\int_{\Omega} \delta u f\, \mathrm{d}\Omega + \int_{\Gamma_N} \delta u\, g\, \mathrm{d}\Gamma \tag{22}$$

M

where $\delta u(\boldsymbol{x})$ is a test function and $u(\boldsymbol{x})$ is a trial function. After selecting an appropriate shape function, the discrete form becomes

$$\sum_J \left(\int_\Omega \nabla\varphi_I \, \nabla\varphi_J \, \mathrm{d}\Omega \right) u_J = -\int_\Omega \varphi_J f \, \mathrm{d}\Omega + \int_{\Gamma_N} \varphi_J \, g \, \mathrm{d}\Gamma \,. \tag{23}$$

This again gives a system of linear equations for a set of unknowns u_J for $J = 1, \ldots, n$.

An important step in implementation of meshless methods is the way integrals are computed. An approach which is frequently used employs the following form

$$\int_\Omega f(\boldsymbol{x}) \, \mathrm{d}\Omega = \sum_{I=1}^{n} f(\boldsymbol{x}_I) \, \Delta V_I \,. \tag{24}$$

There are however other approaches which exploit a background grid to compute integrals. Such approaches are therefore not truly meshless.

Key Research Findings

The meshless methods have found their applications in various fluid mechanics and solid mechanics as well as multi-disciplinary problems. They have also been successfully used for multi-physics problems such as the use of magnetohydrodynamcis (MHD) to control turbulence and the study of non-Fourier heat conduction.

Meshless methods like the Dissipative Particle Dynamics (DPD) methods are especially suitable for mesoscopic analyses involved in combined nanofluidics and mircofluidics problems because the discrete representation of the underlying physics can be inherently linked to interacting particles. These methods provide a unifying formulation for both continuum and discrete systems enabling systematic and robust multiscale simulations [5]. Meshless methods are also appealing for emerging technologies such as Microelectromechanical Systems (MEMS) and microdevices because they can eliminate the need for various meshes to analyze different physical phenomena. The use of meshless methods for numerical simulation of electro-osmotic transport and microfluid in the capillary electrophoresis has already been reported in the literature. The meshless methods have been successfully used in free-surface flow and moving boundaries problems. The methods have also proven to be very powerful in dealing with interfacial flow problems enabling simulation of multi-phase and multi-fluid flows. The effect of surface tension has also been investigated.

In recent years, the SPH methods in particular have gone through major improvements and their application was expanded into a wider range of engineering problems. These include both more advanced physical models and more advanced engineering processes. For example, SPH was successfully used to simulate non-Newtonian fluid flows and viscoelastic materials. It has been also used for the analysis of fluid-structure interaction problems, fluid flow in porous media and fractures, heat transfer and reacting flow problems.

The meshless methods are particularly useful in dealing with large deformations involved in solid mechanics applications where mesh-based methods face significant difficulties. These methods have been successfully used for simulation of crack propagation under various loading conditions.

Figures 3 and 4 show typical solutions obtained by the SPH method. In Fig. 3, the results of SPH simulation for the impact of a liquid droplet with a horizontal rigid wall are shown. The droplet originally has a circular shape of diameter 1.0 cm and is dropped from a distance 4.0 cm above the plate with a vertical speed −1.0 m/s. The fluid is considered to be a viscoelastic Maxwell fluid. The SPH results show capabilities of the method in representing complex features such as elasticity of the fluid, deformations of the droplet and the bouncing up phenomenon.

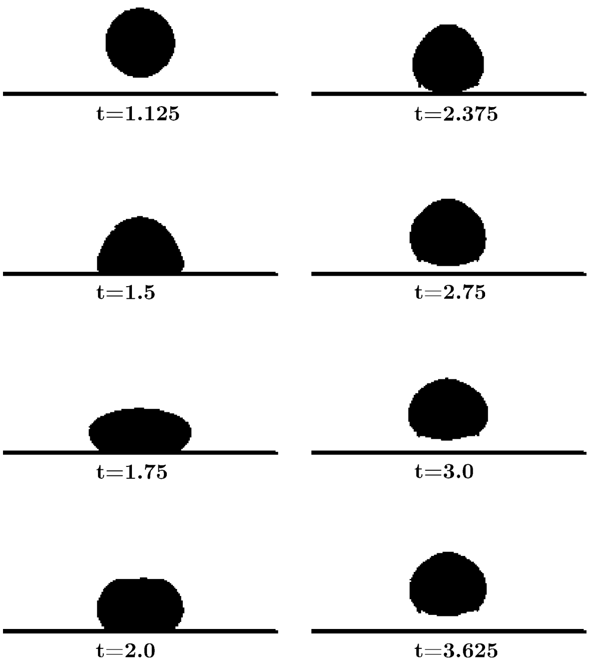

Meshless Methods, Figure 3 Impacting droplet – results of SPH simulations for a Maxwell viscoelastic fluid at various times

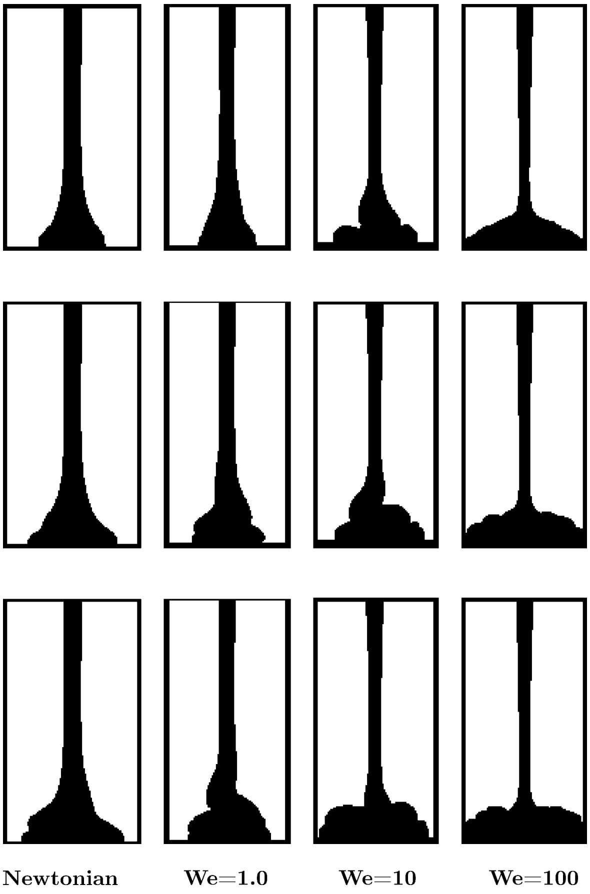

Meshless Methods, Figure 4 Jet buckling – results of SPH simulations for various fluids at three different times

In Fig. 4, the results of SPH simulation for the so-called jet buckling problem are shown. The problem was solved for both Newtonian and viscoelastic fluids. For the viscoelastic analyses, the problem was solved using the Oldroyd-B fluid model over a wide range of Weissenberg (We) numbers. The jet buckling problem involves transient flow of a jet injected downwards from a height $H = 10\,\text{cm}$ into a rectangular cavity. The gravitational force acts downwards with $g = 9.81\,\text{m/s}^2$. The jet is injected into the cavity from a nozzle of width $D = 0.5\,\text{cm}$ and a uniform injection velocity $V = 50\,\text{cm/s}$. It is seen that the SPH method has been able to solve this problem over a wide range of flow regimes and fluid properties.

Future Directions for Research

Only during the past six years from the beginning of the 21st century, more than sixteen hundreds papers in the field of meshless methods have appeared in the literature. Despite their recent fast growth, the meshless methods still require some improvements before they can be an appropriate substitute for the standard methods such as FEM and FDM. Above all, meshless methods need a better computational speed as well as improved robustness. The computational efficiency can be increased by using parallel computing techniques as the meshless methods are naturally parallelizable. An improvement in robustness is problem dependent and needs a more thorough investigation.

Meshless methods have high potentials to be employed in simulation of fluid-structure interactions. Complex geometries and interaction history can be defined using meshless methods requiring far less efforts.

The SPH method seems a viable method to study multiphase flow problems. In this context, effects such as surface tension, surface wetting and miscibility need better and more general algorithms.

It is also important to develop more efficient techniques to handle interface problems including fluid–fluid, fluid–solid and solid–solid contact interfaces.

More efficient contact algorithms also need to be devised if more complex impact or penetration problems are to be solved.

Coupling of the meshless methods with other standard methods such as the Finite Element Method and the Finite Volume Method can enhance the capabilities of both sides significantly. Such couplings can especially offer advantages in modeling problems with extreme deformations within a Lagrangian framework. This area of research can be expanded much further.

Cross References

► Finite Volume and Finite Difference Methods for Modeling and Simulation
► Molecular Dynamics
► Lattice Boltzmann Method (LBM)
► Dissipative Particle Dynamics
► Monte Carlo Method

References

1. Lucy LB (1977) A numerical approach to the testing of the fission hypothesis. Astrono J 82(12):1013–1024
2. Gingold RA, Monaghan JJ (1977) Smoothed Particle Hydrodynamics: theory and application to non-spherical stars. Mon Not Roy Astron Soc 181(2):375–389
3. Liu GR (2003) Mesh Free Methods: Moving beyond the finite element method. CRC Press, Boca Raton
4. Belytschko T, Krongauz Y, Organ D, Fleming M, Krysl P (1996) Meshless methods: An Overview and Recent Developments. Comp Meth Appl Mech Engrg 139(1–4):3–47
5. Koumoutsakos P (2005) Multiscale Flow Simulations using Particles. Annu Rev Fluid Mech 37:457–487

6. Babuska I, Banerjee U, Osborn JE (2002) Survey of Meshless and Generalized Finite Element Methods: A Unified Approach. TICAM Report 02–40, University of Texas at Austin
7. Gavete L, Gavete ML, Benito JJ (2003) Improvements of generalized finite difference method and comparison with other meshless method. Appl Math Model 27:831–847
8. Monaghan JJ (1992) Smoothed Particle Hydrodynamics. Ann Rev Astron Astrophys 30:543–574

Mesicopter

► Microrotorcraft

Mesomorphic State

Definition

The mesomorphic state is a mesophase between a crystalline solid and an isotropic liquid where the molecules are separated in parallel layers of quasi crystalline order. Here the molecules show the optical activity. In this state transition and supercooling is possible.

Mesoscopic Method

► Dissipative Particle Dynamics

Metalorganic Chemical Vapor Deposition (MOCVD)

Definition

Thin-film deposition technique that uses metalorganic vapor-phase precursors to form a solid thin film on substrate surfaces. The metalorganic precursor provides a volatile source of inorganic elements to a growth surface which are then thermally disassociated from their organic components on the substrate surface.

Cross References

► Fabrication of Self-Assembled Catalytic Nanostructures

MGA

► Gas Chromatography

Microactuators

Dan Popa
Automation & Robotics Research Institute,
The University of Texas at Arlington, Fort Worth,
TX, USA
popa@uta.edu

Synonyms

MEMS actuators

Definition

Microactuators are small-scale active devices capable of generating mechanical motion of solids or fluids. Motion is generated via converting one form of energy (for instance electrical) into kinetic energy. Typical sizes of microactuators vary from a few millimetres to a few micrometers, but total sizes can reach centimetres when packaged. When generating mechanical motion of solids, typical displacements are in the nanometer to millimeter range, and typical forces generated are in the nanoNewton to miliNewton range. For microfluidic actuators, typical flow rates generated are in the picoLiter/minute to microLiter/minute ranges.

Overview

Microactuators operate by converting one form of energy (e. g. electrical, thermal, electromagnetic) into kinetic energy of movable components. They are sometimes referred to as Micro-Electro-Mechanical-Systems (MEMS) actuators, but the later term is more commonly used in the United States to denote microactuators made from Silicon. Microactuators are not simply scaled-down versions of typical macroactuators (the later are usually called mini-actuators). Instead, microactuators are fabricated using specially developed fabrication and packaging technology including established techniques from the semiconductor industry such as lithography, etching, or deposition [7]. They can also be fabricated using precision versions of conventional machining such as laser machining, electro-discharge machining (EDM), or micromilling [2]. There are numerous materials that have been used to fabricate microactuators, including Crystalline Silicon, Poly-Silicon, Silicon-on-Insulator (SOI), Piezo Ceramics (PZT), Shape Memory Alloys (SMA), and Electro-Active Polymers (EAP). Microactuators exploit various physical conversion effects in order to generate motion such as: electrostatic, electrothermal, piezoelectric, electromagnetic, thermal expansion, or metallurgical phase change [10].

Microactuators can be implemented in one or more degrees of freedom, leading to another way to classify them as: linear (or prismatic), rotary (or revolute), in-plane (1D to 3D), and out-of-plane (1D to 6D). A micromotor contains several movable parts, including the microactuator and a transmission system. The transmission system consists of bending (or flexture) joints and links, rigid links, stick-and-slip contact elements, or micromechanical hinges. Like macroscale actuators, microactuators are chosen for different applications based on tradeoffs between:

- range of motion,
- precision (resolution, repeatability, accuracy),
- force characteristics,
- power consumption,
- bandwidth and transient effects,
- nonlinear effects.

Microfluidic actuators generate motion of fluids, which can be accomplished directly, by means of peristaltic motion from actuated solid membranes, or indirectly, by means of hydrodynamic or osmotic effects. Microfluidic actuators are typically used in micropumps and microvalves. The primary characteristic that distinguishes a micropump from other types of fluid delivery systems is that the primary driving force for delivery by a pump is a pressure difference, rather than a concentration/molecular gradient. This difference can be generated by pressurizing a fluid reservoir using a gas, by osmotic action, or by direct mechanical actuation. Flow rates in the range of picoLiter/minute to microLites/minute have been demonstrated [5].

Basic Methodology

Major Types of Microactuators

Electrostatic Actuation

Motion is generated by electrostatic attraction force between electrically charged surfaces. Examples of electrostatic MEMS actuators are in-plane comb drives (Fig. 1a), and out-of-plane parallel plate actuators (Fig. 1b) [4]. Both types of actuators require large driving voltages (hundreds of Volts), and can achieve displacements of tens of microns or less. In-plane electrostatic actuators exhibit small force capability (microNewton range), while out-of-plane actuators exhibit regions of instability limiting their range of motion (pull-down effects). Typical bandwidths are in the KHz to MHz ranges. Electrostatic actuators are fabricated using various clean-room compatible micromachining processes, including surface micromachining (such as MUMPS) or bulk micromachining (such as Deep Reactive Ion Etching – DRIE).

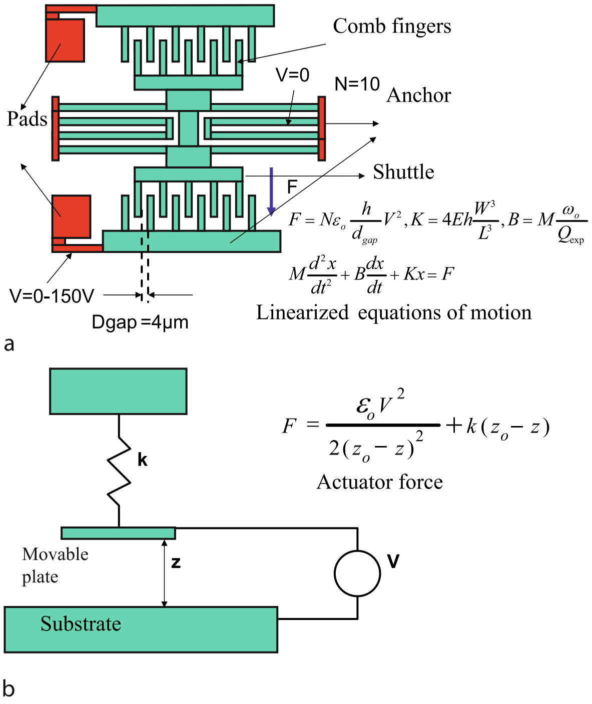

Microactuators, Figure 1 Diagrams of (**a**) in-plane electrostatic comb-drive actuator and actuation force, and (**b**) out-of-plane parallel plate electrostatic actuator

Electrothermal or Thermal Actuation

Motion is generated by differential thermal expansion in materials such as Silicon or Metals, while heat is typically injected into the actuator by means of Joule heat dissipation. Some actuator components expand more than others due to different cross-sections, and therefore electrical resistance. Typical microactuator configurations include in-plane bimorph elements (Fig. 2a), out-of-plane bimorph plates, in-plane Chevron, or bent-beam elements (Fig. 2b) [3]. These types of actuators exhibit larger force capabilities (in mN range), can achieve displacements of 100 μm or less, but generally consume a lot of power (hundreds of mW), and have low bandwidth (Hz to KHz). Common methods of fabrication for electrothermal microactuators include surface micromachining (such as MUMPS) and bulk micromachining (Metal MUMPS, LIGA) or DRIE.

Piezoelectric Actuation

Motion is generated by the piezo-electric effect in certain crystalline materials (for instance Quartz), ceramics such as PZT – Pb(ZrTi)O_3, and polymers (Polyvinylidene fluoride – PVDF). In addition, thin films with piezo-electric properties such as Aluminum Nitride (AlN)

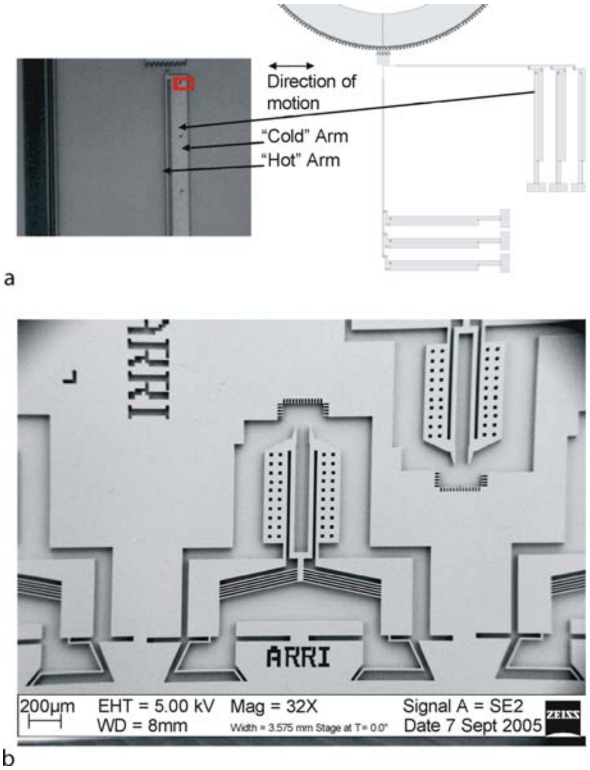

Microactuators, Figure 2 Pictures and diagrams of (**a**) in-plane, surface micromachined electrothermal bimorph MEMS actuator and microactuator bank, and (**b**) in-plane microgripper consisting of an Chevron beam electrothermal actuator, and two bimorph MEMS actuators (Image courtesy of Texas Microfactory Lab, ARRI-UTA)

have been demonstrated in MEMS [8]. The application of a large electrical field produces mechanical actuation along crystal planes. This effect is reversible (mechanical displacement produces an electric field), which is why such materials can be also used as energy harvesters. Typical microactuator configurations include bimorph elements or stacks. These microactuators require large driving voltages (hundreds of Volts), are capable of very large forces (N range), operate at high frequency (KHz to MHz ranges), but generally have limited displacements (nanometer to micrometer ranges). Methods of fabrication includes laser micromachining of bulk materials, or thin film deposition and patterning using lithography.

Magnetic and Electromagnetic Actuation

Motion is generated through magnetic forces generated by placing a magnetic material inside the magnetic field, typically generated by an electromagnet. One type of magnetic microactuator utilizes hard, permanent magnets, composed of rare-earth elements such as Neodymium – $Nd_2Fe_{14}B$, which can be constrained to move by levitation [6]. Other types of microactuators utilize magnetic materials deposited as thin films, that exhibit Magnetostrictive and Giant-Magnetostrictive (GMR) effects. Examples of materials that exhibit a large change in shape when subjected to a magnetic field, is Terfenol-D – Tb(0.3) Dy(0.7) Fe(1.9). Microactuators using magnetic materials are currently not very common, because they are difficult to fabricate, characterize, assemble and control, however, they have the potential to exhibit large bandwidths, low power consumption, large displacements, and large forces.

Shape-Memory Actuation

SMA microactuators are based on alloys that exhibit specific phase transformations when undergoing thermal cycling. The change in phase allows the actuator to remember its original shape when heated. After a SMA sample has been deformed from its original crystallographic configuration, it regains its original geometry by itself during heating by changing between crystal structures known as martensite (at lower temperatures) and austenite (at higher temperatures). An example of SMA material is Nitinol – NiTi. Microactuators made from SMA require a heating source, which can be due to Joule heating of a substrate on which the actuator is attached. Microactuators using SMA materials are currently not very common because they are difficult to manufacture, but laser or EDM micromachined NiTi microgrippers with high force and displacement capabilities have been fabricated [1]. Drawbacks of SMA actuators include low bandwidths (Hz range), and large power consumption (hundreds of mW) due to the need for heating-cooling cycles.

Packaging of Microactuators

In addition to design and fabrication, current research work in microactuation includes aspects related to motion control (open-loop and closed-loop), microassembly (manipulation of small components using robotic devices), packaging (joining, sealing, and interconnecting of actuator components and driving circuitry), and reliability (predicting modes of failure and ensuring operation after repeated cycles) [9]. See Fig. 3 for an example of packaged microactuators.

Microactuators for Microfluidics

Microactuators are also used in microfluidics, for many applications including Lab-on-a-Chip and Implantable Drug Delivery Systems. Such fluidic actuators can be categorized as follows:

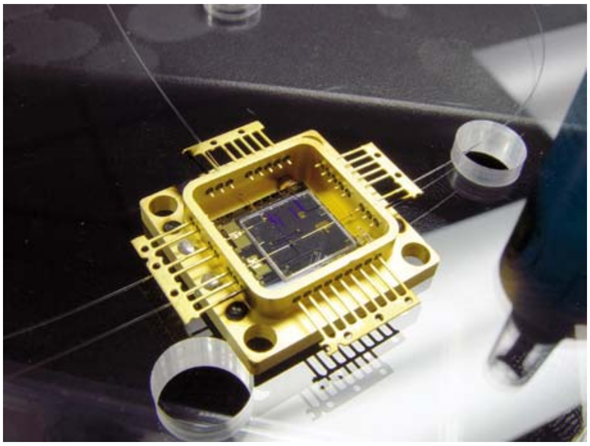

Microactuators, Figure 3 Packaged electrothermal microactuators, including a protective carrier, electrical and optical interconnects (Image courtesy of Texas Microfactory Lab, ARRI-UTA)

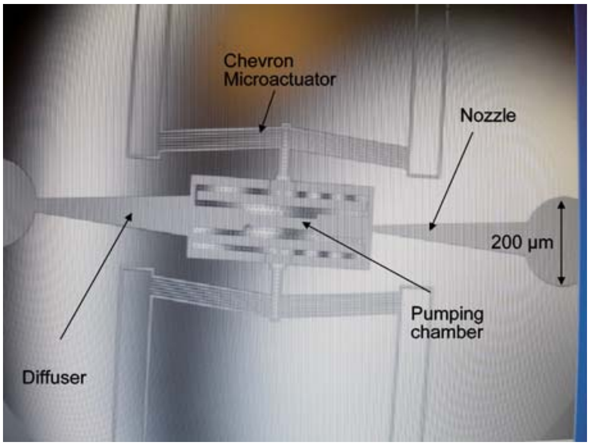

Microactuators, Figure 4 In-plane micropump for drug delivery composed of diffuser, nozzle, pumping chamber, and electrothermal microactuator (Image courtesy of Texas Microfactory Lab, ARRI-UTA)

- Mechanical, including diaphragm actuators (Fig. 4), rotary and reciprocating actuators.
- Pneumatic, including micropistons, microjets and micronozzles.
- Electro-osmotic, e.g. the motion of ions through microchannels, where an applied electrical potential across the channels cause the ion migration.
- Hydrodynamic, for instance, magneto-hydrodynamic pumps for which magnetic fields can induce currents in a moving conductive fluid.

Cross References

► Microactuators
► Micro-Electro-Mechanical Systems
► Micro-Scanners
► Micro-Wave Rotor
► Micro-Pumps
► Microsynthetic Jets

References

1. Bellouard Y (2002), Microrobotics, Microdevices Based on Shape-Memory Alloys. In: Encyclopedia of Smart Materials. Wiley
2. Bruck R, Rizvi N, Schmidt A (2001) Applied Microtechnology: LIGA – Laser – Micro Precision Engineering. Hanser–Gardner
3. Butler JT, Bright VM, Cowan WD (1999) Average Power Control and Positioning of Thermal Actuators. Sens Actuators 99–97
4. Hah D, Toshiyoshi H, Wu MC (2002) Design of Electrostatic Actuators for MOEMS Applications, Design, Test, Integration and Packaging of MEMS/MOEMS. Proc SPIE 4755:200–207
5. Laser DJ, Santiago JG (2004) A review of micropumps, J Micromech Microeng 14
6. Liu C, Yi YW (1999) Micromachined Magnetic Actuators Using Electroplated Permalloy. IEEE Trans Magn 35(3):1976–1985
7. Madou M (1998) Fundamentals of Microfabrication. CRC, Boca Raton
8. Piazza G, Pisano AP (2007) Two-port stacked piezoelectric aluminum nitride contour-mode resonant MEMS. Sens Actuators A 136:638–645
9. Popa DO, Stephanou H (2004) Micro and Meso Scale Robotic Assembly. SME J Manuf Proc 6(1):52–71
10. Senturia S (2000) Microsystem Design. Springer

M

Micro Aerial Vehicles

JEREMIAH HALL, KAMRAN MOHSENI
Department of Aerospace Engineering Sciences,
University of Colorado, Boulder, CO, USA
mohseni@colorado.edu

Synonymns

Miniature aerial vehicles; Small unmammed aerial vehicles; Micro air vehicles

Definition

Micro Aerial Vehicles are a class of aircraft, which are defined by the Defense Advanced Research Projects Agency (DARPA) to have a maximum dimension no greater than 15 cm (approximately 6 in.). A more flexible definition includes aircraft whose flight is characterized by low Reynolds number.

Overview

Recent aircraft design has focused on the development of Unmanned Aerial Vehicles (UAVs). This class of aircraft has been successfully adapted to preform many of

the same roles as manned aircraft but at lower cost. The absence of a pilot eliminates many of the safety and life support requirements, and also changes the control objectives. For example, rapid acceleration or a bumpy trajectory can hinder a pilot's ability to control the aircraft but do not affect the control system of a UAV. Another advantage of UAVs is that they can be used in environments that are undesirable for humans. This may include a combat zone or a toxic chemical plume. Moreover, many mission profiles do not require a large payload, and UAVs can be built much smaller to perform these missions because they do not have to support the extra weight of a pilot. Advancements in miniaturization have simultaneously made it possible to build smaller and smaller aircraft.

Research into small UAVs was given a top priority by DARPA in 1996 with the Micro Air Vehicle (MAV) Program initiative [1]. The goal of the program was to develop the technology for a small reconnaissance and communication microdrone for militarty applications. DARPA defined a MAV as an aircraft with a maximum dimension no greater than six inches. It also set objectives for endurance of approximately two hours and mass around 100 g. This definition of a MAV placed it in a flight regime with small birds, bordering on large insects. The difficulties faced for this type of flight are much different than those encountered at conventional scales, and consequently researchers had to come up with novel designs, in many cases learning directly from flying animals themselves.

In response to this project, many independent research groups have researched, designed, and tested their own solutions to the problem. The result was a wide variety of concepts for flight at small scales. A brief overview of some of the most successful and well-known MAVs is presented here to give a picture of the state of MAV design.

AeroVironment MAV Family

AeroVironment is a technology company that was founded in 1971 by Paul MacCready. The company focuses on energy technologies and Unmanned Aircraft Systems (UAS). They are perhaps best-known for the solar-powered Helios Prototype that was built for NASA. They have also built and produced a wide range of UAVs.

Dragon Eye is a tactical reconnaissance and surveillance UAV that is currently used by the U.S. Marine Corps. While it does not fit within the MAV classification, Dragon Eye is smaller than most commercially available UAVs, with a wingspan of 1.1 m and a mass of 2.3 kg. AeroVironment's most famous MAV is the Black Widow, show in Fig. 1a. Due to the desire to have the maximum possible wing area, but still fit within the MAV definition, the originial design had a circular planform. The initial flight lasted 9 s, and by November of 1997 the duration had increased to 16 min. Multidisciplinary Design Optimization (MDO), combined with a genetic algorithm, led to an optimized design with a wingspan of 15.2 cm and a total mass of approximately 80 g, with an endurance of around 30 min and video downlink to the operator. The Black Widow demonstrated the capability for flight in the MAV regime, and also showed that direct propulsion with an electric was more efficient than using a gearbox [2]. A third MAV developed by AeroVironment is called Wasp (Fig. 1b). Similar to the Black Widow, Wasp has a low-aspect ratio wing, meaning that the ratio of the wingspan chord is on the order of unity; however, Wasp's 41 cm. wingspan places it outside the technical definition of a MAV. Wasp's unique characteristic is the use of batteries as structural members.

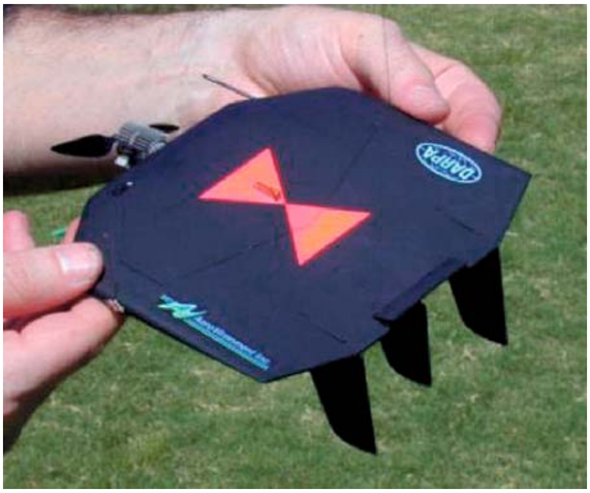

Micro Aerial Vehicles, Figure 1 AeroVironment's Black Widow MAV [2]

NRL MITE

The Naval Research Lab began development of a MAV in 1996. The MITE, for Micro Tactical Expendable, came to designate a family of MAVs based on a similar design concept. The MITE features a low-aspect ratio wing with twin propellers mounted at leading edge wingtips, and vertical triangle-shaped control surfaces at the wingtips (Fig. 2). The propellers rotate in the opposite direction of the wingtip vortices, thus reducing the induced drag effects. Once again, the low-aspect ratio planform is chosen to obtain the required wing area while fitting within the maximum dimensions specified for a MAV. A series of design configurations were built and tested, ranging in span from 8 in. (20.3 cm) to 18 in. (45.7 cm).

Micro Aerial Vehicles, Figure 2 MITE2, developed by Naval Research Lab [3]

Micro Aerial Vehicles, Figure 3 MAV prototype built and flown by University of Florida research group [5]

NRL researchers used Computational Fluid Dynamics (CFD) as an aid in the design process and to evaluate the aerodynamic coefficients needed for automatic control. The propellers were modeled as an actuator disk with the proper distribution of momemtum sources. The NRL team is currently investigating various control schemes, ranging from a simple technique with only pressure-based altitude and magnetic heading as sensors, to a more complex full autopilot including three axis rate gyros. They are also looking at the use of optical sensors for control, and contol of swarms of MAVs [3].

University of Florida

In recent years the University of Florida has developed a very strong MAV program. Their fleet of MAVs and small UAVs, which differ from one another in both size and shape, has been highly successful in competition (Fig. 3). Their first vehicle has a near-circular planform with a 6 in. span. They also have a smaller version which has a 4 in. span. These two aircraft feature membrane wing construction. There are two other aircraft which have more conventional design, including medium-aspect ratio wings, fuselage, and tail. They are designed with semi-flexible wings that can be morphed for control. All vehicles are driven by single nose-mounted propellers. The primary focus of their research has been on the use of flexible membrane wings. Most of their MAVs are designed with low-aspect ratio wings to fit the MAV criteria. The idea for the flexible wing comes from nature and materials science. Many flying animals in the low-Reynolds number regime use some from of passive morphing to perform flow control, i. e. membrane wings on bats and dragonflies. At the same time, composite materials are very effective for constructing lightweight aircraft frames. The UF team combined the two by building carbon fiber skeletons, over which a membrane of latex rubber was stretched. The result was a light wing capable of deforming based on the local flow conditions. One effect of the flexible wing design is to provide adaptive washout to smooth the effect of wind gusts [4]. They have reported that the flexible wing makes the aircraft easier to control than a similar vehicle with a rigid wing. The UF team has also demonstrated that flexible wings can attain greater lift than their rigid counterparts.

The UF group has also researched extensively computational techniques for MAVs with flexible wings [5]. Their simulations showed that a membrane wing generates more lift at high angles of attack, which leads to better stall properties. They have done numerical and experimental investigations of the deformation of the membrane wings during flight conditions and the pressure redistribution which results. The UF researchers investigated the stability and control properties of MAVs as well. They were able to control the MAV with elevons – elevators when actuated symmetrically, ailerons when actuated asymmetricallys – and throttle. They also used wing morphing for control [6].

University of Colorado

Researchers at the University of Colorado are developing a vehicle for the investigation of toxic chemical plumes. This mission requires relatively long endurance, which corresponds to a high lift-to-drag ratio. Early designs were similar to those of the University of Florida and other groups in that they used a low aspect ratio (Fig. 4), but this resulted in poor endurance. In order to extend the flight duration, the 15 cm restriction was abandoned in favor of

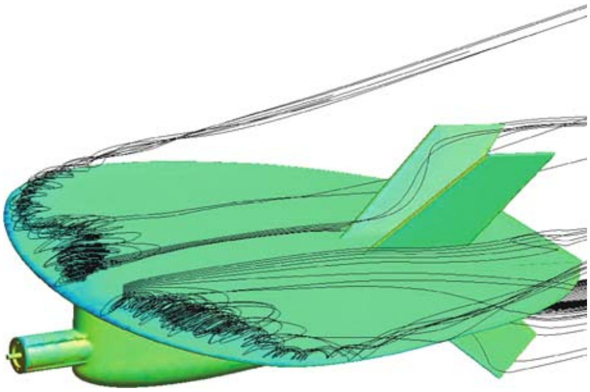

Micro Aerial Vehicles, Figure 4 Streamlines around the first-generation Colorado MAV, computed from CFD [8]

a high aspect ratio, which results in a better lift-to-drag ratio. However, because of the small chord length and the low cruise speed, the aircraft still operates in the low Reynolds number flight regime. Research has been performed on cooperative control of large flocks of MAVs, as well as the aerodynamic performance of various MAV designs [7, 8].

Basic Methodology

As mentioned briefly above, the flow regime which MAVs occupy is much different than that of conventional manned aircraft. Due to the combination of small length scale and slow flight speed, the Reynolds number for a typical MAV is on the order of 10^5, while for a jet airliner it is on the order of 10^7.

There is a stark change in aerodynamic efficiency, measured with lift-to-drag ratio L/D, as Reynolds number decreases below about 3×10^5 (Fig. 5). The decreased efficiency has a significant impact on the mechanics of flight in this regime. For example, eagles and hawks can be seen to soar without flapping, sometimes for long durations; however, bees and hummingbirds must beat their wings at a high frequency to remain airborne. Long endurance flight is difficult to achieve for MAVs because of this. Design of MAVs must focus on achieving the desirable flight characteristics while considering the low Reynolds number effects, unsteady flow, and the typical aerodynamic concerns such as balance and stability.

The primary cause of decreased efficiency at low Reynolds numbers is a laminar separation of the flow from the airfoil surface. This leads to a phenomenon known as a laminar separation bubble. The shape of the airfoil and pressure distribution have a significant impact on the location and size of the separation bubble, and so design and testing of airfoils can dramatically improve MAV performance.

As demonstrated in the examples given above, most MAVs have a low aspect ratio. The reason for this type of wing design is not based on aerodynamics, but simply the desire to fit within the specifications set forth by DARPA for a MAV. Consequently, to get the maximum amount of lift for an aircraft which fits in a 15 in. diameter sphere, a low aspect ratio is preferrable. There are a variety of planforms (i. e., wing shapes) which can accomplish this goal. The most obvious is a circular planform. However, many designs incorporate a modified delta wing or a Zimmerman planform, which is widest at the leading edge and tapers smoothly towards the rear.

If meeting the strict definition of a MAV is not a design requirement, a large aspect ratio is more advantageous. This is due to the induced drag, $C_{D,i} \propto 1/AR$, where AR is the aspect ratio. It is relevent to note that there is a trade-off between induced drag and the drag caused by low Reynolds number effects. Reynolds number is defined as $\mathrm{Re} \equiv \rho v c/\mu$, where ρ is the fluid density, v is the free stream velocity, c is the chord length, and μ is the dynamic viscsity. For the flight regime of MAVs, the profile drag on an airfoil increases as this parameter decreases. Thus, one way to increase the Reynolds number is to make the chord longer, i. e. increase c. If the wing area and cruise velocity are maintained constant while c increases, then AR must decrease. There is a value of AR which will balance the induced drag effects with the low Reynolds number effects.

To illustrate this point, one must look at the derivative of drag with respect to chord length. We wish to treat velocity, area, and lift coefficient as constants, so the span must be a function of aspect ratio. Using the definition for aspect ratio and defining the average chord length $\bar{c} \equiv A/b$, we obtain:

$$AR = \frac{b^2}{A} = \frac{b}{\bar{c}} = \frac{A}{\bar{c}^2} \tag{1}$$

Now we express the drag coefficient in terms of $\bar{c}$:

$$\begin{aligned} C_D = C_{D,0} + C_{D,i} &= k_1\,\mathrm{e}^{-k_2\mathrm{Re}} + \frac{{C_L}^2}{\pi\,\mathrm{e}AR} \\ &= k_1\,\mathrm{e}^{-k_3\bar{c}} + k_4\bar{c}^2 \end{aligned} \tag{2}$$

Here we have made the approximation that $C_{D,0}$ at a given C_L scales as a decreasing exponential of Reynolds number. The k's represent collections of constant scalar values. The next step is to take the derivative with respect to $\bar{c}$. The optimal shape is characterized by $\partial C_D/\partial\bar{c} = 0$.

$$\frac{\partial C_D}{\partial x\bar{c}} = -k_1 k_3\,\mathrm{e}^{-k_3\bar{c}} + 2k_4\bar{c} \tag{3}$$

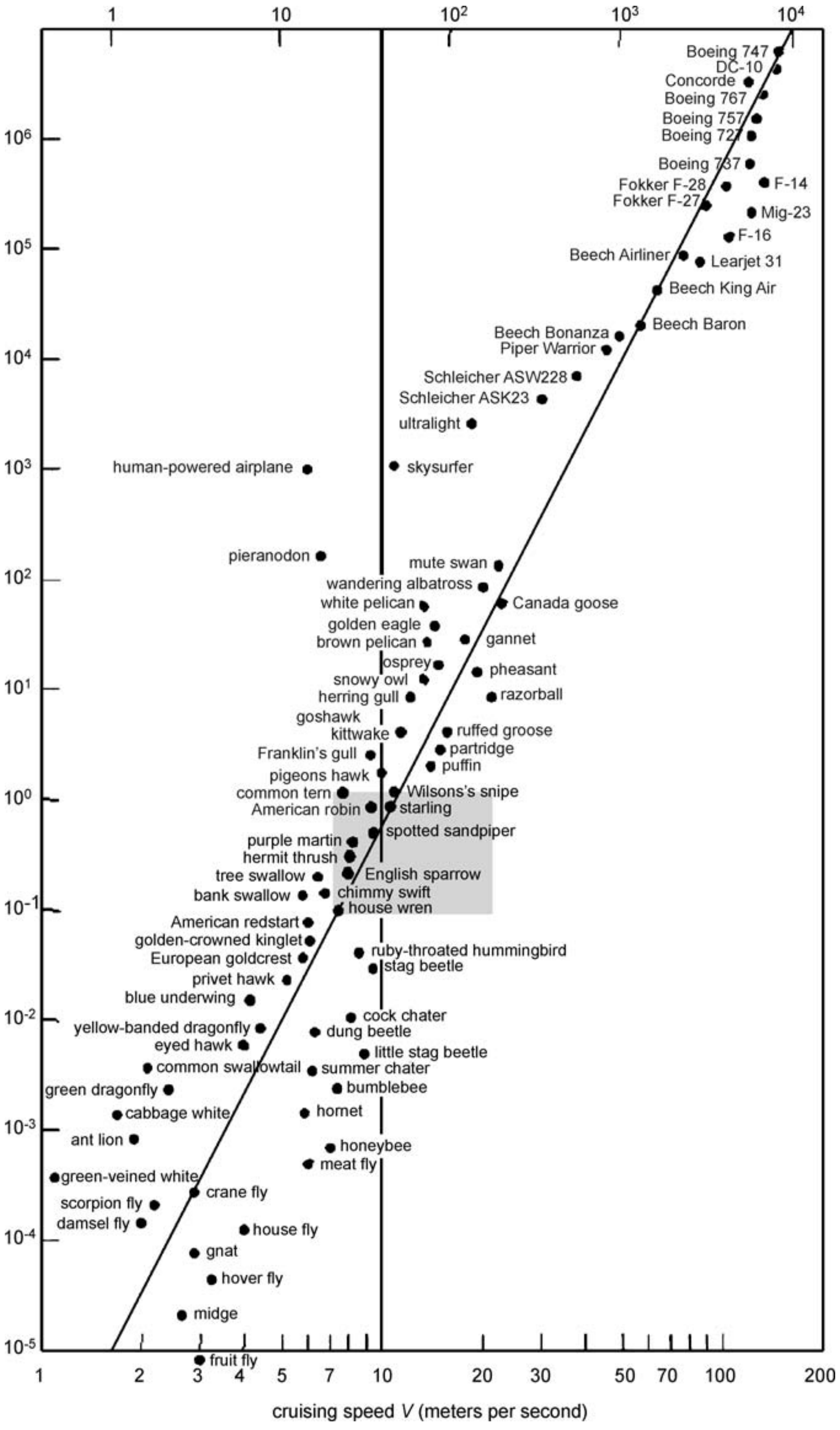

Micro Aerial Vehicles, Figure 5 Weight vs. cruising velocity for various aircraft and animals [14]

For a MAV with a six inch diameter circular wing flying at 25 mph, we find that the rate of change of $C_{D,0}$ with respect to Re is not great enough to overcome the change in induced drag. However, as the length scale and

Reynolds number decrease further, there is a point where the change of $C_{D,0}$ with respect to Re is great enough to make a smaller aspect ratio profitable.

Other considerations for designers are balance and stability. For longitudinal stability (pitch and vertical motion), the center of gravity should be placed in front of the aerodynamic center, through which the lift vector passes. If the MAV incorporates a flying wing design, the wingtips should be swept back and twisted, or an airfoil specific to flying wings should be employed, in order to balance the moments produced by the lift force. Because the aerodynamic forces scale with the square of characteristic length while the mass scales with the cube, inertial forces are much smaller for MAVs than conventional aircraft. Because of this, the control is often simpler. Many MAVs utilize either rudder or ailerons for lateral control surfaces, rather than both.

Key Research Findings

There are many areas of research which are related to MAVs; of notable interest are the effects of low Reynolds number flow, unsteady flow, and flapping wings. A compilation of research on MAV aerodynamics can be found in [9].

Low-Reynolds Number Flow

As mentioned above, laminar separation bubbles affect the aerodynamic performance of MAVs. At higher Reynolds numbers, the transition occurs closer to the leading edge, and the mixing caused by turbulence transfers momentum from the free stream to the boundary layer, delaying separation of the flow. As Reynolds number decreases, the location of the transition point moves toward the trailing edge until the pressure gradient becomes unfavorable, and the flow separates. The resulting shear layer is initially laminar, but Kelvin-Helmholtz instability triggers a transition to turbulent flow. If the angle of attack is not too high, or the adverse pressure gradient is not too strong, the separated shear layer will gain enough momentum through entrainment to reattach to the surface of the airfoil. The region between the separated flow and the airfoil is called the laminar separation bubble, or LSB [10]. Figure 6 diagrams the streamlines of a laminar separation bubble.

The upstream portion of the LSB is sometimes referred to as the "dead air region". Here the flow is nearly stagnant. Slightly downstream from this region is the point in the separated shear layer where instabilities begin to grow. As the instabilities reach a critical size, they detach as vortices and begin to move downstream. Depending on Reynolds number and local flow conditions which are dependent on the particular airfoil, these vortices may "roll up", or pair

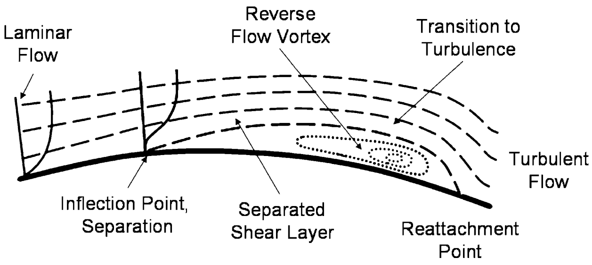

Micro Aerial Vehicles, Figure 6 Diagram of time-averaged view of a laminar separation bubble

to form larger vortices. Eventually they move downstream to the trailing edge, where they are shed from the airfoil and are advected by the wake to form a vortex street. The LSB can be seen in the time-averaged velocity field as a region of recirculation.

Reynolds number has a significant impact on the structure of the LSB. Below approximately Re = 50,000, the separated shear layer may not transtition to turbulence in time to reattach to the airfoil. The attendant increase in pressure drag significantly diminishes the airfoil's efficiency. Between Re = 50,000 and Re = 200,000, the size of the LSB decreases and hence performance increases.

Angle of attack also plays a large roll in the size and effect of the LSB, especially at low Reynolds numbers. For the midrange of angle of attack, i. e. from 4° to 8°, the LSB covers a large portion of the chord. As C_L approaches 1.0, the bubble moves toward the leading edge and transition occurs earlier, shortening the bubble. The result is a decrease in drag due to LSB. This can be seen on the drag polar for most airfoils at low Reynolds number as an increase in drag over the midrange of C_L, which is referred to as the laminar separation bucket.

Many studies have been performed on the flow over airfoils at low Reynolds number. One airfoil which has received significant attention due to its interesting behavior is the Eppler 387. McGhee et al. studied the airfoil experimentally and reported on lift and drag for various Reynolds number, ranging from 60,000 to 400,000, and angles of attack [11]. They also found the separation and reattachment points on the airfoil, and tabulated pressure data versus chordwise position. Other experiments were performed by Selig et al. on a wide range of airfoils at low Reynolds numbers [12]. At very low Reynolds numbers, the discrepancy between defferent sets of experimental data grows large. One possible cause for the experimental scatter is the three-dimensionality of the flow during the vortex shedding; moreover, because of the small resultant forces on the airfoil a wake survey is usually employed for drag calculation, and the spanwise location of these mea-

surements can be a factor. There have also been a number of numerical studies of low Reynolds number flow. Elimelech et al. studied NACA-0009 and Eppler 61 airfoils both numerically and in a water tunnel, and reported on the structure of the vortex shedding [13]. They also found that reasonable accuracy could be obtained without the use of a turbulence model for the numerical simulations.

Unsteady Effects

Unsteady effects become more pronounced as vehicle size decreases. First, the unsteady forces due to vortex shedding and the LSB become stronger in magnitude and percentage of mean force. The unsteady pressure distribution is probably responsible for the observed vibration at $\sim 100\,\text{Hz}$ on membrane wings. However, it is currently unclear what effect these forces have on the global quantities of lift and drag. The second and more significant effect of unsteadiness comes from variations in the free stream flow due to wind gusts and turbulence. As aircraft decrease in size, the inertial effects decrease with the cube of length scale while wing area decreases with the square of length scale. This means that MAVs and other small aircraft have low wing loads, and are therefore more likely to undergo severe acceleration in the presence of unsteady flow. Also, for a large aircraft, a wind gust might only cause a 10% change in airspeed, while the same gust could cause a change of 100% for a MAV.

The techniques devised at the University of Florida directly address the issue of wind gusts. When the local airspeed over the wing changes suddenly, the increased pressure causes the membrane to deform and lose camber. As a result the C_L decreases, but the increase in velocity yields a nearly constant value of lift. This type of passive morphing is referred to as load spilling.

Biomimetics and Flapping Wings

A great deal about flight at low Reynolds numbers can be learned from the study of birds and insects. The difference between the flight of eagles and hummingbirds is a direct result of the changing aerodynamics and decreasing lift-to-drag ratio as Reynolds number decreases [14]. Application of the lessons learned from nature is called biomimetics.

A third type of unsteady effect can be observed in insects and very small birds: flapping. These animals move their wings in a cyclic fashion to produce and usteady flow, which they use to create lift. Wing deformation is also very important for this type of flight. In fact, dragonflies and other insects do not have cambered wings at all, but rather membrane wings attached to flexible skeletons. The combination of aeroelasticity and unsteady flow are crucial to flight at these ultra-low Reynolds numbers.

Future Directions for Research

Many fields related to MAVs still require a great deal of research. While the low Reynolds number flight regime has received some attention, values of Re below 30,000 are still largely unexplored. Biomimetics has the potential to greatly improve the knowledge base of MAV flight. As researchers develop a better understanding of the aerodynamic properties of MAV flight, new control techniques will evolve as well. For example, microsynthetic jets could be used to control the vortex shedding over the wing, or vary the lift and drag along the wings for roll and yaw control. Advances in materials also have potential to change MAV design. As actuators become smaller and batteries lighter, MAV flight will progress to even smaller scales.

Cross References

► Biomimetics
► MEMS-Based Biosensor
► Microactuators
► Microsynthetic Jets

M

References

1. McMichael JM, Francis MS (1997) Micro air vehicles – toward new dimension in flight. Tactical Tech Office DARPA, http://www.darpa.mil/tto/MAV/mav_auvsi.html
2. Grasmeyer JM, Keennon MT (2001) Development of the black widow micro air vehicle, AIAA paper 2001–0127. AIAA
3. Kellog J (2001) The NRL MITE air vehicle, Tech report. Naval Research Laboratory
4. Ifju PG, Jenkins DA, Ettinger S, Lian Y, Shyy W, Waszak MR (2002) Flexible-wingbased micro air vehicles. In: AIAA paper 2002–0705, 40th Aerospace Sciences Meeting Exhibit. AIAA, Reno
5. Lian Y, Shyy W, Wiieru D, Zhang B (2003) Membrane wing aerodynamics for micro air vehicles. Prog Aero Sci, 39(6–7):425–465
6. Garcia H, Abdulrahim M, Lind R (2003) Roll control micro air vehicle using active wing morphing. AIAA Paper 2003–5347, AIAA Guidance, Navigation Control Conference, 11–14 Aug 2003
7. Lawrence DA, Mohseni K, Han R (2004) Info energy for sensor-reactive UAV flock control. AIAA paper 2004–6530, 3rd AIAA Unmanned Unlimited Technical Conference, Workshop Exhibit, Chicago, 20–23 Sept 2004
8. Gyllhem D, Mohseni K, Lawrence D, Geuzaine P (2005) Num simulation of flow around the colorado micro aerial vehicle. AIAA paper 2005–4757, 35th AIAA Fluid Dynamics Conference Exhibit, Toronto, 6–9 June 2005
9. Mueller TJ (ed) (2001) Fixed and flapping wing aerodynamics for micro air vehicle applications. AIAA, Reston
10. Mueller TJ, Delaurier JD (2003) Aerodynamics of small vehicles. Ann Rev Fluid Mech 35:89–111
11. McGhee RJ, Jones GS, Jouty R (1988) Performance characteristics from wind-tunnel tests low-Reynolds number airfoil. AIAA paper, AIAA 26th Aerospace Sciences Meeting, 11–14 Jan 1988

12. Selig MS, Guglielmo JJ, Broeren AP, Giguére P (1995) Summary of low-speed airfoil data. SoarTech, Virginia Beach
13. Elimelech Y, Arieli R, Iosilevskii G (2005) Onset of transition at low Reynolds number flow over airfoils. AIAA Paper 2005–5311, 4th AIAA Theoretical Fluid Mechanics Meeting, Ontario, 6–9 June 2005
14. Shyy W, Berg M, Ljungqvist D (1999) Flapping flexible wings for biological and micro air vehicles. Prog Aerosp Sci 35:455–505

Microair Vehicle (MAV)

► Microrotorcraft

Microarray

Synonyms

DNA array; Protein array and cell array

Definition

Microarrays constitute highly parallel biosensors used in biomedical applications for studying a multitude of complex biological interactions simultaneously to determine the presence and/or amount (quantitation) of nucleic acids and proteins in biological samples, respectively, to investigate gene expression levels or for proteomics studies (e. g. in blood, cell extract, tissue extract). These miniaturised two-dimensional arrays contain a large number (hundreds up to hundreds of thousands) of different unique biological capture agents [nucleic acids (e. g. oligonucleotides, genes, gene fragments), proteins (e. g. antibodies)] on a solid substrate that are arranged in small chemical reaction areas (spots) in a predetermined spatial order (ranging from the hundreds of micrometre down to the sub-micrometre range). Typical substrates are glass, membranes, or silicon wafers.

The complex biological interactions are identified by the specific location of the capture molecules on the microarray. The arranged multitude of biological agents acts as capture probes to bind molecules out of a complex biomedical sample to be analysed in a high-throughput, and parallel manner. After hybridization of labelled complementary molecules, i. e. binding of sterically compatible molecules, a scanning microscope detects the bound, labelled sample and measures the visualised probe to ascertain the presence and/or amount of the specific type of complementary molecule in the complex sample.

Cross References

► Biochip
► Cell Culture (2D and 3D) on Chip
► Cell Patterning on Chip
► DNA Micro-arrays
► DNA Microarrays
► Droplet Dispensing
► Droplet Evaporation
► Evanescent-Wave Sensing
► Fluorescence Measurements
► Fluorescent Labelling
► Hydrophilic/Hydrophobic Patterning
► Methods for Surface Modification
► Micronozzles, Proteomics in Microfluidic Devices
► Surface Tension Capillarity and Contact Angle
► Van der Waals Interaction Forces

Microarray Fabrication

► Bioprinting on Chip

Microbial Fuel Cell

► Biofuel Cell

Microbiosensor

► MEMS-Based Biosensor

Microchannel

Definition

Although the concept of microchannel has been in the field literature for some time now, a clear definition of it has not yet been enunciated. However, it is the general understanding that any channel that has a characteristic dimension is between 500 microns and 1 micron is considered to be a microchannel. Most of the microchannels discussed in the literature are manufactured through microfabrication techniques, but not exclusively.

Cross References

► Confocal Microscopy, Detection
► Shock Wave in Microchannel
► Single-Phase Gaseous Flow

Microchannel Flow

► Combined Pressure-Driven Flow and Electroosmotic Flow

Microchannel Glow Discharge

► Plasma in Microchannel

Microchannel Heat Sinks (MCHS)

► Microscale Cooling Devices

Microchannel Surface Modification

► Plasma in Microchannel

Microchannel Surface Sterilization

► Plasma in Microchannel

Microchemical Systems

► Microfluidics for Biochemical and Chemical Reactions

Micro Chemlab

► Integrated Microdevices for Biological Applications

Micro Coolers

► Micro Energy Conversion Devices

Microdialysis

YI-CHENG HSIEH, JEFFREY D. ZAHN
Department of Biomedical Engineering, Rutgers,
The State University of New Jersey, Piscataway, NJ, USA
jdzahn@rci.rutgers.edu

Definition

Microdialysis is a continuous sampling technique based on controlling the mass transfer rate of small molecules across a semipermeable membrane while excluding the larger ones. For biochemical monitoring, microdialysis systems are usually placed (inserted or implanted) inside the tissue of interest with an isotonic perfusion fluid flowing through the system and diffusional exchange occurring between the perfusate and the surrounding interstitial fluid (ISF). Since the dialysis process does not change or affect the surrounding fluid, it is viewed as a tool for continuous monitoring. Microdialysis systems have recently been adapted to microfluidic technologies for sample preparation prior to sample analysis or for miniaturized biochemical probes.

Overview

Researchers have been interested in the biochemical functions of the body in vivo, especially in the extracellular compartment where signaling chemicals can affect cellular function. Neuroscientists were the pioneers in developing microdialysis techniques due to their interest in analyzing neuron signaling processes within intact brains. The technique was originally used in neuroscience for the measurement of neurotransmitters. It allows sampling of brain regions in conscious, freely moving animals and directly delivering drugs into specific areas. There have been experimental attempts to analyze the tissue of interest without changing or affecting the surrounding fluid environment. The concept of introducing a semipermeable membrane into the tissue of interest to dialyze or continuously sample molecules was first introduced in the late 1960s and early 1970s. In 1966, Bito and colleagues implanted membrane-lined *dialysis sacs* containing 6% dextran in a saline solution into the cerebral hemispheres of dogs. The sacs were surgically removed after ten weeks postimplantation and analyzed for amino acid content. This experiment introduced the idea of using a membrane dialysis compartment to monitor the extracellular environment. In 1972, Delgado and colleagues developed the first-generation version of present-day microdialysis probes, which they called a *dialytrode*. The dialytrode consisted of two stainless steel tubes soldered together forming a push–pull cannula terminating with a small permeable bag. They were the first research group to perfuse the dialysis membrane in vivo in monkeys and the first to practice the technique which has since become known as *microdialysis*.

Development of microdialysis from a long-term dialysis sac implantation, to the push–pull cannula, and finally to the current continuous perfusion flow sampling/monitoring emerged in the neuroscience field in

1974 when Ungerstedt and Pycock first developed a linear, hollow-fiber probe design to continuously monitor neurotransmitter concentration within rat brains [1, 2]. They implanted the probe by drilling holes in each temporal bone of rats and guided the fiber into an area of the brain known to be devoid of a blood–brain barrier. Since then, more designs of microdialysis probes have been presented and utilized not only in neuroscience but also in other fields where continuous sampling/monitoring is needed. Today, the technique is widely applied to body organs and fluids, including blood, heart, liver, kidney, bile, lung, bone, eye, muscle and breast. Microdialysis has been used in the medical community to continuously monitor various metabolites (glucose, lactate, sodium, etc.) in patients.

Glucose microdialysis is of particular interest in diabetes treatment. In diabetics, the consistently high glucose levels results in long-term complications including retinopathy, nephropathy and neuropathy which often leads to amputation of extremities. Studies have shown that tight glycemic control reduces the complications dramatically. In diabetes treatment, these probes are usually inserted subcutaneously into either the abdomen or forearm, sampling glucose from the interstitial space. A large amount of research has been performed on creating a microdialysis sampling system where the dialysate exiting from the probe is then transferred to a glucose sensor by a tubing connection for continuous monitoring in vitro or in vivo. The ability to continuously monitor blood glucose levels in a diabetic patient is especially important for a patient undergoing continuous insulin infusion therapy from an insulin pump, so that the patient does not become severely hypoglycemic. During in vivo microdialysis studies, the microdialysis probes used to dialyze glucose from interstitial tissue were connected to glucose sensors, where the glucose concentration of the dialysate from the probe was determined. The true glucose concentration is back-calculated by using a calibration curve as described in the next section.

Aside from monitoring biomolecules in humans and animals, the microdialysis technique is also utilized in the area of environmental research. Probes are inserted into freshwater systems or soil for real-time and continuous sampling with minimum disturbance of the outer environment [3].

Basic Methodology

Basic Principles

The most common type of microdialysis probe is constructed as a concentric tube as shown in Fig. 1. The probes usually consist of a semipermeable membrane, such as polysulfone, polyethersulfone, polyamide, polycarbonate–polyether copolymer or cuprophan [4], glued between the tip of the inner cannula and the outer shaft, which are made of steel or plastic. The perfusion fluid (perfusate) enters the inlet flowing through the inner tube to its distal end and exits the inner tube to enter the space between the inner tube and the outer dialysis membrane where molecular exchange takes place. After the exchange, the fluid containing the molecules of interest (dialysate) is transferred towards the proximal end of the probe and is collected at the outlet for later analysis. Several different types of microdialysis probe construction are commercially available, including linear, loop, concentric and side-by-side [5] (Fig. 2).

In order to conduct microdialysis experiments several other components are required. Syringe pumps are often used to control the perfusate flow rate. The pump has to be able to deliver flow rates precisely in the microliter per minute range. Tubing is needed to connect between the probe and the pump which drives the perfusion flow and, in some cases, between the probe and a sample collector as well. The total dead volume of tubing should also be maintained as small as possible to have better time resolution. The perfusion fluid is a medium resembling the composition of extracellular fluid with minimal or zero concentration of the molecules of interest. Dialysate exiting from the outlet of the microdialysis probe is usually collected in a vial for later analysis. It is also possible to connect the outlet directly to an analysis instrument without using a collector, which is usually preferred, if possible, for its convenience and usually faster analysis results.

The concentration gradient between the perfusate and the component of interest in the ISF (e. g., glucose) is the driving force to transport molecules to the lumen of the probe. The concentration of the molecules of interest in the perfusion fluid at the output of the microdialysis probe is a representative of the ISF and can be correlated to the concentration within the ISF. The term recovery is defined as

$$\text{Recovery} = \frac{C_{\text{d,out}} - C_{\text{d,in}}}{C_{\text{r}} - C_{\text{d,in}}} \tag{1}$$

where $C_{\text{d,in}}$, $C_{\text{d,out}}$ and C_{r} are the concentration of the analyte of interest in the inflow perfusate, outflow dialysate and the exterior surroundings. When $C_{\text{d,in}}$ equals zero, the recovery can be simplified as

$$\text{Recovery} = \frac{C_{\text{out}}}{C_{\infty}} \tag{2}$$

where C_{out} equals $C_{\text{d,out}}$ the outlet concentration and C_{∞} equals C_{r} the bulk concentration in the surrounding fluid.

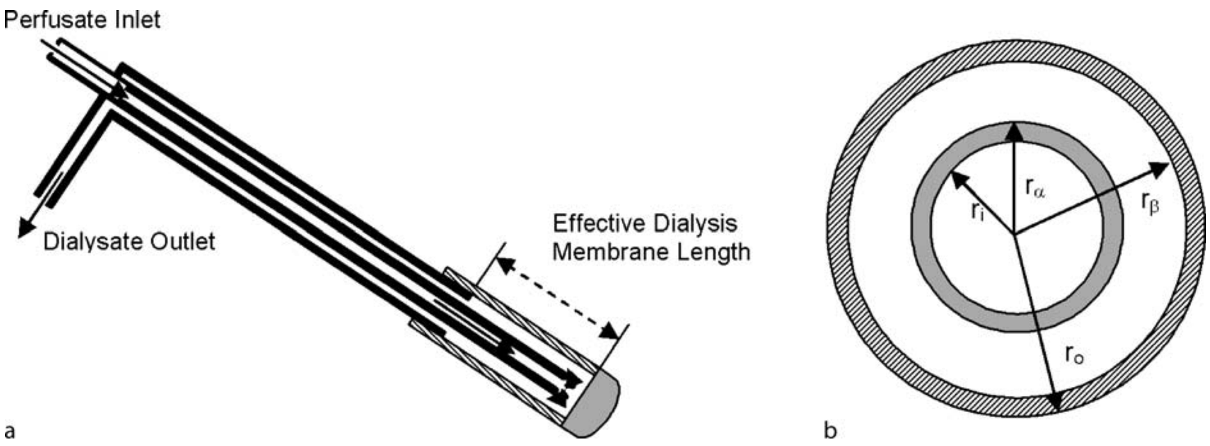

Microdialysis, Figure 1 (**a**) Concentric microdialysis probe design. (**b**) A schematic of the cross-section of a concentric microdialysis probe. Image adapted from [4]

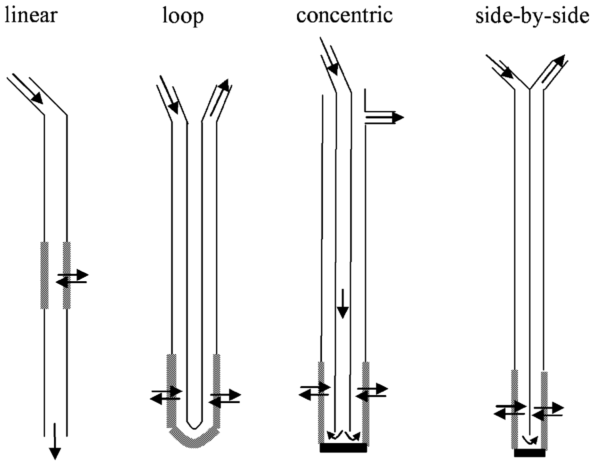

Microdialysis, Figure 2 Different probe designs of commercially available microdialysis probes. Image adapted from [5]

Quantitative Microdialysis Models

Concentric Microdialysis Probe

When a microdialysis probe with perfusion fluid flowing at a flow rate of Q_d is placed in a bath of analyte of concentration C_r, the microdialysis recovery, also known as *dialysate extraction fraction*, is described by a balance of the diffusion of the analyte across the microdialysis membrane into the perfusion fluid with the convective flux due to the perfusion flow:

$$\mathrm{Recovery} = \frac{C_{\mathrm{d,out}} - C_{\mathrm{d,in}}}{C_r - C_{\mathrm{d,in}}} = 1 - \exp\left[-\frac{1}{Q_\mathrm{d}(R_\mathrm{d} + R_\mathrm{m} + R_\mathrm{ext})}\right] \quad (3)$$

where $C_{\mathrm{d,in}}$, $C_{\mathrm{d,out}}$ and C_r are as previously defined in Eq. (1), R_ext is the external mass transfer resistance, R_m is the membrane resistance and R_d is the perfusion fluid resistance. Q_d is the perfusate/dialysate flow rate. This equation was proposed and demonstrated by Bungay and colleagues assuming that the membrane hydraulic conductivity and transmembrane pressure differences are sufficiently small so that no appreciable transmembrane fluid flow was produced [6, 7].

The overall product of permeability of the microdialysis probe (K) and surface area (A) is defined as

$$KA = \frac{1}{R_\mathrm{d} + R_\mathrm{m} + R_\mathrm{ext}} \quad (4)$$

It is governed by the resistance of analyte transport through three regions: the external surrounding medium (R_ext), the membrane (R_m) and the dialysate (R_d). Since they are in series and the mass transfer is the same across the three regions, the three resistances are additive.

A schematic of a cross-section of a microdialysis probe is shown in Fig. 1b, in which r_i is the inner radius of the inner cannula, r_α is the outer radius of the inner cannula, r_β is the inner radius of the membrane and r_0 is the outer radius of the membrane. The dialysate resistance, R_d, may be described as

$$R_\mathrm{d} = \frac{13(r_\beta - r_\alpha)}{70\pi L r_\beta D_\mathrm{d}} \quad (5)$$

where L is the effective dialysis membrane length and D_d is the diffusion coefficient through the dialysate. The membrane resistance, R_m, is described as

$$R_\mathrm{m} = \frac{\ln\left(r_0/r_\beta\right)}{\pi L D_\mathrm{m} \phi_\mathrm{m}} \quad (6)$$

M

where D_m is the diffusion coefficient through the membrane and ϕ_m is the void fraction of the membrane.

It is not possible to generalize the external mass transfer resistance, R_{ext}, based on the knowledge of the analyte molecular weight, shape and charge or the probe dimensions. Knowledge of other factors such as the analyte efflux to the microvasculature, metabolism and cell membrane transport processes are required. However, under most operating conditions R_{ext} is much smaller than R_m. This is especially true when the tissue analyte concentration is constant and does not vary over the sampling time.

Microfluidic Microdialysis Systems

Most microfluidic microdialysis systems consist of a two-compartment system with a sample flow channel and perfusion flow channel separated by the microdialysis membrane. A two-compartment cocurrent mass transport model of microdialysis is shown in Fig. 3. For this microdialysis system, molecules inside the sample channel are dialyzed across the membrane into the perfusion flow channel. Again, this system may be modeled by balancing the sample and perfusion convective fluxes with the diffusion of analyte across the membrane. Assuming the overall permeability is constant, K, over the diffusion path, the mass transfer along the membrane diffusional area, A, can be described as

$$\ln \frac{C_{r,out} - C_{d,out}}{C_{r,in} - C_{d,in}} = -KA\left(\frac{1}{Q_r} + \frac{1}{Q_d}\right) \tag{7}$$

where $C_{d,in}$, $C_{d,out}$ and C_r are as previously defined in Eq. (1). Q_r is the flow rate of the sample flow channel and Q_d is the perfusion flow rate. K is the overall molecular permeability and A is the diffusional surface area.

Under most operating conditions, $C_{d,in}$ is zero, and the sample channel acts as an infinite reservoir where $C_{r,in}$ and $C_{r,out}$ are assumed to be equal to C_∞, because Q_r is much larger thanQ_d so there is minimal mass loss from the sample flow channel. In addition, when Q_r is larger than Q_d ($1/Q_r \ll 1/Q_d$), the $1/Q_r$ term can be ignored on the left of the equation. Therefore, Eq. (7) can be simplified to

$$\ln\left(1 - \frac{C_{out}}{C_\infty}\right) = -KA\left(\frac{1}{Q}\right) \tag{8}$$

where Q stands for Q_d and $C_{d,out}$ is simply C_{out}. Equation (8) can be rearranged to represent recovery as a function of perfusion flow rate as

$$\frac{C_{out}}{C_\infty} = 1 - e^{-\frac{KA}{Q}} \tag{9}$$

By plotting the left side of Eq. (8) as a function of perfusion flow rate ($1/Q$), the permeability of the membrane to the molecule of interest (the slope is KA) may be determined to characterize the system functionality.

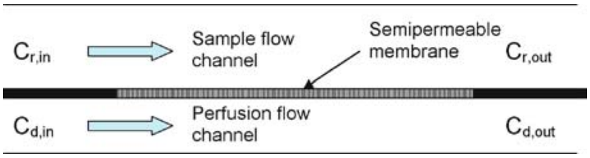

Microdialysis, Figure 3 Schematic of the mass transfer of a two-compartment cocurrent microdialysis system

Factors Affecting Recovery

In general, it is desirable to operate microdialysis systems at the highest recovery possible. There are several factors which affect the recovery rate of analytes.

Perfusate Flow Rate

Because recovery is determined by a competition between a diffusional and perfusion convective flux, it is perfusate flow rate dependent. As demonstrated in Eq. (3), recovery increases as the flow rate decreases. Even though low flow rates result in high recovery, it is often restricted by the reproducibility of low flow rates supplied by syringe pumps and the sample volume needed for solution analysis. Therefore, extremely low flow rates are often not applicable due to limited analysis time resolution because of the long times needed to collect the appropriate solution volume for analysis.

Dialysis Membrane Area and Membrane Material

The dialysis membrane chosen plays an important role in controlling the recovery. The dialysis area of the membrane can be increased to achieve high recovery without sacrificing time resolution. Larger diffusional area can enhance recovery, but in most cases, a minimal tissue disturbance by small microdialysis probes is favored. Recovery can be improved by selecting membranes with a higher permeability, K. Overall permeability mainly depends on the properties of the microdialysis membrane, such as pore size, pore density, tortuosity and analyte particle size. Membranes are commonly available with different molecular weight cutoffs (MWCOs), which determine the size of recovered particles. Molecules beyond the MWCO are too large to fit in the microdialysis pores. Membranes with lower MWCOs usually have lower permeability to

all species due to a smaller pore size. Recovery of certain analytes can also vary by as much as 20% between dialysis membranes made from different materials with the same MWCO. Microdialysis membranes are made from organic polymers. Several different types of membrane are used: polysulfone, polyethersulfone, polyamide, polycarbonate–polyether copolymer, cuprophan, polycarbonate, regenerated cellulose, cellulose acetate and polyacrylonitrile. They come in different thicknesses, where a thicker membrane decreases the permeability and hence recovery.

Diffusion Coefficient

One of the parameters that affects recovery is the diffusion coefficient of molecules of interest, which can be estimated by the Stokes–Einstein equation:

$$D = \frac{k_B T}{6\pi \eta r} \tag{10}$$

where k_B is the Boltzmann constant, T is the absolute temperate (K), η is the viscosity of the solvent and r is the particle radius. The diffusion coefficient of molecules is approximately inversely proportional to its radius and hence to the cube root of its molecular weight. This relationship can be described as

$$\frac{D_{\text{molecule.A}}}{D_{\text{molecule.B}}} \propto \frac{r_{\text{molecule.B}}}{r_{\text{molecule.A}}} \propto \frac{\sqrt[3]{MW_{\text{molecule.B}}}}{\sqrt[3]{MW_{\text{molecule.A}}}} \tag{11}$$

Therefore most microdialysis membranes will allow the rapid passage of small molecules but usually struggle for higher recoveries of larger molecules due to their smaller diffusivity. It is also obvious that the diffusion coefficient is directly proportional to the temperature. Empirically, the diffusion coefficient for small molecules increases $1-2\%$ per degree centigrade. Thus, it is crucial to carry out the entire microdialysis experiment at a constant temperature.

Calibration Techniques

As the relative recovery will never reach 100%, the dialysate concentrations are only a fraction of the true concentration of the analyte of interest in the surrounding fluid. Before using a microdialysis probe for continuous sampling or monitoring, the true concentration of the analyte of interest in the surrounding environment and the recoveries at certain perfusate flow rates have to be obtained. There are many different methods for calibration, which are discussed in the following [1].

Perfusate Flow Rate Variation

Calibration is accomplished by placing a probe in the tissue of interest and varying the perfusate flow rate. At low flow rates, the dialysate concentration will reach a plateau, which is assumed to be near 100% recovery. Recoveries at different perfusate flow rates can then be calculated.

No-Net Flux Method

This is a method enabling the estimation of the in vivo recovery of an analyte of interest introduced by Lonnroth in 1987. The procedure involves adding the analyte of interest into the perfusion solution at different concentrations at a fixed perfusate flow rate and measuring the difference between perfusate and dialysate analyte concentration. The recovery represented by the left term of Eq. (3) can be assumed to be an unknown value P since the perfusate flow rate and resistance are left unchanged. When it is rearranged

$$C_{\text{d,out}} - C_{\text{d,in}} = -P(C_{\text{d,in}} - C_r) \tag{12}$$

By varying $C_{\text{d,in}}$ and determining $C_{\text{d,out}}$, and plotting Eq. (12) as a function of $C_{\text{d,in}}$, the x-axis intercept is the actual recovery concentration C_r and the slope reflects the recovery at the selected perfusate flow rate.

M

Retrodialysis

This technique is less time-consuming than those mentioned above and the recoveries can be measured continuously during the experiment. It is also called the delivery method, and is operated by using a perfusate spiked with the analyte of a known concentration. It is recommended that the perfusate concentration be at a minimum ten times greater than the concentration of the analyte around the probe since the recovery is basically determined by neglecting C_r with the assumption that it is small enough compared with the known $C_{\text{d,in}}$, as

$$\text{Recovery} = 1 - \frac{C_{\text{d,out}}}{C_{\text{d,in}}} \tag{13}$$

Another variation of this method is adding a marker or internal standard to the perfusate. The marker should match the diffusion characteristics of the analyte and therefore the recovery can be obtained in vivo by measuring its relative loss through the microdialysis process.

Key Research Findings

For the past 10 to 15 years, semipermeable membranes have been utilized in microfluidics [8]. The concept of a micro total analysis system (μTAS) was introduced by

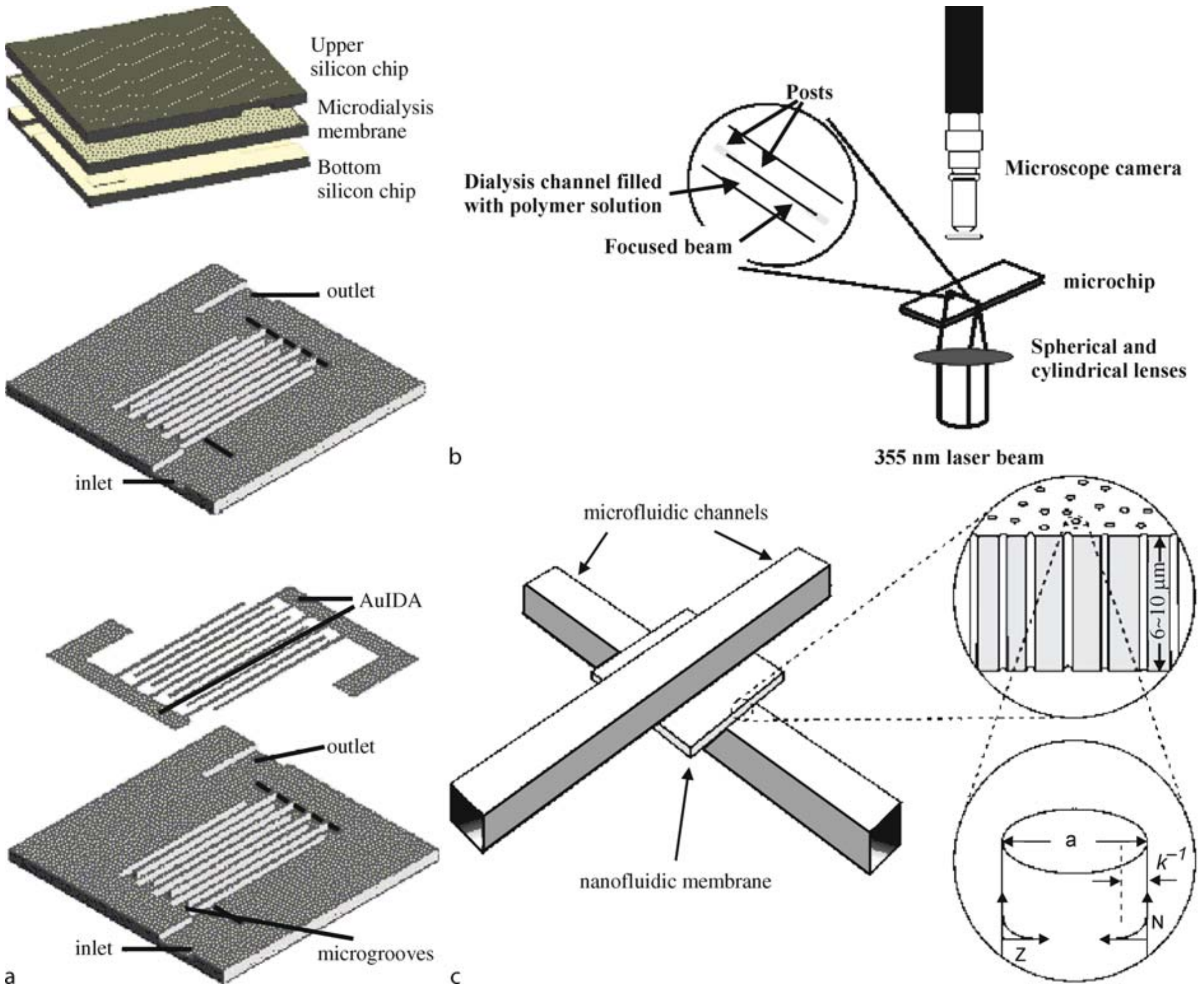

Microdialysis, Figure 4 (**a**) Microdialysis membrane sandwiched between two etched sets of silicon microchannels with interdigitated sensing electrodes. Image taken from [10]. (**b**) Schematic of optical setup for phase separation polymerization to define the microdialysis membrane. Image taken from [11]. (**c**) Schematic of crossed microfluidic channels separated by a nanoporous microdialysis membrane. Image taken from [12]

Widmer and colleagues in 1990, in which silicon chip analyzers which incorporate sample pretreatment, separation and detection played a fundamental role [9]. The advantages of microchip analysis include the ability to analyze minute samples, speed of analysis, reduced cost and waste and portability. Ever since, the μTAS has drawn a huge amount of attention and researchers have been attempting to incorporate a microdialysis-based continuous sampling component. Some of the devices which have been fabricated are shown in Fig. 4.

One approach towards integrating microdialysis membranes with microfluidic systems has been to sandwich a commercially available dialysis membrane between two microfluidic chips. Pan and colleagues adopted this approach for continuous glucose monitoring [10]. In their experiment a commercially available microdialysis probe was used to continuously collect glucose from an analyte solution and the dialysate from the microdialysis probe was introduced into an analysis module consisting of two sets of microfluidic channels with a patterned interdigitated electrode array separated by a microdialysis membrane (Fig. 4a). The dialysate containing the glucose is introduced into one set of channels and allowed to diffuse through the microdialysis membrane into the other set of channels containing glucose oxidase (GOx) enzyme which oxidizes the glucose into gluconic acid and hydrogen peroxide. The hydrogen peroxide is subsequently oxidized on the electrode surface to produce a working current which is proportional to the glucose concentration in the dialysate. The microdialysis membrane was sandwiched between the two sets of channels to prevent the GOx from diffusing into the glucose dialysate and being depleted from the system

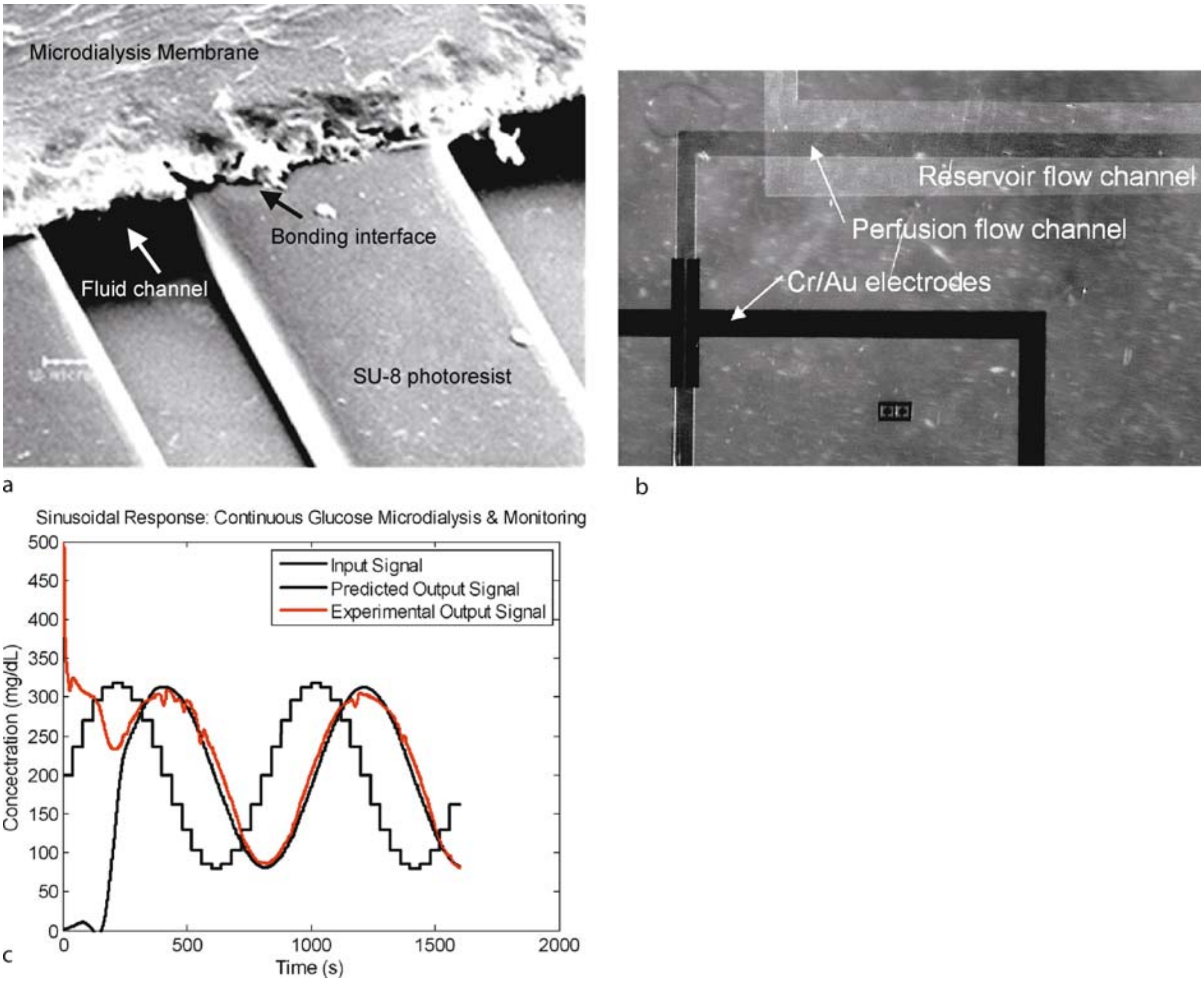

Microdialysis, Figure 5 (**a**) SEM image of a polycarbonate microdialysis membrane bonded onto microfluidic channels formed in SU-8 photoresist. Image taken from [13]. (**b**) Two-compartment system with integrated conductance sensing electrodes. The reservoir and perfusion flow channels are separated by a bonded microdialysis membrane. Image taken from [14]. (**c**) The response to a sinusoidal input demonstrated with a glucose microdialysis system. The perfusion flow rate is 0.5 μl/min and the device is operated at a recovery of 99%. Image taken from [15]

and thus improves sensor lifetime. In this system the layers are held together by mechanical pressure.

A second approach by Kirby and colleagues [11] to integrating microdialysis membranes with microfluidic channels used a UV laser photopolymerization technique to lithographically define a patterned nanoporous dialysis membrane within a microfluidic channel (Fig. 4b). A prepolymer solution is allowed to flow through the microfluidic structure and patterned by phase separation photopolymerization using a shaped UV laser beam. The microdialysis membrane was defined along a series of posts which separated to compartments within a microfluidic network. By changing polymer precursors, the degree of crosslinking could also be adjusted to affect the membrane MWCO. Countercurrent flow operation was demonstrated. The first dialysis demonstration used a membrane with a MWCO below 5700 which was designed for desalting of protein solutions. A low molecular weight rhodamine dye was observed to freely penetrate across the membrane which a higher molecular weight (MW 5700) insulin protein could not. Next, a higher MWCO membrane was defined for fractionation of a mixed protein solution. Using this membrane, lactalbumin (MW 14,000) was seen to permeate across the membrane.

A final approach to integrating microdialysis membranes with microfluidics is based on direct bonding of microdialysis membranes with the microchannel structures. One such structure was developed by Bohn and colleagues [12] and is shown in Fig. 4c. Here microchannels are defined in polydimethylsiloxane (PDMS) in the soft lithography pro-

cess, activated in an oxygen plasma and directly bonded to a nanoporous track-etched polycarbonate membrane. Bohn and colleagues used this device for electrically controlling sample manipulation after capillary electrophoresis (CE) separation of arginine and glutamate. After they were separated, either the arginine or glutamate was collected through the microdialysis membrane into a different microfluidic channel by controlling the time at which the gate was biased to collect the sample flowing through that area of the CE column.

Finally, a novel on-chip microdialysis system for glucose sensing based on direct microdialysis membrane bonding onto microfluidic channels (Fig. 5a) has been developed by Hsieh and Zahn [13–15]. The microdialysis device is designed as a miniaturized probe for direct contact between the dialysis membrane and tissue of interest. The system is designed to allow high recovery of analytes with a smaller diffusional surface area and lower flow rates resulting in a less invasive, more precise microdialysis probe. In addition, the large dialysis surface area to microchannel volume ratio and short diffusional path allow higher recoveries and faster equilibration times for higher frequency sampling rates. Hsieh and Zahn have demonstrated glucose microdialysis [13, 15] using this system. They have also integrated an in situ glucose biosensor directly with the microdialysis system (Fig. 5b, c) and demonstrated continuous sensing in a solution where the solution concentration changed sinusoidally in time [15]. The system was able to track the glucose changes with minimal phase lag at a recovery of 99% (Fig. 5c).

Future Directions for Research

Microdialysis still has great potential to impact many research areas. The designs of probes and the choice of dialysis membrane are crucial. Future research effort must be used to characterize the mass transfer characteristics of different membrane materials and their fouling properties, especially in the context of biofouling when dialyzing biological solutions such as blood. Part of the success of microdialysis is due to the development of chemical analysis methods. A combined sampling device and analytical instrument allow continuous monitoring with minimal disturbance to the surroundings. In the future, microfabrication technology holds promise to integrate these two components and improve temporal resolution with higher analytical throughput. Such systems could also be exploited to produce miniaturized reverse osmosis or ultrafiltration devices. Another area of opportunity lies in the integration of active membranes for selective separations such as the use of ion exchange membranes to allow electrodialysis to separate positively and negatively charged chemical species. The ability to perform on-chip microdialysis with electrical conductivity feedback to determine ionic strength allows very sophisticated manipulation of solution properties for biochemical reaction engineering. In this way enzymatic reactions may be tailored with feedback control to proceed effectively. By monitoring ionic concentration in the reaction chamber and enzyme reaction rate, salt may be removed or added to a reaction as needed to improve the efficiency of the enzymatic reactions. Ultimately dialysis biochips may be integrated with other microfluidic components such as micropumps, micromixers and microreaction chambers to allow real-time processing of biological materials. Finally, by utilizing the high surface to volume ratio and highly parallel fluidic channels, these devices may allow use in a low-cost, low flow rate continuous kidney dialysis module. The microdialysis devices may be assembled in a parallel fashion to fluid reservoirs to continuously filter blood and remove waste for patients suffering from kidney failure.

Cross References

► Diffusion
► Microfilters

References

1. Plock N, Kloft C (2005) Microdialysis – theoretical background and recent implementation in applied life-sciences. Eur J Pharm Sci 25(1):1–24
2. Ungerstedt U (1991) Introduction to Intracerebral Microdialysis. In: Robinson TE, Justice JB (ed) Microdialysis in the Neurosciences. Elsevier, Amsterdam, pp 3-22
3. Miró M, Frenzel W (2005) The potential of microdialysis as an automatic sample-processing technique for environmental research. Trends Anal Chem 24(2):324–333
4. Torto N, Mwatseteza J, Laurell T (2001) Microdialysis Sampling – Challenges and New Frontiers. LCGC Eur 19(3):462–475
5. Benveniste H, Hansen AJ (1991) Practical aspects of using microdialysis for determination of brain interstitial concentrations. In: Robinson TE, Justice JB (eds) Microdialysis in the Neurosciences. Elsevier, Amsterdam, pp 81-100
6. Bungay PM, Morrison PF, Dedrick RL (1990) Steady-state theory for quantitative microdialysis of solutes and water in vivo and in vitro. Life Sci 46(1):105–119
7. Morrison PF, Bungay PM, Hsiao JK, Mefford IN, Dykstra KH, Dedrick RL (1991) Quantitative Microdialysis. In: Robinson TE, Justice JB (ed) Microdialysis in the Neurosciences. Elsevier, Amsterdam, pp 47-80
8. de Jong J, Lammertink RG, Wessling M (2006) Membranes and microfluidics: a review. Lab Chip 6(7):1125–1139
9. Manz A, Graber N, Widmer HM (1990) Miniaturized total chemical analysis systems: A novel concept for chemical sensing. Sens Actuators B 1(1–6):244–248

10. Pan M, Guo X, Cai Q, Li G, Chen Y (2003) A novel Glucose Sensor System with Au Nanoparticles Based on Microdialysis and Coenzymes for Continuous Glucose Monitoring. Sens Actuators A: Phys 108(1–3):258–262
11. Song S, Singh AK, Shepodd TJ, Kirby BJ (2004) Microchip Dialysis of Proteins Using in Situ Photopatterned Nanoporous Polymer Membranes. Anal Chem 76(8):2367–2373
12. Kuo TC, Cannon DM Jr, Chen Y, Tulock JJ, Shannon MA, Sweedler JV, Bohn PW (2003) Gateable Nanofluidic Interconnects for Multilayered Microfluidic Separation Systems. Anal Chem 75(8):1861–1867
13. Hsieh YC, Zahn JD (2005) Glucose recovery in a microfluidic microdialysis biochip. Sens Actuators B: Chem 107(2):649–656
14. Hsieh YC, Zahn JD (2006) On-chip microdialysis system with flow through sensing components. Biosens Bioelectron 22:2422–2428
15. Hsieh YC, Zahn JD (2007) On-chip Microdialysis System with Flow-through Glucose Sensing Capabilities. J Diabetes Sci Technol 1(3):375–383

Microdrone

► Microrotorcraft

Microdroplet Transport

► Thermocapillary Pumping

Micro-Encapsulation

Synonyms

Encapsulation

Definition

Micro encapsulated TLCs have a shell of polymer and are spherical particles which can be put into liquids (which do not chemically attack the encapsulation) or – with a binder – sprayed onto surfaces. Micro-encapsulated TLCs are less vulnerable to environment effects but show worse temperature indicating properties than pure TLC substance.

Micro Energy Conversion Devices

Luc G. Fréchette
Department of Mechanical Engineering, Université de Sherbrooke, Sherbrooke, QC, Canada
luc.frechette@USherbrooke.ca

Synonyms

Micro power generation; Power MEMS; Micro heat engines; Microengines; Micro fuel cells; Micro energy harvesting; Micro energy scavenging; Micro propulsion; Micro coolers

Definition

Micro energy conversion devices are miniature systems that convert available energy into a more useful form, such as the conversion of chemical, thermal, or solar energy into electrical power, propulsion or cooling. They usually integrate fluidic, thermal, mechanical, and/or electrical components on-chip to achieve the desired output. Typical energy conversion microsystems, or *power MEMS*, include micro heat engines (microturbines, internal combustion engines), micro fuel cells, vibration energy harvesters, micro rocket engines, and micro coolers.

Overview

The availability of energy in the form of electricity or storable fuels has shaped the way we live and drastically improved our quality of life. For example, energy has been an enabling factor for the industrialization of our society, has allowed the development of planes, trains, and automobiles for transportation, and provides heating, cooling, and cooking in our homes. At smaller scales however, the availability of portable power sources or propulsion is limited. Electric power sources are mostly based on electrochemical storage, such as primary and rechargeable batteries, which are characterized by limited energy density, shelf life, and disposal restrictions. A need for more compact and long lasting power sources stems from the growing range and functionality of portable consumer electronics, such as mobile phones, handheld multimedia players, and laptop computers, as well as handheld biomedical or chemical instruments. Wireless sensors are also constrained by energy requirements, which holds back the implementation of distributed sensors for pervasive intelligence and monitoring of our environment. Similarly, the applications of small mobile robots and micro air vehicles remain marginal since power sources for their propulsion can only allow short duration missions and limited autonomy.

An alternate approach to traditional batteries consists of using MEMS (microelectromechanical systems), microfabrication, and nanotechnologies to implement a variety of energy conversion microsystems. These *power MEMS* could provide electrical power, propulsion, or cooling based on traditional operating principles or on novel prin-

ciples enabled by the small scale or the semiconductor's properties. This chapter will outline the energy conversion principles available and illustrate their MEMS implementation, following a discussion on energy sources and metrics.

Energy and Power Sources

Energy is available in a wide range of forms from our environment, as outlined in Table 1. Conventional energy conversion approaches are well developed at the macroscale to provide electricity, propulsion, heating, or cooling from these sources. A power source can be defined as the combination of an energy *source* with an energy *conversion* unit. An energy *storage* element can also be included in order to accommodate differences between the rate of energy (i. e. power) required by the load and that available from the source. For example, a photovoltaic solar cell can charge a battery such that electrical power remains available after the sun sets. Storage is also required for mobile systems that are not collocated with the energy source, such as the fuel tank of an automobile. Power sources are also characterized by their centralized or distributed nature. Large-scale thermal power plants and hydroelectric stations provide power generation from a central location; the useful energy is then transported to the points of use. Alternatively, solar cells arrays powering individual homes are distributed power sources, collocated with the load.

Scale and Metrics

The size of the energy conversion element is scaled according to the power required by the load, $\dot{W}_{\text{load}}$. For watt or sub-watt level applications, such as wireless sensors and portable electronics, miniature power generation units would be sufficient, suggesting the applicability of MEMS technology to meet this need.

For systems with stored energy (batteries or fuel), the volume of storage scales with the amount of energy required between replenishments, ΔE_{fuel}. The energy required is simply the product of the average rate of energy consumption, $\mathrm{d}E_{\text{fuel}}/\mathrm{d}t = \dot{E}_{\text{fuel}}$, by the time of operation, $\Delta t : \Delta E_{\text{fuel}} = \dot{E}_{\text{fuel}} \Delta t$. For a given specific energy of the fuel, h_{fuel}, expressed in J/kg or Whr/kg (1 Whr = 3600 J), the mass of stored energy is then $m_{\text{fuel}} = \Delta E_{\text{fuel}}/h_{\text{fuel}}$. Energy density of the fuel is defined as the energy per unit volume of storage, typically expressed in J/cm^3 or Whr/cm^3, and calculated as the mass of stored energy divided by its gravimetric density.

The rate of energy consumption from the source is however greater than the power delivered to the load, since the conversion process is never 100% efficient. One can define the energy conversion efficiency, η, as the ratio of power delivered over the rate of energy consumption:

$$\eta = \frac{\dot{W}_{\text{load}}}{\dot{E}_{\text{fuel}}} \tag{1}$$

This metric is important for power sources with stored energy since low conversion efficiency will increase the energy consumption and reduce the time between replenishments, for the same storage volume and same average power to the load. From the first law of thermodynamics, the inefficiency in the conversion process will translate into heat rejection to the surroundings, either by convection, conduction or radiation:

$$\dot{Q}_{\text{rejected}} = \dot{m}_{\text{fuel}} h_{\text{fuel}} - \dot{W}_{\text{load}} \tag{2}$$

Systems that directly extract their source of energy from the environment are referred to as energy *scavenging* or *harvesting* approaches. In this case, minimal or no storage is required since the system is continuously replenished in energy. The concept of energy density becomes less relevant because the energy is not stored in the system. This has the benefit of reducing the size of the power source, but at the expense of loosing some autonomy since the energy availability is subject to changing environmental conditions. A combination of energy storage and scavenging can offer an interesting compromise.

Specific power and power density are also an important metrics, defined as the ratios of power delivered per unit mass or volume, respectively. For power sources that are not dominated in size by the storage unit, such as energy scavenging systems or high power application with short duration, the power density will define the scale of the device to meet a given power requirement.

Basic Methodology

A broad range of micro energy conversion systems can be implemented based on MEMS technology and microfabrication processes. Many large scale energy conversion systems operate using a working fluid either to implement a thermodynamic cycle or to transport thermal and chemical energy. The implementation of micro energy conversion systems based on these principles requires the miniaturization of fluidic and thermal components, raising new challenges in the related fields. Alternatively, the use of semiconductor processing introduces materials with interesting solid-state physics that can also be leveraged for energy conversion. This section will outline the underlying

Micro Energy Conversion Devices, Table 1 Available sources of energy and examples of power generation approaches

Energy Sources	Power Generation	Usable Energy
Mechanical • Wind, Hydro, Tides • Structural Vibrations • Sound	• Wind mills • Hydroelectric plants • Vibration harvesting	• Electricity
Chemical • Hydrocarbon fuels • Glucose, Biofuels • Battery chemistries	• Engines, turbines • Human body • Batteries, fuel cells	• Propulsion • Electricity • Muscular activity
Radiation • Solar • Nuclear	• Photovoltaic cells • Solar collectors • Nuclear power plant	• Electricity • Heating
Thermal • Geothermal • Waste heat	• Heat pumps • Thermoelectrics	• Heating & cooling • Electricity

principles and engineering approaches for micro energy conversion.

Direct Solid–State Energy Conversion

Photovoltaics

A photovoltaic cell is a solid-state device that directly converts light into electricity. Upon absorption of incident light, electrons in the material gain sufficient energy to rise in the conduction band, and are free to travel. When generated at the junction of a diode, the free electrons will travel only in one direction, creating a useful current. Most solar cells are tailored to absorb the sun wavelengths and are based on silicon. Efficiencies of solar to electrical energy conversion range from 6% for low-cost amorphous silicon cells to over 30% for exotic semiconductor cells with multiple junctions (each tailored to absorb and generate electrons in a distinct band of the sun's spectrum). Power per unit surface area is limited by the incident radiation, ranging from $0.1\ \mathrm{W/cm^2}$ in direct sunlight to $0.1\ \mathrm{mW/cm^2}$ for indoor lighting. For a cell efficiency of 10%, the output electrical power per unit area would be a factor of 10 lower than these values.

Photovoltaic cells are currently manufactured using silicon processing technologies and novel approaches are in development using polymers and nanostructures. By achieving cost reductions, photovoltaics are expected to take an important role in macro power generation. They can also be used as micro power sources, as long as the power and size meet the needs of the application.

Thermophotovoltaics

Photovoltaics can also be used to directly convert thermal radiation into electricity. Here, a photon emitting surface is heated in the range of 1200 – 1600 K, by combustion or nuclear reactions. It is coupled with a photovoltaic cell specifically chosen to absorb the photons in the near infrared and infrared range of the spectrum, emitted by the hot surface. This approach requires a high temperature heat source and careful thermal management and isolation.

Thermoelectrics

Thermoelectric materials generate a current or potential when they are subjected to a temperature gradient. They typically consist of heavily doped semiconductors, with free carriers that carry both heat and charge. The free carriers are electrons in an n-type materials and holes (or electron vacancies) in p-type materials. Carriers in the hot region are faster and tend to travel further, leading to a higher density of carriers in the colder region of the material. Since the carriers are charged (− electrons and + holes), the non-uniform density of carriers induces an electric potential in the material. This phenomenon was first discovered by the German physicist T. J. Seebeck in 1821. The thermoelectric power, or Seebeck coefficient, S, represents the thermoelectric potential induced per unit temperature difference:

$$S = \frac{\Delta V_{\mathrm{TE}}}{\Delta T} \tag{3}$$

The efficiency of thermoelectric power generation is the ratio of electrical power produced to the heat rate conducted through the material. The non-dimensional figure of merit typically used for thermoelectric materials is:

$$zT = \frac{S\sigma^2}{k} T \tag{4}$$

where σ is the electrical conductivity of the material and k is its thermal conductivity. Thermal power generation efficiency will be a function of the material and operating temperatures. Interesting performance is achieved typically by alloying or nano-structuring the material to scatter the phonons and therefore reduce the thermal conductivity, without affecting the carrier mobility (electrical conductivity). Such materials include heavily doped bismuth telluride (Be_2Te_3) for applications below 450 K or SiGe for temperatures up to 1300 K, which have demonstrated thermal to electrical conversion efficiencies up to 4.5% and 7%, respectively.

Thermoelectric devices can also be used for cooling. By forcing a current through the material, a temperature gradient is created. This is the inverse of the Seebeck effect, and is referred to as the Peltier effect.

Thermoelectric devices are traditionally fabricated by assembling small blocks of n-type and p-type material in an array, interconnected in series with electrodes. A successful system implementation is the radioisotope thermoelectric generator (RTG) for deep space probes. Microfabrication technologies for thermoelectric materials are however being developed to create low-cost integrated power and cooling microsystems.

Thermionics

Electrons on a very hot surface (1000 – 3000 K) can reach sufficient thermal vibration energy to overcome the electrostatic forces holding it on the surface and escape the solid. Useful electric power can be created by collecting the emitted electrons on a cooler electrode at a slightly higher potential overcome by the electrons (0.5 – 1 V).

Electromechanical Micro-Generators

Vibration Energy Harvesting

Mechanical vibrations are omnipresent in our surroundings, ranging from the large amplitude vibrations in rotating machinery to barely noticeable vibrations of windows and walls. For wireless sensor nodes or other distributed applications, these vibrations can be a constant source of energy by converting the mechanical motion into electricity. This process is commonly referred to as *vibration energy scavenging or harvesting*. Inertial harvesters use the vibration of a structure to excite a miniature spring-mass-damper system attached at one point, such as an anchored cantilever beam with an end mass. Ideally, the natural frequency of the harvester will coincide with the frequency of the excitation, such that resonance will amplify the displacement. A limitation of this approach is the need for a known and constant source of vibrations. The induced displacement is then converted to electricity through electromagnetic, electrostatic, or piezoelectric principles. An alternate approach is strain-based vibration energy harvesting, which consists of deforming a device attached to a structure by at least two points, again producing electricity according to the same principles. A disadvantage of strain-based harvesting is the need to be closely coupled to the structure. On the other hand, it can operate over a wide range of frequencies, unlike inertial harvesters.

Radioisotope

Radioactive materials can be used as energy sources for long-lasting compact power sources. The most common approach is thermal, where the alpha particles are stopped very easily and their decay energy is converted into thermal energy. Heat can then be converted to electricity using thermoelectric modules or thermodynamic micro heat engines. An alternate approach is to collect the charged particles emitted from the radioactive material on a flexible structure. The accumulated charges can induce an electrostatic force on the structure, therefore inducing a deflection. This deflection can then produce electrical power by electromagnetic, piezoelectric or electrostatic principles.

Wind Energy Harvesting

Ambient air flow or forced convection can also be a source of energy for distributed environmental sensors or similar autonomous devices exposed to a flow. The airflow can induce the rotation of a microturbine (similar to large-scale wind mills) or the oscillation of a structure. This mechanical energy can then be converted to electricity by electromagnetic, piezoelectric or electrostatic principles.

Electrochemical Power Generation

Micro Fuel Cells

Direct chemical to electrical energy conversion can be accomplished in fuel cells. Many types of fuel cells have been implemented at small scale, including low temperature ($< 100\,°C$) proton exchange membrane fuel cells (PEMFC), direct methanol fuel cells (DMFC), and formic acid fuel cells, as well as high temperature ($> 600\,°C$)

solid oxide fuel cells (SOFC). Micro fuel cell configurations are typically planar, consisting of layered cathode, electrolyte, and anode materials with flow field plates covering both electrodes. A fuel, such as hydrogen, is continuously provided to the anode, where it is oxidized to form protons (H^+) and electrons. Oxygen from ambient air is reduced at the cathode, at a different electric potential. Both half-reactions are catalytic, typically requiring the presence of a noble metal such as platinum, palladium and/or ruthenium on the electrodes. Electrons are allowed to flow from the anode to the cathode through an external circuit, providing the electrical power. The reaction is completed by allowing the ions to flow through an electrolyte that separates the anode and cathode compartments. In solid oxide fuel cells, the O^{2-} ions diffuse through a ceramic electrolyte, whereas in most other types of fuel cells, the H^+ protons travel through the polymer or liquid electrolyte. Water is formed at the cathode as a product of the reaction, as well as CO_2 at the anode for methanol fuel cells.

The performance of a fuel cell is characterized by its output voltage and current density, which is defined as the current per unit area of the cell. The fuel cell voltage drops at higher currents due to increasing catalytic activation losses, ionic and electronic resistances in the cell, and mass transport limitations. The cell efficiency is therefore proportional to the ratio of measured voltage to the ideal cell voltage (1.23 V and 1.21 V for hydrogen and methanol at 25 °C, respectively).

From a system perspective, micro fuel cell power sources must include auxiliary components in addition to the fuel cell itself. Hydrogen-based PEMFCs require high pressure hydrogen gas reservoir and pressure regulation or metal-hydride storage with temperature control. Methanol-based fuel cells can either operate by reforming the fuel in a reactor upstream to liberate the hydrogen, or directly breaking down the fuel catalytically at the anode. Either approach also requires flow supply and water management auxiliary equipment, as well as electrical circuits and/or storage.

Microbatteries

In contrast to fuel cells, batteries do not consume the reactants or emit products. The electrodes in a battery store the chemical energy and change as the battery is discharged. Microbatteries leverage thin film deposition processes to form planar configurations that can be more readily integrated with MEMS and microelectronics. Lithographic patterning and micromachining are also used create advanced electrode geometries that enhance the recharging capabilities and power densities of batteries.

Thermodynamic Micro Heat Engines and Coolers

Micro heat engines are miniature systems that implement a thermodynamic power cycle at the microscale. The approach consists of using a fluid, gas or liquid, to convert thermal energy into mechanical energy. The fluid is sequentially compressed, heated, expanded and cooled, such that more work is done by the fluid during the expansion compared to that required for its compression. The result is net mechanical power generation from the heat engine, which can be used for propulsion or electrical power generation. This output power is equal to the difference between the heat added to the fluid and the heat removed during cooling. The efficiency of a heat engine is defined at the ratio of net power output to heat rate input:

$$\eta = \frac{\dot{W}_{\text{out}}}{\dot{Q}_{\text{in}}} \tag{5}$$

The maximum achievable efficiency for a thermodynamic power cycle is that of the Carnot cycle, which adds and removes heat from the working fluid at constant temperatures, T_h and T_c respectively:

$$\eta_{\text{carnot}} = 1 - \frac{T_c}{T_h} \tag{6}$$

Work from heat engines typically scales as the product of mass flow through the engine and the change of enthalpy during the (adiabatic) expansion. Since, fundamentally, thermodynamics are scale independent, one can expect similar enthalpy changes for macro and micro scale engines. The power therefore scales as the mass flow, itself proportional to the cross sectional area of the engine (for similar flow velocities): $\dot{W} \propto \dot{m} \propto A \propto l^2$. Power density of the engine therefore scales as the inverse of its characteristic length scale, l:

$$\frac{\dot{W}}{V} \propto \frac{l^2}{l^3} \propto \frac{1}{l} \tag{7}$$

By miniaturizing heat engines, we therefore expect larger power levels per unit volume. In practice however, the technological challenges of implementing a thermodynamic cycle will differ with scale since heat transfer, friction, and leakage losses tend to be more important in microsystems compared to their large scale brethren. This would reduce the achievable power density and efficiency. Various types of micro heat engines are possible, characterized by their thermodynamic cycle and their mechanical implementation, as described next.

Micro Internal Combustion Engines (Otto Cycle)

A piston moves with a reciprocating motion to alternatively compress and expand an enclosed gas. Upon compression, fuel is burnt with the gas to release heat. The high temperature gas expands by pushing on the piston, which provides mechanical work. The combustion products are then exhausted to the atmosphere and replaced with fresh cool air before the next compression process. High temperatures, and therefore efficiency, can be achieved since heat is generated by combustion directly within the enclosed chamber. Cooling is accomplished externally to the engine, by rejecting the hot combustion products to the atmosphere. Challenges due to miniaturization include: sealing around the movable piston to allow sufficiently high pressure ratios; friction and lubrication between the movable parts given the alternating loads; mass transfer and heat transfer during the combustion process that can lead to insufficient time for combustion or quenching of the flame by heat loss to the nearby walls. Expected power densities range from 0.1 to 10 $\mathrm{W/cm^3}$.

Micro Gas Turbine Engines (Brayton Cycle)

A continuous flow of air is drawn from the ambient into a rotating compressor. The pressurized air is then mixed with fuel and burnt as it flows through a combustor. The hot gases expand through a turbine, imparting torque on it to drive the compressor, and potentially a generator, that are attached to the turbine by a common shaft. The rotating motion instead of an alternating motion reduces the mechanical complexity compared to internal combustion engines. Furthermore, the continuous flow rate and high temperatures suggest higher power densities, on the order of $1-100\ \mathrm{W/cm^3}$. High tangential speeds are however required to achieve sufficient efficiency of the turbomachinery components, to compensate the effect of scale reduction on the Reynolds number.

Micro Steam Turbines (Rankine Cycle)

Steam turbines differ from gas turbines mainly by pressurizing the working fluid in liquid state with a pump, instead of in gaseous state with a compressor. The pressurized water is then evaporated from an external heat source. The steam is expanded through a turbine, which drives the pump and a generator. Component efficiency is less critical compared to a gas turbine since pressurizing a liquid requires dramatically less power per unit flow rate than compressing a gas. Lower rotation speeds are therefore acceptable. There is however a trade-off of lower power density and efficiency since the achievable cycle temperature is limited by heat transfer to the working fluid and by the challenges of managing two-phase flow in a microsystem. Heat must also be rejected to the atmosphere through a heat exchanger since the device must operate on a closed cycle, if fresh water is not available.

Micro Coolers

Refrigeration cycles can also be implemented in microsystems. The vapor compression cycle, which is the inverse of the Rankine cycle *(Micro steam turbine)*, consists of compressing a gas and consequently rising its temperature above ambient conditions. The high pressure fluid is then condensed by rejecting heat to the surroundings. The fluid pressure is then reduced as it flows across a valve, which also drops its temperature below the ambient temperature. The fluid can then absorb heat from the region to be cooled, as it evaporates at low pressure. Challenges include developing efficient compressors at microscale and managing two-phase flows.

Micro Propulsion

In addition to power generation, microsystems can be used for propulsion in small scale applications, such as attitude control of nanosatellites and thrust for micro air vehicles. Micro thrusters or rocket engines consist of a chamber that feeds a convergent–divergent nozzle through which mater is ejected at high speed to provide thrust in the opposite direction. By applying Newton's second law to a control volume enclosing the thruster and the propellant reservoir, one can express the thrust, F, as a function of the total mass, m, and exit velocity, $\boldsymbol{V}_\mathrm{e}$. Noting that the mass decreases due to the flow rate of propellant through the nozzle, $\dot{m}_\mathrm{p}$, the thrust is expressed as:

$$\boldsymbol{F} = \frac{\mathrm{d}\left(m\boldsymbol{V}_\mathrm{e}\right)}{\mathrm{d}t} = \frac{\mathrm{d}m}{\mathrm{d}t}\boldsymbol{V}_\mathrm{e} = -\left|\dot{m}_\mathrm{p}\right|\boldsymbol{V}_\mathrm{e} \tag{8}$$

Assuming that similar exit velocities can be achieved at micro and macro scales, the thrust is proportional to the mass flow, hence to the cross section area or to the square of a characteristic length scale: $F \propto \dot{m} \propto A \propto l^2$. The thrust to weight ratio of a micro thruster is therefore expected to increase as it is miniaturized:

$$\frac{F}{mg} \propto \frac{l^2}{l^3} \propto \frac{1}{l} \tag{9}$$

Another metric for propulsion systems is the specific impulse, I_sp, which represents the thrust per unit mass flow rate of propellant. Ideally, I_sp is not a function of scale, but depends mostly on the type of propellant used. In practice, aerodynamic losses due to lower Reynolds number

flows in the nozzle and non-ideal nozzle geometries (constrained by microfabrication) can reduce the achievable I_{sp} in micropropulsion systems.

The source of energy can be in the form of a compressed gas, electricity, or a chemical fuel. Cold gas thrusters simply exhaust a compressed gas through a convergent-divergent nozzle to reach supersonic velocities at the exit. Higher thrust and I_{sp} can be achieved by heating the gas, either through resistive heating or combustion. Two types of reactants can be used for combustion: solid or liquid fuels. For space applications, fuel and oxidizer must both be carried on-board. On the other hand, air-breathing applications can use oxygen from the ambient air, leading to dramatically higher I_{sp}.

In contrast to gas thrusters, ion thrusters accelerate charged particles with an electrostatic field. This approach leads to the highest I_{sp} but typically very low thrust levels.

Thrusters can be used in either continuous or pulsed operation, according to the application. Miniature rocket launchers and micro air vehicles require a continuous thrust and are best served by a unique thruster or engine with a continuous feed of propellant. Alternatively, digital micropropulsion refers to an array of single-use thrusters that provide a small impulse (short burst of thrust) to accurately orient a small spacecraft or correct a vehicle's trajectory.

Auxiliary Components

Many micro energy conversion systems require a host of auxiliary components along with the core elements mentioned above. These can include: micro heat exchangers and combustors to provide heat; valves and flow regulators to control the flow of fuel or coolant; temperature, pressure, or speed sensors along with electronics to control the device operation; as well as power electronics and electrical energy storage.

Key Research Findings

As described above, many approaches can be taken to convert energy at small scales. This section describes some of the achievements and challenges identified in three of the most researched areas for which microfluidics are of central importance: micro fuel cells, micro heat engines, and micro thrusters. The focus will be on device implementations that leverage MEMS and microfabrication technologies.

Micro Fuel Cells

Although standard techniques can be used to fabricate miniature fuel cells, microfabrication approaches have been increasingly used to implement various components and subsystem of fuel cells power sources. Initially, most attention was devoted to microchannel flow fields for fuel and oxidizer delivery, leveraging the increase in mass transport at small scale, but at the cost of increased pressure drop. Since miniature pumps and blowers to force air through the cell are neither efficient nor small enough for watt-scale applications, air-breathing configurations driven by free convections have gained interest. Unfortunately, this configuration emphasizes the challenge of water accumulation at the cathode. Microfabrication has then been used to replace standard gas diffusion layers that cover the electrodes, such as carbon cloth or paper, by tailored silicon structures for water management. Micro and nanostructures, such as porous silicon, have also been studied to create the porous electrodes and ionic transfer media. Although to date, the best performance of μPEMFC and μDMFC have been demonstrated with traditional carbon-based porous electrodes and polymer electrolyte membranes, novel configurations enabled by micro and nanofabrication offer the promise of increased control over the multiple transport phenomena that must coexist in a fuel cell, such as gas diffusion, water removal, electronic conduction, and ionic conduction. Micro fuel cells operating in laboratory settings on hydrogen have been demonstrated up to $300\,\mathrm{mW/cm^2}$ and average voltages of $0.4-0.7\,\mathrm{V}$, while those operating on methanol have shown a maximum of $100\,\mathrm{mW/cm^2}$ and voltages in the range of $0.2-0.3\,\mathrm{V}$ [1]. Micro-DMFCs have the benefit of using a liquid fuel with high energy density, but suffer from relatively low efficiency ($< 30\%$) and power density. Methanol unfortunately has a tendency to crossover the membrane, from the anode to the cathode, so it is commonly diluted in water (to approx. 7%) to reduce this loss. To ensure proper mass transport of reactants at the electrodes, it is also important to ensure removal of the gaseous CO_2 generated at the anode and liquid water at the cathode. The management of two-phase flow and bubbles in microchannels is therefore of importance. Micro-PEMFCs have demonstrated higher efficiencies ($> 40\%$) and power densities than methanol fuel cells, suggesting more compact power sources. The main challenge for practical applications is the fuel: hydrogen. Although hydrogen has the highest specific energy (per unit mass), its gaseous state leads to very low energy density (per unit volume). Metal-hydride storage or compressed hydrogen tanks remain to be developed at small scale. An alternate approach consists of using a micro reformer to extract hydrogen from a liquid fuel. Such chemical microsystems are being studied, but face the challenge of providing sufficiently pure hydrogen to prevent poisoning of the Pt catalyst. Micro solid oxide fuel cells (SOFC) of planar, tubular, or swiss roll configurations are also under development [2]. They accept a wider range of fuels, but their high

M

operating temperatures (up to 800 °C) introduce material challenges and stringent thermal insulation requirements with the surroundings for viable implementation.

Micro Heat Engines

Two main approaches have been used to implement micro heat engines: precision machining of metals (mesoscale) or silicon-based microfabrication [3]. Mesoscale heat engines are typically miniature versions of their large scale counterparts and operate in the 10 – 1000 W range. Microfabricated heat engines must however be reinvented to comply with the geometric constraints imposed by the planar nature of lithographic and etching processes. They can be further miniaturized to meet the needs at lower power levels.

Internal combustion engines implementing the Otto cycle have been studied based on the rotary engine with a triangular rotor (Wankel), as well as free and spring loaded linear pistons. Challenges in terms of sealing, wear/lubrication, and combustion have led the research towards the mesoscopic implementation however. MEMS-based high speed rotating microturbines have also been developed for propulsion and power generation [4]. Millimeter-scale rotors in the shape of a disk are micromachined from the bulk silicon using deep reactive ion etching (DRIE) and integrated with fluid film bearings, combustors and electromagnetic or electrostatic machinery using wafer bonding. Air-driven microturbines have been operated over 1.4 million RPM, demonstrating the feasibility of air bearings, the mechanical strength of single crystal silicon, and sufficient precision to make adequately balanced rotors to reach the high speeds required for microturbomachinery [5]. Efficient combustion using hydrogen and hydrocarbon fuels has been demonstrated in microfabricated chambers of less than 1 cm^3, with complete combustion and exit gas temperatures over 1800 °C. Permanent magnet and induction generators have also been demonstrated at power levels on the watt scale and with conversion efficiencies near 50%. These building blocks require further development for stand-alone and high temperature operation. Their integration into complete microsystems is also in progress to make micro gas turbines engines (Brayton cycle, [4]) and micro steam turbines (Rankine cycle, [6]). Predicted performance levels range from 1 – 100 W/cm^3 depending on the operating conditions, with overall conversion efficiencies up to 10%. One main challenge is thermal isolation approaches and materials to prevent heat leakage between the hot and cold portions of the thermodynamic cycle. For micro gas turbines, conduction from the turbine to the compressor can dramatically reduce the compressor efficiency and the power output of the cycle. For micro steam turbine cycles, sufficient insulation must be ensured to prevent evaporation in the pump and condensation in the turbine. These thermal challenges are preponderant in microsystems due to the short length scales and the high thermal conductivity of silicon and silicon carbide. Lubrication of the rotating components must be done with the working fluid (air or steam), typically using internally pressurized hydrostatic or hydrodynamic fluid film bearings. This approach prevents solid friction and wear in steady operation, but is not unconditionally stable and requires some initial rotation to become active. Sealing is also important, but not as critical as for internal combustion engines.

Micro Thrusters

Various types of micro-thrusters have been developed, both for continuous and pulse operation. Silicon microfabricated cold gas and heated gas (resistojets) thrusters have been demonstrated with specific impulses (I_{sp}) of 66 s and 90 s respectively, at thrust levels up to 12 mN [7]. Supersonic flows in two-dimensional, deep reactive ion etched micro nozzles exhibit noticeable viscous losses due to the moderate Reynolds number ($1000 < Re_t < 3000$), which impacts the achievable I_{sp}. Liquid bipropellant micro rocket engines have also been studied to achieve higher I_{sp} and thrust, reaching 150 s and 1 N respectively [8]. These consisted of a stack of six micromachined silicon wafers that are bonded to enclose a contoured 2D nozzle with a combustion chamber and integrated cooling passages. Challenges include the temperature limitation of silicon which imposes stringent cooling requirements, as well as aerodynamics of high speed internal micro flows.

Digital micropropulsion, consisting of an array of single-shot thrusters, has also been developed to provide short impulses for attitude control of miniature spacecraft. The approach consists of enclosing an explosive or propellant between a resistive heater and a burst diaphragm that leads to a nozzle etched in silicon. Impulse levels of 10^{-4} N/s for mm^2-scale thrusters have been demonstrated, with an I_{sp} of 11 s [9]. There is potential for finer impulse levels and better fuel utilization as the combustion process is mastered.

Future Directions for Research

Most of the micro energy conversion approaches described above still require significant research and development before reaching the level of performance and reliability of a commercial product. Certain engineering challenges are common to many approaches and worth listing:

- Fluid dynamics, heat transfer, and mass transfer in developing moderate Reynolds number flows

(1 < Re < 1000) in complex microfluidic geometries

- Liquid-gas flows with phase change and capillary forces in complex microchannels
- Materials and configurations for thermal insulation in microsystems
- Novel microfabrication processes and materials to meet the needs of power MEMS, ranging from high strength and high temperature ceramics to stable hydrophilic/hydrophobic coatings.

Opportunities also arise to pursue innovative concepts and leverage micro and nanoscale phenomena for energy conversion. The MEMS tool set provides a framework to invent new concepts for energy conversion that may not be feasible or practical at the macroscale. Examples include microfluidic fuel cells that leverage laminar flow in microchannels to implement a purely diffusive, membrane-less fuel cell, and thermal expansion or phase change heat engines that can cycle at high frequencies due to low thermal mass and high heat transfer rates at microscale. Also, piezoelectrics and electrostatics principles complement more traditional electromagnetic approaches for mechanical to electrical conversion, given the established fabrication processes using MEMS technology. Opportunities also arise in the use of biochemical energy sources and biological approaches inspired from living organisms, as well as in leveraging nanoscale materials and phenomena to meet micro energy system needs.

Not only is further development required to improve the performance of core components, but significant effort is required at the system level. Integration of power generation elements with the required balance-of-plant components and the energy storage remains a technical challenge and a barrier towards commercialisation. Finally, the experimental development of power MEMS also raises unique difficulties in packaging and testing. Instrumentation development has not kept the pace with the microsystems they are meant to characterize, to the point where critical measurements inside the microsystems are replaced by external, global measurements. Only by understanding their physical behaviour will micro energy conversion systems take a predominant role in our every day lives.

Cross References

- ► Micro Cooling Devices
- ► Water Management inMicro DMFCs
- ► Microfluidic Fuel Cells
- ► Micro Hydrogen Fuel Cells
- ► Supersonic Micro-Nozzles
- ► Microrockets
- ► Microturbines

References

1. Nguyen NT, Chan SH (2006) Micromachined polymer electrolyte membrane and direct methanol fuel cells—a review. J Micromech Microeng 16:R1–R12
2. La O' GJ, In HJ, Crumlin E, Barbastathis G, Shao-Horn Y (2007) Recent advances in microdevices for electrochemical energy conversion and storage. Int J Energ Res 31:548–575
3. Dunn-Rankin D, Martins Leal E, Walther DC (2005) Personal Power Systems. Prog Energ Combust Sci 31:422–465
4. Epstein AH (2004) Millimeter-Scale, Micro-Electro-Mechanical Systems Gas Turbine Engines. J Eng Gas Turbines Power 126:205–226
5. Fréchette LG, Jacobson SA, Breuer KS, Ehrich FF, Ghodssi R, Khanna R, Wong CW, Zhang X, Schmidt MA, Epstein AH (2005) High-Speed Microfabricated Silicon Turbomachinery and Fluid Film Bearings. J Microelectromech Syst 14(1):141–152
6. Fréchette LG, Lee C, Arslan S, Liu YC (2003) Design of a Microfabricated Rankine Cycle Steam Turbine for Power Generation. In: Proceedings of the ASME International Mechanical Engineering Congress, Washington D.C., 16–21 Nov 2003
7. Bayt R, Breuer K (2001) Systems Design and Performance of Hot and Cold Supersonic Microjets. 39th AIAA Aerospace Sciences Meeting and Exhibition, Reno, Nevada, 8–11 Jan 2001
8. London AP, Epstein AH, Kerrebrock JL (2000) High-Pressure Bipropellant Microrocket Engine. J Propuls Power 17(4):780–787
9. Lewis DH, Janson SW, Cohen RB, Antonsson EK (2000) Digital MicroPropulsion. Sens Actuators A 80(2):143–154

Micro Energy Harvesting

► Micro Energy Conversion Devices

Micro Energy Scavenging

► Micro Energy Conversion Devices

Microengines

► Micro Energy Conversion Devices

Microfabricated Coulter Counter

► Flow Cytometer Lab-on-Chip Devices

Microfabricated Flow Cytometer

► Flow Cytometer Lab-on-Chip Devices

Microfabricated Needles

► Microneedles – Applications & Devices

Microfabrication

► Laser Based Micromachining

3D Microfabrication

► Fabrication of 3D Microfluidic Structures

Microfabrication of Three-Dimensional Microstructures

► Fabrication of 3D Microfluidic Structures

Microfilters

SHRAMIK SENGUPTA, HSUEH-CHIA CHANG
Department of Chemical and Biomolecular Engineering,
University of Notre Dame, Notre Dame, IN, USA
hchang@nd.edu

Synonyms

Filters; Microporous membranes; Microporous materials; Blood–plasma separators

Definition

Filters with pore size ∼1 μm located within microfluidic systems/channels, typically used to separate blood cells from plasma and to confine micrometer-sized beads within a microfluidic system.

Overview

Biomarkers (molecules of clinical significance) are often present in blood plasma, and the goal of many commercial systems under development is to rapidly estimate the concentration of these molecules – either in batches or continuously. Since one can draw only a limited quantity of blood from a patient for analysis, one is compelled to use as small an amount as possible for each analysis. This is especially true if one wants to either assay for multiple biomarkers, or one is interested in tracking the concentration of a particular biomarker frequently, or both.

Microfluidic systems, with their small volumes and sample requirements are inherently well suited to such tasks. In these systems, various optical, electrochemical, and electrical sensing elements are placed within microchannels. However, since the presence of particulates (like blood cells) can clog up microchannels, these systems are unable to operate for significant periods of time. Although some commercial microfluidic systems [1] have worked around this drawback by utilizing disposable systems, such disposable systems cannot be used for continuous monitoring – which is required in many cases. For instance, it is widely known [2] that during long operations like cardiac bypass surgery, a number of immunological pathways are initiated, and that these immunological responses lead ultimately to many adverse outcomes such as organ dysfunction [3]. This lack of a method to monitor the said responses in real time prevents a better understanding of the problem, and has consequently led to a lack of protocols for early corrective intervention [4]. Similarly, recent research has indicated that if the blood sugar levels of diabetic patients admitted to the intensive care unit (ICU) is kept under "tight glycemic control" [5] by measuring the blood glucose levels of patients once every five minutes and administering appropriate doses of insulin, then the mortality rate for such patients can be reduced by over 40%. Since diabetics, diagnosed or otherwise, make up a disproportionate fraction of those admitted to the ICU (as high as 56% according to one study [6]) a technology that would enable the widespread practice of tight glycemic control could have an enormous impact on overall outcomes in the ICU. In the latter case, though there are "continuous" glucose monitoring systems that rely on using cell-free interstitial fluid (ISF) already available on the market, they are not well suited for this applications on account of the time-lag between the levels of glucose in the blood and in the ISF. In cases like the former (monitoring immune response), there is a more fundamental drawback to using ISF instead of blood – i. e. that a large number of clinically relevant biomarkers may not be found in the ISF, or their concentrations there may not correlate to that in the blood in a clinically significant manner. Thus we are compelled to devise filters (and other technologies) that will remove the interfering cells prior to analysis or assay. A similar logic applies for food, environmental, and other samples – where one wishes to remove various particu-

late matter that may interfere with the detection of the target biomolecules. Another purpose for which microfluidic filters are widely used is to confine micrometer-sized beads to specific regions in a microfluidic network. These beads, typically tagged with antibodies/complementary sequences to target bioparticles or biomacromolecules, are being increasingly used in microfluidic systems on account of their high surface area (leading to better binding probability of the target species) and ease of handling [7].

Basic Methodology

In general, for diagnostic applications, the requirements for blood cell removal are extremely onerous, i. e. a 100% cell removal efficacy. Even a few cells (out of the millions present in a typical sample) have the ability to clog up microchannels and adversely affect sensitive biosensors downstream. The sensitivity of the biosensor and the concentration ranges of the target biomarkers also determine by how much the original solution may be diluted. For low abundance biomarkers, any dilution may be undesirable. At the same time, the need for continuous, or even "once every few minutes" measurements may require a throughput of the order of a few microliters per second. And finally, a filter that meets these requirements must also be such that it can be housed within a chip, whose choice of material may be dictated by other concerns, including, but not limited to, biocompatibility and the ability to fabricate and/or house the downstream sensors in the chip.

The system requirements for most other applications are much less stringent – a 5 – 10% loss of beads may not be catastrophic, and the presence of a small number of particulates may be tolerated in many assay procedures.

Despite the obvious differences in the applications for which they are designed, research in the microfilters area is directed towards answering two basic questions:

- How can one make a filter with the desired pore size distribution within a microchannel carved out in the material of choice?
- How should the filter be sized, positioned, and operated for it to meet the design objectives?

Of course, like all design questions, these two questions need not be completely independent. For instance, the ability to fabricate the filter out of a tougher material that is able to withstand a higher pressure could enable a filter of a particular design to meet more demanding design requirements. Nevertheless, they not only represent two themes on which recent investigators have tended to focus, but also provide a way to classify new designs along two axes.

Key Research Findings

Making the Filter

Given the different types of materials (glass, silicon, poly(dihydroxymethyl silicate) (PDMS), different types of other polymers) used in microchannel fabrication, various techniques have been adopted to achieve the goal mentioned above. Three broad types of filters are seen frequently:

- microporous or nanoporous membranes incorporated as one of the walls of a microfluidic channel (usually the "floor" or "roof") allowing the filtrate to flow into a chamber or channel on the other side of the membrane;
- arrays of pillars, usually arranged in a regular geometric pattern, within a microchannel; and
- porous beds, with a distribution of pore sizes, embedded within a microchannel.

Porous Membranes

Since micro- or nanoporous membranes are routinely used in the macro- or milliscale for many of the same goals as those desired for microfluidic systems, it is not surprising that they have been incorporated into the latter. The membranes used to effect the separation in the microfluidic systems may either be manufactured specifically using microfabrication techniques, or may be bought off the shelf. Using bulk microfabrication techniques (wet etching), it is possible to obtain micrometer-sized pores in a variety of shapes in silicon nitrate membranes. These pores can also be coated with polymers (such as parylene) to impart desired physical properties such as hydrophobicicty or hydrophillicity [8]. Even smaller pore sizes (~ 25 nm) can be obtained by focused ion beam drilling [9].

These membranes, and other commercially available membranes, can be incorporated within microfluidic devices by having open channels (or ports) fabricated in two separate pieces, and then sandwiching the membrane while fusing/gluing together the former. Examples of devices obtained in this manner are shown in Fig. 1.

While these devices are often able to meet their design targets of performing a crude separation at a low cost, they are often not very well suited for complex tasks such as those involving the separation of multiple samples along multiple channels. The very fact that these devices have to be "assembled" (the membranes often being put into position often by hand) limits how many different membranes (with different pore sizes) one can incorporate within a single chip. An alternative to the above is to fabricate the "membranes" within the chip. This can be accomplished in silicon microfluidic devices using the same bulk micro-

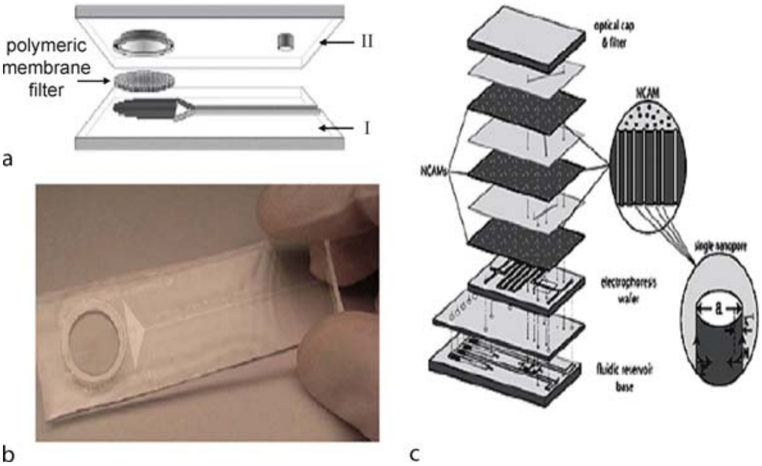

Microfilters, Figure 1 *Left:* (**a**) schematic and (**b**) picture of a microfluidic blood filtration device [32]. The top and bottom pieces are made up of PDMS, and the membrane is a commercially available hydrophilic polypropylene filter. *Right:* schematic of another device fabricated similarly, but with multiple layers of nanoporous membranes [33]

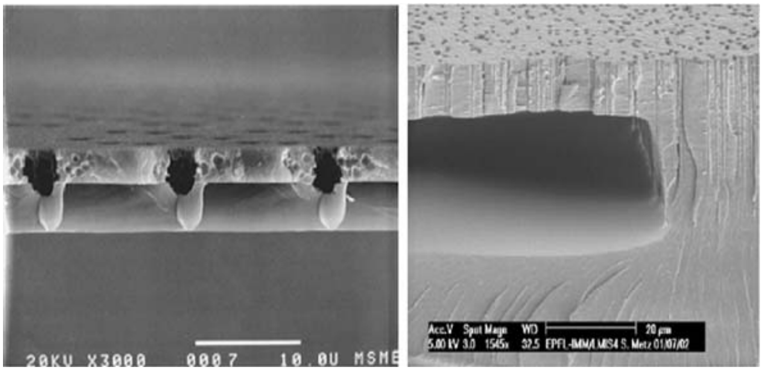

Microfilters, Figure 2 Pores fabricated on top of a channel in a silicon-based device using bulk micromachining [34] *(left)* and in a polyimide channel using track etching by lasers [35] *(right)*

machining techniques (wet-etching and deep reactive ion etching (DRIE)) that are used to make free-standing SiN microporous membranes. More advance fabrication techniques (surface micromachining) are needed to fabricate nanoporous membranes on top of selected regions of microfluidic channels housed in silicon wafers [10, 11]. Similar sized nanopores have also been fabricated by track etching polyimide microchannels (as also shown in Fig. 2). These in situ fabricated membranes are able to overcome most of the drawbacks associated with the devices that use prefabricated membranes. In addition, depending on the material, designers have a high degree of flexibility with respect to the pore size distribution of the membrane. Moreover, the location of their pores is such that these membranes can be used in a cross-flow mode – a mode of operation that (as will be discussed later in the article) is more effective than the other commonly used (dead end) mode. The main drawback is that fabricating devices with such pores is difficult and expensive. Also, and perhaps more importantly, it has been possible to fabricate such devices in only a few limited materials.

Arrays of Pillars

The *arrays of pillars* design has been adopted in microfluidic systems made out of a variety of materials, and the fabrication process adopted is formulated accordingly. In silicon-based microfluidic devices, the channels are typically formed either by wet etching or by DRIE. In either case, selective patterning of photoresist (or oxide) is used to define the channel regions. On exposure to wet etchant or reactive ion radiation, areas on the silicon wafer not covered by the resist or oxide are etched away, leaving open trenches. When the top is covered by another silicon or

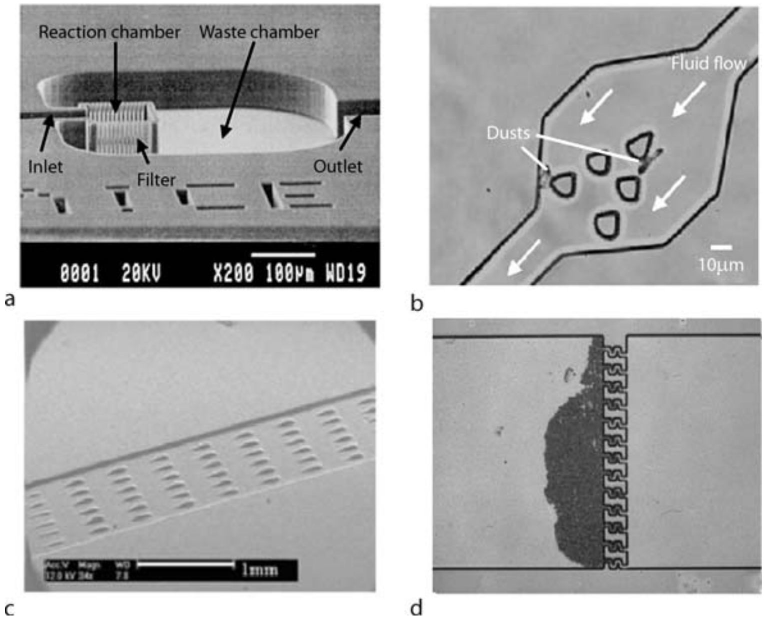

Microfilters, Figure 3 "Arrays of pillars" created in different microfluidic systems. These pillars serve as filters with well-defined pore size. (**a**) 50 μm high pillars with a spacing of 2 μm obtained through DRIE of a silicon wafer [36]. (**b**) 25 μm high posts with a separation of ∼ 15 μm in PDMS [37]. (**c**) Tilted scanning electron microscopy image of trapezoidal shaped pillars (120 μm high, 50 – 200 μm wide) with a separation of ∼ 50 μm injection molded on a cyclic olefin copolymer (Topas 5013-S04) substrate [38]. (**d**) Array of complex microposts (73 μm wide) spaced by 7 μm wide tortuous channels spanning a 500 μm wide ×5.3 μm deep silicon channel [39]

M

glass wafer, and bonded to the former using anodic or thermal bonding, closed microchannel networks are obtained. Here the original resist or oxide pattern itself is used to define islands that will not be attacked by the etchant or reactive ion radiation. These islands give rise to pillars within the microfluidic trench when the channel network is formed by etching – an example of which is shown in Fig. 3a. Subsequent anodic or thermal bonding yields covered channels with pillars within them that stretch from the channel floor to the channel roof. Similar structures have been fabricated in PDMS and other materials also – and examples are shown in Fig. 3. In all these cases, the pillars are fabricated along with the main channels.

The main advantage of using this design is that one can obtain monodisperse "pores" of the desired size with ease. The lower limit of the pore size is determined by the feature size resolution of the fabrication process used to make the channels, and thus pores ∼ 1 μm can be easily fabricated. However, higher throughput microfluidic devices can require channel depths of ∼ 100 μm – and not only is making pillars with a spacing of about a micrometer in such channels difficult and expensive, but such posts, once made, are liable to buckle more easily than shorter ones. The failure of even a few posts may compromise the filtration process. The latter concern may be ameliorated to an extent by fabricating "wider" posts that run for a distance along the direction of fluid flow, and thereby effectively create smaller channels into which larger particles cannot enter. In addition (as seen in Fig. 3d) these "channels" can be designed to be tortuous to further aid the filtration process.

Packed Beds and Porous Monoliths

Packed beds consist of a large number of solid particles packed into a conduit. These particles may be either of the same material, shape, and size (e. g. latex microspheres of 1 μm diameter) or vary by size, shape, and/or material. They are typically held in place by a frit or some other structure downstream of the bed that allows fluid to flow through while holding them in place. Typically, the downstream frit is fabricated/placed first, the bed is then packed at high pressure, and finally another frit is placed upstream to hold the structure in place. A packed bed typically has a large number of interconnected pores, with a distribution of sizes, through which the particle-laden fluid is driven. The interconnected network of pores of different sizes often prevents particles whose diameter is larger than that of the modal pore size from passing through the bed. Even in the macroscopic world, packed beds and membranes are the two most common methods for filtering solutions. So it is not surprising that packed beds are also used for the

same purpose in microfluidic systems. In microchannels, in addition to frits [12], weirs [13], surface coatings [14], and channel constrictions [15] have also been used to hold the particles in place. However, placing the upstream frit (or other structure) after packing the bed in place remains a difficult task to accomplish in microfluidic channels. Hence, for practical reasons, porous monoliths are more commonly used instead of packed beds.

Porous monoliths, as the name suggests, are single pieces of porous material (like a pumice stone). When placed within conduits, they function in the same manner as packed beds and share many of their characteristics as well – primarily the interlinked network of pores with a distribution in pore size. It is possible to fabricate such materials within microchannels, and to ensure that the monolith is bonded to the wall. Thus, the need for frits (and other structures) to hold the "bed" in place is eliminated. In addition, depending on the method used for fabrication, it may also be possible to tailor the modal pore size.

It has been possible to fabricate porous monoliths within silicon [16], glass [17], and polymer [18, 19] microchannels. Within silica and glass channels, porous monoliths can be fabricated by a thermally aided sol–gel reaction. Photopolymerization of acrylate monomers in the presence of porogens (inert organic solvents) has also been used to obtain porous monoliths. By varying the composition of the monomer blend, the composition of the porogen mixture, and the ratio of monomer to porogen it is possible to control the porosity of the monolith and the modal size of its pores. In addition, if the channels are made out of acrylate polymers, or have been coated with such material, the monolith bonds to the surface, and the filter can be operated without any extra arrangements (like frits) to hold the monolith in place.

The main advantage of these porous monoliths is the ease with which they can be fabricated. The fabrication process also allows for the fabrication of multiple porous monoliths with different characteristics (porosity and pore size distribution) within the same microchannel network, and to rapidly modify these characteristics on an as-needed basis with a minimum change in fabrication procedure (changing the composition of the pre-reaction mixture used to fabricate the pores, and/or the reaction temperature and duration for the same). Figure 4 shows two different monoliths fabricated from the same material. They can also be tailored to withstand higher pressures by the simple means of increasing the bed length and/or changing its shape. There are two main disadvantages, though. Firstly, due to the large surface area of the solid, it is possible for a relatively larger number of molecules (relative to the other structures), some of which are likely to be the target molecules in the downstream analysis section of the overall device, to adsorb onto its surface – though one can physically or chemically coat the material with molecules like poly(ethylene glycol) (PEG) or its derivatives to reduce this. Secondly, the characteristic pore sizes are limited to the micrometer range. Not only is making a monolith with smaller pore sizes difficult, but a monolith with a modal pore size in the nanometer range would require extremely high pressures to drive liquid through it. However, this is not an issue for a large number of applications – including that of blood cell removal from plasma.

Operating the Filter

As shown in Fig. 5, there are two main modes in which a filter may be operated – the dead end mode and the cross-flow mode. In the dead end mode, the particle-laden fluid is directed normally against the filter surface. While particles of size larger than that of the pores are prevented from passing through, all of the fluid passes through the filter. The particles being excluded remain on the upstream end of the filter, and when a large number of them are accumulated, they impede further fluid flow. Hence dead end filtration is typically used for small sample volumes, or suspensions with a small number of suspended solids.

In the cross-flow mode, the particle laden fluid flows tangentially past a filter. However, by suction, or by other means, a fraction of the fluid is pulled through the filter. Like in the dead end case, particles whose size is larger than that of the pores are excluded by the filter – but unlike the previous case, are not allowed to accumulate there since the tangential cross-flow sweeps them along and away from the surface of the filter. In practice, the cross-flow is never 100% efficient in sweeping away the excluded particles, and these particles do build up over time, causing the same set of problems (increased pressure drop, damage to the filter, etc.) as in the dead end mode. But a decreased volumetric recovery efficiency of the fluid (only a fraction is pulled through the filter) buys the user a longer operating time.

For most microfluidic applications involving beads, and for removing contaminant particulates from environmental samples, filters are operated in the dead end mode. Also to purify small volumes ($\sim 100\,\mu l$) for "one-shot" diagnostic applications [18], the dead end mode suffices. But for blood-diagnostic applications requiring continued operation and/or larger volumes (milliliters) of blood, one needs to resort to cross-flow [20, 21].

Future Directions of Research

The migration of deformable blood cells towards the low shear filter region [22], however, causes the beneficial

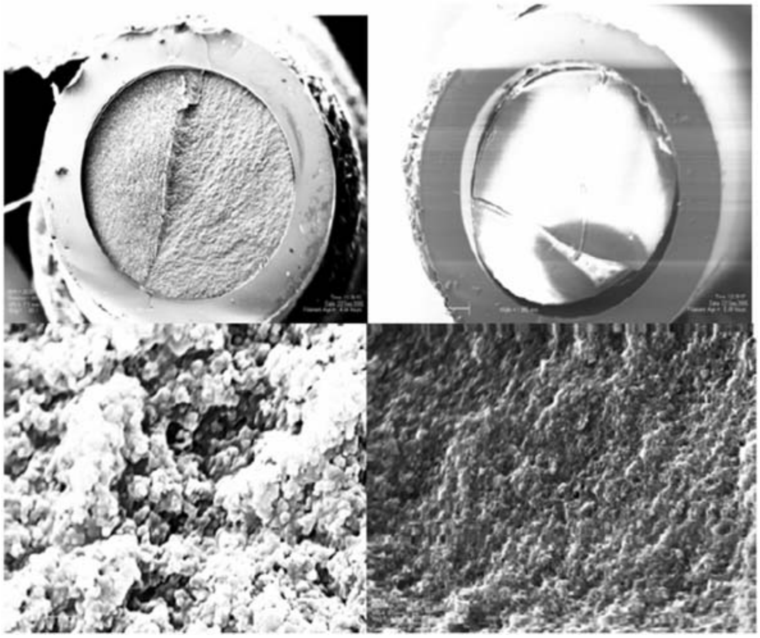

Microfilters, Figure 4 Porous monoliths with different porosities and pore size distributions created by the photopolymerization of a blend of acrylate monomers and porgens

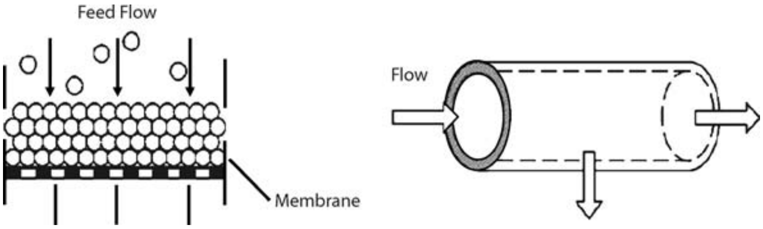

Microfilters, Figure 5 Dead end *(left)* and cross-flow *(right)* modes of filtration [40]

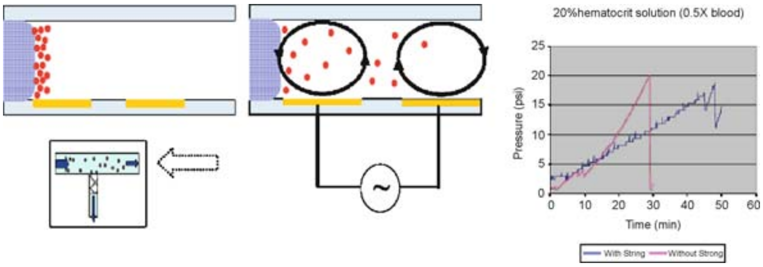

Microfilters, Figure 6 Schematic *(left)* of an AC electro-osmotic stirrer placed at the edge of a monolith filter that generates microvortices to break up the excluded red blood cell “filter cake”, and pressure buildup data *(right)* demonstrating the beneficial effects of stirring (reducing pressure buildup rate and consequent time to failure of the system)

effect of the cross-flow to be less pronounced for microfilters than in their macroscale counterparts and realized performance characteristics fall short of desired goals. An active area of research has been to explore means to enable the cross-flow to be more effective at removing the layer of excluded material on the upstream surface of the filter. Modification of the surface of the filter to make the excluded material less strongly adherent to it [23], the use of acoustic pulses to break up the “filter cake” [24], and the use of a sinusoidal flow field for the cross-flow [25]

have been tried previously to varying degrees of success. Recent research in our laboratory has focused on enhancing the rate at which excluded material can be removed by the cross-flow by placing electrodes at the edge of the filter and generating AC electro-osmotic vortices to break up the filter cake, and, as shown in Fig. 6, we have been able to extend the operation time of the filter by close to 50% as a consequence.

Additional drawbacks of using filters, especially upstream of bioanalytical procedures for detecting low-abundance molecules, include the potential losses of the target molecule due to adsorption on the high surface areas typically associated with filters. Current research has focused on reducing this problem by using thinner membranes [26] – but this general approach comes at a cost (the ability of the membrane to withstand lower pressures). Making the membrane of a stronger material (glass or silicon as opposed to polymer) can also adversely affect the overall bioanalytical goal if it may lead to increase lysis of cells, and consequent perturbation of the composition of the plasma.

To conclude, one may say that while the building blocks are largely available to build blood cell filters, a cake-free and high-throughput blood cell microfilter is still unavailable, and much work remains to be done to make it possible for blood cell filters to meet the performance desired of them in blood diagnostic chips. Other competing technologies exist (and are in development) that seek to remove blood cells and other undesired particulates from suspensions without damaging the cells and/or adversely affecting the composition of the liquid. A large number of technologies, including, but not limited to, dielectrophoresis [27], electrophoresis [28, 29], centrifugal force [30], and differential diffusion rates [31] have and/or are being explored. However, they also suffer from various drawbacks that make them individually unsuitable for the most demanding applications such separating blood cells from plasma in whole blood. One area that has not been explored is to use filtration in combination with one or more of these techniques to effect the desired separation.

Cross References

► AC Electro-Osmotic Flow
► Bead-Based Microfluidic Platform
► Biosample Preparation Lab-on-a-Chip Devices
► Cell-Based Assays Using Microfluidics
► Lab-on-Chip Devices for Particle and Cell Separation
► Integrated Microfluidic Systems for Medical Diagnostics

References

1. Turner APF, Chen B, Piletsky SA (1999) In Vitro Diagnostics in Diabetes: Meeting the Challenge. Clin Chem 45(9):1596–1601
2. Asimakopoulos G (1999) Mechanisms of the systemic inflammatory response. Perfusion 14:269–277
3. Westaby S (1987) Organ dysfunction after cardiopulmonary bypass: A systemic inflammatory reaction initiated by the extracorporeal circuit. Intensiv Care Med 13(2):89–95
4. Yang S, Undar A, Zahn JD (2005) Biological Fluid Separation in microfluidic channels using flow rate control. In: ASME International Mechanical Engineering Congress, Orlando
5. Van den Berghe G et al (2006) Intensive Insulin Therapy in the Medical ICU. N Engl J Med 354:449–461
6. Goldberg PA et al (2004) Implementation of a Safe and Effective Insulin Infusion Protocol in a Medical Intensive Care Unit. Diabet Care 27:461–467
7. Verpoorte E (2003) Beads and Chips: New recipes for analysis. Lab Chip 3:60N–68N
8. Yang X et al (1993) Micromachined membrane particle filters. Sens Actuators A Phys 73:184–191
9. Tong HD et al (2004) Silicon Nitride Nanosieve Membrane. Nanoletters 4(2):283–287
10. He R, Kim CJC (2004) Post-deposition porous etching of polysiclicon: fabrication and characterization of free standing structures. In: ASME International Mechanical Engineering Congress and Exposition, Anaheim
11. Okandan M et al (2001) Development of Surface Micromachining Technologies for MIcrofluidics and BioMEMS. In: SPIE Micromachining and Microfabrication Conference, San Francisco
12. Zeng S et al (2002) Electroosmotic flow pumps with polymer frits. Sens Actuators B Chem 82:209–212
13. Seong GH, Zhan W, Crooks RM (2002) Fabrication of Microchambers Defined by Photopolymerized Hydrogels and Weirs within Microfluidic Systems: Application to DNA Hybridization. Anal Chem 74(14):3372–3377
14. Han J et al (2005) An on-chip blood-serum separator using self-assembled silica microsphere filter. In: TRANSDUCERS-05: The 13th International Conference on Solid-State Sensors, Actuators and Microsystems, Seoul
15. Pregibon DC, Toner M, Doyle PS (2006) Magnetically and Biologically Active Bead-Patterned Hydrogels. Langmuir 22:5122–5128
16. Chen Z, Wang P, Chang HC (2005) An electro-osmotic micropump based on monolithic silica for micro-flow analyses and electro-sprays. Anal Bioanal Chem 382:817
17. Wang P, Chen Z, Chang HC (2006) A new electro-osmotic pump based on silica monoliths. Sens Actuators B Chem 113:500–509
18. Moorthy J, Beebe DJ (2003) In-situ fabricated porous filters for microsystems. Lab Chip 3:62–66
19. Fintschenko Y et al (2003) Monolithic Materials: Miniature and Microchip Technologies, in Monolithic Materials: Preparation, Properties, and Applications. Elsevier, Amsterdam
20. Crowley TA, Pizziconi V (2005) Isolation of plasma from whole blood using planar microfilters for lab-on-a-chip applications. Lab Chip 5:922–929
21. He B, Tan L, Regnier F (1999) Microfabricated Filters for Microfluidic Analytical Systems. Anal Chem 71:1464–1468
22. Zhou R et al (2006) Role of Erythrocyte Deformability during Capillary Wetting. Biotechnol Bioeng 93(2):201–211
23. Wang Y, Ferrari M (2000) Surface modification of micromachined silicon filters. J Mater Sci 35:4923–4930

24. Caton PF, White RM (2001) MEMS microfilter with acoustic cleaning. In: The 14th IEEE International Conference on Micro Electro Mechanical Systems, Interlaken
25. Mielnik MM et al (2005) Sinusoidal crossflow microfiltration device—experimental and computational flowfield analysis. Lab Chip 5:897–903
26. Striemer CC et al (2007) Charge- and size-based separation of macromolecules using ultrathin silicon membranes. Nature 445:749–753
27. Minerick AR et al (2003) Manipulation and characterization of red blood cells with alternating current fields in microdevices. Electrophoresis 24:3703–3717
28. Tsuda T, Yamauchi N, Kitagawa S (2000) Separation of Red Blood Cells at the Single Cell Level by Capillary Zone Electrophoresis. Anal Sci 16:847–850
29. Sengupta S, Todd P, Thomas N (2002) Multistage Electrophoresis II: Treatment of a kinetic separation as a pseudo-equilibrium process. Electrophoresis 23:2064–2073
30. Arifin DR, Yeo LY, Friend JR (2007) Microfluidic blood plasma separation via bulk electrohydrodynamic flows. Biomicrofluidics 1(1). doi:10.1063/1.2409629
31. Holl MR et al (1996) Optimal design of a microfabricated diffusion-based extraction device. In: American Scociety of Mechnical Engineers Meeting
32. Thorslund S et al (2006) A hybrid poly(dimethylsiloxane) microsystem for on-chip whole blood filtration optimized for steroid screening. Biomed Microdev 8:73–79
33. Gatimu EN et al (2007) Three-dimensional integrated microfluidic architectures enabled through electrically switchable nanocapillary array membranes. Biomicrofluidics 1(2). doi:10.1063/1.2732208
34. Chu WH et al (1999) Silicon Membrane Nanofilters from Sacrificial Oxide Removal. J Microelectromech Syst 8(1):34–42
35. Metz S et al (2004) Polyimide microfluidic devices with integrated nanoporous filtration areas manufactured by micromachining and ion track technology. J Micromech Microeng 14:324–331
36. Andersson H et al (2000) Micromachined flow-through filter-chamber for chemical reactions on beads. Sens Actuators B Chem 67:203–208
37. Takahashi K et al (2004) Non-destructive on-chip cell sorting system with real-time microscopic image processing. J Nanobiotechnol 2(5). doi:10.1186/1477-3155-2-5
38. Kim DS et al (2006) Disposable integrated microfluidic biochip for blood typing by plastic microinjection moulding. Lab Chip 6:794–802
39. Wilding P et al (1998) Integrated Cell Isolation and Polymerase Chain Reaction Analysis Using Silicon Microfilter Chambers. Anal Biochem 257:95–100
40. Geiser D et al (1998) Innovative Technology Summary Report: Crossflow Filtration. Office of Science and Technology, US Department of Energy

Microflaps

YANDONG GAO , DONGQING LI
Department of Mechanical Engineering, Vanderbilt University, Nashville, TN, USA
yandong.gao@vanderbilt.edu

Synonyms

Microflow actuator; Flow control

Definition

Flaps are types of flow actuators, which are hinged surfaces on the wings of air vehicles used to generate sufficient moments for aerodynamic control. The flow separation is very sensitive to small perturbations at its origin. This fact makes it possible to control vortices at the leading edge separation line by small force and/or displacement at appropriate locations. Taking advantage of microelectromechanical systems (MEMS) technology, an array of microflaps, together with a shear stress sensor, can be fabricated to manipulate the thin boundary layer near the leading edges, consequently allowing control of the global flow field [1]. Because the thickness of the boundary layer is of the order of millimeters, microflaps are typically required to be able to deliver an out-of-plane displacement of several millimeters and sustain a load of the order of several hundred micronewtons.

M

Overview

Micromachined flaps are attractive because of the possibility of integration of both microsensors and microactuators in a single device. In addition, microflaps have fast frequency responses and fine spatial resolutions with low power consumption because of their small length scales. The use of a large number of small and simple actuators also makes these systems fault-tolerant. To achieve a large actuation displacement and large output force, the most suitable actuating scheme is based on electromagnetic principles [2, 3].

Liu et al. [4] developed an integrated coil-type magnetic micromachined flap, which achieved a vertical deflection larger than 100 μm and an applied magnetic force of about 1 μN. However, the coil-type microflap requires high currents, and the thermomechanical bending strongly influences its performance due to the significant Joule heating. Liu et al. [3] developed millimeter-scale magnetically actuated microflaps moving in the out-of-plane direction based on a permanent magnet. The displacements of their microflaps achieve vortex symmetry breaking. Therefore, the rolling motion of a delta-wing airfoil could be controlled. Sherman et al. [5] presented electrostatically driven in-plane microflaps made from silicon-on-insulator wafers. Due to their small size ($60 \times 200\,\mu m^2$), they are of low power consumption ($< 1\,\mu$W) and high operating frequency ($500 - 1000$ Hz).

Cross References

► Microactuators
► Shear Stress Sensors
► Turbulence Control

References

1. Lee G et al (2000) Sensing and control of aerodynamic separation by MEMS. Chin J Mech 16:45–52
2. Wagner B et al (1992) Microactuators with moving magnets for linear, torsional or multiaxial motion. Sens Actuators A 32:598–603
3. Liu C et al (1999) Out-of-plane magnetic actuators with electroplated permalloy for fluid dynamics control. Sens Actuators 78:190–197
4. Liu C et al (1994) Surface micromachined magnetic actuators. 1994 IEEE Workshop on MEMS, pp 57–62
5. Sherman F et al (1999) Flow control by using high-aspect-ratio, in-plane microactuators. Sens Actuators 73:169–175

Microflow Actuator

► Microflaps

Microflow Switch

► Bubble Actuated Microfluidic Switch

Microfluidic Analysis System

► Microfluidic Systems

Microfluidic Assembly

Bonnie Gray
School of Engineering Science, Simon Fraser University, Burnaby, BC, Canada
bgray@sfu.ca

Synonyms

Microfluidic systems assembly; Microfluidic component assembly; Microfluidic integration; Microfluidic systems packaging

Definition

Microfluidic assembly refers to the realization of devices and systems for handling and analyzing microliter or nanoliter amounts of fluid through the combination of smaller subunits, including the combining of discrete microfluidic devices and components to realize complex microfluidic instrumentation. Microfluidic assembly uses various integrated and modular packaging and interfacing techniques to combine microfluidic subunits together, including bonding, mechanical press-fits, robotic manipulation, and self-assembly.

Overview

Microfluidic components and systems are utilized whenever the manipulation of microliter or (usually) nanoliter amounts of fluid is beneficial or where small size for fluidic systems is needed. Examples of microfluidic applications include the miniaturization of laboratory instrumentation for bed-side rapid diagnosis of disease; implantable monitoring and drug delivery devices such as glucose sensors and insulin pumps for diabetes; bioanalytical instrumentation for studying cells or molecules in new ways; and other Lab-on-a-Chip devices for performing complete laboratory analysis on a sample using a portable instrument. However, these and other microfluidic systems can be very complex, requiring the interfacing of many different passive and active components such as micro channels, valves, pumps, filters, and chemical reaction chambers, as well as detection systems and other sensors operating on electrical, mechanical, or optical principles. Most research in microfluidics has centered around the optimization of particular components or subsystems utilizing well-known or newly developed principles, e. g., polymerase-chain reaction (PCR) for increasing the quantity of DNA in a sample; electrode-based biosensors for determining the amount of a biological component in a sample; DNA microarrays for performing multiple DNA tests simultaneously; and microneedles for painless biofluid sampling and drug delivery. Less research has focused on efficient and cost-effective schemes for component interconnect, assembly, and interfacing between microfluidic components and macroscale devices, although such microfluidic assembly has been widely recognized as crucial to the realization of complex microinstrumentation for bed-side diagnostics and Lab-on-a-Chip devices [1].

Many individually microfabricated fluidic devices have been demonstrated and even marketed commercially. As sample volumes become smaller, and the analysis of individual cells or molecules is desired, the research instrumentation itself decreases in size and new methods of interconnection and assembly are required. Microfluidic components must often first be assembled from smaller subunits (e. g., channels, actuators) and then further assembled together to form microfluidic systems and instrumen-

tation. Although integration of subunits or components during fabrication is a worthwhile goal from the standpoint of simplicity, it is often at the cost of device performance. Methods to efficiently interconnect components that have been fabricated separately, often using vastly different techniques and materials specific to each device, are more complex but are required for full microfluidic component and systems assembly. For many components and systems, a combination of integrated and modular approaches results in the most easily packaged and best performing devices.

This article will cover the main microfluidic assembly methods for components and systems, including integrated and modular approaches, as well as key research findings and example systems from academia and industry that demonstrate these approaches in practical systems. This article will discuss relevant tools and techniques of general microsystems assembly, including bonding, robotics and fluidic microassembly. This article will also focus on interconnection and assembly between disparate materials, including silicon, glass, and polymers.

Basic Methodology

Microassembly Philosophies

Integrated Approaches

Integrated approaches seek to use a single fabrication process for the entire device or system, including all components, interconnect, and packaging. Although using a single process simplifies device interconnection, it can be at the expense of device performance, or can limit the devices and interconnect that is possible. Components cannot be individually optimized using different material platforms or technologies, although interfacing problems between different materials can be minimized.

Surface micromachining is a process whereby multiple layers of a structural material (e. g., thin film polysilicon) are separated by layers of another sacrificial material (e. g., silicon dioxide) that is removed at the end of the fabrication process resulting in free-standing structures in the structural material (see cross-referenced article on surface micromachining). In addition to mechanical structures, electrodes and other electronics can be fabricated in the same (usually silicon) substrate. Some materials combinations for surface micromachining are listed in Table 1, with materials and fabrication processes heavily dependent on the device or system function. Although widely used for more traditional microelectromechanical systems (MEMS) devices, e. g., accelerometers and resonating sensors, integrated approaches can also be employed for microfluidics provided components and interconnect can be realized in the chosen technology.

Microfluidic Assembly, Table 1 Surface micromachining materials

Structural Material	Sacrificial Material	Sacrificial Etchant
Polysilicon	SiO_2, other silicon dioxides (e. g., PSG, LTO)	HF
Al	Photoresist	O_2 plasma
SiO_2	Polysilicon	XeF_2 gas
Al	Silicon	EDP, TMAH, XeF_2 gas
SU-8	Polystyrene	O_2 plasma

Other integrated approaches rely on sequential bonding and patterning of multiple bulk layers rather than film deposition and patterning. One popular approach involves patterning all microchannels and microfluidic structures for one layer using, e. g., deep reactive ion etching (DRIE) of silicon, alternated with silicon fusion bonding of patterned or unpatterned wafers that can then be further structured in the integrated process (e. g., [2]). As with surface micromachining, such approaches can be limited in the realizable structures and are usually limited to a set number of materials.

Modular Approaches

In the macroscopic world, fluidic devices are attached together using various plumbing fixtures, and readily interfaced to electronic, mechanical, and optical devices using wires, mechanical fasteners, and lenses. Fluidic components (e. g., pumps) are also fabricated using a variety of mechanical attachments, gaskets, plumbing parts, and molded plastic or machined metal housing. On the microscale, modular approaches have employed a variety of techniques adapted to or developed for the microscale, including: microfluidic circuit boards with attachable components; gasketed stacked modules where each layer performs a specific function; permanent bonding; quick-connect modular assembly using specially developed interfacial structure between components; and cartridge-based modularity for interfacing reusable control and detection circuitry to disposable microfluidic cartridges.

Microfluidic Boards Microfluidic board interconnection technologies seek to mimic the electronic printed circuit board for ease of use, reliability, and versatility. In microfluidic board technologies, the substrate contains the passive microfluidic channels and reservoirs, with active components (e. g., sensors, valves) mounted

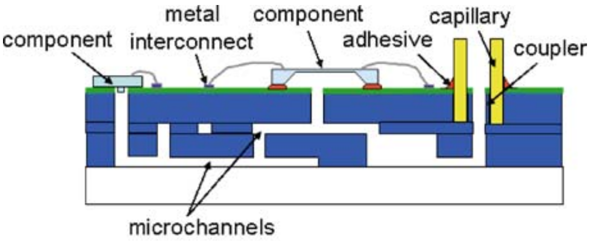

a

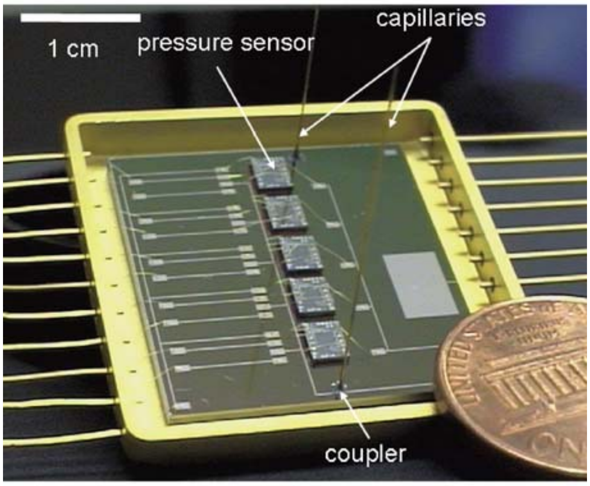

b

Microfluidic Assembly, Figure 1 Modular microfluidic board approach: (**a**) illustration of example board technology with electronic and fluidic routing between surface mounted components and coupling to off-chip devices; (**b**) photograph of example microfluidic board in silicon with five mounted pressure sensors, embedded microchannels, surface electronic routing, and couplers to capillary tubing [2]

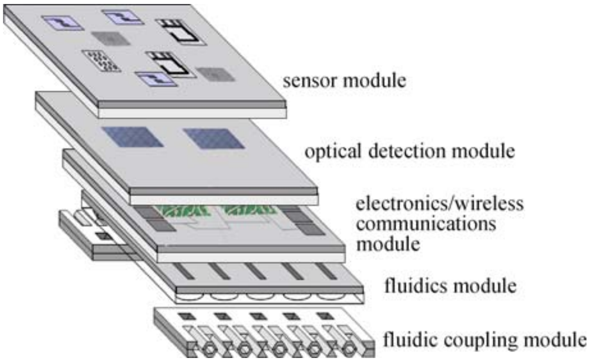

Microfluidic Assembly, Figure 2 Illustration of stacked-module approach, where the microfluidic system is composed of stacked modules that each perform specific functions and are aligned and assembled together vertically in a jig

on top (e. g., [2]) (see Fig. 1) similarly to electronic components mounted on a printed circuit board (PCB) or multichip modules (MCM) in surface mount technologies (SMT). Electronic connections between components are provided on top of the board, while fluidic interconnection is usually provided in the board material itself. Microfluidic circuit boards can be made from a variety of materials, including silicon, glass, and polymers, e. g., polydimethyl siloxane (PDMS), epoxy, or polymethyl methacrylate (PMMA). Microfluidic boards can be as simple as a single packaged component socket or as complex as a full Lab-on-a-Chip analysis system, with size and complexity constrained mainly by mounting technique (e. g., bonding or adhesive) and via hole fabrication method.

Stacked Modules Microfluidic systems composed of modules, where each module forms a layer that is stacked on previously layered modules, is a simple solution to interfacing components fabricated using different materials or for producing components from alternating passive (e. g., microchannels) and active (e. g., sensors, actuators for valves and pumps) layers. Each module (layer) performs a specific function and can be interfaced to the modules above and below it electrically, optically, or fluidically, provided suitable electronic and optical interfaces and fluidic gaskets are used (see Fig. 2). The modules are usually compressed together in a jig, with modular replacement requiring complete disassembly of all modules. Stacked modules can be made of many different materials, including silicon, glass, and both thermoplastic and thermosetting polymers, provided compliant polymer gaskets (e. g., PDMS) are used to interface layers for fluid-tight seals.

Embedding of Components Most of the earliest packaging of individual microsensors centered around a concept taken directly from microelectronics: the embedding of the device in a molded polymer package with simple electronic (e. g., dual-in-line package pins or surface mount bumps) and/or optic (e. g., transparent windows for LEDs) or fluidic (e. g., access holes for pressure sensors) interconnect as needed. This concept has been extended to microfluidic systems whereby many components are assembled in a jig and embedded into a relatively inexpensive polymer package all at the same time. The most commonly used polymer in academia is PDMS as it is readily molded, easy to work with, and in use by many researchers already that utilize soft lithography, or molding against a photoresist master, as a primary method of fabrication of microdevices and systems. However, thermoplastic polymers, e. g., PMMA and polycarbonate (PC), are utilized for embedded packaging by industry and other researchers with access to techniques such as injection molding.

Cartridge-Based Modular Assembly The use of disposable, usually hard polymer cartridges containing microfluidics that are interfaced temporarily to reusable components, e. g., optics or control electronics, is an assembly approach that is widely used in industry for microfluidic systems involving DNA chips and biofluid analysis. In this approach, the cartridge containing the fluidic sample is slid into the instrument by the user, the desired tests performed on the sample, then slid out and disposed of such that the sample does not interfere with the re-usable and more expensive parts of the instrument. This also avoids washing steps, as the cartridge is the only part of the machine in contact with the liquid and is disposable. Smooth motion and lock-in-place mechanisms between the disposable and reusable portions of the instrument must be incorporated into the system design.

Structures to Facilitate Modular Assembly For many modular approaches and techniques, including microfluidic circuit boards, stacks, or freely joined modules assembled via robotic techniques, alignment keys and mechanical joints may facilitate microassembly, joint strength, or reworkability.

Alignment keys can be used for bonding of two substrates, parts, or components such that they line up in some useful manner (e. g., a through-hole lines up with the end of a microchannel or an actuator lines up with a membrane used in a micropump). Alignment keys are similar to those used for photolithography processes, although they may be larger to facilitate manual or robotic assembly. Alignment keys are widely used for assembly of both components and systems.

Mechanical joints for assembling microfluidic components and systems often involve insertion of one part into another. The afore-mentioned cartridges are a simple example, and structures must be included on both the cartridge and inside the instrument to allow smooth insertion. Such structures can include micro-rails to aid such sliding assembly on-chip. Care must be taken in choosing materials for properties such as friction and wear. Friction is defined as the force of motion or tendency toward such of two surfaces in contact, defined by the equation:

$$F = \mu N \quad (1)$$

where μ is the coefficient of friction, which is an empirical property of the contacting materials, and N is the normal force exerted between the surfaces. For surfaces in relative motion, μ is the coefficient of kinetic friction. For surfaces initially at rest relative to each other, μ is the coefficient of static friction (generally larger than its kinetic counterpart). The direction of the frictional force on a surface is opposite to the motion that surface would experience in the absence of friction.

Other structures can be used to facilitate the actual joining of parts. Such structures are based on mechanical press-fits, including simple fits of one part into another, and structures based on micro peg-in-hole or beam-spring assembly. The inserted part is held in contact with the mating part via friction and the spring force from either the beams or material compliancy holding the parts together. Prediction of how well a snap-together interface will work is based on mechanics (e. g., beam equations) and contact modeling, with mechanical materials characteristics such as Young's modulus and yield strength of paramount importance. It should be noted that polymer characteristics can be heavily dependent on processing, which complicates prediction of structure behavior. A compliant cylindrical peg inserted into a hole can provide microfluidic interconnect between two microchannel-containing substrates. Such a structure both mechanically holds the substrates together while providing fluid-tight interconnection.

Hybrid Approaches

Many practical/commercial microfluidic systems use a combination of integrated and modular approaches for systems assembly. In these cases, portions of the system, such as capillary electrophoresis microchannels with integrated electrodes, or microsensors with integrated pumps and valves, may be combined with a modular approach towards the optics or other microfluidic elements. Such combinations of integrated and modular systems can be very effective resulting in the *best of both worlds* for a microfluidic system.

Coupling to the Macroscale World (World-to-Chip Coupling)

A major issue with many microfluidic interconnect technologies is the coupling of the fluidic circuits to the macroscopic world. Such couplers allow fluid to be pumped on-chip, and waste to be removed off-chip in a controlled manner. Couplers can be integrated into the fabrication process, or assembled to the device as a separate component.

The simplest fluidic couplers involve a tube directly glued into a hole at the end of an on-chip microchannel, e. g., fluidic couplers consisting of a capillary tube glued into an insertion channel which is etched into the silicon substrate (see Fig. 3a). These couplers do not have accurately fitted insertion channels resulting in difficult handling and leakage of adhesive into the microchannels. Couplers fabricated by more geometrically versatile techniques, such

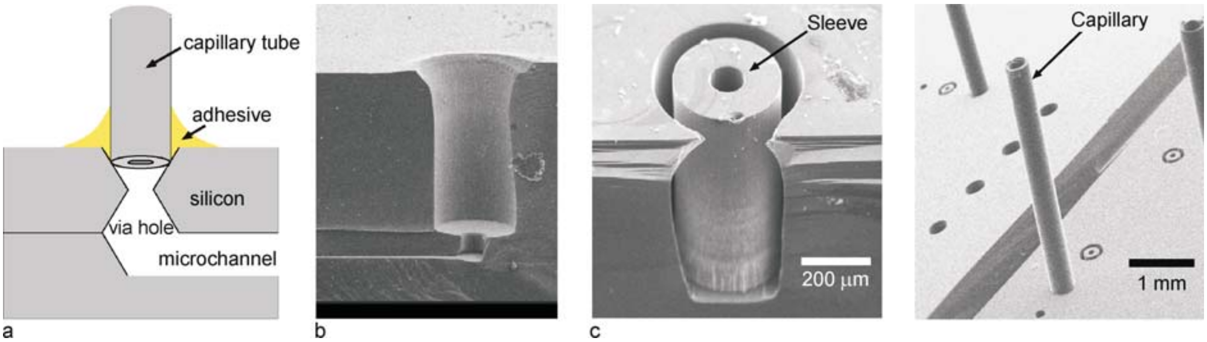

Microfluidic Assembly, Figure 3 Examples of glued couplers between on-chip and off-chip devices: (**a**) illustrations of capillary tube glued in microchannel fabricated by wet anisotropic etching of silicon; (**b**) capillary tubing coupler with holes etched in silicon by DRIE such that the inner and outer diameters of the capillary tubing are matched; (**c**) *sleeve*-type coupler that fits inner and outer diameter of capillary tubing and prevents adhesive seeping into the microchannel [2]

as DRIE of silicon, may have high density insertion channels that accurately fit the outer diameter of capillary tubing [2] (see Fig. 3b). However, such couplers are often still sealed with adhesive.

Couplers featuring exchangeable interconnect utilize mechanical press-fits similar to press-fits used to join modules. Press-fits utilize the elastic forces of the coupling parts to seal the fluidic connection, which is adequate provided high pressure and/or very high density coupling is not required. Press-fit type couples can be designed such that the tubing fits on a coupler parallel to the on-chip microchannels, or such that the tubing couples perpendicularly to the microchannel-containing chip surface.

Microassembly Tools and Techniques

This section will cover several tools and techniques utilized for microsystems assembly, including microfluidic systems assembly, primarily of modular systems although bonding can be considered as either integrated or modular depending on how it is employed. Manual assembly is still the most commonly used microfluidic systems and microinstrument assembly method, but suffers from problems of scale-matching, reproducibility, accuracy, and speed. Manual assembly can be used successfully for prototyping if parts are large enough, although methods of batch and automated assembly are necessary for parts that are too small to be manipulated by a person or for manufacture of multiple units.

Microassembly is the discipline of positioning, orienting, and assembling of micrometer-scale components into complex microsystems [3]. Although some attention has been given to developing techniques and tools for microsystems assembly, much of this has been aimed at combining electrical, mechanical, and optical components, but not microfluidics. Thus, although the robotic and self assembly techniques discussed below are utilized for microsystems assembly, they have not necessarily been utilized for microfluidic systems assembly. Bonding, on the other hand, has been widely used to assemble both microfluidic components from integral parts (e. g., actuator membranes, channels) as well as assemble together microfluidic components into systems (e. g., components adhesively bonded to microfluidic circuit boards).

Bonding

Bonding is the joining of two materials either directly or through the use of an intermediate layer. Various bonding methods can be used for basic assembly and packaging of components fabricated on the same or different technology platforms, including silicon, glass, ceramics, metals, and polymers. These bonding methods usually result in a permanent joining of the two materials that cannot be easily reworked.

► Anodic Bonding is a method of using high voltages and elevated temperature to bond glass to silicon. The glass must contain a mobile ion, such as sodium or potassium, for the bonding to proceed. Many glass making companies sell glass wafers in conventional sizes (e. g., 4 in. diameter and 0.5 mm thick) that are suitable for silicon-to-glass bonding (e. g., Corning 7740 Pyrex, Schott 8329). Typical bonding temperature is about 400 °C, with a typical voltage of 1 kV. It is of note that anodic bonding can be performed over thin metal electrodes on the glass or silicon surface. Anodic bonding can also be used for silicon-to-silicon bonding provided an intermediate glass layer deposited by, e. g., chemical vapor phase deposition or spin-on techniques, is used. Anodic bonding is very useful in situations where channels or active devices (e. g.,

pumps, valves, sensors) have been fabricated in silicon, but it is necessary to visualize the fluid flow through the glass, or an insulating materials is desired between the silicon and its further packaging.

Silicon can be bonded to silicon using fusion bonding. This bonding results in a very strong bond and is accomplished through surface modification and heating of the silicon substrates. The surfaces are thoroughly cleaned and hydrated (e. g., using ammonium hydroxide or sulfuric acid and hydrogen peroxide) to form hydroxyl groups (OH) on the surfaces. The surfaces can be aligned and then contacted. The bonding is then accomplished through an annealing step at elevated temperatures (e. g., 1000 °C).

Glass can also be directly bonded to itself thermally. Cleaned glass wafers are soaked in a solution of water, NH_3 or HCl, hydrogen peroxide, and then thermally bonded at approximately 600 °C for 6 to 8 h.

Polymers require joining processes that are different than those for silicon and glass, and are performed at lower temperatures. In most cases, a form of adhesive bonding is used either through direct adhesion of the two polymers or using a separate adhesive intermediate layer. Other polymer bonding techniques rely on surface chemistry (e. g., plasma bonding, solvent welding) or heat (e. g., thermal welding).

Thermal polymer bonding results when two parts are heated under compression. The joining of the materials takes place by fusing them through direct liquid phase interaction. The heating can be either radiative thermal, or supplied using another method, such as ultrasonics. Some polymers are degraded and soften under radiative light energy, e. g., PMMA under UV light. This property can be exploited to realize reduced-temperature thermal bonding.

Solvent welding is another method of bonding polymers by first degrading and softening them, only in this case a solvent is used to degrade the surfaces before bonding them together.

Plasma activated bonding modifies the polymer's surface to facilitate bonding. PDMS can be irreversibly bonded to itself and various other materials (e. g., silicon, glass, silicon nitride, and several other polymers) through the use of surface-oxygenation. The materials to be bonded are placed in an oxygen plasma. In the case of PDMS, this generates silanol groups by oxidation of the surface methyl groups of the PDMS structure.

Adhesive bonding is essential the *gluing together* of two materials using an adhesive such as epoxy, thermoplastic polymer adhesives, photoresists, benzocyclobutene (BCB), etc. Care must be taken to join the two surfaces while not clogging channels, producing voids, or otherwise not properly controlling the adhesive location.

Robotic Microassembly

Robotic microassembly covers both assembly by telemanipulation and automated robotic assembly such as pick-and-place or the use of a levitation table for part manipulation. Micro-grippers, -robots, and assembly tables are themselves very sophisticated microinstruments, with complex visual and/or tactile feedback to accomplish relatively simple tasks, such as pick-and-place or peg-in-hole insertion.

Manipulator-Based Robotic Microassembly Pick-and-place robotic manipulator systems employ visual and/or force feedback for precise placement of force and monitoring of micropart force interaction (see Fig. 4). These systems can either be macroscale with microscale precision, or themselves built on the microscale, although the latter results in a system that is often more complicated to assemble than the systems intended to be built by the

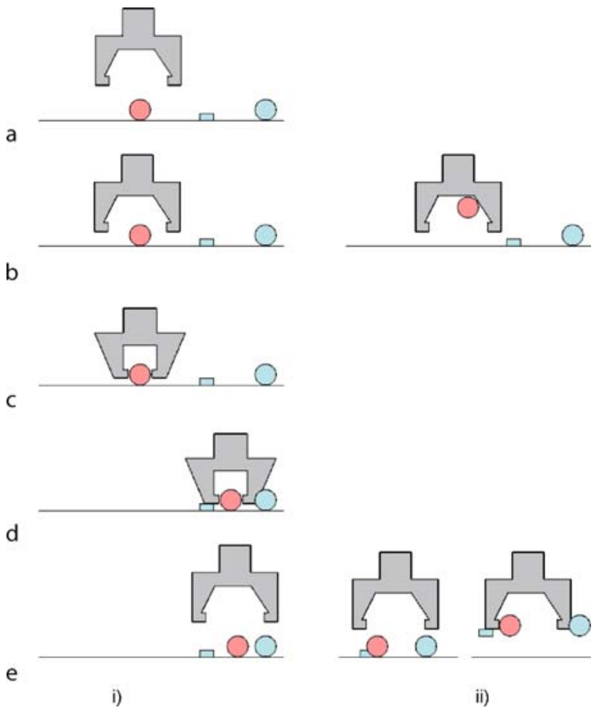

Microfluidic Assembly, Figure 4 Illustration of microassembly by microgripper. The first column (**i**) illustrates the desired microassembly, while the second column (**ii**) illustrates problems that can commonly occur: (**a**) approach; (**b**) close proximity positioning of microgripper. Electrostatic attraction may cause the micropart to *jump* onto the microgripper prematurely causing incorrect placement; (**c**) grasp; (**d**) moving micropart to desired location; (**e**) placement of micropart. The micropart may adhere better to the microgripper than the substrate, causing inaccurate placement or even remain attached to the microgripper after it is removed from the substrate

micro-robotic system. A combination of micro and macro components can also be used, whereby a microgripper less than a millimeter in size is precisely positioned for its task using macroscale equipment such as motors and x-y stages with micrometer precision. Relative placement of parts over the long range is monitored via a visual system, while force sensors provide precise feedback on the interactions among parts during contact.

Manipulation of microparts uses physical characteristics, such as friction, adhesion of micro-scale parts, or suction forces. Once the parts have been grabbed by the device, the components need to be assembled, and this task may require a complex control system. Adhesive forces between microgripper and micropart can be significant compared to gravitational and inertial forces and are primarily due to Van der Walls forces, surface tension, and electrostatic attraction. For example, a micropart may "jump" onto the microgripper prematurely due to electrostatic attraction, but may be difficult to release from the microgripper once in place due to adhesion forces. Electrostatic forces are due to charge accumulation or transfer during contact. Van der Walls forces are due to quantum mechanical polarization of atoms and molecules, while surface tension arises from residual moisture on the microgripper and micropart.

A good review of microassembly adhesion forces can be found in [3] by considering the force between a spherical object and the surface of a microgripper finger, which can be modeled as a plane. We repeat the analysis here for this simple yet instructional case:

The electrostatic force between these objects can be modeled as:

$$F_{\mathrm{es}} = \frac{q^2}{4\pi\varepsilon(2r)^2} \tag{2}$$

where q is the charge, ε is the permittivity of the dielectric, and r is the object radius. Very high electrostatic densities and forces can be generated on the microscale especially as r becomes very small.

The van der Walls force between a sphere and plate is modeled by:

$$F_{\mathrm{vdW}} = \frac{hr}{8\pi z^2} \tag{3}$$

where h is the Lifshitz–van der Walls constant, and z is the atomic separation between the surfaces. This formula is only an approximation in that it assumes smooth surfaces; severe corrections must be made for rough surfaces as the actual contacted area is much different.

Surface tension force in a humid environment with hydrophilic surfaces (e. g., glass, oxidized silicon) may be very high due to a thin layer of liquid present between the object and the plane of the microgripper finger. Surface tension between these objects can be modeled as:

$$F_{\mathrm{st}} = \frac{\gamma\,(\cos\theta_1 + \cos\theta_2)\,A}{d} \tag{4}$$

where γ is the surface tension, A is the shared area, d is the gap between the surfaces, and $\theta_{1,2}$ are contact angles. This can be further simplified assuming completely hydrophilic surfaces (zero contact angles) and $d \ll r$:

$$F_{\mathrm{vdW}} = 4\pi r\gamma \tag{5}$$

These forces can be compared to the gravitation force of a micropart (sphere), given by:

$$F_{\mathrm{g}} = \frac{4}{3}\pi r^3 \rho g \tag{6}$$

where g is gravity and ρ is density for the micropart (sphere) material.

Consider the case of a silicon microsphere ($\rho = 2300\,\mathrm{Kg/m^3}$), with surface tension of water $73\,\mathrm{mN/m^2}$, van der Walls over a contact area of 1% of the apparent area, and charge density of $1.6\times10^{-19}\,\mathrm{C/m^2}$. For microparts ranging in size from 1 μm to 1 mm, surface tension forces will dominate, with gravity overtaking van der Walls and electrostatic forces as micropart size increases. Thus, for microgripper/part release, it is beneficial to assemble parts in as dry an environment as possible. Care must also be taken to utilize materials and methods that minimize surface tension, electrostatic charging, and van der Walls effects, including: materials with small contact potential difference, conductive materials, and roughened materials to minimize contact area.

Telemanipulation for Microassembly Telemanipulation is the utilization of a device which allows a mechanism to be controlled by a human operator for the manipulation of remote objects. In the case of microassembly, the objects are not so much remote in location as a scale mismatch exists that facilitates the need for telemanipulation. The manipulator may be a microgripper or microneedle used to then position and assemble microscale parts and/or devices. The same problems with adhesion forces discussed in the previous section may plague teleoperated microgrippers. Usually, a camera and/or force feedback are provided for the operator who takes the place of the computer in automated robotic microassembly.

Other Robotic Microassembly Platform based micromanipulation, where parts are placed and assembled in a known environment using methods other than pick-

and-place microgripper style manipulation, is popular for microscale systems. An example of a platform-based micromanipulation approach to microassembly would be laying the parts out on a table and using levitation methods, such as an air bearing table where parts are suspended on air and moved around using, e. g., air jets or magnetic coils, to orient and combine the parts. Such systems require complex global control over the entire system and sufficient manipulation force to combine components.

Macroscale X-Y stages and needle-like micromanipulator probes such as those used for electronic test can be used to assemble microscale systems. The X-Y stage can be used to move components in two dimensions, via a macroscale robotic platform and control system, and then forces exerted to assemble the components together using the microneedle.

Micro Self-Assembly

Self-assembly is the spontaneous formation of higher ordered structures from basic units and, unlike the deterministic robotic manipulation discussed thus far, is a stochastic process. In the case of micro self-assembly, many different forces can be used to assemble components together, including surface tension, electrostatic forces, magnetic forces, and gravity. Micro self-assembly is usually performed in a fluidic environment (fluidic micro self-assembly) and often relies on a shape matching of parts, either into a crystal-like structure or components onto matched *binding sites* on a surface. Thus, micro self-assembly relies on two things: 1) a force to induce the parts to assemble and 2) a method of recognizing parts and orienting them correctly at the binding sites.

Most micro self-assembly processes are performed in a fluid medium and use gravity and/or surface tension for assembly. A prime example is self-assembly of small (submillimeter) flat parts that can be formed into a crystal-like structure on a fluid surface caused by minimization of interfacial surface tension (otherwise known in layperson's terms as the *Cheerios effect*). Another prime example is the utilization of gravitational forces to flow parts over a surface, where shape-recognition is used to place parts and surface tension and van der Walls forces hold the parts in place during subsequent processing.

Key Research Findings

Microassembly Philosophies

Integrated Approaches

Surface micromachining has been employed for integrated microfluidic systems. However, most surface micromachining processes involve deposition and patterning of thin films (limited to several microns in thickness) located only on the substrate surface. Thus, utilization of silicon-based and other thin-film surface micromachining for microfluidics has been limited in application. On example is development of an integrated closed-loop drug delivery system at UC Berkeley, with integrated microneedles, fluid manipulation, and analysis fabricated all using the same surface micromachining process.

Several new surface micromachining processes utilize the thick-film polymer SU-8 for fabrication of channels, wells, and other passive microfluidics that are integrated with electronics or optical detection devices. The development of actuation schemes and interconnect technologies may make integrated polymer microfluidic systems more attractive, although more research is needed for these components as well as the integration of the polymers with other materials to realize truly integrated systems.

Approaches that rely on sequential bonding and patterning of multiple bulk layers rather than film deposition and patterning have been utilized successfully. Complex devices and systems have been realized by alternating DRIE of silicon and fusion bonding [2]. A variation of this approach is, of course, to pattern all the layers individually and then bond them together, an approach which can border on modular depending on the specific device or system in question and how the different layers are used. Complex microdevices, e. g., microturbines, can be realized through DRIE patterning and bonding of five different silicon wafers. Polymer example utilizes surface-activated bonding of multiple layers of patterned PDMS with through holes to build up a mutlilevel microchannel system (e. g., [4]).

Modular Approaches

Many microfluidic circuit boards have been demonstrated in epoxy printed circuit board technologies, polymers, ceramics, glass and silicon. A common problem with board technologies is that components are usually permanently mounted using various bonding techniques (e. g., anodic, adhesive), making replacement difficult. Even still, microfluidic board technologies have been utilized in the development of many microfluidic systems including chemical mixing, pH regulation, and analysis systems.

Verpoorte et al., produced one of the first microfluidic systems based on stacked silicon modules with polymer gaskets forming interfacial layers [5]. Since then, many other researchers have successfully utilized this concept for the assembly of even more complex microfluidic devices and systems.

A major drawback of the embedding of components in a package is that the assembly is usually permanent.

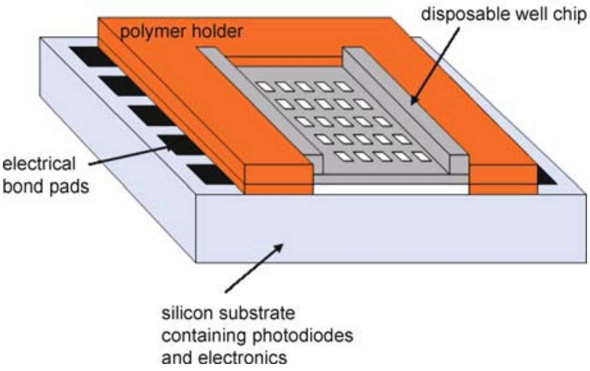

Microfluidic Assembly, Figure 5 Example of disposable microfluidic cartridge interfaced to re-usable instrumentation: disposable well array aligned over re-usable photodiode array using on-chip alignment structures (polymer holder). Chip is used for integrated high-speed screening by monitoring fluorescence changes as chemical reactions proceed inside the wells [7]

An example of such a system combines a small fluidic pump with a glass dielectrophoresis chip, and polymer microchannels [6]. Several other devices successfully combine microchannels with optics for fluorescent activated cell sorting, a closed-loop systems where cells that are tagged with different fluorescent markers can be sorted according to color. Fiber optics or light-emitting diodes and detectors are embedded in a polymer package containing microchannels. Other examples can be found in industry, such as the iSTAT whole blood gas analyzer, a hand held plastic device for manipulating the blood sample into which are embedded simple sensors.

Figure 5 shows an example of a cartridge based integrated high speed screening array, where photodiodes are located under each well for fluorescence detection, but the wells themselves are located on a disposable cartridge that is slid into place using on-chip polymer guides [7]. Other examples include DNA chip cartridges and blood sample analysis cartridges.

Quick-connects were developed in silicon [8] to aid in modular manual assembly. Both finger-joint interconnects perpendicular to the wafer surface, as well as peg-in-hole interconnects parallel to the silicon substrate surface (see Fig. 6b), were realized using KOH anisotropic etching along crystal planes. As these interconnects were developed in silicon, polymer gaskets were needed, complicating the fabrication process. Micro peg-in-hole assembly has been investigated for use in microfluidics, where instead of a simple peg a cylinder is used and assembled into a fluidic hole making a fluid tight connection (see Fig. 6). Fluid-tight interconnects in both deep reactive ion etched (DRIE) silicon [9] and polymers [10] have been developed and used to combine micro-channel containing substrates. The polymer interconnects represent a significant improvement over their silicon interconnects, requiring no additional gaskets and being compatible not only with silicon and glass but polymer substrates, as well, provided suitable bonding/embedding techniques are employed. Polymer interconnects are also superior in that the restoring spring force used to hold the cylinder in the hole is the result of material compliancy, rather than rigid beams, and provides a more uniform joining force [10].

Other noteworthy examples of modular microfluidic systems approaches include 3D MCM chips [11], and multiple layers of integrated systems with electronic, fluidic, and mechanical functionality [12], with new technologies constantly being investigated.

Coupling to the Macroscale World (World-to-Chip Coupling)

Coupling between on-chip channels and off-chip devices is a scale-matching problem that seems universal in the field of microfluidics. Whether a researcher wishes to study flow through a new micromixer, or manipulate and analyze cells for Lab-on-a-Chip, most researcher eventually run across the coupling problem. As a result, a large number of solutions have been developed for providing fluid flow between on-chip microfluidic systems and off-chip devices. A few example devices will be discussed here.

Many reversible press-fit couplers have been developed. One successful design involves a press-fit between a soft tube and a more rigid microstructure on the microchip surface, such as the hexagonal ports shown in Fig. 6f. These ports are fabricated parallel to microchannel flow using KOH anisotropic etching, and have been fabricated in an array of five ports. These ports are usable as is for low pressure flows; at higher pressure flows, adhesive such as RTV silicone must be used in addition to the press-fit. Vertical tubing couplers, where the tubes are perpendicular to the substrate surface, have also be made using press-fits (see Fig. 7). A good discussion of these different couplers can be found in [13]. Example include injected molded plastic couplers, soft molded polymer couplers and compression molded couplers that can be used to hold and seal a fused silica or metal capillary tube in place. Couplers with integrated o-rings have also been developed using a combination of DRIE of silicon and molded silicone o-rings that are squeezed into place. Higher-pressure microfluidic couplers have also been developed that do not rely on adhesives for sealing.

Many glued couplers have been demonstrated, e. g., Fig. 3, where the capillary tube is simply placed in the hole

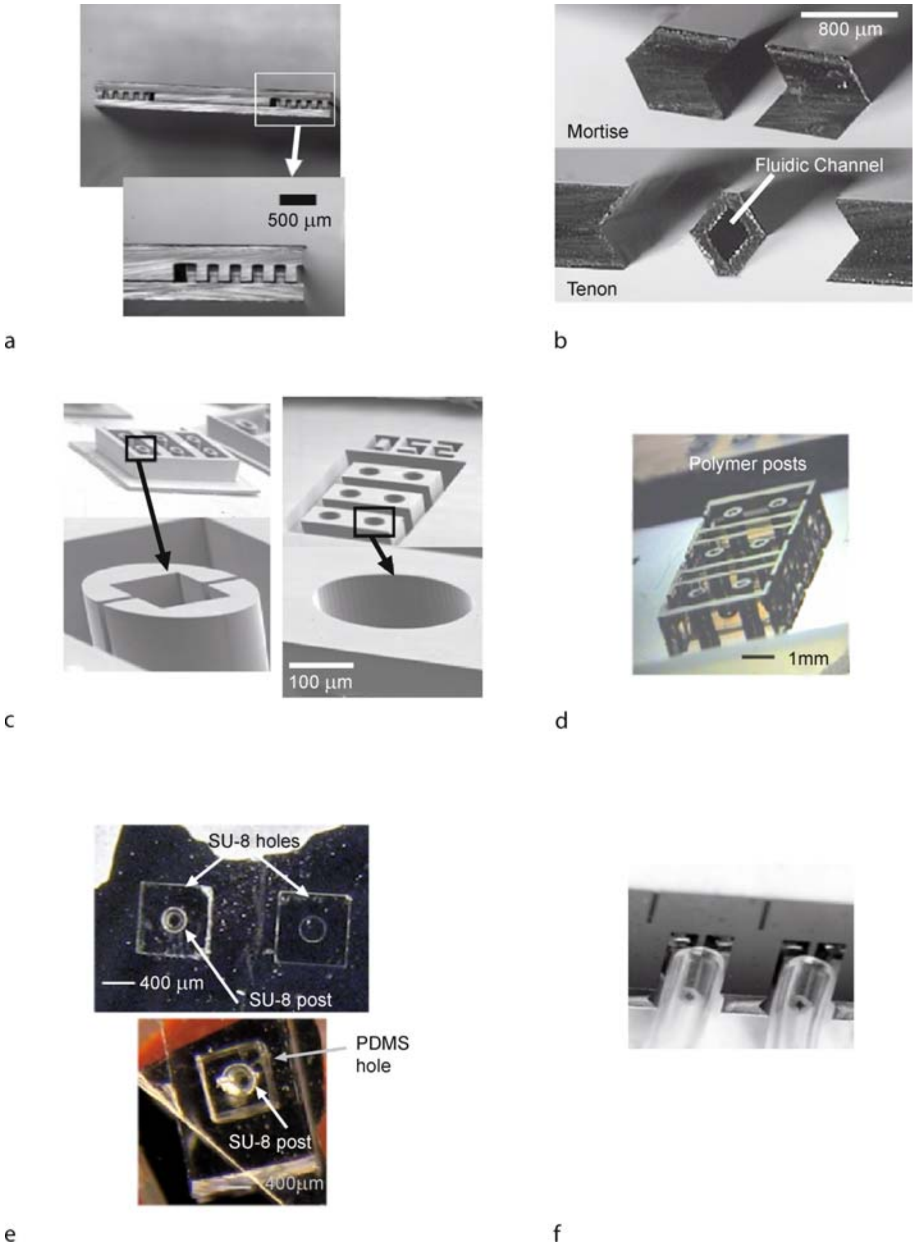

Microfluidic Assembly, Figure 6 Photographs of example press-fit interconnect structures: (**a**) arrays of interlocking silicon fingers; (**b**) silicon hexagonal interlocking interconnects; (**c**) mating silicon notched cylinders and silicon holes; (**d**) polymer cylinders do not require notches; (**e**) polymer cylinders in polymer holes; (**f**) structure in photograph 6b used instead as a soft-tubing press-fit coupler [8–10]

and adhesive used to hold the tube in place and provide a fluid-tight seal. Figure 3c shows a type made by DRIE, where the integrated sidewalls around the tube prevent leakage of the adhesive into the microchannels. A combination of surface roughening, compression molding, and adhesive bonding have also been used to make fluid-tight interconnects [13].

Microassembly Tools and Techniques

Bonding

Bonding has been a key ingredient in many successful microfluidic devices and systems. In fact, most microfluidic devices and systems involve some sort of bonding for at least one part, whether silicon-to-silicon bonding

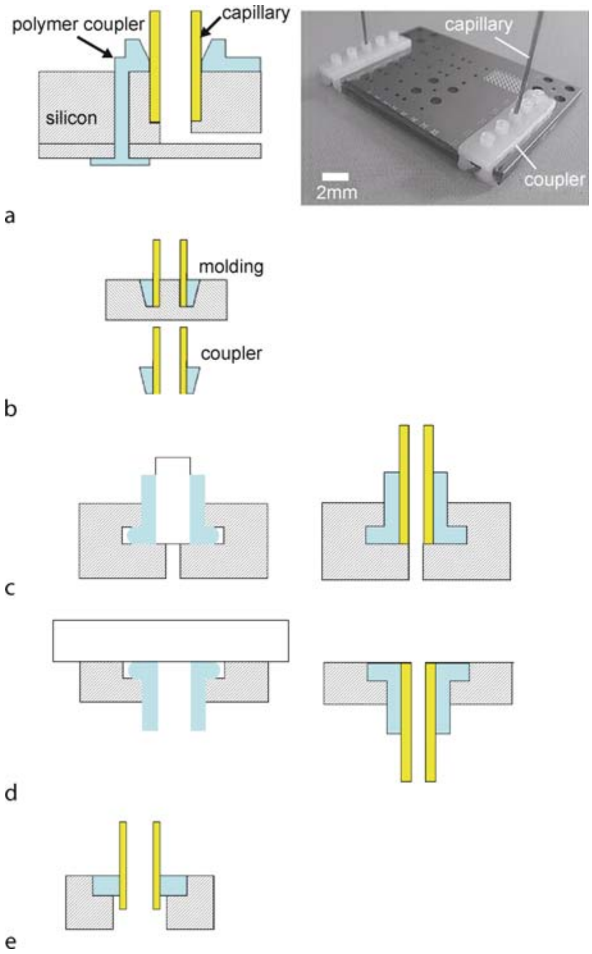

Microfluidic Assembly, Figure 7 Illustrations of press-fit couplers: (**a**) combination silicon DRIE and injected molded polymer coupler [2]; (**b**) PDMS coupler molded to tip of capillary tube; (**c**), (**d**) flanged thermoplastic tube couplers created by thermocompression molding; (**e**) integrated o-ring coupler

to build up multiple channel layers or simple adhesive bonding to hold the system together. Only a few examples are mentioned here. Bonding has been used for microfluidic systems where multiple wafers are patterned, e. g., using deep silicon etching, with microchannels and other fluidic structures, and then bonded together using, e. g., silicon fusion bonding. Silicon-to-glass and silicon-to-silicon bonding has been used for microvalves, micropumps [14], and many other component, as well as combinations of components for complete systems. Bonding has also been used to mount components on microfluidic circuit boards. Polymer bonding of microfluidic parts and components has been similarly utilized for many microfluidic devices and systems, e. g., multiple microchannel layers in PDMS (e. g., [4]), disposable microfluidic circuits using laminate bonding and multiple fluidic and electrical connections using adhesive tape [1], and PMMA bonded microfluidic systems.

Robotic Microassembly

Many robotic microgrippers have been demonstrated, some with accompanying systems that use either teleoperation or automated microassembly. Using a vision system combined with force sensors, researchers (e. g., [15]) have demonstrated systems to automate microassembly. MINIMAN is an example microassembly system with the ability to transfer objects between robots, bond, etc., and perform task planning, which is led by a user via the graphical user interface [16]. The MINIMAN-series design is a translation from conventional macro-scale sensors and control to the micro-scale. Micro peg-in-hole insertion using microgripper has also been demonstrated.
Other robotic microassembly has successfully used air jets, magnetic actuation, or vibrational energy to supply the forces for assembly. In most instances, a global vision system is used to monitor part placement on the two-dimensional assembly grid. Yet another approach popular in Japan is the microfactory which is based on macroscale concepts of fabricating and assembling parts.

Micro Self-Assembly

Due to the difficult and slow nature of assembling complicated microscale devices and systems in a serial and/or deterministic way, self-assembly has generated a lot of research interest as a possible solution to overcome these problems. Many researchers have demonstrated self-assembly on the microscale. Some notable examples include self-assembly of optical components, self-assembly on non-planar surfaces, and self-assembly of microfluidic devices. One group of researchers in Taiwan has even proposed using a microfluidic system for the self-assembly of microfluidic components. Although self-assembly is utilized by many researchers, further research is needed before self-assembly becomes a commonplace microassembly method of microfluidic systems of increasing complexity.

Future Directions

The field of microassembly of microdevices and systems has a long way to go. The addition of the fluidic dimension that is required for microfluidic devices and systems complicates finding a solution, as not only must parts and/or components be joined together mechanically, electrically, and optically as for other systems, but fluid-tight interconnection between parts, devices, or off-chip must all be

provided. One problem is that unlike macroscale devices, systems standards for microfluidics, or a *microfluidic toolbox*, does not yet exist. The necessity for joining disparate materials and processes further complicates matters, especially as surface effects become increasingly important as scale decreases. Other issues, such as dead volume associated with sudden changes in microchannel cross-sections, problems with electrokinetics over changing surface materials, as well as microassembly adhesion force problems, require research solutions before microfluidic systems will become industrially viable.

Cross References

- ▶ Anisotropic Etching
- ▶ Anodic Bonding
- ▶ Fabrication of 3D Microfluidic Structures
- ▶ Integrated Microfluidic Systems for Medical Diagnostics
- ▶ Materials Used in Microfluidic Devices
- ▶ Methods for Surface Modification
- ▶ Microfabrication Techniques
- ▶ Micromolding
- ▶ Packaging (Including Wire Bonding)
- ▶ Self-Assembly Fabrication
- ▶ Soft Photolithography
- ▶ Surface Tension Capillary and Contact Angle
- ▶ Thick Resist Lithography
- ▶ Van der Walls Attraction

References

1. Velten T, Ruf HH, Barrow D, Aspragathos N, Lazarou P, Jung E, Malek CK, Richter M, Kruckow J, Wackerle M (2005) Packaging of bio-MEMS: strategies, technologies, and applications. IEEE Transaction Adv Packaging 28(3):533–46
2. Gray BL, Jaeggi D, Mourlas NJ, van Drieuizen BP, Williams KR, Maluf NI, Kovacs GTA (1999) Novel interconnection technologies for integrated microfluidic systems. Sens Actuators A77(1):57–65
3. B?nger KF, Fearing RS, Goldberg K (1998) Microassembly, In: Nof S (ed) The Handbook of industrial robotics, 2nd edn. Wiley and Sons, p 1045
4. Jo BH, van Lerberghe LM, Motsegood KM, Beebe DJ (2000) Three-dimensional micro-channel fabrication in polydimethylsiloxane (PDMS) elastomer. J Microelectromech Syst 9(1): 76–81
5. Verpoorte EMJ, van der Schoot BH, Jeanneret S, Manz A, Widmer HM, de Rooij NF (1994) Three-dimensional micro flow manifolds for miniaturized chemical analysis systems. J Micromech Microeng 4:246–256
6. Krulevitch P, Benett W, Hamilton J, Maghribi M, Rose K (2002) Polymer-based packaging platform for hybrid microfluidic systems. Biomedic Microdevices 4:301–308
7. Young IT, Moerman van den Doel RLR, Iordanov V, Kroon A, Dietrich HRC, van Dedem GWK, Bossche A, Gray BL, Sarro L, Verbeek PW, van Vliet LJ (2003) Monitoring enzymatic reactions in nanolitre wells. J Microsc 212(2):254–263
8. Gonzalez C, Collins SD, Smith RL (1998) Fluidic interconnects for modular assembly of chemical micro systems. Sens Actuators B 49:40–45
9. Gray BL, Collins SD, Smith RL (2004) Interlocking mechanical and fluidic interconnections for microfluidic circuit boards. Sens Actuators A 112:18–24
10. Jaffer S, Gray BL (2007) Mechanically assembled polymer interconnects with dead volume analysis for microfluidic systems. Proceedings of the SPIE: Microfluidics, BioMEMS and Med Microsyst 6465:1–12
11. Morrissey A, Kelly J, Alderman J (1997) 3D packaging of a microfluidic system with sensory applications, Proc SPIE 3224:161–168
12. Moss ED, Han A., Frazier AB (2007) A fabrication technology for multi-layer polymer-based microsystems with integrated fluidic and electrical functionality. Sens Actuatuators B 121: 689–697
13. Nguyen NT, Wereley ST (2002) Chapter 3 Fabrication techniques for microfluidics, Section 3.5.2 Device level packaging. In: Nguyen NT, Wereley ST (eds) Fundamentals and applications of microfluidics. Artech House, Boston, pp 124–127
14. Nguyen NT, Wereley ST (2002) Chapter 6 Microfluidics for internal control: microvalves, Microfluidics for internal control: micropumps. In: Nguyen NT, Wereley ST (eds) Fundamentals and applications of microfluidics. Artech House, Boston, pp 247–337
15. Zhou Y, Nelson B, Vikramaditya B (1998) Fusing force and vision feedback for micromanipulation. Proceedings International Conference Robotics and Automation, pp 1220–1225
16. Wörn H, Seyfried J, Fahlbusch S, Bürkle A (2000) Flexible Microrobots for Micro Assembly Tasks. Proceedings of the International Symposium on Micromechatronics and Human Science, 22–25 Oct 2000

M

Microfluidic Bioreactors

DOMINIC S. PETERSON
Chemistry Division, Los Alamos National Laboratory,
Los Alamos, NM, USA
DominicP@lanl.gov

Synonyms

Enzymatic bioreactor; Immobilized microfluidic enzyme reactor (IMER); Immobilized enzyme reactor; Immobilized enzyme biosensor; Membrane reactor

Definition

Microfluidic bioreactors are miniaturized systems that are designed to perform a biological transformation on a sample. For instance, a bioreactor with an enzyme will convert the substrate into product when the substrate is present in the sample. Specifically, a protylytic enzyme can be placed in a microfluidic device in order to digest analyte proteins

to facilitate rapid and effective protein sequence mapping. Microfluidic bioreactors are typically fabricated by immobilizing a biologically active enzyme within the microfluidic device. The range of devices that can be made in this way include biosensors, immunoassays, affinity chromatographic stationary phase, and immobilized enzyme reactors. Microfluidic bioreactors are very useful because they have high enzymatic activity and the activity in the device is typically very stable and can be useful over a long time frame.

Overview

Microfluidic bioreactors are a variety of devices that can be made by immobilizing a variety of biologically active substrates within a microfluidic device [1]. The ability to create a variety of biologically important devices is critical to enabling the true total analytical system. The variety of devices that can be made in this way ranges from immobilized enzyme reactors to enzymatic biosensors, immunoassys, and affinity chromatographic stationary phases. In order to form a microfluic bioreactor it is necessary to immobilize the active molecule within the device; either directly onto the channel or onto a solid support within the channel such as a bead or a monolith.

Basic Methodology

The key to making a microfluidic bioreactor is immobilizing a biologically active compound in the microfluidic system. This can be accomplished in a variety of ways, but the two primary categories are covalent immobilization and non-covalent immobilization. Once a micorfluidic bioreactor is made, it can be applied to a wide range of applications including protein mapping and biosensors. In covalent immobilization techniques a covalent bond is formed between the surface of the micorfluidic device and the active molecule. The surface can be either the bare microfluidic channel or it can be a solid support within the device such as a monolith or a bead. Most commonly the immobilization of a enzyme onto a surface will involve forming a linkage between an amine group within the enzyme and a functional group on the surface of the microfluidic device. A wide range of chemical modifications can be used in order to make this covalent linkage. The chemical steps required can require a relatively simple step or it can require a multi-step synthetic strategy in order to make the linkage to the biological compound. The requirement of a synthetic route to make the covalent linkage introduces a significant level of complexity to a system such as a bare microchannel or a monolithic structure. This complexity is due to the need to perform the synthesis within the microfluidic channel, which can be extremely difficult. Beads on the other hand can be modified in a batch process and then introduced to the microfluidic system in a variety of ways.

Non-covalent immobilization typically involves the physical adsorption of a protein onto a solid support. This binding approach is based on ionic interactions, hydrogen bonding, hydrophobic interactions, etc to bind the protein to the solid support. This approach has the advantage that the active molecule is not modified in any way and will therefore retain its full activity. In addition to nonspecific binding, it is also possible to attach a bioactive species to the surface through bio-active interactions, such as an affinity adsorption. This approach is similar to that required for covalently attaching a bioactive compound to the microchip or onto a monolith or bead. The difference is that the compound attached to the microfluidic system has a strong affinity for a complexing biomolecule, which is attached to the active biological compound. The active compound can then be immobilized by passing it through the microfluidic system and allowing the affinity interactions to immobilize the biomolecule. These affinity techniques have been widely used. The advantage is that the active site is typically accessible to the solution and therefore maintains high activity. The last technique that can be used to make a microfluidic bioreactor is by physically confining the biological molecule. This is typically accomplished by encapsulating the protein in a sol–gel structure. This leaves the structure of the protein intact and allows it to maintain a high activity.

Microfluidic bioreactors have a wide range of useful applications that have been demonstrated. The most common application is for immobilized microfluidic enzyme reactors (IMER). IMERs are most commonly used for protein analysis by peptide mapping. Microfluidic bioreactors have also been widely used for biosensing applications. This typically involves immobilizing a enzyme that enables the detection of the analyte of interest. Immunoassays are also a common method to enable the detection of a specific biologically active analyte in a microfluidic system.

Key Research Findings

The most important factor in making microfluidic bioreactors is in the immobilization technique that is used to couple a biologically active functionality into the microfluidic system. In order to incorporate such a functionality into a system the biological compound must be attached to the microfluidic system. This can be accomplished in either an open channel or on a solid support within the microfluidic system. Immobilizing a biologically active compound to an open channel is relatively simple, however limiting

the active functionality to a specific portion of a channel is difficult. In addition, the relatively low surface to volume ratio results in a low overall activity of the bio-active functionality. In order to improve the biological activity of the system it is often necessary to use a solid support to immobilize the biological compounds to [2]. One solid support approach that has been used is monolithic materials [3]. These materials can either be formed by a porous polymer structure or a sol-gel structure. The other approach that can be used to immobilize a biofunctional compound into a microfluidic system is with beads. The great advantage of beads is that the biological functionality can be immobilized in a batch and then be incorporated into the microfluidic system. The incorporation of the beads into the system then becomes the difficult part.

One useful method that is used to immobilize biologically functional compounds into a microfluidic system is to covalently attach a protein or enzyme to the surface or onto the solid support in the microfluidic system [1]. This involves coupling the protein to the surface through a immobilizing site such as the amino, carboxyl, or thiol groups that are present in a protein. In order to make a covalent bond with these groups it is necessary to have a functional group that will be able to react. A wide variety of syntheic strategies have been developed to enable these reactions, as seen in Fig. 1. These reaction approaches include via alcohol groups, amino groups, epoxy groups, carboxylate groups, or other functionalities. Including the necessary functionalities in the microfluidic system simply involves the appropriate organic or silica chemistry depending on the support material that is used in the system. Once the surface chemistry is appropriate the immobilization reactions can be used to incorporate the biological functional compounds into the system. The greatest disadvantage of this approach is that the reactions that are required to immobilize the compounds are difficult to perform in a microfluidic system. This is why using beads, which can be functionalized outside of the system, often provide for a preferred approach to produce the microfluidic bioreactor.

The other major approach to making a microfluidic bioreactor is to use non-covalent techniques. One non-covalent approach involves non-specific adsorption of a biomolecule to the solid support in the bioreactor [4]. This relies on the non-specific physical adsorption of the protein to the surface of the solid support within the microfluidic device. This binding relies on forces such as hydrogen bonding, ionic interactions, hydrophobic interactions, van der Waals forces and so on. Because there is no chemical reaction, the bioactive molecule is not changed and it can therefore retain its full activity for use in the system. However, because the binding forces are relatively weak, the bioactive compound can also wash out of the system and therefore the activity of the system is lost because the active compound is removed from the system. Another non-covalent technique that is used to attach a bioactive species to the microfluidic system is through an affinity (bio-specific) interaction [5]. In this approach, a complimentary pair of proteins are used, with one of the pair immobilized within the microfluidic system and the other attached to the bioactive species of interest. The bioactive species can then be immobilized in the microfluidic system by placing the active compound into the system. Several bio-specific pairs have been used in this approach including Protein A, streptavidin, or the biotin-avidin technique. The great advantage of this oriented immobilization is that good access to the active site of the bioactive protein is maintained. There are other non-covalent methods of placing bioactive compounds in microfluidic system which involve the physical confinment of the protein. For instance, an enzyme can be encapsulated within a sol-gel [6]. This involves placing the enzyme in the sol solution and then forming the sol-gel through the polycondensation of the alkoxysiloxane monomers. This approach is gentle on the encapsulated protein and allows it to completely retain its structure and also maintain high activity.

A wide variety of applications for microfluidic bioreactors have been developed. One of the most common is immobilized enzyme reactors that are used for applications such as biosensors, medial diagnosis and synthetic applications. Most of the applications for immobilized microfluidic enzyme reactors (IMERs) is in protein mapping [7]. This approach is accomplished by incorporating a proteolytic enzyme into the IMER system. Using a microfluidic system for the enzymatic functionalities is ideal because it enables rapid sample handling on small samples. The microfluidic system is also ideal because it allows the reaction time to be significantly reduced, which allows the analysis time to be greatly accelerated. The enzymatic functionality in the IMER is then used to digest a protein. A variety of enzymes have been used in IMER systems including Endoproteinase, Pepsin, and Trypsin. The digested enzyme can then be analyzed in the microfluidic system. This approach can be used not only for mapping of a protein, but it can also be useful in post-translational modifications. This enables the detailed study of cellular functions that exhibit themselves as protein modifications. The real strength of IMER methods is when they are coupled with mass spectrometry methods, particularly when the IMER is coupled directly with the mass spectrometer [8]. This approach enables the identification of the peptide fragments that result when a pro-

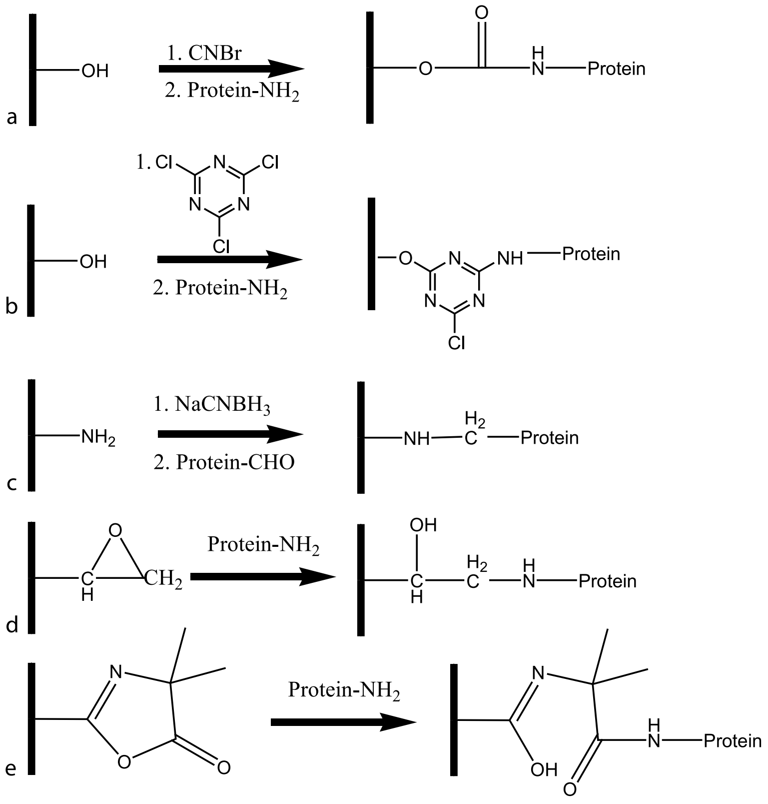

Microfluidic Bioreactors, Figure 1

tein is digested in the microfluidic bioreactor. The identification of the peptide fragments enables the total protein to be identified and mapped. These methods are very powerful and are finding widespread use in proteomics. These IMERs can also be coupled with separation methods such as capillary electrophoresis and micro high performance liquid chromatography. Separation methods allow complex samples to be handled by introducing different proteins in the sample to the bioreactor at different times. Coupled with protein mapping techniques it is then possible to identify the proteins in a sample. It is also possible to identify post-translational modifications.

Microfluidic bioreactors have also been widely used to make immobilized enzyme biosensors. In this application the bioreactor is applied as a part of a detection device for a biologically important analyte. For instance, glucose can be detected by having a bioreactor that contains glucose oxidase immobilized in a microfluidic system [9]. The enzyme enables detection of glucose by electrochemical detection of the products of the bioreactor.

Another application that microfluidic bioreactors have been used for is in immunoassays. These are based on antigen-antibody interactions and is a powerful technique because these interactions have very high selectivity and are extremely sensitive. Typically, an immunoassay is performed by immobilizing one of the binding partners is placed within the system. The corresponding pair is then incubated within the device. The advantage of this approach is the ability to very specifically concentrate molecules on the active surface of the device. This enables enhanced reaction efficiencies, simplified analytical procedures, and reduced consumption of reagents. These immunoassay methods are often coupled with separation methods such as capillary electrophoresis in order to further increase the utility of the method [10].

The use of affinity interactions was described earlier as a method to immobilize a bioactive species within a microfluidic device. Affinity methods can also be used as a way to make a stationary phase in a microfluidic system [11]. This approach relies on the formation of strong, but reversible interactions between the analyte and the stationary phase. Because the binding interactions are reversible it is possible to concentrate the analyte of interest into a very narrow band, which further enables the introduction of high purity compounds into subsequent portions of the analytical device.

Future Directions for Research

Microfluidic bioreactors is a technology that is becoming fairly widespread. The number of applications that they are applied will continue to expand in the future. Advances will continue to be made in coupling the microfluidic within more complex microfluidic systems. This should include separation methods so that the reactions in the bioreactor can either be performed on specific analytes in a mixture or so that the products of the bioreactor can be separated to further enable analysis of the products. New and more efficient methods of incorporating the bioactive compounds into microfluidic bioreactors still will have great applicability.

Cross References

- ▶ Bead-based Microfluidic Platform
- ▶ Biomolecular Synthesis in Microfluidics
- ▶ Bioprinting on Chip
- ▶ Infrared Imaging and Mapping for Biosensors
- ▶ Cell Patterning on Chip
- ▶ Mass Spectroscopy
- ▶ Integrated Micro Devices for Biological Applications
- ▶ Integrated Microfluidic Systems for Medical Diagnostics
- ▶ Lab-on-Chip Devices for Immunoassay
- ▶ Lab-on-Chip Devices for Protein Analysis
- ▶ Mass Spectrometry on Chip Devices
- ▶ MEMS-Based Biosensor
- ▶ Methods for Surface Modification
- ▶ Nanoscale Biosensors
- ▶ Proteomics in Microfluidic Devices

References

1. Krenkova J, Foret F (2004) Electrophoresis 25:3550–3563
2. Peterson DS (2005) Lab Chip 5:132–139
3. Jungbauer A, Hahn R (2003) Catalysts and Enzyme Reactors. In: Svec F, Tennikova TB, Deyl Z (eds) Monolithic Materials. Elsevier Science, Amsterdam
4. Gao J, Xu J, Locascio L E, Lee CS (2001) Anal Chem 73:1067–1074
5. Amankwa LN, Kuhr WG (1992) Anal Chem 64:1610–1613
6. Sakai-Kato K, Kato M, Toyo'oka T (2002) Anal Chem 74:2943–2949
7. Gevaert K, Vandekerckhove J (2000) Electrophoresis 21:1145–1154
8. Cooper JW, Chen J, Li Y, Lee CS (2003) Anal Chem 75:1067–1074
9. L'Hostis E, Michel PE, Flaccabrino GC, Strike DE, de Rooij NF, Koudelka-Hep M (2000) Sens Actuators B 64:156–162
10. Dodge A, Fluri K, Verpoorte E, de Rooij NF (2001) Anal Chem 73:3400–3409
11. Pan Z, Zou H, Mo W, Huang X, Wu R (2002) Anal Chim Acta 466:141–150

Microfluidic Cell Culture

▶ Microfluidic Devices in Tissue Engineering

Microfluidic Chip

▶ Electrochemical Techniques
▶ Transferring Samples to Chips, Techniques

Microfluidic Circuits

PRASHANTA DUTTA[1], KEISUKE HORIUCHI[2], TALUKDER Z. JUBERY[1]

[1] School of Mechanical and Materials Engineering, Washington State University, Pullman, WA, USA

[2] Mechanical Engineering Research Laboratory, Hitachi, Ltd., Hitachinaka, Ibaraki, Japan

dutta@mail.wsu.edu

Synonyms

Flow field-effect transistor; Field-effect flow control; Fluerics; Fluidic logic; Fluidic amplification and oscillation

Definition

A microfluidic circuit is a configuration of microscale fluidic components such as microchannels, individually addressable valves, and chambers through which fluid is allowed to flow. This definition is similar to the description of an electric circuit, which is a configuration of electronic components through which electricity is made to flow. A microfluidic circuit can control flow rates, flow directions, particle separation, mixing and reaction of chemicals, etc. on a single microdevice for lab-on-a-chip operations. Individual components of microfluidic circuits are often described using a model analogous to an electric circuit.

Overview

Like electric circuits, fluidic circuits can consist of individual components such as fluidic resistors, capacitors, inductors, and transistors. Brief descriptions of various components of microfluidic circuits are given below in this section.

Fluidic Resistance

The fluidic resistance is the pressure differential required to obtain a unit flow rate in a fluidic channel. The general formula for the fluidic resistance can be given as

$$R_{\mathrm{f}} = \frac{\Delta P}{Q} \tag{1}$$

where ΔP is the pressure difference and Q is the flow rate. Thus, by comparing Eq. (1) with Ohm's law for a DC circuit, assuming that the flow is steady and there is no energy dissipation in the system, it can be shown that ΔP is analogous to an electric potential difference, and the flow rate Q to an electric current. For a planar microfluidic conduit of length L, width W, and height H, the fluidic resistance is given by

$$R_{\mathrm{f}} = 12\frac{\mu L}{WH^3}, \tag{2}$$

where μ is the viscosity of the fluid. Fluidic resistance is also known as fluidic impedance.

Fluidic Inductance

The fluidic inductance is defined by

$$L_{\mathrm{f}} = \frac{\Delta P}{\mathrm{d}Q/\mathrm{d}t}, \tag{3}$$

where t is the time. The physical meaning of the fluidic inductance is that it describes how fast the flow rate follows the pressure signal. In a fluidic circuit, the characteristic response time can be expressed as

$$t_{\mathrm{L}} = \frac{L_{\mathrm{f}}}{R_{\mathrm{f}}}. \tag{4}$$

A typical value of the characteristic response time for water in an 800 μm capillary is approximately 20 ms, and so the typical frequencies in a microfluidic circuit are on the order of 100 Hz.

Fluidic Capacitance

The fluidic capacitance is the pressure-dependent volume change under isothermal (or adiabatic) conditions, and can be expressed as

$$C_{\mathrm{f}} = \frac{\partial \forall}{\partial P} = -\beta \forall \tag{5}$$

where $\forall$ is the volume of interest and β is the compressibility, or bulk modulus of elasticity. The physical meaning of the fluidic capacitance is that it describes how much the volume of interest changes with respect to a pressure change. The fluidic capacitance is normally used in the case of applications that involve elastic membranes and/or compressible fluids.

Fluidic Transistors

These are also known as flow field effect transistors (flow FETs). Fluidic transistors make use of the surface charge conditions to control the flow in a microfluidic chip. They are generally used with electrokinetically based microflows to modulate the zeta potential at the shear plane. Fluidic transistors can be used to control the flow both locally and globally in a microfluidic channel.

Fluidic Amplifiers

A fluidic amplifier controls the pressure and the flow rate in a microchip through the interaction of multiple fluid streams or jets. Fluidic amplifiers can be used for both analog (proportional) and digital (bistable) control. They can also be used to perform various Boolean functions in a microfluidic chip for the purpose of control logic.

Fluidic Logic

A logic circuit can be formed in a microfluidic chip by incorporating appropriate resistances and/or valves into the flow paths [1]. The various logical functionalities that can be integrated into a chip are OR, AND, NOR, NAND, conversion, and inversion. Fluidic logic can be designed to control the flow and/or mixing of droplets in a microchip.

Basic Methodology

A number of microfluidic circuits have been developed; their principles of operation depend on the mechanism of fluid flow in the microchip. In this article, we shall describe only the fluidic circuits used with pressure-driven flow and electrokinetically driven flow, as these are the two main pumping methods for continuous-flow microfluidic devices. Pressure-driven flow can be obtained by connecting the channel to a syringe pump or a compressed gas. Electrokinetic flow of an ionized electrolyte can be obtained by applying an electric field along the flow direction.

Fluidic Circuits for Pressure-Driven Flow

In a microfluidic channel, the flow becomes laminar because the viscous force is dominant over the inertia of the fluid. Hence, the effects of turbulence used to control flow in regular-scale devices cannot be applied in a microchannel. Most fluidic circuits used for pressure-driven microflow are based on fluid resistance. For

a microflow conduit, a general expression for the fluid resistance is [2]

$$R_{\mathrm{f}} = C\frac{\mu L}{A_{\mathrm{c}}^{2}}\,, \tag{6}$$

where A_{c} is the cross-sectional area, and C is a constant. Values of C for several different channel geometries are listed in Table 1.

Fluidic control can be achieved by changing the impedance of the fluid path and/or by modulating the mass flow rate of the incoming fluid streams. The working principles of some recently tested pressure-driven microfluidic circuits are presented below.

Fluidic Logic Circuit

In a complex microfluidic network, the direction of fluid or particle flow can be controlled effectively by changing the resistances of individual flow conduits. Equation (6) shows that the flow resistance of any particular channel can be modulated by changing the channel dimensions, such as the cross-sectional area and the channel length, or by varying the fluid viscosity. The fluidic resistance can also be altered by inserting a bubble or a droplet of another liquid (other than the fluid flowing in the microchannel). In this case, the interface between the two fluids (between the bubble(s) and the flowing fluid) increases the fluidic resistance. Using this principle, Parkash and Gershenfeld [3] developed a type of microfluidic logic gate called "bubble logic". In the logic circuit that these authors constructed, the binary symbols "0" and "1" were represented by the absence and presence, respectively, of a bubble in a microchannel.

The basic operating principle of a bubble logic gate [3] is shown in Fig. 1. This microfluidic circuit consists of two input channels (A and B) and two output channels (X and Y). Channel X is slightly wider than channel Y, i. e. channel X has a lower fluidic resistance than Y. Hence, if a bubble reaches the junction by way of input channel A or B then it will always take the output channel X owing to the lower fluidic resistance. But if two bubbles arrive simultaneously from input channels A and B, then the first bubble will take the output channel X. This first bubble increases the fluidic resistance of channel X and causes the other bubble to flow through channel Y. For detailed information on other microfluidic logic circuits, readers are advised to consult [3].

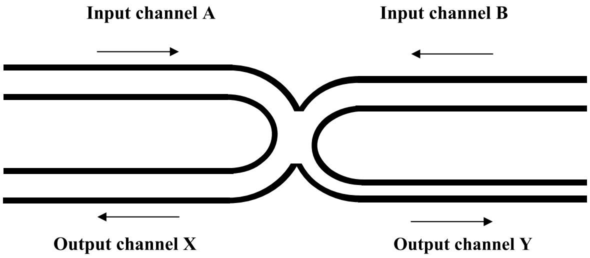

Microfluidic Circuits, Figure 1 Schematic view of a four-channel microfluidic logic gate [3]. The lengths and cross-sectional areas of the input channels A and B are the same. The flow resistance of the output channel Y is higher than that of X owing to its smaller cross-sectional area

Microfluidic Circuits, Table 1 Typical channel geometries used in microfluidic circuits [2]

Cross section	Class	C
	Capillary tube	$8\pi = 25.13$
	Equilateral triangle	$\frac{60}{\sqrt{3}} = 34.64$
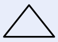	KOH-etched triangle ⟨100⟩	35.12
	KOH-etched trapezoid	$\frac{12-1.38A_{\mathrm{c}}+4A_{\mathrm{c}}^{2}}{A_{\mathrm{c}}-0.85A_{\mathrm{c}}^{2}+0.28A_{\mathrm{c}}^{3}}$

Fluidic Amplifier Circuit

The primary goal of a microfluidic amplifier is to increase the pressure at a set of outlet ports by modulating some control pressures. Microfluidic amplifiers can be primarily classified into two types: analog and digital. The first type uses the effect of jet interaction, whereas the second type makes use of the wall attachment effect in a fluid.

A schematic view of an analog or jet interaction amplifier is shown in Fig. 2a. The device consists of a supply nozzle, two inlet (control) ports, two outlet ports, and two vents. This device is geometrically symmetric about its vertical axis. A uniform jet is supplied to the amplifier via the supply nozzle. Depending on the flow rates at the control channels, there can be three types of scenario at the output channels. First, if there is no flow through the control inlet(s), the fluid jet exiting from the nozzle will flow in a straight line, and it will be equally divided into two outlet streams. Second, if the flow rates of the control inlets are the same, the resultant jet will also travel in a straight line and will split symmetrically between the output ports. Third, if a differential pressure is applied between the two inlet ports, the resultant jet will be deflected from a straight line and the flow rates through the outlet ports will change. The difference between the pressures at the output ports will increase with increasing differential input pressure.

The digital amplifier works on the basis of the Coanda, or wall attachment, effect [4]. In 1930 Henri Coanda observed that a moving fluid has a tendency to attach itself to a surface and flow along it, even if the direction of

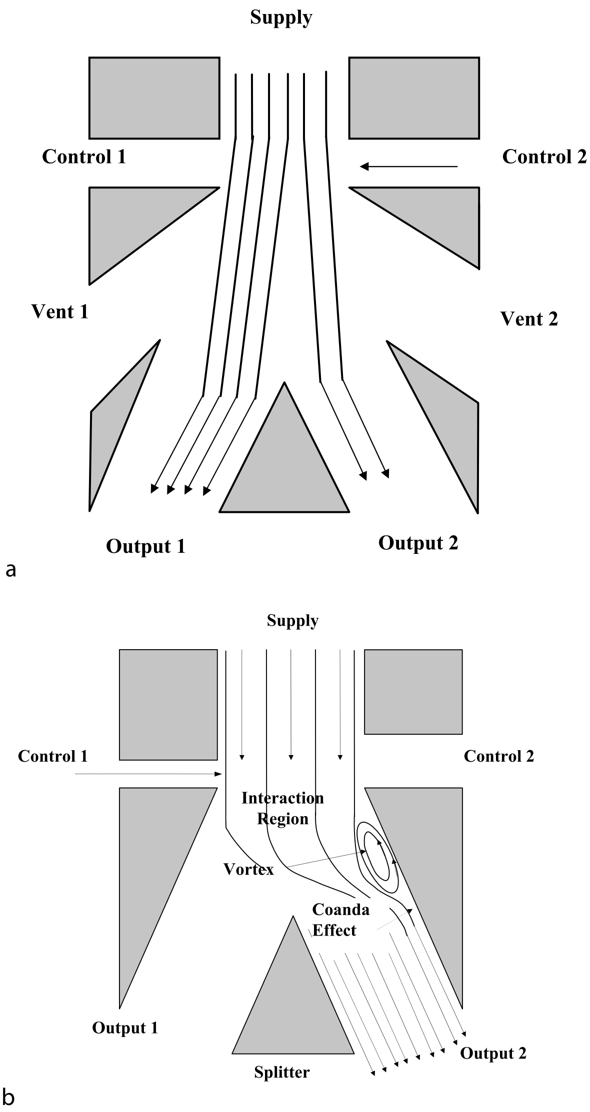

Microfluidic Circuits, Figure 2 (**a**) Schematic view of an analog, or jet, interaction amplifier [11]. The supply jet exits through both of the outputs 1 and 2. The ratio of the mass flow rate at output 1 to that at output 2 is determined by the control ports 1 and 2. (**b**) Schematic view of a digital, or wall attachment, amplifier and its working principle [11]. The supply jet exits through either output 1 or output 2. Switching between these outputs is guided by the control ports 1 and/or 2

curvature of the wall is away from the primary axis of flow. Figure 2b shows a schematic view of a digital wall attachment amplifier. If a constant jet is supplied from the entry nozzle, it will be attached to one of the attachment walls owing to the Coanda effect and will eventually exit through that outlet (#2 in Fig. 2b). However, the exiting jet can be toggled to the other output port if a temporary flow at a small pressure is applied through the control port next to the attached jet. Thus, this wall effect amplifier switches a large flow from one output port to the other by means of a small control flow. In this fluidic circuit, two vent ports are used to decrease the internal pressure and also to control the loading of the output by the control flow [5].

Fluidic Circuits for Electrokinetically Driven Flow

Flows in microfluidic channels are often driven by electrokinetic means. In an electrokinetic flow, an ionized liquid can be forced to move in a dielectric capillary or microchannel under the action of an externally applied field. Electrokinetic flow is an attractive option for driving samples because (a) it can be integrated within a single microchip, (b) the flow rate can be controlled very precisely using an externally applied electric field, (c) no mechanical parts are required, (d) it is useful for a wide range of electrical conductivity of the sample, and (e) the velocity distribution across the microchannel is plug-like. In a planar microchannel, the electrokinetic velocity distribution can be represented by the Helmholtz–Smoluchowski velocity as follows [6]:

$$u \cong u_{\mathrm{HS}} = \frac{\varepsilon \zeta E_x}{\mu}\,, \tag{7}$$

where ζ is the zeta or electrokinetic potential, ε is the permittivity, and E_x is the electric field. The equation above shows that the magnitude of the electrokinetic flow velocity in a microchannel can be controlled either by changing the external electric field applied along the flow direction or by modifying the electrokinetic potential at the shear plane. For control of the global flow in the entire microchannel, the applied electric field is generally altered; this method is relatively straightforward to implement in a microchannel. On the other hand, selective manipulation of the zeta potential can be implemented to obtain local flow control in a microchannel or capillary. However, this technique is quite challenging because the zeta potential depends on the solution pH, the buffer concentration, and the surface charge density.

One commonly used device for controlling the zeta potential is the flow FET [7–9]. The basic principle of the flow FET is that a constant perpendicular electric field from a side channel is used to modify the local zeta potential. A schematic of a typical flow FET is shown in Fig. 3. The device consists of a main channel and a side channel, separated by a very thin wall (nanometer to micron size). In a flow FET, the working fluid moves only through a main microchannel (horizontal) from the source reservoir to the drain reservoir. A gate potential generates a perpendicular electric field that controls the zeta potential, which locally alters the flow in the channel. The change in zeta potential

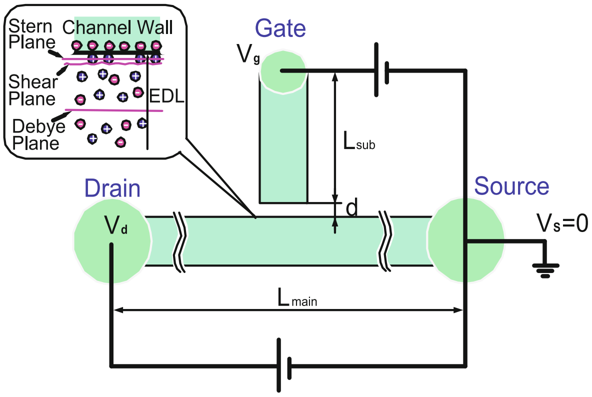

Microfluidic Circuits, Figure 3 Schematic view of a field-effect-controlled microfluidic device for application in a straight channel [9]. The main (horizontal) channel is separated from the subchannel (vertical) by a micrometer-scale distance (d). The potentials at the drain and gate reservoirs are V_d and V_g, respectively, and the source reservoir is connected to a common ground ($V_S = 0$). The inset shows the formation of an electric double layer (EDL) next to the channel surface

for a particular gate voltage V_g can be expressed as [9]

$$\Delta\zeta = \zeta - \zeta_0 = \frac{C_{total}}{C_{EDL1}} \Delta V_C = \frac{C_{total}}{C_{EDL1}} R \left(V_g - V_{g0}\right), \quad (8)$$

where ζ_0 and V_{g0} are the reference zeta potential and the gate voltage for which there is no current from the side channel to the main channel, respectively. R is a system constant that depends on the electrical resistances of the main channel, side channel, and separation wall. The total capacitance of the flow FET (C_{total}) can be expressed as [8]

$$C_{total} = \left(C_{wall}^{-1} + C_{EDL1}^{-1} + C_{EDL2}^{-1}\right)^{-1}, \quad (9)$$

where C_{EDL1} and C_{EDL2} are the capacitances of the electric double layers in the control (side) channel and in the main channel, respectively, and C_{wall} is the capacitance of the separation wall.

Key Research Findings

Microfluidic Logic Gate

A microfluidic logic gate eliminates the need for external valves to control the flow and mixing in microchannels. It also increases the speed of response of the control mechanism: this speed is about 100 times faster than that of external control devices. Figure 4 shows experimental results obtained from a bubble-based logic gate in a microfluidic chip [3]. The microfluidic channels were formed on polydimethylsiloxane (PDMS) using standard soft-lithography techniques, and a Pyrex substrate was used to cover the channel. In this experiment, water was used as the working fluid, and nitrogen bubbles (0.5 psi) were introduced into the water. In order to obtain dominant surface tension effects in the microchannels, bubbles of low capillary number $\mathrm{Ca} = \mu U/\sigma$, where σ is the surface tension and U is the flow velocity, were used. At low capillary number, surface tension dominates over viscous stress, which ensures that there is no splitting of bubbles at a point of bifurcation [10]. Three different cases of logic control, listed in Table 2, are presented in Fig. 4.

Microfluidic Circuits, Table 2 Logical outputs of AND and OR gates for various inputs in the channels A and B shown in Fig. 1. Here, the presence and absence of a nitrogen bubble in water are represented by binary states "0" and "1", respectively [3]. An AND gate returns an output of "1" if both inputs are "1". An OR gate returns an output of "1" if either or both inputs are "1"

	Input channel		Output channel	
	A	B	Y	X
			AND gate	OR gate
Case 1	0	1	0	1
Case 2	1	0	0	1
Case 3	1	1	1	1

- *Case 1 (top row).* One nitrogen bubble and water were introduced through channel A, while only water was allowed to flow through channel B. When the nitrogen bubble reached the junction it took the output channel X owing to the low fluidic resistance and low capillary number. Hence, channel X functions as an OR gate, while channel Y functions as an AND gate.
- *Case 2 (middle row).* In this case water and one nitrogen bubble were introduced through channel B, but only water was introduced through channel A. As in Case 1, the bubble at the junction took the low-resistance output channel X, and so the output of channel X was 1 and that of channel Y was 0.
- *Case 3 (bottom row).* One nitrogen bubble was allowed to flow with water from each of the channels A and B. At the junction, the first bubble took the path of the wider channel X. The presence of the first bubble in channel X increased its fluidic resistance, and so the other bubble was forced to take the output channel Y. Therefore, the outputs of X and Y were both 1.

Microfluidic Amplifier

Schomburg et al. [11] have demonstrated the feasibility of a microfluidic-based jet interaction amplifier. A scan-

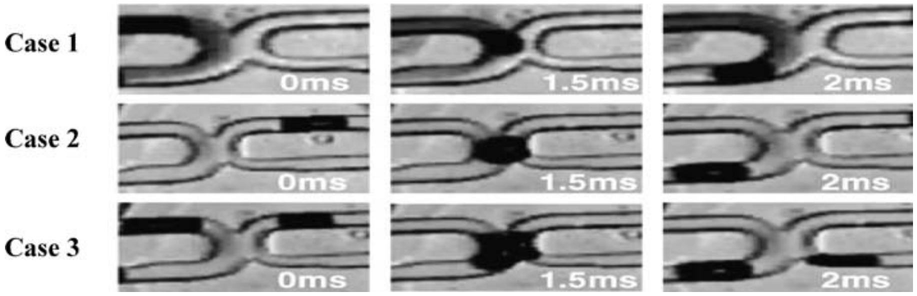

Microfluidic Circuits, Figure 4 Operation of four-channel bubble logic (AND and OR) gates, from Parkash and Gershenfeld [3]. Reprinted with permission from AAAS. The nomenclature used to identify channels *A*, *B*, *X*, and *Y* is identical to that used in Fig. 1. *Left column:* a bubble is flowing through an input channel (*A* and/or *B*) towards the four-way junction. *Middle column:* the bubble reaches the junction of the two input channels. *Right column:* the bubble travels through output port *X* or *Y*, depending on the flow resistances in the output channels. The images for the left, middle, and right columns were taken at 0 ms, 1.5 ms, and 2.0 ms, respectively [3]

ning electron microscope (SEM) image of a microscale analog jet interaction amplifier is shown in Fig. 5a. This microamplifier was formed on PMMA using the well-known LIGA process. Figure 5b shows experimental results [11] obtained using nitrogen gas. A jet of 20 hPa pressure and 45 m/s mean velocity was supplied by the main nozzle. The flows through the control ports were varied to obtain a pressure differential at the outlet ports. Figure 5b shows that the output differential pressure varied linearly within a certain range of the differential control (input) pressure. The amplification of the input pressure in this amplifier depends on discharge of the supply jet.

The same research group also introduced a microfabricated digital wall attachment amplifier [11] for bistable control of flow. An SEM image of a microscale digital wall attachment amplifier formed on PMMA is illustrated in Fig. 6a. The pressure in one of the output ports (opposite to the control port used) is shown in Fig. 6b for various values of the control port pressure. The output pressures were measured at output 2 while the input control pressure was varied at inlet 1. In the experiment, a jet of 330 hPa pressure was supplied through the main nozzle, while the pressures at the control ports were varied from 0 to 12 hPa. The experimental results showed that if the jet was attached to the wall next to a control port, then temporary application of pressure (12 hPa) to that control port guided the jet to the opposite wall. The jet continued to flow along that wall after the removal of the control jet. A minimum supply pressure was needed for the action of this amplifier. The experimental results also showed that the supply pressure had no effect on the pressure recovery (ratio of maximum output to input pressure) and flow recovery (ratio of maximum output to input flow) in this amplifier.

Flow Field Effect Transistor

A schematic of a flow FET for a T-junction is presented in Fig. 7a. The drain and gate reservoirs were connected to positive voltages, while the source reservoir was grounded. The branch channel reservoir was electrically floating. Initially, the pressure head at each reservoir was maintained at the same value so that there was no movement of the fluid before an external electric field was applied. Figure 7b shows the fluid flow behavior for the no-control scenario. In this case, the drain, source, and gate potentials were 48, 0, and 25 V, respectively. The streamlines shown in Fig. 7b indicate the direction of the flow in both the main and the branch channel for the above-mentioned electrical conditions. These streamlines imply that a pressure is induced along the main channel owing to an electrokinetic pumping action, and the balance of pressure among the three reservoirs is broken.

To control the flow, we intentionally created a leakage current by changing the value of the gate voltage from its equilibrium state. This leakage current modified the zeta potential in the controlled region. The change in the zeta potential on one side of the channel wall resulted in a transverse electric field, which created a cross-stream velocity component. Figure 7c shows the velocity vector distribution in a control case for which the gate voltage was 18 V ($\Delta V_g = -7$ V). In this case, almost no sample enters the branch channel, and this specific scenario is particularly useful if one desires to transport a sample such as protein or DNA through a T-junction with minimum band distortion. Here, the effect of the field on the flow at the T-junction acts like an electroswitching valve using the benefits of the crossstream velocity component [9].

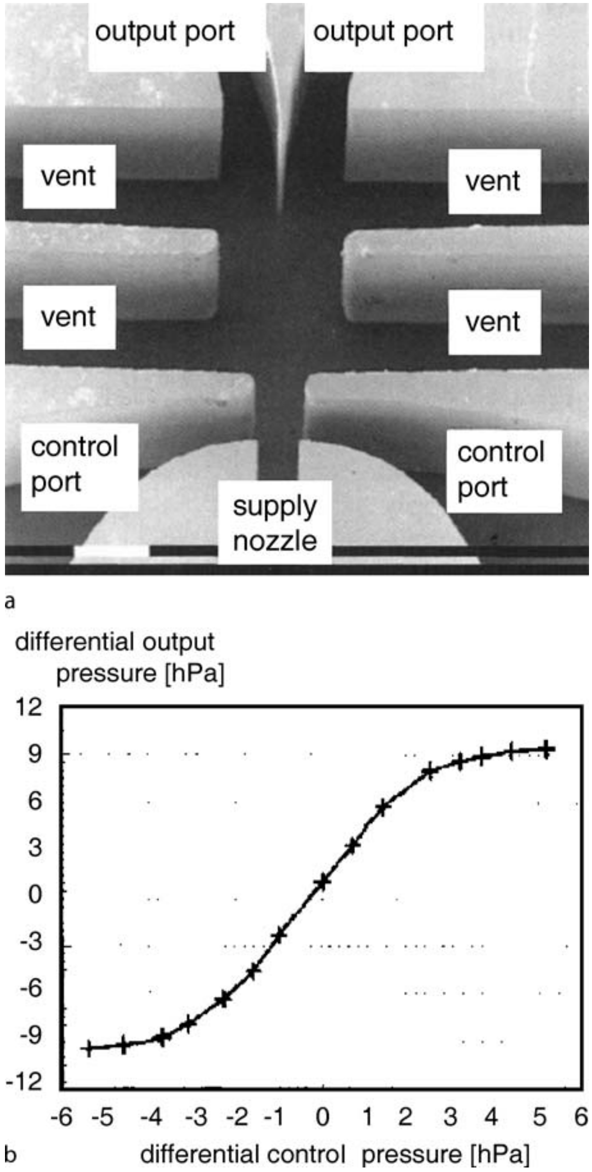

Microfluidic Circuits, Figure 5 (**a**) SEM image of an analog jet interaction amplifier (supply nozzle width 55 μm, amplifier height 500 μm) fabricated on PMMA using the LIGA techniques [11]. (**b**) Pressure differential between the output ports as a function of input pressure difference between the control ports [11]. Reproduced from [11] with permission from IOP. The supply pressure was 2 hPa and the working fluid was nitrogen gas [11]

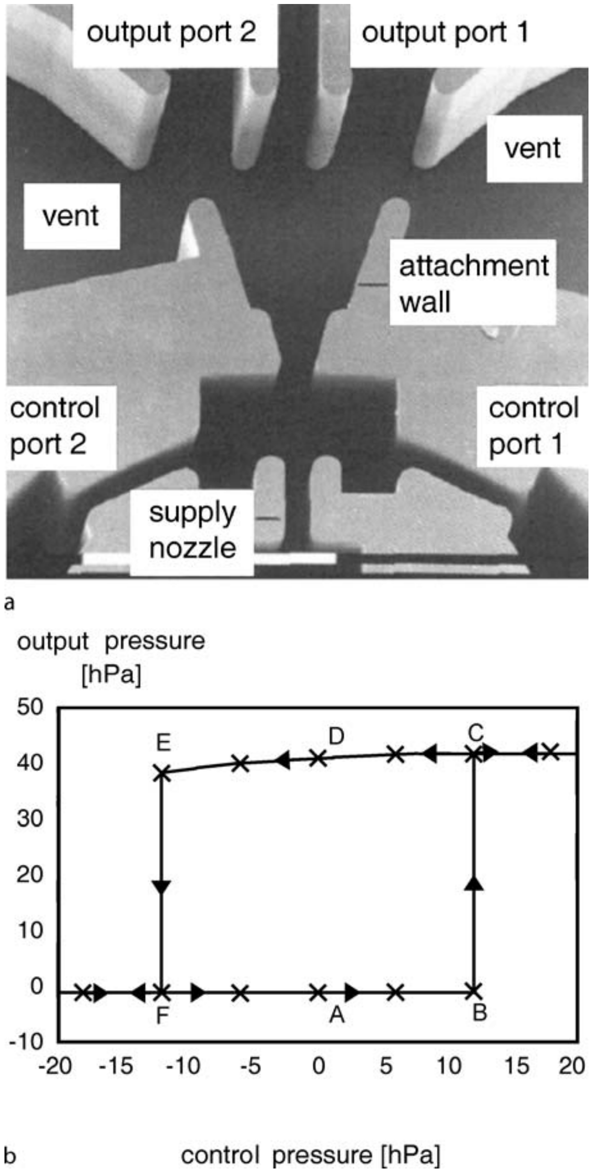

Microfluidic Circuits, Figure 6 (**a**) SEM image of a digital wall attachment amplifier (supply nozzle width 32 μm, amplifier height 500 μm) fabricated on PMMA using the LIGA techniques [11]. (**b**) Switching behavior of digital wall attachment amplifier. Reproduced from [11] with permission from IOP. The supply pressure was 330 hPa and the working fluid was nitrogen gas [11]

Future Directions for Research

Microfluidic circuits have enormous potential for the control of flow and ionic concentration, separation of proteins and DNA, and sensing of single molecules in a complex microfluidic chip. For instance, the microfluidic transistor presented in Fig. 7 could be used to control the flow rate in a number of branch (side) channels. Moreover, an array of flow FETs could be used to dynamically modify the zeta potential along a channel during an electrophoretic separation process. However, to maximize the effects on the zeta potential via an externally applied gate voltage, a very thin channel wall (which acts as an insulator or capacitor) is needed because the wall capacitance is inversely propor-

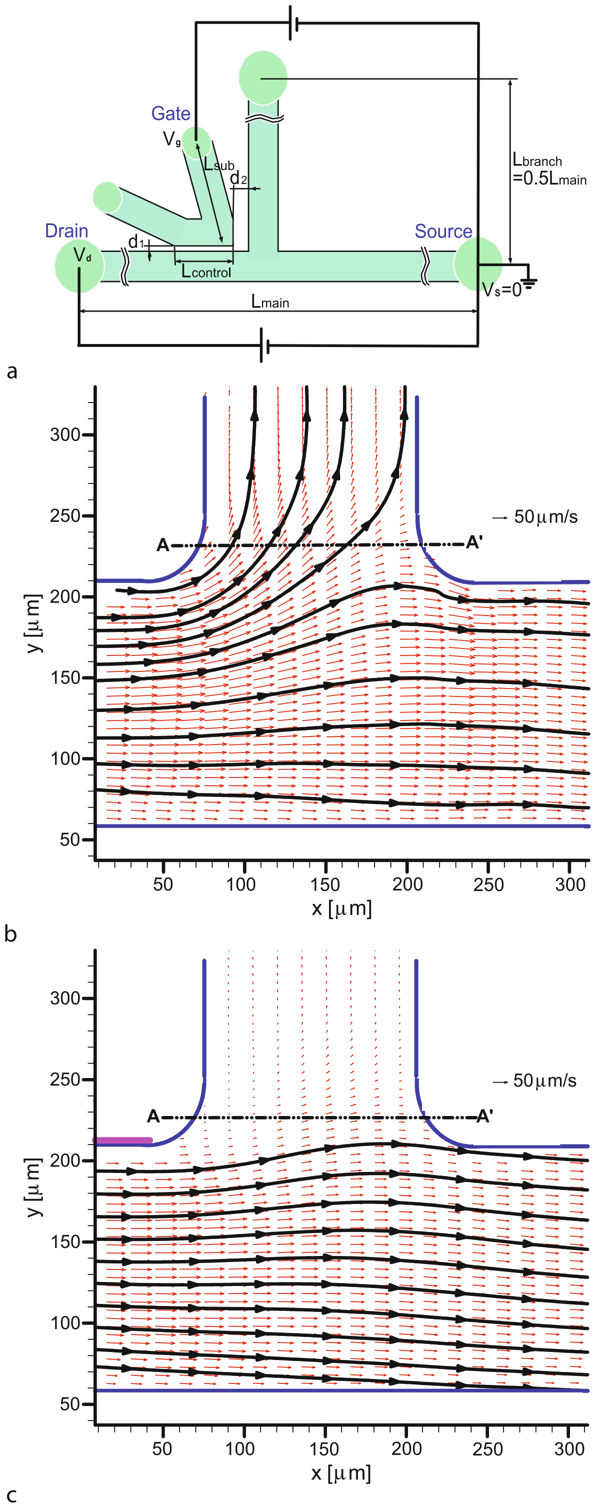

Microfluidic Circuits, Figure 7 (**a**) Schematic view of experimental setup for local flow control at a T-channel junction [9] (reproduced by permission of the Royal Society of Chemistry). Microchannel structures and a flow FET were formed on PDMS using soft-lithography techniques. The length, width, and height of the main channel are 2 cm, 150 µm, and 10 µm, respectively, and the geometric parameters are $d_1 = 50$ µm, $d_2 = 125$ µm, $L_{sub} = 3$ mm, and $L_{control} = 1$ mm. The drain voltage was set to $V_d = 48$ V. (**b**), (**c**) Vector plots of flow velocity in T-channel junction for (**b**) $V_g = 25$ V and (**c**) $V_g = 18$ V. The streamlines (black solid lines) show the net flow direction in the microchannel

tional to the thickness of the wall (in the case of a rectangular channel). Recently, Karnik et al. [12] examined the effects of the perpendicular electric field originating from the gate voltage in a nanofluidic channel. These authors found that both the zeta potential and the ionic concentration were influenced when the channel size was comparable to or smaller than the Debye length. In addition, a number of research groups have been working on nanofluidic diodes using the flow FET concept.

Cross References

- ► Microfluidic Mixing
- ► Bubble-Actuated Microfluidic Switches
- ► Bubble Dynamics in Microchannels

References

1. Vestad T, Marr DWM, Munakata T (2004) Flow resistance for microfluidic logic operations. Appl Phys Lett 84:5074–5075
2. Schaedel HM (1979) Fluidische Bauelemente und Netzwerke. Vieweg, Braunschweig
3. Prakash M, Gershenfeld N (2007) Microfluidic bubble logic. Science 315:832–835
4. Krishner JM, Katz S (1975) Design Theory of Fluidic Components. Academic Press, New York
5. Simoes EW, Furlan R, Pereira MT, Choi DH (2002) Flow-based characterization of the operation of a microfluidic amplifier. Micro Thermophys Eng 6:141–153
6. Dutta P, Beskok A (2001) Analytical solution of combined electroosmotic and pressure driven flows in two-dimensional straight microchannels: Finite Debye layer effects. Anal Chem 73:1979–1986
7. Lee CS, Blanchard WC, Wu CT (1990) Direct control of the electroosmosis in capillary zone electrophoresis by using an external electric field. Anal Chem 62:1550–1552
8. Schasfoort RBM, Schlautmann S, Hendrikse J, van den Berg A (1999) Field-effect flow control for microfabricated networks. Science 286:942–945
9. Horiuchi K, Dutta P (2006) Electrokinetic flow control in microfluidic chips using a field-effect transistor. Lab Chip 6:714–723
10. Link DR, Anna SL, Weitz DA, Stone HA (2004) Geometrically mediated breakup of drops in microfluidic devices. Phys Rev Lett 92:054503
11. Schomburg WK, Vollmer J, Bustgens B, Fahrenberg J, Hein H, Menz W (1994) Microfluidic components in LIGA technique. J Micromech Microeng 4:186–191
12. Karnik R, Fan R, Yue M, Li DY, Yang PD, Majumdar A (2005) Electrostatic control of ions and molecules in nanofluidic transistors. Nano Lett 5:943–948

Microfluidic Component Assembly

► Microfluidic Assembly

Microfluidic Devices

► Biosample Preparation by Lab-on-a-Chip Devices

Microfluidic Devices in Tissue Engineering

PALANIAPPAN SETHU, ROBERT S. KEYNTON
Department of Bioengineering, University of Louisville, Louisville, KY, USA
p.sethu@louisville.edu, rob.keynton@louisville.edu

Synonyms

Cell and tissue culture; Microfluidic platforms; Cellular microenvironments; Microfluidic cell culture; Organ fabrication; Organ or tissue augmentation

Definition

Tissue Engineering

Tissue engineering collectively refers to efforts used to augment, repair or replace tissue or organ using cellular substitutes that have appropriate structural organization and function behavior. This is a highly inter disciplinary field and has received significant contributions from researchers from various fields of engineering and life sciences. Several interpretations of phrase *tissue engineering* exist today, including commonly used definitions coined by *Skalak* and *Fox*

> "Tissue engineering is the application of the principles and methods of engineering and the life science toward the fundamental understanding of structure-function relationships in normal and pathological mammalian tissue and the development of biological substitutes to restore, maintain or improve functions,"

Langer and *Vacanti*

> "an interdisciplinary field that applies the principles of engineering and life sciences toward the development of biological substitutes that restore, maintain, or improve tissue function or a whole organ, and"

MacArthur and *Oreffo*

> "understanding the principles of tissue growth, and applying this to produce functional replacement tissue for clinical use."

In this chapter however, we will limit our discussion to microfluidic devices used to engineer tissues.

Microfluidics

Microfluidics deals with the behavior, control and manipulation of microliter and nanoliter volumes of fluids. The behavior of fluids at the microscale differs significantly from fluidic behavior at the macroscale. At these scales (channel dimensions of around 10 to 100 sμm) some interesting and unintuitive properties appear primarily due to the fact that the Reynolds number which is the ratio of inertial forces to viscous forces, becomes extremely small resulting in highly organized laminar flow and diffusion, becomes the primary mechanism of mixing. Surface to volume ratios also become extremely large. Factors such as surface tension, energy dissipation, and fluidic resistance begin to play an important role whereas effects due to other factors like turbulence, inertia and friction that dominate fluid flow in the macroscale become negligible. Microfluidics is the study of how these behaviors change, understanding the effects of this change and then exploiting them for new applications. In this chapter, the discussion of microfluidic devices extends beyond devices used primarily for fluid flow and includes all types of devices and microscale technologies used for various types of fluidic manipulations.

Overview

Within the body there are different levels of structural organization and complexity. The lowest level of organization is *molecular*. In our body we have a wide variety of *molecules* with different structures and functions including proteins and nucleic acids. The size ranges of the different biomolecules vary from 5 to 100 nm. *Cells* are the smallest independent units of living matter capable of sustaining life. Our bodies are made up of millions of different cells that perform different structural and biological functions. Cells are typically in the size range of a 2 – 30 μm. In complex organisms such as humans, cells with similar structures and functions are typically found together in our bodies forming *tissues*. Cells that make up a single tissue typically interact with each other to function synergistically to perform specific functions. *Organs*, the next level of complexity are made up of different tissues and perform specialized bodily functions. Examples of organs include the kidney, liver, pancreas and the heart.

Further, different organs and tissues work together as a *system* to carry out one or more functions essential for the survival of the organism. Finally, the *organism* relies on the proper functioning of all the different systems in the body to sustain life.

As a field, tissue engineering emerged in the early 1990's through efforts in Robert Langer's laboratory, primarily based on initiatives by chemical and biomedical engineers. The earliest approaches focused on development of suitable scaffolds for cell attachment and culture. These approaches were successful in generating basic tissue constructs but stopped short of achieving tissue complexity in terms of vasculature and innervation into the engineered tissue. The nervous system and the circulatory system are the predominant mechanisms via which the body maintains homeostasis. Successful engineered tissues to date include non-angiogenic tissue including bone and skin. More complex tissue requires integration of vasculature and nervous tissue to achieve exact replication of in vivo tissue architectures. More recently, several efforts have focused on generation of blood vessels in vitro. However, integration of blood vessels and nerves with functional engineered tissue requires technology that can ensure exact replication of in vivo tissue architecture along with delivery of signals with sub-cellular resolution.

Microfluidics deals with the behavior, control and manipulation of microliter and nanoliter volumes of fluids. In most cases microfluidics involves the use of microfabricated systems that contain channel networks, reservoirs, cell culture areas, electrodes for stimulation, temperature controllers, sensors and detectors. The primary advantage of microfluidics over macroscale technologies is the ability to control interactions at the cellular and molecular level. Tissue and organs require well defined architectures, precise control over molecular and chemical signals and controlled microenvironments with appropriate extracellular matrix (ECM). Cellular events such as proliferation, differentiation, migration or apoptosis are facilitated via multiple surface cues from the extra-cellular environment and soluble signals triggering transmembrane signaling proteins, which in turn, activate intracellular signaling pathways. In organisms that reproduce sexually, a sperm fertilizes an egg cell resulting in a cell called the zygote. In the early stage of development (embryonic stage), the embryo can be considered the ultimate microfluidic environment for tissue engineering.

The zygote exists in an extremely well-defined microenvironment with necessary extracellular matrix (ECM) for support, signals with micro/nano scale spatial and temporal resolution, resulting in its development into different germ layers, tissue, organs and finally a mature organism. Microfluidics technology provides us with the tools to accomplish all of these tasks, most of which cannot be accomplished in the macroscale. Microfluidic approaches for tissue engineering work primarily at the molecular and cellular levels of complexity through which we use a bottom up approach to tissue engineering similar to early stages of development in the body. Using fluidics technology at these size scales, we can accomplish a wide variety of functions which will be discussed in detail in this chapter. We can organize cells spatially using microfluidic printing technologies by placing one cell at a time at defined locations; create extra cellular matrices (ECMs) at precisely defined locations for cellular attachment; pattern cells side-by-side to mimic the architectures in the body; create vasculature for continuous supply of nutrients and essential factors while at the same time providing a mechanism for removal of toxic metabolic wastes; and, deliver signals with the spatial and temporal resolution necessary for differentiation and development of certain progenitor cell types. Overall, the type of control and manipulation possible using microfluidic technology is not possible using conventional techniques.

Use of microfluidics technology for tissue engineering has a lot of advantages. However, a lot of work still needs to be done before tissues generated via this technology can be used as a functional replacement or augmentation in the body. Tissues generated in microfluidic devices are, in most cases, too small to be of functional value. Additional technology must be developed that will combine the precise microenvironments available through microtechnology together with a process to reliably scale up the production of useful engineered tissue.

Basic Methodology

We begin with an introduction to microfluidic technology available for creating controlled microenvironments (i. e.) surface modification for cell attachment and techniques for delivery of soluble signals to cells. Construction of the extracellular environment is extremely critical. Small variations in shape, size and composition of surfaces to which cells attach, changes in growth medium, soluble signaling factors, arrangement of neighboring cells as well as the temporal control over delivery of signals can play a huge role in the survival, function, proliferation, and differentiation of cells. The first step towards creating a controlled microenvironment is patterning of cells and ECM proteins to mimic the architectures in the body. Several microfluidic patterning techniques exist that can be used to accomplish cellular and extracellular patterning. Following establishment of a suitable environment, biochemical signals in the fluid medium, including soluble factors, need to be delivered with high spatial and tempo-

ral resolution. This chapter will detail techniques currently employed, that strive to achieve biomimetic patterning of cells and extracellular matrices (ECMs) followed by techniques to deliver biochemical signals with high spatial and temporal resolution as seen in the body.

Cells, Extracellular Matrix (ECM) and Soluble Biochemical Signals

Spatial Resolution

Microfluidics technology offers unparalled spatial resolution for the creation of cellular and extracellular microenvironments that cannot be reproduced with conventional technology. Using micropatterning techniques like photolithography, microcontact printing, microfluidic printing, stencil printing etc., spatial cues in the form of ECM proteins and ligands can be presented to cells with micrometer/sub-micrometer resolution. Growth medium, soluble signaling molecules and growth factors can be presented to cells by taking advantage of fluid flow behavior at the same size scales as present in the body. In tissue, different cells, and sometimes even different locations in a single cell, are exposed to multiple biochemical signals with high spatial resolution An attractive feature of microfluidic platforms is the ability to design systems that can deliver multiple signals simultaneously with similar cellular and/or sub-cellular resolution. Thus, these microfluidic platforms can be valuable tools for investigating or mimicking processes responsible for different cellular functions such as cell proliferation, differentiation, migration, apoptosis, etc.

2D and 3D Cell and ECM Patterning Techniques

Cellular patterning relies heavily on the generation of surfaces favorable for cell attachment (typically coated with ECM proteins), in conjunction with, the ability to ensure that the surface regions where attachment is undesired suppress non-specific interactions between the proteins and the cells. Advances in surface chemistry have made possible the synthesis of biologically inert surfaces which minimize or eliminate the non-specific adsorption of proteins and other biomolecules from biological fluids such as cell culture media as well as cell adhesion. Surfaces that promote cell adhesion are typically charged, hydrophilic surfaces. Biocompatible hydrophilic surfaces are often patterned with ECM proteins like agrin, collagen, fibronectin and vitronectin as well as other molecules like poly-L and -D lysine. Hydrophobic surfaces, on the other hand, typically inhibit cell attachment and prevent the adsorption of proteins. Molecules such as carbohydrates (e. g. agarose and mannitol) and proteins (e. g. albumin) generally reduce the adsorption of proteins at the surface. To overcome limitations with respect to efficiency and stability of naturally occurring biomolecules, a number of synthetic materials have been developed. The most commonly used molecule is poly (ethylene glycol) or PEG with the monomeric repeat unit [–CH_2–CH_2–O]. Other approaches include the use of lipid bilayers tailored with different charged lipids, embedded with peptides and proteins, and polyelectrolytes deposited using layer-by-layer assembly techniques.

The advent of the printing press has been hailed as one of the most significant technological advances in human history. Modifications of those same techniques have found their way into microfluidics technology for patterning surfaces and structures for the creation of cellular and extracellular microenvironments. Much of these techniques and their adaptations for cell and protein patterning are a result of technology developed in George Whitesides's laboratory at Harvard University. Several other researchers have also contributed to development of surface patterning technology pertaining to ECM and cell patterning [please refer to review articles by Andersson [1], Folch [6], and Kane [7] for additional information related to these techniques]. A summary of these different techniques is presented below.

M

Photolithographic Patterning Photolithography involves the formation of geometric features in a substrate through the use of light and a mask in a fashion similar to photography (Fig. 1a). The patterns on the mask (equivalent to a film negative) are transferred via UV illumination onto the substrate (similar to photography paper) which is coated with a photosensitive polymer (called photoresist). The substrates are coated with the photoresist by spinning the substrate at a predetermined speed to achieve the desired thickness of photoresist. Some biocompatible molecules like PEG can be modified to become photosensitive in order to directly pattern surfaces using photolithography techniques. Other biological molecules are patterned indirectly using a lift-off process (the removal of unwanted material on the surface of a photoresist by dissolving the photoresist). Following photoresist patterning, the open spaces are back filled with the molecules of interest. The remaining photoresist is subsequently removed using a solvent, such as acetone, together with sonication. Depending on the application and biomolecules involved, exposure to solvents might not be desirable since denaturation or scission of the biomolecules may result in some cases.

To circumvent the above mentioned limitation, photolithographic patterning can be extended to accomplish generation of selective, molecular assembly patterning. For

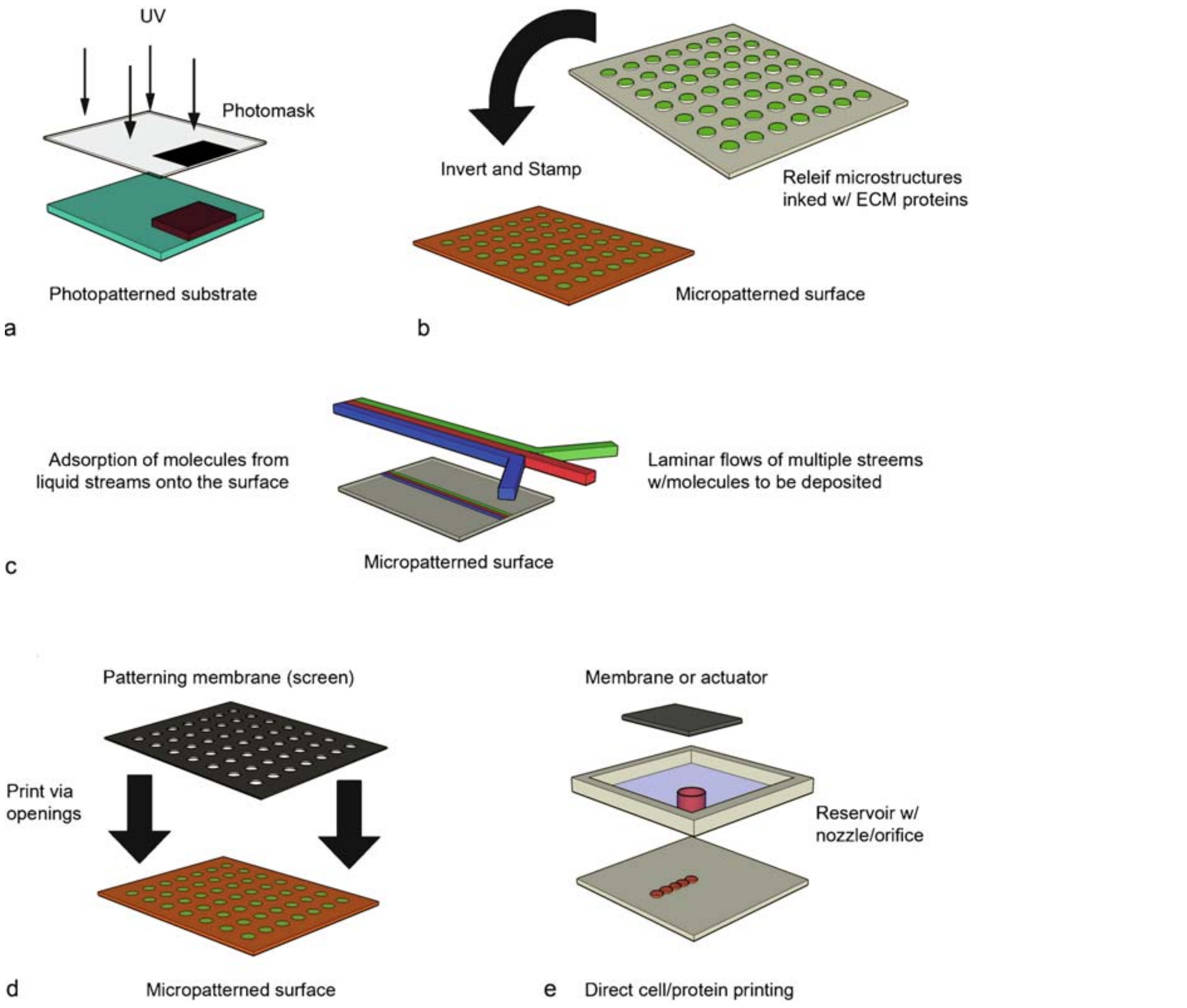

Microfluidic Devices in Tissue Engineering, Figure 1 Commonly used micropatterning techniques for creation of precisely defined cellular and extracellular microenvironments. (**a**) Photolithography, (**b**) Relief or Microcontact printing, (**c**) Microfluidic Patterning or Liquid Phase Printing, (**d**) Stencil or Screen Printing and (**e**) Inkjet or Droplet Printing

example, metal oxides, like titanium dioxide or silicon dioxide, can be patterned using a combination of thin film deposition, lithography and etching. The non-patterned regions can be treated with oxygen plasma to become hydrophilic, modified with molecular linkers, and linked with the molecules of choice. Alternatively, metals like gold or platinum can be patterned the similarly, so molecules like thiols, or modified-thiols with different tail groups, can be self-assembled onto the patterned metal layer.

Relief or Microcontact Printing Microcontact printing is the most widely used technique for surface modification (Fig. 1b). Though primarily intended for microelectronics applications, microcontact printing has been successfully adapted to cellular patterning. This technique is simple, cost effective, and flexible, while at the same time, capable of producing patterns with sub-micron resolution. First, an elastomeric stamp (generally constructed from polydimethyl siloxane (PDMS) material) is formed by casting a liquid-phase polymer over a patterned master (e. g., silicon). After curing, the stamp is released from the master and inked with a solution containing the molecules of choice. Next, the desired surface is stamped by transfering the ink to the substrate. The substrate is patterned with the molecular ink and the geometry of the patterned surface is determined by the geometry of the micropatterned stamp. A bonus feature of this technique is the ability to backfill

the empty spaces between patterned areas with a second molecule to further promote selectivity of the surface.

Microfluidic Patterning or Liquid Phase Printing Microfluidic channels can also be used to selectively pattern surfaces (Fig. 1c). In microfluidic patterning, channels are used to selectively deliver fluids to specific areas of the substrate based on channel geometry. The substrate with the fluidic channels can be reversibly bonded to the substrate to be patterned. The channels are filled with a fluid containing the molecules of interest that can be deposited onto the substrate at specific locations. This technique is similar to microcontact printing, except for the fact that the fluid is delivered via microchannels instead of ink on a stamp. This type of microfluidic arrangement allows for sequential and combinatorial delivery of different molecules in solutions which can be delivered to the desired locations through the proper alignment of the microfluidic channels. Further, this method can draw on the advantages of laminar flow and controlled diffusion in microfluidic channels to pattern gradients of different molecules to mimic similar signaling mechanisms in the body that use gradients to control different cellular activities. Diffusion of molecules can be accurately determined using Fick's Law (1) where J the diffusive flux is dependent on the diffusion co-efficient and concentration of the molecule. The biggest disadvantage to this technique is its limitation to closed network structures.

$$J = -D\left(\frac{\partial \phi}{\partial x}\right) \tag{1}$$

Stencil or Screen Printing Stencil Printing involves the generation of patterns through the use of a rigid or flexible sheet or membrane with openings through the sheet in the shape of the desired patterns (Fig. 1d). When the stencil is brought in close contact with the substrate, it can be used to locally modify the surface while the areas covered by the sheet or membrane material remain protected. The stencil can be used to add material to a substrate via mechanisms similar to microcontact printing or microfluidic patterning followed by a wash step and removal of the stencil. Stencils can also be used to selectively remove material from a substrate to yield specific patterns via chemical etching or physical ablation. Most commonly used stencils are constructed from thin layers of PDMS. Major advantages of PDMS stencils include their ability to be easily aligned and reversibly bonded to the substrate while used for patterning. This technique is also amenable to sequential and combinatorial deposition of different molecules to create complex 3D structures more accurately representing in vivo architectures.

Inkjet or Droplet Printing Technology used in commercial ink jet printers is amenable for use in tissue engineering to directly print or write molecules and proteins onto surfaces in a rapid and controlled fashion [3] (Fig. 1e). Recently, this technology has also been employed to directly print or write cells, but cell death, due to dehydration, has been associated with this technique. However, this issue has been addressed via printing cells in larger droplets. Spatial arrangement, with micron scale resolution, is also possible via ejection from more than one nozzle. 2D architectures as seen in the body can be replicated in vitro via printing, using a combination of molecular and cellular deposition nozzles. This technology potentially represents a step forward since molecular and cellular architecture can be precisely printed and replication of the cellular microenvironment is possible, as opposed to molecular surface patterning followed by self-assembly of cells.

Laser Guided Positioning of Cells or Optical Tweezers Optical tweezers are capable of manipulating nanometer and micrometer-sized dielectric particles by exerting extremely small forces via a highly focused laser beam. The beam is typically focused by sending it through a microscope objective with the narrowest point of the focused beam, known as the beam waist, containing a very strong electric field gradient. Cells and particles are attracted to the region of the strongest electric field, known as an optical trap. The cell can be moved by spatial movement of the laser relative to the substrate and the cell can then be released at any specified location. It is also possible to continuously propel cells along a light path, $\sim 300\,\mu m$ in length, and to create clusters of cells on a target surface. This technique is slow, complicated and time consuming; however, precise alignment can be accomplished one cell at a time.

Layer-by-Layer Assembly Most techniques discussed above are restricted to generation of 2D surface or cell patterning. A simple procedure to generate 3D tissue architecture is the layer-by-layer approach. A surface can be patterned with proteins or other molecules in liquid phase to create cell specific regions using any of the techniques described above, followed by cell patterning which self-assembles to form 2D tissue. This layer, with live cells, can be preserved by cryopreservation or biopreservation, or maintained alive via encapsulation in a hydrogel-like collagen gel or commercially available matrigel. Different layers patterned in 2D can then assembled on top of each other resulting in the desired 3D architecture.

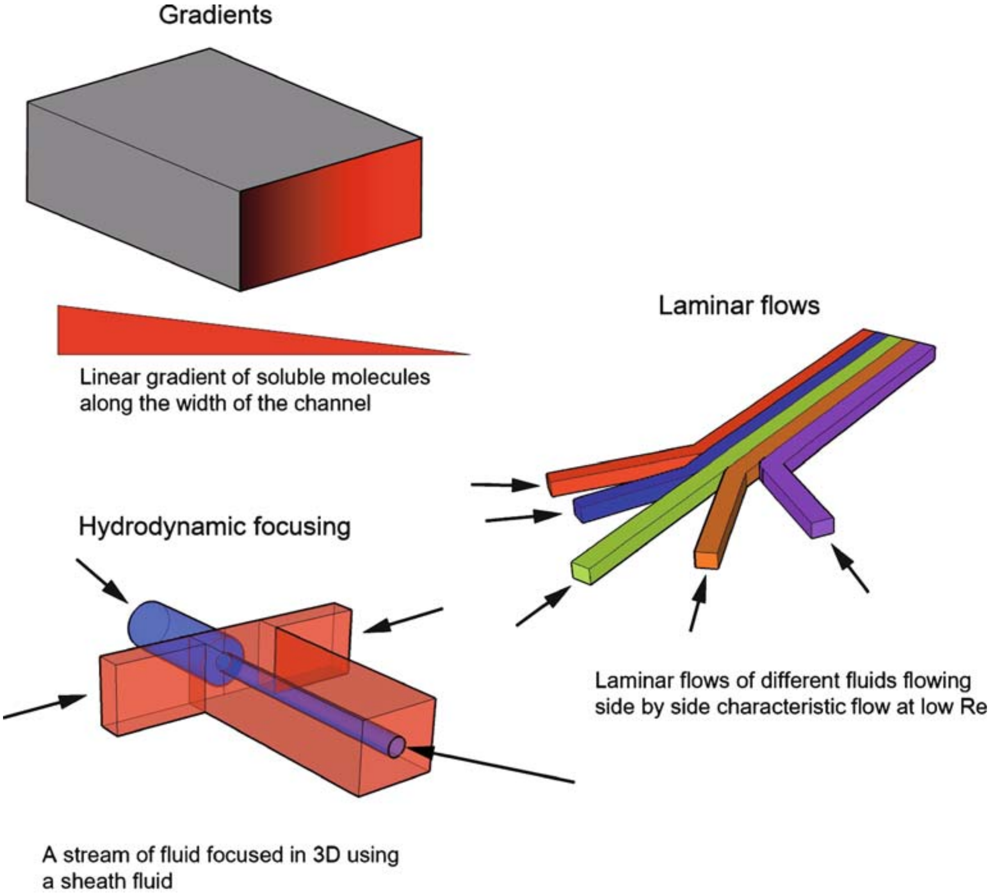

Microfluidic Devices in Tissue Engineering, Figure 2 Due to low Re numbers in microfluidic systems it is possible to accomplish (**a**) controlled and predictable diffusion, (**b**) laminar flows and (**c**) hydrodynamic focusing of streams of fluids

Stereolithography of Biodegradable Polymers Stereolithography is a commonly used tool for layer by layer direct writing of polymers for rapid prototyping of machine parts. This technique can be used to accomplish direct writing of a biodegradable scaffold onto which cells can then be seeded. During the process of writing the scaffold can be modified with compatible surface modified techniques discussed above to define areas for cell attachment and self assembly.

Delivery of Soluble Signals

Thus far we have limited our discussion to microfluidics technology for patterning of ECM proteins and cells. Tissue culture is a dynamic process where a basic tissue construct is first assembled and then continuously remodeled until it resembles in vivo tissue architecture with cellular and extracellular organization. The surrounding extracellular (aqueous) environment provides the necessary signals for tissue remodeling. In static macroscale cultures it is often not possible to deliver these soluble signals with cellular/subcellular resolution necessary to accomplish delivery of multiple molecules, gradients of molecules and simultaneous delivery of two or more molecules to different locations of the same cell. To accomplish this we can use microfluidics technology that exploits flow phenomenon at these size scales to deliver complex signals with extremely high spatial resolution.

Control Using Flow Phenomenon in the Microscale In channel structures with dimensions < 200 mm (microfluidic devices) fluids (liquids) follow predictable laminar paths characteristic of low Reynolds numbers. This allows two or more layers of fluid to flow next to each other without any mixing other than by molecular or particulate diffusion. As a result of this property it is possible to have multiple inputs into a single channel and have them flow side by side in an orderly fashion (Fig. 2b). Since

the channels dimensions in many cases are comparable to the size of single cells we can use laminar flow patterning to expose subcellular regions to specific signals. Also it is possible to allow different regions of the same cell to different conditions.

A consequence of laminar flows and the fact that mixing in microfluidic channels is almost exclusively due to molecular or particular diffusion is the development of devices that can generate stable gradients of different solutions and molecules. Based on the size and shape of a molecule or particle a diffusion coefficient for that particle can be calculated. Based on this coefficient, length of channels necessary for complete diffusion can also be estimated. Several devices using passive structures or networks for combinatorial splitting and mixing of fluids have been developed to generate both linear and non-linear gradients (Fig. 2a). Several cellular processes like cell migration and alignment that respond to molecular gradients can be accomplished using microfluidic technology. Generation of microfluidic gradients can also be accomplished via controlled diffusion of molecules in conjunction with porous or biodegradable materials. These materials can be used to pattern reservoirs, channels or passive structures to contain and deliver at predetermined rates gradients of different molecules, with the highest concentration closest to the structure.

Further exploiting laminar flows in microfluidic systems, a stream of fluid can be focused in 2D and 3D using additional focusing fluids in what is called hydrodynamic focusing (Fig. 2c). Buffers can be used to focus a stream of solution containing signaling molecules. The width of this stream can be controlled to dimensions much smaller than that of the channels itself obtaining 2 or 3D positioning a delivery of signals.

Temporal Resolution

Microfluidic Control Sequential and combinatorial delivery of signals to cells or tissue in microfluidic devices can be accomplished by using built-in control systems. Several microfluidic tools including valves, pumps, mixers, fluidic oscillators, fluidic diodes, etc., have been developed to accomplish fluidic control in these devices. These components can either be passive or active. Examples of passive elements include one way valves (flap, ball) and hydrophobic patches which take advantage of the interaction between the chemical surface properties of the substrate and liquid. Active elements, on the other hand, typically require some type of actuation mechanism. Several mechanisms for force transduction in microfluidic devices include mechanical, thermal, electrical, magnetic, and chemical actuation systems as well as and the use

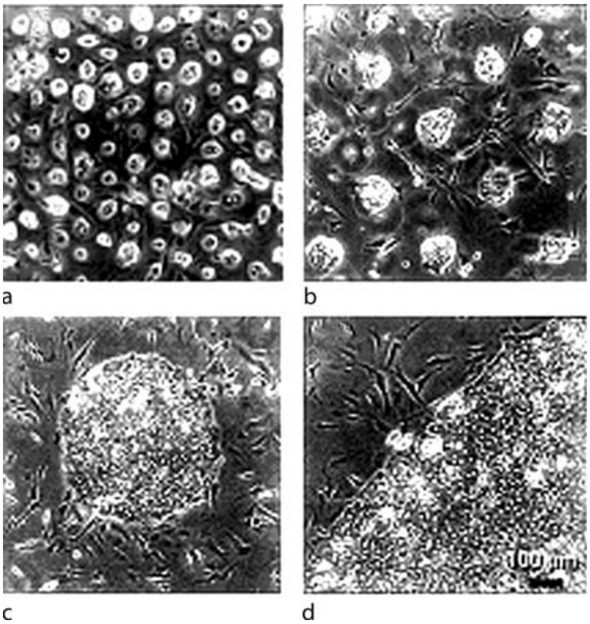

Microfluidic Devices in Tissue Engineering, Figure 3 The figure shows at different magnifications co-cultures of hepatocytes with surrounding stromal cells (fibroblasts). Co-culture is necessary to establish the necessary heterotypic interactions for performance of liver specific functions. Hepatocytes and fibroblasts were patterned using microcontact printing [12]

of biological transducers. There has been a significant amount of work in this area that has been presented in a review by Erickson and Li [5].

Stephen Quake's laboratory at Caltech and more recently at Stanford, developed a technique for creating pneumatically controlled valves and pumps. This technique involves the use of thin microstructured membranes which employs pneumatic force for actuation. Using this technique, valves (normally open or close), pumps (peristaltic), fluidic oscillators, etc., have been fabricated. More recently, complicated microfluidic circuits have been realized using techniques similar to large scale integrated circuits. These technologies and several others, offer the ability to accomplish switching and change in flow or culture conditions rapidly (in the order of milliseconds). Microfluidics, therefore, can not only accomplish delivery of signals with subcellular resolution but also with extremely high temporal resolution.

Integrating Feedback Mechanisms via Electrodes, Sensors and Detectors

Microfabrication technologies originated from the microelectronics industry and these techniques have been extensively applied to other fields including microfluidics and

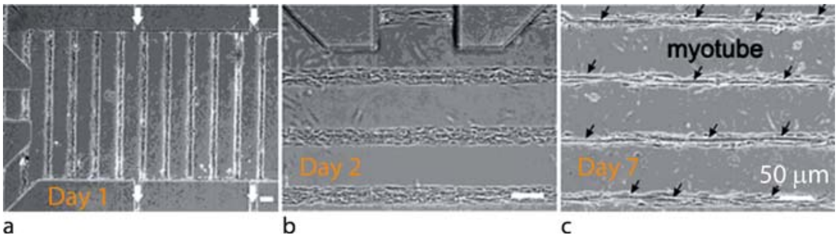

Microfluidic Devices in Tissue Engineering, Figure 4 The formation of skeletal muscle tissue in vivo requires initiation of precursor cells into the myoblastic pathway. To accomplish this, alternating cell-adhesive and cell-repellent microdomains are patterned for attachment of precursor cells which mimics in vivo spatial cues for muscle cell assembly through fusion of myoblasts into aligned, isolated multinucleated myotubes. Figure shows differention of precursor cells into smooth muscle cells constrained in micropatterned regions over a period of 7 days [13]

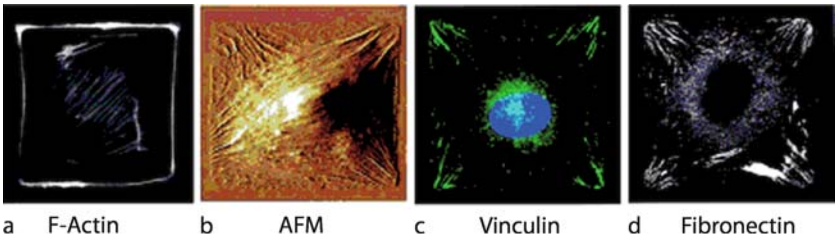

Microfluidic Devices in Tissue Engineering, Figure 5 ECM islands of defined size and shape on the scale of individual cells separated by non-adhesive regions allow cell types adhere and spread on these islands, but extend only up to the limiting boundary along the periphery. By physically constraining cells to square islands, the formation of cell focal adhesions can be controlled. Culture of cardiomyocytes on these islands results ensures that cytoskeletal tension necessary for beating is available to produce a 2D, cellular electrophysiological model of cardiac muscle. Figure shows cardiomyocytes on patterned ECM islands [14]

microelectromechanical systems (MEMS). MEMS technologies have been widely used to develop sensors and detectors to monitor pressure, shear stress, temperature, pH, oxygen, glucose along with many other chemical and biological molecules. Our body has several feedback mechanisms including the circulatory system and nervous system to obtain feedback to constantly adjust its physiological functions in response to alterations in its environmental conditions. In vivo tissue culture typically lacks these feedback mechanisms. By integrating sensors and detectors within microfluidic systems, the tissue microenvironment can be monitored to enable a closed feedback loop to constantly modify the culture conditions. Again, the review by Erickson and Li provides a good overview of integrated microfluidic systems [5].

Key Research Findings

Hepatocyte – Stromal Cell Co-Cultures

Bhatia and colleagues [2] used microscale techniques to exert spatial control over cell adhesion at the 1 – 100 μm scale to study diverse phenomena in hepatocytes such as the effect of cell spreading on cell behavior and surface topology on cell migration. They developed a photolithographic cell patterning technique to study the relative role of homotypic (hepatocyte-hepatocyte) and heterotypic (hepatocyte-stroma) interactions on the stabilization of liver-specific functions in vitro (Fig. 3). Co-cultures were created in which the heterotypic interface varied over three orders of magnitude, while keeping the ratio of cell populations, as well as total cell number constant. It was found that identical cell populations (co-cultivation of hepatocytes with stromal cells (i. e. fibroblasts)) when rearranged spatially can produce different levels of function in the resultant tissue. Arrangement of co-cultures of hepatocytes and fibroblasts mimics in vivo architecture and helps maintain hepatocyte function and phenotype in vitro as determined by urea and albumin synthesis.

Microfluidic Smooth Muscle Cell Culture and Differentiation

The formation of skeletal muscle tissue in vivo involves the determination of precursor cells to the myoblastic pathway, fusion of myoblasts into multinucleated myotubes, and maturation into muscle fibers. Tourovskaia and colleagues [10] have developed a microfluidic cell culture system for myogenesis studies that provides control over the external environment to fully recapitulate myogenic differentiation in vivo and allows the manipulation of subcellular domains within mature myotubes for simulation of postsynaptic differentiation and further modula-

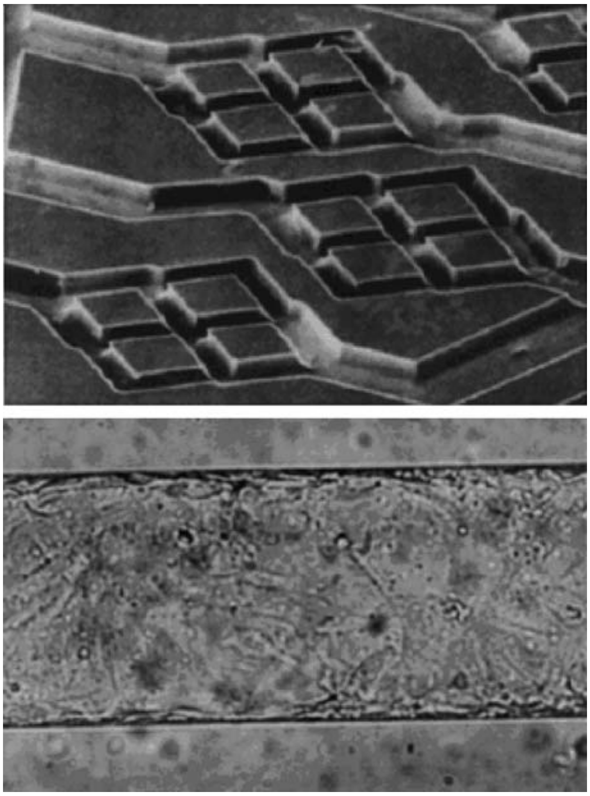

Microfluidic Devices in Tissue Engineering, Figure 6 Microfluidic channels in many ways resemble the vascular network in our body. Microfluidic networks made out of degradable materials like PLGA can be used to provide a structural backbone for seeding and culture of endothelial cells with perfusion and further construction of complex 3D organ and tissue architectures. Shown are the microfluidic network and endothelial cells seeded within the network [15]

tion of muscle differentiation. They accomplished spatial organization of the myotubes to resemble in vivo morphology, grew well-defined, isolated myotubes within the microfluidic channels and demonstrated the selective surface receptor tagging. The cells were successfully cultured for 2 weeks under constant perfusion at a low flow rate and no significant change in the growth rates was observed compared to the traditional non-microfluidic control cultures (Fig. 4).

Cardiomyocyte Model for Electrophysiological Studies

Parker and colleagues [9] used a microcontact printing approach to create adhesive ECM islands of specifically defined size and shape, on the scale of individual cells, separated by non-adhesive regions. They found that various cell types adhere and spread on these islands, but extend only up to the limiting boundary along the periphery (Fig. 5). Individual cells were shown to take on the shape of the island which they adhered to, although the cells were able to locally extend lamellipodia over the non-adhesive boundary regions. Whereas, cells on symmetrical circular islands extended new cell processes at random along their periphery. Cells on square islands were found to extended lamellipodia, filopodia, and microspikes at the corners. By physically constraining cells to square islands, the cells were able to consistently reorient themselves to where their focal adhesions formed, which tension on the exerted cytoskeletal. This structural reorientation resulted in consistent control of the direction of lamellipodia extension: cell processes were redirected to the corners of these cells where the greatest tractional stresses were observed. Application of this technique to cardiomyocytes resulted in a cellular-level model for functional electrophysiological studies of cardiac muscle.

Vascular Tissue Engineering

Borenstein and colleagues [4] developed a microfluidic device for vascular tissue engineering. Using standard photolithography and a replica molding process, they developed a biodegradable scaffold made of poly (lactic-co-glycolic acid) or PLGA with microfluidic channels for seeding with endothelial cells. Endothelial cells were successfully seeded and cultured in the PLGA channels for periods as long as 4 weeks, demonstrating that these cells successfully attach, proliferate and migrate in small channels with closed geometries (Fig. 6). The endothelial cells were maintained in culture under constant perfusion using an external pump. This work is considered a critical first step towards development of microvasculature for enabling bulk organ tissue engineering.

Microfluidic Embryo Cultures

Microfluidic systems have also been used for in-vitro fertilization (IVF) and subsequent embryonic development by Zeringue and colleagues [11]. Using their device, the oocyte was anchored within a microfluidic channel (Fig. 7). The surrounding microenvironment was manipulated using microfluidic channels to deliver medium, molecular signals and growth factors. Microfluidic systems have been used to accomplish various oocyte manipulations including in-vitro maturation (IVM), in-vitro fertilization (IVF), in-vitro embryo culture (IVC), embryo biopsy, and nuclear transfer. In addition to providing a more in vivo-like culture environment, microfluidic technology was demonstrated to be more ideally suited for complex embryo manipulations, such as removal of the zona pellucida and stripping of the cell cumulus.

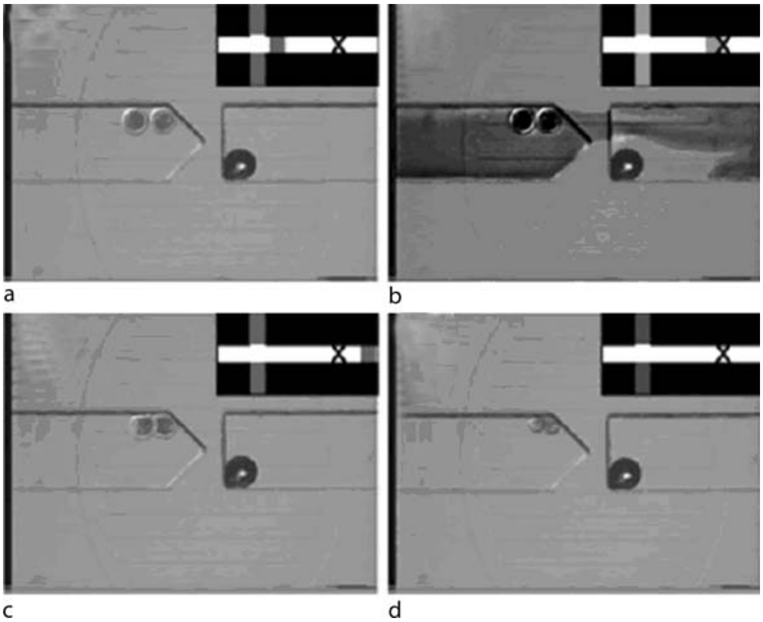

Microfluidic Devices in Tissue Engineering, Figure 7 Microfluidic systems have also been used for positioning, manipulation, fertilization and development of embryos for in vitro fertilization. Shown in this figure are different stages involved in stripping of the cumulus from a captured embryos using a lysis plug [16]

Drosophila Embryonic Development

Lucchetta and colleagues [8] have developed a technique for generating radical temperature variations using laminar flows and microfluidic channels to expose one-half of a drosophila embryo to one temperature and the other half of the embryo to a different temperature to investigate the effects of temperature on embryonic development (Fig. 8). They found that the warmer region initially experienced a more rapid development when compared to the colder region as evidenced by the higher rate of cell division. However, the embryo was found to have compensatory mechanisms in which normal embryonic development was still achieved when the embryos were returned to normal body temperature, even after a 2.5 h exposure to temperature differences.

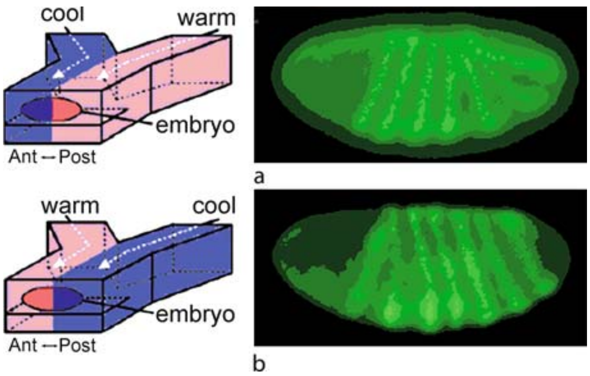

Microfluidic Devices in Tissue Engineering, Figure 8 Biochemical networks in cells and tissue are sensitive to external factors such as temperature. Shown is a microfluidic device used for thermal patterning of a drosophila embryo with hot and cold liquid. Warmer regions show faster development when compared to the colder regions as shown by the staining of nuclei [17]

Future Directions for Research

Microfluidics provides the bioengineering and life science communities with an unprecedented opportunity to engineer tissues at the cellular and molecular level by creating microenvironments with extremely high spatial and temporal resolution. Microfluidic devices for tissue engineering are still in their infancy. Application of techniques and exploitation of phenomenon that occur at these size scales have been used to create complex cellular architectures and deliver spatial cues and soluble signals, but to date, generation of functional tissue using these devices and approaches has not been realized. Rather, these tools have served to help us understand at a molecular and cellular level, heterotypic and homotypic cell–cell interactions, cell–ECM interactions, cell–scaffold interactions and the effects of complex spatial and soluble signals. In terms of integrating more complexity into the engineered tissues, nervous and vascular tissue structures similar to

architectures seen in the body must be incorporated into the engineered tissues to ensure similar functional and structural characteristics of tissue found in vivo. To date, available technology in terms of integration of feedback mechanisms that utilize sensors, detectors and electrodes to monitor and provide information similar to homeostatic mechanisms in our own body have not been exploited. Microfluidics, therefore, provides tools and devices to start building from the bottom up, complicated cellular and extracellular architectures and environments necessary to enable the construction of tissues and organs. However, these techniques will need to be integrated with supporting technology to accomplish 3D architectures and scaled-up to produce functionally viable tissue that can be used to repair, replace or augment tissue in our bodies.

References

1. Andersson H, van den Berg A (2004) Microfabrication and microfluidics for tissue engineering: state of the art and future opportunities. Lab Chip 4(2):98–103
2. Bhatia SN, Balis UJ et al (1999) Effect of cell–cell interactions in preservation of cellular phenotype: cocultivation of hepatocytes and nonparenchymal cells. FASEB J 13(14):1883–1900
3. Boland T, Xu T, Damon B, Cui X (2006) Application of inkjet printing to tissue engineering. Biotechn J 1(9):910–917
4. Borenstein JT, Terai H, King KR, Weinberg EJ, Kaazempur-Mofrad MR, Vacanti JP (2002) Microfabrication Technology for Vascularized Tissue Engineering. Biomed Microdev 4(3):167–175
5. Erickson D, Li D (2004) Integrated microfluidic devices. Anal Chim Acta 507(1):11–26
6. Folch A, Toner M (2000) Microengineering of cellular interactions. Ann Rev Biomed Eng 2:227–256
7. Kane RS, Takayama S, Ostuni E, Ingber DE, Whitesides GM (1999) Patterning proteins and cells using soft lithography. Biomaterials 20(23–24):2363–76
8. Lucchetta EM, Lee JH et al (2005) Dynamics of Drosophila embryonic patterning network perturbed in space and time using microfluidics. Nature 434(7037):1134–1138
9. Parker KK, Brock AL et al (2002) Directional control of lamellipodia extension by constraining cell shape and orienting cell tractional forces. FASEB J 16(10):1195–1204
10. Tourovskaia A, Figueroa-Masot X, Folch A (2005) Differentiation-on-a-chip: a microfluidic platform for long-term cell culture studies. Lab Chip 5(1):14–9
11. Zeringue HC, Rutledge JJ, Beebe DJ (2005) Early mammalian embryo development depends on cumulus removal technique. Lab Chip 5(1):86–90
12. http://lmrt.mit.edu/research/cell-cell_interactions.asp
13. http://faculty.washington.edu/afolch/FolchLabResearchProjects.htm#
14. http://www.seas.harvard.edu/diseasebiophysics/research_mechanotransduction.html#mechanical_stress
15. http://www.draper.com/biomedtech/biomedtech.html
16. http://mmb.bme.wisc.edu/
17. http://ismagilovlab.uchicago.edu/research.html

Microfluidic Flow Visualization

► Microscale Flow Visualization

Microfluidic Fuel Cells

ERIK KJEANG, NED DJILALI, DAVID SINTON
Institute for Integrated Energy Systems (IESVic) and Department of Mechanical Engineering, University of Victoria, Victoria, BC, Canada
dsinton@me.uvic.ca

Synonyms

Laminar flow-based fuel cells; Membraneless fuel cells

Definition

Small ►fuel cells are considered a strong candidate for the next generation of portable power supplies. A microfluidic fuel cell is defined as a fuel cell with fluid delivery and removal, reaction sites and electrode structures all confined to microfluidic channels. This type of fuel cell can use both metallic and biological catalysts and normally operates without a physical barrier, such as a membrane, to separate the electrodes. Other types of small fuel cells, such as microstructured polymer electrolyte membrane-based fuel cells, will not be covered in this entry.

Overview

A fuel cell [1] is an electrochemical device that converts chemical energy stored in a fuel and an oxidant into electrical energy. The fundamental difference between a fuel cell and a battery is that fuel is supplied from outside the reaction chamber and waste products are removed. The heart of the fuel cell contains an anode and a cathode, separated by an electrolyte, as shown in Fig. 1. Its operation is conceptually straightforward. The fuel is oxidized at the anode, releasing protons (H^+ ions) and electrons. The protons travel through the electrolyte, which conducts ions but is electrically insulating, and recombine with the oxidant at the cathode. The electrons, that are required for the cathodic reaction, are conducted from the anode to the cathode through external wiring, thereby generating an electrical current used to drive a load. The electrochemical reactions are heterogeneous and facilitated by an electrochemical solid-liquid interface. Fuel cell electrodes are commonly made porous in order to establish three-phase contact: the solid phase that conducts electrons to or from the electrode, the liquid or gaseous fuel

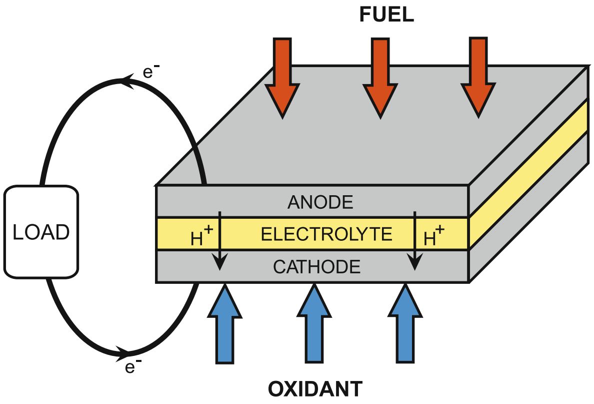

Microfluidic Fuel Cells, Figure 1 Basic fuel cell design showing its core components: anode and cathode separated by an electrolyte and connected to an external load

or oxidant phase, and the liquid or solid polymeric electrolyte phase; all three phases need to be in contact at the active sites to facilitate heterogeneous electrochemical reactions that produce a useful current. Although energy is released in a fuel cell, the reactions are typically slow and have large activation energy that needs to be supplied for the reactions to proceed. There are three main ways to enhance the reaction rates: the use of catalysts, raising the temperature, and increasing the effective electrode area by incorporating microstructured materials. Most fuel cells operate at low temperatures and therefore require an electrochemical catalyst to reduce the activation energy of the chemical reactions. The choice of catalyst depends on the fuel or oxidant. Platinum is arguably the best electrocatalyst available for a wide range of reactants, in particular for hydrogen and oxygen. Other transition metals such as palladium and ruthenium, or combinations of these with platinum, provide good catalytic properties for formic acid and methanol oxidation. The performance of a fuel cell is normally quantified in terms of cell voltage (ΔE_{cell}), and current density (i). Cell voltage is defined as the difference in electrochemical potential between cathode and anode, with a maximum at the reversible open-circuit voltage ($E_{\text{cathode}} - E_{\text{anode}}$). This maximum voltage can be calculated from the Gibbs' free energy of the reactants and products at their standard states. The actual cell voltage achieved is in practice significantly lower than the reversible potential due to various losses (also referred to as overpotentials). The operational cell voltage is determined by Eq. (1)

$$\Delta E_{\text{cell}} = (E_{\text{cathode}} - E_{\text{anode}}) - |\eta_{\text{anode}}| - |\eta_{\text{cathode}}| - iR_{\text{cell}} - \eta_{\text{trans}} \qquad (1)$$

where the last four terms correspond to losses caused by activation overpotentials due to irreversibilities at the electrodes (η), ohmic resistance of the cell (R_{cell}), and concentration overpotentials from mass transport limitations (η_{trans}). Power density (mW cm^{-2}), which is an overall measure of fuel cell performance, is obtained by multiplying cell voltage and current density (current output divided by the geometrical surface area of the electrode).

Fuel cells that utilize biological catalysts are collectively termed ►biofuel cells [2, 3]. There is a common misunderstanding that biofuel cells are named as such because they use biological fuels, which is ambiguous as the same fuel (e. g., methanol) can be produced from both biological and non-biological sources. That said a biofuel cell mimics electrochemical processes occurring in nature to harvest a useful electrical current, without the use of precious electrocatalysts such as platinum. The oxidative metabolism of ethanol in the human liver, principally catalyzed by the alcohol and aldehyde dehydrogenase enzymes, exemplifies a bioanodic process. There are two main categories of biofuel cells: microbial biofuel cells and enzymatic biofuel cells. Microbial fuel cells utilize entire living cells or microorganisms combined with redox intermediates to catalyze the oxidation of a fuel. Enzymatic biofuel cells, on the other hand, catalyze the chemical reactions by biological redox enzymes that can be isolated and purified from suitable organisms, thus extracting the actual part of the cell that enables catalytic operation. Batches of enzymes can be produced by standardized methods from naturally abundant organisms using low-cost fermentation techniques. The enzymatic type of biofuel cell is preferable from an engineering perspective, due to its relatively high power density, compatibility with fluidic networks, and ease of miniaturization. Redox enzymes have an important advantage compared to traditional electrocatalysts: their selectivity towards a specific substrate (fuel). Each enzyme is coupled to the decomposition of a particular substrate, and the presence of other substances in its vicinity does not (in general) influence the turnover rate (the rate at which it oxidizes or reduces the substrate). The specific nature of biocatalysts is particularly attractive from an engineering perspective as both fuel and oxidant may share a fluid delivery manifold. Further advantages include: biocatalytic enzymes are available for a variety of substrates; the optimum temperature for enzymatic activity is near ambient; and the inherent overpotentials for biocatalysis are generally low.

Many different types of fuel cells are currently under development, with a variety of targeted applications ranging from miniature power supplies to large-scale combined heat and power plants. With the exception of limited small scale commercialization of some stationary units, most of

these fuel cells have not yet been commercialized past the field trials stage. Small fuel cells for portable electronic equipment are considered rather close-to-market for a number of reasons: it is unlikely that the technical development of batteries will keep pace with the accelerating power demands; small, microstructured fuel cells have higher energy density than batteries; and the market for portable electronics has an inherently higher cost tolerance. There are still some technical challenges, though, related to small fuel cell development. Hydrogen-based fuel cells require hydrogen storage units that are currently too bulky for portable device applications, and alcohol-based fuel cells, with compact fuel storage solutions, suffer from reduced cell voltage due to fuel crossover from anode to cathode.

In this entry, we describe how established fuel cell principles can be combined with microfabrication techniques and microfluidic networks to develop alternative microfluidic fuel cells using both metallic and biological catalysts, and how they can be operated without polymer electrolyte membranes.

Basic Methodology

Microfluidic fuel cells, sometimes called laminar flow-based fuel cells or membraneless fuel cells, describes a group of fuel cells capable of operation within the framework of a microfluidic chip. This type of fuel cell utilizes the laminar flow characteristic of microfluidics to delay convective mixing of fuel and oxidant. Two aqueous streams, one containing the fuel (anolyte) and one containing the oxidant (catholyte), are allowed to flow side-by-side down a single microfluidic channel (see Fig. 3, 4). The lack of convective mixing ensures the separation of the streams without the use of a physical barrier such as a membrane. The anolyte and catholyte also contain supporting electrolyte that facilitates ionic transport within the streams, thereby eliminating the need for a separate electrolyte. Mixing of the two streams occurs by transverse diffusion only, and is restricted to an interfacial width at the center of the channel. This inter-diffusion region has an hourglass shape, with a maximum width at the channel walls scaling as the cube root of diffusion coefficient (D), channel height (H), downstream position (z), and inverse mean velocity (U):

$$\delta_x \propto \left(\frac{DHz}{U}\right)^{\frac{1}{3}} \tag{2}$$

Anode and cathode are integrated on the walls of the manifold sufficiently far away from the co-laminar inter-diffusion zone in order to prevent fuel crossover. As will be discussed later, the placement of the electrodes also influences fuel utilization as well as ohmic resistance in the channel.

The microfluidic fuel cell design avoids many of the issues encountered in polymer electrolyte membrane-based fuel cells: membrane humidification and degradation, water management, and fuel crossover, to name a few. In addition, the co-laminar configuration allows the composition of the anolyte and catholyte streams to be chosen independently, thus providing an opportunity to improve reaction rates and cell voltage. The open-circuit voltage can thereby be increased by tweaking the reversible half-cell potentials by pH modification of individual streams. For example, the reversible potential (E) of the oxygen reduction reaction

$$O_2 + 4H^+ + 4e^- \longleftrightarrow 2H_2O$$

depends on pH according to the Nernst equation [1]

$$E = E^0 - \frac{RT}{F}\ln\frac{\coprod_{\text{products},i} a_i^{\upsilon_i}}{\coprod_{\text{reactants},j} a_j^{\upsilon_j}} = E^0 - \frac{RT}{F}\ln\frac{1}{a_{O_2}(a_{H^+})^4} \tag{3}$$

where E^0 is the reversible potential at standard state and a the activity of each species ($a = 1$ at standard state), which for aqueous species can be approximated by the concentration. By reducing the pH of the cathode stream (adding more H^+), the cathodic reversible potential becomes more positive and thereby yields larger open-circuit cell voltage.

In addition to compactness, miniaturization of fuel cells has a further advantage: since electrochemical reactions are surface-based, the performance of the fuel cell benefits from a high surface-to-volume ratio, which scales as the inverse of the characteristic length. The most prominent benefit related to microfluidic fuel cells, however, is the economical aspect. Microfluidic fuel cells can be manufactured by inexpensive, well-established micromachining and microfabrication methods and the cost associated with membrane and auxiliary systems, which is significant for most other fuel cells, is eliminated.

Currently, microfluidic fuel cells are typically fabricated using standard photolithographic and soft lithographic methods, see for example Kjeang et al. [4] for a detailed description. In short, this fuel cell consisted of two layers: a structurally rigid base layer containing the electrodes, and a polymeric top layer containing the channel structure. A standard photolithographic technique using UV-light, transparent photomasks and spin-coated layers of photoresist was applied to etch custom gold electrode patterns on

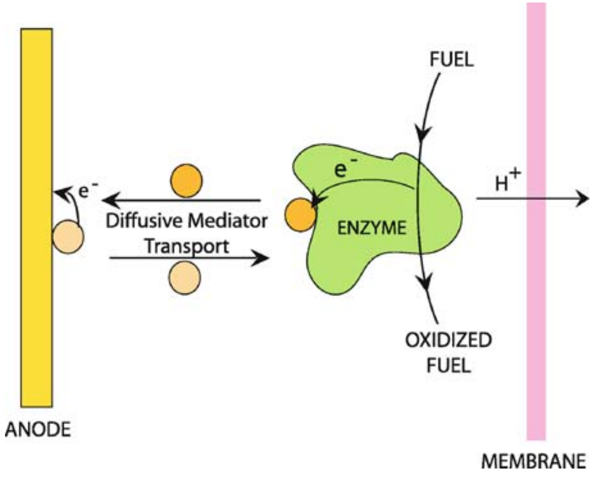

Microfluidic Fuel Cells, Figure 2 Anodic half-cell of a biofuel cell based on biocatalytic enzyme proteins, fuel and redox mediators in solution

a commercial gold slide, used as the base layer. Catalyst was plated on the gold patterns by traditional electrodeposition, and electrical wiring was attached using conductive epoxy. Similar photolithography was used to produce a master with a positive imprint of the channel network patterned on a glass slide, and a copy of the master was cast and cured into a slab of PDMS to mold actual channels for the top layer. Holes were punched in the polymeric layer for fluid delivery and the two layers were plasma treated which renders hydrophilic surfaces and creates an irreversible seal upon assembly of the fuel cell.

The microfluidic fuel cell design may also be implemented for biofuel cells based on enzyme catalysis. Enzymatic biofuel cells are traditionally compartmentalized into two half-cells separated by a salt bridge or ion exchange membrane [2]. Figure 2 shows the anodic half cell of a two-compartment biofuel cell based on mediated electron transfer. Enzyme proteins, fuel, and redox mediators are all dissolved in an ion-conducting electrolyte. In simplified terms, the enzyme (in the anodic compartment) oxidizes the substrate (fuel), thereby harvesting electrons. The enzyme cannot accumulate electrons internally. Instead, each oxidation event requires the docking of a cofactor (or redox mediator) in the proximity of the active site. The electrons are transferred to the cofactor, which is then released into the solution and allowed to diffuse to the electrode. This shuttling of electrons from the enzymes to the electrode can be carried out directly by the cofactor or in a relay with additional redox mediators. Depending on the type of redox mediator, the electrode may need to be functionalized with a self-assembled monolayer or film capable of oxidizing the redox mediator at low overpotentials.

Biofuel cells based on enzymes in solution are largely limited by the rate of diffusion of the intermediate species [2]. Furthermore, the lifetime of enzymes in solution is typically only a few days. These limitations can be addressed by immobilization of the enzyme directly on a conductive support (carbon or gold). Many immobilization schemes have previously been developed for biosensors including the following: self-assembled monolayer-functionalized electrodes with redox polymers and/or conductive polymers bound to the enzyme by covalent linking or affinity interactions combined with cross-linking; or direct encapsulation of enzymes in hydrogel films. Upon conformational fixation of the enzyme attributed to its immobilization, the stability (lifetime) may be extended to weeks or even months. Biofuel cells have more advanced requirements than biosensors however (fast electron transfer, low overpotentials, and maintained enzymatic activity), which makes the development of efficient immobilization schemes more challenging. Only certain types of enzymes, with active sites located on the periphery of the enzyme, are capable of direct electron transfer to the electrode without redox mediators [3].

The immobilization of enzymes on conductive supports enables integrated microfluidic biofuel cell designs. Biofuel cells with non-selective electrochemistry, i. e. cells using diffusional redox mediators, can utilize the co-laminar microfluidic fuel cell design previously described, which also enables the tailoring of independent anolyte and catholyte compositions. Full selectivity of both anodic and cathodic half-cells, i. e. co-immobilized redox relays and enzymes based on suitable linking schemes with electronic coupling, allows microfluidic biofuel cell operation in a single, combined fuel and oxidant channel with mixed reactants.

Key Research Findings

Proof-of-concept microfluidic fuel cells have been developed based on hydrogen, methanol, formic acid, hydrogen peroxide and vanadium redox species as fuel. The majority of these devices employed a Y- or T-shaped channel design featuring two aqueous co-laminar streams with fuel and oxidant dissolved in a supporting electrolyte, similar to the one shown in Fig. 3a, with electrodes on opposite channel walls parallel to the inter-diffusion zone. The power density of these fuel cells was predominantly limited by the rate of mass transport to the active sites, typically in the cathodic half-cell. For cells using dissolved oxygen in the cathodic stream, the maximum power density reported to date, 5 mW cm^{-2}, was primarily restricted by the low solubility of oxygen (2 – 4 mM). One way to avoid this limitation is to integrate an air-breathing porous cath-

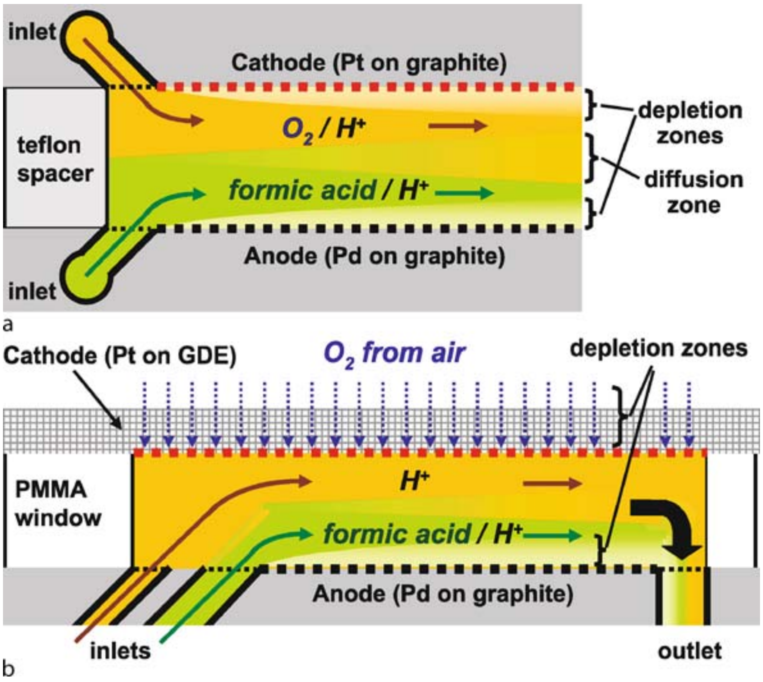

Microfluidic Fuel Cells, Figure 3 Microfluidic fuel cell designs with oxygen-saturated catholyte (**a**) and air-breathing cathode (**b**) Reproduced with permission from [5])

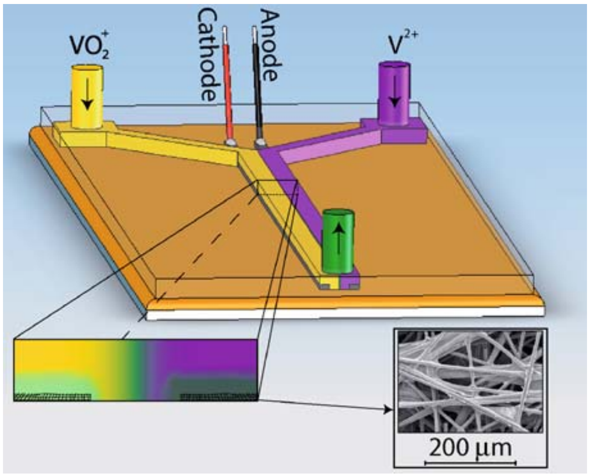

Microfluidic Fuel Cells, Figure 4 Schematic of a microfluidic vanadium redox fuel cell with porous carbon electrodes, using aqueous V^{2+} fuel (purple, dark grey in the print version) and VO_2^+ oxidant (yellow, light grey in the print version) (Reproduced with permission from [6])

ode structure that allows gaseous oxygen transport from the ambient air, a source of oxygen that has significantly higher diffusivity and concentration than dissolved oxygen. Jayashree et al. [5] introduced the first microfluidic fuel cell with integrated air-breathing cathode, shown in Fig. 3b. This cell used a graphite plate anode covered with Pd black nanoparticles and a porous carbon paper cathode covered with Pt black nanoparticles. Peak power density, 26 mW cm^{-2}, was achieved with 1 M formic acid in 0.5 M sulfuric acid anolyte and a blank 0.5 M sulfuric acid catholyte. The cathodic electrolyte stream was required to maintain an inter-diffusion zone with sufficient separation from the cathode and to facilitate ionic transport to the cathodic active sites.

The use of alternative oxidants, soluble at higher concentrations than dissolved oxygen, provides another avenue towards improved performance of mass-transfer limited microfluidic fuel cells. Kjeang et al. [4] evaluated the feasibility of a formic acid anolyte combined with a hydrogen peroxide catholyte. The electrodes consisted of Au strips that were plated with high-surface area dendritic structures of pure Pd (anode) and Pt on Pd (cathode) by potentiostatic electrodeposition. The power densities obtained with the hydrogen peroxide cell was similar to that of the air-breathing cell. An interesting side effect is the decomposition reaction of hydrogen peroxide into oxygen and water that occurs spontaneously on Pt and Pd, causing gaseous oxygen evolution on the cathode. This feature creates an instability leading to unsteady current generation. Interestingly, it also leads to enhanced time-averaged mass transport and reaction rates, and provides an alternative

source of oxygen that is not restricted by the solubility limit.

A microfluidic fuel cell design based on soluble vanadium redox species was recently introduced (Fig. 4). Vanadium redox fuel cells utilize two different aqueous vanadium redox couples, V^{2+}/V^{3+} and VO^{2+}/VO_2^+, as fuel and oxidant, respectively, dissolved in dilute sulfuric acid. This combination of vanadium redox pairs offers several advantages for microfluidic fuel cell operation: they provide well-balanced electrochemical half-cells in terms of reaction rates and transport characteristics; they have high solubility and enable relatively high redox concentrations up to 5.4 M; they have a large difference in formal redox potentials resulting in a high open-circuit voltage (up to ∼1.7 V at uniform pH); and the reactions are facilitated by plain carbon electrodes without requiring precious metal catalysts such as Pt or Pd. These advantages, together with the use of inexpensive microfabrication methods, enable very cost-effective fuel cell units with relatively high performance. Kjeang et al. [6] investigated the effects of high-surface area porous carbon electrodes for a microfluidic vanadium redox fuel cell (Fig. 4), and found that its performance was significantly improved compared to an otherwise similar cell with planar electrodes, attributed to enhanced rates of transport and increased active area. Using 2 M vanadium in 2 M sulfuric acid, a peak power density of 70 $mW\,cm^{-2}$ was obtained at 1 $mL\,min^{-1}$ flow rate per stream, which is the highest power density for microfluidic fuel cells reported to date. The fuel cell was operated at flow rates spanning four orders of magnitude, showing operational flexibility and durability. Operation in the low-flow rate regime (1 – 10 $\mu L\,min^{-1}$) resulted in single-pass fuel utilization up to 55%, with a corresponding decrease in power density. This high rate of fuel utilization was attributed to the high-aspect ratio geometry with electrodes perpendicular to the inter-diffusion zone (Fig. 4) and effective use of low-range flow rates. A consequence of the high-aspect ratio geometry is that the ohmic resistance in the channel is proportional to the average charge transfer distance between anode and cathode. For this reason, ohmic resistance in microfluidic fuel cells is generally higher than in membrane-based fuel cells due to a larger separation of the electrodes, but can be reduced by increasing the concentration of the supporting electrolyte.

The development of enzymatic biofuel cells has mostly focused on the immobilization of redox-active enzymes on conductive supports and the corresponding electron transfer mechanisms. It is common practice to present biofuel cell research findings based on individual bioanodes or biocathodes (versus a more conventional non-biological counter-electrode), and to extrapolate their feasibility towards fuel cell applications. In this entry, we focus on complete biofuel cells as well as advanced bioanodes and biocathodes developed exclusively for fuel cell applications. For more information on enzyme immobilization and linking schemes, see for example Katz et al. [2] and Bullen et al. [3].

Biofuel cells based on enzymes *wired* to tiny carbon fibers (7 μm diameter) have recently been introduced [7]. Cross-linked electrostatic adducts of enzyme were wired to the carbon fibers within a redox hydrogel comprising conductive polymer with complexed osmium redox centers. Glucose was oxidized by glucose oxidase at the anode and oxygen was reduced by bilirubin oxidase or laccase at the cathode. Operation of the fuel cell was shown in a non-compartmentalized configuration in a physiological buffer solution as well as in a grape with naturally available reactants inside its skin. The highest power density achieved was 0.48 $mW\,cm^{-2}$ at 0.60 V (in physiological buffer), which provides a good benchmark for biofuel cell development. The stability, however, was limited to the order of weeks. The laccase-based biocathode was also shown to outperform Pt as an oxygen reduction catalyst, due to its lower overpotential. The current generated by this biocathode was 90% limited by mass transport of oxygen at only −70 mV overpotential when operated in pH 5 citrate buffer.

Moore et al. [8] developed a bioanode based on NAD-dependent alcohol dehydrogenase enzymes immobilized in a tetrabutylammonium bromide treated Nafion membrane. A thin film of methylene green, which is an electrocatalyst for NADH oxidation, was electropolymerized onto a carbon ink electrode, upon which the enzyme/Nafion mixture was cast. The bioanode was assembled on a glass substrate under a PDMS microchannel that was used to deliver the fuel solution containing ethanol and NAD^+ in phosphate buffer. NADH was produced during the oxidation of ethanol by alcohol dehydrogenase in the presence of NAD^+. The NADH diffused through the membrane to the methylene green layer, where it was oxidized back to NAD^+ while transferring two electrons to the carbon electrode. The bioanode produced an open-circuit voltage of 0.34 V and a maximum current density of 53 $\mu A\,cm^{-2}$, expected to be limited by the rate of diffusion of NADH within the membrane, while operated versus an external Pt cathode. This performance was later enhanced by adding aldehyde dehydrogenase and NAD^+ to the previously described Nafion casting mixture suspended on a high-surface area carbon felt electrode. Power densities up to 2.0 $mW\,cm^{-2}$ were reached in a two-compartment U-cell setup with a Pt cathode. This bioanode was also paired with a bilirubin oxidase-based biocathode in a noncompartmentalized complete biofuel

cell arrangement [9]. The biocathode was assembled using a similar procedure with bilirubin and bilirubin oxidase suspended in the Nafion membrane together with preconcentrated $Ru(bpy)_3^{2+}$ redox mediator. The open circuit potential and maximum power density obtained with the membrane-less system (0.51 V and 0.39 mW cm^{-2}) were lower than for the corresponding two-compartment cell with a membrane separator (0.68 V and 0.83 mW cm^{-2}), due to incomplete specificity of the system. Enzymes encapsulated in a modified Nafion membrane are expected to have a lifetime of more than 90 days, though the lifetime of the biofuel cells was reduced to about 30 days due to the degradation of $Ru(bpy)_3^{2+}$.

A swell of research interest in biocatalysis and biofuel cell technology is apparent from the large number of recent contributions in this area. The overall objective of biofuel cell research is still, however, to determine whether biofuel cells are real contenders for practical use. Some future directions for research in this area are described in the next section.

Future Directions for Research

The development of co-laminar microfluidic fuel cells to date has been tremendous, given that it is a relatively new invention. Research so far has resulted in operational devices with promising performance in terms of power density and open-circuit voltage, but little has been done in order to design practical, efficient and competitive devices with high energy density and high fuel utilization. The most prominent constraint identified for current microfluidic fuel cells is their low energy density, defined as energy output per system volume or mass. The core physics of the co-laminar flow configuration requires that both streams are liquid and contain an electrolyte. Although reactants may be added to the system at high concentration, the energy density of all devices presented hitherto has been low compared to other small fuel cells due to the impractical single-pass use of liquid electrolyte without any form of recirculation or recycling. The implementation of a recirculation system for the electrolyte is a challenging task, not only due to the space constraint. Dual outlets can partly solve this issue, but there will always be some degree of mixing of unused fuel and oxidants at the outlet(s) that would influence the open-circuit voltage negatively upon recirculation. Moreover, although fuel utilization data up to 55% per single pass have been presented, the fuel utilization at practical flow rates with useful power generation is generally less than 10%. Reaching overall fuel utilization beyond 20 – 40% is quite a challenging issue that may require an innovative system for separation and recycling of unused fuel and oxidant. In addition, there is a lack of engineering solutions for important functions such as the integration of fuel and oxidant storage solutions, waste handling, and low-power microfluidics-based fluid delivery (normally driven by a syringe pump via external tubing) using integrated micropumps and microvalves. In this context, the microfluidic fuel cells based on vanadium have an important advantage: the opportunity of regeneration. Provided that all reactants and products are vanadium redox species, the waste solutions could be collected from the outlet reservoir and transferred to an electrolytic cell that regenerates the initial fuel and oxidant species by an applied current (recharging), and when fully charged, transfer them back to the fuel cell for another discharge cycle. This technology would benefit from further research into the on-chip integration of a regeneration system with on-board reactant storage.

Another important engineering challenge is the scale-up and tailoring of electric current and voltage output from microfluidic fuel cell systems to meet the specific power requirements of target applications. Most research so far has been directed entirely towards the development of single cells, which despite a lack of optimization, is quite mature. The feasibility of scaling up a single cell, i. e. increasing the geometrical area of electrodes and microchannel, is mainly restricted by structural constraints introduced by flexible materials (e. g., PDMS), increasing inter-diffusion width, and escalating ohmic losses if the average distance between anodic and cathodic active sites becomes large. Stacking of multiple cells may be performed in both planar and sandwich configurations, and wired in either series or parallel configurations to match power and voltage specifications. Finally, the successful integration of well-developed and inexpensive microfabrication methods and MEMS technologies in order to reduce the cost of batch production is a key component for the development of competitive microfluidic fuel cells.

None of the biofuel cells presented to date have utilized microfluidic channels, despite the opportunity of improved performance by the addition of convective transport. Microfluidic designs would be particularly well-suited for biofuel cells using efficient oxygen-reducing biocatalysts, previously shown to be limited by the rate of oxygen transport. Furthermore, microfluidic networks enable the patterning of multiple, consecutive enzymes for the complete decomposition of fuels such as methanol to carbon dioxide. Figure 5 demonstrates a possible configuration. Kjeang et al. [10] projected in a modeling study of enzyme kinetics coupled with multi-component species transport in a microfluidic channel that consecutive enzymatic reactions may be engineered by strategic electrode patterning of multiple enzymes. A mixed enzyme pattern-

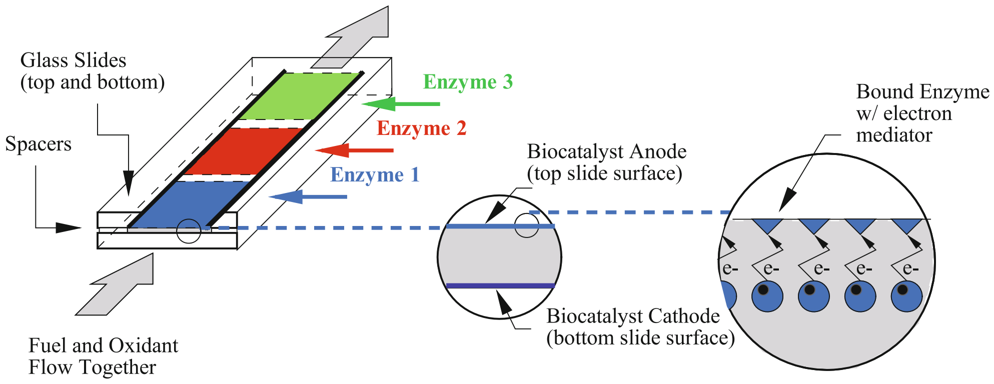

Microfluidic Fuel Cells, Figure 5 Microfluidic biofuel cell with consecutive reactions catalyzed by an array of different enzymes (Reproduced with permission from [10])

ing strategy that accounts for individual turnover rates was recommended, as intermediate fuel becomes available from previous reactions in the direct proximity of the consecutive enzymes further down the chain. A microfluidic system would also be favourable for stability studies since the reactant concentrations can be kept constant by continuous flow. Future research would benefit from an experimental study that demonstrates the capabilities of microfluidics with respect to biofuel cell development.

The performance of current bioanodes and biocathodes must be improved in order for microfluidic biofuel cells to reach their full potential and become competitive on the small fuel cell market. Improved immobilization and redox mediation schemes, more efficient wiring, improved alignment and orientation; all can help increase both stability and current density. Another possible avenue would be to identify and develop new enzyme proteins with higher turnover rates by genetic engineering. From a practical perspective, it is important to realize that early applications are going to be limited to specialized systems where the specific advantages of biocatalysis come into play. For example, biofuel cells are promising candidates for certain biochemical applications related to labs-on-chip or micro total analysis systems since they can use existing solutions specifically to generate power on-chip. Given their compatibility with physiological conditions, biofuel cells are also considered for low-power in vivo biomedical applications such as self-powered glucose sensors and power supplies for prosthetic valve actuators as well as skin-patch-based power sources for receiver-amplifier-transmitter units and miniaturized drug delivery systems. Implantable biofuel cells have effectively infinite energy capacity when utilizing blood-supplied glucose and oxygen available in the subcutaneous interstitial fluid. Unlike batteries, these devices can be miniaturized without packaging and sealing due to their non-compartmentalized operational characteristics. The combination of inexpensive microfabrication, low-cost enzymatic catalyst, and the absence of precious metals and other expensive components, would enable integrated biofuel cell units that can be disposed of and replaced at the end of their lifetime. Pending on the success of these specialized demonstrations, biofuel cells may be scaled up to meet the power and lifetime requirements of more widespread applications.

Cross References

- ► Biofuel Cell
- ► MEMS-Based Biosensor
- ► Microscale Energy Conversion Devices
- ► Micro-structured Hydrogen Fuel Cells

References

1. Larminie J, Dicks A (2003) Fuel Cell Systems Explained. John Wiley and Sons Inc., Hoboken
2. Katz E, Shipway AN, Willner I (2003) Biochemical fuel cells. In: Vielstich W, Lamm A, Gasteiger HA (ed) Handbook of Fuel Cells. John Wiley and Sons Inc., Hoboken
3. Bullen RA, Arnot TC, Lakeman JB, Walsh FC (2006) Biofuel cells and their development. Biosens Bioelectron 21:2015–2045
4. Kjeang E, Brolo AG, Harrington DA, Djilali N, Sinton D (2007) Hydrogen peroxide as an oxidant for microfluidic fuel cells. J Electrochem Soc 154(12):B1220–B1226
5. Jayashree RS, Gancs L, Choban ER, Primak A, Natarajan D, Markoski LJ, Kenis PJA (2005) Air-breathing laminar flow-based microfluidic fuel cell. J Am Chem Soc 127:16758–16759
6. Kjeang E, Proctor BT, Brolo AG, Harrington DA, Djilali N, Sinton D (2007) High-Performance Microfluidic Vanadium Redox Fuel Cell. Electrochimica Acta 52(15):4942–4946
7. Mano N, Mao F, Heller A (2004) A miniature membrane-less biofuel cell operating at +0.60 V under physiological conditions. ChemBioChem 5:1703–1705

8. Moore CM, Minteer SD, Martin RS (2005) Microchip-based ethanol/oxygen biofuel cell. Lab Chip 5:218–225
9. Topcagic S, Minteer SD (2006) Development of a membraneless ethanol/oxygen biofuel cell. Electrochimica Acta 51:2168–2172
10. Kjeang E, Sinton D, Harrington DA (2006) Strategic enzyme patterning for microfluidic biofuel cells. J Power Sources 158:1–12

Microfluidic Imaging

► Microscale Flow Visualization

Microfluidic Integration

► Microfluidic Assembly

Microfluidic Mixer

► Microfluidic Mixing
► Passive Micromixers

Microfluidic Mixing

ROHIT KARNIK
Department of Mechanical Engineering, Massachusetts Institute of Technology, Cambridge, MA, USA
karnik@mit.edu

Synonyms

Blending; Homogenization; Microfluidic mixer

Definition

Mixing is the process by which uniformity of concentration is achieved. Depending on the context, mixing may refer to the concentration of a particular component or set of components in the fluid.

Overview

Importance of Mixing

A mixer is one of the basic building blocks in microfluidics, along with components such as pumps and valves, and is a critical component in several microfluidic devices. For example, mixing of reaction components is essential for providing homogeneous reaction environments for chemical and biological reactions. The efficiency of many devices such as biosensors depends on mixing. In other applications, rapid and controlled mixing is essential for studying reaction kinetics with much better time resolution as compared to microscale techniques. Microfluidic mixers are thus integral components essential for proper functioning of microfluidic devices for a wide range of applications.

Fundamentals of Mixing

In the context of microfluidics, mixing is the process through which uniformity of concentration is achieved. Depending on the application, the concentration may refer to that of solutes (ions, small molecules, biomolecules, etc.), solvents, or suspended particles such as colloids. Microfluidics typically involves incompressible aqueous or organic solutions, and we will consider only these systems here.

Molecules in solution undergo random motions, giving rise to the process of diffusion. Under a concentration gradient, diffusion results in flux (J) of molecules that tends to homogenize the concentration (c) of that molecular species.

$$J = -D\nabla c \qquad (1)$$

Here D is diffusivity of the species under consideration, and varies from approximately 10^{-9} m^2/s for small molecules and ions to 10^{-11} m^2/s for large biomolecules. Therefore, an isolated system with non-uniform concentrations ultimately achieves a state of uniform concentration, i. e., it will be completely mixed. The mixing time depends on the diffusivity (D) and length scale over which diffusion must act in order to homogenize the concentration, known as the striation length (l_{st}). The mixing time is then given by

$$t_{mix} \sim \frac{l_{st}^2}{D} \qquad (2)$$

From this equation, it is clearly seen that for rapid mixing, it is necessary to reduce the striation length (Fig. 1). This concept leads to two ideas intimately connected with the process of mixing: (a) the process of decreasing the distance over which diffusion must act, and (b) the process of diffusion itself. The former process of decreasing the striation length is accomplished by stretching and folding of the fluid or by breakup and rejoining. These processes decrease striation length and increase the area across which diffusion takes place, thus enabling diffusion to rapidly homogenize the solution.

Mathematically, the concept of mixing is rather unwieldy, and is built upon the concepts of ergodicity and dynamical systems theory. The reader is referred to [1] for an introduction to the mathematical treatment of mixing, and

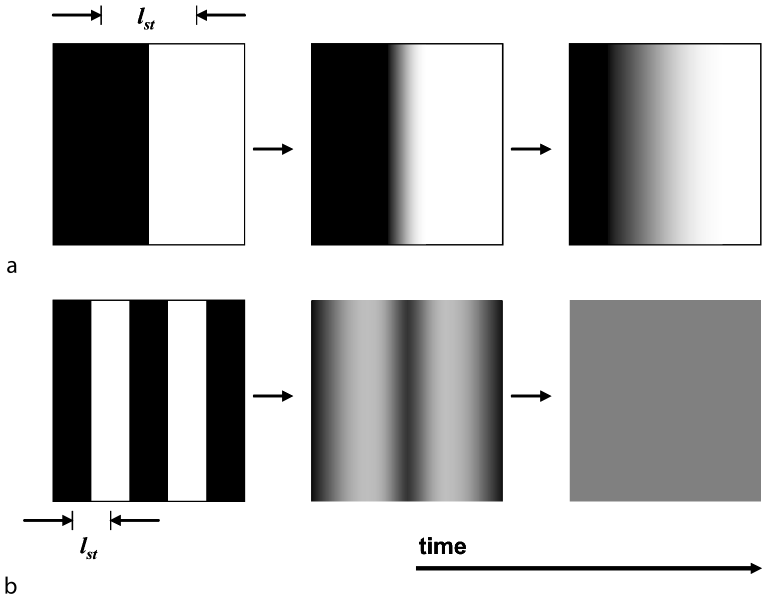

Microfluidic Mixing, Figure 1 Striation length (l_{st}) and mixing time. The striation length characterizes the distance over which diffusion must act in order to homogenize the solution. (**a**) An unmixed solution with a large striation length takes time to mix by diffusion alone. (**b**) A 5-fold reduction in the striation length decreases the mixing time 25-fold

to [2] for a comprehensive treatment. Here we describe two types of flows or transformations with a mathematical basis that aid in understanding and designing mixers: The Baker's transformation is useful for understanding mixing involving the process of breakup, and blinking flows are useful for understanding the process of mixing in designs that do not involve breakup.

Consider a rectangular domain, with half of the domain marked with black points (Fig. 2a). The Baker's transformation consists of stretching, cutting, and rejoining such that the striation length decreases uniformly everywhere in the domain. In the first step, the domain is stretched uniformly in one direction. In the second step, the domain is cut and rejoined. The striation length decreases by a factor of two each time the transformation is applied, therefore an exponential decrease in the striation length is achieved (Fig. 2b). Mixing achieved in this transformation satisfies the strongest mathematical definition of mixing and is therefore highly desirable [1]. The Baker's transformation illustrates how the process of breakup can be used to exponentially decrease the striation length, and is useful for designing systems where fluid streams or droplets split and rejoin.

In a seminal paper in 1984, Aref [3] pointed out that simple time-varying two-dimensional flows can result in non-integrable particle trajectories, beautifully illustrated in the book by Ottino [2] (Fig. 2c). This concept was the starting point of what is now widely called chaotic advection. While chaotic advection is not precisely defined, it is associated with exponential stretching and folding of the fluid. Aref considered mixing in an idealized bounded two-dimensional domain with blinking flows. Blinking flows switch instantaneously from one streamline pattern to another in a periodic fashion. The relevance of this idealized concept to continuous-flow mixing in microfluidics is that flows transverse to the primary flow direction can be made to switch between two patterns as the fluid travels along the channel. Thus, a three-dimensional steady flow with periodicity in space may be understood in terms of a two-dimensional blinking flow with periodicity in time. An intuitive design criterion for such flows is that effective mixing corresponds to maximum crossing of streamlines of the two flows of the blinking flow. The mathematical basis of this design criterion is the linked twist map, described by Wiggins and Ottino [1]. Proper design of mixers incorporating the principles of chaotic advection can result in striation lengths that exponentially decrease in time.

Basic Methodology

Mixing in Microfluidics

The design and implementation of mixers in microfluidics differs considerably from than that on the macroscale. The small length scale leads to different physical phenomena being dominant at the microscale: First, inertial effects

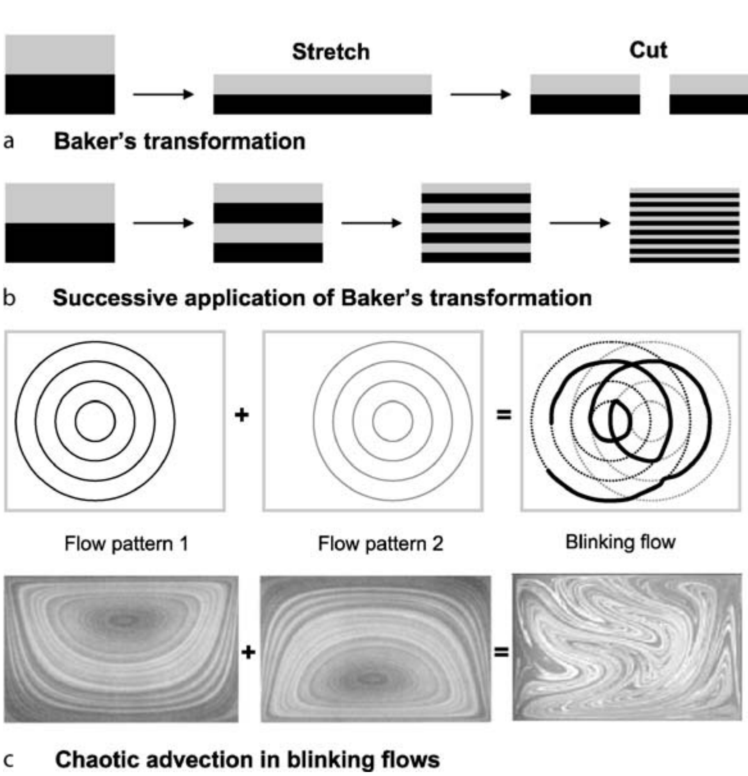

Microfluidic Mixing, Figure 2 (**a**) Baker's transformation consists of stretching, cutting, and rejoining the domain. After each transformation, the striation length decreases by a factor of 2. (**b**) Successive application of the Baker's transformation results in exponential decrease of the striation length. (**c**) Blinking flows alternate periodically between two flow patterns. While each flow pattern exhibits simple streamlines and particle trajectories, the blinking flow itself exhibits chaotic advection and non-integrable particle trajectories. Images of cavity flow are reproduced from [2]

that typically result in turbulence and good mixing on the macroscale are weak in microfluidics, while methods of actuation based on electrokinetics, surface tension or other phenomena that are not relevant on the macroscale become feasible on the microscale. Secondly, many mechanical designs such as stirrers that can be easily implemented on the macroscale are very difficult to implement on the microscale. A useful mixer is therefore often the one that is simple to fabricate and integrate with other microfluidic components.

The Reynolds number (Re) characterizes the relative importance of inertial to viscous forces, and is given by

$$\mathrm{Re} = \frac{\rho U l}{\eta} \tag{3}$$

Here ρ is the density, U is flow velocity, l is the characteristic length scale (e. g., channel height), and η is the dynamic viscosity of the fluid.

In macroscale systems, the effect of inertia is often significant, resulting in a large Re and turbulence, which can be harnessed for mixing. However, due to the small channel size (l), microfluidic flows are characterized by a low Reynolds number, typically in the range of 0.01 to 100, and the effects of inertia are often negligible. Turbulence is therefore typically not encountered and microfluidic flows are usually laminar. Mixing due to diffusion alone is also not sufficient for rapid mixing in microfluidics. For example, a small molecule with a diffusivity of $10^{-9}\,\mathrm{m}^2/\mathrm{s}$ will take approximately 10 s to diffuse across a 100 µm microchannel, while a large macromolecule with a diffusivity of $10^{-11}\,\mathrm{m}^2/\mathrm{s}$ will require about 1000 s.

The Peclet number (Pe), a dimensionless number that characterizes the relative importance of diffusion to convection, is often used in the context of mixing of continuously flowing streams. The Peclet number is given by

$$\mathrm{Pe} = \frac{l^2/D}{l/U} = \frac{t_{\mathrm{diff}}}{\tau_{\mathrm{conv}}} = \frac{lU}{D} \tag{4}$$

Here D is diffusivity, l is the characteristic length scale (typically channel height) and U is the flow velocity. The Peclet number can thus be viewed as the ratio of characteristic time for diffusion (t_{diff}) to the characteristic convection time (τ_{conv}). When mixing occurs only

via diffusion in a microchannel with a flat velocity profile, $t_{mix} = t_{diff} = \tau_{conv}\mathrm{Pe}$. The channel length required for mixing (l_{mix}) is then given by

$$l_{mix} = U\,t_{mix} = l\,\mathrm{Pe} \qquad (5)$$

A linear relationship between the mixing time and the Peclet number implies that the channel length needed for mixing increases linearly as the flow velocity is increased, or as the diffusivity is decreased (for different species). In order to minimize the channel length required for mixing, it is desirable to design mixers in which the mixing time increases only weakly with the Peclet number. For a microchannel with $l = 100\,\mu\mathrm{m}$, the Peclet number is 1000 for diffusivity (D) of $10^{-9}\,\mathrm{m^2/s}$ (typical of small molecules) and flow speed of 1 mm/s. If mixing occurs purely due to diffusion, the channel length must be 1000 times the channel height for two streams to mix in the channel, i. e., the channel length must be 10 cm. However, if larger biomolecules with a diffusivity of $10^{-11}\,\mathrm{m^2/s}$ are to be mixed, the required channel length increases 100-fold to 10 m!

Clearly, in the absence of turbulence, other methods of microfluidic mixing must be devised. Since mixing ultimately occurs by diffusion, the goal of all mixers must be to decrease the striation length across which diffusion takes place in order to mix more efficiently.

Mixer Performance

The criteria used to measure mixing vary widely. One of the more common measures for mixing known as the mixing variance coefficient (MVC) [4] is based on the concentration distribution inside the channel or volume. For this purpose, the volume under consideration is divided into sub-volumes, and the deviation of concentrations in each sub-volume from the average concentration in the volume is computed as follows:

$$MVC = \frac{1}{N}\sum\left(c_i - c_{avg}\right)^2 \qquad (6)$$

Here N is the number of sub-domains, c_i is the concentration in the ith sub-domain, and c_{avg} is the average concentration for the entire domain. MVC approaches zero when mixing is complete. Division of the domain into sub-domains for computing the MVC is shown in Fig. 4a.

Experimentally, a commonly used method for characterizing mixing uses chemical reactions with fast kinetics. Such reactions may include reactions such as ion-binding fluorescent dyes that change fluorescence intensity upon binding the ion or pH indicators that change color. However, it must be noted that mixing characterized using these methods depends on reactant concentrations as well as diffusivities. Therefore, care must be exercised when attempting to evaluate mixing of the molecular species of interest using other species as indicators.

The criteria for evaluating the performance of microfluidic mixers vary widely depending on the application. However, for many applications, the most important criterion that determines the usefulness of the mixer is ease of fabrication. Mixers that can be easily incorporated with other microfluidic components are more likely to be used than those that require special fabrication procedures. Active mixers are generally more difficult to fabricate than passive mixers, and therefore find use only in certain applications. Apart from ease of fabrication, different applications may have different requirements that may be used to judge the performance of the mixer. Applications such as study of reaction kinetics demand rapid mixing and ease of observation of the ensuing reaction. Here, the primary consideration is usually mixing time. For combinatorial synthesis or other applications, it may be necessary to have a small space footprint and ease of integration with other components. In certain cases, pressure drop in the mixer may be important.

Key Research Findings

Mixer Classification

Mixers are broadly classified as active or passive mixers based on the method of actuation. Active mixers employ *active* elements such as external pressure perturbations, small actuators, or other methods in addition to the applied pressure that drives flow. Passive mixers rely solely on the pressure gradient (or other mechanisms such as electroosmosis) that drives the flow in combination with *passive* elements such as channel geometry or other properties in order to achieve mixing. Note that the definition of passive mixers applies only to continuous flow systems, and mixers that mix stationary and bounded volumes of fluid are typically active mixers. Some passive mixers may operate at moderate Reynolds numbers and use inertial effects for mixing, while others use channel geometry or other effects to mix effectively at low Reynolds numbers. Typically, passive mixers are easy to fabricate and more robust than active mixers, and are therefore more widely used by researchers. Other methods of classification may be based on the physical phenomena driving the flow (electrokinetics, magnetohydrodynamics, ultrasound, inertia, etc.), single phase or multi-phase flows, fabrication complexity, continuous flow versus discrete volumes, etc. The following sections classify mixers as active/passive and further based on flow patterns, and other classifications are either self-evident or pointed out in specific cases of interest.

Passive Mixers

Passive mixers may be broadly classified as focusing/injection mixers, lamination mixers, and chaotic advection mixers. Focusing/injection mixers rely on diffusion alone to cause mixing. These mixers are effective if one stream with a small flow rate is to be diluted into another stream with a large flow rate. Lamination mixers typically split the streams to be mixed into multiple streams that are then interdigitated and brought together. Splitting into several streams decreases the striation length and therefore enhances mixing. In these cases, the striation length remains fixed during the process of mixing, and mixing time is approximately independent of the flow rate. Chaotic advection mixers, on the other hand, cause exponential thinning of the striation length. Achieving chaotic flows in passive microfluidic mixers typically requires three-dimensional channel geometry, use of weak inertial effects, or two-phase flows.

Focusing/Injection Mixers

Focusing or injection mixers are not true mixers; rather, they are very efficient at diluting one stream in another. In the hydrodynamic focusing mixer, three streams converge and flow into one microfluidic channel. Fig. 2a shows a cartoon of the hydrodynamic focusing mixer [5]. The inlet stream can be focused into a very thin stream by the adjoining side streams, either by controlling pressures of the three streams or by controlling the flow rates of each stream using a syringe pump. Sub-micron focusing of the inlet stream enables species from the side streams to rapidly diffuse into the focused stream. Homogeneity of concentration is achieved as far as species in the adjoining streams are concerned. However, species in the focused stream take much longer to distribute uniformly across the channel cross section. Mixing time in this mixer depends only upon the width (w_f) of the central focused stream, which defines the striation length in this case:

$$t_{mix} \sim \frac{w_f^2}{D} = \left(\frac{w_f}{l}\right)^2 \tau_{conv}\mathrm{Pe} \qquad (7)$$

It is seen that mixing time scales linearly with the Peclet number. However, the mixing time is decreased dramatically since $w_f \ll l$. For $D = 10^{-9}\,\mathrm{m^2/s}$ (typical of small molecules or ions) and $w_f = 100\,\mathrm{nm}$, the mixing time is only $10\,\mu\mathrm{s}$. This mixer is a very effective tool for rapidly changing the chemical environment of species in the central focused stream, at the same time consuming a smaller sample volume due to the low flow rate of the inlet stream. Hydrodynamic focusing mixers find applications in the study of fast kinetics such as protein folding.

Injection mixers are similar to flow focusing mixers in that they also dilute one stream into another stream; however they differ from focusing mixers in that a small aperture is used to inject a thin stream into another stream. These mixers enable multiple flow streams to be injected, and may be more desirable when flow rates or pressures cannot be controlled. Mixing time depends on the method of injection and device geometry. However, construction of small apertures or the use of a membrane with apertures is required, making injection mixers harder to fabricate compared with focusing mixers.

Lamination Mixers

Lamination mixers employ parallel lamina across which diffusion can take place. The simplest mixer is the classic T-mixer that brings together two fluid streams and allows diffusive mixing as they flow parallel in a channel. In the absence of turbulence, the effective striation length is of the order of the channel size. Therefore, the mixing time in this case is given by

$$t_{mix} \sim \frac{l^2}{D} = \tau_{conv}\mathrm{Pe} \qquad (8)$$

Mixing time scales linearly with the Peclet number, and mixing time is equal to the characteristic time for diffusion across the channel cross-section. This mixer requires long mixing times, but is very simple to implement and hence becomes a practical multi-purpose mixer in cases where there are no severe demands on mixing time and channel length. An improvement over the T-mixer is the parallel lamination mixer (Fig. 2b). This mixer splits the streams to be mixed into multiple streams, which are interdigitated and recombined. If each stream is split into N streams, the striation length is decreased by a factor of N and mixing time is consequently decreased by a factor of N^2.

$$t_{mix} \sim \frac{(l/N)^2}{D} = \frac{\tau_{conv}\mathrm{Pe}}{N^2} \qquad (9)$$

For example, with $D = 10^{-9}\,\mathrm{m^2/s}$, $l = 100\,\mu\mathrm{m}$, and $N = 10$, the mixing time decreases from approximately 10 s to just 100 ms, and the channel length required for mixing also decreases by two orders of magnitude. This mixer is therefore more effective than the T-mixer, even though mixing time scales linearly with the Peclet number. However, interdigitation involves crossing over of channels, requiring a two-level fluidic architecture that is harder to fabricate than the single-level fluidic architecture of the T-mixer.

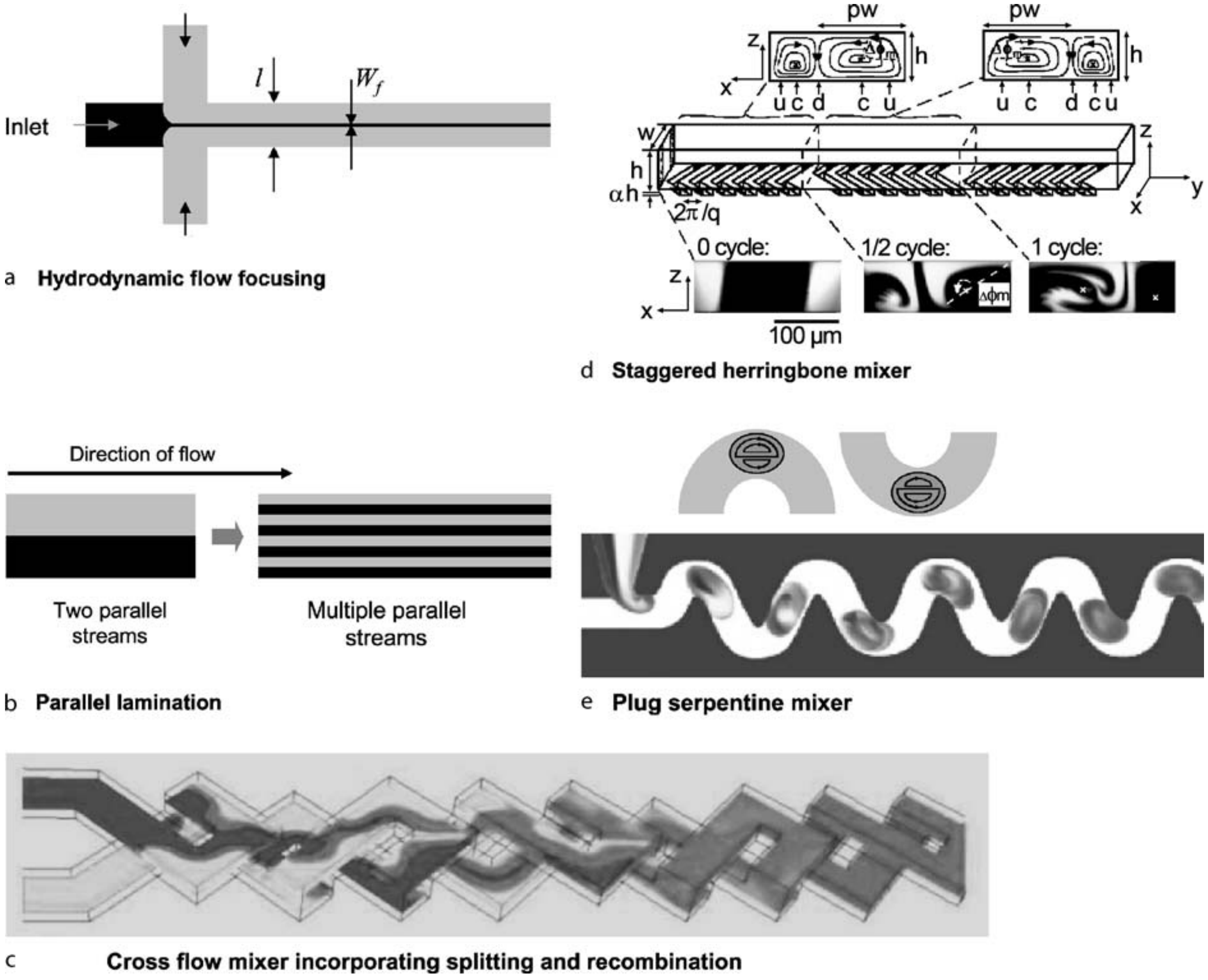

Microfluidic Mixing, Figure 3 (**a**) Hydrodynamic flow focusing mixer. (**b**) Concept of parallel lamination. Rapid mixing is achieved by splitting two streams to be mixed into multiple parallel streams, thereby decreasing the striation length. (**c**) A passive chaotic advection mixer employing splitting and recombination. (from [7]) (**d**) Staggered herringbone mixer uses grooves on channel walls to drive chaotic advection in microchannels. Alternating groove patterns result in asymmetric circulating flows similar to blinking flows. (from [8]) (**e**) Plug serpentine mixer uses a curved microchannel to induce chaotic advection inside plugs (droplets). Inset cartoon depicts alternating flow patterns inside individual plugs as they traverse through the channel. (from [9])

Passive Chaotic Advection Mixers

Proper design of mixers incorporating the principles of chaotic advection can result in striation lengths that exponentially decrease in time. Since steady two-dimensional flows cannot exhibit chaotic advection [1], passive chaotic advection mixers need either three-dimensional geometries or use of weak inertial effects in order to achieve chaotic advection. Alternatively, flow in the third dimension can be imparted using two-phase flows in channels with two-dimensional geometries (i. e., obtained by extrusion of a two-dimensional pattern). Continuous flow chaotic advection mixers usually consist of repeating units that perform stretching and folding or breakup and rejoining operations in each unit. After each unit, the striation length decreases by a constant factor (e. g., by a factor of 2), and exponential decrease in the striation length is achieved as the fluid stream traverses multiple units. The mixing length scales only as the logarithm of the Peclet number, making chaotic advection mixers highly effective in mixing at high Peclet numbers (low diffusivity or high velocity). For example, consider a mixer in which the striation length decreases by a factor of two after every unit. If τ_{conv} is the time required to traverse one unit of the mixer,

$$l_{\mathrm{st}} = l\, 2^{-t/\tau_{\mathrm{conv}}} \tag{10}$$

Mixing may be said to be complete when the time required for diffusion across the striation length equals the time

required to traverse one unit of the mixer [6].

$$\frac{l_{st}^2}{D} \sim \tau_{conv} \tag{11}$$

The mixing time and mixing length are then given as follows:

$$\begin{aligned} t_{mix} &\sim \tau_{conv} \log \mathrm{Pe} \\ l_{mix} &\sim l \, \log \mathrm{Pe} \end{aligned} \tag{12}$$

It is thus seen that mixing time now scales logarithmically with the Peclet number instead of linearly as in the case of the T-mixer or flow focusing mixer.

Low Reynolds Number Chaotic Advection Mixers Microfluidic mixers can be designed to mix using the principles of chaotic advection even in the purely viscous flow regime. Xia et al. [7] reported a mixer that splits, reorients and recombines flows using crossing channels (Fig. 3c). While several mixers with three-dimensional geometries mix flows at intermediate Reynolds numbers, this mixer is one of the few mixers that can mix in the regime of purely viscous flow. The three-dimensional architecture is essential for reorienting the fluid elements before recombination. The mixer was fabricated using two-level microchannels using PDMS, a silicone polymer commonly used for fabrication of microfluidic devices. Good mixing was possible at very small Reynolds numbers down to 0.01.
Stroock et al. [8] reported a staggered herringbone mixer that uses grooves on channel walls to drive transverse flows. An asymmetric herringbone groove structure results in two asymmetric circulating flows in the channel. Circulating flows that alternate periodically along the channel are established by alternating the herringbone pattern (Fig. 3d). Effectively, it results in a time-dependent two-dimensional blinking flow with intersecting streamlines, resulting in chaotic advection. In this mixer, the mixing length was shown to scale logarithmically with Peclet number over a range of 6 orders of magnitude of the Peclet number. Unlike other chaotic advection mixers that require a two-level fluid architecture, this mixer only requires grooves on the substrate, greatly simplifying the fabrication process. This mixer has therefore found wide application in microfluidics.

Two-Phase Flow Mixers Three-dimensional geometries are inherently more difficult to fabricate than two-dimensional channel geometries. However, steady two-dimensional viscous flows are inherently integrable, and chaotic advection is not possible. Two-phase flows overcome this obstacle by introducing circulating flows inside fluid segments or droplets, which can be used to convert the inherently two-dimensional flows to three-dimensional chaotic flows under suitable conditions. The serpentine mixer reported by Song et al. [9] is the most prominent mixer in this category (Fig. 3e). This mixer consists of a wiggly serpentine channel in which droplets of one phase (usually aqueous) flow in another continuous phase (usually oil). When the droplets occupy nearly the entire channel cross-section, they are termed as plugs. As a plug traverses a serpentine channel, the flow inside each plug alternates between two flow patterns with crossing streamlines. This flow pattern results in chaotic advection and rapid mixing. The same principle can be applied to mix liquid segments separated by gas bubbles. Millisecond mixing timescales are possible with this mixer, and sub-millisecond timescale kinetics can be probed, making the it one of the fastest mixers for mixing fluid streams in any given flow ratio. While increasing flow speed can decrease mixing time, this mixer is limited by break-up of the plugs/fluid segments that occurs at high flow speeds. In order to sustain plug flows without breakup of the plug or bubble, surface tension (γ) must be sufficiently large compared to shear forces. This phenomenon is characterized by the Capillary number:

$$\mathrm{Ca} = \frac{\eta l U}{\gamma} \tag{13}$$

For $\mathrm{Ca} > 1$, plugs may be sheared into smaller droplets that destroy proper flow in the mixer. Two-phase mixers are well-suited for studying reaction kinetics because each plug or fluid segment acts as an individual reactor, and there is no dispersion along the flow direction. With increasing use of two-phase systems, this mixer has found wide application in areas ranging from chemical synthesis to biochemistry.

Intermediate Reynolds Number Mixers Based on Weak Inertial Effects While turbulence sets in at Reynolds numbers greater than about 2300, even at low Reynolds numbers inertial effects can induce transverse flows that impart three-dimensionality to a flow that is otherwise two-dimensional at lower Reynolds numbers. At still higher Reynolds numbers, inertial effects can produce flow separation, vortex formation, and vortex shedding. These effects can be harnessed for mixing, and proper design can even lead to chaotic advection at intermediate Reynolds numbers. The simplest mixer in this category is the serpentine mixer that consists of a zigzag channel. Sharp bends in the mixer create cross-flows that enhance mixing. Mixing is due to diffusion alone at Reynolds numbers below about 80, and it improves at higher Reynolds

numbers [5]. Another class of mixers based on Tesla structures employ in-plane splitting and recombination of streams and can mix at Re > 5 [5]. Liu et al. [5] reported a three-dimensional serpentine mixer that uses C-shaped segments. The device has two fluidic layers, and was fabricated in silicon and glass. Chaotic advection was found to occur at Reynolds numbers higher than 20. Mixers operating at intermediate to high Reynolds numbers are especially useful when comparatively high flow rates are required, such as in chemical synthesis. However, these mixers are typically not used for biological applications, where the samples are usually smaller and more expensive.

Mixers Based on Other Instabilities Mixing in turbulent flows that occur at high Reynolds numbers is an illustration of mixing due to instability induced in the flow by inertial effects. Similarly, other phenomena may lead to instabilities in microfluidic flows and may be harnessed for mixing. The only known examples of mixing using other instabilities are the electrokinetic instability mixer and the viscoelastic instability mixer [6]. The electrokinetic instability mixer uses instabilities induced in the charged region at the junction of two fluid streams with differing ionic compositions when an electric field is applied parallel to the junction. The viscoelastic intability mixer exploits non-Newtonian fluid properties in order to achieve mixing.

Active Mixers

In addition to pressure gradients and inertial effects, several other mechanisms can be used to drive fluid flow for mixing. These mechanisms can range from simple pressure disturbances to more complicated systems utilizing miniature actuators.

Pressure/Velocity Field Disturbance Mixers These mixers rely on external pressure or velocity disturbances to change the flow pattern inside the channel and thereby enable faster mixing. Bottausci et al. [4] reported a shear superposition mixer that employs actuating side channels that are perpendicular to the main channel (Fig. 4a). An oscillating pressure or velocity disturbance in these channels affects flow in the main channel and causes mixing. With the correct choice of driving frequencies and amplitudes in the side channels, it is possible to induce chaotic advection and rapid mixing. Another simple design is a modification of the T-mixer. Instead of a steady flow in the two input channels, the driving pressure or flow rates are oscillated so that the mixing channel receives alternating longitudinal bands of fluid from each input channel. The parabolic flow then stretches these bands, algebraically decreasing the striation length and enabling faster mixing.

Rotary Mixer Rotary mixers [6] are very useful in integrated microfluidics, pioneered by the group of Stephen Quake. This microfluidic architecture uses a control layer of fluidic channels that can squeeze an underlying layer of channels, just as stepping on a garden hose clamps it shut. The operation of such elements requires a flexible material such as PDMS for device fabrication. A single element can function as a valve, and three elements operating together can function as a pump. With this basic design of externally actuated valves and pumps, it is possible to perform complex multiplexed fluidic manipulation. The mixer works by driving fluid flow in a circular microchannel using a pump. Fluid volumes to be mixed are first metered into the circular channel, forming bands shaped like arcs in the circular microchannel. Driving fluid flow around the circular channel results in linear stretching of the fluid inside the channel and the striation length decreases algebraically with time. Complete mixing can be achieved within one second. Rotary mixers are useful in such architectures for mixing metered volumes of fluid in a serial fashion or for continuous stirring in confined volumes, and have found applications in chemical synthesis and combinatorial screening.

Induced Field Electroosmosis Mixers Induced field electroosmosis (sometimes known as AC electroosmosis) is electroosmotic flow generated under AC excitation in an electrolyte solution due to tangential migration of induced charges at the electrode-solution interface. This method is relatively simple for driving fluid flow because it does not involve any moving parts and planar electrodes can be easily fabricated using conventional lithographic techniques. Sasaki et al. [10] demonstrated one such mixer that involves asymmetric patterned electrodes inside a mixing microchannel. AC electroosmosis drives asymmetric circulating flow that results in rapid mixing. Mixing was observed to occur in 0.18 s, approximately independent of the flow velocity and 20 times faster than that in the absence of AC electroosmosis. While this mixer was not designed for chaotic advection, induced field electroosmosis offers a wide variety of design possibilities by changing the device geometry. The main drawback of induced field electroosmosis is that it is sensitive to the presence of buffers and biomolecules in the solution.

Other Types of Mixers Apart from the methods described above, there are several different ways in which microfluidic flows can be driven [5]. Several of these methods have been used for microfluidic mixing including

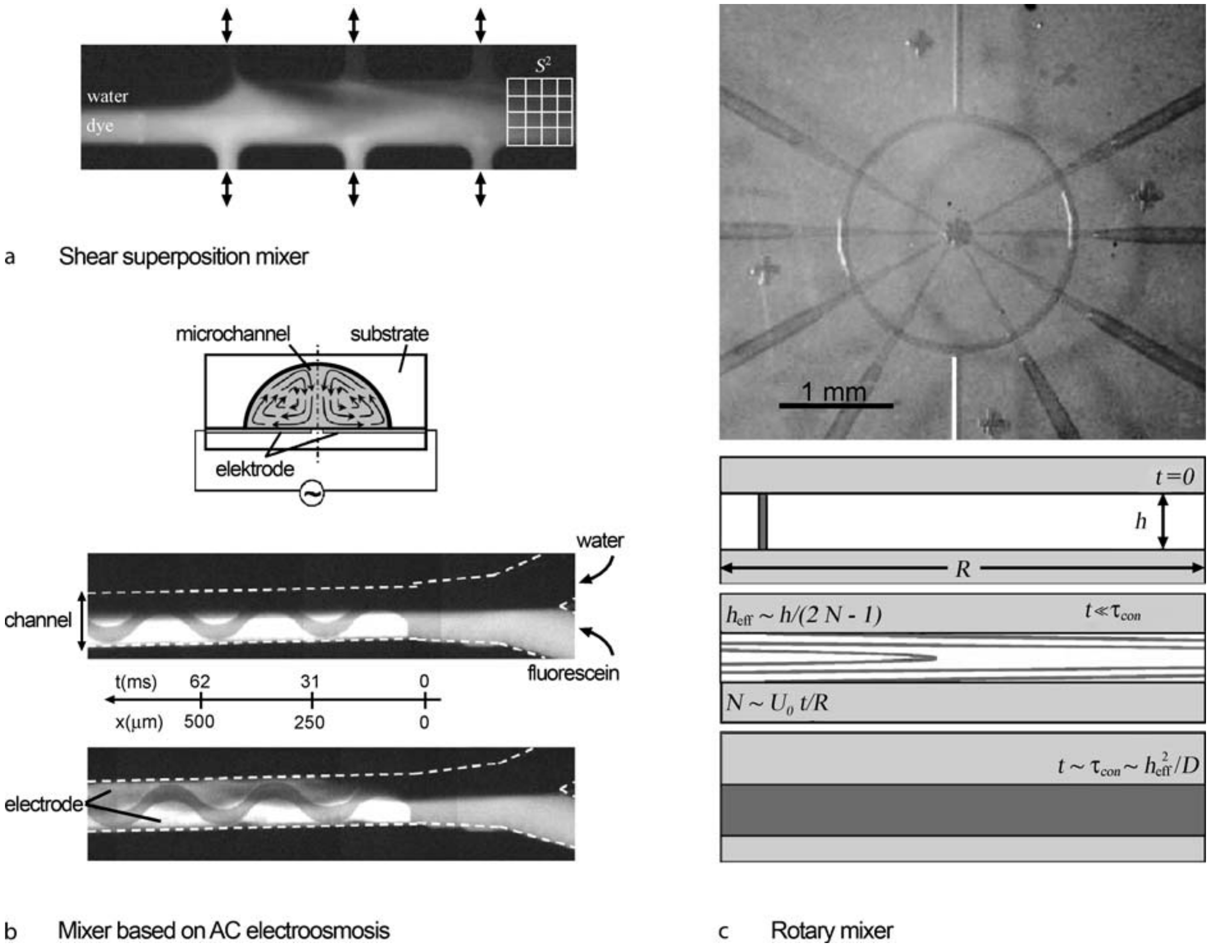

Microfluidic Mixing, Figure 4 (**a**) The shear superposition mixer employs side channels to drive oscillating flow and induce chaotic advection in the main channel. The micrograph depicts six side channels mixing a stream of water and dye solutions in the main microchannel. The grid shown is used for computing mixing using the mixing variance coefficient (MVC). (from [4]) (**b**) A mixer based on AC electroosmosis to mix by driving asymmetric circulating flows inside a microchannel. Cartoon depicts circulating flow; water and dye streams are shown in the absence and presence of AC electroosmosis. (from [10]) (**c**) A rotary mixer uses pumps to drive flow in a circular microchannel. Algebraic stretching of the fluid results in a rapid decrease in the striation length (h_{eff}) and thus enables mixing. (from [9])

dielectrophoresis (migration of polarizable particles under an electric field gradient), electrokinetics (fluid flow driven by migration of charges at microchannel surfaces under an electric field along the channel), acoustic actuation, thermally generated bubbles, magnetohydrodynamics (flow in a current-carrying fluid in a magnetic field induced by Lorentz forces) among others. Most of these mixers are highly specialized and do not find broad applications.

Future Directions for Research

Recent years have seen rapid progress in application of the theory of mixing as well as in the innovative design of new microfluidic mixers. The design space available for innovation in this field is vast, and new mixers are constantly being developed. The mathematical foundations of mixing are being used to optimize the design of mixers. Theorists have developed models and guidelines for mixer design that can be easily adapted by researchers who use microfluidic mixers, but are typically not involved in the theory of mixing. In the future, we may see innovative mixer designs that are effective yet easy to implement, and rest on the mathematical foundations of mixing.

Cross References

- ► Active Mixer
- ► Browning Motion and Diffusion
- ► Chaotic Flow
- ► Chaotic Mixing Based on Viscoelasticity

► Compute Mixing Efficiency
► Curved Microchannel Flow
► Droplet Based Lab-on-Chip Devices

References

1. Wiggins S, Ottino JM (2004) Foundations of chaotic mixing. Philos Trans Royal Soc London Series A – Math Phys Eng Sci 362(1818):937–970
2. Ottino JM (1997) The kinematics of mixing: stretching, chaos and transport. Cambridge University Press, Cambridge
3. Aref H (1984) Stirring by Chaotic Advection. J Fluid Mech 143(Jun):1–21
4. Bottausci F, Mezic I, Meinhart CD, Cardonne C (2004) Mixing in the shear superposition micromixer: three-dimensional analysis. Philos Trans Royal Soc London Series A – Math Phys Eng Sci 362(1818):1001–1018
5. Nguyen NT, Wu ZG (2005) Micromixers – a review. J Micromech Microeng 15(2):R1–R16
6. Squires TM, Quake SR (2005) Microfluidics: Fluid physics at the nanoliter scale. Rev Modern Phys 77(3):977–1026
7. Xia HM, Wan SYM, Shu C, Chew YT (2005) Chaotic micromixers using two-layer crossing channels to exhibit fast mixing at low Reynolds numbers. Lab Chip 5(7):748–755
8. Stroock AD, Dertinger SKW, Ajdari A, Mezic I, Stone HA, Whitesides GM (2002) Chaotic mixer for microchannels. Science 295(5555):647–651
9. Song H, Tice JD, Ismagilov RF (2003) A microfluidic system for controlling reaction networks in time. Angew Chem – Int Ed 42(7):768–772
10. Sasaki N, Kitamori T, Kim HB (2006) AC electroosmotic micromixer for chemical processing in a microchannel. Lab Chip 6(4):550–554

Microfluidic Optical Devices

BARBAROS CETIN, DONGQING LI
Department of Mechanical Engineering,
Vanderbilt University, Nashville, TN, USA
barbaros.cetin@vanderbilt.edu

Definition

Microfluidic optical devices are classified into two groups of devices: (1) devices using microscale on-chip optical methods/components for biochemical sensing or for manipulation of fluids or particles in Lab-on-a-Chip devices; and (2) devices using microfluidics to manipulate light at the microscale.

Overview

Microfluidic optical devices (MODs) represent an emerging technology that combines today's microfluidics technology with optics. Devices based on optofluidics – manipulating fluids and light at the microscale – are examples belonging to this class of microfluidic devices. (An excellent review on optofluidics can be found elsewhere [1].)

In many biological applications, microfluidics and optics technology are already being used in combination: microfluidics for control and manipulation of samples and optics for sensing. However, MODs can be classified as the integration of these two technologies rather than the combination of them. This integration results in integrated detection systems for microfluidic application (which increases the portability of the entire system) [2–4], a sensitivity increase for the existing detection system [5, 6], cell manipulation [7–9], tunable optical fibers [10] and variable-focus liquid lenses [11].

Chabinyc et al. [2] succeeded in the integration of a fluorescence detector based on a microavalanche photodiode into a polydimethylsiloxane (PDMS)-based microfluidic device. Their detection system was reusable, and the microfluidic device was disposable. The elimination of the index matching problem which occurs in some micromachined devices, the elimination of the need for collection optics and the inexpensiveness are the superiority of the design. Those authors also addressed some further improvements for the performance of the device.

Mazurczyk et al. [3] fabricated an integrated fluorescence detection system with a microfluidic Lab-on-a-Chip device. Various arrangements were tested for the fluorescence beam detection: free space optics, fiber optics and fully waveguiding optics. Free space optics was found to have the higher sensitivity, but it needed a bulk microscope-based detection system. Fiber and fully waveguiding optics seemed to be a possible option to overcome the need for a bulk microscope setup, but their sensitivity was not found to be sufficient especially for high-sensitivity applications. Anyhow, those authors showed the feasibility of their device for electrophoretic separations by performing some preliminary experiments. They proposed usage of soda lime glass for the fabrication of their device and envisaged fabrication of more sophisticated systems.

Heng et al. [4] developed a novel on-chip microscope system, which was called an optofluidic microscope (OFM). The feasibility of the OFM was demonstrated. Its images were comparable to those of a conventional microscope. Those authors suggested the possible use of multiple OFMs on a single microfluidic chip either for increasing imaging throughput in the case of parallel usage or sequential imaging of the same target in the case of serial usage.

Camou et al. [5] used two-dimensional optical PDMS lenses to improve the performance of fluorescence spectroscopy detection carried out on a portable chip using optical fibers. The fibers were directly inserted into chan-

nels ending with PDMS optical lenses. Compared to convention flat interfaces, these optical lenses increased the intensity of the fluorescent response close to the fiber which leads to a higher sensitivity of the on-chip detection method for fluorescence spectroscopy. Chen et al. [6] implemented a simple, on-chip arrayed waveguide excitation and detection scheme based on scattering. Detected signals were processed, and not only was sensitivity enhancement observed, but particles moving with different velocities were also detected accurately.

Kruger et al. [7] proposed a miniaturized flow cytometer using the latest photonics technology to perform detection, enumeration and sorting of fluorescent species. They successfully performed sample injection, single-file flow through the detection system and sorting of fluorescent microbeads. They could not achieve fully autonomous cell sorting, but they indicated that as a future direction. They also demonstrated the feasibility of high-gain avalanche photodiodes for more sensitive measurements of fluorescent signals compared to conventional detection techniques.

Optical tweezers are devices that use the force of strongly focused light to trap and move small objects whose dimensions are below tens of micrometers. The exerted force range and the resolution for optical tweezers are very suitable for biological and macromolecular systems. They have been used in many applications [8]. A detailed review on optical tweezers can be found elsewhere [8]. Besides optical tweezers, Mandal and Ericson [9] illustrated the optical transport of microparticles in a liquid core waveguiding structure over long lengths, which has great potential for much more precise particle separation and particle transport without flow field manipulations. The light–particle interaction length of their proposed technique was orders of magnitude larger than that of existing systems.

Mach et al. [10] presented microfluidics-based fiber optics. They demonstrated a multifunctional all-fiber filter. They achieved independent tuning over a broad range of both transmission wavelength and attenuation by locating and manipulating the locations of microfluidic plugs with adjustable position and optical properties.

Another interesting application of microfluidics and optics is the use of variable-focus liquid lenses, which was developed by Philips Research Eindhoven [11]. The lenses which are composed of two immiscible liquids of different refractive indices can be manipulated by electrowetting. By electrowetting, the meniscus curvature of the lenses can be changed, which also changes the effective focal length of the lenses.

Ruano-Lopez et al. [12] demonstrated a simple, inexpensive, new and reliable fabrication process for optical Lab-on-a-Chip devices. They used SU-8 waveguides as sensing elements, and fabricated their cladding by diluting SU-8-50 in a liquid aliphatic epoxy resin.

Cross References

► Optofluidics–Applications
► On Chip Waveguides

References

1. Monat C, Domachuk P, Eggleton J (2007) Integrated Optofluidics: A new river of light. Nat Photonics 1:106–114
2. Chabinyc ML, Chiu DT, McDonald JC, Stroock AD, Christian JF, Karger AM, Whitesides GM (2001) An integrated Fluorescence detection system in poly(dimethylsiloxane) for microfluidic applications. Analyt Chem 18:4491–4498
3. Mazurczyk R, Vieillard J, Bouchard A, Hannes B, Krawczyk S (2006) A novel concept of the integrated fluorescence detection system and its application in a lab-on-a-chip microdevice. Sens Actuators B 118:11–19
4. Heng X, Erickson D, Baugh LR, Yaqoob Z, Sternberg PW, Psaltis D, Yang C (2006) Optofluidic microscopy – a method for implementing a high resolution optical microscope on a chip. Lab Chip, 6:1274–1276
5. Camou S, Fujita H, Fujii T (2003) PDMS 2D optical lens integrated with microfluidic channels: principle and characterization. Lab Chip 3:40–45
6. Chen CH, Tsai F, Lien V, Justis N, Lo YH (2007) Scattering-based cytometric detection using integrated arrayed waveguides with microfluidics. IEEE Photonics Tech 19(6):441–443
7. Kruger J, Singh K, O'Neill A, Jackson C, Morrison A, O'Brien P (2002) Development of a microfluidic device for fluorescence activated cell sorting. J Micromech Microeng 12:486–494
8. Grier DG (2003) A revolution in optical manipulation. Nature 424:21–27
9. Mandal S, Ericson D (2007) Optofluidic transport in liquid core waveguiding structure. Appl Phys 90(184103):1–3
10. Mach P, Dolinsky M, Baltvin KW, Rogers JA, Kerbage C, Windeler RS, Eggleton BJ (2002) Tunable microfluidic optical fiber. Appl Phys 80(23)4294–4296
11. Psaltis D, Quake SR, Yang C (2006) Developing optofluidic technology through the effusion of microfluidics and optics. Nature 442:381–386
12. Ruhano-Lopez JM, Aguirregabiria M, Tijero M, Arroyo MT, Elizalde J, Berganzo J, Aranburu I, Blanco FJ, Mayora K (2006) A new SU-8 process to integrate buried waveguides and sealed microchannels for a lab-on-a-chip. Sens Actuators B 114:542–551

Microfluidic Platforms

► Microfluidic Devices in Tissue Engineering

Microfluidic Reactor for Biomolecular Synthesis

► Biomolecular Synthesis in Microfluids

Microfluidic Reactor for Polymer Synthesis

► Polymer Synthesis within Microfluidic Reactor

Microfluidic Rotary Pump

BARBAROS CETIN, DONGQING LI
Department of Mechanical Engineering,
Vanderbilt University, Nashville, TN, USA
barbaros.cetin@vanderbilt.edu

Synonyms

Viscous pump; Micro/Nanofluidics

Definition

Conventional mechanical pumps based on centrifugal or axial turbomachinery are not suitable for micro and nano scales where the Reynolds numbers are usually small. Centrifugal and inertial forces are negligible, and viscous forces dominate the flow field in this length scale (an excellent review can be found on the physics of fluid flow at microscale in [1]). A microfluidic rotary pump, which is proposed by Sen et al. [2], is a device that is used for pumping fluids in microfluidic applications at extremely low Reynolds number. This miniature device consists of a rotating cylinder placed eccentrically inside a microchannel where the axis of the cylinder is perpendicular to the flow direction (see Fig. 1). Since it is placed asymmetrically, there exists a viscous resistance difference between the small and large gaps between the cylinder and the walls (i. e. unequally distributed shear force on the upper and lower surface of the rotating cylinder), which causes a net flow along the channel. They are capable of pumping very small flow rates which is desired for many medical and biological applications such as drug delivery.

Overview

The operation of the rotary pump depends on the viscous forces and can operate in any situation where viscous forces are dominant. Therefore, they are suitable for flow of low viscosity liquids in micro ducts as well as the flow of highly viscous liquids such as heavy polymers in macro ducts. Together with its simplicity from design point of view and this viscous nature makes rotary pumps suitable for scientific and industrial applications of MEMS (Micro-Electro-Mechanical-Systems), NEMS (Nano-Electro-Mechanical-Systems) and LOC (Lab-on-Chip) technologies.

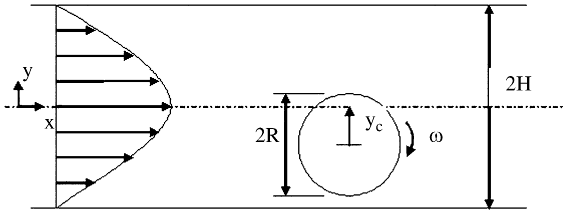

Microfluidic Rotary Pump, Figure 1 Schematic drawing of microfluidic rotary pump. Eccentricity, $\varepsilon = y_c/(H - R)$. $\varepsilon = 0$ means the cylinder is at the center, $\varepsilon = 1$ means the cylinder touches the bottom wall

The channel height, eccentricity (i. e. degree of asymmetry, $\varepsilon = y_c/(H - R)$, see Fig. 1), Reynolds number, channel cross-section and the angular velocity of the rotating cylinder have the effect on the performance of the pump. These effects are extensively studied by many researches [2–8]. Sen et al. [2] first proposed the use of microfluidic rotary pump and conducted some experiments for circular, square and rectangular cross-section rotating rotors. 2D, steady [3] and transient [4, 5], and 3D, steady [6] numerical analysis of the rotary pump is studied for circular as well as the square and rectangular [5] cross-sectional rotors. Thermal effects due to viscous dissipation on pump performance are also analyzed by considering the temperature dependent fluid properties [7]. Closed form, analytical expressions are derived for the flow rate and pressure drop along the channel are derived by using lubrication approximation [8]. The effect of slip-flow boundary condition is also investigated [3]. Another challenging application of this eccentric cylinder inside a microchannel is proposed by DeCourtye et al. [6] as a microturbine which can be used as a microsensor for measuring exceedingly small flow rates in micro/nanofluidic applications.

Cross References

► Centrifugal Microfludics
► Electrical Pumps
► Magnetic Pumps
► Thermocapillary Pumping

References

1. Gad-El-Hak M (1999) The Fluid mechanics of microdevices- the Freeman scholar lecture. J Fluid Eng 121:5–33
2. Sen M, Wajerski D, Gad-El-Hak M (1996) A novel pump for MEMS applications. J Fluid Eng 118:624–627
3. Sharatchandra MC, Sen M, Gad-El-Hak M (1997) Navier–Stokes simulation of a novel viscous pump. J Fluid Eng 119:372–382
4. Abdelgawad M, Hassan I, Esmail N (2004) Transient behavior of the viscous micropump. Microscale Thermophy Eng 8:361–381

5. Phutthavong P, Hassan I (2004) Transient performance of flow over a rotating object placed eccentrically inside a microchannel-numerical study. Microfluid Nanofluid 1:71–85
6. DeCourtye D, Sen M, Gad-El-Hak M (1998) Analysis of viscous micropumps and microturbines. Int J Comput Fluid Dyn 10:13–25
7. Sharatchandra MC, Sen M, Gad-El-Hak M (1998) Thermal aspects of a novel viscous pump. J Heat Transf 120:99–107
8. Day RF, Stone HA (2000) Lubrication analysis and boundary integral simulations of a viscous micropump. J Fluid Mech 416:197–216

Microfluidics

► Control of Micro-Fluidics
► Lattice Poisson–Boltzmann Method, Analysis of Electroosmotic Microfludics
► Microfluidics for Studies of Apoptosis

Microfluidic Sample Manipulation

RUEY-JEN YANG, CHIH-CHANG CHANG,
JIA-KUN CHEN, YU-JEN PAN
Department of Engineering Science, National Cheng Kung University, Tainan, Taiwan
rjyang@mail.ncku.edu.tw

Synonyms

Sample handling; Sample preparation; Sample transport

Definition

The term *microfluidic sample manipulation* refers to the processes involved in controlling the movement of small volumes of fluid or particles around a network of interconnected microchannels. These processes include sample introduction, injection, mixing, reaction, dispensing, separation, and detection, and are typically performed in a fully integrated micro total analysis system or a Lab-on-a-Chip device.

Overview

Recent advances in the field of microelectronics have made possible the miniaturization of microfluidic systems on a microchip to carry out analytical analytes. Such microfluidic systems are generally known as a Lab-on-a-Chip or a micro total analysis system (μTAS). These systems perform a complete, integrated, and automated analysis of the target analyze in a complex sample matrix. In general, μTAS devices are designed to carry out the following functions: sample introduction, injection, mixing, reaction, dispensing, separation, and detection. Figure 1 presents a schematic illustration of a typical Lab-on-a-Chip. The sample of interest is introduced via port 1 and subsequently interacts with a reagent injected via port 2. The sample is then mixed with the reagent to facilitate the subsequent chemical reaction process. Finally, the reacted product is dispensed into a separation channel for component separation and detection using optical instrumentation.

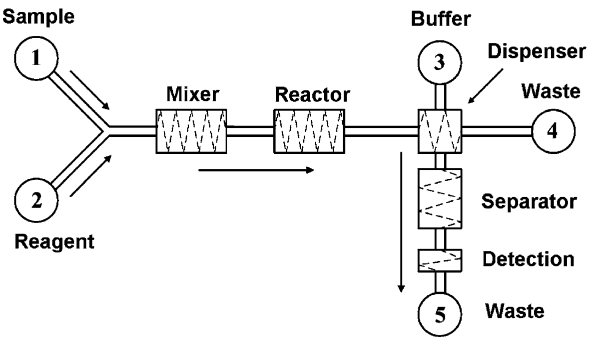

Microfluidic Sample Manipulation, Figure 1 Illustration of microfluidic components in typical Lab-on-a-Chip device

Basic Methodology

Sample Introduction/Storage/Injection

To support the requirements of typical biochemistry applications, current micro-analytical systems are generally designed to manipulate aqueous liquid samples. The sample introduction process includes both sample preparation and sample storage in a suitable reservoir. Four major categories of sample preparation can be identified: separation of the sample from the sample matrix, sample preconcentration, sample derivatization, and sample pretreatment. The original sample generally contains large organic or inorganic particles, which must be removed using some form of cell membrane rupture technique. If the sample analyte is only available in trace amounts, the sample is generally preconcentrated prior to analysis by squeezing the available analyte molecules into a smaller volume to enhance the detection sensitivity. Sample derivatization involves the chemical transformation of the analyte to render it detectable by the particular detection system employed in the microchip. In the biochemical domain, the biomolecules of interest are commonly pretreated by labeling them specifically or nonspecifically with fluorescent labels. In the genomic research field, the DNA sample is often amplified using either polymerase chain reaction (PCR) or cleavage by restriction enzymes. Following the sample preparation process, the sample is introduced into

the microfluidic chip via a reservoir. This reservoir is generally left open to enable the release of gas bubbles generated via electrolysis at the electrodes during electrokinetic manipulation.

The injection process introduces the prepared sample or reagent into the flowing carrier stream within the manifold. Ideally, the injector system should be designed so as to provide a high sample flow rate. Injection systems typically employ electrokinetic mobility or hydrodynamic pressure techniques. In the former systems, the sample flow into the microchannel is controlled by the application of an external electric field to the reservoir, while in the latter systems, a pressure difference is created in the reservoir using either a positive pressure (piston-type) technique or a suction pressure (vacuum) technique.

Mixing/Reaction

Mixing of two or more miscible fluids in microfluidic systems is important in a variety of applications, e. g., to achieve a homogenized solution of the reagents used in chemical reactions. Furthermore, biological processes such as cell activation, enzyme reaction, and protein folding commonly involve reactions which require the mixing of reactants for initiation. Achieving a rapid and efficient mixing effect is an essential but challenging task when developing microfluidic devices for chemical and biological analysis applications.

Since viscous forces dominate the flow in microfluidic devices and the flow is limited to the low Reynolds number regime, turbulence does not readily occur. In electrokinetically driven flow in microfluidic systems, the Reynolds number is typically less than unity (i. e., Stokes flow). In a conventional straight microchannel, the Stokes flow is generally unidirectional. Even in curved or twisted channels, the transverse flow component (i. e., the secondary flow) is very small compared to the streamwise component since the inertial effect is very weak. Therefore, mixing of two fluid streams within the microchannel takes place mainly as the result of molecular diffusion. The rate of diffusive mixing in microscale channels is very slow compared to the convection of the fluid along the channel since the Peclet number ($\mathrm{Pe} = Ul/D$, where U is the average flow velocity, l is the channel dimension, and D is the molecular diffusivity) of typical microchannel flows is very high. The diffusive mixing time is given by $\tau_D \sim l^2/D$ and the mixing length (L_m) along the downstream channel increases linearly with the Peclet number (i. e., $L_\mathrm{m} \sim \mathrm{Pe} \times l$). In practice, many biochemical applications, e. g., immunoassays and DNA hybridization, require the rapid mixing of macromolecules with relatively low molecular diffusivity (e. g., $40\,\mu\mathrm{m}^2/\mathrm{s}$ for small proteins). Typical values in conventional straight microchannel devices are that: an average electroosmotic flow (EOF) velocity is $500\,\mu\mathrm{m/s}$ and a channel dimension is $100\,\mu\mathrm{m}$, the mixing time and mixing length required to achieve a complete mixing are approximately 250 s and 125 mm, respectively. However, this mixing performance is unacceptable for rapid biochemical analysis in microfluidic systems. These values can be improved by increasing the interfacial contact area between the two species and reducing the diffusion length (l) between them. Adopting this approach, various micromixers have been developed to enhance the mixing effect in microfluidic systems. In general, these micromixers can be categorized as either passive or active in nature. Active mixers use either moving components or externally applied forcing functions to achieve mixing, whereas passive mixers induce a mixing effect simply by virtue of their particular geometry topologies or surface properties.

Mixing in micromixers relies primarily on molecular diffusion or chaotic advection (laminar chaos) mechanisms. As discussed above, the diffusive mixing effect can be improved by increasing the interfacial contact area between the different fluids and reducing the diffusion length between them. The use of unstable electrokinetic flow fields to achieve chaotic mixing effect can also be adopted.

Loading and Dispensing

In a microchip, the sample is transferred into the separation channel via pressure-driven or electrokinetically driven loading and dispensing processes. In microfluidic systems, the latter technique provides a particularly effective means of transporting reagents. The velocity of the EOF induced by electrokinetic driving schemes is governed by the Smoluchowski relation, i. e., $V_\mathrm{slip} = \varepsilon\varepsilon_0\zeta\nabla\phi/\mu$, where ε is the dielectric permittivity of the solvent, ε_0 is the vacuum permittivity, ϕ denotes the externally applied electrical potential, ζ is the surface zeta potential, and μ is the viscosity of the fluid. According to this relation, the EOF velocity is independent of the channel size and is governed primarily by the intensity of the applied electrical voltage.

Separation

Capillary electrophoresis (CE) is used to separate ionic species by exploiting their frictional forces and differences in the charges of the respective species. In traditional electrophoresis, electrically charged analytes move in a conductive liquid medium under the influence of an electric field. CE has proved to be highly successful in enabling the analysis of DNA fragments and other

biomolecules. Another commonly used method is the chromatographic technique which is performed in a chromatography column fabricated by immobilizing reversed-phase stationary-phase particles using sol–gel technology. In capillaries filled with a stationary phase the separation occurs on the basis of the different partition of the analytes between the stationary and the mobile phase. Applications include the separation of small neutral molecules, peptides, and proteins.

Key Research Findings

Sample Introduction/Storage/Injection

Before carrying out the analytical process, it is necessary to prepare the sample or reagent [1]. Since optical detection continues to be the method of choice, the compound of interest in the sample is generally labeled with fluorescent dye using a postcolumn reactor incorporated within the microfluidic system. Such a microfluidic system typically consists of a CE structure with an additional side channel intersecting the separation channel at right angles 6 mm downstream from the sample injection region. The labeling reagent is introduced through this channel and subsequently comes into contact with the separated analyte band. However, most species are not easily labeled. Hence, an alternative analytical method utilizing UV-visible absorbance detection and an electrochemical method has been proposed. Before a sample can be analyzed using this method, the species must be preconcentrated to ensure that trace amounts of the analytes can be reproduced quantitatively. The field amplification stacking (FAS) technique provides an effective approach for stacking analytes with a length of 400 μm, creating volume-defined sample plugs, and stacking a full column of the sample. In the FAS approach, preconcentration is achieved by generating a high electrical field within the injected sample plug in order to drive and stack sample ions at the end of the plug. Figure 2 shows a microchip structure for FAS [2], which allows the formation of comparatively long, volumetrically defined, sample plugs with a minimal electrophoretic bias.

Field-amplified injection (FAI) is an alterative preconcentration method. Although both methods are relatively straightforward in terms of their implementation, they are applicable only to the preconcentration of charged analytes. Accordingly, a number of recent studies have proposed methods for the stacking of neutral analytes for separation using micellar electrokinetic chromatography in fused silica capillaries. The polymerase chain reaction (PCR) is a fundamental technology in bioanalytical research. Microchips designed for the PCR (see Fig. 3) incorporate an etched reaction chamber with a volume of the order of several microliters [3].

Generally, the samples considered in microfluidic applications contain large organic or inorganic particles. Therefore, these particles must be removed prior to analysis to prevent fouling or blockage of the analytical system. Accordingly, various techniques have been proposed for separating the sample from the sample matrix, including physical filtering and retention of the particles using

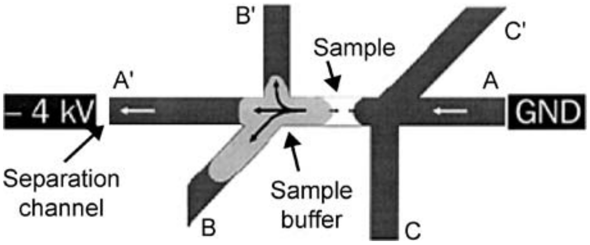

Microfluidic Sample Manipulation, Figure 2 Illustration of different effects during sample stacking in the microchip structure (reproduced from [2])

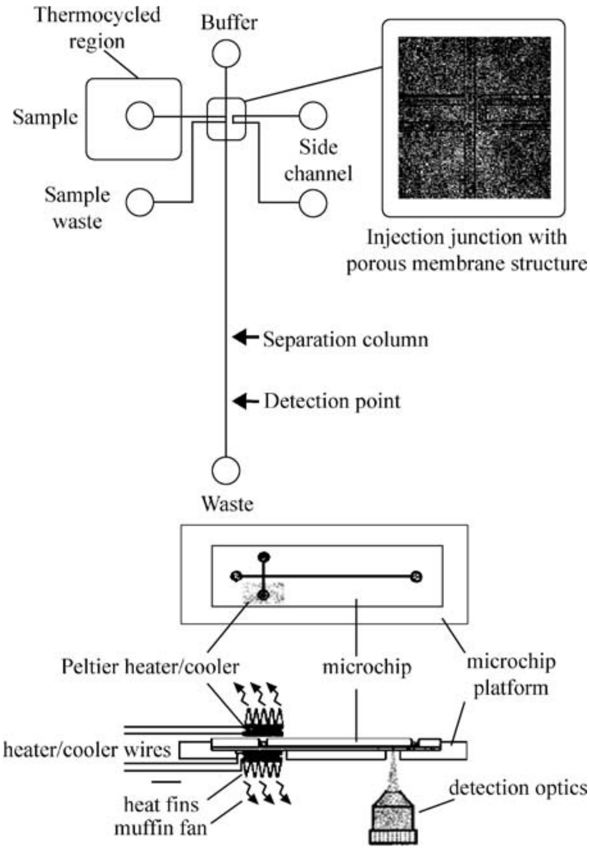

Microfluidic Sample Manipulation, Figure 3 Microchannel design used for integrated rapid PCR analysis on-chip (reproduced from [3])

M

integrated flow restrictors within the microchip, filtering by diffusion in laminar flow, microdialysis, liquid–liquid extraction, free-flow electrophoresis, cell lysis and purification.

Reservoirs are simply storage units designed to hold the reagents and samples used within the manifold. Reservoirs are commonly fabricated by drilling via holes into a flat glass plate using mechanical or (more commonly) ultrasonic methods and then bonding this plate onto a lower plate containing an etched or laser-ablated reservoir structure.

Electrokinetic injection schemes for microfluidic systems are generally designed to perform one of two different injection functions, namely time-based or discrete volume-based [4]. Time-based injection (also known as gated injection) allows for the introduction of the sample into the carrier stream over a controlled period of time. This technique has several key advantages, including a straightforward control and a variable injection volume, and allows for both continuous and sequential injection for on-line measurement applications.

Mixing

Passive micromixers

Passive mixers can be categorized according to the arrangement of the mixed phases, i. e., parallel lamination mixers, serial lamination mixers, injection mixers, chaotic mixers, etc. [5].

Parallel lamination mixers split the inlet stream into two or more substreams, and then join them horizontally as individual laminae in a single stream. Such mixers commonly have the form of a long microchannel with two inlets arranged in either a T- or a Y-form configuration. Hydrodynamic focusing can also be used to reduce the diffusion length for parallel lamination mixers. In this technique, the microfluidic device is designed with three inlets. The sample (solute) flow is introduced through the middle inlet, while the solvent streams are fed through the side inlets and function as sheath flows to restrict the width of the sample flow and consequently to reduce the diffusion length. Knight et al. [6] have reported that the sample stream width can be focused to 50 nm, resulting in a mixing time of no more than a few microseconds. This rapid diffusion-based mixer has been successfully integrated with microfluidic platforms to enable the accurate description of fast reaction kinetics such as protein folding. Serial lamination mixers apply a similar approach to that of parallel lamination mixers. However, in this case, the inlet streams are joined horizontally in the first stage of the mixer and are then joined vertically in the following stage. Adopting a different approach, injection mixers split only the sample (solute) flow into many streams and then inject these streams into the solvent flow. Using an array of nozzles positioned over one of these streams, solute microplumes are produced which increase the contact area between the solute and the solvent and reduce the diffusion length between them.

In contrast to parallel lamination, serial lamination and injection mixers, chaotic mixers produce an effective increase in the interfacial contact area of the mixing species without splitting the inlet streams. Generally, chaotic advection is induced by manipulating laminar flow in microchannels via the use of specific topologies or surface properties. The resulting chaotic flow patterns cause the fluid elements to be repeatedly stretched and folded, resulting in a significantly increased interfacial contact area and a reduced diffusion length. Stroock et al. [7] have investigated the use of groove structures on the channel wall in pressure-driven chaotic advection mixing at very low Reynolds numbers. They considered two different groove patterns, namely a slanted groove structure and a staggered herringbone structure. The results showed that the latter structure provided a particularly significant improvement in the mixing performance at low Reynolds numbers. Various authors have successfully demonstrated electrokinetically driven mixers in which a chaotic mixing effect is induced by patterning the surface charge distribution on the microchannel walls [8, 9]. In addition, Song et al. [10] have proposed an efficient droplet-based reac-

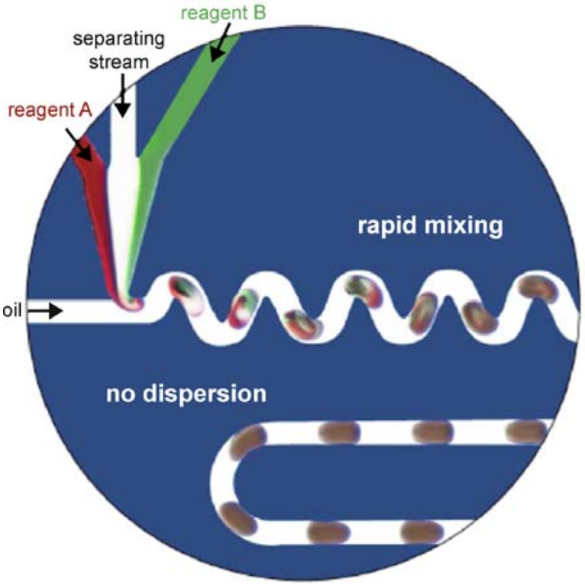

Microfluidic Sample Manipulation, Figure 4 An example of chaotic mixing: mixing of discrete droplets moving in a twisted microchannel (reproduced from [4])

tor in which chaotic mixing occurs as discrete droplets move in a twisted microchannel at low Reynolds number, as shown in Fig. 4. The droplet-based reactors have been successfully demonstrated in the study of fast chemical kinetics.

Active micromixers

Active micromixers require an external disturbance energy source such as pressure, ultrasound, acoustic, electric, or magnetic fields [5]. These external disturbance functions generate chaotic flow patterns at low Reynolds numbers, resulting in a repeated stretching and folding of the fluid elements. Consequently, the interfacial contact area is increased and the diffusion length is reduced. Oddy et al. [11] have employed AC electric fields to induce an electrokinetic instability phenomenon in microscale channels. This instability phenomenon is similar to the electrohydrodynamic instability induced by AC or DC electric fields when an electrical conductivity gradient exists in the bulk flow. The instability effect causes the induced flow field to be more chaotic, and therefore enhances the mixing performance in electrokinetic-based microfluidic systems.

Loading/Dispensing

Advances in the microfluidics field have enabled many devices to be integrated into a single microfluidic chip, thus realizing the concept of a μTAS. However, this increased level of integration requires the assay performance to be optimized and the microchip architectures to be designed with improved sophistication and efficiency. Sample loading and dispensing are essential fluid manipulation tasks in microfabricated devices. The quality of the final results of many on-chip processes is critically dependent on the characteristics of the injected samples. In general, these characteristics tend to be application specific. Since the length of the channel required to separate two analytes via CE is directly proportional to the initial length of the sample, many researchers have developed on-chip dispensing schemes specifically designed to provide tightly focused samples. Typically, these schemes have been implemented in T-form, double-T form and conventional cross-form microchannels. The best sample loading and dispensing results are generally obtained by carefully controlling an eternally applied electric field in order to induce electroosmotic flow within the microchannel [12]. Using this approach, conventional cross-form microchips can function both as a constant-volume valve (i. e., pinched injection mode) and a variable-volume valve (i. e., a gated injection mode). The injected samples produced using these valving techniques enable high performance, electrokinetically driven separation to be performed in applications such as: CE, synchronized cyclic electrophoresis, capillary gel electrophoresis, open channel electro-chromatography, and micellar electrokinetic chromatography.

Separation

One of the biggest challenges for current μTAS devices is analyzing complex and heterogeneous samples such as whole blood or contaminated environmental specimens. Gel electrophoresis is a typical electrophoresis application in the field of molecular biology. This process is used to determine the different sizes of high density lipoproteins in order to establish an accurate representation of their effectiveness. A free-flow electrophoresis device was fabricated on a glass wafer. Separation of standard fluorescent markers was demonstrated by applying a focused free-flow zone electrophoresis technique and free-flow isoelectric focusing (IEF). Proteins focused by IEF were electrokinetically transferred into an array of orthogonal microchannels and then resolved by gel electrophoresis.

IEF is a zone electrophoresis technique, and is most commonly applied for the separation of proteins. IEF separates molecules according to their respective electric charges (assuming that they have a charge), exploiting the fact that the charge carried by a molecule changes as the pH of its surroundings changes. Cui et al. [13] have improved the resolving power of IEF by first focusing proteins in a straight channel using broad-range ampholytes and then refocusing segments of the first channel into secondary channels branching off the primary channel at T-junctions. DNA electrophoresis is an analytical technique used to separate DNA fragments in accordance with their size. In this technique, an electric field is applied to force the fragments to migrate through a gel. The DNA molecules normally migrate from a negative to a positive potential due to the net negative charge of the phosphate backbone of the DNA chain. Finally, chromatography is a collective term applied to a family of laboratory techniques designed to separate mixtures. Chromatography involves passing a mixture containing the analyte through a stationary phase, which separates the analyte from the other molecules in the mixture and allows it to be isolated. Reversed-phase capillary electrochromatography in a 5 mm C_{18} fully packed capillary was employed to optimize the separation of negatively charged nonsteroidal anti-inflammatory drugs [14]. In addition, researchers have shown that a μ-enzyme reactor can be coupled on-line with μ-membrane chromatography to realize an integrated micro-analytical tool enabling rapid protein digestion, high resolution peptide separation, and sensitive protein

M

identification using Electrospray Ionization Mass Spectrometry (ESI-MS).

Future Directions for Research

The task of integrating sample pretreatment processes into microfluidic chips is rendered complex by the enormous variation in the samples to be analyzed. Moreover, the pretreatment technique must be compatible with the analytical devices to which it is coupled in terms of time, reagent consumption, power supply requirements, and sample volume. Although electrokinetic injection has many advantages, it is necessary to address the limitations of this technique as regards applicable pH values, appropriate solvents, and so on. Furthermore, in pressure-driven techniques, problems remain to be resolved in providing samples of sufficiently small volume and making the miniaturized devices sufficiently robust to withstand the significant back-pressure created during the injection process.

Pressure- or electrokinetically driven flows in microfluidic devices are generally limited to the low Reynolds number regime and typically involve the transportation of biomolecules with low molecular diffusivity. Hence, micromixers are obliged to function under conditions of low Reynolds number and high Peclet number. However, current diffusion-based micromixers, e. g., parallel lamination and serial lamination mixers, only provide an acceptable mixing result at low Peclet numbers. By contrast, the performance of chaotic advection mixers is not largely dependent on the Peclet number. Accordingly, the development of future micromixers should focus particularly on passive or active chaotic mixing schemes.

Loading, dispensing, and separation are essential processes in many microfluidic systems. The feasibility of applying microfabrication techniques to manufacture biochips has been well established, and numerous applications have been demonstrated. For practical purposes, the loading and dispensing devices tend to manipulate the picovolumetric reagents. Electrokinetic manipulation makes possible the loading of small-volume sample plugs, the separation of charged species, and a high degree of control over the reaction processes in the microchip. However, the electrokinetic technique is limited to certain conditions, e. g., certain pH values, particular solvents, a limited set of compatible chip materials, etc.

Cross References

- ► Biosample Preparation Lab-on-a-Chip Devices
- ► Electrokinetic Sample Injection
- ► Pressure-Based Sample Injection
- ► Active Mixer
- ► Chaotic Flow
- ► Chaotic Mixing Based on Viscoelasticity
- ► Compute Mixing Efficiency
- ► Microfluidic Mixing
- ► Droplet Dispensing
- ► Electrokinetic Dispensing
- ► Lab-on-a-Chip Devices for Particle and Cell Separation
- ► Lab-on-a-Chip Devices for Separation-Based Detection
- ► Optofluidics – Techniques for Fabrication and Integration

References

1. Lichtenberg J, de Rooij NF, Verpoorte E (2002) Sample pretreatment on microfabricated devices. Talanta 56:233–266
2. Lichtenberg J, Verpoorte E, de Rooij NF (2001) Sample preconcentration by field amplification stacking for microchip-based capillary electrophoresis. Electrophoresis 22:258–271
3. Khandurina J, McKnight TE, Jacobson SC, Waters LC, Foote RS, Ramsey JM (2000) Integrated system for rapid PCR-based DNA analysis in microfluidic devices. Anal Chem 72:2995–3000
4. Haswell SJ (1997) Development and operating characteristics of micro flow injection based on electroosmotic flow: a review. Analyst 122:1R–10R
5. Nguyen N-T, Wu Z (2005) Micromixers – a review. J Micromech Microeng 15:R1–16
6. Knight JB, Vishwanath A, Brody JP, Austin RH (1998) Hydrodynamic focusing on a silicon chip: mixing nanoliters in microseconds. Phys Rev Lett 80:3863–3866
7. Stroock AD, Dertinger SKW, Ajdari A, Mezic I, Stone HA, Whitesides GM (2002) Chaotic mixer for microchannels. Science 295:647–651
8. Biddiss E, Erickson D, Li D (2004) Heterogeneous surface charge enhanced micromixing for electrokinetic flows. Anal Chem 76:3208–3213
9. Chang CC, Yang RJ (2006) A particle tracking method for analyzing chaotic electroosmotic flow mixing in 3-D microchannels with patterned charged surfaces. J Micromech Microeng 16:1453–1462
10. Song H, Tice JD, Ismagilov RF (2003) A microfluidic system for controlling reaction networks in time. Angewandte Chemie Int Ed 42:768–772
11. Oddy MH, Santiago JG, Mikkelsen JC (2001) Electrokinetic instability micromixing. Anal Chem 73:5822–5832
12. Fu LM, Yang RJ, Lee GB, Liu HH (2002) Electrokinetic injection techniques in microfluidic chips. Anal Chem 74:5084–5091
13. Cui H, Horiuchi K, Dutta P, Ivory CF (2005) Multistage isoelectric focusing in a polymeric microfluidic chip. Anal Chem 77(24):7878–7886
14. De Rossi A, Desiderio C (2003) Separation of negatively charged nonsteroidal anti-inflammatory drugs by reversed-phase capillary electrochromatography. J Chromatogr A 984:283–290

Microfluidics-Based Surface Patterning Tools

► Microfluidic Systems for High-Throughput Screening

Microfluidics for Biochemical and Chemical Reactions

Adarsh D. Radadia
University of Illinois at Urbana-Champaign,
Urbana, IL, USA
radadia@uiuc.edu

Synonyms

Microreactor; Microreaction technology; Microchemical systems

Definition

A chemical reaction is said to have taken place when a detectable number of molecules have lost their identity and assumed a new form by a change in the kind or number of atoms in the compound and/or by a change in structure or configuration of the atoms. Microfluidic channels, which have critical length ranging from several microns to a millimeter, provide high heat and mass transfer rates, which can be used beneficially to carry out reactions selectively, for production or analytical purposes. A device containing such channels is termed a microreactor. Depending on how relevant a reaction is to living organisms, a reaction may be called a biochemical or a chemical reaction.

Overview

Introduction

Microfluidic reaction systems called *differential reactors* were reported before the 1960s and were used to measure the kinetics of catalytic reactions. The key early findings indicated that if the reactor volume was made small enough, the temperature and concentration gradients within the reactor would become negligible. This allowed more accurate measurement of reaction kinetics. Reactions involving microfluidic effects have been carried out in large-scale reactors with integrated packing and monolithic structures designed to give higher reaction yields. Such reaction systems have been studied and characterized mostly by empirically determined macroscale models. The advent of micromachining allows us to build low-volume reactors with a systematic channel design on a chip, and is helping us to study reaction kinetics on a scale at which they are much simpler.

The reasons why small-volume microfluidic synthesis is preferred are:

- *Low reactant/product quantity* The pharmaceutical and biotechnology industries produce drugs, enzymes, and biomaterials in small quantities. The production of these materials is done industrially on a batch scale. Microfluidics enables the continuous production of chemicals in small quantities while maintaining consistency in quality, a common problem associated with batch production. Production on demand is more profitable, especially for chemicals with a limited lifetime. Some radiolabeled tracers need to be produced a short time before they are administered to a patient. Microfluidic systems also, owing to their small size, provide a portable platform for producing drugs on site and on demand. Microfluidics can be used to carry out rapid permutation and combination of reagents to create a library of synthetic chemicals. Such technology can be used to advantage to screen drugs and catalysts.
- *Safety* Some reactions involve hazardous chemicals as reactants or products. These unsafe chemicals need to be handled carefully. Microfluidics allows the safe handling of small amounts of hazardous chemicals. Hazardous reactions involving high exothermicity or damaging radiation exposure can be carried out safely.
- *Greater control over reactions* The diffusion paths for heat and mass transfer in microfluidic systems are very short, making such systems ideal candidates for heat- or mass-transfer-limited reactions. The surface-to-volume ratio of microscopic structures is very high. Thus, surface effects are likely to dominate over volumetric effects, increasing selectivity and yield.

An industrial batch reactor has neither an inflow nor an outflow of reactants or products while the reaction is being carried out. Batch reactions can be carried out in droplet microreactors, where nanoliters of fluid are individually manipulated using techniques such as electrowetting on dielectric (EWOD) and surface tension control. Semibatch reactors are used in cases where a by-product needs to be removed continuously and to carry out exothermic batch reactions where a reactant has to be added slowly. Microfluidics allows precise control of concentration and temperature, which allows batch and semibatch reactions to be carried out in a continuous manner. Figure 1 shows the general components of a simple industrial-reactor setup, compared with a laboratory-scale setup to carry out a reaction with microfluidic chips.

Modeling

The Reynolds number in microreaction systems usually ranges from 0.2 to 10. In contrast to the turbulent flow patterns that occur on the macroscale, viscous effects govern the behavior of fluids on the microscale and the flow is always laminar, resulting in a parabolic flow profile. In microfluidic reaction systems, where the characteristic length is usually greater than 10 μm, a continuum

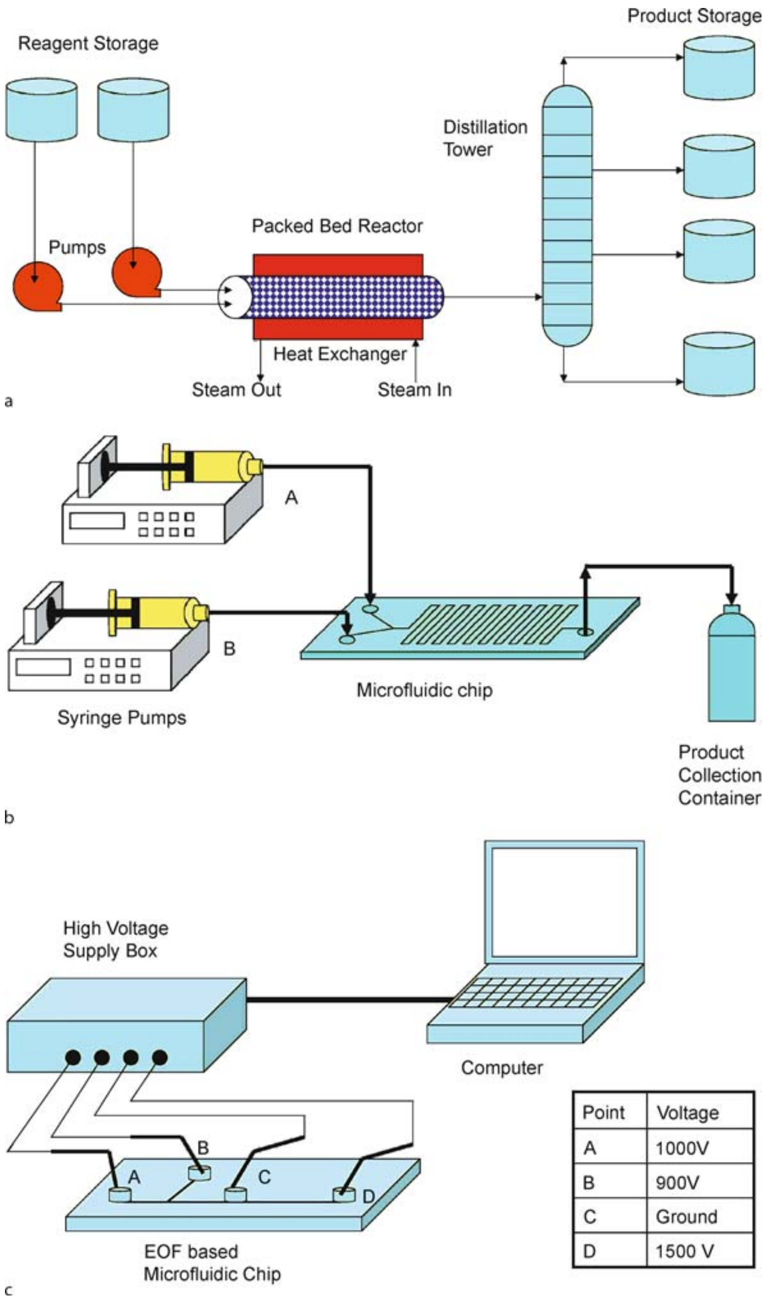

Microfluidics for Biochemical and Chemical Reactions, Figure 1 Schematics of a typical reaction setup (**a**) in industry; (**b**) in laboratory, using hydrodynamic force; and (**c**) in laboratory, using electroosmotic force

description can be used to predict the flow characteristics. This allows commercially written Navier–Stokes solvers such as FEMLAB and FLUENT to model liquid flows in microreaction channels. However, modeling gas flows may require one to take account of boundary slip conditions (if $10^{-2} < \mathrm{Kn} \leq 10^{-1}$, where Kn is the Knudsen number) and compressibility (if the Mach number Ma is greater than 0.3). Microfluidic reaction systems can be modeled on the basis of the Navier–Stokes equation, in conjunction with convection–diffusion equations for heat and mass transfer, and reaction-kinetic equations.

Examples of Microfluidic Reactions

What follows is not an exhaustive compilation of all known examples, but rather a sample of sufficient variety

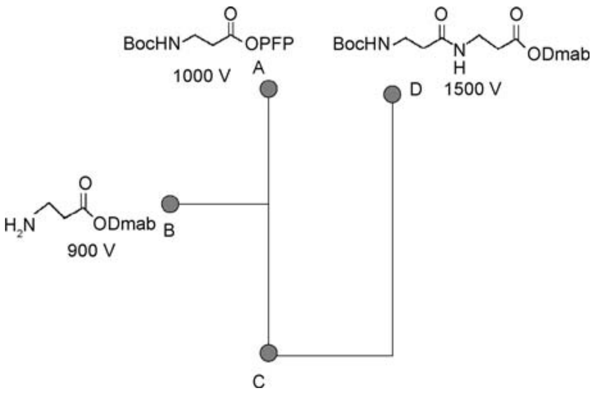

Microfluidics for Biochemical and Chemical Reactions, Figure 2
Layout of microfluidic chip for simultaneous synthesis and separation of dipeptide

to illustrate the extent to which microfluidics has been used to perform biochemical and chemical reactions. Examples of the use of microfluidics for nanoparticle and polymer synthesis have been reported elsewhere.

Ease of Manipulation

A newcomer to the field of microfluidics would find it easiest to operate a microreaction device with hydrodynamic control, using syringe pumps to move liquids within the microfluidic network. The disadvantage of using hydrodynamic forces is that this requires large external pumps. The pumping system becomes complex when one is manipulating more than three reagents in the device. An elegant way to manipulate solutions in a network of channels is the use of electroosmotic flow (EOF). One of the disadvantages of using EOF is the high voltages involved in moving fluids through microchannels.

Watts and Haswell have demonstrated dipeptide and tripeptide synthesis, as the first example of EOF-based multistep synthesis, in a borosilicate glass microfluidic channel, as shown in Fig. 2. A T-shaped microreactor with 200 μm × 50 μm channels was fabricated; the overall reactor dimensions were 20 mm × 20 mm × 25 mm. The channels were filled with microporous silica frit to reduce hydrodynamic effects. After deprotection with one equivalent of hydrazine, tripeptide synthesis was also demonstrated. An offline high-pressure liquid chromatograph (HPLC) was used to determine the results of the synthesis.

Increased Safety

Hazardous Product. The synthesis of hydrogen cyanide (HCN) is an example of a fast, high-temperature process that generates a hazardous gas. Researchers at the Institut für Microtechnik Mainz, Germany, aimed to develop a portable on-site, on-demand HCN-generating unit [2]. The Andrussov process was selected for generating HCN on the microscale. The reaction can be written as

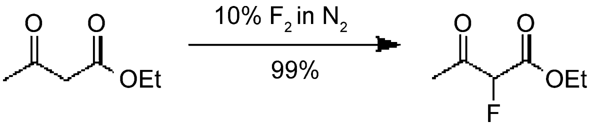

Microfluidics for Biochemical and Chemical Reactions, Figure 3
Fluorination of ethyl acetoacetate

$$CH_4 + NH_3 + 1.5O_2 \underset{Pt}{\rightarrow} HCN + 3H_2O\,.$$

To carry out the above reaction, the reactant gases were heated to 600 °C before being mixed and exposed to a supported platinum catalyst structure in a 70 μm diameter channel. The reaction led to an increase in the gas temperature to 1000 °C; the gas was then cooled to 120 °C in a microscale heat exchanger.

Hazardous Reagent Elemental fluorination of organic compounds provides an example of the safe handling of hazardous gaseous reagents. Fluorination reactions are less selective than others and highly exothermic in nature. Chambers and Spink demonstrated the fluorination of β-dicarbonyl compounds in a microfluidic channel as per Fig. 3 [1]. The reactor consisted of a 500 μm wide, 500 μm deep channel machined into a nickel block and sealed with polychlorotrifluoroethene, which provided inertness and visual access to the reaction zone. 10% fluorine in nitrogen was introduced at 10 mL/min along with ethyl acetoacetate (a β-dicarbonyl compound) at 0.5 mL/h in formic acid into the 17 cm long reaction zone (reactor plus tubing length), which was maintained at 0 °C. The liquid was pumped with a syringe pump and the gas flow was controlled using a mass flow controller. The results were analyzed using an offline gas chromatograph.

Fast Operation with Unstable Intermediates Diazotization of aromatic amines poses hazards including light, heat, and shock sensitivity, which can all lead to uncontrolled decomposition of the diazonium salt, creating an explosion. Lower alkyl nitrites have been known to blow up the container even when refrigerated. The explosion hazard is related to the pressure increase caused by nitrogen generation and to the highly exothermic nature of the reaction. De Mello et al. minimized the transportation time between two sequential steps of a synthesis by incorporating reagent mixing, quench addition, and heated decomposition operations into a single device; transport distances and dead volumes were minimized, preventing precipita-

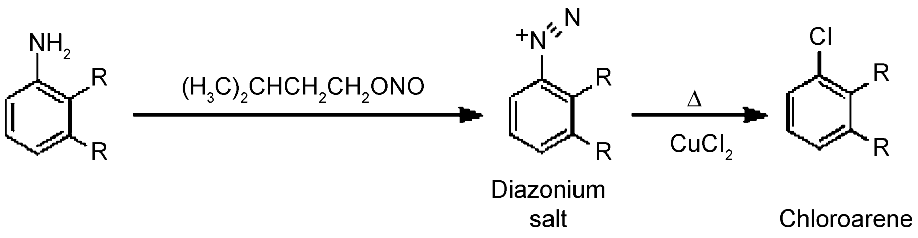

Microfluidics for Biochemical and Chemical Reactions, Figure 4 Chloro-dediazotization: the Sandmeyer reaction

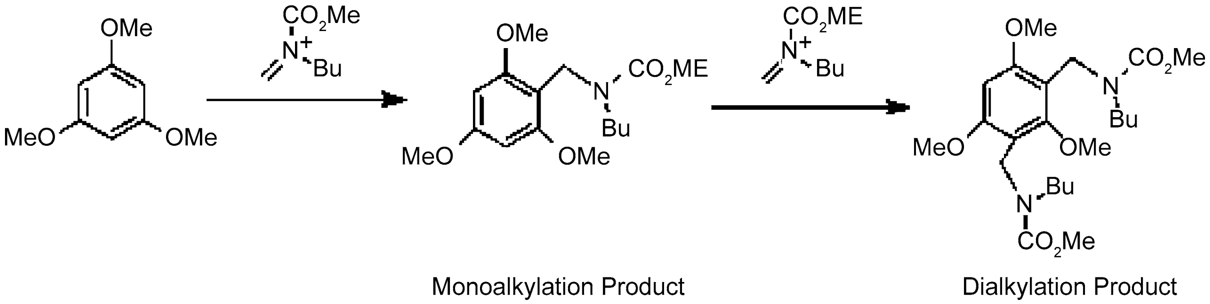

Microfluidics for Biochemical and Chemical Reactions, Figure 5 Competitive consecutive reactions of trimethoxybenzene with *N*-acyliminium ions

tion [1]. The synthesis of chloroarenes was investigated in a pressure-driven glass microreactor with a 150 μm wide, 50 μm deep, 3.6 cm long channel.

The reaction (Fig. 4) was carried out by mixing aniline with isoamyl nitrite at room temperature in the first 80 mm of the channel length and heating the resulting solution with copper chloride at 65 °C in the remaining channel length. A moving stream of air cooled the first section to room temperature. The second section of the microreactor was contacted to a heated metal block to achieve a temperature of 65 °C. The results were analyzed using an offline gas chromatograph.

Increased Yields and Selectivity Control

The Friedel–Crafts alkylation of aromatic and heteroaromatic compounds often suffers from a polyalkylation problem owing to competitive, consecutive alkylation reactions. Owing to the large exothermicity of the reaction, the product distribution has proved difficult to control on the macroscale, resulting in synthesis of a large proportion of dialkylated products (the monoalkylated : dialkylated ratio may be 1 : 1). Yoshida et al. carried out an alkylation reaction in a microchannel at −78 °C as per Fig. 5 [3].

Yoshida et al. also demonstrated the effect of mixing on alkylation yields and selectivity by using an efficient multilamination micromixer (supplied by IMM; channel width = 25 μm) and a T-mixer (500 μm).

Electrosynthesis Microfluidic fuel cells are a good example of microfluidic reaction systems where a reaction is performed catalytically to obtain electrical energy. Vice versa, electrical energy can also be used to form anion and cation radical intermediates and cleanly synthesize chemicals without the need for additional chemical reagents. Using microfluidics, microflow electrolysis reactions have been developed for carrying out electrosynthesis. Yoshida et al. have demonstrated the use of a microflow cell consisting of a porous carbon fiber anode and cathode separated by a porous Teflon spacer (3 μm pores, 75 μm thick) to carry out anodic methoxylation of several organic compounds, including *p*-methoxytoluene [1]. The reaction scheme and a schematic of the reactor are shown in Fig. 6. A *p*-methoxytoluene solution was fed through the anodic chamber and the spacer, and was collected as the solution left the cathode. The design of the reaction system allowed the process to be conducted in the absence of any intentionally added electrolyte.

Time and Temperature Reduction

The polymerase chain reaction (PCR) method is commonly used to create copies of specific DNA fragments. First, the individual strands of DNA are unwound and separated by heating (melting) to 90 – 96 °C. This is followed by cooling (annealing) to 50 – 60 °C, which allows primers to bind to the DNA strands. The primers allow the duplica-

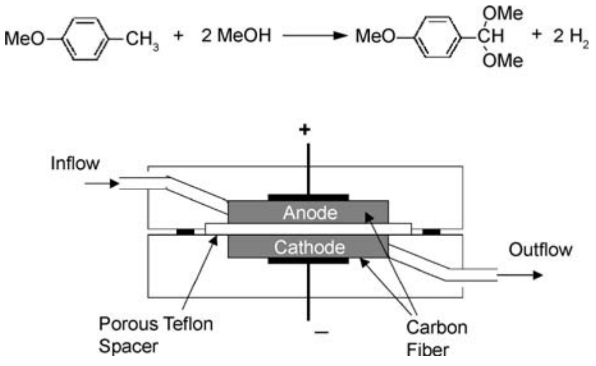

Microfluidics for Biochemical and Chemical Reactions, Figure 6 Reaction scheme and reactor construction for electrosynthesis of dimethoxytoluene

tion process to start at a specific point on the DNA. Finally, the temperature is raised to 72 °C and *taq*-polymerase is used to grow two strands of DNA (extension) from the original single strand. Each cycle duplicates the DNA strand. Generally, the cycle is repeated perhaps 30 times to produce an increase in the DNA concentration by a factor of 2^{30} times.

In a conventional-scale device, each cycle takes 5 – 10 min, and the total time is 150 – 300 min. However, it is possible to do more rapid thermal cycling in a microfluidic channel owing to the high heat transfer rates possible, thus reducing the analysis time. Figure 7 shows a schematic of a PCR device reported by Kopp et al [4]. This utilizes a flow channel that repeatedly passes through three different temperature-controlled zones on the chip to perform the required thermal cycling; 20 cycles could be performed in a time ranging from 90 s to 18.7 min, depending on the flow rate through the microchannel. A more rigorous treatment of the above subject is given in the article ► PCR lab-on-chip devices.

Radiosynthetic Chemistry Positron emission tomography (PET) is a radiotracer imaging technique used to provide quantitative information on physiological and biochemical phenomena in animals and human subjects in vivo. PET uses carbon-11 ($t_{1/2} = 20.4$ min) or fluorine-18 ($t_{1/2} = 109.7$ min), which are usually obtained from [^{11}C]carbon dioxide and [^{18}F]fluoride, respectively. The challenge lies in the reliable and regular production of PET radiotracers, which requires to be performed in a lead-shielded hot cell with remotely controlled automated equipment. The radiotracers have to be synthesized with high yields, purified, and formulated for intravenous injection, all within only two to three half-lives of the radioisotope. Lu et al. demonstrated the feasibility of synthesizing a series of radiolabeled compounds with a T-shaped glass microfluidic reactor (with a 220 μm wide, 60 μm deep, 1.4 cm long channel) [1]. A premixed solution of 3-pyridin-3-yl-propionic acid (0.01 M) and tetra-*n*-butylammonium hydroxide (0.01 M in dimethylformamide (DMF)) was introduced from one inlet and a solution of $^{11}CH_3I$ (0.01 M in DMF) from a second inlet. The reaction products were quenched in methyl cyanide upon collection, and analyzed and purified by an offline HPLC.

Reduction of Chemoselective Reaction Time Panke et al. demonstrated enhanced reaction control in the crucial step of nitration of the pharmaceutically relevant intermediate 1-methyl-3-propyl-1*H*-pyrazole-5-carboxylic acid, a precursor to the lifestyle drug sildenafil citrate (Viagra) [5]. Control of the reaction temperature is absolutely necessary because the decay of the product above 100 °C creates excess CO_2 pressure and heat buildup. A standard 70 mL CYTOS microreactor was fed with reagents using external pumps. A flow rate of 1 mL/min was maintained within each channel, with the reaction temperature maintained at 90 °C.

Microchannel Enzyme Reactor Enzymatic conversion is receiving attention because it is an environmentally friendly approach to synthesizing chemicals. Reactions can be carried out enzymatically in the solution phase or by immobilizing enzymes on microfluidic walls. Use of the latter type of reaction has the same mass and heat transfer advantages as the use of a microfluidic synthetic reactor. More information can be found in a published review article [6] and in the article ► microfluidic bioreactors in this encyclopedia.

M

Improving Microfluidic Devices for Reactions

Microscale reactions have been studied mostly to demonstrate proofs of concept. There is a lack of reaction optimization studies on the microscale with respect to flow rates, stoichiometry, concentrations, mixing design, residence time distribution, and temperature. Conditions obtained from conventional-scale synthesis do not necessarily apply to microscale reactions. Only a few systematically studied reactions have been translated into real industrial technology. The mixing strategy, the parameters of the channel geometry, and the fabrication tolerance affect the microreaction conditions. The effects of the microscale on reactions are detailed in the following sections.

Basic Methodology

Figures of Merit

The percentage yield or percentage atom economy is a widely reported quantitative metric for evaluating

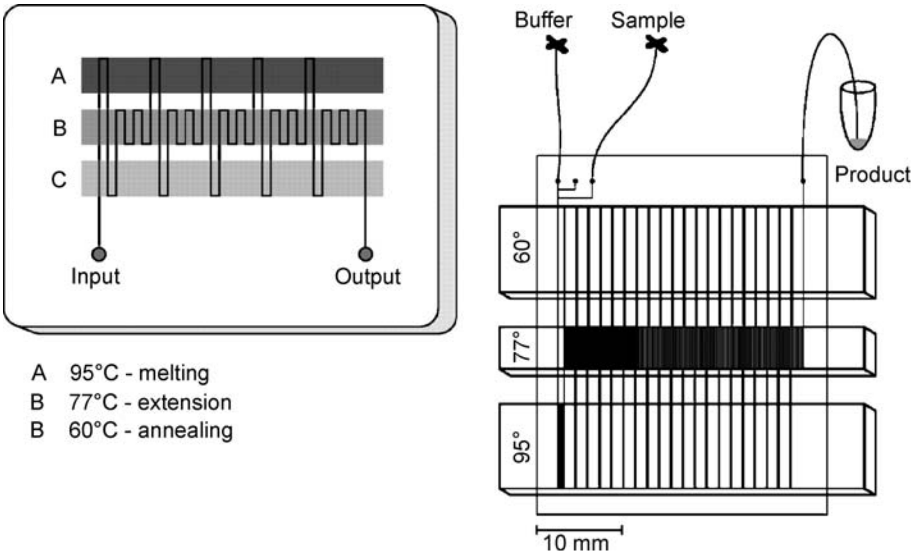

Microfluidics for Biochemical and Chemical Reactions, Figure 7 Layout of a PCR chip reported by [4]. (**a**) Schematic of a chip for flow-through PCR. (**b**) Layout of the device used in the PCR study

a microfluidic synthesis route and comparing it with conventional-scale synthesis. In the case of parallel reactions, the evaluation criterion with respect to obtaining the desired product is the percentage selectivity. The figures of merit are defined below:

$$\text{Reaction yield (\%)} = \frac{\text{(actual quantity of products achieved)}}{\text{(theoretical quantity of products achievable)}} \times 100 \tag{1}$$

$$\text{Reaction selectivity (\%)} = \frac{\text{(yield of desired products)}}{\text{(amount of reagent converted)}} \times 100 \tag{2}$$

$$\text{Atom economy (\%)} = \frac{\text{(Mole weight of desired product)}}{\text{(Mole weight of all products)}} \times 100 \tag{3}$$

Offline analytical techniques such as gas chromatography and high-pressure liquid chromatography are utilized to determine the minuscule amounts of reaction products produced. In cases where the products were not separated with these techniques, the percentage yields are sometimes reported in terms of the substrate used or remaining instead of the product produced. Measurement of the peak area or height is the most commonly utilized method for estimation of the substrate used before and after the reaction.

Control of Reaction Conditions

Chemical synthesis on chip involves dispensing and mixing reagents at a set temperature, pressure, and time, and purification of the products. Similarly, analysis on chip also usually starts with chemical reaction of a marker for the sample, followed by separation and detection. The purification and analysis of products on a chip is outside the scope of this discussion.

Fluid Manipulation

Reactions require accurate dosage of reactants to achieve the optimum stoichiometry. An array of components for fluid manipulation have been developed over the last decade for micrototal analysis systems (μTAS) and microreaction technology. Pumping of fluids is carried out using microfluidic components, which can be classified as either mechanical or nonmechanical. Mechanical pumps are distinguished from nonmechanical pumps by the presence of a moving physical part.

- *Mechanical pumping* Micromechanical pumps are usually based on the movement of a membrane, which results in periodic delivery of a fluid. The actuation schemes utilized for moving the membrane of a pump include piezoelectric, electrostatic, thermopneumatic, pneumatic, and electromagnetic devices, and shape memory alloys and electrowetting. The resulting fluid motion is pulsed, not continuous. The rotary displacement micropump is an example of a mechanical pump not based on membrane movement. External syringe

pumps have found widespread use at the research level. However, this results in challenges in obtaining leak-free connections and a low dead volume between the displacement pump and the device.

- *Nonmechanical pumping* Micropumps in this class are usually continuous and include the use of effects such as electrochemical displacement (bubble generation), thermal expansion, electrohydrodynamics, capillarity, and evaporation forces. The most commonly used nonmechanical pumping method is based on electrokinetic flow. In comparison with mechanical micropumps, field-induced flow is advantageous as it acts as both a valve and a pump, enabling both the direction and the magnitude of the flow to be controlled.

We recommend that readers consult other publications on microfluidic pumping for a comprehensive understanding of this topic.

Kinetic Regimes

Competitive parallel reactions (Fig. 8a) and competitive consecutive reactions (Fig. 8b) are common in chemistry. Here R1 and R2 are two different reagents, S is the substrate, and k_1 and k_2 are reaction rate constants.

Selectivity is governed by kinetics and thermodynamics. The thermodynamic selectivity is not affected by the method of mixing. If, however, the reactions are kinetically controlled and there is no equilibrium between products, the product selectivity is determined by the ratio of the rate constants of the competing reactions. If $k_1 \gg k_2$, the reactions have to be ultrafast for mixing to play a role in the selectivity.

In reactions with rates that are fast compared with the rate of mixing, the reaction rate is independent of the rate constant (k) and is entirely dependent on the rate of mixing and the residence time distribution. The volume available for reaction is reduced from the volume of the entire reaction vessel to a plane between reacting streams. In this situation, designated the *diffusion regime*, the potential for the formation of secondary products is the greatest. In comparison, the mixing time in the *chemical regime* is fast compared with the reaction rate, and therefore mixing is complete before significant amounts of products are present. The entire reaction vessel is available for reaction, and only the smallest amounts of secondary products are formed.

Control of Mixing on the Microscale

On the macroscale, mixing is achieved using agitation provided by mechanical or magnetic stirrers, where large

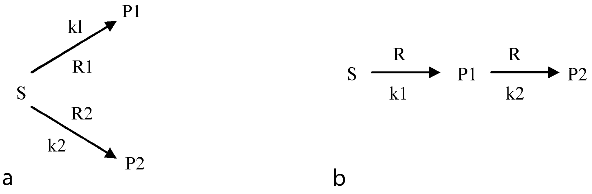

Microfluidics for Biochemical and Chemical Reactions, Figure 8 Two competitive parallel reactions. (**b**) Two competitive consecutive reactions. k_1 and k_2 are rate constants

eddies are generated, allowing bulk diffusion to take place. On the microscale, viscous forces dominate and mixing is mainly governed by molecular diffusion, defined by Fick's first law,

$$J = D\frac{\partial c}{\partial x}\,, \qquad (4)$$

where J is the diffusive flux and D is the molecular diffusion coefficient. The molecular diffusion coefficients of complex biomolecules such as myosin, hemoglobin, and enzymes are two orders of magnitude lower than those of most liquids. From the molecular point of view, mixing is an unsteady-state mass transfer process described by a dimensionless diffusion time, or Fourier number, Fo_D, which is defined over a characteristic length l (usually the smallest of the cross-sectional dimensions) as

$$\mathrm{Fo}_D = \frac{D \times t}{l^2}\,. \qquad (5)$$

Typical values of the molecular diffusion coefficient are 1 to $10^{-2}\,\mathrm{cm^2/s}$ in gases and 10^{-4} to $10^{-6}\,\mathrm{cm^2/s}$ in liquids.

Microfluidic-based mixers allow ultrafast reactions to take place in the kinetically limited regime by achieving faster mixing, which is usually obtained by a complex coupling of increases in the advective flux and interfacial area. The micromixers that have been developed can be categorized into active and passive mixers.

- *Active mixers* Energy is input to control the reagent flow by the use of moving parts or varying pressure gradients. The energy for active mixing is obtained using a pressure disturbance, electrohydrodynamic forces, dielectrophoresis, electrokinetics, magnetohydrodynamics, or acoustic or thermal energy.
- *Passive mixers* No energy is input other than that used to mobilize the fluid within the device. The passive mixers that have been developed use serial or parallel lamination, injection, chaotic advection, or droplet formation. The most popular approaches to the mixing step for biochemical and chemical reactions involve increasing the contact area between two reagent streams. This

involves splitting the two reagent streams into thin laminae and subsequently bringing them back together to allow a greater degree of diffusive mixing at the point of confluence. The greater the number of laminae that are formed from the reagent streams, the faster the mixing occurs. With the ability to efficiently mix reagent streams, the reactions performed in miniaturized systems are limited simply by the inherent reaction kinetics.

Readers are referred to the article ▶ microfluidic mixing in this encyclopedia for a deeper understanding of this topic.

Residence Time and Residence Time Distribution

Flows through microfluidic reaction channels are typically characterized by their mean residence time τ_R, which is defined by

$$\tau_R = \frac{V}{Q} = \frac{L}{v}, \qquad (6)$$

where V is the reactor volume, Q is the volumetric flow rate, L is the reactor length, and v is the plug velocity. The residence time is optimized on the basis of the reaction rate, which is a function of the reaction rate constants and the chemical concentrations. Different atoms spend different amounts of time in the channel. This creates a residence time distribution (RTD). The RTD is indicative of the dispersion, back-mixing, and dead zones present in the microfluidic system. The presence of the latter zones leads to undesired by-products in the case of parallel reactions and consecutive competitive reactions. As a measure to be used for quality control, the RTD should be as narrow as possible if one wishes to run reactions in sequence within a short time. Neglecting axial dispersion, the peak width at half height of the RTD for a Dirac pulse at the inlet is given by

$$\mathrm{PW}_{1/2} = 0.241 \times \tau_R \times \mathrm{Fo}_D^{-0.515}. \qquad (7)$$

A quick estimate of the degree of conversion that can be achieved in a continuous-flow reactions is given by the Damkohler number Da, defined by

$$\mathrm{Da} = \frac{\text{rate of reagent consumption}}{\text{rate of transport of reagent by convection}}. \qquad (8)$$

The rule of thumb is that if Da > 10 then the conversion is greater than 90%, and if Da < 0.1 then the conversion is less than 10%.

Microfluidics for Biochemical and Chemical Reactions, Table 1 Surface-area-to-volume ratios for some common cross-sectional shapes

Cross-sectional shape		Surface area/volume
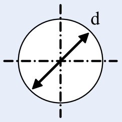	Circle	$\frac{4}{d}$
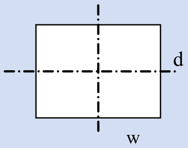	Rectangle	$\frac{2\,[1 + A.R.]}{A.R. \cdot w}$ where $A.R. = \frac{d}{w}$

Temperature Control on the Microscale

Because of the kinetics, temperature forms one of the important criteria for controlling the reaction rate, yield, and selectivity of product formation. Reactions can generally be classified thermodynamically into exothermic (heat-generating) and endothermic (heat-utilizing) reactions. In traditional large-scale reactors, reaction temperature fluctuations are difficult to correct, as any alterations made take time to have an effect on the system as a whole. Temperature control is needed in the case of exothermic reactions to prevent the reactor from going to a higher temperature, which may lead to undesirable by-products or, in severe cases, lead to an explosion.

From Table 1, the surface-area-to-volume ratio is inversely proportional to the critical cross-sectional dimension. Decreasing the channel width or depth results in an increase in the surface-area-to-volume ratio, which also reduces the heating and cooling times. The reaction rate is more uniform over the cross section owing to the minuscule thermal gradients across the walls in a microflow reactor. In systems such as PCR systems, thermal cycling of the fluid takes place by passing through different zones. Fick's law implies that the time needed for heat dissipation is directly proportional to the square of the channel depth (when $d < w$) for a flat rectangular channel, assuming that the chip and heating element have an infinite heat capacity relative to the heated fluid element.

The heat transfer characteristics on the microfluidic scale depend on the ability to heat the material of construction quickly, which is often characterized by the thermal diffusivity, defined as follows:

$$\alpha = \frac{\kappa}{\rho \times C_p}, \qquad (9)$$

Microfluidics for Biochemical and Chemical Reactions, Table 2 Thermal diffusivities of common construction materials for microreactors

Material	Thermal diffusivity ($cm^2 s$ at 300 K)
Air	0.24
Water	1.3×10^{-3}
Silicon	0.8
Pyrex 7740	0.7×10^{-2}
Aluminum	9
Copper	1.3
Gold	1.3
Nickel	0.24
Alumina	0.119
Teflon	0.34×10^{-2}
PMMA	0.124×10^{-2}

where κ is the thermal conductivity, ρ is the bulk density, and C_p is the heat capacity. Substances with a high thermal diffusivity adjust their temperature rapidly to that of their surroundings, because they conduct heat quickly in comparison with their thermal *bulk*. Table 2 lists the thermal-diffusivity properties of some materials used in constructing microreactors. Changes are observed almost immediately in a microscale reactor, which allows more precise control of reaction temperature.

The heating rate of a flowing fluid is usually reported as the Nusselt number instead of giving the solution to the temperature field across the channel cross section. The Nusselt number is a dimensionless quantity characterizing the efficiency of heat transfer and is defined by

$$\mathrm{Nu} = \frac{h \times D_h}{\kappa}, \tag{10}$$

where D_h is the hydraulic diameter and h is the heat transfer coefficient, measuring the transmitted thermal power per unit area divided by a characteristic temperature difference. The hydraulic diameter is given by $4A/P$, where A is the cross-sectional area of the channel and P is its perimeter.

Fabrication of Microreactors

Microstructured reactors have been fabricated from a variety of substrates, including silicon, quartz, metals, polymers, ceramics, and glass. The choice of substrate is largely dependent on the following parameters:

- chemical compatibility with reactants and solvents;
- thermal and pressure resistance;
- cost and ease of fabrication.

Fabrication methods such as DRIE (deep reactive ion etching) and laser ablation have been widely used owing to the exceptional surface quality and reproducibility that they provide. However, high-precision machining and serial processing increase the cost of mass production. Therefore rapid-prototyping processes, such as injection molding, microlamination, and hot embossing for polymeric, ceramic, and metal-based devices, and powder blasting and wet etching for glass, are finding more popularity for high-volume production. Researchers at IMM have demonstrated fabrication of a microreactor for portable HCN synthesis using conventional precision milling and electrode discharge machining [2].

The fabrication of a typical silicon microreactor starts with the reactor design, followed by the design of masks. The masks are printed on high-resolution transparencies or laser-written on chrome–soda-lime glass. The silicon etch pattern is transferred photolithographically to a photoresist-coated silicon wafer, and the latter is etched using DRIE. The silicon wafer is cleaned and anodically bonded to Pyrex 7740. Then, either the microreactor die is connected to a manifold or suitable connectors such as Nanoports® are epoxied to it for connection to the pumping device. A glass microreactor can be fabricated by a similar procedure, with wet etching replacing the DRIE. The etched glass channel is sealed to another glass surface using fusion bonding. In cases where injection molding and hot embossing are used, molds need to be prepared from masks. The resulting master/template is utilized to rapidly make multiple replicas of the microreactor. The main advantage of microfabrication is parallel fabrication, as compared with serial fabrication in the case of molding techniques. However, molding techniques are cheaper than microfabrication.

Surface Engineering and Functionalization of Reactor Walls

In the case of gas–solid and liquid–solid heterogeneous reactions, catalyst nanoparticles themselves or a catalyst supported on nanoparticles can be suspended in a liquid phase and passed through the reactor. Doing so, however, may lead to clogging of microchannels. A solution to the latter problem is to coat the catalyst layer onto the microfluidic walls. The formation of a catalyst layer on a reactor wall can be achieved using sol–gel layer formation. The sol–gel deposition method provides a high catalyst surface area owing to the high porosity of the resulting layer.

Catalyst impregnation can also be carried out by engineering the microfluidic walls to be porous enough to anchor catalyst nanoparticles. Ganley et al. have demonstrated that anodization of aluminum helps to create a porous surface that can anchor ruthenium catalyst particles for ammonia reforming [8]. Drott et al. have shown that anodizing a silicon channel creates

a high surface area for enzyme immobilization and hence higher enzyme activity [6]. A typical silicon anodization takes place at 0.25 A/cm^2 in a 1 : 1 hydrofluoric acid and ethanol electrolytic bath. Aluminum is optimally anodized at 30 V in a batch of 0.6 molar oxalic acid maintained at 18 °C. Anodization creates a semipermeable membrane with a high surface-area-to-volume ratio (10^8 m^{-1}). Borosilicate glasses can be rendered porous using treatment with concentrated hydrochloric acid at high temperature. This is a common practice in the manufacture of silica columns for gas chromatography to increase the surface-area-to-volume ratio of the stationary phase.

Oxide surfaces can be functionalized using a silane-based self-assembled monolayer. Amine functional groups are commonly utilized for functionalizing surfaces with biomaterials, by forming amide bonds. A common method is to expose the surface to 0.1 M aminopropyltrimethoxysilane (APTS) in toluene at 100 °C for 10 min to 1 h. This treatment renders the surface linkable with many biomaterials with a carboxylic group (–COOH). Various silanes can be utilized to decorate the surface with desired functional groups. Readers are referred to the article ▶ methods for surface modification for further understanding.

Process Intensification

A microreactor is advantageous for synthesizing small quantities of chemicals. Industry is always interested in large-scale production owing to the associated larger profit. In order to avoid changes in conditions due to scaling up, multiple microreactors can be put together to increase the production quantity as shown in Fig. 9. The surface-area-to-volume ratio remains the same, and hence so do the thermal and mass transport properties of the reaction.

This process is often referred to as *scale-out* or *numbering-up*. Replication of successful reaction units ensures that the product quality is consistent with that obtained with the laboratory-based optimizations. Currently, as cheaper mass production of microreaction units becomes a reality, the gap between research and industrial application is closing.

Key Research Findings

Three characteristic features of microreactors that have been found to be effective for the enhancement of chemical selectivity and yield are fast mixing, efficient heat exchange, and precise residence time control. However, it is rather difficult to completely separate the effects of these three factors on the outcome of chemical reactions.

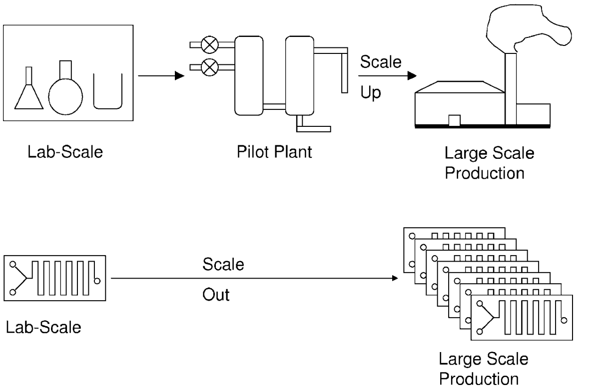

Microfluidics for Biochemical and Chemical Reactions, Figure 9 Schematic comparison of scaling-up and scale-out processes towards large-scale production

Mass Transfer Rate Effects

The high mass transfer rates in microfluidic devices can be attributed to the high surface-to-volume ratio. Small volumes of reagents experience faster diffusive mixing. Watts and Haswell reported nearly 100% formation of dipeptide in 20 min, as compared with the 50% yield obtained by batch synthesis in 24 h [1]. This demonstrates the atomic efficiency of carrying out reactions inside microfluidic channels.

De Mello et al. found that the chloro-dediazotization reaction proceeded to 71% conversion, as compared with the 40 – 49% reported for traditional batch approaches [1]. This higher conversion was attributed to the high heat and mass transfer associated with microfluidics. Raman spectroscopy combined with a microreaction device was used to optimize the residence time for chloro-dediazotization on chip. The optimum time was found to be 600 s, which is significantly longer than the residence time required for complete mixing in a microfluidic reactor as defined by the Fourier number for the system (0.55 for a flow rate of 3.1 μL/min through each inlet). This indicates that the reaction was occurring in the kinetics-governed regime, rather than the diffusive domain. The halogen abstraction efficiency of the reaction with $CuCl_2$ was 100%.

The liquid–gas flow conditions used for fluorination by Chambers et al. gave rise to an annular flow of gas (in the center), with the liquid flowing at the walls [1]. This condition utilizes the high surface-area-to-volume ratio of microfluidic reactors, unlike the case of slug flow (alternate slugs of liquid and gas). Microfluidic fluorination of ethyl acetoacetate resulted in 98% conversion, with a 71% yield of monofluorinated product.

Interfacial areas per unit volume in falling-film microreactors have been reported to be as high as 25,000 m^2/m^3, as

Microfluidics for Biochemical and Chemical Reactions, Table 3 Effect of the method of mixing on the product selectivity of the alkylation reaction

Method of mixing	Product ratio (monoalkylated : dialkylated)
Batch reactor	37 : 32
T-shaped mixer	36 : 31
IMM single mixer	92 : 4

compared with the values of $1-200\ m^2/m^3$ typical in bubble columns. This effect is particularly important in gas–liquid reactions because the rate of mass transfer from the gas to the liquid limits the reaction rate. For the hydrogenation of cyclohexene to cyclohexane in this type of reactor, the mass transfer rate constant ($K_L a$) was found to be in the range $3-7\ s^{-1}$, which is two orders of magnitude higher than that for conventional reactors.

The mixing efficiency and complete mixing time play an important role in ultrafast reactions. Yoshida et al. compared two micromixers to see the effect of the mixing ability on reactions [3]. By use of a multilamination micromixer, a dramatic increase in product selectivity was obtained as compared with a T-mixer. Table 3 quantifies the effect of mixing on selectivity. The amount of monoalkylated products obtained depends highly on the mixing method. If a large amount of alkylation agent is available in relation to a small amount of reagent, dialkyl or trialkyl substitution can take place. Thus efficient mixing in less time also plays an important role.

Control over reagent diffusion is also an important microscale effect. Slow diffusive times can be used to advantage. Yoon et al. have shown that the effects of slow diffusive mixing can be used to advantage when laminar fuel cells are operated [7]. This is a case where a reaction is driven in the mass transfer domain to operate without an electrolyte membrane.

Heat Transfer Rate Effects

The presence of high heat transfer rates is another effect which is also attributed to the high surface-to-volume ratio. Heat transfer coefficients up to $41{,}000\ W/m^2K$ have been reported in silicon microreactors, as compared with $2500\ W/m^2K$ in conventional-scale reactors. In the case of low-thermal-mass microsystems, convective heat loss to the environment can be much more significant in microreactors than in conventional systems owing to their high surface-to-volume ratios. A consequence of this is that insulation generally enhances heat loss rather than mitigating it. The critical radius of a tube below which the use of an outer insulation layer will increase heat losses is given by the ratio of the thermal conductivity of the insulation layer (k) to the heat transfer coefficient at the interface between the insulation and the ambient (h_0), $r_{critical} = k/h_0$. For the most commonly used microfluidic materials and ambient air, this critical radius has been found to be on the order of 1 mm [9]. Localized hot spots occurring in conventional fluorination reactors can lead to undesired side reactions, including the formation of fluorine radicals and nonselected free-radical side reactions. Chamber et al. were able to carry out temperature control of a fluorination reactor at −78 °C, leading to unprecedented control over the reaction rate and process safety [1]. Yoshida et al. were able to run a Friedel–Crafts reaction at −78 °C, giving a selectivity of 96 : 4 (monoalkylated : dialkylated) [3]. During temperature optimization, an increase in temperature from −78 °C to −10 °C decreased the yield of monoalkylated products from 92% to 30%, and the selectivity also decreased.

At high temperatures, hydrogen cyanide can hydrolyze to ammonia. Hessel et al. were able to produce hydrogen cyanide isothermally in a microreactor via the Andrussov route and avoid this undesired reaction [2]. Air was used as the cooling medium, and cooling of the reaction products from 1000 °C to 120 °C was calculated to be achieved in 100 μs. Another example is the production of the antibiotic ciprofloxacin, which requires a complex 20–30 step synthesis to avoid explosions in conventional reactors [10]. CPC Systems has patented a synthesis route utilizing a microreactor to produce ciprofloxacin via a five-step synthesis, where the first step is a highly exothermic and potentially explosive cycloaddition.

Panke et al. carried out nitration at 90 °C, higher than the temperature of the usual laboratory-scale synthesis (50 °C) but below the product decomposition temperature (100 °C) [5]. The process was operated with a residence time 35 min, resulting in a throughput rate of 5.5 g/h. The high surface-to-volume-ratio (channel width $< 100\ \mu m$) inside the microreactor provided improved heat exchange compared with a batch vessel. A reaction yield of 73% was obtained. On the laboratory scale, the nitrating agent was added over 2 h, followed by 8 h of reaction time at 50 °C, to produce a 96% yield. No optimization was performed in order to increase the yield. The above exemplifies the reduction in time achieved by carrying out nitration in a microreactor at elevated temperatures with high control.

Other Small-Scale Effects

An ethyl acetoacetate fluorination reaction in a nickel reactor resulted in 98% conversion to give ethyl 2-fluoroacetoacetonate. A negligible amount of perfluorinated product was observed. This result suggested that the high surface

area of the nickel microreactor had a catalytic effect and promoted formation of the enol form, which reacts very rapidly with fluorine. Chambers et al. showed that selection of the solvent system matters [1]. The reagent and the product should be soluble, or else precipitation may cause the reactor to be blocked. Chambers et al. also demonstrated scale-out from one to three microchannels while maintaining the reaction yield.

Ganley et al. anodized alumina surfaces to create a high surface area for loading with a ruthenium catalyst in microchannels [8]. Their results show increased conversion and production rates for hydrogen synthesis via ammonia reforming in a small-scale microreactor.

Yoshida et al. have shown that electrosynthesis creates faster reactions, forming ions at a faster rate [1]. Here, the only rate-limiting step is the reaction step, where ions react with a molecule. Electrosynthesis also results in an environmentally clean process. Incorporating electrosynthesis into microfluidics enables an electrolyteless process and hence less use of chemicals. Yoshida et al. found that the oxidation of *p*-methoxytoluene in methanol resulted in a 70% yield of the dimethoxylated product. Scale-out of this kind of reaction system to cleanly produce oxidized organic products in large amounts with higher selectivity will be relatively easy.

Performing reactions on a small scale provides a high amount of safety along with portability. HCN synthesis in a microreactor resulted in a 31% yield of HCN, which is half the industrial value [2]. Although this is not a remarkable yield, the result exemplifies the ability to generate dangerous gaseous products portably. Lu et al. found that operating a microreactor at 1 μL/min could produced a radiolabeled ester with a radiochemical yield of 88.0%, and the total processing time amounted to 10 min [1]. As the preparation time was in the same range as that for the laboratory-scale reaction, microfluidics provided a safer alternative for PET tracer synthesis.

Process Optimization

Changes in the operation parameters of a microfluidic system are reflected in a very short time at the product end. An advantage of this is that optimization can be done rapidly. The ease of process optimization has been clearly demonstrated by Ehrfeld and Lowe [2]. These authors investigated a very fast, highly exothermic, homogeneously catalyzed reaction, which yields a vitamin precursor. During this reaction a side product is formed, causing a considerable decrease in yield. Optimization of the industrial procedure has already been accomplished by replacing a semibatch process (70% yield) with a process using a continuous mixer/heat exchanger reactor (80 – 85% yield). Yields of 85% were obtained with a residence time of 4 s at a reactor temperature of 50 °C. Because of the scale-out process associated with microreaction systems, optimization of the reactor conditions can be done on the laboratory scale and directly implemented on the industrial scale.

Future Directions for Research

The relatively low acceptance of microreaction in industry is due to the presence of an existing infrastructure and its inflexibility toward incorporating newer technology. The acceptance of microreactor technology will depend on its compatibility with the already existing infrastructure. Microfluidic tools will replace the conventional laboratory glassware used in biochemical and chemical research work when low-cost, well-characterized reaction systems are widely available. Some areas where microreactors may find faster adoption are in the drug discovery and biotechnology industries, where new drugs and assays need to synthesized and money is not a restriction in starting a new research setup. In such industries, the success rate is proportional to the rate at which permutations and combinations can be studied. Combinatorial research work will require microfluidics to integrate operational accessories of microreactors on chip, including valves and pumps, in a much simpler way than is current. External valves and pumps result in high dead volumes and a slower response to automatic control. PDMS has been used as a material on the laboratory scale for developing device layer microvalves for microreactor control. However, PDMS-based technology suffers from two big disadvantages:

- limited solvent compatibility and
- limited temperature range of operation.

Current state-of-the-art valve and pump microfabrication technology using rigid materials such as silicon, steel, and glass is difficult to use, and completely new development strategies are needed. On-chip analytical instrumentation will also allow microfluidics to be adopted faster in the drug-screening and biotechnology industries.

Cross References

► Droplet Microreactors
► Nanoparticle Synthesis in Microreactors
► Polymer Synthesis Within Microfluidic Reactors

References

1. Watts P, Wiles C (2007) Recent advances in synthetic micro reaction technology. Chem Commun 2007:443–467
2. Ehrfeld HV, Lowe W (2000) Microreactors: New Technology for Modern Chemistry. Wiley, Weinheim

3. Yoshida J, Nagaki A, Iwasaki T, Suga S (2005) Enhancement of chemical selectivity by microreactors. Chem Eng Technol 28:259–266
4. Kopp MU, de Mello AJ, Manz A (1998) Chemical amplification: Continuous-flow PCR on a chip. Science 280:1046–1048
5. Panke G, Schwalbe T, Stirner W, Taghavi-Moghadam S, Wille G (2003) A practical approach of continuous processing to high energetic nitration reactions in microreactors. Synth Stuttg 2003(18):2827–2830
6. Miyazaki M, Maeda H (2006) Microchannel enzyme reactors and their applications for processing. Trend Biotechnol 24:463–470
7. Yoon SK, Fichtl GW, Kenis PJA (2006) Active control of the depletion boundary layers in microfluidic electrochemical reactors. Lab Chip 6:1516–1524
8. Ganley JC, Seebauer EG, Masel RI (2004) Porous anodic alumina microreactors for production of hydrogen from ammonia. AIChE J 50:829–834
9. Arana LR, Schaevitz SB, Franz AJ, Schmidt MA, Jensen KF (2003) A microfabricated suspended-tube chemical reactor for thermally efficient fuel processing, J Microelectromec Syst 12:600–612
10. Taghavi-Moghadam S, Kleemann A, Golbig KG (2001) Microreaction technology as a novel approach to drug design, process development and reliability. Org Process Res Dev 5:652–658

Microfluidics on a CD

► Centrifugal Microfluidics

Microfluidics and Magnetism

► Magnetic Field-Based Lab-on-Chip Devices

Microfluidics and Nanofluidics

► Micro- and Nanoscale Gas Fluidics

Microfluidics for Stem Cell Therapy

Michael R. King
University of Rochester, Rochester, NY, USA
mike_king@urmc.rochester.edu

Synonyms

Microfluidic stem cell culture; Stem cell tissue engineering; Stem cell isolation; Stem cell reprogramming

Definition

Stem cells are immature, undifferentiated biological cells that can multiply to create exact copies of themselves, and also differentiate into the various specific cells that comprise different tissues such as skin, muscle, blood, or brain. This encyclopedia entry refers to recent applications developed to measure, culture (i. e., grow for expansion), and control stem cell function using microfluidic systems. Microfluidic flow environments present several advantages for the manipulation and study of stem cell behavior, including therapeutic applications that are currently in development.

Overview

There is much hope that fundamental research into stem cell biology can eventually be translated into cell-based therapies to treat human disease. Stem cells possess the ability of self-replication, and can be expanded in culture. Stem cells can also be genetically modified, and differentiated into all of the cells comprising tissues that may one day be replaced or repaired via tissue-engineering applications. Rapid advances in materials chemistry, photolithography, microfabrication, and microfluidics have provided important new analytic approaches, and have led to new insights into the physical chemistry of biological behavior at the subcellular and molecular levels [1].

In the majority of stem cell research using microfluidics to date, standard fabrication of channels out of PDMS has been used, coupled with pressure-driven fluid flow of cell suspensions and cell media. The small volume of some of the successfully implemented stem cell culture microchannels allows biological experiments to be carried out for many days, while using only a single mililiter of media. It is often desirable to culture cells in *nonrecirculating* media, i. e., with cells continually contacting fresh media. This can be prohibitively expensive in a macroscale cell culture chamber, but is quite readably accomplished with microfluidics. For comparison, even using 384 well plates with a well volume of 20 µl, a 7 day experiment without recycling of media would use well over a liter of cell media.

Several in vitro strategies for controlled differentiation of embryonic stem cells have been attempted previously. Cell-based therapies are limited by the difficulty in precisely controlling the behavior of stem cells in culture. The precise control of stem cell proliferation and differentiation in culture remains an unsolved problem. In static culture, the chemical composition of the microenvironment cannot be controlled over space and time. Microfluidic technology can help address this, by providing much better control over the cell microenvironment. In addition,

the mechanical-stress environment can affect the state of adherent cell growth, and this is also easily regulated using microfluidics. Additionally, several research groups have pursued combined approaches to stem cell manipulation, using microfluidics combined with micropatterned matrix proteins and conducting large-scale parallel screening of optimal protein combinations. This approach builds on previous work to screen various extracellular matrix proteins for their effects in guiding embryonic stem cell differentiation, using robotic surface deposition. However, to motivate the study of cellular behavior and connect it to clinical outcomes, it is also necessary to concern oneself with the next higher length scale from single cells: that of cell aggregates and tissues [1]. The co-culture of stem cells with another cell type such as feeder cells is another active area of research that can benefit from microfluidic geometries.

Modern approaches to interventional medicine can generally be thought of as having three camps: chemical therapies (including drugs and biologics), devices, and more recently, cellular therapies. Stem cell therapies are among the best-known cell therapies, but a precedent in this area was set by bone marrow transplants, now a standard procedure. Numerous companies are developing stem cell lines for therapies ranging from neural regeneration in Parkinson's disease to prevention of scarring after myocardial infarction. The number of stem cell sources cited as starting materials is expanding steadily; they include adult marrow, blastocyst-derived fetal mass, embryos, and fusion products of adult nuclei and unfertilized eggs. Among all the promising news lie several problems associated with cell therapies:

- tissue compatibility;
- regulatory and ethical concerns;
- lack of control in situ.

Several approaches are being taken to tissue compatibility, ranging from engineered antigen silencing in stem cell lines to the harvesting of autologous adult cells from an individual's marrow or fat. Self-sourcing has become a popular idea for dealing with ethical and regulatory issues, too.

The technical challenges of in situ control are much more difficult to solve. Typically, stem cells are injected as a bolus into the artery feeding a target tissue area, such as a ventricle of the heart. Data from most stem cell companies show that just a few percent of the injected stem cells remain at the trauma site moments later. The majority of the cells pass through the target tissue capillaries and then enter the veins to be carried to other parts of the body. Stem cell markers and debris are typically traced to the lung and the liver. Tracking the migration of stem cells through microfabricated networks of channels could provide insight into the biophysical determinants which control the fate of implanted stem cells.

Basic Methodology

Single-Cell Assay

In a single-cell assay, cells can be confined inside a volume as small as 100 pl, formed by the compression of a flow channel by two adjacent control channels [2]. Actuation of two adjacent valves in the control layer defines the cell chamber volume, which may be as small as $100 \times 100 \times 100\ \mu$m. Fluorescent product molecules to be quantified accumulate in the small volume of the chamber. In miniature cell chambers, fast efflux rates and short mixing times ensure that the overall fluorescence signal in the cell surroundings accurately corresponds to the enzymatic activity within the stem cell. It is expected that 100 such single-cell chambers could be scanned in under 2 min, using a tightly focused laser beam that does not directly illuminate the cell to prevent photoinduced damage of the cell during measurement.

Stem Cell Culture

Lee et al. [3] have used a simple microfluidic device to manipulate transplanted embryonic stem cells while observing differentiation of the cell mass. The chambers were created with a fluid channel structure, constructed from PDMS and SU-8 photoresist. Others have used gradient-generating microfluidic systems to control and achieve proliferation and differentiation of neural stem cells [4]. Such a system exposes cells to a concentration gradient of growth factors under continuous flow, which acts to minimize autocrine (extracellular feedback from the same cell) or paracrine (chemical communication between nearby cells) signaling. Chung and coworkers have constructed gradient chambers out of PDMS using rapid prototyping and soft lithography as pioneered by George Whitesides. One such gradient-generating microchannel network, the "Christmas tree" configuration, uses laminar flow and diffusive mixing to create smoothly varying mixtures of two or more solutes. Neural stem cells retain the ability of self-renewal and can differentiate into the three main types of the central nervous system: neurons, astrocytes, and oligodendrocytes. It is hoped that one day cultured neural cells could be transplanted to alleviate degenerative diseases of the brain such as Alzheimer's and Parkinson's diseases, or be used to reconnect the spinal cord following injury.

Researchers have also built microfluidic devices for culturing adherent stem cells while simultaneously exposing those cells to a logarithmically varying range of flow rates

and to logarithmically varying concentration gradients [5]. One such implementation of this features four microscale culture chambers connected to a network of fluidic resistances, and perfused with a syringe pump (see Fig. 1). To create a 4×4 array of chambers with the flow rate varying along one axis and the concentration along the other axis, devices can be fabricated as four interconnected microfluidic layers:

- a mixer layer of depth 30 μm,
- a delivery layer of depth 100 μm,
- a via layer of depth 100 μm, and
- a chamber layer of depth 100 μm.

This design is straightforward and does not require on-chip valves, and can be scaled up to feature additional culture chambers and wider ranges of flow rates. For rectangular microchannels with an $O(1)$ aspect ratio, the fluidic resistance of each component of the network can be designed using the following expression:

$$R = \frac{12\mu L}{wh^3}\left[1 - \frac{h}{w}\left(\frac{192}{\pi^5}\sum_{n=1,3,5}^{\infty}\frac{1}{n^5}\tanh\left(\frac{n\pi w}{2h}\right)\right)\right]^{-1},$$

where μ is the fluid viscosity, L is the channel length, and w and h are the channel width and height, respectively. In direct analogy with Kirchhoff's current and voltage laws, the individual flow rates through the four parallel branches are given by

$$Q_i = Q_{\text{total}}\left[(R_{\text{ch}} + R_i)\sum_j \frac{1}{R_{\text{ch}} + R_j}\right]^{-1}.$$

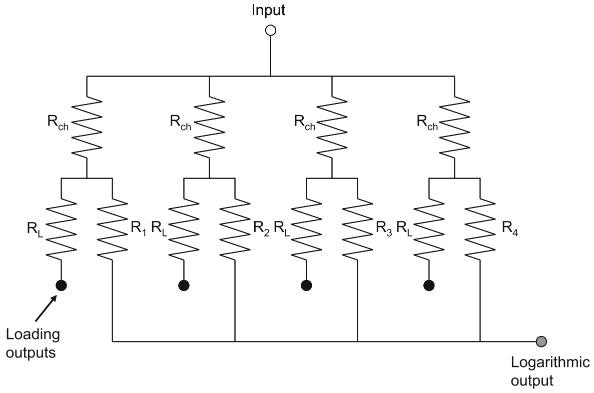

Microfluidics for Stem Cell Therapy, Figure 1 Resistance schematic for the logarithmic microfluidic device of Kim et al. [5]. A similar approach has been used to generate a logarithmically varying local shear rate and solute concentration gradient in a 2×2 array of culture chambers. R_{ch} denotes the flow resistance of each of the four culture chambers, R_{L} denotes the loading-mode flow resistances, and R_1–R_4 are the four logarithmically scaled flow resistors

The above combined device with varying flow rate and simultaneously varying solute concentration helps to control the transport of molecules toward and away from the cells of interest. Embryonic stem cells, for example, are particularly sensitive to their microenvironment. Logarithmically varying concentration gradients have also been used for pharmacological testing on patch-clamped cells.

Stem Cell Tissue Engineering

A long-term goal of tissue engineering is to construct a bioartificial organ containing a dense collection of living cells that can effectively replace the function of a diseased pancreas, liver, kidney, or heart muscle. Such a device, even with only short-term effectiveness, would be extremely valuable for providing temporary support for patients awaiting a matched donor organ. The main engineering challenge in developing a bioartificial liver replacement is that the organ is home to nearly 250 billion hepatocyte cells, each around 25 μm in diameter [6]. Other applications of tissue engineering aim to enhance, rather than fully replace, existing tissues. The three main approaches to tissue engineering have been described in a recent review [7]:

- the use of isolated cells or cell substitutes as cellular replacement components,
- the use of acellular biomaterials that can elicit a tissue regeneration response in the host organism, and
- a combination of cells and materials, i. e., a polymeric scaffold seeded with biological cells.

Two of the preferred biodegradable materials for use in microfabricated capillary networks are poly(DL-lactide-*co*-glycolide) (PLGA) and poly(glycerol sebacate) (PGS). Biodegradable PLGA microfluidic devices that serve as cell scaffolds have been created by stacking multiple layers after microfabrication steps. Functioning microvasculature can then be produced by coating the interior surfaces with fibronectin (an extracellular matrix protein) and then introducing endothelial cells, which grow to form confluent blood vessels within several days. In two dimensions, PLGA substrates can be micropatterned with ligand molecules, whereas 3D patterning has been less effective to date. Molecular micropatterning, when used to control the shape of adherent cells, can be used to control stem cell differentiation. For instance, when human mesenchymal stem cells are allowed to spread across a surface they are observed to differentiate into osteoblasts (cells which build bone), while cells confined so as to maintain a spherical shape mostly become adipocytes (fat cells). Biologists have determined that such a correlation between cell shape, mechanics, and stem cell differentiation is associated with the RhoA intracellular signaling pathway.

M

Multiphenotype cell arrays have been created by capturing cells in a connected network of reversibly sealed microfluidic channels [8]. Elastomeric PDMS molds can be reversibly sealed on a surface to sequentially deliver fluids or cell suspensions to specific locations on a substrate. Khademhosseini et al. [8] have used this technique to capture and immobilize embryonic stem cells in low-shear-stress microwells within microfluidic channels. Orthogonal alignment of a secondary array of channels was then used to perfuse the cell patterns with media.

Stem Cell Isolation

About 200,000 people currently live with leukemia in the US, with about 35,000 new cases and 23,000 deaths each year. Leukemia treatment typically involves high doses of chemotherapy, which kill both cancerous cells and blood-regenerating marrow progenitors. To restore bone marrow function after therapy, physicians perform bone marrow transplants of CD34+ hematopoietic stem cells (HSCs). Transplanted marrow can be sourced autologously (from the patient) or allogenically (from another person). Allogenic stem cells are usually sourced from a close relative, but only about one patient in three finds a donor whose tissue is compatible for a transplant. Autologous transplants have been rare in the past because of the danger of reintroduction of cancerous cells into the patient. However, stem cell isolation techniques are improving and autologous transplants are increasing in frequency.

The HSCs can be harvested by aspiration of marrow, or by isolation from peripheral blood. Studies have shown that peripheral blood stem cell transplants (PBSCTs) result in shorter hospital stays, and are safer and more cost-effective than bone marrow transplants. Donations for the purpose of PBSCTs are currently performed with the use of apheresis, where the white blood cells are separated out by centrifugation. The procedure typically takes 4 h each day over several days. Gambro and Baxter are the market leaders in apheresis instruments, sharing 70% of a market estimated at $145 million in 2002. Miltenyi Biotech markets anti-CD34 antibodies immobilized onto magnetic beads that can precipitate HSCs from the white cell fraction. Clinical applications including this isolation technique are in progress. A new medical device company, CellTraffix [9], is advancing commercial applications of adhesion technology by replicating an in vivo mechanism to build microfluidic devices and instruments capable of isolating HSCs from peripheral blood (see Fig. 2). This in vivo mechanism mediates leukocyte rolling on the vascular endothelium via the weak affinity between P- and E-selectin expressed by the vascular endothelium, and selectin-binding carbohydrate ligands expressed on circulating HSC and leukocytes. P-selectin in combination with specific antibodies is used as a coating on a solid support, over which blood flows at a rate that allows HSCs to roll slowly and all other cells to flow rapidly without rolling. This differential rolling is leveraged to isolate the HSCs in a manner akin to the chromatography of molecules.

Key Research Findings

Single-Cell Assay

Cai et al. [2] have developed a microfluidic assay to perform real-time measurement of the expression of proteins in living stem cells with single-molecule sensitivity. They observed that protein production took place in bursts, with the number of molecules per burst (quantified as enzymatic rate) following a Poisson distribution. The single-cell, single-molecule microfluidic system that they developed was applied to study the mouse embryonic stem cell lines ES54A and ES17. The cells were cultured in a defined medium to prevent differentiation. Although stochastic gene expression had been demonstrated previously for higher expression levels using flow cytometry and fluorescence microscopy, the study of Cai et al. with a microfluidic system was the first to confirm such behavior with single-copy sensitivity.

Stem Cell Culture

Mouse P19 embryonic carcinoma stem cells have been xenotransplanted into an emptied chorion (the transparent envelope of a fertilized zebrafish egg) [3]. The chorion is a useful biological vessel for developing stem cells, owing to its relatively large size of 1 mm in diameter, and also to the presence of penetrating nanopores of dimensions 500 – 700 nm. In experiments by Lee et al. [3], a stem cell/chorion construct was transported using a microfluidic channel though one of ten rectangular culture wells. A thin microhole layer was used to perfuse nutrients to the chorion via microholes of diameter 300 μm, with cell media exchanges occurring every 48 hours. By day 15 of the experiment, Lee et al. determined that the outer layer of the cell mass had successfully differentiated into neural cells, while the inner layer of the large embryoid body had differentiated into beating cardiomyocytes (heart muscle cells). Cell types were verified using immunostaining.

In the growth factor gradients generated by Chung et al. [4], human neural stem cells from a developing cerebral cortex were cultured for over 1 week in a microfluidic chamber under continuous exposure to a smooth gradient of a growth factor mixture comprising

- epidermal growth factor,
- fibroblast growth factor 2, and
- platelet-derived growth factor.

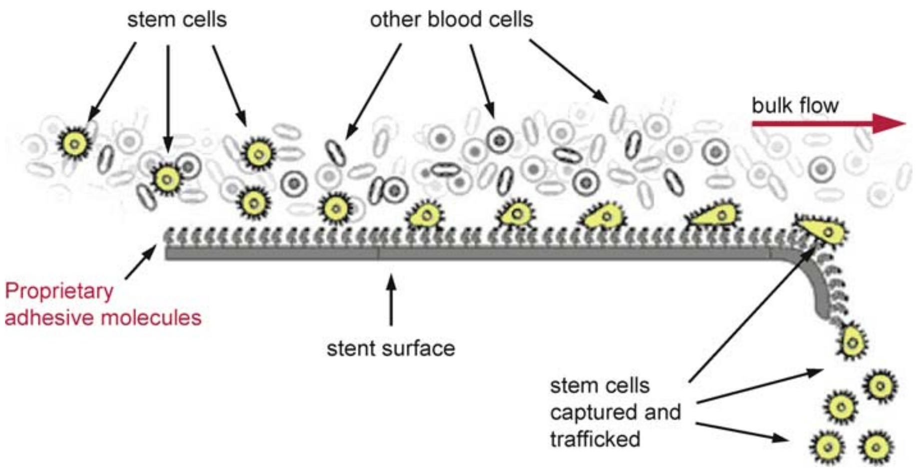

Microfluidics for Stem Cell Therapy, Figure 2 Medical devices are being developed that use the adhesive properties of lectins, which are similar to antibodies in that their binding is highly selective [9]. Unlike antibodies, lectins bind rather weakly, allowing cells to roll over a surface without becoming permanently bound to it. Biomimetic adhesion technology harnesses this rolling behavior to control the movement of captured stem cells in the bloodstream. The advantages of lectins over antibodies include the fact that lectins are not consumed in the adhesion process, promising lower costs and simplicity in the isolation of rare stem cells from dilute solutions

The human neural stem cells were observed via time-lapse microscopy to proliferate and differentiate into astrocytes (star-shaped glial cells in the brain). The cell phenotype was verified by immunohistochemistry. The cells were found to be healthy during the entire week of culture, and the proliferation and differentiation of the cells followed directly from the local concentration of growth factor as expected. Chung et al. found a strong correlation between the total cell number and the local concentration of growth factor.

Logarithmically varying concentration gradients have been studied by Kim et al. [5], and verified with fluorescent measurement. In the presence of different solute concentrations and flow rates covering a range of a factor of 300, murine embryonic stem cells were cultured for up to 4 days. Kim et al. found that the stem cells did not proliferate at the slowest flow rate tested, whereas colonies grown at higher flow rates exhibited a healthy round morphology. The chambers operating at higher flow rates showed a smaller number of colonies, although the individual colonies were much larger in size.

Stem Cell Tissue Engineering

Khademhosseini et al. [8] have successfully cultured murine embryonic stem cells in a microfluidic array of reversibly sealed channels. These authors have proposed to position microwells 100 μm apart using standard soft-lithography techniques, leaving sufficient room to overlay individual microchannels addressing each pattern. Thus, the total required area per microwell would be $200 \times 200\ \mu$m, with each well possibly operating under different culture conditions. Thus, 2500 unique tests could be performed in a 1 cm^2 area, far exceeding the capabilities of existing multiwell plates.

Stem Cell Isolation

The effects of immobilized P-selectin chimeras in the presence and absence of antibodies on the rolling velocities of normal cells (neutrophils and HSCs) and leukemic cell lines (Kg1a and HL60 cells) have been investigated [10]. This research aimed to compare the behavior of the leukemic cell lines with normal cells on P-selectin alone, and then to selectively reduce the rolling velocities of cells expressing the CD34 antigen on their surface (HSCs and Kg1a cells) using a combination of immobilized monoclonal antibodies against CD34 and P-selectin. A microfluidic channel assembly comprising polystyrene and acrylic layers was used, where a suspension of the cells in question was perfused at physiological shear rates over functionalized surfaces using methods developed for the study of neutrophil and platelet adhesion under flow. Movies of the rolling cells could be digitized and subsequently analyzed using a MATLAB program to determine the rolling velocity of each cell.

Cells of the similar sizes (HSCs and neutrophils; Kg1a and HL60 cells) rolled at similar rolling velocities on various concentrations of the immobilized P-selectin. The rolling velocities of cells expressing CD34 antigen (HSCs and Kg1a cells) were significantly reduced in the presence of the antibody and P-selectin, while the veloc-

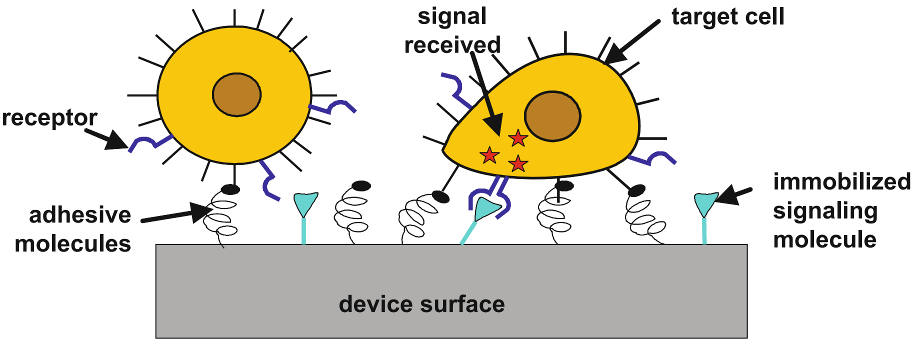

Microfluidics for Stem Cell Therapy, Figure 3 Cell adhesion technology enables highly specific cellular signaling. If a signaling molecule is immobilized on the surface and only the targeted stem cells are rolling on the surface, then only the targeted stem cells will receive the signal

ities of cells that did not express CD34 were unaffected – the antibody alone did not support rolling. The success of these experiments suggests the use of a functionalized selectin/antibody surface to facilitate cell separation. Kg1a cells have been successfully isolated from a mixture of Kg1a and HL60 cells on the basis of their differential rolling velocities on immobilized P-selectin and anti-CD34, and this work has been extended to demonstrating effective separation protocols for a mixture of HSCs and mature blood components [11, 12]. Through the product development activities currently under way, this technology will have clinical and research applications as a low-stress method for purifying cells without significantly affecting their surface antigen profile, and will facilitate cell isolation for stem cell therapies [9].

Future Directions for Research

Single-stem-cell assays based on microfluidics can be scaled up to allow characterization of gene expression on the whole-genome scale, particularly in the limit of low expression levels [2]. Two-dimensional arrays of stem cells will, hopefully, lead to high-throughput screening of drugs and optimal conditions for tissue engineering. In the field of stem cell culture and tissue engineering, one new frontier of controlling the cell microenvironment is to expose an individual cell to multiple microenvironments by placing it at an interface between two adjacent flow streams [7]. While the discussion in this article has focused on the chemical microenvironment and local mechanical shear stress, temperature can also have a profound effect on the dynamics of embryonic development. Multiple research groups have explored the idea of using microfluidics to transport a growing embryonic body from one temperature environment to another as a simulation of in vivo conditions.

Stem Cell Reprogramming

Bone marrow was once thought unique among organs because of its regenerative ability. Since the discovery of stem cells, the marrow has been recognized as the largest of several stem cell sources. Stem cells routinely leave the marrow and circulate in the peripheral blood, trawling for signals that indicate a need for repair before homing back to the marrow. Biotechnology companies are currently developing applications around the concept of artificial marrow that collect and grow stem cells over time in the body [9]. Here, microfluidic capillary networks are placed in the peritoneal cavity, as a venous bypass, using laparoscopic procedures. This implant can be removed with minimally invasive techniques when an acute need for stem cells arises, for example after a heart attack. The idea of in situ stem cell storage overcomes a major obstacle associated with external storage: the cost of liquid nitrogen. The age-related decline in circulating stem cell numbers is well documented, suggesting a regenerative value to deliberately increasing circulating stem cell numbers as an antiaging therapy. Microfabricated flow channels could also enable the controlled release of stem cells from an artificial marrow device. A small number of stem cells circulate in our bodies at all times. Future work in this area will most likely be aimed at developing implants that capture these autologous cells and traffic or reprogram them to a site in need of regeneration (see Fig. 3). In combination with the technologies developed for artificial marrow, these implants could substantially accelerate healing. Likely indications include skin ulcers and peripheral vascular disease, which are chronic and likely to require continuous healing assistance.

Cross References

► Cell Adhesion and Detachment
► Cell Culture (2D and 3D) on Chip

► Cell Patterning on Chip
► Cell Sorting
► Microfluidic Devices in Tissue Engineering

References

1. King MR (ed) (2006) Principles of Cellular Engineering: Understanding the Biomolecular Interface. Academic, San Diego
2. Cai L, Friedman N, Xie XS (2006) Stochastic protein expression in individual cells at the single molecule level. Nature 440(04599):358–362
3. Lee JW, Na DS, Kang JY, Lee SH, Ju BK (2006) Differentiation of mouse P19 embryonic carcinoma stem cells injected into an empty zebrafish egg chorion in a microfluidic device. Biosci Biotec Biochem 70(6):1325–1330
4. Chung BG, Flanagan LA, Rhee SW, Schwartz PH, Lee AP, Monuki ES, Jeon NL (2005) Human neural stem cell growth and differentiation in a gradient-generating microfluidic device. Lab Chip 5:401–406
5. Kim L, Vahey MD, Lee HY, Voldman J (2006) Microfluidic arrays for logarithmically perfused embryonic stem cell culture. Lab Chip 6:394–406
6. King MR (2005) Biomedical applications of microchannel flows. In: Kandlikar SG, Garimella S, Li D, Colin S, King MR (eds) Heat Transfer and Fluid Flow in Minichannels and Microchannels. Elsevier, London
7. Khademhosseini A, Langer R, Borenstein J, Vacanti JP (2006) Microscale technologies for tissue engineering and biology. Proc Nat Acad Sci USA 103(8):2480–2487
8. Khademhosseini A, Yeh J, Eng G, Karp J, Kaji H, Borenstein J, Farokhzad OC, Langer R (2005) Cell docking inside microwells within reversibly sealed microfluidic channels for fabricating multiphenotype cell arrays. Lab Chip 5:1380–1386
9. Fitzgerald TM, Naab D, Bibens WT, Wojciechowski J (2008) Technology. http://www.CellTraffix.com. Accessed 23 Jan 2008
10. Charles N, Liesveld JL, King MR (2007) Investigating the feasibility of stem cell enrichment mediated by immobilized selections. Biotech Prog 23(6):1463–1472
11. Narasipura SD, Wojciechowski JC, Charles N, Liesveld JL, King MR (2008) P-selectin coated microtube for enrichment of CD34+ hematopoietic stem and progenitor cells from human bone marrow. Chin Chem 54(1):77–85
12. Wojciechowski JC, Narasipura SD, Nichola CN, Mickelsen D, Blair ML, King MR (2008) Capture and enrichment of CD34-positive haematopoietic stem and progenitor cells from blood circulation using P-selectin in an implantable device. Brit J Haematology (in press)

Microfluidics for Studies of Apoptosis

Jianhua Qin, Nannan Ye, Bingcheng Lin
Department of Biotechnology
Dalian Institute of Chemical Physics, Chinese Academy of Sciences, Dalian, China
jhqin@dicp.ac.cn

Synonyms

Apoptosis; Programmed cell death; Microfluidics; Lab-on-a-Chip; Micro total analysis system (μTAS); Cell membrane changes; Surface lipid translocation; Translocation of phosphatidylserine; Externalization of phosphatidylserine; Flip of phosphatidylserine; Internucleosomal DNA fragmentation; DNA fragmentation; DNA ladders; Caspase activation; Changes of caspase activity; Intracellular Ca^{2+} concentration changes; Intracellular Ca^{2+} fluxes; μTAS

Definition

► Microfluidic systems, ► Lab-on-a-Chip systems or micrototal analysis systems (μ-TAS) allow the miniaturization of various functional units, such as pumps, valves, and reactors, and make it possible to build novel integrated microsystems for various biological applications. These systems have been well recognized as a possible *enabling technology* that may play important roles in biology in the future. This observation is supported by the efforts that have been made to build functional microsystems for various studies of cells, including studies of apoptosis.

Apoptosis or programmed cell death, is the outcome of a metabolic cascade that results in cell death in a controlled manner. Apoptotic cells are characterized by a distinct set of morphological and biochemical characteristics, which are typically monitored in a multiwell culture plate, and, more recently, microfluidic devices have been employed.

In the early stages of apoptosis, mitochondria suffer specific damage that results in alteration of their integrity and function, for example release of cytochrome *c*, changes in electron transport, loss of the mitochondrial transmembrane potential, altered cellular oxidation and reduction, and participation of pro- and anti-apoptotic bcl-2 family proteins. A unique microfabricated device has been presented for the continuous separation of intact and compromised-membrane-potential mitochondria in apoptotic Hela cells by microscale isoelectric focusing, microIEF.

Phosphatidylserine is a membrane phospholipid, which is normally restricted to the inner leaflet of the plasma membrane. The translocation of phosphatidylserine from the inner to the outer leaflet of the plasma membrane is an early event in apoptosis. Annexin V, an endogenous human protein with a high affinity for membrane-bound phosphatidylserine, can be used in vitro to detect apoptosis. An annexin V assay in a microfluidic system has been developed for flow cytometric analysis of apoptosis using a minimal number of cells.

A shift in the cellular reduction/oxidation (redox) state has been found to be involved in the process of apoptosis.

M

Generally, the cellular redox state is a balance between the relative quantities of the intracellular oxidative substances (reactive oxygen species, ROS) and reductive substances (reduced glutathione, GSH). A microfluidic-device method with laser induced fluorescence, LIF detection for simultaneous, rapid determination of intracellular ROS and GSH in apoptotic leukemia cells has been described.

Internucleosomal DNA fragmentation is the result of activation of the endogenous endonuclease in apoptotic cells. The traditional gel electrophoresis method for the analysis of DNA fragmentation is labor-intensive. However, a microfluidic device has been developed which integrates the selection of individual cells, the lysis of cells, and separation of the released apoptotic DNA fragments.

Caspases are intracellular proteases and cleave their substrate proteins specifically behind an aspartate residue. Caspases are normally present as inactive proenzymes. However, during apoptosis, caspase activation is induced by cleavage at specific internal aspartate residues. Activation of the initiator caspases by pro-apoptotic signals leads to proteolytic activation of the execution caspases, which cleave a set of vital proteins and thus initiate and execute the apoptotic degradation phase. A self-contained on-chip cell culture and pretreatment microdevice system has been developed for the screening of caspase-3 expression in apoptotic cells.

Cytochrome *c* is a component of the mitochondrial electron transfer chain. The release of cytochrome *c* from mitochondria initiates caspase activation during apoptosis. A microchip-based system has been developed for direct monitoring of the cytochrome *c*distribution during the apoptosis process.

Alterations in the cytosolic Ca^{2+} concentration and/or intracellular Ca^{2+} compartmentalization are involved in the regulation of apoptosis. These apoptosis-associated Ca^{2+} fluxes are critical targets of evolutionarily conserved actions. A microfluidic device has been constructed for ionophore-mediated intracellular Ca^{2+} flux measurements and multistep receptor-mediated Ca^{2+} measurements at the single-cell level.

Overview

Apoptosis (programmed cell death) is a complex and tightly regulated process by which a cell orchestrates its own destruction in response to specific internal or external triggers. Apoptotic processes are crucially involved in the development of cells, maintenance of tissue homeostasis, regulation of the immune system, and elimination of damaged cells. Enhanced or inhibited apoptotic cell death can result in severe pathological alterations, including developmental defects, autoimmune diseases, neurodegeneration, and cancer. Owing to its importance in such biological processes, there has been explosive progress toward dissecting its molecular basis, with an exponential increase in PubMed citations. Recently, system-level understanding of biological systems has been pursued. Research into system-level characteristics by discovering the response of cells (die or live) to certain chemicals by studying cell death regulation, and efforts to model cell processes are of great interest in the emerging field of systems biology. These studies have become powerful drivers for new technologies designed to acquire ever more comprehensive information from single cells and cell populations.

Apoptotic cells are characterized by a distinct set of morphological and biochemical characteristics observed exclusively with this mode of cell death. These apoptotic features include loss of cell volume or cell shrinkage, chromatic condensation, internucleosomal DNA fragmentation, and the formation of *apoptotic bodies* that are then phagocytized by macrophages or neighboring cells to rid the body of the dying cells, thus preventing the induction of an inflammatory response. The existence of differential expression patterns or alternate mechanisms in apoptosis pathways among tissues and cell lines makes it necessary to perform two or even three parallel experiments to confirm and compare the kinetic events associated with cell death.

Basic Methodology

The techniques designed to identify, quantify, and characterize apoptosis are numerous. Some examples are fluorescence microscope, flow cytometry, and microplate analysis. Of these, flow cytometry remains the methodology of choice for studying the apoptotic cascade in relation to cell type, triggering, and timing. However, these methods still have some limitations:

- a large number of cells are required for each flow cytometric assay ($> 10^4$/mL);
- the cell preparation prior to analysis is time-consuming, requiring additional time for cell culture, cell staining, and washing steps, and thus real-time monitoring of cell death kinetics is problematic;
- cells are often fixed and destroyed so that intact single living cells cannot be analyzed. These restrictions make current assays of apoptosis cumbersome and impractical for clinical use.

Key Research Findings

The development of miniaturized (microfabricated, microfluidic-based) analytical devices and their integration to create micrototal analysis systems [1] is one of the directions that is being pursued to address future analytical

needs. Microfluidic technologies allow the miniaturization of various functional units, such as pumps, valves, and reactors, and make it possible to build novel integrated microsystems for various biological applications. Microfluidics has been well recognized as a foreseeable "enabling technology" that may play important roles in biology in the future. This observation is partly demonstrated by the efforts that have been made to build functional microsystems for various types of cellular analysis, including apoptosis analysis [2]. Some typical work in this field [3, 4] has shown that novel schemes could be applied on a microfluidic platform to investigate cellular behaviors, schemes which would not be possible with a conventional analytical system. It may be said that contemporary microfluidic technologies provide a bridge between biological materials and systems biology through large-scale multiparameter analysis, with applications ranging from molecular dissections of single cells and very small cell populations to multiparameter disease diagnostics from cells and blood.

Apoptosis is a complex biological process, which is regulated by several cell signal transduction pathways. The study of apoptosis involves the measurement of biological and morphological hallmarks at a variety of stages in the apoptotic cascade. Apoptotic assays in microfluidics can be classified into five themes:

1. alterations of the integrity and function of mitochondria;
2. changes in cell membranes (surface lipid translocation);
3. shifts in the cellular redox state;
4. caspase activation;
5. internucleosomal DNA fragmentation; and
6. intracellular Ca^{2+} concentration changes.

Alterations of Integrity and Function of Mitochondria

A variety of key events in apoptosis are related to mitochondria, such as the release of cytochrome *c*, changes in electron transport, loss of the mitochondrial transmembrane potential, altered cellular oxidation and reduction, and the participation of pro- and anti-apoptotic bcl-2 family proteins. Of these, the disruption of the mitochondrial transmembrane potential is one of the earliest intracellular events that occur following the induction of apoptosis.

Lu et al. [5] have presented a unique microfabricated device for the continuous separation of intact and compromised-membrane-potential mitochondria in apoptotic Hela cells by microIEF. A schematic of field-flow IEF and a photograph of the microfabricated device are shown in Figs. 1a–c. The device was fabricated using a combination of photolithography, thin-film metal deposition/patterning, and electroplating techniques. In a microIEF experiment using JC-1-stained whole-cell lysate, Hela cells were treated with TNF and cycloheximide to induce apoptosis. The different isoelectric points, *pI*s for intact and compromised-membrane-potential mitochondria could potentially be used to assay the fraction of mitochondria that lose their membrane potential when cells undergo apoptosis (Fig. 1d). This microdevice provides fast separation in very small samples while avoiding the large voltages and heating effects typically associated with conventional electrophoresis-based devices.

Cell Membrane Alterations (Surface Lipid Translocation)

One of the earliest events in programmed cell death is the externalization of phosphatidylserine, a membrane phospholipid normally restricted to the inner leaflet of the lipid bilayer. Annexin V, an endogenous human protein with a high affinity for membrane-bound phosphatidylserine, can be used in vitro to detect apoptosis before other well-described morphological or nuclear changes associated with programmed cell death.

Calipter Technologies and Agilent have developed an annexin V assay in a microfluidic system, which allows flow cytometric analysis of apoptosis with a minimal number of cells [6, 7]. In this setup, the cells are moved by pressure-driven flow inside a network of microfluidic channels and are analyzed individually by two-channel fluorescence detection. As only a small number of cells (as few as 50 – 100) are consumed per assay, this setup is particularly suitable for working with cells of limited availability, for example primary cells. The system has been applied to evaluate staurosporine-induced apoptosis and annexin V binding in human umbilical vein endothelial cells (HUVECs) and normal human dermal fibroblasts (NHDFs). The results are in good correlation with results obtained using conventional flow cytometry but demonstrate new dimensions in low reagent and cell consumption.

Shift in Cellular Redox State

The cellular reduction/oxidation (redox) state has been found to be involved in the regulation of cell proliferation, differentiation, and apoptosis. Generally, the cellular redox state is a balance between the relative quantities of the intracellular oxidative substances (reactive oxygen species) and reductive substances (reduced glutathione). Conventionally, intracellular ROS and GSH can only be determined by flow cytometry, HPLC, or enzymatic methods. Qin et al. [8] have described a microfluidic device method with LIF detection for simultaneous, rapid determination of intracellular ROS and GSH in apoptotic

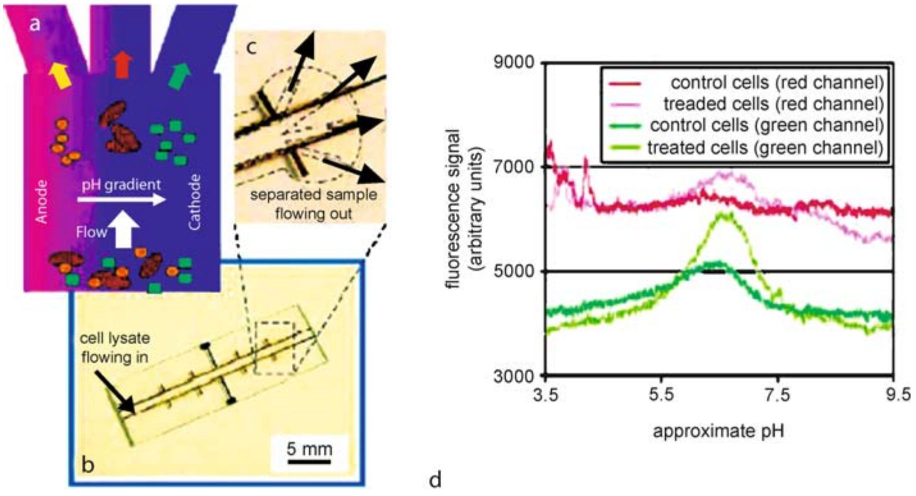

Microfluidics for Studies of Apoptosis, Figure 1 (**a**) Schematic of field-flow IEF of mitochondria. (**b**) Photograph of a microfabricated device before final assembly; (**c**) enlarged view of the fractionation end of the device. The device consists of electroplated gold electrodes and microfluidic channels formed in a photopatternable epoxy. (**d**) IEF of JC-1-labeled mitochondria from apoptotic Hela cells showing larger signals (in both the red and the green channel near neutral pH), which suggests that a number of mitochondria from the apoptotic cell population have lost their transmembrane potential. Reprinted from [5], with permission

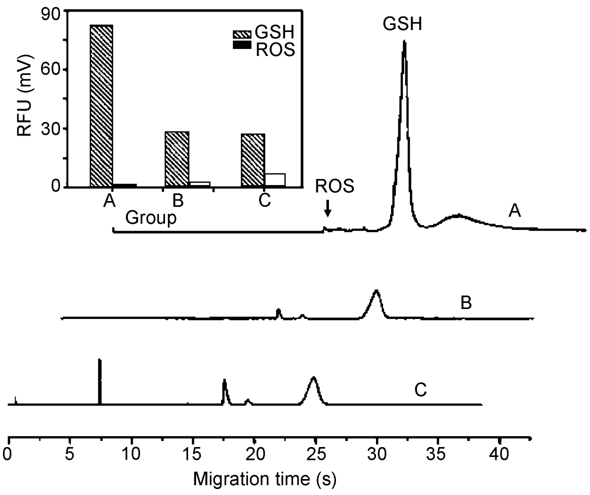

Microfluidics for Studies of Apoptosis, Figure 2 Microchip electropherograms of ROS and GSH in apoptotic NB4 cells. (A) control; (B) 1.0 mM As_2O_3; (C) 1.5 mM As_2O_3. The cells were exposed to As_2O_3 for 72 h

leukemia cells on a glass chip. Both quantitative and qualitative information about the compounds investigated can be obtained, and the two analytes can be detected in just 27 s by using this method. Depletion of GSH and generation of ROS were observed in apoptotic NB4 cells after triggering with arsenic trioxide (As_2O_3) (Fig. 2), showing that the proposed microchip method can readily evaluate the production of ROS, which occurs simultaneously with the consumption of the inherent antioxidant.

DNA Fragmentation

The most familiar biochemical feature of apoptosis is endogenous endonuclease activation. This results in the production of domain-sized large (50 – 300 kb) DNA fragments and oligonucleosomal cleavage products commonly referred to as "DNA ladders". The traditional gel electrophoresis method is labor-intensive, requiring additional time for cell lysing and extraction of genomic DNA. Kleparnik and Horky [9] performed detection of doxorubicin-induced apoptosis in individual cardiomyocytes in a microfluidic device. Microstructures integrated on a CD-like plastic disk were adapted for selection of individual cells, lysis of cells in an alkaline environment, and separation of the released apoptotic DNA fragments. The fragments with the typical 180 bp ladder pattern were electrophoretically resolved in a 2% solution of linear polyacrylamide on a polycarbonate chip. The causal relation between the enhanced doxorubicin concentration and the extent of DNA fragmentation in a single cell was confirmed.

In addition to the use of electrophoresis for identification of the characteristic DNA ladders, DNA content analysis by flow cytometry is often employed to identify cells undergoing DNA fragmentation. This method is based on the fact that permeabilized apoptotic cells release fragmented DNA, resulting in a DNA content that is less than that in live diploid cells. Sohn et al. [10] developed a novel microfluidic technique – capacitance cytometry – that can be used to quantify the polarization response of

DNA within the nucleus of a single eukaryotic cell and to analyze the cell cycle kinetics of populations of cells. The fundamental basis of capacitance cytometry is an AC capacitance measurement. It has been found that there is a linear relationship between the DNA content of eukaryotic cells and the change in capacitance that is evoked by the passage of individual cells across a 1 kHz electric field. By monitoring the DNA content of populations of cells with this technique, one can produce a profile of their cell cycle kinetics. Thus, this might be advantageous in tumor cell detection and in real-time monitoring of the effects of a pharmacological agent on cell cycles and cell death.

Changes in Caspase Activity

A number of specific changes in enzyme activity occur during apoptotic programmed cell death. The protease caspase-3 increases in activity during apoptosis and participates in the degradation of several cellular proteins essential for DNA repair. Tabuchi and Baba [11] have developed a self-contained on-chip cell culture and pretreatment microdevice system, which was used for screening of caspase-3 expression in stress-shock-triggered apoptosis of Jurkat cells. The pretreatment microdevice included 96 hand-made wells and a 12-well inner cup, requiring no external pipetting or centrifugation steps for cell culture and washing. The cells were placed into the inner cup and inserted into wells that were filled with a culture medium. During exchange of the medium, the inserted cups containing cells were moved into the next row of wells, which were filled with new buffer or reagent. By connecting devices for all procedures to an electrophoretic separation chip, the cell culture, cell-washing, stimulation, protein extraction, and electrophoretic separation processes could be integrated. The microdevice could manipulate 12 samples simultaneously, and the total analysis time was around one-eighth of that of the conventional analytical method. Using this microdevice, an annexin V assay of cells treated with camptothecin or heat shock was also performed.

Protein Release from Cells

The release of cytochrome *c* from mitochondria to the cytosol is thought to be a key event for signal transduction in the apoptotic process. It has been suggested that it induces a series of biochemical reactions that result in caspase activation and subsequent cell death. Tamaki et al. [12] have developed a microchip-based system for direct monitoring of cytochrome *c* distribution during the apoptosis process. This system incorporated microscale cell culture, chemical stimulation, and a scanning-thermal-lens detection system under a microscope, which resulted in secure cell stimulation and coincident in vivo observation of the cell responses. Monitoring of the cytochrome *c*distribution in a neuroblastoma–glioma hybrid cell was performed in a microflask fabricated in a glass microchip. Cytochrome *c* was detected with an extremely high sensitivity ($\sim$ 10 zmol) without using any labeling substrate.

Intracellular Ca^{2+} Concentration Changes

Several lines of evidence indicate that alterations in the cytosolic Ca^{2+} concentration and/or intracellular Ca^{2+} compartmentalization are involved in the regulation of apoptosis. These apoptosis-associated Ca^{2+} fluxes are critical targets of evolutionarily conserved actions. Wheeler et al. [13] have developed a microfluidic device constructed from poly(dimethylsiloxane) (PDMS) for ionophore-mediated intracellular Ca^{2+} flux measurements and multistep receptor-mediated Ca^{2+} measurements at the single-cell level. A schematic diagram of the microfluidic device and results showing measurements of the ionomycin-mediated Ca^{2+} flux in Jurkat T-cells are presented in Fig. 3. The microfluidic network enabled passive, gentle separation of a single cell from the bulk cell suspension, and integrated valves and pumps enabled the precise delivery of nanoliter volumes of reagents to that cell. The method of cell trapping and perfusion with focusing and shield buffers provides an innate "washing", minimizing reagent consumption, analysis time, and stress on the cell. Thus, it might be useful for measuring intracellular Ca^{2+} concentrations in individual cells during apoptosis.

In addition, a microfluidic device for monitoring cellular Ca^{2+} uptake reactions has been developed by Yang et al. [14]. The device allows cell transport and immobilization, and dilution of an analyte solution to generate a concentration gradient. The ATP-dependent calcium uptake reaction of HL-60 cells was monitored, demonstrating the feasibility of using a microchip for real-time monitoring of cellular Ca^{2+} flux during apoptosis upon treatment with a concentration gradient of test solution.

Future Directions for Research

The central component of apoptosis is a genetically programmed network within cells, which is driving the development of new technology for system-level study. As already described above, microfluidic devices have been employed to characterize most of the key hallmarks of apoptotic processes. Also, there has been an attempt to integrate an ability to make multiple measurements on one microfluidic chip. However, in view of technical considerations, there is still enough space for this technology to be

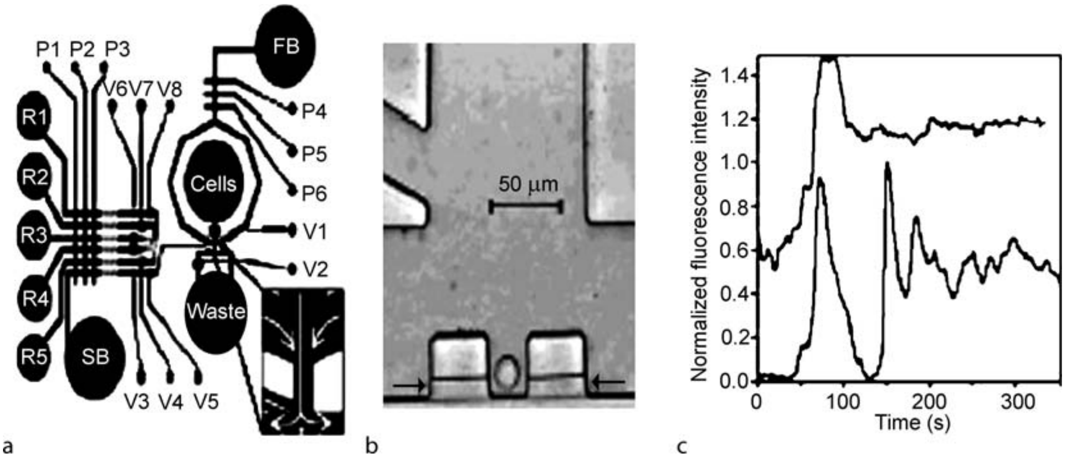

Microfluidics for Studies of Apoptosis, Figure 3 (**a**) Schematic of single-cell analysis device. The fluidic channels are shown as dark, and the control channels as light. R1–R5 are reactant inlets, and SB and FB are the shield and focusing buffer inlets, respectively. Valves are actuated by applying pressure to the control inlets V1–V8. Pumps are activated by actuating P1–P3 or P4–P6 in series. Inset: close-up of cell-trapping region. Cells are pushed by hydrostatic pressure from the cell inlet to waste. They are focused to the center of the stream by the focusing buffer. (**b**) CCD image of an individual Jurkat T-cell trapped in a cell dock. (**c**) Measurements of ionomycin-mediated calcium flux in Jurkat T-cells. After perfusion with ionomycin, the cells responded typically with ringing (lower trace) or with sustained [Ca^{2+}] elevation (upper trace). The traces have been normalized and offset for comparison. Reprinted from [13], with permission

explored further in relation to the following aspects of the study of apoptosis.

Single-Cell-Analysis

Apoptosis is found to proceed in different cells at different times after an initial stress is applied. However, the current experimental measurements on apoptotic processes in particular cells are typically performed on large cell populations. Such experiments necessarily lead to measurements of an inhomogeneous distribution of cell responses. Therefore, it is particularly attractive to be able to carry out external perturbations at the single-cell level.

Microfluidic technology appears to offer an effective platform for single-cell analysis [15], and many efforts are under way to mimic the properties of single cells and to design chips that are as efficient as cells. Various techniques, such as the use of hydrostatic pressure heads in device inlets, electrokinetic pumping with usage of multiple integrated off-chip pumps, and optical or dielectrophoretic traps, have been tried to control liquids or manipulate individual cells in a microdevice. The development of multilayer soft-lithography fabrication has greatly improved the control of fluids and cells in microfluidic devices, with the advantage of forming valves with near-zero dead volume. An integrated microfluidic process on a single chip using mechanical microvalves to achieve parallel, nanofluid processing in a highly integrated system has been demonstrated by Quake's group [16]. This system is capable of trapping mammalian cells, performing lysis, and purifying measurable amounts of mRNA from as little as a single cell. These studies are preparing the ground for the further study of cell death behavior using single cells whose behavior deviates from that of the bulk population, which otherwise would not be possible owing to the complexity of the system.

In Situ Dynamic Apoptosis Analysis

Apoptosis is a dynamic physiological process in the normal development and homeostasis of multicellular organisms. The ability to monitor cell death events over time provides a unique tool for the evaluation of the therapeutic efficacy of experimental therapeutic agents, and for studies on the role of apoptosis in various disease processes. Conventionally, apoptosis in a population is determined at a specific time by microscopic examination or flow cytometry. However, apoptotic cells exist in vitro for a limited time and occur only in a relatively narrow temporal window, after which they promptly disintegrate. Thus, an accurate determination of apoptosis in a population of cells requires either frequent determinations or continuous monitoring.

Microfluidic devices enable one to incorporate cell culture, manipulation of living cells, or cell lysing into a microchip-based platform, making it possible to investigate cell death events in the same cell or in a population of cells after stimuli over time. Recently, there has

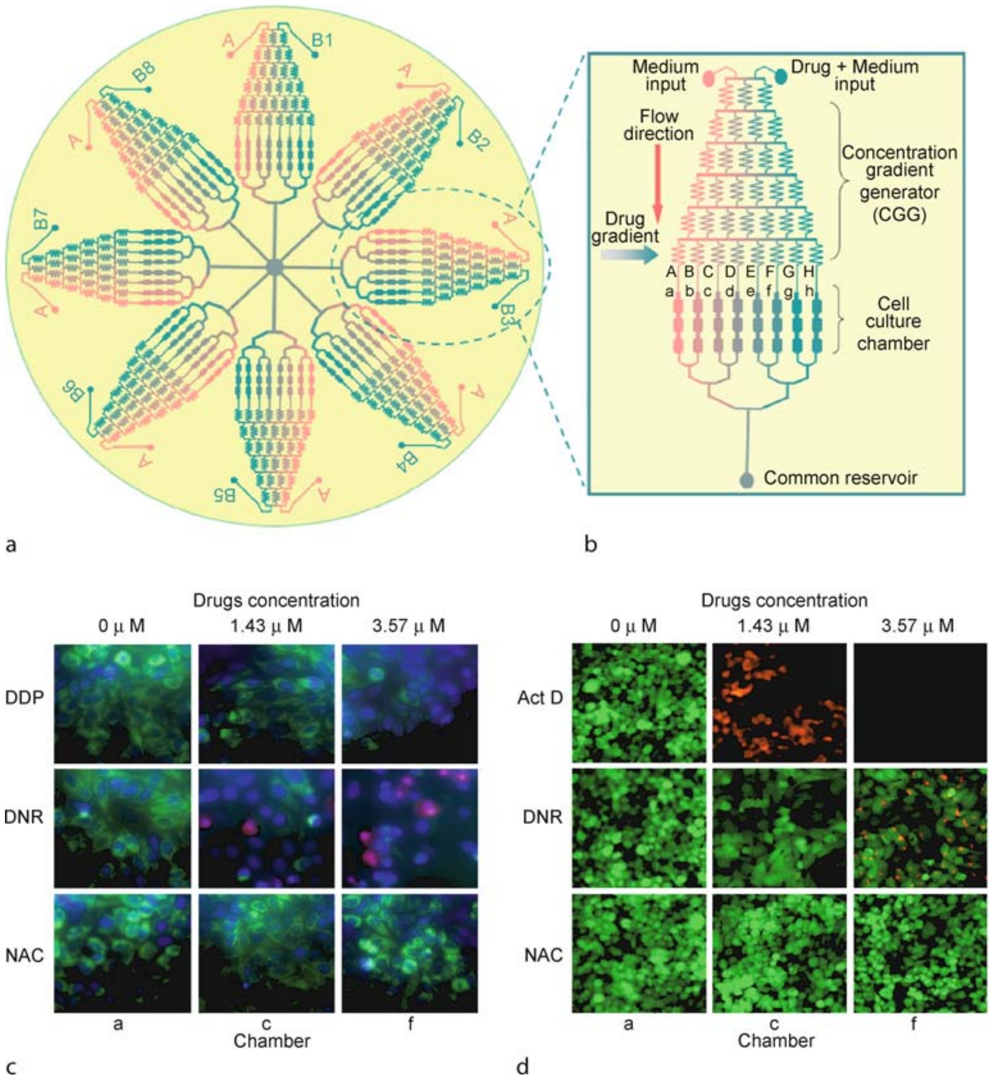

Microfluidics for Studies of Apoptosis, Figure 4 (**a**) Schematic of the integrated microfluidic device, which consists of eight uniform structure units and each unit is connected by a common reservoir in the centre of device. (**b**) Magnified section of the single structure unit containing an upstream concentration gradient generator (CGG) and downstream parallel cell culture chambers. (**c**) Representative composite images from multiparametric apoptosis analysis in HepG2 cells by monitoring mitochondrial transmembrane potential (Rh-123, Green), membrane permeability (PI, Red) and nuclear morphology (Hoechst 33342, blue), respectively. (**d**) Representative composite images associated with parameters of GSH (green) and ROS (red) in HepG2 cells after exposure to tested compounds. Reprinted from [19], with permission.

been some work dealing with dynamic apoptosis analysis in real time with microfluidic devices. Muñoz-Pinedo et al. [17] have designed a microfluidic chip with a filter structure so that a certain number of cells could be retained in a microchamber, while the well-defined height of the chamber (25 mm) could confine the cells within the focal plane of a confocal microscope. This technology was used to monitor and image cell death events in human leukemic U937 cells over time. Multiple apoptosis events such as loss of mitochondrial transmembrane potential, exposure of phosphatidylserine, membrane blebbing, and permeabilization of the cell membrane have been observed, in real time, in individual cells.

High-Throughput Apoptosis Assays

Moving apoptosis and toxicity testing to an earlier stage in pharmacological screening for drug candidates has become a major focus in drug discovery. In the case of cancer cells, the goal is to develop chemotherapeutics that pro-

mote differential cell death. This search is often a quest to screen for triggers of apoptosis in a high-throughput assay. In addition, investigation of the comparative effectiveness of antiviral and antimicrobial compounds and examination of the general cytoxicity of new drugs are also important reasons to analyze cell death in high-throughput assays. Microfluidic technology enables the sorting of cells on the basis of dynamic functional responses to stimuli, and the manipulation of smaller volumes and cells while performing more complex biological experiments. Recently, Valero et al. [18] have presented the design and fabrication of a microfluidic cell-trapping device for potential high-throughput analysis of apoptosis. This microfluidic cell-trapping device consists of two channels, which join together in a crossway. The cross-flow devices introduced in this study offer tools to characterize single cells in a format that allows integration of high-throughput techniques with unique assay functionality. The microfluidic silicon–glass chip enables the immobilization of cells and real-time monitoring of apoptosis processes. The tumor necrosis factor TNF-a, in combination with the cycloheximide-induced cell death dynamics of HL-60 cells, was studied using this chip.

Recently, Ye et al. [19] developed a microfluidic device for high throughput and high content evaluation of anti-cancer drugs with apoptosis inducing capabilities in hepatocellular carcinoma (HepG2) cells. The device consists of multiple drug gradient generators and parallel cell culture chambers, in which the processes of liquid dilution and diffusion, micro-scale cell culture, cell stimulation and cell labeling can be integrated into a single device. The simple assay provides multi-parametric measurements of plasma membrane permeability, nuclear size, mitochondrial trans-membrane potential and intracellular redox states (GSH and ROS) in anti-cancer drug-induced apoptosis of HepG2 cells. The established platform is able to rapidly extract the maximum information in tumor cells in response to various drugs varying in concentrations with minimal sample and less time, which is very useful for basic biomedical research and cancer treatment.

Cross References

► Intracellular Ca^{2+} Concentration Changes
► Cell Culture (2D and 3D) on Chip
► Single Cell Analysis in Microfluidics Devices

References

1. Manz A, Graber N, Widmer HM (1990) Miniaturized total chemical analysis systems: A novel concept for chemical sensing Sens Actuators B 1:244–248
2. Andersson H, van den Berg A (2003) Microfluidic devices for cellomics: A review. Sens Actuators B 92:315–325
3. Takayama S et al (2001) Laminar flows – Subcellular positioning of small molecules. Nature 411:1016–1016
4. Lucchetta EM, Lee JH, Fu LA, Patel NH, Ismagilov RF (2005) Dynamics of Drosophila embryonic patterning network perturbed in space and time using microfluidics. Nature 434:1134–1138
5. Lu H, Gaudet S, Schmidt MA, Jensen KF (2004) A microfabricated device for subcellular organelle sorting. Anal Chem 76:5705–5712
6. Buhlmann C, Valer M, Mueller O (2004) Combination of DNA laddering and annexin-V and caspase assays on one system – Multiple apoptosis parameters analysis with a microfluidic chip-based system. Tissue Antigens 64:392–392
7. Chan SDH, Luedke G, Valer M, Buhlmann C, Preckel T (2003) Cytometric analysis of protein expression and apoptosis in human primary cells with a novel microfluidic chip-based system. Cytometry 55(A):119–125
8. Qin JH et al (2005) Simultaneous and ultrarapid determination of reactive oxygen species and reduced glutathione in apoptotic leukemia cells by microchip electrophoresis. Electrophoresis 26:1155–1162
9. Kleparnik K, Horky M (2003) Detection of DNA fragmentation in a single apoptotic cardiomyocyte by electrophoresis on a microfluidic device. Electrophoresis 24:3778–3783
10. Sohn LL et al (2000) Capacitance cytometry: Measuring biological cells one by one. Proc Natl Acad Sci USA 97:10687–10690
11. Tabuchi M, Baba Y (2004) Self-contained on-chip cell culture and pretreatment system. J Proteome Res 3:871–877
12. Tamaki E et al (2002) Single-cell analysis by a scanning thermal lens microscope with a microchip: Direct monitoring of cytochrome c distribution during apoptosis process. Anal Chem 74:1560–1564
13. Wheeler AR et al (2003) Microfluidic device for single-cell analysis. Anal Chem 75:3581–3586
14. Yang MS, Li CW, Yang J (2002) Cell docking and on-chip monitoring of cellular reactions with a controlled concentration gradient on a microfluidic device. Anal Chem 74:3991–4001
15. Andersson H, van den Berg A (2004) Microtechnologies and nanotechnologies for single-cell analysis. Curr Opin Biotechnol 15:44–49
16. Hong JW, Studer V, Hang G, Anderson WF, Quake SR (2004) A nanoliter-scale nucleic acid processor with parallel architecture. Nat Biotechnol 22:435–439
17. Muñoz-Pinedo C, Green DR, van den Berg A (2005) Confocal restricted-height imaging of suspension cells (CRISC) in a PDMS microdevice during apoptosis. Lab Chip 5:628–633
18. Valero A et al (2005) Apoptotic cell death dynamics of HL60 cells studied using a microfluidic cell trap device. Lab Chip 5:49–55
19. Ye NN, Qin JH, Shi WW, Liu X, Lin BC (2007) Cell-based high content screening using an integrated microfluidic device. Lab Chip 7:1696–1704

Microfluidic Stem Cell Culture

► Microfluidics for Stem Cell Therapy

Microfluidic System Control Modules

► Temperature Control in Microfluidic Systems

Microfluidic Systems

Synonyms

Lab-on-a-Chip; Miniaturized total analysis system (μ-TAS); Microfluidic analysis system; Integrated microfluidic devices

Definition

Microfluidic systems manipulate or process tiny (10^{-9} to 10^{-18} l) volumes of fluids in channels with dimensions of tens to hundreds of micrometers. These systems, built using various *microfabrication techniques*, offer a number of advantages for chemical and biological analysis compared to standard laboratory instrumentation including low consumption of samples and reagents, low cost for mass production, short times for analysis, flexibility and dimensional precision, and separations and detections with high resolution and sensitivity. They can also probe physical phenomena and mechanisms that are not observable on the macroscopic scale. In addition, one key feature of these systems is the integration of different functional units for sampling, sample pre-treatment, sample transport, biochemical reactions, analyze separation, product isolation and detection in a microchannel network. *Microfluidic systems* enable serial processing and analysis, and furthermore, can accomplish massive parallelization through efficient miniaturization and multiplexing.

Cross References

- ► Control of Microfluidics
- ► DC-Dielectrophoresis Lab-on-a-Chip Devices
- ► Droplet Based Lab-on-a-Chip Devices
- ► Flow Cytometer Lab-on-Chip Devices
- ► Integrated Microfluidic Systems for Medical Diagnostics
- ► Lab-on-a-Chip (General Philosophy)
- ► Lab-on-a-Chip Devices for Biodefense Applications
- ► Lab-on-a-Chip Devices for Chemical Analysis
- ► Lab-on-a-Chip Devices for Immunoassay
- ► Lab-on-a-Chip Devices for Particle and Cell Separation
- ► Lab-on-a-Chip Devices for Protein Analysis
- ► Lab-on-a-Chip Devices for Sample Extraction
- ► Lab-on-a-Chip Devices for Separation Based Detection
- ► Microfabrication Techniques
- ► Microfluidic Bioreactors
- ► Lab-on-a-Chip Devices for Chemical Analysis
- ► Microfluidic Devices in Tissue Engineering
- ► Microfluidic Systems for Combinatorial Chemistry
- ► Microfluidic Systems for High-throughput Screening
- ► Microfluidic Systems in Space Science
- ► Microfluidics for Bio- and Chemical Reactions
- ► PCR Lab-on-a-Chip Devices

Microfluidic Systems Assembly

► Microfluidic Assembly

Microfluidic Systems for Combinatorial Chemistry

VÁCLAV TESAŘ
Department of Thermodynamics,
Institute of Thermomechanics, Academy of Sciences
of the Czech Republic, Prague, Czech Republic
tesar@it.cas.cz

Synonyms

High-throughput chemical testing

Definition

Microfluidic systems for combinatorial chemistry are used to discover and optimise the chemical reactions used to produce novel materials, in particular catalysts and drugs. They may also be used to optimise the reaction conditions. The systems are designed to perform a large number of reactions in parallel, each differing – usually only a little – in some variable (or variables), like presence of reagents, their mixing ratio, composition of catalysts, etc., while other variables are kept invariant. The test results, such as properties of the reaction products, are evaluated and stored in the form of combinatorial libraries. Information extracted from the libraries is used to identify optimum reaction conditions.

Overview

The advantage of using microfluidics [1, 16] for combinatorial testing is the small size of the reactors [5] and other devices and the consequent possibility of high throughput by running a very large number of test reactions simultaneously. Most often, the evaluation of the results is made by composition analysis of reaction products. The essential part of a typical microfluidic system for this purpose

is a ▶sampling unit, taking one sample at a time and delivering it to the analyser. This task is complicated by strict requirements of sample purity. With the no-moving-part fluidic valves for sample flow control, a complete separation of the cavities containing different samples is impossible and maintaining sample purity requires a special design of the fluidic circuits, with generation of protective cleansing and ▶guard flows.

Combinatorial chemistry has been and is likely to remain for the foreseeable future an indispensable approach to the discovery of new materials and also the optimisation of their properties. It is particularly important in areas like the development of catalysts [3] and enzymes, where empirical testing is practically the only path to further progress. Essentially, the tests are done by performing similar chemical reactions under conditions identical in all other aspects, with the exception of a single variable (or a small number of variables). These variables may be qualitative (absence of some reagents or components) or quantitative, such as the mixing ratio of the input reagents, or the times at which the reaction is quenched. The quantitative changes are preferably made in small steps. Sometimes more refined steps are then used in subsequent test series. The result of the tests is a set of reaction products differing in the value of a pursued performance criterion or criteria.

The results are stored in combinatorial libraries. They may be in material form, consisting of stored actual reaction products themselves – usually in small wells on a tray or, if they are volatile or perishable, in small closed vials. More convenient is, of course, the library consisting of just stored resultant data as a table in a computer memory. The great advantage of the material library is the availability at a later time for repeated analysis or analysis by a different method, perhaps evaluating a different property of the compounds than was done in the original investigation. Considerable theoretical effort has been devoted to the procedures of using the information stored in the combinatorial libraries for identifying the desirable optimum – the compound with the best properties [2]. The approaches to the search for the optimum are based on combinatorial strategies which originated in pharmaceutical research. They often use advanced mathematical methods, such as genetic algorithms – function optimisation based on the genetic principle of natural selection and survival of the fittest [15]. These work well on mixed (qualitative *and* quantitative variables) optimisation problems and are robust against locking to local peaks. The search for he optimum is often complicated by requirements to meet several, sometimes contradictory optimality criteria. There are traditionally at least two criteria – yield and selectivity – in the case of catalysts, and five ones known as ADMET properties (adsorption, distribution, metabolism, elimination and toxicology) in the case of medicinal drug candidates.

Basic Methodology

Tests

The reliability, usefulness and general quality of the information that may be extracted from a ▶combinatorial library are critically dependent on the number of entries, i. e., the number of compounds produced by the reactions, and on the accuracy of maintaining identical conditions for the reaction. The safest way of securing uniformity of the conditions is to perform the tests at the same time in parallel, perhaps in the same thermostat. Obviously, the spatial requirements make it desirable to perform the large number of combinatorial tests in reactors of a minimum size and with the minimum amounts of reactants and reaction products.

The chemical reactions themselves as used in combinatorial chemistry do not differ substantially from standard reactions elsewhere. The design of the reactors is mainly influenced, as usual, by the reaction conditions. There is a difference between processing proteins at room temperature and testing catalysts at very high pressure and temperature levels. The desirability of minimum size very early led to the use of microreactors. They may be easily stowed in a thermostat and thus kept under the same temperature. Their large surface-to-volume ratio brings the additional advantage of making possible an extremely close temperature control. Many tests producing durable compounds as the reaction products are made in small wells on the surface of a solid support tray. The reaction product may remain on the support, subsequently stored as a combinatorial library in material form. A more progressive approach is, in general, performing the reactions in microchannel reactors. Typically, they are used in arrays made by etching in silicon substrates stacked on top of one another together with another system of channels used for flow of thermostatic fluid.

Also the tests and analyses used for evaluation of the reaction products (or, perhaps, by-products) do not differ significantly from standard test procedures. The testing may be done off-line, when the reactions are finished. With organic samples on the tray, the test may consist of laser irradiation of the whole tray and detection of individual sample properties using their luminiscence. The library then consists of a photograph of the tray with various light intensities in the well locations. For the microfluidic approach it is typical to perform the tests on-line using samples brought from the reactors while the reaction is in progress. Also, there is a trend to

use very small instruments, commensurate with the small microreactors; some of the earliest gas chromatographs were developed in miniature size for this purpose. Another typically used method is mass spectrography. Due to the small analysed sample amounts, there is often a requirement of exceptional sensitivity of the test instruments. This makes them rather expensive. Because of the price there is almost always – provided the reaction is not too fast – just a single instrument performing the tests on all samples one after another even with a very large number of microreactors. After all, using a single analyser instrument brings the advantage of performing all tests under the same conditions and with the same instrument setting. If there are two or more instruments used, they more often than not are used to test different aspects of the samples. The ADMET properties of drugs traditionally required expensive and time-consuming tests on live animals. This is nowadays replaces by tests in microfluidic test devices using, for example, entrapped living human cells.

Sample Transfer

The use of a single test station places a particular emphasis on the transport of the sample to the analysis. There is still a strong tendency even in highly advanced systems to simply simulate the activity of a human operator. The characteristic feature of this approach is storing the reaction products in vials on a tray and transferring them to the analyser by a dedicated robot that opens the vials with its arm one by one by unscrewing their lids and then takes, perhaps by another arm, the sample from each vial, e. g. using a pipette, since the samples are usually liquid or dissolved solid, and carrying it to the analyser.

Even in tests performed in a more modern approach on-line, the traditional approach with mechanical motion, based on the idea of the robotic arm, still survives. Sample transfer to the analyser is still often made by a sampling unit with a moving probe [3]. In this case, the reactors are of the open exit type, with the reaction products issuing into the common space where there is the probe and its traversing gear. The probe is connected to the analyser by a flexible tube and moved from one reactor exit to another by a mechanical servomechanism positioner.

The approach typical for modern microfluidic systems, which is cheaper, faster and less prone to failure, is characterised by the reactor outputs directly connected to the analyser by means of a system of channels or cavities. Again, an essential part is the ►sampling unit between the reactors and the analyser. In its fluidic version, sometimes called a fluidic *selector or multiplexer*, it is an array of valves which open, one by one, the passage leading to the analyser. The sampling unit essentially performs spatiotemporal conversion according to Fig. 1.

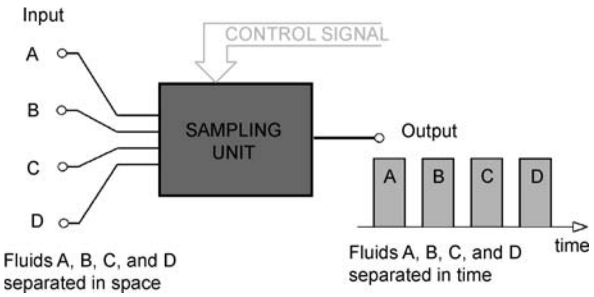

Microfluidic Systems for Combinatorial Chemistry, Figure 1 The task of the sampling unit in principle is a conversion of the spatial distribution of the samples (each available at a different location) into the temporal distribution admitted into the measurement device

There are a large number of possible variants. The fluid flows not selected at a particular instant of time may be halted (turning-down action), or dumped to a vent outlet (diverting action). The latter is preferable because it upsets less the basic requirement of sameness of all reactor conditions. The individual time steps need not be of the same duration, though they most often are. The sequence of the samples at the output is mostly of the simple repetitive periodic character, though the sequence may be varied according to some programme.

There are, nevertheless, features common to all sampling unit designs:

- The unit has several input terminals and a single output (an exception being aggregate designs with two or more outputs serving two or more analysers).
- The operation is controlled by an external signal (though the signal generator may be integrated into the unit – even to the degree of sharing some of its components).
- There is the essential requirement to eliminate any possibility of cross-contamination between the samples.

The sampling units consist of two essential constituent parts: the array of valves and the flow junction circuit. More conventional sampling units use mechanical valves – a single special multiposition scanning valve, or an array of common two-position on–off or diverting valves. In the mechanical on–off valves case, the junction circuits are rather trivial, because the mechanical closure ensures there is no communication between the cavities containing different samples. All valve outlets may be simply connected together. Nevertheless, the sections of the channels downstream from the valves should be as short as possible or eliminated altogether, because they contain different samples, and even though there is no flow in them, the escape

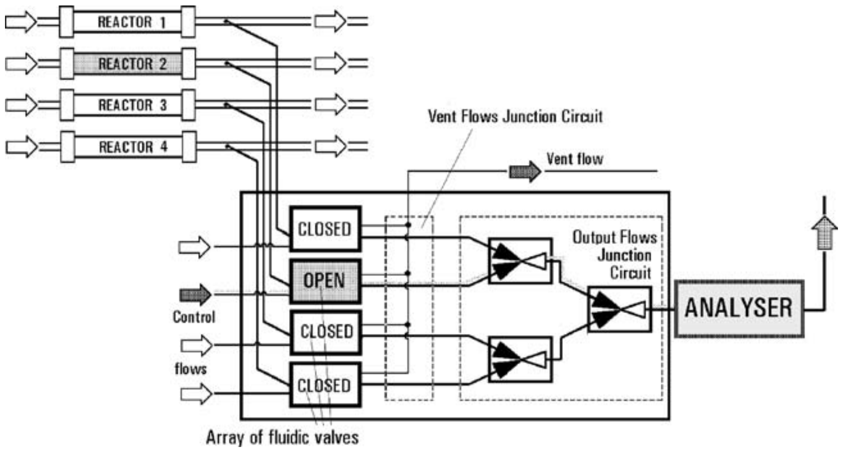

Microfluidic Systems for Combinatorial Chemistry, Figure 2 Schematic of the sampling unit consisting of an array of controlled valves and a junction circuit

from the *dead* cavities by some convection or diffusive mechanisms cannot be altogether excluded.

Pure Fluidic Layouts

Chemical reactors not infrequently operate at high temperature and/or with aggressive fluids. This makes the conditions for the valves rather difficult. The small size of microreactors, calling for correspondingly small valves, makes the demands even more formidable. Although microvalves with moving parts are available, they are expensive, not easy to manufacture and prone to breakage. In direct contrast to mechanofluidic solutions, especially at the small size end of the spectrum of dimensions, are the advantages offered by purely fluidic valves [4]. These are suitable for easy manufacturing by the methods used in microengineering, may be made from heat- and corrosion-resistant material and have an almost unlimited operating life, even under extreme conditions, because there is nothing to stick, jam, or break.

There are many variants, mainly dependent on the driving mechanism and operating conditions. In principle, the flow in the valves may be driven by electrokinetic phenomena, such as electro-osmosis. This, however, limits the use to a rather narrow group of fluids – to polar liquids. More widely applicable are valves in which the fluid flow is pressure assisted or pressure driven [16]. They can operate with any liquid or gas. Designs of these valves depend mainly on the operating Reynolds number. Figures 3 and 4 present what may be a typical example of a no-moving-part pure fluidic valve suitable for operation at the high end of the Reynolds numbers range as used in present-day microfluidics. This valve is of the jet-deflection diverter type employing the Coanda effect. The sample flow is accelerated in the main nozzle and directed as a jet towards the two collectors placed opposite to the nozzle. One of them is connected to the analyser output. The jet is deflected into it in the *open* state of the valve if there is no acting control signal. This state is presented in Fig. 3. The other collector is connected with the vent, into which the sample flow is dumped in the *closed* state by the action of the control flow. This state is shown in Fig. 4. In the schematic representations, nozzles are drawn as black (filled) triangles. Their cross-section decreases in the direction of the flow and this means the pressure energy of fluid is converted into kinetic energy. The white triangles in the schematics are diffusers. Their cross-section increases in the direction of flow. They are usually used in the collectors for re-converting the kinetic energy of captured fluid to pressure energy.

While many fluidic valves are symmetric, the example in Figs. 3 and 4 is a monostable asymmetric valve with the attachment wall guiding the sample fluid to the main collector. Figure 5 shows an example of the use of these valves in the sampling unit. Only four valves are shown in this example – of course, modern sampling units for combinatorial chemistry sometimes contain hundreds of reactors and therefore also hundreds of the flow-control valves. These valves are basically just a shaped constant-depth cavity, easily made by standard microengineering manufacturing techniques, such as etching. There is no expensive assembly of moving components, nothing to break or seize. They may well operate without maintenance at extremely high temperature. It is easy to make them even from refractory materials with high corrosion and abrasion resistance. As shown in Fig. 5, a large number of these

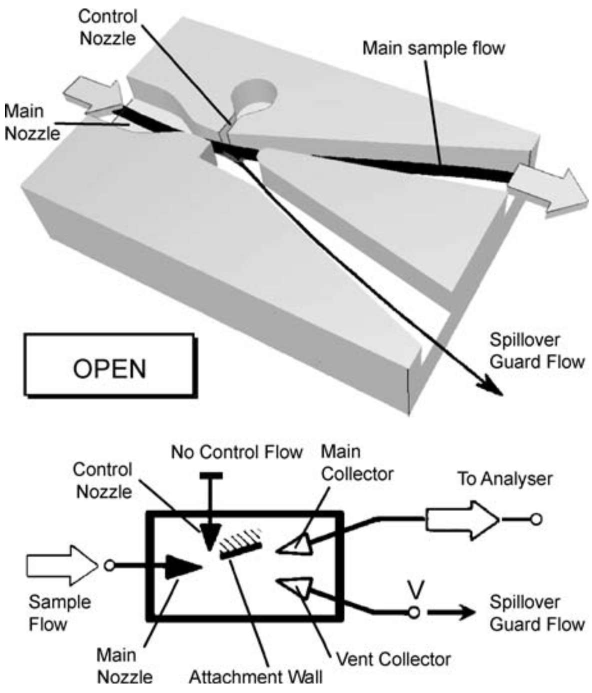

Microfluidic Systems for Combinatorial Chemistry, Figure 3 An example of a monostable diverter valve based on the Coanda attachment and its schematic representation. In this *open* state the jet of sample fluid leaving the main nozzle attaches to the attachment wall and is led, via the main collector, to the analyser. Some sample fluid, spilled over into the vent, forms the *guard* flow

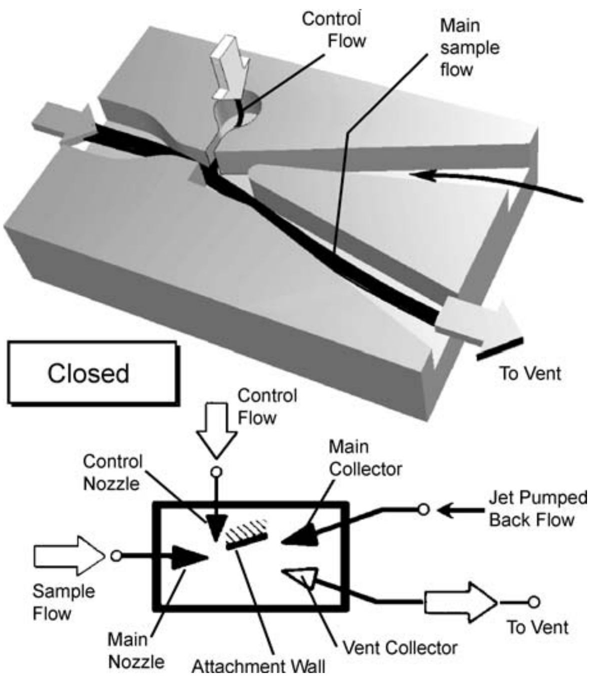

Microfluidic Systems for Combinatorial Chemistry, Figure 4 The valve from Fig. 3, the usual building block of the sampling unit, in the *closed* state with the jet of sample fluid diverted into the vent. The jet-pumping effect (entrainment into the jet) causes a return flow through the main collector

valves may be made in parallel on the same substrate plate. Since the shape of the valves is transferred optically, any shape, however complicated, can be manufactured with equal ease.

Guard Flows and Auxiliary Small Cleaning Flows

In mechanofluidic valves, flow is controlled by a mechanical component blocking the flow passage. In the absence of such components, fluidic valves do not secure directing all the sample fluid into just one of the two outlets. In principle, there is always a possibility of some of the supplied fluid overspilling into the other output terminal. On the other hand, some fluid may be sucked into the valve through the inactive terminal. This effect is caused by entrainment into the jet – the same phenomenon on which is based the operation of jet pumps.

The cavities through which the sample fluid passes in fluidic valves are open to the common vent outlets. All but one sample flows and all the control flows coming from the *closed* valves meet in the common vent cavities and freely mix there. This uncontrollable mixture must be prevented from coming into contact with the sample passing through the only *open* valve. The sample purity requirements call for another small auxiliary protective flow to be generated [13]. This *guard flow* is obtained by sacrificing a small amount from the sample flow and letting it to overspill into the vent, as shown in Fig. 3.

However, similar overspilling into the main or analyser collector in the *closed* state is unacceptable. The overspilled fluid would contaminate the tested sample coming through another, parallel valve. Here, however, it is the ►jet pumping effect (due to the entrainment into the jet) in the *closed* state, Fig. 4, which is useful. The channels and all other ►dead volumes downstream from the closed valves remain full of the earlier delivered samples, different from the sample which should come to the analyser at the particular instant of time. The small reverse flows back into all *closed* valves due to the jet-pumping effect remove the contaminating fluid from these volumes – and thus ensure high sample purity [13].

This capability to generate the *guard* flows and the cleaning reverse flows is another important advantage of purely fluidic sampling units. Of course, they mean a loss of a part of the sample flow. To keep the resultant total loss acceptable, these cleaning flows must be very small. To generate the *guard* flow in the *open* valve and the *cleaning reverse flow* in the *closed* state of the same valve is not easy – due

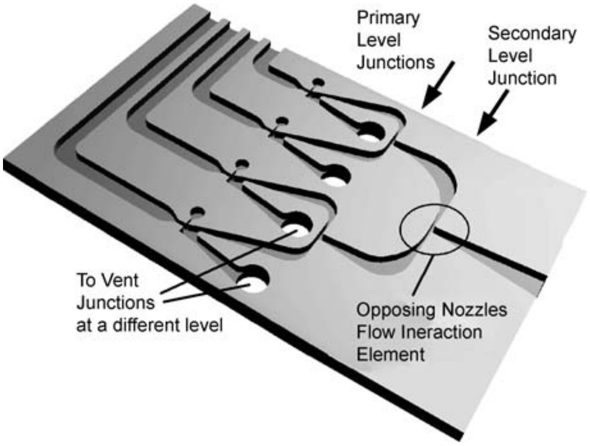

Microfluidic Systems for Combinatorial Chemistry, Figure 5 An example of a microfluidic integrated circuit using an array of the valves from Fig. 3, to define the sample flows into the analyser output

to the mutually opposite requirements. It requires a careful adjustment of the pressure conditions in the circuit.

Flow Junction Circuits: Flow-Enhancing and Flow-Inhibiting Elements

The task of getting the desired orientations of the small auxiliary flows may be made easier and less dependent on precise adjustments by proper shaping of the fluidic elements in the junctions of the valve exits [6]. This results in special flow junction circuits (Figs. 5 and 6). The fluidic elements there are also no-moving-part devices (sharing the advantages of easy manufacture and extreme reliability under adverse conditions). Their task is to generate a specified mutual interaction of the flows that meet in them. The effects are dependent upon dynamic effects in flowing fluids, which – similarly as in the valves – limits the use of these elements to higher Reynolds numbers, of the order of at least 10^2.

There are two basic arrangements of these flow interaction elements. Both consist of two nozzles and one collector and differ only in the angle at which the nozzle exits meet. If the angle is small, the jet generated in one nozzle induces flow in the other inlet by jet pumping action.

The very opposite effect is achieved if the angle at which in the nozzles meet is large, near and preferably equal to π. This is shown in Fig. 5 and schematically in Fig. 6. The flow admitted into one of the nozzles tends to generate a flow of opposite sign in the other inlet. This element is usefully connected to the output terminals of two adjacent diverter valves. The sample flow from the valve in its *open* state generates the desired backward flow through the output collector of the other valve, which is in the *closed* state. Of course, specific requirements of pressure and flow balancing in the junction circuit may call for devices in between, with intermediate values of the angle.

Complete Sampling Unit

A simple, four-valve design of a unit built from the elements described above is shown in the circuit diagram Fig. 6. There are flow reversing interaction elements connected to the main output terminals, leading to the analyser. Also flow-enhancing junction elements are used. They are connected to the vent outlets of the valves.

The outlets from each pair of interaction elements of the neighbouring valves are seen in Fig. 6 connected to the interaction elements of the secondary level junctions. A similar tree-like connection principle [6] at higher levels is applied to build sampling units for a larger number of sample flows. The disadvantage of this layout is the inevitable crossing of the valve outlet channels, requiring multi-layer design of the unit.

Such complete junction circuits – with both kinds of flow interaction elements – are, however, rare. At least one of the desirable small protective flows (and sometimes both) may be generated just by proper adjustment of the pressure levels making these elements superfluous. The example in Fig. 5 has the vents simply open to the common space below the substrate plate. This makes possible building the whole sampling unit on a single plate.

Low Re Microfluidic Sampling Units

A characteristic trend of present-day microfluidics [1], associated with the progress in micromachining, is decreasing size of devices. Together with the often high viscosity (due to the use of viscous biological fluids as used when working with enzymes, or due to high temperature of the gas in ►catalyst testing) and the small flow rates (demanded by the requirements of residence time in the reactor) this means that devices have to be designed for operation at low Reynolds number Re. This dimensionless characterisation quantity is the product of flow velocity and a characteristic length dimension (usually the main nozzle width) divided by viscosity. Reynolds number may be interpreted as the ratio of inertial forces to viscous forces acting on the fluid. If it is low, the dynamic effects even in the accelerated fluid downstream from a nozzle are weak and the flow is dominated by viscous damping. Inertial effects, however, are the very phenomena upon which the operation of fluidic valves and other elements as described above is based. Below about $Re = 40$, the flow issuing from a nozzle forms no jets at all. The fluid simply spreads equally in all available directions. In this ►subdynamic regime [4], the operation of the above described

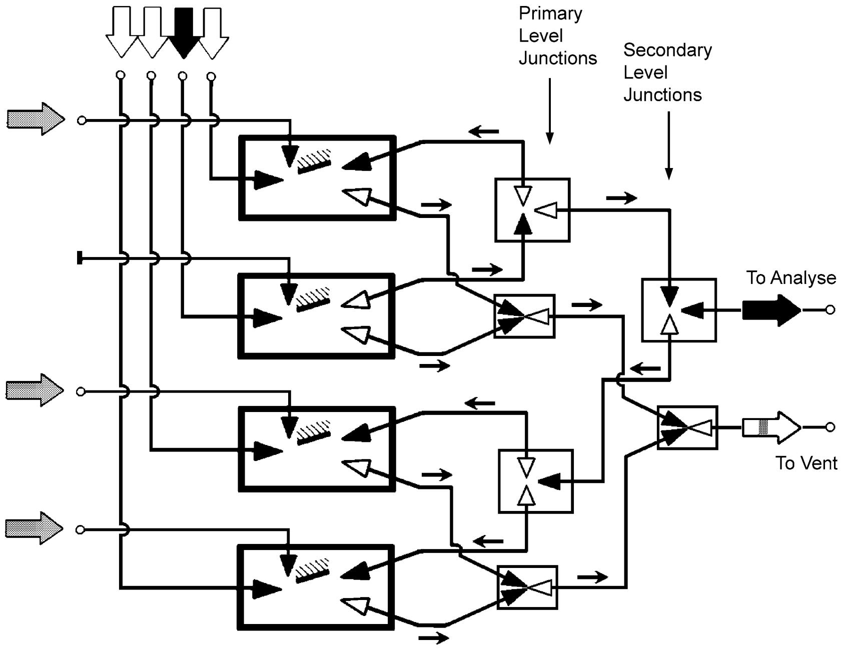

Microfluidic Systems for Combinatorial Chemistry, Figure 6 Schematic representation of the microfluidic circuit using an array of the valves from Fig. 3, to control the sample flows and the junction circuits. Basically similar to the layout from Fig. 5, this circuit has a more complicated way of leading the fluids into the vent. Arrows indicate the protective flows

M

jet-type fluidic elements ceases to be possible. In fact, the Coanda effect attachment to a wall employed in the valves from Figs. 3 and 4 is usually almost absent already below about $Re = 800$.

This means that with the present tendency towards smaller size, new operating principles are needed. *Pressure-driven* valves [16], instead of relying on the inertia of fluid accelerated in a nozzle, force the sample flow by pressure difference maintained between vent V and output terminal Y. Generating and maintaining this pressure difference may require addition of a pressure regulator to the chip. This is not a problem in the context of MEMS, of which microfluidic sampling units form a part, often made by etching directly on a silicon chip together with the electronic control circuits, which are thus readily available.

At low Re there is no point in using flow interaction elements. Instead, all the vent terminals V on the one hand and all the output terminals Y in the unit on the other hand are usually simply mutually connected. The driving pressure difference ΔP_{YV} is acting simultaneously in all the valves. It acts also in those valves which are in the *closed* state. To obtain in the *open* state the small desirable spillover *guard flow* into the vent terminal V requires just a careful adjustment of the driving pressure. In contrast, in the *closed* state, it is difficult to generate the desirable cleaning back flow, since it must overcome the pressure difference ΔP_{YV} acting in the opposing direction. Moreover, there is no hope of producing this reverse flow by the jet pumping effect of the sample flow, which at low Re is too slow and lacks the developed turbulent eddies on its outer boundary, which otherwise in the entrainment play an important role.

Jet Pumping by a Powerful Control Flow

One solution of this problem with the cleaning back flow circumvents the weak entrainment effect of the sample flow by using another available fluid flow [11, 12]. The only one present with the proper timing is the control flow. Standard valves for larger Re are fluidic amplifiers – the control flow, because of the amplification property, may be much less powerful than the controlled main sample flow. The ratio of the supply flow rate to the control flow rate is called the *flow gain*. As Re decreases, so does the values of the gain. In low Re microfluidics it is often necessary to use relatively powerful control flows. Fractional gain values of less than 1.00 are no exception. This does not cause difficulties because the absolute magnitudes of the handled fluid are almost negligibly small anyway. The valves do not operate as fluidic amplifiers, but this property is not used.

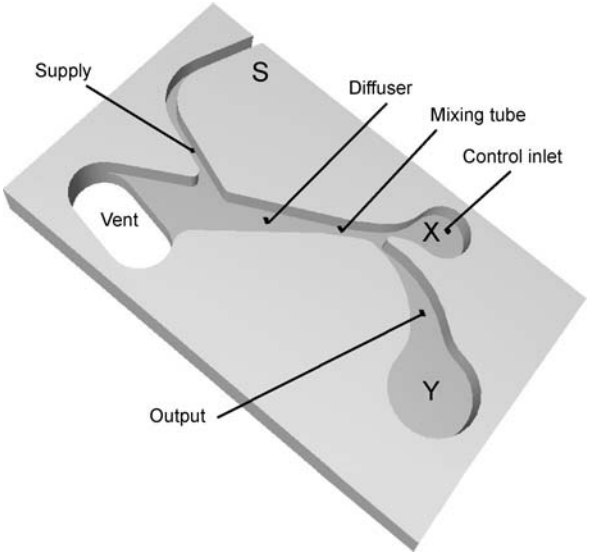

Microfluidic Systems for Combinatorial Chemistry, Figure 7 An example of a microfluidic valve for pressure-driven operation at very low Reynolds numbers. The flow deflection principle is combined with an integral jet pump used to generate the protective back flow in the absence of a significant entrainment into the low-Re sample flow

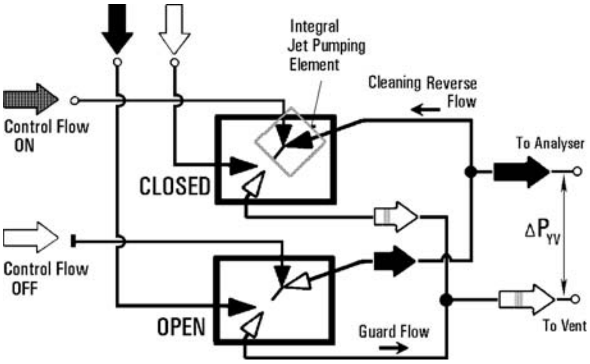

Microfluidic Systems for Combinatorial Chemistry, Figure 8 Schematic representation of a part of a sampling unit with two neighbour valves with the integral jet pumps. One of them is in the *closed* state and the other is in the *open* state. Flows are driven by the pressure difference ΔP_{YV}

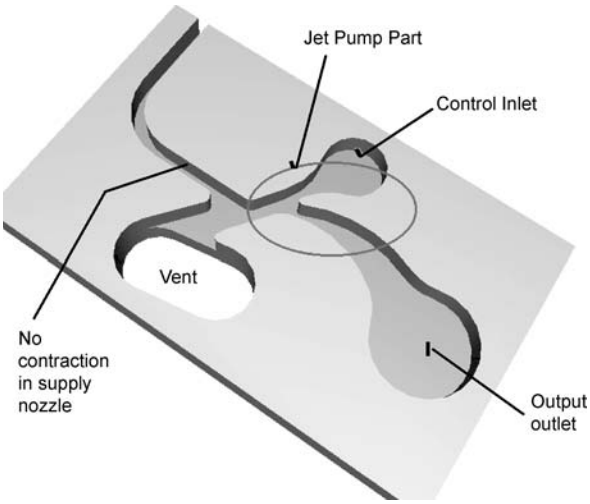

Microfluidic Systems for Combinatorial Chemistry, Figure 9 A valve with rudimental integral jet pump and more straight main flow into the output than in the version from Fig. 7

An example of a valve designed for these regimes is presented in Fig. 7. It operates with very low Re of the main, sample flow, but incorporates a classic, large Re fluidic element: a jet pump driven by the powerful control flow. This generates the desired cleaning return flow in the *closed* state. The exit from the jet pump is directed towards the vent. At the same time, the powerful jet pump exit flow sweeps the sample into the vent as well. The axes of the jet pump and vent collector are inclined with respect to the main (sample supply) nozzle axis. This is a useful feature, since jet momentum interaction studies indicate that optimum jet deflection is achieved with the control jet inclined to have a velocity component opposed to the supply flow velocity. The inclination is even more useful in the *open* valve state as well. The sample flow has to pass through the valve into the output terminal Y, and it is advantageous to have the path towards this terminal as straight as possible in order to operate with a lower value of the driving pressure drop ΔP_{YV}.

Application Example of a Low Re Sampling Unit

Designing a microfluidic valve based on this principle is a question of finding the best compromise between the conflicting requirements of the *closed* and the *open* states. An efficient layout of the jet pump part is shown in Fig. 7. This improves the achievable clearing backflow in the *closed* state, but because of the ensuing complexity of the sample path, this means a higher necessary driving pressure loss ΔP_{YV} in the *open* state to be maintained by the pressure regulator – and to be overcome by stronger *closed* state jet pumping. In the compromise example shown in Fig. 9, no attempt is made to have a really efficient geometry of the integral jet pump. Instead, there is no diffuser of the jet pump, which is reduced to only a very short collector. The idea is to make the flow path through the *open* state valve shorter and easier, with lower pressure loss ΔP_{YV} to be overcome in the *closed* state by the jet pumping. Typical for low-Re microfluidic devices is the missing cross-sectional area contraction in the supply (*main*) nozzle, as there is no point in trying to accelerate the sample flow there.

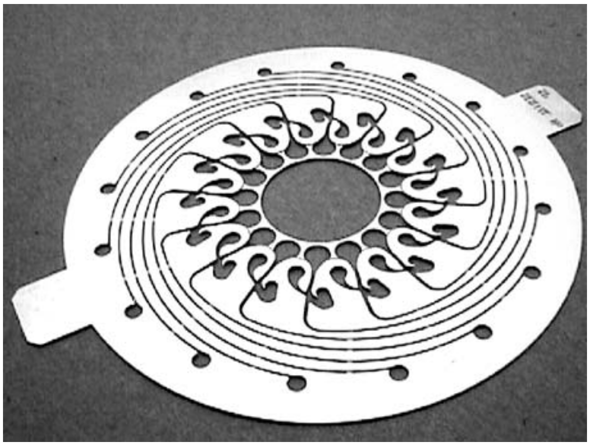

Microfluidic Systems for Combinatorial Chemistry, Figure 10 A sampling unit with 16 valves in the version from Fig. 9. This example of a microfluidic integrated circuit was made by etching in stainless steel [12]

The operation of the sampling unit using these valves may be followed in the circuit diagram of the basic valve pair shown in Fig. 8. To recognise the degenerated character of the jet pump the collector symbols in this schematic diagram are replaced by just a symbol of a short channel. There are no flow interaction fluidic elements in the valve exit junctions. As a consequence, maintaining the driving pressure difference ΔP_{YV} is easier – it has to be kept just between the final exit terminals of the complete sampling unit circuit. An early example of a sampling unit, with a mere 16 valves [12], is shown in Fig. 10. It was built for a research facility and used in combinatorial development of catalysts for the Fischer–Tropsch reaction (hydrogenation of carbon monoxide to ethanol). The reaction conditions are characterised by high temperature (400 °C) and high pressure (4 MPa). The valves are switched by essentially cold nitrogen control flows. The unit was made by etching in a 0.25 mm thin stainless steel foil, together with flow-equalising restrictors. To achieve a higher aspect ratio of the cavities, two-sided etching was used. This would unduly free the central parts of the foil held on long flexible strips. Structural integrity was obtained by braces (seen in Fig. 10) located downstream from the valves. The braces are etched only from one side so that there is a space above them allowing sample flow into the central cavity, which is connected to the analyser. The valves are not very small – the supply nozzle channel width is 340 μm – but they operate at very low Re of about 32 because of the small velocity and high gas viscosity. The sample fluid is *syngas* – fuel synthetisation gas, a mixture of hydrogen and carbon monoxide. Its pressure before reaching the valves drops to 0.5 MPa. Despite cooling of the valve plate by the nitrogen control flows, the kinematic viscosity of the sample gas – also due to its large contents of H_2 – is as high as 40×10^{-6} m^2/s. The nozzle exit bulk velocity is only about 3.8 m/s – in spite of the favourable fact of full reaction product flow being available for composition analysis. The ▶ guard flow magnitude is adjusted by the choice of driving pressure, kept by an external pressure regulator, so that 6% of the sample flow in the *open* state is spilled over into the vent. Only 3% return flow in the *closed* state is chosen (which still means sacrificing in total more than half of the available sample, from which the return flow is taken). The control flow rate needed to generate the jet-pumping effect is about 40 times the sample mass flow rate supplied into the valve (flow gain of 0.025, an absurdly small number from point of view of large-scale fluidics). With lower viscosity of the control nitrogen gas and a narrower, 0.27 mm wide, control nozzle to get higher control jet velocity (around 55 m/s), the Reynolds number of the control jet is around Re = 1000, just high enough to get some vortex entrainment effect.

Key Research Findings

In some areas, often as intellectual property of a particular manufacturer, extensive combinatorial libraries have already been accumulated. However, considering the huge, theoretically infinite number of possible combinations, there is still a vast space for continuing research. Substantial research activity has been directed to the development of the procedures for processing the library data so as to identify the optimum outcome. The mathematics of the search for the optimum is complicated by there being usually a number of optimality criteria. These results, however, are in principle more widely applicable and not particularly specific to the application of microfluidics.

The microscale aspect of combinatorial chemistry has already been proven to be the main road to follow. Earlier rather crude designs with the tested substances typically positioned in wells on a tray, with moving probes sequentially positioned into the wells, have generally been replaced by the approach using no-moving-part microfluidic circuits controlling the flow into an analyser. Successful designs of sampling units, consisting of these circuits, have been already developed [12] and are in everyday use, especially for developments in inorganic chemistry and non-biomedical areas of organic chemistry. Special fluid flow control valves have been developed for operation ensuring minimum cross-contamination between various samples.

Future Directions for Research

Continuing the already extensive past effort, more effective methods have to be developed for processing the

obtained combinatorial data so as to minimise the necessary extent of expensive tests to be performed. The continuing development of microfluidic devices for performing combinatorial testing has to meet more demanding requirements usually associated with processing biological material, such as proteins, and especially when handling living cells. The current microfluidic circuits, often pressure driven and using operating principles based on the inertial effects in flowing fluids, will become more difficult to develop as the smaller size and higher viscosity of biological samples will lead to lower values of flow Reynolds number. This may lead to the development of valves based on different, new flow control principles.

Cross References

- ► Amperometric Techniques
- ► Biosample Preparation Lab-on-a-Chip Devices
- ► Infrared Imaging and Mapping for Biosensors
- ► Biosensors Using Laser
- ► Biosensors Using Magnetics
- ► Biosensors Using Surface-Enhanced Raman Scattering
- ► Nanofluidics in Carbon Nanotubes
- ► Cell Culture (2D and 3D) on Chip
- ► Chromatographic Chip Devices
- ► Mass Spectroscopy
- ► Pyroelectric Flow Sensors
- ► Electro Chemo Luminescence (ECL)
- ► Detection Using Thermal Lensing
- ► Active Mixer
- ► Electrocapillary
- ► Electrochemical Techniques
- ► Gas Analyzers
- ► Gas Chromatography
- ► Lab-on-a-Chip Devices for Chemical Analysis
- ► Liquid Chromatography
- ► Mass Spectrometry
- ► Mass Spectrometry on Chip Devices
- ► Mechanical Nanosensors
- ► Lab-on-a-Chip Devices for Chemical Analysis
- ► Microfluidic Optical Devices
- ► Microfluidic Systems for High-Throughput Screening
- ► Microfluidics for Bio- and Chemical Reactions
- ► On-Chip Detection Using Optical Fibers

References

1. Zimmerman WBJ (ed) (2006) Microfluidics: History, Theory, and Aplications. CISM courses and lectures No 466. Springer-Verlag, Wien, New York
2. English LB (ed) (2002) Combinatorial Library Methods and Protocols. Methods in Molecular Biology, Vol 201. Humana Press, Totowa, New Jersey
3. Zech T, Hönicke D, Lohf A, Golbig K, Richter T (2000) Simultaneous Screening of Catalysts in Microchannels: Methodology and Experimental Setup. In: Ehrfeld W (ed) Microreaction Technology: Industrial Prospects. Springer, Berlin
4. Tesař V (2001) Microfluidic Valves for Flow Control at Low Reynolds Numbers. J Vis 4(1):51–60
5. Charpentier JC (2005) Process intensification by miniaturization. Chem Eng Technol 28(3):255
6. Tesař V (2006) Multi-Level Flow Branching. Proc of Conf Engineering Mechanics, Svratka, May 2006
7. Zhang H, Hoogenboom R, Meier MAR, Schubert US (2005) Combinatorial and High-Throughput Approaches in Polymer Science. Measurement Science and Technology 16:2003
8. Wilkin OM, et al (2002) High Throughput Testing of Catalysts for the Hydrogenation of Carbon Monoxide to Ethanol. In: Derouanne EG, et al (eds) Principles and Methods for Accelerated Catalyst Design and Testing. Kluwer Academic, Netherlands
9. Konrad E, et al (2000) Disposable Electrophoresis Chip for High Throughput Analysis of Biomlecules. In: Ehrfeld W (eds) Microreaction Technology: Industrial Prospects. Springer, Berlin
10. Pihl J, Karlsson M, Chiu DT (2005) Microfluidic Technologies in Drug Discovery. Drug Discovery Today 10(20):1337
11. Tesař V, Tippetts JRT, Allen RWK (2000) Fluid Multiplexer. GB Patent 0019767.9
12. Tesař V, Tippetts JR, Low YY, Allen RWK (2004) Development of a Microfluidic Unit for Sequencing Fluid Samples for Composition Analysis. Chem Eng Res Design 82(A6):708
13. Tesař V (2002) Sampling by Fluidics and Microfluidics. Acta Polytechnica - J Adv Eng 42(2):41
14. Ludwig A, et al (2005) MEMS Tools for Combinatorial Materials Processing and High-Throughput Characterization. Instr Sci Technol 16:111
15. Goldberg DE (1989) Genetic algorithms in search, optimization & machine language. Addison-Wesley, Reading
16. Tesař V (2007) Pressure-Driven Microfluidics. Artech House, Boston/London

Microfluidic Systems for High-Throughput Screening

JONGIN HONG, JENNIFER R. LUKES
Department of Chemistry, Imperial College London, London, UK
hong.jongin@gmail.com, jrlukes@seas.upenn.edu

Synonyms

Ultra high-throughput screening system; Cell-based high-throughput assays; Integrated nanoliter system; Miniaturized fluorescence-activated cell sorting devices; Microfluidics-based surface patterning tools

Definition

► High-throughput screening (HTS) is a method of scientific experimentation widely used in drug discovery and relevant to the fields of biology and chemistry. A screen

is a large experiment designed to test for the presence or absence of particular chemical compounds or biological markers. ►Microfluidic systems are well suited for HTS due to their small size, which allows massively parallel experimentation.

Overview

►Microfluidic systems manipulate or process tiny (10^{-9} to 10^{-18} liters) volumes of fluids in channels with dimensions of tens to hundreds of micrometers. These systems, built using various microfabrication techniques, offer a number of advantages for chemical and biological analysis compared to standard laboratory instrumentation including low consumption of samples and reagents, low cost for mass production, short times for analysis, flexibility and dimensional precision, and separations and detections with high resolution and sensitivity. They can also probe physical phenomena and mechanisms that are not observable on the macroscopic scale. In addition, one key feature of these systems is the integration of different functional units for sampling, sample pre-treatment, sample transport, biochemical reactions, analyte separation, product isolation and detection in a microchannel network. ►Microfluidic systems enable serial processing and analysis, and furthermore, can accomplish massive parallelization through efficient miniaturization and multiplexing.

During the past decade there has been tremendous development in microfluidic systems and related applications. Recent advances in genomics, proteomics and combinatorial chemistry have provided an opportunity for the pharmaceutical industry to accelerate the pace of drug discovery using high throughput techniques. The sequencing of the human genome has generated a number of new molecular targets with unknown function (*new targets*) as well as those with known function (*established targets*). Rapid progress in protein biochemistry and combinatorial chemistry has enabled the arrangement of chemical building blocks into all possible combinations, generating a library of millions of compounds. This increase in experimental complexity demands the organization, interpretation and utilization of experimental data in a methodical and rational manner. *High throughput screening (HTS)* technologies have emerged to meet this demand, and the need for reliability has motivated advances in throughput, accuracy and ease of use.

High throughput screening (HTS) is a method for scientific experimentation widely used in drug discovery and relevant to the fields of biology and chemistry. Modern *HTS* consists of robotics, data processing and control software, liquid handling devices and sensitive detectors to perform millions of biochemical, genetic or pharmacological tests on samples in parallel, allowing screening at significantly higher rates than convential serial screening methods. It facilitates the understanding of human biological pathways that require large experimental data sets to study genes, proteins and metabolites. The primary ways to save time and minimize usage of chemical compounds involve miniaturization of existing technologies like high-density wells on assay plates and nanoliter dispensing systems. However, current robotic systems have limitations in dispensing very small liquid volumes quickly and accurately. Rapid evaporation of the dispensed liquid and high cost are other challenges in modern *HTS* systems. Microfluidic systems are capable of resolving many of these issues and offer the possibility of technological breakthroughs in *HTS*. Herein, novel microfluidic technologies for developing *HTS* are reviewed.

Basic Methodology

Microfluidic Physics

Microfluidics is a large field involving numerous disciplines such as microfabrication, chemistry, biology, and physics. Reviewed below are basic concepts from microfluidic physics relevant to *HTS*. A fluid is a substance that deforms continuously when acted on by a shear stress of any magnitude.

In general, fluid velocity is given by the Navier-Stokes and continuity equations. For fluids that are Newtonian (shear stress linearly related to fluid shear rate) and incompressible, the Navier-Stokes equation is written as

$$\frac{\partial \boldsymbol{V}}{\partial t} + \boldsymbol{V} \cdot \nabla \boldsymbol{V} = \boldsymbol{B} - \frac{1}{\rho}\nabla p + \frac{\mu}{\rho}\nabla^2 \boldsymbol{V}\,, \tag{1}$$

and the continuity equation is written as

$$\nabla \cdot \boldsymbol{V} = 0\,, \tag{2}$$

where $\boldsymbol{V}$ is the velocity of the fluid flow, $\boldsymbol{B}$ is the body force per unit mass, p is pressure, ρ is the density of the fluid, and μ is the viscosity of the fluid. The small characteristic dimensions of microfluidic systems lead to high surface-to-volume ratios, small diffusion distances, and significant surface and interfacial tension effects. Nondimensionalization of Eq. (1) using the characteristic fluid velocity V_c and characteristic microfluidic channel dimension L leads to a dimensionless parameter called the Reynolds number:

$$\mathrm{Re} = \frac{\rho V_c L}{\mu}\,. \tag{3}$$

The Reynolds number represents the ratio of inertia forces to viscous forces acting on a fluid. For water as a working

M

fluid, assuming typical velocities and channel dimensions in the ranges $1\,\mu\text{m/s} - 1\,\text{cm/s}$ and $1 - 100\,\mu\text{m}$, respectively, the Reynolds numbers range between 10^{-6} and 1. These low values indicate that viscous forces overwhelm inertia forces in microfluidic systems, and that the fluid flow is laminar. For these low Reynolds numbers the nonlinear term of the Navier-Stokes equation can be neglected:

$$\frac{\partial \boldsymbol{V}}{\partial t} = \boldsymbol{B} - \frac{1}{\rho}\nabla p + \frac{\mu}{\rho}\nabla^2 \boldsymbol{V}. \quad (4)$$

For certain microfluidic applications, the characteristic time and body force scales may be such that the time derivative and/or body force terms in Eq. (4) are also negligible.

One of the consequences of laminar flow is that mixing in the fluid occurs primarily by diffusion. This is illustrated by the low values of the Péclet number

$$\text{Pe} = \frac{V_\text{c} L}{D}, \quad (5)$$

which is the important dimensionless parameter governing mixing and which represents the ratio of convective mass transport to diffusive mass transport. In Eq. (5), D represents the diffusion coefficient of a molecule in liquid. The characteristic time t for a molecule to diffuse a distance x is proportional to x^2/D. As an example, a protein with a molecular weight of 20 kDa ($1\,\text{Da} = 1.66 \times 10^{-27}\,\text{kg}$) and one hydration layer has a diffusion constant $D \sim 10^{-10}\,\text{m}^2/\text{s}$ at ambient temperature, and will diffuse a distance of $1\,\mu\text{m}$ in approximately 10 ms. To control mixing, a microfluidic system should be designed with these diffusion times in mind. For instance, fast mixing is required for chemical reactions, so the characteristic dimensions of the microchannels should be made small to enable diffusion to occur quickly. In separation processes, mixing should be suppressed, so the dimensions should be made large enough to prevent significant diffusion on the time scale of the experiment.

Thus far, the key dimensionless parameters useful in the design of microfluidic systems for *miscible* fluids have been discussed. For *immiscible* fluids, surface tension σ also becomes important; this parameter affects the dynamics of the free surface. This gives rise to two additional dimensionless quantities: the capillary number and the Weber number. The capillary number represents the ratio of viscous forces to the surface tension forces acting across an interface between a liquid and a gas or between two immiscible liquids. It is defined as

$$\text{Ca} = \frac{\mu V_\text{c}}{\sigma}. \quad (6)$$

The Weber number, which is the ratio of inertial to surface tension forces, is also useful for analyzing fluid flows where there is an interface between two different fluids. It is defined as

$$\text{We} = \frac{\rho V_\text{c}^2 L}{\sigma}. \quad (7)$$

In multiphase microfluidic systems, the complicated interplay between interfacial, viscous and inertial forces corresponds to phase distributions and flow patterns. At low velocities and small channel sizes, interfacial forces dominate over inertial and viscous forces. However, at very high flow rates or in the presence of very large accelerations, inertial forces can affect the dynamic behavior of multiphase flows. Thus, both the capillary and Weber numbers are useful for predicting multiphase flow behavior in microchannel networks and designing multiphase microsystems. Most multiphase microfluidic systems take advantage of flow regimes in which the two phases are segregated (called segmented flows). The flow regime depends on geometry, flow rates and instabilities that occur at the interface between two immiscible liquids. Segmented flows in microfluidic networks enable us to overcome transport limitations in single-phase microflows with high throughput rates. Further details of microfluidic physics are reviewed in [1].

The control of fluids in microfluidic systems can be accomplished using active pumping, passive forces or electrical forces. Active control of fluid flow is often achieved simply by direct connection to external pressure and/or vacuum sources, for example programmable syringe pumps or peristaltic pumps. Micropumps due to thermopneumatic, electrostatic and piezoelectric actuation have also been used for manipulating and transporting fluids within a microfluidic network. In addition, compact disc-type systems based on centrifuge platforms can provide a wide range of flow rates depending on disc geometry, rotational rate and fluid properties. Alternatively, passive forces such as capillary forces provide a means to create a pressure difference in small conduits. If the microchannel has a rectangular cross section of height d and width w, then the resulting capillary pressure P_c of a liquid-air meniscus is expressed as

$$P_\text{c} = -\gamma \left(\frac{\cos\theta_b + \cos\theta_t}{d} + \frac{\cos\theta_l + \cos\theta_r}{w} \right), \quad (8)$$

where γ is the surface tension of the liquid, $\theta_{b,t,l,r}$ are the contact angles of the liquid on bottom, top, left and right sides of the microchannel, respectively. The wettable ($\theta < 90°$) wall induces a negative pressure in front of the liquid and then draws the liquid into the channel. Thus,

tailoring interfacial energies can enable capillary-driven pumping and may remove the need for other peripherals to transport fluids. Recently, capillary forces have been used for processing surfaces and miniaturizing assays.

Electrokinetic techniques are another popular method for manipulating fluids non-mechanically in microfluidic systems. When exposed to electrolyte, the channel wall tends to develop surface charge, which attracts oppositely charged counter-ions and repels similarly charged co-ions. The resulting electric double layer (EDL) screens the surface charge over a characteristic length called the Debye length λ_D. When an external electric field E is applied, the fluid in this charged layer acquires a momentum which is then transmitted to adjacent layers of fluid through the effect of viscosity. In microfluidic systems, this momentum is enough to cause bulk fluid flow in a phenomenon known as electroosmotic flow (EOF). The bulk EOF velocity is proportional to the applied electric field and the electro-osmotic mobility μ_{EOF}.

$$u_{\mathrm{EOF}} = \mu_{\mathrm{EOF}} E \tag{9}$$

The electro-osmotic mobility and bulk EOF velocity are sensitive to the physicochemical properties of the solution and channel walls. Because electroosmosis is a surface-driven phenomenon, EOF fluid transport is characterized by *plug flow*. Except in the thin EDL, there is no shear in the fluid flow and so the velocity profile is flat. At the same time, the individual species charged permanently or spontaneously in the bulk fluid also undergo electric forces. These effects are classified as either electrophoresis (EP) or dielectrophoresis (DEP). Whereas EP arises from the interaction of a fixed charge and an electric field, DEP results from the interaction of an induced charge and the spatial or temporal gradient of the electric field. In EP, direct current (DC) or low-frequency fields, usually homogeneous, are applied. On the other hand, in DEP, alternating current (AC) fields over a wide range of frequencies are used.

Drug Discovery and Current Novel HTS

Drug discovery entails a series of serial and/or parallel processes including candidate identification, synthesis, characterization, screening and assays for therapeutic efficacy. These processes are shown in Fig. 1. First, both natural products and chemical libraries are screened to determine which compounds bind to a particular target protein or inhibit a particular enzymatic reaction. The successful compounds (called *hits*) that exceed a certain threshold value in a given assay are progressed into *leads* by more complicated assessments of chemical integrity, accessibility, functional behavior, structure-activity-relationships (SAR) as well as bio-physicochemcal and absorption, distribution, metabolism and excretion (ADME) properties. The lead series that demonstrate activity and selectivity in the secondary screens are tested in progressively more complex systems from cells to whole animals before reaching clinical trials. Therefore, robust and fast methods are needed to vet an extremely large number of candidates and to minimize the attrition of chemical entities in the costly clinical phases of drug discovery. Based on these demands, *HTS* technologies including small-molecule library design and assembly, robotics, assay development and data handling have developed since the 1980s. Presently, libraries of millions of compounds are screened routinely with single compounds of high purity in 384- and 1536-well formats. Fully automated robotic systems improve screening data quality. Figure 2 shows the configuration of the integrated Ultra-High Throughput Screening System (UHTSS™ platform. This platform integrates several microfluidic dispensing devices into appropriate wells of the 3456-well NanoWell™ assay plates (Aurora BioSciences, San Diego, CA, USA). One primary purpose of this system is the automated screening of over 100,000 compounds and 2400 re-tests per day in a miniaturized assay format. However, robotic *HTS* has been faced with several challenges, including high cost of the technology, poor reliability of data, standardization of data types, rapid and accurate dispensing of very small volumes, and quick evaporation of the dispensed liquid.

Alternatively, microchip technologies offer other platforms for *HTS* such as microarrays and microfluidic devices. Microarrays allow the simultaneous analysis of thousands of parameters within a single experiment and for this reason have become crucial tools in drug discovery and life sciences research. They consist of immobilized biomolecules spatially addressed on planar surfaces, microchannels or microwells, or an array of beads immobilized with different biomolecules. Biomolecules commonly immobilized on microarrays include oligonucleotides, polymerase chain reaction (PCR) products, proteins, lipids, peptides and carbohydrates. Currently, in situ synthesized microarrays can be purchased or they can be custom fabricated in the laboratory. During the past few years, chemical compound microarrays with different surface chemistries and activation strategies have emerged in drug screening and discovery. By contrast, microfluidic devices can perform screening assays in a continuous flow that allows serial processing and analysis on a single chip. They require a series of generic components for introducing reagents and samples, moving the fluids within a microchannel network, combining and mixing them, and various other functional units such as valves, pumps, detectors, sorters and purifiers. So far this field

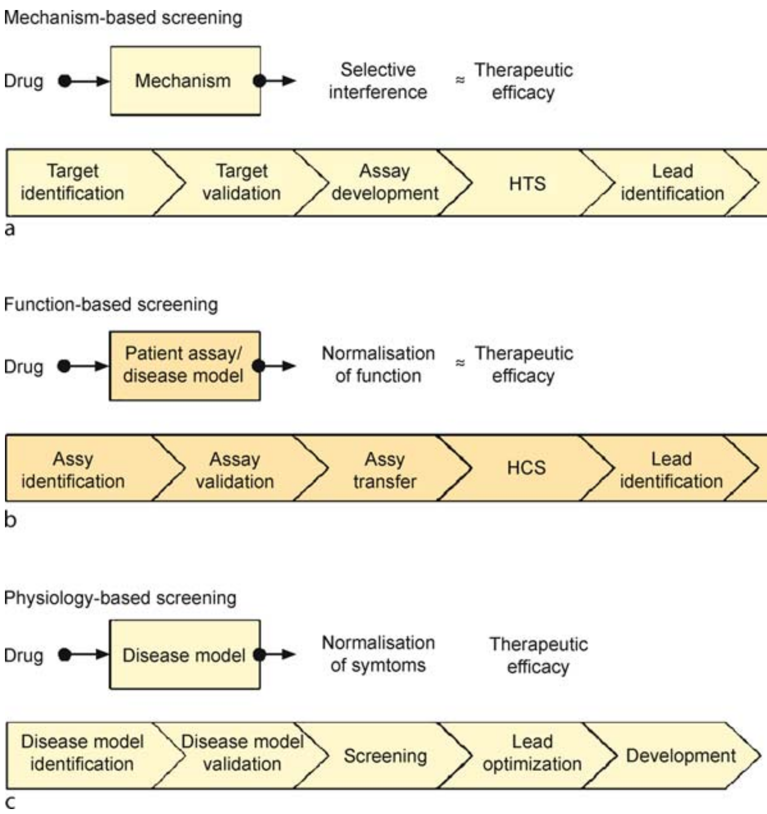

Microfluidic Systems for High-Throughput Screening, Figure 1 Drug discovery approaches: (**a**) mechanism-based drug discovery seeking to produce a therapeutic effect by targeting a specific mechanism, (**b**) function-based drug discovery seeking to induce a therapeutic effect by normalizing a disease-specific functional abnormality, and (**c**) physiology-based drug discovery seeking to induce a therapeutic effect by reducing disease-specific symptoms or physiological changes [11]

has focused on demonstrating concepts for these components and integrating them into a single chip. The majority of microfluidic devices are simple planar microfluidic chips fabricated on substrates such as glass, silicon or polymers using microfabrication techniques. Custom-made planar microfluidic chips and entire measuring systems have been launched commercially (Agilent Technologies, Evotec Technologies, Caliper Life Sciences, Fluidigm, Gyros). Recently, because of the several advantages of microfluidic technology mentioned above, the pharmaceutical industry has begun investing substantially in this technology as a way to expand screening capacity at several stages in drug discovery. The unique physical behavior of fluids within a microfluidic network can give insight into new ways to resolve the current challenges of HTS and to revolutionize all stages of drug discovery.

The testing of analyte on living cells is also an important part of high throughput drug discovery. Microfluidic devices enable manipulation of cells, maintentance of cellular environments close to the physiological conditions typically found in biological systems, simultaneous characterization of cells under comparable conditions, and subsequent analysis. A fundamental paradigm shift in drug discovery, coined *high-content screening* by Cellomics, has motivated the development of cell-based high throughput assays for simultaneous analysis of individual cells and subcellular processes under complex physiological parameters. Below, recent progress in novel microfluidic devices for cell treatment, especially with high throughput rates, is discussed. Additionally, recent progress in microarraying strategies based on microfluidics will be discussed, but the current status and challenges are beyond the scope of this entry. Further information in this area can be found in [2].

Key Research Findings

Novel Surface Patterning

Inkjet and other non-contact droplet formation technologies are able to dispense nanoliter-sized drops onto surfaces, but they offer no control once the liquid has left the confinement of the ejection nozzle and, consequently, suffer from problematic drying and spreading of the ink on

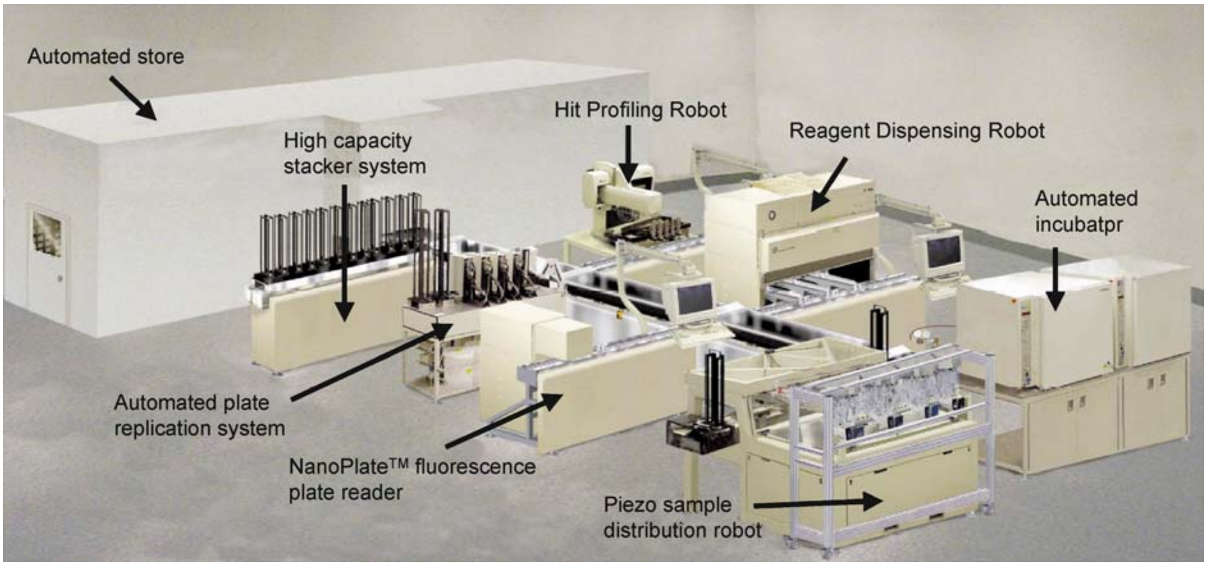

Microfluidic Systems for High-Throughput Screening, Figure 2 A schematic visualization of the UHTSS™ configuration (Aurora Biosciences, San Diego, CA, USA): a working compound solution store, an automated plate replication system, microfluidic dispensing systems, high density 3456-well NanoWell™ assay plates, automated incubators and a high-performance fluorescence plate-reader [12]

the surface. Patterns can also be formed using pins or pen-like devices loaded with the appropriate solute and solvent to draw individual spots or lines. However, the friction and resulting mechanical wear between the pen and the substrate during drawing have limited the resolution of writing techniques to a few hundreds of micrometers. The extension of the pen concept to the micro- and nano-scale using cantilevers is dip-pen nanolithography (DPN) based on atomic force microscope (AFM) technologies. In the DPN process, molecular inks coated on an AFM tip are transferred to a substrate while the tip is held or laterally moved along a surface as programmed. Feature sizes less than 15 nm can be routinely patterned by molecular self-assembly of the ink on the substrate. However, the necessity of molecular-ink replenishment in the DPN technique leads to limited throughput and inevitable realignment during the patterning process.

In the viewpoint of dispensing technologies, Espinosa and co-workers [3] have demonstrated a novel microfluidic AFM probe called the *Nanofountain Probe (NFP)* with a sub-100 nm patterning capability. It consists of a hollow tip, integrated microchannels and on-chip reservoir (Fig. 3a). When an ink solution is fed into the reservoir, it is driven by capillary action through the microchannel to the tip to form a liquid-air interface around the tip core. Molecules are transferred by diffusion from the interface to a substrate and a water meniscus is formed by capillary condensation. Although the NFP is the state-of-the-art patterning technology, massively parallel probe arrays and integration of multiple reservoirs over large areas with multiple inks still are key challenges for high throughput screening applications. Henderson and co-workers (Bioforce Nanoscience Inc., Ames, IA, USA) have commercialized multiple microcantilevers with open microfluidic channels constantly delivering a supply of liquid to be transferred onto the surface for multiplexed biomolecular arrays. As illustrated in Fig. 3b, fluids from the reservoir, down the channel, to the end of the cantilever where the channel narrows to a tiny gap. Upon contact with the surface, a small volume of liquid held in the gap by surface tension is directly transferred to the surface in an event typically requiring less than 1 ms. Capillary fluid flow down the channel instantly replenishes the volume at the gap, and the device is then ready to write the next feature. Recently, they launched the Nano eNabler™ system, which prints proteins and other biological and non-biological materials onto silicon and other surfaces with spot sizes from 20 μm to 1 μm.

Delamarche and co-workers [4] proposed a new format for surface patterning and biological assays using capillary forces. Fluids fill the microstructure of microfluidic networks (μFNs) due to the capillary pressures generated by the small dimensions of the channels and the hydrophilicity of their walls. One example for immunoassays using a μFN is shown in Fig. 4a. A μFN patterns a series of antigens as narrow stripes onto a planar substrate. After a blocking step with bovine serum albumin (BSA), the antigens in each line may be recognized

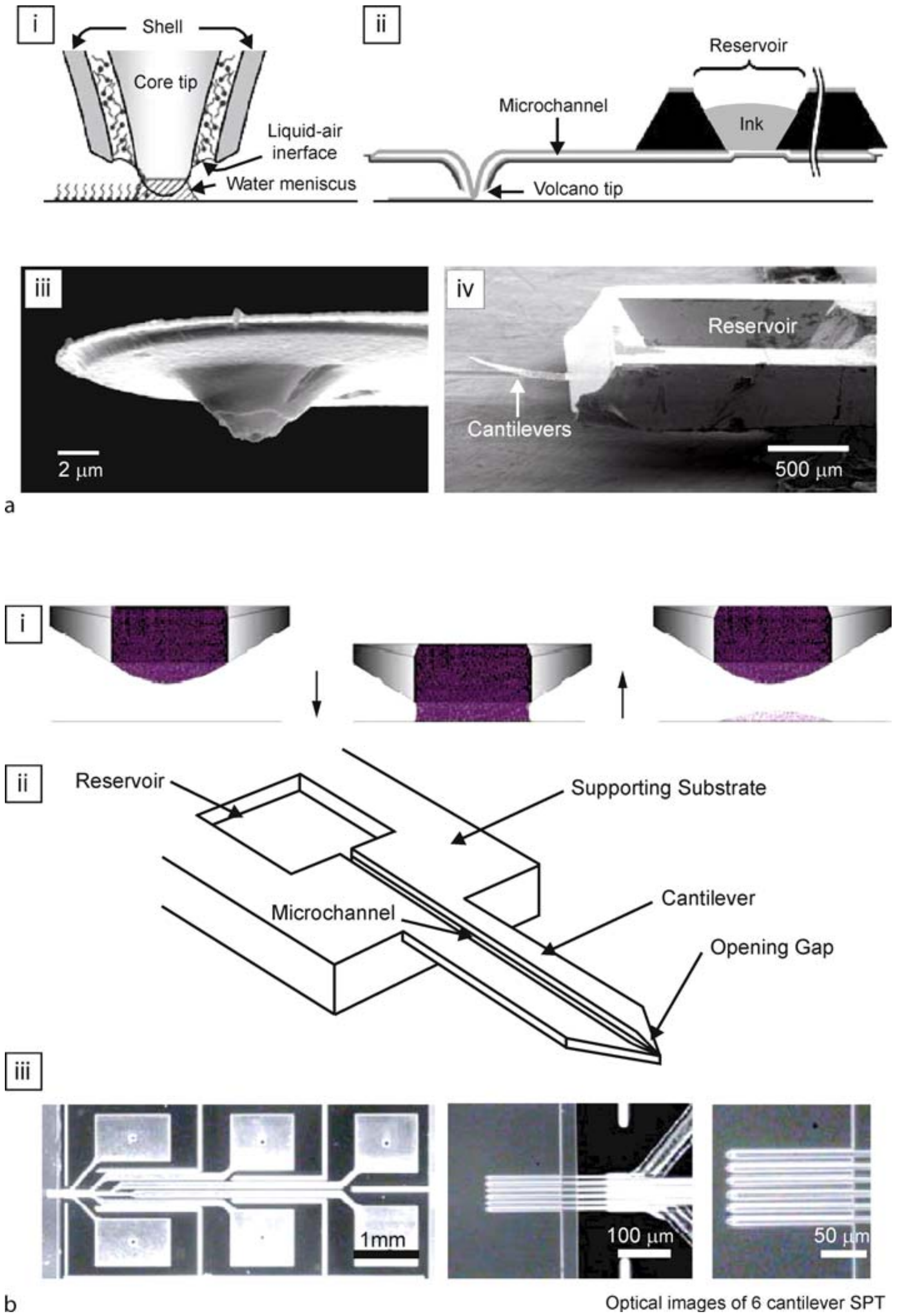

Microfluidic Systems for High-Throughput Screening, Figure 3 Novel microfluidic surface patterning: (**a**) nanofoundation probe (NFP) (i. writing mechanism of the NFP device, a molecular ink fed from the reservoir forms a liquid-air interface at the annular aperture of the volcano tip. Molecules are transferred by diffusion from the interface to a substrate and a water meniscus is formed by capillary condensation; ii. ink from the reservoir is delivered to the dispensing tip via capillary force; iii., iv. SEM images of a dispensing tip and an on-chip reservoir, respectively [3]) and (**b**) multiple microcantilever array with open microfluidic channels (i. surface patterning mechanism; ii. a schematic diagram of a microcantilever with a microfluidic channel and a reservoir; iii. optical images of 6 microcantilever array.) Courtesy of [13]

by specific analytes from a sample solution also guided over the substrate with a second μFN. This procedure is called a *micromosaic immunoassay (μMIA)* because it places a series of ligands and analytes along micrometer-

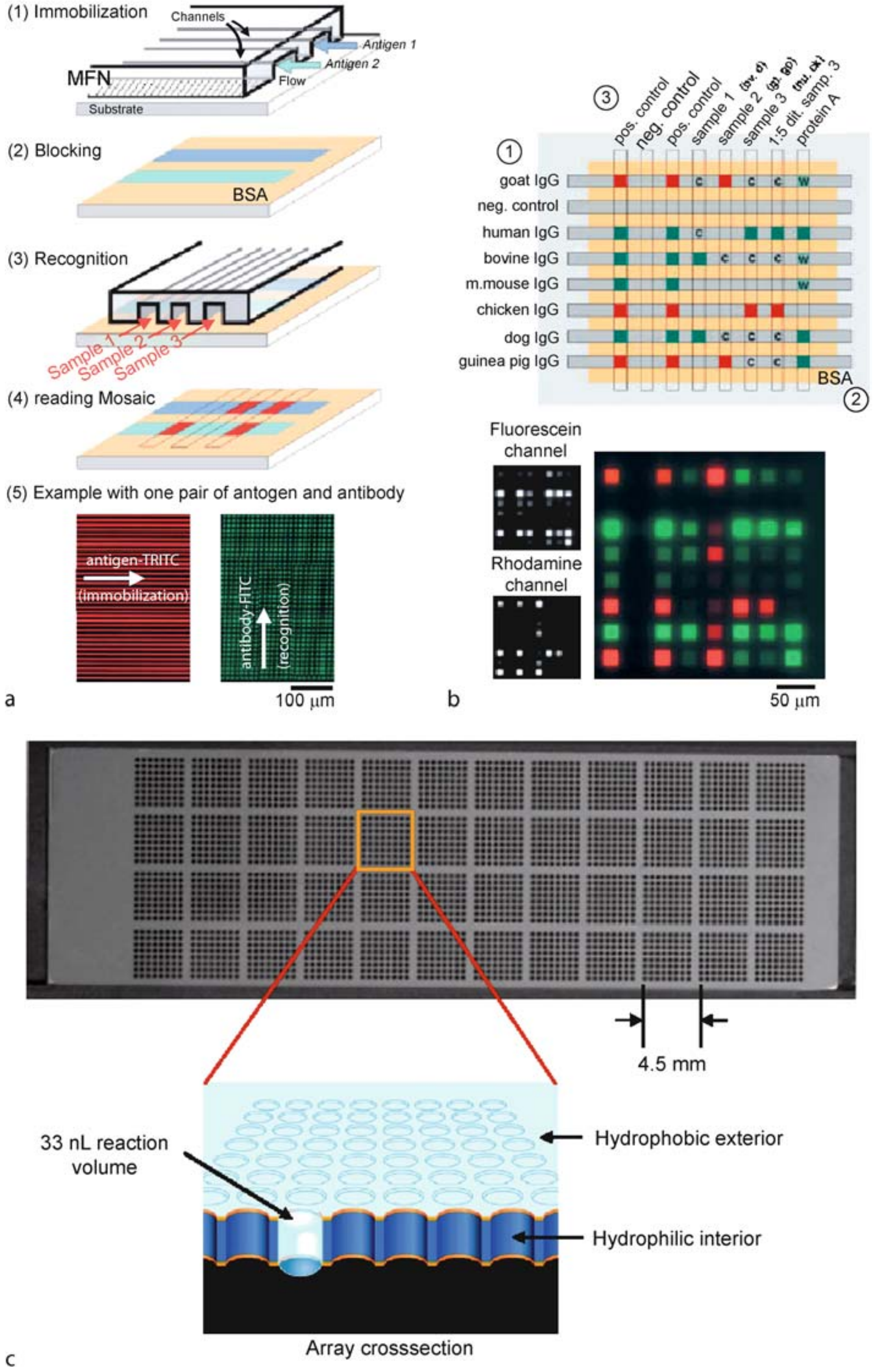

Microfluidic Systems for High-Throughput Screening, Figure 4 A new concept of surface pattering based on a microfluidic network (μFN): (**a**) principle of *micromosaic immunoassay* to localize surface-binding events taking place in the independent microchannels of a μFN, (**b**) combinatorial micromosaic immunoassay used to interrogate the binding between surface-immobilized receptors with fluorescently labeled detection antibodies, which can be done in less than 20 min [4] and (**c**) high-density array of through-hole with hydrophobic exterior and hydrophilic interior. Courtesy of [14]

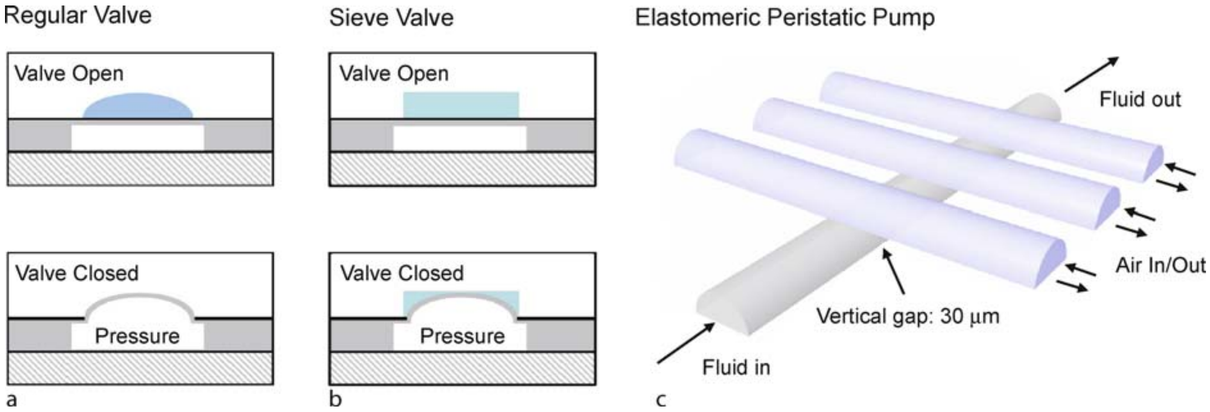

Microfluidic Systems for High-Throughput Screening, Figure 5 Schematic diagrams of the operational mechanisms of (**a**) a regular valve having a round-profile fluidic channel, (**b**) a sieve valve having a square-profiled fluidic channel and (**c**) an elastomeric peristaltic pump from three valves arranged on a single channel [6]

wide intersecting lines, thus providing a mosaic of signals from cross-reacted zones. Figure 4b shows the feasibility of µMIAs for high throughput screening. Using n and m microchannels for a µMIA yields $n \times m$ binding sites but only requires $n + m$ pipetting steps. Delamarche et al. [4] claim that the µMIA would necessitate ~10 times less time, ~100 times less volume of samples and reagents, and ~1000 times less area per site than an assay done using a 1536-well microtiter plate. Recently, µMIAs and similar approaches have been developed to screen for biological analytes in combinatorial fashion with various detection schemes. In addition, thermoplastic microtiter plates with high-density wells, which are commonly used for conventional high-throughput screening systems, can be replaced with a novel approach based on nanoliter through-hole arrays [BioTrove Inc., Woburn, MA, USA] (Fig. 4c). A series of vapor and liquid deposition steps covalently attaches a polyethylene glycol (PEG) hydrophilic layer amine-coupled to the interior surface of each through-hole, and a hydrophobic fluoroalkyl layer to the exterior surface of the platen. Capillary pressure draws fluids into microchannels and surface tension holds the liquids in place, isolated from neighboring channels. The differential hydrophilic-hydrophobic coating facilitates precise loading and isolated retention of fluid in each channel. This platform can reduce capital cost of a thermal cycler and a plate reader, technician labor and expense, reagent consumption and time compared to those of microwell-based *HTS* systems.

Novel Microfluidic Devices

One key feature of microfluidic systems is the integration of different functional units for sampling, sample pre-treatment, sample transport, biochemical reactions, analyte separation, product isolation and analysis in a continuous-flow manner. The technology has centered on proof-of-concept studies for these components and it is still maturing. Two particular contributions have accelerated the development of an integrated microfluidic system. One is soft lithography in poly(dimethysiloxane) (PDMS) as a method for fabricating prototype devices [5]. This allows quicker, less expensive fabrication of prototype devices that test new ideas as compared to devices made using silicon technology. The other is a simple method for fabricating pneumatically actuated valves, mixers and pumps by multilayer soft lithography [6]. Monolithic elastomer actuators restrict fluid flow in a channel by pressurization of an adjacent channel under pressure. Figure 5 shows schematic operation mechanisms of monolithic elastomer valves and pumps. When pressure is introduced into the control channels, the elastic membranes expand into the fluidic channel. In a regular valve having a round-profiled fluidic channel, the fluidic channel is completely sealed because of the perfect fit between the expanded membrane and the fluidic channel. In a sieve valve having a square-profiled fluidic channel, the fluidic channel is partially closed and so fluid flow is allowed along the edges. A peristaltic pump with three elastomer valves works by applying air pressure sequentially in each air channel. These elastomer actuators have enabled the design and realization of integrated microfluidic systems for high throughput processing of increasingly smaller volumes with higher degrees of parallelization.

Quake and co-workers [7] have developed high-density microfluidic chips that contain plumbing networks with thousands of micromechanical valves and hundreds of individually addressable chambers. They demonstrated

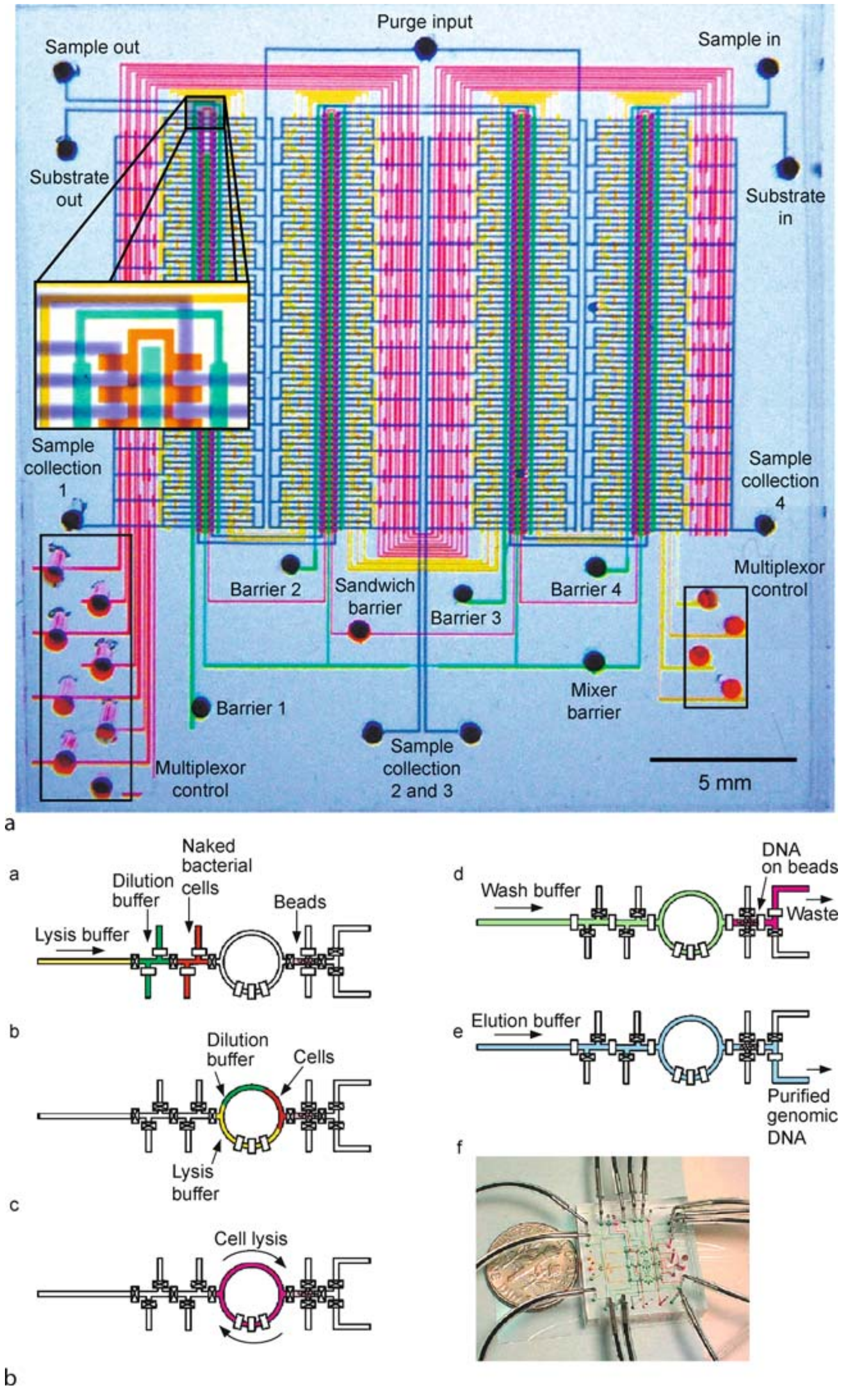

Microfluidic Systems for High-Throughput Screening, Figure 6 Integrated nanoliter systems: (**a**) optical micrograph of a chip for parallelized high-throughput screening of fluorescence-based single-cell assays and (**b**) an integrated processor for DNA purification from cell culture to DNA recovery scheme [7]

a microfluidic system for highly parallel high-throughput screening which integrated 2056 valves with 256 compartments containing bacterial cells expressing an enzyme of interest that could be combined on a pairwise basis with 256 other compartments containing a fluorogenic substrate used to assay for a desired activity (Fig. 6a). In following

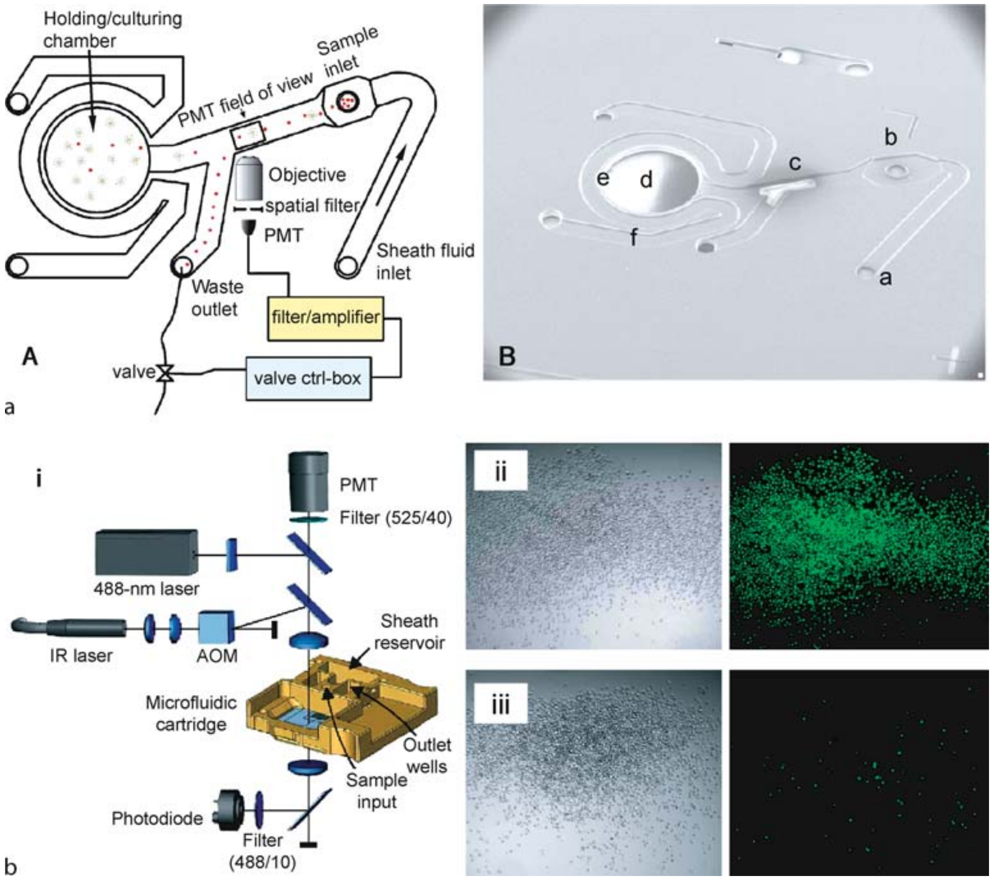

Microfluidic Systems for High-Throughput Screening, Figure 7 High throughput cell sorters: (**a**) an optically switched microfluidic fluorescence-activated cell sorter [15] and (**b**) a micro cell sorter chip with integrated holding/culturing chamber [16] ►Flow Cytometer Lab-on-Chip Devices

work, they developed mechanical valve-based systems for automation of serial and parallel bioprocesses including cell isolation, cell lysis, DNA purification and DNA recovery without any pre- or post-sample treatment on a single microfluidic chip (Fig. 6b). Meanwhile, much effort has been made to develop miniaturized fluorescence-activated cell-sorting devices (μFACS) with high throughput rates. Wolff et al. designed and developed a novel pressure-driven μFACS device with advanced functional components including a chamber for holding and culturing the sorted cells and monolithically integrated waveguides for cell analysis (Fig. 7a). They achieved a 100-fold enrichment of fluorescent beads at a throughput of 12,000 cells per second while sorting a mixture of fluorescent latex beads and chicken red blood cells. Wang et al. demonstrated a high throughput cell sorter with all-optical control switch for living cells (Fig. 7b). The optical forces, which depend on the optical power and relative optical properties of the particle and its surrounding medium, were used to deviate the cell from the flow stream to a sufficient degree to that it was directed toward the target output channel. They showed that sorting runs of cell populations ranging from as few as 1000 cells up to 280,000 cells can be completed in less than an hour. More detailed information on novel flow cytometer based on microfluidic technologies can be found in the entry ►Flow cytometer Lab-on-a-Chip devices in this volume.

The manipulation of multiphase flows is another application for high throughput rate microfluidic systems. These systems enable the generation and manipulation of monodisperse bubbles or droplets of a dispersed gas or liquid phase in a continuous stream. These techniques have been applied to many different types of biochemical reactions that are performed in parallel as well as in series. For instance, single-cell enzymatic assays have been achieved by encapsulating single cells inside droplets (Fig. 8a). A single droplet of controlled femtoliter volume was generated by specially designed *T* channels. Before

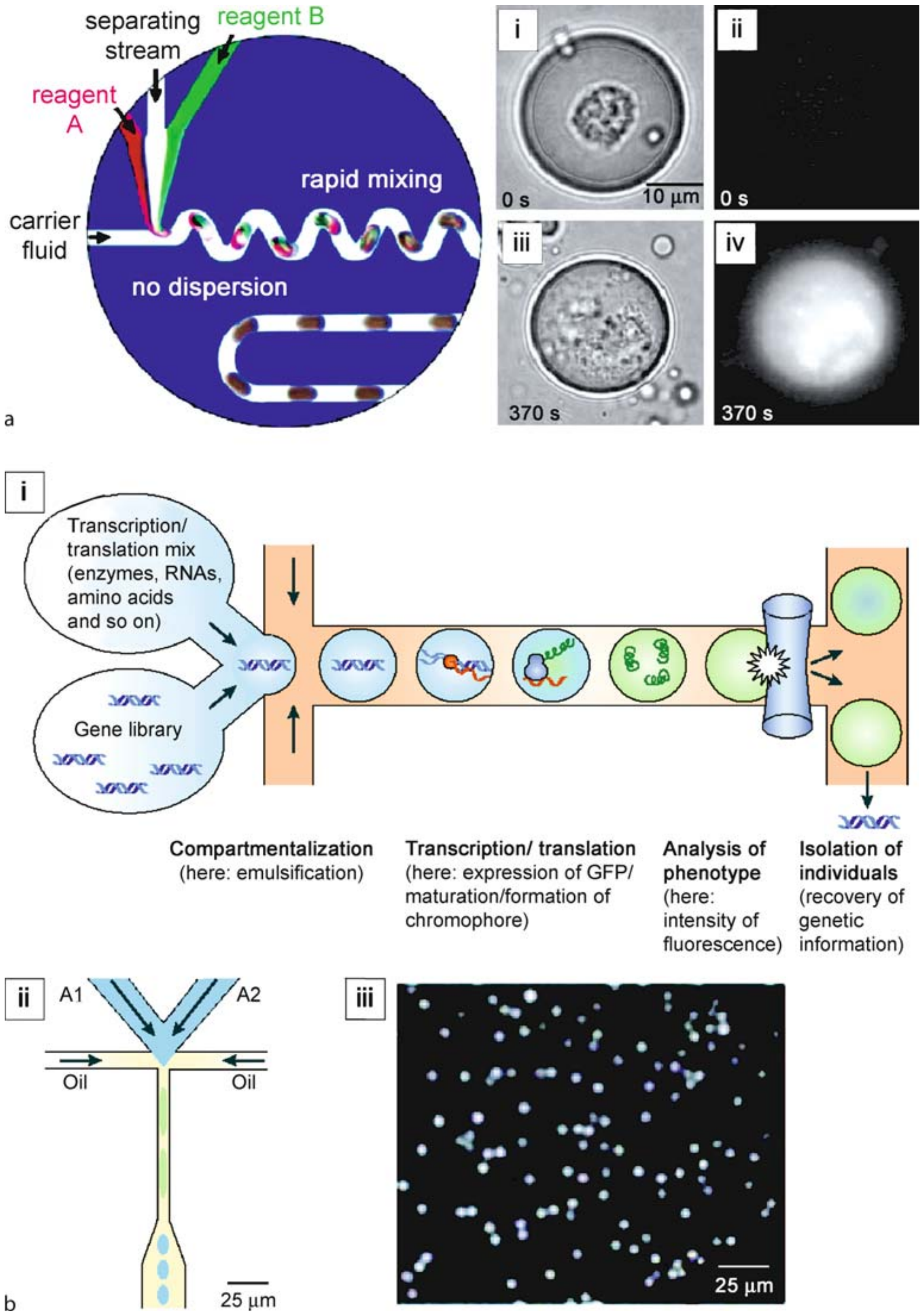

Microfluidic Systems for High-Throughput Screening, Figure 8 Droplet-based microfluidic systems: (**a**) Droplets formed with microfluidic channels (an enzymatic assay for a single mast cell within a droplet. i., iii. brightfield images; ii., iv. fluorescence images [8]) and (**b**) in vitro evolution of proteins in a microfluidic channels (i. the concept [9]; ii. a schematic diagram of the microchip (A1 and A2: aqueous solution containing the translation/transcription mix and a green fluorescent protein(GFP)-encoding plasmid, respectively) [8]; iii. Fluorescence microphotograph of the droplets after GFP expression [9]

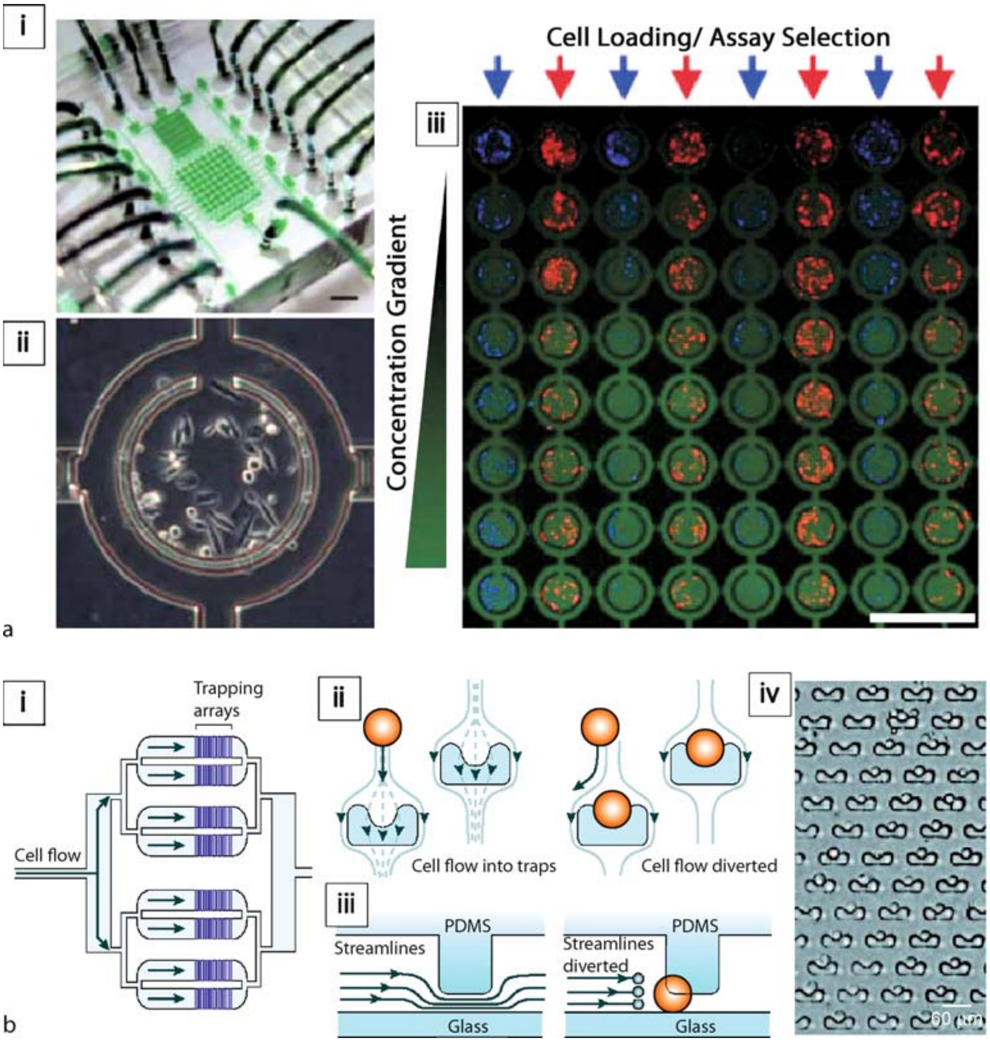

Microfluidic Systems for High-Throughput Screening, Figure 9 Cell-based microfluidic systems: (**a**) microfluidic cell-culture arrays with integrated concentration gradient generators (i. entire cell culture device; ii. close up of HeLa cells growing in a single culture chamber; iii. 8 by 8 cell culture grid. A concentration gradient of media was perfused across the device (left to right) [10]) and (**b**) dynamic single cell culture arrays (i. a schematic diagram; ii., iii. a concept of trapping arrays, top and side views, respectively; iv. trapping HeLa cells [9])

the formation of the droplet, a single cell was selected from the aqueous solution and moved by optical trapping to the interface between the aqueous phase and the carrier fluid. These techniques make it possible to investigate each cell under controlled, physiologically relevant environments. Droplet-based microfluidics is also a useful tool for molecular evolution that is particularly interesting for the optimization of drug candidates. Aqueous droplets form cell-sized compartments that keep together the genes, the RNAs and proteins that they encode, and the products of their activity. In vitro expression of green fluorescent protein (GFP) to directly analyze the contents of individual droplets has been achieved on a microfluidic system (Fig. 8b). More detailed information on droplet-based microfluidics can be found in [8].

In addition, laminar flow within microchannels can be exploited to deliver compounds to a local area of one cell, potentially allowing the evaluation of the stochastic nature of cellular responses or the effect of chemical gradients or drug interactions within a single cell. Recently, Lee and co-workers [10] have developed a microfluidic cell-culture array with an integrated concentration gradient generator for long-term cellular monitoring (Fig. 9a). The gradient generation permits many growth conditions to be analyzed in a combinatorial fashion and is thus well suited for high-throughput experimentation, where a large number of con-

ditions need to be screened in parallel with minimal consumption of analytes and reagents. Lee et al. also demonstrated high-density regular arrays of single cells isolated in a purely hydrodynamic fashion within a microfluidic device (Fig. 9b). Cells were held by obstacles incorporated into the channel while the fluid passed above and around both sides of the cells in the microchannel. Using obstacles of appropriate shape and size, just one cell per obstacle was trapped. The trapped cells were used for studies of enzyme kinetics on a single-cell level.

Future Directions for Research

The field of microfluidic systems for high throughput screening continues to mature. Before microfluidic devices replace existing assays and systems, several challenges still remain: standardization, interfacing between micro- and macro-worlds, ease of handling and robustness of systems, massive parallelization and cost. With these problems surmounted, future microfluidic systems will be capable of performing extensive processing and analysis for biological and drug discovery applications, on components ranging from DNA fragments to entire cells. The processing and analysis functions will be performed on a single chip, with high throughput rates in a continuous-flow manner, and in near-physiological environments as close to in vivo conditions as possible. Furthermore, microfluidic systems combined with computational tools and nanobiotechnologies will make technological breakthroughs in the near future. For instance, personalized medicine could be realized to treat an individual patient with the exact drug with optimal efficacy and safety.

Cross References

- ► Cell Culture (2D and 3D) on Chip
- ► Cell-Based Assays Using Microfluidics
- ► Control of Microfluidics
- ► Droplet Based Lab-on-a-Chip Devices
- ► Droplet Dispensing
- ► Flow Cytometer Lab-on-Chip Devices
- ► Lab-on-a-Chip (General Philosophy)
- ► Microfabrication Techniques

References

1. Squires TM, Quake SR (2006) Microfluidics: Fluid physics at the nanoliter scale. Rev Mod Phys 77:977–1026
2. Venkatasubbarao S (2004) Microarrays – status and prospects. Trends Biotechnol 22(12):630–637
3. Kim KH, Moldovan N, Espinosa HD (2005) A nanofountain probe with sub-100 nm molecular writing resolution. Small 1(6):632–635
4. Delamarche E, Juncker D, Schmid H (2005) Microfluidics for processing surfaces and miniaturizing biological assays. Adv Mater 17:2911–2933
5. McDonald JC, Duffy DC, Anderson JR, Chiu DT, Wu H, Schueller OJA, Whitesides GM (2000) Fabrication of microfluidic systems in poly(dimethylsiloxane). Electrophoresis 21:27–40
6. Unger MA, Chou H-P, Thorsen T, Scherer A, Quake SR (2000) Monolithic microfabricated valves and pumps by multilayer soft lithography. Science 288:113–116
7. Hong JW, Quake SR (2003) Integrated nanoliter systems. Nat Biotechnol 21(10):1179–1183
8. Song H, Chen DL, Ismagilov RF (2006) Reactions in droplets in microfluidic channels. Angew Chem 45:7336–7356
9. Dittrich PS, Manz A (2006) Lab-on-a-chip: microfluidics in drug discovery. Nat Rev Drug Discov 5:210–218
10. Breslauer DN, Lee PJ, Lee LP (2006) Microfluidics-based systems biology. Mol Biosyst 2:97–112
11. Sams-Dodd F (2006) Drug discovery: selecting the optimal approach. Drug Discov Today 11(9/10):465–472
12. Mere L et al (1999) Miniaturized FRET assays and microfluidics: key component for ultra-high-throughput screening. Drug Discov Today 4(8):363–369
13. Henderson E (2003) Surface pattering tools (SPTs™), Bioforce Nanoscience Inc, Ames, IA, USA
14. Kanigan TS (2004) OpenArray™, BioTrove Inc, Woburn, MA, USA
15. Wolff A, Perch-Nielsen IR, Larsen UD, Friis P, Goranovic G, Poulsen CR, Kutter JP, Tellemen P (2003) Integrating advanced functionality in a microfabricated high-through put fluorescent-activated cell sorter. Lab Chip 3:22–27
16. Wang MM, Tu E, Raymond DE, Yang JM, Zhang H, Hagen N, Dees B, Mercer EM, Forster AH, Kariv F, Marchand PJ, Butler WF (2005) Mircrofluidic sorting of mammalian cells by optical force switching. Nat Biotechnol 23(1):83–87

M

Microfluidic Systems Packaging

► Microfluidic Assembly

Microfluidic Systems in Space Science

David Brutin
Poytech Marseille, IUSTI Laboratory, Marseille, France
david.brutin@polytech.univ-mrs.fr

Synonyms

Micro- and nanotechnologies; Microsystems

Definition

Microfluidics is the science of designing, manufacturing, and formulating devices and processes that deal with volumes of fluid of the order of nanoliters. The devices themselves have dimensions ranging from millimeters down to

micrometers. The microfluidic systems are initially developed at a larger scale and then miniaturized for technological applications such as in space science. They have diverse and widespread potential applications. Some examples of particular systems and processes that might use this technology include inkjet printers, blood cell separation equipment, etc.

Overview

During the past 10 years, the concepts of miniaturization have been successfully applied to chemical and biological problems. The development and application of microfluidic or 'Lab-on-a-Chip' technology has been of particular interest. A few studies are developed on earth for future use in space considering the mass reduction benefit of the microscale [1, 2]. But at this stage, the main difficulty is to understand fluid behavior inside the Lab-on-Chip when biological or chemical reactions occur. On earth microfluidic systems have been used in a wide variety of applications including nucleic acid separations, protein analysis, process control, and small-molecule organic synthesis; from a fundamental point of view, chip-based analytical systems have many advantages over their macroscale analogues. These advantages *for space use* concern an improved efficiency in respect to the sample size, response times, cost, analytical performance, process control, integration, throughput, and automation. The idea that microfabricated analysis systems could be used in extraterrestrial environments is not new. The small size and low power requirements of the first silicon 6sgas chromatograph fabricated at Stanford University in 1975 were seen at the time as ideal characteristics for better utilizing spacecraft resources. Chip-based analysis systems possess many distinct advantages in comparison to their conventional counterparts for spaceflight purposes.

References

1. deMello AJ, Stone BM (2004) Unit Operations & Application of Microfluidic Systems for Remote Analysis. http://astrobiotech.arc.nasa.gov/abstracts/abstract_pdfs/deMello42.pdf Accessed Nov 2004
2. Pimprikar M (2003) Integration of micro and nano technologies for space exploration: challenges, opportunities and vision Merging. Micro and Nanotechnologies, pp 6–7

Micro Fluorescently-Activated Cell Sorting (μFACS)

► Droplet Based Lab-on-Chip Devices

Micro Fuel Cells

► Micro Energy Conversion Devices
► Microstructured Hydrogen Fuel Cells

Micro Gas Analyzers

► Gas Chromatography

Micro Gas Chromatography

► Gas Chromatography

Micro Gas and Liquid Chromatography

► Chromatographic Chip Devices

Micro Gas Turbine Engines

► Microturbines

Micro Gas Turbines

► Microturbines

μGC

► Chromatographic Chip Devices
► Gas Chromatography

Microgravity

Definition

Very low gravity conditions, encountered in space flights.

Cross References

► Boiling and Evaporation in Microchannels

Micro Heat Engines

► Micro Energy Conversion Devices
► Microturbines

Micro-Heat Exchangers

► Microscale Cooling Devices

Micro Heat Pipes

HONGBIN MA
Department of Mechanical & Aerospace Engineering,
University of Missouri, Columbiao, MO, USA
mah@missouri.edu

Synonyms

Miniature heat pipes

Definition

The heat pipe is a device that utilizes evaporation heat transfer in the evaporator and condensation heat transfer in the condenser, in which the vapor flow from the evaporator to the condenser is caused by the vapor pressure difference and the liquid flow from the condenser to the evaporator is produced by capillary force, gravitational force, electrostatic force, or other forces directly acting on it. A *micro heat pipe* is so small that the mean curvature of the liquid–vapor interface is comparable in magnitude to the reciprocal of the hydraulic radius of the total flow channel. Mathematically, the definition of micro heat pipe can be expressed as

$$\frac{r_c}{r_h} \geqslant 1 \tag{1}$$

where r_c is the meniscus radius of the mean curvature of liquid–vapor interface, and r_h is the hydraulic radius of the flow channel. A typical micro heat pipe consists of a small noncircular channel that utilizes the sharp angled corner regions or micro grooves as liquid arteries.

Overview

The first heat pipe concept utilizing a wicking structure as part of a two-phase heat transfer device capable of transferring large quantities of heat with a minimal temperature difference was first introduced by Gaugler [1] in 1942. The heat pipe concept received relatively little attention, however, until Grover et al. [2] first applied the term *heat pipe* to describe a *synergistic engineering structure which is equivalent to a material having a thermal conductivity greatly exceeding that of any known metal*. In 1984, Cotter [3] initialized the concept of micro heat pipes. Since that time, micro heat pipes have been extensively investigated resulting in numerous applications ranging from temperature control of the human body to the thermal management of microelectronic systems and components.

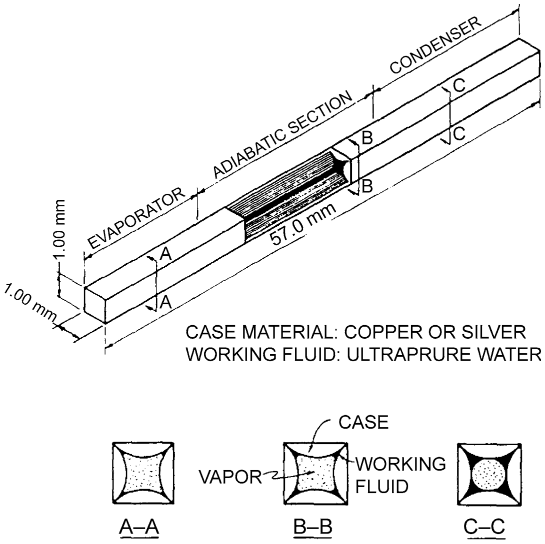

Micro Heat Pipes, Figure 1 Schematic of a micro heat pipe [4]

Figure 1 illustrates a typical micro heat pipe consisting of three sections: an evaporator or heat addition section, an adiabatic section, and a condenser or heat rejection section. A micro heat pipe, which is similar to a conventional heat pipe, consists of three major components: the container, which can be constructed from plastics, ceramics, or metals; a wicking structure constructed from sharp angled corner regions or micro grooves; and a working fluid, which remains at saturation conditions as long as the operating temperature is between the triple point and the critical state. Heat pipes operate on a closed two-phase cycle and only pure liquid and vapor are present in the cycle. Each of these three components is equally important with careful consideration given to the material type, thermophysical properties, and compatibility. For example, the container material must be compatible with the working fluid, and strong enough to withstand pressures associated with the saturation temperature encountered during storage and normal operation. In addition, the container material must be resistant to corrosion resulting from interaction with the environment and must be malleable enough to be formed into the appropriate size and shape. The sharp angled corner region directly formed from the container wall, as shown in Fig. 1, has two functions in heat pipe operation: it is the vehicle through which the working fluid is returned from the condenser to the evaporator. It also ensures that the working fluid is evenly distributed over

the evaporator surface. Because the basis for operation of a heat pipe is the vaporization and condensation of the working fluid, selection of a suitable fluid is an important factor in the design and manufacturing of the micro heat pipes. Care must be taken in selecting the working fluid to ensure that the operating temperature range is adequate for the application.

The fundamental operating principles of micro heat pipes are essentially the same as those occurring in larger more conventional heat pipes. Heat applied to one end of the heat pipe vaporizes the liquid in that region and forces it to move to the cooler end where it condenses and gives up the latent heat of vaporization. This vaporization and condensation process causes the liquid–vapor interface in the liquid arteries to change continually along the pipe, as illustrated in Fig. 1 and results in a capillary pressure difference between the evaporator and condenser regions. This capillary pressure difference promotes the flow of the working fluid from the condenser back to the evaporator through the sharp angled corner regions or micro grooves. These corner regions or micro grooves serve as liquid arteries. Because the conventional wick structures such as meshes and sintered particles do not exist in the micro heat pipe, the vapor flow will significantly affect the liquid flow in the cornered region due to the frictional shear stress, which directly influences the capillary limitation. In addition, the thin film evaporation, wetting characteristics, and condensation heat transfer significantly affect the heat transport capability in a micro heat pipe.

Basic Methodology

Capillary Limitation

For a micro heat pipe to function, the capillary pressure difference occurring in the heat pipe must always be greater than the summation of all the pressure losses occurring throughout the liquid and vapor flow paths. When the heat transfer rate increases, the pressure losses increase, which will be overcome by the increase of the capillary pressure difference. The continuous increase of the heat transfer rate in a heat pipe will significantly increase the pressure losses, and at one heat transfer rate the total capillary pressure difference is no longer equal or greater than the total pressure losses. This relationship, referred to as the capillary limit, can be expressed mathematically as [4]

$$\Delta p_{c,\max} \geqslant \Delta p_l + \Delta p_v + \Delta p_g \tag{2}$$

where

$\Delta p_{c,\max}$ = maximum capillary pressure difference generated within sharp angled corner region

Δp_l = sum of inertial and viscous pressure drops occurring in liquid phase

Δp_v = sum of inertial and viscous pressure drops occurring in vapor phase

Δp_g = hydrostatic pressure drop

When the maximum capillary pressure difference is equal to or greater than the summation of these pressure drops, the capillary structure is capable of returning an adequate amount of working fluid to prevent dry-out of the evaporating section. This condition varies according to the micro channel shape, working fluid, heat flux in the evaporator, vapor flow channel, and operating temperature.

Capillary Pressure

When a meniscus radius exists at a liquid–vapor interface, there is a pressure difference across the interface, which can be determined by the Laplace-Young equation, i. e.,

$$p_{\mathrm{I}} - p_{\mathrm{II}} = \sigma\left(\frac{1}{r_1} + \frac{1}{r_2}\right) \tag{3}$$

where r_1 is the meniscus radius along the x-direction and r_2 is the meniscus radius along the y-direction. In order to generalize the application, the maximum capillary pressure occurring in a micro heat pipe can be expressed as

$$\Delta p_{c,\max} = \sigma\left(\frac{1}{r_{e,\min}} - \frac{1}{r_{c,\max}}\right) \tag{4}$$

where $r_{e,\min}$ and $r_{c,\max}$ are the minimum meniscus radius occurring in the evaporator and the maximum meniscus radius in the condenser, respectively. Both values depend on the shape of the corner region and the amount of liquid charged to the heat pipe.

Liquid Pressure Drop

The liquid pressure drop is the result of the combined effect of both viscous and inertial forces. If the flow rate in the corner regions of the micro heat pipe is very small, the effect of inertial force can be neglected, and the pressure difference in the liquid phase is caused only by the frictional forces at the liquid–solid interface and the liquid–vapor interface due to the vapor flow effect. The total liquid pressure drop can be determined by integrating the pressure gradient over the length of the flow passage, or,

$$\Delta p_l(x) = -\int_0^x \frac{\mathrm{d}p_l}{\mathrm{d}x}\mathrm{d}x \tag{5}$$

where the limits of integration are from the evaporator end ($x = 0$) to the condenser end ($x = L$), and $\mathrm{d}p_l/\mathrm{d}x$ is the liquid pressure gradient resulting from the frictional forces

from the solid wall and vapor flow at the liquid–vapor interface, which can be written as

$$\frac{dp_l}{dx} = -\left(\frac{\mu_l}{KA_l\rho_l}\right)\dot{m}_l \tag{6}$$

where $\dot{m}_l$ is the local mass flow rate in the corner region, and K, the permeability, can be expressed as

$$K = \frac{2r_{h,l}^2}{c_{f,l} \cdot \mathrm{Re}_l} \tag{7}$$

The hydraulic radius, $r_{h,l}$, in Eq. (7) is defined as twice the cross-sectional area divided by the wetted perimeter, or, $r_{h,l} = 2A_l/P$. It should be noted that Eq. (7) is valid for both the circular and non-circular channels/grooves. If the Reynolds number of the working fluid flowing through the corner region is less than the critical value, then laminar flow is assumed. The product of the friction coefficient and Reynolds number, $c_{f,l} \cdot \mathrm{Re}_l$, for laminar flow is constant and depends only on the passage shape. It should be noticed that when the liquid–vapor interface is affected by the vapor flow, the friction coefficient Reynolds number product, $c_{f,l} \cdot \mathrm{Re}_l$, depends on the vapor flow in addition to the contact angle and channel angle [5]. For uniform heat addition and rejection, Eq. (5) can be expressed as

$$\Delta p_l = \left(\frac{\mu_l}{KA_l h_{fg}\rho_l}\right) L_{eff} q \tag{8}$$

where the effective heat pipe length, L_{eff}, can be found as

$$L_{eff} = 0.5L_e + L_a + 0.5L_c \tag{9}$$

Vapor Pressure Drop

If the heat pipe is charged with an appropriate amount of working fluid and the wetting point occurs at the cap end of condenser, the vapor pressure drop can be calculated by the approach recommended by Peterson [4]. Based on the one-dimensional vapor flow approximation, the vapor pressure drop can be determined by

$$\Delta p_v = \left(\frac{C(c_{f,v} \cdot \mathrm{Re}_v)\mu_v}{2r_{h,v}^2 A_v \rho_v h_{fg}}\right) L_{eff} q \tag{10}$$

where C is the constant that depends on the Mach number defined by

$$\mathrm{Ma}_v = \frac{q}{A_v \rho_v h_{fg}(R_v T_v \gamma_v)^{1/2}} \tag{11}$$

The ratio of specific heats, γ_v, in Eq. (11) depends on the molecule types, which is equal to 1.67, 1.4, and 1.33 for monatomic, diatomic, and polyatomic molecules, respectively. Previous investigations summarized by Peterson [4] have demonstrated that the friction coefficient Reynolds number product, $c_{f,v} \cdot \mathrm{Re}_v$, and the constant, C, shown in Eq. (10) can be determined by

$$\begin{aligned} &\mathrm{Re}_v < 2300 \quad \text{and} \quad \mathrm{Ma}_v < 0.2 \\ &c_{f,v} \cdot \mathrm{Re}_v = \text{constant}, \quad C = 1.0 \end{aligned} \tag{12}$$

$$\begin{aligned} &\mathrm{Re}_v < 2300 \quad \text{and} \quad \mathrm{Ma}_v > 0.2 \\ &c_{f,v} \cdot \mathrm{Re}_v = \text{constant}, \quad C = \left[1 + \left(\frac{\gamma_v - 1}{2}\right)\mathrm{Ma}_v^2\right]^{-1/2} \end{aligned} \tag{13}$$

$$\begin{aligned} &\mathrm{Re}_v > 2300 \quad \text{and} \quad \mathrm{Ma}_v < 0.2 \\ &c_{f,v} \cdot \mathrm{Re}_v = 0.038\left(\frac{2r_{h,v}q}{A_v \mu_v h_{fg}}\right)^{3/4}, \quad C = 1.0 \end{aligned} \tag{14}$$

It should be noted that Eq. (14) was determined based on a round cross section. Because the equations used to evaluate both the Reynolds number and the Mach number are functions of the heat transport capacity, it is first necessary to assume the conditions of the vapor flow, and an iterative procedure must be used to determine the vapor pressure drop.

Although the capillary limitation governs the heat transport capability in a micro/miniature heat pipe, several other important mechanisms might limit the maximum heat transport capability. Among these are the viscous limit, sonic limit, entrainment limit, boiling limit, and thermal resistance limit. The viscous limits deal with the pressure drop occurring in the vapor phase. The sonic limit results from the occurrence of choked flow in the vapor passage, while the entrainment limit is due to the high liquid vapor shear forces developed as the vapor passes in a counterflow direction over the liquid flow. The boiling limit is reached when the heat flux applied in the evaporator portion is so high that nucleate boiling occurs in the evaporator liquid channels. This creates vapor bubbles that partially block the return of fluid and may ultimately lead to premature dry-out of the evaporator. The thermal resistance limit is related to the thermal resistance occurring in the condenser section.

Heat Pipe Fabrication Methods

Conventional wick structures such as meshes, sintered particles do not exist in the micro heat pipe. The sharp angled corner regions or channels formed by the heat pipe wall are used to pump the condensate from the condenser

to the evaporator. Because of the vapor flow effect and thermal resistance, the heat transport capability shown in Fig. 1 is limited. Micro heat pipe arrays or miniature heat pipes have been extensively investigated and developed. As a result, a number of fabrication techniques have been advanced. The typical fabrication processes include the formation of a series of parallel triangular grooves using directionally dependent etching [6], a multisource vapor deposition process [7], and low-cost fabrication techniques which utilize the grooved tubes with a thermally-shaping method.

In the first method, anisotropic or orientation dependent etching is used to produce a series of parallel micro channels in a silicon wafer. While wet chemical etching processes have been used extensively in semiconductor processing, Peterson [4] utilized an orientation dependent etching processes which allowed etching of silicon wafers in one particular direction at a higher rate as compared to the other directions. This orientation dependent etching occurs because the crystal structure of silicon is in the diamond cubic group, which causes the crystallographic directions, indicated by the notation ⟨hkl⟩, to be perpendicular to the crystal planes, indicated by the notation (hkl). As a result, the packing density is considerably higher in the ⟨111⟩ direction which is perpendicular to the (111) plane as compared with the ⟨100⟩ direction. This results in an etching rate that is faster in the ⟨100⟩ direction than in the ⟨111⟩ direction. If an orientation dependent etchant is used on a (100) oriented slice covered by an oxide mask, it will create V-shaped grooves limited by the (111) planes. The etching process will stop at the point where the (111) planes intersect and the (100) surface reduces to a line. Once the micro channels are etched into the silicon wafer, a clear glass cover plate is bonded to the surface to form the closed triangular channels using either an ionic bonding process (for bonding silicon to silicon) or an ultraviolet bonding process (for bonding silicon and glass).

The second fabrication technique utilizes a dual source vapor deposition process. The process begins with the fabrication of a series of square or rectangular grooves either machined or etched in a silicon wafer. Then, using a dual E-Beam vapor deposition process, the grooves are closed creating an array of long narrow channels of triangular cross-section and open on both ends. Figure 2 shows a photo micrograph of the end view of a vapor deposited micro heat pipe which has not quite been completely closed at the top. As shown, the micro heat pipes are lined with a thin layer of copper, significantly reducing problems associated with the migration of the working fluid (methanol) throughout the semiconductor material. Using copper as the material for the vapor deposited heat pipes on silicon substrate, ensured less than 2.0% differential expansion during the deposition process.

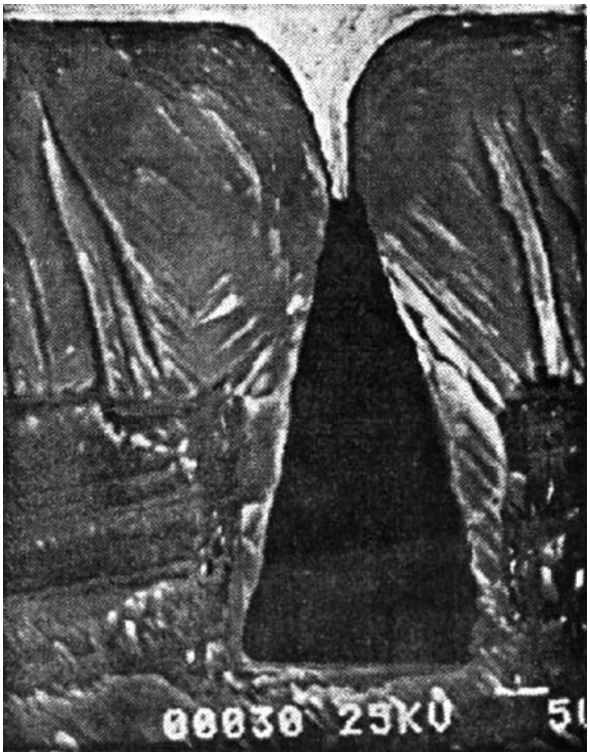

Micro Heat Pipes, Figure 2 A vapor deposited micro heat pipes [4]

The third typical fabrication technique, which is currently and widely used for the mass production of micro/miniature heat pipes, utilizes the commercially available grooved tubes or channels. Using the extrusion or forging processes, the micro grooves are formed on the inside surface of the tubes. Based on the required dimensions for a given application, the grooved tube is cut into the appropriate length. Using the tubing shrinking machine, both ends of cut tubes can be shrunk. One end is directly sealed and another end is reduced to a diameter ranging from 0.5 mm to 1.5 mm for charging. After cleaning, the heat pipe is charged with a working fluid. Once the heat pipe is fabricated, the heat pipe will be thermally shaped into a flat micro/miniature heat pipe.

Cleaning and Charging All of the materials used in a micro heat pipe must be clean. Cleanliness achieves two important objectives: it ensures that the working fluid will wet the materials and that no foreign matter is present which could hinder capillary action or create incompatibilities. The presence of contaminants either in solid, liquid, or gaseous state may be detrimental to heat pipe performance. If the interior of a heat pipe is not clean, degra-

dation of the performance can result over time. Solid particles can physically block the liquid flow in the corner region due to the very small flow channel, decreasing the capillary limit. Oils from machining or from the human hand can decrease the wettability in the heat pipe. Oxides formed on the inside surface of wall can also decrease the ability for the liquid to wet the surface. Therefore, proper cleaning of all of the parts in contact with the interior of the heat pipe is necessary for maximum reliability and performance. Several steps are needed in order to properly clean the heat pipe container and sharp corner regions, such as solvent cleaning, vapor degreasing, alkaline cleaning, acid cleaning, passivation, pickling, ultrasonic cleaning, and vacuum baking. Many of these steps are used in a single cleaning operation [4].

It is necessary to treat the working fluid used in a heat pipe with the same care as that given to the heat pipe container. The working fluid should be the most highly pure available, and further purification may be necessary following purchase. This may be carried out by distillation. The case of low temperature working fluids, such as acetone, methanol, and ammonia in the presence of water, can lead to incompatibilities, and a minimum possible water content should be achieved. The amount of working fluid required for a heat pipe can be approximately calculated by estimating the volume occupied by the working fluid in the sharp corner regions. The amount of working fluid charged to a heat pipe significantly affects the heat transfer performance of the heat pipe. For example, the heat transfer performance of a grooved micro/miniature heat pipe currently being used in the laptop computer is very sensitive to the charging amount of the working fluid.

Once the amount of working fluid required is determined, the working fluid can be introduced into the heat pipe by an evacuation and back-filling technique, a liquid fill and vapor generation technique, a solid fill and sublimation technique, or a supercritical vapor technique [4]. The most common among those for the low or moderate temperature working fluids currently being used for the electronics cooling is the evacuation and back-fill techniques. All these charging methods are to prevent noncondensable gases from entering the heat pipe during the charging process. In order to charge the working fluid in, a suitable evacuation/filling apparatus must be applied. The apparatus must be able to evacuate the container to 10^{-4} torr or less. The filling device is used to evacuate the pipe and charge it with the proper amount of working fluid. Details of the charging process depend on the state of the working fluid at the ambient temperature. The material of construction is generally glass, copper, or plastic materials. Glass has advantages when handling liquids in that the presence of liquid droplets within the ductwork can be observed and their vaporization under vacuum noted. Copper has obvious strength benefits. If plastic materials are chosen, the working fluid used in the charging process would have to not react with the plastic materials. Because the micro heat pipe is so small, several special charging methods have been developed. The most reliable of these is to place the micro heat pipe array in a high pressure chamber. After evacuating the chamber, a predetermined amount of working fluid is added and the chamber is heated to a point above the critical temperature of the working fluid. In this state all of the working fluid exists as a vapor and is uniformly distributed throughout the chamber and micro heat pipe array. The heat pipes are then sealed using an ionic or ultraviolet bonding process. When the chamber is then opened and the temperature reduced, a portion of the working fluid condenses. By controlling the volume of the pressure vessel and the quantity of the working fluid added after initial evacuation, the final amount of fluid in each heat pipe can be precisely controlled. An alternative method, which is simpler but somewhat less accurate has been developed by Peterson [4] and consists of sealing one end of the micro heat pipe array and positioning the wafer in a vacuum chamber vertically with the open end of the micro heat pipes approximately 1 mm above a small charging trough. After evacuating the vacuum chamber, a small amount of working fluid is slowly injected into the charging trough using a micro syringe. As the chamber pressure increases and approaches the saturation pressure corresponding to the temperature of the chamber, the working fluid forms a pool in the charging trough and wicks up into the heat pipe channels effectively sealing off the channel and trapping vapor in the upper portion of the heat pipe. The micro heat pipes can then be removed from the vacuum chamber and the open ends sealed. The final amount of liquid and vapor present in the microgrooves after sealing can be controlled by varying the temperature of the wafer, the height of the wafer above the bottom of the charging trough, and the rate at which the working fluid is injected into the vacuum chamber.

Working Fluid Selections Because a micro heat pipe cannot function below the freezing point or above the critical temperature of its working fluid, the selected working fluid must be within this temperature range. Peterson [4] has listed some working fluids which can be used in the heat pipe for a given operating temperature. In addition, the vapor pressure, surface tension, contact angle, and viscosity in the heat pipe must be considered in the selection of working fluid. For example, the vapor pressure in the heat pipe should not be less than 0.1 atm or higher than 10 atm. Typical working fluids for cryogenic heat pipes include helium, argon, oxygen, and krypton. For

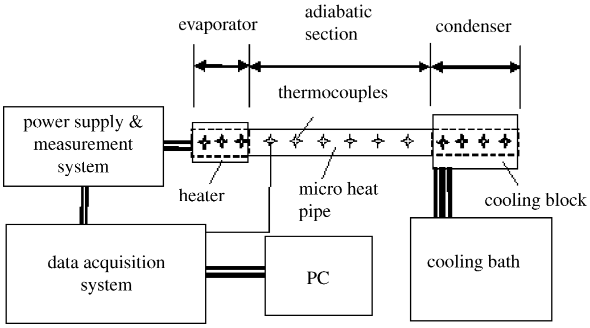

Micro Heat Pipes, Figure 3 Schematic of a heat pipe test setup

most common low-temperature heat pipes ranging from 200 – 550 K, ammonia, acetone, and water are commonly employed. The typical working fluids being used in the high-temperature heat pipes are sodium, lithium, silver, and potassium. Furthermore, a more important factor in the selection of working fluid is the compatibility with the case and wick materials. Some results of compatibility tests of materials with some working fluids can be found from the reference [4].

Testing The test facility needs to be established to test the heat transfer performance and heat transport limitations. Both transient and steady-state tests should be conducted for a micro heat pipe. For low-temperature heat pipes, however, the steady-state test is of most concerned. A typical experimental system for low-temperature heat pipes similar to the one shown in Fig. 3 would normally be used. The test facility shown in Fig. 3 consists of the heat pipe, a heat power supply and measuring unit, a cooling unit, and a data acquisition unit for the temperature measurements. The operating temperature of heat pipe can be controlled by a cooling block connected to a cooling bath, where the temperature of the coolant is maintained at a constant temperature based on the designed operating temperature. The heat source is directly connected to the evaporator. Power input can be supplied by an AC or DC power supply and recorded by multimeters with signals sent directly to a personal computer which can be used to control the entire system. The heat source should be well insulated to reduce convective losses to the environment. A number of temperature sensors are attached to the heat pipe surfaces to measure the temperature distribution along the heat pipe and temperature variation with power input. All of the measured data are sent to a data acquisition system controlled by a personal computer. Prior to the start of the experiment, the system is allowed to equilibrate and reach steady-state such that the temperatures of the cooling media and the heat pipe are constant. When the desired steady-state condition has been obtained, the input power is increased in small increments. Previous tests indicate that a time of approximately 5 – 30 min is necessary to reach steady-state. To obtain the data for the next successive power level, the power is incremented every 5 – 30 min. During the tests, the power input and the temperature data are simultaneously recorded using a data acquisition system controlled by a personal computer.

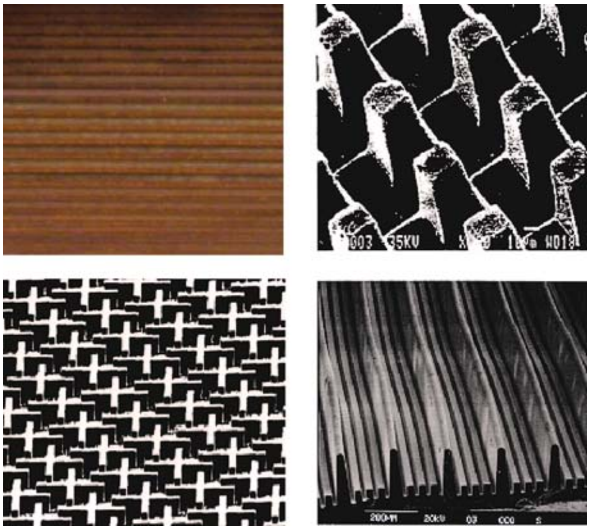

Micro Heat Pipes, Figure 4 Some examples of wicks for micro/miniature heat pipes

Key Research Findings

Since the initial conceptualization in 1984 [3] and the first real micro heat pipe in 1992 [4], numerous analytical and experimental investigations of micro heat pipes have been conducted resulting in a wide variety of applications in microelectronic systems or components.

Vapor Flow Effect For a relatively large conventional heat pipe, the wick structures existing in the heat pipe help to reduce the vapor flow effect on the liquid flow. For a micro/miniature heat pipe, the vapor space in the micro heat pipe is so small and the ratio of the hydraulic diameter of the vapor flow channel to the hydraulic diameter of liquid flow in the corner regions is much larger than a conventional heat pipe. The vapor flow has a larger effect on the heat transport capability than the conventional heat pipe. Ma et al. [5] have conducted a detailed investigation of the vapor flow effect on the liquid flow. The friction coefficient Reynolds number product, i. e., $c_{f,l} \cdot \mathrm{Re}_l$, for the liquid flow in the corner region must include the vapor flow effect, which depends on the vapor flow rate,

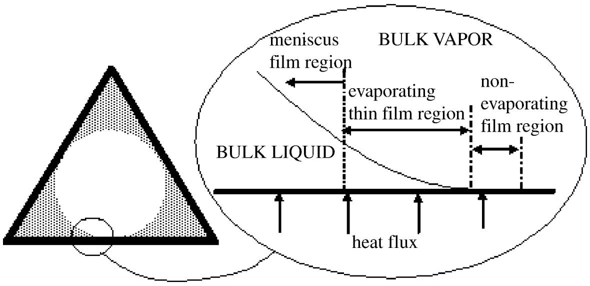

Micro Heat Pipes, Figure 5 Thin film evaporation in the evaporator section of a micro heat pipe

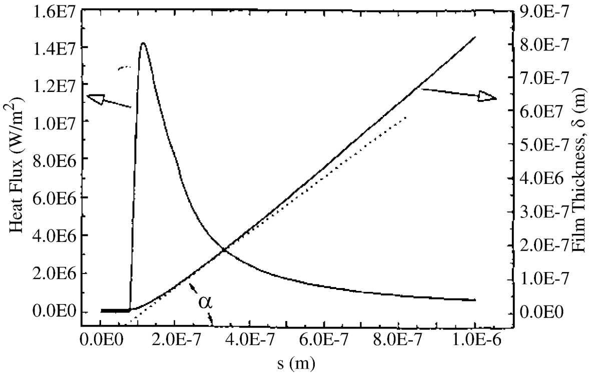

Micro Heat Pipes, Figure 6 Heat flux distribution in the thin film region (superheat = 1.0 C°, water)

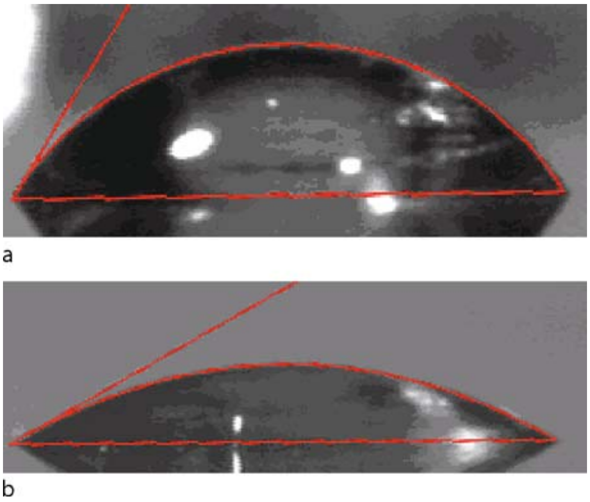

Micro Heat Pipes, Figure 7 Surface treatment effect on the contact angle of water drop on a copper surface (**a**) contact angle = 56.8°; (**b**) contact angle = 33.1°

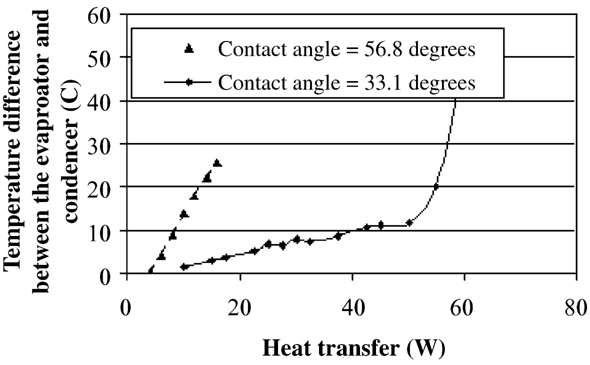

Micro Heat Pipes, Figure 8 Wetting characteristics effect on the heat transport capability in a miniature heat pipe

channel angle, contact angle, and fluid properties. Results show that the vapor flow effect significantly reduces the heat transport capability in a micro heat pipe. As a result, a number of new wick structures for micro/miniature heat pipes have been developed. Figure 4 illustrates several of these wick structures, which can significantly reduce the vapor flow effect.

Thin Film Evaporation When heat is applied to the evaporation region of a micro heat pipe, the heat will travel through the wall of the solid container and reach the working fluid. Most of the heat will pass through a thin-film region consisting of three regions: the non-evaporating thin film region, the evaporating thin film region, and the meniscus thin film region, as shown in Fig. 5. In the presence of a thin film, a majority of the heat will be transferred through a very small region [8]. When thin film heat transfer is compared to boiling heat transfer, it is found that thin film evaporation can provide significantly higher overall heat transfer coefficients. The heat transfer rate at the evaporating surface in a pool boiling system depends on the mechanisms of liquid supply to and vapor escape from the phase-change interface. Due to the presence of liquid, the resistance to vapor flow exists and directly limits the further enhancement of boiling heat transfer in the pool boiling systems. When the thin liquid film is formed in the micro heat pipe as shown in Fig. 5, the evaporating heat transfer rate through the evaporating thin film region can occur at a very small superheat. For example, the heat flux level through the thin film region can reach up to 1400 W/cm^2 with a superheat of 1.0 °C, as shown in Fig. 6. Thin film evaporation plays a key role in a micro heat pipe. There are several ways to increase the thin film evaporation. For example, when the surface wetting characteristics changes, while the capillary pumping capability increases, the thin-film-evaporation heat transfer can be significantly increased. For example, when the surface wetting characteristics changes, i. e., the contact angle changes from 56.8° to 33.1° as shown in Fig. 7, the

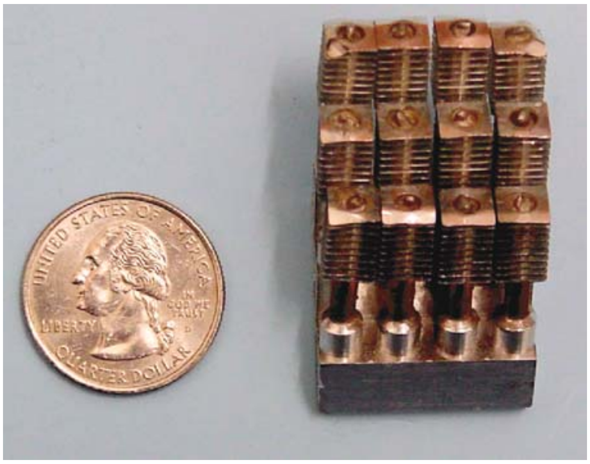

Micro Heat Pipes, Figure 9 Micro heat pipe arrays in electronics cooling

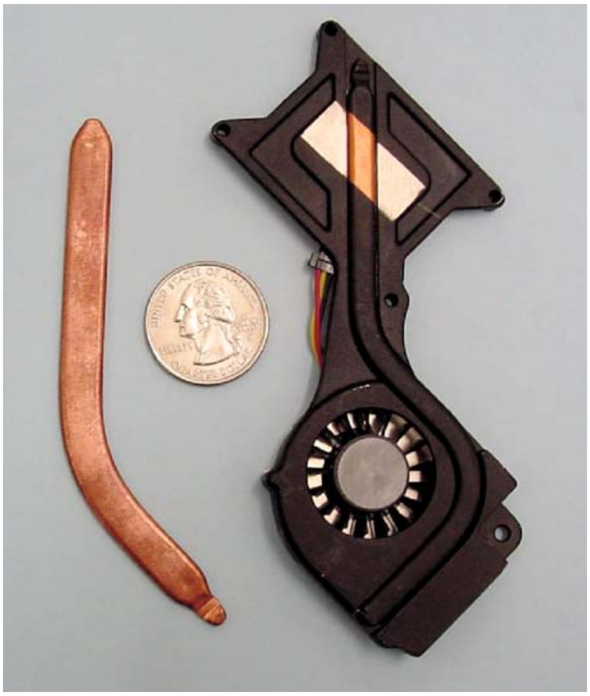

Micro Heat Pipes, Figure 10 Miniature heat pipes in a laptop computer cooling

heat transport capability in a miniature grooved heat pipe can be significantly increased as shown in Fig. 8.

Effective Thermal Conductivity The effective thermal conductivity provided by a heat pipe is the key factor for designing a highly-efficient heat pipe cooling device. For the conventional heat pipe, the thermal resistance in the heat pipe is mainly from the wick structure. Because the conventional wicks do not exist in a micro heat pipe, the prediction of thermal resistance occurring in the micro heat pipe is different from the conventional heat pipe. Peterson and Ma [9] developed a detailed mathematical model to predict the effective thermal conductivity, k_{eff}, in the micro heat pipe. While the expression of effective thermal conductivity, k_{eff}, for the micro heat pipe is similar to the conventional heat pipe, the thermal resistances occurring in the evaporating thin film and condensation film are the primary contribution to the total thermal resistance. Special attention will be given to the capillary flow [9, 10] and heat transfer occurring in the liquid films of both the evaporator and condenser sections. When the heat transfer rate is high, the thermal resistance occurring in the condenser section will become the primary factor affecting the heat transport capability in a micro heat pipe.

Samples of Application

Since Peterson [4] developed the first real micro heat pipe, a wide variety of micro/miniature heat pipes have been developed and utilized in microelectronic systems or components. Figure 9 illustrates an array of micro heat pipe application in an electronic component cooling. In order to reduce the vapor flow effect, increase the condensation heat transfer, and enhance the thin-film-evaporation heat transfer, the size of micro heat pipe must become larger. Figure 10 shows a micro or miniature heat pipe application in laptop computer chip cooling.

Future Directions for Research

Because the vapor space in the micro heat pipe is so small and the vapor flow directly acts on the liquid–vapor interface, the vapor flow significantly reduces the heat transport capability in a micro heat pipe. New kinds of structures for both liquid and vapor flows should be developed to reduce the vapor flow effect, in particular, when the heat transfer rate increases. And the new structures for the liquid flow should significantly increase the capillary pumping capability at the same time. The thin film evaporation in a micro heat pipe plays a key role and an extensive investigation to increase the thin film evaporating region should be conducted in order to significantly increase the evaporating heat transfer rate, in particular, for a high-heat-flux application. While the wetting characteristics will help to increase the capillary pumping capability, a better wetting surface will significantly enhance the evaporating heat transfer. Extensive investigations should be conducted to develop a cost effective approach treating the surfaces in the evaporator and condenser to significantly increase the heat transport capability in a micro/miniature heat pipe.

Nomenclature

A	cross-sectional area, m^2
C	constant
c_f	friction coefficient
h_{fg}	latent heat, J/kg
k	thermal conductivity, W/mK
K	permeability, m^{-2}
L	length, m
Ma	Mach number
$\dot{m}$	mass flow rate, kg/s
r	radius, m
R	universal constant, J/kg-K
p	pressure, N/m^2
P	perimeter, m
q	heat transfer, W
Re	Reynolds number
T	temperature, °C
x	coordinate, m

Greek Symbols

γ	ratio of specific heats
μ	dynamic viscosity, N-s/m^2
ρ	mass density, kg/m^3
σ	surface tension, N/m

Subscripts

a	adiabatic section
c	capillary, condensation, condenser
e	evaporation, evaporator
eff	effective
g	gravity
h	hydraulic
l	liquid
max	maximum
min	minimum
v	vapor
w	wall

Cross References

► Electronics Cooling
► Boiling and Evaporation in Microchannels
► Heat Transfer in Microchannel Flows
► Wetting and Spreading
► Wafer Bonding
► Thermal Capillary
► Thermal Bubble
► Surface Tension, Capillary and Contact Angle
► Surface Tension Driven Flow
► Surface Directed Capillary Flow Systems
► Silicon Micromachining
► Microscale Cooling Devices

References

1. Gaugler RS (1942) Heat Transfer Device. US Patent 2,350,348, 21 Apr 1942
2. Grover GM, Cotter TP, and Erikson FF (1964) Structures of Very High Thermal Conductance. J Appl Phys 35:1990–1997
3. Cotter TP (1984) Principles and Prospects of Micro Heat Pipes. Proc 5th Int Heat Pipe Conf, Tsukuba, Japan, pp 328–335
4. Peterson GP (1994) An Introduction to Heat Pipes. John Wiley & Sons, New York
5. Ma HB, Peterson GP, Lu X (1994) The Influence of Vapor-Liquid Interactions on the Liquid Pressure Drop in Triangular Microgrooves. Int J Heat Mass Transf 37(15):2211–2219
6. Lee M, Wong M, Zohar Y (2003) Integrated Micro-Heat-Pipe Fabrication Technology. J Microelectromech Syst 12(2):138–146
7. Peterson GP (1992) An Overview of Micro Heat Pipe Research. Appl Mech Rev 45(5):175–189
8. Demsky S, Ma HB (2004) Thin Film Evaporation on a Curved Surface. Microscale Thermophys Eng 3(3):285–299
9. Peterson GP, Ma HB (1999) Temperature Response and Heat Transport in a Micro Heat Pipe. ASME J Heat Transf 121(2):438–445
10. Suman B (2006) the Fill Charge and the Sensitivity Analysis of a V-Shaped Micro Heat Pipe. AIChE 52(9):3041–3053

Micro Hot-Wire Anemometer

► Thermal Anemometer

Microhypodermic Needles

► Microneedles – Applications & Devices

Microjets

► Microrockets

Micro Laser Doppler Velocimetry (μ-LDV)

JÜRGEN CZARSKE, LARS BÜTTNER
Professorship of Measuring and Testing Techniques, Dresden University of Technology, Dresden, Germany
juergen.czarske@tu-dresden.de

Synonyms

Laser Doppler anemometry; Laser Doppler sensor

Definition

Laser Doppler velocimetry is a technique for measuring the local velocities of flows.

Overview

In laser Doppler velocimetry (LDV) [1] based on the differential technique, two coherent laser beams, which are usually generated by beam splitting, are made to intersect at a small angle 2θ. In the area of intersection (the measurement volume) an interference fringe pattern with nearly parallel planes arises. The normal vector of these planes lies in the plane spanned by the LDV partial beams and is aligned perpendicular to the optical axis, which is the crossing half angle of the beams. The spacing d of the interference fringes is given by the laser wavelength λ and the crossing half angle of the partial beams θ:

$$d = \frac{\lambda}{2 \sin \theta} \tag{1}$$

For flow measurements, the fluid usually has to be seeded with small particles ("tracers"), having typical diameters in the nano- or micrometer range and following the flow with negligible slip. As the particles pass through the interference fringes they scatter light at only the bright fringes such that the scattered light shows an amplitude modulation with the frequency f_D, which is known as the Doppler frequency. Photodetectors are used to generate an electrical signal from the scattered light. Signal processing techniques calculate the Doppler frequency from it. The velocity component lying parallel to the normal vector of the interference fringes is then given by

$$v_x = f_D \cdot d \tag{2}$$

In order to measure two or all three velocity components two or three different interference fringe systems have to be overlapped with orthogonal alignment of their optical axes in the ideal case. If the optical axes can for some reasons not be aligned orthogonally, a coordinate transform algorithm has to be included in the signal processing software. The different fringe systems have to be physically distinguishable and usually either wavelength division multiplexing (WDM) or frequency division multiplexing (FDM) is applied for this purpose.

For applications of conventional LDV in nano- and microfluidics the spatial resolution is a crucial point. Since usually no information about the position of the tracer particle can be gained, the spatial resolution is determined by the size of the measurement volume. A high spatial resolution can be achieved by beam stops or by strong focusing of the laser beams, e. g. by means of a microscope objective resulting in a small measurement volume of e. g. 20 μm × 20 μm × 20 μm. However, the focusing of the laser beams is accompanied by two disadvantages: a reduced working distance and an increased uncertainty of the velocity determination. The latter effect is caused by the wavefront curvature of the focused laser beams resulting in fringes being no longer parallel. This variation of fringe spacing will increase the relative velocity uncertainty by several percent. This uncertainty relation between spatial resolution and uncertainty of velocity strongly limits the application of conventional LDV for microfluidic tasks [2].

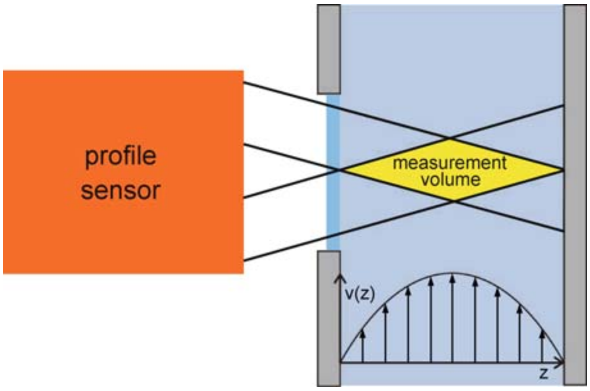

Micro Laser Doppler Velocimetry (μ-LDV), Figure 1 Application of a profile sensor(one concept of micro-LDV): velocity profile measurement in a microchannel

Micro-LDV was developed to overcome these drawbacks. One successful concept is the velocity profile sensor [3]. Along a line, which generally is the optical axis, the lateral velocity component of tracers is resolved with axial position resolution inside the measurement volume. Since the tracer particles are in general distributed statistically in the fluid, the velocity profile can be determined by measuring a sufficient number of tracers whose velocity and position are determined. Of note is the fact that the spatial resolution is no longer limited by the dimension of the measurement volume, so that a significantly higher spatial resolution up to about 100 nm results. Here, the measurement volume can be as large as the flow region of interest, e. g. the cross-section of a microchannel (see Fig. 1), and the velocity profile can be measured without mechanically traversing the sensor head.

Various principles exist as to how a profile sensor can be realized [2]. In the following the profile sensor invented by the authors of this overview will be described as an example [3, 4].

The profile sensor employs two superposed interference fringe systems (Fig. 2). In contrast to conventional LDV with parallel fringes, the fringe systems are fanlike with one being convergent and the other being divergent. They are described by the fringe spacing functions $d_{1,2}(z)$.

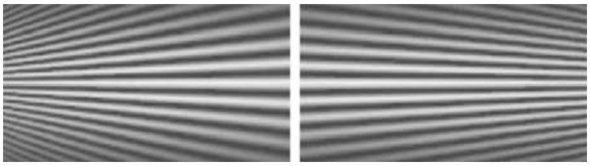

Micro Laser Doppler Velocimetry (μ-LDV), Figure 2 Fringe systems of the laser Doppler velocity profile sensor

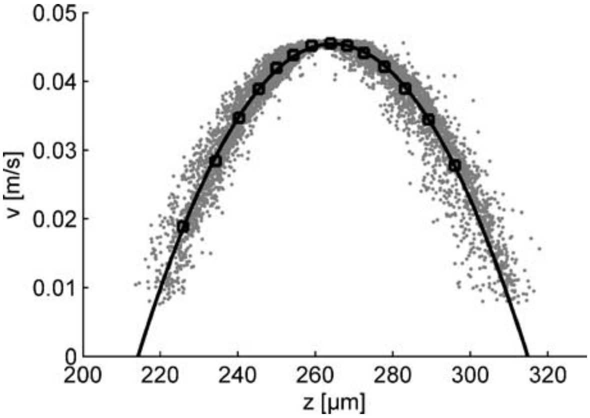

Micro Laser Doppler Velocimetry (μ-LDV), Figure 3 Measured velocity profile of a laminar water flow in a 100 μm microchannel

The z-position of the tracers is determined by the quotient of two measured Doppler frequencies:

$$q(z) = \frac{f_2(v_x, z)}{f_1(v_x, z)} = \frac{v_x/d_2(z)}{v_x/d_1(z)} = \frac{d_1(z)}{d_2(z)} \qquad (3)$$

The calculated z-position allows one to determine the actual fringe spacings $d_1(z)$ and $d_2(z)$, resulting in a precise measurement of the velocity:

$$v_x(z) = f_1(v_x, z)d_1(z) = f_2(v_x, z)d_2(z) \qquad (4)$$

Figure 3 shows the measurement result of an application of the profile sensor at a microchannel flow obtained without traversing the sensor. Each point corresponds to a single tracer whose position and velocity were determined. A good agreement with the expected parabolic velocity profile of the laminar channel flow was achieved. The spatial resolution was approximately 3.5 μm (which is the standard deviation of the tracer position). It was limited by sensor properties and the size of the tracers, which was about 2 μm. Using submicrometer tracers as well as improved sensor properties a spatial resolution in the nanometer range will be possible.

An extension of the profile sensor is the field sensor, which measures a two-dimensional velocity distribution of a flow. It is based on the combination of two profile sensors, which are arranged orthogonally. The features are analogous to micro-PIV (particle image velocimetry). However, since the velocity image is determined without having to use a digital camera, the tracers do not need to be imaged and digitization effects do not occur. In particular, a high relative velocity resolution of around 0.1% and a high temporal resolution in the millisecond range can be achieved. Precise flux measurements are one task of the velocity field sensor in micro- and nanofluidics.

Cross References

► μ-PIV

References

1. Albrecht H, Borys M, Damaschke N, Tropea C (2003) Laser-Doppler and phase-Doppler measurement techniques. Springer, Heidelberg
2. Vennemann P, Lindken R, Westerweel J (2007) In vivo whole-field blood velocity measurement techniques. Exp Fluids 42(4):495–511 (review article)
3. Czarske J, Büttner L, Razik T, Müller H (2002) Boundary layer velocity measurements by a laser Doppler profile sensor with micrometre spatial resolution. Meas Sci Techn 13(12):1979–1989
4. Czarske J (2006) Laser Doppler velocimetry using powerful solid-state light sources. Meas Sci Technol 17:R71–91 (review article)

M

Microlayer

Definition

Thin layer of liquid present on the heated wall underneath a vapor bubble, plug or core.

Cross References

► Bubble Dynamics in Microchannels

Micro-LC

► Chromatographic Chip Devices

Microlithography

► Photolithography

Micromachined Coulter Counter

► Flow Cytometer Lab-on-Chip Devices

Micromachined Flow Cytometer

► Flow Cytometer Lab-on-Chip Devices

3D Micromachining

► Fabrication of 3D Microfluidic Structures

Micromixer

► Passive Micromixers

Micromixing Chip

► Passive Micromixers

Micromolding

IAN PAPAUTSKY, ERIK T. K. PETERSON
Department of Electrical and Computer Engineering,
University of Cincinnati, Cincinnati, OH, USA
Ian.Papautsky@uc.edu

Synonyms

Injection molding; Hot embossing; Polymer casting; Thermoforming; Compression molding; Hot press molding; Replica molding

Definition

Micromolding is a set of fabrication techniques for replicating microstructures in polymers using molds (also commonly known as masters or tools) to define features. The three most common micromolding techniques are *injection molding*, *hot embossing*, and *casting*. Micromolding involves four primary steps: microfabrication of the mold containing a negative or inverse of the desired pattern geometry, introduction of polymer material to the mold, curing or cooling of the polymer material, and release or separation of the molded polymer from the mold.

Overview

Polymer microfabrication has become a popular alternative to the well-established silicon and glass-based microelectromechanical system (MEMS) fabrication technologies, particularly for microfluidic and Lab-on-a-Chip (LOC) applications. Polymers have several major advantages that are not immediately available in silicon and glass, including a wide range of material characteristics, biochemical compatibility, ease of processing and prototyping, and lower costs. Micromolding replication technologies are well suited for these applications because the principles behind these processes are already well established in the macroscale world. Microfluidic systems have been recently demonstrated in polymers for biomedical applications, including miniaturized electrophoresis chips, microfluidic mixers, pumps, valves, switches, and devices for cell culture or protein patterning [1–3].

Generally, micromolding encompasses three established polymer microfabrication technologies: injection molding, hot embossing, and casting.

Injection molding is probably the most well known technology due to its popularity in macroscale plastic processing. In injection molding, polymer pellets are melted in a heated screw and injected at high pressure into a mold (also known as master or tool) to replicate features. The process is typically automated and can be used to very rapidly fabricate LOCs, but is limited by the tool materials and the availability of appropriate substrate polymers. Polymers such as polymethylmethacrylate (PMMA) and polycarbonate (PC) are commonly used to fabricate LOCs by injection molding [4–6]. Although tools can be fabricated with conventional micromachining techniques, there are significant design considerations associated with equipment-specific molding tool design.

Casting is the most popular of the three micromolding methods for fabrication of microfluidic LOCs [7, 8]. This is by far the least expensive and simplest method, and its use is widespread in academia. The polymer (elastomer precursor) and the curing agent are typically mixed at a specific ratio and poured over the mold (also known as template or master). The system is thermally cured, allowing the elastomer to be peeled off once it sets. The most prominent elastomer is polydimethylsiloxane (PDMS), and the casting template can be fabricated with conventional micromachining techniques [9]. Micromolding in capillaries (MIMIC) [10] is a popular variation of the technique, in which PDMS is cast on a mold containing a relief pattern, which is then released and used as the mold in a second step. The mold is formed by placing the PDMS casting in conformal contact with a substrate to create a network of channels, which are then filled with a liquid pre-polymer by capillary action or vacuum and cured. Once cured, the mold is removed leaving the microstructures. MIMIC has been used to fabricate complex microstructures in thermally and UV-curable polymers.

Hot embossing is a reasonably fast and moderately expensive technique used to replicate microfluidic LOCs in thermoplastics [5, 6, 11]. In the embossing process, the polymer and mold (also known as master or tool) are heated above the glass transition temperature (softening point) of the thermoplastic and a controlled force is applied. The assembly is then cooled below the glass transition temperature (T_g) and de-embossed or de-molded. Hot embossing is used in a wide range of applications from rapid prototyping to high volume fabrication. Polymers such as PMMA, PC and cyclic olefin copolymer (COC) are commonly used to emboss microfluidic LOCs using tools fabricated with conventional micromachining techniques.

Material Properties of Micromolded Polymers

Polymers can be broadly classified into three groups, according to the interconnection of the monomer units in the polymer chain, which will substantially affect their properties and thus the molding behavior. The first category is the *thermoplastic polymers*, which consist of unlinked or weakly linked linear chain molecules. Above the glass transition temperature, these materials become plastic and can be molded into specific shapes, which they retain once cooled below the *glass transition temperature* (T_g). Thermoplastics that contain very long polymer chains with strong intermolecular interactions do not melt and flow, but remain soft until they decompose. The glass transition temperature may be lowered through the addition of softeners, or raised by adding plasticizers during the polymerization process. Thermoplastics are commonly used in hot embossing (e. g., PMMA and PC). Thermoplastics have also been dissolved in organic solvents and poured into molds, leaving rigid replicas once the solvent is driven out. The second group is the *elastomeric polymers*, which also contain weakly cross-linked polymer chains. Under an applied stress, molecular chains can be stretched to high extent, but relax and return to the initial state once the force is removed. Elastomers such as PDMS do not melt before reaching the decomposition temperature and are typically processed by casting. The third category are the *duroplastic polymers* (also known as *thermoset polymers*), which contain heavily cross-linked polymer chains and therefore do not easily change shape. Thermosets are normally cast or injection molded into the final shape, and are harder and more brittle than thermoplastics. The majority of the hot embossing work and microscale injection molding to date, particularly in microfluidic applications, has been performed in PMMA (also known as Plexiglas or Lucite) and PC (also known as Lexan, GE or Makrolon, Bayer). Both of these materials offer high optical transmission above 400 nm and have a long history as biomedical materials. PMMA is available in a broad range of molecular weights. This thermoplastic polymer has a relatively low T_g of 106 °C, which makes it better suited for hot embossing than PC ($T_g = 150$ °C). Other physical properties of the two materials, such as the density, modulus of elasticity, thermal conductivity, and water absorption, are quite similar. The refractive index of PC is 1.586, higher than that of PMMA, making PC a good material for applications using optical detection [12]. COC (also known as Topas, Ticona) is a relatively new polymer material that has been gaining popularity in hot embossing and micro injection molding due to its excellent physical and chemical properties [4, 6]. COC is a thermoplastic copolymer consisting of ethylene and bicyclic olefin (norbornene) monomers. Due to the olefinic characteristics, COC has a good chemical resistance to hydrolysis, acids and bases, and most organic polar solvents such as acetone, methanol, and isopropyl alcohol, although it is soluble in nonpolar organic solvents including toluene and naphtha. COC has a lower density than PMMA ($\rho_{COC} = 1010 - 1020\,kg/m^3$ vs. $\rho_{PMMA} = 1170 - 1200\,kg/m^3$) [5, 13], which makes it easier to emboss. However, its glass transition temperature is higher ($T_g = 134$ °C for Topas 5013S-04 and TKX-0001), requiring higher temperatures when injection molding. Overall, based on its material properties, COC is ideally suited for molding of microfluidic LOCs and devices, especially if optical signal detection is required [4, 5].

PDMS is perhaps the most widely used polymer for liquid casting of microfluidic channels with the Sylgard 184 (Dow Corning) formulation being the most frequently reported in the literature. This elastomer is optically transparent above ~230 nm, making it compatible with a variety of optical detection and microscopy techniques including DIC and epifluorescence. It is CO_2 permeable, relatively biocompatible, and has good chemical resistance, although it swells in many organic solvents [12, 13]. PDMS remains flexible and stable over a wide range of temperatures from −50 °C to +200 °C; a property not available in most materials. Furthermore, PDMS surfaces can be modified through adsorption of proteins or via plasma processing to obtain specific surface characteristics. Cured PDMS can easily be bonded to smooth PDMS or glass substrates using a brief O_2 plasma treatment.

Each micromolding method has specific constraints with regard to the material properties of the molded polymers. Detailed material properties and chemical resistances of polymers can be found in [13–16]. The most critical parameters to successful replication in hot embossing are T_g and the thermal expansion coefficient. Controlling the system temperature relative to T_g is critical. Raising the

temperature above T_g results in a viscous state, and the surface is easily deformed by the tool. For de-embossing, the material is cooled below T_g and becomes rigid, although the geometric stability of embossed features can suffer due to relaxation during de-embossing. Thermal expansion coefficient is also important in the microchannel sealing process where different materials are thermally bonded. In injection molding, shrinkage of the molded part following cooling is a major problem, especially if micrometer tolerances are necessary. This is remedied by adding reinforced fillers, such as glass beads which also increase stiffness. Critical material parameters in injection molding include the coefficient of thermal expansion, heat capacity, and the viscosity as a function of temperature. Critical processing parameters include precise temperature control of the melt and mold block, and the injection pressure. In casting, the most critical parameter is the low liquid pre-polymer viscosity, which is key to ensuring that template patterns are easily and completely filled. If liquid pre-polymer contains solvents, it is important that they do not degrade the mold materials. Finally, for all techniques, it is critically important that the micromolded polymer does not form chemical bonds or have strong adhesion to mold materials to facilitate mold release at the end of the process.

Basic Methodology

Fabrication of Masters

The underlying principle of micromolding is the replication of a microfabricated master, which represents the negative (inverse) structure of the desired polymer structure. Thus, microfabrication is only necessary one time for the fabrication of this master structure, which then can be replicated many times in the polymer substrate. This offers substantial cost advantages and freedom of design since master molds can be fabricated with a large number of different microfabrication technologies.

The success of any micromolding technique is largely dependent on the master since any surface defect will be replicated faithfully in the polymer. Thus, these processes have specific constraints with regard to masters that must be considered. First, since the molded part must be released from the master, undercuts in the pattern cannot be tolerated or the interlocking geometry would cause damage to the master or the molded part. Second, fidelity of the replication and lifetime depend strongly on the surface quality of the master. Smoother sidewall master surfaces result in lower frictional forces during separation or mold release. Roughness values below 100 nm RMS are necessary for reliable high-quality replication [5].

The master material should not form any kind of chemical or physical bond during replication. If mold release is difficult, release agents can be used. Some commonly used release agents include dilute liquid soap, silanization coatings, and plasma deposited fluorocarbon films. Specialized release agents are available from a variety of manufacturers. It is possible for release agents to modify the polymer surface or diffuse into the polymer matrix, which could adversely affect biological samples or increase the autofluorescence of the polymer, causing difficulties if the device uses fluorescence-based detection.

There are a number of methods used to fabricate tools, which can be broadly categorized as traditional micromachining methods (e. g., milling), bulk micromachining (e. g., etching Si), surface micromachining (e. g., nickel electroplating in photoresist or LIGA molds), and mold micromachining (e. g., PDMS or polyester tools). Surface morphology, adhesion properties to the molded materials, lifetime, feature sizes, and costs are critical factors to be considered in master fabrication.

Microscale Machining

Modern microscale machining technologies, such as sawing, cutting, and computerized numerically controlled (CNC) milling, are capable of producing masters with structures on the order of a few tens of micrometers. One key advantage of these techniques is the wide range of materials that can be machined, particularly stainless steel which cannot be processed with other microfabrication techniques but offers excellent master lifetimes. Relatively simple geometries with straight walls are a good fit for these techniques. However, high aspect structures (height vs. width ratio greater than 2), very deep holes, or very small structures (less than 10 μm) cannot be fabricated. Further, with surface roughness around several micrometers, these techniques typically do not produce smooth surface finishes. These machining methods are best for large features, often greater than 50 μm, with tolerances around 10 μm [5]. Because the master is machined from a single piece of material, adhesion problems between the substrate and features are entirely avoided. However, all of these prototyping fabrication processes are labor intensive and slow.

Bulk Micromachining

In bulk micromachining, the master is created by etching the substrate wafer, typically silicon. Silicon is an excellent material for use as an embossing master [5]. It has a high modulus of elasticity and high thermal conductivity, properties that are desirable in a hot embossing tool. In addition, there is a large variety of mature silicon microfabrication techniques available.

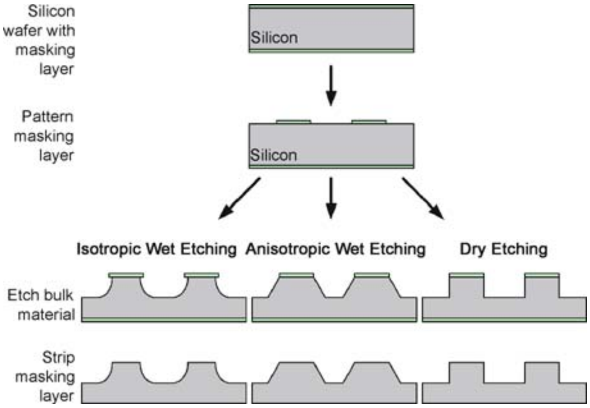

Micromolding, Figure 1 Bulk micromachining of silicon masters

To make a silicon master, a pattern is first created using CAD software, and the image is transferred to a photomask [9]. A Si wafer is coated with a masking material such as silicon dioxide or silicon nitride, and then coated with a layer of photoresist. The process is schematically illustrated in Fig. 1. Following UV exposure, the photoresist is developed revealing the transferred image. The image is then transferred to the exposed masking layer using either wet or dry etching. The exposed silicon is then etched anisotropically using potassium hydroxide (KOH), tetramethylammonium hydroxide (TMAH), or ethylenediaminepyrocatechol (EDP). If silicon with crystallographic orientation ⟨100⟩ is used, the resulting microstructure has a trapezoidal shape with a wall angle of 54.74°. The slant in the wall allows for good mold release and the surface roughness of well-oriented wet etched silicon wafers is excellent. The height and the width of the tool features are controlled by the amount of time the wafer is etched. In the final step, the mask layer is then stripped in hydrofluoric acid or phosphoric acid.

Dry etching methods, such as deep reactive ion etching (DRIE) and the Bosch process [9] can be used to fabricate deep structures with vertical sidewalls. However, scalloping or high surface roughness due to non-optimized or fast etches can result in problems during mold release. Typical depths range from 10 to 40 μm, although through holes have been achieved using the Bosch process.

Although silicon masters are simple to fabricate and offer good resolution and surface properties, they suffer from a number of disadvantages. Silicon masters may be too fragile for typical hot embossing pressures and may need some form of reinforcement (e. g., by anodic bonding to glass wafers). Silicon masters may also adhere to polymers depending on their surface chemistry, which would reduce the number of possible replication cycles. For greater master durability and replication performance, masters are often surface micromachined.

Surface Micromachining

In surface micromachining, a master is created by first patterning a mold on the wafer surface, followed by electroplating nickel, and finally removing the mold producing the nickel master [9]. This is the most commonly used method for hot embossing tools, and has also been used to make tools for injection molding. It is popular since a nickel tool can be made with low surface roughness, high durability, and has the ability to replicate small and high aspect ratio features.

There are two reincarnations of this method, schematically illustrated in Fig. 2. The first method uses a silicon or glass wafer as a substrate material, while the second method uses a nickel plate. A silicon or glass wafer is coated by evaporation or sputtering with a conductive seed layer (∼100 nm) such as Ni or Cu or Au. A thin layer (∼50 nm) of Ti or Cr is used to enhance adhesion of the conducting layer to the silicon substrate. The wafer is then coated with a layer of photoresist, which is subsequently exposed to UV light and developed so that the areas to be electroplated are free of resist. The wafer is placed into a nickel galvanic bath, where due to the migration of metal ions between the electrolyte and the seed layer, nickel is deposited in the photoresist structure. Low stress nickel films are important for developing thick structures, and can be deposited from a nickel sulfamate galvanic solution. Such solutions are commercially available (e. g., Technics Inc.) or can be mixed (e. g., 375 g of nickel sulfamate, 7.5 g nickel bromide, and 37.5 g boric acid per 1 l of deionized water). Electrodeposition is performed at ∼50 °C to reduce stress, with current density on the order of 20 mA/cm^2. Plating is allowed to proceed long enough for the metal to grow higher than the resist and form the master base. To ensure that the plating takes place on top of the photoresist, a thin layer of seed metal can be sputtered on the top surface. Following metal deposition, the resist and seed layers can be dissolved and the resulting metal structure can be used for hot embossing or injection molding.

In the second incarnation, photoresist is deposited and patterned on a nickel substrate rather than Si. Electroplating is performed using the same conditions as described above until nickel completely fills all microstructures. In this method, it is necessary to mechanically polish the nickel microstructures to the desired height prior to embossing. Photoresist is stripped off to complete the fabrication process. The height of the metal structure is determined by the thickness of the photoresist mold. Positive thick

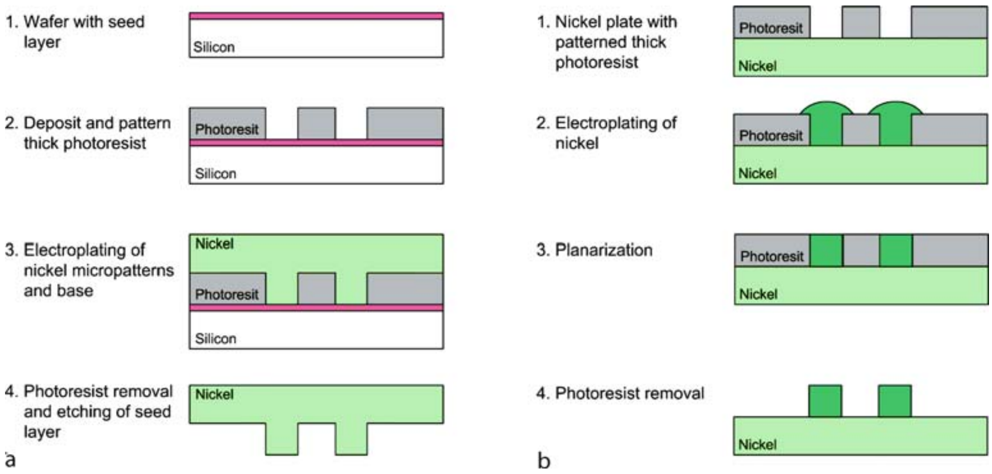

Micromolding, Figure 2 Fabrication of surface micromachined masters by photolithography and nickel electroplating using a silicon wafer as a substrate (**a**) and a nickel plate as a substrate (**b**).

photoresists allow structural heights in the order of 10–40 µm (e. g., AZ P4620, Clariant Inc.). Deep patterns, up to 1 mm, can be obtained using negative thick photoresist (e. g., SU-8, MicroChem Corp.). X-ray LIGA (German for Lithographie, Glavanoformung, Abformung) [9] is a well-established technique, where PMMA resist layers are exposed with synchrotron radiation, and can yield high aspect ratio structures and molds thicker than 1 mm. The electroplating method produces master surfaces with very low roughness (about 10 nm RMS for LIGA).

Conventional lithography, X-ray or UV LIGA followed by electroplating nickel or nickel alloys on silicon or nickel substrates is a common technique for fabricating tools with very small and complex features [4, 11, 17]. The electroplated nickel surface is very smooth and compatible with most polymers. However, electroplating of tall, high aspect ratio structures requires very long times and increasing the current density to speed up the process typically increases stress levels and surface roughness.

Polymer Casting

Casting liquid pre-polymers on microfabricated molds is the simplest and cheapest method of replication. Masters can be fabricated as discussed above or by simply defining structures in photoresist on a variety of substrate materials. Once the masters have been fabricated, they are often treated with a mold release agent prior to use. The liquid polymer is poured over the molds and placed under vacuum in order to completely fill the features and remove any air bubbles. Finally, the material is thermally cured and the replica is cut or peeled from the mold. This process is schematically represented in Fig. 3.

PDMS is one of the most popular polymers used in micromolding and is simple and inexpensive to process in any laboratory, requiring only a balance, a vacuum chamber, and a hot plate or oven [3]. PDMS is mixed at a 10 : 1 (m/m) ratio of base to curing agent, as recommended by the manufacturer, and remains a viscous liquid for several hours at room temperature. Liquid PDMS will easily fill sub-micron features, and any imperfections in the master, such as cracks, will be replicated. Therefore, a high quality replication requires a high quality master. In order to ensure that PDMS will release from the masters, molds may be treated with dilute soap, a fluorocarbon plasma, Sigma Cote (Sigma Aldrich, SL-2), or using perfluoro-1,1,2,2-tetrahydrooctyltrichlorosilane. PDMS is poured over the molds, which are then placed in a vacuum chamber until no air bubbles remain. Finally, the molds are heated to accelerate the curing process. PDMS will cure at room temperature, although it may take 24 h or longer depending on the thickness of the molded material. For PDMS with a thickness less than 5 mm, Table 1 provides typical curing times and temperatures. For increased thickness, either times or temperatures must be increased, however temperatures must be compatible with the mold materials, especially if photoresist molds are used. Once cured, PDMS castings are cut and peeled from the molds.

Micromolding, Table 1 PDMS curing times for 1–5 mm thick films

Temperature	Curing Time
20 °C	24 hrs
65 °C	4 hrs
80 °C	2 hrs
100 °C	1 hr

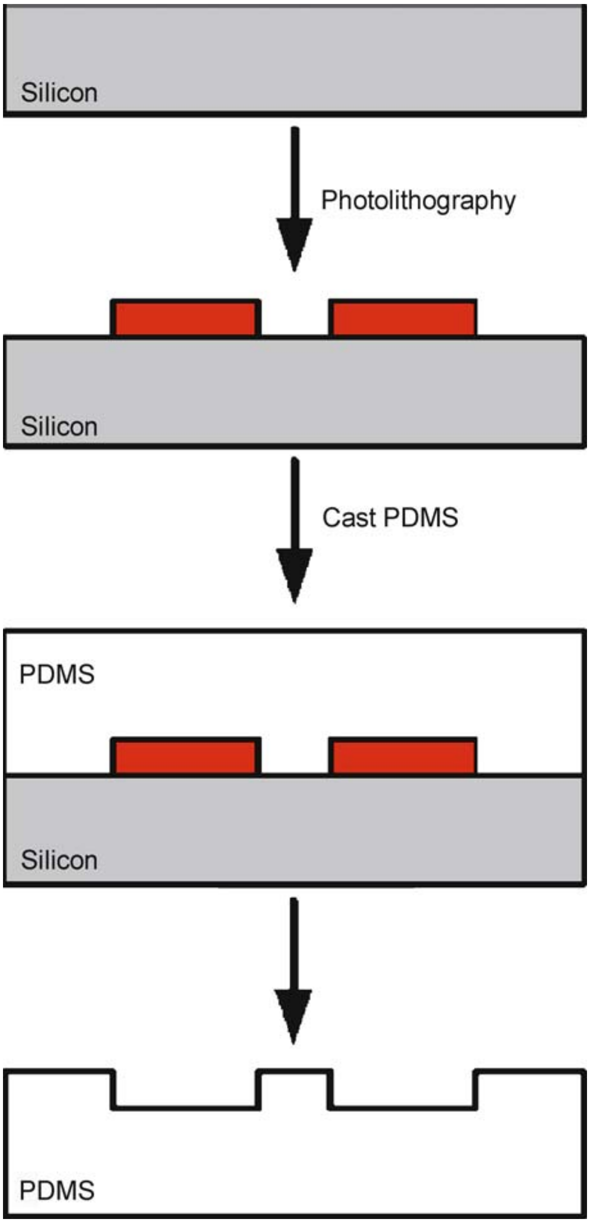

Micromolding, Figure 3 Process sequence for casting PDMS

Hot Embossing

The microfabrication process of hot embossing is rather straightforward. Once an embossing master is fabricated, it is mounted inside the embossing system together with a planar polymer substrate. An embossing machine, schematically illustrated in Fig. 4, consists of a vacuum chamber containing two temperature controlled plates, one of which is hydraulically actuated to deliver the embossing force. The embossing tool and the planar polymer sub-

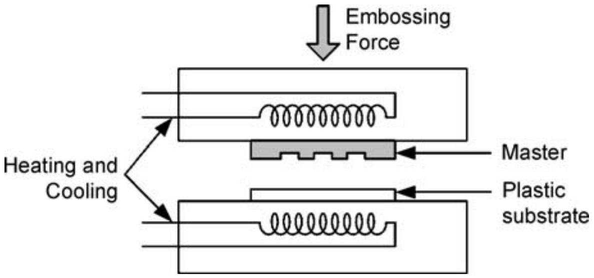

Micromolding, Figure 4 Schematic diagram of the hot embossing machine

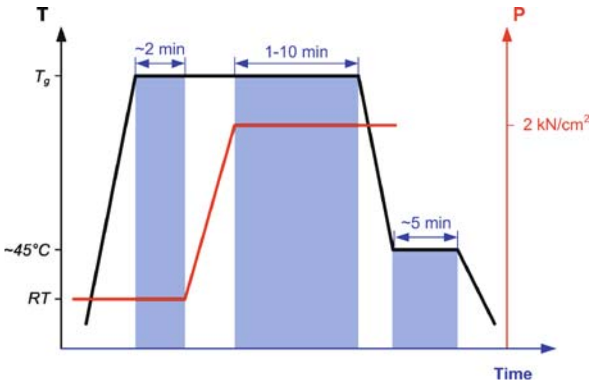

Micromolding, Figure 5 Graphical representation of the temperature and pressure program in a typical hot embossing process

strate are mounted between the plates, which are used for thermal cycling.

Conventional Hot Embossing Process

There are three basic steps in hot embossing, schematically represented in Fig. 5. At the beginning of the embossing cycle, the master and polymer substrate are heated independently in a vacuum chamber at < 100 mTorr to a temperature just above the T_g of the polymer. For most thermoplastics, this temperature is typically in the range of 100 – 180 °C. Vacuum is necessary to prevent trapping of air bubbles in microstructures and to remove water vapor driven out from the polymer substrate during the process. Vacuum also increases lifetime of metal masters by preventing corrosion at elevated temperatures. For most applications, the master and the substrate are heated to the same temperature. However, it is possible to independently control each heating plate to attain optimum embossing results.
In the second step, the master is brought into contact with the substrate and then embossed by applying a controlled force. Typical embossing pressures are on the order of $0.5 – 2\ \mathrm{kN/cm^2}$. While applying the embossing pressure, the tool-substrate sandwich is cooled to just below T_g. In

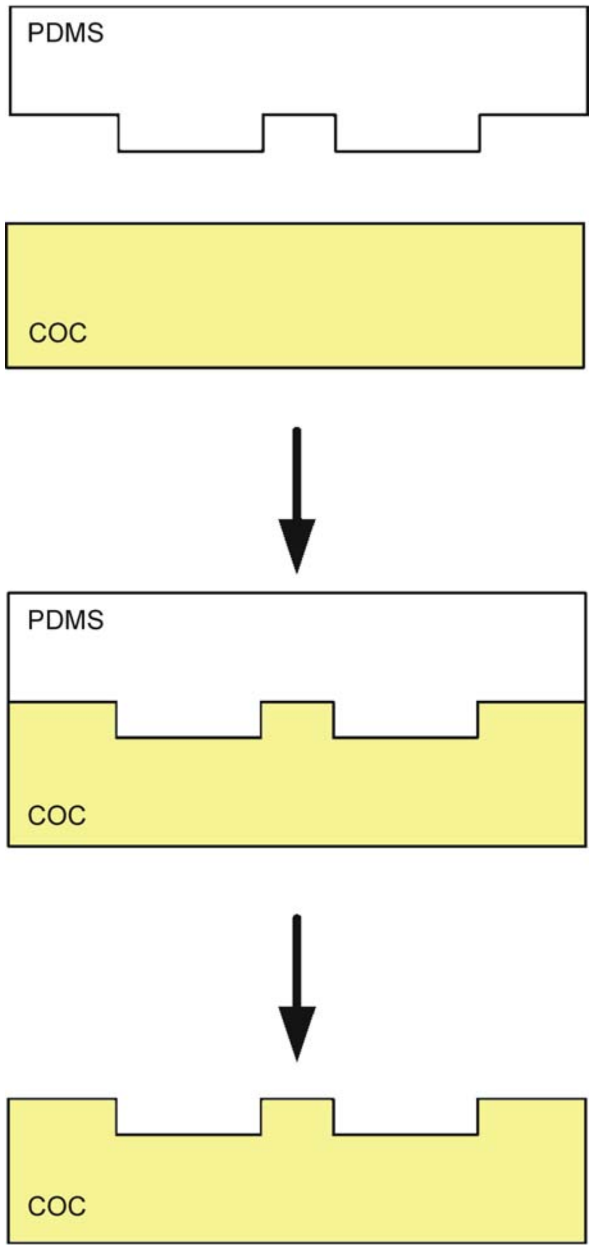

Micromolding, Figure 6 Hot embossing of COC with a PDMS tool

order to minimize thermally induced stress in the material and replication errors due to mismatch in thermal expansion coefficients of the master and the substrate, the temperature differential in the thermal cycle should be as small as possible. Typical values of the thermal expansion coefficient of polymers are on the order of $7 \times 10^{-5}\,\mathrm{K}^{-1}$, while silicon is approximately $2.5 \times 10^{-6}\,\mathrm{K}^{-1}$ and nickel is around $1.3 \times 10^{-5}\,\mathrm{K}^{-1}$.

In the final step, the embossed substrate is cooled to a temperature below the T_g, where the plastic material transitions back to the rigid state. After reaching this lower cycle temperature, the embossing master is mechanically separated from the polymer substrate that now contains the desired microfeatures. Separation is a critical step due to the large forces that act on the polymer structure and mold. This is particularly true for microstructures with vertical sidewalls and high aspect ratios. The overall cycle time of the embossing process is typically 1 – 10 min.

For every microfluidic chip design, however, the process conditions vary slightly. Geometry of the structures is an important factor that includes feature size, aspect ratio, radius of curvature, and whether the structure is freestanding or connected, and can significantly influence the process parameters. Layout properties of the design, such as the distribution of large and small features over the wafer area and the total wafer area to be processed, also must be considered.

Hot Embossing with Polymer Masters

Recently, polymer masters have been demonstrated for molding plastics. Microstructures formed in thick negative resist on silicon can be used directly as a tool for replicating parts in PC and PP [18]. However, lifetime of these tools was very short, only a few replications, due to the poor adhesion of SU-8 to the underlying base substrate during de-embossing. Alternatively, photoresist (AZP 4620 or SU-8) can be used to define a template for casting PDMS to form the embossing tool. The process is schematically illustrated in Fig. 6.

Mechanical properties of PDMS affect the hot embossing process. PDMS masters are not rigid like the nickel or silicon tools discussed earlier and have a much lower Young's modulus [16]. Thus, embossing pressure is very important. PDMS has a higher thermal expansion, and will expand and deform considerably more than conventional tools. Thus optimizing temperature is equally important in order to reduce discrepancies in replication. Overall, the use of PDMS masters can substantially reduce time, complexity, and costs involved in fabricating prototype microfluidic chips, but limits the master lifetime to approximately 20 cycles.

Injection Molding

Injection molding is the most widely used production technique for molding thermoplastics, and is also capable of molding thermosets and elastomers. Injection molding is perhaps the most expensive and complex process used to produce microstructures in polymers due to the specialized equipment, tooling, and process variables. In an injec-

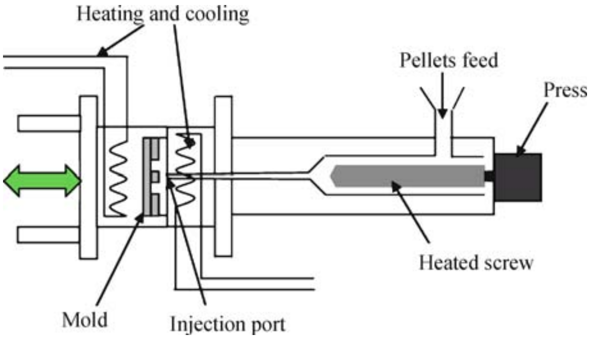

Micromolding, Figure 7 Schematic of a typical injection molding machine

Micromolding, Table 2 Typical parameters for injection molding COC in a reciprocating screw system

Typical Process Conditions for Injection Molding of COC	
Feed Zone	$T_F \leq 100\,°C$
Barrel Zones	$T_1 = 230 - 260\,°C$
	$T_2 = 240 - 270\,°C$
	$T_3 = 250 - 280\,°C$
	$T_4 = 260 - 290\,°C$
Nozzle and Sprue	$T_N = 240 - 300\,°C$
Mold-temperature:	$T_D = 95 - 125\,°C$
Max. residence time	< 15 min
Injection pressure:	$P_{Sp} = 500 - 1100$ bar
Hold on pressure:	$P_N = 300 - 600$ bar
Back pressure:	$P_{St} = 150$ bar max.
Screw speed:	$n_S = 50 - 200$ rpm
Injection speed:	moderate to fast (50 mm/sec – 150 mm/sec)

tion molding process, a molten polymer is injected into a mold at high pressure and temperature and then cooled to solidify the part before the mold is opened and the part is ejected. While there are several different configurations of injection molding machines, a reciprocating screw driven system is the most common. Detailed discussion of injection molding systems is given in [19].

A reciprocating screw driven injection molding machine is schematically illustrated in Fig. 7. Solid polymer pellets are first loaded into the hopper which feeds into the barrel. The barrel contains a rotating screw which transfers the polymer from the hopper to the mold, and shears and compresses the material at the same time through a tapered geometry. Injection barrels are water jacketed or contain electrical heating elements for temperature control through multiple zones, transitioning from room temperature to the process injection temperature. The temperature at the nozzle is often set to the maximum processing temperature of the plastic. Hydraulics then actuate the reciprocating

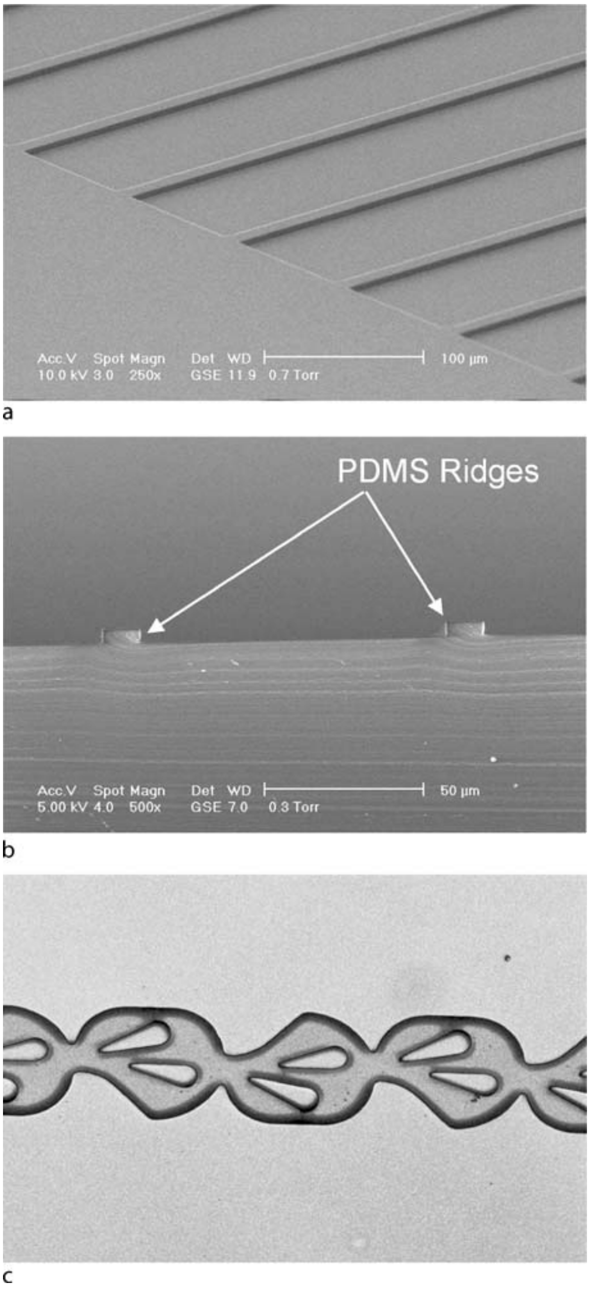

Micromolding, Figure 8 Top view (**a**) and cross section (**b**) SEM images of a PDMS substrate containing an array of microchannels with 10 µm ridges, 100 µm width channels, and 5 µm depth. From [3]. (**c**) An example of passive micromixer fabricated by casting PDMS (bright field image at 20×). The channel is 55 µm deep. Teardrop obstructions to enhance mixing are 100 µm long and span the entire height of the microchannel

screw to rapidly force the liquid polymer out of the nozzle of the barrel, through the injection channel, or sprue, and into the mold cavity. Some injection molding machines have the capability of evacuating the mold block prior to

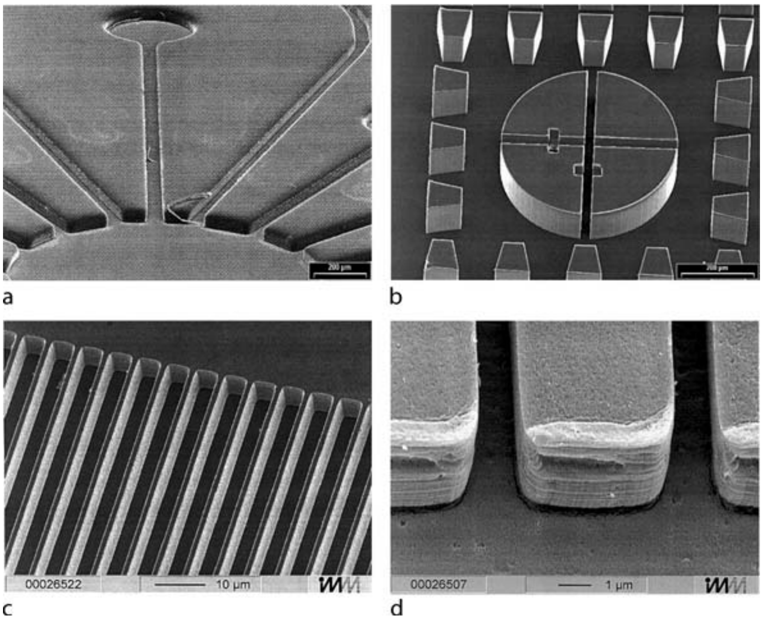

Micromolding, Figure 9 Examples of embossing tools and structures. SEMs of (**a**) a microchannel array of a flow cytometry system in PC fabricated with a silicon RIE-tool, (**b**) a high aspect ratio test structure embossed in PC using a master fabricated with LIGA and nickel electroplating, (**c**) a silicon tool for a two-dimensional channel array for 2D-capillary electrophoresis, and (**d**) the replicated PMMA structure. From [17]

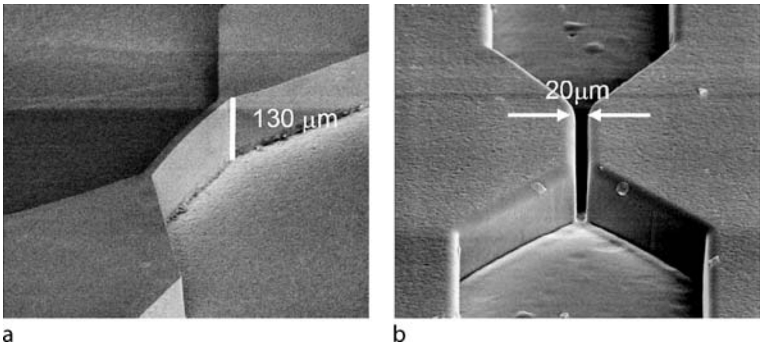

Micromolding, Figure 10 Example of injection molding tool fabricated using Ni electroplating (**a**), and the resulting features in COC (**b**). From [20]

injection which facilitates improved/complete filling of the cavity and eliminates trapped air bubbles. A mold block consists of two halves, one of which is stationary and maintained at the injection temperature, while the other is actuated using hydraulics and contains the relief pattern and ejection pins. Tooling containing the micropatterns is installed in the mold base, and is micromachined using the methods discussed previously. As in hot embossing, a positive draft angle is required along with minimal surface roughness to facilitate mold release upon ejection.

Process variables for injection molding are specific to the molded polymer. These parameters are typically provided by the polymer and machine manufacturers, although minor adjustments will be necessary to fine tune the process for different machines and mold geometries. For example, injection molding parameters for Topas COC grade 5013S-04 in a typical system are summarized in Table 2. Perhaps the greatest challenge in injection molding is filling high aspect ratio microstructures, and often simulation software is used to assist in the design of tooling and process parameters. While injection molding can be advantageous in high volumes, it may be cost-prohibitive for rapid prototyping or small runs if a new mold base is required to accommodate unique geometries. An injection molding process can be completed in a time frame of seconds to tens of minutes depending on the geometry of the mold and polymer material properties.

Key Research Findings

Microstructures in a wide range of shapes and aspect ratios can be replicated with micromolding techniques. For example, replication through liquid casting of PDMS has been used to make microchannels with a wide range of geometries [3, 7, 8, 10, 13]. Figure 8 shows an array of microchannels in PDMS which was cast using a photoresist master. The channels are 100 µm wide, 5 µm deep, and separated by 10 µm ridges. Channels in PDMS can be made with islands of various shapes for passive mixing, as illustrated in Fig. 8c. In most cases masters are planar, yielding planar microfluidic devices. Nevertheless, multilayer 3D microfluidic systems can be formed using multilayered photoresist structures created by repeating the photolithography process or by staking patterned thin films of PDMS.

High-resolution transparencies can be used as photomasks to rapidly prototype patterned photoresist masters, from which PDMS films can be replicated. Using transparency photomasks, the feature sizes are usually limited to ∼10 µm and larger. For smaller feature sizes, a chrome mask, which can be substantially more expensive (approximately 100×) is typically required.

Representative results of microdevices fabricated with hot embossing are illustrated in Fig. 9. An SEM of a microchannel array of a flow cytometry system embossed in PC using an RIE etched silicon master [17] is illustrated in Fig. 9a. Small micrometer sized channels (50 µm × 50 µm in cross-section) and large (hundreds of micrometers) reservoirs can be replicated equally well. Fig. 9b illustrates the high aspect ratio capabilities of the process. The test structure was embossed in PC using a master fabricated with LIGA and nickel electroplating [17]. The channel in the circular middle structure has an aspect ratio of 7, and is 20 µm wide and 140 µm deep. Fig. 9c illustrates a silicon tool for a two-dimensional channel array for 2D-capillary electrophoresis. The ridges are 0.8 µm wide and 5 µm high with a 5 µm pitch. The resulting sub-micrometer channel array pattern replicated in PMMA is shown in Fig. 9d. Similar results can be obtained with micro injection molding. Figure 10 illustrates a high aspect ratio injection molding tool fabricated using nickel electroplating and the resulting microchannel structure in COC [20].

High structural resolution and density are achievable micromolding. Figure 11 illustrates images of a grid pattern of approximately 150 nm wide trenches spaced at a 1 µm obtained with hot embossing [21]. The height of the silicon master fabricated using an advanced silicon etch process and height of the resulting PMMA structures are 200 nm.

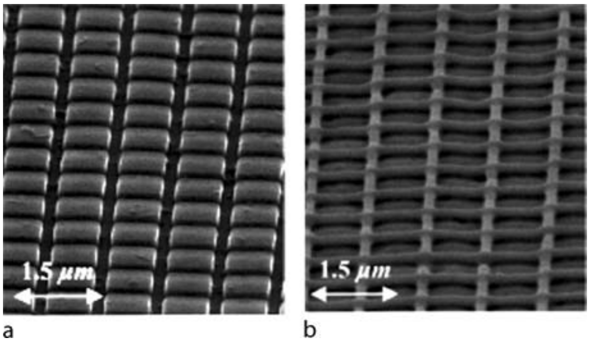

Micromolding, Figure 11 SEMs of (**a**) a silicon master and (**b**) the resulting PMMA structure. Features are 150 nm wide and 200 nm deep at 1 µm spacing. From [21]

Figure 12 shows examples of PDMS masters and the embossed microstructures in PMMA and COC [22, 23] Both large and small features can be replicated using this technique. For example, the PDMS master in Fig. 12(a) is 90 µm thick with an array of 150 µm wide features at 250 µm center-to-center spacing. The PMMA structure is 250 µm deep, containing an array of 600 µm wide microchannels at 1 mm center-to-center spacing. Figure 12 also illustrates a 5 µm thick PDMS master with 10 µm wide ridges and 10 µm spacing, and a 20 µm deep COC pattern with 30 µm wide channels at 10 µm spacing.

The use of PDMS tools can also be extended to fabrication of multi-height structures [24]. This is schematically shown in Fig. 13a. The process involves two lithography steps, (e. g., one with SU-8 and one with AZP 4620 photoresists). A passive micromixer fabricated using this process is shown in Fig. 13b. The mixing channel width is 200 µm at the widest point and 100 µm at the narrowest, with diamond obstructions 100 µm in width. Channel height is 55 µm with 15 µm high obstructions.

Future Directions for Research

Future directions for micromolding research, especially in hot embossing and injection molding, are involved with accurate replication of features with high aspect ratios, reduction of the process cycle time, and the investigation of new polymer materials and additives with improved characteristics. Rapid and accurate replication of nanoscale features, especially over large area, is another critical issue in micromolding that will need to be addressed in the future.

Cross References

► Bulk Micromachining
► Lab-on-a-Chip (General Philosophy)
► LIGA

M

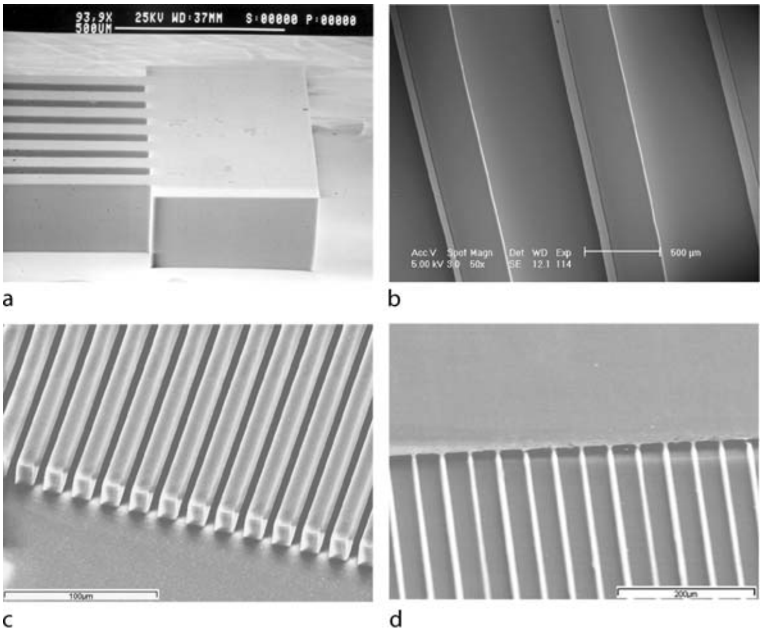

Micromolding, Figure 12 SEM images of PDMS masters and embossed structures. (**a**) A 90 μm thick PDMS master containing an array of 150 μm wide features with 250 μm center-to-center spacing. (**b**) A 250 μm deep PMMA structure containing an array of 600 μm wide microchannels with 1 mm center-to-center spacing. (**c**) A 5 μm thick PDMS master containing 10 μm wide ridges with 10 μm side-to-side spacing. (**d**) A 20 μm deep COC pattern containing 30 μm wide channels with 10 μm spacing spacing. From [22, 23]

► LIGA Like Techniques
► Materials Used in Microfluidic Devices
► Micromolding (Injection and Compression Molding)
► Photomask
► Silicon Micromachining
► Soft Photolithography

References

1. Manz A, Becker H (1999) Microsystem Technology in Chemistry and Life Science. Springer, New York
2. Nguyen NT, Wereley ST (2006) Fundamentals and Applications of Microfluidics, 2nd edn. Artech House, Boston
3. Minteer SD (ed) (2006) Microfluidic Techniques: Reviews and Protocols. Humana Press, Totowa
4. Ahn CH, Choi JW, Beaucage G, Nevin JH, Lee JB, Puntambekar A, Lee JY (2004) Disposable smart lab on a chip for point of care clinical diagnostics. Proc. IEEE, 92:154–173
5. Becker H, Gartner C (2000) Polymer microfabrication methods for microfluidic analytical applications. Electrophoresis 21:12
6. Rötting O, Röpke W, Becker H, Gärtner C (2002) Polymer microfabrication technologies. Microsyst Technol 8:32
7. McDonald JC, Duffy DC, Anderson JR, Chiu DT, Wu H, Schueller OJ, Whitesides GM (2000) Fabrication of microfluidic systems in poly(dimethylsiloxane). Electrophoresis 21:27
8. Duffy DC, Schueller OJA, Brittain ST, Whitesides GM (1999) Rapid prototyping of microfluidic switches in poly(dimethylsiloxane) and their actuation by electro-osmotic flow. J Micromech Microeng 9:211
9. Madou MJ (2002) Fundamentals of Microfabrication: The Science of Miniaturization, 2nd edn. CRC, Boca Raton
10. Kim E, Xia Y, Whitesides GM (1995) Polymeric Microstructures Formed by Moulding in Capillaries. Nature 376:581–584
11. Wang W, Soper SA, (eds) (2007) BioMEMS: Technologies and Applications. CRC, Boca Raton
12. Mark JE (1999) Polymer Data Handbook. Oxford University Press, New York
13. Lee JN, Park C, Whitesides GM (2003) Solvent compatibility of poly(dimethylsiloxane)-based microfluidic devices. Anal Chem 75:6545–6554
14. Kaplan WA (1998) Modern Plastics Encyclopedia. McGraw-Hill, New York
15. Harper CA (2000) Modern Plastics Handbook. McGraw-Hill, New York
16. Lide DR (2003) CRC Handbook of Chemistry and Physics. CRC press, Florida
17. Becker H, Heim U (2000) Hot embossing as a method for the fabrication of polymer high aspect ratio structures. Sens Actuators A 83:130–135
18. Edwards TL, Mohanty SK, Edwards RK, Thomas CL. Frazier AB (2002) Rapid micromold tooling for injection molding microfluidic components. Sens Materials 14:167
19. Berins ML (1991). SPI Plastics Engineering Handbook of the Society of the Plastics Industry, 5th edn. Kluwer, Norwell
20. Trichur R (2003) Development of polymer MEMS structures for lab-on-a-chips using UV-LIGA and injection molding techniques. MS Thesis, University of Cincinnati
21. Studer V, Pepin A, Chen Y (2002) Nanoembossing of thermoplastic polymers for microfluidic applications. Appl Phys Lett 80:3614
22. Narasimhan J, Papautsky I (2004) Polymer embossing tools for rapid prototyping of plastic microfluidic devices. J Micromech Microeng 14:96

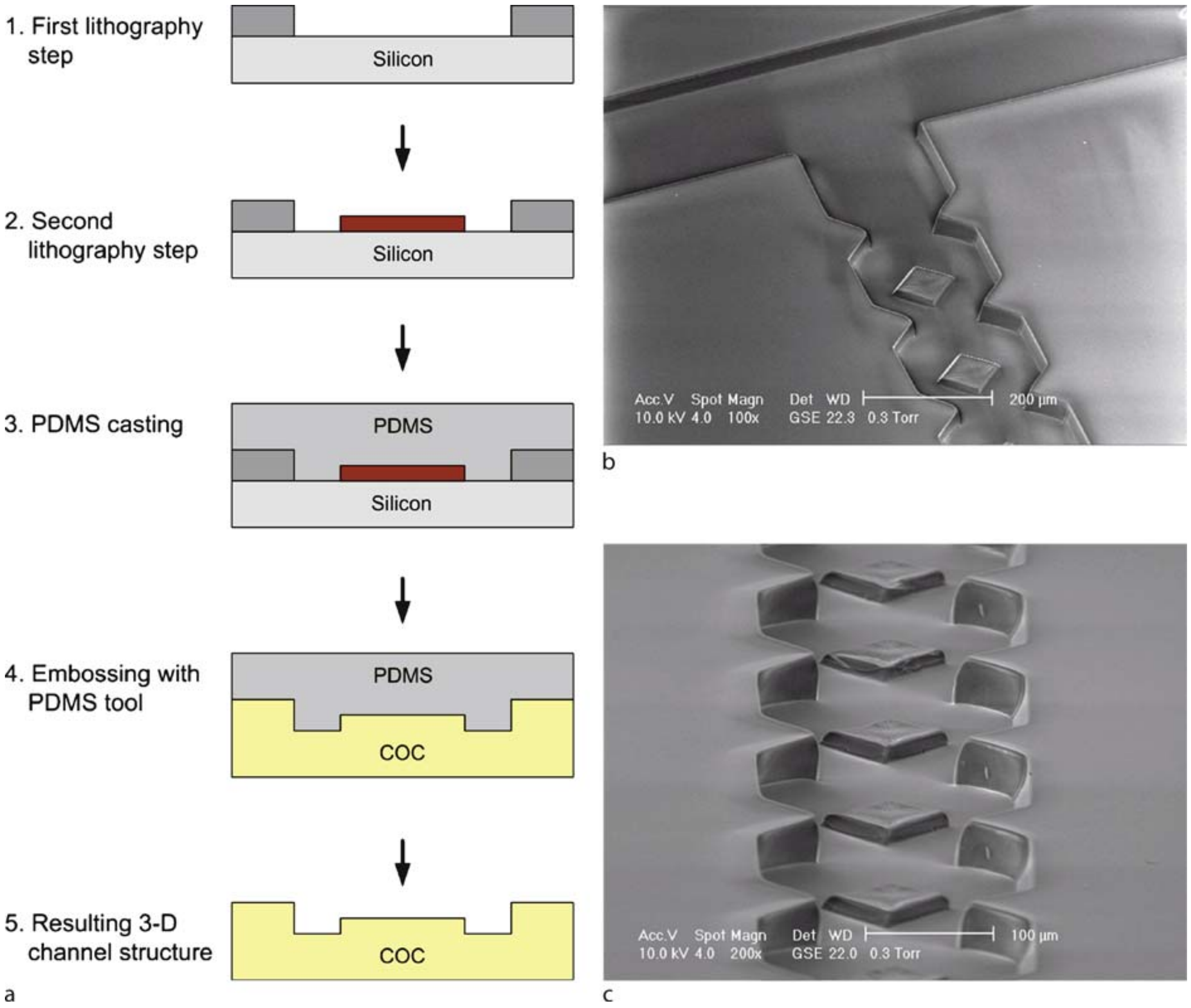

Micromolding, Figure 13 Hot embossing with multi-height PDMS tools (**a**). ESEM images of a micromixer fabricated in COC using this process at the (**b**) input and (**c**) channel regions. The 55 µm high mixing channel is 200 µm at the widest point and 100 µm at the narrowest. The diamond obstructions are 15 µm in height and 100 µm in width [24]

23. Lee JH, Peterson ETK, Dagani G, Papautsky I (2005) Rapid prototyping of plastic microfluidic devices in COC. Proc SPIE 5718:82–91
24. Bhagat AAS, Dagani G, Peterson ETK, Lee JH, Papautsky I (2005) Passive micromixer with obstructions for lab-on-a-chip applications. Proc SPIE 5718:291–297

Micromolding (Injection and Compression Molding)

Blake A. Simmons
Energy Systems Department, Sandia National Laboratories, Livermore, CA, USA
basimmo@sandia.gov

Synonyms

Injection molding; Polymer replication; Compression molding

Definition

Micromolding is one of the key technologies for microfluidic device production because of its mass-manufacturing capability and relatively low component cost. Micromolding is defined as a process similar to traditional commercial injection molding and/or compression molding that allows researchers and manufacturers to produce small features, typically ranging from 1 – 1000 µm, for microfluidic and microelectromechanical applications. This process typically involves the injection or compression of

a molten thermoplastic/thermoset material into a mold cavity that contains tooling with the features to be replicated into the plastic. These features can be channels, ridges, posts, vias, and/or any other component that lends functionality to the manufactured microfluidic device. These features can typically achieve tolerances of 0.01 to 5 μm, depending on the size of the replicated dimension of interest.

Overview

One of the primary drivers behind the commercial success of any microfluidic device and/or component is the cost of manufacturing. While glass is currently the dominant fabrication material in the microfluidics community, the process costs associated with these devices can be prohibitively high. Polymer micromolding offers an attractive alternative fabrication route to low-cost, high-performance microfluidic devices. This approach has been demonstrated to be highly effective in replicating the very fine features that lie at the core of any microfluidic device. Micromolding has its foundation in the commercial manufacturing of plastic parts, primarily injection and compression molding. Injection molding is a process in which a thermoplastic is heated above its glass transition temperature, injected into a mold cavity that contains the features to be replicated, and then cooled below its glass transition temperature to allow for efficient demolding. Compression molding is a process in which a thermoset is compressed in a mold cavity and then cured to consolidate the part and replicated features. In both cases, the tooling that contains the very fine features to be replicated is a critical compo-

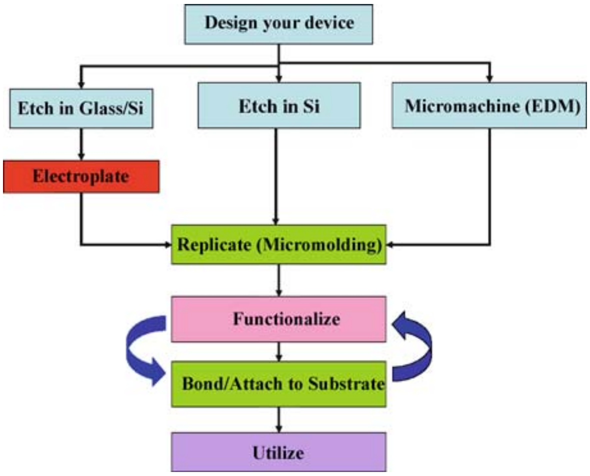

Micromolding (Injection and Compression Molding), Figure 1 Process diagram depicting the steps necessary to move from initial design stage to replication of microfluidic device using micromolding technique

Micromolding (Injection and Compression Molding), Figure 2 Examples of commercial injection molding machines: (**a**) Nissei electric horizontal injection molding machine, (**b**) Nissei hydraulic vertical injection molding machine (image source: [15])

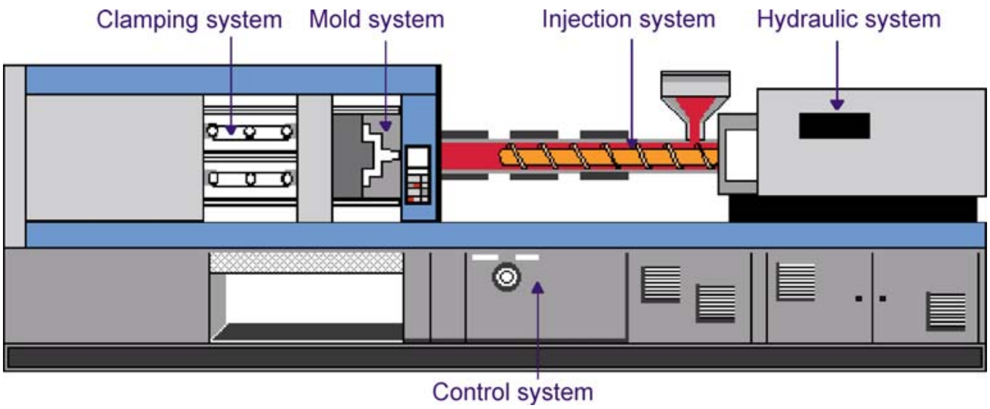

Micromolding (Injection and Compression Molding), Figure 3 Typical components located within an injection molding machine

nent that must be created through established microfabrication techniques.

Two other significant costs in the manufacture of micromolded parts are material costs and operational costs. The material cost associated with micromolding is primarily the cost of the plastic from which each part is made. Therefore, the excess volume of the part should be minimized so as to use the minimum amount of material. The operational cost is directly related to the cycle time for each part. In typical micromolding runs, 70 – 80 % of the total machine cycle time is spent waiting for the molten thermoplastic to cool and solidify in the mold before part ejection. In addition to cost, the production of microfluidic devices through micromolding offers other advantages. These include a wide range of materials to select from with tailored properties for the specific application, the fabrication of composite parts with embedded functionalities (i. e., embedding a sensing such as a fiber optic cable within the polymer substrate itself during micromolding) that enhance performance, and increased mechanical properties when compared with silicon or glass microfluidic devices.

Basic Methodology

Micromolding represents the most efficient method of producing microfluidic devices through mass manufacturing. The process by which tooling can be developed is presented in Fig. 1. We present here a summary of the injection and compression molding techniques that can be used for micromolding applications.

Injection Molding

Injection molding is a plastic-forming process used in the production of most commercially available of plastic parts. Injection molding is generally used in the high-speed manufacture of low-cost, high-volume parts, such as videocassette cases, plastic cups, or children's toys. There are several advantages associated with injection molding: the lower price per part, the wide selection of properties available in molded plastics cannot be duplicated by any other practical process, optically transparent materials can be molded with a smooth finish to produce microfluidic devices that are amenable to optical, fluorescent, and UV diagnostics, and the fabrication of delicate and flexible parts may be easily realized through injection molding that are difficult to consistently achieve hold for conventional machining processes. Injection molding is generally a high-volume manufacturing process, with one mold producing millions of parts. A small change in the design of a mold, or a defect that is present in the initial features to be replicated, is therefore significantly amplified during this process. There are several thousand types of plastic material that can be used in this process, including polymethylmethacrylate (PMMA), polycarbonate (PC), polyethylene (PE), polystyrene (PS), polyamide (PA), polypropylene (PP), polyphenylene ether (PPE), polyester terephthalate (PET), polyetheretherketone (PEEK), polyetherimide (PEI), cycloolefin copolymer (COC), and polyimide (PI). To date, polycarbonate and polymethylmethacrylate are the most widely used materials for injection molding of microfluidic devices.

There are several types of injection molding machines (Fig. 2) that are available from numerous commercial vendors (Nissei, Sumitomo, Polimoon, Milacron, Mikrotech, and Makuta, to name a few). These machines can vary greatly in terms of size, clamping pressure, hydraulic or electrical drives, and degrees of automation and robotic handling. There are two basic types of mold operation: vertical and horizontal. Both have advantages in terms of process flexibility that must be matched to the microfluidic device to be replicated. Injection molding machines can

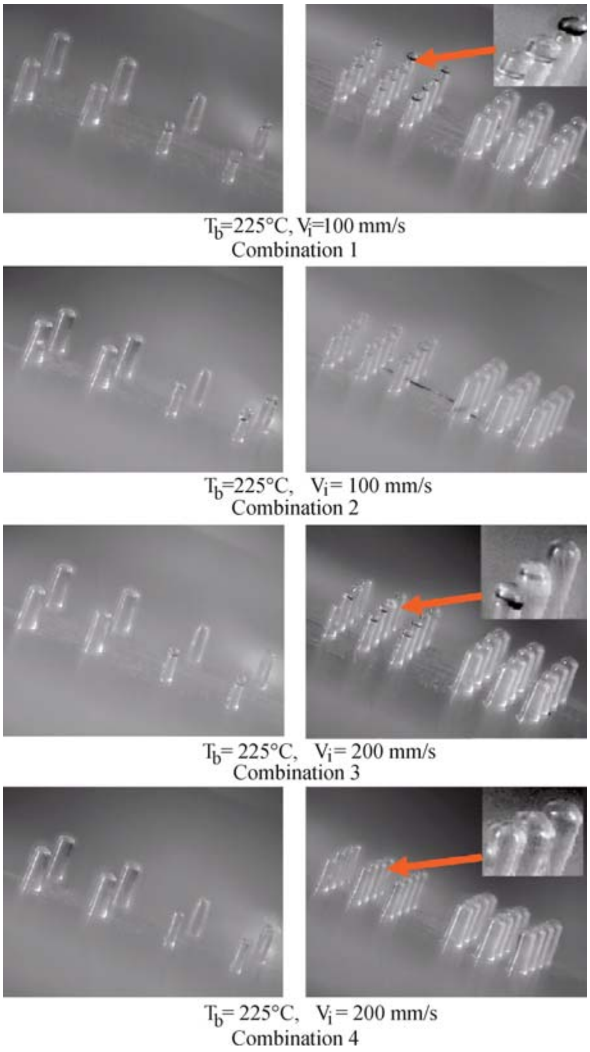

Micromolding (Injection and Compression Molding), Figure 4 Images taken of injection molded polypropylene replicates as a function of barrel temperature (T_b) and injection velocity (V_i) (Images taken from [13])

be classified as semiautomatic, in which the press follows a programmed cycle but the operator manually loads and unloads the press and/or places inserts into the mold cavity; and automatic, which operate under a fully automatic press cycle with robotic loading and unloading.

Any injection molding machine (Fig. 3) can be broken down into the following basic components: (1) injection units, (2) clamping unit, (3) control system, and (4) tempering devices. The process of injection molding typically consists of the following steps:

- Filling the injection barrel: The screw rotates and transports the molten thermoplastic from a hopper to the screw chamber.
- Closing the mold: The clamping unit moves forward until the two platens are in close contact to provide a barrier to polymer leakage. Typical clamping pressures range from 25 to 5000 t.
- Injection: The screw moves forward and injects the molten thermoplastic into the mold cavity. The polymer material fills the mold cavity and the features of the microfluidic device are replicated into the melt.
- Cooling: The melt is allowed to cool below the glass transition temperature and the part solidifies.
- Ejection: The mold opens and the cooled part containing the replicated features is ejected from the mold.

The mold defines the overall shape of the part, as well as the path by which the molten plastic flows from the barrel into the mold cavity. In most microfluidic applications, the mold cavity is in the form of a wafer or a die that will contain the microfluidic features on one of its exterior surfaces. The mold is the most complex element present in the injection molding process and typically represents the highest cost element. A simple mold has several features:

- Fixed and moving platens – These are rectangular blocks of aluminum or steel into which the shape of the part is cut.
- Cavity – When the fixed and moving platens are compressed together, the space formed by the cut-out portions, called the *cavity*, defines the overall shape of the part.
- Sprue – The sprue is a hole cut into the center of the fixed platen. Molten plastic flows from the sprue to fill the cavity.
- Runners – Runners are channels cut into the platens that direct molten plastic from the sprue to the gates.
- Gates – Gates are small openings between runners and cavities. These are the points at which plastic enters the cavity. They are generally small so that the finished part may be easily broken away from the useless sprue and runner material. (You can tell if a plastic part is manufactured by injection molding because it will have a small nubs where the gates were located.)
- Tooling – This mold insert contains the fine features of the microfluidic device to be replicated. This tooling can be created using micromachining, microlithography, or electroforming.

Several injection molding operating parameters must be optimized in order to produce a microfluidic device with a high degree of feature fidelity. Figure 4 presents the impact of the feature fidelity of different micron-sized post features as a function of barrel temperature and injection velocity. It is also important to note that computational modeling can be employed to predict optimal injection molding conditions.

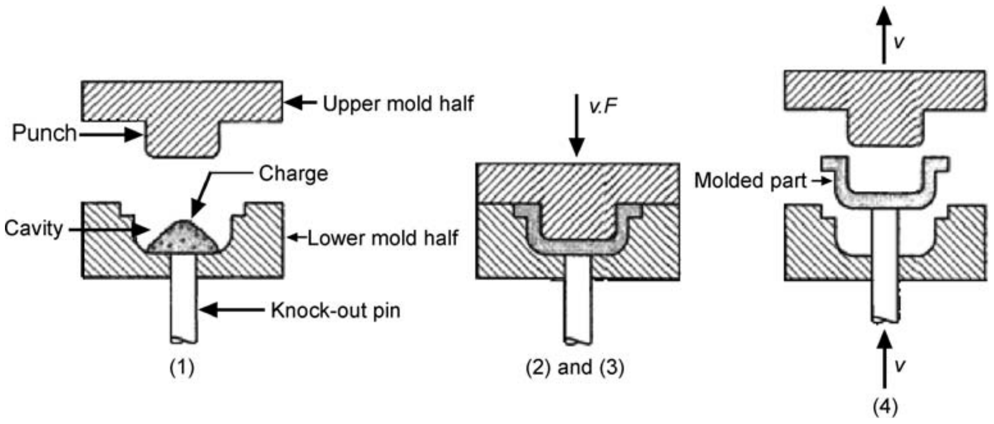

Micromolding (Injection and Compression Molding), Figure 5 General process flow for compression molding

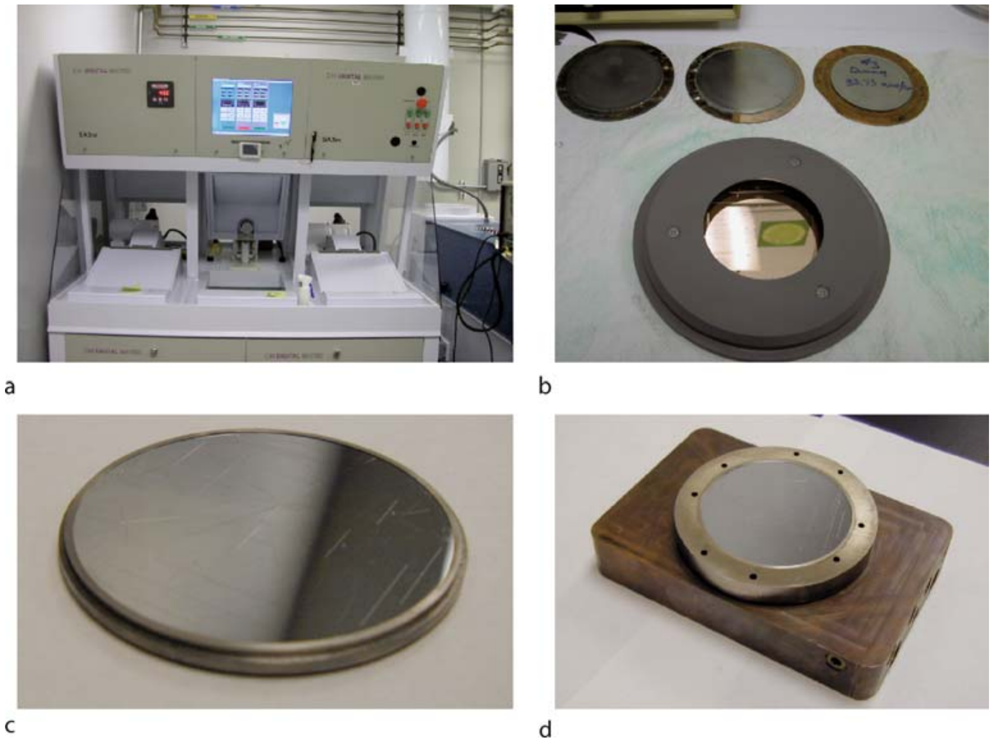

Micromolding (Injection and Compression Molding), Figure 6 Images taken of (**a**) commercial electroforming instrument, (**b**) wafers containing microfluidic features in holders for electroforming instrument, (**c**) Ni stamp containing the desired microfluidic features, and (**d**) Ni stamp placed within mold insert for injection molding machine (images courtesy of Sandia National Laboratories)

In addition to the standard processes of injection molding, there exist variants that may be applicable to a particular microfluidic device. These include reaction injection molding (a.k.a. RIM) where a monomer mixture is injected directly into a production mold where it polymerizes in the mold cavity and is then injected; resin transfer molding (a.k.a. RTM); gas-assisted injection molding; transfer molding; intrusion injection molding; ceramic injection molding.

Compression Molding

Compression molding is an old and widely used molding process for thermosetting plastics. These materials cure

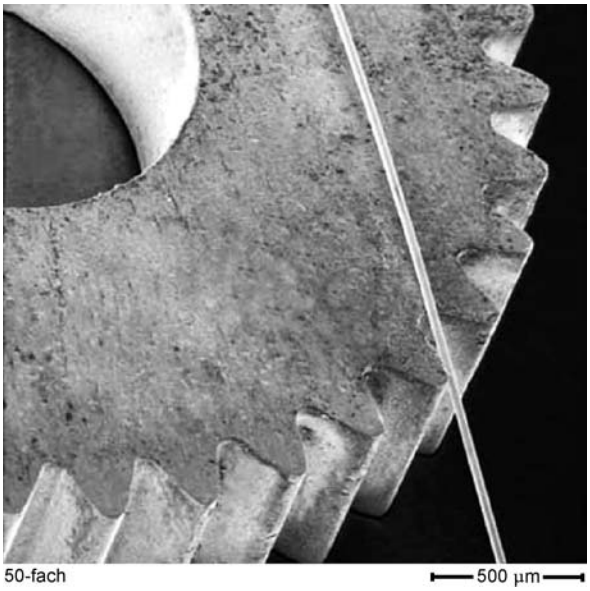

Micromolding (Injection and Compression Molding), Figure 7 SEM image taken of a micromachined part created through wire-EDM process (taken from [14])

at elevated temperatures and are then consolidated into a bulk material as a function of time. This technique can be used to create microfluidic devices with unique chemical and mechanical properties. Other applications of this technique include phonograph records, rubber tires, and various polymer matrix composite parts. The process (Fig. 5) typically consists of (1) loading a precise amount of molding compound, called the charge, into the bottom half of a heated mold; (2) bringing the mold halves together to compress the charge, forcing it to flow and conform to the shape of the cavity; (3) heating the charge by means of the hot mold to polymerize and cure the material into a solidified part; and (4) opening the mold halves and removing the part from the cavity. The initial charge of molding compound can be in any of several forms, including powders or pellets, liquid, or cut preforms of material. The amount of polymer must be precisely controlled to obtain repeatable consistency in the molded product. It is common practice to preheat the charge prior to its placement into the mold; this softens the polymer and shortens the production cycle time. Preheating methods include infrared heaters, convection heating in an oven, and use of a heated rotating screw in a barrel. The latter technique (borrowed from injection molding) is also used to meter the amount of the charge.

Compression molding presses are oriented vertically and contain two platens to which the mold halves are fastened. The presses involve either of two types of actuation: (1) upstroke of the bottom platen or (2) downstroke of the top platen, the former being the more common machine configuration. They are generally powered by a hydraulic cylinder that can be designed to provide clamping capacities up to several hundred tons. Molds for compression molding are generally simpler than their injection mold counterparts. There is no sprue and runner system in a compression mold (in direct contrast to an injection molding system), and the process itself is generally limited to simpler part geometries and channel configurations due to the lower flow capabilities of the starting thermosetting materials. However, provision must be made for heating the mold, usually accomplished by electric resistance heating, steam, or hot oil circulation. Compression molding machines can be classified as hand molds, used for trial runs; semiautomatic, in which the press follows a programmed cycle but the operator manually loads and unloads the press; and automatic, which operate under a fully automatic press cycle (including automatic loading and unloading).

Materials for compression molding typically include phenolics, melamine, urea-formaldehyde, epoxies, urethanes, and elastomers. All of these possess intrinsic chemical and mechanical properties that can be used to tailor the performance of the microfluidic device depending on the specific application. Typical commercial compression molding thermoset plastic parts include electric plugs, sockets, and housings; pot handles, and dinnerware plates. Advantages noted for compression molding in these applications include: (1) molds that are simpler, less expensive, and require low maintenance; (2) minimal residual material; and (3) low residual stresses in the molded that may enable thin-film polymeric microfluidic devices. A typical disadvantage is longer cycle times and therefore lower production rates than injection molding.

Micromolding Tooling Fabrication Techniques

The most expensive and time consuming part of the entire process is the making of the mold, for once the mold is made, a great number of parts may be produced very rapidly. It is this speed of production, and the fact that the cost of the mold can be amortized over a large number of parts, that makes injection molding an inexpensive process for producing large numbers of parts. An injection molding machine is capable of producing 100 or more parts per hour, compared to conventional machining which may produce a half dozen parts per hour. There are several techniques available to produce stamps suitable for micromolding. The most common of these is electroforming, where microfluidic features that have been created using standard microfabrication techniques such as wet

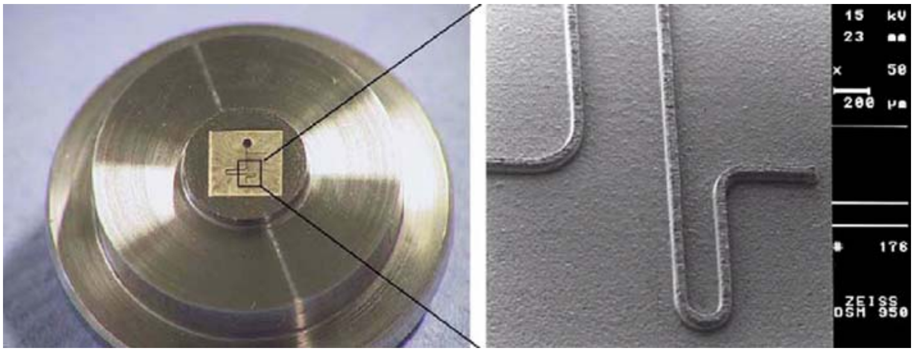

Micromolding (Injection and Compression Molding), Figure 8 Images taken of micromachined tooling to be used to create polymeric channels through micromolding that has been created through plunge-EDM process (taken from [14])

etching and reactive ion etching are used as the master. A metal seed layer is deposited on the surface of these features to create an electroplating base. The coated wafer is then placed in an electroplating bath (Fig. 6) where a bulk metal, typically nickel, is electroplated on top of the original features. After the electroplating process is complete, the Ni is released and then used as a replication tool for injection or compression molding. Another common micromachining technique is electrode discharge machining (EDM, Figs. 7 and 8). This technique creates robust, fine features in a bulk material (typically graphite or copper) that is suitable for use in micromolding machines.

Key Research Findings

It is clear from an extensive examination of the literature, as well as the available information from numerous commercial vendors, that micromolding is an efficient and cost-effective approach for the mass production of polymeric microfluidic devices. The economic advantages, from a manufacturing perspective, are tremendous when compared with other microsystem fabrication techniques. This technique is capable of producing microfluidic devices very rapidly with a high degree of fidelity, with feature deviation typically in the range of $0.1-2\%$. The number of devices that can be produced by micromolding on a time-averaged basis is at least an order of magnitude higher than any other microfluidic manufacturing technique. The highest cost associated with this process is the initial capital cost of purchasing the micromolding equipment, followed by the costs associated with developing the proper tooling that allows for high-fidelity replication. Several different techniques exist to create robust tooling, such as micromachining, lithography, and electroforming. All of these techniques can reliably manufacture the micro-scale features that are required for proper microfluidic device operation. Injection molding is by far the most common technique of producing large numbers of polymeric microfluidic devices. Compression molding is a specialized technique that is very powerful in applications where non-traditional thermoplastics and elastomers are the material of choice.

Future Directions for Research

Micromolding is a proven and growing area in microfluidic device fabrication. As this field becomes more mature in terms of commercial applications, the drivers for low-cost mass manufacturing will continue to grow. As such, there will be increased demand for micromolding manufacturing techniques. The majority of the future directions for research in this field will be found in producing advances in tool design and manufacture, systems engineering and process flow improvements, process design that enable mutli-component (fluidic interconnects, optical lenses, optical fibers for on-chip instrumentation, and multi-level features) integration within a single manufacturing step. One nascent field is the development of micromolding techniques that can efficiently replicate nanometer features for nanofluidic devices.

Cross References

► Micromolding
► Fabrication of 3D Microfluidic Structures

References

1. Weber L, Ehrfeld W (1999) Micromoulding-market position and development. Kunststoffe 89(10):192–202
2. Yao D, Kim B (2004) Scaling issues in miniaturization of injection molded parts. Manuf Sci Eng 126:733–739
3. Mönkkönen K, Hietala J, Paakkonen P (2002) Replication of sub-micron features using amorphous thermoplastics. Polym Eng Sci 42(7):1600–1608

4. Zhao J, Mayes RH, Chen G, Xie H, Chan PS (2003) Effects of process parameters on the micro molding process. Polym Eng Sci 43(9):1542–1554
5. Yoshii M, Kuramoto H, Kato K (1994) Experimental study of transcription of minute width grooves in injection molding. Polym Eng Sci 34(15):1211–1218
6. Wimberger-Friedl R (2001) Injection molding of sub-μm grating optical elements. In: Heim HP, Potente H (eds) Specialized Molding Techniques, Plastic Design Library. Norwich, New York
7. Yu L, Lee LJ, Koelling KW (2004) Flow and heat transfer simulation of injection molding with microstructures. Polym Eng Sci 44(10):1866–1876
8. Arlø UR, Kjær EM (2001) Transcription of small surface structures in injection molding – an experimental study. In: Heim HP, Potente H (eds) Specialized Molding Techniques, Plastic Design Library. Norwich, New York
9. Shen YK, Yeh SL, Chen SH (2002) Three-dimensional non-newtonian computations of micro-injection molding with the finite element method. Int Commun Heat Mass Transf 29(5):643–652
10. Spennemann A, Michaeli W (2001) Process analysis and injection molding of microstructures. In: Heim HP, Potente H (eds) Specialized Molding Techniques, Plastic Design Library. Norwich, New York
11. Yu L, Koh CG, Lee J, Koelling KW, Madou MJ (2002) Experiment investigation and numerical simulation of injection molding with micro-features. Polym Eng Sci 42(5):871–888
12. Shen YK, Wu WY (2002) An analysis of the three-dimensional micro-injection molding. Int Commun Heat Mass Transf 29(3):423–431
13. Sha B, Dimov S, Griffiths C, Packianather MS (2007) Investigation of micro-injection moulding: Factors affecting the replication quality. J Mater Process Technol 183:284–296
14. Uhlmann E, Piltz S, Doll U (2005) Machining of micro/miniature dies and moulds by electrical discharge machining – Recent development. J Mater Process Technol 167:488–493
15. www.NisseiAmerica.com Accessed 5 March 2008

Micro/Nano Anemometers

Synonyms

Thermal flow sensors

Definition

Hot-wire anemometers have traditionally been applied in the fields of experimental fluid mechanics and aerospace engineering. Despite the possibilities to measure real-time physical parameters such as temperature, velocity, flow rates, and shear stress, the spatial resolution is limited to the device dimension. The advent of MicroElectroMechanical system (MEMS) and nano-scale thermal sensors has revolutionized the spatial and temporal resolution critical to gain entry into micro-fluidics, micro-circulation, biomedical sciences, and cardiovascular medicine. These micro/nano devices are fabricated with the semiconductor-based sensing elements having the physical property of a resistor and the dimension at one tenth (or hundredth) of a string of hair. Basede on the Joule effect, these resistant elements are heated by passing electric current through the elements. As air or fluid flow past by the surface of the elements, the changes in temperature alter the resistivity of the sensing elements, from which physical parameters are obtained.

Cross References

► Heat Transfer in Microchannel Flows

Micro/Nanofluidics

► Flow by Surface Acoustic Waves
► Microfluidic Rotary Pump

Micro- and Nanoscale Anemometry: Implication for Biomedical Applications

Mahsa Rouhanizadeh, Hongyu Yu, Lisong Ai, Jennifer Xu, Tzung K. Hsiai
Department of Biomedical Engineering
& Cardiovascular Medicine, School of Engineering & School of Medicine
University of Southern California, Los Angles, CA, USA
rouhaniz@usc.edu

Synonyms

Thermal flow sensors; Hot wire; Hot-wire anemometer

Definition

Hot-wire anemometers (► micro/nano anemometers) have been developed for a wide spectrum of applications from experimental fluid mechanics to aerospace engineering to measure physical parameters such as temperature, flow rates, and shear stress. The advent of microelectromechanical systems (MEMS) and nanoscale thermal sensors has provided an entry point to microfluidics, biomedical sciences, and micro-circulation in cardiovascular medicine. These MEMS and nanoscale devices are fabricated with semiconductor-based sensing elements which harbor the physical property of a resistor and have the dimension of one-tenth of a strand of hair. On the basis of the heat transfer principle, these resistant elements are heated by the Joule effect due to the passage of electric current. As the

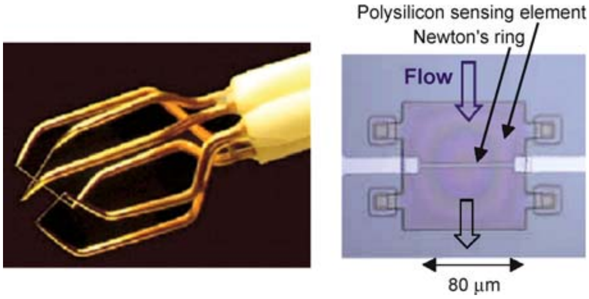

Micro- and Nanoscale Anemometry: Implication for Biomedical Applications, Figure 1 (**a**) Conventional hot-wire anemometry. The arrows indicate the thin hot wires connected to the electrodes with both ends. (**b**) MEMS shear stress sensor supported by an underneath cavity to reduce the heat loss to the substrate as shown by the presence of a Newton's ring

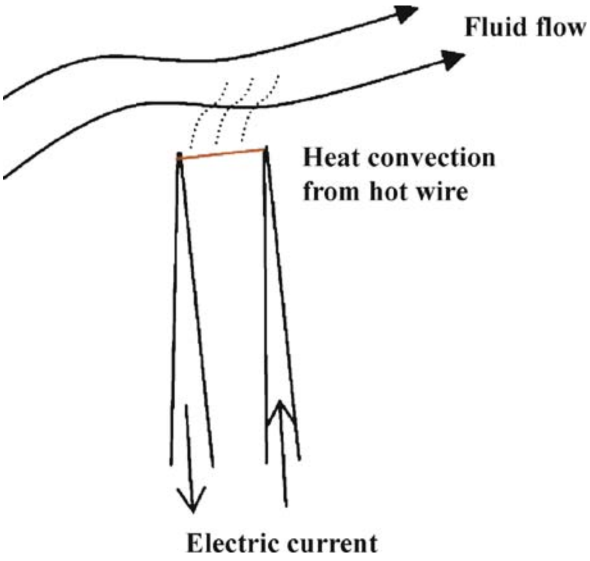

Micro- and Nanoscale Anemometry: Implication for Biomedical Applications, Figure 2 The operating principle of hot-wire anemometry. The electric current is passed to the hot wire via the electrodes. The changes in resistance of the hot wire in response to the fluid flow are calibrated for temperature, flow rate, and shear stress

air or fluid flows past their surfaces, the decrease in temperature alters the resistance of the sensing elements, from which physical parameters can be obtained.

Overview

The concept of hot-wire or hot-film anemometry was first conceived in the early 1900s [1]. Due to the technical difficulty in developing and testing hot-wire anemometers, published experimental data have remained scarce. Boussinesq was one of the first to have validated the theory of hot-wire anemometry [2], followed by other investigators, including Ziegler [1] who was the first to develop the constant-temperature anemometer to enhance the sensitivity. Later, King designed hot-wire anemometers coupled with the theory of heat convection using cylinders immersed in a fluid flow [3]. Recently, Ho and coworkers [4] as well as Sheplak et al. [5] have developed MEMS thermal sensors for aerospace applications. Overall, these investigators have contributed to the basics of hot-wire anemometry for biomedical and clinical applications [6–8]. By virtue of their high temporal and spatial resolution, micro- and nanoscale thermal sensors have ushered in the possibility to acquire the time- and spatial-varying components of physical parameters in vivo.

Shear stress is measured by direct and indirect methods [9]. One of the direct methods is floating element sensing based on both piezoresistive [10] and capacitive [9] readout schemes. The floating element sensors are complicated to fabricate, consisting of fragile mechanical devices and requiring accurate transduction of minute motions. The piezoresistive readout schemes in response to shear stress under low Reynolds numbers or creeping flow are likely below the threshold of the percent changes in piezoresistive elements. The high impedance and capacitive readout scheme also generates high levels of drift in resistance when the sensor is exposed to turbulence in environments such as a wind tunnel.

The indirect methods include ultrasonic Doppler, magnetic resonance imaging (MRI) and thermal anemometry, which measure the shear stress indirectly by correlating this parameter to flow rate. The ultrasonic Doppler method and MRI are non-invasive; however, the spatial resolution near the wall is not as good. Another indirect method is to correlate shear stress with convective cooling of a heated element based on the heat transfer principle. The advent of MEMS technology has made possible advances in microfluidics and biomedical applications.

The advantages of MEMS thermal anemometry are twofold:

- simplicity in the microfabrication and
- high sensitivity in detecting the shear stress through the correlation with heat transfer coefficient.

In response to pulsatile blood flow in complicated arterial geometry, MEMS sensors are able to provide spatial resolution to minimize flow disturbance and time resolution to measure shear stress in unsteady flow fields.

Basic Methodology

Operating Principle

Traditionally, hot-wire or hot-film anemometry has been developed to directly measure the fluid velocities under unsteady state or in the presence of turbulent flow [11].

Hot-wire anemometry consists of an electrical conductive wire or wires functioning as the thermistance that is heated by passage of electrical current (Fig. 2). The heated wire forms a thermal boundary layer in the flow field mainly by convective heat transfer. In this context, the changes in electrical resistance of the hot wire in response to fluid flow past the hot wire are calibrated electrically for obtaining flow velocity, pressure, shear stress, and temperature. Assuming that the rate of heat loss due to conduction to the electrodes and radiation is negligible, a relation for energy balance is described as follows:

Stored thermal energy
= Electrical energy input
− Thermal loss due to heat convection .

This relation is further expressed in terms of power as follows:

$$C\frac{\mathrm{d}T}{\mathrm{d}t} = \frac{V^2}{R} - P_1 \quad (1)$$

where C denotes the specific heat of the wire, t the time, T the temperature, V the electrical voltage, R the electrical resistance, and P_1 the thermal loss to the fluid.

For a practical micro- or nanoscale anemometer, the sensor consists of a resistive element patterned on the surface of a supporting substrate (Fig. 3). The thermal element resides within the velocity boundary layer in which the velocity changes from zero at the wall to the mean flow velocity of the upper boundary. The rate of heat loss from the heated resistive element to the medium flow (air or liquid) depends on the velocity profile in the boundary layer. The temperature gradient develops above the sensing element, and a thermal boundary layer forms in response to air or fluid flow (Fig. 3). Within the thermal boundary layer, the thermal gradient decreases away from the heated element surface until the temperature reaches that of the mean stream flow [4].

The relationship between τ and the temperature of the heated resistor has been extensively studied under the assumption that the thermal boundary layer of the thermal element lies within the velocity boundary layer [4]. The ▶ wall shear stress is defined to be linearly proportional to the stream-wise pressure gradient. Given that electrical power (P) is expressed as $P = V^2/R$, a linear relationship between V^2 and $\tau^{1/3}$ is established as [4]:

$$P = \frac{V^2}{R} = \left(A_\mathrm{T} + B_\mathrm{T}\tau^{1/3}\right) \quad (2)$$

where A_T represents a combination of effective area and length of the thermal element, heat capacity, thermal conductivity, and ▶ viscosity of the fluid, B_T denotes the conductance of heat loss to the surface and R the electrical resistance at the fluid temperature. The relationship between shear stress and heat transfer element is valid under the assumption that the thermal boundary layer of the thermal element lies within the velocity boundary layer, and that the thickness of the thermal boundary layer is small in relation of the dimension of the sensing element. However, this assumption may not be valid for certain microscale devices. By empirical data parameterization and modeling, others have arrived at a linear relations as expressed by $\Delta p \propto \tau^{0.77}$ for microscale sensors [12], where Δp denotes power.

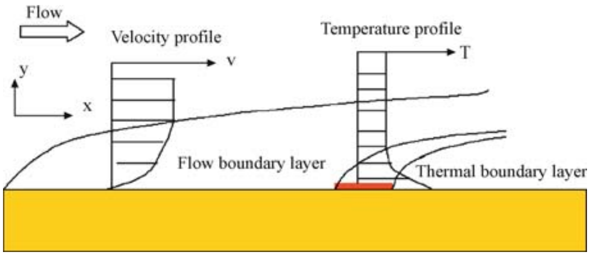

Micro- and Nanoscale Anemometry: Implication for Biomedical Applications, Figure 3 Two-dimensional physics model for MEMS/nanoscale anemometry. The fluid flow is denoted in the x-direction. At steady state, a parabolic velocity profile reflects the fully developed flow. The heat generating/sensing element is denoted in a red rectangular block which is heated by the electric current to form a thermal boundary layer

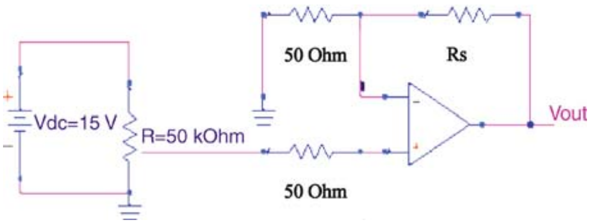

Micro- and Nanoscale Anemometry: Implication for Biomedical Applications, Figure 4 Constant current circuit. Note that Rs denotes the sensing element

The relationship in Eq. (2) further allows for the measurement of shear stress through the hot-wire resistance as follows:

$$\frac{R}{R_0} = 1 + \alpha(T - T_0) \quad (3)$$

where R_0 is the resistance at ambient temperature T_0 and α is the ▶ temperature coefficient of resistance (TCR). The resistance overheat ratio is expressed as $(R - R_0)/R_0$.

To detect the resistance changes due to the thermal loss to the fluid, many laboratories have designed electrical circuits for

- constant temperature (CT),

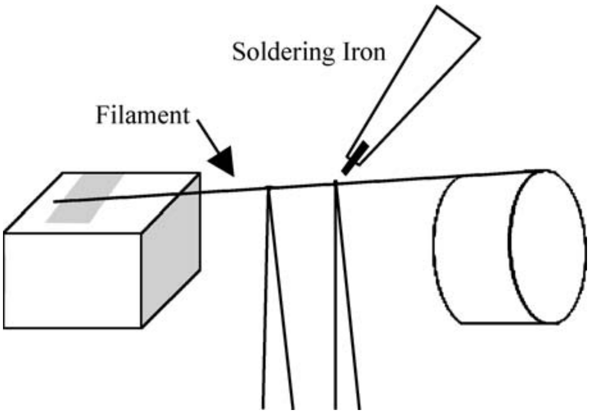

Micro- and Nanoscale Anemometry: Implication for Biomedical Applications, Figure 5 The conventional hot-wire anemometry fabrication by soldering the hot wire to the electrodes

- constant current (CI),
- constant voltage (CV), and
- pulsed signal (PS) methods.

The first three circuit designs entail the use of a single wire working as both heating source and sensing element for direct measurement, whereas the PS mode requires more than two wires, one for the source and another for the sensing element. Specifically, the first wire receives the pulsed input while the second detects the output of voltage responses so that the time delay and amplitude are calibrated to the fluid velocity. Albeit it has complicated circuitry, the CT mode is able to achieve high frequency bandwidth ideal for investigation of turbulent flow.

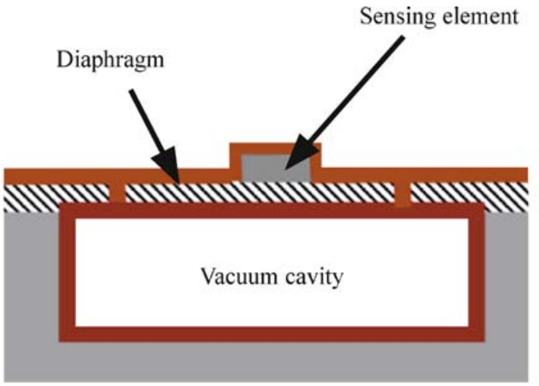

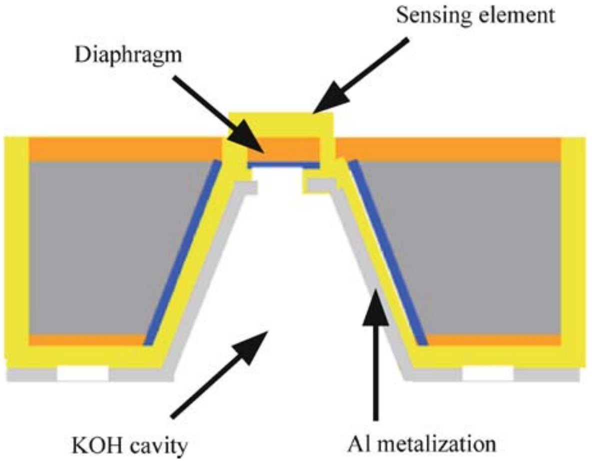

Micro- and Nanoscale Anemometry: Implication for Biomedical Applications, Figure 6 (**a**) MEMS shear stress sensor with vacuum cavity underneath. (**b**) Backside wire bonding for reducing the disturbance to the flow

Fabrication

Traditionally, anemometer wire is made of tungsten, platinum or a platinum–iridium alloy. Tungsten is presently the more popular hot wire material. Soldering and acidic bubble are the two methods (Fig. 5). Because of low resistance in the metal, a high current is required to drive the device. Several experimental disadvantages remain with the utilization of the conventional anemometers:

- low sensitivity,
- high power dissipation due to ineffective insulation of the heating filament from the substrate, and, most notably,
- local flow disturbance in the region of direct measurement.

MEMS Thermal Sensors and Nanofabrication

The semiconductor-based micro- and nanoscale sensors have ushered in the possibility to resolve the engineering challenges in developing and applying the conventional hot-wire anemometer. By virtue of their small dimension, the inherent issues such as flow disturbance and packaging have been minimized. Furthermore, fabrication of multiple devices has been made possible for high-throughput analyzes. The heavily doped polysilicon strip or nanowire for the sensing element has given rise to a higher resistivity than that of metal, resulting in superior sensitivity at low power consumption.

A vacuum cavity was created by both surface and bulk microfabrication to insulate the sensing element from the solid substrate (Fig. 6a). The presence of a cavity further maximizes unidirectional heat transfer in the flowing medium. A KOH-etched cavity was created by bulk micromachining to generate backside wire bonding (Fig. 6b). The design of backside wire bonding has advanced the application of MEMS devices for cardiovascular medicine where catheter-based sensors are deployed into the arterial circulation. While the surface of the sensing element is exposed to the biological fluid, the microelectronics is

M

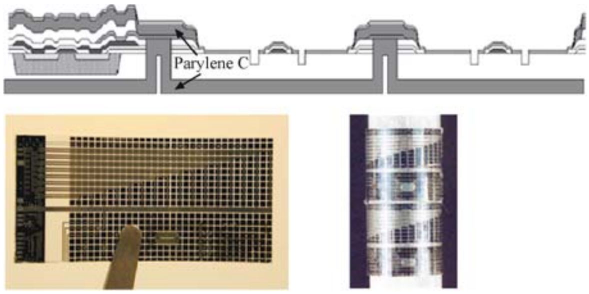

Micro- and Nanoscale Anemometry: Implication for Biomedical Applications, Figure 7 (**a**) Cross-section of a flexible shear stress sensor. (**b**) Shear stress sensors are coated in a 1 cm × 2 cm flexible parylene skin. The arrays of sensors reside on the opaque silicon islands. (**c**) Two flexible sensor skins are wrapped around a cylinder

insulated on the back side via contact between the backside aluminum metalization and the sensing element.

Finally, packaging micro- and nanoscale sensors is critical to translate the bench laboratory technology to biomedical applications. Parylene C is a commonly used biocompatible polymer for surface coating. Given its conformal property, this polymer has recently been explored as a structural and packaging material for flexible MEMS devices (Fig. 7). Parylene can be conformed on the non-flat surface of micro- and nanoscale devices, thereby opening an entry point to the complicated anatomic structures such as human arterial circulation.

Key Research Findings

The hot-wire anemometer has been extensively applied in the area of fluid mechanics. It allows for direct measurement of physical parameters such as flow rate and temperature, from which fluid shear stress can be calibrated for a known geometry. The dimension of a conventional hot wire lies in the range 4 – 10 μm in diameter and 1 mm in length, and its frequency response is relatively low. The advent of micro- and nanofabrication has enabled the miniaturization of hot-wire anemometers to 2 μm in width and 40 μm in length, and the semiconductor-based property of the sensing elements has enabled devices to operate at a high frequency cut-off of 71 kHz [13]. Micromachined thermal shear stress sensors for underwater applications have been developed by applying silicon nitride as the insulating layer on the diaphragm [14]. Parylene C coating and backside wire bonding techniques are two engineering solutions to insulate microelectronics for underwater applications. These techniques have enabled the sensors to be used for naval submarines and cardiovascular circulation. Because of their high spatial and temporal resolution, micro- and nanoscale sensors have enabled investigators to overcome engineering challenges otherwise difficult with conventional technology, and to advance the fields in cardiovascular research, aerospace engineering, and flexible packaging for biological systems.

Applications for Cardiovascular Research

Cardiovascular disease, namely coronary artery disease, remains the leading cause of death in the developed nations. Over the last few years, MEMS sensors have advanced the understanding of blood flow, namely fluid shear stress, in arterial circulation. Fluid shear stress is defined as the frictional force acting tangentially on the surface of a blood vessel wall. Furthermore, the measurement of wall shear stress is important to study the durability of prosthetic valves, and to monitor thrombosis or blood clots in cardiopulmonary bypass machines, artificial hearts, and left ventricular assist devices. Luminal shear stress measurement predicts the development of atherosclerotic plaque in patients at risk for acute heart attacks. In this context, the application of microscale hot-wire anemometry bridges fluid mechanics of blood flow with vascular biology.

Real-time wall shear stress is difficult to monitor precisely because it varies in space and time. MEMS sensors provide high spatial resolution to resolve variations in shear stress in a 3D bifurcation model for small-scale hemodynamics. The application of MEMS sensors with backside wire bonding (Fig. 6b) captured the spatial variations in shear stress in a 3D bifurcation model (Fig. 8). The measured skin friction coefficients at various positions correlated well with values derived from the exact Navier–Stokes solution of the flow within the bifurcation [13]. Therefore, the development of MEMS sensors has enabled the precise measurements of spatial variations in shear stress for small-scale hemodynamics otherwise difficult with conventional technologies such as computed tomography (CT scan), magnetic resonance imaging (MRI), ultrasound, and laser Doppler velocimetry.

Applications for Aerodynamics

The design and development of aerodynamic vehicles require precise measurements of shear stress and boundary layer for turbulence control. The application of MEMS sensors has enabled the localization of flow separation where drastic variation in shear stress develops on the air foils. Ho and Tai [11] have demonstrated the utilization of the MEMS shear stress sensors for an aerodynamic aircraft by fabricating an IC-integrated skin, which is flexible and conformal to the surface of air foils [15]. For instance, a network of sensors has been implemented in different structural sections of a delta-wing (Fig. 9a) via ►flexible shear stress sensors (Fig. 9b) in an unmanned

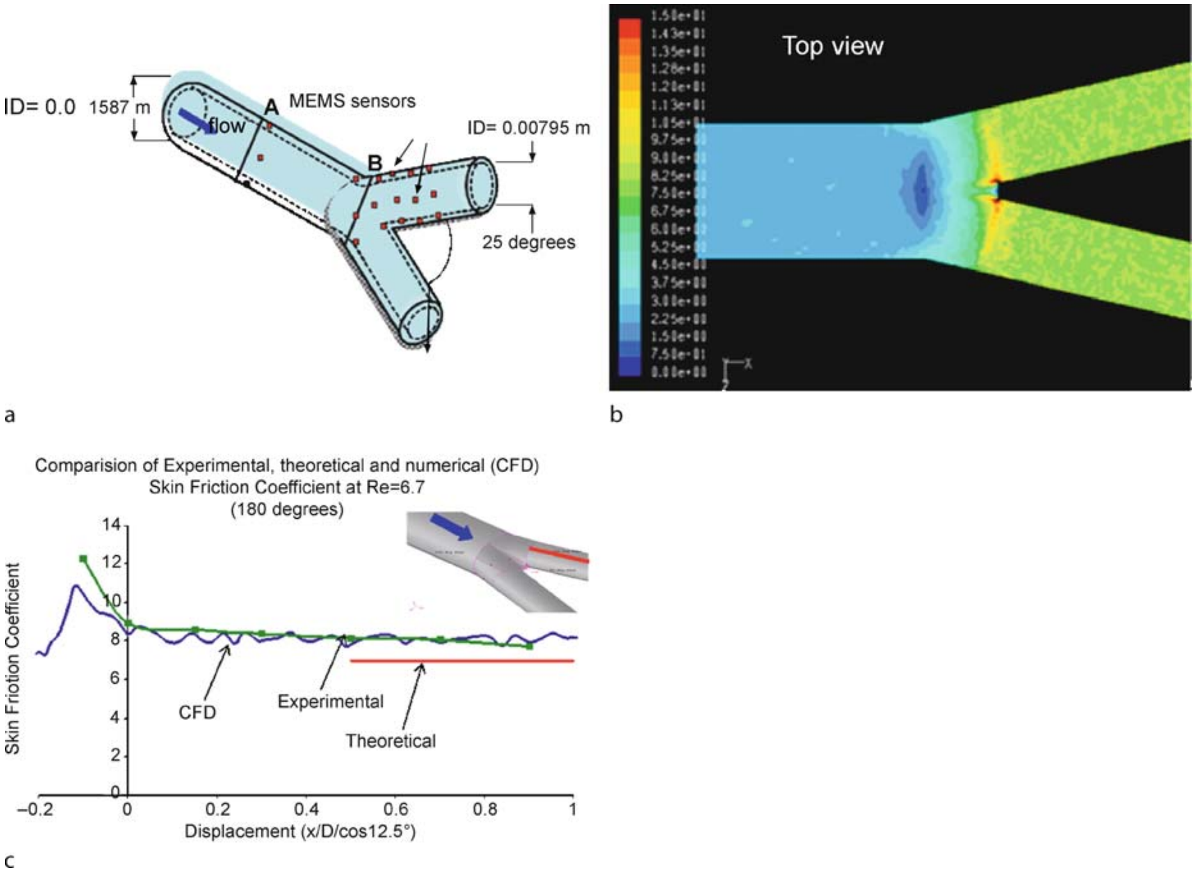

Micro- and Nanoscale Anemometry: Implication for Biomedical Applications, Figure 8 (**a**) An array of MEMS sensors embedded in a 3D bifurcation model. (**b**) Computational fluid dynamics (CFD) solutions for skin friction coefficient (C_f) at a Reynolds number of 6.7. C_f represents local wall shear stress values normalized by the upstream dynamic pressure. C_f values are shown along the interior surface of bifurcation. (**c**) Comparison of the CFD (in blue), experimental (in green), and theoretical (in red) skin friction for the 180° edge. $x/D/\cos(12.5)$ is the x distance normalized to the diameter of the inlet pipe and parallel to the centerline of the outlet pipes

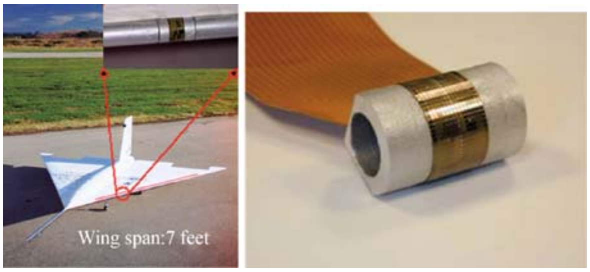

Micro- and Nanoscale Anemometry: Implication for Biomedical Applications, Figure 9 (**a**) An unmanned aerial vehicle installed with shear stress sensor skin along the leading edge of the delta-wing. The inset illustrates the shear stress sensor skin mounted on a 0.5 inch diameter aluminum cylinder. (**b**) Magnification of flexible sensor sheet that is wrapped around the aluminum cylinder

aerial vehicle (UAV). This application of MEMS sensors has advanced the investigation of the air flow separation on the leading edge of the delta-wing.

Flexible Polymer Packaging for Shear Stress Sensors

Packaging micro- and nanoscale devices entails two main challenges:

- insulation of the electronics and
- design of flexible devices conformal to the biological systems.

As a biocompatible coating [16], parylene C has recently been explored as a structural and packaging material for miniaturized biomedical devices. Parylene protects the sensors and serves as electrical isolation. In order to package an array of sensors in a catheter, a microelectric interconnect has been established via a flexible polymer (Fig. 10). The electrical leads are attached to sensors embedded in parylene film (Fig. 10b). Platinum or gold wires are sandwiched in the parylene film to make the connections to the sensors either by wire bonding or flip-chip bonding (Fig. 10c).

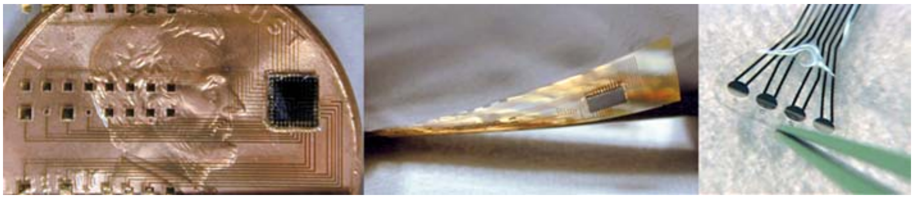

Micro- and Nanoscale Anemometry: Implication for Biomedical Applications, Figure 10 (**a**) Top view of transparent parylene skin with Au wires connected to a single silicon island. (**b**) Side view of flexed parylene skin with Au wires and silicon island. (**c**) Flexed parylene skin with platinum (Pt) wires

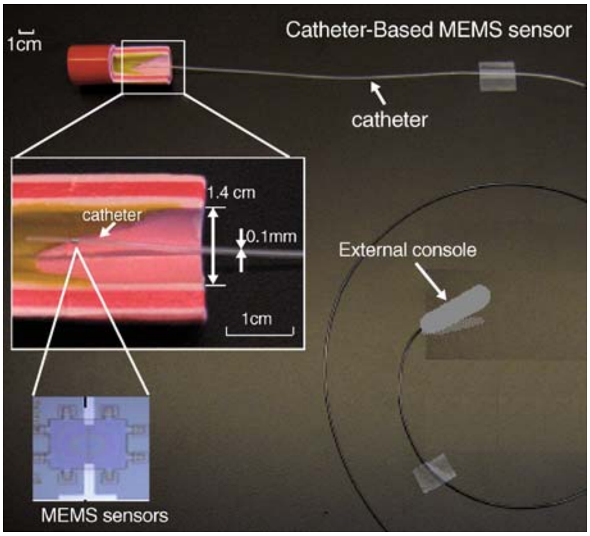

Micro- and Nanoscale Anemometry: Implication for Biomedical Applications, Figure 11 A catheter-based sensor platform in an aortic model. The inset shows the diameter the catheter in relation to that of the aorta

Future Directions for Research

The emerging role of micro- and nanoscale hot-wire anemometry would likely accelerate the translation of in vitro devices to in vivo applications, thereby bridging the lab-to-patient gap. Real-time measurements of intravascular physical parameters, specifically shear stress, temperature, pressure, and flow rate, provide a basis to link hemodynamics with biochemical events in blood vessels. The complex curvature of the vascular system requires small, minimally invasive sensors to discretely measure in real time intravascular physical parameters with minimal blood flow disturbance. To achieve this, flexible micro- and nanoscale sensors would allow for steering in the complicated anatomy in biological systems (Fig. 11). In summary, the utilization of micro- or nanoscale sensors provides a quantitative assessment of vascular hemodynamics. This approach lends itself to applications in broad areas of medicine and physiology and is particularly relevant to quantitative studies of cancer biology as well as cardiovascular medicine. Future development and application of micro- and nanoscale sensors for the in situ assessment of biochemical markers in blood vessels would provide a basis for physical and chemical analyzes of oxidative stress, drug delivery, and regenerative therapy.

Cross References

- ► Heat Transfer in Microchannel Flows
- ► Thermoresistive Flow Sensors

References

1. Comtebellot G (1976) Hot-Wire Anemometry. Ann Rev Fluid Mech 8:209–231
2. Stainback PC, Nagabushana KA (1996) Review of Hot-Wire Anemometry Techniques and the Range of their Applicability for Various Flows. Electron J Fluids Eng, Transaction of the ASME
3. King LV (1914) Phil. Trans R Soc, London
4. Liu CJ, Huang J, Zhu Z, Jiang F, Tung S, Tai YC, Ho CM (1999) A Micromachined Flow Shear-stress Sensor Based on Thermal Transfer Principles. J MEMS 8(1):90–99
5. Sheplak M, et al (2002) Characterization of a silicon-micromachined thermal shear-stress sensor. AIAA J 40(6):1099–1104
6. Hsiai TC, SK Wong P, Ing M, Salazar A, Hama S, Navab M, Demer L, Ho CM (2003) Monocyte Recruitment to Endothelial Cells in Response to Oscillatory Shear Stress. FASEB J 17:1648–1657
7. Rouhanizadeh M, Lin TC, Arcas D, Hwang J, Hsiai TK (2005) Spatial variations in shear stress in a 3-D bifurcation model at low Reynolds numbers. Ann Biomed Eng 33(10):1360–74
8. Goldstein S (1996) Fluid Mechanics Measurements. 2nd ed. Hemisphere, New York
9. Schmidt MA, et al (1988) Design and Calibration of a Microfabricated Floating-Element Shear-Stress Sensor. IEEE Trans Electron Devices 35(6):750–757
10. Padmanabhan A, et al (1996) A wafer-bonded floating-element shear stress microsensor with optical position sensing by photodiodes. J Microelectromech Syst 5(4):307–315
11. Jiang F, Tai Y-C, Huang J-B, Ho C-M (1995) Polysilicon structures for shear stress sensors. In: TENCON '95. IEEE Region 10 International Conference on Microelectronics and VLSI
12. Qiao Lin YX, Tai Y-C, Ho C-M (2005) A parametrized three dimensional model for MEMS thermal shear stress sensors. J Microelectromech Syst 14(3):625–633
13. Rouhanizadeh M, et al (2006) MEMS sensors to resolve spatial variations in shear stress in a 3D blood vessel bifurcation model. IEEE Sens J 6(1):78–88

14. Xu Y, et al (2005) Micromachined thermal shear-stress sensor for underwater applications. J Microelectromech Syst 14(5):1023–1030
15. Xu Y, Jiang F, Newbern S, Huang A, Ho C-M, Tai Y-C (2003) Flexible Shear-Stress Sensor Skin and its Application to Unmanned Aerial Vehicle. Sens Actuators A 105:321–329
16. Meng E, Tai Y-C (2003) A parylene MEMS flow sensing array. In: The 12th International Conference on Solid Slate Sensors, Actuators Microsystems Boston

Micro- and Nanoscale Gas Dynamics

FELIX SHARIPOV
Departamento de Física, Universidade Federal do Paraná, Curitiba, Brazil
sharipov@fisica.ufpr.br

Synonyms

Kinetic theory of gases; Kinetic Boltzmann equation

Definition

► Knudsen number (Kn) is the ratio of mean free path ℓ of fluid molecules to a typical dimension of gas flow a, i. e. $\mathrm{Kn} = \ell/a$. ► Rarefaction parameter δ is the inverse Knudsen number. ► Velocity distribution function is defined so that the quantity $f(t, \boldsymbol{r}, \boldsymbol{v})\, \mathrm{d}\boldsymbol{r}\, \mathrm{d}\boldsymbol{v}$ is the number of particles in the phase volume $\mathrm{d}\boldsymbol{r}\, \mathrm{d}\boldsymbol{v}$ near the point $(\boldsymbol{r}, \boldsymbol{v})$ at the time t.

Chemical and Physical Principles

The main parameter determining the gas rarefaction is the *Knudsen number* $\mathrm{Kn} = \ell/a$, where ℓ is the ► mean free path of fluid molecules and a is a typical dimension of gas flow. If the *Knudsen number* is sufficiently small, say $\mathrm{Kn} < 10^{-2}$, the Navier–Stokes equations are applied to calculate gas flows. For intermediate and high values of the *Knudsen number* the Navier–Stokes equations break down and the implementation of ► rarefied gas dynamics methods is necessary. In practical calculations usually the *rarefaction parameter* defined as the inverse *Knudsen number*, i. e.

$$\delta = \frac{a}{\ell} = \frac{1}{\mathrm{Kn}} \tag{1}$$

is used to characterize the gas rarefaction. Here, the ► equivalent mean free path will be used, which is calculated via the shear viscosity as

$$\ell = \frac{\mu v_0}{P}, \qquad v_0 = \left(\frac{2k_\mathrm{B} T}{m}\right)^{\frac{1}{2}}, \tag{2}$$

where v_0 is the most probable molecular speed, $k_\mathrm{B} = 1.380662 \times 10^{-23}$ J/K is the Boltzmann constant, m is the molecular mass of the gas in kg, T is the temperature of gas in K, P is its pressure in Pa, and μ is the shear viscosity in Pa s. For instance, if nitrogen is maintained at $P = 1$ atm and $T = 300$ K, then $\ell = 0.073$ µm.

The state of a monoatomic gas is described by the one-particle *velocity distribution function* $f(t, \boldsymbol{r}, \boldsymbol{v})$, where t is the time, $\boldsymbol{r}$ is the position vector, and $\boldsymbol{v}$ is a velocity of molecules. The function $f(t, \boldsymbol{r}, \boldsymbol{v})$ is defined so that the quantity $f(t, \boldsymbol{r}, \boldsymbol{v})\, \mathrm{d}\boldsymbol{r}\, \mathrm{d}\boldsymbol{v}$ is the number of particles in the phase volume $\mathrm{d}\boldsymbol{r}\, \mathrm{d}\boldsymbol{v}$ near the point $(\boldsymbol{r}, \boldsymbol{v})$ at the time t. All macro-characteristics of gas flow can be calculated via the *velocity distribution function*:

number density

$$n(t, \boldsymbol{r}) = \int f(t, \boldsymbol{r}, \boldsymbol{v})\, \mathrm{d}\boldsymbol{v}, \tag{3}$$

hydrodynamic (bulk) velocity

$$\boldsymbol{u}(t, \boldsymbol{r}) = \frac{1}{n} \int \boldsymbol{v} f(t, \boldsymbol{r}\boldsymbol{v})\, \mathrm{d}\boldsymbol{v}, \tag{4}$$

temperature

$$T(t, \boldsymbol{r}) = \frac{m}{3nk_\mathrm{B}} \int V^2 f(t, \boldsymbol{r}, \boldsymbol{v})\, \mathrm{d}\boldsymbol{v}, \tag{5}$$

pressure tensor

$$P_{ij}(t, \boldsymbol{r}) = m \int V_i V_j f(\boldsymbol{r}, \boldsymbol{v})\, \mathrm{d}\boldsymbol{v}, \quad i, j = x, y, z, \tag{6}$$

heat flux vector

$$\boldsymbol{q}(t, \boldsymbol{r}) = \frac{m}{2} \int \boldsymbol{V} V^2 f(t, \boldsymbol{r}, \boldsymbol{v})\, \mathrm{d}\boldsymbol{v}, \tag{7}$$

where $\boldsymbol{V} = \boldsymbol{v} - \boldsymbol{u}$ is the peculiar velocity. The *velocity distribution function* obeys the ► Boltzmann equation which in the absence of external forces reads

$$\frac{\partial f}{\partial t} + \boldsymbol{v} \cdot \frac{\partial f}{\partial \boldsymbol{r}} = Q(ff_*), \tag{8}$$

where $Q(ff_*)$ is the collision integral having a cumbersome expression.

If the gas is in equilibrium then the *velocity distribution function* is given by the absolute Maxwellian

$$f_0^\mathrm{M} = n_0 \left(\frac{m}{2\pi k_\mathrm{B} T_0}\right)^{\frac{3}{2}} \exp\left(-\frac{mv^2}{2k_\mathrm{B} T_0}\right), \tag{9}$$

where n_0 and T_0 are equilibrium number density and temperature, respectively. We also will use the local Maxwellian distribution function given by

$$f^{\mathrm{M}}(n,T,\boldsymbol{u}) = n(t,\boldsymbol{r})\left[\frac{m}{2\pi k_{\mathrm{B}}T(t,\boldsymbol{r})}\right]^{\frac{3}{2}} \cdot \exp\left\{-\frac{m[\boldsymbol{v}-\boldsymbol{u}(t,\boldsymbol{r})]^2}{2k_{\mathrm{B}}T(t,\boldsymbol{r})}\right\}, \quad (10)$$

where the density $n(t,\boldsymbol{r})$, temperature $T(t,\boldsymbol{r})$, and the bulk velocity $\boldsymbol{u}(t,\boldsymbol{r})$ are functions of the time t and position $\boldsymbol{r}$.

Usually, the so-called ▶model kinetic equations are applied in practical calculations. They maintain the main properties of the exact collision integral and, at the same time, they reduce significantly the computational efforts. The most usual *model kinetic equation* was proposed by Bhatnagar, Gross and Krook (BGK) [1]

$$Q_{\mathrm{BGK}}(ff_*) = \nu\left[f^{\mathrm{M}} - f(t,\boldsymbol{r},\boldsymbol{v})\right], \quad (11)$$

Note, the local values of the number density $n(t,\boldsymbol{r})$, bulk velocity $\boldsymbol{u}(t,\boldsymbol{r})$ and temperature $T(t,\boldsymbol{r})$ being a part of the local Maxwellian f^{M} are unknown. They are calculated via the function $f(t,\boldsymbol{r},\boldsymbol{v})$ in accordance with the definitions (3)–(5). Thus, Eq. (8) together with (11) is non-linear integro-differential equation. The quantity ν is the collision frequency assumed to be independent of the molecular velocity. The expression

$$\nu = P/\mu \quad (12)$$

is most used because it provides the correct description of shear stress flows. However, this model does not describe correctly a heat transfer.

The S-model proposed by Shakhov [10] is a modification of the BGK model providing the correct description of both momentum and heat transfer. The collision integral of this model is written down as

$$Q_{\mathrm{S}}(ff_*)\nu\left\{f^{\mathrm{M}}\left[1+\frac{2m}{15\,n\,(k_{\mathrm{B}}\,T)^2}\,\boldsymbol{q}\cdot\boldsymbol{V}\left(\frac{mV^2}{2k_{\mathrm{B}}T}-\frac{5}{2}\right)\right] - f(t,\boldsymbol{r},\boldsymbol{v})\right\}. \quad (13)$$

Thus, if one needs to calculate isothermal flows one may use the BGK model. Otherwise, the S-model must be used.

On a boundary surface the *velocity distribution function* of incident particles f^- is related to that of reflected molecules f^+ as

$$v_{\mathrm{n}} f^+(\boldsymbol{v}) = -\int_{v'_{\mathrm{n}}\le 0} v'_{\mathrm{n}} f^-(\boldsymbol{v}') R(\boldsymbol{v}',\boldsymbol{v})\,\mathrm{d}\boldsymbol{v}', \quad v_{\mathrm{n}} \ge 0, \quad (14)$$

$v_n = \boldsymbol{v}\cdot\boldsymbol{n}$ is a normal velocity component, $\boldsymbol{n}$ is the unit vector normal to the surface directed to the gas, $R(\boldsymbol{v}',\boldsymbol{v})$ is a ▶gas-surface scattering kernel satisfying the normalization condition

$$\int_{v_{\mathrm{n}}\ge 0} R(\boldsymbol{v}',\boldsymbol{v})\,\mathrm{d}\boldsymbol{v} = 1, \quad (15)$$

and the reciprocity property,

$$|v'_{\mathrm{n}}|\exp\left[-\frac{m(\boldsymbol{v}'-\boldsymbol{u}_w)^2}{2k_{\mathrm{B}}T_w}\right]R(\boldsymbol{v}',\boldsymbol{v}) = |v_{\mathrm{n}}|\exp\left[-\frac{m(\boldsymbol{v}+\boldsymbol{u}_w)^2}{2k_{\mathrm{B}}T_w}\right]R(-\boldsymbol{v},-\boldsymbol{v}'), \quad (16)$$

where T_w and $\boldsymbol{u}_w$ are the surface temperature and velocity, respectively.

The well known diffuse scattering (cosine law) corresponds to the following kernel

$$R_{\mathrm{d}}(\boldsymbol{v}',\boldsymbol{v}) = \frac{2v_{\mathrm{n}}}{\pi}\left(\frac{m}{2k_{\mathrm{B}}T_w}\right)^2\exp\left(-\frac{m\,v^2}{2k_{\mathrm{B}}T_w}\right). \quad (17)$$

The specular reflection is given by the kernel

$$R_{\mathrm{s}}(\boldsymbol{v}',\boldsymbol{v}) = \delta(\boldsymbol{v}'_{\mathrm{t}}-\boldsymbol{v}_{\mathrm{t}})\delta(v'_{\mathrm{n}}+v_{\mathrm{n}}), \quad (18)$$

where $\boldsymbol{v}_{\mathrm{t}}$ is the two-dimensional vector of the tangential velocity. The diffuse-specular kernel

$$R_{\mathrm{ds}}(\boldsymbol{v}',\boldsymbol{v}) = \alpha R_{\mathrm{d}}(\boldsymbol{v}',\boldsymbol{v}) + (1-\alpha)R_{\mathrm{s}}(\boldsymbol{v}',\boldsymbol{v}) \quad (19)$$

is widely used. Here, α is the part of molecules reflected diffusely. However, some experimental data contradict to theoretical results based on the kernel (19). Recently, more physical *gas-surface scattering kernels* became to be applied. One of them is the Cercignani–Lampis (CL) [6] model given as

$$R_{\mathrm{CL}}(\boldsymbol{v}',\boldsymbol{v}) = \frac{v_{\mathrm{n}}}{\pi^2\alpha_{\mathrm{n}}\,\alpha_{\mathrm{t}}(2-\alpha_{\mathrm{t}})}\left(\frac{m}{2k_{\mathrm{B}}T_w}\right)^2 \times\exp\left\{-\frac{m[v_{\mathrm{n}}^2+(1-\alpha_{\mathrm{n}})v_{\mathrm{n}}'^2]}{2k_{\mathrm{B}}T_w\alpha_{\mathrm{n}}} - \frac{m[\boldsymbol{v}_{\mathrm{t}}-(1-\alpha_{\mathrm{t}})\boldsymbol{v}'_{\mathrm{t}}]^2}{2k_{\mathrm{B}}T_w\alpha_{\mathrm{t}}(2-\alpha_{\mathrm{t}})}\right\} \times\int_0^{2\pi}\exp\left(\frac{m\,v_{\mathrm{n}}\,v'_{\mathrm{n}}}{k_{\mathrm{B}}T_w}\frac{\sqrt{1-\alpha_{\mathrm{n}}}}{\alpha_{\mathrm{n}}}\cos\phi\right)\mathrm{d}\phi,$$

where $0 \le \alpha_n \le 1$ has the physical sense of the accommodation coefficient of energy corresponding to the normal velocity v_n, $0 \le \alpha_t \le 2$ is the accommodation coefficient of the tangential momentum. In the particular case $\alpha_n = \alpha_t = 1$ this kernel coincides with the diffuse one (17). If $\alpha_n = \alpha_t = 0$ the CL kernel becomes the specular one (18). The combination $\alpha_n = 0$ and $\alpha_t = 2$ corresponds to the back scattering, which can occur on a rough surface.

The linearized kinetic equation will be written in terms of following dimensional coordinates and molecular velocity

$$\tilde{\boldsymbol{r}} = \boldsymbol{r}/a, \qquad \boldsymbol{c} = \boldsymbol{v}/v_0\,, \tag{20}$$

respectively. Here a is a characteristic size used in the definition of the gas rarefaction (1).

If the state of the gas is weakly non-equilibrium, we may linearize the *Boltzmann equation* representing the *velocity distribution function* as

$$f(\tilde{\boldsymbol{r}}, \boldsymbol{c}) = f_R^M [1 + \xi\ h(\tilde{\boldsymbol{r}}, \boldsymbol{c})]\,, \qquad \xi \ll 1\,, \tag{21}$$

where ξ is a small parameter of the linearization, f_R^M is the reference Maxwellian given by Eq. (10) with the reference number density n_R, temperature T_R and bulk velocity $\boldsymbol{u}_R$, i. e.

$$f_R^M = f^M(n_R, T_R, \boldsymbol{u}_R)\,. \tag{22}$$

Substituting (21) into (8) the linearized *Boltzmann equation* is obtained as

$$\boldsymbol{c} \cdot \frac{\partial h}{\partial \tilde{\boldsymbol{r}}} = \hat{L}h + g(\tilde{\boldsymbol{r}}, \boldsymbol{c})\,, \tag{23}$$

where $\hat{L}$ is the linearized dimensionless collision operator and g is the source function given as

$$g(\tilde{\boldsymbol{r}}, \boldsymbol{c}) = -\frac{\boldsymbol{c}}{\xi} \cdot \frac{\partial \ln f_R^M}{\partial \tilde{\boldsymbol{r}}}\,. \tag{24}$$

The quantities n_R, T_R and $\boldsymbol{u}_R$ are chosen so that to reduce the computational efforts. Particularly, they can be constant and equal to their equilibrium values. The operator $\hat{L}$ in its exact form has a cumbersome form, that is why just the model linearized operators will be given. With the help of Eqs. (1), (11), (12), and (20) the linearized BGK collision operator takes the form

$$\hat{L}_{BGK}h = \delta\left[\varrho + 2\boldsymbol{c} \cdot \tilde{\boldsymbol{u}} + \tau\left(c^2 - \frac{3}{2}\right) - h\right]. \tag{25}$$

By the same way the linearized S-model is obtained from Eq. (13)

$$\hat{L}_S h = \delta\left[\varrho + 2\boldsymbol{c} \cdot \tilde{\boldsymbol{u}} + \tau\left(c^2 - \frac{3}{2}\right) + \frac{4}{15}\tilde{\boldsymbol{q}} \cdot \boldsymbol{c}\left(c^2 - \frac{5}{2}\right) - h\right],$$

where ϱ, τ, and $\tilde{\boldsymbol{u}}$ are the deviations from their reference values, i. e.

$$\varrho = \frac{n - n_R}{\xi n_R}\,, \quad \tau = \frac{T - T_R}{\xi T_R}\,, \quad \tilde{\boldsymbol{u}} = \frac{\boldsymbol{u} - \boldsymbol{u}_R}{\xi v_0}\,. \tag{26}$$

Moreover, the dimensionless heat flux and stress tensor are introduced

$$\tilde{\boldsymbol{q}} = \frac{\boldsymbol{q}}{\xi P_0 v_0}\,, \qquad \tilde{P}_{ij} = \frac{P_{ij}}{2\xi P_0}\,, \tag{27}$$

where $P_0 = n_0 k_B T_0$ is the equilibrium pressure.

Substituting (21) into Eqs. (3)–(7) with the help of Eqs. (26) and (27) we express the moments in terms of the perturbation function as

$$\varrho = \frac{1}{\pi^{3/2}} \int e^{-c^2} h\, d\boldsymbol{c}\,, \tag{28}$$

$$\tilde{\boldsymbol{u}} = \frac{1}{\pi^{3/2}} \int \boldsymbol{c}\, e^{-c^2} h\, d\boldsymbol{c}\,, \tag{29}$$

$$\tau = \frac{1}{\pi^{3/2}} \int \left(\frac{2}{3}c^2 - 1\right) e^{-c^2} h\, d\boldsymbol{c}\,, \tag{30}$$

$$\tilde{P}_{ij} = \frac{1}{\pi^{3/2}} \int c_i c_j\, e^{-c^2} h\, d\boldsymbol{c}\,, \quad i, j = x, y, z\,, \tag{31}$$

$$\tilde{\boldsymbol{q}} = \frac{1}{\pi^{3/2}} \int \boldsymbol{c}\left(c^2 - \frac{5}{2}\right) e^{-c^2} h\, d\boldsymbol{c}\,. \tag{32}$$

The linearized boundary conditions are obtained substituting (21) into (14) combining with (15) and (16)

$$h^+ = \hat{A}\, h^- + h_w^+ - \hat{A}\, h_w^-\,, \tag{33}$$

where h_w is the perturbation of the surface Maxwellian

$$h_w = \frac{1}{\xi}\left[\frac{m}{k_B T_R}\boldsymbol{v} \cdot (\boldsymbol{u}_w - \boldsymbol{u}_R) + \frac{T_w - T_R}{T_R} \cdot \left(\frac{mv^2}{2k_B T_R} - \frac{5}{2}\right)\right]. \tag{34}$$

The scattering operator $\hat{A}$ is defined as

$$\hat{A}h^- = -\int_{v'_n \le 0} \frac{v'_n}{v_n} \exp\left[\frac{m(v^2 - v'^2)}{2k_B T_0}\right] h(\boldsymbol{v}')R(\boldsymbol{v}', \boldsymbol{v})\, d\boldsymbol{v}' \,. \tag{35}$$

To solve numerically the linearized kinetic Equations (23) with the boundary condition (33) a set of values of the velocity $\boldsymbol{c}_i$ is chosen. The collision operator $\hat{L}h$ is expressed *via* the values $h_i(\tilde{x}) = h(\tilde{x}, \boldsymbol{c}_i)$. Thus, Eq. (23) is replaced by a system of differential equations for the functions $h_i(\tilde{x})$, which can be solved numerically by a finite difference method. First, some values are assumed for the moments being part of the collision operator. Then, the distribution function moments are calculated in accordance with Eqs. (28)–(32) using some quadrature. The differential equations are solved again with the new moments. The procedure is repeated up to the convergence.

Key Research Findings

Plane Poiseuille Flow in Microchannels

Consider two infinite plane plates fixed at $x = \pm a/2$. A monoatomic gas confined between them flows along the axis y due to a pressure gradient, which is used as the small parameter, i. e.

$$\xi = \frac{a}{P}\frac{dP}{dy} \,. \tag{36}$$

We are interested in the velocity profile $u_y(x)$ and mass flow rate $\dot{M}$ through a cross section of the channel defined as

$$\dot{M} = \int_{\frac{-a}{2}}^{\frac{a}{2}} m\, n\, u_y(x)\, dx \,. \tag{37}$$

Such a flow is known as Poiseuille flow.

The following reference quantities being part of the Maxwellian (22) are as used in the linearization: $n_R = n_0\,(1 + \xi\, y/a)$, $T_R = T_0$, $\boldsymbol{u}_R = 0$. According to Eqs. (26) we have $\varrho = 0$ because $n = n_R$ and $\tau = 0$ because the flow is isothermal. Then, the perturbation function depends only on the coordinate $\tilde{x}$, i. e. $h = h(\tilde{x}, \boldsymbol{c})$. The source function defined by Eq. (24) takes the form $g = -c_y$. Since the flow is isothermal we use the BGK model, which is reduced to

$$c_x \frac{\partial h}{\partial \tilde{x}} = \delta\left(2c_y \tilde{u}_y - h\right) - c_y \,, \tag{38}$$

where $\tilde{u}$ is given by Eq. (29) and related the the bulk velocity by Eq. (26). Note, the solution of this equation is even

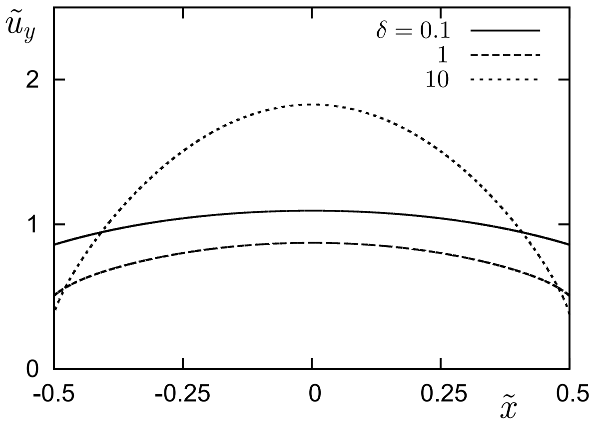

Micro- and Nanoscale Gas Dynamics, Figure 1 Velocity profiles $\tilde{u}_y$ in Poiseuille flow

with respect to c_y, i. e.

$$h(\tilde{x}, c_x, c_y, c_z) = -h(\tilde{x}, c_x, -c_y, c_z) \,. \tag{39}$$

Since $\boldsymbol{u}_w = \boldsymbol{u}_R = 0$ and $T_w = T_0 = 0$, the surface perturbation $h_w = 0$ according to Eq. (34). Thus, the boundary condition (33) is reduced to

$$h^+ = \hat{A}h^- \quad \text{at} \quad \tilde{x} = \pm\frac{1}{2} \quad \text{and} \quad c_y \lessgtr 0 \,. \tag{40}$$

In case of the diffuse reflection we obtain $\hat{A}\, h^- = 0$ using the property (39).

Solving the integro-differential Eq. (38) with the boundary condition (40) we obtain the velocity profile $\tilde{u}$ and then the reduced flow rate

$$G_P = -2\int_{-1/2}^{1/2} \tilde{u}(\tilde{x})\, d\tilde{x} \,, \tag{41}$$

which is called as ► Poiseuille coefficient and related to the mass flow rate as

$$\dot{M} = -G_P \frac{aP}{v_0}\xi = -G_P \frac{a^2}{v_0}\frac{dP}{dy} \,. \tag{42}$$

The last expression is obtained with the help of Eqs. (20), (26), (36), and (37). Note, the coefficient G_P is always positive.

Typical velocity profiles are presented in Fig. 1. For the large value of the *rarefaction parameter* ($\delta = 10$) the profile is very close to the parabolic shape. In the transition ($\delta = 1$) and small ($\delta = 0.1$) values the profiles are practically flat.

The *Poiseuille coefficient* G_P for the diffuse scattering is presented in Table 1. It tends to infinity in both limits

Micro- and Nanoscale Gas Dynamics, Table 1 Poiseuille coefficient G_P vs. rarefaction parameter δ, diffuse scattering

δ	G_P	δ	G_P
0.001	4.274	1.1	1.538
0.01	3.052	1.2	1.540
0.02	2.711	1.4	1.548
0.04	2.397	2.0	1.595
0.1	2.033	4.0	1.846
0.2	1.808	8.0	2.451
0.4	1.640	10.	2.769
0.8	1.548	20.	4.397
0.9	1.542	40.	7.708
1.0	1.539	100.	17.69

Micro- and Nanoscale Gas Dynamics, Table 2 Poiseuille coefficient G_P vs. accommodation coefficients α_t and α_n (Reprinted with permission from [13])

		G_P		
δ	α_t	$\alpha_n = 0.5$	0.75	1.
0.01	0.5	5.014	4.893	4.824
	0.75	3.726	3.675	3.642
	1.	3.052	3.052	3.052
1.	0.5	3.352	3.338	3.326
	0.75	2.157	2.150	2.144
	1.	1.554	1.554	1.554
100.	0.5	19.49	19.47	19.46
	0.75	18.30	18.29	18.29
	1.	17.70	17.70	17.70

$\delta \to \infty$ and $\delta \to 0$. In the transition regime the coefficient G_P has the well known Knudsen minimum.

To give an idea how does the gas-surface interaction affect the flow rate, some values of G_P for the CL scattering kernel obtained in [13] are given in Table 2. In all regimes the influence of the energy accommodation coefficient α_n on the flow rate is weak, while the momentum accommodation coefficient α_t affects significantly the flow rate in the transition ($\delta = 1$) and near the free molecular ($\delta = 0.01$) regimes.

Momentum Transfer in Microscale

Here, we again consider the two plates fixed at $x = \pm a/2$, but the pressure is constant between them. The gas is disturbed by a motion of the plates, namely, the left plate is moving down with a speed $u_w/2$, while the right one is moving up with the same speed. This is the so-called Couette flow. We are interested in the velocity profile $u_y(x)$ between the plates and the shear stress P_{xy}. If we assume the plate speed u_w to be significantly smaller than the most

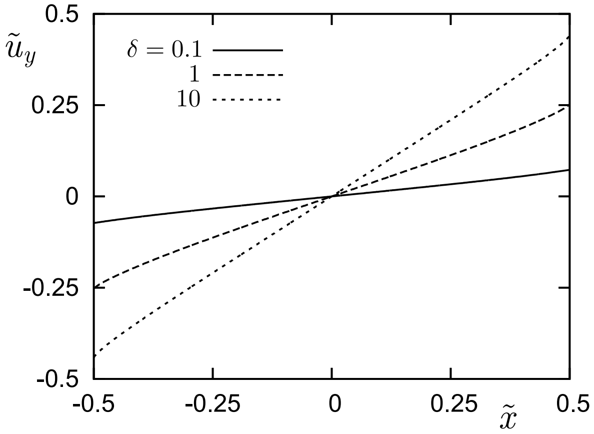

Micro- and Nanoscale Gas Dynamics, Figure 2 Velocity profiles $\tilde{u}_y$ in plane Couette flow

probable speed v_0, the ratio

$$\xi = \frac{u_w}{v_0} \tag{43}$$

can be used as the small parameter for the linearization. The reference quantities in the Maxwellian (22) are as follows $n_R = n_0$, $T_R = T_0$, $\boldsymbol{u}_R = 0$. According to Eqs. (26) we have $\varrho = \tau = 0$ because the density and temperature are constant. Then, the source function (24) is given as $g = 0$. Since the flow is isothermal the BGK model is applied, which reads

$$c_x \frac{\partial h}{\partial \tilde{x}} = \delta \left(2 c_y \tilde{u}_y - h\right) . \tag{44}$$

From Eq. (34) we obtain $h_w = \pm c_y$ on the right/left plate. In case of the diffuse reflection we obtain the explicit boundary condition

$$h = \pm c_y \quad \text{at} \quad \tilde{x} = \pm \frac{1}{2} \quad \text{and} \quad c_y \lessgtr 0 . \tag{45}$$

Solving Eq. (44) with the boundary condition (45) the perturbation function h is obtained. Then the bulk velocity $\tilde{u}_y$ and shear stress $\tilde{P}_{xy}$ are calculated according to Eqs. (29) and (31), respectively.

Typical velocity profiles are presented in Fig. 2. For the large value of the rarefaction ($\delta = 10$) the velocity $\tilde{u}_y$ varies linearly from -0.5 to 0.5, i. e. it is close to the solution in the hydrodynamic regime. By decreasing the *rarefaction parameter* δ the slope of the velocity profile becomes smaller. The shear stress is shown in Table 3. Note, it is negative because the velocity gradient

Micro- and Nanoscale Gas Dynamics, Table 3 Shear stress $\tilde{P}_{xy}$ vs. rarefaction parameter δ

δ	$-\tilde{P}_{xy}$	δ	$-\tilde{P}_{xy}$
0.001	0.2818	1.0	0.1695
0.01	0.2797	2.0	0.1252
0.02	0.2773	4.0	0.0830
0.04	0.2730	10.0	0.0416
0.1	0.2612	20.0	0.0227
0.2	0.2447	40.0	0.0119
0.4	0.2189	100.0	0.0049

is positive. The magnitude of the shear stress monotonely decreases by increasing the *rarefaction parameter* δ.

Heat Transfer in Microscale

Now, we consider the plates being at rest but the left one is maintained at the temperature $T_0 - \Delta T/2$, while the right one has the temperature $T_0 + \Delta T/2$. We are interested in the temperature profile $T(x)$ between the plates and the heat flux q_x. Assuming that $\Delta T \ll T_0$ the ratio

$$\xi = \frac{\Delta T}{T_0} \tag{46}$$

can be used as the small parameter for the linearization. The reference quantities in the Maxwellian (22) are equal to their equilibrium values $n_R = n_0$, $T_R = T_0$, $\boldsymbol{u}_R = 0$. Then, the source function (24) is given as $g = 0$. Since the gas is being at rest we have $\tilde{\boldsymbol{u}} = 0$. For the problem in question the S-model is more appropriate because we are interested in the heat transfer. Finally, the kinetic Eq. (23) is reduced to

$$c_x \frac{\partial h}{\partial \tilde{x}} = \delta \left[\varrho + \tau \left(c^2 - \frac{3}{2} \right) + \frac{4}{15} c_x \tilde{q}_x \left(c^2 - \frac{5}{2} \right) - h \right] . \tag{47}$$

From Eq. (34) we obtain $h_w = \pm(c^2 - 3/2)$ on the right/left plate. In case of the diffuse reflection we obtain the explicit boundary condition

$$h = \pm(\varrho_w + c^2 - 2) \quad \text{at} \quad \tilde{x} = \pm\frac{1}{2} \quad \text{and} \quad c_y \lessgtr 0 , \tag{48}$$

where $\varrho_w = (2/\pi) \int_{c_x \geq 0} c_x e^{-c^2} h \, d\boldsymbol{c}$ at $\tilde{x} = 1/2$. Typical temperature profiles are presented in Fig. 3. Their behaviors are quite similar to those of the velocity profiles in the previous example. The heat flux $\tilde{q}_x$ is shown in Table 4. It is negative because the temperature gradient is positive.

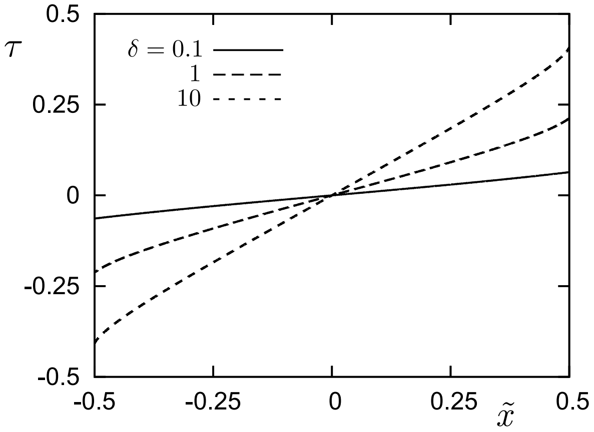

Micro- and Nanoscale Gas Dynamics, Figure 3 Temperature profiles τ between parallel plates

Micro- and Nanoscale Gas Dynamics, Table 4 Heat flux $\tilde{q}$ vs rarefaction parameter δ

δ	$-\tilde{q}_x$	δ	$-\tilde{q}_x$
0.001	0.5638	1.0	0.4001
0.01	0.5608	2.0	0.3236
0.02	0.5575	4.0	0.2383
0.04	0.5514	10.0	0.1348
0.1	0.5351	20.0	0.0784
0.2	0.5122	40.0	0.0427
0.4	0.4754	100.0	0.0180

The magnitude of the heat flux decreases by increasing the *rarefaction parameter* δ.

Examples of Application

Consider two parallel plates with the clearance $a = 0.217\,\mu\text{m}$ between them containing helium at the pressure $P = 10^5$ Pa and at the temperature $t = 20\,°\text{C}$. Under such conditions the gas viscosity is $\mu = 19.73 \times 10^{-6}$ Pa s and the most probable speed is $v_0 = 1.10 \times 10^3$ m/s. Substituting these values into Eq. (2) the *equivalent mean free path* is obtained $\ell = 0.217\,\mu\text{m}$, i. e. the *rarefaction parameter* δ defined by Eq. (1) is equal to unity. According to Tables 1, 3, and 4 for $\delta = 1$ we have $G_P = 1.539$, $\tilde{P}_{xy} = -0.1695$, and $\tilde{q}_x = -0.4001$, respectively. Let us assume the dimensionless pressure gradient $\xi = -0.01$, see Eq. (36), to be maintained along the plates. Using Eq. (42) the mass flow rate is calculated as $\dot{M} = 3.04 \times 10^{-7}$ kg/(m s). Now, let us consider the constant pressure, but one plate moves parallelly the other with a relative speed $u_w = 10$ m/s, then according to Eq. (43) we have $\xi = 9.09 \times 10^{-3}$. With the help of Eq. (27) the shear stress magnitude is obtained

$P_{xy} = 308$ Pa. If one plates has its temperature $t = 10\,°C$ and the other is maintained at $t = 30\,°C$ then, $\xi = 0.0682$ in accordance with Eq. (46). Substituting the corresponding values into Eq. (27) the heat flux magnitude is obtained $q_x = 3.00 \times 10^6$ W/m^2.

Cross References

- ► Control of Microfluidics
- ► Curved Microchannel Flows
- ► Developing Flows
- ► Flow in Channels with 3D Elements
- ► Gas Flow in Nanochannels
- ► Heat Transfer in Microchannel Flows
- ► Methods for Flow Rate Measurements
- ► Supersonic Micro-Nozzles
- ► Rarefied Gas Dynamics
- ► Roughness Effect on Microscale Transport
- ► Single-Phase Gaseous Flow

References

1. Bhatnagar PL, Gross EP, Krook MA (1954) A model for collision processes in gases. Phys Rev 94:511–525
2. Bird GA (1994) Molecular Gas Dynamics and the Direct Simulation of Gas Flows. Oxford University Press, Oxford
3. Cercignani C (1975) Theory and Application of the Boltzmann Equation. Scottish Academic Press, Edinburgh
4. Cercignani C (1988) The Boltzmann Equation and its Application. Springer, New York
5. Cercignani C (2000) Rarefied Gas Dynamics. From Basic Concepts to Actual Calculations. Cambridge University Press, Cambridge
6. Cercignani C, Lampis M (1971) Kinetic model for gas-surface interaction. Transp Theory Stat Phys 1:101–114
7. Chapman S, Cowling TG (1952) The Mathematical Theory of Non-Uniform Gases. Cambridge University Press, Cambridge
8. Ferziger JH, Kaper HG (1972) Mathematical Theory of Transport Processes in Gases. North-Holland, Amsterdam
9. Kogan MN (1969) Rarefied Gas Dynamics. Plenum, New York
10. Shakhov EM (1968) Generalization of the Krook kinetic equation. Fluid Dyn 3(1):142–145
11. Sharipov F (1999) Rarefied gas flow through a long rectangular channel. J Vac Sci Technol A 17(5):3062–3066
12. Sharipov F (1999) Non-isothermal gas flow through rectangular microchannels. J Micromech Microeng 9(4):394–401
13. Sharipov F (2002) Application of the Cercignani-Lampis scattering kernel to calculations of rarefied gas flows. I. Plane flow between two parallel plates. Eur J Mech B / Fluids 21(1):113–123
14. Sharipov F, Seleznev V (1998) Data on internal rarefied gas flows. J Phys Chem Ref Data 27(3):657–706
15. Sharipov FM, Subbotin EA (1993) On optimization of the discrete velocity method used in rarefied gas dynamics. Z Angew Math Phys (ZAMP) 44:572–577
16. Sone Y (2002) Kinetic Theory and Fluid Mechanics. Birkhäuser, Boston

Micro- and Nanoscale Gas Fluidics

MORAN WANG[1], ZHIXIN LI[2]

[1] NEAT, Department of Biological & Agricultural Engineering, University of California Davis, Davis, CA, USA

[2] Department of Engineering Mechanics, Tsinghua University, Beijing, China

mmwang@ucdavis.edu

Synonyms

Gas flow; Microfluidics and nanofluidics; Numerical simulation

Definition

Micro- and nanoscale gas fluidics concerns the behavior of gas flows and the heat transfer mechanisms in micro- and nanoscale devices. Correct understanding and accurate prediction of the characteristics of micro- and nanoscale gas flow and heat transfer are very important for optimization and design of micro- and nanoscale systems. In micro- and nanoscale gas flow, the Knudsen number is high owing to the very small characteristic length, even though the gas density may be not low, which leads to behavior similar to the well-known rarefied-gas flow. Atomistic numerical methods, such as direct-simulation Monte Carlo methods, are available for microscale gas flows and heat transfer. However, when the gas density is so high that the perfect-gas assumption breaks down, both the theories and the simulation methods for rarefied gases are not valid anymore. A generalized Enskog Monte Carlo method has been developed to take account of the effects of a dense, nonideal gas. Using this method, gas microfluidics and nanofluidics have been analyzed.

Overview

The flow of rarefied gases has been investigated in detail because of its important applications in aeronautical and astronautical engineering. Rarefied-gas flows differ from those of classical gas dynamics in that the continuum hypothesis is no longer valid; therefore, the continuum hypothesis cannot be used to analyze rarefied-gas flows. Rarefied-gas flows are characterized by the Knudsen number, which is defined as the ratio of the molecular mean free path to a characteristic geometric length or a length over which very large variations of a macroscopic quantity may take place [1]. Flow regimes can be classified on the basis of the Knudsen number as:

- continuum flow ($\mathrm{Kn} \le 0.001$),

- near-continuum flow ($0.001 < \mathrm{Kn} < 0.01$),
- slip flow ($0.01 < \mathrm{Kn} < 0.1$),
- transition flow ($0.1 < \mathrm{Kn} < 10$),
- free molecular flow ($\mathrm{Kn} \geq 10$).

In recent years, micro/nanoelectromechanical systems (M/NEMS) have been rapidly developed for important applications in navigation, space flight, and industry [2]. The characteristics of microscale gas flows differ from those of macroscale flows. For example, at normal temperatures and pressures, velocity slip and temperature jumps, which are considered as rarefied-gas effects, occur at the wall surfaces in microchannels. Rarefied-gas flows and microscale gas flows exhibit many other similar phenomena. Previous work has shown that most traditional simulation and analysis methods used for rarefied-gas flows are also effective for analyzing microscale gas flows [2]. Various studies have analyzed the similarities between microscale gas flows and macroscale rarefied-gas flows. Since the Knudsen numbers of microscale gas flows are as high as those of rarefied-gas flows, it is very important to build a bridge between them so that the large number of achievements in the field of rarefied-gas flow can be applied in the analysis of microscale gas fluidics. On the other hand, although the Knudsen number of a microscale gas flow may be of the same magnitude as that of a rarefied-gas flow, the reasons in the two cases are different. In microscale flows, the large Knudsen number is caused by the small characteristic length, whereas in rarefied-gas flows, the large Knudsen number is due to the large molecular mean free path. Therefore, the mechanisms may be different despite the fact that the phenomena are similar. How to analyze and predict gas flow and heat transfer in these situations is a very important but challenging problem, in terms of both theory and practice.

Basic Methodology

Direct-Simulation Monte Carlo (DSMC) Method

The DSMC method is a molecule-based statistical simulation method for rarefied-gas flows introduced by Bird [3]. The method solves the dynamical equations for the gas flow numerically, using thousands of simulated molecules. Each simulated molecule represents a large number of real molecules. Assuming molecular chaos and a rarefied gas, only binary collisions need be considered, and so the molecular motion and the collisions are uncoupled if the computational time step is smaller than the physical collision time. Interactions with boundaries and with other molecules conserve both momentum and energy. The macroscopic flow characteristics are obtained by statistically sampling the molecular properties in each of the cells used in the method. At the beginning of the calculation, the simulated particles are uniformly distributed in the cells. During each time step, all particles move according to their individual velocities, interact with the boundaries, and are then indexed. A number of collision pairs are selected in each cell using the no-time-counter (NTC) method for the calculation of collisions. These steps are repeated with increased sample sizes until the statistical errors are small. The DSMC method can simulate nonequilibrium and unsteady gas flows. A steady-state flow field is obtained with a sufficiently long simulation time. The variable-hard-sphere (VHS) model that is most popular in DSMC simulations incorporates the hard-sphere scattering law for collisions and treats the molecular cross sections as functions of the relative translational energy during the collision. In this model, the gas molecules are actually treated as hard spheres with only a repelling force, which is consistent with the perfect-gas assumption. The time step used in the DSMC method should be less than the mean collision time, and the cell (or subcell) size should be less than the mean free path in the simulated situation. Violation of this condition may produce solutions that are not physically realistic [4].

For an isothermal wall, when a simulated particle collides with the wall, a diffuse-reflection model is used to determine the result of reflection, whereby the outgoing velocity is randomly assigned according to a half-range Maxwellian distribution determined by the wall temperature. This is also known as the full thermal and momentum accommodation method.

In traditional DSMC simulations of supersonic flows, the Dirichlet type of velocity boundary conditions has generally been used. This approach is often applied in external-flow simulations, which require the downstream boundary to be far away from the base region. However, the flows in microscale systems are often subsonic flows, and the boundary conditions which can be obtained from the experiment always refer to pressure and temperature, instead of velocity and number density. Wang and Li [5] have proposed a new implicit treatment for a pressure boundary condition, inspired by the characteristic theory of low-speed microscale flows. This new implementation of boundary conditions not only overcomes the instability of particle-based approaches, but also has a higher efficiency than any other existing methods. The new method is easy to extend to gas flows where the downstream and upstream directions are not opposite, such as in L-shaped and T-shaped channels.

Generalized Enskog Monte Carlo (GEMC) Method

High-Knudsen-number nonideal-gas flows have two distinctive characteristics that require a different type of anal-

ysis from rarefied-gas flows: the collisions are much more frequent and the van der Waals force cannot be ignored. Alexander et al. [6] have developed a consistent Boltzmann algorithm (CBA) to expand the DSMC method to dense gases and even liquids by introducing an additional displacement after the molecular collisions. This modification uses the gas properties described by the van der Waals equation instead of those described by the equation of state for a perfect gas. This method has been applied to the modeling of nonideal-gas flows in micro- and nanochannels [7]. However, the additional displacement changes not only the equation of state but also the gas transport characteristics. As a result, when the ratio of the molecular volume of the gas to the whole volume is relatively high, the gas transport characteristics become unrealistic and the predictions fail [8]. Other methods have been developed on the basis of the Enskog dense-gas theory. Enskog developed the Enskog equation for hard spheres to incorporate finite-density effects, where the two significant changes were the finite distance between the centers of a colliding pair and the increased collision frequency due to excluded-volume effects [9]. Montanero and Santos [10] then developed an Enskog simulation Monte Carlo (ESMC) method, which extended Bird's DSMC method to a hard-sphere fluid at finite densities. However, the ESMC method did not include attractive interactions between molecules, and therefore the transport properties predicted by the ESMC method did not agree well with either the experimental data or the theoretical values. Recently, a generalized Enskog Monte Carlo method has been developed [11]. In the new method, a Lennard–Jones (L–J) potential between molecules is introduced, with a generalized collision model, into the Monte Carlo method, and the effects of finite density on the molecular collision rate and transport properties are considered so as to obtain an equation of state for a nonideal gas. The resulting transport properties agree better with the experimental data and theoretical values than do those obtained by any other existing method.

In actual gases, the force between two molecules is repulsive at small distances and weakly attractive at larger distances. This behavior is most simply described by an L–J (6–12) potential [12],

$$\varphi(r) = 4\varepsilon\left[\left(\frac{\sigma}{r}\right)^{12} - \left(\frac{\sigma}{r}\right)^{6}\right], \tag{1}$$

where σ denotes the low-velocity diameter and ε is the depth of the potential well, these being constants characteristic of the chemical species of the colliding molecules, and r is the intermolecular separation. This potential has been found to be adequate for a number of nonpolar

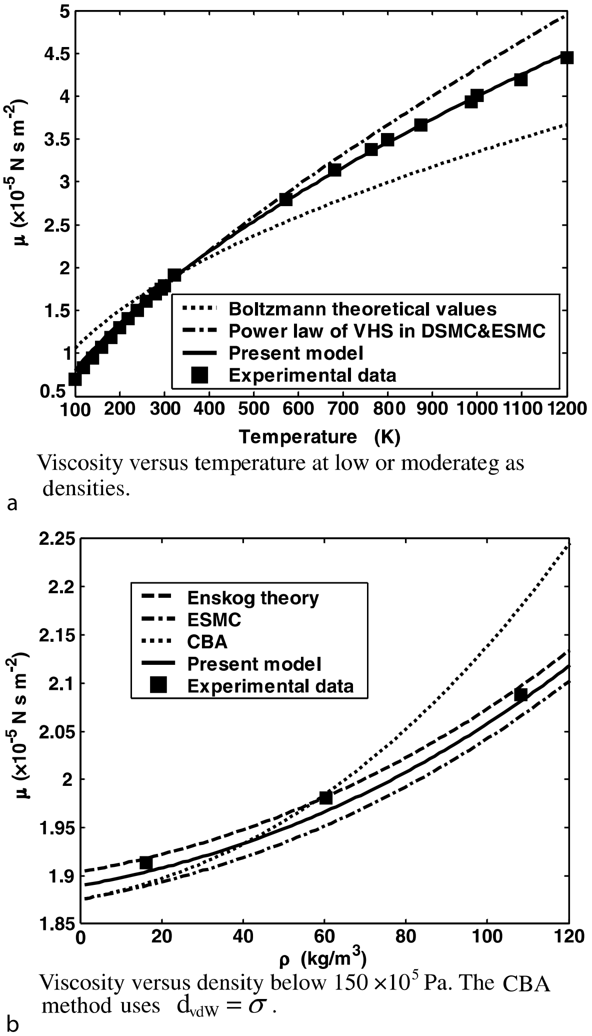

a Viscosity versus temperature at low or moderateg as densities.

b Viscosity versus density below 150 ×10^5 Pa. The CBA method uses $d_{vdW} = \sigma$.

Micro- and Nanoscale Gas Fluidics, Figure 1 Viscosities predicted by the present method compared with experimental data and other models

molecules. Many efforts have been made to establish collision models that include an L–J potential in the molecular interaction process [13, 14]. These models have defined the total collision cross section as

$$\frac{\sigma_T}{\sigma^2} = \sum \alpha_j \left(\frac{E_t}{\varepsilon}\right)^{-\omega_j}, \tag{2}$$

where σ_T is the total collision cross section, E_t denotes the relative translational energy, the parameters ω_j are related to the L–J potential, and the α_j are determined from transport property data, depending on whether the interaction is between like or unlike molecules.

The coefficients of viscosity and self-diffusion of a simple gas, to a first approximation, can be expressed as functions

of temperature by [12]

$$\mu = \frac{5}{16}\left(\frac{(\pi mkT)^{\frac{1}{2}}}{\pi\sigma^2\Omega^{(2,2)*}}\right) , \quad (3)$$

$$D = \frac{3}{16}\left(\frac{(2\pi kT/m_r)^{\frac{1}{2}}}{n\pi\sigma^2\Omega^{(1,1)*}}\right) , \quad (4)$$

where m is the particle mass, k is the Boltzmann constant, n is the number density, and $\Omega^{(1,1)*}$ and $\Omega^{(2,2)*}$ are integrals for calculating the transport coefficients using an L–J potential. For an L–J gas model with a total collision cross section given by Eq. (2), the self-diffusion and viscosity integrals are

$$\Omega^{(1,1)*} = \frac{1}{\pi(\alpha^* + 1)} \sum \alpha_j \Gamma(3 - \omega_j) T_*^{-\omega_j} , \quad (5)$$

$$\Omega^{(2,2)*} = \frac{\alpha^*}{\pi(\alpha^* + 1)(\alpha^* + 2)} \sum \alpha_j \Gamma(4 - \omega_j) T_*^{-\omega_j} , \quad (6)$$

where α^* denotes the scattering coefficient for a soft-sphere model, $T_* = kT/\varepsilon$, and $\Gamma(\ldots)$ denotes the gamma function. These parameters can be determined by numerical fitting using data on $\Omega^{(2,2)*}$ [12]. This task has been done in the case of the GSS model [14]. We have employed the following set of parameter values: $\alpha_1 = 3.962$, $\alpha_2 = 4.558$, $\omega_1 = 0.133$, $\omega_2 = 1.25$, and $\alpha^* = 1.5$. These values are generally suitable for simple nonpolar gases.

On the basis of the Enskog equation for dense gases, when a gas is so dense that the *co*volume of the molecules is comparable to the total volume of the system, the assumptions of point particles and binary collisions are no longer applicable. After considering the scattering and screening effects of intermolecular scattering and screening effects, a collision enhancement factor dependent on the gas density has been derived, with the following third-order form [9]:

$$\chi(\eta) = 1 + 0.625\eta + 0.2869\eta^2 + 0.1103\eta^3 , \quad (7)$$

where $\eta = 2\pi n\sigma^3/3$ represents the molecular volume ratio. In the standard Enskog theory, the pressure in a dense gas is

$$p = knT[1 + \eta\chi] . \quad (8)$$

However, Enskog preferred a different procedure, based on the close relation between $\eta\chi$ and the compressibility. He observed that if hard-sphere molecules were surrounded by weak attractive fields of force, the equation of state would be modified to the following form:

$$p + a_v\rho^2 = knT[1 + \eta\chi] , \quad (9)$$

where a_v denotes the strength of the attraction, which is independent of the temperature and dependent on the gas properties; it is given by

$$a_v = \frac{27}{64}\frac{R^2T_c^2}{p_c} , \quad (10)$$

where R denotes the gas constant, T_c the critical temperature, and p_c the critical pressure.

This method solves the Enskog equation for a dense gas statistically while keeping the gas transport properties in good agreement with experimental data. The viscosity obtained from this method is compared with predictions from other methods and experimental data [12] in Fig. 1a, which shows the variation of viscosity with temperature at low and moderate gas densities. The present method gives much better agreement with experimental data at both lower and higher temperatures than does the Boltzmann theory or the viscosity–temperature power law used in the VHS model in the DSMC and ESMC methods. The variation of viscosity with density below a pressure of 150×10^5 Pa is shown in Fig. 1b. The results of the present method agrees well with the experimental data and the Enskog theory, whereas the results of the CBA and DSMC methods deviate from the experimental data at high gas densities. Therefore, the present method gives the best agreement with the experimental data over a large of temperatures and densities.

Since the main procedure in this GEMC method is similar to other Monte Carlo methods for gas flows, the program for it can therefore use many techniques borrowed from the DSMC method, such as the indexing and sample techniques; the codes were developed on the basis of the standard DSMC code of Bird [3]. The internal energy exchange model, i. e. the Borgnakke–Larsen model, for the generalized collision model was also modified on the basis of Parker's formula [13].

Key Research Findings

Similarity Analysis

Both microscale gas flows and rarefied-gas flows have three dimensionless numbers that characterize the flow: the Reynolds number Re, the Mach number Ma, and the Knudsen number Kn. However, these three parameters are not independent in rarefied-gas flows but instead are

related by

$$\mathrm{Kn} = \sqrt{\frac{\pi\gamma}{2}}\frac{\mathrm{Ma}}{\mathrm{Re}} . \tag{11}$$

Several researchers have used this relationship for rarefied-gas flows in the analysis of microscale gas flows [2]. However, this relationship has limited application to microscale gas flows. Wang and Li [15] found that Eq. (11) is based on a relationship between the viscosity and the mean free path. On the basis of the kinetic theory of gases, when the gas molecules are treated as smooth, rigid spheres with only a repelling force, the kinetic viscosity can be simply related to the molecular mean free path by

$$\nu = \frac{1}{2}\lambda v_{\mathrm{m}} , \tag{12}$$

where v_{m} is the mean molecular speed, which is somewhat higher than the speed of sound a:

$$v_{\mathrm{m}} = \sqrt{\frac{8}{\pi\gamma}}a . \tag{13}$$

With this assumption for Eq. (12), if the gas is a perfect gas, the three dimensionless numbers are not independent. As a result, gas flows at different scales can be similar (if other similarity conditions are also satisfied, such as similar geometries and boundary conditions). Since rarefied-gas flows have been studied extensively, owing to their important applications in astronautics and aeronautics, many theories and much experimental data can be used for the analysis of microscale gas flow by making use of this similarity, which has been numerically validated by a series of standard DSMC simulations [15].

However, the perfect-gas assumption does not always hold for micro- and nanoscale gas flows. When the gas density is high or the temperature is low, intermolecular attractions become significant as the effect of denseness changes the characteristics of the gas flow. According to Enskog's theory, the molecular mean free path in a dense gas, λ, is given by [12]

$$\lambda = \left[\sqrt{2}\pi n\chi\sigma^2\right]^{-1} . \tag{14}$$

The dynamic viscosity μ' of a dense gas is related to the dynamic viscosity μ of a perfect gas by

$$\mu' = \mu \cdot \eta\left[(\eta\chi)^{-1} + 0.8 + 0.7614(\eta\chi)\right] . \tag{15}$$

From classical thermodynamic theory, the speed of sound in a dense gas is enhanced as follows:

$$a' = a\left[1 + 8\eta\chi + \frac{4}{5}\eta^2\left(8\chi^2 + 3\frac{\mathrm{d}\chi}{\mathrm{d}\eta}\right)\right]^{\frac{1}{2}} . \tag{16}$$

For convenience, let us assume that Re and Ma have the same values in two systems; we can then obtain the ratio of the Knudsen numbers of the two systems as follows:

$$\frac{\mathrm{Kn}_1}{\mathrm{Kn}_2} = \frac{\sqrt{T_1}}{\sqrt{T_2}} \cdot \frac{\left[1 + 8\eta_1\chi_1 + \frac{4}{5}\eta_1^2\left(8\chi_1^2 + 3\frac{\mathrm{d}\chi_1}{\mathrm{d}\eta}\right)\right]^{\frac{1}{2}}}{\left[1 + 8\eta_2\chi_2 + \frac{4}{5}\eta_2^2\left(8\chi_2^2 + 3\frac{\mathrm{d}\chi_2}{\mathrm{d}\eta}\right)\right]^{\frac{1}{2}}} \cdot \frac{\left[1 + 0.8\eta_2\chi_2 + 0.7614\,(\eta_2\chi_2)^2\right]}{\left[1 + 0.8\eta_1\chi_1 + 0.7614\,(\eta_1\chi_1)^2\right]} . \tag{17}$$

A detailed data analysis has indicated that the characteristic lengths must be the same if the two dense-gas flows are to be treated similarly. That is to say, the three dimensionless parameters for two dense-gas flows with different scales cannot be the same in both flows. The similarity fails for dense-gas flows.

The high gas density influences the properties of the gas such as the viscosity and the speed of sound. Therefore, a critical density can be specified such that for densities below this critical density, the perfect-gas assumption and the similarity between gas flows hold. The critical density can be calculated for a specified error tolerance of 5%. For nitrogen gas, the critical density for the perfect-gas assumption is

$$\rho_{\mathrm{c}} \approx 4.5\rho_0 , \tag{18}$$

where ρ_0 is the density in the standard state. Equation (18) indicates that the effect of denseness must be considered when the density of the microscale flow is larger than 4.5 times the standard-state density.

High-Knudsen-Number Nonideal-Gas Flow

With the rapid development of M/NEMS techniques, gas flows in micro- and nanochannels are often encountered in practice. The large flow resistance caused by the huge aspect ratios of micro- and nanochannels usually requires a large driving pressure, which actually make the gas dense. However, the small characteristic length of the channel leads to a high Knudsen number, which causes continuum-based theories and prediction methods to break down. Such flows with both high Knudsen numbers and high densities have never been effectively and correctly predicted, though many efforts have been made in the past decade [6–8, 10]. In the present contribution, we describe the results of simulation of dense-gas flow in micro- and

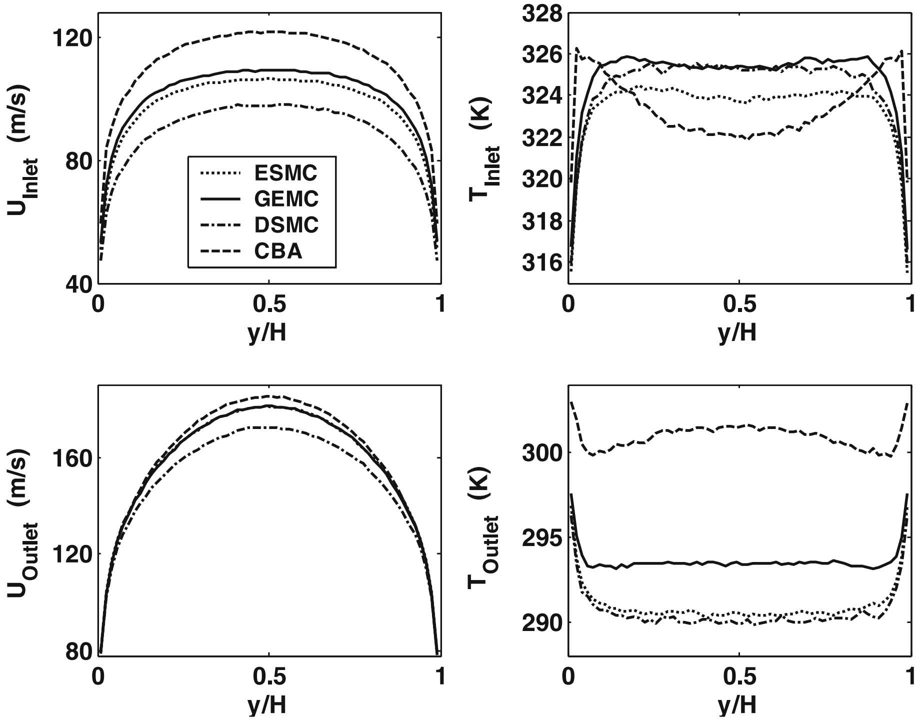

Micro- and Nanoscale Gas Fluidics, Figure 2 Effect of density on gas flow and heat transfer calculated by the GEMC method at $\eta_\infty = 0.135$ and $Kn_\infty = 0.06$, compared with DSMC, CBA, and ESMC results

nanochannels by the GEMC method, and the results are compared with previous studies.

We considered the flow of nitrogen gas in a microchannel. The density and temperature of the incoming gas were $n = 100\,n_0$ and $T = 300$ K, which lead to $\eta_\infty = 0.135$ and $Kn_\infty = 0.06$. The velocity of the incoming gas and the wall temperature were $U = 200$ m/s and $T_w = 300$ K, respectively. Figure 2 compares the simulation results for the velocity and temperature profiles at the inlet and outlet. Results obtained from the ESMC, DSMC, and CBA methods are also plotted in the figure. The results show that the high gas density affects the flow and heat transfer characteristics, which deviate from those predicted by the perfect-gas assumption. The ESMC algorithm modified the enhanced particle collision greatly but made little change to the internal energy exchange. Therefore, its results agreed well with the GEMC results for the velocity profiles at the inlet and outlet but deviated greatly from the GEMC results for the temperature field. At the same time, the reversal of the temperature distribution near the wall surface that occurred in the CBA simulations did not occur in the GEMC results [7], which indicates that the collision process needs to be modified to deal with the interaction between molecules and wall surfaces after the additional displacement that occurs in the CBA method. As a result, the present GEMC method works better than the other two numerical methods for modeling high-Knudsen-number nonideal-gas flows.

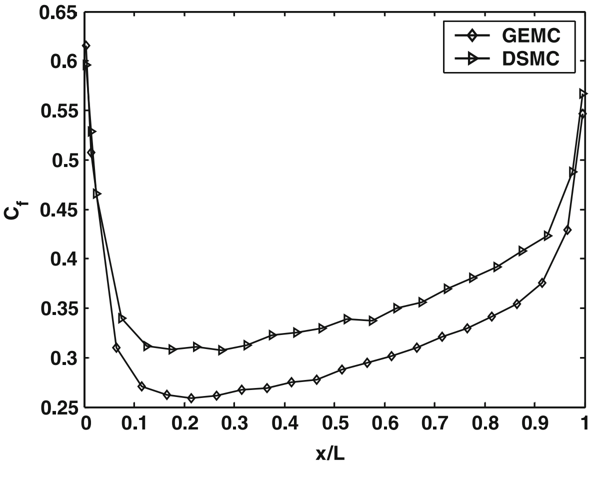

Micro- and Nanoscale Gas Fluidics, Figure 3 Distributions of the skin friction coefficient along the wall surfaces predicted by the GEMC and DSMC methods at $\eta_\infty = 0.135$ and $Kn_\infty = 0.06$

Figure 3 compares the distributions of the skin friction coefficient along the wall surfaces predicted by the GEMC

and DSMC methods. The results show that the density effect reduces the friction below the predictions of the perfect-gas assumption; this will need more theoretical and experimental validation.

Gas Flow and Heat Transfer in N/MEMS Devices

Since the development and application of atomistic computational methods in recent years, our understanding of gas microfluidics and nanofluidics has been greatly improved. If the flow and thermal behavior can be correctly analyzed and accurately predicted, optimal design of microsystems is possible. Related work can be found in analyses of the performance of microscale air slide bearings in hard disk drives [16], the propulsion efficiency of micronozzles in microsatellites [17], flows through orifices and orthogonal channels in microchips [5], gas mixing in microchannels, and heat transfer in vacuum-packaged MEMS devices [4]. Micro- and nanoscale gas fluidics has been a *hot* area, and numerous papers are being published every month owing to its importance, and therefore we cannot list all of the achievements in this area in these limited pages.

Future Directions for Research

Although the numerical tools for the simulation and analysis of gas microfluidic systems are now well developed, there are still many hard challenges ahead. Here, we list a few imperative and promising directions for the near future:

- *Hybrid multiscale simulation.* Although hybrid continuum/DSMC methods for multiscale gas flows have been proposed and developed for over ten years [19], these methods are far from completely established. The balance between accuracy and efficiency is still a problem. Recently, it has been found that the full-particle hybrid method may provide the best accuracy for the problem of coupling. The approach of finding efficient solvers for both continuum and high-Knudsen-number flows and then coupling them is promising. Another promising direction is coupling of the DSMC method for microscale gas flow to the MD method for special interfaces so as to deal with the unknown boundary conditions at the interfaces [20].
- *Multiphase processes.* Although the above Monte Carlo methods were developed for simulations of gas flows, they can also be used to analyze gas–particle interactions in granular flows, gas–liquid phase interactions in a liquid drop, and particle coagulation and aggregation. The proposed GEMC method will be very helpful for the analysis of multiphase processes in microscale gas flows.

Cross References

▶ Gas Flow in Nanochannels
▶ Micro- and Nanoscale Gas Dynamics
▶ Pressure-Driven Single-Phase Gas Flows
▶ Single-Phase Gaseous Flow
▶ Microfluidic Mixing
▶ Monte Carlo Method
▶ Multiscale Modeling and Numerical Simulations
▶ Supersonic Micro-Nozzles

References

1. Tsien H S (1946) Superaerodynamics, mechanics of rarefied gases. J Aero Sci 13(12):653–664
2. Gad-el-Hak M (1999) The fluid mechanics of microdevices: The Freeman Scholar Lecture. J Fluid Eng 121:5–33
3. Bird GA (1994) Molecular Gas Dynamics and the Direct Simulation of Gas Flows. Clarendon, Oxford
4. Wang MR, Li ZX (2006) Gas mixing in microchannels using the direct simulation Monte Carlo method. Int J Heat Mass Transf 49(9–10):1696–1702
5. Wang M, Li ZX (2004) Gas simulations for gas flows in microgeometries using the direct simulation Monte Carlo Method. Int J Heat Fluid Flow 25(6):975–985
6. Alexander FJ, Garcia AL, Alder BJ (1995) A consistent Boltzmann algorithm. Phys Rev Lett 74:5212–5215
7. Wang M, Li ZX (2003) Non-ideal gas flow and heat transfer in micro and nano channels using the direct simulation Monte Carlo method. Phys Rev E 68:046704
8. Wang M, Li ZX (2005) Monte Carlo simulations of dense gas flow and heat transfer in micro- and nano-channels. Sci China Ser E 48(3):317–325
9. Schram PPJM (1991) Kinetic Theory of Gas and Plasmas. Kluwer Academic, Dordrecht
10. Montanero JM, Santos A (1996) Monte Carlo simulation method for the Enskog equation. Phys Rev E 54:438–444
11. Wang M, Li ZX (2007) An Enskog based Monte Carlo method for high Knudsen number non-ideal gas flows. Comput Fluid 36(8):1291–1297
12. Chapman S, Cowling TG (1970) The Mathematical Theory of Non-uniform Gases, third edition. Cambridge Univ Press, Cambridge
13. Hash DB, Moss JN, Hassan HA (1994) Direct simulation of diatomic gases using the generalized hard-sphere model. J Thermophys Heat Transf 8:758–764
14. Fan J (2002) A generalized soft-sphere model for Monte Carlo simulation. Phys Fluid 14(12):4399–4405
15. Wang M, Li ZX (2003) Similarity of ideal gas flow at different scales. Sci China Ser E 46(6):661–670
16. Wenski TE, Olson T, Rettner CT, Garcia AL (1998) Simulations of air slider bearings with realistic gas–surface scattering. J Tribol ASME 120(3):639–641
17. Wang MR, Li ZX (2004) Numerical simulations on performance of MEMS-based nozzles at moderate or low temperatures. Microfluid Nanofluid 1(1):62–70
18. Liu HW, Wang MR, Wang JK et al (2007) Monte Carlo simulations of gas glow and heat transfer in vacuum packaged MEMS devices. Appl Therm Eng 27:323–329

19. Wijesinghe HS, Hornung RD, Garcia AL et al (2004) Three-dimensional hybrid continuum-atomistic simulations for multi-scale hydrodynamics. J Fluid Eng ASME 126(5):768–777
20. Nedea SV, Frijns AJH, van Steenhoven AA et al (2005) Hybrid method coupling molecular dynamics and Monte Carlo simulations to study the properties of gases in microchannels and nanochannels. Phys Rev E 72(1):016705

Microneedles – Applications & Devices

JIE WU
Department of Electrical Engineering and Computer Science, The University of Tennessee, Knoxville, TN, USA
jaynewu@utk.edu

Synonyms

Microfabricated needles; Microscale needles; Microhypodermic needles; Microprojections; Microtips and microspikes

Definition

Microneedles are a type of micromachined structure that promote the transport of substance through an interface or media, via enhanced permeability or microchannels. In most cases, microneedles are similar in shape to hypodermic needles, but are much smaller in size, enabling localized and painless delivery of drugs into cells or tissues. Microneedles, which can be either singular or grouped in arrays, are prepared using micro electro mechanical systems (MEMS) technology, and therefore can be produced in large batches from inexpensive metal, semiconductor, and polymer materials.

Overview

The microneedle concept was first proposed as a technique for transdermal drug delivery in the 1970s [1], and the recent advances in the microelectronics industry have provided the technical capability to make microneedles into reality. The first microneedle experiments were reported in 1998 [2]. Since then, there has been a rapid increase of interest in the field. Much of this effort concerns the development of novel needle fabrication technologies by adopting various needle designs and materials for use in biological and pharmaceutical applications.

Modern pharmaceutical technology is exploring a new generation of macromolecular medicines that are intended for applications in DNA research or directly as protein drugs. For these types of applications oral delivery is not a viable option because of the degradation of macromolecules in the stomach, intestines, or liver. In contrast, microneedles provide the means to locally and precisely deliver drugs, to take biomedical/neural measurements, and to perform microbiological sample analysis.

Currently, the smallest needles commercially available for injections are 30 gauge needles used in conventional syringes (305 um outer diameter), and 31 gauge used in pen injectors (254 um outer diameter). Microneedles, created by modern microfabrication technology, can be orders of magnitude smaller in diameter. The fabrication of microneedles involves one or more of the technologies in the area of MEMS (micro-electro-mechanical systems) including wet etching, reactive ion etching, chemical vapor deposition, and electroplating for casting of materials such as metals, and polymers. These needles are produced with high precision and, typically, are comparable to (or smaller than) the diameter of a human hair. Because of their small sizes, the injection is highly localized and damage to the tissue is minimal.

Applications

The applications of microneedles are many and varied. In the fields of genetic engineering, molecular and cell biology, it is desired to develop a method to introduce peptides, proteins, oligonucleotides, DNA and other probes into cells to alter their functions. For this purpose, microneedles can be applied for the delivery of molecules through impermeable membranes into cells. It has been demonstrated that microfabricated needle arrays could be used to deliver DNA into plant and mammalian cells, inducing cell transformation.

Another important application of microneedles is minimally invasive drug delivery. The small cross sectional area of microneedles, typically several hundreds of square micrometers, reduces any possibility of detrimental effects. At the same time, the drug delivery can be limited to a specific and localized region or tissue in the body. For this reason, microneedles have been used to study neural activities with very limited trauma to the tissue [3]. The short shaft of microneedles presents another advantage in drug delivery. Microfabrication technology allows the length of needle shafts to be controllable at a microscopic scale. The needles can be designed to penetrate just under the stratum corneum (the outer layer of the skin that has very low permeability). Since the nerve endings occur at a depth of about 100 μm, delivery at this location will reduce pain, infection or injury as well. In addition, because of the presence of a large number of capillaries in this layer of skin, the drug will be readily absorbed into the body, thereby enabling rapid treatment.

Microneedles can also be used to extract samples, thus finding significant applications in the field of health monitoring and biochemical analysis. For example, with diabetic patients, frequent use of needles is necessary for blood sampling to test glucose levels and to administer multiple doses of insulin. The use of microneedles can make it a virtually pain-free and a much more palatable experience to patients.

The applications of microneedles have expanded into electronics and sensors. They have been used as probes for surface modification and profiling, for example, in atomic force and scanning tunneling microscopes, and *Millipede* data storage. Microneedles have being applied in microdialysis where the microneedles are made permeable only to small molecular weight compounds. This protects the sensors from higher molecular weight compounds like proteins helping maintain the operational viability of the medical monitors. Other applications include printer heads and electrospray emitter nozzles.

Types of Microneedles

Microneedles can be classified into two groups, *solid microneedles* and *hollow microneedles*, depending on whether or not they contain a hollow bore for fluid transport. Solid microneedles increase the permeability of the skin or membrane by punching microscopic holes in the material. The transport of drugs or chemicals happens by diffusion or is assisted by applying an electric field, i. e., iontophoresis. These holes act as molecular pathways, readily permitting the transport from macromolecules to microparticles. On a clinical length scale, the holes are tiny compared to those from regular hypodermic needles and are therefore expected to be safer than their larger counterparts. With solid microneedles, transdermal drug delivery can basically be implemented in two approaches. One is to first make holes with microneedles to increase skin permeability, then remove the needles and apply drugs on the skin such as a patch. The other method is to coat the needles with drugs, then insert the needles into the skin and leave them there to release drugs. For the second method, people have investigated making microneedles with biodegradable polymers, into which drugs are incorporated. Once inside the skin, the polymer microneedle will disintegrate and be absorbed by living tissues gradually as a means of drug release.

Hollow microneedles work in a way similar to regular hypodermic microneedles. Fluids flow through the needle bore and into the tissue. The rate of fluid delivery is much faster than with solid microneedles, and the flow rate can be monitored and controlled over time. Using microfabrication technology, it is possible to build several bores or channels within one needle shaft with outlet ports at different locations along the shaft, so that more than one fluid can be injected at close spacing [4]. Also it is possible to integrate micropumps with microneedles onto a single microchip to further miniaturize the drug delivery system [3].

As far as microfabrication is concerned, especially with silicon-based processes, microneedle design can be classified as *out-of-plane* or *in-plane* depending on the orientation of the needle relative to that of the substrate material. Out-of-plane design refers to the microneedle configuration that protrudes perpendicularly from the plane of the substrate material (e.g. a silicon wafer), while in-plane refers to the design where the resulting needle lies lengthwise in the substrate plane. Examples of various microneedles (solid and hollow, out-of-plane and in-plane) are shown in Figs. 1a–d.

Because microfabrication is a two-dimensional (2D) technology in essence, microstructures are built from planar patterns projected onto the substrates by photolithography. Consequently, out-of-plane microneedles tend to have the same geometry along their length, since photolithography projects the needle cross-section onto the substrate. In contrast, in-plane microneedles can have various needle shapes, such as a bended needle shaft, because it is the needle side view being projected onto the substrate. In-plane needles have the possible advantage of building electrical, microfluidic, or optical functionalities on the needle shaft, which up to now has not been done with out-of-plane microneedles. With out-of-plane design, the micro-needle length is limited to be less than the substrate thickness, which is usually several hundred micrometers. If long microneedles are required, for example in the millimeter range, then the in-plane design is preferred. If it is desired to have a 2D array of microneedles that have repetitions of single needles in both x and y directions, then it is probably more efficient to fabricate with the out-of-plane design. With in-plane design, building a 2D-array requires additional fabrication steps, such as wafer bonding, which can be difficult and time consuming.

Failure Mechanisms

Penetration of microneedles into the tissue is essential to transdermal drug delivery. During the insertion, mechanical stress is induced onto the microneedles and causes them to break (fail). The failure modes of microneedles include buckling (compressive force), bending (from transverse tip force) and shear, since needles may not be perfectly aligned during insertion. Analysis has shown that shear is the least likely to cause failure, and bending is determined to be the critical failure mode [4]. For a 2 mm

M

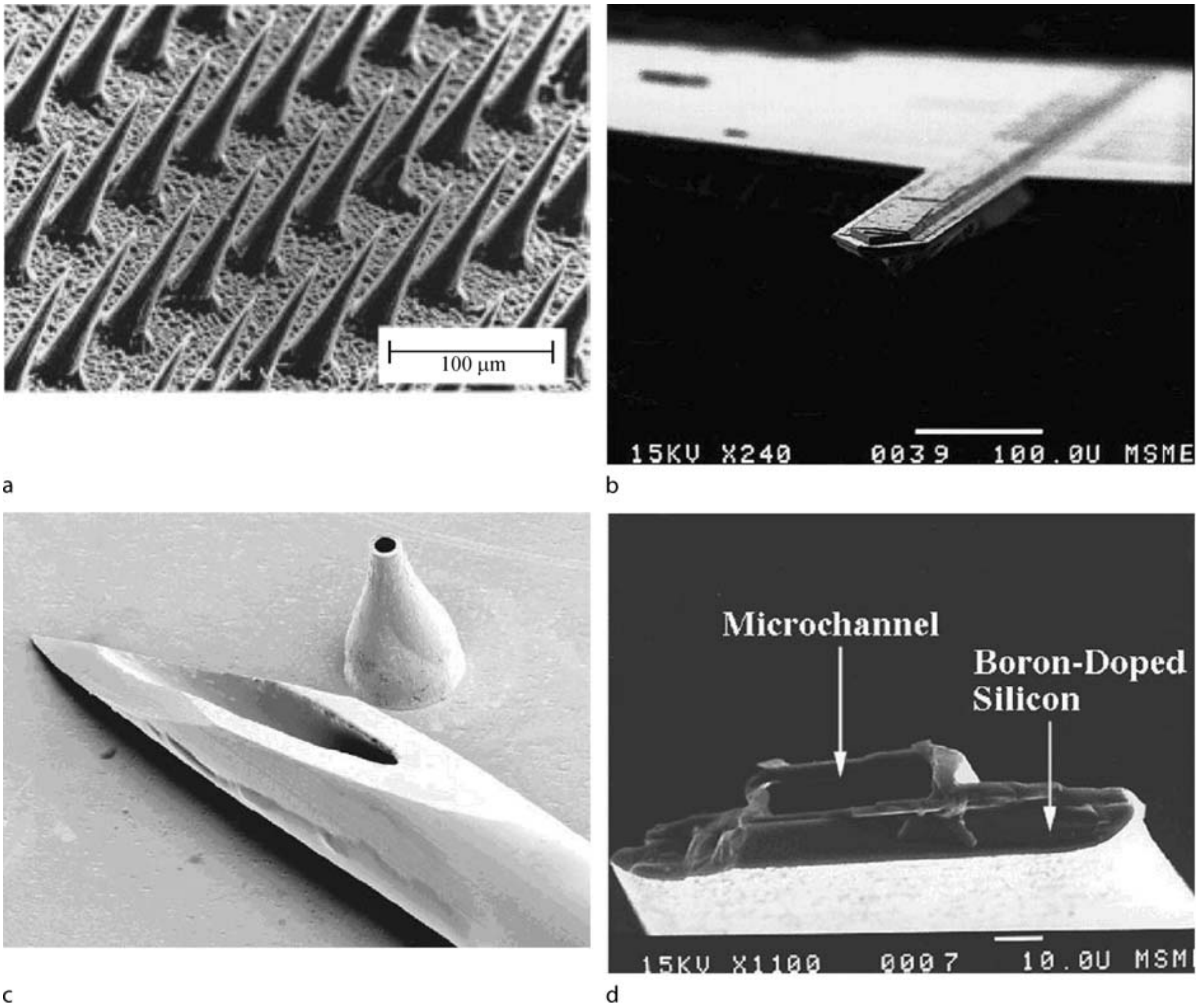

Microneedles – Applications & Devices, Figure 1 (**a**) Solid out-of-plane microneedle array [2]; (**b**) Hollow in-plane microneedle [8]; (**c**) In-plane microneedle [3]; (**d**) Microchannel of the in-plane microneedle, produced by silicon surface micromachining [3]

long silicon microneedle with a cross-sectional area of 100 µm by 100 µm, the maximum transverse force at the tip (out-of-plane bending) is 0.124 N (force required to break the microneedle shaft). For in-plane buckling, it can sustain a force of 6.28 N compared to the 0.0809 N needed to penetrate chicken breasts [5].

Flow Characteristics

Flow rate of fluids through hollow microneedles is an important design criterion in meeting the dosing requirements of drugs. Therefore it is important to model fluid flow characteristics within the bores/channels of microneedles. Typically, channels within microneedles have dimensions around a few micrometers. The flow within such a microchannel is laminar, i. e., the fluid flow follows streamlines and is free of turbulence. The transition between laminar and turbulent flow generally occur when the Reynolds number is around 2300. Reynolds number is defined as

$$R_\mathrm{e} = \frac{\rho u D_\mathrm{h}}{\mu} ,$$

where ρ is the fluid mass density (kg/m^3), u is the average flow velocity through the channel (m/s), D_h is the hydraulic diameter (= 4×Cross-sectional Area/Perimeter) (m) and μ is the dynamic viscosity (Ns/m^2). Representative values of the Reynolds number in a microchannel ranges from 1 to 100, well below the transition number.

When external pumps are used to deliver fluids through the needles, the flow within the microchannel is pressure

driven *Poiseuille* flow at steady state. The pressure losses from flowing through a microchannel can be divided into three regions: entrance losses, pressure decrease due to the drag that fully developed flow exerts on the duct walls, and losses due to specific microneedle geometry (expansions, constriction, bends, etc.).

At entry point, the fluid flow profile can be significantly different from the parabolic profile of *Poiseuille* flows. There is a characteristic distance before the steady state *Poiseuille* profile can be established. This distance, between the entry point and the fully establishment of *Poiseuille* flow, is called the *entrance length*. At the end of the entrance length, the pressure gradient matches that of the fully developed flow. The entrance length, l_e, can be expressed in term of the dimensionless *entrance length number El*:

$$l_e = El \times D_h \,.$$

For laminar flow, the entrance length number is correlated with the Reynolds number as

$$El_{la\min ar} = 0.06 R_e \,.$$

So l_e can be expressed as

$$l_e = 0.06 \frac{\rho u D_h^2}{\mu} \,.$$

The entrance pressure drop (Pa, N/m^2) can be found by the following relationship:

$$\Delta P_{ent} = \frac{2.656}{D_h} \sqrt{\rho \cdot \mu \cdot u^3 \cdot l_e} \,,$$

where l_e is the entrance length or the channel length, whichever is shorter.

After the entrance length, the pressure loss in the fully developed parabolic region can be found by the *D'Arcy–Weisbach* equation:

$$\Delta P_{dev} = \lambda \cdot \frac{L - l_e}{D_h} \cdot \frac{\rho \cdot u^2}{2} \,,$$

where λ is *D'Arcy–Weisbach friction coefficient* and L is the length of microchannel (m).

Pressure loss due to geometry can be generally expressed as

$$\Delta P_{geom} = K_{Loss} \cdot \frac{\rho \cdot u^2}{2} \,,$$

where K_{Loss} is the geometric loss factor. The overall pressure loss is the sum of these factors.

$$\begin{aligned} \Delta P_{tot} &= \Delta P_{ent} + \Delta P_{dev} + \Delta P_{geom} \\ &= \frac{2.656}{D_h} \sqrt{\rho \cdot \mu \cdot u^3 \cdot l_e} + \lambda \cdot \frac{L - l_e}{D_h} \cdot \frac{\rho \cdot u^2}{2} \\ &\quad + K_{Loss} \cdot \frac{\rho \cdot u^2}{2} \end{aligned}$$

Basic Methodology

The fabrication of microneedles, in and of itself, is the the main challenge in microneedle development. The task involves finding fabrication techniques that are capable of defining materials precisely in three-dimensions at the micro scale and are amenable to mass production. Addtionally, the material used to produce the microneedles must be compatible with the fabrication tools and offer sufficient resistance to buckling, bending and shear forces. Microfabrication techniques (a.k.a. MEMS techniques) that evolved from integrated circuit technologies provide the capability to define needle features with submicron precision for both in-plane and out of plane needle design, providing a high degree of flexibility with respect to the creation of different needle designs. These technologies also allow many needles to be fabricated on a single substrate, thereby achieving repeatability and reproducibility.

Microfabrication

Microfabrication techniques can be roughly categorized into surface micromachining, bulk micromachining, and micromolding. Surface micromachining is an additive process, which consists of depositing thin films, such as silicon nitride, polycrystalline silicon and other materials, onto substrates and dissolving sacrificial materials to form micromechanical structures. The thickness of the microstructures is limited to no more than several microns. The thickness restriction is directly related to the time period for processing that is determined by the deposition rate, etch rate, etc., and internal stresses introduced during the processing. As a result, surface micromachined structures tend to be fragile. In microneedle fabrication, surface micromachining is largely used for making microchannels. Bulk micromachining is a subtractive process that selectively removes significant amounts of material from a substrate to form microstructures. In bulk micromachining, the desired pattern is transferred onto the surface of a substrate from the mask by photolithography, and then, starting at the surface of the substrate, the pattern is etched into the substrate until the desired depth is reached. In most cases, the body of the microneedle is defined by bulk micromachining, i. e., three-dimensional features are etched into the bulk of the crystalline or

non-crystalline material. Finally, the microstructures are released from the substrate by dicing or dissolving the excess substrate material. Bulk micromachining can be achieved by using both dry and wet etching processes. Both surface and bulk micromachining techniques have been derived from their application in silicon-based technologies. Silicon was initially the material of choice in microfabricated devices because of its favorable electrical and mechanical properties. Recently, other materials, such as metals and polymers, have been applied in the fabrication of microdevices because of their desirable properties (e. g. biocompatibility and price). For those materials, techniques from outside the realm of silicon processing can be used, such as laser drilling, electroplating or a combination of techniques. Among them, micromolding is becoming increasingly popular as an unconventional fabrication method. With this method, typically a mold needs to be built first, which can be made from metal or silicon by bulk micromachining. The needle material is then cast into the mold to produce microneedles. With micromolding, microneedles can be easily mass-produced with a variety of materials.

Microchannel Fabrication

Hollow microneedles have microchannels to transport fluids, and those microchannels are enclosed within the microneedle shafts. To produce a closed microchannel, the following methods have been reported: substrate-to-substrate bonding such as anodic bonding, surface micromachining with a sacrificial layer, and a type of bulk micromachining known as *buried channel technology* by de Boer et al. [6]. Figure 2 and Fig. 1d show the microchannels produced by the above-mentioned methods, respectively. Bonding processes form a closed channel by joining two substrates with chemical or physical means. Alignment and a clean environment are critical to the bonding process, since particles and micro voids may be introduced during the process, which can change or even destroy the functional performance of the device. Surface micromachining produces closed microchannels by overlaying thin-film microstructures around a suitable sacrificial material on the surface of a substrate. The sacrificial material is later dissolved to leave an enclosed microchannel, thus avoiding the need for aligned bonding. The dimensions of such channels are generally restricted by the maximum sacrificial layer thickness. The third method, called buried channel technology (BCT), is a bulk micromachining method that makes trenches into the substrate, then selectively expands the trench bottoms into channels. Depositing a layer of dielectric over the substrates seals the channels.

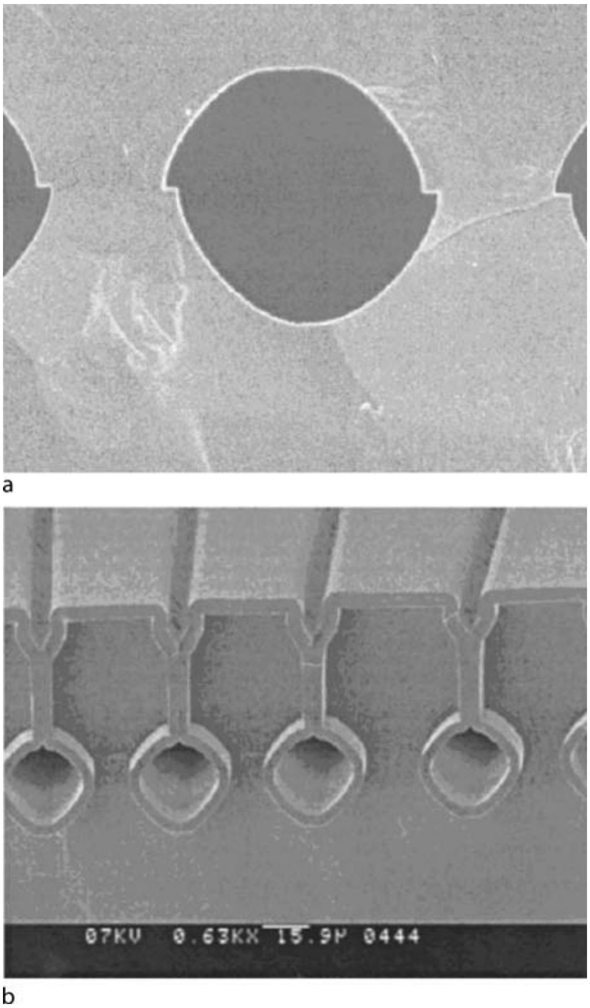

Microneedles – Applications & Devices, Figure 2 (**a**) Microchannel formed by bonding [6]; (**b**) Microchannels formed by buried channel technology (BCT) [6]

Key Research Findings

Effectiveness of Microneedles

The most prevalent use of microneedles is in the delivery of drugs. It has been shown that solid microneedles can increase skin permeability to a broad range of molecules and nanoparticles in vitro by up to four orders of magnitude [7]. In vivo animal studies have demonstrated delivery of oligonucleotides and vaccines (Macroflux®), as well as induction of immune responses from protein and DNA vaccines [8, 9]. The functionality of hollow microneedles has also been demonstrated, including fluid transport in vitro and microinjection of insulin in diabetic rats to induce reduction of blood glucose levels [10]. Microneedles have also been used to extract interstitial fluid from skin for glucose measurement [11].

Mechanics of Microneedle Insertion

The mechanics of microneedle insertion are fundamentally important to practical applications. Only microneedles with the correct geometry and physical properties can be inserted into tissues. When the force required for insertion is too large compared with needle strength, microneedles can break or bend before insertion occurs. Two mechanical events play a critical role in microneedle insertion: the force required to insert microneedles and the force needles can withstand before fracturing. The fracture force must be larger than the insertion force for the microneedles to be functional.

Davis et al. [12] have investigated the insertion of microneedles over a range of geometries (tip radii between 30 – 80 μm and constant length of 500 μm). In their experiments, the insertion force was found to vary linearly with the interfacial area of the needle tip. Thin-walled hollow needles and solid needles with the same outer tip radii required the same force of insertion. Measured insertion forces ranged from approximately 0.1 – 3 N, which is sufficiently low to permit insertion by hand. The force required to fracture microneedles was found to increase with increasing wall thickness, wall angle, and possibly tip radius. For almost all geometries considered, the ratio of fracture force to insertion force, termed the margin of safety, was much greater than one and was found to increase with increasing wall thickness and decreasing tip radius. Thus, the margin of safety was found to be optimal for needles with small tip radius (to facilitate insertion) and large wall thickness (to provide strength).

Future Directions for Research

Up to now, the development of microneedles has focused on microfabrication techniques for Si and other biocompatible materials. Currently, there are several commercially available microneedle products, such as MTS® (Microstructured Transdermal System) by 3M, Macroflux® by ALZA and Micro-Trans™ by BioValve Technologies, and most of them are designed to increase skin permeability and adopt passive delivery methods (i. e., capillary force). As the feasibility of microneedles is well established, the next step is to understand the characteristics of fluid transport by microneedles, especially in vivo, and to interface microneedles with external dosing control for active drug delivery. A very important aspect in microneedle development is to become closely involved with pharmaceutical research. Microneedle injection can control well the depth of drug delivery to receptive intradermal, junctional or subcutaneous tissues, and some medicines of large molecule seem to have better and faster absorption when given intradermally rather than subcutaneously. Also the pharmacokinetics may change, e.g. medicine may preferentially migrate to the lymphatic system, and this could potentially help in the treatment of many types of cancer, including certain types of leukemia, lymphomas, melanomas, etc. By investigating microneedle design and fabrication in conjunction with drug delivery mechanism, revolutionizing changes may be brought about in the medicine field.

Cross References

- ► Pressure-Based Sample Injection
- ► Electrokinetic Sample Injection
- ► Supersonic Micro-Nozzles
- ► Silicon Micromachining
- ► Micromolding

References

1. Gerstel MS, Place VA (1976) Drug delivery device, US Patent No. 3,964,482
2. Henry S, McAllister D, Allen MG, Prausnitz MR (1998) Microfabricated microneedles: a novel method to increase transdermal drug delivery. J Pharm Sci 87(8):922–925
3. Lin L, Pisano A (1999) Silicon processed microneedles. J Microelectro-mech Syst 8(1):78–84
4. Zahn JD, Talbot NH, Liepmann D, Pisano A (2000) Microfabricated polysilicon microneedles for minimally invasive biomedical devices. Biomed Microdev 2(4):295–303
5. Paik S-J, Byun S, Lim J-M, Park Y, Lee A, Chung S, Chang J, Chun K, Cho D (2004) In-plane single-crystal-silicon microneedles for minimally invasive microfluid systems. Sens Actuators A 114(3):276–284
6. de Boer MJ, Tjerkstra RW, Berenschot JW, Jansen HV, Burger GJ, Gardeniers JGE, Elwenspoek M, van den Berg A (2000) Micromachining of buried micro channels in silicon. J Microelectromech Syst 9(1):94–103
7. McAllister DV, Wang PM, Davis SP, Park J-H, Canatella PJ, Allen MG, Prausnitz MR (2003) Microfabricated needles for transdermal delivery of macromolecules and nanoparticles: fabrication methods and transport studies. Proc Natl Acad Sci 100(24):13755–13760
8. Lin WQ, Cormier M, Samiee A, Griffin A, Johnson B, Teng C-L, Hardee GE, Daddona PE (2001) Transdermal delivery of antisense oligonucleotides with microprojection patch (Macroflux) technology. Pharm Res 18(12):1789–1793
9. Matriano JA, Cormier M, Johnson J, Young WA, Buttery M, Nyam K, Daddona PE (2002) Macroflux microprojection array patch technology: A new and efficient approach for intracutaneous immunization. Pharm Res 19(1):63–70
10. Minokoshi Y, Haque MS, Shimazu T (1999) Microinjection of leptin into the ventromedial hypothalamus increases glucose uptake in peripheral tissues in rats. Diabetes 48(2):287–291
11. Prausnitz MR (2004) Microneedles for transdermal drug delivery. Adv Drug Deliv Rev 56(5):581–587
12. Davis SP, Landis BJ, Adams ZH, Allen MG, Prausnitz MR (2004) Insertion of microneedles into skin: measurement and prediction of insertion force and needle fracture force. J Biomech 37:1155–1163

µPEMFC

► Microstructured Hydrogen Fuel Cells

Micro-PIV-Based Diffusometry

PRAMOD CHAMARTHY, STEVEN T. WERELEY
Department of Mechanical Engineering,
Purdue University, West Lafayette, IN, USA
pramodc@purdue.edu, wereley@purdue.edu

Synonyms

Brownian noise

Definition

Brownian motion of submicron-sized tracer particles is a significant source of error in µPIV measurements, which can be substantially reduced by ensemble averaging over multiple images. This unbiased noise can be measured to obtain temperature, viscosity, or particle size information.

Overview

Microparticle imaging velocimetry (µPIV) is an established nonintrusive technique to obtain accurate velocity data with high spatial resolution and is widely used as a design tool for most microfluidic devices. In typical µPIV experiments, the fluid is seeded using submicron-sized particles, which are small enough to exhibit Brownian motion. It was recognized very early on that the random movement of these particles contributed a significant source of error for low-velocity flows. This undesirable error was substantially minimized through ensemble averaging over multiple images. The precise effect of Brownian motion on the spatial cross-correlation function must be understood in order to make useful measurements.

Basic Methodology

In PIV analysis, the cross-correlation function between two ideal images would have a single peak. The location of the peak gives an estimate of the mean velocity of the fluid, and the shape of the cross-correlation function contains information about the particle size, and about any fluctuations in the velocity. Brownian motion of the tracer particles introduces an error into the location of the correlation peak. Since Brownian motion is an unbiased noise source, ensemble averaging over multiple correlation peaks should help to minimize this error. However, as a result of the averaging process, the peak width of the correlation function is broadened. Olsen and Adrian [9] performed a theoretical study of the effect of Brownian motion on the µPIV correlation signal peak and derived a function quantifying the broadening of the correlation function.

Brownian Motion in a Stationary Fluid

As described by Hohreiter et al. [6], the idea of PIV *diffusometry* is based on the theory of Brownian motion. The Eq. (1)

$$D = \frac{\mathrm{k}T}{3\pi \mu d_{\mathrm{p}}} \tag{1}$$

defines the diffusivity D of particles with diameter d_{p} immersed in a liquid with absolute viscosity μ and temperature T; k is Boltzmann's constant. The mean square of the expected distance traversed by a particle with diffusivity D within a time Δt is given by the Eq. (2)

$$\left\langle s^2 \right\rangle = 2D\Delta t \tag{2}$$

In a typical PIV experiment, two snapshots of the flow field are obtained at times t_1 and $t_2 = t_1 + \Delta t$. If these two images are denoted by $I_1(X)$ and $I_2(X)$, then the cross-correlation function can be obtained using the convolution integral (Keane and Adrian [7])

$$R(s) = \int I_1(X) I_2(X+s)\,\mathrm{d}X\,. \tag{3}$$

$R(s)$ can be decomposed into three components as follows:

$$R(s) = R_{\mathrm{C}}(s) + R_{\mathrm{F}}(s) + R_{\mathrm{D}}(s)\,, \tag{4}$$

where $R_{\mathrm{C}}(s)$ is the convolution of the intensities of the two images with its diameter equal to the particle diameter, $R_{\mathrm{F}}(s)$ is the fluctuating noise component, and $R_{\mathrm{D}}(s)$ is the displacement component of the correlation function and gives the distance traveled by the particle during a time Δt. Hence $R_{\mathrm{D}}(s)$ is the component of the correlation function which contains the velocity information.

The displacement and width of the correlation function depend on the probability function $f\left(x', t_2; x, t_1 \middle| u(x), T\right)$, where f denotes the probability that a particle initially at (x, t_1) will move into the volume $(x', x' + \mathrm{d}x)$ at t_2 for a known velocity field $u(x)$ and temperature T. In the absence of Brownian motion, $\Delta x = u(x, t_1)\Delta t$ is the displacement undergone by a particle at (x, t_1). Since for a given velocity field there can only be one final location for the particle, the probability function f becomes the delta function

$$f\left(x', t_2; x, t_1 \middle| u(x), T\right) = \delta\left(x' - x - \Delta x\right)\,. \tag{5}$$

However, in the presence of Brownian motion, an exact value of the displacement Δx cannot be defined and, as a result, f is no longer a delta function. Instead, f is now a probability distribution function centered at $x' = x + \Delta x$, and its shape is defined by the space–time correlation for Brownian motion given by Chandrasekhar [5],

$$f\left(x', t_2; x, t_1 \middle| u(x), T\right) = (4\pi D\Delta t)^{-3/2} \times \exp\left[-\frac{\left(x' - x - \Delta x\right)^2}{4D\Delta t}\right] . \quad (6)$$

This change in f due to Brownian motion has the effect of broadening the correlation function and reducing its height. The increase in the width of the correlation function contains information that yields the temperature. This effect is demonstrated in Fig. 1, which shows correlation functions with and without Brownian motion.

Olsen and Adrian [9] derived analytical expressions to define the shape and height of the correlation function in the presence of Brownian motion for both light-sheet PIV and volume-illumination PIV. In both cases, the correlation function assumes a Gaussian shape and its center is located at the mean particle displacement. In light-sheet PIV, the field of view of the camera can be set to be greater than the thickness of the laser sheet so that all of the particles in the image can have the same diameter and peak intensity. The characteristics of the imaging optics play an important role in defining the relationship between the actual cross section of a particle and that of its image (Adrian [1]). Given a diffraction-limited lens, the image of a particle is the convolution of the geometric image of the particle and the point response function of the imaging system. The point response function is an Airy function with a diameter given by

$$d_s = 2.44(1 + M) f^{\#} \lambda , \quad (7)$$

where M is the magnification of the lens, $f^{\#}$ is the f-number of the lens, and λ is the wavelength of the light used to image the particles. Adrian and Yao [2] found that the Airy function and the image of a particle can be approximated by Gaussian functions, in which case the diameter of the particle image can be expressed by the formula

$$d_e = \left(M^2 d_p^2 + d_s^2\right)^{1/2} , \quad (8)$$

where d_p is the particle diameter and M is the magnification of the lens used.

In volume-illumination PIV (for example μPIV), the particle images are more complex. Since the entire channel is illuminated, all of the particles within the depth of field of the camera contribute to the resulting image. The particles close to the focal plane form sharp images, while the particles away from the focal plane form dim, blurred images. Olsen and Adrian [10] proposed that the particle image diameter in μPIV can be approximated by

$$d_e = \left(M^2 d_p^2 + d_s^2 + d_z^2\right)^{1/2} , \quad (9)$$

where

$$d_z = \frac{M z D_a}{x_0 + z} \quad (10)$$

and D_a is the aperture diameter of the microscope objective, z is the distance of the particle from the focal plane, and x_0 is the object distance.

From an analysis of cross-correlation PIV, Olsen and Adrian [10] found that for light-sheet PIV, the width of the correlation peak Δs_0, taken as the diameter of the Gaussian function measured at a height of $1/e$ times the peak value, can be expressed as

$$\Delta s_{o,a} = \sqrt{\frac{2 d_e^2}{\beta^2}} \quad (11)$$

in the absence of Brownian motion. When Brownian motion is present, the peak width $\Delta s_{o,c}$, can be expressed as

$$\Delta s_{o,c} = \sqrt{\frac{2\left(d_e^2 + 8M^2\beta^2 D\Delta t\right)}{\beta^2}} . \quad (12)$$

Equation (12) reduces to Eq. (11) when the Brownian motion $(D\Delta t)$ is assumed to be zero. The constant β is a parameter arising from approximating the Airy function by a Gaussian function and was found to be equal to $\beta^2 = 3.67$ (Adrian and Yao [2]).

In the case of volume illumination, Eqs. (11) and (12) still hold, except that the term for the particle image diameter d_e must be replaced by an integral over the depth of the device. The cumbersome calculation of the integral term for d_e can be avoided by manipulation of Eqs. (11) and (12). Squaring Eq. (11) and subtracting it from the square of Eq. (12) gives the equation

$$\left\langle s^2 \right\rangle = \frac{\Delta s_{o,c}^2 - \Delta s_{o,a}^2}{8M^2} = \frac{2k\Delta t}{3\pi d_p} \cdot \frac{T}{\mu} , \quad (13)$$

which can be used directly to calculate the temperature.

M

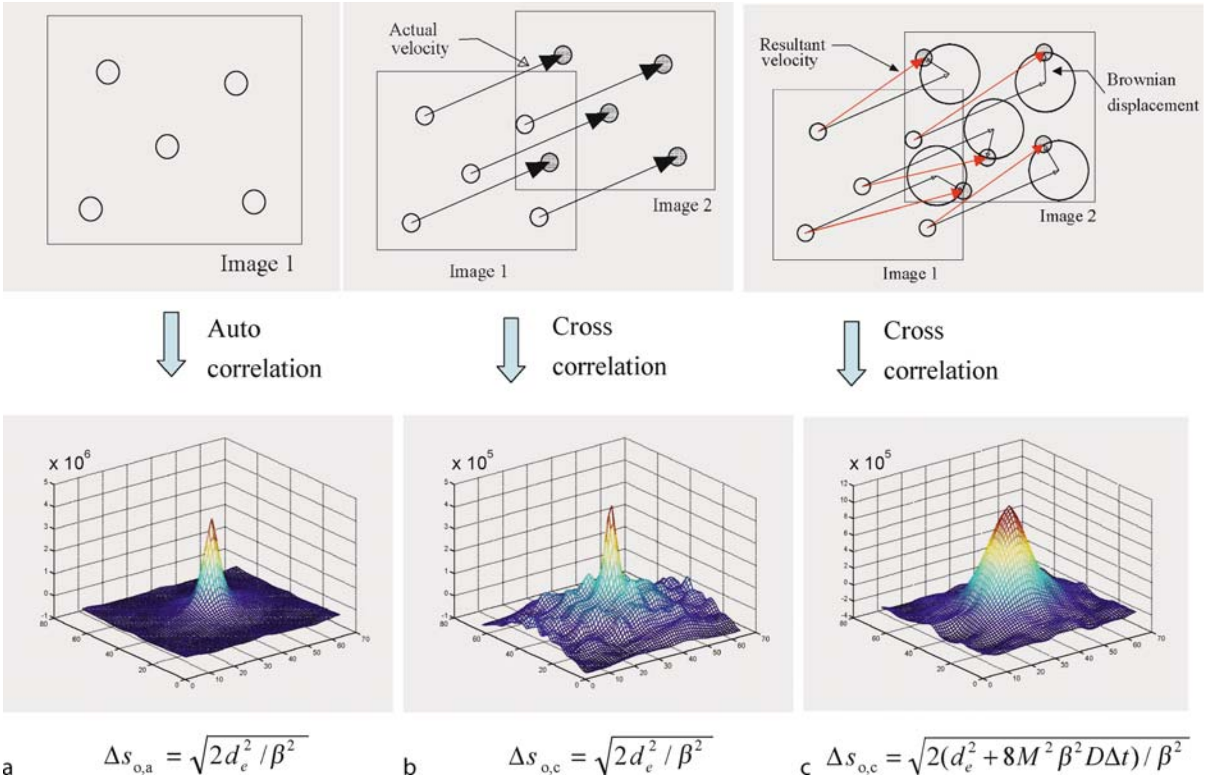

Micro-PIV-Based Diffusometry, Figure 1 Comparison of (**a**) autocorrelation function, (**b**) cross-correlation function without any Brownian motion, and (**c**) cross-correlation function with Brownian motion

Brownian Motion in a Moving Fluid

In the presence of a nonuniform velocity field, if there is a velocity gradient present across the interrogation window, the correlation function is deformed accordingly. In the case of a Poiseuille flow, the velocity gradient is nonuniform across the channel. As a result, the probability distribution function f has a Brownian-motion component and a velocity distribution component. For simple flows, if the velocity profile is known, the probability distribution of velocities and the resulting broadening of the cross-correlation function can be computed. This can be subtracted from the total measured value to obtain the broadening due to Brownian motion alone. In this analysis, a steady flow is assumed.

The feasibility of this method will be illustrated here with the help of a numerical experiment, as described below. Figure 2a shows the velocity profile across the channel; the red lines show the velocity gradients present in the interrogation window at different locations. A uniform Brownian motion (temperature profile) is assumed across the channel. Figure 2b shows the broadening in the cross-correlation function for different amounts of Brownian motion. The x-axis shows the increase in the peak width in pixels, and the y-axis shows the radial location across the channel. It can be seen that the peak width increase is greatest near the walls, where the maximum velocity gradient is also present. In the absence of Brownian motion, the increase in peak width is due only to the velocity gradients present. As the amount of Brownian motion increases, the curve becomes flatter. The peak width increase due to Brownian motion alone can be obtained by subtracting the peak width increase caused by the velocity gradient alone. Figure 2c shows this subtracted value. It can be seen that by subtracting the velocity gradient information, information about the Brownian motion can be obtained.

The peak widths of the cross-correlation function in the streamwise direction and the perpendicular direction are shown in Fig. 3. The cross-correlation function in the streamwise direction near the wall is broader than the cross-correlation function near the center of the channel, owing to the high velocity gradients near the walls. Since there are no velocity gradients present in the radial component of velocity, the peak width of the cross-correlation function in the perpendicular direction is uniform across the channel.

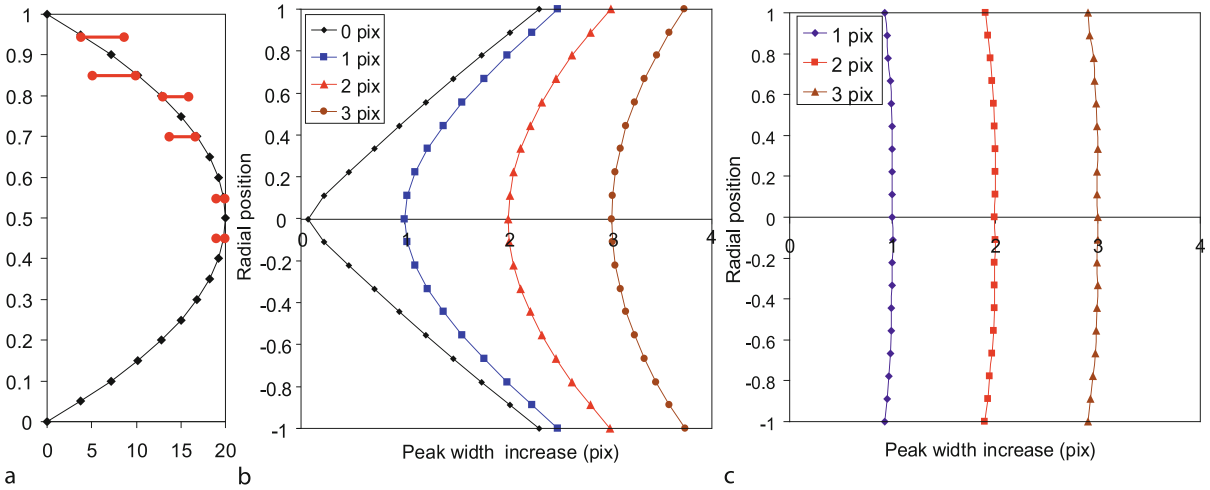

Micro-PIV-Based Diffusometry, Figure 2 Broadening of the correlation function due to a velocity gradient

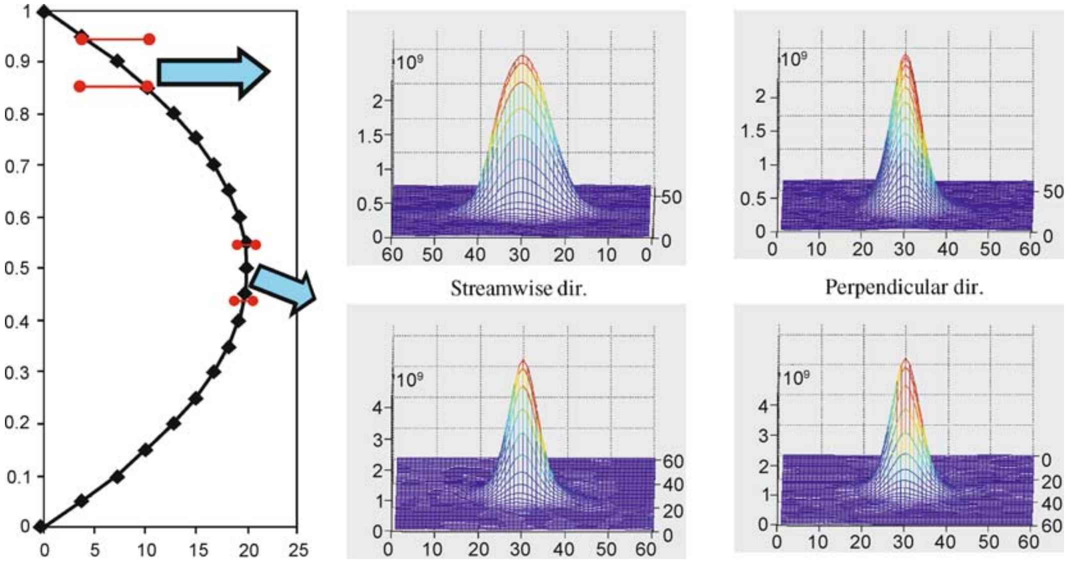

Micro-PIV-Based Diffusometry, Figure 3 Illustration of the effect of a velocity gradient on the cross-correlation function

Prior knowledge of the velocity field is required for this method to work. In practice, this can be achieved by measuring the velocity field first and then using that information to measure the temperature field. Since the velocity information is decoupled from the temperature information, this does not pose a problem.

Key Research Findings

Temperature Measurement Using Brownian Motion

Combining Eqs. (1) and (2), it can be seen that, if all other variables are held constant, the mean square displacement $\langle s^2 \rangle$ is dependent only on the temperature, as given by the relationship $\langle s^2 \rangle \alpha T/\mu$, since the absolute viscosity μ is a strong function of temperature. For a gas, increasing the temperature increases the absolute viscosity, which in turn, might increase or decrease the value of T/μ, depending on the fluid. For a liquid, increasing the temperature decreases the absolute viscosity, and hence the value of T/μ is always increased. Hence, if the diffusion coefficient of a particle and its diameter are known along with the viscosity of the fluid, the temperature of the fluid can be determined.

This method was proposed by Santiago et al. [11] and experimentally verified by Chamarthy et al. [3]. The image was split into smaller windows of a specified size. An

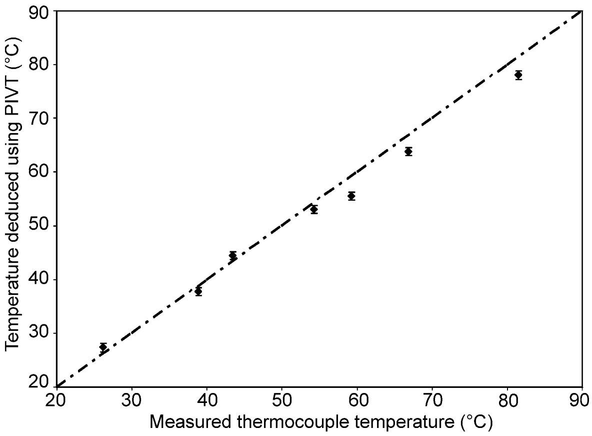

Micro-PIV-Based Diffusometry, Figure 4 Temperatures in a stationary fluid deduced using the PIV based Thermometry (PIVT) method plotted against the temperatures measured with a thermocouple. The average difference between the predicted and measured temperatures was ±2.1 °C

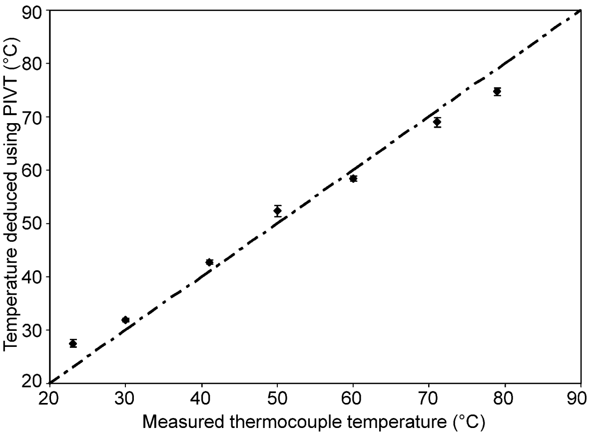

Micro-PIV-Based Diffusometry, Figure 5 Temperatures in a moving fluid deduced using the PIV based Thermometry (PIVT) method plotted against the temperatures measured with a thermocouple. The average difference between the expected and average temperatures was ±2.6 °C

interrogation window size of 128×128 px was used so that there would be particles present in every window. Evaluation functions were then read and processed in MATLAB. The evaluation functions were averaged over the entire image, and a 2D Gaussian fitting program was used to measure the peak width of the evaluation function. In order to fully characterize a 2D Gaussian function, given by the Eq. (14)

$$G(x, y) = A \exp\left(\frac{-(x - x_0)^2}{2\sigma_x^2}\right) \cdot \exp\left(\frac{-(y - y_0)^2}{2\sigma_y^2}\right), \tag{14}$$

five parameters must be defined: the peak height A, the coordinates locating the peak center x_0 and y_0, and the values of the standard deviation in the x and y directions σ_x and σ_y. If σ_x is equal to σ_y then the Gaussian function has a circular cross section; otherwise, it has an elliptical cross section. The standard deviation is related to the peak width by $\Delta s^2 = 8\sigma^2$, and contains the Brownian-motion information. In the case described here, since the images were taken far from the walls of the channel, the Brownian motion should be identical in all directions, resulting in a circular Gaussian function.

The temperatures were calculated using Eq. (13) and are plotted in Fig. 4. The advantage of this method is that a high concentration of particles can be used as long as the particles do not interact with each other, yielding the highest possible number of data points. Also, for the purpose of measuring temperature in the presence of a flow field, this method would be much less cumbersome than a particle-tracking technique. The main disadvantage of this method is the error introduced into the measurement of the shape of the correlation function owing to uneven illumination and background noise in the image. Standardized image-processing techniques must be used to eliminate this noise. Also, advanced algorithms such as those for central difference image correction (CDIC) and continuous window shifting (CWS) cannot be used, as they distort the shape of the correlation function.

PIV-based temperature measurement in a moving fluid was experimentally verified by Chamarthy et al. [4]. Since the Brownian motion along each coordinate axis is independent of that along the other axes, the diffusion in the x and y directions was measured separately at each location. The x-axis was taken as the axial direction and the y-axis as the radial direction. As a uniform temperature was applied across the channel, the Brownian motion in the x and y directions should be uniform along the radial direction. Since the velocity gradient affects only the standard deviation in the x direction (σ_x), σ_y is a measure of the Brownian motion alone and should be uniform across the channel. The value of σ_x contains both Brownian-motion and velocity-gradient information and varies according to the gradients present in each window.

The temperature values obtained from the mean increase of the peak width in the y direction are plotted against the expected values in Fig. 5. The average difference between the measured and expected temperatures was found to be ±2.6 °C.

Brownian-Motion-Based Biosensor

Brownian motion of suspended particles can be used as a means for the detection of biological agents. If the tem-

perature of the fluid is known, the diffusion is a function only of the viscous drag acting on a particle. In this method, fluorescent particles are functionalized with antibodies against a specific analyte and are introduced into a sample containing that analyte. As the analytes bind to the particles the hydrodynamic drag is increased, causing a decrease in the diffusion coefficient, which can be measured using μPIV techniques.

The common methods for biological-agent detection measure binding events using fluorescence, bioluminescence, surface plasmon resonance, changes in impedance, changes in the resonance of a microbalance, and changes in the conductance of nanowires. Typically, such biosensors use "sandwich" assays for detection and measurement. The disadvantage of using sandwich assays is that it is difficult to produce two antibodies that each bind to different sites of an antigen. Also, the probability of two binding events occurring on a single antigen is much less than that of a single binding event.

The advantage of a diffusion-based biosensor is that it avoids the need for a sandwich assay by directly measuring the reduction in the diffusion coefficient of antibody-functionalized submicron particles caused by the binding of complementary antigens. This technique should be useful for bioanalytical techniques for drug discovery, and for pathogen detection in complex media.

Microrheology Using Brownian Motion

Studying rheological properties within cells and complex fluids is an important step in understanding biological motility. Cell biologists have discovered that many aspects of a cell's gene expression, such as locomotion, differentiation, and apoptosis, are also governed by the stress and elasticity of its surroundings. However, standard mechanical and optical rheological techniques cannot be applied at such small length scales.

Recently, Brownian-motion-based techniques have been developed to measure local rheological properties and resolve microheterogenities inside such complex fluids. Particle-tracking techniques have been used to measure the displacements of individual particles and calculate their diffusion using Eq. (2). The disadvantage of single-particle tracking is that a large volume of data needs to be taken to obtain a statistically averaged result. Moreover, the probability of a particle diffusing out of the region of interest increases as the measurement time increases. A large number particles can be used in PIV-based methods, so that the measurement time can be reduced. Also, the loss of a few particles due to diffusion out the region of interest does not severely affect the measurement.

Future Directions for Research

The PIV-based diffusometry method is still in its infancy and has the potential to be developed into a powerful tool that can be used across several different disciplines. The sensitivity of the technique can be increased by increasing the magnification, decreasing the size of the pixels in the camera, and increasing the number of images obtained. The particle size and the time between a pair of images need to be chosen such that the particles diffuse by more than the linear dimensions of a pixel. The technique is especially sensitive to particle clumps present in the measurement region. An efficient, easy-to-use algorithm for diffusometry techniques needs to be developed in order to increase the usage of the technique.

Cross References

► Microparticle Imaging Velocimetry (μPIV)
► Fundamentals of Diffusion in Microfluidic Systems

References

1. Adrian RJ (1991) Particle-imaging techniques for experimental fluid mechanics. Annu Rev Fluid Mech 23:261–304
2. Adrian RJ, Yao CS (1985) Pulsed laser technique application to liquid and gaseous flows and the scattering power of seed materials. Appl Opt 24:44–52
3. Chamarthy P, Wereley ST, Garimella SV (2005) Assessment of alternate approaches for temperature measurement using Brownian motion. 6th Int Symp Particle Image Velocimetry, Pasadena
4. Chamarthy P, Wereley ST, Garimella SV (2006) Simultaneous measurement of temperature and velocity using μPIV. Proc ASME Int Mech Eng Congress Exposition, IMECE2006–14079, Chicago
5. Chandrasekhar S (1941) Stochastic problems in physics and astronomy. Rev Mod Phys 15:1–89
6. Hohreiter V, Wereley ST, Olsen MG, Chung JN (2002) Cross-correlation analysis for temperature measurement. Meas Sci Technol 13:1072–1078
7. Keane RD, Adrian RJ (1992) Theory of cross-correlation analysis of PIV images. Appl Sci Res 49:1–27
8. Kumar A, Gorti V, Wereley ST (2006) Biological agent detection using optical diffusometry methods. Proc ASME Int Mech Eng Congress Exposition, IMECE2006–13267, Chicago
9. Olsen MG, Adrian RJ (2000) Brownian motion and correlation in particle image velocimetry. Opt Laser Technol 32(7–8):621–627
10. Olsen MG, Adrian RJ (2000) Out-of-focus effects on particle visibility and correlation in microscopic particle image velocimetry. Exp Fluids 29:166–174
11. Santiago JG, Wereley ST, Meinhart CD, Beebe DJ, Adrian RJ (1998) A particle image velocimetry system for microfluidics. Exp Fluids 25:316–319

Microplug Transport

► Thermocapillary Pumping

Microporous Materials

► Microfilters

Microporous Membranes

► Microfilters

Micropowder Blasting

► Powder Blasting

Micro Power Generation

► Micro Energy Conversion Devices

Microprojections

► Microneedles – Applications & Devices

Micro Propulsion

► Micro Energy Conversion Devices

Microreaction Technology

► Microfluidics for Biochemical and Chemical Reactions

Microreactor

► Microfluidics for Biochemical and Chemical Reactions

Microreactor for Synthesis of Biomolecules

► Biomolecular Synthesis in Microfluids

Microrockets

KENNETH S. BREUER
Division of Engineering, Brown University, Providence, RI, USA
kbreuer@brown.edu

Synonyms

Microthrusters; Microjets

Definition

Microrockets are microfluidic systems that generate a high speed (supersonic) jet of gas, used either for propulsion, materials processing or other applications.

Overview

Microrockets generate high speed gas jets by expanding a gas (or vapor) through a converging-diverging nozzle to generate high speed supersonic jet at the exit. The appeal of microrockets derives from the *cube-square* law. In general, the thrust of a rocket is determined by the plenum pressure, P_c, and the nozzle throat area of the rocket, while the mass of propellant used is proportional to the plenum pressure and the *volume* of the system. Thus the thrust-to-weight ratio of a rocket will increase as the characteristic scale decreases:

$$\frac{F}{m} \propto \frac{P_c L^2}{P_c L^3} = \frac{1}{L}\,.$$

However, at the microscale, the performance of the microrocket is limited by viscous losses due to the low Reynolds number of the expanding flow. These losses are characterized by the thrust efficiency which compares the observed momentum flux to the momentum flux predicted for an ideal (zero viscosity) fluid. Computations and experiments (for example, Bayt and Breuer 2000 [1]) confirmed supersonic exit flow and have found efficiencies ranging from 10% - 80%, depending on the Reynolds number of the system, which in turn depends directly on the size of the throat and the fluid temperature and pressure as it passes through the nozzle, prior to supersonic expansion. The performance of the system can be improved by raising the temperature of the gas. Examples include using an electrical heater in the plenum upstream of the throat (Bayt and Breuer 2001 [2]), and using a chemical reaction, such as combustion (London et al. 2001 [3]).

Cross References

► Micro- and Nanoscale Gas Dynamics
► Micronozzles

References

1. Bayt RL, Breuer KS (2000) Fabrication and Testing of Micron-Sized Cold-Gas Thrusters. In: Micci M, Ketsdever AD (eds) Micropropulsion for Small Spacecraft. Progress in Astronautics and Aeronautics 187 AIAA
2. Bayt RL, Breuer KS (2001) Analysis and testing of a silicon intrinsic point heater in a micro propulsion application. Sensors Actuators A 91:249–55
3. London AP, Epstein AH, Kerrebrock JL (2001) High-Pressure Bipropellant Microrocket Engine. J Propulsion Power 17(4):780–787

Microrotorcraft

LAURA SCHAEFER
Mechanical Engineering and Materials Science Department, University of Pittsburgh, Pittsburgh, PA, USA
las149@pitt.edu

Synonyms

Microair vehicle (MAV); Unmanned rotorcraft; Miniature unmanned air vehicle (UAV); Mesicopter; Microdrone

Definition

Microrotorcraft are small scale vehicles for which both the thrust and the directional control are provided using rotors. Although the rotorcraft themselves do not fall within the traditional length scales of microsystems, micromanufacturing techniques must be applied to create the rotors and motors, and microscale effects dominate the aerodynamic behavior.

Overview

Specifications and Aerodynamics

Microrotorcrafts are a subcategory of microair vehicles (MAVs), other permutations of which include fixed-wing MAVs, flapping-wing MAVs, and microrockets. In 1996, the Defense Advanced Research Projects Agency (DARPA) defined the principal characteristics of MAVs to be that they must not exceed 15 – 20 cm in length, width, or depth and have a flight speed of 10 – 20 m/s. Additionally, MAVs must weigh less than 100 g and be capable of carrying a payload of up to 20 g for 20 – 60 min over a distance of up to 10 km. Each unit should also cost less than $ 1000 to produce. In addition to satisfying these requirements for MAVs, microrotorcrafts must rely solely on two or more rotors to supply both the thrust and directional control for their flight. Although there is currently no microrotorcraft (or any other MAV) that satisfies all of these requirements, progress has been made over the past ten years toward achieving some of these goals.

Microrotorcrafts could be used for a variety of missions. Their portability and hovering capabilities make them well-suited for military surveillance missions (also categorized as hover-and-stare missions), as well as for other data gathering activities. Furthermore, clusters of microrotorcrafts could be used to provide insight into weather phenomena, pollution dispersal, wave patterns, etc. Finally, because microrotorcrafts are unmanned, they could also be used in hazardous environments (whether due to biological, chemical, or other causes) or for extra-planetary or low-gravity missions, such as exploration of Mars.

The dimensions of microrotorcrafts (as with other MAVs) mean that these vehicles operate in a relatively low Reynolds number regime, on the order of 10^4 (in comparison to large aircraft, which may have Re values in excesses of 10^9). At low Re, viscous effects become dominant. In this regime, the aerodynamic efficiency of microrotors is significantly smaller than is seen for conventional rotorcraft on the macroscale [1]. Other aerodynamic consequences of low Re flow are that the thermal boundary layer thickness is large compared to the airfoil chord size, and can affect the potential flow region, and that the pressure will not necessarily be constant throughout the boundary layer.

There are limited theoretical or numerical analysis tools available for low-Re aerodynamic effects and many of the predicted phenomena must be verified experimentally. For example, in the design of his mesicopter, Kroo evaluated two potential codes that might be able to apply to microrotorcraft modeling [2]. Both codes are Navier–Stokes solvers: the FLO103 (which is a Reynolds-averaged Navier–Stokes solver) and the INS2D (which solves the incompressible Navier–Stokes formulation). He also studied the applicability of the MSES program, which divides the flow field into an outer and an inner flow region. Other researchers (such as [1]) have relied on commercially-available codes such as FLUENT, despite some of that solver's limitations at low Reynolds numbers.

Comparison of Microrotorcrafts and Fixed-Wing MAVs

Some of the advantages of microrotorcrafts over fixed-wing MAVs are their potential agility, hovering capabil-

ity, and vertical take-off. The largest disadvantage is their lower endurance. Green and Oh showed this mathematically as a simple function of thrust for two different configurations, as outlined below [3].

For both a fixed-wing MAV and a microrotorcraft, the endurance (or active flight time) of the craft can be characterized as the capacity of the power source divided by the current draw of the motor. For a rotorcraft, the thrust (T) generated by the propeller is:

$$T_{\text{rotor}} = C_{\text{T}} \rho A (\omega R)^2 , \tag{1}$$

where C_{T} is the thrust coefficient, ρ is the density, and ω is the angular velocity. It is clear that T is directly proportional to the square of ω. The propeller is powered by the motor, and the motor's shaft speed is directly proportional to its current draw, so that:

$$E \propto \frac{1}{\sqrt{T}} , \tag{2}$$

where E is endurance.

For a fixed-wing craft, the thrust is equal to the drag on the craft:

$$T_{\text{fixed}} = D = \frac{1}{2} \rho V_{\infty}^2 S C_{\text{D}} , \tag{3}$$

where V_{∞} is the free-stream velocity, S is the wing area, and C_{D} is the coefficient of drag. Therefore, combining Eqs. (1)–(3), the resulting ratio of the fixed-wing and rotorcraft endurance is:

$$\frac{E_{\text{fixed}}}{E_{\text{rotor}}} = \sqrt{\frac{T_{\text{rotor}}}{T_{\text{fixed}}}} . \tag{4}$$

The thrust required for a rotorcraft will be equal to its weight, while the thrust required for a fixed-wing craft will be significantly less than the weight, even given a poor span efficiency. Therefore, from Eq. (4), the endurance of the fixed-wing craft will be greater than the endurance of the rotorcraft.

Another simpler way of considering this issue is the familiar comparison of thrust to the lift-to-drag ratio:

$$T = \frac{W}{\text{Ratio}_{\text{LD}}} , \tag{5}$$

where W is the weight. Since typical fixed-wing vehicles can achieve lift-to-drag ratios of $20-100$, their required thrust is much less than that of rotorcrafts. However, since the lift-to-drag ratio will decrease with the scale of a MAV, it has been theorized that the endurance characteristics of microrotorcrafts may at some scales become competitive with fixed-wing MAVs.

Example Microrotorcraft Configurations

Proposed microrotorcraft designs can generally be grouped into categories depending on the number of rotors that are utilized. These include single rotor configurations (such as tip-jets), ducted or unducted twin rotors (for example, the Cypher and Cypher II), and crafts with four or more rotors (the Gyronsaucer, Roswell Flyer, Stanford's Mesicopter, etc.) [4].

There have been a variety of microrotorcraft designs hypothesized and prototyped. These include the Kolibri model, which had a ducted fan design. Although the diameter of the Kolibri rotor fell within the aforementioned DARPA specifications, it could only hover for a maximum of 20 min, and its weight was 320 g. The ISTAR configuration also uses a ducted fan, but weighs over 1.8 kg [1].

Kunz proposed two potential microrotorcraft designs. The first had a gross take-off mass of only 17 g. It utilized four four-blade ducted rotors, each with its own rotor, and arrayed around a control circuit. Each rotor unit was only 2.5 cm in diameter. This device was not self-powered, however, an issue that would add considerable weight to the final design, given that the hover power was calculated to be 16 W. Kunz also developed a 65 g microrotorcraft. Again, this craft used 4 rotors around a central control circuit. However, the rotors were not ducted, and consisted of 2 blades apiece, with a total rotor diameter of 6.35 cm. The hover power requirement was 15 W, which could be maintained for one minute, given the on-board power supply. Finally, Kunz also developed a much larger prototype that weighed 150 g, utilized four unducted two-blade rotors (10 in diameter), and could carry a 20 g payload for 5 to 20 min [5].

Oh et al. designed and built a two-blade, backpackable microrotorcraft specifically designed for hover-and-stare operations [6]. Their device was longer (17" × 8" × 4") and heavier (450 g) than the DARPA guidelines, but was capable of hovering for up to 90 s using standard lithium poly batteries while delivering image data from an on-board camera.

Young et al. have provided a review of a number of their proposed microrotorcraft designs [7]. These include a quad-rotor tail sitter, which uses rotor speed control for vehicle trim, and can engage in hovering or forward flight; a mini-morpher, which can change shape to operate as either a ducted-fan flier or a hybrid rotorcraft/fixed-wing vehicle; a tandem twin-fuselage tiltrotor, which employs two rotors mounted between two joined fuselages; and a coaxial helicopter, where two two-blade rotors are mounted coaxially are controlled by two coupled drive trains.

Bohorquez et al. designed, built, and tested both single rotor and coaxial dual-rotor vehicles they dubbed MICOR [4]. The single rotor device had a takeoff weight off 100 g, and was able to hover for 3 m using its on-board power supply.

Improving Microrotorcrafts

Some of the primary obstacles to meeting the original DARPA guidelines are a satisfactory level of power for the microrotorcraft motor(s), device durability, flight control technologies and strategies, sensor weight and secure and reliable communication, and not just understanding, but also capitalizing on low-Re aerodynamic phenomena. More details on the methodology for addressing these areas, current research findings, and future challenges are provided in the following sections.

Basic Methodology

Figure of Merit

The figure of merit for a rotor is a simple ratio of the ideal power to the actual power required to hover. While the ideal power is simply a function of thrust and velocity, the actual power accounts for both the ideal power and the profile power. Neglecting induced power (the power needed to overcome the drag that results from changes in the flow caused by the lift), the figure of merit for a hovering rotorcraft then becomes:

$$FM \approx \frac{P_{\text{ideal}}}{P_{\text{ideal}} + P_{\text{profile}}} . \tag{6}$$

The ideal power is simply:

$$P_{\text{ideal}} = T v_{\text{hover}} = T\sqrt{\frac{T}{2\rho A}} = \frac{T^{3/2}}{\sqrt{2\rho A}} , \tag{7}$$

while the profile power (the power required to overcome form drag and skin friction) is:

$$P_{\text{profile}} = N_{\text{b}}\Omega \int_0^R \frac{1}{2} C_{\text{D}} \rho V_d^2 c y \, \text{d}y , \tag{8}$$

which can be approximated as [5]:

$$P_{\text{profile}} \approx \frac{\rho \sigma C_{\text{D}} (\omega R)^3 A}{8} , \tag{9}$$

where σ is the rotor solidity:

$$\sigma = \frac{N_{\text{b}} c}{\pi R} . \tag{10}$$

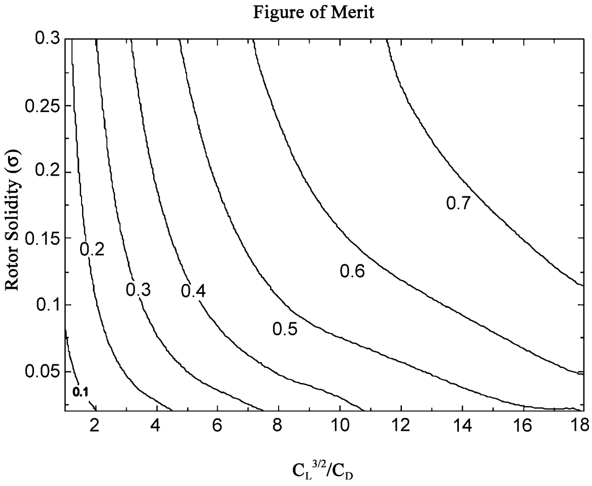

Microrotorcraft, Figure 1 The figure of merit for a microrotorcraft plotted as a function of rotor solidity (σ) and $C_{\text{L}}^{(3/2)}/C_{\text{D}}$ for a coefficient of lift of 0.5

The thrust (see Eq. (1)) can also be approximated as a function of these variables:

$$T \approx \frac{\rho \sigma \pi C_{\text{L}} (\omega R)^2 R^2}{6} . \tag{11}$$

Combining Eqs. (6), (7), (9) and (11) yields [5]:

$$FM \cong \frac{1}{1 + \left(\frac{3}{2}\frac{C_{\text{D}}}{C_{\text{L}}}\sqrt{\frac{3}{\sigma C_{\text{L}}}}\right)} . \tag{12}$$

It should be noted from Eq. (12) that for rotorcraft, although the general trend is the same, the maximum of the ratio of $C_{\text{L}}^{(3/2)}/C_{\text{D}}$ is more important to the figure of merit than the L/D ratio [1]. For a coefficient of lift of 0.5 (which is reasonable for microrotorcraft), it can be seen in Fig. 1 that the figure of merit increases with increasing $C_{\text{L}}^{(3/2)}/C_{\text{D}}$.
If the induced power is accounted for, the figure of merit can instead be expressed as [4]:

$$FM = \frac{\sqrt{\frac{C_{\text{T}}^3}{2}}}{\kappa\sqrt{\frac{C_{\text{T}}^3}{2}} + \frac{\sigma \bar{C}_{\text{D}}}{8}} . \tag{13}$$

Where C_{T} is the thrust coefficient, $\bar{C}_{\text{D}}$ is the mean drag coefficient, and κ is the induced power factor.
In addition to this rigorous statement of the figure of merit, there are also other criteria that can be used to quantify the effectiveness of a microrotorcraft [8]. These include how well the inherent properties of a microrotorcraft can be utilized by the operator, whether the performance fits

M

the needs of a particular task, what is the short term performance (or bandwidth), the speed at which the microrotorcraft can make moderate attitude changes, and what is the achievable attitude rate. Further considerations include the simplicity of the vehicle, the ease of payload packaging, and the compactness of folding [4].

Control Methods

Development of control methodologies for microrotorcrafts is complicated on a number of levels. The rotors provide both the thrust and the directional control for the vehicles, and the resulting microrotorcraft motion is affected by the user's inputs, by interactions between the rotors, and by external/environmental factors. For a microrotorcraft, controls must be designed and implemented for the vertical, longitudinal, and lateral directions, as well as for the yaw (the rotation about a craft's vertical axis). While yaw and thrust can be changed by varying the speed of the rotor motors, more sophisticated techniques are required for lateral control. Three potential methods for accomplishing this are flaps, a gimbaled drive train, and reaction jets [4]. Although microrotorcraft controls are still in the development stage, there are well-established linear control laws for macroscale rotorcrafts that could potentially be adapted to microrotorcraft design and operation. It is likely that the most effective control laws for microrotorcrafts will come from the intersection of first principle modeling and system identification. In both hover and flight modes, the operative degrees of freedom for microrotorcrafts results in a large number of interrelated states and design parameters. Mettler [8] has enumerated microrotorcraft control issues as falling into six main categories: the changing flight dynamics, multivariable (six degrees of freedom and four control variable) and unstable (the attitude dynamics) vehicle behavior, rotor-fuselage coupling, and sensitivity to disturbances. The six degrees of freedom of a microrotorcraft (a simplified version of which is shown in Fig. 2) can be expressed using the standard Newton–Euler equations of motion for a body-fixed frame of reference:

$$\begin{aligned} \boldsymbol{F} &= m\frac{\mathrm{d}\boldsymbol{v}}{\mathrm{d}t} + m(\boldsymbol{\omega}\times\boldsymbol{v}) \\ \boldsymbol{M} &= \mathbf{I}\frac{\mathrm{d}\boldsymbol{\omega}}{\mathrm{d}t} + (\boldsymbol{\omega}\times\mathbf{I}\boldsymbol{\omega})\,, \end{aligned} \tag{14}$$

where $\boldsymbol{F}$ is the external force vector, m is the mass, $\boldsymbol{v}$ is the velocity vector, $\boldsymbol{\omega}$ is the angular velocity vector, $\boldsymbol{M}$ is the external moment vector, and $\mathbf{I}$ is the inertial tensor. These relations can be used to develop three interrelated differential equations for the translational motion and three equations for the angular motions. Finding a closed-form solution for these equations is problematic, however, so the system identification method instead develops simplified forms of these expressions.

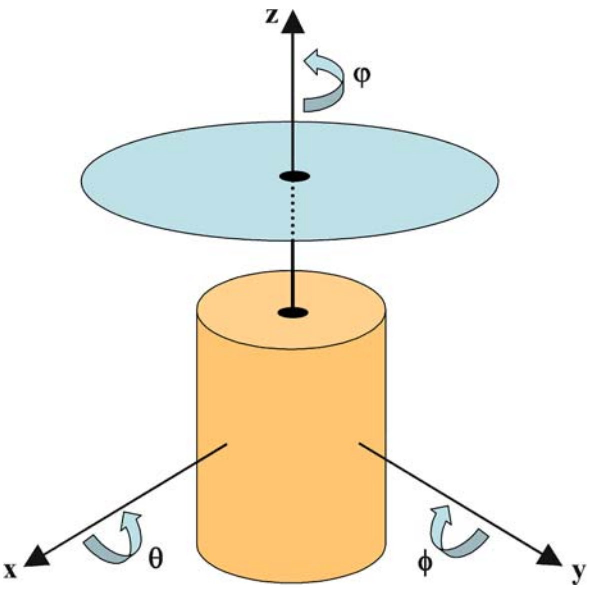

Microrotorcraft, Figure 2 Six degrees of freedom for a basic microrotorcraft

Small Scale Effects

Heat Transfer

Given the importance of low-Re, viscous flow on microscale aerodynamics, it is possible to take advantage of the dominant heat transfer effects to enhance microrotorcraft flight. These heat effects can be characterized using the standard transport equations and a Navier–Stokes solver. In order to accurately apply the physical properties, it is important to include the effect of temperature on the viscosity (using, for example, Sutherland's, Wilke's, or Keyes' laws), thermal conductivity, and specific heat of the surrounding fluid (air).
Heat transfer effects can be used to improve microrotorcraft performance through the introduction of a temperature gradient over the airfoil. Both the temperature and velocity boundary layers are relatively thicker for small-scale airfoils, and a lower temperature on the upper surface will accelerate the flow, while a higher temperature on the lower surface will decelerate the flow. The resulting changes to the pressure distribution on the airfoil can increase the lift and reduce the drag. From the standard governing equations and asymptotic matching, Kim [1] developed an approximation for the pressure coefficient

along a microrotorcraft's airfoil as:

$$\begin{aligned}&Cp\left(\frac{x}{c}; \mathrm{M}, \alpha, \delta, \mathrm{Re}, \mathrm{Pr}, \frac{T_{\mathrm{wu}}}{T_\infty}, \frac{T_{\mathrm{wl}}}{T_\infty}\right)\\&= Cp^*\left(x^*; \mathrm{M}, \alpha_{\mathrm{M}}, \mathrm{Re}_{\mathrm{M}}, \mathrm{Pr}, \frac{T_{\mathrm{wu}}}{T_\infty}, \frac{T_{\mathrm{wl}}}{T_\infty}\right)\\&+\left[Cp_{\mathrm{u,l}}\left(\frac{x}{c}\right) - Cp_{\mathrm{cp}}\left(\frac{x}{c}; \mathrm{M}, \delta, A\right)\right] V^*(x^*)\rho^*(x^*)\,, \end{aligned} \tag{15}$$

where Cp_{cp} is the pressure coefficient in the overlap region, and is equal to:

$$Cp_{\mathrm{cp}} = (-1)^m \frac{2\alpha w_0 \sqrt{\frac{c}{x}}}{\beta}\,, \tag{16}$$

while $Cp_{\mathrm{u,l}}$ is derived from classical subsonic linear airfoil theory:

$$\begin{aligned}Cp_{\mathrm{u,l}} = &-2\frac{\delta}{\beta}\Bigg\{h(1+2\cos\theta)\\&+2\sum_{k=2}^{\infty} A_{2k-1}\left[\frac{\sin(2k-1)\theta - \sin\theta}{\sin\theta}\right]\\&+2\sum_{k=2}^{\infty} A_{2k}\left[\frac{\sin 2k\theta - \sin 2\theta}{\sin\theta}\right]\\&+(-1)^m\left[w_0\frac{1+\cos\theta}{\sin\theta} - \sum_{n=1}^{\infty}(-1)^n w_n \sin n\theta\right]\Bigg\}\,.\end{aligned} \tag{17}$$

Cp^* cannot be expressed in closed form, but is derived from a computational solution of the dimensionless equations for mass, momentum, and energy, where the fluid properties are governed by the ideal gas equation of state. In Eqs. (15)–(17), x is the location; c is the chord length; M is the Mach number; α is the angle of attack; δ is the airfoil thickness ratio; T is the temperature, where wu is the upper wall, wl is the lower wall, and ∞ is the free stream; $*$ represents a dimensionless variable; A is the thickness function; m is a surface determinant, and equals $+1$ for the upper surface and -1 for the lower surface; w is the camber line; β is a function of the Mach number such that $\beta^2 = \mathrm{M}^2 - 1$; and h is a function of the nose radius of curvature R_c, such that $h^2 = R_c/2\delta^2 c$. The thickness function can be expressed as its coefficients of the Fourier series expansion:

$$A_n = \frac{2n}{\pi}\int_0^{\pi} t\frac{x}{c}\sin(n\theta)\,\mathrm{d}\theta\,, \tag{18}$$

as can the airfoil's camber line:

$$\begin{aligned}w_0 &= 1 - \frac{1}{\pi A}\int_0^{\pi} \mathrm{Ca}'\frac{\xi}{c}\,\mathrm{d}\theta\,,\\ w_n &= \frac{2n}{\pi A}\int_0^{\pi} \mathrm{Ca}'\frac{\xi}{c}\cos(n\theta)\,\mathrm{d}\theta\,.\end{aligned} \tag{19}$$

Finally, the dimensionless velocity and density in Eq. (15) are at the edge of the thin boundary layers in the inner region, and are given by:

$$\begin{aligned}V^* &= \sqrt{1 - 2\frac{\left(1 + \frac{\gamma \mathrm{M}_\infty^2}{2} - Cp^*\right)^{\gamma-1/\gamma} - 1}{(\gamma-1)\mathrm{M}_\infty^2}}\\ \rho^* &= \left(1 + \frac{\gamma \mathrm{M}_\infty^2}{2} Cp^*\right)^{1/\gamma}\,.\end{aligned} \tag{20}$$

The solution of these equations, and the resulting effect on microrotorcraft lift, drag, and endurance, is discussed in the Key Research Findings section.

Viscous Swirl Effects

In addition to amplified heat transfer effects, understanding microrotorcraft operation at low Reynolds numbers also requires better modeling of viscous swirl effects. There are numerous enhanced viscous swirl models that could be utilized, a review of some of which has been provided by Kunz [5]. The average wake deficit viscous swirl model is based on using a power-law fit of computationally-modeled airfoil wake profiles at low Re (using INS2d data):

$$\begin{aligned}v_{\mathrm{v}} &= v_{\mathrm{v1}}\,\mathrm{arclength}^{v_{\mathrm{v2}}}\,,\\ v_{\mathrm{v1}} &= -3\,\mathrm{e}^{-10}\mathrm{Re}_{\Omega\mathrm{r}}^2 - 3\,\mathrm{e}^{-6}\mathrm{Re}_{\Omega\mathrm{r}} + 0.241\,,\\ v_{\mathrm{v2}} &= 3\,\mathrm{e}^{-9}\mathrm{Re}_{\Omega\mathrm{r}}^2 - 7\,\mathrm{e}^{-5}\mathrm{Re}_{\Omega\mathrm{r}} - 0.372\,,\end{aligned} \tag{21}$$

where v_{v} is rotor viscous tangential induced velocity and $\mathrm{Re}_{\Omega\mathrm{r}}$ is the Reynolds number calculated using the rotor angular velocity multiplied by the local section radius. This model is simple and straightforward, but it has been found that it overestimates the viscous swirl effects.

A second viscous swirl model that accounts for downstream rotor effects is the Gaussian wake viscous swirl model:

$$\frac{u}{U_\infty} = \frac{u_{\mathrm{mid}}}{U_\infty}\exp\left(-\frac{(\bar{y}-\mu)^2}{2\sigma}\right)\,, \tag{22}$$

where U_∞ is the free-stream velocity, σ is the wake deficit standard deviation, and μ is the mean of u/U_∞.

Finally, there is also the simple and familiar conservation of angular momentum viscous swirl model:

$$v_{\mathrm{V}} = 2u\left(\frac{C_{\mathrm{D}}}{C_{\mathrm{L}}}\right). \tag{23}$$

Kunz found that this model has reasonable extensions to low-Re flows.

Key Research Findings

Heat Transfer and Fluid Flow Effects

As predicted by both low-Re theory and computational modeling of Eq. (15), experimental testing of microrotorcrafts with an induced temperature difference over the blade thickness verified that heat transfer effects can significantly affect aerodynamic performance. Kim [1] constructed a microrotorcraft that utilized a thermoelectric alloy material for the rotor blades. By applying a voltage at the centerline of the airfoil section, he was able to utilize the ►peltier effect to create a temperature difference of 65.5 K across each blade. He tested the blades at a range of angles of attack, and found that there was decent agreement with the numerical predictions. For example, at an angle of attack of 4.5°, upper surface temperature of 290.5 K, and lower surface temperature of 356 K, Eq. (15) predicted an increase in the lift coefficient of 5.5%, and experimental testing found an increase in the lift coefficient of 7.7%.

While the magnitude of this error shows the need for more refined computational predictions, the qualitative result remains that heat transfer effects can be important to the efficiency of microrotorcraft in their highly viscous, low-Re operating regime. However, when there is an induced temperature difference over the rotor blades, Kim also found computationally that increasing either the Mach number or the Reynolds number decreased the improvement in the lift coefficient. Furthermore, an additional complication remains in evaluating the magnitude by which the increase in the aerodynamic efficiency is offset by the increased power needed to activate the Peltier effect in a thermoelectric rotor blade.

Blade Geometry and Configuration

To evaluate the effects of blade geometry and configuration, Kim [1] performed a number of microrotorcraft spin tests on a single-rotor device using a load cell to measure thrust and a laser to measure rotor speed. The motor was driven using an external power supply. Kim tested blades with varying aspect ratios, cambers (the asymmetry of an airfoil's top and bottom shape), and thicknesses, tapers, pitches, and configurations.

In terms of the overall aerodynamic efficiency of the device, he found that it was desirable to employ a moderate camber (4 – 6%), low thickness (5 – 6%), high aspect ratio, and pitch setting in the range of 12 – 15 degrees. He also concluded that changing the blade tapering had only minor consequences for the efficiency. (Young et al. [7] also found that changes in tapering had a minimal effect on the aerodynamic performance.) Finally, increasing the number of rotor blades did increase the thrust, but it also increased the power consumption, which is a critical issue for microrotorcrafts, and is discussed in more detail in the next subsection. Kim's optimal configuration resulted in a lifting capacity (C_T/σ) of 0.16, a figure of merit of approximately 0.5 (which represents a poor hovering efficiency), and a lift-to-drag ratio of around 10.

Kunz [5] also tested a number of blade configurations. He examined a five-blade 2.2 cm diameter rotor, a four-blade 2.5 cm diameter rotor, and two-blade 10 in diameter rotor. These designs were based on an optimization methodology that Kunz developed for microrotorcraft design. He found that the errors between the predicted and tabulated values were less 10% for all of the rotor designs except the five-blade rotor. One reason for this, as well as for some of the errors found in the other rotor predictions, was the role of structural deformation. All of the rotors exhibited some degree of static deflection from manufacturing and/or handling, and also torsional deflection due to rotational mass effects during operation. While, theoretically, a reduced airfoil thickness can increase the aerodynamic efficiency of a microrotorcraft, a thinner airfoil is also subject to greater torsional deflections, and this must be accurately accounted for in any numerical model to optimize the rotor design.

Power

One of the largest challenges in designing microrotorcrafts has been providing adequate power for both the lift-off and hover modes of operation. Bohorquez et al. [4] calculated that a two-rotor vehicle that meets the DARPA requirements for size and weight would require a power draw of 15 W to ascend, hover, and maneuver. This power could be provided by fuel cells, batteries, IC engines, chemomechanical engines, compressed gas, etc., with the first two options proving to be the most likely choices.

Thomas et al. [9] further quantified the flight endurance time (t_{E}) as a function of available energy as:

$$t_{\mathrm{E}} = \eta_{\mathrm{P}}\left(\frac{E_{\mathrm{Avail}}}{W^{3/2}}\right) \times \left(\frac{\rho S C_{\mathrm{L}}^3}{2C_{\mathrm{D}}^2}\right)^{1/2}, \tag{24}$$

where η_P is the propeller efficiency, E_{Avail} is the available energy (from a battery or other source), and W is the weight of the microrotorcraft and its payload. Note the familiar ratio of $C_L^{(3/2)}/C_D$ from the figure of merit (Eq. (12)). They proposed to provide the required power through the use of laminated polymer lithium ion bicell materials with barrier-layer packaging. The bicell is 0.5 mm thick with a mass density of 0.14 g/cm^2. It demonstrates a 3.7 V discharge and 7.2 mAh/cm^2 charge storage capacity. Furthermore, the packaging is only 0.1 mm thick with a mass density of 0.013 g/cm^2. By building the payload or packaging systems out of this material, it may be possible to greatly increase microrotorcraft endurance times. Thomas et al. tested this type of battery on a fixed-wing MAV rather than a microrotorcraft, and were able to achieve endurance times of up to 107 min for a 171 g vehicle (which included 98 g of battery weight).

Controls and Sensors

In evaluating control systems for microrotorcrafts, Mettler [8] found that frequency domain identification served as a better method than time domain identification. This is because in frequency domain identification, the output measurement noise does not affect the results, it is possible to focus on a precise frequency range (which minimizes the disparity between the modes of motion), and frequency responses can completely describe the system's linear dynamics. Mettler also determined that the rigid body equations of motion needed to be expanded through use of the hybrid formulation to generate a more accurate control system. This method models the rotor motion using a tip-path plane model, and expresses the rotor forces and moments in terms of the rotor states. The rotor and fuselage motions are then dynamically coupled.

Oh et al. have proposed the use of two optic flow sensors to provide real-time feedback on both obstacles and altitude [10]. The sensor model that they tested weighed just 4.8 g, had an optic flow rate of 20 rad/s, and was approximately the size of a U.S. quarter. One sensor should be placed on a gimbal so that it is always facing directly toward the ground, and the other should be forward facing. For the sensors, the rate of optic flow (rad/s) is equal to:

$$\mathrm{OF} = \frac{V}{D}\sin\theta - \omega\,, \tag{25}$$

where V is the forward velocity, D is the distance from an obstacle, θ is the angle between the obstacle and the microrotorcraft's direction of travel, and ω is the angular velocity. Since it is likely that changes in the vehicle's pitch will be much smaller than changes in its forward motion, ω can be neglected, further simplifying Eq. (25).

Coupling the optic flow sensors with control loops allows a microrotorcraft to perform both autonomous landing and autonomous collision avoidance. For example, when providing feedback to the ground-facing sensor, Eq. (25) reduces to $\mathrm{OF} = V/D$. In order to keep a constant rate of optic flow, the velocity of the microrotorcraft must decrease as its distance from the ground decreases, which results in a smooth landing.

Future Directions for Research

In order to create a durable, flexible, and autonomous microrotorcraft that can be used in a variety of applications, more work is needed on a number of fronts. Additional experimental data should be gathered on the effects of blade design, and these data should be used to both improve existing 2-D microrotorcraft representations and to generate more detailed 3-D Navier–Stokes computational models. These data could be created using actual small rotor systems, or through the use of scale models.

Improvements are also needed in the endurance time of microrotorcrafts. Further energy sources should be investigated, and the trade-offs of materials that improve aerodynamic efficiency but require power (such as thermoelectric or piezoelectric rotors) should be quantified. Endurance time could also be increased by improving the efficiency or lowering the weight of auxiliary systems such as the micromotor, control circuits, and sensors. Hybrid configurations, such as the prop-hanging vehicle proposed by Green and Oh [3], could also be developed.

Finally, improved communications and control mechanisms are needed. For example, ▶ neural networks could be used to train optic flow sensor controls to react appropriately to changes in light intensity, diffuse objects (such as fog), and low contrast obstacles (such as a white wall) [10]. Beyond the control of single microrotorcrafts, strategies should also be developed to control communications and reactions for groups of these vehicles.

Cross References

▶ Temperature Control in Microfluidic Systems
▶ Micro Aerial Vehicles
▶ Microactuators
▶ Turbulence Control

References

1. Kim J (2004) Flow Control Strategies for Improved Aerodynamic Efficiency of Microrotorcraft. PhD Dissertation, Rensselaer Polytechnic Institute, Troy, New York

M

2. Kroo I (1999) The Mesicopter: A Meso-Scale Flight Vehicle. NASA Institute for Advanced Concepts, Phase I Final Report
3. Green WE, Oh PY (2005) A MAV That Flies Like an Airplane and Hovers Like a Helicopter. Proc 2005 IEEE/ASME Int Conf Adv Intell Mechatron, Monterey, California, pp 699–704
4. Bohorquez F, Samuel P, Sirohi J, Pines D, Rudd L, Perel R (2003) Design, Analysis and Performance of a Rotary Wing MAV. J Am Helicopter Soc 48(2):80–90
5. Kunz PJ (2003) Aerodynamics and Design for Ultra-Low Reynolds Number Flight. PhD Dissertation, Stanford University, Palo Alto, California
6. Oh PY, Joyce M, Gallagher J (2005) Designing an Aerial Robot for Hover-and-Stare Surveillance. IEEE Int Conf Adv Robot, Seattle, Washington, pp 303–308
7. Young LA, Aiken EW, Johnson JL, Demblewski R, Andrews J, Klem J (2002) New Concepts and Perspectives on Micro-Rotorcraft and Small Autonomous Rotary-Wing Vehicles. 20th AIAA Appl Aerodyn Conf, St. Louis, Missouri
8. Mettler B (2001) Modeling Small-Scale Unmanned Rotorcraft for Advanced Flight Control Design. PhD Dissertation, Carnegie Mellon University, Pittsburgh, Pennsylvania
9. Thomas JP, Keennon MT, DuPasquier A, Qidwai MA, Matic P (2003) Multifunctional Structure-Battery Materials for Enhanced Performance in Small Unmanned Air Vehicles. Proc 2003 ASME Int Mech Eng Congr Expo, Washington, DC, IMECE2003-41512
10. Oh PY, Green WE, Barrows G (2004) Neural Nets and Optic Flow for Autonomous Micro-Air-Vehicle Navigation. Proc 2004 ASME Int Mech Eng Congr Expo, Anaheim, California, vol 2, IMECE2004-62262

Microscale Cooling Devices

CLEMENT KLEINSTREUER, JIE LI
Mechanical and Aerospace Engineering,
North Carolina State University, Raleigh, NC, USA
ck@eos.ncsu.edu

Synonyms

Miniature heat-removal devices; Micro-heat exchangers; Microchannel heat sinks (MCHS); Flow of coolants in micro-conduits; Nanofluid flow in microchannels

Definitions

A microscale cooling device consists of a coolant flowing through a large number of parallel, micromachined or etched conduits to remove heat from and generate uniform temperature distributions in microelectromechanical systems, integrated circuits boards, laser-diode arrays, high-energy mirrors and other compact products with high transient thermal loads. Key is the very large heat transfer surface-to-volume ratio of the device. The coolant can be a pure fluid or a very dilute mixture of distilled water (or ethylene glycol, engine oil, etc.) and nanoparticles, such as metals, metal-oxides, and carbon-based materials. Heat transfer occurs via forced convection, which includes impinging jets of the coolant and liquid-to-vapor phase change due to boiling or condensation. The microchannels are typically silicon-, metal-, or plastic-based and often feature circular, rectangular or trapezoidal cross sections, ranging in terms of the hydraulic diameter from 100 nm to 1000 μm. Alternatively, porous media, such as foam, has been employed as micro-conduits with pure fluids.

Overview

Fundamental to the understanding of the dynamics of microscale cooling devices is the description of convection heat transfer in these micro-conduits. The most rigorous approach would be to analyze the behavior of each coolant molecule in terms of simultaneous mass, momentum and heat transfer. Even for microchannels this would imply tracking billions of *particles*; hence, for most engineering applications the coolant is treated as a continuum. The continuum mechanics assumption is valid as long as the size and mean-free-path of the molecules (or particles) are small enough compared to the device dimensions, e. g., channel height or tube diameter. This is basically assured when the Knudsen number, defined for gas flow as the ratio of mean-free-path distance to characteristic system length, is less than 0.1 and then macro-level modeling equations can be used (see, for example, review chapter 12 by Zohar [1] in The MEMS Handbook). Nevertheless, a number of phenomena unique to micro-conduits still prevail, causing pressure drops, flow rates and/or friction factors to differ from results obtained for macro-channels [2]. Examples include dominant entrance effects because the conduits are very short, significant surface roughness effects due to the closeness of the channel walls, earlier onset of turbulence because of induced instabilities, measurable viscous dissipation effects resulting from steep velocity gradients, possible fluid-slip on channel walls depending upon the physical-chemical characteristics of the (coated) surfaces, and significant effects of low-level forces usually not relevant in macro-devices, such as surface tension and electrostatics.

Already in 1981, Tuckerman and Pease [3] achieved heat transfer rates of about $10^5\ \mathrm{W/m^2K}$ for water flow in small cooling channels etched in a silicon substrate. A representative microchannel heat sink (MCHS) is shown in Fig. 1. Typically, a coolant is forced through a large number of parallel channels, which are in contact with a hot surface, to convect evolving heat away and provide a near-uniform temperature field in the device to be cooled. An MCHS can generate such elevated heat transfer rates because of its high surface-to-volume ratio and enhanced

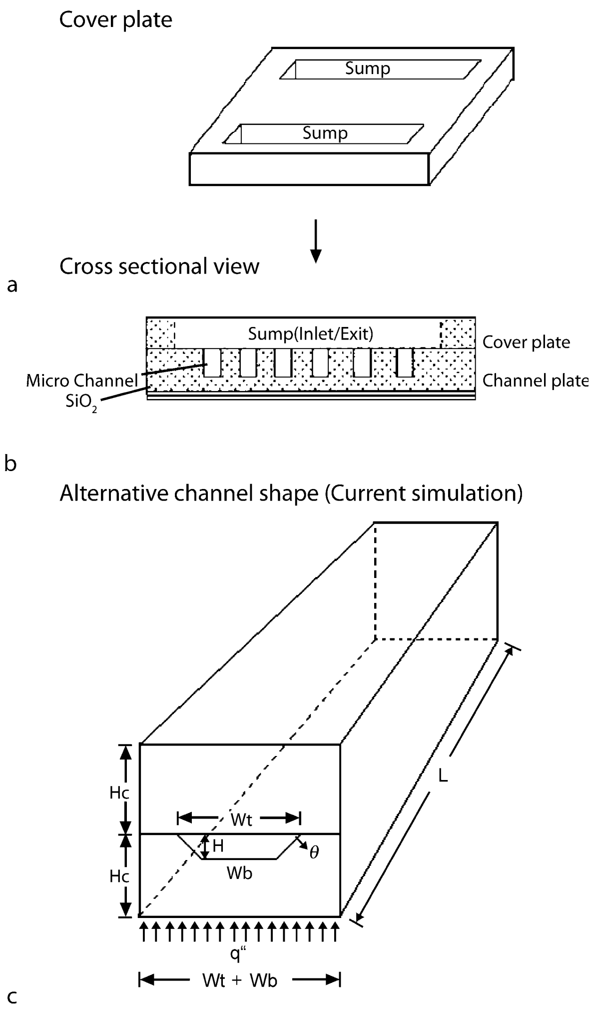

Microscale Cooling Devices, Figure 1 Typical microchannel heat sink elements and the current computational trapezoidal microchannel unit

thermal conductivity of the coolant (i. e., when using a nanofluid), while being very small in size and having relatively low coolant-volume and pumping-power requirements. Clearly, channel geometry/configuration, type of coolant with associated flow regime (or thermodynamics) and required pumping power are some of the more important system parameters determining MCHS performance. The underlying microfluidics for flow in microchannels is outlined in [4] and [5] while MCHS performance has been discussed by Kandlikar and Grande [6], Li et al. [7], and Koo and Kleinstreuer [8], among others. Li and Peterson [9] focused on MCHS performance improvements considering nanofluids vs. pure water as well as geometric parameters, especially the channel aspect ratio, H/W (see Fig. 1). Nanofluids are very dilute suspensions of metal, metal-oxide or carbon-based nanoparticles (0.01 to 4% by volume) in liquids, such as water, ethylene glycol, etc. These mixtures exhibit thermal conductivities which are 30 to 300% higher than the one of the carrier fluid [10].

Basic Methodology

In order to provide some physical insight into the dynamics of microchannel heat sinks (MCHS), steady laminar water flow in a smooth single trapezoidal microchannel is discussed and compared with measured data sets. Then the effects of nanofluids on augmented MCHS heat transfer are introduced, employing very simple correlations for the enhanced thermal conductivities of the mixtures. The fluid flow and heat transfer simulations have been carried out with the commercial software CFX-10 (Ansys, Inc., Canonsburg, PA) and user-supplied pre- and post-processing software.

Theory

Figure 1c depicts the representative microchannel under consideration. The top width W_t, bottom width W_b and depth of the channel H are 500 μm, 358.4 μm and 100 μm, respectively. The base angle, which is the angle between the channel side wall and bottom wall, is 54.7°. The length of the channel L is 27 mm. The heights of the cover and base substrate are both $H_c = 500\,\mu\text{m}$. A constant heat flux, i. e., $q'' = 431{,}466\ \text{W/m}^2$, from below and adiabatic conditions at the other boundaries were assumed. First, a smooth channel with pure de-ionized water as the working fluid is considered. The hydraulic diameter for the present case is:

$$D_h = \frac{4 \times 0.5 \times (W_t + W_b) \times H}{W_t + W_b + 2 \times H/\sin\theta} = \frac{2 \times 858.4 \times 100}{858.4 + 245.1} = 155.6\,\mu\text{m}\,. \tag{1}$$

Other important geometric channel parameters are the aspect ratio as well as the aspect factor, defined respectively as (see Fig. 1c):

$$A = W_b/W_t \tag{2}$$

and

$$\alpha = H/W_b\,. \tag{3}$$

Assuming steady laminar 3D flow and heat transfer with constant material properties, the continuum mechanics equations are:

$$\nabla \cdot \boldsymbol{u} = 0\,, \tag{4}$$

$$\rho_f(\boldsymbol{u}\cdot\nabla\boldsymbol{u}) = -\nabla p + \nabla\cdot(\mu_f\nabla\boldsymbol{u}) \tag{5}$$

and

$$\rho_f c_{p,f}(\boldsymbol{u}\cdot\nabla T) = k_f\nabla^2 T + \mu_f\Phi\,, \tag{6}$$

where

$$\Phi = \left(\frac{\partial u_i}{\partial x_j} + \frac{\partial u_j}{\partial x_i}\right)\frac{\partial u_i}{\partial x_j}\,. \tag{7}$$

In the solid region:

$$k_s\nabla^2 T = 0\,. \tag{8}$$

Here, ρ is the density; k is the thermal conductivity; μ_f is the fluid dynamic viscosity; p is the pressure; T is the temperature; $\boldsymbol{u}$ is the velocity vector; c_p is the specific heat capacity, and Φ is the viscous dissipation; the subscripts f and s represent fluid and solid, respectively. For nanofluids, the corresponding effective thermal conductivities and effective fluid dynamic viscosities will be introduced.

When using CFX-10, the solid and fluid are treated as a unitary computational domain. The interface between the solid and fluid is automatically connected by equal temperature magnitudes and heat flux values; thus, only the boundaries for the unit cell are needed. Specifically, for the hydraulic boundary conditions, a uniform velocity is applied at the channel inlet:

$$u = 0,\quad v = 0,\quad w = U_{in}\quad \text{for}\quad x = 0\,,\quad (y, z) \in \text{channel region}\,. \tag{9}$$

The outlet pressure is the static pressure, i. e.,

$$p_{out} = 0\,. \tag{10}$$

The no-slip boundary condition was enforced at all solid walls.

The thermal boundary condition at the bottom is:

$$q'' = C\,. \tag{11}$$

Adiabatic boundary conditions are applied at all other sides of the walls:

$$\frac{\partial T}{\partial n} = 0\,. \tag{12}$$

In the fluid region:

$$T = T_{in}\quad \text{for}\quad x = 0,\quad (y, z) \in \text{channel region}\,. \tag{13}$$

Results

Pure Water Flow

For comparison purposes, a steady global energy balance based on the temperature difference between the channel inlet and outlet was performed, i. e.,

$$\rho_f u_m c_p A_c (T_{out} - T_{in}) = q'' A_{bottom}\,. \tag{14}$$

Here, u_m is the mean velocity, A_c is the area of the channel cross section, and A_{bottom} is the area of the heated substrate wall.

Figure 2a depicts the simulated water temperature rise between the channel inlet and outlet as a function of inlet Reynolds number and the theoretical values predicted by Eq. (14), where $\text{Re} = u_m D_h/\nu_{fluid}$. Figure 2b shows the dimensionless entrance length at different Reynolds numbers in comparison with the experimental result of Hao et al. [11]. When the Reynolds number is less than 1000, the entrance length dependence can be expressed as a linear correlation of the form:

$$L_{e,d} = L_e/D_h = (0.08 \sim 0.09)\text{Re}\,. \tag{15}$$

For noncircular conduits the channel aspect ratio or aspect factor (see Eqs. (2) and (3)) have a profound influence on the friction factor $C_f = f\text{Re} = \Delta p D_h^2/2\mu_f uL$, which has a constant value of 16 for circular conduits. For example, Fig. 2c provides a comparison of the simulation results with an empirical correlation of Wu and Cheng [12], i. e.,

$$f\text{Re} = 11.43 + 0.80\exp(2.67 W_b/W_t)\,. \tag{16}$$

The bar-height of the numerical data represents the range of the friction factor for different hydraulic diameters and different Reynolds numbers, which are clearly less important than the aspect ratio.

Nanofluid Flow With Heat Transfer

In order to investigate the heat transfer characteristics of a nanofluid in the trapezoidal microchannel, we employed a CuO-water combination as the working fluid. Clearly, the thermal fluid properties of the nanofluid have to be updated. Thus, in the governing Eqs. (5) and (6), the following expressions were introduced, replacing the previous μ_f and k_f parameters. Typically, for a very dilute suspension, the effective viscosity, density and specific heat capacity have the following forms:

$$\mu_{nf} = \mu_f\frac{1}{(1-\varphi)^{2.5}} \tag{17}$$

$$\rho_{nf} = \varphi\rho_p + (1-\varphi)\rho_f \tag{18}$$

$$c_{p,nf} = c_{p,p}\varphi + c_{p,f}(1-\varphi) \tag{19}$$

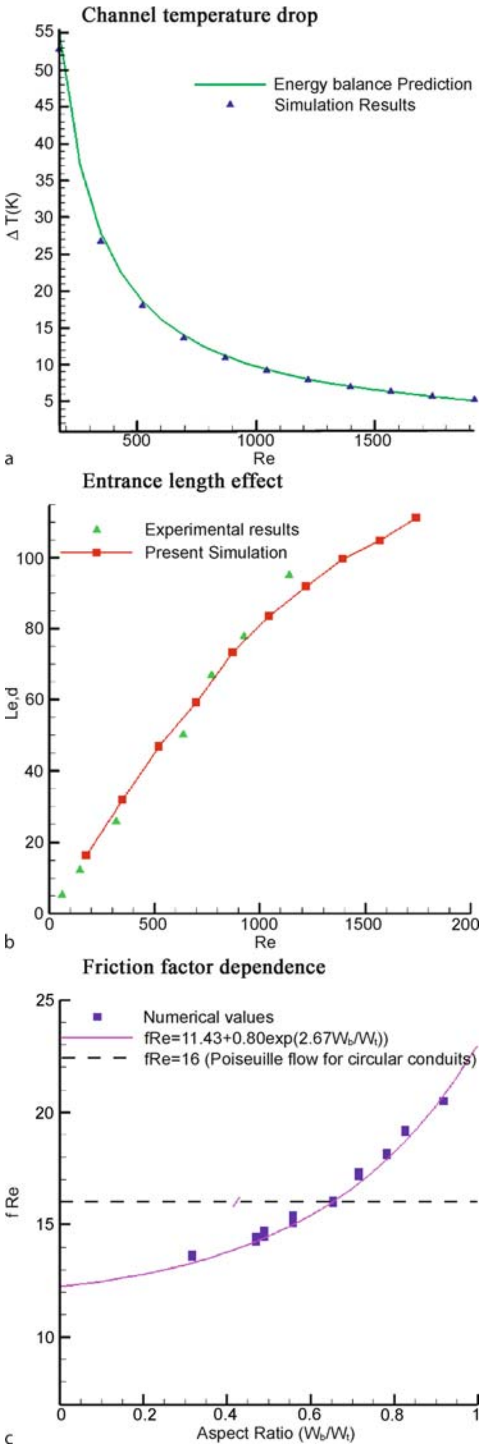

Microscale Cooling Devices, Figure 2 Model validations: (**a**) temperature rise from heat sink inlet to outlet; (**b**) dimensionless entrance length as a function of inlet Reynolds number [11]; (**c**) comparison of the numerical friction coefficient with an experimental correlation [11]

here, ρ_{nf} is the nanofluid density, μ_{nf} is the nanofluid viscosity, $c_{p,nf}$ is the specific heat capacity, φ is the volume fraction, $c_{p,p}$ is the particle specific heat capacity and $c_{p,f}$ is the specific heat capacity of the base fluid.

The most elusive parameter is the effective thermal conductivity. At present, there is no single expression for k_{eff} representing all nanofluids. Thus, in order to be somewhat realistic and computationally efficient, we chose the correlations based on experimental results of Das et al. [13] as our effective thermal conductivities:

$$k_{eff} = 1.19 k_f \quad \text{for} \quad \varphi = 1\% \tag{20}$$

$$k_{eff} = 1.27 k_f \quad \text{for} \quad \varphi = 4\%\,. \tag{21}$$

The base fluid temperature was set to 36 °C.

The calculated pressure gradient results for the CuO-water mixture at different volume fractions and two experimental data sets of Qu et al. [14] for trapezoidal microchannels as a function of inlet Reynolds number are given in Fig. 3a. The measured data points for pure water flow in two trapezoidal silicon channels with hydraulic diameters $D_h = 142.0\,\mu m$ and $168.9\,\mu m$ envelope the result for the present channel geometry which falls right between the two sets of measured data points. When adding nanoparticles at three different volume fractions, it clearly shows that the pressure gradient increases slightly with volume fraction, which is in line to the results of Chein and Huang [15].

In order to investigate heat transfer enhancement for nanofluids, the average Nusselt numbers for different volume fractions are compared. The average Nusselt number is defined as:

$$Nu_{ave} = \frac{q'' D_h}{(T_{w,ave} - T_{f,ave}) k_f} \tag{22}$$

where

$$T_{w,ave} = \frac{1}{A_{int}} \iint_A T \mathrm{d}A \tag{23}$$

and

$$T_{f,ave} = \frac{1}{V} \iiint_{V_f} T \mathrm{d}V \tag{24}$$

$T_{w,ave}$ is the surface-averaged temperature at the fluid–solid interface of area A_{int}, $T_{f,ave}$ is the volume-averaged temperature of the fluid field and k_f is the thermal conductivity of the pure water.

Figure 3b compares the average Nusselt numbers for different channels with different nanoparticle volume fractions and different Reynolds numbers. It shows that

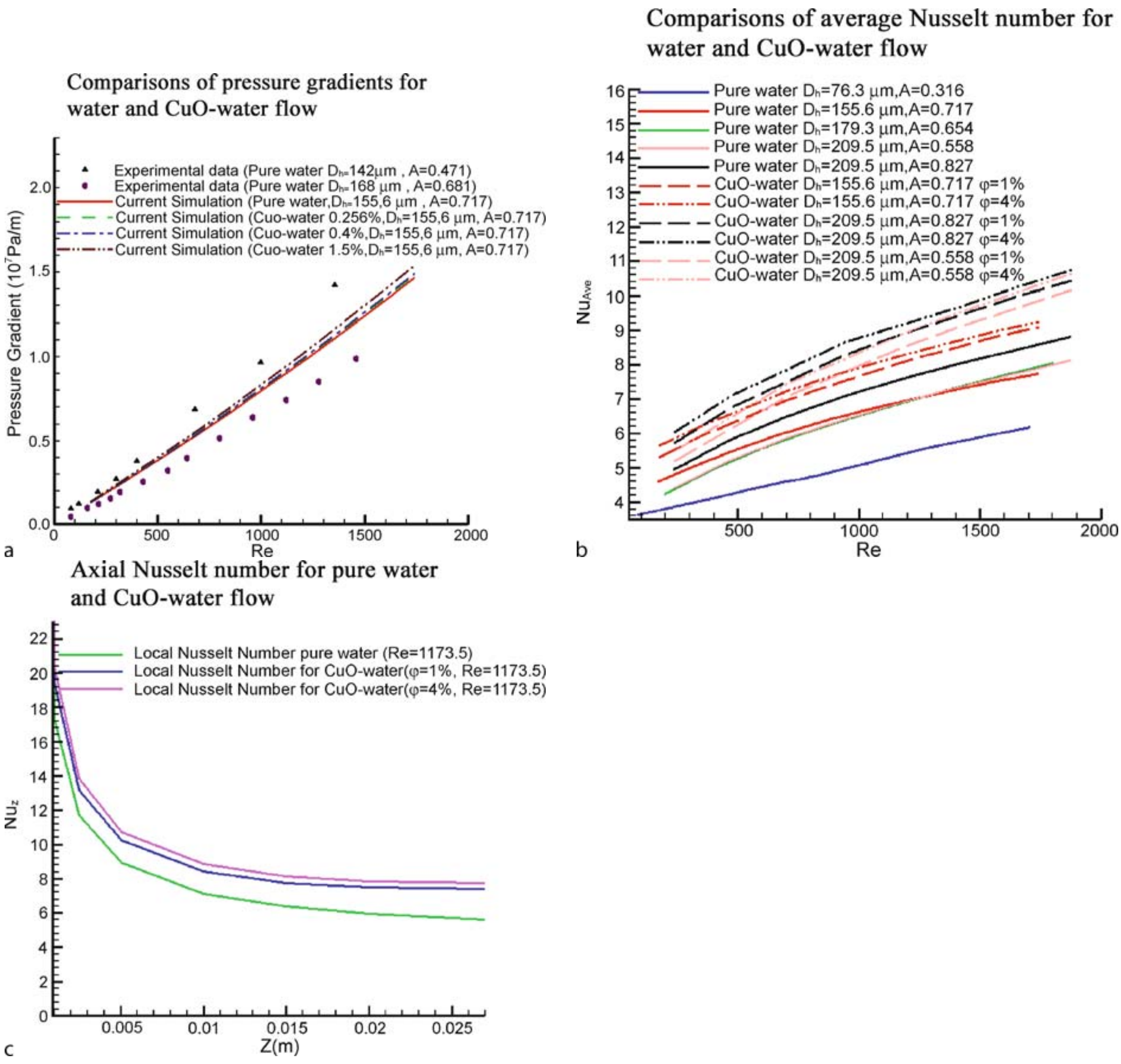

Microscale Cooling Devices, Figure 3 Computational results: (**a**) pressure gradient vs. Reynolds number; (**b**) thermal properties for different channels with different fluids; (**c**) local Nusselt number in the axial microchannel direction for different fluids

nanofluids can improve the thermal performance of microchannels:

- the larger the volume fraction of nanoparticles, the higher is the thermal performance;
- the channel shape has a strong influence on thermal performance; and
- a large aspect ration appears to be beneficial for low Reynolds number flows.

Considering the same hydraulic diameter ($D_\mathrm{h} = 209.5\ \mu\mathrm{m}$), the smaller aspect ratio case ($A = 0.558$) Nu_ave increases more rapidly when compared to the larger aspect ratio case ($A = 0.827$). There is a $20-30\%$ heat transfer enhancement in microchannels when employing nanofluids. The aspect ratio (or hydraulic diameter) measurably influences thermal enhancement when using nanofluids.

The axial Nusselt number, based on the local surface temperature and fluid temperature cross-sectionally averaged were investigated as well. The use of nanofluids greatly decreases both the channel wall temperature and fluid temperature for the same wall heat flux. Thus, it can improve the thermal dissolve capability of microchannels. In Fig. 3c, the local Nusselt numbers along the microchannel are displayed. The local Nusselt number is defined as:

$$\mathrm{Nu}_z = \frac{q'' \cdot D_\mathrm{h}}{(T_{\mathrm{w},z} - T_{\mathrm{f},z})k_\mathrm{f}} \tag{25}$$

Here $T_{w,z}$ and $T_{f,z}$ are the average wall temperature and fluid temperature as a function of axial coordinate z. Again, the local Nussels numbers are enhanced when nanofluids are employed. Figure 3c also indicates the higher thermal performance in the entrance region, especially near the inlet. As the fluid flow develops, the local Nusselt number approaches a constant value for each case. Because the entrance range of microchannels can be quite substantial, a strong entrance influence on thermal performance of microchannels can not be neglected.

Key Research Findings

Microchannel Heat Sinks

Heat removal and control has become a challenging task with the application of various high power, high speed Micro-Electro-Mechanical Systems (MEMS) in electronics or mechanical equipment. As discussed, most solutions are based on microchannel heat sinks which commonly consist of an array of microchannels.

Colgan et al. [16] described a practical implementation of single-phase Si-microchannel devices designed for cooling very high power chips. The 3D rendering of their assembled microchannel cooler is shown in Fig. 4, where the manifold chip is on top and shown semi-transparent. The test results indicated Nusselt numbers as high as 25 for reasonable flow velocities ($\sim 2.52\,\text{m/s}$). The staggered fin arrangements were at a pitch of $100\,\mu\text{m}$, channel width of 65 or $75\,\mu\text{m}$, and fin lengths of 210 to $250\,\mu\text{m}$. The strong entrance effect of the microchannel was considered to be one important factor to support the elevated average Nusselt number, which is in line with corresponding to the laminar convective heat transfer theory. The resulting heat transfer coefficients were as high as $130\,\text{kW/m}^2\cdot{}^\circ\text{C}$. The resulting pressure drop was less than 35 kPa.

Kandlikar et al. [17] presented an optimization scheme for designing microchannel heat exchangers for cooling high-heat flux silicon chips with water. An offset strip-fin construction was analyzed for dissipating heat fluxes above $3\,\text{MW/m}^2$. The continuous fin in the microchannels was broken down into several smaller fins that were placed offset to each other in the flow direction. In this arrangement, a higher heat transfer coefficient was obtained; but, with an increase in pressure as well because of the stronger fluid-development effect. In order to reduce the pressure drop of the system, a split-flow arrangement was employed to replace the single-pass arrangement, which is shown in Figs. 5a, 5b. The fluid was introduced at the center and exited on the two sides. The reduction of the flow length through the channel passages resulted in a lower pressure drop, as displayed in Fig. 5c. The heat dissipation capacity for a specified pres-

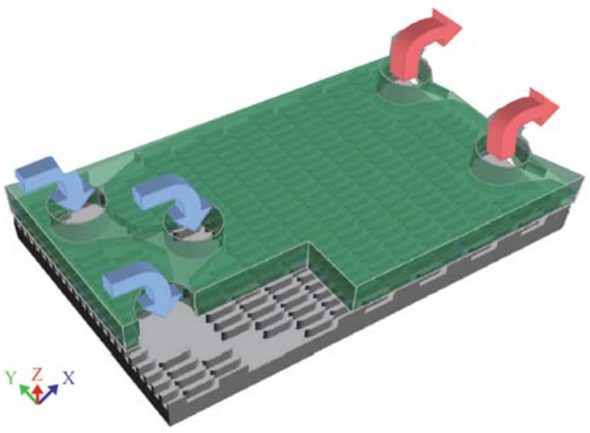

Microscale Cooling Devices, Figure 4 3D rendering of assembled microchannel cooling device [16]

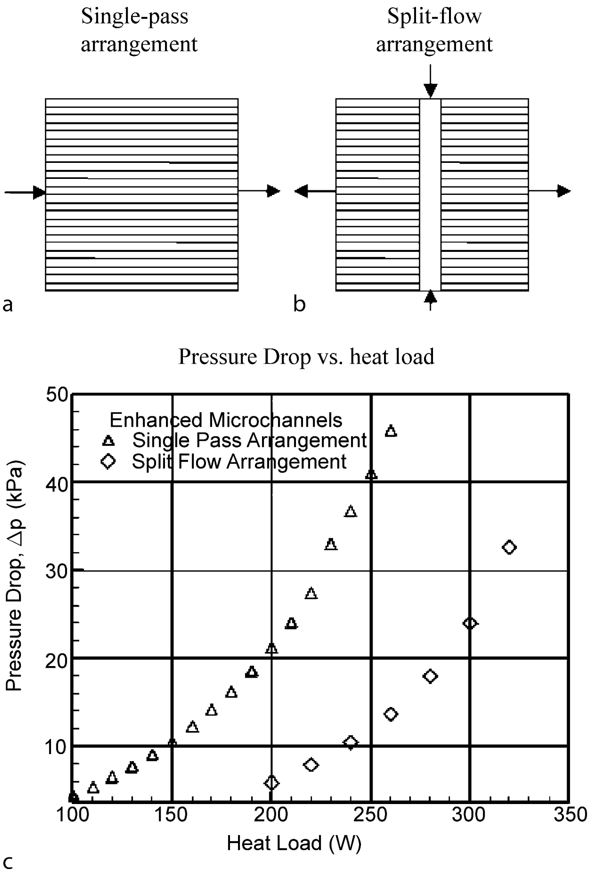

Microscale Cooling Devices, Figure 5 Microscale cooling device applications for pure water: (**a**) schematics of single-pass and split flow arrangements showing fluid flow through microchannels; (**b**) comparison of pressure drops for microchannels with offset strip-fins (l=0.5 mm) in single-pass and split-flow arrangements on a 10 mm × 10 mm chip [17]

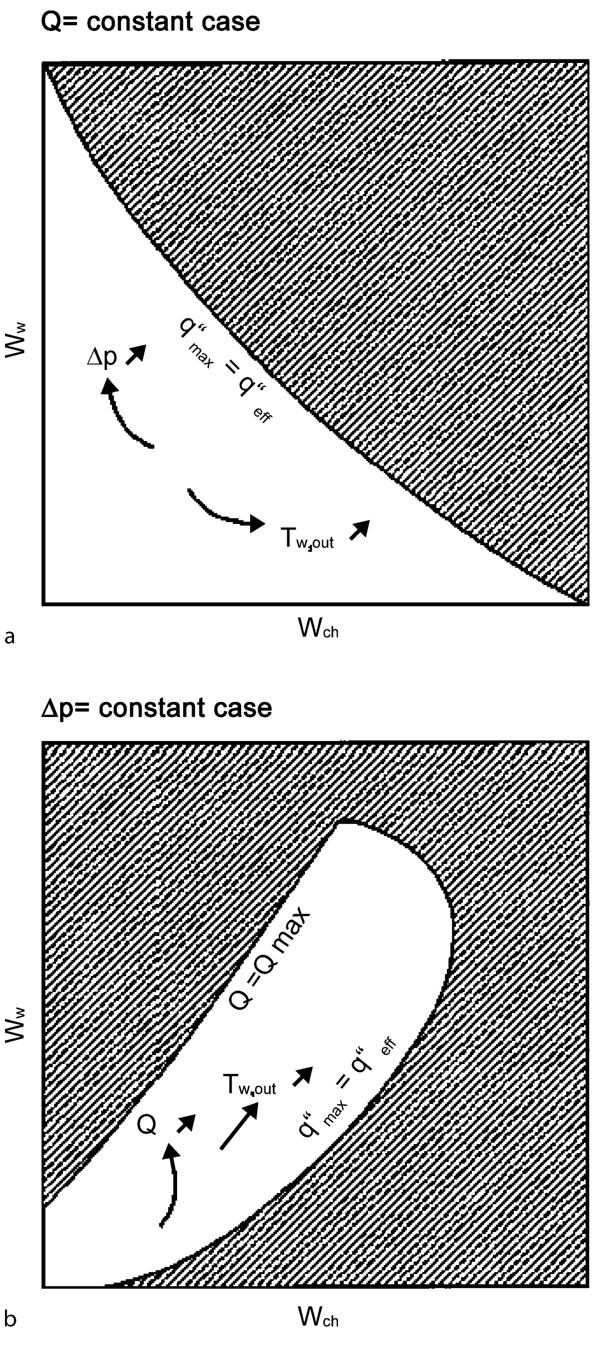

Microscale Cooling Devices, Figure 6 Map of general performance trends for a typical two-phase microchannel heat sink: (**a**) fixed total volume flow rate and (**b**) fixed pressure drop [19]

sure drop was significantly enhanced. The improvement can be attributed to the increased heat transfer coefficient leading to a reduced mass flow rate, and the reduced fluid flow length for each fluid stream. This offset strip-fin configuration in a split-flow arrangement provides an interesting option for extending the heat flux limit in direct chip cooling applications. More recently, Kandlikar [18] presented a system for cooling a high-power density processor chip which included two coolant loops. The actual heat generating device is cooled by the primary microchannel heat sink and the primary coolant was cooled by the second cooling system. In their solution, the building HVAC system was connected to the secondary cooling loop. With the current single-phase enhanced microchannel technology, a heat dissipation rate as high as $10\,\text{MW/m}^2$ was predicted. The microchannel fluid flow boiling heat transfer was also considered in the study, but the author thought that the operational instability and the resulting low critical heat flux levels had prevented their implementation in practical devices. Single-phase cooling should be more promising because of its reliable operation and ability to handle different imposed heat fluxes.

Qu and Mudawar [19] discussed a comprehensive methodology for optimizing the design of a two-phase microchannel heat sink. In their study, flow rate or pressure drop were key constraints in the design of microchannel heat sinks which often demanded specialized micro-pumps with performances dictated by either flow rate or pressure drop. For a fixed flow rate of $Q = 60\,\text{ml/min}$ and a device heat flux of $q''_{\text{eff}} = 500\,\text{W/cm}^2$, the acceptable range of two-phase operation was confined so that the dissipative heat flux will not exceed the maximum dissipative heat flux of the microchannel heat sink. For two-phase microchannel heat sinks, the minimum dissipative heat and maximum dissipative heat are defined as:

$$q''_{\text{min}} = \frac{\rho Q c_{\text{p,f}}(T_{\text{sat}} - T_{\text{in}})}{WL} \quad (26)$$

$$q''_{\text{max}} = \frac{\rho Q \left[c_{\text{p,f}}(T_{\text{sat}} - T_{\text{in}}) + h_{\text{fg}}\right]}{WL}\,. \quad (27)$$

Here T_{sat} and T_{in} are the fluid saturation temperature and inlet temperature, respectively; W and L are the width and length of the microchannel heat sink, respectively; h_{fg} is the latent heat of vaporization. Finally, they provided the numerical procedure for the optimal design of two-phase microchannel heat sink either by fixing flow rate or fixing pressure drop. The general performance map trends for fixed total volume flow rate and fixed pressure drop are shown in Figs. 6a and 6b. It provides a reference for optimizing two-phase microchannel heat sink.

Jang and Kim [20] investigated experimentally fluid-flow and heat-transfer characteristics of a microchannel heat sink, again subject to an impinging jet. This type of heat sink retains the high heat transfer coefficient asso-

ciated with a typical microchannel heat sink and experiences a low pressure drop compared to the microchannel heat sink with parallel flow. The authors modeled the microchannel heat sink, subject to an impinging jet, as a porous medium. Based on their experimental results, they suggested correlations for the pressure drop across a microchannel heat sink subject to an impinging jet as well as its thermal resistance as follows:

$$\Delta p = \rho \left(\frac{V_0}{H}\right)^2 \left(\frac{L^2}{8}\right) \left(1 + \frac{12}{\mathrm{Re}_{\mathrm{wc}}}\frac{H}{Wc} + \frac{C_{\mathrm{E},x}\varepsilon^2 L}{3K^{1/2}}\right) - \rho \left(\frac{V_0}{H}\right)^2 \left(2 - \frac{24}{\mathrm{Re}_{\mathrm{wc}}}\frac{H}{Wc} - \frac{4C_{\mathrm{E},x}\varepsilon^2 L}{3K^{1/2}}\right) \quad (28)$$

$$\theta = \frac{1}{\dot{m}C_{\mathrm{p}}} + 0.028\frac{1}{k_{\mathrm{f}}L}\left(\frac{w}{L}\right)^{0.332}\left(\mathrm{Re}_{\mathrm{dp}} \times Ar\right)^{-0.324} \quad (29)$$

for $3 \leq Ar \leq 11$ and $0 < \mathrm{Re}_{\mathrm{dp}} < 500$, where

$$Ar = \frac{H}{Wc}\,. \quad (30)$$

Here, Δp is the pressure drop across a microchannel heat sink subject to an impinging jet, ρ, V_0, ε, K, C_{E}, H, Re, Wc, Ar are density, impinging velocity at the inlet of the microchannel heat sink, fluid dynamic viscosity, porosity, permeability, Ergun coefficient, and channel height, Reynolds number, channel width and aspect ratio, respectively. The correlations for the pressure drop, the thermal resistance were compared with experimental results, and both match with experimental results within ±10%.

Zhang et al. [21] experimentally investigated the fluid flow and heat transfer of liquid-cooled foam heat sinks (FHS). As indicated in Fig. 7, eight open-cell copper foam materials with two pore densities of 60 and 100 PPI (pores per inch) and four porosities varying from 0.6 to 0.9 were bonded onto copper base plates, which formed the FHS. The authors focused on the characterization of a foam heat sink with high pore density and heat exchange area for cooling high-performance electronic chips in comparison with a microchannel heat sink. The thermal resistances and pressure drops were measured for the FHS subject to fixed heating power of 60 W and maximum pressure drop around 0.5 bar. As expected, the thermal resistance in each case decreased with the increase of the flowrate. This porosity effect on the thermal resistance can be attributed to characteristics inherent in the foam structure. Porous foams with lower porosities have a higher interstitial velocity and thus a higher local heat transfer coefficient. For the four 60 PPI FHS, the one with the lowest porosity of 0.6 was found to possess the lowest thermal resistance level accompanied by the largest pressure drop. Plotting the thermal resistance against the pressure drop and pumping power (see Fig. 8) revealed that 0.8 is the optimal porosity for the FHS at 60 PPI with a minimal thermal resistance 0.31 °C/W. For the 100 PPI case, the porosity of 0.9 was identified to be the optimal porosity with a minimum thermal resistance of 0.34 °C/W, due to the bypassing through the gap on the foam, which partially offsets the high pressure drop related to the high pore density.

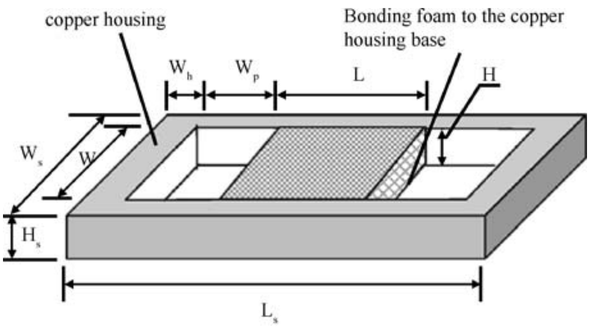

Dimensional details for the Foam Heat Sink (FHS) and the microchannel Heat Sink (HS) (Unit: mm)

Parameters	FHS 60/100PPI	Microchannel HS
Foam or finned array width W	12.2	12.2
Foam or fin length L	13	15
Faom or fin height H	2	2
Heat sink width W_s	26	24
Heat sink length L_s	52	52
Heat sink height H_s	3.5	2.8
Housing width W_h	10.5	11
Plenum width W_p	9	7.5
Unit cell scale	0.42/0.25	0.6

Microscale Cooling Devices, Figure 7 Schematic of a metallic foam heat sink (FHS) design compatible with geometric data table [21]

Peles et al. [22] investigated heat transfer and pressure drop phenomena over a bank of micro-pin fins in a micro-heat sink. The dimensionless total thermal resistance was expressed as a function of Reynolds number, Prandtl number and the geometrical configuration of the pin-fin micro-heat sink. They compared their theoretical model with their experimental results and concluded that very high heat fluxes can be dissipated at a low wall temperature rise using a microscale pin-fin heat sink. Thus, forced convection over shrouded pin-fin arrays is a very effective cooling device. In many cases, the primary cause for the rise in wall temperature is the increase of the fluid tempera-

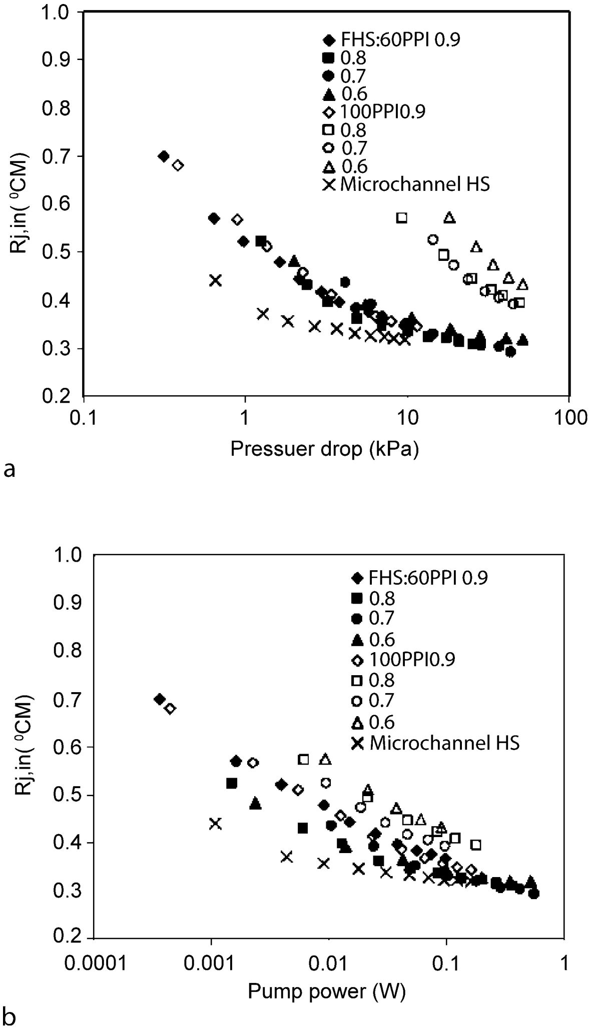

Microscale Cooling Devices, Figure 8 Thermal resistances for FHS of both 60 and 100 PPI and the microchannel heat sink with respect to: (**a**) the pressure drop and (**b**) the pumping power [21]

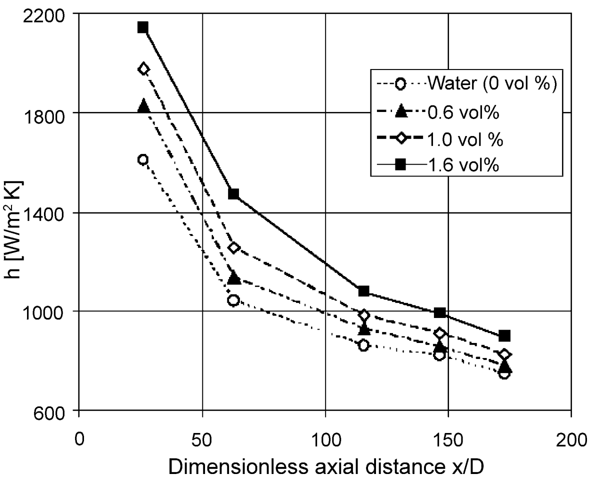

Microscale Cooling Devices, Figure 9 Nanofluid flow application in microchannel heat sink: axial profile of local heat transfer coefficient ($Re = 1050 \pm 50$) [23]

ture as it flows through microchannels. To suppress the convective thermal resistance at high Reynolds numbers, dense pin-fin configurations are preferable, while for low Reynolds numbers more sparse arrangements are advisable. The thermal resistance is less sensitive to changes in the tube diameter at larger diameters, so very low tube diameters (below $\sim 50\,\mu$m) should be avoided. To increase efficiencies, pins should be relatively short. However, correlations for heat transfer coefficients at low Reynolds numbers, as applicable to microscale systems, using intermediate pin lengths are not available.

Li and Peterson [9] investigated numerically the thermal performance of silicon-based microchannel heat sinks using a simplified heat transfer model, i. e., 2D fluid flow and 3D heat transfer analysis. The tested rectangular microchannels had widths ranging from 20 μm to 220 μm and depths ranging from 100 μm to 400 μm. The effect of microchannel geometry on the temperature distribution was discussed, assuming constant pumping power. Their model was validated with previously published experimental results and theoretical analyses. It was found that both the physical geometry of the microchannel and the thermo-physical properties of the substrate are important parameters in the design of these microchannel heat sinks. The optimal number of channels was found to be N=120 per cm with an aspect ratio as large as possible (i. e., very deep grooves), while still meeting the constraints imposed by

- the strength of the microchannel heat sinks and
- a ratio of $W_{\text{channel}}/W_{\text{pitch}} \approx 0.7$ for deep grooves.

Nanofluid Flow in Microchannel Heat Sinks

As mentioned, nanofluids exhibit unusual thermal and fluid properties, which in conjunction with microchannel systems provide enhanced heat transfer performance in heat transfer and fluid flow. For example, Wen and Ding [23] reported a considerable convective heat transfer augmentation when employing γ-Al_2O_3 nanoparticles in water flow in a copper tube based on their experimental results. The test γ-Al_2O_3 nanoparticles had a size range of 27 – 56 nm. Figure 9 depicts the local heat transfer coefficient vs. axial distance from the entrance of the test section, which clearly shows that the enhancement of the local heat transfer coefficient is much more dramatic than the enhancement of the effective thermal conductivity in the

main section of the test tube. The classical theory fails to predict the peculiar heat transfer behavior of nanofluids, mainly because of the migration of nanoparticles as well as particle-induced disturbance of the boundary layer in the entrance region.

Chein and Huang [15] analyzed the silicon microchannel heat sink performance using $Cu-H_2O$ nanofluid. Two specific geometries, one with $W_{ch} = W_{fin} = 100\,\mu m$ and $L_{ch} = 300\,\mu m$, the other with $W_{ch} = W_{fin} = 57\,\mu m$ and $L_{ch} = 365\,\mu m$ were examined. The particle volume fraction φ of the nanofluid was in the range of $0.3-2\%$. They postulated for laminar nanofluid flow in microchannels:

$$\mathrm{Nu_{nf}} = \mathrm{Nu_{CNF}} + c_3\varphi^{n_1}\,\mathrm{Pe_d^{n_2}}\,\mathrm{Re_{nf}^{n_3}}\,\mathrm{Pr_{nf}^{n_4}}\,, \tag{31}$$

where $\mathrm{Nu_{CNF}} = D_h h/k_{nf}$ and $c_3, n_1 - n_4$ are constants that were determined from experimental data, i. e., c_3, n_1, n_2, n_3 and n_4 are 4.884, 0.754, 0.218, 0.333 and 0.4, respectively. They showed that Nu increases significantly with the increase in Re and φ when compared with pure water. The enhancement of the nanofluid thermal conductivity was contributed to the increase in thermal conductivity of the coolant and the nanoparticle thermal dispersion effect. The experimental results also showed that there is almost no extra pressure drop occurring when using nanofluids as coolants.

Koo and Kleinstreuer [8] investigated laminar nanofluid flow in microheat-sinks using the effective nanofluid thermal conductivity model they had established [24]. For the effective viscosity due to micromixing in suspensions, they proposed:

$$\begin{aligned}\mu_{\text{effective}} &= \mu_{\text{static}} + \mu_{\text{Brownian}}\\ &= \mu_{\text{static}} + \frac{k_{\text{Brownian}}}{k_f} \times \frac{\mu_f}{\mathrm{Pr}_f}\,.\end{aligned} \tag{32}$$

The impact of volume fraction in laminar flow of water and ethylene glycol with CuO-nanoparticles on the microchannel pressure gradient, temperature profile and Nusselt number was analyzed. Based on their experimentally validated results, the following was recommended: Use of high Prandtl number carrier fluids, high aspect ratio channels, high thermal conductivity nanopaticles, and treatment of channel surface to avoid nanoparticle accumulation.

Yang et al. [25] experimentally measured convective heat transfer coefficients of several nanoparticle-in-liquid dispersions for laminar flow in a horizontal tube heat exchanger. Graphite nanoparticles with an aspect ratio of 0.02 (l/d) were selected, with an average diameter of about $1-2\,\mu m$ and lengths of $20-40$ nm. The test tube had an inside diameter of 0.457 cm and 45.7 cm in

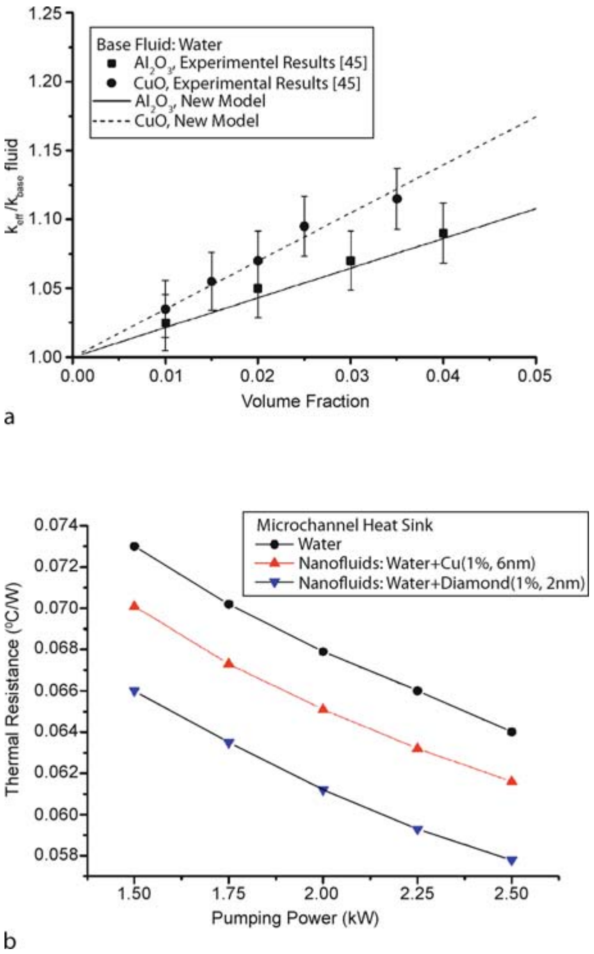

Microscale Cooling Devices, Figure 10 Nanofluid flow applications in microchannel heat sinks: (**a**) comparison of model predictions with experimental thermal conductivity data for copper oxide-in-water and aluminum-in-water nanofluids [27]; (**b**) thermal resistances of microchannel heat sinks with water-based nanofluids containing copper and diamond particles [26]

length. Although the graphite nanoparticles increased the static thermal conductivity of the mixture significantly at low weight fraction loadings, the authors found that the experimental heat transfer coefficients showed lower increases than predicted by either conventional correlations for homogeneous fluids or correlations developed for particle suspensions with aspect ratios close to one. The type of nanoparticles, particle loading, base fluid chemistry, and the process temperature are all important factors influencing the thermal performance of nanofluids.

Jang and Choi [26] numerically investigated the cooling performance of a microchannel heat sink with nanofluids. Two kinds of nanofluids were investigated in this study, i. e., $d_p = 6$ nm nanoparticles in a copper-water mixture and $d_p = 2$ nm diamond-in-water nanofluid. A the-

oretical model was employed for the thermal conductivity of nanofluids that accounts for four modes of energy transport: the thermal diffusion in the base fluid, the thermal diffusion of nanoparticles, the collision between the nanoparticles, and the nanoconvection due to Brownian motion. Specifically,

$$k_{\text{nanofluids}} = k_{\text{f}}(1-\phi) + \beta k_{\text{p}}\phi + 3C\frac{d_{\text{f}}}{d_{\text{p}}}k_{\text{f}}\text{Re}_{d_{\text{p}}}^{2}\,\text{Pr}\,, \quad (33)$$

where β is a constant related to the Kapitza resistance, being in the order of 0.01; d_{f} and d_{p} are the equivalent diameters of a base fluid molecule and a nanoparticle, respectively; $\text{Re}_{d_{\text{p}}}$ and Pr are the Reynolds number and the Prandtl number, and $C = 6 \times 10^{6}$.

Figure 10a compares the previous experimental findings [27] with the results of the new model. With the new effective thermal conductivity model, the cooling performance of the microchannel heat sink with nanofluids was considered. The cooling performance of a microchannel heat sink with nanofluids was evaluated in terms of the thermal resistance θ, which is defined as:

$$\theta = \frac{T_{\max} - T_{\text{in}}}{q''}\,, \quad (34)$$

where q'', T_{in}, and $T_{\max}$, are the heat flux generated, temperature of the inlet coolant and the maximum temperature at the bottom surface of the microchannel heat sink, respectively. Figure 10b shows the thermal resistance of microchannel heat sinks with water-based nanofluids containing copper and diamond particles. Clearly, the cooling performance of a microchannel heat sink with water-based nanofluids containing diamond (1 vol.%, 2 nm) at the fixed pumping power of 2.25 W is enhanced by about 10% when compared to that of a microchannel heat sink with water. The numerical results show that the nanofluids reduce both the thermal resistance and the temperature difference between the heated microchannel wall and the coolant.

Microchannel heat sink (MCHS) performance using copper-water and carbon nanotube-water nanofluids as coolants was analyzed by Tsai and Chein [28]. The microchannel heat sink was modeled as a porous medium. The MCHS performance was characterized by the thermal resistance which was divided into the conductive thermal resistance and convective thermal resistance. When employing a nanofluid as the coolant, the convective thermal resistance was found to increase due to the increase in viscosity and decrease in thermal capacity. The reduction of the total thermal resistance was contributed to the reduced temperature difference between the MCHS bottom wall and bulk pure fluid or nanofluids which produced a reduction in conductive thermal resistance. For the pure fluid, it was found that the higher aspect ratio decreased the thermal resistance which confirmed the results of Li and Peterson [9]. However, the nanofluid has a significant effect on MCHS performance only when the channel aspect ratio and porosity are low. For the MCHS with high channel aspect ratio and porosity, it was found that using the nanofluid does not produce significant MCHS performance enhancement. Under the condition of a given pressure drop, an optimum MCHS design was investigated. It was found that using nanofluid can enhance the MCHS performance when the porosity and aspect ratio are less than the optimal porosity and aspect ratio. The optimal aspect ratio had a value of 5–6 for different pressure drops, i.e., 50 kPa and 200 kPa. The authors compared the performance of the pure fluid cooled and nanofluid cooled MCHS with the optimized channel geometry of Tuckerman and Pease [3]. It was found that a 23% and 25% reduction of thermal resistance was achieved by using the nanofluids of Cu-water and CNT-water with a 4% volume fraction, respectively.

Future Directions for Research

Nanofluids are one of the most promising candidates for optimal microscale cooling devices. Thus, ongoing research is focusing on the thermal and fluid properties of nanofluids as well as such mixture flow in microchannels. How to optimize the cooling capabilities of nanofluids in microchannel heat sinks will be a challenging task. Alternative approaches include fluid-jet impingement and two-phase, i.e., liquid–vapor, flow with boiling heat transfer.

Cross References

► Microscale Cooling Device
► Microchannel Heat Sinks
► MEMS-Based Biosensor

References

1. Zohar Y (2006) Microchannel heat sinks. In: Gal-el-Hak M (ed) MEMS Applications. CRC Press, Boca Raton
2. Koo J, Kleinstreuer C (2003) Liquid flow in microchannels: Experimental observations and computational analyses of microfluidics effects. J Micromech Microeng 13:568–579
3. Tuckerman DB, Pease RFW (1981) High-performance heat sinking for VLSI. IEEE Electron Device Lett 2(5):126–129
4. Nguyen N-T, Wereley ST (2002) Microfluidics. Artech House, Boston
5. Tabeling P (2005) Introduction to Microfluidics. Oxford University Press, Oxford
6. Kandlikar SG, Grande WJ (2004) Evaluation of single phase flow in microchannels for high heat flux chip cooling – Thermo-

hydraulic performance enhancement and fabrication technology. Heat Transf Eng 25(8):5–16
7. Li J, Peterson GP, Cheng P (2004) Three-dimensional analysis of heat transfer in a micro-heat sink with single phase flow. Int J Heat Mass Transf 47:4215–4231
8. Koo J, Kleinstreuer C (2005) Laminar nanofluid flow in microheat-sinks. Int J Heat Mass Transf 48:2652–2661
9. Li J, Peterson GP (2006) Geometric optimization of a micro heat sink with liquid flow. IEEE TRANS On Comp Pack Tech 29:145–154
10. Choi ES, Brooks JS, Eaton DL, Al-Haik MS, Hussaini MY, Garmestani H, Li D, Dahmen K (2003) Enhancement of thermal and electrical properties of carbon nanotube polymer composites by magnetic field processing. J Appl Phys 94(9):6034–6039
11. Hao PF, He P, Zhu KQ (2005) Flow characteristics in a trapezoidal silicon microchannel. J Micromech Microeng 15:1362–1368
12. Wu HY, Cheng P (2003) Friction factors in smooth trapezoidal silicon microchannels with different aspect ratios. Int J Heat Mass Trans 46(14):2519–2525
13. Das SK, Putra N, Thiesen P, Roetzel W (2003) Temperature dependence of thermal conductivity enhancement for nanofluids. J Heat Transf 125:567–574
14. Qu W, Mohiuddin M, Li D (2000) Pressure-driven flows in trapezoidal silicon. Int J Heat Mass Transf 43:353–364
15. Chein R, Chuang J (2005) Analysis of microchannel heat sink performance using nanofluids. Appl Therm Eng 25:3104–3114
16. Colgan EG, Furman B, Gaynes M, Labianca N, Magerlein JH, Polastre RJ, Rothwell MB, Bezama RJ, Choudhary R, Martson K, Toy H, Wakil J, Zitz J, Schmidt R (2005) A practical implementation of silicon microchannel coolers for high power chips. Invited Paper presented at IEEE Semi-Therm 21, San Jose, 15–17 Mar 2005, pp 1–7
17. Kandlikar SG, Upadhye HR (2005) Extending the heat flux limit with enhanced microchannels in direct single-phase cooling of computer chips. Invited Paper presented at IEEE Semi-Therm 21, San Jose, 15–17 Mar 2005, pp 8–15
18. Kandlikar SG (2005) High flux heat removal with microchannels – A roadmap of challenges and opportunities. Heat Transf Eng 26(8):5–14
19. Qu W, Mudawar I (2005) A systematic methodology for optimal design of two-phase micro-channel heat sinks. J Electron Packag 127:381–390
20. Jang SP, Kim SJ (2005) Fluid flow and thermal characteristics of a microchannel heat sink subject to an impinging air jet. J Heat Transf 127:770–779
21. Zhang HY, Pinjala D, Joshi YK, Wong TN, Toh KC, Iyer MK (2005) Fluid flow and heat transfer in liquid cooled foam heat sink for electronic packages. IEEE Trans Compon Packag Technol 28(2):272–280
22. Peles Y, Kosar A, Mishra C, Kuo C-J, Schneider B (2005) Forced convective heat transfer across a pin fin micro heat sink. Int J Heat Mass Transf 48:3615–3627
23. Wen D, Ding Y (2004) Experimental investigation into convective heat transfer of nanofluids at the entrance region under laminar flow conditions. Int J Heat Mass Transf 47:5181–5188
24. Koo J, Kleinstreuer C (2004) A new thermal conductivity model for nanofluids. J Nanopart Res 6:577–588
25. Yang Y, Zhang ZG, Grulke EA, Anderson WB, Wu G (2005) Heat transfer properties of nanoparticle-in-fluid dispersions (nanofluids) in laminar flow. Int J Heat Mass Transf 48:1107–1116
26. Jang SP, Choi SUS (2006) Cooling performance of a microchannel heat sink with nanofluids. Appl Therm Eng 26:2457–2463
27. Lee S, Choi SUS, Li S, Eastman JA (1999) Measuring thermal conductivity of fluids containing oxide nanoparticles. J Heat Transf – Trans ASME 121(2):280–289
28. Tsai TH, Chein R (2007) Performance of nanofluid cooled microchannel heat sink. Int J Heat Fluid Flow 28:1013–1026

Microscale Flow Visualization

Ian Papautsky, Ali Asgar S. Bhagat
Department of Electrical and Computer Engineering,
University of Cincinnati, Cincinnati, OH, USA
Ian.Papautsky@uc.edu

Synonyms

Microfluidic flow visualization; Microfluidic imaging

Definition

Flow visualization is a branch of fluid mechanics that provides visual perception of the dynamic behavior of fluids flows. The fundamental principle of any flow visualization technique lies in the detection of fluid transport by altering the fluid properties while leaving the fluid motion unaltered. *Microscale flow visualization* focuses on imaging microscale flows microfluidic flows, with the most common techniques broadly classified into particle-based and scalar-based methods.

Overview

The concept of Lab-on-a-Chip (LOC) has triggered an avalanche of developments and discoveries leading to an exponential growth of the microfluidics field in both industry and academia [1]. The reduction in dimensions that accompanies miniaturization results in flows through microchannels which are drastically different from macroscale flows and theory. Fluid motion at these small scales, integrated with nonlinear interaction between macromolecules can create complex phenomena which are difficult to predict and simulate theoretically. Rapid development of microfluidic technologies has been augmented by parallel progress of various visualization techniques for assessing the transport phenomena occurring at these scales. Although flow visualization on the macroscale was pioneered in the late 19th century, microscale flow visualization techniques were not demonstrated until the early 1990's. Since then, a number of methods have been developed, which are reviewed in detail in several recent publications [1–3].

Microscale flow visualization has played a key role in the development of the microfluidics and LOC fields. It is central to fundamental understanding of microflows, developing novel microfluidic processes, investigating non-ideal and non-linear behaviors, and providing data for numerical simulations. Many microfluidic applications such as mixing, pumping, and filtering require flow visualization to characterize device efficiency. To date, most microscale flow visualization techniques have focused on determination of flow velocity in liquids (or velocimetry). The most common microscale flow visualization techniques can be broadly classified into particle-based and scalar-based methods.

Particle Based Techniques

Particle based flow visualization techniques introduce marker particles into the flow field to study the motion of the bulk by determining the velocity vectors associated with these particles. Laser Doppler velocimetry (LDV), optical Doppler tomography (ODT) and particle image velocimetry (PIV) are the different methods that have been developed in this regard. However, of these methods microscale PIV (μ-PIV) is the most well-developed and popular microscale flow visualization technique.

Laser Doppler Velocimetry (LDV)

LDV relies on detection of light reflected from particles within a flow. Two cross-collimated laser beams creating an interference pattern pass through a small sampling volume. A microscopic pattern of bright and dark stripes forms in this intersection volume. Particles in the flow passing through this pattern reflect light towards a detector with a characteristic frequency indicative of the particle velocity, based on the Doppler effect. One of the drawbacks of this technique is the dependence on the size of the probe volume. As the volume decreases, the probability of a particle passing through the volume decreases, thus limiting the accuracy of the velocity measurements. Also, stray reflections near microchannel walls may corrupt the signal at the detector. LDV was successfully used by Tieu et al. [4] to measure laminar flows in 175 μm thick channels using diode lasers (Fig. 1a). The system offered a wall resolution of 18 μm, while higher resolution could be achieved by correcting the astigmatism of the laser diode using cylindrical lens.

Optical Doppler Tomography

ODT has been developed to accurately resolve the location and velocity of particles in highly scattering medium, especially useful in medical diagnosis. For example, knowledge of in vivo blood flow under the skin allows clinicians to determine depth of burns [5]. ODT combines single beam Doppler velocimetry with optical coherence tomography using a low-coherence Michelson interferometer. Light in an ODT system is broken into a target arm (containing the sample) and a reference arm (usually a mirror). The combination of backscattered light from the target arm and reference light from the reference arm gives rise to an interference pattern only when optical path lengths of light in the target and reference arms match to within the laser coherence length. Particle velocity is determined by measuring the frequency shift of the backscattered interference pattern at the detector. The ODT system developed by Chen et al.[6] exhibited a lat-

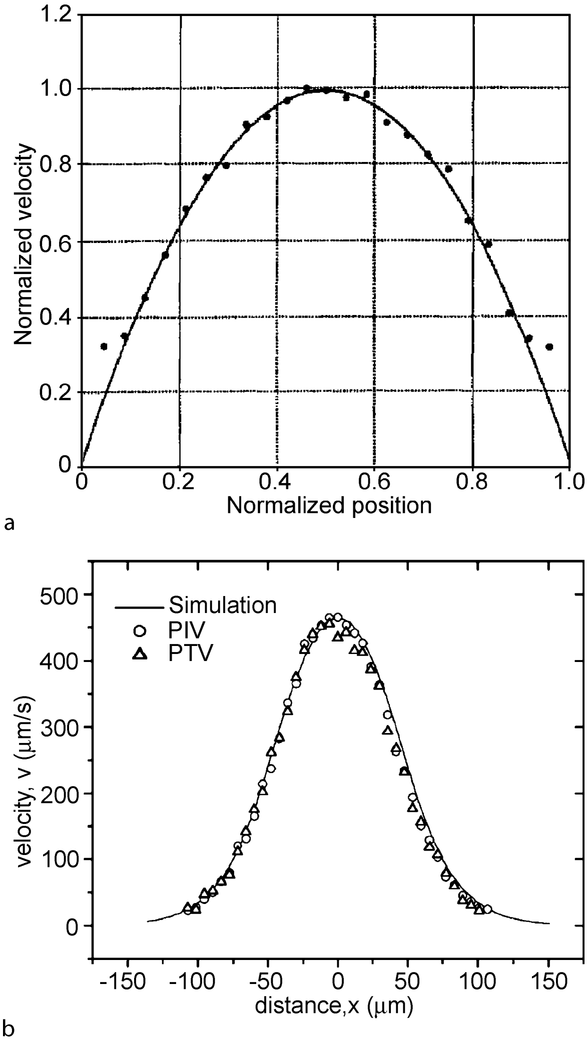

Microscale Flow Visualization, Figure 1 (**a**) Velocity profile across 175 μm wide glass microchannel obtained by LDV [4]. (**b**) Velocity field across a 120 μm wide acrylic microchannel, obtained experimentally with both PIV and PTV and compared with simulation data [18]

eral and axial resolution of 5 μm and 15 μm limited by the beam spot size.

Particle Image Velocimetry (PIV)

PIV is an optical whole-field, non-intrusive measurement technique to measure fluid velocity by recording the displacement of small tracer particles added to the fluid. PIV has been extensively reviewed in past [5], and can be divided into pattern matching velocimetry (PMV) and particle tracking velocimetry (PTV). PIV offers more flow information per interrogation, and thus substantially more work has been done in this field compared to LDV and ODT.

In PMV, the velocity vectors are estimated by tracking patterns of particles in a small interrogation area. PMV measures the velocity field from images obtained at two different times with a know time delay governed by the delay between the pulses of the laser. The two images are then cross-correlated to extract information about flow. In PTV, the velocity vectors are estimated by tracking individual particles in a small interrogation area. In comparison to the PMV technique, the PTV technique offers better resolution as individual particles are tracked and not the overall pattern. Figure 1b shows typical velocity filed obtained using PIV and PTV techniques.

Application of PIV to microflows, or microscale PIV (μ-PIV), was first successful demonstrated by Santiago et al. [7] in 1998. Today, it is rapidly becoming the preeminent technique for visualizing velocity in liquid flows in microfluidic devices. However, there are three fundamental aspects differentiating macroscale and microscale PIV (discussed in detail by Wereley et al. [8]). First, as the particles become small compared to the wavelength of the illuminating light (i. e. $d \ll \lambda$), the amount of light scattered by such a particle (which varies as d^6 due to Rayleigh scattering [9]) places significant constraints on the imaging optics. To overcome this problem, fluorescently-tagged microspheres are commonly used for better imaging. Second, when the seed particle size becomes very small, the effects of particle-particle and particle-fluid molecule interactions become significant, preventing the particles from following the flow to some degree. This error in the resulting velocity vector is substantially reduced by averaging multiple image interrogations. The third significant difference is that the flow is volume illuminated due to use of high numerical aperture microscope objectives that have a narrow depth of focus.

Scalar Based Techniques

Scalar based techniques using molecular tracers (fluorescence or phosphorescence) have been widely employed for visualization of microflows. To obtain velocity information, images at two instances in time are obtained and correlated to determine the displacement. Perhaps the most common visualization technique is using conventional food dye visualization. Food dyes are preferred over other molecular tracers as they are safe, cheap and available in most supermarkets. Most food dyes are sold as concentrated solution with a specific gravity greater than one. To make the dye buoyant such that it follows the flow field, they are generally mixed with a small quantity of alcohol. Another common indicator which is often used to visualize flows is milk. Milk is frequently preferred over dye solutions due to good reflective properties which improve image contrast. When using milk as a flow indicator, it is essential to flush the injection system after the experiment as any milk left in the system may curdle and can cause flow blockage.

Scalar image velocimetry (SIV) is the technique used to determine the vector velocity fields by recording images of a passive scalar quantity and inverting the equation of motion for a passive, conserved scalar. The technique was originally developed by Dahm et al. [10] to measure the velocity field in a turbulent jet. Later, Tokumaru and Dimotakis [11] developed image correlation velocimetry (ICV), which uses correlation of two successive scalar images to measure fluid velocity vectors. Since then, a variety of methods for tracking scalar tracers have been developed including laser-induced fluorescence (LIF), flow-tagging velocimetry (FTV), molecular tagging velocimetry (MTV), laser-induced molecular tagging (LIMT), laser induced photochemical anemometry (LIPA), photobleached fluorescence (PF), microbubble lensing induced photobleaching (μBLIP), IR thermal velocimetry (ITV) and photo-activated nonintrusive tracking of molecular motion (PHANTOMM). However, the basic mechanisms employed in these techniques are fluorescence, photobleached fluorescence, phosphorescence, caged fluorescence, and IR heating [2].

Fluorescence

Fluorescence techniques have been widely used to determine the velocity of flows by imaging the elapsed displacement in a given time interval. Fluorescence is the phenomenon by which electromagnetic excitation of a molecule results in the emission of a photon. The emitted light has a wavelength longer than the light absorbed. This shift in the wavelengths, called the Stoke's shift, was first observed by Stokes in 1852 and forms the basis of fluorescence microscopy. The typical lifetime of a fluorophore in the excited state is 1 – 10 ns. This inhibits the use of fluorescence as a flow visualization tech-

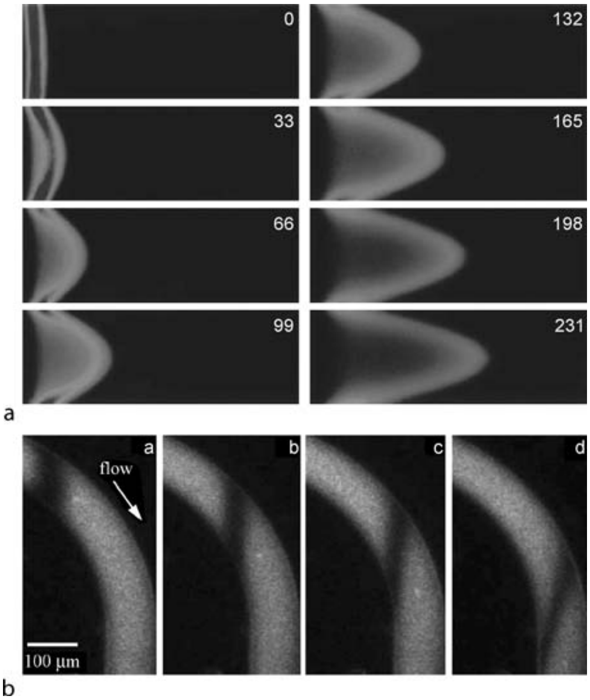

Microscale Flow Visualization, Figure 2 (**a**) Images of pressure-driven flow through an open 100 µm i.d. fused-silica capillary using a caged fluorescein dextran dye. Pressure differential of 5 cm of H_2O per 60 cm of column length. Viewed region 100 µm × 200 µm. The frames are numbered in ms as measured from the uncaging event [13]. (**b**) Electroosmotic flow profile from top to bottom in a curved acrylic microchannel at time a) $t = 0$ s, b) $t = 1.2$ s, c) $t = 1.8$ s, and d) $t = 3.2$ s, studied by Mosier et al. [14]. The electric field is 30 Vcm^{-1}. The photobleached region helps to study the stretching and tilting of the flow profile due to the 'racetrack' effect

nique on its own. Instead, fluorophores are used along with caging molecules to facilitate tagging, or are permanently tagged by overexposure (photobleaching). For example, the absorption maxima of fluorescein molecule is 490 nm and the emission maxima is 513 nm. Similarly, the absorption maxima of another popular fluorophore, Rhodamine 6G, is 530 nm and the emission maxima is 566 nm.

Caged Fluorescence

Caged-fluorescent or photoactivated fluorescent (PAF) dye molecules are fluorophores with additional chemical groups that quench the fluorescence of the dye. Upon exposure to electromagnetic radiation, the chemical group is cleaved (photolysis) and fluorescence is recovered, known as an uncaging event. The first demonstration of measuring flow velocity in macrochannels ~ 1 cm in diameter using caged-fluorescent dyes was shown by Lempert et al. [12] in 1995. He named his scheme as "PHoto-Activated Nonintrusive Tracing Of Molecular Motion" (PHANTOMM). However, it was Paul et al. [13] in 1998 who applied caged fluorescence to visualize and characterize microscale flows. The technique was demonstrated for pressure- and electrokinetically driven flows in capillaries. Light from a 355 nm tripled Nd:YAG laser was used to un-cage the caged fluorophores. The resulting sheet of uncaged fluorescein was then excited using a second laser (Argon ion laser, and later doubled Nd : YVO_4 laser). Fluorescent images indicating dye transport were then captured using an attached CCD camera. Representative images are shown in Fig. 2a.

Photobleaching

Photobleaching is the permanent destruction of fluorescence by over exposure to a high-intensity light. Photobleaching is a common problem in time-lapse microscopy. However, it can be employed to visualize microscale flows using the fluorescence recovery after photobleaching (FRAP) technique. Mosier et al. [14] employed photobleaching of fluorescein to visualize electroosmotic and pressure driven fluid flow fields (Fig. 2b). A brief exposure to a laser sheet photobleaches a fraction of the fluorophores present in the diluted fluorescein solution flowing in the microfluidic device. The development of this photobleached region is then used to determine flow field conditions and transport coefficients such as velocity vectors and electro-osmotic mobility. A distinct advantage of this technique is the ability to use visible light and standard dyes as opposed to caged-dyes that typically require ultraviolet light to activate the dye molecules. However, the signal-to-noise ratio that defines image contrast of this technique is almost an order of magnitude inferior when compared to caged-fluorescence imaging.

Phosphorescence

Phosphorescence is a process, similar to fluorescence, by which electromagnetic excitation of a molecule results in the emission of a photon. However, unlike fluorophores, which have a lifetime of about 1 – 10 ns, a phosphorescent molecule does not immediately discharge the absorbed radiation. Typically, the emission lifetimes of phosphorescence emission can be as long as several milliseconds. Although a variety of phosphorescence techniques are available, analogous to fluorescence, they are not as popular as their fluorescence counterparts due to the much longer tracer lifetimes. These longer tracer lifetimes also limit their applicability to relatively fast flows ($Re > 10$),

which are not very characteristic of microscale flows (typically Re < 1).

IR Heating

IR-based velocimetry technique involves measurement of small volume flows using a non-invasive, simple design. A small volume of flow is heated by repeated exposures to IR radiation and detected at a short distance downstream using heat indexing, thermal imaging or laser induced interferometric backscatter. IR heating based flow monitoring was demonstrated by StClaire and Hayes [15] in a 184 μm diameter capillary over a velocity range of 2 – 25 cm/s (500 nl/s to 7 ml/s). A small volume of fluid was heated using a NiCr heating coil driven by a variable AC controller. By heating, one can change the refractive index of the fluid and thus determine the flow velocity by measuring the laser light backscattered from the capillary at a fixed length downstream. Markov and Bornhop [16] employed similar technique to measure linear flow velocity within filled capillaries. In their case, an infrared laser diode was used to repeated heat a small volume of fluid and measuring the thermally induced change of refractive index using a micro-interferometric back-scatter detector (MIBD).

Summary

Selection of an appropriate microscale visualization technique depends primarily on the application of interest. Both particle-based and scalar-based measurement techniques can be applied to most microscale flows. However, one advantage of scalar-based techniques is that the molecular tracer will not be trapped in even the smallest passages, thus avoiding issues arising from channel blockage. Also, with an increasing trend towards soft polymeric microfluidic devices, particle based techniques could probably be difficult to implement due to the problem of particles sticking to the walls of the device which can possibly decrease the resolution of the measurement. Another limitation of particle based methods, typically PIV, is that while characterizing electroosmotic flows the particles can acquire substantial charge (due to their larger size as compared with molecular tracers) and become influenced by both the hydrodynamic and the electrical forces. However, one major limitation of scalar-based techniques is that the diffusivity of the molecular tracers can be typically much higher than individual particles, thereby lowering the spatial and velocity resolution of the measurements. The following section will discuss in detail experimental methodologies of two most commonly used methods for microscale visualization: μ-PIV and fluorescence. We will limit our discussion to pressure driven flows.

Basic Methodology

Microscale Particle Image Velocimetry (μ-PIV)

The principle of μ-PIV lies in recording of images of the flow field with a well-defined time-delay with the help of small fluorescently-tagged particles as illustrated in Fig. 3. Unlike traditional tracking schemes where individual particles are tracked, in μ-PIV sets of particle images are tracked with a high particle density. The particles are assumed to have densities similar to the surrounding fluid and are small enough so that they follow the flow faithfully without influencing it. By recording the position of a particle at two separate time instants the local fluid velocity can be determined using following equitation:

$$u = \frac{x_2 - x_1}{t_2 - t_1} = \frac{\Delta x}{\Delta t} \tag{1}$$

where x_1 is particle position at time t_1, and x_2 is particle position at time t_2. By extending this concept to the entire flow field, high spatial resolution and accuracy can be obtained. As a single image pair may contain hundreds of particles, the images are typically divided into smaller sub-areas called interrogation regions.

The first successful μ-PIV system was demonstration by Santiago et al. [7] in 1998, who recorded the velocity vector in a Hele-Shaw flow around a 30 μm cylindrical obstruction. The system utilized an inverted epi-fluorescent microscope (e. g., Nikon TE2000 or Olympus IX71), a Hg arc lamp for continuous illumination, and a intensified CCD camera to image 100 – 500 nm diameter fluorescently-tagged polystyrene particles. Flow was injected into the microfluidic device using a conventional syringe pump (e. g., Harvard Apparatus). Meinhart et al. [17] demonstrated an improved μ-PIV system consisting of the same general components with the exception that the continuous light source was replaced by dual 5 ns pulsed Nd:YAG lasers (e. g., New Wave, Minilase System) along with beam expanding optics. High accuracy and spatial resolution (~ 1 μm) using this technique were reported.

Figure 4 shows a typical experimental setup to conduct μ-PIV measurements in microfluidic devices. Imaging is typically performed using 60× water or oil immersion objectives. For microchannels incorporating 3-D structures, a microscope with z-translation is commonly used to capture images at varying height within the channel. The microscope must be equipped with a high-speed camera capable of capturing thousands of images per second. A computer with large processing power is then used to analyze these images and extract flow information.

Characteristics of the particle imaging system largely determine the achievable resolution in a μ-PIV system. Two critical parameters here are the total magnification

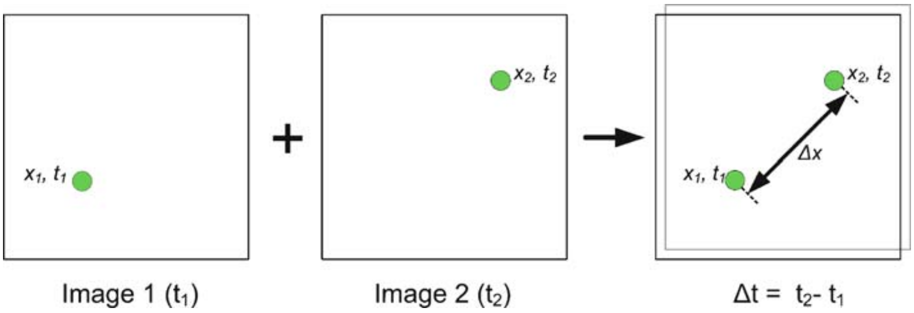

Microscale Flow Visualization, Figure 3 Schematic illustrating the principle of flow characterization using PIV technique. By calculating the displacement of a particle in a known time delay, the flow velocity vectors can be calculated

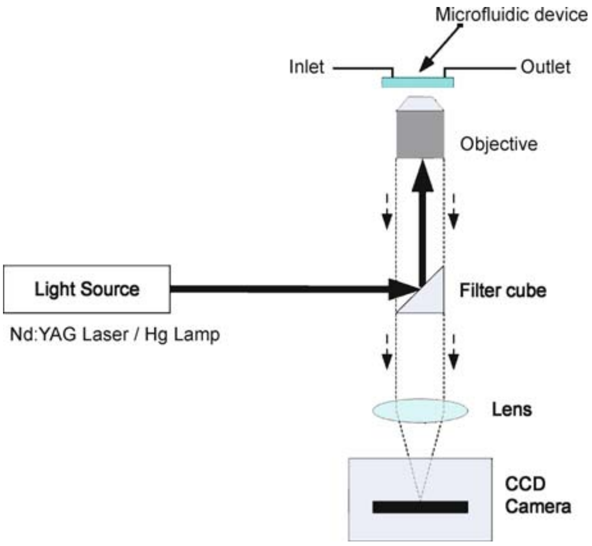

Microscale Flow Visualization, Figure 4 Schematic of the experimental set-up used to carry out μ-PIV measurements. A pulsed Nd:YAG laser or a continuous Hg arc lamp is used to excite fluorescently tagged polystyrene particles on an inverted epi-fluorescent microscope. A CCD camera is used to capture the particle images at regular well-defined time intervals. A filter cube is selected based on the fluorophore used (i. e. FITC for fluorescein or TRITC for rhodamine)

and the numerical aperture of the objective lens. For a 60 × objective lens with a numerical aperture of 1.4, the image diameter of 500 nm diameter spherical particles is 700 nm in the object plane [7]. By resolving the particle image over an area in the detector that is 3 to 4 px across, the uncertainty associated with determining the center of the cross-correlation peak is approximately 10% of the particle image diameter, which translates to approximately 70 nm in the object plane [18].

Particle size is an important consideration in any particle tracking method. Particles should be small compared to the dimensions of the microfluidic channels, and should be much smaller in size (less than 1% of the hydraulic diameter of the microchannel) than the distance over which spatial velocity gradients are to be measured. Another important consideration is the optical signal produced by the particles. The particles should be large enough to be visible above background noise without producing unnecessarily large images which may limit the spatial resolution of the measurements. Inertial particle effects are typically not important in μ-PIV (500-nm diameter polystyrene spheres have a response time of 10^{-8} s).

Since the probe area in μ-PIV is volume illuminated rather than sheet illuminated, it limits the number density of particles that can be traced to characterize the flow. If the particle density is too low, then cross-correlation techniques fail to provide an adequate signal, making the measurements noisy and inaccurate. On the other hand, if the particle density is too high, then out-of-focus particles can reduce the visibility of in-focus particles making the signal noisy. One of the possibilities to overcome this limitation is by averaging the correlation function over a large number of PIV recording pairs. This concept of averaging correlation functions can also be applied to other evaluation algorithms such as Minimum Quadratic Difference method. Wereley and Meinhart [19] developed a second-order accurate PIV technique based on adaptive central difference interrogation (CDI) algorithm. The adaptive CDI algorithm provides better accuracy compared to traditional adaptive forward difference interrogation (FDI) algorithms, especially at large time delays between camera exposures. The technique was used to study pressure driven flow around a red blood cell. An excellent review by Wereley et al. [8] highlights the various advanced algorithms developed to obtain maximum spatial resolution with the μ-PIV technique.

Fluorescence-Based Flow Visualization

The fluorescence process is a three-stage process involving excitation of a fluorophore from ground state S_0 to

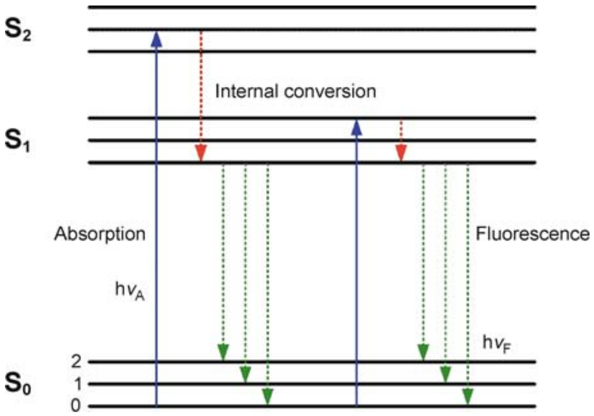

Microscale Flow Visualization, Figure 5 Jablonski diagram illustrating the principle of fluorescence excitation. The diagram shows the possible routes by which an excited molecule can return to its ground state via unstable triplet states

any one of the excited states S_1, S_2, or S_n (Fig. 5) by the absorption of a photon depending on the wavelength of the radiation. At each of these electronic energy levels the fluorophores can exist in a number of vibrational states denoted by 0, 1, 2 etc. The fluorophore stays in the excited state for a finite time, typically $1-10$ ns and then returns to its ground state by the emission of a photon of lower energy. Because of their short lifetime, the measurement of time-resolved emission requires sophisticated optics and electronics.

As mentioned earlier, most microscale flow visualization techniques have focused on determination of flow velocity in liquids (or velocimetry). Fluorescence based techniques, e. g. LIF and PF, have been extensively used for this application. However, in this section, we will look at another microfluidic application for which the development of microscale flow visualization techniques has been critical—micromixing.

In many miniaturized biological systems (e. g., LOCs) mixing is needed in microchannels for blending, emulsification and suspensions of two or more fluids, or mixing of reactants for process initiation. For example, biochemical sensing techniques such as immunoassays and hybridization analysis require rapid and homogeneous mixing of macromolecular solutions such as DNA or globular proteins. Many investigators have used reactions between acids and bases to observe mixing (via change in pH and thus color of the indicator such as phenolphthalein). Although this technique is rather simple and inexpensive, fluorescence offers an efficient and more accurate method that is not influenced by reaction kinetics and reaction types (endothermic or exothermic). Further, the size of the fluorophores is comparable with most protein molecules that are commonly used in biological analysis.

The experimental set-up to capture real-time images of the two-fluid mixing is similar to that used for μ-PIV (Fig. 4). It also consists of an inverted microscope, but a continuous light source, such as Hg arc lamp is used. The microscope filter cube, color filter assembly, is selected for the specific dye to be used as tracer. Fluorescein is the most common and inexpensive fluorescent dye with the absorption maxima of 490 nm and the emission maxima of 513 nm. For fluorescein, a FITC filter cube must be used. The standard FITC filter set from Chroma Technology consists of a 480 nm bandpass exciter filter, a 505 nm dichoric beam splitter, and a 535 nm bandpass emission filter. For another popular fluorophore, rhodomine 6G (absorption maxima of 530 nm and emission maxima of 566 nm), a TRITC filter cube must be used. The standard TRITC filter set from Chroma Technology consists of a 540 nm bandpass exciter filter, a 565 nm dichoric beam splitter, and a 605 nm bandpass emission filter. Higher quality filters improve fluorescence imaging since these filters offer wider excitation and emission with steeper passbands. Such filters provide more excitation and capture more fluorescence, resulting in greater signal to noise ratio, and allow for the cube assembly to be placed closer together for those dyes with a very short Stoke's shift.

To measure mixing characteristics, 1 μM dye solution is injected in one of the inlets of the microfluidic micromixer using a syringe pump while water is pumped into the other. The dye solution is prepared using deionized water. Higher concentration dye solutions can be used, but are not desirable due to CCD camera saturation and higher exposure times which reduce response time. To quantify mixing by visualizing fluorescence intensity, images of the channel with the two fluids are acquired using an automated image acquisition system at various positions along the channel. Typically, the images are captured with a ~ 1 μm resolution in z direction and $1-2$ μm resolution in the $x-y$ plane.

Following image capture, the images are analyzed to extract the intensity value at each pixel. The two most common commercial image processing software packages are Metamorph® (Universal Imaging) and Image Pro Plus (Media Cybernetics). Alternatively, a public domain Java image processing program ImageJ (developed by the National Institutes of Health, USA) can be used. From the captured images, grey-scale line scans indicating pixel intensity across the microchannel width are recorded. The intensity values must be normalized to 1 using the highest intensity value. The extent of mixing is determined based on the standard deviation of the pixel intensity distribution across the microchannel. To calculate standard deviation, the following equation is used:

M

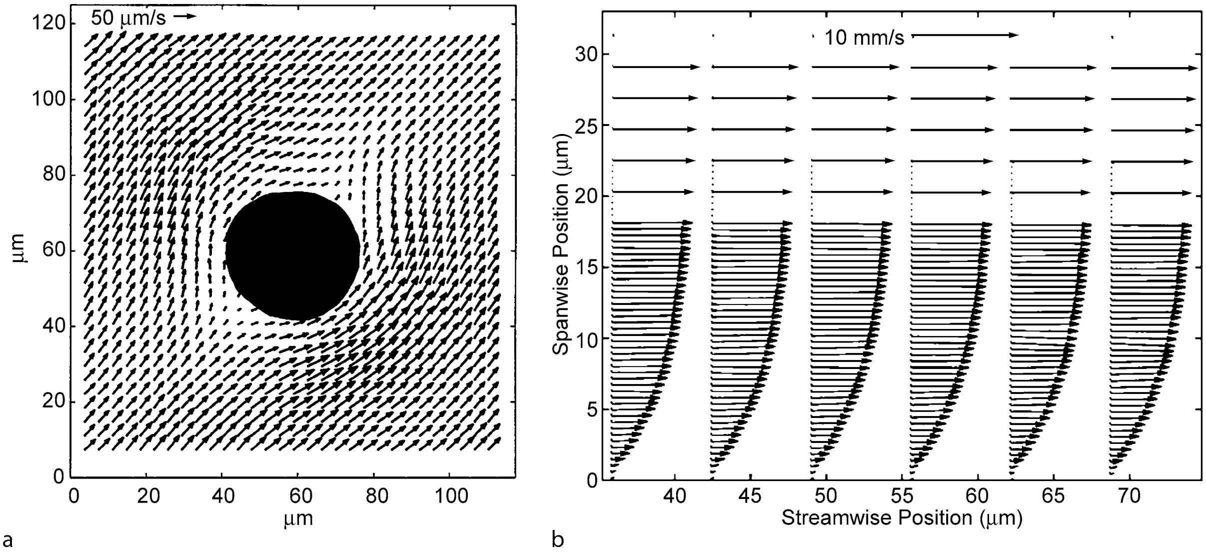

Microscale Flow Visualization, Figure 6 (**a**) μ-PIV velocity map of a Hele-Shaw flow [7]. The velocity vector field shown contains over 900 velocity vectors, with a spatial resolution of 6.9 × 6.9 × 1.5 μm for each vector measured using an eight image ensemble-average. (**b**) Ensemble-averaged near-wall velocity vector field measured using μPIV technique in a 30 μm (high) × 300 μm (wide) × 25 mm (long) channel by Meinhart et al. [17]. The spatial resolution is 13.6 μm × 4.4 μm away from the wall and 13.6 μm × 0.9 μm near the wall. A velocity vector spacing of 450 nm in the wall-normal direction is obtained due to a 50% overlap between interrogation spots

$$\sigma = \left[(I_{\text{low}} - I_{\text{ave}})^2\right]^{\frac{1}{2}} \tag{2}$$

where I_{low} is the lowest grey scale pixel intensity, I_{ave} is the average overall the pixels in the image and σ is the standard deviation [20]. Using this definition, standard deviation is 0.5 for completely separated flow streams at mixer entrance and 0 for perfect mixing.

Although a fully mixed channel should have a standard deviation of 0, in practice however even fully mixed channels exhibit some noise in the pixel intensity. Thus, the background noise for each image is based on the variation in fluorescence intensity for a fully mixed channel. Noise values of ~ 0.1 are typical. Thus a fully mixed channel can exhibit a standard deviation of ~ 0.1.

Standard deviation can be related to percent mixing efficiency E by the following equation:

$$E = (1 - 2\sigma) \times 100\% \tag{3}$$

Complete mixing of two flow streams is characterized by a mixing efficiency of 100%. Thus, $\sigma = 0.2$ implies 60% mixing.

Key Research Findings

The field of microscale flow visualization has been receiving wide attention in the recent years due to developments in microfluidics and LOCs. Most of the developed techniques are capable of high spatial and velocity resolution, with μ-PIV and fluorescence imaging being the most widely used.

Figure 6a illustrates a typical result obtained with the μ-PIV technique—an instantaneous velocity field of a Hele-Shaw cell [7]. The velocity field vectors were measured by averaging an eight image ensemble recorded using a CCD array exposed for 2 ms with a 68.5 ms time delay between successive images and 300 nm polystyrene particles. Spatial resolution was 6.9 μm × 6.9 μm × 1.5 μm. Figure 6b shows an ensemble-averaged near-wall velocity vector field measured using μ-PIV technique in a 30 μm (high) × 300 μm (wide) × 25 mm (long) channel [17]. Using a Nd:YAG pulsed laser to illuminate fluorescently tagged particles and camera capable of capturing images within a 500 ns time interval, high spatial resolution of 13.6 μm × 4.4 μm away from the wall and 13.6 μm × 0.9 μm near the wall was obtained. By overlapping the interrogation regions 50%, a velocity vector spacing of 450 nm in the wall-normal direction is obtained.

Recently Sinton et al. [21] developed a technique based on photobleached fluorescence microflow visualization. Their technique, called micro bubble lensing-induced photobleaching (μ-BLIP), takes advantage of the change in properties of a gas bubble – liquid interface creating an optical arrangement in which light incident on the bubble is focused into the surrounding liquid, resulting in locally

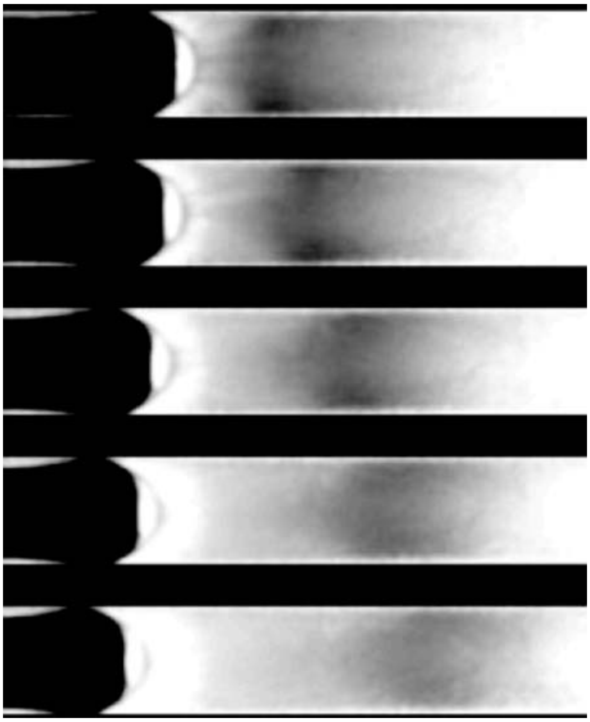

Microscale Flow Visualization, Figure 7 A μ-BLIP generated flow marker indicating electroosmotic transport inside a 100 μm fused silica capillary. The five image sequence is captured using a CCD camera running at 15 Hz with individual exposures times of 1/60 s [21]

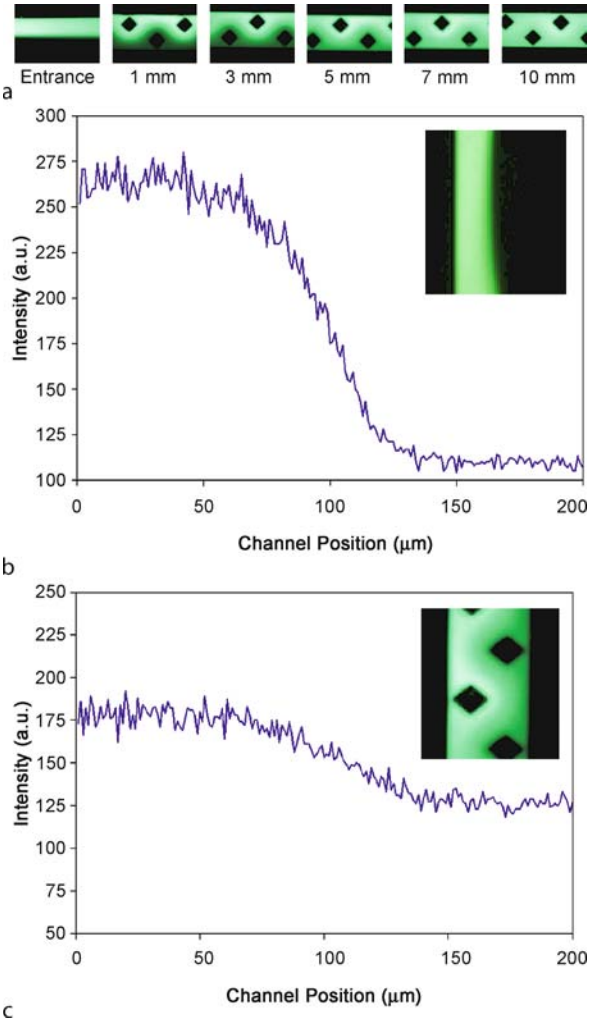

Microscale Flow Visualization, Figure 8 (**a**) Mixing visualization using 1 μM fluorescein solution in mixer with break-up obstructions at increasing distances downstream. Fluorescein solution is flowing in the upper portion of the images (pseudo colored green) and water in the lower portion. Pixel intensity line-scans across the microchannel cross-section at (**b**) the entrance and (**c**) 5 mm downstream [22]

increased total light exposure. The technique was used to analyze the electrokinetic transport of a photobleached marker by measuring the cross-channel velocity profile. A five image sequence showing the transport of a μ-BLIP generated flow marker is shown in Fig. 7.

Figure 8a illustrates typical fluorescent images of a micromixer, indicating the mixing behavior at increasing distance downstream at $Re = 0.1$. The obstruction micromixer is a planar passive microfluidic mixer with diamond-shaped obstructions within the mixing channel to break-up and recombine (i. e., laminate) the flow [22]. The images were captured using an inverted microscope (Nikon TE2000) equipped with a 12-bit CCD camera (CoolSNAP ES). Figures 8b and 8c show representative cross-sectional scans indicating the pixel intensities of the two fluids at entrance and 5 mm along the channel. At the channel entrance, since no mixing occurs, the fluorescent intensity curve is similar to a step function with half the channel filled with a 1 μM fluorescein solution (Sigma-Aldrich) and the other half with water. At 5 mm downstream, the fluorescence intensity curve tends to flatten out indicating mixing. Figure 9 shows mixing intensity of a typical T-mixer and an obstruction mixer calculated using Eq. (2). A T-mixer is a basic passive micromixer with two inputs opposite to each other and orthogonal to the straight mixing channel with no obstructions. In a T-mixer, two liquids flow next to each other and mix by diffusion across their interface. T-mixer is a commonly used benchmark when comparing micromixer performance.

Future Directions for Research

The discussed microscale flow visualization methods discussed here were divided into particle- and scalar-based approaches. However, as hybrid techniques are developed

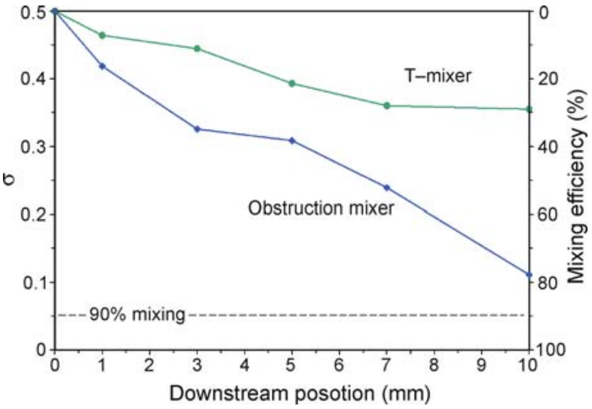

Microscale Flow Visualization, Figure 9 Mixing intensity of a typical T-mixer and an obstruction mixer calculated using Eq. (2) for increasing distance downstream

and marker sizes begin approach single molecule dimensions (e. g., quantum dots), these distinctions will become progressively blurred and no longer meaningful. Although the developed techniques help us understand the nature of flows on the microscale, they cannot be readily applied to nanoscale. Resolving nanoscale features with visible light presents a fundamental challenge. Integrating optical detectors on-chip, such as a high-speed high-resolution CCD array, may minimize coupling losses and maximize signal intensity permitting to resolve nanoscale flow features. Current monitoring techniques could be used to characterize bulk velocity in nanochannels for electroosmotic flows. Reducing wavelength of tracer emission (e. g., deep UV or radioactive traces) may also offer a way to image flows on the nanoscale.

Cross References

- ► Micro-PIV-Based Diffusometry
- ► Fluorescent Labeling
- ► Interface Capturing Schemes for Free-Surface Flows
- ► Microfluidic Mixing
- ► Micro Laser Doppler Velocimetry (μ-LDV)

References

1. Nguyen NT, Wereley ST (2002) Fundamentals and Applications of Microfluidics. Artech House, Norwood
2. Sinton D (2004) Microscale flow visualization. Microfluid Nanofluid 1:2–21
3. Smits AJ, Lim TT (2000) Flow Visualization: Techniques and Examples. Imperial College Press, London
4. Tieu AK, Mackenzie MR, Li EB (1995) Measurements in microscopic flow with a solid-state LDA. Exp Fluids 19:293–294
5. Chen Z, Milner TE, Dave D, Nelson JS (1997) Optical doppler tomographic imaging of fluid flow velocity in highly scattering media. Opt Lett 22:64–66
6. Raffel M, Willert C, Kompenhans J (1998) Particle Image Velocimetry: A Practical Guide, 3rd edn. Springer, New York
7. Santiago JG, Wereley ST, Meinhart CD, Beebe DJ, Adrian RJ (1998) A particle image velocimetry system for microfluidics. Exp Fluids 25:316–319
8. Wereley ST, Gui L, Meinhart CD (2002) Advanced algorithms for microscale particle image velocimetry. AIAA J 40:1047–1055
9. Born M, Wolf E (1997) Principles of Optics. Pergamon, Oxford
10. Dahm WJA, Su LK, Southerland KB (1992) A scalar imaging velocimetry technique for fully resolved four-dimensional vector velocity field measurements in turbulent flows. Phys Fluids 4:2191–2206
11. Tokumaru PT, Dimotakis PE (1995) Image correlation velocimetry. Exp Fluids 19:1–15
12. Lempert WR, Magee K, Ronney P, Gee KR, Haugland RP (1995) Flow tagging velocimetry in incompressible flow using photoactivated nonintrusive tracking of molecular motion (PHANTOMM). Exp Fluids 18:249–257
13. Paul PH, Garguilo MG, Rakestraw DJ (1998) Imaging of pressure and electrokinetically driven flows through open capillaries. Anal Chem 70:2459–2467
14. Mosier BP, Molho JI, Santiago JG (2002) Photobleached-fluorescence imaging of microflows. Exp Fluids 33:545–554
15. StClaire JC, Hayes MA (2000) Heat index flow monitoring in capillaries with interferometric backscatter detection. Anal Chem 72:4726–4730
16. Markov DA, Bornhop DJ (2001) Nanoliter-scale non-invasive flow-rate quantification using micro-interferometric back-scatter and phase detection. Fresenius J Anal Chem 371:234–237
17. Meinhart CD, Wereley ST, Santiago JG (1999) PIV measurements of a microchannel flow. Exp Fluids 27:414–419
18. Devasenathipathy S, Santiago JG, Wereley ST, Meinhart CD, Takehara K (2003) Particle imaging techniques for microfabricated fluidic systems. Exp Fluids 34:504–514
19. Wereley ST, Meinhart CD (2001) Second-order accurate particle image velocimetry. Exp Fluids 31:258–268
20. Stroock AD, Dertinger SKW, Adjari A, Mezic I, Stone HA, Whitesides GM (2002) Chaotic mixer for microchannels. Science 295:647–651
21. Sinton D, Erickson D, Li D (2003) Micro-bubble lensing induced photobleaching (μ-BLIP) with application to microflow visualization. Exp Fluids 35:178–187
22. Bhagat AAS, Peterson ETK, Papautsky I (2007) A passive planar micromixer with obstructions for mixing at low Reynolds numbers. J Micromech Microeng 17:1017–1024

Microscale Needles

► Microneedles – Applications & Devices

Microscopic Lenses

Definition

Microscopic lenses are used to enlarge objects. They can be purchased as complete lens systems in microscopic objectives.

Microsegmented Flow

Michael Köhler
Institut für Physik, Technische Universität Ilmenau, Ilmenau, Germany
michael.koehler@tu-ilmenau.de

Synonyms

Taylor flow; Microslug flow; Droplet flow

Definition

Microsegmented flow is the formation of a series of small moving liquid volumes of one phase embedded in a linear order in a liquid forming a second phase due to the immiscibility with the first one. Segmented flow is applied in microtubes, capillaries and microchannels for the definition of small process volumes to be operated serially or in parallel.

Overview

Microsegmented flow describes the phenomenon of the formation of fragments of a liquid column inside a microchannel or capillary, if the liquid is injected into an immiscible liquid. The formed sections of the liquid are called slugs or segments. For many applications – namely in synthetic chemistry – the slug formation itself is of interest, for example in order to realize local mixing and plug-flow transport characteristics. Beside these aspects, the formed segments of a liquid embedded in a linear order in a second immiscible inert liquid can also be applied for the definition of separate reaction volumes. In this case, the segments can be addressed and, therefore, generated and manipulated individually. Microslugs, which are addressable inside a sequence of slugs, are understood as microfluid segments in the narrow sense. Microsegmented flow is based on the principle of spontaneous separation of phases between immiscible liquids. This effect is well known from the separation of oil and water. Such combinations of liquids form separated droplets or segments in capillaries and microchannels. This formation of certain small volumes of one liquid separated from each other by segments of the second liquid occurs spontaneously and with high reproducibility. The specific of liquid separation in microfluidics consists in the phenomenon that the diameter of formed segments or droplets corresponds to the diameters of the applied channel. This effect results in each process of segment or droplet generation in a linear order of small liquid volumes.

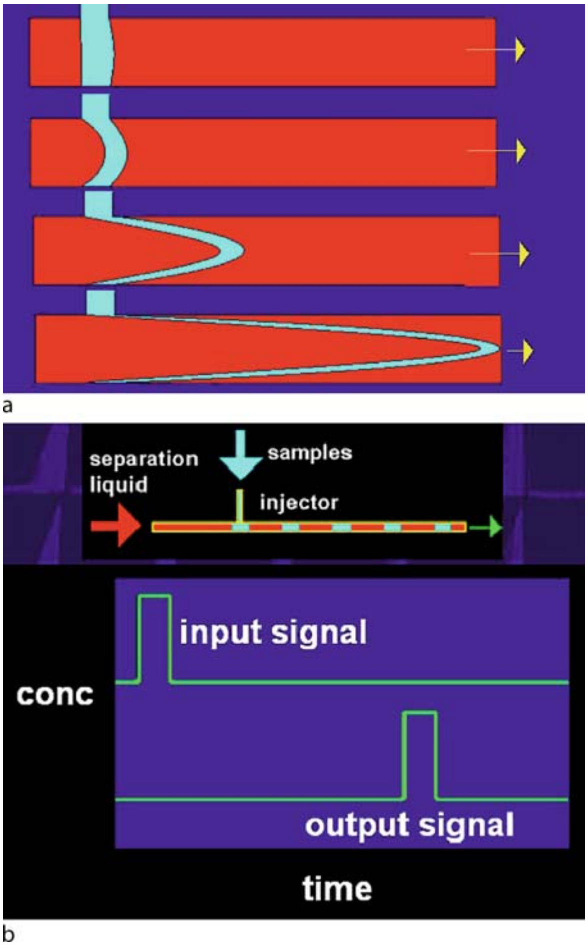

Microsegmented Flow, Figure 1 Flow behaviour in homogenous and heterogeneous liquid systems: (**a**) fluidic dispersion of a concentration pulse after injection into a homogeneous laminar flow in a microchannel (schematic); (**b**) plug-like transport of a concentration pulse in the case of a segmented flow

The formation of segments is accompanied by several crucial advantages for microfluidics. The first is that microfluid segments result from a regular subdivision of larger volumes into small partial volumes. This represents the simplest way for technical compartmentation. The second is the addressability. The microfluid segments in a capillary or microchannel are in a linear order and each segment can be identified by its number in this order. The third is the stability. Microfluid segments possess a size-dependent stability against pressure and shear forces. Thus, they can be transported and manipulated in different ways. The fourth is the suppression of fluidic dispersion in case of slug flow behaviour during transport of segments in capillaries (Fig. 1).
The microfluid segments are always handled in capillaries and microchannels. In consequence, they are sepa-

rated from the environment. Problems caused by contact to air like undesired evaporation of solvent and complete drying out are avoided. Undesired influences of humidity and oxygen from air on oxidation-sensitive compounds of anaerobic cells can be excluded or strongly suppressed. Also, undesired effects of contact between the components of handled samples and the wall surfaces can be significantly reduced or suppressed by the separation of samples inside segments from the walls due to the carrier liquid.

The completely new quality of microfluid segments in comparison with microtiterplates (MTPs) and nanotiterplates (NTPs) is marked by their operability in fluidic systems and networks. Microfluid segments are the best adapted form of sample handling in microflow-through systems. And in contrast to NTPs, the stability of segments increases with decreasing sample volume. So, it is to expect that microfluid segments will be particularly important for future applications with sample handling in the lower nanolitre and in the picolitre range. Probably, microfluid segments will be a very promising technique for future picolitre and femtolitre fluidics.

Basic Methodology

In mixtures of miscible liquids, the free energy of mixing results from an overcompensation of a decrease of interaction energy between the molecules of both liquids by the mixing entropy. Such an overcompensation of interaction energy reduction by entropy gain does not take place if the interaction between molecules of two different species is much lower than the interaction energy of molecules of the single types. This is exactly the case if protic liquids with high dipole moments and a strong tendency of forming of hydrogen bridges come together with molecules interacting exclusively by van der Waals forces (lipophilic interactions). The miscibility increases in general with increasing temperature because the entropic energy gain increases with increasing temperature.

$$\mathrm{d}G(\mathrm{mix}) = \mathrm{d}H(\mathrm{mix}) - T\mathrm{d}S(\mathrm{mix}) \tag{1}$$

The stability of fluid segments is due to the interface tension in the system. Each increase of interface area leads to an increase of energy inside the system.

$$E(\mathrm{interface}) = A(\mathrm{interface}) \times \sigma(l1,\ l2) \tag{2}$$

Microfluid segments always have a tendency to minimize their surface to volume ratio. The effect can be defined by a density of interface energy $D(\mathrm{interface})$:

$$D(\mathrm{interface}) = \frac{E(\mathrm{surface})}{V(\mathrm{segment})} = \frac{\sigma(l1,\ l2)}{d} \tag{3}$$

where $d = V(\mathrm{segment})/A(\mathrm{surface})$. The ratio d of segment volume to liquid interface (segment surface) is a shape-dependent characteristic length parameter of the fluid segment.

The tendency of minimization of the interface energy corresponds to the maximization of the curvature of segment surface. As a result, the behaviour of microfluid segments can be controlled by tuning their geometry and applying appropriate shear forces on them.

Laminar homogenous flow causes a large fluidic dispersion of concentration signals in microchannels. In contrast, microfluid segments show a nearly ideal slug-flow behaviour.

If the volume of the segments embedded in a carrier liquid is small enough in comparison with the diameter of the fluid channel, the best relaxed shape is a sphere. Deviations in shape of segments from a sphere indicate larger volumes, wall contact or deformations by shear forces. The deformation of a segment during the transport from a channel of larger diameter to a smaller one or the passage of any kind of fluid resistance or barrier is always connected with an increase in interface energy. An enhancement of interface energy is a precondition for the initiation of interface-changing processes like splitting of segments.

The fluidic dispersion can be completely suppressed if the wetting tendency against the wall surfaces is reduced. Such a reduction of wetting can easily be achieved by using appropriate wall materials or by surface modification. So, the covering of silicon or glass surfaces by alkylsilane residues (silanization) leads to a large increase of contact angle of aqueous phases and can suppress wetting and cross-talk between fluidic segments completely, if the aqueous fluid segments are embedded in a non-polar organic phase.

Microfluid segments can be generated simply by merging two streams of two immiscible liquids. In this case, a resulting liquid column containing alternating segments of both liquids is formed automatically. Segments can be produced with high frequencies. They can be fused, split and shifted in their position. Different concentrations inside segments can be realized by double- or multi-injector arrangements, by fusion of two or more segments or by coupling micromixing with segment generation. The motion of segments can induce very efficient mixing inside the segments. Sequences of segments can be merged in order to generate complex microsegment patterns.

The shape and transport behaviour of segments are strongly dependent on the wetting behaviour of the segment liquid on the walls. Wall segment-induced internal convection takes place at high wetting tendency (low contact angles). The wetting of the walls always causes an induction of segment-internal fluid motion. Vortices are

formed. A back streaming occurs in the centre of the segment. The segment can be completely separated from the wall if no wetting takes place (contact angle 180°). In this case, interactions between components inside the segment and the wall surface can suppressed completely. The existence of segment-internal convection depends on the shear forces and on the viscosity ratio of the segment liquid and the embedding liquid outside the segment.

Cross-talk between fluid segments of the same phase can take place if the contact area of the separating phase with the wall does not form a closed ring. This is always the case for the embedding phase (carrier phase) if the embedded phase is without wall contact.

Key Research Findings

The Size of Segments

The size of segments is mainly determined by the geometry of the channel in the segment-forming region and the applied shear forces. At low shear forces, the liquid injected through a T-injector or through a nozzle into the carrier liquid tends to fill the complete diameter of the main channel. A regular formation of microsegments of a volume corresponding to a sphere with the diameter of the main channel is observed (Fig. 2). The volume of generated segments can be significantly larger than the volume of a sphere with the diameter of the channel in the case of large nozzle diameters and low viscosity of carrier liquid. The segments become the shape of a slug.

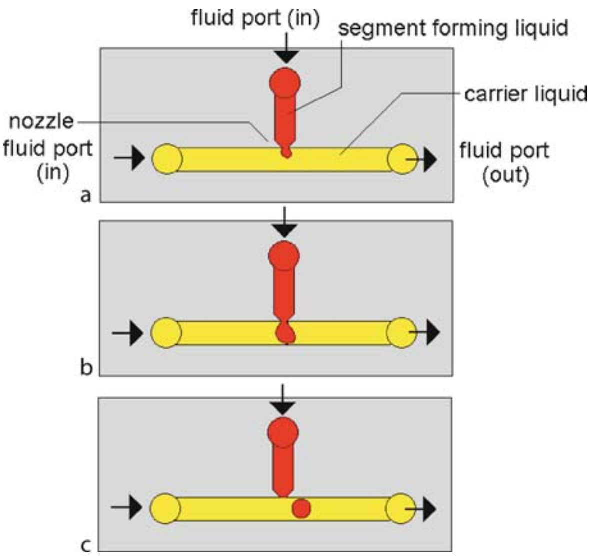

Microsegmented Flow, Figure 2 Formation of a fluid segment during injection at a T-junction with aperture

The volume of the formed droplets injected into a carrier liquid can be lower than the volume of a sphere with a diameter of the main channel, if high shear forces (high flow rate of carrier liquid) and a small diameter of the nozzle are applied. Small droplets relaxing into a nearly ideal spherical shape are delivered in this case. They can be small and move through the channel like solid particles. The size of these particles increases with increasing diameter of the nozzle aperture and decreasing flow rate of the carrier liquid.

Beside the flow rate of the carrier liquid, the viscosity of the carrier also affects the size of segments. In general, an increase in viscosity results in a decreased size of generated segments. The size of generated segments can be well reproduced if the segments are released from the wall of the main channel. However, the behaviour of segment-forming liquids can become very complex and unpredictable, if local or partial wetting takes place.

Formation of Series of Segments

A regular formation of fluid segments takes place if the segment-forming liquid is non-wetting and is brought together with the wetting carrier liquid with constant volume flow rates. Such a regular segmentation is marked by a constant size of segments as well as a by a constant frequency. Fluctuations in segment size and distance observed in real experiments can be smaller than 1% and are mainly due to shifting or fluctuating flow rates, small pressure fluctuations or particles passing the injector.

Characterization of Segments

Size and distance of segments can be characterized by the relative distance of alternating phase boundaries (liquid–liquid interfaces). These positions can be determined by photographic imaging. Electrical or optical methods can much easier be applied for automated recording of the quality of segment sequences. The measurements can use the differences in physical properties of segment liquid and carrier liquid.

In case of coloured liquids, photometry represents a very simple method for the determination of the alternating liquids. Microphotometric arrangements easily allow measurement frequencies up to 5 kHz. This means that the size of segments passing the detector with a frequency of 25 Hz can be measured with an accuracy of about 1%.

Carrier liquid and segment liquid consist normally of substances or mixtures with very different electrical properties. For example, the dielectric constants of an oil or a perfluorinated alkane (typical carrier liquids for aqueous segments) are much smaller than those of water. Electrical measurements can use differences in specific resistances

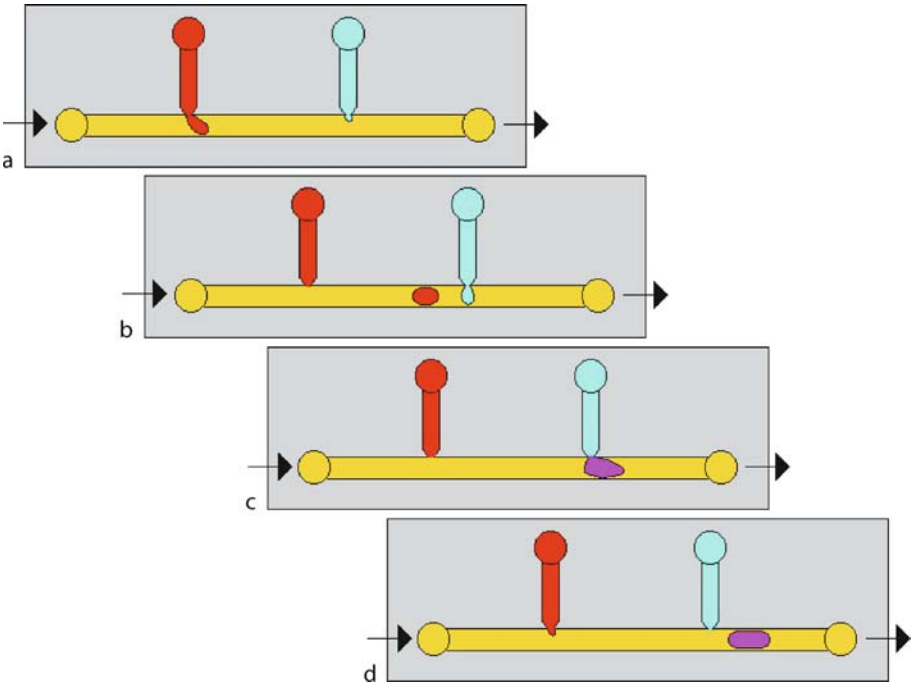

Microsegmented Flow, Figure 3 Mixing of two miscible liquids inside a segment formed and transported in a carrier stream of a third immiscible liquid

of direct or alternating current. In principle, changes in electrochemical properties like media-dependent electrode potentials or Faraday currents can also be used for the detection of the interfaces.

For practical purposes, the characterization of the components of segments is of interest beside the size and distance between segments. Optical methods are preferred due to their easy applicability. Other sensoric functions like electrochemical methods can only be used if there is a contact between segment and wall. This contact is often suppressed by a film of carrier liquid between the segment and the wall.

Dosing to Preformed Segments

The addressability of segments can be used for the formation of segment sequence pattern. Pattern can be expressed by changing size, distance or compositions. Alternating size or alternating colour represent, for example, two simple forms of patterns.

Changes in composition can be achieved either by changing concentrations in the injected liquid or by changing the concentration of a component inside a segment by injecting additional solution of another composition to a preformed segment. This dosing is preferably realized by using a second injector with an injection nozzle.

Double-injector devices are well suited for the generation of patterned segment sequences. They are particularly suited for making segment series with stepwise varied volumes and concentration ratios. Dosing can also be used for the unification of two different educt solutions in order to start chemical reactions inside segments (Fig. 3).

Segment sequences with larger stepwise varied concentrations or concentration ratios can easily be realized by including mixer structures in the inlet channels before the segment generating injector. Changing the composition, but with constant size of segments formed, is achieved if the two inlets of the injector are conducting fluid streams of different concentration and complementary changed flow rates.

Mixing by Induction of Segment-Internal Convection

The mixing of the original segment liquid with an added liquid is a precondition for the initiation of chemical reactions inside segments and for other operations with segments with homogenous distributed substances. In the case of particle-like transport behaviour of spherical segments, the mixing inside segments is only driven by diffusion if no external forces are inducing segment-internal convection. This process can be slow, in particular in the case of dissolved macromolecules, nanoparticles and cells. Such a convection can be caused by fields generated outside

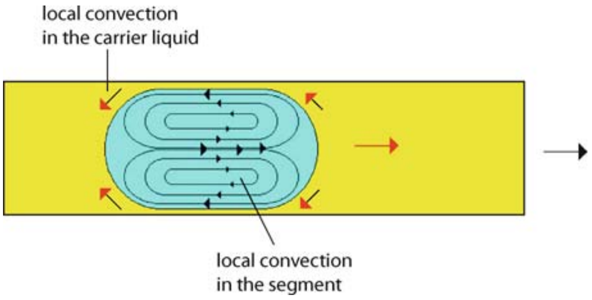

Microsegmented Flow, Figure 4 Internal convection inside a moving fluid segment

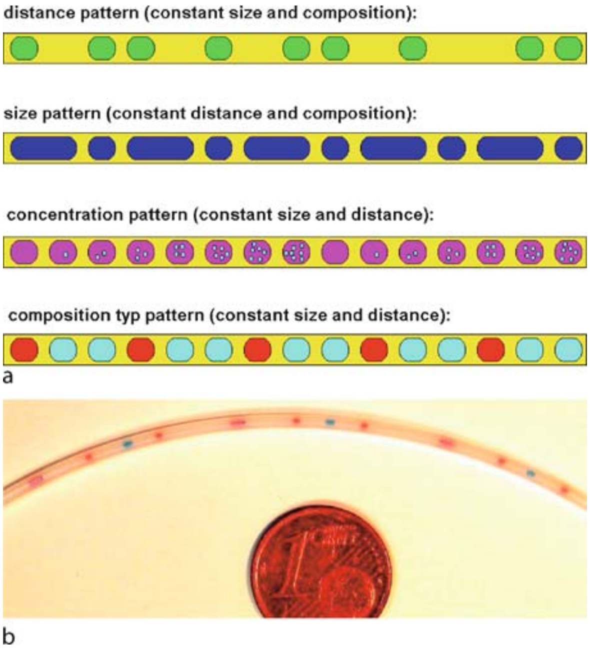

Microsegmented Flow, Figure 5 Pattern formation in microfluid segment sequences: (**a**) pattern types (schematic); (**b**) periodic pattern of segments with different size and composition after merging of two simple segment sequences with different period and composition

the segmented fluids, for example by magnetic fields or mechanic oscillations like surface acoustic waves (SAWs), if the liquid is sensitive to these forces (magnetic properties, local density differences).

A simple induction method for internal convection is the transfer of shear stress from the embedding carrier liquid into the embedded liquid of the segments (Fig. 4). This is always the case if the viscosity of the liquid inside the segments is not much greater than the viscosity of the carrier liquid. A particularly intense segment-internal convection is induced if segments pass curved channels or capillaries. Series of loops lead regularly to good internal mixing after dosing to segments. Loop or meander structures are often used as mixer elements for segment-internal mixing in microfluidic devices for segment operations.

Segment Merging (Fusion) and Segment Sequence Patterns

The generation of composition and size patterns in fluid segment sequences can also be realized by fusion of segments of different original composition. In the absence of surfactants, the contact of two segments of the same solvent leads to an immediate coalescence. Molecular layers formed by surfactant molecules at the fluid interfaces can suppress or delay the coalescence and, therefore, segment fusion.

The fusion of segments can be initiated by the joining of two or more segment streams, for example in a Y- or T-element. The regularity of fusion is often disturbed by fluctuations in segment distances in the original sequences. Then, devices with hydrodynamic self-controlling of segment transport can support a synchronization of segment pairs arriving from both input streams at the junction structure.

Segment fusion can also be realized in inline structures, if one segment stops at a fluid resistance or in a stopping chamber, so that it is united with a following segment. The larger segment so formed can move on in the case of appropriate stopping structures. A regular pairwise fusion in a linear chain of segments demands good adaptation of flow rate, viscosity and stopping structure. A regular mixing of segments from two original segment streams can be achieved in an alternative to the one-step fusion at a T- or V-junction by a two-step process consisting of segment stacking by a branched structure (T- or V-shaped) and a subsequent linear fusion structure.

Fusion and splitting of segments can result in complex, but regular patterns. In principle different types of sequence pattern can be realized (Fig. 5a):

- distance patterns;
- size patterns;
- concentration patterns;
- segment type patterns; and
- mixed variants of these types.

An example of a nearly periodic, but complex pattern with segments varying in distance, size and composition is shown in Fig. 5b.

Surfactants affect the transport behaviour and the fusion behaviour of fluid segments. The contact between microfluid segments leads regularly to an immediate coalescence. This coalescence can be delayed or completely suppressed if surfactants are involved (Fig. 6). Segments can be pressed against each other in a T-junction without coalescence, for example (Fig. 6a). In some cases, a strong deformation occurs without coalescence or destruction of

M

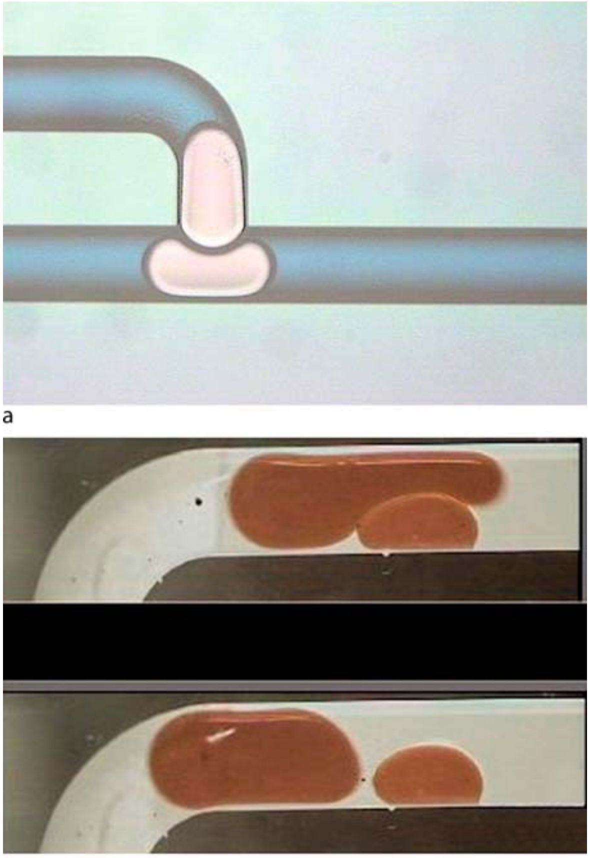

a

b

Microsegmented Flow, Figure 6 Influence of surfactants on segment transport behaviour: (**a**) deformation of a segment under contact with another segment without fusion; (**b**) separation, contact without coalescence and deformation of two fluid compartments of the same phase type (dark) in the surrounding of an immiscible carrier liquid (bright) in the presence of surfactants

segments, as is observed in an example where one fluid segment is adsorbed at the wall, whereas a second segment passes under strong deformation (Fig. 6b). It is assumed that in these cases the presence of surfactants leads to membrane-like molecular double layers in the contact region of segments.

Applications

Microfluid segments are applied both in microchemistry and in biotechnology. They are used, for example, in chemical synthesis in liquid phase, for the preparation of nanoparticles, for analytical chemistry, for cell cultivation and screening and for DNA amplification by polymerase chain reaction. Cell technology, molecular biotechnology, medical and environmental diagnostics as well as the development of new materials and active agents demand new methods for the characterization and optimization of substances and microscopic biological objects like cells, cell organelles, viruses and biomacromolecules. This demand can be regarded as a need for read-out and optimization of information incorporated in molecules, solids and biosystems. Laboratory techniques and equipment get more and more the character of an information interface between chemical and biological objects on the one side and measurement devices and computers on the other. No large amounts of substances are needed for this information exchange and optimization. The applied number of biological or chemical objects involved in the information exchange processes can be reduced to the minimal value which is necessary for initiation of processes, detection of interactions or read-out of data. In contrast, instead of single samples, large sets of samples must be operated in order to maximize the information throughput. Therefore, several miniaturization and parallelization strategies have been developed during the last few decades.

Series of microfluid segments represent an important alternative to the microchamber arrays like MTP and NTP technology. MTPs and NTPs were introduced for highly parallelized handling of liquid samples. However, there are several disadvantages in the application of such microchamber arrays. First, the filling of the chambers demands a liquid dispensing or pipetting system. So, the generation of larger sample sets is always connected with a complex mechanical system and more or less sophisticated handling. Second, the application, processing and characterization of liquids inside the microchambers of MTPs and NTPs become increasing difficult and less reproducible in the case of decreasing liquid volumes. Third, the further manipulation after application of liquids into the chambers is difficult. MTPs and NTPs do not support complex operations with liquids. So, automation of processes with several process steps is connected with much effort in roboting and micropipetting or completely impossible. All these problems can be overcome by the application of microfluid segments. The constant volume and composition and the comparatively high stability of a certain segment make these fluid elements well suited for massive serial or highly parallel processing.

Future Directions of Research

Recent research is focussed on understanding the transport behaviour and the phenomena of induced convection inside the segments and in the carrier liquid. The understanding of different influences on the convection pattern is important for mixing control, minimization of mixing time inside segments and understanding the role of material and process parameters like viscosity and flow rate on

internal mixing. Particular attention is paid for the incorporation of particles and cells, which can influence the internal convection on one side, but can be damaged or destroyed by shear stress due to the internal convection.

Particular importance attaches to the wetting behaviour of the segments. This is responsible for the transport behaviour and influences strongly the deformation behaviour in the case of geometry change as well as fusion and splitting processes. Therefore, the control of changes in interface tensions is very important. Considerable changes can be induced by addition of surfactants or other amphiphilic chemicals, chemical reaction and also by biological activity.

There is much research concerned with different applications of the segmented flow principle. It reaches from chemical synthesis to analytical procedures in inorganic and organic chemistry and molecular biology to miniaturized screenings with bacteria, eucaryotic cells and multicellular organisms. The investigations deal with the formation and transport behaviour of the fluid segments under the particular application conditions, with the behaviour of treated objects like cells, particles and biomolecules inside the segments and with the improvement of different conventional methods by transferring them into microfluid segments. Therefore, improvements of yield and selectivity in chemical reactions, efficiency and reproducibility in analytical procedures and the efficiency of highly parallelized screenings are under investigation.

The development of (1) new handling tools for fluidic segments, (2) the improvement of the characterization of segment contents, (3) the control of segment operations in complex networks, (4) the use of microfluid segments as models for biological compartmentation and (5) the ultraminiaturization of the segmented flow principle will be the main challenges for further research besides the recent basic investigations on segment formation, microfluidic behaviour and applications.

It is comparatively easy to generate and process larger series of fluid segments. However, there is an urgent need for segment-on-demand techniques in order to realize well-controlled automated processes for the generation of segment patterns and for dosing and fusion processes with different treatment of single segments. The individually addressed stopping, switching and other manipulation of well-selected single segments from larger segment sequences are a second demand on the development of new microfluidic actuators. The development of microstructured actuators for addressing single segments must be accompanied by the development of appropriate miniaturized sensors. In principle, several sensor developments during the last few decades for other purposes can be applicable, but they are not adapted for microfluid segment control and operations and must be adapted and integrated in functional modules or microfluidic networks for microsegmented flow applications.

Sensors relevant to the above discussion are mainly necessary for identifying segments and measuring the position, size and speed of them. Additional information can be supplied by measuring pressure drops, pressure fluctuations, electrical conductivity, dielectric properties, temperature, thermal capacity and heat conductivity. In addition to this sensing, more detailed information from microfluid segments must be extracted in order to characterize the content and the change of content of segments during chemical and biological processes inside the segments. Therefore, different spectroscopic and other analytical techniques have to be adapted to microfluid segment systems. Optical techniques are favoured for this purpose, because they work without direct mechanical or chemical contact with the segment liquids. Unfortunately, spectrophotometry and fluorimetry in the UV and visible range of light supply only raw information about chemical and biological changes. More information could be gained by mid-infrared and Raman spectrometry. Possibly, turbidimetric measurements, light scattering, microscopic techniques and relaxation measurements using thermal pulses and laser-impulse techniques would probably be suited for gaining supplementary information about changes inside fluid segments.

It is expected that more interest will be focused on the segment behaviour in complex networks of segment elements if control of transport and manipulation of individual elements is improved. Particular processes including several steps of splitting and fusion will be of interest. However, the development of such complex systems, which could be applied for analytical or screening procedures, must be strictly founded on strong control of the previous history of the content of single segments (segment process reports) and is therefore dependent not only on the architecture of networks but also on the successes of the development of integrated sensors and actuators for segment addressing.

A particularly interesting field is the ultra-miniaturization of fluid segments. The further decrease of segment volumes into the picolitre and sub-picolitre range leads to segments which are much more robust than larger ones due to the high surface to volume ratios. Also, interface properties and interface changes will become increasingly important in such systems. It is expected that a lot of exciting new effects will be discovered during this ultraminiaturization process. Future developments will probably include the treatment of high numbers of robust spherical picolitre and femtolitre droplets dependent on changing physical and chemical parameters and gradients of them in embedding liquids. They will involve a drastic

enhancement of mobility of medium and higher viscosity liquids in very small channels by transporting them in the form of segments or droplets in embedding liquids of very low viscosity (for example by pressure-liquified inert gases), switching of segment properties and segment interactions by radiation-induced switching of molecular interface layers, "tunnelling" of liquid phases through other phases and many other effects. Of particular importance could be studying segment behaviour in small environments like nanocapillary slits and inside nanotubes. Besides simply structured fluidic segments, the embedding of micelles, vesicles, colloidal phases and nanoemulsions as well as the generation, handling and manipulation of complex hierarchically structured segments (nested phases) will be of particular importance for this research direction.

The application of different types of amphiphilic substances in connection with a variety of segment manipulations opens the possibility to construct microfluidic segments as models for spontaneously formed vesicles, biological cells, cell organelles, viruses and other particles and compartments. This gives the possibility of preparing cell-like microcompartments with selected groups of cellular functions and to make different functional models of living cells. In this way, addressable populations of "artificial cells" equipped with different sets of functions could be operated. Fluidic networks for the handling of these compartments will probably be particularly suited for studying cellular interactions and chemical communications, and also the interactions between the artificial cell-like compartments and cells. Processes like endocytosis and exocytosis, cell division and penetration through membranes could be statistically studied in populations of well-designed nanofluidic objects embedded in fluidic segments which allow all required manipulations. It is imaginable that the technique of segmented flow will not only be able to contribute to a lot of new cell-oriented techniques, but also could contribute to the understanding and future technical reproduction of the mystery of life.

Cross References

► Digital Microfluidics
► Droplet Based Lab-on-Chip Devices
► Lab-on-a-Chip (General Philosophy)
► Stationary Phases in Microchannels

References

1. Köhler JM, Dillner U, Mokansky A, Poser S, Schulz T (1998) Micro channel reactors for fast thermocycling. In: American Institute of Chemical Engineers (ed) Proc 2nd proces Miniaturization: 2nd International Conference on Microreaction Technology New Orleans. New Orleans, p 241
2. Thorsen T, Roberts RW, Arnold FH, Quake SR (2001)Dynamic pattern formation in a vesicle-generating microfluidic device. Phys Rev Lett 86:4263
3. Burns JR, Ramshaw C (2001) The intensification of rapid reactions in multiphase systems using slug flow in capillaries. Lab Chip 1:10
4. Hessel V, Löwe H (2002) Microtechnology: Components – plant concepts – user acceptance. Chem Ing Tech 74:17
5. Nisisako T, Torii T, Higuchi T (2002) Droplet formation in a microchannel network. Lab Chip 2:19
6. Song H, Tice JD, Ismagilov RF (2003) A microfluidic system for controlling reaction networks in time. Angew Chem 115:792
7. Martin K, Henkel T, Baier V, Grodrian A, Schön T, Roth M, Köhler JM, Metze J (2003) Lab Chip 3:202
8. Shestopalov I, Tice JD, Ismagilov RF (2004) Multi-step synthesis of nanoparticles performed on millisecond time scale in a microfluidic droplet-based system. Lab Chip 4:316
9. Köhler JM, Henkel T, Grodrian A, Kirner T, Roth M, Martin K, Metze J (2004) Digital reaction technology by micro segmented flow – components, concepts and applications. Chem Eng J 101:201

Micro-Shock Tube

► Shockwaves in Microchannels

Microslug Flow

► Microsegmented Flow

Micro Steam Turbines

► Microturbines

Microsterolithography

Clifford L. Henderson
Georgia Institute of Technology, School of Chemical and Biomolecular Engineering, Atlanta, GA, USA
cliff.henderson@chbe.gatech.edu

Synonyms

Stereolithography

Definition

► Stereolithography (SL) is a special type of additive fabrication process, in the general class of techniques known

as solid freeform fabrication (SFF), that is used to produce solid objects directly from computer design data. Solid freeform fabrication refers to techniques in which a solid object is manufactured by the sequential delivery of energy and/or material to specific points in space to produce that solid part. SFF is also sometimes referred to as solid freeform manufacturing (SFM), rapid prototyping (RP), rapid manufacturing (RM), additive fabrication (AF), or layered manufacturing (LM). In stereolithography, manufacturing of the desired part is accomplished by using a vat of liquid photocurable resin and a light source that can produce pattern-wise exposure in the vat to build up the solid polymer object via localized polymerization of the photocurable resin. ►Microsterolithography (MSL) simply refers to SL processes which possess feature resolutions that are significantly higher than the tens of micron accuracies that are typically possible with conventional SL tools.

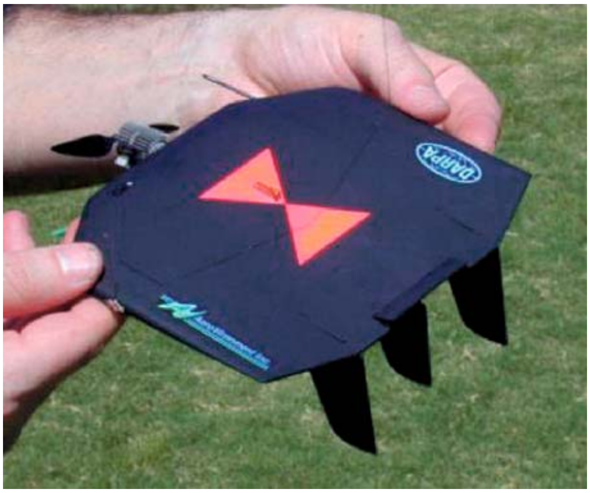

Microsterolithography, Figure 1 Schematic of a scanning-based stereolithography apparatus

Overview

►Stereolithography (SL) is one type of layer-by-layer manufacturing process, based on photopolymerization of a photocurable resin, that was first reported in 1981 by teams from the United States [1], Europe [2], and Japan [3]. It is a 3D manufacturing technique that can directly build a solid 3-dimensional part directly from a computer data file containing the information on the part size and shape in electronic format. Such electronic data can be generated either directly from computer aided design (CAD) software when an object is designed, or can be generated from existing solid objects through imaging techniques that can measure and record the shape and size of an object in a three dimensional data format such as magnetic resonance imaging (MRI).

The SL process begins with the generation of the 3D data file containing a model of the shape and size of the object that is to be built. This model of the object is then sliced into a series of closely spaced planes that represent two-dimensional (2D) cross-sections of the 3D object, each at a slightly different coordinate along one axis of the object. These 2D slices are then translated into numerical control codes and combined together to generate a data file that can control the stereolithography apparatus (SLA) that is used to build the part. Most commonly, this data file is used to control elevator position and laser beam scanning path in a scanning laser SLA tool. A simple schematic of how such a scanning laser SLA tool works is shown in Fig. 1. First, an elevator platform that will support the part that is being built is brought within some close distance to the surface in a vat of a photocurable resin. A laser is scanned over the surface of the vat and initiates polymerization where the resin is exposed to the light. Two main types of polymerization reactions are used in SL processes:

- radical induced chain propagation polymerizations (often of acrylic monomers) and
- ionic chain propagation polymerization (often with epoxy or urethane monomers).

Examples of the basic chemistry involved in such polymerizations is shown in Fig. 2. In conventional SLA tools, the laser beam diameter is typically on the order of 100 μ in size and the focused beam has a large depth of focus such that a relatively consistent beam diameter can be maintained as the beam is scanned across large areas of the vat. After the first layer of the object is polymerized, the elevator is lowered down by some small incremental distance into the vat, the liquid resin is allowed to flow over the top of the first layer, and the laser is scanned over the surface to initiate polymerization of the second layer of the part in this new resin layer. This process is repeated over-and-over for each layer of the part until the object is completed. Once the object has been made, the part is raised from the resin vat on the elevator, drained and washed of the unreacted photocurable resin, and subjected to various treatments to finish hardening the object. The first commercially available SLA system was produced by 3D Systems in 1987 and SL is now a widely used technique in industries such as automotive and aerospace. In these industries, SL was originally used to fabricate an array of objects from basic design verification parts to "show and tell" objects at low cost before significant more expense was invested to mass produce or make any actual application-ready mechani-

Radical Polymerization

$$PI + h\nu \rightarrow R\bullet$$

$$R\bullet + M \rightarrow RM_1\bullet \qquad \text{"Photoinitiation"}$$

$$RM_1\bullet + M \rightarrow RM_2\bullet$$

$$\ldots\ldots$$

$$RM_{n-1}\bullet + M \rightarrow RM_n\bullet \qquad \text{"Propagation"}$$

$$RM_n\bullet + RM_m\bullet \rightarrow RM_{m+n} \qquad \text{"Termination"}$$

Cationic Polymerization

$$PI + h\nu \rightarrow H^+X^-$$

$$H^+X^- + M \rightarrow HM_1{}^+X^- \qquad \text{"Photoinitiation"}$$

$$HM_1{}^+X^- + M \rightarrow HM_2{}^+X^-$$

$$\ldots\ldots$$

$$HM_{n-1}{}^+X^- + M \rightarrow HM_n{}^+X^- \qquad \text{"Propagation"}$$

$$HM_n{}^+X^- + M \rightarrow HM_nX \qquad \text{"Termination"}$$

Microsterolithography, Figure 2 Examples of the basic chemistry involved in the photopolymerization processes used in stereolithography

cal parts. Instead of waiting the days, weeks, or months that were common at the time for production of a complex mechanical part using milling or other machining and molding techniques, SL allowed for the direct production of such parts on the time scale of hours. For this reason, it was termed a *rapid prototyping* method. The first SL materials consisted of mixtures of monomers, oligomers, and photoinitiators that could be cured into high moleular weight polymers by exposure to ultraviolet light, and these compounds were used to make purely polymeric solid objects. However, to meet the demands of various applications, especially in terms of transitioning the method from a rapid prototyping technique to a true *rapid manufacturing* method, new photocurable resins that could be used to produce ceramic or metallic parts were developed [4]. Such new resin developments allowed the parts produced by SL to be directly used in applications such as rapid tooling.

Microstereolithography (MSL) is a more recent augmentation to conventional SL techniques that allows for parts with much higher spatial part resolution and surface finish to be produced. In MSL techniques, much more tightly focused light (i. e. exposure sources with a much smaller effective pixel size are used, generally with pixel or spot sizes on the order of 1 μ or better) is used to initiate polymerization and cure the part. There have been two basic types of MSL techniques reported:

- scanning-based MSL methods and
- projection-based MSL methods.

Additional details of these methods are provided in the next section.

Basic Methodology

As mentioned previously, microstereolithography systems can be divided into two general categories:

- scanning-based systems and
- projection-based systems.

Scanning-based MSL systems are basically modified versions of the classical SLA tools originally developed for SL. They generally involve scannning a very tightly focused laser beam over or within a vat of liquid photocurable resin to produce a solid 3D object. A schematic example of a possible configuration for an MSL tool that is analogous to the SLA apparatus described earlier is shown in Fig. 3. Such a tool and technique are also referred to as a vector-by-vector MSL apparatus or method. The main difference between the MSL tool in Fig. 2 and the original SLA tool shown earlier in Fig. 1 is that a dynamic lens is shown in the MSL tool to maintain a very tightly focused beam. The disadvantage in such an MSL tool is that the plane of best focus for such a tightly focused beam being moved by means of a series of rotating mirror is a spherical surface whereas the liquid monomer surface to be cured is planar in nature. This requires the use of such a dynamic focusing lens that can be used to adjust the focal length of the beam as the beam is scanned so as to maintain the desired small beam diameter on the resin vat surface as each layer of the object is drawn. Even though it is in principle possible, published reports show that this issue of dynamic focusing is critical to producing a high resolution process using such a tool and that it is in fact quite difficult to achieve the desired resolutions using such a configura-

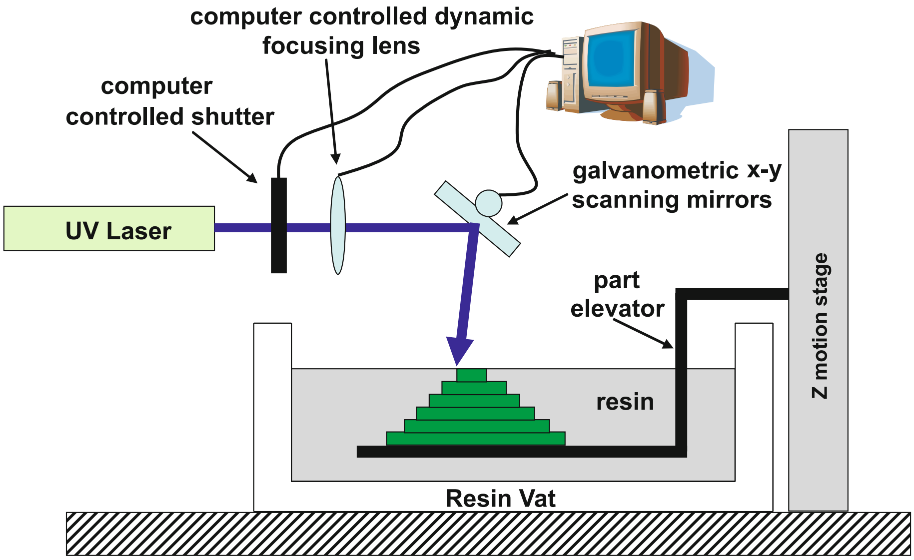

Microsterolithography, Figure 3 Schematic of a basic microstereolithography apparatus

tion. Due to these difficulties, a series of other types of scanning MSL tools have been reported in the literature as described in the following sections.

The Integrate Harden (IH) Polymer Stereolithography Process

The first reported MSL technique was in fact introduced by Professo Ikuta and coworkers in 1993 and was used for making microelectromechanical system (MEMS) parts [5]. In their Integrated Harden Polymer Stereolithography process (IH process), a tightly focused beam was scanned over a resin vat. In their case, a window was placed on the surface of the vat and exposure occurred through the window. The position of the window was translated in the *Z*-direction to change the location of the surface at which polymerization occured. Due to the focusing problem mentioned earlier and the fact that commercial galvanometric scanning mirrors did not possess the scanning resolutions needed, a different *X*-*Y* scanning and *Z*-scanning approach was used in the original IH method. The focal point of the apparatus remained fixed in space relative to the window by directly attaching the exposure source, lens, and optical window that defined the resin surface to a motorized *Z*-stage so as to achieve the tightest possible focus. To produce the object, the vat was translated in the *X*-*Y* plane and the window and focused spot was translated in the *Z*-direction to cause local polymerization and solidify the object being manufactured (see Fig. 4). The main disadvantage of this technique is that the scanning speeds possible when moving the entire resin vat are significantly lower than the scanning speed possible when simply moving the beam around using galvanometric mirrors. However, high aspect ratio, 3D parts were made using this type of method. Another disadvantage of this technique is that it is possible for the part being polymerized can stick to the optical window in such a constrained surface configuration, and thus free surface versions of this type of system have also been produced and used, whereby the resin vat is translated in all three directions (*X*-*Y*-*Z*) while the exposure source and focal spot remain fixed in space. Feature resolutions on the order of 1 μ have been demonstrated using such systems.

The Mass-IH Process

In order to address the speed issue with the original IH process, Prof. Ikuta developed and reported the so-called Mass-IH process in 1996 [6]. In this new version of the IH technique, the exposure source was tightly focused onto a fiber optic bundle, and each of the fiber ends was placed into a ordered array that was used to generate a series of exposure point sources in the resin vat that were scanned by again moving the entire object and resin vat (see Fig. 4). The advantage in the Mass-IH process is that it can be made reasonably parallel in nature using this multi-exposure source approach to offset the slow scanning speed of the resin vat. Both the IH and Mass-IH processes suffered from a number of problems though including:

- the depth of resolution of the object is determined by the thickness of the layer slices stacked together to build the object and

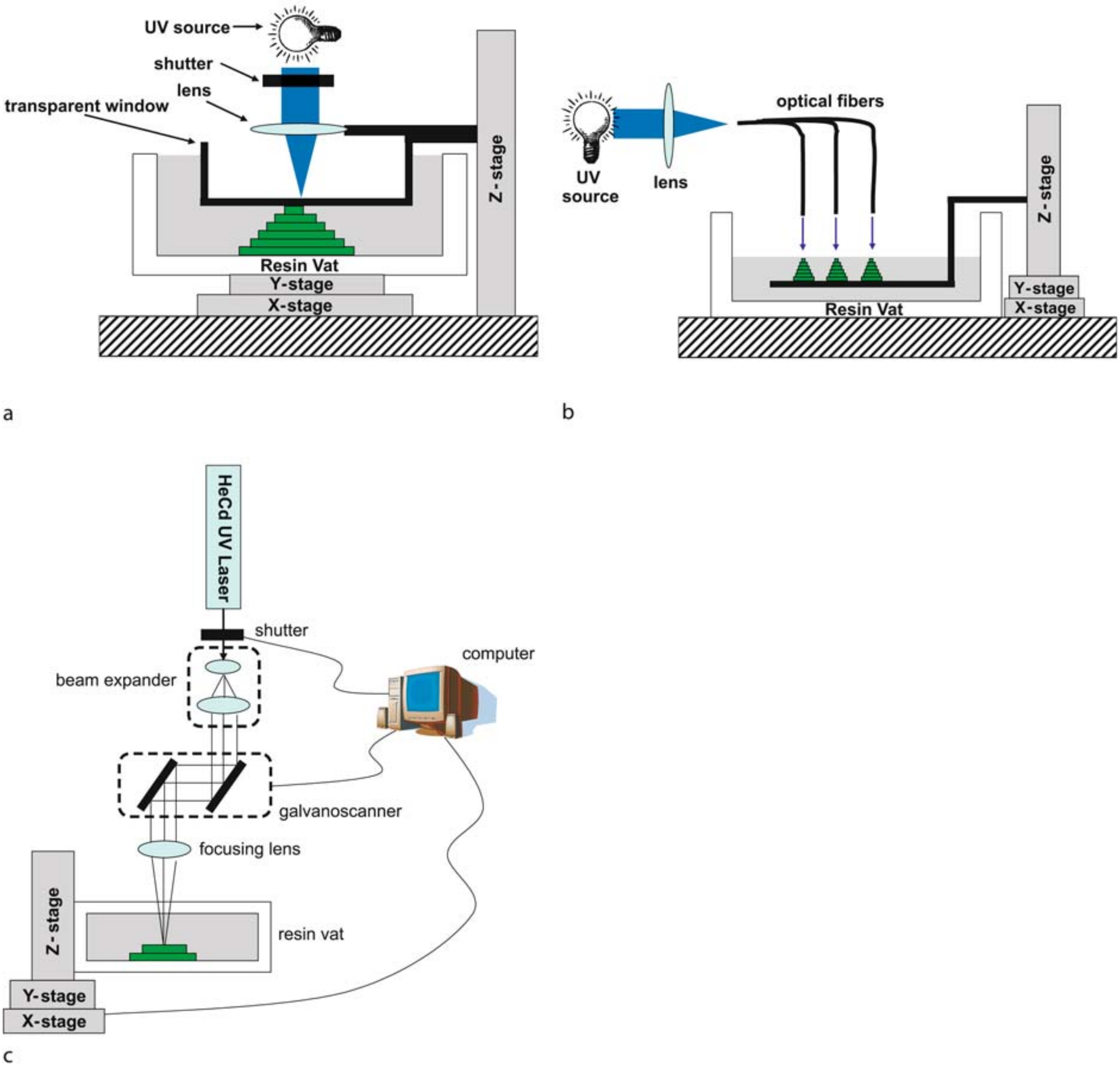

Microsterolithography, Figure 4 Schematic of the apparatus used for the (**a**) IH process, (**b**) Mass-IH process, and (**c**) Super-IH process developed by [3]

- surface tension effects and other phenomena can lead to deformation or destruction of small microscale parts during fabrication and processing.

The Super-IH Process

Due to the limitations of the IH and Mass-IH processes, Professor Ikuta and coworkers developed and reported the so-called Super-IH process in 1998 in which a broad beam is tightly focused into the volume of the resin vat and is used to cause local polymerization at the focal spot of the beam (see Fig. 4). A 3D object is produced by translating the focal spot of the beam inside the vat to draw out the desired shape. This movement away from surface polymerization in the resin vat in favor of polymerization in the volume can allow one to eliminate the need for support or sacrificial structures that are common in conventional SL processes that rely on surface polymerization. Furthermore, since the polymerization of material does not occur at a free resin surface in the super IH process, surface tension effects and other problematic phenomena associated with polymerization at the resin surface can be minimized or eliminated. However, there are a number of challenges associated with such a technique. First, the beam used for

exposure passes through the vat on its way to the focal point, and so regions of the resin vat in addition to the focal point of the beam received light energy while the material at the beam focus is being polymerized. Although the intensity of the beam is lower in these other regions than at the focal spot, avoiding extensive polymerization in these other regions can be challenging. By using carefully designed resins that exhibit a very non-linear response to exposure dose it was shown to be possible though to use such methods to produce very small, complex 3D parts with feature resolutions well below 1 micron.

Two-Photon Microstereolithography

As mentioned in the discussion of the Super IH technique, a challenge in doing microstereolithography via polymerization in the resin volume (i. e. as opposed to surface polymerization) with a tightly focused beam is that the material being polymerized needs to have a highly non-linear response to either total exposure dose or to local light intensity. Such a non-linear response allows one to achieve polymerization with high spatial resolution without spurious polymerization in regions of the vat that are unavoidably exposed by the unfocused beam as it propagates through the vat on its way to the focal point. So-called two-photon processes can provide such a highly non-linear response to local light intensity that can help confine polymerization to the beam focal region. As described earlier in Fig. 2, in conventional photopolymerization processes, one photon is absorbed the polymerization initiator and results in the production of a radical, acid, or base that initiates polymerization of the monomer/oligomer mixture. This means that the rate of initiation locally in the resin is proportional to the local light intensity (I). In two-photon polymerization, a so-called two-photon absorption process is used that requires two photons to be absorbed by the photoinitiator to produce an active initiator (i. e. a radical, acid, or base). There are two general types of two-photon excitation processes. The first type of two photon reaction process is termed *sequential excitation* or *resonant two-photon absorption*. In this case, the photoinitiator first absorbs a photon and an intermediate excited state of the molecule of the photoinitiator is created that typically has lifetimes in the range of 10^{-4} to 10^{-9} s. However, the excited state intermediate created is not capable of going on to further produce the active initiator radical, acid, or base without additional energy. A second photon must be absorbed by the excited intermediate within its lifetime to result in the desired photochemical reaction and initiate polymerization. Therefore, it should be clear that the rate of initiation of polymerization in such a two-photon process will be proportional the local light intensity squared (I^2), which provides the desired non-linear dependence on local light intensity that helps to confine polymerization to the tightly focused region of the beam in an MSL tool. The other type of two-photon absorption process is termed *simultaneous two-photon absorption* or *non-resonant two-photon excitation*. In this case, no excited intermediate is produced and instead both photons must be absorbed essentially simultaneously, i. e. within the interaction time of the photon with the photoinitiator which is on the order of 10^{-15} s. The requirement that two photons arrive at the photoinitiator in such short times scales requires very high intensity laser sources for either type of two-photon process. An example of a schematic of such a two-photon MSL tool is shown in Fig. 5. Such two-photon systems have produced the smallest MSL manufactured objects to date, with feature resolutions in the tens of nanometers having been demonstrated.

Real Mask Projection Microstereolithography

In this MSL technique, a part is built by irradiating the photopolymerizable resin through a physical or "real" patterned mask in a manner similar to traditional photolithography. The mask in this case is generally either a glass or quartz plate that has been coated with an optically opaque film (e. g. metal) that has been removed in a pattern-wise fashion representing the cross-section of the object to be built. Fig. 6 shows a schematic of an apparatus that can be used for mask projection MSL. Although it is possible to simply use the mask to shadow mask the resin during exposure without the use of any lens elements in a manner similar to the proximity printing processes used in photolithography, the resolution of such processes is typically limited to many tens or hundreds of microns due to diffraction effects and difficulty in bringing the mask close to the liquid resin surface and maintaining a constant gap width. Therefore, most mask projection MSL systems use lens elements to focus an image of the mask onto the resin surface. This focusing of the mask image onto the resin surface can significantly improve the resolution of the process and offers the possibility to use a reduction lens system in which the size of the features on the mask is reduced in the projected image, thereby improving the resolution of the features in the manufactured part relative to the original mask patterns. After exposure of the resin surface through the mask, a new layer of resin is prepared on the surface of the resin vat in some manner and the exposure process is repeated. For example, in Fig. 6 an elevator arrangement similar to those shown earlier in the scanning MSL techniques is used to move the object lower into the resin vat and a fresh layer of resin flows over the object after each exposure. The main advantage of mask projection MSL

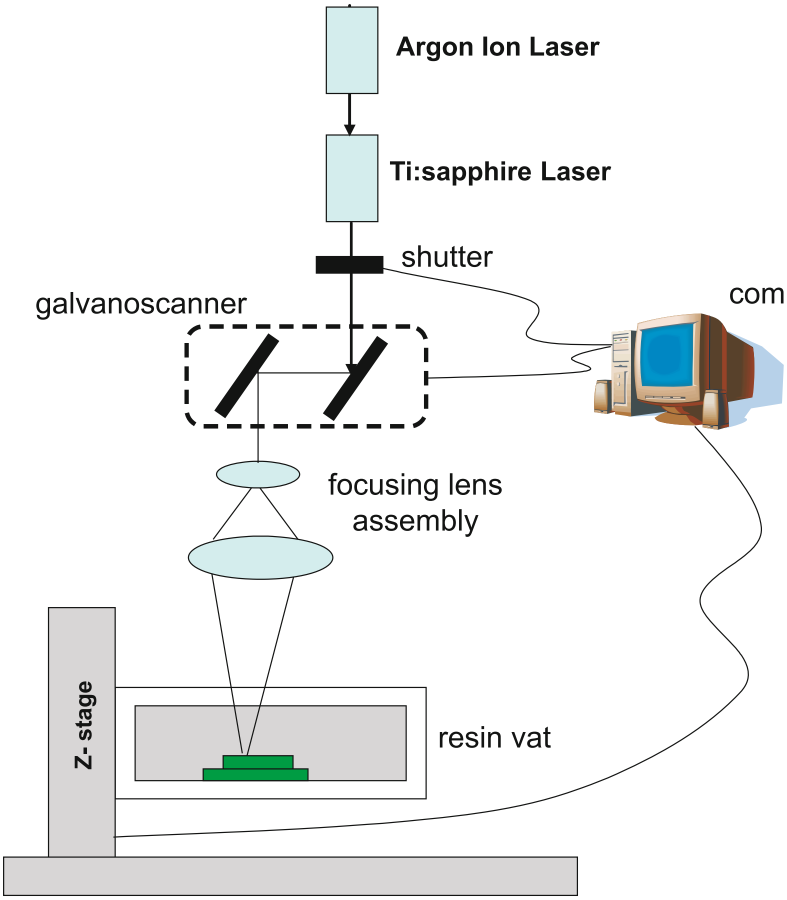

Microsterolithography, Figure 5 Schematic of an apparatus that can be used for direct volumetric fabrication of objects using two-photon photopolymerization

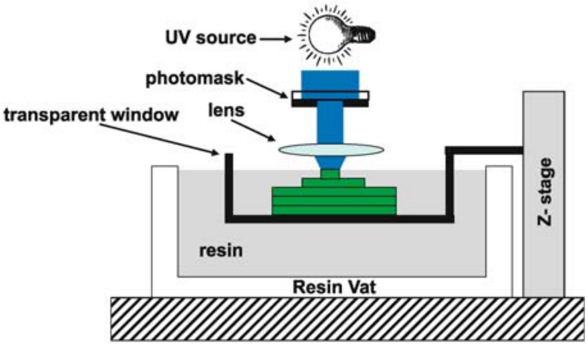

Microsterolithography, Figure 6 Schematic of an apparatus for real mask projection stereolithography

over scanning MSL techniques is that large areas of resin can be exposed simulataneously, resulting in much faster build times per layer and per total part. The main disadvantage of mask projection MSL is that a physical mask must be created for each different cross-section of the object that is to be built. For this reason, only objects with a constant cross-section or a few different cross-section profiles are built using this method. For producing very small scale objects, the cost of producing the physical masks can become significant.

Dynamic Mask Projection Microstereolithography

Dynamic mask projection MSL is in principle the same type of process as real mask MSL except that in this case a *dynamic mask* is used instead of a physical mask. The dynamic mask is capable of being changed arbitrarily for each layer that is exposed, thus allowing parts with any number of different cross-sections to be fabricated by such methods. A schematic of a dynamic mask projection MSL apparatus is shown in Fig. 7. The dynamic mask used in such methods generally consists of one of two types of systems:

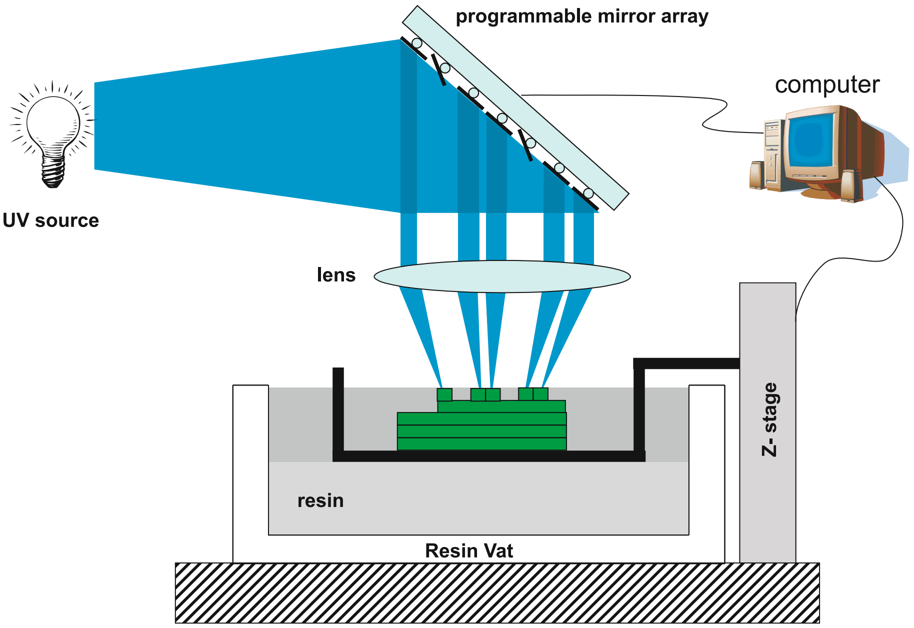

Microsterolithography, Figure 7 Schematic of an apparatus for dynamic mask projection stereolithography

- a transmissive liquid crystal display (LCD) that is sometime referred to as an LCD light valve or
- a micromirror array similar those now common in optical computer projector systems (e. g. the micromirror arrays produced by Texas Instruments and referred to as digital light projection or DLP systems).

In either the LCD or micromirror dynamic mask, the LCD or micromirror array consists of a large number of individually controllable pixels. For example, current micromirror arrays that contain more than 800,000 individually addressable mirrors are available where each mirror in the array is a square mirror that is roughly 15 μ long on each side. Therefore, again using lens-based projection optical systems it is possible to produce complex 3D objects with feature resolution down in the micron scale range and below quite easily.

Light Propagation and Cure Modeling in Photopolymerization During Scanning-Based Stereolithography

In processes where photopolymerization is used to achieve part fabrication using scanning-based stereolithography, the two critical paraemeters that must be controlled are the line width and the line cure depth. Both of these qualities of the photopolymerized line of material formed as the laser or light spot is scanned across the resin are determined by the radiation absorption in the resin, radiation distribution in the resin, exposure energy or dose given to the material, and the photochemical response of the resin to the exposure energy.

The transmission of light through an absorbing medium such as the photopolymerizable resin used in stereolithography can be described by the Beer–Lambert law as

$$I(z) = I(0)\,\mathrm{e}^{-\alpha z} = I(0)\,\mathrm{e}^{-z/D_\mathrm{p}}\,, \qquad (1)$$

where z is the distance light has traveled in the absorbing medium, $I(z)$ is the light intensity at the point z, $I(0)$ is the incident light intensity at the surface of the absorbing medium, α is the absorption coefficient of the absorbing medium, and D_p is termed the depth of penetration of light into the resin. D_p is simply defined as the depth into the absorbing medium at which point the light intensity at that depth is equal to $1/\mathrm{e}$ of the intensity at the surface of the medium. D_p is one of the common parameter used to describe a photopolymerization process used for stereolithography. For a Gaussian irradiance distribution beam source, such as a laser that could be used to expose the resin in a scanning stereolithography apparatus, the intensity distribution at any point inside the resin volume for normal incidence of the beam at a point $(0, 0, 0)$ on the resin surface can be expressed as

$$I(x, y, z) = \frac{2P}{\pi W_0^2}\,\mathrm{e}^{-2r^2/W_0^2}\,\mathrm{e}^{-z/D_\mathrm{p}}\,, \qquad (2)$$

$$r = \sqrt{x^2 + y^2}\,, \qquad (3)$$

where P is the laser power and W_0 is the Gaussian half width. Now, for a beam that scans along a single axis, in this case the x-axis, it is possible to express the laser exposure energy in the resin volume along the scan line as

$$E(y, z) = \sqrt{\frac{2}{\pi}} \frac{P}{W_0 V} \mathrm{e}^{-2y^2/W_0^2} \mathrm{e}^{-z/D_\mathrm{p}}, \quad (4)$$

where V is the beam scanning speed along the scan axis (i. e. in this case along the x-axis). Obviously the maximum exposure dose or energy will be dpeosited into the resin at the resin surface in the center of the beam along the scan line. If one calls this maximum exposure energy $E_{\max}$, it can be defined as

$$E_{\max} = E(0, 0) = \sqrt{\frac{2}{\pi} \frac{P}{W_0 V}}. \quad (5)$$

If one uses a threshold model for polymerization in which resin receiving more than a certain dose will become solid polymer, which is of course a gross oversimplification but which works reasonably well for SL process design, it is possible now to quantitatively describe the size and shape of the cured part due to SL exposure. Let us define the threshold exposure dose or energy required to turn the resin into solid polymer as E_c (i. e. the *critical exposure or critical energy*), then the so-called *cure depth* C_d, which represents the height of the single cured line formed due to the scanning beam, can be defined as

$$C_\mathrm{d} = D_\mathrm{p} \ln\left(\frac{E_{\max}}{E_\mathrm{c}}\right). \quad (6)$$

The line width (L_w) for a single cured line can also be obtained using the E_c criteria as

$$L_\mathrm{w} = W_0 \sqrt{2 \ln\left(\frac{E_{\max}}{E_\mathrm{c}}\right)}. \quad (7)$$

Figure 8 shows a schematic of the exposure process and result for a single line in cross-section. More generally, by using Eq. (4) in conjunction with the threshold criteria that resin which receives an exposure dose higher than E_c will become part of the polymerized solid object, it is possible to simulate the shape and size of a cured part. Such models are used in practice on stereolithography tools to perform the inverse process design needed to translate an object's CAD data into a beam scanning and exposure time recipe for making the desired solid object from the CAD data. In cases where the exposure beam is not Gaussian, similar results can be obtained assuming a different beam irradiance function.

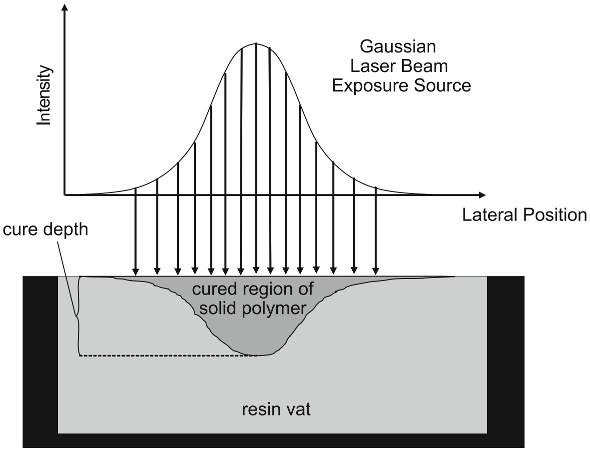

Microsterolithography, Figure 8 Schematic of scanning stereolithography exposure process and resulting solid polymer line object produced from such methods during a single scan

It should be clear from this discussion that the two parameters, E_c and D_p can be used to provide a basic description of the SL or MSL process for a particular resin and exposure source combination. Experimentally, these parameters can be derived for a particular resin on a particular SL exposure tool by performing a series of experiments in which single line parts are made by varying $E_{\max}$ (i. e. by changing the laser scan speed for modulating the exposure source intensity). By measuring the cure depth of the resulting single line parts, it is possible to perform a nonlinear fitting of Eq. (6) to this data to determine E_c and D_p. It is also possible to derive these parameters from similar experiments using slightly different part types and SL protocols. Once these parameters are determined, they can then be used for the process planning required to fabricate a particular object from CAD data as mentioned earlier.

Key Research Findings

Stereolithography and microstereolithography techniques provide the ability to produce arbitrary objects directly from computer aided design data. Such methods have found widespread use in rapid prototyping applications and are beginning to see some application in rapid manufacturing applications. In scanning based systems, part feature resolutions on the order of 100 µ is common in commercial laser scanning systems. Two-photon photopolymerization methods can be used to significantly increase the resolution of such scanning based systems and to allow for direct 3D volumetric fabrication of object (i. e. as opposed to the layer-by-layer approach common to most SL and MSL methods). However, two-photon based SL and MSL has not been widely used commercially yet.

Dynamic mask projection SL and MSL tools have been recently developed and allow for the fabrication of objects at higher speeds and higher resolutions than single beam scanning tools, and such tools are likely to become more common in commercial applications in the coming years. Part feature resolutions on the order to one to 10 μ is relatively easy to obtain using such dynamic mask projection SL and MSL tools.

Future Directions for Research

As mentioned earlier, scanning-based stereolithography and microstereolithography are used quite widely for the rapid prototyping of objects. The main research directions for stereolithography include:

- finding ways to increase the speed with which parts are built,
- increasing the resolution and surface finish of built parts,
- developing new materials that can be used in conjunction with SL tools to produce functional parts, and
- using such advancements in materials and techniques to transition the methods to rapid manufacturing applications.

Research in two-photon MSL techniques is also very active, with current research directions including:

- developing better two-photon initiators,
- developing better apparati for two-photon MSL, and
- using the methods to perform tasks beyond traditional MSL part building, such as for the in situ fabrication of objects inside living cells and living systems.

Currently, mask projection microstereolithography is still much less common that scanning-based methods due to the fact that the micromirror arrays, which are now the most common form of dynamic mask used for such methods, are a relatively recent invention and have been commercially available for purchase for only a few years at this point.

Cross References

► MEMS-Based Biosensor

References

1. Andre JC, Le Methaute A, de Wittee O (1984) French Patent 8,411,241
2. Hull C (1983) US Patent 4,575,330
3. Ikuta K, Hirowatari K (1993) Real three dimensional microfabrication using stereolithography and metal molding. Proc IEEE MEMS 42–47
4. Ikuta K, Maruo S, Kojima S (1998) New microstereolithography for freely moved 3D micro structure-super IH process with submicron resolution. Proc IEEE MEMS 290–295
5. Ikuta K, Ogata T, Tsubio M, Kojima S (1996) Development of mass productive microstereolithography (Mass-IH process). Proc IEEE MEMS 301–305
6. Kodama, H (1981) Automatic method for fabricating a three-dimensional plastic model with photo-hardening polymer. Rev Sci Instrum 52:1770–1773
7. Varadan VK, Jiang X, Varadan V (2001) Microstereolithography and other fabrication techniques for 3D MEMS. Wiley, Chichester

Microstructured Hydrogen Fuel Cells

LUC G. FRÉCHETTE
Department of Mechanical Engineering,
Université de Sherbrooke, Sherbrooke, QC, Canada
Luc.Frechette@USherbrooke.ca

Synonyms

Micro fuel cells; Proton exchange membrane fuel cells; Polymer electrolyte membrane fuel cells; μPEMFC

Definition

Micro fuel cells are miniature electrochemical energy conversion devices that generate a continuous electrical current from the flux of electrons exchanged between two half-reactions (reduction and oxidation) occurring in distinct regions of the cell. Microstructured hydrogen fuel cells are specifically implemented using microfabrication technologies and directly use hydrogen as a fuel.

Overview

Micro fuel cells are considered as promising power sources, offering longer autonomy for portable electronics and other devices traditionally powered by batteries. In contrast to electrochemical batteries, fuel cell power sources have distinct energy storage and power conversion components. The fuel cell can generate a constant level of power, as long as it is replenished with reactants and as long as products are removed. Hydrogen fuel cells typically have a planar layout consisting of anode and cathode electrode layers separated by a polymer electrolyte membrane, as illustrated in Fig. 1. Each electrode consists of a porous structure loaded with catalytic particles, such as platinum. They are covered by a diffusion layer and flow channels that deliver hydrogen or oxygen to the reaction sites. For fuel cells fed with hydrogen and oxygen (typically from the ambient air), the anode and cathode reactions are, respectively

M

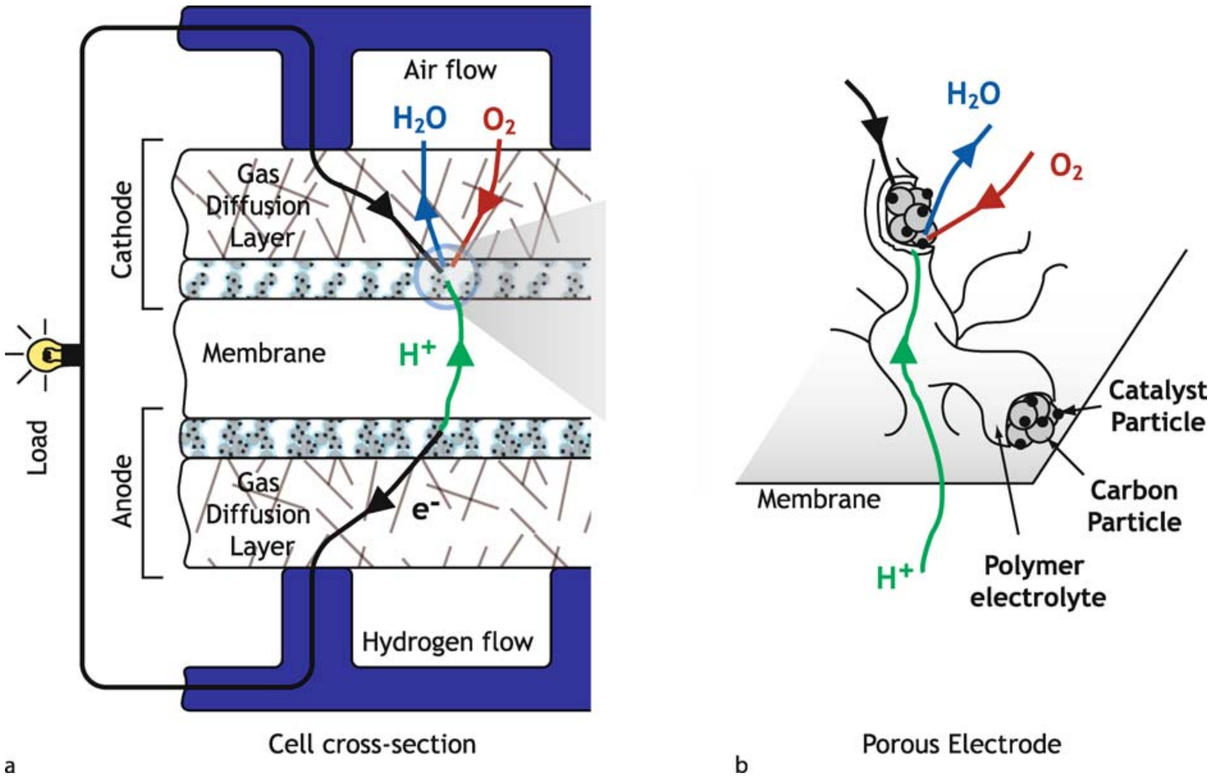

Microstructured Hydrogen Fuel Cells, Figure 1 Operating principle and cross-section schematic of a hydrogen fuel cell

$$\begin{aligned} &\text{Anode:} && H_2 \overset{\text{Pt}}{\rightarrow} 2H^+ + 2e^- \\ &\text{Cathode:} && \frac{1}{2}O_2 + 2H^+ + 2e^- \overset{\text{Pt}}{\rightarrow} H_2O \end{aligned} \tag{1}$$

The protons (H^+) generated at the anode travel across the polymer electrolyte membrane to form water at the cathode. Electrons also travel to the cathode, but through an external circuit, providing the desired output electrical power.

The ideal cell potential between the two half-reactions for H_2/O_2 is 1.23 V at 25 °C. The actual cell voltage will be lower due to losses in the cell. As the current is increased from the open circuit condition, catalytic activation losses (dominant at the cathode) will initially reduce the voltage to ~ 1 V. Ohmic losses due to ionic resistance through the membrane and electrical resistance in the assembly (to a lesser extent) will further reduce the voltage in a linear fashion with current. The most common polymer electrolyte is Nafion (trademark of DuPont), which is a perfluorinated ionomer that must be humid to maintain good ionic conductivity. A limiting current will then be achieved, beyond which the mass transport of reactants (typically oxygen at the cathode) becomes insufficient to match the current, and the voltage drops to zero. Water accumulation at the cathode can restrict oxygen diffusion and lead to premature current limitation. Since power is the product of current and voltage, the maximum power level of the cell will be achieved before reaching the limiting current.

Micro Polymer Electrolyte Membrane Fuel Cells (μPEMFC) and their Challenges

Small hydrogen fuel cells can be similar to their large-scale counterparts, but some challenges differ [1]. For example, the mechanical assembly must apply sufficient pressure between the layers to ensure proper sealing and low electrical resistance, but upon miniaturization, this can easily dominate the fuel cell volume. The flow channels can be machined into the mechanical plates in a serpentine shape or in parallel channels aiming to provide uniform air and fuel delivery. In small-scale channels, however, the pressure drop can become important. Unfortunately, miniature blowers are not efficient and can often be as large as the fuel cell itself. The challenge of finding appropriate auxiliary components for watt-scale fuel cells suggests the use of air-breathing con-

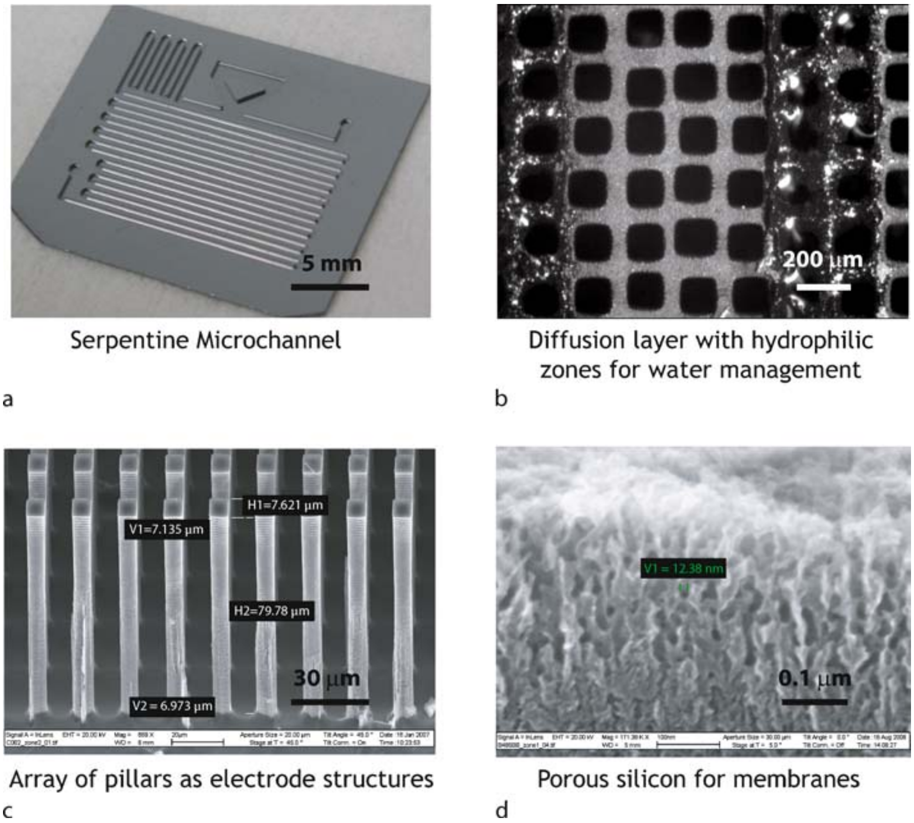

Microstructured Hydrogen Fuel Cells, Figure 2 Examples of microstructures for hydrogen fuel cells: (**a**) microchannel flow field; (**b**) silicon micromachined diffusion media with porous coating for water management; (**c**) silicon pillars as electrode structures; (**d**) porous silicon as a membrane support material

figurations, where temperature gradients induce natural convection of the ambient air over the cathode to provide oxygen and remove the water generated. Although this approach simplifies the balance of plant, one has less control over the critical cathode flows. If the cell is too cold, weak natural convection will not succeed in removing water at the rate it is generated, so the cell will have a tendency to flood. In contrast, if the cell heats up too much, it will likely dry out and lead to increased ionic resistances. Although not discussed here, hydrogen storage and fuel delivery also remain critical roadblocks for the viability of hydrogen-based power sources.

Microfabricated Structures for PEMFC

Microfabrication techniques allow the patterning of large arrays of complex features down to the micrometer scale, without the cost associated with high-precision manufacturing. Figure 2 shows examples of silicon microfabricated structures for fuel cells, ranging from meso- to nanoscale. Photolithography can be used to transpose microchannel shapes or other microstructures on the surface of a silicon wafer or within photosensitive polymers. Deep reactive ion etching or laser micromachining allow the creation of these shapes in silicon, glass or metal substrates. The shapes can also serve as molds to form microchannel plates from flexible polymers, such as PDMS. These approaches have been explored to make microflow channel plates with enhanced mass transfer performance due to small channel diameters ($\sim 100\,\mu\text{m} \times 100\,\mu\text{m}$) [2]. Polymer approaches will often require bonding, while additional clamping plates may be necessary when using fragile silicon.

The gas diffusion layers are typically carbon paper or cloth, treated to be hydrophobic in order to prevent pooling of liquid water. Silicon plates with microfabricated perforations can be used instead, with the potential for integrating more advanced water management strategies. For example, specific regions of a silicon mesh can be treated to be hydrophilic, with the rest being hydrophobic. This approach tends to keep some water in the cell to prevent drying out, but wicks water out of the hydrophobic zones to allow unrestricted oxygen diffusion [3].

Traditional electrodes typically consist of a porous layer that combines platinum nanoparticles (diameter ~ 3 nm) supported on carbon particles, all covered with a thin Nafion layer. This layer must not only contain the catalyst but also act as an electronic conductor (carbon), ionic conductor (Nafion), gas diffusion media (oxygen) and prevent water from accumulating. Replacing such a structure with a microfabricated equivalent is a daunting task. Many configurations have been explored, such as high aspect ratio silicon columns covered with platinum and a thin Nafion layer [4], or simply covering the flow channel structures or membrane with a film of catalyst. These approaches have typically led to lower power densities than traditional porous electrodes, mainly due to the lower effective catalytic surfaces and the challenge in achieving the multifunctional specifications for the electrode.

Finally, silicon processing techniques have also been leveraged to make novel ion conducting membranes. Porous silicon can be readily created in a silicon substrate by an anodization process in HF. The result is a nanoporous structure with over 50% porosity. By forming thick membranes of porous silicon ($> 40\,\mu$m) loaded with sulfonic acid, ionic conductivities similar to Nafion were attained ($10^{-2} - 10^{-1}$ S/cm) [5].

Microfabrication therefore appears to be a viable approach to monolithically integrate the electrolyte with the electrodes, gas diffusion, water management structures and the flow fields. Based on examples of other microelectromechanical systems the microfabrication approach may lead to cost-effective manufacturing in large volumes of microstructured hydrogen fuel cells.

Performance Levels of μPEMFC

The best performance levels achieved to date are for micro fuel cells based on traditional membranes and electrodes, and using forced convection [6, 7]. For example, power levels of over 300 mW/cm^2 have been shown for pure pressurized oxygen, whereas 130 mW/cm^2 was achieved for free convection of ambient air. Significant efficiencies, or voltages, have also been demonstrated at the peak power values, ranging from 0.4 to 0.7 V for various implementations. Most demonstrations were, however, done in a laboratory setting with external control and monitoring.

Future Needs for Research and Development

Only a small spectrum of the broad range of device configurations and materials has been explored, so there is significant opportunity for innovation. Advances in nanomaterials for electrodes, such as carbon nanostructures [8], and other fuel cell fabrication approaches can have a significant impact on the field of μPEMFC. Innovative fabrication must be accompanied by judicious optimization at the meso-/micro-/nanoscales, ranging from two-phase flow in microchannels to diffusion in nanoporous structures. Future developments will best be served by an increased understanding of the multiple functions that must be met by the various fuel cell elements. Further studies of transport and electrochemical phenomena in micro- and nanofabricated structures specifically designed for test purposes could take an important role in the learning process. Finally, commercialization will only be possible by addressing the challenges in system-level design, fuel supply, power management, packaging and testing.

Cross References

► Microscale Energy Conversion Devices
► Microfluidic Fuel Cells
► Silicon Micromachining
► Microfabrication Techniques
► Photolithography

References

1. Meyers JP, Maynard HL (2002) Design considerations for miniaturized PEM fuel cells. J Power Sources 109:76–88
2. Cha SW, O'Hayre O, Prinz FB (2004) The influence of size scale on the performance of fuel cells. J Power Sources 175:789–795
3. Modroukas D, Calabrese Barton S, Modi V, Fréchette LG, (2005) Water Management And Mass Transport Studies In Free Convection Proton-Exchange Membrane Fuel Cells. In: 208th Meeting of the Electrochemical Society, Los Angeles, 16–21 Oct 2005
4. Beloin-St-Pierre D, Paquin M, Fréchette LG (2007) Design, Fabrication, and Characterization of Microfabricated Electrodes for a Proton Exchange Membrane Fuel Cell. In: Canadian Workshop on MEMS and Microfluidics (CWMEMS (2007)), Montreal, 13 Aug 2007
5. Gold S, Chu KL, Lu C, Shannon MA, Masel RI (2004) Acid loaded porous silicon as a proton exchange membrane for micro-fuel cells. J Power Sources 135:198–203
6. Nguyen NT, Chan SH (2006) Micromachined polymer electrolyte membrane and direct methanol fuel cells—a review. J Micromech Microeng 16:R1–R12
7. La O' GJ, In HJ, Crumlin E, Barbastathis G, Shao-Horn Y (2007) Recent advances in microdevices for electrochemical energy conversion and storage. Int J Energy Res 31:548–575
8. Kim C, Kim YJ, Yanagisawa T, Park KC, Endo M (2004) High performance of cup-stacked-type carbon nanotubes as a Pt – Ru catalyst support for fuel cell applications. J Appl Phys 96:5903–5905

Microsynthetic Jets

KAMRAN MOHSENI
Department of Aerospace Engineering Sciences,
University of Colorado, Boulder, CO, USA
mohseni@colorado.edu

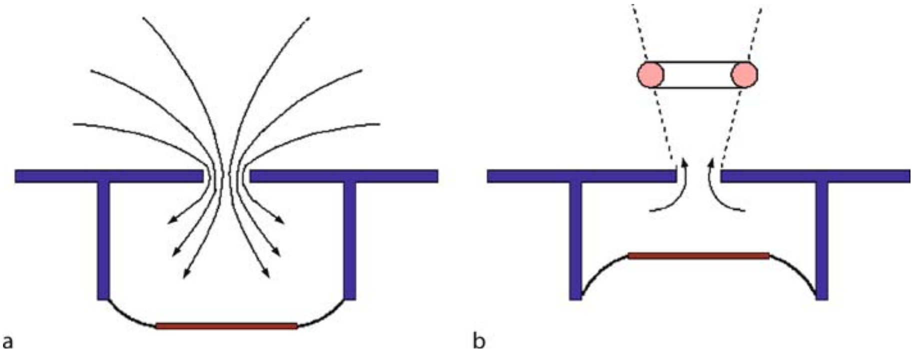

Microsynthetic Jets, Figure 1 Synthetic jet actuator concept: (**a**) ingestion phase; (**b**) expulsion phase

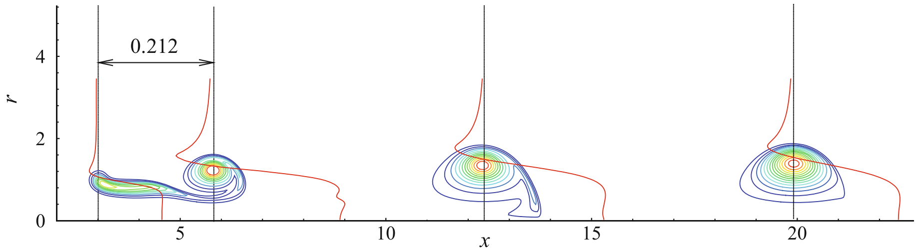

Microsynthetic Jets, Figure 2 Nondimensional vorticity contours and axial velocity profiles at three times during vortex ring formation: before the vortex pinch-off, during the pinch-off, and after the pinch-off. Axial velocities at the axial center of the vortex ring regions and close to the orifice are also plotted. Notice that the axial velocity before the pinch-off shows two maximums, one due to the shear layer and one due to the vortex. The shear layer is weakened and forced toward the axis of symmetry while the leading vortex ring grows. From Mohseni et al. [1]

Synonyms

Synthetic jet; Vortex ring; Vortex pair

Definition

Synthetic jets are jets with no net mass but a finite momentum flux. A common technique for creating a synthetic jet is using actuation of a Helmholtz cavity as depicted in Fig. 1. The cavity has an orifice and at least one flexible wall that can be actuated by various means. The jet formation is due to cyclic motion of the flexible wall in two distinct phases: ingestion and expulsion. During the ingestion phase the cavity is expanded and low-momentum fluid is ingested inside the cavity (Fig. 1a). The subsequent outward diaphragm movement expels the fluid, forming a vortex ring or a jet depending on the formation number (Fig. 1b). Repetition of this cycle results in a pulsatile jet. Because of the asymmetry of the flow during the inflow and outflow phases, a net fluid impulse is generated in each cycle, even though there is no net mass flow through the chamber over one cycle. Furthermore, the expelling jet will entrain additional fluid, adding to the net fluid momentum that is generated.

Figure 2 shows the direct numerical simulation of vortex ring formation at the exit of a nozzle. The vortex rings entrain surrounding fluid and travel downstream from the orifice because of self-induced velocity. The flow field of a synthetic jet might be initially comprised of a periodic array of vortex rings that are created at the exit orifice. A jet is formed by the interacting vortices. The vortices could be initially laminar or turbulent, but the final jet is often turbulent and the flow at the far field resembles that of conventional continuous and pulsed jets (see Fig. 3).

Overview

The formation and evolution of synthetic jets are dominated by vortex formation and interactions. In this respect, a synthetic jet is similar to a pulsed jet. However, a synthetic jet is distinguished from a pulsed jet in that the synthetic jet is entirely formed by the working fluid of the surrounding fluid. As a result in a synthetic jet a net momentum is added to the flow without a net mass injection across the system boundary. Synthetic jets are also distinct from classical streaming flows, as the mean induced motions are often of the same order as the oscillation amplitude, while for streaming flows the mean motion is of second order.

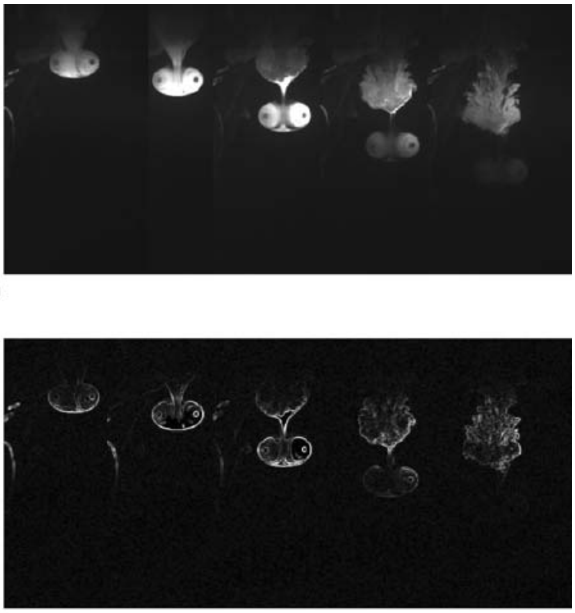

Microsynthetic Jets, Figure 3 Starting synthetic jet. The first two ingestion/expulsion cycles are visualized. In the first cycle a laminar vortex ring emanates from the orifice in a stationary domain. The following vortex ring is turbulent due to chaotic motion inside the cavity after the ingestion period. (**a**) Original LIF visualization. (**b**) After postprocessing calculation to identify sharp gradient lines

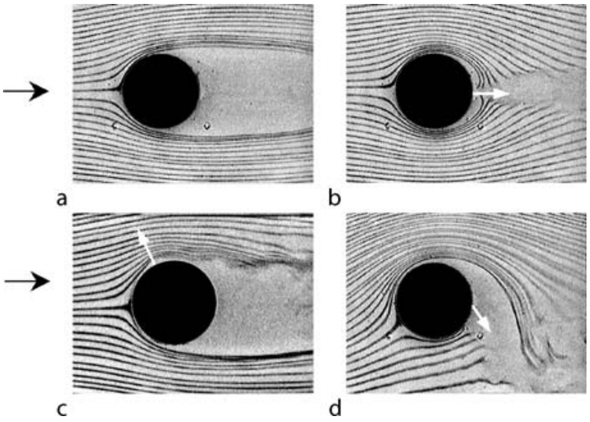

Microsynthetic Jets, Figure 4 Smoke visualization of flow around a circular cylinder in a uniform cross stream. A pair of synthetic jets are closely spaced from each other and are flush with the cylinder surface. (**a**) No jet. Base flow appears to separate at $\theta \sim 80°$. (**b**) In-phase actuation of jets at 60°. (**c**) Jets located at 180°. The external flow appears to be almost attached to the cylinder. (**d**) Jets are still located at 180° but operate out of phase by 120°. Out-of-phase operation of adjacent synthetic jets results in vectoring the combined jet toward the jet that is leading in phase. From Glezer and Amitay [3]

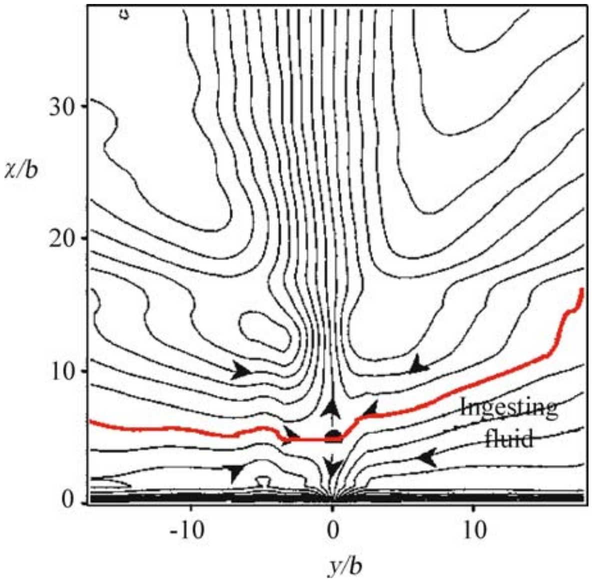

Microsynthetic Jets, Figure 5 Phase-averaged streamlines for a two-dimensional synthetic jet. The stagnation point in this case in located at $x/b = 5$. The stagnation streamline that passes through the stagnation point and separates the flow that is driven by the expulsion phase and the ingestion phase is marked in bold red. From Glezer and Amitay [3]

This entry is mostly focused on isolated synthetic jets. Interaction of synthetic jets with a cross flow is not covered. The reader is referred to [2, 3] and references therein.

Actuation Techniques

Imposing an oscillating pressure drop across an orifice can result in the formation of a synthetic jet. The oscillating pressure drop can be created by acoustic waves or by mechanical means such as boundary movement. Various actuation techniques can be employed for forcing the movement of the flexible wall. These include, but are not limited to, electrostatic, electromagnetic, and piezoelectric actuation. Each of these actuation technologies has advantages, disadvantages, and trade-offs in terms of performance metrics such as force capability, total displacement, actuation bandwidth, ease of integration to particular applications, and manufacturability. In electrostatic or magnetic actuations, the energy is stored in the gap between the flexible wall and an electrode. Electromagnetic actuators are often more effective in producing high-amplitude deflection of the deformable wall due their high stored energy density; at microscales the energy density of electromagnetic actuation is typically three orders of magnitude higher than that of electrostatic actuation. However, creating a magnetic field is often achieved by passing current through an electric coil, resulting in heat dissipation. An effective actuation technique at the microscale is piezoelectric actuation. Piezomaterials operate with high force and speed and the motion is fully reversible and repeatable.

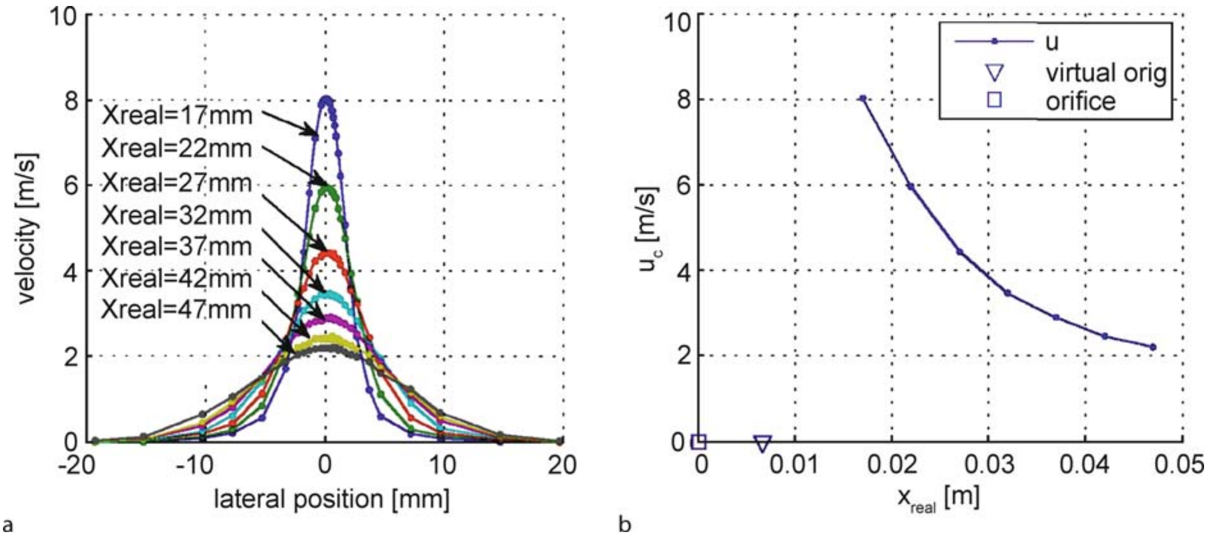

Microsynthetic Jets, Figure 6 (**a**) Averaged velocity profiles at various distances from the actuator. (**b**) Centerline velocity drop as a function of distance from the actuator. X_{real} is the distance of the measurement position from the orifice and u_c is the centerline velocity

Applications of Synthetic Jets

Synthetic jets have attracted significant interest in recent years due to their potential application in flow control (see Fig. 4), in particular performance control of aerodynamic surfaces through fluidic modification of their apparent aerodynamic shape. Application of synthetic jets can move the local streamlines in the vicinity of a synthetic jet and cause an apparent modification in the shape of the boundary. Such shape modifications are often achieved by operating a synthetic jet at timescales that are below the characteristic time scales of the mean flow. Synthetic jets are also employed for forced cooling of electronic devices, steering mechanism for capsule endoscopy, thrust generation, and jet noise reduction, among others.

Key Research Findings

The characteristic dimension of a synthetic jet scales with the orifice diameter. As a result, is it in principle possible to form jets over a wide range of length scales. The axisymmetric vortex rings, including those created at the exit of a Helmholtz cavity, may be characterized by two main parameters: one is the Reynolds number of the flow and the other is the formation number. The formation number is defined as the ratio of the stroke length to the orifice diameter, $L = \int_0^T u_0(t)dt$, where T is the expulsion time, $u_0(t)$ is the averaged streamwise velocity at the orifice, and D is the orifice diameter. Some other parameters that affect the resulting jet are the geometry of the cavity and orifice, actuation frequency, and actuation profile.

The time-averaged static pressure near the orifice plane is often lower than the far-field pressure. As a result, in the absence of a radial mean momentum there will be a net entrainment toward the jet center. The periodic flow direction reversal during the ingestion and expulsion phases creates a saddle stagnation point on the centerline closely downstream of the orifice that moves along the centerline during the ingestion stroke (see Fig. 5).

The frequency response of a synthetic jet often has a signature of two natural frequencies that mainly depend on the device dimensions and material properties. One of these frequencies is associated with the natural frequency of the vibrating membrane and the other is associated with the natural frequency of the Helmholtz cavity. The resonant frequency of Helmholtz resonators f_H, to a first approximation, is given by

$$f_H = \frac{c}{2\pi}\sqrt{\frac{A}{VL}}\,, \tag{1}$$

where c is the speed of sound, A is the orifice cross-sectional area, L is the length of the orifice, and V is the cavity volume. The maximum result is achieved by designing the cavity dimensions so that the two frequencies are matched. The natural frequency of the diaphragm can be calculated from well-known formulas for membrane vibrations.

Rathnasingham and Breuer [4] developed the first low-order model of a synthetic jet using a control volume model for the flow and an empirical model for the structural dynamics of the diaphragm. A lumped element model

of a piezoelectric-driven synthetic jet actuator was derived in [5].

Flow Modeling of a Synthetic Jet

An important aspect of the recent surge in investigations of synthetic jets is in modeling the spreading rate, centerline velocity drop, and average velocity profile at various distances away from the orifice. This is, of course, important when predicting the actuator response to control inputs. Figure 6 shows the gradual spreading of a synthetic jet as the measurement location is moved away from the orifice. The decay of the averaged centerline velocity u_c is also shown. If the radial distance is nondimensionalized by the virtual location of momentum source $x_{virtual} = x_{real} - x_0$, and the velocity is normalized by the centerline velocity, the experimental data collapse to an almost single curve, as shown in Fig. 7. This suggests self-similar behavior.

The classical model of a normal turbulent jet was recently extended to a synthetic jet [6, 7]. This is summarized in this section. Axisymmetric free turbulent jets can be solved analytically by using the Prandtl mixing-length model. The model findings are summarized by

$$u = \frac{3}{8\pi}\frac{J}{\rho\epsilon_0 x}\left(1+\frac{\xi^2}{4}\right)^{-2}, \quad (2)$$

$$v = \sqrt{\frac{3J}{16\pi\rho}}\frac{\xi}{x}\left(1-\frac{\xi^2}{4}\right)\left(1+\frac{\xi^2}{4}\right)^{-2}, \quad (3)$$

where u is the axial velocity, v the radial velocity, ρ the fluid density, x the axial coordinate, r the radial coordinate, $\xi\sqrt{\frac{3J}{16\pi\rho}\epsilon_0^2}\frac{r}{x}$ the similarity variable, and $J/\rho = 2\pi\int_{r=0}^{\infty} u^2 r dr$ the momentum flux per unit density (kinematic flux). Note that in eq. (2) the jet centerline velocity is inversely proportional to the distance from the jet origin. This could be employed to determine the virtual origin of a synthetic jet; i.e. a point of zero cross-section.

Vargas et al. [6] found that the main difference between a normal turbulent jet and a turbulent synthetic jet, to a first approximation, is in the apparent difference in virtual viscosity. This was attributed to the pulsatile nature of a synthetic jet that results in higher mixing, more effective spreading, and consequently higher turbulent viscosity. They directly used experimental data to estimate the virtual viscosity ϵ_0 to be 0.0361 ± 0.002. This value is more than twice the value of 0.0161 reported in the literature for a normal turbulent jet. Therefore, for a turbulent synthetic jet $\epsilon_0 = 0.0361\sqrt{J/\rho}$. This analytical model is shown in Fig. 7 where good agreement with the experimental data is observed. For comparative reasons, analytical results for a normal jet are also shown in Fig. 7. As expected and depicted in Fig. 8 a synthetic jet spreads at a much faster rate than a normal jet.

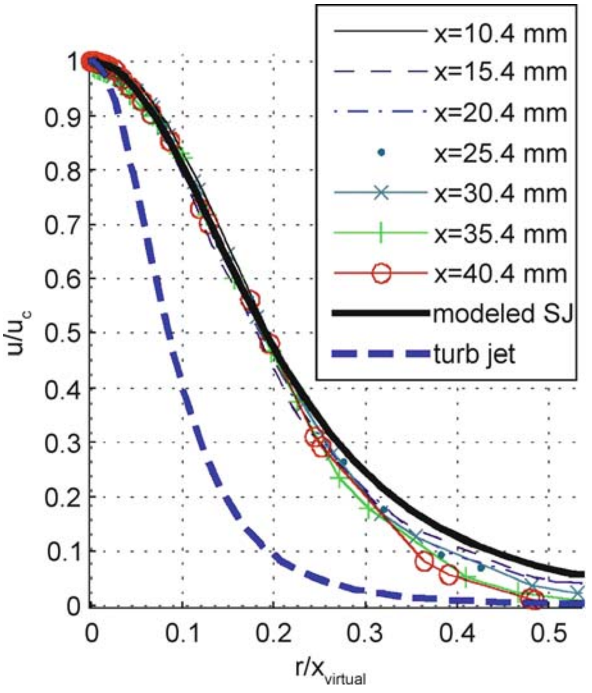

Microsynthetic Jets, Figure 7 Normalized velocity profiles for experimental and analytical data for a synthetic jet and a conventional turbulent jet. Note that $x_{virtual} = x_{real} - x_0$ and u_c is the centerline velocity

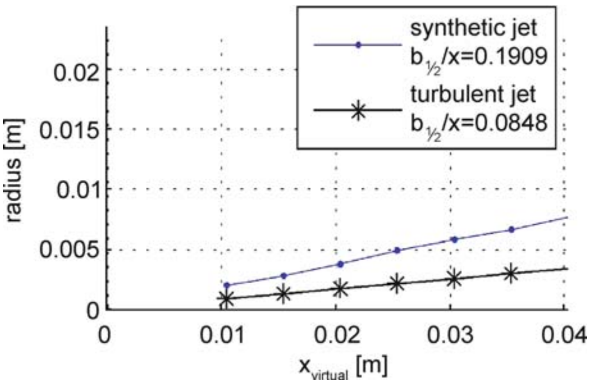

Microsynthetic Jets, Figure 8 Spreading rate of synthetic and normal turbulent jets

The flow volume per second can be calculated to be

$$Q = 2\pi\int_0^{\infty} u r dr = 8\pi\epsilon_0 x = 0.907\sqrt{J/\rho}x\,, \quad (4)$$

Note that this quantity for a laminar jet is $8\pi\nu x$ independent of the jet momentum; that is, independent of the

excess of pressure under which the jet leaves the orifice. For a synthetic jet, the virtual viscosity and the flow volume per second are not constant and are functions of the jet momentum.

Further Reading

This brief list of further reading is limited to 10 citations. A general review of single and multiple synthetic jet flows is presented in [3]. The flow field of a two-dimensional synthetic jet that is formed normal to an orifice in a flat plate was studied in detail by Smith and Glezer [2]. Mittal and Rampunggoon [8] studied synthetic jets numerically and investigated the virtual aeroshaping effect of synthetic jets. Analytical modeling of turbulent synthetic jets and self-similar solutions are presented in [6]. The effect of formation number (the ratio of the length of the ejected fluid slug during the expulsion phase to the orifice diameter) on the flow and thrust generation in a synthetic jet was investigated in [7]. Lumped element analysis of synthetic jet actuators is considered in [5]. Using synthetic jets for jet vectoring is proposed in [9] and application of an array of synthetic jets to vector and modify the cross-section of an axisymmetric continuous jet is presented in [10].

References

1. Mohseni K, Ran H, Colonius T (2001) Numerical experiments on vortex ring formation. J Fluid Mech 430:267–282
2. Smith BL, Glezer A (1998) The formation and evolution of synthetic jets. Phys Fluids 10(9):2281–2297
3. Glezer A, Amitay M (2002) Synthetic jets. Ann Rev Fluid Mech 34:503–529
4. Rathnasingham R, Breuer K (1997) Coupled fluid structure characteristics of actuators for flow control. AIAA J 15:832–837
5. Gallas Q, Holman R, Nishida T, Carroll B, Sheplak M, Cattafesta L (2003) Lumped element modeling of piezoelectric-driven synthetic jet actuators. AIAA J 41(2):240–247
6. Vargas Y, Finley T, Mohseni K, Hertzberg J (2006) Flow characterization of a synthetic jet. AIAA paper 2006–1422, 44th AIAA Aerospace Sciences Meeting and Exhibit, Reno, 9–12 Jan 2006
7. Vargas Y, Mohseni K (2006) Characterization and thrust optimization of synthetic jets. FEDMS2006 2006–98312, 2006 ASME Joint US-European Fluids Engineering Summer Meeting, Miami, Florida, 17–20 July 2006
8. Mittal R, Rampunggoon P (2002) On the virtual aeroshaping effect of synthetic jets. Phys Fluids 14(4):1533–1536
9. Smith BL, Glezer A (2002) Jet vectoring using synthetic jets. J Fluid Mech 458:1–34
10. Pack LG, Seifert A (2001) Periodic excitation for jet vectoring and enhanced spreading. J Aircraft 38(3):486–495

Microsystems

► Biosample Preparation by Lab-on-a-Chip Devices

μTAS

► Droplet Based Lab-on-Chip Devices
► Lab-on-a-Chip Devices for Chemical Analysis
► Microfluidics for Studies of Apoptosis

Microthermocyclers

► PCR Lab-on-Chip Devices

Microthrusters

► Microrockets
► Supersonic Micro-Nozzles

Microtips and Microspikes

► Microneedles – Applications & Devices

Micro Total Analysis System (μTAS)

► Droplet Based Lab-on-Chip Devices
► Lab-on-a-Chip Devices for Chemical Analysis
► Lab-on-Chip Devices for Separation-Based Detection
► Lab-on-a-Chip (General Philosophy)
► Microfluidics for Studies of Apoptosis
► On-Chip Detection Using Optical Fibers

Microturbines

Luc G. Fréchette
Department of Mechanical Engineering, Université de Sherbrooke, Sherbrooke, QC, Canada
Luc.Frechette@USherbrooke.ca

Synonyms

Micro heat engines; Micro gas turbines; Micro gas turbine engines; Micro steam turbines

Definition

Microturbines are miniature rotating machines that convert fluid energy into mechanical energy, implemented using microelectromechanical systems technologies or other

small scale manufacturing approaches. They are characterized by the use of fluid flow to set a mechanical component (rotor) into rotation, to drive a compressor, pump, generator or other rotating components. Microturbine-based systems include micro gas turbine engines for propulsion and micro steam turbines for power generation.

Overview

Rotating machinery is commonly used at large scale to meet our society's daily needs for electric power generation, propulsion, cooling, and pumping, to name a few. The implementation of systems that include turbines, generators and pumps at very small scale, say a few millimeters or less, is however challenging from engineering and manufacturing perspectives. Silicon microfabrication processes and other technologies developed to create microelectromechanical systems (MEMS) can be leveraged to enable the miniaturization of rotating machinery. For example, photolithographic patterning, etching and wafer bonding have been shown as viable approaches to create millimeter scale microturbines, as illustrated in Fig. 1.

This chapter addresses the design and use of microturbines by discussing the main types of devices based on microturbomachinery and the key fluidic components that compose them. Specifically, the operating principles and characteristics of microturbines and fluid film bearings will be presented.

Cube-Square Law

As a thermal and fluidic system is miniaturized, certain physical phenomena become more or less predominant with scale, according to the *Cube-Square law*. Let's consider a machine with a characteristic dimension of length scale l, such as its length or diameter. Surface forces and fluxes, such as friction, pressure, heat transfer, and mass flow, will decrease proportionally to a characteristic area of the machine, hence as l^2. Volumetric effects, such as inertia, gravity or mass, will decrease as l^3. With respect to each other, the volumetric effects will decrease more rapidly than surface phenomena as the machine is miniaturized:

$$\frac{\text{Surface}}{\text{Volume}} \alpha \frac{l^2}{l^3} = \frac{1}{l}; \text{ ratio} \uparrow \text{ as } l \downarrow \tag{1}$$

For aerodynamic machines, the Cube-Square law implies that friction forces will tend to become more important compared to inertial forces. This is captured by the Reynolds number:

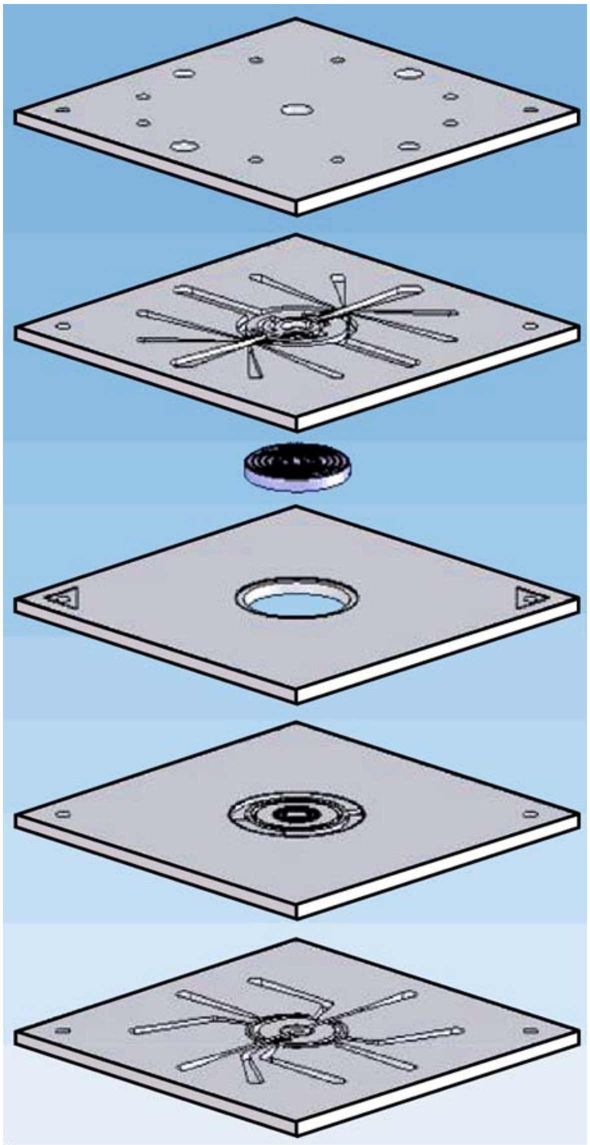

a

Microturbines, Figure 1 (**a**) Exploded view of a microturbine-driven micropump as the core rotating component for a Rankine steam turbine power plant-on-a-chip. The device is fabricated using deep reactive ion etching and wafer bonding of 5 wafers.

$$\text{Re} = \frac{\text{Inertial forces}}{\text{Viscous forces}} = \frac{\rho V l}{\mu}; \downarrow \text{ as } l \downarrow \tag{2}$$

expressed as a function of the fluid density ρ, dynamic viscosity μ, and a characteristic flow velocity V. Small scale turbomachinery is therefore expected to operate at low Re, typically characterized by predominantly laminar flow and low adiabatic efficiency.

Heat transfer will also become more important at small scales. The Stanton number is a non-dimension quantity that measures the ratio of heat transferred between a fluid

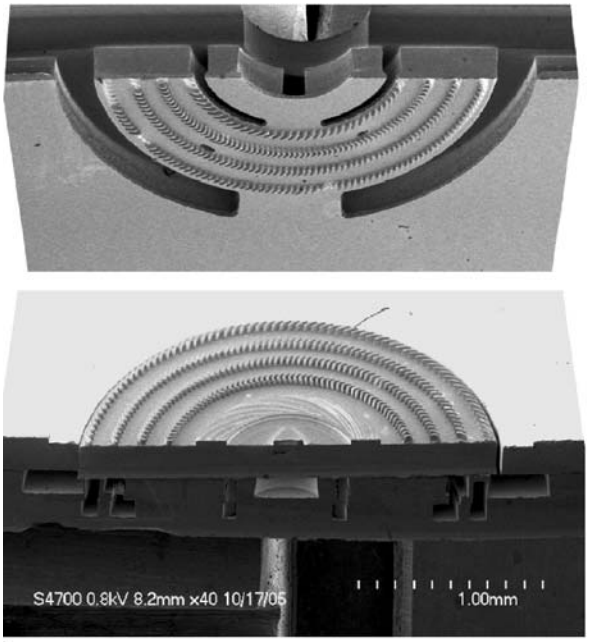

b

Microturbines, Figure 1 (**b**) Perspective view of an opened and sectioned device. The 4 mm diameter rotor is shown with four microturbine blade rows. The top portion of the device with stator blades is raised for visual access

and its adjacent structure to the heat capacity of the flow. It can be expressed as:

$$\mathrm{St} = \frac{\text{Heat transfer to wall}}{\text{Heat transport by flow}} = \frac{h}{\rho C_\mathrm{p} V} \tag{3}$$

where C_p is the fluid's specific heat. The convective heat transfer coefficient, h, typically increases at smaller scales [1], so for similar fluid properties and flow velocities, the Stanton number will increase. The impact is that flows in microturbomachinery can rarely be considered adiabatic.

Furthermore, conduction in the structures also tends to becomes predominant. The Biot number represents the ratio of heat transferred by convection to heat conduction in the solid:

$$\mathrm{Bi} = \frac{\text{Heat transfer to wall}}{\text{Heat conduction in solid}} = \frac{hl}{k_\mathrm{s}} \tag{4}$$

expressed as a function of the thermal conductivity of the solid, k_s. When using thin microfabricated layers and high thermal conductivity materials (such as silicon), the thermal resistance in the solids is diminished; this enhances conduction in the structures. This suggests that a conjugate heat transfer representation that combines convection in the fluid and conduction in the structures may need to be solved to predict the temperature distributions and performance of microturbomachinery.

Power Density of Microturbomachinery

The Cube-Square law can also guide the evaluation of power density for microturbines. The fluid to mechanical power conversion for a turbine is expressed as the product of mass flow and change of specific total enthalpy across the turbomachine, Δh_t. Thermodynamic properties of a fluid, such as pressure, temperature, and enthalpy do not fundamentally change with scale. For equivalent thermodynamic cycles, the power of a turbine therefore scales simply as the mass flow, which can be expressed in terms of an average flow velocity, V, through a characteristic flow area, A, proportional to l^2. For constant thermodynamic and flow properties, the power density of a turbine therefore scales as:

$$\frac{\text{Power}}{\text{Volume}} = \frac{\dot{m}\Delta h_\mathrm{t}}{\text{Volume}} = \frac{(\rho AV)\Delta h_\mathrm{t}}{\text{Volume}} \alpha \frac{l^2}{l^3} = \frac{1}{l} \tag{5}$$

Miniaturization from meters to millimeters should therefore lead to turbomachines with 1000× higher power per unit size or weight. In practice, this gain will not be as dramatic since low Re flows, heat loss and less flexible manufacturing capabilities at small scale will reduce the efficiency and diminish the output power per unit flow rate compared to large scale turbines. Current achievements to date confirm however that a gain in power density clearly results from miniaturization [6].

Applications of Microturbines

Microturbines, pumps and compressors are key components used to implement thermodynamic cycles for power generation, propulsion, or cooling. Thermodynamic power cycles use a working fluid that changes state (pressure and temperature) in order to convert heat into mechanical work. To achieve high power density, the pressures and temperatures of the fluid in the cycle should be kept to the high levels common at large scale. Common cycles are the Brayton gas power cycle and the Rankine vapor power cycle, described next.

Brayton Cycle

The pressure of a low temperature gas is first raised by the work of a compressor before entering a combustion chamber where it is mixed with a fuel and ignited to raise its temperature. The hot and high pressure gases are then expanded across a turbine. The turbine therefore extracts energy from the flow and converts it into mechanical power that is available to drive the compressor. In

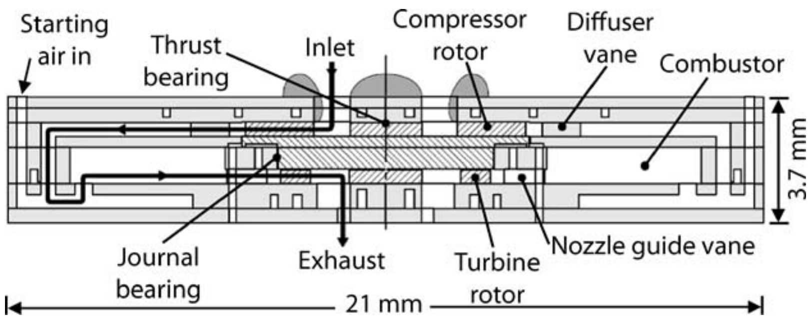

Microturbines, Figure 2 Cross section schematic of the MIT H_2 demo micro gas turbine engine constructed of six silicon wafers [2]

the case where the component efficiencies are sufficient, the power provided by the turbine is equal or exceeds the power required by the compressor. The turbine exhaust gases can either provide thrust for propulsion of an aircraft or can be further expanded through a turbine to drive a generator. To complete the cycle, the Brayton cycle can reject the turbine exhaust gases to the atmosphere and breathe in fresh air. Conventional gas turbine generators and jet engines implement the Brayton cycle at macro-scale. At micro-scale, one can use MEMS technology to create millimeter scale microturbines as electric power generators for portable electronics or for the propulsion of micro air vehicles.

Rankine Cycle

The main difference between the Rankine and Brayton cycles is the compression process. In the Rankine cycle, the fluid is pumped in liquid phase instead of gas phase. This requires significantly less power, leaving more turbine output power for useful work. Water is typically used as the working fluid, both in liquid an vapour state, so phase change processes are therefore required (evaporation and condensation). Unless a source of cool water is readily available, the Rankine cycle must be implemented as a closed cycle with heat rejection to condense the steam at the exit of the turbine, before pumping it. Two-phase flow heat exchangers are therefore required. Heat is added to the fluid to evaporate and superheat it before it enters the turbine using another two-phase flow micro heat exchanger. At macro-scale, steam turbine generators are used in nuclear and coal power plants to convert the thermal energy released by the reactions into electricity. The heat source is external to the device, providing significant flexibility for the source. At small scale, micro steam turbine power plants-on-a-chip can also convert heat from various sources into electricity. Heat can either come from the combustion of a fuel in an external combustor or as waste heat from the exhaust of vehicles or industrial processes. Microturbines can therefore provide a means to improve the efficiency of automobiles and manufacturing plants by converting waste heat in electricity.

Other than for implementing thermodynamic power cycles, microturbines can be used in situations where natural flows exists, including environmental, industrial or biological flows. Coupled with a generator, the microturbines could provide power for implantable or distributed sensors, for example. They could also simply provide a measurement of the flow rate through it. Finally, microturbines provide an alternative to electric/magnetic motors by providing an approach to set a rotor in rotation by simply providing a pressurized fluid. The rotor could then perform various functions, such as optical scanning or modulation for example.

Basic Methodology

Two main approaches have been taken to implement microturbines: semiconductor batch processing or traditional precision manufacturing.

Traditional Precision Manufacturing

Miniature turbine-based systems can be fabricated using high precision machining. Relatively standard configurations can be implemented such as miniature gas turbine generators, that consist of a shaft to which is attached the turbine rotor, generator, compressor and supported by ball bearings. Approaches to make the small parts include high-precision milling of metals and ceramics, electro-discharge machining (EDM) of metals, and micro-molding of ceramics. Although many of the concepts presented herein apply to such miniature turbines, the focus will be on silicon MEMS-based microturbines.

Silicon Batch-Processed Microturbines

This approach was initiated by Epstein [2] at the Massachusetts Institute of Technology (MIT) in the mid-

1990s, in the context of building micro gas turbine engines in silicon using microfabrication technologies. Although the realizable geometries and materials available are limited with this approach, the MEMS implementation of microturbines promises low cost, high volume batch fabrication, and the ease of integration of instrumentation and other electromechanical elements. Silicon is a well adapted material for high speed rotating micromachinery, since it has a high strength and relatively low density to minimize centrifugal loads. Since it is a brittle material, surface defects and cracks can lead to catastrophic failure of the device. Thankfully, single crystal silicon wafers, the starting material prepared for the semiconductor industry, are virtually defect free and polished to submicron precision. Furthermore, most etching techniques lead to smooth, well defined surfaces, with average fracture strength up to 4 GPa. Thermally, silicon is a high thermal conductor (like a metal), which tends to reduce the probability of thermal stresses in the structure. Unfortunately, this also make thermal insulation an important challenges in applications where heat loss is detrimental, such as micro heat engines. Although glass or quartz could be of interest from a thermal isolation perspective, etching techniques remain limited in comparison to silicon.

The main processes typically used to build silicon microturbines are: deep reactive ion etching (DRIE) of silicon to form the turbine blades, rotor, or microchannels in the bulk of the substrate; and aligned wafer bonding to assemble multiple substrates (previously etched) to form the bearings components adjacent to the rotor. Figure 1 illustrates the exploded view of a 5-wafer device and a cross section of the fabricated device with a 4 mm rotor. Given the two-dimensional nature of photolithography and deep reactive ion etching, the blades of a typical microturbine configuration are defined in the plane of the wafer and are laid out for radial flow. Here, fluid film bearings support the rotor by applying a distributed pressure field on it. The small gaps required are created once again by deep reactive ion etching and wafer bonding. A journal bearing is formed around the rotor by etching a narrow circumferential trench that defines the rotor and provides space for a film of air around its periphery. Air bearings above and below the rotor are created by etching a shallow recess on the wafers on either side of the rotor before bonding. The following sections will describe these components in more detail.

Turbomachinery

In a planar turbine configuration, the flow expands radially through circumferential rows of blades. Stator blade rows are fixed and tend to deviate the flow in the tangential direction. The swirling flow then enters the next blade row that is attached to the disk, the rotor. The curved rotor blades turn the flow in the opposite direction, which imparts a reaction force on the rotor. With respect to the center of the disk, this force is a moment, or torque T, that sets the rotor in motion. This process of fluid to mechanical energy conversion is best described by the conservation of angular momentum applied to a control volume enclosing a blade row:

$$T_{\text{blade row}} = (\dot{m} r V_\theta)_{\text{out}} - (\dot{m} r V_\theta)_{\text{in}} \tag{6}$$

where $\dot{m}$ is the mass flow, r is the radius, and V_θ is the tangential component of the flow velocity. The mechanical power extracted by a rotor blade row is the product of the torque and the rotational speed Ω. For a turbine with multiple pairs of rotors and stators (i. e. stages), the total power of the turbine, $\dot{W}_\text{T}$, will be the sum for all rotor blade rows:

$$\begin{aligned} \dot{W}_\text{T} &= \sum\nolimits_{\text{rotors}} \Omega \cdot T \\ &= \Omega \cdot \sum\nolimits_{\text{rotors}} \left[(\dot{m} r V_\theta)_{\text{out}} - (\dot{m} r V_\theta)_{\text{in}}\right] \end{aligned} \tag{7}$$

The turbine power can also be related to the flow properties using the first law of thermodynamics, $\dot{W}_\text{T} = \dot{m}\Delta h_\text{t} - \dot{Q}$, defined as a function of the change of the fluid's total (or stagnation) enthalpy h_t, and the rate of heat transfer to the flow $\dot{Q}$. For a constant mass flow through the turbine, the total power per unit mass flow can be expressed as the Euler turbine equation:

$$\frac{\dot{W}_\text{T}}{\dot{m}} = \Delta h_\text{t} - \frac{\dot{Q}}{\dot{m}} = \Omega \cdot \sum\nolimits_{\text{rotors}} \left[(r V_\theta)_{\text{out}} - (r V_\theta)_{\text{in}}\right] \tag{8}$$

For incompressible, adiabatic flow with negligible change in flow velocity throughout the turbine, the change in total enthalpy can be approximated as $\Delta h_\text{t} \approx \Delta h = \Delta (u + P/\rho) \approx P/\rho$, where ΔP is pressure drop. The power per unit mass flow becomes:

$$\frac{\dot{W}_\text{T}}{\dot{m}} = \frac{\Delta P}{\rho} = \Omega \cdot \sum\nolimits_{\text{rotors}} \left[(r V_\theta)_{\text{out}} - (r V_\theta)_{\text{in}}\right] \tag{9}$$

Equation 9 relates the turbine power and mass flow to the pressure drop and flow velocities, so it is the starting point for turbine design and analysis.

Conservation of mass is also used to define the average radial flow velocities V_r, as a function of geometry. At a given radial location r of flow passage height h, the mass flow is simply expressed as:

$$\dot{m} = \rho A V_r = \rho (2\pi r h) V_r = \text{constant} \tag{10}$$

M

The flow angles are defined by the blade angles in the relative reference frame of the blade row of interest.

For adequate design and performance predictions, nonideal effects such as blockage, pressure loss, deviation, and endwall secondary flows should also be considered. If the wall and flow temperatures differ, significant heat transfer can also occur and should be considered, especially for compressible flows. Extensive literature and a solid design basis on the aerodynamics of microturbomachinery are not yet available since the range of Re encountered $(100 < \mathrm{Re} < 10{,}000)$ is not common in past applications. Furthermore, experimental measurements are challenging at the microscale with traditional instrumentation. The use of computational fluid dynamic (CFD) modeling is therefore required for advanced microturbine design.

Bearings

Based on Eqs. 9 and 10, we note that turbine power essentially scales as the cube of a characteristic velocity. This implies that high rotational speeds are of paramount interest to achieve the power density levels promised by the Cube-Square law. The challenge is however to provide a bearing solution for high speed rotation with minimal friction and wear, that will support the axial and radial loads, and be readily microfabricated and integrated in the microsystem. Other rotating MEMS devices found in the literature typically rely on dry friction in pin-hole bearings, which are only viable for low speed operation. Ball bearings are commonly used for rotating machinery at macroscale, as well as for small turbine engines. An alternate approach for high speed microturbines is to support the rotor on fluid film bearings, which will be described here.

Thin films of pressurized air, steam or water (depending on the working fluid available in the microsystem) separate the rotor from the static structure all around it. They are referred to as *hydrostatic* bearings when the pressurized fluid is provided externally to the bearing or as *hydrodynamic* bearings when the pressure field is directly created by the relative motion of the bearing surfaces. Thrust bearings provide forces along the axis of the rotor, while a journal bearing on the periphery of the rotor supports radial loads. Thrust bearings can consist of steps or spiral groove patterns for hydrodynamic operation, or arrays of holes (restrictors) that pressurize a narrow gap in hydrostatic operation. In its simplest form, the journal bearing can consist of a uniform cylindrical gap. More advanced configurations include wave shaped clearances, foil bearings, or tilting pad bearings. The main difference with conventional macroscale bearings is the shape factor, dictated by microfabrication. For example, the journal bearing is typically a trench etched by deep reactive ion etching through a silicon wafer. The axial length is therefore limited to the wafer thickness, leading to low ratios of length to rotor diameter, $L/D < 0.1$. The resulting high speed, short journal bearing is well outside the range of experience found in the literature.

The bearings (i. e. support system for the rotor) play two main roles for microturbines: force balance and dynamic centering. In steady-state operation, the rotor will position itself in order to balance the axial forces on it. This implies that as the turbine pressure is increased, a proportional and opposite force must act on the rotor to maintain its axial position and prevent non-lubricated friction. This can be achieved with a balance piston (i. e. an area of the rotor on the side opposite to the turbine over which a pressure is applied) that scales with the turbine inlet pressure. Alternatively, one can design a symmetric rotor to balance forces (with a turbine on both sides of a disk), but at the cost of fabrication complexity. The second role is to maintain the rotor away from the static structures when subjected to shock, vibrations, and other external excitations. The bearings must therefore provide sufficient stiffness and damping. The stiffness of a fluid film bearings results from a change in the pressure field when the rotor is displaced slightly. The bearing provides a restoring force by reducing its internal pressure as the rotor moves away from the bearing surface. This creates an imbalanced net force on the rotor (normal to the bearing surface) that tends to push the rotor back to its initial position. This restoring principle can be implemented with hydrodynamic or hydrostatic bearings. In hydrodynamics, a larger gap reduces the shear forces and therefore lowers the pressure build up. In hydrostatics, a constant pressure reservoir supplies flow to the bearing surfaces through restrictors, hence the pressure in the bearing depends on the pressure drop across the restrictors. One approach to vary the pressure drop across the restrictor is to change the flow rate through it, by connecting the restrictor in series with a variable flow resistance, for example. Consider the case where the variable resistance is formed by a gap between the rotor and the bearing surface. As the rotor moves to increase the gap, the flow resistance decreases and a larger flow rate will pass through. The pressure drop across the upstream restrictors will therefore increase due to the higher flow rate. The pressure in the bearing clearance therefore drops, lowering the force on the rotor, and providing a restoring net force opposite to the rotor motion.

Key Research Findings

Development efforts to date have demonstrated most of the components required to create microturbine-based power

MEMS. System-level studies have also been done to provide design guidelines for component development and to predict overall performance. This section describes the results achieved to date and the main conclusions that can be drawn from this work.

Traditional Precision Manufacturing

Using high precision metal miling and ceramic molding, 10 – 12 mm diameter turbine rotors supported on ball bearings or fluid film bearings have been demonstrated up to 870,000 rpm [3]. The turbines typically consist of mixed flow single stage impellers or axial flow configurations. Target power levels for miniature gas turbine generators are on the order of 100 W with overall efficiencies of 5%. Performance levels demonstrated by a simpler air-driven turbine-generator device (10 mm diameter, axial flow, ball bearings) were 44 W of electrical power generation with a compressed air-to-electricity conversion efficiency of 16% [4]. These preliminary results suggest that the technical challenges using this approach are achievable, but sufficient components efficiencies will be required to implement the Brayton gas turbine power cycle. The complex manufacturing and assembly of this approach are most amenable for low volume, high cost, specialized applications.

Silicon Batch-Processed Microturbines

The turbomachinery configurations are significantly different when implemented using lithography-based microfabrication techniques. The layout is purely radial, with the blade shapes defined in the plane of the wafer by lithography and etching. Similarly, the bearings and other components must be reinvented to comply with the constraints of microfabrication and integration. Research and development efforts on the core components of a micro gas turbine engine have been extensively studied under the micro gas turbine engine program at MIT over the past decade [2]. In addition, research programs on devices implementing alternate cycles, such as the Rankine microturbine by Fréchette et al. [5], have explored the core technologies for microturbine-based systems with different requirements. The primary findings from this work are presented here.

Microturbomachinery

Single-stage microturbines on 4.2 mm diameter rotors have been demonstrated at rotational speeds of over 1.4 million rpm, which corresponds to 5 W of mechanical power [6]. The power density of the turbine is calculated to be 3500 MW/m^3, which is a least twice that of high performance turbines in commercial transport jet engines, supporting the trend proposed by the Cube-Square law. The performance matches well with CFD predictions, suggesting that current numerical modeling is adequate at this stage of development. Turbine isentropic efficiency at this scale is predicted to be in the range of 55 – 70%, which is acceptable for a Rankine power cycle, but marginal to close the Brayton cycle. Since the Rankine cycle typically operates at very high pressure ratios, multistage turbines are required to expand the working fluid. Multi-stage turbines with significantly shorter blade chord (100 µm vs. 1 mm) were also demonstrated on 4 mm rotors. Turbine isentropic efficiency of 35% was measured at 330,000 rpm (average $Re = 266$) [7]. Predictions suggest an increase in efficiency up to 63% at a design rotor speed of 1.1 million rpm due to the increase in Re at higher speed.

These experimental demonstrations confirm that silicon microfabrication is a valid approach to implement microturbines. The relatively simple structures survived the centrifugal loads at high speeds. In addition, rotor balancing was not required after fabrication, a required step for traditional high speed rotors.

M

Bearings

These high speed demonstrations also confirm the ability of fluid film bearings to be implemented in power MEMS. The journal bearing was operated in a hydrostatic mode by forcing air axially along the cylindrical bearing gap. Pressure drop at the entrance of the gap was found to vary as a function of the radial clearance, leading to a restoring radial force. Modeling and experimental investigations of very short plain journal bearings suggest that stable hydrodynamic operation would require the rotor to be offset radially, to within a clearance of $1 - 2$ µm. This close proximity is not practical, hence hydrostatic operation is preferred. Alternate journal bearing designs, such as foil bearings and tilted pad bearings deserve further investigation.

Various thrust bearing configuration have been successfully demonstrated, including central and annular hydrostatic thrust bearings with $1 - 2$ µm operating gaps and 8 – 10 µm diameter restrictors, as well as hydrodynamic spiral groove thrust bearings. Since the ratio of clearance to radial extent is not as small as traditional bearings, developing flows in the entrance region of the bearings are not necessarily negligible. Beyond these entrance regions, well-established lubrication theory, such as the Reynolds equation for lubrication films, is found to be appropriate. The representation of the gas as a continuum becomes questionable for clearance of less than 1 µm, however. Slip

boundary conditions should therefore be considered below this scale.

Other Components

Electromechanical Generators

Microfabricated generators on the millimeter and watt scales have also been demonstrated for mechanical to electrical energy conversion. Electrostatic induction micromotors operating above 2 MHz and 100 V have been fabricated and integrated with microturbomachinery and fluid film bearings [8]. Performance levels to date are however limited to the sub-watt range. These require a small clearance between the disk and the stator, leading to high viscous losses. They are however fabricated with standard semiconductor materials (dielectrics and conductors), which facilitates their integration. Electromagnetic induction and permanent magnet generators have also been fabricated and characterized with an external drive. The fabrication processes for magnetic machines is however challenging, since they require laminated cores, coils with multiple windings, and the integration of permanent magnet materials. Their operation is limited in temperature due to the Currie point of the magnetic materials and their mechanical strength is less than single-crystal silicon. Their use in high speed, high temperature power MEMS must therefore be considered carefully. To their advantage, they operate with large clearance, which reduces the viscous losses in the generator and have been demonstrated to generate over 1 W of electrical power at 40% of mechanical-to-electrical conversion efficiency [9].

Microcombustors

As a heat source, micro-combustors have been developed to burn hydrogen or a hydrocarbon fuel with oxygen from the ambient air. Combustion requires mixing of the fuel and air, followed by a chemical reaction. The time required for combustion to occur defines the length of the combustion chamber. Although the mixing time can be reduced with miniaturization, the reaction time is independent of scale. Furthermore, a miniature combustion chamber will be prone to heat loss since the surface area dominates over the reaction volume at smaller scale. Nevertheless, complete combustion of hydrogen in $0.2\,cm^3$ micro-combustors has been successfully demonstrated, without noticeable effects to the silicon structures [2]. In the Brayton cycle, combustion occurs directly in the working fluid, allowing high operating temperatures. In the Rankine steam cycle, heat from the combustor must be transferred to the working fluid through a heat exchanger, limiting the operating temperatures.

Microfabrication

Most of the MEMS-based microturbine devices demonstrated to date consisted of deep reactive ion etched, single-crystal silicon wafers that are fusion bonded. Stacks of up to six such wafers have been assembled to create micro-combustors and microturbines. The main fabrication challenges stem from the need to achieve the level of tolerances required for the proper operation of the rotating components. The journal bearing designs prone high aspect ratio trenches with minimal taper, such as 15 μm wide trenches of 400 μm in depth. Etch uniformity is also important to minimize the imbalance of the silicon rotors. As the turbine blades are etched, a non-uniformity in etch rate across a rotor would lead to a center of mass that would be offset from the geometric center. This offset must be significantly less than the journal bearing clearance to prevent a wall strike as the rotor is accelerated through its natural frequency. An offset on the order of 2 μm has been readily achievable for 4 mm diameter rotors with 150 mm tall blades on a 300 μm thick disk [2]. At increased dimensions of 8 mm diameter and 400 μm tall blades, the level of imbalance becomes excessive and often prevents high speed operation as fabricated.

From a thermal perspective, silicon has noticeable limitations. First, since silicon transitions from a brittle to a ductile behavior in the proximity of 950 K, high speed rotors could experience creep from the centrifugal loads above this temperature. To address this issue, fabrication approaches to reinforce silicon rotors with silicon carbide have been explored. A second challenge is thermal management, which stems from the high thermal conductivity of silicon and the short length scales separating hot and cold streams. The approach to date has focused on allowing heat to conduct through the structures and recuperate the heat loss with the working fluid. This fluidic cooling approach facilitates the fabrication, since silicon can still be used, but to the detriment of performance and efficiency. Alternatively, silicon could be replaced by less conductive materials, such as glass or alumina, but at the expense of mechanical strength and ease of micromachining. The integration of non-traditional MEMS materials in the process flow is also a challenge for magnetic machinery.

Micro Power Generation Systems

Based on the core components and technologies described above, various turbine-based microsystems are at different stages of development. Given the complexity of these microsystems, their development requires an incremental

approach where the core components are initially developed independently (as described above), then gradually integrated as subsystems of increased functionality. Each step typically requires the redesign and fabrication of the components that are combined on a single chip, given their strong interaction. The value of establishing a solid design base at each stage of development is therefore important.

Micro Gas Turbine Engines

The MIT H_2 demo micro gas turbine engine, illustrated in Fig. 2, is designed as a 6-wafer stack that encloses an 8 mm single stage compressor and 6 mm turbine bonded to form the rotor [2]. The design speed is 1.2 million rpm with a mass flow of 0.36 g/s of air. It is predicted to deliver 0.1 N of thrust or 17 W of shaft power. Envisioned applications include jet propulsion for micro air vehicles and portable power generation. The core rotating component, acting as a turbocharger, has been demonstrated at speeds above 400,000 rpm with an external air supply. Further development to operate the engine in close cycle with combustion is required.

Rankine Microturbine

A Rankine steam turbine power plant-on-a-chip for power generation from waste heat is also under development [5]. The device design consists of 4 mm rotors with multi-stage microturbines, magnetic generators and a spiral groove viscous micropump, integrated with two-phase flow microchannel evaporators and condensers. The 1 cm^2 chips are predicted to deliver up to 12 W of electrical power with thermal-to-electrical conversion efficiency of 1 – 10%, according to the temperature of the heat source. This technology could be used for waste heat recovery from automobile exhaust or industrial processes. The rotating subsystem (turbopump shown in Fig. 1) has been demonstrated up to 330,000 rpm, validating the multistage turbine models, micropumps design, and seal functionality. Thermal insulation is required in the device to prevent heat leakage from the hot steam in the turbine to the liquid in the pump.

Other Microturbine Applications

Air-driven microturbines could also find applications other than power generation. For example, an optical modulator based on a rotating grading machined on the rotor has been demonstrated up to speeds of 60,000 rpm, driven by compressed air. The device integrated glass and silicon wafers to form the wafer stack.

Future Directions for Research

Microfabrication

Since microfabrication is one of the most limiting factors in the development of microturbines and power MEMS in general, further research in this area is required. Of most importance are:

- Insulating materials, such as glass, quartz, alumina, and porous silicon and their microfabrication methods to create high aspect ratio structures compatible with wafer bonding;
- Integration of electromagnetic machinery into the process flow;
- Understanding the materials issues related to durability of high speed rotating micromachinery and their failure modes;
- Process control to achieve the tolerances in bond alignment and deep reactive ion etching of critical structures.

System and Components

- Losses and heat transfer in moderate Reynolds number flows ($10 < Re < 10000$);
- Advanced fluid bearings with broad stability margins, high speed capability, and self-sustained operation;
- System level integration of on-chip and off-chip components;
- Address a broader range of applications, such as micro-compressors for cooling, rocket pumps, flow metering, and biochemical processing.

M

Cross References

- ▶ Micro Energy Conversion Devices
- ▶ Microscale Energy Conversion Devices
- ▶ Supersonic Micro-Nozzles
- ▶ Microrockets
- ▶ Pressure Driven Single Phase Gas Flows
- ▶ Heat Transfer in Microchannel Flows
- ▶ Silicon Micromachining
- ▶ Anisotropic Etching
- ▶ Wafer Bonding
- ▶ Microfabrication Techniques
- ▶ Photolithography
- ▶ Plasma Etching

References

1. Jacobson SA (1998) Aerothermal challenges in the design of a microfabricated gas turbine engine. 29th Fluid Dynamics Conf, Albuquerque AIAA 98–2445
2. Epstein AH (2004) Millimeter-scale micro-electro-mechanical systems gas turbine engines. J Eng Gas Turbines Power 126:205–226

3. Isomura K, Tanaka S, Togo SI, Esashi M (2005) Development of high-speed micro-gas bearings for three-dimensional micro-turbo machines. J Micromech Microeng 15:222–227
4. Peirs J, Reynaerts D, Verplaetsen F (2003) Development of an axial microturbine for a portable gas turbine generator. J Micromech Microeng 13:190–195
5. Fréchette LG, Lee C, Arslan S, Liu YC (2003) Design of a microfabricated rankine cycle steam turbine for power generation. Proc ASME Int Mech Eng Congress Expo, Washington
6. Fréchette LG, Jacobson SA, Breuer KS, Ehrich FF, Ghodssi R, Khanna R, Wong CW, Zhang X, Schmidt MA, Epstein AH (2005) High-speed microfabricated silicon turbomachinery and fluid film bearings. J Microelectromech Syst 14(1):141–152
7. Lee C, Fréchette LG (2005) Demonstration and characterization of a multi-stage silicon microturbine. Proc ASME Int Mech Eng Congress Expo, Orlando
8. Fréchette LG, Nagle SF, Ghodssi R, Umans SD, Schmidt MA, Lang JH (2001) An electrostatic induction micromotor supported on gas-lubricated bearings. IEEE 14th Int Micro Electro Mechanical Systems Conf MEMS, Interlaken
9. Arnold DP (2004) Magnetic Machines for Microengine Power Generation. Ph.D. thesis, School of Electrical and Computer Engineering, Georgia Institute of Technology, USA

Microvalve

► Electrostatic Valves
► Piezoelectric Valves

Micro-Wave Rotor

Definition

Wave rotor is a promising technology which uses unsteady waves to create a self cooled dynamic pressure exchange between fluids. For high-pressure, high-temperature topping cycles, it results in an engine overall pressure ratio and temperature increase which in turn generate higher efficiency and lower specific fuel consumption. The microscale version of the wave rotor has applications for portable power generation, small propulsion equipment and microscale heat exchangers.

Cross References

► Shock Wave in Microchannel

Millikan's Resistance Factor

► Cunningham's Correction

Miniature Heat Pipes

► Micro Heat Pipes

Miniature Heat-Removal Devices

► Microscale Cooling Devices

Miniature Unmanned Air Vehicle (UAV)

► Microrotorcraft

Miniaturized Analysis Systems

► Lab-on-a-Chip (General Philosophy)

Miniaturized Fluorescence-Activated Cell Sorting Devices

► Flow Cytometer Lab-on-Chip Devices
► Microfluidic Systems for High-Throughput Screening

Miniaturized Ion Mobility Spectrometry

MAGGIE TAM[1], PRASHANTA DUTTA[2],
HERBERT H. HILL JR.[1]
[1] Department of Chemistry, Washington State University, Pullman, WA, USA
[2] School of Mechanical and Materials Engineering, Washington State University, Pullman, WA, USA
dutta@mail.wsu.edu

Synonyms

Plasma chromatography; Ion mobility spectrometer; Time of flight ion mobility spectrometry; Field asymmetric ion mobility spectrometry; Differential ion mobility spectrometry

Definition

Ion mobility spectrometry is an analytical technique that separates ions based on their mobilities through an electric field in a non-ionic medium. Ion mobility spectrometry

separates compounds based on the differences in mobilities, which depends on the size and charge of the ion, electric field, and interaction between the ions and the medium. Ion mobility spectrometry is an established method of choice for the detection of explosives and illicit drugs. Commercial ion mobility spectrometers are available and are widely employed in public areas.

Overview

In an ion mobility spectrometer analyte ions are moved by an applied electric field along a tube, where the ions experience multiple collisions with neutral drift gas molecules. Ion mobility spectrometry offers milliseconds-fast analysis time, simple operation and maintenance, low cost instrumentation, and portability. Ion mobility spectrometry is now the method of choice in drug and explosive detection, and is widely employed in public areas like airports, customs, courthouses and correctional institutions. There are more than ten commercial companies that manufacture bench-top, portable and hand-held ion mobility spectrometry devices. Moreover, there are currently more than forty major research groups worldwide that focus on different aspects of ion mobility spectrometry research: studying the fundamentals of ion mobility spectrometry, expanding the technique for new applications, and coupling with new ionization and separation techniques.

Schematic of a typical ion mobility spectrometer is shown in Fig. 1. An ion mobility spectrometer consists of an ionization source, an ion mobility drift tube, a detector, and supporting electronics. The samples are usually ionized by radioactive Nickel-63, electrospray ionization source, corona discharge, or photoionization source. The ions travel through the drift tube while colliding with the medium molecules, usually air or nitrogen, at atmospheric pressure. The resulting ion velocity is proportional to the applied electric field and mobility of the ion.

The ion mobility, K, is the ratio of the ion velocity, v_d, to the magnitude of the applied electric field, $\boldsymbol{E}$. The ion mobility is constant under low-field conditions where the $\boldsymbol{E}/N$ quotient is typically less than 2 Td ($1\,\text{Td} = 10^{-17}\,\text{Vcm}^2$). Ion mobility can be determined from the experimental parameters as:

$$K = \frac{v_d}{E} = \frac{L^2}{Vt_d} \tag{1}$$

where the drift length, L, is the lengthwise distance from the ion shutter to the detector, the drift time, t_d, essentially is the time an ion takes to travel this distance, and V is the electric potential.

A theoretical relation between ion mobility and the charge and size of the ion was developed by Revercomb and

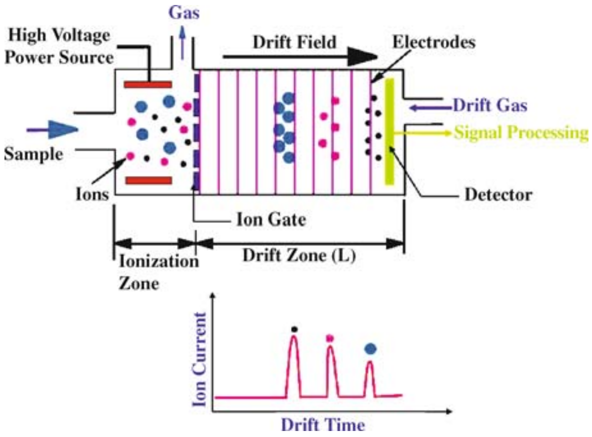

Miniaturized Ion Mobility Spectrometry, Figure 1 Schematic of an ion mobility spectrometer, showing the location of the ionization region and drift region, which are separated by an ion gate. In the ionization zone, sample vapor is ionized using an ionization source. Ions are then gated by an electronic shutter into the drift zone. Ions move down the drift region due to the electric field (also known as drift field) and collected by the detector. Smaller ions move faster than larger ions, hence require less drift time

Mason [1]:

$$K = \frac{3}{16N} \cdot \left(\frac{2\pi}{\mu kT}\right)^{1/2} \cdot \frac{ze}{\Omega_D} \tag{2}$$

where N is the number density of the drift gas, μ is the reduced mass, k is the Boltzmann constant, z is the charge of the ion, e is the elementary charge, and Ω_D is the collision cross section of the ion. To account for the dependence on temperature, T, and pressure, P, and to facilitate comparison among different experimental settings, the mobility constant is commonly normalized to 273 K and 760 mm Hg and reported in literature as the reduced mobility, K_0:

$$K_0 = K \times \left(\frac{273}{T}\right) \times \left(\frac{P}{760}\right). \tag{3}$$

Separation Efficiency and Resolution

Several expressions are used to describe the separation efficiency of ion mobility spectrometry. These include the peak width at half height, $w_{1/2}$, the resolving power, R_p, and the number of theoretical plates, N. These terms can be expressed in theory and from experimental data. The peak width at half height is the width of a mobility peak at 50% of its height, and it has units of milliseconds. The experimental resolving power of an ion mobility spectrometer is determined by measuring the drift time (t_d) and peak

width at half height ($w_{1/2}$) of a single mobility peak:

$$R_p = \frac{t_d}{w_{1/2}} . \tag{4}$$

The typical resolving power obtained from a commercial 3.9 cm long ion mobility spectrometer is about 30, and the resolving power obtained from a research grade 20 cm long ion mobility spectrometer is around 100. The resolving power of ion mobility spectrometry is related to the chromatographic theoretical plate numbers by the following equation:

$$N = 5.55 \left(R_p\right)^2 . \tag{5}$$

Therefore, a commercial ion mobility spectrometer has roughly 5000 theoretical plates, whereas a research grade ion mobility spectrometer has approximately 55,000 theoretical plates.

The diffusion limited resolving power can be expressed as:

$$\text{Diffusion Limited } R_P = \left(\frac{V\,ez}{16kT \ln 2}\right)^{1/2} = \left(\frac{E \cdot L \cdot ez}{16kT \ln 2}\right)^{1/2} . \tag{6}$$

While the diffusion limited resolving power estimates the possible separation power of an ion mobility spectrometer, the theoretical resolving power determines its separation power by taking the additional consideration of the actual operation parameters, such as the ion shutter pulse width and pressure as:

$$\text{Theoretical } R_P = \frac{\frac{L^2}{V \cdot K_0} \times \frac{P}{760} \times \frac{273}{T}}{\sqrt{\left(t_g^2 + \left(\frac{16kT \ln 2}{V\,ez}\right) \cdot \left(\frac{L^2}{V \cdot K_0} \times \frac{P}{760} \times \frac{273}{T}\right)^2\right)}} \tag{7}$$

The efficiency of an ion mobility spectrometer can be computed by expressing the experimental resolving power as a percentage of the theoretical resolving power as

$$\text{Efficiency} = \frac{\text{Experimental } R_P}{\text{Theoretical } R_P} \times 100\% \tag{8}$$

Basic Methodology

There are two major types of ion mobility spectrometers. The first type is the gas phase time-of-flight ion mobility spectrometer, which detects the analyte signal as a function of the arrival time. The second type is the gas phase differential mobility spectrometer, which measures the analyte signal as a function of the compensation voltage. The separation in gas phase time-of-flight ion mobility spectrometry is based on the mobility of the analytes, with the analytes having faster mobility reaching the detector sooner. On the other hand, in gas phase differential mobility spectrometer, the separation is based on the variance in mobility as a function of changing electric field. Both time-of-flight ion mobility spectrometry and differential mobility spectrometry have been reviewed extensively in the past. For detail and advanced information on ion mobility spectrometry, readers are advised to consult references [1–6].

Gas Phase Time-of-Flight Ion Mobility Spectrometer

Figure 1 shows a schematic view of a gas phase time-of-flight ion mobility spectrometer. There are two sections, separated by an ion shutter, in an ion mobility spectrometer: the ionization or desolvation region and the drift region. A typical ion mobility drift tube (Fig. 1) contains individual metal guard rings, connected in series with resistors (not shown here), which establish a homogeneous electric field along the drift tube. Bradbury–Nielsen gate and Tyndall gate are the most common versions of ion shutter.

The ion shutter opens periodically to let in a pulse of ions into the drift region of the spectrometer. The length of time that the ion shutter remains open is called the pulse width, t_g. The gated ions collide with neutral drift gas molecules at atmospheric pressure while traveling down the drift region due to a uniform electric field along the drift channel. The purpose of the drift gas is to sweep off neutral species out of the system. Ions finally strike the detector and generate an electrical signal for identification. Separation in ion mobility spectrometry is based upon the differences in the size, shape and charge of the ions, as well as the physical and chemical interaction between the ions and the drift gas molecules. It is obvious that smaller ions move faster than larger ions due to their smaller cross-sectional areas, and hence require less drift time than that of larger ions.

Separation of Trinitrotoluene Using Ion Mobility Spectrometry – An Example

In this section, trinitrotoluene (TNT), a common military explosive, is selected as the analyte of interest to show the typical parameters of an ion mobility spectrometry analysis. Trinitrotoluene, with its molecular weight of 227.1 Da, has a reduced mobility of 1.54 $cm^2V^{-1}s^{-1}$ in air. In ion mobility spectrometer with a 3.9 cm drift tube and an applied electric field of 250 Vcm^{-1}, operating at 200 °C

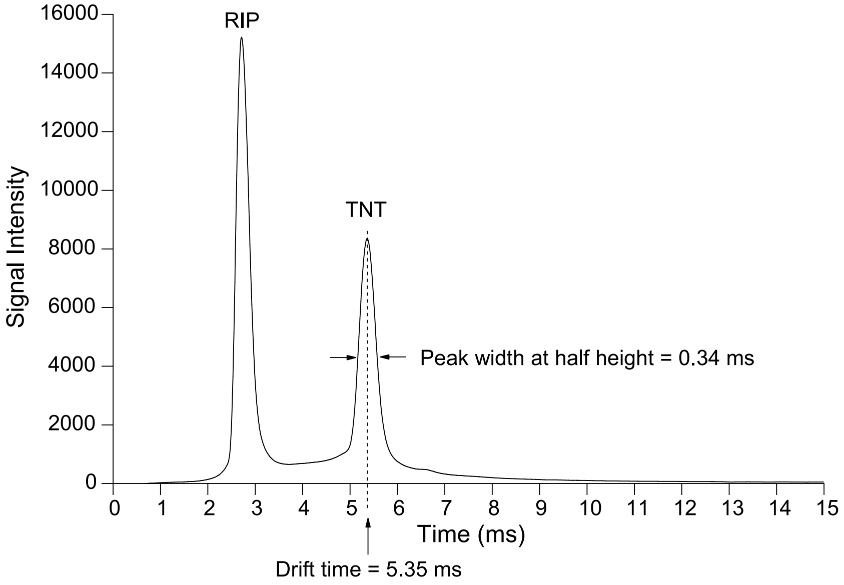

Miniaturized Ion Mobility Spectrometry, Figure 2 Ion mobility spectrum of 100 ng trinitrotoluene as analyzed by ITEMISER (GE Interlogix), a commercial ion mobility spectrometer. Two peaks were observed, the chloride reactant ion peak (RIP) and the trinitrotoluene (TNT) peak. The TNT peak had a drift time of 5.35 ms, with a peak width of 0.34 ms

and 700 torr, trinitrotoluene would have a drift time of 5.4 ms with a detection limit in the ppb range. Fig. 2 shows an ion mobility spectrum of trinitrotoluene analyzed by ITEMISER (GE-Interlogix), a commercial bench-top ion mobility spectrometer with a 3.9 cm long drift tube and a diffusion limited resolving power of 47. From Eq. (1), the experimental mobility of TNT can be calculated as $2.90\,\mathrm{cm^2V^{-1}s^{-1}}$ and reduced mobility of TNT can be determined from Eq. (3) as $1.54\,\mathrm{cm^2V^{-1}s^{-1}}$. The experimental peak width at half height, as shown in Fig. 2, was 0.34 s. The experimental resolving power is therefore 16 and the experimental number of theoretical plates is 1400. The theoretical resolving power of this instrument is 23 and the efficiency of the instrument is 68%.

Gas Phase Differential Mobility Spectrometer

The working principle of differential mobility spectrometry (DMS), also known as field asymmetric waveform ion mobility spectrometry (FAIMS), is significantly different from that of conventional drift tube time-of-flight ion mobility spectrometry (TOFIMS). In DMS, sample ions are allowed to move through a carrier gas under specialized waveform electric fields. Generally a rectangular shaped wave with a high positive field ($\boldsymbol{E}_{\mathrm{high}}$) is applied for a shorter period (t_{high}) and a low negative field ($\boldsymbol{E}_{\mathrm{low}}$) is used for a longer time (t_{low}). Figure 3a shows a schematic of a DMS for analytes separation; the associated waveform electric field distribution is shown in Fig. 3b. This technique takes advantages of differences in mobility during high and low electric field periods. Experimental results show that mobility of ions changes nonlinearly with applied electric field if the ratio of electric field to gas density exceeds 40 Td [7]. For instance, at atmospheric pressure, some ions such as CO^+CO demonstrate increase in mobility with increasing electric field, while others (N_4^+, N_3^+, N^+) show decrease or no change in mobility with increasing electric field strength [7]. Therefore, in a gas phase, the electric field dependent ion mobility can be written as

$$K(\boldsymbol{E}) = K(0)\,[1 + \alpha(\boldsymbol{E})] \tag{9}$$

Where $K(0)$ is the mobility of ions at low electric field, and its value remains constant for a particular ion. Equation (9) indicates that the value of α will determine whether the mobility of ions will change with increasing electric field. The net displacement of an ion in the y-direction over one cycle of asymmetric field can be expressed as

$$\Delta y_{\mathrm{cycle}} = K(\boldsymbol{E}_{\mathrm{high}})\,\left|\boldsymbol{E}_{\mathrm{high}}\right|\,t_{\mathrm{high}} - K(\boldsymbol{E}_{\mathrm{low}})\,\left|\boldsymbol{E}_{\mathrm{low}}\right|\,t_{\mathrm{low}} \tag{10}$$

Hence, under the action of waveform electric field, shown in Fig. 3b, the ions with $\alpha > 0$ will have a net drift toward positive y-direction after each cycle, and these ions will

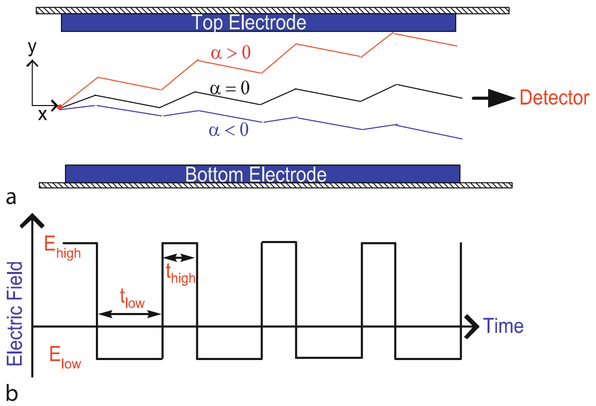

Miniaturized Ion Mobility Spectrometry, Figure 3 (**a**) Schematic view of a differential ion mobility spectrometer. For ions of positive α, the effective ion mobility increases with increase in electric field, while for ions with $\alpha < 0$, the mobility decreases with increase in electric field. It is important to note that at low electric field strength ($\boldsymbol{E} < 10{,}700$ V/cm at atmospheric pressure) the value of α is zero. (**b**) Cyclic waveform electric field used to generate asymmetric field in the drift tube

eventually hit the top wall. On the other hand, the ions with $\alpha < 0$ will reach bottom wall by drifting in the negative y-direction due to the waveform electric field. The net drifting, of a particular type of ions in a cycle, in the vertical direction can be stopped by applying a DC compensation electric field depending on the direction of drifting. For instance, a negative compensation electric field is required if $\alpha > 0$, and vice versa. Therefore, a mixture of ions in a carrier gas can be completely separated by ramping or sweeping of DC electric field applied to the system.

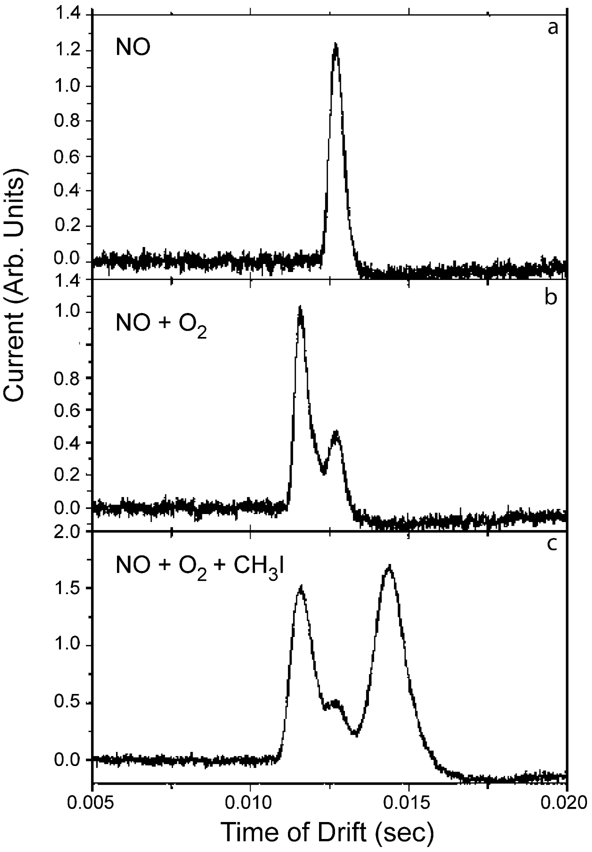

Miniaturized Ion Mobility Spectrometry, Figure 4 Mobility spectra of negative ions: (**a**) NO, (**b**) NO + impurity, and (**c**) NO + impurity + CH_3I. Reprinted with permission from [8]. Photoionization method was used to form the free electrons, and the drift gas was maintained at atmospheric temperature. These spectra were averaged over 20 scans, and the drift times were adjusted for a uniform drift potential of −500 V

Key Research Findings

Gas Phase Time-of-Flight Ion Mobility Spectrometer

Current research in miniaturized gas phase time-of-flight ion mobility spectrometry can be categorized by its drift tube design. The most common type is still the stacked-ring design with multiple guard rings. Additionally, there is the *cigarette-rolled* design, fabricated with low-temperature cofired ceramics.

Stacked-Ring Design

The stacked-ring design stemmed from the work of Earl W. McDaniel at Georgia Institute of Technology [7]. This design consists of a stack of guard rings which are connected in series with resistors, establishing a uniform electric field. The ring electrodes are insulated from one another by physical distance and insulating spacers, such as ceramic rings or sapphire balls.

Currently there are four commercial companies offering handheld and portable gas phase time-of-flight ion mobility spectrometers, with drift tubes shorter than 5 cm: Smiths Detection, Bruker-Daltonics, GE-Interlogix, and G.A.S. Gesellschaft für analytische Sensorsysteme mbH. Table 1 presents their respective instruments and their major applications. These instruments generally use an applied electric field of around 250 $\mathrm{V\,cm^{-1}}$, and they operate at either ambient or elevated temperature, and at atmospheric pressure. The samples are ionized by radioactive nickel-63 source mostly, but also by corona discharge and photo-ionization source.

Besides the commercial spectrometers, there are also reports of novel prototypes of miniaturized gas phase time-of-flight ion mobility spectrometers. Xu et al. [8] fabricated a miniature ion mobility spectrometer; their miniature IMS device was 35 mm in length having a 1.7 mm diameter drift channel. There were 25 metal electrodes

Miniaturized Ion Mobility Spectrometry, Table 1 List of commercially available miniaturized gas phase ion mobility spectrometers

Company	Instrument	Application
Bahia-21	MO-2M	Explosives
Bruker-Daltonics	RAID-1	Chemical warfare agent
	RAID-M	Chemical warfare agent
GE-Interlogix	Itemiser	Explosives and narcotics
	Vapor Tracer	Explosives and narcotics
Gesellschaft für analytische Sensorsysteme mbH	μIMS-ODOR	Odorization additive of natural gas
	UV-IMS Portable	Volatile organic compounds
	Ni-IMS Portable	Volatile organic compounds
	TEIMS-SF6	Decomposition products of SF6
Implant Sciences	Quantum Sniffer QS-H150	Explosives
	Quantum Sniffer QS-BTS	Explosives
Smiths Detection	APD2000	Chemical warfare agent
	CAM	Chemical warfare agent
	LCD	Chemical warfare agent
	MCAD	Chemical warfare agent
	SABRE 4000	Explosives, chemical warfare agents, toxic industrial chemicals, and narcotics
Thermo Electron	EGIS Defender	Explosives

stacked in the channel and separated by insulator spacers. The electrodes were made of oxygen-free high density copper (OFHC) with a thickness of 0.33 mm. The insulator spacers were made of Macor with an inner diameter of 3 mm, outer diameter of 15.7 mm, and thickness of 1.1 mm. Total 24 miniature resistors were connected between the electrodes to form a voltage divider. Each resistor had 1 MΩ with 1% uncertainty. To apply the drift voltage along the channel, a power supply was connected to end electrodes and the voltage was distributed to sequential electrodes through these resistors. They observed a linear decrease in potential along the channel which indicated a nearly homogeneous electrostatic field produced in the drift region. The electrode next to the detector plate was ac-grounded through a capacitor so the electric current due to ion movement would not be coupled to the detector.

They used a frequency-quadrupled Nd:YAG laser as an ionization source, and negative ions were formed by binding free electrons with NO, O_2 and methyl iodide (CH_3I) [8]. Figure 4 illustrates the mobility spectra of negative ions obtained from the aforementioned miniaturized IMS. A single peak (Fig. 4a) was found when nitric oxide was provided in the ionization region and argon was used as a drift gas. Two ion peaks (Fig. 4b), one due to NO^- and the other due to the residual oxygen, appeared when the drift gas was switched to nitrogen (with 1.2 ppm oxygen and 1.1 ppm moisture) from argon. Figure 4c presents the mobility spectrum when a mixture of nitric oxide and methyl iodide was introduced in the ionization region, and nitrogen was used as the drift gas [8].

The multipurpose sensor project at Washington State University and Boise State University involves design and construction of a miniaturized ion mobility device for measuring sub-surface organic contaminants. The remote controlled capability of the miniaturized ion mobility device is suitable for long-term monitoring at contamination sites. Their ion mobility device featured stainless steel guard rings, insulated by Macor ceramic rings, with a 6.8 cm drift length and an electric field of 452 $V cm^{-1}$. The ion mobility device, including its sampling module, supporting electronics and wireless data transmission, was housed inside a cone penetrometer that was pushed into the ground by a hydraulic jacking system. Figure 5 shows the cross-sectional view of the cone penetrometer, which can be pushed down to forty feet below ground. The cone penetrometer was tested at a field site known to have trichloroethylene contamination. Figure 6 illustrates the ion mobility spectrum, with trichloroethylene detected from the contaminated soil sample. This sub-surface ion mobility device has a detection limit of 6 ppb_v-trichloroethylene, and is capable of detecting trichloroethylene in a mixture with gasoline, jet fuel, and diesel.

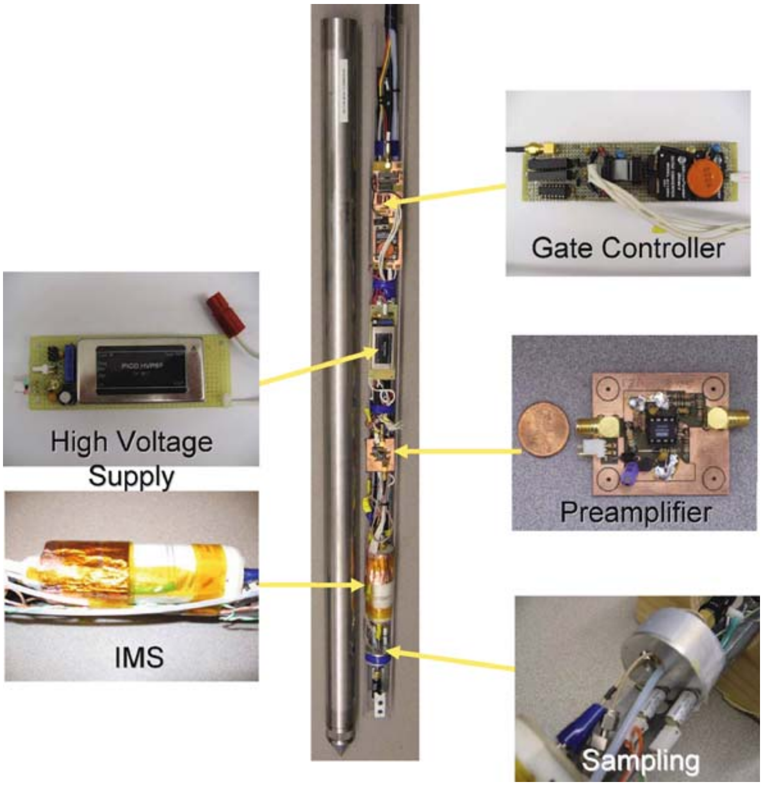

Miniaturized Ion Mobility Spectrometry, Figure 5 Miniaturized ion mobility spectrometer for sub-surface measurement

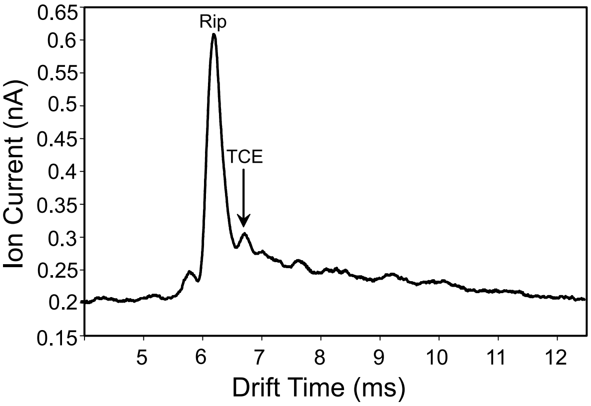

Miniaturized Ion Mobility Spectrometry, Figure 6 Ion mobility spectrum of sub-surface soil sample, known to be contaminated with trichloroethylene (TCE). A peak for trichloroethylene was observed, at a reduced mobility of 1.89 $cm^2V^{-1}s^{-1}$

LTCC Cigarette Roll Design

Although the stacked-ring design has dominated for four decades, the design is not suitable for miniaturization in terms of mass production. An ion mobility spectrometer, even at miniature size, can easily have over a hundred parts and required labor-intensive construction. For example, an ion mobility spectrometer of 20 electrodes requires 20 insulating spacers, 20 resistors, an ion gate, and over 20 electrical connections among the electrodes, the resistors, and the ion gate. The ultimate goal of a miniaturized system is one that can be mass produced cost effectively by automation. Sandia National Laboratory explored low temperature co-fire ceramic as a potential solution for mass-producing miniaturized ion mobility spectrometers [9]. The rolled design, that replaced the stacked-ring design, eliminated many parts by using machine to print electrodes and resistors onto an unfired sheet of pliable low temperature co-fire ceramic. The low temperature co-fire ceramic is made of glass and proprietary organic compounds, which burn off during the firing process. The printed low temperature co-fire ceramic can then be rolled into the required size. After being fired, the rolled tube with the printed electrodes and resistors fused with the ceramic into one piece. Only minimal manual connections are required for this fabrication process.

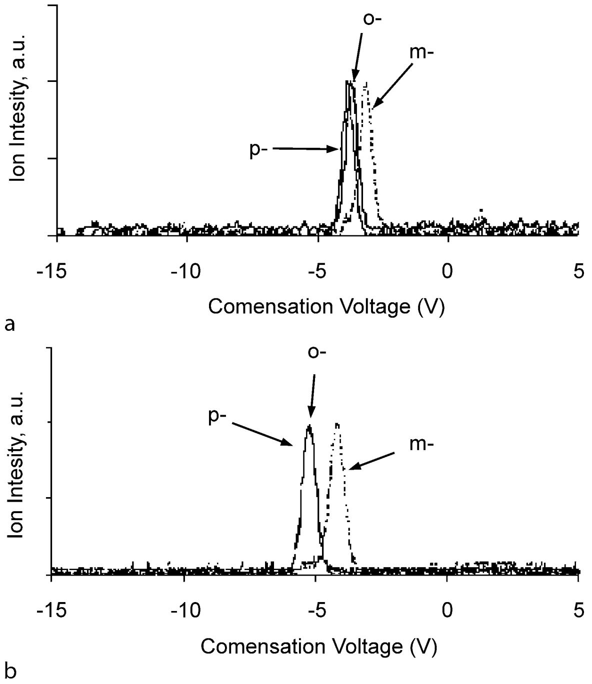

Miniaturized Ion Mobility Spectrometry, Figure 7 DMS spectra for m-, o- and p-xylene ions. A miniature 10.6 eV ($\lambda = 116.5$ nm) UV light source was used to produce the photons for ionization. (**a**) $E_{high} = 18$ kV/cm and (**b**) $E_{high} = 24$ kV/cm. Reprinted from [10] with permission from Elsevier

Gas Phase Differential Mobility Spectrometer

A miniaturized drift chamber is particularly useful for proper functioning of DMS since this technique requires very high electric field. In miniaturized drift tube, the distance between top and bottom electrodes is scaled down to microns. Hence, a very high electric field can be obtained by applying relatively low voltages across the electrodes.

Miller and co-workers [10] first fabricated a miniaturized DMS using Pyrex substrates and heavily boron doped silicon wafer. Silicon wafer of 500 μm thick was placed in between the two Pyrex substrates and determined the thickness of the drift tube. Titanium (40 nm) and Gold (120 nm) were deposited on the Pyrex substrates to form ion filter, a deflector electrode and a detector electrode. Patterning of Ti/Au electrodes was performed by conventional lift off process using Shipley 1822 photoresist. Once the electrodes were formed, silicon wafers were diced into strips and bonded with Pyrex by the anodic bonding process. A photo-ionization source (10.6 eV photo discharge lamp, $\lambda = 116.5$ nm was connected to the device to provide a means for the photons to enter the ionization region [10].

Figure 7 shows the spectra for xylene isomers obtained from a micro fabricated radio-frequency DMS described above [10]. It is important to note that the structural isomers of xylene (meta-, para-, and ortho-) have the same molecular weight, but they differ in position of the second methyl group. Ortho-xylene is 1,2-dimethylbenzene, meta-xylene is 1,3-dimethylbenzene, and para-xylene is 1,4-dimethylbenzene. At low electric field, they have similar cross-section and can only be separated by an ion mobility spectrometer with ultra-high resolving power. However, owing to the differences in mobilities at high electric field, m-xylene could be separated from p- and o-xylenes, although p- and o-xylenes were inseparable [10].

Future Directions for Research

One shortcoming of gas phase ion mobility spectrometry is its inability to maintain high resolving power at small scale. The separation efficiency of time-of-flight ion mobility spectrometry is limited by the low-field requirement, the speed of ion shutter gate relative to the drift time of analyte ion, and the space charge effect.

In order to maintain the desired high resolving power, the drift length must be increased when higher voltages are used. As a result, gas phase ion mobility spectrometry suffers from low resolving power when the instrument size is reduced. While laboratory-size gas phase ion mobility spectrometry instruments, with a drift length of 20 cm, routinely achieve a resolving power of 100, miniaturization of gas phase ion mobility spectrometry results in much lower resolving power. Thus, gas phase ion mobility spectrometer could not be scaled down to function as a micro sensor without sacrificing resolving power.

To circumvent this problem, researchers ventured away from signal averaging to employing time-dispersive data acquisition, such as Fourier transformation and Hadamard transformation, and reported an increase in signal-to-noise ratio and an improvement in resolving power.

Adding a separation dimension in tandem with ion mobility spectrometry improves the separation power of a miniaturized device, in terms of increasing the number of peaks that it can separate. Multicapillary columns and gas chromatograph had been coupled at the front end of miniaturized ion mobility spectrometers to pre-separate otherwise co-eluting mobility peaks. The added dimension is ideal for separating analytes with close mobilities and also for separating complex samples.

Cross References

► Chromatography
► Electrophoresis
► Electroosmotic Flow (DC)

M

References

1. Revercomb HE, Mason EA (1975) Theory of Plasma Chromatography/Gaseous Electrophoresis. Anal Chem 47(7):970–983
2. Eiceman GA, Karpas Z (2005) Ion Mobility Spectrometer, 2nd edn. CRC Press, Boca Raton
3. Guevremont J (2004) High-field asymmetric waveform ion mobility spectrometry: A new tool for mass. J Chromatogr A 1058(1-2):3–19
4. Collins DC, Lee ML (2002) Developments in ion mobility spectrometry – mass spectrometry. Anal Bioanal Chem 372(1):66–73
5. Ewing RG, Atkinson DA, Eiceman GA, Ewing GJ (2001) A critical review of ion mobility spectrometry for the detection of explosives and explosive related compounds. Talanta 54(3):515–529
6. St Louis RH, Hill HH Jr (1990) Ion Mobility Spectrometry in Analytical Chemistry. CRC Crit Rev Anal Chem 21(5):321–355
7. McDaniel EW, Mason EA (1973) The mobility and Diffusion of Ions in Gases. Wiley, Hoboken
8. Xu J, Whitten WB, Ramsey JM (2000) Space Charge Effects on Resolution in a Miniature Ion Mobility Spectrometer. Anal Chem 72:5787–5791
9. Pfeifer KB, Rumpf AN (2005) Measurement of Ion Swarm Distribution Functions in Miniature Low-temperature Co-fired Ceramic Ion Mobility Spectrometer Drift Tubes. Anal Chem 77:5215–5220
10. Miller RA, Nazarov EG, Eiceman GA, King AT (2001) A MEMS Radio-frequency Ion Mobility Spectrometer for Chemical Vapor Detection. Sens Actuators A 91:301–312

Miniaturized Systems

► Lab-on-Chip Devices for Protein Analysis

Miniaturized Total Analysis System (μ-TAS)

► Microfluidic Systems

Minichannels

Definition

Channels with the smallest passage dimension D between 3 mm and 200 μm.

Cross References

► Boiling and Evaporation in Microchannels

Mixing Effectiveness

► Mixing Measures

Mixing Efficiency

► Mixing Measures

Mixing Enhancement

► Turbulence Control (Microflap, Microballoon, Microsynthetic Jet)

Mixing Measures

Mark A. Stremler
Department of Engineering Science and Mechanics,
Virginia Polytechnic Institute and State University,
Blacksburg, VA, USA
mark.stremler@vt.edu

Synonyms

Degree of mixing; Mixing effectiveness; Mixing efficiency; Mixing performance; Mixing quality

Definition

Mixing is the homogenization of an initially heterogeneous substance through bulk motion and/or molecular diffusion. In the development of mixing processes, it is necessary to evaluate the ability of each process to mix rapidly and uniformly. Mixing measures quantify the degree to which a substance is homogenized.

Overview

Mixing is a crucial process in many micro- and nanofluidic systems. Despite the small length scales involved, molecular diffusion alone is often insufficient to rapidly produce a uniform mixture. The small length scales also make it impractical to produce turbulent flow, which is typically used to mix rapidly in macroscale systems. Special consideration has thus been given to the design of small-scale devices that rapidly mix fluid under laminar flow conditions. A key requirement of this development is the ability to consistently quantify the degree to which fluid is mixed in a device by a given protocol.

Fluid mixing has been discussed in the scientific literature for over a century. In 1894, O. Reynolds described fluid mixing as a three-step process [10], which is consistent with the modern view [8, 9]. First, the substance is

stretched in at least one direction and, due to volume conservation, attenuated in an orthogonal direction; second, the substance is folded, piled, or wrapped back upon itself; and third, in a miscible fluid mixture, molecular diffusion completes the homogenization. The first two steps, namely stretching and folding, are often performed concurrently and can be viewed as a result of stirring. Through fluid motion, stirring breaks up large-scale inhomogeneities, stretching out interfaces and layering together distinct regions of fluid. In miscible fluids, the third step, namely molecular diffusion, is also occurring concurrently. In many cases, however, the effects of stirring dominate in the early stages of the mixing process. Furthermore, every process does not include all three steps: immiscible fluids inhibit or prevent diffusion across interfaces, and some techniques, such as hydrodynamic focusing (see passive mixing), stretch the fluid but do not fold it. How best to produce these steps in an effective mixing device depends on the properties of the components, the initial state of the system, the desired outcome, and the available technology.

Despite the long history of fluid mixing as a subject of scientific inquiry, the best tools for quantifying the mixedness of a system are not clearly determined. To quote J. Ottino, a mixing measure "should be selected according to the specific application and it is futile to devise a single measure to cover all contingencies" [8]. Nevertheless, it is useful to identify a few measures that provide a basis for evaluating device performance. The context for this discussion will be systems relevant to micro- and nanofluidic applications, with focus on mixing fluid containing a diffusing (and perhaps reacting) ▶ tracer such as a dye. The measures discussed here require the ability to observe and measure variations in the spatial distribution of this tracer.

Numerous mixing measures have been proposed through the years. The most often used measures are based on the variance of the concentration of a tracer substance, with Danckwerts' intensity of segregation [4] being the most common. These measures have been in use for decades and are considered the standard. However, practical implementation of these measures depends on a somewhat arbitrary course-graining of the domain, and in the ideal limit of a smooth distribution they do not account satisfactorily for the important effects of stirring. Measures based on the Shannon entropy [3] display similar behavior and are less commonly used, so these are not discussed here in detail.

A recent development are multi-scale measures of mixing that can be defined as weighted sums of the coefficients in a Fourier decomposition of the concentration field. These measures, including the mix-variance [5] and multi-scale mixing efficiencies [11], do not depend on a choice of ▶ coarse-graining scale, they are able to capture the effects of stirring even when diffusion is negligible, and they show promise for evaluating mixing in micro- and nanofluidic devices.

Most of the experimental setups used to characterize small-scale mixing devices use miscible fluids containing a passive diffusive tracer such as dye. This tracer will have a spatially and temporally varying concentration $c(\boldsymbol{x},t)$, where $\boldsymbol{x}$ is the vector position and t is time. A stirring mechanism (see, e. g., ▶ microfluidic mixing) will impose a velocity distribution $u(\boldsymbol{x},t)$ that advects the tracer, and the tracer will diffuse with a molecular diffusivity D. If the flow is incompressible and the domain of interest does not have sources or sinks of concentration, or a net concentration flux at the boundary, then the total concentration in the domain is conserved and the average concentration, namely

$$c_{\text{ave}} = \frac{1}{V}\int c(\boldsymbol{x},t)\,\mathrm{d}V\,, \tag{1}$$

is constant in time. In this case one can consider, without any loss of generality, the scalar field $\theta(\boldsymbol{x},t) = c(\boldsymbol{x},t) - c_{\text{ave}}$. For incompressible fluid, $\theta(\boldsymbol{x},t)$ evolves according to the advection–diffusion equation

$$\frac{\partial\theta}{\partial t} + \boldsymbol{u}\cdot\nabla\theta = D\,\nabla^2\theta\,. \tag{2}$$

Multiplying Eq. (2) by θ and integrating this product over the fluid domain gives

$$\frac{\mathrm{d}}{\mathrm{d}t}\,\|\theta\|_2^2 = -2D\,\|\nabla\theta\|_2^2\,, \tag{3}$$

where $\|\theta(\cdot,t)\|_2$ is the L_2-norm given by

$$\|f(\boldsymbol{x})\|_2 = \int |f(\boldsymbol{x})|^2\mathrm{d}V\,, \tag{4}$$

which is proportional to the scalar variance

$$\sigma^2 = \frac{1}{V}\int |f(\boldsymbol{x})|^2\mathrm{d}V\,. \tag{5}$$

That is, by Eq. (3) the variance of a conserved scalar concentration will decrease with time when that scalar is diffusive. The rate of decrease in $\|\theta\|_2^2$ is proportional to the molecular diffusivity D and depends on the variance of the concentration gradients, and the long-time, steady-state limit of the system is a uniform concentration, $c(\boldsymbol{x},t)\to c_{\text{ave}}$ or $\theta(\boldsymbol{x},t)\to 0$. A more rapid decay indicates better mixing, which is the basis for using the intensity of segregation and related quantities as mixing measures. Stretching and folding by the flow field do not appear explicitly in Eq. (3), but this deformation acts to

M

increase local concentration gradients and improve mixing. In the absence of diffusion, $\|\theta\|_2^2$ is constant in time, which seems to indicate that no mixing occurs. However, it is clear that stirring will mix up the fluid even in the absence of diffusion, and it would be useful if the applied mixing measure captured this behavior. In micro- and nanoscale systems, mixing is often needed on time scales for which bulk diffusion is negligible, which makes it important to accurately quantify the effects of stirring. Addressing this role of stirring in the mixing process is a major motivation for the development of multi-scale mixing measures.

A key requirement for proper mixing evaluation is to clearly define better or more efficient mixing. In most micro- and nanoscale applications the objective is to obtain a sufficiently homogeneous substance as quickly as possible using whatever means available, in which case the mixing time or mixing length is of primary interest. This definition of better mixing is assumed here. In contrast, energy expenditure is crucial in many macroscale applications, and a slower mixing protocol may be considered more efficient. The mixing measures considered here do not account for the energy used during the mixing process.

One approach to developing laminar flow mixing devices is to design for chaos using mathematical models and tools from dynamical systems theory. In this approach, the quality of the system is determined using chaos measures such as Poincaré sections and Lyapunov exponents, which are based on passive particle kinematics. The underlying assumption in this approach is that there is a strong connection between the generation of chaos and efficient mixing. For more information on chaos and its measures, see ► chaotic flow.

Basic Methodology

Mixing measures quantify the spatial homogeneity or, similarly, inhomogeneity in a (fluid) system initially comprised of multiple distinct regions or species. The exact computation of any measure depends in part on how one distinguishes between different species and on what one means by a homogeneous mixture. The evolution of the measure as the system is mixed can depend significantly on the initial distribution of the different species, and the final state of the system depends on whether not the mixing process involves a chemical reaction or a concentration source. Thus, accurately quantifying the ability of a system to mix well, particularly if comparison is to be made with other systems, requires consistent use of initial conditions and careful characterization of the fluid (in)homogeneity, in addition to a good choice of mixing measure.

Determining the Scalar Field

The mixing measures discussed here quantify the spatial distribution of some scalar field that becomes homogenized by a mixing process. Accurately computing a mixing measure requires quantifying the local values of this scalar. In both experimental and computational analyses of mixing, measurement or prediction of the continuous scalar field $c(\boldsymbol{x}, t)$ almost always results in a discrete set of N values $c_\mathrm{i}(t)$ that each represent the average of $c(\boldsymbol{x}, t)$ within a small element of area $\mathrm{d}A_\mathrm{i}$. This forced binning has some effect on the computation and interpretation of the mixing measures.

One common approach of making an experimental measurement is to use a colored or fluorescent dye in a transparent device, shine light through the device, and record the image with a camera. In this optical method, the quantity being measured is, for example, the intensity of light captured by each pixel in a charge-coupled device (CCD) array. The dependence of this intensity on the local dye concentration should be determined through a controlled calibration process, including the minimum observable concentration and the functional relationship between intensity and concentration. Background noise due to flaws or features in the device should be removed by subtracting out the image containing no dye. The analysis is simplest if the calibration results are uniform across the region being evaluated; if this region has varying fluid depth, for example, then this uniformity is not likely. The lighting and camera settings must be consistent throughout the experiment for these steps to give reliable data. Of course, if something other than optical sensing is used, it is still necessary to calibrate the measurements, account for background noise, and maintain consistent experimental settings.

Note that in some cases the substance being mixed cannot be viewed as a continuously varying concentration field. For example, in a suspension of large biomolecules it is (usually) desirable for these molecules to maintain their integrity, which forces even a fully mixed system to remain inhomogeneous at length scales on the order of the molecule size. Obviously, the definition of the scalar field or the implementation of a mixing measure must be adjusted for situations such as this.

The imaging technique described above produces a planar image. Pixel intensities are a result of light passing through the full depth of the device, and thus depend on the depth-averaged concentration. The distribution in Fig. 1a, when sensed using a light below and CCD array above, i. e. averaged in the y-direction, cannot be distinguished from the fully mixed case. Care must be taken so that a case such as this is not misinterpreted. If features of a distribution

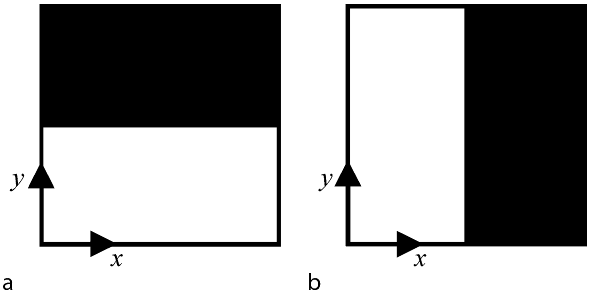

Mixing Measures, Figure 1 Example initial distributions

through the depth of a device must be resolved in order to accurately evaluate the mixing process, then an alternate technique such as confocal microscopy should be considered. Another option in this case is to test the device by monitoring the product of a chemical reaction that depends on the level of mixing [6].

Initial Distributions

The choice of initial inhomogeneity, such as the concentration distribution, can have a significant influence on how rapidly a system becomes well mixed. Consider, for example, mixing with the linear shear flow

$$u(y) = U y \tag{6}$$

in the domain $0 \le y \le 1$, where u is the velocity component in the x-direction. If the initial distribution is that shown in Fig. 1a, the flow has no effect on it and mixing is due solely to diffusion. If instead the initial distribution is that shown in Fig. 1b, the length of the interface between the black and white fluids increases linearly in time, and mixing progresses faster than for Fig. 1a. In general, the appropriate choice of initial distribution will depend on the design of the device, the intended use of the system, and the results of the calibration process. Ideally this distribution will allow observation of both strengths and weaknesses in the mixing device. Placing dye only in a poorly mixed region (such as in a regular, or elliptic, island; see ▶ chaotic flow) will lead to a poor characterization of the device; conversely, placing too much dye over a large portion of the domain may lead to overestimating the device's capability.

Comparisons between devices are best made when the initial distributions are all similar for both, but it can be difficult to determine similar initial distributions for different mixing protocols. If the initial distributions are significantly different, care must be taken when making any device comparisons. One approach is to characterize the mixing performance of a device for several relevant initial distributions, something that currently is not standard practice in the evaluation of micro- and nanoscale mixers.

Reference States

Mixing measures are typically defined with respect to a reference state c_{ref}. This state may be the average of the concentration field being considered, $c_{\mathrm{ref}} = c_{\mathrm{ave}}$, the average concentration of the final well-mixed state, $c_{\mathrm{ref}} = c_{\mathrm{mix}}$, or it may be a more complicated function of position. When there are sources or sinks of concentration [11], chemical reactions involving the observed species [7], or variations in the thickness of the region of interest, the system does not necessarily become completely homogeneous even when fully mixed, and a non-uniform field $c_{\mathrm{ref}}(\boldsymbol{x})$ should be used to accurately measure mixing.

Mixing measures are often normalized with respect to the initial distribution. This normalization gives a dimensionless measure and helps account for some variation in the initial distribution, such as small changes in concentration levels between tests. As discussed above, however, a dimensionless measure cannot account for large or fundamental differences in initial distribution.

In a closed system, the initial distribution, the well-mixed reference state, and the progression of mixing are all imaged at the same location. Obviously this is not possible in an open system such as a microchannel, in which the mixing progresses as the fluid moves axially. The initial distribution is present only at the inlet of the channel and thus serves to normalize the result at every location considered in the analysis. The well-mixed reference state, however, can often be determined at each location by passing a mixed solution through the system.

Variance-Based Mixing Measures

The *intensity of segregation* introduced by Danckwerts [4] is defined as

$$\Phi_1 = \frac{\sigma^2}{\sigma_0^2}, \tag{7}$$

where σ^2 is the variance of the instantaneous scalar field $c(\boldsymbol{x})$ being considered, namely

$$\sigma^2 = \frac{1}{A} \int |c(\boldsymbol{x}) - c_{\mathrm{ref}}|^2 \, \mathrm{d}A, \tag{8}$$

σ_0^2 is the variance of the initial distribution, and c_{ref} is the reference state (see above). It is assumed here that the scalar field is planar and defined over a region with area A.

M

This measure is initially $\Phi_1 = 1$ and decays to zero as the domain becomes homogeneous.

The distribution $c(\boldsymbol{x})$ is typically not a continuous function but rather a discrete set of N values c_i, such as the pixel intensities in a CCD array. Each c_i can be viewed as the average value of $c(\boldsymbol{x})$ within a *bin* with size $\mathrm{d}A_i$. If the bin size distribution is consistent between the current and reference states, then the variance is given by the sum

$$\sigma^2 = \frac{1}{N}\sum_{i=1}^{N} |c_i - c_{\mathrm{ref}}|^2 . \tag{9}$$

Thus, in practice this measure is based on a course-grained representation of the scalar field, and the results will depend on the choice of bin size [3]. In some investigations this bin size is taken to be the resolution of the imaging measurement, but this choice is somewhat arbitrary. An advantage of course graining is that it gives the ability to dictate the scale at which mixing is considered important. Also, bin sizes can be chosen to capture the effects of stirring even when diffusion is negligible. However, since the results depend on the choice of scale, whether or not the system appears well mixed is somewhat arbitrary, and consistent comparison between experiments is difficult.

One occasional modification of the intensity of segregation is to use the *coefficient of variation* [1]

$$\mathrm{COV} = \frac{\sigma}{c_{\mathrm{ave}}} , \tag{10}$$

where c_{ave} is the average of the instantaneous scalar field $c(\boldsymbol{x})$ and $c_{\mathrm{ref}} = c_{\mathrm{ave}}$. The mixing measure is thus

$$\Phi_1' = \frac{\mathrm{COV}}{\mathrm{COV}_0} = \frac{(c_{\mathrm{ave}})_0}{c_{\mathrm{ave}}} \sqrt{\Phi_1} , \tag{11}$$

although sometimes COV is used directly. This measure is typically used to evaluate mixing for cases in which the average concentration is not conserved.

There are at least 36 other related statistical measures [2], two of which are

$$\Phi_2 = 1 - \frac{\sigma^2}{\sigma_0^2} , \tag{12}$$

and

$$\Phi_3 = 1 - \frac{\sigma}{\sigma_0} . \tag{13}$$

Both of these measures have an initial value of zero and increase to one as the system becomes homogeneous. Boss [2] conducted a comparison of these measures using 9 evaluation criteria. The measures Φ_2 and Φ_3 rank the highest in that comparison, with their primary advantage over Φ_1 being that they increase in value as mixing increases. Boss [2] concludes that Φ_3 is the best of these indices for determining the state of any mixture.

Multi-Scale Mixing Measures

Multi-scale mixing measures can be viewed as an extension of the course-graining approach to the above measures. Instead of quantifying the homogeneity of the system using a single course-grain scale, or bin size, the multi-scale measures average over a range of scales. These measures can be computed directly as an average over different bin sizes, or as weighted sums of the coefficients in the Fourier decomposition of the instantaneous concentration field [5]

$$c(\boldsymbol{x}) = \sum_{\boldsymbol{k}} \hat{c}_{\boldsymbol{k}} \exp\{\mathrm{i}\, 2\pi\, (\boldsymbol{k}\cdot\boldsymbol{x})/L\} , \tag{14}$$

where $\boldsymbol{k} = (k_1, \dots, k_n)$ is the n-dimensional wave-number vector. Differences between these measures lie in the weighting assigned to different scales.

The current definitions of these measures require the scalar field to be spatially periodic. Since this is almost never the case, the analysis takes place on a periodic continuation of the domain; i. e. it is assumed that the domain consists of an infinite number of periodically arranged copies of the original.

The Mix-Norm [5] is the measure that results from averaging over all possible scales. This measure is given in terms of the Fourier coefficients $\hat{c}_{\boldsymbol{k}}$ as

$$\Phi_4(c) = \sqrt{\sum_{\boldsymbol{k}} \Lambda_{\boldsymbol{k}} |\hat{c}_{\boldsymbol{k}}|^2} , \tag{15}$$

where $\Lambda_{\boldsymbol{k}}$ is the weighting factor. For a one-dimensional scalar field (e. g. data from a single line of pixels), the weighting factor is given by

$$\Lambda_k = \int_0^1 \frac{\sin^2(k\pi s)}{(k\pi s)^2}\, \mathrm{d}s , \tag{16}$$

and for a two-dimensional scalar field it is

$$\Lambda_{\boldsymbol{k}} = 2\Gamma(1) \int_0^1 \frac{J_1^2(s\pi k)}{(s\pi k)^2}\, \mathrm{d}A , \tag{17}$$

where Γ is the gamma function, J_1 is a Bessel function of the first kind, and k is the magnitude of $\boldsymbol{k}$. In both cases, $\Lambda_{\boldsymbol{k}}$ must be computed numerically, and the values decay monotonically with increasing k. The *Mix-Variance* is then defined as $\Phi_4^2(c - c_{\mathrm{ref}})$. Note that these two measures as defined in [5] are not normalized by the initial values.

The multi-scale mixing efficiencies [11] are obtained by noting that weighting the Fourier coefficients, as in Eq. (15), is related to examining the variance of concentration gradients. The authors in [11] examine the following gradients of the relative scalar field

$$||\nabla\theta||_2^2 = \sum_{\boldsymbol{k}} k^2 |\hat{\theta}_{\boldsymbol{k}}|^2 , \tag{18}$$

which focuses on small scales, and

$$||\nabla^{-1}\theta||_2^2 = \sum_{\boldsymbol{k}} \frac{|\hat{\theta}_{\boldsymbol{k}}|^2}{k^2} , \tag{19}$$

which focuses on large scales. The multi-scale mixing efficiencies are defined as

$$\Phi_5 = \frac{||\nabla\theta_0||_2^2}{||\nabla\theta||_2^2} \tag{20}$$

and

$$\Phi_6 = \frac{||\nabla^{-1}\theta_0||_2^2}{||\nabla^{-1}\theta||_2^2} . \tag{21}$$

These measures give a somewhat arbitrary weighting to the various scales in the problem, but separating large and small scale effects can lend important insight into the progression of the mixing.

Mixing Time, Mixing Length, and Mixing Rate

In many cases it is useful and practical to define an index that quantifies how long it takes for the fluid to become well mixed. These indices require the choice of a measure to characterize the time-dependent evolution of mixing in the system, and the results depend on this choice of measure.

For the mixing time or mixing length, a threshold level is defined, say 95% mixing, and this index gives the time or length needed for the system to reach this threshold. For example, choosing the measure Φ_3 and a threshold level of 95% mixing, the mixing length L_{95} gives the length of microchannel needed to achieve $\Phi_3 \geq 0.95$ using a given mixing protocol. As with all the measures, the result will also depend on the initial distribution.

For the mixing rate, it is assumed that efficient mixing will lead to exponential decay or increase in the mixing measure. For example, again choosing the measure Φ_3, which increases with mixing, the mixing rate R is defined by fitting the curve $1 - \exp(-Rt)$ to the data.

Future Directions for Research

In general, the investigation and development of small-scale mixing devices would benefit from a more careful and consistent evaluation of mixing quality. Regardless of which measure is used, the importance of initial condition and system calibration make it difficult to directly compare the current mixing studies of different devices developed and tested in different laboratories. A single study that examines mixing in several competing devices using a consistent, carefully documented procedure would likely be quite instructive.

Further development and application of multi-scale mixing measures are needed. Work is currently being done to formulate the mix-norm and mix-variance for arbitrary domains [5], which will make this tool more widely applicable. Multi-scale measures are slightly more difficult to compute than the traditional single-scale measures based on the variance of concentration, but they can capture the effects of stirring and they show promise for quantifying mixing quality. However, this multi-scale approach is new enough that its application is currently quite limited. Comparisons need to be made between the different multi-scale measures and with the traditional measures to clearly establish which is the more appropriate and useful tool.

Cross References

- ► Active Mixer
- ► Chaotic Flow
- ► Chaotic Mixing Based on Viscoelasticity
- ► Microfluidic Mixing

References

1. Aubin J, Fletcher D, Bertrand J, Xuereb C (2003) Characterization of the mixing quality in micromixers. Chem Eng Technol 26:1262–1270
2. Boss J (1986) Evaluation of the homogeneity degree of a mixture. Bulk Solids Handl 6(6):1207–1215
3. Camesasca M, Manas-Zloczower I, Kaufman M (2005) Entropic characterization of mixing in microchannels. J Micromech Microeng 15:2038–2044
4. Danckwerts P (1952) The definition and measurement of some characteristics of mixtures. Appl Sci Res A3:279–296
5. Mathew G, Mezić I, Petzold L (2005) A multiscale measure for mixing. Phys D 211:23–46
6. Munson M, Yager P (2004) Simple quantitative optical method for monitoring the extent of mixing applied to a novel microfluidic mixer. Anal Chim Acta 507:63–71
7. Muzzio F, Liu M (1996) Chemical reactions in chaotic flows. Chem Eng J 64:117–127
8. Ottino J (1989) The Kinematics of Mixing: Stretching, Chaos, and Transport. Cambridge University Press, Cambridge
9. Ottino J, Wiggins S (eds) (2004) Transport and mixing at the microscale: Papers of a Theme Issue. Philosophical Trans R Soc London A 362:1818

10. Reynolds O (1894) Study of fluid motion by means of coloured bands. Nature 50:161–164
11. Shaw T, Thiffeault JL, Doering C (2007) Stirring up trouble: Multi-scale mixing measures for steady scalar sources. Phys D 231(2):143–164

Mixing Performance

► Mixing Measures

Mixing Quality

► Mixing Measures

MLPA

► Multilayer Piezoelectric Actuator

Mn

► Number-Average Molecular Weight

Model Kinetic Equation

Definition

Model kinetic equation is the Boltzmann equation with a simplified form of the collision integral.

Cross References

► Gas Flow in Nanochannels
► Heat Transfer in Microchannel Flows
► Micro- and Nanoscale Gas Dynamics
► Lattice Poisson-Boltzmann Method, Analysis of Electroosmotic Microfluidics

Model Order Reduction (MOR)

Yi Wang[1], Aditya S. Bedekar[1],
Siva Krishnamoorthy[2],
Shivshankar Sundaram[1], Ashok K. Singhal[1]
[1] CFD Research Corporation, Huntsville, AL, USA
[2] Baxter Healthcare Corporation, Round Lake, IL, USA
yxw@cfdrc.com

Synonyms

Model reduction

Definition

Model Order Reduction (MOR) is a set of theories and techniques that reduce the order of a complex dynamic system while preserving its essential properties and input-output behavior for efficient and accurate simulation and design.

Overview

Microfluidics technology holds great promise for a wide spectrum of applications in the realm of genomics, proteomics, diagnostics, and drug discovery. In contrast to the sophisticated analysis and processing functionalities that have been achieved to date, efficient modeling and design of microfluidic devices continues to be a challenge. This is primarily attributed to the increasing complexity of today's microfluidic chips, arising from the integration of more components and functions, and accompanied by the interplay of multiple physicochemical phenomena, such as fluid flow, heat transfer, mass transport, electrokinetics, biochemistry, and structural mechanics.

Currently, multiphysics-based high fidelity numerical analysis is the dominant technique that allows coupled analysis of these phenomena and provides detailed information of spatio-temporal variations of the field variables. However, prohibitive CPU time and memory requirements make it unsuitable for system-level modeling and design of entire microfluidic devices. Therefore, in order to truly enable simulation-based chip design with rapid turnaround time, compact models with substantially reduced computational expense (while capturing the underlying physicochemical phenomena, remaining basic conservation laws, and accounting for chip complexity) are highly desired.

In general, compact models are classified into three categories: ►primitive models, ►macromodels, and ►behavioral models [1]. A primitive model is the constituent element (e. g., capacitors, inductors, and resistors etc.) in a complex system and is typically represented as a single Differential-Algebraic Equation (DAE) derived from basic conservation laws in different domains. The difference between macromodels and behavioral models is subtle, and both describe the dynamic response of a device via a set of equations. Macromodels are constructed via assembly of primitive models or a set of DAEs in a system-level representation, while the behavioral models are more generic and effective forms and built on the underlying domain-physics [1].

Strictly speaking, Model Order Reduction (MOR) refers to compact model generation procedures that lump the

spatial dependency of device behavior, extract the most typical characteristics of the governing equations, and, hence, reduce the order of the problem. MOR originally derives from control theory and is widely used in electronic and MEMS design. Many of the techniques are based on subspace projection (such as Arnoldi approach and Proper Orthogonal Decomposition). In addition to these well-established methods, we will also introduce some other useful approaches, such as ► Artificial Neural Networks (ANNs) and analytical methods (e. g., Method of Moments), which have been recently reported for modeling of microfluidics systems.

Basic Methodology

Electric Analogy

The electric analogy is one of the most extensively used methods for flow and species transport modeling in channel-based microfluidic systems. A microfluidic network is equivalent to an electric circuit, of which each component can be individually described by resistors, conductors, and inductors Eqs. (1) and (2) show the *RLC* circuit models in electric and fluidic domain,

$$\Delta\Phi = L_e \frac{dI}{dt} + R_e I + \frac{1}{C_e}\int I\,dt \quad \text{(electric)} \tag{1}$$

$$\Delta P = L_f \frac{dQ}{dt} + R_f Q + \frac{1}{C_f}\int Q\,dt \quad \text{(fluidic)} \tag{2}$$

where subscripts e and f are, respectively, for the electric and fluidic quantities; P is pressure and ϕ is potential; t is the time, I is the electric current; Q is the volumetric flow rate. L, R, and C represent the inductance, resistance, and capacitance of the component, which for fluidics arise from the fluid inertia (momentum acceleration), viscous shear force at channel walls, and fluid compressibility. Depending on the physical phenomena involved and component types of interest, Eq. (2) can be further simplified, e. g., in microfluidics the fluid compressibility is normally absent and the third term on the R.H.S of Eq. (2) can be neglected. Next, we will discuss typical cases that are often encountered in electric analogy-based microfluidic modeling.

Transient Pressure Driven Flow in a Channel of Constant Cross-Section

For a channel with a constant cross-section, its fluidic resistance is written as

$$R_f = \begin{cases} \dfrac{12\beta l \mu}{d^4\left[1 - \frac{192\beta}{\pi^5}\sum\limits_{i=1,3,5\ldots}^{\infty}\frac{\tanh(i\pi/2\beta)}{i^5}\right]} & \text{(rectangular channel)} \\ \dfrac{8\mu l}{\pi r_c^4} & \text{(circular channel)} \end{cases} \tag{3}$$

where μ is the dynamic viscosity of the fluid, l is the channel length, $\beta = d/h$, d, and h are the aspect ratio, width, and depth of the rectangular channel. r_c is the radius of the circular channel. The fluidic inductance is given by [2],

$$L_f = \frac{\rho l}{A_c} \tag{4}$$

where ρ is the fluid density and A_c is the cross-sectional area of the channel.

Coupled Pressure Driven and Electroosmotic Flow (EOF) at Steady State

When flow in a microchannel is driven by both electric potentials and pressure gradients that are externally applied or internally induced, electroosmotic flow (EOF) and streaming current need to be taken into account. Streaming current is caused by the effective movement of the counter-ions in the diffuse layer of the Electric Double Layer (EDL) due to pressure gradients. Equations (1) and (2) are then rewritten as,

$$\begin{cases} Q = \frac{\Delta P}{R_f} + \frac{\Delta\Phi}{R_{EOF}} = G_f\Delta P + G_{EOF}\Delta\Phi \\ I = \frac{\Delta P}{R_{st}} + \frac{\Delta\Phi}{R_e} = G_{st}\Delta P + G_e\Delta\Phi \end{cases}$$

$$\text{or}\quad \begin{bmatrix} Q \\ I \end{bmatrix} = \begin{bmatrix} G_f & G_{EOF} \\ G_{st} & G_e \end{bmatrix} \cdot \begin{bmatrix} \Delta P \\ \Delta\Phi \end{bmatrix} \tag{5}$$

where the inductance term is neglected for steady-state flow; G refers to the conductance, the reciprocal of the resistance; G_f is the fluidic conductance; G_{EOF} reflects the flow rate contribution from EOF; G_{st} the electric conductance of the streaming current due to pressure-driven flow; and G_e the electric conductance attributed to the EOF convection and conduction of species under electric field. Equation (5) is a generalized form and obtained by cross-sectional integration of the pressure-induced and electroosmotic flow velocity and current density. The expression for G_f, G_{EOF}, G_{st} and G_e depends on the cross-sectional shape of microchannels, buffer and species properties [3].

Elastic Structural Elements in Microfluidics

In addition to the fluid flow, electric analogy can be also applied to modeling elastic structural elements (e. g.,

valves and membrane chambers) and their coupling to flow in microfluidic devices. For valves, the interaction between the movable structure and the surrounding flow is strong and normally categorized into reverse and forward flow modes. In the reverse flow mode zero flow rate or a constant leakage is assumed, while in the forward flow mode a non-linear pressure-flow static characteristic (i. e., fluidic resistance) is used [2], which is given in Eq. (6)

$$Q = \frac{\gamma}{\mu} \Delta P^3 \tag{6}$$

where γ is a factor depending on the geometry and stiffness of the valve. The clamped membrane is another widely used structural element in micropumps. Activated by external forces (e. g., electrostatic and piezoelectric etc.), it propels the fluid flow through its volumetric change due to the membrane compliance. Therefore, elastic membranes are typically modeled as capacitors (storing fluid mass),

$$\Delta P = \frac{1}{C_{\text{mem}}} \int_s \delta \, \mathrm{d}\Gamma \tag{7}$$

where C_{mem} is the capacitance of the membrane, δ is the spatial deflection of the membrane, Γ is its total surface area, and ΔP is the net pressure applied to it. The models for structure elements are often assembled to the fluidic element models to achieve system-level simulation and design of the entire microfluidic device [2].

In practice, a lot of microfluidic devices often involve irregular component geometry (e. g., junctions and channels with variable cross-sections) and, hence, their R, L and C values in Eqs. (1) and (2) are not directly available. In this case, high-fidelity simulations that enable spatio-temporal analysis and/or an ensemble of experimental data are used to identify and extract these values. Usually, an interface linking the detailed device simulation and macro-model generation needs to be established to automate *RLC* value extraction. Such a procedure is called automatic macromodel extraction [1].

Arnoldi-Based Model Order Reduction

Arnoldi-based algorithm is a classical Krylov subspace-based [4] MOR technique. In particular it is suited to investigate linear transport problems in microfluidics, such as heat transfer, species diffusion, and low-Reynolds flow (negligible fluid inertia). The underlying philosophy of Arnoldi-based algorithm is to reduce the dimension of the spatially semi-discretized form of the original governing PDEs using moment-matching of transfer functions.

Before presenting Arnoldi-based algorithm, we introduce fundamentals of the projection subspace. Consider a system of first-order ODEs given below

$$\begin{cases} \frac{\mathrm{d}\boldsymbol{X}}{\mathrm{d}t} = \mathbf{A} \cdot \boldsymbol{X} + \mathbf{B} \cdot \boldsymbol{Z} \\ \boldsymbol{Y} = \mathbf{C} \cdot X \end{cases} \tag{8}$$

where $\boldsymbol{X}(t) \in \mathrm{Re}^n$ is the state vector of unknowns (a function of time), n is the dimension of the system and the total number of ODEs. $\mathbf{A} \in \mathrm{Re}^n \times \mathrm{Re}^n$ is the system matrix, $\boldsymbol{Z} \in \mathrm{Re}^m$ is the input vector. $\mathbf{B} \in \mathrm{Re}^n \times \mathrm{Re}^m$ is the scatter matrix relating the input function to each state $\boldsymbol{X}$. $\boldsymbol{Y} \in \mathrm{Re}^p$ is the output vector containing quantities of interest, and $\mathbf{C} \in \mathrm{Re}^p \times \mathrm{Re}^n$ is the gather matrix, which links the system state to the output. Often the number of Eq. (8) is so large that it is prohibitively expensive for an efficient system-level simulation. Hence, we seek for a transformation matrix $\mathbf{V}$ that projects the behavior of the state vector $\boldsymbol{X}$ into a subspace with low-dimension r, which is given by

$$\boldsymbol{X} = \mathbf{V} \cdot \boldsymbol{X}_r + \varepsilon\,, \ \ \boldsymbol{X}_r \in \mathrm{Re}^r\,, \ \ r \ll n\,, \ \ \varepsilon \approx 0 \tag{9}$$

where $\mathbf{V} \in \mathrm{Re}^n \times \mathrm{Re}^r$ consists of r n-dimensional vectors that contain a basis for the reduced subspace. $\boldsymbol{X}_r \in \mathrm{Re}^r$ represents the equivalent of $\boldsymbol{X}$ in the reduced subspace, $\varepsilon \in \mathrm{Re}^n$ is a small error. When the subspace is located (i. e., $\mathbf{V}$ is determined), Eq. (8) can be projected on it to obtain a system with lower dimensions (that is $r \ll n$) while the essential behavior is still preserved. This can be expressed as

$$\begin{cases} \frac{\mathrm{d}\boldsymbol{X}_r}{\mathrm{d}t} = \mathbf{A}_r \boldsymbol{X}_r + \mathbf{B}_r \boldsymbol{Z} \\ \boldsymbol{Y} = \mathbf{C}_r \boldsymbol{X}_r \end{cases} \tag{10}$$

Note that even through projection, the input $\boldsymbol{Z}$ and output $\boldsymbol{Y}$ vector of the system remain unchanged. For large-scale system, an effective and prevalently used projection subspace is the Krylov subspace [4].

The Arnoldi-based algorithm begins with a spatial discretization of the governing PDEs to attain the dynamic system equations as Eq. (8). Specifically, here $\boldsymbol{X}(t)$ is the state vector of unknowns (a function of time) on the discrete nodes and n is the total number of nodes; $\mathbf{A}$ is formulated by the numerical discretization; $\boldsymbol{Z}$ defines the functions of boundary conditions and source terms; $\mathbf{B}$ relates the input function to each state $\boldsymbol{X}$. Equation (8) can be recast into the frequency domain in terms of transfer function $T(s)$. $T(s)$ then is expanded as a Taylor series at $s = 0$ yielding,

$$T(s) = \sum_{k=0}^{\infty} m_k s^k \tag{11}$$

where m_k is the k-th moment of the transfer function $T(s)$. To match the moments between the original (Eq. (8)) and the reduced system (Eq. (10)) up to degree r (i. e., $m_k = m_{rk}$, where m_{rk} is the k-th moment of the transfer function for the reduced system, $k = 0, \ldots r-1$), we can calculate the first r orthogonal bases $\boldsymbol{v}_i$, $i = 1, \ldots, r\}$ that span the Krylov space [5]

$$\mathbf{K}_r(\mathbf{A}^{-1}, \mathbf{b}) = span\left\{\mathbf{b},\ \mathbf{A}^{-1}\mathbf{b},\ \mathbf{A}^{-2}\mathbf{b},\ \ldots \mathbf{A}^{-(r-1)}\mathbf{b}\right\} \tag{12}$$

where $\mathbf{b} = -\mathbf{A}^{-1}\mathbf{B}$. The transformation matrix $\mathbf{V}$ is then explicitly obtained by $\mathbf{V} = [\boldsymbol{v}_1, \boldsymbol{v}_2, \ldots \boldsymbol{v}_r]$. Projecting Eq. (8) onto the Krylov subspace, the reduced system characteristics is given by

$$\mathbf{A}_r = \mathbf{V}^{\mathrm{T}}\mathbf{A}\mathbf{V},\ \mathbf{B}_r = \mathbf{V}^{\mathrm{T}}\mathbf{B},\ \mathbf{C}_r = \mathbf{V}^{\mathrm{T}}\mathbf{C} \tag{13}$$

The detailed implementation steps for ►Arnoldi-Based Model Order Reduction are illustrated and summarized in Fig. 1.

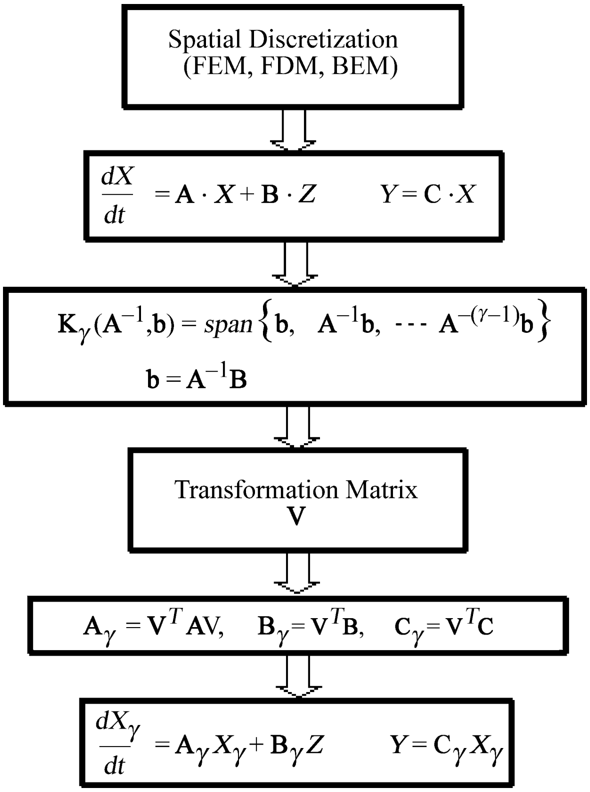

Model Order Reduction (MOR), Figure 1 Flow chart for Arnoldi-Based MOR

Proper Orthogonal Decomposition (POD) Based MOR

For microfluidic systems with strong non-linear effects, ►Proper Orthogonal Decomposition (POD) based MOR (also called Karhunen–Loève decomposition) is employed to locate the low-dimensional subspace for modeling. POD is a technique that extracts the orthogonal basis function spanning the reduced subspace using an ensemble of data from numerical simulations of the original full systems. This is different from the Arnoldi-based MOR algorithm, which relies only on the system matrix from numerical discretization of the original full equations without solving them.

The POD-based MOR begins with a computationally expensive but accurate analysis (e. g., finite element, finite difference or finite volume), which yields an ensemble of vector or scalar fields (*snapshots*) $X_k(\boldsymbol{x})$ and $k = 1, \ldots N_\mathrm{s}$, where X is the state variables (such as velocity fields, pressure distribution, and fluid temperature etc.), X_k is the k-th snapshot in time, $\boldsymbol{x}$ is the spatial coordinates, and N_s is the total number of the snap shots. We then seek for the most characteristic basis function ϕ that best matches the given snapshots $X_k(\boldsymbol{x})$, which is written in a mathematic form as

$$\min\ \lambda = \sum_{k=1}^{N_\mathrm{s}} (\phi(\boldsymbol{x}) - X_k(\boldsymbol{x}))^2 \tag{14}$$

where λ is the objective function. Note that $(\phi(\boldsymbol{x}) - X_k(\boldsymbol{x}))^2$ in Eq. (14) represents the sum of its value at all grid points on $\boldsymbol{x}$. Equation (14) is mathematically equivalent to

$$\max\ \lambda = \frac{1}{N_\mathrm{s}} \sum_{k=1}^{N_\mathrm{s}} \frac{(\phi, X_k)^2}{(\phi, \phi)} \quad \text{subject to} \quad (\phi, \phi) = 1 \tag{15}$$

where $(g, q) = \int_\Omega g(\boldsymbol{x})q(\boldsymbol{x})\,\mathrm{d}\Omega$ defines the inner product of g and q. Equation (15) implies that ϕ with the maximum mean square projection on the ensemble set of X_k is the most characteristic basis functions that are desired. Define linear operator $\boldsymbol{R}$:

$$\boldsymbol{R}\phi = \frac{1}{N_\mathrm{s}} \sum_{k=1}^{N_\mathrm{s}} \int_\Omega X_k(\boldsymbol{x})X_k(\boldsymbol{x}')\phi(\boldsymbol{x}')\,\mathrm{d}\boldsymbol{x}' \tag{16}$$

then

$$(\boldsymbol{R}\phi, \phi) = \frac{1}{N_\mathrm{s}} \sum_{k=1}^{N_\mathrm{s}} \int_\Omega \int_\Omega X_k(\boldsymbol{x})\phi(\boldsymbol{x})X_k(\boldsymbol{x}')\phi(\boldsymbol{x}')\,\mathrm{d}\boldsymbol{x}\,\mathrm{d}\boldsymbol{x}'$$

$$= \frac{1}{N_s} \sum_{k=1}^{N_s} (\phi, X_k)^2 \tag{17}$$

Substitute Eq. (17) into Eq. (15), we can obtain

$$\max\ \lambda = \frac{(\boldsymbol{R}\phi, \phi)}{(\phi, \phi)} \tag{18}$$

It can be easily proven that maximization of λ in Eqs. (15) and (18) is essentially equivalent to the following eigenvalue problem [6]

$$\boldsymbol{R}\phi = \lambda\phi \tag{19}$$

Equation (19) can be solved using the method of snapshots, that is, ϕ is expressed as a linear combination of the original data ensemble,

$$\phi(\boldsymbol{x}) = \sum_{i=1}^{N_s} w_i X_i(\boldsymbol{x}) \tag{20}$$

where w_i is the weight for each snapshot and will be determined to yield the maximum in Eqs. (15) and (18). Substituting Eq. (20) into Eq. (19), it is straightforward to obtain

$$HW = \lambda W \tag{21}$$

where

$$H_{ki} = \frac{1}{N_s} \int_\Omega X_k(\boldsymbol{x}) X_i(\boldsymbol{x})\, \mathrm{d}\boldsymbol{x}, \quad W = [w_1\ w_2\ \ldots\ w_{N_s}]^{\mathrm{T}} \tag{22}$$

H_{ki} is the correlation matrix for snapshots, and is symmetric and positive definite. Once the eigenvectors of Eq. (21) are determined, they can be substituted into Eq. (20) to obtain the basis functions. We can sort the eigenvalues of Eq. (21) in descending order ($\lambda_1 > \lambda_2 > \cdots > \lambda_{N_s}$). From Eq. (15), we can have

$$\lambda_k = \frac{1}{N_s} \sum_{k=1}^{N_s} (\phi_k, X_k)^2 \tag{23}$$

It shows that the eigenvalue λ_k is a measure of how well the basis function ϕ_k represents the snapshots. The first basis function ϕ_1 corresponding to λ_1 represents the most typical characteristics of the snapshots. Therefore, by examining the relative magnitude of λ_k, we can determine the appropriate number r of ϕ for the model that lowers its dimension while still retaining modeling accuracy.

In addition, an alternative approach based on Singular Value Decomposition (SVD) technique to find out the orthogonal basis function is also used on many occasions and is proven mathematically equivalent to the method presented above. The key concept of this approach is to minimize a least-squares measure of the *error* between the state variables projected on the original and reduced subspace, which can be described by

$$\min \sum_{k=1}^{N_s} \left| X_k - \mathrm{proj}\big(X_k, \mathrm{span}\{\phi_1 \cdots \phi_r\}\big) \right| \tag{24}$$

It has been shown that the basis function ϕ is simply the column vectors of Ψ, which as shown in Eq. (25) is obtained by taking the SVD of the matrix containing the snapshot ensemble $\widetilde{X} = (X_1, \cdots, X_{N_s})$ [7],

$$\widetilde{X} = \Psi \Theta \Pi^T \tag{25}$$

Given the known orthogonal basis function ϕ, subsequent macromodeling is straightforward. We first approximate the exact solution X of the original equations as a series superposition of the basis function ϕ and the time-dependent coefficients $\alpha_i(t)$

$$\hat{X}(\boldsymbol{x}, t) = \sum_{i=1}^{r} \alpha_i(t)\phi_i \tag{26}$$

where $\hat{X}(\boldsymbol{x}, t)$ is the approximate solution. Assuming all the governing equations (e. g., Navier–Stokes, continuity, convection–diffusion etc.) can be formulated using a differential operator $\boldsymbol{L}$,

$$\boldsymbol{L}(X) = f \tag{27}$$

where f is the source term. Typically a Galerkin method is employed to reduce the original PDEs into dynamic system ODEs with low dimensions. Apply the Galerkin condition [6], we can obtain

$$\big(\phi, \boldsymbol{L}(\phi) - f\big) = 0 \tag{28}$$

Equation (28) yields a set of ODEs, which are summarized as

$$\mathbf{M}\dot{\alpha}(t) + \mathbf{K}\alpha(t) + \alpha^T \mathbf{N}\alpha + \mathbf{F} = 0 \tag{29}$$

where $\alpha(t) = \left[\alpha_1(t), \alpha_2(t), \ldots \alpha_r(t)\right]^T$; $\mathbf{M}$ is the mass matrix; $\mathbf{K}$ is the diffusion matrix; $\mathbf{F}$ arises from external sources, and $\mathbf{N}$ is the inertia matrix for fluid flow. For linear transport phenomena (e. g., species transport and heat transfer in known flow field), $\mathbf{N}$ is absent and the convection effects are included in $\mathbf{K}$. The time dependent vector $\alpha(t)$ is readily obtained by time integration, and then substituted into Eq. (26) for $\hat{X}(\boldsymbol{x}, t)$. Fig. 2 summarizes the POD and Galerkin method-based MOR procedure.

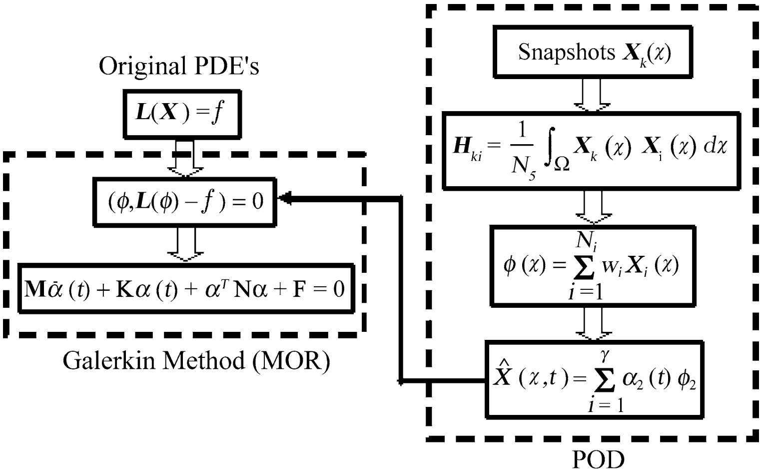

Model Order Reduction (MOR), Figure 2 Flow chart for POD and Galerkin method-based MOR

Artificial Neural Networks

The Artificial Neural Network (ANN) methodology is particularly useful for capturing the complex multiphysics nature of microfluidic devices. An ANN is an information processing paradigm inspired by the way the human nervous system processes information. The ANN consists of a network of processing elements called neurons. Depending upon the connections between these elements and element parameters, the ANN can exhibit a complex global behavior. The ANN is determined by its topology, number of layers, number of neurons per layer, neuronal transfer functions and interconnecting weights. Figure 3(a) shows an example of the most common type of ANN topology, consisting of several layers of neurons: an *input* layer connected to the layer of *hidden* units, which are in turn connected to a layer of *output* units. The activity (output) of the input neuron represents the raw information that is fed into the network. The activity of each hidden unit is determined by the activities of the input units (z_i) and the weights (w_i) on the connections between the input and the hidden units [8]. Figure 3b shows the general principle of determination of output Y_k of a neuron k as a function (func) of the weighted inputs to the neuron from the previous layer's activations, which is described by

$$Y_k = \text{func}\left[\sum_{i=1}^{N_i} w_i z_i\right] \qquad (30)$$

where N_i is the number of inputs to the neutron k. ANNs can be trained to generate an arbitrary number of outputs in response to an arbitrary number of inputs. This flexibility allows them to be used to model complex multiphysics phenomena without significantly compromising on accuracy of the model.

Analytical Approaches

Currently, analytical approaches are still the most preferred tools for model reduction in microfluidic research community. While it is impossible to enumerate all of them in this chapter, we will discuss one particular technique – the Method of Moments, which has been systematically investigated for species dispersion modeling [9, 10]. The Method of Moments was originally proposed to study Taylor dispersion in a circular tube under hydrodynamic flow. Later it was successfully applied to investigate the analyte band dispersion in microfluidic chips (in particular electrophoresis chip). Essentially, the Method of Moments is employed to reduce the transient convection–diffusion equation that contains non-uniform transverse species velocity into a system of simple PDEs governing the spatial moments of the species concentration. Such moments are capable of describing typical characteristics of the species band (such as transverse mass distribution, skew, and variance).

For the sake of brevity, we consider the species band in a 2D channel (while it can be readily extended to the 3D case). Its concentration c is governed by

$$\frac{\partial c}{\partial t} + u\frac{\partial c}{\partial x} = D\left(\frac{\partial^2 c}{\partial x^2} + \frac{\partial^2 c}{\partial y^2}\right) \qquad (31)$$

where t is the migration time of the species band; x and y are the axial and widthwise coordinates; u is the axial species velocity and is a function of y; D is the species diffusion coefficient. We define the dimensionless axial coor-

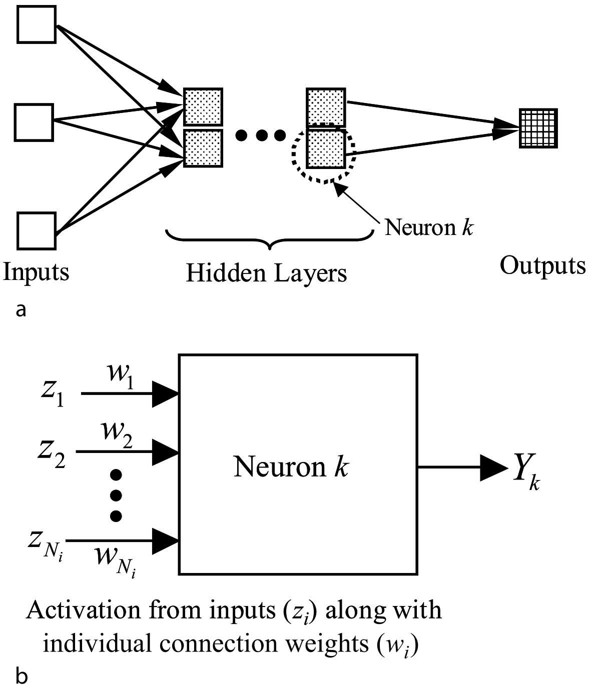

Model Order Reduction (MOR), Figure 3 (**a**) An example of a general feed-forward network with multiple hidden layers and a single output layer. (**b**) Output of a single neuron k with incoming neural activations (z_i) and connection weights w_i

dinate ξ, widthwise coordinate η, and time τ in a new coordinate frame that moves at the average velocity U of the species band

$$\xi = (x - Ut)/d, \quad \eta = y/d, \quad \tau = Dt/d^2 \tag{32}$$

where d is the channel width. In terms of these dimensionless variables, Eq. (31) is formulated as the following form in concentration $c(\xi, \eta, \tau)$:

$$\frac{\partial c}{\partial \tau} = \frac{\partial^2 c}{\partial \xi^2} + \frac{\partial^2 c}{\partial \eta^2} - \mathrm{Pe}\chi \frac{\partial c}{\partial \xi} \tag{33}$$

where $\mathrm{Pe} = Ud/D$ is the Péclet number, characterizing the ratio of axial convective and transverse diffusive transport rates, and χ is the normalized species velocity relative to the average:

$$\chi(\eta) = (u - U)/U \tag{34}$$

If the species band is entirely contained in the channel, Eq. (33) holds effectively over the axial domain $-\infty < \xi < \infty$ and $c \to 0$ as $\xi \to \pm\infty$. Thus, we can define the

Model Order Reduction (MOR), Table 1 Different MOR techniques and compact models

Method	Numerical Simulation	Type
Electric Analogy	No	Primitive/Macromodel
Extraction	Yes	Macromodel
Arnoldi	No	Macromodel
POD	Yes (snapshots)	Macromodel
ANN	Yes (training data)	Macromodel
Analytical	No	Behavioral

spatial moments of the species concentration as

$$c_p(\eta, \tau) = \int_{-\infty}^{\infty} \xi^p c(\xi, \eta, \tau)\, \mathrm{d}\xi\,, \quad m_p(\tau) = \int_0^1 c_p\, \mathrm{d}\eta \tag{35}$$

Here, c_p is the p-th moment of the species concentration in the axial filament at η, and m_p is the p-th moment of the average concentration of the band. For species dispersion modeling, it is sufficient to obtain the moments up to the second order. Specifically, c_0 provides the transverse distribution of the species mass in each axial filament within the channel and m_0 is the total species mass and can be chosen as $m_0 = 1$ without losing generality. c_1 gives the axial locations of the centroid of the axial filaments in the species band, and hence indicates the skew of the band. m_1, the transverse average of c_1, is the axial location of the centroid of the entire species band in the moving frame (ξ, η). Finally, m_2 can be used to determine the variance σ^2 of the species band by $\sigma^2 = d^2\left(m_2/m_0 - m_1^2/m_0^2\right)$ [10]. Table 1 summarized different MOR techniques and corresponding compact models features.

Key Research Findings

The ultimate goal of MOR is to obtain reduced models for fast and efficient simulation and design of microfluidic devices. In this section, we consider key research findings of MOR in fluid flow and species transport that have proven useful for system-level simulation and design.

Fluid Flow

For coupled pressure-driven and electrokinetic flow, Xuan and Li [3] obtained the conductance coefficients (Eq. (5)) for a microfluidic channel of circular cross section, although the approach can be generalized to a variety of microchannels. Specifically, $G_\mathrm{f} = -\pi r_\mathrm{c}^4/8\mu l$, $G_\mathrm{EOF} = G_\mathrm{st} = \pi \varepsilon_r \varepsilon_0 r_\mathrm{c}^2 \zeta J_1/\mu l$, and $G_\mathrm{e} = -\pi \varepsilon_r^2 \varepsilon_0^2 \zeta^2 J_2/\mu l - \pi r_\mathrm{c}^2 \tilde{\sigma} J_3/l$, where ε_r is the rela-

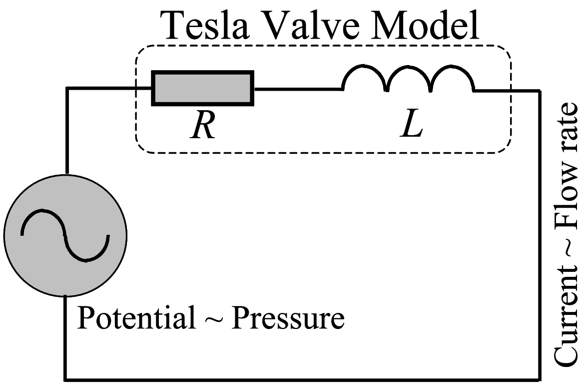

Model Order Reduction (MOR), Figure 4 The equivalent *RL* electronic circuit of a microfluidic circuit including the Tesla valve

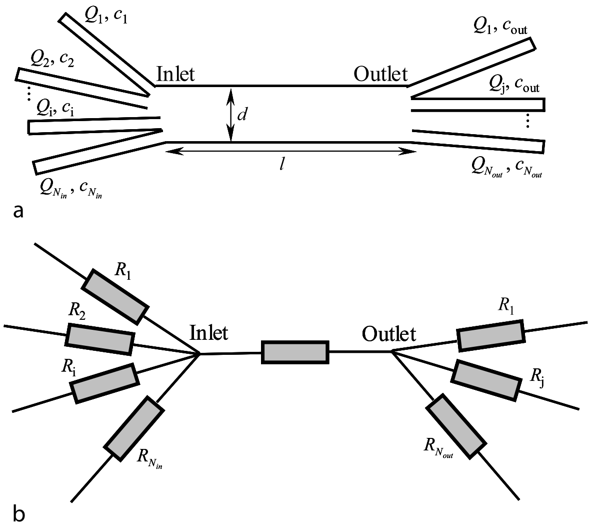

Model Order Reduction (MOR), Figure 5 (**a**) Schematic of the multi-input and multi-output microfluidic channels. (**b**) Equivalent electric resistor network for flow computation

tive permittivity of the fluid, ε_0 the permittivity of vacuum, $\tilde{\sigma}$ the electric conductivity of the liquid, $J_i (i = 1, 2, 3)$ are constants depending on fluid properties and channel size. In many cases the streaming effects are negligible, the coexistent pressure-driven and electrokinetic fluid flow are completely decoupled and their flow rate and electrical current can be calculated independently using simple resistor Kirchhoffian networks.

Automatic macromodel extraction that takes advantage of high-fidelity device simulations (e. g., FEM, FVM, and BEM) to extract *RLC* values in irregular microchannel geometries has also been reported. Turowski et al. [11] approximate the microfluidic *Tesla valve* as a *RL* circuit (serial connection of a resistor *R* and an inductor *L* in Fig. 4) and performed both steady and transient analysis to extract its fluidic resistance and inductance. The macromodels are then stitched together for an overall system simulation on the pumping performance.

Projection subspace-based MOR techniques, such as Arnoldi algorithm and POD, have also been used. Yang et al. [5] considered the lateral air damping effects in MEMS devices. The Navier–Stokes equation governing airflow at the microscale is reduced into a parabolic-typed PDE by neglecting the inertia term, and then solved using the Arnoldi approach. Yang et al. [6] applied the POD to extract the basis function using snapshots from CFD analysis of a single 3D L-Shaped Channel. The reduced ODE set is then obtained by applying the Galerkin method to Navier–Stokes and continuity equations. System-level simulation of serpentine channels that are constructed by concatenating constituent L-shaped channels was also demonstrated with 1% error and at least three orders of speedup. As an alternative approach, Qiao et al. [7] used the SVD algorithm to extract the basis function and investigated electrokinetic flow at irregular geometries, such as cross-, T-, and L-shaped microchannels.

Species Transport

The electric analogy also played a major role in evaluating the steady-state species concentration in microfluidic networks. By applying the principle of flow and species balance to a multi-input and multi-output microchannel involving no reaction, we can obtain

$$\sum_{i=1}^{N_{\text{in}}} Q_i = \sum_{j=1}^{N_{\text{out}}} Q_j \quad \text{and} \quad \sum_{i=1}^{N_{\text{in}}} Q_i c_i = c_{\text{out}} \sum_{j=1}^{N_{\text{out}}} Q_j \qquad (36)$$

where N_{in} and N_{out} are the total number of the braches at the channel inlet and outlet, Q_i and Q_j, respectively, are the flow rates at the i-th flow-in branch and the j-th flow-out branch (Fig. 5a). In order to calculate the distribution of the flow rate Q, the microfluidic network is typically modeled as an assembly of fluidic/electric resistors (Fig. 5b) and solved using the Kirchhoff's law as discussed above. Given the species concentrations in the most-upstream inlet reservoirs, those at downstream channels then can be explicitly determined. For Eq. (36) to be valid, a constraint of transversely complete mixing and uniform species concentration at the end of each channel (a single value c_{out} is used for all outgoing streams in Eq. (36)) is imposed, i. e., $\text{Pe} \times d/l \ll 1$.

ANNs have been used to develop behavioral models to enable efficient system-level simulation of integrated microfluidic devices. Magargle et al. [8] reported a feed-forward ANN-based model for an injector device that is used in electrophoretic separation chips. They used the Buckingham-π theorem to select dimensionless groups

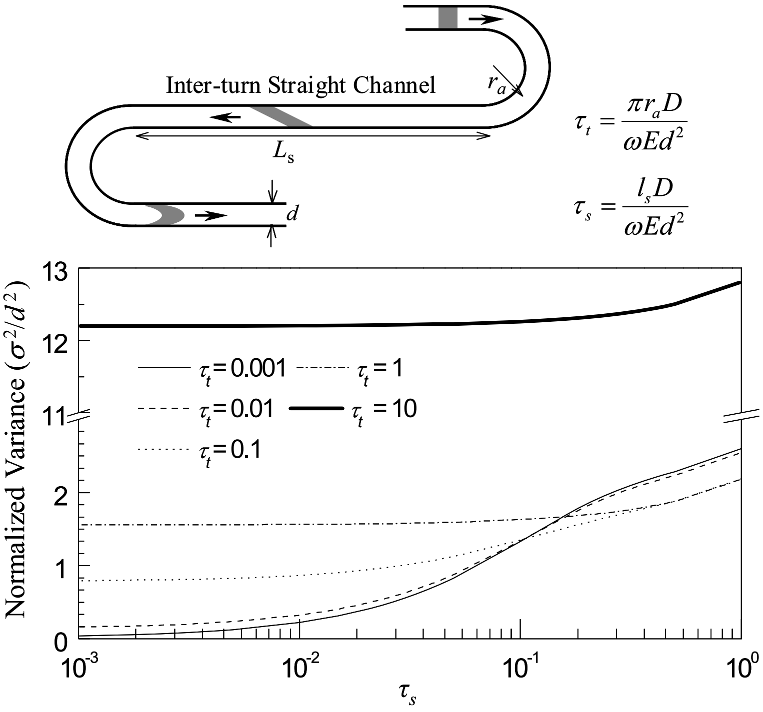

Model Order Reduction (MOR), Figure 6 Dependence of dispersion variance of species band on dimensionless times (τ_t and τ_s)

that aided in reducing the size of the variable space for the training simulations. Finite-element analysis of the governing equations was performed to train the ANN. This model was then used to extract an explicit analytical equation that can be used in a system-level modeling and simulation of complex electrophoresis microchips. The model achieved a computational speedup of more than four orders of magnitude over the numerical solution.

To predict the transient behavior of species bands in microchannel networks, Wang et al. [10] developed a generalized, analytical dispersion models using method of moments. The model takes into account of several factors contributing to species band-broadening, such as Joule heating- and geometry-induced non-uniformity in axial velocity along the channel's cross section, as well as non-uniformity in traveling distance at turns. By neglecting appropriate terms of χ in Eq. (34), the model could be reduced to the special cases including Joule heating dispersion in straight channels or turn-geometry induced dispersion in complex (i. e., serpentine, spiral, and their combinations) electrophoresis microchips. Figure 6 illustrates the dependence of dispersion variance of the species band on the dimensionless times τ_t and τ_s in the widely used complementary-turn electrophoresis chips with Joule heating dispersion neglected. As shown in Fig. 6, both dimensionless times lump the combinational effects of the material properties (species electrokinetic mobility ω and diffusivity D), channel sizes (d, l_s, and mean turn radius r_a), and operational parameter (electric field E) and characterize the ratio of the migration time to the transverse diffusive time constant of the species band. It shows that when τ_t and τ_s are small (i. e., when species convection is dominant), the band distortion caused by the first turn is largely cancelled by the second turn, leading to minor overall dispersion variance. On the other hand, at large τ_t, species diffusion is more significant and the band is uniformly distributed across the turn, the foregoing canceling effect is not present and the total band variance increases markedly.

Future Directions for Research

In contrast to the rapid growth of microfluidic technology, the microfluidic MOR techniques, have not kept pace. The application of MOR techniques exhibits an obvious imbalance. Electric analogy and analytical approaches are still the mainstream tools prevalently used in microfluidic modelling and design. Other MOR techniques (e. g., Arnoldi method, Artificial Neural Network, and POD) that derive from control theory and other disciplines receive less attention, even although they are effective in addressing the inherent complexities arising from high dimensions, irregular geometries, and multiphysics.

Therefore, efforts that bridge these MOR and multidisciplinary research in microfluidics are strongly desired. Recently, Vasilyev et al. [12] demonstrated an elegant work on macromodeling of non-linear system behavior of complex BioMEMS components based on a stabilized balanced truncation plus trajectory piecewise-linear approach, which can be considered as a meaningful step toward the direction. In addition, inadequate effort has been focused on the development of MOR techniques dedicated to the segments of the species transport and biochemical reactions in microfluidics. To a major extent, this limits the utility of the current microfluidic CAD tools to achieve the goal of establishing microfluidics as an efficient platform for the detection, analysis, and manipulations of bio-samples.

Cross References

► Model Order Reduction (MOR)
► Macromodel
► Artificial Neural Network
► Proper Orthogonal Decomposition
► Singular Value Decomposition

References

1. Chakrabarty K, Zeng J (2006) Design Automation for Microfluidics-Based Biochips. ACM J Emerging Technol Comput Syst 1(3):186–223
2. Bourouina T, Grandchamp JP (1996) Modeling micropumps with electrical equivalent networks. J Micromech Microeng 6(4):398–404
3. Xuan X, Li D (2004) Analysis of electrokinetic flow in microfluidic networks. J Micromech Microeng 14(2):290–298
4. Rudnyi EB, Korvink JG (2002) Review: Automatic Model Reduction for Transient Simulation of MEMS-based Devices. Sens Update 11(1):3–33
5. Yang YJJ, Yen PC (2005) An efficient macromodeling methodology for lateral air damping effects. J Microelectromech Syst 14(4):812–828
6. Kuo CW, Chein CM, Yang YJ (2006) Macromodeling for Microfluidic Channels. 9th NSTI Nanotechnology Conference and Trade Show, Boston, MA, pp 517–520
7. Qiao R, Aluru NR (2003) Transient analysis of electro-osmotic transport by a reduced-order modelling approach. Int J Numer Methods Eng 56(7):1023–1050
8. Magargle R, Hoburg JF, Mukherjee T (2006) Microfluidic injector models based on artificial neural networks. IEEE Transactions on Computer-Aided Design of Integrated Circuits and Systems 25(2):373–380
9. Bedekar AS, Wang Y, Krishnamoorthy S, Siddhaye SS, Sundaram S (2006) System-level simulation of flow-induced dispersion in lab-on-a-chip systems. IEEE Transactions on Computer-Aided Design of Integrated Circuits and Systems 25(2):294–304
10. Wang Y, Lin Q, Mukherjee T (2004) A model for Joule heating-induced dispersion in microchip electrophoresis. Lab Chip 4(6):625–631
11. Turowski M, Chen ZJ, Przekwas A (2001) Automated generation of compact models for fluidic microsystems. Analog Integr Circuits and Signal Process 29(1-2):27–36
12. Vasilyev D, Rewienski M, White J (2006) Macromodel generation for bioMEMS components using a stabilized balanced truncation plus trajectory piecewise-linear approach. IEEE Transactions on Computer-Aided Design of Integrated Circuits and Systems 25(2):285–293

Model Reduction

► Model Order Reduction (MOR)

Molecular Beam Epitaxy (MBE)

Definition

Thin-film deposition technique in which a material is formed from a beam of sublimated atoms. The MBE process is valued for its precise control of atomic species to the growth surface, both for desired and undesired species.

Cross References

► Fabrication of Self-Assembled Catalytic Nanostructures

Molecular-Continuum Simulation

► Multiscale Modeling and Numerical Simulations

Molecular Dynamics

Definition

Computer simulation of a fluid or large molecule where the position and velocity of every atom is tracked in time as they interact.

Cross References

► Electrokinetic Flow and Ion Transport in Nanochannels

Molecular Dynamics Simulation Method

Dongyan Xu, Deyu Li
Department of Mechanical Engineering,
Vanderbilt University, Nashville, TN, USA
dongyan.xu@vanderbilt.edu, deyu.li@vanderbilt.edu

M

Synonyms

Atomistic computer simulation; Particle dynamics simulation; Molecular modeling

Definition

Classical molecular dynamics is a computer simulation method to study the equilibrium and transport properties of a classical many-body system by solving Newton's equations of motion for each component. The hypothesis of this methodology is that the properties of the matter or the transport phenomena can be understood through the observation of statistical properties of a small molecular system under certain microscopic interactions among its constituents. The main justification of the classical molecular dynamics simulation method comes from statistical mechanics in that the statistical ensemble averages are equal to the time averages of a system.

Overview

Many challenges in understanding the nature and developing new technologies are related to the classical many-body problem, i. e., the behavior of a system composed of many particles. Even though modern physics has provided powerful theoretical and experimental techniques to study the behavior of individual particles at the atomic or molecular level, the behavior of a many-body system remains a difficult problem because of its inherent complexity. Emerging in the 1950s, and starting to receive widespread attention from the mid-1970s, molecular dynamics has become a promising tool to solve complex many-body problems, as the rapid developments of digital computers are making this methodology more and more powerful. Today, the molecular dynamics simulation method is well accepted as an important research approach in addition to theoretical and experimental investigations. Molecular dynamics can be used to verify a theoretical result by performing a numerical experiment or to explain an experimental observation by modeling the situation and extracting detailed information to provide a physical insight. Using the molecular dynamics simulation method to study the properties of liquids has a long and rich history. The efforts in the early stages mainly focused on development of models that reflected more realistically the interactions between molecules, and the work focused on modeling physical properties such as density, enthalpy of evaporation, critical points, etc. Modeling of micro- and nanofluidic transport phenomena such as electroosmotic flow started more recently during the mid-1990s, and now using molecular dynamics to study the fundamentals of micro- and nanofluidic phenomena is well accepted.

There are two main classes of molecular level simulation techniques, namely the Monte Carlo simulation method and molecular dynamics simulation method [1]. The Monte Carlo method is a stochastic method that extracts system properties by solving for the statistical average of stochastically generated ensemble microconfigurations (microstates) under a certain macrostate (the description of the system at macroscopic level using properties such as temperature and pressure). Because of the stochastic manner in the generation of microstates in Monte Carlo simulations, it is difficult to reflect the dynamical properties of the system. On the other hand, molecular dynamics is a more deterministic method that monitors the motion of each molecule in the system under certain intermolecular potentials by solving the equations of motion, and hence can reveal the dynamical properties of the system. Both Monte Carlo and molecular dynamics methods can be used to determine equilibrium properties of a system, and the Monte Carlo method has the advantage of being easier to code and more efficient for systems in which the intermolecular force is difficult to derive from the potential function. However, molecular dynamics is more powerful in the sense of its capabilities of studying transport coefficients and time correlation functions.

Molecular dynamics itself can be further divided into two classes: classical molecular dynamics and ab initio molecular dynamics. Classical molecular dynamics treats molecules as point masses and the interactions between molecules are represented by simple potential functions, which are based on empirical data or from independent quantum mechanical calculations. The so-called ab initio molecular dynamics unifies classical molecular dynamics and density-function theory, and takes into account the electronic structure when calculating the forces on atomic nuclei. In this entry, we only present a brief summary of the classical molecular dynamics simulation method. Readers interested in Monte Carlo or ab initio molecular dynamics simulation methods are referred to other entries such as ▶ Monte Carlo Method or *Car-Parrinello Molecular Dynamics*.

Molecular dynamics studies the properties of matter or transport phenomena by constructing an atomic or molecular system with the initial microscopic state of a system specified in terms of the positions and momenta of the constituent atoms or molecules, which can be obtained either from theoretical consideration or from experimental results. Molecular dynamics also requires a model potential to simulate the interactions among atoms and molecules, in which way physics comes in to play a role. The model interaction potential should obey the fundamental laws of physics and chemistry, and capture the important features of the intermolecular interactions that

determine the property of interest. It needs to be remembered that the model is just an approximation to the interactions in the real world and the results from the molecular dynamics simulation have to be tested against proved theoretical or experimental findings, i. e., it should be able to reproduce some properties of matter like density distribution, transport coefficients and so on. Starting from the initial set-up of the system with given intermolecular potentials, Newton's equations of motion are integrated for each atom or molecule to calculate the positions and velocities of the Atoms or molecules in the system as time progresses. After the system reaches equilibrium, the properties of the model system can be extracted from the motion of the atoms or molecules using statistical mechanics methods.

Molecular dynamics provides a methodology for detailed microscopic modeling at the molecular level, which is becoming an indispensable tool for both fundamental studies and applied research. Today, molecular dynamics simulation is widely applied in physics, chemistry, biochemistry and materials sciences, studying the behavior of various kinds of solids, liquids and gases. The applications of molecular dynamics in the micro- and nanofluidics field widely span different topics such as electric double layer structures, electroosmotic flow, interactions between liquids and macromolecules, etc. Over the past two to three decades, several well-accepted molecular dynamics simulation codes have been developed by different research groups. Even though all these codes can model fluidic systems, different codes may be more pertinent to different problems because of the research interest of the developers. The most popular simulation packages include AMBER, CHARMM, NAMD, LAMMPS, DL-PLOY and GROMACS, which are available online and some of them are free to download. Molecular dynamics codes developed and used only by the developers' groups are also applied to many micro- and nanofluidic studies.

It is certainly impossible to cover every aspect in detail of even just the classical molecular dynamics simulation method in this short entry. Quite a few books on the general molecular dynamics simulation method have been published [1–3], which contain much more detailed information for interested readers.

Basic Methodology

For a system composed of N atoms, after constructing the initial microscopic state by specifying the positions and momenta of all atoms under certain constrains such as the given total energy and volume, the behavior of the system is fully determined by the classical equations of motion for the atoms

$$m_i \ddot{\boldsymbol{r}}_i = \boldsymbol{f}_i \tag{1}$$

$$\boldsymbol{f}_i = -\frac{\partial V}{\partial \boldsymbol{r}_i} \tag{2}$$

where m_i and $\boldsymbol{r}_i$ are the mass and Cartesian coordinates of atom i and $\boldsymbol{f}_i$ represents the total force acting on atom i by all other atoms in the system and the external force field, which can be derived from the potential energy function $V(r_1, r_2, \cdots, r_N)$.

Interaction Potential

A set of realistic intermolecular potentials are arguably the most important part of a successful molecular dynamics simulation. For a simple atomic system, the potential energy can be written in terms of the coordinates of individual atoms, atom pairs, atom triplets, etc.:

$$V(r_1, r_2, \cdots, r_N) = \sum_i v_1(r_i) + \sum_i \sum_{j>i} v_2(r_i, r_j) + \sum_i \sum_{j>i} \sum_{k>j>i} v_3(r_i, r_j, r_k) + \cdots \tag{3}$$

The notation $\sum_i$ in the first term indicates a summation over all atoms in the system and $v_1(r_i)$ represents the potential in an external force field. The second term, usually called the pair potential, is probably the most important energy term in a molecular dynamics simulation. The pair potential sums over all distinct atom pairs i and j without counting any pair twice. The function $v_2(r_i, r_j)$ depends only on the separation between atoms i and j and hence can also be expressed as $v_2(r_{ij})$. Three-body and other multi-body potentials are normally avoided in molecular dynamics simulations since they are not easy to implement and can be extremely time consuming. The multi-body effects are usually taken into account by modifying the pair potential, i. e., using an *effective* pair potential, which is not the exact interaction potential between the two atoms. According to the range of the interactions, the pair potential can be divided into two categories, i. e. short-range interaction potentials and long-range interaction potentials. Different algorithms are adopted to treat the short-range and long-range interaction potentials.

Short-Range Interaction Potentials

Short-range interaction potentials apply to those interactions that attenuate rapidly as the distance between the atoms increases. The most commonly used short-range

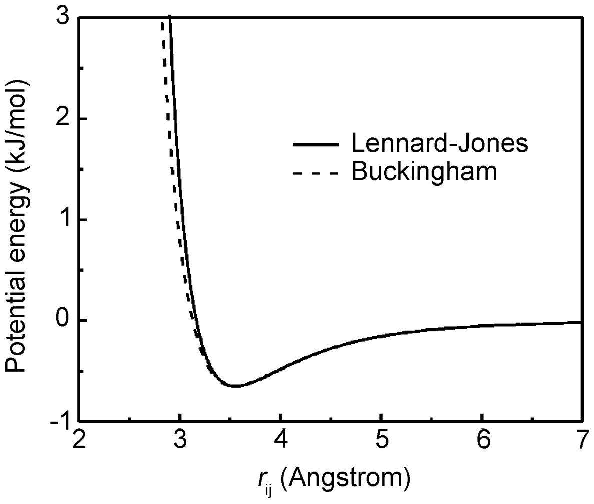

Molecular Dynamics Simulation Method, Figure 1 The Lennard–Jones and Buckingham interaction potentials

interaction potential is probably the Lennard–Jones $12-6$ potential (as shown in Fig. 1):

$$v_2^{\mathrm{LJ}}(r_{ij}) = 4\varepsilon_{ij}\left[\left(\frac{\sigma_{ij}}{r_{ij}}\right)^{12} - \left(\frac{\sigma_{ij}}{r_{ij}}\right)^{6}\right] \tag{4}$$

The Lennard–Jones potential includes a strongly repelling term proportional to $1/r_{ij}^{12}$, which represents the excluded volume by an atom, and a long attractive tail of the form $-1/r_{ij}^{6}$, which models the effect of attractive interactions between induced dipoles due to fluctuating charge distributions. This potential provides reasonable simulation results for the properties of liquid argon. The parameters σ_{ij} and ε_{ij}, the effective diameter and the depth of the potential well between different atoms, can be calculated by using the combination rules since normally the effective diameter and the depth of the potential well are only available for the atoms of individual elements. The most frequently used combination rule is the Lorentz–Berthelot formula:

$$\sigma_{ij} = \frac{\sigma_{ii} + \sigma_{jj}}{2}\,, \tag{5}$$

$$\varepsilon_{ij} = \sqrt{\varepsilon_{ii}\varepsilon_{jj}}\,. \tag{6}$$

Another commonly used potential function, the Buckingham potential (also shown in Fig. 1), has a more flexible and realistic repulsion term than the Lennard–Jones potential, but it is also more expensive to compute. The potential can be written as

$$v_2^{\mathrm{BH}}(r_{ij}) = A_{ij}\exp(-B_{ij}r_{ij}) - \frac{C_{ij}}{r_{ij}^{6}} \tag{7}$$

where the constants A_{ij}, B_{ij} and C_{ij} are in general different for different atom pairs.

In a molecular dynamics simulation, it takes a double loop to calculate the potential energy or force and the time for this calculation is proportional to N^2, which is the most time-consuming and computationally expensive part in the simulation and limits the speed of the program execution. For short-range interactions, since the potential value drops to zero very rapidly as the distance increases, it is a common practice to restrict the evaluation of the interaction potential to a limited region of space. A cutoff radius, R_{c}, is usually introduced, beyond which the interaction potential is set as zero. A common choice is $R_{\mathrm{c}} = 2.5\sigma_{\max}$. The cutoff radius approach reduces the computation time significantly since the potential/force calculations are skipped for those atoms that are not in the cutoff sphere. However, the separations of all distinct pairs still have to be calculated at each time step to examine if they are in the interaction range or not, which also takes a lot of time. The situation gets worse rapidly for larger systems since this calculation scales with N^2. In order to solve this problem, Verlet introduced a technique in 1967 [4] and the strategy is to construct a neighbor list for each atom, which stores the indices of all neighbor atoms falling in the sphere with a radius of $R_{\mathrm{c}} + R_{\mathrm{s}}$. Here R_{s} is called the skin radius. Therefore, in a force routine, not all atoms but only those in the neighbor list will be tested to see if they are in the range $r_{ij} < R_{\mathrm{c}}$. The neighbor list is reconstructed as less frequently as possible but has to be done before any unlisted atoms come into the interaction region.

Long-Range Interaction Potentials

Long-range interaction potentials apply to those interactions that attenuate slowly as the distance between the atoms increases. A very common long-range interaction potential is the Coulomb potential, which scales as $1/r_{ij}$. Therefore, for a system containing ions or polarizable molecules such as water, the Coulomb potential must be taken into account for all atoms in the system and can be expressed by

$$v^{\mathrm{C}} = \frac{1}{2}\sum_{i\neq j}\frac{q_i q_j}{|\boldsymbol{r}_{ij}|} \tag{8}$$

where q_i and q_j are charges on atom i and j, respectively.

The trouble with long-range interaction potentials is not only the time-consuming calculation over all atom pairs in the simulation system, but also the fact that when simulating bulk liquids with a small system, periodic boundary

conditions must be used to avoid surface effects. The simulation box is replicated throughout the space to form an infinite lattice. During a simulation, when an atom moves in the central box, its periodic images in other replicated boxes move exactly in the same way. In this case, not only the long-range interactions among the atoms in the central box but also those between the atoms in the central box and the image atoms in all replicated boxes must be taken into account in the Coulomb potential calculation. Therefore, a lattice sum has to be calculated as

$$v^{\mathrm{C}} = \frac{1}{2}\sum_{\boldsymbol{n}}{}' \sum_{i,j=1}^{N} \frac{q_i q_j}{\left|\boldsymbol{r}_{ij} - \boldsymbol{n}L\right|} \tag{9}$$

where $\boldsymbol{n}$ is a lattice vector and L is the length of the simulation box which is assumed to be cubic here. The prime on the first summation means $i \neq j$ for $\boldsymbol{n} = 0$. It is known that the above lattice sum is only conditionally convergent and the result depends on the summation order. Different techniques have been developed in the literature to overcome this difficulty, which can be classified into three categories: the Ewald summation method, the particle-mesh method and the multipole method. For brevity, only the Ewald summation method will be briefly described here; the details of the particle-mesh method and multipole method can be found in a review paper [5].

The basic idea of Ewald summation is to break down the lattice sum in Eq. (9) into two parts: a short-range potential that can be treated with a simple cutoff scheme and a long-range potential that is periodic, slowly varying, which can be represented to an acceptable accuracy by a finite Fourier series. The strategy is to construct a cloud of screening charge of opposite polarity so that each charge in the system is screened by this charge cloud, which makes the electrostatic potential due to the charge at position $\boldsymbol{r}_i$ decay rapidly to nearly zero at a short prescribed distance. This approach makes the potential of this composite charge distribution a short-range interaction and can be calculated in real space. The screening charges are compensated using a smoothly varying periodic charge density that can be summed up in the reciprocal Fourier space. The final form of the Ewald summation can be written as [5]

$$v^{\mathrm{C}} = \frac{1}{2}\left[\sum_{\boldsymbol{n}}{}' \sum_{i,j=1}^{N} \frac{q_i q_j \operatorname{erfc}\left(\alpha \left|\boldsymbol{r}_{ij} - \boldsymbol{n}L\right|\right)}{\left|\boldsymbol{r}_{ij} - \boldsymbol{n}L\right|} + \frac{4\pi}{L^3}\sum_{\boldsymbol{k}\neq 0}\sum_{i,j=1}^{N} \frac{q_i q_j}{|\boldsymbol{k}|^2} \mathrm{e}^{-|\boldsymbol{k}|^2/4\alpha^2} \mathrm{e}^{i\boldsymbol{k}\boldsymbol{r}_{ij}} - \frac{2\alpha}{\sqrt{\pi}}\sum_{i=1}^{N} q_i^2\right] \tag{10}$$

Bonded Interaction Potentials within Molecules

For a system consisting of molecules composed of multiple atoms, in addition to the short-range and long-range interactions discussed above, the intramolecular bonded interactions between the atoms can also play an important role. These bonded interactions can have different contributions corresponding to the energy coming from bond vibrations (two covalently bonded atoms), angular vibrations (varying bond angle between three bonded atoms), improper dihedrals (four bonded atoms in the same plane) and proper dihedrals (torsional deformation of four bonded atoms). The typical form of the bonded interaction potentials is

$$\begin{aligned} v^{\mathrm{Bonded}} &= \sum_{\mathrm{Bonds}} k_r (r - r_{\mathrm{eq}})^2 \\ &+ \sum_{\mathrm{angles}} k_\theta (\theta - \theta_{\mathrm{eq}})^2 \\ &+ \sum_{\mathrm{improper}} k_\xi (\xi - \xi_0)^2 \\ &+ \sum_{\mathrm{proper}} k_n (1 + \cos(n\varphi - \varphi_0)) \,. \end{aligned} \tag{11}$$

At the beginning of the simulation, a fixed list can be established which contains all indices of atom pairs, atom triplets and atom quadruples that participate in the bonded interactions. The bonded interaction potentials can be calculated on the basis of this fixed list at each time step instead of checking all the atoms in the system.

Integration Algorithm

From the initial configuration and the given potential functions, the equations of motion can be integrated using finite difference methods. The integration algorithm, which is normally called the integrator, must be accurate since it determines the accuracy of the simulation results. However, no integration algorithm can provide an exact solution due to the roundoff of the finite number representation and the finite difference scheme. The integrator must be accurate in the sense of approximating the true trajectory of the system as closely as possible, which requires the use of a short time step. On the other hand, the integrator also has to pursue the use of a long time step δt for the computing efficiency. Therefore, there is a tradeoff between accuracy and efficiency when selecting the integration time step.

The most widely used integration algorithm for the equations of motion is the Verlet algorithm. Various versions of the Verlet algorithm exist in the literature, including

the original Verlet scheme, the leap-frog scheme and the velocity Verlet algorithm. They are essentially equivalent and we will briefly introduce the leap-frog and velocity Verlet algorithms here. The leap-frog scheme can be written as

$$\boldsymbol{v}\left(t+\tfrac{1}{2}\delta t\right)=\boldsymbol{v}\left(t-\tfrac{1}{2}\delta t\right)+\delta t\cdot\boldsymbol{a}(t) \tag{12a}$$

$$\boldsymbol{r}(t+\delta t)=\boldsymbol{r}(t)+\delta t\cdot\boldsymbol{v}\left(t+\tfrac{1}{2}\delta t\right) \tag{12b}$$

where $\boldsymbol{r}$, $\boldsymbol{v}$ and $\boldsymbol{a}$ are the position, velocity and acceleration vectors, respectively. In this scheme, the stored quantities are the current position $\boldsymbol{r}(t)$, acceleration $\boldsymbol{a}(t)$ and the half-step velocity $\boldsymbol{v}(t-1/2\,\delta t)$. In order to calculate the kinetic energy at time t, the current velocity may be calculated by

$$\boldsymbol{v}(t)=\frac{1}{2}\left[\boldsymbol{v}\left(t+\tfrac{1}{2}\delta t\right)+v\left(t-\tfrac{1}{2}\delta t\right)\right]. \tag{13}$$

The velocity Verlet algorithm takes the following form:

$$\boldsymbol{v}\left(t+\tfrac{1}{2}\delta t\right)=\boldsymbol{v}(t)+\tfrac{1}{2}\delta t\cdot\boldsymbol{a}(t) \tag{14a}$$

$$\boldsymbol{r}\,(t+\delta t)=\boldsymbol{r}(t)+\delta t\cdot\boldsymbol{v}\left(t+\tfrac{1}{2}\delta t\right) \tag{14b}$$

$$\boldsymbol{v}\,(t+\delta t)=\boldsymbol{v}\left(t+\tfrac{1}{2}\delta t\right)+\tfrac{1}{2}\delta t\cdot\boldsymbol{a}(t+\delta t)\,. \tag{14c}$$

This scheme stores the information of positions, velocities and accelerations all at the same time step.

Statistical Ensemble

If there is no time-dependent external force, the dynamics of a molecular system will evolve on a constant-energy surface. Therefore, a natural choice of the statistical ensemble in molecular dynamics simulation is the microcanonical ensemble (NVE). Other types of ensembles, such as the canonical ensemble (NVT) and the isothermal–isobaric ensemble (NPT), can also be realized by controlling corresponding thermodynamic variables. For the last two ensembles, the temperature of the ensemble needs to be controlled and four different control mechanisms, namely differential control, proportional control, integral control and stochastic control, have been developed in the literature. As an example, a proportional thermostat for the NVT ensemble will be briefly discussed as follows.

In order to correct the deviation of the actual system temperature from the prescribed T_0, Berendsen et al. introduced a proportional method in which the system is weakly coupled to an external heat bath, and at each time step the velocities of the atoms in the system are multiplied by a scaling factor

$$\lambda=\left[1+\frac{\delta t}{\tau}\left(\frac{T_0}{T}-1\right)\right]^{\frac{1}{2}}. \tag{15}$$

In this way, the kinetic energy of the system is scaled and the temperature of the system is forced to approach the prescribed temperature. The coupling time constant τ represents the time scale in which the system reaches the prescribed temperature. Using the Berendsen thermostat, the system temperature is allowed to fluctuate instead of being set as a constant. At each time step, the temperature is corrected to a value closer to T_0. For a larger time constant (τ), it takes longer time for a system to reach the prescribed temperature.

Key Research Findings

The molecular dynamics simulation method has seen a rapid development and been applied to model solids, liquids and gases. Applications of molecular dynamics simulations to micro- and nanofluidics have been an active research topic over the past decade including studies of the structure of water, ion distribution in the electric double layers, electroosmotic flow, etc. Because of the complex structure of water molecules, significant efforts have been made to develop models and potential functions to accurately represent the intermolecular interactions. Most of these studies tried to calculate water properties such as density, enthalpy of evaporation, diffusivity, critical point, etc., to verify the accuracy of the model. A large number of water models, such as SPC/E, TIP3P and TIP4P, have been developed and extensively examined against experimental results, which laid a solid foundation for studying micro- and nanofluidic phenomena with the molecular dynamics simulation method.

Using molecular dynamics to study the electric double layer structure started a little over a decade ago, with the hope of determining more accurate structures because the classical description of an electric double layer based on the Poisson–Boltzmann equation is accurate only for low surface potential and dilute electrolytes. The Poisson–Boltzmann equation only considers the electrostatic interactions between the charged surface and ions in the solution, but not the ion–ion interactions in the solution and the finite molecule size, which can be taken into account in molecular dynamics simulations. It was shown [6, 7] that the ion distribution in the near-wall region could be significantly different from the prediction of classical theory. Typical molecular dynamics simulation results of counter-ion and co-ion concentrations in a nanochannel are shown

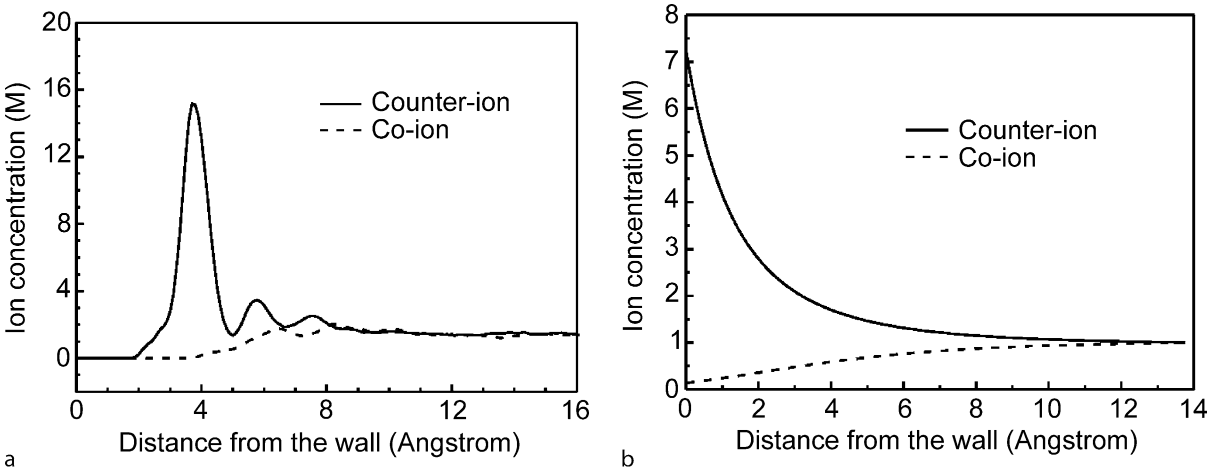

Molecular Dynamics Simulation Method, Figure 2 Counter-ion and co-ion concentrations across a nanochannel obtained from the molecular dynamics simulation (**a**) and the Poisson–Boltzmann equation (**b**)

in Fig. 2a. The ion distribution obtained from the Poisson–Boltzmann equation is also shown in Fig. 2b for comparison. Different from the traditional Poisson–Boltzmann prediction, both counter-ions and co-ions are depleted in the near-wall region (2 Å from the channel wall) due to the finite sizes of wall atoms and ions. Also, the counter-ion and co-ion concentrations from the molecular dynamics simulation do not change monotonically to their values in the channel center, but fluctuate with peaks and valleys, resulting from the molecular stacking near the channel wall. Molecular dynamics was also used to simulate electroosmotic flow, and it was found that the viscosity near the wall could be much higher than the bulk viscosity [7] and the continuum theories had to be corrected to agree with the molecular dynamics results [8]. To date, molecular dynamics studies of micro- and nanofluidic phenomena have just started and many fundamental issues still need to be investigated.

Future Directions for Research

Future research efforts relating to molecular dynamics simulation in micro- and nanofluidics could be devoted to two areas, i. e., development of the simulation methodology itself and fundamental studies of the phenomena in micro- and nanofluidics. With the advent of massively parallel computers, it is possible to increase both the length scale and the time scale of molecular dynamics simulations to model larger and more complex systems. However, the current parallel molecular dynamics codes do not scale well enough to use thousands of processors provided by modern computer clusters. Therefore, parallel algorithms with better scalability are highly desirable.

Many issues in micro- and nanofluidics require a fundamental understanding of the interactions among ions, fluid, surface charges and biomolecules. For example, in recent experiments [9, 10] using nanopores or nanochannels as biosensors, both ion current enhancement and ion current blockade were observed when DNA molecules were translocated through the nanopore/nanochannel. This was explained by the competition of two effects: conductance decrease due to the volume occupied by the DNA molecule of lower mobility, and the increased ions adsorbed on the DNA to shield the charge on the DNA backbone. The crossover from current enhancement to current blockade occurred at different concentrations in different experiments. This indicates that the complex charge interactions inside the nanopore/nanochannel may not be fully reflected by the simple models developed in the literature. It can be imagined that molecular dynamics, as a powerful research tool for an assembly of molecules, could greatly contribute to fundamental issues such as the complex charge interactions among ions, fluid, surface charges and macromolecules such as DNAs and proteins.

M

Cross References

► Monte Carlo Method
► Multiscale Modeling and Numerical Simulations

References

1. Allen MP, Tildesley DJ (1989) Computer Simulation of Liquids. Oxford University Press, New York
2. Rapaport DC (2004) The Art of Molecular Dynamics Simulation, 2nd edn. Cambridge University Press, New York
3. Haile JM (1992) Molecular Dynamics Simulation: Elementary Methods. Wiley, New York

4. Verlet L (1967) Computer Experiments on Classical Fluids I, Thermodynamical Properties of Lennard–Jones Molecules. Phys Rev 159:98–103
5. Gibbon P, Sutmann G (2002) Long-Range Interactions in Many-Particle Simulation. In: Grotendorst J, Marx D, Muramatsu A (eds) Quantum Simulations of Complex Many-Body Systems: From Theory to Algorithms. John von Neumann Institute for Computing, Jülich
6. Qiao R, Aluru NR (2003) Ion Concentration and Velocity Profiles in Nanochannel Electroosmotic Flows. J Chem Phys 118:4692–4701
7. Freund JB (2002) Electro-Osmosis in a Nanometer-Scale Channel Studied by Atomistic Simulation. J Chem Phys 116:2194–2200
8. Zhu W, Singer SJ, Zheng Z, Conlisk AT (2005) Electro-osmotic Flow of a Model Electrolyte. Phys Rev E 71(041501):1–12
9. Fan R, Karnik R, Yue M, Li D, Majumdar A, Yang P (2005) DNA Translocation in Inorganic Nanotubes. Nano Lett 5:1633–1637
10. Smeets RMM, Keyser UF, Krapf D, Wu M, Dekker NH, Dekker C (2006) Salt Dependence of Ion Transport and DNA Translocation through Solid-State Nanopores. Nano Lett 6:89–95

Molecular Flow

► Single-Phase Gaseous Flow

Molecular Method

► Non-Continuous Approaches

Molecular Modeling

► Molecular Dynamics Simulation Method

Molecular Self-Assembly Fabrication

► Self-Assembly Fabrication

Monoclonal

Definition

Monoclonal antibodies are antibodies which have been artificially produced against a specific antigen. They are extremely specific and bind to their target antigens.

Monostability

Definition

Capability to remain, without an external control action, in one of its two stable regimes.
This is a useful property in fluidic diverter valves with two outlets operated so that most of the time the fluid has to leave mainly through the preferred outlet and only exceptionally and for a short period of time the fluid has to leave through the other outlet. The regime with flow directed into the non-preferred outlet has to be maintained a the control input. In microfluidic valves operating at higher Reynolds numbers, more than ~ 1000, the monostability is usually obtained without by using the Coanda effect of attachment of a fluid jet to an attachment wall leading towards the preferred outlet. The monostable valves may be a very useful part of sampling units used in microfluidic systems for combinatorial chemistry testing.

Cross References

► Microfluidic Systems for Combinatorial Chemistry
► Sampling Unit

Monte Carlo Method

William W. Liou
Western Michigan University, Kalamazoo, MI, USA
William.liou@wmich.edu

Synonyms

Monte Carlo simulation method; Statistical sampling method; Random method

Definition

The Monte Carlo method generally refers to approaches that generate a simulated system with randomness introduced to the variables in the system. The integrated properties are built by sampling the field and the accuracy depends on the size of the sample subjecting to statistical scatter.

Overview

Monte Carlo methods belong to the category of probabilistic methods that can be used in problems of significant uncertainties in initial or input values. Early pioneers [1], with reference to the activities of similar processes in casinos for the repetitive occurrences of chances, or random-

ness, fronted the name Monte Carlo for the famous casinos in Monaco. As the method requires a large number of calculations, it was not widely used until the advent of modern computers.

The Monte Carlo method has been applied to problems in many different fields. It has been found useful in solving multidimensional differential–integral equations. Computational physicists often use it as an alternative to molecular dynamics approaches to examine nuclear and particle physics. Ray tracing in graphics uses a version of the Metropolis–Hastings Monte Carlo algorithm. Financial analysts use the method to generate data for investment portfolios and risk assessment. Engineering applications in reliability prediction, optimization, environmental impact studies, semiconductors behavior, and light transport modeling can also be found.

In microfluid mechanics, the direct simulation Monte Carlo (DSMC) method has been applied to study gas flows in microdevices [2]. DSMC is a simple form of the Monte Carlo method. Bird [3] first applied DSMC to simulate homogeneous gas relaxation problem. The fundamental idea is to track thousands or millions of randomly selected, statistically representative particles, and to use their motions and interactions to modify their positions and states appropriately in time. Each simulated particle represents a number of real molecules. Collision pairs of molecule in a small computational cell in physical space are randomly selected based on a probability distribution after each computation time step. In essence, particle motions are modeled deterministically while collisions are treated statistically. The backbone of DSMC follows directly classical kinetic theory, and hence the applications of this method are subject to the same limitations as kinetic theory. These limitations are associated with the fundamental assumption of molecular chaos and dilute gases. DSMC has been shown to be accurate at the Boltzmann equation level for monatomic gases undergoing binary collisions [4]. The statistical error of a DSMC solution is inversely proportional to the square root of the sample size N. A large sample size is needed to reduce the statistical error. The primary drawback of DSMC is the significant computer resources required for simulating a practical flow. A significant advantage of DSMC is that the total computation required is proportional to the number of molecules simulated N, in contrast to N^2 for molecular dynamics simulations.

Basic Methodology

The feature that separates Monte Carlo methodology from deterministic methods is mainly the use of random numbers, or pseudo-random number sequences in the algorithm. The use of random number differs in the various Monte Carlo methods. A simple Monte Carlo method can be programmed in a few lines of coding or by using existing software, while a general-purpose routine can be quite complicated.

The most common use of Monte Carlo methods is Monte Carlo integration. This can be best illustrated by a simple integration $\int_\Omega f\,\mathrm{d}x$, where x represents multidimensional variable defined in the region Ω. The integration can be started by identifying a region V, of which Ω is a subset. The region V can be randomly sampled in x. For sample points that fall in Ω, f assumes its value. For sample points that are not in Ω, take f as zero. For a total of N samples, the basic Monte Carlo integration algorithm gives

$$\int_\Omega f\,\mathrm{d}x = \frac{\Omega}{N}\sum_{i=1}^{N} f(x_i)$$

The statistical error of such sampling is proportional to $1/\sqrt{N}$. Therefore, the accuracy of the method increases with the sample size. More advanced adaptive Monte Carlo methods use, for instance, importance sampling to enhance the convergence and the accuracy over that of the basic Monte Carlo integration.

The DSMC method often used in micro gas flow simulations was originally developed for high Knudsen number rarefied gas flow. The procedures involved in applying DSMC to steady and unsteady flow problems are presented in Fig. 1 [2, 5].

Execution of the method requires the physical domain to be divided into a distribution of computational cells. The cells provide geometric boundaries and volumes, which are used to sample macroscopic properties. Also, only molecules located within the same cell, at a given time, are allowed to collide. The DSMC simulation proceeds from a set of prescribed initial condition. The molecules randomly populate the computational domain. These simulated molecules are assigned random velocities, usually based on the equilibrium distribution. The simulated representative particles move for a certain time step. This molecule motion is modeled deterministically. This process enforces the boundary conditions. With the simulated particles being appropriately indexed, the molecular collision process can be performed. The collision process is modeled statistically, which is different from deterministic simulation methods such as the molecular dynamics methods. In general, only particles within the same computational cell are considered to be possible collision partners. Within each cell, collision pairs are selected randomly and a representative set of collisions is performed. The post-collision velocities are determined. There are several

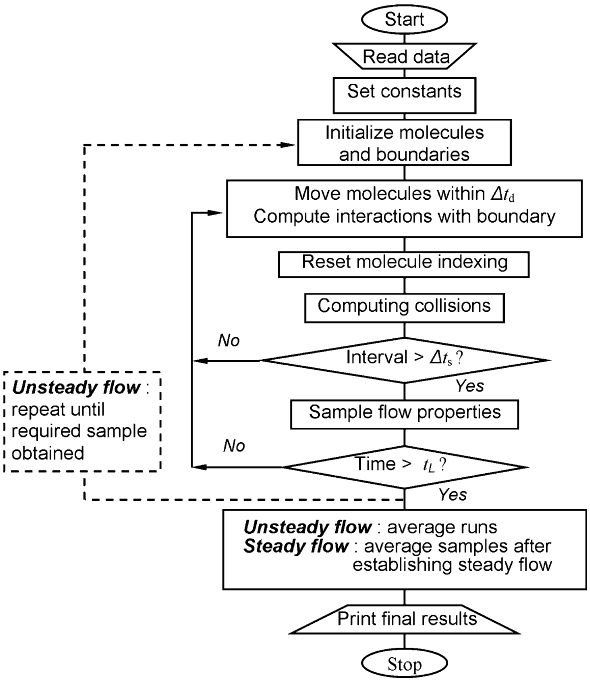

Monte Carlo Method, Figure 1 DSMC flow chart [2]

collision-sampling methods that have been used successfully. The currently preferred model is the *no-time-counter* (NTC) technique used in conjunction with the sub-cell method [6]. Figure 2 [2] shows the velocity phase plane in a cell for a typical microflow simulation. The sample size is 17,370.

Key Research Findings

For microflow simulations, the statistical scatter associated with DSMC limits its applications to microflows with extremely low velocity. The information preservation (IP) method has been developed to address this issue. The method [7, 8] introduces preserved information velocities. It has been applied to low-speed Couette, Poiseuille and Rayleigh flows in the slip, transition and free-molecular flow regimes, and to low-speed microflows. For convergence, the computation time of an IP scheme can be several orders of magnitude smaller compared with a regular DSMC simulation. Figure 3 [2] shows the IP velocity phase plane results for the same microflow as shown in Fig. 2 obtained by DSMC. The reduction of the scattering is significant.

Future Directions for Research

Monte Carlo methods are inherently parallel and can be readily parallelized compared with deterministic

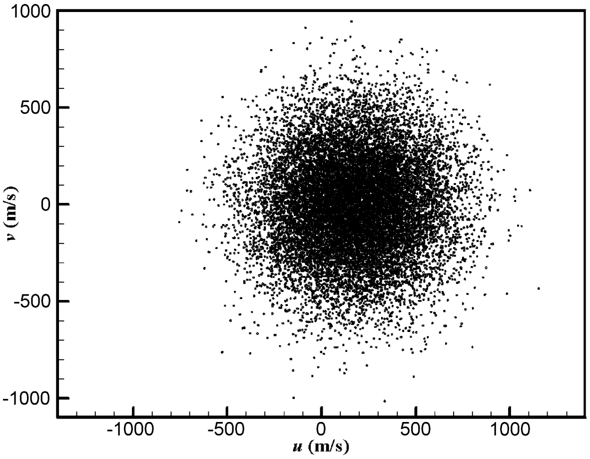

Monte Carlo Method, Figure 2 Velocity phase plane from a DSMC simulated microflow

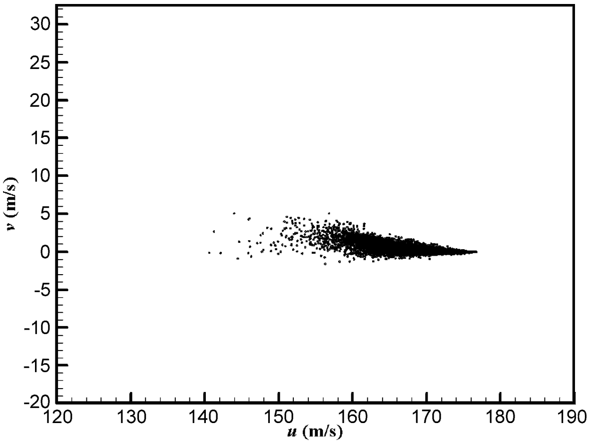

Monte Carlo Method, Figure 3 Velocity phase plane from an IP simulated microflow

approaches. With the advent of low-cost, PC-based cluster computing, the parallel nature of Monte Carlo method should be further explored. Simulations of fluid behavior and properties at micro- and nanoscales may be facilitated with hybrid types of method employing both Monte Carlo and molecular dynamics techniques. This combination allows the simultaneous exploration of, for instance, thermal properties and local phase space.

Cross References

- ► Chaotic Flows
- ► Lattice Boltzmann Method (LBM)
- ► Micro- and Nanoscale Gas Dynamics
- ► Micro- and Nanoscale Gas Fluidics
- ► Multiscale Modeling and Numerical Simulations
- ► Non-continuous Approaches

References

1. Metropolis N, Ulam S (1949) The Monte Carlo method. J Am Stat Assoc 44(335)
2. Liou WW, Fang YC (2006) Microfluid Mechanics. McGraw-Hill
3. Bird G (1963) Approach to translational equilibrium in a rigid sphere gas. Phys Fluid 6:1518–1519
4. Bird G (1970) Breakdown of translational and rotational equilibrium in gaseous expansions. Am Inst Aero Astro J 8:1998–2003
5. Bird GA (1976) Molecular Gas Dynamics. Clarendon Press, Oxford
6. Bird GA (1994) Molecular Gas Dynamics and the Direct Simulation of Gas Flows. Clarendon Press, Oxford
7. Fan J, Shen C (1999) Statistical simulations of low-speed unidirectional flows in transition regime. In: Brun et al (ed) Rarefied Gas Dynamics Cepadus-Editions, Toulouse 2:245
8. Sun Q, Boyd ID (2002) A direct simulation method for subsonic microscale gas flows. J Comput Phys 179:400–425

Monte Carlo Simulation Method

► Monte Carlo Method

Morphotropic Phase Boundary

Definition

The boundary in a composition diagram along which there are a maximum number of polarization states. With PZT, for example, the choice of x in the relative concentration of Pb_x versus Zr_{1-x} is typically set near 0.52, along the *morphotropic phase boundary*, to increase the ability of the material to be polarized in response to an externally applied electric field or stress. Usually the material is doped with either acceptor or donor ions to give either a low-loss *hard* material at the expense of polarization difficulty and reduced piezoelectric coupling or a lossy *soft* material with greater piezoelectric coupling.

Motional Branch

Synonyms

Motional leg; Motional circuit

Definition

The portion of the electrical circuit representation of a system that delivers the oscillatory resonance behavior at one or more resonance frequencies (► resonance and antiresonance frequencies).

Cross References

► Piezoelectric Microdispenser

Motional Circuit

► Motional Branch

Motional Leg

► Motional Branch

Motion of a Deformable Drop in Microchannels

► Droplet Dynamics in Microchannels

M

MS

► Mass Spectrometry

MS/MS

► Mass Spectrometry

Multi-Channel Micro Liquid Dosing System

► Bubble Actuated Microfluidic Switch

Multi-Channel Micro Switch Pumping

► Bubble Actuated Microfluidic Switch

Multilayer Piezoelectric Actuator

Synonyms

MLPA; Stack actuator

Definition

Piezoelectric materials of thicknesses of 1 mm or more require applied voltages in excess of 100 V to reach maximum strain, depending on the frequency of excitation and the nature of the piezoelectric material. To reduce the voltages needed for full strain, thin (∼ 50 um) layers of piezoelectric material may be stacked with Pt electrodes in a green, presintered state and then sintered to form a complete piezoelectric element with internal electrodes.

Cross References

- ► Piezo/PZT for Microfluidics
- ► Piezoelectric Valves

Multiphase Flows

- ► Cavitation in Microdomains

Multiphase Pumping

- ► Thermocapillary Pumping

Multiplexed Time Etching

- ► ICP Etching

Multiscale Modeling

- ► Multiscale Modeling and Numerical Simulations

Multiscale Modeling and Numerical Simulations

GUOQING HU, DONGQING LI
Department of Mechanical Engineering, Vanderbilt University, Nashville, TN, USA
guoqing.hu@vanderbilt.edu, dongqing.li@vanderbilt.edu

Synonyms

Multiscale modeling; Hybrid simulation; Molecular-continuum simulation

Definition

Microfluidic and nanofluidic phenomena arising from Lab-on-a-Chip microdevices are characterized by hierarchal multiscale nature with respect not only to space but also to time. In the area of microfluidics and nanofluidics, multiscale modeling aims to develop a viable multiscale computational methodology to study fluid mechanics in spatial and temporal domains ranging from the molecular level to the continuum level.

Overview

Size generally means the physical dimensions, proportions, magnitude, or extent of an object. In the real world, length is one of the most important dimensions of measurement, spanning from 10^{25} m (our entire universe) down to 10^{-15} m (proton and neutron). Many fundamental processes of biology, however, do not cover quite as large a range of sizes as mentioned above. For instance, translation, gene regulation, and cell communication occur on the micrometer to nanometer scale. Table 1 lists the typical length scales of some of biological objects. In order to study the various biological phenomena and processes at the molecular level and at the cellular level, researchers must be able to access these relevant length scales. This requires the experimental devices to have characteristic sizes of a few nanometers up to several micrometers. During the past decade, micromachining and microfabrication technology has become available to make nano- and micron-sized devices, thus enabling studies of objects with these length scales.

Multiscale Modeling and Numerical Simulations, Table 1 Length scale of typical objects in biology

Objects	Length
Diameter of glucose molecule	1 nm
Diameter of DNA helix	2 nm
Diameter of insulin molecule	5 nm
Thickness of cell wall (gram negative bacteria)	10 nm
Size of typical virus	75 nm
Diameter of the smallest bacterium	200 nm
Diameter of red blood cell	8.4 μm
Diameter of average cell in human body	10 μm
Diameter of the largest bacterium	750 μm

Since the introduction of the concept of miniaturized total analysis system (μTAS) or Lab-on-a-Chip, the miniaturization of biological or chemical devices has attracted substantial attention and remarkable progress has been achieved. An integrated Lab-on-a-Chip device can incor-

porate many of the necessary components and functionality of a typical room-sized laboratory into a small chip that perform a specific biological or chemical analysis, including sample treatments, transport, reactions and detection. Originally it was thought that the most significant benefit of the miniaturization would be the analytical improvements associated with the scaling down of the size. Further development revealed other advantages such as minimized reagents, increased automation, and reduced manufacturing costs.

Lab-on-a-chip devices are not just a simple small version of the conventional instruments. Miniaturization raises many new challenges. Fluid and sample transport is a crucial issue in these Lab-on-a-Chip devices because many biological and chemical processes and experiments take place in aqueous environments. The fundamental properties of fluidics in micro/nanoscale may differ significantly from those in larger devices [1]. In microscale (100 nm $\sim$ 100 μm), the fluidic phenomena still can be described by continuum theory, but the decrease of length scale makes surface force and electrokinetic effects important and inertial force unimportant. One of the well-known examples is that mass transportation in microfluidic device is normally dominated by viscous force rather than inertial force. Dimensions of fluidic channels continue to be scaled down to below 100 nm, entering the region of nanofluidics. In these scales, the surface-to-volume ratio is very high, the non-slip boundary condition does not hold fully, and fluid constitutive relations are strongly affected by the existence of the boundary. The study of micro/nanoscale fluid mechanics is important for the understanding and development of the Lab-on-a-Chip devices at the corresponding scales.

Fluid flow in small devices acts differently from those in macroscopic scale. The Reynolds number (Re) is the most often mentioned dimensionless number in fluid mechanics. The Re number, defined by $\rho UL/\mu$, represents the ratio of inertial forces to viscous ones. In most circumstances involved in micro- and nanofluidics, the Re number is at least one order of magnitude smaller than unity, ruling out any turbulence flows in micro/nanochannels. Inertial force plays an insignificant role in microfluidics, and as systems continue to scale down, it will become even less important. For such small Re number flows, the convective term $(\rho \boldsymbol{u} \cdot \nabla \boldsymbol{u})$ of Navier–Stokes equations can be dropped. Without this nonlinear convection, simple micro/nanofluidic systems have laminar, deterministic flow patterns. They have parabolic velocity profile in pressure-driven flows, plug-like velocity profile in electroosmotic flows, or a superposition of both. One of the benefits from the low Re number flow is that genomic material can be transported easily without shearing in Lab-on-a-Chip devices. It is worth noting, however, that other mechanisms, such as capillary effects, viscoelasticity, and electrokinetic effects may complicate the flow phenomena since their nonlinearity increases in small scales [1].

Along with experimental and theoretical studies, numerical simulation has been an indispensable tool in almost every research and application field for many years. It also provides great help in the design of microfluidic and nanofluidic devices. Simulations allow researchers to rapidly determine how design change will affect chip performance, thereby reducing the number of prototyping iterations. However, there are several factors that complicate the numerical simulation of micro/nanoscale phenomena and thus distinguish it from the macroscale counterpart. The first and most important one is the large range of relevant length scales, which can vary up to seven orders (from Debye layer, nm, to channel length and substrate thickness, cm). Secondly, the downscaling of the size dramatically increases the relative importance of surface and interfacial phenomena. Rapid and localized changes of fluidic and material properties often occur in the miniature devices. Another challenge in numerical simulation is the intrinsic multi-physics phenomena that usually combine less or more fluid mechanics, heat transfer, electrokinetics, and chemical and biological thermodynamics and reaction kinetics. In general, one must consider all these aspects in order to provide a numerical picture for a true Lab-on-a-Chip device and therefore there is emerging need to develop multiscale modeling methods.

It is well known that the continuum theory in the Navier–Stokes equations only validates when the mean free path of the molecules is smaller than the characteristic length scale of the gas flow. Otherwise, the fluid will no longer be in thermodynamic equilibrium and the linear relationship between the shear stress and rate of shear strain cannot be applied. The commonly used no-slip boundary condition at the fluid-solid interface is not fully valid, and a slip length has to be introduced,

$$\Delta\, u|_w = u_{\text{fluid}} - u_{\text{wall}} = L_{\text{s}} \left.\frac{\partial u}{\partial y}\right|_w \tag{1}$$

where $\Delta\, u|_w$ is the tangential velocity at the solid wall, L_s is the constant slip length determining the degree of slip, and $\partial u/\partial y|_w$ is the strain rate computed at the wall. It should be noted that so far there is no well-established theory for treating slip boundary at liquid-solid interface in small scales.

Fortunately, for normal liquid flows with the characteristic scale above 10 nm, the continuum assumption still holds practically. For example, modeling and simulation of electrokinetic flow, based on the classical Poisson–

Boltzmann equations and the continuum Navier–Stokes equations, have explained many experimental results and guided the design of Lab-on-a-Chip systems. However, as the device scale shrinks further to several nanometers, or if the local effects such as surface roughness of molecular size and ion-surface interaction must be considered, one needs to resolve the atomistic details of the flow because these effects are neglected in the classical continuum. One example is the fluid density. Continuum theory assume that the density does not vary significantly over intermolecular distance, but fluctuations of density in the vicinity of the solid surface have been confirmed by molecular dynamics simulation and experiment. Therefore, molecular-based computer simulations, mainly Molecular Dynamics (MD) method and direct simulation Monte Carlo (DSMC) method, are necessary for improving our understanding of the flows at these scales.

Basic Methodology

There are two basic models of simulating a flow filed: the continuum model and the molecular model. The continuum model, in form of the Navier–Stokes equations or Euler equations, is able to describe the microfluidic phenomena where the channel sizes are in the micrometer range. It should be noted that many liquid flows in the nano regime can still be treated by continuum models (with appropriate boundary conditions), whereas this is no longer true for nanoscale gas flows. As the length scale decreases further to naonometer range, the continuum assumption begins to break down and molecular-based models, such as Molecular Dynamics method and direct simulation Monte Carlo, are needed to address the effects of the discrete particles: molecules, atoms, ions, and electrons.

Navier–Stokes/Stokes Simulation

The flow of incompressible liquids in continuum state can be described by the Navier–Stokes equations,

$$\begin{aligned} \rho(\partial_t \boldsymbol{u} + \boldsymbol{u}\cdot\nabla\boldsymbol{u}) &= -\nabla p + \mu\nabla^2\boldsymbol{u} + \boldsymbol{F} \\ \nabla\cdot\boldsymbol{u} &= 0 \end{aligned} \tag{2}$$

where $\boldsymbol{u}$ is the flow velocity vector, ρ is the fluid density, μ is the fluid viscosity, p is the pressure, and $\boldsymbol{F}$ is the body force acting on the liquid.

Computational Fluid Dynamics (CFD) based on the continuum Navier–Stokes equations Eq. (2) has long been successfully used in fundamental research and engineering design in different fluid related areas. Naturally, it becomes the first choice for the simulation of microfluidic phenomena in Lab-on-a-Chip devices and is still the most popular simulation model to date. Due to the nonlinearity arising from the convention term, Eq. (2) must be solved numerically by different discretization schemes, such as finite element method, finite difference method, finite volume method, or boundary element method. Besides, there are a variety of commercially available CFD packages that can be less or more adapted to model microfluidic processes (e. g., COMSOL (http://www.femlab.com), CFD-ACE+ (http://www.cfdrc.com), Coventor (http://www.coventor.com), Fluent (http://www.fluent.com), and Ansys CFX (http://www.ansys.com). For majority of the microfluidic flows, Re number is always very small and thus the flows are Stokes type. The full Navier–Stokes equations thus can be linearized as Stokes equations, which greatly reduces the computational cost. The Navier–Stokes/Stokes equations, coupled with other equations, have been applied in study of many kinds of phenomena in the microfluidic systems: electrokinetic flow with Poisson–Boltzmann equation, species transportation with species transport equation, chemical reaction with reaction equation, and thermal analysis with heat transfer equation.

Molecular Dynamics Simulation

Molecular Dynamics method was first used in thermodynamics, physical chemistry, and average thermochemical properties of gases, liquids, and solid. The basic idea of the MD method is straightforward: atoms or molecules are described as a system of interacting material points, whose motion is determined dynamically by a vector of instantaneous positions and velocities. The velocities $\boldsymbol{v}_i = (v_{x,i}, v_{y,i}, v_{z,i})$ and positions $\boldsymbol{r_i} = (x_i, y_i, z_i)$ of the single atoms evolve according to Newton's law of motion,

$$\begin{aligned} m_i \frac{\partial \boldsymbol{v}_i}{\partial t} &= \sum_{j\neq i} \nabla V(r_{ij}) \\ \frac{\partial \boldsymbol{r}_i}{\partial t} &= \boldsymbol{v}_i(t) \end{aligned} \tag{3}$$

where m_i is the mass and $V(r_{ij})$ is the interaction potential that models the physics of the system under consideration. Among a wide range of potentials employed in MD simulations, the Lennard–Jones $12-6$ potential is typically used to represent inter-atomic interactions,

$$V(r_{ij}) = 4\varepsilon\left[\left(\frac{\sigma}{r_{ij}}\right)^{12} - \left(\frac{\sigma}{r_{ij}}\right)^{6}\right] \tag{4}$$

where $r_{ij}$is the distance between atoms i and j, ε is the energy scale, and σ is the Lennard–Jones diameter. The

set of Eq. (3) can be integrated in time, with initial conditions and specified boundary conditions. MD simulations are usually employed for homogeneous system where periodic boundary conditions are used. However, sometimes it is also necessary to impose arbitrary non-periodic boundary conditions. For example, interactions between the liquid and solid walls can be taken into account by adding different wall atoms, either fixed on a lattice or coupled to a lattice with large spring constant.

Direct Simulation Monte Carlo Method and Lattice–Boltzmann Method

MD simulations are highly inefficient for dilute fluid (gas) where the molecular interactions are infrequent. Alternative statistical approaches, such as direct simulation Monte Carlo method (DSMC) or Lattice–Boltzmann method (LBM), are more suitable for dealing with such a situation. DSMC is a direct particle simulation method based on kinetic theory and its basic idea is to track a large number of statistically representative particles. Unlike exactly calculating collisions in MD simulations, DSMC models collisions stochastically using scattering rates and postcollision velocity distributions based on kinetic theory. DSMC simulations are not correct at atomic scale, but they are accurate at scales smaller than mean free path. Most of DSMC methods are based on the following Boltzmann equation,

$$\frac{\partial nf}{\partial t} + \boldsymbol{c} \cdot \frac{\partial nf}{\partial \boldsymbol{r}} + \boldsymbol{F} \cdot \frac{\partial nf}{\partial \boldsymbol{c}} = \int_{-\infty}^{\infty} \int_{0}^{4\pi} n^2 (f^* f_1^* - ff_1) c_r \sigma \, \mathrm{d}\Omega \, \mathrm{d}\boldsymbol{c}_1 \quad (5)$$

where nf is the product of the number density n and the velocity distribution function f, $\boldsymbol{c}$ is the molecular velocity vector, $c_r$is the relative molecular speed, $\boldsymbol{F}$ is an external force, the superscript * denotes postcollision values, f and f_1 represent two different kinds of molecules, σ is the collision cross section, and Ω is the solid angel. The right hand side term of Eq. (5) represents the collision of molecules. In the DSMC simulations, the physical flow domain is discretized into a grid of cells, structured or unstructured. The size of the cells should be sufficiently fine so that the change of flow properties across the cell is small. The time step is chosen so that the molecules do not move across more than one cell during a time step. With initial conditions and imposed boundary conditions, Eq. (5) can be numerically solved. The macroscopic flow parameters, such as density, velocity, and temperature, are obtained by averaging the corresponding velocity functions over all particles in a single cell.

LBM has been developed to simulate flows in microchannels based on kinetics equations and statistical physics. In LBM, the motion of the fluid is modeled by a lattice Boltzmann equation for the distribution function of the fluid molecules. The discrete velocity Boltzmann equation corresponding to the Navier–Stokes equations can be written as,

$$\frac{\partial f}{\partial t} + \boldsymbol{c} \cdot \nabla f = \Omega + \boldsymbol{F} \quad (6)$$

where f is the single-particle distribution function for particles moving at velocity $\boldsymbol{c}$, $\boldsymbol{F}$ is the external force term, and Ω is collision operator representing the change rate resulting from collisions in f. The most commonly used collision operator is the BGK (Bhatnagar–Gross–Krook) model which uses a single relaxation time approximation,

$$\Omega(f(\boldsymbol{x}, t)) = -\frac{f(\boldsymbol{x}, t) - f^{\mathrm{eq}}(\boldsymbol{x}, t)}{\tau} \quad (7)$$

The appropriately chosen equilibrium distribution, denoted by f^{eq}, depends on the local fluid variables, and $1/\tau$ is the rate of approach to this equilibrium.

Originated from the lattice gas automata (LGA), the LBM has been widely applied in simulating the rarefied gaseous flow in microchannel. Recently the LBM has also found success in applications to the liquid microflows, particularly the electrokinetic flows. For the continuous liquid, the Navier–Stokes equations can be recovered from the Boltzmann equation by Chapman–Enskog expansion or multiscale analysis, in which the Boltzmann equation is split into different scales for space and time variables. The lattice that an LBM operates is usually designated by an identifier of DdQq where d is the number of dimensions and q is the number of velocity vectors. The geometry of the lattice should be symmetrical to satisfy the isotropic requirement of fluid properties. To correctly recover the Navier–Stokes equations, it also requires sufficient lattice symmetry. For a 2D LBM, there are three lattice models: D2Q5, D2Q7, and D2Q9. For a 3D LBM, there are three lattice models: D3Q15, D3Q19, and D3Q27. Although not a real mesoscale method, the LBM for the incompressible flow has comparable computing efficiency to a Navier–Stokes solver yet has the potential of providing accurate results beyond the slip-flow regime. Moreover, external force field (e. g., applied electric field) can be more easily added to the lattice Boltzmann equation than to the Navier–Stokes equations.

Multiscale Simulation

Molecular-based simulations have already become a powerful tool for studying nanoscale physical phenomena.

However, the length and time scales that molecular-based simulations can probe are still very limited (tens of nanosecond and a few nanometers), due to computer memory and CPU power limitations. On the other hand, nanoscale flows are often a part of larger scale devices that could contain both nanochannels and microfluidic domains. The dynamics of these systems depends on the intimate connection of different scales from nanoscale to microscale and beyond. MD simulation cannot simulate the whole systems due to its prohibitive computational cost, whereas continuum Navier–Stokes simulation cannot elucidate the details in the small scales. These limitations and the practical needs arising from the study of multiscale problems have motivated research on multiscale (or hybrid) simulation techniques that bridge a wider range of time and length scales with the minimum loss of information. A hybrid molecular-continuum scheme can make such multiscale computation feasible. A molecular-based method, such as MD for liquid or DSMC for gas, is used to describe the molecular details within the desired, localized subdomain of the large system. A continuum method, such as finite element or finite volume based Navier–Stokes/Stokes simulation, is used to describe the continuum flow in the remainder of the system. Such hybrid method can be applied to solve the multiscale phenomena in gas, liquid, or solid.

The key issue of the multiscale simulations is the coupling (exchanging information) between the molecular scale and the continuum scale. There are two classes of coupling schemes for liquids: direct flux exchange [2] and the domain decomposition method (Schwartz alternating method) [3]. O'Connell and Thompson's scheme [2] implemented a finite overlap region between the molecular domain and continuum domain to avoid sharp density oscillation and therefore allow two solutions to relax before coupled together. Hadjiconstantinou and Patera [3] proposed a Maxwell demon method for simulating incompressible flow. They introduced a particle reservoir to conserve mass flux across the MD-continuum interface. Several extensions of the model have been made but without much improvements on outputs. The most critical problem with the model is how to determine the empirically coupling parameter. Recently, a dynamic coupling model was proposed to simultaneously calculate the free parameter without any a priori input in computation, which yielded satisfactory results for the Couette flow and the Stokes flow. Various multiscale simulations have been used in studying the fluid flow with localized molecular characteristics. Qiao and Aluru [4] presented embedding multiscale simulation techniques for analysis of electroosmotic flow in nanochannels. The multiscale results were compared to direct MD simulations and found good agreement in ion distribution and velocity profile. Their simulations also indicated that the classical continuum theory significantly overestimates the average velocity at a high-bulk concentration. Werder et al. [5] developed an MD simulation coupled to a continuum Navier–Stokes solver based on finite volume discretization. The two regions were combined through Schwarz alternating method to exchange information. They used this hybrid method to study the flow of liquid argon past a carbon nanotube, and found that the resulting flow field agreed with a fully molecular reference solution.

Key Research Findings

While experimental evidence indicates that fluid flow in microdevices differs from flow in macroscale, existing experimental results are often inconsistent and contradictory because of the difficulties associated with such experiments and the lack of a guiding rational theory. Koo and Kleinstreuer [6] summarized experimental observations of liquid microchannel flows and computational results concerning channel entrance, wall slip, non-Newtonian fluid, surface roughness, and other effects. Those contradictory results suggest the need for applying molecular-based models to help establish a theoretical frame for the fluid mechanics in microscale and nanoscale.

Thompson and Troian [7] presented results from MD simulations of Newtonian liquids under shear and found a general nonlinear relationship between the slip boundary condition and the local shear rate at a solid surface. Werder et al. [8] conducted parallel MD simulations to investigate the wetting behavior of water droplets confined in carbon nanotubes and found that pure water showed a nonwetting behavior in nanotubes. Kalra et al. [9] used MD to study osmotically driven transport of water molecules through hexagonally packed carbon nanotube membranes and revealed several distinct features of the nanoflows. The thermal fluctuations become significant at the nanoscale and the flow is stochastic in nature. The flow also appears frictionless and is limited mainly by the barrier at the inlet and outlet of the nanotube. Yeh and Hummer [10] studied the electrophoresis of single-stranded RNA molecule through 1.5 nm-wide pore of carbon nanotube membranes using MD simulations. They found that translocation kinetics of RNA through nanotube membranes is sequence-dependent, which suggests the possibility of extracting sequence information from synthetic-pore translocation data.

Future Directions for Research

As advancements in microfabrication techniques allow for further shrinking Lab-on-a-Chip devices from the micron

regime to the nanometer regime, much nontraditional physics is still to be discovered and many exciting applications of Lab-on-a-Chip devices are yet to be exploited. For example, fast sequencing of DNA strands with a nanopore device need the knowledge of the conformations of DNA inside the pore in atomic detail. Due to difficulties associated with the nanoscale experiments, molecular-based simulation, as well as multiscale modeling, will play a more and more important role in development and optimization of such devices. The computer models must be able to cover length scale from nanometer to micron, and time scale from femtosecond to microsecond. Therefore considerable research effort should be put to construct the foundations for the multiscale methodology and to develop computational capability to realize such multiscale simulation. Meanwhile, it is also essential to develop novel experimental techniques for direct measurement and visualization of flow fields and molecular transport in the nanoscale. Such techniques will not only generate first-hand observation in nanometer regime, but also provide validation and improvement for the molecular-based models and multiscale simulations.

Cross References

► Boundary Slip of Liquids
► Gas Flow in Nanochannels
► Molecular Dynamics Simulation Method
► Monte Carlo Method
► Nanofluidics in Carbon Nanotubes

References

1. Squires TM, Quake SR (2005) Microfluidics: Fluid physics at the nanoliter scale. Rev Mod Phys 77:977–1026
2. O' Connell ST, Thompson PA (1995) Molecular dynamics-continuum hybrid computations: A tool for studying complex fluid flow. Phys Rev E 52:R5792–R5795
3. Hadjiconstantinou NG, Patera AT (1997) Heterogeneous atomistic-continuum representations for dense fluid systems. Int J Mod Phys C 8:967–976
4. Qiao R, Aluru NR (2004) Multiscale simulation of electroosmotic transport using embedding techniques. Int J Multiscale Comput Eng 2:173–188
5. Werder T, Walther JH, Koumoutsakos P (2005) Hybrid atomistic-continuum method for the simulation of dense fluid flows. J Comput Phys 205:373–390
6. Koo J, Kleinstreuer C (2003) Liquid flow in microchannels: experimental observations and computational analyses of microfluidics effects. J Micromech and Microeng 13:568–579
7. Thompson PA, Troian SM (1997) A general boundary conditions for liquid flow at solid surfaces. Nature 389:360–362
8. Werder T, Walther JH, Jaffe RL, Halicioglu T, Noca F, Koumoutsakos P (2001) Molecular dynamics simulation of contact angles of water droplets in carbon nanotubes. Nano Letters 1:697–702
9. Kalra A, Garde S, Hummer G (2003) Osmotic water transport through carbon nanotube membranes. Proc Nat Acad Sci USA 100:10175–10180
10. Yeh IC, Hummer G (2004) Nucleic acid transport through carbon nanotube membranes. Proc Nat Acad Sci USA 101:12177–12182

Mw/Mn

► Polydispersity

Nanoarrays

► Nanoscale Biosensors

Nanobiosensors for Nano- and Microfluidics

► Impedimetric Biosensors for Nano- and Microfluidics

Nanocatalyst

► Fabrication of Self-Assembled Catalytic Nanostructures

Nanochannel Fabrication

DEYU LI
Department of Mechanical Engineering,
Vanderbilt University, Nashville, TN, USA
deyu.li@vanderbilt.edu

Synonyms

Nanopores; Nanofluidic channels; Nanopore fabrication

Definition

A nanochannel is a hollow channel with at least one dimension of its cross-section in the 1 – 100 nm range. Depending on the cross sectional configuration, a nanochannel can be classified as a twodimensional (2D) nanochannel or a nano-slit with one side of its cross-section in the nanometer regime, or a onedimensional (1D) nanochannel or a nanotube with its diameter (or both width and depth) in the nanometer regime. Short nanochannels are usually denoted as nanopores.

It is worth noting that some confusion exists at present in classifying nanochannels as 1D or 2D. Nano-slits are also referred to by some researchers as 1D confined nanochannels, and sometimes simplified as 1D nanochannels, while nanotubes are called 2D confined nanochannels. This is exactly opposite to the above classification so caution must be used to find out what a researcher means by 1D and 2D nanochannels in his writing. Here the definition follows the common practice in naming low dimensional structures, for example, thin films are usually denoted as two dimensional and nanowires are usually denoted as one-dimensional.

Overview

Nanochannels or nanopores are interesting nanostructures due to the fact that their sizes are comparable to either the size of DNAs or proteins or the Debye screening length of electric double layers. Current interest in nanochannels or nanopores in nanofluidic research was largely inspired by the pioneering work of single molecule sensing with a naturally occurring protein nanopore, α-hemolysin, which is a nanopore of about 10 nm long and has an smallest inner diameter of about 1.4 nm. The nanopore was embedded in a lipid bilayer membrane separating two fluid cells and a baseline ion current was set up under an electric bias across the nanopore. When single stranded DNA or RNA molecules were translocated through the nanopore, the ion current was partially blocked, making an extremely sensitive single molecule detector. These promising results motivated the development of robust and size-tunable inorganic nanopores as single molecule sensors with solid-state microfabrication techniques. Nanopores of about 2 nm in diameter have been fabricated and ion current modulation was observed when DNA molecules translocated through these solid-state inorganic nanopores.

Long nanochannels can be used as single molecule sensors in a similar way as nanopores, as has been demonstrated in several recent studies. In addition to the application as single molecule sensors, long nanochannels and their arrays can be used as filters for molecule separation, membranes for electroosmotic pumping, templates for nanowire synthesis, electrodes for supercapacitors, and

proton exchange membranes in fuel cells. Novel and complex transport phenomena can occur in nanochannels, leading to improved performance or new functions for devices made of nanochannels.

The promising applications of nanochannels in nanofluidics have excited great interest in fabrication of various kinds of nanochannels. In general, nanochannels can be made by either top down approach based on micro- and nanofabrication techniques, or the bottom up approach based on chemical self-assembly to build up nanostructures with chemical reactions [1]. The top down approach takes advantage of the rapid development of micromachining techniques, and can make nanopores or nanochannels as small as one to two nanometers. The fabrication process is usually based on lithography and etching on a silicon or glass substrate, making it possible to directly integrate the nanochannel with microfluidic components to make integrated nanofluidic devices. The disadvantage of the top down approach is that it could be very expensive, especially for nanochannels of ultra small size such as ~ 2 nm. The bottom up technique is based on chemical synthesis, which is usually cost-effective and can make very small pores. However, chemical synthesis usually makes an array of nanochannels either by anodization through a membrane, or by growing an array of nanochannels on a substrate. It may be difficult to separate a single nanochannel for certain applications. Integration with other components to make integrated nanofluidic devices may also pose challenges.

Many techniques have been developed to fabricate nanochannels or nanochannel arrays. Several general approaches of nanochannel fabrication relevant to nanofluidics are summarized in the following sections.

Basic Methodology

Nanochannel Fabrication with Solid-State Fabrication Techniques

Top down nanochannel fabrication techniques are developed mainly over the last decade with state-of-the-art micromachining facilities. Various kinds of nanochannels, such as short nanopores, 2D nanoslits, and 1D nanotubes have been fabricated and tested for different applications. Small nanopores are made based on the reflow of surface atoms under the irradiation of focused ion or electron beams. 2D nanoslits can be easily batch-fabricated with either etching of enclosed sacrificial lines or bonding of two chips with one having etched nanometer deep open channels on it. 1D nanochannels need advanced lithography capability and many techniques are not suitable for batch fabrication. Some more details of making these three types of nanochannels are as follows.

Fabrication of Inorganic Nanopores

Inorganic nanopores of about 2 nm pore size for single molecule sensing are fabricated with advanced microfabrication techniques and further processed by either focused ion beams or focused electron beams. To date, two processes have been developed to make either SiN_x nanopores with focused ion beams or SiO_2 nanopores with focused electron beams.

To make ~ 2 nm diameter SiN_x nanopores, a layer of nitride film is first deposited on top of a silicon wafer and the silicon wafer is then etched from the backside with KOH to leave a small region of free standing SiN_x membrane. Either an electron beam lithography or ion milling step will create a nanopore of tens of nanometers. Further exposure of the nanopore to focused ion beam will gradually shrink the pore to $1-2$ nm in diameter.

To make the ~ 2 nm SiO_2 nanopores, the typical process starts with a silicon-on-insulator (SOI) wafer. The silicon substrate is anisotropically etched by KOH to leave a small region of free-standing silicon film. E-beam lithography is then performed to create a hole in the device silicon layer, and the size of the hole is further reduced by thermal oxidation to grow a layer of SiO_2 from the device layer silicon. This process will lead to a nanopore of less than 20 nm diameter, which is subsequently shrunk to $2-3$ nm in a transmission electron microscope by focus electron beam mediated reflow of the SiO_2.

The size of these SiN_x or SiO_2 nanopores is comparable to the naturally occurring protein nanopores and ion current modulations through these solid-state nanopores have been observed when single DNA molecules are translocated through these pores. The single molecule detection experiments are performed by embedding the membrane with the nanopore between two bulk fluid cells and applying an electric bias on the order of hundreds millivolts with Ag/AgCl electrodes. The concentration of the electrolyte used is on the order of 0.1 M to 1 M and a baseline ion current on the order of 100 pA to 1 nA is observed. Single DNA molecule translocation through these nanopores will cause a current modulation of the baseline ion current that is significant enough to observe.

Fabrication of 2D Nanochannels

Fabrication of 2D nanochannels can be easily done with state-of-the-art microfabrication facilities based on either sacrificial lines or bonding of a flat chip with a chip with etched grooves of nanometer depth. These nanochannels can be batch-fabricated and easily integrated with other components to make integrated nanofluidic devices. While other techniques may be available to make 2D nanochannels, we will only briefly introduce the two most com-

mon techniques, namely those based on sacrificial lines and bonding because they can be readily made with easily accessible microfabrication facilities.

The sacrificial line method starts with deposition of the sacrificial thin film on selected substrates. Standard photolithography can then be used to pattern the sacrificial thin film into lines of different widths, depending on the available lithography tool and requirement. Another thin film will be subsequently deposited to cover the sacrificial lines and form closed channels with the substrate. Finally the sacrificial lines can be selectively etched away while the wall materials of the nanochannel are intact. In the design of the fabrication process with the sacrificial line technique, attention needs to be paid on selecting the sacrificial materials. The sacrificial material must be able to be deposited uniformly to a height of tens of nanometers and must be able to be selectively etched by some chemicals that do not attack the material that forms the channel wall. If the fabrication of the nanochannel is only part of a process to make integrated nanofluidic devices, then the sacrificial material must be compatible with other process steps. One example of this method is fabricating SiO_2 nanochannels with poly-silicon as the sacrificial material, which can be uniformly deposited by low pressure chemical vapor deposition (LPCVD) at a slow rate.

The bonding technique makes 2D nanochannels by bonding a flat chip with another chip with open nanochannels, usually made by lithography and etching. The bonding will produce a nanochannel enclosed by the two chips. Microchannels connected to the nanochannel and open holes through one of the chip are usually pre-made before the bonding process to provide access to the nanochannel. Different bonding processes are available to bond two different chips together, but anodic bonding and fusion bonding are usually the techniques adopted to make nanochannels. Anodic bonding is a bonding technique to bond silicon and sodium-rich glass with the assistance of high electric field. The advantage of anodic bonding is that the process can be carried out at relatively low temperatures (as low as about 180 °C). Fusion bonding can be used to bond silicon and silicon, and glass and glass at relatively high temperature to achieve desired bonding strength.

Fabrication of 1D Nanochannels

2D nanochannels provide the platform to study novel effects such as those due to overlapped electric double layers. However, the large lateral dimension (usually over 1 μm) could render the 2D nanochannel incapable of manipulating single macromolecules, so fabrication of 1D nanochannels is necessary for some single molecule sensing and manipulation purpose. Because 1D nanochannels need to control the size in both lateral and vertical directions, more advanced lithography techniques are needed to shrink the width of the nanochannel to be comparable to the height of the nanochannel. Much less efforts have been carried out to make 1D nanochannels, so only a couple of examples and some possible approaches are summarized as follows.

In principle, 1D nanochannels should be able to be made in the same ways as those for 2D nanochannels as long as advanced lithography tools are accessible to make sacrificial lines or open channels of tens of nanometers or even smaller in width. This can be done by state-of-the-art e-beam lithography to pattern sacrificial lines or by focused ion beam to dig open nanochannels on one chip for binding.

Making 1D nanochannels with nanoimprint lithography has been demonstrated and shown great promise for batch fabrication of integrated nanofluidic devices. Nanoimprint lithography makes a rigid mold with e-beam lithography and press the mold into a thin resist film and the shape of the film is subsequently solidified by being either exposed to UV light or cooled down below the glass transition temperature of the resist film. The ultra-fine resolution of nanoimprint lithography, as small as 10 nm, provides great potential of making 1D dimensional nanochannels for single molecule sensing and manipulation.

Since advanced lithography tools with resolution down to sub 100 nm may not be readily available, some novel techniques to fabricate 1D nanochannels have been developed and reported. One of these techniques uses standard microfabrication process and has the potential to make integrated nanofluidic devices [2]. This technique is similar to the *spacer technique* developed in solid-state electronic device fabrication. A spacer is the thin side wall achieved by conformal deposition of selected thin film on the side wall of a sacrificial structure. With the fine control of the LPCVD deposition process, a spacer as thin as 10 nm can be made. After removing the sacrificial structure, a spacer as thin as 10 nm is left on the substrate, which can be subsequently used as a mask to pattern nanometer lines or used as a sacrificial line to make a nanochannel. Other novel techniques involve shrinking a larger channel made by standard micromachining to smaller sizes by methods such as filling the channel with other materials [3].

One point that is worth noting is that the solid-state fabrication technique can be integrated with soft-lithography to make poly-dimethylsiloxane (PDMS) nanochannels, as commonly referred to as mold-machining. This method can be used to make both 1D and 2D nannochannels, depending on the mold fabricated. The mold is fabricated either with optical lithography or e-beam lithography to make the inverse shape of the desired chan-

nel. Then PDMS films with desired nanochannel structures can be made by pouring a liquid precursor over the mold and cured into the solid form, which can then be peeled off the mold and bonded to glass substrate to form enclosed nanochannels. The nature of soft lithography technique makes PDMS nanochannels cost effective; however, the polymer nature of PDMS renders weak mechanical strength to PDMS nanochannels, which limits the smallest feature size of PDMS nanochannels to about 200 nm. Even smaller PDMS nanochannels tend to collapse, which is the reason that most small nanochannels are made of inorganic materials such as SiO_2 or SiN_x.

Nanochannel Fabrication by Chemical Self-Assembly

Nanochannel fabrication with microfabrication techniques takes advantage of the rapid development of semiconductor industry and provides the opportunities of fabricating nanochannels of various configurations. In addition, it is relatively easy to integrate the nanochannel with other microscale components to make integrated nanofluidic devices. However, this approach is usually expensive and needs access to advanced fabrication facilities in a cleanroom. In contrast, chemical synthesis of nanochannels is much cheaper and can be realized with relatively simple set-up. The drawback of chemical synthesis is that usually only arrays of nanochannels can be made in a certain pattern and the nanochannels are of certain cross-sectional configuration determined by the synthesis mechanism. In addition, the integration of chemically synthesized nanochannels into a Lab-on-a-Chip device might pose significant challenges. Numerous kinds of nanochannels can be made by chemical synthesis and it is difficult to exhaust every nanochannel structure made by chemical synthesis. Here the fabrication of three kinds of nanochannels, i. e., carbon nanotubes, SiO_2 nanotubes, and anodic porous alumina, all have been used for nanofluidic studies, will be briefly described as follows.

Synthesis of Carbon Nanotubes

Carbon nanotubes have attracted huge attention ever since they were discovered because of their unique structures. The studies are mainly focused on the mechanical, electrical, and thermal properties of carbon nanotubes and the applications of their novel properties. Fluid behavior inside carbon nanotubes and fluid transport through carbon nanotubes have been investigated only recently and novel fluidic phenomena, such as abnormally low flow resistance, have been observed. Carbon nanotubes are usually synthesized by arc-discharge, laser ablation, and Chemical Vapor Deposition (CVD) [4]. The arc-discharge and laser ablation methods involve the condensation of carbon atoms generated from evaporation of solid carbon sources. The temperatures involved in these methods are close to the melting temperature of graphite, 3000 – 4000 °C. In arc-discharge, carbon atoms are evaporated by plasma of helium gas ignited by passing high currents through opposing carbon anode and cathode. By controlling the growth conditions such as the chamber pressure and arc current, high quality multi-wall carbon nanotubes (MWCNTs) can be obtained. To grow single wall carbon nanotubes (SWCNTs), a metal catalyst is added to the arc-discharge system by using a carbon anode with a small percentage of cobalt catalyst. In laser ablation, intense laser pulses are used to ablate a carbon target containing a small percentage of nickel or cobalt catalysts. Usually the target is placed in a tube-furnace heated to 1200 °C. During laser ablation, a flow of inert gas is passed through the growth chamber to carry the grown nanotubes downstream to be collected. The CVD growth involves heating a catalyst material to high temperatures in a tube furnace and flowing a hydrocarbon gas through the tube reactor for a period of time. Nanotubes grown over the catalyst are collected after cooling the system to room temperature. By carefully selecting the hydrocarbon, catalysts, and tuning the growth temperature, both SWCNTs and MWCNTs can be synthesized by the CVD method.

SiO_2 Nanochannels Made From Silicon Nanowires

SiO_2 capillaries have been extensively used in microfluidic and nanofluidic devices so an efficient and cost-effective approach of fabricating SiO_2 nanochannels can greatly facilitate the development of nanofluidic devices. A fabrication process of SiO_2 nanochannels based on partial oxidation of silicon nanowires have been developed recently. The process starts with synthesis of single crystalline silicon nanowires with the vapor-liquid-solid (VLS) method. Once the silicon nanowires are synthesized, a timed dry oxidation process is applied to partially oxidize the silicon nanowires into silicon-core/SiO_2-sheath nanowires. Finally the core/sheath nanowires are exposed to XeF_2 gas to etch away the silicon cores and SiO_2 nanotubes are formed. The diameter of these SiO_2 nanotubes can be as small as 10 nm and the length can be more than 20 μm.

Alumina Nanochannels by Anodization

Alumina nanochannel array has been made for long time and has been used as filters in various applications. More recently, alumina nanochannels have been used as template to synthesize various kinds of nanostructures such as different nanowires. In addition, the nanochannel array has been used to provide nano-environment for biological related studies. The alumina nanochannel membrane pro-

vides a great flexibility because it has easily tunable pore diameter (from 7 – 300 nm), easily tunable pore length (from ~100 nm to more than 100 μm), and high pore densities (up to 7×10^{10} /cm^2).

Fabrication of the alumina nanochannel array is a straightforward process involving anodization of aluminum sheets. To achieve high quality, the aluminum is usually mechanically and electrochemically polished to produce as smooth a surface as possible. The anodization can be done with different acid solutions such as oxalic acid, sulfuric acid, or phosphoric acid. The anodization of aluminum involves the initial formation of oxide layer on the surface, and the oxygen will then transport through the oxide only preferentially at sites that provides low resistance conduction path. The oxide at those sites will start to dissolve, leading to the nucleation of pores, which then grow perpendicular to the surface of the aluminum because of equilibrium between the field-enhanced oxide dissolution at the interface of the electrolyte/oxide, and the oxide growth at the aluminum/alumina interface until the pore grows deep into the aluminum.

To make highly ordered alumina nanochannel array, modifications of the standard anodization process have been made. Successful techniques include pre-pattern to make small dimples on the surface of aluminum to initiate anodization only at specified sites, and a two step anodization process in which the first step serves as an initiation of the regular pattern of tiny dimples on the surface. With these modifications, highly ordered parallel alumina nanochannel arrays have been fabricated.

Key Research Findings

Fabrication of ~1.8 nm diameter nanopores in a SiN_x membrane by ion-beam sculpting was invented rather accidentally around the year 2001 when Jiali Li et al. [5] attempted to dig nanometer holes with focused ion beam but failed with no nanopore open even after excessively long ion beam exposure. They later found that by exposing a 60 nm diameter pore to the focused ion beam, the pore size could be shrunk from 60 nm to ~1.8 nm under the irradiation of energetic Ar^+ ion, which helped the flow of SiN_x molecules along the surface. SiO_2 nanopores of around 3 nm have been fabricated also rather accidentally when Storm et al. [6] used a 300 kV transmission electron microscope to observe a ~20 nm diameter pore made of SiO_2. They found that the pore shrunk under the irradiation of the focused electron beam and the shrinking process can be controlled very precisely since the shrinking rate is at 0.3 nm per minute. The pore shrinking mechanism is believed to be the viscous flow of the amorphous SiO_2 under the irradiation of energetic electrons.

Making nanochannels by combined sacrificial layer and e-beam lithography was reported by Harnett et al. [7], and later nanochannel arrays of 10 nm by 50 nm cross-sectional dimensions were fabricated with nanoimprint lithography by Cao et al. [8]. Mao and Pan reported a thorough investigation of using bonding techniques to make nanochannels of different aspect ratios with glass–glass and glass–silicon [9]. They showed if the nanochannels survived or collapsed under different aspect ratios. Fabricating SiO_2 nanotubes based on partial dry oxidation of silicon nanowires and etching of the intact silicon core was realized in the year of 2003 by Fan et al. [10].

Future Directions for Research

Nanochannel fabrication is an important step to make integrated nanofluidic devices. Solid-state nanochannel fabrication technique can easily integrate the nanochannel with other components to make integrated nanofluidic devices because the channel is made with lithography at specified position. However, the cost of solid state fabrication is usually high so methods to reduce the cost and to remove the requirement of advanced nanolithography tools can greatly lower the barrier of making integrated nanofluidic devices. The cost of chemical synthesis is usually low but it can be a big challenge to separate one nanochannel from the massively synthesized nanochannels by chemical methods to make integrated nanofluidic devices, so approaches to realize this is highly desirable. On the other hand, the array of nanochannels prepared by chemical synthesis could be of great advantage for applications that need massively parallel nanochannels.

N

Cross References

- ► Microfabrication Techniques
- ► Nanochannels
- ► Nanofluidic Systems for Single Molecule Detection
- ► Nanoscale Biosensors

References

1. Mijatovic D, Eijkel JCT, van den Berg A (2005) Technologies for Nanofluidic Systems: Top-down vs Bottom-up-A Review. Lab Chip 5:492–500
2. Lee C, Yang EH, Myung NV, George T (2003) A Nanochannel Fabrication Technique without Nanolithograph. Nano Lett 3:1339–1340
3. Ilic B, Czaplewski D, Zalalutdinov M, Schmidt B, Craighead HG (2002) Fabrication of Flexible Polymer Tubes for Micro and Nanofluidic Applications. J Vac Sci Technol B 20:2459–2465
4. Dai H (2001) Nanotube Growth and Characterization. In: Dresselhaus MS, Dresselhaus G, Avouris P (eds) Carbon Nanotubes: Synthesis, Structure, Properties, and Applications. Springer, Berlin

5. Li J, Stein D, McMullan C, Branton D, Aziz MJ, Golovchenko JA (2001) Ion-Beam Sculpting at Nanometer Length Scales. Nature 412:166–169
6. Storm AJ, Chen JH, Ling XS, Zandbergen HW, Dekker C (2003) Fabrication of Solid-State Nanopores with Single-Nanometer Precision. Nature Mater 2:537–540
7. Harnett CK, Coates GW, Craighead HG (2001) Heat-Depolymerizable Polycarbonates as Electron Beam Patternable Sacrificial Layers for Nanofluidics. J Vac Sci Technol B 19:2842–2845
8. Cao H, Yu Z, Wang J, Tegenfeldt JO, Austin RH, Wu W, Chou SY (2002) Fabrication of 10 nm Enclosed Nanofluidic Channels. Appl Phys Lett 81:174–176
9. Mao P, Han J (2005) Fabrication and Characterization of 20 nm Planar Nanofluidic Channels by Glass–Glass and Glass–Silicon Bonding. Lab Chip. 5:837–844
10. Fan R, Wu Y, Li D, Yue M, Majumdar A, Yang P (2003) Fabrication of Silica Nanotube Arrays from Vertical Silicon Nanowire Templates. J Am Chem Soc 125:5254–5255

Nanochannels

Definition

Channels with the smallest passage dimension D below 0.1 μm.

Cross References

► Boiling and Evaporation in Microchannels
► Nanochannel Fabrication

Nanochips

► Nanoscale Biosensors

Nanoclusters

► Nanoparticles
► Nanoparticle Synthesis in Microreactors

Nanocrystals

► Nanoparticles
► Nanoparticle Synthesis in Microreactors

Nanofluid Flow in Microchannels

► Microscale Cooling Devices

Nanofluidic Channels

► Nanochannel Fabrication

Nanofluidics

► Nanoscale Biosensors

Nanofluidics in Carbon Nanotubes

HYUNG GYU PARK, OLGICA BAKAJIN
Lawrence Livermore National Laboratory,
Livermore, CA, USA
bakajin1@llnl.gov

Definition

This entry describes recent advances in understanding of fluid (gas & liquid) flow through graphitized carbon nanotubes. We discuss both simulation and experimental results.

Overview

Carbon nanotubes are tubules that consist of a graphene sheet rolled up into a seamless cylinder with diameters of the order of a few nanometers. Carbon nanotubes have unique properties such as extraordinary strength and unique electrical properties, and are efficient conductors of heat. Carbon naotubes also act as extraordinary pipes in the true nanofluidic regime.

When studying molecular properties inside carbon nanotubes we need to consider the applicability of the continuum physics. A liquid fluid particle is defined as a volume containing a relatively large number of molecules. Since less than 1% statistical fluctuation (1% statistical resolution in other words) of a physical property can be obtained for more than 10,000 particles, we may regard this number of liquid as a continuum limit of fluid particle. A sphere containing 10,000 equidistant molecules would have a diameter corresponding to about 25 molecules. Since a water molecule has a diameter of ~ 0.24 nm, the diameter of the 10,000-molecule sphere will have diameter of 6 nm. A system with spatial size of its domain much larger than 6 nm can thus allow the fundamental hypothesis of hydrodynamics to work. In the range of sizes of carbon nanotubes, continuum theories start to break apart. Molecular dynamics simulations have first predicted and, more recently, a growing body of experimental evidence has started to verify the unique molecular structure and

unique transport mechanisms of molecules confined in the interior of graphitic carbon nanotubes. Water and gas transport in nanometer-size nanotube pores is orders of magnitude faster than predicted by classical theories that do not take in account unique surface properties and the scale of carbon nanotubes. The novel transport phenomena have important implications for technological developments such as the energy efficient filtration membranes and drug delivery platforms. Understanding of molecular structure and transport in carbon nanotubes directly enhances our understanding of the fundamentals of transport at the nanoscale and of the way the biological channels function.

Basic Methodology

The developments in this field have been motivated by a large number of simulations. A central question in nanofluidics concerns the extent to which the classical equations describing the way fluids interact with nanomaterials hold at the nanoscale. Molecular simulation is ideally suited to shed light on this problem. They provide a way of probing static and dynamic behavior of molecules by taking in account both intermolecular and molecule–nanotube interactions in a carbon nanotube environment that is commensurable with molecular size. In the first simulation of fluid flow in a simple nanotube using a realistic model for the solid, Sokhan et al. [1] in 2001 showed that fluids flowing through carbon nanotubes experience very low surface friction, that is very small Maxwell coefficients (~ 0.01) or equivalently large slip boundary conditions, whereas pores made from other materials show higher values and stick boundary conditions. Multiple other simulations have since then revealed interesting phenomena related to flow of gases, water, ions, and polymers (such as DNA and proteins) through carbon nanotubes.

Experimental work can be divided into work that examines structure of fluids inside of the carbon nanotubes using

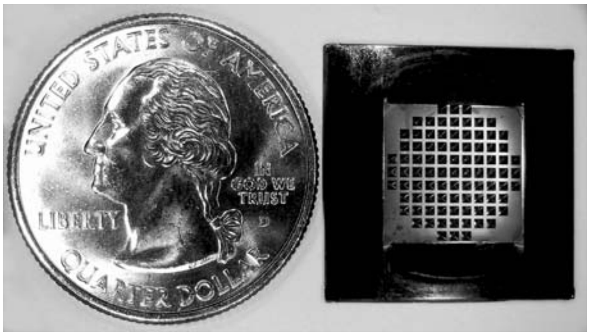

Nanofluidics in Carbon Nanotubes, Figure 1 Sub-2 nm carbon nanotube membrane chip, from [16]

techniques such as neutron diffraction, NMR and in situ TEM, and the studies that examine transport properties using specially fabricated devices in which carbon nanotubes serve as pores (Fig. 1). Two experimental groups have so far demonstrated devices that allow studies of transport through graphitic carbon nanotubes. As synthesized carbon nanotube mats have considerable spacing between individual carbon nanotubes. Researchers have, therefore developed methods to fill those spaces with a dense material and confine transport through carbon nanotubes. B. Hinds group at U. of Kentucky has fabricated carbon nanotube membranes utilizing multiwall carbon nanotubes with ID $\sim 6-7$ nm and a polystyrene as the matrix material. O. Bakajin's group at Lawrence Livermore National Laboratory is using membranes that have both sub-2 nm ID double wall carbon nanotubes and multiwall ones as pores and use silicon nitride to fill interstitial spaces between the nanotubes.

Key Research Findings

Simulations of Gas Transport

MD simulations showed that the transport rates in nanotubes are orders of magnitude faster than in other materials, attributing the exceptionally high transport rates in nanotubes to the inherent smoothness of the nanotube walls.

As an example, see Skoulidas et al. [2]. They reported atomistic simulations for both self- and transport diffusivities of light gases in carbon nanotubes and compared them with transport rates in zeolites with comparable pore sizes.

Simulations of Water and Ions

There have been numerous reports of the simulations of water and ions through carbon nanotubes. This entry does not intend to present a comprehensive review of the field, but rather give examples of major research developments. Koga et al. [3, 4] studied solid and liquid phases of water confined in narrow arm chair carbon nanotubes ($1.1-1.7$ nm in diameter) and the phase transition at various fixed temperatures ($240-320$ K) and pressures ($50-500$ MPa). They found that solid phases of confined water are different from those of any known bulk ice structure and determined by the confining geometry. Hummer et al. [5] reported the first report of molecular dynamics simulations showing spontaneous and continuous filling of a nonpolar carbon nanotube with a 1D ordered chain of water molecules (Fig. 2). The simulation suggest fast water transport through a single-walled nanotube 13.4 Å long with a small diameter of 8.1 Å. In another study, Kalra et al. [6] reported a through carbon nanotube comparable

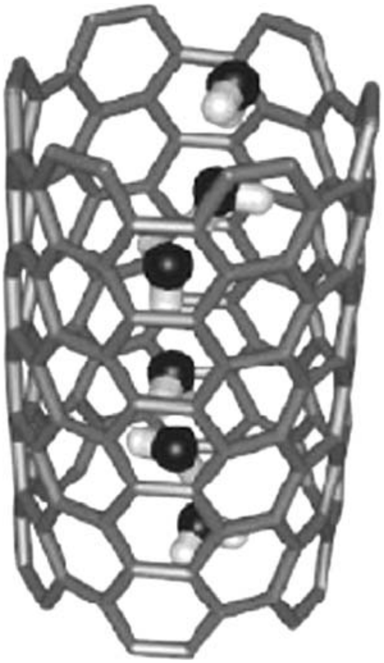

Nanofluidics in Carbon Nanotubes, Figure 2 Structure of the hydrogenbonded water chain inside the nanotube [5]

to the flow rate measured for the transmembrane protein aquaporin-1, and are practically independent of the length of the nanotube, in contrast to predictions of macroscopic hydrodynamics. A study by N. Aluru's group [7] examined ionic flow in carbon nanotubes with the goal of using carbon nanotubes as artificial protein channels found in cell membranes. They suggest that cationic or anionic selectivity could be obtained by symmetrical placement of the functional groups.

Simulations of Polymers

Wei, C. and D. Srivastava [8] reported diffusion of polymers to be several orders of magnitude faster than through the zeolite channels (of comparable size). Also report that translocation time through the nanotube scales as N^2, where N is the number of monomers in a polymer. Gao et al. [9] calculated that a single stranded DNA will spontaneously insert into the nanotubes from water solutions provided that the nanotube is big enough, attributing the mechanism to Van der Waals attraction. Yeh and Hummer studied electrophoretic transport of nucleic acids through 1.5 nm carbon nanotubes. Their simulation showed that without electric field RNA would remain trapped in the hydrophobic pores. Sorin & Pande [10] recently also demonstrated that confinement inside a nanotube denatures protein helices.

Experimental Observations of Structure of Fluids

Y. Gogotsi's group [11, 12] has reported in situ TEM observations of water inside carbon nanotubes filled using autoclave treatment at different temperatures and pressures. The TEM observations of the 2 – 5 nm-diameter nanotubes confirm the successful filling of and reveal disordered gas/liquid interfaces contrasting the smooth curved menisci visualized previously in MWNT with diameter above 10 nm. They demonstrated a wet/dry transition on the nanometer scale by means of external heating. Their TEM results suggest that when ultrathin channels such as carbon nanotubes contain water, fluid mobility is greatly retarded compared to that on the macroscale. This observation does not agree with the measurements of flow through carbon nanotube membranes.

Argonne National Laboratory group [13] used neutron diffraction and scattering methods to observe confined water molecules in a 1.4 nm diameter carbon nanotube. The water structure inside the tube is observed. They observed a single-file of water within an ice-tube-layer inside the internal nanotube wall at a temperature more than a hundred degrees lower than the room temperature.

Experimental Observations of Fluid Transport

Hinds et al. [14] published the first account of experiments involving fluid flow through a membrane composed of graphitic carbon nanotubes. The paper claimed that the gas flow through these MWNT membranes with pore sizes in the 6 – 7 nm range followed Knudsen theory. Later revision of the density of the open pores revealed enhancement of flow rates over the predictions of the Knudsen model. Hinds et al. also studied diffusion of aqueous ionic species ($Ru(NH_3)_6^{3+}$ diameter $= 0.55$ nm) and noted that the diffusion coefficient was near the bulk aqueous-solution diffusion for the Ru cation, inferring only limited interaction between the ion and the nanotube tip and walls. More recently the same group reported measurements of flow rates of water, ethanol, and alkanes [15]. The results demonstrate dramatically enhanced flow through ~ 7 nm-diameter nanotube cores compared with conventional fluid flow theory. Observed flow rates were four to five orders of magnitude greater than predicted by hydrodynamics based on macroscale behavior. The implied slip lengths (3 to 70 μm), which are much greater than the tube diameter, are consistent with a nearly frictionless interface.

Holt et al. [16] measured water and gas flow through the pores of double walled carbon nanotubes. These tubes had inner diameters less than 2 nm with nearly defect-free graphitic walls. Five hydrocarbon and eight non-hydrocarbon gases were tested to determine flow rates and to demonstrate molecular weight selectivity compared

with helium. Water flow was pressure-driven at 0.82 atm and measured by following the level of the meniscus in a feed tube. The results for both gas and liquid show dramatic enhancements over flux rates predicted with continuum flow models. Gas flow rates were between 16 and 120 times that expected according to the Knudsen diffusion model in which fluid molecule–wall collisions dominate the flow. Water flow rates were 560 to 8400 times greater than those calculated according to the Hagen–Poiseuille equation. Minimum slip lengths are estimated in the range of 140 to 1400 nm. To express these findings in a practical context, the nanotube membranes showed flow rates several orders of magnitude greater than those of conventional membranes, despite having pore sizes an order of magnitude smaller.

Future Directions for Research

The field of carbon nanotube nanofluidics is very young. Fundamental question about physical principles that govern fast flow of gases and liquids in carbon nanotubes are still not fully answered. There will be more simulation and experimental work on this topic.

Cross References

► Biomimetics
► Boundary Slip of Liquids
► Gas Flow in Nanochannels
► Ion Channel
► Micro- and Nanoscale Gas Dynamics
► Micro- and Nanoscale Gas Fluidics
► Nanochannel Fabrication

References

1. Sokhan VP, Nicholson D, Quirke N (2001) Fluid flow in nanopores: An examination of hydrodynamic boundary conditions. J Chem Phys 115(8):3878
2. Skoulidas AI, Ackerman DM, Johnson JK, Sholl DS (2002) Rapid transport of gases in carbon nanotubes. Phys Rev Lett 89:185901
3. Koga K, Gao GT, Tanaka H, Zeng XC (2001) Formation of ordered ice nanotubes inside carbon nanotubes. Nature 412(6849):802–805
4. Koga K (2004) Hydrophobic effect in the pressure-temperature plane. J Chem Phys 121(15):7304
5. Hummer G, Rasaiah JC, Noworyta JP (2001) Water conduction through the hydrophobic channel of a carbon nanotube. Nature 414(6860):188–190
6. Kalra A, Garde S, Hummer G (2003) Osmotic water transport through carbon nanotube membranes. Proc Nat Acad Sci 100:10175–10180
7. Joseph S, Mashl RJ, Jakobsson E, Aluru NR (2003) Electrolytic transport in modified carbon nanotubes. Nano Lett 3(10):1399–1403
8. Wei X, Srivastava S (2003) Theory of transport of long polymer molecules through carbon nanotube channels. Phys Rev Lett 91:235901
9. Gao H, Kong Y, Cui D, Ozkan CS (2003) Spontaneous Insertion of DNA Oligonucleotides into Carbon Nanotubes. Nano Lett 3(4):471–473
10. Sorin EJ, Pande VS (2006) Nanotube confinement denatures protein helices. J Am Chem Soc 128:6316–6317
11. Naguib N, Ye H, Gogotsi Y, Yazicioglu AG, Megaridis CM, Yoshimura M (2004) Observation of Water Confined in Nanometer Channels of Closed Carbon Nanotubes. Nano Lett 4(11):2237–2243
12. Megaridis CM, Yazicioglu AG, Libera JA, Gogotsi Y (2002) Attoliter fluid experiments in individual closed-end carbon nanotubes: Liquid film and fluid interface dynamics. Phys Fluid 14(2):L5
13. Kolesnikov AI, Zanotti JM, Loong CK, Thiyagarajan P, Moravsky AP, Loutfy RO, Burnham CJ (2004) Anomalously soft dynamics of water in a nanotube: A revelation of nanoscale confinement. Phys Rev Lett 93(3)
14. Hinds BJ, Chopra N, Rantell T, Andrews R, Gavalas V, Bachas LG (2004) Aligned Multiwalled Carbon Nanotube Membranes. Science 303(5654):62–65
15. Majumder M, Chopra N, Andrews R, Hinds BJ (2005) Enhanced flow in carbon nanotubes. Nature 438:44
16. Holt JK, Park HG, Wang YM, Stadermann M, Artyukhin AB, Grigoropoulos CP, Noy A, Bakajin O (2006) Fast mass transport through sub-2-nanometer carbon nanotubes. Science 312(5776):1034–1037

Further Reading

• Whitby M, Quirke N (2007) Nat Nanotech 2:87–94
• Hummer G (2007) Mol Phys 105(2–3):201–207

Nanofluidic Single Molecule Detection

► Nanofluidic Systems for Single Molecule Detection

Nanofluidic Single Molecule Sensors

► Nanofluidic Systems for Single Molecule Detection

Nanofluidic Systems for Single Molecule Detection

Deyu Li
Department of Mechanical Engineering, Vanderbilt University, Nashville, TN, USA
deyu.li@vanderbilt.edu

Synonyms

Nanofluidic single molecule sensors; Nanofluidic single molecule detection

Definition

Nanofluidic systems are integrated microdevices with at least one component in the devices having length scales in the range of one to hundreds of nanometers. The critical dimension of nanofluidic systems is comparable to relevant length scales such as diffusion lengths of molecules, sizes of molecules and Debye screening lengths of electric double layers. Nanofluidic systems are ideally suitable for single molecule detection because the systems have the capability of either constraining an individual molecule in a nanochannel for optical detection or providing electrical signals reflecting the presence of an individual molecule inside a nanochannel of the system.

It is worth noting that there is still debate on whether nanofluidic systems should be strictly used for systems with channels of tens of nanometers or smaller in all cross-sectional dimensions, or they can include systems with micro-sized channels that contain nanoliter volumes. The definition here emphasizes the comparable sizes of channels with nanoscale physical length scales, which may lead to interesting phenomena and applications.

Overview

Microfluidic Lab-on-a-Chip technology has been a focus of research over the past two decades and is now making a great impact with the commercial applications of various novel devices in rapid diagnosis, drug discovery and drug delivery. Microfluidics uses microfabricated fluid channels with dimensions of the order of tens to hundreds of micrometers to deliver liquids of nanoliters and work with a small ensemble of molecules. Introducing nanoscale channels into microfluidic Lab-on-a-Chip devices, to make nanofluidic systems, leads to a new breakthrough in creating new functions such as single molecule detection and manipulation. Nanofluidic systems for single molecule detection emerged in the mid-1990s with the demonstration of detecting single DNA molecules with a nanofluidic system composed of a naturally occurring protein nanopore, α-hemolysin, embedded in a lipid bilayer. Since then, nanofluidic single molecule detection has seen great progress as advanced nanofabrication techniques allow the fabrication of small nanochannels or nanopores with dimensions of the order of one to hundreds of nanometers, providing human-made nanofluidic systems.

Fabrication of nanofluidic systems usually involves fabrication of nanochannels and integration of the nanochannels with microfluidic components to make functional nanofluidic systems. Microfluidic component fabrication is usually done with either solid-state fabrication on silicon or glass substrates, or soft-lithography fabrication with polymers such as polydimethylsiloxane (PDMS), which is a transparent, biologically compatible, elastomeric polymer. Nanochannel fabrication is more challenging and usually involves advanced microfabrication techniques such as e-beam lithography or nanoimprint lithography. Top-down nanofluidic system fabrication based on solid-state fabrication techniques can readily integrate the fabricated nanochannel with microchannels by alignment in the lithography step during device fabrication process. Integration of nanochannels synthesized massively via bottom-up chemical reactions with microfluidic components for single molecule detection can be a significant challenge in device fabrication.

To date, nanofluidic single molecule detection has been done in two ways. One takes the advantage of the comparable size of nanochannels and macromolecules, and detects the modulation of ion current through a nanochannel or a nanopore when an individual macromolecule enters the nanochannel/nanopore. This method ist well-known as resistive-pulse sensing or the Coulter principle. The other uses a nanochannel as a confined region to limit the number of molecules inside the nanochannel and uses other methods such as optical microscopy to sense a single molecule inside the nanochannel. Both approaches have demonstrated successful detection of single molecules inside nanofluidic channels. However, to date, only a few examples for each approach have been reported since nanofluidic systems have been developed only within the last decade.

Basic Methodology

Nanofluidic Single Molecule Detection Based on the Comparable Size of the Nanochannel and the Molecule

Nanofluidic single molecule detection based on the comparable size of the nanochannel and the molecule is based on the measurement of the electrical current through a nanochannel. In this approach, a nanochannel connects two fluid cells at each side of the nanochannel and an ion current is set up by applying an electric bias across the nanochannel. When a macromolecule of comparable size to the nanochannel enters the nanochannel, it will alter the electrical resistance of the nanochannel, and hence results in a modulation of the electrical current through the nanochannel. Therefore, a nanofluidic system can detect single molecules as long as there is a nanoscale channel in the system with comparable size to the molecules of interest. Figure 1 shows a schematic diagram of nanofluidic

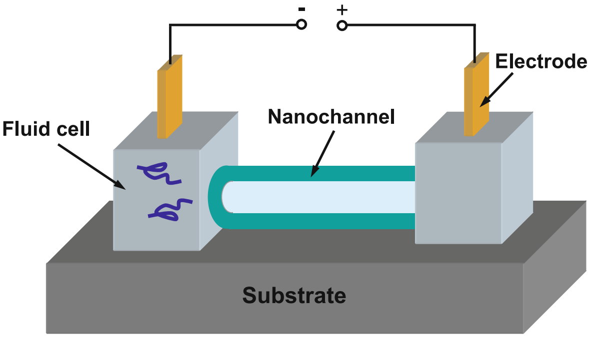

Nanofluidic Systems for Single Molecule Detection, Figure 1
A schematic diagram of nanofluidic system for single molecule detection based on electrical current modulation when macromolecules are translocated through the nanochannel

systems that detect single molecules based on this sensing mechanism.

This simple concept was first implemented in pioneering work [1] on single DNA molecule sensing with a naturally occurring protein nanopore, α-hemolysin, which is a nanopore of about 10 nm in length and has a smallest inner diameter of about 1.4 nm. The detection is based on the ion current blockade when DNA molecules transport through the nanopore. The nanopore was embedded in a lipid bilayer membrane separating two fluid cells and a baseline ion current was set up under an electrical bias across the nanopore. When single stranded DNA or RNA molecules were translocated through the nanopore, the ion current was partially blocked, making an extremely sensitive single molecule detector.

The promising results and simple concept motivated development of robust and size-tunable inorganic nanopores as single molecule detectors and two types of nanopores of $\sim 2-3$ nm in diameter have been made based on the reflow of amorphous SiN_x or SiO_2 under the irradiation of focused ion or electron beams. It was found that the molecules of SiN_x or SiO_2 amorphous films could undergoes viscous flow under the bombardment of energetic ions or electrons and a $2-3$ nm pore could be made on a SiN_x or SiO_2 film by exposing the film with an initial pore of tens of nanometers to focused ion or electron beams. Successful single molecule detection with nanofluidic systems composed of a nanopore embedded between two fluid cells was demonstrated by measuring the ion current modulations from the translocation of DNA molecules through the nanopore [2].

These nanopores were not fabricated in batches but made individually in expensive tools and the fluid cells at each side of the nanopore are bulk fluid cells, which may consume a significant amount of sample. Efforts of making on-chip nanofluidic systems for single molecule detection based on the same principle started with a 3 μm long, 200 nm in diameter PDMS nanochannel on a glass substrate [3]. The channel size (200 nm) is much larger than a typical nanopore (< 10 nm) due to the limitation of the mechanical strength of PDMS. Instead of two terminal measurements, four electrodes were patterned with two on each side of the nanochannel, enabling four probe electrical measurements to detect the small current change. Current blockade of the order of 30 pA induced by single DNA molecules ($\sim$ 16 μm long) was observed in a baseline ion current of 15 nA. The volume occupied by the DNA is estimated to be about 0.16% of the volume of the channel and the nanofluidic system is not suitable for the detection of even smaller molecules since the current modulation will be too weak to be distinguished from the noise of the baseline current. Even smaller nanochannels can be made with inorganic materials such as SiO_2 or SiN_x, which has been demonstrated in a nanofluidic system that has SiO_2 nanochannels of 20 μm in length with inner diameters of $40-60$ nm [4]. The nanofluidic system has been used to detect the presence of single DNA molecules inside the nanochannel.

The detection mechanism looks straightforward: macromolecules will block the ion current through nanochannels, which indicates the presence of macromolecules in the nanochannel. However, it turns out that the phenomena can be much more complex. It was found [5] that when DNA molecules moved through a $4-5$ nm diameter, $50-60$ nm long nanopore in 0.1 M buffer solutions, current enhancement instead of current blockade was observed. Later, Fan et al. [4] observed that when λ-DNA molecules passed through ~ 50 nm SiO_2 nanochannels, ion current enhancement occurred in low-concentration (0.5 M) buffer solutions, but ion current blockade occurred in high-concentration (2 M) solutions. The reason is believed to be that the current blockade in 2 M solutions is due to the geometrical exclusion of high concentration ions by the DNA molecules, while the current enhancement in 0.5 M solutions can be attributed to the increased counter-ions in the nanochannel to shield the DNA backbone. This is the first observation of current crossover as the solution concentration changes, which has been confirmed by other more recent experiments with nanopores. Simple models have been proposed to explain the current modulation but a thorough understanding of the complex interactions between the surface charge, the ions in the solution and the charged DNA molecules has not been achieved yet. For example, the crossover from current enhancement to current blockade occurred at different concentrations for different experiments. More interestingly, in the experiment with the 200 nm PDMS channel [3], current blockade instead of current enhancement

N

occurred even though the concentration of the buffer used (0.1 M) is lower than the crossover concentration in other experiments, which means a current enhancement should have been observed for a 0.1 M buffer solution, as shown in the experiment [5] using 0.1 M buffer solutions. This indicates that the complex charge interactions inside the nanochannel may not be fully reflected with the simple models developed in the literature.

The more ambitious goal of single molecule detection with nanofluidic systems is the detection of not only the presence of single molecules but also the structure, morphology and dynamics of the molecules, such as DNA sequencing or protein structure sensing. Therefore, sensing of more subtle details of the molecules than just the presence of the molecules is being actively pursued. Soon after the detection of single molecules with α-hemolysin, an attempt [6] at DNA sequencing was made by tethering an oligonucleotide inside the α-hemolysin, and single base pair mismatch between DNA strands of up to 30 nucleotides was discriminated. In fact, the idea was proposed back in 1989 by David Deamer, who conceived that the DNA sequence can be read out by passing a single stranded DNA through a nanopore with built-in sensors to detect the DNA sequence through the changing electrical pattern. Similar ideas should also be applicable to the detection of protein structures under different conditions. The rapid development of more powerful nanofluidic systems in recent years has certainly made the technique closer to the detection of the structure, morphology and dynamics of single molecules. However, many challenging problems still need to be solved by research breakthroughs. For example, the sensitivity is still not good enough to distinguish signals from different DNA bases for DNA sequencing. This is especially true considering the fact that the length of the nanopore is usually much larger than the length of each DNA base and tens or even hundreds of DNA bases may present in the nanopore. Breakthroughs in novel and more sensitive detection techniques other than simple ion current modulation and better control of the translocation of DNA molecules must be achieved before DNA sequencing can be realized. Similar challenges also exist for the detection, structural study and spectroscopy of protein molecules with nanofluidic systems.

Nanofluidic Single Molecule Detection Based on the Confinement of Nanochannels on Molecules

Nanofluidic systems could also combine with other single molecule detection techniques to provide unprecedented opportunities to achieve high resolution and acquire information that is not easily accessible in bulk solutions. Single molecule detection with scanning probe microscopy and optical microscopy has been an active research field for about three decades. Many interesting and powerful techniques have been developed to explore the structure, composition, and other properties of single molecules. To date, nanofluidic systems have been mainly combined with fluorescent single molecule detection techniques to sense the presence and properties of single molecules, as schematically shown in Fig. 2.

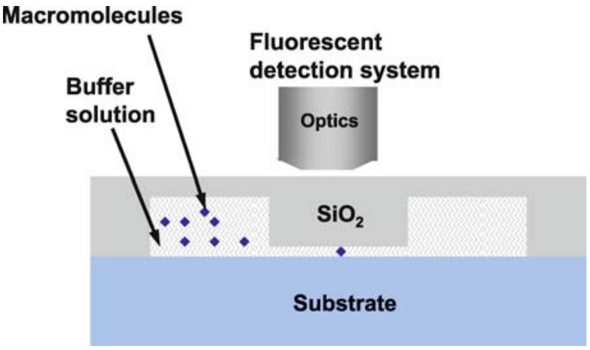

Nanofluidic Systems for Single Molecule Detection, Figure 2
A schematic diagram of nanofluidic systems for single molecule detection based on fluorescent microscopy. The nanochannel isolates single molecules for detection and helps to increase the signal to noise ratio

Nanofluidic systems constructed for fluorescent single molecule detection are relatively simple with nanochannels connected to microchannels at each side of the nanochannels and molecules of interest are usually introduced into the nanochannels through electrophoresis for fluorescent detection. Various kinds of nanochannel fabrication techniques such as focused ion beam milling and nanoimprint lithography have been used to fabricate the nanofluidic channels. The fabricated nanofluidic system is usually positioned on a fluorescent microscope for fluorescent single molecule detection.

The nanoscale dimension of a nanofluidic system can provide several advantages for fluorescent single molecule detection. One is the capability of nanochannels to hold tiny volumes of solutions, which can contain only one molecule for detection. Optical single molecule detection observes volumes of femtoliters so in bulk systems, pico- to nanomolar concentrations of molecules are required in order to isolate individual molecules in the volume under observation. The low concentration requires patience when introducing the molecules of interest into the detection range and limits the study of properties only to those that are not sensitive to the concentration. Nanofluidic systems allow single molecule detection in solutions of much higher concentrations since nanochannels confine the liquid from two dimensions and provide the possibility of having only one molecule in the focal

volume even in a high concentration solution. In addition, molecules in nanochannels have a slow diffusion coefficient up to 50 – 100 times smaller than that in bulk [7], which helps the molecule to reside in the focal volume for an observation of much longer time.

Single molecule detection in nanofluidic systems also provides the possibility of achieving detection with higher resolution. Nanofluidic systems can help to reduce the background noise from other molecules and impurities in the solution to achieve higher signal-to-noise ratio. The fluorescent signal of a single molecule is independent of the detection volume, while the noise in the detection generated from impurities of the sample, Rayleigh straylight and Raman scattering scales linearly with the size of detection volume. Therefore, single molecule detection in nanoscale channels, which contain a tiny volume of the solution, can help to achieve a high signal-to-noise ratio.

Nanofluidic systems are also ideally suitable for certain single molecule detection techniques such as total internal reflection fluorescence (TIRF) microscopy. TIRF utilizes evanescent waves, which are generated by total internal reflection of a laser beam, to excite the fluorescence signal, and since evanescent waves decay exponentially, the molecule of interest must locate to the close proximity of the interface of the glass and liquid. Nanofluidic systems confine molecules of interest in nanochannels, which is well in the evanescent field of TIRF microscopy.

Another advantage of nanofluidic systems for single molecule detection is due to the fact that the small dimension of nanochannels can force DNA molecules to stretch, enabling analysis that is not possible for DNA molecules in a random coil configuration in a free solution. For example, through fluorescent molecule detection, the lengths of single DNA molecules in different size nanochannels have been measured [8], which helps to infer the statics and dynamics of DNA molecules in highly confined nanoenvironments. Investigation of protein–DNA interactions can also benefit from the nano-confinement provided in nanofluidic systems. For example, the numbers of proteins bound to DNA molecules have been counted by introducing DNA molecules into nanochannels [9], which stretch the DNA molecules and allow the count of the number of proteins bound to the DNA molecules. It is difficult to do this in bulk solutions since the random coil configuration of DNA molecules will prevent the count of proteins attached to a DNA molecule. The above mentioned advantages are just some that have been recognized in the past. More advantages of nanofluidic systems for single molecule detection may be found in the near future since using nanofluidic systems for single molecule detection is attracting more attention as advanced nanofabrication techniques are making nanofluidic systems more readily available.

Given all the advantages of using nanofluidic systems to confine single molecules for further detection and investigation, it is worth noting that this comes with the efforts of fabricating nanofluidic systems. Nanochannel fabrication usually requires advanced solid-state fabrication techniques in a cleanroom, which can be expensive if the required nanofluidic systems contain nanochannels of tens of nanometers or even smaller in all cross-section dimensions. In addition, the fundamental physics of fluid flow in nanochannels of around ten nanometers or even smaller in diameter is still not fully understood, which may add more complexity to the study of single molecules in nanochannels.

Key Research Findings

Using α-hemolysin embedded in lipid bilayer to sense single DNA molecules was reported by Kasianowicz et al. in 1996 [1]. Later, sequence-specific DNA molecule detection was demonstrated with an individual oligonucleotide tethered inside the α-hemolysin [6], in which single base pair mismatch between DNA strands of up to 30 nucleotides was discriminated.

Single DNA molecule detection with nanofabricated inorganic SiN_x nanopores was first demonstrated by Li et al. [2] and the ion current blockade resulting from DNA molecule translocation through nanopores was demonstrated. Chang et al. [5] later observed ion current enhancement induced by DNA molecules through a SiO_2 nanopore in 0.1 M buffer solutions, which indicates that complex charge interactions can happen inside nanochannels.

Single DNA molecule detection with long nanochannels was first demonstrated by Saleh and Sohn [3] with a PDMS nanochannel of 200 nm in diameter. They observed current blockade in 0.1 M buffer solutions. Later, Fan et al. [4] first reported the crossover of ion current modulation from current enhancement in low-concentration solutions to current blockade in high-concentration solutions.

Lyon and Nie [7] confined single molecules in a pulled silica capillary of submicrometer dimension (500 – 600 nm inner diameter) and detected single molecules with a confocal fluorescence microscope. They found that the diffusion of molecules in the silica capillary was much slower than that in bulk solution, allowing 50 – 100 times longer observation period. Foquet et al. [10] reported a nanofluidic system made by microfabrication for fluorescent single molecule detection in 2004 and demonstrated that nanochannels could be used to isolate a single molecule for fluorescent detection. Tegenfeldt et al. [8] measured the

lengths of genomic-length DNA molecules in nanochannel arrays and examined the dynamics of DNA molecules in confined nanochannels. Later, Wang et al. [9] counted the number of proteins bound to DNA molecules by stretching DNA molecules in nanochannels. The low occupancy level they found indicates that the proteins on the DNA may have some long-range interactions.

Future Directions for Research

Nanofluidic systems were developed only recently and their potentials for single molecule detection have not been fully explored. Single molecule detection based on the comparable size of nanochannels and molecules has been very successful in sensing the presence of single molecules. However, using this technique to acquire more information of the molecules, such as the sequence of DNA molecules and the structure and morphology of protein molecules, is still at very early stage. So investigation is urgently needed to further develop this technique, enabling acquisition of information beyond the presence of single molecules.

Nanofluidic systems made for fluorescent single molecule detection have shown several advantages such as isolating single molecules for detection and manipulating single molecules to detect desirable information. The research is still in the early stage and the potential of using nanofluidic systems to manipulate single molecules to extract useful information is still far from being fully explored. Therefore, it is time to perform research to design novel nanofluidic systems to manipulate single molecules and obtain information beyond the presence of single molecules.

For both detection approaches, it is of great interest to study the complex interactions between the molecules of interest and the nano-environment. The high surface area to volume ratio in nanochannels can change the behavior of molecules significantly from that in bulk solutions. The complex interactions between the molecules of interest and the ions and surface charges are still not fully understood yet. These effects must be clarified before extensive applications of nanofluidic systems for single molecule detection.

Cross References

► Nanochannel Fabrication
► Nanoscale Biosensors

References

1. Kasianowicz JJ, Brandin E, Branton D, Deamer DW (1996) Characterization of individual polynucleotide molecules using a membrane channel, PNAS 93:13770–13773
2. Li J, Stein D, McMullan C, Branton D, Aziz MJ, Golovchenko JA (2001) Ion-beam sculpting at nanometer length scales. Nature 412:166–169
3. Saleh OA, Sohn LL (2003) An artificial nanopore for molecular sensing. Nano Lett 3:37–38
4. Fan R, Karnik R, Yue M, Li D, Majumdar A, Yang P (2005) DNA translocation in inorganic nanotubes. Nano Lett 5:1633–1637
5. Chang H, Kosari F, Andreadakis G, Alam MA, Vasmatzis C, Bashir R (2004) DNA-mediated fluctuations in ionic current through silicon oxide nanopore channels. Nano Lett 4:1551–1554
6. Howorka S, Cheley S, Bayley H (2001) Sequence-specific detection of individual DNA strands using engineered nanopores. Nature Biotech 19:636–63
7. Lyon WA, Nie S (1997) Confinement and detection of single molecules in submicrometer channels. Anal Chem 69:3400–3405
8. Tegenfeldt JO, Prinz C, Cao H, Chou S, Reisner WW, Riehn R, Wang YM, Cox EC, Sturm JC, Silberzan P, Austin RH (2004) The dynamics of genomic-length DNA molecules in 100-nm channels. PNAS 101:10979–10983
9. Wang YM, Tegenfeldt JO, Reisner W, Riehn R, Guan XJ, Guo L, Golding I, Cox EC, Sturm J, Austin RH (2005) Single-molecule studies of repressor-DNA interactions show long-range interactions. PNAS 102:9797–9801
10. Foquet M, Korlach J, Zipfel WR, Webb WW, Craighead HG (2004) Focal volume confinement by submicrometer-sized fluidic channels. Anal Chem 76:1618–1626

Nanofluids

► Plasma Treatment of Nanoparticles for Nanofluids

Nanolithography

► Photolithography

Nanometer

Definition

Unit of length defined as 10^{-9} meters.

Cross References

► Fabrication of Self-Assembled Catalytic Nanostructures

Nano-Particle Controllable Assembly

TONGXIANG FAN, HAN ZHOU, DI ZHANG
State Key Lab of Metal Matrix Composites, Shanghai Jiaotong University, Shanghai, China
txfan@sjtu.edu.cn

Synonyms

Aggregation of nanoparticles; Assembly of nanoparticles into controlled nanostructures

Definition

Nanoparticle controllable assembly refers to the assembly of nanoparticles into controlled nanostructures (wires, rods, belts, rings, tubes, thin films, superlattices, and sophisticated 3D nanostructures) via interactions like electrostatic interaction, covalent-interaction, metal–ligand interaction, etc.

Overview

Nanoparticle (NP) controllable assemblies are of considerable interest for both fundamental research and applications, since they provide direct bridges between nanometer-scale objects and the macroscale world. Generally speaking, nanoparticle (NP) controllable assemblies can be classified into three categories: one-dimensional (1D), two-dimensional (2D) and three-dimensional (3D) NP assemblies. These controllable assemblies are likely to play critical roles in the improvement of the efficiencies of various electronic, optoelectronic, magnetic, and other devices, and also nanostructure based micro-nano fluidic systems.

In this context, we present a systemic review of current research on NP controllable assemblies. Their basic methodologies are classified and key research findings of novel characteristics of NP assemblies, such as novel properties in electronics, optics, magnetics, etc., are elucidated. Problems and promise of NP controllable assembly are also indicated.

Basic Methodology

One-Dimensional Assemblies of Nanoparticles

1D assemblies of nanoparticles refers to the controlled assembly of nanoparticles into wires, rods, belts, rings and tubes, which have become the focus of intensive research owing to their unique application in mesoscopic physics and fabrication of nanoscale devices. The basic method for 1D assemblies can be divided into template-directed method and template-free method which will be introduced in the following text.

Template-Directed Methods

Template-directed synthesis represents a straightforward route to 1D NP assemblies. In this approach, the template simply serves as a scaffold with (or around) which a different material is generated in situ and shaped into a nanostructure with its morphology complementary to that of the template. A wealth of templates including organic polyelectrolytes and biomolecules (so-called *soft templates*), inorganic wires and tubes (so-called *hard templates*), pores, and step edges, have been employed successfully to produce 1D NP assemblies. It is generally accepted that template-directed synthesis provides a simple, high-throughput, and cost-effective procedure that also allows the complex topology present on the surfaces of a template to be duplicated in a single step. Here we review the results for 1D NP assemblies using the most common linear templates.

Polyelectrolytes Linear polyelectrolytes in solution can provide a scaffold for the adsorption of metal ions with opposite charges. Thereafter, the ion-absorbed polyelectrolyte templates can transform to 1D metal or semiconductor-NP assemblies either by a reduction reaction or by chemical combination of ion pairs. Minko and co-workers explored this strategy to prepare 1D Pd NP assemblies. Colfen and co-workers adopted double-hydrophilic block copolymers (DHBCs) with more complex structures, in which one hydrophilic block interacted strongly with appropriate inorganic materials and the other hydrophilic block mainly promoted solubility in water, to synthesize 1D NP assemblies of materials such as $CaCO_3$, $CdWO_4$.

Biomolecules Biomolecules, including DNA, proteins, and microorganisms, are superior templates for the synthesis of 1D NP assemblies. Among biotemplates, DNA is probably the most frequently used molecule owing to its strong electrostatic and coordation interactions with NPs. Different kinds of NPs, such as Ag, Pd, Au, and Pt have been organized using this technique. Taking advantage of electrostatic interactions between metal or semiconductor NPs with DNA, 3 nm wide chains from CdS have been prepared while ribbon-like and even branched Au NP assemblies could also be prepared on DNA templates. Well-defined silver nanorings (100 nm in diameter) dispersed in water, have been simply synthesized based on the use of dilute solutions of DNA condensates as nanostructured templates.

Besides DNA, linear fibrous biomacromolecules like fibrin, dextran, and collagen are excellent candidates for producing 1D NP arrays. Double helical arrays by assembling Au and Pd NP on peptide nanofibrils under different PH conditions were obtained. Using dextran as a template a variety of metal and metal–oxide NP chains have been synthesized. TiO_2 and SnO_2 NPs can self-assemble onto linear collagen peptides to form 1D aggregares.

N

Linear microorganisms have also been employed. Dujardin et al. and Mann and co-workers used the tobacco mosaic virus, which has the shape of a linear tube, for assembly of various kinds of NPs inside and outside the tubes. Belcher and co-workers utilized bacteriophage to obtain oriented CdS, ZnS, CoPt, and FePt nanowires (NWs). Au and Ag NWs were also obtained by depositing Au and Ag solutions onto the surface of the yeast *Saccharomyces cerevisiae*.

Bacteria can form minerals intra-, inter- and extracellularly, nanoparticles formed in the bacteria cell can be assembled by manipulating the bacteria. External fields can be utilized to direct the assembly of the particles. Chains and rings from magnetic particles formed by controlling motion of the magnetotactic bacteria (MS-1) in external magnetic field, using microelectromagnets. Cellular membranes of the bacteria were removed by cell lysis, leaving the assemblies of magnetic nanocrystals.

Inorganic Nanowires and Nanotubes Carbon nanotubes (CNTs) and inorganic nanowires (NWs) are probably the most logical nanostructures to use as structure-directing matrices for the preparation of 1D NP assemblies.

Both the inner cavities and outer surfaces of hollow CNTs can serve as templates for 1D NP assemblies. Almost a decade ago, Ajayan, and Iijima reported encapsulating 1D Pd NP arrays in CNTs made via capillary induced filling. Afterwards, various types of 1D metal and metal–oxide NP arrays were prepared inside CNT cavities, and an appropriate review can be found in the publication of Ugarte et al. [1]. In general, the preparation methods can be classified into three types: the first is direct chemical or physical vapor deposition of metal or semiconductor NPs onto the surfaces of the CNTs and NWs, the second is sol-gel decoration of metal complexes onto the surfaces of CNTs and NWs and the last one is the modification of the surface properties of CNTs and NWs followed by specific adsorption of NPs. Using the above strategies, many 1D arrays of varying types of metal and semiconductor NPs such as Au, Ag, Pt, SnO_2, TiO_2, have been formed.

Other Templates Linear pores and channels inside polymers, alumina, and silica templates are also used to make linear agglomerates of NPs.

Template-Free Self-Assembly Methods

Template methods for the preparation of 1D NP assemblies have several intrinsic disadvantages. For instance, linear templates may have a considerable effect on both the photonic and electronic properties of the resulting 1D NP assemblies. Although post-synthetic physical or chemical treatment can help remove the templates, it is possible that they also cause morphological and structural alterations to the NP chains, which are detrimental to their application. There has been a growing realization in the research community that templates may not at all be necessary for the formation of 1D NP structures because, under certain conditions, they may self-assemble due to the inherent anisotropy of NP–NP interactions. Self-assembly has been extensively explored as a bottom-up approach for generating complex nanostructures on various scales. In particular, monodispersed colloids have been pursued as building blocks for the formation of wire-like structures through self- or externally manipulated assembly.

Magnetic Dipole Moments Chain formation and anisotropy of magnetic NPs have been well-known in nature for a long time. For instance, an anisotropic chain-like structure of maghemite NPs has been observed in terrestrial magnetotactic bacteria as shown in Fig. 1. These chain structures within the bacterium, which give rise to the formation of permanent magnetic dipoles, act as a critical orientation system. Moreover, a similar biomineralization process also occurs in the human brain, which might provide a theory for the mechanism of interaction of environmental magnetic fields with the human central nervous system. For references on the preparation of 1D NP chains by utilizing magnetic moments, one may refer to the review of Prof. M. P. Pileni [2].

Electric-Dipole Moments Electric-dipole moments are prevalent in semiconductor NPs due to either the presence of an anisotropic crystal lattice or surface defects. However, strong electrostatic or steric repulsion from stabilizers overcompensates electric-dipole attractions between NPs. Semiconductor NPs, silver and gold NPs were discovered to spontaneously form 1D chains. However, the origin of the dipole interaction and the driving forces of chain formation in metallic colloids remain unknown.

Oriented Aggregation The crystallographically specific orientation among primary nanocrystals also results in the formation of self-assembled NP chains, which was first explored by Banfield and co-workers. Some concrete examples can be referred to the review on oriented aggragation of NPs [3].

Langmuir–Blodgett Assembly The Langmuir–Blodgett (LB) technique has been used to assemble 1D nanoscale building scale. Various superstructures can be obtained as a result of different interactions between the

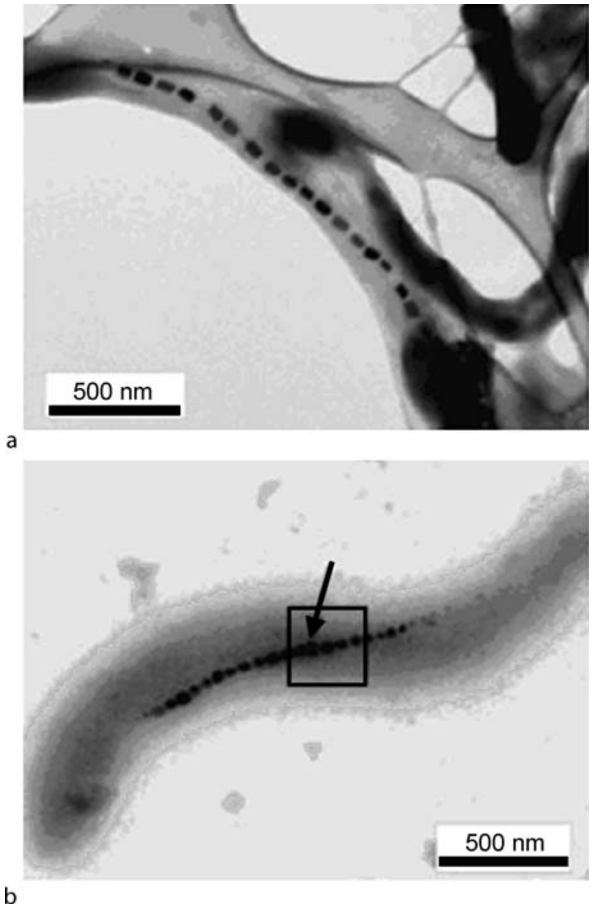

Nano-Particle Controllable Assembly, Figure 1 TEM images of the (**a**) MV-1 strain, and (**b**) MS-1 strain of terrestrial magnetotactic bacteria. Reproduced with permission from [11]

individual nanostructures and different surface pressure applied.

Previously, Langmuir–Blodgett films of various nanoparticles such as Ag, Au, and CdS have been prepared. Typically, the surface of the nanocrystals are functionalized by organic molecules (usually long alkyl chains) in order to prevent particle aggregation and also to ensure the nanoparticles float on the subphase surface (usually water). The nanoparticles are dispersed in organic solvents such as toluene, and this solution is spread dropwise onto the subphase surface. The nanoparticles form a monolayer on the water–air interface, which is slowly compressed. This monolayer can be transferred during the compression process using either horizontal or vertical liftoff to substrates such as transmission electron microscopy (TEM) grids or silicon wafers in order to be inspected with electron and optical microscopy.

Applying Langmuir–Blodgett technique, the assembly of one-dimensional nanostructures such as nanorods and

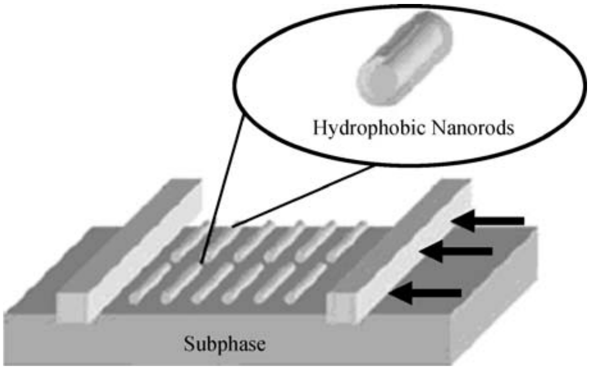

Nano-Particle Controllable Assembly, Figure 2 Schematic illustration of the Langmuir–Blodgett apparatus for nanorod assembly. Nanorods are generally rendered hydrophobic through surface functionalization. Reproduced with permission from [12]

nanowires have been synthesized successfully. These 1D nanostructures are rendered hydrophobic by surfactant surface functionalization before the LB experiments. Figure 2 schematically shows the experimental apparatus.

2D and 3D Assemblies of Nanoparticles

2D and 3D assemblies have been made by using a large variety of techniques, such as template-directed assembly, solvent evaporation, Langmuir–Blodgett (LB) transfer, producing self-assembled monolayers and multilayers, and layer-by layer assembly, etc.

Template-Directed Assembly

Template-directed assembly refers to the use of some templates (including synthetic templates and natural templates) to assembly preformed nanoparticle building blocks, forming sophisticated and complex architectures. Various methods are used including sol–gel, chemical vapor deposition, chemical vapor infiltration, atomic layer deposition, dip-coating, evaporation and deposition, LBL, sonochemical assembly and biological-assisted assembly.

Sol–Gel The sol–gel process involves the transition of a system from a liquid (the colloidal *sol*) into a solid (the *gel*) phase. The sol is made of solid particles of a diameter of few hundred nm, usually inorganic metal salts, suspended in a liquid phase. In a typical sol–gel process, the precursor is subjected to a series of hydrolysis and polymerization reactions to form a colloidal suspension, then the particles condense in a new phase, the gel, in which a solid macromolecule is immersed in a solvent. Various materials have been synthesized applying sol–gel method

by using different templates. For example, metal oxides can be formed by oxidation of the sol containing metal in the form of metal salts, metal alkoxides, etc. Sulfides can be formed by introducing S (aqueous or gaseous), into a sol containing ions like Cd(II), Zn(II), Fe(II), ect. Metals can be formed by reducing metal-containing sol covering the template. Still more materials, like nitride, zeolite, phosphor are also synthesized using sol–gel.

Chemical Vapor Deposition (CVD) and Chemical Vapor Infiltration (CVI) Chemical vapor deposition (CVD) is a chemical process used to produce high-purity, high-performance solid materials. The process is often used in the semiconductor industry to produce thin films. In a typical CVD process, the wafer (substrate) is exposed to one or more volatile precursors, which react and/or decompose on the substrate surface to produce the desired deposit. Frequently, volatile byproducts are also produced, which are removed by gas flow through the reaction chamber. Microfabrication processes widely use CVD to deposit materials in various forms, including: monocrystalline, polycrystalline, amorphous, and epitaxial. These materials include: silicon, carbon fiber, carbon nanofibers, filaments, carbon nanotubes, SiO_2, silicon-germanium, tungsten, silicon carbide, silicon nitride, silicon oxynitride, titanium nitride, and various high-k dielectrics.

Templates with complex structures can be used to controllable assembly of nanoparticles using gaseous reactants of good flowing properties, and near net-shaping is possible. G. Cook et al. have demonstrated the controlled vapor-phase oxidation of silanes on the surface of butterfly wings, producing an exact, inorganic oxide replica of natural form. The experimental apparatus for the chemical vapor deposition of silica is shown in Fig. 3. While CVD deposits materials onto a surface, chemical vapors in CVI can penetrate porous structures and deposit materials within the "body". Most materials that can be deposited by CVD can also be deposited by CVI. Here CVI has the edge when it comes to bulky templates like wood tissues, eg. Thickness of the coatings can be controlled by the number of deposition or infiltration cycles, and there is no background deposition which commonly occurs in sol–gel. Despite the many advantages of CVD and CVI, they are relatively expensive.

Evaporation and deposition is a straightforward method to assembly nanoparticles as a thin coat by replicating surface features of templates. Evaporation and deposition can produce fine structures from bio-templates. Au microshells showing diatom frustule morphologies and complex structures at the nanoscale; continuous Au nanowires as thin as 10nm can be formed on DNA by evaporation, while those grown from solution are no thinner than 30nm due to the stochastic metal deposition in solution. Metals of various kinds can be used for evaporation and deposition as long as they are suitable for evaporation. Compound coatings can be formed by surface reactions of synthetic vapors, eg. ultra-thin and compact TiO_2 coatings formed on diatom frustules via surface reactions of volatilized $TiCl_4$ and H_2O alternatively flown onto the template surface.

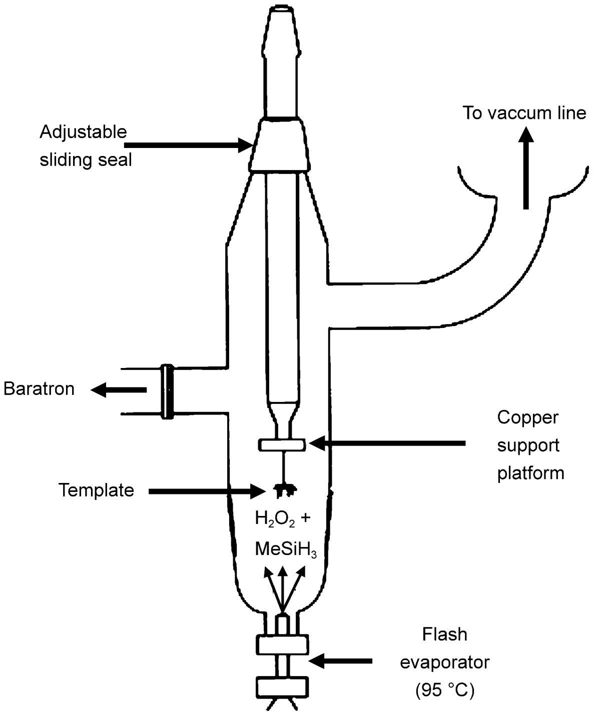

Nano-Particle Controllable Assembly, Figure 3 Experimental apparatus for the chemical vapor deposition of silica. Reproduced with permission from [13]

Atomic Layer Deposition (ALD) Atomic Layer Deposition (ALD) is a self-limiting, sequential surface chemistry that deposits conformal thin-films of materials onto substrates of varying compositions. ALD is similar in chemistry to chemical vapor deposition (CVD), except that the ALD reaction breaks the CVD reaction into two half-reactions, keeping the precursor materials separate during the reaction. ALD film growth is self-limited and based on surface reactions, which makes achieving atomic scale deposition control possible. By keeping the precursors separate throughout the coating process, atomic layer control of film grown can be obtained as fine as ~ 0.1 angstroms per monolayer. ALD has unique advantages over other thin film deposition techniques, as ALD grown

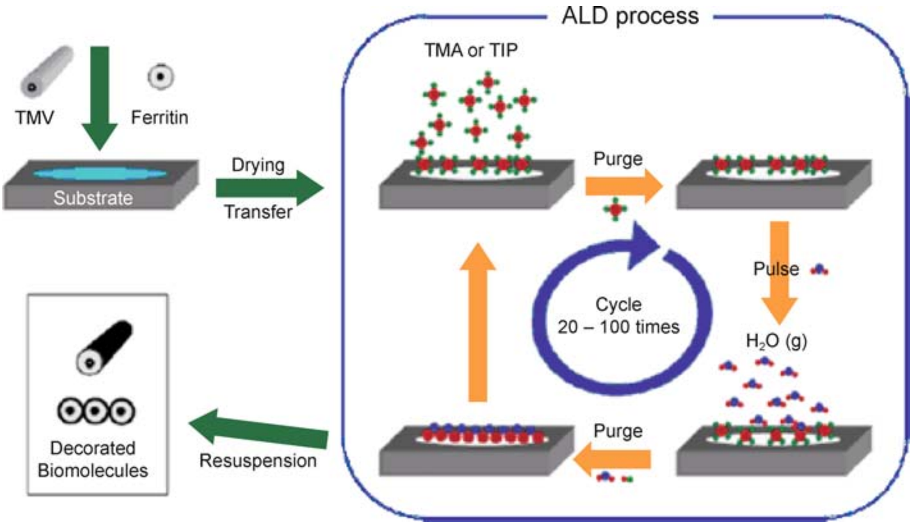

Nano-Particle Controllable Assembly, Figure 4 Schematic illustration of the ALD process. Reproduced with permission from [14]

films are conformal, pin-hole free, and chemically bonded to the substrate. With ALD it is possible to deposit coatings perfectly uniform in thickness inside deep trenches, porous media and around particles. The film thickness range is usually 1 – 500 nm. ALD can be used to deposit several types of thin films, including various ceramics, from conductors to insulators.

M. Knez et al. showed the application of atomic layer deposition, a gas-phase thin film deposition process, to biological macromolecules (Tobacco Mosaic Virus and Ferritin), which are frequently used as templates in nanoscale science, and the possibility to fabricate metal oxide nanotubes and thin films with embedded biomolecules, the experimental process is shown in Fig. 4.

Dip-Coating Dip coating refers to the immersing of a substrate into a tank containing coating material, removing the piece from the tank, and allowing it to drain. The coated piece can then be dried by force-drying or baking. It is a popular way of creating thin film coated materials along with the spin coating procedure. The dip coating process can be, generally, separated into 3 stages:

1. Immersion: the substrate is immersed in the solution of the coating material at a constant speed preferably judder free – sometimes cheese is applied to help fluid stick to material.
2. Dwell time: the substrate remains fully immersed and motionless to allow for the coating material to apply itself to the substrate.
3. Withdrawal: the substrate is withdrawn, again at a constant speed to avoid any judders. The faster the substrate is withdrawn from the tank the thicker the coating material that will be applied to the board.

The dipping is slow and the substrate is withdrawn from the tank at a uniform velocity to obtain a uniform coating. In template-directed synthesis, the template is used as the substrate, e. g. hollow mesoporous silica fibers with hierarchical order were fabricated by dip-coating a single strand of spider silk in liquid crystalline silica-surfactant mesophase. A high degree of alignment of the mesochannels was observed, which was created along the fiber due to the shear flow along the silk direction when dip-coated under gravity.

Biological-Assisted Assembly The aggregation of NPs induced by specific biological interactions has attracted huge interest in the assembly of nanoscale components into controlled and sophisticated nanostructures. Biological systems possess inherent functional groups with material specificity or polarity, which greatly facilitate assembly onto these templates. Biomolecules, bacteria, fungus, virus, diatom, etc. are widely used as templates to assemble NPs into controlled nanostructures. Interactions like electrostatic interaction, metal–ligand interaction, streptavidin-biotin (antigen–antibody) interaction, DNA-intercalator interaction, etc. are utilized.

For example, two-dimensional iron-oxide nanoparticle array can be prepared using ordered ferritin molecules as the template. Au and CdSe – ZnS quantum dots can assemble into ordered arrays using a chaperonin protein template, which was modified with thiol groups to bind the nanoparticles via metal–ligand interactions. Au nano-

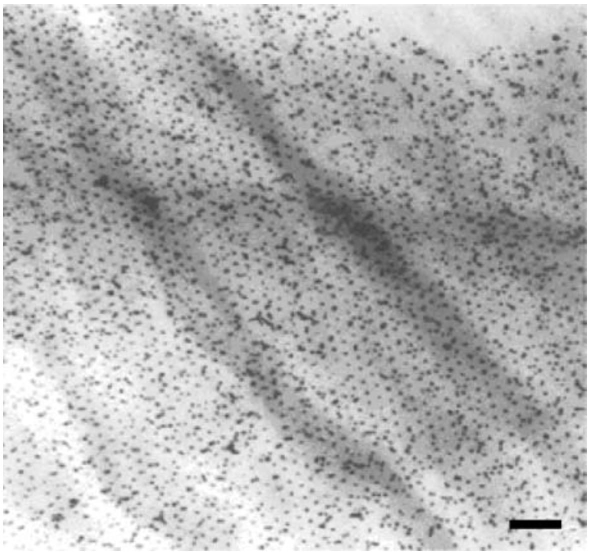

Nano-Particle Controllable Assembly, Figure 5 TEM image showing S-layer templated periodic array of 5 nm sized gold nanoparticles. Scale bar is 100 nm. Reproduced with permission from [15]

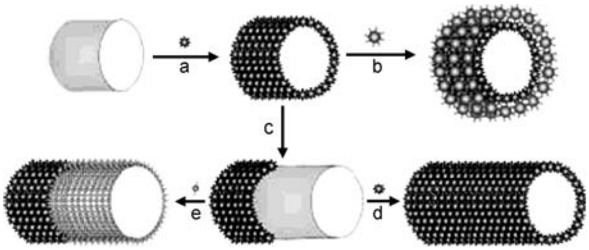

Nano-Particle Controllable Assembly, Figure 6 Schematic illustration of the use of a living hypha of a filamentous fungus as the template for the assembly of oligonucleotide-funtionalized Au nanoparticles into ordered microscopic structures. (**a**) As the living fungal hypha grows, the Au nanoparticles (functionalized with single-stranded DNA) bind to its cell walls and a microscopic tube-shaped nanoparticle assembly is formed. (**b**) Additional layers of nanoparticles functionalized with complementary oligonucleotide strands can be assembled onto the surface of the microscopic nanoparticle tube through DNA hybridization. (**c**) The fungal hypha will continue to grow in a favorable environment and generate unmodified hyphae ends. (**d**) and (**e**) These fresh ends can be modified with new particles, thus providing control of the architecture along the growth axis. Reproduced with permission from [16]

clusters can be formed using IgGs (immuno-globulin Gs) aggregates as the template.

Viruses are similar to biomolecular templates because the viral capsid is in fact a complex composed of protein subunits. Viruses coupled with nanoparticles can be used as building blocks to form nanoparticle assemblies, or virus assemblies of two- and three-dimension can be used as templates. Virus is advantageous as a building block because identical viruses can be produced in large amounts at low cost, and nanoparticles templated by viruses generally have a high monodispersity. Viruses may have inherent self-assembly, for example, nanowires mineralized using TMV templates are often found to be longer than individual TMV particle, indicating a higher-order assembly of the TMV particles. It is a reversible head-to-tail assembly of TMV, attributable to the complementary hydrophobic interactions between the dipolar ends of the helical structure, and the trend of the head-to-tail assembly may be favored in acidic environments.

Self-assembled 2D crystals of a bacterial surface layer protein (S-layer) were used to fabricate highly ordered superlattice arrays of gold nanoparticles by deposition from pre-formed colloids [4]. The S-layer template consisted of hexameric units arranged in a periodic (P6) hexagonal structure with lattice constant, 18 nm. Each hexamer was in the form of a hollow cone with a 2 nm wide positively charged central channel, and this site-specific surface periodicity was used to control the periodic assembly of negatively charged gold nanoparticles by electrostatic binding as shown in Fig. 5. Besides 2D nanostructures, bacteria can also used as templates for the assembly of nanoparticles into 3D nanostructures. For example, preformed ceramic (SiO_2), magnetic (Fe_3O_4), and semiconducting (CdS) inorganic nanoparticles were incorporated into macroscopic threads of *Bacillus subtilis* by reversible swelling of the superstructure in colloidal sols [5].

Nanoparticle assembly on living fungi can lead to structures of interesting forms. Z. Li et al. used the living hypha of a filamentous fungus, *Asprgillus niger*, for Au nanoparticle assembly. The schematic illustration is shown in Fig. 6. The Au particles are modified with oligonucleotides which bind to the hypha surface. As the hypha keep growing, the fresh uncovered ends continue to bind Au particles, forming a continuous Au coating. Nanoparticles (not necessarily Au) modified with complementary-oligonucleotides can be assembled onto the first layer of particles via DNA complementary coupling, thus multilayered coatings can be formed.

Layer-by-Layer (LBL) Assembly LBL assembly, largely developed by Decher, Lvov, and Mohwald in the 1990s, is a popular technique for the fabrication of organized, multilayer organic–inorganic films based on the alternating adsorption of oppositely charged materials as shown in Fig. 7. LbL assembly, which was initially based on alternating electrostatic absorption, has successfully been extended to encompass different kinds of driving forces, such as hydrogen bonding, covalent bonding, and other weak intermolecular interactions. It is now widely

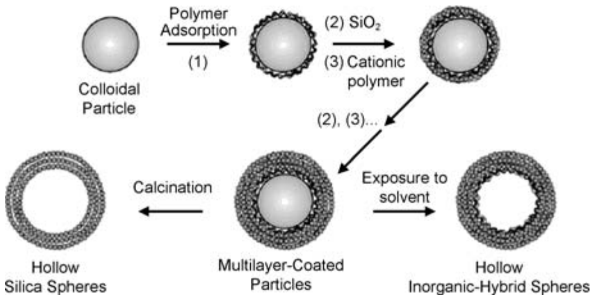

Nano-Particle Controllable Assembly, Figure 7 Illustration of procedures for preparing hollow inorganic silica and inorganic-hybrid spheres through colloid-templated electrostatic LBL assembly of silica NP polymer multilayers, followed by the removal of the templating core and, optionally, the polymer. Reproduced with permission from [17]

accepted that LbL assembly can be a powerful approach for assembling functional building blocks into ultrathin films with controlled internal organization, thickness, and molecular structure on planar solid substrates.

LBL assembly also been extended to construct freestanding nanostructures by controllable assembling nanoparticles. Freely suspended flexible LbL structures with different shapes, compositions, and properties can be fabricated by using sacrificial substrates (planar, spherical, and cylindrical). Depending upon the fabrication procedure, freestanding LbL microcapsules, microtubules, microcubes, microcantilevers, and planar films can be obtained as shown in Fig. 8.

These structures can be classified into three broad groups according to the media surrounding them:

- LbL structures in air,
- LbL structures at the air/liquid interface, and
- LbL structures at the liquid/liquid interface.

Since the first report by Möhwald and co-workers in 1998, the fabrication of LbL microcapsules has become one of the hottest areas in this field. LbL assembly, nanocapsules, nanoreactors, responsive films and capsules, biomimetic microcapsules, the mechanical properties of the microcapsules, and the permeability of these capsules are also hot research areas.

Sonochemical Assembly Sonochemistry is emerging as a promising approach for the controllable assembly of nanoparticles due to the application of powerful ultrasound radiation ($20\,\text{kHz} - 10\,\text{MHz}$) which can break chemical bonds. The chemical effects of ultrasound arise from acoustic cavitation: the formation, growth, and implosive collapse of bubbles in liquid. The implosive collapse of the bubble generates localized hot spots through adiabatic compression or shock wave formation within the gas phase of the collapsing bubble. The conditions formed in these hot spots have been experimentally determined, with transient temperatures of 5000 K, pressures of 1800 atm, and cooling rates in excess of $1010\,\text{K/s}$. These extreme conditions attained during bubble collapse have been exploited to prepare nanoparticles of metals, metal carbides, metal oxides, and metal sulfides and to the further surface assembly of nanoparticles on the templates by forming chemical bonds or chemical interactions with the substrate and cannot be removed by washing.

A variety of templates have been used for the sonochemical assembly of nanoparticles including silica and PS spheres, wool, microorganisms etc. Controllable assembly of ZnS, CdS, CdSe, metals (Ag, Au, Pd, Pt), etc. onto silica or PS spheres have been demonstrated.

H. Zhou et al. [6] developed a novel bacteria-templated sonochemical route for the controllable assembly of ZnS nanoparticles into desired hollow nanostructures. It is based on artificial mineralization and cell disruption under ultrasound. Two shapes of bacteria cocci and bacillus were used as templates to direct the formation of corresponding ZnS hollow spheres and hollow nanotubes, respectively. The inorganic replicas retain the original morphologies of the templates faithfully. This bacteria-templated sonochemical method can be extended to the synthesis of various ZnS hollow assemblies by templating other shapes of bacterium such as vibrios, spirillum, square bacteria, etc. Meanwhile, this method is expected to be a generic means to the simple synthesis of hollow assemblies of various materials.

Template-Free Self-Assembly

Self-assembled nanocrystals have attracted an increasing interest over the last ten years. The level of research activity is growing seemingly exponentially, fueled in part by the observation of physical properties that are unique to the nanoscale domain. The first two-dimensional (2D) and three-dimensional (3D) superlattices were observed with Ag_2S and CdSe nanocrystals. Since then, various self-organized lattices of silver, gold, cobalt, and cobalt oxide have been prepared successfully. It has been demonstrated that three-dimensional superlattices of nanocrystals are often organized in a face-centered cubic (FCC) structure. In other cases, the particles pack in a hexagonal lattice. The template-free self-assembly is simple and straightforward compared with template-directed assembly. Here, we focus on the fabrication modes of self-assemblies in 2D and 3D superlattices.

Solvent Evaporation M. P. Pileni reported the solvent evaporation method for the self-assembly of nanoparticles. With silver and silver sulfide, the nanocrystals are able to self organize in 2D and 3D super lattices to form "supra"

N

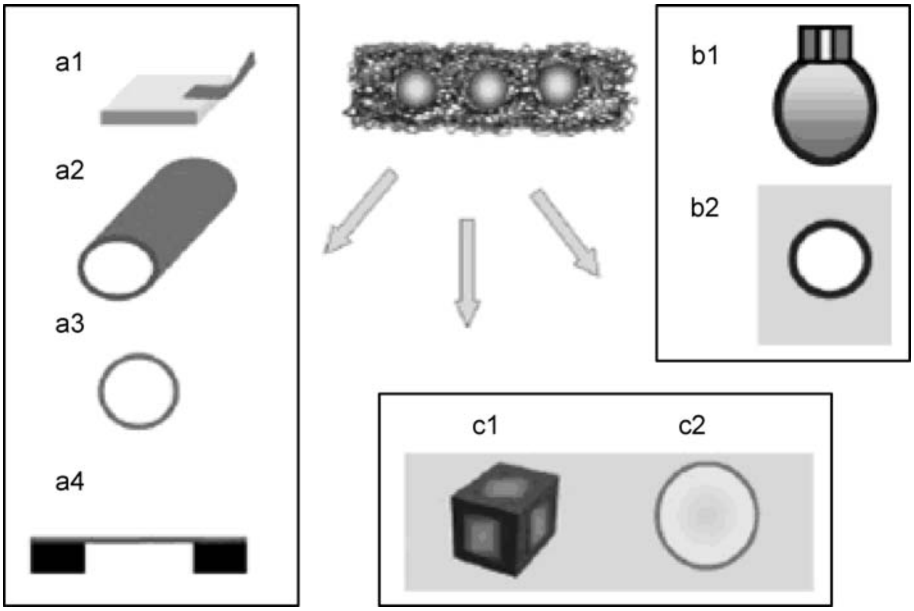

Nano-Particle Controllable Assembly, Figure 8 Three different types of freestanding LBL nanostructures. (**a**) LbL structures in air: (a1) microcantilever (a2) microtubule; (a3) hollow microcapsule; and (a4) thin planar film. (**b**) LBL structures at the air/liquid interface: (b1) LBL structures within a pendant drop; and (b2) gas-filled microcapsules in solution. (**c**) LBL structures at the liquid/liquid interface: (c1) microcubes and (c2) microcapsules. Reproduced with permission from [18]

crystals. The process is as follows: Immediately after the solution containing the nanocrystals is deposited on the substrate, the solvent begins to evaporate and droplets form. The Ag_2S nanocrystals themselves are fully solvated by the heptane, which prevents their assembly into dense structures. As the droplets grow and begin to merge, some of the Ag_2S nanocrystals (which are still mobile because of the thin solvent layer present on the HOPG surface) are expelled away from the merge center as shown in Fig. 9. These dressed particles form compact monolayer islands, whose density increases after all of the solvent evaporates and interdigitation of the alkyl chains on the Ag_2S nanocrystal occurs. Other particles are caught in the center of the droplet merge point. The pressure exerted on these particles by the droplet menisci is large, and while a monolayer initially forms, continued droplet coalescence engenders the formation of a 3D structure.

Field-Directed Self-Assembly By applying an external field (including electric-field, thermal-field, magnetic-field, fringing-field, etc.) during the deposition process of nanocrystals, the particles can be oriented along the direction of the applied field.

A new gas-phase integration process has been developed to assemble nanomaterials into desired areas using localized fringing fields. This process is expected to work with any material that can be charged, including organic and inorganic, metallic, semiconducting, and insulating materials.

Electric-field-directed self-assembly of higher-order structures with more than 50 layers of nanoparticles can be carried out in a rapid and highly parallel format using a CMOS electronic microarray device. Control of the current, voltage, and activation time of each of the 400-microarray electrodes allows a combinatorial approach to optimize nanoparticle binding. Under optimal conditions, nanoparticle layers form within 15 s of microelectrode activation, and the directed assembly of more than 50 alternate layers of nanoparticles is complete within an hour. The final multilayered structures are removed from the support by a relatively simple lift-off process. The electric-field process allows the parallel patterned assembly of multilayer structures using extremely low concentrations of nanoparticles and produces minimal nonspecific binding to unactivated sites. These results are significant for the development of rapid, maskless nanofabrication and hierarchical integration of biomolecular-derivatized nanocomponents into higher-order materials and devices.

By applying a magnetic field during the deposition process of nanocrystals, the easy axes of the particles are oriented along the direction of the applied field, inducing again the

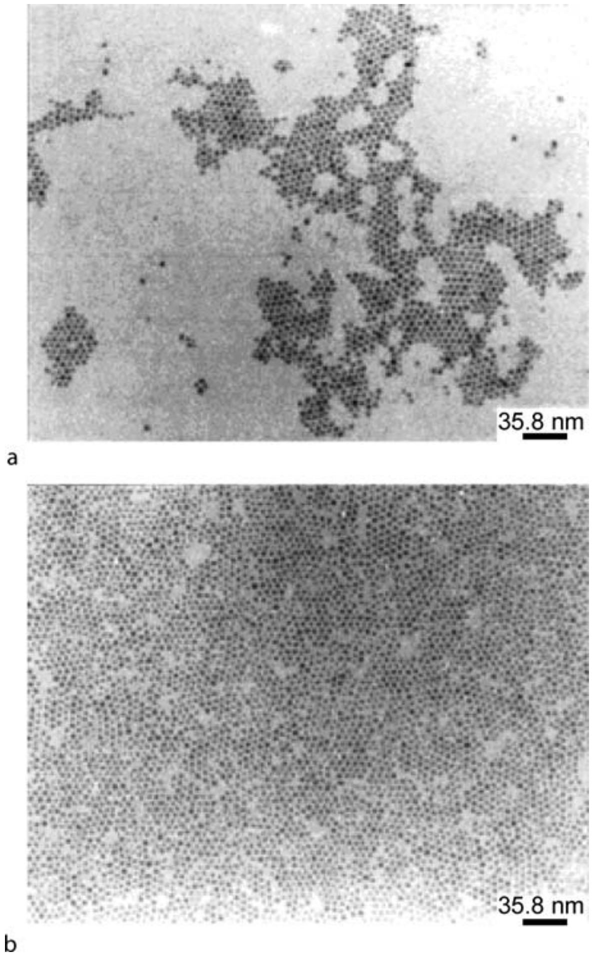

Nano-Particle Controllable Assembly, Figure 9 TEM images of a monolayer of 5.8 nm diameter silver sulfide nanocrystals deposited on amorphous carbon, observed at various nanocrystal concentration. Reproduced with permission from [19]

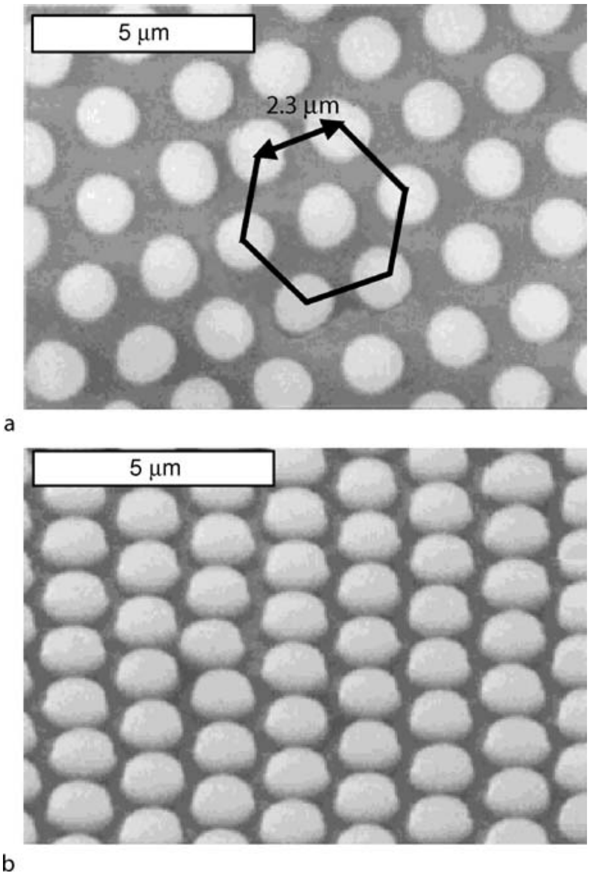

Nano-Particle Controllable Assembly, Figure 10 (**a**) SEM patterns at different magnifications of superlattices obtained on HOPG substrates, with an applied field of $H = 0.27$ T. The hexagonal network is visible. (**b**) Titled SEM pattern showing the 3D structures. The deduced height is 1 μm for each pillar. Reproduced with permission from [19]

collective magnetic properties. Enhancement of the SEM grid shows that these dots are organized in a well-defined hexagonal network (Fig. 10).

Langmuir–Blodgett (LB) Transfer Langmuir–Blodgett (LB) films have been investigated, extensively, over the past 70 years. In the 1930s, Irving Langmuir and Katherine Blodgett introduced a method for fabricating monolayer and multilayer arrays of surfactants. Since that time, this Langmuir–Blodgett (LB) technique has been used, extensively, to construct a wide variety of organized thin films. Typically, LB films are fabricated by dipping a solid support, vertically, through a surfactant monolayer at an air–water interface. For example, a single "down-trip" of a hydrophobic support from air into water results in the monolayer being transferred, such that the hydrocarbon tails are in intimate contact with the support and the polar head groups extend outward towards the bulk aqueous phase (Fig. 11). A subsequent "up-trip" generally deposits a second monolayer with a head-to-head orientation with the first deposited monolayer. Further dipping can then lead to multilayers of the surfactant.

In recent years, there has been a steady shift away from the LB technique towards self-assembly methods for the fabrication of monolayer and multilayer arrays (Fig. 12). In contrast to the LB method, which requires a film balance and careful control over surface pressures during dipping and transfer, self-assembly is carried out by simple immersion of a suitable support into a solution containing an excess of monomer. The formation of multilayer arrays via self-assembly has also become popular. Most commonly, a charged surface is dipped into a solution containing a polyionic species, followed by dipping into a second solution that contains a polymeric counterion. Repeti-

tion of such dipping then produces the desired material in a layer-by-layer manner.

Micro Force Driven Self-assembly of nanoparticles into 2D and 3D nanostructures can also be achieved by virtue of micro forces like capillary force, dielectrophoretic force, hydrophobic force, etc.

N. Bowden et al. realized self-assembly of topologically complex, millimeter-scale objects into ordered two-dimensional arrays driven by capillary forces, with the shapes of the assembling objects and the wettability of their surfaces determining the structure of the arrays. The system was composed of solid objects floating at the interface between perfluorodecalin and water and interacting by lateral capillary forces; patterning of the wettability of the surfaces of the objects directs these forces. Self-assembly results from minimization of the interfacial free energy of the liquid–liquid interface. Calculations suggest that this strategy for self-assembly can be applied to objects on a micrometer scale.

A new class of microwires can be assembled by dielectrophoresis from suspensions of metallic nanoparticles. The wires are formed in the gaps between planar electrodes and can grow faster than 50 μm per second to lengths exceeding 5 mm. They have good ohmic conductance and automatically form electrical connections to conductive islands or particles. The thickness and the fractal dimension of the wires can be controlled, and composite wires with a metallic core surrounded by a latex shell can be assembled. The simple assembly process and their high surface-to-volume ratio make these structures promising for wet electronic and bioelectronic circuits.

Key Research Findings

In the former section we have introduced the basic methods for controllable assembly of nanoparticles systematically, some typical examples have been given as well. The preparation of NP assemblies should serve the exploration of their novel properties and applications. So, in this section we will list some key research findings focusing on their novel properties and potential applications.

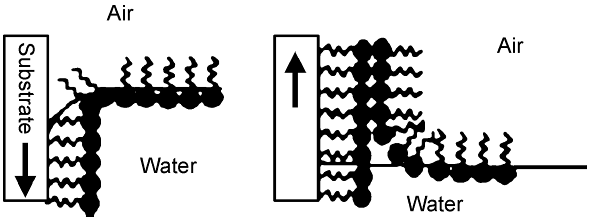

Nano-Particle Controllable Assembly, Figure 11 A stylized illustration showing a single surfactant monolayer being transferred to a hydrophobic support on a down-trip, followed by the transfer of a second monolayer on the up-trip, to form a bilayer. Reproduced with permission from [20]

Indeed, 1D NP assemblies exhibit many collective properties in optics, magnetics, electronics, and so forth. For instance, 1D magnetic NP arrays showed anisotropic and collective magnetic properties. Pileni and co-workers obtained 1D chains of 8 nm Co NPs by applying a magnetic field (1 T) parallel to a highly oriented pyrolytic graphite (HOPG) substrate during the evaporation process. Magnetic measurement results demonstrated that, with respect to partially disordered NP aggregates, the reduced remnant magnetization and coercivity of the 1D Co chains increased from 0.52 and 0.13 T to 0.60 and 0.14 T, respectively. The increase of both remnant magnetization and coercivity of the 1D Co NP chains were attributed to the enhanced orientation of their magnetic moments along the direction of the applied magnetic field.

1D NP arrays have been utilized as gas sensors. Favier et al. [7] fabricated parallel 1D Pd NP arrays using the electrochemical reduction method (Fig. 13a). adsorption of H_2 gas caused a reversible expansion of the crystalline lattice of Pd. As a result, the gaps between the Pd NPs in the linear arrays decreased, thus improving electron transport along the chains (Fig. 13b). The gaps opened up again when hydrogen was vented from the sensors, and such reversible responses make 1D Pd NP arrays good prototypes of reproducible gas sensors.

2D and 3D assemblies of nanoparticles also show some novel and unique properties in optics, electronics, magnetics, etc. For instance, Recently, Z. L. Wang and coworkers [8] demonstrated the fine structure of the wing scale of a Morpho Peleides butterfly was completely replicated by a uniform Al_2O_3 coating through a low-temperature ALD process. An inverted structure was achieved by removing the butterfly wing template at high temperature, forming a polycrystalline Al_2O_3 shell structure with precisely controlled thickness. Other than the copy of the morphology of the structure, the optical property, such as the existence of PBG, was also inherited by the alumina replica. Reflection peaks at the violet/blue range were detected on both original wings and their replica, while a simple alumina coating shifted the reflection peak to longer wavelength because of the change of periodicity and refraction index. The alumina replicas also exhibited similar functional structures as waveguide and beam splitter, which may be used as the building blocks for photonic ICs with high reproducibility and lower fabrication cost compared to traditional lithography techniques. The "waveguide" properties of the alumina replicas is shown in Fig. 14.

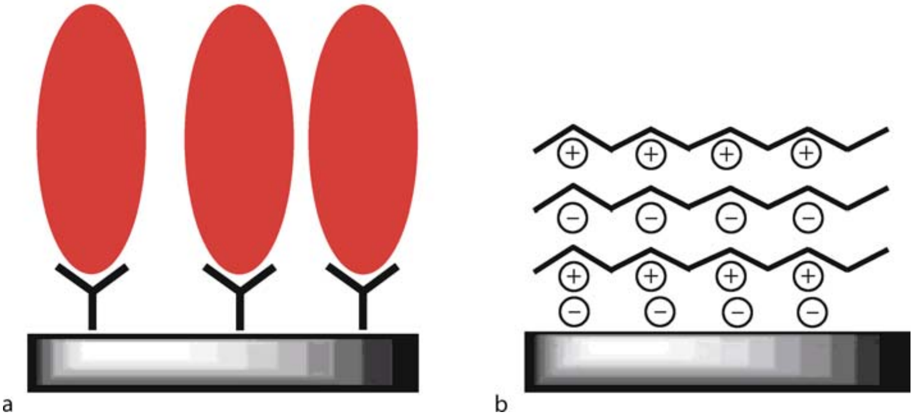

Nano-Particle Controllable Assembly, Figure 12 Illustration showing (**a**) self-assembled monolayer and (**b**) and alternating array of polycations and polyanions supported on a negatibely-charged substrate. Reproduced with permission from [20]

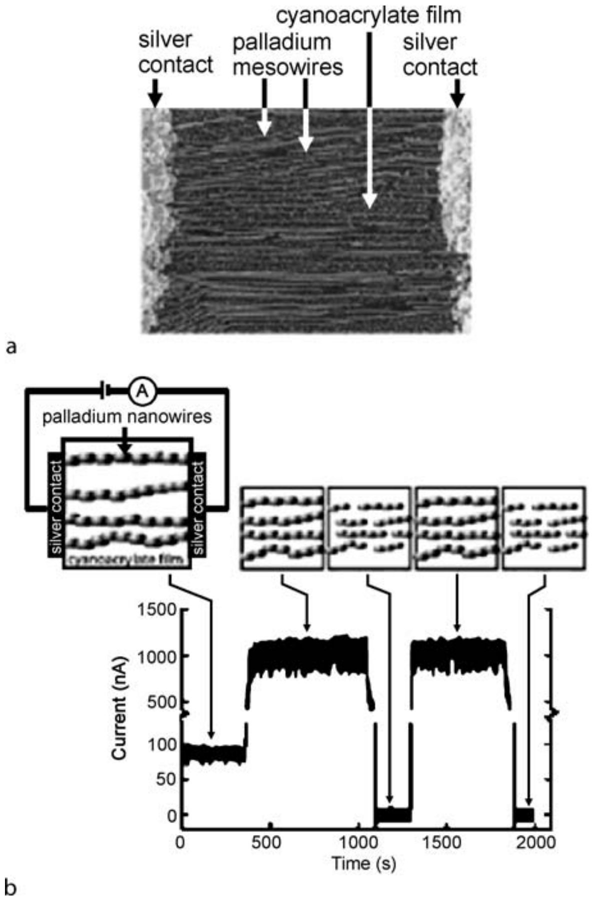

Nano-Particle Controllable Assembly, Figure 13 (**a**) SEM image of the active area of a hydrogen sensor based on chains of Pd NPs; area: 400 μm × 600 μm. (**b**) schematic of the operation of a hydrogen sensor based on chains of Pd NP with corresponding current response measurements. Reproduced with permission from [21]

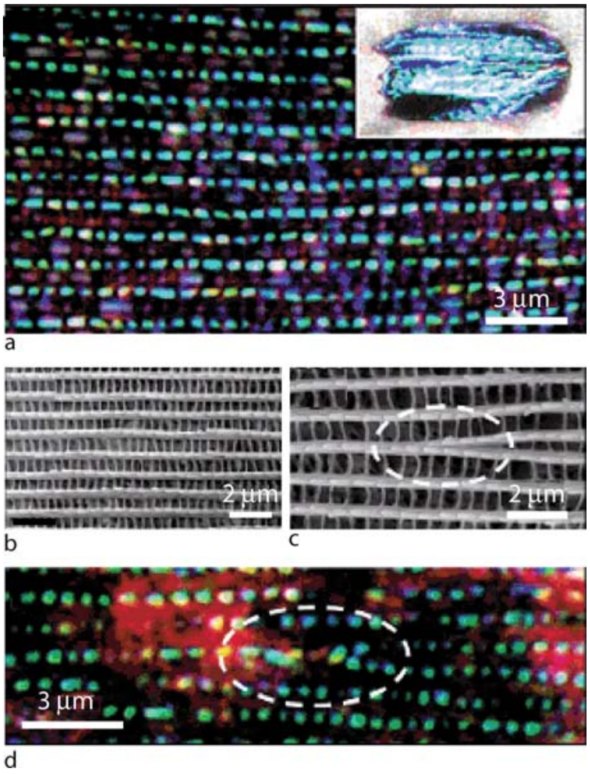

Nano-Particle Controllable Assembly, Figure 14 "Waveguide" properties of the alumina replicas. (**a**) A dark field optical microscope image of an alumina replica of the lamella rows; the inset is an optical image of an individual scale. (**b**) The SEM image of the replica structure corresponding to optical microscopy image shown in part a. (**c**) The SEM image of the bifurcated lamella structure. (**d**) the corresponding dark field optical microscope image showing the potential application as a beam splitter. Reproduced with permission from [22]

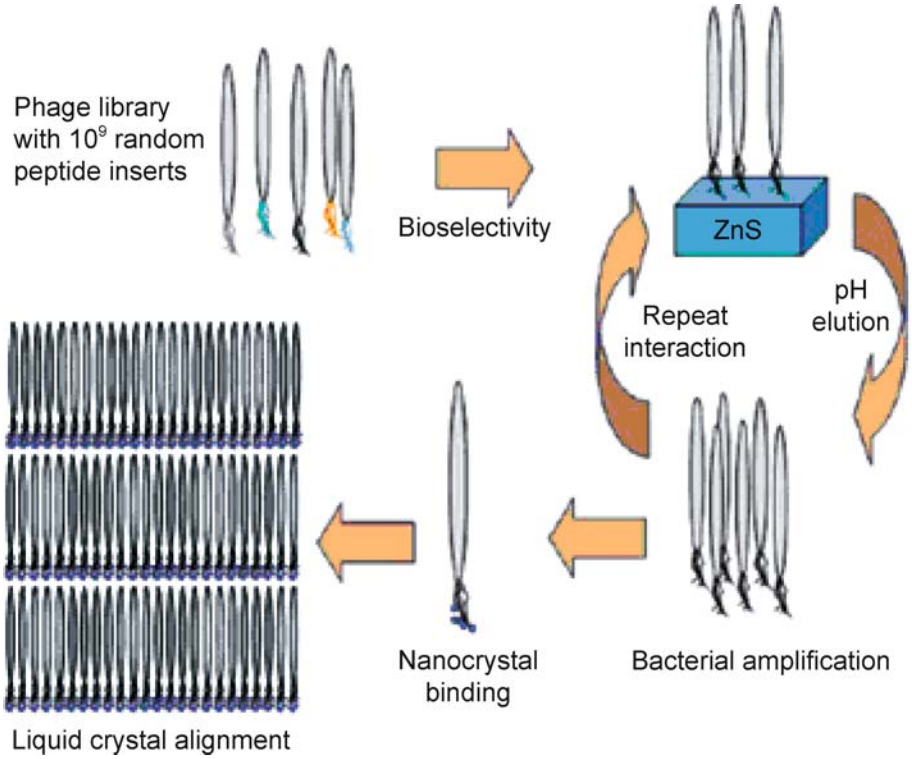

Nano-Particle Controllable Assembly, Figure 15 Schematic diagram of the process used to generate nanocrystal alignment by the phage display method. Reproduced with permission from [23]

Rod-shaped viruses can form liquid crystalline phases, which can be controlled by factors like virus suspension concentration, ionic strength of solution, external fields, etc. For example, M13 phages are found to randomly orientated in an isotropic concentration range, but transform to nematic, cholesteric, and smetic phases with increased concentrations, solid-phase films and 1D fibers can be obtained at much higher concentrations. Belcher et al. [9] utilized liquid crystal system of M13 to arranged ZnS nanocrystals into ordered domains at the nano- and micrometer scale under an external magnetic field, forming a self-supporting biological-semiconducting hybrid film. The schematic illustration of the process is shown in Fig. 15. The films were typically $\sim 15\,\mu$m thick and several centimeters in extent. Optical characterization revealed that the films were composed of $\sim 72\,\mu$m periodic dark and bright band patterns which corresponded to the chiral smectic C structure. The films showed smectic-like lamellar morphologies between the ZnS nanocrystals and M13 viral layers when imaged by SEM. A periodic length of 895 nm was observed, corresponding to the combination of virus length (860 – 880 nm) and nanocrystal aggregates (~ 20 nm). Surface morphology of the viral film exhibited zig-zag chiral smectic O patterns due to the long rod shape of the viruses conjugated to an inorganic head group composed of ZnS nanocrystals. The viral film cast on an ITO substrate showed smectic B morphologies when imaged by atomic force miscroscopy (AFM) (Fig. 16). TEM images of microtomed cross sections of the viral film revealed 2 – 3 nm nanocrystals that were aligned and were extended to more than $2\,\mu$m in length. The $2\,\mu$m bands formed in parallel were separated by ~ 700 nm, corresponding to the length scale imposed by the virus in a tilted smectic alignment. Based on the similar mechanism, other forms of assemblies can also be obtained as shown in Fig. 17.

Fibrous assemblies like nanofibers, nanopipes, nanotubes may have applications in micro/nano-fluidic systems. Vertically aligned carbon nanofibers grown by plasma-enhanced chemical vapor deposition are used as sacrificial templates for nanopipes with internal diameters as small as 30 nm and lengths up to several micrometers that are oriented perpendicular to the substrate. Such nanopipes can be implemented as functional elements in gas- and liquid-phase micro/nano-fluidic devices. The functionality of nanopipes has been demonstrated by observing fluidic transport between two fluid regions that were physically separated by a membrane containing the nanopipe pores.

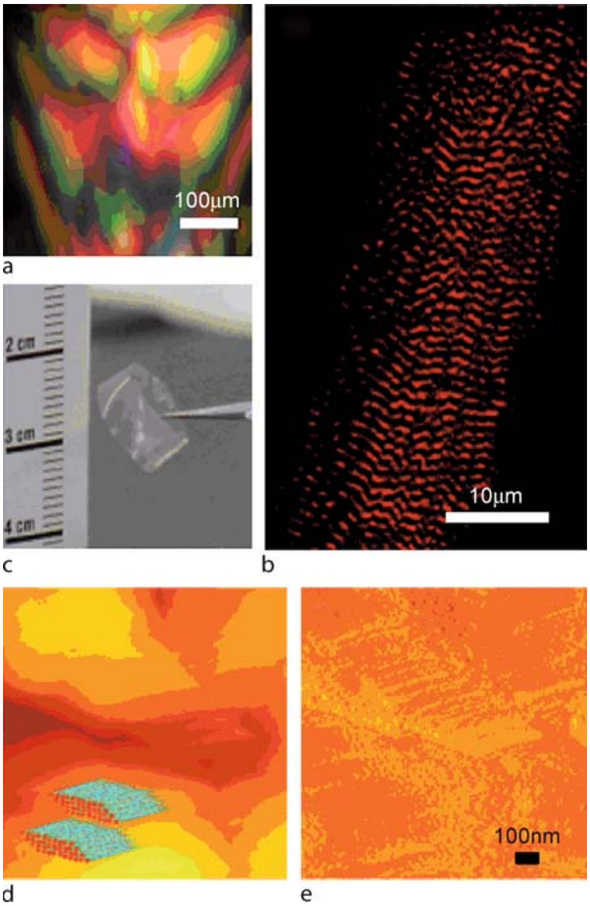

Nano-Particle Controllable Assembly, Figure 16 (**a**) Smectic phase of M13 virus liquid crystal suspension conjugated with ZnS nanocrystals observed using polarized optical microscope. (**b**) Self-supporting composite film of M13 virus crystal conjugated with ZnS nanocrystals. (**c**) One micrometer stripe patterns of phycoerythrin linearly aligned by anti-streptavidin viruses observed using confocal microscopy. (**d**) Height and (**e**) phase AFM images of a viral film cast on an ITO substrate. Inset in (**d**) illustrates the viral packing. Reproduced with permission from [23]

Several applications of nanopipes can be envisioned, including highthroughput sensing, analysis of molecular species, drug delivery systems, and fluidic interfaces to live cells.

Future Directions for Research

As described in this text, significant developments have been made in nanoparticle controllable assembly during the last year. The field continues to grow internationally and contribute to new interdisciplinary areas concerned with the synthesis, properties and applications.

Although 1D NP chains are ubiquitous in nature, research into their preparation and properties are still in their early stages. There are plenty of unknown phenomena awaiting exploration and there are also many problems requiring resolution. Practical application of devices based on 1D NP requires large-scale production as well as precise positioning of 1D NP arrays. Although numerous methods have been developed to prepare 1D NP chains, attaining precise arrangement of these chains remains highly desirable. Recent research has demonstrated that 1D NP chains could be accurately positioned and assembled into complex patterns by DNA templates on solid substrates [10] which also can be utilized in the practical fabrication of NP devices. The exploration of new properties and applications of 1D NP assemblies is strongly dependent on their preparation methods. We believe that, in the future, two issues should be addressed in order to understand the properties of 1D NP chains. One important issue is to control the interparticle distances in NP chains, so that distance-dependent photonic and electronic transfer along the NP chains could be realized, which will have applications in electronic and photonic devices, telecommunications, and sensors. Another critical issue is to produce NP chains consisting of multiple components, which are of considerable interest for both the fundamental-research and application communities.

As for 2D and 3D NP assemblies, prospects for the future include the development of novel transcription methodologies, as well as the creation of new transcribable templates which present a greater degree of structural complexity or can give rise to extended, patterned architectures. One of the principal challenges remaining consists of finding novel methodologies for obtaining transcribed structures with a high degree of order at the 2D or 3D level. Particularly, biological assemblies of nanoparticles may play an important role in the preparation of NPs assemblies due to the opportunities that are opening up with regard to biological coding of the assembly process. Besides, the exploration of the relationship between the sophisticated structures and the corresponding specific functionality is highly appealing and urgent. Complex assemblies of nanoparticles by using sophisticated biological systems would probably provide great opportunities and potentials for the extensive study of the relationship between the sophisticated structures and the corresponding specific functionality. This area is still in an early phase of development and many fantastic phenomena remain unknown and awaiting exploration.

Assembling and design of nanostructures for micro- and nano-fluidics systems has led to a wide range of microchemical applications. Material properties are crucial in the fabrication, assembly, and operation of micro- and

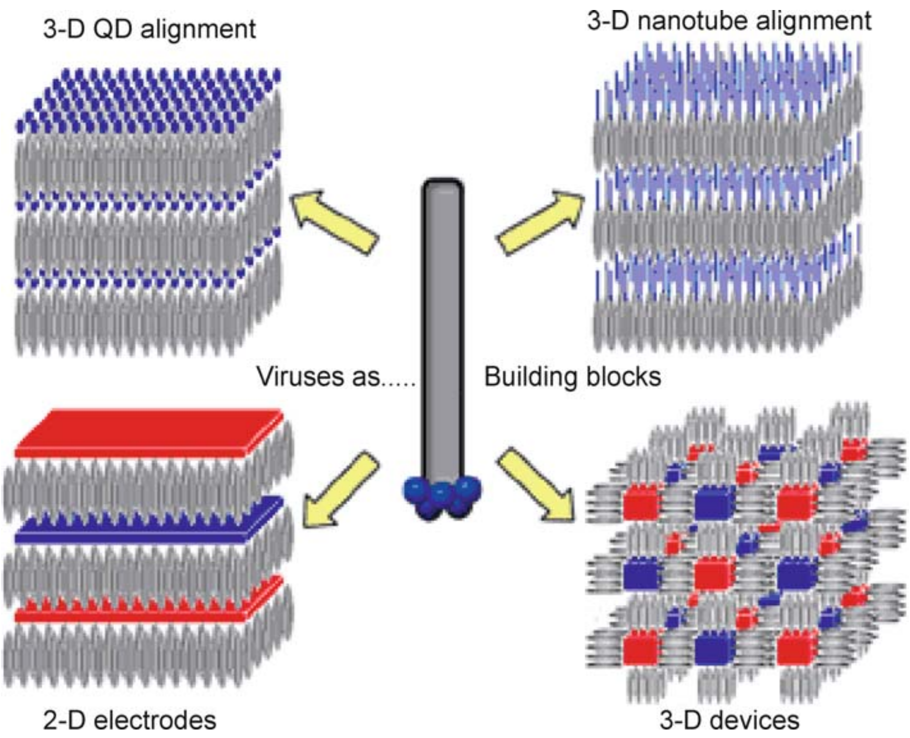

Nano-Particle Controllable Assembly, Figure 17 Schematic diagram of various self-assemble structures using one dimensional viruses with zere dimensional quantum dots (QD), one dimensional nanowires/nanotubes, two dimensional plate-shaped devices and three dimensional components. Reproduced with permission from [24]

nanofluidic systems. Thus, development of new methods for manufacturing nanoparticles assemblies with good properties for micro and nanofluidic devices is highly important. Choice-of-material considerations range from an assessment of whether a desired channel design can be microfabricated in a certain material to whether the material is compatible with the operating conditions (i. e., pressure, temperature) and the chemical composition (solvent, solutes) of the fluid used. Moreover, in certain cases, specific surface can be used to the benefit of the application of the device. For example, these materials can be equipped with functional nanofeatures such as nanogrooved surfaces, patchy hydrophobic-hydrophilic nanopatterns, and stimuli-responsive nanocoatings. Therefore, these materials are expected to form a new economically-viable nanofluidic platform. This platform provides novel capabilities that could not be realized with the existing or improved photo-lithographically manufactured platforms.
There are almost unlimited research opportunities that are being, and will be explored by many labs around the world in this general area of NPs controllable assembly. However, one should also realize that some potential environmental and health issues might arise. In this regard, a systematical evaluation on how these nanostructures will impact our environment and health is urgently needed!

Cross References

- ► Chemical Vapor Deposition for Film Deposition
- ► Quantum Dots
- ► Self-Assembled Monolayers
- ► Self-Assembly Fabrication
- ► Sol–Gel Technique

References

1. Ugarte D, Stoeckli T, Bonard JM, Charelain A, De Heer WA (1998) Filling carbon nanotubes. Appl Phys A 67:101–105
2. Pileni MP (2001) Nanocrystal self-assemblies: fabrication and collective properties. J Phys Chem B 105:3358–3371
3. Penn RL (2004) Kinetics of oriented aggragation. J Phys Chem B 108:12707–12712
4. Hall SR, Shenton W, Engelhardt H, Mann S (2001) Site-specific organization of gold nanoparticles by biomolecular templating. Chem Phys Chem 2:184–186
5. Davis SA, Patel HM, Mayes EL, Mendelson NH, Franco G, Mann S (1998) Brittle bacteria: A biomimetic approach to the formation of fibrous composite materials. Chem Mater 10:2516–2524

6. Zhou H, Fan T, Zhang D, Guo Q, Ogawa H (2007) Novel bacteria-templated sonochemical route for the in situ one-step synthesis of ZnS hollow nanostructures. Chem Mater 19:2144–2146
7. Favier F, Walter EC, Zach MP, Benter T, Penner RM (2001) Hydrogen sensors and switches from electrodeposited palladium mesowires arrays. Science 293:2227–2231
8. Huang J, Wang X, Wang ZL (2006) Controlled replication of butterfly wings for achieving tunable photonic properties. Nano Lett 6:2325–2331
9. Lee SW, Mao C, Flynn CE, Belcher AM (2002) Ordering of quantum dots using genetically engineered viruses. Science 296:892–895
10. Nakao H, Gad M, Sugiyama S, Otobe K, Ohtani T (2003) Transfer-printing of highly aligned DNA nanowires. J Am Chem Soc 125:7162–7163
11. Dunin-Borkowski RE, McCartney MR, Pósfai M, Frankel RB, Bazylinski DA, Buseck PR (2001) Off-axis electron holography of magnetotactic bacteria: magnetic microstructure of strains MV-1 and MS-1. Eur J Miner 13:671–684
12. Peidong Y, Franklin K (2002) Langmuir–Blodgett Assembly of One-Dimensional Nanostructures. Eur J Chem Phys Chem 3:503–506
13. Cook G, Timms PL, Göltner-Spickermann C (2003) Exact Replication of Biological Structures by Chemical Vapor Deposition of Silica. Angew Chem Int Ed 42:557–559
14. Knez M, Kadri A, Wege C, Gösele U, Jeske H, Nielsch K (2006) Atomic Layer Deposition on Biological Macromolecules. In: Metal Oxide Coating of Tobacco Mosaic Virus and Ferritin. Nano Lett 6:1172–1177
15. Hall SR, Shenton W, Engelhardt H, Mann S (2001) Site-Specific Organization of Gold Nanoparticles by Biomolecular Templating. Eur J Chem Phys Chem 2:184–186
16. Li Z, Chung SU, Nam JM, Ginger DS, Mirkin CA (2003) Living Templates for the Hierarchical Assembly of Gold Nanoparticles. Angew Chem Int Ed 42:2306–2309
17. Crespo-Biel O, Ravoo BJ, Reinhoudt DN, Huskens J (2006) Noncovalent nanoarchitectures on surfaces: from 2D to 3D nanostructures. J Mater Chem 16:3997–4021
18. Jiang C, Tsukruk VV (2006) Freestanding Nanostructures via Layer-by-Layer Assembly. Adv Mater 18:829–840
19. Pileni MP (2001) Nanocrystal Self-Assemblies: Fabrication and Collective Properties. J Phys Chem B 105:3358–3371
20. McCullough DH, Regen SL (2004) Don't forget Langmuir–Blodgett films. Chem Commun 2787–2791
21. Favier F, Walter EC, Zach MP, Benter T, Penner RM (2001) Hydrogen Sensors and Switches from Electrodeposited Palladium Mesowire Arrays. Science 293:2227–2231
22. Huang J, Wang X, Wang ZL (2006) Controlled Replication of Butterfly Wings for Achieving Tunable Photonic Properties. Nano Lett 6:2325–2331
23. Lee SW, Mao C, Flynn CE, Belcher AM (2002) Ordering of Quantum Dots Using Genetically Engineered Viruses. Science 296:892–895
24. Flynn CE, Lee SW, Peelle BR, Belcher AM (2003) Viruses as vehicles for growth, organization and assembly of materials. Acta Mater 51:5867-5880

Nanoparticles

Synonyms

Nanocrystals; Nanoclusters; Clusters

Definition

A *Nanoparticle* is generally defined as a particle whose diameters are between 1 to 100 nm.
It does not make any distinction regardless of the material. It can be metals, metal compounds, organic compounds, or polymers.

Cross References

► Nanoparticle Synthesis in Microreactors

Nanoparticle Synthesis in Microreactors

HIROYUKI NAKAMURA
Nanotechnology Research Institute, National Institute of Advanced Industrial Science and Technology (AIST), Tosu, Japan
nakamura-hiroyuki@aist.go.jp

N

Synonyms

Nanocrystals; Nanoclusters; Clusters

Definition

A ►nanoparticle is generally defined as a particle whose diameter is between 1 and 100 nm. No distinction is made according to the material: nanoparticles can be metals, metal compounds, organic compounds, and polymers. A ►composite nanoparticle is a nanoparticle which has a composite structure, including core-shell structure, onion-like structure, or gladiate composition.

Overview

Nanoparticle Properties and Applications

►Nanoparticles are generally defined as particles with diameters ranging from 1 to 100 nm. Recently, synthesis methods for nanoparticles have been rapidly developed. Nanoparticles are expected to find applications in various fields, i. e., biology, electronics, optics, informatics, and environmental engineering, as tags for biomolecules, quantum transistors, LEDs, super mass storage media, and

electrodes for wet-type solar cells [1]. Nanoparticles often exhibit unique properties, such as superparamagnetism in magnetic particles, surface plasmon shift in metallic particles, and quantum size effects in semiconductor particles. In particular, the quantum size effect for *semiconductor nanoparticles* with a particle radius of less than the Bohr radius (in most cases, less than 5 nm), contributes to the ability to control their band gap energy, and this is expected to be relevant for many of the unique applications listed above.

Most of the features listed above are affected by particle size. Therefore, in many cases, it is necessary to control a homogeneous particle size to fully utilize particles' unique and pre-eminent properties. Moreover, tuning particle size often enables tuning of particle properties. Some efforts have been made to classify nanoparticles of wide particle size distribution; however, it is still difficult to achieve high efficiency together with high yield. Furthermore, other properties such as shape and crystallinity can often affect nanoparticle properties and direct control of these properties is also required. Therefore, much effort has been made to control these nanoparticle properties.

As will be described in the following sections, property (size and size distribution, morphology, crystallinity, and so on) control implies precise process control, i. e., control of reaction conditions. Here, a microreactor is a useful tool that can control reaction conditions flexibly and accurately. Furthermore, a microreactor can be an easy setup on-line reaction analyzer, in particular allowing in situ observation of article properties, for example optical spectroscopy.

This article introduces some applications of microreactors for nanoparticle preparation and growth analysis.

Nanoparticle Synthesis Method

The methodology of particle synthesis can be categorized into three phases: gas-, liquid-, and solid-phase methods. In order to control the properties of nanoparticles, it is necessary to precisely control the synthesis process. The *colloidal process*, in which solvents and surfactants are of great help in preventing particle aggregation and deposition on the wall, is the most reported for nanoparticle synthesis in a microreactor. This method is also one of the most utilized methods for nanoparticle synthesis that allows control of particle size, shape, and even crystal structure and crystallinity by controlling particle ► nucleation and growth.

Generally, particle size control by the colloidal method requires nucleation and growth control. Furthermore, aggregation control is also important. Nucleation is considered to be affected by the free energies of nuclei (affected by properties of nuclei, such as size, structure, morphology, chemical bonding strength, surface properties, etc.), and nucleation kinetics (which is also affected by attachment and collision frequency of reaction species, dissolution rate of embryos (clusters), etc.). However, in the current state of understanding, the mechanism of nucleation is still in a "black box" and is hardly well controlled.

Even so, there is a classic but still often utilized model that explains nucleation with a balance between surface free energy and volume free energy. When a small particle is generated from solution, its total free energy change (ΔG) can be expressed as the sum of surface free energy change (ΔG_s) and volume free energy change (ΔGv):

$$\Delta G = \Delta G_s + \Delta G_v = 4\pi r^2 \gamma + \frac{4}{3}\pi r^3 \Delta g_v \qquad (1)$$

Here, r is the particle radius, γ is the surface energy of particles, and Δg_v is specific volume energy change. From this formula, it can be understood that the solubility of nuclei depends on particle size and they cannot exist stably in a solution when their size is less than the critical size, whereas they are stable when their size exceeds it. The particles of critical size are generally called critical nuclei. Nucleation rate (J) can be determined by saturation ratio as shown in the following formula:

$$J = J_0 \exp\left[-16\gamma^3 {V_s}^2 / 3k^3 T^3 (\ln S)^2\right] \qquad (2)$$

where J_0 is the nucleation constant, γ is the surface energy, V_s is the volume of a monomer (precursor), k is the Boltzmann constant, T is absolute temperature, and S is the degree of supersaturation, i. e., $(C - C_s)/C_s$ (where C is the concentration of monomer and C_s the saturating concentration of monomer).

Particle growth is more studied than nucleation and some growth kinetic models such as the surface reaction-limited model, diffusion-limited model, and Ostwald ripening model have been proposed, and their growth kinetics can often be well explained solely or by a combination of some kinetic models. Shape and size distribution of the particles are often influenced by kinetics. For example, diffusion-limited growth kinetics gives a larger growth rate for smaller particles and can reduce the coefficient of variation (CV) of particle size distribution while particles are growing (when diffusion layer thickness $> 2D$ (where D is particle diameter)). In contrast, Ostwald ripening usually increases the CV of *monodispersed* particles because smaller particles dissolve while larger particles grow.

Various processes are proposed for particle synthesis. Among them, for nanoparticle synthesis by the colloidal process, the nucleation-growth process (where one nuclei of particle grows into one particle), aggregation growth process, and confined growth process (e. g., particle growth in microemulsions) are often taken. The aggregation growth model is a rather new model proposed by Zukoski which explains the growth of monodispersed particles by a sol–gel method (such as SiO_2 and TiO_2), by balance of aggregation and repulsion of large and small particles. In the aggregation growth model, monodispersed particles can be obtained under diffusion-limited growth by attachment of small particles to a large particle. In this case, surface properties of small particles largely affect the growth kinetics. In addition, controlled aggregation gives anisotropic shaped particles similar to those reported for ZnO nano-rods. The confined space growth process has a rather long history. This process makes particles in a confined space such as a microemulsion. In this case, the collision frequency, stability, and shape of the emulsions affect the particle size distribution and shapes.

For the nucleation-growth model, narrow particle size distribution cannot be obtained solely by growth kinetics control: nucleation timing control is also very important. An ideal model for monodispersed particles using this process was proposed in the 1950s known as the La Mer model (shown schematically in Fig. 1). Under an assumption that particle aggregation can be ignored, shorter nucleation time can reduce fluctuation of particle growth duration, and thus reduce particle size distribution. In this case, during growth, it is very important to control the monomer concentration at a level not exceeding the critical nucleation concentration. On the other hand, under the same reaction yield, a larger number of particles can produce smaller particle size. Therefore, following this model, a rapid increase in the concentration of the nucleation stage is necessary to obtain a larger number of nuclei as can be deduced from Eq. (2). Considering this, in order to obtain monodispersed nanoparticles (especially of small size) a rapid and precise chemical reaction control is required, in addition to prevention of particle aggregation. As a matter of fact, despite the reported large number of nanoparticle syntheses, many of them set the solution volume to a few tens of milliliters. This is because a larger solution volume makes it more difficult to uniformly control the reaction condition (Fig. 2). Even though the La Mer model has been considered as "ideal" for monodispersed particle synthesis, only a few materials including silver halide were said to follow this model for microparticles. Recently, however, fairly stable nanoparticles are reported to follow this model. In addition to efficient surfactant employment, possibly the high

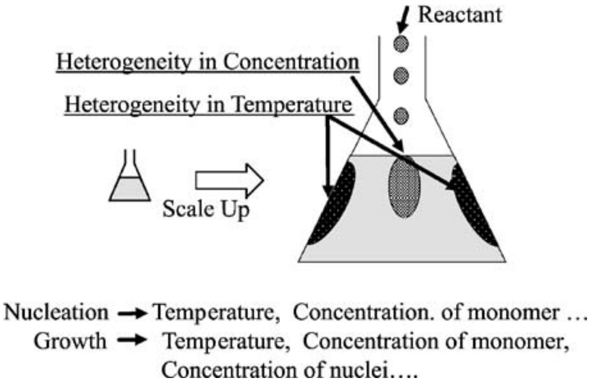

Nanoparticle Synthesis in Microreactors, Figure 1 La Mer diagram

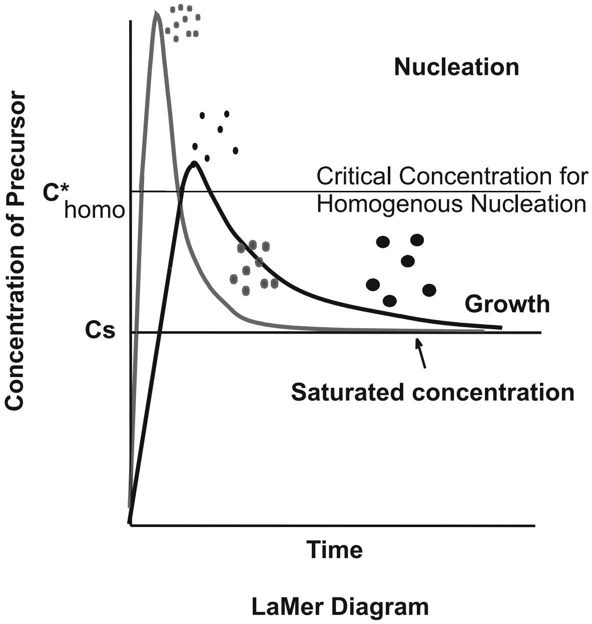

Nanoparticle Synthesis in Microreactors, Figure 2 Schematic image of condition fluctuations arising from scaling up

numeric concentration of particles was helpful in preventing free particle generation (second nucleation) during the reaction.

As such, for nanoparticle preparation, homogeneous and precise control of reaction conditions are important to obtain well-defined nanoparticles with controlled properties. To achieve this, appropriate choice of reaction process is important as well as appropriate choice of reaction systems including solvents and capping agents.

Nanoparticle Synthesis Using a Microreactor

The small channel size of a microreactor is of particular advantage for ►reaction condition control. The high sur-

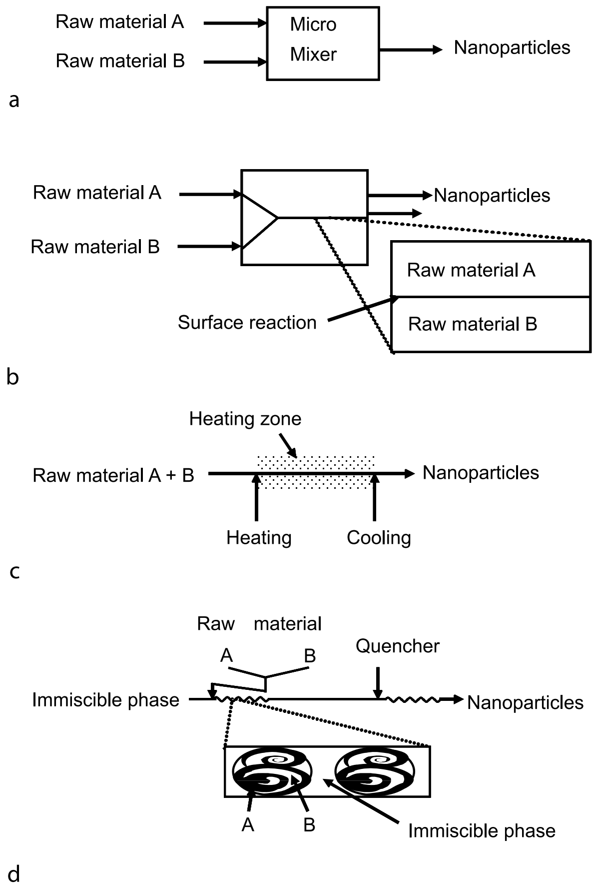

Nanoparticle Synthesis in Microreactors, Figure 3 Schematic images of representative microreactor designs for nanoparticle synthesis

face/volume ratio and small heat capacity of a microchannel can make rapid control of temperature possible in order to control the reaction. For example, a thermo-conductive simulation showed that 0.3 s was enough to raise the solution temperature from 20 to 300 °C, when the reactor was placed in a 300 °C heating media [2]. Additionally, another important unit operation, mixing, is also reported to be enhanced by a properly designed micromixer because the fine flow pattern control makes it possible to reduce the mutual diffusion length of the flows to be mixed rapidly. These rapid and prompt controls of the reaction can lead to the control of nucleation and growth kinetics in nanoparticle preparation as shown in the following.

Basic Methodology

Nanoparticle Synthesis Method Using a Microreactor

As mentioned above, microreactors are expected as small-size industrial reactors for nanoparticle synthesis. A number of reports on nanoparticle synthesis in a microreactor have been published following the reports of De Mello's group and Maeda's group in 2002. Among them, the most dominant and currently being employed in nanoparticle synthesis using a microreactor is the nucleation-growth model. Therefore, this section mainly focuses on this process.

Nanoparticle synthesis by a colloidal process has four steps which include nucleation, growth, ripening, and aggregation. To control the properties of particles, a precise control of these four processes is necessary. The nucleation process is often triggered by mixing raw material solution and precipitant, or by heating the mixed solution especially when the room temperature reaction rate is negligible. To control the nucleation state by this method it is necessary to control concentration and temperature of reactants within a short period of time (i. e., sufficiently shorter than nucleation time), preferably in a controlled fashion. However, nanoparticles of high crystallinity often require high temperature [1] where reaction rate is high. Therefore, for most batch reactions, scaling up makes control of the process difficult, because fluctuations easily arise due to high reaction rate. To effectively utilize this model, high reaction controllability is required which in turn can be provided by microreactors.

Taking into account the above discussions, several groups, including us, have studied nanoparticle synthesis in a microreactor, and the following three methods were reported in 2002 (Fig. 3a–c):

(a) Mixing-triggered reaction by applying rapid mixing provided by a micromixer [3].
(b) Interface reaction between two liquid phases that were stably generated in a microchannel [4].
(c) Temperature-triggered reaction by applying rapid heating in a microchannel [5].

Method (a) was reported by Edel et al. They rapidly mixed aqueous solutions of Na_2S and $Cd(NO_3)_2$ by a micromixer to obtain CdS nanoparticles, and showed that CdS nanoparticles with a similar quality to that of a batch reaction could be continuously produced. They also showed that the particle size distribution got wider when the flow rate was low, because of poor mixing quality which led to inhomogeneous concentration of reactant causing inhomogeneous nucleation and growth condition. This report is the first for a controlled nanoparticle synthesis showing the importance of mixing state for the mixing-triggered reaction.

Method (b) was reported by Wang et al. They used titanium isopropoxide cyclohexane solution (oil phase) and aqueous solution of alkali (water phase) as raw material solutions. These two solutions flowed from different inlets and were made to meet in a microreactor to react at the interface between these solutions. Here, the microreactor

Temp.: 300°C, Excitation wave length: 360nm

Flow rate (μL/min)	750	500	250	200	150	100	50	20	10
Reaction time(s)	1.9	2.8	5.6	7	9.3	14	28	70	140
Average size (nm)	2.0	2.2	2.4	2.9	3.1	3.4	3.7	4.1	4.5
PL wave length (nm)	516	532	542	563	572	584	598	616	630

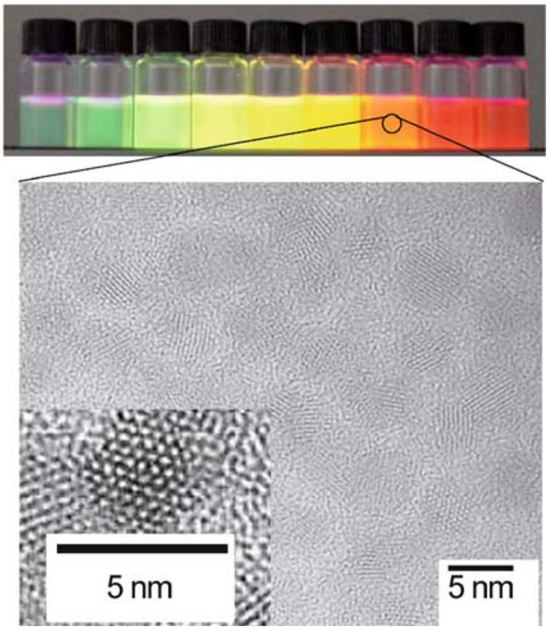

Nanoparticle Synthesis in Microreactors, Figure 4 Size and luminescence wavelength control of CdSe nanoparticles by a microreactor

was mainly used to obtain a stable interface for nanoparticle generation. It was reported that a thin mixed phase (∼1 nm) existed in the oil–water interface where the reaction mainly occurred. In this case, they utilized easily hydrolyzable titanium alkoxide as Ti source; however, the interface reaction made the reaction condition sufficiently slow. Here, they focused on the reaction field control rather than the control of reaction time. By using this method, a continuous synthesis of anatase-type TiO_2 nanoparticles, whose reproducible production is difficult in a batch system, became possible.

Method (c) was performed by Nakamura et al. of the same group as Wang. They utilized high temperature controllability of the microreactor. Here, they previously mixed all reaction solutions (reaction at room temperature was negligible) and heated to the reaction temperature to initiate particle generation. In the temperature-triggered reaction, it was easily possible to stop the reaction by quenching the reaction solution. The reaction time can be tuned by controlling the reactor volume and flow rate in an easy and exact fashion, and it was possible to tune the product particle size very easily (Fig. 4). Furthermore, they introduced inert gas bubbles into the reactor to obtain narrow residential time distribution. They also showed that the reproducibility of the reaction, when they used the identical reaction solution, was extremely high (Fig. 5a, b) [2], showing reproducible nucleation and growth process. The high reproducibility of the nucleation process, in particular, is not easy for a batch reactor. The fairly high reproducibility was also found in optical properties (Fig. 5c) [2]. They used a commercial quartz capillary tube as a microreactor. The tube had thin walls (a few tens of micrometers) and had high heat conductivity, and fabrication of the microreactor was easy.

These three reports have succeeded in showing the possibility of nanoparticle synthesis using a microreactor. Especially, method (c) showed that a dimension of time, which is not easy to control, can be controlled by space, which is much easier to control, for nanoparticle synthesis.

On the other hand, a segmented reaction solution like the one in method (c) can produce eddies in the solution

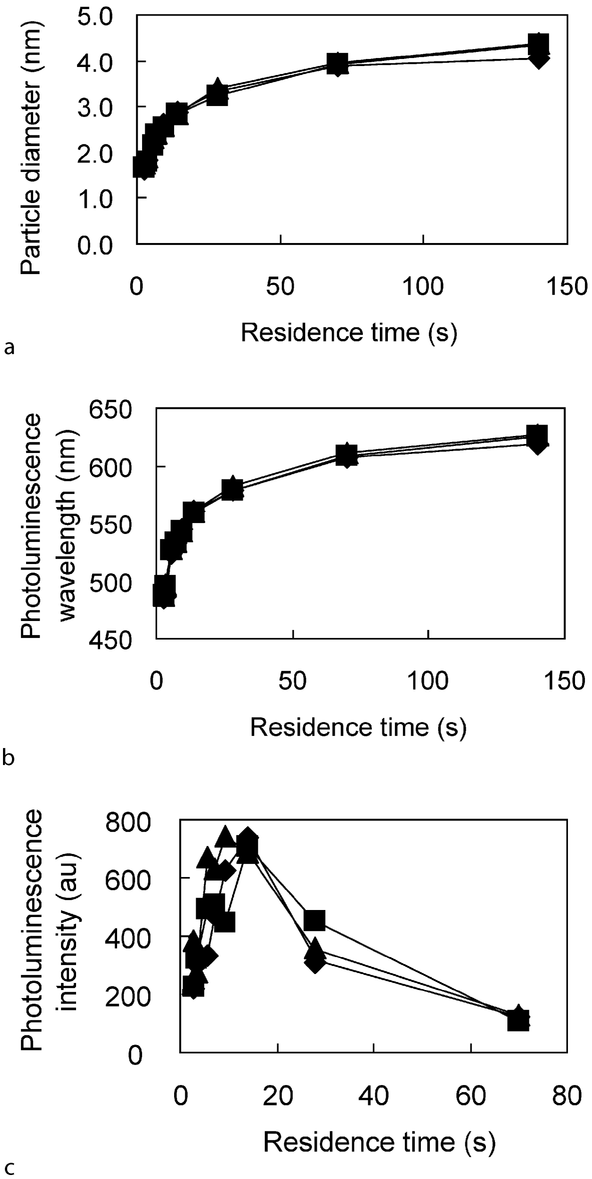

Nanoparticle Synthesis in Microreactors, Figure 5 Reproducibility of CdSe nanoparticle properties: (**a**) band edge peak location, (**b**) photoluminescence wavelength, (**c**) photoluminescence intensity

caused by the friction between channel wall and the solution. The eddies can stir the solution, mixing it rapidly at almost millisecond time scales.

In 2004, Shestopalov et al. [6] reported another method:

(d) Segmentation of reaction solution for rapid and sequential mixing of reaction solutions (Fig. 3d).

In this method, to stop the particle growth reaction, the authors rapidly mixed a capping agent (surfactant) which strongly coordinates the products and/or raw materials. (Diluting was also effective to quench the reaction.) This kind of method can control the growth time of the

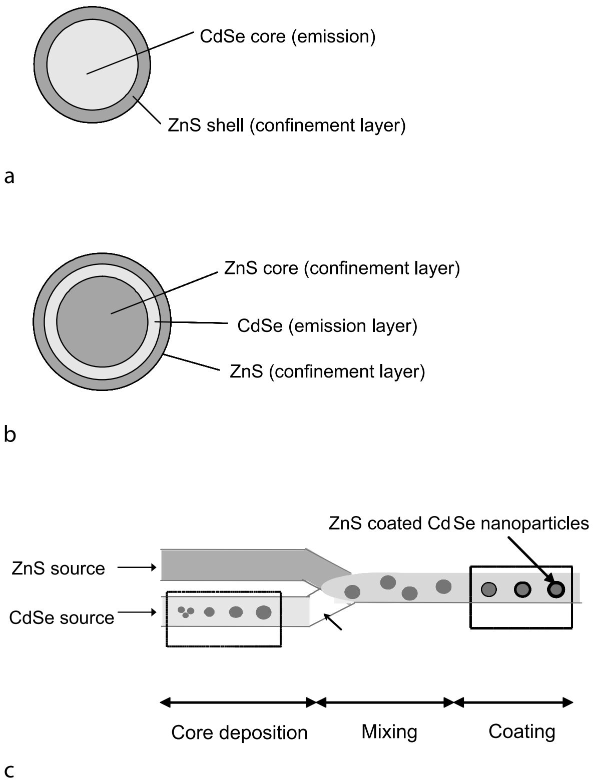

Nanoparticle Synthesis in Microreactors, Figure 6 Schematic images of composite nanoparticles (**a, b**), and sequential mixing process for CdSe/ZnS composite nanoparticle synthesis (**c**)

order of a millisecond. As mentioned above, to control nanoparticle synthesis, it is important to control the reaction homogeneously in a sufficiently short time. Therefore, this kind of method is expected to be an excellent way to control the reaction condition of nanoparticles especially where strict reaction condition control is required.

Many works have since reported the expansion of applicability and optimization of operation, but still most of the work can be roughly categorized into the four methods above. Several kinds of processes are utilized in microreactors for nanoparticle synthesis, including organometallic route, sol–gel, supercritical, reduction, and polyol methods. Moreover, a wide range of materials including metal chalcogenides, multinary compounds, metal oxides, metals, and organic pigments are synthesized, showing the wide applicability of this method for various nanoparticle syntheses.

Composite Nanoparticle Synthesis Using a Microreactor

Composite structure of nanoparticles largely affects their properties, as can be seen in semiconductor nanoparti-

cles [1]. Therefore, if it is possible to control the structure of composite nanoparticles, it could be possible to provide a wide range of particles with high-valued properties. From this point of view, some works have reported the composite structure control of nanoparticles. Here, the high reaction controllability of microreactors is expected to be helpful for composite structures and property control.

Photoluminescence (PL) intensity of CdSe nanoparticles is improved drastically by a wide bandgap material coating like ZnS (Fig. 6a) [1]. However, PL wavelength shifts with coating layer thickness, and too great a thickness of the coating layer induces interfacial defects between the core and shell to reduce PL intensity. Therefore, in order to improve PL intensity by maintaining monochromaticity of luminescence spectra, control of coating layer thickness by maintaining a homogeneous amount of coating is necessary. Demonstrating this, Wang et al. utilized a microreactor to synthesize ZnS-coated CdSe (CdSe/ZnS), and showed that it was possible to increase the intensity by maintaining narrow PL intensity [7] (Fig. 7). This method can control only one condition (i. e., temperature, reaction time) by fixing other conditions. Therefore, optimization of reaction condition can be easily done. Furthermore, this method can be utilized in a multi-step method by sequential addition of raw materials (Fig. 6c).

In our group, we found it was possible to synthesize a nanoparticle, in which a CdSe inner shell was sandwiched between ZnS core and outer shell (QDQW structure nanoparticle; Fig. 6b), by sequential deposition of the ZnS core, then the CdSe shell, and finally the ZnS outer shell. The particle had a high quantum yield with blue PL, and furthermore it was possible to control bandgap and PL wavelength by controlling CdSe shell thickness which was controlled by the quantum size effect.

These results show the ability of a microreactor to control the composite structure as well as the size of nanoparticles. A segmentation flow was also reported for the synthesis of CdSe/CdS composite nanoparticles using a similar strategy [6].

Optimization and Analysis of Particle Growth Kinetics Using Microreactors

As described above, numerous kinds of nanoparticles and composite nanoparticles are being developed, and these require optimization of synthesis conditions. Actually, numerous reports on nanoparticle synthesis using microreactors discussed reaction condition optimization or its possibilities. Furthermore, analysis of nucleation and growth kinetics will be helpful for deeper understanding of the particle generation and further development or alterations of the synthesis method. The above-mentioned high reaction condition controllability and reproducibility of microreactors will benefit quick reaction analysis. For example, the flexible reaction time tuneability of microreactors can be used for particle growth analysis [2]. By this method, as shown in Fig. 8, CdSe nanocrystal synthesis was confirmed, and the growth kinetics fit a diffusion-limited growth formula

$$\mathrm{d}r/\mathrm{d}t = DV_\mathrm{m}\,(1/r + 1/d)\,(C_\mathrm{b} - C_\mathrm{e})$$

where D is the diffusion coefficient of the monomer, V_m is the molar volume of the monomer, r is the particle diameter, d is the thickness of the diffusion layer, C_b is the bulk concentration of the monomer, and C_e is the equilibrium concentration of the monomer at the particle surface.

It is worth mentioning that all of the sample for data shown in Fig. 8 was obtained in a 1-day experiment, and this plainly shows the advantage of a microreactor as a kinetics analyzer. Moreover, it was shown that synthesis conditions affect the particle number, which would be induced by nucleation frequency.

Additionally, on-line analysis can enhance the speed of reaction analysis. Therefore, reaction condition optimizations by microreactors are effective. For example, in a report in 2003, Chan et al. mixed previously heated Cd and Se source in a micromixer, and stopped the reaction by cooling and diluting. The properties of the product were determined on-line using a spectrometer, showing that online monitoring of the product properties was possible. Similarly, the on-line monitoring of properties of nanoparticles whose morphology offers optical properties (e. g., semiconductors) is straightforward. Other techniques like IR and Raman spectroscopy can be used on-line, and it is expected that these on-line methods will enhance new materials and process development for nanoparticle synthesis by microreactors.

N

Problems in Nanoparticle Synthesis by Microreactors and their Solutions

The realization of industrial production of nanoparticles by microreactors still faces some problems, and several papers point out these problems and possible approaches to solve them.

One of the main problems is the scale of the reaction system. So far, with some exceptions, production rates of reactors are less than 1 ml/min. Therefore, the industrial production of nanoparticles requires piling up of the reactors or further optimization of the reactor design by maintaining the above outstanding features. For organic pigment nanoparticles, a pilot plant targeting 100 t/year has

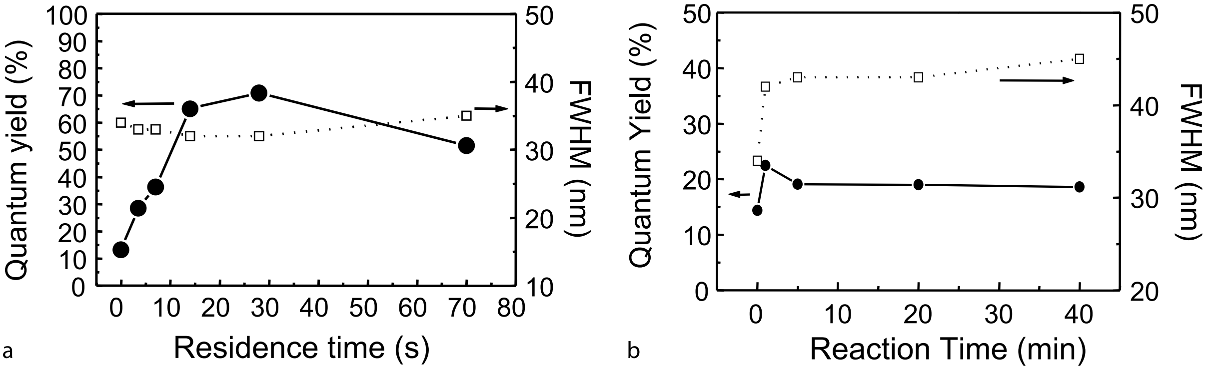

Nanoparticle Synthesis in Microreactors, Figure 7 Effect of coating time on quantum yield and full width at half maximum of fluorescence spectra of CdSe/ZnS composite particles: (**a**) microreactor; (**b**) batch reactor

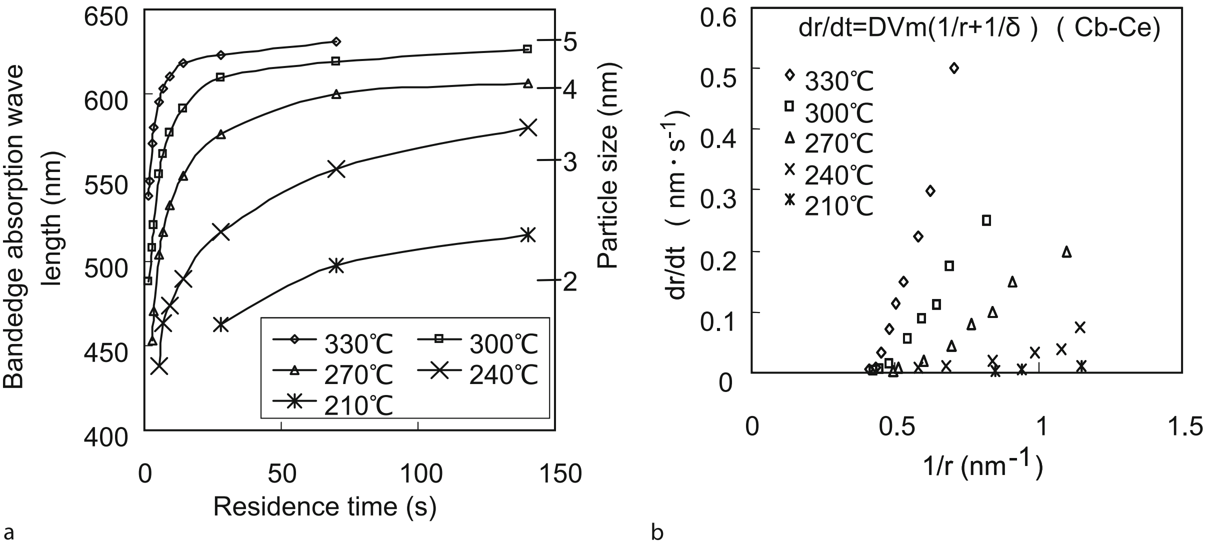

Nanoparticle Synthesis in Microreactors, Figure 8 Particle growth kinetics analysis of CdSe nanoparticles: (**a**) average particle size development; (**b**) fitting result to diffusion growth model

been launched, showing the great potential of microreactors as industrial reactors for nanoparticle synthesis.

Despite the productivity of the reactors, at least two problems are found: one is the residential time distribution and the other is depositions on the reactor wall. The effects of residential time distribution on the particle size distribution was analytically discussed for CdSe nanoparticle synthesis by Krishnadasan et al. [8] As mentioned above, the growth mode of CdSe is diffusion limited, and normally gives a narrower particle size distribution for longer particle growth time (as far as particle growth is limited by monomer diffusion). However, in experiments, higher flow rate (i. e., shorter reaction time) gave a narrow particle size distribution. Krishnadasan et al. explained that the phenomenon is caused by the enlargement of absolute reaction time distribution. They also mentioned that mixing by transverse diffusion requires a long time for nanoparticles, because their size, which is much larger than small molecules, caused a reduction of diffusion rate, and was not helpful in equalizing their residential time by transverse diffusion for a practical size (i. e., of the order of 100 μm). On the other hand, a similar reaction system with higher temperature and higher flow rate gave a narrower particle size distribution [2, 5]. In this case, the absolute time was much shorter than in the work of Krishnadasan et al., and therefore the particle growth followed the batch system, thus showing that the particle growth kinetics as well as residential time distribution determined the particle size distribution. To solve the problem, a segmentation, achieved by introducing immiscible inert gas

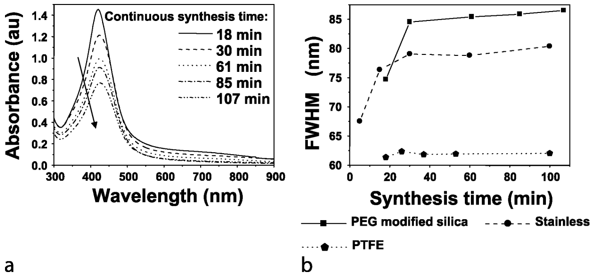

Nanoparticle Synthesis in Microreactors, Figure 9 (**a**) UV–visible spectra of silver nanoparticle colloids at different synthesis times when a polyethylene glycol-modified silica tube was used. (**b**) Plots of corresponding full width at half maximum of surface plasmon peak of silver nanoparticles synthesized in microreactors with different wall surfaces

or liquid into the flow system, was effective [5, 6]. This method is widely applicable for many reaction systems and temperatures.

As mentioned above, precise reaction control can be realized by the high reactor surface area to reactor volume ratio of the microchannel. On the other hand, it can also cause one of the other critical problems, that is, deposition of reactants on the reactor channel wall. Obviously, a large amount of deposition will lead to clogging or uncontrollable flow in the reactor channel. However, even a small amount of deposition, which does not affect the flow pattern, can give a larger particle size distribution as He et al. reported [9]. In our experience, this is a general phenomenon and is presumed to be caused by longer residence time by adsorption deposition, or aggregation of clusters on the surface.

Deposition has serious effects in practical applications. To solve this problem, at this point, we can only suggest to *choose proper channel wall material for the reaction system*. The material can be chosen based on affinity balance between particle–particle, particle–solvent, and solvent–wall. Beside the physical or physicochemical affinities, chemical affinities such as solidification by surface reaction between adsorbed ions and dissolved ions can also induce deposition. If the affinity between particle and wall is smaller than that between solvent and wall, particles are expected not to be deposited on the wall. Therefore, proper choice of reactor wall or surface modification can be good options (Fig. 9) [9]. Also, proper choice of surfactants is also helpful. However, as far as our knowledge is concerned, it is very difficult to obtain general solutions to the deposition problem, and a good combination of reactor material, reaction system, and operation conditions is required.

Takagi et al. [10] reported a plausible method. They applied sheath flow, where raw material was dissolved only in the inner flow, and synthesized TiO_2 nanoparticles by a sol-gel method. The outer flow can be regarded as "liquid wall" and can prevent the produced particles from attaching to the wall. In the report by Shestopalov et al. on a segmented flow reactor, they mentioned that almost no deposition was found in the reactor [6]. These reports suggest that reactor design, other than the choice of reaction system and wall surface, can also solve the problem, although intrinsic resolution for long stable operation may still require the proper reaction system.

Key Research Findings

Generally, nanocrystal synthesis consists of four processes: nucleation, growth, ripening, and aggregation. To control nanocrystal properties such as particle size and distribution, it is necessary to control these processes. Precise reaction control can be realized by utilizing a microreactor. Owing to the small size dimension, this useful tool can achieve control of temperature and mixing rate in a sufficient time scale (i. e., of the order of 100 ms) as shown by the reported results. Therefore, a microreactor can tune nanocrystal properties by ensuring precise control of reaction parameters such as temperature and reaction time. Furthermore, the high controllability can help one achieve a homogeneous structure of composite particles and at the same time tune their structure. The reproducible result for particle size control also show that the nucleation and growth processes can be well controlled for the said processes. Based on the attained high reaction controllability and reproducibility by the microreactor, it is suggested that this convenient tool can be applied to particle growth analysis. Especially for systems that can combine with online monitoring, e. g., semiconductor nanoparticles which show quantum size effects, the tool could enhance the development of the synthesis process by rapid optimization and analysis. Presently, microreactor-based methods are applied to many reaction systems including aqueous methods, organometallic route, sol–gel process, hydrothermal process, and polyol process, and to the synthesis of various materials such as metals and their oxides or chalcogenides, and organic pigments.

There are some problems encountered such as residential time distribution and deposition on the wall. The residential time distribution can induce widening of the particle size distribution. This can be solved by proper design of the reactor or designing the operation such that the reaction time is reduced or by introducing segmented flow. The deposition of reactant on the wall can cause critical problems because it can induce clogging, uncontrollable flow, particle size distribution widening, and reduction of product yields. To solve these problems, proper choice of reaction systems and wall materials is necessary. Furthermore,

sheath flow and segmented flow have been reported to be considerably effective in preventing deposition.

Future Directions for Research

As discussed, precise and reproducible reaction control can be realized by using microreactors for nanoparticle synthesis. Continuous production of nanoparticles by microreactors can be made possible by maintaining their morphology and structure which consequently determine the nanoparticle properties. Therefore, microreactors can be expected to be on-site on-demand production reactors, i. e., small but flexible in operation condition, with the capability to produce the required material properties in the required amount. It should be possible to pile up or design microreactors for small-scale industry without losing the preciseness and flexibility in control of reaction conditions. For nanoparticles of high value and with properties dependent on their morphology and structure, it would be possible to establish a flexible, on-demand production process, that is, tuning properties and providing product as required. Particularly for semiconductor nanoparticles, their properties can undergo slight fluctuations in the experimental conditions including the quality of raw materials or contaminations. Therefore, equipments that tune the properties by monitoring and optimizing the properties of the products are expected, as in the *flexible on-demand process*.

By using microreactors, it is also possible to utilize an easy set-up for condition optimization and particle growth analysis. Therefore, it would also be possible to make experimental tools capable of optimization of various kinds of new nanoparticle syntheses. The small size of the reactor will make it possible to set up a combinatorial system, which would greatly enhance the methodology development speed. Therefore, this kind of reactor can also be utilized for better understanding of particle generations, for example nucleation. This kind of basic research would be helpful for further development of nanoparticle science. Such a highly efficient analyzer which can be used to realize a process design will play a major role in nanoparticle industries. After the achievement of scale-up to the industrial level, it would be possible to convey the optimized conditions directly to industry. Furthermore, these applications and basic research will help to find effective ways for nanoparticle R&D; for example, designing and producing optimum morphology and structure of nanoparticles and composite nanoparticles to control their properties such as electronic and magnetic properties, finding a reliable condition of raw material synthesis for reproducible production, and reliable and effective surface modification of nanoparticles.

Cross References

► Droplet Microreactors
► Temperature Control in Microfluidic Systems
► Microfluidic Mixing
► Droplet Microreactors
► Nanoparticles
► Nanoparticle Synthesis in Microreactors
► Quantum Dots

References

1. Schmid G (2004) Nanoparticles: From Theory to Application. Wiley-VCH, Weinheim
2. Nakamura H, Tashiro A, Yamaguchi Y, Miyazaki M, Watari T, Shimizu H, Maeda H (2004) Application of a microfluidic reaction system for CdSe nanocrystal synthesis: their growth kinetics and photoluminescence analysis. Lab Chip 4:237–240
3. Edel JB, Fortt R, deMello JC, deMello AJ (2002) Microfluidic routes to the controlled production of nanoparticles. Chem Comm 2002:1136–1137
4. Wang H, Nakamura H, Uehara M, Miyazaki M, Maeda H (2002) Synthesis of titania particles utilizing the insoluble phase interface in a microchannel reactor. Chem Comm 2002:1462–1463
5. Nakamura H, Yamaguchi Y, Miyazaki M, Maeda H, Uehara M, Mulvaney P (2002) Synthesis of CdSe nanocrystals in a microflow-reactor. Chem Comm 2002:2844–2845
6. Shestopalov I, Tice JD, Ismagilov RF (2004) Multi-step synthesis of nanoparticles performed on millisecond time scale in a microfluidic droplet-based system. Lab Chip 4:316–321
7. Wang H, Nakamura H, Uehara M, Yamaguchi Y, Miyazaki M, Maeda H(2005) Highly luminescent CdSe/ZnS nanocrystals synthesized by a single molecular ZnS source in a microfluidic reactor. Adv Funct Mater 15:603–608
8. Krishnadasan S, Tovilla J, Vilar R, deMello AJ, deMello JC (2004) On-line analysis of CdSe nanoparticle formation in a continuous flow chip-based microreactor. J Mater Chem 14:2655–2660
9. He S, Kohira T, Uehara M, Kitamura T, Nakamura H, Miyazaki M, Maeda H (2005) Effects of Interior Wall on Continuous Synthesis of Silver Nanoparticles in Micro-Capillary Reactor. Chem Lett 34:748-749
10. Takagi M, Maki T, Miyahara M, Mae K (2004) Production of titania nanoparticles by using a new microreactor assembled with same axle dual pipe. Chem Eng J 102:269–276

Nanophotonic Characterization in a Microfluidic System

► Nanoscale Optofluidic Characterization Techniques

Nanopore Conductance

► Electrokinetic Flow and Ion Transport in Nanochannels

Nanopore Fabrication

► Nanochannel Fabrication

Nanopores

► Nanochannel Fabrication

Nanorods

► Fabrication of Self-Assembled Catalytic Nanostructures

Nanoscale Biosensors

DONGQING LI, GUOQING HU
Department of Mechanical Engineering, Vanderbilt University, Nashville, TN, USA
Dongqing.li@vanderbilt.edu

Synonyms

Nanosensors; Nanochips; Nanoarrays; Nanofluidics

Definition

Sensors with immobilized bioreceptor probes selective for target analyte molecules are called biosensors. Next-generation biosensor platforms will require significant improvements in sensitivity, specificity, and throughput. The emergence of nanotechnology opens new horizons for biological diagnosis at single cell and molecule level. Because of the small dimension, nanoscale biosensors may overcome many drawbacks of the conventional biosensors and lead to a new future in molecular diagnostics, detecting proteins, DNA, and viruses with high sensitivity and selectivity. Nanoscale biosensors can function independently or be integrated into more complex systems, for example so-called microfluidic Lab-on-a-Chip devices, to provide point-of-care detection.

Overview

Based on the detection principle, the major nanoscale biosensors are classified into the following types: electrical nanobiosensors, optical nanobiosensors, and mechanical nanobiosensors. Comprehensive descriptions of nanoscale biosensors can be found in two recent reviews [1, 2].

Electrical Nanobiosensors

Nanomaterials, such as carbon nanotubes and semiconductor or polymer nanowires, can be functionalized with appropriate chemical or biological capture probes [3, 4]. A unique property of these materials is the very high surface-to-volume ratio. The chemical binding event on their surface causes a change of the conductance of the nanotube or nanowire and thus can be identified via electrical measurement. Electrical nanobiosensors are capable of realizing sensitive, label-free, and real-time detection of a wide range chemical and biological species.

Optical Nanobiosensors

These biosensors utilize the optical properties of lasers to monitor and quantify the interactions of biomolecules that occur on functionalized surfaces or in solutions. They are further subdivided into evanescent field-based devices [5], photonic crystal devices [6], and surface plasmon resonance devices [7].

Mechanical Nanobiosensors

These biosensors exploit mechanical effects, for example the resonant frequency of materials. Cantilever-based devices [8] and acoustic devices [9] are two types of widely used nanobiosensors. After binding of molecules to the detection surface, the amount of bound mass can be determined by observing changes in the resonant frequency of the oscillator or the piezoelectric crystal.

Cross References

► Nanofluidics in Carbon Nanotubes
► Pyroelectric Flow Sensors
► Nanoscale Biosensors
► Fluidic Nanosensors
► Mechanical Nanosensors
► Nanochannel Fabrication
► Impedimetric Biosensors for Nano- and Microfluidics

References

1. Jain KK (2005) Nanotechnology in clinical laboratory diagnostics. Clinica Chimica Acta 358:37–54
2. Erickson D, Mandal S, Yang AHJ, Cordovez B (2007) Nanobiosensors: Optofluidic, electrical and mechanical approaches to biomolecular detection at the nanoscale. Microfluid Nanofluid 4:33–52
3. Patolsky F, Zheng GF, Hayden O, Lakadamyali M, Zhuang XW, Lieber CM (2004) Electrical detection of single viruses. Proc Natl Acad Sci USA 101:14017–14022
4. Lieber CM, Wang ZL (2007) Functional nanowires. MRS Bull 32:99–108

N

5. Marazuela MD, Moreno-Bondi MC (2002) Fiber-optic biosensors - an overview. Anal Bioanal Chem 372:664–682
6. Skivesen N, Tetu A, Kristensen M, Kjems J, Frandsen LH, Borel PI (2007) Photonic-crystal waveguide biosensor. Opt Express 15:3169–3176
7. Karlsson R (2004) SPR for molecular interaction analysis: a review of emerging application areas. J Mol Recognit 17:151–161
8. Ilic B, Craighead HG, Krylov S, Senaratne W, Ober C, Neuzil P (2004) Attogram detection using nanoelectromechanical oscillators. J Appl Phys 95:3694–3703
9. Rabe J, Buttgenbach S, Schroderr J, Hauptmann P (2003) Monolithic miniaturized quartz microbalance array and its application to chemical sensor systems for liquids. IEEE Sens J 3:361-368

Nanoscale Optofluidic Characterization Techniques

Seung-Man Yang, Seung-Kon Lee,
Chul-Joon Heo, Jong-Min Lim, Se-Heon Kim,
Se Gyu Jang
National CRI Center for Integrated Optofluidic Systems and Department of Chemical and Biomolecular Engineering, Korea Advanced Institute of Science and Technology, Daejeon, Korea
smyang@kaist.ac.kr

Synonyms

Nanoscale optofluidic measurement; Nanophotonic characterization in a microfluidic system

Definition

Optofluidics refers to the complementary hybridization of photonics and fluidics. Optofluidic characterization is the analysis of a fluidic system by photonics, and vice versa. In particular, nanoscale optofluidic characterization is related to photonic phenomena based on the nanostructures. The photonic bandgap properties, surface plasmon resonance or surface-enhanced Raman scattering sensitively change with the refractive index of the surrounding fluid or the specific binding of chemicals and biomolecules on the nanostructures.

Overview

Recent advances in chemistry, biotechnology and materials science have generated an immense amount of biological and chemical information, which calls for the development of novel devices that can efficiently process the vast amount of information. An enormous amount of research has been directed toward the development of micro-total analysis systems (μ-TAS) that carry out ultra-high fidelity sensing and analysis much faster than previous devices for processing only infinitesimal amounts of chemicals and bioactive substances. A microfluidic device for precision transport and manipulation of femtoliter-scale materials is an ideal platform to put high-throughput μ-TAS to practical use. However, the current μ-TAS built on a fluidic-device platform employs conventional electrochemical and electronic detection tools, which are especially inferior to optical detection methods in terms of sensitivity and resolution. In addition, microfluidic device technology is limited to using photolithography to fabricate and integrate fluidic circuits. Although fabrication techniques have made great advances to materialize actuation parts such as microscale pumps, microvalves and complex channel geometries, the characterization system remains primitive and the system size is much larger than fluidic chips. Consequently, Lab-on-a-Chip technology such as μ-TAS that can synthesize, analyze, and refine substances with truly high efficiency is still in its early stages.

Optical systems have been widely used for high-speed communication, data processing and high-resolution sensors. However, today's optical systems are not nearly as flexible as electronic systems, and the fabrication of robust and durable optical devices has been a demanding issue for decades. The key idea to meet the increasingly important demands is the introduction of microscopic flows of liquids, i. e., microfluidic devices in the optical structures. Micro- and nano-fluidics have been used for the precise processing of extremely small amounts of liquids. These techniques perform various functions including the reconfiguration of functionality, the adjustment of properties and the transport of functional materials. In optofluidic devices, precise tuning of optical properties such as those of photonic band-gaps can be achieved by injecting liquids with different refractive indices through microfluidic channels.

At the nano-level scale, optofluidics is closely related to the nanostructures. For the dielectric materials, the photonic bandgap property can be generated by periodic nanostructures. Analogous to the X-ray diffraction phenomena in the atomic crystals, the interference of regularly diffracted light waves creates special reflection condition that can be described by Bragg's law. Bragg's reflection condition is sensitively changed by the refractive index, the lattice spacing, and the crystal structure of the materials. Each parameter can be modulated by swelling the nanostructures or filling solvents, as well as by physical adsorption or a chemical reaction of the analytes.

For metallic materials, surface plasmon resonance (SPR) and surface-enhanced Raman scattering (SERS) are the

most significant phenomena related to the nanostructures. At the interface of the dielectric and the metal, the intensity of the electromagnetic field is strongly amplified and localized by their structural characteristics. The SPR mode varies sensitively with a small refractive index change of the binding molecules. In addition, SERS enables the qualitative analysis of infinitesimal amounts of analytes. The Raman signal provides a fingerprint of the specific chemicals that originate from the chemical bonding and the molecular vibration of the analytes.

The relationship between nanostructures and light is the basis of nanophotonic characterization. High sensitivity in a nanophotonic characterization is adequate for single molecule detection without florescence labeling. Detection of a fluorescence signal requires highly sensitive detectors and signal processing units due to the weak signal intensity. Therefore, label-free indicates not only simplicity with sample preparation but also a great advantage for integrated analysis devices.

The objective of nanoscale optofluidic characterization is to combine different nanophotonics technologies with microfluidic devices, and thereby explore and develop photonic analysis techniques based on the microscopic flows of liquids and on nanophotonic properties. The optofluidic characterization techniques will be powerful new tools for a wide range of applications in optical information processing and the miniaturization of chemical and biological processes for synthesis, analysis, and recognition [1].

The optofluidic devices can be very effective in microscopic analysis just as typical optical equipment such as UV, IR, Raman, visible light spectrometers or fluorescence spectrometers are used to analyze molecular information. Therefore, optofluidic systems are more appropriate for constructing μ-TAS and have much greater levels of high-fidelity analytic resolution and sensitivity compared to existing microfluidic devices using electrical, electrochemical and thermal detection methods. Moreover, the use of fluidics provides an order of magnitude increase in the achievable refractive index modulation of the optical components compared with the application of traditional electric, acoustic and mechanical strain fields, as manipulations of the rates of the flows and the compositions of the liquids will tune the characteristics of these photonic systems in real time. These fluidically adjustable and unique properties enable flexible fine-tuning and even dynamic reconfiguration of the optical circuits. The most important technological advantage of this new optofluidic device is that it has unique features that individual devices cannot demonstrate.

Basic Methodoloy

Photonic Band-Gap Property

A photonic crystal is the special material whose refractive index is periodically modulated on a length scale of visible light. With structural periodicity, the propagation properties of photons can be controlled by changing the design of the photonic crystals intentionally. In general, wave propagation is affected by structures when the light enters the materials. Inside of the periodic photonic crystals, the photons scatter coherently at every interface of the two different refractive index regions. Consequently, the behavior of the lightwaves depends on the propagation direction through the photonic crystal. Photons of certain frequencies and directions can be forbidden in a photonic crystal. If the photons of certain energy bands are forbidden regardless of their propagation direction, they are known as photonic band-gaps (PBGs). Recently, photonic crystals were incorporated with microfluidic chips for optofluidic characterizations of chemical and biological analytes. As the band-gap properties of photonic crystals are changed sensitively by various control variables, band-gap engineering enables an effective optofluidic characterization.

The study of photonic crystals rests on the foundation of electromagnetics and solid-state physics. Analogous to the propagation of electrons in a periodic crystal potential described by the Schrödinger equation, the propagation of light is described by the well-known Maxwell equation under the periodic boundary condition. The master equation for a harmonic mode in photonic crystal can be derived from four macroscopic Maxwell equations with assumptions for simplification [2].

$$\nabla \times \left(\frac{1}{\varepsilon(\mathrm{r})} \nabla \times H(\mathrm{r}) \right) = \left(\frac{\omega}{c} \right)^2 H(\mathrm{r}) \tag{1}$$

Solving the master equation is sufficient to obtain an electromagnetic field at a certain position. For a multidimensional calculation of various symmetries, a numerical method should be applied. There are three methods to calculate photonic band structures; the plane wave expansion method (PWM), Green's function expansion and the finite difference time domain (FDTD) method.

Controlling Parameters in Photonic Crystals

In order to develop an optofluidic characterization technique based on a photonic crystal, parameters for band-gap engineering must be established.

- *Dimensionality:* According to the periodicity of dielectric materials along one or more axes, the dimension of

N

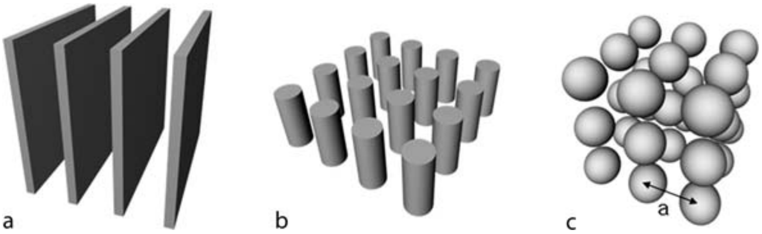

Nanoscale Optofluidic Characterization Techniques, Figure 1 Multidimensional photonic crystal structures with dielectric constants that vary along the x, y and z axes. (**a**) 1D, (**b**) 2D and (**c**) 3D photonic crystal structures

photonic crystal is determined. This defines the working direction of photonic crystals to the incident lightwaves. Figure 1 shows examples of multidimensional photonic crystal structures whose refractive indices vary as a periodic function in the length scale.

- *Symmetry:* Analogous to the crystalline lattice of atomic structures, photonic nanostructures may have different symmetries. According to the structural symmetry of photonic crystals, different scattering symmetries are caused, leading to a variation of the photonic band-gap properties.
- *Lattice parameter:* The length scale of a photonic crystal is closely related to the lattice constant of scattering building blocks. The working range of the photonic crystal in the wavelength domain is proportional to the lattice parameter (a).
- *Effective refractive index:* The relative amount of one scattering material to another is known as the filling fraction. The effective refractive index (n_{eff}), which is calculated as the square root of the average dielectric constant, varies with changes in the filling fraction. The working range of the photonic crystal also depends on n_{eff}.
- *Refractive index contrast:* the scattering strength of photonic crystal structures depends on a value known as the refractive index contrast. The refractive index contrast is defined by the ratio of the materials composing the structures: the high dielectric constant to the low dielectric constant. As the refractive index contrast increases, fewer dielectric layers are needed to achieve photonic band-gap properties.

Therefore, change in these factors cause a band-gap modulation in photonic crystals, which can be characterized optically.
Surface Enhanced Raman Scattering

Raman Scattering

Raman scattering, or the *Raman effect*, was first demonstrated by Indian physicist Chandrasekhara Venkata Raman and his colleagues in 1928 [3]. It is the inelastic scattering that occurs when light is scattered from an atom or molecule. In contrast to elastic Rayleigh scattering, incident photons are inelastically scattered from a molecule and shifted in frequency by the energy of its characteristic molecular vibration and rotation. The inelastic interaction of incident light with a molecule in its vibrational or rotational ground state induces a red-shifted Stokes Raman spectrum, and a molecule in a vibrational or rotational ground state absorbs energy from the incident light. On the other hand, when the incident light interact with a molecule in its vibrational or rotational excited state, a blue-shifted anti-Stokes Raman spectrum is produced and molecules in vibrational or rotational excited state lose energy to incident light. As the absolute value of the frequency shift does not depend on the process type and because it is only dependent on the number of molecules that occupy different vibrational or rotational states, the Raman spectrum is symmetric relative to the Rayleigh scattering band. The relative intensity of Raman scatterings in the Stokes and anti-Stokes Raman spectra can be determined using a Boltzman distribution; in most cases, Stokes scattering related to lower energy levels is stronger than anti-Stokes scattering. Raman scattering interacts with the vibrational and rotational levels of the molecule, which depend on atomic species and their bond arrangements and strengths in a specific molecule. Therefore, a Raman spectrum can provide a structural *fingerprint* of the target molecule.

Surface Enhanced Raman Scattering (SERS)

However, Raman spectrum shows weak signal intensity compared with conventional Rayleigh scattering and fluorescence, which is a widely used technique for molecular detection. Raman scattering cross-sections imply that the scattering intensities are between 10^{-31} and 10^{-29} cm/molecule (for comparison, the maximum fluorescence cross-section is 10^{-16} cm^2/molecule). Resonance Raman scattering (RRS) can increase the cross-section when a molecule is excited by a laser with a resonance frequency. However, RSS still has an insufficient

cross-section compared with other optical characterization techniques; additionally, it shows strong fluorescence, which interrupts the observation of Raman scattering. In 1974, Fleischman and his colleges observed the surface-enhancing effect of Raman scattering at a roughened silver electrode, and found that the signal of Raman scattering can be dramatically enhanced by *Surface-enhanced Raman spectroscopy* (SERS) [4]. After this historical discovery, Van Duyne [5], Creighton [6] and their coworkers pointed out that the intensification of the effective Raman cross-section was far in excess of the increased surface effect. Moskovits [7] proposed that the huge increase in the Raman cross-section was a result of electromagnetic field enhancement.

The Electromagnetic Theory of SERS

Raman enhancement by SERS is mainly attributed to an electromagnetic (EM) field enhancement via localized optical fields of the metallic nanostructures that are related to plasmon resonance excitation. The increase of the cross-section with contact between the metal nanostructure and a molecule induces an additional enhancement. Without enhancement by the electrical resonance between incident light and molecules, the total Stokes–Raman signal $P^{RS}(\nu_S)$ is proportional to the number of molecules in the scattering volume N, the Raman cross-section without surface enhancement σ^R_{free}, and the excitation laser intensity $I(\nu_L)$.

$$P^{RS}(\nu_S) = N\sigma^R_{free} I(\nu_L) \tag{2}$$

For a Stokes–Raman signal enhanced by SERS, the above equation should be modified to consider the electromagnetic enhancement effects of metal nanostructures on Raman scattering.

$$P^{SERS}(\nu_S) = N'\sigma^R_{ads} \,|A(\nu_L)|^2 \,|A(\nu_S)|^2 \, I(\nu_L) \tag{3}$$

Here, N' is the number of molecules involved in the SERS process and σ^R_{ads} is the increased cross-section of the enhanced Raman process of the adsorbed molecule. For a given excitation laser and Raman scattered field, $A(\nu L)$ and $A(\nu S)$ are the enhancement factors determined by the intensity ratio of the incident field and the scattered field at a position [8].

Although the first reported signal enhancement in SERS was a factor of $10^3 - 10^5$, a further enhancement up to 10^9 becomes possible, which originates from the effect of shape and geometry together with chemical resonant mode (although why is not yet fully understood). Now, these additional factors are of practical importance because Raman signal is basically so weak as to be covered by unwanted signals and noises. Therefore, the design of SERS active substrates, the selection of suitable chemical compositions and the development of integrated SERS systems are the most important issues in today's Raman scattering research.

Key Research Findings

Bragg's Law for Simple Optofluidic Characterization of Photonic Crystals

Although the band-gap properties of photonic crystals are soluble according to Maxwell equations, classical Bragg's law provides sufficient approximations. If only one-dimensional periodicity is considered, Bragg's law provides a simplified prediction of the peak position in terms of the effective refractive index, periodicity and incident angle.

$$\lambda_{Bragg} = 2n_{eff} d \sin\phi \tag{4}$$

Here, the peak wavelength of reflected light is proportional to the effective refractive index n, structural period d and incident angle of a given light source, $\sin\phi$.

The effective refractive index of composite materials can be represented as follows:

$$n_{eff} = \sqrt{f_a n_a^2 + (1 - f_a) n_b^2} \tag{5}$$

This shows that the photonic bandgap shifts with a change in the refractive indexes of materials or the interparticle distance. Therefore, replacement of the surrounding media and swelling of the colloidal lattice is expressed by changes in the reflection color. Given that all liquid fluids have a higher refractive index compared to air, the bandgap position shifts to a longer wavelength when the fluid flows through the built-in colloidal crystal part of microfluidic chips. This means that small changes in the refractive index caused by chemicals or biomaterials can be detected by a shift in the reflection peak position. Variation of the lattice parameter under specific chemical or physical conditions can also be estimated by a simple Bragg's law.

Hydrogel is a smart material whose volume changes with the environmental condition; temperature, pH, or solvent concentration. Thus, the interparticle distance of colloidal photonic crystals combined with hydrogel can be tuned by varying these conditions. In this case, the Bragg's condition gives a simple estimation of the band-gap shift base upon a variation of the lattice constant. Asher reported the hydrogel base tuning of photonic crystals under various swelling conditions [9]. Specially synthesized hydrogel photonic crystals showed a significant change in their

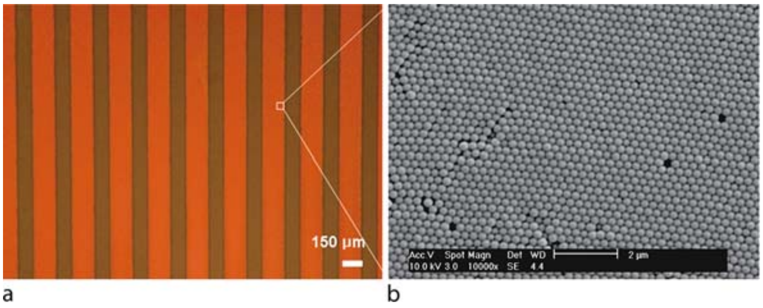

Nanoscale Optofluidic Characterization Techniques, Figure 2 Colloidal crystals in centrifugal microfluidic chips. (**a**) Optical micrograph of colloidal photonic crystal patterns. (**b**) Scanning electron micrograph of crystallized colloidal crystals whose lattice constant is 260 nm

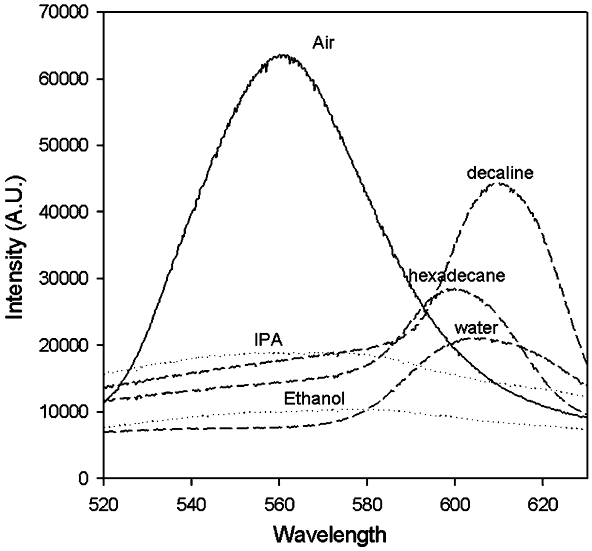

Nanoscale Optofluidic Characterization Techniques, Figure 3 Experimental data for a glass surface with (**a**) de-ionized ultra-filtered water and (**b**) a 10^{-3} M aqueous NaCl solution

reflection color with changes in the pH, temperature, heavy metals and glucose concentration. As the lattice parameter of a photonic crystal increased, the peak position of the reflectance spectra shifted toward a longer wavelength. Xia et al. showed similar results using an expansion of a PDMS/silica composite material by solvent swelling [10].

The Ozin group reported an optical chromatography method using colloidal crystal capillary columns [11]. The stop bands of colloidal crystal columns were tuned by filling the colloidal crystals with Alkanes; Octane, Nonane and Decane. Although they have similar molecular structures and weights, a reflectance peak shift was detected from small refractive index variations. This is applicable to a novel liquid-chromatography column with a higher resolution and a shorter processing time than a currently existing column. Lee et al. reported the in situ crystallization of colloidal particles in microfluidic chips under a centrifugal force field [12]. The colloidal crystallization speed was accelerated by a centrifugal force that supplied colloidal particles at a 50-fold rate. Although the processing time was dramatically reduced, the crystallinity was not seriously affected, as the colloidal arrangement time scale is still larger than crystallization scale. The sedimentation rate is proportional to the density difference that can be controlled by the selection of dispersing media. Figure 2 shows optical and scanning electron microscope images of crystallized colloidal crystal patterns inside of a centrifugal microfluidic chip. The photonic bandgap of the colloidal photonic crystals could be modulated by refractive index mismatching between the solvent and the colloidal particles. Given that all liquid fluids have a higher refractive index compared to air, the bandgap position shifted to a longer wavelength when the fluid flowed through a built-in colloidal crystal part in the microfluidic chips. However, when the refractive index of the outside materials is similar to that of the core materials, the refractive index contrast is minimized and the photonic band-gap disappears. Therefore, this cannot be used as an optofluidic characterization tool. With colloidal photonic nanostructures composed of two different refractive index materials, the undetectable ranges of one material can be eliminated by a second photonic crystal. The bandgap shift is visualized by the reflectance spectra of silica and polystyrene colloidal crystals with various solvents, as shown in Fig. 3.

As mentioned earlier, colloidal photonic crystal devices were fabricated through a self-assembly process. This process is the most economic method to produce 3D nanostructures. When the size of a colloidal building block is half the wavelength of visible light, a physical change of the photonic crystals caused by the analytes converts into a color change. However, the width of the reflectance peak is usually broad, which disturbs the high sensitive characterization.

Photonic Crystal Cavities

A defect in the photonic crystal leads to allowed states for particular frequencies and a strong localized mode in the band-gap, as shown in Fig. 4. Point defects have great importance for the control of spontaneous emission and light localization events [13]. These can be created by removing one unit structure, changing the local refractive index or by modifying the size of the structures.

In general, 2D photonic crystals are fabricated by drilling an array of holes onto high index substrates. Since Painter et al. first reported lasing from a single-defect photonic crystal cavity, many researches have attempted to create a triangular lattice, a square lattice and a quasi-periodic lattice for large quality factor in a small mode volume. In a 2D photonic crystal slab, photons are confined by the total internal reflection in the vertical direction and by the photonic band-gap effect in the in-plane direction. Consequently, compact and effective optical cavities are achieved. The characteristics of photonic crystal cavities can be modulated by introducing fluids through nanochannels [14]. As the resonance mode of a photonic crystal cavity is very narrow and sensitive to the environment, even very small changes in effective refractive of medium are clearly detectable. The specific binding of analytes onto the cavity enables sub-femtoliter scale sensitivity, which originates from variations in the effective refractive index, hole radius or surface evanescent mode. When the surrounding medium of photonic crystal cavities change from air ($n = 1$) to a liquid medium ($n > 1$), the refractive index contrast reduces and band-gap shifts to a longer wavelength. Consequently, a small change in the refractive index is represented as a shift of the lasing peak.

To fabricate 2D photonic crystal cavities, expensive e-beam lithography should be used. In addition, a bulky and complicated detection setup is required to catch the lasing signals. In spite of all the disadvantages, photonic crystal lasing units show a sub-1-nm resolution, which is required for single-molecule level detection of analytes [15].

SERS-Active Colloidal Particles

Recently, synthesis processes for colloidal dispersions have been expanded from dielectric materials to metals and semi-conductors. In addition, core-shell particles with multi-layer coatings can be synthesized via chemical processes. When metal nanostructures are located with nanoscopic gaps among them, hot spots can exist that result from strong localizations of the electromagnetic field. Core-shell particles with dielectric cores and metal shells are a representative of these nanogap structures, and such colloidal nanoshell particles exhibit strong SPR and SERS activity [16]. This originates from the interaction of electromagnetic waves and oscillating surface charges generated on the inner and outer surfaces of the metal shells. In particular, the thickness of gold and silver shells onto colloidal particles can be controlled to nanometer-scale accuracy. According to the charge distribution, plasmon resonance has differing plasmon energy states of bonding plasmons with low energy and anti-bonding plasmons with relatively higher energy. This is analogous to the molecular orbital theory of quantum mechanics.

The plasmon effect enables highly sensitive SERS detection at the single molecule level. The Halas group reported experimental and simulated results of SERS activity with various colloidal structures that included spherical particles, nanoshells, dimer clusters and nanoshell clusters. According to their results, nanoshells enhanced the signal-to-noise (S/N) ratio 548 times relative to the general particles. For dimer clusters of nanoshells, the S/N ratio was increased by 95,238 times when the polarization of the incident light was in the axial direction of the clusters.

SERS-Active Substrates

It is well known that surface-enhanced Raman scattering is observed for molecules close to surface of silver or gold nanostructures due to the existence of surface plasmon resonance. The maximum values for an electromagnetic enhancement for isolated single colloidal silver and gold nanoparticles are $\sim 10^6 - 10^7$. From theoretical studies, further enhancement can be achieved for sharp features and large curvature regions such as the junctions or edges of colloidal aggregates or nanocrystals. Moreover, closely spaced particles (inter-particle distances less than 10 nm) can produce extra Raman enhancement up to 10^{11} at the midpoint between separated particles.

SERS-active colloidal clusters show both localized surface plasmon resonance (LSPR) and extended plasmon resonance (EPR) in the extinction spectrum, unlike a single nanosphere, in which EPR can be identified from the broadened extinction peak that appears at longer wavelengths relative to LSPR. EPR induces very strong field only in a very short length scale of a few nanometers and consequently the induced field distribution is highly inhomogeneous. The highly localized surface plasmon with very strong fields termed *hot spots* plays an important role in the total electromagnetic enhancement of metal nanostructures. This can be used for single-molecule detection. The location and size of hot spots depend on the local geometry and the wavelength and polarization of the incident beam. Strongly localized hot spots provide an opportunity to detect a single selected molecule within a larger population or to probe selectively parts of large molecules such as DNA or proteins. These hot spots can

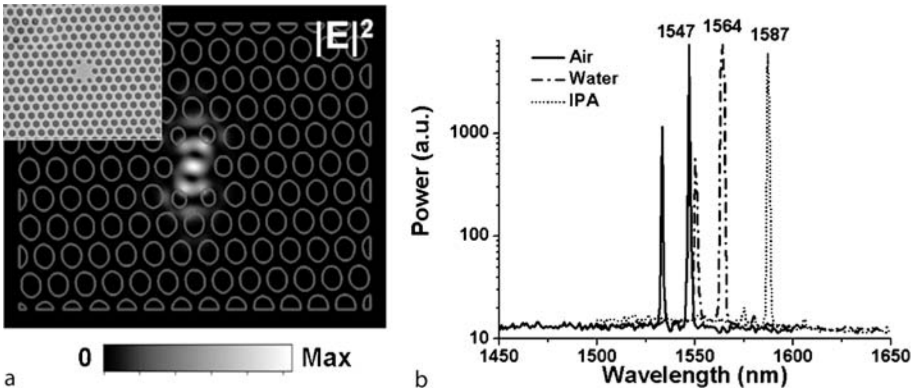

Nanoscale Optofluidic Characterization Techniques, Figure 4 Nanoscale characterization in a 2D photonic crystal cavity. (**a**) Resonance mode of a 2D photonic crystal cavity laser calculated using the FDTD method. (**b**) Red shift of the lasing mode with varying refractive indexes of the surrounding media

produce very large electromagnetic enhancements, and the overall Raman enhancement factor is as large as 10^{14} with chemical enhancement. Therefore the cross-section enhanced by SERS is comparable with that of fluorescence and other optical characterization techniques. Transmission electron microscopy (TEM) combined with Raman spectroscopy can be used to study hot spots of immobilized nanoparticles in nanoscale by comparing their structures and Raman enhancement characteristics. In addition, a metal-coated nanoscale microscope tip such as an atomic force microscopy (AFM) tip can be combined with Raman spectroscopy for single molecule detection with extremely high resolution. This tip-based SERS characterization technique is known as tip-enhanced Raman scattering (TERS).

SERS-Based Optofluidic Detection Technique

Optofluidic detection techniques based on SERS can be used as a highly sensitive biomedical and chemical sensor. Combining a microfluidic device with Raman spectroscopy provides an opportunity to analyze target molecules in real time without labeling at the single molecular level. There are several methods for combining SERS-based detection techniques with a microfluidic chip. Highly sensitive detection can be achieved by flowing biomolecules with SERS-active metal nanoparticles in a microfluidic mixer. Biomolecule-adsorbed metal nanoparticles are then analyzed by Raman spectroscopy downstream of the channel, and quantitative analysis of the Raman spectra is also possible [17]. SERS-active nanostructures with large enhancements are integrated on a microfludic chip that functions as a sample delivery device and are used for label-free biomolecular detections [18]. In addition, by using these types of optofluidic detection techniques, ultrasensitive real-time analyses down to the femto-molar level is possible. By combining a micro Raman set-up and optical tweezers with a microfluidic system, analysis of a single trapped cell can be achieved. This technique provides analysis of reaction processes in cellular systems, and has high potential for in vivo monitoring of cellular drug responses [19]. Figure 5a shows the scheme of an optofluidic SERS or SPR device and Fig. 5b is the example of Raman shift caused by benzenthiol molecules.

Integrated Optofluidic Devices

The sizes of microfluidic devices are becoming smaller and smaller for automatic, inexpensive and accurate characterizations of infinitesimal amounts of samples. However, to characterize chemical and biomedical samples, expensive and bulky instruments have been always attached to microfluidic chips. Various optical units, such as detectors, light sources, cameras, monochromators, focusing lenses, add-drop filters, amplifiers, optical fibers and microscopes should be integrated and aligned in a single chip in order to obtain a proper signal.

Optofluidic Microscope

The development of a miniaturized microscope system that can be integrated with microfluidic devices is a hot issue in the optofluidic characterization field. Lange et al. [20] succeeded in obtaining the image of *C. elegans* from a CMOS array bounded to a sample chamber. However, the resolution was poor (10 μm) compared to conventional microscopy because the resolution of the image was defined by the pitch size of the detector array. Recently, Heng et al. [18] introduced a nanofabrication technique to achieve an optofluidic microscope with high throughput

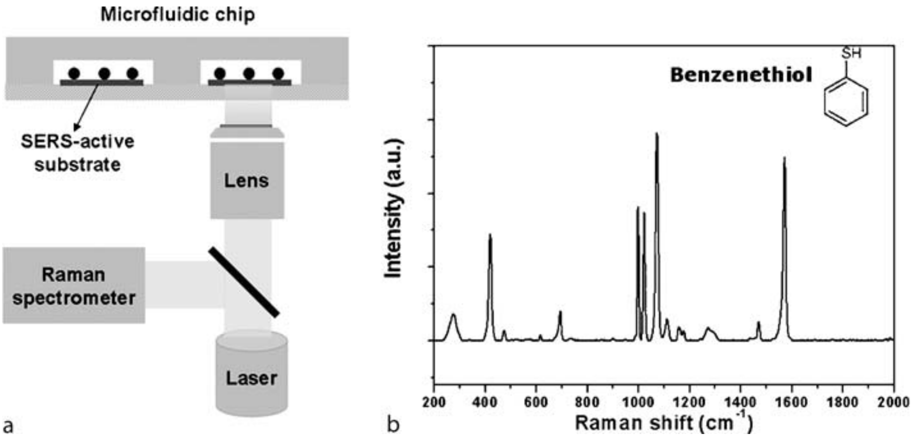

Nanoscale Optofluidic Characterization Techniques, Figure 5 Scheme of in situ optofluidic SPR and SERS devices. (**a**) Conceptual diagram of a 2D nanohole-array-based SPR or SERS sensor (**b**) Resonance peak position shift versus a refractive index change

and high resolution. When samples pass through PDMS microchannels, images are taken by a CCD array located at the bottom. To increase the spatial resolution of an image, 600 nm holes drilled by electron beam lithography are arranged in a diagonal direction with 5 μm intervals. Images are focused on the CCD array through a skewed array of apertures, which enables the production of full-size images by integrating spot images along the translation of the sample. Final images taken by the optofluidic microscope with the nanoscale hole-array showed a high resolving power equivalent to a commercial microscope. This demonstrates the potential for imaging various biological objects as well as *C. elegans* inside of microfluidic channels [21].

Future Directions for Research

Recently, most research groups have focused on the MEMS process based on microelectronics to materialize microfluidic device technology. This is one of the essential elements of optofluidics. Although microelectronics is able to manipulate fluidics at a microscopic scale, there is a serious shortcoming associated with this method. The electronic circuit to actuate fluidics on the microfluidic channels inevitably scatters or reflects light, which is a fatal weakness for an optofluidic device in which transmission of light is critical for optical functions. Novel methods including capillary, centrifugal and photothermal actuation should be applied to actuate fluidics without introducing an electronic circuit pattern to a fluidic device substrate.

From a fabrication point of view, a simple and versatile strategy for constructing nanophotonic structures is required to create fluidically tunable and robust 3D photonic band gap structures. Conventional photolithography can create a uniform pattern mostly in 2D with no defect over a large area, but it does not provide significant advantages to the proposed optofluidic device technology, as an optofluidic device requires photonic structures of very limited length scales. Furthermore, it is impossible to manipulate light in 3D space with photolithographically achievable 2D photonic crystals. Self-organization of photo-responsive complex colloids inside of microfluidic devices enables the fabrication of 3D nanophotonic structures. The efficiency of building 3D photonic structures significantly improves when photonic crystals are made by self-assembly in confined geometries of microfluidic channels with preferable crystal orientations and a lower defect density. In this case, no additional process is needed for the integration of photonic devices with microfluidic devices.

One of the most important factors is to diversify the materials constituting optofluidic devices. Physico-chemical functionalities of mobile fluids should be exploited to manipulate the optical and fluidic properties of optofluidic devices. Current optofluidic device technology has used a very limited number of materials for mobile and immobile phases of optofluidic devices; consequently, the required flexibility has not yet been achieved. As for compatibility with fluidic devices, proper affinity between liquids and substrates poses many challenges to the application of optofluidic characterization devices.

Especially for nanoscale optofluidic characterizations, the physical, chemical, biological, and electromagnetic functionalities of structures and surfaces are very important, as the optical phenomena are deeply related to these aspects in nanophotonics and fluidics.

Cross References

► Surface Plasmon Resonance Sensors
► Surface Enhanced Raman Scattering (SERS)

References

1. Psaltis D, Quake SR, Yang CH (2006) Developing optofluidic technology through the fusion of microfluidics and optics. Nature 442(7101):381–386
2. Joannopoulos JD, Meade RD, Winn JN (1995) Photonic Crystals: Molding the Flow of Light. Princeton University Press
3. Raman CV, Krishnan KS (1928) A New Type of Secondary Radiation. Nature 121:501–502
4. Fleischm M, Hendra PJ, Mcquilla AJ (1974) Raman-Spectra of Pyridine Adsorbed at a Silver Electrode. Chem Phys Lett 26(2):163–166
5. Jeanmaire DL, Vanduyne RP (1977) Surface Raman Spectroelectrochemistry, 1. Heterocyclic, Aromatic, and Aliphatic-Amines Adsorbed on Anodized Silver Electrode. J Electroanal Chem 84(1):1–20
6. Albrecht MG, Creighton JA (1977) Anomalously Intense Raman-Spectra of Pyridine at a Silver Electrode. J Am Chem Soc 99(15):5215–5217
7. Moskovits M (1978) Surface-Roughness and Enhanced Intensity of Raman-Scattering by Molecules Adsorbed on Metals. J Chem Phys 69(9):4159–4161
8. Kneipp K, Kneipp H, Itzkan I, Dasari RR, Feld MS (2002) Surface-enhanced Raman scattering and biophysics. J Phys: Condens Matter 14(18):R597–R624
9. Holtz JH, Asher SA (1997) Polymerized colloidal crystal hydrogel films as intelligent chemical sensing materials. Nature 389(6653):829–832
10. Fudouzi H, Xia YN (2003) Colloidal crystals with tunable colors and their use as photonic papers. Langmuir 19(23):9653–9660
11. Kamp U, Kitaev V, von Freymann G, Ozin GA, Mabury SA (2005) Colloidal crystal capillary columns – Towards optical chromatography. Adv Mater 17(4):438–443
12. Lee SK, Yi GR, Yang SM (2006) High-speed fabrication of patterned colloidal photonic structures in centrifugal microfluidic chips. Lab Chip 6(9):1171–1177
13. Park HG, Hwang JK, Huh J, Ryu HY, Kim SH, Kim JS, Lee YH (2002) Characteristics of modified single-defect two-dimensional photonic crystal lasers. IEEE J Quantum Electron 38(10):1353–1365
14. Loncar M, Scherer A, Qiu YM (2003) Photonic crystal laser sources for chemical detection. Appl Phys Lett 82(26):4648–4650
15. Erickson D, Rockwood T, Emery T, Scherer A, Psaltis D (2006) Nanofluidic tuning of photonic crystal circuits. Opt Lett 31(1):59–61
16. Malinsky MD, Kelly KL, Schatz GC, Van Duyne RP (2001) Chain length dependence and sensing capabilities of the localized surface plasmon resonance of silver nanoparticles chemically modified with alkanethiol self-assembled monolayers. J Am Chem Soc 123(7):1471–1482
17. Park T, Lee S, Seong GH, Choo J, Lee EK, Kim YS, Ji WH, Hwang SY, Gweon DG, Lee S (2005) Highly sensitive signal detection of duplex dye-labelled DNA oligonucleotides in a PDMS microfluidic chip: confocal surface-enhanced Raman spectroscopic study. Lab Chip 5(4):437–442
18. Liu GL, Lee LP (2005) Nanowell surface enhanced Raman scattering arrays fabricated by soft-lithography for label-free biomolecular detections in integrated microfluidics. Appl Phys Lett 87(7):074101
19. Ramser K, Enger J, Goksor M, Hanstorp D, Logg K, Kall M (2005) A microfluidic system enabling Raman measurements of the oxygenation cycle in single optically trapped red blood cells. Lab Chip 5(4):431–436
20. Lange D, Storment CW, Conley CA, Kovacs GTA (2005) A microfluidic shadow imaging system for the study of the nematode Caenorhabditis elegans in space. Sens Actuators B 107(2): 904–914
21. Heng X, Erickson D, Baugh LR, Yaqoob Z, Sternberg PW, Psaltis D, Yang CH (2006) Optofluidic microscopy - a method for implementing a high resolution optical microscope on a chip. Lab Chip 6(10):1274–1276

Nanoscale Optofluidic Measurement

► Nanoscale Optofluidic Characterization Techniques

Nanosensors

► Nanoscale Biosensors

Nanostructures

► Fabrication of Self-Assembled Catalytic Nanostructures

NEMS-Based Biosensors

► Impedimetric Biosensors for Nano- and Microfluidics

Neural Network

Definition

A neural network is a type of computational model that can be used to analyze complicated events or phenomena. They are based on the architecture of biological brains, and consist of a collection of *neurons* (or simple processing elements) that are connected in an adaptive manner. Neural networks can be trained with existing data to generate a robust model.

Cross References

► Artificial Neural Networks

Nitrides

► Non-Metallic Inorganic Materials

No-Moving-Part Pumps

► Valve-Less Rectification Pumps

No-Moving-Part Valves

► Piezoelectric Valves

Non-Centrosymmetric

Definition

A centrosymmetric material has points of inversion symmetry throughout its volume. A material that does not is said to be non-centrosymmetric. This is a key requirement for piezoelectric materials: they must be non-centrosymmetric. Not all non-centrosymmetric materials are piezoelectric, however (the exception is materials with class 432).

Cross References

► Inversion Symmetry
► Hermann–Mauguin Notation
► Piezoelectric

Non-Continuous Approaches

William W. Liou, Oluyinka O. Bamiro
Western Michigan University, Kalamazoo, MI, USA
William.liou@wmich.edu,
oluyinka.o.bamiro@wmich.edu

Synonyms

Molecular method; Discrete method

Definition

The fluid media are not considered continuum in a non-continuous approach. The molecular nature of fluid is recognized and explicitly considered in the development of methodologies.

Overview

An intrinsic length scale in dilute gases is the mean free path, which measure the average distance the gas molecules travel between collisions. The ratio of the molecular mean free path of gas λ to a flow characteristic length scale L is defined as the Knudsen number Kn.

$$\mathrm{Kn} = \frac{\lambda}{L} \tag{1}$$

For gas flows found in conventional macro-scale devices at atmospheric conditions, the flow characteristic length scale L in Eq. (1) can be orders of magnitude larger than the molecular mean free path, which is in the order of 10^{-8} m, and the Knudsen number approaches zero. For micro- and nano-scaled devices that operate with gases in atmospheric conditions, the scaling relation can be quite different. For example, for a micro channel that is one micron deep and one micron wide, the Knudsen number based on the cross sectional dimension is then 10^{-2}, which is four to five orders of magnitude larger than those typically found in macroscaled devices. The Knudsen numbers of micro gas flows are significantly larger than that in the macro-scaled devices. For micro flows where there are localized regions of large gradients of flow property, the device dimension can not be used as the length scale for the entire flow filed and different length scales may be required to characterize the flow in these regions. In this case, the magnitude of the Knudsen number can be even higher when a local length scale of the flow is used, instead of the global length scale. Since the mean free path varies inversely with gas density, the Knudsen number can be quite large for micro and nano fluidic devices that operate in low-pressure or low-density environment.

The kinetic theory of liquid is less well-developed compared as the gas kinetic theory. Continuous approaches in micro/nano fluidics are often used in practice with modifications to the wall boundary conditions and the surface-flow interaction mechanisms.

At zero or extremely small Knudsen number, the physical domain is large compared to the mean free path. For dilute gases, there are then a large number of molecules and, for a time period that is large compared to the mean collision time (about 10^{-10} s for air in standard atmospheric condition), a large number of collisions occur among the molecules. With sufficiently large number of molecules the statistical variation of the number of molecules in the volume can be neglected. Without external forcing, there is then no gradient in the macroscopic flow properties with both time and space due to the large number of molecular collisions. The gas is in an equilibrium state. The fraction of molecules in a velocity class remains unchanged with time, even though the velocity of the individual molecule

varies with collisions. The velocity distribution function for equilibrium gases is represented by the Maxwellian distribution function. A local equilibrium can be established when the gradient of the macroscopic properties is infinitesimal such that, with sufficiently high collision rate, the velocity distribution of the volume of gas can adjust to the local equilibrium state. The gas flows with such small Knudsen numbers can be regarded as a continuous distribution of matter where the local macroscopic properties can be determined by the sample average values of the appropriate molecular quantities, such as mass, velocity, and energy. Since the statistical fluctuations can be neglected, such averages are defined. The applications of the conservation of mass, momentum, and energy further provide a set of differential equations that regulate the changes of these quantities. By assuming linear relationship between stress and strain, and between heat transfer and temperature, the familiar Navier–Stokes equations can then be obtained. The linear constitutive relationship can also be derived from the Boltzmann equation by using, for instance, the Chapman–Enskog expansion. At large Knudsen numbers, such a constitutive relationship fails, resulting in the breakdown of continuous approaches.

For flow with high Knudsen number, the number of molecules in a significant volume of gas decreases and there could be insufficient number of molecular collisions to establish an equilibrium state. The velocity distribution function will deviate away from the Maxwellian distribution and is non-isotropic. The properties of the individual molecule then become increasingly prominent in the overall behavior of the gas as the Knudsen number increases. The implication of the larger Knudsen number is that the particulate nature of the gases needs to be included in the study. The continuum approximation used in the small Knudsen number flows becomes invalid. At the extreme end of the Knudsen number spectrum is when its value approaches infinity where the mean free path is so large or the dimension of the device is so small that intermolecular collision is not likely to occur in the device. This is called collisionless or free-molecule flows.

Non-continuous approach can be deterministic or stochastic. In deterministic approaches, such as the molecular dynamics (MD) method and the lattice Boltzmann method (LBM), the particle or molecule's trajectory, velocity and intermolecular collision are calculated or simulated in a deterministic manner. In the stochastic approaches, such as the direct simulation Monte Carlo (DSMC) method, randomness is introduced in to the solution variables.

MD was conceived in the field of theoretical physics in the 1950's. It is multidisciplinary with laws and theories stemming from mathematics, physics, and chemistry. The method simulates the movement of atoms and molecules and allows them to interact under force field or potential.

DSMC method is one form of Monte Carlo type of method that has been applied to study gas flows in microdevices (Liou and Fang [1]). Bird [2] first applied DSMC to simulate homogeneous gas relaxation problem. The fundamental idea is to track thousands or millions of randomly selected, statistically representative particles, and to use their motions and interactions to modify their positions and states appropriately in time. Each simulated particle represents a number of real molecules. Collision pairs of molecule in a small computational cell in physical space are randomly selected based on a probability distribution after each computation time step. In essence, particle motions are modeled deterministically while collisions are treated statistically. A significant advantage of DSMC is that the total computation required is proportional to the number of molecules simulated N, in contrast to N^2 for the molecular dynamics simulations.

LBM was originally proposed by McNamara and Zanetti [3] to circumvent the limitations of statistical noise that plagued Lattice Gas Automata (LGA). LBM is a simplified kinetic (mesoscopic) and discretized approximation of the continuous Boltzmann equation. LBM is mesoscopic in nature because the particles are not directly related to the number of molecules like in DSMC or MD but representative of a collection of molecules. Hence, the computational cost is less demanding compared with DSMC and MD. Typical LBM consist of the Lattice Boltzmann Equation (LBE), Lattice structure, transformation of lattice units to physical units and boundary conditions.

Basic Methodology

Molecular Dynamics

In a typical MD implementation, the trajectory $\boldsymbol{x}$ and the velocity $\boldsymbol{V}$ of N number of particles are solved using the classical laws of mechanics. The intermolecular interactions between the particles are modeled via a two body interaction potential ϕ. In obtaining the time evolution of the trajectories and velocities of the particles, initial conditions are required. The initial velocity is assigned a Boltzmann distribution at the initial temperature. After application of the initial conditions, the time evolution of the velocity $\boldsymbol{V}$ and trajectory $\boldsymbol{x}$ is solved by integration of Eqs. (2) and (3) respectively.

$$\boldsymbol{F} = -\nabla\phi = m\frac{\partial \boldsymbol{V}}{\partial t} \tag{2}$$

$$\boldsymbol{V} = \frac{\partial \boldsymbol{x}}{\partial t} \tag{3}$$

Equation (2) is the Newton's second law. There are different potentials ϕ that are use in MD. The most popular one, arguably, is the Lennard–Jones 12–6 potential as shown in Eq. (4)

$$\phi(r) = 4\varepsilon\left[\alpha\left(\frac{\sigma}{r}\right)^{12} - \beta\left(\frac{\sigma}{r}\right)^{6}\right] \quad (4)$$

where r represents the molecular separation while σ and ε the length scale and energy values, respectively. The coefficients α and β are chosen in order to simulate fluid–fluid or fluid–solid interactions. The first term in Eq. (3) represents the short range repulsive force while the other term is the long range attractive force. MD suffers from the drawback or limitation that it is computationally expensive. The computational cost scales with the square of the number of particles or molecules O(N^2) since the computation of a particle's trajectory requires consideration of other particles as possible collision partners. Due to the high computational cost and small simulation time scales, MD simulations is not usually used in many practical micro/nanofluid applications.

Lattice Boltzmann Method

The lattice Boltzmann equation (LBE) consists of two steps, representing the streaming and collision components. During the streaming step, the particles move to the neighboring lattice points in the direction of its velocity. During the collision step, the particles arriving at the neighboring lattice site interact with each other according to scattering rules and change their velocity directions. The Bhatnagar, Gross and Krook (BGK) LBE (LBGK) is the most widely used form of LBE and it is stated below as

$$\begin{aligned} f_i(x + e_i\Delta t,\ t + \Delta t) \ - \ f_i(x,t) \\ = -\frac{1}{\tau}\left(f_i(x,t) - f_i^{\mathrm{eq}}(x,t)\right) \end{aligned} \quad (5)$$

where f_{eq} represents the Maxwellian distribution function, f_i and e_i the distribution function and the particle speeds for particle i.

The lattice pattern in the LBM helps in the discretization of the fluid domain into nodes/particles and also in describing the microscopic motion of the particles. For a 2D model the lattice can either have a square or hexagonal lattice. The square lattice can have 4 or 5 or 8 or 9 speed models while the hexagonal lattice can have the 6 or 7 speed models.The general nomenclature used for describing the lattice structure or pattern is DxQy, the letter x and y represents the dimensions and speed model respectively. The lattice pattern shown in Fig. 1 is the D2Q9 model. The

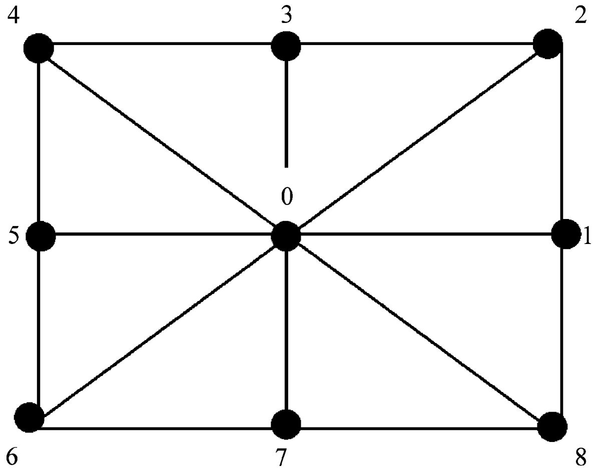

Non-Continuous Approaches, Figure 1 D2Q9 lattice pattern

D2Q9 and D2Q7 are the most widely used 2D lattice pattern due to their symmetry (isotropy) and ability to recover the Navier–Stokes equation. For the D2Q9 lattice pattern, the lattice speed e_i can be represented as found in Fig. 1 of

$$e_i = (0,0) \quad \text{for i = 0 (rest particle)}$$

$$e_i = e\left[\frac{\cos(i-1)\pi}{4}, \frac{\sin(i-1)\pi}{4}\right]$$

$$\text{for i = 1, 3, 5 and 7} \quad (6)$$

$$e_i = \left(\sqrt{2}\right)e\left[\frac{\cos(i-1)\pi}{4}, \frac{\sin(i-1)\pi}{4}\right]$$

$$\text{for i = 2, 4, 6, 8 (for diagonal particles)}$$

Due to the kinetic nature of LBE, phenomenon or physics that involves molecular interaction can easily be applied and hence makes LBM a good tool for micro/nano fluidics simulation. Fewer sets of discrete velocities and particle density distribution function in phase space is used in LBM as opposed to a continuous velocity or distribution function in the complete functional phase space of the Boltzmann equation.

Direct Simulation Monte Carlo Method

The DSMC method often used in micro gas flow simulations was originally developed for high Knudsen number rarefied gas flow. The procedures involved in applying DSMC to steady or unsteady flow problems can be found Fig. 1 of the entry ►Monte Carlo method. Execution of the method requires the physical domain to be divided into a distribution of computational cells. The cells

N

provide geometric boundaries and volumes used to sample macroscopic properties. Also, only molecules located within the same cell, at a given time, are allowed for collision. The DSMC simulation proceeds from a set of prescribed initial condition. The molecules randomly populate the computational domain. These simulated molecules are assigned random velocities, usually based on the equilibrium distribution. The simulated representative particles move for a certain time step. This molecule motion is modeled deterministically. This process enforces the boundary conditions. With the simulated particles being appropriately indexed, the molecular collision process can be performed. The collision process is modeled statistically, which is different from deterministic simulation methods such as the molecular dynamics methods. In general, only particles within the same computational cell are considered to be possible collision partners. Within each cell, collision pairs are selected randomly and a representative set of collisions is performed. The post-collision velocities are determined. There are several collision-sampling methods that have been used successfully. The currently preferred model is the *no-time-counter* (NTC) technique used in conjunction with the sub-cell method (Bird [4]). Figure 2 of the entry ▶Monte Carlo method shows the velocity phase plane in a cell for a typical microflow simulation. The sample size is 17,370.

Key Research Findings

LBM is well suited for microflow and it has been applied to both gas and liquid flows. Pioneering applications of LBM were geared towards developing suitable boundary conditions and Kn number relations to the mesoscopic variables particularly for gas microflows using classical flows, such as Couette and Poiseuille flows. LBM has gradually matured and it has being applied to capture physics occurring in microflows such as the Knudsen layer in the transition regime. LBM has been successfully applied to capture multiphysics and multiscale phenomenon, such as reactive flows, electroosmotic flows in the presence of the Electric Double Layer (EDL), chaotic mixing using magnetohydrodynamics, surface related physics (like hydrophobicity and hydrophilicity) and thermal related flows. For microflow simulations, the statistical scatter associated with DSMC limits its applications to microflow with extremely low velocity. The information preservation (IP) method was developed to address this issue. The method [5, 6] introduces preserved information velocities collected based on inelastic collision model. Application has been applied to low-speed Couette, Poiseuille, and Rayleigh flows in the slip, transition and free-molecular flow regimes, and low-speed microflows. The computation time of an IP scheme can be several orders of magnitude lower compared with a regular DSMC simulation for convergence. Figure 3 in the entry ▶Monte Carlo method show the IP velocity phase plane results for the same microflow shown in the previous figure obtained by DSMC. The reduction of the scattering is significant.

MD in micro/nano scale fluids has generally been used as a means to validate other simulation approaches (DSMC or LBM) and it is also used for liquid microflows. The lack of wide usage of MD in practical applications is due to its high computational cost.

Future Directions for Research

The fundamental advantages of LBM such as the ease of parallelization, coding, its ability to incorporate molecular interaction, and cheaper computational cost compared to other non continuous approaches will make LBM a promising approach to the modeling of multiphysics and multiscale phenomenon with an interdisciplinary flair. The extents and limitations of LBM particularly with regards to liquid microflows need further investigation. Monte Carlo methods are inherently parallel and can be readily parallelized. With the advent of low-cost PC-based cluster computing, the parallel nature of Monte Carlo method should be further explored. Simulations of fluid behavior and properties at micro and nanoscales may be facilitated with hybrid types of method employing both Monte Carlo and molecular dynamics techniques. This combination allows the simultaneous exploration of, for instance, thermal properties and local phase space.

Cross References

- ▶ Chaotic Flows
- ▶ Micro- and Nanoscale Gas Dynamics
- ▶ Monte Carlo Method
- ▶ Multiscale Modeling and Numerical Simulations

References

1. Liou WW, Fang Y (2006) Microfluid Mechanics-Principles and Modeling. McGraw-Hill, New York
2. Bird G (1963) Approach to translational equilibrium in a rigid sphere gas. Phys Fluid (6):1518–1519
3. McNamara GR, Zanetti G (1988) Use of Boltzmann equation to simulate lattice-gas automata. Phys Rev Lett (61):2332–2335
4. Bird GA (1994) Molecular Gas Dynamics and the Direct Simulation of Gas Flows. Clarendon Press, Oxford, United Kingdom
5. Fan J, Shen C (1999) Statistical simulations of low-speed unidirectional flows in transition regime. In: Brun et al (ed) Rarefied Gas Dynamics, Cepadus-Editions, Toulouse (2):245
6. Sun Q, Boyd ID (2002) A direct simulation method for subsonic microscale gas flows. J Comput Phys (179):400–425

Non-Covalent Bonding

► Non-Covalent Interactions

Non-Covalent Forces

► Non-Covalent Interactions

Non-Covalent Interactions

Synonyms

Non-covalent bonding; Non-covalent forces

Definition

Noncovalent interactions refer to a variety of interactions that are not covalent in nature between molecules or parts of molecules that provide force to hold the molecules or parts of molecules together, usually in a specific orientation or conformation. These noncovalent interactions include: ionic bonds, hydrophobic interactions, hydrogen bonds, Van der Waals forces (aka London dispersion forces), and Dipole-dipole bonds.

Cross References

► Biosensor

Non-Directional Etching

► Isotropic Etching

Non-Equilibrium Diffuse Charge

► Space Charge

Non-Equilibrium Electrical Double Layer

► Space Charge

Nonlinear Electrokinetic Phenomena

Martin Z. Bazant[1,2]
[1] Department of Mathematics and Institute for Soldier Nanotechnologies, Massachusetts Institute of Technology, Cambridge, MA, USA
[2] Ecole Superieure de Physique et Chimie Industrielles, Paris, France
bazant@math.mit.edu

Synonyms

AC electro-osmosis (ACEO); Nonlinear electrophoretic mobility

Definition

Nonlinear electrokinetic phenomena are electrically driven fluid flows or particle motions, which depend nonlinearly on the applied voltage. The term is also used more specifically to refer to induced-charge electro-osmotic flow, driven by an electric field acting on diffuse charge induced near a polarizable surface.

Chemical and Physical Principles

Linear Electrokinetic Phenomena

A fundamental electrokinetic phenomenon is the ►electro-osmotic flow of a liquid electrolyte (solution of positive and negative ions) past a charged surface in response to a tangential electric field. ►Electrophoresis is the related phenomenon of motion of a colloidal particle or molecule in a background electric field, propelled by electro-osmotic flow in the opposite direction. The basic physics is as follows:

Electric fields cause positive and negative ions to migrate in opposite directions. Since each ion drags some of the surrounding fluid with it, any significant local charge imbalance yields an electrostatic stress on the fluid. Ions also exert forces on each other, which tend to neutralize the bulk solution, so electrostatic stresses are greatest in the ►electrical double layers, where diffuse charge exists to screens surface charge. The width of the diffuse part of the double layer (or "diffuse layer") is the Debye screening length ($\lambda \sim 1 - 100\,\text{nm}$ in water), which is much smaller than typical length scales in microfluidics and colloids. Such a "thin double layer" resembles a capacitor skin on the surface.

Electro-osmosis produces an effective slip of the liquid outside the double layer past to the solid surface. In the classical continuum model of the diffuse layer, the

slip velocity is given by the Helmholtz–Smoluchowski formula,

$$u_s = -\frac{\varepsilon\zeta}{\eta}\boldsymbol{E}_\mathrm{t} \tag{1}$$

where $\boldsymbol{E}_\mathrm{t}$ is the tangential electric field just outside the double layer, ε and η are the permittivity and viscosity of the liquid (both assumed constant), and ζ is the zeta potential, a measure the electro-osmotic mobility with units of voltage. In Smoluchowski's theory, the zeta potential corresponds to the potential difference ψ between the slip plane and the neutral bulk solution, just outside the double layer, but this need not be the case (see below).

Classical electrokinetic phenomena are *linear* ($u \propto \boldsymbol{E}$) since the zeta potential is assumed to be a material constant, reflecting chemical equilibrium at the liquid–solid interface:

$$u = -\frac{\varepsilon\zeta}{\eta}\boldsymbol{E} = -b\boldsymbol{E} \quad \text{(non-polarizable surface)} \tag{2}$$

The electro-osmotic mobility b is the coefficient of linear response. This ubiquitous approximation, which can be justified in the limits of thin double layers and/or weak fields, greatly limits possible flows and particle motions. With constant zeta and thin double layers, for example, electro-osmosis in a capillary is irrotational (free of vortices), and particles of different shapes and sizes have the same electrophoretic mobility $b = U/\boldsymbol{E}$ and thus cannot be separated.

Induced-Charge Electrokinetic Phenomena

The possibility of *nonlinear* electro-osmotic flow, varying as $u \propto \boldsymbol{E}^2$, seems to have been first described by Murtsovkin [1, 16], who showed that an alternating electric field can drive steady quadrupolar flow around a polarizable particle (Fig. 1a). This effect has recently been unified with other nonlinear electrokinetic phenomena in microfluidics [2], such as ►AC electro-osmotic flow (ACEO) at microelectrodes [4, 11, 12] (Fig. 1b), DC electrokinetic jets at dielectric corners [5] (Fig. 1c), and nonlinear flows around metal posts [3] (Fig. 1d–e). These are all cases of ►induced-charge electro-osmosis (ICEO) – the nonlinear electro-osmotic flow resulting from the action of an electric field on its own induced diffuse charge near a polarizable surface.

The simplest example of ICEO involves a metal sphere (1) or cylinder (2) in a suddenly applied field, sketched in Fig. 2. Conceptually, there two steps: electrochemical relaxation in response to the field, and electro-osmotic flow driven the induced charge.

1. *Charge relaxation.* When the field is turned on, electrons on the metal surface immediately drift toward one pole to induce a dipole moment making the surface equipotential (Fig. 2a). This is an unsteady configuration in an electrolyte, however, since the field drives ionic current, any normal component transports charge in or out of the diffuse layer. Ignoring surface conduction through the double layer (for thin double layers) and Faradaic reactions passing current through the particle (at low voltage), the normal current locally charges double layer, like a capacitor, until all the field lines are expelled in steady state (Fig. 2b). The time scale for this process is the "RC time" for the equivalent circuit of the bulk resistance coupled to the double layer capacitance [2–4, 12]

$$\tau = \frac{L}{\sigma}\frac{C_D}{(1+\delta)} = \frac{\lambda L}{D(1+\delta)} \tag{3}$$

where $\delta = C_D/C_S$ is the ratio of the diffuse-layer capacitance to that of the compact layer (e. g. a Stern monolayer or dielectric coating), σ and D are the bulk conductivity and diffusivity, and L is the length (radius) of the object. In microfluidic devices, the double layer charging time (Eq. (3)) (ms) is much larger than the Debye relaxation time $\varepsilon/\sigma = \lambda^2/D$ for bulk ionic screening (µs) and much smaller than the diffusion time L^2/D for the relaxation of bulk concentration gradients (s). In nano-channels, however, all of these time scales can be comparable (µs).

2. *Fluid flow.* The tangential field acts on the non-uniform induced-charge (or ζ) distribution to produce quadrupolar ICEO flow, sucking fluid at the poles and ejecting it at the equator (Fig. 2c). The scaling of the flow can be easily understood as follows. Capacitive charging transmits a non-uniform voltage to the double layer of order EL, a fraction $(1+\delta)^{-1}$ of which is dropped across the diffuse part and contributes to the induced zeta potential. If Eq. (2) holds, then ICEO flow scales as

$$u \propto \frac{\varepsilon L E^2}{\eta(1+\delta)} \quad \text{(ideally polarizable surface)} \tag{4}$$

The flow builds up over the time scale τ in Eq. (3); if an AC field of frequency ω is aplied, then the flow decays above the RC frequency as $\left[1+(\omega\tau)^2\right]^{-1}$, assuming constant double-layer capacitance [3].

In this canonical example, broken symmetries generally lead to fluid flow past the object, if it is held fixed, or motion by ►induced-charge electrophoresis (ICEP), if it is freely suspended [2, 17]. For example, if the object

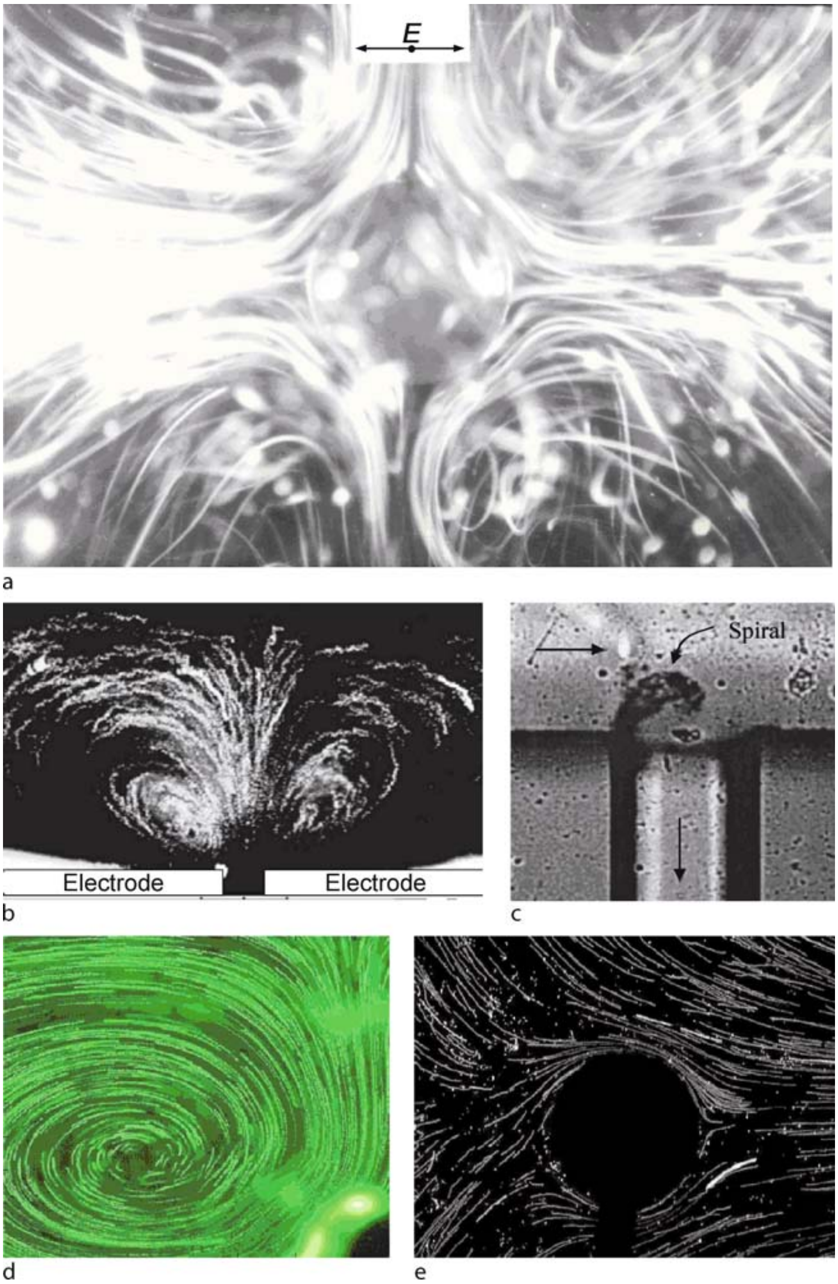

Nonlinear Electrokinetic Phenomena, Figure 1 Experimental photographs of induced-charge electro-osmosis, imaged by streaks of tracer particles. (**a**) Nonlinear flow around a 500 μm spherical ionite particle driven by a weak 10 V/cm 80 Hz background AC electric field [2]; (**b**) AC electro-osmosis at a pair of titanium electrodes applying a 2 V 100 Hz AC voltage (from [4]); (**c**) DC electrokinetic jet at a dielectric microchannel corner [5]; (**d**) one roll of quadrupolar ICEO flow around a 100 μm cylindrical gold post in a 100 V/cm 300 Hz electric field and (**e**) fixed potential ICEO flow around a gold post connected to one electrode supplying the background AC field [8] (d,e image credit: Jeremy Levitan)

has a nonzero total charge, then the ICEO flow is superimposed on the familiar streaming flow of linear electrophoresis (Fig. 2d). Whenever Eq. (2) holds, the two effects are additive, since the total charge corresponds to a constant ζ offset, relative to the background potential.

In fixed-potential ICEO (Fig. 3b), the potential of a conductor controlled so as to induce total charge in phase with a (steady or oscillating) background field [3]. The effective L in Eq. (4) is then set by the distances between the object and the electrodes supplying the background

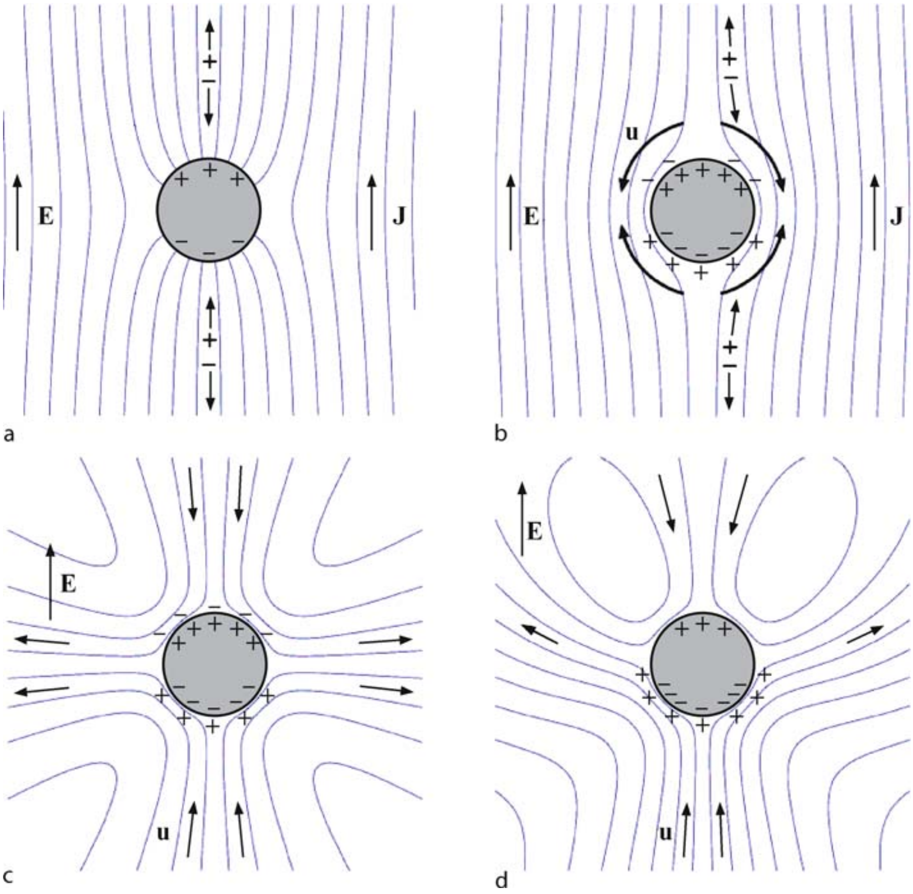

Nonlinear Electrokinetic Phenomena, Figure 2 Physical mechanism for induced-charge electro-osmosis around an ideally polarizable metal cylinder in a suddenly applied electric field (from [2]). (**a**) When the field is turned on, electronic charges relax to make the surface an equipotential, but the normal current drives double-layer charging. (**b**) After charging, the field lines are expelled by a nonuniform distribution of induced double-layer charge. (**c**) The tangential field acts on the induced charge to drive quadrupolar ICEO flow around a neutral cylinder. (**d**) If the cylinder has a nonzero total charge, then the dipolar flow of linear electrophoresis is superimposed on the quadrupole

field, so fixed-potential ICEO flow can be much faster than the quadrupolar ICEO flow and has a different frequency response.

Other broken symmetries include irregular shapes (e. g. rods, polyhedra, etc.), non-uniform surface properties (e. g. partial dielectric or metallic coatings), and non-uniform background electric fields [17]. In each case, net pumping of the fluid by ICEO results if the object is held fixed, which requires a certain force and torque. Conversely, if the object is a colloidal particle, then broken symmetries cause it to translate and rotate ICEP, as described in companion articles on the ►electrokinetic motion of polarizable particles and heterogeneous particles.

Nonlinear Electrokinetic Phenomena Involving Dielectrics

The example above assumes an "ideally polarizable" metal surface, where the double layer charges capacitively to sustain the entire voltage applied to the object, but the phenomenon of ICEO is much more general and occurs at any polarizable surface, to varying degrees [1–3]. For example, if the metal object described above has a thin dielectric coating of width h and permittivity ε_d, then the quadrupolar ICEO flow scales as Eqs. (3)–(4) with $\delta = (\varepsilon/\varepsilon_d)(h/\lambda)$. This shows that dielectric coatings, which are thicker than the Debye length, can substantially reduce ICEO flows at metal surfaces. In the opposite limit of a purely dielectric object of length $L \gg \lambda$, the flow scales as

$$u \propto \frac{\varepsilon_d \lambda \boldsymbol{E}^2}{\eta} \quad \text{(dielectric surface)} \tag{5}$$

which is smaller than for an ideally polarizable object Eq. (4) by a factor $(\varepsilon_d/\varepsilon)(\lambda/L)$.

Although often small, ICEO flows at dielectric surfaces need not be negligible in microfluidic devices, due to

large local fields. For example, an electric field passing around a sharp corner in a dielectric microchannel can drive a strong "nonlinear electrokinetic jet" of ICEO flow due to the corner field singularity [5], as shown in Fig. 1b. In very simple terms, this phenomenon can be understood as half of the quadrupolar flow around a polarizable particle, where the jet corresponds to the outward flow at the equator in Fig. 2c.

Dielectric objects can also experience electrostatic forces. The uniform component of a background electric field induces a dipole on the object, which then feels a torque to align it with the field. A field gradient can also apply a force to the induced dipole. Higher-order multipoles in the background field can likewise cause forces and torques by acting on higher-order induced multipole moments on the object. In the case of colloidal dielectric particles, these forces and torques (balanced by hydrodynamic drag) produce translation $u \propto \varepsilon a^2 \nabla \boldsymbol{E}^2/\eta$ and rotation $\Omega \propto \varepsilon \boldsymbol{E}^2/\eta$, respectively. This general effect, known as ▶*dielectrophoresis* (DEP), is perhaps the best-known nonlinear electrokinetic phenomenon. The theory of DEP has mostly been developed for dielectric liquids, but in electrolytes, however, ICEO flows also occur, with the same scalings. The net ▶electrokinetic motion of polarizable particles results from a competition between DEP and ICEP.

Nonlinear Electrophoretic Mobility

Prior to the discovery of ICEO flow in the 1980s, the possibility of field-dependent electrophoretic mobility for charged, polarizable particles was demonstrated by several groups in the 1970s [14, 15]. A theory predicting an $\boldsymbol{E}^2$ correction to the mobility of a highly charged particle was first proposed by Simonova and Dukhin in 1976:

$$b(\boldsymbol{E}) = \frac{U(\boldsymbol{E})}{\boldsymbol{E}} \sim \frac{\varepsilon}{\eta}\left(\zeta + \alpha(\boldsymbol{E}a)^2 + \ldots\right) \tag{6}$$

It has recently been proposed to refer to this nonlinear correction as the ▶Stotz–Wien effect [14]. It can be understood as a phenomenon of induced-charge electrophoresis due to the nonlinear differential capacitance $C(\psi)$ of the diffuse layer, as a function of its voltage drop ψ, given by $\psi = (\phi - \phi_{\text{surface}})/(1+\delta)$ for a constant compact-layer capacitance. In that case, for example, the coefficient of the leading nonlinear term in a weak electric field ($\boldsymbol{E}a \ll kT/e$) is given by $\alpha = -9/8(\mathrm{d}/\mathrm{d}\psi \log C)_{\psi=\zeta}$ for an ideally polarizable sphere with a thin dielectric coating (which could model a biological cell) [15]. The basic idea is that the redistribution of diffuse charge around a polarizable particle, which is induced in response to an applied field, leads to a shift of its potential $\phi_{\text{surface}} \propto \boldsymbol{E}^2$, and thus its electrophoretic mobility, in order to maintain the same total charge with a non-constant $C(\psi)$.

In principle, the Stotz–Wien effect can be used to separate colloidal particles using an unbalanced AC field, which has zero time average $\langle \boldsymbol{E} \rangle = 0$, but nonzero time-averaged higher moments, such as $\langle \boldsymbol{E}^3 \rangle \neq 0$. An unbalanced AC field leads to a size-dependent nonlinear electrophoretic velocity for a highly charged polarizable particle

$$\langle U \rangle = \alpha \frac{\varepsilon a^2}{\eta} \left\langle \boldsymbol{E}^3 \right\rangle \quad \text{(highly charged, polarizable particle)} \tag{7}$$

This method of particle separation was first proposed by Chimenti in a US patent (5,106,648, filed in 1985) and independently in Ukraine by Dukhin's group, who called the technique "▶aperiodic electrophoresis", around the same time [14].

Electrokinetic Phenomena of the Second Kind

All of the examples above involve "blocking" surfaces, which do not pass any electrical current. If current can enter the surface, e. g. due to Faradaic reactions at a metal electrode or ionic conduction through a perm-selective porous material, then ICEO flows can be substantially modified. Electrical conduction through the surface tends to "short-circuit" the capacitive charging mechanism, so time-dependent ACEO flows tend to be reduced by Faradaic reactions. If a steady DC voltage is applied, then current into a surface can deplete the bulk salt concentration, leading to concentration polarization (breakdown of Ohm's law) and ▶diffusio-osmosis (slip driven by bulk concentration gradients). If the current is large enough to nearly deplete the bulk concentration, at the diffusion-limited current, then the diffuse-charge in the electrical double layer loses thermal equilibrium and expands into the bulk. A ▶super-limiting current causes the formation of extended ▶space charge, which can alter the nature of ICEO flow.

The possibility of nonlinear electro-osmotic flow driven by non-equilibrium space charge at large currents was predicted by S.S. Dukhin in the 1980s [6, 13]. He coined the term ▶electroosmosis of the second kind, to distinguish it from electrokinetic phenomena of the first kind (whether linear or nonlinear), which involve quasi-equilibrium double layers and non-zero bulk concentrations. In spite of appealing to very different physical mechanisms, the maximum velocity of second-kind electro-osmosis is argued to be the same as that described above for ICEO flow (Eq. (4)):

$$u \propto \frac{\varepsilon L \boldsymbol{E}^2}{\eta} \quad \text{(surface at limiting current)} \tag{8}$$

N

The reason is that in both cases the applied voltage is transferred to a charged layer near the surface as an induced zeta potential, $\zeta_{\text{induced}} \approx \boldsymbol{E}L$, either by space charge formation at large currents or by capacitive charging of the diffuse layer, respectively.

In spite of similar scaling, electro-osmosis of the second kind is fundamentally different from ICEO flow below a limiting current. Second-kind electro-osmosis requires near-total depletion of the bulk salt concentration by a large current, so it arises at the slow time scale of bulk diffusion, L^2/D, which is much greater than the capacitive double-layer charging time (Eq. (3)). It is essentially a DC effect. The passage of current through the surface also breaks symmetry in a different way in the ► electrokinetic motion of polarizable particles by ► electrophoresis of the second kind. For example, if the particle in Fig. 2c could pass a large current of counterions, then only its lower portion (facing the field) would form space charge and drive second-kind flow propelling the particle toward the field (roughly half of the quadrupolar flow field of ICEO). This picture is oversimplified, however, since experimentally observed second-kind flows can be more complicated, as sketched in Fig. 3 [6].

Space charge formation and second-kind electro-osmosis can also be observed in microfluidic devices and porous materials at interfaces between nanochannels and microchannels, as sketched in Fig. 4 [7]. Nano-scale pores with overlapping double layers act as filters, allowing the passage of only counterions. The applied electric field drives a current, which can be strong enough to deplete the nearby bulk salt concentration, resulting in a nonequilibrium space-charge layer of counterions. Tangential electric fields near the nanopore opening can then drive (often chaotic) second-kind flows in the surrounding micro-pore.

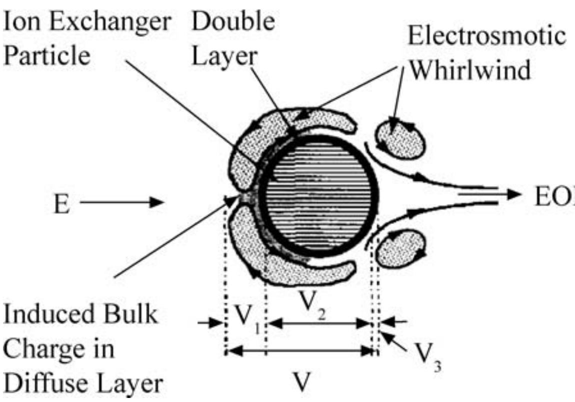

Nonlinear Electrokinetic Phenomena, Figure 3 A sketch of electro-osmotic flow of the second kind around an ion-permselective particle from experiments (from [6])

Other Nonlinear Electrokinetic Phenomena

Induced-charge and second-kind electrokinetic phenomena arise due to electrohydrodynamic effects in the electric double layer, but the term *nonlinear electrokinetic phenomena* is also sometimes used more broadly to include any fluid or particle motion, which depends nonlinearly on an applied electric field. In the classical effect of ► dielectrophoresis mentioned above, electrostatic stresses on a polarized dielectric particle in a dielectric liquid cause ► dielectrophoretic motion of particles and cells along the gradient of the field intensity ($\propto \nabla \boldsymbol{E}^2$). In ► electrothermal effects, an electric field induces bulk temperature gradients by Joule heating, which in turn cause gradients in the permittivity and conductivity that couple to the field to drive nonlinear flows, e. g. via Maxwell stresses $\propto \boldsymbol{E}^2 \nabla \varepsilon$. In cases of flexible solids and emulsions, there can also be nonlinear electro-mechanical effects coupling the motions of different fluid and/or solid phases, driven by electric fields. Electric fields applied to diffuse interfaces between liquid phases, e. g. at different salt concentrations, can also produce ► electrokinetic flow instability, which depends nonlinearly on the field amplitude through the electric Rayleigh number ($\propto \boldsymbol{E}^2 \nabla \sigma$). All of these nonlinear electrokinetic phenomena can further be modified by the simultaneous application of a magnetic field, which drives fluid flow and particle motion due to the Lorentz force ($J \times B$) acting on ionic currents in solution.

Key Research Findings

Induced-Charge Electrokinetic Phenomena

The first experiments demonstrating field-dependent electrophoretic mobility of colloids (Stotz–Wien effect) were reported by several groups in the 1970s [14], and the possibility of using this effect for particle separation using unbalanced AC fields has begun to be explored [14]. This work focused on nonlinear corrections to the classical phenomenon of electrophoresis, where a particle moves in the direction of the applied electric field, $U = b(\boldsymbol{E})\boldsymbol{E}$, rather than on the associated ICEO flows and more complicated ICEP motion.

In a series of pioneering experiments on polarizable colloids, Murtsovkin and collaborators studied ICEO flows around tin, quartz, and ionite particles and liquid mercury drops in alternating electric fields and compared with the theory [1]. The scalings of the fundamental quadrupolar flow with the electric field squared and the particle size [4] were roughly verified (e. g. Fig. 5a), although in some cases the flow was observed in the opposite direction from the theory, at large induced voltages. The ► electrokinetic motion of polarizable particles and ► heterogeneous parti-

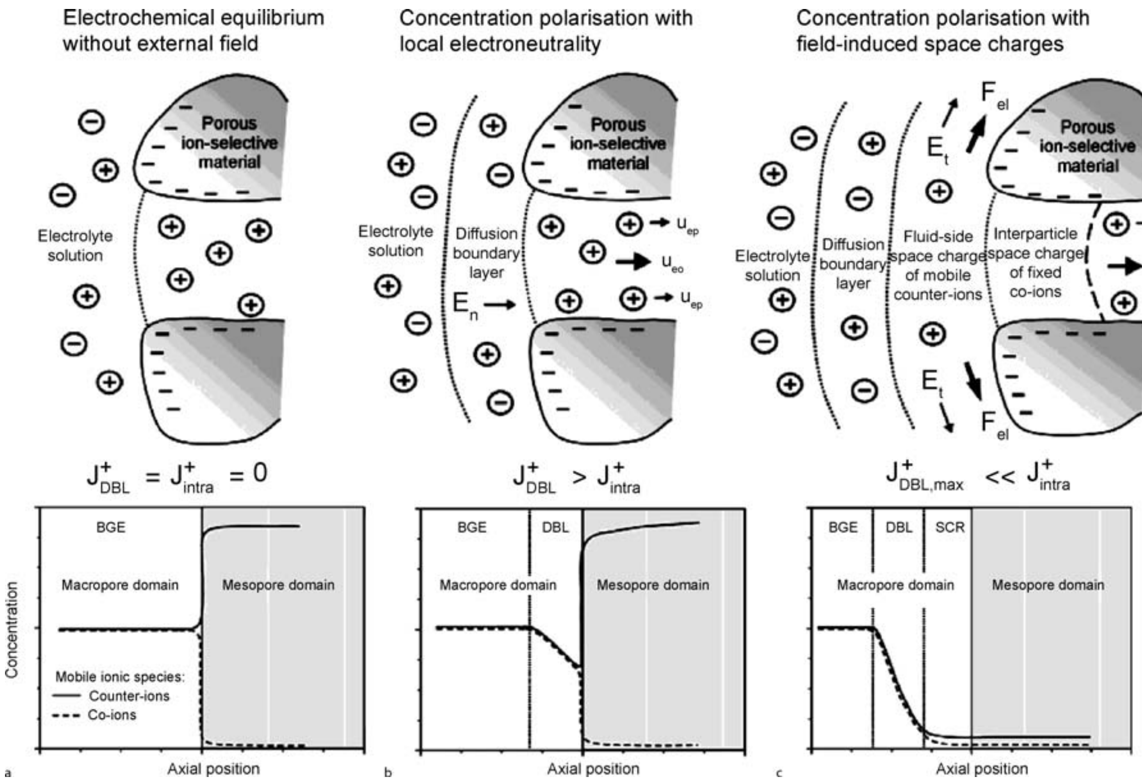

Nonlinear Electrokinetic Phenomena, Figure 4 Sketch of space charge formation and second-kind flow at the junction between a nanopore and a micropore in a microfluidic device or porous material (from [7]). (**a**) In equilibrium, the micropore contains neutral electrolyte, while the nanopore has overlapping double layers containing mostly counterions. (**b**) When an electric field is applied, the nanopore conducts a current of counterions, which depletes the nearby salt concentration in the micropore, forming a bulk diffusion layer. (**c**) If the field is strong enough, the bulk concentration goes to zero, leading to space charge formation and second-kind electro-osmotic flow in the micropore

cles by ICEP has also begun to be observed and analyzed in experiments, including unusual motion perpendicular to a uniform AC field, but much remains to be done.

Detailed three-dimensional measurements of ICEO flows are now possible in microfluidic devices. Using particle-image velocimetry applied to thin optical slices, the ICEO flow field around a platinum cylinder has recently been reconstructed experimentally (Fig. 5b) and found to agree well with the theory, up to a scaling factor which could perhaps be attributable to compact-layer effects [8]. There has also been extensive experimental work on ▶ AC electro-osmotic flows in microfluidic devices, discussed in a separate article.

Experiments lend some support to the simplest theory of ICEO, used in nearly all calculations, which describes the bulk as an Ohmic resistor coupled to thin double layer capacitors. The mathematical model consists of Laplace's equation for the bulk electrostatic potential, $\nabla^2\phi = 0$, with an "RC" boundary condition equating the change in diffuse-layer charge density with the current entering from the bulk solution,

$$C(\psi)\frac{d\psi}{dt} = n \cdot (\sigma \nabla \phi) \tag{9}$$

Once the electrochemical problem is solved, the ICEO flow is obtained by solving Stokes' equations, $\nabla p = \eta \nabla^2 \boldsymbol{u}$ and $\nabla \cdot \boldsymbol{u} = 0$, with electro-osmotic slip given by Eq. (1) with the induced zeta potential, $\zeta = \psi$. Although this set of approximations can only be justified at low voltages in a dilute solution [3], it has had many successes in predicting induced-charge electrokinetic phenomena in experiments outside this regime.

There is, however, a need to extend the theory of ICEO to "large voltages", $\psi \gg kT/e$, where the induced diffuse-layer potential greatly exceeds the thermal voltage (25 mV at room temperature). Experiments on ▶ AC electro-osmotic flows involve micro-elecrode arrays applying several volts ($\approx 100kT/e$), and indeed many features of the data cannot be explained by the low-voltage theory, such

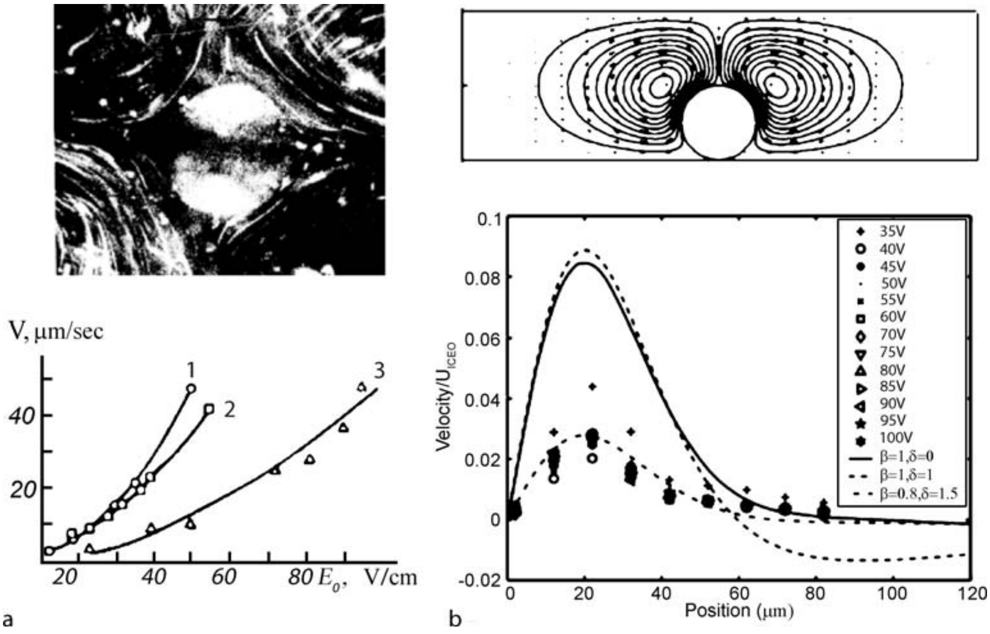

Nonlinear Electrokinetic Phenomena, Figure 5 Some experimental data on induced-charge electrokinetic phenomena. (**a**) The fluid velocity at different points around a tin particle in an AC field versus the applied electric field, demonstrating the quadratic scaling of Eq. (4) (from [1] and references therein). (**b**) The velocity profile at different voltages, measured by micro-particle-image velocimetry, in an optical slice above a platinum cylinder in a transverse AC field, plotted with the scaling (Eq. (4)) to demonstrate data collapse. The simulated streamlines are shown above. (from [8])

as flow reversal at high frequency and flow suppression with increasing salt concentration as $u \sim \log(c_{\max}/c)$ extrapolating to zero around 10 mM. Similarly, experiments on the ►electrokinetic motion of polarizable particles and ►heterogeneous particles at somewhat lower voltages also exhibit flow reversal and the same, seemingly universal concentration dependence.

The primary consequence of a large applied voltage is the crowding of counterions near a highly polarized surface, which violates the assumptions of the classical dilute solution theory. By considering steric constraints and increased viscosity due to counterion crowding, a modified electro-osmotic slip formula has recently been derived for large induced diffuse-layer voltages in a symmetric z:z electrolyte, where

$$\bar{\zeta} = \psi - \operatorname{sgn}(\psi)\frac{kT}{ze}\log\left[1 + 4\frac{c_{\max}}{c}\sinh^2\left(\frac{ze\psi}{2kT}\right)\right] \quad (10)$$

is the apparent zeta potential in Eq. (1) and $c_{\max} = a^{-3}$ is a counterion concentration (charge density) where the viscosity is postulated to diverge [9]. The critical separation a is at least the solvated ion radius, but could be effectively larger due to under-estimation of steric effects in this lattice-gas-based model and (poorly understood) correlation effects on the viscosity. This theory reduces to Smoluchowski's at low voltages $\left(\bar{\zeta} \sim \psi \text{ for } |\psi| \ll \psi_c\right)$, but the electro-osmotic mobility saturates $\bar{\zeta} \sim \operatorname{sgn}(\psi)\psi_c$ at a concentration-dependent value,

$$\psi_c = \frac{kT}{ze}\log\left(\frac{c_{\max}}{c}\right) \quad (11)$$

at large voltages $|\psi| \gg \psi_c$. This model seems to qualitatively capture the basic features of ICEO flows in experiments, but a complete quantitative theory is still lacking. It may be necessary to go beyond the mean-field approximation (i. e. Poisson's equation for the electrostatic potential in the diffuse layer). Atomistic simulations and nanoscale experiments should be crucial to guide the further development of a modified theory of ICEO at large applied voltages.

Electrokinetic Phenomena of the Second Kind

There is growing body of experimental literature on nonlinear electro-osmotic flows around highly conductive, permselective ionite particles and porous structures in microfluidics [6, 7]. The basic velocity scaling (Eq. (8)) has been verified, and the time scale for the onset of the flow has been shown to be diffusive (L^2/D = minutes), not capacitive (Eq. (3)) (milliseconds). Imaging of second-kind flow around ionite particles with submicron tracers has shown that the largest electro-osmotic slip is near

the surfaces sustaining the largest incoming current density, resulting in a flow profile around a spherical particle, which resembles a shifted dipole or the structure in Fig. 3. Space–charge formation and concentration gradients have also been directly imaged in porous structures using charged and neutral tracers.

The mathematical theory of electro-osmosis of the second kind is still in its infancy. Scaling arguments modifying Eq. (8) have been made to quantify various effects in second-kind electrophoresis, such as advection-diffusion (large Péclet number), but precise flow fields and particle motions have not yet been calculated (or even approximated) starting from the underlying nonlinear partial differential equations of electrochemical hydrodynamics. Mathematical modeling of space charge formation has also mostly been restricted to one-dimensional conduction (as in Fig. 4).

An exception is the case of ▶electrokinetic/hydrodynamic flow instability at electro-dialysis membranes, where mathematical modeling has recently implicated second-kind electro-osmosis as a likely mechanism for super-limiting current. Starting from the classical Poisson–Nernst–Planck and Navier–Stokes equations, Rubinstein and Zaltzman have shown that one-dimensional conduction is stable until the bulk concentration approaches zero at the classical Nernst limiting current, due to fast Faradaic reactions limited by bulk diffusion [10]. In particular, hydrodynamic instability due to classical “first-kind” electro-osmotic and diffusio-osmotic flow does not occur. At the limiting current, the double layer expands, while remaining “thin” compared to the typical geometrical length scale, and assumes a non-equilibrium structure altered by the passage of normal current. In this thin space-charge layer, hydrodynamic instability occurs via second-kind electro-osmotic flows, and the resulting electro-convection brings concentrated fluid to the surface to enhance the reaction rate and exceed the diffusion-limited current.

A novel aspect of this theory is the derivation of a modified slip formula for second-kind electro-osmosis,

$$u_s = -\frac{\varepsilon V^2}{8\eta} \nabla_s \ln\left(\hat{n} \cdot \nabla c\right) \quad \text{(surface at limiting current)} \tag{12}$$

where V is the applied voltage on the surface [10]. The slip is thus given by the surface gradient of the normal diffusive flux entering the space charge layer. A unified theory of electro-osmotic slip at all applied voltages has also been derived and applied to the problem of hydrodynamic instability at electro-dialysis membranes. However, it has not yet been applied to second-kind electro-osmotic flows in other experimental situations of electrophoresis and microfluidic devices.

In spite of the complications resulting from concentration gradients and normal current, the classical transport equations used in this analysis are likely to remain valid for second-kind electro-osmosis. The reason is that the normal current prevents the overcharging of the diffuse layer, and instead most of the voltage drop occurs in the extended space charge layer, where the counterion concentration is small (and the co-ion concentration is negligible). Complicated effects of ion crowding, which are crucial in induced-charge electrokinetics at large voltages (e. g. Eqs. (9)–(11), are thus not important. This further underscores the difference between first-kind and second-kind induced-charge electrokinetic phemomena.

Examples of Applications

There are many applications of nonlinear electrokinetic phenomena in microfluidics. For example, the ▶dielectrophoretic motion of particles and cells is used for separating and concentrating biological samples. ▶Electrokinetic flow instability and ▶electrothermal effects can be used for microfluidic mixing.

Induced-charge electrokinetic phenomena are finding many new applications as well. ▶AC electro-osmotic flow is a promising means of microfluidic pumping and mixing in portable or implantable devices, since it requires low voltage and low power. ACEO has also been used in conjunction with DEP to trap, concentrate, and release particles and cells. ▶Induced-charge electro-osmosis can also be used for mixing, due to easy electrical control of complex flow patterns in space and time. ▶Induced-charge electrophoresis leads to complicated new behavior of polarizable colloids, e. g. perpendicular to an AC field, which can be exploited in new kinds of separations. In all of these cases, the use of relatively weak AC voltages, enabled by nonlinearity, is a major advantage over the large DC voltages required for linear electrokinetics, since it can greatly reduce unwanted Faradaic reactions, gas bubbles, electrode dissolution, and sample contamination.

Electrokinetic phenomena of the second kind have received mostly academic interest, but there may be important and unexpected applications. Already, second-kind electro-osmosis has been implicated as a mechanism for superlimiting current in electrodialysis. Space-charge formation at nanochannel/microchannel junctions has also been exploited to trap biomolecules, although in that case the flow is undesirable since it interferes with trapping. The speed of second-kind electrophoresis may be useful in separation or mixing, but the need to apply a large DC voltage may limit its applicability.

Cross References

- ► Aperiodic Electrophoresis
- ► AC Electro-Osmotic Flow
- ► Dielectrophoresis
- ► Dielectrophoretic Motion of Particles and Cells
- ► Diffusiophoresis
- ► Electrical Double Layers
- ► Electrokinetic/Hydrodynamic Flow Instability
- ► Electrokinetic Motion of Heterogeneous Particles
- ► Electrokinetic Motion of Polarizable Particles
- ► Electroosmotic Flow (DC)
- ► Electroosmosis of the Second Kind
- ► Electrophoresis of the Second Kind
- ► Electrophoresis
- ► Electrothermal Effects
- ► Induced-Charge Electro-Osmosis
- ► Induced-Charge Electrophoresis
- ► Space Charge
- ► Stotz–Wien Effect
- ► Super-Limiting Current
- ► Unbalanced AC Field

References

1. Murtsovkin VA (1996) Nonlinear flows near polarized disperse particles. Colloid J 58:341–349
2. Bazant MZ, Squires TM (2004) Induced-charge electrokinetic phenomena: theory and microfluidic applications. Phys Rev Lett 92:066010
3. Squires TM, Bazant MZ (2004) Induced-charge electro-osmosis. J Fluid Mech 509:217–252
4. Green NG, Ramos A, Gonzalez A, Morgan H, Castellanos A (2002) Fluid flow induced by nonuniform ac electric fields in electrolytes on microelectrodes. III. Observation of streamlines and numerical simulation. Phys Rev E 66:026305
5. Thamida SK, Chang HC (2002) Nonlinear electrokinetic ejection and entrainment due to polarization at nearly insulated wedges. Phys Fluid 14:4315–4328
6. Rathore AS, Horvath C (1997) Capillary electrochromatography: theories on electroosmotic flow in porous media. J Chromatogr A 781:185–195
7. Leinweber FC, Tallarek U (2004) Nonequilibrium electrokinetic effects in beds of ion-permselective particles. Langmuir 20:11637–11648
8. Levitan JA, Devasenathipathy S, Studer V, Ben Y, Thorsen T, Squires TM, Bazant MZ (2005) Experimental observation of induced-charge electro-osmosis around a metal wire in a microchannel. Colloid Surf A: Physicochem Eng Asp 267:122–132
9. Bazant MZ, Kilic MS, Storey B, Ajdari A (2007) Nonlinear electrokinetics at large applied voltages. http://www.arxiv.org/abs/cond-mat/0703035. (preprint)
10. Zaltzman B, Rubinstein I (2007) Electro-osmotic slip and electroconvective instability. J Fluid Mech 579:173–226
11. Ajdari A (2000) Pumping liquids using asymmetric electrode arrays. Phys Rev E 61: R45-R48
12. Ramos A, Morgan H, Green NG, Castellanos A (1999) AC electric-field-induced fluid flow in microelectrodes, J Colloid Interface Sci 217:420–422
13. Dukhin SS (1991) Electrokinetic phenomena of the 2nd kind and their applications. Adv Colloid Interface Sci 35:173–196
14. Dukhin AS, Dukhin SS (2005) Aperiodic capillary electrophoresis method using an alternating current electric field for separation of macromolecules. Electrophoresis 26:2149–2153
15. Dukhin AS (1993) Biospecific mechanism of double layer formation and peculiarities of cell electrophoresis. Colloid Surf A: Physicochem Eng Asp 73:29–48
16. Gamayunov NL, Mursovkin VA, Dukhin AS (1986) Pair interactions of particles in electric field. 1. Features of hydrodynamic interaction of polarized particles. Colloid J USSR 48:197–203
17. Squires TM, Bazant MZ (2006) Breaking symmetries in induced-charge electro-osmosis. J Fluid Mech 560:65–101

Nonlinear Electro-Osmosis

► Induced-Charge Electro-Osmosis

Nonlinear Electrophoresis

► Aperiodic Electrophoresis
► Electrophoresis of the Second Kind
► Induced-Charge Electrophoresis
► Stotz–Wien Effect

Nonlinear Electrophoretic Mobility

► Nonlinear Electrokinetic Phenomena

Non-Metallic Inorganic Materials

Synonyms

Glass; Ceramics; Oxides; Nitrides

Definition

In microfluidic systems, non-metallic inorganic material can be found as a bulk material (e. g., a glass chip or a quartz chip) or a coating (e. g., a dielectric transition metal oxide or nitride coating, or a natural silicon oxide layer on a silicon chip which is chemically similar to glass). Because of their ionic or heteropolar (dipoles) bonding character, non-metallic inorganic materials are usually hydrophilic, i. e. they are wetted rather well by water because the water molecules have also strong dipole character.

Cross References

► Glass-Polymer-Bonding

Non-Newtonian

► Chaotic Mixing Based on Viscoelasticity
► Viscoelasticity

Non-Newtonian Fluid

Definition

Any fluid that does not obey the Newtonian relationship, i. e. the Newton law of viscosity, is termed as a non-Newtonian fluid.

Cross References

► Turbulence in Microchannels
► Viscoelasticity
► Non-Newtonian Fluids in Microchannel
► Non-Newtonian Fluids in Microfluidics

Non-Newtonian Fluids in Microchannel

SUMAN CHAKRABORTY
Department of Mechanical Engineering, Indian Institute of Technology, Kharagpur, India
suman@mech.iitkgp.ernet.in

Synonyms

Rheological fluid flow in microchannels

Definition

Non-Newtonian fluids are characterized by the fact that the shear stresses in the fluids are not linearly proportional to the rate of deformation. It is well known that the mechanics of non-Newtonian fluids differs from the classical Newtonian fluid mechanics in many respects. One of the contrasting features of the non-Newtonian constitutive behavior is a rather non-generic nature of the pertinent governing equations, whereas for Newtonian fluids the Navier–Stokes equations are accepted without question as the appropriate conservation equations.

Chemical and Physical Principles

Biomedical micro-assay systems are continuously being developed to perform rapid clinical chemistry using minimal sample volumes. These systems are expected to improve the medical diagnostics and the patient monitoring system considerably, by eliminating the conventional protocols that are often slow and cumbersome. Other Lab-on-a-Chip based micro total analysis systems (which achieve fluid delivery, mixing, concentration and separation in a single chip, as fundamental fluidic operations) are also offering great promises in improving the sensitivity, specificity and the processing rates in several biochemical and biotechnological applications. For most of the bio-fluids that are routinely employed in these kinds of applications, Newtonian behavior appears to be an exception rather than the rule.

It is well known that the mechanics of non-Newtonian fluids differs from the classical Newtonian fluid mechanics in many respects. One of the contrasting features of the non-Newtonian constitutive behavior is a rather non-generic nature of the pertinent governing equations, whereas for Newtonian fluids the Navier–Stokes equations are accepted without question as the appropriate conservation equations.

Fundamentally, it is possible to characterize a class of fluids known as simple fluids [1], by postulating a functional relationship between the stress tensor at time t and the strain history of the material point with respect to its current configuration. For such fluids, the Cauchy stress tensor, $\boldsymbol{\tau}_{ij}$, can be expressed as [2]

$$\boldsymbol{\tau}_{ij} = -p\delta_{ij} + \mathbf{T}_{ij}\left(C_{\mathrm{mn}}^{-1}(t-s), 0 \leqslant s \leqslant \infty\right) \tag{1}$$

where $\mathbf{T}_{ij}$ is a tensor functional of the deformation history. The term in the bracket denotes the components of the Finger strain tensor of the fluid configuration at time $(t-s)$ with respect to the configuration at time t. A constitutive equation of this form implies the existence of a natural relaxation time scale λ, which can be compared with the corresponding time scale of flow, L/V. The ratio of these two quantities, known as the Weissenberg number ($\mathrm{W} = \lambda V/L$), turns out to be a key parameter in devising the mathematical forms of the non-Newtonian constitutive equations in certain cases, to be discussed later. Although somewhat generic in nature, a rather abstract form of the constitutive relationship depicted by Eq. (1) may not be sufficient to provide tractable equations for practical computations, even for the simplest of the flow problems. Physically, it may be more convenient to describe the mathematical models of constitutive behavior of non-Newtonian fluids by classifying them in terms of certain

distinctive flow features and addressing each class of fluid in a somewhat separate manner. A simple classification of non-Newtonian flows, in that perspective, is obtained as follows [2].

Flows Dominated by Shear Viscosity

For such flows, the range of flow rates is such that the variations in normal stresses are inconsequential relative to the shear stresses. Even when the fluid is highly elastic, the flow geometry and confinement may be such that the fluid elasticity has only a minor influence on the streamline orientations. On the other hand, shear-thinning effects upon the flow characteristics and the pressure distribution may appear to be quite important, even for low values of the shear rate. Such flow problems can be solved by considering constitutive equations that are of analogous (although, not necessarily the same) forms as those adopted for Newtonian flows, as follows:

$$\boldsymbol{\tau}_{ij} = -p\boldsymbol{\delta}_{ij} + 2\eta_a(I_2)D_{ij} \tag{2}$$

where $\mathbf{D}_{ij}$ is the rate of deformation tensor, η_a is the apparent viscosity and I_2 is a suitable form of the second invariant of $\mathbf{D}_{ij}$. The exact functional expressions of $\eta_a(I_2)$ are often fitted on the basis of experimental grounds; the well-known power-law fluids being just special cases of this functional behavior.

Slow Flows (Slightly Elastic Liquids)

In case the viscoelastic liquid is only slightly elastic, the general constitutive behavior depicted by Eq. (1) can be substantially simplified, by obtaining an asymptotic series of approximation in W, which can be taken as small under these conditions. As a consequence, one may arrive at the following second order constitutive model, for example [2]:

$$\boldsymbol{\tau}_{ij} = 2\eta\mathbf{D}_{ij} - \nu_1 \overset{\nabla}{\underset{ij}{D}} + 4\nu_2\mathbf{D}_{ik}\mathbf{D}_{kj} \tag{3}$$

where η, ν_1 and ν_2 are material constants and the overhead ∇ denotes the contravariant derivative, defined as

$$\overset{\nabla}{\underset{ij}{D}} = \frac{\partial \mathbf{D}_{ij}}{\partial t} + u_m \frac{\partial \mathbf{D}_{ij}}{\partial x_m} - \frac{\partial u_i}{\partial x_m}\mathbf{D}_{mj} - \frac{\partial u_j}{\partial x_m}\mathbf{D}_{im} \tag{4}$$

Substitution of Eq. (3) in the Navier's equation of motion and a subsequent expansion of the terms based on the small parameter, W, leads to a series of partial differential equations having the same structure as the Navier–Stokes equation (although, substantially more complicated in the details). However, this approach is only limited to the situations in which W can be taken as small.

Nearly Viscometric Flows

Such flows can be regarded as perturbations about basic viscometric flows, such as the Poiseuille flows or the Couette flows. Commonly, a suitable perturbation parameter is evident in nearly-viscometric flows and the problems classically solved by a perturbation expansion in that small parameter, the zero-order solution being the solution appropriate to viscometric flows. A general constitutive equation for all types of viscometric flows, however, cannot be trivially established.

Complex flows Involving Highly Elastic Fluids

These types of flows deal with fluids having a finite memory (i. e., the relaxation time, λ, is small) and the flow geometry and rates are such as to rule out the hierarchy of equations and the related constitutive expansions.
From a unified viewpoint, regardless of the class of flow, a general strategy for the solution of non-Newtonian flow problems may be to resort to the constitutive equations that are special cases of the general statement of Eq. (1) and at the same time are tractable enough to allow for numerical computations. A common approach towards achieving this goal is either to use a differential model or an integral model, relating the stress with the rate of deformation tensors. A commonly used differential model is the so-called *upper convected Maxwell model*, which has its constitutive equation in the form

$$\boldsymbol{\tau}_{ij} + \lambda \overset{\nabla}{\underset{ij}{\tau}} = 2\eta\mathbf{D}_{ij} \tag{5}$$

which is an implicit equation in the stress tensor, so that the stress components also need to be considered as dependent variables (along with the velocity components and pressure). The same model can also be expressed in an integral form, which is explicit in the stress tensor, for example

$$\boldsymbol{\tau}_{ij}(\boldsymbol{x}, t) = \frac{\eta}{\lambda^2}\int_{-\infty}^{t} \exp\left[-(t-t')/\lambda\right]\left[\mathbf{C}_{ij}^{-1}(t') - \boldsymbol{\delta}_{ij}\right] \mathrm{d}t' \tag{6}$$

where $\mathbf{C}_{ij}^{-1}$ is the Finger tensor, defined as

$$\mathbf{C}_{ij}^{-1} = \frac{\partial x_i}{\partial x_{m'}}\frac{\partial x_j}{\partial x_{m'}} \tag{7}$$

and x_i' is the position at time $t^/$ of the element that is instantaneously at the point x_i at time t'. This special form

is applicable to 'rubber-like' elastic beads, for which one needs to solve additional equations for obtaining the displacement functions (x_i'). These displacement functions can be obtained by setting $Dx_i'/Dt = 0$, for $i = 1$ to 3. The unknowns in the integral model, therefore, are the pressure, velocity and the displacement components.

Out of the various classes of non-Newtonian flows discussed as above, shear-viscosity dominated fluid flows are possibly the most common ones for typical bio-microfluidic applications. The Carreau viscosity model is one of the standard constitutive models used for many such applications. The apparent viscosity, as per this model, is given by [3]

$$\eta_a = \eta_\infty + (\eta_0 - \eta_\infty)\left[1 + (\lambda\dot{\gamma})^2\right]^{\frac{1}{2}} \tag{8}$$

The four parameters of this model, namely, $\eta_0, \eta_\infty, \lambda$ and n are the apparent viscosity at zero shear rate, apparent viscosity at infinite shear rate, time shear relaxation constant and the exponential index, respectively. The parameter λ has a unit of time and can assume any value in the range $(0, \infty)$. The index n is dimensionless, with $0 < n < 1$. Equation (8) is graphically represented in Fig. 1, for illustration. Various parameters assumed for obtaining the plots appearing in Fig. 1 are as follows: $\eta_0 = 900, \eta_\infty = 0.1$, and the non-dimensional time shear relaxation constant is defined as $\lambda^* = \lambda V/L$. From Fig. 1, it is apparent that for low values of λ^*, the constitutive behavior is practically Newtonian. For high values of λ^*, on the other hand, only marginal values of shear strain rates induce a significant non-Newtonian character. Some representative values of the Carreau parameters for different fluids are reported in the book of Tanner [3]. Based on typical values of these parameters, Zimmerman et al. [4] designed a two-dimensional finite elements model for non-Newtonian electrokinetic flows in microchannel T-junctions. Their studies revealed that the fluid experiences a range of shear rates as it turns around the corner, and the flow field was found to be extremely sensitive to the Carreau model parameters. These authors also obtained a one-to-one mapping between the model parameters and the end wall pressure, by employing a statistical analysis of the pressure profile for a wide range of operating and physical parameters. Such a mapping potentially allows one to determine the Carreau parameters of an unknown fluid if the end wall pressure profile is known, thereby establishing the working principle of a highly efficient viscometric device for microfluidics. However, the effects of viscous heating, Joule heating, net charges on the species and varying electrical properties were not considered in their study. Some of the common practical examples of non-Newtonian flows in microchannels involve the transport and manipulation of blood and blood-components in biomedical microdevices. While it has long been well-established that blood is essentially a *shear-thinning fluid'*(i.e., apparent viscosity decreases with increase in shear rate), the validity of existing constitutive models for different flow geometries at the microscale remains yet to be rigorously tested and justified. Terebotich et al. [5] investigated the use of a simple power law model for blood flow between 2.5 and 100 ml/min in microchannels with 200 μm × 60μm cross sections and having characteristic bends/sudden contractions. Including this model, in the literature, in general, there are four common models to describe the blood reheology, as follows:

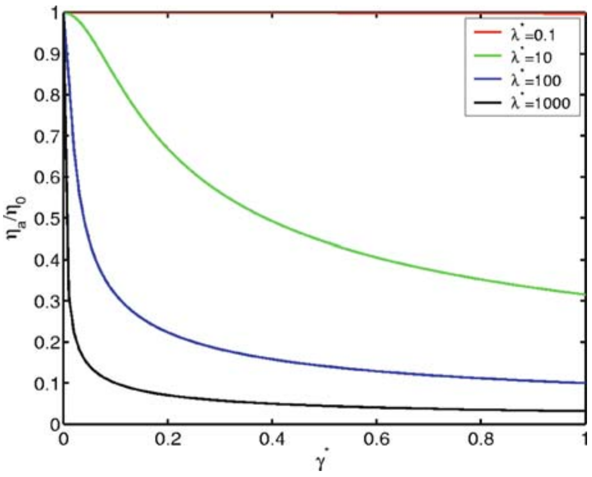

Non-Newtonian Fluids in Microchannel, Figure 1 Apparent viscosity as a function of the rate of shear strain, for the Carreau viscosity model

- Casson model: $\tau = \eta_c\dot{\gamma}^{\frac{1}{2}} + \tau_Y^{\frac{1}{2}}$, for $|\tau| \geqslant \tau_Y$ and $\dot{\gamma} = 0$, otherwise; where τ, $\dot{\gamma}$, η_c and τ_Y denote shear stress, shear rate, Casson viscosity and yield stress, respectively.
- Power law model: $\tau = k|\dot{\gamma}|^{n-1}\dot{\gamma}$, where k is the consistency parameter and n is the power-law index.
- Bingham plastic model: $\tau_{ij} = 2\left(\eta_B + \tau_y/\sqrt{2P}\right)D_{ij}$ if $1/2\tau_{ij}\tau_{ji} \geqslant \tau_y^2$, and $D_{ij} = 0$, otherwise. Here η_B is the plastic viscosity, and $P = D_{ij}D_{ji}$.
- Bi-viscosity model [6]: $\tau_{ij} = 2\left(\eta_B + \tau_y/\sqrt{2|P|}\right)D_{ij}$ if $|P| \geqslant P_c$, and $\tau_{ij} = 2\left(\eta_B + \tau_y/\sqrt{2|P_c|}\right)D_{ij}$, otherwise. The parameter P_c is based on the fact that $\beta = \eta_B\sqrt{2P_c}/\tau_Y$ controls the effective viscosity in the plug region. If β is small enough, the viscosity in the plug region is so large that the predictions from the bi-viscosity model and the Bingham plastic model are virtually identical. However, if β is too small then the viscosity changes drastically at the boundary of the plug region.

N

Various criticisms have been put forward in the literature in the favor or against some of the above-mentioned models. For example, in the power law model, the apparent viscosity diverges when $\dot{\gamma} = 0$, for pseudoplastic fluids ($n < 1$). On the other hand, in the Bingham plastic model, the apparent viscosity coefficient diverges if the shear rate becomes zero. Further, the constitutive forms of the Casson model and the Bingham plastic model are greatly modified by the shear stress distributions in the fluid and in fact, explicit equations for shear stress cannot be written for very low shear rates. The bi-viscosity model, on the other hand, gives a finite apparent viscosity even in the low shear rate regimes, and therefore has been preferred by some researchers. Typical bio-fluids, in reality, are somewhat complex in constitutive behavior, and possibly any single constitutive model might not be adequate enough to represent the corresponding rheological characteristics. For example, the case of blood, which is one of the most common bio-fluids can be cited. It is well known that blood is a nonhomogeneous, anisotropic, composite fluid, composed of a suspension of many asymmetric, relatively large viscoelastic particles carried in a liquid medium, which contains high molecular weight, asymmetric, polarized, long-chain polymers that behave in a complicated way under shear loading. Thus, blood typically shows nonlinear, time-dependant (viscoelastic) flow characteristics. Some researchers prefer to describe blood as a Bingham plastic, a power law fluid, or a Casson fluid. Nevertheless, in more simple terms, blood can be described as a pseudo-plastic fluid, with non-Newtonian behavioral index (n) lying between 0 and 1. Human blood, however, can show only a very slight Bingham plasticity, attributable mainly to the presence of the protein fibrinogen [7], but only appearing in blood samples having relatively higher hematocrit percentages. Therefore, in general, for all practical purposes the Bingham plastic characteristics of human blood can be neglected, and blood can approximately be modeled either as a power law fluid or a Casson fluid.

In the power-law models of blood rheology, the indices k and n are primarily dependent on the hematocrit fraction, which is a measure of the number and size distribution of red blood cells in the sample. The above functional dependence may take the following form under time-independent circumstances [7]:

$$k = C_1 \exp(C_2 h) \tag{9}$$

and

$$n = 1 - C_3 h \tag{10}$$

where h is the hematocrit fraction in the blood cells and C_1, C_2, C_3 are species specific coefficients that can be experimentally determined [8]. These coefficients, however, are not universal constants, but are rather dependant on several biological factors. For example, C_1 depends on the plasma globulin concentration and on the hematocrit. The parameter C_2 also depends on the plasma protein. Moreover, both C_1 and C_2 show more sensitivity to viscosity of blood plasma than to any other factors related to blood cells. On the other hand, C_3 is virtually independent of plasma chemistry and is remarkably constant for a given animal species. However, C_3 correlates directly with the cellular haemoglobin concentration. Haemoglobin content being the major determinant of intracellular erythrocyte viscosity, one can assume that C_3 is somewhat related to the latter.The dependence of C_1 on plasma composition and on hematocrit can be summarized by the equation [7]:

$$C_1 = C_1^* \exp[C_4(\mathrm{TPMA})/h^2] \tag{11}$$

where TPMA is total protein minus the albumin fraction of blood, $C_1^* = 0.00797 dPa(s)^n$ and $C_4 = 145.85 d\,\mathrm{lg}^{-1}$. Typically, total protein content of human blood is around 8% and albumin constitutes 60% of the blood protein. This means that standard value of TPMA fraction in blood is 0.032. Again, the average value hematocrit in human male is 45% [8]. From this information, one may directly estimate the value of C_1. For estimation of the other rheological parameters, one may appeal to suitable experimental correlations, for example, the one variable power law of Walburn and Schneck [8], which yields the following values: $n = 0.785$ and $k = 0.0134\,Pas^n$, at 37 °C.

Key Research Findings

In a very recent study, Chakraborty [7] demonstrated the influence of non-Newtonian rheological characteristics on the dynamics of flow of blood in a microfluidic channel. In his work, special attention was devoted to estimate the effects of variable hydraulic resistance over different flow regimes, influence of suspended RBC particulates on the non-Newtonian flow characteristics and implications of a dynamically-evolving contact angle. An expression of modified viscosity was employed in the above-mentioned study, based on the consideration that blood contains a suspension of particles, length scale of which can be characterized by characteristic dimension of a typical RBC (δ, say). Accordingly flow through a microchannel of hydraulic radius r_h can be thought of as flow through r_h/δ number of concentric layers of annular laminae, each having a finite layer thickness of δ. This gives rise to

a modified apparent viscosity, given by

$$\eta_a = \frac{\eta}{\left(1 + \frac{\delta}{r_h}\right)^2} \tag{12}$$

It can easily be observed here that for δ/r_h 1, the above effect is clearly inconsequential. However, in typical microscale circulations, order of δ may approach that of r_h, which would reduce the apparent viscosity by about half of its macroscale value, and would enhance the volumetric flow rate by about 4 times, in an order of magnitude sense. Such effects can be of significant consequence in case the bio-fluid sample contains a few number of relatively large suspension particles, even though the characteristic channel dimensions might otherwise preclude microcirculation. It can be noted here that the relatively large-sized suspended particles in a bio-fluid can have other interesting implications as well. To appreciate the pertinent implications, one first needs to appreciate that the streamlines that are closer to the centerline of the microchannel represent fluid velocities that are faster than the ones associated with fluid streamlines close to the wall. This gradient in velocity across any suspended particulates (say, RBC) starts the cell spinning in such a way that the side of the cell facing the channel centerline moves in direction of the flow, whereas the side of the cell facing wall of the vascular channel moves in a direction against the flow. This leads to a drift in the particulates away from the wall, resulting in existence of a region primarily constituted of the bulk fluid within a so-called skimming layer. This implies that near the walls (where viscous effects are most predominant), the effective viscosity becomes less, and the axial pressure gradients do not have to work as hard as it would have otherwise required (if particulates were densely populated near the walls) to drive the flow, and hence, the whole bio-fluid appears to be less viscous. This can effectively be modeled by dividing the entire flow cross section into two distinct zones, which are (i) a cell-rich central zone of thickness $(r_h - \delta)$, with an averaged mixture viscosity of μ_{av} and a cell free skimming zone of thickness δ near the wall, with a liquid viscosity of μ_l. The net effect is a modified apparent viscosity, which can be computed analogous to (12) as [7]

$$\eta_a = \frac{\eta_l}{1 - \left[1 - \left(\frac{\delta}{r_h}\right)\right]^4 \left[1 - \frac{\eta_l}{\eta_{av}}\right]} . \tag{13}$$

A third consequence of presence of suspension particulates can also be realized, by referring to the blood flow morphology, as an example. After the RBCs drift toward the channel centerline (due to reasons as explained earlier), the cells eventually equilibrate at some characteristic radial location. As they do so, they align with the flow streamlines in such a way that they offer least profile drag in the direction of flow. Thus, with progressive shearing, the apparent viscosity of blood tends to decrease.

Based on the above considerations, Chakraborty [7] developed a capillary-filling model for the transport of blood through microchannels. From his study, following major conclusions were drawn, regarding the implications of the non-Newtonian characteristics on the microchannel transport:

- Blunting of velocity profiles due to an axial accumulation of RBCs, as well as a streamline-RBC alignment strongly influences motion of blood into the channel.
- Axial accumulation of RBCs leaves behind a lower viscosity plasma skimming layer near the microchannel wall, which is, otherwise, a region of higher rates of strain. Consequently, the apparent viscosity of the whole blood sample decreases, and effects of this reduction become significantly prominent as size of the RBCs approaches hydraulic radius of the microchannel, leading to enhanced rates of fluidic transport.

In a more recent study, Das and Chakraborty [9] presented analytical solutions for velocity, temperature and concentration distribution in electroosmotic flows of non-Newtonian fluids in microchannels. A brief description of their transport model is summarized here, for the sake of completeness. A schematic diagram of the parallel plate microchannel configuration, as considered by the above authors, is depicted in Fig. 2. The bottom plate is denoted as $y = -H$ and top plate as $y = +H$. A potential gradient is applied along the axis of the channel, which provides the necessary driving force for electroosmotic flow. The governing equations appropriate to the physical problem are the equations for conservation of mass and linear momentum, potential distribution equation within the Electric Double Layer (EDL), energy conservation equation, and the species conservation equation for the transported solute. These equations can be described as follows:

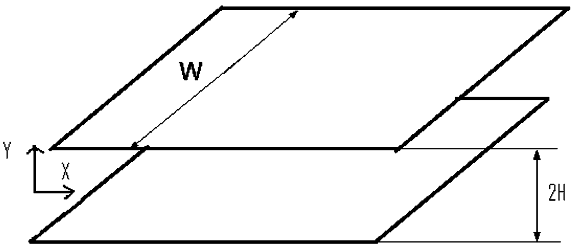

Non-Newtonian Fluids in Microchannel, Figure 2 Schematic diagram depicting a parallel plate microchannel

Continuity Equation

$$\frac{\partial\rho}{\partial t} + \nabla\cdot(\rho \boldsymbol{V}) = 0 \quad (14)$$

where ρ is the density of the fluid and $\boldsymbol{V}$ is the flow velocity.

Linear momentum equation

$$\frac{D}{Dt}(\rho \boldsymbol{V}) = \nabla\cdot(\tau) + \boldsymbol{b} \quad (15)$$

where τ is the stress tensor and $\boldsymbol{b}$ is the body force per unit volume, given as

$$\boldsymbol{b} = \rho_e \boldsymbol{E} \quad (16)$$

In Eq. (16), ρ_e is the net electric charge density and $\vec{E}$ is the applied external electric field.

Poisson–Boltzmann equation for potential distribution within EDL

$$\nabla\cdot(\nabla\psi) = -\frac{\rho_e}{\varepsilon} \quad (17)$$

where ψ denotes the EDL potential and ε is permittivity of the fluid. The net electric charge density, ρ_e, can be described as:

$$\rho_e = -2n_0 ez \sinh\left(\frac{ez\psi}{k_B T}\right) \quad (18)$$

where, n_0 is the ion density (in molar units), e is the electronic charge, z is the valence, k_B is the Boltzmann constant, and T is the absolute temperature. To depict the relationship between the net electric charge density and Debye length, n_0 can be expressed as a function of the Debye length, λ, as follows:

$$n_0 = \frac{\varepsilon k_B T}{8\pi e^2 z^2 \lambda^2} \quad (19)$$

Energy conservation equation

$$\frac{D}{Dt}(\rho C_P T) = \nabla\cdot(k_{Th}\nabla T) + \boldsymbol{\tau}\cdot\mathbf{D} + \dot{q} \quad (20)$$

where $\mathbf{D}$ is the strain rate tensor, k_{Th} is the thermal conductivity of the fluid, and $\dot{q}$ is the heat generation per unit volume due to Joule heating (which is a consequence of application of an electric field across a conductive liquid), given by:

$$\dot{q} = \frac{(\rho_e \boldsymbol{V} + \sigma\boldsymbol{E})\cdot(\rho_e \boldsymbol{V} + \sigma\boldsymbol{E})}{\sigma} \quad (21)$$

Here, σ is the electrical conductivity of the fluid.

Species conservation equation for the transported solute

$$\frac{D}{Dt}(\rho C) = \nabla\cdot(\rho D\nabla C) \quad (22)$$

where C denotes the instantaneous concentration of the solute being transported and D is the diffusion coefficient of the solute in the fluid.

The above equations were analytically solved under the following simplifying assumptions:

- The flow is incompressible and the fluid properties are independent of temperature.
- The velocity field is steady and fully developed, i.e., $u = u(y)$ and $v = 0$.
- There is no externally imposed pressure gradient, i.e., $-\partial p/\partial x = 0$.
- The temperature field is steady and fully developed, i.e., $\partial/\partial x(\frac{T-T_W}{T_m-T_W}) = 0$, subjected a constant surface heat flux, q_s'', where $T_W(x)$ is the wall temperature and $T_m(x)$ is the bulk mean flow temperature.
- The fluid obeys a power-law constitutive model, with n as the index.
- The flow is subjected to a constant axial concentration gradient, i.e., $\partial C/\partial x = \text{cons}\tan t = M(\text{say})$.
- The charge density field is calculated on the basis of an averaged temperature (T_{av}), for the sake of analytical treatment.
- The electric double layers formed at the microchannel walls do not overlap, and the Debye–Hückel linearization principle remains as valid.

Under the above assumptions, the final forms of the governing differential equations become:

$$kn\left(\frac{du}{dy}\right)^{n-1}\frac{d^2u}{dy^2} = -\rho_e E_x \quad (23)$$

$$\frac{d^2\psi}{dy^2} = -\frac{\rho_e}{\varepsilon} \quad (24)$$

$$uM_T = k\left(\frac{du}{dy}\right)^{n+1} + k_{Th}\frac{\partial^2 T}{\partial y^2} + \dot{q} \quad (25)$$

where $\partial T/\partial x = dT_m/dx = dT_W/dx = M_T$, which is a constant for a thermally fully developed flow with constant wall heat flux boundary condition. An explicit expression for M_T is discussed later. The simplified form of the species conservation equation is as follows:

$$\frac{\partial C}{\partial t} + u\frac{\partial C}{\partial x} = D\frac{\partial^2 C}{\partial y^2} \quad (26)$$

The boundary conditions consistent with the above mentioned governing equations, with one symmetric half of the

microchannel taken as the problem domain, are as follows:

$$u = 0 \quad \text{at} \quad y = -H \quad \text{and} \quad \frac{\mathrm{d}u}{\mathrm{d}y} = 0 \quad \text{at} \quad y = 0$$

$$\psi = \psi_0 \quad \text{(zeta potential) at} \quad y = -H \quad \text{and}$$

$$\frac{\mathrm{d}\psi}{\mathrm{d}y} = 0 \quad \text{at} \quad y = 0 \tag{27}$$

$$q_s'' = -k_{\mathrm{Th}} \frac{\partial T}{\partial y} \quad \text{at} \quad y = -H \quad \text{and}$$

$$\frac{\partial T}{\partial y} = 0 \quad \text{at} \quad y = 0$$

$$D \frac{\partial C}{\partial y} = \mu(t) \quad \text{at} \quad y = -H \quad \text{and}$$

$$\frac{\partial C}{\partial y} = 0 \quad \text{at} \quad y = 0 \tag{28}$$

where $\mu(t)$ typically describes the reactions taking place at the channel surface and can be expressed as:

$$\mu(t) = -E_1 C_{\mathrm{WALL}} \tag{29a}$$

where C_{WALL} is the instantaneous wall concentration of the solute at the given axial location and E_1 is a constant. Again time dependence of C_{WALL} can be expressed as:

$$C_{\mathrm{WALL}} = E_2 \exp(-Ft) \tag{29b}$$

where E_2 and F are time-independent constants. Equations (31a, b) can be combined to yield an equation of the following form:

$$\mu(t) = E \exp(-Ft) \tag{29c}$$

where E and F are some time-independent constants. It can be noted here that for non-reactive channel walls, $\mu(t) = 0$.

The initial condition for the unsteady concentration field is taken as follows:

$$C = 0 \quad \text{at} \quad t = 0 \tag{30}$$

Analytical solutions for the velocity, temperature and concentration field, consistent with the above-mentioned physical considerations, can be obtained as a parametric function of the Debye–Hückel parameter, $\omega = \sqrt{2n_0 e^2 z^2 / \varepsilon k_{\mathrm{B}} T_{\mathrm{av}}}$, as follows:

$$u = u(y) = \left(\frac{\varepsilon \omega E_x \psi_0}{2k \cosh(\omega H)} \right)^{\frac{1}{n}} \times \begin{bmatrix} \frac{n}{\omega}\{\exp(\frac{\omega y}{n}) - \exp(-\frac{\omega H}{n})\} \\ -\frac{1}{\omega - 2\omega n}\Big\{ \exp\left(\frac{\omega y}{n} - 2\omega y\right) \\ - \exp(-\frac{\omega H}{n} + 2\omega H)\Big\} \end{bmatrix}, \tag{31a}$$

for $-H \leqslant y \leqslant 0,\ n \neq \frac{1}{2}$

$$= \left(\frac{\varepsilon \omega E_x \psi_0}{2k \cosh(\omega H)} \right)^2 \times \begin{bmatrix} \frac{1}{2\omega}\{\exp(2\omega y) - \exp(-2\omega H)\} \\ -2(y + H) \end{bmatrix}, \tag{31b}$$

for $-H \leqslant y \leqslant 0,\ n = \frac{1}{2}$.

To obtain the temperature field, it is assumed that in comparison to the electric field, the velocity field does not contribute significantly towards Joule heating. This implies

$$\dot{q} = \sigma E_x^2 \tag{32}$$

Further, the constant M_{T} can be evaluated by performing an overall energy balance for an elemental control volume, to obtain

$$\dot{m} C_P \frac{\mathrm{d}T_m}{\mathrm{d}x} = 2(q_s'' + \sigma E_x^2 H) \tag{33}$$

which yields,

$$\frac{\mathrm{d}T_m}{\mathrm{d}x} = \frac{2(q_s'' + \sigma E_x^2 H)}{\dot{m} C_P} = M_{\mathrm{T}} \tag{35a}$$

where $\dot{m}$ is the mass flow rate (per unit width of the plates), which can be evaluated as

$$\dot{m} = 2\rho \int_{-H}^{0} u \mathrm{d}y = 2\rho \left(\frac{\varepsilon \omega E_x \psi_0}{2k \cosh(\omega H)} \right)^{\frac{1}{n}} \begin{bmatrix} \frac{n}{\omega^2}\left\{ n - (n + H\omega)\exp\left(-\frac{H\omega}{n}\right) \right\} - \\ \frac{1}{(\omega - 2\omega n)^2} \left(\begin{array}{c} n - \exp\left[-\frac{H\omega}{n} + \frac{H\omega(2n-1)}{n} \right] \\ \left\{ n \exp\left(\frac{H\omega}{n}\right) + H\omega \exp\left[2H\omega - \frac{H\omega(2n-1)}{n} \right] \right. \\ \left. -2Hn\omega \exp\left[2H\omega - \frac{H\omega(2n-1)}{n} \right] \right\} \end{array} \right) \end{bmatrix} \tag{34a}$$

for $n \neq \frac{1}{2}$,

$$= 2\rho\left(\frac{\varepsilon\omega E_x\psi_0}{2k\cosh(\omega H)}\right)^2 \cdot\left[\frac{1}{4\omega^2} - \frac{1}{4\omega^2}\exp(-2\omega H) - \frac{H}{2\omega}\exp(-2\omega H) - H^2\right] \tag{34b}$$

for $n = \frac{1}{2}$.

A variation in T_w (or equivalently, T_m) can now be obtained by noting that $\mathrm{d}T_m/\mathrm{d}x = \mathrm{d}T_w/\mathrm{d}x = M_\mathrm{T}$, in conjunction with the inlet condition given as: $T_\mathrm{W} = T_\infty$ at $x = 0$, to yield:

$$T_\mathrm{W}(x) = M_\mathrm{T}x + T_\infty \tag{36}$$

Equation (25) can be subsequently solved, with the aid of following conditions:

$$T = T_\mathrm{W}(x) \quad \text{at} \quad y = -H \quad \text{and} \quad \frac{\partial T}{\partial y} = 0 \quad \text{at} \quad y = 0 \tag{37a}$$

to obtain a temperature distribution in the following form:

$$T = T(x,y) = -\frac{k}{k_\mathrm{Th}}\left(\frac{\varepsilon\omega E_x\psi_0}{2k\cosh(\omega H)}\right)^{\frac{n+1}{n}} \cdot\left[\begin{array}{c} \frac{n^2}{(n+1)^2\omega^2}\left\{\exp\left(\frac{n+1}{n}\omega y\right) - \exp\left(-\frac{n+1}{n}\omega H\right)\right\} \\ -\frac{(n-1)^2}{4\omega^2 n(n+1)}\left\{\exp\left(\frac{n+1}{n}\omega y - 2\omega y\right) - \right. \\ \left.\exp\left(-\frac{n+1}{n}\omega H + 2\omega H\right)\right\} - \frac{n^2+1}{2\omega n(n+1)}(y+H) \end{array}\right]$$

$$+ \frac{M_\mathrm{T}}{k_\mathrm{Th}}\left(\frac{\varepsilon\omega E_x\psi_0}{2k\cosh(\omega H)}\right)^{\frac{1}{n}} \left[\begin{array}{c} \frac{n^3}{\omega^3}\left\{\exp\left(\frac{\omega y}{n}\right) - \exp\left(-\frac{\omega H}{n}\right)\right\} - \frac{n}{2\omega}\exp\left(-\frac{\omega H}{n}\right) \\ (y^2 - H^2) \\ -\frac{n^2}{(\omega-2\omega n)^3}\left\{\exp\left(\frac{\omega y}{n} - 2\omega y\right) - \exp\left(-\frac{\omega H}{n} + 2\omega H\right)\right\} \\ \frac{1}{2\omega(1-2n)}\exp\left(\frac{\omega H}{n} - 2\omega H\right)(y^2 - H^2) \\ -\left\{\frac{n^2}{\omega^2} - \frac{n}{(\omega-2\omega n)^2}\right\}(y+H) \end{array}\right]$$

$$+ M_\mathrm{T}x + T_\alpha - \frac{\sigma E_x^2}{2k_\mathrm{Th}}(y^2 - H^2) \tag{36a}$$

for $-H \leqslant y \leqslant 0,\ n \neq \frac{1}{2}$,

$$= -\frac{k}{3\omega k_\mathrm{Th}}\left(\frac{\varepsilon\omega E_x\psi_0}{2k\cosh(\omega H)}\right)^3 \times\left[\frac{1}{3\omega}\{\exp(3\omega y) - \exp(-3\omega H)\} - (y+H)\right]$$

$$+ \frac{3k}{2\omega^2 k_\mathrm{Th}}\left(\frac{\varepsilon\omega E_x\psi_0}{2k\cosh(\omega H)}\right)^3 \times\left[\frac{1}{\omega}\{\exp(\omega y) - \exp(-\omega H)\} - (y+H)\right]$$

$$+ \frac{M_\mathrm{T}}{k_\mathrm{Th}}\left(\frac{\varepsilon\omega E_x\psi_0}{2k\cosh(\omega H)}\right)^2 \times\left[\begin{array}{c} \frac{1}{8\omega^3}\{\exp(2\omega y) - \exp(-2\omega H)\} - \frac{y+H}{4\omega^2} - \\ \frac{\exp(-2\omega H)}{4\omega}\left(y^2 - H^2\right) - \frac{1}{3}\left(y^3 + H^3\right) - H\left(y^2 - H^2\right) \end{array}\right]$$

$$+ M_\mathrm{T}x + T_\alpha - \frac{\sigma E_x^2}{2k_\mathrm{Th}}\left(y^2 - H^2\right) \tag{36b}$$

for $-H \leqslant y \leqslant 0,\ n = \frac{1}{2}$.

Analogously, the solutal concentration field can be obtained as

$$C = C(y,t) = \sum_{r=1}^{\infty}\left[\frac{w_0}{\exp(M_1 t)} + \frac{B_2}{M_1}\{1 - \exp(-M_1 t)\} + \frac{2EH\cos(r\pi)F}{D(r\pi)^2(M_1 - F)}\{\exp(-Ft) - \exp(-M_1 t)\}\right] \times\cos\left(\frac{r\pi y}{H}\right) - \frac{E\exp(-Ft)}{2HD}y^2 \tag{37a}$$

for $-H \leqslant y \leqslant 0,\ n \neq \frac{1}{2}$,

$$= \sum_{r=1}^{\infty}\left[\frac{w_0}{\exp(M_1 t)} + \frac{B_2'}{M_1}\{1 - \exp(-M_1 t)\} + \frac{2EH\cos(r\pi)F}{D(r\pi)^2(M_1 - F)}\{\exp(-Ft) - \exp(-M_1 t)\}\right] \times\cos\left(\frac{r\pi y}{H}\right) - \frac{E\exp(-Ft)}{2HD}y^2 \tag{37b}$$

for $-H \leqslant y \leqslant 0,\ n = \frac{1}{2}$.

The other terms appearing in the above equation are defined as follows:

$$M_1 = \left(\frac{r\pi}{H}\right)^2 \quad (37c)$$

$$w_0 = -\frac{2E}{HDM_1}\cos(r\pi) \quad (37d)$$

$$B_2 = M\left(\frac{\varepsilon\omega E_x\psi_0}{2k\cosh(\omega H)}\right)^{\frac{1}{n}} S_6 \quad (37e)$$

$$B_2' = M\left(\frac{\varepsilon\omega E_x\psi_0}{2k\cosh(\omega H)}\right)^{2} S_6' \quad (37f)$$

where $M = \frac{\partial C}{\partial x} = \cos\tan t$,

$$S_6 = \frac{2H^2n^2\left\{1-\exp\left(-\frac{H\omega}{n}\right)\cos(r\pi)\right\}}{H^2\omega^2+n^2r^2\pi} + 2\frac{\left(\begin{array}{l}\exp\left(-\frac{H\omega}{n}\right)\left\{-Hn\exp\left(-\frac{H\omega}{n}\right)\right. \\ \left.+2Hn^2\exp\left(\frac{H\omega}{n}\right)\right\} \\ +\exp\left(-\frac{H\omega}{n}+2H\omega\right)\left\{-Hn\cos(r\pi)\right. \\ \left.+2Hn^2\cos(r\pi)\right\}\end{array}\right)}{(1-2n)\left\{(2Hn\omega-H\omega)^2+(rn\pi)^2\right\}} \quad (37g)$$

$$S_6' = \frac{1}{4\omega H}\left[\frac{2\omega}{4\omega^2+M_1^2}(1-\exp(-2\omega H)\cos(M_1H))\right] - \frac{1}{HM_1^2}[1-\cos(M_1H)] \quad (37h)$$

For the cases in which the solute does not undergo any chemical reaction at the channel walls, Eq. (39) reduces to the following simplified form:

$$C = C(y,t) = \sum_{r=1}^{\infty}\left[\frac{B_2}{M_1}\{1-\exp(-M_1t)\}\right]\cos\left(\frac{r\pi y}{H}\right)$$

$$\text{for } -H \leqslant y \leqslant 0,\ n \neq \frac{1}{2} \quad (38a)$$

$$C = C(y,t) = \sum_{r=1}^{\infty}\left[\frac{B_2'}{M_1}\{1-\exp(-M_1t)\}\right]\cos\left(\frac{r\pi y}{H}\right)$$

$$\text{for } -H \leqslant y \leqslant 0,\ n = \frac{1}{2} \quad (38b)$$

Examples of Application

The applications related to non-Newtonian fluid flow through microchannels are mostly associated with the transport of biofluids, with blood as the most common example. Utilizing the mathematical model outlined as above, recent efforts have been directed to understand the implications of various rheological characteristics of blood on electrokinetically driven microfluidic transport [9]. The simulation studies based on the above-mentioned mathematical model clearly revealed that although changes in hematocrit fraction have relatively insignificant impacts on temperature distribution, their effects on concentration distribution are rather profound. As such, due to stronger dispersive effects in the velocity profile, the maximum concentration was observed to decrease with an increase in hematocrit fraction. Although the above simulation studies were executed on the basis of a fairly general framework, outlines were given on the possibilities of extending the simulation results to analyze more complicated bio-fluidic transport mechanisms. Other than understanding these basic rheological mechanisms behind microscale-transport processes of blood samples, results from the above study might also be utilized to design optimal micro-devices for blood diagnostics, by characterizing the segregation and aggregation effects of the transported solute, which can greatly influence the operating efficiency of micro-devices. For instance, the significance of leukocyte interactions with platelets, RBCs, and endothelial cells can be well characterized, by coupling the appropriate macromolecular interaction characteristics with the present generic model. The processes of leukocyte activation, adhesion and sequestration play major roles in exacerbating malperfusion associated with tissue injury and in the early stages of development of cardiovascular diseases, and this model can be extended to a basic fluid-dynamic characterization of the same. With a basic understanding of the relation between leukocyte rolling and adherence under different flow conditions, one might probe into the kinetics of interstitial accumulation of leukocytes during ischemia and after reperfusion. In fact, the increased adherence of leukocytes seen during low-flow conditions might be an important mechanism in the overall pathophysiology of inflammatory states that are accompanied by reduced blood flow. In essence, one might obtain deeper understandings regarding the effects of non-Newtonian properties of blood, nonuniform hematocrit distribution and leukocyte adhesion on flow in small vessels, by extending the general formulation to more specific cases. In particular, to trace the evolution of the core region as the blood passes by the leukocytes, an immiscibility condition between the plasma phase and RBC core phase may be imposed by introducing a solute conservation equation, of the same form as the species conservation equation employed in this study. This can also be employed to obtain a hematocrit distribution, as the same is convected along the streamlines. The species conser-

vation model can also be utilized for theoretical evaluation of concentration distribution of fluorescent particles, which are often employed for the measurement of plasma velocity in blood samples. The above-mentioned generic model can also be aimed to analyze macromolecular (such as DNA, RNA) transport characteristics within electroosmotically driven non-Newtonian microflows, with a special emphasis towards understanding the consequences of interaction between the applied electric field with the EDL potential, and the resultant temperature rises owing to Joule heating effects, which can be of utmost practical significance. Such studies, therefore, can be of particular consequence towards understanding the role of erythrocyte density on the rate of macromolecular transport through microchannels under electroosmotic effects, for designing of biomicrofluidic systems as solutal carriers.

The examples of non-Newtonian microchannel flows cited in the present article so far inherently assume that the continuum hypothesis is not disobeyed, so far as the description of the basic governing equations is concerned. This, however, ceases to be a valid consideration in certain fluidic devices, in which the characteristic system length scales are of the same order as that of the size of the macromolecules being transported. Fan et al. [10], in a related study, used the concept of finitely extended nonlinear elastic (FENE) chains to model the DNA molecules and employed the dissipative particle dynamics (DPD) approach to simulate the underlying flow behaviour in some such representative cases. From their results, it was revealed that simple DPD fluids essentially behave as Newtonian fluids in Poiseuille flows. However, the velocity profiles of FENE suspensions could be fitted with typical power-law curves, especially for dilute suspensions. More detailed investigations, indeed, need to be executed to establish and generalize this proposition for many complex fluids, possibly by drawing analogies from other theoretical viewpoints as well (the micropolar fluid theory, for instance). These system level predictions can also be substantiated by executing comprehensive molecular dynamics simulations for nano-scale flow geometries.

Cross References

- ► Electrical Double Layers
- ► Electrokinetic Flow and Ion Transport in Nanochannels
- ► Electrokinetic Flow in Porous Media
- ► Electrokinetic Motion of Polarizable Particles
- ► Electrokinetic Motion of Cells and Nonpolarizable Particles
- ► Electroosmotic Flow (DC)
- ► AC Electro-Osmotic Flow
- ► Electroviscosity
- ► Heat Tansfer in Microchannel Flows
- ► Microfluidic Bioreactors
- ► Viscous Dissipation

References

1. Truesdell C, Noll W (1965) The non-linear field theories of mechanics. In: Flügge S (ed) Encyclopedia of Physics. vol III, Springer, Berlin, Göttingen, Heidelberg
2. Crochet MJ, Walters K (1983) Numerical methods in non-Newtonian fluid mechanics. Ann Rev Fluid Mech 15:241–260
3. Tanner RI (2002) Engineering rheology. Oxford University Press, Oxford
4. Zimmerman WB, Rees JM, Craven TJ (2006) Rheometry of non-Newtonian electrokinetic flow in a microchannel T-junction. In: Microfluidics and Nanofluidics. DOT 10.1007/s10404-006-0089-4
5. Trebotich D, Chang W, Lippmann D (2001) Modelling of blood flow in simple Microsystems, in proc. In: Of Modeling and Simulation of Microsystems 2001, ISBN 0-9708275-0-4
6. Nakamura M, Sawada T (1987) Numerical study on the laminar pulsatile flow of slurries. J non-Newtonian Fluid Mech 22:191–206
7. Chakraborty S (2005) Dynamics of capillary flow of blood into a microfluidic channel. Lab Chip 5:421–430
8. Schnek DJ, Lucas CL (1990) Biofluid mechanics. New York University Press, New York
9. Das S, Chakraborty S (2006) Analytical Solutions for Velocity, Temperature and Concentration Distribution in Electroosmotic Microchannel Flows of a Non-Newtonian Bio-fluid. Anal Chim Acta 559:15–24
10. Fan X, Phan-Tien N, Yong NT, Wu X, Xu D (2003) Microchannel flow of a macromolecular suspension. Phys Fluid 15:11–21

Non-Newtonian Fluids in Microfluidics

SHELLEY L. ANNA
Department of Mechanical Engineering, Carnegie Mellon University, Pittsburgh, PA, USA
sanna@cmu.edu

Synonyms

Rheology; Complex fluids; Polymer solutions; Suspensions

Definition

Non-Newtonian fluids exhibit complex flow behavior, typically because they contain additives such as polymers or particles that alter the response of the fluid. Unlike Newtonian fluids, which have constant viscosity (resistance to flow), the viscosity of a non-Newtonian fluid is not constant. The viscosity depends on the shear rate and the amount of strain accumulated, as well as the nature of the additives, including the concentration of additives, the

polymer molecular weight, and the particle size. In addition, flexible polymers stretch in a flow, leading to an elastic response. Development of microfluidic devices has centered on miniaturizing assays to analyze the biological, physical, and chemical properties of DNA, proteins, and biopolymers in solution, as well as suspensions of cells and bioparticles. Since the analysis is typically performed in the liquid state, non-Newtonian flow behavior must be considered. This entry discusses how biomolecules alter the flow behavior of a liquid, and how microfluidics can be used to characterize the molecular properties and the flow or *rheological* behavior.

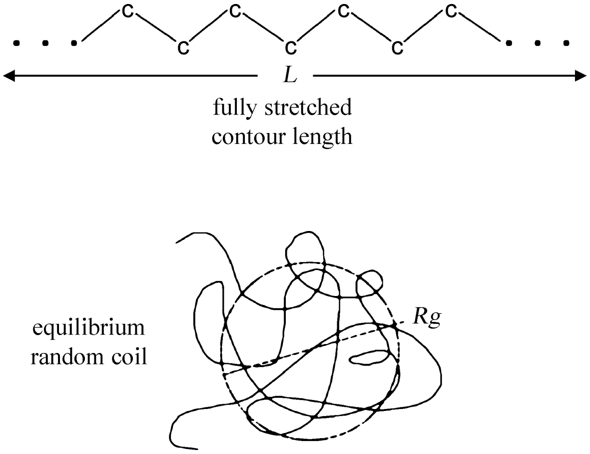

Non-Newtonian Fluids in Microfluidics, Figure 1 Schematic illustration of the molecular conformation of a polymer, including a fully stretched chain with contour length L and an equilibrium random coil with radius of gyration R_g

Overview

The viscosity of a liquid is a parameter that measures the resistance of that liquid to flow. For example, water has a very low viscosity, while honey has a much larger, or 'thicker' viscosity. Newtonian fluids have constant values of viscosity, which means that the stress in a flowing liquid is proportional to the rate of strain of the flow. Non-Newtonian liquids do not have constant viscosity, but rather have viscosities that can be functions of the rate of strain, the total amount of strain, and other flow characteristics. Fluids are usually non-Newtonian as a result of microscopic additives such as polymers or particles. These additives alter the viscosity of a liquid and impart nonlinear flow behavior, such as viscoelasticity. The non-Newtonian behavior of many complex liquids is described thoroughly in several texts, for example [1]. In this entry we focus on behavior and applications of polymer solutions in microfluidic devices. For example, DNA is a biopolymer that is common in microfluidics applications such as gene sequencing and amplification.

A *polymer* is a long, chain-like molecule consisting of many *monomers*, or building blocks, connected together via covalent bonds. Among biologically interesting polymers used in microfluidics, DNA contains building blocks consisting of nucleotide base pairs, and proteins are built from amino acids. The *contour length* L of a polymer chain is the maximum length of the chain when fully stretched. This length is proportional to the molecular weight M. However, the fully stretched conformation is not energetically favored at equilibrium. Rotational freedom about each bond leads to flexibility and a large number of possible configurations. When the persistence length λ_p, a measure of the polymer stiffness, is much shorter than the contour length, $\lambda_p \ll L$, the polymer is said to be flexible, and its equilibrium shape is modeled as a sphere with *radius of gyration*, R_g, depicted schematically in Fig. 1. The radius of gyration depends on the molecular weight and the polymer interaction with the surrounding solvent, or the *solvent quality*. At *theta conditions*, which are conditions in which the segments of the polymer chain have equal preference to be near other polymer chain segments or solvent molecules, the polymer adopts a *random coil* conformation, in which R_g is given by

$$R^2_{g,\theta} = C_\infty n\ell^2 \tag{1}$$

where C_∞ is the characteristic ratio, which is a constant coefficient whose values are tabulated for various polymers. The characteristic ratio allows for short-range interactions due to the chemistry of the polymer chain. Also, $n = M/M_0$ is the number of bonds in the backbone, λ is the length of a bond, and M_0 is the monomer molecular weight. In a good solvent, the polymer chain has a greater affinity for the solvent molecules and the coil is expanded relative to the theta chain. The coil size is related to solvent quality through an excluded volume exponent, ν, where $R_g \sim M^\nu$. For a theta solvent, $\nu = \frac{1}{2}$, consistent with Eq. (1). For good solvents, $0.5 < \nu < 0.6$. For example, double-stranded DNA has a persistence length of about $\lambda_p = 50 - 70$ nm, and forms a random coil when the length is $50 - 1000$ kbp. T4 DNA containing 169 kbp has a contour length $L = 70$ μm, and a radius of gyration $R_g \approx 1.5$ μm [8].

Polymers increase the solution viscosity, and the *intrinsic viscosity*, $[\eta]$, is a measure of the contribution of a single polymer molecule to the overall viscosity. The intrinsic viscosity is defined by writing a Taylor expansion for the solution viscosity η as a function of concentration c,

$$\eta = \eta_s \left(1 + [\eta]\, c + k_H\, [\eta]^2\, c^2 + \dots\right) . \tag{2}$$

The intrinsic viscosity is determined by extrapolating the viscosity to infinite dilution, $c \to 0$. In Eq. (2), η_s is the solvent viscosity and k_H is a constant [2]. Thus, the solution viscosity can be written as the sum of the solvent viscosity η_s and the polymer contribution to the viscosity, $\eta = \eta_s + \eta_p$. For an equilibrium coil R_g is related to the intrinsic viscosity by the Flory–Fox equation, $[\eta] = \Phi_0 R_g^3/M$, where $\Phi_0 = 3.67 \times 10^{24}\,\text{mol}^{-1}$ is a universal constant.

When a polymer chain is placed in a flow field, the coil stretches out of its equilibrium state and rotates in the flow field. These conformation changes dramatically impact the global flow response of a polymer solution, beyond simply enhancing the viscosity of the solution. *Shear thinning* and *viscoelasticity* are two key behaviors observed in polymer solution flows. Rotation of the polymer chain in a shear flow leads to shear thinning, in which the viscosity decreases with increasing shear rate. The power law model is a simple model used to describe this behavior, where the viscosity is given by

$$\eta = m\dot{\gamma}^{n-1} \tag{3}$$

where $\dot{\gamma}$ is the shear rate and m and n are constants [3]. In reality, the viscosity of a polymer solution varies from a zero-shear-rate plateau value, η_0, to a high shear rate plateau value, $\eta_\infty \approx \eta_s$.

When a polymer chain stretches, entropy tends to return the coil to its equilibrium configuration, leading to an elastic restoring force. Thus, elastic stresses are generated as the polymer chain stretches and relaxes in response to flow. A liquid exhibiting both elastic and viscous stresses is *viscoelastic*. We note that the ratio of a viscosity η to an elastic modulus G yields a characteristic *relaxation time* $\lambda \sim \eta/G$ characterizing the 'memory' of a fluid of its past deformation history, or the timescale for a stretched polymer chain to relax toward equilibrium.

The relaxation time λ and the polymer contribution to the viscosity η_p depend strongly on the polymer molecular weight, concentration, and equilibrium conformation. Kinetic theory can be used to obtain scaling behavior for these quantities. At dilute concentrations, for example, the Zimm bead-spring model predicts the relaxation time as a function of the drag on polymer chain segments,

$$\lambda \sim \frac{6\pi\eta_s}{k_B T} R_g^3 \sim M^{3\nu}, \tag{4}$$

where k_B is the Boltzmann constant and T is the solution temperature [1]. Similarly,

$$\eta_p \sim \frac{c N_A k_B T \lambda}{M} \sim M^{3\nu-1} \tag{5}$$

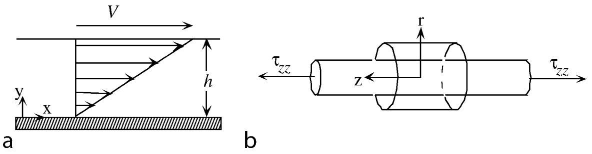

Non-Newtonian Fluids in Microfluidics, Figure 2 Schematic diagram of two simple flow types. (**a**) Simple shear flow between parallel rigid surfaces with gap *h*. (**b**) Uniaxial elongational flow in a cylindrical fluid filament stretching along its axis *z*

where N_A is Avogadro's number. For example, T4 DNA containing 169 kbp dissolved in buffer with $\eta_s = 1$ cP has a relaxation time of $\lambda = 1.7$ s [8].

It is useful to describe non-Newtonian flows in terms of the *Deborah number*, a dimensionless group describing the ratio of the viscoelastic relaxation time, λ, and a characteristic timescale for the flow, t_{flow},

$$\text{De} = \frac{\lambda}{t_{flow}} \tag{6}$$

The flow timescale can be defined in terms of an inverse shear rate or a residence time, for example. When De is small, polymer chains have ample time to relax toward equilibrium, and the fluid behavior is viscous. When De is large, the polymer chains elongate in the flow and do not have time to relax. In this limit, the fluid behavior is predominantly elastic. The *coil-stretch transition* occurs at $\text{De} = \frac{1}{2}$, above which a majority of polymer chains elongate with the flow. Below this limit, a majority of polymer chains do not deform significantly away from the equilibrium coil size.

In addition to the flow 'strength', characterized by the Deborah number, non-Newtonian flows can also be characterized by the *flow type*. Any flow can be described in terms of contributions from three basic deformations: pure rotation, pure shearing (or sliding) motions, and pure stretching (or elongational) motions. For example, the simple shear flow depicted in Fig. 2a is described by a rate-of-strain tensor containing only off-diagonal components, while the uniaxial elongational flow depicted in Fig. 2b is described by a rate-of-strain tensor containing only diagonal components. Many useful flows contain a mixture of rotation, shearing, and stretching, which can be quantified in terms of a *flow type parameter* ξ,

$$\xi = \frac{|\mathbf{E}| - |\mathbf{\Omega}|}{|\mathbf{E}| + |\mathbf{\Omega}|} \tag{7}$$

where $|\mathbf{E}|$ and $|\mathbf{\Omega}|$ are the magnitudes of the deformation and vorticity tensors [5]. This parameter varies from $-1 < \xi < +1$, encompassing the full spectrum of flow types, where $\xi = -1$ corresponds to pure rotation, $\xi = 0$

corresponds to pure shearing, and $\xi = +1$ corresponds to pure straining. Intermediate values denote *mixed flows*.

Polymer solutions respond in dramatically different ways to pure shearing and pure straining deformations. For example, the elongational viscosity of a polymer solution can be up to 1000 times larger than the shear viscosity. Although the flow in a straight microchannel segment is a pure shearing flow, microfluidic devices often contain complex geometric elements such as contractions, expansions, and cross-flows. Flows in these geometries contain significant elongational components, and thus, characterizing the flow type in a given geometry is essential to predicting and controlling the polymer solution behavior in that device. In summary, non-Newtonian flows can be characterized by at least two key parameters: the dimensionless strain rate De, and the flow type parameter ξ. In the following sections we will describe applications of non-Newtonian flows in microfluidics that utilize the full spectrum of these parameters.

Basic Methodology

Non-Newtonian liquids are used in numerous microfluidics applications, including microscale viscosity and rheology measurements, amplification and sequencing of DNA, fundamental investigations of elastic flows, and development of fluidic memory and control devices. Although these applications span a wide range of flow conditions and non-Newtonian fluid properties, similar experimental methods are used. In this section we summarize some of the experimental considerations for driving non-Newtonian flows, controlling the nature of these flows through the device geometry, and characterizing the non-Newtonian flow behavior.

Methods available to control non-Newtonian flows are the same as for Newtonian flows, including pressure-driven flows via syringe pumps, capillary driven flows, and electrokinetic flows. These methods and others are covered in more detail in other entries. In many cases the behavior of polymer solutions subject to a driving force is similar to that of the corresponding Newtonian solvent as long as the characteristic strain rate remains below the coil-stretch transition, or $\mathrm{De} < \frac{1}{2}$. Above this critical value, shear thinning and elasticity are important.

Pressure-driven flow is one of the most common methods of driving non-Newtonian flows. Below the coil-stretch transition, a polymer solution in a straight microchannel behaves as a Newtonian liquid, exhibiting a parabolic velocity profile $u(x, y)$ and a pressure gradient $\Delta \mathrm{p}$ along the channel axis that is linearly proportional to the volumetric flow rate Q and the total viscosity of the solution $\eta = \eta_\mathrm{s} + \eta_\mathrm{p}$, given by Eq. (2). In a channel with rectangular cross-section, this pressure drop–flow rate relationship is given by

$$\frac{\Delta \mathrm{p}}{L} \cong \frac{12\eta Q}{wh^3}\left[1 - 6\left(\frac{2}{\pi}\right)^5 \frac{h}{w}\right]^{-1} \tag{8}$$

where L is the length of the channel segment, w is the width of the channel, and h is the depth of the microchannel [3]. The approximate expression given here is valid when $h/w < 0.7$. In a pressure-driven flow, the shear rate varies across the channel, with the maximum shear rate occurring at the channel walls. Thus, the dimensionless shear rate is approximately

$$\mathrm{De} = \lambda \dot{\gamma}_\mathrm{w} = \lambda \left.\frac{\partial u}{\partial y}\right|_\mathrm{wall} \approx \frac{6\lambda Q}{wh^2} \tag{9}$$

where y is the dimension across the channel depth (the smallest dimension).

When $\mathrm{De} > \frac{1}{2}$, shear thinning and elasticity influence the velocity and pressure distributions. For example, in a shear thinning liquid described by Eq. (3), the wall shear rate is modified by the exponent n such that

$$\dot{\gamma}_\mathrm{w} = \frac{6Q}{wh^2}\left(\frac{2}{3} + \frac{1}{3n}\right) \tag{10}$$

and the pressure drop for a given volumetric flow rate is modified by the viscosity index m,

$$\frac{\Delta \mathrm{p}}{L} = \frac{2m}{h}\left[\frac{6Q}{wh^2}\left(\frac{2}{3} + \frac{1}{3n}\right)\right]^n \tag{11}$$

In general, an appropriate stress-strain constitutive relationship is needed in order to predict the velocity profile, stress distribution, and pressure drop for a given non-Newtonian liquid [1].

Geometric features such as contractions and expansions can lead to pronounced non-Newtonian flow responses. For example, in a planar contraction with a ratio $\beta = w/w_\mathrm{c}$ of the upstream and downstream channel widths w and w_c, the fluid along the centerline accelerates into the contraction, leading to a significant elongational flow component. The strain rate within the contraction can be estimated by $\dot{\varepsilon}_\mathrm{c} \approx 2Q/w_\mathrm{c}^2 h$. In reality, the local strain rate reaches values several times larger than the characteristic value $\dot{\varepsilon}_\mathrm{c}$ within the contraction [10]. Elastic stresses generated by the predominantly elongational flow through the contraction lead to a pressure drop exceeding the Newtonian value.

In addition to De, which characterizes the role of elasticity in the non-Newtonian flow response, the Reynolds number Re describing the relative magnitudes of inertia and

viscous stresses remains an important parameter in contraction flows,

$$\mathrm{Re} = \frac{\rho \bar{V}_c D_h}{\eta} = \frac{2\rho Q}{\eta\,(w_c + h)} \tag{12}$$

where $\bar{V}_c$ is the average velocity in the contraction, ρ is the density of the liquid, and D_h is the hydraulic diameter of the contraction, $D_h = 2w_c h/(w_c + h)$. Since both Re and De are linearly dependent on the flow rate Q, these two parameters do not vary independently in experiments. Thus, as elastic effects become more important with increasing De, inertial effects also become more important since Re is also increasing. The ratio of the two dimensionless parameters is the Elasticity number, El,

$$\mathrm{El} = \frac{\mathrm{De}}{\mathrm{Re}} = \frac{\lambda\eta\,(w_c + h)}{\rho w_c^2 h} \tag{13}$$

Note that El depends only on fluid properties and device geometry, and its magnitude describes the rate at which Re changes with De [10].

Electric fields can also be used to drive flows of aqueous polymer solutions, and since most water-soluble polymers carry some charge, it is possible to drive both electrophoretic and electro-osmotic motions. At low field strengths, electrophoretic motions of DNA molecules in electric field gradients can be analyzed exactly analogously to hydrodynamic motions [8]. In addition, some disadvantages of microscale pressure-driven flows can be avoided by using electric fields, including the large shearing components that inevitably accompany such flows, and device failure due to large applied pressures. By placing electrodes at strategic locations within the microfluidic device, one can achieve purely elongational stretching of DNA molecules in the absence of shearing, with an equivalent stretching rate $\dot{\varepsilon}_{EL}$ and $\mathrm{De}_{EL} = \lambda\dot{\varepsilon}_{EL}$.

In all of these approaches to driving non-Newtonian flows in microfluidic devices, the geometry of the device itself plays a key role in determining the nature of the resulting flow. In pressure-driven flow, a straight channel results in pure shearing flow, while a contraction generates a significant elongational component in addition to strong shearing. Stretching flows are accomplished in several other microfluidic geometries including opposing flows in a cross-slot geometry [6], and a hyperbolic converging channel used in conjunction with electric fields [8]. More complex geometries have been designed specifically to create a range of flow types (Eq. (7)) [4, 5]. Microfluidic lithographic fabrication methods offer a significant advantage in these efforts since it is possible to design arbitrarily complex patterns. On the other hand, lithographic fabrication methods are limited to planar patterns, and a given device typically has a uniform depth throughout. In this sense, microfluidic geometries are sometimes more complicated than desired, since the cross-section of the device is rectangular and the aspect ratio of the cross-section varies throughout the device. The complex geometries in most microfluidic devices render interpretation of experiments using simple theories difficult, especially when nonlinear behavior such as non-Newtonian rheology is involved. Many recent studies have employed complementary numerical computations, experiments, and theoretical arguments to aid in the design and analysis of devices.

Finally, measurement and visualization methods are needed in order to analyze and utilize non-Newtonian microfluidic flows. Transparent materials such as glass and PDMS enable a host of optical techniques to be used. Many of these have been used to analyze non-Newtonian flows in microfluidic devices, most notably micro-PIV and related particle imaging techniques, and flow visualization using fluorescent dyes. Pressure taps have also been integrated to measure the non-Newtonian flow response simultaneous to flow visualization [9, 10].

An important visualization technique in non-Newtonian microfluidic flows is single molecule imaging of DNA via fluorescent labeling. The dynamics of bacteriophage DNA have been examined in numerous flow studies, in which DNA chains ranging in length from 2 – 140 μm have been stained with a fluorescent dye. DNA types that have been imaged include T2, T4, T7, λ-phage, and *E. Coli* DNA, and fluorescent dyes that have been used typically come from the YOYO family [7]. The large size of these molecules permits visualization using a fluorescence microscope with a high NA objective; an intensified CCD camera is needed in order to image individual molecules. At high salt concentrations in aqueous buffer solution, DNA molecules have a persistence length of $l_p \approx 50$ nm, and are therefore flexible at these lengths. Using these techniques, the dynamics of DNA molecules have been visualized in a wide range of conditions including microscale hydrodynamic flows [6, 7] and electric field gradients [8].

Key Research Findings

Non-Newtonian effects are important in numerous microfluidics applications. In some cases, microfluidic devices have been designed specifically to characterize the molecular properties and the response of a non-Newtonian liquid in a flow. Other applications involve the use of polymer molecules for specific functions, such as gene amplification and sequencing, in which the non-Newtonian behavior may also play an important role. Still others have

used non-Newtonian effects to design functional microfluidic elements. We highlight a few examples here.

Numerous microscale devices and techniques have been developed to characterize the flow behavior of polymer solutions. The principal motivation for this broad class of techniques is to enable characterization of tiny liquid volumes for which samples are costly or difficult to obtain in large quantities. These microfluidic "rheometers" fall into three categories, organized in order of increasing De: devices to measure intrinsic viscosity, shear-rate dependent viscosity, and non-Newtonian behavior for a range of flow types.

At low shear rates De $< \frac{1}{2}$, polymer chains do not stretch in a flow, but they modify the viscosity according to Eq. (2). Thus, by controlling either the pressure gradient or the volumetric flow rate in a straight microchannel, it is possible to deduce the absolute viscosity of the liquid flowing in that channel using Eq. (8). Furthermore, Eq. (2) shows that the total viscosity of a polymer solution increases relative to the solvent viscosity and the solute concentration. By successively decreasing the concentration of a solute and measuring incremental changes in the viscosity relative to η_s, one can extrapolate the value of intrinsic viscosity $[\eta]$ as the limit of the ratio $\eta_p/c\eta_s$ at infinite dilution $c \to 0$. Lee and Tripathi recently reported on a microfluidic network that successively dilutes a sample by mixing two streams, one containing a polymer solution and the other containing a dyed stream of the base solvent [2]. By applying a known pressure at the inlet of each stream and analyzing the flow rate distribution within the network using an electric circuit analogy, the authors show that the ratio of flow rates entering the mixed stream is related to the concentration of polymer in that stream, allowing the authors to measure the fluorescence intensity of the dye and infer the concentration. The device yields intrinsic viscosity measurements for polymer solutions with volumes as small as 3 μL, opening the possibility to characterize high value molecules of biological and pharmaceutical interest, and eliminating the need for manual dilutions that are typical of standard $[\eta]$ measurements.

The flow of a liquid in a microcapillary can also be used to characterize the shear-rate dependent viscosity for larger De values. Srivastava and Burns have reported on a device that draws a liquid droplet into a microchannel via capillary filling [3]. Due to the changing radius of the entering droplet, the pressure gradient within the channel changes with time, and therefore the filling rate and the length of the filled region of the capillary also vary with time and with the viscosity of the liquid. The authors monitored the filling length with time, and used Eqs. (10) and (11) to deduce the viscosity of the liquid as a function of the changing shear rate during the experiment. A reference channel allows the device to self-calibrate, and the results agree well with measurements from a conventional rheometer. The approach taken in this example is also useful because the method of sample loading circumvents the usual "world-to-chip" interface problem faced in many microfluidic devices.

Pressure-driven flows in straight microchannels with uniform cross-section are purely shearing flows ($\xi = 0$ in Eq. (7)). Thus, although the micro-viscometers described in the previous two examples will provide useful information about molecular conformation (through $[\eta]$) and shear flow behavior, they cannot yield information about a liquid's response to any flow that contains elongational components, encompassing many complex microfluidic geometries. Two recent microfluidic devices have been designed to address this need; both devices mimic a conventional, bulk-scale device called a *four roll mill* in which it is possible to generate a wide range of flow types $-1 \le \xi \le +1$. In one microfluidic analog, six channels meet in a cross configuration at a junction [4]. Two pairs of channels are positioned opposite each other with asymmetric baffles in between to offset the opposing flows. The remaining two channels are exit channels oriented perpendicular to the inlet pairs. By adjusting the ratio of the volumetric flow rates entering through the inlet channel pairs, one can vary the flow type parameter from a maximum of $\xi = +1$ to a minimum near $\xi \approx -1$. In this device it is not possible to achieve purely rotational flow. An alternate design reported by Lee et al. offers a similar concept, with opposing flows meeting at a central stagnation region, but in this case both incoming and outgoing channels contain *symmetric* baffles [5]. In this case, varying the flow rate ratio spans the complete range of flow types, including pure rotational flow $\xi = -1$. The performance of both devices is sensitive to the aspect ratio of the channels, requiring validation of the concept using flow visualization experiments and numerical computations. The first device has been used to investigate complex flows of wormlike micelle solutions, but in general neither device has been extensively validated against data from conventional devices.

The previous examples show that various microfluidic geometries can be used to successfully measure the viscoelastic properties of polymer solutions. Together with some of the advantages highlighted above, microfluidic devices offer the benefit that the devices are closed systems with no free surfaces, placing few limitations on the range of fluid viscosities that can be used, beyond pressure limitations on the device materials. On the other hand, there are also potential disadvantages. Most notably, the large surface areas lead to unavoidable shearing effects, which are difficult to de-couple when interpreting the response to

elongational or mixed flows. In this vein, shearing within the inlet regions of a device will lead to 'pre-conditioning' of the polymer chain conformations prior to entering the region of interest. Memory of past deformation history can dramatically alter a fluid's response to a flow, which can be either advantageous or detrimental depending on the application.

The ability to fluorescently tag individual DNA molecules and visualize their dynamics in these flows can considerably enhance the information we obtain from these flows. Numerous single molecule visualization experiments have already led to significant advancements in our understanding of polymer chain dynamics in viscous flows. In addition, these experiments have recently been combined with Brownian dynamics simulations, which simulate the motion of bead-rod chains in viscous flows and can quantitatively predict the chain conformation for given flow conditions. This powerful combination has allowed for the validation of detailed molecular scale physics, as well as the development of new physical insights. These conclusions are described in a recent review [7]; we summarize a few of the salient conclusions here.

Arguably the most important new concept to result from single molecule visualization experiments is that of "molecular individualism". In a set of groundbreaking experiments, Perkins, Smith, and Chu placed DNA molecules in a variety of flow conditions and tracked the dynamics of the polymer chains individually. Their observations confirmed several assumptions that had formed the basis for polymer dynamics theories in the absence of the ability to directly measure the chain conformation (although many other measurements supported these hypotheses). Among these, one study observed the dynamics of DNA molecules in dilute solution as they passed through the predominantly elongational flow in a microfluidic cross-slot geometry [6]. The authors collected measurements of the elongation of many individual DNA molecules, and noted several distinct conformation types including folded, kinked, and dumbbell-like configurations. An important observation from these measurements is that the configuration realized by an individual chain is highly sensitive to its initial configuration. This sensitivity to the initial configuration, dubbed 'molecular individualism', leads to highly heterogeneous conformation 'trajectories' as the chains stretch in a flow. Molecular individualism also leads to the idea that 'pre-conditioning' the polymer chains prior to stretching can result in a different flow response. For example, Brownian dynamics simulations have shown that exposing the polymer solution to shearing prior to stretching leads to fewer kinked and folded conformations among the stretched chains. Other studies have shown that in mixed flows, the elongational strain determines the amount of stretching, but the rate of stretching is much slower in mixed flows than in purely elongational flows [7].

Statistics computed from individual measurements form the link between single molecule observations and bulk flow measurements. In the study of Perkins et al. described above, the statistics indicate that the distribution of chain sizes is Gaussian during the majority of stretching; however, when the chains approach full stretch, the statistical distribution becomes highly non-Gaussian. This observation is essential to the development of stress-strain constitutive relationships for polymer solutions. It also helps explain such important observations as 'stress-conformation hysteresis'. Microfluidic devices incorporating non-Newtonian flow have played a central role in developing these conclusions [7].

A novel method for gene sequencing builds upon the ideas developed from single molecule experiments. The idea is to sequence individual DNA strands by directly detecting each base pair along the backbone [8]. To implement this concept, the DNA strand must be fully elongated. While this can be accomplished by exposing the molecules to an elongational flow, the sensitivity of the stretching profile to the initial chain conformation and the degree of shearing in the flow renders hydrodynamic methods impractical. Instead, it has been noted that electric field gradients can efficiently stretch DNA molecules using the charge along the backbone, as we described earlier. Randall and Doyle have presented a method to use electrophoretic motions of DNA in electric field gradients to stretch long DNA strands [8]. In particular, electric fields can be used to achieve pure stretching in the absence of uncontrolled shear flows, such as those that occur in hydrodynamic flows due to the no-slip condition at the walls. Randall and Doyle present a two-step microfluidic process that is designed to control molecular individualism by pre-conditioning the molecular conformation using a gel matrix to pre-stretch the molecules upstream, and then using electric field gradients to further stretch the molecules inside a hyperbolic contraction downstream. The authors show that this method is an efficient alternative to hydrodynamics for achieving continuous stretching of long strands of DNA.

Many microfluidic geometries are not as simple as those described above, and the *mixed* flow type within complex geometries can lead to other interesting flow behaviors, especially at elevated De values. For example, contraction flows of highly elastic non-Newtonian fluids can be unstable due to the interaction of elastic stresses with streamline curvature in the vortices upstream of the contraction. The upstream vortices grow relative to the New-

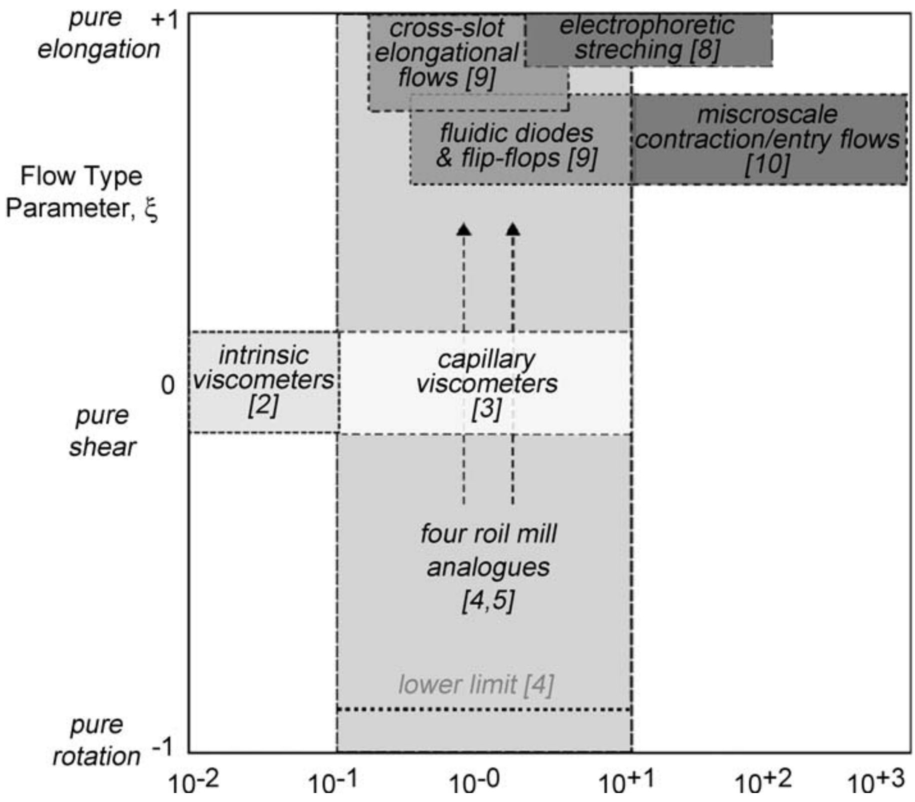

Non-Newtonian Fluids in Microfluidics, Figure 3 Deborah number – flow type phase diagram depicting the range of flow conditions utilized in each of the examples discussed

tonian case as De increases. At high enough flow rates, the vortex structure becomes unstable and begins to fluctuate, contributing to the measured overall pressure drop. As described earlier, De and Re do not vary independently in these flows (see Eqs. (12) and (13)), and their ratio contains a geometric length scale, suggesting that microscale contractions can be useful in accessing new regions of the De–Re phase space. Recently, Rodd and McKinley utilized this control over the geometric length scale to perform fundamental studies of viscoelastic contraction flows, measuring the pressure drop and the vortex lengths as functions of De, mapping the steady flow patterns as a function of De and Re, and characterizing the onset of inertio-elastic flow transitions [10]. These nonlinearities and instabilities have also been utilized to design functional microfluidic components. For example, as elastic instabilities develop and grow at larger De values, the flow becomes chaotic and has the ability to enhance mixing (see ► chaotic mixing based on viscoelasticity). In addition, the nonlinearity inherent in viscoelastic contraction flows has led to the design of microfluidic memory and control devices, including a 'fluidic diode' in which flux is significantly easier in one direction, and a bistable 'flip-flop' which utilizes an elastic instability to modulate the direction of flow at a junction [9].

Based on the examples described, it is clear that at least two essential factors determine the nature of a microscale non-Newtonian flow: the dimensionless strain rate, or De, and the device geometry or the flow type. The utility of each device relies on the ability to operate within a particular range of De and ξ values. Fig. 3 shows a schematic diagram of the De–ξ phase space for non-Newtonian flows, indicating the region of interest for the applications described.

Future Directions for Research

Non-Newtonian flows will remain important in microfluidic applications as long as there is the need to transport and characterize long chain molecules such as DNA and proteins. In fact, increasingly longer strands of DNA are becoming common in gene sequencing and amplification. Thus the development of new ideas for manipulating and characterizing those molecules will be essential to the success of future microfluidic devices. In

addition, an understanding of the non-Newtonian behavior in microfluidic devices can be helpful in optimizing the performance of newly developed assays incorporating large macromolecules and particles. Most of the applications highlighted here are just in their beginning stages, and future research will inevitably focus on further development, validation, and uses for these techniques.

Cross References

- ► Capillary Filling
- ► Chaotic Mixing Based on Viscoelasticity
- ► Electrophoresis
- ► Fluorescent Labeling
- ► Lab-on-a-Chip Devices for Particle and Cell Separation
- ► Microscale Flow Visualization
- ► Non-Newtonian Fluids in Microchannel
- ► PCR Lab-on-Chip Devices
- ► Polymer Synthesis within Microfluidic Reactors
- ► Pressure-Driven Single Phase Liquid Flows
- ► Viscoelasticity

References

1. Larson RG (2000) Structure and Rheology of Complex Liquids. Oxford Univ Press, New York
2. Lee J, Tripathi A (2005) Intrinsic viscosity of polymers and biopolymers measured by microchip. Anal Chem 77:7137–7147
3. Srivastava N, Burns MA (2006) Analysis of non-Newtonian liquids using a microfluidic capillary viscometer. Anal Chem 78:1690–1696
4. Hudson SD, Phelan FR, Handler MD, Cabral JT, Migler KB, Amis EJ (2004) Microfluidic analog of the four-roll mill. Appl Phys Lett 85:335–337
5. Lee JS, Dylla-Spears R, Teclemariam NP, Muller SJ (2007) Microfluidic four-roll mill for all flow types. Appl Phys Lett 90:074103
6. Perkins TT, Smith DE, Chu S (1997) Single Polymer Dynamics in an Elongational Flow. Science 276:2016–2021
7. Shaqfeh ESG (2005) The dynamics of single-molecule DNA in flow. J Non-Newtonian Fluid Mech 130:1–28
8. Randall GC, Schultz KM, Doyle PS (2006) Methods to electrophoretically stretch DNA: microcontractions, gels, and hybrid gel-microcontraction devices. Lab Chip 6:516–525
9. Groisman A, Enzelberger M, Quake SR (2003) Microfluidic memory and control devices. Science 300:955–958
10. Rodd LE, Scott TP, Boger DV, Cooper-White JJ, McKinley GH (2005) The inertio-elastic planar entry flow of low-viscosity elastic fluids in micro-fabricated geometries. J Non-Newtonian Fluid Mech 129:1–22

Nucleation

Definition

Initiation of any material growth process where atoms cluster together to provide the starting point for further growth. The nucleation process is governed by the energetics of atomics clusters.

Cross References

- ► Bubble Dynamics in Microchannels
- ► Fabrication of Self-Assembled Catalytic Nanostructures

Nucleation and Growth

Synonyms

Deposition; Precipitation; Crystallizaiton

Definition

A process of nanoparticle generation. Raw materials for nanoparticles (monomers) transform to make embryos, forming under which can grow to particles. Here, embryos and nuclei can be distinguished by its thermodynamic stability. Embryos have smaller size than the nucleus and thermodynamically unstable. The nuclei are said to be thermodynamically stable and grow into larger particles.

Cross References

- ► Nanoparticle Synthesis in Microreactor

Nucleic Acid Detection

- ► SNP on Chip – Micro- and Nanofluidics for Single Nucleotide Polymorphism Discrimination

Nucleus

- ► Kernel Function

Number-Average Molecular Weight

Synonyms

Mn

Definition

It is determined by measuring the molecular weight of n polymer molecules, summing the weights, and dividing by n.

Cross References

► Polymer Synthesis within Microfluidic Reactor

Numerical Discretization

► Discretization

Numerical Simulation

► Lattice Poisson–Boltzmann Method, Analysis of Electroosmotic Microfludics
► Micro- and Nanoscale Gas Fluidics

Numerical Solution of Boltzmann Equation

RAMESH AGARWAL[1], FELIX G. CHEREMISIN[2], SUBRATA ROY[3]
[1] Aerospace Research and Education Center (AeREC) and Aerospace Engineering Program, Washington University, St. Louis, MO, USA
[2] Russian Academy of Science, Moscow, Russia
[3] University of Florida, Gainesville, FL, USA
rka@me.wustl.edu, cherem@ocas.ru, roy@ufl.edu

Synonyms

Wang-Chang–Uhlenbeck equation; Generalized Boltzmann equation; Flow simulations in transitional and rarefied regimes

Definition

The Boltzmann equation describes the behavior of gas flows in non-equilibrium due to molecular motion. It is applicable for all mean free paths λ between the molecules, that is, for all Knudsen numbers Kn ($= \lambda/L$, where L is a characteristic dimension in the flow). Thus it can be employed to calculate the flow fields in a variety of applications ranging from hypersonic flow past a space shuttle to flow in microdevices, where all the flow regimes – continuum (Kn $\to 0$), transitional (Kn $\sim O(1)$) and rarefied (Kn $\gg 1$) – may be encountered. The classical Boltzmann equation (CBE) describes the flow of monatomic gases (such as argon and helium) in translational non-equilibrium. The behavior of polyatomic gases (such as nitrogen and oxygen) is described by the generalized Boltzmann equation (GBE) or Wang-Chang–Uhlenbeck equation (WC–UE) [1], wherein the internal (rotational and vibrational) and translational degrees of freedom are considered in the framework of quantum and classical mechanics respectively. The molecular motion in the Boltzmann equation is described by a distribution function f which describes both the motion of the molecules and their collisions. The motion of the molecules is described by a convective differential operator while the molecular collisions result in an integral in molecular velocity space. Thus the Boltzmann equation is an integrodifferential equation whose numerical solution becomes quite a difficult task. One of the most widely used methods for the numerical solution of the Boltzmann equation is due to Cheremisin and his colleagues at the Russian Academy of Science in Moscow [2]. In this method the convective operator is discretized by an explicit scheme and the collision integral is solved by the method of discrete ordinates. A two-step method for time integration is employed that sequentially includes the convective step and the collision step.

Overview

In principle, the Boltzmann equation describes the flow at all Knudsen numbers Kn. For very small values of Kn (say < 0.01), the flow approaches the continuum regime, while for very large values of Kn (say > 10), the flow can be considered free molecular. When Kn $= O(1)$, the flow is in the continuum transition regime. In the continuum regime, Navier–Stokes equations can accurately predict the flow field, while for Kn > 1, the direct simulation Monte Carlo (DSMC) method [3] can be successfully employed. However in a variety of applications ranging from hypersonic flow past a space shuttle to flow in microdevices, part of the flow field may be in the transition regime. In the transition regime, both the Navier–Stokes equations and the DSMC method have significant limitations. Navier–Stokes equations are no longer accurate because of significant departure from equilibrium and the DSMC method becomes computationally prohibitive because of the large number of particles required for accurate simulations. A number of alternative approaches have been proposed and investigated in the literature such as the Burnett equations, Grad's moment equations or Eu's equations. These equations collectively are known as the extended hydrodynamics (EHD) equations. However, the progress has been limited and furthermore the accuracy of the EHD equations remains questionable because of

the asymptotic nature of the Chapman–Enskog expansion (e. g. for the Burnett equations), the issues related to regularization and the difficulty in imposing the exact kinetic boundary conditions on the surface of the body.

Physically, gas flows in the transition regime, where Kn is $O(1)$, are characterized by the formation of narrow, highly non-equilibrium zones (Knudsen layers) of thickness of the order of the molecular mean free path λ; the flow structure is then determined by the fast kinetic processes. Moreover, in the case of unsteady flows, an initial Knudsen time interval is of the order $\tau_0 = \lambda/v$, where v is the molecular velocity. Thus, the Knudsen layer can be computed accurately only by directly solving the Boltzmann equation.

For calculating the non-equilibrium flow of polyatomic gases, the DSMC method is currently the most widely used technique. In the DSMC approach, one usually employs some empirical models [4], which very much resemble a BGK type relaxation model with a constant relaxation time. There are only a few attempts due to Koura [5] and Erofeev [6], for example, which employ the so called *trajectory calculations*, where a realistic modeling of inelastic collisions with translational–rotational (T–R) transfer of energy is made. These computations require enormous CPU time. For vibrational excitations, no trajectory calculations with the DSMC method have been attempted to date. The physical reality is such that the vibrational term becomes important at much higher temperature than the rotational term. For the N_2 molecule the quanta of vibrational temperature is 3340 K and the quanta of rotational temperature is 2.89 K; the corresponding quanta for the O_2 molecule are 2230 and 2.1 K respectively. Therefore, rotational energy levels are important at all temperatures, but the vibrational energy levels are important only at high temperatures. Thus, each vibration energy level splits into a high number of rotational energy levels. The characteristic relaxation times for T–T, T–R, and T–V transfer of energy are in the proportion of about $1:5:100$ (or several thousands). A good physical assumption is that the translational and rotational energy are in thermodynamic equilibrium during the vibrational relaxation process.

Taking into account the above observations, let us consider hypersonic flow at different Knudsen numbers. If $\mathrm{Kn} > 1$, then no internal energies need to be taken into account, except the reactions at the boundaries. If $0.1 < \mathrm{Kn} < 1$, only the rotational levels play a role. For $\mathrm{Kn} < 0.01$, in the majority of the flow field the rotational and translational energies can be considered in equilibrium, but the vibrational relaxation continues. What can therefore be expected in the case of a shock wave (SW) at high Mach number? At the beginning, the SW structure will be formed by T–T and R–T transfers and the structure should be the same as in a gas having no vibrational levels. This SW structure with a characteristic length of about 10 mean free paths will be followed by a large zone of the size of several hundreds of mean free paths formed by the vibrational excitation. Therefore, the computation of the SW structure including the vibrational excitation becomes much more difficult than that with only T–R exchange. The computations with both the rotational and vibrational energy levels will include $N_{\mathrm{total}} = N_{\mathrm{r}} \times N_{\mathrm{v}}$ levels (N_{r} = number of rotational levels and N_{v} = number of vibrational levels) which are equivalent to a gas with N_{total} components. These computations thus require significant computational resources. It is therefore important to reduce the numbers N_{r} and N_{v} for efficient calculations without sacrificing the accuracy. Further increase in the efficiency can be obtained by exploiting the big difference between the rotational and vibrational characteristic times. As mentioned before, vibrational degrees of freedom become important when the flow is in rotational–translational equilibrium. Therefore, under such conditions, $N_{\mathrm{total}} = N_{\mathrm{v}}$. Further efficiency can be achieved by using the simplified molecular potentials, for example the inverse power potential and simple R–T cross-sections.

The solution of the GBE at high Mach numbers requires both large memory and CPU time. Following Cheremisin's work on a monatomic gas [2], one can employ a large time step in velocity space (of the order of the mean thermal velocity) ahead of the SW in the GBE code. It is also possible to use fewer levels (6 to 10) in the rotational spectrum to reduce both the memory and CPU requirements as described by Agarwal et al. [7]. Another source of large CPU time in the currently used time-explicit algorithm for solution of the Boltzmann equation is the requirement of a very small time step which results from the condition that the distribution function remains positive after the relaxation stage. For example, for a monatomic gas, at Mach 20, the time step is of the order of 0.001 of the mean free path time. In order to overcome this problem, two strategies can be employed: (a) use a filter that excludes the negligibly small contributions to the collision integral and (b) modify the algorithm to a mixed explicit–implicit scheme to increase the time step by at least a factor of 10. All these improvements result in an accurate and efficient GBE solver for computing the flow field of a diatomic gas at high Mach numbers including the rotational and vibrational excitations.

Basic Methodology

It should be noted that the GBE [8] replaces the classical WC–UE for the case when energy levels are degenerate. In its mathematical form, the GBE is similar to WC–UE and differs from the latter by a factor related to the statistical

weights of the levels. Thus, the GBE gives the equilibrium spectrum different from WC–UE. The GBE has the form

$$\frac{\partial f_i}{\partial t} + \xi \frac{\partial f_i}{\partial \boldsymbol{x}} = R_i \,. \tag{1}$$

The collision operator is given by

$$R_i = \sum_{jkl} \int_{-\infty}^{\infty} \int_0^{2\pi} \int_0^{b_m} \left(f_k f_l \omega_{ij}^{kl} - f_i f_j \right) P_{ij}^{kl} g b \, \mathrm{d}b \, \mathrm{d}\varphi \, \mathrm{d}\xi_j \,. \tag{2}$$

Here f_i is the distribution function for the energy level i, P_{ij}^{kl} is the probability of the transfer from levels i, j to levels k, l, and the factor $\omega_{ij}^{kl} = (q_k q_l)/(q_i q_j)$ (q_i being the degeneracy of the energy level). For simple levels, the GBE changes to the WC–UE; therefore it can also be considered as a more general form of the latter. In [8] the GBE was obtained directly from WC–UE by grouping the q_i single levels that have the same energy and form a degenerate level.

Let us consider molecular nitrogen having the Lennard–Jones potential (6–12), given in Ferziger and Kaper [9], with the depth of the energy hole $\varepsilon = 91$ K, degeneracy of rotational level $q_i = 2i + 1$, $i = 0, 1, \ldots \infty$, and the rotational energy of the level $e_{ri} = \varepsilon_0 i(i+1)$, $\varepsilon_0 = 2.9$ K. The molecular interaction during the collision consists of two phases. In the first phase, the molecules interact in an elastic manner according to the molecular potential. This stage determines the deviation angle of the relative velocity. In the second stage, the modulus of the relative velocity changes according to the energy conservation equation. For the transition probabilities P_{ij}^{kl} we apply the formulas given in [7] that are obtained by fitting the experimental data of molecular dynamics simulations of interactions of rigid rotors that model N_2 molecules:

$$P_{ij}^{kl} = P_0 \omega_{ij}^{kl} \left[\alpha_0 \exp\left(-\Delta_1 - \Delta_2 - \Delta_3 - \Delta_4\right) + \frac{1}{\alpha_0} \exp\left(-\Delta_3 - \Delta_4\right) \right],$$

where

$$\Delta_1 = \frac{|\Delta e_1 + \Delta e_2|}{e_{tr0}}, \qquad \Delta_2 = 2\frac{|\Delta e_2 - \Delta e_1|}{e_{\mathrm{tot}}},$$

$$\Delta_3 = 4\frac{|\Delta e_1|}{(e_{tr0} + e_{ri})}, \qquad \Delta_4 = 4\frac{|\Delta e_2|}{\left(e_{tr0} + e_{rj}\right)},$$

$$\Delta e_1 = e_{ri} - e_{rk}\,, \qquad \Delta e_2 = e_{rj} - e_{rl}\,,$$

$$\alpha_0 = 0.4\frac{e_{\mathrm{tot}}}{e_{tr0}}, \qquad e_{tr0} = \frac{mg^2}{4},$$

$$e_{\mathrm{tot}} = e_{tr0} + e_{ri} + e_{rj}\,.$$

The energy conservation law in a collision selects virtual collisions with nonzero probability. From the equation

$$\frac{mg_{ij}^2}{4} + e_{ri} + e_{rj} = \frac{mg_{kl}^2}{4} + e_{rk} + e_{rl}$$

it can be shown that $P_{ij}^{kl} > 0$, if $g_{kl}^2 \geq 0$, otherwise $P_{ij}^{kl} = 0$. The elastic collision is a particular case of the collision. The probabilities obey the normalization condition $\sum_{k,l} P_{ij}^{kl} = 1$. The kinetic equation (1) is solved by the splitting scheme described by Cheremisin [2]. At a time step $\tau < \tau_0$, where τ_0 is a mean intercollision time, Eq. (1) is replaced by the sequence of equations

$$\text{(a)} \quad \frac{\partial f_i}{\partial t} + \xi \frac{\partial f_i}{\partial \boldsymbol{x}} = 0\,, \quad \text{(b)} \quad \frac{\partial f_i}{\partial t} = R_i\,.$$

The collision operator R_i is evaluated at the uniform grid S_0 in the velocity space by the conservative projection method proposed in [2].

Sample Results on Computation of Shock Structure

Some sample results on the computation of shock structure in nitrogen in rotational and vibrational non-equilibrium are presented here in two parts: (a) the computations are presented for shock structure in nitrogen including the rotational degrees of freedom up to Mach 15 by solving the complete WC–UE with a number of energy levels, and (b) the computations are presented for shock structure in nitrogen with both rotational and vibrational degrees of freedom by solving the complete WC–UE for V–T relaxations and employing the two-level kinetic model for R–T relaxations. Some of the details of this two-level kinetic model for R–T relaxations are not given here but can be obtained from Morse [10]. The model reproduces the results obtained by the complete WC–UE.

(a) The SW structure is formed as a final stage of the evolution of discontinuity in the initial distribution function. The problem is considered for the interval $-L_1 \leq x \leq L_2$ with the discontinuity at $x = 0$. The initial distribution function on both sides of the discontinuity is described by the velocities and spectral levels. It has the form

$$f_i^{1,2}(\xi, x) = n^{1,2} \left[\frac{m}{2\pi T^{1,2}} \right]^{\frac{3}{2}} \left[-\frac{m\left(\xi - u^{1,2}\right)^2}{2T^{1,2}} \right] \times \frac{2i+1}{Q_r} \exp\left(-\frac{e_{ri}}{T^{1,2}} \right)$$

where Q_r denotes the statistical sum. Parameters $(n, T, u)^{1,2}$ are defined by the Rankine–Hugoniot relations with $\gamma = 7/5$. At the boundary the initial distribution function is kept constant.

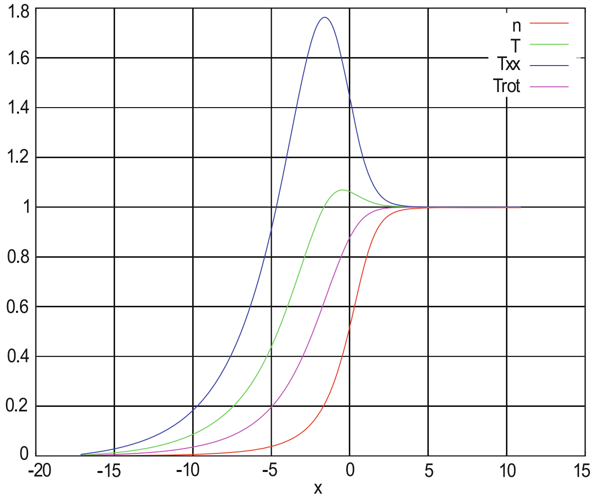

Numerical Solution of Boltzmann Equation, Figure 1 Shock wave structure in nitrogen for $M = 15$; n = density, T = translational temperature, Txx = longitudinal translational temperature, Trot = rotational temperature (normalized)

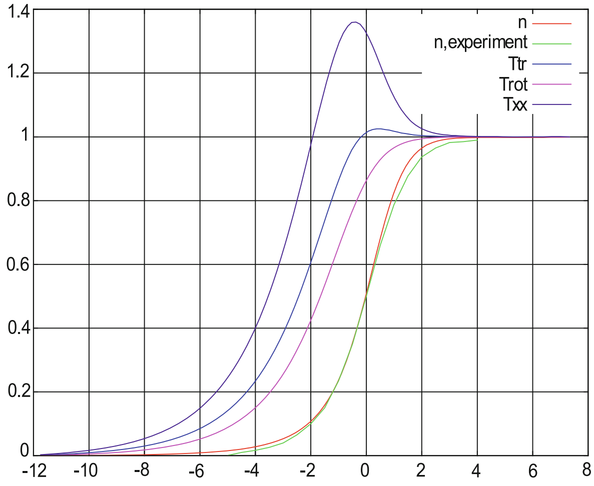

Numerical Solution of Boltzmann Equation, Figure 2 Shock wave structure in nitrogen for $M = 10$; n = computed density, n, experiment = experimental density, T = translational temperature, Txx = longitudinal translational temperature, Trot = rotational temperature (normalized)

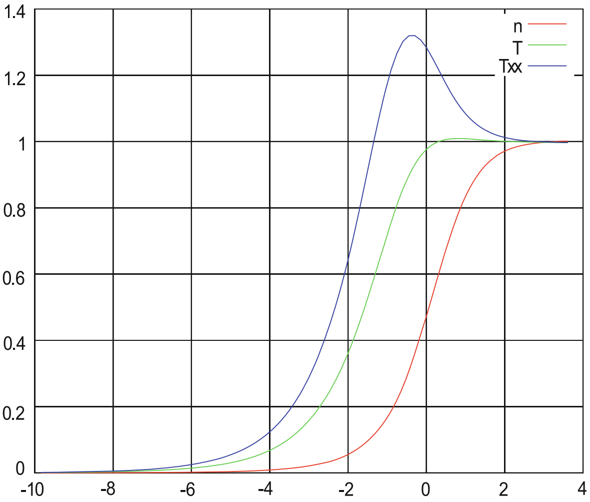

Numerical Solution of Boltzmann Equation, Figure 3 Shock wave structure in a monatomic gas for $M = 25$; n = density, T = translational temperature, Txx = longitudinal translational temperature (normalized)

For moderate Mach numbers, the SW structure in nitrogen can be computed with real values of the spectral energy gap ε_0, but for the hypersonic case the needed number of levels becomes too high (up to 50 – 70 levels) and therefore the computations become very time consuming. To facilitate this problem it is possible to increase this energy gap and thereby reduce the number of levels. By conducting numerical experiments at Mach 4, it was determined that this increase in spectral energy gap does not influence the results of calculations in any significant way. Figure 1 shows an example of hypersonic SW structure in nitrogen at Mach 15, computed with 16 levels instead of nearly 70 "natural" levels. These types of calculations compare well with the experiments of Alsmeyer [11] for density n for reported Mach numbers up to 10. Figure 2 shows the comparison for density distribution at Mach 10 between the computation and experimental data; excellent agreement is obtained.

Figure 3 shows the hypersonic SW structure in a monatomic gas at $M = 25$. It should be noted that for this case, the temperature behind the SW increases about 200 times, which makes the computation very difficult; it required an important improvement to the algorithm.

(b) In this part we consider the gas with both rotational and vibrational degrees of freedom. The interaction potential is the Lennard–Jones potential with parameters of nitrogen taken at room temperature of 300 K. The vibrational spectrum corresponds to nitrogen with energy gap of 3340 K. For the rotational spectrum the energy quantum was increased against the actual (which is equal to 2.9 K) for reducing the number of the levels as described before in part (a). The probabilities of R–T transfers are taken from the data of mathematical simulation by Beylich [8]. The probabilities of V–T transfers are generally accepted to be much smaller than those of the R–T transfers and are in the range of 0.005 – 0.001 of the elastic collision probability. As mentioned above, V–T transfers are computed using WC–UE and the R–T transfers are computed using the two-level kinetic model to simplify the computations. Computations are performed at Mach 6 and 10.

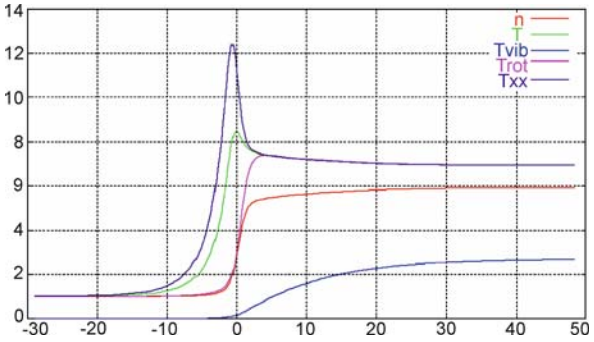

Numerical Solution of Boltzmann Equation, Figure 4 Shock wave structure in nitrogen at $M = 6$; $n =$ density, $T =$ translational temperature, Tvib = vibrational temperature, Trot = rotational temperature, Txx = longitudinal translational temperature

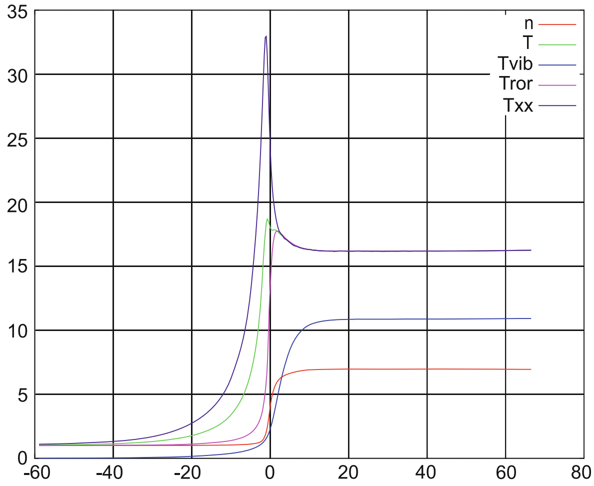

Numerical Solution of Boltzmann Equation, Figure 5 Shock wave structure in nitrogen at $M = 10$; $n =$ density, $T =$ translational temperature, Tvib = vibrational temperature, Trot = rotational temperature, Txx = longitudinal translational temperature

In Figs. 4 and 5, the density, total translational, parallel translational, vibrational and rotational temperatures are shown. It is important to note that the vibrational temperature does not reach the equilibrium state with translational and rotational temperatures. This is due to the large energy quantum of the vibrational spectrum. The deviation from the equilibrium diminishes when Mach number increases. The SW structure is characterized by two phases. In the first phase, the elastic and R–T collisions are essential and the influence of V–T transfers is negligible. The translational temperature here rises above the equilibrium value. The rotational and translational temperatures reach the equilibrium at the end of this stage. At the second stage the gas energy goes to the vibrational degrees of freedom and the above indicated temperatures decrease.

At Mach 6, the vibrational spectrum consists of four levels which are sufficient to cover the entire energy range. At Mach 10, the number of needed levels is eight. In Figs. 4 and 5, a part of the x-axes is shown. The computations were made for $x = (-120, 250)$. The deviation of the final vibrational temperature from the equilibrium T–R temperatures decreases when the Mach number increases and thus the temperature behind the SW increases.

Key Research Findings

For computing the non-equilibrium flow fields of polyatomic gases in all flow regimes ranging from continuum to transitional to rarefied, the WC–UE or GBE can be successfully solved numerically to account for both the RT and VT energy transfers in very high Mach number flows. The biggest challenge is the computational efficiency for high Mach number flows using the complete GBE or WC–UE including both the RT and VT energy transfers. This issue has been addressed by reducing the number of energy levels for RT relaxations by increasing the ground state energy quantum (e. g. for Mach 15 flow, we have demonstrated that it is possible to reduce the number of levels from 70 to 16), by coarsening the grid in the velocity space without compromising the accuracy, and by treating the convective operator implicitly.

In addition, a newly developed BGK type 2-level model for R–T energy transfers (2LRT) can be employed to reproduce the calculations of the complete WC–UE; however 2LRT is 20 times faster. Thus the computations including both the R–T and V–T relaxations can be performed efficiently using the 2LRT since the number of vibrational energy levels required is usually four to six even at high Mach numbers. For example, at Mach 15, the complete solution of the WC–UE will require total number of levels $= N_r \times N_v = 70 \times 6 = 420$. With 2LRT, we require only 12.

Furthermore, it is important to note that the quantum of rotational energy for diatomic gases such as nitrogen and oxygen is much smaller than that of vibrational energy; therefore accounting for the rotational spectra is important for all Mach numbers for flows with Kn below 0.3 or so. The influence of vibrational energy should be taken into account for high Mach numbers and much smaller Kn. For Kn > 0.3, the CBE can be applied.

Future Directions for Research

The basic methodology presented here should be extended to a mixture of reactive gases. In addition, several improvements can be made for increasing the efficiency of the computations:

- implicit treatment of the convective operator,
- efficient treatment of collision integral in velocity space by employing the conservative projection method,
- increasing the ground state energy quantum of rotational energy to reduce the number of energy levels required at high Mach numbers, and
- including the adaptive meshing and parallelization in the Boltzmann solver.

Cross References

► Lattice Boltzmann Method (LBM)
► Molecular Dynamics Simulation Method
► Monte Carlo Method
► Multiscale Modeling and Numerical Simulations

References

1. Cheremisin FG (2002) Solution of the Wang Chang–Uhlenbeck Master Equation. Doklady Phys 47:872–875
2. Cheremisin FG (2004) Solution of the Boltzmann Kinetic Equation for High Speed Flows of a Rarefied Gas. In: Proceedings of the 24th international symposium on rarefied gas dynamics, Bari, Italy, 10–16 July 2004
3. Bird GA (1994) Molecular Gas Dynamics and the Direct Simulation of Gas Flows. Oxford Science Publications, New York
4. Koura K (1994) A Set of Model Cross-Sections for the Monte Carlo Simulation of Rarefied Real Gases: Atom-Diatom Collisions. Phys Fluid 6:3473–3486
5. Koura K (1997) Monte Carlo Direct Simulation of Rotational Relaxation of Diatomic Molecules Using Classical Trajectory Calculations: Nitrogen Shock Wave. Phys Fluid 9:3543–3549
6. Erofeev AI (2002) Study of a shock Wave Structure in Nitrogen on the Basis of Trajectory Calculations of Molecular Interactions. Fluid Dyn 6:134–147
7. Agarwal RK, Chen R, Cheremisin FG (2007) Computation of Hypersonic Shock Wave Flows of Diatomic Gases Using the Generalized Boltzmann Equation. AIAA Paper 2007–4541 presented at the 39th AIAA Thermophysics Conference, Miami, FL, 25–28 June 2007
8. Beylich AA (2000) An Interlaced System for Nitrogen Gas. In: Proceedings of CECAM Workshop, ENS de Lyon
9. Ferziger JH, Kaper HJ (1972) Mathematical Theory of Transport Processes in Gases. North Holland, Amsterdam–London
10. Morse TF (1964) Kinetic Model for Gases with Internal Degrees of Freedom. Phys Fluids 6:159
11. Alsmeyer H (1976) Density profiles in Argon and Nitrogen Shock Waves Measured by the Absorption of an Electron Beam. J Fluid Mech 74:497–513

Numerical Stability

► Stability

Numerical Techniques for Free Surface Flows: Interface Capturing and Interface Tracking

ALI JAFARI, NASSER ASHGRIZ
Department of Mechanical and Industrial Engineering,
University of Toronto, Toronto, ON, Canada
ashgriz@mie.utoronto.ca

Synonyms

Volume tracking; Surface tracking; Surface capturing; Interfacial flow modelling

Definition

Numerical techniques for free surface flows refer to methods for solving multiphase flows of liquids and gases with sharp moving and deforming interfaces. The solution of these types of flows is complex since the boundary between the two phases is not known a priori and it is part of the solution. In addition, the problem usually involves fluid flows with very large density, viscosity and velocity ratios. This makes the solution of the governing partial differential equations (PDEs) very difficult. Several numerical techniques have been developed to tackle this complex fluid flow. They can be categorized based on the type of flow modeling (Eulerian, Lagrangian or mixed), type of interface modeling (capturing or tracking), type of flow–interface coupling (integrated or segregated) and type of spatial discretization (meshless, finite difference, finite volume, finite element or others).

Overview

Free surface flows and interfaces between two or more immiscible fluids or phases are observed in many natural and industrial processes at macro- and microscales. Different numerical techniques are developed to simulate these flows. However, due to the complexity of the problem, each technique is tailored to a particular category of flows. Finite element (FE), finite volume (FV) and finite difference (FD) methods are all potentially applicable to generalized Navier–Stokes equations. However, they have to be coupled with a technique to track moving fluid boundaries and interfaces. The difficulty in tackling interfacial flows is inherently related to the complexity of interface topology and the fact that the interface location is unknown.

There are two main categories of interface solvers. The first category of methods involve mesh motion and deformation while the second group are based on fixed grids. In the moving mesh methods, the grid points move according

to the local flow characteristics. In most cases where all grid points are moved, the method is Lagrangian; otherwise, it is a mixed Lagrangian–Eulerian approach. These include methods such as FE-based Lagrangian [1], interface fitting (or boundary-fitted coordinate) [2] and boundary integral [3] approaches. In these methods, the grid points near the interface essentially play the role of marker points. Thus, these techniques are confronted with difficulties when applied to large surface deformations, surface breaking and merging.

Interface fitting methods, Fig. 1a, are efficient and accurate in the study of shaping processes of viscous materials. However, these methods rapidly become inappropriate, indeed impossible, to apply with less viscous materials that undergo large deformations. Mesh regenerations are necessary when mesh cells and elements become highly skewed, to prevent computational failures. This can make the interface fitting scheme and other moving mesh techniques become very complicated and inefficient.

The fixed grid methods, on contrast, operate in the pure Eulerian and, sometimes, combined Lagrangian–Eulerian framework. The main distinction between moving mesh and fixed mesh lies in the fact that fixed mesh methods use an additional agent such as a Lagrangian marker or indicator function to follow the interface motion instead of grid points used by moving mesh methods. The fixed grid methods are divided into three main categories: interface capturing (Fig. 1b), interface tracking (Fig. 1c) and combined interface capturing–interface tracking techniques. Examples of interface capturing methods include marker and cell (MAC) [4], volume of fluid (VOF) [5, 6], level set (LS) [7], and diffuse interface (DI) (or phase field) [8] methods. The most widely used interface tracking method is Glimm's front tracking method [9]. The notable combined techniques which inherit from both interface capturing and interface tracking methods are Tryggvason's front tracking [10], sharp interface (SI) [11], immersed boundary (IB) [12] and immersed interface (II) [13] methods.

Techniques based on interface tracking and interface capturing avoid the grid-related problems associated with interface fitting methods by employing a grid which is fixed and by defining the location of the liquid and gas regions relative to the fixed grid. This practice requires an enlargement of the computational domain to encompass the entire container, since the free surface can potentially occupy any position within the fixed grid. In general, interface capturing methods can handle complex interfacial regions more easily, but interface tracking methods give a more accurate description of the free surface because of their Lagrangian nature. In interface tracking methods, the position of the free surface is described in a direct way; either by specifying a set of marker points located on the free surface [9] or by introducing a height function which explicitly describes the free surface position [14]. Furthermore, in interface tracking schemes, implementation of the surface tension force is straightforward given the location and curvature of the free surface. The limitation of these methods, unlike interface capturing methods, is their inability to cope naturally with folding or rupturing interfaces.

In the interface capturing techniques, the interface motion can be reproduced using different approaches. In MAC, hundreds of massless marker particles are added to the fluid. These particles are then advected in Lagrangian sense using the average of Eulerian velocities in their vicinity. In the VOF method, the use of volume fractions to mark the fluid regions is adopted because of its efficiency and simplicity and the natural way in which complex interfaces can be treated as internal moving boundaries. The volume fractions are convected through the flow domain by solving a scalar convection equation. In the level set method, a smooth distance function is used as the indicator function for the interface. A similar approach is taken in the diffuse interface method, by devising an equation which governs the continuity of mass concentration. The methods of using volume fractions, level sets or mass concentration are robust enough to handle the breakup and coalescence of fluid masses.

The advantage of LS and DI techniques over the VOF method is that their indicator functions are smooth, rather than discontinuous, and are easier to solve. Another advantage of the LS and DI methods over the MAC method is that these two techniques do not suffer from the lack of divisibility that discrete particles exhibit. There are highly accurate numerical schemes that can be applied to the level set equation. The disadvantage of level set method, however, is that the level set needs to be reset periodically which is not strictly mass conservative. The DI method models interfacial forces as continuum forces by smoothing interface discontinuities and forces over thin but numerically resolvable layers. This smoothing allows use of conventional numerical approximations, sometimes even central differencing, of interface kinematics on fixed grids with acceptable accuracy. This is because the DI method relies on the physical mechanisms on which it is based, rather than special numerical schemes to capture the interface.

Given the shortcoming of different interface solution techniques such as interface tracking and capturing methods and considering their strengths, progress has been made by combining different methods and taking advantage of the best features of each technique while removing or alleviating their drawbacks. A class of promising techniques is the combined Eulerian–Lagrangian meth-

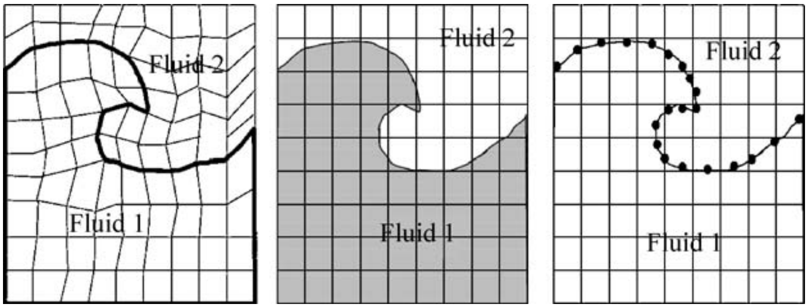

Numerical Techniques for Free Surface Flows: Interface Capturing and Interface Tracking, Figure 1 Different interfacial flow solution methodologies: (**a**) interface fitting; (**b**) interface capturing; (**c**) interface tracking [15]

ods which have the potential to deliver both accuracy and efficiency. This class of methods combines some features of the Eulerian and Lagrangian approaches. The interface is tracked explicitly as curves (or surfaces in three dimensions). The computations are performed on fixed meshes whose topology is independent of that of the interface. One example of this type of method is the immersed boundary technique used for a range of multi-fluid problems [10, 11] and for fluid–structure interaction problems. While explicitly tracking the interface, this method transmits the information regarding the discontinuity across the interface to the grid in much the same way as purely Eulerian methods, i. e. by casting the surface forces into a body force term in the governing equations. Therefore the solution reverts to a single-fluid approach, i. e. the solver does not see a discontinuity at the location of the interface, but experiences distributed forces and material properties in the vicinity of the interface. On the other hand, the cut-cell treatment [11] proceeds to reconstruct the domain on either side of the interface with attention to the immersed boundary and its geometry overlying the grid. Phases are treated separately and no smearing of the interface takes place at the formulation level.

In the following sections, first, different formulations of interfacial flows are presented. Then, different interface solution techniques are presented with the details of each method to the extent possible.

Basic Methodology

Fluid Flow Formulations

Let us consider an arbitrary control volume Ω with boundary $\partial\Omega$ containing a portion of the two fluids. Both fluids divide the volume into two sub-volumes Ω_1 and Ω_2 by the interface Γ. The flow equations can be written in two different forms: two-fluid and single-fluid formulations.

Two-Fluid Formulation

The two-fluid formulation consists of solving the governing equations in both phases independently and then matching the interfacial boundary conditions at the interface, which usually requires an iterative algorithm. This approach keeps the interface as a discontinuity, consistent with the continuum mechanics concept. For each phase, we can write the following momentum equation along with the incompressibility constraint:

$$\frac{\mathrm{D}(\rho_i \boldsymbol{u}_i)}{\mathrm{D}t} = \nabla \cdot \boldsymbol{\Pi}_i + \rho_i \boldsymbol{g}$$
$$\nabla \cdot \boldsymbol{u}_i = 0 \quad \boldsymbol{x} \in \Omega_i\,, \quad i = 1, 2 \tag{1}$$

where $\mathrm{D}/\mathrm{D}t$ is the material derivative $\partial/\partial t + \boldsymbol{u}_i \cdot \nabla$. The subscript i denotes fluids 1 and 2 respectively. The stress tensor is defined as

$$\Pi_i = -p_i \boldsymbol{I} + \mu_i \big(\nabla \boldsymbol{u}_i + (\nabla \boldsymbol{u}_i)^T\big) \tag{2}$$

where ρ and μ are density and viscosity respectively. The last term in Eq. (1) is the body force due to gravity and buoyancy effects. The fluid interface Γ is impermeable and assuming no mass transfer between the two fluids yields a continuous velocity condition at the interface:

$$\boldsymbol{u}_1 = \boldsymbol{u}_2 \quad \text{for} \quad x \in \Gamma\,. \tag{3}$$

The jump in normal stresses along the fluid interface is balanced with the surface tension. Neglecting the variations of the surface tension coefficient, σ, gives the following Laplace–Young boundary condition for momentum conservation at the interface:

$$\boldsymbol{\Pi}_1 - \boldsymbol{\Pi}_2 = \sigma \kappa \boldsymbol{n} \quad \text{for} \quad x \in \Gamma \tag{4}$$

where σ is surface tension coefficient and $\boldsymbol{n}$ is the unit normal vector along the interface pointing outwards from

fluid 2 into fluid 1. The curvature κ of the interface is given as $-\nabla \cdot \boldsymbol{n}$.

Single-Fluid Formulation

The two-fluid formulation is in general demanding in computational operations and complex to implement. A more popular method is the single-fluid formulation of interfacial flows. In the single-fluid approach, one set of equations are solved in the whole domain making use of appropriate physical properties of each phase. The conservation of total momentum for the body of fluid in control volume Ω can be written as

$$\int_\Omega \frac{\mathrm{D}(\rho \boldsymbol{u})}{\mathrm{D}t}\,\mathrm{d}x = \int_\Omega \nabla \cdot \boldsymbol{\Pi}\,\mathrm{d}x + \int_\Gamma \sigma\kappa\boldsymbol{n}\,\mathrm{d}s + \int_\Omega \rho\boldsymbol{g}\,\mathrm{d}x\,. \tag{5}$$

It is assumed that the velocity field is continuous across the interface and the interface boundary conditions are implicitly contained within the equation of motion.

An important aspect of the surface tension is that it creates a jump in pressure across a curved interface. The pressure jump is discontinuous and located only at the interface. This singularity creates difficulties when deriving a continuum formulation of the momentum equation. The interfacial conditions should be embedded in the field equations as source terms. Once the equations are discretized in a finite-thickness interfacial zone, within which the flow properties change smoothly. It is therefore necessary to create a continuum surface force equal to the surface tension at the interface, or in a transitional region, and zero elsewhere.

Thus, the surface integral term in Eq. (5) could be rewritten into an appropriate volume integral:

$$\int_\Omega \sigma\kappa\delta(\chi)\nabla\chi\,\mathrm{d}x \tag{6}$$

where $\delta(\chi)$ is a one-dimensional Dirac delta function which is equal to 1 at the interface and 0 elsewhere. After replacing the surface integral with the obtained volume integral, the final form of unsteady Navier–Stokes equations for a system consisting of two incompressible phases is

$$\frac{\partial(\rho\boldsymbol{u})}{\partial t} + \nabla \cdot (\rho\boldsymbol{u}\boldsymbol{u}) = \nabla \cdot \boldsymbol{\Pi} + \sigma\kappa\delta(\chi)\nabla\chi + \rho\boldsymbol{g} \tag{7}$$

with the incompressibility constraint

$$\nabla \cdot \boldsymbol{u} = 0 \tag{8}$$

The single-fluid approach has been undertaken utilizing Eulerian methods such as the VOF, level set, and mixed Eulerian–Lagrangian methods [10, 11].

Interface Advection Equation for Single-Fluid Formulation

For most interface capturing schemes, which use the single-fluid formulation, an additional equation is solved to obtain the interface evolution and topology. This equation governs the advection of a variable that can be attributed to the interface. The equation of interface motion is as follows:

$$\frac{\partial\chi}{\partial t} + \boldsymbol{u} \cdot \nabla\chi = 0 \tag{9}$$

where χ is an indicator (or color) function which represents the location of interface. The scalar χ is defined differently in different interface capturing techniques. For example, χ is a volume fraction in the VOF volume tracking method, a distance function in the level set method or a Heaviside (step) function in the front tracking method.

The normal vector and curvature are computed from the indicator function using the following formulas:

$$\boldsymbol{n} = \frac{\nabla\chi}{|\nabla\chi|} \quad \kappa = -\nabla \cdot \boldsymbol{n}\,. \tag{10}$$

The physical properties, such as density and viscosity, used in the single-fluid approach are dependent on the value of χ in the cells throughout the computational domain. For example, if χ is a normalized color function such as volume fraction in the VOF method which changes between 0 and 1 throughout the domain, the following formulas determine the density and viscosity:

$$\rho = \rho_2 + (\rho_1 - \rho_2)\chi \tag{11}$$

$$\mu = \mu_2 + (\mu_1 - \mu_2)\chi \tag{12}$$

where subscripts 1 and 2 refer to the first and second fluids, respectively.

Interface Solution Methodologies

Moving and Deforming Mesh Methods

FE-Based Lagrangian Methods While FD- and FV-based techniques have been commonly used to simulate large surface deformations including the breakup and merging of liquids, the FE-based techniques have been more common in simulating less complicated surface deformations. FE performs on either fixed or deforming spatial meshes (see Fig. 2a). Deforming meshes are more

N

popular and are divided into three sub-categories. The first is based on a three-stage iterative cycle by guessing the location of the free surface, solving the governing equations and updating the free surface. Iterations are repeated until the difference between the two successively updated free surface locations becomes less than some desired convergence tolerance. The second approach eliminates the iterations by introducing the position of the nodes on the free surface as a degree of freedom. The third technique is the height flux (HF) method. In this technique, neither iterations are involved for locating the free surface nor is one degree of freedom added to the set of the unknowns. The free surface is found by using the volume of fluid inside sub-volumes which are updated at any time step using the velocity field.

As a sample simulation using the Lagrangian FE method, Fig. 3 shows the deformation of a droplet after impaction on a flat substrate simulated by Fukai et al. [1]. The deformation of the grid as the droplet spreads can be observed. For low to moderate interface deformations, this method gives accurate results and sometimes is even more efficient than interface capturing simulations with high grid resolutions since in FE-based methods, the region near interface can be adapted locally and reduce the number of cells required.

Interface Fitting (Boundary-Fitted Coordinate) Method In the interface fitting, or boundary-fitted method (Fig. 1a), the interface is tracked by attaching it to a mesh surface which is forced to move with the interface. This can be considered a Lagrangian mesh method. The motion of the free surface is accounted for by a coordinate transformation which maps the moving, body-fitted coordinate system in physical space to a uniformly spaced coordinate system in computational space. If the free surface becomes highly distorted, a new mesh may have to be generated in order to prevent both grid singularities and highly skewed grid point distributions.

For the low-deformation bubble simulations where the boundary-fitted method is most widely used, it is assumed that Reynolds number ($\mathrm{Re} = \rho U D/\mu$) is low, the gas flow inside bubbles is neglected and a constant gas pressure assumed. The following boundary conditions are applied at the interface:

- velocity continuity,
- zero tangential stress, and
- balance of normal stress (Π) contributions by pressure, viscous and capillary forces.

The interface position is tracked by introducing a curvilinear interface-fitted non-orthogonal coordinate system. By means of a coordinate transformation, the physical domain is converted to a computational domain with known boundaries that are coordinate isolines. A boundary-fitted grid is generated around the deformed interface at each iteration by a pair of Poisson equations associated with spacing control functions.

The major difficulty arising in free surface flow computation is that the interface location is unknown together with the velocity and pressure fields. Therefore, one has to obtain the physical velocity boundary conditions and the interface position from the boundary conditions.

The following iterative procedure is used in boundary fitted method:

1. Choose an initial state (bubble shape, velocity and pressure fields) with desired values of Reynolds and Weber ($\mathrm{We} = \rho U^2 D/\sigma$) numbers.
2. Compute a curvilinear coordinate interface-fitted grid by carrying out some iterations on the mapping equations.
3. Calculate the velocity boundary conditions from the velocity continuity and tangential stress.
4. Solve Navier–Stokes equations using the fractional steps method.
5. Check the normal stress condition: if not satisfied, displace each interfacial point proportionally to the current normal stress excess Π^n; a new interface position X^{n+1} is then defined at each iteration (Fig. 4).
6. Continue the iterative process from step 2 until boundary conditions and incompressibility condition are satisfied.

The interface position correction at step 5 is given by

$$k_\Pi \Pi^n \boldsymbol{n}^n \tag{13}$$

where k_Π is a constant coefficient, and Π^n and $\boldsymbol{n}^n$ are respectively the current normal stress excess and interface normal vector at iteration n. The iterative process is stopped when

$$\Pi^n \leqslant \varepsilon_\Pi \tag{14}$$

with $\varepsilon_\Pi = 10^{-2}$. The value of k_Π depends on the Weber number and varies between $k_\Pi = 10^{-1}$ (for small Weber numbers) and $k_\Pi = 10^{-3}$ (for large Weber numbers). Conservation of the bubble volume is controlled at each iteration after the interface position correction step (step 5) in order to avoid accumulation of numerical errors and to ensure the convergence of the whole procedure.

This method is best suited and gives very accurate results for relatively simple geometries especially those encountered in two-dimensional and axisymmetric problems. However, application of the boundary-fitted method to complex fully three-dimensional problems with unsteady deforming phase boundaries is very rare [17].

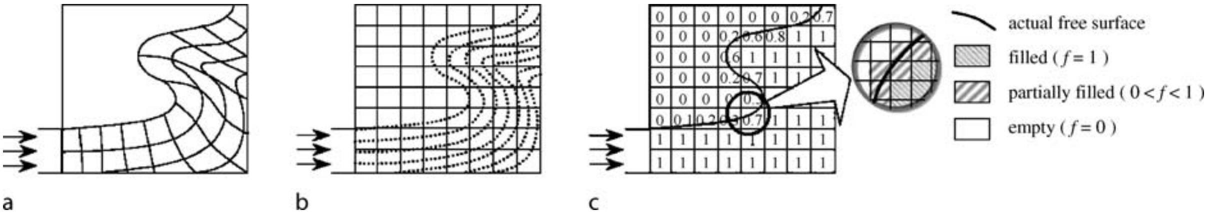

Numerical Techniques for Free Surface Flows: Interface Capturing and Interface Tracking, Figure 2 Numerical methods for the fluid flow with moving free surface. Moving grids: (**a**) Lagrangian FE method. Fixed grids: (**b**) MAC method and (**c**) VOF method [16]

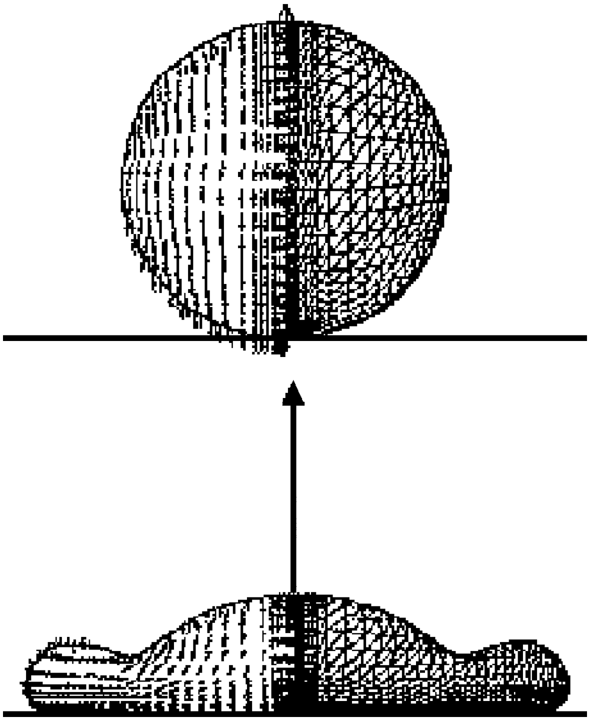

Numerical Techniques for Free Surface Flows: Interface Capturing and Interface Tracking, Figure 3 Impact of a droplet on a substrate at two different time instances using Lagrangian FE method [1]

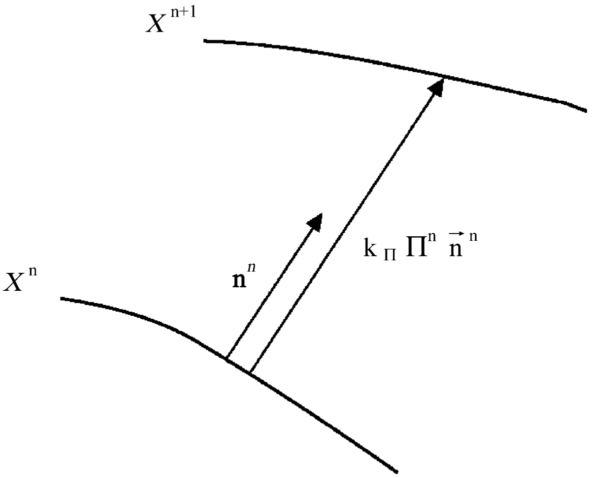

Numerical Techniques for Free Surface Flows: Interface Capturing and Interface Tracking, Figure 4 Definition of the new interface location [2]

Boundary Integral (BI) Method The low Reynolds number approximation of the Navier–Stokes equations (also known as Stokes equations) is an acceptable model for a number of interfacial flow problems. For instance, the typical example of drop coalescence also belongs to this case. A boundary integral method [3] arises from a reformulation of the Stokes equations in terms of boundary integral expressions and the subsequent numerical solution of the integral equations.

The main advantage of the boundary integral methods, compared with other methods (e. g. FD, FE), is that for a number of multiphase flow problems its implementation involves integration on the interfaces only. Thus, discretization is required only for the interfaces, which allows for higher accuracy and performance, especially in three-dimensional simulations. An important feature of the mathematical model used in the BI method is that the velocity at a given time instant depends only on the position of the interfaces at that time instant.

For a system of two incompressible Newtonian fluids separated by an immiscible interface, and neglecting inertial forces, the two-fluid system of Eq. (1) can be simplified to

$$\nabla \cdot \boldsymbol{\Pi}_i = 0\,,$$
$$\nabla \cdot \boldsymbol{u}_i = 0 \quad x \in \Omega_i\,, \quad i = 1, 2 \tag{15}$$

where $\boldsymbol{\Pi}_i = -p_i \boldsymbol{I} + \mu_i(\nabla \boldsymbol{u}_i + (\nabla \boldsymbol{u}_i)^T)$ is the stress tensor. The boundary conditions at the interface $S = \Omega_0 \bigcap \Omega_1$ are the stress balance boundary condition and continuity of the velocity across the interface,

$$(\Pi_1(\boldsymbol{x}) - \Pi_2(\boldsymbol{x})) \cdot \boldsymbol{n}(\boldsymbol{x}) = f(\boldsymbol{x})\boldsymbol{n}(\boldsymbol{x})\,, \quad \boldsymbol{u}_1(\boldsymbol{x}) = \boldsymbol{u}_2(\boldsymbol{x}) \tag{16}$$

where $\boldsymbol{n}(\boldsymbol{x})$ is the unit vector normal to S. The present formulation is limited to interfacial forces, such as capillary effects, that are normal to the interfaces:

$$f(\boldsymbol{x}) = 2\sigma\kappa(\boldsymbol{x}) \tag{17}$$

where $k(\boldsymbol{x}) = 0.5(1/R^1 + 1/R^2)$ is the mean curvature of the interface, and R^1 and R^2 are the main radii of the curvature.

The velocity at infinity is prescribed via a boundary condition,

$$\boldsymbol{u}_\infty(\boldsymbol{x}) = \boldsymbol{L} \cdot \boldsymbol{x}, \quad ||\boldsymbol{x}|| = \infty \tag{18}$$

where $\boldsymbol{L}$ specifies the type of linear flow.

The evolution of the interface $S(\boldsymbol{x}, t)$ is given by the kinematic condition

$$\frac{\mathrm{d}\boldsymbol{x}}{\mathrm{d}t} = \boldsymbol{u}(\boldsymbol{x}, t) + \boldsymbol{w}(\boldsymbol{x}, t), \quad \boldsymbol{x} \in S \tag{19}$$

where $\boldsymbol{w}$ can be an arbitrary velocity, tangential to S.

For a given position of the interfaces S the solution of the mathematical model (Eqs. (15)–(17)) for the velocity $\boldsymbol{u}(\boldsymbol{x}_0)$ at a given point $\boldsymbol{x}_0$ can be obtained by means of the boundary integral formulation. The equations are nondimensionalized and, for simplicity, the same notations for the dimensionless velocity, pressure, space and time variables are used as those for the corresponding dimensional variables from the previous equations.

$$\begin{aligned}\boldsymbol{u}(\boldsymbol{x}_0) = {} & \frac{2}{\lambda+1}\boldsymbol{u}_\infty(\boldsymbol{x}_0) \\ & - \frac{2}{\lambda+1}\frac{1}{8\pi}\int_S f(\boldsymbol{x})\boldsymbol{G}(\boldsymbol{x}_0, \boldsymbol{x}) \cdot \boldsymbol{n}(\boldsymbol{x})\,\mathrm{d}s(\boldsymbol{x}) \\ & - \frac{\lambda-1}{\lambda+1}\frac{1}{4\pi}\int_S \boldsymbol{u}(\boldsymbol{x}) \cdot \boldsymbol{T}(\boldsymbol{x}_0, \boldsymbol{x}) \cdot \boldsymbol{n}(\boldsymbol{x})\,\mathrm{d}s(\boldsymbol{x})\end{aligned} \tag{20}$$

where the integration is over the total interfacial area $S = \bigcup_i S^i$. Here, λ is the non-dimensional viscosity. Tensors $\mathbf{G}$ and $\mathbf{T}$ are the Stokeslet and stresslet, respectively:

$$\mathbf{G}(\boldsymbol{x}_0, \boldsymbol{x}) = \frac{\boldsymbol{I}}{r} + \frac{\hat{\boldsymbol{x}}\hat{\boldsymbol{x}}}{r^3}, \quad \mathbf{T}(\boldsymbol{x}_0, \boldsymbol{x}) = \frac{-6\hat{\boldsymbol{x}}\hat{\boldsymbol{x}}\hat{\boldsymbol{x}}}{r^5} \tag{21}$$

where $\hat{\boldsymbol{x}} = \boldsymbol{x} - \boldsymbol{x}_0$, $r = |\hat{\boldsymbol{x}}|$.

The main advantage of a boundary integral method is that it involves integration only on the interfaces. The main problem, however, regarding the numerical implementation of Eq. (20) is due to the singularities of the kernels $\mathbf{G}$ and $\mathbf{T}$ at $\boldsymbol{x} = \boldsymbol{x}_0$, which is described in detail elsewhere [3].

Among the numerical methods for interfacial flow problems the boundary integral method seems to be one of the most appropriate for problems involving interfaces in close approach. Such situations are typical for most of the practically important multiphase flows including drop deformation and drop-to-drop interaction. Well-known examples are neck formation and its thinning during breakup as well as film formation and drainage during drop coalescence. A simulation of these processes requires a good resolution and accuracy in the neck and film regions. However, the main difficulty for the implementation of a boundary integral method is due to the singularity of the free-space Green's kernels and sensitivity of the method to numerical instabilities. Another disadvantage of this method is that the topological changes do not occur naturally, rather by algorithm intervention.

Interface Capturing

Marker and Cell (MAC) Method The first method capable of modeling gas–liquid flows, separated by a moving interface, was the MAC of Harlow and Welch [4]. In the MAC method, as shown in Fig. 2b, the massless markers are used to define the location and track the movement of free surface. This is in fact a combination of a Eulerian solution of the basic flow field, with Lagrangian tracking of marker particles. The computational cycle in the MAC method consists of the advancement of discrete field variables from an initial time t_0 to the subsequent time $t_0 + \Delta t$ by accomplishing the steps below. The computation starts with a predictor–corrector algorithm for the determination of velocity field at $t_0 + \Delta t$. In the predictor stage of the solution algorithm, the pressure is replaced by an arbitrary pseudo-pressure β (which in most cases is set equal to zero at full cells), and tentative velocities are then calculated. A pseudo-pressure boundary condition is applied in surface cells to satisfy the normal stress condition. Since pressure has been ignored in the full cells, the tentative velocity field does not satisfy the incompressible continuity equation. The deviation from incompressibility is used to calculate a pressure potential field ψ, which then is used to correct the velocity field. In the final steps, the velocity boundary conditions are calculated, the new location of free surface is determined by tracking the markers and the velocity boundary conditions associated with the new fluid cells are assigned (Fig. 5).

The MAC method, which allows arbitrary free surface flows to be simulated, is widely used and can be readily extended to three dimensions. Its drawback lies in the fact that it is computationally demanding to trace a large number of particles, especially in three-dimensional simulations. In addition, it may result in some regions void of par-

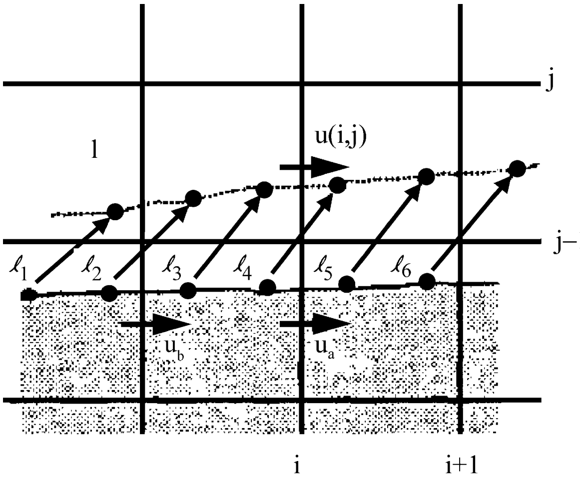

Numerical Techniques for Free Surface Flows: Interface Capturing and Interface Tracking, Figure 5 Free surface and velocity distribution in MAC family of interface tracking schemes. The circles represent surface markers, while continuous and dotted lines show the old and new free surface topology. $u(i,j)$ is a new fluid cell velocity [18]

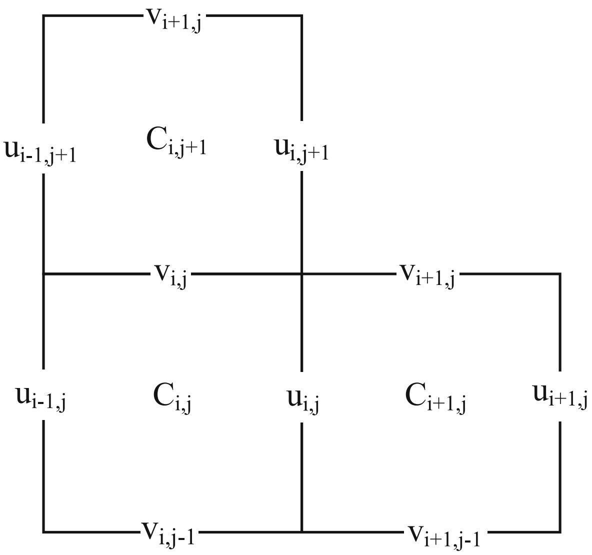

Numerical Techniques for Free Surface Flows: Interface Capturing and Interface Tracking, Figure 6 Variable arrangement for staggered grid according to the MAC method [4]

ticles because the density of particles is finite. The impact of the MAC method is much beyond its interface capturing scheme. The staggered mesh layout (Fig. 6) and other features of MAC have become a standard model for many other Eulerian codes (even numerical techniques involving mono-phase flows).

Volume of Fluid (VOF) Technique In the VOF method [5, 6], free surface is represented on fixed grids using fractional fluid volume in a cell. Each rectangle in Fig. 2c denotes a unit cell. The fractional volume-of-fluid, C, is defined such that it is equal to unity at any point occupied by the heavier fluid and zero elsewhere. As the free surface moves, the fractional volume of fluid of each cell is updated. In a numerical sense, every cell is classified into three categories according to the value of C (see Fig. 2c). If a cell is completely filled with the first (heavier) fluid, the fractional volume of fluid of the cell is unity ($C = 1$). If a cell is filled with the second (lighter) fluid, its volume of fluid is zero ($C = 0$). A cell is considered to be on the free surface when the values of C lie between 0 and 1 ($0 < C < 1$). Discontinuity in C propagates according to the following transport equation [5, 6]:

$$\frac{\partial C}{\partial t} + \boldsymbol{u} \cdot \nabla C = 0 . \tag{22}$$

By solving Eq. (22), distribution of C is obtained and thus free surface location can be identified. In a physical sense, the equation implies mass conservation of one phase in the mixture. Numerically, this equation is characterized as a hyperbolic or pure convection equation.

The formulation of the VOF model requires that the convection and diffusion fluxes through the control volume faces be computed and balanced with source terms within the cell itself. The interface will be approximately reconstructed in each cell by a proper interpolating formulation, since interface information is lost when the interface is represented by a volume fraction field. The application of Eq. (22) to the interface cells is not trivial and requires certain knowledge of the interface shape. The problem of reconstructing an interface by using the volume fraction field data (updated or given at the start) has generated a multitude of approaches and methods. The geometric piecewise linear interface calculation (PLIC) scheme is commonly employed because of its accuracy and applicability for complex flows, compared to other methods such as the donor–acceptor, Euler explicit and implicit schemes. An interface is viewed as comprised of line segments. This is acceptable when the grid system is fine enough. Inside of each cell, this line segment determines uniquely what the volume fraction inside that cell is. However, the reverse correlation is not unique, since more than one location of the interface may determine the same volume fraction in the cell. One has to take into account a group of neighboring cells in order to reconstruct the interface accurately.

A VOF geometric reconstruction scheme is divided into two parts: a reconstruction step and a propagation step. The key part of the reconstruction step is the determination

of the orientation of the segment. This is equivalent to the determination of the unit normal vector $\boldsymbol{n}$ to the segment. Then, the normal vector $\boldsymbol{n}_{i,j}$ and the volume fraction $C_{i,j}$ uniquely determine a straight line. Once the interface has been reconstructed, its motion by the underlying flow field must be modeled by a suitable algorithm.

In the PLIC method, the interface is approximated by a straight line of appropriate inclination in each cell. A typical reconstruction of the interface with a straight line in cell (i,j), which yields an unambiguous solution, is perpendicular to an interface normal vector $\boldsymbol{n}_{i,j}$ and delimits a fluid volume matching the given $C_{i,j}$ for the cell. A unit vector $\boldsymbol{n}$ is determined from the immediate neighboring cells based on a stencil $C_{i,j}$ of nine cells in two dimensions. The normal vector $\boldsymbol{n}_{i,j}$ is thus a function of $C_{i,j}$, $\boldsymbol{n}_{i,j} = \nabla C_{i,j}$. Initially, a cell-corner value of the normal vector $\boldsymbol{n}_{i,j}$ is computed. For a uniform grid, an example at $(i+1/2,\ j+1/2)$ in two dimensions is as follows:

$$n_{x,i+\frac{1}{2},j+\frac{1}{2}} = \frac{1}{2h}(C_{i+1,j} - C_{i,j} + C_{i+1,j+1} - C_{i,j+1}) \tag{23}$$

$$n_{y,i+\frac{1}{2},j+\frac{1}{2}} = \frac{1}{2h}(C_{i,j+1} - C_{i,j} + C_{i+1,j+1} - C_{i+1,j}) \tag{24}$$

where $h = \Delta x = \Delta y$ is the computational cell size. Similar relations are used in other interface capturing schemes such as level set or diffuse interface method to calculate the interface normal vector from the proper indicator function. The required cell-centered values are given by averaging

$$\boldsymbol{n}_{i,j} = \frac{1}{4}(\boldsymbol{n}_{i+\frac{1}{2},j-\frac{1}{2}} + \boldsymbol{n}_{i-\frac{1}{2},j-\frac{1}{2}} + \boldsymbol{n}_{i+\frac{1}{2},j+\frac{1}{2}} + \boldsymbol{n}_{i-\frac{1}{2},j+\frac{1}{2}}) . \tag{25}$$

The most general equation for a straight line on a Cartesian mesh with normal $\boldsymbol{n}_{i,j}$ is

$$n_x x + n_y y = \alpha . \tag{26}$$

The normal vector $\boldsymbol{n}_{i,j}$ is defined by the vector gradient of $C_{i,j}$, which can be derived from different finite difference approximations which directly influence the accuracy of algorithms. These include Green–Gauss, volume-average, least-squares, minimization principle and Young's gradients. It is noted that a wide, symmetric stencil for $\boldsymbol{n}_{i,j}$ is necessary for a reasonable estimation of the interface orientation.

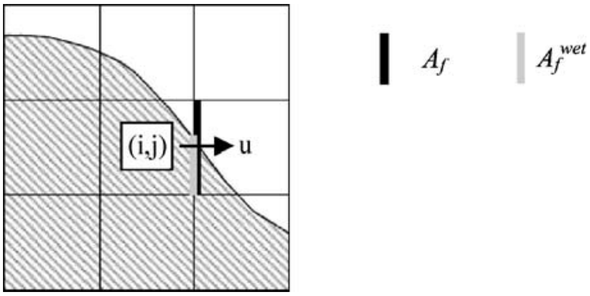

Numerical Techniques for Free Surface Flows: Interface Capturing and Interface Tracking, Figure 7 Definitions of wet-out fraction for the k-th face of cell (i,j), $C_{\Gamma k}$

Geometrical VOF Advection Algorithm In order to trace the free surface location on a fixed mesh using a volume flux-based scheme, fluid volume fluxes through every cell boundary should be calculated. To handle the time derivative in Eq. (22), explicit and implicit time integration can be adopted. Generally, implicit integration gives a solution with higher accuracy, but requires more complex and time-consuming algorithm. In the explicit integration, in contrast, values at the new time step are updated from those at the old time step using the known flow field. In most studies, explicit integration is adopted due to its simplicity in updating the free surface location. After the divergence theorem is applied and the time integration is performed, Eq. (22) is reduced to

$$C_{i,j}^{n+1} = C_{i,j}^{n} + \frac{\Delta t}{V_{i,j}}\left[-\sum_k (C_{\Gamma k}\boldsymbol{u} \cdot \boldsymbol{n})\, A_k \right] \tag{27}$$

where the subscripts (i,j) and k represent the cell and the face numbers, respectively; $C_{i,j}^{n+1}$ and $C_{i,j}^{n}$ denote the values of C in the (i,j) cell at the new and the old time steps; Δt is the size of time increment; $V_{i,j}$ is the volume of the cell and A_k is the area of its k-th face; and $\boldsymbol{u}$ and $\boldsymbol{n}$ are the velocity and the unit outward normal vectors at the k-th face, respectively. From Eq. (27), it can be stated that the change in fluid volume in a cell during a given time interval is equal to the net fluid volume flux through every cell boundary. Here, $C_{\Gamma k}$ represents the *actual fractional volume-of-fluid* at the k-th face of the cell during a given time increment. Also, it can be interpreted as the wet-out fraction at a cell boundary, which indicates to what extent the cell boundary is wetted by the fluid (see Fig 7). In two dimensions, it can be expressed as $C_{\Gamma k} = A_f^{\text{wet}}/A_{\text{f}}$.

In general, $C_{\Gamma k}$ in Eq. (27) is dependent upon the free surface orientation and the value of f in the cell as well as the size of time increment Δt. However, due to the explicit

nature of the time integration illustrated here, dependency of $C_{\Gamma k}$ on Δt becomes out of question. As a result, $C_{\Gamma k}$ is a function of the free surface orientation (or normal vector $\boldsymbol{n}$) and $C_{i,j}$ so that

$$C_{\Gamma k} = C_{\Gamma k}(\boldsymbol{n}, C_{i,j}) \tag{28}$$

The relations between $C_{\Gamma k}$ and volume fraction and normal vector components for three-dimensional interfaces can be found in Jafari et al. [19]. In the VOF-PLIC method, the fluxes are calculated using geometric approaches.

VOF Advection Based on High-resolution Difference Schemes It becomes complicated to use a geometric line reconstruction scheme on unstructured grids and more difficulty is encountered in extending it to three-dimensional calculations. To circumvent this limitation in VOF methods, a class of high resolution difference schemes is utilized, instead of geometric calculations, to capture the interface motion. Using standard convection schemes, the advection operator will lead to significant smearing of the interface (an effect of upwind scheme) or unbounded values of volume fraction (a result of using central difference schemes). A variety of compressive advection schemes have been devised to minimize the diffusion and promote boundedness. The compressiveness is often obtained by using a controlled downwinding of the fluxes. Controlled downwinding schemes have compressive characteristics which depend upon the time step, and therefore require small time steps to achieve sharp interfaces even for steady-state free surface flows.

One of the most widely used difference-based VOF schemes is the high-resolution interface-capturing scheme (HRIC) [21]. It is a normalized variable diagram (NVD) scheme based on a nonlinear blending of the bounded downwind (BD) and upwind differencing (UD) schemes, with the aim of combining the compressive property of the BD scheme with the stability of the UD scheme.

The normalized cell value of volume fraction $\tilde{C}_\mathrm{c}$ which is used to find the normalized face value $\tilde{C}_\mathrm{f}$ for face f is defined as follows:

$$\tilde{C}_\mathrm{c} = \frac{C_\mathrm{D} - C_\mathrm{U}}{C_\mathrm{A} - C_\mathrm{U}} \tag{29}$$

where U, D, and A represent upwind, donor and acceptor cells respectively. The normalized functional relationships

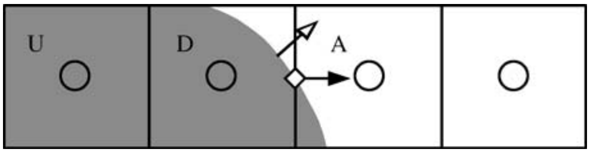

Numerical Techniques for Free Surface Flows: Interface Capturing and Interface Tracking, Figure 8 Interface and volume fraction distribution in neighboring cells [20]

of the BD and UD schemes are given by

$$\tilde{C}_\mathrm{f}^\mathrm{BD} = \begin{cases} 2\tilde{C}_\mathrm{c} & 0 < \tilde{C}_\mathrm{c} \leqslant 0.5 \\ 1 & 0.5 < \tilde{C}_\mathrm{c} \leqslant 1 \\ \tilde{C}_\mathrm{c} & \text{otherwise} \end{cases} \tag{30}$$

$$\tilde{C}_\mathrm{f}^\mathrm{UD} = \tilde{C}_\mathrm{c} \tag{31}$$

The functional relationship of the HRIC scheme is also function of the angle θ between the normal to the interface and the normal to the cell face (Fig. 8). For an interface aligned with the cell face ($\theta = 0$) the bounded downwind scheme is used, while for an interface perpendicular to the cell face the upwind scheme is used. For an interface with θ between these two limits, $f(\theta)$ is chosen to be $\sqrt{\cos\theta}$ and the blending formula is given by

$$\tilde{C}_\mathrm{f} = \tilde{C}_\mathrm{f}^\mathrm{BD}\sqrt{\cos\theta} + \tilde{C}_\mathrm{f}^\mathrm{UD}(1 - \sqrt{\cos\theta}) \tag{32}$$

where

$$\cos\theta = \frac{\nabla \boldsymbol{C} \cdot \boldsymbol{d}}{|\nabla \boldsymbol{C}|\,|\boldsymbol{d}|} \tag{33}$$

and $\boldsymbol{d}$ is a vector connecting cell centers adjacent to the face f. With this formulation, Eq. (32), the blending of the upwind and downwind schemes is dynamic and accounts for the spatial distribution of the C field.

The face volume fraction is now obtained from the normalized value computed above as follows:

$$C_\mathrm{f} = \tilde{C}_\mathrm{f}(C_\mathrm{A} - C_\mathrm{U}) + C_\mathrm{U}\,. \tag{34}$$

The use of high-resolution schemes in interfacial flow calculations is promising, but existing schemes are still too diffusive for the capturing of sharp interfaces. Implementation in multiple dimensions is also restricted to the technique of operator splitting. A generalization for implementation on unstructured meshes is still required.

N

Surface Tension Calculation in VOF Method Modeling interfacial tension effects is important because it is a potentially large force which is concentrated on the interface. There are two different approaches to modeling surface tension forces. The first one is continuum surface force (CSF) defined as

$$F^{\mathrm{st}} = -\sigma\kappa \boldsymbol{n}\delta_{\mathrm{s}} = \sigma\nabla\cdot\left(\frac{\nabla C}{|\nabla C|}\right)\frac{\nabla C}{[C]} \tag{35}$$

where the normal vector and curvature are calculated from Eq. (10). The delta function is approximated as $\delta_{\mathrm{s}} = |\nabla C|/[C]$ and $[C] = C_1 - C_2$ is the difference between maximum and minimum values of C.

The second approach is the continuous surface stress (CSS) model where the surface force is expressed as the divergence of a surface tension tensor:

$$\mathbf{T} = -\sigma(\boldsymbol{I} - \boldsymbol{n}\otimes\boldsymbol{n})\,|\nabla C|\,,$$

$$F^{\mathrm{st}} = -\nabla\cdot\mathbf{T} = \sigma\nabla\cdot\left(|\nabla C|\boldsymbol{I} - \frac{\nabla C\otimes\nabla C}{|\nabla C|}\right) \tag{36}$$

An advantage of the CSS model is that it does not explicitly contain the curvature term since curvatures calculated from the VOF method are less accurate than those calculated from other methods such level set. This is because curvature evaluation in effect requires the second derivative of the discontinuous volume fraction field. Therefore, care must be taken in order to avoid errors in curvature calculations.

Since the movement of free surface is accomplished by solving Eq. (22) in the VOF method, instead of deforming the mesh as in the Lagrangian method or tracing marker particles as in the MAC method, an overall solution algorithm becomes simple and efficient. Combined with advantages of fixed grids which can accommodate complex geometry, the VOF method is adaptable to any existing CFD codes regardless of the solution methods such as FD, FV or FE. For this reason, the VOF-based methods have been used extensively in the simulation of general free surface flow problems. There are several extended or modified versions of the VOF method [22]. If mass conservation is a design constraint, geometrically based algorithms tend to result rather than simpler algebraically based techniques. Geometrically based algorithms, on the other hand, tend to exhibit *numerical surface tension* when interface features are not resolved [23].

The basic idea behind the VOF method is to discretize the equations for conservation of volume in either conservative flux or equivalent form resulting in near-perfect volume conservation except for small over and under shoots. The main disadvantage of the VOF method, however, is that it suffers from the numerical errors typical of Eulerian schemes such as the level set method. The imposition of a volume preservation constraint does not eliminate these errors, but instead changes their symptoms replacing mass loss with inaccurate mass motion leading to small pieces of fluid non-physically being ejected as flotsam or jetsam, artificial surface tension forces that cause parasitic currents and an inability to calculate accurately geometric information such as normal vector and curvature. Due to this deficiency, most VOF methods are not well suited for surface tension-driven flows unless some improvements are made [19].

Level Set (LS) Method In the level set method, the interface between the two phases is represented by a continuous scalar function $\phi(\boldsymbol{x}, t)$, which is set to zero at the interface, is positive on one side and negative on the other. This way both phases are identified, and the location of the physical interface is associated with the surface $\phi = 0$. The function ϕ is called the level set function and is typically defined as the signed distance to the interface; i. e. $\phi = -d(\boldsymbol{x}, t)$ on one side of the interface and $\phi = +d(\boldsymbol{x}, t)$ on the other, where $d(\boldsymbol{x}, t)$ is the shortest distance from the point $\boldsymbol{x}$ to the interface.

When the interface is advected by the flow, the evolution of the level set function is given by

$$\frac{\partial\phi}{\partial t} + \boldsymbol{u}\cdot\nabla\phi = 0 \tag{37}$$

The level set Eq. (37) moves the interface along its normal vector field with the normal speed $v^n = \boldsymbol{u}\cdot\boldsymbol{n}$. Note that any tangential component will have no effect on the position of the front. Using the normal vector $\boldsymbol{n}$ given as $\nabla\phi/|\nabla\phi|$ we can rewrite Eq. (37) as

$$\frac{\partial\phi}{\partial t} + v^n\,|\nabla\phi| = 0 \tag{38}$$

This is called the *Hamilton–Jacobi* formulation and yields the motion of the front $\Gamma(t)$ with normal velocity v^n on the zero level set, $\phi = 0$.

In the level set formulation, the density and viscosity are typically interpolated across the interface as follows:

$$\rho(\boldsymbol{x}, t) = \rho_2 + (\rho_1 - \rho_2)H_\varepsilon(\phi(\boldsymbol{x}, t)) \tag{39}$$

$$\mu(\boldsymbol{x}, t) = \mu_2 + (\mu_1 - \mu_2)H_\varepsilon(\phi(\boldsymbol{x}, t)) \tag{40}$$

where subscripts 1 and 2 denote the values corresponding, respectively, to the two different phases. Here, $H_\varepsilon(\phi)$ is

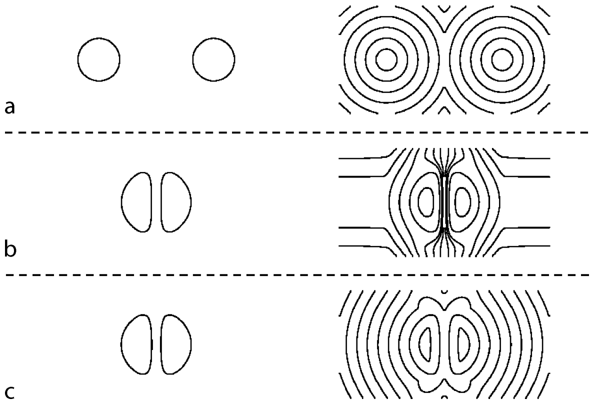

Numerical Techniques for Free Surface Flows: Interface Capturing and Interface Tracking, Figure 9 Effect of re-initialization for two merging bubbles. Left columns show the interface and right columns show contours of the level set function ϕ. (**a**) Initial configuration; (**b**) just before merging (time step $n = 100$) with no re-initialization; (**c**) just before merging ($n = 100$) with re-initialization back to a distance function [24]

a smoothed Heaviside function, which is defined as

$$H_\varepsilon(\phi) = \begin{cases} 0 & \text{if } \phi < -\varepsilon \\ \frac{(\phi+\varepsilon)}{(2\varepsilon)} + \frac{\sin(\frac{\pi\phi}{\varepsilon})}{(2\pi)} & \text{if } |\phi| \leqslant \varepsilon \\ 1 & \text{if } \phi > \varepsilon \end{cases} \quad (41)$$

where ε is a small parameter of the order of the size of a mesh cell close to the interface. By using the smoothed Heaviside function, one effectively assigns the interface a fixed finite thickness of 2ε, over which the phase properties are interpolated. Hence, the value of ε can be considered to be the half-thickness of the numerical interface.

The level set function will not necessarily remain a distance function as the front propagates. For large time computations this distortion will give a non-uniform thickness of the interface causing a randomness in the distance over which fluid properties change and surface tension forces are distributed.

There are basically two reasons for this distortion. Standard differencing schemes introduce numerical diffusion to the initial distance function. This problem can be reduced by using higher order numerical methods. The second reason is that the flow field is very rarely of that character so that the level set function ϕ would be kept as a distance function. For example, the maximum and minimum values of the level set function will remain the same throughout the computations. For two merging interfaces (e. g. two bubbles) this will cause a steep gradient and an impenetrable sheet between the two merging interfaces (see Fig. 9). It is therefore necessary to reinitiate the distance function after each time step.

Re-Initialization Procedure Maintaining ϕ as a distance function becomes important for providing a uniform thickness at the interface with a fixed width in time and to avoid steep gradients. It is also essential that the level set function is re-initialized to a distance function without changing its zero level set. An iterative procedure is used to maintain ϕ as a distance function. Their re-initialization procedure is based on solving the following partial differential equation to steady-state solution at each time step:

$$\frac{\partial d}{\partial \tau} = sign(\phi)(1 - |\nabla d|) \quad (42)$$

with initial condition

$$d(\boldsymbol{x}, 0) = \phi(\boldsymbol{x}, t)\,, \quad (43)$$

where τ is an artificial time. It has also been proposed to use a smooth sign function in order to eliminate numerical oscillations,

$$sign_\varepsilon(\phi) = \frac{\phi}{\sqrt{\phi^2 + \varepsilon^2}}\,. \quad (44)$$

The steady-state solution of Eq. (42) is a distance function and, since $sign(\phi = 0) = 0$, the zero level set of $d(\boldsymbol{x}, \tau)$ and $\phi(\boldsymbol{x}, t)$ are the same. When the steady-state solution of Eq. (42) is obtained at $\tau = \tau_S$, we simply replace $\phi(\boldsymbol{x}, t)$ by $d(\boldsymbol{x}, \tau_S)$.

Surface Tension Solution in Level Set (LS) Methods As for the discontinuous Heaviside function there will be numerical difficulties with discretization of the singular Dirac delta function. This function is therefore smoothed over the interface thickness and commonly defined as

$$\delta_\varepsilon(\phi) = \frac{\partial H_\varepsilon(\phi)}{\partial \phi} \quad (45)$$

or

$$\delta_\varepsilon(\phi) = \begin{cases} \frac{1}{(2\varepsilon)}\left[1 + \cos\left(\frac{\pi\phi}{\varepsilon}\right)\right] & \text{if } |\phi| \leqslant \varepsilon \\ 0 & \text{otherwise.} \end{cases} \quad (46)$$

Introducing the regularized delta function δ_ε into Eq. (6) smears out the surface tension force across the interface. The level set formulation of Eq. (6) takes the form

$$F^{\text{st}} = -\sigma \nabla \cdot \left(\frac{\nabla\phi}{|\nabla\phi|}\right)\delta_\varepsilon(\phi)\nabla\phi\,, \quad (47)$$

where we have expressed the curvature in terms of ϕ. This is similar to the widely used continuum surface force (CSF) model.

Diffuse Interface (Phase Field) Method The diffuse interface (DI) model, also known as partial miscibility or phase field method, is based on the idea that a fluid–fluid interface has a finite thickness over which various thermodynamic variables change continuously. The concept was first used by van der Waals in 1893 to explain why equilibrium interfaces have surface tension and, hence, the DI method is endowed with capillarity. The thickness of the interface is closely related to the finite range of molecular interactions. The finite interaction range is represented by a non-local effect in the free energy: the local free energy density not only depends on the local composition but also on the composition of the immediate environment. By using a mean-field approximation, the non-local effect in the free energy is represented by the dependence on the local composition gradients rather than on the non-local composition. This free energy determines both the interfacial thickness and the surface tension that now appears in the equations of motion as a distributed stress over the interfacial region. The position and the shape of the interface is a part of the solution that is continuous throughout the system but may have large variations in the interfacial region of the governing equations of DI. Originally designed to model the initial stages of spinodal decomposition, the DI approach has recently been used to model a wide range of hydrodynamic and interfacial phenomena.

The following Cahn–Hilliard equation governs the continuity of mass concentration:

$$\frac{\partial C}{\partial t} + \boldsymbol{u} \cdot \nabla C = \nabla \cdot (M(C) \nabla \xi) \tag{48}$$

$$\xi = F'(C) - \varepsilon^2 \Delta C \tag{49}$$

where $M(C) = C(1-C)$ is the mobility and $F(C) = 1/4C^2(1-C)^2$ denotes Helmholtz free energy, and ε is the interface thickness which is a measure of gradient energy. This equation can be solved using ordinary difference schemes and it is an advantage of the DI method.

Surface Tension Simulation in Diffuse Interface Method Similar to surface tension modeling in the VOF method, both CSF and CSS methods are applicable, with minor adjustments, to the diffuse interface method. The CSF method is as follows:

$$F^{\mathrm{st}} = -\alpha \sigma \varepsilon \nabla \cdot \left(\frac{\nabla C}{|\nabla C|} \right) |\nabla C| \; \nabla C \tag{50}$$

The CSS formulation of surface tension force is given as

$$F^{\mathrm{st}} = \alpha \sigma \varepsilon \nabla \cdot \left(|\nabla C|^2 \boldsymbol{I} - \nabla C \otimes \nabla C \right) \tag{51}$$

Here, α is constant and has the value of $6\sqrt{2}$.

The diffuse interface method is rapidly developing into a reliable technique for investigation of multiphase and interfacial flows. Its advantages are automatic handling of topological changes, the possibility of easy implementation of physical phenomena and its applicability for treating multiphase flows involving more than two phases, miscible and immiscible [25].

Interface Tracking Methods

Glimm's Front Tracking Method In Glimm's front tracking method [9], the discrete representation of the flow is based on a composite grid that consists of a spatial grid representing the flow field in the bulk fluid, together with a lower dimension grid that represents the fronts. Figure 1c shows a two-dimensional schematic of a time step snapshot of such a grid. The front is represented by a piecewise linear curve, the sections of which are called bonds. In contrast to the spatial grid, which is fixed in time (i. e. Eulerian), the fronts move according to the dynamics of the wave fronts that they represent. A single time step is divided into two processes: the propagation of the fronts and the updating of the solution on the spatial grid.

Front tracking has several features in common with the arbitrary Lagrangian Eulerian (ALE) family of methods in which the solution grid is adapted to the flow. ALE methods are based on a moving mesh formulation of the flow equations where the mesh motion is chosen to maintain desirable features of both the Lagrangian (fluid following) or Eulerian (fixed grid) formulations. Front tracking is a special case where adaptivity is used on a lower dimensional manifold corresponding to wave fronts.

Two key features are exploited by the tracking. When the orientation and position of a front is known, one can locally rotate into a coordinate system that is aligned with the wave front so that the normal and tangential directions to the front are grid lines in the local coordinate system. Such a grid substantially improves the quality of the solution near the front.

A tracked interface is a collection of geometric objects describing the location of a set of fronts at a given time. They consist of discrete representations of points, curves and surfaces. A curve is a connected oriented piecewise linear list of bonds, which are connectors between adjacent points. A surface is a connected oriented piecewise

linear collection of triangles, which are in turn connectors between three adjacent points. Both bonds and triangles are linking objects in the sense that they contain pointers to their neighbors. Each bond points to both the previous and following bonds that share its endpoints. It is assumed that a valid interface is non-intersecting in the interior of the surfaces and curves. Thus curves may only intersect along nodes or surfaces along curves. Front intersections produced during propagation correspond to wave interactions and require special treatment to resolve the interaction and untangle the interface.

This technique has been extensively developed by Glimm and collaborators. Details can be found in Glimm et al. [9]. Front tracking is accurate in locating interfaces. However, it is difficult to implement and simulation of rupturing and merging interfaces is not automatically done and needs algorithm intervention.

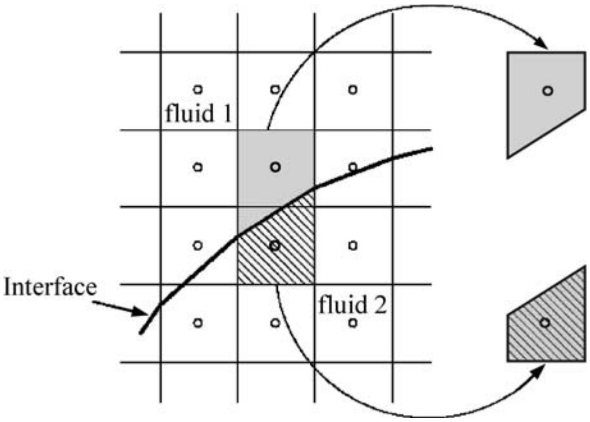

Numerical Techniques for Free Surface Flows: Interface Capturing and Interface Tracking, Figure 10 Illustration of the cell–interface intersection in the sharp interface method. Trapezoidal cells are formed near the interface [27]

Combined Interface Capturing–Interface Tracking Methods

Tryggvason's Hybrid Method Although this method is also called front tracking, it is a hybrid between interface capturing and interface tracking techniques. A stationary regular grid is used for the fluid flow, but the interface is tracked by a separate grid of lower dimension, similar to Glimm's method. This grid is usually called the front. However, unlike interface tracking method of Glimm [9] where each phase is treated separately, Tryggvason's method follows front capturing methods and treats all phases by a single set of governing equations throughout the whole flow field [10]. Interfacial source terms such as surface tension are computed on the front and transferred to the fixed grid. Advection of fluid properties such as density is done by following the motion of the front.

Although the front tracking method has been successfully applied to different interfacial flows, there are problems associated with these kinds of interface tracking methods. The main drawback is that the marker points will be non-uniformly distributed as the interface evolves. Also, relatively high computer storage is needed to maintain the interface continuous and smooth. The need to provide element connectivity for a moving, adaptive surface mesh significantly complicates three-dimensional interface tracking. To alleviate this problem, Shin and Juric [26] developed a method which automatically provides for element addition/deletion and topology change.

Sharp Interface Method The sharp interface (SI) method [27] employs a combined Eulerian–Lagrangian strategy. It uses the finite volume method and solves two sets of governing equations instead of using the single set of governing equations for the entire domain of all phases/materials. This enables the method to handle large property (such as density) ratios across the interface with relative ease. The interface is sharp with almost no numerical smearing. In SI method, interfacial constraints are imposed as the distinct boundary conditions, instead of being incorporated through source terms in the governing equations. The cubic B-spline curve fitting method is employed to represent the interface.

An illustration of the cell and interface intersection treated in the sharp interface method is depicted in Fig. 10. It is noted that the small fragments of cut-cells are absorbed into the neighboring cells in the same phase to form larger, trapezoid cells. The interface, represented by suitable geometric representations based on massless markers, intersects with the underlying, fixed Cartesian grid. A compact interpolation method near the interface is adopted to retain second-order accuracy and conservation property. The SI is accurate in capturing interface evolution. However, it is in general demanding in computational operations and complex to implement.

Immersed Boundary (IB) and Immersed Interface (II) Techniques The immersed boundary technique [28] is a combined Eulerian–Lagrangian method in the sense that the flow is solved using a Eulerian approach on a fixed Cartesian mesh, and the interface is represented by a discrete set of points and advected in a Lagrangian way. In this method, a single set of conservation equations valid for both phases is solved. The interface conditions are incorporated into the governing field equa-

tion as source terms using the continuum surface force (CSF) method [22]. As a result, the interface is considered to be of small nonzero thickness within which the values of the properties change smoothly. The immersed boundary method tracks the interface explicitly instead of reconstructing it as a posteriori measure. Furthermore, the fluid properties are not advected but prescribed based on the known interface position, therefore keeping the transitional zone on both parts of the interface constant and avoiding any numerical diffusion. This method is suitable for solving bubble and drop dynamics that often encounter large deformation, as has been proved in the existing literature.

In the immersed boundary method, the information between the moving interface and the field variables is exchanged through interpolation. Since the locations of the marker points in general do not coincide with the underlying grid points employed to solve the field equations, the velocity of the field equation, defined according to the Cartesian grid system, is interpolated to obtain the marker velocity. Furthermore, the interfacial force acting on the marker points is spread to the nearby grid points. The concept is illustrated in Fig. 11b. The interpolations are performed via a discrete Dirac delta function taken in this study as Eq. (46) where the interface half-thickness of $\varepsilon = 2h$ with h as grid size is used.

Interface Tracking in Immersed Boundary Method The immersed boundary or interface denoted by $C(t)$ (a curve in two dimensions or a surface in three dimensions), see Fig. 11a, is represented by K markers of coordinates $\boldsymbol{x}_k(s)$ with $k = 1, 2, \ldots, K$. The markers are uniformly distributed along $C(t)$ at some fraction of the grid spacing, $0.5h < ds < 1.5h$. The interface is parameterized as a function of the arclength s by fitting quadratic polynomials $\boldsymbol{x}_k(s) = \boldsymbol{a}_k s^2 + \boldsymbol{b}_k s + \boldsymbol{c}_k$ through three consecutive marker points of coordinates $\boldsymbol{x}_{k-1}, \boldsymbol{x}_k, \boldsymbol{x}_{k+1}$.

The II method [29] is similar to the IB technique with some differences. The IB method uses a set of discrete delta functions to spread the entire singular force exerted by the immersed boundary to the nearby fluid grid points. However, the II method instead incorporates part of this force into jump conditions for the pressure, avoiding discrete dipole terms that adversely affect the accuracy near the immersed boundary.

Hybrid Techniques

There are a number of hybrid techniques which integrate different methodologies. These include (a) coupled level set–volume of fluid (CLSVOF) which combines mass conserving properties with accurate normal and curvature calculation of level set, (b) particle level set which uses particles to enhance mass conservation, (c) mixed markers and volume of fluid with which one obtains a smooth motion of the interface, typical of the marker approach, with a good volume conservation, as in standard VOF methods and (d) hybrid immersed interface–level set which, instead of tracking the interface explicitly, captures the interface similar to level set method (purely Eulerian technique). There are a number of other hybrid techniques which have been less widely used.

Other Methods

There are other methods which are used in some studies of multiphase and interfacial flows. These include particle-based methods and also techniques that do not rely on Navier–Stokes equations for flow solution.

Particle-based methods are roughly divided into two main categories: those that use particles in conjunction with a grid, namely particle-in-cell (PIC) methods; and those that are massless, such as smoothed particle hydrodynamics (SPH). The most striking feature of particle-based methods is their ease of implementation. They are essentially as easy to implement on three-dimensional unstructured meshes as on two-dimensional structured meshes. However, they are very demanding in terms of memory and processing power that has caused their limited use in interfacial flows so far.

There are methods which are not based on Navier–Stokes equations. These include molecular dynamics (MD) and lattice Boltzmann (LB) methods applied to two-phase flows. A MD study of any physical phenomenon attempts to simulate the real behavior of nature by identifying each molecule and following its motion in time through the basic laws of classical mechanics. The system behavior and temporal evolution of its thermodynamic and transport properties are, therefore, nothing more than the cumulative result of individual molecular motion. The simulation of macroscopic multiphase flow phenomena such as droplet evaporation using MD is not yet possible due to the prohibitively large computational requirements both in terms of CPU time and memory. However, a system involving a submicrometer droplet is small enough to successfully apply MD. Consolini et al. [30] studied evaporation of submicrometer droplets in a gaseous surrounding using MD.

The LB method [31] is a relatively new computational method for fluid dynamics. It is based on the foundations of kinetic theory and involves the solution of a kinetic equation, a simplified form of the Boltzmann equation.

This equation describes the evolution of the distribution of the population of particles whose collective behavior reproduces fluid behavior. The distribution of the popu-

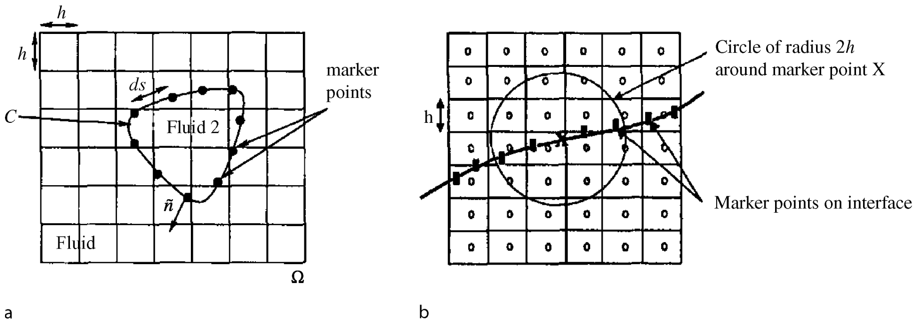

Numerical Techniques for Free Surface Flows: Interface Capturing and Interface Tracking, Figure 11 Immersed boundary method: (**a**) computational domain composed of two immiscible fluids; (**b**) grid points considered for the interface velocity around the marker X [12]

lation of particles is modified by the movement and collisions of the particles simulated on a lattice. This lattice restricts the movement and interaction of particles to selected discrete directions such that in the continuum, i. e. longer length and time scales, the collective behavior of the particle populations corresponds to the dynamics of fluid flow described by the Navier–Stokes equations. In contrast to the conventional computational methods for fluid dynamics, which solve macroscopic equations, the LB method effectively simulates macroscopic fluid flow by solving the kinetic equations at the mesoscopic level. This modeling of physics at a smaller scale relative to the macroscopic scale enables it to naturally incorporate physical properties needed to compute complex flows. In the case of multiphase flows, phase segregation and interfacial dynamics can be simulated by incorporating appropriate intermolecular attraction forces or by employing concepts based on the free-energy approach. LB-based methods do not track interfaces, but can maintain sharp interfaces without any artificial treatments. Also, the LB method is accurate for the mass conservation of each component of the fluid. Recently, Inamuro et al. developed a LB method which is applicable to real interfacial flows with density ratios as high as 1000 [32].

Key Research Findings

Despite advances in moving and deforming mesh methods, it remains the case that these methods are useful primarily when the interface topology is straightforward. Effects such as splashing, breaking and colliding remain difficult challenges.

Eulerian methods perform well for a variety of moving boundary problems. However, in these problems, particularly when surface forces are to be included in the flow calculations, the interface is diffused and occupies a few grid cells in practical calculations. This is undesirable in many problems both from an accuracy as well as physical realizability/modeling standpoint.

In the Lagrangian methods, the grid adapts to the interface and hence grid rearrangement and motion terms have to be incorporated. When the interface begins to distort, the grid needs to be regenerated each time. The resulting grid on which the field variables are computed may be skewed and unevenly distributed, thus influencing the accuracy of the field solver. The Eulerian methods have an advantage in this regard since the computations are performed on a fixed grid, hence obviating the need for grid rearrangement. In these methods, mergers and fragmentations are taken care of automatically, merely by updating the values of the phase fraction. However, when the interface is arbitrarily shaped, improved resolution in desired regions is difficult to obtain due to smearing of information, unless complicated local refinements are adopted [33].

As also mentioned by Prosperetti and Tryggvason [17], no method can be regarded as the best technique for handling interfacial flows. This is because each method is tailored for a certain range of flows and it depends on the level of detail that is expected from the numerical simulations.

Future Directions for Research

It is predicted that in the short term, the well-known interface simulation techniques such as VOF and level set will continue to dominate interfacial flow investigations. The algorithmic improvements of these methods are still being made. However, newer techniques which combine Eulerian and Lagrangian features, such as sharp interface and particle level set methods, seem to be the more promising ones. They are conceptually based on a more rigorous flow solution paradigm. Although the new combined methods have not been extensively tested for real flow problems, they show promise in handling interface motions accurately. They still need more developments regarding effi-

ciency and feasibility to solve three-dimensional complex interface motion, breakup and merging.

Turning attention to multiphase micro- and nanoflows, the interface simulation techniques are used to simulate different phenomena encountered in micro- and nanofluidic devices. These include liquid dispensing, handling, breakup into droplets and merging, compound droplet and bubble encapsulation and, finally, formation of slug bubbly flows. In some cases where thin ligaments are formed, such as film formation on the surface or necking of microjets and microdroplets upon breakup, the adaptive grid methods become important to implement into the interface simulation technique. In cases where heat transfer or phase change is involved, the proper form of energy equation should be added to the system of flow equations and coupled accordingly.

Since in most microfluidic applications wall effects are important, development of accurate contact angle handling techniques is vital. Care should be given on implementation and coupling of flow, heat transfer and electric effects. For example in electro-wetting processes, the voltage and temperature dependence of contact angle should be taken into account in the numerical model. Since micro- and nanoscale devices may have complex shapes, development of proper numerical methods, which can handle such geometries, seems inevitable. In these devices, and also in devices with moving components such as micro-dispensing devices, the free surface may interact with the structure. In such cases, a method that can treat fluid–structure interaction with free surface flows is desirable. For simulation of three-phase interfacial microflows, such as formation of double emulsion and compound bubbles, appropriate interface solvers which account for the third phase are necessary to be developed.

Cross References

- ► Finite Volume and Finite Difference Methods for Modeling and Simulation
- ► Boundary Element Method and its Application to the Modelling of MEMS Devices
- ► Immersed Boundary Method
- ► Lattice Boltzmann Method (LBM)
- ► Meshless Methods
- ► Molecular Dynamics Simulation Method
- ► Non-Continuous Approaches
- ► Pressure-Driven Two Phase Flows
- ► Surface Tension Driven Flow
- ► Wetting and Spreading
- ► Electrokinetic Two Phase Flows

References

1. Fukai J, Zhao Z, Poulikakos D, Megaridis CM, Miyatake O (1993) Modeling of the deformation of a liquid droplet impinging on a flat surface. Phys Fluid A 5(11):2588–2599
2. Raymond F, Rosant JM (2000) A numerical and experimental study of the terminal velocity and shape of bubbles in viscous liquids. Chem Eng Sci 55:943–955
3. Pozrikidis C (1992) Boundary-Integral and Singularity Methods for Linearized Viscous Flow. Cambridge Univ Press, Cambridge
4. Harlow FH, Welsh JE (1965) Numerical calculation of time dependent viscous incompressible flow with a free surface. Phys Fluid 8:2182–2189
5. Hirt CW, Nicholls BD (1981) Volume of fluid (VOF) method for the dynamics of free boundaries. J Comput Phys 39:201–225
6. Ashgriz N, Poo JY (1991) FLAIR: flux line-segment advection and interface reconstruction. J Comput Phys 93(2):449–468
7. Osher S, Fedkiw RP (2001) Level set methods. J Comput Phys 169:463–502
8. Anderson DM, McFadden GB, Wheeler AA (1998) Diffuse-interface methods in fluid mechanics. Ann Rev Fluid Mech 30:139–165
9. Glimm J, Grove JW, Li XL, Shyue KM, Zhang Q, Zeng Y (1998) Three-dimensional front tracking. SIAM J Sci Comput 19:703–727
10. Tryggvason G, Bunner B, Esmaeeli A, Juric D, Al-Rawahi N, Tauber W, Han J, Nas S, Jan YJ (2001) A front tracking method for the computations of multiphase flow. J Comput Phys 169:708–759
11. Udaykumar HS, Mittal R, Shyy W (1999) Computation of solid-liquid phase fronts in the sharp interface limit on fixed grids. J Comput Phys 153:535–574
12. Francois M, Shyy W (2003) Computations of drop dynamics with the immersed boundary method, part 1: numerical algorithm and buoyancy-induced effect. Numer Heat Transf B 44:101–118
13. Lee L, Leveque RJ (2003) An immersed interface method for incompressible Navier-Stokes equations. SIAM J Sci Comput 25:832–856
14. Veldman AEP (1979) Liquid sloshing under low-g conditions: mathematical model and basic numerical method. NLR Report TR 79057 U, National Aerospace Laboratory, The Netherlands
15. Zhao Y, Tan HH, Zhang B (2002) A high-resolution characteristics-based implicit dual time-stepping VOF method for free surface flow simulation on unstructured grids. J Comput Phys 183:233–273
16. Kim MS, Lee W (2003) A new VOF-based numerical scheme for the simulation of fluid flow with free surface. Part I: new free surface-tracking algorithm and its verification. Int J Num Methods Fluid 42:765–790
17. Prosperetti A, Tryggvason G (2003) Appendix 3: report of study group on computational physics. Int J Multiph Flow 29:1089–1099
18. Chen S, Johnson DB, Raad PE (1995) Velocity boundary conditions for the simulation of free surface fluid flow. J Comput Phys 116:262–276
19. Jafari A, Shirani E, Ashgriz N (2007) An improved three-dimensional model for interface pressure calculation in free-surface flows. Int J Comput Fluid Dyn 21(2):87–97

20. Darwish M, Moukalled F (2006) Convective schemes for capturing interfaces of free-surface flows on unstructured grid. Numer Heat Transf B 49:19–42
21. Muzaferija S, Peric M, Sames P, Schellin P (1998) A two-fluid Navier-Stokes solver to simulate water entry. Proceedings of Twenty-Second Symposium on Naval Hydrodynamics, Washington, DC
22. Scardovelli R, Zaleski S (1999) Direct numerical simulation of free-surface and interfacial flow. Ann Rev Fluid Mech 31:567–603
23. Kothe DB (1997) Perspective on Eulerian finite volume methods for incompressible interfacial flows. LANL Report LA-UR-97-3559, Los Alamos National Lab., Albuquerque, NM
24. Berthelsen PA (2002) A short introduction to the level set method and incompressible Two-Phase Flow: A Computational Approach, NTNU Report, Norway
25. Kim J (2005) A continuous surface tension force formulation for diffuse-interface models, J Comput Phys 204:784–804
26. Shin S, Juric D (2002) Modeling three-dimensional multiphase flow using a level contour reconstruction method for front tracking without connectivity. J Comput Phys 180:427–470
27. Ye T, Shyy W, Tai CF, Chung JN (2004) Assessment of sharp- and continous-interface methods for drop in static equilibrium. Comp Fluid 33:917–926
28. Peskin CS (1977) Numerical analysis of blood flow in the heart. J Comput Phys 25:220–252
29. Li Z (1997) Immersed interface methods for moving interface problems. Numer Alg 14:269–293
30. Consolini L, Aggarwal SK, Murad S (2003) A molecular dynamics simulation of droplet evaporation. Int J Heat Mass Transf 46:3179–3188
31. Succi S (2001) The Lattice Boltzmann Equation for Fluid Dynamics and Beyond. Clarendon, Oxford, UK
32. Inamuro T, Ogata T, Tajima S, Konishi N (2004) A lattice Boltzmann method for incompressible two-phase flows with large density differences. J Comput Phys 198:628–644
33. Shyy W, Francois M, Udaykumar HS (2001) Cartesian and Curvilinear Grid Methods for Multi-domain, Moving Boundary Problems. In: Debit M et al (eds) 13th Int. Conf. on Domain Decomposition Meth. CIMNE, Barcelona

Ohmic Heating

► Joule Heating and Chip Materials
► Joule Heating in Electrokinetic Flow: Theoretical Models

Ohnesorge Number

Definition

To account for the liquid viscosity in droplet formation, the appropriate nondimensional number is the *Ohnesorge number* which represents the ratio of internal viscosity dissipation to the surface tension energy. The *Ohnesorge number* may be written in terms of the square root of the ►Weber number divided by the Reynolds number. The *Ohnesorge number* is sometimes also referred to as stability number, viscosity number, Laplace number, or Z number. It is independent on the velocity and therefore only adequate to describe droplet ejection in conjunction with the *Weber number*.
The lower the *Ohnesorge number* the weaker are the friction losses due to viscous forces. This means that most of the inserted energy converts into surface tension energy, i. e. a droplet can be formed. The higher the *Ohnesorge number* the more dominant is the internal viscous dissipation. This means that most of the inserted energy converts into internal viscous dissipation, i. e. that a droplet formation is critical or even impossible.

Cross References

► DNA Micro-arrays
► Droplet and Bubble Formation in Microchannels
► Electrokinetic Dispensing
► Piezoelectric Microdispenser

On-Chip Cell Culture

► Cell Culture (2D and 3D) on Chip

On-Chip Cell Lysis

Arpita Bhattacharyya[1],
Catherine M. Klapperich[2]
[1] Biomedical Engineering Department, Boston University, Boston, MA, USA
[2] Biomedical and Manufacturing Engineering Departments, Boston University, Boston, MA, USA
abhatta@bu.edu, catherin@bu.edu

Synonyms

Cell disruption; Permeabilization of cells

Definition

Cell lysis is the process of releasing intercellular biological molecules into the extracellular milieu by disrupting the cellular membrane. On-chip cell lysis is the process of lysing a cellular sample on a biochip.

Overview

On-chip cell lysis is a crucial component of integrated micro total analysis systems (μTAS). In order to perform biochemical analysis of intercellular molecules (i. e. proteins, lipids and nucleic acids), the cells at first have to be disrupted releasing the biomolecules from inside the cell. The molecules of interest can then be separated or purified from the cell lysate using affinity purification, charge- and size-based separation, filtration, precipitation etc. The process of on-chip cell lysis followed by extraction of the desired biomolecules is collectively referred to as on-chip sample preparation.

Several approaches have proven useful in releasing biomolecules from inside a cell. The most commonly used techniques are

- chemical lysis or permeabilization of the cells,
- physical disruption of the cell wall and cell membrane.

The most commonly used chemical lysis methods include the use of detergents (such as Triton-X, sodium dodecyl sulphate (SDS) etc.), and chaotropic agents (such as guanidinium thiocyanate (GuSCN), guanidine hydrochloride (GuHCL), ethanol, etc.).

Detergent-based lysis is the easiest and mildest form of cell lysis. Detergents disrupt the lipid bilayer surrounding cells by solubilizing proteins and disrupting lipid-protein interactions. Salts, chelating agents (e. g. EDTA) and reducing agents (e. g. dithiothreitol (DTT)) can be added for more efficient lysis. Detergents are comprised of a polar hydrophilic head and a non-polar hydrophobic tail. The nature of the head group is used to categorize the detergent as either ionic (cationic or anionic), non-ionic or zwitterionic. Non-ionic detergents (such as the Triton-X series) and zwitterionic detergents (such as CHAPS) are less denaturing than ionic detergents and retain native protein functions. Ionic detergents (such as sodium dodecyl sulphate (SDS)) are strong solubilizing agents and tend to denature proteins.

Chaotropes are strong protein denaturants and induce cell permeabilization by weakening the hydrophobic interactions of the membrane. In case of bacterial cells, chaotropic agents also inhibit the assembly of cross-linked peptidoglycans in the cell wall. Another common method of disrupting bacterial cell walls is enzymatic digestion using lysozyme, which hydrolyzes the polysaccharide component of the cell wall.

For microchip-based chemical treatments, optimal lysis depends on mixing of the lysis agent with the cell sample. Due to laminar flow in microfluidic channels, mixing occurs solely due to diffusion, which limits the exposure of individual cells to the lysis agent. To enhance the cell lysis efficiency, microfluidic mixing mechanisms can be introduced on the chip. Toner et al. have successfully demonstrated a continuous flow microfluidic system where lysis is achieved by flanking the cell suspension on both sides by the chemical reagent (Sethu et al. [1]). Bhattacharyya and Klapperich demonstrated continuous lysis by mixing chaotropic buffer (GuSCN) and cell suspension in serpentine mixing channel with sharp turns that enhances diffusive mixing (Bhattacharyya and Klapperich, [2]). Lee et al. presented a novel method of chemical cell lysis on-chip using hydroxide ions that porate the cell membrane and cause cell lysis (Di Carlo et al. [3]). A combination of one or more lysis methods may produce optimal lysis in some cases. Bau et al. demonstrated a microfluidic cassette where lysis of gram-positive bacteria was achieved by incubation of the bacteria sample with a solution containing detergents and lysozme, followed by incubation in chaotropic buffer (GuHCl) and proteinase K (Wang et al. [4]).

In addition to these various chemical treatment methods, a number of physical methods of cell disruption can be used in a chip-based system. These physical methods include osmotic shock, which occurs when cells are suspended in a hypotonic solution; shearing and fracturing of cells walls and membranes using microfabricated needles or spherical particles (beads); application of an electric field that causes electroporation; ultrasonication of the cell sample; and thermal lysis.

Lee et al. implemented a mechanical lysis device in which cells were lysed using a microfluidic filter with nanostructured barbs which they refer to as *nano-knives* (Di Carlo et al. [3]). Madou et al. demonstrated disruption of mammalian, bacterial and yeast cells on a microfluidic compact disc platform using spherical beads in a lysis chamber (Kim et al. [6]). Klapperich et al. demonstrated lysis of bacteria using carbon nanotubes embedded in a porous polymer monolith within a microfluidic channel (Klapperich et al. [7]). Jensen et al. demonstrated the electrolysis of human carcinoma cells in a micro-electroporation device to release the subcellular materials. They also demonstrated using simple circuit models that electrical lysis is selective towards plasma membrane and leaves organelle membranes undamaged (Lu et al. [8]). Lysis of white blood cells and murine clonal cells by electroporation in a continuous flow microfluidic device has also been demonstrated (Ramadan et al. [9]). Ultrasonication is frequently used for cell lysis. Ultrasonication is particular advantageous for lysing bacterial or fungal spores. Northrop, et al. performed ultrasonic lysis of bacterial spores trapped in a microfilter. However, in this application the ultrasonic horn was not incorporated in the microfluidic device due to its large size (Taylor et al. [10]). Northrop et al. went on to successfully implement ultrasonication lysis of epithelial and sperm cells on a microfluidic cartridge with an integrated sonication module (Devitt et al. [11]). Grodzinski et al. demonstrated thermal lysis of trapped E. coli cells using embedded heaters (Liu et al. [12]). A single step thermal cell lysis and PCR amplification of E. coli in a microreactor has also been presented (Ke et al. [13]).

The choice of cell lysis method depends to a large extent on sample type. Mammalian cells, bacteria and yeast all have different requirements for lysis depending on the presence or absence of a cell wall. In some cases, a combination of chemical and mechanical disruption may yield best results. Another important factor in the choice of lysis

method is the sample size of cells to be disrupted. If only a very small volume of sample is available, care must be taken to reduce loss and avoid cross-contamination. Consideration should also be given to the compatibility of the chosen method with downstream applications.

Cross References

► Biosample Preparation Lab-on-a-Chip Devices

References

1. Sethu P, Anahtar M, Moldawer LL, Tompkins RG, Toner M (2004) Continuous flow microfluidic device for rapid erythrocyte lysis. Anal Chem 76:6247–6253
2. Bhattacharyya A, Klapperich CM (2005) Polymeric microfluidic device for on-chip cell lysis and extraction of nucleic acids from biological samples. Proc 9th Int Conf Miniaturized Syst Chem Life Sci Boston pp 1167–1169
3. Di Carlo D, Ionescu-Zanetti C, Zhang Y, Hung P, Lee LP (2005) On-chip cell lysis by local hydroxide generation. Lab chip 5:171–178
4. Wang J, Mauk MG, Chen Z, Bau HH (2005) A disposable microfluidic device for cell lysis and DNA isolation. Proc 9th Int Conf Miniaturized Syst Chem Life Sci Boston pp 289–291
5. Di Carlo D, Jeong HK, Lee LP (2003) Reagentless mechanical cell lysis by nanoscale barbs in microchannels for sample preparation. Lab Chip 4:516–522
6. Kim J, Hee Jang S, Jia G, Zoval JV, Da Silva NA, Madou MJ (2004) Cell lysis on a microfluidic CD (compact disc). Lab Chip 4:516–522
7. Klapperich CM, Kaufman JD, Kulinski MD, Altman DH (2007) Method for bacterial lysis. Pending. USSN 60/921,404
8. Lu H, Schmidt MA, Jensen MF (2005) A microfluidic electroporation device for cell lysis. Lab Chip 5:23–29
9. Ramadan Q, Samper V, Poenar D, Liang Z, Yu C, Lim TM (2005) Simultaneous cell lysis and bead trapping in a continuous flow microfluidic device. Sens Actuators B 113:944–955
10. Taylor MT, Belgrader P, Furman BJ, Pourahmadi F, Kovacs GT, Northrop MA (2001) Lysing bacterial spores by sonication through a flexible interface in a microfluidic system. Anal Chem 73:492–496
11. Devitt AJ, Aflatooni N, Vinas M, Loh N, Pourahmadi F, Yuan R, Northrop MA (2005) Differential extraction of male and female DNA in an automated microfluidic device. Proc 9th Int Conf Miniaturized Syst Chem Life Sci Boston pp 7–9
12. Liu RH, Yang J, Lenigk R, Bonanno J, Grodzinski P (2004) Self-contained, fully integrated biochip for sample preparation, polymerase chain reaction amplification and DNA microarray detection. Anal Chem 76:1824–1831
13. Ke C, Kelleher AM, Berney H, Sheehan M, Mathewson A (2007) Single step cell lysis/PCR detection of Escherichia coli in an independently controllable silicon microreactor. Sens Actuators B 120:538–544

On-Chip Detection

► On-Chip Micro-Optical Detection

On-Chip Detection Using Optical Fibers

Lonnie J. Lucas, Jeong-Yeol Yoon
Department of Agricultural & Biosystems Engineering, The University of Arizona, Tucson, AZ, USA
jyyoon@email.arizona.edu

Synonyms

Fiber optics; Lab-on-a-Chip; Micro total analysis system (μTAS)

Definition

Using optical fibers to perform detection *on-chip* is an excellent example of two completely different technologies merging together to produce a synergistic result. In this entry, *on-chip* refers to a Lab-on-a-Chip (LOC) or micro total analysis system (μTAS). The optical fiber or fibre is a thin, transparent strand, usually made of glass or plastic, for transmitting light. Optical fibers integrated with an LOC, may be used to detect particles, chemicals, biomaterials, or other analytes, typically in an aqueous medium. The fibers are used to deliver source light to the chip and to collect emitted light from the sample located in the detection zone of the chip.

O

Overview

The phenomenon of total internal reflection confines light in one material surrounded by another material of lower refractive index. In the 1840's, physicists showed that light could be guided along jets of water for fountain displays. Later, inventors realized that bent quartz rods could carry light, and patented them as dental illuminators and lighted tongue depressors. During the 1920's, Baird and Hansell patented arrays of glass rods for transmitting television images. These early fibers were *bare*, with total internal reflection at a glass–air interface. Later, fibers were coated with *cladding* of lower refractive index to protect the surface and reduce light leakage [1].

By 1960, fibers had reached signal attenuation of about one decibel per meter, much too high for communication distances. In 1970, Corning Inc. produced fibers with attenuation below 20 dB/km and Bell Laboratories produced the first semiconductor diode laser. In the 1980's, carriers built telephone systems of single-mode fiber with 1300 nm sources. Those technologies spread to other communication platforms and remain the standard for most fiber optic systems today [2].

By the mid 1990's, the need for portable chemical and/or biological detection systems has emerged, as later rein-

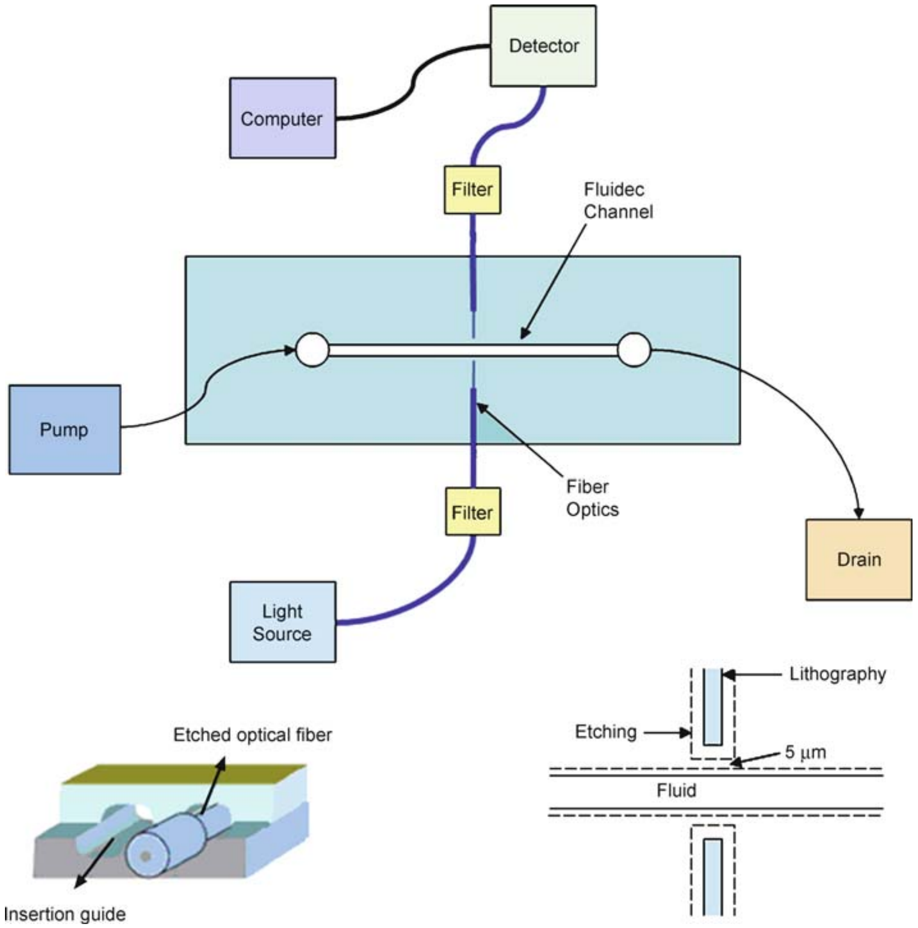

On-Chip Detection Using Optical Fibers, Figure 1 Embedded fiber device with source and detection fibers adjacent to microchannel (top). Etched fiber placed into an insertion guide (bottom left). Embedded fibers located within 5μm of the fluid channel (bottom right)

forced by research supports for portable biochemical warfare agent detection systems (e. g. U.S. DARPA, Defense Advanced Research Projects Agency) [3].

Initially, fiber ends were conjugated with biomolecule sensing layers and dipped into test tubes while reactions occurred and were monitored with photomultiplier tubes (PMTs). These types of devices are called fiber optic biosensors (FOB) and are not performed *on-chip*. Many experiments and devices were developed throughout the 1990's using FOB techniques [4].

In the early 2000's, researchers began to incorporate fiber optics with the LOC for doing *on-chip* detection. The number of publications involving on-chip detection using optical fibers has been growing exponentially each year [5].

This entry reviews the basic fabrication methods for various LOCs using optical fibers. A description of fiber optics technology used with LOC applications is discussed. Light sources, detectors, filters and lenses are also discussed.

Basic Methodology

Similar to any bench-scale optical detections, there are multiple measurement modes commonly used with optical fibers, including fluorescence (excite at a certain wavelength and detect the emission at a longer wavelength); colorimetry (color detection); Raman (inelastic scattering detection of a laser); luminescence (light generation at low temperature). Also, changes in intensity, spectral shifts, time-domain parameters (fluorescence decay time), as well as polarization (with appropriate polarization-preserving fiber bundles and configuration) can all be used with optical fiber detections.

The approaches for integrating fiber optics with Lab-on-a-Chip devices can be grouped according to fiber location and are classified as: embedded fibers, proximity fibers, or wetted fibers. Table 1 provides a summary of the characteristics of embedded fiber sensors. Tables 2

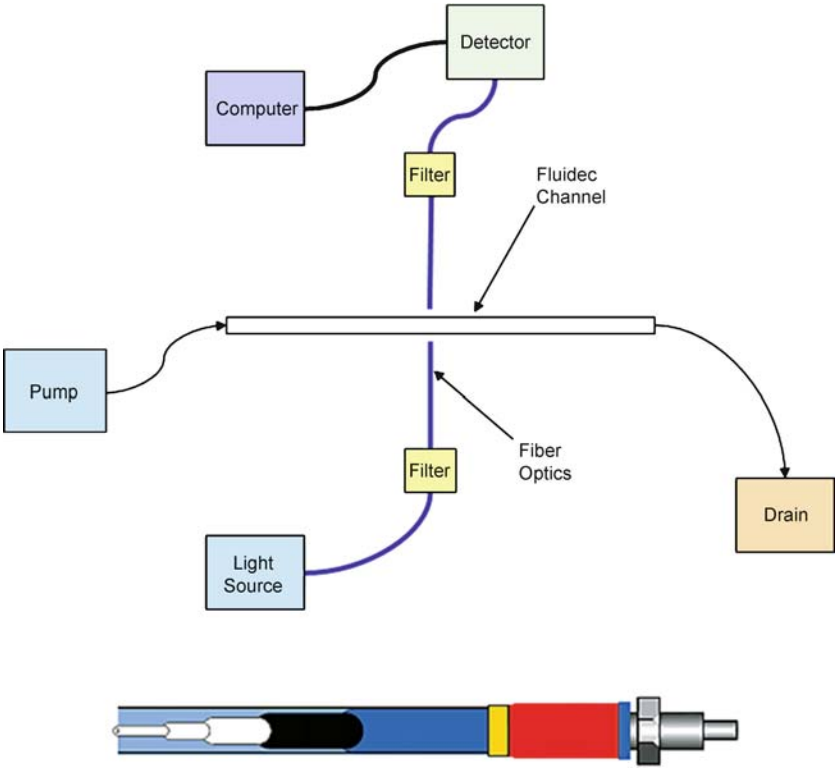

On-Chip Detection Using Optical Fibers, Figure 2 Proximity fiber device with source and detection fibers above and below the detection zone on the chip (top). Example of a commercial fiber with jacketing, color coding and connectors (bottom)

and 3 lists the key parameters for proximity and wetted fiber sensors. Each of these three unique *on-chip* fiber optic sensor configurations will be described in the following.

Embedded Fibers

The most common configuration for performing on-chip detection has been the embedded fiber type of device as listed in Table 1. A typical setup, shown in Fig. 1, includes a light source and fiber for delivery, exit fiber connected to a detection system, microfluidic channel, and liquid delivery components. The fibers are usually embedded in chip materials consisting of polydimethylsiloxane (PDMS), SU-8 epoxy, polymethyl methacrylate (PMMA) or glass [3].

An *insertion guide* is used to accurately locate an etched optical fiber. Fiber distal ends are chemically etched to reduce the diameter by removing fiber cladding for easier insertion into the LOC. The plastic or rubber jacket of optical fiber should be moved before this etching. One of the keys to fabrication involves accurately setting the distance from the fiber channel to the microfluidic channel shown in Fig. 1.

Proximity Fibers

The next most popular configuration for performing on-chip detection uses optical fibers in close proximity to the detection zone as summarized in Table 2 and shown in Fig. 2. The input fiber and the receiving fiber tips are usually within 1 mm of the chip surface. In some cases, lenses and filters are used to focus and/or collect the light. Other system components such as light sources, detectors, and computers are the same as those used with the embedded fiber devices.

There are many commercial fiber types, jacketing options, and connectors which can be used such as the example shown in Fig. 2. Fiber accessories and fixtures allow one to easily connect fibers, and integrate them into experimental set-ups. Bulk fibers and fiber assembly-making kits and components are also readily available.

The main advantage of the proximity fiber detection system is that fabrication is much easier due to the fact that the fibers are not connected directly into the chip. This greatly simplifies the chip fabrication process. One disadvantage is that it is more difficult to achieve the maximum intensity of light entering and exiting the detection zone because the fiber tips are further away from the chip. Lenses and filters

On-Chip Detection Using Optical Fibers, Table 1 Embedded fiber types of on-chip detectors (to be continued)

Principal Investigator (Country)	Journal Year	Vol. Page	Fiber Type	Source Light	Lens	Detected Light	Detector	Filters	Fluid Channel ($h \times w$), μm	Motive Force	Chip Mat'l	Analyte	LOD	Application
A. Llobera (Germany)	Lab Chip 2005	5: 506	multimode fiber core 230 μm/ clad 250 μm material: silica	blue LED $\lambda = 460$ nm	biconvex	absorbance	spectrometer	none	100×230	syringe pump	PDMS	fluorescein methylorange	mM range for both	pH measurement
A. Wolff (Denmark)	Lab Chip 2004	4: 372	multimode fiber core 70 μm/ clad 100 μm material: silica	red laser $\lambda = 633$ nm	elliptical	forward light scattering	PMT	none	100×600	syringe pump	SU-8 and PDMS	polystyrene microspheres	50 – 65 beads per second	flow cytometry
D. Li (Canada)	Instrum Sci Technol 2005	33: 597	multimode fiber #1 core 50 μm/ clad 125 μm multimode fiber #2 core 100 μm/ clad 125 μm material: silica	red laser diode $\lambda = 640$ nm	none	transmitted light	Si PIN photodiode	none	80×80	syringe pump	PDMS and glass	polystyrene microspheres	10 μm particles	flow cytometry
G.M. Whitesides (United States)	Anal Chem 2001	73: 4491	multimode fiber core 100 μm, clad 140 μm $NA = 0.29$ material: silica	blue LED $\lambda = 470$ nm	none	fluorescence	micro-avalanche photodiode	dichroic	50×100	electrokinetic	PDMS	fluorescein	25 nM	spectro-fluorometry; spectrophotometry
G.-B. Lee (Taiwan)	Sens Actuators A 2003	107: 125	multimode fiber #1 core 63 μm, clad 100 μm single mode fiber #2 core 9 μm, clad 100 μm material: silica	red laser $\lambda = 633$ nm mercury vapor $\lambda =$ spectral	none	fluorescence	PMT	band-pass	50×70	syringe pump	soda lime glass	Rhodamine B + Cy3; FITC-labeled polypeptides	multimode fiber $= 10^{-7}$ M singlemode fiber $= 10^{-6}$ M	capillary electrophoresis
G.-B. Lee (Taiwan)	Anal Chim Acta 2004	507: 163	singlemode fiber core 9 μm, clad 100 μm material: silica	red laser $\lambda = 633$ nm	10*x* objective	transmitted light	avalanche photodiode	none	40×80	electrokinetic	soda lime glass	polystyrene microspheres; red blood cells	10 μm particles	flow cytometry
G.-B. Lee (Taiwan)	Biosens Bioelectron 2004	20: 83	multimode fiber core 50 μm, clad 125 μm material: silica	mercury vapor $\lambda =$ spectral	none	fluorescence	PMT	band-pass	50×100	electrokinetic	soda lime glass	X-174 DNA marker; Rhodamine B + Cy3	none reported	capillary electrophoresis
H.-P. Loock (Canada)	Proc SPIE 2005	5969: 1	singlemode fiber core 9 μm, clad 125 μm $NA = 0.13$ material: silica	laser diode $\lambda = 810$ nm	convex fiber	phase shift	InGaAs photodiode	none	100×360	syringe pump	glass	cyanine dye ADS805WS	240 nM	capillary electrophoresis
J. Hubner (Denmark)	Rev Sci Instrum 2001	72: 229	singlemode fiber core 9 μm, clad 125 μm $NA = 0.12$ material: silica	deuterium halogen $\lambda =$ spectral	none	fluorescence	PMT	band-pass filters	50×500	syringe pump	silicon wafer	fluorescein; bodipy 650X	fluorescein 250 pM; bodipy 100 nM	spectro-fluorometry; spectrophotometry

Principal Investigator (Country)	Journal Year	Vol. Page	Fiber Type	Source Light	Lens	Detected Light	Detector	Filters	Fluid Channel ($h \times w$), μm	Motive Force	Chip Mat'l	Analyte	LOD	Application
L.J. Golonka (Poland)	Int J Appl Ceram Technol 2006	3: 150	multimode fiber core 63 μm, clad 125 μm material: quartz	blue-green LED $\lambda = 502$ nm	none	transmitted light	photodiode	band-pass filters	125×125	peristaltic pump	low-temperature cofired ceramic (LTCC)	dye (Ponceau IV)	10 μg/ml	spectro-fluorometry; spectrophotometry
L.J. Golonka (Poland)	Sens Actuators B 2005	111-112: 396	multimode fiber core 63 μm, clad 125 μm material: silica	red LED $\lambda = 630$ nm	none	transmitted light	PMT	none	125×125	peristaltic pump	low-temperature cofired ceramic (LTCC)	fluorescein; creatinine $Cu(NH_3)_4$	none reported	spectro-fluorometry; spectrophotometry
S. Bargiel (Poland)	Sens Actuators A 2004	115: 245	multimode fiber #1 core 63 μm, clad 125 μm material: silica multimode fiber #2 core 750 μm clad 850 μm material: PMMA	blue LED $\lambda = 490 nm$	none	fluorescence	spectrometer	none	200×500	peristaltic pump	silicon wafer & glass	fluorescein + erythrosine; phosphate	0 – 0.2 mg/ml of fluorescein + erythrosine; 0.2 – 1.6 g/ml phosphate	spectro-fluorometry; spectrophotometry
S.A. Soper (United States)	Lab Chip 2002	2: 88	singlemode fiber #1 core 8 μm, clad 125 μm multimode fiber #2 core 40 μm, clad 125 μm material: silica	red laser diode $\lambda = 750 nm$	none	fluorescence	avalanche photodiode	band-pass filters	20×80	electrokine	PMMA	near-IR dye; NN382 fluorescence; intercalating dye TOPRO-5	1.4×10^{-20} *moles*	capillary electrophoresis
T. Fujii (Japan)	Lab Chip 2003	3: 40	multimode fiber core 105 μm, clad 125 μm $NA = 0.22$ material: silica	incandescent tungsten $\lambda =$ spectral	PDMS 2D lenses	fluorescence	CCD camera	band-pass filters	50×130	syringe pump	PDMS on glass	FITC-labelled albumin	170 mM FITC solution	spectro-fluorometry; spectrophotometry
Z. Cui (United Kingdom)	Biomed Microdevices 2005	7: 323	multimode fiber core 63 μm, clad 125 μm material: silica	green LED $\lambda = 568$ nm	none	absorption	Si PIN photodiode	none	150×250	syringe pump	SU-8 and PDMS	lactate	50 mg/l	spectro-photometry

On-Chip Detection Using Optical Fibers, Table 2 Proximity fiber types of on-chip detectors

Principal Investigator (Country)	Journal Year	Vol. Page	Fiber Type	Source Light	Lens	Detected Light	Detector	Filters	Fluid Channel ($h \times w$), μm	Motive Force	Chip Mat'l	Analyte	LOD	Application
J.-Y. Yoon (United States)	Biosens Bioelectron 2007	22: 2216	multimode fiber core 400 μm, clad 500 μm $NA = 0.22$ material: silica	blue LED $\lambda = 470 nm$ red laser diode $\lambda = 635 nm$	none	forward light scattering	mini-spectrometer	none	150 × 150	syringe pump	PDMS on glass	anti-PR3 vasculitis marker	50 ng/mL	immunoassay
A. Okubo (Japan)	Anal Sci 2004	20: 209	multimode fiber core 800 μm, clad 1000 μm material: silica	xenon arc λ = UV spectrum	10x objective	fluorescence	PMT	none	50 × 500	syringe pump	PDMS	sulfite and nitrite	sulfite 10^{-6}M; nitrate 10^{-7}M	spectro-fluorometry; spectrophotometry
D. Li (Canada)	Biosens Bioelectron 2006	21: 2006	multimode fiber core 200 μm, clad 350 μm material: silica	red laser diode $\lambda = 640 nm$	none	fluorescence	Si PIN photodiode	filter cube dichroic; band-pass	20 × 100	electrokine	PDMS	Escherichia coli O157:H7	0.3 ng/μL	immunoassay
H. Mihara (Japan)	Mol Biosyst 2005	1: 363	multimode fiber core 1000 μm, clad 1200 μm material: PMMA	quartz halogen λ = spectral	none	reflectivity	Si PIN photodiode	none	1000 × 1000	syringe pump	glass	calmodulin (CaM) as model protein	30 nM	immunoassay
J. N. McMullin (Canada)	Appl Photon Technol 2003	6: 114	multimode fiber core 1000 μm, clad 1200 μm $NA = 0.50$ material: PMMA	green LED $\lambda = 570 nm$ red laser diode $\lambda = 640 nm$	ball lens	fluorescence	PMT	band-pass filters	150 × 150	syringe pump	glass	fluorescent polystyrene microspheres	15 μm spheres	flow cytometry
J. N. McMullin (Canada)	Rev Sci Instrum 2003	74: 4145	multimode fiber core 1000 μm, clad 1200 μm $NA = 0.50$ material: PMMA	red laser diode $\lambda = 700 nm$	ball lens	fluorescence	PMT	band-pass filters	20 × 50	syringe pump	glass	fluorescent polystyrene microspheres	15 μm spheres	flow cytometry
R. Bruce (United States)	Biosens Bioelectron 2006	21: 1893	fiber array width: 50 mm $NA = 0.66$ material: silica	mercury vapor λ = spectral red laser diode $\lambda = 640 nm$	none	fluorescence	PMT	dichroic filters	not reported	syringe pump	glass	Circulating tumor cells	10^{-6}M to 10^{-7}M	immunoassay
S. M. Cramer (United States)	J Chromatogr A 2004	1044: 277	multimode fiber core 600 μm, clad 630 μm $NA = 0.22$ material: silica	deuterium halogen λ = spectral	10x objective	absorbance	CCD array	none	40 × 150	peristaltic pump	quartz	three peptides (Trp–Ala, Leu–Trp and Trp–Trp); thiourea	thiourea 167 μM	electro-chromatography; spectrophotometry

On-Chip Detection Using Optical Fibers, Table 3 Wetted fiber types of on-chip detectors

Principal Investiga-tor (Country)	Journal Year	Vol. Page	Fiber Type	Source Light	Detector	Filters	Fluid Channel $(h \times w)$, μm	Motive Force	Chip Mat'l	Analyte	LOD	Application
R. Irawan (Singapore)	Lab Chip 2006	6: 1095	multimode fiber #1 core 1000 μm, clad 1010 μm material: PMMA multimode fiber #2 core 600 μm, clad 750 μm material: silica	blue LED $\lambda = 470nm$	mini-PMT	band-pass	100×210	syringe pump	acrylic	fluorescein	0.005 mg/L	spectro-fluorometry; spectropho-tometry
A. Dybko (Poland)	Analyst 2003	128: 523	multimode fiber core 1000 μm, clad 1200 μm material: PMMA	red LED $\lambda = 630nm$	spectrometer	none	1000×1000	peristaltic pump	PDMS	saccharose	none reported	refractometry; spectro-photometry
A. Dybko (Poland)	Proc SPIE 2003	5576: 314	multimode fiber core 1000 μm, clad 1200 μm material: PMMA	blue LED $\lambda = 470nm$ red LED $\lambda = 640nm$	spectrometer	none	1000×1000	peristaltic pump	PDMS	erythrosine; saccharose; bromothymol blue	none reported	refractometry; spectro-photometry
A. Dybko (Poland)	Sens Actuators B 2005	107: 184	multimode fiber core 1000 μm, clad 1200 μm material: PMMA	blue LED $\lambda = 470nm$ red LED $\lambda = 640nm$	spectrometer	none	1000×1000	peristaltic pump	PDMS	glucose; fluorescein	none reported	refractometry; spectrop-hotometry; spectro-fluorometry
D. Walt (United States)	Anal Chem 2005	77: 5583	fiber array 50,000 fibers diameter: 1 mm material: silica	xenon arc $\lambda = UV$ spectrum	CCD camera	dichroic	1000×1000	syringe pump	PMMA	Bacillus thuringiensis Kurstaki (BTK), biowarfare agent simulant.	10 aM	immunoassay

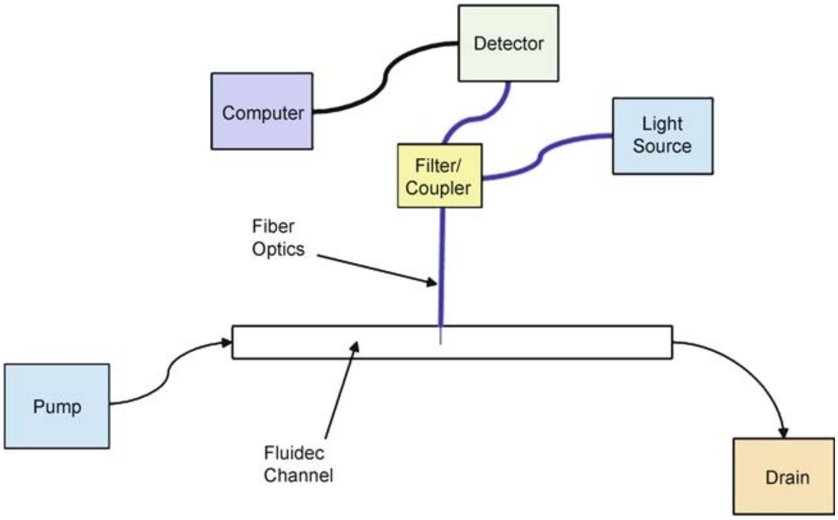

On-Chip Detection Using Optical Fibers, Figure 3 Wetted optical fiber device with the end of a fiber inserted directly into the analyte flow stream

are sometimes used to compensate for this light traveling distance issue.

Wetted Fibers

Table 3 lists another type of on-chip detection that is performed using *wetted* optical fibers. In this case, the ends of the fibers are inserted directly into the analyte flow stream as shown in Fig.3. Prior to insertion, an indicating layer of biomolecules must be immobilized as sensing elements on the fiber tips as shown in Fig. 4. The ends of the fibers are first decladded and polished, followed by incubation in a labeled antibody/protein solution. Fluorophore labeling is the most common, but chromophore or Raman reporter can also be used. This produces a sensing region on the surface of the fiber. This fluorescent indicating layer responds to the presence of analyte by changing its optical properties. The change in the indicator's properties affects the light which is transmitted back through the fiber to a detector. The change in intensity or spectral properties of the returning light correlates with analyte concentration. Similar to any optical immunoassays, labels (e. g. fluorophore) can be located not only on the fibers but within solution and/or other biomolecules (thus sandwich assay configuration). Competitive binding assay or various other assay formats are all possible in wetted fiber configuration. Wetted fiber optic sensors are created using either a single fiber or a fiber array bundle. A fiber array bundle may contain thousands of individually clad fibers, each $3-10\,\mu$m in diameter. An imaging fiber bundle is able to transmit light signals and images concurrently, while a single-core fiber can carry light, but not images.

Fiber Optics Technology

An optical fiber is simply a very thin piece of glass or plastic which acts as a pipe, through which light can pass. The light that is passed down the fiber can be turned on and off to transmit digital information, or changed in amplitude, frequency, or phase to transmit analog information. This is an important distinction, since telecommunication fibers are based in digital applications while sensor fibers are based in analog applications. On-chip bioreactions emit analog signals, not digital. This is one reason why signal attenuation is a lesser issue for sensor applications than with telecommunications.

Digital signals are sent as square waves, with high frequency components. The bandwidth of a fiber is set by the maximum frequencies it can handle. In sensor applications (analog), high frequencies are generally not an issue except when fluorescence decay time is of interest; and thus, signal attenuation due to bandwidth is typically not an issue. Also, signal attenuation over hundreds of kilometers (dB/km), which is a key parameter for telecommunications, is not a factor for LOC fiber optic sensors which usually travel less than a few meters.

Signal flow direction in fiber optics consists of simplex or duplex methods as illustrated in Fig. 5. The simplex method allows data to flow in one direction only. This is the common case where one fiber is used to transmit the light source while another fiber is used to receive and send the emitted signal to a detector. The duplex method allows simultaneous flow of information in both directions. When detection is performed using wetted optical fibers, it is usually done using the duplex method, where light delivery

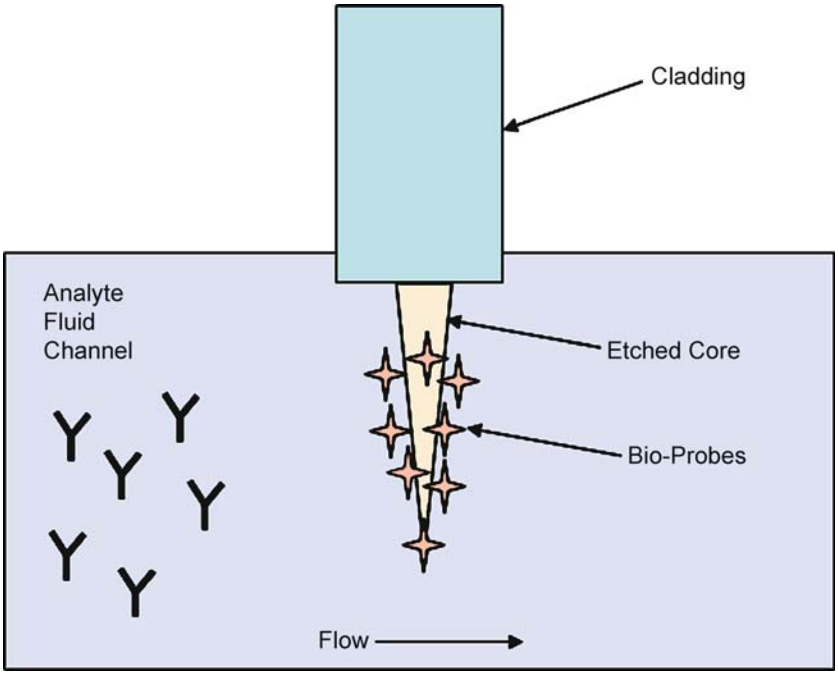

On-Chip Detection Using Optical Fibers, Figure 4 An indicating layer of biomolecules are immobilized as sensing elements on the fiber tips. Here an antibody-antigen immunoassay is shown

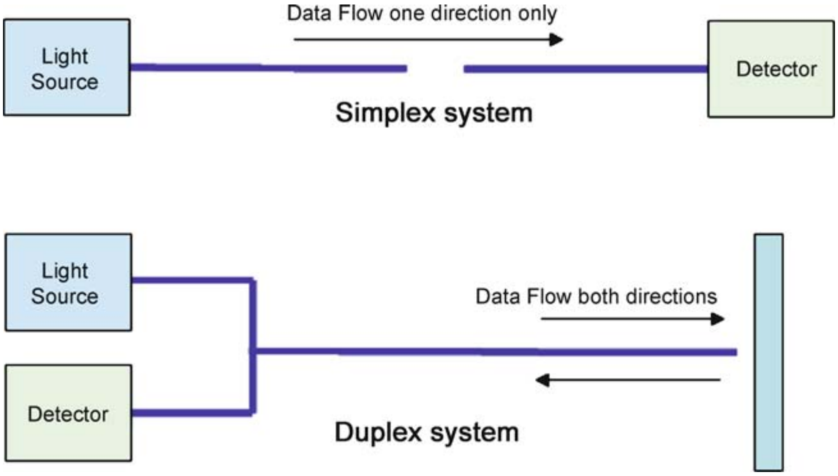

On-Chip Detection Using Optical Fibers, Figure 5 The simplex fiber arrangement is normally used for embedded and proximity fibers (top). The duplex setup is used with wetted fiber optic devices (bottom)

and detection both occur simultaneously in opposite directions. There is no problem using the same fiber for sending and receiving light waves. The larger core diameters of multimode fibers are capable of handling thousands of light modes without interference.

The optical region of the spectrum where fiber optic devices operate is from 300 nm to 2 µm wavelengths. The wavelengths used in fiber optic systems are matched to the particular characteristics of the system. Plastic fibers operate best at visible wavelengths, non-silica glass fibers are designed to operate at infrared wavelengths, and special grades of doped silica are used in the near-ultraviolet region. Most optical fibers use silica glass, which is most transparent to light in the near-infrared region from 700 – 1600 nm.

Most LOC devices require detection in the UV-VIS spectrum for biomaterial applications. These wavelengths require quartz or doped silica core fibers, since glass and

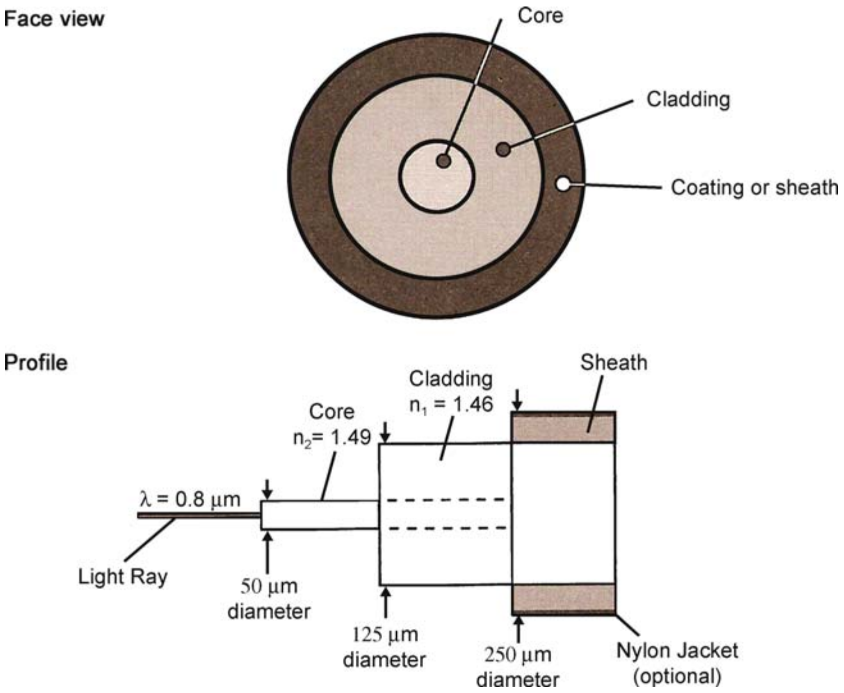

On-Chip Detection Using Optical Fibers, Figure 6 Cross section of a typical multimode, step index fiber. Some LOC detection devices employ fibers with cores up to 1mm in diameter

plastic will not transmit very efficiently below 400 nm. Doped silica fibers with high hydroxyl (−OH) content for UV-VIS, or low hydroxyl (−OH) content for VIS-NIR are often used in biosensor fibers. When working in the UV wavelengths, the cladding of the fiber must be chosen such that it will not fluoresce and create noise. The cladding material also affects the light-acceptance angle of the fiber.

Construction of an optical fiber begins with a tube of glass consisting of a number of layers of concentric rings as shown in Fig. 6. Each ring of glass has a different refractive index. Total internal reflection (TIR) is required to send light down the center of these concentric glass tubes. To achieve TIR, the outer glass rings must have a lower refractive index than the inner glass core in which the light is traveling. The core (50 μm) and cladding (125 μm) diameters shown are typical of the fibers used in some LOC devices. TIR should be achieved for successful use of optical fibers, and there exist maximum allowable bending and strain (both extension and compression) as well as maximum/minimum operating temperatures. The ultimate tensile strength of glass is also of important interest.

Numerical aperture refers to the maximum angle of light allowed into the fiber tip. For light to travel down a fiber, it must enter and reflect off the cladding at greater than the critical angle. Due to refractive changes in the direction of light as it enters the fiber core, there is a limit to the angle at which light can enter the core and propagate down the optic fiber. Any light striking the cladding at greater than the critical angle will penetrate the cladding and leak out as illustrated in Fig. 7 (top).

For light entering within the cone in Fig. 7 (bottom), all the rays will strike the cladding at less than the critical angle and transmit down the fiber. This is referred to as the acceptance cone and the half angle (θ) of this cone is referred to as the acceptance angle. The value of the acceptance angle depends on the refractive indices of the core, cladding, and air. A light ray entering the core at an angle greater than (θ) will disperse into the cladding. The term used to specify the light collecting ability of a fiber is the numerical aperture (NA). NA is the sine of the acceptance angle θ, that is: $\mathrm{NA} = \sin 11.5° = 0.20$ for the example shown.

Optical fibers with high NAs will accept more light than fibers with low NAs. High NA fibers must be used when weaker light sources such as LEDs are used. Low NA fibers generally require more expensive light sources, such as lasers, to achieve sufficient intensity for high quality transmission.

Modal dispersion is a phenomenon which affects the clarity of light transmission. A fiber with a large diameter and high NA will have a large number of modes (rays of light) operating along its length. Optical fibers are classified according to the number of rays of light that can be carried down the fiber simultaneously. This is referred to

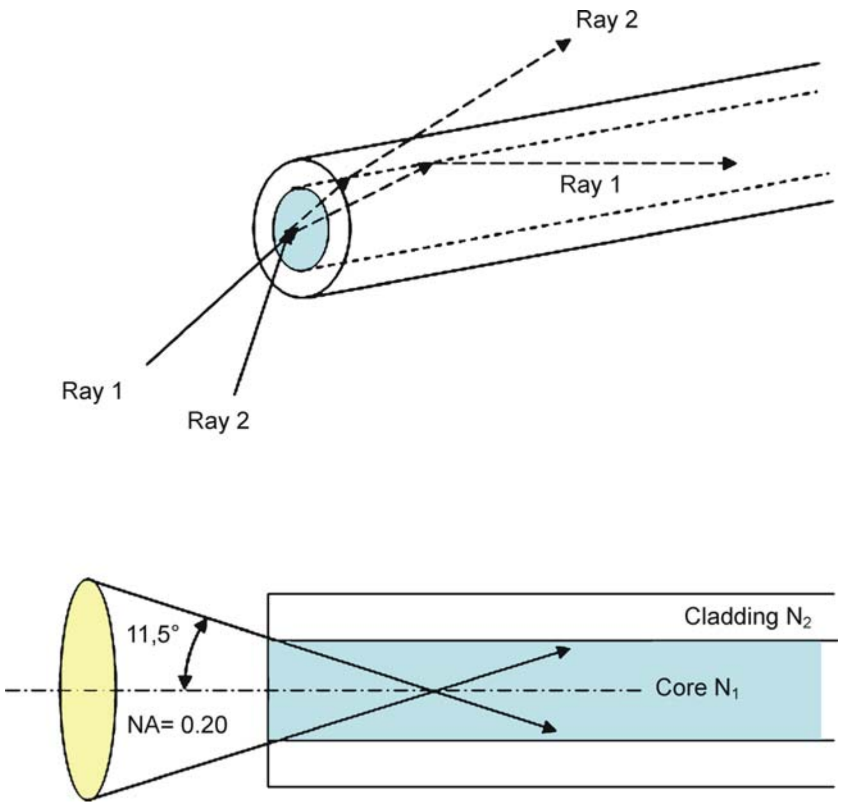

On-Chip Detection Using Optical Fibers, Figure 7 Light rays striking the core at less than the critical angle will penetrate the cladding and leak out (top). Light entering within the acceptance cone will strike the cladding at greater than the critical angle and transmit down the fiber (bottom)

as the *mode of operation* of the fiber. A mode of light is simply a single light ray. The higher the mode of an optical fiber, the more rays of light that can travel down the core. It is possible for a fiber to carry as many as several thousand modes or as few as only one.

An omnidirectional light source (i. e. one that radiates light rays equally in all directions) such as an LED, emits several thousand rays of light in a single pulse. Because an LED injects a broad beam angle into the core, each mode of light travels at a different angle as it propagates down the fiber, and will travel different total distances over the length of the fiber. Therefore, it takes different lengths of time for each light ray to travel from one end of the fiber to the other. The light source will launch all modes into the fiber at exactly the same time, and the signal will appear at the beginning of the fiber as a short sharp pulse. By the time the light reaches the end of the fiber, it will spread out and appear as an elongated pulse. This is referred to as *modal dispersion*. Modal dispersion increases with higher NA, while the bandwidth of a fiber decreases with higher NA.

A specific number of modes are allowed to propagate down the length of a fiber. When the core and cladding each have a constant refractive index across their cross sections, but the core refractive index is different than the cladding refraction index, then they behave like an optical waveguide. This is referred to as *step index* and in this fiber type, only a specific number of modes can propagate.

As the diameter and the NA decrease, so do the number of modes that can propagate down the fiber. The decrease in modes is affected more by reduction in diameter than by reduction in NA. As the diameter decreases to the wavelength of light, then only one mode will travel down the fiber. This state is referred to as *single mode* propagation or a *single mode* fiber.

Multimode fibers generally refer to fibers with a core diameter of 50 μm or more. Because of their large diameter, multiple modes of light are able to travel down the core. The wider diameter of the multimode fibers makes them suitable for use with LED light sources. This normally produces a lower cost system than single mode fibers, which have a small diameter and require the use of lasers. However, allowing multiple modes of light to travel down

a fiber may cause modal dispersion. The good news is that the short optical fiber lengths in most LOC systems make problems with modal dispersion unlikely.

Step and graded index fibers differ in the gradients of their refractive indices. A step index fiber has a glass core of constant cross-sectional refractive index, surrounded by a cladding of a different but constant cross-sectional refractive index. Because of this sudden change in the refractive index, light will reflect off the core/cladding interface and transverse its way down the core. The refractive index of the core (N_1) is typically 1.48 while the cladding is 1.46 (N_2). The acceptance angle (θ_a) is typically near 14°. Step index fibers used in telecommunications exhibit modal dispersion which limits their transmission bandwidth and speed. However, step index fibers are often used in chip sensor applications, where fiber lengths and data rates are much lower than in communication applications.

Graded index (GRIN) multimode fiber has a core with a gradually changing cross-sectional refractive index. The highest refractive index is in the core center and then gradually reduces, as it moves to the outer edge of the core. Because of this gradually changing refractive index, the light rays refract (rather than reflect as in step index fibers) as they move through the core, and produce sinusoidal light wave patterns in the fiber. The practical effect of this curved refractive index profile is that light rays that are traveling further from the center axis of the core will have further to travel, but are traveling through the lowest refractive index and will therefore be traveling the fastest (Snell's law). Light rays that are traveling near the center of the core are moving the shortest distance but going through the highest refractive index and therefore traveling the slowest. The result is that all the rays tend to arrive at the end of the core at the same time, which means that modal dispersion is greatly reduced in graded index fibers.

Single-mode fibers are used to reduce the number of modes traveling down a fiber and therefore reduce modal dispersion. A single-mode fiber is basically a step index fiber with a very small core diameter, generally 8 – 9 μm. To reduce the number of modes, the fiber is constructed with very little difference between the refractive indices of the core and the cladding. As the difference between the refractive indices of the core and cladding decrease, the critical angle increases. Therefore, only light approaching at a very large angle of incidence is internally reflected and all other rays will dissipate into the cladding. Because of this, only a single mode of light is able to traverse down the fiber (i. e. the fundamental mode).

When using a single-mode fiber, light must be precisely aimed down the center of the core, or light will be lost to the cladding. With only the fundamental mode traveling down the fiber, there can theoretically be no modal dispersion in single-mode fiber. The signals input at one end of the fiber appear at the output of the fiber with exactly the same shape. As optical biosensors move toward single molecule detection, single-mode fibers may be required.

Alignment of fibers is a major concern with all on-chip detection using optical fibers. There are many issues involved in aligning fibers and connecting fibers. The main concern when connecting two optical devices together is *attenuation*, the fraction of optical power lost in the connection process. Attenuation is the sum of the losses from a number of factors including: misalignment of fibers, differing core diameters, numerical aperture differences, reflection from fiber ends, spacing between the ends of the fibers, fiber tip end finish and cleanliness, and bends in the fibers. Theoretical analysis of the losses caused by these factors is complicated by the fact that the distribution of power across the face of a fiber is usually unknown and varies according to the type and length of fiber, method of excitation, etc.

Plastic fibers such as PMMA have also been used successfully with both communications and sensor applications. Plastic fibers are, however, limited to step index, multimode construction. Because of the nature of plastics, the fabrication process produces a core and cladding with significantly different refractive indices. Most plastic fibers have a core refractive index of 1.50 and a 1.40 cladding refractive index. A typical NA is 0.50, which represents an acceptance angle of 30° (an acceptance cone of 60°) for plastic fibers, which allows them to collect a great deal of light.

There are several other advantages associated with using plastic fibers. First, they are more robust than glass fibers. They can sustain significantly more shock, pressure and stress than glass fibers. Second, they are far more flexible, easier to handle and to terminate than glass fibers. Finally, they are generally cheaper than glass.

However, plastic also some disadvantages. Plastic fibers have a much higher attenuation than glass and can only be used over very short distances. Plastic has an optimum operating wavelength of 650 nm, which may not match the sensor application. Plastic fibers also have very limited operating bandwidth. Another issue for some sensor applications is that plastics are limited to much lower temperatures than glass fibers.

Light Sources

The light-emitting diode (LED) is a semiconductor device that emits incoherent, narrow-spectrum light. The color of the emitted light depends on the semiconducting material used, and can be near-ultraviolet, visible or infrared.

The laser light is monochromatic, i. e., consisting of a single wavelength or color, and emitted in a coherent beam, contrary to common light source.

A laser diode is a laser where the active medium is a semiconductor similar to that found in a light-emitting diode. Laser diodes are used in devices for optical storage, laser pointers, and fiber optics.

The quartz halogen lamp contains a tungsten filament surrounded by a halogen gas such as iodine or bromine. Halogen lamps can be run at higher temperatures, allowing for higher luminous efficacy, apparent brightness, and whiter color temperature. Because the lamp must be very hot to create this reaction, the halogen lamp's envelope must be made of quartz.

The deuterium halogen lamp is a low pressure gas discharge light source often used in spectroscopy when a full spectrum source of illumination in the ultraviolet region is needed. The origin of the continuum ultraviolet radiation extends from around 160 nm to 400 nm.

A mercury-vapor lamp is a gas discharge lamp which uses mercury in an excited state to produce light. They also offer a very long lifetime, as well as intense lighting. Like fluorescent lamps, mercury vapor lamps usually require a starter which is usually contained within the mercury vapor lamp itself.

Xenon arc lamp uses ionized xenon gas to produce a bright white light that closely mimics natural daylight. Xe lamp, however, have a significant amount of spectral fine structure in many parts of the spectrum, as this is one factor to consider when choosing between a halogen and a Xe source. The white, continuous light generated with this arc is of daylight quality and all movie projectors in theaters employ these lamps.

The incandescent tungsten lamp is a source of light that works by passing an electric current through a thin filament, heating it and causing it to emit light. This is the typical light bulb for home use.

Light Detectors

Photomultiplier tubes (PMTs) are extremely sensitive detectors of light in the ultraviolet, visible and near infrared. These detectors multiply the signal produced by incident light by as much as 10^8, from which single photons can be resolved. The PMT benefits from a combination of high gain, low noise, high frequency response and large area of collection.

The photodiode is a semiconductor diode that functions as a photodetector. Photodiodes are packaged with either a window or optical fiber connection, in order to let in the light to the sensitive part of the device. They may also be used without a window to detect vacuum UV or X-rays.

Avalanche photodiodes (APDs) are photodetectors that can be regarded as the semiconductor analog to photomultipliers.

Si PIN photodiodes feature low capacitance, which enables them to deliver a wide bandwidth with only a low bias voltage, making them ideal for high-speed photometry as well as optical communications. Some PIN diodes have a mini-lens, which increases fiber coupling efficiency and enhanced sensitivity for violet laser detection.

The spectrometer measures light over a specific range of wavelengths, from gamma- and X-rays into the far infrared. The variable measured is most often the light's intensity but could also, for instance, be the polarization state. Spectrometers are used for producing spectral lines and measuring wavelengths and intensities.

The charge-coupled device (CCD) detector array is an image sensor, consisting of an integrated circuit containing an array of linked or coupled capacitors sensitive to light. CCDs are used in digital photography, astronomy, photometry, optical and UV spectroscopy and other high speed techniques.

The complementary metal-oxide-semiconductor (CMOS) detector array is another type of an image sensor. Although less sensitive than the CCD array, it is increasingly used in sensor and Lab-on-a-Chip applications due to: much lower power consumption, much lower cost, easier compatibility with digital electronics, and the fact that for many Lab-on-a-Chip applications the background levels are sufficiently high that the higher sensitivity of the CCD does not confer a significant advantage.

Optical Filters

An optical filter is a device which selectively transmits light having certain properties (often, a range of wavelengths), while blocking the remainder. Filters are commonly used in many optical instruments including LOC sensors.

A *longpass (LP) filter* is a colored glass filter that attenuates shorter wavelengths and transmits longer wavelengths over the active range of the target spectrum. In fluorescence, longpass filters are frequently utilized in dichroic mirrors and barrier (emission) filters.

A *shortpass (SP) filter* is a colored glass filter that attenuates longer wavelengths and transmits shorter wavelengths over the active range of the target spectrum. In fluorescence, shortpass filters are often employed in dichromatic mirrors and excitation filters.

A *band-pass filter* is a device that passes frequencies within a certain range and rejects (attenuates) frequencies outside that range. The filter does not attenuate all frequencies outside the desired frequency range completely. This

is known as filter roll-off, and is usually expressed in dB of attenuation per octave of frequency.

A *dichroic filter* is a very-accurate color filter used to selectively pass light of a small range of colors while reflecting other colors. By comparison, dichroic mirrors and dichroic reflectors are characterized by the colors of light that they reflect rather than the colors they pass. Because unwanted wavelengths are reflected rather than absorbed, dichroic filters don't absorb much energy during operation and so don't become nearly as hot as the equivalent conventional filter.

Filter wheels and *filter cubes* usually contain four or more individual filters which can be rotated into position. Since all filters are the same thickness, no refocusing is required when changing filters. Filter wheels and cubes are designed to closely and rigidly couple to CCD cameras or other optical equipment.

Applications of On-Chip Detection Using Optical Fibers

Nearly all of the published studies in on-chip detection using optical fibers were conducted after the year 2000. Most of the work to date has been performed at universities in North America (Canada and United States), Europe (Denmark, Germany, Poland and United Kingdom), and East Asia (Japan, Singapore and Taiwan).

Fiber Types

There have been three main types of optical fibers used for on-chip detection as listed in Tables 1–3. The vast majority of researchers have chosen multimode fibers made from fused silica (glass).

Most of the embedded fiber devices (Table 1) contain small diameter (50 – 100 μm) multimode fibers. Many researchers further reduce the size of the fiber by acid etching to remove much of the cladding. For example, when starting with a 63 μm core and 125 μm cladding, the fiber may be acid etched to reduce the cladding size to perhaps 70 μm. This facilitates assembly of the fibers into the micro dimensions of the device. Several embedded fiber devices have been made from the singlemode type (9 μm core), but it has been challenging to deliver or gather sufficient amounts of light while being limited to a single mode and low NA. Lee et al. were able to obtain an order of magnitude lower LOD by using multimode fibers compared to singlemode (Table 1, 5th row) [6].

One advantage of using a proximity type fiber arrangement (Table 2) is that a much larger diameter multimode fibers can be used. Most of these chips are based on fiber cores from 400 μm to 1000 μm. The silica fibers usually have NAs of 0.22, while plastic fiber NAs of 0.50 are common. The proximity fibers can gather more light, but there is a greater distance between the analyte and the fiber which reduces the signal strength.

The wetted fiber types listed in Table 3 have been based on multimode fibers or fiber array bundles. In Fig. 4, the large diameter (1000 μm) multimode cores are acid etched or stretched to create a sharp probe tip. In either case, the fiber surface is treated for binding proteins or other molecular probes. Walt et al. [7] (Table 3, 5th row) developed a chip using a wetted fiber optical array of thousands of individual fibers in a coherent bundle. By etching the core at the fiber bundle's tip, an array of microwells was created and loaded with microspheres. The microspheres are coated with various sensing materials such as antibodies. Resulting changes in fluorescence intensity correspond to analyte concentration.

Lighting and Detection

The most common light source for all applications has been the blue LED (470 nm) and red LED (635 nm), generally used with multimode fibers. Lasers are used with singlemode fibers because the small core requires more intense power. For spectrophotometry, devices utilize full spectral light sources such as mercury vapor, halogen, or tungsten lamps. This allows detection of light absorbance or transmission over the spectrum.

Lenses are sometimes used to focus both source and detected light. Concave, convex, bi-convex and other converging lenses have been used. Loock et al. [8] formed a convex lens directly onto the ends of the fibers (Table 1, 8th row). Fujii et al. [9] fabricated lenses into the chip PDMS structure (Table 1, 14th row). In some cases, filters are also used to sharpen the signal. The most popular filters are the band-pass and dichroic variety.

Chip Fabrication

The chips themselves are most commonly made from SU-8 molds and polydimethylsiloxane (PDMS) which is a silicon-based organic polymer. It is optically clear, inert, and non-toxic, which makes it well suited for Lab-on-a-Chip applications. Other glasses, silicon wafers, and acrylics have also been used. Recently, Golonka et al. have used low-temperature cofired ceramic (LTCC) technology to produce electrical, optical, and fluidics within an LOC structure (Table 1, 10th and 11th rows) [10, 11].

The microfluidic channels in these LOC systems are typically 100 μm depth and width. The liquids are moved with syringe pumps, peristaltic pumps, or some type of electrokinetic method. The syringe pump generally provides a low cost, yet accurate solution.

Analyte Detection

Much of the early work in this area was done for flow cytometry applications using embedded or proximity fiber systems. These devices typically measured the counts and velocities of microspheres in liquids. These systems are able to detect 10 μm spheres at a rate of 65 particles per second (Table 1, 2nd row) [12].

Another application involves capillary electrophoresis (CE) used to separate ionic species based on their size-to-charge ratio in microchannels filled with electrolytes. Various dyes have been used such as Rhodamine B, Cy3, and Topro-5 to detect biomolecules and DNA. LOD's of 100 – 200 nM have been reported (Table 1, 5th, 8th and 13th rows) [6, 9, 13].

The most popular applications have been in the areas of spectrophotometry and/or spectrofluorometry involving the measurement of light intensity as a function of wavelength. These devices have been used to measure chemical concentrations, amino acids, and fluorescent species down to an LOD of 25 nM (Table 1, 4th row) [14].

Most recently, researchers have begun using these chips to conduct immunoassays. An immunoassay is a test that measures the level of a substance in a bio-sample, typically serum or urine, using the specific binding reaction of an antibody or antibodies to its antigen. LOC's have been used to detect protein markers for vasculitis and cancer (Table 2, 1st and 7th rows) [15, 16] at LOD's in the 100 nM range. They have also been used to detect *E. coli* and BTK-a biowarfare agent simulant (Table 3, 5th row) [7].

Future Directions for Research

Lab-on-a-Chip detection using optical fibers will be guided by two major driving forces: molecular analysis and molecular biology, and microelectronics and optical telecommunications. Most Lab-on-a-Chip technologies to date have focused primarily on molecular analysis by miniaturizing capillary electrophoresis (CE), chromatography, flow cytometry, and sensing conditions such as pH, ionic strength, and concentrations of analytes. Currently in the U.S., biodefense funding from DOD and DARPA are driving much of the LOC academic research in universities. These defense programs tend to focus on detection and immunoassays for bioterror prevention. The recent emphasis on high-throughput sequencing for genomics and proteomics has also begun to use microfluidics devices. Current commercial development, in the meantime, is driven to a much greater extent by the real need (and real market for) in vitro diagnostics and drug discovery tools. While the manufacturing technologies being developed in microelectronics will continue to pace the fabrication of microelectromechanical systems (MEMS) in the future [3].

Fiber optics technology has always been dominated by the telecommunications markets and this will certainly continue. Fibers will continue to increase in speed and bandwidth by using new methods such as dense wavelength-division multiplexing (DWDM). Future fibers will be even more pure, and conduct light and images with more clarity. Recent growth in the sensors industry has spawned several new companies which focus strictly on fibers for optical detection. While the communications industry has focused on longer IR wavelengths, the sensor fiber optics companies will work on improving light transmission down into the UV range for biodetection.

Embedded fiber optics will continue to be successful only as microfabrication methods are simplified and commercialized. The original hope of microfluidics was that photolithography and associated technologies that had been so successful in silicon microelectronics, and in microelectromechanical systems (MEMS), would be directly applicable to microfluidics. Some of the earliest work in fluidic microsystems did, in fact, use silicon and glass, but these materials have largely been displaced by plastics. For analyses of biological samples in water, devices fabricated in glass and silicon are usually inappropriate. Silicon, in particular, is expensive, and opaque to visible and ultraviolet light, and cannot be used with optical methods of detection. It is easier to fabricate the components required for microanalytical systems in elastomers than in rigid materials but these methods have not been commercialized. Exciting future research areas will involve embedding light sources and micro-detectors directly into the chip.

Proximity fiber optics should continue to grow in popularity as light sources and detectors become smaller and portable. Companies are now producing low cost LEDs, lasers, and spectrometers that make it relatively easy to set-up on-chip detection devices. These systems will require better and lower cost lenses, filters, light sources and detectors especially in the near-UV wavelengths. Again, this is because almost all research to date has focused on the IR wavelengths used for telecommunications and the internet. Future work in proximity fiber optics will focus on lowering signal-to-noise ratios and increasing the sensitivity of distinguishing different wavelengths.

Wetted fibers on-chip have only recently been attempted and shows great promise. Like embedded fibers, the wetted fibers require very sophisticated microfabrication techniques. Microfluidics has seen the rapid development of new methods of fabrication, and of components such as microchannels that serve as pipes, and other structures that form valves, mixers, and pumps that are essential elements

of microchemical ’factories’ on a chip. Wetted fibers will require easier ways of inserting and removing the fibers from the chip as well as simpler methods of preparing the fiber tips with biomolecules for detection.

An LOC system must have a number of generic components: a method of introducing reagents and samples; methods for moving these fluids around on the chip, and for combining and mixing them; and various other items such as detectors for most microanalytical work, as well as components for purification of products for systems used in synthesis. The field has, so far, centered on demonstrating concepts for these components. In the future there will be sufficient methods of fabrication, and a range of components which will make it possible to apply microfluidic systems to the resolution of problems rather than simply to the demonstration of principles [3].

Cross References

► Flow Cytometer Lab-on-Chip Devices
► Spectrophotometric Analysis
► Capillary Electrochromatography
► Spectrofluorometry
► Immunoassay
► Capillary Electrophoresis

References

1. Bailey D, Wright E (2003) Practical Fiber Optics. Elsevier, Burlington
2. Shotwell RA (ed) (1997) An Introduction to Fiber Optics. Prentice Hall, Englewood Cliffs
3. Whitesides GM (2006) The origins and the future of microfluidics. Nature 442(27):368–373
4. Grattan KTV, Sun T (2000) Fiber Optic Sensor Technology: Introduction. In: Grattan KTV, Meggitt BT (eds) (2000) Optical Fiber Sensor Technology. Kluwer Academic, Dordrecht
5. Zhang ZY, Grattan KTV (1998) Commercial activity in optical fiber sensors. In: Grattan KTV, Meggitt BT (eds) (1998) Optical Fiber Sensor Technology. Kluwer Academic, Dordrecht, pp 257–306
6. Lin CH, Lee GB, Chen SH, Chang GL (2003) Micro capillary electrophoresis chips integrated with buried SU-8/SOG optical waveguides for bio-analytical applications. Sens Actuators A 107:125–131
7. Bowden M, Song L, Walt DR (2005) Development of a microfluidic plattform with an optical imaging microarray capable of attomolar target DNA detection. Anal Chem 77:5583–5588
8. Treflak NR, Barnes J, Rask F, Courtney DG, Walford R, Li R, Oleschuk RD, Loock HP (2005) Absorption measurements in microfluidic devices using ring-down spectroscopy. Proc SPIE 5969:59690O
9. Camou S, Fujita H, Fujii T (2003) PDMS 2D optical lens integrated with microfluidic channels: principle and characterization. Lab Chip 3:40-45
10. Golonka LJ, Zawada T, Radojewski J, Roguszczak H, Stefanow M (2006) LTCC microfluidic system. Int J Appl Ceram Technol 3:150–156
11. Golonka LJ, Roguszczak H, Zawada T, Radojewski J, Grabowska I, Chudy M, Dybko A, Brzozka Z, Stadnik D (2005) LTCC based microfluidic system with optical detection. Sens Actuators B 111–112:396–402
12. Wang Z, El-Ali J, Engelund M, Gotsaed T, Perch-Nielsen IR, Morgensen KB, Snakenborg D, Kutter JP, Wolf A (2004) Measurements of scattered light on a microchip flow cytometer with integrated polymer based optical elements. Lab Chip 4:372–377
13. Qi S, Liu X, Ford S, Barrows J, Thomas G, Kelly K, McCandless A, Lian K, Goettert J, Soper SA (2002) Microfluidic devices fabricated in poly(methylmethacrylate) using hot-embossing with integrated sampling capillary and fiber optics for flourescence detection. Lab Chip 2:88–95
14. Chabinyc ML, Chiu DT, McDonald JC, Stroock AD, Christian JF, Karger AM, Whitesides GM (2001) An integrated fluorescence detection system in poly(dimethylsiloxane) for microfluidic applications. Anal Chem 73:4491–4498
15. Lucas LJ, Han JH, Chesler N, Yoon JY (2007) Latex immunoagglutination assay for a vasculitis marker in a microfluidic device using static light scattering detection. Biosens Bioelectron 22:2216–2222
16. Hsieh HB, Marrinucci D, Bethel K, Curry DN, Humphrey M, Krivacic RT, Kroener J, Kroener L, Ladanyi A, Lazarus N, Kuhn P, Bruce RH, Nieva J (2006) High speed detection of circulating tumor cells. Biosens Bioelectron 21:1893–1899

On-Chip Electrospray

Leslie Yeo, James Friend
Micro/Nanophysics Research Laboratory
Department of Mechanical Engineering, Monash University, Clayton, VIC, Australia
leslie.yeo@eng.monash.edu.au

Synonyms

Electrospray ionization-mass spectrometry (ESI-MS); Electrospray mass spectrometry; Electrospray emitter on-chip; Chip electrospray mass spectrometry

Definition

Electrospraying utilizes an applied electric field to generate micron or nanometer sized aerosol drops. If DC fields are employed, the emitted drops carry a net charge which allows electrosprays to function as ionization sources, in particular, for mass spectrometry. With electrospray ionization (ESI), interfacing between microfluidic separation technology such as on-chip high performance liquid chromatography (HPLC) and capillary electrochromatography (CEC) with mass spectrometry (MS) is now realizable.

Overview

The concept of employing electrostatic charging to atomize a liquid source was first observed by John Zeleny in

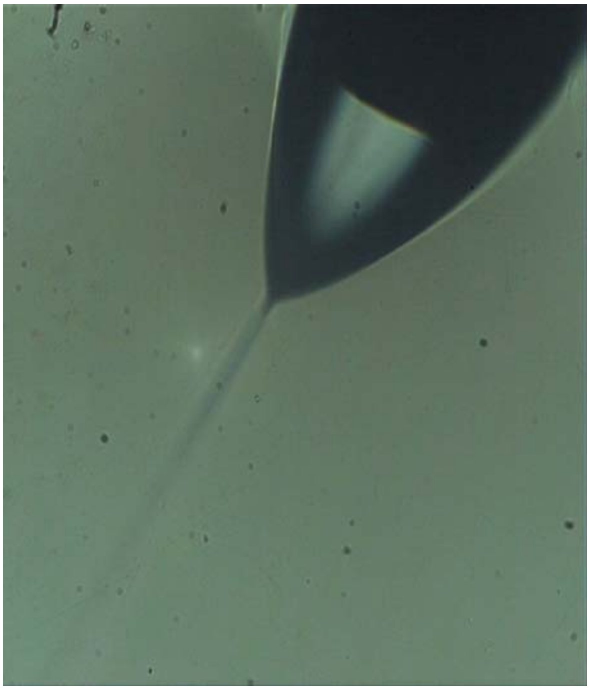

On-Chip Electrospray, Figure 1 Taylor cone formation at the tip of a 100 μm capillary across which a 3 kV DC voltage is applied. A slender jet issues from the tip of the Taylor cone as a result of Rayleigh fission, subsequently breaking up to form aerosol droplets

1914. If the liquid is flowing through a metal capillary, the surface of which is raised to a potential with respect to a grounded source placed a small distance away, the electric field acts to stretch and deform the liquid meniscus at the capillary tip. The fluid physics under the influence of an electric field in such circumstances was described by Sir Geoffrey Ingram Taylor in 1964, who observed the meniscus to deform into a sharp cone with a specific half angle of 49.3° for highly conducting liquids. This Taylor cone, depicted in Fig. 1, arises due to the separation of electrical charges within the liquid or ambient phase to form a thin polarized layer of counter-ions near the meniscus interface; these counter-ions then drift towards the tip of the meniscus by tangential electromigration.

The counter-ion accumulation at the tip then creates a Coulombic repulsion force which causes the tip to disintegrate into a thin jet that emanates from meniscus when the surface tension force holding the drop together is exceeded, as shown in Fig. 1. This jet subsequently breaks up due to hydrodynamic or Coulombic instabilities to form a spray of small liquid drops. As the accumulated charge at the tip is transferred from the meniscus tip to the jet and subsequently to the drops, each individual drop carries a net charge. Since the size of the ejected drop shrinks during its flight due to evaporation, the repulsive force builds up due to the increase in the charge density. Coulombic fission then occurs once again when the Rayleigh limit

$$q > 64\pi^2 \varepsilon_m a^3 \gamma \, , \qquad (1)$$

is reached. In Eq. (1), q is the charge, ε_m the permittivity of the surrounding medium, a the drop diameter and γ the surface tension. The drop disintegrates to produce even smaller droplets, which themselves undergo similar disintegration cycles, as depicted in Fig. 2; this Rayleigh instability fission cascade eventually leads to charged drops with dimensions down to 10 nm orders.

The ability of the electrospray to produce very small, monodispersed charged drops then naturally lends itself as a powerful soft ionization technique for the mass spectrometry of large, complex and non-volatile biomacromolecules (e. g., DNA, peptides and proteins) which are otherwise denatured by other ionization techniques. Electrospray ionization (ESI) also has several advantages over matrix-assisted laser desorption/ionization (MALDI), which is another soft ionization technique. The use of lasers requires fine tuning of optical properties in order to ensure quality and reproducibility in the results; signals are dependent on the laser wavelength, pulse energy, time between pulses and impact angle, amongst others. Moreover, the inorganic salts in proteins can interfere with the ionization and hence elaborate sample preparation to remove these components is a vital step in MALDI. The small size of the laser spot compared to the sample also requires multiple laser pulses targeted at different sample regions in order to obtain a statistical average of the local concentration within the sample, which is further complicated by inhomogeneity due to partitioning of the analyte molecules as a result of non-uniform solvent evaporation. Sample dispensing onto MALDI target plates also requires the integration of complex components such as piezoelectric microdispensers or centrifugal delivery systems.

ESI was first proposed by Malcolm Dole in 1968 who noticed that the Coulombic fission cascade would eventually lead to sufficiently small drops which contained a single solute molecule that retained some of the drop charge such that a fully desolvated gas phase ion would ultimately be left once all the solvent evaporates, this mechanism being known as the charge residue model (CRM). These efforts were, however, largely unsuccessful practically due to the use of an ion-drift spectrometer to which the electrospray was interfaced. It was John Fenn, then at Yale University, who later developed a practical method for electrospray ionization mass spectrometry (ESI-MS) that allowed the identification and structure analysis of biomacromolecules of virtually unlimited molecular weights to an accuracy of 0.01% by averaging

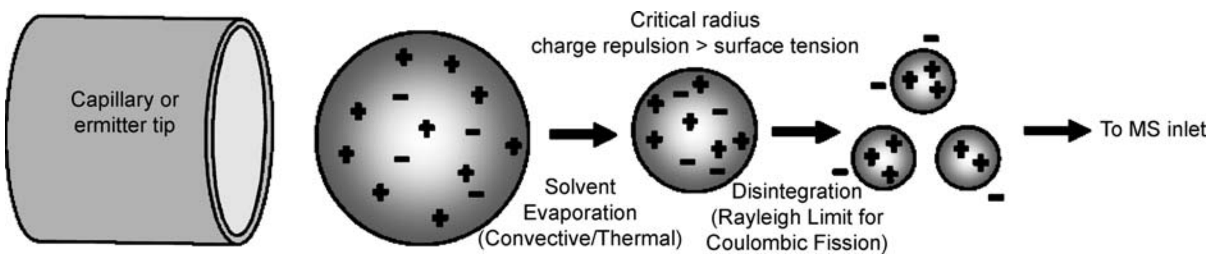

On-Chip Electrospray, Figure 2 Schematic illustration of the Coulombic fission process occurring during DC electrospraying giving rise to successively smaller charged drops

over the signals generated by the multiple ions which are associated with the high mass-to-charge ratios of large, complex molecules [1]. In recognition of this significant contribution and its impact on genomic, proteomic and drug discovery research, Fenn was awarded the Nobel Prize in Chemistry in 2002. It should however be noted that the term *electrospray ionization* is somewhat misleading as the process is not akin to electron ionization in which electroneutral molecules are converted into ions. Instead, the electrospray essentially allows the transfer of analytes, already ionized in the liquid phase, into the gas phase [2]. Nevertheless, we will retain the term due to its widespread use in the literature.

The recent progress in micro/nanofabrication technology as well as microfluidics has spurred efforts to interface chip-based separation devices with electrospray ionization mass spectrometers. As frontiers in the ability to miniaturize the mass analyzers are being extended further, an integrated field portable microdevice that couples both on-chip separation (e. g., capillary electrophoresis, capillary electrochromatography and high-performance liquid chromatography) and analytical technology with an electrospray interface to produce a complete tool, which is both reliable and can be easily replicated, is increasingly realizable. Such a device would be extremely attractive for in-situ analysis in environmental, chemical or biological monitoring and remediation, offering the advantage of reduced analyte quantities and separation times, higher flow rate capabilities, low cost, increased precision and repeatability. At the time of writing, an ESI-MS microdevice for high performance liquid chromatography known as the HPLC-chip which is marketed by Agilent Technologies is commercially available. The HPLC-chip integrates the HPLC column with a sample enrichment column and an electrospray tip, which can then be mounted onto a mass spectrometer.

Basic Methodology

A review of DC electrospraying is given by Grace & Marijnissen [3]. It should be noted that the use of high frequency ($> 10\,\text{kHz}$) AC electric fields gives rise to completely different drop dynamics and characteristics [4], the most important distinction perhaps being the larger $1-10\,\mu\text{m}$ drops generated which are electroneutral. For the purposes of on-chip electrospray devices for analyte separation and detection, we will focus on the use of DC electrospraying henceforth as the AC electrospray has only recently been discovered and hence the use of AC fields for various applications and devices is currently work-in-progress (see, for example, [5]).

The most stable DC electrospray mode required for ionization is the cone-jet mode [3] described above and depicted in Fig. 1. The appearance of this characteristic conical meniscus and its stability has therefore been generally, and more likely than not, universally, adopted as the benchmark criterion for stable electrospray ionization. This stability is most commonly disrupted intermittently by gas bubbles aggregating into large slugs, thus temporarily causing cessation in the spraying. Once the slug is released, the spraying resumes. The formation of gas bubbles is a common problem in DC electrokinetics as a result of electrolytic reactions occurring to balance the charge induced by the applied voltage at the metal capillary, leading to a reduction in throughput and hence stable electrospray disruption due to the enormous capillary pressures. Joule heating and the generation of ionic contaminant as a result of Faradaic reactions at the electrodes are also additional problems accompanying the use of large DC voltages. Alternatively, stable electrospraying can also be disrupted by stray electric fields, mechanical perturbations (e. g., vibration) or flow variation.

The critical voltage V_c required for stable electrospraying can be estimated through a balance between the capillary stress, of order γ/R, where $R \sim 10^{-3} - 10^{-4}$ m is the principal curvature of the meniscus, of the same order as the radial capillary dimension, and the electric stress $\varepsilon_l V^2/d^2$, where ε_l is the liquid permittivity, V the applied voltage and d the electrode separation:

$$\frac{V_c}{d} \sim \sqrt{\frac{\gamma}{\varepsilon_l R}} \quad . \tag{2}$$

Typically, $\gamma \sim 10^{-2}\,\text{kg/s}^2$, $d \sim 10^{-2}\,\text{m}$ and $\varepsilon_1 \sim 10^{-10}\,\text{C}^2/(\text{Jm})$, thus suggesting that extremely large critical fields in excess of 1 kV are required.

Taylor, by considering a static balance between capillary and electric stresses, showed the existence of a conical meniscus with a half angle of 49.3° at equilibrium for a perfectly conducting liquid. In this limit, the meniscus behaves as a constant potential body and hence the field is external to the drop; the field lines intersect the interface orthogonally. The normal gas phase electric field E_n then scales as $1/\sqrt{R}$, and hence the normal electric stress $p_E \sim E_n^2$ scales as $1/R$. At every point R along the interface, the normal electric stress exactly balances the azimuthal capillary pressure $p_C \sim \gamma/R$. This exact balance and absence of a specific length scale, is responsible for the formation of a static Taylor cone [6].

The perfectly conducting limit was later relaxed to allow for the effect of finite liquid conductivity [7]. In these cases in which the liquid meniscus is assumed to be sufficiently slender such that the longwave approximation can be assumed, the field that arises is predominantly in the liquid phase, tangential to the interface. Nevertheless, this tangential liquid phase electric field E_t also scales as $1/\sqrt{R}$ and thus an exact balance between the normal electric stress $p_E \sim E_t^2$ and the capillary stress $p_C \sim \gamma/R$ again yields a stable equilibrium cone-like meniscus. The cone angle, however, depends crucially on the liquid to gas permittivity ratio $\varepsilon_1/\varepsilon_m$, wherein the Taylor angle is recovered in the perfectly conducting limit as $\varepsilon_1/\varepsilon_m \to \infty$ [6].

An alternative ionization mechanism to Dole's charge residue model (CRM) above has been proposed, in part to account for the inadequacy of CRM to account for the excess of analyte molecules over the observed charges in the electrospray flux. The CRM predicts that the relative number of drops for each species is proportional to the species relative concentration. The difficulty lies conceptually in the unlikely possibility for the successive drop subdivisions during the disintegration process to end up with the observation that all the daughter drops contained only a single analyte molecule for each of the ionizable species, especially in the presence of strong evaporation currents. Even if this were possible, a spectral peak for each species would always be obtained, which is not true. The alternative model, in contrast, proposes that the singly charged or multiply charged gas phase ions are generated by the evaporation of small, highly charged liquid drops of the analyte species [8].

On-Chip ESI-MS Interfacing

Progress in the development of on-chip electrospray interfaces for mass spectrometry has grown exponentially over the past two decades. Whilst there are many different designs and methods proposed, it is possible to summarize these developments in general into three broad categories based on the nature of the electrospray emitter type employed: Blunt edge, transfer capillary attachment, and, emitter tip. Early developmental work employed the blunt edge configuration. However, there appeared to be a subsequent parallel divergence thereafter, in which either the transfer capillary or the emitter tip interfaces were employed. Most of the recent on-chip electrospray interface designs therefore fall generally into either of these two latter categories.

On-chip ESI-MS devices were initially fabricated onto quartz or silica substrates. In addition to problems due to the hydrophobicity (discussed below), fabrication on glass is relatively labor-intensive. The shapes and dimensions available for patterning on glass are also limited. Silicon has also been commonly used because of its amenability to fabricating relatively small high aspect ratio features such as needle tip structures. In addition, semiconductor processing techniques such as deep reactive ion etching (DRIE) can be carried out for mass production of silicon chips [9]. However, silicon being semi-conducting has the disadvantage of current leakage.

Recently, the use of polymer-based substrates such as parylene, poly(dimethylsiloxane) or PDMS, polycarbonate (PC), polyimide (PI), poly(methylmethacrylate) or PMMA, poly(ethylene terephthalate) or PET, amongst others, has become increasingly attractive due to the availability of a wide range of plastics at low costs and the relatively simple and rapid microfabrication (rapid prototyping) techniques involved. The flexibility, superior optical properties and the ability to bond readily to glass after exposure to plasma of some plastics also make these materials attractive. Plastics, and glass for that matter, however, often have to be treated with hydrophobic surfactants to eliminate wetting and capillary ballooning at emitter tips. Other methods to avoid emitter tip wetting are discussed in the next section.

Electrospray tips from SU-8 photoepoxy have also been fabricated. Nevertheless, solvent resistance of polymer-based substrates is a critical issue, with poor resistance resulting in the swelling and distortion of the channels. A comparison between the performance of fused silica, parylene and borosilicate glass is discussed in Licklider et al. [10].

Blunt Edge Orifice

The first miniaturized on-chip electrosprays consisted of a planar glass microchip with 60 μm wide and 10 μm deep etched channels [11]. The open-end channel exit

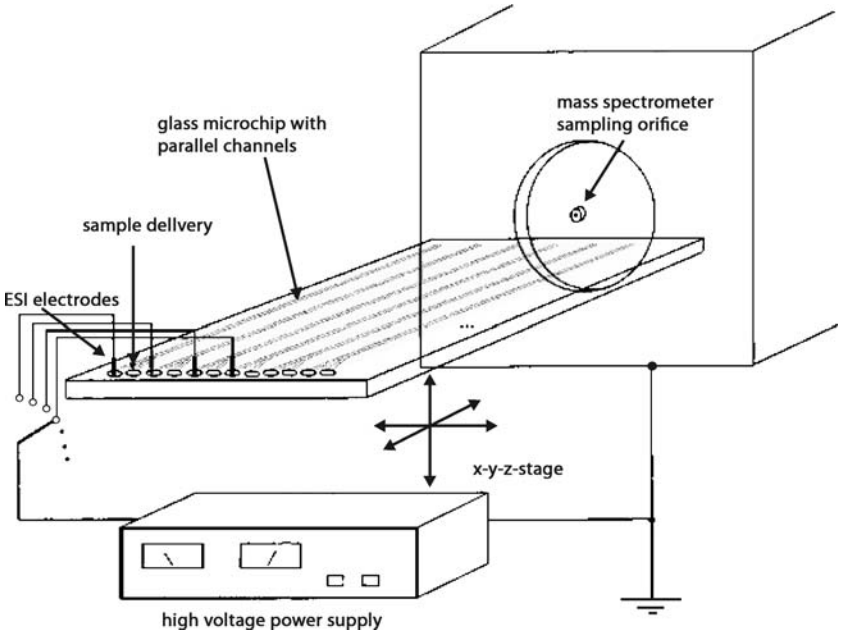

On-Chip Electrospray, Figure 3 Schematic diagram representing the multichannel ESI-MS chip device in Xue et al. [12]. Each channel was connected to two reservoirs for sample injection and delivery. A syringe pump attached to the second reservoir of each channel was used to deliver the sample through the channels and electrodes were placed in one of each two buffer reservoirs to provide the electrical contact with the solution. The electrospray orifices consisted of the blunt edges of the open-ended channels. Reprinted with permission from [12]

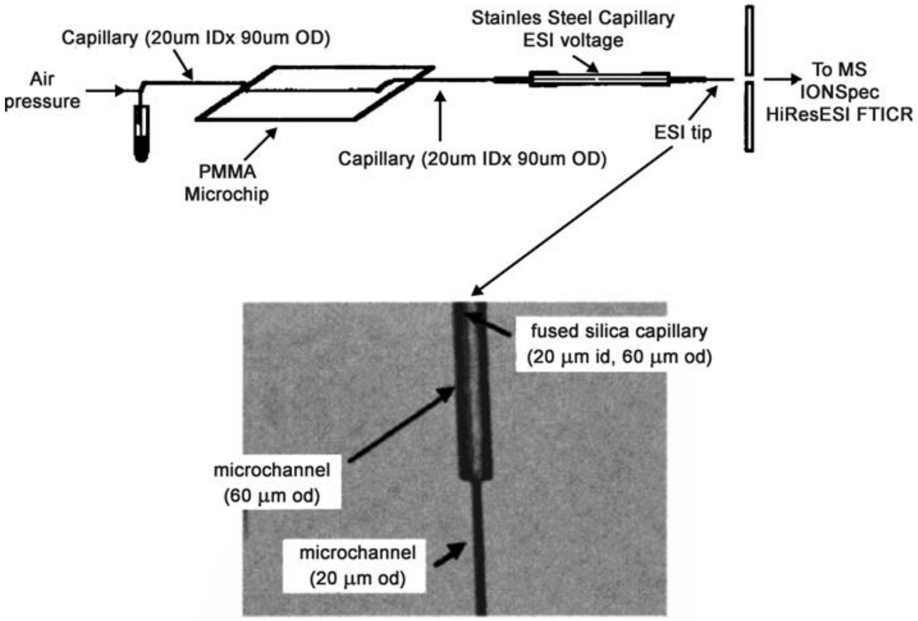

On-Chip Electrospray, Figure 4 On-chip ESI-MS device employing a fused silica transfer capillary. The electrical contact was established through a stainless steel capillary connected to the silica capillary using a poly(tetrafluoroethylene) sleeve. Another fused silica capillary connected to the other end of the stainless steel capillary was used as the electrospray emitter, as shown by the enlargement in the bottom image. Reprinted with permission from [16]

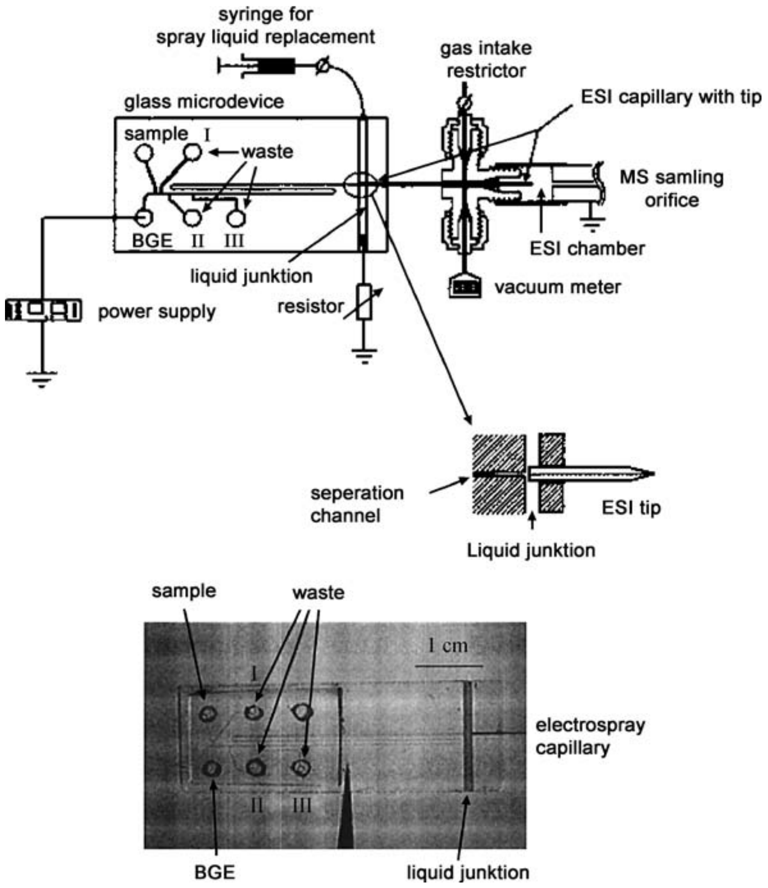

On-Chip Electrospray, Figure 5 Schematic diagram (top) and image (bottom) of the ESI-MS device involving a transfer capillary and a subatmospheric liquid junction. Reprinted with permission from [17]

functioned as the electrospray orifice from which a Taylor cone was observed, thus avoiding the necessity of a dedicated electrospray tip. The coning and spraying is still possible as the electric field intensity at the exposed liquid surface was sufficiently high, above the critical value estimate given by Eq. (2). The blunt edge functioning as the electrospray orifice was formed by either breaking off the scored chip or by cutting the chip using a dicing saw. A similar but parallel multichannel electrospray microchip (Fig. 3) for increased throughput was also developed [12].

Whilst the blunt edge configuration is simple to fabricate, there were several challenges associated with such a design. The low currents associated with electrospraying are insufficient to generate electroosmotic flow (EOF) and hence required the flow to be pressure-driven. The absence of flow regulation however resulted in meniscus ballooning at the orifice which disrupted the electrospray stability and led to the formation of a dead volume; this dead volume introduces hydrodynamic dispersion and hence band broadening of the sample, reducing the efficacy of the separation. Even with application of ancillary electric potentials to drive the flow electroosmotically, the low EOF flow rate made regulation difficult. The electrical connection to the electrospray tip, established by insertion of a metal wire into the sample reservoir, also introduced flow perturbations which aggravated the problem of the lack of flow regulation.

In addition, the ballooning problem was intensified by the hydrophilic glass substrate. This was overcome by surface modification or applying a hydrophobic coating around the edges of the exit end. Nevertheless, this was only a partial remedy as it was possible that the corona discharge affected the chemical stability of the coating [13]. Alternatively, it is possible to bond a porous poly(tetrafluoroethylene) or PTFE membrane at the edge of the microchannel exit acting as the electrospray orifice. The hydrophobic membrane acts to constrain lateral dispersion of the liquid emanating from the orifice. The hydrophobic surface of such a membrane being consis-

tently hydrophobic and hence the hydrophobicity can be easily controlled [14].

The ballooning problem was also addressed by attaching a pneumatic nebulizer and introducing an ancillary liquid (e. g., acetonitrile, methanol or 2-propanol) sheath flow downstream prior to the electrospray exit [15]. This was carried out by coupling an integrated nebulizer to a subatmospheric liquid junction. The role of the nebulizer gas (e. g., nitrogen) is four-fold, directly removing the ballooning meniscus and hence minimizing the dead volume, controlling the flow rate of the ancillary sheath flow, aiding in the evaporation of the electrosprayed drops, and, providing cooling to the sheath flow at high currents. The role of the sheath flow is two-fold, providing an electrical connection and reducing the ballooning effect and hence dead volume by constraining the flow of the sample. Sheath flow interfaces also enjoy the advantage of wide flexibility in analyte solution selection and enhanced reliability. However, a major drawback of sheath flows is the dilution of the sample and the introduction of background noise from the ancillary flow, both of which compromise the detection sensitivity. The position at which the nebulizer channel merges with the separation channel is however crucial. If this is too far from the exit, the gas pressure results in a back flow whereas non-merger of the channels will result in the failure of the gas flow to disperse the liquid at the exit [15].

Subsequent developments in the on-chip electrospray then involved using either a transfer capillary or a microfabricated emitter tip as a dedicated electrospray orifice in order to more efficiently address these problems.

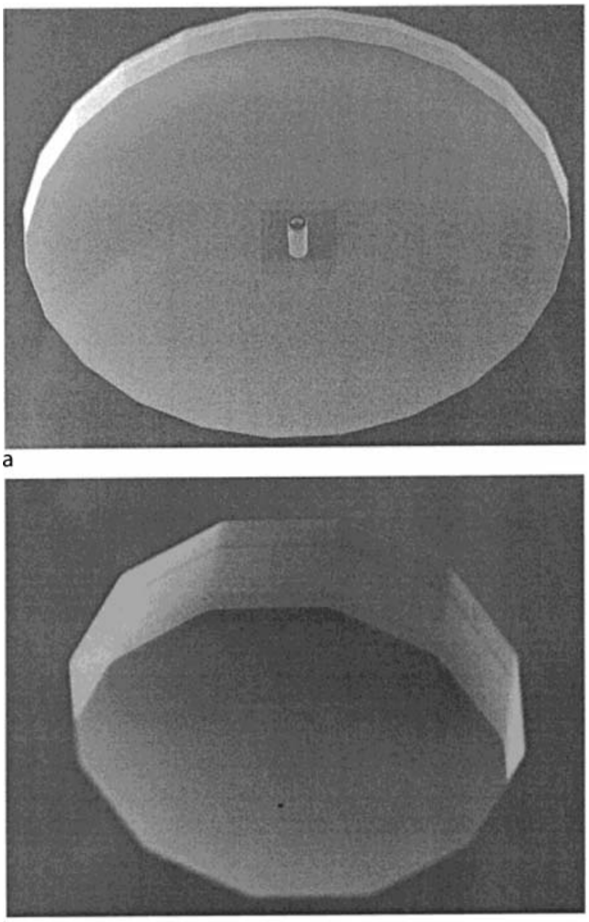

a

b

On-Chip Electrospray, Figure 6 Scanning electron microscopy images of an out-of-plane needle electrospray emitter tip fabricated at the bottom side of a liquid chamber etched into a silicon wafer. The view from the bottom is depicted in image (**a**) showing the 10 μm diameter needle protruding from the underside of the substrate. The view from the top of the substrate is depicted in image (**b**) showing the 600 μm liquid chamber. Reprinted with permission from [9]

Capillary Transfer Attachment

A transfer capillary to which a high voltage is applied can be attached to the edge of a microchannel to act as the electrospray interface. This allows the orifice to be smaller in dimension than that of the blunt edge, thus increasing the stability and hence the performance of the electrospray. In addition, the use of transfer capillaries, the majority constructed from quartz or fused silica, simplifies the construction of the device. Since the capillary is external to the microchannel and chip device, the ESI can be optimized externally. The transfer capillary can also be attached to different chip devices, extending its lifetime and eliminating contamination [13]. An example of the transfer capillary is shown in Fig. 4 in which a long 20 cm fused silica capillary affixed tightly with epoxy to one end to the microchannel was connected to a stainless steel capillary at its free end with a PTFE tube, which in turn, was connected using the PTFE tubing to an electrospray tip pulled from a fused silica capillary [16].

The capillary attachment setup is, however, difficult to control and does not produce good reproducibility. To circumvent these issues, the transfer capillary can also incorporate the sheath flow and liquid junction components discussed above (Fig. 5) to provide the electrical connection, reduce the dead volume as well as to act as a buffer zone such that the separation is not affected by the nebulizer gas flow. Transfer capillaries however require time-consuming alignment and end-to-end butting; poor alignment reintroduces more dead volume instead, resulting in a reduction in the detection sensitivity and separation efficiency. Another deficiency associated with transfer capillary devices is the clogging of the capillary due to contaminants.

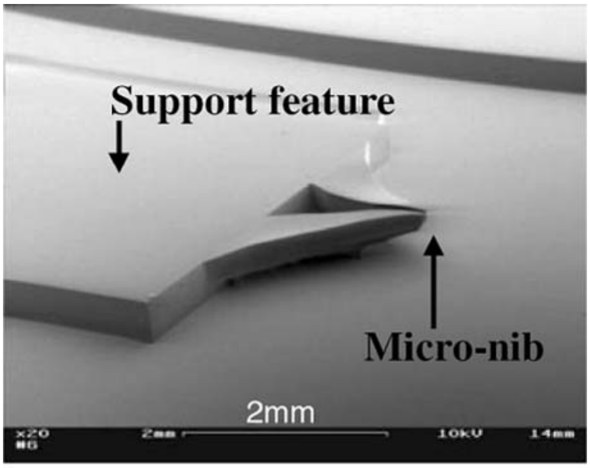

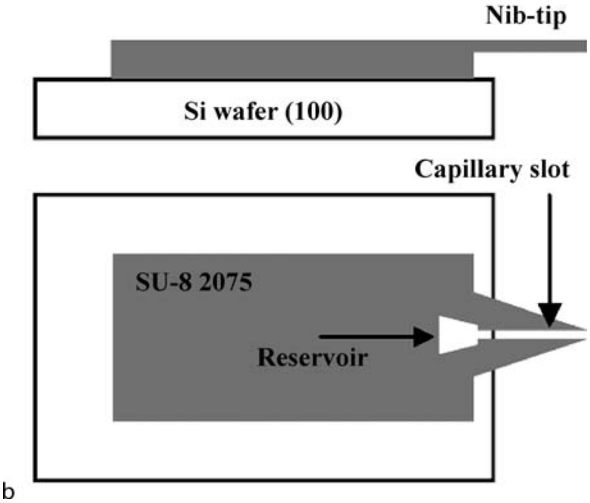

On-Chip Electrospray, Figure 7 Scanning electron microscopy image (**a**) and schematic plan and side views (**b**) of the nib-like in-plane electrospray emitter tip fabricated in SU-8 epoxy using double exposure lithography [21]. Reprinted with permission from [21]

Sheathless interfaces have also been developed to eliminate the dilution effect. To achieve a stable electrospray in the absence of nebulizer flow, the capillary tip is often tapered to provide a reduced orifice size. Electrical connection is provided either by applying a conductive coating (e. g., gold, carbon black or a conductive polymer) to the capillary tip, insertion of a wire electrode through a small opening drilled in the capillary wall or with an additional stainless steel capillary connected via a sleeve tubing shown in Fig. 4 [16]. The conductive layer coating is susceptible to damage due to corona discharge and deterioration due to friction. Moreover, these connections suffer the disadvantage of bubble generation due to electrolytic reactions at the electrode, which could disrupt the spraying and suppress the output signal. To avoid this, a Nafion® housing design was employed in a novel sheathless interface device which provides an escape route to relieve the flow of undesirable electrolytic products [18]. Nafion® is a conducting polymer which acts as a charge-selective salt bridge, thus permitting current penetration through the Nafion® membrane, which in itself has negligible polarization due to the small operating current. The external housing of the electrodes thus permits any gas bubbles to escape through the vent. In this same work, an efficient electroosmotic pump is also integrated into the device using silica monoliths, thus enhancing the stability of the electrospray.

Emitter Tips

Direct electrospraying via emitter tips, also known as nanoelectrospray or nanospray tips, were developed almost as a parallel technique to the transfer capillary interface in an attempt to address the problems associated with direct electrospraying using a blunt edge. The use of emitter tips has the advantage of parallelization in which multiple arrays of emitter tips (over 100 in number) can be fabricated very cheaply and attached onto a microchip, which makes them amenable to high throughput delivery [19]. In general, the development of such tips has taken two routes, namely, out-of-plane tips and in-plane tips. Early work on these emitter tips were almost always out-of-plane, in which the main flow direction and hence emitter is in a direction perpendicular to the device substrate. The first emitter tips comprised of a needle tip, about 50 μm at the large end and 5 μm at the emitting end, blunt cut to about 2 cm in length and glued on to the underside of the substrate at a drilled opening where it meets the bottom of the microchannel [20]. The next generation devices consisted of an integrated nozzle fabricated at the bottom of a liquid chamber, as shown in Fig. 6 [9]. Electrical connection was obtained through the use of a conductive coating or a conducting emitter. In another design, an array of 30 μm holes was machined into the substrate by laser ablation to function as emitters; the inherent taper of low demagnification factor laser etching processes naturally gives rise to conical orifices [19]. The surfaces of these holes were treated to increase the hydrophobicity.

In-plane emitter tips in which the tips are embedded at the end of the microchannel at the edge of the chip devices have been heralded mainly by recent advances in microfabrication technology by which low cost disposable chips are now close to reality. The smaller dimensions of these emitter tip devices were observed to produce more stable electrosprays over longer times. These emitter tip devices consist of an open capillary slot, connected at one end of

the chip to a reservoir, which tapers in diameter at the emitting end to form a nib-like structure resembling that of a calligraphic pen, as illustrated in Fig. 7 [21]. This tapered tip is intentionally designed to minimize liquid spreading and to reduce the characteristic orifice length scale and hence the critical voltage required, as stipulated by Eq. (2). In this design, a platinum wire is inserted into the nib to establish the electrical connectivity and sample delivery was achieved using capillary infusion. A drawback of this design, however, is that a large reservoir is required due to evaporation from the open channel. A star-shaped chip device containing eight arms, each with a similar open channel and tip for sequential analysis via rotation of the chip has been built [22]. Other tip designs, e. g., groove structures, triangular tips, point tips and enclosed SU-8 tips have also been proposed. To reduce contamination, the insertion of a triangular parylene sheet between a bottom substrate and a top substrate incorporating the channel and tip has been suggested to confine the liquid at the outlet.

Future Directions for Research

Although a commercially on-chip device for ESI-MS is now available, there still remains several design problems related to enhancing electrospray stability, ionization efficiency, detection sensitivity, separation efficiency, speed, accuracy and spectra quality that need to be addressed. In addition, efforts need to be concentrated to minimize and eliminate sample loss and cross-contamination. Despite significant progress, there is still some way to go before a robust, optimized, cost-effective, high-throughput microdevice providing flexibility for coupling to different MS configurations can be realized. Whilst the high duty cycle of MALDI-MS enables large number of samples deposited on a single target plate, high throughput can only be achieved on chip based ESI-MS devices through the use of multiple channels or emitter tip arrays (see previous section), which themselves are limited by the allotted chip substrate area. The use of high voltage DC electric fields is also a critical safety issue for portable field deployment of miniaturized consumer devices. A possibility around this is to explore the feasibility of employing high frequency AC electric fields [4, 5].

Perhaps the main challenge, however, is the sequential or simultaneous handling of multiple streams (multiplexing) and the integration of multistep processes to allow analyte separation and detection onto a single microchip device [23]. Miniaturization and integration of the mass spectrometer onto the microchip is one goal; some advances have been achieved in scaling down ion trap and quadrupole mass analyzers although the complexity of the tandem mass spectrometer poses a significant challenge for its reduction to a chip-based system. The other goal is upstream miniaturization and complete integration of various other processes such as flow-through sampling, and, sample preparation and enrichment. Such a total analysis microsystem would require complete compatibility and connectivity between the various microfluidic components.

Cross References

- ▶ Interfacial Electrokinetic Flow
- ▶ Lab-on-Chip Devices for Chemical Analysis
- ▶ Lab-on-Chip Devices for Protein Analysis
- ▶ Mass Spectrometry
- ▶ Mass Spectrometry on-Chip Devices

References

1. Fenn JB, Mann M, Meng CK, Wong SF, Whitehouse CM (1989) Electrospray ionization for mass spectrometry of large biomolecules. Science 246:64–71
2. Gaskell SJ (1997) Electrospray: Principles and practice. J Mass Spectrom 32:677–688
3. Grace JM, Marijnissen JCM (1994) A review of liquid atomization by electrical means. J Aerosol Sci 25:1005–1019
4. Yeo LY, Lastochkin D, Wang S-C, Chang H-C (2004) A new ac electrospray mechanism by Maxwell-Wagner polarization and capillary resonance. Phys Rev Lett 92:133902
5. Yeo LY, Gagnon Z, Chang H-C (2005) AC electrospray biomaterials synthesis. Biomaterials 26:6122–6128
6. Yeo LY, Chang H-C (2006) High frequency AC electrosprays: Mechanisms and applications. Advances in Fluid Mechanics VI, Skiathos, Greece. WIT Press, Southampton
7. Stone HA, Lister JR, Brenner MP (1999) Drops with conical ends in electric and magnetic fields. Proc R Soc Lond A 455:329–347
8. Thomson BA, Iribarne JV (1979) Field induced ion evaporation from liquid surfaces at atmospheric pressure. J Chem Phys 71:4451–4463
9. Schultz GA, Corso TN, Prosse SJ, Zhang S (2000) A fully integrated monolithic microchip electrospray device for mass spectrometry. Anal Chem 72:4058–4063
10. Licklider L, Wang X-Q, Desai A, Tai Y-C, Lee TD (2000) A micromachined chip-based electrospray source for mass spectrometry. Anal Chem 72:367–375
11. Ramsey RS, Ramsey JM (1997) Generating electrospray from microchip devices using electroosmotic pumping. Anal Chem 69:1174–1178
12. Xue Q, Foret F, Dunayevskiy YM, Zavracky PM, McGruer NE, Karger BL (1997) Multichannel microchip electrospray mass spectrometry. Anal Chem 69:426–430
13. Sung W-C, Makamba H, Chen S-H (2005) Chip-based microfluidic devices coupled with electrospray ionization-mass spectrometry. Electrophoresis 26:1783–1791
14. Wang Y-X, Cooper JW, Lee CS, DeVoe DL (2004) Efficient electrospray ionization from polymer microchannels using integrated hydrophobic membranes. Lab Chip 4:363–367

15. Zhang B, Liu H, Karger BL, Foret F (1999) Microfabricated devices for capillary electrophoresis–electrospray mass spectrometry. Anal Chem 71:3258–3264
16. Meng Z, Qi S, Soper SA, Limbach PA (2001) Interfacing a polymer-based micromachined device to a nanoelectrospray ionization Fourier transform ion cyclotron resonance mass spectrometer. Anal Chem 73:1286–1291
17. Zhang B, Foret F, Karger BL (2000) A microdevice with integrated liquid junction for facile peptide and protein analysis by capillary electrophoresis/electrospray mass spectrometry. Anal Chem 72:1015–1022
18. Wang P, Chen Z, Chang H-C (2006) A new electro-osmotic pump based on silica monoliths. Sens Actuat B 113:500–509
19. Tang K, Lin Y, Matson DW, Kim T, Smith RD (2001) Generation of multiple electrosprays using microfabricated emitter arrays for improved mass spectrometric sensitivity. Anal Chem 73:1658–1663
20. Lazar IM, Ramsey RS, Sundberg S, Ramsey JM (1999) Subattomole-sensitivity microchip nanoelectrospray source with time-of-flight mass spectrometry detection. Anal Chem 71:3627–3631
21. Arscott S, Le Gac S, Druon C, Tabourier P, Rolando C (2004) A planar on-chip micro-nib interface for NanoESI-MS microfluidic applications. J Micromech Microeng 14:310–316
22. Yuan C-H, Shiea J (2001) Sequential electrospray analysis using sharp-tip channels fabricated on plastic chip. Anal Chem 73:1080–1083
23. Oleschuk RD, Jed Harrison D (2000) Analytical devices for mass spectrometry. Trends in Anal Chem 19:379–388

On-Chip Free-Flow Magnetophoresis

► Magnetophoresis

On-Chip Laboratory

► Lab-on-a-Chip Devices for Chemical Analysis

On Chip Light Confiners

► On Chip Waveguides

On Chip Light Guiding

► On Chip Waveguides

On Chip Light Propagator

► On Chip Waveguides

On-Chip Micro-Optical Detection

Holger Schmidt
University of California, Santa Cruz, CA, USA
hschmidt@soe.ucsc.edu

Synonyms

On-chip detection

Definition

On-chip micro-optical detection describes the collection of optical signals created in a micro- or nanofluidic device on the same chip. The wavelengths of the optical signals to be detected are typically in the visible or near-infrared part of the spectrum ranging from 0.4 to 2 μm. This sets the length scale for the detection elements and results in the use of micro-optical methods for on-chip detection. The detection process is an integral part of a fully integrated Lab-on-a-Chip and has to be optimized in the context of the entire chip. In this chapter, we will survey the most common approaches to on-chip micro-optical detection in the context of the complete integrated microfluidic system.

Overview

A large number of microfluidic devices with applications in analytical chemistry, biology, and biomedicine rely at least in part on optical methods for sample analysis. At the same time, the overarching goal for building microfluidic systems is to create miniaturized, portable, and self-contained Labs-on-a-Chip that perform all desired functions in as small a volume as possible. If optical analysis is to be part of the fluidic system, all optical components should be miniaturized as well. This situation is schematically depicted in Fig. 1a that shows the components of a Lab-on-a-Chip with focus on the optical parts. In general terms, light has to be brought in contact with liquid sample material. To this end, the outputs of light and fluid sources are guided via optical waveguides and fluidic channels, respectively, to an interaction region denoted by "I" where the sample analyte creates a characteristic optical signal, typically fluorescence, scattering, or absorption. This optical signal needs to be recorded by the detector, and to this end may pass additional functional optical elements such as filters, beam splitters, or gratings. Fig. 1b shows a recent example for an optofluidic chip that incorporates all these elements in a single device, resulting in almost complete integration [1]. In the remainder of this article, we will first give a brief overview of the optical components preceding the detector stage before focusing on proposed and cur-

rently implemented solutions for incorporating the detector with the microfluidic system to create a true optofluidic Lab-on-a-Chip.

Basic Methodology

Integrated Light Source

Due to the generally small amount of sample volume, optical analysis methods in microfluidic systems require only moderate to low amounts of optical power in the range from microwatts to milliwatts. These power levels can easily be achieved by incoherent sources such as light emitting diodes (LEDs). Coherent radiation as produced by a laser has, however, numerous advantages such as high spectral purity and long coherence lengths so that most studies are carried out with laser sources. The main challenge has been that the electronic properties of silicon cause it to be an extremely poor light emitter and preclude the realization of an electrically pumped laser built on a pure silicon platform. There are several ways around this limitation. Either a more efficient semiconductor material, typically alloys from III-V systems such as GaAs or InP or organic dyes that emit light in the desired wavelength range are used. Dye lasers have the advantage that they do not require a silicon-based substrate and that advanced laser structures such as single wavelength distributed feedback (DFB) lasers can be built [1, 2]. Current limitations to this technology include the need for an off-chip optical pump source for exciting the dye molecules and the additional fluidic infrastructure required to control the laser dye.

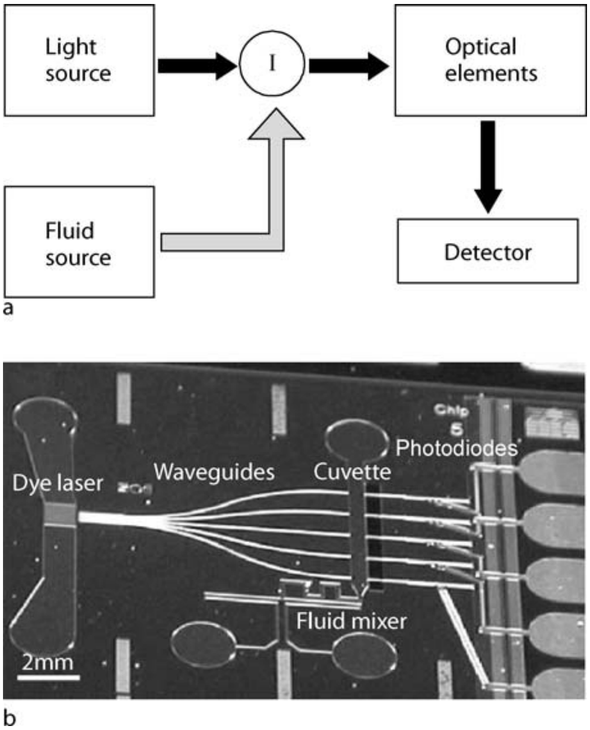

On-Chip Micro-Optical Detection, Figure 1 (**a**) Schematic layout of optical components in a fully integrated Lab-on-a-Chip (I: interaction region of light with fluidic sample material). (**b**) Photograph of state-of-the-art optofluidic chip with on-chip micro-optical detection (after [1])

Optofluidic Architectures

Once light is generated at the source location on the chip it needs to be guided to the interaction volume to excite the particles of interest. This light transport occurs in optical waveguides and leads to two fundamentally different approaches to the optofluidic device architecture. Light can be guided using conventional index guiding based on total internal reflection from the material surrounding the waveguide core. In this case, it interacts with the fluid either via the evanescent component of the light field that extends into the liquid surrounding the waveguide, or the waveguides are intersected by the fluidic channels and light is recollected after passing the liquid. This approach is represented in Fig. 2a which shows a layered optofluidic device in which microfluidic controls, microfluidic channels, and optical structures (sources, waveguides, sensors) are vertically separated from each other [3]. This architecture is particularly suited for hybrid material approaches where the optical layer is made of different materials (e. g. silicon based) than the fluidic layers (e. g. polymer based). In the second approach, both light and liquids are guided through the same physical fluidic channels. This appears difficult to achieve at first because the low refractive index of typical analyte liquids (around 1.3 to 1.4) precludes the use of conventional index guiding as used in silica fibers. In the context of chip-based integration, two methods to solve this problem have recently been developed. Liquid-core/liquid-cladding (L^2) waveguides are based on flowing two non-mixing liquids through the same channel. If the index of the innermost liquid is higher than that of the cladding liquid, regular index guiding is possible over millimeters of length [4] and additional functionalities such as optical switching can be added. Alternatively, light can be confined in the low-index liquid using dielectric multilayer confinement based on the antiresonant reflecting optical waveguide (ARROW) principle. In this case, light that is refracted out of the liquid is efficiently reflected back into the core by several layers of dielectric materials of appropriate thickness, typically silicon nitride (SiN) and oxide (SiO_2). This principle has been implemented on silicon platforms using wafer bonding for channels with $\sim$150 μm diameter [5], and monolithic fabrication for channels with

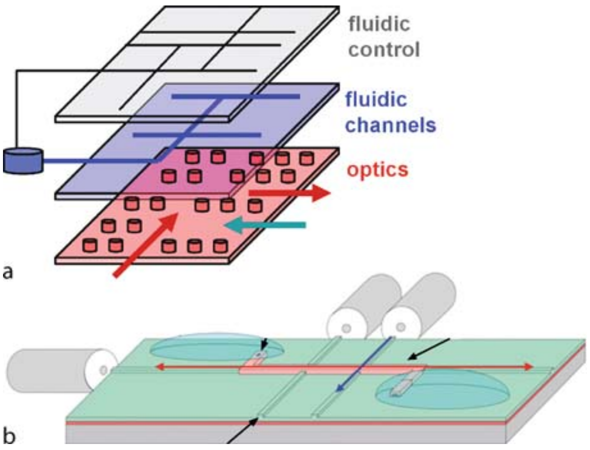

On-Chip Micro-Optical Detection, Figure 2 (**a**) Three-layer architecture of optofluidic chip with separate fluidic and optical layers (after [3]). (**b**) Planar optofluidic architecture with integrated liquid-core ARROW waveguides (after [7]). Fluid and light (indicated by arrows) are guided through the central channel connecting fluidic reservoirs. Solid-core waveguides interface to the edges of the chip

5 – 15 μm diameter [6]. It has also been shown that the latter approach can be extended to designing 2D networks of hollow and solid core waveguides that allow for fully planar optical beam geometries as the light can be coupled in and out of the fluidic channels in different locations [7]. This scheme is shown schematically in Fig. 2b.

Integrated Optical Elements

When considering the on-chip optical detection process in a microfluidic device, it is not sufficient to consider the detector region alone. Most optical detection methods, in particular the most popular fluorescence detection schemes, require isolation of a weak generated signal from a much stronger excitation beam. In bulk systems, this separation is accomplished in the wavelength domain because the exciting and generated signals have different wavelengths. The most common wavelength selective optical elements are spectrometers, dichroic mirrors, and bandpass interference filters. If efficient on-chip detection is to occur, these elements need to be transferred to the optofluidic chip or alternative solutions need to be found.

The most versatile and sophisticated wavelength selective element is a spectrometer, and substantial efforts to develop integrated microspectrometers on a chip have been made [8]. A key figure of merit for the performance of a spectrometer is the spectral resolution $R = \lambda/\Delta\lambda$ which is defined as the ratio of wavelength λ and the 3 dB power bandwidth $\Delta\lambda$. High-performance grating spectrometers can reach spectral resolutions up to 10^6. Spectrometers work by spatially separating different wavelengths via the combination of a dispersive element and subsequent propagation. Several approaches have been taken to implement this concept on a chip. These include metal gratings and Fabry–Perot resonators as dispersive elements. Fabrication is done with MEMS-based silicon bulk micromachining which can cause compatibility problems for an optofluidic chip. All of these approaches suffer from the short separation path length on a small chip and no spectral resolutions higher than $R \sim 15$ have been achieved [8].

Perhaps a more promising approach for pre-detection signal conditioning is to emulate an interference filter on a chip. These filters are used to pass only fluorescence signals over a few to tens of nanometers while rejecting the excitation spectrum. Interference filters are characterized by the ratio of transmitted power at the excitation and detection wavelengths which is typically on the order of 10^5. It has been shown that the ARROW waveguide based optofluidic platform discussed above can be used as an interference filter [7]. The waveguiding efficiency of these structures depends both on wavelength and thickness of the dielectric cladding layers. If properly designed, the hollow channels in Fig. 2b can be designed to guide light efficiently at the detection wavelength while being extremely lossy at the excitation wavelength. This principle allows for implementation of the filter function without adding additional fabrication steps or chip area. Narrowband wavelength transmission and subsequent separation can also be achieved with interference based integrated elements including microrings or Mach–Zehnder interferometers. There, the challenges lie mainly in minimizing optical losses that occur in curved structures.

Finally, an entirely different, filterless approach can be taken. In this case, the entire optical signal reaches the detector. Its wavelength dependence is recovered by applying different control voltages to the photodetector that result in different detection depths of the detector material [9]. The spectrum can then be reconstructed because the penetration of the optical signal into the detector is wavelength dependent. This approach has been implemented using standard 5 μm CMOS technology and was verified using DNA solution with SYBR-Green labeling. It may have limited use when a large dynamic range is required, i. e. when the excitation and generated signal differ strongly in intensity as is the case when low concentrations of analyte are to be detected.

Integrated Micro-Optical Detection

The optical detection process consists of turning light into an electrical signal that can be recorded, amplified, and stored for further processing and analysis. This signal con-

version is carried out via the photoelectric effect in which photons generate mobile charge carriers, i. e. an electrical current. In bulk detection systems, this can be done using photomultiplier tubes (PMTs) or semiconductor photodetectors. In a PMT, the photons impinge on a metal cathode to release electrons that are subsequently amplified in a high voltage cascade. In a photodiode, light incident on a semiconductor transfers electrons to a different electronic state, creating both a positive (hole) and negative (electron) charge in the process that can contribute to electrical current. If this generation process occurs inside or in the vicinity of a p/n-junction – semiconductor regions that have mostly free holes/electrons, respectively – the generated electrons and holes are separated in an applied electric field and can be detected as a photocurrent. Both photodiodes and PMTs can be extremely sensitive and reach the single photon detection limit. Semiconductor detectors with this sensitivity are called avalanche photodetectors (APDs) that include an amplification process similar to PMTs after creation of the initial electron-hole pairs.

Semiconductor photodiodes are the natural choice for building an optofluidic device with integrated on-chip detection. The immediate consequence is that the chip has to be either entirely semiconductor based or be a hybrid system with soft material fluidic components and a solid-state detection layer as shown in Fig. 2a. The detectable wavelength range is determined by the semiconductor material properties. Silicon absorbs light with wavelengths shorter than 1.1 µm and is therefore a good choice for detection in the visible and near-infrared. Longer wavelengths, in particular 1.55 µm, can be reached using different absorbing layers such as InGaAs.

The main challenges for an on-chip detection system are to guide the light to the active detector area, couple as much light as possible into the detector, and find a system fabrication process that is compatible with producing the required photosensitive p/n junctions.

Figure 3 shows different approaches that have been taken to create the optical signal in on-chip semiconductor photodiodes. Common to all of these is the principle of coupling light from the waveguides (these could be any of the types discussed above) into a detector region that consists of different materials. All of these methods were first demonstrated in solid-state integrated optical devices without fluidic components. Fig. 3a shows lateral coupling, which is perhaps the most intuitive approach as the optical signal symbolized by the black arrows remains in the same plane during the coupling process. This concept was implemented using SiON waveguides and laterally structured p-i-n photodiodes yielding light coupling efficiencies on the order of 85% [10].

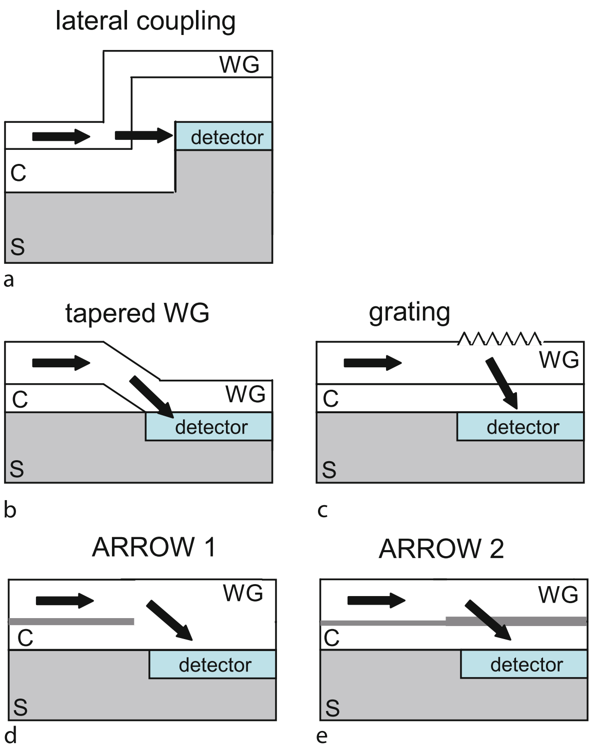

On-Chip Micro-Optical Detection, Figure 3 Overview of different approaches to on-chip micro-optical detection (details see text, WG: waveguide, C: cladding)

All other methods shown in Fig. 3 utilize vertical coupling and require a way to efficiently scatter light from the waveguide into an underlying photodiode. This scattering process is cumulative and the coupling efficiency increases with the length of the detector region. In Fig. 3b, the waveguide cladding is gradually tapered until being completely absent over the detector region. Without the cladding, the waveguide becomes leaky and light is scattered into the bottom detector. In Fig. 3c, the scattering process is accomplished by a surface grating, otherwise the principle is similar to Fig. 3b. Figs. 3d and 3e are examples for variations of the ARROW waveguiding principle described earlier to accomplish efficient coupling. In Fig. 3d, the thin gray dielectric layer that ensures light confinement in the guiding region is removed over the detector and the waveguide becomes leaky. Radiation is lost quickly through the bottom interface and collected by the detector. In Fig. 3e, the thickness of the ARROW confinement layer is altered above the detector. As mentioned earlier, the ARROW guiding effect depends on the layer thickness and can vary from being highly reflective (waveguiding) to highly transmissive (leaky).

The coupling efficiencies κ of approaches 3b, 3d, and 3e can be expressed analytically as

$$\kappa = 2.17\left(\frac{\lambda}{d_C}\right)^3\left[n_C\sqrt{n_S^2 - n_C^2}\right]^{-0.5}$$

[dB · λ/m] (tapered waveguide, Fig. 3b)

$$\kappa = 0.643\left(\frac{\lambda}{d_C}\right)^3\left[n_C\sqrt{n_S^2 - n_C^2}\right]^{-0.5}$$

[dB · λ/m] (ARROW 1, Fig. 3d)

$$\kappa = 0.879\left(\frac{\lambda}{d_C}\right)^3\left[n_C\sqrt{n_S^2 - n_C^2}\right]^{-0.5}$$

[dB · λ/m] (ARROW 2, Fig. 3e),

where λ is the optical wavelength, d_C is the effective waveguide core thickness, and n_C and n_S are the refractive indices of the core and substrate layers, respectively.

Typical values for the radiation loss for all three structures are in the range of 10 dB/cm for a 5 μm thick waveguide (index 1.46) coupled to silicon (index 3.85) and several hundreds dB/cm for a 1 μm thick core. It should be emphasized that the coupling efficiency can be substantially increased by adding an antireflection layer on top of the detector that ensures efficient transmission of the scattered light into the high index silicon detection region. Experimentally, coupling efficiencies of 85% within a detector length of only 300 μm have been observed [11].

Key Research Findings

The recent development of a Lab-on-a-Chip with integrated optical detection described by Balslev et al. illustrates the combination of the individual optical and fluidic components described in the previous sections and represents the state of the art for on-chip micro-optical detection in a larger fluidic system [1]. An image of the fluidic device was already presented in Fig. 1b. It is built on a p-type silicon substrate which also contains the electrical detection layer (photodiode). Light is guided in SU-8 waveguides surrounded by SiO_2 and PMMA resist cladding layers. Sealing of the channels is provided by a borofloat glass layer on top. The device also contains a fluidic dye laser with external optical pumping, and a fluid mixer. The sample analyte is contained in a cuvette that is horizontally intersected by the SU-8 waveguides. Coupling to the photodetector is accomplished by removing the SiO_2 layer above the detector, corresponding to the tapered waveguide configuration of Fig. 3b. The photodiodes are 50 μm wide and 2 mm long and optimized for detection at 600 nm with a 1 μm deep p/n junction. They exhibit good detection characteristics with a noise equivalent power (NEP) of 7×10^{-13} W (10 Hz bandwidth) and a sensitivity of 0.39 A/W at 580 nm. The device was used for an absorption measurement on xylenol orange dye, and sensitivity to different dye concentrations was demonstrated qualitatively. Note that due to the lack of a wavelength sensitive optical element, fluorescence detection is not feasible on this chip. Such an element could be added using the techniques discussed above, e. g. a microring or Mach–Zehnder interferometer section. Also, up to now no avalanche photodiodes have been integrated on a chip. These would be required for detection on the single molecule level. This work shows that while a fully integrated optofluidic Lab-on-a-Chip has not become reality yet, this goal is now within reach. In particular, the addition of on-chip micro-optical detection represents a key step along this way.

Future Directions for Research

The large payoff for developing completely self-contained micro- or optofluidic Labs-on-a-Chip will continue to drive future research on the optical components of the system, and new developments are bound to occur in all aspects. Integration of both the light source and detector on the chip will represent major breakthroughs along this road. Research on sources will focus on electrically pumped emitters that eliminate the need for off-chip optical pumps. Electrically pumped fluidic DFB lasers, silicon lasers or bonded light emitting diodes are all candidates for suitable sources. Fully planar optical approaches based on ARROW waveguides also hold a lot of promise as single molecule detection sensitivity on a chip has already been demonstrated [6], and the concept can be extended to adding wavelength filtering and efficient detector coupling with little additional effort. Future developments in the area of on-chip micro-optical detection will likely occur in incorporating ultrasensitive avalanche photodetectors (APD) and the required circuitry on the chip [12]. This requires the use of solid-state-only or hybrid silicon-plastic chip architectures and will allow for single molecule sensitivity on a fully self-contained chip. It was discussed that for most applications – in particular fluorescence detection and Raman spectroscopy – additional optical elements such as filters with high extinction ratio must be integrated on the chip along with the detector element itself to produce a useful signal. Finally, more developments on the back-end of the detection process in the areas of on-chip signal processing and data analysis using elaborate CMOS-based circuitry can be expected.

Cross References

- ► Detection using Confocal Microscopy
- ► Fluorescence Measurements
- ► Lab-on-a-Chip (General Philosophy)

► On-Chip Waveguide
► Optofluidics – Applications

References

1. Balslev S, Jorgensen AM, Bilenberg B, Morgensen KB, Snakenborg D, Geschke O, Kutter JP, Kristensen A (2006) Lab-on-a-chip with integrated optical transducers. Lab Chip 6:213–217
2. Li ZY, Zhang ZY, Emery T, Scherer A, Psaltis D (2006) Single mode optofluidic distributed feedback dye laser. Opt Express 14:696–701
3. Psaltis D, Quake SR, Yang C (2006) Developing optofluidic technology through the fusion of microfluidics and optics. Nature 442:381–386
4. Wolfe DB et al (2004) Dynamic control of liquid-core/liquid-cladding optical waveguides. PNAS 34:12434–12438
5. Campopiano S, Bernini R, Zeni L, Sarro PM (2004) Microfluidic sensor based on integrated optical hollow waveguide. Opt Lett 29:1894–1896
6. Yin D, Barber JP, Deamer DW, Hawkins AR, Schmidt H (2006) Single molecule sensitivity using planar integrated optics on a chip. Opt Lett 31:2136–2138
7. Schmidt H, Yin D, Barber JP, Hawkins AR (2005) Hollow-core waveguides and 2D waveguide arrays for integrated optics of gases and liquids. IEEE J Selected Top Quantum Elect 11:519–527
8. Wolfenbuttel RF (2004) State-of-the-art in integrated optical microspectrometers. IEEE Trans Inst Meas 53:197–202
9. Maruyama Y, Sawada K, Takao H, Ishida M (2006) A novel filterless fluorescence detection sensor for DNA analysis. IEEE Trans Elect Dev 53:553–558
10. Wunderlich S, Schmidt JP, Muller J (1992) Integration of SiON waveguides and photodiodes on silicon substrates. Appl Opt 31(21):4186–4189
11. Baba T, Kokubun Y (1990) High efficiency light coupling from antiresonant reflecting optical waveguide to integrated photodetector using an antireflective layer. Appl Opt 29(18):2781–2792
12. Niclass C, Rochas A, Besse PA, Popovic R, Charbon E (2006) A 4μs integration time imager based on CMOS single photon avalanche diode technology. Sens Actuators A 130–131:273–281

On Chip Waveguides

Ian Papautsky, Andrea Pais
Department of Electrical and Computer Engineering,
University of Cincinnati, Cincinnati, OH, USA
Ian.Papautsky@uc.edu

Synonyms

Integrated waveguides; Buried channel waveguides; On chip light guiding; On chip light propagator; Integrated light guiding; Integrated light propagator; Integrated light confiners; On chip light confiners

Definition

An *optical waveguide* is a structure that guides light waves. It traditionally consists of an inner core layer, a dielectric material with high permittivity and thus high refractive index, and an outer cladding layer, a material with lower refractive index than the core. Such a structure guides optical waves by total internal reflection. Waveguides that are integrated with microfluidic/Lab-on-a-Chip devices for the purpose of delivering excitation light and/or transmitting signal light to a detector are called *on-chip waveguides*.

Overview

A critical component for almost any miniaturized analytical device is perhaps the detection system. Among the possible detection methods and principles, optical detection is the most common in modern bio/chemical analysis. In particular, fluorescence is the most frequently used optical detection method in microfluidic systems. Fluorescence occurs when a fluorophore or quantum dot relaxes to its ground state after being excited. In biotechnology applications, for example, fluorophores or quantum dots can be used to label antibodies which tag molecules of interest in order to visualize their presence. Traditionally, this approach includes bulk optical equipment such as light sources, lenses, and microscope objectives, and requires precise mechanical alignment.

Waveguides can be integrated on-chip with microfluidic systems to improve optical detection. The general advantages of integrating waveguides on-chip are that microfluidic channels and optical elements can be aligned during fabrication, and that very compact devices can be created when light sources and detectors are integrated on-chip.

Waveguide Fundamentals

The key principle behind the waveguiding function of an optical waveguide is the phenomenon of *total internal reflection* [1, 2]. A light wave incident on an interface between two materials will refract and reflect, as schematically shown in Fig 1. Such behavior is described by Snell's law:

$$n_1 \sin\theta_1 = n_2 \sin\theta_2 \quad (1)$$

where θ are input and output angles with respect to the normal plane, and n are refractive indices of the two materials. Refractive index is a material property, defined by the ratio between the velocities of light traveling in vacuum and in the material. The refractive index of a solid material, a liquid, or a gas would thus be always greater than 1. Different

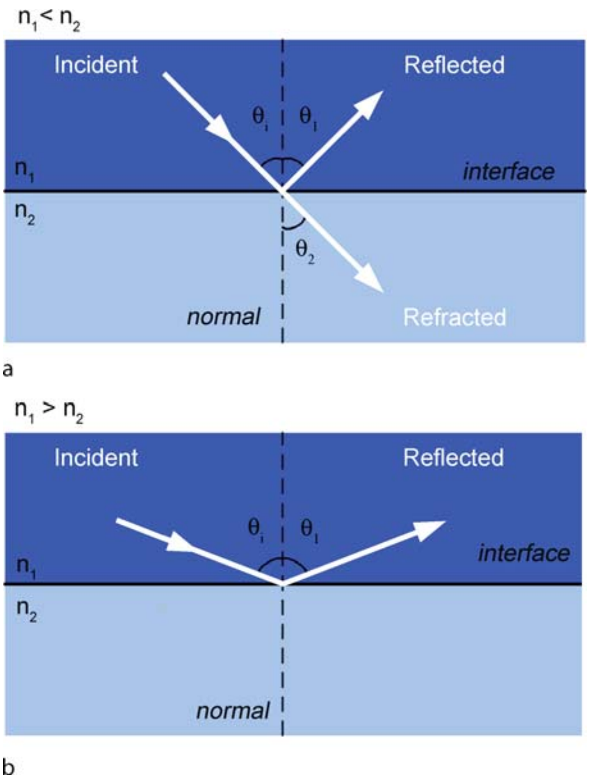

On Chip Waveguides, Figure 1 Behavior of a light wave incident on an interface with (**a**) $n_1 < n_2$ and (**b**) $n_1 > n_2$.

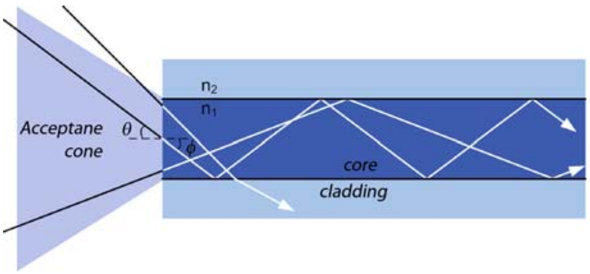

On Chip Waveguides, Figure 2 Total internal reflection of light in a waveguide ($n_1 > n_2$). Light entering the waveguide core within the acceptance cone is guided, while light entering at a steep angle results in coupling losses

wavelengths of light travel at different speeds through the same material, thus index of refraction of a given material is dependant on the wavelength.

Eq. 1 offers insight into the properties of optical waveguides. When the reflected angle equals 90° (i. e., $\theta_2 = \frac{\pi}{2}$), $\sin\theta_2 = 1$, and Snell's law can be rewritten as:

$$\sin\theta_1 = \frac{n_2}{n_1} \qquad (2)$$

Since the sin of a non-imaginary angle can never be greater than 1, the incidence medium must have a greater index of refraction than the transmission medium (i. e., $n_1 > n_2$) and

$$\theta_1 = \sin^{-1}\left(\frac{n_2}{n_1}\right) \qquad (3)$$

At this incidence angle, there is no longer any light transmitted though the interface and the output light would travel along the interface boundary itself. However, if the medium of incidence has a lower refractive index than the transmission medium (i. e., $n_2 > n_1$), there is refraction (external reflection). In other words, *total internal reflection* occurs when $n_1 > n_2$.

For waveguiding, the index of refraction of the core material must be grater than the index of refraction of the cladding material (Fig. 2) [1, 2]. Total internal reflection confines light in the optical waveguide core. The angle in Eq. 3 is called the angle of total internal reflection or the interface's *critical angle*. For visible light traveling from glass into air (or vacuum), the critical angle is approximately 41.5°. The critical angle for diamond is about 24.4°, which means that light is much more likely to be internally reflected within a diamond (diamonds for jewelry are cut to take advantage of this, achieving high total reflection of entering light).

A light beam propagating in waveguide core (internally) reflects off the core-cladding interface at an angle greater than the critical angle. A nearfield standing wave (called *evanescent wave*) propagates along the boundary and decays exponentially with increasing distance from the interface. Thus, as light is conducted along an on-chip waveguide, the transverse energy field extends past the waveguide core boundaries into the surrounding cladding layer.

Critical angle at the core-cladding interface at the front surface of a waveguide is the *acceptance angle*. If angle of the input light is larger than the acceptance angle, the incident light will not be totally internally reflected and will enter the cladding, causing losses (termed *coupling losses*). If the angle of the incident light is less than the acceptance angle, the light is guided.

The condition for total internal reflection at the core-cladding interface (Fig. 2) is given by:

$$n_1 \sin\left(\frac{\pi}{2} - \phi\right) \geq n_2 \qquad (4)$$

Since the angle ϕ is related to the incident angle θ by equation

$$\sin\theta = n_1 \sin\phi \leq \sqrt{n_1^2 - n_2^2} \qquad (5)$$

critical condition for total internal reflection is that:

$$\theta \leq \sin^{-1}\left(\sqrt{n_1^2 - n_2^2}\right) \equiv \theta_{\max} \quad (6)$$

where $\theta_{\max}$ denotes the maximum light acceptance angle of the waveguide and is known as the numerical aperture (NA). The acceptance angle can then be approximated by

$$\theta_{\max} \approx \sqrt{n_1^2 - n_2^2} \quad (7)$$

A typical refractive index difference between the core and cladding is on the order of 0.01 or greater.

Depending on the various possible patters of propagating or standing electromagnetic fields, optical waveguides are either *single-mode* or *multi-mode* [1, 2]. Each mode is characterized by its frequency, effective refractive index, polarization, power distribution, electric field strength, and magnetic field strength. A single mode waveguide has a narrow core, typically less than 20 μm in critical dimension. As its name suggests, it has only one mode of transmission. Single mode waveguides carry higher bandwidth than multi mode waveguides but require a light source with a narrow spectral width. Using a small core and single light-wave reduces signal attenuation and distortions from overlapping light pulses and increases transmission speeds. A multi mode waveguide has a core at least 50 μm in critical dimension (100 μm is typical). Since it has higher numerical aperture, it can support more than one propagation mode. Light waves are dispersed into numerous paths, or modes, as they travel through the waveguide's core.

In optical communications, long-distance transmissions are accomplished over cylindrical dielectric waveguides (optical fibers). For on-chip integration with planar microfluidic devices, *planar optical waveguides* in the form of films or strips are required. Planar waveguides confine light in one dimension and propagate it in any direction parallel to the surface. Such waveguides can be produced by simply depositing a thin film with a higher refractive index than the substrate, trapping light inside this film.

The boundary between the waveguide core and cladding may either be abrupt or gradual. Waveguides where the refractive index changes sharply or in discrete steps are called *step-index (SI)* optical waveguides, whereas those with a gradual transition in the refractive index are called *graded-index (GI)* optical waveguides. Figure 3a shows a typical three-layer SI planar waveguide formed by depositing a think layer of material with a higher refractive index on a substrate with a lower index. The third layer is

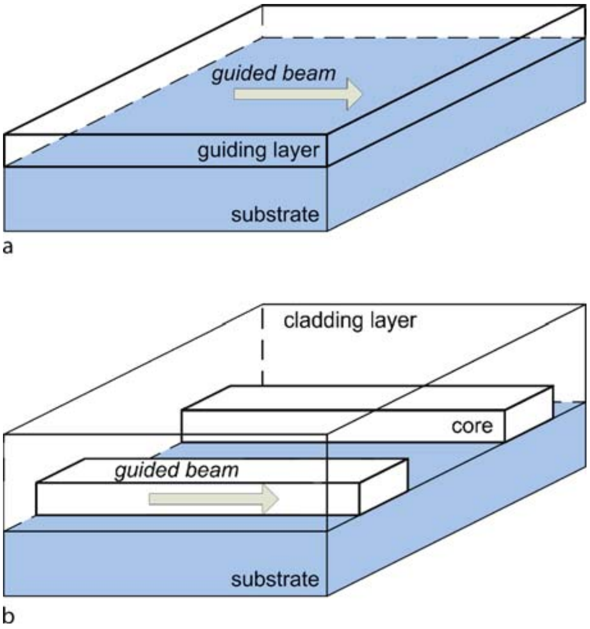

On Chip Waveguides, Figure 3 Structures of (**a**) planar and (**b**) channel waveguides

either air or an additional lower-index cladding layer. Planar waveguides trap light in the direction of the film thickness, but allow light to spread in horizontally. To facilitate integration with microfluidic devices, 3D optical waveguides (or optical channel waveguides, Fig. 3b) that trap light in both vertical and transverse directions have been fabricated. Although waveguides come in various forms and with a variety of functions, optical waveguides that are uniform in the direction of propagation are the most basic type. Thus, the following discussion will be limited to optical waveguides in which material properties do not change in the direction of propagation.

Transmission Losses in Waveguides

Transmission loss (or attenuation) is an important characteristic of a waveguide. To measure *attenuation*, a cut back test is performed [1, 2]. Laser light is coupled into one end of a waveguide, and the other end is cut flat (e. g., with a razor blade) to allow light to exit directly to the photodetector. The waveguide length is progressively reduced (cut) and for each time the corresponding light intensity measurements are taken. Attenuation is then calculated as:

$$A = -10 \log\left(\frac{P_{\text{out}}}{P_{\text{in}}}\right) \quad (8)$$

where A is the attenuation in dB, P_{in} is the power injected into the waveguide, and P_{out} is the power measured by the

photodetector. Attenuation level of 3 dB means roughly half the power (P_{out}/P_{in} approximately equal to a ratio of 1/1.995).

One of the main causes of attenuation is absorption of energy (or photons). Absorption is caused by atomic defects which result when the waveguide is exposed to radiation, *extrinsic* absorption by impurity atoms, and *intrinsic* absorption by constituent atoms of the material [1, 2]. The dominant mechanism is extrinsic absorption, primarily by metallic ions (iron, cobalt, etc.) and OH^- ions. In early glass optic fibers, transmission distance was primarily limited by absorption by OH^- ions. These ions were introduced in the material from the presence of water or water vapor during the manufacture process. Attenuation caused by this ion is greatest at 1400 nm, 950 nm, and 725 nm, leaving *windows* for transmission between these wavelengths. Today, the vapor phase axial deposition (VAD) manufacturing method tremendously reduces the OH^- concentration in fibers. However, for waveguides microfabricated on-chip, high OH^- content can still be problematic.

Losses in modern glass optic fibers are caused by ultraviolet absorption, infrared absorption, and scattering [1, 2]. The scattering losses, modeled by Rayleigh scattering, are caused by the interaction of the light wave with the constituent molecules which are on the order of the light wavelength. Rayleigh scattering loss is $1/\lambda^4$, so it can be reduced by increasing the wavelength. On the other hand, infrared absorption losses tend to increase with λ, and are usually the greatest at wavelengths above 1.5 μm.

Imperfections in the surface of the waveguide can also cause losses. Imperfections with dimensions of several wavelengths cause perturbation in the field, leading to coupling to higher order modes which do not have the desired transmission characteristics, and also causes power loss. Losses in modern commercial optic fibers can be kept down to as little as 0.01 dB/km, but for microfabricated waveguides losses in the order of 1 – 10 dB/cm for polymer and 0.1 – 1 dB/cm for glass cores are more common.

Basic Methodology

Overview

Generally, the motivation for integration of waveguides in microfluidic devices is to improve the detection, either by focusing the light in the channel to increase the excitation power for fluorescence measurements or by increasing the optical path length for absorbance detection. Further advantages are that optical and fluidic elements can be aligned during fabrication, reducing the number of interfaces and minimizing coupling losses, and that array of elements for multi-point/multi-analyte detection can be easily produced. In addition, on-chip waveguides can enable very compact devices when integrated with light sources and photodetectors.

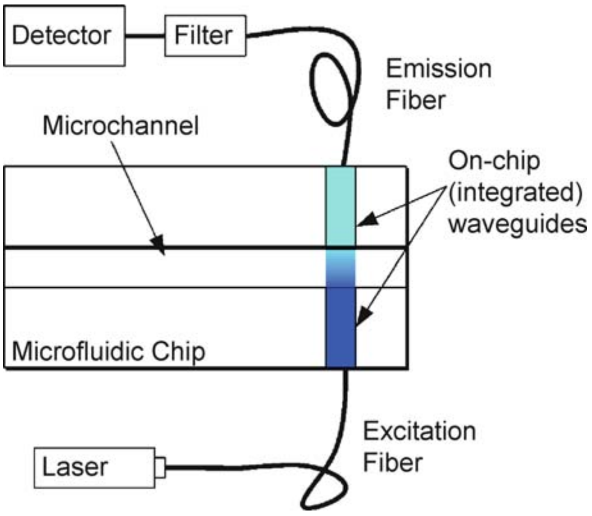

On Chip Waveguides, Figure 4 Schematic illustrating typical placement of on-chip optical waveguides in a microfluidic system

On-chip optical waveguides are placed within the microfluidic system such that the waveguide is either perpendicular or alongside microchannels. In a typical setup, illustrated in Fig. 4, light from a light source (e. g., laser or Hg arc lamp) is coupled to on-chip (integrated) waveguides via optical fiber. After light traverses the microchannel, it is transmitted by another optical fiber to a photodetector.

Alternatively, microfluidic systems can be designed to take advantage of the evanescent field by immobilizing analyte-sensitive fluorescent dye on the surface of the on-chip waveguide. In this configuration, the evanescent energy field excites the dye molecules resulting in fluorescence emission, and this emitted energy is superimposed on the transmitted light signal. Thus, the emitted signal from the waveguide contains components of the residual excitation signal and the fluorescent emission. Using filtering, chemical effects on the immobilized dye resulting in a change in fluorescent emission intensity and output spectra can allow determination of specific interactions occurring on the waveguide surface. For the evanescent waveguide sensor to operate effectively, the waveguide must confine the light by total internal reflection while allowing transmission of a substantial portion (at least 80% for short waveguide structures) of the light at both excitation and emission frequencies [3].

On-chip waveguides can be fabricated from different types of core materials. Traditionally glass has been a popular choice, but recently polymers have gained popularity

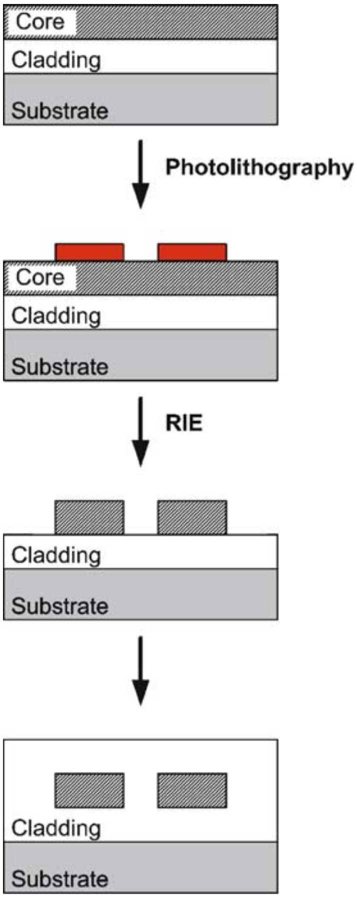

On Chip Waveguides, Figure 5 Process flow for farbciation of glass core waveguides

due to lower costs and excellent transmittance characteristics [4]. Furthermore, polymeric waveguides can now be easily integrated with microfluidic devices, which are now commonly made in polymers.

Glass core waveguides

Glass (or silica) is very well suited as a core material because of its high optical transparency, the stability of silica glass, and its chemical robustness. Silica can be thermally grown on a silicon wafer or deposited by plasma enhanced chemical vapor deposition (PECVD) from the gas phase onto the silicon wafer. Deposition rates of 160 nm/min are typical for high quality films. Figure 5 illustrates a typical process flow. To form waveguides, a bottom cladding layer consisting of pure silica glass is first deposited on top of the substrate. A core layer is then deposited on top if the bottom cladding layer. To achieve light guiding by total internal reflection, the index of the core layer is adjusted to be 1.0 – 1.5 % higher than the surrounding cladding layers. This is achieved by doping the core layer with germanium and nitrogen during PECVD deposition. The core layer is patterned using photolithography and reaction ion etching (RIE). The entire structure is then covered by a cladding layer consisting of pure silica glass. Once waveguides have been fabricated, microchannels are fabricated by etching trenches in glass and bonding with another wafer. Most of such on-chip glass waveguides are single mode, with core thicknesses of 5 – 10 μm and cladding layer thickness of approximately 10 – 20 μm.

Polymer Core Waveguides

A common and simple approach to creating cladding around a polymer core is to sandwich it between two substrates. These substrates form cladding on top and bottom surfaces of the waveguide. Side cladding layers are formed by microchannels filled with air. This approach, schematically illustrated in Fig. 6, can be used to fabricate on-chip waveguides in a variety of polymers.

For a photosensitive polymer, the core is fabricated first directly on a cladding substrate. The second substrate is bonded directly on top of the polymer core (Fig 6a). The cladding is then formed by glass substrates on top and bottom, and air on both left and right sides of the waveguide. Photosensitive epoxy SU-8 (Microchem Corp.) has been growing in popularity as a core material for on-chip waveguides due to simplicity of fabrication. To fabricate waveguide core, SU-8 ($n = 1.59$ at $\lambda = 633$ nm) is simply spin-coated to a desired thickness and photolithographically patterned. Using this approach, single mode or multimode waveguides single to hundreds of micrometers in width and height can be fabricated, limited in height by SU-8 layer thickness and in width by photomask design. SU-8 waveguides, like many polymer waveguides, exhibit higher losses than those fabricated from glass. Nevertheless, unlike in optical waveguides for telecommunications, higher losses are not as problematic in on-chip waveguides for microfluidic Lab-on-a-Chip (LOC) sensing due to their short length.

For a non-photosensitive polymer, such as polydimethylsiloxane (PDMS, Sylgard 184, Dow Corning), a master is first fabricated in SU-8 by photolithography or in silicon by deep reactive ion etching (DRIE) (Fig. 6b). PDMS ($n = 1.41$ at $\lambda = 633$ nm) is then cast to form the core, followed by bonding of a cladding layer. The polymer structure is removed from the SU-8 master, and a second cladding layer is bonded. The resulting structure is schematically illustrated in Fig. 6c.

PDMS has many advantages over other core materials like SU-8 and glass. In addition to low cost, it has a very high light transmittance (> 95%) over a large frequency

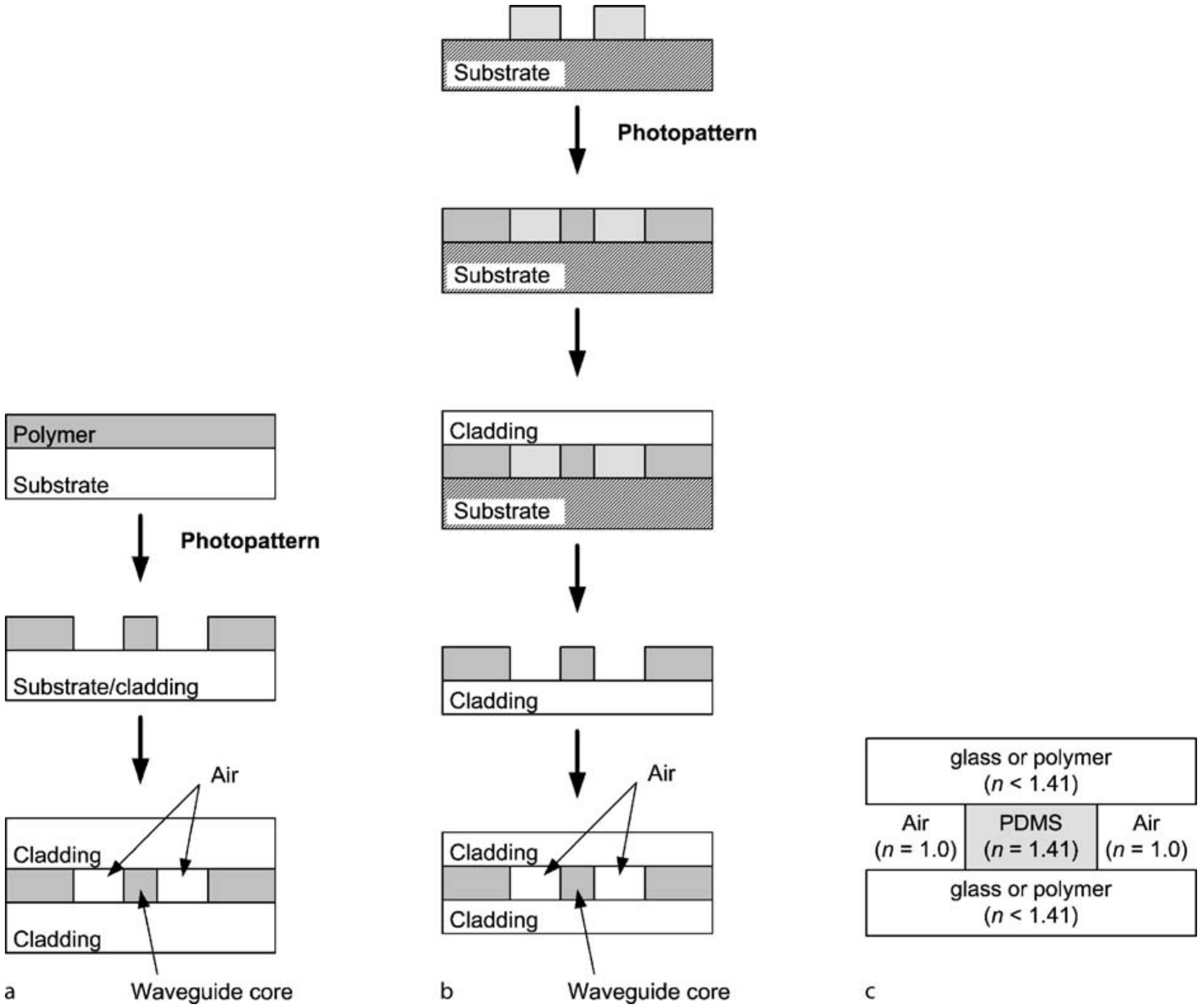

On Chip Waveguides, Figure 6 Fabrication of polymer core waveguides using (**a**) photosensitive and (**b**) non-photosensitive materials. (**c**) Resulting waveguide cross-section structure

O

range. It is also biocompatible, robust, and has a rapid and repeatable mold fabrication process [5]. Even though SU-8 optical sensors designed for biochemical applications have been demonstrated successfully, the need for simpler and more biocompatible materials makes PDMS superior [6]. PDMS devices can be fabricated using soft lithography techniques [5], which do not require the use of a clean room.

Similar to glass core waveguides discussed earlier, buried waveguides can also be fabricated in polymers (Fig. 7). In this case, two different polymers with appropriate refractive indexes must be used. For example, an on-chip waveguide can be fabricated using a SU-8 core and PDMS cladding ($n_{SU-8} = 1.59$ vs. $n_{PDMS} = 1.41$ at $\lambda = 633$ nm). Alternatively, if using the same polymer for both core and cladding, differences in refractive index must be induced. For instance, curing PDMS at room temperature yields a slightly lower refractive index than curing at 150 °C ($n_{150\,°C} = 1.47$ vs. $n_{25\,°C} = 1.45$ at $\lambda = 460$ nm) [7].

Liquid Core Waveguides

As an alternative to the traditional buried channel waveguides, liquid core waveguides can be formed using microfluidic channels. In this case, microfluidic channel walls serve as cladding. By flowing liquid of higher refractive index than the microchannel material, light can be guided within the core. Liquid waveguides can also be composed of a liquid core and a liquid cladding (L^2 waveguides) [8, 9]. By selecting the inner core liquid to be of higher refractive index than the refractive index of

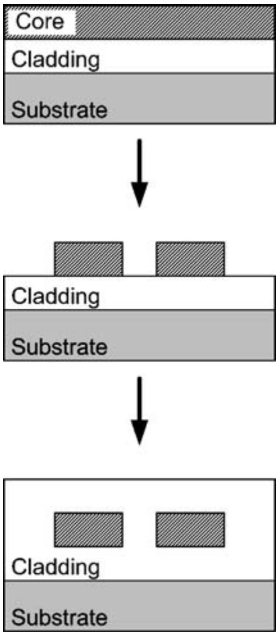

On Chip Waveguides, Figure 7 Fabrication of polymer core waveguides using two polymer materials

the surrounding media, light can be confined to the inner core. In these waveguides, the direction of light propagation can be easily altered by altering the differential flow rates for the liquids to steer the inner core liquid.

Key Research Findings

Mogensen et al. reported microfluidic devices for capillary electrophoresis (CE) and electrochromatography (CEC) with glass on-chip waveguides for optical detection [10]. The devices were fabricated from silicon substrates by DRIE and subsequent oxidation to form optical and microfluidic structures. Figure 8 illustrates the CEC device and shows a cross-section of an optical waveguide fabricated by oxidizing a thin lane of silicon, leaving a 22 µm wide stripe of pure SiO_2. The two air channels on both sides of the SiO_2 core constitute the lower refractive index regions of the waveguide. The depth of the air channels was ∼100 µm, which was also the depth of the microfluidic network. PDMS was used as the top cladding layer of the waveguide, due to its low refractive index and the need to seal the microfluidic channels. Light was not confined in the bottom part of the waveguide, which is a limitation of this approach (although the bottom footprint of the waveguide is small compared to the rest of the structure). Figure 8c shows the measured transmission losses for the waveguide. The propagation loss increased from about 0.2 dB/cm at 800 nm to about 0.8 dB/cm at 250 nm, which was attributed to surface scattering at the glass-air interface due to the waveguide sidewall roughness [10]. This kind of wavelength dependence is expected, since scattering generally is more pronounced at shorter wavelengths [1].

Polymers have been gaining popularity in on-chip waveguide fabrication as core and cladding materials. The use of polymers for on-chip waveguides often makes fabrication of a polymer microfluidic system substantially simpler, as both microfluidic and optical components can be fabricated in a single step. For example, Fleger et al. [11] developed a polymer microfluidic chip for capillary electrophoresis with multimode polymer waveguides for optical analytical applications. The microchannels 50 µm in width and 60 µm in depth were fabricated in polymethylmethacrylate (PMMA) using hot embossing. The on-chip waveguides were formed by fabricating 80 µm wide and 60 µm deep waveguide channels in the PMMA substrate (at the time of the microfluidic channel fabrication) and filling them with core material (NOA72, Norland Optical). NOA72 is a highly transparent UV curing adhesive, with low viscosity and good wetting of PMMA. The refractive index of NOA72 is $n=1.56$ and is suitable as a core material inside PMMA ($n=1.49$) cladding. Figure 9 shows top view and cross-section of the microfluidic channel and polymer waveguides. The transmission spectrum measured with a cooled photomultiplier (Fig. 9c) proves the suitability of the devices for optical detection in the range 440–800 nm, with a propagation loss of only 1 dB/cm [11].

Fleger et al. [12] also described a PDMS microfluidic chip for capillary electrophoresis with integrated waveguides for optical detection (Fig. 10). The waveguide core was composed of a special formulation of polysiloxane ($n=1.43$ at $\lambda=633$ nm). The waveguide cladding was formed by PDMS ($n=1.41$ at $\lambda=633$ nm) and air. Dimensions of the microfluidic channel and the waveguide channels were 70×70 µm^2; distance between the microfluidic channel and the waveguides was 50 µm. Optical loss in the whole system at $\lambda=633$ nm was approximately 1.27 dB, which included propagation loss in the 25 mm waveguides and coupling losses between the waveguides and the microfluidic channel.

Buried on-chip waveguides using the same polymer for both core and cladding can also be fabricated. Chang-Yen et al. demonstrated a method of fabricating a monolithic PDMS waveguide system using soft lithography [7]. An SU-8 master was first prepared to define waveguide core, and PDMS was cast and allowed to flow into the pattern. The excess PDMS that did not fill the SU-8 pattern was carefully removed using a razor blade. PDMS was cured

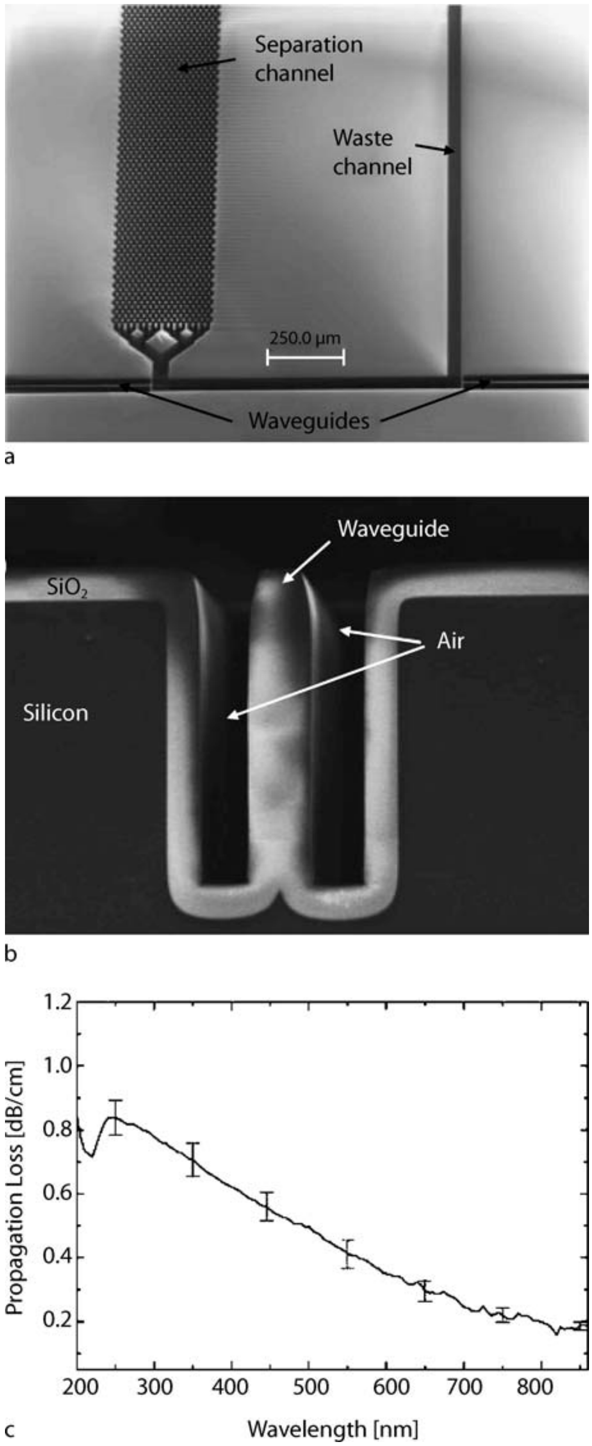

On Chip Waveguides, Figure 8 Microfluidic CEC device with on-chip waveguides for optical detection. (**a**) Scanning electron micrograph of the detection region. (**b**) SiO_2 stripe that forms the on-chip waveguide. (**c**) Propagation loss between 200 and 860 nm. From [10]

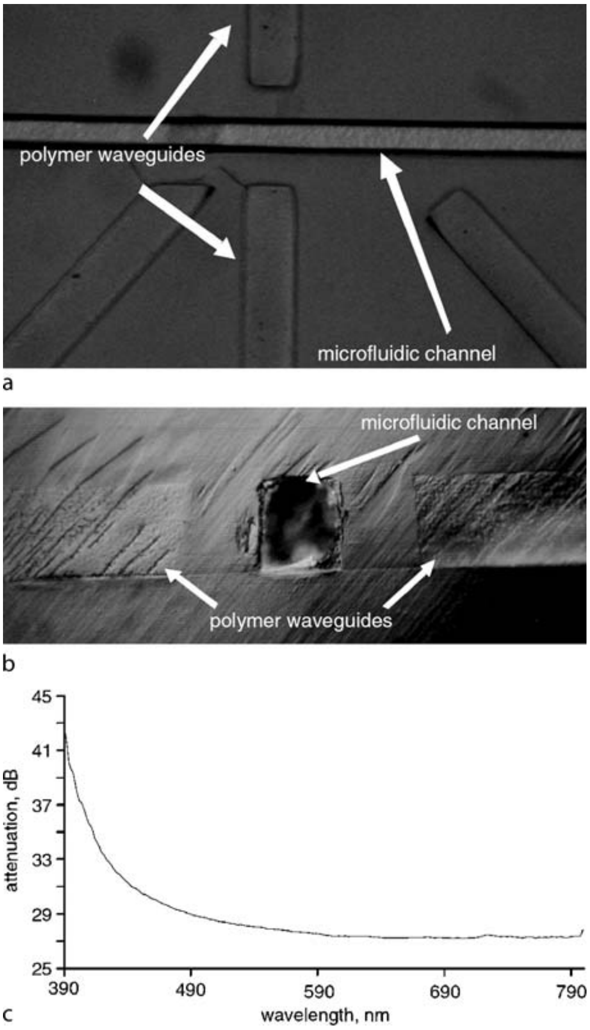

On Chip Waveguides, Figure 9 PMMA capillary electrophoresis chip with on-chip waveguides for optical detection. (**a**) Top view of the optical detection site illustrating the microfluidic channel and polymer waveguides (additional two waveguides were added for designed for specialized fluorescence measurements). (**b**) Cross-section of the microfluidic channel and polymer waveguides. (**c**) Attenuation spectrum of on-chip polymer waveguides, which includes propagation losses due to coupling between the waveguides and the microfluidic channel. From [11]

at 150 °C for 60 min, which yielded the waveguide core with $n = 1.47$ at $\lambda = 460$ nm. The baked layer was then cooled to room temperature and more PDMS was poured over it. The entire wafer was allowed to cure at room temperature to a refractive index of 1.45 (at $\lambda = 460$ nm), forming the cladding layer. A change of 0.02 in refractive index was sufficient for waveguiding. The cutback procedure was used to measure the attenuation of the waveguide demonstrated a loss of approximately 0.40 dB/cm at $\lambda = 460$ nm [7].

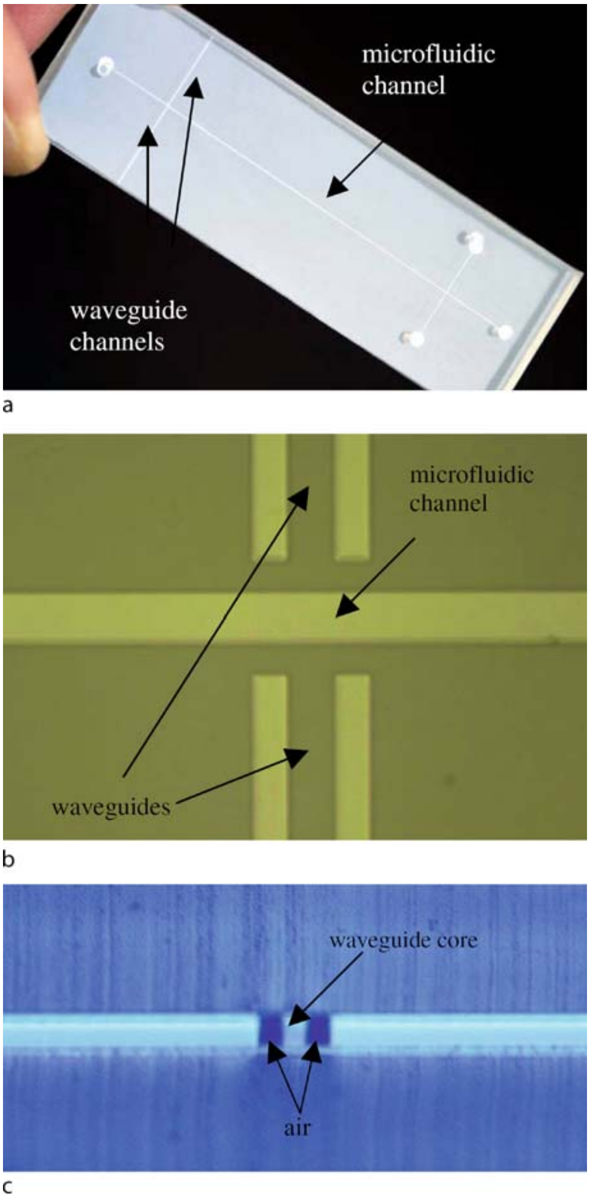

On Chip Waveguides, Figure 10 (**a**) PDMS capillary electrophoresis chip with on-chip waveguides. (**b**) Top view of the optical detection site, illustrating the microfluidic channel and waveguides. (**c**) On-chip waveguide cross-section. From [12]

Alternatively, photosensitive epoxy SU-8 can be used as both the core and cladding layer. The refractive index of SU-8 can be reduced by mixing it with at least 2.7% (by weight) liquid aliphatic epoxy resin DER 353TM from Dow Plastics [13]. The SU-8/aliphatic resin mixture was measured to have $n = 1.590$ at $\lambda = 633$ nm, as opposed to $n = 1.595$ for the un-modified SU-8. The aromatic groups from the aliphatic resin are absorbed in the SU-8 polymeric mesh, inhibiting high cross-linking of the SU-8. Therefore, the refractive index of the blend was lower than the pure SU-8 epoxy. The fabrication process consisted of three successive photolithographic steps to deposit sub-cladding (lower RI), core (higher RI) and top-cladding (lower RI) layers. Both cladding layers had microfluidic channels patterned in them.

Future Directions for Research

Fabrication of waveguides on-chip is important in microfluidic devices, since optical detection is used for many applications. While microfluidics has made it possible to integrate many fluidic casts on a single chip, most optical components such as light sources and sensors remain off-chip. On-chip waveguides provide an interface between these off-chip optical components and on-chip microfluidics. With the drive towards portable microfluidic systems for point-of-care diagnostics or on-site analysis, it is highly desirable to integrate these components on-chip with minimal coupling and transmission losses. This becomes especially important as limits of detection of miniaturized analytical systems improve and analyte concentrations decrease, resulting in ever smaller optical signals.

Cross References

► Evanescent-Wave Sensing
► Fluorescence Measurements
► Microfluidic Optical Devices
► Micromolding
► On-Chip Micro-Optical Detection
► Thick Resist Lithography
► Soft Photolithography

References

1. Saleh BEA, Teich MC (1991) Fundamentals of Photonics. Wiley, New York
2. Kasap SO (2001) Optoelectronics and Photonics: Principles and Practices. Prentice Hall, Old Tappan, NJ
3. Chang-Yen DA, Gale BK (2003) An integrated optical oxygen sensor fabricated using rapid-prototyping techniques. Lab Chip 3:297–301
4. Ma H, Jen AKY, Dalton LR (2002) Polymer-based optical waveguides: materials, processing and devices. Adv Mater 14:1339–1365
5. Sia SK, Whitesides GM (2003) Electrophoresis 24:3563–3576
6. Mogensen KB, El-Ali J, Wolff A, Cutter JP (2003) Integration of polymer waveguides for optical detection in microfabricated chemical analysis systems. Appl Opt 42:4072–4079
7. Chang-Yen DA, Gale BK (2005) A monolithic PDMS waveguide system fabricated using soft-lithography techniques. J Lightwave Technol 23:2088–2093

8. Psaltis D, Quake SR, Yang C (2006) Developing optofluidic technology through the fusion of microfluidics and optics. Nature 442:381–386
9. Wolfe DB, Conroy RS, Garstecki P, Mayers BT, Fischbach MA, Paul KE, Prentiss M, Whitesides GM (2004) Dynamic control of liquid-core/liquid-cladding optical waveguides. PNAS 101:12434–12438
10. Mogensen KB, Eriksson F, Gustafsson O, Nikolajsen RPH, Kutter JP (2004) Pure-silica optical waveguides, fiber couplers, and high-aspect ratio submicrometer channels for electrokinetic separation devices. Electrophoresis 25:3788–3795
11. Fleger M, Siepe D, Neyer A (2004) Microfabricated polymer analysis chip for optical detection. Proc Nanobiotechnol 151:159–161
12. Fleger M, Neyer A (2006) PDMS microfluidic chip with integrated waveguides for optical detection. Microelec Eng 83:1291–1293
13. Ruano-Lopez JM, Aguirregabiria M, Tijero M, Arroyo MT, Elizalde J, Berganzo J, Aranburu I, Blanco FJ, Mayora K (2005) A new SU-8 process to integrate buried waveguides and sealed microchannels for a Lab-on-a-Chip. Sens Actuators B 114:542–551

Optical Coherence Imaging

► Optical Coherence Tomography and Optical Doppler Tomography

Optical Coherence Tomography and Optical Doppler Tomography

ZHONGPING CHEN
Department of Biomedical Engineering, University of California, Irvine, CA, USA
z2chen@uci.edu

Synonyms

Optical Doppler tomography (ODT); Doppler OCT; Optical coherence imaging; Optical Doppler velocimetry

Definition

Optical coherence tomography (OCT) is an interferometric, non-invasive, non-contact optical tomographic imaging modality based on coherence-domain optical technology [1–6]. OCT uses the short coherence length of a broadband light source to perform cross-sectional imaging with micrometer-scale axial and lateral resolutions. Optical Doppler tomography (ODT), also named Doppler OCT, combines the Doppler principle with OCT to obtain simultaneously high resolution tomographic images of structure and flow velocity of scattering samples [7, 8].

Overview and Basic Methodology

Optical Coherence Tomography

OCT is a recently developed interferometric imaging modality that uses short coherence length of broadband light sources to perform micrometer-scale, cross-sectional imaging of biological tissue and other sample. Variations in sample scattering due to inhomogeneities in the optical index of refraction provide imaging contrast. OCT is analogous to ultrasound imaging except that it uses light instead of sound wave. The short coherence length of the broadband light source makes it possible to achieve spatial resolution one or two orders of magnitude better than what can be achieved with ultrasound. OCT was initially developed for imaging biological tissue for medical applications [2]. Since then, OCT has been used for imaging and quantifying biomaterials, microchannels, and nanostructures [3, 5, 8].

There are two basic implementations of OCT, time domain OCT (TD-OCT) and Fourier domain OCT (FD-OCT). TD-OCT is based on a Michelson interferometer with a broadband light source (Fig. 1). Light from a broadband partial coherent source is incident on the beam splitter and splits equally between reference and target arms of the interferometer. Light backscattered from the turbid sample recombines with light reflected from the reference arm and forms interference fringes. High axial spatial resolution is possible because interference fringes are observed only when the pathlength differences between the sample arm and reference arm are within the coherence length of the source. Axial scans are performed by scanning the reference arm, and lateral scans are performed by scanning the sample beam. A two-dimensional, cross-sectional image is formed by performing an axial scan followed by a lateral scan. Axial resolution is determined by the coherence length of the source, and lateral resolution is determined by the numerical aperture of the focusing lens [1–6].

Fourier domain OCT measures interference fringes in the spectral separated domain either by a spectrometer with a high speed line-scan camera (Fig. 2) or a swept laser source based system that uses a single detector [3, 6, 8]. Modulation of the interference fringe intensity in the spectral domain is used to determine the location of all scattering objects along the beam propagation direction by a Fourier transformation without scanning of the reference arm. FD-OCT has the advantages of high sensitivity and fast imaging speed. The significant increase in imaging speed and sensitivity of FD-OCT makes it possible to acquire three-dimensional OCT images with high spatial resolution.

An example of OCT applications in microfluidics is the investigation of Laminar dispersion in a serpentine

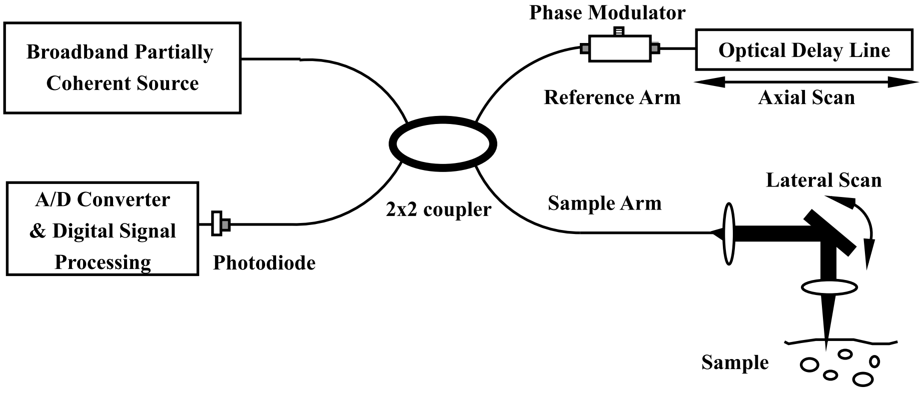

Optical Coherence Tomography and Optical Doppler Tomography, Figure 1 Schematic of a time domain OCT system consisting of a fiber-based Michelson interferometer with a partially coherent light source

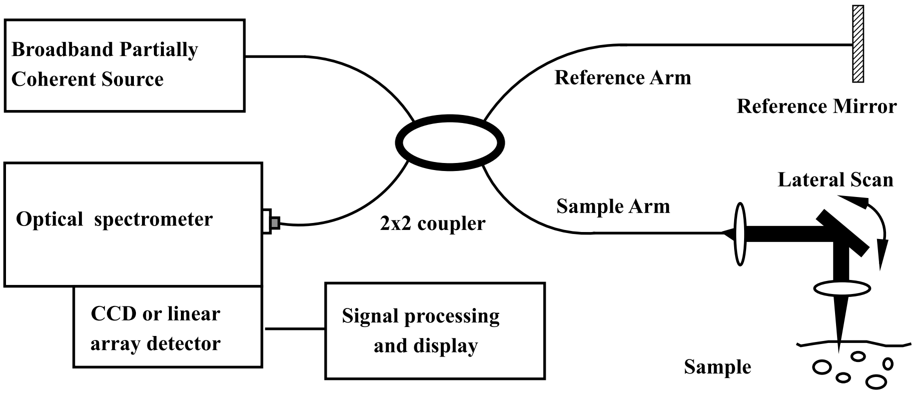

Optical Coherence Tomography and Optical Doppler Tomography, Figure 2 Schematic of a spectrometer based Fourier domain OCT system

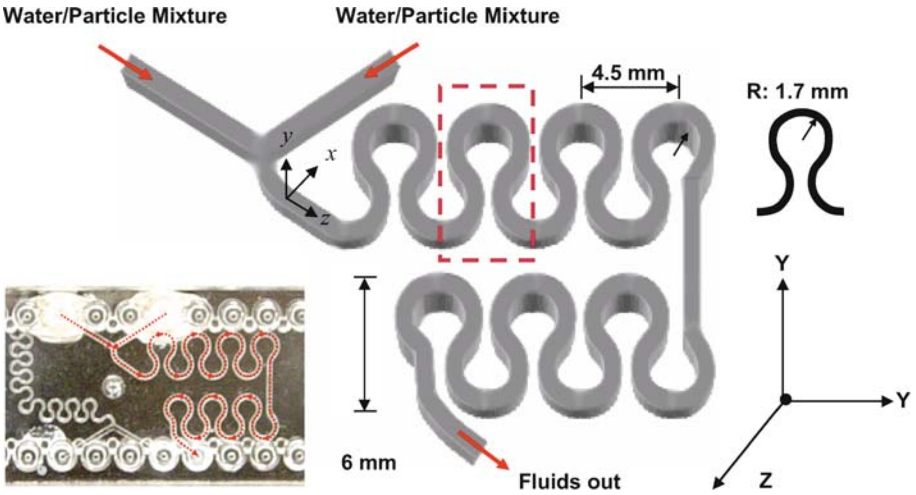

Optical Coherence Tomography and Optical Doppler Tomography, Figure 3 Picture and schematic of a meandering square micro-channel made of cyclo-olefin copolymer. It has a Y branch at the beginning and the dimension of cross-section between confluence and outlet is 600 μm $\times$ 600 μm. The radius of curvature R is 1.7 mm. The red dotted line indicates area of interest

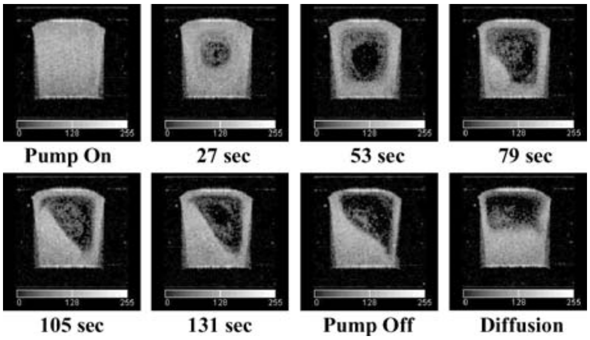

Optical Coherence Tomography and Optical Doppler Tomography, Figure 4 OCT images of transient two-fluid mixing in a meandering square micro-channel as shown in Fig. 3. Initially, the entire channel was filled with a particle/water mixture, and the dual syringe pump (one with the particle/water mixture, and the other with water only) was turned off. As soon as the pump was turned on with a programmed flow rate, OCT images were acquired at 1 frame per second. When the initial mixing was stabilized and reached a dynamic steady state, the pump was turned off again. At the dynamic steady state, sedimentation was observed macroscopically. Stratification between the water and particle/water mixture was developed, and a clear interface was observed in the transverse plane. Secondary flow at the dynamic steady state is clearly visible. Finally, the concentration reached a static steady state where scattering particles occupied the lower half cross-section which resulted from sedimentation

microchannel with a Y-shape inlet (Fig. 3). Transient two-fluid mixing in microfluidic devices can be clearly observed (Fig. 4) [9].

Optical Doppler Tomography

ODT combines the Doppler principle with OCT to obtain high-resolution tomographic images of static and moving constituents simultaneously in scattering samples [5, 8, 10, 11]. When light backscattered from a moving particle interferes with the reference beam, a Doppler frequency shift f_D occurs in the interference fringe:

$$f_D = \frac{1}{2\pi}(\boldsymbol{k}_s - \boldsymbol{k}_i) \bullet \boldsymbol{v}\,, \qquad (1)$$

where $\boldsymbol{k}_i$ and $\boldsymbol{k}_s$ are wave vectors of incoming and scattered light, respectively, and $\boldsymbol{v}$ is the velocity vector of the moving particle (Fig. 5). Since ODT measures the backscattered light, assuming the angle between flow and sampling beam is θ, the Doppler shift equation is simplified to:

$$f_D = \frac{2V\cos\theta}{\lambda_0}\,, \qquad (2)$$

where λ_0 is the vacuum center wavelength of the light source. Therefore, measurement of Doppler shift of the backscattered light allows quantification of flow velocity of scattering particles.

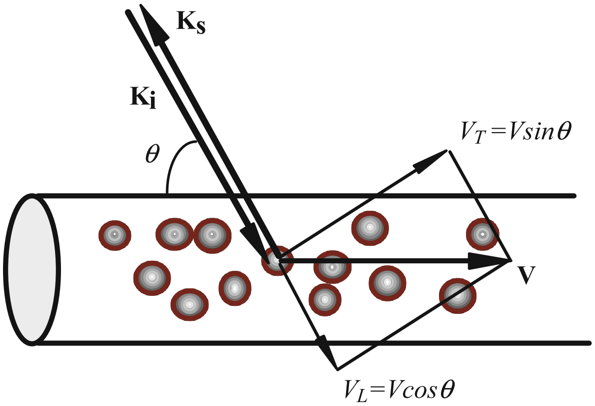

Optical Coherence Tomography and Optical Doppler Tomography, Figure 5 Schematic of flow direction and probe beam angle in ODT

The optical system of ODT is similar to that of OCT. The primary difference is in signal processing. The first two-dimensional in vivo ODT imaging was reported using the spectrogram method [10, 11]. The spectrogram method uses a short time fast Fourier transformation or wavelet transformation to determine the power spectrum of the measured fringe signal [10, 11]. Although spectrogram methods allow simultaneous imaging of in vivo tissue structure and flow velocity, the velocity sensitivity is limited for high-speed imaging. Phase-resolved Doppler OCT was developed to overcome these limitations [12]. This method uses the phase change between sequential A-line scans for velocity image reconstruction [8, 12]. Phase-resolved Doppler OCT decouples spatial resolution and velocity sensitivity in flow images and increases imaging speed by more than two orders of magnitude without compromising spatial resolution and velocity sensitivity [8, 12]. In phase resolved ODT, the phase information of the fringe signal can be determined from the complex analytical signal $\tilde{\Gamma}(t)$, which is determined through analytic continuation of the measured interference fringe function, $\Gamma(t)$, using a Hilbert transformation [8]:

$$\tilde{\Gamma}(t) = \Gamma(t) + \frac{\mathrm{i}}{\pi} P \int_{-\infty}^{\infty} \frac{\Gamma(\tau)}{\tau - t} \mathrm{d}\tau = A(t)\mathrm{e}^{\mathrm{i}\phi(t)}\,, \qquad (3)$$

where P denotes the Cauchy principle value, i is the complex number, and $A(t)$ and $\phi(t)$ are amplitude and phase term of $\tilde{\Gamma}(t)$, respectively. Because the interference signal $\Gamma(t)$ is quasi-monochromatic, the complex analytical signal can be determined by:

$$\tilde{\Gamma}(t) = 2\int_0^{\infty}\int_0^{\tau} \Gamma(t')\exp(-2\pi\mathrm{i}\boldsymbol{v}t')\,\mathrm{d}t' \exp(2\pi\mathrm{i}\boldsymbol{v}t)\,\mathrm{d}\boldsymbol{v}\,, \qquad (4)$$

where τ is the time duration of the fringe signal in each axial scan.

The Doppler frequency shift f_n at nth pixel in the axial direction can be determined from the average phase shift between sequential A-scans. This can be accomplished by calculating the phase change of sequential scans from the individual analytical fringe signal [8]:

$$f_n = \frac{\Delta\phi}{2\pi T} = \frac{1}{2\pi T}\sum_{m=(n-1)M}^{nM}\sum_{j=1}^{N}\left[\tan^{-1}\left(\frac{\mathrm{Im}\,\tilde{\Gamma}_{j+1}(t_m)}{\mathrm{Re}\,\tilde{\Gamma}_{j+1}(t_m)}\right) - \tan^{-1}\left(\frac{\mathrm{Im}\,\tilde{\Gamma}_{j}(t_m)}{\mathrm{Re}\,\tilde{\Gamma}_{j}(t_m)}\right)\right]. \quad (5)$$

Alternatively, the phase change can also be calculated by the cross-correlation method [8]:

$$f_n = \frac{1}{2\pi T}\tan^{-1}\left(\frac{\mathrm{Im}\left[\sum_{m=(n-1)M}^{nM}\sum_{j=1}^{N}\tilde{\Gamma}_j(t_m)\tilde{\Gamma}^*_{j+1}(t_m)\right]}{\mathrm{Re}\left[\sum_{m=(n-1)M}^{nM}\sum_{j=1}^{N}\tilde{\Gamma}_j(t_m)\tilde{\Gamma}^*_{j+1}(t_m)\right]}\right). \quad (6)$$

where $\tilde{\Gamma}_j(t_m)$ and $\tilde{\Gamma}^*_j(t_m)$ are the complex signals at axial time t_m corresponding to the jth A-scan and its respective conjugate; $\tilde{\Gamma}_{j+1}(t_m)$ and $\tilde{\Gamma}^*_{j+1}(t_m)$ are the complex signals at axial time t_m corresponding to the next A-scan and its respective conjugate; M is an even number that denotes the window size in the axial direction for each pixel; N is the number of sequential scans used to calculate the cross correlation; and T is the time duration between A-scans. Because T is much longer than the pixel time window within each scan used in the spectrogram method, high velocity sensitivity can be achieved.

In addition to the local velocity information, the standard deviation of the Doppler spectrum gives the variance of local velocity and can be determined from the measured analytical fringe signal [8]:

$$\sigma^2 = \frac{1}{(2\pi T)^2} \times \left(1 - \frac{\left|\sum_{m=(n-1)M}^{nM}\sum_{j=1}^{N}\tilde{\Gamma}_j(t_m)\tilde{\Gamma}^*_{j+1}(t_m)\right|}{\frac{1}{2}\sum_{m=(n-1)M}^{nM}\sum_{j=1}^{N}\left[\tilde{\Gamma}_j(t_m)\tilde{\Gamma}^*_j(t_m)+\tilde{\Gamma}_{j+1}(t_m)\tilde{\Gamma}^*_{j+1}(t_m)\right]}\right), \quad (7)$$

The σ value depends on the flow velocity distribution. Variations in flow velocity will broaden the Doppler frequency spectrum and result in a large σ value. Thus, the Doppler variance image can be an indicator of flow variations and can be used to study flow turbulences. In addition, standard deviation imaging can also be used to determine the transverse flow velocity [8].

The significant increase in velocity sensitivity of phase resolved ODT makes it possible to image in vivo tissue microcirculation. Recently, the development of FD-OCT has significantly increased imaging speed and sensitivity. Combination of FD-OCT with the phase-resolved method has been demonstrated by a number of groups [8]. Because the dynamic range of the phase-resolved ODT depends on the speed of the line scans, Fourier domain ODT has an advantage over the time domain method in terms of imaging speed and velocity dynamic range [8].

ODT can provide cross-sectional imaging of channel geometry and flow velocity simultaneously. It has been used to measure osmotic mobility, quantify size of the scattering particle, and study flow dynamics of microfluidic devices of different materials, geometry, junction, and surface treatment [8, 13]. ODT has also been used to image and quantify two-phase flow and flow mixing [8, 9, 14, 15]. An example of ODT applications to simultaneously image and quantify the secondary flow and mixing pattern in microchannels is shown in Fig. 6 [15]. Aqueous suspension of polystyrene beads with a diameter of 0.2 μm and concentration of 20.5 mg/cc was injected into both inlets of the Y branch device of a meandering microchannel with a square cross section as shown in Fig. 3. The probe beam of the FD-ODT was adjusted to be approximately perpendicular to the plane of the microchannel (x-y plane). Because primary flow is in the x-y plane and the probe beam is in the z direction, ODT is not sensitive to the primary flow in such a probe configuration. Consequently, only the secondary flow will contribute to the Doppler signal. The z-component of the secondary flow velocity $V_z(x, y, z)$ was imaged and quantified with FD-ODT. Fig. 6i–m shows cross-sectional mapping of secondary flow velocity $V_z(x, z)$ in the x-z plane at different y positions as indicated. The velocity field at x-z plane shows a pair of counter rotating vortices. Since the curvature is alternating, the rotational direction of the vortices is also alternating as shown by comparing Fig. 6i–m. Figure 6n–p shows cross sectional mapping of secondary flow velocity $V_z(x, y)$ at different z positions. Alternating flow direction of the secondary flow at different depth in the x-y plane can be clearly visualized. The inset in Fig. 6o is a cross-sectional mapping of secondary flow velocity $V_z(y, z)$ in the y-z plane at the center of the channel as indicated by the white line. The velocity field at the y-z plane shows a pair of counter rotating vortices. This result clearly demonstrates that ODT can be used to image and quantify secondary flow [15].

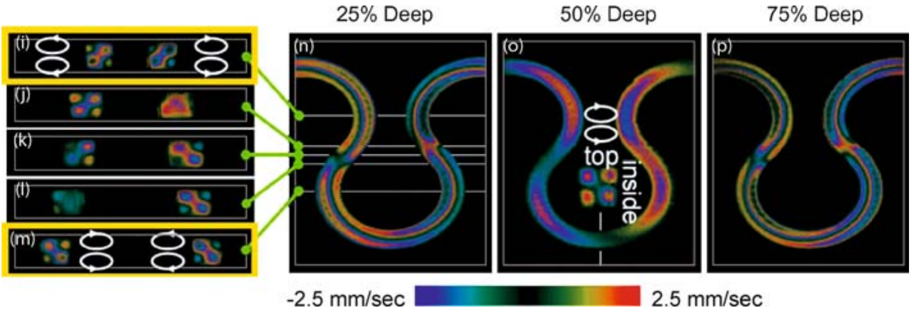

Optical Coherence Tomography and Optical Doppler Tomography, Figure 6 ODT images of secondary flow in a meandering square micro-channel as shown in Fig. 3. The measured z components of the flow velocity $V_Z(x, y, z)$ in the area of interest was projected into different cross-sectional planes, where the z axis is perpendicular to the micro channel plane (x-y plane) and along the direction of the ODT probe beam. (**i**)–(**m**): cross-sectional mapping of secondary flow velocity $V_Z(x, z)$ at different y positions. (**n**)–(**p**): cross-sectional mapping of secondary flow velocity $V_Z(x, y)$ at different z positions (depth). Inset (**o**) is a cross-sectional mapping of secondary flow velocity $V_Z(y, z)$ at the center of the channel as indicated by the white line

Future Directions for Research

OCT and ODT are rapidly developing technologies with many potential applications for imaging and quantifying microfluidic flow dynamics in BioMEMS devices. New developments in all components of an OCT/ODT system, including light sources, detection electronics, and phase resolved processing algorithms can further increase imaging speed and sensitivity. Given its non-invasive and non-contact nature and exceptionally high spatial resolution and velocity sensitivity, OCT/ODT will be a powerful metrology tool for investigating complex flow dynamics in various bioMEMS devices that involve microfluidics.

Cross References

► Micro-PIV-Based Diffusometry
► AC Electro-Osmotic Flow
► Active Mixer
► Velocity Sensor

References

1. Huang D et al (1991) Optical Coherence Tomography. Science 254(5035):1178–1181
2. Bouma BE, Tearney GJ (2002) Handbook of Optical Coherence Tomography. Dekker, New York
3. Fercher AF, Hizenberger CK (2002) Optical Coherence Tomography. In: Wolf E (ed) Progress in Optics. Elsevier, p 215
4. Chen Z (2003) Functional optical coherence tomgoraphy. In: Hwang NHC, Woo SLY (eds) Frontiers in Biomedical Engineering. Kluwer Academic/Plenum, New York, pp 345–364
5. Chen Z (2004) Tomography and Optical Imaging. In: Guenther BD (ed) Encyclopedia of Modern Optics. Elsevier, New York
6. Brezinski ME (2006) Optical Coherence Tomography. Elsevier, New York
7. Chen Z et al (1997) Optical Doppler tomographic imaging of fluid flow velocity in highly scattering media. Opt Lett 22:64–66
8. Chen Z (2004) Optical Doppler tomography. In: Tuchin VV (ed) Coherent-Domain Optical Methods for Biomedical Diagnostics, Environmental and Material Science. Kluwer Academic, Boston, pp 315–340
9. Ahn YC et al (2005) Investigation of laminar dispersion with optical coherence tomography and optical Doppler tomography. Opt Express 13:8164–8171
10. Chen Z et al (1997) Noninvasive Imaging of in vivo blood flow velocity using optical Doppler tomography. Opt Lett 22:1119–1121
11. Izatt JA et al (1997) In vivo bidirectional color Doppler flow imaging of picoliter blood volumes using optical coherence tomography. Opt Lett 22:1439–1441
12. Zhao Y et al (2000) Phase-resolved optical coherence tomography and optical Doppler tomography for imaging blood flow in human skin with fast scanning speed and high velocity sensitivity. Opt Lett 25:114–116
13. Wang RK (2004) High-resolution visualization of fluid dynamics with Doppler optical coherence tomography. Meas Sci Technol 15:725–733
14. Ahn YC, Jung W, Chen Z (2006) Tubid two-phase slog flow in a microtube simultaneous visualizaion of structure and velocity field. Appl Phys Lett 89:064109
15. Ahn YC, Jung W, Chen Z (2008) Optical sectioning for microfluidics: secondary flow and mixing in a meandering microchannel. Lab Chip 8:125–133

O

Optical Doppler Tomography (ODT)

► Optical Coherence Tomography and Optical Doppler Tomography

Optical Doppler Velocimetry

► Optical Coherence Tomography and Optical Doppler Tomography

Optical Lithography

► Photolithography
► Photo Patterned

Optical Narrow Passband Filter

► Fabry-Perot Optical Filter

Optical Trapping

► Optofluidics: Optics Enabling Fluidics

Optical Traps

► Optical Tweezers for Manipulating Cells and Particles

Optical Tweezers for Manipulating Cells and Particles

ALOKE KUMAR, ANDREW H. EWING,
STEVEN T. WERELEY
Department of Mechanical Engineering,
Purdue University, West Lafayette, IN, USA
wereley@purdue.edu

Synonyms

Optical traps

Definition

Optical tweezing is the stable three-dimensional trapping of dielectric substances by the creation of strong light intensity gradients such as by focusing a laser beam to a diffraction-limited spot. Although originally created using counter-propagating laser beams, most optical tweezers today use a single beam of laser light which is focused to a diffraction-limited spot, the spot being the trapping zone.

Overview

Optical trapping refers to the manipulation of extremely small objects using forces generated by light. The field was pioneered by Arthur Ashkin in the 1970s at Bell Labs. His groundbreaking work demonstrated that forces generated by light could capture micrometer-sized particles in a stable three-dimensional trap. Although Ashkin in his early work used counter-propagating laser beams to capture such miniature particles, present day optical traps generally employ only single laser beams. What exactly causes particles to get 'caught' in laser beams depends on the size of the particle, and different theories have been developed to explain the existence of trapping forces according to particle sizes. Diverse mechanisms for the phenomenon exist because of the extremely wide range of particle sizes that have been captured. Atoms, macromolecules, micrometer-sized beads and entire cells, such as viruses, have been shown to be capable of being optically trapped. The mechanisms not only depend on the particle size but also on the wavelength of laser used.

Optical trapping in all cases requires a gradient to be present across the cross-section of the light beam and wavelength control is often necessary in case of biological particles. Lasers, which are strongly monochromatic light sources with a Gaussian intensity profile across the cross-section, are ideal candidates for such purposes. The trapping of micrometer-sized particles is explained with regards to forces arising from the change in momentum of light passing through particles. The momentum change requires a force to be exerted on particles and these forces have transverse (radial) components which confine a particle to a domain. In normal circumstances such forces would be too small to be of any significance but they become increasingly important at lower length scales. These forces are usually in the piconewton range and are large enough for small particles to cause a change in their motion. Also, such a net non-zero transverse trapping force on a particle exists only for a gradient-based light source.

Application of this technology has been extremely wide and varied. The 1997 Nobel Prize in Physics was awarded to scientists who developed methods to cool and trap atoms with laser light. Researchers have used such traps/tweezers to manipulate a whole gamut of particles. The advantages laser tweezers offer over most other confining methods is the non-invasive nature and that the particles only need to have a different refractive index compared to the surroundings for the trap to work. Non-invasiveness can be a critical factor when dealing with biological particles where remote-execution is desirable.

Basic Methodology

Theoretical Principles

To trap a particle in three dimensions with a single beam requires the spatial variation of the light to satisfy two important conditions. The first requirement is that an intensity gradient in the direction perpendicular to the opti-

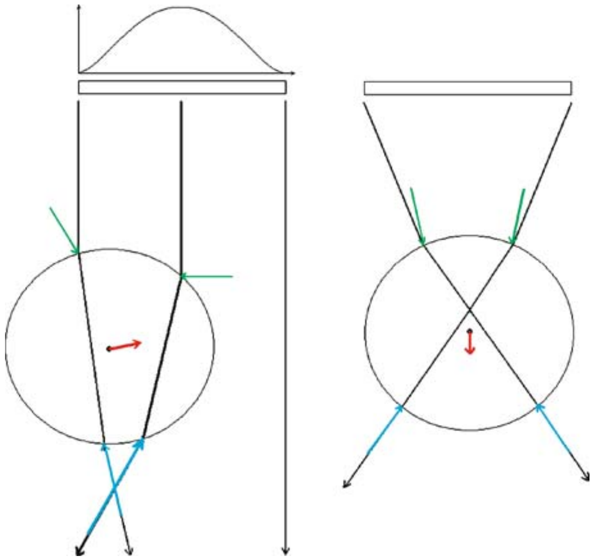

Optical Tweezers for Manipulating Cells and Particles, Figure 1 On the left-hand side the radial gradient force is illustrated for a particle near the axis of a Gaussian beam. The right-hand side depicts the axial gradient force acting on a particle near the focus of a divergent beam. Red lines represent the gradient forces while blue and green lines represent the forces due to refracting and reflecting rays, respectively

cal axis be present in the beam. This radial intensity gradient is responsible for trapping in the radial direction of the beam and is inherent in most laser systems. Figure 1 shows how a ray of high intensity from the core of a beam contributes a greater degree to the trapping force than a ray of low intensity. In practice, a TEM_{00} mode laser beam is used because of the Gaussian intensity gradient present in such a laser beam. The radial stiffness of the trap depends primarily on the magnitude of the radial intensity gradient. The second condition required for three-dimensional, single-beam trapping is that the laser must be tightly focused, or highly divergent, in the region where trapping is desired. A divergent beam has an intensity gradient in the direction of the optical axis due to the variation in the cross-sectional area of the beam. Trapping in the axial direction can occur near the focus of a divergent beam due to this form of spatial variation, as shown in Fig. 1. Focusing a beam to create an axial intensity gradient large enough to trap particles is easily achieved using an objective lens of high numerical aperture (NA).

Gradient Forces: Mie and Rayleigh Regimes

Optical gradient forces are the fundamental physical phenomena responsible for optical tweezers. There exist two separate theories which accurately describe the origin of the optical gradient forces for two different physical extremes. These two physical extremes, known as the Mie and Rayleigh regimes, refer to the magnitude of the wavelength of the trapping laser with respect to the characteristic size of the particle being trapped. The Mie regime assumes wavelength of the impinging laser beam, λ, is much smaller than the size of the particle, s, so that a geometric approximation of the optics and Newton's third law of motion are all that is required for a quantitative description of the gradient forces. Photons from the laser beam undergo a change in direction when they are refracted or reflected, which constitutes a change in the momentum of the photons. From Newton's third law, the material causing this direction change experiences an equal and opposite change of momentum, which manifests itself in the form of an external force acting on the material, as seen in Fig. 1. Certain rays of light will contribute disproportionately to this external force compared to others in the presence of a spatial intensity gradient. Depending on their intensity and direction before and after interacting with the specimen, each ray will contribute to the external force to a varying degree. The sum of the forces applied by each photon being scattered or transmitted by the specimen is the gradient force which acts as a potential well to trap the specimen. The differential force contribution of a ray, dF, is given by Eq. (1), where n_1 is the refractive index of the surrounding medium and c is the speed of light in a vacuum [1]:

$$dF = \frac{n_1 R\,(I \cdot dA)}{c} \tag{1}$$

In Eq. (1), I and A are the intensity and area of the incident ray, respectively, and R is either the reflectance or the transmittance of the ray in question depending on whether the ray is being reflected or transmitted as it interacts with the trapped object. In Eq. (2), the gradient force, F_∇, is found by integrating dF over the surface of the specimen [1]:

$$F_\nabla = \int_s dF \tag{2}$$

This method is particularly useful – when implemented numerically for computing the gradient force for bodies of arbitrary shape.

The other physical extreme for which an accurate theoretical treatment exists is known as the Rayleigh regime. Here the size of the specimen is assumed to be much smaller than the wavelength of light; therefore geometric approximations are no longer adequate for describing the behavior of light. Calculation of trapping forces in the Rayleigh

regime requires an electrodynamics approach to calculate the optical forces. This approach assumes the gradient force arises from the fact that a dipole in an inhomogeneous electric field experiences a force in the direction of the field gradient. In optical tweezers, the laser induces a fluctuating dipole in a dielectric particle which interacts with the inhomogeneous electric field within the beam. In the presence of an electric field gradient, a dielectric particle with dipole moment, $\boldsymbol{p}$, will experience a force given by

$$\boldsymbol{F} = (\boldsymbol{p} \cdot \nabla)\boldsymbol{E} \tag{3}$$

This is done by treating the particle as a point dipole and using Maxwell's equations to solve for the electric field within the beam. It is convenient to analyze the trapping force in terms of two separate components: the scattering force, F_{scat}, and the gradient force, F_{∇}. The scattering force arises due to absorption and re-radiation by the dipole, whereas the gradient force arises due to the interaction between the induced dipole and the electric field. The dipole moment can be calculated by

$$\boldsymbol{p} = 4\pi n_2^2 \varepsilon_0 a^3 \left(\frac{m^2 - 1}{m^2 + 2}\right)\boldsymbol{E} \tag{4}$$

where $m = n_1/n_2$ is the ratio of refractive indices. The electric field vector for the lowest order Gaussian beam approximation is

$$\begin{aligned}\boldsymbol{E} = E_0 \frac{ikw_0^2}{ikw_0^2 + 2z} \exp(-ikz) \\ \cdot \exp\left[-i\frac{2kz(x^2 + y^2)}{\left(kw_0^2\right)^2 + 4z^2}\right] \\ \cdot \exp\left[\frac{(kw_0)^2(x^2 + y^2)}{\left(kw_0^2\right)^2 + 4z^2}\right]\end{aligned} \tag{5}$$

where k is the wave number and w_0 is the minimum radius of the beam. The gradient force acting on the dielectric particle is found by substituting Eqs. (4) and (5) into Eq. (3), which yields

$$F_{\text{grad}} = 4\pi n_2^2 \varepsilon_0 a^3 \left(\frac{m^2 - 1}{m^2 + 2}\right) \tfrac{1}{2} \nabla E^2 \tag{6}$$

where a is the radius of the trapped sphere [2]. The scattering component of the optical forces must be calculated in order to find the total trapping force. The scattering force, F_{scat}, is equal to the energy density of the electromagnetic wave impinging on the scattering cross section, C_{scat}, of the sphere. The scattering force and cross-section are found using Eqs. (7) and (8) [2]:

$$F_{\text{scat}} = \left(\frac{n_2}{c}\right) C_{\text{scat}} I(x, y, z) \tag{7}$$

$$C_{\text{scat}} = \tfrac{8}{3}\pi (ka)^4 a^2 \left(\frac{m^2 - 1}{m^2 + 2}\right)^2 \tag{8}$$

The total trapping force acting on the trapped sphere is the sum of the trapping and scattering forces:

$$F_{\text{total}} = F_{\text{grad}} + F_{\text{scat}} \tag{9}$$

The theoretical treatments described above are very accurate for the extreme cases to which they apply. Unfortunately, most practical cases fall in the intermediate regime where the wavelength of the incident light is roughly the same size as the trapped particle. This intermediate case requires more complex theoretical models and is currently an area of interest for researchers.

Experimental Principles

As discussed earlier, single optical traps are characterized by a single laser beam focused to a high diffraction-limited spot using a high-magnification lens. The lens usually is the objective lens of a microscope, which serves to integrate the imaging and trapping systems. The imaging can serve as a data acquisition system, a monitoring system and a positioning device which helps focus the trap onto the region of interest. As stated before, optical traps have become an important tool for very diverse activities and as such have undergone numerous modifications to suit those diverse activities. The simplest form of optical trap consists of the following optical components.

Laser

The laser is the basic and most important component of the trapping system. Lasers are perhaps the most easily available sources of highly collimated, high-energy and monochromatic light beams. Also the transverse intensity gradient provides the necessary means to capture micro/nanoparticles. Being such an important component of the setup, the laser needs to be selected properly, the selection being based on a number of factors. These factors are usually output beam shape, beam astigmatism, power and wavelength. The most important requirement is that the output beam should be single mode (Gaussian TEM_{00} mode). This ensures that the beam is focused, by the objective lens, to the smallest beam diameter thus producing the

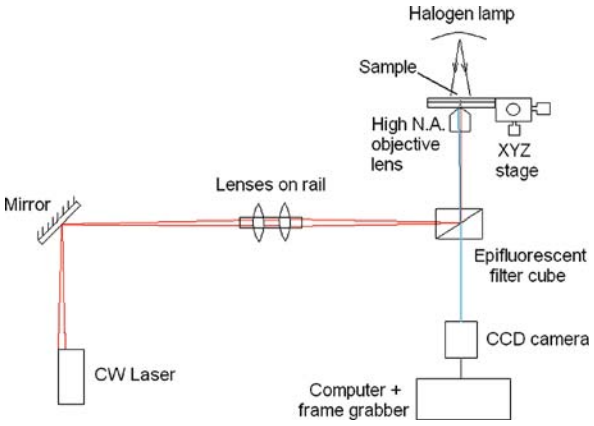

Optical Tweezers for Manipulating Cells and Particles, Figure 2 A typical experimental setup for optical trapping. The lenses on the rail focus the beam onto a diffraction-limited spot and the epi-fluorescent cube filters the unwanted part of the spectrum and hence enhances image quality

most efficient trap. Beam astigmatism also prevents convergence of the laser beam to a small spot and hence needs to be eliminated if present before the laser is deployed. The maximum power of the laser and the final output power determine the maximum attainable strength/stiffness for the laser trap. The required wattage is usually calculated allowing for the losses and taking into account the actual power required for trapping an object. The actual trapping power required might not be easy to calculate and in many cases a review of existing literature should give an order of magnitude estimate. A laser power of the order of 20 – 100 mW is usually sufficient for many basic trapping experiments. The wavelength is another important parameter when it comes to trapping biological specimens. For non-living objects any part of the spectrum works fine but the visible region is usually preferred due to the relative ease in aligning the various other optical components. There is a broad consensus that when dealing with biological elements infrared lasers should be used. The primary concern behind using a laser with an emission peak in the visible spectrum is possible "opticution" (death by light). Such opticution was first observed by Ashkin [3] when working with viruses and bacteria. Even if low-power lasers are used for trapping purposes, very high energy levels are developed due to focusing of the laser beam, and high absorption of the laser wavelength by biological specimens might lead to their extermination. There is a wide consensus that lasers in the infrared region are far less damaging to live biological specimens and the current choice of laser is the neodymium:yttrium-aluminium-garnet (Nd:YAG) laser and its close cousins [4, 5]. This is because of the low absorption of radiation of the infrared part of the spectrum by biological species in general, and wavelengths between 750 and 1000 nm are usually recommended. Nd:YAGs, although a popular choice, are more expensive compared to diode-pumped solid-state lasers. However usage of any infrared laser does not guarantee prevention of opticution and laser wavelength should be determined after a thorough literature survey.

Most of the lasers employed for trapping purposes are continuous-wave (CW) lasers but femtosecond lasers have also been shown to be effective for trapping purposes. Diode lasers are usually inexpensive but the beam quality usually necessitates correcting optics which adds to the cost and makes the optical train more complex. The output beam in the case of diode lasers is elliptical and also astigmatic. Symmetry can be restored by correcting with an anamorphic prism. Spatial filtering by pinholes or single-mode optical fibers can also achieve the same goal albeit with large losses.

Objective

The objective lens is another important component of the system and its use is primarily to focus the laser beam to a diffraction-limited spot. The objective lens is an influencing parameter with regard to the final trap stiffness and depends on its numerical aperture (NA) and transmittance. The NA is usually a measure of the light-gathering ability of a system and hence higher NA lenses are preferred. The lenses should be chosen so as to minimize the refractive index mismatch between the immersion medium and the trapping medium. Some of the higher NA lenses are oil-immersed while water-immersed lenses are also available. As aberrations have a degrading effect on the trap quality, the choice of objective lenses should be made judiciously [4]. In many trap setups the objective serves a dual purpose of trapping and viewing the particles.

Microscope

Inverted and upright microscopes have both been used for trapping purposes and usually integration with the trapping optics is straightforward. Single-beam trapping integrated with confocal microscopy has also been achieved. The microscope also serves as the imaging system which might be achieved visually or using a video-based system. Eyepieces can be used to view the sample or the light might be redirected by a dichroic to a CCD camera. Care has to be taken that the laser light is filtered out before it reaches either the eyepiece or the camera. Highly focused laser beams pose a serious hazard to the observer and hence should be removed using appropriate optical filters. Microscopes also enable different imaging techniques such as differential interference contrast and epi-fluorescence. Figure 2 shows such an arrange-

ment where an epi-fluorescent cube has been deployed for imaging. Like most other designs, it focuses a suitably expanded and shaped laser beam through a high-NA microscope objective. The laser beam is focused by an optical train to a diffraction-limited spot which is also the location for trapping particles. The optical path consists of lenses, directing mirrors and a filter cube, which is set up to specifically enable fluorescent imaging with a setup based on an inverted microscope. Bechhoefer and Wilson [6] and Smith et al. [7] discuss in detail the various practical and theoretical aspects involved in setting up a laser trap. The sample is held on an XYZ translational stage that serves to laterally displace the sample. The sample is illuminated using a halogen lamp placed directly above the sample, which can serve to provide the excitation frequency of the fluorescent microparticles. Finally, the image from the microscope is fed directly to a camera sensor. The microscope (not shown) is represented by the cube and XYZ stage.

Lenses and Other Trapping Optics

Lenses are required to expand the initial laser beam so that it totally fills the back aperture of the objective lens. Beam expanders can either be bought or constructed for specific use, by using individual lenses. The latter allows for the flexibility of a variable output if three lenses are used. Mirrors help to steer the beam. Other optics might be required depending on the specific task. Position detection might be achieved by a variety of techniques with each having its own merits and demerits. An exhaustive treatment of the same can be found in [4].

Key Research Findings

Since their invention, optical tweezers have proved themselves to be very powerful interdisciplinary tools. Today they are used extensively in biophysics, as they serve as delicate tools to manipulate and study single molecules of DNA [8, 9]. Optically trapped beads have been successfully used to measure local elasticities and viscosities, for example inside cells. Ashkin [5] provides an overview of the diverse uses of optical traps as an important tool in the important areas of research. Isolation and detection of sparse cells; concentration of cells from dilute suspensions; separation of cells according to specific properties; and trapping and positioning of individual cells for characterization are the key areas of research due to their possible impact. The non-invasive nature of particle manipulation being a key requirement, forces like hydrodynamic, optical, ultrasonic and electromagnetic have been employed for such purposes. Successful examples of the use of these optical forces for biological applications are determination of motility forces, 3-dimensional multi-gene detection and non-invasive optical sectioning of tissues [10] amongst many others.

Future Directions of Research

An optical trap behaves, at its simplest approximation, like a spring. The further a particle travels from the center of an optical trap, the greater the force it feels back to the center of the trap. Single optical traps make use of the Gaussian intensity profile in a laser to trap particles. Such traps are characterized by linear stiffness constants and hence the resulting potential well has a parabolic profile. Such systems are hence not suitable for creating arbitrary trap geometries. Fortunately recent technological advancements in holographic optical trapping have made possible generation of trap geometry based on individual preference and necessity. Optical tweezers implemented by SLMs are usually computer controllable which bestows upon them the important quality of being easily repeatable. The computer-driven liquid–crystal spatial light modulators create holograms, which correspond to various arrays of traps that can be designed, calculated and optimized on a computer. The traps can be controlled and reconfigured by writing these holograms on an SLM in real time. SLM optical traps have the advantage that they can switch traps independently. Such trapping systems show a lot of promise for future applications because of their many advantages over single optical traps.

Cross References

► AC Dielectrophoresis Lab-on-Chip Devices
► Dielectrophoretic Motion of Particles and Cells
► DC-Dielectrophoresis Lab-on-Chip Devices
► Dielectrophoresis

References

1. Gauthier RC (1995) Ray Optics model and numerical computations for the radiation pressure micromotor. Appl Phys Lett 67(16):2269–2271
2. Harada H, Asakura T (1996) Radiation forces on a dielectric sphere in the Rayleigh scattering regime. Opt Comm 124(5–6):529–541
3. Ashkin A (1970) Acceleration and Trapping of Particles by Radiation Pressure. Phys Rev Lett 24(4):156
4. Neuman KC, Block SM (2004) Optical trapping. Rev Sci Instrum 75(9):2787–2809
5. Ashkin A (1997) Optical trapping and manipulation of neutral particles using lasers. Proc Natl Acad Sci USA 94(10):4853–4860
6. Bechhoefer J, Wilson S (2002) Faster, cheaper, safer optical tweezers for the undergraduate laboratory. Am J Phys 70(4):393–400

7. Smith SP, Bhalotra SR, Brody AL, Brown BL (1999) Inexpensive optical tweezers for undergraduate laboratories. Am J Phys 67(1):26–35
8. Kurachi M, Hoshi M, Tashiro H (1995) Buckling of a single microtubule by optical trapping forces: Direct measurement of microtubule rigidity. Cell Motil Cytoskeleton 30(3):221–228
9. Felgner H, Frank R, Schliwa M (1996) Flexural rigidity of microtubules measured with the use of optical tweezers. J Cell Sci 109:509–516
10. Konig K (2000) Laser tweezers and multiphoton microscopes in life sciences. Histochem Cell Biol 114:79–92

Optofluidics – Applications

SUDEEP MANDAL, DAVID ERICKSON
Sibley School of Mechanical and Aerospace Engineering, Cornell University, Ithaca, NY, USA
sm445@cornell.edu, de54@cornell.edu

Synonyms

Photofluidics

Definition

Optofluidics is the marriage of optics, optoelectronics and nanophotonics with fluidics. Such integration represents a new approach for dynamic manipulation of optical properties at length scales both greater than and smaller than the wavelength of light with applications ranging from reconfigurable photonic circuits to fluidically adaptable optics to high sensitivity bio-detection and analysis currently under development. In this article we present a comprehensive review of some of the emerging applications and technologies for optofluidics.

Overview

The capabilities in terms of fluidic control, mixing, miniaturization and optical property tuning afforded by micro-, nano- and electro-fluidics provides an ideal platform upon which to build versatile optofluidic devices. In this article we provide a general overview of some of the emerging applications of optofluidic technology. Providing a comprehensive overview of all the research in this field is outside the scope of this review. Rather we will provide a number of representative examples of the state of the art.

Basic Methodology

The basic methodology behind optofluidics is described in detail in the ►optofluidics – fluidics enabling optics, ►optofluidics – optics enabling fluidics and ►optofluidics – fabrication and integration techniques. Here we focus primarily on providing an overview of the some of the recent applications for optofluidics and refer readers to those articles for more detailed information.

Key Research Findings

Optofluidic Particle and Cell Sorting Techniques

The discovery that laser radiation could transfer its momentum to microscopic particles and thus be used to manipulate them led to many innovative applications. Optical tweezing was a direct consequence of this and has been vastly refined over the years. Recently there have been various advanced implementation of such techniques to achieve optical control and sorting of particles into advanced and highly integrated microfluidic systems. These techniques range from traditional optical trapping (see a recent review by Grier [1]), to massively parallel handling of particles and cells using electro-optic tweezers, rotational manipulation of components based on form birefringence, to optical force based cell sorting. The advantage of these optical approaches lies in their ability to provide remote operation and handle individual particles directly as opposed to indirect manipulation of the surrounding flow field (as with electrokinetic and pressure driven effects).

Active Sorting

As an example of a direct device integration, Wang et al. [2] developed an optical force based cell sorting technique whereby radiation pressure was used to direct rare cells into separate streams following a green florescent protein (GFP) detection event. A schematic of the operating procedure for this device is shown in Fig. 1. The mixture of cells was made to flow through a microfluidic channel and was aligned into a narrow stream using hydrodynamic focusing. The initial alignment was such that these cells would flow into the waste outlet. Prior to this the cells were made to first pass through an interrogation region. If fluorescence was detected, indicating the presence of a target cell, the optical switch was activated and a focused laser spot was used to deflect the target cell laterally. This lateral displacement of the target cell caused it to follow a streamline which would carry it into the collection outlet. Sorting speeds as high as 200 cells per second were achieved.

Passive Sorting

Though very complex optical manipulations have been demonstrated in literature, the majority of these imple-

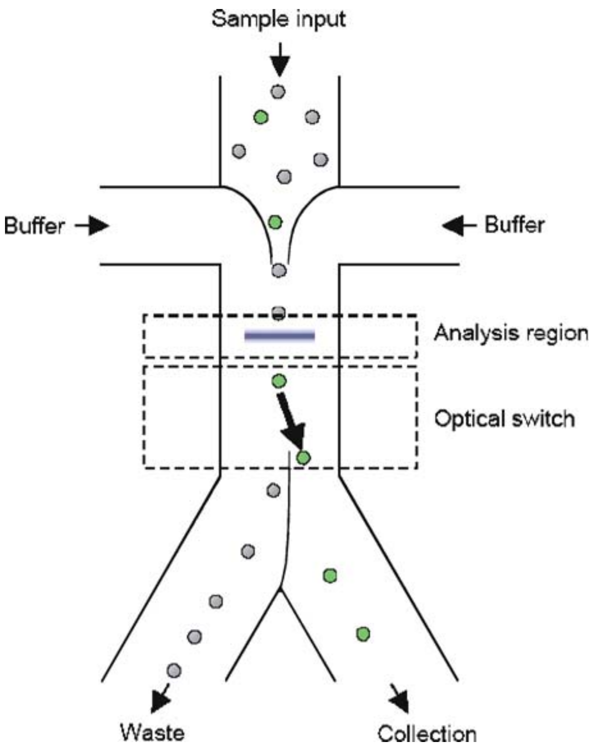

Optofluidics – Applications, Figure 1 Layout of the microfluidic sorting junction and the optical switch for the optofluidic cell sorter described by Wang et al. [2]. After being aligned to the center of the channel by flow focusing, cells are analyzed and then switched based on their detected fluorescence. Target cells are directed by the laser to the collection output while all other cells flow to the waste output. Figure and Caption reprinted with permission from Wang et al. [2]

mentations tend to be *binary*. This means that they rely on either the ability to trap or not trap a particle based on whether the conditions for trapping stability are met. Recently however a number of works have extended these ideas to exploit the dependence of this trapping potential on the particle properties, enabling much more advanced and subtle operations. As an example, Macdonald et al. [3] demonstrated an optical lattice technique where particles of different sizes were sorted into different streams depending on their strength of repulsion to regions of high optical intensity. The method relies upon the principle of a periodic optical gradient that is designed to deterministically guide smaller particles. The field is designed to temporarily trap small particles, while using hydrodynamic force to push particles out of the trapped state into an adjacent trapping location in the field. Careful planning of the periodicity of the field leads to a deterministic motion of smaller particles in a specified direction, while larger particles continue nearly unimpeded.

Optical Chromatography

In a series of papers, Imasaka and coworkers [4] provided the initial foundations for optically driven separation techniques, which they termed optical chromatography. The advantage of this technique lies in that it is the most sensitive technique known to date for separation of particles based on their size. Table 1 below compares various bio-analytical separation techniques, the operating principles behind the techniques and the dependence of the separation velocity on the particle radius a.
Work in this area has recently been extended by Terray et al. [5] who have recently integrated this into a microfluidic device format for pathogen detection, demonstrating very precise separation between very closely related bacteria *Bacillus anthracis* and *Bacillus thuringiensis* and millimeter scale separation. In their work a loosely focused laser beam propagates in a direction opposite to the fluid flow in the Poly(dimethysiloxane) (PDMS) channel. As a result of the difference in the optical forces on the cells they come to rest at different points along the length of the channel. At present however, such systems are practically limited by the fundamentals of the free-space optics on which they rely. Specifically, the light-particle interaction length is limited by either the focal depth or the spot size of the objective lens.

Evanescent Field Based Particle Trapping and Manipulation

Waveguide based optical structures serve to confine light within solid structures from the visible to the IR spectrum. A waveguide relies upon the principles of total internal reflection to confine light within the solid waveguide structure. Such confinement separates optical energy into guided modes and evanescent modes. While the guided modes represent the confined optical energy in the waveguide, the evanescent modes represent leaked optical energy, which exhibits an exponential decay as the distance from the waveguide surface increases. A waveguide trap/propulsion device is designed such that the evanescent mode interacts with particles to generate scattering/absorption and gradient forces which pull the particle towards the waveguide. There have been some experimental works of waveguide based particle propulsion. Gaugiran et al. [6] published a paper based on silicon nitride waveguide and demonstrated the trapping and propulsion of biological cells along these waveguides. The paper also presents the use of a finite-element analysis as a means of predicting the optical forces for a dielectric particle interacting with a waveguide. The difficulty with these waveguide techniques is that one is limited to interaction with

Optofluidics – Applications, Table 1 Comparison of Bioanalytical Separation Techniques

Technique	Operating Principle	Separation Velocity
Optical	Scattering and adsorption force dependence on particle size and refractive index. Driving force is intensity of EM field, $V_{op} \propto I$.	$V_{op} \propto a^5$ $V_{op} \propto (\varepsilon_p - \varepsilon_m)^2$
Electrophoresis	Differences in species charge to drag ratio represented by electrophoretic mobility. Driving force is electric field, $V_{ep} \propto E$.	$V_{ep} \propto \zeta \neq f(a)$ * (thin EDL) $V_{ep} \propto 1/a$ * (thick EDL)
Dielectrophoresis	Lorenz force dependence on particle size and polarizability. Driving force is the gradient of E^2, $V_{dep} \propto \nabla(E^2)$.	$V_{dep} \propto a^2$ $V_{dep} \propto (\varepsilon_p - \varepsilon_m)$
Centrifugation and Sedimentation	Differences in density. Driving force is gravitational or centrifugal acceleration field, $V_{cent} \propto g$.	$V_{cent} \propto (\rho_p - \rho_m)a^2 \approx a$
Size Exclusion Chromatography	Size dependence on permeability through packed column. Typically pressure is used as driving force, $V_{SEC} \propto \Delta P$.	$V_{SEC} \propto -\log(a^3)$ **

* For free solution electrophoresis. Gel based electrophoresis results in a non-linear drag which can increase the dependence of V_{ep} on a.
** Approximate, based on assumption of proportionality between hydrodynamic volume and molecular weight.

the evanescent mode which tend to be much weaker than direct interactions with the mode.

Optoelectronic Tweezers

As an alternate approach Chiou et al. [7] recently demonstrated massively parallel manipulation of single cells and microparticles using optical images. This was achieved by high resolution patterning of electric fields by projection of an optical image on a photoconductive surface. In these optoelectronic tweezers (OET), high resolution dielectrophoretic electrodes were patterned optically which enabled single cell manipulations and sorting. By varying the frequency of the AC signal applied between the two electrodes, one can switch between negative dielectrophoresis (DEP) and positive DEP regimes. Since the images used to pattern the electrodes are generated on a computer they can be dynamically modified in real-time. Thus this technique allows for highly parallel cell manipulations, sorting and trapping. The only limitation with this technique is that the resolution of the images that are projected on the photoconducting surface is fundamentally limited because of diffraction. As a result manipulation, with submicron resolution is not possible, though this is well below the precision required for cell based manipulations.

Optofluidic Imaging Techniques

At present one of the significant hindrances towards the development of fully portable, stand alone Lab-on-Chip devices, is the reliance on macroscale infrastructure such as pumps, power sources and most importantly external optics. To tackle the latter of these, Heng et al. [8] have developed an integrated optofluidic microscope (OFM) which integrates a high resolution imager, in the form of a slanted nanohole array, directly into a microfluidic network. Figure 2 provides an overview of the operating procedure for the OFM. The target object is made to flow through the microfluidic channel at a constant velocity using either electrokinetic control or pressure driven flow and confined to the center of the imager through upstream focusing. In the arrangement the imager consists of a slanted nanohole array defined in an opaque layer (typically aluminum) which spans the width of the channel. As is shown in the current arrangement the device is epi-illuminated and the transmission through the holes is monitored as the target flows over the imager. For the length of time the target flows over each individual well the transmission is reduced. Given that the flow rate is known the transmission traces can be used to reconstruct an image of the target. This technique enables the correct shape and size of the target to be extracted which should be sufficient for high speed phenotyping.

Using an entirely different approach, Kuiper and Hendriks [9] demonstrated a variable-focus liquid lens that has immense potential for application in miniature cameras and other optical devices. The lens consists of the meniscus between two immiscible liquids. In their experiment the two liquids were oil and water. By changing the curvature of this meniscus one can change the focal length of this liquid lens. To achieve this change in curvature they used the technique of electrowetting. Electrowetting refers to the phenomena of changing the interfacial contact angle between an electrolyte and solid through application of an applied potential difference. By varying this applied potential difference, the curvature of the fluidic lens could be continuously varied from convex to concave thereby adjusting the focal length of the lens.

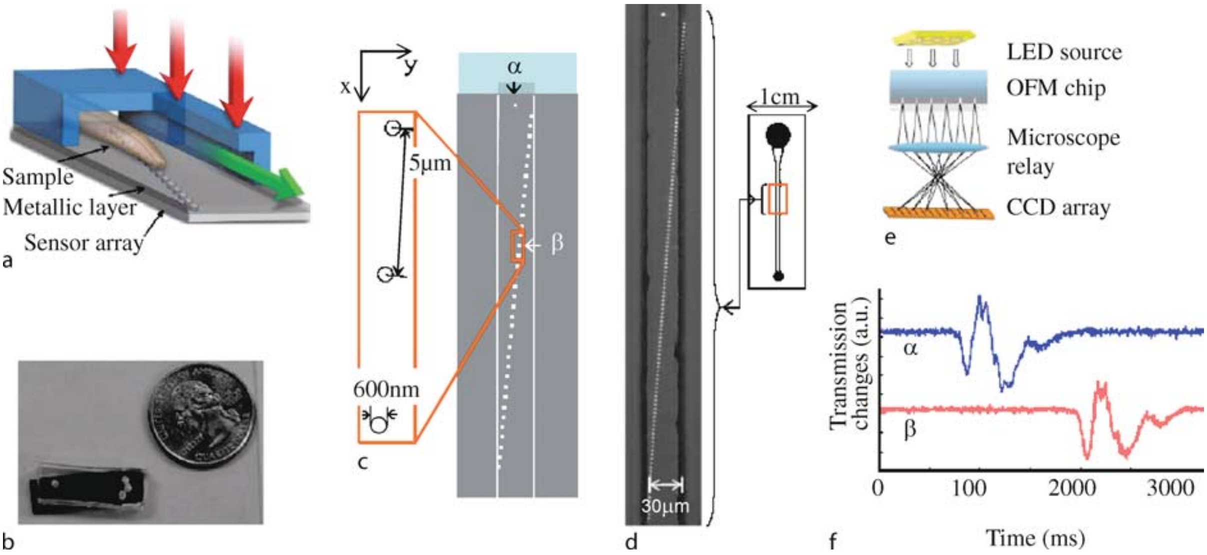

Optofluidics – Applications, Figure 2 **(a)** Architecture of the optofluidic microscope (OFM); set of three arrows: illumination; single arrow: flow direction. **(b)** Photograph of the OFM prototype compared with a U.S. quarter. The actual nanoaperture array is 600 mm long. **(c)** The top view of the OFM; a denotes the isolated aperture; b denotes the corresponding aperture, as explained in the text. **(d)** Photograph of the orientation of the aperture array with respect to the channel. **(e)** Experimental scheme for the OFM prototype. **(f)** Transmission time traces from aperture α and β associated with the transition of a C. elegans. Figure and Caption reprinted by permission from Heng et al. [8]

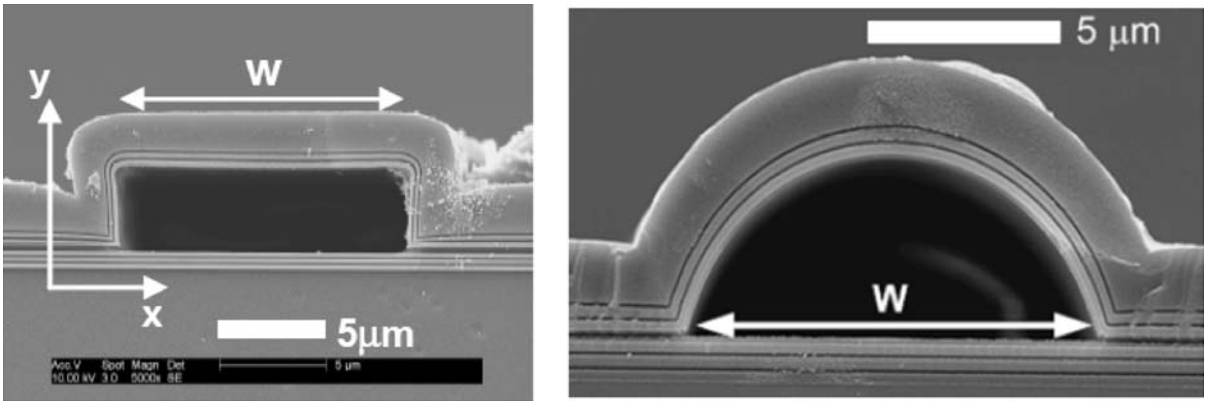

Optofluidics – Applications, Figure 3 SEM images of hollow-core ARROWs with rectangular and arch-shaped cross sections. Figure and Caption reprinted with permission from Yin et al. [11]

Optofluidic Lasers

Another limitation of existing Lab-on-Chip devices is the inability to encorperate active optical components directly into the same inexpensive structure that contains the microfluidic components. As a result of the widespread adoption of PDMS as a material of choice for microfluidic systems, there has been a large thrust towards creating structures which can be easily cast into the soft elastomer fluidics and provide this more advanced functionality. One such example was presented by Li et al. [10] who demonstrated an optofluidic dye laser. In their implementation, a solution of Rhodamine 6G lasing dye in a Methanol, Ethylene Glycol solution is introduced into a microfluidic channel. The refractive index of the solution ($n = 1.42$) is slightly higher than that of PDMS (1.406) at visible wavelengths so that the dye solution and PDMS act as the core and the cladding of an optical waveguide respectively. To provide the feedback mechanism, a Bragg grating is fabricated on the sidewall of the channel. Tunable laser output can be obtained by either changing the index of the dye solution or mechanically varying the grating period. In this work, lasing was demonstrated around the 585 nm point. Such lasers would be of great interest for on-chip spectroscopy and cell sorting applications.

Liquid Core Waveguides

Liquid core waveguides are of great importance in the field of optofluidics since they allow the optical and fluidic structures to be fundamentally intertwined. Recently Yin et al. [11] have demonstrated such a liquid core waveguide which works on the principle of antiresonant reflecting optical waveguides (ARROW), see Fig. 3. ARROW waveguides with solid cores have been used for semiconductor lasers and other applications in the past. The technique uses multiple layers of materials of precise thicknesses as cladding such that an antiresonant Fabry–Perot reflector is created causing the light at the design wavelength to reflect back into the core. Silicon nitride and silicon dioxide are used as the cladding layers because of their compatibility with microfabrication techniques and the potential for integration with silicon-based electronics. The cladding layers are deposited over a sacrificial layer that is later etched away to create a rectangular shaped hollow core. This hollow core can be filled with liquids or gases and has shown exceptional promise for low level, single molecule detection in fluidic systems. The architecture is also amenable to massively parallel integration by creating numerous waveguides on the same chip.

Another approach towards creating liquid core waveguides was demonstrated by Wolfe et al. [12]. They managed to manipulate light in waveguides comprising of a liquid core and a liquid cladding. These waveguides are dynamic and can be reconfigured and adapted in a continuous manner which is a big advantage over solid-state waveguides. The liquids are introduced into a microfluidic channel in such a manner so that the higher refractive index core liquid is sandwiched between two sheaths of the lower refractive index cladding fluid. Thus the light is guided via total internal reflection within the liquid core. Since the flow is laminar the liquid-liquid interface is optically smooth resulting in low optical losses. By varying the rate of flow and the fluid compositions the characteristics of these optical systems can be tuned.

Future Directions for Research

The technologies we have described above represent, in our opinion, those which show the most promise for future commercial development. Of what we have described here liquid lenses (such as that described by Kuiper and Hendriks liquid lenses [9]) are likely the closest to being mass produced and broadly commercially available. Though less well developed at present the other optofluidic imaging techniques may also serve to solve some of the fundamental downsizing challenges (those related to imaging) which have to date largely prevented the demonstration of a truly portable Lab-on-Chip. The inherent advantages of optical chromatography coupled with the very large size of the bio-analytical separations market seem to suggest that this could hold commercial potential in the near future.

Cross References

► Optofluidics – Optics Enabling Fluidics
► Optofluidics – Fluidics Enabling Optics
► Optofluidics – Fabrication and Integration Techniques

References

1. Grier DG (2003) A revolution in optical manipulation. Nature 424(6950):810–816
2. Wang MM, Tu E, Raymond DE, Yang JM, Zhang HC, Hagen N, Dees B, Mercer EM, Forster AH, Kariv I, Marchand PJ, Butler WF (2005) Microfluidic sorting of mammalian cells by optical force switching. Nature Biotechnology 23(1):83–87
3. MacDonald MP, Spalding GC, Dholakia K (2003) Microfluidic sorting in an optical lattice. Nature 426(6965):421–424
4. Imasaka T (1998) Optical chromatography. A new tool for separation of particles. Analusis 26(5):M53–M55
5. Terray A, Arnold J, Hart SJ (2005) Enhanced optical chromatography in a PDMS microfluidic system. Opt Express 13(25):10406–10415
6. Gaugiran S, Getin S, Fedeli JM, Colas G, Fuchs A, Chatelain F, Derouard J (2005) Optical manipulation of microparticles and cells on silicon nitride waveguides. Opt Express 13(18):6956–6963
7. Chiou PY, Ohta AT, Wu MC (2005) Massively parallel manipulation of single cells and microparticles using optical images. Nature 436(7049):370–372
8. Heng X, Erickson D, Baugh LR, Yaqoob Z, Sternberg PW, Psaltis D, Yang CH (2006) Optofluidic microscopy - a method for implementing a high resolution optical microscope on a chip. Lab on a Chip 6(10):1274–1276
9. Kuiper S, Hendriks BHW (2004) Variable-focus liquid lens for miniature cameras. Appl Phys Lett 85(7):1128–1130
10. Li ZY, Zhang ZY, Emery T, Scherer A, Psaltis D (2006) Single mode optofluidic distributed feedback dye laser. Opt Express 14(2):696–701
11. Yin DL, Schmidt H, Barber JP, Lunt EJ, Hawkins AR (2005) Optical characterization of arch-shaped ARROW waveguides with liquid cores. Opt Express 13(26):10564–10570
12. Wolfe DB, Conroy RS, Garstecki P, Mayers BT, Fischbach MA, Paul KE, Prentiss M, Whitesides GM (2004) Dynamic control of liquid-core/liquid-cladding optical waveguides. Proceedings of the National Academy of Sciences of the United States of America 101(34):12434–12438

Optofluidics – Fluidics Enabling Optics

David Erickson
Cornell UniversitySibley School of Mechanical Engineering, Ithaca, NY, USA
de54@cornell.edu

Synonyms

Photofluidics

Definition

Optofluidics is the marriage of optics, optoelectronics and nanophotonics with fluidics. Such integration represents a new approach to the dynamic manipulation of optical properties at length scales both greater than and smaller than the wavelength of light. Broadly speaking optofluidic devices can be split into two distinct classifications: optics enabling fluids and fluids enabling optics, the latter of which is the focus of this article.

Chemical and Physical Principles

The concept behind optical devices which incorporate liquids as a fundamental part of the optical structure can be traced at least as far back as the 18th century where rotating pools of mercury were proposed as a simple technique to create smooth spherical mirrors for use in reflecting telescopes. Modern microfluidics has enabled the development of a present day equivalent of such devices, the development of which we now refer to as Optofluidics. As will be described below, the capabilities in terms of fluidic control, mixing, miniaturization and optical property tuning afforded by micro-, nano- and electro-fluidics combined with soft lithography based fabrication provides an ideal platform upon which to build such devices.

Broadly speaking optofluidic devices can be classified into two distinct categories: *Optics enabling Fluidics* and *Fluidics enabling Optics*. As mentioned above in this article we focus on the latter of these two and refer readers to the ►optofluidics – optics enabling fluidics article within this encyclopedia for more detail. In this article we begin by describing the core fluid dynamics which describe the transport of fluids and behavior of interfaces in optofluidic devices. In the key research findings section we describe in detail the core advantages and applications of optofluidic devices (specifically looking at adaptive optics, biosensor and thermal stabilization). Following that provide a detailed example of the application of optofluidics to the tuning of photonic crystal circuits at the 200 nm scale.

The Fluid Dynamics of Optofluidic Devices

In the broadest sense, optofluidics involves the manipulation of the optical properties of a system using fluidics and conversely the manipulation of fluidic properties of a system with optics. It is thus is inherently concerned with both the optical and thermophysical properties of the fluid and the dynamics of how both the optical and flow fields change in response to external stimuli. In this section we will provide a brief overview of some of the fluids of particular interest in optofluidics and some of their important optical and thermophysical properties. The following subsection will provide a brief overview of the relevant microfluid dynamics with a focus on the issues of relevance to optofluidics.

Optofluids

Table 1 provides an overview of a small sampling of liquids of the relevant properties for a few common optofluidic liquids. Note that this represents a non-comprehensive list, other parameters of particular interest include: fluid–fluid surface tension, fluid–solid surface energy, contact angle, fluid–solid electroosmotic mobility, compatibility with soft elastomers (or other materials of interest), and numerous others.

Optofluid Dynamics

On length scales relevant to optofluidic devices (between 10 nm and 5 mm), fluid flow and species transport can be accomplished using numerous different techniques, a few of which include: traditional pressure driven flow, electrokinetic transport, buoancy, magnetohydrodynamics, capillarity, electrowetting and thermocapillarity (see Stone et al. [1] for a comprehensive overview). In general all flows can be classified as either body force driven (as in the former four of those listed above) and surface force driven (as in the latter three). Although examples exist to the contrary in general body force driven flows have been more successfully exploited in confined channel geometries, whereas free surface techniques are more popular for discrete droplet techniques. It is important to note that this statement is a general trend and by no means a rule (as capillarity, electrowetting and thermal manipulation of surface forces have all been used in channel driven geometries).

In either case fluid motion is governed by the momentum (Navier-Stokes) Eq. (1a) and continuity equations Eq. (1b) shown below,

$$\rho\left(\frac{\partial \boldsymbol{v}}{\partial t}+\boldsymbol{v}\cdot\nabla\boldsymbol{v}\right)=-\nabla p+\eta\nabla^2\boldsymbol{v}+f\,, \tag{1a}$$

$$\nabla\cdot\boldsymbol{v}=0\,, \tag{1b}$$

where $\boldsymbol{v}$, t, p, η, and ρ are velocity, time, pressure, viscosity and density respectively and f represents an applied body force. Though it is beyond the scope of this paper to provide a comprehensive review of the equations for all transport mechanisms mentioned above we will provide

Optofluidics – Fluidics Enabling Optics, Table 1 Some fluids used in optofluidic devices*

Fluid	Optical Properties: Refractive index, n	Temperature derivative, dn/dT (10^{-4} 1/K)	Non-linear refractive index, γ (10^{-20} m^2/W)	Thermophysical Properties: Viscosity, η (mPas)	Density, ρ (kg/m^3)	Thermal conductivity, k (W/mK)
Water, H_2O	1.33299	−0.8	2.7[b]	0.890	997.05	0.6071
Heavy Water, D_2O	1.32828	–	6.4[c]	–	1104.4	–
Methanol, CH_4O	1.33118	−4.68[a]	4.7[b]	0.544	787.2	0.200
5.03M Aqueous $CaCl_2$	1.4420	–	–	8.997	1395.7	–
Ethylene glycol, $C_2H_6O_2$	1.4318	−3.06[a]	–	16.1	959.8	0.256
Carbon disulfide, CS_2	1.6319	−8.00	310–360[b]	0.35 2	1255.6	0.149

* Except where indicated properties are given at room temperature conditions and measured at 590 nm. [a] = measurement reported at 600 nm, [b] = measurement reported between 530 nm and 532 nm, [c] = measurement reported at 1060 nm

a brief overview of some of those mechanisms which may be most appropriate for optofluidics.

Pressure driven flow, for which f is zero in Eq. (1a), tends to be the simplest transport mechanism to implement and is accomplished by applying a mechanical pressure difference between an inlet and an outlet port. For the simplest case of pressure driven flow in a microchannel with low aspect ratio it can be shown that the average velocity in the channel is described by Eq. (2) below,

$$v_{\text{ave}} = \frac{h^2}{12\eta}\nabla P\,, \tag{2}$$

where h is the channel height. The geometric dependence of velocity shown in Eq. (2) represents the most significant weakness of pressure driven fluidics in that as one approaches the nanoscale the flow velocity either becomes debilitatingly small or the required pressure exceedingly high.

Alternatively a different transport mechanism can be used which does not exhibit such a fundamental limitation. In electrokinetic transport results from the interaction of an externally applied electric field, $\nabla\phi$, with the net charge density ρ_e, in the electrical double layer (the body force term in Eq. (1a) becomes $f = \rho_e\nabla\phi$). The electrical double layer is a very thin region of non-zero net charge density near the interface (in this case a solid–liquid interface) and is generally the result of surface adsorption of a charged species and the resulting rearrangement of the local free ions in solution so as to maintain overall electroneutrality. In general it can be shown that for electroosmotic flow in a channel with uniform properties Eq. (1a) reduces to a flat velocity profile (as opposed to the parabolic velocity profile associated with pressure driven flow) whose velocity is described by that below,

$$v_{\text{ave}} = \frac{\varepsilon_w\varepsilon_o\zeta}{\eta}\nabla\phi = \mu_{eo}\nabla\phi \tag{3}$$

where μ_{eo} is the electroosmotic mobility and ε_o and ε_w are the dielectric permittivity of a vacuum and the local relative dielectric permittivity (or dielectric constant) of the liquid respectively. In general μ_{eo} is of the order 10^{-4} cm^2/Vs and flow velocities on the order of 1 mm/s are achievable with applied potential fields of 1000 V/cm. The advantage of electrokinetic flow are that the flow velocity does not scale with channel height (outside the limit of double layer overlap and then only weakly until the extreme cases) and thus is more appropriate for nanoscale fluidics. The most significant disadvantage is that μ_{eo} is highly sensitive to the conditions at the solid liquid interface and is thus only applicable to a limited class of fluids, typically aqueous based solution. Even within this class μ_{eo} is strongly dependent with on ionic concentration and becomes exceedingly small in the high molarity (i. e. high refractive index) solutions listed in Table 1. Electrokinetics in high molarity solutions also tends to have other difficulties such as joule heating. The coupling of these effects complicates the use of electrokinetics for optofluidic devices.

As mentioned above, the other class of fluidic manipulation of particular interest in optofluidic applications are surface force driven techniques. In such techniques fluidic motion is induced applying an external perturbation to the equilibrium conditions at the interface between two phases. The normal stress conditions at the interface between two phases is described by Eq. (4) [2].

$$(p - \tau_{nn})_a - (p - \tau_{nn})_b = \sigma\left(\frac{1}{R_1} + \frac{1}{R_2}\right) \tag{4}$$

where the subscripts a and b represent the two phases τ_{nn} is the stress normal to the interface, σ is the surface tension and R_1 and R_2 are the principal radii of curvature. The applied perturbation, which most commonly is either electrically (i. e. electrowetting), thermally or chemically

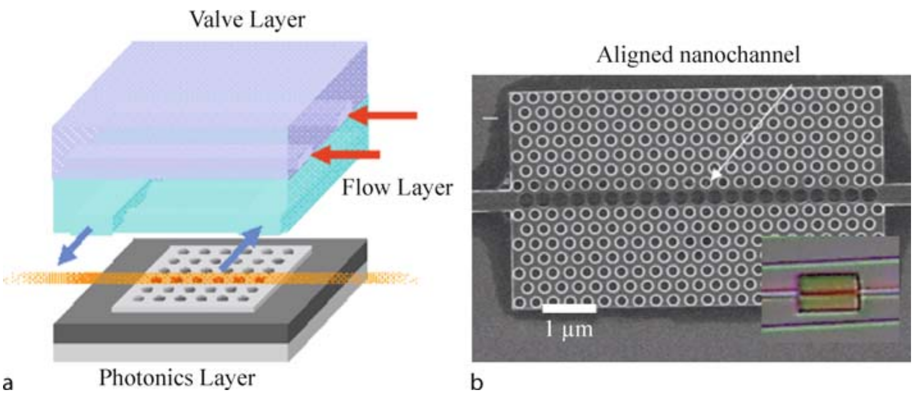

Optofluidics – Fluidics Enabling Optics, Figure 1 Nanoscale Optofluidic Integration. Multilayer soft lithography is used to fluidically address and tune photonic structures at the nanoscale. (**a**) shows schematic of multi-layer soft-lithography coupling with nanophotonics. (**b**) SEM image of nanoscale precision fluidic addressability in a photonic crystal

based, induces a local change in either the surface tension or curvature (often observed as a change in the solid–fluid contact angle) which, from Eq. (4), in turn results in a pressure gradient and subsequent motion within at least one of the phases. While such techniques have proven extremely successful for both optical and Lab-on-Chip type devices, the activation energy required to overcome surface roughness tends to limit such effects to relatively large droplet sizes.

Key Research Findings

As mentioned above the focus of this section is to describe some of the core applications for optofluidic devices.

Optofluidics for Adaptive Optics

A key factor for high performance adaptive optical system is the capability to dynamically control either the physical layout or the refractive indices of the optical components. Recent advancements in optical MEMS technology [3] has provided significant functionality and flexibility to the former of these (e. g. optical switching and reconfigurable mirror arrays). Traditional techniques for manipulating the refractive index through the application of electric, acoustic or mechanical strain fields are limited in this respect by the achievable $\Delta n/n$, as is shown in Table 2. Optofluidics offers an order of magnitude jump in this quantity allowing for the development of an entirely new class of adaptive optical system in which, when combined with soft lithography based nanofluidics, the index of refraction can in principal be arbitrarily reconfigured at scales significantly smaller than the wavelength of light. At present modulation speeds for such tuning can be in the millisecond range but are ultimately limited by the viscous nature of the process and the mechanical actuation techniques that are popularly used. Alternative transport mechanisms such as electrokinetics (discussed in the following section) could be used to reduce the time response even further, though likely not to the scale required for high speed optical switching applications.

Optofluidics – Fluidics Enabling Optics, Table 2 Comparison of optofluidics with traditional optical tuning techniques

Technology	$O(\Delta n/n)$	Time response (s)
Optofluidics	**1**	$\mathbf{10^{-3}}$
Liquid crystal	0.1	10^{-3}
Injection current	0.02	10^{-9}
Temperature	0.02	1
Photorefractive	0.001	10^{-1}–10^{-5}
Electrooptic (10 kV/cm)	0.002	10^{-12}
Photoelastic/ Acoustooptic (10 W)	0.0001	10^{-6}–10^{-7}

Optofluidic Biosensors

The integration of microfluidics with optical detection techniques has been a field of active interest for several years (see Prasad [4] for an overview of optical biosensors and Erickson and Li [5] for an overview of integrated microfluidic devices). In addition to traditional florescence based detection, techniques relying on the incorporation of planar waveguides, evanescent wave fields or surface plasmons are particularly suitable for integration with microfluidics. While such techniques have proven exceptionally successful, a particularly fruitful path for future research in optofluidics is in the development of resonant cavity sensors. Such sensors can take advantage of the extremely high quality factor to mode volume ratios (Q/V) achieved in nanophotonic structures to perform single or few molecule sensing. The challenges here will be to not only develop techniques for deliver-

ing, attracting or concentrating bioentities into the resonant cavities, but being able to perform highly specific detection as well.

Optofluidics for Thermal Stabilization

The incorporation of liquids directly into the optical structure also has inherent advantages in terms of temperature stabilization. In general the heat transfer coefficient (which is the proportionality constant between heat rejection and surface temperature) for systems immersed in air ranges from 10 W/m^2K to 100 W/m^2K, depending strongly on the geometry and flow velocity. As a result of the higher density, specific heat capacity and thermal conductivity of water immersed systems, heat transfer coefficients typically range from 500 W/m^2K to 10,000 W/m^2K thus representing at least an order of magnitude decrease in the temperature rise for a given heat rejection requirement. It is important to note that while this represents a general rule for global heat transfer, more detailed modeling is required to accurately predict the local heat transfer enhancement.

Examples of Application

Since the emergence of optofluidics as a distinct field around 2002, a number of prominent examples of the fusion of these technologies have been developed including: liquid crystal infused photonic crystal lasers, fluid-fluid waveguides and florescent light sources, polarization independent fluidic switches, microfluidically tuned optical fibers and interferometers, and electrowetting based adaptable fluidic lenses and electronic paper. Rather than providing a cursory overview of these different devices in the limited space available here, we choose to focus on our recent work on nanofluidically tunable photonic crystal circuits [6] as a representative example. Readers looking for broader detail should consult the article within this encyclopedia entitled ► optofluidics – fabrication and integration or the recently published work by Psaltis et al. [7]. As mentioned above and shown in Table 2, at present techniques for local refractive index modulation in photonic structures are limited to the exploitation of relatively weak non-linearities, where $\Delta n/n$ on the order of 10^{-3} or lower. The consequence of this is that they require long interaction lengths, high operational power, or the incorporation of resonant elements to enhance the effect. The advantage of these techniques is that they can be, in general, applied locally to single devices (a necessity for device integration). Alternative techniques such as mechanical deformation, thermooptics, liquid crystal infusion and liquid-fluid infusion (amongst others) offer much higher effective $\Delta n/n$. At present, however, these methods rely on globally modifying the refractive index of the entire

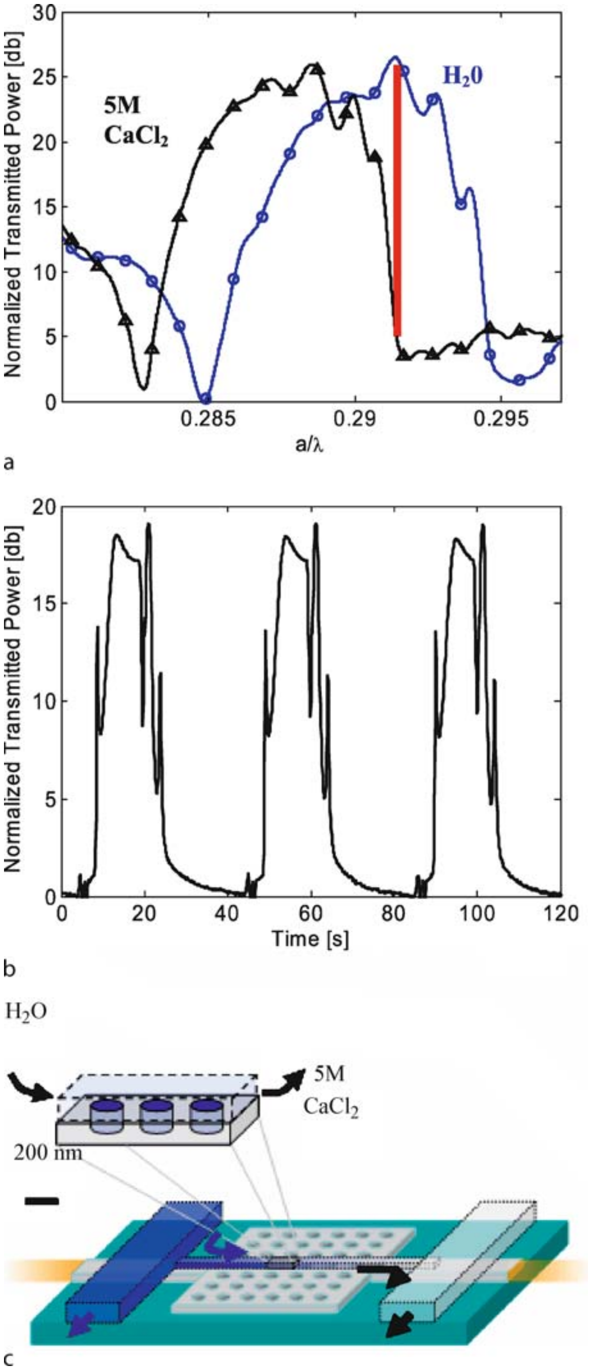

Optofluidics – Fluidics Enabling Optics, Figure 2 TE-like transmission through photonic crystal with aligned nanochannel. (**a**) Shift in transmitted power spectrum when aligned nanochannel filled with H_20 ($n = 1.33$) and 5M $CaCl_2$ ($n = 1.44$) (**b**) Dynamic switching at $a/\lambda = 0.291$ (shown as *red line* in (**a**)) (**c**) Rendition of the switching process

device. Thus whereas local tunability over small interaction lengths requires the high $\Delta n/n$ afforded by these

global approaches, the ability to perform such manipulations with the sub-micron scale precision required for advanced photonic devices remains elusive. The development of such a technique could enable the creation of a new class of ultra-compact adaptable photonic circuits.

Nanofluidics provides a solution that enables both localized control and high refractive index modulation. As a first step in the development of two dimensional reconfigurable photonic circuits, here we demonstrate the nanofluidic addressing and tuning of individual defects within planar photonic crystals. Photonic crystals are attractive for controlling optical propagation by introducing pre-engineered defects into an otherwise regular lattice to create spectral filters, tight bend waveguides, resonant cavities and highly efficient lasers. Figure 1 outlines our approach which follows a three level nanoscale optofluidic integration architecture approach comprising of:

1. a nanophotonic level. Fabricated in silicon on insulator with the appropriate device structure.
2. a ► nanofluidic level, which serves to deliver fluids directly into the photonic structure and
3. a microfluidics control engine that performs all the major fluidic manipulations.

Assembly of the structure is performed by first defining the nanofluidic layer in positive relief on SOI and then defining the microfluidic structure on the same device using standard photolithography. At the same time a microscale valve layer is also defined in positive relief using photolithography on a separate silicon wafer. The two layers are then cast in PDMS, aligned and bonded together using standard multilayer soft lithography techniques [8]. The assembled fluidic structure is then aligned and bonded (through plasma oxidation) to the photonics layer. Using this structure fluids with different linear and non-linear optical properties can be infused directly into the nanophotonic structure with excellent precision and without significant leaking as shown in Fig. 1.

Figure 2 shows the normalized quasi-TE mode transmission through the photonic crystal with a fluidically modulated waveguide for DI ($n = 1.33$) water and 5M $CaCl_2$ ($n = 1.44$). The results show a shift in the peak transmission of the guided mode from $a/\lambda = 0.291$ to $a/\lambda = 0.289$ (corresponding to $\lambda = 1491$ nm and 1502 nm respectively) when the lower index liquid is displaced by the higher index salt solution. The high $\Delta n/n$ afforded by nanofluidic modulation demonstrated here enables consistently high contrast over a relatively wide range of wavelengths. Increasing the $\Delta n/n$ of the switching solutions would provide a greater shift in the peak transmission of the guided mode, however it would not provide for a much higher extinction ratio. Dynamic modulation of the transmitted power is demonstrated in Fig. 2 at $a/\lambda = 0.291$ by fluidically switching between the DI water and $CaCl_2$ solutions. For reasons described above, the modulation speed is inherently limited by the use of pressure driven flow. While the length of the nanochannels could be reduced the most fundamental limitation on the speed of such device is the nanochannel width section which is fixed by the lattice constant of the photonic crystal. Alternative fluidic transport mechanisms such as electroosmotic flow are mentioned above as a possibility, however here the low electroosmotic mobility of the $CaCl_2$ solution made such an approach not feasible.

Cross References

► Optofluidics – Optics Enabling Fluidics
► Optofluidics – Fabrication and Integration

References

1. Stone HA, Stroock AD, Ajdari A (2004) Engineering flows in small devices: Microfluidics toward a lab-on-a-chip. Ann Rev Fluid Mech 36:381–411
2. Panton R (1996) Incompressible Flow. John Wiley & Sons, New York
3. Lin LY, Goldstein EL (2002) Opportunities and challenges for MEMS in lightwave communications. IEEE J Selec Topics Quantum Electron 8(1):163–172
4. Prasad P (2004) Nanophotonics. Hoboken, John Wiley and Sons, Inc, New Jersey
5. Erickson D, Li DQ (2004) Integrated microfluidic devices. Anal Chimica Acta 507(1):11–26
6. Erickson D, Rockwood T, Emery T, Scherer A, Psaltis D (2006) Nanofluidic tuning of photonic crystal circuits. Opt Lett 31(1):59–61
7. Psaltis D, Quake SR, Yang CH (2006) Developing optofluidic technology through the fusion of microfluidics and optics. Nature 442(7101):381–386
8. Unger MA, Chou HP, Thorsen T, Scherer A, Quake SR (2000) Monolithic microfabricated valves and pumps by multilayer soft lithography. Science 288(5463):113–116

Optofluidics: Optics Enabling Fluidics

ALLEN YANG, DAVID ERICKSON
Cornell UniversitySibley School of Mechanical Engineering, Ithaca, NY, USA
ay38@cornell.edu, de54@cornell.edu

Synonyms

Photofluidics; Waveguide trapping; Waveguide propulsion; Radiation pressure; Optical trapping

Definition

In the broadest sense, Optofluidics involves the manipulation of the local optical properties of a system using fluids and flow behavior and, conversely, the manipulation of fluids and particles within a flow through optical forces. The latter is inherently concerned with both the optical and thermophysical properties of the fluid and the dynamics of how both the electromagnetic and flow fields change in response to external stimuli. Optical forces used to manipulate fluid and particle behavior can arise either from focused beams in free space or from guided light confined to defined planar structures though total internal reflection. This emerging field of study is currently focused on the understanding of the fundamental coupling between optical dynamics and hydrodynamics, and developing methods to exploit the unique advantages optically derived forces have for micro and nanoscale systems.

Chemical and Physical Principles

The idea of using optical forces for particle manipulation was pioneered by Arthur Ashkin [1] in 1970, when he detailed the scattering and gradient force effects for small particles in the presence of optical energy. Since then, the field has developed to include many other methods to confine and move particles/fluids through the use of optical energy. The first experiments conducted using optical traps dealt with the manipulation of spherical beads within a stagnant liquid and the characterization of the forces observed acting on particles due to the presence of a focused laser beam [2]. With the development of microfluidics, experiments and studies of flow behavior could be conducted on scales similar to those on which optical phenomena occur. Thus, it becomes possible to study systems where coupled fluid and optical dynamics become important. The end goal is to develop nanoscale systems where optics can be exploited as a fundamental transport mechanism.

Free-space optical manipulation techniques in microfluidic systems have recently generated a significant amount of interest. Classically the advantage of these optical approaches lies in their ability to provide remote operation and handle individual particles directly as opposed to indirect manipulation of the surrounding flow field. The precision with which particles can be transported and separated with these optical techniques makes them particularly useful for bio-medical analysis devices. While extremely flexible and relatively easy to implement (see the section on ► optofluidics – applications and ► optofluidics – techniques for fabrication and integration), these systems are ultimately limited by the fundamentals of the free-space optics. Specifically, the light-particle interaction length is

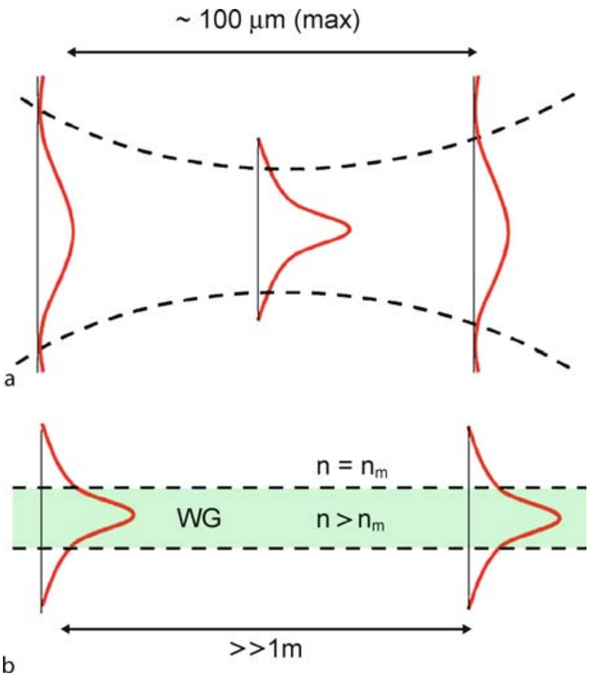

Optofluidics: Optics Enabling Fluidics, Figure 1 Comparison between optical energy concentration for (**a**) free space and (**b**) a dielectric waveguide. WG = waveguide, n = refractive index

O

limited by either the focal depth or the spot size of the objective lens to usually a few hundred microns, as shown in Fig. 1. Using a more loosely focused lens with a larger spot size can increase the interaction length to as much as a millimeter. The intensity however scales with the square of the beam radius and as such relatively large optical power is required to perform manipulations over even these relatively small length scales.

A waveguide relies upon the principles of total internal reflection to confine light within the solid waveguide structure [3]. Though the light is confined to propagate in a single direction, an exponentially decaying component of the optical mode, known as the evanescent field, extends outside the waveguide. The degree of this extension depends on the refractive index contrast between the waveguide and the surrounding media, however is generally on the order of a few 100 nm for visible and near infrared light. The optical gradient in the evanescent field partially polarizes the particle near the waveguide, resulting in an extremely strong gradient force. This serves to attract the particle to the waveguide surface, where the electric field strength is highest. Waveguides for visible light can be fabricated from many types of materials and in different forms. For infrared light, silicon is a better material due to its relatively high transparency in the 1550 nm range and well defined fabrication methods. Planar waveguides are of

unique interest for optofluidics for the relatively simple methods for incorporating both microfluidic and optical elements on the same chip.

Optical Forces

There are three types of forces associated with electromagnetic fields, the scattering and absorption forces which account for radiation pressure, and the gradient trapping force. The scattering and absorption propagation forces can be physically described as the momentum transfer associated with the scattering and absorption of a photon from an incident electromagnetic source. For a dielectric particle, these forces can be described as an electromagnetic stress using the Maxwell stress tensor [4]:

$$\boldsymbol{F}_{\mathrm{EM}} = \oint_S \left(\langle \mathbf{T}_{\mathrm{EM}} \rangle \cdot \boldsymbol{n}\right) \mathrm{d}S \tag{1}$$

$$\mathbf{T}_{\mathrm{EM}} = \varepsilon\varepsilon_0 \boldsymbol{E}\boldsymbol{E} + \mu_0 \boldsymbol{H}\boldsymbol{H} - \frac{1}{2}\left(\varepsilon\varepsilon_0 \boldsymbol{E}\cdot\boldsymbol{E} + \mu_0 \boldsymbol{H}\cdot\boldsymbol{H}\right)\mathbf{I} \tag{2}$$

where $\boldsymbol{T}_{\mathrm{M}}$ represents the Maxwell stress tensor and $\boldsymbol{n}$ is the surface normal vector, $\boldsymbol{E}$ and $\boldsymbol{B}$ are the instantaneous electric and magnetic fields respectively, $\mathbf{I}$ is the identity tensor, ε_0 and μ_0 are the electric permittivity and magnetic permeability in vacuum and ε is the dielectric constant of the surrounding medium. It can be shown that the time averaged stress tensor then becomes,

$$\langle \mathbf{T}_{\mathrm{EM}} \rangle = \frac{1}{2}\,\mathrm{Re}\left[\varepsilon\varepsilon_0 \boldsymbol{E}(r)\boldsymbol{E}^*(r) + \mu_0 \boldsymbol{H}(r)\boldsymbol{H}^*(r) - \frac{1}{2}\left(\varepsilon\varepsilon_0 \left|\boldsymbol{E}(r)\right|^2 + \mu_0 \left|\boldsymbol{H}(r)\right|^2\right)\mathbf{I}\right] \tag{3}$$

where $\boldsymbol{E}^*$ and $\boldsymbol{H}^*$ represent complex conjugates. In Eq. (1) the integration is performed in a surface which encloses the particle of interest and returns the total electromagnetic force on the particle, including scattering, absorption and gradient forces. The latter of these physically results from the temporary polarization of a dielectric particle by the electric field. The instantaneous interaction of the dipole with a non-uniform electric field results in a force directed towards the high-intensity regions of the electric field.

Analytical Simplification: As mentioned above, the mechanism for propulsion in the proposed system is based on the summation of the scattering and absorption forces applied to a particle trapped, expressed most generally through Eq. (1) through Eq. (3) above. We can simplify these equations significantly by considering the case of a Rayleigh particle, as described by Svoboda and Block [7] (amongst others). For such a case we can derive analytical expressions for these forces given by Eq. (4a) and (4b) respectively,

$$F_{\mathrm{scat}} = \frac{8\pi^3 I_0 \alpha^2 \varepsilon_{\mathrm{m}}}{3c\lambda^4} \tag{4a}$$

$$F_{\mathrm{abs}} = \frac{2\pi\varepsilon_{\mathrm{m}} I_0}{c\lambda} Im(\alpha) \tag{4b}$$

where $\alpha = 3V(\varepsilon - \varepsilon_{\mathrm{m}})/(\varepsilon + 2\varepsilon_{\mathrm{m}})$, V is the particle volume, c and λ are the speed and wavelength of light, ε_{p} and ε_{m} are the dielectric constants of the particle and material and I_0 is the incident intensity.

Fluid Mechanics

The details of fluid mechanics on the micro- and nanoscales are well described throughout this encyclopedia and thus to minimize duplication here we will focus primarily on introducing the governing equations relevant to the remainder of our discussion. As is well known fluid motion is governed by the momentum Eq. (5) and continuity equations Eq. (6) shown below [8],

$$\rho\left(\frac{\partial \boldsymbol{v}}{\partial t} + \boldsymbol{v}\cdot\nabla\boldsymbol{v}\right) = -\nabla p + \eta\nabla^2\boldsymbol{v} + f\,, \tag{5}$$

$$\nabla\cdot\boldsymbol{v} = 0\,, \tag{6}$$

where v, t, p, η, and ρ are velocity, time, pressure, viscosity and density respectively and f represents an applied body force. Flow in channels with the low Reynolds number regime (which is almost exclusively the case in nanometer and micrometer scale confined geometries) is dominated by the diffusive transport terms, leading to the Stokes equation:

$$\nabla p = \eta\nabla^2\boldsymbol{v} + f \tag{7}$$

In optofluidic transport we are typically concerned with the interaction of the flow field with the transported species and thus the hydrodynamic quantity of interest is typically the total flow force on the particle. This is described by the integral of the normal component of the total stress tensor, $\mathbf{T}_{\mathrm{f}}$, around the particle boundary given by,

$$\boldsymbol{F}_{\mathrm{FLOW}} = \oint_s \left(\mathbf{T}_{\mathrm{f}}\cdot\boldsymbol{n}\right)\mathrm{d}S \tag{8a}$$

$$\boldsymbol{F}_{\mathrm{FLOW}} = \oint_s \left([p\boldsymbol{I} + \eta\nabla\boldsymbol{v}]\cdot\boldsymbol{n}\right)\mathrm{d}S \tag{8b}$$

where $\boldsymbol{n}$ is the surface normal. In the absence of any interaction with the confining geometry (which is commonly the case for free space optofluidics, but rarely the case for planar or waveguide based optofluidics) an analytical solution to Eqs. (8a) and (8b) is available in the form of Stokes drag law:

$$F_{\text{stokes}} = 6\pi\eta a U_0 \tag{9}$$

where U_0 is the particle velocity. Note that variants on Eq. (9) have been derived to account for the added influence of the channel side walls on the viscous drag (Faxen's law).

Key Research Findings

In this section we split recent research findings into two sections. In the first of these we will present a series of calculations illustrating the potential velocities achievable through optofluidic propulsion. In the second section we will discuss the trapping stability of a particle in an evanescent field subject to a cross flow.

Propagation Velocity

When this particle interacts with an optical field, a certain percentage of the photons which flow through the system are either scattered (radiated in a random direction) or absorbed when they contact the particle. Each of these photons has a momentum given by Planck's constant multiplied by the frequency, $h\nu$. These scattering and absorption events result in momentum transfer to the particle and a net forward velocity which is proportional to intensity and impeded by fluid drag. By equating the scattering and absorption forces exerted by a Gaussian optical front, Eqs. (4a) and (4b) on a Rayleigh (i. e., sub wavelength) particle with Stokes drag, Eq. (9) we obtain,

$$U_0 = \frac{\varepsilon_m I_0}{6ac\eta}\left(\frac{8\pi^2\alpha^2}{3\lambda^4} + \frac{2I\,m(\alpha)}{\lambda}\right), \tag{10}$$

In Eq. (10) the first term in brackets represents the scattering force and the second the absorption.

Figure 2 shows the computed propagation velocities from Eq. (10) for a (a) silica nano-particle ($\varepsilon_p = 2.4$), which is weakly absorbing, and (b) a gold nanoparticle, which is strongly absorbing ($\varepsilon_p = -80 + 10i$). From this figure it is apparent that at moderate optical powers, relatively high velocities are possible even at relatively long wavelengths (the scattering velocity scales with $1/\lambda^4$). Note that in the caption of Fig. 2 we refer to the peak intensity used to calculate the above ($0.8\,\text{W}/\mu\text{m}^2$) as being equivalent to 100 mW of power in a 200 nm by 600 nm silicon waveguide. For this comparison we have assumed an optimized system such that the peak in optical intensity occurs directly at the interface between the waveguide and surrounding medium (a technique developed by Ng et al. [9]). This comparison also ignores the influence of the surface on the drag force (see above) and this Eq. (10) is likely to overestimate the actual propulsive velocity for the waveguide system. This result however is accurate for the free space system and can provide some estimates of the expected performance for waveguide based propulsion. Also note that the absorption component of

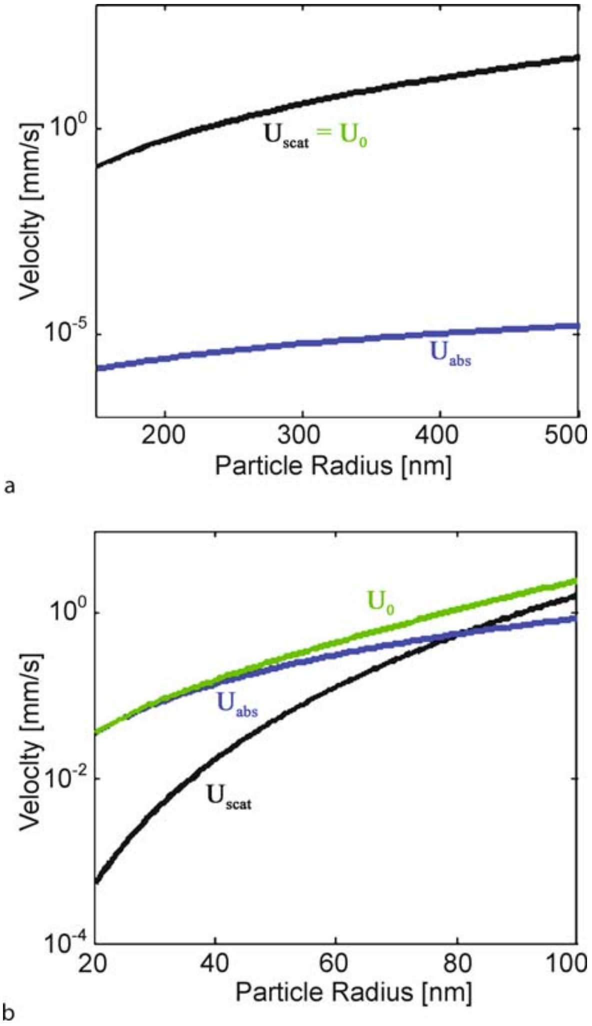

Optofluidics: Optics Enabling Fluidics, Figure 2 Propagation velocity estimates for Silica (**a**) and Gold Nanoparticles (**b**) on a Silicon Waveguide. U_{abs} and U_{scat} represent the absorption and scattering components of Eq. (10) and U_0 is the summation of the two. Velocities are for calculated for a peak intensity of $0.8\,\text{W}/\mu\text{m}^2$ at 1550 nm. This is approximately equivalent to that obtainable for 100 mW of power in a 200 nm by 600 nm silicon waveguide shown in Fig. 3

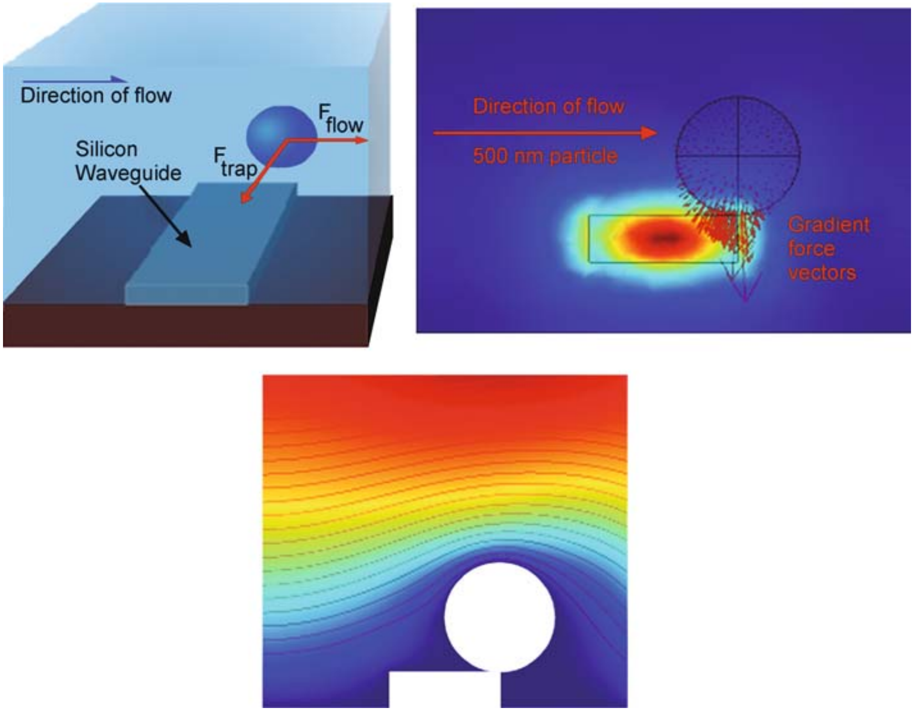

Optofluidics: Optics Enabling Fluidics, Figure 3 Optofluidic architecture for waveguide based transport (**a**) diagram of fluid/electro-magnetic coupling at waveguide interface. (**b**) Cross Section of guided mode with arrows showing surface normal electromagnetic forces (Simulation is 3D). (**c**) Cross section image of the magnitude of fluid velocity along with calculated streamlines

velocity for the silica particle results from the imaginary component of the dielectric constant of water at 1550 nm. For smaller absorping particles, such as gold, the scattering force becomes less significant below 100 nm and the absorption forces begin to dominate.

As mentioned above, in a waveguide system, the optical intensity (power/area) is governed by the geometry cross section of the waveguide which can be much smaller than the diffraction limit for a tightly focused free space spot (these calculations are done for the 200 nm tall waveguide shown in Fig. 3 which compares with the diffraction limited spot size which is on the order of 620 nm diameter). As such much lower optical power is required. At the same time the index contrast confines the energy over an indefinite spatial length. As this waveguide is made smaller the intensity increases and with it the net velocity. As such smaller devices have the potential for faster transport, which could impact emerging nanofluidic devices.

Particle Trapping in an Evanescent Field

Although estimates can be made regarding the propagation velocity of a particle once it has been trapped, one of the key questions which must be addressed in order for this to be a translated into a useful technology is the strength of the Lorenz trapping force compared with Brownian motion and the presence of a cross flow. We have examined this here by performing a series of numerical simulations that examine the waveguide/dielectric particle geometry shown in Fig. 3 subject to a pressure driven cross flow. As can be seen in Fig. 3b, the evanescent mode extends outside the waveguide decaying exponentially into the surrounding medium with a portion of it interacting with the particle. For the electromagnetic simulations, Maxwell's equations were solved for the electric and magnetic fields in the waveguide, and the forces on a spherical glass particle were evaluated using Eq. (1). Continuity of the electromagnetic equations are maintained for all internal boundaries, while the surrounding boundaries allow the flux of scattered light, as would be expected in a unbounded fluid medium. The inlet and outlet boundary conditions use the numerical solution from an eigenvalue solver used to determine the guided and evanescent mode profiles.

Simulation results for a glass bead of varying size were evaluated at different positions along the surface of the waveguide. The magnitude of the trapping force on a particle is determined largely by the size and position of the particle relevant to the evanescent field. As seen in Fig. 4,

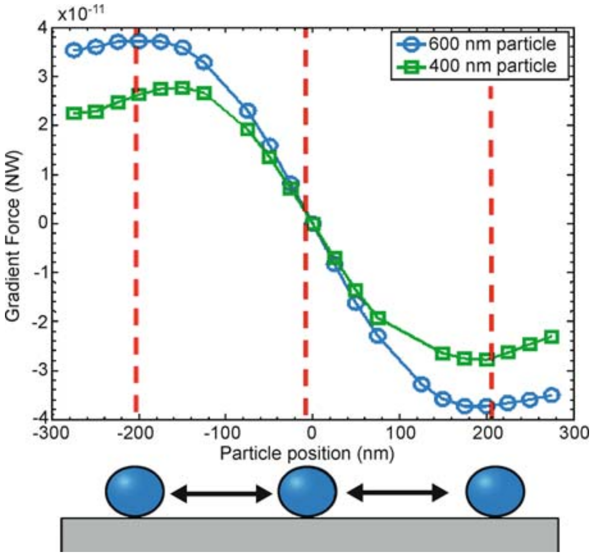

Optofluidics: Optics Enabling Fluidics, Figure 4 Electromagnetic force on a particle as a function of position. Gradient force calculated for 600 and 400 nm spherical glass particles on a silicon waveguide. A critical maximum in the trapping force is observed for positions ~ 175 nm from the center of the waveguide

for a 600 and 400 nm glass bead, the strongest forces are 200 nm from the center of the waveguide. Note that the forces are directed towards the center of the waveguide, the region of highest intensity (as seen in Fig. 3b). The reason the maximum force does not correspond to the edge of the waveguide surface results from the size of the particle relative to the evanescent field and the radius of curvature of the particle. Smaller particles, and thus those which have a larger radius of curvature have a sharper peaks compared to larger particles. Additionally, the hydrodynamic force as a function of particle position can be considered. In the region from $x = 150$ to $x = 300$, where the critical trapping region would be, the hydrodynamic force on the particle remains constant with respect to position.

Simulations were conducted to determine the relationships describing the electromagnetic and hydrodynamic forces acting on a single sphere in the waveguide geometry. For particles ranging in size from 50 – 600 nm in diameter, the forces in the trapping direction acting on the particle were evaluated. Shown in Fig. 5, the gradient forces at the stable point with respect to size exhibit a near-linear relationship for particle sizes larger than 200 nm. This arises from the positioning of the particle at the edge of the waveguide, thus allowing large portions of the surface area of the particle to sample lower field intensities (in the region beyond the waveguide edge) relative to areas near the waveguide surface, creating a large gradient in the surface force profile. On the other hand, the hydrodynamic force

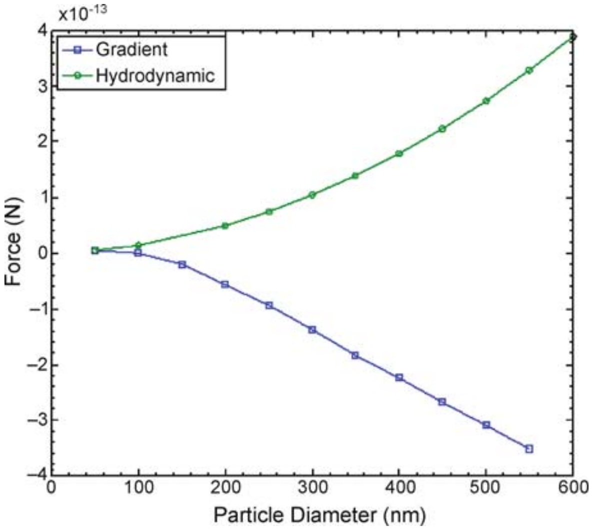

Optofluidics: Optics Enabling Fluidics, Figure 5 Gradient and Hydrodynamic Forces. Forces plotted for glass particle sizes from 50 to 1000 nm. Forces evaluated at edge of waveguide, as illustrated in Fig. 3

exhibits a non-integer power-law relationship. In the standard stokes drag scenario, the hydrodynamic drag on a particle has a linear relationship with respect to size, but this is in the presence of a uniform velocity field. In the presence of a parabolic flow profile, along with a waveguide geometry that serves to disturb the flow field, it is highly probable that a higher order relation exists in this case.

O

Examples of Application

Please see experimental application article ► optofluidics – fluidics enabling optics which details the use of direct and indirect optical forces in the manipulation of particles for a variety of applications.

Cross References

► Optofluidics - Fluidics Enabling Optics

References

1. Ashkin A (1970) Acceleration and Trapping of Particles by Radiation Pressure. Phys Rev Lett 24(4):156
2. Svoboda K, Block SM (1994) Biological Applications of Optical Forces. Ann Rev Biophys Biomol Struc 23:247–285
3. Saleh DEA, Teich MC (1991) Fundamentals of photonics. Wiley, New York
4. Jackson JD (1975) Classical electrodynamics. Wiley, New York
5. Melcher JR (1981) Continuum electromechanics. MIT Press, Cambridge
6. Gaugiran S, Getin S, Fedeli JM, Colas G, Fuchs A, Chatelain F, Derouard J (2005) Optical manipulation of microparticles and cells on silicon nitride waveguides. Opt Exp 13(18):6956–6963
7. Svoboda K, Block SM (1994) Optical Trapping of Metallic Rayleigh Particles. Opt Lett 19(13):930–932

8. Panton RL (2005) Incompressible Flow. Wiley, New York
9. Ng LN, Luf BJ, Zervas MN, Wilkinson JS (2000) Forces on a Rayleigh particle in the cover region of a planar waveguide. J Lightwave Technol 18(3):388–400

Optofluidics – Techniques for Fabrication and Integration

Roman Akhmechet, David Erickson
Sibley School of Mechanical Engineering,
Cornell University, Ithaca, NY, USA
ra224@cornell.edu, de54@cornell.edu

Synonyms

Photofluidic devices

Definition

Optofluidic devices integrate within themselves elements of microfluidics, optics, and electronics. Although methods for fabricating each of the components separately are reasonably well known, difficult challenges exist in developing architectures that enable the integration of all these functionalities onto a single device. Though approaches differ from device to device, the goal is to make fabrication as easy and affordable as possible. In this article we present an overview of the fabrication technologies and integration architectures for optofluidic devices. We will also discuss these techniques in the context of a sampling of the state of the art from the literature.

Overview

Choosing an appropriate fabrication process and integration architecture for optofluidic devices requires the designer to consider a number of different issues ranging from: material restrictions (e. g. optical transparency range, electrical insulation and compatibility with various fluids and functionalization chemistry), desired feature sizes (e. g. are features required on the same scale as the wavelength of light), power consumption, and of course cost (e. g. smaller feature sizes require more elaborate fabrication techniques and more careful handling and treatment of substrates increasing device cost). While these issues have been exhaustively examined independently within the electronics, optics/photonics and fluidics fields, it is unclear what the optimal device structure will be for optofluidics. For example it is reasonably well accepted that for disposable microfluidic devices, polymeric materials and fabrication techniques (such as elastomeric devices fabricated through soft lithography or hard plastic devices fabricated using embossing techniques) are likely to yield the most commercially viable products. This trend towards simplicity conflicts with the complex multilayer lithography and etching techniques commonly used in the electronics and integrated photonics industries. As such it is unclear whether the most fruitful path will be to develop a single fabrication technology that enables the incorporation of each of these elements or whether integration architectures should be developed which enable us to combine, for example, polymeric micro- and nanofluidic structures with silicon photonic devices.

The goal of this article will be to largely explore this question. In the "Basic Methodology" section below we will provide a brief overview of existing fabrication techniques, focusing on those of relevance to optical devices and microfluidics, followed by a discussion on integration techniques. To properly address integration methodology, several examples of optofluidic devices are presented in the "Key Research" section with their challenges and the advantages of techniques that were chosen.

Basic Methodology

As discussed above in this section we will begin by providing a brief review of fabrication techniques for optical and fluidic devices (we focus on these two here as they constitute the most fundamental aspects, electronics will be covered incidentally, but not directly). We will focus primarily on the different sets of tools required and, to a lesser extent, materials required for each. As will be described, the tools are closely interconnected with materials from which the components are made, as well as the sizes of features that are to be included in the optofluidic device.

Techniques for Optical Component Fabrication

Fabrication Procedures

The optical elements of optofluidic devices include such components as waveguides, photonic crystals, optical resonators and active components such as lasers. The order of magnitude of feature size for these elements can range from roughly the scale of the wavelength of light – hundreds of nanometers, to tens of microns or larger. For these smaller features (commonly required in single mode waveguides and photonic crystals for example) techniques such as electron-beam lithography (e-beam) or focused ion beam (FIB) are appropriate. Briefly for e-beam, a focused beam of high energy electrons is used to expose an e-beam resist which can subsequently be developed and the system etched so as to create features of sizes as small as tens of nanometers. Electron beam processes are well developed for silicon on insulator (SOI) type devices and represent

a good choice for fabrication of optical waveguides that include smooth bends or circular resonators. In focused ion-beam lithography, samples are bombarded with ions so as to directly etch features into the substrate. An important difference in FIB is that it has a much lower scattering, but a higher chance to damage sensitive electronics though similar feature sizes are available. The ultimate limitation of both e-beam and FIB fabrication procedures is that they are serial in nature and thus while suitable for device prototyping, they are not particularly useful for mass production. Photolithography, on the other hand, allows for much more parallel fabrication once an exposure mask is fabricated. There is a great variety of positive and negative photoresists available to achieve different feature heights. Though only cost effective for mass produced runs, state of the art fabrication lines can now reach feature sizes on the order of 100 nm and below.

Materials

The range of available active and passive optical materials is much too extensive to be described in detail and thus we will focus on the handful which are of broadest interest to optofluidics and separate them into those which are usable in the infrared and visible spectra. Within the former of these silicon specifically, silicon on insulator, tends to be the material of choice, primarily due to the well developed fabrication procedures, simplicity of integration with electronics and high refractive index. The underlying oxide layer serves to isolate the optical components but also as a convenient surface for biochemical functionalization. While generally compatible with most fluids, the conductivity of silicon can lead to some difficulties with electrically driven flow mechanisms such as electrokinetics.

A much more diverse set of materials is available within the visible regime for creating optical elements compatible with fluidics. In most cases devices are fabricated on either a glass or hard plastic base to facilitate photolithography steps and device handling; however techniques borrowed from the flexible optoelectronics communities are becoming more popular. For optical components, silicon nitrides are relatively popular due to the relatively high achievable refractive indices. Commonly however polymeric materials such as SU-8, PMMA and more recently PDMS are preferred due to the relatively easy fabrication procedures (SU-8 devices for example require only simple photolithography and developing steps, whereas silicon nitride devices require more complex etching steps) and slightly higher than glass refractive indices. Though often used to create multimode waveguides for delivering excitation light or capturing emitted light, because the index difference between these polymers and aqueous liquids, it is usually possible to create single mode devices without too much difficulty.

As mentioned above materials processing varies strongly from material to material as well. There are other numerous types or dry and wet etching that work for these different materials, each with its own unique characteristics. For example, reactive ion etches can create well defined, high aspect ratio features with straight, smooth sidewalls in numerous materials, but typically require much more handling and equipment. Wet etches are much simpler but less precise techniques that compatible with both silicon and glass materials. Because etching is time dependent, is it important to properly time the process to achieve appropriate depths. In chemical etching the materials can be layered, so that when the chemical reaches the next layer the process will stop.

In order to create micron scale mirrors or electrical functionality, evaporation of metals such as gold, chrome, titanium and silver are used [1]. The two types of vapor deposition are thermal evaporation, which works by physically boiling material, and sputtering, which includes ion bombardment. Although sputtering works on a much larger variety of materials, it is slower and more expensive than evaporation and, thus, should be used when precision counts or choice of material requires it.

Techniques for Fluidic Component Fabrication

At the onset of modern microfluidics in the early 1990's glasses, quartz and silicon were the materials of choice for microfabrication, primarily due to the well established wet etching and lithography based micromachining techniques developed by the electronics and semiconductor industries. Though silicon based devices found a variety of niche markets, particularly those that benefit from its high thermal conductivity, its high electrical conductivity proved to be a problem for the high voltages required for on-chip electrokinetic transport (as mentioned above). As such the first chips for electrokinetic processes such as capillary electrophoresis were typically constructed from glass which also offered good optical qualities, well defined surface chemistries and a high electroosmotic mobility (i. e. it supports a high ζ-potential). In general however high quality glass is reasonably expensive, at $\$\,4000/m^2$, and fabrication is very expensive, largely due to the costs associated with establishment and maintenance of clean room facilities. Additionally, usable structures must be thermally bonded to a cover plate made from a similar material at temperatures over 400°C, which precludes the possibility of incorporating a biological agent in to the chip prior to sealing.

As a result of these difficulties with traditional microfabrication materials and techniques, there has been a recent trust to manufacture microfluidic systems and biochips from low-cost polymeric materials such as poly(dimethsiloxane) (PDMS), poly(methylmethacrylate) (PMMA) and others. The primary attractiveness of these materials is that they tend to involve simpler and significantly less expensive manufacturing techniques (e. g. casting, injection and replica molding, or hot embossing), however they are also amenable to surface modification and the wide variety of physiochemical properties allows the matching of specific polymers to particular applications. While the development of these systems has reduced the time from idea to chip from weeks to days, and the per unit cost by a similar ratio, the low thermal conductivities inherent in these materials (0.18 W/mK for PDMS which is an order of magnitude lower than that of glass) retards the rejection of internally generated heat during electroosmosis (Joule heating).

Though there are many microfabrication processes for manufacturing microfluidic systems in soft polymers and hard plastics, one of the most promising is the Soft Lithography and Rapid Prototyping of Masters process developed by Professor Whitesides' group at Harvard University [2]. Through this process complex microfluidic systems can be manufactured in soft elastomer substrates (primarily PDMS) very rapidly and at a fraction of the cost or traditional glass manufacturing. After the initial investment in processing equipment, this technique can reduce the cost per custom microchannel system to several dollars per unit and reduce the lag time from several weeks (or months as outlined above) to 2 or 3 days. Briefly the process consists of producing positive, reusable, masters of the desired microfluidic design on a glass or silicon substrate, by first spin coating a film of photoresist onto the substrate, hardening it through a baking procedure, expositing it to UV light through a transparency mask containing the channel pattern, inducing cross linking of the polymers through a second bake procedure, then dissolving the unexposed portion of the film in a developer solution. PDMS replica molds of the channel design are then prepared by pouring the uncured liquid elastomer over the master and allowing it to cure in a vacuum oven. This yields a negative cast of the microchannel pattern in the PDMS slab. To form the enclosed, sealed chip the PDMS cast is typically plasma treated, aligned, and then placed in direct contact with either a glass substrate or another PDMS slab. Both the lithography mask and the final master can be reused multiple times with PDMS casting to mass-fabricate fluidic layers.

A slight extension of the above involves the use of glass or silicon as mask materials in various soft lithography techniques which can be used in fabrication of fluidic components as well as optical ones. Features as small as 30 nm can be achieved. An example is micro-transfer molding where a mold is filled with a polymer and is pushed against a substrate. The polymer is then cured forming structures on the substrate after the mold is removed. These structures of rectangular cross section can be used as waveguides in optical layers, or walls of microfluidic channels. The main disadvantage of soft lithography is its accuracy limit from thermal deformations.

Photolithography is probably the most widely used technique for making simple microfluidic devices or masters for embossing and casting of polymer devices. A combination of appropriate photoresist and an appropriate developer are needed to fabricate positive or negative relief fluidic channels. Despite its relatively low resolution achievable with photolithography, it is very convenient for channels with features sizes on the order of 2–5 μm or larger. For smaller features e-beam or FIB techniques (see above) are more commonly used. Currently there is a development to move away from placing a physical mask in proximity of the substrate with photoresist and instead use photomask created by a system of high resolution lenses. This will allow photolithography to work on non-planar surfaces.

Sealing of fluidic components to optical/electrical devices can be an issue, particularly when using pressure driven flow. High temperature bonding processes are often undesirable as they can damage electrical/optical devices or any biological functionalization which may be pre-deposited inside devices. Similarly bonding of hard fluidics (glass, silicon) to irregular surfaces is notoriously difficult. Fortunately, the technology has progressed in a direction such that a number of "optofluidically compatible" material systems have been developed. An example is wide use of PDMS because it is easy to bond with glass, silicon or other PDMS layers. Commonly air or oxygen plasmas are used to activate the bonding surface and expose the free oxygen in PDMS. Temperature treatments, such as baking or hot plates, rely on diffusion processes to bond materials. Similarly for PDMS under moderate temperatures, the polymer chains inside the two layers can inter-diffuse between themselves strengthening the bond.

Key Research Findings

Given the well developed fabrication techniques describe above, the key research directions on the fabrication side are focused on developing the techniques which integrate the optical and fluidic layers. Though this will be discussed below in the context of a series of case studies

we will also try to provide some global insight in each case. When it comes to choosing appropriate techniques and materials to fabricate these devices, it is important to make decisions based not only on equipment availability, but also on cost. Some of the devices presented below are successful because of their simplicity and cost efficiency. Here we focus on techniques for enabling the fusion of optical and fluidic layers, generally made from different materials, without deforming any of the components and preserving the function of the multilayer device.

Optofluidic Attenuator

The first device we will consider is the optical attenuator presented by Lin Zhu et al. [3]. The device is comprised of two layers, which can be used to reduce the power level of an optical signal in a waveguide. Thus, the two layers are an optical layer that contains straight waveguides with cladding, and a fluidic layer. An opening was made in the top cladding of the waveguides which is filled with a fluid from the fluidic channel on top of it. By changing the refractive index of the fluid occupying the cladding opening, it is possible to change the output power from the waveguides.

The optical layer is manufactured by first thermally growing silicon oxide on a silicon wafer to serve as the lower cladding, and then defining waveguides photolithographically in SU-8. Another photosensitive material serves as the top cladding with an opening defined by a second photolithography process. The fluidic channel is made from PDMS that is cast over a negative resist master fabricated by standard photolithography. To ensure the bonding of PDMS to the top cladding of the optical layer, the device is treated with high power oxygen plasma for 30 s and then baked for an additional 8 h. Experimental results included power output depending on the refractive index of the fluid in the channel and are in agreement with numerical simulations.

The fabrication is based mostly on soft photolithography, which is easy to facilitate and is very cost efficient. The device itself is simple to operate and reproduce. The materials used are completely inert, which is important when using chemically reactive fluids. The sizes of features make what is commonly a complex part of the fabrication process – alignment – relatively simple. Attenuation of optical signals is very sensitive to refractive indexes of the cladding materials. Thus, the main challenge in designing such a device is to allow for fabrication processes which will not only work with materials whose properties are well known, but also guarantee those properties remain relatively constant throughout the sampled volume.

Integration of Nanofluidics with Photonic crystals

A different type of optofluidic device was presented by Erickson et al. [4] and comprised of a silicon photonic crystal integrated with soft-lithography nanofluidics. A photonic crystal is a regular periodic array of varying dielectric constant that exhibits a bandgap (a range of wavelengths which cannot propagate within the structure). In the case of a silicon photonic crystal where the periodicity comprises of a series of nanoholes etched into the base silicon, the output power from the crystal and the range of the bandgap will vary depending on the refractive index of the fluids occupying the wells. The goal of the device developed in this paper was to address individual features within the photonic crystal.

This device consists of three layers: a photonic crystal layer, a nanofluidic delivery layer to deliver proper fluid into the photonic crystal structure, and a microfluidic control level to perform required fluidic manipulations. Photonic crystals have features on the order of a 100 nm and thus require electron-beam lithography for definition. The structure can then be dry etched in silicon-on-insulator substrate. In this case the nanofluidic level (which required similar feature sizes to those in the photonic crystal) was also fabricated in positive relief using e-beam lithography and the microfluidic structures (which had features closer to 10 μm) were superimposed using photolithography. Control fluidic layers were fabricated with standard soft lithography. In order to ensure that at least one channel is delivery layer is aligned with a photonic crystal, the spacing between the photonic structure is constantly varied. Immediately before the assembly of different layers, the whole device was exposed to a short duration air plasma treatment in order to aid with sealing. Figure 1 shows an overview of the device fabrication and integration techniques.

The incorporation of a multilayer microfluidic structure in this device allows for precise control of fluid delivery to the crystal. Thus, experiments require less fluid by volume and can steady state results faster (important for future sensing applications). Further integration with electric components can allow for electrokinetic trapping and other fluidic or sample manipulations. Compared to the previously discussed attenuator, this device requires a number of additional fabrication steps, including bonding between different types of materials, but it achieves versatility beyond its primary function. The final device allows for sub-wavelength usability. It is useful for very localized (sub-wavelength) control and modulation with high refractive indexes, but requires nanoscale flows, which take relatively long time to process.

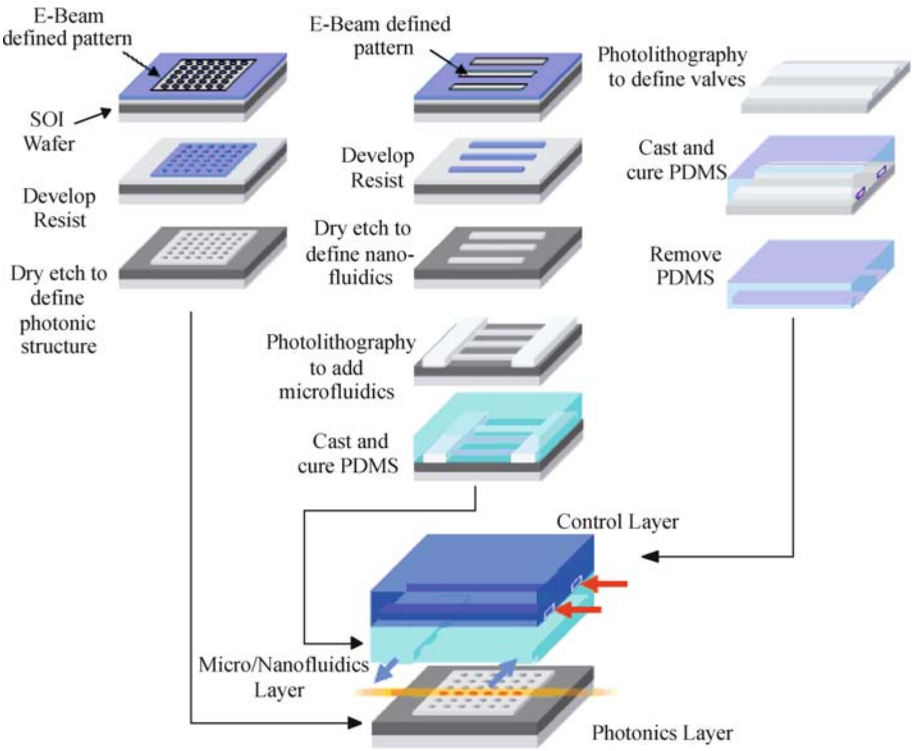

Optofluidics – Techniques for Fabrication and Integration, Figure 1 Nanoscale optofluidic integration. Sample fabrication procedure for combining micro- and nanofluidics with nanophotonic structures

Label Free Biosensor

The above two devices functionally integrate optics and fluidics on the micro- and nano-scales respectively however the often cited goal of these optofluidic devices is the integration of binding reactions for biomolecular detection. An example of such a device is the label-free biochemical sensor based on a Mach–Zehnder interferometer developed by Blanco et al. [5]. A biosample occupies a chamber on one arm of the interferometer formed by a multilayer process. A waveguide in the chamber has an evanescent field which extends from it and the speed at which light passes through the waveguide arm depends on the refractive index shift caused by the presence or absence of a binding event at the waveguide surface.

The device is fabricated by bonding two separately prepared parts with multiple layers each. One part includes the interferometer with a waveguide as part of one arm. They are fabricated using photolithography on a silicon wafer. The waveguide surface has to be sufficiently pure in order for the evanescent field to interact with the fluid. Since photolithography usually leaves contaminants on the surface, the waveguide was treated with oxygen plasma. The other part consists of two temporary layers to allow for easy lift off and pealing, and an SU-8 layer on which the inlet and outlet holes are photo-patterned and developed. All of the layers of this part are transparent, so as to facilitate alignment. The materials are dehydrated on a hot plate to ensure good adhesion of the two parts.

Since the device is based on a Mach–Zehnder interferometer, the second arm is used to lower or eliminate external perturbations such as temperature fluctuations. This allows for higher accuracy and detection of smaller concentrations. The adhesion of different layers was good enough to sustain fluid pressure of up to 500 kPa. Several additional integration steps and choice of materials were made in order to satisfy this requirement. In general, this sensing mechanism is used to allow compatibility with complementary metal-oxide semiconductors (CMOS). This property, together with compactness of the device, makes it attractive for further integration with MEMs into a complete lab-on-chip device.

Integration of Fluidics and Semiconductor Lasers

The ultimate degree of optofluidic integration involves the integration of fluidics, passive and active optics, and electronics into a single device. The device presented by Cran-

McGreehin et al. [6] is an example of a device that uses electrical current to create light with wavelength of about 1290 nm. The light is trapped in waveguides and is used to optically move and trap particles in a microfluidic channel. This device can also be used for simultaneous particle detection and manipulation thought scattering and absorption forces. Such integration of microfluidics and semiconductor lasers is not done in distinct components as above. Rather a device is etched and covered with other materials to achieve proper shapes and properties in each part of the device.

The light is emitted from electrically excited layers of quantum dots. The active layer is covered with thermally grown conductive cladding on top and bottom. In order to allow waveguiding, ridges are photo-defined and etched with specific dimensions to support only the zero-order mode. To isolate adjacent waveguides, a layer of SU-8 is added and heated to reflow from the top of the ridges and harden between them. The top electrode for the electrical component is then deposited with an electron beam evaporator through a lift-off mask. The fluidic channel is etched separately to be deeper than the space between the ridges in order to accommodate larger particles. Because it is essential to isolate the pn junction from the fluid, the ridges and the contacts are covered with another layer of SU-8 polymer. This layer is also used to photo-define the walls of the channel. The last step is to deposit a thin metallic layer on the bottom of the channel to prevent particle adhesion. In order to operate, the device requires a relatively large heat sink due to heat generation from electrical currents.

This device allows for exploration of how semiconductor lasers interact with different materials. The experimental data is the power drop when the particle blocks a pair of oppositely positioned lasers. The device itself contains a large variety of fabrication techniques and materials and has a large range of applications. The advantage of this device is the ability to simultaneously manipulate and detect single particles using optical functionality. It is also likely the most prominent example of integration of different components, including electronic ones, directly into the fluidic layer instead of fabrication of different layers followed by their bonding to each other. The advantage of including so much "infrastructure" right on the device (e. g. having optical pressure generated within the microchip as opposed to using an external laser) is largely related to the idea of developing portable devices.

Future Directions for Research

What has inspired initial research in microfluidics is similarly driving the research into optofluidics today. The goal is to make smaller features going from micro- to nano-scales in order to fill the gap between top-down and the bottom-up fabrication techniques [7]. Because most devices consist of multiple planar layers, there is motivation to develop 3-D fabrication or assembly methods for both optical and electrical components. The ultimate goal is an easy and simple technique which works well with a variety of materials and on different scales. The most successful devices up to date rely on fundamental principles of both optics and fluidics in order to avoid as many of components as possible, leaving those devices only with essentials to carry out their functions.

Cross References

► Optofluidics – Fluidics enabling optics
► Optofluidics – Optics enabling fluidics
► Optofluidics – Applications

References

1. Vezenov D, Mayers B, Conroy R, Whitesides G, Snee P, Chan Y, Nocera D, Bawendi M (2005) A low-threshold, high-efficiency microfluidic waveguide laser. J Am Chem Soc 127(25):8952–8953
2. Xia Y, Whitesides G (1998) Soft lithography. Annu Rev Mater Sci 28:153–84
3. Zhu L, Huang Y, Yariv A (2005) Integrated microfluidic variable optical attenuator, Opt Express 13(24):9916–9921
4. Erickson D, Rockwood T, Emery T, Scherer A, Psaltis D (2006) Nanofluidic tuning of photonic crystal circuits. Opt Lett 31(1):59–61
5. Blanco F, Agirregabiria M, Berganzo J, Mayora K, Elizalde J, Calle A, Dominguez C, Lechuga L (2006) Microfluidic-optical integrated CMOS compatible devices for label-free biochemical sensing, J Micromech Microeng (16):1006–1016
6. Cran-McGreehin S, Dholakia K, Krauss T (2006) Monolithic integration of microfluidic channels and semiconductor lasers. Opt Express 14(17):7723–7729
7. Madou M (2002) Fundamentals of microfabrication. CRC, Boca Raton

Ordinary Least Square

► Least Square

Organ Fabrication

► Microfluidic Devices in Tissue Engineering

Organic Material

► Polymer

Organ or Tissue Augmentation

► Microfluidic Devices in Tissue Engineering

Orthorhombic Crystal

► Perovskite

Over/Under/Perfectly-Expanded Nozzle Flow

Definition

A comparison of the theoretical exit pressure for an isentropic nozzle with the level of the ambient back-pressure. For isentropic exit pressures below the ambient, the flow is ‘over-expanded’; for isentropic exit pressures exceeding the ambient value, the flow is ‘under-expanded’ ; when the pressures are matched, the flow is ‘perfectly expanded’.

Oxidation/Reduction

► Amperometric Techniques

Oxidation (of Silicon)

CHE-HSIN LIN
Department of Mechanical and Electromechanical Engineering, National Sun Yat-sen University, Kaohsiung, Taiwan
chehsin@mail.nsysu.edu.tw

Synonyms

Thermal oxidation; Oxide growth; Oxide deposition; Silicon dioxide growth

Definition

Oxidation of silicon to create a silicon dioxide layer on the silicon surface can be done either by the thermal growth methods or the undesired native growth process. The process is an adding procedure which adds oxygen to react with silicon to form silicon dioxide on the silicon surface. The process consumes silicon during the oxidation procedure. In general, the oxide layer can be grown either by wet or dry oxidation processes in a furnace at a temperature of 750 – 1100 °C. The reaction can be expressed as: $Si_{(s)} + O_{2(g)} \rightarrow SiO_{2(s)}$.

Overview

Silicon dioxide is a form of pure glass with a melting temperature of 1730 °C which is similar to fused silica. It exhibits excellent dielectric properties and has a good adhesion to silicon such that silicon dioxide is ideal to be used as a dielectric or barrier layer. Silicon dioxide is also very useful in the MEMS and semiconductor industry due to its excellent material properties. A grown oxide layer is conformal on the silicon surface, which makes it an ideal surface coating or passivation layer for MEMS structures. The electric resistivity is up to $1 \times 10^{20}\ \Omega.\mathrm{cm}$ and the energy band gap is around 9 eV. A well-grown silicon oxide layer can sustain a high electric field of up to 10^9 V/m without breakdown [1]. Further more, the ease of formation and its excellent interface with the underlying silicon material make it the most popular thin film in VLSI technology. Essentially, silicon is reactive to oxygen at room temperature such that most silicon exists in the form of silicon dioxide like quartz sand in nature. In this regard, oxidation of silicon occurs immediately to form amorphous silicon dioxide film by exposing a silicon surface to oxygen in atmospheric environment. Silicon dioxide is a dense material that fully covers the silicon wafer to prevent the inner silicon from further oxidation. The thickness of this native oxide will reach to an upper limit of about 40 Å even over a long period of time. The native oxide layer grown from air is not uniform and is usually considered a contaminant in semiconductor processing. This native oxide can be simply removed in seconds using dilute HF solution.

Alternatively, a thermally grown oxide layer is thickness-controllable and has various applications in the semiconductor industry. The thickness ranges for thermal oxide layers may vary, depending on the particular application. For example, the thickness for an oxide capacitor dielectric is as thin as several angstroms but the thickness of a field oxide layer can be up to several micrometers. Since the grown oxide layer will fully cover the silicon surface to prevent it from further oxidation, it is common to elevate the temperature to drive the oxidant molecules to diffuse across the formed oxide layer to continue the oxidation process. In general, an oven or a furnace with high-purity oxygen supplied is usually adopted for the oxidation process. The oxidant can be either pure oxygen gas or water vapor. If the growth procedure occurs with dry oxygen, then the oxidation process is called *dry oxidation*. If the oxygen is introduced to the reaction chamber with water vapor, then the oxidation process is known as *wet oxidation*. The reaction mechanism of these two oxidation approaches is different such that the growth rate and the grown film quality of these two approaches are also

different. In general, the wet oxidation process is faster than the dry oxidation process but the density of the grown oxide layer obtained is lower when using the wet oxidation process. Higher temperature will significantly increase the growth rate of the oxide layer. The equipment for performing the oxidation processes, a mathematical model for evaluating the growth rate and a well-known pattern of bird's beak effect in local oxidation of silicon (LOCOS) process are described in this entry.

Basic Methodology

Oxidation Modeling

Silicon dioxide is usually grown by consuming silicon during oxidation process at high temperature from 750 to 1100 °C. Figure 1 shows the basic process for the oxidation of silicon. For successive oxidation, oxidants must diffuse across the formed oxide layer then react with silicon at the SiO_2/Si interface. The chemical reactions for both dry and wet oxidation processes can be described as follows:

$$\text{Dry: } Si_{(s)} + O_{2(g)} \rightarrow SiO_{2(s)}$$

$$\text{Wet: } Si_{(s)} + 2H_2O_{(g)} \rightarrow SiO_{2(s)} + 2H_{2(g)}$$

Apparently, silicon is consumed to form silicon dioxide in both the dry or wet oxidation process. The thickness of the silicon consumed is around 0.44 of the total oxide thickness. This value can be simply calculated using the following equation:

$$\frac{t_{Si}}{t_{SiO_2}} = \frac{V_{Si/mole}}{V_{SiO_2/mole}} = \frac{M_{Si}/\rho_{Si}}{M_{SiO_2}/\rho_{SiO_2}}$$

$$= \frac{28.09(\text{g/mole})/2.33(\text{g/cm}^3)}{60.08(\text{g/mole})/2.21(\text{g/cm}^3)} \approx 0.44$$

where t is the thickness, V is the volume, M is the molecular weight and ρ is the material density. The growth rate of oxide depends on the parameters for the oxidation process such as temperature, gas pressure, oxidizing condition (wet or dry), silicon crystal orientation and the dopant concentration in silicon. The model for oxide growth on silicon was first described by Deal and Grove in 1965 [2]. The Deal–Grove model describes two growth stages of the linear stage and the parabolic stage during oxidation. Figure 2 illustrates the one-dimensional model for the oxidant flux from the gas phase to the silicon surface during thermal oxidation. Three first-order equations describing the three series parts of the sample fluxes, i. e., F_1, F_2 and F_3, in the one-dimensional model are presented in Eqs. (1)–(3), where F_1 is the gas transport flux in number of molecules

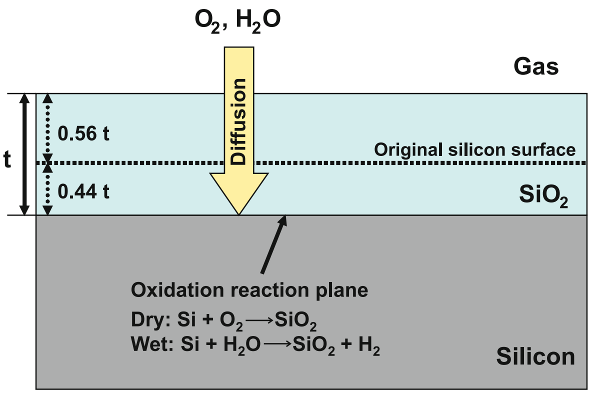

Oxidation (of Silicon), Figure 1 The basic process for the oxidation of silicon

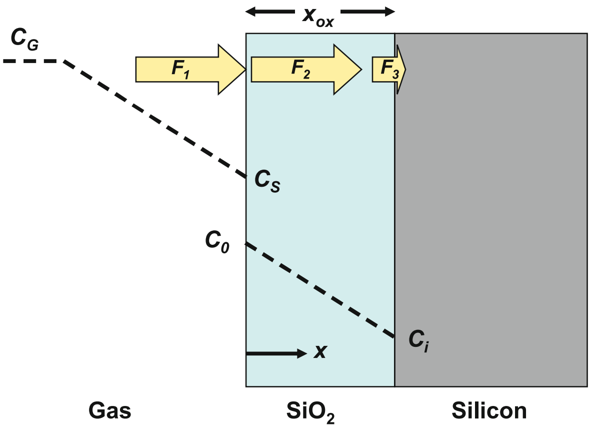

Oxidation (of Silicon), Figure 2 Flux model for oxidant diffusion from the gas phase to silicon surface during thermal oxidation

per square centimeter per second, F_2 is the diffusion flux through the oxide layer and can be expressed using Fick's first law and F_3 is the reaction flux at the SiO_2/Si interface:

$$F_1 = h_G(C_G - C_S) \tag{1}$$

$$F_2 = -D\frac{\partial C}{\partial x} = D(\frac{C_0 - C_i}{x_0}) \tag{2}$$

$$F_3 = k_s C_i \tag{3}$$

where h_G is the mass transfer coefficient (molecules per cm^2 s), C_G is the concentration of oxidant, C_S is the concentration at the surface, D is the oxidant diffusivity in the oxide (cm^2/s), C_0 and C_i are the concentrations at the two interfaces, x_0 is the oxide thickness and k_s is the reaction rate constant (cm/s). The concentration of the oxidant just inside the oxide surface C_0 and C_S can be related using

O

Henry's law:

$$C_0 = \mathrm{H}P_\mathrm{S} \tag{4}$$

where H is Henry's constant and P_S is the partial pressure of oxidant at the surface. From the ideal gas law, $PV = NkT$, Eq. (4) can be expressed as

$$C_0 = \mathrm{H} \times kT(\frac{N_\mathrm{S}}{V}) = \mathrm{H}(kTC_\mathrm{S}) \tag{5}$$

where the subscript s denotes at surface. Rearranging Eq. (5) will give

$$C_\mathrm{S} = \frac{C_0}{\mathrm{H}kT} \tag{6}$$

where k is the Boltzmann constant (1.38×10^{-23} J/K) and T is the temperature in K. C^* is defined to be the oxidant concentration in the oxide that would be in equilibrium with the bulk gas pressure P_G, which is known:

$$C^* = \mathrm{H}P_\mathrm{G} = \mathrm{H}(kTC_\mathrm{G})$$

$$\text{then } C_\mathrm{G} = \frac{C^*}{\mathrm{H}kT} \tag{7}$$

Substitution of Eqs. (6) and (7) into Eq. (1), leads to the result that

$$F_1 = h_\mathrm{G}\left(\frac{C^*}{\mathrm{H}kT} - \frac{C_0}{\mathrm{H}kT}\right)$$

$$\equiv \frac{h_\mathrm{G}}{\mathrm{H}kT}\left(C^* - C_0\right) \equiv h\left(C^* - C_0\right) \tag{8}$$

where $h = h_\mathrm{G}/\mathrm{H}kT$, which is a large value because experimental results show that wide changes in gas flow rates in oxidation furnaces, changes in the spacing between wafers on the carrier in the furnace and changes in the wafer orientation make little difference to oxidation rates. Under steady-state conditions, mass must balance such that the three flux equations representing the oxidation process must be equal. Thus $F_1 = F_2 = F_3$. Solving the two unknowns C_i and C_0 from the two equations of $F_1 = F_2$ and $F_2 = F_3$, then we have

$$C_i = \frac{C^*}{1 + \frac{k_\mathrm{s}}{h} + \frac{k_\mathrm{s}x_\mathrm{ox}}{D}} \tag{9}$$

$$C_0 = C^*\left(1 + \frac{K_\mathrm{s}x_\mathrm{ox}}{D}\right) \tag{10}$$

Substitution of Eq. (9) into Eq. (3) leads to

$$F(= F_1 = F_2 = F_3) = \frac{k_\mathrm{s} \cdot C^*}{1 + \frac{k_\mathrm{s}}{h} + \frac{k_\mathrm{s}x_\mathrm{ox}}{D}} \tag{11}$$

Let M be the number of molecules of the oxidant in a unit volume of the oxide. The rate of the thickness change of the oxide layer with time is then given by oxidizing flux divided by the number of molecules M of the oxidizing species (O_2 or H_2O) that are incorporated into a unit volume of the resulting oxide:

$$\frac{\mathrm{d}x_\mathrm{ox}}{\mathrm{d}t} = \frac{F}{M} = \frac{k_\mathrm{x} \cdot C^*}{M(1 + \frac{k_\mathrm{s}}{h} + \frac{k_\mathrm{s}x_\mathrm{ox}}{D})} \tag{12}$$

where $M = 2.2 \times 10^{22}\ O_2/\mathrm{cm}^3$ for the dry oxidation process and $M = 4.4 \times 10^{22}\ H_2O/\mathrm{cm}^3$ for the wet oxidation process. Note that $M = \text{density}/(\text{Avogadro's number} \times$ molecular weight of SiO_2). Take the boundary condition of $x_\mathrm{ox} = x_i$ at $t = 0$. The oxide growth kinetics can be obtained by integrating Eq. (12) from an initial oxide thickness x_i to a final thickness x_ox. The result is described as

$$\frac{x_\mathrm{ox}^2}{B} + \frac{x_\mathrm{ox}}{B/A} = (t + \tau) \tag{13}$$

where

$$A = 2D\left(\frac{1}{k_\mathrm{s}} + \frac{1}{h}\right),\ B = \frac{2DC_\mathrm{A}}{M} \text{ and } \tau = \frac{x_i^2 + Ax_i}{B}$$

The terms B and B/A can be referred to as the parabolic and linear rate constants for describing the oxide growth kinetics. The physical meanings of the rate constants B and B/A are the oxidant diffusion and interface reaction rate, respectively. The corresponding values for B and B/A for dry and wet oxidation of ⟨111⟩ silicon are plotted in Fig. 3. For ⟨100⟩ silicon, these values should be divided by 1.68. These expressions are better fit for the cases of a very

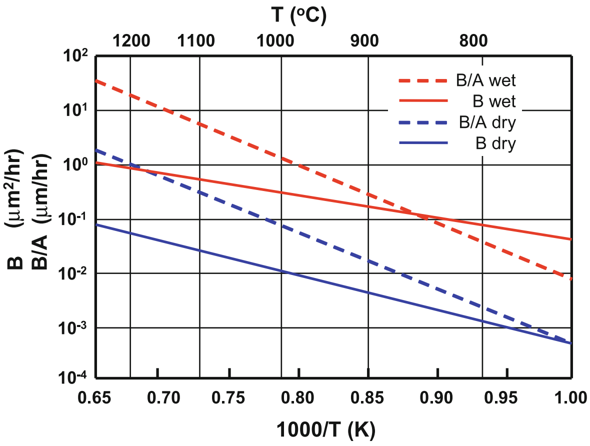

Oxidation (of Silicon), Figure 3 Plot of B and B/A versus temperature for dry and wet thermal oxidation of ⟨111⟩ silicon

thin oxide layer and in dry O_2 conditions. Solving Eq. (13) leads to the relationship between the oxide thickness and the growth time:

$$x_{ox} = \frac{A}{2}\left\{\sqrt{1+\left[\frac{t+\tau}{A^2/4B}\right]}-1\right\} \tag{14}$$

Considering two limiting cases of $t \to 0$ (small x_{ox}) and $t \to \infty$ (large x_{ox}), we have the following expressions corresponding to Eq. (14):

$$x_{ox} \to \frac{B}{A}t \quad \text{when} \quad t \to 0$$

and

$$x_{ox} \to \sqrt{Bt} \quad \text{when} \quad t \to 0$$

It is clear that the thickness of the grown oxide layer varies linearly with time at the initial stage of oxidation. In this stage, the oxide growth rate is controlled by the reaction occurring at the SiO_2/Si interface and is called the *reaction rate-controlled region*. The linear stage of oxide growth is valid up to about 150 Å of oxide thickness [3]. The growth of the oxide layer slows down after the linear stage because the oxidant must diffuse across a longer distance to reach the interface where the oxidation reaction occurs. The equation generates the shape of a parabola such that it is called the parabolic stage. In the parabolic stage, the growth rate of oxide is controlled by the mass transportation of the oxidant and is called the *diffusion-controlled region*. Figure 4 illustrates the general curve for both the linear and parabolic stages for dry oxidation at 1100 °C [4]. It is noted that the linear stage is only at the very beginning of the thermal oxidation process.

In practical applications, it is not necessary to calculate the thickness of the grown oxide layer using the kinetic model described above. Users can simply obtain the approximate thickness from a chart which plots the oxide thickness for oxidation versus temperature and time, as an example shown in Fig. 5. Another simple way to estimate the thickness of the grown oxide layer is to use the well-developed simulator available on the internet [5]. In addition, the dopant concentration in silicon is also a factor that influences the growth rate of oxide. Here also a minor parameter which may affect the oxide growth rate is doping during the oxidation process. In general, heavily doped silicon oxidizes at a faster rate than a lightly doped substrate. In the parabolic stage, boron doping will oxidize faster than phosphorus. However, the growth rate shows little difference in the linear rate constant between boron and phosphorus doping [6].

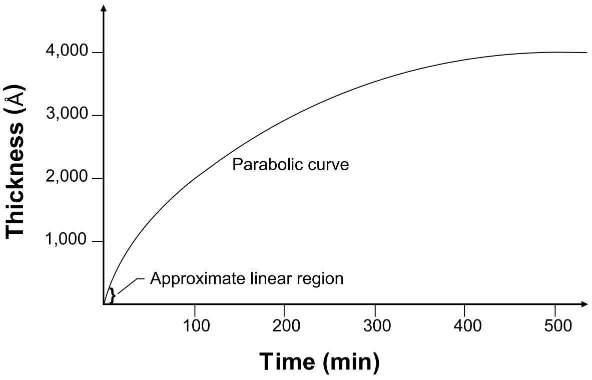

Oxidation (of Silicon), Figure 4 Linear and parabolic stages for dry oxidation process at 1100 °C

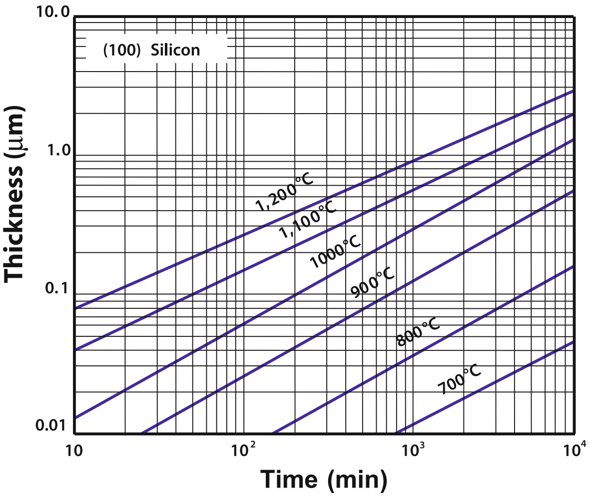

Oxidation (of Silicon), Figure 5 The thickness of a grown oxide layer for different temperature and time

In summary, the growth of thermal oxide follows a linear growth stage up to about 150 Å, followed by a slower parabolic growth stage. The chemical reaction for the thermal oxidation of silicon consumes silicon and oxidant and the growth rate of the oxide layer is faster when using wet oxidation. Factors including dopant concentration, crystal orientation, pressure and temperature may affect the oxide growth rate during oxidation.

LOCOS Process

The abbreviation LOCOS stands for *local oxidation of silicon*, in which selective areas on a wafer are oxidized for electrical insulation purposes in semiconductor technology. This process is used for isolating two adjacent devices with a feature size of greater than 0.25 μm.

0

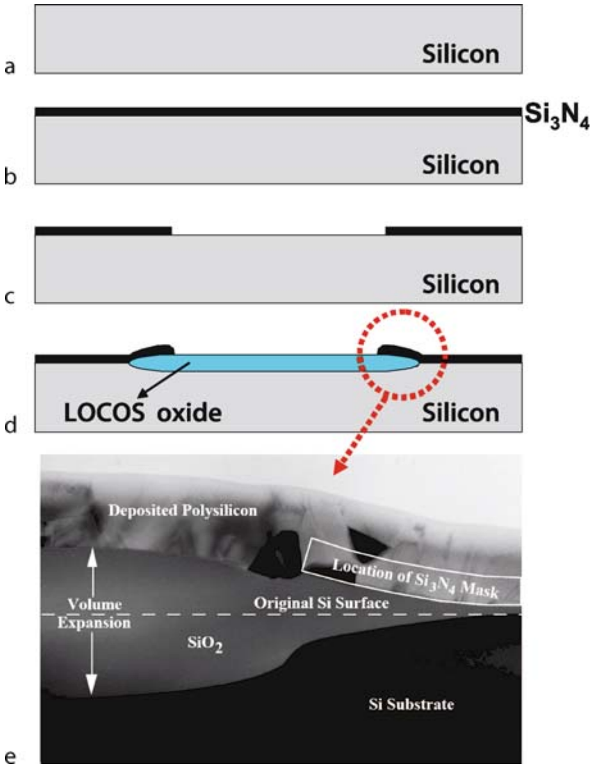

Oxidation (of Silicon), Figure 6 (**a–d**) Schematic of a typical LOCOS formation process. (**e**) SEM image of a LOCOS structure. Note that the silicon nitride layer on the right-hand side was stripped and a polysilicon layer has been deposited on top of the structure to provide better contrast in the image. (Image courtesy of J. Bravman, Stanford University.)

Figure 6 presents a simplified schematic for the LOCOS process. A deposited silicon nitride layer is patterned and etched to expose the selective area for the oxidation process. The patterned Si_3N_4 layer serves as the oxidation barrier (Fig. 6a–c). There is a slight lateral growth of the oxide beneath the nitride oxidation barrier because the oxidants move in all directions when diffusing through the grown oxide. Since the oxidation is an adding procedure and the grown oxide is thicker than any silicon consumed, the oxide grown beneath the nitride layer serves to push up the nitride edge (Fig. 6d). The LOCOS process results in a non-planar Si/SiO_2 interface between the nitride oxidation barrier and oxidized regions. This phenomenon is known as the *bird's beak effect* due to its shape. The bird's beak effect is an undesired by-product of LOCOS processes since it increases the area required for building a semiconductor device. Figure 6e illustrates a SEM image showing the cross-section of a LOCOS process, the bird's beak shape being clearly observed in the image.

Furnace Equipment and Oxidation Processes

Furnace equipment serves as a workhorse in thermal processing and is among the simplest type of processing equipment in the semiconductor industry. The equipment is conceptually constituted of an oven capable of temperatures from 600 to 1200 °C and a simple gas distribution system capable of introducing the oxygen or water molecule oxidants. Since the growth rate of the oxide layer is highly dependent on the temperature, precise temperature control is essential for oxidation furnaces. Modern furnaces are easy to handle up to several hundred 8 in. wafers, with a temperature uniformity of ±0.5 °C [7]. There are three basic types of furnace, horizontal furnace, vertical furnace and rapid thermal processor (RTP), used for thermal processing. Figure 7 shows two images of a conventional horizontal furnace and a RTP chamber. Simple construction and ease of maintenance are the major advantages of the horizontal furnaces such that they are popular in academic institutes and industries which require only small production volumes. The horizontal furnace is so named because of the horizontal position of the quartz tube where wafers are located and heated. This furnace was largely replaced in the early 1990s by the vertical furnace in the semiconductor industry, mainly because the vertical construction is easier to automate, has improved operator safety and reduces particular contaminations [8]. Oxidation processes operated in the horizontal and vertical furnaces are batch processes, which are capable of processing large quantities of wafers (tens to 200 wafers) in one process cycle. The furnace process is considered a hot-wall procedure such that it requires more thermal budget for heating the furnace.

Figure 8 illustrates schematically the setup of a typical oxidation furnace which shows the conceptual configurations for both the dry and wet oxidation processes. The main body of the system is a quartz process tube surrounded by a resistance heating element which can be controlled to produce multiple heating zones. It is common to form three to seven symmetric hot zones over the process tube. The temperature zones thus formed facilitate control of the furnace tube to attain a flat zone near the middle of the tube where the thermal oxidation takes place. The outer zones are designed to help compensate for heat losses out of the ends of the tube. The wafers are normally loaded into the furnace on quartz *boats* which hold 10–50 wafers in parallel. The boats are carried into the center section of the hot zones by the operator or the loading system. The wafers are normally loaded at a moderate temperature (600 – 800 °C) in order to prevent crystallographic defects caused by large thermal gradients across the wafers; thermal budget for this process can be saved as well. Nowa-

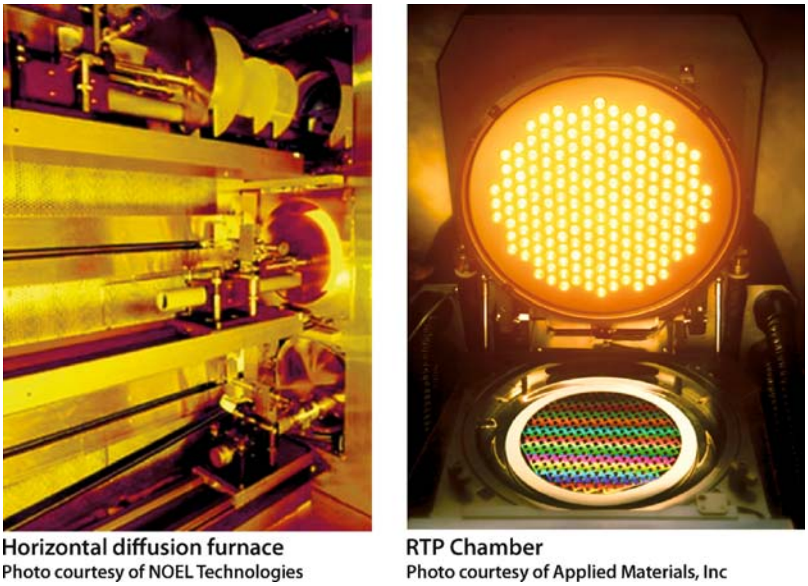

Oxidation (of Silicon), Figure 7 Images of a conventional horizontal furnace (left) and a RTP chamber (right)

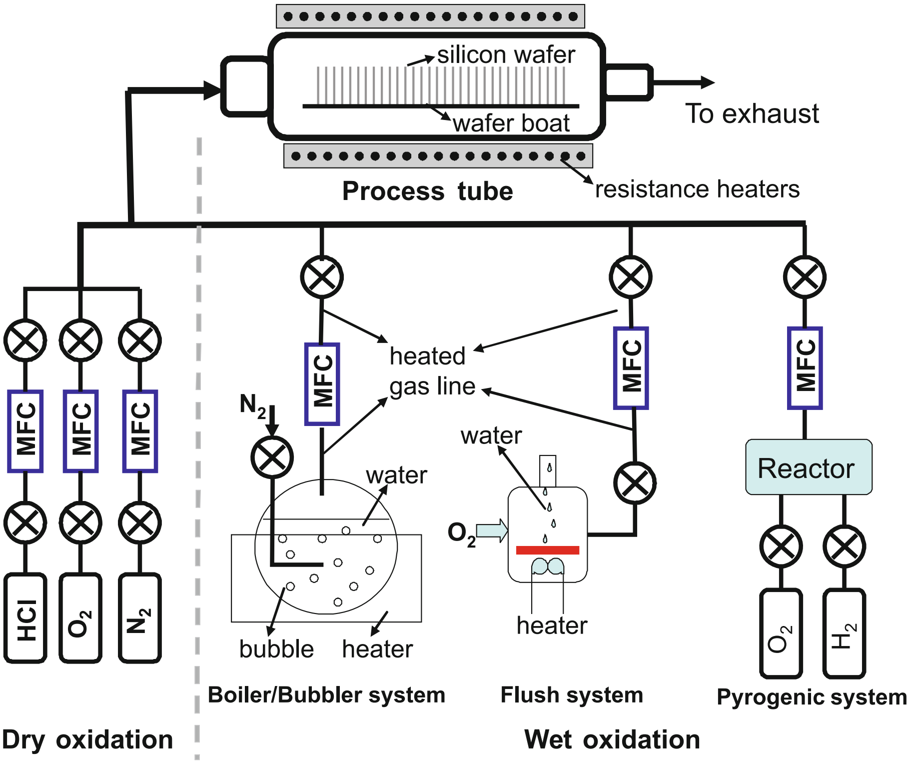

Oxidation (of Silicon), Figure 8 Schematic for the conceptual construction of an oxidation furnace

days, these furnaces are most commonly operated at atmospheric pressure. However, if necessary, one is able to increase the tube pressure to increase the growth rate of oxide film.

Dry Oxidation

The furnace structure for the dry oxidation process is simple and straightforward. Usually, high-purity oxygen gas is used to oxidize silicon. Nitrogen gas in the oxidation system is used as the process gas during system idle, temperature ramping, wafer loading steps and chamber purging, because nitrogen does not react with silicon at the processing temperature. In dry oxidation, the process gas is usually introduced into the furnace with a trace amount of hydrogen chloride gas. The existence of chloride ions during oxidation is very important because chloride ions react with the mobile metallic ions, such as sodium ions, to form immobile chloride compounds. The undesired oxide charge occurring at the Si/SiO_2 interface can be neutralized by the use of HCl gas. In addition, the existence of hydrogen chloride will also allow some chlorine atoms to be integrated into the oxide film and bind with silicon at the silicon–oxide interface. This process minimizes the number of dangling bonds and improves IC device reliability. Another important advantage of adding chloride ions to the thermal oxidation process is that they tend to increase the oxidation growth rate by about 10 – 15% [9]. However, the concentration of chlorine ions should not be high (usually $< 3\%$); otherwise the electric properties (e. g., bias voltage) of the electronic device would become unstable. Instead of using toxic and corrosive HCl gas, chlorine compounds such as dichloroethylene (DCE) or trichloroethylene (TCE) can be used to introduce the chlorine ions into the process tube [10]. Oxide films grown by dry oxidation have better quality than films grown by wet oxidation. Therefore, high-quality thin oxide layers such as gate oxide, screen oxide or pad oxide are usually grown using the dry oxidation process.

Wet Oxidation

The wet oxidation process uses water molecules instead of dry oxygen as the oxygen source to oxidize silicon. As a matter of fact, water molecules contact the silicon furnace in a normal wet oxidation process. Water molecules dissociate at high temperature and form hydroxide (HO) prior to reaching the silicon surface. Hydroxide has faster diffusion mobility in silicon dioxide than pure O_2, which explains why wet oxidation has a higher growth rate than dry oxidation. Wet oxidation is used to form thick oxides such as the LOCOS oxide, masking oxide and field oxide. As shown in Fig. 7, several systems have been used to deliver water vapor into the process tube. The boiler system is the simplest setup which vaporizes ultra-pure water then drives the water vapor in to the process tube via heated gas lines. However, it is difficult to have precise control of the vapor flow with this method. In addition, the water in the boiler is not *fresh* after a long boiling procedure and contaminants may be dissolved in the water. A modified setup is called a bubbler system which flows nitrogen gas into a hot water bath to generate wet nitrogen bubbles and carry vapor into the process tube. This scheme is the most commonly adopted in academic fields due to its simple structure and more precise flow control than a boiler system. The flush system is an alternative choice for introducing water vapor in to the process tube. This system uses small water droplets on a quartz hot plate, which vaporizes the water. The vaporized steam is then carried in to the process tube by flowing oxygen gas. However, this method has the problem that the steam generation is not a steady process. In order to have better control of the vapor flow rate, a pyrogenic system called *Dryox* was developed, which burns hydrogen gas to generate water vapor right at the inlet port of the process tube. The vapor flow can be precisely controlled since no liquid and vapor handling is required in this system. However, it needs extreme care to handle this process since hydrogen gas is flammable and explosive. The pyrogenic reaction is operated at a temperature of about 400 °C at which hydrogen automatically reacts with oxygen and forms water vapor. The typical mixing molar ratio for hydrogen and oxygen is 1.8 : 1 to 1.9 : 1, in order to completely consume the hydrogen gas [9]. Otherwise, hydrogen can accumulate inside the process tube and cause an explosion. A burn box and a scrubber system for exhaust gas treatment are necessary for operating a pyrogenic system.

Rapid Thermal Process (RTP)

The rapid thermal process (RTP) is a method which heats a single wafer to a temperature range of 400 – 1300 °C in a very short time under atmospheric conditions or at low pressure. This process is usually referred to as rapid thermal oxidation (RTO). The RTP has a gas handling system, an optical pyrometer for fast temperature measurement and a computer for controlling process operation. In order to achieve this fast heating process, a tungsten halogen lamp array located nearly at the top and bottom of the wafer is used as the radiant heating source. The temperature ramp up and down in a furnace is typically about 20 °C/min or less. Alternatively, the RTP can incorporate a fast-heating system which provides ramp-up rates up to 250 °C/min. In order to keep the temperature uniformity across the reaction surface, the RTP usually treats a single wafer at a time. The wafer-to-wafer uniformity of a RTP system is also better than that of a conventional furnace system. The silicon wafers are

heated by selectively absorbing radiation from the lamps, which produce short-wavelength radiation. The energy from the lamps is mainly absorbed by the silicon but not the chamber wall such that the RTP is considered as a cold-wall process. In this manner, heat-generated contaminants from the chamber wall can be reduced. The RTP also uses less thermal budget than a furnace system but the throughout is an issue. More importantly, the oxidation process achieved using the RTP can minimize dopant movement in wafers due to the shorter process time. This advantage makes the RTP ideal for processes like the barrier-layer formation and the oxide reflow process.

Future Directions for Research

Oxidation processes have been studied for more than 50 years and they still attract lots of interests from researchers who are working in this area. For example, in order to prevent gate leakage and dielectric breakdown, growth of thinner and denser dielectric layers with high dielectric constant for gate structures is an ongoing trend. The RTP will play a more important role in the semiconductor process since it offers better process control, less thermal budget, less processing time and better wafer-to-wafer uniformity. The RTP incorporated with on-line film monitoring, rapid thermal annealing and even rapid thermal chemical vapor deposition (RTCVD) processes has shown its potential for fabricating high-quality thin films with various material choices. Finally, an automation system to handle the multi-function RTP system is essential for improving the throughput of this system.

Cross References

► Rapid Thermal Oxidation (RTO)

References

1. DiMaria DJ, Arnold D, Cartier E (1992) Degradation and breakdown of silicon dioxide films on silicon. Appl Phys Lett 61:2329–2331
2. Deal BE, Grove AS (1965) General relationship for the thermal oxidation of silicon. J Appl Phys 36:3770–3778
3. Ganem JJ, Battistig G, Rigo S, Trimaille I (1993) A Study of the Initial Stages of the Oxidation of Silicon Using O_{18} and RTP. Appl Surf Sci 65/66:647–653
4. Quirk M, Serda J (2001) Semiconductor manufacturing technology. Prentice-Hall, Inc., New Jersey
5. http://www.lelandstanfordjunior.com/oxcalcfaq.html
6. Choi SS, Numan MZ, Chu WK, Irene EA (1987) Anomalous oxidation rate of silicon implanted with very high doses of arsenic. Appl Phys Lett 51:1001–1003
7. Plummer JD, Deal MD, Griffin PB (2000) Silicon VLSI technology: Fundamentals, Practice and Modeling. Prentice-Hall, New Jersey
8. Singer P (1997) Furnaces evolving to meet diverse thermal processing needs. Semiconduct Int 20:84–88
9. Xiao H (2001) Introduction to semiconductor manufacturing technology. Prentice-Hall, New Jersey
10. Higashitani M, Hikazutani K (1997) Semiconductor device manufacturing method including dry oxidation, US Patent 5,637,528

Oxide Deposition

► Oxidation (of Silicon)

Oxide Growth

► Oxidation (of Silicon)

Oxides

► Non-Metallic Inorganic Materials

Packaging (and Wire Bonding)

MU CHIAO
Department of Mechanical Engineering,
University of British Columbia, Vancouver,
British Columbia, Canada
muchiao@mech.ubc.ca

Synonyms

Electronic packaging; IC packaging; MEMS packaging

Definition

Packaging provides electrical or mechanical access to microdevices from the outside world. Packaging also provides protection to microdevices from being damaged by the elements, such as dust, moisture and chemicals from the environment.

Wire bonding is a technology that connects microdevices to the outside world electrically using small metal wires.

Overview

Historically, packaging technology was developed by the integrated circuit (IC) industry. When semiconductor microdevices such as transistors are fabricated on a semiconductor wafer, electrical signals can only be accessed through many micrometer-sized metal lines and contacts using specialized equipment such as a probe station, equipped with an optical microscope and micromanipulators with fine tungsten needles. In order to provide low cost, general access to the microdevices, semiconductor wafers are first diced into small chips (or dies) and small metal wires are used to connect the metal contacts to a *carrier case*. The carrier case has millimeter-sized pins that can be accessed using standard circuit boards.

In IC packaging, the carrier case also provides a moisture barrier. Often, failure in a microdevice is the contact between the metal wires and the metal contacts on the substrate due to moisture-induced corrosion. For microelectromechanical system (MEMS) devices, moisture presents more of a threat than for conventional IC devices [1]. Many micromechanical MEMS components (such as a microcantilever beam) are positioned a few micrometers from the substrate. Moisture condensing on the surface of the substrate will pull down the MEMS devices due to surface tension. The micromechanical component will no longer be functional.

For microfluidic devices, packaging not only provides electrical access to the metal electrodes in the microchannels, but also provides mechanical access. Small tubing is used to connect the fluid ports on the microfluidic device to syringe pumps or other external devices.

Wire bonding is a technology that uses small gold or aluminum wires with a diameter around 20 to 50 μm to build electrical connections to the MEMS/IC devices. The wires are fed through a small aperture on the tip of an ultrasound actuator (or horn). The tip presses the wire to the metal contact surface on the device substrate. Ultrasound energy is applied to vibrate the tip, making the wire rub against the metal contact surface. The vibration-induced friction can (1) create a clean interface between the wire and the metal surface and (2) provide thermal energy that bonds the wire to the metal surface.

Basic Methodology

DIP (Dual In-Line Package)

DIP technology uses moisture-resistant plastic compounds to encapsulate MEMS/IC devices [2]. As shown in Fig. 1a (Courtesy of Shinko Electric Industries Co. Ltd), the two row of pins commonly seen in IC devices that extended out from the plastic body are used for electronic connections, hence the term *dual in-line*.

After IC devices are manufactured on a substrate wafer, a dicing saw is used to break the wafers into smaller chips. The chips are then bonded to a metal frame (called a lead frame) using epoxy. The lead frame is often made of Cu – Ni – Fe alloys with a thermal expansion coefficient matched with that of the silicon substrate as well as of the plastic compound. Wire bonding is used to connect con-

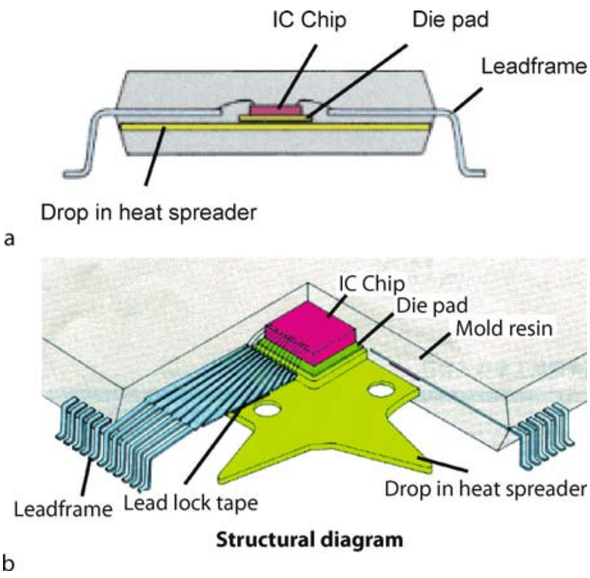

Packaging (and Wire Bonding), Figure 1 (**a**) Cross-section of a DIP package; (**b**) exploded view of a QFP package

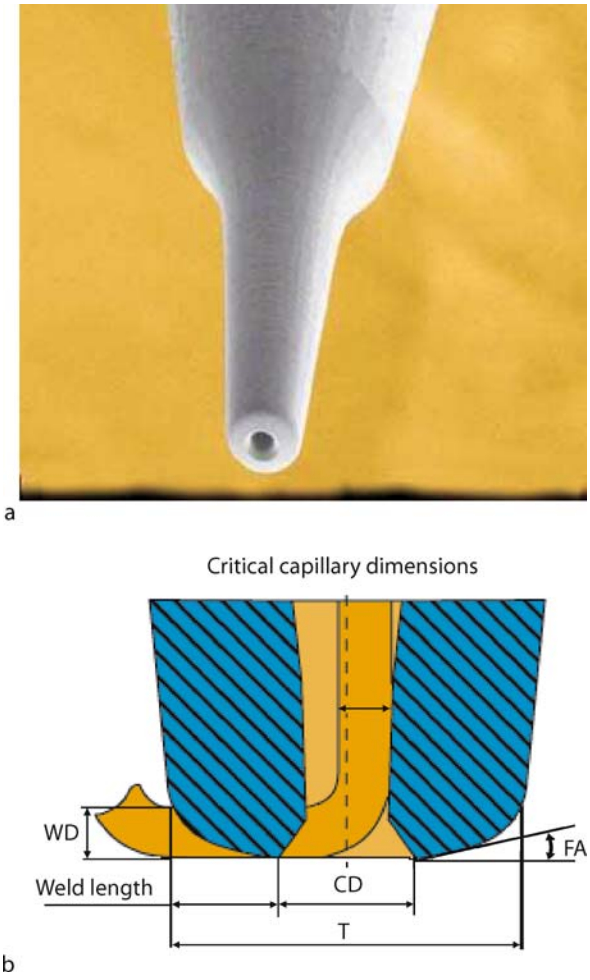

Packaging (and Wire Bonding), Figure 2 Ultrasound horn for wire bonding

tact pads on the device to the lead frame. The device (and the lead frame) is then put into a mold. The plastic compound, with a thermal expansion coefficient matched with silicon, is molded around the device/lead frame to form a protective case.

Many other variations of DIP technology are readily available, such as SH-DIP (shrink DIP), SIP (single in-line package), SOP (small out-package) and QFP (quad flat pack, as shown in Fig. 1b (Courtesy of Shinko Electric Industries Co. Ltd)). The basic techniques are the same as DIP but the variants provide different form factors and different arrangement of the pins.

Wafer Bonding

MEMS devices need to be separated from the substrate using a wafer dicing machine before they can be packaged. However, unlike IC devices, water used in the dicing operation will destroy micromechanical components. Moreover, DIP technology cannot be used since the molding process will also destroy the micromechanical part of the MEMS devices.

The wafer bonding technique has been used to encapsulate MEMS devices before the dicing process. Wafers (silicon or glass) with recessed microcavities are used to bond to the MEMS device wafer. The microcavity provides a protection cap to the micromechanical component. The hermetic sealing between the bonded wafers will prevent water (during dicing operation) from coming into the cavity. It will also delay moisture diffusion from the environment into the cavity. Furthermore, the strength of the sealing will need to be high enough to sustain the subsequent molding in a DIP process.

Anodic Bonding

Anodic bonding has been widely used to form a pressure reference chamber in silicon pressure sensors. Borosilicate glass wafers with a thermal expansion coefficient matched with silicon are often used to bond with silicon wafers using a strong electric field and high temperature. The glass wafer is first chemically etched or sand blasted to form small cavities. Each cavity will accommodate one or more MEMS devices. The glass wafer is made contact with a silicon surface on a hot plate at 400 °C. An electric field is applied between the glass and the silicon such that sodium ions drift away from the glass–silicon interface.

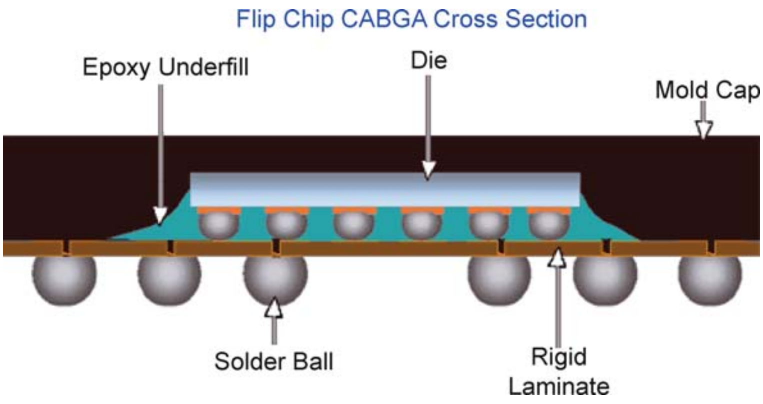

Packaging (and Wire Bonding), Figure 3 Flip-chip technology for electric interconnection

Dissolved oxygen in the glass moves towards the glass–silicon interface and forms silicon dioxide that bonds the silicon surface and glass wafer (also silicon dioxide).

Silicon–Silicon Wafer Bonding

A clean and polished silicon wafer can be bonded to another silicon wafer at room temperature [3]. Two bonding mechanisms exists: (1) hydrophilic silicon surfaces will allow hydrogen bonds to form between two wafers with thin silicon dioxide layers and (2) hydrophobic silicon surfaces will allow van der Waals interactions between two clean silicon surfaces. Thermal annealing at high temperature ($> 1000\,°C$) is then required to permanently bond the silicon wafers.

Wafer Bonding with Intermediate Layers

Wafers can be bonded using intermediate layers such as metals to form hermetic seals. Polymers, in general, do not provide water-tight sealing, and are hence less important in the field of MEMS packaging. Soft metals such as indium can be bonded with silicon with a gold passivation [4]. Aluminum has been used to bond with silicon dioxide [5] and silicon nitride [6] to form hermetic seals.

Fluid Interconnects for Microfluidic Devices

In Lab-on-a-Chip applications, not only electrical, but also mechanical access (fluids) needs to be realized to the outside world. Flexible tubing such as polyimide tubes is often used to connect the small opening in microfluidic chips [7]. The sealing between the tube and the device opening has to be leak-tight. Most methods involve the use of placing a tube into the small fluid access via and sealants, such as polysiloxane [14] or polydimethylsiloxane [8], are then poured in to form seals. However, the sealants must not clog the tubing.

Many fluid interconnect techniques have been demonstrated to address the issues with the blocking of the tubing as a result of sealant application. These methods include the use of polymer membranes that prevent the seal from clogging [9] and the use of thermal shrink plastic tubing [10]. The published methods have been demonstrated in research and academic settings; much is still needed to be done for industry-relevant scale [15].

Electrical Interconnection

Wire bonding has been used in IC packaging for many years. Ultrasound energy is used to bond small metal wires on the metal pads on silicon wafers. As shown in Fig. 2a (Courtesy of Dr. I.W. Qin, Advanced Packaging, PennWell, Inc.), an ultrasound horn has a small opening at its tip. A small metal wire is fed through the opening, as shown in Fig. 2b (Courtesy of Dr. I.W. Qin, Advanced Packaging, PennWell, Inc.). The horn then makes contact with the surface and bonds the wire to the surface using ultrasound energy. The pitch size is often determined by the precision of the ultrasound horn placement, the size of the ultrasound horn and the size of the metal wires. As IC and MEMS I/O densities increase, it is becoming more and more challenging for wire bonding technology to meet the need of high-density I/O.

Other electric interconnection techniques such as wafer bumping and *flip-chip* bonding have emerged [11]. As shown in Fig. 3 (Courtesy of Amkor Technology, Inc.), small metal balls (Ag/Sn or Sn/Pb) are directly electroplated on the metal pads of the device chip. The chips are then "flipped over" and bonded to a printed circuit board (PCB) or a substrate with prefabricated metal connections. An epoxy underfill is then used to fill the space

between the chip and the PCB. A plastic compound is then molded over the chip for protection.

Packaging Reliability and Testing

A major characteristic of a MEMS or IC package is reliability. One often asked question is "how long will the device be operational"? From a packaging perspective, the protection and electrical/mechanical interconnection must withstand the elements. For example, for an accelerometer, the moisture from the environment must be stopped or delayed by the packaging seal so that the accelerometer sitting in the package will function properly. Furthermore, the temperature cycling often seen in automotive applications may raise concerns over the electric interconnection. The metal-to-metal contacts may form intermetallic compounds that are thermally mismatched with the surroundings and cracks will form when the package goes through temperature cycling. The metal contact resistance will then increase and eventually form an open circuit.

Many testing methods are available to evaluate the reliability of an IC/MEMS package. For example, if the dominant failure mode of a MEMS device is water condensation in the package, *autoclave* tests are available to test the reliability of the devices [1]. In an autoclave test, pressurized water is used to fill bonding imperfections and small crevasses that may exist in a package to accelerate the device failure.

Key Research Findings

In recent years, low-cost, localized "welding" has demonstrated reliability and possibilities for packaging of MEMS devices [5, 12]. One of the emphases has been on vacuum packaging for MEMS resonators and gyroscopes for high quality factor performance in a vacuum. Vacuum packaging for MEMS resonators using aluminum-to-silicon nitride bonding was shown to maintain the vacuum level in a harsh environment (130°C, 2.7 atm and 100% relative humidity) for a long period of time [6]. A specialized metallization process was also demonstrated to produce a vacuum package [13].

Future Directions for Research

Due to the diversity of MEMS devices, MEMS packaging methodology is device and application dependent. Compromise solutions between cost, reliability and process compatibility need to be considered.

Cross References

► Anodic Bonding
► Micromolding
► Techniques for Transferring Samples to Chips
► Wafer Bonding

References

1. Chiao M, Lin L (2004) Sealing Technologies. In: Hsu TR (ed) MEMS Packaging. IEE, Stevenage, Herts., UK
2. Kamath SM, Tummala RR (2001) Fundamentals of Single Chip Packaging. In: Tummala RR (ed) Fundamentals of Microsystems Packaging. McGraw-Hill, Boston
3. Tong QY, Gosele U (1999) Semiconductor wafer bonding: sciences and technology. Wiley, New York
4. Cheng YT, Lin L, Najafi K (2000) Localized silicon fusion and eutectic bonding for MEMS fabrication and packaging. J Microelectromec Syst 9(1):3–8
5. Cheng YT, Hsu WT, Najafi K, Nguyen CTC, Lin L (2002) Vacuum packaging technology using localized aluminum/silicon-to-glass bonding. J Microelectromec Syst 11(5):556–565
6. Chiao M, Lin L (2006) Device-Level Hermetic Packaging of Microresonators by RTP Aluminum-to-Nitride Bonding. J Microelectromec Syst 15(3):515–522
7. Puntambekar A, Ahn CH (2002) Self-aligning microfluidic interconnects for glass- and plastic-based microfluidic systems. J Micromech Microeng 12:35–40
8. Li S, Chen S (2003) Polydimethylsioxane fluidic interconnects for microfluidic systems. IEEE Trans Adv Packag 26(3):242–247
9. Tsai JH, Lin LW (2001) Micro-macro fluidic interconnectors with an integrated polymer sealant. J Micromech Microeng 11:577–581
10. Tingrui P, Baldi A, Ziaie B (2006) A reworkable adhesive-free interconnection technology for microfluidic systems. J Microelectromec Syst 15(1):267–272
11. Al-Sarawi SF, Abbott D, Franzon PD (1998) A review of 3-D packaging technology. IEEE Trans Compon Packag Manuf Technol, Part B: Adv Packag 21(1):2–14
12. Lin L (2000) MEMS post-packaging by localized heating and bonding. IEEE Trans Adv Packag 23(4):608–616
13. Stark BH, Najafi K (2004) A low-temperature thin-film electroplated metal vacuum package. J Microelectromec Syst 13(2):147–157
14. Gonzalez C, Collins SD, Smith RL (1998) Fluidic interconnects for modular assembly of chemical microsystems. Sens Actuators B 49:40–45
15. Han KH, Frazier AB, (2005) Reliability aspects of packaging and integration technology for microfluidic systems. IEEE Trans Device Mater Reliab 5(3):452–457

Parallelization

Definition

Simultaneous implementation of several chemical/biological analyses in an on-chip format generally from a single reagent source.

Cross References

► Surface-Directed Capillary Flow Systems

Parallel (Stratified) Flow

Definition

Stratified flow is that multiphase flow where the phases flow along each other in distinct strata or layers.

Cross References

► Pressure-driven Two Phase Flows

Partial Differential Equations (PDEs)

Definition

A partial differential equation (PDE) is a relation involving an unknown function of several independent variables and its partial derivatives with respect to those variables. Partial differential equations are used to formulate and solve problems that involve unknown functions of several variables, such as the propagation of sound or heat, electrostatics, electrodynamics, fluid flow, elasticity, or more generally any process that is distributed in space, or distributed in space and time. (Definition taken from wikipedia: http://en.wikipedia.org/wiki/Partial_differential_equation)

Particle Dynamics Simulation

► Molecular Dynamics Simulation Method

Particle Image Thermometry

Definition

Particle Image Thermometry (PIT) is a method to determine two dimensional temperature fields of fluids. The particles carry the temperature information and are seeded into the fluid. Thermochromic Liquid Crystals (TLCs) are often used for that.

Particle Image Velocimetry (PIV)

Definition

PIV is used to estimate two-dimensional velocity fields of fluid flows. The fluid is seeded with ► tracer particles (able to follow the flow) whose motion gives information about the motion of the fluid. Therefore two images taken at two times are divided into ► interrogation areas. The interrogation areas belonging together are correlated (image processing algorithm) which leads to a pixel displacement. With the time interval between the capture of the two pictures, the pixel displacement, and the pixel length the velocity of the considered interrogation area can be calculated.

Particle Manipulation

► Bead Based Microfluidic Platforms

Particle Manipulation Using Ultrasonic Fields

Nick R. Harris[1], Martyn Hill[2]
[1] School of Electronics and Computer Science, University of Southampton, Highfield, Southampton, UK
[2] School of Engineering Sciences, University of Southampton, Highfield, Southampton, UK
nrh@ecs.soton.ac.uk

Synonyms

Ultrasonic separation; Ultrasonic concentration; Ultrasonic particle manipulation; Acoustic separation

Definition

Ultrasonic fields, particularly standing waves or pseudo standing waves, can be used to manipulate particles within fluids. Typically particles in aqueous media will move to pressure nodes of the field, which can be planes, lines or points, depending on the standing wave geometry. By control of the standing wave patterns, it is possible to agglomerate particles, separate particles from the medium, wash particles from one fluid to another or fractionate populations of particles. In this article, techniques that have been used in microfluidic applications will be discussed, although many of the techniques can also be used at the macro scale.

Overview

It has been known for many years that acoustic standing waves can influence the behaviour of particles in either a liquid or gaseous medium. This effect relies on acoustic radiation forces that act on particles and other acoustic discontinuities (such as second phase fluids) within an ultrasonic field [1]. These forces are generally larger

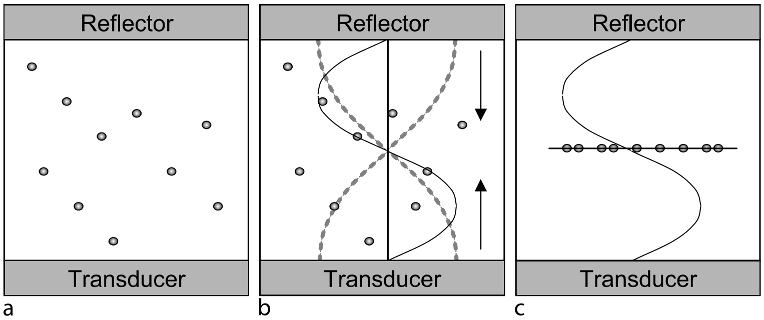

Particle Manipulation Using Ultrasonic Fields, Figure 1 Movement of particles within an ultrasonic standing wave (USW). (**a**) Before a standing wave is generated, particles are evenly distributed throughout the fluid (**b**) a standing wave is excited by driving a transducer at a thickness resonance of the fluid layer, generating a pressure node in the centre of the fluid layer (dotted grey lines). A net force profile is established as per the solid line (in the direction of the arrows) (**c**) particles aggregate at the pressure node, driven by the force

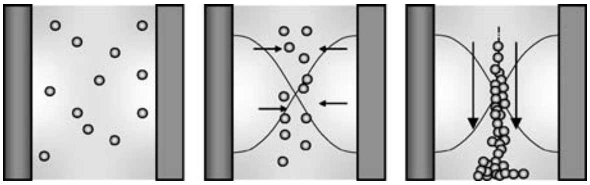

Particle Manipulation Using Ultrasonic Fields, Figure 2 Enhanced sedimentation. Particles within an ultrasonic field (left) are agglomerated by the field (centre) and then tend to sediment under gravity (right)

in an ultrasonic standing wave (USW) than in a progressive wave and so it is mainly standing waves that are used for particle manipulation. The magnitude of this force is dependent upon the distance from the node of the standing wave and causes particles to move to the nodal plane. Use in microfluidic systems concentrates on active dimensions comparable with an acoustic wavelength. Acoustic frequencies of a few megahertz have wavelengths of the order of a few hundred micrometres. For example, a 3MHz acoustic wave in water has a wavelength of 500 μm. Many of the devices to be discussed here actually use sub-wavelength active dimensions and so it can be seen that ultrasonic waves of this order of frequency are compatible with the dimensional scale typically used in microfluidic systems. Consider the system represented in Fig. 1, in which particles within a fluid are bounded by an ultrasonic transducer and a reflective boundary. If the transducer is driven so as to excite a resonance frequency of the cavity (in this case, a half wavelength mode as shown by the pressure profile) a standing wave will be set up, with associated pressure maxima and minima. Particles will, in general, be transported towards pressure nodes within the field, by radiation forces. Figure 1b shows the relative magnitude and direction of the force across the depth of the chamber. The arrows show the net force direction, and the black curve gives an indication of relative magnitude. The dotted curve shows the acoustic pressure profile (in this case a half wavelength) with a resulting node in the centre of the fluid layer.

The magnitude of the force seen by the particles is dependent on

- the radius of the particle
- the energy density in the standing wave
- the distance of the particles from the nodal plane
- the acoustic contrast factor of the particles.

This last factor is a function of the differences in mass density and compressibility of the fluid and the particle.

By considering these factors, it can be seen that particles can be either all concentrated in one place, or by making use of the different size of particle populations and a competing force such as viscous drag, fractionated by size. It is also possible, by making use of acoustic contrast factor variations to fractionate similar sized populations.

Basic Methodology

Particle Concentration or Filtration

An obvious application of this technique is in a particle concentration or filtration system. There are two main approaches adopted

- Particle agglomeration
- Flow through separation.

In a particle agglomeration system (see [2]), devices are typically operated in a vertical direction (see Fig. 2). Particles are driven to the standing wave nodes by the acoustic radiation forces, and start to form agglomerates. Agglomerates form due to secondary radiation forces (see *key research findings*). As agglomerates grow, the relative importance of gravitational forces over viscous drag forces grows until the clumps of particles are able to sediment under gravity. Alternatively, once particles have been

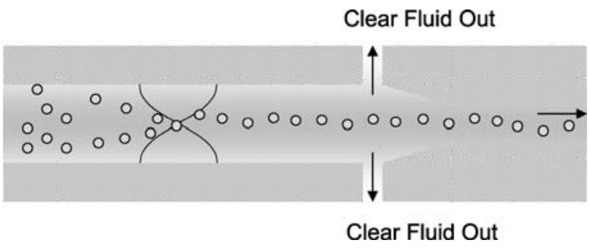

Particle Manipulation Using Ultrasonic Fields, Figure 3 Flow through concentration based on technique described by Hawkes and Coakley [3]

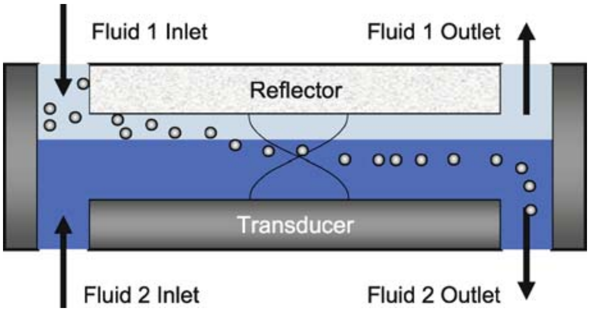

Particle Manipulation Using Ultrasonic Fields, Figure 4 Particle Washing by forcing particles from one medium to another under laminar flow conditions

trapped, the field can be removed and the particle agglomerate falls.

Although as described, this technique has obvious application in batch processing, it can be modified to work as a flow-through device.

Flow-through systems are used in a continuous mode of operation in which a mix of fluid and particles is pumped through the device and the ultrasonic standing wave field concentrates the particles into a nodal plane. In this way a barrier-free filter is created.

This allows concentrated particles to be drawn off from the centre of the flow and clarified fluid to be drawn from either the upper or lower outlet, or from both as shown in Fig. 3. In this configuration, a mixture of particles and fluid are input from the left and flow through the device. In the main chamber an acoustic field concentrates the particles into a nodal plane in the centre. Clear fluid is then drawn out through the top and bottom outlets while the concentrated particles are allowed to proceed to the third exit.

This approach relies on the particles remaining at the centre of the channel due to the ordered nature of the highly laminar flow in a microchannel. The device developed by Hawkes and Coakley [3] was fabricated using traditional techniques and a microfabricated device has been developed using channels that are wet etched into silicon and Pyrex layers anodically bonded together [4].

An alternative technique that sorts particles into discrete patterns within a microchamber has been used by Neild et al. [5]. In the devices used by this group, acoustic energy is coupled into a fluid by first exciting flexural waves in a glass plate that bounds the fluid. Changing the excitation frequency, and in some cases using different transducers to excite the plate, allows particles to be aligned and manipulated within the fluid. Work described in reference [5] uses the acoustic pattern to align particles prior to further manipulation by a mechanical microgripper.

While most work has used planar resonators, it is also possible to manipulate particles in alternative geometries such as cylindrical tubes [6].

Particle Washing

Applications have also been developed whereby particles can be driven acoustically from one fluid to another, making use of the laminar flow inherent in microfluidic systems. This precludes turbulent mixing, and so fluids can be in physical contact with minimal mixing. Figure 4 shows the principle. A fluid with particles in is fed in through fluid 1 inlet, and the acoustic force drives the particles from fluid 1 to fluid 2. Fluid 2 can then be withdrawn from outlet 2 with the particles. The ability to wash cells and particles and to move them from one medium to another is a critical element of many forms of analysis and hence an important component of a Lab-on-a-Chip toolbox.

A microfabricated device that works in a manner similar to that shown in Fig. 4 has been developed by Peterson et al. [7]. Three inlet and three outlet channels feed a single parallel sided channel anisotropically wet etched into a silicon substrate. This channel is excited at its half-wave resonance by a transducer mounted in the plane of the silicon, perpendicular to the axis of the standing wave. Similar devices have been used by the same group for a number of applications, including the separation of lipids from blood (in which the lipids move to the pressure antinode and the red cells to the pressure node) and fractionation of different size beads.

Biosensor Performance Enhancement

Ultrasonic particle manipulation can also be used to enhance biosensor performance, by using the ultrasound to drive the particles of interest to the biosensor surface. In this implementation (Fig. 5), a resonant reflector layer is used to generate a pressure node at a boundary, (effectively creating a quarter wave resonance within the fluid layer), rather than in the centre of the chamber, as previously described.

Such a device was demonstrated by Martin et al [8], who forced spores in a 135 μm deep chamber on to an antibody

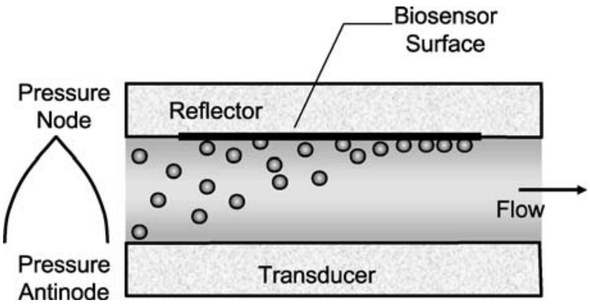

Particle Manipulation Using Ultrasonic Fields, Figure 5 Enhancing biosensor performance based on technique of Martin et al [8]

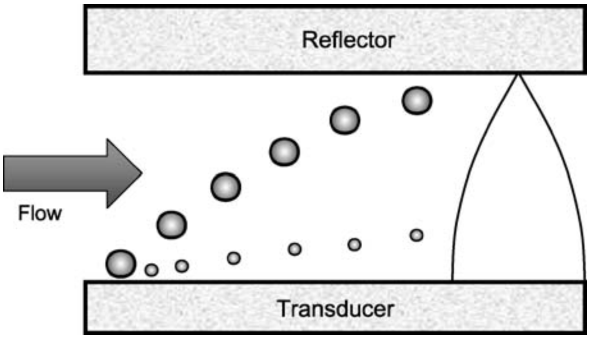

Particle Manipulation Using Ultrasonic Fields, Figure 6 Fractionation of particles, making use of the net larger force on larger particles

coated surface and increased the capture of those spores by a factor of 70 when compared with the same system without ultrasonic actuation. This has the potential to overcome the diffusion limit on detection in microfluidic biosensor systems and significantly increase sensor sensitivity.

Fractionation

A further illustration of the use of ultrasonic fields is shown in Fig. 6. This demonstrates the principle of particle fractionation using acoustics. Different sized particles of the same material will experience different magnitudes of force within the same field. Thus larger particles, experiencing a larger force, will move more rapidly to the nodal plane. As long as the lateral flow is balanced against the vertical particle movement, the population of particles will be fractionated as shown. If the residence time in the field is too long though, all the particles will end up at the nodal plane.

Again, a quarter wave structure is used here to spread the particles across the width of the chamber, and the pressure profile is shown in the diagram. This requires the whole particle population to be input at the bottom of the channel, requiring some pre-conditioning of the particle distribution before the particles are introduced to this device, as the particles are driven from bottom to top in this case.

Key Research Findings

Calculation of Radiation Forces within the Fluid Layer

For a more detailed description of the background, including key references, see Gröschl's 1998 paper [1]. King provided the first comprehensive calculation of acoustic radiation forces on a small particle within a standing wave in 1934. This theory was developed for rigid spheres in an inviscid fluid and predicts that particles will move toward either the node or antinode of the field depending on the ratio of the fluid and particle densities. When the ratio of the incompressible particle density to the fluid density is less than 0.4, the acoustic force will act towards the pressure antinode. If the density ratio is above 0.4 (which is the general case for real particles) the acoustic radiation force will act towards the pressure node of the standing wave. King's predictions have been shown to be in good agreement with experimental results for solid spheres suspended in a gas, but are subject to significant errors for spheres which are not rigid in comparison to the fluid medium, which is the case of bubbles within a resonant field.

In the light of this, King's theory was extended by Yosioka and Kawasima to allow for compressible spheres in 1955. They demonstrated that the time-averaged acoustic radiation force on a spherical particle of radius a, at position x within a one dimensional standing wave of acoustic energy density ε is:

$$F(x) = 4\pi k\varepsilon a^3 \Phi(\beta\rho)\sin(2kx) \tag{1}$$

The *acoustic contrast factor*, $\Phi(\beta\rho)$ is given by:

$$\Phi(\beta\rho) = \frac{\rho_p + \frac{2}{3}(\rho_p - \rho_f)}{2\rho_p + \rho_f} - \frac{\beta_p}{3\beta_f} \tag{2}$$

where β and ρ are the compressibility and the mass density of the fluid and the particle, indicated by subscripts f and p respectively. The wave number, k is equal to $2\pi/\lambda$ where λ is the wavelength of the standing wave.

For most applications of interest, including cells in aqueous solution, the acoustic force will act towards the pressure node, however in the case of bubbles that are smaller than resonant size, and certain two-phase fluid mixtures, the bubble, or second phase fluid, will experience an acoustic force acting towards the pressure antinode.

Particle Positions Under Gravity and Other Forces Yosioka and Kawasima also considered the direction in which an acoustic force will act on a particle in suspension. The equilibrium position of a particle within the

field will be determined by the resolution of this acoustic force and any other forces acting on the particle. Typically this would be gravity, although it applies to any force. In the case of a planar resonant field in which the positive x-axis points vertically upwards, the particle will be in equilibrium when:

$$3k\varepsilon\Phi(\beta\rho)\sin(2kx) = (\rho_p + \rho_f)g \quad (3)$$

The equilibrium position, for this case (in which the particle is small compared to the acoustic wavelength) is independent of the size of the particle, but dependent upon the acoustic contrast factor and the strength and frequency of the ultrasonic field. This offers a means of characterizing the acoustic field, the pressure amplitude of which is often difficult to determine in microsystems, by balancing acoustic and gravitational forces on an acoustically levitated particle. Particles that are not neutrally buoyant will have a minimum acoustic energy density required to hold the particle against buoyancy forces.

In many applications, including the manipulation of biological cells, particles are close to neutrally buoyant and the equilibrium position given by Eq. 3 will be very close to the pressure node. However for heavy particles, or for bubbles, this buoyancy offset may be significant.

Lateral Forces Real standing wave fields do not only exhibit pressure variations along the axis of the standing wave. They also have variations in the lateral directions leading particles to move not just to the axial pressure nodes, but also to particular points within those energy nodal planes. The practical effect of this is that instead of having a homogeneous layer of particles, the layer can organise itself into stripes, or striations, or other patterns. These inhomogeneities in the field may be caused by a number of phenomena including a decrease in acoustic energy towards the edges of axial fields, near field effects [9] due to geometric interference patterns, multi-dimensional acoustic modes within the enclosure, the coupling of structural (for example bending) modes into the fluid or inhomogeneity of the ultrasonic source.

In some cases these lateral variations provide a desirable feature of the device operation, particularly in systems designed to trap particles, while in others, the variations are not desirable and may be detrimental to the device performance, such as flow through concentrators. In real devices lateral forces may well exist due to a combination of the above causes. The magnitude and distribution of the lateral forces within resonators has been measured and shown to compare well with calculations using Gorkov's formulation for radiation forces (described by Gröschl in [1]).

Secondary Radiation Forces In addition to the axial and lateral radiation forces attributable to the primary acoustic field, secondary acoustic forces are produced between particles themselves. These particle-particle interactions, known as Bjerknes forces, aid the formation of aggregates within a standing wave, but such effects are negligible until the particles are in close proximity.

Some Practical Considerations

The Influence of Particles on the Field Resonant chambers for particle manipulation (including microfluidic chambers) are designed to provide specific acoustic characteristics. However, the chambers must work when filled with a fluid-particle mix which will have acoustic characteristics that differ from the particle-free fluid. Many applications will need to work over a range of particle concentrations that will modify the acoustic field. In cases where the particles are very different acoustically from the fluid medium, agglomerations can cause localized breakdown of the acoustic field resulting in a disruption of the ordered collection of particles at the pressure nodes.

Temperature Changes The temperature of an acoustic resonator will typically rise during use due to energy dissipation in the transducer and acoustic absorption within the layers of the resonator. The temperature rise will depend on the input power, the size of the resonator, the transducer material, and the material characteristics of the resonator layers. Hence there are significant differences in the thermal behaviour of resonators reported in the literature, with, for example, Hawkes and Coakley [3] reporting less than 1 K temperature increase in micro-scale chambers, while at the other extreme, Doblhoffdier et al. [2] required an integrated cooling circuit to avoid significant temperature rises in their rather larger chamber designed for the retention of mammalian cells.

Cell Viability Many of the uses envisaged for USW manipulation of particles are based upon manipulation of biological cells and so cell viability after treatment with ultrasound becomes an important issue. This has been reported on by several studies which have found that viability is maintained. For example Doblhoffdier et al. [2] suspended mammalian cells in a large resonator at different power levels and reported no significant loss in viability.

Hultström et al. [10] trapped cells in a 260 μm deep microfluidic chamber constructed from glass and PDMS. It was demonstrated that cell viability was not significantly impeded by 75 min exposure to a 0.85 MPa 3 MHz USW field. Indeed, tests on the cells following exposure

suggested that the exposure to ultrasound enhanced the cells' ability to proliferate. The same group has demonstrated the ability of ultrasound traps to enhance bioanalysis in a number of different microchambers and has constructed microdevices that integrate ultrasonic and dielectrophoretic manipulation.

Future Directions for Research

Radiation forces as generated by low MHz ultrasonic standing waves offer a method of manipulating particles in a fluid, with particular application at the microscale. This gives tremendous potential for trapping and manipulating larger particles and groups of particles, perhaps prior to finer manipulation from other techniques. In addition, the evidence that ultrasound can manipulate and control the position of cells without adversely affecting cell viability suggest that ultrasonic standing waves hold significant potential in the manipulation of biological cells. The field is still relatively immature and requires work on the characterisation and optimisation of chambers and defining the scale limits of manipulation in practical devices.

Cross References

► Acoustic Streaming
► Acoustics Based Biosensors
► Biosample Preparation Lab-on-a-Chip Devices
► Cavitation in Microdomains
► Cell Sorting
► Lab-on-chip Devices for Particle and Cell Separation
► Piezo/PZT in Microfluidics

References

1. Gröschl M (1998) Ultrasonic separation of suspended particles – Part I: Fundamentals. Acustica 84(3):432–447
2. Doblhoffdier O, Gaida T, Katinger H, Burger W, Groschl M, Benes E (1994) A Novel Ultrasonic Resonance Field Device for the Retention of Animal-Cells. Biotechnol Progress 10(4):428–432
3. Hawkes JJ, Coakley WT (2001) Force field particle filter, combining ultrasound standing waves and laminar flow. Sens Actuators B Chem 75(3):213–222
4. Harris NR, Hill M, Beeby SP, Shen Y, White NM, Hawkes JJ, Coakley WT (2003) A Silicon Microfluidic Ultrasonic Separator. Sens Actuators B 95(1-3):425–434
5. Neild A, Oberti S, Beyeler F, Dual J, Nelson BJ (2006) A micro-particle positioning technique combining an ultrasonic manipulator and a microgripper. J Micromech Microeng 16(8):1562–1570
6. Goddard G, Kaduchak G (2005) Ultrasonic particle concentration in a line-driven cylindrical tube. J Acoust Soc Am 117(6):3440–3447
7. Petersson F, Nilsson A, Jonsson H, Laurell T (2005) Carrier medium exchange through ultrasonic particle switching in microfluidic channels. Anal Chem 77(5):1216–1221
8. Martin SP, Townsend RJ, Kuznetsova LA, Borthwick KAJ, Hill M, McDonnell MB, Coakley WT (2005) Spore and microparticle capture on an immunosensor surface in an ultrasound standing wave system. Bio-sens Bioelectron 21(5):758–767
9. Lilliehorn T, Simu U, Nilsson M, Almqvist M, Stepinski T, Laurell T, Nilsson J, Johansson S (2005) Trapping of microparticles in the near field of an ultrasonic transducer. Ultrasonics 43(5):293–303
10. Hultström J, Manneberg O, Dopf K, Hertz HM, Brismar H, Wiklund M (2006) Proliferation and viability of adherent cells manipulated by standing-wave ultrasound in a microfluidic chip. Ultrasound Med Biol 33:175–181

Particle Methods

► Meshless Methods

Passive Micromixers

CHIA-YEN LEE[1], CHE-HSIN LIN[2], LUNG-MING FU[3]
[1] Department of Mechanical and Automation Engineering, Da-Yeh University, Chung-Hua, Taiwan, ROC
[2] Department of Mechanical and Electromechanical Engineering, National Sun Yat-sen University, Kaohsiung, Taiwan, ROC
[3] Department of Materials Engineering, National Pingtung University of Science and Technology, Pingtung, Taiwan, ROC
loudyfu@mail.npust.edu.tw

Synonyms

Microfluidic mixer; Micromixing chip; Micromixer; Passive mixer

Definition

A passive micromixer is one of the microfluidic devices. It utilizes no energy input except the mechanism (pressure head) used to drive the fluid flow at a constant rate. Due to the dominating laminar flow on the microscale, mixing in passive micromixers relies mainly on chaotic advection realized by manipulating the laminar flow in microchannels or molecular diffusion with increasing the contact surface and time between the different fluid flows.

Overview

Microfluidic devices have had a considerable impact in the fields of biomedical diagnostics and drug development, and are extensively applied throughout the food and chemical industries. The very small scale of the flow

channels in microfluidic systems increases the surface to volume ratio, and is therefore advantageous for many applications. However, the characteristic Reynolds number ($\mathrm{Re} = l\rho v/\eta$) of liquid flows in such microchannels is very small. For example, the Reynolds number in a typical water-based microfluidic system with a channel width of 100 μm, a liquid flow rate of 1 mm/s, a fluid density of 1 g/cm^3 and a viscosity of 0.001 N s/m^2 is of the order of 0.1. In such low Reynolds number regimes, turbulent mixing does not take place, and hence species mixing occurs primarily as a result of diffusion, which is an inherently slow process. Consequently, the aim of microfluidic mixing schemes is to enhance the mixing efficiency such that a thorough mixing performance can be achieved within shorter mixing channels, thus reducing the characteristic size of microfluidic devices. Furthermore, developing efficient mixing schemes is essential to increase the throughput of microfluidic systems in general and to realize the concept of micro-total-analysis systems and Lab-on-a-Chip systems in particular.

In micromixers, two operating parameters are of importance: the Reynolds number Re and the Péclet number Pe. The Reynolds number, given by

$$\mathrm{Re} = VL_h/\upsilon \quad (1)$$

represents the ratio of momentum to viscous friction, where V is the average flow velocity, L_h is the hydraulic diameter and υ is the kinematic viscosity. A turbulent flow can be indicated by a high Reynolds number above a critical value (around 2300 on the macroscale). In most cases of microfluidics, a laminar flow can be expected with a low Reynolds number. The Péclet number, given by

$$\mathrm{Pe} = VL/D \quad (2)$$

represents the ratio of the mass transport due to convection and that of diffusion, where L is the mixing path and D is the diffusion coefficient. Convection is dominant at higher Péclet numbers.

The theory reported on mixing began with Einstein's investigation of Brownian movements [1]. The common mixing methods are the generation of chaotic advection and turbulence. Fluid motions vary irregularly so that quantities such as pressure and velocity show a random variation in space and time. The random movement quickly disperses the mixed components. Chaotic advection can be generated by stirring the flow, which is very effective for low Reynolds numbers. The concepts of splitting, stretching, folding and breaking up play an important role in the mixing quality.

In contrast to the passive mixing schemes presented above, in which the microchannel configuration is specifically designed to increase either the contact area or the contact time (or both) of the multiple species, active mixing schemes improve the mixing performance by applying external forces to the sample flow in order to accelerate the diffusion process. Typically, active schemes are implemented by incorporating some form of mechanical transducer within the microfluidic device using microfabrication techniques. It has been shown that microfluidic mixers which use embedded ultrasonic transducers to generate acoustic waves to stir the samples are capable of achieving a high mixing performance. However, the acoustic vibrations also generate considerable heat, which is undesirable since it may lead to unwanted reactions between the samples. Various microfluidic devices with embedded microelectrodes designed to mix the sample fluids dielectrophoretically have been presented. It has also been shown that the use of embedded electrode pairs to change the surface energy of the microchannel walls provides an efficient means of enhancing species mixing by inducing local instabilities in the flow stream. Compared to other active mixing schemes, the use of embedded electrode pairs has the advantage that moving components are not required, and hence the resulting microfluidic devices are not only cheaper, but also more reliable.

Besides chaotic advection, molecular diffusion is another important form of mass transfer in passive micromixers. In such scales where the flow is strictly laminar, the mixing is entirely ensured by molecular diffusion between layers of different concentrations. Consequently, when the thickness of each fluid layer is larger than the characteristic diffusion length, an effective and rapid mixing is difficult to achieve. The diffusion length is often approximated by $\sqrt{Dt}$, where t is the residence time of the species. To overcome the limitations by integrating particular designs of microchannels on the basis of different fluidic mechanisms, the most common approach is based on increasing the contact surface between the different fluids and decreasing the diffusion path between them. In general, passive micromixers can be categorized as lamination, chaotic advection and special designs, based on the arrangement of the mixed phases.

Basic Methodology

Theory of Lamination

Mixing in general follows a two-step sequence. The first is segmentation where a heterogeneous mixture of substantially homogeneous flows of the two fluids is formed by convection; the second is interdiffusion of molecules between nearby flows. Segmentation procedures, well

known from the macroscopic world, such as stirring or creation of turbulent flow, cannot be scaled down to microsystems with dimensions so small that Reynolds numbers exceeding 2000 (the limit for turbulent flow) are not feasible.

Perfect lamination can be obtained in a flow with a sufficiently low Reynolds number provided that the channel system guiding the fluid is designed in such a way that the pressure gradients in the flow channels will force the two fluids to laminate. Figure 1 shows a generic channel arrangement laid out in a free three-dimensional space. When considering symmetry it is obvious that a perfect lamination and a split into two channels is obtained. Depending on the flow direction, either horizontal (Fig. 1a) or vertical (Fig. 1b) lamination will be the result [2].

A detailed theoretical description of flow and diffusion phenomena in the laminar regime is very useful during design and testing of mixers for microsystems. The fully developed velocity profile for laminar flow in a straight channel of rectangular cross-section of dimensions $W \times H$ is easily found by numerical methods. For channels having width (W) significantly larger than height (H) the velocity profile turns out to be very close to parabolic in the direction of the short dimension and almost similar to H from the channel walls. This is also expected intuitively, as the distance to the nearest walls is the only physically important parameter for laminar flow. In Ref. [2], it was found that the peak velocity (v_{peak}) in the middle of the channel is related to the average velocity (v_{average}) (as calculated from the volume flow rate) as

$$v_{\mathrm{peak}} = \frac{3}{2}\left(\frac{1}{1-0.62H/W}\right) V_{\mathrm{average}} \tag{3}$$

within 1.5% when $W \geq 3H$.

When solving the diffusion problem for a laminated structure, it is useful to consider Fourier expansion of the initial concentration profile, as it is well known that the time evolution of the concentration profile is given by the time evolution of each of the Fourier components. Each Fourier component κ decays exponentially during the diffusion process with a time constant τ_k given by

$$\tau_k = (2\pi)^{-2}\frac{L_k^2}{D} \tag{4}$$

where L_k is the *wavelength* of the Fourier component and D is the diffusivity.

This explains concisely what is also expected from quantitative arguments that a 2^n-layer structure can mix 4^{n-1} times faster than a 2-layer structure, as the wavelength of the Fourier component of longest wavelength and thus slowest decay rate scales with the layer thickness [2].

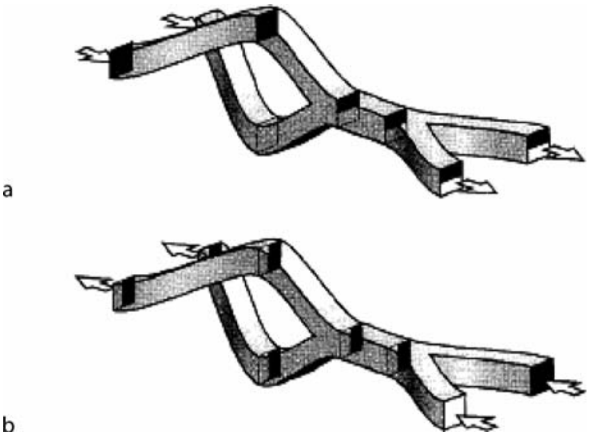

Passive Micromixers, Figure 1 A generic two-input two-output mixer including lamination and splitting shown in free three-dimensional space. (**a**) Horizontal lamination and (**b**) vertical lamination [2]

Meanwhile, the Fourier argument makes a small but important detail of mixing by lamination very clear: The lamination has to be symmetric, i. e. the top- and bottommost layer should be of only half thickness compared to the other layers. Otherwise, i. e. if the lamination is asymmetric, the Fourier expansion of the initial profile will contain a component with a wavelength twice the channel dimension, no matter how thin the laminated layers are. The component will sooner or later become dominant because of its slow decay, and only a minor benefit is obtained by lamination. The qualitative counterpart of this argument is that, unless the outermost layers are of half thickness, half of their content of the diffusing species has to be distributed over all of the inner layers before full mixing is achieved. When being of only half thickness, they are balanced by their neighboring layer as are all the other layers.

However, a simple cascade of two-input two-output mixers results in an asymmetric lamination. Symmetric lamination can be obtained with a modification of the first mixer into a three-input two-output mixer which builds up a $(H/4, H/2, H/4)$ type of laminate. This initial mixer can be followed by as many regular two-input two-output mixers as desired for the particular application.

Micromixers Based on Lamination

In miniature flow systems with Reynolds numbers varying from 2 to 100, flow structures can be artificially induced which assist in flow segmentation through inertia effects. Wu et al. [3] presented an analytical model of diffusive

mixing in microchannels. The dimensionless analysis generalizes the solution for different channel sizes and different diffusion coefficents by varying the Peciet numbers. It could be seen that the nonlinear model described well the diffusive mixing process in the microchannels and the mixing performance was improved with lower Peciet numbers due to the stronger diffusion effect. Another lamination micromixer using inertia forces was reported in the literature, involving a coaxial mixer containing an inner core liquid stream with a low flow rate and an outer flow stream with a higher flow rate.

Jacobson et al. [4] proposed micromixers for electrokinetically driven parallel and serial mixing. To simplify the voltage control hardware, electrokinetic mixing is effected using a single voltage source with the channels dimensioned to perform the desired voltage division. In addition, the number of fluid reservoirs is reduced by terminating multiple buffer, sample or analysis channels in single reservoirs. The parallel micromixer (Fig. 2a) was designed with a series of independent T-intersections, and the serial micromixer (Fig. 2b) was based on an array of cross intersections and sample shunting. The parallel micromixer has the advantages that each set of channels is independent of the others. Consequently, a failure in one set of channels does not affect the operation of the others. The dynamic range of the serial micromixer is larger especially if the sample shunting is carried out with additional cross intersection added to the channel manifold beyond the fifth cross intersection. Wong et al. [5] presented a micro T-mixer fabricated on a silicon substrate and bonded to a Pyrex glass plate (Fig. 3). The experimental results revealed that a mixing channel with a hydraulic diameter of 67 μm and an applied pressure of 5.5 bar were sufficient to result in complete species mixing in less than 1 ms following the initial contact between the two species flows with Reynolds numbers of 400 – 500.

Micromixers Based on Intersecting Channels

Micromixers with intersecting channels can be used to split, rearrange and combine component streams in order to enhance their mixing. He et al. [6] proposed a picoliter-volume mixer (Fig. 4) with intersecting channels of various lengths and a bimodal width distribution. In the proposed design, all of the channels running parallel to the flow direction had a width of 5 μm, while those intersecting the parallel channel network had a width of 27 μm and were aligned at an angle of 45°. The microchannels were designed such that the two species streams merged into one larger stream and then flowed together along a mixing channel of length 300 μm. The results showed that this configuration enabled a complete species mixing within a distance of 200 μm, representing a considerable

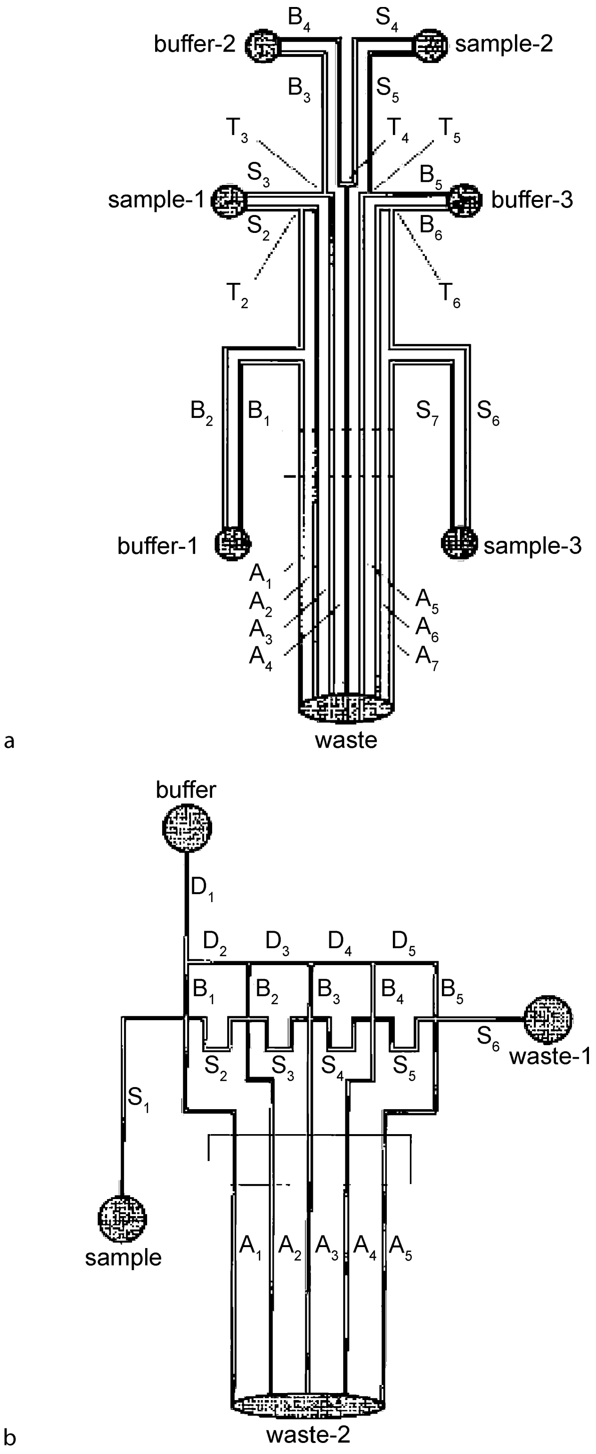

Passive Micromixers, Figure 2 (**a**) Schematic of the microchip for parallel electrokinetic mixing. (**b**) Schematic of the microchip for serial electrokinetic mixing [4]

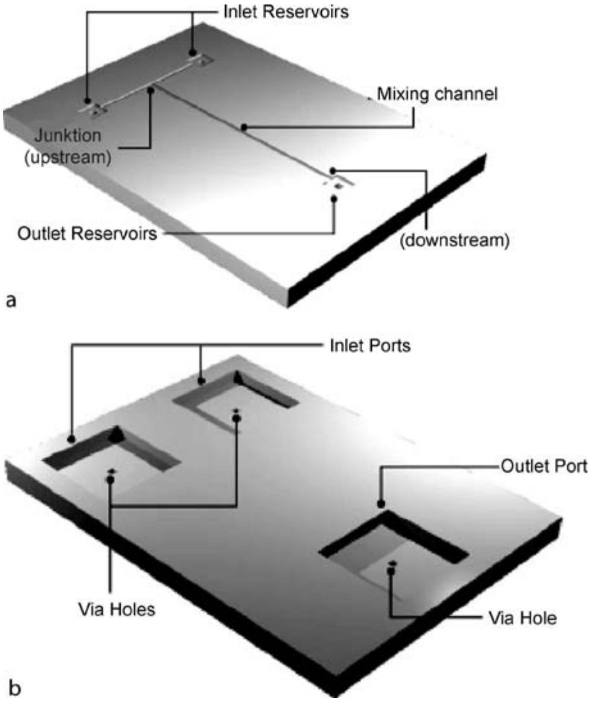

Passive Micromixers, Figure 3 (**a**) The front face of the micro T-mixer test chip. (**b**) The back face of the micro T-mixer [5]

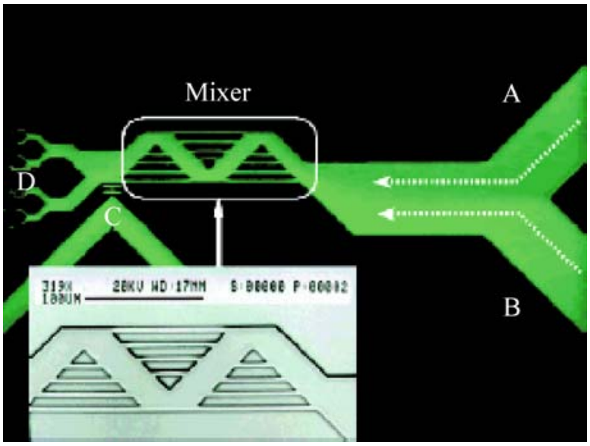

Passive Micromixers, Figure 4 Photomicrograph of a microfabricated mixer. The small image in the lower left corner is the SEM of the mixer. This mixer is about 100 by 200 μm wide and 10 μm in depth. Effect of mixing is evaluated by bringing in two fluids from channels A and B, and flowing to D. Channel C is not used in this work [6]

improvement compared to the mixing distance of 3000 μm required to fully mix the two streams in a conventional straight channel. Melin et al. [7] presented a micromixer in which a constantly changing, time-dependent flow pattern was created within a two-sample liquid plug as the plug passed through a planar mixer chamber. It was shown that the micromixer created a larger mass transfer within the liquid plug than that achieved in many of the passive devices presented previously. The proposed mixing chamber comprised a main meandering channel with perforated walls, which formed connecting channels between parallel segments of the main meandering channel. In the mixing process, two discrete liquid samples are fed into the mixing chamber in a laminar manner. When the liquid wets one side of the first perforated wall segment, it enters the perforation, but is prevented from exiting by surface tension effects. However, as the bulk of the liquid proceeds to the next main channel segment, the other side of the perforated wall becomes wetted. As a result, the liquid/air interface at the exit of the perforation is replaced by a liquid/liquid interface, and hence the liquid flows freely through the perforation. The same phenomenon is repeated in each of the main channel segments as the liquid flows progressively through the mixing chamber. The resulting constantly changing flow lines within the liquid plug cause a self-folding effect within the plug which yields a significant improvement in the mixing performance.

Micromixers Based on Zigzag Channels

Mengeaud et al. [8] presented a 100 μm wide zigzag microchannel integrating a "Y" inlet junction (Fig. 5). The effect of the periodic step value (s) on the mixing efficiency was investigated in a series of experimental trials. The results indicated that for $\mathrm{Re} = 0.26$, the mixing efficiency increased from 65% to 83.8% when the geometry ratio was increased from 1 to 8. For low values of s/w, the number of angles increases, resulting in an increase in the effective width and a reduction in the effective length. For low Reynolds number flows, it was found that the most efficient zigzag configuration, corresponding to $s = 800$ μm, gave a mixing efficiency of 83.8%. For $\mathrm{Re} = 267$, the mixing efficiency increased rapidly to 98.6% as the geometry ratio was increased to 4, but reduced slightly to 88.1% as the geometry ratio was further increased, thus indicating the existence of an optimal zigzag geometry. After the research, the zigzag passive micromixer showed a modified Tesla structure. The species streams flowed close to the angled surface as a result of the Coanda effect, and this effect was used to guide the fluid streams such that they collided with one another. Mixing cells in opposite directions were then used to repeat the transverse dispersion caused by the flow impact. In the micromixer, one of the fluids was divided into two sub-streams and one of these two sub-streams was then merged with the second fluid stream from the main channel in the micromixer. The two streams were then

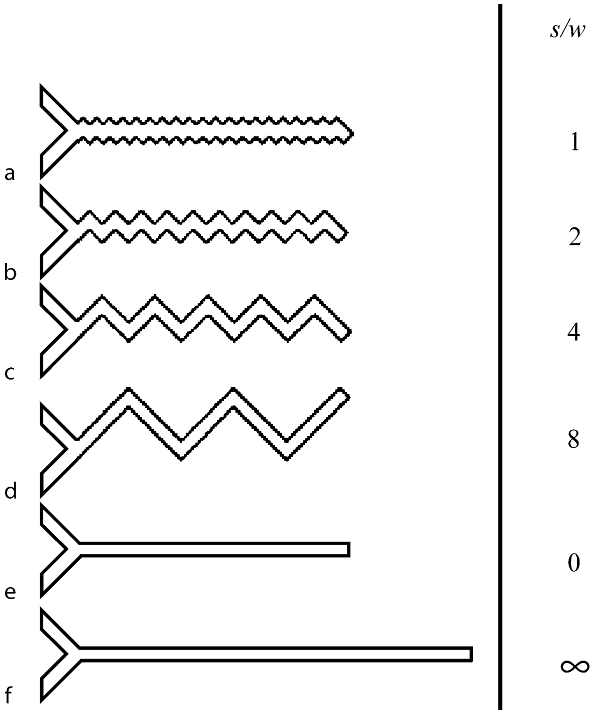

Passive Micromixers, Figure 5 Different geometries of a microchannel. (**a**) $s/w = 1$, (**b**) $s/w = 2$, (**c**) $s/w = 4$, (**d**) $s/w = 8$, (**e**) $s/w \to 0$, and (**f**) $s/w \to \infty$ [8]

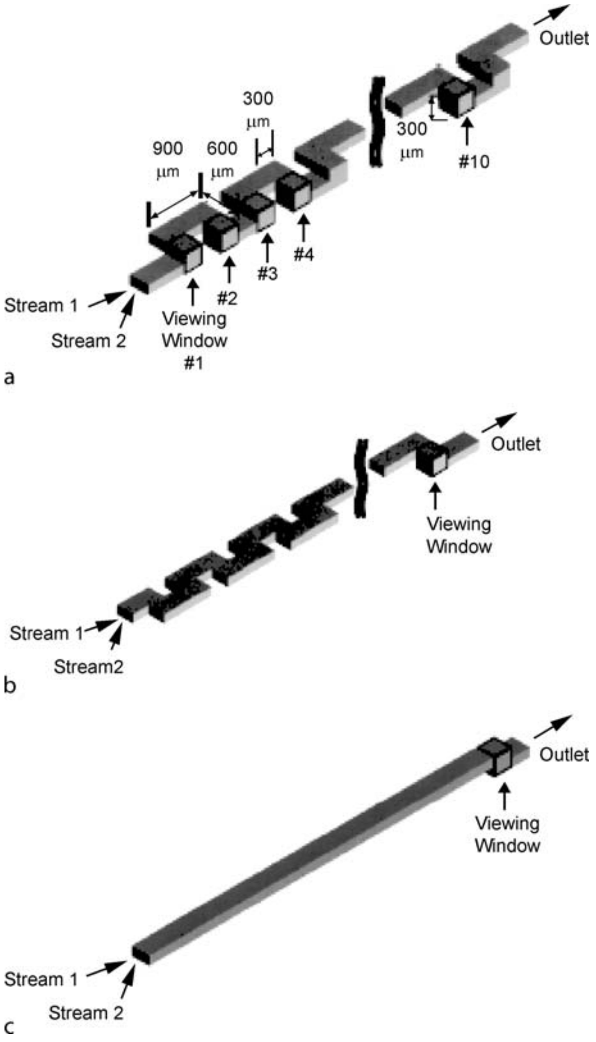

Passive Micromixers, Figure 6 (**a**) Schematic of the three-dimensional serpentine channel. "Viewing windows" in the channel are labeled 1–10. (**b**) Schematic of zigzag channel. (**c**) Schematic of straight channel [9]

mixed with the second sub-stream, resulting in a strong impact around the sub-channel of the micromixer.

Micromixers Based on Three-Dimensional Serpentine Structures

The three-dimensional serpentine micromixer was designed to induce a chaotic mixing effect. It was found that the mixing efficiency of the serpentine microchannel was twice that obtained in a conventional straight microchannel. Liu et al. [9] fabricated a three-dimensional serpentine micromixer (Fig. 6) featuring a "C"-shaped repeating unit designed to induce chaotic advection. Mixing in the serpentine channel relies on the flow field being sufficiently three-dimensional, with secondary flows stretching and folding the fluid, greatly increasing the interfacial area across which diffusion occurs. The results showed that for flows with a Reynolds number of 70, the mixing efficiency in the serpentine channel was 16 times better than that in a conventional straight channel and 1.6 times better than that in a zigzag channel.

Micromixers Based on Embedded Barrier

Based on the combination of multilamination and chaotic advection effects, Kim et al. [10] developed barrier embedded micromixers for pressure-driven flow in which chaotic flow was induced by applying periodic perturbations to the velocity field via periodically inserted barriers along the upper surface and helical-type flow structures were induced by slanted grooves on the lower surface of the microchannel. Observations using a confocal microscope revealed cross-sectional mixing behaviors in several locations of the micromixer. The proposed design was validated experimentally at a flow rate corresponding to a Reynolds number of 2.28 (corresponding to $Pe = 1.24 \times 10^4$ with a Rhodamine diffusivity of $2.8 \times 10^{-10}\ m^2\ s^{-1}$). Laser scanning around the entrance zone of the micromixer identified a bright image only in the half-zone containing Rhodamine. Bright images

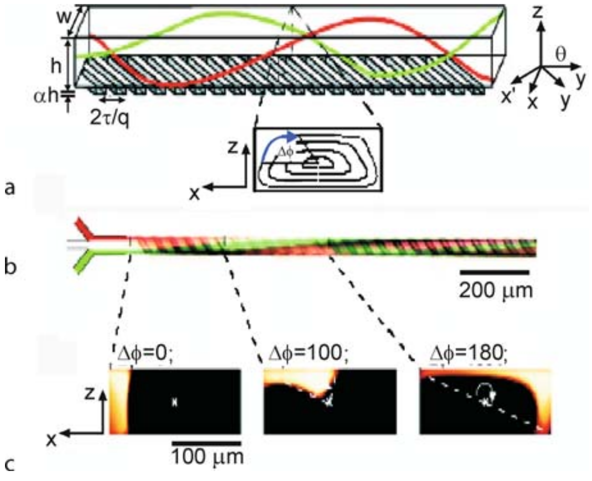

Passive Micromixers, Figure 7 Three-dimensional twisting flow in a channel with obliquely oriented ridges on one wall. (**a**) Schematic of channel with ridges. (**b**) Optical micrograph showing a top view of a red stream and a green stream flowing on either side of a clear stream in the channel. (**c**) Fluorescent confocal micrographs of vertical cross-sections of a microchannel such as in (**a**) [11]

were also observed at the no-barrier zone in the first half-cycle, thus confirming the cross-sectional rotating flow effect induced by the slanted grooves. When the streams entered the barrier zone in the next half-cycle, laser scanning showed that the flow was rotated yet further. The experimental results confirmed that the barrier embedded micromixer yielded an excellent species mixing within a short channel length.

Micromixers Based on Slanted Well

Stroock et al. [11] presented chaotic mixers (Fig. 7) designed to mix streams of steady pressure-driven flows in microchannels at low Reynolds numbers. The authors considered two different microchannel designs, namely one channel with straight ridges on one wall and a second channel with a staggered herringbone pattern on one wall. The mixing performances of the two microchannels were compared with that of a smooth microchannel. In the evaluation experiments, cross-sectional images taken at the same distance (3 cm) from the junction were acquired and the mixing efficiency was assessed by computing the standard deviation σ of the fluorescence intensity in the confocal images as a function of the distance along the mixing channel length, Δy. The deviation maintained a constant value of approximately 0.5, indicating a poor mixing performance. The results revealed that the micromixer with straight ridges on one microchannel wall yielded a poor mixing performance. The standard deviation profile for a low Pe number was approximately 0, which signifies an almost complete mixing. Others investigated the effects of the asymmetry index p and depth ratio α of the groove on the mixing performance of a staggered herringbone mixer with patterned grooves. Since the two vortices within the mixing channel are determined by the asymmetry index p, vortices with dissimilar scales were shown to provide a better mixing performance than two equally sized vortices. Furthermore, the results showed that the intensity of the vertical fluid motions at the side edges of the grooves increased with increasing groove depth α, resulting in a significant improvement in the mixing effect.

Micromixers Based on Twisted Channels

In twisted microchannel applications, the micromixer featured is a three-dimensional structure of twisted microchannels designed to induce a chaotic mixing effect within the fluid streams. The twisted microchannels were designed such that the angle of the channels' lower surfaces alternated in each longitudinal subsection of the mixing channel. The fluid flow sways from side to side as it travels along the microchannel, resulting in a chaotic advection effect. Park et al. [12] presented a breakup method based on passive rotation for enhancing the mixing efficiency of micromixers. The proposed method not only actively generated interfaces between the mixing species, but also enhanced the diffusion process at the interface. The micromixer actually incorporated two separate mixing regions, namely one region with short segments of length 200 μm and a second region with long segments of length 400 μm (Fig. 8). The results showed that this design caused a rotation of the fluids flowing through the channel. It was found that the fluids were mixed well and their interface was distorted at high Reynolds numbers. Conversely, at low Reynolds numbers, the fluids were hardly mixed and the interface was not distorted, i. e. only the respective positions of the two fluid streams were changed.

Key Research Findings

Grooved Staggered Herringbone Micromixers

Grooved staggered herringbone micromixers are based on the original design proposed by Aubin et al. [13] and have an off-centered herringbone pattern on the lower surface of the microchannel, which creates a transverse velocity component in the flow field. Such mixers have several mixing cycles, where each cycle comprises two sequential regions of grooves, i. e. two half-cycles. The direction of asymmetry of the herringbone pattern switches with respect to the centerline of the microchannel every half cycle. In order to improve the mixing efficiency, the depth of the grooves in staggered herringbone micromixers should be specified

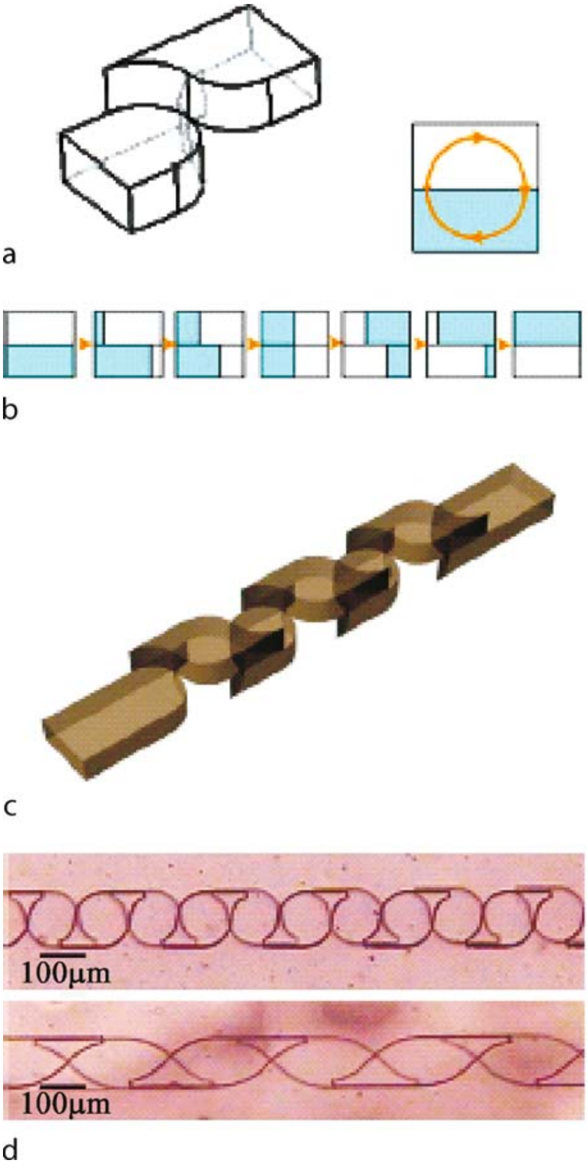

Passive Micromixers, Figure 8 Schematic diagrams of (**a**) one mixer segment and (**b**) flows in the microchannel recirculating along the walls. (**c**) Schematic of mixer 1. (**d**) Optical micrograph of mixer 1: top, micromixer composed of short mixer segments; bottom, micromixer composed of long mixer segments [12]

as 30% of the channel height. This promotes both spatial homogenization and a reduction of the striation thickness without increasing the pressure drop across the mixer.

Surface Chemistry Technology in Microchannels

In microfluidic systems, very high pressure gradients are generally required to drive and manipulate the fluid flow. Due to the small characteristic scale of the microchannels in typical microfluidic devices, surface forces dominate, and high friction effects are generated. Conventionally, microchannels are fabricated using silicon dioxide. Silicon dioxide surfaces are typically negatively charged due to their deprotonated silanol groups ($\equiv$Si–O^-). When these surfaces come in to contact with a solution containing ions, the positive ions are attracted to the surface, forming an important layer and a diffuse layer on the surface. If an electrical field is then applied, the positive ion diffuse layer moves in the direction of the applied field. The movement of the diffuse layer drags the bulk fluid into motion via momentum coupling, resulting in the so-called electroosmotic flow (EOF) phenomenon [14].

Future Directions for Research

Mixing in electro-osmotic flow is generally diffusion-dominated. However, it has been shown that the introduction of electrically charged surface heterogeneities enhances the mixing efficiency by creating localized flow circulation regions. By selectively patterning positively charged molecules on a negatively charged channel wall, flow vortices can be induced as a result of the differences in electrostatic potential between the homogeneous and heterogeneous surfaces. It has been shown that these localized flow vortices can be exploited to yield a significant improvement in the mixing performance in a variety of microchannel configurations, including in-line, staggered, serpentine, herringbone and diagonal arrays [15]. In their numerical investigations, the authors specified the patch length and spacing parameters in such a way as to maintain a constant ratio of the heterogeneous-to-homogeneous surface areas over a channel length of 1.8 mm. The results revealed that the nonsymmetrical heterogeneous patterns, namely the staggered and diagonal patterns, generated a better mixing performance than either the symmetrical herringbone pattern or the in-line arrangement. With a theoretical mixing efficiency of 96%, the staggered configuration provided the best mixing performance, outperforming the diagonal, herringbone and serpentine configurations by 8%, 31% and 36%, respectively. Furthermore, compared to the homogeneous case, the staggered configuration provided a 61% improvement in the mixing efficiency. The use of heterogeneous surface charge patches to manipulate electrokinetic flows provides a simple, low-cost solution to mixing problems in Lab-on-a-chip systems, and is therefore likely to receive increasing attention in future studies.

Cross References

► Microfluidic Mixing
► Fundamentals of Diffusion in Microfluidic Systems
► Passive Micromixer

P

References

1. Einstein A (1956) Investigations on the theory of the Brownian movements. New York, Dover
2. Branebjerg J, Gravesen P, Krog JP, Nielsen CR (1996) Fast mixing by lamination. In: Proc IEEE MEMS'96, pp 441–446
3. Wu Z, Nguyen NT, Huang X (2004) Nonlinear diffusive mixing in microchannels: theory and experiments. J Micromech Microeng 14:604–611
4. Jacobson SC, McKnight TE, Ramsey JM (1999) Microfluidic devices for electrokinetically driven parallel and serial mixing. Anal Chem 71:4455–4459
5. Wong SH, Ward MCL, Wharton CW (2004) Micro T-mixer as rapid mixing micromixer. Sens Actuators B 100:359–379
6. He B, Burke BJ, Zhang X, Zhang R, Regnier FE (2001) A picoliter-volume mixer for microfluidic analytical systems. Anal Chem 73(9):1942–1947
7. Melin J, Gimenez G, Roxhed N, van der Wijngaart W, Stemme G (2004) A fast passive and planar liquid sample micromixer. Lab Chip 4:214–219
8. Mengeaud V, Josserand J, Girault HH (2002) Mixing processes in a zigzag microchannel: finite element simulations and optical study. Anal Chem 174(16):4279–4286
9. Liu RH, Stremler MA, Sharp KV, Olsen MG, Santiago JG, Adrian RJ, Aref H, Beebe DJ (2000) Passive mixing in a three-dimensional serpentine microchannel. J Microelectromech Sys 9(2):190–197
10. Kim DS, Lee SW, Kwon TH, Lee SS (2004) A barrier embedded chaotic micromixer. J Micromech Microeng 14:798–805
11. Stroock AD, Dertinger SKW, Ajdari A, Mezić I, Stone HA, Whitesides GM (2002) Chaotic mixer for microchannels. Science 295:647–651
12. Park SJ, Kim JK, Park J, Chung S, Chung C, Chang JK (2004) Rapid three-dimensional passive rotation micromixer using the breakup process. J Micromech Microeng 14:6–14
13. Aubin J, Fletcher DF, Xuereb C (2005) Design of micromixers using CFD modelling. Chem Eng Sci 60:2503–2516
14. Zeng S, Chen CH, Mikkelsen J, Santiago JG (2000) Fabrication and characterization of electrokinetic micro pumps. Proc. of 7th International Conference on Thermal and Thermomechanical Phenomenon in Electronic Systems 2:31–36
15. Biddiss E, Erickson D, Li D (2004) Heterogeneous surface charge enhanced micromixing for electrokinetic flows. Anal Chem 76(11):3208–3213

Passive Mixer

► Passive Micromixers

Patch Clamp Measurements On-Chip

HUI YAN, HONGKAI WU
Department of Chemistry, Hong Kong University of Science and Technologyi, Hong Kong, China
chhkwu@ust.hk

Synonyms

Patch clamp technique; Voltage clamp; Patch voltage clamp technique; Cell-attached (single-channel) voltage clamp

Definition

Ion channels, like molecular pores that open and close in response to stimuli, allow electrically charged atoms – such as sodium, potassium and calcium ions – to pass in and out of a cell through the cell's outer membrane by opening and closing like tiny gates. The *patch clamp technique*, a dominant technique providing valuable information for ion channels, including their electrophysiological properties, molecular structures and the mechanism of drug action in cellular electrophysiology with high resolution, involves the fabrication of a pipette with a micrometer-sized tip which is filled with a conducting solution and the tip gentle suction directed towards the cell membrane with a micromanipulator in order to form a gigaseal between the pipette tip and the cell membrane. A *gigaseal* is a tight seal between the membrane and pipette rim with a resistance in the range of gigaohms (10^9 Ω).

Overview

The patch clamp technique, as a dominant technique, provides valuable information for ion channels, including their electrophysiological properties, molecular structures and the mechanism of drug action in cellular electrophysiology with high resolution. The rationale for using *patch pipettes* and the principles of patch clamp recording, including the information provided, are elaborated in detail first to understand the mechanism of the technique. The advantages and disadvantages of four configurations of this technique, i. e. on-cell patch clamp, whole cell patch clamp, inside-out patch clamp and outside-out patch clamp, are then described in the following. Two different methods for preparation of pipette on-chip and patch clamp device on-chip fabrication and electrophysiology recordings are given to provide reference for the reader. There are some simple but perspicuous figures presented to allow an easier grasp of the patch clamp technique. Finally, the key research findings about this technique are summarized and future directions for research are proposed.

Ion channels provide pores for the passive diffusion of ions across biological membranes. They are often highly selective for a particular ionic species, leading to a classification into sodium (Na^+), potassium (K^+), calcium (Ca^{2+}), chloride (Cl^-) and unspecific cation channels. The direc-

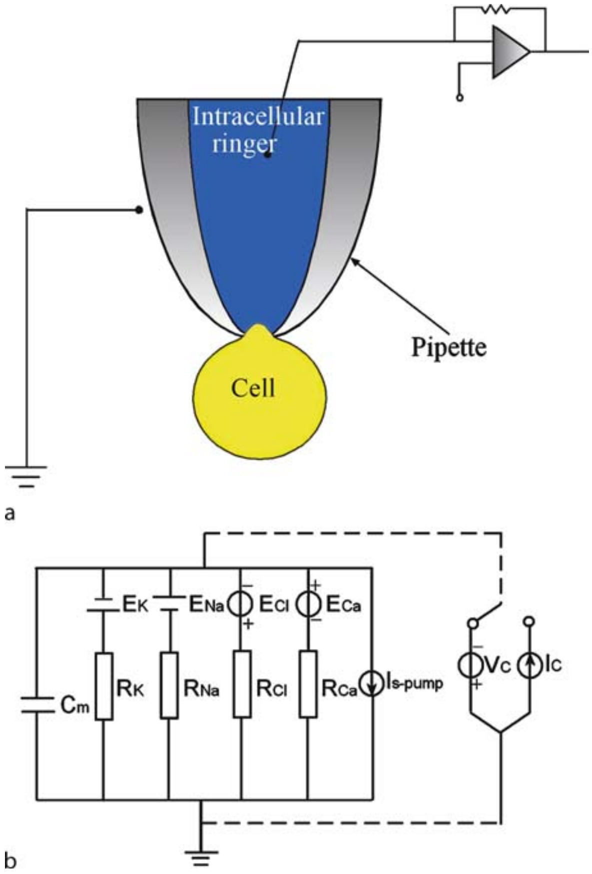

Patch Clamp Measurements On-Chip, Figure 1 Patch clamp technique and an amended equivalent circuit

tion of net ion transport, which is associated with an electric current, depends on the electrochemical gradient (established by interplay of active pumps, co-transporters and ion channels) for the relevant ionic species. Channels occur not only in the external (plasma) membrane, but also in membranes of intracellular organelles. Ion channels are essential for many of the cell's functions, such as impulse conduction in the nervous system or pace-making in the cardiac system, and their dysfunction is pivotal in many diseases. The list of human diseases known to be associated with defects in ion channels has grown considerably during the past few years. Hence, there is a great interest in ion channels not only from academia to understand the biophysics of their function but also from the biotechnology and pharmaceutical industries to develop drugs that modulate ion channels to correct any malfunction.

Several methods are available today to test candidate ion channel active drugs (ICADs): electrophysiology (patch clamp), binding assays, radioactive flux assays, membrane potential-sensitive fluorescent dyes, ion-sensitive dyes and voltage sensing based on fluorescence resonant energy transfer (FRET).

Giving an unsurpassed information content and having high sensitivity, the patch clamp technique, developed by Erwin Neher and Bert Sakmann at the Max Planck Institute, Germany (they were awarded the Nobel Prize in Medicine for this discovery; see Fig. 1), is a powerful tool for studying the electrophysiological properties of biological membranes. It is mainly used to detect currents that pass a patch of cell membrane. This *patch* can be a large one, as large as almost the whole cell membrane; or a small one, so small as to contain only several or even one ion channel. *Clamp* mainly refers to fixing the voltage across the membrane, i. e. membrane potential, at a constant level, or at different levels stepwise, under which conditions transmembrane currents are measured (i. e. voltage clamp mode). Also, the patch clamp technique can sometimes be used to observe the membrane potential when a constant current (usually zero), on which sometimes a squarewave current is superposed, is injected into the cell (i. e. current clamp mode). And furthermore, with this technique cell secretion ions can also be studied by measuring the capacitance of the cell membrane (C_{m}), which, used as an indicator of the area of cell membrane, may change during cell secret ion.

Basic Methodology

Mechanism

Rationale for Using Patch Pipettes

A basic limitation for any current measurement, disregarding instrumentation noise, is the Johnson or thermal noise of the signal source, which for a simple resistor is given by

$$\sigma_n = \sqrt{4kT\Delta f/R}$$

where σ_n is the root-mean-square deviation of the current, k the Boltzmann constant, T the absolute temperature, Δf the measurement bandwidth and R the resistance. From this equation, it is clear that the internal resistance of a signal source (or, more generally, the complex impedance) should be very high for low-noise current recording. Specifically, to record a current of 1 pA at a bandwidth of 1 kHz with 10% accuracy, the internal resistance of the signal source should be about 2 GΩ or higher. We now know that the input resistances of small cells can be as high as that. But in the early 1970s the conventional microelectrode techniques required large cells for reliable current measurements, and these typically had input resistances in the range 100 kΩ to 50 MΩ. Thus, it seemed impossible to reach the required resolution with

standard techniques and standard preparations. What was required was a smaller signal source.

It was clear that they should be good tools for single-channel measurements, if only the *pipette-to-membrane seal* could be made good enough. The impedance of the patch itself should be higher than required, even for a patch as large as 10 μm in diameter. An incomplete seal, however, is "seen" by the measuring amplifier in parallel to the patch, and its noise is superimposed onto the patch signal.

Principles of Patch Clamp Recording

As is known, there is a resting potential (RP) across the membrane of most cells, and based on it action potentials (AP) or local responses can occur. All these electric phenomena involve specific states or activities of different ion channels and pump proteins in the membrane. The commonly cited explanation can be found in any textbook of general physiology, so we only present an amended equivalent circuit (Fig. 1) for a membrane patch, which is useful for understanding various electric phenomena that occur in the cell membrane.

This circuit includes multiple branches but only two nodes. Channels for different ions are equivalent to voltage sources, whose electromotive forces are equal to their respective equilibrium potentials determined by the Nernst formula, and whose internal resistances depend on the permeability of the membrane for, and the diffusion coefficients as well as the concentrations of, respective ions, etc. The ion pumps can be represented by corresponding current sources, all of which can be summed up forming one current source as shown in Fig. 1. If there exist transporters in the membrane, they can be electrically modeled (omitted in Fig. 1) in the same way as pumps. The capacitor represents the effect of the lipid bilayer of the membrane together with the extracellular solution (or the bath solution under artificial conditions) and intracellular solution. All these branches are arranged in parallel.

If no external circuit acts on the membrane, and the membrane potential is constant or changes very slowly, its value can be given by the node voltage formula:

$$V_{\mathrm{m}} = \frac{E_{\mathrm{K}} g_{\mathrm{K}} + E_{\mathrm{Na}} g_{\mathrm{Na}} + E_{\mathrm{Ca}} g_{\mathrm{Ca}} + E_{\mathrm{Cl}} g_{\mathrm{Cl}} - I_{s-\mathrm{pump}}}{g_{\mathrm{K}} + g_{\mathrm{Na}} + g_{\mathrm{Ca}} + g_{\mathrm{Cl}}} = \frac{\sum E_j g_j - I_{s-\mathrm{pump}}}{\sum g_j}$$

Incidentally, if g_{K} is much larger than the conductance for other ions, and the contribution of the net pump current to V_{m} is small enough to be omitted, which is the case for most cells at rest, it can be seen that RP = $V_{\mathrm{m}} \approx E_{\mathrm{K}}$.

If the state of a certain kind of ion channel changes, there generally occurs a change in more than one channel current, accompanied by a change in the membrane potential, i. e. hyper- or hypo-charge of the membrane capacitance.

What interests us most is what ion channels mediate a certain cellular electric activity caused by a certain factor such as alteration in V_{m} or a chemical (ligand) stimulus. Some ion channels are voltage dependent, that is, their permeability changes with the alteration of V_{m}. By holding and changing V_{m} artificially to measure the currents through these channels we can get the details of their voltage-dependent characteristics. On the other hand, many channels such as ligand gated ion channels and G-protein coupled ion channels are chemical dependent, and also respond to V_{m} alteration passively (i. e. voltage independent: the response current is linear with V_{m} alteration with the permeability or conductance of the ion channel remaining constant) or even actively (i. e. voltage dependent as explained above). Under normal circumstances, the activity of these channels caused by a chemical is accompanied by the change in membrane potential. To distinguish between the effect of a chemical and that of V_{m} alteration, it is necessary to fix V_{m} at a constant level to remove the influence of the V_{m} alteration, or at different levels stepwise to observe the amplitude and configuration of the channel current traces for analyzing its ionic mechanisms. The following is a further discussion using some concise and explicit formulae.

V_m is set at a constant level. Once V_{m} is set constant, the capacitive current is zero. This means that the current recorded via the recording pipette equals the transmembrane current (current carried by ions flowing through channels and ions transported by pumps); or briefly speaking, the current recorded is the transmembrane current.

In this case, the current via each kind of ion channel can be expressed as

$$I_j = (V_{\mathrm{m}} - E_j) g_j$$

And the active current caused by the activity of this kind of channel is

$$\Delta I_j = (V_{\mathrm{m}} - E_j) \Delta g_j$$

The whole transmembrane current (including that carried by ion pump s) is

$$I = \sum (V_{\mathrm{m}} - E_i) g_j + \sum I_{s-\mathrm{pump}}$$

and the whole active transmembrane current is

$$\Delta I = \sum (V_{\mathrm{m}} - E_j) \Delta g_j + \sum \Delta I_{s-\mathrm{pump}}$$

It is clear that the term $\Sigma(V_m - E_j)\Delta g_j$ represents the current response caused by the activity of ion channels, and the term $\Sigma\Delta I_{s-\text{pump}}$, by the activity of ion pumps.

V_m *is set dynamically from one definite level to another.* If V_m clamped jumps from an initial level to a new one, that is, an artificially controlled step voltage $g\Delta V_m$ occurs across the cell membrane, and it causes the activity of some ion channels, the transmembrane current will change from $\Sigma(V_m - E_j)g_j$ to $\Sigma(V_m + \Delta V_m - E_j)(g_j + \Delta g_j)$ (pump currents are omitted here for simplifying the discussion), and the alteration of the transmembrane current will be

$$\Delta I = \sum \Delta V_m g_j + \sum (V_m + \Delta V_m - E_j)(\Delta g_j)$$

The term $\Sigma\Delta V_m g_j$ is the linear transmembrane current change caused by the step voltage, i.e. the passive current response. It can be removed using leak subtraction function for a better observation of the current change caused by the activity of ion channels, i.e. the active current response, which is represented by the term $\Sigma(V_m + \Delta V_m - E_j)(\Delta g_j)$.

Based on the above important concept, the reversal potential V_{rev} is easily accessible. It generally refers to the membrane potential at which the active current response to a kind of stimulus disappears, and beyond which it reappears but flows in the opposite direction. So, let $\Sigma(V_m - E_j)\Delta g_j$ be zero in case (1), or let $\Sigma(V_m + \Delta V_m - E_j)(\Delta g_j)$ be zero in case (2), and we arrive at: $V_{rev} = (\Sigma E_j \Delta g_j)/(\Sigma\Delta g_j)$ (pump currents are omitted, and note that V_{rev} refers to V_m in case (1) and to $V_m + g\Delta V_m$ in case (2)). This is a general formula for discussing reversal potential, and it is helpful in exploring the mechanism underlying a current response that has been observed.

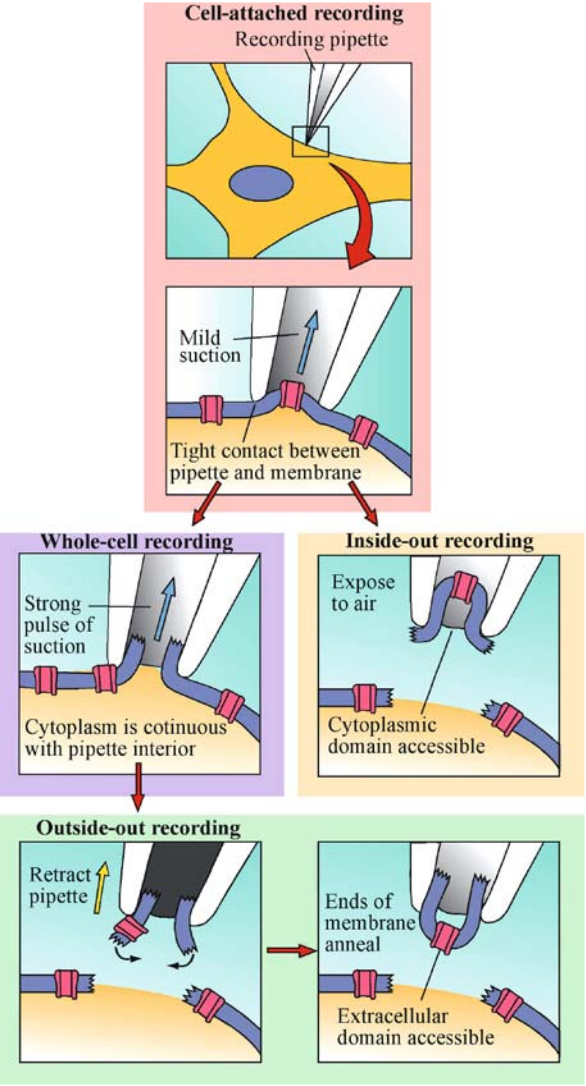

Patch Clamp Measurements On-Chip, Figure 2 Four configurations of patch clamp

Four Configurations

Figure 2 shows the four configurations of patch clamp technique. They are discussed as following.

On-Cell Patch Clamp

A cell-attached (single-channel) voltage clamp is a form of patch clamp when the voltage of only a small part of the cell is controlled allowing current flowing through individual ion channels to be distinguished.

This technique is based on a very simple idea. A pipette with a very small opening is used to make tight contact with a tiny area, or patch, of neuronal membrane. After the application of a small amount of suction to the back of the pipette, the seal between pipette and membrane becomes so tight that no ions can flow between the pipette and the membrane. Thus, all the ions that flow when a single ion channel opens must flow into the pipette. The resulting electrical current, though small, can be measured with an ultrasensitive electronic amplifier connected to the pipette. Based on the geometry involved, this arrangement usually is called the cell-attached patch clamp recording method.

As with the conventional voltage clamp method, the patch clamp method allows experimental control of the membrane potential to characterize the voltage dependence of membrane currents.

Whole Cell Patch Clamp

A whole cell voltage clamp is a form of patch clamp where electrical access is gained to the whole of the cell (usually

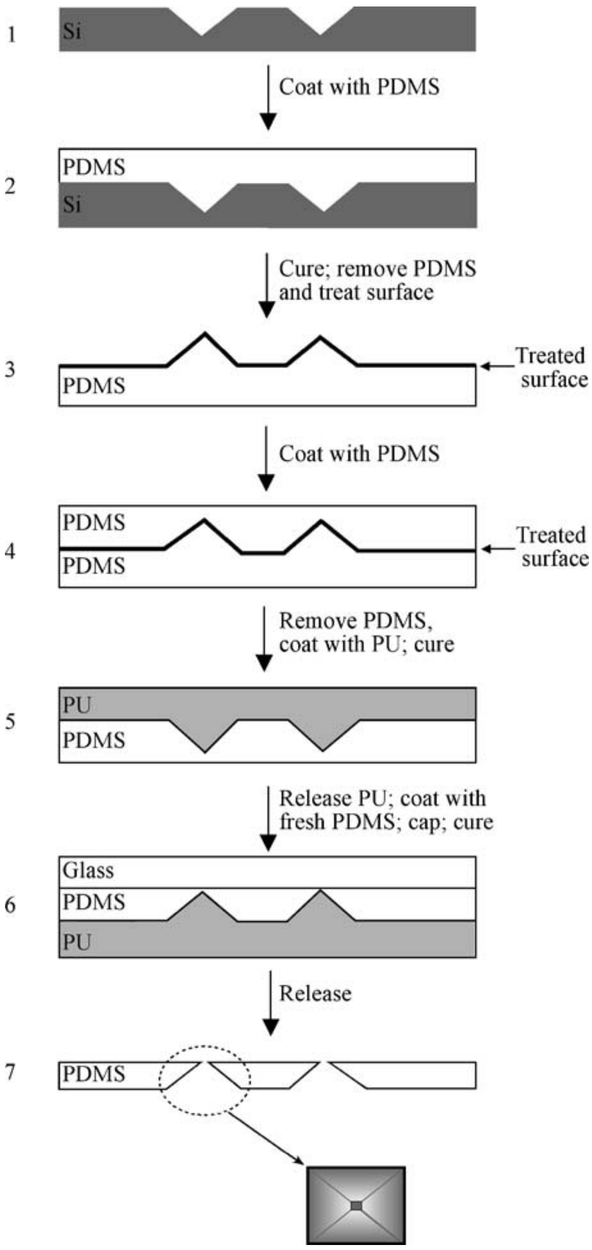

Patch Clamp Measurements On-Chip, Figure 3 Multi-pipette tip on-chip fabrication

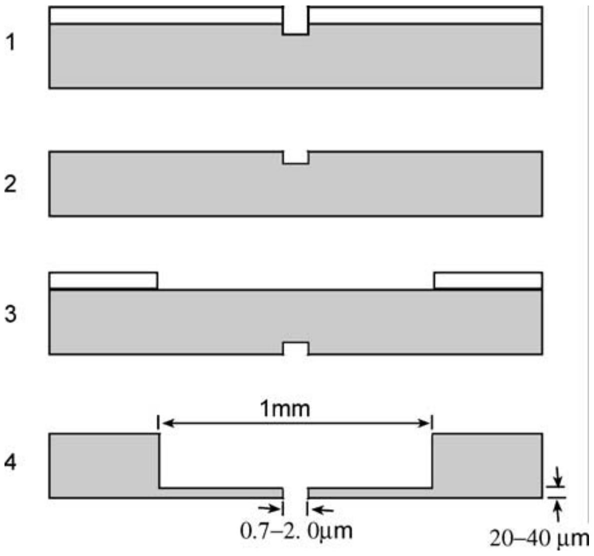

Patch Clamp Measurements On-Chip, Figure 4 The steps in fabricating a silicon substrate for use as a planar patch clamp. Circles (2 μm diameter) were defined in a photoresist (white layer) using optical lithography and then etched to a depth of 20–40 μm using deep reactive ion etching. The SU-8 resist was then stripped off with an acid bath and the wafer was inverted for back-side processing. A 1 mm diameter well, centered on the 2 μm pore, was defined using optical lithography. Deep reactive ion etching was used to etch the 1 mm well to a depth such that a small pore was formed connecting the base of the well to the other side of the wafer. A 0.5–1 μm thick SiO_2 film was then deposited over the surface of the entire wafer (using PECVD). This film electrically isolates the front side of the wafer from the back and reduced the pore diameter to 1.5–1.8 μm. The deposition conditions could be varied to deposit thicker oxides and thereby reduce pore diameters as small as 0.7 μm

by disrupting the membrane underneath the pipette by suction), allowing the electrical activity of the whole cell to be measured.

If the membrane patch within the pipette is disrupted by briefly applying strong suction, the interior of the pipette becomes continuous with the cytoplasm of the cell. This arrangement allows measurements of electrical potentials and currents from the entire cell and is therefore called the whole cell recording method. The whole cell configuration also allows diffusional exchange between the pipette and the cytoplasm, producing a convenient way to inject substances into the interior of a *patched* cell.

This is a powerful technique for studying ionic currents at the level of the whole cell membrane.

Inside-Out Patch Clamp

Once a tight seal has formed between the membrane and the pipette, small pieces of membrane can be pulled away from the cell without disrupting the seal; this yields a preparation that is free of the complications imposed by the rest of the cell. Simply retracting a pipette that is in the cell-attached configuration causes a small vesicle of membrane to remain attached to the pipette. By exposing the tip of the pipette to air, the vesicle opens to yield a small patch of membrane with its (former) intracellular surface exposed. This arrangement is called the inside-out patch recording configuration.

This is a true single-channel patch clamp mode allowing the measurement of single-channel currents with the

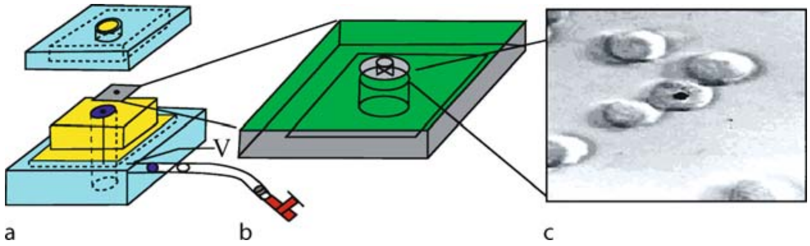

Patch Clamp Measurements On-Chip, Figure 5 Assembly of the patch clamp device. (**a**) Aligning and sealing the processed silicon chip (grey wafer) between an upper and lower chamber (yellow and blue) electrically isolates one side of the chip from the other (except through the pore in he silicon), and enables independent experimental manipulation of each side. The top and bottom chambers are composed of cured PDMS (yellow) coupled to machined polycarbonate (light blue) supports. The bottom polycarbonate support interfaces the lower PDMS vertical channel to a syringe which is used to apply negative pressure. (**b**) Except for the area immediately surrounding the pore on the topside and the 1 mm well on the underside of the chip, the entire top and bottom surfaces of the silicon wafer were stamped with SU-8 photoresist (green) to enable sealing to the PDMS layers and reduce the chip capacitance to as low as 15 pF. (**c**) A single RIN m5F cell is drawn onto the pore (black spot) following suction. A few seconds after landing on the pore, an individual cell tends to center itself over the pore. This image is of a chip that was recycled after being previously used to patch clamp a cell

added benefit of making it possible to change the medium to which the intracellular surface of the membrane is exposed. Thus, the inside-out configuration is particularly valuable when studying the influence of intracellular molecules on ion channel function, like calcium or ATP.

Outside-Out Patch Clamp

If the pipette is retracted while it is in the whole cell configuration, a membrane patch is produced that has its extracellular surface exposed. This arrangement is called the outside-out recording configuration.

This is a true single-channel recording mode. The patch can be superfused on the extracellular side with solutions containing materials such as neurotransmitters, agonists like GABA or glutamate to activate receptor channels in the patch. This range of possible configurations makes the patch clamp method an unusually versatile technique for studies of ion channel function.

Examples of Patch Clamp On-Chip Design and Fabrication

Multi-Pipette Tip On-Chip Fabrication Based on Polydimethylsiloxane (PDMS)

To scale up fabrication of the planar PDMS, as a typical example, a 4×4 on-chip array described in literature is given here.

The 4×4 array of 400 μm deep, self-terminated pits spaced 1 mm apart was anisotropically etched in a silicon wafer. The strategy was to use the precision of silicon micromachining to create a master structure e with good ordering that would define a shape similar to the tip of a glass micropipette in a thin sheet of molded PDMS. That shape was then transferred through two PDMS molding steps into an array of pyramids in polyurethane (see Fig. 3). An important step in forming the PDMS in step 4 of the figure was the treatment of the first PDMS mold so that the two PDMS layers could be separated. The final PDMS electrode partition was formed by pouring freshly prepared PDMS onto the polyurethane mold and then capping the polyurethane pyramids with a glass slide (step 6). The contact between the tip of the polyurethane pyramid and the glass slide excluded the PDMS to form small apertures. The size and shape of the aperture depended on the amount of contact with the glass slide. The authors chose polyurethane because it deforms sufficiently when contacting the glass slide to make holes 4 – 20 μm in size.

P

For patch clamp measurements the PDMS planar electrode array was plasma-oxidized then mounted in the recording system shown in Fig. 6. To electrically isolate each electrode, the partition was sealed onto the chamber bottom over an array of openings that each contained an Ag–AgCl wire and suction tubing. The Ag–AgCl wire was connected to the multiplexer chip mounted on the circuit board under the chamber. The multiplexer then connected to the input of the amplifier. The tubing connected to a suction manifold that permitted individual or global suction.

The electrode resistance values were measured to confirm that the electrodes were electrically isolated and that the apertures were open. Fig. 6 shows a *macro-patch* recording obtained when a devitellinized oocyte, expressing Shaker potassium channels, was dropped onto an aperture. The ionic currents carried by a population of ~ 80 Shaker channels were measured in response to positive step changes in membrane potential. The overall success rate for forming a gigaseal on a xenopus oocyte using a planar PDMS patch electrode was 13% (10 out of 75). This is lower than the ~ 40 % success rate for the conventional patch electrodes with or without PDMS coating and surface treatment.

In general, a planar electrode has many advantages over the conventional patch pipette electrode. First, the planar electrode can be easily scaled to an array of electrodes to permit multi-cell or multi-site measurements. Second, the planar electrode has the potential for integrating microfluidic lines that would permit exchange of the electrode solution, something rarely achieved with a micropipette. The amplifier electronics can also be integrated into the substrate of the electrode for improved noise performance. Third, a planar electrode can be mounted over a fluorescence microscope to simultaneously record electrical and optical signals.

Also, micromolding a planar electrode from PDMS has advantages over the other microfabricated planar electrodes under development. First, the fabrication is simple and economical so that the electrodes are disposable, therefore eliminating the difficult step of cleaning the device. Second, microfluidic lines can be micromolded in the same structure or added by bonding PDMS layers. Third, PDMS is optically transparent so that alignment to underlying components can be done visually. The transparency of the material may also be advantageous when integrating an optical recording system. Fourth, the PDMS surface can be chemically modified to facilitate seal formation.

However, the probe nature of the conventional patch pipette still has its advantages. Most importantly, it can penetrate the top layers of tissue to permit patch clamp measurement on a cell within a tissue. Second, the electrode can be pulled away from a cell to make an *excised patch* recording, useful for applying modifying agents to the patch of membrane. Third, the pipette can be moved quickly between lines of solution flow for quick changes in modifying agents. Integrated microfluidics may negate the need for these last two points but more complicated micromachining may be required to fabricate planar patch electrodes that can penetrate tissue.

The need to plasma-treat the PDMS surface just before use may be a disadvantage of the planar electrode. This would add a plasma system to the required equipment for patch clamp experiments. However, the planar electrodes do not require use of the high-quality optical microscope and micromanipulators currently required for patch clamp recording. In addition, conventional patch pipettes commonly require several processing steps before use including heat polishing and coating.

Patch Clamp Device On-Chip Fabrication

As another typical example, a method for silicon chip-based patch clamp electrodes integrated with PDMS microfluidics is given in the following.

Silicon Chip Microfabrication. Up to 80 silicon chips to be used for patch clamping experiments were parallel fabricated in a single sequence of steps (Fig. 4) using standalone processing tools. Patterns for pores were defined using a photoresist in concert with a custom-designed mask and a mask aligner (operating with 365 and 405 nm radiation lines and in constant power mode). The patterns were developed to etch out the pores using a plasmatherm deep reactive ion-etching system. In the region surrounding the pore, the silicon wafer was thinned to about $20-40\,\mu$m for the micropores ($1.5-2\,\mu$m diameter) and $10-20\,\mu$m for the nanopores ($0.7-1\,\mu$m diameter). Each wafer was fabricated with a small array of usable pores. In the following, only one device was used for any given experiment, and so the chips were diced into 8×8 mm sections, each containing a single pore. The chips were acid cleaned, rinsed using copious amounts of 18 MΩ H_2O and dried under flowing nitrogen. The chips were then coated with a $0.5-1.0\,\mu$m thick insulating film of SiO_2 using plasma-enhanced chemical vapor deposition (PECVD). The top side of the chip was exposed for $20-40$ min and the bottom side was exposed for $10-20$ min. This procedure shrunk the pore diameters by about 0.4 μm. For the nanopores, the oxide was deposited at lower pressure. Deposition at lower pressure was necessary in order to increase the oxide density, deposit a thicker layer of SiO_2, and to conserve the circular symmetry of the nanopores. At this point, the tip fabrication process was essentially complete. *PDMS Microfluidic Fabrication.* Fluidic platforms for both the front and back sides of the wafer were prepared from micromolded PDMS. For most measurements, the chambers simply allowed for separate chemical access to the front and back sides of the micropore. The minimum microfluidic channel widths were 100 μm and the typical channel heights were 100 μm. A mold master was photolithographically patterned into a spin-coated film of photoresist on silicon as described in the literature. The microfluidic channels that were used for cell focusing consisted of two layers of micromolded PDMS that formed one final microchannel network component. The bottom layer of the PDMS microchannel network defined the focusing channels which interfaced the silicon substrate, and the top layer interfaced the focusing channel to larger channels that had inlet and outlet ports. Modified syringe needles were pierced through the top layer to connect the input and output ports with Teflon tubing for the introduction and extraction of cells and solutions. The focusing channel was designed to allow for optical access to the micropore region when the syringes were in place.

Device Assembly. The molded PDMS fluidic chambers were pressure bonded to the silicon chips (Figs. 5a,b). This chemically isolated one side of the pore from the other,

thereby creating a device that enabled independent experimental control of each side of the pore (or membrane sealed over the pore). To prevent electrical leak around the silicon chip, SU-8-5 photoresist was applied around the edges of the surface of the chip with a cotton swab (Fig. 5b) or by transferring the SU-8-5 with a PDMS stamp, and then cured. This coating not only permitted a quick, greaseless method for sealing the chip surface to the PDMS surfaces of the experimental cell-chip chamber (Fig. 5a), but it also reduced the chip capacitance. Chip capacitance values as small as 15 pF were achieved when the stamping technique was utilized. However, for the devices that were integrated with PDMS microchannels, little or no SU-8 resist was applied, since the PDMS channels themselves prevented solution leak around the silicon chip and minimized stray capacitance. In order to recycle the same batch of chips several times, the SU-8 resist and oxide layers were sequentially stripped away using standard oxidizing solutions. First, an oxidizing clean (2:1 concentrated H_2SO_4:H_2O_2 (30 %)) was used to remove the SU-8-5 resist. Next, the oxide was stripped using a buffered oxide etching (BOE) solution. The oxide layer was then re-deposited using PECVD.

Electrophysiology recordings. To record currents from sealed cells, the silicon chip assembly was used as a chamber for a voltage clamp setup (Fig. 6). Each half of the chamber (top and bottom) was connected to the electrodes of a headstage. The top chamber was connected to the input of the patch clamp amplifier and the bottom chamber was connected either to either the ground or the command voltage depending on the amplifier used.

The silicon chip device, coupled to a voltage clamp setup was prepared for cells by adding external and internal solution to the top and bottom chamber, respectively. An amount of 50 μl of cell solution (about 5×10^4 cells) was introduced into the top chamber with a syringe that had a 2 cm piece of Teflon tubing on its tip. The cells were tracked by viewing the top surface of the chip with a microscope and by monitoring the electrical resistance across the pore. Once the cells covered 20 – 30 % of the chip surface, gentle suction was applied from the bottom chamber side. The progress and quality of the seal of a cell over the pore was monitored visually through the microscope and by measuring the capacitance and resistance across the pore. Once the seal reached maximum resistance, the suction was released and electrophysiological recordings from the cell were made.

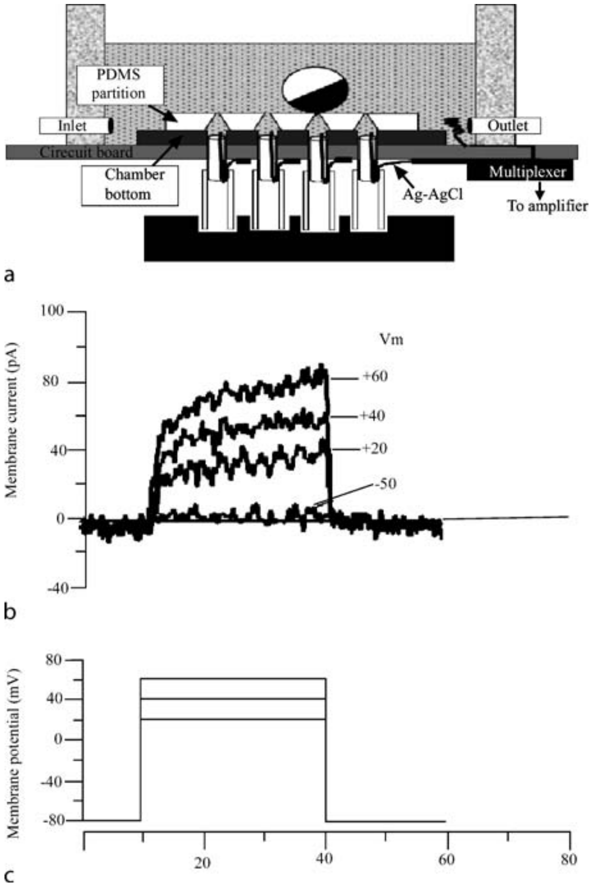

Patch Clamp Measurements On-Chip, Figure 6 Planar PDMS patch electrode array recording of Shaker potassium channel currents. (**a**) Schematic of planar patch electrode array recording system. The 400 mm thick, oxidized PDMS partition is sealed onto the chamber bottom with vacuum grease. The chamber bottom contains an array of openings, each containing tubing and an Ag–AgCl wire. The tubing connects to a suction manifold and the Ag–AgCl wire connects to a multiplexer chip on the circuit board under the chamber bottom. The multiplexer connects each contact to the amplifier electronics. Another Ag–AgCl wire in the bath solution connects to the ground of the amplifier. Bath solution is exchanged through solution lines into and out of the bath chamber. A devitellinized oocyte is dropped onto the aperture to make a patch clamp recording. (**b**) Current traces recorded from a xenopus oocyte expressing inactivation-removed Shaker potassium channels. Each trace represents a step change in membrane potential from rest, 80 mV. Voltage steps are to 50, 20, 40 and 60 mV, as noted, before returning to 80 mV. Leakage currents were subtracted from the raw data by a P/4 protocol (Penner, 1995).

Key Research Findings

The inherent complexity of the technique limits its uses in high-throughput screening for drug discovery and drug safety. To meet high-throughput screening requirements, many efforts have been made to improve the patch clamp system. Planar patch clamp electrodes, scalable and easy to use, have been fabricated using silicon oxide-coated nitride membranes, deep reactive ion etched silicon holes coated with PECVD oxide, polyimide films, track-etched quartz, silicon oxide nozzles, glass substrates and oxygen

P

plasma-treated PDMS. Microfluidics have also been integrated with patch clamp systems using PDMS or glass. Those devices have made possible fast fluid exchange for single electrodes.

Some patch clamp setups with more advantages have been developed to be used more easily. For example, a lateral-based patch clamp setup is compatible with high-resolution microscopy (with a working distance in the $100-300\,\mu$m range). The idea is to trap a cell onto a lateral microchannel in a manner which makes it easier in terms of fabrication and fluidic integration. Niels Fertig has made use of state-of-the-art microstructuring techniques to define three-dimensional micro-openings in planar substrates, with the geometry of an inverted patch clamp pipette tip.

Future Directions for Research

The on-chip-based patch clamp technique broadens the possibilities of ion channel analysis by transferring the classic patch clamp principle onto a microstructured chip format. The planar patch clamp technique enables the automation and parallelization of ion channel measurements. This is an example of the beneficial integration of microtechnological processes in the field of cellular electrophysiology. The chip-based patch clamp technique not only improves ease of use as well as throughput capability compared to conventional patch clamping, but also opens new experimental possibilities for the biophysical characterization of ion channels such as intracellular perfusion or optical accessibility of the chips for combined optical and electrical recordings from ion channels. The automated and parallel patch clamp methods should be further developed in the near future for academia and industry.

Cross References

► Ion Channel

References

1. Neher E (1991) Ion channels for communication between and within cells. Nobel Lect 9 1991:10–25
2. Sakmann B (1992) Elementary steps in synaptic transmission revealed by currents through single ion channels. Nobel Lect 9 1992:31–59
3. Hübner CA, Jentsch TJ (2002) Ion channel diseases. Hum Mol Genet 11:2435–2445
4. Wood C, Williams C, Waldron GJ (2004) Patch clamping by numbers. Drug Discov Today 9:434–441
5. Pantoja R, Nagarah JM, Starace DM, Melosh NA, Blunck R, Bezanilla F, Heath JR (2004) Silicon chip-based patch-clamp electrodes integrated with PDMS microfluidics. Biosens Bioelectron 20:509–517
6. Klemic KG, Klemic JF, Reed MA, Sigworth FJ (2002) Micromolded PDMS planar electrode allows patch clamp electrical recordings from cells. Biosensors and Bioelectronics 17:597–604
7. Fertig N, Blick RH, Behrends JC (2002) Whole Cell Patch Clamp Recording Performed on a Planar Glass Chip. Biophys J 82:3056–3062
8. Li X, Klemic KG, Reed MA, Sigworth FJ (2006) Microfluidic System for Planar Patch Clamp Electrode Arrays. Nano Lett 6:815–819
9. Brüggemann A, Stoelzle S, George M, Behrends JC, Fertig N (2006) Microchip technology for automated and parallel patch-clamp recording. Small 2:840–846
10. Lau AY, Hung PJ, Wu AR, Lee LP (2006) Open-access microfluidic patch-clamp array with raised lateral cell trapping sites. Lab on a Chip 6:1510–1515

Patch Clamp Technique

► Patch Clamp Measurements On-Chip

Patch Voltage Clamp Technique

► Patch Clamp Measurements On-Chip

PCR Lab-on-Chip Devices

Michael Köhler
Stiftungslehrstuhl der Deutschen Bundesstiftung Umwelt, Institut für Physik, Technische Universität Ilmenau, Ilmenau, Germany
michael.koehler@tu-ilmenau.de

Synonyms

Microthermocyclers; Chip thermocyclers

Definition

PCR Lab-on-Chip devices are microfluidic instruments for the biochemical amplification of DNA by thermocycling using the polymerase chain reaction at the microscale.

Overview

PCR Lab-on-Chip devices are miniaturized fluidic systems for fast DNA amplification. The polymerase chain reaction (PCR) is a molecular biological technique for addressing and exponentially amplifying a DNA fragment. The PCR process is based on temperature cycles with an enzymatic amplification step. It works without the use of a living cell. For PCR, a liquid mixture of an analyte

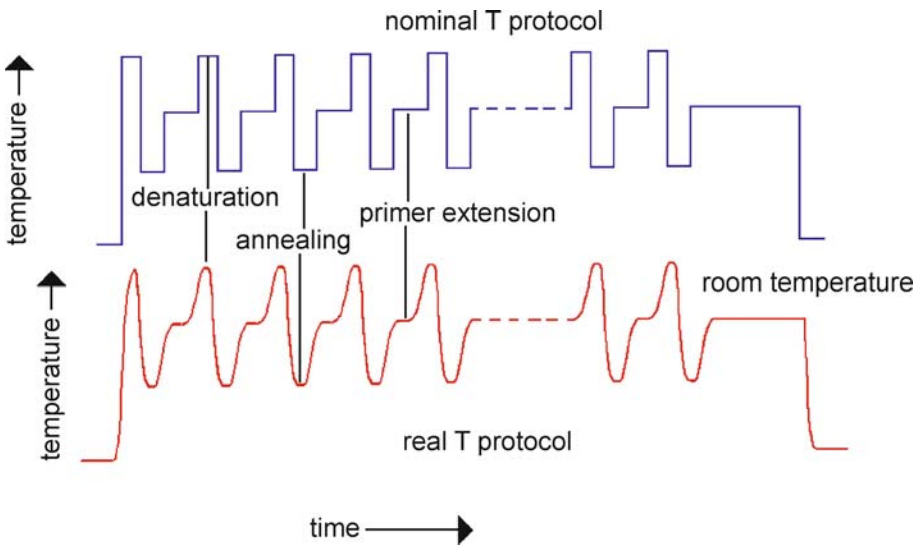

PCR Lab-on-Chip Devices, Figure 1 Temperature protocol for PCR with repeated thermal addressing of process steps; nominal and real temperature tracks (double-strand separation, primer annealing, primer extension)

containing DNA with an amplification buffer solution containing nucleoside triphosphates (building units for DNA synthesis), primers (starter molecules), catalyst (the enzyme polymerase) and some additives is applied. The exponential increase of concentration of the sequence of interest is due to the doubling during each temperature cycle. The synthesis of a daughter strand of DNA on a mother single strand (template) occurs by template-directed condensation of nucleotides. The primers are applied for addressing a selected sequence part of DNA template molecules from the analyte sample carrying the genetic information of interest. Very small amounts of interesting DNA are required. Under optimized conditions, a single template DNA molecule is sufficient for starting the process. DNA fragments up to about 10,000 base pairs can be amplified by PCR.

The addressed sequence is identically replicated to a large extent during the thermocycling process. The miniaturization by transferring the technology from classic block thermocyclers into Lab-on-Chip devices is associated with a miniaturization of sample and with a large reduction of process time. In addition, Lab-on-Chip PCR allows the integration of sample preparation and post-amplification treatments including labelling and/or separation in order to realize a completely automated process chain in a miniaturized system. DNA microanalysis systems can be built, in which the micro PCR is the key operation for getting the molecular information carrier in a concentration suited for convenient signal readout.

Amplification of DNA by Lab-on-Chip PCR is mainly used for genotyping. In connection with a reverse transcription process using RNA-dependent DNA polymerase, this technique can also be applied for the characterization of RNA, in particular for the identification and measurement of messenger RNA. As a result, the Lab-on-Chip PCR devices can be also applied for gene expression studies.

The application of PCR chip devices is connected with several important advantages with respect to conventional systems:

- low sample volumes
- very fast process steps
- low power consumption, suited for point-of-care diagnostics
- well reproducible temperature protocols
- processing of larger sample series under the same conditions
- low space requirements of devices
- integration of functions like reverse transcription process (for gene expression studies), on-line measurement of double-strand DNA concentration or real-time measurement by multi-sensor arrangements.

Hence, miniaturized PCR devices are very interesting for a broader application of PCR in laboratories as well as for point-of-care diagnostics, screenings or investigations for food safety and environmental protection.

Basic Methodology

The basic technique is the PCR invented by K. Mullis in 1983. This technique allows one to replicate DNA identically without any living cell. The PCR has developed

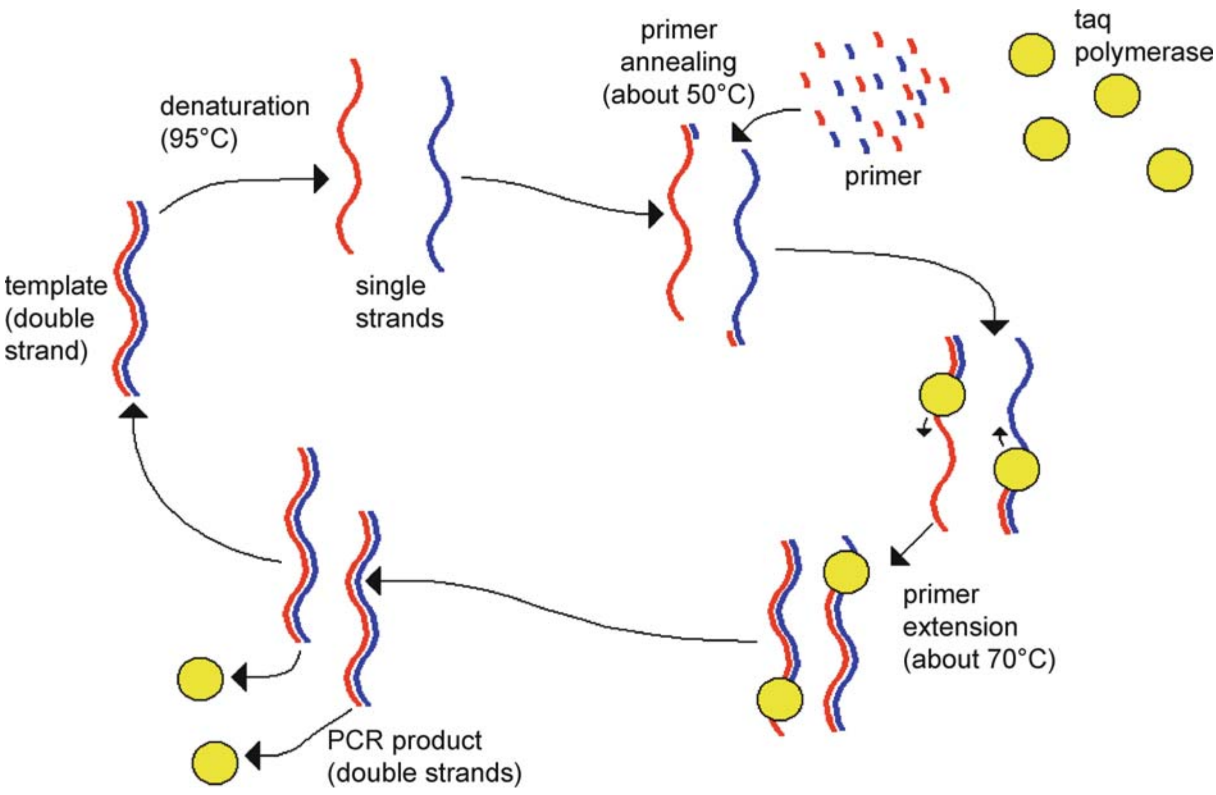

PCR Lab-on-Chip Devices, Figure 2 Principal molecular processes of PCR during thermocycling

into a common technique used in medical and biological research and diagnostics as well as in forensic, archaeological and other investigations. It is the key method for sequencing of genes, for the diagnosis of hereditary diseases, for paternity testing and for molecular identification of infectious microorganisms.

The PCR technique succeeds by the use of the DNA-dependent DNA polymerase from bacteria living in hot sources (taq-polymerase). This enzyme is able to elongate primers (oligonucleotide starter molecules) in a complementary pattern to a template DNA single strand at a temperature of about 70 °C. This high temperature is necessary in order to create a temperature-controlled three-step process. The whole process includes the following steps:

1. the initialization step for denaturation of DNA double strand into two single strands at about 95 °C by thermal disruption of the hydrogen bonds between the complementary bases in the double strand;
2. the addressing of a short well-known sequence pattern by base-pairing of primers (*primer annealing*) at suitable temperatures in the range between about 45 and 65 °C depending on primer length, AT/CG ratio and desired selectivity; and
3. the elongation of the primers with the complementary order of nucleotides by the synthesis of the new DNA strand by the enzymatic activity of the taq-polymerase (*primer extension*).

Two suitable primers are applied in order to generate both new complementary single strands of a selected DNA sequence in the replication during one temperature cycle. The repeated application of temperature (Fig. 1) cycles leads to a fast increase of the concentration of the selected DNA sequence by doubling the DNA in each cycle (Fig. 2). As a result, the selected sequence can be amplified by a factor of about 1000 in 10 temperature cycles, by a factor of about 1 million in about 20 temperature cycles and about 1 billion in 30 temperature cycles. This amplification is high enough for all characterization techniques like fluorescence detection, electrophoretic characterization, sequencing or chip hybridization. PCR bridges the gap between the molecular diversity in living nature using small numbers of key molecules and the analytical tools of chemistry and sensorics (Fig. 3).

Classic PCR is performed in Eppendorf tubes, microtiterplates or similar repositories by conventional thermocyclers with thermostatted blocks. The typical time required

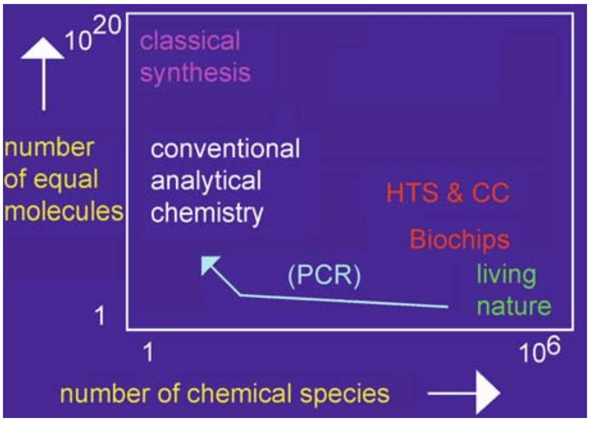

PCR Lab-on-Chip Devices, Figure 3 Schematic of PCR as gap bridging technology between the biomolecular and chemical worlds: number of molecular species (types) and number of molecules of the same type in chemical and biological systems

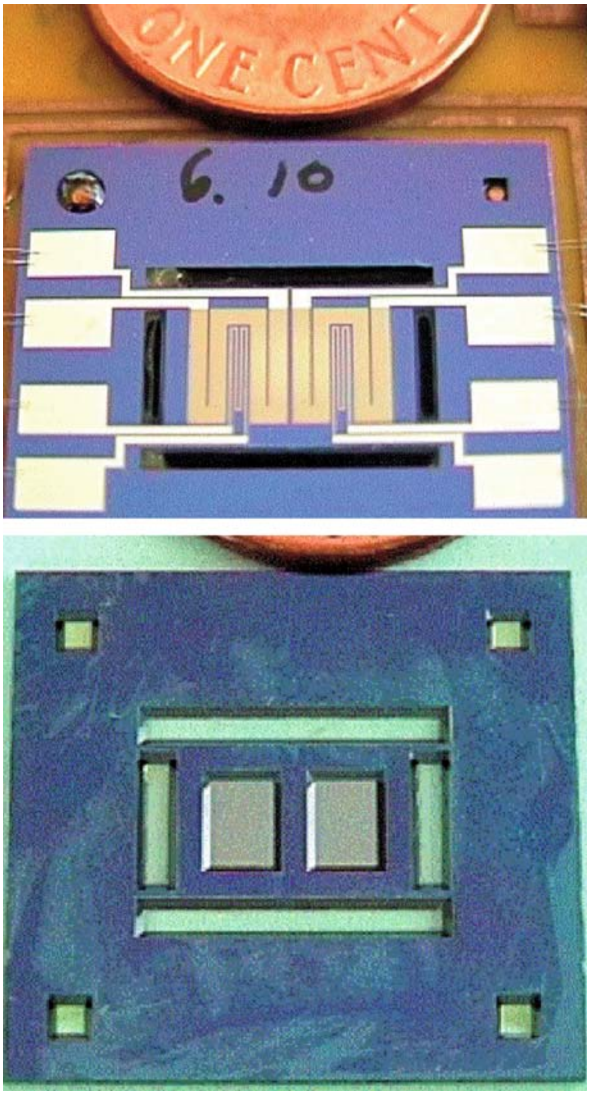

PCR Lab-on-Chip Devices, Figure 4 Example of a silicon chip thermocycler (IPHT Jena, Germany): microlithographically patterned thin-film transducers at the back side (above), liquid chambers and air chambers for heat transfer control at the front side (below)

is in the range of about 90 min up to about 3 h. Faster working thermocyclers need powerful heaters as well as coolers in order to realize high heating and cooling rates.

The temperature control can be realized by alternating mechanical contact to heating/cooling plates, by fluidic switching between heating and cooling liquids or by Joule heating using thick-film or thin-film microheaters. The latter method is frequently combined with passive cooling by heat conduction or convective cooling. In several chip devices, microheaters and thermal microsensors are prepared in close proximity in order to realize efficient feedback loops in electrical heating.

Despite the high amplification factor, the volumes can be small that have to be operated in thermocycling for PCR. So, DNA amplification can be done with volumes in the lower μl or in the nl range. The reduction of sample volume gives the possibility to apply chip devices or other miniaturized systems for the PCR. The reduction of size allows a crucial enhancement of heating and cooling rate and at the same time a reduction of power consumption. Power reduction and process rate enhancement become possible due to the lowering of parasitic heat capacitances and by efficient transfer of heat inside the system. So, miniaturized PCR devices can work at high process speed with low power requirement. Therefore, they are particularly applicable for hand-held devices, mobile analytical systems and microautomated systems.

Microtechnology offers two different strategies for Lab-on-a-Chip PCR. The first is the stationary concept. This concept corresponds to the classic thermocycler. The core element is a miniaturized chamber for PCR liquid equipped with heaters and temperature sensors (Fig. 4). Fast PCR is realized by fast heating and cooling the whole system. The maximum process rate is mainly determined by the ratio of heating and cooling power to the heat capacity of chamber and sample. The second strategy is based on a microflow-through concept. The device contains a long microchannel, which is conducted in meanders through three temperature zones (Fig. 5). Thus, the three regions of the device remain at constant temperature, and the temperature cycling is realized by changing contact of the liquid with the three different temperature zones. The maximum process rate is mainly determined by the heat capacity of the streaming liquid itself and by the heat conduc-

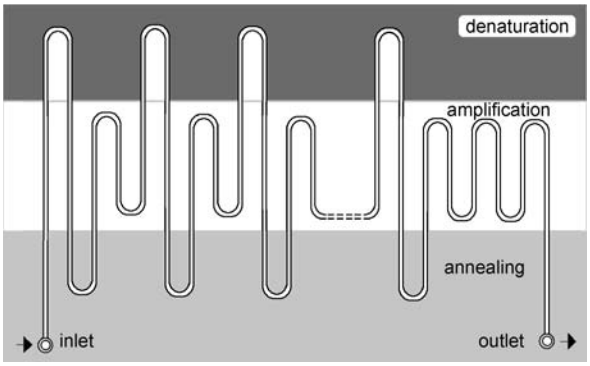

PCR Lab-on-Chip Devices, Figure 5 Principle of construction of a flow-through chip thermocycler

tivity between sample and walls. In principle, the time for single temperature cycles can be reduced down to a few seconds. The whole PCR process with 20 – 40 cycles can be done in time scales between a few minutes and about half an hour.

The acceleration of the PCR process is a very important advantage of PCR Lab-on-a-Chip systems. A second advantage is in the possibility to integrate further functions into the microdevice. Thus, steps of sample preparation as well as separation and detection supporting process steps can be integrated. In this way, miniaturized DNA analysis systems are constructed, in which the Lab-on-Chip amplification by PCR is the central process.

Key Research Findings

The motivation for miniaturization of PCR was driven by several factors. First, PCR should be made faster in order to get results more quickly. Second, larger sets of samples should be processed. Third, DNA-based diagnostics should be evolved from a laboratory technique requiring experienced specialists to an automated on-site diagnostic method operated after brief instructions by anybody. Finally, the amplification by PCR should be integrated in a diagnostic chain (μ-TAS concept) and implemented in a miniaturized transportable system. The power consumption of the thermocycling process should be as low as possible.

The simplest way for meeting the requirements mentioned above and realizing micro-PCR on-a-Chip consists in a transfer of the conventional PCR technique into a microchamber chip. Therefore, microchambers for liquid volumes between a few μl and several hundred nl were etched anisotropically in silicon wafers. A lithographically micropatterned metallic thin-film system at the backside of the wafer was applied in order to control temperature by Joules heating and thermoresistive temperature measurement. Metal film thicknesses of about 1 μm or several hundred nm were sufficient for achieving all temperatures necessary for PCR. The bottom membrane of the chamber carrying the metal transducers was built by the residual silicon thickness after time-controlled chamber etching. The high heat conductivity of the material guaranteed a fast heat transfer between the thin-film transducers and the liquid.

The cooling steps of PCR could be realized by direct contact of the bottom membrane with a cooling element (e.g. a Peltier cooler) or by indirect cooling using the passive heat transfer from the silicon chamber to ambient. For the second method, the fine tuning between temperature homogeneity in the core region of the PCR chamber and temperature gradients between core region (with PCR chamber) and the outer frame region of the microsystems were of particular importance. The problem was solved by the definition of spatially restricted areas *(heat conduction beams)* for passive heat transfer between core and frame by etching holes into the silicon. Optimized chips supplied high temperature homogeneity in the core region of PCR chips and heating and cooling rates of 40 – 80 K/s. Cycle times could be downscaled to a few seconds. The time required for the whole PCR process could be reduced down to 30 – 10min.

An important advantage of microchamber chips, beside the good dynamics, is the flexibility. Temperature/time protocols can easily be adapted and varied. Thus, this technique is useful for the development and optimization of protocols.

Microtiterplates (MTPs) are the most commonly used chamber arrays for PCR. The open chambers have to be covered by oil or sealed by membranes in order to suppress evaporation of water during the process. A fast working PCR in arrays can be realized, if small chamber volumes are applied and the wall thickness of the plate material is thin enough for fast heat transfer. Such chamber arrays can be prepared by in situ forming of array plates by means of a thermostatted block suitable as metal master. A further miniaturization of chamber volumes is possible by using nanotiterplates (NTPs). Microlithography allows the preparation of chambers in the lower μl range as well as over the whole nl and pl range. There are technologies for preparation in silicon as well as in glass. Polymer carriers are made in many cases by replication from microstructured silicon or glass master chips. A wide spectrum of materials is available for NTPs. The thermostatting can be realized by the conventional incorporation of the sealed NTPs in metal block devices or by integration of thermal transducers in the carrier systems. The application of micropatterned thin-film heaters

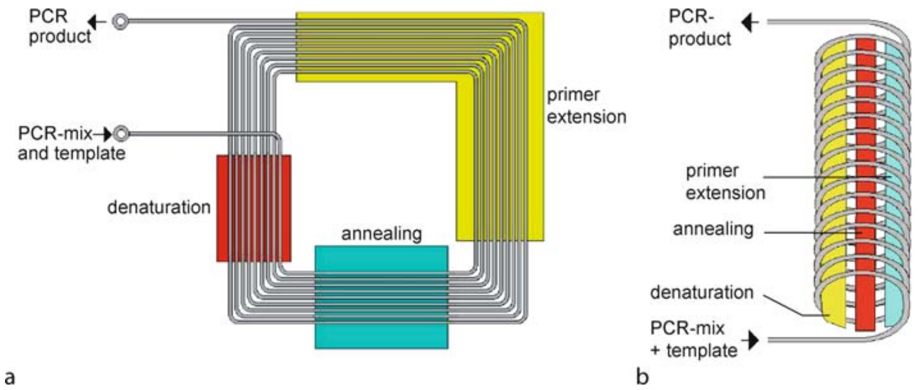

PCR Lab-on-Chip Devices, Figure 6 Micro-flow-through PCR in tube arrangements: (**a**) spiral-like arrangement (two-dimensional), (**b**) helical arrangement (three-dimensional)

and thin-film sensors for direct thermostatting of NTPs is compatible with well-established microsystem technologies using glass and silicon substrates. It is more difficult in the case of polymer materials. The high conductivity of silicon is responsible for the attractiveness of using these materials for all processes connected with fast temperature changes. Silicon carriers are of particular interest for NTPs used in PCR. The comparatively high affinity of silicon against proteins is a disadvantage and demands special surface covering or chemical surface modifications (see below).

The power consumption for heating and cooling of samples can be reduced if the temperatures in the device are kept constant in three different regions and the sample is moved between these three regions. This movement can be operated at the surface of a thermostatting chip, for example by electrostatic manipulation or by surface acoustic waves (SAWs). Therefore fluidic transport paths (hydrophilic areas) are defined lithographically in a hydrophobic environment on a piezoactive substrate like lithium niobate. The excitation of SAWs is realized by microlithographically prepared thin-film electrodes. SAW systems are of particular interest due to the fast manipulation and the very efficient mixing processes, which can be applied also for sample preparation. The small volumes of droplets make the evaporation of water a serious problem. This can be overcome to a certain extent by oil covering.

The evaporation of solvent can be avoided completely if closed microchannels are used for a micro-PCR with moving of samples between different temperature zones. The simplest variant consists of a flow-through PCR realized in a tube, which is conducted repeatedly through the three temperature zones. There are two principal geometries for the arrangement of tubes. In one variant the tube is coiled in one plane like a spiral (Fig. 6a). This geometry can be easily realized. But, this arrangement suffers from increasing or decreasing residence times in all three temperature zones due to the changing diameter of the tube loops. The alternative is a three-dimensional, helical arrangement of the tube. In this geometry, the conditions at all temperature cycles can be kept equal (Fig. 6b).

A certain disadvantage of using tubes is the low heat conductivity of polymer tube materials and the comparatively high thicknesses of tube walls. This leads to low temperature gradients. As a result, the outside temperature must be adapted to the flow rate-dependent heat required inside the tube and the heat transfer conditions in the tube wall.

The principle of flow-through PCR can further be miniaturized and optimized with respect to heat transfer conditions by realizing flow-through chip thermocyclers. These are devices for flow-through PCR on silicon, glass or polymer chips. The use of silicon (high thermal conductivity) and glass (low heat conductivity) in one device allows convenient control of temperatures in the three process zones by choosing a suitable local heat capacity and heat exchange conditions. In analogy to chip chamber cyclers, etched holes in silicon support the thermal separation of temperature zones, and thin-film resistors are applied for heating and electroresistive temperature measurements.

DNA amplification can occur either in a continuous flow mode or in a serial flow mode. In the continuous flow mode, a template is mixed continuously with the PCR mix and transported through the flow thermocycler. This mode is well suited for preparing amplificates of a certain DNA sequence in constant quality. In contrast to continuous amplification, most PCR applications are found in analytics. Therefore, the enhancement of throughput of samples in one analytical system is the deciding parameter. In principle, series of template-containing samples can be applied in a certain clock pulse in a flow-through system. But, the subsequent injection of different samples in

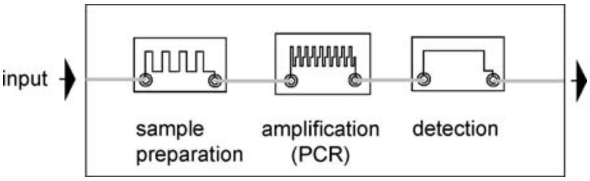

PCR Lab-on-Chip Devices, Figure 7 Schematic of integration of PCR in a μ-TAS arrangement with sample pre-treatment and separation/detection unit

continuous flow leads to strong cross-talk effects due to the fluidic dispersion which is caused by the laminar flow behaviour in the microtubes and microchannels. This fluidic cross-talk is particularly critical due to the exponential character of the amplification process during PCR.

A crucial improvement of sample separation in serial processing can be achieved by the application of a segmented flow in the micro-PCR. The separation of aqueous fluid segments containing the PCR mix and the different templates by immiscible organic liquids converts the laminar flow to a plug flow. If the inner surface of the wall is hydrophobic, the chemical cross-talk between fluid segments can be suppressed completely. Thus, the segmentation of flow improves the transport behaviour as well as inhibiting effects of the wall. In addition, the plug flow guarantees constant residence times for all samples and all volume parts of one sample in all temperature regions and in all cycles. The segmented flow principle can be applied for both microtube PCR and on-chip PCR.

Serial PCR using flow segments allows comparatively high sample frequencies. The generation of segments can occur up to frequencies of some tens per second. Reconsidering a certain redundancy (several segments of the same sample), it is possible to process in the order of 10^4 samples per hour. This high throughput power of serial flow micro-PCR makes this technique interesting for screening procedures with well-standardized protocols. The fixed definition of temperature protocols is necessary because the length of capillaries or tubes in the different temperature zones is fixed. Changing of flow rate leads only to a proportional change in all temperature zones. The ratio of residence times is fixed by the design of the flow-through device. So, flow-through thermocyclers are much more efficient than chamber thermocyclers, but less flexible. Flow-through PCR is therefore preferably applied for well-defined analytical problems with high numbers of analogue samples.

A big additional advantage of flow-through processes in comparison with stationary processes consists in the possibility of implementation of process chains (Fig. 7). In this way, complete microanalytical systems can be designed. They can include sample pre-treatment like cell separation, cell lysis or chemical separation. Reverse transcription processes can be directly connected on-chip with the DNA amplification by thermocycling (RT-PCR). The analytical chain can also include post-amplification steps like fluorescence labelling, separation by capillary electrophoresis or hybridization on DNA chips.

Chemical compatibility is a particularly important problem for Lab-on-Chip PCR devices. The taq-polymerase possesses a certain surface affinity due to their amphiphilic character. In addition, the low start concentrations of DNA for amplification are critical if the molecules are adsorbed at wall surfaces. The molecule–surface interactions are particularly critical due to the high surface-to-volume ratios in chip devices. The suppression of undesired adsorption demands inert materials. Polymers like polypropylene or polytetrafluoroethylene are much better suited than glass or silicon. The OH groups at the surface of native glass, silicon or silicon dioxide surfaces are mainly responsible for disturbing adsorption. The affinity of surfaces against the biomolecules can be suppressed by surface treatments. Therefore, alkylsilanization (by alkyltrichlorsilanes or alkyltrimethoxysilanes for example) is particularly suited. The surface properties change during the exposure of walls against cell suspensions and PCR solutions. Certain rinsing, cleaning and resilanization protocols are applied in order to achieve a high reproducibility in the case of reused Lab-on-Chip PCR systems.

Micro-flow-through PCR has been investigated in the last few years for several biological and medical applications. They relate to the identification of DNA in different research experiments, for genotyping of microorganisms, in particular the identification of pathogens, as well as for genotyping of tissue material, gene expression studies using a preceding reverse transcription step for conversion of messenger-RNA into DNA and for adaptation and development studies of insect embryos.

Future Directions of Research

Further research for Lab-on-Chip PCR devices is focused on four main topics: the improvement of the performance of the amplification process, the integration of new functions in PCR-based analytical chip devices, the integration of PCR in microautomated diagnostic systems and the extension of PCR-based nucleic acid microdiagnostics to new applications.

The improvement of heat transfer by optimized channel and wall geometries and the choice of best-suited materials contribute to the enhancement of process speed and to a better control of selectivity. Adapted selectivity can be achieved by realizing well-defined temperature proto-

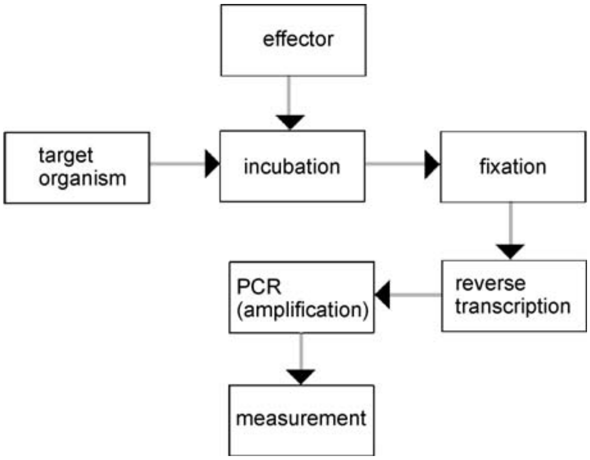

PCR Lab-on-Chip Devices, Figure 8 Process scheme for use of Lab-on-Chip PCR for expression diagnostics in drug screening

cols for the primer annealing step. Therefore, steep cooling and heating ramps are of interest. Special material combinations and the adaptation of manufacturing technologies are under investigation for the improvement of speed and surface compatibility.

Sample throughput is particularly important for screening processes with large numbers of samples. Low-cost DNA diagnostic tools are necessary for biomedical screenings in order to identify genotype-determined health risks in the human population. They are also of interest for screenings for dangerous microbial genotypes. Despite biomedical, environmental and agricultural screenings, high sample throughput is also required for pharma screenings. Here, expression studies depending on drug concentrations and drug combinations demand low-cost solutions including fast RT-PCR (Fig. 8). Highly parallelized systems and in particular fast working serial PCR systems are of interest for such pharma screenings.

The specific fields of recent and future applications of rapid flow-through chip PCR demand the development of PCR-based chip devices with additional integrated functions for sample pre-treatment, on-line sensing, process control and real-time measurement, for referencing and reproducibility tests. Therefore, further efforts for integration of transducers as well as additional fluid manipulation functions are required.

Process speed, sample throughput as well as selectivity could be improved by ultra-miniaturization of Lab-on-Chip PCR. In nature, DNA amplification takes place in reaction volumes (cells) down to the sub-micrometre level. This corresponds to volumes in the sub-femtolitre range. In principle, the PCR process could be down-scaled to this region. Recently, most PCR Lab-on-hip devices are working with sample volumes in the sub-μl and in the nl range. By ultra-miniaturization, these volumes could be reduced by factors of between 10^{-3} and 10^{-7}. Therefore, special strategies of liquid handling and, in particular, microencapsulation techniques, vesicle techniques or ultra-miniaturized segmented flow techniques are necessary.

The very different possibilities of using information from nucleic acids for health care, drug development, environmental control, product and process safety, food control, control of trade and transport and so on demand cost-efficient special solutions with microsystems for DNA or RNA analysis. So, further research will address a wide spectrum of different special diagnostic solutions integrating Lab-on-Chip PCR. The questions of universality, reusability, safety and recyclability will become important, in future, like the questions of costs, operability, robustness and reliability.

Cross References

► Droplet-Based Lab-on-Chip Devices
► Lab-on-Chip Devices for Biodefense Applications
► Microfluidics for Bio- and Chemical Reactions
► Microsegmented Flow

References

1. Auroux PA, Koc Y, DeMello A, Manz A, Day PJR (2004) Miniaturised nucleic acid analysis. Lab Chip 4:534–546
2. Curcio M, Roeraade J (2003) Continuous segmented-flow polymerase chain reaction for high-throuput miniaturized DNA amplification. Anal Chem 75:1
3. Easley CJ, Karlinsey JM, Landers P (2006) On-chip pressure injection for integration of infrared-mediated DNA amplification with electrophoretic separation. Lab Chip 6:601–610
4. Fukuba T, Yamamoto T, Naganuma T, Fujii T (2004) Microfabricated flow-through device for DNA amplification – towards in situ gene analysis. Chem Eng J 101:151–156
5. Guttenberg Z, Müller H, Habermüller H, Geisbaurer A, Pipper J, Felbel J, Kielpinski M, Scriba J, Wixforth A (2005) Planar chip device for PCR and hybridization with surface acoustic wave pump. Lab Chip 5:308–317
6. Kopp MU, DeMello AJ, Manz A (1998) Chemical amplification: Continous-flow PCR on chip. Science 280:1046–1048
7. Lee JG, Cheong KH, Huh N, Choi JW, Ko Ch (2006) Microchip-based one step DNA extraction and real-time PCR in one chamber for rapid pathogen identification. Lab Chip 6:886–895
8. Liu CN, Toriello NM, Mathies RA (2006) Multichannel PCR-CE microdevice for genetic analysis. Anal Chem 78:5474–5479
9. Mullis KB, Ferré F, Gibbs RA (1994) The polymerase chain reaction, Birkhäuser, Boston
10. Poser S, Schulz T, Dillner U, Baier V, Köhler JM, Schimkat D, Mayer G, Siebert A (1997) Temperature controlled chip reactor for rapid PCR. Sens Actuators A 62:672
11. Schneegaß I, Köhler JM (2001) Flow-through polymerase chain reactions in chip thermocyclers. Rev Mol Biotechnol 82: 101–121

12. Wilding P, Shoffner MA, Kricka LJ (1994) Clin Chem 40:1815
13. Wooley AT, Hadley D, Landre P, DeMello AJ, Mathies RA, Northrup MA (1996) Anal Chem 68:4081

Peclet Number

Definition

Peclet number is a dimensionless number relating the rate of advection of a flow to its rate of thermal diffusion.

Cross References

- ► Polymer Synthesis within Microfluidic Reactor
- ► Microfluidics for Bio- and Chemical Reactions

Peltier Effect

Synonyms

Thermoelectric effect

Definition

The Peltier effect occurs when an electric current passes through two different connected materials (metals or semiconductors) and thereby generates a temperature difference across the materials.

Perfect Slip

- ► Boundary Slip of Liquids

Peristalsis

Definition

Peristalsis is transport in a flexible duct via traveling contraction waves. Peristalsis is the process by which material is moved through anatomical passages, for example of the digestive tract, by the contraction of smooth muscle in rhythmic waves. In biological systems, peristalsis moves liquids or solids. Micropumps based on the principle of peristalsis have been designed to move liquids and gases.

Cross References

- ► Linear Peristaltic Pumps
- ► Peristaltic Pumps
- ► Rotary Peristaltic Pumps

Peristaltic Pumps

JORDAN M. BERG[1], TIM DALLAS[2]
[1] Nano Tech Center & Department of Mechanical Engineering, Texas Tech University, Lubbock, TX, USA
[2] Nano Tech Center & Department of Electrical & Computer Engineering, Texas Tech University, Lubbock, TX, USA
jordan.berg@ttu.edu

Synonyms

Flexible member pump; Membrane pump; Diaphragm pump; Valveless pumps

Definition

Peristaltic pumps are mechanical displacement pumps that induce flow in a fluid-filled, flexible-walled conduit through ►peristalsis – transport due to traveling contraction waves. While macroscale peristaltic pumps appear in a variety of configurations, micropumps based on this principle almost exclusively use the sequenced contraction and expansion of a small number of discrete actuators – typically three – placed along the fluid channel.

Overview

Peristaltic pumps emulate the biological process of peristalsis, in which material is moved through the esophagus or other anatomical passage by the contraction of smooth muscle in rhythmic waves. Figure 1 is a schematic of a typical ►rotary peristaltic pump, as implemented at the macroscale, in which a set of revolving contact elements creates a traveling compression wave in a section of a flexible tube. Figure 2 is a schematic of a macroscale implementation of a ►linear peristaltic pump, in which a number of translating piston actuators cyclically compress a flexible tube. In either case, a moving boundary displaces fluid and induces a flow, placing peristaltic pumps in the class of positive-displacement pumps. Increasing the tube diameter or the pumping cycle frequency increases the flow rate. A major attraction of macroscale peristaltic pumps is cleanliness. The fluid is completely isolated from the pump components since it never leaves the tube. Furthermore, it is a simple matter to change the tubing to avoid cross-contamination between fluids, and the tubing material may be tailored to ensure compatibility with a particular application. The pumping action is relatively gentle, making peristaltic pumps suitable for reactive liquids or cell suspensions. Also, the pumps may be self-

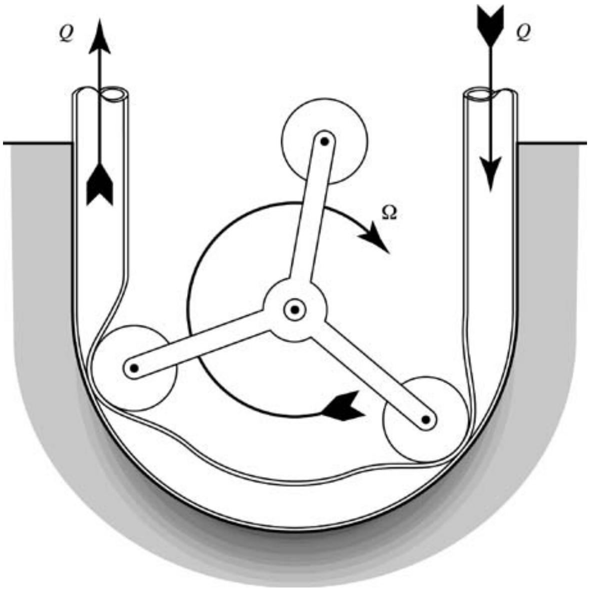

Peristaltic Pumps, Figure 1 A typical macroscale rotary peristaltic pump design. A set of rotating contact elements cyclically compresses a flexible tube. The elements may roll or slide along the tube; the number of contact elements may also vary. The fluid never leaves the tube, protecting the fluid from contamination by the pump elements, and the pump elements from corrosion or abrasion by aggressive fluids. The tube itself is easily replaced. Tube size and composition may be adjusted to accommodate different fluids, or to change the flow rate. Changing the rotation rate Ω changes the flow rate; changing the sign of Ω reverses the flow direction

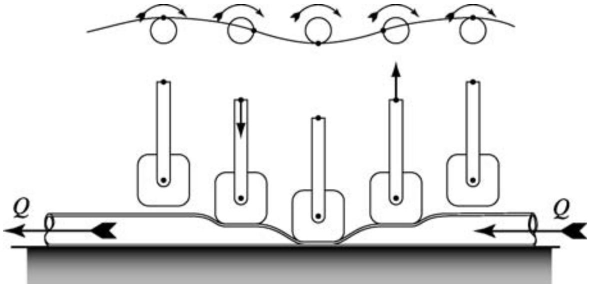

Peristaltic Pumps, Figure 2 A typical macroscale linear peristaltic pump design. A set of translating actuators cyclically compresses a flexible tube. The number of actuators may vary. Features of macroscale rotating peristaltic pumps also apply to microscale linear peristaltic pumps. Linear peristaltic pumps are used in applications such as drug delivery, when accurate flow rate control is needed

priming due to the low-pressure region created behind the moving constriction, and the flow direction can be easily reversed. At the macroscale, use of rotary peristaltic pumps is widespread, while linear peristaltic pumps are found mainly in niche applications, such as intravenous drug delivery.

Cleanliness considerations do not translate to the microscale, nor does the notion of interchangeable components. Therefore, use of peristaltic micropumps must be justified for other reasons. Self-priming and bidirectionality remain appealing features, but perhaps the main benefit is simplicity of design. Any mechanism providing volume change in a chamber or channel is a candidate actuator for a peristaltic pump. For example, a typical active microvalve involves a membrane that can be forced against a seal to close, or pulled away from the seal to open [1, 12]. Two or more active microvalves can be arranged in sequence and actuated with the appropriate phasing to create a linear peristaltic micropump. The principles of peristaltic pumping apply to liquid or gas, and micropumps for both have been demonstrated. The ease with which an actuator can be transformed into a pump accounts for the wide variety of linear peristaltic micropumps that have been reported, including an early micromachined silicon and glass version by Smits (as reviewed in [3, 12], or see the original paper referenced therein).

In this article we refer to an actuator as *closed* when the associated chamber or channel volume is minimized, and as *open* when that volume is maximized. The volume in the closed position is called the ► dead volume, and the difference between the volume in the open position and the dead volume is the ► stroke volume. The ► stroke volume divided by the dead volume is the ► compression ratio. Compression ratio is particularly important when pumping gases, since the amount of gas ejected from the actuator is reduced by the compressibility of the fluid. In pure liquids this effect is much less, but compression ratio plays an important role in determining how severely bubbles impact a particular pump. In classifying micropumps, a distinction is sometimes made between ► integrated actuators – fabricated along with the other components of the microfluidic system – and ► external actuators – fabricated separately and attached later. It is common to see peristaltic micropumps of either kind.

While a linear pump can easily be built up from two or more basic actuation units, microscale rotary mechanisms face significant fabrication challenges. Accordingly, rotary peristaltic micropumps have seen very limited implementation. While several rotary mechanical micropumps are described in the literature (see the summaries in [1], [3] and [12], for example), to our knowledge there is only one example in the literature of a true rotary peristaltic micropump; Kim et al. (Sensors and Actuators A 128:43–51, 2006) use a silicone membrane for the deformable channel surface, and a rotating ferrofluid plug driven by an external magnet for actuation. Also notable is a miniature rotary peristaltic pump by Bar-Cohen and Chang (*Smart Structures and Materials 2000: Active Materials:*

P

Behaviors and Mechanics, *Proceedings of SPIE 3992, 2000*) that employs a traveling flexural wave in a piezoelectric ring. Reflecting their dominance in the literature, the subsequent discussion will consider only linear peristaltic micropumps, which for brevity are henceforth referred to simply as peristaltic micropumps. Most reported microscale implementations approximate continuous peristaltic action using two or more (most commonly three) discrete collapsible chambers. A notable exception, and one which does not fit well into the analysis scheme presented here, is the colloidal peristaltic pump presented in [15]. There a large number (approximately twelve) of 3 μm colloidal silica particles are oscillated sinusoidally in a 6 μm deep polydimethylsiloxane (PDMS) channel using external actuation by optical trapping with a scanned 532 nm laser. Flow rate on the order of 1 nl/h are induced in an aqueous solution by the resulting traveling wave. Peristaltic actuation through movable suspended particles is, to our knowledge, unique to [15]. The remainder of this paper focuses on the much more common case of discrete collapsible chambers.

Peristaltic pumps have found wide application in microfluidic systems based on PDMS, due to their ease of fabrication and versatility in operation. PDMS is a popular material for microfluidics for several reasons. Compared to traditional semiconductor industry fabrication schemes, both the materials and processing tools are inexpensive. PDMS is biocompatible, resistant to many chemicals, and transparent to wavelengths of light useful in chemical and biochemical analysis. Figure 3 shows a typical actuator design, similar to that first reported in [4], with the fluid channels formed between a thin PDMS layer and a glass, silicon, or PDMS substrate, and actuator channels formed at right angles to the fluid channels in a thicker PDMS layer, bonded to the planar side of the fluid layer. We refer to the area of the fluid channel under an actuator channel as a pump chamber, even though it is geometrically identical to the rest of the channel. The actuator channels are inflated from an external pressure source to close the pump chamber; when the pressure is removed the natural elasticity of the PDMS restores the channel to its original shape. As suggested by the figure, due to the low modulus of elasticity of PDMS, the pump chambers may be designed to collapse completely when closed, allowing them to act either in concert for pumping, or in isolation as pure valves.

In a peristaltic pump, the volume of fluid displaced by the individual actuators is rectified, that is, directed in the desired direction of flow, solely by the phasing of multiple actuators. Other types of displacement pumps rectify flow differently. A passive check-valve pump uses two passive, one-way check valves incorporating moving flaps or other components. One such valve at the pump inlet permits fluid to enter the chamber as the pump chamber expands, but prevents it from leaving as the chamber contracts. Likewise, a passive check valve at the outlet prevents backflow on the expansion stroke, but permits fluid to exit the chamber on the contraction stroke. Valveless rectification pumps are similar, but use flow diodes instead of mechanical check valves. Flow diodes are diffuser/nozzle structures or so-called Tesla valves that have no moving parts, but exhibit a preferential flow direction due to their geometry. More detail on passive check-valve or valveless rectifier pumps may be found in [1], [3] or [12]. Since these require only a single actuator, versus two or more for peristaltic pumps, they are natural design alternatives. Reasons to prefer a peristaltic design include ease of integration onto the microchip, with no special fabrication steps or external connections. For example, [13] presents an electrostatically-actuated peristaltic micropump suitable for incorporation into a micro-total analytical system (μTAS) with no additional special considerations. Peristaltic pumps avoid the more complex microfabrication typically required for passive check valves, and the susceptibility of such valves to fouling by particles or bubbles. Valveless rectifiers are simple to fabricate, and not prone to fouling, but may have a larger footprint than peristaltic designs. Finally, peristaltic pumps may be used to generate forward or reverse flow by modifying the actuator phasing, while bidirectional versions of the other two options are difficult to realize. Some guides to peristaltic pump design advise adding series passive check valves to aid in rectification if the application allows [1], though this reduces to some extent the operational and fabrication benefits that peristaltic designs offer over check-valve designs.

In many peristaltic micropump implementations identical actuators provide both stroke displacement and flow valving. However, these functions may also be divided between actuators of different design. One analysis reported in the literature treats a large stroke displacement actuator with a low flow resistance, flanked by active valves with small stroke displacement [5]. While similar in concept to a passive check-valve diaphragm pump, the valving actuators in this case are actively opened and closed by external commands, and flow direction is determined by the phasing of these commands with regard to actuation of the central diaphragm. Hence, this design may properly be classified as a peristaltic pump.

Due to a combination of surface tension and viscosity effects, the pressure drop per unit length along a channel with characteristic length l (radius or hydraulic diameter) scales unfavorably (as $1/l^3$ or $1/l^2$, depending on the analysis). Thus mechanical pumps must generate extremely high pressures to maintain flow rates as channel diameters

shrink. For this reason, it is widely accepted that mechanical pumping mechanisms, including peristaltic pumps, are not suitable for very small channels. Nguyen and Wereley survey the literature, and, using water as a working fluid, give 10 µl/min as the flow rate below which nonmechanical pumping principles are preferred [1]. However, that boundary is somewhat arbitrary, as demonstrated by flow rate of 0.14 µl/min reported in [4] for pneumatically-actuated peristaltic pumping of water in PDMS channels, the flow rate of 1.7 nl/min for electrostatically-actuated peristaltic pumping of ethanol in parylene channels [13], and the flow rate of 1 nl/h reported in [15] for optically-actuated peristaltic pumping by colloidal particles suspended in an aqueous solution.

Basic Methodology

A linear peristaltic micropump consists of two or more actuators arranged along a channel, and driven in a particular sequence. Important parameters that quantify pump performance are the maximum flow rate, denoted here by Q^*, the maximum pressure that can be generated between the pump inlet and outlet (called the ►pump head), denoted here by p^*, and the efficiency with which the pump converts external power into flow power, denoted here by η. Given a particular actuator, or set of available actuators, pump design consists of selecting the number of actuators, the actuation sequence, and the frequency of actuation. Important information about the individual actuators includes the stroke volume, V, the dead volume, V_0, the flow resistance in open and closed configurations, R_o and R_c, respectively, the maximum pressure the actuator can generate, p^*_{act}, called the ►closing pressure, the minimum time required for the actuator to either open or close completely, T_{min} (the minimum time to open and the minimum time to close are typically different; here T_{min} would be the larger of the two) and the energy or power required to operate an actuator. Almost any mechanical transducer can be used as an actuator in a peristaltic micropump, making generalizations about pump performance difficult. For example, the response time of a thermopneumatic actuator may be dominated by heat transfer out of the actuator, while that of a piezoelectric actuator is primarily determined by material stiffness and membrane geometry. As another example, a thermal actuator may require continual power to remain in the closed position, while – once closed – an electrostatic or pneumatic actuator may be held closed with little or no additional power consumption.

In this article we focus on those considerations that are common to all peristaltic pump designs. This rules out detailed physical analysis. However, some broad assumptions about actuator and system characteristics allow rough comparisons for pump design purposes. We begin by assuming ideal actuators, with infinite flow resistance in the closed position and zero dead volume. The first property allows easier accounting of the movement of fluid, the second allows issues related to fluid compressibility to be ignored.

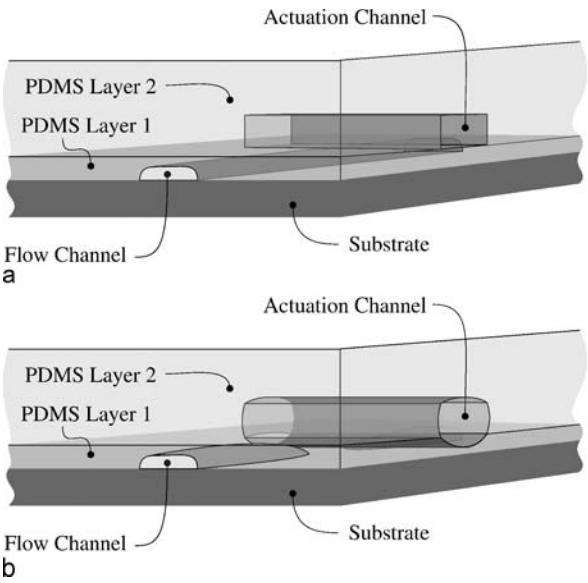

Peristaltic Pumps, Figure 3 A typical pump chamber in a multilayer PDMS implementation (similar to those of [4]). The chamber is open by default, as shown in (**a**). Inflating the actuation channel with compressed air closes the chamber, as shown in (**b**). PDMS layer 1 defines the fluid channels (sometimes called the working channel), while PDMS layer 2 defines the actuation channels. In both cases casting or spinning PDMS on a negative mold creates the channel structures. The molds are defined photolithographically, with standard positive resists used for thin channels (on the order of a micrometer) and negative resists such as SU8 used for thicker channels (up to one millimeter). The patterned side of the fluid layer is bonded to a glass, silicon, or PDMS substrate, and the patterned side of the actuation layer is bonded in turn to the planar side of the fluid layer. For convenience, we refer to the area of the fluid channel under the actuation channel as the pump chamber, even though it is otherwise indistinguishable from the rest of the channel. Baking the fluid layer mold at high temperature after the pattern is developed causes the photoresist to *reflow*, yielding rounded corners in the fluid channels. These rounded corners reduce leakage when the chamber is closed

The first step in this simplified analysis is estimating the volume of fluid transported in a complete pumping cycle. To do this, we apply the following rules:

1. When an actuator closes, the fluid within is completely expelled.
2. When an actuator opens, it completely fills with fluid.
3. If an actuator remains closed during a step in the sequence, no fluid may pass across it.
4. If, in a single step, some actuators open while others close, and there is a path for fluid to flow between them, then fluid is transferred from the latter to the former.

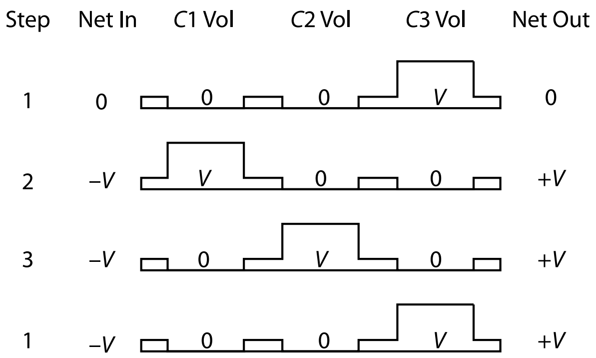

Peristaltic Pumps, Figure 4 A three-step, three-actuator pumping sequences, used in numerous pumps, including thermopneumatic pumps by Grosjean and Tai (see the reference in [1]) and Jeong, et al. [9]. The stroke volume is designated V. Chambers 1, 2, and 3 are abbreviated $C1$, $C2$, and $C3$. At every step two chambers are closed, reducing leakage. Note that Grosjean and Tai use a similar looking figure to define the pump sequence, but in their paper the raised level indicates actuation, which corresponds to *closing* the chamber

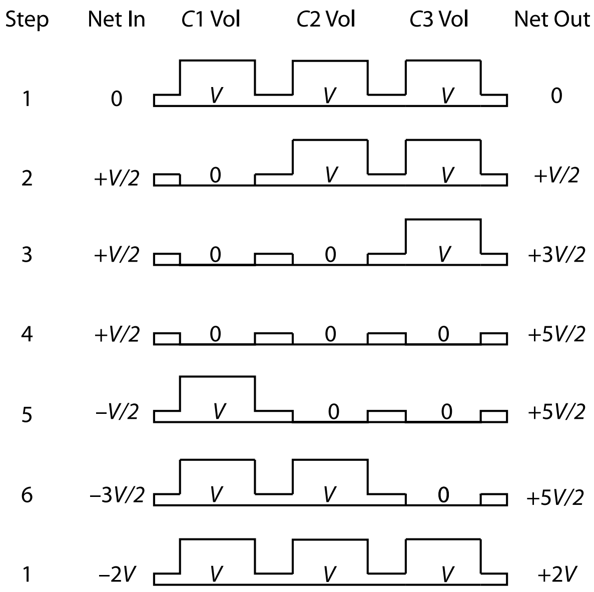

Peristaltic Pumps, Figure 5 A six-step, three-actuator pumping sequences proposed in the literature [6]. At step 1 all chambers are open, allowing backflow which will reduce the net flow rate

5. If an actuator opens or closes with no closed actuators between it and either the inlet or the outlet, the transfer of fluid is made equally from or to both sides. Once the fluid volume is computed, the flow rate flows from the actuation frequency. Maximum head is taken to be the maximum pressure exerted by an actuator (though this is not often known), and efficiency is estimated from the actuation sequence. Often, an estimate of flow rate is all that is desired. It must be noted that these estimates are very coarse, with for examples, errors of a factor of two reported, and attributed to unmodeled valve leakage [6].

Simplified Sequence Analysis

As an illustration of the simplified analysis, consider the three-step cycle shown in Fig. 4 for a pump consisting of three identical ideal actuators with stroke volume V. At the start of the cycle, no fluid has yet been transferred. In step 2, chamber $C1$ opens while chamber $C3$ closes. By rules 1 and 2, $C1$ must fill with volume V while $C2$ expels volume V. Since the intervening chamber $C2$ is closed, by rule 3 $C1$ must take volume V from the inlet, while $C3$ must expel volume V to the outlet. In step 3 $C1$ closes while $C2$ opens. By rule 4, since there is an open path between them, this transfers volume V from $C1$ to $C2$. Likewise the return to step 1, which completes the cycle, transfers volume V from $C2$ to $C3$. We conclude that, ideally, volume V is pumped per complete three-step cycle. At the final step the net fluid volume increase at the outlet must equal the net decrease at the input. This is a useful check that the analysis was done correctly.

Maximum Flow Rate

If each step requires time T, the pumping rate is $V/3T$. The maximum flow rate Q^* then corresponds to the minimum cycle time, $T_{\min}$: $Q^* = V/3T_{\min}$.

Maximum Head

In step 2, $C3$ is emptied to the outlet. If the outlet pressure is greater than p^*_{act}, the maximum pressure the actuator can provide, the chamber will be unable to close. Thus, the maximum head can be approximated as the closing pressure, $p^* = p^*_{\text{act}}$.

Efficiency

Fluid power is the product of flow rate by head. In an ideal ►positive displacement pump, flow rate is independent of head. Therefore, the maximum fluid power is approximately $P^* = p^*Q = p^*_{\text{act}}V/3T$. One actuator closes at each step, and two actuators must be held closed at each step. If energy E_{act} is required to close an actuator, and power P_{act} is required to hold it closed, we see that each cycle requires total energy $3E_{\text{act}} + 6P_{\text{act}}T$ (we assume no energy is required to open an actuator). The total power consumed per cycle is $(E_{\text{act}}/T) + 2P_{\text{act}}$, and the maximum efficiency is $\eta = p^*_{\text{act}}V/(3E_{\text{act}} + 6P_{\text{act}}T)$.
Experiments suggest that a linear relation between flow rate and pump head may be a more appropriate model [5]. In that case, the maximum fluid power is given by $P^* = p^*Q^*/4$.

Design Comparison

To illustrate the use of the simplified analysis in design, we compare the actuation sequence analyzed above to a six-step three-chamber sequence also reported in the literature [6], and shown in Fig. 5. The analysis is similar to the three-step sequence, except for steps 1 and 6, where an actuator closes with no closed actuators between it and either the inlet or the outlet. By rule 5, the expelled fluid is divided evenly between the inlet and the outlet. Two considerations make application of the simplified model more problematic in this case. The first is the all-actuators-open configuration in step 1. If there is significant head across the pump, this may produce an unmodeled backflow. The second is the assumption mentioned above, that the flow splits evenly in step 1 and 6. If the external system flow resistances as seen from the input and output are different, or if there is significant head, the split will *not* be even. These issues aside, we find that a volume $2V$ is pumped in each six-step cycle.

If each step requires time T, the pumping rate is $2V/6T$, or $V/3T$. The maximum flow rate is $Q^* = V/3T_{\text{min}}$. This is the same as for the three-step sequence.

In steps 2, 3, and 4 chambers are emptied to the outlet. The maximum head can again be approximated as the closing pressure.

The maximum fluid power is approximately $P^* = p^*Q = p^*_{\text{act}}V/3T$. In each cycle, energy $3E_{\text{act}}$ is required for actuator closings, and energy $9P_{\text{act}}T$ is needed to hold actuators closed, for a total cycle power requirement $(E_{\text{act}}/2T) + (2P_{\text{act}}/3)$. The maximum efficiency is $\eta = 2p^*_{\text{act}}V/(3E_{\text{act}} + 9P_{\text{act}}T)$.

To the level of modeling accuracy applied, the two designs have the same maximum flow rate and maximum head. The six-step sequence is more power efficient, but there are unanswered questions about how well this design will perform, particularly if there is significant backpressure. If power usage is more important than maximum head, the six-step design may be preferable, but further investigation will be required. If efficiency is not important, the three-step sequence should be chosen for its higher resistance to backflow. An advantage of the six-step sequence is that only one chamber is actuated per step. This makes the sequence insensitive to asymmetries in opening versus closing actuators. For example, if the actuators close ten times faster than they open, fluid may not transfer smoothly between chambers in the sequence of Fig. 4, but instead may leak out of the chamber. Avoiding this risk by adding intermediate steps, as for example, in the five-step sequence used by Smits [2] will reduce the maximum flow rate, and make the sequence of Fig. 5 more attractive.

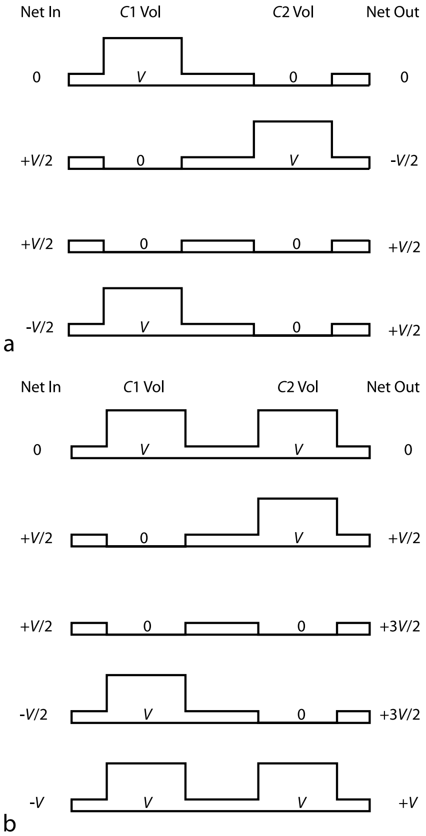

Peristaltic Pumps, Figure 6 Pumping sequences for two-actuator peristaltic pumps [7]. Sequence A has at least one actuator closed at all times. Sequence B has a higher maximum flow rate, but may have problems with backflow under high head conditions

Most reported peristaltic micropump designs use three actuators. A few use more, but typically not more than five. Since the actuators take up potentially valuable space, and require connections for power and switching, it is desirable in many applications to use the minimal possible number. Some authors have stated that three chambers are the fewest possible for peristaltic pumping. However, the sequences shown in Fig. 6 have been shown to provide peristaltic pumping using only two chambers [7].

Diagrams like Figs. 4–6 are easy to grasp visually, but a more compact description of pumping sequences is also useful. One method used in the literature (for example, in [8]) is to indicate an actuated (closed) chamber by a 1 and an un-actuated (open) chamber by a 0. Thus the sequence in Fig. 4 is written $\{110, 011, 101\}$, that of Fig. 5 becomes $\{000, 100, 110, 111, 011, 001\}$, and those of Fig. 6 A and B are $\{01, 10, 00\}$ and $\{00, 10, 11, 01\}$, respectively. The five-step sequence used by Smits [2] is, following the convention of 1 for closed, 0 for open, $\{011, 001, 101, 100, 110\}$. (This sequence does involve an

actuator closing simultaneously with another opening, but they are separated by a closed chamber.) Some care is required in using this notation, since some mechanisms close when actuated (e. g. thermopneumatic), while others open (e. g. piezoelectric).

Dynamic Modeling

Leaks, backpressure, and actuator dynamics all influence the performance of peristaltic pumps. Leaks and backpressure effects will alter the distribution of fluid as actuators open and close. The dynamics of the actuators determines the maximum actuation rate, which in turn limits the maximum flow rate. These effects can be incorporated into lumped-parameter models for analysis and simulation. We do not pursue this further in this article, but refer the reader to the literature. One general approach is presented in [5]. Also relevant for further study are [6], [13] and [14], which present dynamic models for pneumatic and electrostatic pumps, respectively. All of these works are applied to liquid pumps. For gas pumps, or robustness to bubbles, compressibility becomes a factor. Some considerations of micropumps for compressible fluids may be found in [1]. Finite-element analysis of individual chambers can also be used to obtain detailed predictions of pump dynamic performance.

Key Research Findings

Fabrication Materials and Actuator Types

Peristaltic pumps have been demonstrated in all materials common for microfluidic applications, using a variety of physical principles. Space constraints prevent a comprehensive listing, but [1], [3], and [12] provide good overviews. Summarizing here just the main fabrication materials, the operating principle, and the working fluid, these include for silicon and/or glass devices, piezoelectric, thermopneumatic, and electrostatic actuators pumping water. For PDMS devices only pneumatic pumping of water is reported. For plastic or mixed-type devices, electrostatic, thermopneumatic, and pneumatic actuators are reported, pumping water and air. A novel traveling wave pump implemented using optically-actuated colloidal silica spheres is reported in [15]. Recently, Husband et al. (Microelectronic Engineering 73–74:858–863, 2004) report a piezoelectric silicon-glass device pumping water and air, Pan et al. (Proceedings of the 26th Annual International IEEE EMBS Conference, 2004) report a magnetically driven PDMS pump for water, and Jeong et al. report a thermopneumatic PDMS pump for water [9]. Electrostatic pumps implemented in parylene for integration with μTAS devices are reported in [13].

Reducing Device Complexity

Peristaltic pumps already offer simpler fabrication than passive check-valve pumps. Even the simplest actuators, however, require at least two patterned layers, as, for example, in the PDMS device of Fig. 3. However peristaltic pumping was recently demonstrated in a device with a single patterned layer of PDMS on an un-patterned glass or PDMS substrate [10]. The single patterned layer incorporates both pneumatic actuation lines and the water-filled working channels. Rather than press on the fluid channel from above, the actuation lines in this device squeeze the working channel from the sides. While these actuators provide enough stroke and increased resistance for pumping, cell sorting, and mixing, in their closed configuration they are still quite leaky, and do not completely seal the channel. However, the elimination of the second layer, along with the associated alignment and bonding tasks, should yield a significant reduction in device cost.

Reducing Number of Off-Chip Connections

Each actuator in a peristaltic pump is an active element, requiring switching and power. In applications such as Lab-on-a-Chip, the number of required off-chip connections can become very large. As mentioned above, one means for doing this is by using two actuators instead of three [7]. The proliferation of pumps and valves is a particular problem in pneumatically actuated pumps that require external valving. An innovative approach to ameliorating this problem is described in [11] for pneumatically actuated pumps fabricated in PDMS. Here, a single pneumatic actuation channel has a serpentine shape, crossing over the straight channel containing the working fluid at multiple intersections. The phasing of the actuation is provided by the natural delay associated with the propagating inflation zone in the serpentine channel. In this way the equivalent of a three-, five-, or seven-actuator peristaltic pump is realized using a single actuator line.

Multifunction Components

The individual actuators in a peristaltic pump can also serve as individual valves. Additional flexibility in integrating peristaltic pumps into large microfluidic systems can be gained from providing components with multiple functions. An example of this is the rotary mixer described in [8], which can serve as an effective dynamic micromixer, or as a peristaltic pump, depending on the actuation pattern of the individual valves.

Future Directions for Research

Progress in peristaltic pump design has paralleled the advancement of microfluidics as a field. As new materials and applications have been developed, peristaltic pump designs have soon followed. This trend seems likely to continue.

Peristaltic pumps are commonly used in PDMS-based systems. As those systems have attracted increasing amounts of research effort, due to their biocompatibility and demonstrated success in manipulation of cells, genetic material, and proteins, new innovations in PDMS-based pumps have followed. Progress has been made in reducing the need for external connections, but improvement would be welcome in the area of fully integrated pumps of reasonable cost and low complexity.

Cross References

- ► Electromagnetic Valves
- ► Electrostatic Valves
- ► Magnetic Pumps
- ► Membrane Actuation for Micropumps
- ► Microactuators
- ► Microfluidic Mixing
- ► Piezoelectric Valves
- ► Piezo/PZT in Microfluidics
- ► Pneumatic Valves
- ► Soft Photolithography
- ► Thermomechanical Valves
- ► Thermopneumatic Valves
- ► Water Management in Micro DMFCs

References

1. Nguyen NT, Wereley ST (2002) Fundamentals and Applications of Microfluidics. Artech House, Boston
2. Smits JG (1990) Piezoelectric Micropump with 3 Valves Working Peristaltically. Sens Actuators A Phys 21(1–3):203–206
3. Laser DJ, Santiago JG (2004) A review of micropumps. J Micromech Microeng 14:R35–R64
4. Unger MA, Chou HP, Thorsen T, Scherer A, Quake SR (2000) Monolithic Microfabricated Valves and Pumps by Multilayer Soft Lithography. Sci 288:113–116
5. Goldschmidtböing F, Doll A, Heinrichs M, Woias P, Schrag HJ, Hopt UT (2005) A generic analytical model for micro-diaphragm pumps with active valves. J Micromech Microeng 15:673–683
6. Goulpeau J, Trouchet D, Ajdari A, Tabeling P (2005) Experimental study and modeling of polydimethylsiloxane peristaltic micropumps. J Appl Phys 98(044914):1–9
7. Berg J, Anderson RC, Anaya M, Lahlouh B, Dallas T, Holtz M (2003) A Two-Stage Discrete Peristaltic Micropump. Sens Actuators A 104:6–10
8. Chou HP, Unger MA, Quake SR (2001) A Microfabricated Rotary Pump. Bioméd Microdevices 3:323–330
9. Jeong OC, Park SW, Yang SS, Pak JJ (2005) Fabrication of a Peristaltic PDMS Micropump. Sens Actuators A 123–124:453–458
10. Sundararajan N, Kim D, Berlin AA (2005) Microfluidic operations using deformable polymer membranes fabricated by single layer soft lithography. Lab Chip 5:350–354
11. Wang CH, Lee GB (2006) Pneumatically driven peristaltic micropumps utilizing serpentine-shape channels. J Micromech Microeng 16:341–348
12. Nguyen NT, Huang X, Chuan TK (2002) MEMS-Micropumps: A Review. J Fluids Eng 124:384–392
13. Xie J, Shih J, Lin Q, Yang B, Tai YC (2004) Surface Micromachined Electrostatically Actuated Micro Peristaltic Pump. Lab Chip 4:495–500
14. Lin Q, Yang B, Xie J, Tai YC (2007) Dynamic Simulation of a Peristaltic Micropump Considering Coupled Fluid Flow and Structural Motion. J Micromech Microeng 17:220–228
15. Terray A, Oakey J, Marr DWM (2002) Microfluidic Control Using Colloidal Devices. Sci 296:1841–1844

Permeabilization of Cells

► On-Chip Cell Lysis

Perovskite

Synonyms

Calcium titanium oxide; Orthorhombic crystal

Definition

Defines calcium titanium oxide in particular and generally all crystalline materials that exhibit a crystal structure similar to it, as with the crystalline structure of PZT.

Phase-Change Heat Transfer in Microchannels

► Condensation in Microchannels

Phase Field Method

► Interface Capturing Schemes for Free-Surface Flows

Phase Separation Kinetics

► Demixing

Phase Shift

► Frequency Response

pH Control Device

► pH-Sensitive Hydrogel

Phenol Extraction

► Lab-on-a-Chip Devices for Sample Extractions

Phenotypic Assay

► Cell Assays

Phenotypic Screening in Microfluidic Devices/on-Chip

► Cell Assays in Microfluidics

Phosphorescence

Definition

Phosphorescence is the emission of light from triplet-excited states, whereby one set of electron spins is unpaired. This means that electrons in the excited orbital have the same spin as the ground state electrons. Therefore, transition to ground state is not possible and emission rates are slow (in the region of $10^3 - 10^1\ s^{-1}$. Phosphorescent life-times have durations in the millisecond range. Following exposure to light, phosphorescent substances glow for several minutes as the excited phosphors return to the ground state very slowly.

Cross References

► Fluorescent Labeling

Photo-Activated Nonintrusive Tracking of Molecular Motion

► Visualization Based on Molecular Tagging Methods

Photobleached Fluorescence

► Visualization Based on Molecular Tagging Methods

Photobleaching

Synonyms

Photochemical decomposition; Photochemical degradation

Definition

Photobleaching is the decrease of the emitted fluorescence intensity by the excited fluorophores as a result of the decay of dye molecules due to their prolonged exposure to high-intensity incident light.

Cross References

► Fluorescent Thermometry
► Fluorescence Labeling

Photochemical Decomposition

► Photobleaching

Photochemical Degradation

► Photobleaching

Photofluidic Devices

► Optofluidics – Techniques for Fabrication and Integration

Photofluidics

► Optofluidics – Applications
► Optofluidics – Fluidics Enabling Optics
► Optofluidics: Optics Enabling Fluidics

Photolithography

Mauris De Silva
Bascom Palmer Eye Institute, University of Miami, Miami, FL, USA
mdesilva@med.miami.edu

Synonyms

Optical lithography; Microlithography; Nanolithography

Definition

Photolithography is a process mainly used but not limited to manufacturing integrated circuits, and involves the photographic transfer of a desired pattern to a surface for further processing (e. g. etching).

Overview

Photolithography is the most popular method among various forms of lithography when transferring patterns from a mask (reticle) onto a surface of a substrate. Photolithography is widely used in the integrated circuit (IC) industry. However, it has other potential important applications such as developing methods for controlling the position of cells on a substrate or micropatterning of cells that has many bioengineering applications including the design of biosensors that can be used for drug and toxicity sensing devices and environmental monitoring devices, tissue engineering applications, and basic biology studies.
Photolithography is widely used in the semiconductor industry to perform a series of successive patterning on a given substrate to achieve an electronically functioning product. Although, this pattering method is limited to planar surfaces, it can provide accurate patterning feature sizes at the submicrometer level.

Basic Methodology

Photolithography is comprised of sequential process steps that are schematically summarized in Fig. 1. The process begins by choosing or preparing a substrate for the photolithography process. The ideal substrate should be dehydrated before any application of photoresist. This dehydration is usually done by a baking step called *dehydration bake* to remove adsorbed water from the substrate, usually a silicon wafer. Thereafter, the dehydrated substrate is spin coated with a photoresist adhesion promoter using a spinner. Usually, hexamethyldisilazane (HMDS) is used for this step, which is called priming. Then, the primed substrate is spin coated placing excess amount

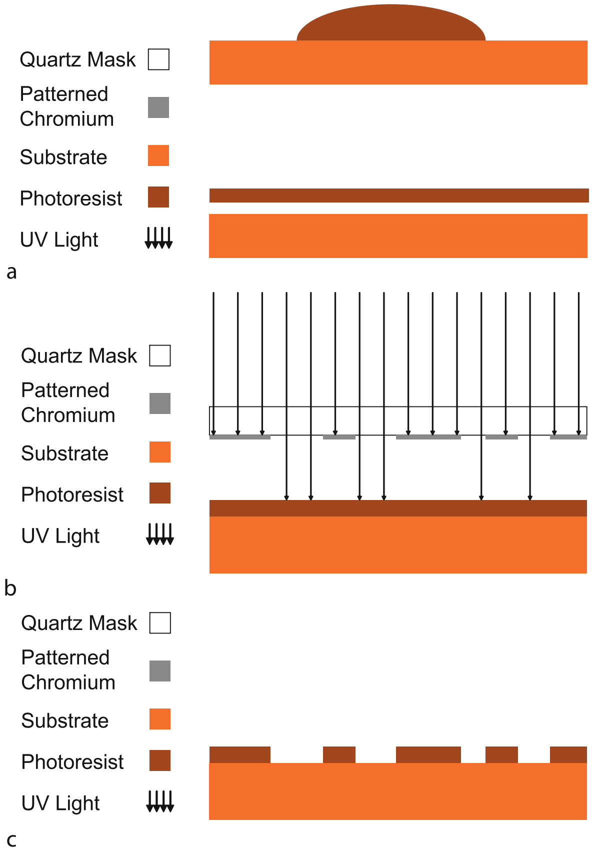

Photolithography, Figure 1 (**a**) The top image shows the deposition of photoresist on a dehydrated and then primed wafer. The image below shows the coated wafer with uniform layer of photoresist. (**b**) The photoresist-coated wafer is exposed to UV light with an intact mask. (**c**) The pattern is developed by rinsing the substrate in a developing solution or using a spray developer. This process will remove the unwanted photoresist and leaves the pattern on the surface of the substrate.

of a photoresist, a photosensitive material. The photoresist will be spread uniformly on the surface of the substrate by centrifugal force. This process is one of the most important parts of the process, as the quality of the pattern transfer depends on effective spin coating of photoresist material. The most important requirements of spin coating are having a known uniform thickness of the photoresist material throughout the substrate, and this should be optimized for different substrate–photoresist combinations to determine the appropriate amount of photoresist and spinning velocity to use during the spin coating step. The thickness of photoresist may be varied according to the spinning speed and the viscosity of the photoresist-containing fluid. Usually, photoresist vendors provide information on how thickness may vary according to the spinning velocity of a given photoresist. The photoresist-coated substrates are subjected to a prebaking

step or soft baking step before being exposed to UV light with an intact stencil called a *photomask*. This prebaking step is usually done at 80 – 110 °C for 5 to 10 min depending on the thickness of the photoresist layer. This step will enhance the adhesion of the photoresist to the substrate by removal of the solvent in the photoresist and any built in stresses.

The exposure can then be conducted using an aligner. An aligner is comprised of a light source including any reflecting and/or refracting optics needed for collecting, collimating, filtering, and focusing the light onto the mask with the desired image. The most common aligners are contact printers and projection printers. In the contact printer approach the mask is held against the photoresist; in the projection printing method a set of lenses (projector/objective) is placed between the mask and the wafer to refocus light onto the photoresist. After exposure, the pattern is developed by rinsing the substrate in a developing solution or using a spray developer. This process will remove the unwanted photoresist and leaves the pattern on the surface of the substrate. This is also a very important step as it is very temperature sensitive, and will affect control and maintenance of line widths of the pattern, resist contrast, and resist profiles. There are two types of pattern transfer: positive and negative. In the positive form, the photoresist pattern on the substrate is the positive image of the mask pattern; in the negative form, the image of the photoresist pattern is the inverse image of the photomask pattern.

After developing, the substrate is subjected to a hard baking process to harden the photoresist. The hardening of the photoresist is done as the patterned substrates may be used for further processing such as plasma etching or ion implantation. Once all the processing is complete, any remaining/developed photoresist can be removed using a commercially available organic photoresist stripping solvent. This substrate can be used for further patterning by starting another photolithography step.

Future Directions for Research

The future directions for research in photolithography will be in improving minimum feature size. The variables that involve improving minimum feature size include photoresist, mask, and exposing wavelength. Thus, one can think that the future improvement in photolithography will depend on improving resist types, and designing better mask-refining technology and better laser technology.

Cross References

- ► Cell Patterning on Chip
- ► Photo Patterned
- ► Photoresist SU-8
- ► Photoresist Reflow

References

1. Campbell SA (2001) The Science and Engineering of Microelectronic Fabrication. Oxford Univ Press, New York
2. Madou MJ (2002) Fundamentals of Microfabrication: The Science of miniaturization. CRC, Boca Raton

Photoluminescence

► Fluorescent Thermometry

Photomask

Definition

A plate of opaque material that has been patterned with transparent regions.

Cross References

► Sputtering for Film Deposition

Photometer

Kenji Yasuda
Department of Biomedical Information,
Division of Biosystems Institute of Biomaterials and Bioengineering, Tokyo Medical and Dental University, Tokyo, Japan
yasuda.bmi@tmd.ac.jp

Synonyms

Photometry; Illuminance; Irradiance; Scattered light intensity; Absorption; Spectroscopy; Spectrophotometer

Definition

The instrument used to measure illuminance or irradiance of light. It is the general term covering instruments for detecting scattered light intensity, absorption, fluorescence applied in the field of photometry. Spectroscopic techniques using photometer can probe the change of energy, frequency, wavelength and intensity of light caused by the interaction with matter. Most photometers are based on a photoresistor, photodiode, or photomultiplier tubes for photon observation. Either exhibits a change in electrical properties when exposed to light, which can be detected with a suitable electronic circuit.

Photometer, Table 1 Symbols, SI units and abbreviations used in photometer

Quantity	Symbol	SI unit	Abbreviation
Luminous energy	Q_V	lumen second	lms
Luminous flux	F	lumen (= cdsr)	lm
Luminous intensity	I_V	candela (= lm/sr)	cd
Luminance	L_V	candela per square metre	cd/m^2
Illuminance	E_V	lux (= lm/m^2)	lx
Luminous emittance	M_V	lux (= lm/m^2)	lx
Luminous efficacy		lumen per watt	lm/W
Radiant energy	Q	joule	J
Radiant flux	Φ	watt	W
Radiant intensity	I	watt per steradian	Wsr^{-1}
Radiance	L	watt per steradian per square metre	$Wsr^{-1}m^{-2}$
Irradiance	E	watt per square metre	Wm^{-2}
Radiant exitance / Radiant emittance	M	watt per square metre	Wm^{-2}
Spectral radiance	L_λ or L_ν	watt per steradian per metre^3 or watt per steradian per square metre per hertz	$Wsr^{-1}m^{-3}$ or $Wsr^{-1}m^{-2}Hz^{-1}$
Spectral irradiance	E_λ or E_ν	watt per metre^3 or watt per square metre per hertz	Wm^{-3} or $Wm^{-2}Hz^{-1}$
Radiant energy	Q	joule	J

Photometer, Table 2 Comparison of two photodetectors: photodiodes and photomultipliers

Advantages of photodiodes	Advantages of photomultipliers
• Excellent linearity of output current as a function of incident light • Spectral response from 190 nm to 1100 nm (silicon), longer wavelengths with other semiconductor materials • Low noise • Ruggedized to mechanical stress • Low cost • Compact and light weight • Long lifetime • High quantum efficiency • No high voltage required	• Large area • Flexible internal gain • Higher overall sensitivity • Photon counting is possible

P

Overview

The interaction of electromagnetic radiation with matter is essentially a quantum phenomenon and is dependent on the properties of the radiation and on the appropriate structural parts of the material involved. As the origin of the radiation is due to energy changes within the matter itself, an understanding of the properties of electromagnetic radiation and its interaction with matter leads to a recognition of the variety of types of spectrum, and consequently spectroscopic techniques, and their application to the solution of biological problems. Photometry is the science of measurement of light, historically, in terms of its perceived brightness to the human eye. It is distinct from radiometry, which is the science of measurement of light in terms of absolute power; rather, in photometry, the radiant power at each wavelength is weighted by the luminosity function that models human brightness sensitivity. Thus many different units of measure are used for photometric measurements and sometimes that can't be converted from radiometry. For example, in photometric quantities, every wavelength is weighted according to how visible it is, while radiometric quantities use unweighted absolute power. Because the eye responds much more strongly

to green light than to red, a green source will have higher luminous flux than a red source with the same radiant flux would. Light outside the visible spectrum does not contribute to photometric quantities at all, so for example a 1000 W space heater may put out a great deal of radiant flux (1000 W, in fact), but as a light source it puts out very few lumens (because most of the energy is in the infrared, leaving only a dim red glow in the visible). Watts (radiant flux) and lumens (luminous flux) illustrates the distinction between radiometric and photometric units. The watt is a unit of power. As power is not a measure of the amount of light output, power is only a rough guide to light output. In contrast, the lumen is the photometric unit of light output. The lumen is defined as amount of light given into one steradian by a point source of one candela strength; while the candela, a base SI unit, is defined as the luminous intensity of a source of monochromatic radiation, of frequency 540 THz, and a radiant intensity of $1/683\ \mathrm{Wsr}^{-1}$. (540 THz corresponds to about 555 nm, the wavelength, in the green, to which the human eye is most sensitive. The number 1/683 was chosen to make the candela about equal to the standard candle, the unit which it superseded). Combining these definitions, we see that 1/683 W of 555 nm green light provides one lumen. The definition tells us that 1 W of pure green 555 nm light is equal to 683 lm. It should be noted that it does not say anything about other wavelengths. Because lumens are photometric units, their relationship to watts depends on the wavelength according to how visible the wavelength is. Infrared and ultraviolet radiation, for example, are invisible and do not count. That means one watt of infrared radiation is worth zero lumens.

In photometry, illuminance is the total luminous flux incident on a surface, per unit area. It is a measure of the intensity of the incident light, wavelength-weighted by the luminosity function to correlate with human brightness perception. Similarly, luminous emittance is the luminous flux per unit area emitted from a surface. Luminous emittance is also known as luminous exitance. In SI derived units, these are both measured in lux (lx) or lumens per square metre (cdsrm^{-2}). In the CGS system, the unit of illuminance is the phot. One phot is equal to 10,000 lx. Illuminance was formerly often called brightness, but this leads to confusion with other uses of the word.

Irradiance is a radiometry term for the power of electromagnetic radiation at a surface, per unit area, which is used when the electromagnetic radiation is incident on the surface. The SI unit for this quantity is watts per square meter ($\mathrm{W/m}^2$), which is sometimes called intensity. This quantity characterizes the total amount of radiation present, at all frequencies. It is also common to consider each frequency in the spectrum separately. When this is done for radiation incident on a surface, it is called spectral irradiance, and has SI units $\mathrm{W/m}^3$, or commonly $\mathrm{Wm}^{-2}\mathrm{nm}^{-1}$.

Basic Methodology

Photometric Measurements

Photometric measurement is based on photodetectors, devices that produce an electric signal when exposed to light. Simple applications of this technology include switching luminaries on and off based on ambient light conditions, and light meters, used to measure the total amount of light incident on a point. More complex forms of photometric measurement are used for detecting scattered light intensity, absorption, fluorescence.

Light Scattering

Light scattering is one of the two major physical processes that contribute to the visible appearance of most objects, the other being absorption. Major forms of elastic light scattering (involving negligible energy transfer) are Rayleigh scattering and Mie scattering. Inelastic light scattering effects include Brillouin scattering, Raman scattering. Light scattering can also give color to some objects, usually shades of blue, but resonant light scattering in nanoparticles can produce different highly saturated and vibrant hues, especially when surface plasmon resonance is involved. At values of the ratio of particle diameter to wavelength more than about 10, the laws of geometric optics are mostly sufficient to describe the interaction of light with the particle, and at this point the interaction is not usually described as scattering. For modeling of scattering in cases where the Rayleigh and Mie models do not apply such as irregularly shaped particles, there are many numerical methods that can be used. The most common are finite-element methods which solve Maxwell's equations to find the distribution of the scattered electromagnetic field.

Rayleigh Scattering

Rayleigh scattering is a process in which light is scattered by a small spherical volume of variant refractive index, such as a particle, bubble, droplet, or even a density fluctuation. This effect was first modeled successfully by Lord Rayleigh, from whom it gets its name. In order for Rayleigh's model to apply, the sphere must be much smaller in diameter than the wavelength (λ) of the scattered wave; typically the upper limit is taken to be about 1/10 the wavelength. In this size regime, the exact shape of the scattering center is usually not very significant and can often be treated as a sphere of equivalent volume. The inherent scattering that radiation undergoes

passing through matter is due to microscopic density fluctuations as the molecules in matter move around, which are normally small enough in scale for Rayleigh's model to apply. This scattering mechanism is the primary cause of the blue color of the Earth's sky on a clear day, as the shorter blue wavelengths of sunlight passing overhead are more strongly scattered than the longer red wavelengths according to Rayleigh's famous $1/\lambda^4$ relation. Along with absorption, such scattering is a major cause of the attenuation of radiation by the atmosphere. The degree of scattering varies as a function of the ratio of the particle diameter to the wavelength of the radiation, along with many other factors including polarization, angle, and coherence.

Mie Scattering

For larger diameters, the problem of electromagnetic scattering by spheres was first solved by Gustav Mie, and scattering by spheres larger than the Rayleigh range is therefore usually known as Mie scattering. In the Mie regime, the shape of the scattering center becomes much more significant and the theory only applies well to spheres and, with some modification, spheroids and ellipsoids. Closed-form solutions for scattering by certain other simple shapes exist, but no general closed-form solution is known for arbitrary shapes.

Raman Scattering

Raman scattering is the inelastic scattering of a photon. When light is scattered from an atom or molecule, most photons are elastically scattered (Rayleigh scattering). The scattered photons have the same energy (frequency) and, therefore, wavelength, as the incident photons. However, a small fraction of scattered light (approximately 1 in 1000 photons) is scattered from excitations with optical frequencies different from, and usually lower than, the frequency of the incident photons. Raman scattering can occur with a change in vibrational, rotational or electronic energy of a molecule. Raman spectroscopy employs the Raman effect for material analysis. The frequency of light scattered from a molecule is changed based on the structural characteristics of the molecular bonds. A monochromatic light source (laser) is required for sufficient illumination, and a spectrogram of the scattered light then shows the deviations caused by state changes in the molecule.

Doppler Shift

Electromagnetic radiation scattered by moving scattering centers does undergo a Doppler shift, which can be detected and used to measure the velocity of the scattering center/s in forms of techniques such as radar. Both Mie

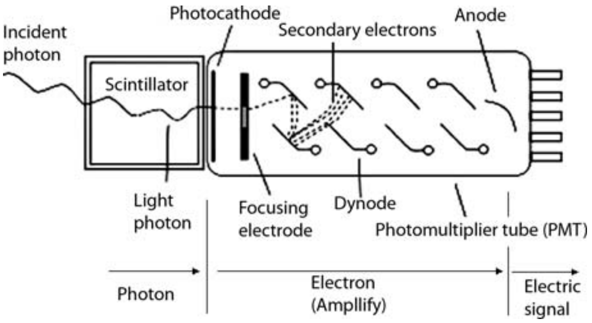

Photometer, Figure 1 Photomultipliers are constructed from a glass vacuum tube which houses a photocathode, several dynodes, and an anode. Incident photons strike the photocathode material which is present as a thin deposit on the entry window of the device, with electrons being produced as a consequence of the photoelectric effect. These electrons are directed by the focusing electrode towards the electron multiplier, where electrons are multiplied by the process of secondary emission

and Rayleigh scattering are considered elastic scattering processes, in which the energy (and thus wavelength and frequency) of the light is not substantially changed. However, this shift involves a slight change in energy.

Absorption (Electromagnetic Radiation)

Absorption is the process by which the energy of a photon is taken up by another entity, for example, by an atom whose valence electrons make transition between two electronic energy levels. The photon is destroyed in the process. The absorbed energy may be re-emitted as radiant energy or transformed into heat energy. The absorption of light during wave propagation is often called attenuation. The absorbance of an object quantifies how much light is absorbed by it. This may be related to other properties of the object through the Beer-Lambert law. For most substances, the amount of absorption varies with the wavelength of the light, leading to the appearance of color in pigments that absorb some wavelengths but not others. For example, an object that absorbs blue, green and yellow light will appear red when viewed under white light. More precise measurements at many wavelengths allow the identification of a substance via absorption spectroscopy.

Fluorescent Measurement

Fluorescent measurement uses the luminescence of fluorescence that is mostly found as an optical phenomenon in cold bodies, in which the molecular absorption of a photon triggers the emission of another photon with a longer wavelength. The energy difference between the absorbed and emitted photons ends up as molecular vibrations or

heat. Usually the absorbed photon is in the ultraviolet range, and the emitted light is in the visible range, but this depends on the absorbance curve and Stokes shift of the particular fluorophore. The fluorescence quantum yield gives the efficiency of the fluorescence process. It is defined as the ratio of the number of photons emitted to the number of photons absorbed. The maximum fluorescence quantum yield is 1.0 (100%); every photon absorbed results in a photon emitted. Compounds with quantum yields of 0.10 are still considered quite fluorescent. The fluorescence lifetime is an instance of exponential decay. Thus, it is similar to a first-order chemical reaction in which the first-order rate constant is the sum of all of the rates (a parallel kinetic model). Thus, the lifetime is related to the facility of the relaxation pathway. If the rate of spontaneous emission, or any of the other rates are fast the lifetime is short (for commonly used fluorescent compounds typical excited state decay times for fluorescent compounds that emit photons with energies from the UV to near infrared are within the range of 0.5 to 20 ns). The fluorescence lifetime is an important parameter for practical applications of fluorescence such as fluorescence resonance energy transfer. There are several rules that deal with fluorescence.

Photodetectors

Photoresistor

A photoresistor is an electronic component whose resistance decreases with increasing incident light intensity. It can also be referred to as a light-dependent resistor (LDR), photoconductor, or photocell. A photoresistor is made of a high-resistance semiconductor. If light falling on the device is of high enough frequency, photons absorbed by the semiconductor give bound electrons enough energy to jump into the conduction band. The resulting free electron (and its hole partner) conduct electricity, thereby lowering resistance. A photoelectric device can be either intrinsic or extrinsic. An intrinsic semiconductor has its own charge carriers and is not an efficient semiconductor, e. g. silicon. In intrinsic devices, the only available electrons are in the valence band, and hence the photon must have enough energy to excite the electron across the entire bandgap. Extrinsic devices have impurities added, which have a ground state energy closer to the conduction band – since the electrons don't have as far to jump, lower energy photons (i. e. longer wavelengths and lower frequencies) are sufficient to trigger the device. If a sample of silicon has some of its atoms replaced by phosphorus atoms(impurities), there will be extra electrons available for conduction. This is an example of an extrinsic semiconductor.

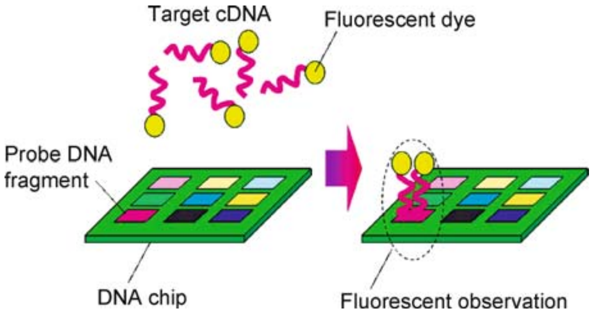

Photometer, Figure 2 DNA microarrays. The probes are complementary fragment oligonucleotides, of target DNA or mRNA are spotted onto the microarray surface. This type of array is typically hybridized with target cDNAs that are labeled with fluorophores. The samples are amplified by PCR and hybridized to the microarray, and then scanned in a microarray scanner to visualize fluorescence of the fluorophores on the chip. Absolute levels of gene expression cannot be determined, but relative differences in expression among different spots can be estimated when we used the two-color array, each color represents two different samples

Photodiode

A photodiode is a semiconductor diode that functions as a photodetector. Photodiodes are packaged with either a window or optical fibre connection, in order to let in the light to the sensitive part of the device. They may also be used without a window to detect vacuum UV or X-rays. A phototransistor is in essence nothing more than a bipolar transistor that is encased in a transparent case so that light can reach the *base-collector junction*. The phototransistor works like a photodiode, but with a much higher responsivity for light, because the electrons that are generated by photons in the base-collector junction are injected into the base, and this current is then amplified by the transistor operation. However, a phototransistor has a slower response time than a photodiode. A photodiode is usually a p-n junction structure. When a photon of sufficient energy strikes the diode, it excites an electron thereby creating a mobile electron and a positively charged electron hole. If the absorption occurs in the junction's depletion region, or one diffusion length away from it, these carriers are swept from the junction by the built-in field of the depletion region, producing a photocurrent. Photodiodes can be used under either zero bias (*photovoltaic mode*) or reverse bias (*photoconductive mode*). In zero bias, light falling on the diode causes a current across the device, leading to forward bias which in turn induces *dark current* in the opposite direction to the photocurrent. This is called the photovoltaic effect, and is the basis for solar cells – in fact, a solar cell is just a large number of big photodiodes. Reverse bias induces only little current (known as saturation or back current) along its direction. But a more important effect of reverse bias is widening of the depletion layer

(therefore expanding the reaction volume) and strengthening the photocurrent. Circuits based on this effect are more sensitive to light than ones based on the photovoltaic effect and also tend to have lower capacitance, which improves the speed of their time response. On the other hand, the photovoltaic mode tends to exhibit less electronic noise.

Photomultiplier Tubes (Photomultipliers, PMT)

Photomultiplier tubes are extremely sensitive detectors of light in the ultraviolet, visible and near infrared. These detectors multiply the signal produced by incident light by as much as 10^8, from which single photons can be resolved. Avalanche photodiodes have replaced photomultipliers in some applications, but photomultipliers are still used in most cases. The electron multiplier consists of a number of electrodes, called dynodes. Each dynode is held at a more positive voltage than the previous one. The electrons leave the photocathode, having the energy of the incoming photon (minus the work function of the photocathode). As they move towards the first dynode they are accelerated by the electric field and arrive with much greater energy. On striking the first dynode, more low energy electrons are emitted and these, in turn, are accelerated toward the second dynode. The geometry of the dynode chain is such that a cascade occurs with an ever-increasing number of electrons being produced at each stage. Finally the anode is reached where the accumulation of charge results in a sharp current pulse indicating the arrival of a photon at the photocathode.

Avalanche Photodiodes (APDs)

Avalanche photodiodes (APDs) are photodetectors that can be regarded as the semiconductor analog to photomultipliers. By applying a high reverse bias voltage (typically 100-200 V in silicon), APDs show an internal current gain effect (around 100) due to impact ionization (avalanche effect). However, some silicon APDs employ alternative doping and beveling techniques compared to traditional APDs that allow greater voltage to be applied (> 1500 V) before breakdown is reached and hence a greater operating gain (> 1000). In general, the higher the reverse voltage the higher the gain. Since APD gain varies strongly with the applied reverse bias and temperature, it is necessary to control the reverse voltage in order to keep a stable gain. Avalanche photodiodes therefore are more sensitive compared to other semiconductor photodiodes. If very high gain is needed (10^5 to 10^6), certain APDs can be operated with a reverse voltage above the APD's breakdown voltage. In this case, the APD needs to have its signal current limited and quickly diminished. Active and passive current quenching techniques have been used for this purpose. APDs that operate in this high-gain regime are in Geiger mode. This mode is particularly useful for single photon detection provided that the dark count event rate is sufficiently low.

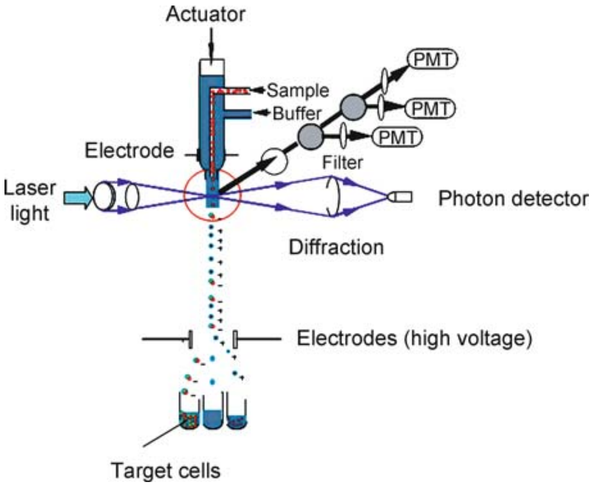

Photometer, Figure 3 Fluorescence-activated cell-sorting (FACS). The cell suspension is entrained in the center of a narrow, rapidly flowing stream of buffer liquid. The flow is arranged so that there is a large separation between cells relative to their diameter. A vibrating mechanism of actuator causes the stream of cells to break into individual droplets. The system is adjusted so that there is a low probability of more than one cell being in a microdroplet. Just before the stream breaks into microdroplets the flow passes through a fluorescence measuring station where the fluorescent character of interest of each cell is measured. An electrical charging ring is placed just at the point where the stream breaks into droplets. A charge is placed on the ring based on the immediately prior fluorescence intensity measurement and the opposite charge is trapped on the droplet as it breaks from the stream. The charged droplets then fall through an electrostatic deflection system that diverts droplets into containers based upon their charge. In some systems the charge is applied directly to the stream and the droplet breaking off retains charge of the same sign as the stream. The stream is then returned to neutral after the droplet breaks off

Key Research Findings

Biochemical and Medical Measurements

There is a wide range of applications for photometer in biochemistry and medicine. Especially, in micro/nano fluidics field, fluorescent chemical groups can be attached with small amount of biological molecules by a chemical reaction, and the fluorescence of the attached tag enables very sensitive detection of the molecule by fluorescent photodetector.

DNA Microarray

A DNA microarray (*gene* chip, DNA chip, or gene array) is a collection of microscopic DNA spots, commonly repre-

senting single genes, arrayed on a solid surface by covalent attachment to chemically suitable matrices. DNA arrays are different from other types of microarray only in that they either measure DNA or use DNA as part of its detection system. Qualitative or quantitative measurements with DNA microarrays utilize the selective nature of DNA-DNA or DNA-RNA hybridization under high-stringency conditions and fluorophore-based photodetection. DNA arrays are commonly used for expression profiling, i. e., monitoring expression levels of thousands of genes simultaneously, or for comparative genomic hybridization. Applications of these arrays include mRNA or gene expression profiling, comparative genomic hybridization (Array CGH), SNP detection arrays, and Chromatin immunoprecipitation (chIP) studies.

Fluorescent-Activated Cell Sorting (FACS)

Fluorescence-activated cell-sorting (FACS) is a specialised type of flow cytometry. It provides a method for sorting a heterogenous mixture of biological cells into two or more containers, one cell at a time, based upon the specific light scattering and fluorescent characteristics of each cell within microdroplet. It is a useful scientific instrument as it provides fast, objective and quantitative recording of fluorescent signals from individual cells as well as physical separation of cells of particular interest. The acronym FACS is trademarked and owned by Becton Dickinson although it is used within the scientific community as a general term.

Future Directions for Research

Photometer is important for identifying the materials in micro- and nano-scale flow, especially when the channel size is small and the flow speed is high. Although photometer itself does not have spatial resolution, the development of nanofluidics for single molecule detection should be desirable to develop new experimental methods and applications for single molecule based applications.

Cross References

- ► Bioprinting on Chip
- ► Infrared Imaging and Mapping for Biosensors
- ► Biosensors Using Laser
- ► Cell Sorting
- ► DNA Microarray
- ► Flow Cytometer Lab-on-Chip Devices
- ► Fluorescence
- ► Microfluidic Optical Devices
- ► SNP on Chip

References

1. Bohren CF, Huffman DR (1983) Absorption and Scattering of Light by Small Particles. Wiley, Hoboken
2. Stover JC (1995) Optical Scattering: Measurement and Analysis. SPIE Optical Engineering Press
3. Schena M, Shalon D, Davis RW, Brown PO (1995) Quantitative monitoring of gene expression patterns with a complementary DNA microarray. Science 270(5235):467
4. Wei C, Li J, Bumgarner RE (2004) Sample size for detecting differentially expressed genes in microarray experiments. BMC Genomics 5:87
5. Shapiro HM (2003) Practical Flow Cytometry. Wiley, Hoboken

Photometry

► Photometer

Photo Patterned

Synonyms

Lithography; Optical lithography

Definition

Photo patterned is a process used in IC and microfabrication to selectively remove parts of a thin film (photoresist). It uses light to transfer a geometric pattern from a photomask to a light-sensitive chemical on the substrate. A series of chemical treatments then engraves the exposure pattern into the material underneath the photoresist.

Cross References

- ► Bulk Micromachining
- ► Photolithography

Photopatterned Materials

► Stationary Phases in Microchannels

Photoresist Reflow

Definition

Photoresist reflow refers to a unique method to generate the photoresist patterns with hemispheric cross-section using heating effect of photoresist for 3-D microstructure fabrications. The 3-D structures are formed by heating up the photoresist to a certain high temperature after the photoresist is patterned by the conventional lithography. When the temperature is higher than the glass transition temperature of the photoresist, the photoresist begins to melt

and reflow. Due to the surface tension of the liquid resist and the surface property of the substrate, the resist always tends to form a convex shape on top of the substrate. This is an effective way to form convex lens, cylinder type channels or round tops of the structures as the replica molds for MEMS applications.

Cross References

- ► Fabrication of 3-D Microfluidic Structures
- ► Photolithography
- ► Soft Photolithography
- ► Photoresist SU-8
- ► Photoresist Reflow
- ► Thick Resist Lithography

Photoresist SU-8

Definition

The photoresist SU-8 is an epoxy-based photosensitive polymer that losses its resistance to chemical etching when exposed to ultra-violet radiation. It is used especially in the transference of a structure pattern to a substrate. It offers properties such as high mechanical strength, good adhesion on many different substrate materials and biocompatibility. The fabrication of SU-8 structures is a low-cost process and ultra-violet lithography semiconductor compatible.

Cross References

- ► Lab-on-a-Chip Device for Chemical Analysis
- ► Microfabrication Techniques
- ► Photolithography
- ► Photoresist SU-8
- ► Photoresist Reflow
- ► Wafer Bonding

Photoresponsive Hydrogels

- ► Photosensitive Hydrogels

Photosensitive Hydrogels

Shu Yang
Materials Science and Engineering, University of Pennsylvania, Philadelphia, PA, USA
shuyang@seas.upenn.edu

Synonyms

Photoresponsive hydrogels; Photoswitchable hydrogels

Definition

A hydrogel is defined as a network of hydrophilic polymer chains that is able to swell and retain large amounts of water. The crosslinks can be produced by chemical reactions to form covalent bonds, or physical interactions, such as hydrogen bonding, van der Waals force and polymer entanglement. Hydrogels can absorb over 99% water in their three-dimensional swollen network. Hydrogels possess a degree of flexibility very similar to natural tissue, due to their significant water content. Responsive hydrogels can reversibly change volume in response to a slight change of external stimulus, including pH, temperature, electric field, ionic strength, salt type, solvent, external stress or light. Photoresponsive is defined as a light-induced reversible change of chemical structures and physical properties.

Chemical and Physical Principles

Definition of Photochromism

Photochromism is the process of light-induced reversible color changes in a medium or more generally of their absorption spectra [1]. Photochromic compounds can exist in two different states, A and B, whose relative concentration depends on the wavelength of the incident light. The thermodynamically stable form A is transformed by irradiation into form B. The back reaction can occur either photochemically or thermally:

$$A \underset{h\nu_2 \text{ or } \Delta}{\overset{h\nu_1}{\rightleftharpoons}} B \tag{1}$$

Photochromic molecules, or light-sensitive chromophores, are chemical species having photochromic properties. Examples of photochromic molecules and photochromic processes are summerized in Table 1.

Chemical Processes Involved In Photochromism

Pericyclic reactions Cycloadditions are found in spiropyrans, spirooxazines, chromenes, hexa-1, 3, 5-triene, diheteroarylethenes, cyclohexa-1, 3-diene and spirodihydroindolizines systems.

Cis–trans isomerizations *Cis–trans* isomerizations occur in stilbenes, azobenzene, azines, thioindigoids, as well as some biological receptors.

Intramolecular hydrogen transfer Intramolecular hydrogen transfer is found in anils, benzylpyridines, tri-

azoles, oxazoles, metal dithizonates and perimidine-spirohexadienones.

Intramolecular group transfers Intramolecular group transfers are found in polycyclic quinones (periaryloxyparaquinones).

Dissociation processes Heterolytic bond cleavages occur in triarylmethanes and related systems.

When incorporating a small amount of photochromic molecules into a hydrogel matrix, either through chemical coupling or physical impregnation, a molecular level conformational change often leads to a macromolecular structural change and then macroscopic change of shape due to swelling and contraction in the hydrogel. Such a photoresponse has many advantages over other stimulation methods because:

- light is readily available;
- the amount of energy conversion can be carefully controlled by the wavelength, intensity of the exciting light, choice of chromophores and choromphore–polymer interactions;
- use of lasers offers high spatial resolution (up to nanometers), large areas and volumes, and fast speed; and
- it produces no waste during the photochemical process.

Key Research Findings

Hydrogels, which are crosslinked polymer networks surrounded with aqueous solution, are *intelligent* soft materials. In response to external stimuli, such as pH, temperature, light, electric potential, chemical agents and biological agents, polymer chains and water molecules will associate or dissociate, resulting in swelling and shrinking respectively, with a change of volume up to several hundred percent and a change of shape of the polymer.

In 1986, Irie and Kungwatchakun reported a synthesis of photosensitive gels by incorporating photosensitive molecules (1 – 4 mol%), such as leucocyanide and leucohydroxide, into the gel network [2]. These gels underwent volume changes upon irradiation; however, no phase transition was observed. In 1990, a photoinduced phase transition was first reported in thermoresponsive *N*-isopropylacrylamide (PNIPAAm) gels, by copolymerizing light-sensitive bis(4-(dimethylamino)phenyl)(4-vinylphenyl)methyl leucocyanide into the gel network [3]. In the absence of light the gels are neutral and undergo a sharp, yet continuous volume change. Upon irradiation by ultraviolet light, the neutral triphenylmethane leuco derivatives are dissociated into triphenylmethyl cations, creating internal osmotic pressure that induces swelling of the gels, showing a discontinuous volume phase transition. This transition process is slow since it depends on the photochemical ionization and subsequent recombination of ions.

Later, a much faster process (response time of the order of milliseconds) was reported. This was achieved by impregnating light-absorbing chromophores, trisodium salt of copper chlorophyllin, into PNIPAAm gels and illuminating with visible light [4, 5]. In this case, the phase transition was induced by local heating of polymer networks. According to the Flory–Huggins mean field theory, at equilibrium with zero osmotic pressure, the gel temperature, T, increases monotonically with the network density, ϕ:

$$T = T_{\mathrm{gel}}(\phi) \tag{2}$$

When illuminated by light, the chromophore absorbs the light and subsequently dissipates heat locally, inducing an increase in the local temperature. The temperature increment is proportional to the incident light intensity and the concentration of chromophore, and therefore also to the network density ϕ. Thus

$$T = T_0 + \alpha I_0 \phi \tag{3}$$

where T_0 is the ambient temperature, I_0 is the illuminating light intensity and α is a constant related to the heat capacity of the gel. Therefore

$$T_0 = T_{\mathrm{gel}}(\phi) - \alpha I_0 \phi \tag{4}$$

The term $\alpha I_0 \phi$ describes the ability of the system to undergo a local volume phase transition upon illumination of light. When the gel is in thermal equilibrium at a fixed gel temperature T, ϕ increase discontinuously with the increase of light intensity, I_0, beyond a threshold value. When I_0 is decreased, ϕ decreases discontinuously and the gel does not exhibit hysteresis as a function of I_0.

Because the increase of local temperature is the result of a balance between absorption of light and heat dissipation, the swelling and shrinking process of the gel in response to light is much faster compared to the response to ionization and ion migration, which requires collective diffusion of the gel network.

When introducing a small amount of ionic charge either through addition of salt or copolymerization of charged monomers in the light-sensitive gels mentioned above, the phase transition temperature was found also to be a function of pH. In ionic gels, the phase transitions are governed by the extent of hydrophobic interactions or the degree of hydrogen bonding induced between the polymer chains. The temperature and/or visible light intensity determine the extent of hydrophobic interactions, whereas pH affects the degree of hydrogen bonding. In the absence of external

Photosensitive Hydrogels, Table 1 Examples of photochromic molecules and photochromic processes

Photochromic molecules	Photochromic reactions
Spiropyrans	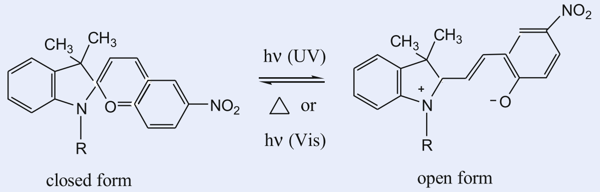
Spirooxazines	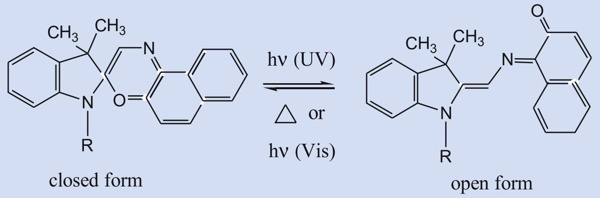
Acridizinium cations	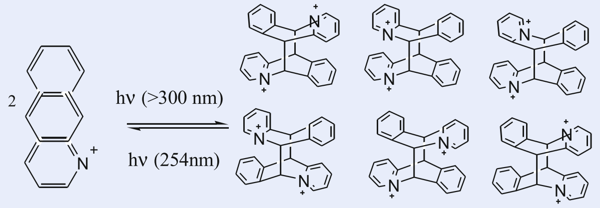
Fulgides and fulgimides	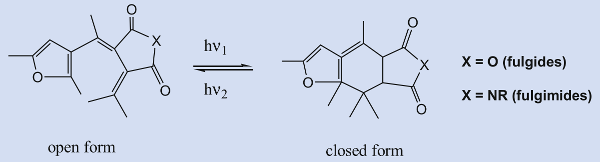
Azobenzene and derivatives	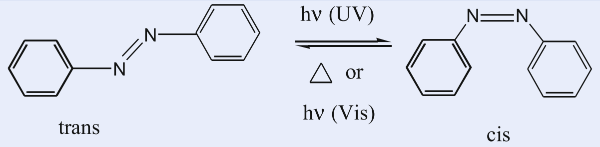
Anils and related compounds (hydrogen transfer)	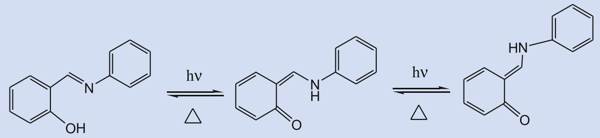
Polycyclic quinones (periaryloxyquinones)	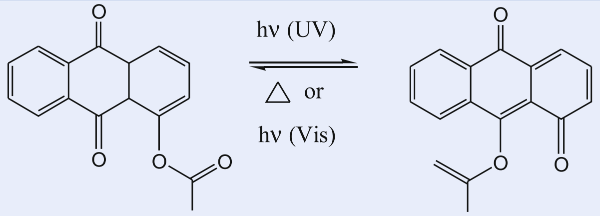
Triphenylmethane leuco derivatives	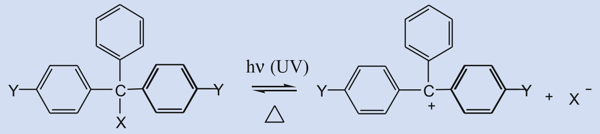

stimulus, the ionic gel exhibits a large hysteresis between the collapsed and swollen states, which is indicative of the existence of two free energy minima. It would, therefore, be possible to control the phase behavior by manipulation of other external factors in addition to visible light.

According to the principle of kinetics of gels, the time needed for swelling and shrinking of a gel is dependent on the diffusion of water in and out of the hydrogel, which is proportional to the square of the characteristic linear dimension of a gel, l^2. It is expected that response time will be decreased to microseconds and nanoseconds if we can shrink the gel size to the submicrometer scale. This also means we need to perturb the environment extremely fast. Using a laser T-jump, a switching time of the order of $\sim$100 ns was observed in individual PNIPAAm nanogels [6].

Another common approach to prepare light-sensitive hydrogels is to covalently couple chromophores either in the polymer side chains or in the main chains [7, 8]. The chromophores undergo crosslinking through photodimerization or *trans–cis* isomerization, which brings about a change of the dipole moment or structure, the dissociation of the chromophore into ions, or change of hydrophilicity of the polymer, thus varying the shape and volume phase transition of the hydrogel network.

Photocrosslinking linear PNIPAAm with photodimerizable chromophores, such as stilbene, stilbazolium and acridizinium cations, has been studied [8]. The reversible photodimerization reactions allow for dynamic tuning of the crosslinking density of the gel network, which in turn influences the phase transition temperature and swelling ratio. The introduction of the chromophores could affect the hydrophobic nature of the polymer. Compared to stilbene and stilbazolium, the positive charge in acridizinium cations compensates the hydrophobicity of aromatic groups, resulting in a smaller decrease of the critical transition temperature of PNIPAAm, $-2.7\,°C$ vs. $-11.0\,°C$ in the stilbazolium photopolymer, and a higher photoreversibility. A complete reversion to monomer will be impossible if the monomer absorption is higher than that of dimers at the irradiation wavelength.

A conformational change of a hydrogel can be induced by photoisomerization of a chromophore group, such as azobenzene and spiropyran. For azobenzene and derivates, the thermodynamically more stable *trans* form is converted into the metastable *cis* isomer by UV light irradiation, and the *cis* isomer can return to the *trans* form by visible light irradiation or thermally in the dark. A spiropyran group is known to undergo photoisomerization from its neutral, *closed* spiro form (colorless and nonpolar) to the *open* merocyanine form (highly polar and zwitterionic) under UV light irradiation, which isomerizes back to the spiro form under visible light irradiation or thermally in the dark [8]. The formation of zwitterionic merocyanines can be further exploited to bind with charged molecules to manipulate the phase transition of hydrogels. Kinetics study suggests that photoisomerization is dependent on solvent, polymer composition and the free volume distribution around the chromophore. A bulky substituent in the polymer chains seems to slow down the *trans–cis* isomerization but increases the thermal recovery rate (the *cis–trans* isomerization). Typically, it requires hundreds of seconds up to minutes of photoirradiation to induce reversible swelling and shrinkage of hydrogels using this approach.

Examples of Application

Because of their interesting properties, such as swellability in water, hydrophilicity, biocompatibility and lack of toxicity, hydrogels have been widely used in biological and biomedical applications. In response to an environmental stimulus, responsive hydrogels undergo various types of volume phase transition, which converts chemical potential energy into mechanical force. Thus, responsive hydrogels have been used in microfluidic devices such as actuators, pumps and valves, artificial muscles, controlled delivery, sensors and separation. Responsiveness to light and the potentially fast response time provide an additional opportunity to design microfluidic devices that can be triggered without disturbing the system. One could design a submicrometer optical switch on a gel surface, and control an on/off nature by focusing the light in a local area of the gel, generating features analogous to *memory* or *display*. When photoresponsive polymers are grafted onto a porous membrane, reversible UV or visible light irradiation induces a change of the polymer solubility in water, leading to photoregulating permeability and mass transport through the membrane [8].

Cross References

► pH-sensitive Hydrogel
► Photolithography
► Photoresist SU-8
► Photoresist Reflow
► Thermosensitive Hydrogel
► Soft Photolithography

References

1. Bouas-Laurent H, Dürr H (2001) Organic Photochromism. Pure Appl Chem 73:639–665
2. Irie M, Kunwatchakun D (1986) Photoresponsive Polymers. 8. Reversible Photostimulated Dilation of Polyacrylamide Gels

Having Triphenylmethane Leuco Derivatives. Macromolecules 19:2476–2480
3. Mamada A, Tanaka T, Kungwatchakun D, Irie M (1990) Photoinduced Phase-Transition of Gels. Macromolecules 23:1517–1519
4. Suzuki A, Tanaka T (1990) Phase-Transition in Polymer Gels Induced by Visible-Light. Nature 346:345–347
5. Suzuki A, Ishii T, Maruyama Y (1996) Optical switching in polymer gels. J Appl Phys 80:131–136
6. Reese CE, Mikhonin AV, Kamenjicki M, Tikhonov A, Asher SA (2004) Nanogel nanosecond photonic crystal optical switching. J Am Chem Soc 126:1493–1496
7. Chung DJ, Ito Y, Imanishi Y (1994) Preparation of Porous Membranes Grafted with Poly (spiropyran-containing methacrylate) and Photocontrol of Permeability. J Appl Polym Sci 51:2027–2033
8. Kuckling D, Ivanova IG, Adler HJP, Wolff T (2002) Photochemical switching of hydrogel film properties. Polymer 43:1813–1820

Photoswitchable Hydrogels

► Photosensitive Hydrogels

Photothermal Effect

► Thermal Lensing, Detection

pH-Sensitive Hydrogel

DOMINIC S. PETERSON
Chemistry Division, Los Alamos National Laboratory, Los Alamos, NM, USA
DominicP@lanl.gov

Synonyms

pH control device; pH-sensitive valve; pH sensor; Valve

Definition

A pH-sensitive hydrogel is a gel structure that is sensitive to changes in pH. Most commonly, the hydrogel will swell or contract in response to a change in the local chemical environment. Hydrogels can be made using in situ polymerization techniques, which makes it very useful in incorporating them into microfluidic systems. These pH-sensitive hydrogels have applications in forming valves that are sensitive to a change in pH or in systems that can release a compound when the pH is changed, and in pH sensors.

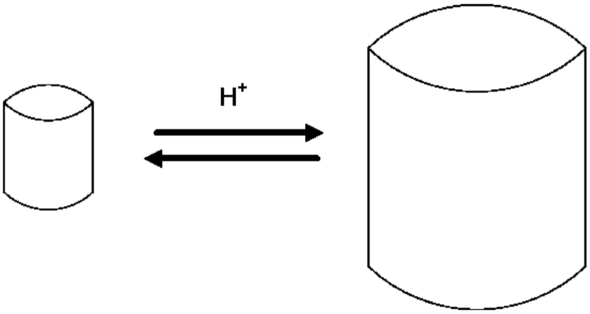

pH-Sensitive Hydrogel, Figure 1 Schematic representation of the reproducible swelling that occurs in a pH-sensitive hydrogel

Overview

A pH-sensitive hydrogel consists of a gel structure which varies with a change in the pH of the system. The basis of a pH-sensitive hydrogel is a structure that swells or contracts depending on the pH of the solution (Fig. 1). The use of a hydrogel structure allows these devices to be easily fabricated within a microfluidic system. Placing these devices in a microfluidic device enables flow control to be accomplished by changing the pH of the solution that is being pumped through the system. Alternatively, a series of these hydrogels make it possible to sort solutions according to pH by placing two different hydrogels sensitive to either basic or acidic solutions into a microfluidic system, or by using a hydrogel to regulate the pH of solutions flowing out of a mixing hydrogel.

Basic Methodology

Hydrogels are polymer structures that contain a high water content. Because they contain a large amount of water, their physical configuration can change in response to the local chemical environment [1]. In particular, hydrogels undergo a change in volume in response to chemical or physical stimuli. Hydrogels that change their structure in response to temperature have been widely studied [2]. Hydrogels can also change in response to chemical conditions. The chemical environment that is often able to induce this type of volume change in a hydrogel is the pH of the system. In this type of a system the swelling of the hydrogel is produced from an ion-driven effect. How fast the gel expands is therefore dependent on the diffusion of ions into and out of the gel. Furthermore, swelling of the gel is an equilibration effect, and will be limited by how fast a steady state can be reached within the gel.
The ability to change in response to pH has been applied to two general applications. The first is as a valve. Because the volume of the hydrogel changes, a valve can be fabricated in which a hydrogel expands to plug a channel under

one set of conditions and contracts to allow flow under another set of conditions. The other application that hydrogels have been applied to is as pH detectors. This approach involves allowing a hydrogel to swell with a change in pH and to detect and measure the swelling of the hydrogel.

One of the great challenges in microfluidics is in preparing functional devices within a microfluidic system. Often, it is necessary to fabricate a functional device within a microfluidic system. Hydrogels are very useful in microfluidic systems because they can be either fabricated in bulk or they can be fabricated in situ. The in situ fabrication approach is particularly important in microfluidics because it greatly simplifies the fabrication of complex devices compared to more traditional methods of fabrication, which are usually based on semiconductor fabrication technology. The in situ synthesis of a hydrogel is usually performed using monomers that are somewhat hydrophilic, such a acrylic acid (AA), or 2-hydroxyethyl methacrylate (HEMA). A hydrophilic monomer allows water to penetrate the hydrogel, and therefore enables the polymer to swell and contract. The crosslinking monomer (such as ethylene glycol dimethacrylate, DGDMA) allows the polymer to retain its cohesiveness with swelling. The amount of crosslinker used affects many parameters in the resulting hydrogel such as how much it can swell, how much water can permeate the gel and the pore structure of the polymer. The actual polymerization step requires an initiator. The use of a photoinitiated monomer enables the hydrogel to be patterned into a specific portion of the microfluidic channel. The fabrication methods for placing a hydrogel into a microfluidic channel are critical in enabling their use in these applications.

Key Research Findings

There are two major areas that pH-sensitive hydrogels are used for in microfluidics. The first of these applications is as a valve. A hydrogel has the ability to change volume. When they expand, the hydrogel has the effect of closing off a channel. When the hydrogel contracts, the channel is opened. An early example of this approach involved introducing a pH-sensitive hydrogel into a microfluidic system in order to regulate the pH in the system [3]. This study utilized a circular chamber with a pH-sensitive hydrogel and included inlet channels that had solutions at a pH of 2 and 12. The outlet of the system was regulated at a pH of 7 by the action of the hydrogel. This study found that the geometry of the hydrogel has a strong effect on the regulation of the outlet pH. When a circular hydrogel is used the outlet pH was observed to oscillate; however, the use of a star-shaped hydrogel greatly reduced the oscillation. Another study fabricated two pH-sensitive hydrogels in a "V" shape in order to mimic a biomimetic valve such as those found in the veins [4]. This valve arrangement has the effect that flow through the valve is enabled in the forward direction, but is restricted in the reverse direction, effectively acting as a check valve. Furthermore, flow regulation is enhanced because the pressure drop across the valve is constant across a wide range of flow rates (0.4 – 1.8 ml/min). This ability to have the same pressure drop across the valve is due to the elasticity of the hydrogel; it enables the hydrogel to act as a pressure regulator in the microfluidic system, while the pH sensitivity enables the valve to be activated and deactivated depending on the solution being used. In another study a pH-sensitive hydrogel sphere was used as the actuating element in a microfluidic valve [5]. This approach involved placing the pH-sensitive hydrogel microsphere in a chamber. The swelling microsphere contacts a thick-centered membrane. This contact causes the membrane to close the valve. This approach allows the valve to be activated without the hydrogel being present in the main microfluidic channel, and the activation of the valve can be performed independently of the solvent in the microfluidic channel. This is because the hydrogel microsphere is in a channel separate from the main channel, and the two channels are isolated from one another via the membrane. The primary drawback is that this approach requires a more complex fabrication process to incorporate the valve into the microfluidic system.

In addition to pH-sensitive hydrogels being used as valves in microfluidic devices, they have also been used as a method to determine the pH of a solution in a microfluidic device. The pH of the solution in a microfluidic system can be very important in performing functions on a solution, such a protein digestion or a synthetic step. However, detection of the pH in a microfluidic channel can be very difficult due to the small volumes involved in these channels. One approach involved incorporating a pH-sensitive dye within a hydrogel [6]. The synthesis of the hydrogel with the pH-sensitive dye is relatively simple because the hydrogel is simply synthesized with the dye incorporated within the polymer gel structure. The pH of the system can then be determined by the color of the dye. Using UV-visible spectroscopy enables very specific determination of the dye state. The primary limitation on the time required to determine the pH is the diffusion of within the hydrogel. Another approach that has been demonstrated to measure the pH in a microfluidic channel involves a hydrogel actuating a piezoresistive device [7]. This approach involves fabrication of a pH-sensitive hydrogel in contact with a bending plate. This plate then actuates a piezoresistor, the electrical signal of which is then read to give an indication of the pH in the microfluidic device. While

the piezoresistor makes fabrication of these systems more complex, it has the advantage of enabling rapid and precise electronic indication of the pH of the system.

A key parameter that has been studied for pH-sensitive hydrogels is their mechanical properties [8]. This is very important because the macromolecular properties will determine how the gel performs in the system. For instance, the mechanical properties in a valve will determine how well it can seal a channel, and can also affect how fast the valve can close. A wide variety of experimental techniques have been developed to characterize the mechanical properties of microgels, particularly the tensile strength [9]. In these studies it was found that the mechanical properties are dependent on the extent of equilibrium swelling as well as the polymerization conditions used to produce the gel. The mechanical properties can be controlled by adjusting the amount of crosslinker that is used in the hydrogel composition. The ability to control the mechanical properties of a pH-sensitive hydrogel will be critical in applying these components into specific microfluidic applications.

Future Directions for Research

While there have been a number of devices demonstrated for pH-sensitive hydrogels, there is a great deal of development work that can still be done. In particular pH-sensitive hydrogels need to be demonstrated in more robust environments, and their reliability and longevity need to be explored. The use of these systems in more robust situations will enable them to be explored in more complex microfluidic systems. In particular, devices will need to be made that can incorporate multiple valves in order to enable complex flow paths to be constructed. While this may be accomplished utilizing pH-sensitive hydrogels, it may be advantageous to incorporate valves in the system that are actuated via different approaches. This may further enable complex systems to be fabricated. The synthesis of pH-sensitive hydrogels will also need to become more refined to enable them to be placed into these more complex systems. Part of this development will include refining the synthetic methods to produce hydrogels with the desired mechanical, physical and chemical properties. In developing hydrogels with specific chemical properties there are two possible approaches. The first is to incorporate specific chemical functionalities into the polymerization mixture of which the hydrogel is made. The other approach is to coat or react a specific chemical functionality on the surface [10]. The ability to control the chemistry will enable these devices to be used with a wide variety of solutions and may improve their versatility.

Cross References

► Capillary Force Valves
► Electrochemical Valves
► Electromagnetic Valves
► Microfluidic Sample Manipulation
► Photosensitive Hydrogels
► Sol–Gel Technique
► Thermosensitive Hydrogel

References

1. Eddington DT, Beebe DJ (2004) Flow control with hydrogels. Adv Drug Deliv Rev 56:199–210
2. Gariepy ER, Leroux JC (2004) In situ-forming hydrogels – review of temperature-sensitive systems. Eur J Pharm Biopharm 58:409–426
3. Eddington DT, Liu RH, Moore JS, Beebe DJ (2001) An organic self-regulating microfluidic system. Lab Chip 1:96–99
4. Yu Q, Bauer JM, Moore JS (2001) Responsive biomimetic hydrogel valve for microfluidics. Appl Phys Lett 78:2589–2591
5. Park JY, Oh HJ, Kim DJ, Baek JY, Lee SH (2006) A polymeric microfluidic valve employing a pH-responsive hydrogel microsphere as an actuating source. J Micromec Microeng 16:656–663
6. Moorthy J, Beebe DJ (2002) A hydrogel readout for autonomous detection of ions in microchannels. Lab Chip 2:76–80
7. Trinh QT, Gerlach G, Sorber J, Arndt KF (2006) Hydrogel-based piezoresistive pH sensors: Design, simulation and output charcteristics. Sens Actuators B 117:17–26
8. Johnson BD, Beebe DJ, Crone WC (2004) Effects of swelling on the mechanical propertis of a pH-sensitive hydrogel for use in microfluidic devices. Mater Sci Eng C 24:575–581
9. Johnson BD, Bauer JM, Niedermaier DJ, Crone WC, Beebe DJ (2004) Experimental techniques for mechanical characterization of hydrogels at the microscale. Experim Mech 44:21–28
10. Kraft ML, Moore JS (2003) n-Alkyl fatty acid modified microgels: ton permeation as a function of chain length. Langmuir 19:910–915

pH-Sensitive Valve

► pH-Sensitive Hydrogel

pH Sensor

► pH-Sensitive Hydrogel

Physical-Chemical Etching

► Anisotropic Etching

P

Physical Domain

Synonyms

Physical region

Definition

This refers to the actual spatial domain under consideration. In computational methods, this is replaced by a computational domain using a simplified geometry and boundary conditions.

Cross References

- ► Meshless Methods
- ► Volume and Finite Difference Method for Modeling and Simulation

Physical Etching

- ► Sputter Etching

Physical Region

- ► Physical Domain

Physical Vapor Deposition

- ► Sputtering for Film Deposition

Picoliter Flow Calibration

ZHANHUA SILBER-LI
LNM, Institute of Mechanics, Chinese Academy of Sciences, Beijing, China
lili@imech.ac.cn

Synonyms

pL; Flow rate

Definition

Flow rate is defined as the volumes or masses of fluids flowing through a special area in unit time. The standard unit of flow rate is m^3/s. Picoliter (pL) is a unit of volume, $1\,pL = 10^{-15}\,m^3$ and transfers to other units as: $1\,pL = 10^{-3}\,nL = 10^{-6}\,\mu L = 10^{-9}\,mL = 10^{-12}\,L$. An example describes the volume of a picoliter: a droplet with a diameter of 20 μm has a volume of about 4.2 pL.

Overview

Classic flow rate measurement tools are mass flowmeter, electromagnetic flowmeter, rotameter and turbine flowmeter, their measurement ranges being normally larger than $10^{-7}\,m^3/s$ (0.1 mL/s). But in microscale flows, the range of flow rate is usually $10^{-7} - 10^{-12}\,m^3/s$, in other words, $10^2\,\mu L/s$–1 nL/s. In nanoscale flows, the flow rate is from 10^{-15} to $10^{-18}\,m^3/s$ (1 pL/s–1 fL/s). So the measurement and calibration methods will be different for micro- or nanoscale flows, compared to classic macroscale flows.

Colin [1] has reviewed some measurement methods in microscale flow, including the weighing method, thermal method, wave reflection method, acoustic vibration method, and so on. Here two common methods, the weighing and displacement methods, are introduced. In the weighing method [2], the total mass M of fluids flowing out within a time Δt are measured, and the flow rate is calculated as:

$$Q_g = \frac{M}{\Delta t} \tag{1}$$

The uncertainty of this method is directly proportion to the accuracies of balance and stopwatch. If a balance with an accuracy of within ±0.001 g is used to measure a kind of flow whose range is larger than 1 μL/s, the measurement accuracy is about ±1%.

The displacement method [1, 3] is another kind of indirect method, which calculates flow rate by measuring the displacement L of a fluid in a capillary tube with a diameter D and interval Δt:

$$Q_m = \frac{\pi D^2 L}{4\Delta t} \tag{2}$$

Because flow rate Q_m is proportion to the second power of diameter D, the uncertainty of flow rate is mainly related to the accuracy of D. The measuring precision of the diameter of capillary tubes using a toolmaker's microscope is ±0.01 mm, so the uncertainty can reach ±2%, for a flow rate range of 1 – 100 nL/s.

For saving samples, reducing cross-contamination and operating fluids with smaller volume in microfluidic devices, designers hope that the dimensions of channels or tubes are as small as possible. When the characteristic dimension of channels decreases to the nanoscale, picoliter-scale flow will occur. De Heij et al. [4] designed a nozzle array of 50 μm diameter, which can produce

100 – 700 pL discrete droplets. Ahmed and Jones [5] controlled dielectrophoretic (DEP) force, capillary force and inertial force by an electrophoresis method, and produced discrete droplets on the substrate of a channel, whose volumes were smaller than 10 pL. He et al. [6] drove water flow through a nozzle of diameter 1.7 µm by electric pulse, and formed 8 – 14 pL water droplets in an oil environment making use of Rayleigh instability. Ellson [7] used focused acoustic energy to spray droplets from the surface of fluids, whose volumes are about 0.1 pL–1 µL. Karnik et al. [8] controlled protein to transmit in nano- and microchannels under the effect of an electrostatic field, the dimension of the channel being 1 – 100 nm, equivalent to the Debye length. The height of the channel cross-section was just 30 nm, so this device can be used to control picoliter-scale flow of protein solution.

From these literature reports we can see that pL flows have been achieved and applied in sampling devices of biology chips, in micro- or nanochannels and two-phase flows, so the measurement and calibration of pL volume fluid flow have great importance attached to them.

Basic Methodology

The methods that are usually used to calibrate ultra small-volume fluids are the static weighing method, comparing method, flow velocity measurement method, and so on. The study of picoliter flows has just begun, so the perfect calibration methods have not been formed yet. This section will review partial methods to produce pL flow, their measurement accuracy and the relevant calibration methods. A fuller coverage is not possible because of space limitations.

Visual Inspection Measurement

As shown in the literatures, pL flows always present as droplet form. So it is important to pay attention to measuring the volume of droplets in pL flow measurement. The common methods are calculating volume by the size of the microvial or microchannel in which droplets are formed, or measuring droplet diameters from their images and calculating volume by the ball volume formula:

$$V_\mathrm{d} = \frac{4}{3}\pi R^3 = \frac{1}{6}\pi D^3 \tag{3}$$

Here, the radius R or diameter D are measured from images captured by a microscope, with a calibrated microruler.

De Heij et al. [4] designed a nozzle array to produce continuous droplets. The diameter of the nozzle is 50 µm.

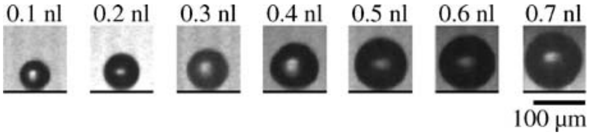

Picoliter Flow Calibration, Figure 1 The droplet volume measured with stroboscope camera [4]

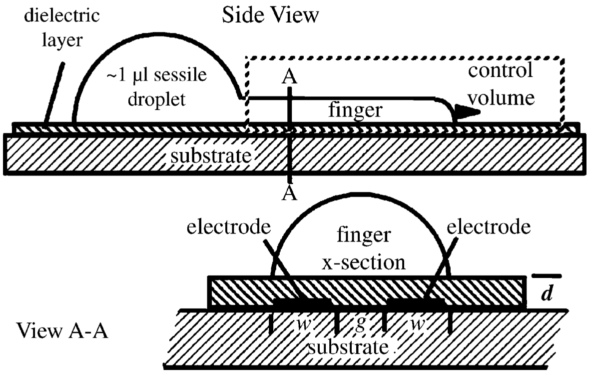

Picoliter Flow Calibration, Figure 2 Side view of a DEP-driven finger emerging from a sessile droplet using parallel co-planar electrode (top) and the cross-sectional (view A–A) [5]

A digital stroboscope (Visit Video Stroboskop MOCRON-RT) was used to record the spraying process of droplets, and then the image processing software was used to calculate the diameter (Fig. 1). The accuracy of image measurement is ±5%. They have measured droplets from 0.1 to 0.7 nL, and the measurement accuracy is ±0.1 pL.

Ellson et al. [7] used the method of focused acoustic energy to eject a pL droplet from a nanoliter-scale well, the droplet diameter being also measured by a digital stroboscope. In their experiment, 20 pL droplets were ejected from 20 nL liquids. The accuracy of liquid volume measurement is determined by the accuracy of image measurement. They used a precisely calibrated micrometer to measure the image size, the accuracy being estimated as about ±5 µm based on the image resolution. The minimum volume of experimental droplets is 20 pL, and the measurement accuracy is ±0.1 pL. Thousands of droplets were produced continuously, and the whole fluid volume divided by the number of droplets calibrated the average volume.

Ahmed et al. [5] proposed a method to produce discrete pL droplets on substrate by an electrophoresis method. A finger will be formed when water is driven by electrophoresis force above an electrode (Fig. 2). The key parameter dominating capillary instability is the Bond number, which is expressed by $\mathrm{Bo} = \rho g R^2 \gamma$, which presents the relation between hydrostatic pressure $\rho g R$ and Laplace pressure

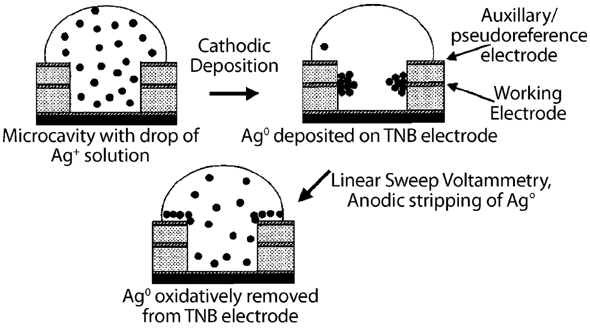

Picoliter Flow Calibration, Figure 3 Schematic diagram of the electrode and the procedure for small volume measurement using anodic stripping voltammetry [9]

γ/R. If the electrical potential is taken out for $\mathrm{Bo} < 10^{-3}$, the capillary force will dominate, and the finger will be broken to form droplets. The front part of the finger is assumed to form a hemispherical shape droplet, whose diameter is about $D = 2w + g$, where w is the width of the electrode and g is the interspace between the electrodes. The volume of the hemispherical droplet can be calculated by reference to formula (3).

Ahmed et al. used a camera to record the droplet forming process at 500 frames/s, 6 continuous frames being used to calculate the extending length of the finger, and compared to the estimated value of droplet diameter. In the experiment, the average volume of 30 droplets is 40 pL. If the size of the microelectrodes decreases further, 10 pL volume droplets would be obtained. The minimum measurable volume is of the order of 10 pL, and the accuracy is about ±5 pL, but the volume measured by this method has not been calibrated.

In the methods discussed above, fluid volumes were measured by visual inspection, so other methods are needed for fluids which cannot be inspected directly or which flow in opaque channels.

Electrical Measurement

Coulometric Method

Vandaveer et al. [9] proposed anodic stripping voltammetry to measure fluids with ultra-small volume. The advantages of this method are avoiding optical detecting devices, fast and easy and suitable for irregular shapes of fluid flows.

A microvial with electrodes in the wall is used in this method. The volume of fluids can be calculated by exhaustive reduction of current under the effect of continuous changed voltage (Fig. 3). Recessed microdisk (RMD) electrode, tubular nanoband (TNB) electrode and reference electrodes were installed on the bottom, sidewall and top of the microvial, respectively. Soluble metal species were added into the sample fluids, and then they were deposited on the electrodes on the sidewall driven by voltage. After that, the deposited metal species were removed under a voltage of -0.6 to 1 V. Droplets volumes can be measured indirectly by the quantity of electricity integrated from the relation between removed current and voltage of reference electrodes, the formula being expressed as [9]:

$$V_s = \frac{Q}{nFC^*} \tag{4}$$

where Q is the total Coulomb value integrated from the anodic removed curve, n is the moles of electrons transferred per mole of metal ions, F is the Faraday constant ($F = 96{,}485$ C/mol) and C^* is the initial concentration of metallic ions in solution.

Electrodes are installed on the wall of the microvial, and as a result the minimum size of the microvial is 8 μm in height and 13 μm in diameter; in other words, 1 pL measurable volume. The accuracy of this method is 1.49 nL ± 20 pL. It is easier for smaller volume fluids to dissipate and deposit, so this method is better for measuring fluid volumes below 1 nL. Also, because the method is coulometric, calibration curves are not required [9].

Impedance Method

Hjelt et al. [10] proposed an integrated, noninvasive method to measure sub-nanoliter volume droplets. Microelectrodes were integrated on the bottom of a reactor and covered with a layer of SiN. According to the impedance characteristic between electrodes, the size of droplet can be obtained. The volumes of the reactor fabricated in the experiment are 60–40 pL. The relation between liquid volumes and electrodes voltages was calibrated, and the accuracy of voltage measurement was ±5%, and the resolution of volume measurement could be up to 1 pL. To calibrate the measurement results of the impedance method, the authors used a fluorescence microscope to inspect the liquid volume inside the reactor, and they concluded an accuracy could be achieved of ±5%. The minimum measuring volume in the experiment is 30 pL, and the measurement accuracy is ±1.5 pL.

Optical Measurement

Markov et al. [11] measured the velocity of the flow in an electrophoresis chip by backscatter interferometry (Fig. 4). An infrared laser with a shutter was used to heat the fluid periodically in an upstream position, and a bicell was used as a position-sensitive device in the detecting section. The

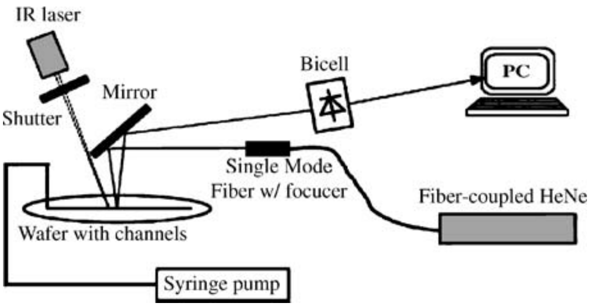

Picoliter Flow Calibration, Figure 4 Diagram of backscatter interferometry for fluid flow measurement [11]

changes of refractive index of fluids as a function of temperature were converted to electrical signals, and these signals had the same frequency as that of the heating laser, but with different phase. The phase difference between the shutter signal and the bicell signal was used to calculate the time interval Δt during which fluids flowed from the heating section to detecting section. Then the velocity can be calculated. The authors also calibrated the relations between the flow rate and the phase difference.

Experiments were carried out in a $200\,\mu$m channel, with a measurement accuracy of $0.833 - 1.66\,\text{nL/s} \pm 0.127\,\text{nL/s}$, but the velocity measurement results were not calibrated.

Key Research Findings

Several methods to obtain and measure pL fluid volumes have been reviewed: visual inspection measurement, electrical measurement and optical measurement. Visual inspection measurement captures a droplet image by microscope or stroboscope, and measures the size of the droplet in the image to calculate its volume. The minimum volume of droplets can reach 10 pL, with a measurement accuracy of ± 0.1 pL. Coulometric and impedance methods were introduced as electrical measurements, which measure the quantity of electricity or impedance of fluids to calculate the droplet volume. The minimum volume of droplets measurable with these methods is 30 pL, with ± 1 pL accuracy. Finally, optical measurement, especially the backscatter interferometric method, was introduced. This method measures the difference of light phase to calculate the velocity of a fluid, and then calculates the volume. Flow rates from 0.833 to 1.66 nL/s were measured in experiments and the accuracy was ± 0.127 nL/s.

Obviously, visual inspection measurement is the easiest method with the highest accuracy to date. The impedance method also uses it for calibration [10].

For calibration, if the cumulative volume of liquid is larger than $1\,\mu$L, the volume weighing method is suggested. But for calibration of single droplet volume, the visual inspection method is simpler.

Future Directions for Research

In principle, calibration methods of ultra small-volume droplets include static weighing method, comparing to standard volume and calibration by high-accuracy velocity measurement. Traditional optical devices, microscopes, stroboscopes, etc., are still the main measurement method for pL fluid volume calibration, and the accuracy is about 0.1 pL. Novel measurement techniques are needed for calibration of sub-picoliter fluid volume.

Cross References

► Fluid Metering
► Droplet Dispensing
► Nanoscale Flow Visualization

References

1. Colin S (2004) Microfluidique. Hermes Science Publications, French 393
2. Sharp KV, Adrian RJ (2004) Transition from laminar to turbulent flow in liquid filled microtubes. Exp Fluids 36:741–747
3. Cui HH, Silber-Li ZH, Zhu SN (2004) Flow characteristics of liquids in microtube driven by high pressure. Phys Fluids 16:1813–1810
4. De Heij B, Steinert C, Sandmaier H, Zengerle R (2003), A tuneable and highly-parallel picolitre-dispeser based on direct liquid displacement. Sens Actuators A 103:88–92
5. Ahmed R, Jones TB (2006) Dispensing picoliter droplets on substrates using dielectrophoresis. J Electrostatics 64:543–549
6. He MY, Kuo JS, Chiu DT (2005) Electro-generation of single femtoliter- and picoliter-volume aqueous droplets in microfluidic systems. Appl Phys Lett 87, 031916
7. Ellson R (2002) Picoliter:enabling precise transfer of nanoliter and picoliter volumes. DDT, 7(5):S32–34
8. Karnik R, Castelino K, Majumdar A (2006) Field-effect control of protein transport in a nanofluidic transistor circuit. Appl Phys Lett 88, 123114
9. Vandaveer WR, Fritsch I (2002) Measurement of ultra-small volumes using anodic stripping voltammetry. Anal Chem 74:3575–3578
10. Hjelt KT, van den Doel R, Lubking W, Vellekoop MJ (2000) High-resolution liquid volume detection in sub-nanoliter reactors. Sens Actuators 83:61–66
11. Markov DA, Dotson S, Wood S, Bornhop DJ (2004) Noninvasive fluid flow measurements in microfluidic channels with backscatter interferometry. Electrophoresis 25:3805–3809

Piezoelectric

Definition

Coupling phenomenon between mechanical strain and stress, and the electric field strength and displacement in

P

a material. Requires a polarization that remains within a material in the absence of the application of an external field, in turn requiring a non-enantiomorphic polar symmetry in the composition of the material.

Cross References

- ► Non-Centrosymmetric
- ► Ferroelectric
- ► Acoustics Based Biosensors

Piezoelectric Drop-on-Demand

► Piezoelectric Microdispenser

Piezoelectric Ink Jet

► Piezoelectric Microdispenser

Piezoelectric Materials for Microfluidics

JAMES FRIEND, LESLIE YEO
Micro/Nanophysics Research Laboratory, Monash University, Clayton, VIC, Australia
james.friend@eng.monash.edu.au

Synonyms

Lead zirconate titanate; PZT; Zinc oxide; Quartz; AlN; Electroactive materials; Electromechanically coupled materials; Artificial muscle materials; Electrets

Definition

Piezoelectricity means *squeeze* or *pressure* electricity, from the Greek *pieze* which means to press or squeeze. The casual definition of piezoelectric materials is that they develop an electric charge differential along an axis of ► piezoelectric polarization if placed under appropriate mechanical strain, called the ► direct piezoelectric effect, and deform if an electric field is applied along the same axis of polarization, the converse piezoelectric effect. The electric field to mechanical strain coupling occurs when the positive and negative charge of the individual ions within the material do not displace symmetrically upon the application of an external strain. Strictly speaking, piezoelectric materials exhibit electric polarization upon the application of a stress and vice versa. Often the casual and strict definitions are the same, though confusion may arise with the casual definition. All piezoelectric materials are ► anisotropic, and there are useful examples of piezoelectric materials that are single crystals, polycrystalline ceramics, and polymers. Many of the known piezoelectric materials have at one time or another been used as sensors or actuators in microfluidics, for which their rapid response and large force transmission have been beneficial, though researchers have had to learn to overcome small strains, thermal losses, aging, and difficulties in fabrication, especially in process compatibility.

Overview

Piezoelectric materials offer the ability to directly transform (transduct) from electrical to mechanical energy and vice versa, convenient for microtechnology in sensing and actuation; a material is said to be piezoelectric if an applied stress generates an electric field within, and vice versa. They may be used to provide static and dynamic deformation at frequencies up to several gigahertz, depending on the motion to be induced, the scale of the device, and the material used. Compared to other methods of power transduction, including electrostatic, electrostrictive, magnetostrictive, and electromagnetic means, piezoelectric transduction typically provides large forces at small strain rates ($< 1\%$ strain typically) for actuation, and relatively large voltages and small currents for sensing. Piezoelectricity is usually treated as a linear interaction between mechanical and electrical phenomena, though this assumption is generally invalid for high-power applications or in materials with either large losses or large deformations (polymers). The ► hysteresis in such conditions is the deviation from linear transduction. This is different than the typically weak ► electrostrictive [2] behaviour of many insulating materials which exhibit a strain proportional to the square of the applied field, though some materials, like ► relaxor ferroelectrics are exceptions. Single crystal materials are usually naturally polarized, implying they may be used without additional treatment, while polycrystalline and polymeric materials must be polarized with either an applied electric field or an applied strain prior to use.

Recognition of the piezoelectric effect has been known since ancient times [6]. Theophrastus noted in 314 BC the attraction of small pieces of straw and wood to tourmaline after heating, but recognition of the presence of an electrostatic field causing the attraction had to wait for the nineteenth century, along with a name provided by Brewster in 1824: ► pyroelectricity. All pyroelectric materials are piezoelectric; Jacques and Pierre Curie studied piezoelectric materials in the 1880's and were able to describe many of the characteristics of the phenomena used in applications today. Once synthetic quartz and high-performance

materials like barium titanate, lead zirconate titanate and subsequent variations became available in the 1950's and 60's, a wide variety of applications beyond sonar became feasible.

Many of the piezoelectric materials used for applications are single crystals or polycrystalline matrices of single-crystal grains. Overall, crystalline media may be organized into thirty-two crystal classes or point groups based on their symmetry; the names of some of these groups are commonly known; triclinic, orthorhombic, cubic, and isotropic are especially well-known. ► Hermann–Mauguin notation [1] is often used to precisely describe the properties of these materials. For example, triclinic materials are represented with either a 1 or –1, depending on whether or not the material has ► inversion symmetry, respectively. Of these thirty-two crystal classes, twenty-one possess no centre of symmetry; they are said to be ► non-centrosymmetric or to lack inversion symmetry, and all but one of these classes are piezoelectric. The exception is class 432, which has other symmetries which negate the non-centrosymmetric nature of the crystal structure. The remaining crystal classes which are piezoelectric are 1, 2, m, 222, mm2, 23, 3, 3m, 32, 4, –4, 422, 4mm, –42m, –43m, 6, –6, 622, 6mm, and –62m.

Out of these twenty piezoelectric classes, ten also lack symmetric characteristics along a particular axis, and are therefore able to retain a natural ionic charge separation in the crystalline structure along that axis—a ► spontaneous polarization—that forms an electric dipole which remains even without an externally applied electric field. This is in contrast to all insulating or dielectric materials which polarize to form such dipoles only with an externally applied field. These crystal groups are *pyroelectric*, including 1, 2, m, mm2, 3, 3m, 4, 4mm, 6, and 6mm. A crystal belonging to one of these crystal groups that has a polarization that may be reversed through the application of an external electric field is said to be ► ferroelectric. A distinct characteristic of ferroelectric materials, in the strictest definition, is the presence of hysteresis. All ferroelectric materials are both piezoelectric and pyroelectric. Lead zirconium titanate (PZT or $Pb_xZr_{(1-x)}O_3$) is one of the most important ferroelectric materials, class 6mm, though PZT is only found in polycrystalline form as a ► perovskite ABO_3.

Most piezoelectric materials tend to be quite capacitive. The pyroelectric nature of all polarized piezoelectric materials can cause the development of significant charging across the material due to thermal expansion coupled to the direct piezoelectric effect causing a charge displacement from the thermal strain; voltages of 1 kV are not unheard of in PZT after a temperature change of 50 °C, and caution is warranted in any application. However, a piezoelectric material will lose its spontaneous polarization if its temperature is raised above the ► Curie temperature, near the temperature of maximum dielectric constant, the ► Curie–Weiss temperature. Since the mechanical and electrical behavior are coupled, a change in boundary conditions in one domain will change the behavior of the material in the other domain. By leaving a polarized piezoelectric element open-circuited, the mechanical stiffness of the material will be higher, called stress stiffening. Similarly, mechanically clamping a piezoelectric element will tend to increase the impedance.

With polycrystalline and amorphous *piezoelectric* materials, a spontaneous polarization can rarely be obtained as a consequence of the natural ordering within the material during fabrication. Some form of applied strain or electric field is necessary to polarize the material before use. A common sensor material, polydivinylfluoride (PVDF), is stretched to polarize it, while standard PZT must have a large ($> 10\,\text{kV/cm}$) electric field applied to it to order the electric Weiss domains, or groups of dipoles, in the general direction of the applied field. It is a common misconception that polarization of these materials implies the dipole polarization is rotated to be aligned with the electric field or that the atomic structure itself is realigned within the material. In reality, the atomic structure is essentially fixed, preventing such rotation or realignment. Once polarized, the material can be said to be a member of the pseudocrystal group ∞ mm, and is often represented as a 6 mm material. Generally, the domains are randomly oriented beforehand.

At times, particularly with amorphous materials, the term *electret* is used instead of *piezoelectric* to describe a material; the term was introduced as an electric counterpart to the magnet, defined as all materials that are able to retain at least a quasi-permanent electric polarization within, and perhaps trap charge on the surface (or within in a porous material). Polytetrafluorethylene (PTFE) is a powerful electret material. The critical difference among the terms is that electrets retain polarization in thermodynamic *non*equilibrium, pyroelectric materials retain polarization in equilibrium, ferroelectrics permit the equilibrium polarization to be reversed along the polarization axis, and piezoelectric materials may or may not have any polarization at all.

Basic Methodology

Modeling Linear Piezoelectricity

Equations for structural dynamics within the solid material, along with the standard equations for electrostatics, are sufficient to model most piezoelectric materials and their applications. The full electromagnetic equations are

P

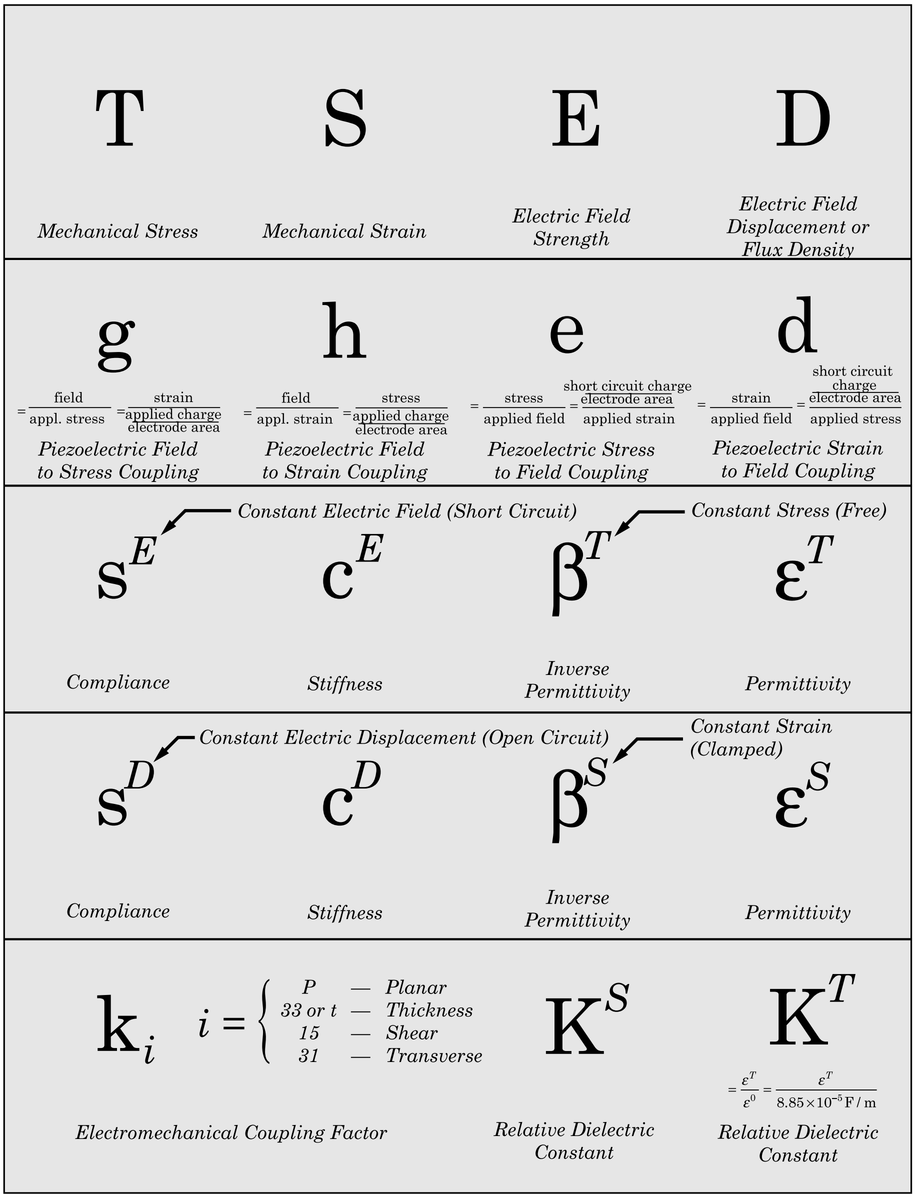

Piezoelectric Materials for Microfluidics, Figure 1 Variables used in linear piezoelectric material analysis

unnecessary since the mechanical motion propagates at $\sim 10^3$ m/s, several orders of magnitude less than the electric field, permitting the so-called *quasistatic* assumption. For the same reason, magnetic fields are typically weak and may be safely ignored. Still, equations to describe the electrical and mechanical behaviour are needed in addition to the constitutive equations for the material.

Using Auld's notation [1], the full tensor form of the linear constitutive equations with the strain and charge displacement as dependent on the stress and applied field may be written as

$$\mathbf{T} = \mathbf{c}^E : \mathbf{S} - \tilde{\mathbf{e}} \cdot \mathbf{E}$$
$$\mathbf{D} = \mathbf{e} : \mathbf{S} + \tilde{\boldsymbol{\varepsilon}}^S \cdot \mathbf{E} \quad (1)$$

where the terms are defined with units in Figs. 1 and 2 (using contracted notation to be described later). The tilde ($\sim$) is a transpose while the single and double dots represent an inner product across one and two dimensions

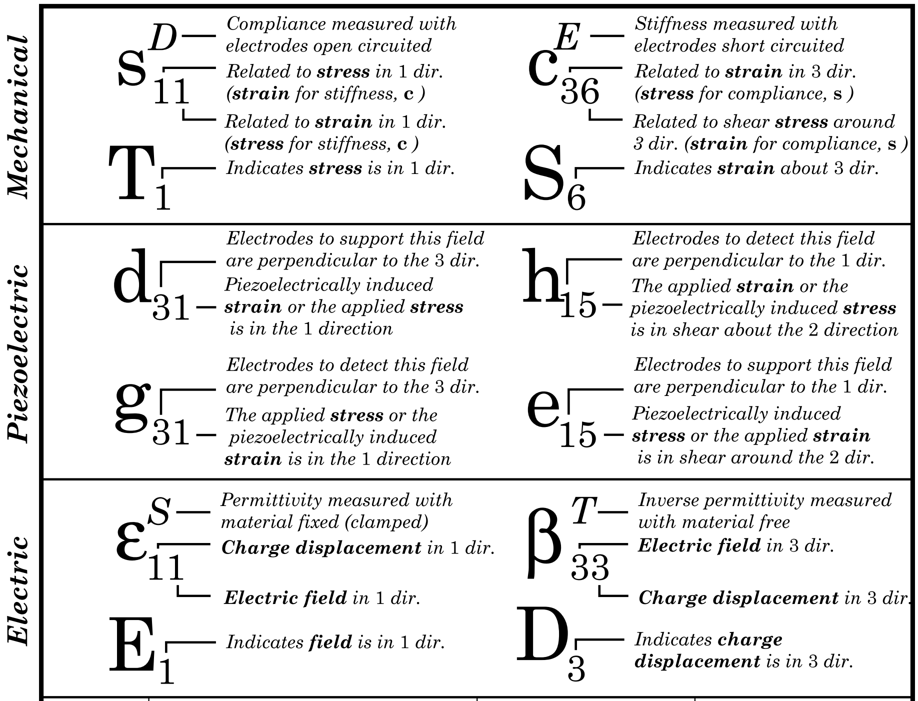

Units

Variable	Name	Derived Units (MKS)	Fundamental Units
c	*Stiffness*	Pa	kg / m • s^2
s	*Compliance*	1 / Pa	m • s^2 / kg
T	*Stress*	Pa	kg / m • s^2
S	*Strain*	—	—
d	*Piezo. Strain Coefficient*	m / V *or* C / N	C • s^2 / kg • m
g	*Piezo. Voltage Coefficient*	m • V / N *or* N • m / C	m^2 / C
e	*Piezo. Stress Coefficient*	C / m^2	C / m^2
h	*Piezo. Stiffness Coefficient*	V / m	kg • m / C • s^2
ε	*Permittivity*	F / m	C^2 • s^2 / kg • m^3
β	*Inverse Permittivity*	m / F	kg • m^3 / C^2 • s^2
D	*Electric Charge Displacement*	F • V / m	C / m^2
E	*Electric Field Strength*	V / m	kg • m / C • s^2
K	*Relative Dielectric Constant* ($\varepsilon/\varepsilon_0$)	—	(ε_0 = 8.85 x 10^{-5} F / m)
k	*Electromechanical Coupling Factor*	—	—

Piezoelectric Materials for Microfluidics, Figure 2 Description of subscripts used in piezoelectric analysis

of the adjacent tensors, respectively. In piezoelectric materials analysis, the contravariant basis vectors are typically Cartesian, therefore orthonormal and so the covariant basis is not needed. Upon choosing a coordinate system, an indicial notation may be adopted [14],

$$T_{ij} = c^E_{ijkl} S_{kl} + e_{mij} E_m$$

$$D_i = e_{ijk} S_{jk} + \varepsilon^S_{ik} E_k \,, \tag{2}$$

where summation is assumed across repeated subscripts in products of terms, i. e., k and l in $c^E_{ijkl} S_{kl}$; all of the subscripts range from 1 to 3. The strain S_{ij} is given by astrain-displacement relationship $S_{ij} = \frac{1}{2}\left(u_{i,j} + u_{j,i}\right)$ where the comma in the subscript represents a spatial derivative ($u_{i,j} = \partial u_i/\partial x_j$). The momentum equation is $T_{ij,i} + f_i = \rho \ddot{u}_j$ where $\ddot{u} = \partial^2 u_j/\partial t^2$ and f_i represents a body force. The time-dependent electric field, E_i, and charge displacement, D_i, may be related through the polarization and permeability equation $D_i = \varepsilon_0 E_i + P_i$ where P_i is the polarization. A scalar potential φ may be defined to represent the electric field, $E_i = \varphi_{,i}$, while the charge displacement is *spatially* constant along a particular direction, $D_{i,i} = 0$.

A piezoelectric Poynting energy flux akin to those defined for nonpiezoelectric acoustic waves and electromagnetic waves is given by $-\left(T_{ij}\dot{u}_j - \varphi \dot{D}_j\right)$.

In attempting to use these equations to solve problems, a complete and consistent set of electromechanical boundary conditions are needed. Tiersten [13] provides such a derivation, though solution of anything beyond simple problems requires computation. Fortunately, the mechanical and electrical boundary conditions are usually separable; $u_i = u_i^*$ or $n_i T_{ij} = n_i T_{ij}^*$, and $n_i D_i = n_i D_i^*$ or $\varphi = \varphi^*$. The starred terms represent constants, time-varying values, or values defined within another media adjacent to the piezoelectric material. The outward vector normal to the boundary surface is given by n_i.

Even in the most anisotropic of materials substantial symmetry exists in Eq. (2), permitting contraction of the subscripts [4] and giving a simpler form for the constitutive equation;

$$\begin{aligned} T_p &= c_{pq}^E S_q + e_{mp} E_m \\ D_n &= e_{nr} S_r + \varepsilon_{nm}^S E_m \,, \end{aligned} \tag{3}$$

where p, q, and r range from 1 to 6, while m and n range from 1 to 3. There is *not* a one-to-one correspondence between the two representations in Eqs. (2) and (3). For example, the strain S_{ij} is $S_p = 2^{|\mathrm{sgn}(i-j)|}$. For this reason and the confusion that can arise in defining the momentum and strain-displacement equations, one must use care in solving problems with the contracted notation. The value of p in terms of i, j varies notoriously between authors, but the IEEE standard [4] is the most commonly accepted version; here $p = \frac{1}{2}(i+j)(1 - |\mathrm{sgn}(i-j)|) + |\mathrm{sgn}(i-j)|(9-i-j)$ for i, j = 1,2,3; here the vertical bars $|\cdot|$ represent an absolute value while sgn($\cdot$) is the *signum*, zero when x is zero and the sign of x otherwise.

Most solutions found by solving the complete set of piezoelectric material equations are very simple approximations. Computation, typically using finite element analysis software, is often necessary for practical cases. The ability to handle piezoelectric materials in commercially available finite element analysis software varies, though ANSYS (ANSYS Inc., Canonsburg, PA, USA) and COMSOL (COMSOL Inc., Burlington, MA, USA) are two well-known packages with decent implementations. However, a one-dimensional model of the piezoelectric material behavior offers many of the salient features without the complexity.

Piezoelectricity in One Dimension: Transducer Equations

If we assume a longitudinal plane wave propagates along the z-axis—assumed to be a principal axis of the material—the only non-zero displacement will also be along the z- or 3-axis, $u = u(z, t)$ and the strain will be $S_{33} = \partial u / \partial z$. Further, assuming the applied electric field is only along the 3-axis, $E_3 = E$ while $E_1 = E_2 = 0$, we may find the resulting constitutive equations from substitution into Eq. (2), closely following the approach used by Dieulesaint and Royer [3]:

$$\begin{aligned} T_{ij} &= c_{ij33}^E S_{33} + e_{3ij} E_3 \\ D_i &= e_{i33} S_{33} + \varepsilon_{i3}^S E_3 \end{aligned} \,, \tag{4}$$

where i must be equal to j. If we set $i = j = 1$, the motion would be transverse to the applied field (setting i and j to 2 would give the same result), while if $i = j = 3$, the motion is parallel. Taking the latter option with Eq. (4),

$$\begin{aligned} T_{33} &= c_{3333}^E S_{33} + e_{333} E_3 \\ D_3 &= e_{i33} S_{33} + \varepsilon_{33}^S E_3 \end{aligned} \rightarrow \begin{aligned} T &= c^E S + eE \\ D &= eS + \varepsilon^S E \end{aligned} \,, \tag{5}$$

where we discard the subscripts here and subsequently. The electric field, E, may be eliminated from Eq. (5):

$$T = \left(c^E + \frac{e^2}{\varepsilon^S}\right) \frac{\partial u}{\partial z} - \frac{e}{\varepsilon^S} D, \tag{6}$$

giving

$$\frac{\partial T}{\partial t} = \left(c^E + \frac{e^2}{\varepsilon^S}\right) \frac{\partial^2 u}{\partial z \partial t} - \frac{e}{\varepsilon^S} \frac{\partial D}{\partial t} \tag{7}$$

if we take a time derivative. The quantity $\left(c^E + \frac{e^2}{\varepsilon^S}\right) \equiv c^D$; this relation is also true for the tensor form, and indicates the relationship between the constant-field stiffness c^E and the constant field displacment c^D. There are relations between all of the coefficients as described later. The current passing through the piezoelectric element is given by $I = \int \frac{\partial D}{\partial t} dA$ where A is the cross-sectional area perpendicular to the z-axis. Since the wave is planar, $\frac{\partial D}{\partial t}$ is a constant across the cross-sectional area A, so $\frac{\partial D}{\partial t} = I/A$, and Eq. (7) simplifies to

$$\frac{\partial T}{\partial t} = c^D \frac{\partial^2 u}{\partial z \partial t} - \frac{eI}{\varepsilon^S A} \,. \tag{8}$$

Differentiating Eq. (8) with respect to z,

$$\frac{\partial^2 T}{\partial t \partial z} = c^D \frac{\partial^3 u}{\partial z^2 \partial t} = c^D \frac{\partial^2 v}{\partial z^2} \,, \tag{9}$$

noting $I = I(t)$ alone, and $v = \partial u/\partial t$. From the momentum equation, if the body force $f = 0$,

$$\frac{\partial T}{\partial z} = \rho \frac{\partial^2 u}{\partial t^2} \implies \frac{\partial^2 T}{\partial z \partial t} = c^D \frac{\partial^2 v}{\partial z^2} = \rho \frac{\partial^2 v}{\partial t^2}, \tag{10}$$

The latter part of Eq. (10), $c^D \partial^2 v/\partial z^2 = \rho\, \partial^2 v/\partial t^2$, may be solved as a wave equation:

$$v(x,t) = e^{\jmath\omega t}\left(V_1 e^{-\jmath kz} + V_2 e^{\jmath kz}\right). \tag{11}$$

where the circular frequency-wavenumber ratio is related to the material properties by $\omega/k = \sqrt{c^D/\rho}$ and $\jmath = \sqrt{-1}$; the first and second parts of the solution in Eq. (11) are waves traveling in the positive and negative z-directions, respectively.

An acoustic impedance may be defined as $Z = T/v = \sqrt{c^D \rho}$ —the latter term found by substituting Eq. (11) into Eq. (10)—and used to describe the stress wave propagation by substitution of Eq. (11) into Eq. (8) and integrating,

$$T = e^{\jmath\omega t} \left[\frac{kc^D}{\omega}\left(-V_1 e^{-\jmath kz} + V_2 e^{\jmath kz}\right) + \jmath \frac{eI_0}{\omega\varepsilon^S A}\right]. \tag{12}$$

Notice that the wave is *electroelastic*, with a propagating electric field wave in addition to the elastic behavior, and that $I = I_0 e^{\jmath\omega t}$.

The relationship between the mechanical and electrical behavior may now be determined using the stress and particle velocity fields for a piezoelectric element of homogeneous composition, finite thickness t, and constant cross-sectional area A as shown in Fig. 3. Note the polarization of the material indicated by the arrow adjacent to P. The stress T, when expressed on the faces of the piezoelectric element normal to the z-axis, becomes the force delivered by the element:

$$\begin{aligned} F_1 = AT|_{z=z_1} &= e^{\jmath\omega t} \cdot \left[\frac{Akc^D}{\omega}\left(-V_1 e^{-\jmath kz_1} + V_2 e^{\jmath kz_1}\right) + \jmath \frac{eI_0}{\omega\varepsilon^S A}\right], \\ F_2 = AT|_{z=z_2} &= e^{\jmath\omega t} \cdot \left[\frac{Akc^D}{\omega}\left(-V_1 e^{-\jmath kz_2} + V_2 e^{\jmath kz_2}\right) + \jmath \frac{eI_0}{\omega\varepsilon^S A}\right]. \end{aligned} \tag{13}$$

The velocities on the faces $z = z_1$ and $z = z_2$ are given by

$$\begin{aligned} v_1 &= -v|_{z=z_1} \\ &= -e^{\jmath\omega t}\left(V_1 e^{-\jmath kz_1} + V_2 e^{\jmath kz_1}\right), \\ v_2 &= v|_{z=z_2} \\ &= e^{\jmath\omega t}\left(V_1 e^{-\jmath kz_2} + V_2 e^{\jmath kz_2}\right) \end{aligned} \tag{14}$$

Using Eq. (14), it is possible to eliminate V_1 and V_2 from the force Eq. (13);

$$\begin{aligned} V_1 e^{\jmath\omega t} &= -\frac{v_1 e^{\jmath kz_2} + v_2 e^{\jmath kz_1}}{2\jmath \sin kd}, \\ V_2 e^{\jmath\omega t} &= \frac{v_1 e^{-\jmath kz_2} + v_2 e^{-\jmath kz_1}}{2\jmath \sin kd} \end{aligned} \tag{15}$$

where $d = z_2 - z_1$, giving

$$\begin{aligned} F_1 &= \frac{kc^D A}{\jmath\omega}\left[\frac{v_1}{\tan kd} + \frac{v_2}{\sin kd}\right] + \jmath \frac{eI_0}{\omega\varepsilon^S} \\ F_2 &= \frac{kc^D A}{\jmath\omega}\left[\frac{v_1}{\sin kd} + \frac{v_2}{\tan kd}\right] + \jmath \frac{eI_0}{\omega\varepsilon^S} \end{aligned} \tag{16}$$

making use of several trignometric identities.

From the field displacement equation in Eq. (5), the applied voltage V is given by

$$\begin{aligned} V &= \int_{z_1}^{z_2} E\, dz \\ &= \int_{z_1}^{z_2}\left(-\frac{e}{\varepsilon^S} S + \frac{D}{\varepsilon^S}\right) dz \\ &= -\frac{e}{\varepsilon^S} u|_{z=z_1}^{z_2} + \frac{1}{\varepsilon^S}\int_{z_1}^{z_2} D\, dz \\ &= \frac{e}{\varepsilon^S}\left(u|_{z=z_1} - u|_{z=z_2}\right) + \frac{I_0 d}{\jmath A\omega\varepsilon^S} \end{aligned} \tag{17}$$

since $D = (1/A)\int I_0\, \mathrm{d}A = I_0/(\jmath\omega A)$, implying $\int_{z_1}^{z_2} D\, \mathrm{d}z = I_0 d/(\jmath\omega A)$. Since $u = -\jmath\omega v$ and the *static* or *shunt capacitance* is $C_0 = \frac{\varepsilon^S A}{d}$,

$$V = -\jmath\left[\frac{\omega e}{\varepsilon^S}(v_1 - v_2) + \frac{I_0}{\omega C_0}\right], \tag{18}$$

forming the third of three equations which may be combined to give a matrix relationship between the input voltage and current and the output forces and velocities on the

P

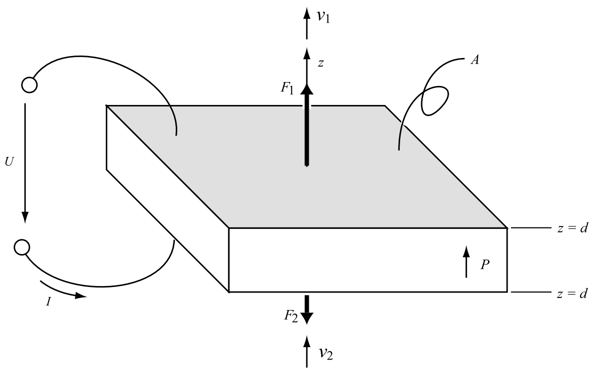

Piezoelectric Materials for Microfluidics, Figure 3 Schematic of a piezoelectric element to illustrate the process of analysis

faces of the piezoelectric element:

$$\begin{bmatrix} F_1 \\ F_2 \\ V \end{bmatrix} = -\jmath \begin{bmatrix} \frac{\zeta}{\tan kd} & \frac{\zeta}{\sin kd} & -\frac{e}{\omega\varepsilon^S} \\ \frac{\zeta}{\sin kd} & \frac{\zeta}{\tan kd} & -\frac{e}{\omega\varepsilon^S} \\ \frac{\omega e}{\varepsilon^S} & -\frac{\omega e}{\varepsilon^S} & \frac{1}{\omega C_0} \end{bmatrix} \begin{bmatrix} v_1 \\ v_2 \\ I \end{bmatrix} \tag{19}$$

if $\zeta \equiv \frac{kc^D A}{\omega}$ as the mechanical impedance, with units of mass/time. Notice that

- The output forces F_1 and F_2 are linearly proportional to the input current I and piezoelectric stress coefficient e, and inversely proportional to the permittivity ε^S and circular frequency ω.
- The change in velocity across the element $v_1 - v_2$ is linearly proportional to the input voltage V and permittivity ε^S, and inversely proportional to the circular frequency ω and piezoelectric stress coefficient e.

Approximating Transducer Behavior with Equivalent Circuit Equations

From the expression in Eq. (19) most forms of equivalent circuit models of piezoelectric elements may be found. The Van Dyke circuit [14] is the simplest, using discrete electrical components combined to approximate the piezoelectric element's behavior. I tis used to represent the electrical impedance about one resonance of a freely suspended piezoelectric element, using a shunt capacitor in parallel with an inductor, resistor, and capacitor placed in series to represent the *motional* or resonance behavior of the element. A multivibrator Van Dyke model may be formed by adding additional motional legs, each representing another resonance. Since it lacks any explicit treatment of the output force and velocity, it is not especially useful beyond electrical characterization (see Smits' method below). Other circuit models incorporate the mechanical behavior, and the most prevalent of these are the *Mason* [14] and Krimholtz–Leedom–Matthaei [7] (KLM) circuits.

The Mason equivalent circuit may be derived directly from Eq. (19). It is sometimes called a *transmission-line* circuit model since the transcendental terms in the matrix appear in the same way when modeling power transmission lines. Most importantly, the circuit represents more than one resonance with these transcendental terms. Consider first an element that does not have piezoelectricity, implying the piezoelectric stress coefficient $e = 0$. The force-velocity relationships in the nonpiezoelectric element would then be

$$F_i = \frac{v_1 + v_2}{\jmath \sin kd}\zeta + (\jmath\zeta \tan kd/2)\, v_i \tag{20}$$

for $i = 1, 2$. This relates the force and velocity on one face of the nonpiezoelectric element to the other face. For an element that is piezoelectric, $e \neq 0$, and we can use the third equation in Eq. (19) to determine the actual force due to the applied voltage by substitution in the top two equations.

Piezoelectric Coefficient Relations

Typically, a piezoelectric material's properties are measured through a series of experiments on a set of samples, and these measurements give results easily substituted into the matrix representations of the material. Unfortunately, very few of the components within each of the matrices are defined with the measured data, but the remaining data may be calculated using relations between the coefficients. At times, not enough data are provided to do this; for whatever reason, the data set is incomplete. This problem is especially common with piezoelectric material manufacturers. Further complicating the problem, companies sometimes provide redundant data that are inconsistent—calculated results from some of the provided data does not match the rest of the data that are provided.

The simplest relationship between the electrical property tensors is the inverse relationship between the permittivity, $\boldsymbol{\varepsilon}$, and the inverse permittivity, $\boldsymbol{\beta}$. The equations are

$$\boldsymbol{\beta}^S = \boldsymbol{\varepsilon}^{S^{-1}} \quad \text{and} \quad \boldsymbol{\beta}^T = \boldsymbol{\varepsilon}^{T^{-1}}. \tag{21}$$

Other relations transform the matrix representation of the permittivity or inverse permittivity from one set of boundary conditions (either fixed stress or fixed strain) to the other; for the permittivity,

$$\boldsymbol{\varepsilon}^S = \boldsymbol{\varepsilon}^T - \mathbf{d}\,\mathbf{c}^E\tilde{\mathbf{d}} = \boldsymbol{\varepsilon}^T - \mathbf{e}\,\mathbf{s}^E\,\tilde{\mathbf{e}}, \tag{22}$$

and for the inverse permittivity,

$$\boldsymbol{\beta}^S = \boldsymbol{\beta}^T + \mathbf{h}\,\mathbf{s}^D\,\tilde{\mathbf{h}} \;=\; \boldsymbol{\beta}^T + \mathbf{g}\,\mathbf{c}^D\,\tilde{\mathbf{g}} \tag{23}$$

Again, there is a simple inverse relationship between the mechanical coefficient matrices, namely, the stiffness, **c** and the compliance, **s**;

$$\mathbf{c}^E = \mathbf{s}^{E^{-1}} \quad \text{and} \quad \mathbf{c}^D = \mathbf{s}^{D^{-1}}. \tag{24}$$

The boundary conditions on the mechanical property matrices may be changed with the following transformations:

$$\mathbf{c}^D = \mathbf{c}^E + \tilde{\mathbf{e}}\,\boldsymbol{\beta}^S\,\mathbf{e} \;=\; \mathbf{c}^E + \tilde{\mathbf{h}}\,\boldsymbol{\varepsilon}^S\,\mathbf{h}, \tag{25}$$

for the stiffness, and

$$\mathbf{s}^D = \mathbf{s}^E + \tilde{\mathbf{g}}\,\boldsymbol{\varepsilon}^T\,\mathbf{g} \;=\; \mathbf{s}^E + \tilde{\mathbf{d}}\,\boldsymbol{\beta}^T\,\mathbf{d}, \tag{26}$$

for the compliance.

Unfortunately, there are no inverse relations between the piezoelectric coefficients. But, there are a wide collection of equations that describe one piezoelectric quantity in terms of the others. The following is a complete list of these equations:

$$\mathbf{d} = \boldsymbol{\varepsilon}^T\mathbf{g} = \mathbf{e}\mathbf{s}^E, \tag{27}$$

$$\mathbf{g} = \boldsymbol{\beta}^T\mathbf{d} = \mathbf{h}\mathbf{s}^D, \tag{28}$$

$$\mathbf{h} = \boldsymbol{\beta}^S\mathbf{e} = \mathbf{g}\mathbf{c}^D, \tag{29}$$

and

$$\mathbf{e} = \boldsymbol{\varepsilon}^S\,\mathbf{h} \;=\; \mathbf{d}\,\mathbf{c}^E. \tag{30}$$

Through substitution between these equations, many more relations between the variables can be expressed. Written differently, the relations are clearer. In the following equation, the dots within the parentheses represent where the variable at the top of each column would be placed to form the equation for the variable on the left side of each row:

$$\begin{array}{ccccc} & \mathbf{d} & \mathbf{g} & \mathbf{h} & \mathbf{e} \\ \mathbf{d} = & (\cdot) & \boldsymbol{\varepsilon}^T(\cdot) & \boldsymbol{\varepsilon}^T(\cdot)\,\mathbf{s}^E & (\cdot)\,\mathbf{s}^E \\ \mathbf{g} = & \boldsymbol{\beta}^T(\cdot) & (\cdot) & (\cdot)\mathbf{s}^D & \boldsymbol{\beta}^S(\cdot)\,\mathbf{s}^D. \\ \mathbf{h} = & \boldsymbol{\beta}^S(\cdot)\,\mathbf{c}^E & (\cdot)\,\mathbf{c}^D & (\cdot) & \boldsymbol{\beta}^S(\cdot) \\ \mathbf{e} = & (\cdot)\,\mathbf{c}^E & \boldsymbol{\varepsilon}^S(\cdot)\,\mathbf{c}^D & \boldsymbol{\varepsilon}^S(\cdot) & (\cdot) \end{array} \tag{31}$$

Experiment and Use

Physically measuring the coefficients of a piezoelectric material can be pursued in several different ways. Two of the most popular are the IEEE method [14] and Smits' technique [11]. Smits' technique has the advantage in that it requires fewer samples to be made by eliminating the radial resonator shape, especially important when considering the time necessary to make, machine, electrode, pole, and test piezoelectric material. Further, Smits' method uses exact equations in the calculation of the material constants, makes possible the calculation of loss data at the same time, and the electric and mechanical constants are measured at the same frequency unlike the IEEE method.

The technique is iterative, but the iteration process is strongly convergent. To determine all of the coefficients of a given piezoelectric material, four different geometries must be used. Each of these geometries encourage a particular vibration mode shape which reduce the number of material coefficients that are participating in the motion to a reasonable number. Named after the desired mode shape, the *thickness/shear* resonator, the *length expansion* resonator with perpendicular field, the *thickness expansion* plate resonator, and the *length expansion* resonator with parallel field provide different material constants when using Smits' technique on each of them. Convergence criteria and proof are provided in Smits' paper [11], but he claims that convergence to the correct values is usually achieved in eight iterations.

P

Manufacturing Methods

There are numerous ways to manufacture piezoelectric materials, roughly divided into crystal-growth methods for the single crystal media and a collection of techniques for polycrystalline piezoelectric media. The most obvious and troublesome difference in fabricating piezoelectric materials is the presence of lead in lead-based polycrystalline piezoelectrics like PZT; the lead is present in solid solution and tends to leach from the ceramic during sintering unless a source of lead is provided to maintain equilibrium. For all piezoelectric materials that exhibit remnant polarization, charging effects can be a problem during processing, enough to cause arcing and device failure or substrate cracking.

Among the crystal-growth techniques, the Czochralski (CZ) crystal growth technique is most common, particularly for lithium niobate, lithium tantalate, barium gallium orthophosphate (BGO), langasite, There are other techniques, and this is an active area of research. The development of single-crystal high-strain relaxor ferroelectrics like lead manganese niobate-lead titanate (PMN-PT) [8]

using the high-temperature flux technique is a notable example of another approach.

For ceramic materials, there are many approaches available to a researcher for fabrication, including the simple pellet press, tape casting, screen printing, sputter deposition (especially PZT and ZnO), sol-gel techniques for thin films, pulsed-laser deposition, and the hygrothermal technique [10] for deposition of quality PZT onto titanium.

Key Research Findings

During World War II, the discovery of PZT was a fortuitous and remarkable improvement on the state of the art in piezoelectric materials engineering. Since then, modest improvements in performance of piezoelectric materials have been made, with the discovery of single-crystal high-strain PMN-PT materials [8] an important milestone. In the past few years, however, methods for studying and manipulating the structure of ceramics on the scale of the unit cell and lower—the grain structure, the ferroelectric domains, and the structure of the unit cells themselves—have appeared [5]. These techniques are especially well-suited for improving the quality of piezoelectric materials; a recent potassium-sodium niobate/lithium tantalate/lithium antimonate ceramic has a piezoelectric performance equivalent to PZT while eliminating toxic lead [12]. Further, given the need to fabricate ► thin-film devices with features measured in nanometers in conjunction with micro- and nanofluidics, an understanding of the nature of polarization and ferroelectric domain growth in materials compatible with fabrication at these scales is vital. The applications for this technology span many disciplines: nonvolatile memory for computer technology, sensors and sensors for medical and biological diagnostics and actuators and microwave devices for consumer applications [9].

Future Directions for Research

The development of characterization and fabrication methods approaching the unit-cell size of known piezoelectric materials has reenergized the area of piezoelectric materials research in the past few years. By tailoring the structure of piezoelectric materials to maximize the polarizability, strength, and maximum strain, major advances are just beginning to appear. Work on applying the replete knowledge of bulk piezoelectric materials to thin-film materials research remains incomplete, from fabrication of PMN-PT to lead-free ceramics at small scales.

Looking beyond ceramic materials to electrets, polymer and elastomeric piezoelectric materials, and so-called electroactive materials, a wide-open field of research in high-strain piezoelectric materials is appearing. Using the same technology to manipulate the chemical and physical structures of complex ionic or nanotube-imbibed polymers, strains of well over 50 % have been obtained in this new class of material, many examples of which are biocompatible. Improvements in reliability, tolerance of extreme ambient conditions, and modeling are important areas that remain to be considered.

Cross References

► Piezoelectric Microdispenser

References

1. Auld BA (1989) Acoustic fields and waves in solids, vol. 1. Krieger, Malabar
2. Bellaiche L, Vanderbilt D (1999) Intrinsic piezoelectric response in perovskite alloys: PMN-PT versus PZT. Phys Rev Lett 83(7):1347–1350
3. Dieulesaint E, Royer D (2000) Elastic Waves in Solids II. Springer, Berlin
4. Hearmon RFS (1956) The elastic constants of anisotropic materials II. Adv Phys 5(19):323–382
5. Hong S, Woo J, Shin H, Jeon J, Pak Y, Colla E, Setter N, Kim E, No K (2006) Principle of ferroelectric domain imaging using atomic force microscope. J Appl Phys 89(2):1377–1386
6. Lang SB (1999) History of pyroelectricity: from ancient greece to space missions. Ferroelectrics 230(1):401
7. Leedom D, Krimholtz R, Matthaei G (1971) Equivalent Circuits for Transducers Having Arbitrary Even-Or Odd-Symmetry Piezoelectric Excitation. IEEE Trans Son Ultrason 18(3):128–141
8. Park S, Shrout T (1997) Ultrahigh strain and piezoelectric behavior in relaxor based ferroelectric single crystals. J Appl Phys 82:1804
9. Setter N, Damjanovic D, Eng L, Fox G, Gevorgian S, Hong S, Kingon A, Kohlstedt H, Park N, Stephenson G et al (2006) Ferroelectric thin films: Review of materials, properties, and applications. J Appl Phys 100(5):51606–51606
10. Shimomura K, Tsurumi T, Ohba Y, Daimon M (1991) Preparation of lead zirconate titanate thin film by hydrothermal method. Jpn J Appl Phys 30(9B):2174–2177
11. Smits J (1976) Iterative Method for Accurate Determination of the Real and Imaginary Parts of the Materials Coefficients of Piezoelectric Ceramics. IEEE Trans Son Ultrason 23(6):393–401
12. Takao H, Tani T, Nonoyama T, Takatori K, Homma T, Nagaya T, Nakamura M (2004) Lead-free piezoceramics. Nature 432:84–87
13. Tiersten HF (1967) Hamilton's principle for linear piezoelectric media. Proc IEEE 55(8):1523–1524
14. Warner AW, Berlincourt D, Meitzler AH, Tiersten HF, Coquin GA, Welsh IFS (1988) IEEE standard on piezoelectricity (ANSI/IEEE standard 176-1987). Technical report, The Institute of Electrical and Electronics Engineers, Inc.

Piezoelectric Microdispenser

James Friend, Leslie Yeo
james.friend@eng.monash.edu.au,
leslie.yeo@eng.monash.edu.au

Synonyms

Piezoelectric ink jet; Piezoelectric drop-on-demand; Droplet generator; Piezoelectric micro/nanoliter droplet dispenser

Definition

A fluid-filled chamber that has one or more exit orifices (nozzles) through which the fluid is driven by piezoelectric material causing either a rapid increase in pressure within the fluid or an acceleration of the orifice with respect to the fluid body. Additional fluid is provided through an inlet orifice by external pressure or through a suction mechanism designed into the microdispenser. The fluid, once forced through the nozzles, forms one or more droplets through an instability mechanism – main and perhaps ► satellite droplets – that propagate away from the nozzle, usually at a speed several times the diameter of the droplet per second at speeds up to 10 m/s. The droplets characteristically have a diameter of the same order as the nozzle diameter, usually 1 to 100 μm, and have a volume of several picoliters to nanoliters as they form over a period of about 100 μs. To deliver the fluidic pressure wave required to form the droplets, a pulse or tailored electric drive signal must be provided to the piezoelectric material at a voltage of 5 to 200 V.

Overview

The ► piezoelectric microdispenser, closely related to ► piezoelectric ink-jet printing, a specific application of the microdispenser traditionally for consumer printing, encompasses three separate operating schemes depending on the intended application. A single ► droplet on demand may be delivered by a dispenser through either impulse excitation of the piezoelectric element or continuous vibration of the nozzle with short-term contact onto an application surface. Continuous droplet generation may be obtained through formation of a long-term Rayleigh instability of the fluid surface at the nozzle. ► Fluid jetting is another method to form fibers or droplets, the latter through subsequent breakup of the jet after it has left the microdispenser's exit nozzle due to Rayleigh or Kelvin–Hemholtz instabilities. Another less common method, ► free-surface atomization, makes use of sessile droplets or relatively large fluid volumes placed on the surface of an ultrasonically vibrating structure which induces breakup through an as-yet poorly understood combination of Rayleigh instability and ► cavitation mechanisms.

Piezoelectric microdispensers have existed since the 1950's, though their use increased dramatically with a need for inexpensive printing from the early 1980's, an application shared with thermoelectric (bubble) microdispensers. Generally, piezoelectric microdispensers offer superior flexibility, simplicity, and scalability compared to other known droplet-forming technologies. However, the use of piezoelectric materials causes problems, particularly in the use of lead zirconate titanate (PZT) and its higher-performance doped variants, which are not generally compatible with standard micromachining processes. As a consequence, scaling down dispensers that make use of PZT is difficult. Though other piezoelectric materials have been used over the years, including quartz, aluminum nitride, and zinc oxide, PZT is favored for its large ► electromechanical coupling and relatively large ► piezoelectric strain coefficients. The generation of a sufficient electric field in the piezoelectric materials, particularly for pulsed drop-on-demand dispensers, can require high voltages not directly compatible with integrated-circuit voltages (5 or 12 V). The placement, diameter, and configuration of the inlet and outlet orifices is critical to obtain suitable droplet formation from input strain pulses along the boundary of the fluid chamber, and microdispenser design is a challenge met through a combination of approximate analytical methods, computational modeling, and experimental development, using many versions of a design to discover the one most suitable for the application. Over the years, different operating schemes have been considered for piezoelectric microdispensers, and current technology [1] is essentially a refinement of the spectrum of configurations available over 25 years ago [2].

Regardless, a majority of the systems operate through direct squeezing of the fluid volume present within the dispenser, and as a consequence the volume of fluid ejected from the dispenser at the nozzle is a linear function of the applied voltage, that is, once the stability of the fluid ► meniscus present across the nozzle is overcome. This is in contrast to the generation of jets and droplets via ► acoustic streaming, which would result in an ejected fluid volume proportional to the square of the applied voltage. Applying low voltage signals to the piezoelectric element will result in a deformation of the meniscus, and as the applied voltage is increased, the deformation grows until the meniscus becomes unstable.

If the capillary wavelength is approximately the same size or larger than the nozzle diameter, the formed droplet diameter will be related to the nozzle diameter, and will increase with an increase in the applied voltage. At a certain threshold voltage, more than one droplet will form from the extension and breakaway of the meniscus. Typically, each of the extra droplets – a ► satellite drop – is smaller in size than the primary droplet, but as the voltage continues to increase, these droplets tend to increase in number and volume. There may be yet another transi-

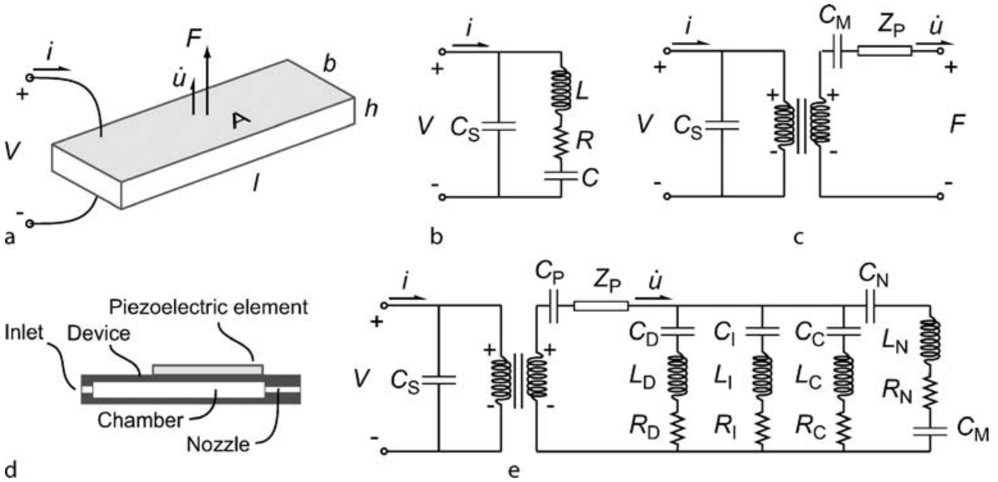

Piezoelectric Microdispenser, Figure 1 Equivalent circuit modeling of (**a**) planar, thickness-polarized, thickness-vibrating piezoelectric transducers using (**b**) a simple lumped-element Van Dyke model and (**c**) a more complex transmission-line model. A model of a piezoelectric microdispenser (**d**) may be formed by connecting the output terminals to the equivalent circuit model of the remaining components (**e**)

tion to chaotic droplet and stream generation as the voltage continues to increase, and cavitation within the chamber or at the nozzle may also occur.

However, if the capillary wavelength is much less than the diameter of the nozzle, the droplet diameter will instead be related to the capillary wavelength: the droplets form from crest instabilities on the free surface of the fluid. The droplet dimensions for this arrangement follow similar trends as the voltage is increased. Using this technique, it is possible to generate droplets less than 1 μm in diameter through the use of frequencies beyond 10 MHz generated from ▶ surface acoustic wave devices.

This review considers the variety of device designs for piezoelectric microdispensers, methods to model their overall behavior, in addition to the characteristics of atomization mechanisms available for dispensing droplets using piezoelectric materials.

Basic Methodology

Device modeling

Equivalent circuit models have been used to represent piezoelectric material behavior for many years, but are not without limitations. The most common representation for a piezoelectric material, as recommended by the IRE/IEEE standards on piezoelectricity, is the Van Dyke model as described in detail in ▶ piezoelectric materials in microfluidics, with a capacitor, resistor, and inductor in series representing a single resonance, or motional component of the piezoelectric element, all set in parallel with a second capacitor, representing the ▶ shunt capacitance. Additional resonances may be included by placing additional capacitor-resistor-inductor sets in parallel, but therein lies some of the limitations of equivalent circuit modeling: accurate determination of the equivalent circuit components requires either a physical prototype or an accurate computational model to provide the data. Further, assuming the loss mechanisms are isolated to a single resistance in the motional component per resonance may lead to error in predicting both the system response and the resonance frequencies. Computational models using finite-element analysis or the like require similar physical data, and so a physical prototype becomes absolutely necessary in the prediction of microdispenser behavior.

Additional matters to consider in using piezoelectric materials that require a physical prototype include the aging of the piezoelectric material and the temperature change during operation. Over time, the resonance frequency and static capacitance will change in an exponential fashion; most of the aging will occur in the first two months, but the subsequent aging can be important in circuit and resonant chamber design. As an electric field is applied to a piezoelectric element, the element will heat due to electromechanical losses in the material. The heating can be significant for soft piezoelectric materials, and can affect the resonance frequencies and capacitance for both hard and soft piezoelectric media.

Equivalent circuit modeling is a useful and commonly applied analysis approach for designing piezoelectric microdispenser systems. The method has limited accuracy, and the ▶ lumped analysis approach requires the wavelength of the input signal to be larger than any characteristic length within the device. In a microdispenser with an internal cavity, for example, the ▶ Hemholtz resonance

of the orifice, nozzle, and cavity structure should be far higher than the frequency of excitation of the device used to perform the dispensing. The time required to transmit a change in the applied electric field on the piezoelectric element to a change in the meniscus shape at the nozzle is therefore negligible. Using ▶transmission-line models of the piezoelectric element, fluid chamber, and other components in the microdispenser permit analysis without the wavelength limitation [3], and provide the ability to analyze the approximate interaction between multiple resonances in the complete system.

In this situation the coupling coefficient of the piezoelectric material is especially important. Though there are many specific forms of the coupling coefficient, an effective coupling coefficient may be used for a transducer operating near a particular resonance;

$$k_{\text{eff}} = \sqrt{\frac{\text{mechanical energy stored}}{\text{electrical energy input}}} = \sqrt{1 - \frac{f_r^2}{f_a^2}}$$

where f_r is the resonance frequency and f_a is the antiresonance frequency (▶resonance and antiresonance frequency) associated with the vibration mode that dominates the motion induced by the applied voltage signal, if one such mode can be assumed to exist. The mechanical energy stored in the piezoelectric device may then be used to perform work on the fluid meniscus, and in this way the amount of energy applied to form a droplet for a microdispenser as a fraction of the input electrical energy may be estimated once one knows the resonance and antiresonance frequencies. The resonance and antiresonance frequencies are typically near the frequencies of minimum and maximum impedance, respectively, for a specific resonance.

Choosing a thickness-polarized, thickness-vibrating piezoelectric element as an example, we can define the applied voltage V, current i, dimensions b, h, and l, and the output force and velocity F and $\dot{u}$; the cross-sectional area bounded by b and l can be defined by A; here it is assumed this area is electroded on the top and bottom faces of the element and that b and l are much greater than h. Treating it as a collection of discrete circuit elements as shown in Fig. 1b, the Van Dyke circuit, allows the analysis of one resonance within the isolated element. Most piezoelectric materials are capacitive insulators, and the ▶shunt capacitance $C_S = bl/\beta_{33}^S h$ is the constant capacitance present across the element. The additional branch in the circuit represents the specific resonance being analyzed, the motional branch with inductance L, resistance R, and capacitance C. Many impedance analyzers provide this circuit as a means to model the electrical behavior of the piezoelectric element. The coupling coefficient for this specific arrangement is $k_T = \sqrt{h_{33}^S \varepsilon_{33}^S / c_{33}^S}$. Unfortunately, the model only accounts for one resonance and provides no information on the output force F and velocity $\dot{u}$. By treating the element as a transmission-line impedance Z_P as shown in Fig. 1c, one can incorporate an arbitrary number of resonances, where $C_M = -h_{33}^S bl/\beta_{33}^S h$ and $Z_P = \frac{k}{j\omega} \frac{\omega h/c}{\tan(\omega h/c)}$ where $c = \sqrt{c_{33}^D/\rho}$ is the longitudinal wave velocity for an open-circuit element. The resonances appear when $(\tan \omega h/c)$ goes to infinity. The quantities h_{33}, β_{33}, e_{33}, and c_{33} represent the piezoelectric field to strain coupling, permittivity, inverse permittivity, and material stiffness along the thickness direction in this model. The S superscript on these quantities represents constant strain (clamped) values, and the D represents constant electric field displacement (open-circuit) values. By connecting the output of the piezoelectric element, or port, to a microfluidics structure (see Fig. 1d) with nozzle, chamber, inlet and compliant structure, a microdispenser can be formed. A simple representation of this situation can be modeled as a collection of RLC resistance-induction-capacitance branches in Fig. 1e connected to the output of the piezoelectric element represented by the open terminals on the right in Fig. 1c. Note the inclusion of RLC sets for the device, inlet, device, and nozzle, each treating a specific resonance of the component. Transmission-line impedances could be used for these components as well to handle multiple resonances. There is an additional capacitor for the meniscus to take into account the formation of capillary waves; the charging of the capacitor is tied to the appearance of the capillary waves and can suggest whether a droplet will be formed as a consequence of an input signal V. The values of the resistance, inductance and capacitance may be related back to the dimensions and configuration of the microdispenser as shown by Berger and Recktenwald [3].

P

Generation

Modeling of piezoelectric microdispensers provides useful information on the potential for further optimization and insights into the operating mechanism underlying their behavior. However, the reliable formation of stable, monodisperse droplets from a device generally requires a tedious process of trial-and-error design of the driving scheme, fluid, nozzle, chamber, and inlet. Many factors affect the behavior of microdispensers, only a few of which can be incorporated into a mathematical model of the overall device at present. Most of the difficulty is associated with the behavior of the fluid at the exit nozzle. Generally, if the fluid to be dispensed has a low viscosity of about $1-50\,\text{cS}$, is slightly hydrophobic, and does

not contain particles greater than 10% of the diameter of the nozzle, droplet generation becomes a function of the design of the microdispenser alone [4].

The generation of droplets can be divided into three schemes depending on the form of the fluid leaving the orifice. Individual droplets may be formed on demand through discrete signals applied to the microdispenser, droplets may be formed continuously, with a short transition to and from steady droplet formation upon the application and removal of the driving signal from the microdispenser, or jets of fluid can be generated from a microdispenser, which may later break up into droplets as the jet interacts with the environment. A comparison of a characteristic length of the fluid leaving the microdispenser with the nozzle meniscus size provides another way to categorize the generation mechanism of a device. If the characteristic length – droplet diameter, for example – and the meniscus diameter are similar, the characteristic length is typically controlled by the meniscus size. If, however, the characteristic length is significantly smaller than the meniscus size, the characteristic length is controlled instead by the instability mechanism that generated it.

Droplets from Nozzles

Piezoelectric microdispensers that generate droplets of a size defined by the nozzle diameter function either through the interaction of a pressure wave induced in the fluid with the meniscus located at the nozzle, or a rapid acceleration of the meniscus. Either way, a column of fluid is pushed from the nozzle into the surrounding atmosphere. If the column reaches a sufficient length before being drawn back into the nozzle after passage of the pressure wave (πd_{noz} as predicted by Rayleigh [5], where d_{noz} is the nozzle diameter), the free surface will become unstable and pinch off, forming at least one droplet; the droplet diameter he predicted as a consequence of this process, $d_{\text{Rayleigh}} = 1.89 d_{\text{noz}}$, represents an upper bound for the actual droplet diameter. This instability mechanism is not the free-surface Rayleigh instability as commonly understood and described later.

Lee and Lal [6] summarize the work of Lord Rayleigh, Weber, Sterling and many others quite well, and consultation of references in their work provides an introduction to the literature. Rayleigh's result represents the upper bound since it ignores the drag on the column and droplet from the surrounding atmosphere, and subsequent research considered these factors in the analysis. Through the inclusion of a drag model, the droplet size prediction can be made to be more accurate. Consider the column of fluid pushed from the nozzle, and treat the velocity of the column as U, the fluid's density, surface tension, and dynamic viscosity as ρ, σ, and μ, respectively, and the ambient atmosphere's density as $\hat{\rho}$. The ► Weber number of the ambient atmosphere and ► Ohnesorge number of the fluid may then be defined as

$$\hat{\text{We}} = \frac{\hat{\rho} U^2 d_{\text{noz}}}{\sigma} \tag{1}$$

$$\text{and } \text{Z} = \frac{\mu}{\sqrt{\rho \sigma d_{\text{noz}}}} \,. \tag{2}$$

Typically, the Weber and Ohnesorge numbers are dimensionless measures of the relative strength of the inertia to the surface tension in a fluid, and the viscosity to the surface tension of a fluid, respectively. Here the Weber number is modified (with a hat, $\hat{\text{We}}$) to consider the inertia of the surrounding atmosphere in comparison to the surface tension of the fluid extending from the nozzle.

As the fluid column extends from the nozzle, the instability of the free surface is exhibited across several length scales, represented by a collection of solutions of Sterling's equation of motion describing the instability. One of these solutions grows in amplitude more rapidly than the others, which caused Sterling to assume that it would come to dominate the droplet formation process. The selected solution describes the maximum column length that can be obtained without actually causing sufficient surface instability to form a droplet. It further describes the diameter of the droplet formed as a consequence of the instability once the fluid column surpasses that maximum length. The wavelength of the instability as it forms a droplet may be written as $\lambda = \pi d_{\text{noz}} \hat{\vartheta}$, where

$$\hat{\vartheta} = \sqrt{2(1 + 3\text{Z})}\, \text{e}^{-0.035\hat{\text{We}}} \tag{3}$$

represents the reciprocal non-dimensional wavenumber of the most rapidly growing disturbance. For water being ejected from a $10\,\mu\text{m}$ diameter nozzle at $U = 1\,\text{m/s}$, the modified Weber number is $\hat{\text{We}} = 1.81 \times 10^{-4}$, the Ohnesorge number is $\text{Z} = 0.0373$, and so $\hat{\vartheta} = 1.49$ and the wavelength of the instability is $\lambda = 46.9\,\mu\text{m}$. The diameter of the droplet may be taken as one-half the instability wavelength, $d = 23.4\,\mu\text{m}$, because one-half of the wavelength forms the droplet while the other half forms the neck region that separates the droplet from the remaining portion of the fluid column. The fluid's density, surface tension, and dynamic viscosity were treated as $\rho = 1002\,\text{kg/m}^3$, $\sigma = 0.072\,\text{N/m}$, and $\mu = 1.002 \times 10^{-3}\,\text{kg/(m} - \text{s)}$, respectively, and the ambient atmosphere's density was set at $\hat{\rho} = 1.3\,\text{kg/m}^3$.

The formation of additional droplets – ► satellite droplets – in addition to the desired or primary droplet for each

extension of the fluid column induced by an applied pressure wave or acceleration of the nozzle is a troublesome problem with microdispensers. Dong, et al., in a thorough work [7], examined the formation of the primary and satellite droplets and suggested a criteria for avoiding the formation of satellite droplets. As the primary droplet forms from the liquid column extending from the nozzle, a fluid thread may form from the neck. In some cases, this fluid thread may become quite long in comparison to the nozzle diameter, the ratio of which could be defined as l_b/d_{noz}. If the fluid thread length is larger than a limiting value l_b^*, the thread will break up into satellite droplets. There is the possibility that the satellite droplets will merge with the primary droplet if the relative velocities are in the correct direction and large enough to induce recombination.

In any case, the limiting value of the fluid thread length may be written as

$$l_b^* = d_{noz}\left(\frac{(C_2 - C_1)a}{2\alpha^*_{max}} + 1\right), \tag{4}$$

where

$$\alpha^*_{max} = \sqrt{\frac{2\vartheta^2 - 2 + 9Z^2}{4\vartheta^4}} \tag{5}$$

is a term related solely to the nozzle and fluid characteristics; $\vartheta = \sqrt{2(1+3Z)}$ here, an approximation similar to Dong, et al., in line with Sterling's analysis given by Eq. (3) with the omission of the Weber-related air drag term. The nondimensional constants C_1 and C_2 are related to the pinch-off time of the liquid thread from the nozzle and primary droplet, respectively, while a represents another nondimensional constant that relates the speed of the wave disturbance along the periphery of the fluid column to the speed of the retreating fluid column back towards the nozzle after the formation of the droplet and fluid thread stretching between the column and droplet. Dong, et al., claim the product $(C_2 - C_1)a$ is between 0.9 and 1.1 for their experiments with water and glycerin compounds ejected into air. For the water/air system considered in this section, the limiting fluid thread length is $l_b^* = 22.8\,\mu m$ if $(C_2 - C_1)a$ is 0.9. Experimental visualization would be necessary to determine the actual fluid thread length. Dong, et al., suggest that the most effective method to eliminate satellite droplet formation is an increase in the fluid viscosity which would increase the Ohnesorge number and reduce α^*_{max}.

Most piezoelectric microdispensers use the single-droplet nozzle ejection mechanism to form droplets. Through careful design, droplets may be rapidly ejected one after another from the meniscus at frequencies of up to 10 kHz, though there are limitations from refill speed, cavitation, bubble ingestion from the nozzle into the fluid chamber, and satellite droplet formation. Generally the piezoelectric material is not a limitation in droplet delivery speed unless soft PZT is used, which has a larger electromechanical transduction loss and is susceptible to heating at operating frequencies above 1 kHz.

Jetting from nozzles in piezoelectric microdispensers is also possible, usually through a combination of constant applied pressure on the fluid with a lesser modulation of the pressure using the piezoelectric element. The modulation introduces an instability in the jet traveling out of the orifice which is amplified to cause the breakup of the jet into droplets through the interaction of the jet with the ambient environment; this instability mechanism is known as the ▶ Kelvin–Helmholtz instability and requires the jet to be moving at several meters per second in air to cause droplet formation [8]. Secondary breakup of the droplets into finer droplets may then occur via the Rayleigh–Taylor mechanism described later, though the conditions under which this can happen do not typically occur on the scales of most piezoelectric microdispensers.

Droplets from Free Surfaces

It is also possible to dispense microdroplets from free surfaces, either formed on a sessile droplet or along the meniscus formed at a nozzle. In the latter case, the critical difference with the previous section is that the primary droplet formed from the nozzle is much smaller than the diameter of the nozzle, eliminating the direct influence of the nozzle's size on the size of the droplet. The study of the formation of droplets from free surfaces has a long and controversial history, which has been suggested to be due to either capillary wave breakup, cavitation, cavitation-induced capillary waves which subsequently break up to form droplets, or even cavitation-screened capillary wave breakup, where a cavitation layer beneath the surface acts to suppress atomization. It is likely that over the wide range of operating frequencies and configurations available each of these physical mechanisms is possible, but for microdispensing fluids, capillary wave breakup appears to be the most likely mechanism [9]. Even so, the complexity of the analysis and nonlinear behavior [10] should not be underestimated in considering the use of free surfaces.

In 1950 Taylor studied the formation of sinusoidal waves on the free surface of a fluid in air undergoing acceleration perpendicular to the free surface and in the direction of the force of gravity, and almost a century prior Rayleigh considered the formation of similar waves if the denser fluid was placed above the free surface; both illus-

trate a similar mechanism that has come to be described by the Rayleigh–Taylor instability. Curiously, the instability will appear between the interfaces of other phases of media, including even solid-solid interfaces, and the form of the equations that describe the instability will remain essentially the same [11]. The formation of droplets from capillary waves may be described by the Rayleigh–Taylor instability.

Loosely following Piriz, et al. [11], if $\xi = \xi(x, t)$ represents the transverse displacement of the inviscid fluid surface where x is the position coordinate along the fluid interface[1], $\ddot{\xi} = A_T \kappa g \xi$ is the equation of motion of the surface if we ignore surface tension and let the ▶ Atwood number be $A_T = \rho_2 - \rho_1/\rho_2 + \rho_1$, $\rho_2 > \rho_1$, where ρ_2 is the density of the fluid above the interface, and g and κ be the gravitational acceleration ($9.8065\ \mathrm{m/s^2}$) and the perturbation wave number, respectively. This can be integrated to give the exponential growth of the interface amplitude at a rate of $\sqrt{A_T \kappa g}$. The wavenumber is related here to the frequency of the applied oscillation through $\kappa = f/c$, where f is the frequency of the applied oscillation and c is the bulk sound speed within the fluid carrying the acoustic energy to the interface. If we place the dense fluid beneath the interface so that now ρ_2 is the density of the fluid below the interface, and incorporate surface tension, dynamic viscosity, and the acceleration of the fluid interface $\ddot{\psi}(t)$ in the direction of the gravity force g, the equation of the transverse displacement of the surface $\xi(t)$ becomes

$$\ddot{\xi} + \left[A_T \kappa \left(g - \ddot{\psi}(t)\right) + \sigma/\rho_1\right] \xi + 2\frac{\mu_1 + \mu_2}{\rho_1 + \rho_2} \rho_2 \kappa^2 \dot{\xi} = 0 . \tag{6}$$

Lamb recognized in 1932 that the surface tension acts to stabilize disturbances with wavenumbers greater than the cutoff value of

$$\kappa_C = \sqrt{\frac{g(\rho_1 + \rho_2)}{\sigma}} .$$

Above this value, oscillations induced on the free surface are stable, while below this value, it is possible to induce instability on the surface and form droplets. Viscosity cannot prevent the instability, but it does increase the acceleration $\ddot{\psi}(t)$ necessary to cause the instability to appear. In the equation of motion (6), acceleration due to gravity, g, also acts to stabilize the interface. There are different ways to destabilize the surface, the simplest of which is to $\ddot{\psi}(t)$ to a constant value above $g + \sigma/(\rho_1 A_T \kappa)$, forming a gravity wave. Other ways include harmonic excitation with $\ddot{\psi}(t) = \Psi\, e^{i 2\pi F t}$ where $i = \sqrt{-1}$, Ψ is the amplitude, and F is the frequency of excitation. Lang [9] found the diameter of the droplets formed from the free surface closely follows Kelvin's equation for the capillary wavelength,

$$\lambda = \sqrt[3]{\frac{2\pi\sigma}{\rho f^2}} , \tag{7}$$

where f represents the frequency of the most easily excited capillary waves on the free surface. Based on experimental results, it has been shown that the frequency of the capillary waves is one-half the excitation frequency F if it is assumed to be harmonic, and Lang showed that the droplet diameter is 0.34 times the capillary wavelength based on experimental results across a wide range of frequencies:

$$d = 0.34 \sqrt[3]{\frac{8\pi\sigma}{\rho f^2}} .$$

Similar to the droplet breakup model in the previous section, many different vibration modes may be excited on the surface by the acceleration $\ddot{\psi}(t)$, but the one represented by λ in equation is assumed to dominate in the generation of droplets. This assumption is valid at powers just sufficient to cause the generation of droplets, but as the amplitude Ψ is further increased, other modes may become large enough to form droplets, increasing the droplet size distribution and the complexity of analysis.

Impulsive excitation may also be used to form droplets from a free surface in this way. Continuous wave excitation can provide very monodisperse distributions of droplets with diameters much less than the characteristic size of the free surface [12], but impulsive excitation has also been used with success in commercial applications by Xerox [4]. A critical part of their success has been in finding ways to form a single droplet from the surface per excitation pulse; typical free surface droplet generators form n droplets where $n = (1/2)\pi(d_{\mathrm{surf}}/\lambda)^2$, d_{surf} is the diameter of the free surface, and λ is the capillary wavelength. Impulsive excitation has the advantage of offering droplet-on-demand operation at the expense of requiring thorough analysis of the free surface to ensure reliable formation of individual droplets.

Jetting from the free surface may also be obtained, and droplets could be formed from these jets through secondary breakup mechanisms if the Ohsenorge number is less than about 0.1 and the Weber number is above 5. The conditions necessary to obtain free-surface jetting from piezoelectric microdispensers are fairly challenging; even though there are examples of high-frequency free-surface

[1] A 2-D assumption is implicit here, as it is throughout most literature on instability calculations.

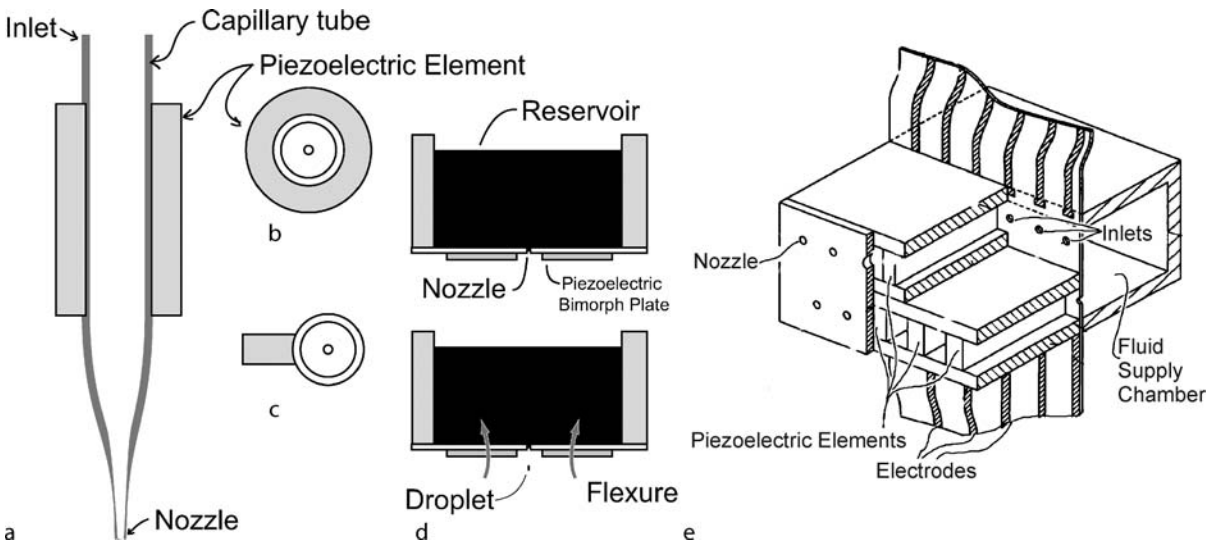

Piezoelectric Microdispenser, Figure 2 The capillary tube microdispenser, viewed from the side (**a**) and top (**b**), with a variation (**c**) by Lee and Lal [6]. Though almost unrecognizable after years of refinement and adoption of a parallel layout scheme, the Konica-Minolta device (**d**) is also a capillary tube microdispenser

jetting [13], they at present remain little more than curiosities.

Droplet Motion After Ejection

Once formed, most piezoelectrically-dispensed droplets have a drag force proportional to their velocity. In contrast to the viscous drag force on macroscopic objects,

$$F_{\text{Viscous Drag}} = \tfrac{1}{2}\rho C_{\text{d}} A v^2 \,, \tag{8}$$

which scales with the square of the velocity of the object relative to the surrounding fluid, the drag force due to Stokes' law scales linearly with velocity:

$$F_{\text{Stokes}} = 6\pi\eta r v \,; \tag{9}$$

$r, v, A, C_{\text{d}}, \rho$, and η are the drop's radius, velocity, and cross-sectional area, the coefficient of drag, and the surrounding fluid's density and viscosity, respectively. The viscous drag scales inversely to the square of the diameter of the droplet, and so is negligible in air for droplets less than about 25 μm in diameter. The most common figure of merit used in choosing the appropriate drag force is the ► Reynolds number.

For droplets in air less than about 5 μm in diameter, the actual drag force is even lower, since the surrounding air is not a continuum at these scales. Millikan's resistance factor (or ► Cunningham's correction) multiplies the terms on the right-hand side of equation (9) to form the corrected drag force

$$F'_{\text{Stokes}} = 6\pi\eta r v\left[1 + \left(\frac{0.130\,\mu\text{m}}{d}\right) \times \left(1.252 + 0.399\,\mathrm{e}^{-1.100 d/0.130\mu\text{m}}\right)\right] \tag{10}$$

A 10 μm diameter droplet moving at 1 m/s in air would have 14.1 pN, 1.72 nN, and 2.00 nN of force on it from viscous drag, uncorrected Stokes' drag, and Cunningham-corrected Stokes' drag, respectively. More importantly, the deceleration of a 10 μm diameter water droplet moving at 1 m/s would be 3820 m/s^2 due to the Cunningham-corrected Stokes drag calculated from

$$\dot{v} = \mathrm{F}'_{\text{Stokes}} \Big/ \left(\frac{\pi}{6}\rho d^3\right) \tag{11}$$

where the term in parentheses is the droplet mass. The deceleration decreases rapidly as the droplet slows; the velocity is an exponential function of time. Under gravity, the terminal velocity can be found by setting the drag force equal to the force of gravity, though this is far less than the ejection velocities for most dispenser systems; for example, a 10 μm droplet has a terminal velocity of only 3 mm/s.

In addition to the correction on the drag force from the noncontiguous surrounding fluid, there is also an randomizing effect on the droplets' motion due to the interaction with the environment: ► Brownian motion. This motion can cause error in droplet placement or

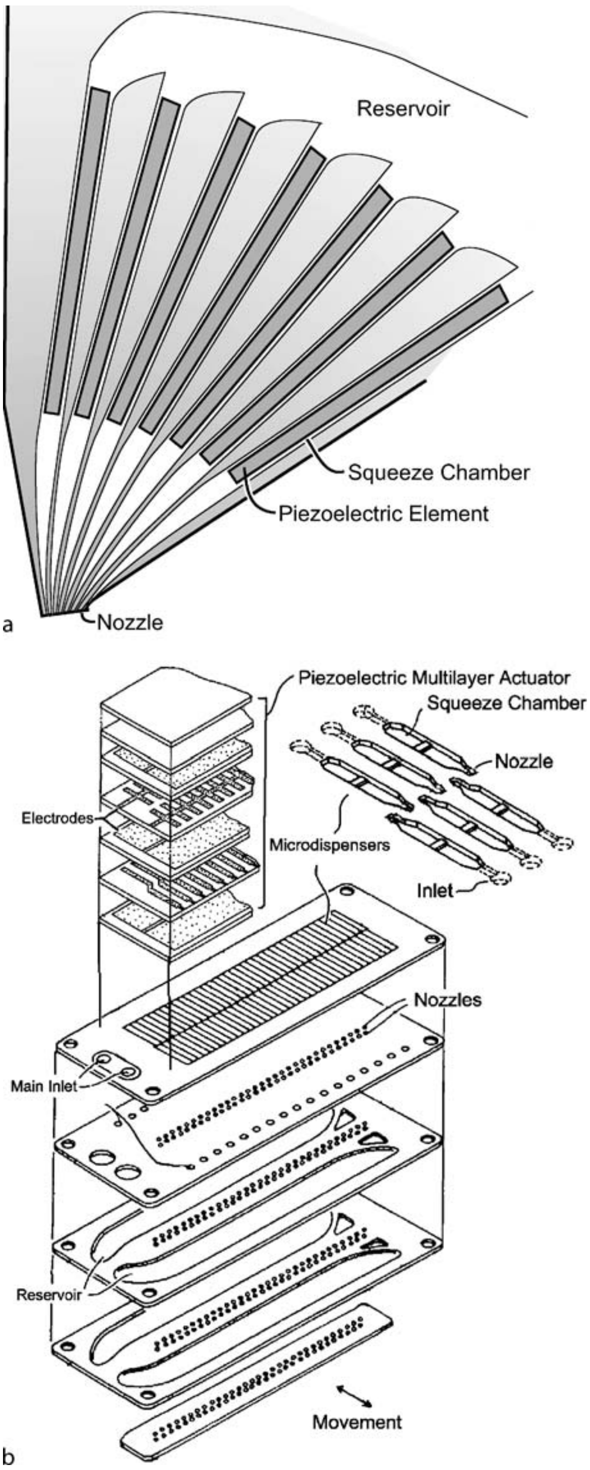

Piezoelectric Microdispenser, Figure 3 The side-shooter design as conceived by Kyser and his associates at Silonics in the 1970's (**a**), and a modern version by Brother (**b**) using planar micromachining technology. Note the dramatic increase in nozzles and the more detailed cross-sectional design. The chamber cross-section in the Kyser design is rectangular

agglomeration of droplets in continuous droplet formation or atomization systems. The mean displacement of a droplet, δ, due to Brownian interaction over time t is a function of the temperature T, ►Boltzmann's constant $k = 1.38065 \times 10^{-23}$ J/K, and drag force, F_{Drag}, which is a choice between Eqs. (8) through (10) suited to the diameter of the droplet under consideration,

$$\delta = \sqrt{\frac{2kTt}{F_{\text{Drag}}}}. \quad (12)$$

For a 5 μm droplet, the average displacement after one second at 20 °C is about 2.66 μm, over half the droplet's radius, using Eq. (10) for the drag force.

Key Research Findings

The devices resulting from the combination of piezoelectric materials and fluidic microstructures to provide dispensing of small amounts of liquid fall into several distinct categories based on their construction. Most common of these is the capillary tube drop-on-demand system, shown in Fig. 2, first developed by Zoltan at Clevite in the early 1970's, and commonly called the Gould or Bogy device. Many variations on this design exist due to the simplicity of the configuration and ease in forming the micropipette tips from which droplets may be dispensed; one can even manufacture their own capillary tube microdispenser for very little cost [4]. Fig. 2a illustrates the typical form of this device, though there have been many variations in the shape of the piezoelectric element used, as shown with the top views in Fig. 2b and c; the latter from Lee and Lal [6], and an interesting variation (see Fig. 2d) from Percin and Khuri-Yakub [14]. Through mass production and microfabrication techniques, the concept has been refined to the form shown in Fig. 2e by Konica-Minolta [15]. The device functions either by squeezing the fluid or accelerating the meniscus through actuation of the piezoelectric material; in most devices both mechanisms are in part responsible for the ejection of droplets. Note even in the Konica-Minolta device the piezoelectric material is a simple shape that may be constructed from machining bulk pieces of PZT. Another design that has been used for microdispensers is the so-called side-shooter design originally developed by Kyser and others in the late 1970's, as illustrated in Fig. 3 in its original configuration, and a modern configuration by Brother making use of planar micromachining technology. A relatively unique version of droplet generation from a free surface is focused acoustic beam ejection by Elrod, et al., at Xerox PARC in the early 1990's [4] illustrated in Fig. 4; it represents a refined version yet lower-frequency ver-

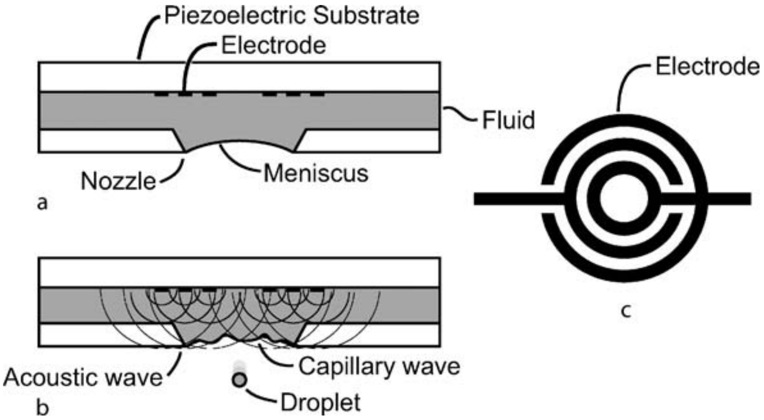

Piezoelectric Microdispenser, Figure 4 Focused acoustic beam ejection technology by Elrod and associates at Xerox PARC. Using a piezoelectric element with electrodes immersed in a thin layer of fluid below a nozzle (**a**), an electrical impulse will induce an acoustic wave that, when interacting with the meniscus, forms a capillary wave that ejects a single droplet (**b**). The form of the electrode (**c**) and the driving signal are two of the features of the design that must be carefully designed

sion of the surface acoustic wave atomizer by Shiokawa et al. [13].

Future Directions for Research

Recently, many new piezoelectric materials have appeared as a consequence of the ability to observe and tailor crystal, polycrystalline, and polymer structures on the nanoscale. Indeed the evolution of high-performance piezoelectric materials like PMN-PT, polypyrrole, IPMC, and other electroactive polymers promise to usher in a new generation of materials that offer advantages over PZT for dispensing applications. Meanwhile, compatibility problems in the fabrication of silicon, PZT, and other standard micromachining materials are being solved, offering the ability to apply PZT in ways not currently possible.

In analysis, most microdispensing work assumes the working fluid is Newtonian, while many fluids that are useful for dispensing in the printing, biomedical and microfabrication industries are strongly non-Newtonian. A return to the fundamentals is in order to revisit the use of these fluids in forming droplets. Improved computational algorithms capable of dealing with the free surfaces and multiple physical phenomena of piezoelectric media, structural deformation, and nonlinear acoustic wave propagation will be central to this effort. As the excitation frequencies and power per unit volume are increased, the incorporation of cavitation models will also be beneficial.

Cross References

► Acoustic Streaming
► Biosample Preparation Lab-on-a-Chip Devices
► Cavitation in Microdomains
► Control of Microfluidics
► Droplet Based Lab-on-Chip Devices
► Droplet Dispensing
► Membrane Actuation for Micropumps
► Microactuators
► Microneedles – Applications & Devices
► Supersonic Micro-Nozzles
► Piezo/PZT in Microfluidics
► Ultrasonic Pumps

References

1. Burgold J et al (2005) Evolution and operating experiences with different drop-on-demand systems. Macromol Rapid Commun 26(4):265–280
2. Wehl WR (1989) Ink-jet printing: the present state of the art. CompEuro'89, VLSI and Computer Peripherals. VLSI and Microelectronic Applications in Intelligent Peripherals and their Interconnection Networks, Proceedings 2, p 2
3. Berger SS, Recktenwald G (2003) Development of an Improved Model for Piezo-Electric Driven Ink Jets. In: NIP19: International Conference on Digital Printing Technologies. The Society for Imaging Science and Technology, New Orleans
4. Lee ER (2003) Microdrop Generation. In: Lyshevski SE (ed) Nano- and Microscience, Engineering Technology and Medicine Series. CRC Press, New York, p 252
5. Rayleigh L (1878) On the instability of jets. Proc London Math Soc 10:4–13
6. Lee CH, Lal A (2004) Single microdroplet ejection using an ultrasonic longitudinal mode with a PZT/tapered glass capillary. Ultrasonics, Ferroelectrics and Frequency Control, IEEE Trans 51(11):1514–1522
7. Dong H, Carr WW, Morris JF (2006) An experimental study of drop-on-demand drop formation. Phys Fluids 18(7):072102

P

8. Tanner FX (2004) Development and Validation of a Cascade Atomization and Drop Breakup Model for High-Velocity Dense Sprays. Atomization Sprays 14(3):211–242
9. Lang RJ (1962) Ultrasonic Atomization of Liquids. J Acoust Soc Am 34:6
10. Shi WT, Goodridge CL, Lathrop DP (1997) Beraking waves: bifurcations leading to a singular wave state. Phys Rev E 56(4):4157–4161
11. Piriz AR et al (2005) Rayleigh-Taylor instability in elastic solids. Phys Rev E 72(056313):1–10
12. Forde G, Friend J, Williamson T (2006) Straightforward biodegradable nanoparticle generation through megahertz-order ultrasonic atomization. Appl Phys Lett 89:064105
13. Shiokawa S et al (1989) Liquid streaming and droplet formation caused by leaky Rayleigh waves. In: IEEE Ultrasonics Symposium. IEEE, Montreal
14. Percin G, Khuri-Yakub BT (2003) Piezoelectric droplet ejector for ink-jet printing of fluids and solid particles. Rev Sci Instrum 74(2):1120–1127
15. Okuno T (2006) Inkjet Print Head and Manufacturing Method Thereof, U.S.P. Office. 2006, Konica Minolta Holdings, Ltd.: United States, US2006/0017778, p 21

Piezoelectric Micro/Nanoliter Droplet Dispenser

► Piezoelectric Microdispenser

Piezoelectric Pumps

► Piezoelectric Valves

Piezoelectric Valves

James Friend, Leslie Yeo
MicroNanophysics Research Laboratory, Monash University, Clayton, VIC, Australia
james.friend@eng.monash.edu.au,
leslie.yeo@eng.monash.edu.au

Synonyms

Microvalve; Piezoelectric pumps; No-moving-part valves

Definition

Structures that regulate the flow of fluids using piezoelectric materials, either composed of active regulation through deflection of a structure to block or allow passage of the fluid using electrically-driven piezoelectric elements, or as a piezoelectric pump in combination with mechanical or passive diffuser valves.

Overview

Active piezoelectric valves offer a unique combination of large closing forces – hundreds to thousands of newtons – against fluid loads and small displacements measured in the tens of microns. Such valves may be designed to close or open upon the application of an electric field to the piezoelectric material, and offer flow rates from nearly arbitrarily low amounts to tens of liters per minute for gases, water, and similar fluids [1]. Given the limited strain, 0.1% or less, available from typical high-performance piezoelectric ceramic materials, a majority of the research and development effort has been in amplifying this strain to permit efficient valving action. Flap or cantilever valves seated across an orifice actuated as a piezoelectric ►bimorph or ►unimorph or ball or grooved structures seated against an orifice and moved using a large-displacement ►linear multilayer piezoelectric actuator is typical of this approach.

Passive piezoelectric valves function in an entirely different manner, though they also make use of piezoelectric bimorph or unimorph structures. Forming one side of a small fluid chamber, or ►Helmholtz cavity, the piezoelectric element can excite chamber resonances when driven at appropriate frequencies via an oscillatory electric field, usually from 10 Hz to 100 kHz depending on the device dimensions and fluid. With two or more orifices connecting the chamber to the outside, fluid may be passed into and out of the chamber; by using orifices with different shapes the flow direction may be regulated without requiring a mechanical blockage of the flow [2] or moving parts. Though these configurations are effective as pumps [3], they also can serve as valves for applications where some leakage is tolerable, or where ball or flap valves may be used as passive mechanical restrictions on the orifices to augment the sealing action and improve performance.

Cross References

► Piezoelectric Microdispenser
► Piezoelectric Materials for Microfluidics

References

1. Oh K, Ahn C (2006) A review of microvalves. J Micromech Microeng 16:13–39
2. Izzo I, Accoto D, Menciassi A, Schmitt L, Dario P (2007) Modeling and experimental validation of a piezoelectric micropump with novel no-moving-part valves. Sens Actuators A 133(1):128–140
3. Laser D, Santiago J (2004) A review of micropumps. J Micromech Microeng 14(6):35–64

pL

► Picoliter Flow Calibration

Planar Laser-Induced Fluorescence

► Laser-Induced Fluorescence (LIF)

Plasma Bonding

► Plasma in Microchannel

Plasma Chromatography

► Miniaturized Ion Mobility Spectrometry

Plasma Etching

CHEN-KUEI CHUNG
Department of Mechanical Engineering, National Cheng Kung University, Tainan City, Taiwan (R.O.C.)
ckchung@mail.ncku.edu.tw

Synonyms

Advanced silicon etching (ASE); DRIE (Deep Reactive Ion Etching); High aspect ratio Si etching

Definition

Plasma etching is the removal process of materials performed using a plasma, which involves the physical, chemical and mixed etching mechanisms. Ion-enhanced ► chemical etching, i. e., a reactive radical dominated etching process with ion assistance, is used in microelectronics and MEMS fabrication. ICP (inductively coupled plasma) etching is the etching process using a high-density plasma generated by the inductive coupling of RF power through an antenna, which is widely used in Si micromachining for high aspect ratio and deep microstructure fabrication. DRIE (deep ► reactive ion etching) is another term for ► ICP etching due to the deep or high aspect ratio microstructure fabricated by RIE principles, which is also called high aspect ratio Si etching or Advanced Silicon Etching (ASE™, a trademark for this technology of the company Surface Technology Systems, STS).

Overview

Etching is used in microelectronic processing and MEMS for pattern transfer during fabrication of devices. The pattern transferred is defined using lithographic techniques by UV exposure on a photoresist through a mask. The photoresist material often loses adhesion in solutions during wet etching processes. Therefore, the pattern dimensions can vary and there can be a lack of control of line width. The process also etches laterally at approximately the vertical rate during wet chemical etching downward into the film and loses the etching directionality. So, wet etching in many semiconductor processes has been replaced by plasma-assisted etching [1, 2]. The driving force of plasma-based etching technology in semiconductor manufacturing is primarily due to the achievement of ► etch directionality and the ability for true pattern transfer from lithographically defined photoresist patterns into underlying layers. The isotropy, undercutting and adhesion problems encountered in wet ► chemical etching can be overcome by anisotropic dry plasma etching; other advantages are its cleanliness and compatibility with automation and vacuum processing technologies. Plasma etching is performed using a discharge gas formed by reactive radicals, ions and electrons to create ion sputtering or reactive radical species that react with surfaces with or without ion assistance to form volatile compounds. The physically sputtered or chemically reacted products evaporate from the surface and proceed to etch the film or substrate. When plasma etching is used, adhesion is no longer a major problem, undercutting can be controlled by varying the plasma chemistry and parameters, and directional or anisotropic profiles can thus be achieved.

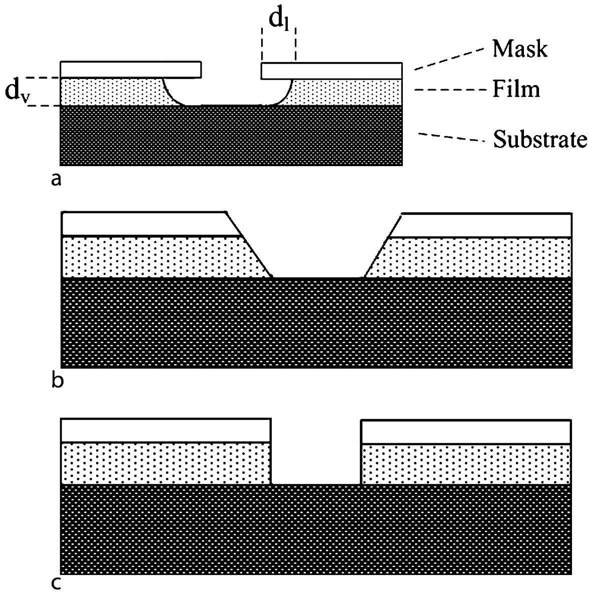

Plasma Etching, Figure 1 Three types of plasma etching of a film on a substrate under a mask: (**a**) isotropic etching, (**b**) sloped wall via etch and (**c**) vertical wall (anisotropic etching)

P

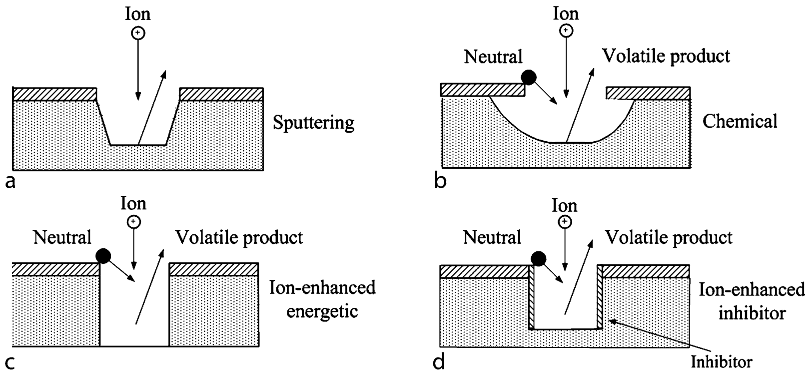

Plasma Etching, Figure 2 Four types of reaction mechanism during plasma etching: (**a**) sputter etching, a purely physical process, (**b**) chemical etching, or chemical volatilization, a purely chemical process, (**c**) ion-enhanced energetic, i. e., ion-enhanced chemical, etching, a combination of physical and chemical processes and (**d**) ion-enhanced inhibitor, i. e., inhibitor ion-enhanced chemical, etching, also a combination of physical and chemical processes but that involves an inhibitor that passivates the surfaces that are not exposed to ion bombardment. The last two types (**c**) and (**d**) are related to reactive ion etching (RIE)

The ►etch directionality in plasma etching is due to directed energy input to an etching reaction at a surface and can be accomplished by radical atoms, electrons, photons or ion bombardment of a surface exposed to a chemical etchant. It can be obtained by controlling the interaction between the plasma physical and chemical mechanisms to achieve the required etching profiles using a suitable reactor and adjusting the plasma parameters. Figure 1 shows three types of plasma-etched profiles of films on a substrate under a mask: isotropic etching, sloped wall via etch and vertical wall (anisotropic etching) [2]. Anisotropic etching occurs when it proceeds much faster in one direction as compared to other directions. The directionality, or anisotropy, is defined by the ratio of vertical to lateral etching rate. The degree of isotropic etching, IE, can be defined in Fig. 1a by equation (1) [2]:

$$\mathrm{IE} = \frac{d_\mathrm{l}}{d_\mathrm{v}} = \frac{V_\mathrm{l}}{V_\mathrm{v}} \tag{1}$$

where d_l is the amount of undercutting due to the lateral etching in rate of V_l, and d_v is the amount of the etched thickness of film due to the vertical etching in rate of V_v. So, the degree of anisotropic etching, AE, is correspondingly given by

$$\mathrm{AE} = 1 - \mathrm{IE} = 1 - \frac{V_\mathrm{l}}{V_\mathrm{v}} \tag{2}$$

In addition to isotropic and/or anisotropic behavior, another important etching characteristic is the ►etch selectivity. Etch selectivity between two materials is defined as the ratio between their etching rates at identical plasma conditions. High selectivity is usually preferred in etching and is related to a high etching rate ratio between chemically different materials or between the etched and the underlying layer. In addition, high selectivity is required between the substrate and etching mask or between different substrate materials.

Also, a plasma etching process should satisfy a number of requirements, including [2]:

- high etching anisotropy for the desired etching profile
- high etching selectivity
- high etching rate
- good uniformity of etching across wafer surface
- minimal material damage
- smooth surface without residues after etching.

Since plasma etching is related to the reactant activated by input energy to active radicals, electrons and ions, it occurs through the following steps for physical or chemical processing [2]:

1. Active species are formed in the plasma from non-reactive gases.
2. The active species formed in the plasma adsorb on the surface of the substrate and react with the surface to form volatile products.
3. The volatile products with a high vapor pressure leave the surface at the substrate temperature and are pumped out with the effluents of the plasma.

The reaction during plasma etching can be categorized into four types of mechanism [2, 3] as illustrated in Fig. 2.

(a) ►Sputter etching, a purely physical process caused by surface bombardment with high-energy ions, leading to anisotropic etching; also with poor selectivity, high surface damage, and low etching rates.

(b) ►Chemical etching, or chemical volatilization, caused by neutral species generated in the plasma, which react with the etched layer to form volatile compounds.

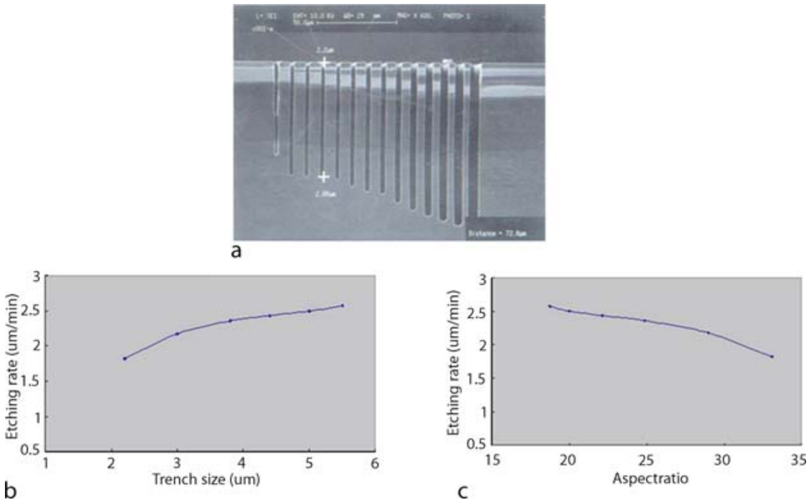

Plasma Etching, Figure 3 High aspect ratio silicon trenches with nearly vertical sidewall profile obtained by inductively coupled plasma (ICP) etching: (**a**) SEM micrograph, (**b**) RIE lag and (**c**) aspect ratio dependent etching phenomena

Chemical etching is typically isotropic and is characterized by high etch rates, usually good ►etch selectivity, and low substrate damage.

(c) Ion-enhanced energetic, i. e., ion-enhanced chemical, etching, a combination of physical and chemical processes in which the chemical reactions at the surface of the processed sample are enhanced by ion bombardment, enabling one to achieve material selective etch anisotropy.

(d) Ion-enhanced inhibitor, i. e., inhibitor ion enhanced, chemical etching, also a combination of physical and chemical processes but that involves an inhibitor that passivates the surfaces that are not exposed to ion bombardment. It is used in the sidewall passivation process for anisotropic etching.

The last two types, types (c) and (d), are related to ►reactive ion etching (RIE).

Plasma chemical etching is generally performed under low ion bombardment and chemical reactions with plasma species under conditions at which the physical effects are negligible and is usually an isotropic etching process. The pressure used in plasma chemical etching is relatively high, greater than 0.2 torr, often about 1 torr [2, 3]. If a parallel plate reactor is used, the substrates are placed on the ground electrode at a low potential relative to the plasma and the ion bombardment on the substrates is very weak. It is also performed in barrel reactors often with an etch tunnel to limit the discharge to a region outside the substrates. The substrates interact only with plasma species diffusing out of the plasma and are only chemically etched by atoms and radicals. RIE is generally performed in a parallel plate reactor. The substrates are placed on an electrode, which is capacitively coupled to a generator, usually operated 13.56 MHz. The pressure used in RIE is intermediate in the range 0.01 – 0.2 torr. The problem is the increase of ion bombardment damage with increasing substrate bias as high RF power is required for a high etching rate. To solve the surface damage problem in RIE, a high-density low-pressure (HDLP) system has been developed with the substrates placed out of the high density plasma region. The plasma diffuses downstream to the substrates biased at low power for etching. The benefits of HDLP are high etching rate with low damage, high selectivity and good directionality control for high anisotropy. Electron cyclotron resonance (ECR) and ICP are the two popular excitation techniques for generating HDLP plasma. In MEMS, ►ICP etching is a very powerful tool for the fabrication of deep and high aspect ratio (HAR) Si microstructures. It will be discussed in detail in the following sections. The common applications of plasma/reactive ion etching in Si technology are listed in Table 1.

Many materials, e. g., single/poly-Si, SiN_x, SiO_x, glass, metals, slicides and polymers, can be etched by plasma-assisted etching to get anisotropic profiles by changing the etching chemistry. A large variety of fluorine-, chlorine-, bromine- and oxygen-based etching plasmas with a few gas additives, e. g., H_2, Ar and He, are used in the semiconductor industry as listed in Table 2 [1–3]. A process recipe involving the specific etching gas mixture and operation parameters is generally based on a large amount of empirical evidence obtained for a particular etching application rather than a real fundamental understanding of the rele-

vant plasma chemistry. In practice, etching is performed by selecting a typical etching recipe and adjusting using a certain basic understanding of plasma physics and chemistry for process improvement.

Basic Methodology

Anisotropic etching is desired in the fabrication of numerous devices, especially the high aspect ratio microstructure (HARM) for MEMS applications. Many phenomena become pronounced in HARM etching compared to the low aspect ratio features ($< 3:1$), e. g., ►RIE lag, ►aspect ratio dependent etching (ARDE), bowing (barreling) of sidewalls, faceting, profile shape dependence, mirotrenching and notching (footing). These effects result from several mechanisms as follows [4]:

- angular dispersion of ions and neutrals as etchants due to collisions within the plasma sheath;
- ion and etchant transport within the feature onto the sidewalls;
- depletion of the reactant as microscopic loading under conditions of high probability at the surface;
- charging of feature sidewalls, as local charging of substrate surface or microstructure sidewalls deflects ions and prevents them from reaching the bottom surface to be etched;
- etching yield dependency upon the angle of incidence;
- deposition of material produced in the discharge within the feature; and
- redeposition of material released by ion-induced etching and reaction of the neutrals on the sidewalls to form passivation layers.

In order to obtain HARM with plasma-assisted etching, the significant issue is to reduce the lateral etching rate by controlling the ratio of ion flux to radical flux and sidewall passivation through the precursor gases and process parameters. Ion-assisted reactions at the bottom surface lead to highly anisotropic etching with the assistance of sidewall passivation or reduction of lateral reactive radical reactions. The key factors for controlling the microscopic etch uniformity in HAR etching are the selection of reactant chemistry, process conditions and the transport behavior of reactant to the surface and product away from the surface. Kassing and Rangelow [4] reported two main etching strategies for reducing the adverse effects listed above: controlled formation of sidewall-inhibitor films, and ►reactive ion etching at low substrate temperatures. Also, Laermer and Schilp [5] used alternating etching and passivation steps in the Si etching process, known as Bosch patented technology, which has become the main technique in the fabrication of Si HARM devices. Based on the Bosch technology, Surface Technology Systems (STS) continues promoting the *ASE* process in equipment design and process enhancement [6], which has been widely used in many universities, research institutes and industries. Figures 3a–c show an SEM micrograph, feature-dependent ►RIE lag and ARDE phenomena of HAR Si trenches with nearly vertical sidewall profile, respectively [7]. The structure was obtained using the *ASE* process with an STS Multiplex ICP system. The feature sizes of trenches from the fourth to the ninth trenches from the left side are between 2.2 μm and 5.5 μm. The etch rates measured range from 1.82 μm/min to 2.58 μm/min while the aspect ratios obtained are from 33.1 to 18.7. The larger the trench size, the higher the etching rate, and the lower the aspect ratio.

In the following, the STS Multiplex ICP system and *ASE* process, etching performance and chemistry, end point detection and experiment will be introduced for anisotropic plasma etching.

Plasma Etching, Table 1 Common applications of plasma/►reactive ion etching in silicon technology

Application	Etch step
Device formation	Polysilicon/polycide gate; sidewall; storage node; emitter contact
Isolation	Deep trench; shallow trench or recessed oxide
Interconnection	Contacts; metal; interlevel vias
Other	Multilayer resist definition; resist strip; backside strip; planarization

STS Multiplex ICP Etching System and ASE Process

Figure 4 shows schematically the STS Multiplex ►ICP etching system. The source plasma is generated by an inductively coupled coil supplied by a 1 – 3 kW 13.56 MHz RF generator. Another 13.56 MHz generator is used to power the platen electrode which allows independent control of the bias potential of the wafer relative to the source plasma. The wafer temperature is maintained at typically less than 80 °C through temperature-controlled, pressurized helium supplied to the back of the wafer. Wafers may be either mechanically or electrostatically clamped to the platen electrode. Typical base pressures are in the 10^{-7} torr range. The system is equipped with an automatic pressure control valve which can operate in one of two modes. In fixed automatic pressure control (APC) mode, the APC position remains constant and the chamber pressure is a function of gas flows and RF powers. In automatic APC mode, the APC valve adjusts to maintain the chamber pressure at a constant value. The tool has been developed to produce excellent

Plasma Etching, Table 2 Materials and reactive gases used for plasma/reactive ion etching in Si technology

Material	Reactive chemistry	Remarks
Si	CF_4/O_2, SF_6, NF_3 Cl_2, BCl_3, CCl_4 HBr, CF_3Br	Anisotropic; difficult Directional; good SiO_2 selectivity Directional
Oxide	CF_4/H_2, CHF_3/C_2F_6, CHF_3/CO_2	Etching selectivity to Si
Nitride	CF_4, CHF_3, SF_6, NF_3	Characteristics intermediate to Si, SiO_2
$TiSi_2$	CCl_2F_2, CCl_4	Control of oxygen impurities
WSi_2	CF_4/O_2, SF_6	
W	CF_4/O_2, SF_6	
Al	Cl_2, BCl_3, CCl_4, $SiCl_4$	Removal of native oxide
Al(Cu)	Cl_2, BCl_3, CCl_4, $SiCl_4$	Cu removal, removal of native oxide
Polymers	O_2, O_2/CF_4	

repeatability from cycle to cycle for the switched *ASE* process.

The ASE process uses sequentially alternating etching and passivation steps based on Bosch technology for anisotropic Si etching with feature sizes ranging from submicrometer to several millimeters. SF_6 and C_4F_8 are the primary gases used for etching and passivation purposes, respectively. O_2 is generally added to SF_6 in the etching step for prolonging the turbo pump life with reduction of sulfide coating on turbo blades [6] and for reducing the bowing profile at high bias with the enhancement of side-wall passivation [8]. The STS *ASE* procedure is shown schematically in Figures 5a–c: (a) passivation step after one cycle, (b) the etching step after one cycle, i. e., the second etching, and (c) profile after four cycles. Fig. 5d shows a cross-sectional SEM micrograph of the etched holes with scalloped surface due to the cycling *ASE* process. The etching and passivation mechanism can be explained with the following Eqs.:

$$C_4F_8 + e^- \rightarrow CF_x^+ + CF_x^{\cdot} + F^{\cdot} + e^- \quad (3)$$

$$nCF_x^{\cdot} \rightarrow nCF_{2(\mathrm{ads})} \text{ (on surface)} \rightarrow nCF_{2(\mathrm{f})} \quad \text{(polymeric passivation film)} \quad (4)$$

$$SF_6 + e^- \rightarrow S_xF_y^+ + S_xF_y^{\cdot} + F^{\cdot} + e^- \quad (5)$$

$$nCF_{2(f)} + F^{\cdot} \xrightarrow{\text{ion energy}} CF_{x(\mathrm{ads})} \rightarrow CF_{x(\mathrm{g})} \text{ (passivation film removed)} \quad (6)$$

$$Si + F^{\cdot} \rightarrow Si - nF \quad (7)$$

$$Si - nF \xrightarrow{\text{ion energy}} SiF_{x(\mathrm{ads})} \quad (8)$$

$$SiF_{x(\mathrm{ads})} \rightarrow SiF_{4(\mathrm{g})} \text{ (final Si etched product)} \quad (9)$$

The ionization and dissociation of C_4F_8 plasma deposits a $n\mathrm{CF}_2$ or $(C_xF_y)_n$ polymeric passivating film on the sidewalls and the base of the features (Eqs. (3) and (4)). This polymer, $nCF_{2(f)}$, is preferentially removed from the base of features by the directional ion bombardment energy during the following etching cycle to expose Si for spontaneous etching (Eqs. (5) and (6)). The sidewalls remain protected by the polymer which receives no ion bombardment and subsequently no ►chemical etching either. SF_6 gas supplies fluorine radicals (Eq. (5)) for spontaneous isotropic etching of exposed Si (Eqs. (7)–(9)). Si is mainly etched by the fluorine radicals ($F^{\cdot}$) and assisted by ion bombardment. The ion bombardment only serves to remove polymer from the base of the features. Then the passivation and etching steps are repeated for Si etching. The balance between etching and passivation determines the final process results and can be controlled by a wide variation of process parameters, e. g., the cycle time, flow rate, coil power, platen power and pressure in the etch-

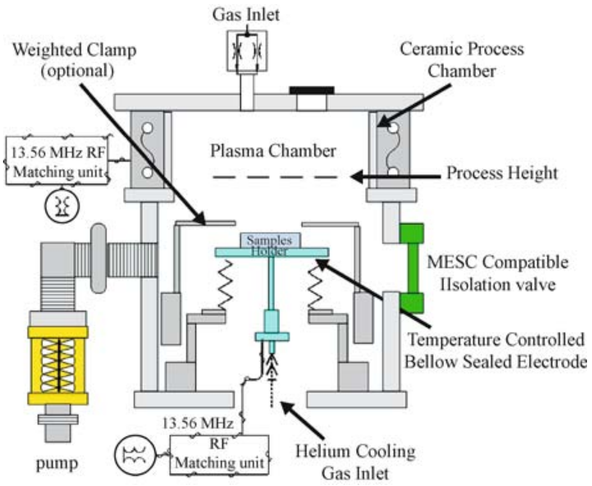

Plasma Etching, Figure 4 Schematic diagram of the STS Multiplex ICP etching system

P

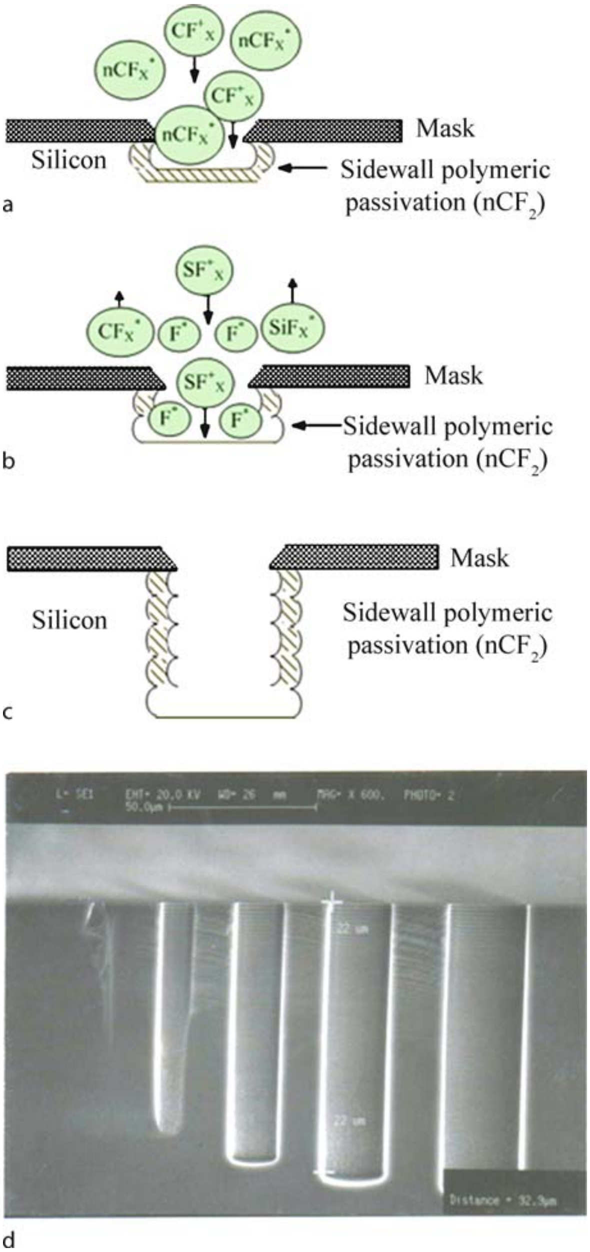

Plasma Etching, Figure 5 Schematic diagram of the STS *ASE* procedure: (**a**) passivation step after one cycle, (**b**) the etching step after one cycle, i. e., the second etching, (**c**) profile after four cycles and (**d**) cross-sectional SEM micrograph of the etched holes with scalloped surface

ing and passivation step, as well as the substrate temperature and the distance from the source plasma. Table 3 lists the typical characteristics of Si etching using the STS *ASE* process [3, 6].

Figures 6a–d show cross-sectional SEM micrographs of etched profiles in different geometry [7]: (a) high aspect ratio microstructure of holes with the same nominal diameter of 1.5 μm and nearly the same etching depth of 69.5 μm, (b) through-wafer etching of 525 μm thick Si holes with a diameter of 200 μm, (c) rectangular and circular donut trenches with constant width or radius of 5 μm and (d) trenches with feature length from 100 to 500 μm at constant width of 5 – 10 μm, respectively. Compared to Fig. 3 with the larger feature width for the deeper etching depth, the larger continuous feature area also leads to the deeper etching depth. The rectangular donut has a larger area than the circular donut, which leads to the higher etching rate or depth. In addition, the etching depth of trenches is nearly the same as the feature width is fixed. But the etching depth varies as the feature width is changed. The feature width of pattern geometry is a dominating factor affecting the ►RIE lag in ►ICP etching while secondary factors are feature area, shape as well as length-to-width ratio. Etching rates of rectangular trenches are sensitive to width while the ring trenches are sensitive to both width and area. Process parameters can be adjusted to control RIE lag magnitude.

Plasma Etching, Table 3 Typical characteristics of Si etching using the STS *ASE* process [3, 6]

SF_6 flow	30 – 150 sccm
C_4F_8 flow	20 – 100 sccm
Etch cycle	5 – 15 s
Deposition cycle	5 – 12 s
Pressure	0.25 – 10 Pa
Temperature	20 – 80 °C
Etching rate	1.5 – 4 μm/min
Aspect ratio	$> 20:1$
Etch depth capability	10 – 800 μm (/through wafer)
Sidewall angle	$90° \pm 2°$
Selectivity to photoresist	50 – 100
Selectivity to SiO_2	100 – 200

Etching Performance and Chemistry

The performance of anisotropy etching can be evaluated from the etching rate, selectivity, profile (directionality), loading effect, ►RIE lag, ►aspect ratio dependent etching (ARDE) and uniformity. Besides the design of equipment configuration, it is related to the process condition, pattern geometry and reactant chemistry. In general, there is a compromise between the etching rate, selectivity and profile. The higher the etching rate, the better the throughput. Etching rate can be enhanced by high plasma power, substrate bias, process pressure and gas flow and a reduced total etching area. But the high ion energy from high bias,

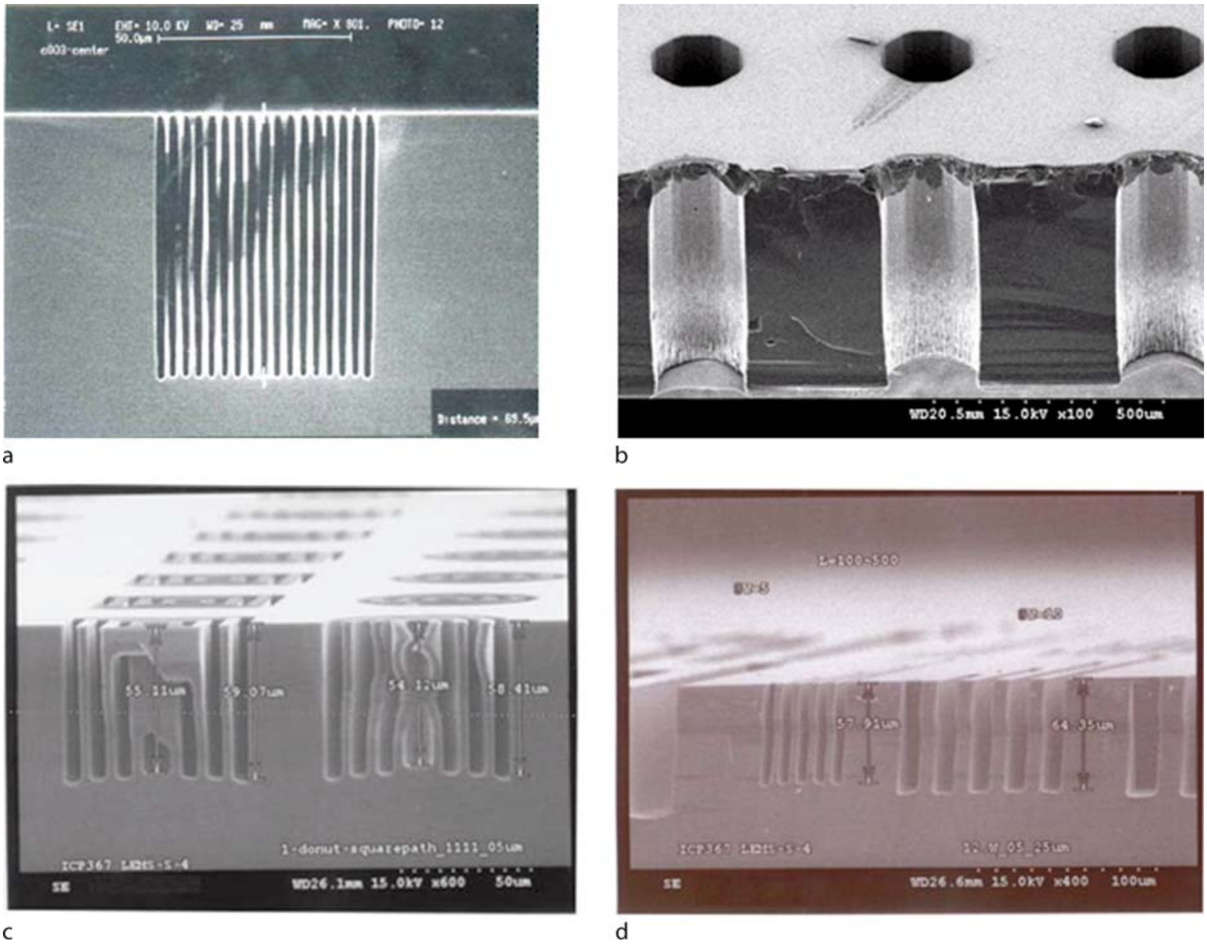

Plasma Etching, Figure 6 Cross-sectional SEM micrographs of: (**a**) high aspect ratio microstructure of holes with the same nominal diameter of 1.5 µm and nearly the same etching depth of 69.5 µm, (**b**) through-wafer etching of 525 µ m thick Si holes with a diameter of 200 µm, (**c**) rectangular and circular donut trenches with constant width or radius of 5 µm and (**d**) trenches with feature length from 100 to 500 µm at constant width of 5 – 10 µm

which is increased with RIE power or independently controlled in ICP, leads to low selectivity and surface damage. Good selectivity, profile control and uniformity are more easily obtained at lower etching rate and shallower depth. In HARM with high etching rate, ►RIE lag and ARDE will become pronounced, thus reducing the uniformity. The larger the feature size, the higher the etching rate while the higher the aspect ratio, the lower the etching rate. Most isotropic etchants, e. g., SF_6 gases, exhibit a loading effect which can be reduced to some extent by using large-volume reactors and be eliminated as etchant loss, i. e., surface reaction instead of diffusion mechanism, dominates the etching behavior [1, 2]. The high ion energy for HAR features will result in bowing of the profile due to the scattering of ions at high pressure, which can be eliminated by enhanced sidewall passivation with the addition of O_2 in the etching gas [8]. In the ASE process [6], the primary dominant factors for etching rate enhancement are increase of etching step time, decrease of passivation step time and decrease of passivation gas flow. Increasing plasma power, etching step pressure and platen power also increase the etching rate. In order to create a vertical sidewall angle, the process parameters may be adjusted by increasing passivation gas flow, substrate bias, substrate temperature and etching gas flow. The reverse adjustment is made to obtain sloped or tapered sidewall profile for a wafer-level package. To reduce the scallop size for a smooth profile, it can be controlled by decreasing the etching step time, increasing the deposition step time and decreasing the etching gas flow. The patented *Parameter Ramping* has been developed to continually adjust the key parameters in ASE to meet the requirements for good profile in HARM etching [6].

As listed in Table 2, a large variety of fluorine-, chlorine-, bromine- and oxygen-based etching plasmas are used in the Si semiconductor industry. Etching of Si can be accom-

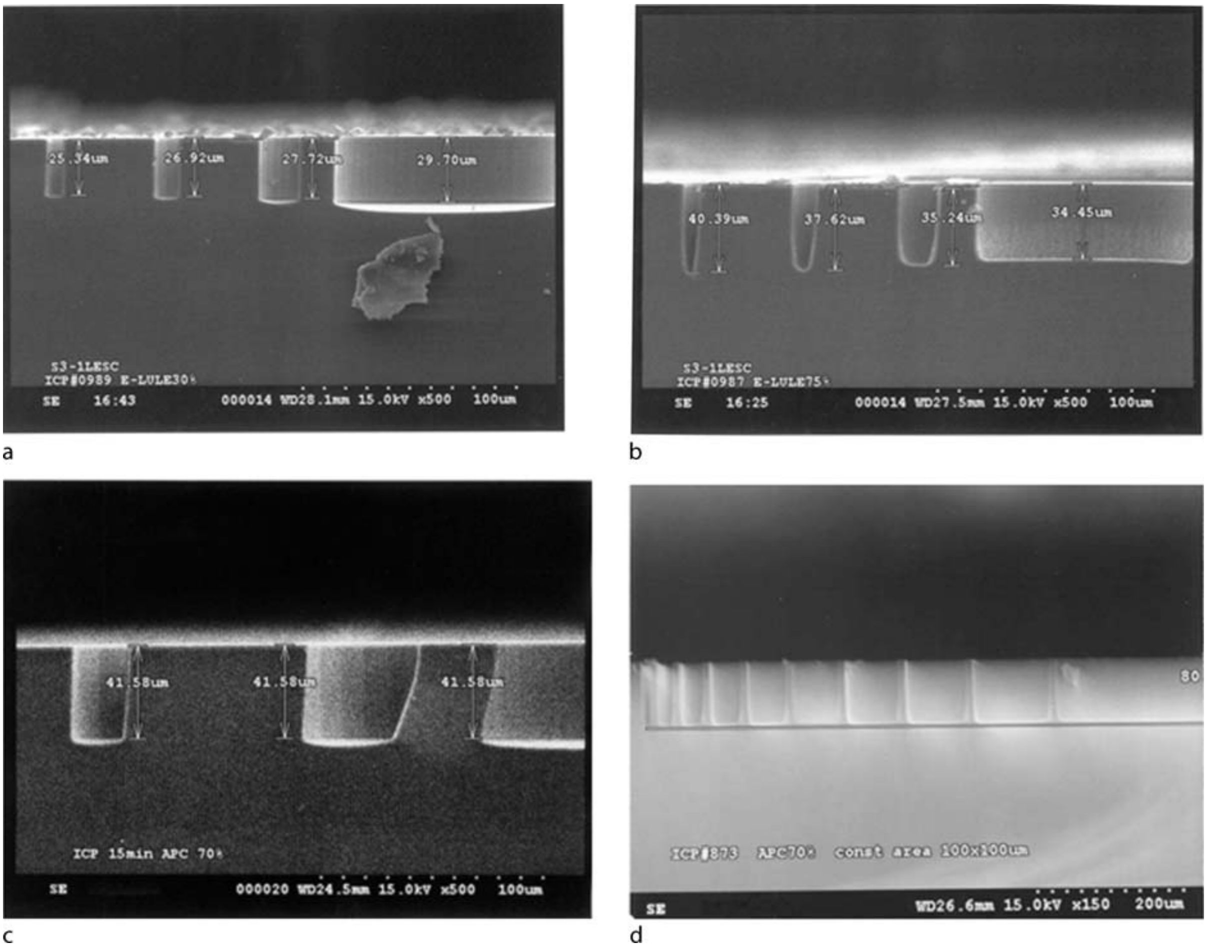

Plasma Etching, Figure 7 Cross-sectional SEM micrographs of etched donut trenches with constant area at pressures: (**a**) APC 30% and (**b**) APC 75% for $\pi \times 52.5^2 \mu m^2$, (**c**) APC 70% for $\pi \times 105^2 \mu m^2$ and (**d**) APC 70% for the etched rectangular trenches with constant area of $100 \times 100 \mu m^2$, in which the width varies from 10 to 100 μm while length varies from 1000 to 100 μm

plished using F-, Cl- and Br-based chemistries and the etch products include volatile SiF_4 and $SiCl_4$. The etching of Si can be carried out in a CF_4 or SiF_6 plasma with negligible ion bombardment of the Si substrate [1]. The correspondence of Si etch rate and atomic fluorine emission is as a function of the RF power through the intensity variation of the 704 nm atomic fluorine-related optical emission. Reactive F atoms are directly involved with Si etching. The gas phase density influences the etching rate in simple CF_4 or SiF_6 plasmas and a large undercut occurs in F-based plasma etching due to the isotropic chemical etch. The directionality in SiF_6 plasma etching can be improved by cooling the substrate to a temperature of −110 to −120 °C, as cryogenic etching enables one to get near vertical profiles [1]. The spontaneous ▶chemical etching reactions are suppressed at *cryogenic* temperatures. The etching at the bottom of the feature dominated by ion-assisted etching reactions is not affected at low substrate temperature while the vertical etching rate increases with decreasing temperature, attributed to condensation of etchant for high density. The drawbacks of Si etching at cryogenic temperature are the cracking of resist mask, the increase of surface contamination (leading to black Si) and the increase of equipment complexity. A hard mask, e. g., oxide or metal, is needed in cryogenic etching. Anisotropic Si etching can also be obtained by Cl- and Br-based plasmas at room temperature. Si and oxide passivation are not spontaneously etched by chlorine and bromine atoms for directionality improvement. The size of the halogen relative to the Si atom plays an important role in the spontaneous etching. The spontaneous etching of Si exposed to large Cl atoms is absent compared to small F atoms for isotropic profiles. Although Cl- and Br-based plasma chemistries may achieve highly anisotropic structures, the shallow depth (< 20 μm) obtained limits the potential for MEMS applications. Modified F-based

plasmas for Si etching by sequentially switching etching and passivation gases, i. e., Bosch technology, demonstrate anisotropic etching for high aspect ratio microstructure and through-wafer at room temperature. It has become the main method in Si etching as described in the previous sections.

End Point Detection (EPD)

The most direct need for plasma diagnostic techniques results from the determination of the etch end point for a given process. In addition, plasma diagnostic techniques are used for process monitoring and provide information on the types of species present in a plasma etching, the concentration and the energy content. Laser interferometry (or reflectance) and optical emission spectroscopy (OES) are two commonly used techniques for EPD and require only an appropriate optical window attached to the chamber. They are easily implemented to obtain information about etching plasmas [1].

Laser Interferometry (Reflectance)

This technique measures the laser light reflected from the surface of a wafer being etched. For transparent films, e. g., SiO_2, an oscillation is observed for the reflected laser light intensity due to interference of the reflected light from surfaces of both the film and the substrate. The spacing between adjacent maxima (or minima) is $\delta d = \lambda/2n$, where λ is the wavelength of the laser light and n is the refractive index of the transparent layer. Etch rates can be examined in real time. For nontransparent films, e. g., metals, one measures the change in reflectivity before and after complete removal of the metallic film. For patterned wafers without an etch stop layer, we determine the depth of the etched pattern in situ through the used pattern as a diffraction grating. There are two principal drawbacks of these techniques. Firstly, they usually require a special test site especially as the features being etched, e. g., contact holes into a SiO_2 film, are too small for measurements. Secondly, the obtained EPD information is only for one specific area on the wafer, and not suitable for batch processing.

Optical Emission Spectroscopy (OES)

OES is the most widely used techniques for etch end point detection. The change in emission from a characteristic species is observed as etching of a film is completed. Either the decrease in emission of a suitable etch product species or the increase in etchant species at the end of the etching process is monitored. By measuring the wavelengths and intensities of the emitted spectral lines, one can identify the end points both in research laboratories and in manufacturing for production control. Some important electronic materials and common optical emission lines of etching gases used for EPD are listed in Table 4. The OES technique is limited to the monitoring if light-emitting species and the emission intensities are not always directly related to the concentration of the species in the plasma. The sensitivity of this technique depends on how much etchant is consumed or how much film material is etched per unit. If the etch rate is too slow or the size of the etched pattern too small, e. g., contact hole etching into SiO_2 layers, this technique may not be suitable for EPD.

Experimental

Si wafers are initially cleaned in a solution of $H_2SO_4 : H_2O_2$ at 3 : 1 ratio. Thick resist or thermal oxide SiO_2 are used as ICP etch mask of Si. Standard lithography and RIE are used to transfer the photo mask pattern to thick resist or oxide mask. Si deep etching is performed using the *ASE* process in an STS Multiplex ICP system. The etching and passivation gases are (SF_6 + O_2) and C_4F_8, respectively, and are switched during the process. Three major kinds of patterns of constant length, constant width and constant area with different feature sizes of 2 to 100 μm are divided to understand the dominating factor of geometry for ► RIE lag in ► ICP etching. Process pressure is adjusted by auto pressure control (APC) from 30% to 75% to understand the process pressure effect on RIE lag. The plasma source is generated by a 600 – 800 W 13.56 MHz RF generator

Plasma Etching, Table 4 Common optical emission lines of etching gases used for EPD [1]

Material	Etchant gas	Emitting species	Wavelength (nm)
Si	CF_4/O_2, SF_6	F (etchant)	704
	CF_4/O_2, SF_6	SiF (product)	440, 777
	Cl_2, CCl_4	SiCl (product)	287
SiO_2	CHF_3	CO (product)	484
Si_3N_4	CF_4/O_2	N_2 (product)	337
	CF_4/O_2	CN (product)	387
	CF_4/O_2	N (product)	674
W	CF_4/O_2	F (product)	704
Al	Cl_2, BCl_3, CCl_4	Al (product)	391, 394, 396
	Cl_2, BCl_3, CCl_4	AlCl (product)	261
Resist	O_2	O (etchant)	777, 843
	O_2	CO (product)	484
	O_2	OH (product)	309
	O_2	H (product)	656

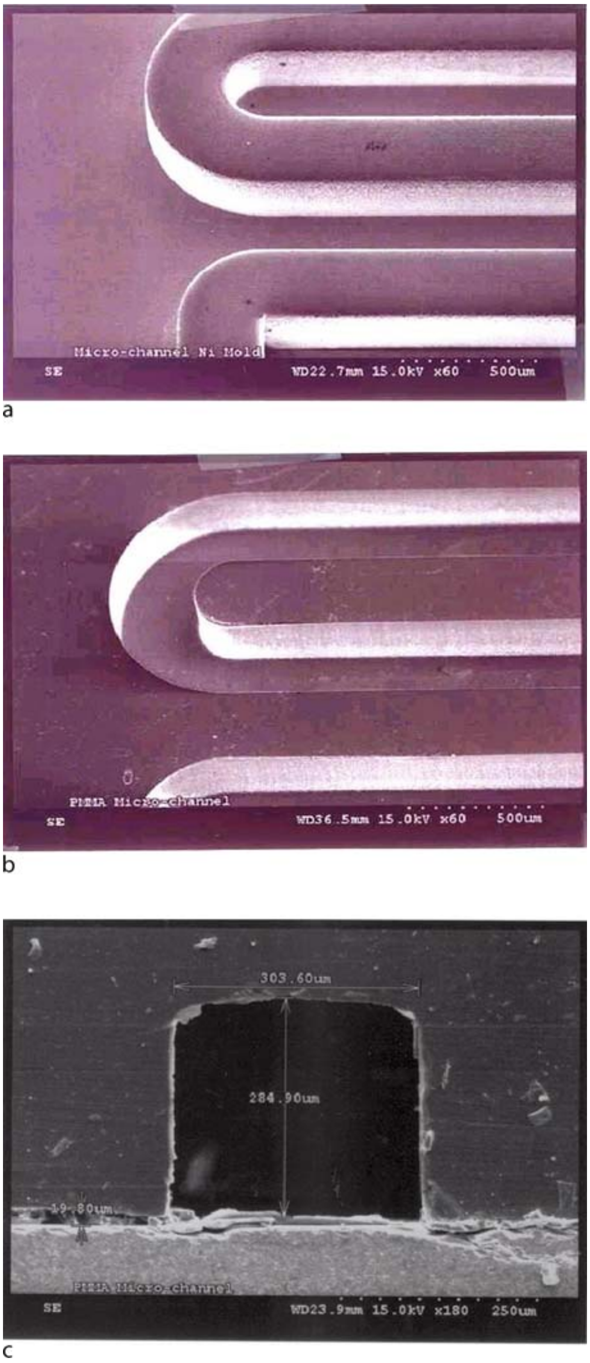

Plasma Etching, Figure 8 SEM images of (**a**) an electroplated Ni mold, (**b**) hot embossed PMMA replica and (**c**) PMMA adhesive bonding in ICP LIGA

and biased by a 10 – 15 W 13.56 MHz RF generator at the platen during the etching step. The wafer is electrostatically clamped and cooled by backside helium flow. Scanning electron microscopy (SEM) is used to examine the etching result after the *ASE* process.

Key Research Findings

Fabrication of Deep/HAR Si Microstructure with High Etching Rate and Good Uniformity to Large Diameter Wafers (Up to 200 mm)

For the requirements of full-scale commercial production, Si DRIE for MEMS applications and advanced packaging are needed for high etching rate with excellent uniformity. The wafer size up to 200 mm is expected and important for high throughput and yield for a cost-effective end product. In mid-2005, STS [6] introduced a new generation of Si etch system, known as Pegasus, for the above purposes. Pegasus employs a revolutionary new de-coupled ICP source design by enhancing both the throughput and the yield to reduce the cost per die.

In conventional plasma processing with the *center-high* spatial profile of both ions and neutral radicals, the density profile variation of the ions will usually be more extreme than for the radicals, leading to large uniformity deviation. Two new de-coupled plasma sources are patented technologies of STS for ramping and SOI modules. They offer the following benefits:

- To reduce the volume of the plasma source for more efficient breakdown of the precursor gas due to the higher power density delivered from the RF power supply.
- To adjust the geometry and volume of the plasma source region to match the silicon's loading characteristics for the ions and neutral radicals diffusing down to the wafer with the desired profiles to obtain high etch uniformity.
- To alter the balance between numbers of ions and neutral radicals reaching the wafer to control selectivity to mask and/or ion damage to feature profiles.

With the appropriate magnitude of parameter values during an etching and precise control of notching at the surface of Si to the insulator, a high etch rate with good uniformity can be achieved. For example, Si etch rates of more than 30 μm/min can be achieved at a more realistic exposed area of around 10% and exceeding 50 μm/min for a 1% exposed area have been observed using the Pegasus source with the *ASE* process. Yield is optimized by improving absolute etch depth uniformity and by reducing trench tilting artifacts observed with conventional ICP plasma sources. The very high etch rate uniformity and feature profile control is relevant for up to 200 mm wafers.

Inverse RIE Lag and Lag Elimination

A ► RIE lag phenomenon occurs in many patterns and becomes more severe at smaller feature width and higher etching depth. In general, the smaller the feature size, the

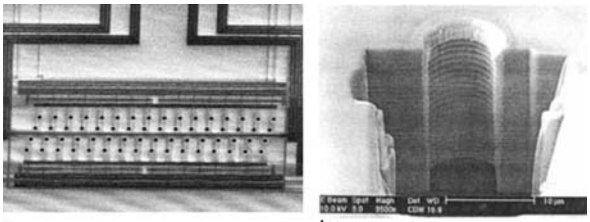

a b

Plasma Etching, Figure 9 SEM micrographs of (**a**) plane-view nozzle array with circuit layout and (**b**) cross-section of one nozzle for a high-resolution inkjet head application

lower the etching rate and the more obvious is the RIE lag. Experimental results reveal that the primary dominating factor is feature width and a secondary factor is feature area together with length-to-width ratio. Chung [7] reported the effect of geometrical pattern and process parameters on the transition between RIE lag, inverse RIE lag and eliminated RIE lag. Figures 7a and b show SEM micrographs of etching donut trench structure with constant area of $\pi \times 52.5^2 \mu m^2$ at a pressure of APC 30% (20 mtorr (etching)/10 mtorr (passivation)) and APC 75% (54 mtorr (etch)/32 mtorr (passivation)) for 30 min, respectively. The RIE lag exists at low pressure of APC 30% while an inverse RIE lag appears at high pressure of APC 75%. The inverse RIE lag means the higher etching rate occurs at smaller feature width. It implies that other mechanism exists in Si DRIE with respect to previous reports [4, 9]. The possible new reaction mechanism is C_xF_y radical dissociated from C_4F_8 passivation gas playing an important role to affect the etching rate ratio of different feature sizes. The formation and removal of C_4F_8 passivation film impedes the increase of etching depth while the arrival of SF_6 etching gas enhances the etching processing. As the pressure increases, the increasing C_xF_y radical density for the formation of passivation film and reducing S_xF_y ion density to remove passivation film at the bottom will delay longer the start of etching of Si surface at the bottom in a large feature than a small one. The etching rate is enhanced more for small width than for large width. This will lead to the reduction of RIE lag. If the pressure is much higher, inverse RIE lag occurs. Since RIE lag and inverse RIE lag have been achieved, we could find an optimum condition at a pressure of APC 70% to obtain the RIE lag-eliminated feature as shown in Fig. 7c and d, respectively, for donut trenches with constant area of $\pi \times 105^2 \mu m^2$ and rectangular trenches with constant area of $100 \times 100\ \mu m^2$.

SOI MEMS and Other Microstructures Using Pure Isotropic Etching or in Combination with Anisotropic Etching

Silicon-on-insulator (SOI) MEMS has the advantages of RIE lag elimination and enabling multilevel HARM for optical MEMS applications. Milanovic [10] reported multilevel beam SOI–MEMS fabrication and its applications to optical scanners. The multilevel beam was fabricated by 4-mask DRIE: two for front-side and two for back-side etching to high degree of freedom motion (both upward and downward vertical pistoning motions as well as bi-directional rotation). One problem of notching or footing will occur at the bottom of Si on oxide due to charging effect. Docker et al. [11] used the notching effect as lateral etching for the fabrication of suspended MEMS structure in one dry single-step process. Mita et al. [12] used DRIE SOI and contour lithography methods for fabrication of nanometer-to millimeter-scale coexisting microsystems. Marty et al. [13] reported that three-dimensional Si structure for Fresnel lens or staircase structure can be fabricated by pure SF_6 isotropic etching in RIE lag condition. In a combination of isotropic and anisotropic etching, a single crystal reactive etching and metalization (SCREAM)-like process has been demonstrated for a suspended Si MEMS structure without the need for an SOI wafer. Other multistep structures from isotropic and anisotropic etching can be fabricated for applications in the photonics and microfluids.

P

ICP LIGA-Like Process and Nanoimprinting

ICP LIGA-like process is a process to duplicate deep polymer microstructure for applications in microfluid or micro-devices at low cost and easy fabrication compared to the X-ray LIGA process. Figures 8a–c show SEM micrographs of an electroplated Ni mold, hot embossed poly(methyl methacrylate) (PMMA) replica and PMMA adhesive bonding, respectively, in ICP LIGA after Si DRIE process. The PMMA channel width is about 300 μm and the depth nearly 285 μm with vertical sidewall profile without any distortion. It indicates that a cheap plastic chip can be obtained for microfluidic applications using the ICP LIGA process. With the development of nanoimprinting, it requires Si or quartz stamps in a nanoscale pattern for nanolithography pattern transfer. ►ICP etching has been used for the manufacture of Si stamps used to pattern the resist in hot embossing or in different etching chemistry for the transparent quartz stamps used in UV light curing the resist [6].

Examples of Applications

Many examples of applications have been reported in the STS Innovations magazine issues 1 – 3 since April 2006 [6]. They include MEMS inertial and pressure sensors, Si springs for luxury wristwatch components, optical switches and resonators for communication, microphones for portable electronic equipment, advanced packages (system-in-package), and inkjet channels and nozzles. For example, Figs. 9a and b show SEM micrographs of a plane-view nozzle array with circuit layout and cross-section of one nozzle, respectively, for high-resolution inkjet head application. It combines the fabrication of backside wet anisotropic etching and front-side dry DRIE etching. The nominal nozzle diameter is 10 μm with vertical profile as well as scallop rings due to the *ASE* switching process. The emerging nanoscale etching has been applied in photonic crystals, magnetic nanostructures (magnetoresistive random access memory, MRAM), high-Q MEMS resonators, sub-micrometer pilar array or HAR structures made of Si for bioanalysis and lab-on-a-chip, microchannels and inkwells for dip pen nanolithography, and Si or quartz stamps for nanoimprint lithography.

Future Directions for Research

ICP is an important technology for micro- and nanoscale patterning processes. High etch rate, high aspect ratio and anisotropic, good profile control, high uniformity and RIE lag elimination are important issues in the development of MEMS and nanotechnology devices. In MEMS fabrication, it is steadily moving from the development and pilot stages to full-scale production. In nanofabrication, it is promising to enable nanometer–micrometer–millimeter multiscale structures in device design and application. In combining isotropic and anisotropic etching, different promising HARM or three-dimensional structures may be realized for the application of Si-MEMS or SOI MEMS. ICP technology will be required in many applications including MEMS inertial and pressure sensors, optical switches and resonators for communication, inkjet channels and nozzles for high-resolution printheads, microphones for portable electronic equipment, advanced packages, and so on.

Cross References

- ► Anisotropic Etching
- ► Dry Chemical Etch
- ► ICP Etching
- ► Isotropic Etching
- ► Laser Ablation
- ► Laser Based Micromachining
- ► LIGA Like Techniques
- ► Plasma in Microchannel
- ► Reactive Ion Etching (RIE)
- ► Silicon Micromachining

References

1. Oehrlein GS (1990) Reactive Ion Etching. In: Rossnagel SM, Cuomo JJ, Westwood WD (ed) Handbook of plasma processing technology. Noyes, Berkshire
2. Grill A (1994) Plasma Assisted Etching. In: Cold plasma materials fabrication: from fundamentals to applications. Wiley/IEEE, Hoboken
3. Madou M (2002) Pattern Transfer with Dry Etching Techniques. In: Fundamentals of Microfabrication, 2nd ed. CRC, Boca Raton
4. Kassing R, Rangelow IW (1996) Etching process for High Aspect ratio Micro Systems Technology (HARMST). Microsyst Technol 3:20–27
5. Laermer F, Schilp A (1994) Method of Anisotropically Etching Silicon. German Patent DE4241045 1996; USA Patent 5501893, 1996
6. http://www.stsystems.com/; STS Innovations news, issues 1–3, April, July and September, 2006
7. Chung CK (2004) Geometrical pattern effect on silicon deep etching by an inductively coupled plasma system. J Micromech Microeng 14:656–662
8. Chung CK, Lu HC, Jaw TH (2000) High aspect ratio silicon trench fabrication by inductively coupled plasma. Microsyst Technol 6:106–108
9. Jansen H, de Boer M, Wiegerink R, Tas N, Smulders E, Neagu C, Elwenspoek M (1997) RIE lag in high aspect ratio trench etching of silicon. Microelectron Eng 35:45–50
10. Milanovic V (2004) Multilevel Beam SOI-MEMS Fabrication and Applications. J Microelectromech Syst 13(1):19–30
11. Docker PT, Kinnell PK, Ward MCL (2004) Development of the one-step DRIE dry process for unconstrained fabrication of releASEd MEMS devices. J Micromech Microeng 14:941–944
12. Mita Y, Kubota M, Harada T, Marty F, Saadany B, Bourouina T, Shibata T (2006) Contour lithography methods for DRIE fabrication of nanometre-millimetre-scale coexisting microsystems. J Micromech Microeng 16:S135–S141
13. Marty F, Rousseau L, Saadany B, Mercier B, Français O, Mita Y, Bourouina T (2005) Advanced etching of silicon based on deep reactive ion etching for silicon high aspect ratio microstructures and three-dimensional micro- and nanostructures. Microelectron J 36:673–677

Plasma in Microchannel

Khanh Dang[1,2], David W. G. Morrison[1,2], Utkan Demirci[1,2], Ali Khademhosseini[1,2]

[1] Harvard-MIT Division of Health Sciences and Technology, Massachusetts Institute of Technology, Cambridge, MA, USA

[2] Center for Biomedical Engineering, Department of Medicine, Brigham and Women's Hospital, Harvard Medical School, Boston, MA, USA

alik@mit.edu

Synonyms

Microchannel glow discharge; Microchannel surface modification; Microchannel surface sterilization; Plasma bonding

Definition

Gas plasma, a fourth state of matter, is a neutral composition of ions, electrons, radicals, and photons that is synthesized by applying energy to a gas at atmospheric pressure or within a vacuum. Gas plasma can be used to enhance the functionality of microdevices for various biological and chemical applications. The effects of plasma in microchannels are regulated by parameters such as the type of gas, power intensity, chamber pressure and duration of the treatment.

Overview

Microchannels that range in diameter from tens to hundreds of microns have emerged as potentially powerful tools for a variety of biomedical applications. They can be used to minimize sample volume and reduce costs, as well as to increase throughput and analysis sensitivity. Since microfluidic devices operate at small length scales, their functionality is greatly dependent on their surface properties, which vary depending on the type of material that is used to fabricate the channel and the subsequent surface modifications.

Microchannels have traditionally been fabricated from commonly used materials from the semiconductor industry, such as silicon. Silicon offers many advantages for microchannel fabrication, such as standardized fabrication procedures and easy integration with electronics. Despite these merits, silicon is opaque and brittle and cannot be used for fabricating transparent microfluidic devices that require light based sensors. To overcome these difficulties, glass microfluidic channels have also been developed, however, the fabrication of these devices, similar to those of silicon microchannels is time consuming, expensive and requires the use of a clean room facility. As a result, polymeric microchannels have recently emerged as potentially valuable alternatives. Polymers that have previously been investigated for microchannels include: polycarbonate (PC), polystyrene (PS), poly(dimethylsiloxane) (PDMS) and poly(methylmethacrylate) (PMMA). One of the main advantages of using polymeric materials to make microchannels is that they can be fabricated from soft lithographic techniques such as micromolding. Furthermore, the ability to tailor the mechanical and optical properties of polymers can be used to fabricate microchannels with a wide range of properties. Despite the great advancements in the materials used to fabricate microchannels, the surface properties of these channels often require additional modifications based on the specific needs of the device. Thus, approaches to activate microchannel surfaces have been of great interest in fully realizing the potential of these techniques.

During the 1920s and 1930s, Dr. Irving Langmuir proposed the term *plasma* while he was studying the physical properties of gases and the balance of charges between ions and electrons. Commonly considered as the fourth state of matter, basic gas phase plasma contains a neutrally charged mixture of negative and positive ions, photons, electrons and radicals that are produced by applying energy to a gas at low pressure (from 10^{-6} to 10^{-4} bar). In this process, the temperature of plasma electrons is extremely high (on the order of 10^4 K), however, the plasma gas remains close to ambient temperature. This is because plasma components found at higher temperatures (such as the sun) are made of equilibrium (thermal) plasmas while low-pressure gas plasmas are non-equilibrium (non-thermal) type. Plasma is formed by the exposure of free electrons to an external energy source that increases the kinetic energy, resulting in the formation of radicals and ions. These excited molecules then form photoemissions, ions and free radicals due to a loss of excess energy from the plasma. The energy released from these chemical species is capable of breaking covalent bonds and altering the surface chemistry of many materials.

The bombardment of a surface with reactive chemical species can be used to drastically change its surface properties and create functional surfaces within microchannels. Traditionally, corona discharge and oxygen plasma treatment have been used. Corona discharge is the formation of sparks at the tip of a wire created by electromagnetic fields that result in the ionization of nearby molecules at low temperatures and pressures. Corona discharge can be used to oxidize a surface near the tip of the wire. Although widely used in various industrial processes, a negative aspect of corona discharge is its tendency to modify the surface non-uniformly. To overcome this limitation, surface plasma treatment can be used. Plasma treatment of microchannel surfaces is particularly attractive, as it does not require the tedious placement of a wire inside microscale channels. In addition, plasma treatment of a surface is faster and more reproducible compared to corona discharge.

The reaction between the plasma and a surface is highly complex and comprised of numerous and simultaneous chemical reactions [1]. Upon the initial application of energy, the gas molecules, such as oxygen, are converted to various unstable intermediates that can react with the surface. Some of the initiation mechanisms between plasma

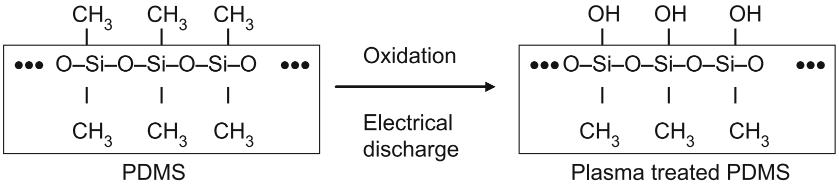

Plasma in Microchannel, Figure 1 Schematic of the oxygen plasma treatment of a PDMS substrate

(which may include oxygen radicals) with a surface are shown below:

$$RH + O\bullet \;\rightarrow\; \begin{matrix} R\bullet + H\bullet + O_2 \\ R_1\bullet + R_2O\bullet \\ R\bullet + OH\bullet \end{matrix}$$

These radical species then induce chain scission, radical transfer, oxidation and disproportionation to generate functional surface groups such as hydroxyl and carboxyl moieties (Fig. 1). For some materials, such as PDMS, these activated surfaces can be bonded to fabricate channels, as shown in Fig. 2. Plasma treatment of microchannels can also be used to control surface properties by incorporating reactive molecules or by increasing the hydrophilicity of the surfaces that eases the flow of fluids and minimizes the formation of bubbles.

In addition to adding surface functional groups, plasma can be used to remove organic contaminants and sterilize surfaces. In this process, plasma radicals break the covalent bonds and oxidize the surface contaminants, which are then cleared by the vacuum. Here, we will outline the basic methodology of gas plasma modification in microchannels, including theory, experimental methods, pertinent process parameters and characterization methods. Additionally, key research findings will be discussed.

Basic Methodology

In this section we will outline the basic methodology of the plasma treatment process. First, the theory behind plasma treatment will be presented. Following this, experimental protocol outlining the treatment process, pertinent parameters and their relevance will be discussed. Finally, surface analysis methods for plasma treated surfaces will be described, such as X-ray photoelectron spectroscopy (XPS), atomic force microscopy (AFM), and contact angle measuring tools.

Theory

To establish an analytical framework of plasma formation and initiation, thermodynamic models have been developed. For example, for low pressures and high frequencies that generate plasma gases at ambient temperatures the power required to generate plasma can be determined from molecular collision analysis. In this model, the reactive species within the plasma process are created from inelastic collisions between electrons and ground-state atoms [2], where electrons have energy, u, given by

$$u = \frac{(mw^2)}{2}$$

where w is the electron velocity and m is the electron mass. The excitation rate coefficient, C_j, of a particular species is then given by

$$C_j = \left(\frac{2}{m}\right)^{\frac{1}{2}} \int_0^\infty \sigma_j(u) F_0(u) u du$$

where $\sigma_j(u)$ is the particular process cross-section and F_0 is the electron energy distribution function. Nearly all processes at this level that are important possess energy threshold, u_j, where

$$\sigma_j(u) \equiv 0, \quad u \le u_j$$

There is also a dependence of the number density $\dot{n}_j$ of species j produced per second in the plasma from ground state molecules (of number density Ncm^{-3}) on the electron density n, where

$$\dot{n}_j = C_j N n.$$

The applied electromagnetic field (where frequency $f = \omega/2\pi$) and the plasma has a power balance that is expressed by

$$P_a = \xi n V,$$

where the power absorbed is P_a, the volume of plasma is V and the average power absorbed per electron is ξ. ξ also refers to the power necessary to sustain an electron–ion pair in the plasma.

Experimental

To plasma treat a surface, samples are initially placed within a plasma vacuum chamber. Gas plasma is then generated using various energy sources such as alternating current (AC), radio frequencies (RF) or microwaves (MW) (Fig. 3). For example, in apparatuses that use RF, two electrodes apply energy in the form of magnetic and electric fields to a gas at low pressure (∼ 266 – 800 mbar) inside the vacuum. The application of appropriate amount of energy to the gas discharge results in the formation of a neutral gas plasma. During this process, a characteristic glow is emitted from the apparatus indicating the plasma state of the gas.

Parameters

There are a number of parameters that affect the surface modification during the plasma treatment process. These parameters can be separated into internal process parameters, which are dependent on the plasma, and external process parameters, which are external to the plasma but within the system. Examples of internal parameters include the type and the degree of dissociation of the gas and the residence time of the active species in the vacuum chamber. Examples of the external parameters include, but are not limited to, the substrate material, amount of time that the material is exposed to the plasma, gas pressure, energy frequency, power and substrate temperature. It is important to note that the internal parameters of the plasma are indirectly controlled by the external process parameters. Figure 4 depicts the relations among several parameters. This entry will discuss how the type of gas, exposure time, gas pressure and power affect the plasma initiated surface modifications and the resulting bonding strengths of substrates.

The type of gas is a key parameter in any plasma surface modification process. Plasma treatments using inert gases, such as argon, have been shown to increase the hydrophobicity of oxygen-containing polymers without adding detectable chemical species to the surface. These properties are a result of the degradation and rearrangement of molecules on the surface of the polymer. Degradation is caused by an increase in the kinetic energy in the plasma treatment chamber when inert plasmas are present. This increased energy breaks molecular bonds on the surface, which result in the degradation of the impurities on the surface of the substrate. Rearrangement of chemical species occurs as a result of cracks that are introduced onto the surface of the substrate. These cracks enable molecules from beneath to rearrange with molecules present on the surface. This is indicated by a decrease in the oxygen/carbon ratio within the treated surface, possibly resulting from loss of CO or CO_2. In contrast, plasma treatment by using reactive gases results in the direct conjugation of the reactive molecule on the surface. For example, in the case of oxygen plasmas, hydroxyl and carboxyl functional groups are formed on the surface and can react with each other between two treated surfaces through a dehydration reaction to produce covalent linkages that result in bonding of two substrates.

The exposure time of the plasma to the surface can greatly affect its surface properties. For example, the bonding of PDMS to PDMS for the fabrication of microchannels has been shown to be time dependent (Table 1). If the substrate is not adequately treated with plasma then there will not be enough functional groups present to achieve bonding. If the substrate exposure exceeds an optimal time. Then there will be excessive oxidation of the PDMS surface and the formation, which leads to the formation of a brittle layer of silica. Thus, prolonged plasma treatment results in polymer reorganization on the substrate surface that causes decreased bonding strength due to induced hydrophobic properties.

It has also been determined that the internal pressure of the treatment chamber has a significant impact on the surface properties of treated substrates (Table 1). When the internal pressure is high, the mean free distance between molecular collisions within the plasma is significantly reduced. For example, for PDMS substrates the upper pressure region is characterized as greater than approximately 0.1 mbar. The molecules within this condensed plasma increasingly interact with the polymer surface molecules, resulting in increased bonding strength. Conversely, if the pressure within the chamber is too low (i. e. less than approximately 0.1 mbar) there is reduced interaction between the plasma and the surface and the bond strength is not optimized.

Finally, power variation has also been shown to affect the surface properties of the substrate (Table 1). In the case of PDMS at low power settings, plasma electron speeds are reduced and there is less interaction between the radicals in the plasma and the substrate. This minimizes the formation of functional groups on the surface. Conversely, extreme voltages result in reduced bonding strengths because of the formation of Si–O–Si groups on the PDMS surface. The dissociation energy of these specific bonds is larger than the dissociation energy of the Si–C bonds in the backbone of the polymer, therefore causing substrate degradation and less functional group formation for PDMS-PDMS bonding. At optimal power levels the number of functional groups present on the surface of the substrate is high enough to encourage bonding but low enough to not affect the siloxane backbone of the PDMS.

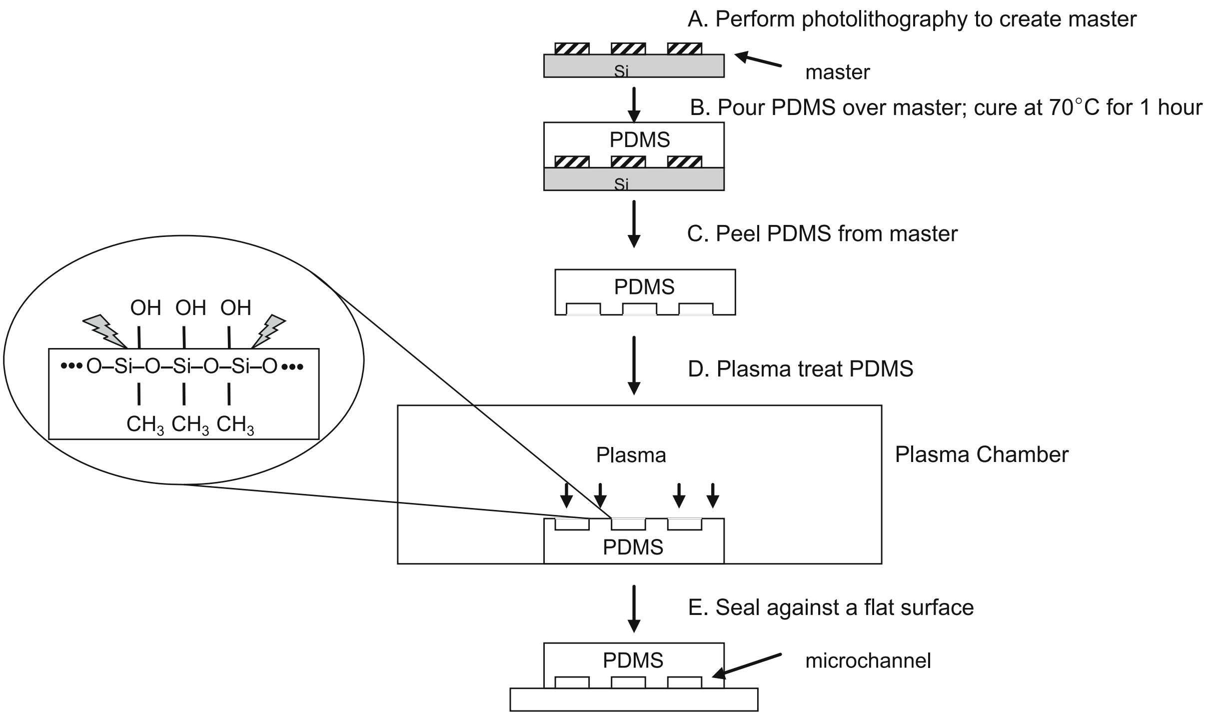

Plasma in Microchannel, Figure 2 Schematic of the process used to fabricate microchannels through a plasma induced bonding process

Plasma in Microchannel, Table 1 Comparison of the bonding results with RIE process parameters for bonding of plasma treated surfaces. Bonding 1 metric based on permanently bonded area after immediate contact (no bonding = 0 ~ whole area bonded = 10). Bonding 2 metric based on permanently bonded area when 3 days have passed after immediate contact. Adapted from [11]

#	1	2	3	4	5	6	7	8	9	10	11	12	13	14	15	16	17	18	19	20	21
Power (W)	70						200						300						400		500
Pressure (mTorr)	65		120		180		65		120		180		65		120		180		120		160
Time (sec)	10	40	10	40	10	40	10	40	10	40	10	40	10	40	10	40	10	40	10	40	20
Bonding 1 (max=10)	10	6	10	9	10	9	10	6	10	7	10	3	4	0	3	0	3	0	2	0	0
Bonding 2 (max=10)	10	10	10	10	10	10	10	8	10	8	10	8	4	0	3	0	3	0	2	0	0

Evaluation of Plasma Treated Surfaces

Surface chemical composition, structure and functional properties can be characterized by various techniques, such as XPS, AFM, and contact angle measurements. XPS measures the short range of photoelectrons leaving the surface. The sensitivity ($\sim 1-10$ nm) is semi-quantitative and detects chemical bonding information at the surface. Composition depth profiles, known as XPS spectra, can be generated from this method. Conversely, AFM utilizes a nanoscale probe to characterize surfaces and produce 3D surface profiles. AFM can determine the surface roughness and elastic modulus through phase imaging and nanoidentations, respectively. In addition to analyzing the surface of substrates, cross-sections can be imaged by using AFM to picture the stiffer surface layer and determine thickness. Furthermore, contact angle analysis can also be used to study surface wetting behavior. Contact angle measuring devices measure the angle of a liquid–vapor interface with a solid surface to assess surface hydrophilicity. Water droplets on hydrophilic substrates spread out and have relatively low contact angle measurements. Conversely, they maintain a more spherical shape on hydrophobic substrates, thereby producing higher contact angle measure-

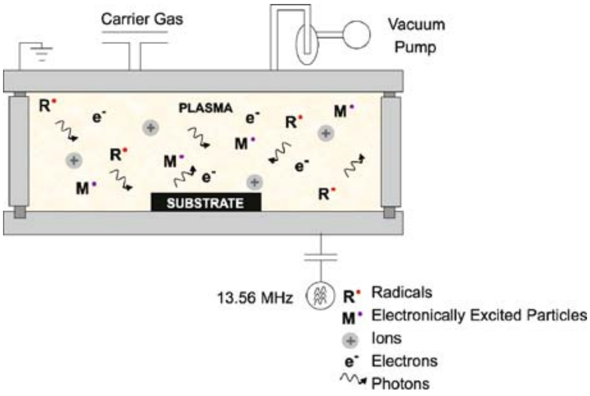

Plasma in Microchannel, Figure 3 Schematic of a radio frequency plasma treatment chamber

ments. Common contact angle analysis methods include drop–bubble, reflective light and interference microscopy.

Key Research Findings

Various research findings on the effects of plasma treatment on microchannels have reported improved surface characteristics within microfluidic channels. Researchers have also been able to adapt plasma treatment technologies to develop novel applications in the field of engineering. Furthermore, applications of plasma in microchannels include the development of on-chip light sources and the fabrication of micropatterns and gradients for cell adhesion studies.

Hydrophobic Recovery and Bonding Enhancement Techniques

As previously mentioned, surface properties of a substrate can be tailored by applying various plasma treatments. The stability of plasma treatment is dependant on the material properties. For instance, for PDMS, oxygen plasma treated surfaces regain their hydrophobicity over time. This may be due to

- surface silanol groups reorienting into the bulk;
- movement of free PDMS chains from the bulk phase to the surface through cracks in the Si–O–Si structure;
- silanol groups at the surface condensing;
- volatile oxygen or other species escaping into the atmosphere;
- changes in the surface roughness [4].

Conversely, other explanations suggest hydrophobic recovery can be described in two distinct phases: adsorption of atmospheric contaminants and surface reorganization. Within the first few hours, the initial phase of adsorption of atmospheric contaminants begins. These atmospheric species react with the surface moieties that were introduced during treatment and reduce their functionality. In the case of PDMS, surface reorganization begins when siloxane groups from the backbone of the polymer migrate through cracks created during surface modification and reorganize to yield the original properties of the polymer. Similarly to hydrophilicity, bonding characteristics are also dependent on time (Table 2). It has been shown that the adsorption of contaminants and surface reorganization also has an adverse effect on the bonding properties of PDMS.

To increase the stability of a surface treated substrate a variety of approaches have been developed. For example, different plasma gases can be applied to reduce the amount of surface reorganization. Specifically, nitrogen treated surfaces maintain their hydrophilicity longer than oxygen plasma treated surfaces. Also, to maintain stable hydrophilic PDMS it is possible to fabricate C-F bonds or react poly(HEMA) bonds on PDMS microchannel surfaces [6].

Enhancing Microchannel Functionality

Plasma treatment of microchannels can be useful for improving the functionality of microdevices. For example, previous studies have shown that PDMS microchannels can be made hydrophilic by the addition of silane molecules with polar head groups [7]. In this process (3-mercaptopropyl)trimethoxysilane (3-MPS) was absorbed to PDMS to increase the hydrophilic properties of microchannels. Additionally, plasma polymerization has been used to induce in the long-term hydrophilic surface modification by covalently bonding a polymer layer to the surface. Barbier et al. [8] describe a method based on plasma polymerization modification with acrylic

Plasma in Microchannel, Table 2 Aging of activated PDMS surfaces. Bonding metric is based on permanently bonded area after aging the activated surfaces (no bonding = 0 ~ whole area bonded = 10). Adapted from [11]

#	1	2	3	4	5	6	7	8	9
Power (W)					70				
Pressure (mTorr)					75				
Etch Time (sec)					10				
Aging (min)	2	3	5	7	10	15	20	25	30
Bonding 1 (max=10)	10	10	10	10	10	10	6	7	8

P

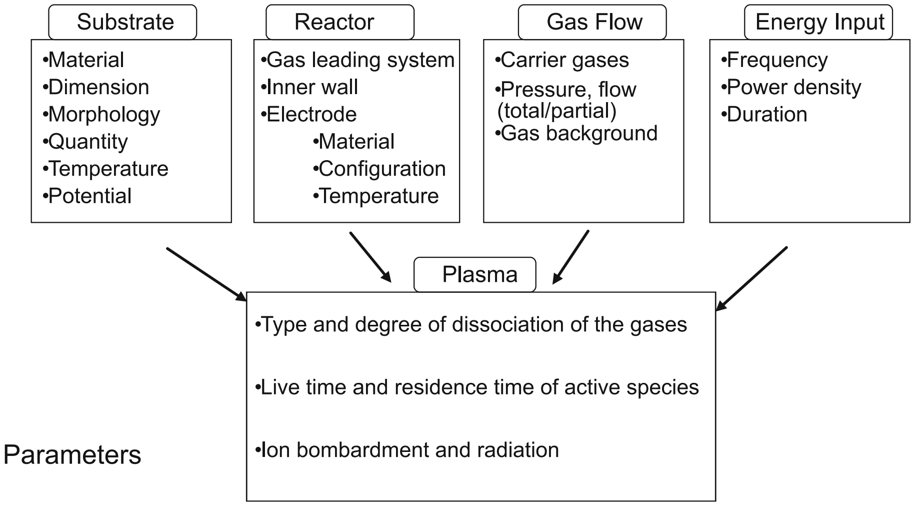

Plasma in Microchannel, Figure 4 External parameters that influence the quality of surface plasma treatment

acid coatings. First, argon plasma pretreatment was used to activate trace oxygen molecules in the chamber, which partially oxidize the top layer of the substrate. This step crosslinked the surface to reduce ablation of silicon during deposition as well as limits the movement of siloxane chains for hydrophobic recovery. Secondly, plasma with acrylic acid was deposited onto the pretreated PDMS. Finally, helium plasma treatment was used to crosslink the deposited polymer film to reinforce the cohesion. This process provides a homogeneous stable hydrophilic polymer layer for robust applications within microfluidics and nanofluidics.

Applications

Applications of plasma in microchannels include the development of chromatography detectors and on-chip light sources. Evju et al. [9] describe the creation of microdischarges or microplasmas by direct current within microfluidic channels on polystyrene. The three different gases tested included helium (He), water-saturated helium (H_2O/He), and hexafluoroethane (C_2F_6/He). These gases were released through a microchannel and ignited at atmospheric pressure. The treatments were completed in several seconds to reduce heat formation. XPS confirmed that oxygen and fluorine on the surfaces contributed to hydrophilic and hydrophobic regions, respectively.

Complex biomolecular micropatterns and microgradients have also been synthesized with the use of plasma treated surfaces, with possible future applications in tissue engineering, biosensors, and immunoassays. Various methodologies, such as microcontact printing and micromolding, have been used to create micropatterns where wettability was controlled through selective plasma treatment. These micropatterns are made up of many ligands and cell types for spatial control and cellular organization. This organization can induce cell–cell signaling and recreate the hierarchy lost in standard in vitro methods to produce more tissue-like structures. These advances are critical in understanding biology and enabling improved tissue culture and tissue engineering techniques.

An application of plasma treated surfaces has also been shown in microcontact printing, where elastomeric stamps are *inked* with chemical species and ligands, which can then be patterned onto different surfaces. Langowski et al. [10] have shown that by applying oxygen plasma to the original *stamp* there is a reduction in low-molecular-weight silicon containing fragments transferred to PMMA substrates. The effect of the treatment increased ligand bioactivity, cell function and proliferation due to reduced contamination from the initial untreated substrate. This finding allows for proper modification for applications desiring the removal of low-molecular-weigh silicon fragments, especially for biological applications.

Microgradient textures within microchannels have also been synthesized by utilizing plasma treatments. By having gradients of ligands, microchannels enable visualization of the effects on cell behavior, such as differentiation, migration and adhesion. Because of the quick and inexpensive nature of soft lithographic techniques and plasma treatments, biological applications can be done more cost effectively and in a faster manner.

Future Directions for Research

Plasma treatment of microfluidic surfaces can be used to improve microdevice functionality, to build devices through bonding processes and to activate and sterilize surfaces. Future directions for this technology include improved modeling of techniques with respect to parameter and surface plasma interaction. The development of refined experimental methods, theoretical models, and experimental studies is required to have more control over plasma treatment within microchannels.

Cross References

► Plasma Treatment Physics
► Plasma Etching
► AFM
► Bioprinting on a Chip
► Cell Adhesion and Detachment
► Control of Microfluidics
► Wetting and Spreading

References

1. Wu S (1982) Polymer Interface and Adhesion. Dekker, New York
2. Liston EM, Martinu L, Wertheimer MR (1997) Plasma surface modification of polymers for improved adhesion: a critical review. Plasma Surface Modification of Polymers: Relevance to Adhesion. VSP Boston
3. Makamba H et al (2003) Surface modification of poly(dimethylsiloxane) microchannels. Electrophoresis 24(21):3607–3619
4. Fritz JL, Owen MJ (1995) Hydrophobic recovery of polydimethylsiloxane after exposure to corona discharge. J Adhesion 54:33–45
5. Jo BH et al (2000) Three-Dimensional Micro-Channel Fabrication in Polydimethylsiloxane (PDMS) Elastomer. J Microelectromech Syst 9(1):76–81
6. Bodas D, Khan-Malek C (2006) Formation of more stable hydrophilic surfaces of PDMS by plasma and chemical treatments. Microelectron Eng 83:1277–1279
7. Pisignano D et al (2004) Rapid Soft Lithography by Bottom-Up Enhanced Capillarity. Langmuir 20(12):4802–4804
8. Barbier V et al (2006) Stable Modification of PDMS Surface Properties by Plasma Polymerization: Application to the Formation of Double Emulsions in Microfluidic Systems. Langmuir 22(12):5230–5232
9. Evju JK et al (2004) Atmospheric pressure microplasmas for modifying sealed microfluidic devices. Appl Phys Lett 84(10):1668–1670
10. Langowski BA, Uhrich KE (2005) Oxygen plasma-treatment effects on Si transfer. Langmuir 21(14):6366–6372
11. BH J, Van Lerberghe LM (2000) Three-Dimensional Micro-Channel Fabrication in Polydimethylsiloxane (PDMS) Elastomer. J Microelectromech Syst 9(1):76–81

Plasma Oxidation

Definition

The treatment of a surface with a plasma containing oxygen generally performed using a vacuum chamber and an RF discharge.

Cross References

► Sputtering for Film Deposition

Plasma Treatment of Nanoparticles for Nanofluids

Young Jo Kim[1], Qingsong Yu[1,2], Hongbin Ma[2]
[1] Department of Chemical Engineering,
Center for Surface Science and Plasma Technology,
University of Missouri-Columbia, Columbia, MO, USA
[2] Department of Mechanical & Aerospace Engineering,
University of Missouri-Columbia, Columbia, MO, USA
yuq@missouri.edu

Synonyms

Diamond nanoparticles; Nanofluids; Thermal conductivity

Definition

Plasma treatment refers to the surface modification processes of materials using non-equilibrium gas plasmas. Non-equilibrium plasmas with a low degree of ionization, so-called cold plasmas or low-temperature plasmas, are mainly composed of electrons, ions, free radicals, and electronically excited atomic and molecular species. These highly reactive plasma species interact non-thermally with material surfaces, and can react with and bond to various substrate surfaces, or combine together to form an ultra thin layer of plasma coating, and consequently alter the surface chemistry and surface properties. The plasma treated nanoparticles with desired surface functionalities can strongly interact with liquid molecules and thus better disperse into the base fluid to form stable suspension.

Overview

Plasma Treatment

Non-equilibrium plasmas, i. e., low-temperature plasmas, which can be easily created by electrical discharges under reduced pressures (e. g., 10 mtorr to 10 torr), are composed of electronically excited atomic, molecular, ionic and free radical species. Depending on the plasma chemistry or gas

P

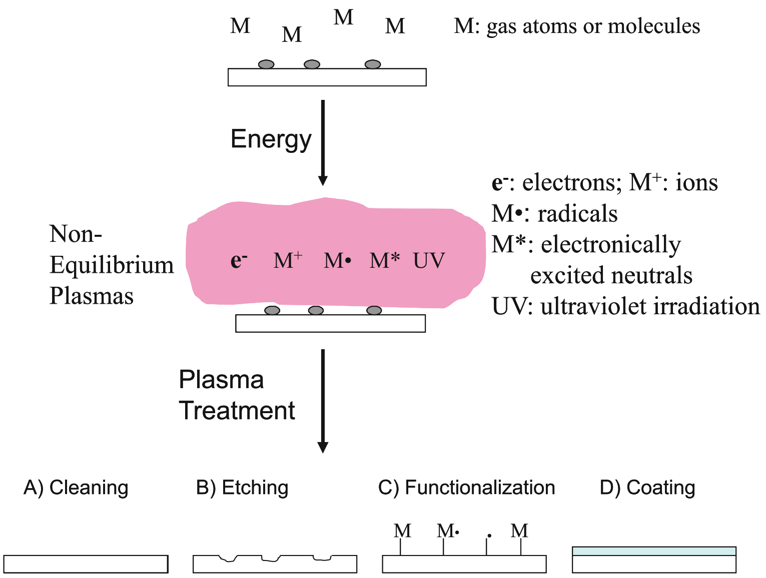

Plasma Treatment of Nanoparticles for Nanofluids, Figure 1 Plasma treatment effects on materials surfaces

composition, these highly reactive plasma species react with, clean, and etch surface materials, bond to various substrates, or combine to form a nanoscale thin layer of plasma coating, and consequently alter the surface characteristics. Figure 1 schematically illustrates the plasma-surface interaction results when a material substrate is exposed to low-temperature plasmas. Such plasma-surface interactions are limited to only the material surface without affecting bulk properties of the substrate materials. Since the gas phase is close to room temperature, low-temperature plasmas are suitable and very efficient in surface modification of various materials such as metals, polymers, and ceramics. Plasma treatments with and/or without deposition are currently being widely used in surface modification of various materials for improving adhesion, wettability, printability, corrosion resistance, surface etching or cleaning, and biocompatibility etc. [1–6].

Plasma treatment for material surface modification can be achieved using either simple gas plasmas without deposition or organic vapor plasmas to deposit an ultra-thin layer of plasma coatings on the surfaces. Plasma treatment possesses many unique advantageous features in surface modification of materials. Among these are:

1. plasma treatment processes are usually reliable, reproducible, non-line-of-sight, and applicable to different sample geometries;
2. plasma deposition creates an ultra-thin (in nano-scale) film coating, which are conformal, chemically inert and robust, corrosion-resistant, and strongly bonded to various substrates including both organic and inorganic materials;
3. plasma treatment is relatively inexpensive, easily operated, dry and rapid;
4. plasma treatment can tailor the surface with desired functionalities and properties through simply adjusting the plasma chemistry.

These advantageous features have been demonstrated in the continuous operation of plasma deposition and plasma etching processes in semiconductor manufacturing industry.

Recently, low-temperature plasma treatment has been explored for surface modification of various nanosized materials [7–13]. Surface functionalization of carbon nanotubes (CNTs) using plasma treatment was recently attempted by several research groups. Oxygen plasmas generated at both radiofrequency (RF) and microwave (MW) were used to treat CNTs [7, 8]. It was found that acidic groups were implemented to the CNT surfaces with improved surface wettability. Several other studies [9, 10, 13] reported the surface modification of both CNTs and nanoparticles using plasma treatment. With a simple fluidized-bed plasma apparatus, plasma coatings of 2 nm from pyrrole and 15 nm from acrylic acid were able to be uniformly deposited on 10 – 150 nm Al_2O_3 and 50 nm ZnO nanoparticle surfaces respectively [11]. It was also reported that uniform plasma coating with 1 – 3 nm thickness was achieved on carbon nanotubes with inner diameter of 20 nm [12].

Plasma treatment of nanoparticles for nanofluids can be obtained by plasma treatment using low-temperature plasmas. The diamond nanoparticle surfaces, for example, can be modified by the low-temperature plasmas of methane

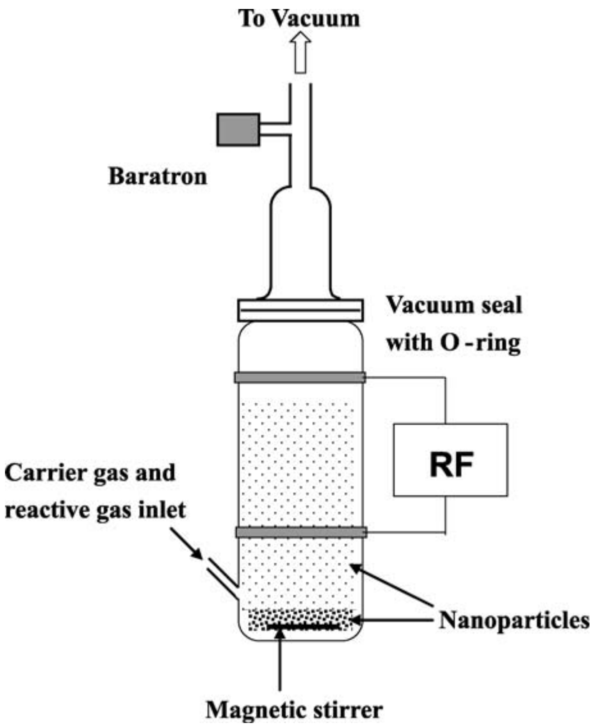

Plasma Treatment of Nanoparticles for Nanofluids, Figure 2 Schematic diagram of the magnetically assisted fluidized bed plasma reactor system

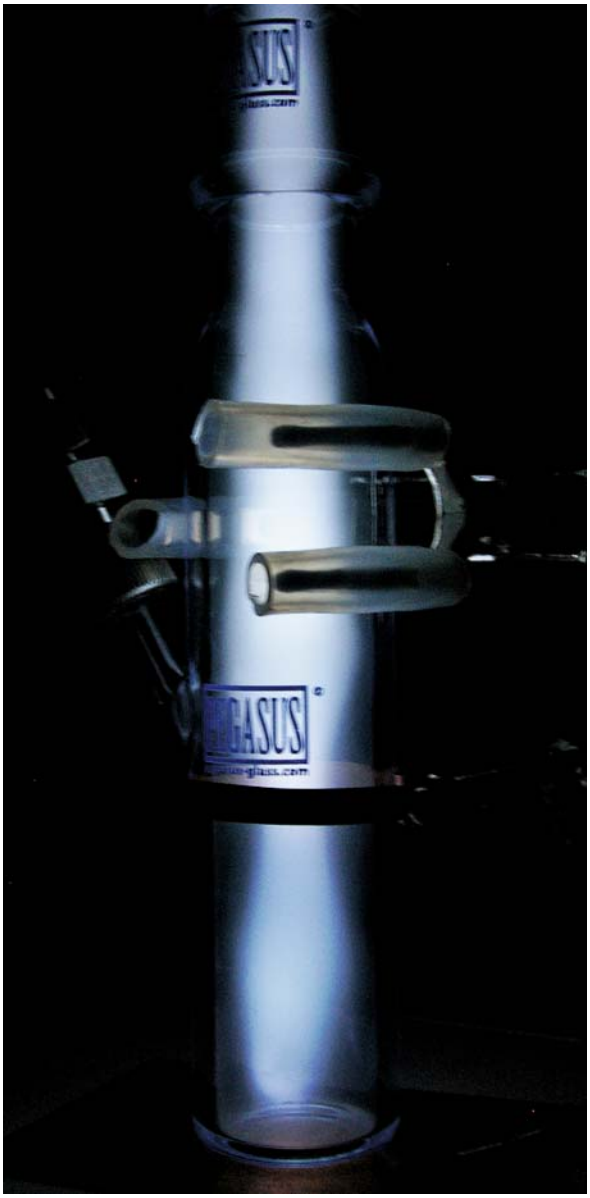

Plasma Treatment of Nanoparticles for Nanofluids, Figure 3 Pictorial view of the plasma reactor system

and oxygen mixtures, which can improve their dispersion characteristics including dispersibility and suspension stability in water for nanofluid. Plasma treatment of diamond nanoparticles with selected plasma chemistry imparted various functional groups on the particle surfaces and tailored the surface energy to the required levels. Plasma coated nanoparticles with desired surface functionalities, e. g., polar and/or charged groups, can strongly interact with water molecules and thus better disperse into water to form stable suspension through mechanism of *electrostatic repulsion* or *steric repulsion*, or combination of both.

Nanofluids

Nanofluids, a concept developed by Choi at Argonne National Laboratory [14], is a new class of heat transfer fluids that are composed of suspended nano-sized metallic or nonmetallic solid particles in liquid media. Nanofluids when properly prepared display significantly enhanced heat transfer capacities relative to those of traditional heat transfer fluids. From the practical application viewpoint, the most critical concerns are the agglomeration and poor suspension stability of the metallic or non-metallic nanoparticles in a given fluid medium.

For most fine powders including nanoparticles, strong interparticle attractions tend to stick the particles into agglomerates, which make the independent dispersion of the powders difficult and, more importantly, deteriorates the final property including the thermal conductivity, viscosity, suspension stability, reliability and reproducibility. There is a great difference of density between metallic particles and fluids. As a result, the stability of the suspension of metallic particles in liquid media is usually poor, especially with the relatively high-density and large-size parti-

cles. The agglomerates of particles have a great tendency to precipitate and thus further worsen the suspension stability. The particle precipitation will not only decreases the heat transfer capacity of the nanofluids but also adversely limits the application of nanofluids in practical devices. The consequence of the agglomerate precipitation may cause clog issues of the nanofluids-based devices in which the fluids need to flow through mini and/or microchannels.

One approach to achieve the homogeneous dispersion and stable suspension of fine particles is using various dispersing agents (or surfactants) to stabilize the particle suspension via a steric and/or electrostatic repulsion [15]. It is well known that, however, the synthesis of stable dispersion of nanosized inorganic materials in liquid requires amounts of stabilizers several orders of magnitude higher than the available space on the surface of nanoparticles can accommodate [16]. The presence of excess amount of stabilizers could significantly alter the fluids characteristics, such as viscosity and thermal conductivity, and could be a big concern in the practical application of the fluids. In contrast, plasma treatment of nanoparticles provides a new promising approach in producing well-dispersed and stably suspended heat transfer nanofluids via fabrication of surface-functionalized nanoparticles without using dispersing agents (or surfactants).

Basic Methodology

Plasma Treatment

A magnetically-assisted fluidized bed plasma reactor, which is schematically shown in Fig. 2 and pictorially shown in Fig. 3, can be used to treat diamond nanoparticles (average size of 50 nm). The reactor shown in Fig. 3 is a long cylinder with an inside diameter of 2.54 cm and a length of 15.24 cm. The plasma reactor is pumped down to a base pressure less than 3 mtorr. Then, methane and oxygen mixture at various ratios is used as the plasma fuel and introduced into the reactor to a preset pressure for plasma treatment. Methane and oxygen gases both have a purity of 99.997%. The flow rates of the methane and oxygen were controlled and adjusted using needle valves. The gas pressure in the reactor was monitored using a Baratron (MKS instruments, Inc.). A radio-frequency plasma source (RFX-600, Advanced Energy Industries, Inc.) was used to ignite the plasmas for plasma treatment of the nanoparticles.

Surface Energy and Polar Interactions of Nanoparticles

The surface energy of diamond nanoparticles can be measured and calculated through Lifshitz–van der Waals/acid-base (LW-AB) approach by surface contact angle measurements using three different liquids with known surface tensions, including HPLC grade water, acetone, and hexane. The surface contact angles of the untreated and plasma treated diamond nanoparticles were determined using sessile drop contact angle measurements with a VCA 2500XE system (Advanced Surface Technologies, Inc., Billerica, MD). Before each measurement, the diamond nanoparticles were sticking to a glass slide with a piece of double-layer tape, and then pressed and smoothened using another glass slide under ~ 1.0 kg weight. For surface contact angle measurement, a sessile droplet of 0.4 μl liquid was placed on the smoothened nanoparticle surfaces to obtain an optical image of the liquid droplet. The computer user manually traced the arc that was created by the droplet and a computer program was used to calculate the contact angles of liquid on the nanoparticle surfaces. Six measurements for each sample were performed and the average number was reported in this study. The experimental error for the static contact angle measurement was within ± 2.0 degree from the average value.

Plasma treatment of diamond nanoparticles can functionalize the nanopartcicles' surfaces with polar groups that have improved interactions with water molecules and thus strong affinity to water medium. Lifshitz–van der Waals/acid-base (LW-AB) approach can be used to quantify the contributions of these plasma-induced polar groups to surface energy increase of the plasma treated nanoparticles. As described by Van Oss et al. [17], the total surface energy of nanoparticle, which combined both Lifshitz–van der Waals and Lewis acid-base (LW-AB) interactions, can be expressed by following expression:

$$\gamma = \gamma^{LW} + \gamma^{AB} \tag{1}$$

In other words, the total potential energy of nanoparticle-liquid interactions is the sum of a Lifshitz–van der Waals interaction (γ^{LW}), which means the surface free energy (dipole–dipole and dipole-induced dipole interaction), and Lewis acid-base interaction (γ^{AB}). The Lewis acid-base interaction (γ^{AB}) for the component i is simply calculated by the geometric mean of electron acceptor (γ^{+}) and donor (γ^{-}):

$$\gamma^{AB} = 2\sqrt{\gamma^{+}\gamma^{-}} \tag{2}$$

In order to calculate the surface energy of nanoparticles from our experimentally measured surface contact angle

data, Young–Dupre equation can be used:

$$(1+\cos\theta)\gamma_L = 2\left(\sqrt{\gamma_S^{LW}\gamma_L^{LW}} + \sqrt{\gamma_S^{+}\gamma_L^{-}} + \sqrt{\gamma_S^{-}\gamma_L^{+}}\right) \quad (3)$$

By measuring the contact angle (θ) of the diamond nanoparticles with three different liquids including at least two polar solvent with known γ_L^{LW}, γ_L^{+}, and γ_L^{-} values, the γ_S^{LW}, γ_S^{+} and γ_S^{-} of the untreated and plasma treated diamond nanoparticles were determined.

Fourier Transform Infrared Spectra (Ftir)

FTIR measurements can be used to identify and semi-quantitatively verify the surface functionalities/polar groups on diamond nanoparticles' surface induced by plasma treatment. Nicolet 6700 FT-IR Spectrometer (Thermo Scientific Inc.) was used to take Fourier Transform Infrared Spectra (FTIR) of the untreated and plasma treated diamond nanoparticles. Well-ground mixtures of nanoparticle and KBr powders (IR grade) were kept in an oven and baked at 200 °C for 48 h to get rid of moisture before performing the FTIR measurements.

Thermal Conductivity Measurement

The transient hot-wire method can be used to measure the thermal conductivity of nanofluids in this study [18]. As schematically shown in Fig. 4, the transient hot-wire measurement system contains a DC power supply, the wheatstone bridge, a data acquisition system, a nanofluid container, and a computer system to analyze the measurement data. The wheatstone bridge was constructed to determine the change of resistance. The input voltage of 5 V was supplied by an Agilent E3645A DC power supply and the output voltage was measured by a National Instruments SCXI-1000 DAQ. This data acquisition system was also used to measure the temperature of the liquid during the measurement. Each dataset was collected at a rate of 500 points per second. The relation between the output voltage and the resistance of the platinum wire is given by following Eq. (4):

$$R_{Pt} = R_2 \frac{\left(\frac{V_{OUT}}{V_{IN}} + \frac{R_3}{R_1+R_3}\right)}{\left(1 - \frac{V_{OUT}}{V_{IN}} - \frac{R_3}{R_1+R_3}\right)} \quad (4)$$

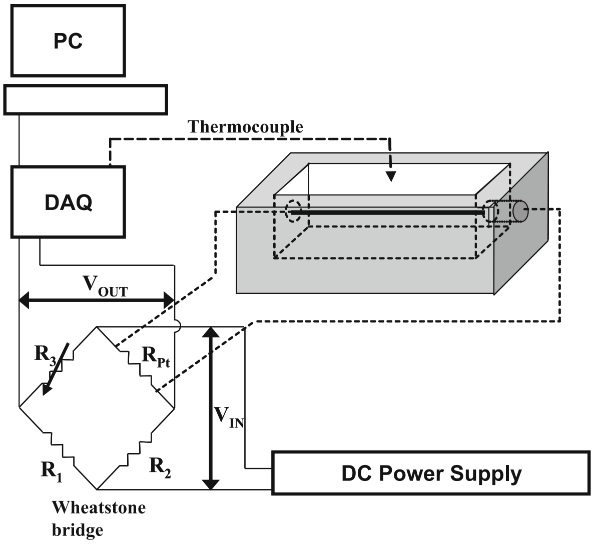

Plasma Treatment of Nanoparticles for Nanofluids, Figure 4 Schematics of the transient hot wire system for thermal conductivity measurement

Using the linear relation between resistance and temperature, Eq. (5) is derived.

$$T = \frac{1}{\alpha}\left(\frac{R_{Pt,T}}{R_{Pt,T=0}} - 1\right) \quad (5)$$

where α is

$$\alpha = \frac{\partial \frac{R_{Pt}}{R_{Pt,T=0}}}{\partial T} \quad (6)$$

Finally, thermal conductivity (k) can be found from the following liner heat source model:

$$k = \frac{q}{4\pi(T_2 - T_1)} \ln\left(\frac{t_2}{t_1}\right) \quad (7)$$

In order to eliminate the effect of convection of the nanofluid, time interval in Eq. (7) must be within the region where thermal conduction is dominant.

The rectangular nanofluid container was designed so that the wire was at least 10 cm long and would contain about 100 ml of fluid. The fluid container was constructed out of 1.49 cm thick Plexiglas. A 1.27 cm diameter hole was drilled through the container wall in each end. A 0.0254 mm diameter pure platinum wire was attached to 12 gage copper wire. The copper wire was crimped onto each end of the platinum wire at a spacing of 10 cm. The connections between platinum and copper wires were soldered to ensure a good contact and the two copper wires were inserted into the fluid container through two rubber stoppers. The copper portion that would be in contact with

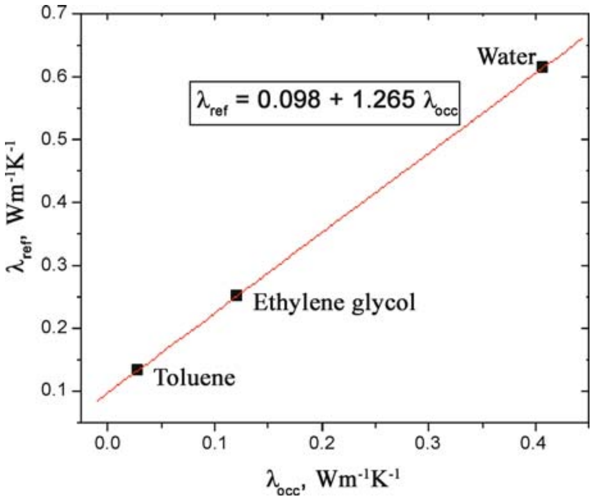

Plasma Treatment of Nanoparticles for Nanofluids, Figure 5 Calibration curve for thermal conductivity measurements of nanofluids

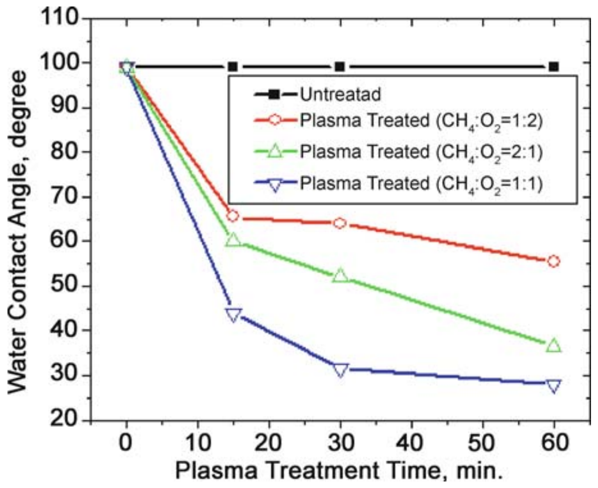

Plasma Treatment of Nanoparticles for Nanofluids, Figure 6 Contact angle change of diamond nanoparticles with plasma treatment time. Plasma treatment conditions were: 60 mtorr pressure, 4 W RF power

the test fluid was covered with Omegabond "100" epoxy to eliminate galvanic corrosion. A T type thermocouple was also placed in the fluid so that the temperature of the fluid could be monitored. The temperature measurements using this thermocouple gave reading with an error of $\pm 1\,°C$. To relate the resistance of the wire to temperature, the resistance of the platinum wire over a range of temperatures should be known. Therefore, HPLC grade water of varying temperatures was placed into the container and the resistances of the platinum wire and the temperature of the water were measured.

The thermal conductivity measurement of nanofluids was conducted with the fluid without any vibration. Each test was conducted at ambient condition and the data were collected for 131 s. After repeated trials it was found that the variable resistor should be balanced slightly above the known resistance of the platinum wire. Once the bridge is properly balanced the variation of voltage with time was measured and recorded. The measured thermal conductivity data was calibrated using three kinds of fluids, which was HPLC grade water, ethylene glycol and toluene. Figure 5 shows the calibration curve obtained by recording the thermal conductivity of those liquids measured. The calibration curve gave a linear calibration equation of $\lambda_{\mathrm{ref}} = \boldsymbol{a} + \boldsymbol{b}\lambda_{\mathrm{acc}}$, with $\boldsymbol{a}$ and $\boldsymbol{b}$ were 0.098 and 1.265. All the measured thermal conductivity data of nanofluids was corrected using this calibration equation.

Key Research Findings

Surface Energy of the Plasma Treated Nanoparticles

Figure 6 shows that the water surface contact angle change of plasma treated diamond nanoparticles with plasma treatment time under different plasma conditions. It can be seen that the untreated diamond nanoparticles had a water surface contact angle of 99°. In contrast, plasma treatment significantly reduced the water surface contact angle to less than 30°, which indicated very hydrophilic surfaces with increased surface energy. Using Lifshitz–van der Waals/acid-base (LW-AB) approach, Table 1 summarized the surface energy data analysis results contributed from Lifshitz–van der Waals interaction (γ^{LW}) and Lewis acid-base interaction (γ^{AB}). Evidenced from the data shown in Table 1, the significant surface energy increase of the plasma treated diamond nanoparticles resulted from the contributions from enhanced Lewis acid-base interaction (γ^{AB}), which includes γ_S^+ and γ_S^-, the surface energies contributed from electron acceptors and the electron donors, respectively. This indicates that increased amount of polar functionalities on plasma treated diamond nanoparticles.

Fourier Transform Infrared Spectra

FTIR measurements were used to determine the surface functionalities induced by plasma treatment. Figure 7 presents the FT-IR spectra of untreated, plasma-treated diamond nanoparticles in plasma gas mixtures of methane and oxygen with ratios of 1 : 1 and 1 : 2. The band at $1630\,\mathrm{cm}^{-1}$ is associated with the vibrations of C = C bonds which is corresponding to the characteristic of diamond. A wide band with its maximum at $3400\,\mathrm{cm}^{-1}$ in the IR spectrum is due to the vibration of OH groups. The peak at $1725\,\mathrm{cm}^{-1}$ is attributed by the vibration of C = O bonds in weak-acid carbonyl. The increased peak

Plasma Treatment of Nanoparticles for Nanofluids, Table 1 The contact angle (θ) and its suface energy of untreated and treated ($CH_4 : O_2 = 1:1$, 60 mtorr, 4 W RF power) diamond nanoparticles. Surface energy of each solvent is $\gamma_l^+ = 71.99$, $\gamma_l^- = 23.46$, $\gamma_l^{LW} = 17.89$. γ_S^+ and γ_S^- are the surface energies contributed from electron acceptors and the electron donors, respectively. γ^{LW} represents Lifshitz–van der Waals interaction and γ^{AB} represents Lewis acid-base interaction

Plasma gases	Plasma time	Contact angle ($\cos\theta$)			Surface energy (mN/m)				
		Water	Acetone	Hexane	γ_S^+	γ_S^-	γ_S^{LW}	γ_S^{AB}	γ_S^{Total}
Untreated		−0.156	0.044	0.019	12.82	6.39	4.64	18.10	22.74
$CH_4 : O_2 = 1:1$	15 min	0.729	0.820	0.175	53.80	19.43	6.17	64.66	70.83
$CH_4 : O_2 = 1:1$	30 min	0.853	0.886	0.559	61.79	20.86	10.87	71.80	82.67
$CH_4 : O_2 = 1:1$	60 min	0.884	0.927	0.643	63.88	21.78	12.07	74.60	86.67

Plasma Treatment of Nanoparticles for Nanofluids, Table 2 FTIR peak ratios for untreated and plasma treated diamond nanoparticles. Plasma treatment conditions were: 60 mtorr pressure, 4 W RF power, 60 min treatment time

FTIR peaks	$C=O/C=C$	$OH/C=C$
(a) Untreated	0.07	2.37
(b) Plasma treated ($CH_4 : O_2 = 1:1$)	0.56	3.59
(c) Plasma treated ($CH_4 : O_2 = 1:2$)	0.82	4.01

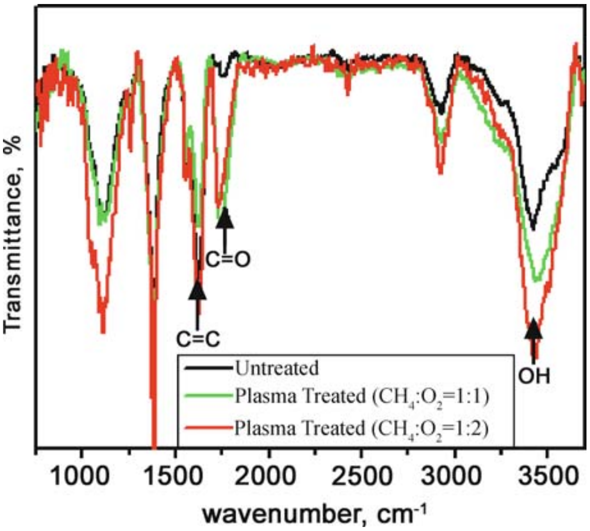

Plasma Treatment of Nanoparticles for Nanofluids, Figure 7 FTIR spectra of untreated and plasma treated diamond nanoparticles. Plasma treatment conditions were: 60 mtorr pressure, 4 W RF power, 60 min treatment time

intensity at 1725 and 3400 cm^{-1} indicates the incorporation of $C=O$ and $-OH$ polar functionalities on plasma treated nanoparticles' surfaces. Table 2 summarizes the peak area comparison of $C=O$ and $-OH$ relative to $C=C$ peaks to semi-quantitatively determine the polar groups on plasma treated nanoparticle surfaces, because the amount of $C=C$ group should be constant before and after the plasma treatment. From the Table 2, it is shown that, in comparison with the untreated control, the ratios of $C=O/C=C$ and $-OH/C=C$ groups for plasma treated diamond nanoparticles were significantly increased.

Thermal Conductivities of the Resulting Nanofluids

Effect of Oxygen/Methane (O_2/CH_4) Ratio in Plasma Gas Mixture

The untreated and plasma treated diamond nanoparticles were dispersed into HPLC grade water with the aid of mechanical agitation using a magnetic stirrer. We have reported that plasma treated diamond nanoparticles showed enhanced dispersibility and improved suspension stability in water as compared with the untreated controls [19]. After settled for one hour, the nanofluids thus prepared were characterized using the transient hot wire system shown in Fig. 4. Figure 8 shows the thermal conductivities of the nanofluids prepared using plasma treated nanoparticles with varying oxygen addition in plasma gas mixtures of methane and oxygen. When O_2/CH_4 ratio increased from 1 : 4 to 1 : 1 in the plasma gas mixture, the plasma treated nanoparticles gave increasing thermal conductivities of the resulting nanofluids with more oxygen addition. Further increasing the oxygen amount above 50% ($O_2/CH_4 = 1:1$), however, the thermal conductivity of the resulting nanofluids with the plasma treated nanoparticles started to decrease.

The thermal conductivity dependence of the resulting nanofluids on O_2/CH_4 ratios in plasma gas mixture shown in Fig. 8 is consistent with the water surface contact angle results shown in Fig. 6. 1 : 1 ratio of O_2/CH_4 gave the lowest water contact angles for the plasma treated diamond nanoparticles as compared with lower or higher O_2/CH_4 ratios. The lower water surface contact angle suggested higher amount of polar functionalities were introduced onto diamond nanoparticles' surfaces through

P

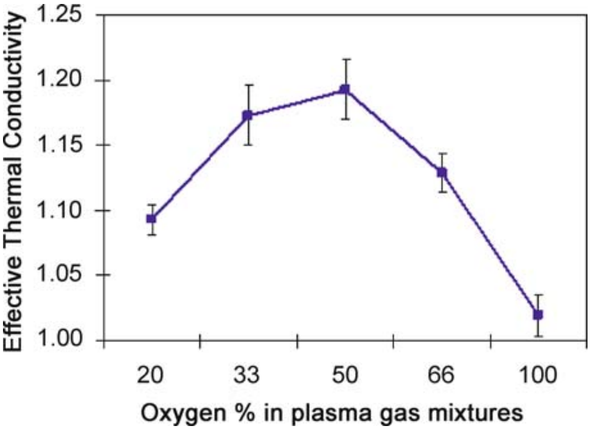

Plasma Treatment of Nanoparticles for Nanofluids, Figure 8 The effects of O_2/CH_4 ratio used for plasma treatment on thermal conductivity of the resulting nanofluids with addition of 0.15 Vol.% plasma treated diamond nanoparticles into water. The thermal conductivities were measured after 1.0 hour settling time. Plasma treatment conditions were: 60 mtorr pressure, 4 W RF power, 60 min treatment time

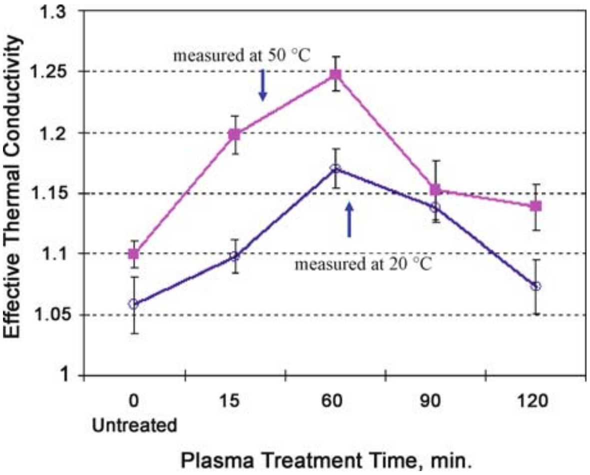

Plasma Treatment of Nanoparticles for Nanofluids, Figure 9 Plasma treatment time effects on thermal conductivity of the resulting nanofluids with addition of 0.15 Vol.% plasma treated diamond nanoparticles into water. The thermal conductivities were measured after 1.0 h settling time. Plasma treatment conditions were: 60 mtorr pressure, 4 W RF power, 1 : 1 ratio of $CH_4 : O_2$

plasma treatment. As a result, a better dispersion of the nanoparticles in water medium was achieved and so was the thermal conductivity of the resulting nanofluids. It is believed that plasma treatment using higher amount of oxygen addition over 1 : 1 ratio of O_2/CH_4 could very likely result in a pronounced surface etching effect and etch the surface polar surface functionalities away.

Effect of Plasma Treatment Time

The water surface contact angle measurement and thermal conductivity measurement showed that plasma treatment of diamond nanoparticles with 1 : 1 ratio of O_2/CH_4 gave rise to the best surface wettability and the highest thermal conductivity of the resulting nanofluids. Using plasma gas mixture with a fixed O_2/CH_4 ratio of 1 : 1, therefore, effects of plasma treatment time on thermal conductivities of the resulting nanofluids were examined. In Fig. 9, the effective thermal conductivities of the resulting nanofluids at both 20 °C and 50 °C were plotted against the plasma treatment time for diamond nanopaticle treatment using plasma gas mixture of $O_2/CH_4 = 1 : 1$. With plasma treatment time varied from 15 to 120 min, plasma treatment of diamond nanoparticles for 60 min gave a nanofluids with the maximum thermal conductivity at both temperatures. The results in Fig. 9 are also consistent with the water surface contact angle measurement results shown in Fig. 6. The thermal conductivity decrease using plasma treatment time longer than 60 min could be due to the over treatment effects often observed in plasma treatment processes.

Stability of the Resulting Nanofluids

We have recently reported that plasma treatment of diamond nanoparticles significantly improved their suspension stability in water [19]. After 45 day sediment test, the nanofluids using plasma treated diamond nanoparticles didn't give any phase separation, while the nanofluids using untreated controls showed clear phase separation of water. In this study, the settling time dependence of the nanofluid thermal conductivity was monitored and the data are shown in Fig. 10. It can be seen that the nanofluids using untreated nanoparticles showed a decreasing trend with settling time. After 120 h settling, the effective thermal conductivity reached to ∼ 1.0, i. e., the same as pure water. In contrast, the nanofluids prepared using plasma treated diamond nanoparticles showed very little change in the effective thermal conductivity with settling time.
From Fig. 10, it was noted that, with the same amount nanopartcile addition of 0.15 Vol.%, nanofluids using plasma treated nanoparticles gave much higher thermal conductivity than that using untreated nanoparticles. It was usually observed that the thermal conductivity of nanofluids is proportional to the volume fraction of nanoparticles added in base liquid media [20]. Results shown in this study suggest that plasma treatment of diamond nanoparticles could well disperse the nanoparticles in water and thus increase the thermal conductivity of the resulting nanofluids. It is suspected that the enhanced interfacial interactions between nanopaticles – base water fluids due to introduction of polar surface functionalities by plasma treat-

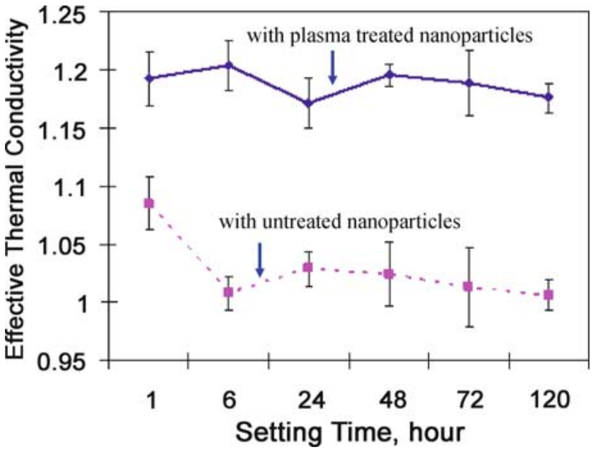

Plasma Treatment of Nanoparticles for Nanofluids, Figure 10 Thermal conductivity change of the resulting nanofluids (with 0.15 Vol.% diamond nanoparticle addition in water) with settling time. Plasma treatment conditions were: 60 mtorr pressure, 4 W RF power, 60 min treatment time, 1 : 1 ratio of CH_4 : O_2

ment could be another important factor contributed to the thermal conductivity increase of the resulting nanofluids.

Future Directions for Research

Plasma treatment provides a new approach to functionalize nanoparticle surface for heat-transfer nanofluid preparation without using stabilizing agents. More experimental investigation is very necessary to optimize the plasma treatment process in term of plasma chemistry, plasma operating conditions, and proper plasma apparatus design. As pointed out in this paper, besides nanoparticle concentration, the enhanced interfacial interactions between nanopaticles – base fluids could be another important factor that contributed to the thermal conductivity increase observed in heat-transfer nanofluids. A detailed characterization of the nanofluids with the aid of theoretical simulations will help us to understand the fundamental mechanisms for the observed heat-transfer enhancement.

Cross References

► Plasma Surface Modification
► Surface Tension Measurements
► Surface Conductivity Measurement

References

1. Shohet JL (1991) Plasma-Aided Manufacturing. IEEE Transf Plasma Sci 19:725–733
2. Yasuda HK (2005) Luminous chemical vapor deposition and interface engineering. Dekker, New York
3. Yu QS, Deffeyes J, Yasuda HK (2002) Corrosion protection of ion vapor deposition (IVD) Al-coated Al alloys by low-temperature plasma interface engineering: Part III: DC Cathodic Polymerization in a Closed Reactor System. Prog Org Coat 44:37–47
4. Yu QS, Reddy CM, Moffitt CE, Wieliczka DM, Johnson R, Deffeyes J, Yasuda HK (2001) Improved Corrosion Protection of Al Alloys by System Approach Interface Engineering: Part IV – Spray Primer Coated Al Alloys. Corrosion 57:802–814
5. Chu PK, Chen JY, Wang LP, Huang N (2002) Plasma-surface modification of biomaterials. Mater Sci Eng R36:143–206
6. d'Agostino R (1990) Plasma Deposition, Treatment, and Etching og polymers. Academic Press, Boston
7. Bubert H, Haiber S, Brandl W, Marginean G, Heintze M, Bruser V (2003) Characterization of the uppermost layer of plasma-treated carbon nanotubes, Diamond and Related Materials 12(3–7):811–815
8. Chirila V, Marginean G, Brandl W (2005) Effect of the oxygen plasma treatment parameters on the carbon nanotube surface properties Sur Coat Techn 200:548–551
9. Khare BN, Wilhite P, Quinn RC, Chen B, Schingler RH, Tran B, Imanaka H, So CR, Bauschlicher CW Jr, Meyyappan M (2004) Functionalization of Carbon Nanotubes by Ammonia Glow-Discharge: Experiments and Modeling. J Phys Chem B 108(24):8166–8172
10. Khare BN, Wilhite P, Meyyappan M (2004) The fluorination of single wall carbon nanotubes using microwave plasma. Nanotechnology 15(11):1650–1654
11. Shi D, He P, Lian J, Wang L, van Ooij WJ (2002) Plasma deposition and characterization of acrylic acid thin film on ZnO nanoparticles. J Mater Res 17(10):2555–2560
12. Shi D, Lian J, He P, Wang LM, van Ooij WJ, Schulz M, Liu Y, Mast DB (2002) Plasma deposition of ultrathin polymer films on carbon nanotubes. Appl Phys Lett 81(27):5216–5218
13. Shi D, Wang SX, van Ooij WJ, Wang LM, Zhao JG, Yu Z (2001) Uniform deposition of ultrathin polymer films on the surfaces of Al_2O_3 nanoparticles by a plasma treatment. Appl Phys Lett 78(9):1243–1245
14. Choi US (1995) Enhancing thermal conductivity of fluids with nanoparticlers. In: Siginer DA, Wang HP (ed) Developments and Applications of Non-Newtonian Flows. FED-Vol. 231/Mid-Vol. 66, ASME, New York
15. Toshima N (2003) Metal nanoparticles for catalysis. In: Liz-Marzan LM, Kamat PV (ed) Nanoscale materials. Kluwer Academic, Boston
16. Hilgendroff M, Giersig M (2003) Assemblies of magnetic particles – Synthesis and production. In: Liz-Marzan LM, Kamat PV (eds) Nanoscale materials. Kluwer Academic, Boston
17. van Oss CJ (2003) Long-range and short-range mechanisms of hydrophobic attraction and hydrophilic repulsion in specific and aspecific interactions. J Mol Recognit 16:177–190
18. Corey W (2006) Experimental Investigation of Nanofluid Oscillating Heat Pipes. M.S. thesis, University of Missouri, Columbia
19. Yu QS, Kim YJ, Ma HB (2006) Plasma treatment of diamond nanoparticles for dispersion improvement in water. Appl Phys Lett 88:231503/1–3
20. Xie H, Lee H, Youn W, Choi M (2003) Nanofluids containing multiwalled carbon nanotubes and their enhanced thermal conductivities. J Appl Phys 94:4967–4971

P

Plastic

► Polymer

Plasticity

► Viscosity

Platinum Resistance Thermometer

► Resistance Temperature Detectors

Plug Flow

► Taylor Flow in Microchannels

Pneumatic Valves

Daniel Irimia
Massachusetts General Hospital, Harvard Medical School, Boston, VA, USA
dirimia@partners.org

Synonyms

Elastomeric valve

Definition

Mechanical structure designed to control the flow of fluids in one channel through changes in pressure in a second channel from which it is separated by a membrane or equivalent structure.

Overview

Pneumatic valves rely on the deformation of a membrane, or other thin structure, by pressure, with the end result of altering the flow of a fluid in a channel. The size of the pneumatic valves is usually comparable to the size of the channels they control and consequently these valves are easy to integrate in the overall design of the microfluidic chips. Although several designs have been proposed over time, using different materials, the most successful valves in terms of applications have been the valves using elastomeric materials. Elastomeric materials are easily deformable, and are already widely used for microfluidic applications, making them ideal for developing pneumatic valves.

In the simplest design, the deformation of a circular membrane under uniform pressure on one side can be described by the following equation:

$$\Delta x = \Delta P \frac{3r^4}{16t^3} \cdot \frac{(1-\nu^2)}{E}$$

where Δx is the deformation of the membrane at its center, ΔP is the pressure difference on the two sides of the membrane, E and ν are characteristics of the membrane material (the Young modulus and the Poisson's ratio, respectively), and r and t are dimensional characteristics of the membrane (the radius and the thickness of the circular membrane, respectively). Although for more complicated shapes of the membrane the dependence of deformation to actuation pressure has to be calculated numerically using specialized software, the formula for the circular membrane already suggests a very important impact from the valve dimensions on valve functionality.

Basic Methodology

Pneumatic valves are fabricated using standard microfabrication and assembly technologies. The membrane of the valve can be one uniform film of elastomeric material, or can have microchannels already imprinted on one side (see ► microfabrication techniques). The actuation chamber is usually in a separate layer, either elastomer or a rigid material. The layer including the controlled microchannel, the membrane, and the layer containing the actuation chamber are then bonded together using standard techniques (e. g. oxygen plasma for elastomer and glass layers see ► microfluidic assembly and microfabrication techniques). The decision for the precise design and integration of pneumatic devices into the manufacturing of microfluidic devices is usually based on several criteria, each of which may have different weight in different applications. The first criterion is usually the compatibility of the technologies for the valve with the rest of the manufacturing. Some valve require the use of positive resist and overflow at higher temperature, other require glass etching, and some can be manufactured using only negative epoxy resist (SU8). Most of the pneumatic valves require the precise aligning and bonding of two layers of elastomeric material. The second criterion is the nature of the fluid to be handled. While most of the elastomeric materials are compatible with water solutions, only few materials could handle solvents and more aggressive chemicals. The third criterion is the number and size of the valves on one device. Smaller valve size is possible when controlling single rounded channels, while larger valves could incorpo-

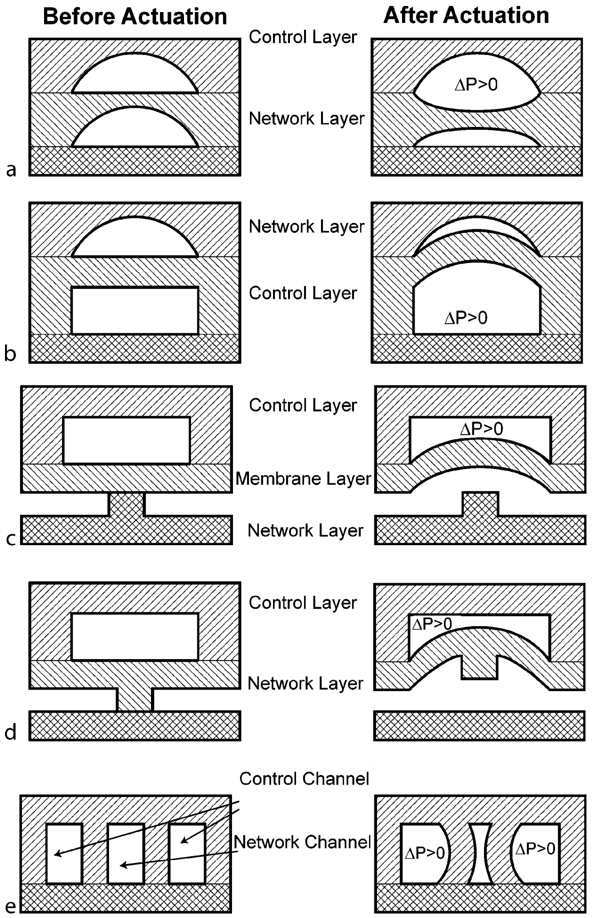

Pneumatic Valves, Figure 1 Schematics of pneumatic valves. (a) Pneumatic valve using the compression of a rounded channel in the network layer. (b) A bulging membrane can be used to control flow in a rounded channel. (c) Negative pressure can deform a membrane and open communication in a network layer. (d) A microstructured membrane could be used to control flow in a complex network layer. (e) In a single layer valve the control channels are placed on the side of the network layer

rate more features or control multiple channels at the same time. Finally, valves that are normally closed or normally open have been described, and the choice depends on the functionality and actuation pressure available for operating the valves.

Key Research Findings

Several approaches have been described for the practical implementation of the pneumatic valves in microfluidic systems. In general, the control and network channels (Fig. 1) are placed in different layers and the membrane structure performing the actuation is in between the layers. Both higher pressure (Fig. 1a,b,e) and vacuum (Fig. 1c,d) have been use to control the fluid in the network layer. In the case of vaccum-actuated valves, the membrane could seal channels in the network layer in the absence of the actuation pressure, only by elasticity of the membrane pressing against the valve seat (Fig. 1c,d).

While smaller aspect ratios of the network layer usually lead to smaller dead volumes for the valves (Fig. 1), various designs that allow the control of higher aspect ratios has been described, especially for applications that require the transport of larger cells or particles (Fig. 1b-e). Pneumatic valves with rounded (Fig. 1a–c) as well as rectangular (Fig. 1d–e) channels in the network layer have been implemented. The control layer could be above or bellow the network layer (Fig. 1a–d), and at least in one implementation the control and network channels were implemented at the same level (Fig. 1 e). Hierarchical arrangements of pneumatic valves in microfluidic devices, where some microscale valves are used to control the operation of other microscale valves, have been demonstrated as a way to reduce the number of control lines and increase the sophistication of actuation patterns.

For most of the designs, the membrane is relatively flat and feature-less and in some implementations it can be different material from the control and network layer materials (Fig. 1c). However, the addition of microstructures to the valve membrane (Fig. 1d) has been demonstrated to result in higher degree of complexity of the functionality that can be achieved using pneumatic actuation.

Future Directions for Research

There are two main challenges for the development of applications using pneumatic valves. The first one has to do with the choice of materials for the valve. Although elastomeric materials are very good for prototyping, scaling up and reducing the fabrication costs would require the use of polymeric materials. Either these new materials would have to have comparable mechanical properties with the current elastomers, or different designs would have to be imagined. The second challenge is related to the control system and pressure generation that is usually off chip. Integrating these on the chip or at least standardizing and miniaturizing these would be needed for compact, reliable miniaturized devices.

Cross References

- ► Capillary Force Valves
- ► Control of Microfluidics
- ► Digital Microfluidics
- ► Electrochemical Valves
- ► Electromagnetic Valves
- ► Electrostatic Valves
- ► Fabrication of 3D Microfluidic Structures

- ► Volume and Finite Difference Method for Modeling and Simulation
- ► Fluid Metering
- ► Lab-on-a-chip (General Philosophy)
- ► Lab-on-chip Devices for Particle and Cell Separation
- ► Membrane Actuation for Micropumps
- ► Microactuators
- ► Microfluidic Assembly
- ► Microfluidic Circuits
- ► Peristaltic pumps
- ► Piezoelectric Valves
- ► Thermopnuematic Valves
- ► Water Management in Micro DMFCs

References

1. Grover WH, Skelley AM, Liu CN, Lagally ET, Mathies RA (2003) Monolithic membrane valves and diaphragm pumps for practical large-scale integration into glass microfluidic devices. Sensors Actuators B 89(3):315–323
2. Hosokawa K, Maeda R (2000) A pneumatically-actuated three-way microvalve fabricated with polydimethylsiloxane using the membrane transfer technique. J Micromech Microeng 10(3):415–420
3. Irimia D, Toner M (2006) Cell handling using microstructured membranes. Lab Chip 6(3):345–52
4. Li N, Hsu CH, Folch A (2005) Parallel mixing of photolithographically defined nanoliter volumes using elastomeric microvalve arrays. Electrophoresis 26(19):3758–3764
5. Studer V, Hang G, Pandolfi A, Ortiz M, Anderson WF, Quake SR (2004) Scaling properties of a low-actuation pressure microfluidic valve. J Appl Phys 95(1):393–398
6. Sundararajan N, Kim DS, Berlin AA (2005) Microfluidic operations using deformable polymer membranes fabricated by single layer soft lithography. Lab Chip 5(3):350–354
7. Unger MA, Chou HP, Thorsen T, Scherer A, Quake SR (2000) Monolithic microfabricated valves and pumps by multilayer soft lithography. Science 288(5463):113–116

Poiseuille Coefficient

Definition

Poiseuille coefficient determines a gas flow induced by a pressure gradient.

Cross References

- ► Gas Flow in Nanochannels
- ► Micro- and Nanoscale Gas Dynamics

Poiseuille Single Phase Gas Flows

- ► Pressure-Driven Single Phase Gas Flows

Polyclonal

Definition

Polyclonal antibodies are antibodies that are derived from several different t B-cell lines. The selections of antibody molecules bind to different parts of the antigen, with different binding affinities. Within a polyclonal sample, some of the antibodies will be specific for the antigen with which the animal was immunised. The rest of the antibodies have been obtained from meetings with other foreign antigens that the animal has been exposed to through its life time.

Poly(dimethylsiloxane) (PDMS)

Definition

PDMS is popular polymer in the microfluidics community; often used for rapid fabrication of microchannel structures. PDMS is optically-transparent and is generally considered to be inert, non-toxic and non-flammable. PDMS is formed by mixing a *base* with a *curing agent* (typically mixed in a 10 : 1 ratio, but this can vary depending on the desired stiffness of the resultant polymer) and curing in a vacuum-oven for several hours. Cured PDMS will form a reversible-bond with various surfaces (glass microscope slides, for example). Irreversible sealing can be achieved by exposing the PDMS to oxygen plasma prior to bonding.

Cross References

- ► Temperature Effects on the Zeta Potential

Polydispersity

Synonyms

Polydispersity index; Mw/Mn

Definition

The distribution of molecular weights in a given polymer sample.

Cross References

- ► Polymer Synthesis within Microfluidic Reactor

Polydispersity Index

► Polydispersity

Polyelectrolyte

Definition

A species (for example, a colloidal particle or a flexible chain) that is partially ionizable when placed in solution. The polyelectrolyte dissociates into a macroion and counterions.

Cross References

► Electrokinetic Flow and Ion Transport in Nanochannels
► Electrophoresis

Polyelectrolyte Patterning Technique

► Surface-Charge Patterning Techniques

Polymer

Synonyms

Plastic; Organic material

Definition

A polymer is a material composed of large macromolecules. These macromolecules are formed by chains of hundreds or thousands of connected (polymerized) monomer molecules. The three main classes of polymers are thermoplastics, elastomers and thermosets. They differ in the degree of cross-linking of their macromolecules – from no cross-linking (thermoplastics) to moderate cross-linking (elastomers, rubbers) to high cross-linking (thermosets). Thermoplastics commonly used in microfluidics include materials like polymethylmethacrylate (PMMA), polycarbonate (PC), polyethylene terephthalate (PET) or cyclic olefin copolymers (COC). Silicones (like polydimethylsiloxane, PDMS) are a typical class of elastomers. Thermosets include photoresist materials like SU-8 and others.

Cross References

► Glass-Polymer-Bonding

Polymer Casting

► Micromolding

Polymer Electrolyte Membrane Fuel Cells

► Microstructured Hydrogen Fuel Cells

Polymerization Reaction in Microreactor

► Polymer Synthesis within Microfluidic Reactor

Polymer Monoliths

► Stationary Phases in Microchannels

Polymer Replication

► Micromolding (Injection and Compression Molding)

Polymer Solutions

► Non-Newtonian Fluids in Microfluidics

Polymer Synthesis within Microfluidic Reactor

Masaya Miyazaki[1,2], Hideaki Maeda[2,3]
[1] Nanotechnology Research Institute, National Institute of Advanced Industrial Science and Technology (AIST), Tosu, Japan
[2] Department of Molecular and Material Science, Interdisciplinary Graduate School of Engineering Sciences, Kyushu University, Kasuga, Japan
[3] CREST, Japan Science and Technology Agency (JST), Kawaguchi, Japan
m.miyazaki@aist.go.jp, maeda-h@aist.go.jp

Synonyms

Synthesis of polymer molecules using microfluidics; Microfluidic reactor for polymer synthesis; Polymerization reaction in microreactor

P

Definition

Polymer synthesis requires strict control of reaction conditions such as temperature, reaction time, and mixing of reagents. Microfluidic reaction systems enable efficient mixing and rapid heat exchange. Moreover, a laminar stream in a microfluidic channel enables control of the resulting shape of a molecule. These features of microfluidic reaction systems are suitable for polymer synthesis.

Overview

Reactions involved in chemical polymerization should be highly controlled because polymer properties such as ►average molecular weight, molecular weight distribution, and size and shape of particles strongly affect the functions of polymer materials. When using polymers of less well known functions, the molecular weight or size and shape should be carefully selected, and the molecular weight or size distribution should be controlled to be as narrow as possible. Such requirements could be satisfied by utilizing microfluidic systems. Microfluidic reaction systems have several distinctive features. One of the unique features is the ability to control molecular weight distribution and simple control of the molecular weight of linear polymers. In addition, microfluidic systems enable efficient emulsification with controlled size and shape. Present-day investigations on polymer materials are directed towards the development of novel functional substances by using high-throughput and combinatorial synthesis methods. The microdevices developed for this purpose should be simple, controllable, and capable of continuous combinatorial synthesis process with high-throughput screening systems for polymer material libraries. Moreover, there is a requirement for accelerated multi-parameter optimization of reaction conditions. In this article, efforts towards the development of microreactors for linear polymer synthesis and preparation of complicated polymer particles are summarized.

Synthesis of Linear Polymers in Microfluidic Reactor

Microreaction systems involve microreaction apparatuses that enable high controllability of chemical reactions. Such controllability results from efficient heat transfer, mass transport, and/or a larger surface/interface area. Recent studies have shown the potential benefits of using microfluidic reactors for various chemical reactions. Reactions using micromixing devices give better results than batchwise reactions. This is because a micromixer enables rapid mixing and therefore yields excellent controllability of rapid reactions.

Application of microreaction technology for linear polymer syntheses was initially performed by several researchers, but the field is still in its infancy. Most of the work utilized a combination of micromixing and reaction parts.

The most popular polymerization method is ►radical polymerization. Wu et al. performed radical polymerization by using a chip-type microreactor [1]. The system is composed of a microstirrer mixer connected to a microchannel reaction part. The molecular mass of the polymer produced is governed by the flow rate or polymerization time. The monomer conversion agrees well with the bulk reaction kinetics reported in the literature. The reactor is convenient and inexpensive to manufacture, with a versatile design that can be reconfigured and prototyped in less than a day. The radical polymerization technique was also applied for ►block copolymerization of poly[(ethylene oxide)-*block*-(2-hydroxypropyl methacrylate)] [2]. A series of well-controlled polymerizations was carried out at different pumping rates or reaction times with a constant ratio of monomer to initiator. The stoichiometry of the reactants was also adjusted by varying relative flow rates to change the reactant concentrations. Another example of radical polymerization in a microreactor was described by Iwasaki and Yoshida, who reported a microreactor consisting of commercially available micromixers (T-shape, 500 μm internal diameter) connected with capillary tubes (500 μm internal diameter) [3]. Thermal decomposition of 2,2-azobis(isobutylronitrile) (AIBN) was examined first and subsequent polymerizations of butyl acrylate (BA), benzyl methacrylate (BMA), methyl methacrylate (MMA), vinyl benzoate (VBz), and styrene (St) were performed. The microreactor was quite effective in controlling the molecular weight distribution for highly exothermic reactions (BA, BMA, and MMA) but not so effective for less thermic polymerizations (VBz and St).

Cationic polymerization was performed in a microreaction system consisting of two micromixers connected by microcapillaries [4]. A method that used irreversible generation and accumulation of highly reactive cations in the absence of nucleophile was applied for polymerization. The molecular weight distribution was controlled by extremely fast micromixing, and the resulting polymer could be used for follow-up reactions.

The benefit of microreaction systems is not limited to cationic or radical polymerization. Amino acid polymerization using α-amino acid *N*-carboxyanhydride (NCA) yielded better molecular weight distribution when performed in a microreactor [5]. Also, the average molecular weight could be controlled by changing the flow rates.

Synthesis of dendric molecules has also been performed. Chang and coworkers synthesized ethylenediamine-cored polyamidoamine (PAMAM) dendrimer using an interdigital micromixer [6]. Using this method, synthesis of generation two through generation five PAMAM dendrimer was confirmed by microchip capillary zone electrophoresis. Furthermore, the synthesized polyamide dendron was deposited onto a functionalized glass surface through the formation of amide bonds using a facile coupling procedure via a microreactor. The dendron deposition process involved two major steps: functionalization of the native glass surface using 3-aminopropyl triethoxysilane, and coupling of the synthesized polyamide dendron with the aminosilanized surface.

Compared with conventional synthesis methods, the microreactor provides better yield and selectivity, and a considerably faster synthesis rate. Nanostructured polyamide G1 dendron thin films could be deposited in minutes using an impinging flux from this microreactor.

Not only have efforts been focused on the synthesis of linear or branched polymer molecules, but theoretical studies have also been performed. Serra et al. conducted numerical simulations of free radical polymerization in microfluidic devices [7]. Three microfluidic devices were modeled: two interdigital multilamination micromixers with a long and short focusing section, respectively, and a simple T-junction followed by a microtube reactor together considered as a bilamination micromixer with a large focusing section. The simulations showed that in spite of the heat released by the polymerization reaction, the thermal transfer in such microfluidic devices was high enough to ensure isothermal conditions. Moreover, for low radial ►Peclet number, microfluidic devices with a large focusing section could achieve better control over the polymerization than a laboratory-scale reactor as the ►polydispersity index obtained was very close to the theoretical limiting value. Serra et al. [7] concluded that the reactive medium cannot be fully homogenized by the diffusion transport before leaving the system resulting in a high polydispersity index and a loss in the control of polymerization as the characteristic dimension of the microfluidic device increases, i. e. for high radial ►Péclet number.

Complicated Polymer Particle Synthesis

There is an increasing demand for polymer particles by industry, particularly for painting formulations and drug delivery applications. A microfluidic reaction system provides superior controllability of fluid because the flow forms simple laminar streams. Thus, efforts have been exerted on polymer particle synthesis using microfluidics because of the unique capacity to generate microdroplets with very narrow size distributions. Polymer particles by simple emulsification have been widely studied and well summarized in other entries. Here, we focus on polymer synthesis by complicated emulsification. Nie et al. reported a novel approach to continuous and scalable production of core–shell droplets and polymer capsules in microfluidic devices [8]. They used laminar flow of three immiscible liquids, aqueous SDS, monomer, and silicon oil, in a microfluidic system. The described method is also useful for the synthesis of polymer particles with nonspherical shapes. They used capillary instability-driven break-up of a liquid jet formed by two immiscible fluids. Precise control of emulsification of each liquid allowed production of highly monodispersed core–shell droplets with a predetermined diameter of cores and thickness of shells. They also achieved control over the number of cores per droplet and the location of cores in a droplet. The authors carried out fast throughput photopolymerization of the monomeric shells and obtained polymer particles with various shapes and morphologies, including spheres, truncated spheres, hemispheres, and single and multicore capsules. Photolithography was also applied for the synthesis of polymer particles. Dendukuri et al. reported a one-phase method using a T-junction microchannel to create solid disk- and plug-shaped particles (Fig. 1) [9]. Snap-off at the junction yielded plugs containing Norland optical adhesive (NOA) 60, a photopolymerizable resin. When an ultraviolet (UV) beam was shone on the plug in the narrow channel, a plug structure was captured, but if the plug was allowed to expand laterally and then polymerized, a disk was formed. Because of the small dimensions of the plugs and disks, the photopolymerization occurred in less than 1 s, using only $3\,\mathrm{J\,cm^{-2}}$ of energy. They also developed an evolutionally advanced microfluidic system by combining the advantages of microscope projection photolithography and microfluidics to continuously form morphologically complex or multifunctional particles down to the colloidal length scale (Fig. 2) [10]. Exploiting the inhibition of free radical polymerization of diacrylate monomers near polydimethylsiloxane (PDMS) surfaces, they were able to repeatedly pattern and flow rows of particles in less than 0.1 s, affording a throughput of near 100 particles per second using the simplest of device designs. Polymerization was also carried out across laminar, co-flowing streams to generate ►Janus particles, which are chemically biphasic particles. They synthesized a Janus polymer by using co-flowing laminar streams of monomer, one of which contained a rhodamine-labeled crosslinker, and forming particles across this interface. The relative proportions of Janus particles could be easily tuned. This new high-throughput technique offers unprecedented control over particle size, shape, and anisotropy.

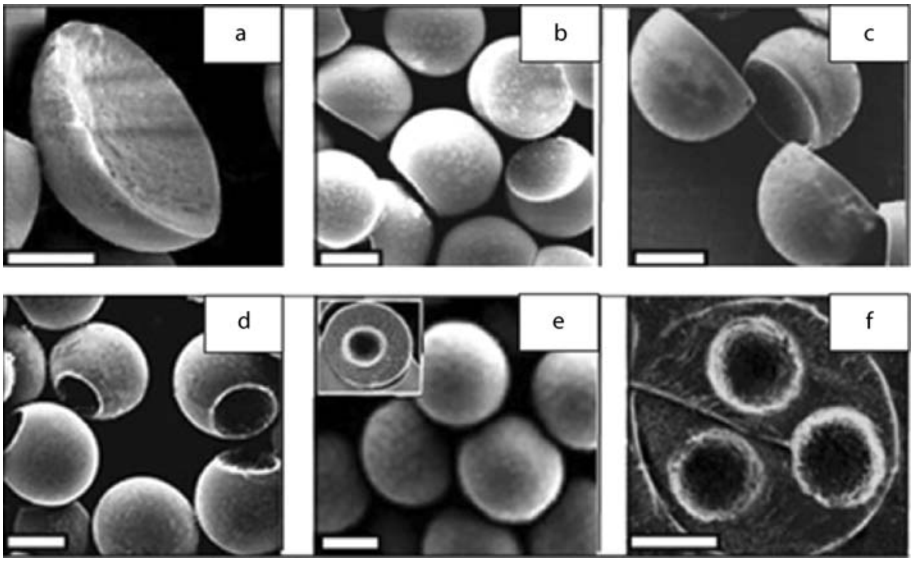

Polymer Synthesis within Microfluidic Reactor, Figure 1 (**a**)–(**e**) Scanning electron microscopy images of polymer microbeads obtained by polymerizing TPGDA in droplets obtained in regimes A, B, C, D, respectively, after removing a SO core. Inset: cross-section of the core–shell particle. (**f**) Cross-section of a polyTPGDA particle with three cores obtained by polymerizing core–shell droplets with three cores. The particle is embedded in epoxy glue. Scale bar is 40 μm. Reproduced from [9]

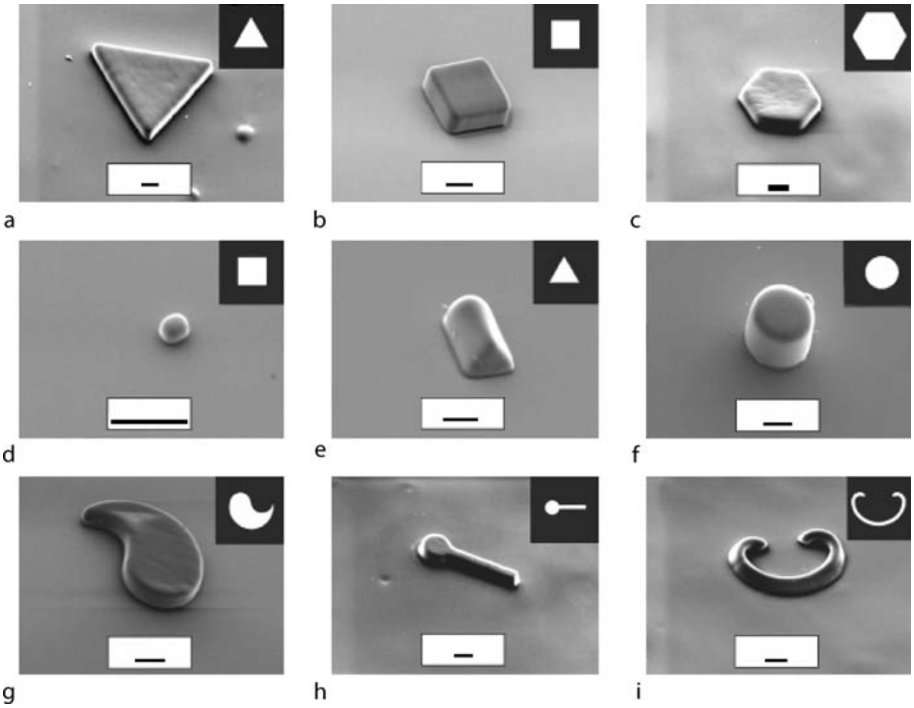

Polymer Synthesis within Microfluidic Reactor, Figure 2 Scanning electron microscope images of particles. Microparticles formed using a ×20 objective (except (**d**), which was formed using a ×40 objective) were washed before being observed. The scale bar in all of the figures is 10 μm. (**a**)–(**c**) Flat polygonal structures that were formed in a 20 μm high channel. (**d**) A colloidal cuboid that was formed in a 9.6 μm high channel. (**e**), (**f**) High-aspect-ratio structures with different cross-sections that were formed in a 38 μm high channel. (**g**)–(**i**) Curved particles that were all formed in a 20 μm high channel. The inset shows the transparency mask feature that was used to make the corresponding particle. Reproduced from [10]

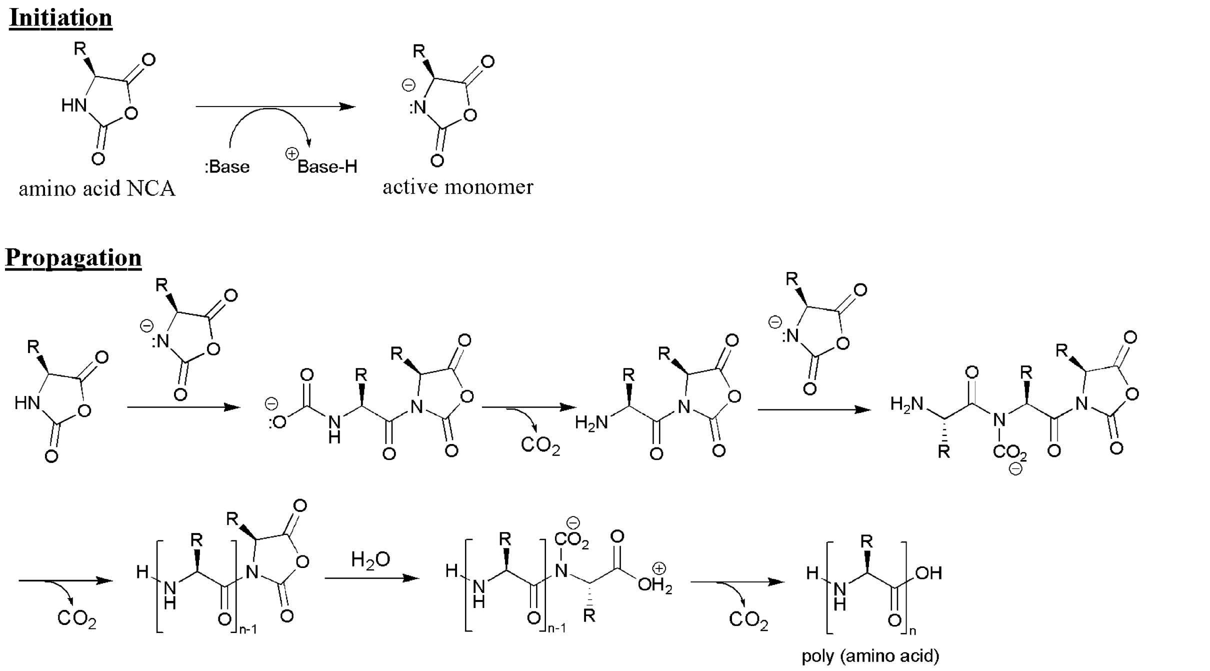

Polymer Synthesis within Microfluidic Reactor, Figure 3 Mechanism of NCA polymerization initiated by a base such as tertiary amine. Reproduced from [5]

Basic Methodology

Basically, a microreaction system for polymerization reaction consists of a microfluidic device for mixing or droplet formation followed by microchannels as reaction parts. In this article, linear amino acid polymerization reaction is used as a basic example of polymer synthesis using microfluidic devices. Amino acid polymer was synthesized using the NCA method. This reaction is an anion ring-opening reaction which consists of two stages (Fig. 3): initiation by tertiary amine, and propagation of the polymer chain. The initiation and NCA anion attack are known to be relatively fast reactions. It is assumed that these steps are important in controlling polymerization of NCA. However, control of polymerization would be difficult in conventional batchwise systems due to the tendency to locally generate concentration gradients of the reagents. As a remedy, strict reaction control of a microreaction system can be employed to synthesize biopolymers.

Preparation of Microreaction Device

Generally, mixing is extremely important in chemical reactions. When using microreactors for chemical reactions, micromixers are often incorporated in the microreactor for effective mixing. Mixing of the monomer and base principally depends on diffusion through the interface of the two solutions. A multilayered micromixer increases the interface area of two fluids and shortens the diffusion length, resulting in an increase in the mixing efficiency of reactants. Also, a characteristic feature of this mixer is that mixing efficiency increases with a decrease in flow rate. In order to gain long residence time required for polymerizations, low flow rate should be used in the microfluidic system; therefore, a multilayered micromixer was employed for NCA polymerizations in a microfluidic system.

Figure 4 shows the setup of a microreaction system. The micromixer was attached to a PTFE microtube (length = 500 cm) and served as a polymer-propagating region. The volume of fluid channel of the micromixer was 4.4 μl, and the total inner product volume of this microreactor corresponded to 250 μl. In the microreactor setup, monomer and initiator solutions were each charged into a 1 ml Hamilton gastight syringe. The solutions were supplied to the microreactor using a syringe pump with a parallel syringe holder, which enable identical pumping rates so that the final mixed solution would have a constant reagent concentration.

Polymerization Reaction

Polymerizations were performed in DMF and initiated by triethylamine. Both solutions of monomer and base were separately introduced into the microreactor (Fig. 4) using a syringe pump. The resulting mixture was heated at

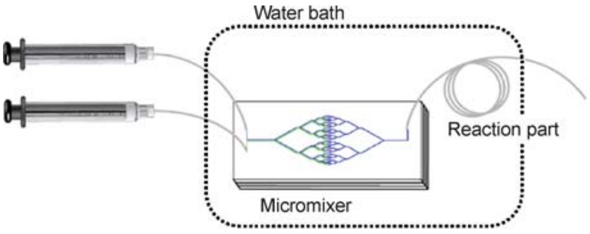

Polymer Synthesis within Microfluidic Reactor, Figure 4 Microreaction system used in this study. The system consists of a PDMS micromixer and PTFE microtubes. Two syringes containing reagents were coupled on the PDMS micromixer by PTFE microtubes (diameter = 250 μm, 10 cm). The PDMS micromixer was attached to a PTFE microtube (diameter = 250 μm, 500 cm) and served as a reaction region. The mixer and reaction region were kept at 30 °C in a water bath. Reproduced from [5]

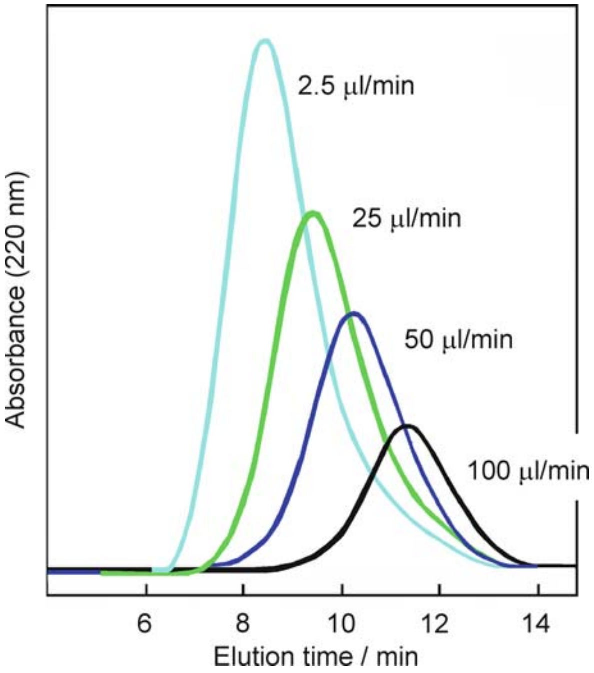

Polymer Synthesis within Microfluidic Reactor, Figure 5 Gel filtration chromatography analysis of poly(Lys) produced by the microreactor. The polymerizations were conducted with 0.1 M monomer and 0.01 M initiator for 1, 5, 10, and 100 min of reaction times corresponding to 250, 50, 25, and 2.5 μl/min flow rates, respectively. Reproduced from [5]

100 °C for termination, then deprotection of the side-chain protective group was performed using HBr in AcOH. The sample was analyzed by gel filtration chromatography after dialysis against water to remove HBr. Figure 5 shows the gel filtration chromatography data for the poly(Lys) produced using the microreactor at different flow rates. The molecular weights of the respective samples regularly increased with a decrease in flow rates, that is, as a consequence of the increase in time required for polymerization to occur. It was found that the molecular mass of the polymer produced using the microreactor is simply governed by the flow (pumping) rate. Also, polymers produced by the microreaction showed narrower molecular weight distribution than that of macroscale reaction in homo- and copolymers (Fig. 6).

Key Research Findings

Many polymers with interesting functionalities have been developed and applied in various fields. At present, a rapid and combinatorial synthesis system with highly controllable polymerization reaction is much required. However, it is generally difficult to control polymerization reactions in conventional batchwise systems. Synthesis of polymer molecules using a microreactor enables strict control of chemical reactions which serves as a model of polymer synthesis. The performance of a microreaction system for polymerization was compared with that of a conventional batchwise system by analyzing the properties of the obtained polymers. In linear polymer products, the M_w/M_n values of the polymers synthesized by the batchwise system obviously increased with increasing concentration of monomer. In contrast, the M_w/M_n values in the microfluidic system remained low with high monomer concentrations [5]. It was demonstrated that the microreactor provided high controllability of polymerization even at concentrations that produced poor control of molecular weight distribution in the case of the batch reaction. The controllability of molecular weight distribution is governed by several factors. The first factor is the mixing efficiency of reactants. In the batchwise system, an increase in reagent concentration tends to decrease the mixing efficiency of reagents, and leads to generation of local concentration gradients of the reagents. In addition, the viscosity rise observed for highly concentrated monomer solutions will cause a decrease in the efficiency of mixing based on turbulent flow in the batchwise system. Consequently, it is assumed that such a decrease in mixing efficiency induces a broadening of the molecular weight distribution. In contrast, it is hypothesized that effective mixing of reactants by the attached micromixer in the microfluidic system enables high control of molecular weight distribution. Not only was linear polymer synthesis performed in the microfluidic reactor, but also synthesis of dendrimer molecules. Although still in their infancy, microfluidic systems open the use of microreactors for branched polymers. Overall, the usefulness of microreactors in controlling the reaction of linear and branched polymer synthesis has been demonstrated. For polymer particle synthesis, microfluidic reaction systems show several

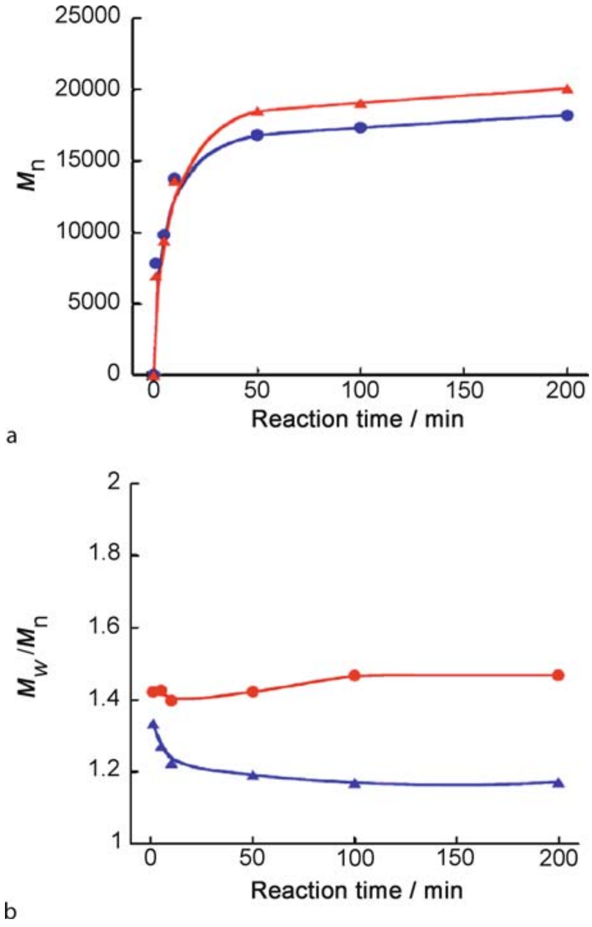

Polymer Synthesis within Microfluidic Reactor, Figure 6 Comparisons of polymer properties in batchwise (circle) and microfluidic (triangle) systems at various monomer concentrations. (**a**) ►number average molecular weight (M_n) and (**b**) polydispersity (M_w/M_n) of the obtained polymers against concentrations of NCA. Polymerizations were carried out for 200 min. Reproduced from [5]

advantages over the conventional reaction systems. These benefits arise from the small dimensions of microdevices which provide predictable thermal and mass transportation properties and unique control over the fluid structure. Enhanced transport characteristics of microreactors allow more precise synthesis of polymers compared to traditional batch reactors. Perhaps most importantly, extreme fluid controllability in a laminar flow system enables synthesis of particles with unique shapes not accessible by other methods. Core–shell type polymers and nonspherical polymers were prepared by controlling the fluidic behavior in microchannels. Also, solid, hollow, and multicored asymmetric and irregularly shaped polymer microparticles as well as membranes and fibers can all be produced with microfluidic devices. These particles are generally monodispersed, and the sizes may be tuned from a few micrometers to hundreds of micrometers, depending on the specific device geometry and flow parameters. The design of fluidic systems therefore becomes quite important. Numerical simulation is useful in designing microreaction devices. Likewise, reproducibility of these particles is quite high when performing the reaction using the same microreaction apparatus because of the simple operation of the reactor and strict control of the reaction conditions provided by the system. The reaction does not require special techniques as in batchwise synthesis. This feature is quite advantageous for production of polymer particles by numbering-up. Utilizing the principle of shape control by fluidic behavior, the elegant technique was applied to control the shape of polymers. Microscope projection photolithographic synthesis of particles is a novel particle formation method [8, 9]. This method enables continuous-flow synthesis of particles with complicated shapes. Polymerization was also carried out across laminar, co-flowing streams to generate Janus particles containing different chemistries, whose relative proportions could be easily tuned. This new high-throughput technique offers unprecedented control over particle size, shape, and anisotropy.

To summarize, polymer synthesis in microfluidic reactors, although in its initial stage, holds a promising future. Many efforts are now in progress in many laboratories to develop generally applicable microreactors for polymer synthesis.

Future Directions for Research

Microreactors will represent an indispensable tool for synthesizing polymers with controlled properties. Microreaction in microfluidic systems will find its way in the shift from conventional batchwise reaction to microreaction strategy. In future, microfluidic devices will find broad applications particularly in linear polymer production aimed at obtaining polymers of desired average molecular weight with narrower molecular weight distribution. In addition, the prospect of making novel polymer particles with unique shapes can be realized by microreaction system via control of specific device geometry and flow parameters. The process of rapid prototyping and the emergence of simple, homemade devices that take only minutes or hours to construct have enabled many groups to explore this exciting field. More and more applications of microfluidic reaction systems for polymer synthesis are required to develop a generally applicable microreactor for polymerization reactions. In addition to simple reactions, an aspect of polymer synthesis that may offer great research opportunity is synthesis of novel particles with unique shapes, and thus the development of microscope

projection photolithography will be necessary. In addition, theoretical studies such as numerical simulations are also required to obtain a generally applicable microreactor. Matching of experimental achievements and theoretical studies may accelerate development of microreactors for polymerization reactions. Still, this field is in its initial stage and has much room for development.

Cross References

- ► Droplet Based Lab-on-Chip Devices
- ► Lab-on-a-Chip Devices for Chemical Analysis
- ► Microfluidics for Bio- and Chemical Reactions
- ► Droplet Microreactors

References

1. Wu T, Mei Y, Cabral JT, Xu C, Beers KL (2004) A new synthetic method for controlled polymerization using a microfluidic system. J Am Chem Soc 126:9880–9881
2. Wu T, Mei Y, Michelle Byrd HC, Beers KL (2005) Block copolymer PEO-*b*-PHPMA synthesis using controlled radical polymerization on a chip. Macromol Rapid Commun 26:1037–1042
3. Iwasaki T, Yoshida J (2005) Free radical polymerization in microreactors. Significant improvement in molecular weight distribution control. Macromolecules 38:1159–1163
4. Nagaki A, Kawamura K, Suga S, Ando T, Sawamoto M, Yoshida J (2004) Cation pool-initiated controlled/living polymerization using microsystems. J Am Chem Soc 126:14702–14703
5. Honda T, Miyazaki M, Nakamura H, Maeda H (2005) Controllable polymerization of *N*-carboxyanhydride in a microreaction system. Lab Chip 5:812–818
6. Abhinkar A, Tennico Y, Liu SH, Rundel JT, Tseng T, Remcho VT, Paul BK, Chang CH (2006) High Rate Convergent Synthesis and Deposition of Polyamide Dendrimers using a Continuous-Flow Microreactor. Chem Eng Technol 30:334–340
7. Serra C, Sary N, Schlatter G, Hadziioannnou G, Hessel V (2005) Numerical simulation of polymerization in interdigital multilamination micromixers. Lab Chip 5:966–973
8. Nie Z, Xu S, Seo M, Lewis PC, Kumacheva E (2005) Polymer particles with various shapes and morphologies produced in continuous microfluidic reactors. J Am Chem Soc 127:8058–8063
9. Dendukuri D, Tsoi K, Hatton TA, Doyle PS (2005) Controlled synthesis of nonspherical microparticles using microfluidics. Langmuir 21:2113–2116
10. Dendukuri D, Pregibon DC, Collins J, Hatton TA, Doyle PS (2006) Continuous-flow lithography for high-throuput microparticle synthesis. Nat Mater 5:365–369

Poor Man's LIGA

► LIGA-Like Techniques

Porous Electrodes

► Three-Dimensional Electrodes

Port Resonance

► Hemholtz Resonance

Positive Displacement Pump

Synonyms

Flexible member pump; Membrane pump; Diaphragm pump

Definition

In a *positive displacement pump* fluid is displaced by a moving boundary. Ideally, this displacement is independent of backpressure, up to the maximum pump head.

Cross References

- ► Compression Ratio
- ► Dead Volume
- ► Electromagnetic Valves
- ► Electrostatic Valves
- ► Magnetic Pumps
- ► Membrane Actuation for Micropumps
- ► Microactuators
- ► Peristaltic Pumps
- ► Piezoelectric Valves
- ► Pneumatic Valves
- ► Stroke Volume
- ► Thermomechanical Valves
- ► Thermopneumatic Valves

Positive Pressure or Suction (Vacuum) Pressure

Definition

Positive pressure or suction (vacuum) pressure is used to generate a pressure difference to the reservoir on chips and drives the sample solution into the microfluidic systems on chip.

Cross References

► Techniques for Transferring Samples to Chips

Potassium Hydroxide (KOH) Etching

► Anisotropic Etching

Powder Blasting

Zheng Cui
Rutherford Appleton Laboratory, Didcot, Oxfordshire, UK
z.cui@rl.ac.uk

Synonyms

Sand blasting; Micropowder blasting

Definition

Powder blasting is a micromachining technique which uses a high-velocity air jet containing microparticles to impinge on and erode material from a surface.

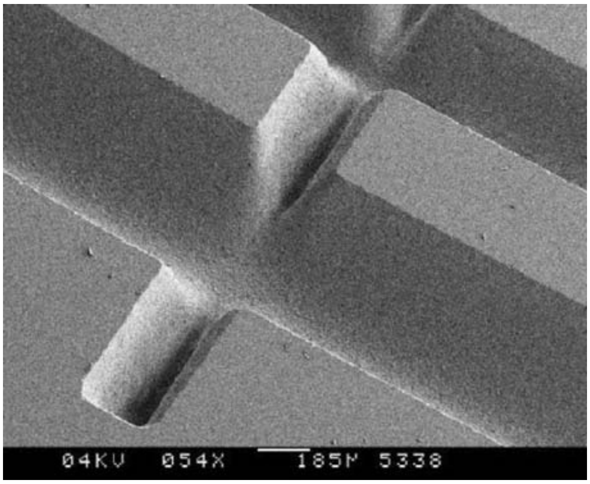

Powder Blasting, Figure 1 Typical etch profile of powder blasting in glass

Overview

Sand blasting is a traditional mechanical processing technique which can be found in a mechanical workshop. Sand blasting has been used commonly for removing rusty surface, dry paints or contaminants from a metal work piece. From the mid-1990s, sand blasting was used to machine large arrays of holes in glass panels for large-area flat panel display devices. Thousands of holes could be machined in the glass at once, which was highly efficient and low cost [1]. Sand blasting was introduced as a microstructuring technique in early 2000, with the name of powder blasting because much smaller particles were used [2]. The principle of power blasting micromachining is that when a powder particle indents the surface of a brittle material such as glass or silicon it generates cracks and a plastic zone around the impact point. There are two types of cracks: lateral and radial. The lateral cracks play a major role in the erosion process because they can reach the surface and remove upper material zone. The radial cracks have no significant contribution in the erosion process, but they weaken the material. The length of such cracks depends on a few parameters like the substrate's Young's modulus and hardness and the indentation volume. These parameters then depend on the kinetic energy of the particle and its shape. Powder blasting has the following features [3]:

- It is only suitable for machining brittle materials, such as glass, silicon and ceramics; it is not suitable for ductile materials, such as metals and polymers. Ductile materials can serve as masking material in powder blasting machining.
- The mask materials for powder blasting are required not only to be ductile but also thick enough. Because high-speed particles inevitably consume the masking layer, even though at a lower rate, when the masking layer reaches a certain thinness the particles with high kinetic energy can penetrate through the mask and damage the work piece surface. The best way of making the mask is to pattern it directly on the work piece surface. For example, a copper layer is deposited by electroplating on the substrate surface and then photolithographically patterned. The selectivity of powder blasting Pyrex glass to copper is 65:1 [4]. Some rubber-like polymers, which are also photon sensitive, can also be used as masking materials.
- Powder blasting is a pure mechanical processing technique. The particle beam from a nozzle is always of the highest speed in the centre, as a result of which the etched profile always has a sloped sidewall. Figure 1 shows typical structure profiles etched by powder blasting [4].
- The resolution of powder blasting is normally above 50 μm. This is mainly attributed to the particle sizes which are around 30 μm. The resolution may increase if smaller particles are used. However, the kinetic energy of particles also reduces for smaller sized particles.
- The roughness of an eroded surface produced by high-speed powder is around the micrometre scale, which is related to the size of the particles.

Powder blasting is not a high-tech machining method. It is for this reason that the technique is less expensive. Powder blasting is particularly useful for making patterns in glass. For micromachining of glass there are no other better techniques apart from wet etching by HF acid. It is well known that HF acid is a hazardous chemical and wet etching by HF is isotropic. Powder blasting is a much better suited

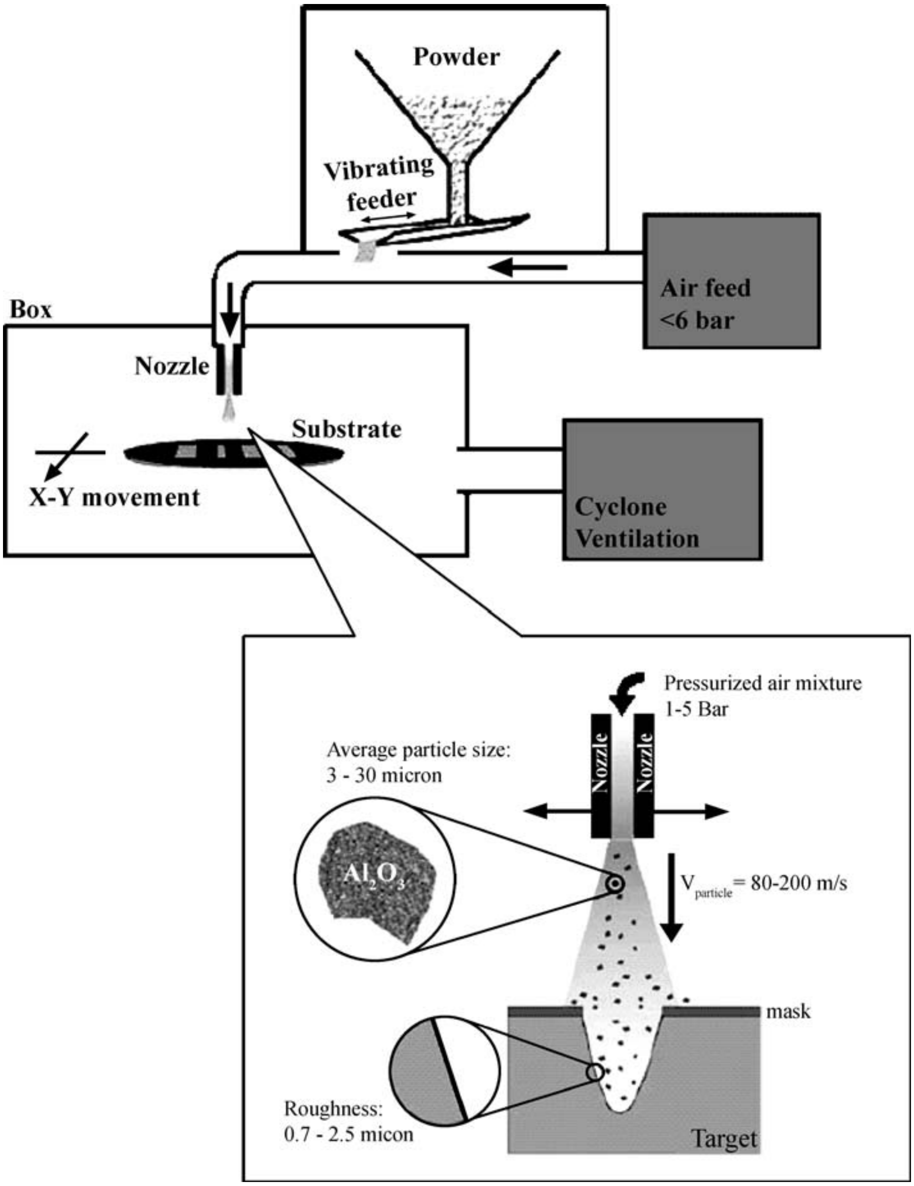

Powder Blasting, Figure 2 Schematic representation of a powder blasting system

method to process glass materials. The structures encountered in microfluidic and biochip systems are normally above a few tens of micrometres, which can be adequately resolved by powder blasting machining [5]. For drilling holes in glass chips, the conventional method is mechanical drilling with a diamond bit. Mechanical drilling can produce chippings on the edge and it becomes extremely difficult to drill thin glass. Powder blasting can machine a large number of holes in glass at once and the quality of the holes is much better than that produced by mechanical drilling.

Basic Methodology

A schematic representation of a powder blasting system is shown in Fig. 2. The microparticles used for powder blasting are not sands, but Al_2O_3 or SiC particles in the size range $20-30\,\mu m$. These are injected from a vibrating feeder into a pressured air flow stream. The pressured particle jet flows through a nozzle and impinge at high velocity normal to the surface of a work piece. The velocity at which the particles impinge on a solid surface is in the range $80-200\,m/s$. These particles with high kinetic

energy can crack and erode the solid surface locally, with etching rate of a few tens to a few hundreds of micrometers per minute, and in extreme cases can be as high as 1 mm/min [2]. The etching rate is directly proportional to the air pressure and the gap distance between the nozzle and surface of the work piece. However, the etching rate becomes saturated when the air pressure is too high and the speed of the air stream approaches the speed of sound. An array of nozzles can be used to etch a large area of surface. The substrate to be blasted is normally mounted on a rotating table, while the nozzle array is fixed. By rotating the table, uniform erosion over a large area of substrate or a number of substrates can be achieved. While the powder jet impinges the substrate, a cyclone ventilation system collects the powders and reuses them. Although small particles can improve the surface roughness of powder blasting, particles smaller than 5 μm cannot be recycled, which is another reason for not using too small powder particles. After powder blasting and removal of the masking layer, the etched surface can be washed clean by water.

There are no commercial powder blasting systems available because there is not such a market. Only a few places worldwide have utilised this technique. There are companies that can make custom designed powder blasting systems. They only make to order. However, there are some companies, such as Micronit in the Netherlands, which provide powder blast micromachining services.

Key Research Findings

Much of the research in powder blasting has been focused on improving resolution and selectivity of masking materials. Currently the resolution of powder blasting is above 50 μm. This is mainly attributed to the particle sizes which are around 30 μm. Using smaller particles can improve resolution and give smaller pattern dimensions. However, there is a limit to the particle size that can be used for powder blasting. As mentioned earlier, there is the sound barrier which limits the velocity of microparticles not to exceed 335 m/s. There is also a threshold kinetic energy above which a particle can crack an eroding material. For powder blasting of soda lime glass with alumina (Al_2O_3) particles, the threshold energy is 25 nJ, from which the minimum size of alumina particles can be estimated to be 6 μm in order to acquire the threshold kinetic energy at the speed of sound [6]. For safety reasons 10 μm alumina particles were used with a velocity of 156 m/s, which helped to achieve a minimum feature size of 30 μm in soda lime glass. However, smaller particles resulted in much less efficiency. Experimental comparison demonstrated that a 10 μm particle is 50 times less efficient than a 30 μm particle in powder blasting. The etch rate is also limited by the mask feature size. The smaller the mask feature size compared to the particle size, the lower the etch rate.

Various photosensitive polymers, as well as metal films, have been used as masking materials. In general, depending on their erosion behaviour, materials can be divided into two classes: one class comprising all materials showing maximum erosion rate at normal impact of particles, and the other class of materials having a maximum erosion rate at a glancing impact angle. Glass belongs to the first class of materials, while metals belong to the second class. Due to their high erosion resistance at normal impact, metals therefore have been used as a masking material. Metallic contact masks can be made by laser ablation or electroplating using a photoresist as a mould. Recent development has shown that elastomers such as polydimethylsiloxane (PDMS) can be used as masking materials [6]. A PDMS mask can be made by casting into a patterned SU-8 mould. The PDMS mask has selectivity of 5000:1 to soda lime glass in powder blasting [7].

Future Directions for Research

Powder blasting as an alterative technique has been increasingly adopted for making microstructures in glass, ceramics or graphite, which are not easy to make by other techniques. Future research will be aimed at improving etching efficiency and resolution by trying out different masking materials or parameters of microparticles and air jet flow.

Cross References

► Plasma Etching

References

1. Ligthart HJ, Slikkerveer PJ (1996) Glass and glass machining in ZEUS panels, Philips J Res 50:475–499
2. Belloy E, Thurre S, Walckiers E, Sayah A, Gijs MAM (2000) The introduction of powder blasting for sensor and microsystem applications. Sensor Actuator 84:330–337
3. Cui Z (2006) Micro-Nanofabrication Technologies and applications. Springer-Verlag
4. Wensink H, Jansen HV, Berenschot JW, Elwenspoek MC (2000) Mask materials for powder blasting. J Micromech Microeng 10:175–180
5. Schlautmann S, Wensink H, Schasfoort R, Elwenspoek M, van den Berg A (2001) Powder-blasting technology as an alternative tool for microfabrication of capillary electrophoresis chips with integrated conductivity sensors. J Micromech Microeng 11:386–389
6. Pawlowski A-G, Sayah A, Gijs MAM (2005) Precision Poly-(Dimethyl Siloxane) Masking Technology for High-Resolution Powder Blasting. J Microelectromech Syst 14(3):619–624

7. Sayah A, Parashar VK, Pawlowski A-G, Gijs MAM (2005) Elastomer mask for powder blasting microfabrication, Sensor Actuator A 125:84–90

Power MEMS

► Micro Energy Conversion Devices

Precipitate

Definition

A phase change which results in the formation of a collection of a material. For example, solid precipitate can be formed in a liquid phase solution as a result of a chemical reaction or a supersaturation condition in the solution.

Cross References

► Fabrication of Self-Assembled Catalytic Nanostructures

Precipitation

► Nucleation and Growth

Precursor Materials

Synonyms

Predecessor material

Definition

A substance that, following a reaction, becomes an intrinsic part of a product chemical. The material must be stable at room temperatures. During CVD process, the precursor material is vaporised. The precursor gas is transported to the surface where it undergoes a chemical reaction to produce the desired thin film.

Cross References

► Chemical Vapor Deposition for Film Deposition
► Plasma-Treatment Physics

Predecessor Material

► Precursor Materials

Preparatory Separation

► Biosample Preparation by Lab-on-a-Chip Devices

Pressure

Synonyms

Absolute pressure; Gage pressure; Differential pressure

Definition

The absolute pressure is referenced to total vacuum (no gas molecule present in a defined volume). The gage pressure is the difference between absolute pressure and atmospheric pressure. The differential pressure is the difference between a measured pressure and a reference pressure. Pressures are measured in Pascal (N/m^2) according to the international standards system (SI). Further commonly used units include bar, Torr (millimeters of mercury column), pounds per square inch and others.

Cross References

► Glass-Polymer-Bonding
► Wall Shear Stress

Pressure-Driven Flow

Definition

Flow driving principle used to create fluid flows through microfluidic channels. By applying pressure at the inlet the fluid is pumped through the channel. The fluid velocity near the walls approaches zero and a parabolic velocity profile is produced within the channel.

Pressure-Driven Single Phase Gas Flows

Stéphane Colin
National Institute of Applied Sciences of Toulouse (INSAT), Toulouse Cedex 4, France
stephane.colin@insa-toulouse.fr

Synonyms

Poiseuille single phase gas flows

Definition

A pressure-driven gas flow is generated by applying a pressure difference between the inlet and the outlet of a fluidic system, for example a channel. Due to very small hydraulic diameters, pressure-driven gas flows in microchannels are laminar. Gas microflows are distinct from gas macroflows by rarefaction effects which appear as soon as the mean free path of the molecules is no longer negligible compared with the hydraulic diameter of the microchannel. For such rarefied flows, the classic Poiseuille model is no longer valid, and other models should be used, according to the rarefaction level, which is quantified by the Knudsen number.

Overview

Rarefaction Effects and Gas Flow Regimes

Usually, the regime of gas flow in a macrochannel refers to viscous and compressibility effects, respectively quantified by the Reynolds number Re and the Mach number Ma. For low Reynolds numbers (typically for $\mathrm{Re} < 2000$), the flow is laminar and it becomes turbulent for higher values of Re. For $\mathrm{Ma} < 1$, the flow is subsonic and for $\mathrm{Ma} > 1$, it is supersonic. Generally, if $\mathrm{Ma} > 0.3$, compressibility effects should be taken into account.

On the other hand, for gas microflows, the main microeffect that results from shrinking down the devices size is rarefaction. Actually, there is a strong – although not complete – analogy between microflows and low pressure flows. Rarefaction, which implies a local thermodynamic disequilibrium, occurs as soon as the mean free path of the gas molecules is no longer negligible compared with a characteristic length of the system.

Thus, it is convenient to differentiate the flow regimes in function of the Knudsen number

$$\mathrm{Kn} = \frac{\lambda}{L}, \tag{1}$$

ratio of the mean free path of the molecules λ over this characteristic length L, and the following classification is usually accepted:

- For $\mathrm{Kn} < 10^{-3}$, the flow is a *continuum flow* **(C)** and it is accurately modeled by the compressible Navier–Stokes equations with classical no-slip boundary conditions.
- For $10^{-3} < \mathrm{Kn} < 10^{-1}$, the flow is a *slip flow* **(S)** and the Navier–Stokes equations remain applicable, provided a velocity slip and a temperature jump are taken into account at the walls. These new boundary conditions point out that rarefaction effects become sensitive at the wall first.

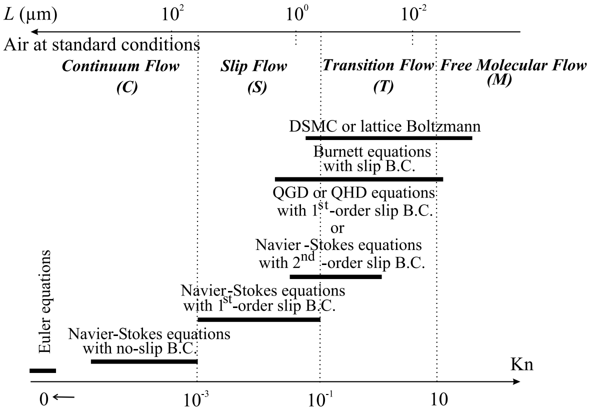

Pressure-Driven Single Phase Gas Flows, Figure 1 Gas flow regimes and main models according to the Knudsen number

- For $10^{-1} < \mathrm{Kn} < 10$, the flow is a *transition flow* **(T)** and the continuum approach of the Navier–Stokes equations is no longer valid. However, the intermolecular collisions are not yet negligible and should be taken into account.
- For $\mathrm{Kn} > 10$, the flow is a *free molecular flow* **(M)** and the occurrence of intermolecular collisions is negligible compared with the one of collisions between the gas molecules and the walls.

The limits of these different regimes are only indicative and could vary from one case to another, partly because the choice of the characteristic length L is rarely unique. For flows in microchannels, L is generally the hydraulic diameter or the depth of the channel. In complex geometrical configurations, it could be preferable to define L from local gradients (for example of the density ρ: $L = 1/|\nabla\rho/\rho|$) rather than from simple geometrical considerations [1]; the Knudsen number based on this characteristic length is the so-called local rarefaction number. The upper axis of Fig. 1 locates these different regimes for air in standard conditions, as a function of a characteristic length, for example a microchannel hydraulic diameter. The lower axis shows the corresponding values of the Knudsen number.

Mean Free Path and Knudsen Number Calculation

Calculating the mean free path requires assumptions about intermolecular collisions. First, the gas is assumed to be a dilute gas, i.e. a gas for which the mean molecular diameter of the molecules is small compared with the mean molecular spacing. This condition is verified with a good precision for all usual gases under standard pressure and temperature conditions. It involves binary collisions between molecules and the mean free path may be expressed as $\lambda = c'/\nu = \sqrt{8RT/\pi}/\nu$, ratio of the mean

P

thermal velocity c' to the collision rate ν. The mean thermal velocity depends on the temperature T and on the specific gas constant R.
For classic collision models, based on an inverse power law (IPL) interaction scheme which only takes into account the repulsion part of the force between two molecules, the expression of ν leads to the general form of the mean free path:

$$\lambda = \frac{k_2 \mu}{\rho \sqrt{RT}} . \tag{2}$$

The mean free path is a function of the temperature T, the density ρ and the dynamic viscosity μ of the gas which itself depends on the temperature as

$$\mu_{(T)} = \mu_{0(T_0)} \left(\frac{T}{T_0} \right)^{\omega} , \tag{3}$$

T_0 being a reference temperature for which the viscosity μ_0 is known.
The values of the dimensionless parameters k_2 and ω for the most classic collision models are given in Table 1. The Maxwell Molecules (MM) model assumes a linear relationship between viscosity and temperature, although for the Hard Sphere (HS) model, the viscosity is proportional to the square root of the temperature. These models could be roughly considered as limits for the real behavior of gases, and the Variable Hard Sphere (VHS) model proposed by Bird [2] is much more accurate. Another sophistication has been proposed by Koura and Matsumoto who developed the Variable Soft Sphere (VSS) model, which introduces via an adjustment parameter α limited corrections – less than 3% – to the evaluation of the mean free path deduced from the VHS model, assuming soft collisions between the molecules. For $\alpha = 1$, the VSS model reduces to the VHS model.
Experimentally deduced values of ω and α are available for different gases (Table 2).

Pressure-Driven Single Phase Gas Flows, Table 1 Mean free path and dynamic viscosity for classic IPL collision models

Model	$\mu \propto T^{\omega}$	$\lambda = k_2 \frac{\mu}{\rho\sqrt{RT}}$
	ω	k_2
Maxwell Molecules (MM)	1	$\sqrt{2/\pi} \approx 0.798$
Hard Spheres (HS)	$\frac{1}{2}$	$\frac{16}{5\sqrt{2\pi}} \approx 1.277$ (sometimes proposed as $\sqrt{\pi/2} \approx 1.253$)
Variable Hard Spheres (VHS)	$\omega = \frac{\eta+3}{2(\eta-1)}$	$\frac{2(7-2\omega)(5-2\omega)}{15\sqrt{2\pi}}$
Variable Soft Spheres (VSS)	$\omega = \frac{\eta+3}{2(\eta-1)}$	$\frac{4\alpha(7-2\omega)(5-2\omega)}{5(\alpha+1)(\alpha+2)\sqrt{2\pi}}$

Ideal Gas Assumption

For a dilute gas in thermodynamic equilibrium, the classic ideal gas equation of state

$$p = \rho RT = nk_{\mathrm{B}} T \tag{4}$$

is valid. If the thermodynamic equilibrium is not verified, Eq. (4) remains valid, providing the thermodynamic temperature T is replaced with the translational kinetic temperature T_{tr}, which measures the mean translational kinetic energy of the molecules. Here, p is the pressure and $\rho = mn$ is the density, $k_{\mathrm{B}} = R'/N = (M/N)(R'/M) = mR = 1.381 \times 10^{-23}\,\mathrm{J\,K^{-1}}$ is the Boltzmann constant, $R' = 8.315\,\mathrm{J\,mol^{-1}\,K^{-1}}$ being the universal gas constant, $N = 6.022 \times 10^{23}\,\mathrm{mol^{-1}}$ the Avogadro's number and M the molecular weight.
As a consequence, for an ideal gas and an IPL collision model, the Knudsen number can be written as

$$\mathrm{Kn} = \frac{k_2 \mu_{(T)} \sqrt{RT}}{pL} , \tag{5}$$

with the value of k_2 given in Table 1.

Modeling Gas Flow in Microchannels

It can be shown from Eq. (5) that for an ideal gas and an IPL collision model,

$$\mathrm{Re} = k_2 \sqrt{\gamma} \mathrm{Ma}/\mathrm{Kn} , \tag{6}$$

since $\mathrm{Re} = \rho u L/\mu$ and $\mathrm{Ma} = u/\sqrt{\gamma RT}$, noting γ the ratio of the specific heats of the gas. As k_2 is of the order of unity (Table 1), the result is that for subsonic microflows, viscous effects are predominant and the flows are laminar.
It can be seen from Fig. 1 that gas flows in micron size channels are typically relevant to the slip flow regime, at any rate for usual pressure and temperature conditions. For lower sizes, i. e. for Knudsen numbers higher than 10^{-1}, the slip flow regime could remain valid, provided that classical velocity slip and temperature jump boundary conditions are modified (taking into account higher order terms as explained below) and/or that Navier–Stokes equations are extended to more general sets of conservation equations, such as the Quasi-Gasodynamic (QGD), the Quasi-Hydrodynamic (QHD) or the Burnett equations [3].
However, for Knudsen numbers higher than unity, as it could be the case in nanochannels (▶ gas flow in nanochannels) or in low-pressure flows in microchannels,

Pressure-Driven Single Phase Gas Flows, Table 2 Molecular weight and dynamic viscosity under standard conditions ($p_0 = 101{,}325$ Pa and $T_0 = 273.15$ K) estimated from a VHS or a VSS model (data from Bird [2]) with corresponding values of ω and α

Gas	$M \cdot 10^3$ (kg mol^{-1})	$\mu_0 \cdot 10^7$ (N s m^{-2})	ω	α
sea level air	28.97	171.9	0.77	–
Ar	39.948	211.7	0.81	1.40
CH_4	16.043	102.4	0.84	1.60
Cl_2	70.905	123.3	1.01	–
CO	28.010	163.5	0.73	1.49
CO_2	44.010	138.0	0.93	1.61
H_2	2.0159	84.5	0.67	1.35
HCl	36.461	132.8	1.00	1.59
He	4.0026	186.5	0.66	1.26
Kr	83.80	232.8	0.80	1.32
N_2	28.013	165.6	0.74	1.36
N_2O	44.013	135.1	0.94	–
Ne	20.180	297.5	0.66	1.31
NH_3	17.031	92.3	1.10	–
NO	30.006	177.4	0.79	–
O_2	31.999	191.9	0.77	1.40
SO_2	64.065	116.4	1.05	–
Xe	131.29	210.7	0.85	1.44

the continuum approach is not longer valid, and molecular methods such as the Direct Simulation Monte Carlo – DSMC – (► Monte Carlo method) or the Lattice Boltzmann methods (► Lattice Boltzmann method) should be used.

Basic Methodology

For moderate pressure levels, and Knudsen numbers up to 0.5 or so, pressure-driven gas microflows can be modeled with the compressible Navier–Stokes equations, slip velocity and temperature jump boundary conditions, considering the gas as an ideal gas.

Compressible Navier–Stokes Equations

The compressible Navier–Stokes equations are the governing conservation laws for mass, momentum and energy. These laws are written assuming that the fluid is Newtonian and follows the Fourier law of diffusion, so that the stress tensor is a linear function of the velocity gradients and the heat flux vector is proportional to the temperature gradient. Adding Stokes' hypothesis, which expresses that the changes of volume do not involve viscosity, the compressible Navier–Stokes equations may be written as:

$$\frac{\partial \rho}{\partial t} + \nabla \cdot (\rho \boldsymbol{u}) = 0 \tag{7}$$

$$\frac{\partial (\rho \boldsymbol{u})}{\partial t} + \nabla \cdot \left(\rho \boldsymbol{u} \otimes \boldsymbol{u} - \mu \left[\nabla \otimes \boldsymbol{u} + (\nabla \otimes \boldsymbol{u})^{\mathrm{T}} - \frac{2}{3} (\nabla \cdot \boldsymbol{u}) \mathbf{I} \right] \right) + \nabla p = \boldsymbol{f} \tag{8}$$

$$\frac{\partial E}{\partial t} + \nabla \cdot \left((E + p) \boldsymbol{u} - \mu \left[\nabla \otimes \boldsymbol{u} + (\nabla \otimes \boldsymbol{u})^{\mathrm{T}} - \frac{2}{3} (\nabla \cdot \boldsymbol{u}) \mathbf{I} \right] \cdot \boldsymbol{u} - k \nabla T \right) = \boldsymbol{f} \cdot \boldsymbol{u} \tag{9}$$

where $\boldsymbol{u}$ is the velocity vector, $\mathbf{I}$ the unit tensor, t the time and k the thermal conductivity. The total energy per unit volume $E = \rho(e + \boldsymbol{u} \cdot \boldsymbol{u}/2)$ is a function of the internal specific energy e that may be written $e = p/[\rho(\gamma - 1)]$ for an ideal gas.

The external volume forces $\boldsymbol{f}$ (gravitational forces, magnetic forces, etc.) are generally negligible in gas flow. It is even more the case in gas microflows, since the volume over surface ratio decreases with the characteristic length L and consequently, in microscale geometries, volume effects may be neglected when compared to surface effects.

P

Knudsen Layer

The Knudsen layer plays a fundamental role in the slip flow regime. This thin layer, between one and two molecular mean free paths in thickness, is a region of local non-equilibrium which is observed in any gas flow near a surface. In non rarefied flows, the Knudsen layer is too thin for having any significant influence, but in the slip flow regime, it should be taken into account.

Although the Navier–Stokes equations are not valid in the Knudsen layer, due to a nonlinear stress/strain-rate behavior in this small layer [4], their use with appropriate boundary velocity slip and temperature jump conditions proved to be accurate for predicting mass flow rates [5] (► methods for flow rate measurements) and velocity profiles out of the Knudsen layer. Classically, the real flow is not simulated within the Knudsen layer, but the influence of the Knudsen layer on the flow outside this non-equilibrium layer is taken into account, replacing the no-slip condition at the wall with a slip-flow condition. For that purpose, a fictitious slip velocity u_{slip} is introduced (Fig. 2). Real slip at the wall, $u_{\mathrm{gas}} - u_{\mathrm{wall}}$, is due to the fact that gas molecules very close to the wall have actually a mean

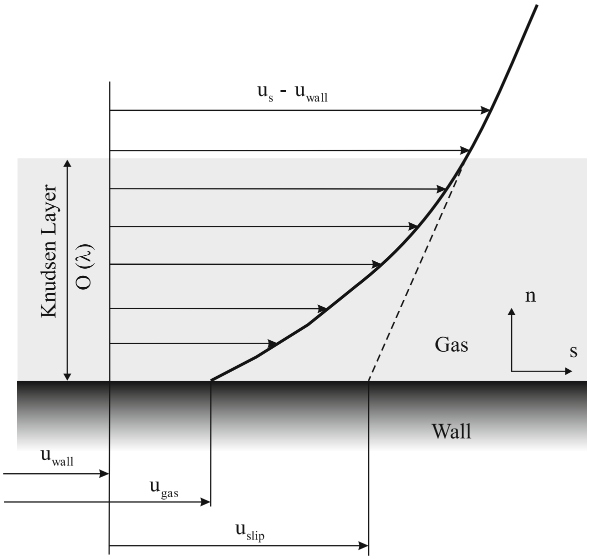

Pressure-Driven Single Phase Gas Flows, Figure 2 Gas flow regimes and main models according to the Knudsen number

tangential momentum partly due to the non zero momentum of molecules coming from the flow and to the momentum of the molecules reflected by the wall. These reflected molecules keep all their tangential momentum if the reflection is specular, loose all their tangential momentum if the reflection is diffuse or more generally keep only a part of it.

Velocity Slip in the Slip-Flow Regime

The classic slip-flow condition, deduced from a momentum balance at the wall, was first proposed by Maxwell and is generally presented in the form

$$u_{\text{slip}} = \frac{2-\sigma}{\sigma}\lambda \left.\frac{\partial u_s}{\partial n}\right|_w + \frac{3}{4}\frac{\mu}{\rho T}\left.\frac{\partial T}{\partial s}\right|_w . \quad (10)$$

In this equation, σ is the tangential momentum accommodation coefficient, equal to unity for perfectly diffuse molecular reflection and zero for purely specular reflection. In Maxwell's model, u_{slip} overestimates the real velocity at the wall but leads to a rather good prediction of the velocity out of the Knudsen layer, as represented in Fig. 2. After non-dimensionalization with the characteristic length L, a reference velocity u_0 and a reference temperature T_0, Eq. (10) is written as follows:

$$u^*_{\text{slip}} = \frac{2-\sigma}{\sigma}\text{Kn}\left.\frac{\partial u^*_s}{\partial n^*}\right|_w + \frac{3}{4\gamma k_2^2}\frac{\text{Kn}^2\text{Re}_0}{\text{Ma}_0^2}\left.\frac{\partial T^*}{\partial s^*}\right|_w , \quad (11)$$

with $u^*_s = u_s/u_0$, $T^* = T/T_0$, $n^* = n/L$ and $s^* = s/L$. Note that this non-dimensionalization is valid only if the reference lengths are the same in the s and n directions, which is generally not the case for a flow in a microchannel. In that case, it is preferable to keep the dimensional form of Eq. (10). The second term on the right-hand side, which is proportional to the square of the Knudsen number, involves the Reynolds number $\text{Re}_0 = \rho u_0 L/\mu$ and the Mach number $\text{Ma}_0 = u_0/\sqrt{\gamma R T_0}$ defined at the reference conditions. This second term is associated with the thermal creep, or transpiration phenomenon. It shows that a flow can be induced by the sole presence of a tangential temperature gradient, without any pressure gradient. In that case, the gas experiences a slip velocity and moves from the colder toward the warmer region. This can also result in a pressure variation inside a microchannel only submitted to tangential temperature gradients. Given that we consider here pressure driven flows, we assume that there is no thermal creep and that the only cause of flow is a pressure gradient. As a consequence, the first-order slip flow boundary condition is written

$$u^*_{\text{slip}} = \beta_u \frac{2-\sigma}{\sigma}\text{Kn}\left.\frac{\partial u^*_s}{\partial n^*}\right|_w = A_1 \text{Kn}\left.\frac{\partial u^*_s}{\partial n^*}\right|_w . \quad (12)$$

A corrective coefficient β_u has been calculated by different authors [6] who have shown that a better prediction of the flow out of the Knudsen layer would be obtained with this corrective coefficient slightly different from unity, unlike as initially proposed by Maxwell. Its value depends on the collision model: for example, $\beta_u = 1.11$ for a HS model [7]. Equation (12) is called first-order slip boundary condition, because it involves the Knudsen number ($\vartheta(\text{Kn})$) and the first derivative $(\partial u^*_s/\partial n^*)_w$.

For $\text{Kn} > 0.1$, experimental [5] or numerical studies with the DSMC method show significant deviations with models based on first-order boundary conditions. Therefore, since 1947, several authors have proposed second-order boundary conditions, hoping to extend the validity of the slip flow regime to higher Knudsen numbers. Second-order boundary conditions take more or less complicated forms, which are difficult to group together in a sole equation. Actually, according to the assumptions, the second-order terms ($\vartheta(\text{Kn}^2)$) may be dependent of σ [8, 9] or involve streamwise second derivatives $(\partial^2 u^*/\partial s^{*2})_w$, in addition to spanwise second derivatives $(\partial^2 u^*/\partial n^{*2})_w$ [10]. For a developed flow between plane plates or in a circular microtube, the tangential second derivatives are zero and one may compare most of the second-order models that take the generic form

$$u^*_{\text{slip}} = A_1 \text{Kn}\frac{\partial u^*_s}{\partial n^*} + A_2 \text{Kn}^2 \frac{\partial^2 u^*_s}{\partial n^{*2}} . \quad (13)$$

Pressure-Driven Single Phase Gas Flows, Table 3 Coefficients of some second-order boundary conditions proposed in the literature, for $\sigma = 1$

Author, Year	A_1	A_2
Maxwell, 1879	1	0
Schamberg, 1947	1	$-5\pi/12$
Chapman and Cowling, 1952	≈ 1	$\approx 1/2$
Deissler, 1964	1	$-9/8$
Cercignani, 1964	1.1466	-0.9756
Hsia and Domoto, 1983	1	$-1/2$
Mitsuya, 1993	1	$-2/9$
Karniadakis and Beskok, 2002	1	$1/2$
Hadjiconstantinou, 2003	1.11	-0.61

In the particular case of a fully diffuse reflection ($\sigma = 1$), some A_1 and A_2 coefficients proposed in the literature are compared in Table 3. We note significant differences, essentially for the second-order term. Recent experimental flow rate data and molecular numerical simulations show that the second order coefficient A_2 should be negative, which corresponds to a slip velocity higher than that predicted by a first-order slip boundary condition.

Pressure Driven Isothermal Flows in Microchannels

We consider here the flow of an ideal gas through different microchannels in the slip-flow regime. The flow is steady, isothermal and the volume forces are neglected. The flow is also assumed to be locally fully developed: the velocity profile in a section is the same as the one obtained for a fully developed incompressible flow, but the density is recalculated in each cross-section and depends on the pressure and the temperature via the equation of state (4). This assumption is no longer valid if the Mach number is greater than 0.3. The main kinds of sections of interest are the rectangular and the circular sections. Microchannels with rectangular cross-sections are easily etched in silicon wafers, for example by reactive ion etching (RIE) or by deep reactive ion etching (DRIE). If the aspect ratio of the section is small enough, the flow may be considered as a plane flow between parallel plates and the modeling is much simpler. Gas flows in circular microtubes are also frequently encountered, for example in chromatography applications. Fused silica microtubes are proposed by different suppliers with a variety of internal diameters, from one micrometer to hundreds of micrometers. Due to their low cost, they are an interesting solution as connecting lines for a number of microfluidics devices or prototypes.

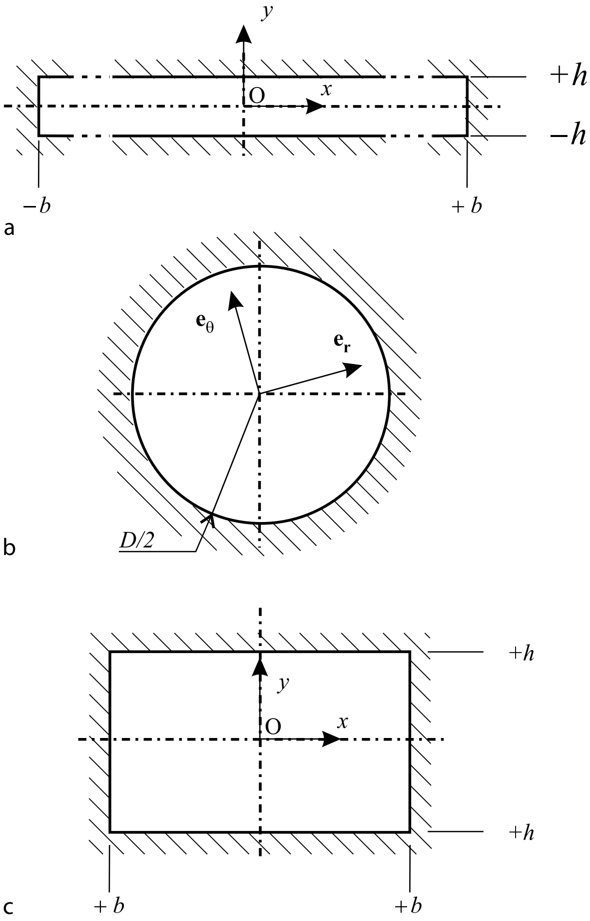

Pressure-Driven Single Phase Gas Flows, Figure 3 Different microchannel sections; **a** plane channel limited by parallel plates ($b \gg h$), **b** circular duct, **c** rectangular channel

The streamwise coordinate is z and the cross-section is in the (x, y) plane. The different considered sections are represented in Fig. 3.

Two different Knudsen numbers are usually defined for microchannel flows:

$$\mathrm{Kn} = \frac{\lambda}{D_{\mathrm{H}}} = \frac{\lambda}{4A/P} \tag{14}$$

is defined from the hydraulic diameter D_{H} as a reference length. The section area is noted A and the wetted perimeter is noted P. On the other hand,

$$\mathrm{Kn}' = \frac{\lambda}{L_{\min}} \tag{15}$$

is defined from the minimal representative length of the section.

Key Research Findings

Pressure Driven Flows Between Parallel Plates

In the case of a plane flow (Fig. 3a), $h/b \to 0$ and the velocity only depends on the transverse coordinate y. With the previous assumptions, the momentum Eq. (8) reduces to

$$\frac{\mathrm{d}^2 u_z}{\mathrm{d}y^2} = \frac{1}{\mu}\frac{\mathrm{d}p}{\mathrm{d}z}\,. \tag{16}$$

The first-order boundary condition (12) for a fixed wall and an isothermal flow is $u_s|_w = A_1\lambda\,(\partial u_s/\partial n)_w$, i.e. for a flow between parallel plates:

$$u_z|_{y=h} = -A_1\lambda \left.\frac{\partial u_z}{\partial y}\right|_{y=h}, \tag{17}$$

to be associated with the condition of symmetry (cf. Fig. 3)

$$\left.\frac{\mathrm{d}u_z}{\mathrm{d}y}\right|_{y=0} = 0\,. \tag{18}$$

The solution of this set of equations is

$$u_z = \frac{1}{\mu}\frac{\mathrm{d}p}{\mathrm{d}z}\left(\frac{y^2-h^2}{2} - A_1\lambda h\right). \tag{19}$$

In a dimensionless form, the velocity distribution can be written as

$$u_z^* = 1 - y^{*2} + 8A_1\mathrm{Kn} = 1 - y^{*2} + 4A_1\mathrm{Kn}'\,, \tag{20}$$

where $y^* = y/h$, $u_z^* = u_z/u_{z0}$ and $u_{z0} = u_{z\,(y=0,\mathrm{Kn}=0)} = -\left(h^2/[2\mu]\right)\left(\mathrm{d}p/\mathrm{d}z\right)$ represents the velocity at the center of the section when rarefaction is not taken into account.
The integration of the velocity distribution given by Eq. (20) over the cross-section leads to the mean velocity

$$\overline{u_z^*} = \frac{1}{2}\int_{-1}^{1} u_z^*\,\mathrm{d}y^* = \frac{\overline{u_z}}{u_{z0}} = \frac{2}{3} + 8A_1\mathrm{Kn} = \frac{2}{3} + 4A_1\mathrm{Kn}'\,. \tag{21}$$

Considering a long microchannel of length l with a pressure p_i at the inlet and a pressure p_o at the outlet and neglecting the entrance effects, we can deduce from Eq. (21) the mass flow rate $\dot{m} = \rho\overline{u_z}A = p\overline{u_z}A/(RT)$, which is independent of z. According to Eq. (5), the quantity ($\mathrm{Kn}p$) is constant for an isothermal flow and it can be written as a function of the outlet conditions: $\mathrm{Kn}p = \mathrm{Kn_o}p_o$. Therefore, the integration of Eq. (21) yields

$$\int_{p_i}^{p_o}\left(\frac{2}{3}p + 8A_1\mathrm{Kn_o}p_o\right)\mathrm{d}p = -\frac{2\mu\dot{m}RTl}{h^2A}\,, \tag{22}$$

which leads to

$$\dot{m}_{\mathrm{NS1,plan}} = \frac{2bh^3p_o^2}{\mu RTl}\left[\frac{\Pi^2-1}{3} + 8A_1\mathrm{Kn_o}\,(\Pi-1)\right], \tag{23}$$

where $\Pi = p_i/p_o$ is the ratio of the inlet over outlet pressures and $\mathrm{Kn_o}$ is the outlet Knudsen number. The subscript NS1 refers to the Navier–Stokes equations with first-order slip boundary conditions. In a dimensionless form that compares the actual mass flow rate $\dot{m}$ with the mass flow rate $\dot{m}_{ns}$ obtained from a no-slip hypothesis, Eq. (23) becomes:

$$\dot{m}^*_{\mathrm{NS1,plan}} = \frac{\dot{m}_{\mathrm{NS1,plan}}}{\dot{m}_{ns,\mathrm{plan}}} = 1 + 24A_1\frac{\mathrm{Kn_o}}{\Pi+1} = 1 + 12A_1\frac{\mathrm{Kn'_o}}{\Pi+1}\,. \tag{24}$$

The pressure distribution along the z-axis can be found by expressing the conservation of mass flow rate through the channel, notably between any section defined by z and the outlet section:

$$\dot{m}_{\mathrm{NS1,plan}} = \frac{2bh^3p_o^2}{\mu RT\,(l-z)} \times \left[\frac{(p/p_o)^2-1}{3} + 8A_1\mathrm{Kn_o}\,(p/p_o-1)\right]. \tag{25}$$

Equation (25) shows that the pressure $p^* = p/p_o$ is the solution of the polynomial

$$p^{*2} + \alpha_1 p^* + \alpha_2 + \alpha_3 z^* = 0\,, \tag{26}$$

where $z^* = z/l$ and $\alpha_1 = 24A_1\mathrm{Kn_o}$, $\alpha_2 = -\Pi(\Pi+\alpha_1)$, $\alpha_3 = (\Pi-1)(\Pi+1+\alpha_1)$.
The solution of Eq. (26) is plotted in Fig. 4, for an inlet over outlet pressure ratio $\Pi = 2$. This figure shows that rarefaction and compressibility have opposite effects on the pressure distribution. Rarefaction effects (characterized by Kn) reduce the curvature in pressure distribution due to compressibility effects (characterized by Ma).
Therefore, the previous model can be improved to remain accurate for higher Knudsen numbers. For this purpose,

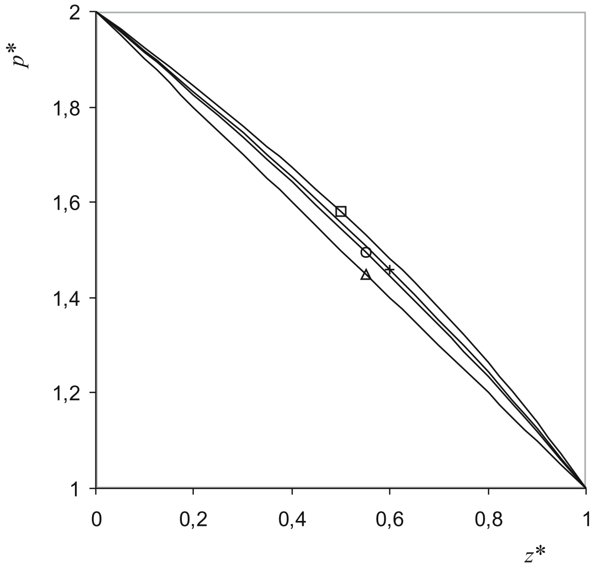

Pressure-Driven Single Phase Gas Flows, Figure 4 Pressure distribution along a plane microchannel, for $\Pi = 2$.
(△): incompressible flow; (□): $\mathrm{Kn_o} = 0$; (+): $\mathrm{Kn_o} = 0.05$; (○): $\mathrm{Kn_o} = 0.1$

second-order – $\vartheta(\mathrm{Kn}^2)$ – models, based on second-order boundary conditions, may be used.

It is easy to verify that the mass flow rate is consequently corrected as:

$$\begin{aligned}\dot{m}^*_{\mathrm{NS2,plan}} &= \frac{\dot{m}_{\mathrm{NS2,plan}}}{\dot{m}_{ns,\mathrm{plan}}} \\ &= 1 + 24A_1\frac{\mathrm{Kn_o}}{\Pi+1} - 96A_2\mathrm{Kn_o^2}\frac{\ln\Pi}{\Pi^2-1} \\ &= 1 + 12A_1\frac{\mathrm{Kn'_o}}{\Pi+1} - 24A_2\mathrm{Kn'_o}^2\frac{\ln\Pi}{\Pi^2-1}\,. \end{aligned} \quad (27)$$

Pressure Driven Flows in Circular Microtubes

With the same general assumptions than in the previous section, the momentum Eq. (8) in polar coordinates reduces to

$$\frac{1}{r}\frac{\mathrm{d}}{\mathrm{d}r}\left(r\frac{\mathrm{d}u_z}{\mathrm{d}r}\right) = \frac{1}{\mu}\frac{\mathrm{d}p}{\mathrm{d}z}\,. \quad (28)$$

The first-order boundary condition (12) for a non-moving wall and an isothermal flow is now (cf. Fig. 3b):

$$u_z|_{r=D/2} = -A_1\lambda\left.\frac{\partial u_z}{\partial r}\right|_{r=D/2}, \quad (29)$$

which leads to the dimensionless velocity profile

$$u_z^* = 1 - r^{*2} + 4A_1\mathrm{Kn} \quad (30)$$

where the Knudsen number $\mathrm{Kn} = \lambda/D_\mathrm{H} = \lambda/D = \mathrm{Kn}' = \lambda/L_\mathrm{min}$ is defined from a characteristic length $L = D$. Here, $r^* = 2r/D$ and $u_z^* = u_z/u_{z0}$ with $u_{z0} = -\left(D^2/[16\mu]\right)(\mathrm{d}p/\mathrm{d}z)$. The integration of the velocity within a section and along the microtube leads to

$$\dot{m}_{\mathrm{NS1,circ}} = \frac{\pi D^2 p_\mathrm{o}^2}{16\mu RTl}\left[\frac{\Pi^2-1}{4} + 4A_1\mathrm{Kn_o}(\Pi-1)\right] \quad (31)$$

for a long microtube, neglecting entrance effects and

$$\dot{m}^*_{\mathrm{NS1,circ}} = \frac{\dot{m}_{\mathrm{NS1,circ}}}{\dot{m}_{ns,\mathrm{circ}}} = 1 + 16A_1\frac{\mathrm{Kn_o}}{\Pi+1}\,. \quad (32)$$

The pressure distribution $p^* = p/p_\mathrm{o}$ along the microtube is the solution of the polynomial

$$p^{*2} + \beta_1 p^* + \beta_2 + \beta_3 z^* = 0\,, \quad (33)$$

where $\beta_1 = 16A_1\mathrm{Kn_o}$, $\beta_3 = (\Pi-1)(\Pi+1+\beta_1)$ and $\beta_2 = -1-\beta_1-\beta_3$, which qualitatively leads to the same conclusions as for a plane flow.

The first-order solution can easily be extended to second-order boundary conditions, following the same reasoning as in the previous section. We find

$$\begin{aligned}\dot{m}^*_{\mathrm{NS2,circ}} &= \frac{\dot{m}_{\mathrm{NS2,circ}}}{\dot{m}_{ns,\mathrm{circ}}} \\ &= 1 + 16A_1\frac{\mathrm{Kn_o}}{\Pi+1} - 32A_2\frac{\mathrm{Kn_o^2}\ln\Pi}{\Pi^2-1}\,. \end{aligned} \quad (34)$$

Pressure Driven Flows in Rectangular Microchannels

A rectangular section is characterized by its aspect ratio $a^* = h/b$, with $0 < a^* \le 1$, assuming $h \le b$ (Fig. 3c). Actually, calculation of the mass flow rate in a rectangular microchannel using the plane flow solution (24) or (27) is inaccurate as soon as the aspect ratio of the section a^* is higher than 10^{-2}, due to non-negligible friction on the side walls of equations $x = \pm b$. Typically, the overestimation $[(\dot{m}_\mathrm{plan} - \dot{m}_\mathrm{rect})/\dot{m}_\mathrm{rect}]_\mathrm{NS2}$ is about 0.5% for an aspect ratio $a^* = 0.01$, it rises to 5.3% for an aspect ratio $a^* = 0.1$ and reaches 112% for a square cross-section for which $a^* = 1$! As a consequence, a real 3D model is required. With the general assumptions of previous sections, the momentum equation takes the dimensionless form

$$a^{*2}\frac{\mathrm{d}^2u_z^*}{\mathrm{d}x^{*2}} + \frac{\mathrm{d}^2u_z^*}{\mathrm{d}y^{*2}} = -1\,, \quad (35)$$

with $x^* = x/b$, $y^* = y/h$ and $u_z^* = -\mu u_z/(h^2(\mathrm{d}p/\mathrm{d}z))$.

P

The first-order boundary conditions are

$$u_z^*\big|_{y^*=1} = -2A_1\text{Kn}' \left.\frac{\partial u_z^*}{\partial y^*}\right|_{y^*=1} , \tag{36}$$

$$u_z^*\big|_{x^*=1} = -2a^*A_1\text{Kn}' \left.\frac{\partial u_z^*}{\partial x^*}\right|_{x^*=1} , \tag{37}$$

with $\text{Kn}' = \lambda/(2h)$ and the conditions of symmetry are $\left(\text{d}u_z^*/\text{d}y^*\right)_{y^*=0} = 0$ and $(\text{d}u_z^*/\text{d}x^*)_{x^*=0} = 0$. The solution of Eqs. (35) to (37), compatible with the conditions of symmetry can be written as

$$u_z^* = -\sum_{i=1}^{\infty} \Psi_i\left(x^*\right)\cos\left(\delta_i y^*\right) , \tag{38}$$

where the eigenvalues δ_i must verify

$$\delta_i \tan\delta_i = \frac{A_1}{2\text{Kn}'} \tag{39}$$

in order to be compatible with the boundary condition (36) without leading to a trivial velocity solution. The x^* dependent Ψ_i functions are found by expanding the right-hand side of Eq. (35), i. e. unity, in terms of the orthogonal functions $\cos\left(\delta_i y^*\right)$:

$$\begin{aligned} -1 &= -\sum_{i=1}^{\infty} \frac{2\sin\delta_i}{\delta_i + \sin\delta_i\cos\delta_i}\cos\left(\delta_i y^*\right) \\ &= -\sum_{i=1}^{\infty} \Omega_i\cos\left(\delta_i y^*\right) . \end{aligned} \tag{40}$$

Therefore, to verify the momentum Eq. (35), the functions Ψ_i must obey

$$\frac{d^2\Psi_i}{dx^{*2}} - \left(\frac{\delta_i}{a^*}\right)^2 \Psi_i - \frac{\Omega_i}{a^{*2}} = 0 . \tag{41}$$

The solution of Eq. (41), with the boundary and symmetry conditions and using Eq. (39), is

$$\Psi_i = -\frac{\Omega_i}{\alpha_i^2}\left(1 - \frac{\cosh\left(\frac{\alpha_i x^*}{a^*}\right)}{\cosh\left(\frac{\alpha_i}{a^*}\right) + 2A_1\text{Kn}'\alpha_i\sinh\left(\frac{\alpha_i}{a^*}\right)}\right) . \tag{42}$$

Consequently, the velocity distribution is given by Eq. (38), where Ψ_i and δ_i are obtained from Eqs. (40) and (42). This solution is given as a function of a Knudsen number $\text{Kn}' = \lambda/(2h)$ based on the channel depth, but it can also be expressed as a function of the Knudsen number $\text{Kn} = \lambda/D_\text{H}$ based on the hydraulic diameter, using the relation $2\text{Kn} = \text{Kn}'\left(1 + a^*\right)$.

The solution of the problem with Deissler [10] second-order boundary conditions is detailed in [3]. These boundary conditions may be written in a dimensionless form as

$$\begin{aligned} u_z^*\big|_{y^*=1} &= -2A_1\text{Kn}' \left.\frac{\partial u_z^*}{\partial y^*}\right|_{y^*=1} \\ &\quad - \frac{9}{4}\text{Kn}'^2\left(\left.\frac{\partial^2 u_z^*}{\partial y^{*2}}\right|_{y^*=1} - 1\right) \end{aligned} \tag{43}$$

and

$$\begin{aligned} u_z^*\big|_{x^*=1} &= -2A_1a^*\text{Kn}' \left.\frac{\partial u_z^*}{\partial x^*}\right|_{x^*=1} \\ &\quad - \frac{9}{4}\text{Kn}'^2\left(a^{*2}\left.\frac{\partial^2 u_z^*}{\partial x^{*2}}\right|_{x^*=1} - 1\right) . \end{aligned} \tag{44}$$

for a locally fully developed flow in a rectangular section. A semi-analytical solution for the mass flow is found as [3]:

$$\dot{m}_{\text{NS2,rect}} = -\frac{4ph^4}{a^*RT\mu}\frac{\text{d}p}{\text{d}z}\left[a_1 + a_2\text{Kn}' + a_3\text{Kn}'^2\right] . \tag{45}$$

Values of a_1, a_2 and a_3 coefficients are given in Table 4, for different aspect ratios and values of A_1.

Temperature Jump and Heat Transfer

As for the velocity, it can be shown that the temperature experiences a jump at the wall, which can be written

$$\begin{aligned} T^* - T^*_\text{wall} &= \beta_T\frac{2-\sigma_T}{\sigma_T}\frac{2\gamma}{\gamma+1}\frac{\text{Kn}}{\text{Pr}}\left.\frac{\partial T^*}{\partial n^*}\right|_w \\ &= B_1\frac{2\gamma}{\gamma+1}\frac{\text{Kn}}{\text{Pr}}\left.\frac{\partial T^*}{\partial n^*}\right|_w , \end{aligned} \tag{46}$$

where Pr is the Prandtl number and σ_T is the energy accommodation coefficient; β_T is a corrective coefficient introduced by Cercignani to improve the original formula proposed by Smoluchowski. This temperature jump must be taken into account as well as the velocity slip if the flow is not isothermal and if heat transfer is considered (►convective heat transfer in microchannels). For example, for a hydrodynamically and thermally developed flow in a plane microchannel (Fig. 3a) with a lower adiabatic

Pressure-Driven Single Phase Gas Flows, Table 4 Values of a_1, a_2 and a_3 coefficients for different values of A_1 and a^*, for Deissler second-order boundary conditions

a^* A_1	3.0000	2.3333	1.8571	1.5000	1.2222	1.0000
0 $a_1 = 0.33333$	$a_2 = 6.0000$ $a_3 = 4.5000$	$a_2 = 4.6667$ $a_3 = 4.5000$	$a_2 = 3.7143$ $a_3 = 4.5000$	$a_2 = 3.0000$ $a_3 = 4.5000$	$a_2 = 2.4444$ $a_3 = 4.5000$	$a_2 = 2.0000$ $a_3 = 4.5000$
0.01 $a_1 = 0.33123$	$a_2 = 5.9694$ $a_3 = 4.4528$	$a_2 = 4.6459$ $a_3 = 4.4542$	$a_2 = 3.7007$ $a_3 = 4.4548$	$a_2 = 2.9917$ $a_3 = 4.4550$	$a_2 = 2.4405$ $a_3 = 4.4549$	$a_2 = 1.9993$ $a_3 = 4.4549$
0.025 $a_1 = 0.32808$	$a_2 = 5.9228$ $a_3 = 4.3840$	$a_2 = 4.6141$ $a_3 = 4.3875$	$a_2 = 3.6797$ $a_3 = 4.3887$	$a_2 = 2.9788$ $a_3 = 4.3895$	$a_2 = 2.4337$ $a_3 = 4.3896$	$a_2 = 1.9977$ $a_3 = 4.3892$
0.05 $a_1 = 0.32283$	$a_2 = 5.8420$ $a_3 = 4.2761$	$a_2 = 4.5591$ $a_3 = 4.2813$	$a_2 = 3.6423$ $a_3 = 4.2843$	$a_2 = 2.9547$ $a_3 = 4.2858$	$a_2 = 2.4201$ $a_3 = 4.2858$	$a_2 = 1.9925$ $a_3 = 4.2853$
0.1 $a_1 = 0.31233$	$a_2 = 5.6774$ $a_3 = 4.0697$	$a_2 = 4.4431$ $a_3 = 4.0832$	$a_2 = 3.5613$ $a_3 = 4.0906$	$a_2 = 2.9000$ $a_3 = 4.0943$	$a_2 = 2.3860$ $a_3 = 4.0952$	$a_2 = 1.9751$ $a_3 = 4.0944$
0.25 $a_1 = 0.28081$	$a_2 = 5.1332$ $a_3 = 3.6073$	$a_2 = 4.0464$ $a_3 = 3.6287$	$a_2 = 3.2675$ $a_3 = 3.6449$	$a_2 = 2.6823$ $a_3 = 3.6560$	$a_2 = 2.2267$ $a_3 = 3.6626$	$a_2 = 1.8626$ $a_3 = 3.6647$
0.5 $a_1 = 0.22868$	$a_2 = 4.2443$ $a_3 = 3.3489$	$a_2 = 3.3519$ $a_3 = 3.3588$	$a_2 = 2.7120$ $a_3 = 3.3708$	$a_2 = 2.2289$ $a_3 = 3.3856$	$a_2 = 1.8487$ $a_3 = 3.4048$	$a_2 = 1.5395$ $a_3 = 3.4292$
1 $a_1 = 0.14058$	$a_2 = 3.1207$ $a_3 = 3.3104$	$a_2 = 2.4552$ $a_3 = 3.3176$	$a_2 = 1.9782$ $a_3 = 3.3287$	$a_2 = 1.6187$ $a_3 = 3.3438$	$a_2 = 1.3364$ $a_3 = 3.3644$	$a_2 = 1.1077$ $a_3 = 3.3908$

wall and an upper wall with constant heat flux, the Nusselt number Nu can be calculated and is given by

$$\mathrm{Nu}^{-1} = \frac{\varsigma^*}{4} + \frac{26 + 147\xi^* + 210\xi^{*2}}{140\,(1 + 3\xi^*)^2}\,, \qquad (47)$$

where $\xi^* = 4A_1\mathrm{Kn}$ and $\varsigma^* = (8\gamma)/(\gamma+1)B_1(\mathrm{Kn}/\mathrm{Pr})$ are the dimensionless slip and temperature jump coefficients. This Nusselt number reduces to the classic value 70/13 when $\mathrm{Kn} = 0$.

Future Directions for Research

Theoretical knowledge on pressure-driven gas microflows is currently well advanced, especially in the slip-flow regime. However, there is yet a need for accurate experimental data, both for steady or unsteady gas microflows, with or without heat transfer. For example, in order to definitely validate the choice of the best boundary conditions in the slip flow regime, we need to isolate the influence of the accommodation coefficients, as it remains an open issue. Relationships between their values, the nature of the substrate and the micro fabrication processes involved are currently not available. There are also few data about flows of gas mixtures in microchannels.

Cross References

- ► Micro-PIV-Based Diffusometry
- ► Convective Heat Transfer in Microchannels
- ► Gas Flow in Nanochannels
- ► Lattice Boltzmann Method (LBM)
- ► Methods for Flow Rate Measurement
- ► Micro and Nanoscale Gas Dynamics
- ► Molecular Dynamics Simulation Method
- ► Monte Carlo Method
- ► Single Phase Gaseous Flow

P

References

1. Gad-el-Hak M (1999) The fluid mechanics of microdevices – The Freeman Scholar Lecture. J Fluid Eng 121:5–33
2. Bird GA (1998) Molecular gas dynamics and the direct simulation of gas flows. Clarendon Press, Oxford
3. Kandlikar SG, Garimella S, Li D, Colin S and King MR (2006) Heat Transfer and Fluid Flow in Minichannels and Microchannels. Elsevier, Oxford
4. Lockerby DA, Reese JM, Gallis MA (2005) Capturing the Knudsen layer in continuum-fluid models of nonequilibrium gas flows. AIAA J 43(6):1391–1393
5. Colin S, Lalonde P, Caen R (2004) Validation of a second-order slip flow model in rectangular microchannels. Heat Transf Eng 25(3):23–30
6. Cercignani C, Illner R, Pulvirenti M (1994) The mathematical theory of dilute gases. Springer-Verlag, New York
7. Hadjiconstantinou NG (2003) Comment on Cercignani's second-order slip coefficient. Phys Fluids 15(8):2352–2354
8. Chapman S, Cowling TG (1952) The mathematical theory of non-uniform gases. University Press, Cambridge
9. Karniadakis GE, Beskok A (2002) Microflows: fundamentals and simulation. Springer-Verlag, New York, pp 340
10. Deissler RG (1964) An analysis of second-order slip flow and temperature-jump boundary conditions for rarefied gases. Int J Heat Mass Transf 7:681–694

Pressure-Driven Single Phase Liquid Flows

Gian Luca Morini
DIENCA, Università di Bologna, Bologna, Italy
gianluca.morini@mail.ing.unibo.it

Definition

The forced mass movement of single phase liquids through microchannels with a hydraulic diameter less than 1 mm induced by a pressure gradient imposed at the ends of the microchannel is called pressure-driven single phase liquid flow.

Overview

Investigation of the flow phenomena in pipes and channels is the most important subject of hydraulics. In the middle of the nineteenth century an exact solution of the hydrodynamic equations was derived for the flow of a fluid through straight tubes of circular cross-section by Hagen [1] and Poiseuille [2] independently. It is interesting to highlight that the original experimental work of Poiseuille was conducted by testing water through glass capillary tubes having an internal diameter down to 15 μm. This work can be considered the first experimental test of pressure-driven single phase liquid flows in microchannels.

Basic Methodology

The behavior of isothermal pressure-driven single phase fluid flows in microchannels can be studied by determining the velocity distribution in the fluid region with the aid of the mass conservation principle (*continuity equation*) and the equations of conservation of fluid momentum [3]:

$$
\begin{aligned}
-\frac{1}{\rho}\frac{D\rho}{Dt} &= \nabla \cdot \boldsymbol{v} \\
\rho\frac{D\boldsymbol{v}}{Dt} &= -\nabla p + \rho \boldsymbol{g} - \nabla \cdot \boldsymbol{\tau}
\end{aligned}
\qquad (1)
$$

in which $\boldsymbol{v}$ is the velocity vector, ρ is the fluid density, t is the time, p is the pressure, D/Dt is the total derivative and $\boldsymbol{\tau}$ is the viscous tensor.

In Table 1 the components of the viscous tensor for Newtonian fluids are reported for Cartesian, cylindrical and spherical coordinates.

In order to solve the continuity and momentum balance equations (Eq. (1)) the following *constitutive laws* have to be taken into account:

$$
\begin{cases}
\rho = \rho(p, T) \\
\mu = \mu(p, T)
\end{cases}
\qquad (2)
$$

Pressure-Driven Single Phase Liquid Flows, Table 1 Components of the viscous tensor for Cartesian, cylindrical and spherical coordinates

Cartesian coordinates (x, y, z)	$\tau_{xx} = -\mu\left[2\frac{\partial v_x}{\partial x} - \frac{2}{3}(\nabla \cdot \boldsymbol{v})\right]$
	$\tau_{yy} = -\mu\left[2\frac{\partial v_y}{\partial y} - \frac{2}{3}(\nabla \cdot \boldsymbol{v})\right]$
	$\tau_{zz} = -\mu\left[2\frac{\partial v_z}{\partial z} - \frac{2}{3}(\nabla \cdot \boldsymbol{v})\right]$
	$\tau_{xy} = \tau_{yx} = -\mu\left[\frac{\partial v_x}{\partial y} + \frac{\partial v_y}{\partial x}\right]$
	$\tau_{yz} = \tau_{zy} = -\mu\left[\frac{\partial v_y}{\partial z} + \frac{\partial v_z}{\partial y}\right]$
	$\tau_{zx} = \tau_{xz} = -\mu\left[\frac{\partial v_z}{\partial x} + \frac{\partial v_x}{\partial z}\right]$
Cylindrical Coordinates (r, θ, z)	$\tau_{rr} = -\mu\left[2\frac{\partial v_r}{\partial r} - \frac{2}{3}(\nabla \cdot \boldsymbol{v})\right]$
	$\tau_{\theta\theta} = -\mu\left[2\left(\frac{1}{r}\frac{\partial v_\theta}{\partial \theta} + \frac{v_r}{r}\right) - \frac{2}{3}(\nabla \cdot \boldsymbol{v})\right]$
	$\tau_{zz} = -\mu\left[2\frac{\partial v_z}{\partial z} - \frac{2}{3}(\nabla \cdot \boldsymbol{v})\right]$
	$\tau_{r\theta} = \tau_{\theta r} = -\mu\left[r\frac{\partial}{\partial y}\left(\frac{v_\theta}{r}\right) + \frac{1}{r}\frac{\partial v_r}{\partial \theta}\right]$
	$\tau_{\theta z} = \tau_{z\theta} = -\mu\left[\frac{\partial v_\theta}{\partial z} + \frac{1}{r}\frac{\partial v_z}{\partial \theta}\right]$
	$\tau_{zr} = \tau_{rz} = -\mu\left[\frac{\partial v_z}{\partial r} + \frac{\partial v_r}{\partial z}\right]$
Spherical coordinates (r, θ, ϕ)	$\tau_{rr} = -\mu\left[\frac{\partial v_r}{\partial r} - \frac{2}{3}(\nabla \cdot \boldsymbol{v})\right]$
	$\tau_{\theta\theta} = -\mu\left[2\left(\frac{1}{r}\frac{\partial v_\theta}{\partial \theta} + \frac{v_r}{r}\right) - \frac{2}{3}(\nabla \cdot \boldsymbol{v})\right]$
	$\tau_{\phi\phi} = -\mu\left[2\left(\frac{1}{r\sin\theta}\frac{\partial v_\phi}{\partial \phi} + \frac{v_r}{r} + \frac{v_\theta \cot\theta}{r}\right) - \frac{2}{3}(\nabla \cdot \boldsymbol{v})\right]$
	$\tau_{r\theta} = \tau_{\theta r} = -\mu\left[r\frac{\partial}{\partial y}\left(\frac{v_\theta}{r}\right) + \frac{1}{r}\frac{\partial v_r}{\partial \theta}\right]$
	$\tau_{\theta\phi} = \tau_{\phi\theta} = -\mu\left[\frac{\sin\theta}{r}\frac{\partial}{\partial \theta}\left(\frac{v_\phi}{\sin\theta}\right) + \frac{1}{r\sin\theta}\frac{\partial v_\theta}{\partial \phi}\right]$
	$\tau_{\phi r} = \tau_{r\phi} = -\mu\left[\frac{1}{r\sin\theta}\frac{\partial v_r}{\partial \phi} + r\frac{\partial}{\partial r}\left(\frac{v_\phi}{r}\right)\right]$

If the flow is isothermal, Eqs. (1) and (2) allow the calculation of the pressure field and of the velocity vector $(p, \boldsymbol{v})$ in the fluid region.

It is possible to demonstrate that, for Newtonian fluids with constant viscosity μ, the following equality is satisfied:

$$
(\nabla \cdot \boldsymbol{\tau})_i = -\mu\left[\nabla^2 v_i + \frac{1}{3}\frac{\partial}{\partial i}(\nabla \cdot \boldsymbol{v})\right] \qquad (3)
$$

where $i = x, y, z$ for Cartesian coordinates.

Combining Eq. (3) and the momentum equation one obtains

$$\rho \frac{\mathrm{D}\boldsymbol{v}}{\mathrm{D}t} = -\nabla p + \rho \boldsymbol{g} + \mu \left[\nabla^2 \boldsymbol{v} + \frac{1}{3} \nabla (\nabla \cdot \boldsymbol{v}) \right] \tag{4}$$

This version of the momentum equation is known as the *Navier–Stokes equation*.

For an incompressible ($\rho = \text{const}$) and Newtonian fluid with constant viscosity ($\mu = \text{const}$) the continuity and the momentum balance equations can be written as follows:

$$\nabla \cdot \boldsymbol{v} = 0$$

$$\rho \frac{\mathrm{D}\boldsymbol{v}}{\mathrm{D}t} = -\nabla p + \rho \boldsymbol{g} + \mu \nabla^2 \boldsymbol{v} \tag{5}$$

The momentum balance equation can be simplified in the case of very slow fluid motion. In this case the total derivative of the velocity and the acceleration due to the gravity can be neglected in the *Navier–Stokes equation*:

$$\mu \nabla^2 \boldsymbol{v} = \nabla p \tag{6}$$

Equation (6) applies to the analysis of fluid behavior in tribology and microchannel flows: this kind of flow is called *Stokes flow*. In this case, the velocities are free of macroscopic fluctuations at any point in the flow field and the flow is defined as *laminar*.

For a laminar flow through a straight microchannel the fluid particles move in definite paths called streamlines and there are no components of fluid velocity normal to the duct axis. The projection of Eq. (6) along the axial direction (z) gives

$$\mu \nabla^2 v_z = \frac{\mathrm{d}p}{\mathrm{d}z} \tag{7}$$

Equations (6) and (7) are valid only far from the inlet section of the microchannel (see ► developing flows and ► entrance region) where the velocity profile can be considered hydrodynamically fully developed. Laminar flow is designated as hydrodynamically fully developed when the fluid velocity distribution at a cross-section is of an invariant form independent of the axial distance z.

Laminar Regime

Let us consider a liquid flowing through a straight microchannel having an axially unchanging and uniform cross-section with an area equal to Ω and the perimeter equal to Γ. It is possible to define the *hydraulic diameter* of the microchannel as follows:

$$D_\mathrm{h} = \frac{4\Omega}{\Gamma} \tag{8}$$

and the *mean fluid velocity* as the integrated average axial velocity over the flow area Ω:

$$W = \frac{1}{\Omega} \int_\Omega v_z d\Omega = \frac{\dot{m}}{\rho \Omega} \tag{9}$$

in which the link with measurable quantities, like the mass flow rate, is highlighted.

It is suitable to introduce the dimensionless quantities

$$\Omega^* = \frac{\Omega}{D_\mathrm{h}^2}; \quad \Gamma^* = \frac{\Gamma}{D_\mathrm{h}}; \quad \nabla^* = D_\mathrm{h} \nabla;$$

$$V_z = \frac{v_z}{W}; \quad c_1 = -\frac{D_\mathrm{h}^2}{\mu W} \frac{\mathrm{d}p}{\mathrm{d}z} \tag{10}$$

Consequently, the dimensionless momentum balance equation is readily obtained in the following form:

$$\nabla^{*2} V_z + c_1 = 0 \tag{11}$$

In order to characterize a liquid flow through microchannels under an imposed pressure gradient Eq. (11) can be used together with the appropriate boundary condition that, for Newtonian liquids, is the no-slip boundary condition at the walls:

$$V_z|_{\Gamma^*} = 0 \tag{12}$$

For a Newtonian liquid flow, this assumption is justified if the microchannel has a hydraulic diameter larger than 1 μm. In fact, for liquids the typical mean free path λ of molecules under ambient conditions is 0.1 – 1 nm. Since the fluid velocity tends to evidence a slip at the microchannel walls for Knudsen numbers, defined as $\mathrm{Kn} = \lambda / D_\mathrm{h}$, larger than 0.001, the no-slip boundary condition has to be abandoned only when the hydraulic diameter of the microchannel becomes less than 1 μm.

On the contrary, for non-Newtonian liquids, like polymer solutions and surfactants, a slip velocity at the walls can be observed even for microchannels having a hydraulic diameter greater than 1 μm.

The solution of Eqs. (11) and (12) yields the velocity distribution inside the microchannel in the laminar regime for fully developed flow. The analytical solution of this differential problem is available only for very simple geometries.

From the velocity distribution obtained by the solution of Eqs. (11) and (12) it is possible to calculate the value assumed by the main flow parameters which can be useful during the design stage of a microfluidic device:

- the *ratio between the maximum and the mean value of the velocity* (V_max):

P

$$V_{\max} = \frac{v_{z,\max}}{W} \quad (13)$$

- the asymptotic value of the *momentum flux correction factor* K_d defined as:

$$K_d = \frac{1}{\Omega^*} \int_{\Omega^*} V_z^2 \, d\Omega^* \quad (14)$$

- the asymptotic *kinetic energy correction factor* K_e defined as:

$$K_e = \frac{1}{\Omega^*} \int_{\Omega^*} V_z^3 \, d\Omega^* \quad (15)$$

- the asymptotic *incremental pressure drop number* $K(\infty)$:

$$K(\infty) = \frac{2}{\Omega^*} \int_{\Omega^*} \left[\left(V_z^3 - V_z^2 \right) \right] d\Omega^* = 2\,(K_e - K_d) \quad (16)$$

- the *Poiseuille number* defined as the product of the Fanning friction factor for fully developed flow (f) and the Reynolds number ($\mathrm{Re} = \rho W D_h / \mu$):

$$(f\mathrm{Re})_{fd} = -\frac{1}{2\Omega^*} \int_{\Gamma^*} \left. \frac{\partial V_z}{\partial n^*} \right|_{\Gamma^*} d\Gamma^* = \frac{c_1}{2} \quad (17)$$

where n^* is the normal direction to the walls.

For Newtonian laminar flows these parameters depend on the geometry of the microchannel cross-section only.

Circular Cross-Section

For a channel with a circular cross-section it is possible to demonstrate that the velocity distribution, written in dimensionless form, is

$$V_z(r^*) = 2(1 - 4r^{*2}) \quad (18)$$

in which r^* is the dimensionless radius defined as r/D_h with D_h being the inner diameter.

In Table 2 the values assumed by $V_{\max}$, K_d, K_e, $K(\infty)$ and $f\mathrm{Re}_{fd}$ are quoted for this geometry.

Elliptical Cross-Section

Microtubes with elliptical cross-section in which fully developed laminar flow occurs are geometrically characterized by the value of the aspect ratio β defined as ratio between the minor (h) and the major (a) axes (see Fig. 1).

Pressure-Driven Single Phase Liquid Flows, Table 2 Analytical laminar fully developed values of $V_{\max}$, K_d, K_e, $K(\infty)$ and of the Poiseuille number ($f\mathrm{Re}_{fd}$) for circular microtubes

$V_{\max}$	K_d	K_e	$K(\infty)$	$f\mathrm{Re}_{fd}$
2	4/3	2	4/3	16

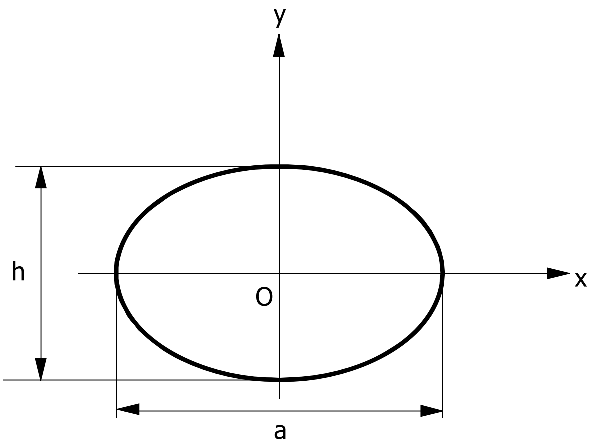

Pressure-Driven Single Phase Liquid Flows, Figure 1 Schematic of the elliptical cross-section and of the Cartesian coordinate system

The fully developed laminar velocity profile is

$$V_z(x^*, y^*) = 8\left(\frac{1}{4} - x^{*2} - y^{*2}\right) \quad (19)$$

in which x^* and y^* are dimensionless coordinates defined as x/a and y/h respectively and the Cartesian coordinate system has its origin at the center of the channel (see Fig. 1).

It is possible to demonstrate by using Eq. (19) that $V_{\max}$, K_d, K_e and $K(\infty)$ assume the same values as those for circular cross-section (see Table 2) for any β.

The fully developed Poiseuille number can be calculated analytically by means of the following relation:

$$f\mathrm{Re}_{fd} = 2\pi^2 \left(1 + \beta^2\right) \left[\frac{1}{E(1 - \beta^2)}\right]^2 \quad (20)$$

where E denotes the complete elliptical integral of the second kind.

In Table 3 the value of the fully developed Poiseuille number is quoted as a function of the aspect ratio β of the elliptical cross-section.

Concentric Annular Cross-Section

The solution of Eq. (11) with the no-slip boundary condition (Eq. (12)) through an annular channel with an inner radius equal to r_i and an outer radius equal to r_o (see Fig. 2) can be written as follows:

$$V_z(r^*) = \frac{2}{\left[1 + \beta^2 - 2r_m^{*2}\right]} \left(1 - r^{*2} + 2r_m^{*2} \ln(r^*)\right) \quad (21)$$

in which β is the aspect ratio of the annuli defined as r_i/r_o, r^* is the dimensionless radius defined as r/r_o and r_m^* is given by

$$r_m^* = \left[\frac{1-\beta^2}{2\ln(\frac{1}{\beta})}\right]^{\frac{1}{2}} \quad (22)$$

and designates the dimensionless radius corresponding to the maximum value of the velocity.

For this geometry a closed form solution for V_{max} and the Poiseuille number is known:

$$\begin{aligned} V_{max} &= 2\frac{\left(1-r_m^{*2}+2r_m^{*2}\ln(r_m^*)\right)}{1+\beta^2-2r_m^{*2}} \\ f_i\mathrm{Re}_{fd} &= 16\frac{(1-\beta)}{\beta\left(1+\beta^2-2r_m^{*2}\right)}\left(r_m^{*2}-\beta^2\right) \\ f_o\mathrm{Re}_{fd} &= 16\frac{(1-\beta)}{\left(1+\beta^2-2r_m^{*2}\right)}\left(1-r_m^{*2}\right) \\ f\mathrm{Re}_{fd} &= \frac{16}{\left(1+\beta^2-2r_m^{*2}\right)}\left(1-r_m^{*2}\right) \end{aligned} \quad (23)$$

where f_i and f_o designate the Fanning friction factors at the inner and outer walls respectively and $f\mathrm{Re}_{fd}$ is the perimeter average Poiseuille number:

$$f\mathrm{Re}_{fd} = \frac{\beta f_i\mathrm{Re} + \beta f_o\mathrm{Re}}{1+\beta} \quad (24)$$

In Table 4 the value assumed by V_{max}, K_d, K_e and $f\mathrm{Re}_{fd}$ are quoted for this geometry as a function of the aspect ratio β. It is evident that, the circular geometry can be considered as the limit case for $\beta = 0$ and the parallel plate geometry for $\beta = 1$.

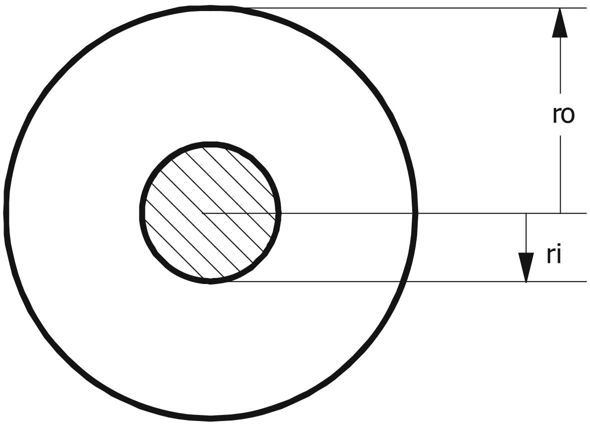

Pressure-Driven Single Phase Liquid Flows, Figure 2 Schematic of the annular cross-section

Pressure-Driven Single Phase Liquid Flows, Table 3 Analytical laminar fully developed values of V_{max}, K_d, K_e, $K(\infty)$ and of the Poiseuille number ($f\mathrm{Re}_{fd}$) for elliptical microtubes as a function of the aspect ratio β

β	$f\mathrm{Re}_{fd}$	β	$f\mathrm{Re}_{fd}$
1	16	0.3	17.896
0.9	16.022	0.25	18.24
0.8	16.098	0.2	18.602
0.75	16.161	1/6	18.847
0.7	16.244	1/7	19.02
2/3	16.311	1/8	19.146
0.6	16.479	1/9	19.241
0.5	16.823	1/10	19.314
0.4	17.294	1/16	19.536
1/3	17.681	1/20	19.598

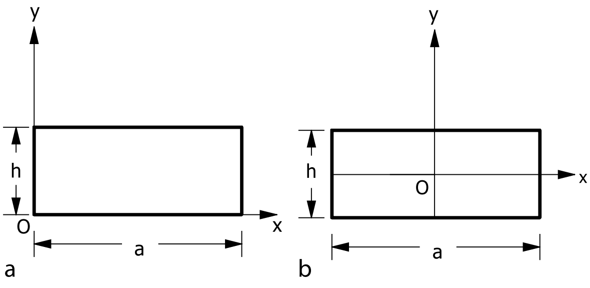

Pressure-Driven Single Phase Liquid Flows, Figure 3 Schematic of the rectangular cross-section with the Cartesian coordinate system used in (**a**) Eq. (25) and (**b**) Eq. (28)

Rectangular Cross-Section

For a rectangular channel with an aspect ratio $\beta = h/a$ (see Fig. 3a), for which a Cartesian system of coordinates x, y, z is assumed, with its origin in the left bottom corner of the inlet rectangular cross-section (y along the side with length h and z perpendicular to the cross-section), the analytical solution of Eqs. (11) and (12) gives the following velocity distribution:

$$\begin{aligned} V_z(x^*, y^*) = &\sum_{n=1,\mathrm{odd}}^{\infty}\sum_{m=1,\mathrm{odd}}^{\infty} v_{n,m}\sin\left(n\pi\frac{2\beta}{1+\beta}x^*\right) \\ &\times \sin\left(m\pi\frac{2}{1+\beta}y^*\right) \end{aligned} \quad (25)$$

Pressure-Driven Single Phase Liquid Flows, Table 4 Analytical laminar fully developed values of r_m^*, V_{max}, K_d, K_e, and of the inner, outer and average Poiseuille number ($f\mathrm{Re}_{fd}$) for annular microtubes as a function of the aspect ratio β

β	r_m^*	V_{max}	K_d	K_e	$f_i\mathrm{Re}$	$f_o\mathrm{Re}$	$f\mathrm{Re}_{fd}$
0.0001	0.233	1.767	1.298	1.863	9742.834	16.973	17.945
0.001	0.269	1.725	1.287	1.823	1352.776	17.337	18.671
0.01	0.329	1.661	1.266	1.753	219.426	18.034	20.028
0.05	0.408	1.598	1.243	1.675	74.459	18.923	21.567
0.1	0.464	1.567	1.230	1.634	50.886	19.489	22.343
0.15	0.508	1.549	1.222	1.610	42.027	19.904	22.790
0.2	0.546	1.537	1.217	1.594	37.264	20.253	23.088
0.3	0.615	1.522	1.210	1.573	32.166	20.850	23.461
0.4	0.677	1.513	1.206	1.561	29.437	21.375	23.678
0.5	0.736	1.508	1.204	1.555	27.719	21.859	23.813
0.6	0.791	1.504	1.202	1.549	26.529	22.318	23.897
0.75	0.872	1.501	1.200	1.546	25.295	22.971	23.967
0.8	0.898	1.501	1.200	1.544	24.978	23.182	23.980
0.9	0.950	1.500	1.200	1.543	24.440	23.596	23.996

in which the series coefficients $v_{n,m}$ are defined as

$$v_{n,m} = \frac{\pi^2}{4mn\left(\beta^2 n^2 + m^2\right)} \frac{1}{\sum\limits_{i=1,\mathrm{odd}}^{\infty} \sum\limits_{j=1,\mathrm{odd}}^{\infty} \frac{1}{i^2 j^2 (\beta^2 i^2 + j^2)}} \tag{26}$$

and x^* and y^* are the dimensionless coordinates defined as x/D_h and y/D_h respectively.
It is easy to demonstrate that for a rectangular cross-section the hydraulic diameter D_h, the aspect ratio β and the length of the sides (a, h) are correlated:

$$a = \frac{1+\beta}{2\beta} D_h; \quad h = \frac{1+\beta}{2} D_h \tag{27}$$

Since Eq. (25) involves considerable computational complexity, a simple approximation in the following form, validated for $\beta \le 0.5$, can be suggested:

$$V_z(x^*, y^*) = \left(\frac{w+1}{w}\right)\left(\frac{k+1}{k}\right)\left[1 - \left(\frac{4}{1+\beta} y^*\right)^w\right] \times \left[1 - \left(\frac{4\beta}{1+\beta} x^*\right)^k\right] \tag{28}$$

but in this case the origin of the Cartesian system of coordinates x, y, z is assumed at the center of the cross-section ($a/2$, $h/2$) (see Fig. 3b).

The exponents w and k can be calculated by means of the following empirical correlations:

$$k = 1.7 + 0.5\beta^{-1.4}$$
$$w = \begin{cases} 2 & \text{for } \beta \le \frac{1}{3} \\ 2 + 0.3\left(\beta - \frac{1}{3}\right) & \text{for } \beta > \frac{1}{3} \end{cases} \tag{29}$$

In Table 5 the values assumed by V_{max}, K_d, K_e, $K(\infty)$ and $f\mathrm{Re}_{fd}$ are quoted for this geometry as a function of the microchannel aspect ratio β. It is evident that, owing to the symmetry of the cross-section, for microchannels having β greater than 1, one can use $1/\beta$ in order to calculate the integral parameters from Table 5.

Parallel Plates

Very shallow rectangular microchannels with $h \ll a$ (or, for symmetry, in the case that $h \gg a$) are characterized by low values of the aspect ratio ($\beta = 0$); in this case the rectangular microchannel can be modeled as two parallel plates. It is possible to demonstrate that for parallel plates with a plate spacing equal to h, the fully developed laminar velocity profile can be written as follows:

$$V_z(y^*) = \frac{3}{2}\left[1 - 16\left(y^*\right)^2\right] \tag{30}$$

in which y^* is the dimensionless coordinate defined as y/D_h with $D_h = 2h$, as obtained by Eq. (27) for $\beta = 0$. As depicted in Fig. 4, in this case the origin of the Cartesian coordinate system is assumed as placed at the center of the channel.

Pressure-Driven Single Phase Liquid Flows, Table 5 Laminar fully developed values of V_{max}, K_d, K_e, $K(\infty)$ and of the Poiseuille number ($f\mathrm{Re}_{fd}$) for rectangular microchannels as a function of the aspect ratio β

β	V_{max}	K_d	K_e	$K(\infty)$	$f\mathrm{Re}$
0	1.500	1.200	1.543	0.686	24.000
0.01	1.510	1.204	1.554	0.7	23.677
0.05	1.549	1.218	1.599	0.762	22.477
0.1	1.601	1.237	1.656	0.838	21.169
0.2	1.715	1.271	1.770	0.998	19.071
0.3	1.829	1.303	1.878	1.15	17.512
0.4	1.924	1.328	1.969	1.282	16.368
0.5	1.992	1.347	2.039	1.384	15.548
0.6	2.038	1.361	2.088	1.454	14.980
0.7	2.067	1.370	2.121	1.502	14.605
0.8	2.085	1.375	2.141	1.532	14.378
0.9	2.094	1.378	2.151	1.546	14.261
1	2.096	1.379	2.154	1.55	14.227

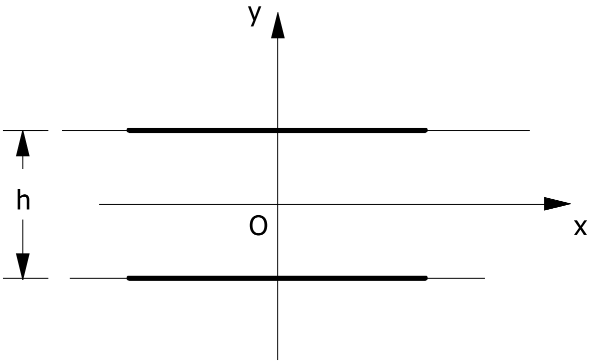

Pressure-Driven Single Phase Liquid Flows, Figure 4 Schematic of the parallel plate cross-section with its Cartesian coordinate system

The values assumed by V_{max}, K_d, K_e, $K(\infty)$ and $f\mathrm{Re}_{fd}$ are given in Table 5 for $\beta = 0$.

Triangular Channels

The fully developed laminar velocity profile for isosceles triangular ducts (see Fig. 5a) can be in general determined by solving numerically Eq. (11) with Eq. (12). Shah and London [4] reported the following approximate closed-form solution for the velocity profile for isosceles triangular channels:

$$V_z(x^*, y^*) = \frac{3(B+2)}{(B-2)}\left[4y^{*2} - x^{*2}\right]\left[x^{*B-2} - 1\right]$$
$$B = \left[4 + \frac{5}{2}\left(\frac{1}{\tan^2\phi} - 1\right)\right]^{\frac{1}{2}} \quad (31)$$

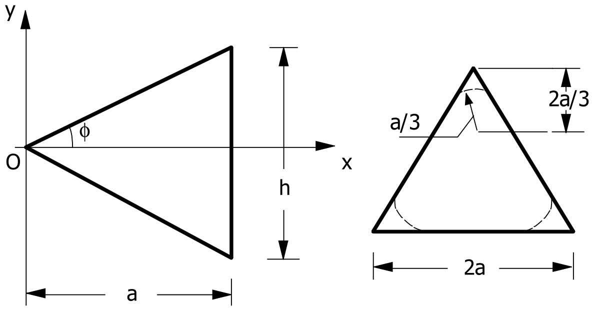

Pressure-Driven Single Phase Liquid Flows, Figure 5 Schematic of (**a**) the isosceles triangular cross-section and (**b**) an equilateral triangular microchannel with rounded corners

where x^* and y^* are dimensionless coordinates defined as x/a and y/h (see Fig. 5a). For the isosceles triangular ducts the hydraulic diameter can be calculated by means of the following equation:

$$D_h = \frac{a\sin\phi}{1+\sin\phi} = \frac{h\cos\phi}{1+\sin\phi} \quad (32)$$

It can be demonstrated that the maximum value of the velocity occurs at $y^* = 0$ (for the symmetry) and

$$x_m^* = \sqrt[B-2]{\frac{2}{B}} \quad (33)$$

The fully developed Poiseuille number can be calculated by means of the following equation:

$$f\mathrm{Re}_{fd} = \frac{12(B+2)(1-\tan^2\phi)}{(B-2)\left[\tan^2\phi + (1+\tan^2\phi)^{\frac{1}{2}}\right]^2} \quad (34)$$

The numerical results obtained by Shah and London [4] for V_{max}, K_d, K_e, $K(\infty)$ and $f\mathrm{Re}_{fd}$ for this geometry are quoted in Table 6.

Because the manufacturing processes employed sometimes produces microchannels of triangular cross-section with one, two or three rounded corners instead of sharp corners, in Table 7 the numerical results obtained by Shah and London [4] for an equilateral triangular microchannel with rounded corners in terms of V_{max}, K_d, K_e, $K(\infty)$ and $f\mathrm{Re}_{fd}$ are quoted. The radius of each rounded corner is considered as $a/3$, as shown in Fig. 5b, with $2a$ as the side length of the base triangle.

Trapezoidal Channels

It is well known that with a photolithographic-based process one can obtain microchannels having a cross-section fixed by the orientation of the wafer crystal planes; for example, the microchannels etched in ⟨100⟩ silicon using

Pressure-Driven Single Phase Liquid Flows, Table 6 Laminar fully developed values of x_m^*, V_{max}, K_d, K_e and of the Poiseuille number (fRe_{fd}) for isosceles triangular microchannels as a function of the apex angle ϕ or the aspect ratio a/h

a/h	ϕ	V_{max}	x_m*	K_d	K_e	fRe_{fd}
8.003	3.58	2.593	0.896	1.545	2.805	12.352
5.715	5.00	2.521	0.871	1.526	2.731	12.474
4.000	7.13	2.442	0.839	1.505	2.64	12.636
2.836	10.00	2.368	0.805	1.482	2.546	12.822
2.000	14.04	2.302	0.766	1.459	2.454	13.026
1.866	15.00	2.29	0.758	1.455	2.438	13.065
1.500	18.44	2.259	0.732	1.443	2.392	13.181
1.374	20.00	2.249	0.722	1.439	2.377	13.222
1.072	25.00	2.228	0.692	1.431	2.347	13.307
1.003	26.50	2.225	0.684	1.43	2.342	13.321
0.866	30.00	2.222	0.667	1.429	2.338	13.333
0.750	33.69	2.225	0.650	1.43	2.342	13.321
0.714	35.00	2.227	0.645	1.431	2.345	13.311
0.596	40.00	2.241	0.626	1.436	2.366	13.248
0.500	45.00	2.264	0.608	1.445	2.4	13.153
0.289	60.00	2.38	0.565	1.489	2.571	12.744
0.251	63.34	2.416	0.559	1.499	2.617	12.622
0.134	75.00	2.587	0.530	1.543	2.815	12.226
0.125	75.97	2.605	0.527	1.548	2.835	12.196

Pressure-Driven Single Phase Liquid Flows, Table 7 Laminar fully developed values of V_{max}, K_d, K_e and of the Poiseuille number (fRe_{fd}) for equilateral triangular microchannels with one, two, three rounded corners

	V_{max}	K_d	K_e	fRe_{fd}
No rounded corners	2.222	1.429	2.338	13.333
One rounded corner	2.172	1.406	2.254	14.057
Two rounded corners	2.115	1.379	2.163	14.899
Three rounded corners	2.064	1.353	2.074	15.993

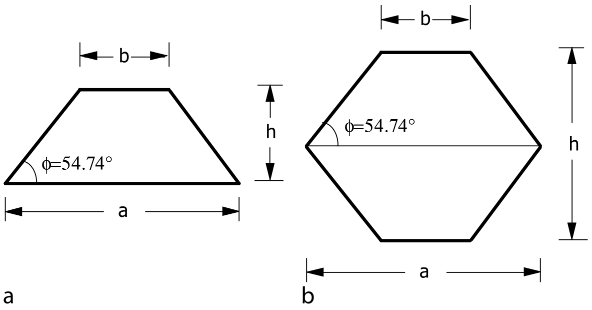

Pressure-Driven Single Phase Liquid Flows, Figure 6 (**a**) KOH-etched trapezoidal cross-section and (**b**) KOH-etched double-trapezoidal cross-section

a KOH solution have a trapezoidal cross-section with an apex angle of 54.74° imposed by the crystallographic morphology of the ⟨100⟩ silicon. By gluing together two KOH-etched trapezoidal silicon microchannels one can obtain microchannels having a double-trapezoidal cross-section (see Fig. 6). These cross-sectional geometries are investigated in this section.

Only numerical solutions of Eq. (11) have appeared in the open literature for this kind of geometry.

In Tables 8 and 9 the numerical results for KOH-etched trapezoidal and KOH-etched double trapezoidal microchannels respectively in terms of V_{max}, K_d, K_e, $K(\infty)$ and fRe_{fd} are given.

Two different definitions of the aspect ratio are used in the literature for trapezoidal channels ($\beta = h/a$ or $\gamma = h/b$ with reference to the symbols quoted in Fig. 6a). In Table 8, both β and γ are quoted in order to simplify the use of the data. For a ⟨100⟩ silicon microchannel the aspect ratio β cannot exceed the value of $\tan(\phi)/2$ (equal to 0.707 for $\phi = 54.74°$) corresponding to the degeneration of the channel cross-section to the triangular geometry ($\gamma = \infty$). The aspect ratio β of a double-trapezoidal channel is defined as the ratio between the height (h) and the maximum width (a); β can assume all the values between 0, the parallel plate configuration, and 1.414, the rhombic configuration.

Comparison Among Microchannel Cross-Sections

The data illustrated in the above sections can be used in order to minimize the pressure drop in a microfluidic

Pressure-Driven Single Phase Liquid Flows, Table 8 Laminar fully developed values of V_{max}, K_d, K_e, $K(\infty)$ and of the Poiseuille number ($f\mathrm{Re}_{fd}$) for KOH-etched trapezoidal microchannels as a function of the aspect ratio $\beta = h/a$ or $\gamma = h/b$

γ	β	V_{max}	K_d	K_e	$K(\infty)$	$f\mathrm{Re}_{fd}$
0	0.000	1.5	1.2	1.543	0.686	24
0.01	0.010	1.511	1.205	1.556	0.702	23.597
0.0277	0.027	1.530	1.212	1.580	0.736	22.931
0.05	0.047	1.555	1.222	1.610	0.776	22.174
0.1	0.088	1.610	1.243	1.674	0.862	20.737
0.2	0.156	1.719	1.279	1.793	1.028	18.650
0.3	0.211	1.822	1.310	1.897	1.174	17.244
0.4	0.255	1.908	1.334	1.984	1.300	16.263
0.5	0.293	1.976	1.354	2.054	1.400	15.565
0.6	0.325	2.027	1.368	2.108	1.480	15.060
0.7	0.352	2.065	1.379	2.150	1.542	14.690
0.8	0.375	2.094	1.388	2.182	1.588	14.417
0.9	0.396	2.116	1.394	2.207	1.626	14.215
1	0.414	2.132	1.399	2.225	1.652	14.063
1/0.9	0.432	2.146	1.403	2.241	1.676	13.940
1.25	0.452	2.158	1.407	2.254	1.694	13.832
1/0.7	0.473	2.168	1.410	2.266	1.712	13.745
1/0.6	0.497	2.177	1.412	2.275	1.726	13.685
2	0.522	2.183	1.414	2.282	1.736	13.654
2.5	0.551	2.189	1.415	2.287	1.744	13.654
1/0.3	0.583	2.196	1.417	2.294	1.754	13.679
5	0.620	2.206	1.420	2.307	1.774	13.694
10	0.660	2.219	1.426	2.330	1.808	13.622
∞	0.707	2.228	1.431	2.346	1.830	13.308

device with microchannels. In Fig. 7 a comparison among rectangular, KOH-etched trapezoidal microchannels and KOH-etched double-trapezoidal microchannels in terms of friction factor as a function of the aspect ratio β is shown. It is evident that, for a fixed value of the aspect ratio, the trapezoidal geometry allows the achievement of lower friction factors than the other cross-sections. The differences among the cross-sections in terms of friction factors decrease when the aspect ratio decreases.

A fifth-order polynomial approximation for calculating $f\mathrm{Re}_{fd}$, K_d and K_e as a function of the channel aspect ratio (β) is given with the aim of offering a very simple but accurate tool for technicians and designers involved in microfluidic applications:

$$f\mathrm{Re}_{fd} \text{ or } K_d \text{ or } K_e = \sum_{n=0}^{5} g_i \beta^n \qquad (35)$$

The values of the constants g_i are listed in Table 10 for microchannels having rectangular, trapezoidal and double-trapezoidal cross-sections;, the maximum relative differ-

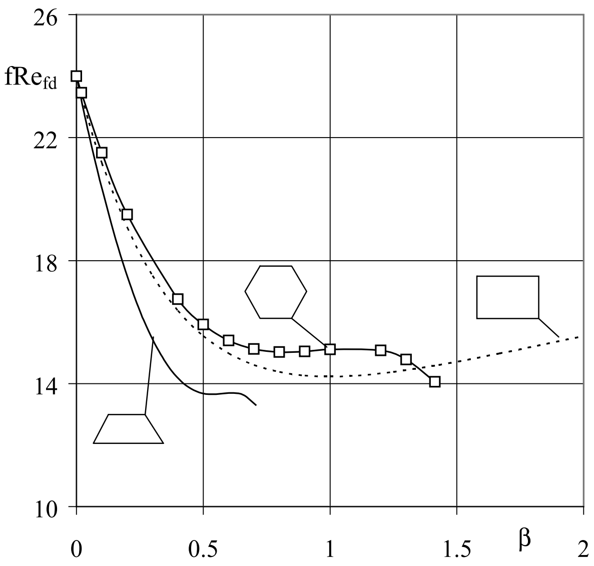

Pressure-Driven Single Phase Liquid Flows, Figure 7 Laminar fully developed Poiseuille number for KOH-etched trapezoidal microchannels, KOH-etched double-trapezoidal microchannels and rectangular microchannels as a function of the aspect ratio

Pressure-Driven Single Phase Liquid Flows, Table 9 Laminar fully developed values of V_{max}, K_d, K_e, $K(\infty)$ and of the Poiseuille number ($f\mathrm{Re}_{fd}$) for KOH-etched double-trapezoidal microchannels as a function of the aspect ratio β

β	V_{max}	K_d	K_e	$K(\infty)$	$f\mathrm{Re}_{fd}$
0	1.500	1.200	1.543	0.686	24.000
0.02	1.518	1.207	1.563	0.712	23.459
0.1	1.598	1.233	1.648	0.830	21.507
0.2	1.717	1.267	1.758	0.982	19.501
0.4	1.931	1.321	1.950	1.258	16.746
0.5	1.989	1.337	2.007	1.340	15.923
0.6	2.019	1.346	2.039	1.386	15.403
0.7	2.030	1.350	2.053	1.406	15.126
0.8	2.033	1.351	2.057	1.412	15.027
0.9	2.036	1.351	2.060	1.418	15.043
1	2.044	1.353	2.068	1.430	15.111
1.2	2.083	1.369	2.123	1.508	15.081
1.3	2.106	1.381	2.164	1.566	14.785
1.414	2.119	1.388	2.188	1.600	14.055

ence Δ quoted in Table 10 is positive when Eq. (35) gives values greater than the rigorous calculation.

Laminar-to-Turbulent Transition

The laminar regime in a channel holds until the Reynolds number reaches a critical value above which the laminar motion becomes unstable and a transition to a turbulent flow will generally occur. It has been demonstrated experimentally that for a microchannel the critical value of the Reynolds number depends on the entrance conditions, on the cross-section geometry and on the wall roughness. The effect of the roughness on the laminar-to-turbulent transition is very important and it can be evidenced by observing Fig. 8 in which the experimental values of the Poiseuille number ($f\mathrm{Re}$) are shown as a function of the Reynolds number for two microtubes made in stainless steel and in fused silica. The stainless steel microtube has an internal diameter of 133 μm and a relative roughness (e/D) equal to 3%, while the tube made in fused silica is characterized by an internal diameter equal to 100 μm and a relative roughness equal to 0.1%. The agreement with the Poiseuille law is confirmed for low values of the Reynolds number ($\mathrm{Re} < 1600$). The stainless steel microtube exhibits an earlier deviation from the Poiseuille law at Re equal to 1600. On the contrary, for the smoother microtube in fused silica the Poiseuille law holds up to Re equal to 2300. In general, for smooth microtubes the critical Reynolds number is about 2000 – 2300, in agreement with the behavior of macrotubes. On the contrary, for rough microtubes it can be concluded that higher relative roughness tends to anticipate the transition and thus decreases the value of the critical Reynolds number down to 1700 – 1800.

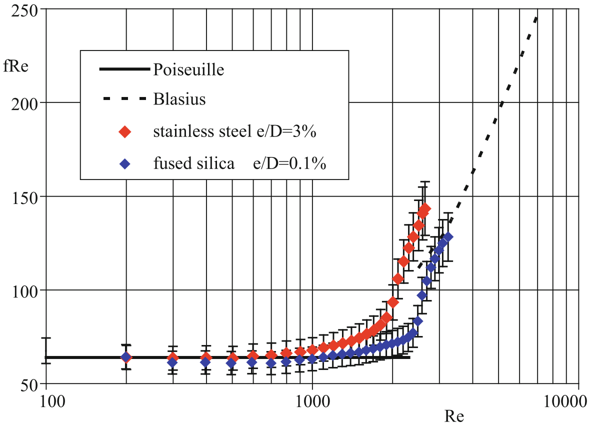

Pressure-Driven Single Phase Liquid Flows, Figure 8 Effect of the relative roughness on the laminar-to-turbulent transition in a microtube

Turbulent Regime

For Reynolds numbers larger than the critical Reynolds number the flow becomes turbulent and the fluid velocity at a point can be defined as the mean value of the velocity at this point with respect to time by taking a time interval t_0 larger than the typical time of one turbulent fluctuation and shorter than the typical time of pressure variations. Since mass and momentum must be conserved in turbulent as well as in laminar flow, the conservation equations (Eq. (1)) hold equally for turbulent flow, provided the velocities and pressures in these equations are interpreted as instantaneous velocities and pressures of the turbulent field. From a practical standpoint such equations are of little value because there is no interest in knowing the complete and complex history of instantaneous velocities and pressures but only their time-mean values that can be measured and observed (see also ▶turbulence in microchannels). In microchannels with hydraulic diameters less than 500 μm the maximum value that the Reynolds number can assume drops to between 10,000 and 30,000. In fact, in order to reach these values of the Reynolds number a very large pressure difference has to be imposed at the ends of the microchannels. For this reason, the analysis of the turbulence in microchannels is bounded to Reynolds numbers less than 30,000.

Circular Cross-Section

The time-mean value of the dimensionless velocity $\langle V_z \rangle$ can be written in fully developed turbulent flow in a micro-

Pressure-Driven Single Phase Liquid Flows, Table 10 Polynomial coefficients appearing in Eq. (35) for rectangular, KOH-etched trapezoidal and double-trapezoidal silicon microchannels

	g_0	g_1	g_2	g_3	g_4	g_5	Δ (%)
Rectangular microchannel $0 < \beta < 1$							
$f\mathrm{Re}_{\mathrm{fd}}$	24	−32.5272	46.7208	−40.8288	22.9536	−6.0888	0.06
K_d	1.2	0.3563	0.1532	−0.8946	0.7953	−0.2312	0.05
K_e	1.543	1.0376	1.1632	−3.8892	3.1821	−0.8831	0.10
KOH-etched trapezoidal microchannel $0 < \beta < 0.707$							
	g_0	g_1	g_2	G_3	g_4	g_5	Δ (%)
$f\mathrm{Re}_{\mathrm{fd}}$	24	−42.267	64.272	−118.42	242.12	−178.79	−0.14
K_d	1.2	0.3962	0.9808	−1.4388	−2.5004	3.3655	−0.27
K_e	1.543	1.1296	3.7251	−2.6799	−14.585	15.496	−0.68
KOH-etched double-trapezoidal microchannel $0 < \beta < 1.414$							
	g_0	g_1	g_2	g_3	g_4	g_5	Δ (%)
$f\mathrm{Re}_{\mathrm{fd}}$	24	−27.471	26.117	−6.6351	−0.2956	−0.5974	0.05
K_d	1.2	0.2833	0.5441	−1.7965	1.5499	−0.4277	−0.1
K_e	1.543	0.8343	2.3859	−6.9184	5.8104	−1.5876	−0.25

tube as follows:

$$\langle V_z \rangle = (1 - 2r^*)^{\frac{1}{m}}$$

$$m = \begin{cases} 6 & 4000 < \mathrm{Re} < 110{,}000 \\ 7 & 110{,}000 \le \mathrm{Re} < 3{,}200{,}000 \\ 10 & \mathrm{Re} > 3{,}200{,}000 \end{cases} \tag{36}$$

in which the following dimensionless quantities are used:

$$\langle V_z \rangle = \frac{\langle v_z \rangle}{\langle W \rangle}; \quad r^* = \frac{r}{D} \tag{37}$$

The ratio $\langle V_{\max} \rangle$ can be computed by using the following equation:

$$\langle V_{\max} \rangle = \frac{\langle v_{z,\max} \rangle}{\langle W \rangle} = \frac{(m+1)(2m+1)}{2m^2} \tag{38}$$

Parallel Plate Cross-Section

For shallow rectangular microchannels, having a low value of the aspect ratio β, the rectangular cross-section can be modeled as a parallel plate geometry (see Fig. 4). In this case one obtains that the velocity distribution for fully developed turbulent flows becomes the following:

$$\frac{\langle v_z \rangle}{v^*} = \frac{1}{k}\left[\ln\left(1 - \sqrt{4y^*}\right) + \sqrt{4y^*}\right] + \frac{\langle v_{z,\max} \rangle}{v^*} \quad \left(0 \le y^* \le \frac{1}{4}\right) \tag{39}$$

in which $y^* = y/D_h$ with $D_h = 2h$, ($\boldsymbol{\tau}_0$ is the wall shear stress) and $k = 0.36$.

Friction Factor

For Newtonian fluids, the Fanning friction factor f is defined in terms of the wall shear stress as

$$f = \frac{\boldsymbol{\tau}_0}{\frac{\rho W^2}{2}} \tag{40}$$

For turbulent fully developed flow ($\mathrm{Re} > 10{,}000$) in a *smooth* microtube, the Fanning friction factor can be calculated from the *Karman–Nikuradse relation*:

$$\frac{1}{\sqrt{4f_{\mathrm{fd}}}} = -0.8 + 0.87 \ln\left(\mathrm{Re}\sqrt{4f_{\mathrm{fd}}}\right) \tag{41}$$

In the range $5000 < \mathrm{Re} < 30{,}000$, in which in general microtubes could work, the *Blasius equation* may be used instead of Eq. (41) for smooth tubes:

$$f_{\mathrm{fd}} = \frac{0.079}{\mathrm{Re}^{0.25}} \tag{42}$$

In *rough* microtubes, like metallic microtubes, the effect of the inner roughness e on the friction factor cannot be neglected and the friction factor can be calculated by using the *Colebrook correlation*:

$$\frac{1}{\sqrt{4f_{\mathrm{fd}}}} = -2.0 \log\left[\frac{\frac{e}{D_h}}{3.7} + \frac{2.51}{\mathrm{Re}\sqrt{4f_{\mathrm{fd}}}}\right] \tag{43}$$

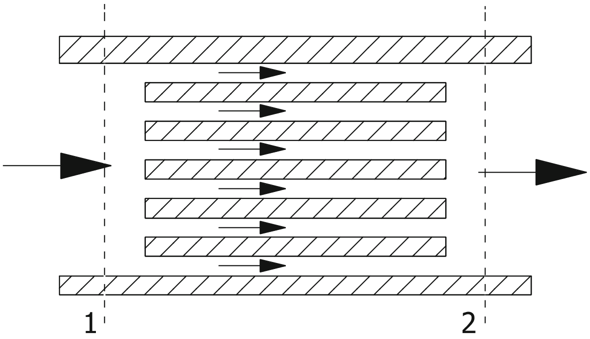

Pressure-Driven Single Phase Liquid Flows, Figure 9 Model for pressure drop analysis of multiple microchannel systems

Since the *Colebrook correlation* is awkward to use, an approximate explicit relation for the friction factor was published by *Haaland*:

$$\frac{1}{\sqrt{4f_{\text{fd}}}} = -1.8\log\left[\left(\frac{\frac{e}{D_{\text{h}}}}{3.7}\right)^{1.11} + \frac{6.9}{\text{Re}}\right] \quad (44)$$

This relation gives values within 2% of the *Colebrook correlation*.

Typical values of the relative roughness defined as the ratio e/D_{h} in microchannels vary between 0.0001 (glass microtubes) and 0.1 (stainless steel microtubes).

Pressure Drop Calculation

Pressure drop evaluation for flow through both single-microchannel and multiple-microchannel systems is very important in the design of microfluidic devices.

The model for the pressure drop analysis is depicted in Fig. 9 in which multiple microchannels with an abrupt entrance and exit are shown. The equations to be presented in this section apply to this model and are not restricted to a particular geometry of the microchannel cross-section.

They are applicable to single-microchannel flow by reducing the appropriate terms. The general relation for flow-stream pressure drop calculations is the following:

$$\Delta p = \frac{\rho_1 W_1^2}{2}\left[\left(K_{\text{c}} + 1 - \sigma^2\right) + 2\left(\frac{\rho_1}{\rho_2} - 1\right) + 4f\frac{L}{D_{\text{h}}}\frac{\rho_1}{\rho} - \left(1 - \sigma^2 - K_{\text{ex}}\right)\frac{\rho_1}{\rho_2}\right] \quad (45)$$

in which L is the microchannel length, W_1 is the average velocity defined by Eq. (9) and based on the minimum free flow area, σ is the free flow/frontal area ratio ($\sigma = 1$ for a single microchannel), K_{c} and K_{ex} represent entrance and exit loss coefficients and ρ is given by

$$\frac{1}{\rho} = \frac{1}{L}\int_0^L \frac{1}{\rho}\,\text{d}z \quad (46)$$

The terms involved in Eq. (45) in order to calculate the total pressure drop represent:

- the entrance effects (see ►developing flow and ►entrance region);
- the flow acceleration effect for a compressible fluid;
- the usual friction pressure drop;
- the exit effects.

In order to investigate only the entrance pressure drop Eq. (45) can be reduced as follows:

$$\Delta p_{\text{inlet}} = \frac{\rho_1 W_1^2}{2}\left(1 - \sigma^2\right) + K_{\text{c}}\frac{\rho_1 W_1^2}{2} \quad (47)$$

in which the first term is the pressure drop which would occur due to a change in the cross-section alone, without friction, and the second term represents the loss due to irreversible free expansion that follows the abrupt contraction. The irreversible component of the pressure drop is contained in the abrupt contraction or entrance coefficient K_{c}. The exit pressure rise is similarly broken into two parts:

$$\Delta p_{\text{exit}} = \frac{\rho_1 W_1^2}{2}\left(1 - \sigma^2\right) - K_{\text{ex}}\frac{\rho_1 W_1^2}{2} \quad (48)$$

The first is the pressure rise which occurs due to the area change alone, without friction, and is identical to the corresponding term in the entrance pressure drop. The second term is the pressure loss associated with the irreversible free expansion following an abrupt expansion and this term in the present case subtracts from the other.

The values of K_{c} and K_{ex} have been established analytically for a number of simple entrance and exit geometries and are quoted in many textbooks [9]. These coefficients have been evaluated on the assumption of essentially uniform velocity in the manifolds linked to the microchannels but by considering a fully established velocity profile in the microchannels (that means $L \gg D_{\text{h}}$). These assumptions can be considered verified for long microchannels for which $L > 100D_{\text{h}}$.

In applying the data related to the values of K_{c} and K_{ex} it should be remembered that these coefficients already include the pressure change associated with change in velocity profile.

Thus the friction factor used in Eq. (45) to evaluate the overall pressure drop should be defined on the basis of the mean wall shear stress after the entrance region and not on the basis of the overall pressure drop.

For liquids for which the incompressible model holds Eq. (45) can be simplified as follows:

$$\Delta p = \frac{\rho_1 W_1^2}{2}\left[K_c + 4f\frac{L}{D_h} + K_{ex}\right] \quad (49)$$

where f is the friction factor based on the mean wall shear stress after the entrance region.

For long microchannels for which $L \gg D_h$ (this condition is very common in microchannels) one can use the fully developed value of the friction factor in the calculation of the pressure drop:

$$\Delta p = \frac{\rho_1 W_1^2}{2}\left[K_c + 4f\mathrm{Re}_{fd}\frac{L}{\mathrm{Re}D_h} + K_{ex}\right] \quad (50)$$

To eliminate the uncertainties caused by estimation of minor losses (K_{ex}, K_c) many authors have suggested performing tests with microchannels of different lengths; in this manner it is possible to even out the inlet and outlet minor losses by subtracting the pressure drop of the shorter tube from that of the longer one for a fixed value of the average Reynolds number. By following this method, the value of the friction factor would be calculated as follows:

$$f_{fd} = \frac{\rho}{2\mu^2}\left(\frac{\Delta p(L_1) - \Delta p(L_2)}{L_1 - L_2}\right)\frac{D_h^3}{\mathrm{Re}^2} \quad (51)$$

where L_1 and L_2 are the lengths of the longer and shorter tube respectively.

It is important to observe that this method is in general valid for liquid flows in microchannels but becomes unsuitable for gaseous flows when the effects of compressibility are strong, as the values of the minor losses at the inlet and at the outlet, even for a fixed average value of the Reynolds number, can be very different.

When the initial velocity profile is uniform and there are no abrupt contraction ($K_c = 0$) and expansion ($K_{ex} = 0$) one can take into account the effects of momentum change in the entrance region by using $K(\infty)$ which includes the increased wall shear in the entrance region but separates out the downstream fully developed flow pressure drop due to wall shear to give

$$\Delta p = \frac{\rho_1 W_1^2}{2}\left[4f\mathrm{Re}_{fd}\frac{L}{\mathrm{Re}D_h} + K(\infty)\right] \quad (52)$$

Experimental Results

As mentioned above, the first experimental work in which water through glass microtubes with an inner diameter down to 15 μm was tested was due to Poiseuille in 1840 [2]. The experimental data obtained by Poiseuille were used to state the famous *Poiseuille law* for laminar flows through circular tubes, according to which for Stokes flows the product of the friction factor times the Reynolds number is a constant (equal to 16 for circular tubes) that depends on the cross-section geometry only.

On the contrary, as evidenced in [10], many experimental works published in the last decade seem to be partially in disagreement with the conventional theory and if these results are used in order to establish the validity of the conventional theory for microchannels in laminar and turbulent regime the answer obtained is not unequivocal. In fact, some authors found that the predictions of the conventional theory agree with the experimental results on the friction factor; however, for the same range of hydraulic diameters, some other authors found the opposite result.

It is possible to sum up the main results quoted in the open literature on the friction factor in microchannels highlighting the peculiarities, proposed by different authors, with respect to the conventional macrochannels:

- the friction factor for laminar fully developed flow is found to be smaller or larger than the conventional value;
- the Poiseuille number for laminar fully developed flow depends on the Reynolds number;
- the fully developed turbulent friction factor seems to be in disagreement with the *Blasius equation* for smooth microchannels and with the *Colebrook correlation* for rough microchannels;
- the friction factor depends on the material of the microchannel walls (metals, semi-conductors and so on) and/or on the test liquid (polar fluid or not), thus evidencing the importance of electro-osmotic phenomena at microscales;
- the friction factor depends on the relative roughness of the walls of the microchannels also in the laminar regime.

However, from a chronological analysis of the experimental results of the literature it is possible to extrapolate how the deviations of the behavior of fluid flow through microchannels from that through large-sized channels are decreasing. This fact can be explained by taking into account the dramatic improvement of the techniques of microfabrication with the consequent reduction of the issues of surface roughness of the microchannels and a more appropriate control of the channel cross-sections; for this reason the results of the older studies may not provide useful comparisons. Another possible explanation of the decrease of the observed deviations is related to the increase of the reliability/accuracy of the more recent experimental data quoted in literature. This seems to be confirmed by the increasing number of experimental results on the friction factor of the last few years, which confirm the success of conventional correlations in pre-

dicting pressure drop for Newtonian liquids in microchannels having inner hydraulic diameters down to 10 μm.

Future Directions for Research

The analysis of the behavior of single phase Newtonian liquid flow through microchannels in laminar and turbulent regime evidenced that the conventional theory validated for large channels holds for hydraulic diameters down to 10 μm. Further investigations are required for non-Newtonian flows, like polymer solutions and surfactants, for which slip velocity at the walls has been observed even for microchannels having a hydraulic diameter greater than 1 μm. In addition, an accurate analysis of the critical Reynolds numbers for which the laminar-to-turbulent transition occurs in microchannels of different cross-sectional geometry (for Newtonian and non-Newtonian liquids) could be important to improve the understanding of the rules of the development of turbulence at the microscale.

Cross References

▶ Entrance Region
▶ Developing Flow
▶ Pressure-Driven Single Phase Gas Flows
▶ Turbulence in Microchannels

References

1. Hagen G (1839) On the Motion of Water in Narrow Cylindrical Tubes. Pogg Ann 46:423
2. Poiseuille JM (1840) Recherches expérimentales sur le mouvement des liquides dans les tubes de très petits diamètres. C R Hebd Acad Sci 11:961–967, 11:1041–1048
3. Bird RB, Stewart WE, Lighfoot EN (1960) Transport Phenomena. Wiley, New York
4. Shah RK, London A (1978) Laminar Flow Forced Convection in Ducts. Adv Heat Transf 14(1):477
5. Jones OC (1976) An Improvement in the Calculation of Turbulent Friction Factor in Rectangular Ducts. Trans ASME J Fluid Eng 98:173–181
6. Obot NT (1988) Determination of Incompressible Flow Friction in Smooth Circular and Noncircular Passages. A Generalized Approach Including Validation of the Century Old Hydraulic Diameter Concept. Trans ASME J Fluid Eng 110:431–440
7. Idelchick IE (1986) Handbook of Hydraulic Resistance, Chap 2. Begell, Redding
8. Celata GP, Cumo M, Guglielmi M, Zummo G (2000) Experimental Investigation of Hydraulic and Single Phase Heat Transfer in 0.130 mm Capillary Tube. Proc Int Conf Heat Transf Transport Phenomena Microscale: 108–113
9. Rohsenow WM, Hartnett JP (1973) Handbook of Heat Transfer, Chap 7. McGraw Hill, New York
10. Morini GL (2004) Single-phase Convective Heat Transfer in Microchannels: a Review of Experimental Results, Int J Therm Sci 43:631–651

Pressure-Driven Two Phase Flows

LINGLING SHUI, JAN C. T. EIJKEL,
ALBERT VAN DEN BERG
BIOS, Lab-on-a-Chip Group, MESA+ Institute
for Nanotechnology, Enschede, Netherlands
L.shui@ewi.utwente.nl

Synonyms

Two-phase flow driven by pressure

Definition

Pressure-driven ▶ two phase flows are flows of two immiscible fluids in the same micro- or nanofluidic conduit driven by a pressure gradient. The fluids can be of different chemical compositions – liquid/liquid, or in different physical states – gas/liquid.

Overview and Theory

In the past decade, micro- and nanofluidics has been studied in great detail because of the increasing availability of methods for fabricating complicated flow configurations and measuring transport phenomena on the micro and nanoscales. The micro- and nanofluidic channel systems with integrated pumps, valves, and detectors, are known as ▶ Lab-on-a-Chip (LOC) or ▶ micro total analysis system (μTAS) [1]. Ideally, each process – e. g., sampling, sample pretreatment, reaction, separation, detection and analysis in an analytical system – is realized on one integrated device. Fluid mechanics studies in these processes therefore are indispensable for the design and fabrication of LOC and μTAS.

Fluids that are of interest in nature, biotechnology and chemistry, are rarely simple single-phase fluids. Most compartmental chemistry, interfacial phenomena and applications employ two-phase flows. It is therefore not surprising that recently a surge of interest has arisen in two-phase microfluidic manipulation.

Compared to single-phase flow systems, when discussing two-phase flow in micro- and nanosystems, there are many questions that arise even in a simple configuration. When two phases flow in the same conduit or channel, the flow patterns change between droplet-base flows and stratified flows depending on the physicochemical properties of fluids and channel surfaces. At the same time, in two-phase flow systems, several flow phenomena, such as film flow, corner flow and slip flow play increasingly important roles with reduction of the dimensions. Both advantages and disadvantages originate from the reduction in dimension

and the coexistence of two phases. In all these phenomena, the fluid manipulation is no doubt the most important factor.

Manipulating fluids in a two-phase flow system is much more complicated than in single-phase systems. Fluid flows can be actuated spontaneously, non-mechanically or mechanically. The most frequently used flow actuation method, till now, is still pressure-driven pumps due to their availability and versatility. Especially, for a two-phase flow system, the naturally existing inhomogeneity makes other methods much more difficult to be applied. Electroosmosis for instance, resulting from the force exerted on a space-charge region in the liquid by an electric field, will not work if the conductivity continuum in the fluid is interrupted by an entrapped dielectric liquid droplet or gas bubble.

Fluid flow in channels of constant cross-sectional shape can be simply described by Poiseuille's law:

$$Q = \int v_i \, dA \approx \frac{\Delta P}{R_{hy}} \tag{1}$$

where Q ($m^3 s^{-1}$) is the volume flow rate, v_i ($m s^{-1}$) is the flow velocity at the position i, A (m^2) is the area of cross section. The hydrodynamic resistance, R_{hy}, can be approximately expressed as:

$$R_{hy} \approx \eta l C^2 A^{-3} \tag{2}$$

where η (Pa s) is the fluid viscosity, l (m) is the channel length, and C (m) is the perimeter of the cross section. ΔP (Pa) is the pressure difference between two ends of the fluid, which is the total pressure acting on the fluids. It is the sum of externally applied pressure ($P_{ex.}$) and the internal (capillary) pressure ($P_{cap.}$):

$$\Delta P = P_{ex.} \mp P_{cap.} \tag{3}$$

If there is a positive capillary pressure in a channel, the externally applied pressure has to exceed it to pump fluid, and inversely fluid can be automatically imbibed in a microchannel if there exists a negative capillary pressure (capillary action). Therefore, pressure-driven flows can be manipulated not only by externally applied pressure but also by the internally generated capillary pressure.

The dynamical response of two-phase flows can be commonly characterized successfully in terms of the dimensionless numbers [2]. Table 1 lists some force-related dimensionless numbers. These dimensionless numbers demonstrate competing phenomena of forces: buoyancy, gravitational, inertial, viscous and interfacial forces. The Grashof number (buoyancy to viscous forces), the Bond number (gravitational to interfacial forces) and the Reynolds number (inertial to viscous forces) scale with the third, the second and the first power of flow dimensions, respectively. The relative importance of the different forces that act on fluids therefore dramatically changes on downscaling. With downscaling, the buoyancy, gravitational and inertial forces become less and less important and viscous and interfacial forces become more and more predominant. In micro-systems, the relative importance of forces, calculated for a water/oxygen two-phase flow, is given by the following order: buoyancy forces < inertial forces < gravitational forces < viscous forces < interfacial forces.

Of these dimensionless numbers, the Reynolds number is the most frequently used number to describe microfluidics. It expresses the ratio of inertial forces to viscous forces:

$$\mathrm{Re} = \frac{\rho v L}{\eta} \tag{4}$$

where ρ ($kg\,cm^{-3}$) is the effective density, v ($m s^{-1}$) is the average flow velocity, L (m) is the characteristic flow dimension, and η (Pa s) is the effective viscosity. In a straight channel, the value of $\mathrm{Re} \approx 10^3$ is accepted as a limit for the transition from a laminar flow to a turbulent flow. In a straight micro- or nanochannel with diameters between 100 nm and 100 μm, where $\eta(H_2O) = 1.025 \times 10^{-3}$ Pa s, $\rho(H_2O) = 10^3\ kg\,m^{-3}$ and $v = 1\ mm\,s^{-1}$, the calculated Reynolds number lies between 10^{-1} and 10^{-4}. For a gas, oxygen for instance, $\eta(O_2) = 20.317 \times 10^{-6}$ Pa s and $\rho(O_2) = 1.429\ kg\,m^{-3}$, the Reynolds number at these channel dimensions ranges from 10^{-5} to 10^{-2}. Therefore, inertial forces are over-

Pressure-Driven Two Phase Flows, Table 1 Important force-related dimensionless numbers in two-phase microfluidics and scaling with device dimension L

Dimensionless number	Definition	Equation	Scaling	Value*
Grashof	Buoyancy/Viscous	$\frac{L^3 \rho^2 g \beta \Delta T}{\eta^2}$	3	10^{-4}
Bond	Gravitational/Interfacial	$\frac{(\rho - \rho_f) g L^2}{G\sigma}$	2	10^{-5}
Reynolds	Inertial/Viscous	$\frac{\rho v L}{\eta}$	1	10^{-1}
Capillary	Viscous/Interfacial	$\frac{\eta v}{G\sigma}$	0	10^{-4}

* For a water-oxygen two-phase flow: $T = 20°$, $\eta(O_2) = 20.317 \times 10^{-6}$ Pa s, $\eta(H_2O) = 1.025 \times 10^{-3}$ Pa s, $\sigma(H_2O) = 72.8\ mN\,m^{-1}$, $\rho(H_2O) = 10^3\ kg\,m^{-3}$, $\rho(O_2) = 1.429\ kg\,m^{-3}$, θ(water and glass) $\approx 50°$, β(water at 20 °C) $= 0.00021\ °C^{-1}$ assuming that $L = 10\ \mu m$, $v = 1\ cm\,s^{-1}$ and $g_c = 1$

L – channel dimension, ρ – fluid density, g – gravity acceleration constant, β – coefficient of expansion, ΔT – temperature difference, η – fluid viscosity, ρ_f – surrounding fluid density, f – subscript of density, G – geometrical constant, σ – interfacial force, v – flow velocity

whelmed by viscous forces in microfluidic devices. Laminar flows are thus expected in micro- and nanochannels for both gas and liquid, and not turbulent or random flows. The forces acting on two-phase fluids can be divided into tangential and normal components. On the micro- and nanoscales, as shown in Table 1, a pair of competitive forces – the viscous force and the interfacial force – become dominant. The viscous forces mainly act tangential to the interface elongating it, whereas the interfacial forces act normal to the interface inducing droplet or bubble formation (minimizing the interfacial area). The capillary number is the ratio of these two competitive forces, and can be expressed as:

$$\mathrm{Ca} = \frac{\eta v}{G\sigma} \tag{5}$$

where η (Pa s) is the viscosity of continuous phase, G is a geometrical constant, and σ ($\mathrm{N\,m^{-1}}$) is the interfacial tension. The capillary number is independent of flow dimensions, and can be controlled by the properties of fluids and channels and the interactions between them. It is the most useful dimensionless number to describe two-phase microfluidic flow phenomena including flow formation, sizing, coalescing, mixing and splitting.

Keeping in mind that two-phase flows include both liquid-liquid systems, and gas-liquid systems, the different behavior of a gas and liquid must be emphasized before discussing two-phase flows. The average distance between molecules in a gas phase is one order of magnitude higher than the diameter of its molecules, while it approaches the molecular diameter in a liquid phase. Therefore, in some microdevices the gas is compressed when the pressure strongly changes. The Mach number Ma is a dynamic measure of fluid compressibility, and is defined as the ratio of flow velocity (v) to sound speed (a):

$$\mathrm{Ma} = \frac{v}{a} \tag{6}$$

The flow of a compressible fluid like air can be treated as incompressible if the local Mach number is less than 0.3. Ma is very small in microfluidic systems due to the low flow velocity. Compression however might still occur in the case of density gradients, for instance by high local pressure changes, wall heating or cooling. In that case, equations for compressible flow must be applied [3]

Basic Methodology

Channel Geometries

Two-phase flows can be easily generated by combining flow of different phases in certain channel geometries. The basic channel configurations used to generate multiphase flows are T, Y or cross junctions (Fig. 1).

Pumping by Externally Applied Pressure

In micro- and nanofluidic devices, a pressure is normally externally applied by syringe pumps or vacuum pumps. The pressure difference, generated at two ends of fluids, pushes or pulls fluid to move, and the resulting volume flow rate is expressed by Eq. (1).

The advantage of syringe or vacuum pumping is its versatility. It can be applied to drive all kinds of fluids (gas, liquid or gas-liquid two-phase fluids), and theoretically, it can also be used on all scales as long as the pressure is high enough to overcome the flow resistance. However, the hydrodynamic resistance in a channel is proportional to flow distance and inversely proportional to the fourth power of the channel size, and therefore, very high pressure is necessary to drive flows in smaller channels. For example, without capillary pressure, calculated from Eq. (1), to have water flow with $1\,\mathrm{cm\,s^{-1}}$, in a $10\,\mu\mathrm{m}$ diameter channel of 1 mm length 10^3 Pa is needed, however, 10^7 Pa has to be applied for the same flow in a 100 nm diameter channel.

Syringe pumping and vacuum pumping remain predominant in microfluidic flows. Fluid flows driven by capillarity become more efficient on downscaling due to its favorable scaling behavior.

Pumping by Capillary Pressure

A hydrophilic liquid, water for instance, *pulls* itself into or through a hydrophilic micro- or nanochannel by capillary action which is induced by interfacial tensions (Fig. 2a). The capillarity-induced pressure pulling the liquid along the channel (Fig. 2a and 2b) is expressed by Young–Laplace's equation:

$$P_{\mathrm{cap.}} = G\sigma_{\mathrm{lg}} \cos\theta\, d^{-1} \tag{7}$$

where G is a geometrical constant, d (m) is the characteristic diameter, σ_{lg} ($\mathrm{N\,m^{-1}}$) is the liquid-gas interfacial tension, and θ (degree) is the contact angle which is set up when a liquid droplet contacts both a solid and a gas (or a solid and a second immiscible liquid) (Fig. 2c and 2d). The liquid curvature of the droplet is caused by the differences among interfacial tensions. The force balance is described by Young's equation:

$$\sigma_{\mathrm{sg}} = \sigma_{\mathrm{sl}} + \sigma_{\mathrm{lg}} \cos\theta \tag{8}$$

where σ_{sg} and σ_{sl} ($\mathrm{N\,m^{-1}}$) indicate the interfacial tensions of solid-gas and solid-liquid, respectively. Fluids,

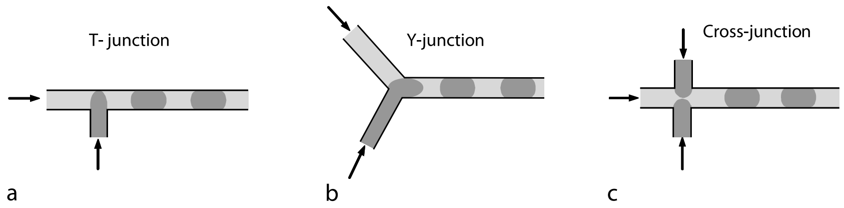

Pressure-Driven Two Phase Flows, Figure 1 Configurations for two-phase flows: (**a**) T-junction, (**b**) Y-junction and (**c**) Cross-junction

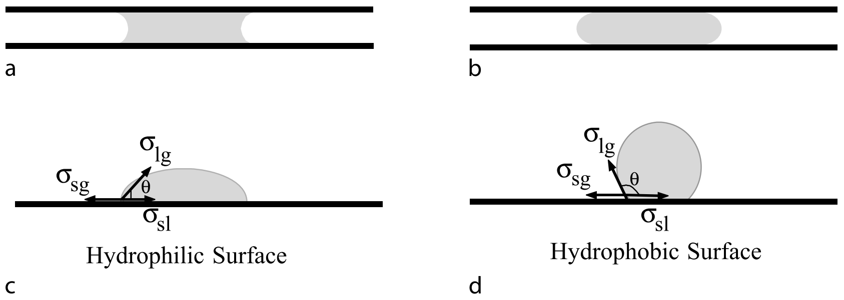

Pressure-Driven Two Phase Flows, Figure 2 Water (**a**) in a hydrophilic channel, (**b**) in a hydrophobic channel, (**c**) on a hydrophilic surface and (**d**) on a hydrophobic surface.

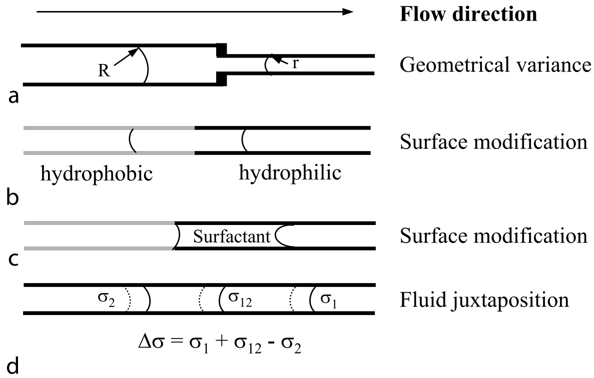

Pressure-Driven Two Phase Flows, Figure 3 Capillary pressure induced by (**a**) Geometrical variance, (**b**) Surface modification (solid), (**c**) Surface modification (liquid), (**d**) Fluid juxtaposition (bi-slug)

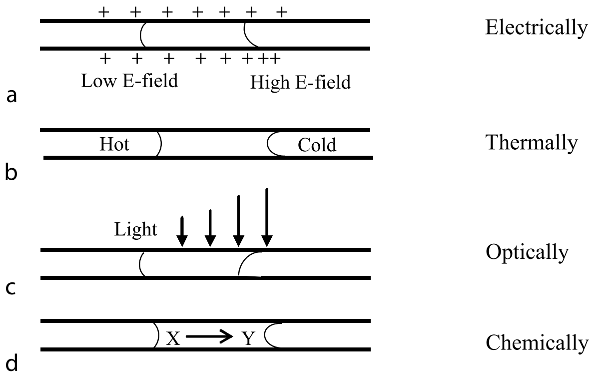

Pressure-Driven Two Phase Flows, Figure 4 Interfacial forces modulated (**a**) Electrically, (**b**) Thermally, (**c**) Optically and (**d**) Chemically

therefore, can be spontaneously propelled by a capillarity-induced pressure gradient.

In a channel, the motion of a fluid segment can result from the capillarity-induced pressure difference between the front and a rear of the fluid column. Such a pressure difference (ΔP) is described by:

$$\Delta P = P_{\mathrm{cap.2}} - P_{\mathrm{cap.1}} = G\sigma_{\mathrm{lg}} \left(\frac{\cos\theta_2}{d_2} - \frac{\cos\theta_1}{d_1} \right) \quad (9)$$

According to the equation, the pressure difference can be obtained by changing the channel diameter (d), the interfacial tension (σ) or the contact angle (θ). Therefore, self-propelling slugs can be realized by careful design, material selection, microfabrication, and surface control and processing. For example, a slug will move from the wide part to the narrow part when the channel diameter changes (Fig. 3a). The movement can also be realized by using different channel materials (Fig. 3b) or fluids (Fig. 3c) with different interfacial energy. Similar phenomena happen for two or more juxtaposed phases (Fig. 3d). The motion can even be inverted by juxtaposing a liquid of low surface tension.

Furthermore, interfacial tensions can be tuned electrically (Fig. 4a), thermally (Fig. 4b), optically (Fig. 4c), chemically (Fig. 4d), or by combinations of them such as optic-electrically.

Flow Phenomena

Flow patterns

Two-phase flow in microfluidic systems is broadly categorized into ► segmented (droplet-based) flow and ► parallel (stratified) flow architectures. Gas-liquid two-phase flows in microchannels have been studied in detail for heat-exchanger applications. Between segmented flows and stratified flows there can be several other flow patterns – bubbly flow, ring flow, lump flow and annular flow (Fig. 5a) [4]. The flow of immiscible liquids has been successfully manipulated to study chemical reactions and for biotechnology purposes. The two-phase microchannel flows change from the droplet-based flows to stratified flows depending on the flow rate and fluid composition, in a manner ultimately dependent on the capillary number (Eq. (5), Fig. 5b) [5].

Immiscible gas-liquid and liquid-liquid mixtures form droplet-based flows over a wide range of flow conditions and channel dimensions without additional control due to interfacial forces. Vice versa, two immiscible streams would flow alongside one-another if there were no interfacial forces between them. Theoretically, a stable elongated interface between two phases only occurs when tangential forces (viscous shear forces) are equal to or greater than normal forces (interfacial forces), i.e, at higher capillary number. Figure 5c shows a typical example of a two-phase flow transition according to the capillary number [6]. Two streams of water are added to a carrier liquid in a cross configuration. The two streams of water coalesce to form a big droplet-based flow at extremely small Ca (~ 0.0004). By increasing Ca, alternating droplet-based flow is generated with decreased droplet size. Droplet size (R) in a two-phase flow depends on the channel size (h) and the capillary number: $R \sim h/\mathrm{Ca}$ [7]. Finally, stratified flow is obtained for $\mathrm{Ca} > 0.15$ at a water fraction of 0.2.

Based on the definition of the capillary number, the two-phase flow patterns in microchannels can be influenced by interfacial forces (σ), fluid viscosity (η), flow velocity (v) and geometric features (G). The interfacial forces can be modulated by adding surfactants, surface coating and patterning techniques, but also by electrical, thermal or optical modulations of the interfacial tensions (see previous section). The fluid viscosity will be changed by changing temperature or adding polymers. The flow velocity is mainly tuned by actuation forces and geometrical tailoring. The geometric features include designing smart geometries and adding microtextures inside micro- and nanofluidic devices.

When two immiscible phases come into contact at a junction, an approximately parabolic flow profile can be obtained for a two-phase stratified flow in a common pressure-driven microfluidic system. On the other hand, in a droplet-based flow, stimulated by the shear between the stationary fluid at the channel wall and the slug axis, there exists internal recirculation in both continuous and dispersed phases [8]. Complex flow patterns may appear under different conditions, depending on the forces acting on the fluids.

Whether a stable two-phase flow can be obtained in a fluidic system depends on both fluid dynamic conditions and surface chemistries. The aim is to open the way to control the flow and to achieve versatility and reproducibility in on-chip flow management. The design will require smart network topologies and interplay of multiple physical and chemical effects.

Slip Flow

Traditional *non-slip* assumptions have been doubted for a long time in microfluidic systems. Recently, the results from molecular dynamics simulations and experiments on micro- and nanoscales strongly indicate the existence of slip flow. Theoretically, fluids will slip when the attraction between fluids molecules is stronger than the wall/fluid molecule attraction. The amount of slip is described as the slip length which is the notional distance inside the surface at which the velocity equals to zero (Fig. 6a).

Molecular dynamics (MD) simulations have shown that slip can occur only when a critical surface shear stress is reached, and that there exists a general relationship (linear or nonlinear given by different results) between the slip length and the local shear rate at a solid surface. Significant slip has been experimentally demonstrated by driving different fluids through micro- and nanochannels. Slip length depends on the interactional parameters between solid and fluid: shear stress, wetting properties, fluid properties (e. g., viscosity and density) and interfacial roughness.

Different fluids have different interactions with each other or with solid surfaces. The fluid/fluid intermolecular interactions can be stronger or weaker than those of fluid/solid surfaces. Therefore, in two-phase flows, boundary conditions are much more complicated. As diagnostic techniques improve our ability to probe the fluid surface at the molecular scale, it is expected that slip flows can be investigated by direct measurement of fluid velocity or the movement of contact lines.

Film Flow

When droplet-based multiphase flow is considered, there are two possible configurations. In the first, a drop forms a distinct contact line with the walls of the channel. In the other, a drop is separated from the boundaries by a thin wetting film. Because of the affinity of fluids and surfaces,

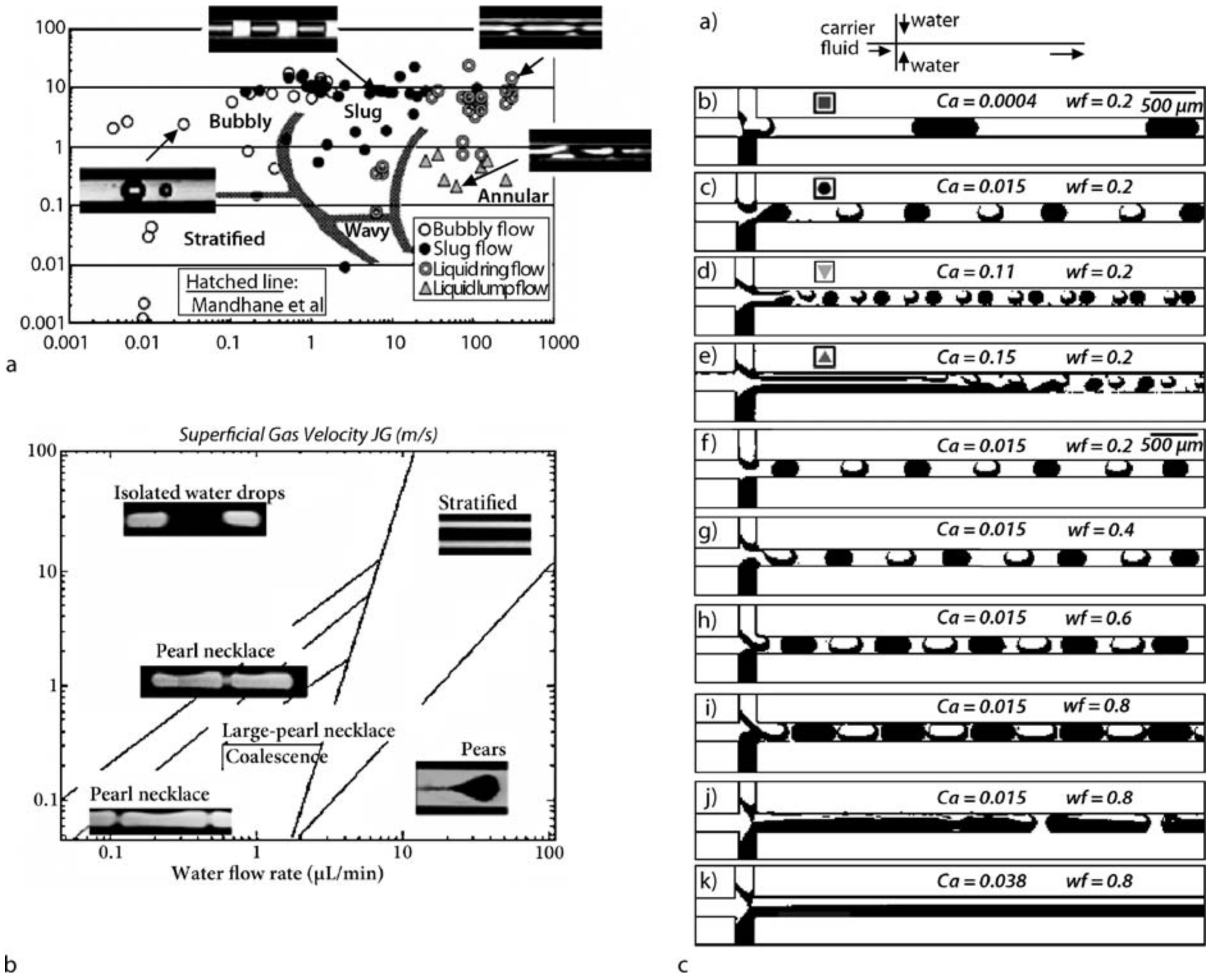

Pressure-Driven Two Phase Flows, Figure 5 (**a**) Phase diagram of a gas-liquid two-phase flow. Reprinted from [4] with permission of Elsevier. (**b**) Phase diagram of a liquid-liquid two-phase flow. Reprinted from [5] with permission of the American Physical Society. (**c**) Two-phase flow patterns transition according to the capillary number. (a) is the schematic illustration of the experimental setup, (b)–(k) are the microphotographs of the observed flow patterns as Ca and wf (water fraction) are varied. Reprinted from [6] with permission of the American Chemical Society

hydrophilic fluids prefer to flow along hydrophilic channel surfaces, and hydrophobic fluids like to flow along hydrophobic surfaces. As hydrophilic liquids are imbibed into hydrophilic channels by capillary force, hydrophobic fluids flow into hydrophobic channels much more easily.

When fluid slugs flow forward in a channel, the trail left by the previous slug act as a lubricant for the following one (Fig. 6b). The film thickness can be theoretically calculated from the ratio of the loss of the fluid volume to the surface area traveled by the fluid. The thickness of a lubricating film experimentally depends on viscosity of neighboring slugs, fluid velocities and surface properties. Viscosity causes the deposition while capillary forces oppose the formation of a film. The film thickness (h_∞) deposited behind a wetting meniscus is therefore a function of Ca. At $10^{-5} < \mathrm{Ca} < 10^{-2}$ it can be expressed by: [9]

$$h_\infty = nR\mathrm{Ca}^{2/3} \qquad (10)$$

where n is a prefactor determined by fluid properties, and R is the channel radius. Although the thickness decreases with flow dimension, the percentage of film flow will still increase with downscaling due to both the decrease of fluid amount and the increase of specific interfacial areas. The greater the capillary number, the larger the film thickness according to Eq. (10), which allows more liquid flow through the film. A stable thin liquid film between the tube wall and gas slugs can appear at high velocities on carefully treated clean surfaces, and vice versa, so that thin films can be decreased in thickness or eliminated by sur-

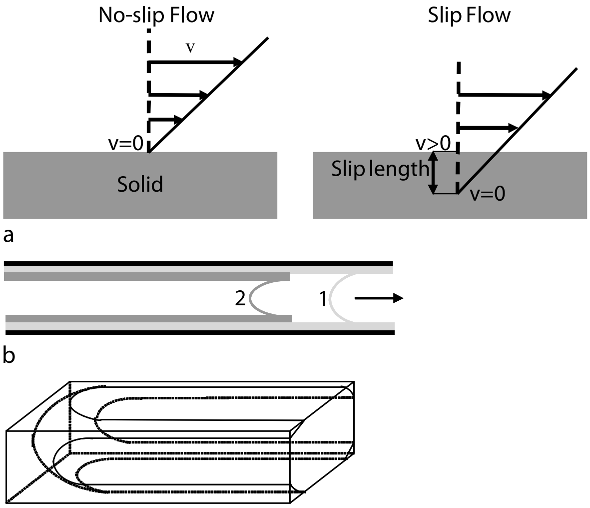

Pressure-Driven Two Phase Flows, Figure 6 Schematics of (**a**) No-slip flow and slip flow. (**b**) Film flow: (1) and (2) are immiscible fluids. (**c**) Corner flow in a rectangular channel

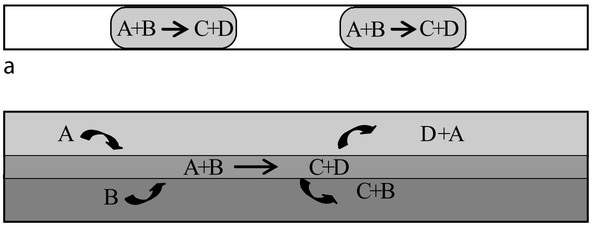

Pressure-Driven Two Phase Flows, Figure 7 Schematic applications of (**a**) Droplet-based flow and (**b**) Stratified flow.

face modification of the channel walls by changing the wetting properties.

Corner Flow

As we know, liquid surface tension is prone to minimize the liquid surface area to minimize the surface energy. Most of the channels fabricated on the micro- or nanoscale possess rectangular or slit-like cross sections. To satisfy the contact angle wetting condition the fluid will curve along the perimeter of the interface, thus minimizing interfacial area, and achieving a lower energy state (Fig. 6c). The polymorphism of the wetting liquid depends on two parameters: the channel geometry, and the interaction between substrate materials and liquids. The corner flow velocity is influenced by a flow resistance coefficient and geometric factors: the corner half-angle and the contact angle [10].

In a two-phase flow system, the different affinity of the two fluids for the wall makes one fluid preferentially flow along corners due to the capillarity. As the number of the polygon sides decreases and the corners sharpen, the cross-sectional area of fluids held in corners increases, and corner flow becomes more important. Therefore, corner flow must be considered carefully in such processes as evaporation and drying of micro- and nanochannels with small angular polygonal cross sections.

Key Research Findings

Applications

Two-phase systems are more complex than their single-phase counterparts, but are ubiquitous in process applications. Both the immiscible individual fluids separated by interfaces and the interfaces themselves provide us with mediums that are very suitable to study microreactions and interfacial phenomena.

Droplet-based Flows

Immiscible gas-liquid and liquid-liquid mixtures form droplet-based flows over a wide range of flow conditions and microchannel dimensions without additional control. There are several advantages for droplet-based flows to be applied in different fields. Specific interfacial areas as large as $9000-50{,}000\,\text{m}^{-1}$ have been obtained by decreasing channel dimensions and droplet (bubble) sizes down to $50\,\mu\text{m}$, which is 100 times larger than generally obtained in macroscopic channels. Thermal and mass transfer is therefore rapid due to the large specific interfacial area and consequently small molecular diffusion distance. Moreover, the process controllability is wide in droplet-based flows. The size, the number, and the composition of droplets can be controlled at each step of the process. By varying the initial composition of droplets, one can assess its effect on reaction yield and kinetics, providing a useful operational research tool for laboratories. Furthermore, in a droplet-based multiphase flow, droplets are separated from channel walls by a thin layer of immiscible (carrier) fluid, therefore the internal compositions of the droplets can not change due to contact with the channel walls, and the internal recirculation inside the droplets makes components mix efficiently in a very short time. This supplies us with more flexibility to employ each droplet as a separate microreactor.

Droplet-based two-phase flows offer controlled picoliter or femtoliter volumes of droplets (Fig. 7a) which are almost ideal chemical reactors and therefore have been utilized in emulsification and encapsulation, microreaction, synthesis, mixing, and bioassay [7].

Stratified Flows

In a multiphase stratified flow, the interfaces between immiscible fluids have several characteristics. Firstly, the specific interfacial area can be very large just as droplet-based flow. It can for example be about 10,000 m^{-1} in a microchannel compared with only 100 m^{-1} for conventional reactors used in chemical processes. Secondly, the mass transfer coefficient can be very high because of the small transfer distance and high specific interfacial area. It is more than 100 times larger than that achieved in typical industrial gas-liquid reactors. Thirdly, the interfaces of a stratified microchannel flow can be treated as nano-spaces. Simulation results show that the width of the interfaces of a stratified flow is in nanometers, and that diffusion-based mixing occurs at the interface. The interface width can be experimentally adjusted by adding surfactants. Finally, reactants only contact and react with each other at the interface. Therefore, the interfaces supply us with mediums to study interfacial phenomena, diffusion-controlled interfacial reactions and extraction.

The ideal 2D "nano-reactors" of the interfaces between immiscible fluids in stratified flows (Fig. 7b) have been used for chemical synthesis, triphase hydrogenation and biological enzymatic degradation, for extraction and separation, and for kinetic studies.

Future Directions for Research

Two-phase flows for a long time have been propelled by externally applied pressure, due to the inhomogeneity of two confined phases in the same system. High external pressure is needed to maintain flow in small devices due to the hydrodynamic resistance which increases with downscaling. This makes syringe pumping and vacuum pumping less suitable at smaller length scales. However, the capillarity-induced flow shows its importance at small flow dimensions. The capillary pressure is induced by interfacial forces which increase with downscaling. Moreover, more and more means have been found to modulate different interfacial forces of gas-liquid, gas-solid, liquid-liquid and liquid-solid. As device size decreases, the capillary pressure-driven flow therefore gains importance and may increasingly be used for systems where externally applied pressure would have to be extremely high.

Cross References

- ► Pressure-driven Flow
- ► Pressure-based Sample Injection
- ► Two-phase Flow

References

1. van den Berg A, Lammerink TSJ (1998) Micro total analysis systems: Microfluidic aspects, integration concept and applications. Springer, Berlin
2. Stone HA, Stroock AD, Ajdari A (2004) Engineering flows in small devices: Microfluidics toward a lab-on-a-chip. Ann Rev Fluid Mech 36:381–411
3. Karniadakis GAB, Aluru N (2005) Microflows and Nanoflows. Springer, New York
4. Serizawa A, Feng Z, Kawara Z (2002) Two-phase flow in microchannels. Exp Therm Fluid Sci 26(6-7):703-717
5. Dreyfus R, Tabeling P, Willaime H (2003) Ordered and disordered patterns in two-phase flows in microchannels. Phys Rev Lett 90(14):1445051–1445054
6. Zheng B, Tice JD, Ismagilov RF (2004) Formation of droplets in microfluidic channels alternating composition and applications to indexing of concentrations in droplet-based assays. Anal Chem 76(17):4977–4982
7. Squires TM, Quake SR (2005) Microfluidics: Fluid physics at the nanoliter scale. Rev Mod Phys 77(2):977–1026
8. Song H, Tice JD, Ismagilov RF (2003) A microfluidic system for controlling reaction networks in time. Angew Chem Int Ed 42(7):768–772
9. Bico J, Quere D (2002) Self-propelling slugs. J Fluid Mech 467:101–127
10. Weislogel MM, Lichter S (1998) Capillary flow in an interior corner. J Fluid Mech 373:349–378

Pressure Drop in Microchannels

► Turbulence in Microchannels

Pressure Injection

Definition

Pressure injection is another important technique for transferring sample to microfluidic chips.

Cross References

- ► Techniques for Transferring Samples to Chips

Pressure Measurements, Methods

BARBAROS CETIN, DONGQING LI
Department of Mechanical Engineering, Vanderbilt University, Nashville, TN, USA
barbaros.cetin@vanderbilt.edu

Synonyms

Pressure sensors

P

Definition

Experimentation and novel measurement techniques are crucial for the further development of microfluidic devices. Pressure is one of the basic parameters involved in microfluidic experiments. However, it is not realistic to apply conventional pressure measurement techniques to microsystems, since the characteristic dimensions of these measurement instruments are already comparable to those of the microdevices used. Therefore, novel pressure methods are needed for pressure measurement on the microscale.

Overview

It is not practical to measure pressures inside microchannels and nanochannels by use of conventional sensors, since it is very difficult or impossible to implement these sensors in microsystems without disturbing the flow field. Therefore, some novel methods are required for pressure measurement on the microscale.

The common practice for measuring the pressure drop along a microchannel is to use pressure transducers in the inlet and exit reservoirs, which gives overall information about the pressure rather than the pressure distribution along the channel. This approach is used in many studies related to fluid flow in microchannels [1–4].

Sekimori et al. [5] have developed a pressure sensor for use in Lab-on-a-Chip (LOC) devices. It has an embedded miniaturized structure and high chemical resistance, and causes no interference in the microflow during the measurement. This pressure sensor element has a volume of 1 mm^3 and was fabricated by using MEMS technology. The pressure sensor element was installed in an LOC without any dead volume or disturbance to the microflow, and the pressure inside the microchannel was measured (see Fig. 1).

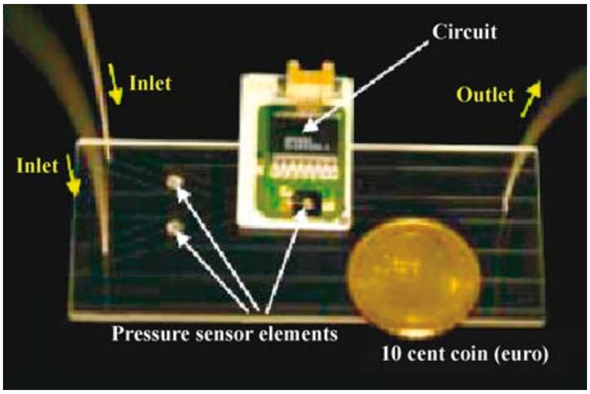

Pressure Measurements, Methods, Figure 1 Installation of the pressure sensor to a microchip. Reprinted from [5] with permission from Dr. Kitamori

Wu et al. [6] proposed the use of single-walled carbon nanotubes (SWNTs) as nanoscale electromechanical pressure sensors. These authors demonstrated computationally a reversible pressure-induced shape transition in armchair SWNTs, which in turn induced a reversible electrical transition from metal to semiconductor. They also discussed the potential long lifetime of this pressure sensor due to the excellent mechanical durability of carbon nanotubes.

Li and Chou [7, 8] proposed the use of SWNTs as mechanical sensors to measure also mass, strain, and temperature, as well as pressure. The principle of sensing was based on the shift of the resonant frequency of a carbon nanotube resonator when it is subjected to changes in attached mass, external loading, or temperature. Li and Chou discussed the feasibility of such a sensor, with the aid of computer simulation using atomistic modeling together with molecular structural mechanics. They concluded that the sensing capability of this nanoscale sensor was superior to that of current microsensors, and that the sensitivity could be further enhanced by using smaller-sized carbon nanotubes.

Kim and Daniel [9] have recently suggested the use of atomic force microscopy (AFM) for measuring pressure profiles in micro/nanochannels. The method is based on measurement of the deflection of a thin plate over the channel surface by topographic imaging of the plate using AFM. Kim and Daniel verified this measurement technique numerically with artificially generated topographic data. Since the topographic imaging takes quite a long time, this technique is only applicable to steady-state processes. Moreover, special attention needs to be paid to providing vibration-free surroundings, since vibrations transmitted via the fluid can cause noise in the data, leading to loss of accuracy.

Matsuda et al. [10] have proposed the use of a pressure-sensitive paint (PSP) technique, which is based on the interaction of atoms or molecules with photons, to measure the pressure inside micro/nanochannels. This technique is limited to gaseous flow, and has drawbacks for high-pressure and low-speed applications. Moreover, the surface where the pressure is to be measured must be visible to the detector. The temperature sensitivity of the PSP technique must also be considered during the calibration.

In conclusion, although several techniques have been suggested by many researchers, the development of measurement techniques for use on the microscale is a challenging topic, and this topic seems likely to remain open-ended in the near future.

Cross References

► Nanofluidics in Carbon Nanotubes
► Control of Microfluidics

► Fluidic Nanosensors
► Velocity Sensors

References

1. Qu W, Mala GM, Li D (2000) Pressure-driven water flows in trapezoidal silicon microchannels. Int J Heat Mass Transf 43:353–364
2. Qu W, Mala GM, Li D (2000) Heat transfer for water flow in trapezoidal silicon microchannels. Int J Heat Mass Transf 43:3925–3936
3. Ren L, Li D, Qu W (2001) Interfacial electrokinetic effects on liquid flow in microchannels. Int J Heat Mass Transf 44:3125–3134
4. Ren L, Li D, Qu W (2001) Electro-viscous effects on liquid flow in microchannels. J Colloid Interface Sci 233:12–22
5. Sekimori Y, Yoshida Y, Kitamori T (2004) Pressure sensor for micro chemical system on a chip. Sens Proc IEEE 1:516–519
6. Wu J, Zang J, Larade B, Guo H, Gong G, Liu F (2004) Computional design of carbon nanotube electromechanical pressure sensors. Phys Rev B 69(15):153406-1–153406-4
7. Li C, Chou T-W (2006) Atomistic modeling of carbon nanotube-based mechanical sensors. J Intel Mater Syst Struct 17:247–254
8. Li C, Chou T-W (2004) Strain and pressure sensing using single-walled carbon nanotubes. Nanotechnology 15:1493–1496
9. Kim SK, Daniel IM (2006) Pressure measurement technique in nano- and micro-channels using atomic force microscopy. Invers Prob Sci Eng 14(7):701–709
10. Matsuda Y, Mori H, Niimi T, Uenishi H, Hirako M (2007) Development of pressure sensitive molecular film applicable to pressure measurement for high Knudsen number flow. Exp Fluid 42:543–550

Pressure Sensors

► Pressure Measurements, Methods

Pressure Wave

► Shockwaves in Microchannels

Primitive Model

Synonyms

Element model

Definition

Primitive model is a single Differential–Algebraic Equation (DAE) derived from basic conservation laws in different domains describing the dynamic response of a constituent element (e.g., capacitors, inductors, resistors, channels, etc.) in a complex system.

Cross References

► Model Order Reduction (MOR)

Probe Microscopy

► Scanning Probe Microscopy

Programmed Cell Death

► Microfluidics for Studies of Apoptosis

Proper Orthogonal Decomposition (POD) Based MOR

Synonyms

Karhunen–Loève (K–L) expansion; Karhunen–Loève (K–L) decomposition; Karhunen–Loève (K–L) approach

Definition

Proper Orthogonal Decomposition is a technique that extracts the orthogonal basis function spanning the reduced subspace using an ensemble of data from experiments or numerical simulation of the original full systems.

Cross References

► Model Order Reduction (MOR)

Protein Adsorption

► Biomolecular Adsorption in Microfluidics

Protein Array

► Biochip
► Bioprinting on Chip

Protein Array and Cell Array

► Microarray

Protein Chip

► Lab-on-Chip Devices for Protein Analysis
► Protein Microarrays

Protein Microarrays

Steven Wong, Samuel K. Kassegne
MEMS Research Laboratory
Department of Mechanical Engineering
College of Engineering,
San Diego State University, San Diego, CA, USA
kassegne@mail.sdsu.edu

Synonyms

Microarrays; Protein chip

Definition

Protein microarrays are small chips made of glass, plastic or silicon that enable the study of protein–protein, protein–antibody and protein–drug interactions in a miniaturized, automated fashion.

Overview

Protein microarrays are chips made of glass, plastic or silicon spotted with an array of known antibodies or peptides onto which a biological sample of immobilized proteins is applied and binding determined (Fig. 1). These microarrays are used for identifying interactions between molecules fixed onto the surface (i. e. antibodies) and proteins in a solution. In a single experiment, these microarrays enable the simultaneous analysis of thousands of molecular parameters [1]. Typical applications of protein microarrays include determining protein–protein, enzyme–substrate, antibody–protein and drug–protein interactions, and determination of protein expression levels. In general, protein microarrays are classified under two broad categories: *analytical protein microarrays* for identifying the contents of an analyte and *functional protein microarrays* for studying the interaction between the protein of interest and other molecules [2]. Analytical protein microarrays often have microfluidic channels where a solution containing the proteins being investigated is pumped into a flow cell containing the microarrays. These types of protein microarrays are mainly used for basic molecular biology research, disease marker identification, toxicological response profiling and pharmaceutical target screening [3]. In contrast, functional protein microarrays have the proteins being investigated attached to the chip itself.

Protein microarrays are very similar to DNA microarrays; however, they are much more difficult to design [4]. DNA is an unstructured linear polymer that hybridizes due to information contained in the nucleic acid sequence. Proteins, however, are much more complex and possess a wide degree of secondary, tertiary and quaternary structures. In addition, protein function is highly dependant on protein structure. As a consequence, protein microarrays must be synthesized in a way that prevents denaturing of the molecule. Maintaining proteins in buffers at appropriate temperatures and pH is crucial in preserving protein shape. In manufacturing protein microarrays several sources of proteins and peptide have been arrayed onto a solid support including synthetic peptides, recombinant proteins, monoclonal antibodies and polyclonal antibodies. Out of these sources, antibody microarrays have been the most developed due to their good biochemical stability.

Basic Methodology

The design and fabrication of a protein microarray parallels that of a DNA microarray. Using a solid support that exhibits low non-specific binding is quite important in the design of a protein microarray. As shown in Fig. 1, typically glass and in some cases silicon and polymer are used as the support for protein microarrays. To increase signal-to-noise ratios, coating with nitrocellulose polymers can be used [4]. Some of the common protein microarray fabrication methods include robotic contact printing, ink-jetting, piezoelectric spotting and photolithography. A microfluidics system for automated sample incubation with arrays on glass slides and washing has also been developed.

In terms of attachment chemistry, covalent bond formation between the protein and the glass slide or affinity interactions are exploited as the means of attaching a protein to the solid support. In the covalent bond formation method, random regions of the protein are used as linkages to bind to the solid support resulting in different sides of the protein being exposed for probing interactions. In the affinity interaction method, the proteins to be plated are expressed as recombinant His-tagged proteins. The tagging of the protein enables the uniform placement of the protein onto the solid support, which can result in a more uniform signal. However, it has been suggested that the tag can artificially enhance some protein–protein interactions. Tagging both N- and C-terminals and comparing the results can resolve this problem.

Several companies have explored different means of attaching an array of proteins onto a solid surface. Schlei-

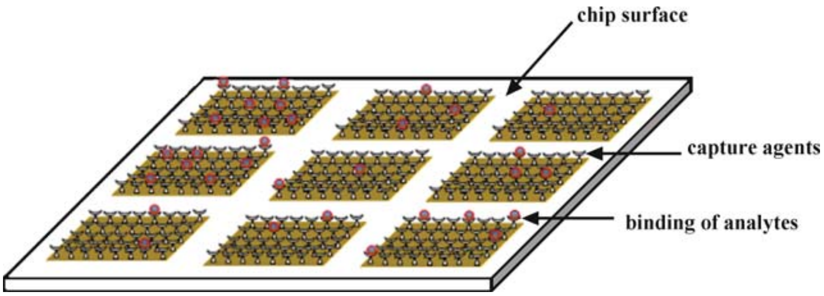

Protein Microarrays, Figure 1 A protein microarray with capture agents spotted on a chip surface. Typically glass and in some cases silicon and polymer are used as the support. Robotic contact printing is often used for spotting the agents on the surface. A microfluidics system for automated sample incubation with arrays on glass slides and washing is included. The analytes of interest are retained by selective binding to the capture agents. Specific binding is monitored by fluorescence or mass spectroscopy.

cher & Schuell and the Pall Corporation have used nitrocellulose-coated FAST and Vivid slides using simple random adsorption. The sensitivity for their antibody microarray has been reported in the range of 1 pg/mL. Xenopore, NoAb, BioDiscoveries, Microsurfaces and TeleChem International have products with surface-reactive groups that can minimize protein denaturation. Perkin Elmer and Biocept have commercially available glass slides coated with a hydrogel that increases the protein loading capacity.

Protein Microarray Applications

Protein microarrays find several uses such as in gene expression, detection of signal transduction, genome mismatch scanning, inflammation, cancer, cell cycle, DNA replication, oxidative stress, hormone action, apoptosis, neurodegenerative disease, infectious disease and cytoskeleton [4]. In broad terms, protein microarrays have found unique and superior advantage in the following areas: expression profiling, protein-protein interactions, drug discovery, and diagnostics.

- *Expression Profiling.* This is one of the main application areas for protein microarrays. The microarrays essentially help in identifying proteins in a sample or mixture. This requires good binding specificity and good binding affinity. In other words, the interactions between antibody and protein must be very specific and strong. Today, this is not done quantitatively, rather qualitatively. As a result, we get a relative difference in expression rather than a quantitative amount. This difficulty in quantifying binding efficiency accurately is due to high non-specific binding such as antibodies binding to proteins at varying degrees. Typically, quantification is done with standard calibration curves on the array for calibration.
- *Protein–protein interactions.* This is another area of protein microarray applications where proteins come to contact with other elements in the cell by binding interactions. These interactions influence the behavior of those elements with which they come in contact (i. e. signal transduction). Studying protein–protein interactions allows deeper understanding of the functionality of cells. Protein microarrays offer a means of directly studying these interactions, unlike DNA microarrays which are indirect in that – for protein expression – extrapolation of genetic sequencing or gene expression is used.
- *Drug discovery.* Drugs are often small molecules and interact with proteins. These proteins become activated or repressed due to the drug–protein interaction. Microarrays are being used to gain more understanding of cross reactivity and toxicity due to a given drug–protein interaction. Microarrays can be used as a means to optimize drug targets and avoid toxicity or side effects from activation of unwanted receptors.
- *Diagnostics.* Two diagnostic formats are generally available. One involves antigens printed onto the microarray with the purpose of identifying antibodies in patients. The other format involves antibodies printed onto the microarray with the intent of identifying proteins expressed as a result of genetic defects or disease.

P

Major Protein Microarrays in the Market

Many microarrays are available on the market, one of which is Clonetech's AB Microarray 500 [5]. This microarray is comprised of over 500 antibodies immobilized onto a glass surface at a high density. This device allows for direct comparison of protein expression in two biological samples. The device uses a fluorescence-based analysis which determines the relative measure of pro-

tein abundance in one sample compared to another. The device is typically used as a screening tool to identify proteins involved in physiological or pathological processes. For example, it can be used to detect proteins involved in signal transduction, cell-cycle regulation and apoptosis. Applications range from toxicity testing, to disease investigation and drug discovery [5].
Several companies are involved in developing protein microarrays for expression profiling and diagnostics. Examples include Zyomyx (Hayward, CA), Axcell Biosciences (Newtown, PA), BioSite (San Diego, CA), LumiCyte (Fremont, CA), Phylos (Lexington, MA) and ProteinOne (Bethesda, MD). Other players in the protein microarray market include BD Biosciences and Invitrogen who actually have leading positions in the market. Other chips on the market address the need for probing for a specific group of proteins rather than a diverse range. Zyomyx (Hayward, CA), for example, has developed a chip specific for human cytokines.

Key Findings and Future Directions for Research

Significant research and product development efforts in protein microarrays are being carried out in the following key areas: development of capture agents, surface attachment chemistry, and better detection methods.

- *Development of capture agents.* Monoclonal antibodies take a long time to develop and are labor intensive. Among some of the ongoing research in improving capture agents is the use of phage display methods that can be used to isolate high-affinity binding agents against protein targets [6]. Phage display is a system in which a protein is displayed on the surface of a phage as a fusion with one of the coat proteins of the virus.
- *Surface substrates and attachment.* The quality of data obtained from protein microarray experiments is severely affected by the nature of the surface substrate and attachment chemistry [7]. The immobilization of biotinylated proteins onto streptavidin surfaces has been demonstrated to lead to an increase in sensitivity over random attachment in a microarray assay. Poly(ethylene glycol) derivates used as coatings have also proved successful in increasing sensitivity.
- *Detection methods.* There are several detection methods currently under development. These include laser scanning, ELISA, phosphorimaging, atomic force microscopy, nanoparticles and rolling circle amplification. Currently, research efforts continue in improving detecting binding events. One promising area is the use of sandwich immunoassay with labeled detection antibodies. For ELISA-based assays that have certain restrictions, a highly sensitive detection strategy that uses rolling circle amplification (RCA) has been introduced [8].

Cross References

► Protein Microarrays
► DNA Microarray
► Lab-on-a-Chip (General Philosophy)
► Lab-on-Chip Devices for Protein Analysis

References

1. Zhu H, Bilgin M, Bangham R, Hall D, Casamayor A, Bertone P, Lan N, Jansen R, Bidlingmaier S, Houfek T et al (2001) Global analysis of protein activities using proteome chips. Science 293:2101–2105
2. Twyman RM (2004) Principles of Proteomics. BIOS Scientific Publishers, Oxon
3. LaBaer J, Ramachandran N (2005) Protein microarrays as tools for functional proteomics. In: Cravatt BT, Kodadek T (eds) Current Opinion in Chemical Biology, vol 9. Proteomics and Genomics pp 14–19
4. Schena M (ed) (2005) Protein Microarrays. Jones and Bartlett, Sudbury ISBN 0-7637-3127-7
5. Clontech http://www.clontech.com Accessed Oct 2006
6. Sheets MD, Amersdorfer P, Finnern R, Sargent P, Lindquist E, Schier R, Hemingsen G, Wong C, Gerhart JC, Marks JD, Lindqvist E (1998) Efficient construction of a large nonimmune phage antibody library: the production of high-affinity human single-chain antibodies to protein antigens. Proc Natl Acad Sci USA 95:6157–6162
7. Sydor JR, Nock S (2003) Protein expression profiling arrays: tools for the multiplexed high-throughput analysis of proteins. Proteome Sci 1:3
8. Lizardi PM, Huang X, Zhu Z, Bray-Ward P, Thomas DC, Ward DC (1998) Mutation detection and single-molecule counting using isothermal rolling-circle amplification. Nat Genet 19:225–232

Protein Profiling

► Lab-on-Chip Devices for Protein Analysis

Proteolysis

Synonyms

Enzymatic or chemical digestion

Definition

Proteolysis is the process of cleaving protein molecules into smaller pieces (peptides) via chemical or enzymatic reactions. Living systems carry out proteolysis to obtain amino acids from protein substrates or as part of the construction of new proteins. In proteomic analyses, it is often

necessary to perform proteolysis in order to facilitate identification of a protein of interest, as digest peptides form a characteristic "fingerprint" of the parent protein.

Cross References

- ► Lab-on-Chip Devices for Protein Analysis
- ► Liquid Chromatography
- ► Mass Spectrometry
- ► Microfluidic Bioreactors
- ► Proteomics in Microfluidic Devices

Proteomics

► Lab-on-Chip Devices for Protein Analysis

Proteomics in Microfluidic Devices

ELIZABETH M. MILLER[2], SERGIO FREIRE[1], AARON R. WHEELER[1]
[1] Department of Chemistry, University of Toronto, Toronto, ON, Canada
[2] Terrence Donnelly Centre for Cellular and Biomolecular Research, University of Toronto, Toronto, ON, Canada
awheeler@chem.utoronto.ca

Definition

Proteomics is the study of the collection of proteins (the proteome) expressed in a given system. The field of proteomics can be divided into three subtypes:

- *profiling* – identification and quantification of the proteins in a sample and drawing comparisons between samples,
- *functional* – the study of the behavior of specific proteins, and
- *structural* – the study of protein folding and the complexes it forms.

Microfluidics is characterized by devices that contain channels or features with dimensions measured in microns, and are capable of transporting and analyzing sample volumes in the nanoliter range.

Overview

Proteomics is a field that first gained prominence in the mid 1990s. The sheer number of proteins as well as the number of variations that comprise the proteome presents a huge challenge for analysis. Serum protein concentrations can vary by several orders of magnitude, and often a single disease will affect both high- and low-abundance proteins to varying degrees. In addition to basic protein structures and sequences, a vast array of post-translational modifications exists that significantly impacts the functionality, structure, and activity of the native proteins. The primary applications of microfluidics in proteomics have been in the profiling and functional subtypes – structural proteomics has not yet been extensively studied on the microscale.

Profiling proteomics is used to identify all of the proteins in a sample or to compare changes in protein expression between several samples. Due to the complexity of the proteome, accurate analysis requires a great deal of sample processing, including proteolytic digestion, followed by multidimensional separations and mass spectrometry. Separations and mass spectrometry are be covered in other chapters of the *Encyclopedia* ►lab-on-chip devices for protein analysis, ►chromatographic chip devices, ►interfaces between microfluidics and mass spectrometry, but chemical processing for profiling proteomics will be discussed here. Readers are encouraged to see Friere and Wheeler [1] for a comprehensive discussion of proteome profiling in microfluidics.

The study of functional proteomics on the microscale comprises an assortment of assays to identify functional groups on proteins and evaluate binding events to determine functional properties of proteins. Functional proteomics is exploited in *enzyme assays* and *immunoassays* to characterize the behavior of a protein within a biological system.

There are a number of ways in which enzymatic studies contribute to the understanding of the proteome. Enzymes are commonly used in proteomics to investigate analytes that are difficult to measure by conventional means. Quantitation of small molecules with enzymatic methods provides insight into the concentration and activity of the proteins associated with those molecules. A great variety of these enzymatic assays have been carried out in microfluidic devices. Another function of enzymatic assays is in kinetics; measurements of properties of enzymes such as the Michaelis–Menten constant (the concentration of substrate when the reaction rate is half the maximum rate) and the turnover number (the number of moles of substrate that are converted to product per catalytic site per unit time) are vital to understanding the mechanics of the proteome, and are used to characterize of the effects of known drugs and discover new ones.

The immunoassay is another widely used technique that has been applied to a diverse set of proteomic applications, including the identification and quantization of protein markers for diagnosis of diseases where laboratory facilities are not readily available. Immunoassays can be

designed to detect very small amounts of antigens and to measure the concentrations quite accurately; in addition, further information about the disease markers, such as the existence of structural changes and posttranslational modifications, can be elucidated. Since immunoassays typically comprise a number of repetitive steps and require expensive reagents, they are a ripe target for adaptation to the microscale format, where sample sizes, reagent quantities, and analysis times are all greatly reduced.

Basic Methodology

The methods used in microscale proteomics applications can be divided into two categories, related to the features of microfluidic devices, and the nature of the analyses and assays themselves.

Features of Microfabricated Proteomic Devices

In proteomics applications, the most important features of microfluidic systems are related to delivery of fluid reagents, immobilization of proteins, mixing and reactions, and geometric microarrays.

Movement of Fluids

A critical decision for any microfluidic system is how to generate and control the flow of fluid. The most common methods rely on external pumps or electrokinetic flow. Conventional pumps are too large for pumping ~nL volumes of solutions, requiring splitters to isolate a fraction of the pressure to apply to the device. Smaller pumps such as syringe pumps are used frequently, but can be difficult to interface with microchannels in a device. Another common option is using electroosmotic (or electrokinetic) flow (EOF) to move analytes through a chip. This method is advantageous because it doesn't require any pressure to be applied on the sometimes fragile chips, it can move fluids at fast rates (exceeding 33 mL/min), and electrodes can easily be integrated into the chip itself. The magnitude of EOF is a function of the density of charge on microchannel walls (or on the surface of packed media); thus, careful consideration must be made in determining the materials used to fabricate devices. If materials without adequate charge density are used (or if the native EOF is too weak or strong), there are a number of coatings that can be used tune the direction and magnitude of EOF (► electroosmotic flow). Electrokinetic effects can also be used to separate the constituents of solutions; however, this can be one of its biggest disadvantages. Any fluid pumped by this method will have its components at least partially separated from one another, creating an inherent bias in any injected sample plug, and flow rates will vary due to protein adsorption on the interior of the chip or with Joule heating in the device. A final disadvantage is that all solutions must contain buffer ions in a particular concentration range, which is not convenient for all applications.

There are several less common alternatives for controlling fluid flow in microchannels. ► Digital microfluidics (DMF) is an alternative fluid handling method that is beginning to be used in proteomic applications. In DMF, discrete droplets are manipulated on a surface (rather than as streams in enclosed channels) via electrowetting and/or dielectrophoretic forces generated when an electrical potential is sequentially applied to electrodes in an array. This technique can be used with a wide variety of different fluids and can be applied to some aspects of sample preparation and purification. Hydrodynamic pumping, in which flow is driven by siphoning from one fluid reservoir to another, is an option for driving flow that does not introduce a sampling bias. It can, however, be difficult to control; consistency and fine-tuning of flow rate are problematic. Centrifugal pressure flow is another attractive option for fluid movement in protein studies, as it is insensitive to pH, ionic strength, and other characteristics of the fluid that may need to be varied for different assays. Centrifugal pumping is also relatively unaffected by the deposition of analytes onto channel walls (unlike EOF, DMF, etc.); however, it typically relies on single-use valves and therefore flow can only be driven one-time, and in one direction.

Immobilized Proteins

There are two basic formats in which assays are incorporated in microfluidic devices: homogeneous, or solution-based, assays, and heterogeneous, or surface-based, assays. Both approaches significantly reduce sample and reagent consumption relative to their macroscale counterparts, but heterogeneous assays are emerging as the dominant method for proteomics, as they can be adapted to many different types of interactions (Fig. 1a–f) [2].

Heterogeneous assays require proteins or other substrates to be immobilized on surfaces, which allows for conservation and repeated use of the immobilized bed, as well as facilitating the analysis of a sample without need for a separate concentration or mixing step. Also, the binding event or interaction between analytes is not restricted by equilibrium conditions or adequate mixing/diffusion of reagents. Finally, immobilization makes it easier to incorporate more than one reaction-zone in a device, increasing the number of analyzes that can be performed on a sample and taking greater advantage of the benefits of a microfluidic system. Several properties are required for useful surface-immobilized proteins, including: the sur-

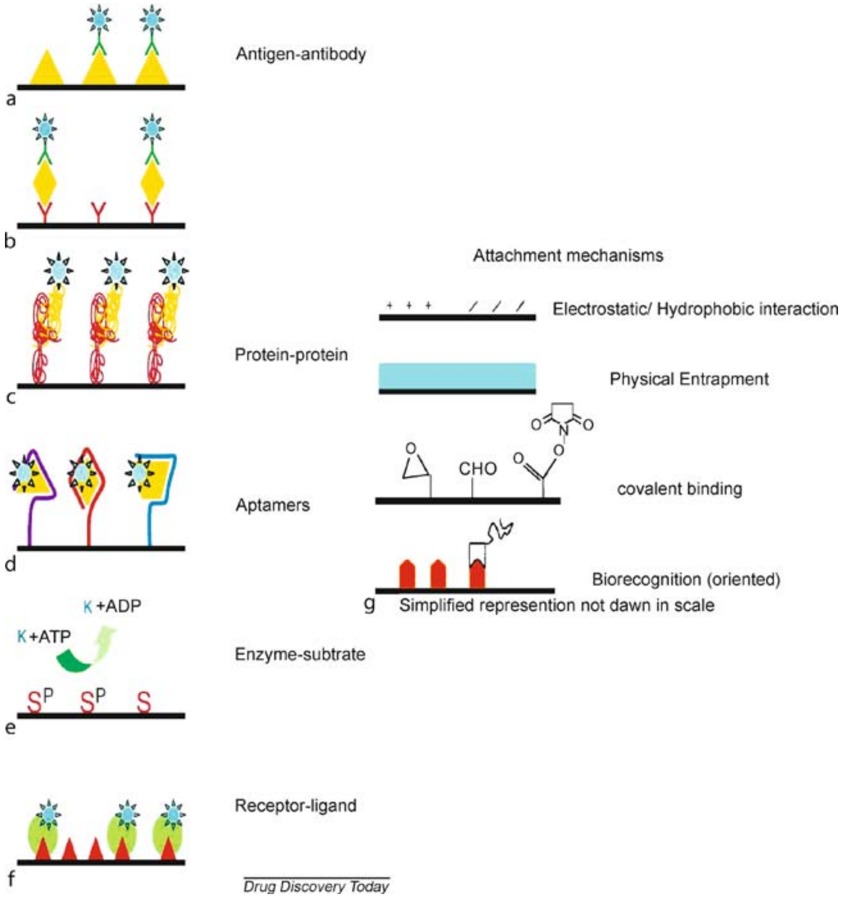

Proteomics in Microfluidic Devices, Figure 1 (**a**)–(**f**) Several heterogeneous protein assay formats (reprinted from [2]). A variety of protein binding events can be studied, ranging from antibody/antigen to protein/protein to enzyme/substrate interactions. (**g**) Strategies for the immobilization of proteins on solid supports (reprinted from [4])

face must have a high binding capacity for the capture protein, the immobilized protein must retain its biological activity, the protein must be spatially accessible, and there must be a low level of *non*specific interactions between proteins in solution and the coated surface.

In microfabricated devices, protein immobilization is most often carried out on glass or silicon supports, using a wide variety of surface chemistries [3]. The most common methods for attachment of proteins to surfaces are depicted in Fig. 1g [4], ranging from simple (e. g., adsorption of proteins via electrostatic or hydrophobic interactions with the surface, entrapment in immobilized polymers, etc.) to more sophisticated techniques, relying on covalent bonding and biological recognition (e. g., biotin/streptavidin). In general, the most robust immobilized protein beds are formed by covalent attachment. One popular method requires two steps: a first layer is formed by silane chemistry such that the surface presents a reactive group (e. g., epoxy, amino, thiol, etc.), and a second layer (e. g., the protein to be immobilized or a linker molecule) is covalently attached via the immobilized reactive groups. Other strategies include covalent attachment to functionalized polymer coatings on the interior of the device or linkage to the free end of a self-assembled monolayer (SAM) on a gold surface. Most of these methods result in incomplete coating of the surface, and some reactive groups are left vulnerable to interaction with target proteins during analysis; this phenomenon is called non-specific interaction, and can negatively impact assay performance. A number of strategies exist for blocking surfaces to prevent nonspecific binding of analytes, most of which involve coatings of polymers (e. g., polyethylene glycol) or proteins (e. g., albumin or casein) that will not interact with the sample. However, even with these precautions, interactions between analytes and the surface of the device are very difficult to eliminate.

P

Mixers and Microreactors

In contrast to heterogeneous assays, in homogeneous assays, solutions of an enzyme and a substrate or an *antibody* and antigen are combined in a channel to evaluate the enzyme kinetics or properties of inhibitors, or measure the amount of displaced antigen, which requires thorough mixing. In low Reynold's Number microfluidic channels, turbulent mixing is not possible, and diffusive mixing dominates. Diffusive mixing is a reasonable technique for small molecules; however, enzymes and other large molecules diffuse much too slowly for adequate mixing in many proteomic applications. A number of passive mixing schemes in microfluidic systems have been developed – for example, a network of interconnecting channels of varying lengths and widths is capable of mixing solutions being pumped by electroosmotic flow, while patterned surface grooves enable mixing in a pressure-flow device.

One solution to the challenges of mixing proteins in microfluidic systems is to immobilize proteins in *microreactors* [5]. These systems typically consist of chambers of enzymes immobilized on beads, micropillars [6], or porous polymer monoliths [7] (Fig. 2a–b). Such systems have large surface area-to-volume ratios, which minimizes diffusion time for reactions with solution-phase reagents. Microreactors can be used either for the conversion of an analyte to another form that is more easily detected, or for direct studies of the properties of enzymes and substrates. One of the most common uses is for the digestion of proteins for proteome profiling, but such systems can also be used for the removal of amino acid residues from peptides or proteins or for enzyme kinetic studies.

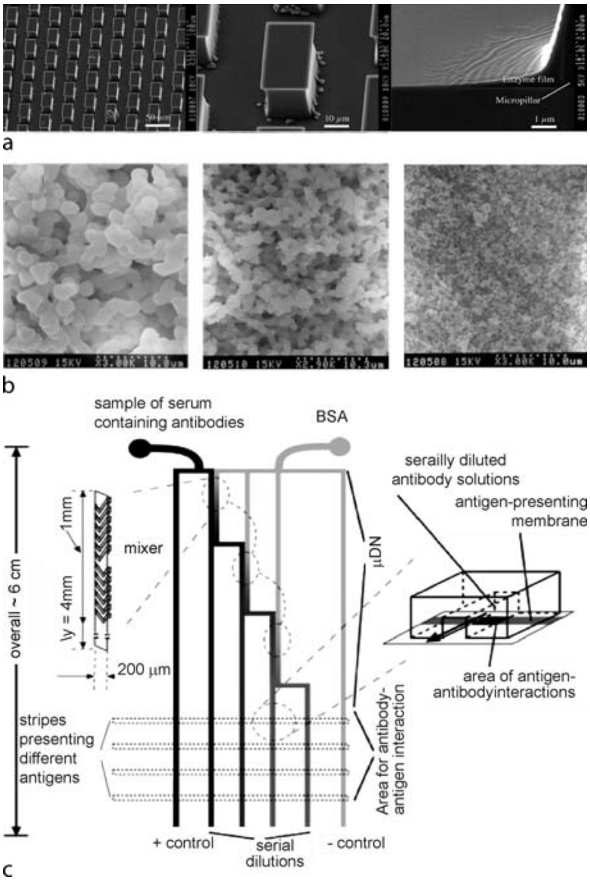

Proteomics in Microfluidic Devices, Figure 2 (**a**) An enzymatic microreactor containing micropillars that have been coated with trypsin for protein digestion. Reprinted from [6]. (**b**) Porous monolith microreactors of various pore sizes. Pore size is determined by the ratio of monomer to porogen (solvent) during polymerization. Reprinted from [7]. (**c**) A microdilution network (µDN) for the quantitation of multiple antigens. The device uses a series of T-intersections to sequentially dilute a serum sample. Herringbone patterned areas are used as mixers in the dilution channels. Several antibodies have been deposited on a membrane using a microfluidic network, and the membrane is incorporated in the bottom of the µDN device. Reprinted from [12]

Microarrays

Biological microarrays are two-dimensional arrangements of immobilized spots of molecules on a surface. When a microarray is exposed to a solution containing unknown analytes bearing an appropriate label, analytes binding to particular spots on the surface can be rapidly identified. DNA microarrays were introduced in the late 1990s, and have become a widely used tool for high-throughput genomic analysis; however the development of similar tools for proteome analysis has been hampered by the diverse properties of proteins. For example, all DNA molecules inherently possess specific capture properties through complementary base-pairing; proteins do not have such a universal property. Additionally, protein capture *ligand*s tend to be more delicate in structure and function than the relatively robust DNA molecule. Finally, small amounts of DNA can be detected quite easily using amplification techniques such as the polymerase chain reaction (PCR); no such amplification technique exists for proteins.

Despite these disadvantages, the promise of multiplexed detection of analytes has made protein microarrays a popular research topic in microfluidic implementations of proteomic analyses.

The immobilized spots used in protein microarrays may contain protein molecules, or smaller molecules such as inhibitors or ligands with which a protein in solution may interact. Very small spots are advantageous in that higher detection throughput can be achieved with minimal amounts of printed material and sample. Spots are typically deposited either by contact methods, such as printing arrayers that use needles to deposit droplets directly on the

surface, or by non-contact methods, including the use of capillaries or ink jet dispensers to deposit droplets with nanoliter-picoliter volumes.

An alternative to microarrays is the use of arrays of multiple parallel channels. Typically, such structures are used to carry out a number of duplicate assays on one or more samples, to perform a serial dilution of a single sample for quantitation of a given protein, or to detect multiple targets in a single sample. In the latter case, an array of channels may be used in conjunction with a printed array of spots or bands – the channel network is used for fluid delivery to the printed array (Fig. 2c).

Analyses and Assays

Microfluidic devices are used in a variety of profiling and functional proteomics applications; the goal in much of this work is to reduce sample and reagent consumption and increase throughput. The primary application in profiling proteomics is in the preparation of protein samples for separations and mass spectrometry, while the major functional proteomics tools are enzymatic and immunological assays.

Sample Preparation for Profiling Proteomics

The identification of unknown proteins often requires that they be digested (or divided) into a group of constitutive peptides, which are interrogated by mass spectrometry. Comparing the masses of the peptides to genomic databases enables absolute identification by means of peptide mass fingerprinting (PMF). Proteins are digested by exposure to proteolytic enzymes (e. g., trypsin), or other lytic reagents (e. g., cyanogen bromide, CNBr); this is often part of a multistep process requiring 12 – 18 h, including mixing the sample with buffer and denaturant, mixing and incubating the sample with reducing agent to reduce disulfide bonds, mixing and incubating the sample with alkylating agent to prevent disulfide bonds from reforming, and finally, mixing and incubating with lytic reagent. This process is extremely tedious and time-consuming, making it an attractive application for microfluidics.

Several device configurations have been used for proteomic processing in microfluidic devices, including open channels, immobilized beads, and other solid phase media. Open-channel devices for tryptic digestion and reduction of disulfides in proteins are capable of achieving complete tryptic digestion in timeframes ranging from 15 min to 5 s. Immobilized beads increase the surface-to-volume ratio further; for example, a bed of trypsin-modified beads immobilized in a microfluidic chamber can be used very effectively for *proteolysis* of relatively large volumes of flowing sample. An alternative method for increasing the surface area-to-volume ratio in microfluidic devices is to use trypsin-modified monoliths, formed from polymer plugs cured in situ, or from membranes sandwiched between channels. Trypsin and other enzymes can also be copolymerized within hydrogel microstructures – the hydrogel is a biocompatible matrix that reduces the likelihood of damage to the enzyme during and after immobilization.

Microfluidics is promising for developing tools with integrated chemical processing of proteomic analytes, by virtue of fast reaction kinetics. Sample purification and concentration can be carried out on the microscale by methods such as solid phase extraction on hydrophobic surfaces ► lab-on-chip devices for sample extraction or affinity chromatography ► chromatographic chip devices. Immunoassays on magnetic beads have been used not just for detection of antigens (described below), but also as a purification method for the isolation of a target for mass spectrometry. However, to our knowledge, there have been no reports of implementing a fully integrated process, including stepwise reduction, alkylation, and digestion. Microfluidic tools for chemical processing will likely not be widely adopted until this critical benchmark is achieved.

Enzymatic Assays

Traditionally, enzymatic assays are performed in microtitre plates (plastic trays containing arrays of isolated wells), where an enzyme and its substrate are mixed in an individual well, and the substrate turnover is measured to determine the activity of the enzyme. Microfabricated devices that can perform enzymatic studies without interference between individual elements are highly desirable, as the macroscale method consumes a great deal of enzyme. There are three basic applications of enzymatic assays in proteomic studies:

1. small molecule detection or sensing via an enzymatic reaction,
2. studies of enzyme–substrate, protein–ligand, and protein–protein interactions, and
3. kinetic studies.

The first type of enzyme application in microfluidics is chemical sensing. Sensors can be constructed in cases where an enzyme turns over a particular small-molecule substrate to produce a product quantifiable by fluorescence, chemiluminescence, absorbance spectroscopy, or electrochemical detectors. In cases where the substrate is not detectable itself, an enzymatic product can often be coupled to another enzyme that produces a detectable product. For example, there are a wide variety of small

molecules (such as nutrients, amino acids, and sugars) that can be coupled to the chemiluminescent reaction of luminol and peroxide in the presence of horseradish peroxidase. These enzyme-substrate assays were the first to be adapted to microfluidic devices – a great number of small-molecule sensors have been developed based on microfluidic channels with electroosmotic or hydrodynamic flow, and pre-loaded microfluidic cartridges containing nanoliter volumes of reagents have shown great promise as a replacement for 96-well plates for high-throughput screening [8].

The second type of enzyme application in microfluidics is protein interaction studies. In order to study interactions between enzymes and substrates, peptides, or other proteins, an alternative to microtitre plates is the microarray. These arrays are very often used in conjunction with microfluidic sample and reagent delivery systems; alternatively, microchannels can be used to deposit spots in an array. By immobilizing substrates or inhibitors on the array, it is possible to screen large numbers of molecules for their relative abilities to bind a particular enzyme. This is typically accomplished by tagging the enzyme with a fluorescent molecule and using the intensity of the array spots to determine the amount of enzyme bound (Fig. 3a). This is a promising approach for the identification of protein drug targets, or for the evaluation of compound libraries in drug discovery. Peptide fragments of proteins of interest have great potential as capture ligands, as they are easy to synthesize, stable, and able to mimic proteins. However, small molecules such as peptides are difficult to immobilize on a surface such that they are still accessible to the sample. Peptide fragments are also not as specific as complete proteins; for some applications, it is preferable to immobilize an entire protein to characterize its interactions with other proteins or enzymes of interest. Sample delivery to the elements of an array via microfluidics enables hundreds of different analyses to be performed on a single sample while reducing the size of that sample from microliter volumes to nanoliters.

A third type of enzyme application in microfluidics is kinetic studies, which may be carried out in either homogeneous or heterogeneous format. In homogeneous assays, adequate mixing of the enzyme, substrate, and any inhibitors that are being studied is crucial – this is done either via the merging of reagent streams at a T- or Y-shaped junction between channels or by means of a microfabricated mixer to ensure complete homogenization. A microfluidic mixer is advantageous – it ensures complete mixing of the enzyme and substrate and a smaller quantity of enzyme is consumed. Electrophoretically-mediated microanalysis, or EMMA, uses electrokinetic forces as the pumping method, which has the added benefit of separating product from substrate as the analysis proceeds. EMMA was first developed in capillary electrophoresis systems, but was readily adapted to microchannel setups [9]. Since a chip disperses Joule heat much more efficiently than a capillary does, the analysis can be run at higher potentials, increasing the speed of measurement. In most cases, a modified substrate is used that is converted to a fluorescent, chemiluminescent, or colored product by the enzyme, and optical methods are used to calculate factors such as the turnover number and Michaelis constant. Kinetic assays have also been carried out in centrifugal flow microfluidic devices [10], which are applicable for a wide variety of biological samples, including whole blood, plasma, and urine, that are incompatible with electroosmotic flow systems. Centrifugal devices are also easily adapted to perform multiple analyses on a single plastic device, reducing the costs of manufacturing. However, fresh enzyme is required for each determination, making enzyme recovery difficult. Heterogeneous enzyme microreactors eliminate the need for recovery

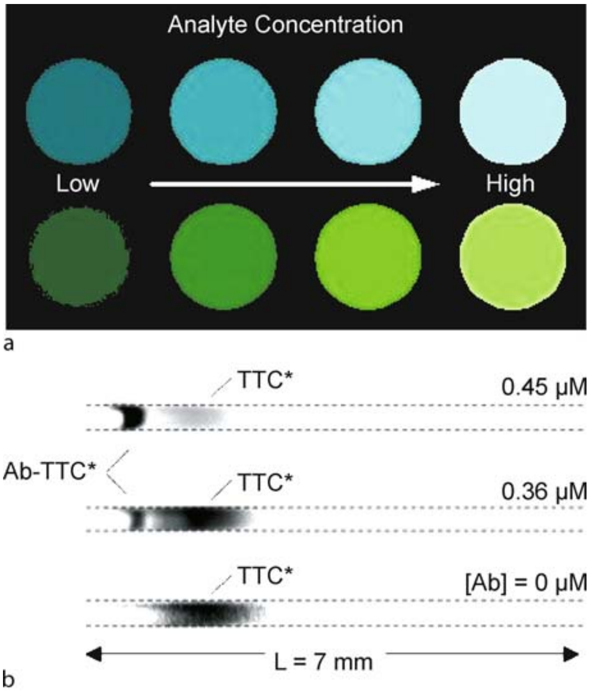

Proteomics in Microfluidic Devices, Figure 3 Detection of binding of a protein analyte in a heterogeneous (**a**) or homogeneous (**b**) assay. In (**a**), the fluorescence intensity of spots on an array reflects the amount of the target protein in the sample solution. Different analytes are tagged with molecules that fluoresce at different wavelengths to simplify identification. In (**b**), the tetanus toxin-C-fragment (TTC) is fluorescently labeled and separated from the antibody-TTC complex in an electrophoretic channel for quantification. Reprinted from [11]

steps and dead time during the measurement. Microfluidic devices containing immobilized enzymes enable the study of kinetics with excellent enzyme recovery and decreased reagent consumption, increasing the overall efficiency of the method and greatly decreasing waste.

Immunoassays

Like enzymatic assays, immunoassays are conventionally implemented in microtitre wells, but they are even more easily adapted to the microscale. Homogeneous immunoassays are typically employed for the study of small molecules, while heterogeneous immunoassays are preferred for large-molecule detection.

A homogeneous assay is carried out by combining an antigenic sample and an antibody by means of electrokinetic flow in a microchannel. After the antigen binds the antibody, the complex can be separated from the remaining free antibody via electrophoresis to determine the amount of antigen present in the sample (Fig. 3b) [11]. On a microfluidic chip, this analysis can easily be multiplexed – a different assay can be performed in different channels on the same sample.

There are two common forms of heterogeneous assays used to detect and quantify disease markers: the direct-labeling method, in which the proteins in a sample are labeled with a detectable tag and isolated from a complex sample by means of a bed of immobilized antibodies, and the indirect-labeling method, in which two antibodies are used for each marker. Sandwich-type immunoassays, such as the enzyme-linked immunosorbent assay (ELISA), require two antibodies: an immobilized antibody used to capture a molecule of interest – a protein, a virus, or a small molecule (e. g., a hormone, pharmaceutical, or environmental pollutant) – and a second antibody in solution that is conjugated to a detectable tag. Immunoassays have also been carried out with detection via surface plasmon resonance microscopy, atomic force microscopy, and electrochemical sensors, eliminating the need for a detectable label. These assays are very useful because the antibody-antigen binding that must occur at each step is highly specific and thus has built-in redundancy – they are very sensitive and capable of quantitation of changes in concentration with a dynamic range of up to 2 – 3 orders of magnitude. As for enzymatic assays, microfluidic channels can be used either to deposit the first antibody onto a surface for immobilization or to direct the sample over the immobilized antibody (concentrating the antigen on the surface in the process) and any subsequent reagents – in some cases, microfluidic systems have been used for both purposes [12]. While basic immunoassays are well-suited for determining the presence of a given molecule in a sample and sometimes the quantity, they do not provide any other information about the target molecule. In recent work, immunoassays have been adapted to provide structural and post-translational modification information on marker proteins, however, these assays have not yet been widely applied to microfluidic devices and are still primarily performed in microtitre wells.

Key Research Findings

In the first report of on-chip proteolytic processing, Gottschlich et al. used open-channel devices for tryptic digestion and reduction of disulfides in proteins, which enabled complete processing in 15 min. More recently, Huang et al. [13] and Liu et al. [14] used surface adsorbed trypsin in channels to enable complete digestion in less than 5 s. In an alternative strategy, Yue et al. used a bed of trypsin-modified agarose beads immobilized in a weir in a glass microfluidic device to digest β-casein [15]. Peterson et al. used the related heterogeneous technique of forming methacrylate plugs cured in situ to increase the surface area-to-volume ratio to achieve tryptic digestion of myoglobin in $\sim$11 s [16]. Sakai-Kato et al. developed similar methods using trypsin immobilized in a sol-gel matrix [17]. Gao et al. reported using a trypsin-modified polyvinylidiene fluoride (PVDF) membrane in a PDMS microfluidic chip, enabling protein digestion in 3 – 10 min [18]. Each of these methods represents a vast improvement over conventional macroscale proteolysis, which typically requires hours-days. One promising approach for sample purification during processing is the use of digital microfluidics to remove hydrophilic impurities from proteomic samples [19].

Hadd et al. performed the first homogeneous assays to determine enzyme kinetics in a microfluidic chip – these assays relied on diffusional mixing of β-galactosidase and resorufin β-D-galactopyranoside (RBG) within a channel electrophoresis system [9]. This assay successfully characterized the kinetics of the enzyme, and reduced reagent consumption by four orders of magnitude over conventional assay methods. The same assay was later modified by Burke et al. by including a passive microfluidic mixer, resulting in a characterization of enzyme kinetics that more closely agreed with that obtained via conventional methods [20]. Puckett et al. developed a centrifugal microfluidic system in which homogeneous protein-ligand binding assays were performed to detect and characterize the binding interaction between phenothiazine antidepressants and calmodulin, a calcium-binding protein known to interact with this class of drugs [21]. This system utilized pre-measured aliquots of reagents,

P

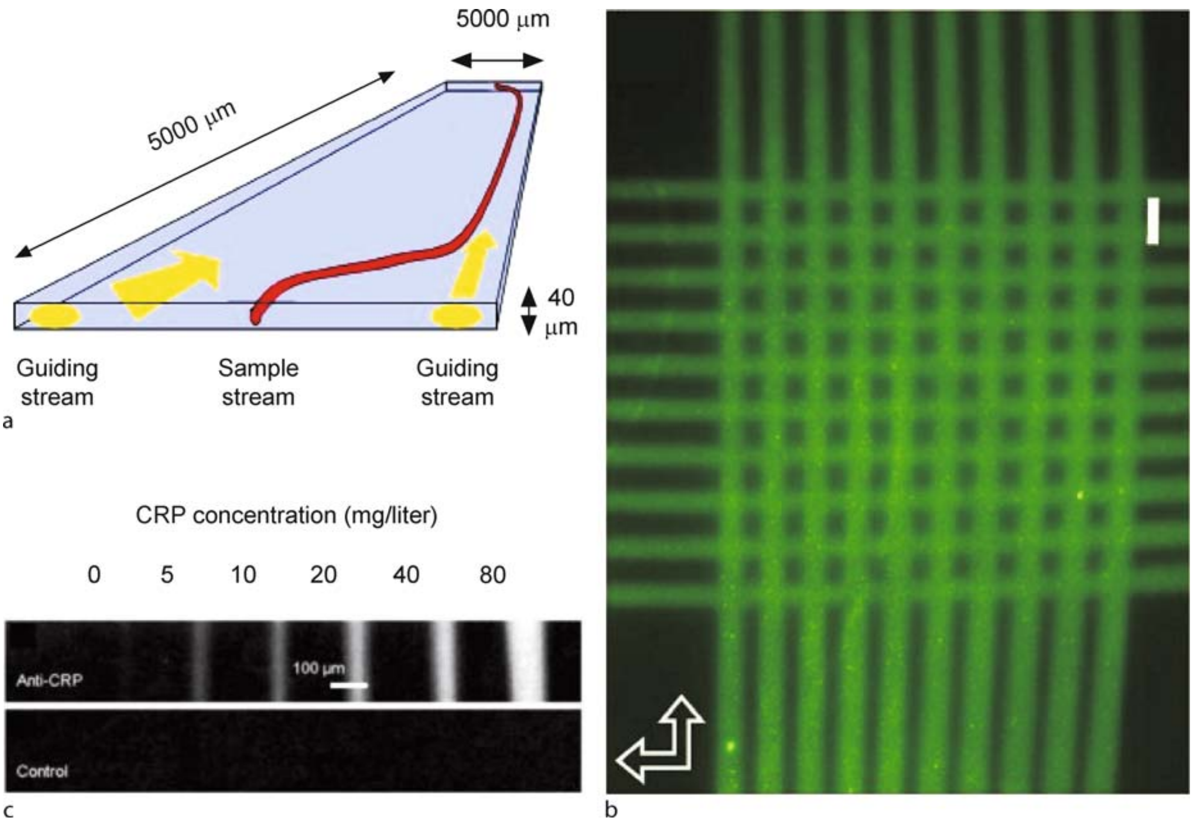

Proteomics in Microfluidic Devices, Figure 4 (**a**) Use of hydrodynamic flow to create a microfluidic stream and direct it to specific areas of a larger channel. (**b**) The flow system is used to deposit biotinylated fluorescein in a grid pattern. The direction of flow during deposition is indicated by arrows. (**c**) Quantitation of C-reactive protein (CRP) in whole blood. Samples of blood were spiked with CRP and the microstream directed across a surface coated with anti-CRP before exposure with a Cy3-labeled secondary antibody. Reprinted from [24] under open access agreement with BioMed Central.

increasing the speed and reproducibility of the analysis for high-throughput applications. In an effort to integrate multiple analyses on one device, Wang et al. incorporated two homogeneous assays into one microfluidic channel: an enzymatic assay for glucose and an immunoassay for insulin [22]. Electrokinetic effects were used for both fluid movement and separation of the components before detection. Through the use of pre- and post-column reactors and an electrophoretic separation of analytes, two independent measurements were made in the same space.

Perhaps the greatest area of interest in microfluidics for proteomics applications is in multiplexed, heterogeneous assays. Kim et al. used microfluidic PDMS channels to pattern sol–gels on polyvinylacetate-coated glass slides under conditions mild enough to retain protein activity [23]. The use of a microfluidic channel system generated a well-defined, intricate pattern of immobilized protein that simplified data collection. Jiang et al. patterned antigens on a membrane via a microfluidic network, and then positioned the membrane under a microdilution network to carry out serially-diluted immunoassays to detect multiple antigens on the patterned surface (Fig. 2c) [12]. This fluidic network enables the simultaneous quantitation of several molecules that vary widely in concentration – a major challenge in proteomics – in a single submicroliter sample. Brevig et al. developed a hydrodynamic microfluidic system that uses two streams of fluid to focus a sample and perform parallel immunoassays to quantitate levels of C-reactive protein, a well-known marker of inflammation (Fig. 4) [24]. As this method effectively creates a microscale stream within a larger chamber, it conserves sample but can also be carried out on whole blood without risk of clogging very small channels. In recent years, a great number of biochips have been made commercially available that use networks of microfluidic channels to perform analyses of over 100 different proteins using only 0.1 μL of whole blood [25]. These chips are capable of separating plasma from blood cells, and then directing the plasma sample across an ELISA array – the heterogeneous

array format and simplified sample prep are advantageous in terms of both speed of analysis and reduced sample consumption. This is very promising, as the cleanup of whole blood is a major bottleneck to the use of microfluidics in medical applications.

Future Directions for Research

The future of miniaturization in proteomic applications lies in achieving greater sophistication of devices. A variety of arrays have been used to investigate post-translational modifications such as phosphorylation and glycosylation, and it is only a matter of time before these are incorporated into microfluidic systems. Factors such as antibody synthesis currently limit the range of proteins that can be incorporated on an array, and devices that are capable of simultaneous quantitation of a protein and the study of its post-translational modifications, activity, etc., are not yet fully realized. Enzymatic microreactors are evolving in directions that will enable rapid screening of enzyme inhibitors for pharmaceutical purposes, industrial-scale synthesis, and environmental applications such as conversion of used grease to diesel fuel. Tools such as biochips mark the beginning of a shift from central laboratory to point-of-care testing, one of the hallmark aims of microfluidic technology. Together, these innovations will enable the development of a true total analytical system capable of greatly increasing the efficiency and throughput of any number of diagnostic, prognostic, and industrial processes.

Cross References

- ► Biosample Preparation Lab-on-a-Chip Devices
- ► Chromatographic Chip Devices
- ► Digital Microfluidics
- ► DNA Micro-arrays
- ► Interfaces between Microfluidics and Mass Spectrometry
- ► Lab-on-Chip Devices for Immunoassay
- ► Lab-on-Chip Devices for Protein Analysis
- ► Lab-on-Chip Devices for Sample Extraction
- ► Microfluidic Bioreactors
- ► Droplet Microreactors

References

1. Friere SLS, Wheeler AR (2006) Proteome-on-a-chip: Mirage or the Horizon? Lab Chip 6(11):1415–1423
2. Templin MF, Stoll D, Schrenk M, Traub PC, Vohringer CF, Joos TO (2002) Protein microarray technology. Drug Discovery Today 7(15):815–822
3. Peterson DS (2005) Solid supports for micro analytical systems. Lab on a Chip 5(2):132–139
4. Cretich M, Damin F, Pirri G, Chiari M (2006) Protein and peptide arrays: Recent trends and new directions. Biomol Eng 23(2–3):77–88
5. Urban PL, Goodall DM, Bruce NC (2006) Enzymatic microreactors in chemical analysis and kinetic studies. Biotechnol Adv 24(1):42–57
6. Kato M, Inuzuka K, Sakai-Kato K, Toyo'oka T (2005) Monolithic bioreactor immobilizing trypsin for high-throughput analysis. Anal Chem 77(6):1813–1818
7. Hayashi K, Iwasaki Y, Kurita R, Sunagawa K, Niwa O, Tate A (2005) The highly sensitive detection of catecholamines using a microfluidic device integrated with an enzyme-modified pre-reactor for interferent elimination and an interdigitated array electrode. J Electroanal Chem 579(2):215–222
8. Linder V, Sia SK, Whitesides GM (2005) Reagent-loaded cartridges for valveless and automated fluid delivery in microfluidic devices. Anal Chem 77(1):64–71
9. Hadd AG, Raymond DE, Halliwell JW, Jacobson SC, Ramsey JM (1997) Microchip Device for Performing Enzyme Assays. Anal Chem 69(17):3407–3412
10. Duffy DC, Gillis HL, Lin J, Sheppard NF, Jr., Kellogg GJ (1999) Microfabricated Centrifugal Microfluidic Systems: Characterization and Multiple Enzymatic Assays. Anal Chem 71(20):4669–4678
11. Herr AE, Throckmorton DJ, Davenport AA, Singh AK (2005) On-chip native gel electrophoresis-based immunoassays for tetanus antibody and toxin. Anal Chem 77(2):585–590
12. Jiang X, Ng JMK, Stroock AD, Dertinger SKW, Whitesides GM (2003) A Miniaturized, Parallel, Serially Diluted Immunoassay for Analyzing Multiple Antigens. J Am Chem Soc 125(18):5294–5295
13. Huang JX, Mehrens D, Wiese R, Lee S, Tam SW, Daniel S, Gilmore J, Shi M, Lashkari D (2001) High-throughput genomic and proteomic analysis using microarray technology. Clin Chem 47(10):1912–1916
14. Liu Y, Lu H, Zhong W, Song P, Kong J, Yang P, Girault HH, Liu B (2006) Multilayer-Assembled Microchip for Enzyme Immobilization as Reactor Toward Low-Level Protein Identification. Anal Chem 78(3):801–808
15. Lin Y, Timchalk CA, Matson DW, Wu H, Thrall KD (2001) Integrated microfluidics/electrochemical sensor system for monitoring of environmental exposures to lead and chlorophenols. Biomed Microdevices 3(4):331–338
16. Peterson DS, Rohr T, Svec F, Frechet JMJ (2002) Enzymatic microreactor-on-a-chip: Protein mapping using trypsin immobilized on porous polymer monoliths molded in channels of microfluidic devices. Anal Chem 74(16):4081–4088
17. Sakai-Kato K, Kato M, Toyo'oka T (2004) Screening of inhibitors of uridine diphosphate glucuronosyltransferase with a miniaturized on-line drug-metabolism system. J Chromatogr A 1051(1–2):261–266
18. Nie S, Han M, Gao X (2001) Lab-on-a-bead: Optically encoded microspheres for massively parallel analysis of genes and proteins. Abstracts of Papers, 221st ACS National Meeting, San Diego, CA, United States, April 1-5, IEC-019
19. Wheeler AR, Bird CA, Loo JA, Garrell RL, Loo RRO, Kim CJ, Moon H (2005) Digital microfluidics with in-line sample purification for proteomics analyses with MALDI-MS. Anal Chem 77(2):534–540
20. Burke BJ, Regnier FE (2003) Stopped-Flow Enzyme Assays on a Chip Using a Microfabricated Mixer. Anal Chem 75(8):1786–1791

21. Puckett LG, Dikici E, Lai S, Madou MJ, Bachas L, Daunert S (2004) Investigation into the Applicability of the Centrifugal Microfluidics Platform for the Development of Protein-Ligand Binding Assays Incorporating Enhanced Green Fluorescent Protein as a Fluorescent Reporter. Anal Chem 76:7263–7268
22. Wang J, Ibanez A, Prakash CM (2003) On-chip integration of enzyme and immunoassays: Simultaneous measurements of insulin and glucose. J Am Chem Soc 125(28):8444–8445
23. Kim Y-D, Park CB, Clark DS (2001) Stable Sol-Gel Microstructured and Microfluidic Networks for Protein Patterning. Biotech Bioeng 73(5):331–337
24. Brevig T, Kruhne U, Kahn RA, Ahl T, Beyer M, Pedersen LH (2003) Hydrodynamic guiding for addressing subsets of immobilized cells and molecules in microfluidic systems. BMC Biotechnology 3(10)
25. Dupuy AM, Lehmann S, Cristol JP (2005) Protein biochip systems for the clinical laboratory. Clin Chem Lab Med 43(12):1291–1302

Proton Exchange Membrane Fuel Cells

► Microstructured Hydrogen Fuel Cells

PRT

► Resistance Temperature Detectors

Pump Head

Synonyms

Backpressure; Differential pressure; Head pressure

Definition

Pump head is the pressure rise from pump inlet to pump outlet. The *characteristic curve* of a pump relates pump head to flow rate. The pump head at which the flow rate is zero is called the *shut-off head* or *maximum head*.

Cross References

► Magnetic Pumps
► Membrane Actuation for Micropumps
► Peristaltic Pumps
► Positive Displacement Pump

Pyroelectric

► Pyroelectric Flow Sensors

Pyroelectric Flow Sensors

HUI YAN, HONGKAI WU
Department of Chemistry, Tsinghua University, Beijing, P. R. China
hkwu@mail.tsinghua.edu.cn

Synonyms

Pyroelectric sensors; Pyroelectric; Thermal flow sensors

Definition

A *pyroelectric* is substance that generates an electrical charge during a temperature change. The *pyroelectric coefficient* is the measured change in the polarization with a variation in the temperature in a single-domain pyroelectric material. *Pyroelectric sensors*, in principle, work as thermal transducers. The pyroelectric sensing element converts a non-quantified thermal flux into an output measurable quantity like charge, voltage or current.

Overview

Pyroelectric Effect

The pyroelectric coefficient (p) of a material under constant stress and electric field is defined by the following expression:

$$p = \left(\frac{\partial P}{\partial T}\right)_{E,\sigma} \tag{1}$$

where P is the polarization, T the temperature, E the electric field and σ ghe elastic stress.

Pyroelectrics can be classified into two main categories:

- non-pyroelectric pyroelectrics, those whose polarization cannot be switched by an application of external electric field (such as some semiconductors and biological materials); and
- pyroelectric pyroelectrics, those whose polarization is obtained by poling and also can be switched by an electric field.

The pyroelectric effect of pyroelectric pyroelectrics usually exists below a certain transition temperature called the *Curie point*, T_c, in proper pyroelectrics and is more temperature dependent than that of the non-pyroelectric pyroelectrics.

Primary and Secondary Pyroelectric Effects

Thermodynamic analysis of the pyroelectric effect yields the expression

$$P_i^\sigma = P_i^\varepsilon + d_{ijk}^T c_{jklm}^{T,E} \alpha_{lm}^\sigma \tag{2}$$

where P_i^σ is the total pyroelectric effect measured at constant stress, and P_i^ε, the pyroelectric effect at constant

strain ε, is called the primary effect. The second term of Eq. (2) is the contribution caused by thermal deformation of the crystal and is known as the secondary pyroelectric effect. Parameters d, c and σ are the piezoelectric, elastic stiffness and thermal expansion coefficients of the crystal, respectively.

In pyroelectric ferroelectrics, generally, the primary effect is large and negative because the spontaneous polarization decreases with increasing temperature. The secondary effect is considerably smaller and may have either sign depending on the values of the constants. And so the experimentally observed pyroelectric coefficients are dominated by the primary effect and are negative in pyroelectric crystals. But in non-ferroelectric pyroelectric crystals there is no simple way to predict the sign and the magnitude of their coefficients. In practice the total pyroelectric effect can be measured and, also, the secondary effect calculated from the constants d, σ and c.

Pyroelectric Currents

Pyroelectric currents are proportional to the time derivative of the temperature and, in case of infrared (IR) detectors, to the changes of IR radiation. In order to assess stationary IR sources as well, a chopper is used to modulate the IR radiation. Signals thus exhibit a well-defined angular chopping frequency ω. The smallest detectable temperature change is limited to the temperature fluctuation of the detector system, the electronics or the intrinsic noise current j_n of the pyroelectric element, given here for a thin film by the expression

$$j_n = \sqrt{\frac{A}{t} 4KT(\sigma + \omega\varepsilon_r\varepsilon_0 \tan\delta \Delta f)} \tag{3}$$

where σ is the leakage conductivity of the pyroelectric thin film (in bulk detectors, the parallel resistor); ω the angular frequency; $\tan\delta$ the loss tangent; Δf the frequency bandwidth; A the surface; and t the thickness of the element.

The crossover frequency $\omega_{el} = \sigma/\varepsilon_r\varepsilon_0 \tan\delta$ between resistor-type noise and dielectric noise is typically $0.1 - 10$Hz. At typical modulation frequencies of 30 Hz, the dielectric noise dominates. The figure of merit of dielectric and pyroelectric material parameters for an optimal detectivity can thus be formulated as

$$F_D = \frac{p}{\sqrt{\varepsilon_0\varepsilon_r \tan\delta}} \tag{4}$$

Essential Materials

Pyroelectrics in Materials with Perovskite Structure

Perovskite oxides have the structural formula ABO in which A may be some large cation, such as Ba^{2+} or Pb^{2+}, and B may be some medium size cation, such as Ti^{4+} or Zr^{4+}. These cations are located in cages formed by the network of the oxygen anions. There is an abundance of perovskites, natural (minerals) and synthetic ones, because of a large number of cations having sizes that can fit into the oxygen cages. Pyroelectric perovskites are a sub-group in the perovskite family.

Lead Zirconate Titanate (PZT)

Because of its high piezoelectric constants, PZT is the most widely used pyroelectric ceramic in sensor applications. PZT is a solid solution of lead titanate and lead zirconate. The substitution of a small fraction ($\sim$1 %) of the PZT cations by other cations can improve the properties. This method is always used to produce PZT that is optimized for different applications. Doping by cations of lower valence, e. g. Fe^{3+} replacing Ti^{4+}, Zr^{4+} and/or Na^{+} for Pb^{2+}, results in oxygen vacancies that stabilize the domain walls. PZT ceramics with dopants of lower valence (acceptors) are very useful for underwater applications and also for high-power and high-voltage applications. Doping with a higher valence than the substituted cations (donors), e. g., Nb^{5+} for Ti^{4+}/Zr^{4+} and/or La^{3+} for Pb^{2+}, increases the concentration of lead vacancies, enhancing the mobility of domain walls. These materials are used for medical transducers and for sensitive pressure sensors. PZT ceramics for pyroelectric applications are rich in titanium. The compositions rich in titanium (e. g., zirconium titanium) have a high pyroelectric coefficient and low permittivity, giving good pyroelectric figure of merit. Additionally, their coercive field is high, reducing the risk of depolarization during use and making this composition useful also in the form of thin films.

Relaxors and Relaxor Pyroelectrics

A large number of lead-containing perovskites, called relaxors, show anomalous characteristics typified by a strong frequency dispersion of the permittivity. Examples are lead magnesium niobate ($PbMg_{1/3}Nb_{2/3}O_3$ or PMN) and lead zinc niobate ($PbZn_{1/3}Nb_{2/3}O_3$ or PZN). These materials have many useful advantages:

- very high permittivity over a wide temperature range,
- large electrostrictive strain and
- strong pyroelectric response under a DC bias field. Solid solutions of relaxors and normal pyroelectrics, which are the subject of much interest, are called relaxor pyroelectrics, such as $PMN - PbTiO_3$ and $PZN - PbTiO_3$.

Layer Perovskites

A large number of pyroelectrics crystallize in the so-called layer perovskite phases. These phases are made of layers of perovskites separated by other layers; a typical example is bismuth oxide. Many pyroelectric layer perovskites have a high T_c, making them interesting for high-temperature piezoelectric applications. In addition, many of them are lead free. A prototype material is bismuth titanate ($Bi_4Ti_3O_{12}$).

Lithium-niobate and Lithium-tantalate

Lithium-niobate (LN) and lithium-tantalate (LT) are uniaxial pyroelectrics, having trigonal structure, with spontaneous polarization arising from asymmetrical displacement of lithium relative to the other ions. These materials' T_c values are 1210 and 620 °C, respectively. They are always produced commercially in single-crystal forms. Both are much used for surface acoustic wave devices (e. g., high-frequency filters), while LT is used for pyroelectric detection due to its large pyroelectric coefficient and low permittivity.

Pyroelectric Polymers

Pyroelectricity is also found in polymers. Polyvinylidenfluoride (PVDF, $(CH_2CF_2)_n$) is used for sensor applications that can benefit from a large sensor area. The pyroelectric polymers have low pyroelectric coefficients d and high coefficients because of the low permittivity. The polymers are light and then have good acoustic impedance matching to water, to organic and biological matter.

Dimensional and Microstructural Aspects of Pyroelectric Materials

Pyroelectric sensors utilize a wide range of material forms: crystals, bulk ceramics, thick layers and thin films. Noteworthy among new compositions with improved performance is the class of relaxor pyroelectrics. Many novel pyroelectric sensors utilize thin and thick films. Bulk pyroelectric ceramics for room temperature, and pyroelectric sensors, are widely available. New compositions with higher permittivity are available now.

Poling of Pyroelectric Materials

After the manufacturing, pyroelectric materials usually do not possess pyroelectric properties, since the pyroelectric domains are randomly oriented. The poling process consists of the application of a DC electric field to align the domains. A remanent polarization persists after the removal of the field and the material is pyroelectrically active. Poling is usually done at elevated temperatures (see below) using fields larger than the coercive field. During use of pyroelectric materials, care should be taken to avoid depolarization under high temperatures, electric fields or stresses.

In summary, pyroelectric materials have found applications in a wide range of fields. For device applications and the convenience of application engineers, several figures of merit criteria are defined. Most of these can be calculated using the thermal, electrical and optical characteristics of the materials available in the literature and various handbooks on the physical constants of materials.

Pyroelectric Flow Sensors

Pyroelectric flow sensors are a kind of thermal flow sensor. They can be classified according to the thermal transfer mechanism, i. e., calorimetric- or boundary-layer-type flow meters and here the latter will be introduced.

Thermal mass-flow meters directly measure the mass-flow rate utilizing the thermal transfer process between a heated element and the flowing mass. According to the thermal transfer mechanism, they can be classified as calorimetric- or boundary-layer-type flow meters. Calorimetric flow meters utilize the simple principle that as the mass flows through the device, power has to maintain the temperature of the incoming mass at a known level. By measuring the supplied power P and the temperature above ambient, ΔT, the mass-flow rate $\dot{M}$ can be calculated as the expression

$$\dot{M} = \frac{1}{c_{pg}} \frac{P}{\Delta T} \tag{5}$$

where c_{pg} is the specific heat of the mass at constant pressure. A typical example of calorimetric flow meters consist of a thin-walled capillary with a heater wire wound around its center. The wire resistor serves both to heat the center section and to provide a measure of the temperature, since the resistance of the heater wire is a function of temperature. Because the capillary has a very small diameter, the mass absorbs heat from the wall and quickly reaches the wall temperature. As the mass follows, additional power has to be supplied to compensate for the energy carried away by the mass. The mass-flow rate may be measured by keeping either the power or the elevated temperature constant.

Another type of capillary flow meter is shown in Fig. 1. A central heater (H) is wound about a thin walled capillary tube. Two resistive sensor elements are mounted on the capillary symmetrically, one upstream (S_1) and the other downstream (S_2) of the heater to monitor the temperature

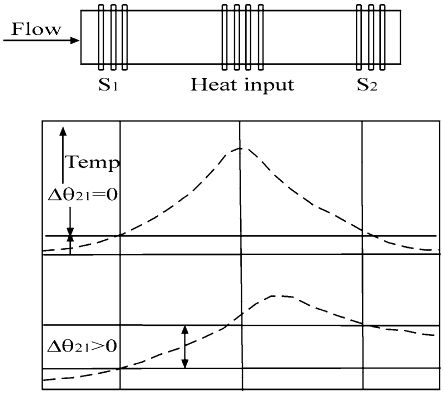

Pyroelectric Flow Sensors, Figure 1 A capillary flow meter with external heater and transducers is depicted at the top with the corresponding temperature profile along the capillary for zero (upper) and nonzero (lower) gas flow

as depicted in the upper portion of Fig. 1. The difference in temperature between the two sensors

$$\Delta T_{21} = \Delta T\,(\mathrm{S}_2) - \Delta T\,(\mathrm{S}_1) \tag{6}$$

is used to determine the flow rate. In the absence of flow, the temperature profile in the capillary is symmetric with $\Delta T_{21} = 0$ as shown in Fig. 1. As mass flows, heat is transferred from the wall to the moving fluid at the upstream position, thereby lowering $\Delta T(\mathrm{S}_1)$. At the downstream electrode, energy is injected into the wall at S_2 by the heated flowing fluid, thereby increasing the temperature $\Delta T(\mathrm{S}_2)$. The net effect is an asymmetric temperature profile in the tube causing $\Delta T_{21} \neq 0$, as indicated at the bottom of Fig. 1. This differential measurement has the advantage of being directional and providing a zero signal at zero flow.

Basic Methodology

Methods for Determination of Pyroelectric Coefficients

There are several methods for measurement of pyroelectric coefficients, but most can be grouped into two kinds. The objective in the first case is to directly measure the pyroelectric current and at the same time change the temperature. In the second method measurements of polarization or charge can be estimated either by the integration of pyroelectric current during the continuous heating of the sample or recording the hysteresis loop at various temperatures by the Sawyer–Tower technique.

In the first approach the changing temperature can be generated by chopping the incoming radiation source or AC heating (known as the Chynoweth technique) of the sample and the pyroelectric response current i can be expressed as follows:

$$i = \frac{p\eta W T_{\mathrm{r}}}{Ct}$$

where η is the power absorbed by the sample, T_{r} is a transfer function depending on the thermal circuit of the sample and the chopping or modulation frequency, t is the thickness of the sample and C is the thermal capacity of the sample. Often a thin layer of highly absorbing material is applied on the sample in order to achieve $\eta = 1$.

The pyroelectric current $i(T)$ at a temperature T can also be measured by uniformly heating or cooling the sample at a constant rate (generally, 1 to 4 °C/min) and the pyroelectric coefficient, p, can be calculated using the following expression (Byer–Roundy technique):

$$i(T) = \frac{Ap}{(\Delta T/\Delta t)^{-1}}$$

where A is the electroded area of the sample and $\Delta T/\Delta t$ is the heating or cooling rate of the sample. Here, the charge release (in either of the two cases mentioned earlier) at a discrete temperature is determined and the pyroelectric coefficient is obtained graphically or by differentiation.

Methods for Thin-Film Deposition

Thin-film deposition techniques such as sol–gel method, hydrothermal route, sputtering, metalorganic chemical vapor deposition (MOCVD) and pulsed laser deposition have been developed and are being adapted in commercial devices. Table 1 lists some advantages and disadvantages of different film deposition techniques. Three major kinds are sol–gel, physical vapor deposition and chemical vapor deposition. In wet methods, the sol–gel technique uses fine powder in gel forming a liquid-like mixture of metal oxides and organic salts to grow transparent ceramic films. It is low energy consuming process at lower crystalline temperature and allows better control of chemistry by mixing of precursors in the liquid state at the molecular level. Most electroactive ceramics and polymers are amenable to this technique. Physical vapor deposition requires vacuum and uses DC or RF magnetron sputtering and pulse laser deposition to provide high quality, uniformity and stability but low deposition rates of materials. Chemical vapor deposition, i. e., MOCVD, on the other hand, uses volatile chemical precursors, which are vaporized on heated substrates. It is proving suitable for conformational deposition of high-quality three-dimensional structures on bottom electrodes and is characterized by high deposition rates.

Pyroelectric Flow Sensors, Table 1 The advantages and disadvantages of different film deposition techniques

	Deposition technique	Advantages	Disadvantages
1	Sol–gel	Lower crystallization temperature, lower cost, better control of mixing of precursors, quickly produce new materials	Lack of phase and composition control, morphology, reproducibility
2	Physical vapor deposition (i) DC sputtering (ii) Pulsed laser deposition (iii) MBE	Compatibility with IC processing Uniformity and scalability, high quality Rapid sampling of materials, quickly produce new materials Composition control, precise atomic layering, extreme flexibility and scalability	High equipment cost Low deposition rate, high point defect concentration Lack of uniformity, high residual stresses Expensive development stage
3	Chemical vapor deposition	High deposition rate, good stoichiometry control, low point defect concentration, high conformity and scalability	Low precursor stability, expensive

Properties to be Considered of an Appropriate Material

While the pyroelectric, dielectric and thermal properties of pyroelectric materials are clearly fundamental in determining the basic performance of a device, there are many other properties to be considered when making a selection of an appropriate material. These are the following:

- Electrical resistivity. The circuit in Fig. 2 shows a resistor R_G connected across the active element. This serves three functions. First, it fixes the electrical time constant τ_E of the device. Second, it allows the gate leakage current of the FET to bias its operating point. If there was no bias resistor here, the FET amplifier would not be stable and would take a long time to settle. Third, it determines the voltage responsivity.
- Piezoelectric properties. At first sight it seems surprising that piezoelectric properties are important in pyroelectric devices. However, all pyroelectric detectors used in a high-vibration or acoustically noisy environment will produce a piezoelectric microphonic noise signal, mostly through flexure, which can be very significant if steps are not taken to suppress it.
- Manufacturability. The ability to make the selected material in a large area at low cost is a very important consideration. Pyroelectric ceramics have an important advantage here over some of the single-crystal materials that are available, as a consequence of their relative ease of manufacture using a range of techniques and their stability during other subsequent manufacturing processes.

Examples for Sensor Design and Fabrication

Many studies had demonstrated that pyroelectric anemometers based on single-crystal $LiTaO_3$ have a very wide range and the promise of interesting response characteristics. The following example was well characterized by a conjugate gas-flow–heat-flow model.

A 200 μm thick, 30 mm diameter, Z-cut, single-crystal $LiTaO_3$ wafer, unpolished on both sides, was used to fabricate the pyroelectric flow sensor. The wafer was first degreased by immersing in trichloroethane, acetone and isopropyl alcohol for 10 min each and then it was rinsed in deionized (DI) water and blown dry with nitrogen. After cleaning, nichrome (NiCr) and gold films were sequentially deposited on the front surface of the wafer. This was done in a cryo-pumped electron-beam evaporator at a pressure of about 10^{-5} Pa without breaking vacuum between the NiCr and Au evaporations. The last step minimized contamination of the devices.

Two masks were prepared to define the nichrome and gold patterns. Using standard photolithography, the Au leads and contact patterns were formed in a photoresist layer. The residual gold was removed with a solution of $4\,g\ KI : 1 g\ I_2 : 40\,mL\ H_2O$. The $KI - I_2$ solution was chosen because it etches the gold film but not the NiCr. The photoresist was then removed using photoresist stripper and rinsed in DI water.

After cleaning and processing, the NiCr pattern was formed in the photoresist by aligning a suitable mask to the Au pattern on the wafer. The NiCr on the wafer was etched using a solution of $310\,g\ (NH_4)_2Ce(NO_3)_6 : 1970\,mL\ H_2O : 120\,mL\ HNO_3$. With the completion of the front side patterning, a 200 nm thick NiCr film was evaporated onto the backside of the wafer. The wafer was then sliced into chips.

The two-electrode element, 3.8 mm × 3.8 mm × 0.2 mm in size, is shown in Fig. 3. The device was mounted on a ceramic carrier with one end of the heater connected to the NiCr common on the other side of the $LiTaO_3$ chip. The assembled unit was then inserted into a standard

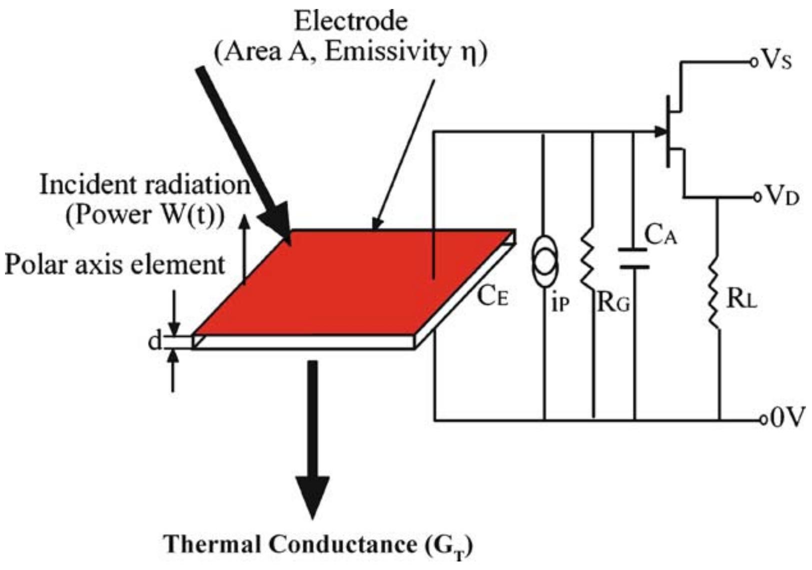

Pyroelectric Flow Sensors, Figure 2 Schematic diagram of a pyroelectric detector element

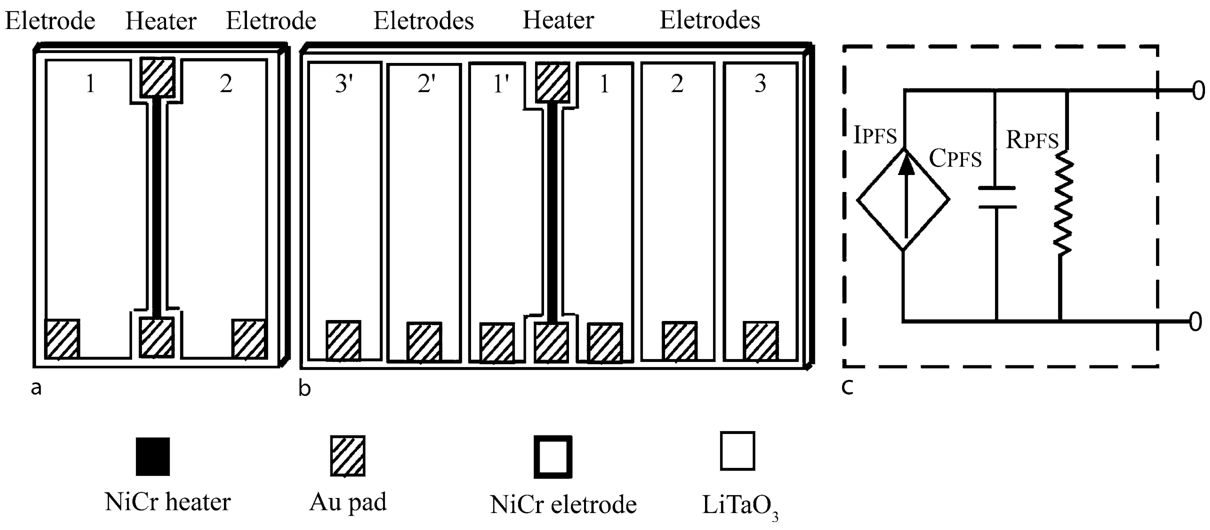

Pyroelectric Flow Sensors, Figure 3 Layer of (**a**) a two-electrode element pyroelectric flow sensor and (**b**) a six-electrode one and (**c**) the equivalent circuit of the pyroelectric electrode

1/4′ Union Tee. For completeness, the equivalent circuit of the pyroelectric flow sensors electrode is shown in Fig. 3. A schematic diagram of the measurement system is shown in Fig. 4. The basic component consists of a function generator that produces the heater current and a computer-controlled two-phase analog lock-in amplifier.

Other parts of the electronic measuring system consisted of a function generator to supply a sinusoidal driving voltage to the heater of the sensor, a buffer, a signal conditioner for the output from the sensor, a two-phase lock-amplifier and a computer. The signals from the two electrodes of the sensor are sent directly to a buffer. The buffer section transforms the high impedance of the sensor signal into a low-impedance signal, which is sent to a signal conditioner through a seven-line cable. Because of the extremely high resistance, R_{PA}, of the sensor chip, the loading by the electronics produces a voltage output signal across the input resistance of the buffer amplifier.

Key Research Findings

Modification of Pyroelectric Materials

As we know, there are many kinds of pyroelectric materials, but all of them have some advantages and disadvan-

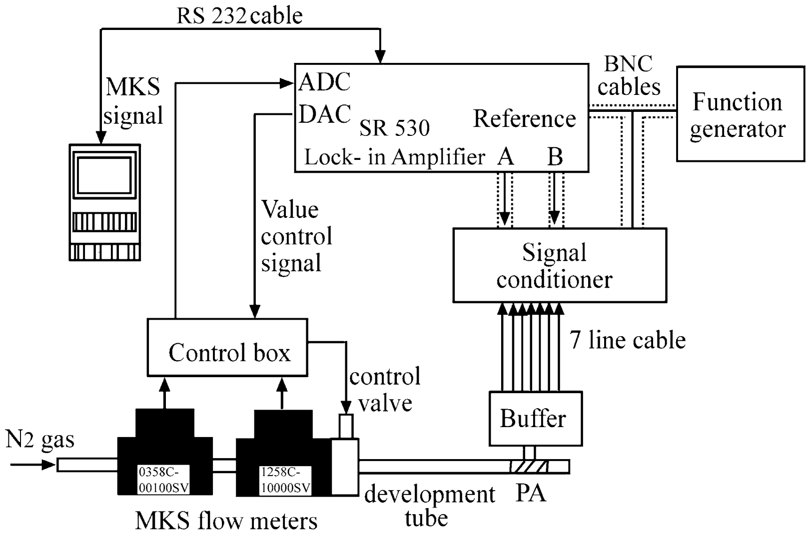

Pyroelectric Flow Sensors, Figure 4 Diagram of the measurement system

tages. For example, as a perovskite-type pyroelectric compound desirable for pyroelectric infrared detectors because of its relatively large pyroelectric coefficient and spontaneous polarization, PT has poor mechanical properties due to its large tetragonal strain which makes poling of PT materials difficult. Much attention has been focused on the modification of PT by doping with the purpose of obtaining improved mechanical and electrical properties. The incorporation of off-valent (La^{3+}, Sm^{3+}, Nd^{3+}, Gd^{3+}) and isovalent ions (Ca^{2+}, Ba^{2+}, Sr^{2+}) into PT ceramics is reported to enhance the pyroelectric properties. Substitution of these ions results in the reduction of lattice anisotropy leading to hard and dense ceramics with high mechanical strength. From the standpoint of thermal responsivity, the performance of a pyroelectric detector is enhanced when it is in the form of a thin film. In recent device applications, it has become increasingly necessary to consider the improvement of these films in their performance in addition to the large component area and connection to many circuit elements. Recently, calcium- and lanthanum-doped lead titanate (PCT and PLT) thin films have been studied due to their possible use in optical waveguides, infrared sensors, dynamic random access memories and non-volatile memories. Thin-film optical devices are especially attractive because of their potential for monolithic integration. In addition, thin films offer the potential for increased speeds, reduced operating voltages and enhanced efficiency.

In order to improve mechanical properties for different applications, many pyroelectric polymer composites have been prepared, such as $BaTiO_3$–PVC composites, $(Bi_{0.5}Na_{0.5})_{0.94}Ba_{0.06}TiO_3$/P(VDF-TrFE), 65PMN-35PT/P(VDF-TrFE) and DTGS:PVDF.

Preparation of Thin Films

The use of bulk pyroelectrics in pyroelectric devices inevitably leads to a situation where the material must be cut, lapped and polished to make a thin, thermally sensitive layer. If an array of detectors is required for a thermal goal, this must be metallized on both faces, processed photolithographically and bonded to a silicon read-out circuit to yield a complete hybrid array. Clearly, it would be desirable if the material could be deposited as a thin film, to remove the requirement for lapping and polishing, if possible directly onto a complete wafer of chips, where it could be processed to yield an array of thin, thermally isolated structures. Fortunately, many techniques have been researched for pyroelectric thin-film deposition, mainly for applications to non-volatile memories. These include chemical solution deposition (CSD), metalorganic deposition (MOD), RF magnetron sputtering, pulsed laser ablation (PLD) and metalorganic chemical vapor deposition (MOCVD).

Pyroelectric flow sensors and chips

Pyroelectric sensors have recently been increasingly employed for sensing purposes. Excellent piezoelectric and pyroelectric properties of pyroelectric materials, combined with design flexibility and miniaturization offered by thin-film geometry and also developments in micro- and nanoscale fluids technologies have generated great

interest in pyroelectric thin films. The multisensing chip utilizes the pyroelectric effect in the following sensing devices: gas-flow sensor infrared detector arrays, chemical reaction sensors and charge-coupled device imagers. A multipurpose integrated sensor chip that responds simultaneously to several different physical and chemical variables has been fabricated.

Also, multifunctional pyroelectric flow sensors have also appeared. As we know, any change in the temperature induces charges on the surface of the material, inducing an electric field, which generates transverse strain and bending deformation (see Fig. 3). A typical example is used for flow sensor and valving purposes.

Future Directions for Research

During recent years, the study of micro- and nanoscale fluids has shown significant opportunities for high detectivity of elementary devices with small size. For pyroelectric flow sensors, it is highly desirable to develop theoretical models, experimental methods for pyroelectric element preparation and sensor fabrication, and higher sensitivity with excellent mechanical properties.

Cross References

► Ferroelectric
► Pyroelectricity
► Piezoelectric Valves

References

1. Damjanovic D, Muralt P, Setter N (2001) Pyroelectric sensors. IEEE Sens J 1(3):191–206
2. Lee MH, Guo R, Bhalla AS (1998) Pyroelectric sensors. J Electroceramics 2(4):229–242
3. Whatmore RW (2004) Pyroelectric arrays: ceramics and thin films. J Electroceramics 13:139–147
4. Chang DH, Yoon YS (2002) Response analysis of multilayer pyroelectric structures. Integr Pyroelectrics 49:275–283
5. Hsieh HY, Zemel JN (1995) Pyroelectric anemometry: frequency, geometry and gas dependence. Sens Actuators A 49:133–140
6. Hsieh HY, Bau HH, Zemel JN (1995) Pyroelectric anemometry: theory of operation. Sens Actuators A 49:125–132
7. Hsieh HY, Spetz A, Zemel JN (1995) Pyroelectric anemometry: vector and swirl measurements. Sens Actuators A 49:141–147
8. Duggirala R, Son IS, Lal A (2003) A pyroelectric-piezoelectric valve for integrated microfluidics. Transducers'03, International Conference on Solid-State Sensors, Actuators and Microsystems, Digest of Technical Papers, 12th, Boston, MA, United States, 8–12 June, vol 2, pp 1554–1557
9. Goel M (2004) Recent developments in electroceramics: MEMS applications for energy and environment. Ceram Int 30:1147–1154
10. Chopra S, Sharma S, Goel TC, Chatterje R, Mendiratta RG (2006) Comparison of Ca-doped and La-doped PT films for pyroelectric sensors. Comput Mater Sci 37:134–140

Pyroelectricity

Definition

Describes the phenomenon of materials that generate an electric field across them due to a change in their temperature. All pyroelectric materials are piezoelectric.

Pyroelectric Sensors

► Pyroelectric Flow Sensors

PZT

► Piezoelectric Materials for Microfluidics

P

Q-Dots

► Semiconductor Nanoparticles

Quadrupole Filter

Synonyms

Electrostatic quadrupole; Quadrupole mass spectrometer

Definition

A mass filter that separates ions according to their trajectories in a two-dimensional hyperbolic electrostatic field with DC and radiofrequency AC components. Ions with stable trajectories transit the filter, while other ions discharge on the electrodes. Unlike a quadrupole ion trap, the quadrupole filter operates continuously.

Cross References

► Mass Spectrometry

Quadrupole Ion Trap

Synonyms

Ion trap mass spectrometer

Definition

A mass filter that separates ions according to their trajectories in a three-dimensional hyperbolic electrostatic field with DC and radiofrequency AC components. Unlike a quadrupole filter, the ion trap does not operate continuously, but on batches of ions that are trapped, stored and then detected in sequence.

Cross References

► Mass Spectrometry

Quadrupole Mass Spectrometer

► Quadrupole Filter

Quantum Box

► Quantum Dot

Quantum Dot

CHAN HEE CHON, DONGQING LI
Department of Mechanical Engineering, Vanderbilt University, Nashville, TN, USA
Chanhee.chon@vanderbilt.edu

Synonyms

Quantum box; Artificial atom

Definition

A quantum dot is a semiconductor nanoparticle that confines the motion of electrons and holes in three spatial directions.

Overview

Quantum confinement is defined as the space where the motions of electrons and holes in a semiconductor are restricted in one or more dimensions. This quantum confinement occurs when the size of semiconductor crystallites is smaller than the bulk exciton Bohr radius. Quantum wells, quantum wires, and quantum dots are confined in one, two, and three dimensions, respectively [1, 2]. The confinement can be created due to electrostatic potentials, the presence of an interface between different semiconductor materials, and the presence of a semiconductor surface. A valence band and a conduction band are separated by an energy range known as the band gap (E_g). These amounts

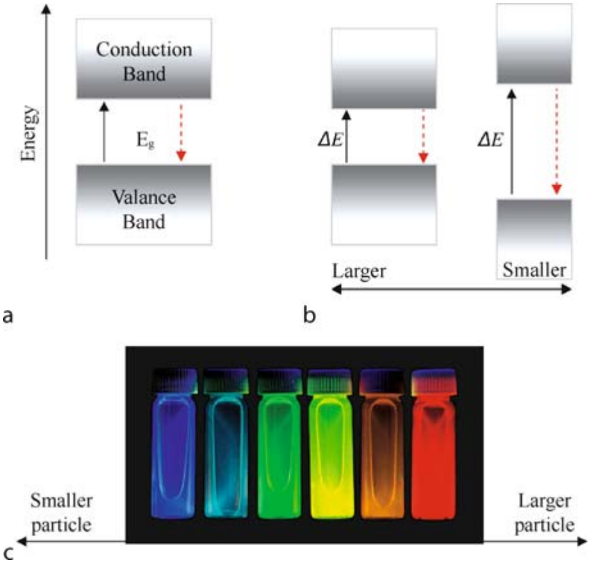

Quantum Dot, Figure 1 Schematics and image of quantum confinement and semiconductor size: (**a**) energy level of high-energy conduction band and low-energy valence band; (**b**) band gap energy increase by decreasing nanoparticle sizes; (**c**) quantum dots of cadmium sulfide in solution fluoresce brightly under ultraviolet light [3]

of energy will be absorbed in order to promote an electron from the valence band to the conduction band and emitted when the electron relaxes directly from the conduction band back to the valence band. By changing the size of the semiconductor nanoparticles the energy width of the band gap can be altered and the optical and electrical responses of these particles are changed (Fig. 1).

A quantum dot containing electrons can be compared to an atom because both have a discrete energy spectrum and bind a small number of electrons. However, a quantum dot different from an atom can be engineered by controlling the geometrical size and shape and the strength of the confinement potential [4].

A quantum dot confines more electrons and holes than those of the bulk semiconductor material. This causes a blue-shift of the interband absorption and a quantum dot of the same material can emit different color light depending on its size [5]. A smaller quantum dot emits shorter wavelength light (bluer) while a larger quantum dot emits longer (redder) wavelength light because of the band gap energy (E_g) levels (Fig. 1a), which determine the fluoresced light. This band gap energy is inversely proportional to the square of the size of the quantum dot. Consequently, a larger quantum dot has more energy and a closer energy band (Fig. 1b). This allows the quantum dot to absorb photons containing less energy, which is closer to red light (Fig. 1c).

The size of a quantum dot is important for the tunable light emission characteristic. A small quantum dot, such as a colloidal semiconductor nanocrystal, can be as small as 2 to 10 nm [6]. A self-assembled quantum dot is typically between 10 and 50 nm in size [7]. A quantum dot defined by lithographically patterned gate electrodes or by etching on two-dimensional electron gases in semiconductor heterostructures can have lateral dimensions exceeding 100 nm [8].

Quantum dots have many promising applications in diode lasers [9], QD-LED for computer displays [10], quantum computing [11], solar cells [12], and biological applications such as medical imaging and disease detection [13].

Cross References

- ► Evanescent Wave Microscopy
- ► Flow Cytometer Lab-on-Chip Devices
- ► Fluorescence Measurements
- ► Fluorescent Labeling
- ► Fluorescent Thermometry
- ► Nanoscale Flow Visualization
- ► Detection Using Confocal Microscope
- ► Detection Using Fluorescence Microscope
- ► Semiconductor Nanoparticles

References

1. Brus LE (1984) Electron–Electron and Electron–Hole Interactions in Small Semiconductor Crystallites: The Size Dependence of the Lowest Excited Electronic State. J Chem Phys 80:4403–4409
2. Norris DJ, Sacra A, Murray CB, Bawendi MG (1994) Measurement of the Size Dependent Hole Spectrum in CdSe Quantum Dots. Phys Rev Lett 72:2612–2615
3. Frankel F (2007) No Small Matter. http://www.nisenet.org/publicbeta/gallery/slideshow001/index.php. Accessed 26 Nov 2007
4. Shiraishi K, Tamura H, Takayanagi H (2001) Design of a Semiconductor Ferromagnet in a Quantum-Dot Artificial Crystal. Appl Phys Lett 78:3702–3704
5. Canham LT (1990) Silicon Quantum Wire Array Fabrication by Electrochemical and Chemical Dissolution of Wafers. Appl Phys Lett 57:1046–1048
6. Murray CB, Norris DJ, Bawendi MG (1993) Synthesis and Characterization of Nearly Monodisperse CdE (E = Sulfur, Selenium, Tellurium) Semiconductor Nanocrystallites. J Am Chem Soc 115:8706–8715
7. Petroff P, Lorke A, Imamoglu A (2001) Epitaxially Self-Assembled Quantum Dots. Phys Today 54:46–51
8. Scherer A, Craighead HG (1986) Fabrication of Small Laterally Patterned Multiple Quantum Wells. Appl Phys Lett 49:1284–1286
9. Zhukov AE et al (1999) Continuous-Wave Operation of Long-Wavelength Quantum-Dot Diode Laser on a GaAs Substrate. Photonics IEEE Tech Lett 11:1345–1347

10. Coe S, Woo WK, Bawendi M, Bulovic V (2002) Electroluminescence from single monolayers of nanocrystals in molecular organic devices. Nature 420:800–803
11. DiVincenzo DP (1995) Quantum Computation. Science 270:255–261
12. Schaller RD, Klimov VI (2004) High Efficiency Carrier Multiplication in PbSe Nanocrystals: Implications for Solar Energy Conversion. Phys Rev Lett 92:186601
13. Michalet X et al (2005) Quantum Dots for Live Cells, in Vivo Imaging, and Diagnostics. Science 307:538–544.

Quantum-Dot Quantum Well (QDQW Nanoparticles)

► Composite Nanoparticles

Quantum Efficiency

Synonyms

Fluorescence efficiency; Quantum yield

Definition

Quantum efficiency is a parameter that is used to quantify the efficiency of the fluorescence emission of a fluorescent dye. For a fluorophore that is excited to its first excited state, the quantum efficiency represents the fractional rate of emission of photons via fluorescence.

Cross References

► Fluorescent Thermometry
► Lab-on-a-Chip Device for Chemical Analysis

Quantum Yield

► Quantum Efficiency

Quartz

► Piezoelectric Materials for Microfluidics

Radiation Pressure

► Optofluidics: Optics Enabling Fluidics
► Transport of Droplets by Acoustics

Radical Polymerization

Definition

A type of polymerization in which the reactive center of a polymer chain consists of a radical.

Cross References

► Polymer Synthesis within Microfluidic Reactor

Radiofrequency (RF) Sputtering

Definition

Thin-film deposition technique which uses a radio frequency (e. g. 13.56 MHz) to create a plasma consisting of ions of a process gas (Ar in the case of this investigation). These ions are accelerated into a target material to remove atoms of the material, which are then deposited onto a substrate to form a thin film.

Cross References

► Fabrication of Self-Assembled Catalytic Nanostructures

Radius of Curvature

Definition

Radius of a theoretical circle (or sphere in three dimensions) that can fit a meniscus of interest. This radius is used to approximate the pressure drop associated to capillary flow.

Cross References

► Surface-Directed Capillary Flow Systems

Random Method

► Monte Carlo Method

Rarefaction Parameter

Definition

Rarefaction parameter is the ratio of a typical size of gas flow a to the equivalent mean free path ℓ, i. e. $\delta = a/\ell$.

Cross References

► Gas Flow in Nanochannels
► Heat Transfer in Microchannel Flows
► Supersonic Micro-Nozzles
► Micro- and Nanoscale Gas Dynamics

Rarefied Flow

Definition

Conditions under which the characteristic length scale for a flow approaches the mean free path of the gas molecules; this flow regime bridges the continuum regime and the gas kinetics regime.

Rarefied Gas Dynamics

Definition

Rarefied Gas Dynamics is a scientific field which aims at describing gas flows on the basis of the kinetic Boltzmann equation considering the whole range of the gas rarefaction covering the free molecular, transitional and hydrodynamic regimes.

Cross References

- ► Gas Flow in Nanochannels
- ► Heat Transfer in Microchannel Flows
- ► Supersonic Micro-Nozzles
- ► Micro- and Nanoscale Gas Dynamics
- ► Lattice Poisson-Boltzmann Method, Analysis of Electroosmotic Microfluidics

Rayleigh Flow

Definition

An idealized steady, I-D compressible duct flow in which heat transfer may occur. The flow is regarded as frictionless and perfect gas behavior with constant specific heat is assumed.

Cross References

- ► Supersonic Micro-Nozzles

Rayleigh Instability

Definition

Taking a force balance between the surface tension along the surface of a fluid and the normal stresses across it, the Rayleigh instability will describe the tendency of a fluid stream to break up into droplets. It is not the same as the Rayleigh-Taylor instability, and not to be confused with Kevin-Helmholtz instabilities.

Cross References

- ► Piezoelectric Microdispenser
- ► Kelvin–Helmholtz Instability
- ► Rayleigh–Taylor Instability
- ► Jetting
- ► Free-Surface Atomization

Rayleigh–Taylor Instability

Definition

Describes the formation of irregularities along an interface, typically fluid-fluid, as it is accelerated in a direction perpendicular to the interface. The phenomenon occurs in microfluidics in the atomization of sessile droplets. It is not the same as the Rayleigh instability (► Rayleigh–Taylor instability), and should not be confused with the ► Kevin–Hemholtz instability.

Cross References

- ► Piezoelectric Microdispenser

Reacting Electrokinetic Flow

► Electrokinetic Transport with Biochemical Reactions

Reaction Condition Control

Synonyms

Temperature control; Concentration control; Reaction time control

Definition

Controlling reaction conditions such as temperature, concentration of chemicals, and reaction time. To obtain well defined products, it is often necessary to control these reaction conditions precisely and uniformly.

Reaction Time Control

► Reaction Condition Control

Reactive Ion Etching (RIE)

SAMI FRANSSILA, LAURI SAINIEMI
Helsinki University of Technology, Helsinki, Finland
sami.franssila@tkk.fi, lauri.sainiemi@tkk.fi

Definition

Reactive ion etching (RIE) is a plasma process where radiofrequency (RF) discharge-excited species (radicals, ions) etch substrate or thin films in a low-pressure chamber. RIE is a synergistic process between chemically active species and energetic ion bombardment. RIE is faster than either pure physical ion bombardment or spontaneous chemical etching. Because ion bombardment is directional, RIE has anisotropic character, with reduced lateral etch rate and vertical (or nearly vertical) sidewalls. RIE is essential when narrow lines or channels are needed, or when high aspect ratio structures need to be fabricated. RIE of silicon is independent of crystal planes, and therefore any shape can be fabricated, unlike anisotropic wet etching. Deep reactive ion etching (DRIE) is an extension of RIE that enables high-rate etching of deep structures.

Overview

Etching has traditionally been divided into wet and dry etching, according to etchant phase. In the case of wet etching, the etch reaction results in soluble products; in the case of dry etching, in volatile etch products:

Solid + gaseous etchant → volatile products

$Si(s) + 2XeF_2(g) \rightarrow SiF_4(g) + 2Xe(g)$

$W(s) + SF_6(g) + O_2(g) \rightarrow WF_6(g) + SO_2(g)$

Etch gases are thus selected on product volatility considerations. Halogens F, Cl and Br are the most widely used etch species, coming from SF_6, CF_4, CHF_3, C_4F_8, Cl_2, BCl_3, $SiCl_4$, HBr. Typical etch products include SiF_4, $SiCl_4$, NF_3, WF_6, $AlCl_3$ [1–3]. Non-volatile etch products like AlF_3 or $CuCl_2$ cause problems in the form of residues, micromasking, roughness and non-uniformity.

Other gases used in RIE include oxygen, hydrogen, argon, helium and nitrogen. These have roles in modifying plasma chemistry and physics, heat transfer and surface chemistry. Oxyhalides typically form WO_xF_y type etch products, and CO_2 and H_2O are generated as photoresist mask is etched.

Additive gases are also important for anisotropy mechanism: for instance deposition of SiO_xF_y film is essential for sidewall passivation in silicon etching in SF_6/O_2 plasmas. Similarly, CHF_3 and C_4F_8 etch gases lead to deposition of $(CF_2)_n$ type fluoropolymer films, which passivate sidewalls and minimize lateral etching. Etch rate and anisotropy are manifestations of balancing properly etching and deposition reactions.

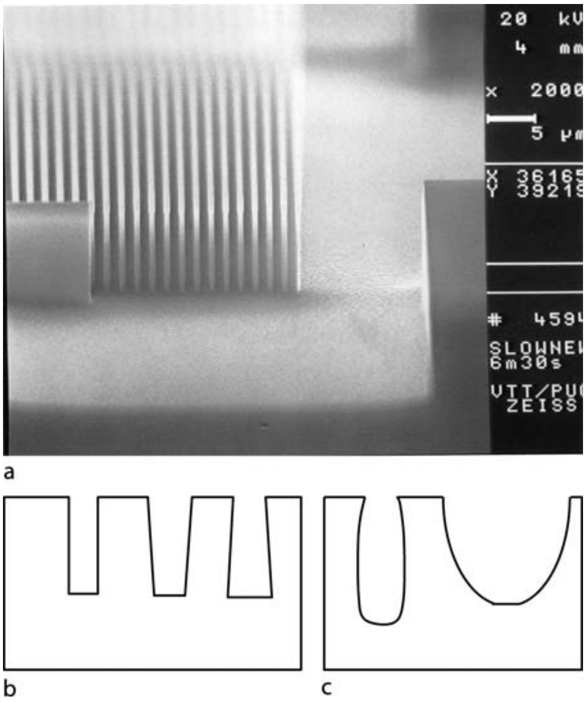

Reactive Ion Etching (RIE), Figure 1 RIE etched sidewall profiles (from left to right): vertical (SEM and schematic); positively sloped; negatively sloped (retrograde); bowing (barrelling); isotropic

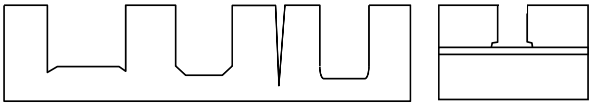

Reactive Ion Etching (RIE), Figure 2 Bottom of etched structures: trenching; faceting; spearheading, rounding; notching (footing) at insulator interface

Etched profiles are depicted in Fig. 1. Perfectly vertical walls are possible, but both positively and negatively sloped and bowing and isotropic profiles can be found. The bottoms of reactive ion etched structures exhibit similarly a wide variety of shapes (Fig. 2): trenching, faceting, spearheading and rounding. At insulator etch stop layers notching (footing) effects can take place.

Ion beam etching (IBE; also known as ion milling) relies on energetic (argon) ions and differs thus from RIE. Chemically active species are absent in ion beam etching, and etch product volatility is not an issue. IBE rates are very low compared to RIE, only 20 – 100 nm/min. Reactive ion beam etching (RIBE) uses reactive ions, e. g. fluorine or chlorine, but the etching mechanism is dominated by physical bombardment at low pressures.

The term dry etching is sometimes used as a synonym for RIE, but there are also processes which are dry etching without ions or plasmas. The XeF_2 example cited above is a case of spontaneous chemical reaction that proceeds without plasma activation.

Basic Methodology

For many materials there is the choice of both wet and RIE processes. Silicon, silicon dioxide, aluminum, tungsten (and other refractory metals) and glass/quartz can be etched by either method. Silicon and its compounds can be etched in both fluorine or chlorine plasmas, with SiF_4 or $SiCl_4$ as the main reaction products, but because of tighter safety requirements chlorine gas is less popular [4]. In integrated circuit fabrication Cl_2 (and HBr) source gases are used routinely in silicon etching because they offer better anisotropy and higher oxide selectivity than fluorine gases. DRIE of silicon using Cl_2 gas is limited because the etch rate is very slow compared with that of fluorine gases, even by a factor of ten. Another drawback is the need for thick metallic masks (e. g. several micrometers thick electroplated nickel). The advantages of Cl_2 plasmas are in smaller RIE lag (see below) and smaller mask undercut.

Silicon nitride is etched in CF_4- or SF_6-based plasmas. The process is fairly straightforward and the main considerations are the etch rate ratios (selectivities) needed. It is impossible to achieve selectivity against silicon in CF_4 and SF_6 plasmas, but nitride-to-oxide selectivity is ca. 2:1 to 10:1. If selectivity between nitride and silicon is needed, plasmas based on CHF_3, C_2F_6 or C_4F_8 are employed. Nitride-to-silicon selectivities can be in the range 5:1 to 50:1. Oxide etching is carried out with these same plasmas. Nitride etch rate is roughly half of oxide etch rate in the same plasma.

Diamond, silicon carbide, titanium carbide and gallium nitride are materials that do not have wet etch processes, but RIE processes do exist. For some materials neither RIE nor wet processes exist and then IBE can be used to pattern them, or else molding or deposition together with polishing can be used for patterning. Platinum and gold (and other noble metals) can be wet and dry etched, but both processes are difficult since the aggressive etch conditions are damaging the resist mask. These materials are often patterned by lift-off rather than by etching.

Releasing structures by isotropic undercut etching in wet solutions is prone to stiction when capillary force exceeds the mechanical spring force of a cantilever, beam or a plate, leading to contact. Dry release techniques avoid stiction by avoiding liquid-phase processing. Dry release methods include vapor etching (HF; oxide sacrificial layer), plasmaless dry etching (XeF_2; silicon sacrificial layer) and isotropic plasmas (SF_6; silicon sacrificial layer).

In RIE the details of thin-film structure or doping can usually be neglected and for instance PECVD nitride and LPCVD nitride are etched at roughly the same rate, and in silicon etching no doping dependence needs to be accounted for.

Equipment

RIE equipment is usually parallel plate reactors in which both plasma and DC bias voltage are created using one capacitively coupled plasma (CCP) source [5]. The wafers are placed on top of the electrode which is typically in direct contact with plasma glow (Fig. 3). This ensures a reasonable etch rate but the controllability of etching is difficult. A major downside of this type of reactor is that the wafers are exposed to heavy ion bombardment because plasma generation and bias voltage are coupled. The etch rate of silicon is typically 0.1 – 1 μm/min and selectivity against the photoresist mask is usually below 5:1. Anisotropy is based on the directionality of ion bombardment and aspect ratios are usually limited to 2:1.

The difference between RIE and DRIE is not unambiguously defined. The division can be made according to etch rate, selectivity, aspect ratio capability or reactor type. DRIE reactors are typically equipped with two RF power generators instead of one (Fig. 3). An inductively coupled plasma (ICP) source generates plasma that has 1 – 2 orders of magnitude higher plasma density than RIE, which roughly translates to 1 – 2 orders of magnitude higher etch rate. In DRIE reactors the wafer is clamped on the bottom electrode of the CCP power source, which is not in direct contact with the plasma. Bias voltage is controlled separately by the second capacitively coupled source. This arrangement allows low bias voltages and therefore much higher selectivities can be achieved. In DRIE selectivity of photoresist mask is 10:1 to 100:1 vs. 1:1 to 10:1 in RIE.

The parameters available for process optimization include:

- etch gas selection
- RF power (coil power in ICP)
- bias voltage (CCP power in ICP)
- pressure
- flow rate
- temperature

The key process outcomes of a (D)RIE process are:

- etch rate
- anisotropy/sidewall angle
- mask selectivity
- substrate selectivity
- etched surface quality
- throughput

A rough order of magnitude estimate of etch rates is as follows: 100 nm/min for simple research reactors; 1 μm/min for production tools and 10 – 50 μm/min for silicon DRIE reactors. Exact values depend on particular reactor design, RF power source and other hardware factors. Silicon etch rate is much faster than oxide or polymer etch rate in the same reactor. More extensive passivation translates to reduced etch rate but also reduced undercut and more vertical sidewalls.

In most DRIE processes aspect ratios of 20:1 can be quite easily achieved. Directionality of ion bombardment is also better in DRIE reactors because wafers are not in direct contact with plasma and process pressure is also lower (typically 10 – 50 mTorr in DRIE). Low process pressure creates high requirements for vacuum pumps because, in order to achieve high etch rates, high gas flows are essential. Temperature of the wafer can be controlled between −150 and +450 °C. Systems with wafer cooling can utilize higher RF power to increase etch rate while keeping photoresist erosion to a minimum.

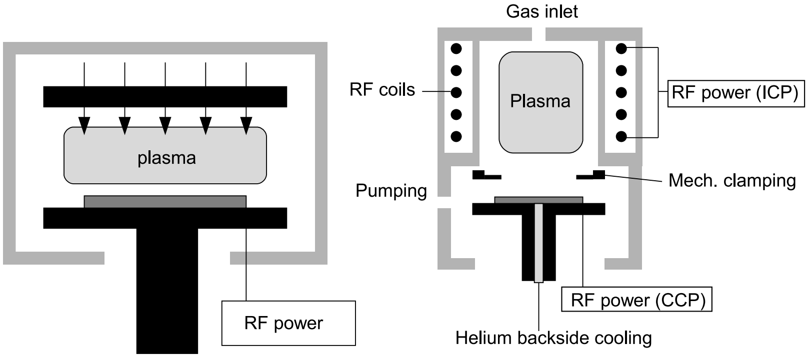

Reactive Ion Etching (RIE), Figure 3 Capacitively coupled RIE reactor (left); inductively coupled DRIE reactor (right)

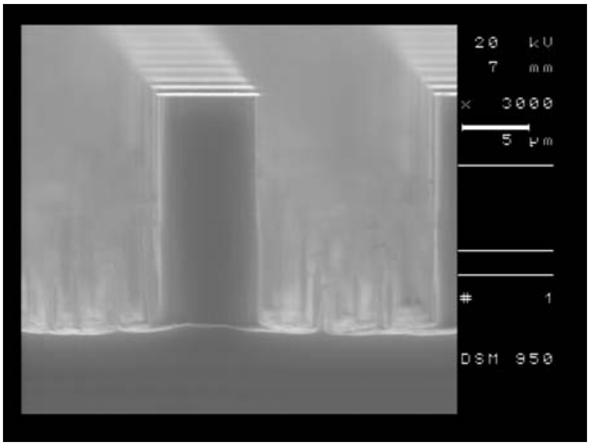

Reactive Ion Etching (RIE), Figure 4 Micromasking from aluminum mask

Mask Selection (Selectivity, Mask Material Effects, Removal)

Photoresist is used as a mask practically whenever it is possible because it is the fastest and the simplest way to create patterns. However, its fairly low selectivity in RIE limits the etch depth. Both elevated and cryogenic temperatures are detrimental to photoresists. During conventional RIE process temperature of the wafer increases because of the heavy ion bombardment and photoresist may burn. At cryogenic temperatures photoresists suffer from cracking.

When high selectivity or wider temperature range is needed hard masks such as silicon dioxide, metals and metal oxides are utilized. The most obvious downside of the hard masks is the increase in process complexity. Deposition of the hard mask material might include high-temperature processes and the non-idealities in hard mask etching process degrade the quality of final structures. The most common hard mask material is silicon dioxide (SiO_2). In conventional RIE silicon to oxide selectivity is 10:1 to 100:1 and in DRIE 100:1 and higher. Metals and metal oxides have usually higher selectivities than SiO_2, but they may create new problems, like generation of microroughness (Fig. 4).

In order to avoid photoresist deposition over severe topography, a peeling mask (nested mask) can be used: two mask patterns are fabricated on a starting surface, using a suitable combination of mask materials, e. g. oxide-resist or oxide-nitride. After the first DRIE step, one of the mask materials is selectively removed (oxygen plasma ashing of resist mask; or HF etching of oxide mask), exposing more etchable area, while the non-etchable mask still protects selected areas. The second DRIE step etches both newly opened area and continues deeper in the original areas (Fig. 5).

Hard masks can be patterned by both wet and dry etching, and in the first approximation they are identical. However, if accurate dimensional control is required and hard mask etch selectivity is not very high, the etch profile of a wet etched hard mask can influence the size and shape of the feature. The thin wedges resulting from wet etching are quickly eroded by plasma, and the edge of the hard mask recedes, widening the trench (or narrowing a ridge). With vertical walled plasma etched hard masks this is not an issue. Redeposition of etched material on the mask sidewalls can lead to dimensional changes, however (Fig. 6).

R

Key Research Findings

Silicon DRIE

By far the two most popular DRIE techniques are the Bosch [6] and cryogenic processes [7].

Bosch Process

The Bosch process was developed and patented by Franz Lärmer and Andrea Schilp in 1994. Because of

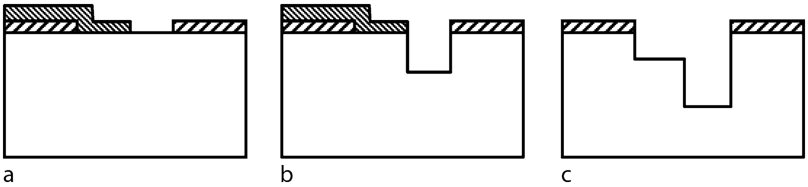

Reactive Ion Etching (RIE), Figure 5 Nested (peeling) mask: (**a**) mask layers patterned; (**b**) after first RIE step; (**c**) after peeling the top mask and second RIE step. Bottom mask, e. g. SiO_2; top mask, resist

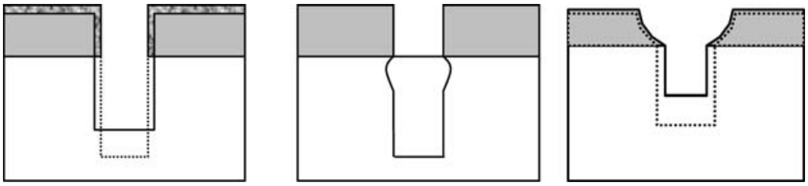

Reactive Ion Etching (RIE), Figure 6 Non-idealities in width control (left to right): redeposition on mask; bowing at trench top; hard mask erosion and trench widening

the nature of the process it is also frequently called the *switched process* and *time domain multiplexed process*. The principle of the Bosch process is shown in Fig. 7. It is based on alternating etch and passivation steps. The etching gas is sulphur hexafluoride (SF_6) that creates fluorine radicals in high-density plasma. After the etch step a thin fluorocarbon film is deposited from cyclic octofluorocyclobutane (c-C_4F_8). This film passivates the surface and prevents etching. At the beginning of the next etch step the fluorocarbon film is removed from horizontal surfaces but sidewalls remain passivated. The SF_6 etch step is not fully anisotropic but the polymer is etched preferentially from the horizontal surfaces due to ion bombardment and the sidewalls remain protected. The repetition of etching and passivation steps results in vertical sidewalls. The microstructure of the etched sidewall, however, shows scalloping (undulation) because of the pulsed nature of the process [8]. The etching and passivation pulse times are typically 5 – 15 s. Etch rate, anisotropy, selectivity and scalloping (sidewall undulation) are all influenced by the duration and overlap of the etch and passivation pulses.

Cryogenic Process

Cryogenic RIE etching was first introduced in 1988 [9]. It was noticed that by cooling the wafer during the RIE the rate of chemical reactions on the sidewalls could be reduced dramatically, leading to improved anisotropy. Selectivity between silicon and masking material is also improved at cryogenic temperatures. The reason for reduced chemical reactions on sidewalls is the silicon oxyfluoride (SiO_xF_y) layer that forms during cryogenic etching process in SF_6/O_2 plasma [10]. Fluorine has very low adsorption coefficient to passivating SiO_xF_y wich therefore inhibits lateral etching. Etching can proceed downwards because ion bombardment removes the passivating layer from horizontal surfaces. Cryo-etched pillars and holes are shown in Fig. 8. Low temperature also reduces spontaneous reactions of free radicals according to the Arrhenius rate law, which also improves anisotropy. Still, the main reason for enhanced anisotropy is the passivating SiO_xF_y layer.

High etch rate in SF_6/O_2 plasma is due to high concentration of fluorine radicals. Oxygen controls the quality of the passivating layer. It is the most important parameter when optimizing the sidewall tapers. If the O_2 content is too low, an isotropic profile results. Too high an oxygen flow leads to overpassivation and formation of so-called black silicon which consists of silicon micrograss.

DRIE Reactor Requirements

The Bosch and cryogenic processes utilize similar DRIE reactors but both processes have their own special requirements [11]. The Switched nature of Bosch-process calls for high speed mass flow controllers, or fast acting valves and buffer tanks. Short step times also necessitate gas line design to minimize delays. In order to reduce the polymer deposition on the chamber walls and pumping lines they should be heated as deposition of fluorocarbon polymer to unwanted surfaces creates particle contamination. In the Bosch process the ratio between the ions and free radicals is important. If relative ion concentration is too high the profile control is lost. By placing the wafer far enough from the plasma glow it is possible to create sufficient ratio

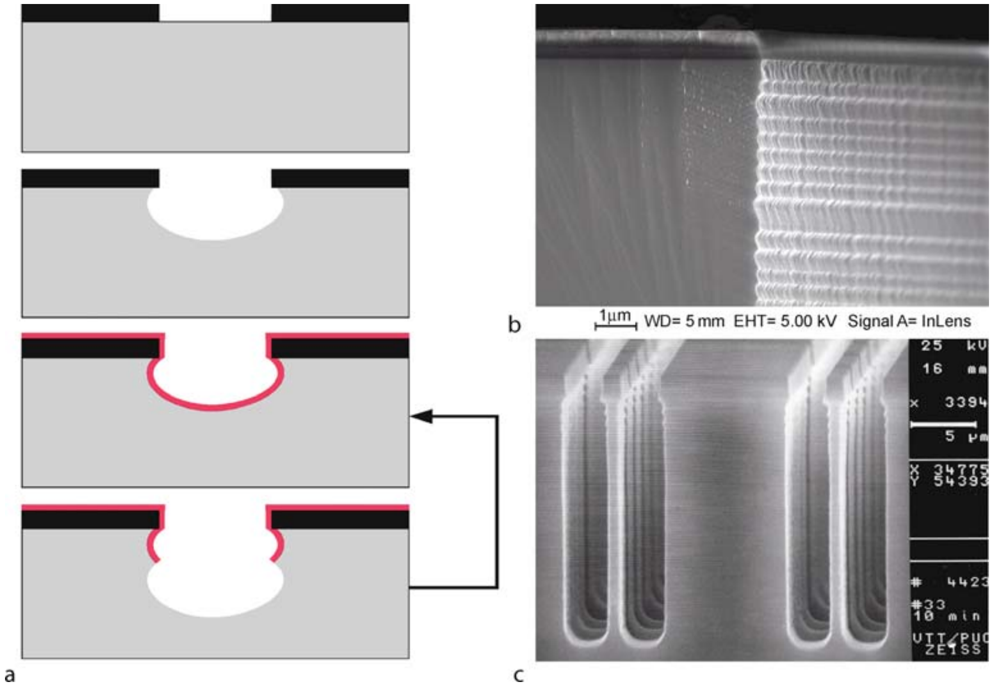

Reactive Ion Etching (RIE), Figure 7 (**a**) Bosch process schematic: repetition of etch and deposit pulses. SEM images of etched structures: (**b**) scalloping of the sidewall; (**c**) perfectly vertical profile

of free radical to ions because of short decay time of ions. Without an ICP source it is impossible to create adequate ratio of free radicals to ions.

In the cryogenic process the temperature of the wafer plays an important role. Accurate wafer temperature control during the process is also essential because the wafer temperature directly affects etch profiles. Cryogenic cooling of the wafer stage is done using liquid nitrogen. The wafer is mechanically or electrostatically clamped on the cooled stage and helium pressure is applied on the backside of the wafer. Because of the high thermal conductivity of the helium, heat transfer from the stage to the wafer is improved. Clamping must be tight to prevent helium leaks to the chamber. Leaks compromise not only the temperature control of the wafer, but also the plasma conditions. In principle a cryogenic process can be operated using a CCP source only, but the etch rate and the selectivity would be considerably lower.

DRIE Special Features

The benefits of the Bosch process are its accurate profile control in high aspect ratio structures and its high etch rate [12]. Etch rates up to 50 µm/min have been reported in special cases, with 10 – 20 µm/min to be considered as more typical production etch rates.

The Bosch process results in scalloping sidewalls due to the pulsed process. This limits its applications in optics, and some fluidic devices are also sensitive to sidewall roughness. The amplitude of scalloping can be minimized by shortening the pulse lengths, and this minimizes the amplitude as well, and 20 nm can be obtained. However, etch rate will be sacrificed. Scallops can also be treated after etching by thermal oxidation or wet etch smoothing.

A notching effect (or footing effect) [13] is seen when high-density plasma etching reaches an insulator surface, e. g. SOI buried oxide or oxide on the backside of the wafer in through-wafer etching (Fig. 2). Charging of the interface leads to ion deflection and ion-enhanced sideways etching at the insulator–silicon interface. This can be minimized by running the end point step in RIE mode (low-density plasma) as opposed to high-density plasma mode, and minimized by having only a single feature size which minimizes overetch time. Reactor design can also help: pulsed CCP power, or low frequency (kHz) power give the electrode time to discharge, thus minimizing the notching effect, but unfortunately affecting sidewall quality. Notching has also been utilized as a release step: joining of two lateral etch fronts acts as a dry release method without the isotropic character of SF_6 plasma release.

With the cryogenic process, sidewalls of the etched structures are smooth, but the etch rate of silicon is some-

R

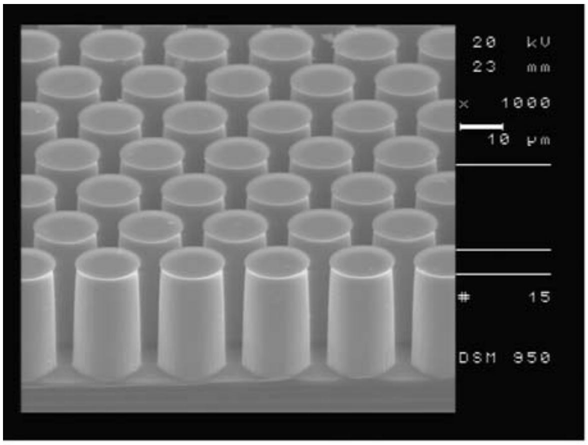

a

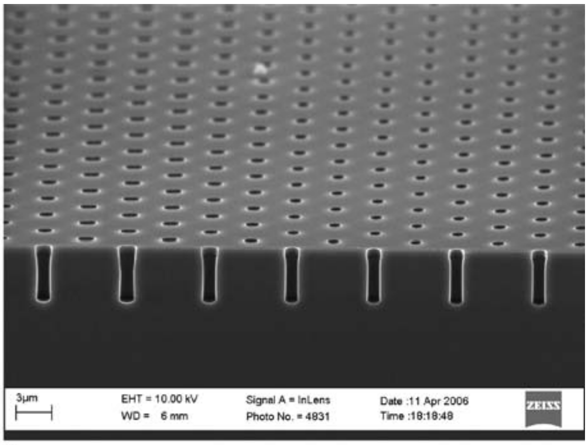

b

Reactive Ion Etching (RIE), Figure 8 Cryo-DRIE etched pillars and holes

what lower than in the Bosch process. Because the thickness of the passivation layer is only ca. 10 nm little ion bombardment is needed to remove it from horizontal surfaces. Therefore applied bias voltage can be very low and extremely high selectivities can be reached. A downside of the cryogenic temperature is that not all photoresists can stand it: they shatter like glass. Thick photoresists are especially prone to cracking. Therefore hard masks such as silicon dioxide must often be employed. Another characteristic feature of the cryogenic process is the possibility to create crystallographic-dependent etch results. Crystallographic dependence appears only at the bottom of the trench (Fig. 2) and it is possible only when using extremely low temperatures and low RF powers.

DRIE Processes for Other Materials

Glasses can be etched by SF_6, CHF_3 or C_4F_8 gases in DRIE but the process is more difficult than with silicon [14]. Silicon–oxygen bonds are stronger than silicon–silicon bonds, and higher power is needed to etch glass with DRIE. Fused silica which is pure SiO_2 can be etched more easily than Pyrex glass which has metal oxides. Increased ion bombardment (and thus power) is needed to prevent residues from metal oxides. This high power leads to problems with masking layers. For shallow etching thin silicon films (PECVD, LPCVD) are suitable as etch masks, but for deep etching thick (electroplated) metals, silicon wafers or thick photoresists (SU-8) must be used. Selectivities of 10:1 are typical for both metal and silicon masks.

Etch rates of Pyrex are typically in the range 1 µm/min, which is considerably lower than that of silicon. Aspect ratios of 10:1 are demanding, and sidewall angle is positively tapered because of extensive mask erosion. Even though 88° sidewall angles have been reported, 80° is more typical, and the sidewall angle is more feature size (anodically bonded or shadow masks) dependent than in the case of silicon DRIE. Increasing sidewall roughness is an additional factor limiting higher etch rates.

Polymers can be etched by oxygen plasmas using silicon, metal and oxide masks. Etch rates of a few µm/min have been demonstrated with 20:1 aspect ratios. A Bosch process for polymer etching involves an O_2 etch step followed by a C_4F_8 passivation step.

SiC is typically etched in high-density SF_6 plasma that results in etch rate of ~ 300 nm/min. A benefit of low reactivity of SiC is that no sidewall passivation is needed to enhance anisotropy. A downside is that heavy ion bombardment (platen power 50 – 100 W) enhances also mask material etch rate and selectivity becomes a problem. Therefore hard masks such as nickel, indium tin oxide and aluminm are used in SiC etching. Because of sputtering and redeposition of mask material etched surfaces are often rough.

(D)RIE Process Limitations and Problems

Practical (D)RIE processes exhibit a number of limitations regarding etch rate, etchable area, feature size and shape, all of which become more prominent for high aspect ratio structures. Also the sidewall profile non-idealities are discussed.

Loading effect [15] refers to etch rate dependence on etchable area. Loading effect has its roots in reactant supply and consumption balance. When etchable area is small, etch gas flow can supply enough reactive specie,

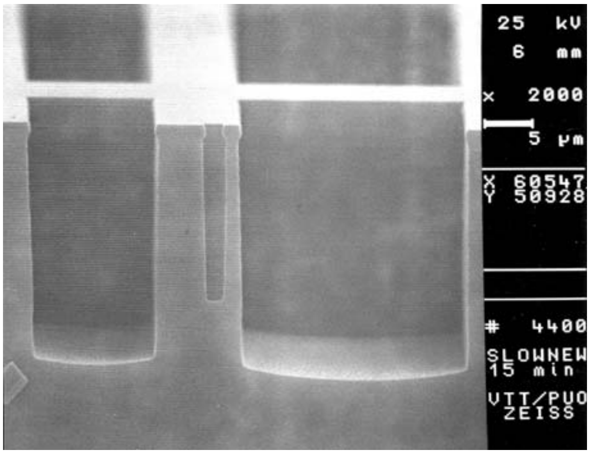

Reactive Ion Etching (RIE), Figure 9 RIE lag: etched depth depends on feature size

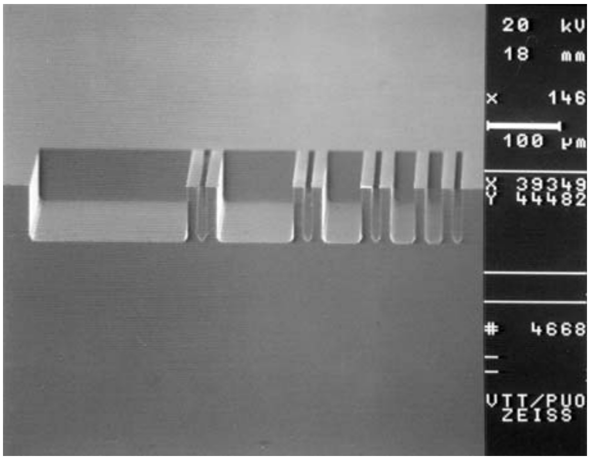

Reactive Ion Etching (RIE), Figure 10 Elimination of RIE lag: DRIE of single sized mosaic subpatterns combined with sidewall removal by TMAH wet etching

but with higher etchable area a deficiency of reactants may develop. Higher gas flow will compensate this but it may be undesirable to increase flow rate for other reasons. Loading phenomenon exhibits itself in various ways: in batch reactors rate depends on the number of wafers in the reactor; in a single-wafer reactor it depends on chip design. On the microscale loading manifests itself between dense and isolated structures. Etchable area also influences etch uniformity: for the Bosch process 1.5% uniformity over a 150 mm wafer has been reported, at 20% loading, with deterioration for higher loads, especially at the edges.

RIE lag refers to the common observation that smaller features are shallower than larger features (Fig. 9). This effect manifests itself in high aspect ratio ($> 1:1$) structures only. Aspect ratio-dependent etching (ARDE) is a similar but not identical effect: etch rate decelerates for longer etching times (i. e. when aspect ratios increase). ARDE occurs for all line widths, and many different etch times are needed to check it, while RIE lag can be seen from one wafer. Reactions (both etching and deposition) are affected as gas transport and ion bombardment change in high aspect ratio structures. At very high aspect ratios, etching of passivation layers also changes.

Combination of RIE lag and wet etching of sidewalls can be utilized either to eliminate RIE lag or to create multidepth microstructures in a single etch step [17]. This necessitates that the larger patterns are redrawn on the mask as a mosaic of smaller structures. If all mosaic elements are the same size, RIE lag is eliminated (Fig. 10); if they are different in size, multiple etched depths are obtained.

The shape of the etchable feature affects etch rate [18]. Holes of 5 μm diameter are etched more slowly than trenches 5 μm wide. This is again related to reactant transport inside the microstructures. Making narrow structures side-by-side with large features, e. g. a pillar filter and a liquid reservoir, or sniffer holes in a microreactor, results in larger areas being deeper than the small ones.

(D)RIE Applications in Microfluidics

In this section RIE applications in fluidics are discussed. Especially, benefits and drawbacks of silicon DRIE processes are highlighted, and special capabilities of DRIE emphasized.

Silicon DRIE is independent of silicon crystal structure, and this enables fabrication of all possible shapes, in contrast to wet chemical anisotropic etching which is limited by silicon crystal planes. In microfluidics this shape freedom has implications for flow profiles, as significantly channel cross-sections can be kept constant on turns, or widened or narrowed. Various microreactors, separation systems, mixers, fuel atomizers and micropower combustion systems make use of meandering, radial or spiralling channels enabled by DRIE. Constrictions of various sorts, converging–diverging structures are essential for example in microthrusters, capillary valves and nozzle-diffuser micropumps. They can be etched easily by DRIE. All sorts of nozzles, emitters and orifices can be optimized for performance when DRIE is used, while wet etched structures are limited in shape. Filters with narrow pass gaps can be made by DRIE (also by bonding and sacrificial layer techniques) but not by wet etching.

DRIE is essential in fabrication of small features. DRIE is capable of reproducing accurately practically any features that have been defined by lithography. Fluid dynamics studies of microflows utilize DRIE for making accurately

R

dimensioned microchannels and orifices. Membrane structures with small holes are useful in many drug delivery, fuel cell and cell probing applications. In a patch clamp application submicrometre apertures have been etched in 20 μm thick silicon membrane. In catalysis studies a small DRIE fabricated capillary leak into a mass spectrometer enabled increased sensitivity and fast response times. Integration of microreactor and mass spectrometer also minimized dead volumes.

DRIE enables high aspect ratio structures. Holes, trenches and pillars with 10:1 to 20:1 aspect ratios can be fabricated, and experimental structures with 40:1 and even higher have been demonstrated. These high aspect ratio structures are limited by RIE lag, however. Applications for high aspect ratio structures include various trapping devices. Depending on feature size, either micro- or nanobeads are trapped, or macromolecules like DNA. For pillars, aspect ratios in excess of 50:1 have been demonstrated: 300 nm feature size, 15 μm structure height.

Random nanopillars can also be utilized in chemical microsystems. Intensity of desorption/ionization on silicon mass spectrometry (DIOS-MS) is dependent on surface area. At first DIOS plate material was porous silicon, but it has been shown that using nanopillars instead of porous silicon, signal intensity can be increased.

Combining DRIE and anisotropic wet etching can produce unique structures. For example, ⟨111⟩ silicon cannot be etched by the standard KOH, TMAH or EDP etchants, but if an initial trench has been etched by DRIE, fast etching crystal planes are exposed, and wet etching can proceed. If this is combined with spacer structures to protect sidewalls and another DRIE step, ⟨111⟩ free-standing silicon structures can be made.

Combination of DRIE and isotropic plasma etching can be used to create channels inside silicon. After the DRIE step, a sidewall passivation step is performed, and etching is then continued with an isotropic etchant. Anisotropic SF_6/O_2 DRIE recipe can quite easily be tailored to be isotropic by for example raising the pressure and eliminating the oxygen. Similarly, isotropic SF_6 plasma release etch can be used to fabricate free-standing silicon structures.

DRIE in combination with electrochemical etching of silicon enhances shape freedom in electrochemical etching. If anisotropic wet etching is used to create the initial pits for electrochemical etching, the usual limitations of crystal plane dependence manifests itself, while by using DRIE complex shapes like circular or curving can be made.

DRIE of silicon is a major method for making masters for polydimethylsiloxane (PDMS) casting and hot embossing. Alternative techniques include silicon wet etching and SU-8 thick photoresist. Silicon offers more durable material properties, but the master fabrication is more tedious. DRIE excels over wet etching because of shape freedom and sidewall profile engineering possibilities, but suffers from inferior surface quality. DRIE process has to be optimized for slightly positively sloping sidewall profile in order to facilitate de-embossing/release. The quality of optimized silicon masters is good, as applications in optofluidic chips demonstrate: PDMS fluidics and optics can be replicated from silicon masters with excellent performance [19].

An DRIE reactor can be used as a CVD-like deposition tool by changing process parameters and gases [20]. An important example is the deposition of $(CF_2)_n$ from CHF_3 or C_4F_8 source gases. This is the basis of anisotropy in the Bosch process but such films have been used in their own right in microfluidics to render surfaces hydrophobic. Patterning on these films can be done by oxygen plasma with standard photoresist masking and acetone resist stripping as Teflon-like films are chemically very tolerant. Alternatively, lift-off techniques or shadow mask techniques with oxygen plasma can be used.

Future Directions for Research

RIE and DRIE are workhorses of micromachining, and they are being applied to an increasing variety of structures. In developing (D)RIE processes, a number of issues have to be dealt with simultaneously: etch rate, mask etch rate, sidewall angle and profile, the various process limitations and process integration issues. There is a need for more robust processes that are insensitive to design changes, and allow small and large areas to be etched with the same rate, sidewall angle and surface roughness. Through-wafer etching still poses challenges, both as regards rate and aspect ratio and process integration. Very high aspect ratio structures still need design-specific optimization. The same challenges apply to other materials even more than to silicon.

Cross References

► Fabrication of 3D Microfluidic Structures
► Bulk Micromachining
► Silicon Micromachining
► Laser Based Micromachining
► Plasma Etching

References

1. Williams KR, Muller RS (1996) Etch rates for micromachining processes. J MEMS 5:256–269
2. Williams KR, Gupta K, Wasilik M (2003) Etch rates for micromachining processes – Part II. J MEMS 12:761–778

3. Franssila S (2004) Introduction to Microfabrication. Wiley, Chichester
4. Tian WC, Weigold JW, Pang SW (2000) Comparison of Cl_2 and F-based dry etching for high aspect ratio Si microstructures etched with an inductively coupled plasma source. J Vac Sci Tech B18:1890
5. Elwenspoek M, Jansen H (1998) Silicon micromachining. Cambridge University Press, Cambridge
6. Lärmer F, Urban A (2003) Challenges, developments and applications of deep silicon reactive ion etching. Microelectronic Eng 67–68:349
7. Murakami K, Wakabayashi Y, Minami K, Esashi M (1993) Cryogenic dry etching for high aspect ratio microstructures. Proc IEEE Microelectromech Syst Conf, Fort Lauderdale, Feb 1993
8. Ayon A et al (1999) Characterization of a time multiplexed inductively coupled plasma etcher. J Electrochem Soc 146:339
9. Tachi S, Kazunori K, Okudaira S (1988) Low-temperature reactive ion etching and microwave plasma etching of silicon. Appl Phys Lett 52:616
10. de Boer MJ, Gardeniers JGE, Jansen HV, Smulders E, Gilde MJ, Roelofs G, Sasserath JN, Elwenspoek M (2002) Guidelines for etching silicon MEMS structures using fluorine high-density plasmas at cryogenic temperatures. J MEMS 11(4):385–401
11. Walker MJ (2001) Comparison of Bosch and cryogenic processes for patterning high aspect ratio features in silicon. Proc SPIE 4407:89–99
12. Marty F et al (2005) Advanced etching of silicon based on deep reactive ion etching for silicon high aspect ratio microstructures and three-dimensional micro- and nanostructures. Microelectronics J 36:673–677
13. Hwang GS, Giapis KP (1997) On the origin of the notching effect during etching in uniform high density plasmas. J Vac Sci Technol B15:70
14. Akashi T, Yoshimura Y (2006) Deep reactive ion etching of borosilicate glass using an anodically bonded silicon wafer as an etch mask. J Micromech Microeng 16:1051
15. Mogab CJ (1977) The loading effect in plasma etching. J Electrochem Soc 124:1262
16. Gottscho RA et al (1992) Microscopic uniformity in plasma etching. J Vac Sci Tech B10:2133–2147
17. Kiihamäki J, Kattelus H, Karttunen J, Franssila S (2000) Depth and profile control in plasma etched MEMS structures. Sens Actuators 82:234–238
18. Kiihamäki J, Franssila S (1999) Pattern shape effects and artefacts in deep silicon etching. J Vac Sci Technol A17:2280
19. Seo J, Lee LP (2004) Disposable integrated microfluidics with self-aligned planar microlenses. Sens Actuators B99:615–622
20. Andersson H, van der Wijngaart HW, Griss P, Niklaus F, Stemme G (2001) Hydrophobic valves of plasma deposited octafluorobutane in DRIE channels. Sens Actuators B75:136–141

Reflective Index

Definition

Materials with a high reflective index reflect a huge amount of the striking light. They appear glittery.

Regular Least Square

► Least Square

Relative Roughness

Definition

Ratio of roughness to the channel hydraulic diameter.

Relaxation

► Viscoelasticity

Relaxation Time of the Viscoelastic Fluid

Definition

Relaxation time is the characteristic time in which a system relaxes under certain changes in external conditions. Here, it refers to the characteristic time required for the polymer coil to relax from a deformed state to its equilibrium configuration. It is a key parameter for characterizing a viscoelastic fluid.

Cross References

► Turbulence in Microchannels
► Viscoelasticity
► Non-Newtonian Fluids in Microchannel
► Non-Newtonian Fluids in Microfluidics

Relaxor Ferroelectrics

Definition

A specific type of electrostrictive material with large electrostrictive coupling coefficients, and important for applications that require high relative permittivities (i. e., supercapacitors) of 20,000 – 35,000, and actuator applications in particular. Single crystal PMN-PT is a popular composition in this class of material.

Cross References

► Electrostrictive

Replica Molding

► Micromolding

Reptation Tube

Definition

A model of the steric constraints provided by a gel during DNA electrophoresis. The DNA is assumed to move by curvilinear motion along the tube axis.

Cross References

► Electrophoresis

Residual Stress

Definition

Residual stresses are stresses that remain after the original cause of the stresses (external forces, heat gradient) has been removed. Residual stresses occur for a variety of reasons, including inelastic deformations and heat treatment.

Resistance Temperature Detectors

CHRIS DAMES
Department of Mechanical Engineering, University of California, Riverside, CA, USA
cdames@engr.ucr.edu

Synonyms

RTD; Platinum resistance thermometer; PRT; SPRT; IPRT

Definition

A resistance temperature detector (*RTD*) is a device to measure temperature by relating it to changes in the electrical resistance of a metallic sensing element. The resistance of a typical RTD increases by about 0.3% to 0.4% of its room temperature value for every degree Kelvin of temperature increase. With care, RTDs can achieve accuracies of better than 0.1 K at temperatures ranging from about 14 K to over 900 °C.

Overview

Resistance temperature detectors (*RTD*s) are widely used for general purpose temperature measurements as well as high-accuracy metrology and research applications such as MEMS and microfluidics[1–6]. The key concept is the fact that the electrical resistance of a pure metal increases almost linearly with temperature over a broad range of temperature. The underlying physical reason for the temperature dependence is the scattering of electrons by lattice vibrations (phonons), which vibrate with larger amplitudes at higher temperatures. For example, the resistance of platinum, the most common RTD material, is shown in Fig. 1a from −200 °C to 600 °C. To use an RTD, the resistance of the metallic sensing element is measured and then its temperature is calculated from a known calibration relation. The most important property of an RTD is its ► temperature coefficient of resistance (TCR), often denoted by α. The TCR is defined as the relative change in resistance per unit change in temperature:

$$\alpha(T) \equiv \frac{1}{R}\frac{dR}{dT}\,, \tag{1}$$

where R is the resistance and T is the temperature. A larger TCR results in a more sensitive RTD. For industrial and standards-grade platinum RTDs, the TCR is approximately 0.0039 K^{-1} near room temperature, although this value can be significantly reduced in microfabricated platinum RTDs due to their different microstructures (Fig. 1b). RTDs are traditionally made of loosely wound platinum wire encapsulated in a ceramic, glass, or metallic housing. RTDs are also made from laser-trimmed films of platinum on a ceramic substrate. These chip-style RTDs are cheaper and smaller than the wire-wound variety and offer a faster response time, but historically they have been slightly less accurate and at greater risk of degraded accuracy due to thermal expansion mismatch and impurity contamination from the underlying substrate. Nickel, copper, and tungsten are less widely used for commercial RTDs. In MEMS and microfluidic devices, it is common to microfabricate small metallic RTDs out of a wide variety of metals, including platinum, nickel, copper, and gold.

Typical Applications

RTDs are used in a great variety of applications. At one extreme, carefully-designed platinum RTDs are used in the very definition of temperature between 13.8033 K and 961.78 °C [2], because of their potential for extreme stability and accuracy (uncertainties of better than ±1 mK). At a more practical level, commercial RTDs are widely used for industrial and research applications from 14 K to around 600 – 700 °C, with typical absolute accuracies of around ±0.15 K to ±2 K uncalibrated, or ±0.1 K or better after calibration. Bare platinum RTDs also have a long and illustrious history as velocity sensors for fluid flow, a technique known as hot-wire anemometry. More recently, special RTD configurations have also been developed to measure the thermal properties of fluids and solids [7–9].

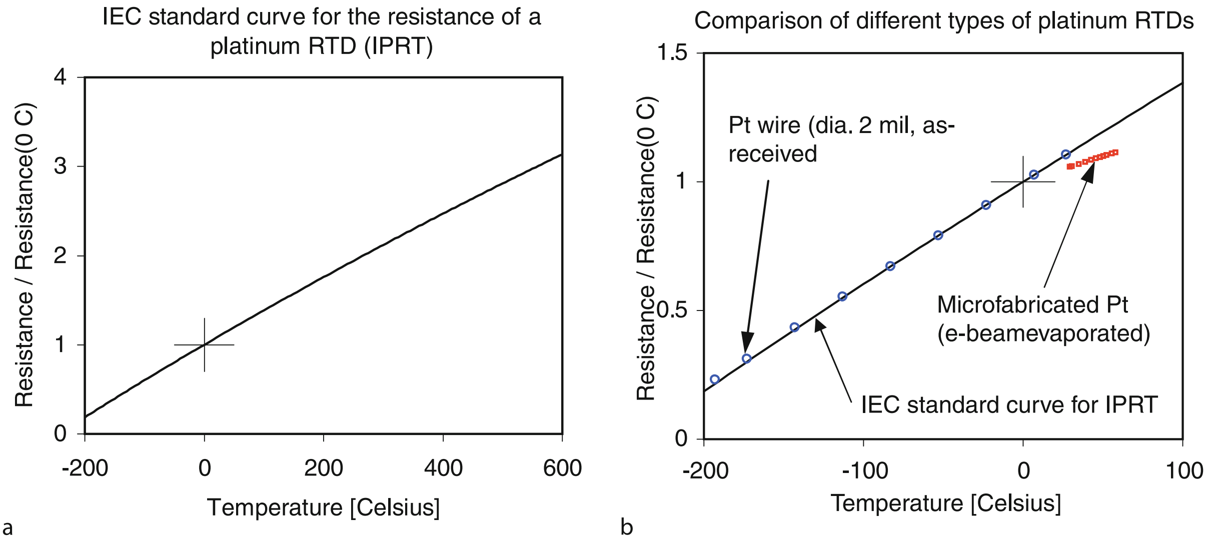

Resistance Temperature Detectors, Figure 1 (**a**) The normalized resistance of an industrial platinum resistance thermometer (IPRT or RTD) as a function of temperature. This curve was calculated using the Callendar-Van Dusen equation with the IEC standard coefficients, Eqs. (2a), (2b) and (3). (**b**) The normalized resistance of representative home-built platinum RTDs (points) as compared to the standard curve given in (Fig. 1a) (solid line). The circles are measurements of an unannealed platinum wire of 2 mil (51 μm) diameter. The squares are measurements of a microfabricated platinum line on a substrate, deposited by e-beam evaporation and patterned with a lift-off technique. Although the data for the wire RTD are fairly close to the standard curve, the data for the microfabricated RTD have a very different slope, highlighting the necessity of calibration

RTDs Compared to Other Temperature Sensors

For general-purpose temperature measurements with the convenience of electronic readout, the three most common technologies are RTDs, thermistors, and thermocouples. Thermistors are close cousins to RTDs because both depend on the temperature dependence of the electrical resistance of the sensor. However, thermistors are based on semiconducting films such as oxides of cobalt, manganese, and nickel. The TCR of typical thermistors at room temperature is around $-0.03\,\mathrm{K}^{-1}$ to $-0.05\,\mathrm{K}^{-1}$, which is of opposite sign and about 10 times larger in magnitude compared to RTDs, making thermistors significantly more sensitive than RTDs. However, thermistors have an inconveniently nonlinear relationship between temperature and resistance (roughly following an Arrhenius-type trend $R \propto \exp(-\theta/T)$, where θ is a constant) and they can be somewhat less uniform in manufacturing and less stable in use compared to RTDs. Thermocouples are formed at the junction between two dissimilar metal wires, and exploit the Seebeck effect which gives an open circuit voltage that can be related to the temperature at the junction. Thermocouples are inexpensive, offer measurements at a small point, are more tolerant of vibrations and high temperatures compared to RTDs, and may be more convenient because of their direct voltage readout. However, compared to RTDs, thermocouples are less accurate, are subject to spurious signals from intermediate metals and temperature drifts elsewhere in the circuit, and are less well-suited to microfabrication.

Basic Methodology

Typical RTD Materials

An ideal material for use as an RTD sensing element would have the following properties:

- Linear $R(T)$ relationship over a broad temperature range.
- Moderate resistivity for ease of resistance measurement ($10-1000\,\Omega$ is a good value).
- High TCR for good sensitivity.
- Minimal thermal expansion; or thermal expansion matched to its substrate.
- Chemically stable and inert in oxidizing, reducing, and corrosive environments.
- Mechanically strong.
- Good solderability for making junctions.
- Commercially available as wires and films with highly reproducible properties.
- Able to be deposited by evaporation and/or sputtering for microfabrication applications.
- Low cost.

The material that comes closest to satisfying these diverse requirements is platinum, which is justifiably the most common RTD material. One noteworthy weakness of plat-

inum is that it is unstable in reducing environments, and so performs best when there is some oxygen in the surrounding ambient. Other common RTD materials include copper, nickel, and gold, although in principle almost any metal can be used. Although some RTDs are also made out of alloys, such as platinum and rhodium, in general alloys are less well-suited to RTDs because alloy scattering of electrons is not as temperature-sensitive as phonon scattering.

Types of Sensing Elements

RTD sensing elements are available in a wide range of packages for various applications. The sensors can be roughly grouped into the following three categories:

Standard Platinum Resistance Thermometers (SPRTs)

Standard platinum resistance thermometers (SPRTs) are the most accurate and most delicate RTDs in existence. Their applications are largely limited to standards laboratories and other applications requiring temperature accuracies of 1 mK or better. SPRTs are the primary interpolation instrument in the very definition of temperature in the International Temperature Scale of 1990 (ITS-90) from 13.8033 K (the triple point of hydrogen) to 961.78 °C (the freezing point of silver) [2]. An SPRT can therefore cover the vast majority of practical temperatures, although extra care is required above about 400 – 500 °C due to risks of contamination, defect generation, and other materials issues [6]. SPRT sensing elements are typically made of platinum wire of diameters from 10 to 100 μm, gently wound on an insulating support such as mica or quartz. The wire and support are housed in an insulating sheath and may be packed loosely with electrical insulation for additional mechanical support. Electrical connections are always of the 4-wire variety to eliminate the influence of lead resistances. These instruments are very sensitive to shock and vibrations, which can plastically deform the platinum sensing element and alter its calibration.

Industrial Platinum Resistance Thermometers (IPRTs)

For the vast majority of applications, the extreme accuracy of SPRTs cannot justify their high cost, large size, and fragile construction. Instead, manufacturers offer a wide selection of industrial platinum resistance thermometers (IPRTs), which are smaller, far more robust, and only slightly less accurate than SPRTs. They can be either wire-wound or made of thin films evaporated on a substrate, and are most commonly provided with 100 Ω resistance at 0 °C. Various package styles are available, including cylinders, washers, and glue-on chips.

Microfabricated RTDs

Standard commercial RTDs (that is, IPRTs) are typically at least several millimeters in size, which is much larger than would be desired for many applications in MEMS and microfluidics. For these applications there is a clear need for integrated temperature sensors that are smaller than commercial sensors. Microfabricated metallic RTDs are the most common solution to this challenge, although microfabricated thermocouples and thermistors (e. g. doped silicon) have also been used. Micron-sized metallic RTDs are easily patterned using standard microfabrication techniques such as wet or dry etching, liftoff, or electrodeposition. Although platinum is probably still the preferred material for microfabricated RTDs, other metals (e. g. Au, Ni, Cu) are also widely used. For simplicity it is common practice to pattern a microfabricated RTD in the same mask step as other metallization required in the microdevice, thus eliminating the need for a separate deposition and lithography step. An important consideration for microfabricated RTDs is that the properties of the deposited metal can differ significantly from the properties of bulk metals. Microfabricated metals often have more defects and grain boundaries than the wires used most macro-scale RTDs. This leads to increased resistivity in the microfabricated metals, and more importantly to a reduced temperature sensitivity. It is not unusual for the TCR of a microfabricated metal to be tens of percent lower than a well-annealed bulk sample (Fig. 1b). Thus, calibration is essential for microfabricated RTDs, and the literature values of TCR for the bulk metal should be considered only as an upper bound.

Describing the Relationship Between Temperature and Resistance

Depending on the application, the relationship between resistance and temperature will be determined using one of two approaches: a standardized $R(T)$ curve, or a calibration by the end user.

Standardized Curves Relating Temperature to Resistance

For general purpose temperature measurements the user will generally select a commercial platinum RTD (that is, an IPRT) which conforms to existing codes and standards for the relationship between temperature and resistance. Several different standards govern the performance

of IPRTs. By far the most widely used is the International Electrotechnical Commission (IEC) standard 60751, which is essentially equivalent to the Deutsches Institut für Normung (DIN) standard 43760 and the American Society for Testing and Materials (ASTM) standard E1137. The uncertainty tolerances on commercial RTD elements are commonly specified as Class A or Class B. As seen from the expressions in Table 1, the uncertainty is minimum at $t = 0\,°C$ and increases linearly with the absolute value of t, where we have followed the usual convention in this field that t denotes temperature in degrees Celsius. Thus, an uncalibrated Class A RTD at 100 °C has an uncertainty of $\pm 0.35\,°C$. The IEC tolerance specifications of Table 1 apply to as-received IPRTs without any calibration, and the uncertainty can be improved to $\pm 0.1\,°C$ or better over all temperatures after calibration.

Manufacturers also sometimes specify RTD tolerances with fractions such as *1/10 Class B*, or *1/10 DIN*. These RTDs have reduced uncertainty at 0 °C but are still subject to the same temperature dependence of the uncertainty given in Table 1 for either Class A or Class B. For example, the tolerance formula for *1/10 Class B* is $\pm (0.03 + 0.005\,|t|)\,°C$.

The IEC/DIN standards are based on platinum with some level of impurities such that the $R(T)$ relationship follows a standard curve known as the European curve (described in more detail below). This curve is also designated by its resistance at 0 °C and 100 °C, such that the quantity $\left[R\,(100\,°C) - R\,(0\,°C)\right] / \left[(100\,°C) \times R\,(0\,°C)\right]$ is approximately $0.00385\,K^{-1}$, which is also known as the European Fundamental Interval. Therefore these RTDs are also known as *385* or *0.00385* type RTDs. Note that although this quantity $0.00385\,K^{-1}$ is also sometimes known as *alpha* and denoted α, it is only approximately equal to the average value of the TCR (as defined in Eq. 1) over this temperature range. Less commonly, IPRTs with higher purity platinum are also available with a value of $0.00392\,K^{-1}$ for the quantity $\left[R\,(100\,°C) - R\,(0\,°C)\right] / \left[(100\,°C) \times R\,(0\,°C)\right]$. This is also known as the American Fundamental Interval or American curve, even though most IPRTs available in the United States now follow the European curve. IPRTs are most commonly available with 3-wire or *Siemens* connections as described below, although 2-wire and 4-wire connections are also available.

Commercial platinum RTDs are almost always described by the following $R(t)$ relationship, known as the Callendar-Van Dusen equation:

$$R(t) = R(0\,°C)\left[1 + At + Bt^2 + C\left(t - 100\,°C\right)t^3\right], \quad -200\,°C < t < 0\,°C \tag{2a}$$

$$R(t) = R(0\,°C)\left[1 + At + Bt^2\right], \quad 0\,°C \leqslant t < 850\,°C \tag{2b}$$

where t is the temperature in degrees Celsius. For the large majority of IPRTs which conform to the IEC/DIN standards, the Callendar-Van Dusen constants are assigned the values

$$A = 3.9083 \times 10^{-3}\left[°C^{-1}\right], \tag{3a}$$

$$B = -5.775 \times 10^{-7}\left[°C^{-2}\right], \tag{3b}$$

$$C = -4.183 \times 10^{-12}\left[°C^{-4}\right], \tag{3c}$$

It is often necessary to invert the Callendar-Van Dusen equation to express t as a function of R. For the high temperature range ($t \geqslant 0\,°C$), the quadratic Eq. (2b) is readily solved for $t(R)$ in closed form:

$$t(R) = \frac{-A \pm \sqrt{A^2 - 4B\left(1 - R(t)/R(0\,°C)\right)}}{2B}, \quad 0\,°C \leqslant t < 850\,°C \tag{4}$$

while below 0 °C numerical or iterative solutions may be preferred. Many commercial meters are available to convert directly from resistance to temperature using these equations with the standard coefficients. However, users should be aware that slightly different values of the coefficients may be provided by an RTD manufacturer, or determined by a user after careful calibration. In particular, RTDs are still commercially available that follow the *American curve* (0.00392-type), and should be used with different values of the Callendar-Van Dusen constants. If one of these 0.00392-type RTDs is mistakenly used with the IEC/DIN standard coefficients given above (0.00385-type), the calculated temperature will be correct at 0 °C, but will be in error by about 3 K at −200 and 200 °C, with errors increasing to nearly 10 K at 600 °C.

Calibration

Because microfabricated metals generally have more defects and grain boundaries than the metals used in commercial RTDs, they will have different $R(t)$ relationships, making it essential to calibrate microfabricated RTDs prior to use. There are many approaches to calibration depending on the desired accuracy. For many MEMS and microfluidics applications it will be satisfactory to calibrate the RTD against a second thermometer with trusted temperature readings. In these calibrations it is important

Resistance Temperature Detectors, Table 1 Temperature accuracy of industrial platinum resistance thermometers (IPRTs) according to the most common standard, which is known variously as IEC, DIN, ASTM, 0.00385-type, and/or the European curve. Note that t is the temperature in degrees Celsius

	Class A	Class B
Temperature Range	$-200\,°C < t < 650\,°C$	$-200\,°C < t < 850\,°C$
Formula for Temperature Uncertainty	$\pm(0.15 + 0.002\,\lvert t\rvert)\,°C$	$\pm(0.3 + 0.005\,\lvert t\rvert)\,°C$
Uncertainty at −100 °C	±0.35 °C	±0.8 °C
Uncertainty at 0 °C	±0.15 °C	±0.3 °C
Uncertainty at 100 °C	±0.35 °C	±0.8 °C
Uncertainty at 500 °C	±1.15 °C	±2.8 °C

that the standard thermometer and RTD to be calibrated are subject to the same temperature. Thus it is important to minimize conduction heat transfer through any leads or supports which will alter the local temperature at the sensing element. Convection and radiation may also be concerns. Calibrations are generally performed in an oven, cryostat, vacuum chamber, or well-stirred bath, often with both RTD and standard thermometer in intimate thermal contact with a common substrate of high thermal conductivity. For example, a copper block may have two holes bored into it to accommodate the RTD and standard thermometer. The practice of taping or gluing the two thermometers to the surface of a substrate which is then placed on a hot plate can result in significant errors, because of the large thermal resistance between thermometer and substrate and potential for large heat transfer along the thermometer leads and supports. For a chip or wafer with microfabricated RTDs, it may be acceptable to firmly attach the wafer to a larger, thermally conducting substrate which is fitted with a standard thermometer in good thermal contact.

The goal of calibration is to obtain data for the temperature-dependent resistance of the RTD being calibrated. This is often done by measuring the RTD resistance at several fixed points, for example at 20, 30, …, 100 °C. It is not unusual for the experimental apparatus used for the calibration to take a long time (from tens of minutes to an hour or more) to reach stable thermal equilibrium at each intermediate temperature. As an alternative calibration procedure, it is sometimes more efficient to slowly sweep the temperature between the minimum and maximum temperatures of interest. In this case the temperature and resistance should both be recorded periodically, or even continuously. If both thermometers are in good thermal contact and the sweep rate is slow enough, the lag in temperature between the two thermometers will be negligible. This can be confirmed by repeating the sweep in the opposite direction and verifying that there is negligible hysterisis in the plot of resistance versus temperature.

After obtaining the calibration data for resistance as a function of temperature at various known temperatures, it is convenient to fit this data with a continuous function for ease of future use. In many cases a linear approximation will be adequate:

$$R(t) = R(0\,°C)\,[1 + c_1 t] \tag{5}$$

where again t is the temperature in degrees Celsius, and R (0 °C) and c_1 are fitting constants determined by the calibration. For example, over the range from 25 °C to 75 °C, a linear approximation for a commercial RTD introduces less than 0.1 °C of error. For improved accuracy a parabolic fit may be used by introducing a third fitting constant c_2:

$$R(t) = R(0\,°C)\left[1 + c_1 t + c_2 t^2\right] \tag{6}$$

This is the same form as the high-temperature Callendar-Van Dusen equation given in Eq. (2b), but in general the constants c_1 and c_2 will be different from A and B. A parabolic fit with the form of Eq. (6) should be adequate for microfabricated metallic RTDs over temperature ranges spanning several hundred degrees. (Recall that *semiconducting* resistance elements are known as thermistors, which are beyond the scope of this article and would be better described by an Arrhenius-type $R(T)$ behavior.)

Measurement Considerations

To achieve a typical accuracy of ±0.1 °C around room temperature with an RTD, the resistance of the sensing element must be measured with accuracies of a few hundredths of one percent. Thus, for typical RTDs with resistances in the range of 10 – 100 Ω, the resistance measurement must have an accuracy of tens of milliohms or even better. This level of accuracy is readily achieved with commercial RTD readers, standard laboratory multimeters, and

bridge circuits, each of which is described later. Regardless of the measurement technology, several additional issues must be considered for a quality measurement:

Lead resistances are unlikely to be negligible compared to the required resistance accuracy. For some simple RTDs, two-wire measurements may still be satisfactory, but most commercial RTDs use a 3-wire connection, and for the utmost in accuracy a 4-wire approach should always be used.

Thermoelectric effects occur whenever more than one type of metal is used in the measurement circuit, which includes the sensing element, the leads, and the readout instrumentation. The typical Seebeck coefficient between different metals is around $10\,\mu V/K$ or more, and it is not unusual for temperature to vary by $5-10\,°C$ between different parts of an apparatus even for room-temperature measurements. Thus thermoelectric effects can be expected to contribute voltages of $100\,\mu V$ or more if no precautions are taken, which may lead to errors of $\pm 1\,°C$ when measuring the RTD temperature around 300 K, and potentially much worse away from 300 K. The first guideline to minimize thermoelectric errors is to minimize the number of junctions between dissimilar metals. When such junctions are necessary, they should be designed as pairs that occur at the same temperature (ideally in a region close to room temperature). For example, if copper leads are connected to a platinum RTD, the two (or 3 or 4) copper-platinum junctions should be placed nearby to each other and thermally anchored to the same common temperature. Thermoelectric voltage errors typically vary slowly with time and are insensitive to the magnitude and direction of the test current. Therefore one effective technique to minimize the impact of thermoelectric voltages in DC measurements is to use a current-reversal method, whereby the true RTD resistance can be estimated from the average of the apparent resistances recorded with both forward and reverse currents. AC measurements are also very good at minimizing thermoelectric errors as well as many other types of noise, and are typically conducted at a few hundred Hertz where inductive and capacitive effects can be neglected.

Self-heating effects occur because the finite measurement current inevitably causes some joule heating (I^2R) within the temperature sensing element. This heating will cause the temperature of the sensing element to rise slightly above that of the surroundings, especially if large sensing currents are used. The heating can be minimized by reducing the sensing current, but this will also reduce the voltage signal thereby increasing the uncertainty in the resistance measurement. As a compromise, common test currents are around 1 mA. It is worth noting that a 1 mA test current through a typical $100\,\Omega$ RTD at room temperature results in a voltage sensitivity of approximately $400\,\mu V/K$, which is about 10 times more sensitive than the common type K thermocouple ($\approx 40\,\mu V/K$). Self-heating errors can also be minimized by ensuring good thermal contact between the sensing element and the fluid or solid being measured. In many cases the strength of this thermal coupling between the sensing element and the fluid can be estimated and expressed as a thermal conductance, G, with units of W/K, in which case the self-heating temperature error is given by

$$\Delta T_{\text{self-heating}} = I^2 R/G \tag{7}$$

where I is the test current and R is the electrical resistance of the sensing region. This simple relationship also provides a means to experimentally estimate the thermal conductance G and ensure that self-heating effects are negligible. For a constant temperature of the surroundings, the sensor resistance can be measured with several different test currents. The resistance is then plotted against the square of the test current(Fig. 2), and is expected to follow the relationship

$$R(T, I) \approx R_0 + \alpha R_0^2 I^2/G \tag{8}$$

where $R_0(T)$ is the actual resistance of the sensor at the temperature T of the surroundings. This resistance R_0 is sometimes known as the *cold-wire* resistance (as opposed to the *hot-wire* resistance used in anemometry). The slope of resistance versus the square of the current gives the thermal conductance:

$$G = \frac{\alpha R_0^2}{\mathrm{d}R / \mathrm{d}\left(I^2\right)} \tag{9}$$

which is useful for estimating the magnitude of the self-heating errors.

Strain gauge effects are an important concern whenever the RTD element is subject to mechanical stress or strain. This can be due to shock, vibration, or damage during handling or operation, or mismatched coefficients of thermal expansion between the RTD and its substrate if they are tightly bonded. For modern commercial RTDs this is not usually an issue.

Non-uniform temperature profiles in the RTD sensing element can occur due to self-heating effects, temperature gradients within the fluid being measured, or thermal losses through the leads and supports of the sensor. Because any such temperature nonuniformities are typically well within the temperature range over which the $R(T)$ relation can be approximated as linear, and the sensing elements have a uniform cross section, it is easily shown that the measured resistance corresponds to the *average* temperature of the sensing element.

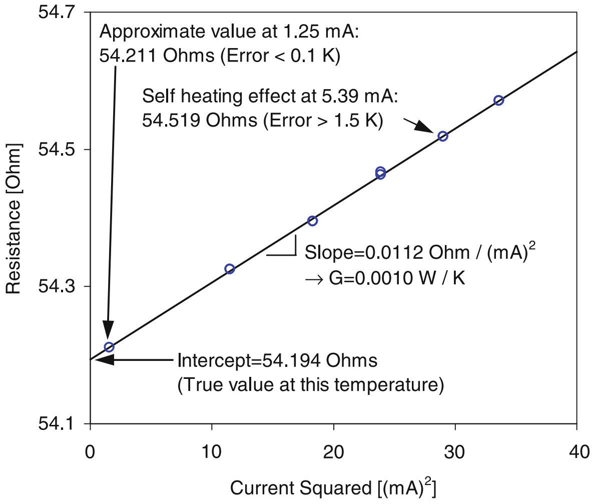

Resistance Temperature Detectors, Figure 2 Representative data to illustrate self-heating effects in an RTD. The true value of the RTD resistance at this temperature is 54.194 Ω. Test currents of around 1 mA cause small self-heating errors of less than 0.1 K. Larger test currents of around 5 mA cause significant self-heating errors of 1.5 K or more. The slope of the curve is related to the thermal coupling G between the sensing element and the fluid or solid being measured

Measurement Hardware

Commercial Temperature Readers

For commercial platinum RTDs that follow the IEC/DIN (0.00385-type) standard, the most convenient method to determine temperature is to use a commercial temperature reader which automatically measures resistance and converts it to temperature by using the standardized Callendar-Van Dusen coefficients given in Eq.(3). Some of the more sophisticated readers are also capable of handling non-standard curves or lookup tables as provided by the RTD manufacturer or determined by a user calibration. Commercial RTDs are used in 2, 3, or 4-wire configurations. The 2-wire configuration is the simplest but is subject to errors from the finite lead resistances. The 3-wire configuration (*Siemens-type*) is the most common, and can remove the effect of lead resistance as long as all 3 leads are identical (Fig. 3a). The 4-wire configuration is used whenever the utmost in accuracy is required (better than around 0.01 °C.

Direct Measurement with a Digital Multimeter or Lock-in Amplifier

In many cases a commercial temperature reader may not be desirable or available, especially for microfabricated RTDs which do not conform to the IEC/DIN standard. In this case it is common to use a digital multimeter to monitor resistance. Four-wire operation is essential to avoid the effect of lead resistances (Fig. 3b). Widely-available benchtop multimeters typically measure 100 Ω resistances with better than ±0.02 % accuracy, and a test current of 1 mA which is appropriate for typical RTD measurements. At room temperature this resistance uncertainty corresponds to a temperature accuracy of approximately ±0.05 °C, which is adequate for many applications. For increased accuracy a nanovoltmeter can be used along with a stable current source, leading to a typical resistance uncertainties of ±0.005% which corresponds to a temperature accuracy of around ±0.015 °C at room temperature. Thermoelectric effects are likely to be important in these measurements, and should be checked by the current reversal method mentioned above. If AC methods are chosen then a sinusoidal current source should be combined with a lock-in amplifier to ensure the best accuracy. Typical lock-in amplifiers can have voltage accuracies better than one part in 10^4, corresponding to a temperature accuracy of around ±0.03 °C at room temperature.

Because voltage sources are much more common than current sources, especially for AC measurements, experimentalists will sometimes place a *ballast resistor* in series with a voltage source in order to approximate a current source [7]. Furthermore the current is sometimes estimated from the ratio of the source voltage to the total resistance of the circuit, as measured separately at a baseline condition. This practice is generally acceptable as long as the ballast resistor is very stable (ideally TCR = 0) and much larger in magnitude than the RTD element being studied. However, if the RTD resistance is *not* negligibly small compared to the total circuit resistance, the temperature-induced voltage changes across the RTD will be smaller than the analysis assumes, leading the experimenter to underestimate the temperature changes. In this situation a simple correction factor can be applied for improved accuracy [7].

Bridges

Bridge arrangements were the standard approach for all RTD measurements circuits prior to the development of highly-accurate digital electronics, and are still used at standards laboratories to achieve the utmost extremes of accuracy. Carefully-made DC and AC bridges can have accuracies of better than 1 part in 10^7, which for a typical platinum RTD at room temperature corresponds to a temperature uncertainty of a few tens of micro-Kelvin. Although a classical Wheatstone bridge can be used in a 2-wire arrangement (Fig. 3c), in practice a 3-wire or 4-wire arrangement is always used in order to compensate for the effects of lead resistances. The 3-wire arrangement

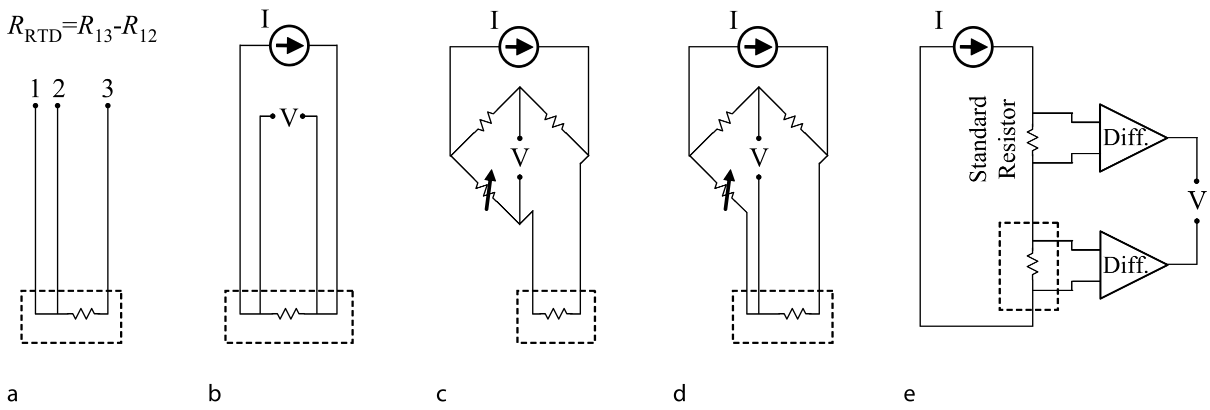

Resistance Temperature Detectors, Figure 3 Several methods for measuring the resistance of an RTD sensing element. (**a**) The 3-wire connection which is most widely used in commercial RTDs. (**b**) A 4-wire arrangement for use with a digital multimeter or lock-in amplifier. (**c**) 2-wire arrangement in a classical Wheatstone bridge, which is subject to errors due to the lead resistances. (**d**) An improved bridge using the Siemens arrangement, a common 3-wire connection where the lead resistances cancel (as long as the leads have the same resistance). (**e**) A half-bridge with two differential amplifiers [8]. The standard resistor is chosen to have nearly the same resistance as the RTD sensing element, resulting in reduced common-mode background voltage for the same RTD signal

is also known as the Siemens arrangement and is shown in Fig. 3d. To the extent that all 3 wires have the same resistance, the unknown lead resistance cancels out at the balance condition. However, because the lead resistances are never truly identical, there is always some residual uncertainty which limits the accuracy of this arrangement to around ±0.01 °C. For the utmost in accuracy, 4-wire arrangements such as the Mueller bridge are used.

It may sometimes be worthwhile to use a half-bridge in combination with simple operational amplifier (op-amp) circuit, as shown in Fig. 3e. The standard (or *series*) resistor should have a very low TCR and its value is chosen and/or adjusted to be close to the value of the RTD resistance at some baseline temperature. The two differential amplifiers remove most of the common-mode background voltage, allowing the output voltage to be dominated only by the *changes* in the RTD voltage due to temperature. This can improve the measurement accuracy by making better use of the available dynamic range of the multimeter or lock-in amplifier and by making the measurement much less sensitive to fluctuations in the current source. A multiplying digital-to-analog converter element (not shown) can also be incorporated to allow computer control of the adjustments of the standard resistor [8].

Key Research Findings

RTDs already have a long history for both industrial and standards-grade thermometry [2–6]. Over the last century the key enabling results have included: the ability to fabricate low-stress platinum sensing elements that are mechanically supported yet free to expand and contract with temperature changes; the evolution of accurate potentiometers and ratio transformers; the evolution of standards such as IEC 60751 which allow industrial RTDs to be interchanged without calibration; and the development of relatively low-cost, highly-accurate digital instrumentation for sourcing current and measuring voltage, with typical accuracies of ±0.005% to ±0.02%.

Future Directions for Research

The state of the art in thermometry research is generally reported at the International Temperature Symposia, with conference proceedings published by the American Institute of Physics [1]. For metrology applications at standards laboratories, an important research direction for platinum RTDs is to extend the upper temperature limit at which the RTDs can be used. For example, the International Temperature Scale of 1968 (ITS-68) only used platinum RTDs up to 630.74 °C, while requiring a Pt-PtRh thermocouple above this temperature. But subsequent research improved the stability and accuracy of platinum RTDs so that they are now used in ITS-90 up to 961.78 °C. It is likely that research will continue to extend the high-temperature limits of platinum RTDs. Applied research continues to improve the accuracy and reliability of thin-film RTDs, making them a good compact, low-cost alternative to the more traditional wire-wound RTDs.

Finally, there is considerable interest in using what are essentially self-heated RTDs as tools to measure thermal properties. Referring back to Eq.(9) and Fig. 2, it is possible to evaluate the thermal conductance G between an RTD and its environment by studying the RTD's resistance

R

as a function of current. For many situations the thermal conductance can be directly related to one or two thermal properties of the surrounding environment. For example, this concept is used in the hot-wire method of measuring the thermal conductivity of a fluid, whereby a long insulated platinum filament is immersed in a fluid and subject to varying electrical currents. The higher the thermal conductivity of the fluid, the smaller the temperature rise of the wire for a given amount of heat dissipation. In many cases additional information can be extracted by studying the response over a range of frequencies. Related methods can be used to study fluid velocity (hot-wire anemometry) and the thermal conductivity and/or specific heat of wires, fluids, and semi-infinite solids both with and without thin films [7–9].

Cross References

- ► Methods for Temperature Measurements
- ► Temperature Control in Microfluidic Systems
- ► Temperature Sensitive Resistor
- ► Thermoelectric Flow Sensors
- ► Thermoresistive Flow Sensors
- ► Contact Temperature Sensors

References

1. Ripple DC (ed) (2003) Temperature: Its Measurement and Control in Science and Industry, Vol. 7. Eighth International Temperature Symposium 21-24 Oct 2002, Chicago, Illinois, AIP Conference Proceedings, Vol. 684, American Institute of Physics, New York
2. Preston-Thomas H (1990) The International Temperature Scale of 1990 (ITS-90). Metrologia 27:3–10 (see also corrections detailed in Metrologia 27:107)
3. McGee TD (1988) Principles and methods of temperature measurement. Wiley, New York
4. Schooley JF (1986) Thermometry. CRC Press, Boca Raton
5. Quinn TJ (1990) Temperature. 2nd edn., Academic Press, London
6. Bentley RE (ed) (1998) Handbook of temperature measurement. Springer, New York
7. Dames C, Chen G (2005) 1ω, 2ω, and 3ω methods for measurements of thermal properties. Rev Sci Instrum 76(12):124902-1–124902-14
8. Cahill DG (1990) Thermal conductivity measurement from 30 to 750 K: the 3ω method. Rev Sci Instrum 61(2):802–808
9. Birge NO, Nagel SR (1987) Wide-frequency specific heat spectrometer. Rev Sci Instrum 58(8):1464–1470

Resistance Thermometers

Definition

A resistance thermometer uses the temperature dependency of the electric resistance of the used material. Therefore a well defined and very low current is applied onto the sensor by measuring the voltage simultaneously. For precise measurements pure platinum is often used since the temperature coefficient is almost constant and the variations of the electric resistance are higher than for alloys. When semiconductors are used, much higher temperature coefficients and therewith higher sensitivity can be obtained; these thermometers are called thermistors.

Cross References

- ► Resistance Temperature Detectors

Resistive Heating

- ► Joule Heating in Electrokinetic Flow: Theoretical Models

Resonance and Antiresonance Frequencies

Definition

The resonance and antiresonance frequencies are associated with the frequencies of minimum and maximum impedance for a particular resonance phenomenon, respectively. A continuous structure, like a cantilever beam, may have many resonance and antiresonance frequencies alternating in an ordered fashion with respect to frequency.

Cross References

- ► Piezoelectric Microdispenser

Reynolds Number

Definition

A characteristic dimensionless number that determines the nature of fluid flow in a given set up.

Cross References

- ► Electrokinetic Flow and Ion Transport in Nanochannels

RGB

Definition

Red, Green and Blue cubic color model. The RGB Values are used in an additive way to describe a color. The color ratio varies from 0 % to 100 %. White is determined by 100 % of the three values.

Rheological Fluid Flow in Microchannels

► Non-Newtonian Fluids in Microchannel

Rheology

► Non-Newtonian Fluids in Microfluidics

Rheometer

Synonyms

Viscometer

Definition

Rheometer is an instrument that measures both the stress and deformation history of a material for the derivation of the viscosity and the viscoelastic properties of materials.

Cross References

► Chaotic Mixing Based on Viscoelasticity
► Non-Newtonian Fluids in Microchannel
► Non-Newtonian Fluids in Microfluidics

RIE Lag

Synonyms

Feature size dependent etching

Definition

RIE lag is the phenomenon of the etching rate related to the feature size. The larger the feature size, the higher the etching rate. As the larger feature size results in the lower etching rate, it is called inverse RIE lag.

Cross References

► Aspect Ratio Dependent Etching
► Anisotropic Etching
► Reactive Ion Etching (RIE)
► Plasma Etching

Rosensweig Instability

► Interfacial Instability

Rotary Peristaltic Pump

Definition

Rotary peristaltic pumps transport fluid through a flexible duct using traveling contraction waves. In a typical rotary peristaltic pump, revolving contact elements close off sections of flexible tube, defining moving volumes of fluid. Because a moving boundary displaces fluid and induces the flow, rotary peristaltic pumps are an example of positive-displacement pumps.

Cross References

► Linear Peristaltic Pumps
► Peristalsis
► Peristaltic Pumps

Rotating Channel Flow

► Centrifugal Microfluidics

Rough Channels

► Roughness Effect on Microscale Transport

Roughness

Definition

Surface irregularity or surface features on the channel walls.

Roughness Effect on Microscale Transport

Satish G. Kandlikar
Department of Mechanical Engineering,
Rochester Institute of Technology, Rochester, NY, USA
sgkeme@rit.edu

Synonyms

Rough channels; Surface features to enhance transport

Definition

► Roughness on the surface of a channel wall directly affects the transport processes at the wall. In fluid mechanics applications, roughness is generally defined in terms of the average roughness parameter *Ra*, which represents the average height of the roughness elements on a surface. Newer parameters are being proposed to capture the roughness effects on fluid flow. Recent experimental evidence indicates that the roughness affects laminar flow and transition to turbulence. Roughness effects become especially important in microfluidics as the roughness features offer a unique opportunity to control the level of transport processes occurring at the wall.

Overview

Our understanding of ► roughness effects on fluid flow at macroscale is largely derived from the experimental data obtained by Nikuradse [1] in 1933. He used sand grain coated pipes of 25 to 5486 mm diameter tubes coated with sand grains in his experiments. The sand grains were coated on the inside of the tube in a monolayer, separated by some unknown distance from each other, with the help of a coating of Japanese lacquer. The diameter of the sand grains was used as the roughness parameter ε, and the ► relative roughness was defined as the ratio ε/D, where D is the root diameter of the pipe. The widely used Moody [2] diagram depicts the effect of Reynolds number and relative roughness ε/D on the friction factor. The relative roughness varied from 0 to 0.05, or 5%, and the Reynolds number ranged from 600 to 10^6. Based on his data, Nikuradse concluded that there is no effect of roughness in the laminar range under the experimental conditions employed in his experiments.

Nikuradse's conclusion on the roughness effect in the laminar region was disputed by Kandlikar [3]. It was shown that the experimental uncertainty in Nikuradse's data was of the same order as the pressure drop measurements between the two adjacent pressure taps. Experiments conducted [4] clearly show a roughness effect on friction factor and transition Reynolds number. A comprehensive summary of the research in this field is given by [4] and [5].

In the microfluidic application, since the flow channel size is small, it is possible to achieve high values of relative roughness with only a modest size rough roughness. For example, in a 200 μm channel, a roughness of 5 μm results in a relative roughness of 2.5%. Relatively large relative roughnesses, on the order of 10%, can be easily fabricated using the microfabrication techniques. Since the Reynolds numbers in the microchannels are generally low, a clear understanding of the roughness effects in laminar and transition regions becomes important.

Basic Methodology

The roughness effects on the transport processes are not well understood. Our current knowledge is mainly based on the experimental data available in the literature. In recent literature, the flow over roughness elements is also being investigated using CFD simulation. Some models are also being considered by incorporating an effective viscosity and slip velocity at the wall. But these formulations are still in very preliminary stages.

Key Research Findings

The effect of roughness on incompressible fluid flow was studied extensively by a number of investigators, with the experimental work of Nikuradse [1] being one of the most noteworthy. He clearly established that the roughness affected the friction factor using turbulent flows in circular channels. Moody [2] presented these results in his well-known Moody diagram. The relative roughness was defined as the diameter of the sand grains used by Nikuradse to make the roughened pipes. The relative roughness was defined as the ratio of the sand grain diameter to the pipe internal diameter without the sand grains, or the root diameter of a rough pipe.

Two key features in the Moody diagram were discussed further by Kandlikar et al. [4]. Firstly, the fully developed rough turbulent flow region at higher Reynolds numbers is seen to be dependent on the relative roughness. As the relative roughness increases, the friction factor increases for a given Reynolds number. Secondly, the laminar region was represented as being unaffected by the wall roughness. A new hydraulic diameter $D_{h,cf}$ was introduced based on the ► constricted flow dimensions. For a circular pipe with wall roughness ε, the constricted flow diameter is

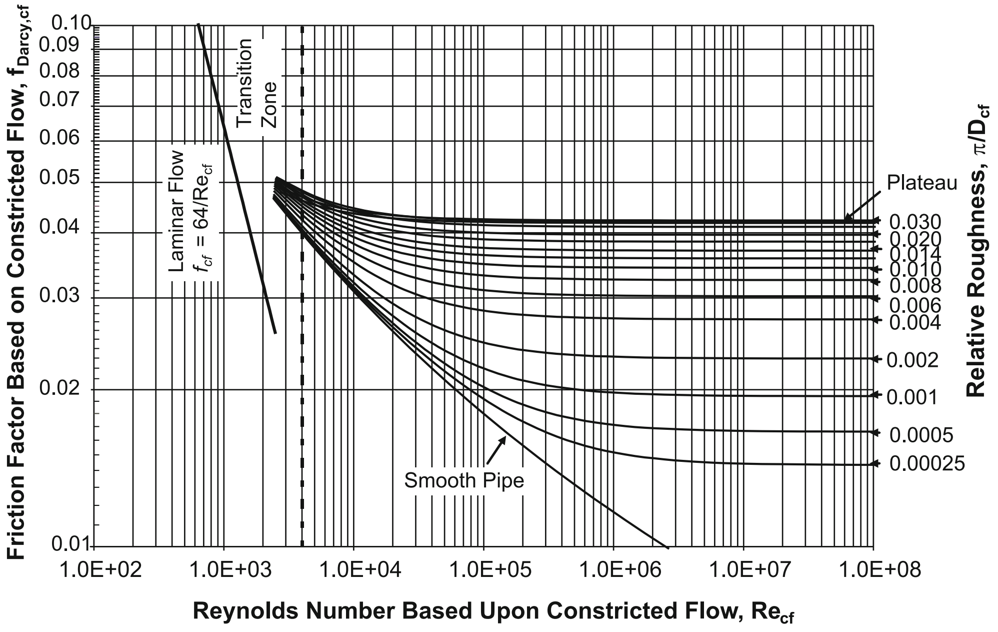

Roughness Effect on Microscale Transport, Figure 1 Variation of transition Reynolds number with relative roughness based on constricted flow diameter, Kandlikar et al. [4]

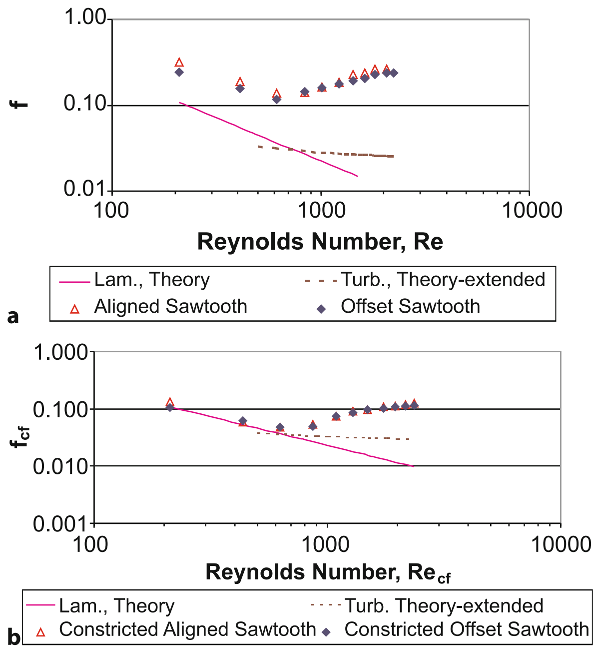

Roughness Effect on Microscale Transport, Figure 2 (**a**) Fully developed friction factor versus Reynolds number for water flow, $D_h = 953\ \mu m$ and $\varepsilon/D_h = 0.0735$, adapted from [4]. (**b**) Fully developed friction factor versus Reynolds number, both based on constricted flow diameter for water flow, $D_h = 953\ \mu m$ and $\varepsilon/D_h = 0.0735$; $D_{h,cf} = 684\ \mu m$ and $\varepsilon/D_{h,cf} = 0.1108$, adapted from [4]

defined as:

$$D_{h,cf} = D - 2\varepsilon \quad (1)$$

Moody diagram is replotted using the new constricted flow diameter in defining the friction factor as well as the Reynolds number. The resulting plot is shown in Fig. 1. It should be noted that all the lines in the fully rough turbulent region for $\varepsilon/D_{h,cf} > 0.03$ collapse on a single line with $f_{Darcy,cf} = 0.042$. This introduces a significant simplification and also provides some insight into the roughness effect on the turbulent flows at high $\varepsilon/D_{h,cf}$ values. Another fact that is introduced in the modified plot shown in Fig. 1 is that the laminar region was represented by a line similar to that in the original Moody diagram, but was modified to include the constriction effect:

$$f_{cf} = \frac{Po}{Re_{cf}} \quad (2)$$

Where f_{cf} and Re_{cf} are constriction based friction factor and Reynolds number respectively, and Po is the Poiseuille number specific to the cross-sectional geometry of the channel, 16 for circular pipes, 14.23 for a square channel and 24 for flow between two parallel plates.

Since Nikuradse's data in the laminar region was obtained with a high degree of uncertainty, the original Moody plot

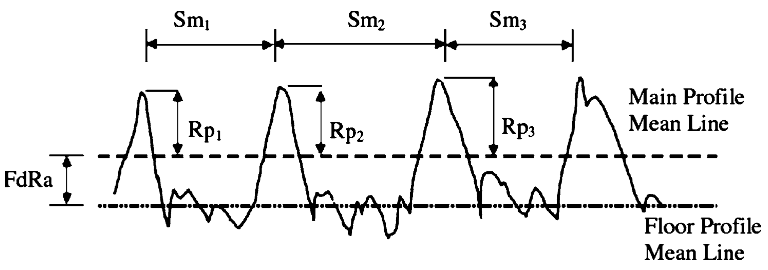

Roughness Effect on Microscale Transport, Figure 3 Roughness parameters for application in fluid flow [4]

erroneously indicates that a relationship of $f = \mathrm{Po}/\mathrm{Re}$, with both f and Re based on the root diameter of the pipe. Extensive experiments conducted by [4, 6] show the validity of the constricted diameter approach as indicated by Eq. (2). Figures 2a and 2b show the plots of the experimental data for water in an artificially roughened rectangular channel with sawtooth ridges. The use of the conventional base channel dimensions in Fig. 2a clearly underpredicts the friction factor significantly, while using the same data with the constricted flow parameters shows excellent agreement with the experimental data.

Roughness representation: A set of three parameters are proposed to represent the roughness compatible with the constricted flow parameters discussed in the earlier sections: Maximum Profile Peak Height (*Rp*), Mean Spacing of Profile Irregularities (*RSm*), and the Floor Distance to Mean Line (*Fp*), as shown in Fig. 3. Two of these parameters (*Rp* and *RSm*) are defined in the ASME B46.1-2002 and the other (*Fp*) is proposed by Kandlikar et al. (2005)

Maximum Profile Peak Height (*Rp*): The distance between the highest point of the profile and the mean line within the evaluation length. The mean line represents the conventional average roughness value (*Ra*).

Mean Spacing of Profile Irregularities (*RSm*): Consists of the mean value of the spacing between profile irregularities within the evaluation length. The irregularities of interest are the peaks, so this is equivalent to the Pitch.

$$RSm = \frac{1}{n}\sum_{i=1}^{n} Sm_i \tag{3}$$

Floor Distance to Mean Line (*Fp*). Consists of the distance between the main profile mean line (determined by *Ra*) and the floor profile mean line. The floor profile is the portion of the main profile that lies below the main profile mean line.

From the above parameters, the equivalent roughness ε can be estimated by the following relationship:

$$\varepsilon = Rp + Fp \tag{4}$$

Future Directions for Research

The concept of constricted flow diameter is seen to be applicable in the laminar and turbulent flows as illustrated in the above sections. The effect of different roughness structure is also important and needs to be investigated further. The roughness parameter ε defined by Eq. 4 is proposed for replacing the conventional average roughness parameter *Ra*. Further work to validate this concept is currently under way [6]. Experiments with biological application are also being conducted and indicate a need for further investigation in this field [7]. Numerical simulation of the flow with rough walls is also being pursued [8–10]. In future, a close tie-in between the numerical simulations and experimental work is expected. The size and shape of the roughness structure and its effect on the flow can be effectively used to create the desired transport effect at the wall, such as enhanced mixing, localized mass transport enhancement or more effective heat transfer surfaces.

Cross References

- ► Developing Flows
- ► Microfluidic Micing
- ► Pressure Drive Single Phase Liquid Flows
- ► Turbulence in Microchannels
- ► Transition to Turbulence in Microchannels

References

1. Nikuradse J (1933) Strömungsgesetze in rauhen Rohren. VDI-Forschungsheft 361, Beilage zu "Forschung auf dem Gebiete des Ingenieurwesens", Ausgabe B, Band 4; English Translation: Laws of Flow in Rough Pipes. NACA Tech Mem 1292, 1937
2. Moody LF (1944) Friction Factors for Pipe Flow. ASME Trans 66:671–683
3. Kandlikar SG (2005) Roughness Effects at Microscale – Reassessing Nikuradse's Experiments on Liquid Flow in Rough Tubes. Bull Polish Acad Sci Tech Sci 53(4):343–349

4. Kandlikar SG, Schmitt D, Carrano AL, Taylor JB (2005) Characterization of surface roughness effects on pressure drop in single-phase flow in minichannels. Phys Fluids 17(10):100606
5. Kandlikar SG, Garimella S, Li D, Colin S, King MR (2005) Flow Boiling in Microchannels and Minichannels. In: Heat Transfer and Fluid Flow in Minichannels in Minichannels and Microchannels. Elsevier, London
6. Brackbill TP, Kandlikar SG (2007) Effect of sawtooth roughness on pressure drop and turbulent transition in microchannels. Heat Transf Eng 28(8-9):662–669
7. Kim YM, Kim WS, Lee SH, Baek JY (2005) Effects of surface roughness on the flow characteristics in PDMS microchannel 3rd IEEE/EMBS Special Topic Conference on Microtechnology in Medicine and Biology, 292–295
8. Rawool AS, Mitra SK, Kandlikar SG (2006) Numerical simulation of flow through microchannels with designed roughnes Microfluid Nanofluid 2(3):215–221
9. Croce G, D'Agaro P (2005) Numerical simulation of roughness effect on microchannel heat transfer and pressure drop in laminar flow. J Phys D: Appl Phys 38(10):1518–1530
10. Baviere R, Gamrat G, Favre-Marinet M, Le Person S (2006) Modeling of laminar flows in rough-wall microchannel. J Fluids Eng, Trans ASME 128(4):734–741

RTD

► Resistance Temperature Detectors

Rutherford Backscattering Spectrometry (RBS)

Definition

Material characterization technique which uses a high-energy beam of He ions to determine the chemical and physical properties of a material. The beam is directed at a sample and the ions which scatter from the sample are collected by a detector. This technique can give both composition and crystallographic information on a material.

Cross References

► Fabrication of Self-Assembled Catalytic Nanostructures

Sample Handling

► Microfluidic Sample Manipulation

Sample Pre-Fractionation

► Biosample Preparation by Lab-on-a-Chip Devices

Sample Preparation

► Microfluidic Sample Manipulation

Sample Purification

► Lab-on-a-Chip Devices for Sample Extractions

Sample Purification Using Magnetic Particles

JUN KEUN CHANG
NanoEnTek Inc. & Digital Bio Technology Co., Inc., Seoul, Korea
jkchang@digital-bio.com

Synonyms

MACS (magnetic-activated cell sorting)

Definition

Isolation of specific content from a cocktail using paramagnetic particles in a magnetic field.

Overview

Under a certain magnetic field, a magnetic particle is forced to move depending on its susceptibility and volume [1]. The magnetic force [2] is

- paramagnetic particle:

$$F_M = \frac{\chi V}{\mu_0} B \nabla B \qquad (1)$$

- superparamagnetic particle (saturation of field in the case of a relatively small particle, in general less than 100 nm in diameter):

$$F_M = m_s \nabla B \qquad (2)$$

where the magnetic field (B) is $\mu_0(H+M)$ and the magnetization (M) is the product of a dimensionless magnetic susceptibility (χ_m) and a uniform external field (H_{app}). The strength of the magnetic source is expressed by the magnetic moment (μ_0 and m_s, respectively, in Eqs. (1) and (2)). The consideration of magnetic property is critical to perform sample purification using magnetic particles.
Magnetic sample purification is conducted by binding magnetic particles on a specific content such as DNA, protein, bacteria or cells in an equivalent contents pool. By applying magnetic particles, a target material which has no magnetic property can be controlled under the magnetic field.
There are three methods in sample purification using magnetic particles [3].
The positive method is to label magnetic particles only with the target molecule. The target molecule is isolated from the others by magnetic force balance under the field. After the isolation process, magnetic particles should be removed from target molecules to reduce the interference during post-processes such as cell culture and gene work. To remove the possibility of this interference clearly, the negative method is used. All other molecules except the target molecule are conjugated with magnetic particles using each specific binding partner. The purifying efficiency of the two methods is reported as 60–90%. The

depletion method, which removes partial unwanted contents but not all from a cocktail in a single step, is also used. The sequential depletion shows 99.9% purifying efficiency in general.

Cross References

► Lab-on-Chip Devices for Particle and Cell Separation
► Magnetic Field Based Lab-on-Chip Devices

References

1. Tondra M, Granger M, Fuerst R, Porter M, Nordman C, Taylor J, Akou S (2001) Design of integrated microfluidic device for sorting magnetic beadsin biological assays. IEEE Transaction Magn 37:2621–2623
2. Inglis DW, Riehn R, Sturm JC, Austin RH (2006) Microfluidic high gradient magnetic cell separation. J Appl Phys 99 08K101-1-3
3. Safarik I, Safarikova M (1999) Use of Magnetic techniques for the isolation of cells. J Chromatograp B, 722:33–53

Sample Transport

► Microfluidic Sample Manipulation

Sampling

► Transferring Samples to Chips, Techniques

Sampling Unit

Synonyms

Fluidic multiplexer; Fluidic sequencing circuits

Definition

A fluidic device performing spatio/temporal conversion of fluid flows in response to a control signal. It allows only one of the inlet fluid flows at a time to progress to the outlet.
Essential part of sampling units is an array of microfluidic valves. There are many advantages in using for the purpose the no-moving-part valves, but their property of the flow paths not being separated by a solid partition requires a somewhat sophisticated design, with the fluid purity ensured by guard flows. Sampling units find an application in microfluidic systems for combinatorial chemistry, where they deliver a sample at a time from several test reactors allowed to flow to the composition analysis connected to the sampling unit outlet.

Cross References

► Microfluidic Systems for Combinatorial Chemistry
► Guard Flows

Sand Blasting

► Powder Blasting

Satellite Droplets

Definition

Droplets about one or more main droplets that are of a smaller size.

Cross References

► Piezoelectric Microdispenser

Saturated Flow Boiling

Definition

Boiling process at the wall while the mean bulk enthalpy of flow is at or above the saturation enthalpy corresponding to the local pressure.

Cross References

► Bubble Dynamics in Microchannels

Scanning Electron Microscopy (SEM)

Definition

Material characterization technique where electrons emitted from a filament (typically tungsten) interact with a material to create secondary electrons. These electrons are collected in a detector and used to create an image of the material. The resolution of this technique approaches hundreds of angstroms and thus shows a material's grain structure.

Cross References

► Fabrication of Self-Assembled Catalytic Nanostructures

Scanning Probe Measurement

► Scanning Probe Microscopy

Scanning Probe Microscopy

DAVID LEE BUTLER
School of Mechanical & Aerospace Engineering,
Nanyang Technological University, Singapore, Singapore
mdlbutler@ntu.edu.sg

Synonyms

Scanning probe measurement; Probe microscopy

Definition

Scanning Probe Microscopy (SPM) is the branch of microscopy concerned with the formation of images of a surface using a physical probe that scans the specimen.

Overview

Scanning probe microscopy originated with the invention of the scanning tunneling microscope (STM) in 1981 by Gerd Binning and Heinrich Rohrer (Nobel Prize for Physics in 1986). The STM relies on the principle of electrons *tunneling* through the gap between a sharpened tip and the sample in a vacuum. For tunneling to take place, both the sample and the tip must be conductors or semiconductors, STMs cannot image insulated materials.

To understand how atomic resolution can be achieved, it is necessary to consider the electronic structure of a metal as illustrated in Fig. 1. The electrons of the metal occupy all the available energy levels up to the energy E_F known as the *Fermi* energy (at this level they precisely compensate the positive charge of the metal ions). For an electron to be able to exit the metal, an additional amount of energy of Φ above the Fermi energy is required. This brings the electron up to the vacuum level, at which point it is free to move away from the metal. The energy Φ is known as the *work function* of the metal.

To allow the electrons to tunnel through the vacuum, a second conductive object needs to be placed a small distance d away from the first. When an electrical voltage V is applied between the specimen and tip, a net electrical current (known as the tunneling current) flows. The current depends on the tip-surface distance d, the voltage V and on the height of the barrier Φ. The relationship is given by Eq. (1).

$$I(d) = \text{constant} \times \text{eV} \exp\left(-2\frac{\sqrt{2m\Phi}}{\text{h}}d\right) \quad (1)$$

The other quantities in Eq. (1) are the electron charge and mass e and m, and Planck's constant h. Eq. (1) shows that

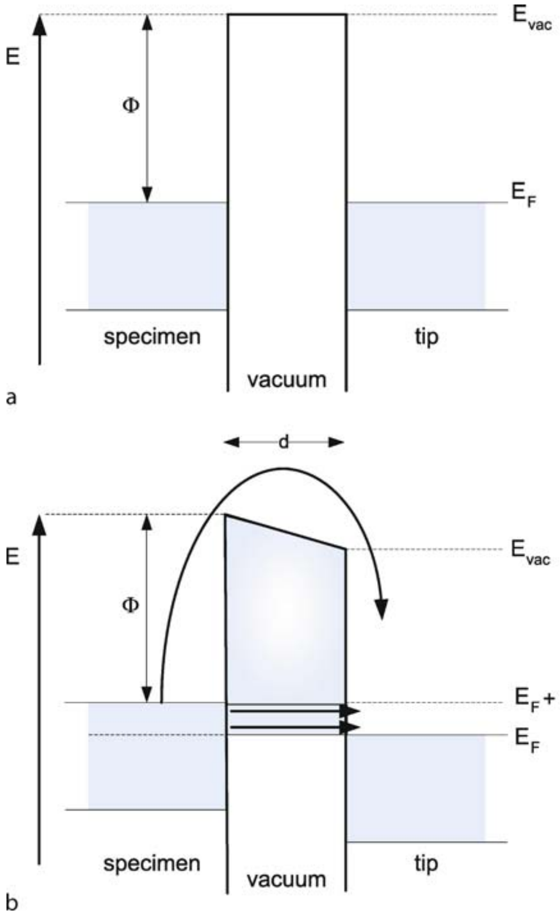

Scanning Probe Microscopy, Figure 1 Schematic illustrating the tunnel phenomena. (**a**) In a metal, the energy levels of the electrons are filled up to a particular energy known as the Fermi energy E_F. In order for electrons to leave the metal and travel to the other body (in this case specimen and tip), an additional amount of energy known as the work function is required. (**b**) If the distance d between the specimen and tip is small enough, electrons can 'tunnel' through the vacuum barrier and with an applied voltage between the specimen and tip, a tunneling current is achieved

the tunneling current obeys Ohm's law (i. e., $I \propto V$). It also depends exponentially on the distance d. For a typical work function value of 4 electronVolts (eV), the tunneling current reduces by a factor of 10 for every 0.1 nm increase in d. Considering a typical atomic diameter to be 0.3 nm the tunneling current would change by a factor of 1000 over this range.

The most common and possible most versatile SPM is the Atomic Force Microscope (AFM). The AFM relies on the principle of the atomic forces exerted between two objects as they are brought close to each other (Fig. 2). At a distance of tens to hundreds of angstroms, the interatomic forces are attractive (predominantly due to long-range van der Waals forces). On approaching the surface

S

to a distance of a few angstroms the force becomes repulsive. To observe this phenomenon, a sharp tip of a few μm in length with a diameter of less than 100 μm is used to probe the surface. The tip is located at the free end of a cantilever (typically 100 to 200 μm in length). The forces between the tip and the sample cause the cantilever to bend or deflect and this movement is measured by a detector. Unlike the STM, the AFM is not restricted to only conducting material.

In comparison with other microscopy techniques such as optical microscopy or scanning electron microscopy, SPM offers a number of advantages in terms of resolution and magnification. However, due to image acquisition by raster scanning, the measurement is slower and the maximum image size is generally smaller as well. Table 1 list some of the more common applications for SPMs.

In addition to the STM and AFM, the SPM family has expanded to include a whole array of instruments for detecting various probe-surface interactions. Figure 3 shows a comparison of the measurement scale of scanning probe microscopes in relation to other types of microscopy.

Basic Methodology

A generalized scanning probe microscope is shown in Fig. 4. The sample is typically mounted on a piezoelectric scanner which allows precise movement in the x-, y- and z-directions. The image is generated by the sample moving under the probe (or vice versa depending on instrument configuration) in a raster pattern. Typical scan step sizes range from a few angstroms to hundreds of nanometres with scan areas ranging from a couple of nanometres to around 50 μm depending on the instrumentation.

Scanning Probe Microscopy, Table 1 Areas of Application for the Scanning Probe Microscopes

Mineral surface morphology
Metal surfaces (roughness)
Microfabrication techniques
Optical and compact discs
Ceramic surface structures
Lipid monolayers (as Langmuir–Blodgett films)
Different layered substances on solids
Self-assembly structures at interfaces
Solid surfaces
Langmuir–Blodgett films
Thin-film technology
Interactions at surfaces of ion beams/laser damage
Nanoetching and lithography, nanotechnology
Semiconductors
Catalyses
Surface adsorption (metals, minerals)
Surface manipulation by STM/AFM
Friction force microscope (FFM)
Polymers
Biopolymers (peptides, proteins, DNA, cells, virus)
Vaccines
Microsensors

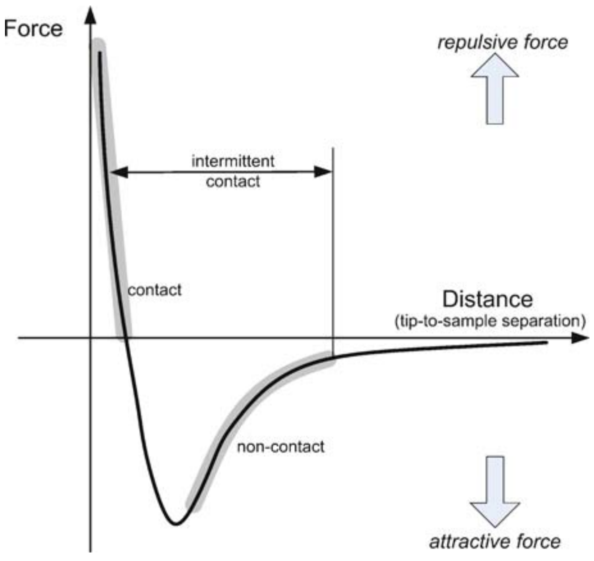

Scanning Probe Microscopy, Figure 2 The variation in inter-atomic forces in relation to separation distance

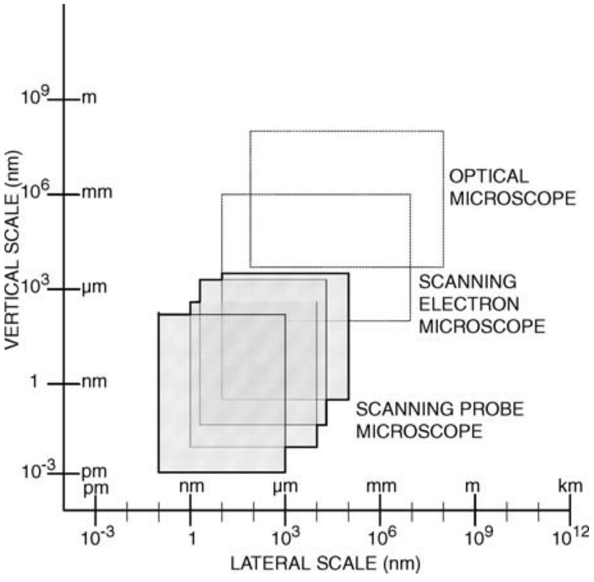

Scanning Probe Microscopy, Figure 3 Lateral and vertical measurement ranges of various microscopes

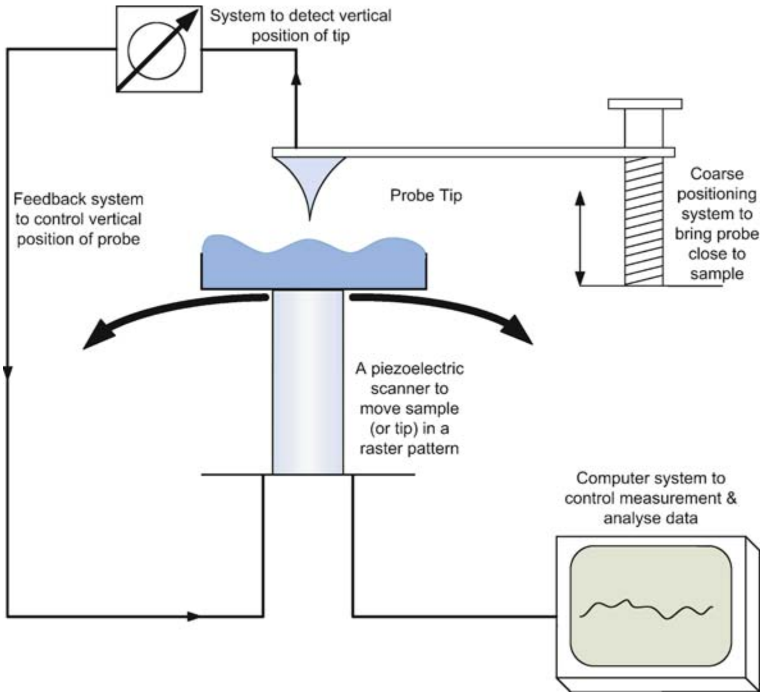

Scanning Probe Microscopy, Figure 4 Schematic of a generalised Scanning Probe Microscope

Depending on what physical phenomena is being measured, the probe will either maintain contact with the surface or remain a fixed distance above the surface. This height control is maintained by a feedback system which inputs and amplifies the tunneling current (low voltage) and drives the piezo scanning tube (high voltage). The shielding and layout of the feedback control is critical to the performance of the system as a whole.

Scanning Tunneling Microscopy

The STM typically employs a probe, made of tungsten (W) or platinum–iridium (Pt–Ir) alloy to scan the surface at a distance of 5 to 10 angstroms. The magnitude of resolution achievable is in the range of a fraction of 1 angstrom. This is highly dependable on the size and shape of the probe tip which will determine the lateral resolution.

The STM has a number of very real limitations. The instrument probes the electron cloud structure of the surface with great precision however, this reveals nothing about other important sample properties. As only the electronic structure is observed, information such as distinguishing between different elemental atoms within a compound is not achievable.

Atomic Force Microscopy

Limitations in the STM and its inability to investigate non-conducting surfaces led to the development of the AFM. Based on similar principles to the STM, the AFM can operate on both conducting and non-conducting surfaces.

A cantilever scans the surface and the deflection of the cantilever is detected by the reflection of a laser beam. The cantilever is typically made of Si_3N_4 of approximately 200 μm in length and with a spring constant of between 0.2 and 40 N/m. In many AFM instruments deflections in the cantilever are measured optically by bouncing a laser off the top of the cantilever, minute changes (as small as 10 angstroms) in the light path can be measured using a photodiode array. An alternative detection technique involves the incorporation of a piezoresistive element into the cantilever which generates a small voltage when deflected.

As the AFM relies on actual contact to sense the sample surface (as opposed to current flow for the STM), it can be used on biological molecules, organic materials, polymers, ceramics and insulating materials like diamond or glass.

Once the AFM has detected the cantilever deflection, it can generate the topographic data by operating one of two modes – *constant height* or *constant force*. In constant

height mode, the spatial variation of the cantilever deflection can be used directly to generate the surface data as the scanner height is fixed as it scans. In constant-force mode, the deflection of the cantilever can be used as input to the feedback circuit so that the scanner is moved up or down vertically in order to keep the deflection constant. In general, the AFM operates under a constant force mode.

For the cantilever, the two most important characteristics which will affect its performance are the spring constant and the resonant frequency. The spring constant for the cantilever is normally measured directly. For a beam with a rectangular cross section loaded at one end, the spring constant is given by Eq. (2).

$$k_{\text{spring}} = E_{\text{Y}} w_{\text{width}} / 4(\text{t}_{\text{thickness}} / l_{\text{length}})^3 \tag{2}$$

Where k_{spring} is the spring constant, E_{Y} is the Young's modulus and w_{width}, $t_{\text{thickness}}$ and l_{length} are the respective beam width, thickness and length. The resonant frequency of the cantilever will be dependant on which measurement mode or AFM variation is employed (these will be discussed in the proceeding sections) and whether a stiff or flexible cantilever is desirable. The formula for determining the resonant frequency is given by Eq. (3) where m is the mass of the cantilever.

$$\text{resonant frequency} = \frac{1}{2\pi}\sqrt{\frac{k_{\text{spring}}}{m}} \tag{3}$$

The AFM has three common modes or regions of operation; these are contact, intermittent contact and non-contact and are shown in Fig. 2.

Contact Mode

In contact AFM mode (also known as repulsive mode), the AFM tip makes soft physical contact with the sample. As the scanner traces the tip across the surface, the contact force causes the cantilever to bend to accommodate changes in topography. From Fig. 2 it can be seen that the slope on the left side of the graph is relatively steep suggesting the force increases significantly for a very small movement towards the surface. In other words, when the cantilever pushes the tip against the surface, the cantilever will bend rather than forcing the tip against the sample.

In addition to the repulsive force between the tip and sample, two other forces are generally present during contact AFM measurement. These are a capillary force exerted by the thin water layer often present in an ambient environment and the force exerted by the cantilever itself. The capillary force arises when water adheres itself to the tip and creates a strong adhesive force (about 10^{-8} N) that holds the tip in contact with the surface. The force exerted by the cantilever on the surface can be likened to that of a compressed spring with the magnitude and force direction dependent on the spring constant. However, as long as the tip is in contact with the surface the capillary force should remain constant. The magnitude of the total force exerted on the sample varies from 10^{-8} N to the typical operating range of 10^{-7} N to 10^{-6} N.

Non-Contact AFM

Non-contact AFM is one of several vibrating cantilever techniques in which an AFM cantilever is vibrated near the surface of a sample. Tip-sample spacing is in the order of tens to hundreds of angstroms.

Non-contact AFM is desirable where little or no contact between the tip and sample is required. The total force between the tip and sample is relatively low at about 10^{-12} N which makes it advantageous for studying soft or elastic samples. As no contact is made, there are no tip contamination issues to consider.

Cantilever selection differs from that for contact mode as they are required to be stiffer to prevent being pulled into the sample surface.

In non-contact mode, the system vibrates a stiff cantilever near its resonant frequency (typically 100 to 400 kHz) with an amplitude in the range of ten to several hundred angstroms. Any change in resonant frequency or vibration amplitude as the tip nears the surface can be detected. The sensitivity of this technique allows sub-angstrom vertical resolution to be achieved.

Intermittent Contact

Intermittent Contact AFM is similar to the non-contact AFM mode except that the vibrating cantilever is brought closer to the sample so that at the maximum amplitude it makes slight contact with the surface (i. e., 'taps' the surface). The intermittent contact region is shown on Fig. 2. As with non-contact measurement, the change in cantilever oscillation amplitude is in response to variation in tip-to-sample spacing.

In some cases, intermittent contact is preferred as it is less likely to damage the sample than contact mode as it eliminates lateral forces (i. e., friction or drag) between the tip and sample. Compared to non-contact measurement, intermittent contact is more effective for imaging larger scan areas that may include greater surface topographic variation. In recent years, intermittent contact AFM has become a popular tool for cell biologists as it can measure hydrated biological samples- overcoming the adhesive forces of the water by vibrating at a sufficiently high frequency.

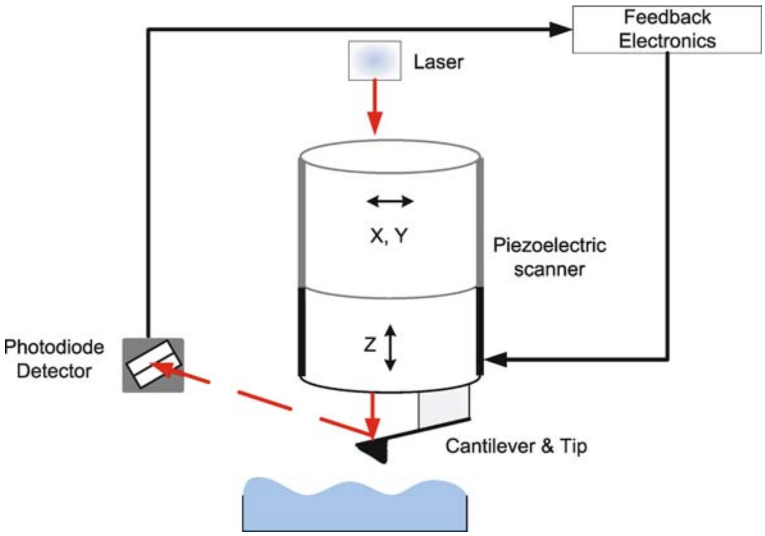

Scanning Probe Microscopy, Figure 5 The basic components of an Atomic Force Microscope showing the stationary sample configuration with the tip mounted on the scanning tube

Calibration

Due to the measurement range that SPMs work in, calibration is an essential procedure which needs to be carried out on a regular basis. The calibration of STM and AFM in the x–y direction is carried out using a standard of regular and known structure such as Highly Oriented Pyrolytic Graphite or a grid. The real challenge has been calibration in the vertical direction. Currently used procedures are based on calibration standards consisting of gold samples with one layer steps of gold, lipid layer deposited on a Langmuir-Blodgett film or macromolecules with known dimensions.

Other Types of SPM

Magnetic Force Microscopy

Magnetic Force Microscopy (MFM) images the spatial variation of magnetic forces on a sample surface. The tip is coated with a thin film of ferromagnetic material. To obtain the necessary surface topographic and magnetic information, a two-pass measurement approach is used. The first measurement pass obtains the topographic data by either contact or intermittent contact mode while the second pass uses the non-contact mode to detect changes in the resonant frequency of the cantilever induced by the magnetic fields influence on the tip.

Lateral Force Microscopy

Lateral Force Microscopy (LFM) measures the lateral deflections in the cantilever that are present from forces on the cantilever parallel to the plane of the sample surface. Lateral deflections of the cantilever are normally attributable to changes in surface friction or changes in slope. The LFM has been used to image variation in surface friction which can arise from inhomogeneity in the surface material.

Force Modulation Microscopy

A further extension to AFM imaging is that of Force Modulation Microscopy (FMM) which characterises the sample's mechanical properties while simultaneously obtaining the surface topographic information.

In FMM mode, the AFM tip is scanned in contact with the sample while a constant cantilever deflection is maintained by the feedback system. In addition, a periodic signal is applied to either the sample or the tip. Any variation in the amplitude of cantilever modulation that results from the applied signal can be attributed to a change in the elastic properties of the sample.

Electrostatic Force Microscopy

Electrostatic Force Microscopy (EFM) works on the same two-pass measurement technique as MFM. Rather than measure the magnetic force, in EFM a voltage is applied between the tip and the surface. Any deflection in the cantilever can be attributed to locally charged domains on the sample surface. EFM can be used to map electrostatic fields in electronic devices when switched on and off in a technique known as voltage probing.

Scanning Probe Microscopy, Table 2 Members of the Scanning Probe Microscopy Family

AFM	Atomic Force Microscopy
EFM	Electrostatic Force Microscopy
FMM	Force Modulation Microscopy
KPFM	Kelvin Probe Force Microscopy
LSTM	Laser Tunneling Microscope
MRFM	Magnetic Resonance Force Microscopy
NSOM	Near-Field Scanning Optical Microscopy
SICM	Scanning Ion Conductance Microscopy
SECM	Scanning Electrochemical Microscopy
SCM	Scanning Capacitance Microscopy
SNM	Scanning Noise Microscopy
SPotM	Scanning Potentiometry Microscopy
SSRM	Scanning Spreading Resistance Microscopy
STAP	Scanning Tunneling Atom Probe
SThM	Scanning Thermal Microscopy
STM	Scanning Tunneling Microscopy
SVM	Scanning Voltage Microscopy

Scanning Thermal Microscopy

The scanning probe based thermal microscope (SThM) gives information about the temperature distributions and allows for quantitative determination of the local thermal conductivity in a sample. A resistive probe is employed which both captures the topographic information as well as the temperature/thermal conductivity profile with a resolution of a few milliKelvin. Table 2 provides a list of the more established members of the scanning probe microscope family.

Future Directions for Research

Research in SPMs appears to follow two distinct directions; one as a characterisation instrument and the other as a nanomanipulation instrument. In terms of characterisation, it has found use in many areas as described in Table 1 however, there are demands on the performance of these instruments to allow them to measure larger, rougher samples with greater speed. This has led to new developments in cantilever design as well control systems which is envisaged to continue to satisfy new areas of application.

As a tool for nanotechnology, the STM has been well publicised in its ability to 'push' or manipulate atoms into specific locations to create nanopatterns. However, this is a relatively slow process and would not be commercially viable. A more feasible approach has been undertaken using the AFM to create nanolithographic patterns by using the tip to remove material from a surface and create the desired pattern.

Cross References

- ► Biosensors Using Atomic Force Microscopes
- ► Dip-Pen Nano Lithography
- ► Enzyme Nanolithography
- ► Roughness Effect on Microscale Transport
- ► Scanning Electron Microscopy (SEM)
- ► Surface Roughness Measurement
- ► Surface Modification

References

1. Samori P (2006) Scanning Probe Microscopies Beyond Imaging: Manipulation of Molecules and Nanostructures. Wiley-VCH, Weinheim
2. Foster A, Hofer W (2006) Scanning Probe Microscopy: Atomic Scale Engineering by Forces and Currents. Springer, New York
3. Morita S, Wiesendanger R, Meyer E (2002) Noncontact Atomic Force Microscopy. Springer, Berlin

Scattered Light Intensity

► Photometer

Segmented (Droplet-Based) Flow

Definition

Segmented flow (or droplet-based flow) means multiphase flow where the individual phases are divided in consecutive segments.

Cross References

► Pressure-driven Two Phase Flows

Segmented Flow

► Taylor Flow in Microchannels

Selective Silicon Etching

► Silicon Micromachining

Self-Assembled Monolayer

Definition

A two-dimensional single layer of molecules induced to spontaneously order upon a surface via covalent bonding at an interface.

Cross References

► Surface-Directed Capillary Flow Systems

Self-Assembly

Definition

Growth method whereby atoms naturally group together into structures due to energy considerations that may form shapes such as nanorods and quantum dots.

Cross References

► Fabrication of Self-Assembled Catalytic Nanostructures

Self-Assembly Fabrication

Zhemin Wu, Dongqing Li
Department of Mechanical Engineering, Vanderbilt University, Nashville, TN, USA
zhemin.wu@vanderbilt.edu

Synonyms

Molecular self-assembly fabrication

Definition

Self-assembly refers to the fundamental principle which generates autonomous organization of components into structural patterns or well-defined structure without external instructions or human interventions. Molecular self-assembly is the spontaneous organization of molecules under thermodynamic equilibrium conditions into stable, structurally well-defined aggregates joined by a number of noncovalent bonds (Whitesides et al. [1]).

Overview

As a fundamental natural principle, self-assembly exists everywhere at all scales from molecules to galaxies. Self-assembly describes the spontaneous association of numerous individual entities into a structural organization without external interventions. It is defined as reversible processes in which pre-existing parts or disordered components of a preexisting system form structures of patterns. Molecular self-assembly is the most well-studied subfield, which refers to the spontaneous organization of molecules under thermodynamic equilibrium conditions into stable, structurally well-defined arrangements through noncovalent interactions such as hydrogen bonds, ionic bonds, hydrophobic interactions, van der Waals interactions and water-mediated hydrogen bonds [1–4].

There are two major types of self-assembly, static and dynamic [5]. Static self-assembly describes the process that the ordered state occurs when the system is in equilibrium and does not dissipate energy. One special example of static self-assembly is the formation of atomic, ionic and molecular crystals [6–8]. In dynamic self-assembly, the process occurs only if the system is dissipating energy. The patterns formed in oscillating chemical reactions are simple examples [9, 10].

In recent years, self-assembly was successfully applied in micrometer scale structures. Self-assembled monolayer (SAM) [11] is the representative example of self-assembly microfabrication, in which surfaces consist of a single layer of molecules on a substrate. SAMs can be prepared simply by adding a solution of the desired molecule onto the substrate surface and washing off the excess. The technique was utilized on the metal substrates with PDMS stamps to form the combined system for controlling of crystal nucleation [12]. Another example involves a fluidic technique based on patterned hydrophobic SAMs and capillary forces to self-assemble micro fabricated silicon blocks onto silicon and quartz substrates [13].

Cross References

► Hydrophilic/Hydrophobic Patterning
► Materials used in Microfluidic Devices
► Methods for Surface Modification
► Microfabrication Techniques
► Self-assembled Monolayers
► Silicon Micromachining
► Surface Modification

References

1. Whitesides GM, Mathias JP, Seto CT (1991) Molecular self-assembly and nanochemistry: a chemical strategy for the synthesis of nanostructures. Science, 254:1312
2. Lehn JM (1993) Supramolecular chemistry. Science 260:1762–1763
3. Ball P (1994) Polymers made to measure. Nature 367:323
4. Zhang S (2003) Fabrication of novel biomaterials through molecular self-assembly. Nature Biotechnol 21:1171
5. Whitesides GM, Grzybowski B (2002) Self-assembly at all scales. Science 295:2418

6. Philip D, Stoddart JF (1996) Self-Assembly in Natural and Unnatural Systems. Angew Chem Int Ed 35:1155
7. Desiraju GR (1989) Crystal Engineering: The Design of Organic Solids. Elsevier, New York
8. Isaacs L, Chin DN, Bowden N, Xia Y, Whitesides GM (1999) Self-assembling systems on scales from nanometers to millimeters: design and discovery. In: Reinhoudt DN (ed) Supramolecular Technology, pp 1–46. Wiley, New York
9. Jakubith S, Rotermund HH, Engel W, von Oertzen A, Ertl G (1990) Spatiotemporal concentration patterns in a surface reaction: Propagating and standing waves, rotating spirals, and turbulence. Phys Rev Lett 65:3013–3016
10. Hess B (2000) Periodic patterns in biology. Naturwissenschaften 87:199–211
11. Kumar A, Abbott NA, Kim E, Biebuyck HA, Whitesides GM (1995) Patterned Self-Assembled Monolayers and Meso-Scale Phenomena. Acc Chem Res 28:219–226
12. Aizenberg J, Black AJ, Whitesides GM (1999) Control of crystal nucleation by patterned self-assembled monolayers. Nature 398:495
13. Srinivasan U, Liepmann D, Howe RT (2001) Microstructure to substrate self-assembly using capillary forces. J Microelectromech Syst 10:17

Self-Diffusion

► Fundamentals of Diffusion in Microfluidic Systems

Semiconductor Nanocrystals

► Semiconductor Nanoparticles

Semiconductor Nanoparticles

Synonyms

Semiconductor Nanocrystals; Q-Dots

Definition

Nanoparticles of semiconductor materials. Many of them absorb light whose energy is larger than their band gap energy and emit fluorescence whose energy corresponds to their band gap. Their band gap can be tuned according to their diameter, composition, and structure, and consequently fluorescence can also be tuned by these properties. Due to their stability and arbitrarity in excitation wave length, they are expected to be used as fluorescence tag for bio materials.

Cross References

► Fluorescence Measurements
► Fluorescent Labelling
► Quantum dots

Sensing and Actuation

► Control of Micro-Fluidics

Serpentine Microchannel Flow

► Curved Microchannel Flow

SERS

Definition

Surface-enhanced Raman scattering

Cross References

► Biosensors Using Surface-Enhanced Raman Scattering

SERS-Based Biosensors

► Biosensors Using Surface-Enhanced Raman Scattering

Shear

► Viscoelasticity

Shear-Driven Flow

Definition

The shear-driven technique is an alternative flow driving principle for the creation of fluidic flows through micro- and nanochannels. It is created when two flat surfaces are translated relative to each other resulting in a movement of the fluid in between the two surfaces. The fluid flow is characterized by a linear flow profile and is independent of the channel size.

Shear-Driven Micro- and Nanofluidics

KRIS PAPPAERT, DAVID CLICQ, VERONIKA FEKETE, GERT DESMET
Transport Modeling & (Bio)analytical Separation Science Group (TMAS[2]), Vrije Universiteit Brussel, Brussel, Belgium
kris.pappaert@gmail.com

Definition

The shear-driven technique is an alternative flow driving principle for the creation of fluidic flows through micro- and nanochannels. It is created when two flat surfaces are translated relative to each other resulting in a movement of the fluid in between the two surfaces. The fluid flow is characterized by a linear flow profile and is independent of the channel size.

Overview

During the last decade, miniaturization has been a major issue in analytical and bio-analytical chemistry. Microsystems have generated a considerable activity at economic and scientific levels and their importance in our everyday life is expected to increase considerably over the next few years. The drive towards miniaturization follows from an ever increasing demand (from such fields as organic (polymer) synthesis, medical diagnostics and therapeutics, genomics, etc.) for analytical tools capable of identifying and quantifying all compounds within small sample volumes. Furthermore, methods should generate more precise results, higher sensitivity and this in the fastest possible way. An efficient handling of minimal sample consumption can become possible by miniaturizing the analysis systems. Miniaturized fluidic systems can have several applications, such as amplification, digestion, and analysis of deoxyribonucleic acid (DNA) sequences or the separation and analysis of single defective cells in order to diagnose specific diseases at early stages. With the completion of the Human Genome Project, the analysis of gene and protein functions creates a huge demand for advanced biotechnological systems. These systems can only be realized using miniaturized fluid handling systems, which allow the rapid and efficient analysis of structures and functions with minimal sample volume. Due to this increasing demand, microfluidics has rapidly turned into an interdisciplinary research field equally including physics, chemistry, materials science and engineering.

The generation of a stable and controllable fluid flow in microfluidic devices is a major issue and a lot of research work has been put into optimizing the flow driving methods. Not only conventional methods (derived from macroscopic applications) like pressure-driven and ►electro-osmotic flows have been scaled down, but also novel methods like ►shear-driven flows (SDF) have been introduced. There are several problems associated with the conventional flow driving methods: ►pressure-driven flows suffer from pressure drop limitations, while electro-osmotic flows suffer from Joule heating, fluctuations of flow velocity and double-layer overlap [1]. Therefore other approaches to evade these problems and limitations have been proposed (centrifugal forces, magneto-hydrodynamic forces, etc.).

The shear-driven fluidic approach is based on a radical modification of the fluidic channel concept. This recently developed technique for the transport of fluids in ultra-thin channels based on the SDF [2] relies on a very basic hydrodynamic effect: the viscous drag. This effect is present in every fluid flow, be it a liquid or a gas flow. In pressure-driven flows, the viscous drag manifests itself in an undesirable manner, as the stationary column and particle surfaces tend to slow down the fluid flow. In SDF, the viscous drag effect is turned into an asset. By conceiving channels with a moving wall element, this part of the channel wall no longer acts as a flow resistance but instead provides a net source of impulse, dragging along the fluid through the channel without the need to apply a pressure- or voltage gradient.

Instead of considering channels which are hermetically sealed along their longitudinal axis, the channels are axially split into two separate surfaces (Fig. 1a). While one of the surfaces is kept stationary, the other one is translated or rotated past the first. A large number of different channel layouts can be used to put this principle into practice. In the “Basic methodology” section the more practical side of this technology is described in more detail.

Pure hydrodynamic considerations [3] easily allow showing that, when the flat wall element is moved (Fig. 1b) relative to the element carrying the open channel, a flow is obtained which does not generate any pressure drop or pressure build up. The flow rate is only determined by the velocity of the moving wall element. As is taught in nearly every basic hydrodynamics course, the axial velocity in a laminar flow between two flat plates displays a perfectly linear profile, going from $u = 0$ near the stationary wall to $u = u_{\mathrm{wall}}$ near the moving wall [4]. As the viscous drag effect sustains this so-called shear-driven flow (SDF) at literally each point of the channel axis, the flow is generated without any pressure-drop or pressure build-up. This also implies that none of the fluid will leak through the axial split, which in turn implies that the use of axially split channels, forming the basis of the SDF concept, does not pose any sealing problem. It can be shown [3]

S

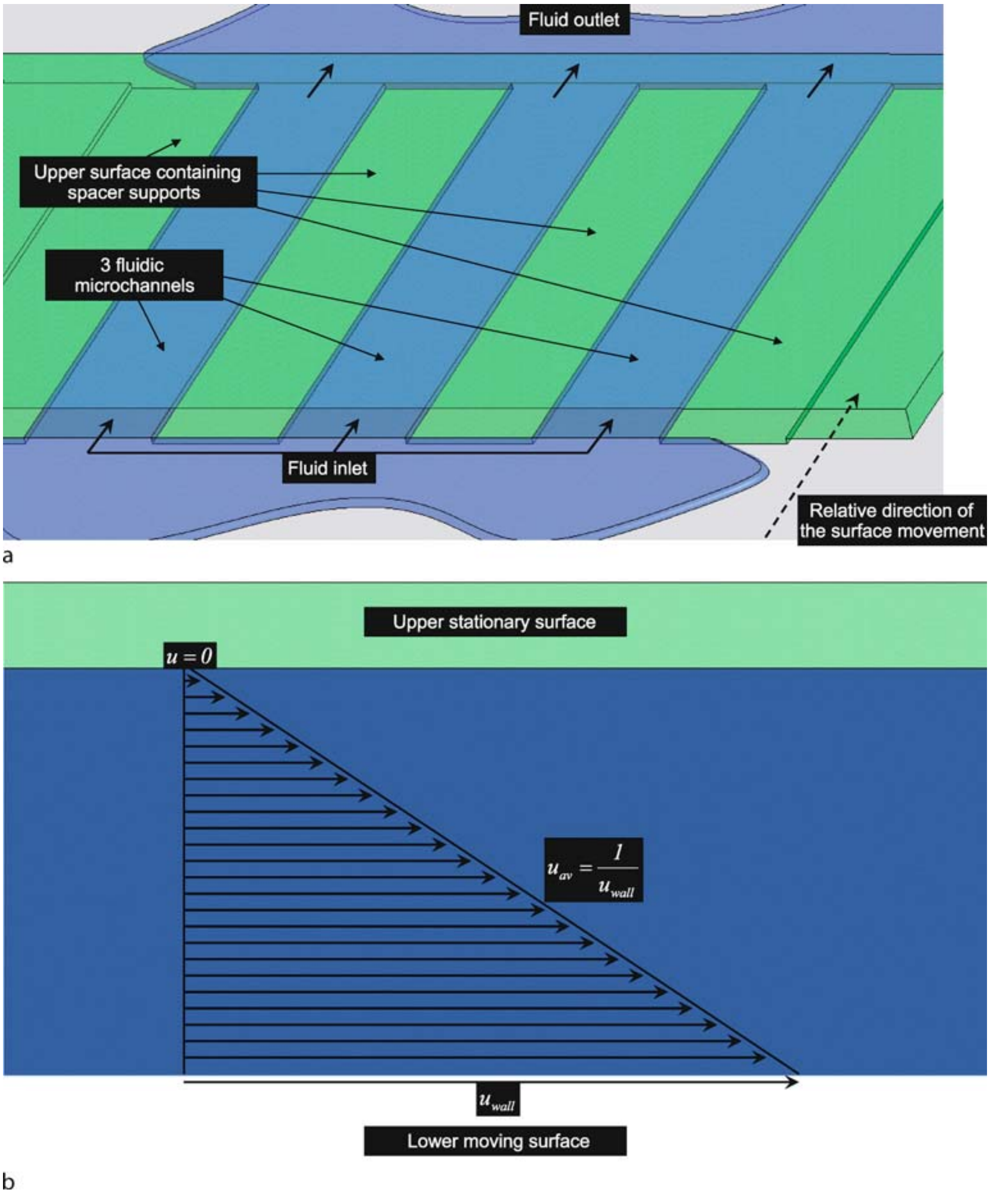

Shear-Driven Micro- and Nanofluidics, Figure 1 Figure showing the basic concept of a shear-driven flow apparatus. (**a**) The upper wall is kept stationary while the lower wall moves (driven by a linear translating stage) at a constant velocity. In this way the fluid in the channel is flown through the channel. The dimensions of width, length, and thickness are not to scale. (**b**) This shear-driven flow technique results in a linear flow profile inside the microchannel with an average fluid velocity that is half the velocity of the moving wall

that in a channel with a flat rectangular cross-section (width $w \gg$ thickness d), if neglecting the small regions (width of order d) near the side walls, a flow with a substantially linear radial velocity profile (Fig. 1b) is established, with the mean fluid velocity (u_m) given by:

$$u_m = \frac{1}{2} u_{wall} \quad (1)$$

wherein u_{wall} is the velocity of the moving wall.

Since the factor 2 in Eq 1 can also be considered as a geometrical factor, representing the ratio of the moving channel wall surface to the total channel wall surface, it should be noted that Eq 1 only holds in a channel with a flat-rectangular cross-section, wide enough to neglect the surface of the side-walls. It also shows that the SDF method intrinsically is an open-tubular technique: the moving wall cannot be used to generate a significant flow through a packed bed, as the stationary surface area

in a packed bed is typically orders of magnitude larger than the surface area of the moving wall ever could be.
The striking difference between Eq 1 and the pressure-driven case that follows from Poiseuille's pressure drop law:

$$\Delta P = \frac{u_{\mathrm{m}} \psi \eta L}{\mathrm{d}^2} \tag{2}$$

is that the fluid velocity is totally independent of the channel diameter (d) and the channel length (L), implying that the SDF concept offers an intrinsic possibility to get around Poiseuille's pressure drop limitation on d and L. The fact that neither the length and/or the thickness of the channels, nor the physical properties of the fluid influence the fluid velocity is one of the most interesting properties of shear-driven flows. The SDF concept also retains all the beneficial characteristics of pressure-driven systems (same choice of stationary- and mobile-phase composition, same ruggedness and same possibility to perform temperature and solvent gradient programming, etc.).
The advantage with respect to the electro-osmotic flow is that SDF does not rely on the generation of an electrical double layer but is purely controlled by mechanical means, allowing for much larger fluid velocities, and as the established velocity field is independent of the nature of the fluid (3), the system also offers a perfect flow rate controllability and repeatability.
It should be noted that, with the basic principle described above, a large number of column shape variants for SDF can be conceived. The use of spiral- or helical shaped channels to increase the path length is such an example.
In our group, this type of flow principle has been researched extensively and one of the most important applications is situated in the field of chromatographic separations [5]. For chromatographic purposes, SDF creates the possibility to use longer and thinner separation channels without any theoretical restriction on the fluid velocity. Other advantages are the perfect predictability, reproducibility of the established flow rates and the selection of the solvent or buffer composition solely on the basis of its ability to maximize selectivity or detection [6]. Shear-driven ►chromatography therefore leads to a high separation efficiency and numerous experimental set-ups have been used to demonstrate the theoretical expected gain.
SDF has also proven to be a successful technique when it comes too enhancing the ►DNA hybridization on ►DNA-microarrays. The DNA microarray technology is a recently developed technique that can be used to study gene expression, mutation detection or genome analysis and allows the analysis of hundreds of thousands of genes or complete genomes in parallel. The power and universality of DNA microarrays as experimental tools are derived from the exquisite specificity and affinity of complementary base-pairing of the nucleic acids (the hybridization process). During the pas decade DNA microarrays have become an important biological tool for obtaining high-throughput genetic information in studies of human disease states, toxicological research and gene expression profiling. However, this technique still suffers from a number of inherent shortcomings such as lack of uniformity and slow hybridization speed. The main cause for these shortcomings is the fact that the hybridization process on the microarrays is governed by the slow diffusion process of the target molecules towards their complementary probes. Using the SDF technique this slow diffusion process could be circumvented by transporting small target volumes over the microarray surface, hence enhancing the hybridization rate and sensitivity of the hybridization process
The flexibility of the SDF fluid transport system in nano- and micrometer thin channels enables to exploit numerous other possible applications, especially if a high degree of spatial confinement or an increase in the diffusion transport rates is required. Vankrunkelsven et al. used the SDF system for the size separation of macromolecules and micro-particles in nano- and micrometer deep channels using micro-steps [7] (Fig. 2). The separation of 0.5 and 1.0 μm carboxylated polysterene beads; mixtures of *Staphylococcus aureus* and *Saccharomyces cerevisiae*; and mixtures of *Saccharomyces cerevisiae* and *Escherichia coli* cells in a micro- or nanochannel that is only slightly larger than the molecules themselves and is narrowed in a stepped structure.

Basic Methodology

Shear-Driven Chromatography (SDC)

As it already has been described in the overview, SDC is based on two well-polished surfaces, slid one at the top of the other generating a fluid flow thanks to the viscous drag. For chromatographic purposes, like in reverse phase-HPLC (RP-HPLC) (►high performance liquid chromatography (HPLC)), the sample solution (present in the mobile phase) needs to flow over a separation surface (the stationary phase) that can adsorb or absorb the sample molecules that need to be separated. The smallest (stationary) plate carries the stationary phase, whilst the longer (moving) plate should either be inert or have an opposite hydrophobicity. Thus far the majority of the conducted separation experiments have been carried out with monolayer coatings of C8 and C18. Given the sub-micron channel heights, these monolayer coatings already provide a sufficient retention capacity to separate a 4 component

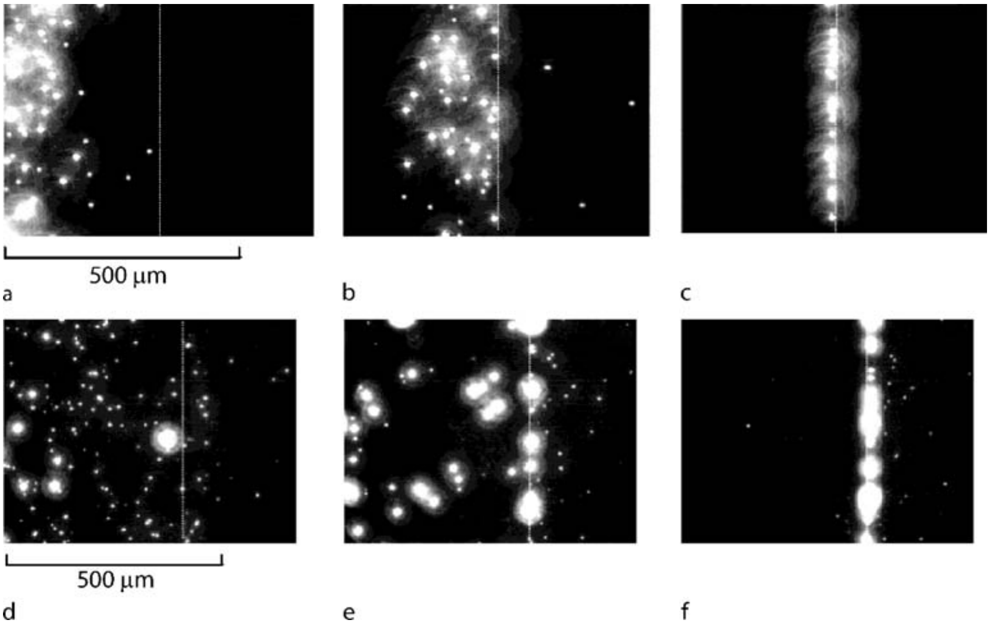

Shear-Driven Micro- and Nanofluidics, Figure 2 Compilation of a series of captured CCD-images (20× magnification) of a micro-step separation experiment of a mixture of 0.5 μm and 1.0 μm polystyrene beads (**a-c**) ($u_{wall} = 100$ mm/s) and a mixture of *E. coli* and *S. cerevisiae* cells (**d-f**) ($u_{wall} = 10$ mm/s, pure PBS). The channel depth changes respectively from 3.3 μm to 0.7 μm (a-c) and from 5.2 μm to 1.6 μm (d-f) at the micro-machined step, indicated by the white dashed line. The relation between the apparent size of the particles and cells does not correspond to the actual size ratio, due to the disproportionately stronger fluorescence of the larger particles and cells (reproduced from [7])

coumarin dye mixture in the first few mm of a C8-coated nano-channel. The stationary plate also contains an etched rectangular nanochannel. These channels are prepared by Deep ► reactive ion etching (RIE) using a state of the art etching machine: the AMS 100 SE (Adixen, France).

During the separation, the stationary channel is placed on top of a well polished fused silica plate (Photox Optical Systems, Sheffield, UK). This plate can be translated along the channel direction while the channel is kept in a fixed position (Fig. 3a). The velocity of the moving channel part is controlled using an automatic translation stage. This translation stage is held in the microscope table. The epi-fluorescence microscope is equipped with an Hg-vapour lamp and a UV-1 filter cube set that allows to excite the components at the right wavelength and to detect the emitted fluorescent light (Fig. 3b). The passage of the excitation and emission light is ensured via the moving bottom part made of fused silica. The SDC channels are positioned above the objective lens of the microscope. The emitted fluorescent light is taped by a ► charge coupled device (CCD) camera.

The actual injection method is semi-automated and consists basically of five successive steps. In the first step, the inlet of the channel is cleaned and all liquid present in front of the channel is removed. In the second step, a small drop of the sample mixture is deposited in front of the channel inlet. During the third step, the moving wall is rapidly displaced over a given prescribed distance depending on the injection volume. This movement forces the sample deposited in front of the inlet into the channel. During the fourth step, the non-entered sample is aspirated and replaced by pure buffer solution. When this is completed, the motion of the translation stage is restarted to perform the actual separation run (step 5). Apart from the second step, everything is automated. Using a computer controlled vacuum switch (needed in steps 1 and 4) and a syringe pump (needed in step 4), the entire injection process is currently completed in a couple of seconds [3].

The efficiency of chromatographic separations can be determined by calculating the plate heights. For the SDC system the theoretical plate height (HETP) can be calculated using Eq 3.

$$HETP = 2 \times \frac{D_m}{u_m} + \frac{2}{30} \times \frac{1 + 7k' + 16k'^2}{(1+k')^2} \times u_m \times \frac{d^2}{D_m} + \frac{2}{3} \times \frac{k'}{(1+k')^2} \times u_m \times \frac{\delta^2}{D_s} \quad (3)$$

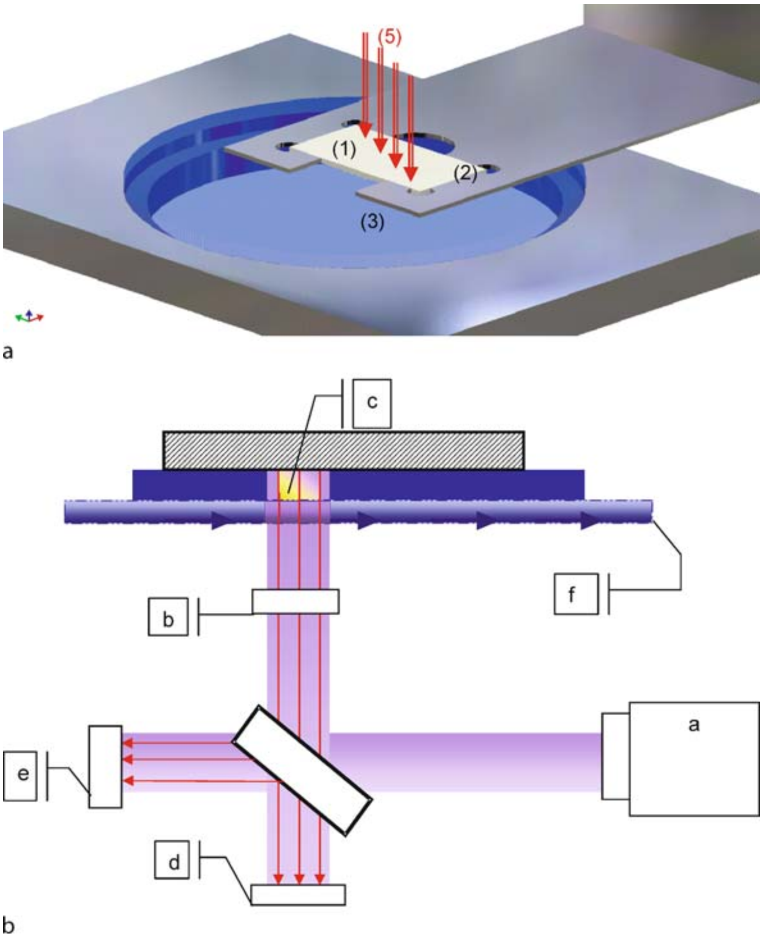

Shear-Driven Micro- and Nanofluidics, Figure 3 (**a**) This figure shows the employed mechanical set-up. The stationary phase is deposited on the bottom surface of a rectangular nanochannel [1]. The channel is placed on top of a well polished fused silica plate [3] which is moved along the channel direction while the channel is kept in a fixed position by a home-made holder [2]. (**b**) The main part of the detection set-up is an inverted epi-fluorescence microscope equipped with a Hg-vapour lamp (**a**) and a UV-1 filter cube set (**b**) to excite the four coumarin dyes (**c**) at the right wavelength (375 nm) The detection system consists of the two detectors, A CCD camera and a PMT device (**d-e**). The organization of the employed flow principle is represented, as well as the orientation and direction of the light paths of the employed fluorescence detection scheme. The passage of the excitation and emission light is ensured via the moving bottom part made of fused silica (**f**)

The plate height is calculated using the molecular diffusion coefficient of the mobile phase (D_m), the mean fluid velocity (u_m), the retention factor (k'), the channel depth (d), the molecular diffusion coefficient of the stationary phase (D_s) and the stationary phase thickness (δ). In general higher plate heights will lead to more efficient separations or the possibility to perform more complex separations.

Shear-Driven Hybridization (SDH)

The system used to perform shear-driven hybridization (SDH) on microarrays consists of a circular microchamber (diameter= 2 cm) etched in the center of a round, flatly polished (flatness= $\lambda/4$ at $\lambda = 512$ nm) borosilicate glass wafer (Radiometer Nederland, The Netherlands) with thickness 6 mm and diameter 5 cm [9]. This wafer was subsequently clamped in a home-built, hybridization device (Fig. 4). The wafer is rotated with an automated rotation stage equipped with a stepper motor (M-060, Physik Instrumente, Karlsruhe, Germany), and controlled with NetMove420-software (Physik Instrumente, Karlsruhe, Germany). The circular PVC holding cup surrounding the glass wafer makes it possible to control the temperature using a Julabo$^{\text{ő}}$ F32-MD Heating (and Refrigerated) Circulator (JD Instruments Inc., Houston, TX, USA), set at T= 42 °C during all the experiments.

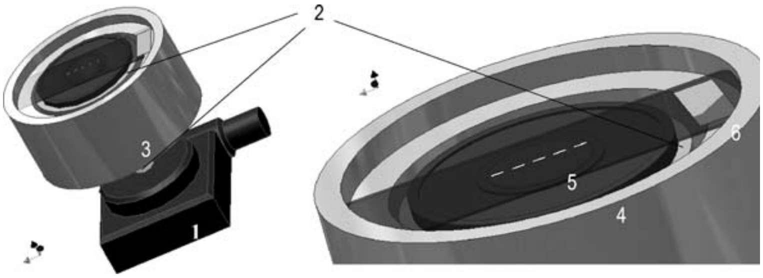

Shear-Driven Micro- and Nanofluidics, Figure 4 Bird's eye view schematic of the rotating micro-chamber hybridization set-up, showing the rotation stage (1) and the stainless holding shaft (2). The PVC-cup (3) is used for temperature control. The etched glass consists of an outer etched ring (4) made to limit the contact area between the rotating bottom substrate and the microarray slide surface, and the microchamber (5). Finally the microarray slide (6) seals the entire system

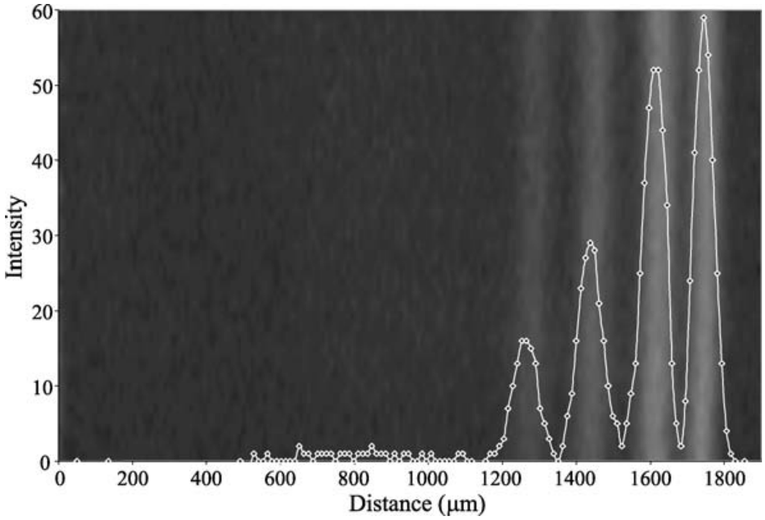

Shear-Driven Micro- and Nanofluidics, Figure 5 Compilation of a series of subsequent CCD-camera images of the separation of a mixture of four coumarin dyes (C440, C450, C460 and C480) injected at a concentration of 10^{-4} M in a channel with $d = 280$ nm

To carry out the hybridization experiments, a freshly spotted microarray slide was gently deposited (spotted surface facing downwards) on the top surface of the glass wafer. A volume of 10 μL was applied in the 3.7 μm deep micro-chamber with diameter 2.0 cm. During the rotation of the glass wafer, the microarray slide was kept stationary and a pressure of 1 bar was used to push the microarray substrate and the microchamber against each other. For other hybridization experiments (coverslip and Slidepro) the standard hybridization procedures of the MicroArray Facility Lab (www.microarray.be) were followed. For the coverslip hybridization 30 μl sample was used to hybridize the microarray slide for an overnight (16 h) period in an incubator at 42 °C. Hybridizations using the Slidepro-system (GE Heatlhcare) are performed in independently temperature-controlled chambers, allowing customized process parameters to be used for each slide. Up to 210 μl can be injected into each chamber.

All hybridization experiments were conducted using conventional microarray procedures and made use of the VIB_Mouse_21K_II chip (MicroArray Facility, Leuven, Belgium). As array elements, mouse spleen and heart total RNA was used (BD Biosciences Clontech, Palo Alto, CA, USA). All different cDNA strands were obtained by PCR amplification and were arrayed on Amersham type 7 star slides (Amersham Biosciences, Buckinghamshire, UK) using a commercial Generation III Array Spotter (Amersham Biosciences, Buckinghamshire, UK). The array elements were all spotted at a concentration of 200 ng/μL. The spots (diameter 100 μm and spaced 20 – 30 μm apart), situated in the circular spotted area were grouped in 2 × 5 different blocks of 21 × 44 spots.

Prior to each experiment the arrays were slightly dampened and UV-crosslinked at 50 mJ followed by a prehybridization in 2xSSPE/0.2%SDS at 26 °C for 30 minutes. After hybridization the slides were washed

3 times for 10 minutes in respectively 1xSSC/0.2%SDS, 0.1xSSC/0.2%SDS and 0.1xSSC/0.2%SDS at 56 °C and 1 time for 1 minute in 0.1xSSC at room temperature. The slides were then scanned at 532 nm using a commercial Array Scanner Generation III (Amersham Biosciences, Buckinghamshire, UK). Image analysis was done using Array Vision 7.0-software (Imaging Research, ON, Canada) and Spotfire 8-software (Spotfire Inc., Somerville, MA, USA).

All experiments were started from 5 µg testis total RNA and 5 µg lung total RNA per sample. This was first amplified by T7-in vitro transcription and 5 µg aRNA was used for every labeling reaction. After labeling with ► Cy3/Cy5-dye, both samples were mixed and for every experiment, identical amounts of sample, i.e. 5, 20 or 40 pmol Cy3/Cy5-dye were applied. The cDNA was further dissolved in a solution containing 50% formamide, 25% buffer, 15% Mouse COT and 7.5% polydT35. This cDNA-mixture was then respectively denatured at 96 °C for 3 minutes, set on ice for 2 minutes, heated to 42 °C for 5 minutes, centrifuged at $\omega = 12.000$ rpm for another 5 minutes and subsequently held on ice before applying it on the microarray slide.

Key Research Findings

Shear-Driven Chromatography (SDC)

In our lab the use of the shear-driven technology to perform chromatographic separation has been investigated since 1999, and the results obtained thus far are remarkable. Yet there is still room for improvement. Especially the enhancement of the detection system and the automation of the injection procedure have been the two main focus points. They are considered as the Achilles' heel of this technique. It has already been proven that a separations of four coumarin dyes is possible in less than 2 s. Figure 5 shows such a separation of a mixture of four coumarin dyes (C440, C450, C460 and C480) in a 300 nm deep channel in 1.8 sec. The velocity of the moving wall is 2 mm/s (i. e., far below the optimal flow velocity which is situated around 10 mm/s) in order to be compatible with the scan rate of the Charge-Coupled Device (CCD) camera. About 2000 plate numbers per second can be achieved. This offers the possibility to yield over 10,000 plates per centimeter in a few seconds. A separation at 8 mm far from the inlet of the channel does not yield unfortunately the hoped 8000 plates per second but 4000. The reason of the drop in efficiency is explained by the channel irregularities and the use of 10 times more concentrated solutions to allow detecting far from the injection region.

Detection Enhancement

The observation that the SDC technique couldn't reach the theoretical predicted efficiency, led us to find a way to enhance the detection system. A very simple idea about locally deepened channels was investigated. By creating a small but 10 to 30 times deeper region (► detection groove, Figure 6a) in the channel structure near to the exit a 10 to 30 times more intense fluorescent signal can be expected. The groove accumulates the fluid passing in the channel and instead of detecting in the 300 nm deep region of the nanochannel, the detection occurs in a small but much deeper region enabling an enhanced detection. An experimental study was carried out in order to proof the efficiency of the detection grooves. A 4.75 µm deep and 4 µm wide detection groove, running perpendicular to the mean flow direction, was etched (Fig. 6a). This resulted in a 5-fold lower detection limit in a 300 nanometer deep nano-channel. This 5-fold gain in S/N-ratio is however about three times lower than the theoretically expected gain, based on the ratio of the channel depth outside and inside the groove. Measurements performed under stationary conditions indicated that this underachievement is due to scattering light losses. The plate number loss accompanying the passage of the peaks through the detection groove in a 1 cm long and 300 nm deep channels coated with a retentive layer would be of order of 20%.

The separation experiments with the detection groove were however still insufficient for more qualitative studies. This can be attributed to the semi-manual injection procedure that is not reproducible enough. The standard variation of three consecutive injections can vary from 1 up to 50% mainly due to the manual handling in this injection procedure.

Fully Automated Injection System

To tackle the injection problems a new automated injection system was tested (Fig. 6b). An ► injection slit etched by Bosch avoids any formation of asymmetric shaped plugs, which typically occurs during loading of the sample in wide channels. The slit is connected to a vacuum system and syringes for the supply of the analyte and the mobile phase. A CFD simulation was first performed to compare different injection well shapes and configurations in order to account for less profitable configurations.

The main problems related to the semi-automated injection method (the definition of plugs is highly dependent on the dicing quality of the substrate, the method is slow which gives rise to peak broadening by diffusion, reproducibility is bad because of uncontrolled dilution and manual handling and no gradient in the mobile phase composi-

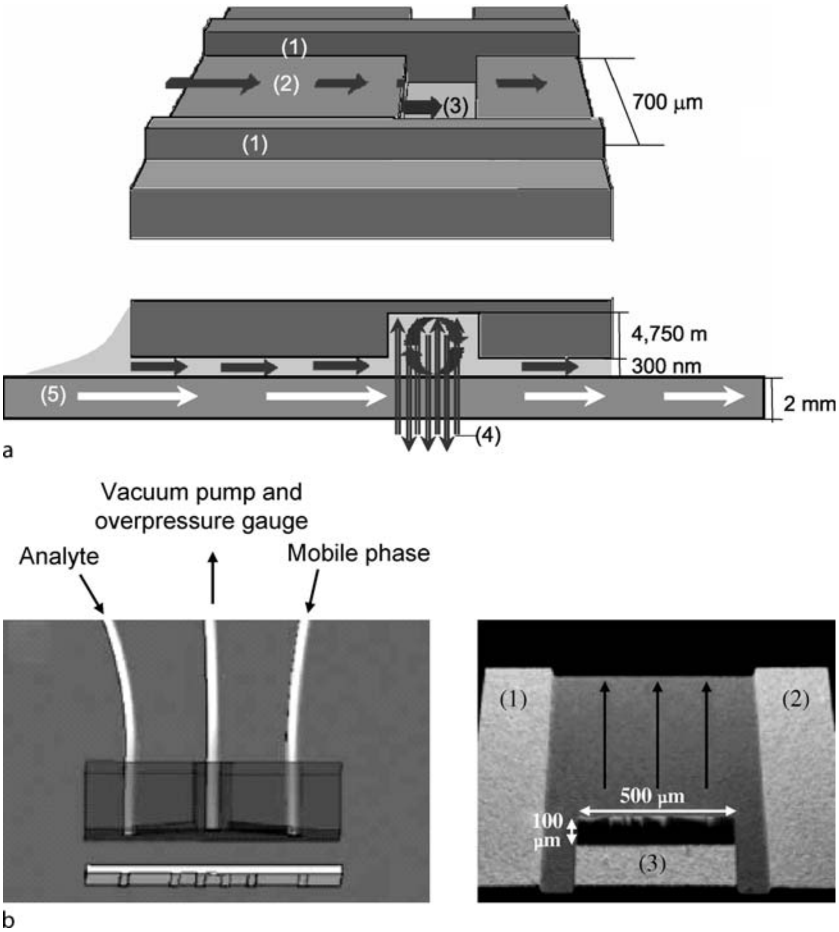

Shear-Driven Micro- and Nanofluidics, Figure 6 (**a**) Schematically overview of the detection groove structure. In the nanochannel structure (1–2) a deeper groove (3) is etched to enhance the detection. With this type of groove (with a depth of 4.75 μm, see side view) a 5 fold decrease in the detection limit could be obtained. (**b**) Outline of the automated injection system. (**a**) The supply channels in the PMMA connect to a cavity above the injection micro-well. (**b**) Wyko (optical profilometry) scan of the backside of the etched well, showing the position of the injection slit in the channel, together with the non-etched channel spacer regions (1, 2) delimiting the lateral extent of the channel and the non-etched region (3) preventing the mobile phase that is present in front of the channel to enter the channel. The flow direction is indicated by the arrows

tion can be created) could be resolved by this new method. It would hence allow performing complex separations.

It was experimentally shown that a good reproducibility occurred both for the peak width as for the sample concentration (standard deviations are max. 4 and 8%, respectively), where as the plug concentration was 80% of the original sample concentration. It was also observed that with the current setup the lower limit of the peak width was 122 μm. This is a consequence of the fact that peak width originating from convection becomes negligible to the contribution of diffusion during filling and flushing. This automated and closed system paves the way for further functionalities in shear driven chromatography, i. e. gradient elution and parallelization.

Shear-Driven Hybridization (SDH)

A second important application of the shear-driven technology based on the microarray technique has been investigated as well in our group. Earlier reports show that the most ideal flow principle for hybridization on the microarrays is an intermitting flow mode where the fluid is kept stationary for a certain period, followed by a short movement of the fluid. The stationary period is necessary to allow the target molecules to form hybrids with their complementary probes, while the short fluid pulses are necessary to refresh the target mixture above the microarray spots.

A further evaluation of the efficiency of the SDH system consisted of a series of hybridizations with complex tar-

get samples (mouse spleen and heart) on slides containing more than 21,000 cDNA fragments. In order to compare SDH with other types of hybridization approaches all experiments started from the same amount of genetic material (i. e. 40 pmol Cy3/Cy5- labeled cDNA) (Table 1). As the amount of labeled sample was kept the same for all experiments, SDH had an immediate advantage as the sample concentration is increased from 3 to 21 fold compared to the conventional coverslip and Slide Pro, respectively. A comparison of these three types of hybridization systems (Table 1) showed that, compared to the results with an automated slide processor (SlidePro, GE Heatlhcare), the relative intensity of the spots increased with a factor 2 for the coverslip hybridization and with a factor 4 for the shear-driven hybridization. Furthermore the total number of spots that could be flagged as being hybridized rose from 67% with the Slidepro system and 80% under the coverslip to 87% with the SDH system. This significant rise in the number of spots points to the great potential of SDH as it will be possible to detect a larger number of hybridized spots with the same amount of sample, or detect the same amount of spots with a smaller sample consumption. An even better gain could be obtained by making the shear driven hybridization last longer than two hours. All experiments with the SDH system lasted two hours while the SlidePro and coverslip hybridizations lasted for 16 hours.

Shear-Driven Micro- and Nanofluidics, Table 1 Comparison of hybridization conditions on the shear-driven rotating micro-chamber system, the diffusion-driven coverslip system and the SlidePro (GE healthcare) for a mouse heart and spleen total RNA sample on the VIB_Mouse_5KI microarray chip

	Shear-driven hybridization-system	Diffusion under cover-slip	SlidePro auto-mated hybridiza-tion
Amount incorporated Cy3/Cy5 (in pmol)	40	40	40
Sample Volume (in μL)	10	30	210
Sample Concentration (in pmol Cy3/ μL)	3.00	1.00	0.14
Hybridization Time (h)	2	16	16
Surface Micro-chamber (in mm^2)	314	1000	1000
Hybridized spots	87%	80%	67%
Relative Intensity	396%	189%	100%

Figure 7 shows images of experiments identical to the ones from table 1. It was clear from these images that the overall intensity of the spots was much greater for the SDH system than for the coverslip and SlidePro hybridization. For this series (Fig. 7a) of experiments the SlidePro hybridization was conducted with a total amount of 40 pmol incorporated Cy3/Cy5 dyes while the SDH and coverslip hybridizations were performed with only 20 pmol incorporated Cy3/Cy5 dyes. It is even possible to drop the concentration even further to 5 pmol incorporated Cy3/Cy5 dyes in the sample (Fig. 7b) and still be able to get good results with the SDH system, compared to SlidePro, where almost no hybridization occurred.

This report shows how a working prototype for microarray hybridizations based on the shear-driven technology has been developed and tested. The key factor for the success of the SDH method was the combination of the mixing, circumvented the slow molecular diffusion, and the reduction of sample volume generated more concentrated samples and higher final intensity values of the microarray spots. The concentration was indeed found a major factor on the effect of convection to reach higher signals intensities.

Future Directions for Research

The investigations into the fundaments of the shear-driven technique and the different applications (SDC, SDH, . . .) is still ongoing. Fundamentally different types of spacer walls are being tested in order reduce the channel depth under the 100 nm boundary. Until now 100 nm has been the limit of the shear-driven fluidics. Other channel designs and etching techniques are now being used to reduce even

S

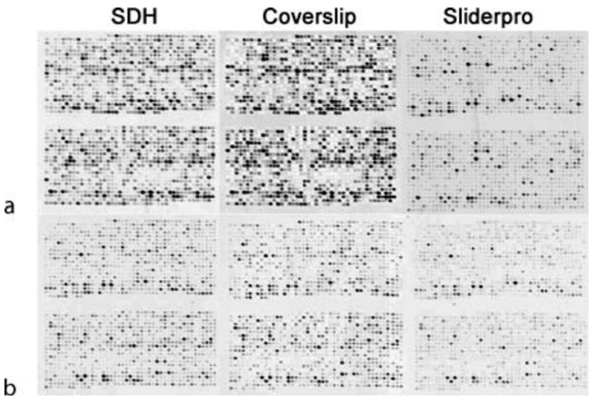

Shear-Driven Micro- and Nanofluidics, Figure 7 A series of different hybridization experiments done with 20 pmol (coverslip and SDH) and 40 pmol (SlidePro) of incorporated Cy3/Cy5 dyes (**a**) and with 5 pmol of incorporated Cy3/Cy5 dyes (**b**). All experiments were done with mouse heart (Cy3) versus spleen (Cy5) total RNA sample on the VIB_Mouse_21KII microarray chip

further the channel depths in order to reach sub 100 nm nanofluidic flows. Also the development towards infinite moving wall elements and high-throughput formats are being studied.

For SDC applications, apart from detection enhancement and the automation of the injection system, much effort is put into the development of novel stationary phases and the application of gradient elutions.

Currently a novel SDH prototype is being developed to enable a 100% coverage of the microarray slide, where our current prototype covers only 30% of the microarray slide. In order to use shear driven convection on standard microarray slides, the prototype needs to be redesigned from a rotating to a lateral movement or change the standard microarray slides to microarrays on round disks.

Cross References

► Electroosmotic Flow (DC)
► DNA-Microarrays
► Pressure-Driven Flow
► Reactive Ion Etching (RIE)

References

1. Bhuiyan LB, Outhwaite CW, Levine S (1979) Chem Phys Letters 66:321
2. Desmet G, Baron GV (2000) Anal. Chem. 72:2160
3. Schlichting H (1958) Boundary Layer Theory. Mc-Graw Hill, London
4. Desmet G, Baron GV (1999) J Chromatogr A 855:57–70
5. Desmet G, Vervoort N, Clicq D, Baron GV (2001) J Chromatogr A 924:111
6. Clicq D, Pappaert K, Vankrunkelsven S, Vervoort N, Baron GV, Desmet G (2004) Anal Chem 76(23):430A–438A
7. Vankrunkelsven S, Clicq D, Pappaert K, Baron GV, Desmet G (2004) Anal Chem 76:3005–3011
8. Clicq D, Pappaert K, Vankrunkelsven S, Vervoort N, Baron GV, Desmet G (2004) Anal Chem 76(23):430A–438A
9. Vanderhoeven J, Pappaert K, Dutta B, van Hummelen P, Desmet G (2005) Anal Chem 77:4474–4480

Shear Flows

Definition

Fluid motion that is characterized by velocity gradients.

Shear Stress

► Wall Shear Stress

Shear Stress Sensors

PRADIPTA KUMAR PANIGRAHI
Department of Mechanical Engineering, IIT Kanpur, Kanpur, India
panig@iitk.ac.in

Definition

Fluid flow past a surface or boundary leads to surface forces acting on it. These surface forces depend on the rate at which fluid is strained by the velocity field. A stress tensor with nine components is used to describe the surface forces on a fluid element. The tangential component of the surface forces with respect to the boundary is known as shear stress. The nature or origin of shear stress depends on the nature of flow, i. e., laminar or turbulent. The stress components for a laminar flow are functions of the viscosity of the fluid and are known as viscous stresses. The turbulent flow has additional contributions known as Reynolds stresses due to velocity fluctuation, i. e., the stresses of a laminar flow are increased by additional stresses known as apparent or Reynolds stresses. Hence, the total shear stresses for a turbulent flow are the sum of viscous stresses and apparent stresses. In a turbulent flow, the apparent stresses may outweigh the viscous components.

Overview

The ► wall shear stress is an essential quantity of interest in a wall-bounded flow. The time averaged value of wall shear stress can be used to determine the skin friction drag acting on the body by the fluid flow. The time-resolved behavior of surface shear stress indicates the unsteady flow structures responsible for individual momentum transfer events and turbulence activities. The instantaneous shear stress values at distributed locations on the surface can be used to feedback control the turbulence events inside a boundary layer. Shear stress measurement also helps in assessment and control of power consumption rate and therefore is an important quantity of interest in various industrial applications.

The importance of shear stress measurement is even more crucial for small-scale devices, i. e., MEMS applications, due to their higher surface to volume ratio. There have been many efforts in literature for successful shear stress measurements. The success of these efforts primarily relies on the complexity of the flow, the nature of solid boundaries and limitations of the measurement techniques. The other drawback of shear stress measurements is its smaller magnitude, i. e., the estimated value of shear stress

of a typical car moving at 100 km/hour is about 1 Pa. Hence, highly sensitive shear stress measuring devices are required for successful measurements of surface shear stress and it is essential to have proper understanding of the various noise sources that can effect shear stress measurements.

Shear stress sensors provide qualitative information about the flow field, i. e., separation, transition, reattachment, etc., and proper calibration of shear stress sensors is required for quantitative measurement/information. Hence, this review concentrates on: principle of operation, noise sources and calibration of various shear stress sensors. The spatial and temporal resolution requirements for turbulent flow applications and the benefit of MEMS sensors are also discussed.

Requirements for Turbulent Flow

Turbulence is characterized by the existence of numerous length and time scales. The time scale is a measure of the fact that at a given point in a turbulent flow field, distinct patterns get repeated regularly in time. Similarly, distinct patterns may be repeated in space at a given instant and the size of the patterns are known as length scales. Different length scales and time scales have been defined for characterization of turbulent flow field. The smallest eddy of turbulent flow is expressed by the Kolmogorov length (l) and time scale (τ) which is uniquely determined by dissipation (ε) and kinematic viscosity (ν):

$$l = \left(\frac{\upsilon^3}{\varepsilon}\right)^{\frac{1}{4}} \tag{1}$$

$$\tau = \left(\frac{\nu}{\varepsilon}\right)^{\frac{1}{2}} \tag{2}$$

Using the inviscid assumption for calculation of the dissipation rate, the non-dimensional length scale and time scale respectively reduce to

$$\frac{l}{l_S} = (\mathrm{Re})^{-\frac{3}{4}} \tag{3}$$

$$\frac{\tau}{l_S} u = (\mathrm{Re})^{-\frac{1}{2}} \tag{4}$$

Here, l_S is the characteristic length of the inertial sublayer, u is the characteristic velocity of the eddy and Re is the Reynolds number (ul_S/ν). Equations (3) and (4) indicate that with an increase in Reynolds number, the length and time scales of eddies decrease. To spatially resolve the small eddies, sensors that are of same size as the Kolmogorov length scale for that particular flow are needed. Hence, smaller sensors are required as the Reynolds number is increased. For a flat plate boundary layer with momentum thickness Reynolds number equal to 4000, the Kolmogorov length scale is of the order of 50 μm. A large-dimension sensor integrates the fluctuation due to small eddies over its spatial extension. Therefore, when measuring fluctuating quantities, small eddies are counted as mean flow and the fluctuating energy is lost. This leads to lower estimated value of turbulence intensity. The other important issue is the spacing between the sensors, which is primarily determined by the spacing between the coherent structures present in the flow. For the turbulent wall boundary layer, the spacing between the sensors needs to be less than the distance between the low-speed streaks, i. e., the near-wall region coherent structures.

Basic Methodology

Classification

Various shear stress measurement techniques have been proposed in the literature. Some of the principal measurement techniques are: Stanton tube, Preston tube, electrochemical technique, velocity measurements, thermal method, floating element sensors, sublayer fence, oil-film interferometry and shear stress sensitive liquid crystal.

The Stanton tube is a rectangular shaped pitot tube located very close to the boundary wall and the mean velocity measured from this pitot tube pressure difference is directly related to the shear stress. The Preston tube is similar to the concept of the Stanton tube using a pitot static tube close to the surface and the difference between the stagnation pressure at the center of the tube from the static pressure is related to the shear stress. The electrochemical or mass transfer probe is flush mounted with the wall and the concentration at the wall element is maintained constant. The measurement of mass transfer rate between the fluid and the wall element is used for determination of the wall shear stress. One of the limitations of the mass transfer probe is that at very high flow rates, the mass transfer rate becomes large and it may not be possible to maintain the wall concentration constant. A detailed discussion on the above three techniques can be found in Hanratty and Campbell [1]. These shear stress measurement techniques are not ideal MEMS-based techniques.

Benefits of MEMS-Based Sensors

MEMS-based shear stress sensors offer many advantages over traditional shear stress sensors. These are:

- MEMS-based shear stress sensors can meet the spatial and temporal requirement of turbulent flow due to their small size.

- MEMS-based sensors have low thermal inertia leading to higher dynamic response.
- MEMS-based sensors are less intrusive compared to the traditional sensors due to their small size and therefore do not effect the flow significantly.
- The energy consumption is low for MEMS-based sensors.
- MEMS-based sensors are ideal for distributed measurements and control, as a large number of sensors can be fabricated on the same chip in a cost-effective manner.

Due to numerous benefits of MEMS-based shear stress sensors, the following shear stress measurement techniques having great promise for future MEMS applications are discussed in the following sections: velocity measurements, thermal sensors, floating element sensors, sublayer fence, oil-film interferometry and shear stress-sensitive liquid crystal.

Velocity Measurements

Velocity measurements close to the wall or the velocity profile measurement in the near-wall region can be used to determine the wall shear stress. Clauser proposed an approach for shear stress measurement of turbulent flow [1]. Here, the mean velocity measurements away from the wall are used with the assumption that the mean velocity ($\bar{U}$) varies with the logarithmic distance from the wall (y), i. e.,

$$\frac{\mathrm{d}\bar{U}}{\mathrm{d}y} = \frac{u^*}{\kappa y} \tag{5}$$

where $u^* = (\tau_\mathrm{w}/\rho)^{1/2}$ is the friction velocity and κ is the von Karman constant. The slope of a semi-logarithmic plot between $\bar{U}$ and y gives u^*/κ and therefore τ_w. The difficulty in this approach is the validity of the logarithmic region assumption and the value of the von Karman constant, which is approximated to be equal to 0.40. For flows with large pressure gradient, a well-defined logarithmic layer does not exist. If the wall is flat and in equilibrium situation Clauser proposed a relationship as

$$\frac{\bar{U}}{u^*} = f\left(\frac{yu^*}{\nu}, \Delta\right) \tag{6}$$

where $\Delta = |\mathrm{d}P/\mathrm{d}x|\left(\nu/u^*\tau_\mathrm{w}\right)$ and $\mathrm{d}P/\mathrm{d}x$ is the pressure gradient. Comparison of measured variation of mean velocity with distance from the wall gives the wall shear stress τ_w.

The Spalding formula represents a good fit to the velocity profile in a turbulent boundary layer, i. e., from the wall to the end of the log region, thus including both the linear sub-layer and the logarithmic region. The Spalding formula is given by

$$y^+ = \frac{yu^*}{\nu} = u^+ + \frac{1}{E}\left[e^{-\kappa u^+} - 1 - \kappa u^+ - \frac{(\kappa u^+)^2}{2} - \frac{(\kappa u^+)^3}{6} - \frac{(\kappa u^+)^4}{24}\right] \tag{7}$$

where $u^+ = u/u^*$ and E is a constant equal to 8.6. An iterative procedure is carried out for curve fitting the experimental velocity profile to the Spalding formula and the shear stress is determined from the best fit. The Spalding formula represents the mean velocity profile in a turbulent boundary layer at all pressure gradients and until about $y^+ = 200$.

Optical techniques, i. e., laser Doppler velocimetry (LDV), particle image velocimetry (PIV) and holographic PIV, have matured as successful non-intrusive velocity measurement techniques for large-scale applications. Panigrahi et al. [2] obtained the shear stress from PIV measurements by assuming the validity of law of the wall for turbulent flow. In recent years, the μ-PIV has matured as a successful velocity measurement technique for MEMS applications [3]. The PIV techniques provide instantaneous velocity field information. The spatial and temporal resolution of PIV can be controlled with proper selection of lighting source, i. e., laser, imaging system, i. e., camera and frame grabber, and optical arrangements/components. The continuous development of this hardware in near future is expected to result in very high spatial and temporal resolution velocity measurements. Therefore the μ-PIV and μ-holographic PIV techniques will develop as high-resolution indirect instantaneous shear stress measurement techniques in the near future.

Thermal Sensors

The operational principle of a thermal sensor is based on the relationship between the heat transfer from the sensor exposed to the flowing fluid and the shear stress. For the heat transfer to take place the sensor element temperature must differ from the temperature of the flowing medium, i. e., the sensor is raised to a temperature above the medium temperature. The thermal sensor forms one of the resistances of a Wheatstone bridge circuit (see Fig. 1a). The resistance of the thermal sensor is given by

$$R = R_0\left(1 + \alpha\,(T - T_0)\right) \tag{8}$$

where R is the sensor resistance at temperature T and R_0 is the sensor resistance at reference temperature (T_0); T is the temperature of the sensor and α is the temperature

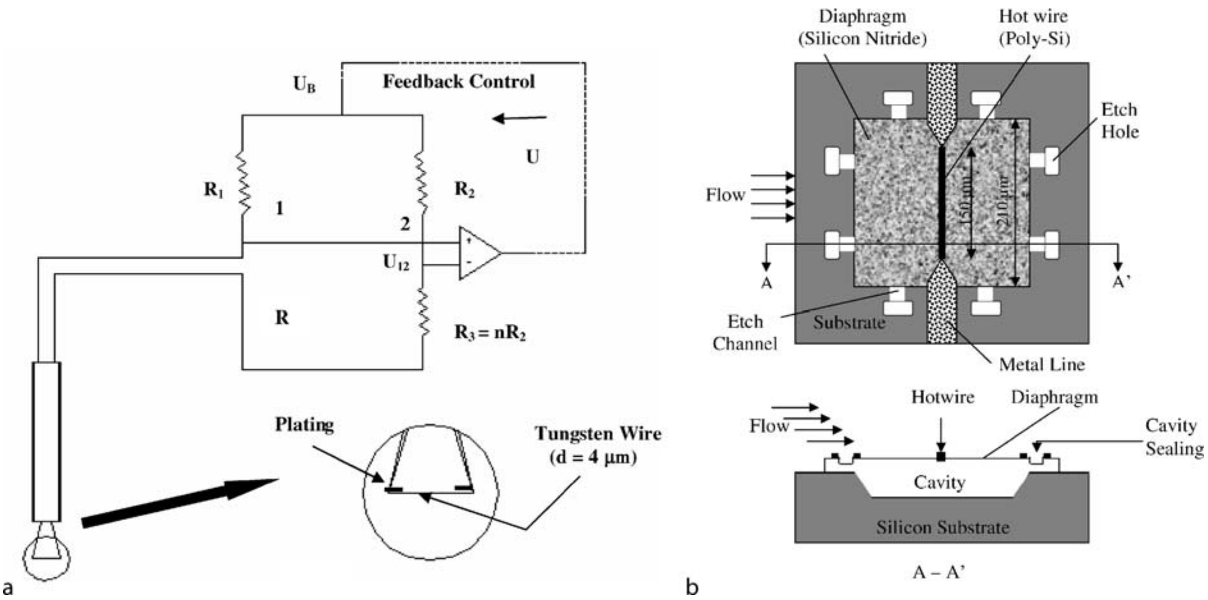

Shear Stress Sensors, Figure 1 (**a**) Schematic of a hot wire sensor connected to a Wheatstone bridge circuit and (**b**) schematic of a flush-mounted thermal shear stress sensor

coefficient of resistance. The heat transfer rate depends on the nature of fluid flow past the sensor leading to drop in temperature of the sensor. The drop in sensor temperature affects the sensor resistance leading to imbalance of the Wheatstone bridge circuit. The relationship between the bridge circuit imbalances and the heat transfer can be obtained from two approaches: deflection method and null method. In the deflection method, the change in bridge balance due to the input signal is measured. In the null method, an electronic feedback is used to keep the bridge balanced. The null method is usually preferred due to better frequency response. For the electronic feedback, there are three possible modes of operation:

- *Constant current mode* (CC). Here the current through the sensor is kept constant and the change in current needed to maintain its constant value is related to the flow signal, i. e., shear stress.
- *Constant voltage mode* (CV). Here the voltage across the sensor is kept constant and the change needed to keep the voltage constant is related to the shear stress.
- *Constant temperature mode* (CT). Here the temperature of the sensor is kept constant and the voltage or current change needed to keep the temperature constant represents the wall shear stress.

The thermal sensors for shear stress measurements can have two principal modes of variation: elevated hot wire probe and surface-mounted hot wire probe. The principle of operation of these two types of thermal shear stress sensors is discussed in the following sections.

Elevated Hot Wire Probe

In the elevated hot wire approach, the hot wire is mounted a small distance away from the wall. The velocity increases linearly with the wall distance in the near-wall region of both laminar and turbulent flow. For turbulent flow, this assumption is valid for the instantaneous velocity profile up to the wall normal location $y^+(yu^*/\nu) < 5$. The linear relationship between the shear stress (τ_w) and the velocity u at distance y from the wall is given as

$$\tau_\mathrm{w} = \frac{\rho \nu u}{y} \tag{9}$$

The true velocity in the near-wall region determined from the hot wire calibrated in the free stream is affected due to the heat conduction in the near-wall region. Therefore, the velocity obtained from the hot wire needs to be corrected based on the empirical relationship. The substitution of this corrected velocity in Eq. (9) provides the wall shear stress. The sensitivity of this approach depends on the wall distance, i. e., there is an optimal wall distance at which the hot wire sensitivity is optimal. In addition to that, the hot wire should be located inside the inertial sublayer to satisfy the basic assumption essential for the shear stress measurement.

Surface-Mounted Hot Wire Sensor

Figure 1b shows a schematic of a flush-mounted thermal shear stress sensor. The sensor element is either positioned

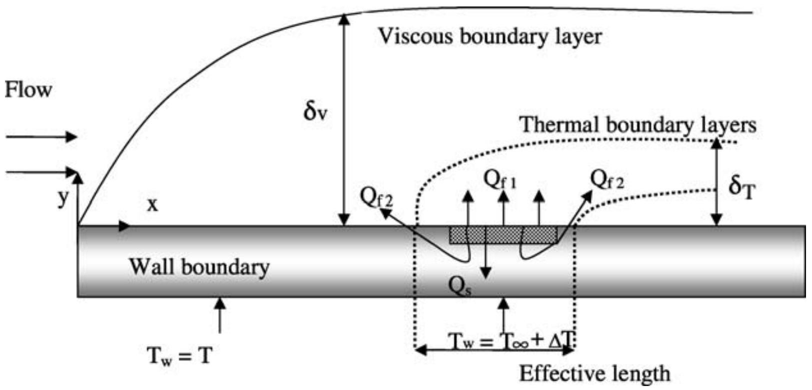

Shear Stress Sensors, Figure 2 The flow and heat transfer mechanism of a flush-mounted thermal shear stress sensor

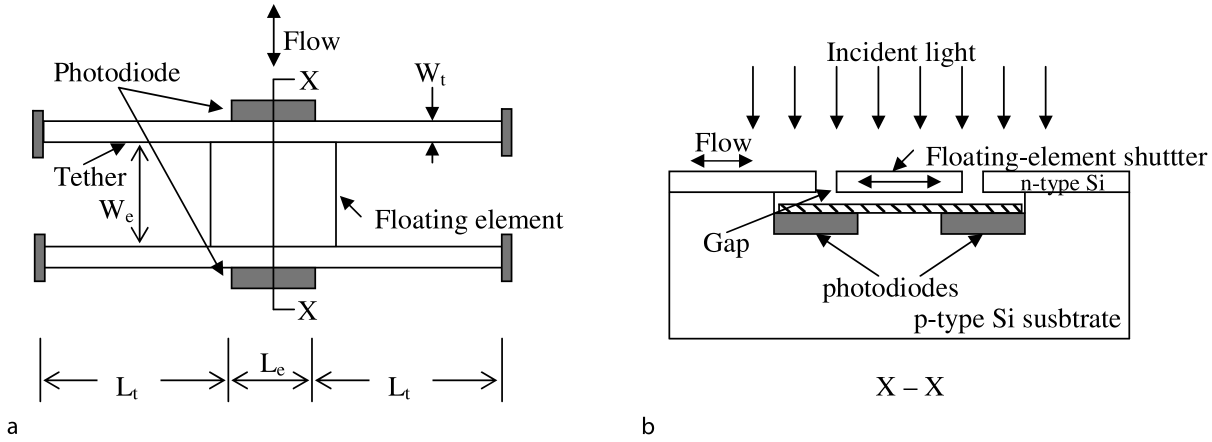

Shear Stress Sensors, Figure 3 Schematic of a floating element shear stress sensor: (**a**) top view and (**b**) cross-sectional view

on the top of a substrate or on a thin diaphragm above a vacuum cavity. As the thermal shear stress sensor is flush mounted along the surface of the wall, this technique is considered as non-intrusive with negligible disturbance to the mean flow. The ohmic heating (Q_{ohmic}) due to the current flow through the sensor element transfers heat to both fluid (Q_{fluid}) and the substrate ($Q_{\text{substrate}}$), i. e.,

$$Q_{\text{ohmic}} = Q_{\text{fluid}} + Q_{\text{substrate}} \tag{10}$$

Figure 2 shows the heat transfer mechanism from a surface-mounted thermal sensor. The total heat transfer to the fluid from the thermal sensor (Q_{ohmic}) has two components, i. e., the heat transfer to the fluid (Q_{fluid}) and the heat lost to the substrate ($Q_{\text{substrate}}$). The heat transfer to the fluid has two parts, i. e., direct heat transfer from the sensor element (Q_{f1}) and the indirect heat transfer from the substrate heated by the conduction of heat from the sensor to the substrate (Q_{f2}). The heat transferred to the fluid via the substrate affects the temperature distribution near the sensor. This affects the net heat transfer rate from the sensor element and limits the performance of thermal shear stress measurement. The effective length of the thermal sensor is higher than the size of the sensor element thus limiting the spatial resolution of shear stress measurement. Therefore, effective thermal isolation between the sensor element and substrate is an important issue for optimum performance, fabrication and packaging of thermal shear stress sensors. For thermal isolation, the resistor of the sensor sits on the top of a diaphragm above a vacuum cavity (see Fig. 2). The presence of the vacuum cavity and thin diaphragm reduces the convective and conductive heat transfer to the substrate. Better insulation improves the thermal sensitivity of the sensor, i. e., higher temperature rise ($T - T_0$) of the thermal sensor is achieved for a particular power input (P).

In experimental aerodynamics, the surface hot wire probe has proved to be the most successful standard measure-

ment technique to determine the laminar-to-turbulent flow transition, local separation and shear stress fluctuations. The flush-mounted thermal shear stress sensor is one of the most successful techniques for shear stress measurement and is available in various forms, i. e., sensor skin, etc. [4], due to the rapid development of MEMS manufacturing processes. The quantitative determination of shear stress depends on the proper calibration with a reference method. The calibration issues are described in a later section.

Floating Element Sensors

Direct measurement of tangential force exerted by the fluid on the sensor element is possible using floating element shear stress sensors. Therefore, the floating element-based shear stress sensor is classified as a direct measurement device. A schematic of a floating element shear stress sensor is shown in Fig. 3. The floating element is connected to the substrate by four tether elements. The movement of the floating element due to the surface force, i. e., shear stress acting on it, is sensed by suitable transducer and is related to the shear stress. The movement of the floating element can be inferred using the capacitive, piezo-resistive and optical detection schemes. The axial compression and expansion of the tethers due to the imposed shear stress cause a change in piezo-resistive effect for piezo-resistive sensing element. The change in resistance is a measure of the shear stress magnitude and direction. In the capacitive scheme, the sensor element displacement leads to change in the capacitance value. In the photodiode-based scheme, photodiodes are integrated below the floating element at its leading and trailing edge. A coherent light source illuminates the sensor element from above. The differential photocurrent generated due to the movement of the floating element is related to its displacement (see Fig. 3).

No assumption regarding the flow field is required for the floating shear stress sensor. The displacement (δ) of the floating element sensor as a function of shear stress (τ_w) can be derived from Euler–Bernoulli beam theory as

$$\delta = \tau_w \frac{L_e W_e}{4Et} \left(\frac{L_t}{W_t} \right)^3 \left(1 + 2 \frac{2 L_t W_t}{L_e W_e} \right) \tag{11}$$

where L_t is the tether length; W_t is the tether width; E is the elastic modulus of the tether; t is the floating element thickness; L_e is the length of the floating element; W_e is the width of the floating element; and g is the recessed gap of the floating element (see Fig. 3). Equation (11) indicates a linear relationship between the displacement of the floating element and the shear stress. The above linear relationship has been verified from the static calibration results of floating element sensors. The flow under the floating element and the pressure gradient acting on its lip introduce error to the measurement of skin friction. This relationship between the effective shear stress (τ_{eff}) and the actual shear stress (τ_w) is given by [5]

$$\tau_{eff} = \left(1 + \frac{g}{h} + \frac{2t}{h} \right) \tau_w \tag{12}$$

where h is the channel height of the wind tunnel used for calibration. The second and third term of the above equation relate to the effect of gap height and pressure gradient on the measurement error respectively. Equation (12) indicates the benefit of MEMS-based shear stress sensors, as both gap height and the floating element thickness can be maintained at a very small value ($\sim 1\,\mu$m) leading to considerable reduction in errors. In addition, the MEMS-based sensor element results in high spatial resolution and higher frequency bandwidth due to lower effective size and mass respectively. Due to the rapid advancement of MEMS-based fabrication techniques, it is also possible to place pairs of sensors in close proximity at right angles to each other for detection of both streamwise and spanwise shear stress.

The capacitive and piezo-resistive sensing-based floating element sensors may show sensitivity to electromagnetic interference due to the impedance of the electronics elements used for detection. The size of the floating element, the misalignment and gaps around the floating element, pressure gradient, sensitivity to acceleration, vibration and thermal expansion are some of the general drawbacks of floating element sensors. The availability of MEMS fabrication techniques has enhanced the capability of floating element sensors.

MEMS Skin Friction Fence

The generic skin friction fence and its principle has been explained by Hanratty and Campbell [1]. Recently, Schober et al. [6] developed a MEMS-based skin friction fence (see Fig. 4a). The surface fence is a fence protruding from the wall. There is a slot below the surface fence with support at both ends. Two pairs of piezo-resistors are located at both ends of the fence. These piezo-resistors are connected to a Wheatstone bridge circuit. The voltage output of the Wheatstone bridge circuit is related to the strain acting on the fence. The strain due to the deflection of the fence is directly related to the pressure difference across the fence. Hence the voltage output is indirectly related to the shear stress acting on the fence. The surface fence should remain inside the viscous sublayer ($y^+ < 5$). However, there is no requirement on the validity of the law of

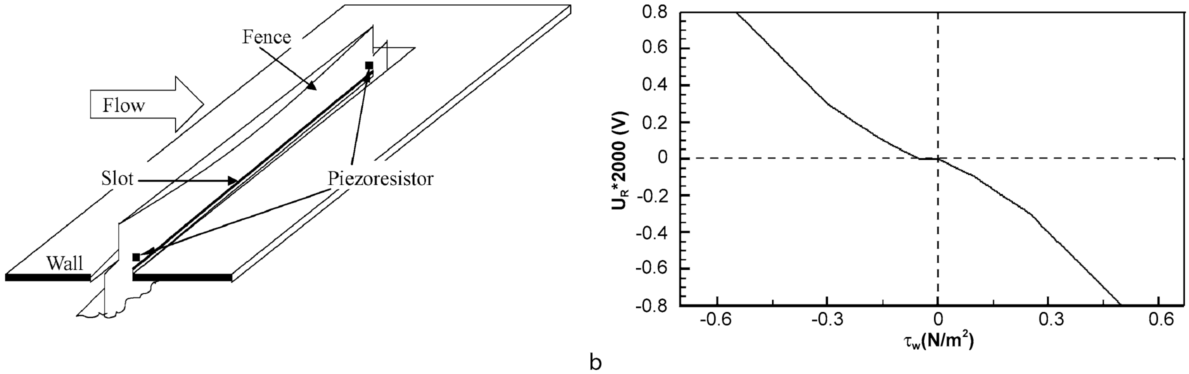

Shear Stress Sensors, Figure 4 Schematic of (**a**) MEMS skin friction fence and (**b**) its calibration curve between the bridge voltage (U_B) and the shear stress (τ_w)

the wall for the turbulent boundary layer. The pressure difference between the front and back of the fence is related to the shear stress, i. e.,

$$\Delta P = A\tau_w + B\tau_w^2 \quad (13)$$

where A and B are constants. From Eq. (13), the measured voltage (V_{br}) from the Wheatstone bridge circuit can be related to the shear stress as

$$V_{br} = A_{br}\tau_w + B_{br}\tau_w^2 \quad (14)$$

where A_{br} and B_{br} are the constants to be obtained from the calibration. Figure 4b shows the calibration curve between the bridge voltage and the shear stress of a micro-fence inside a zero pressure gradient turbulent boundary layer. It may be observed that the sensitivity of the micro-fence is higher at higher shear stress.

Optical Sensors

The optical-based shear stress sensor can be classified into two categories based on the measurement principle: oil-film interferometry and shear sensitive liquid crystal. These techniques are discussed in the following sections.

Oil-Film Interferometry

The oil film technique is a direct method for skin friction measurement based on the movement of interference fringes of a thin film. In this method, an oil film is applied to the smooth solid wall, which spreads out by the flow into a thin layer whose thickness is of the order of 1 μm. The thickness of the oil film is dependent on the shear force acting upon it. Interferometry is used to measure the thickness of the oil film. Monochromatic light of wavelength λ from a light source is incident on the film at an angle θ (Fig. 5a). The light partially gets reflected from the oil/air interface. The remainder of the light passes through the film and reflects from the solid surface and travels back through the oil film. These two beams interfere constructively and destructively with each other in the image plane depending on the phase difference between the two leading to formation of bright and dark bands known as interference fringes.

The local height of the oil film can be obtained from the fringe patterns. The height of the oil film at the kth black fringe is given by

$$h_k = h_0 + k\Delta h\ ;\ k = 0, 1, 2, \ldots \quad (15)$$

where h_0 is the height of the zeroth black fringe at the film edge, i. e., at $k = 0$, and Δh is the difference in height between two consecutive fringes given by

$$\Delta h = \frac{\lambda}{2\left(n^2 - \sin^2\alpha\right)^{1/2}} \quad (16)$$

Here, n is the refractive index of oil and λ is the wavelength of light. A general oil-film interferometry experimental setup is shown in Fig. 5b. Here, the light from preferably a He – Ne laser (wavelength = 632.8 nm) or sodium lamp (wavelength = 589 nm) is incident on the thin oil film through a beam splitter. A camera collects the reflected light from the oil film and a portion of the incident light from the beam splitter against a black background. The motion of the interference fringes is collected by imaging through the camera.

For oil-film interferometry, it is assumed that the oil film is so thin that it does not influence the flow above it and is driven by the skin friction distribution of the flow. Using a control volume analysis of the thin oil film with its height

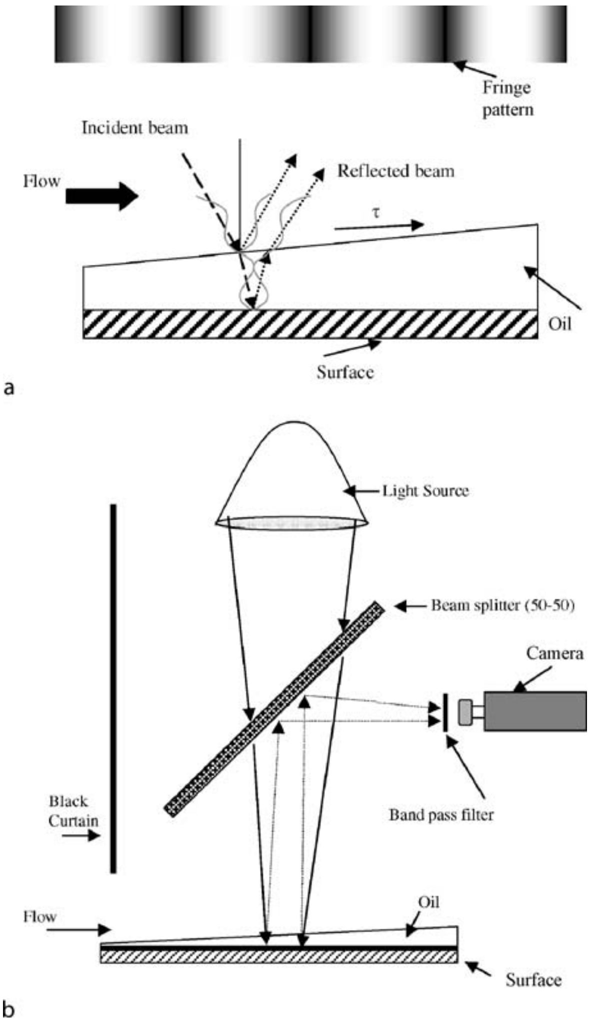

Shear Stress Sensors, Figure 5 Schematic showing (**a**) fringe formation for oil height measurement and (**b**) an experimental setup using oil film interferometry

h in wall normal (y) direction as a function of streamwise (x) and spanwise (z) coordinate and assuming the shear stress contribution to be dominant compared to the pressure gradient and surface tension force, the governing equation for the thin oil-film flow is

$$\frac{\partial h}{\partial t} + \frac{\partial}{\partial x}\left(\frac{\tau_{w,x} h^2}{2\mu}\right) + \frac{\partial}{\partial z}\left(\frac{\tau_{w,z} h^2}{2\mu}\right) = 0 \qquad (17)$$

Using the distribution of oil film height from interferometry measurements and the integration of equation (16) the skin friction can be determined. The benefit of oil-film interferometry is that no calibration is required for measurement of shear stress and the basic analytical expression is used. It can be used for three-dimensional flow situations and provides both magnitude and direction of shear stress. The disadvantage is that it does not possess any temporal resolution and therefore cannot be used for fluctuating skin friction measurements.

Liquid Crystal Sensors

Liquid crystal is a phase of matter that exists between the liquid and solid phase. It exhibits optical properties similar to a solid crystalline material. The molecular arrangement of a liquid crystal is a function of either temperature or shear stress. When the molecular arrangement is sensitive to temperature, the liquid crystal coating can be used for temperature measurement and when the molecular arrangement is sensitive to shear stress, the liquid crystal can be used for shear stress measurement.

Shear sensitive liquid crystal coatings applied to a solid surface consist of helical aggregates of long planar molecules arranged in layers parallel to the coated surface. This molecular arrangement is affected by the application of shear stress on the thin film of liquid crystal. Each layer of molecules is rotated relative to the layer above and below it due to the application of shear stress. The incident light on the coating surface selectively scatters at a wavelength proportional to the pitch of the helix. The local pitch of the helical structure is altered due to application of shear stress relative to the no shear state. The liquid crystal selectively scatters the incident white light as a three-dimensional spectrum in color space depending on the molecular arrangement. The color change observed at a particular direction by the imaging device is a function of both shear stress vector magnitude and direction (see Fig. 6a). The shear vectors with components directed away from the observer exhibits color change responses of the liquid crystal depending on the shear magnitude and direction. At any surface point, maximum color change occurs when the shear stress vector is aligned and directed away from the observer. The location with shear stress directed to the observer exhibits no color change response. The above behavior of the shear sensitive liquid crystal is used for determination of the shear stress magnitude and direction.

A sample experimental setup for the application of shear sensitive liquid crystal is shown in Fig. 6b similar to the one proposed by Fujisawa et al. [7]. The off-axis angles of the camera and the light source with respect to the horizontal are α and β respectively. Two cameras are situated on opposite sides of the axis with an off-axis angle δ. As the color images are acquired at an oblique angle to the test surface, it is important to convert the images at oblique angle to the normal observation angle by using a geometrical transformation technique. The two color cameras

S

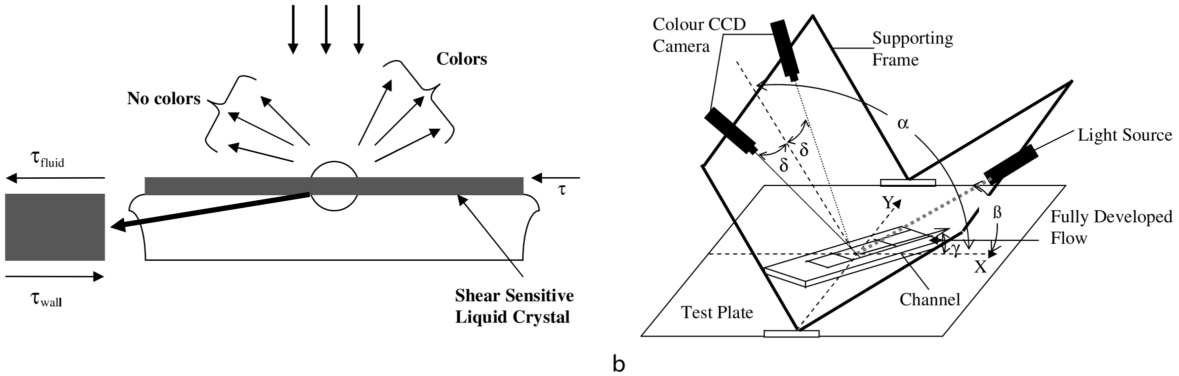

Shear Stress Sensors, Figure 6 Schematic showing (**a**) the principle of shear sensitive liquid crystal and (**b**) the experimental setup for shear stress measurement using shear sensitive liquid crystal

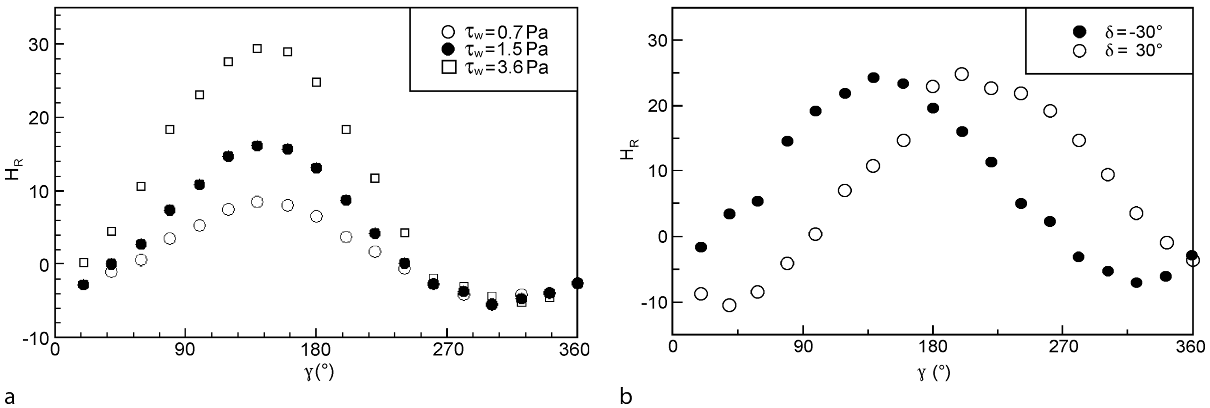

Shear Stress Sensors, Figure 7 (**a**) The relative hue (H_R) versus the shear stress angle (γ) for different shear stress magnitude (τ_w). (**b**) The relative hue (H_R) versus the shear stress angle (γ) for two cameras (left, $\delta = -30°$; right, $\delta = 30°$) at a particular shear stress magnitude

are synchronized with the lighting source. The test section can be rotated leading to variation of the shear stress angle (γ) for calibration. There are different color formats, i. e., RGB, HIS, for quantitative representation of color. The hue has been observed to be the best indicator for expressing the change in color. It can be calculated from

$$H = \left[\pi/2 - \tan^{-1}\left(\frac{2R - G - B}{\sqrt{3(G - B)}}\right) + \pi\right] \Big/ 2\pi ; \; G > B \tag{18}$$

The color change of the liquid crystal depends on the illumination and observation angle with respect to the liquid crystal coating surface. Therefore, the calibration of the liquid crystal is carried out by the relative hue ($H_R = H_\tau - H_{no-\tau}$), where H_τ is the hue value of the liquid crystal with applied shear stress and $H_{no-\tau}$ is the hue value of the liquid crystal without applied shear stress. The hue value for a particular shear stress magnitude and direction depends on the camera and lighting angle. Therefore, two separate calibration curves for two cameras in stereo arrangement can be used to determine the two unknowns, i. e., the shear stress magnitude and direction. Figure 7a shows the calibration curve between the relative hue (H_R) and the shear stress angle (γ) at different shear stress amplitudes (τ_w) for a particular camera and lighting angle. Figure 7b shows the relative hue (H_R) versus the shear stress angle (γ) for two different cameras (left and right). For quantitative determination of the shear stress, the two cameras and lighting source are set at optimum off-axis (δ), observation (α) and illumination (β) angles respectively. The calibration curve between the relative hue of both the cameras (left and right), i. e., $H_{R-left}(\tau_w, \gamma)$ and $H_{R-right}(\tau_w, \gamma)$ with respect to the shear stress magnitude (τ_w) and direction (γ) is established during the calibration process. The determination of shear stress magnitude and direction for an actual measurement is carried out by an iterative process. Initially, the shear stress magnitude (τ_w) and direction (γ) are assumed. The corresponding hue values for both left and right cameras are determined from the

calibration curve. The measured hue value for both left and right cameras $\left(H_{\mathrm{R-left-M}}(\tau,\ \gamma)\right.$ and $\left.H_{\mathrm{R-right-M}}\right)\ (\tau,\ \gamma)$ are compared with the calibrated hue values. The iteration is carried out, i. e., the shear stress magnitude (τ_{w}) and direction (γ) are changed, until the error (E) between the calibrated hue and actual hue value for both left and right cameras is minimized close to a zero value.

$$E = \left(H_{\mathrm{R-left}}(\tau,\gamma) - H_{\mathrm{R-left-M}}(\tau,\gamma)\right)^2 + \left(H_{\mathrm{R-right}}(\tau,\gamma) - H_{\mathrm{R-right-M}}(\tau,\gamma)\right)^2 \quad (19)$$

Calibration Procedure

Calibration is one of the important issues for quantitative determination of the shear stress vector from measurement. The suitability of the shear stress sensor for a particular application is based on the complexity of the calibration procedure. The calibration of thermal-based shear stress sensors and the calibration setup required is described below. Similar setup can be used for calibration of other types of shear stress sensors. The calibration process is categorized as static and dynamic.

Static Calibration

The heat transfer rate from a flush-mounted shear stress tensor depends on the near-wall flow, i. e., the magnitude of the velocity gradient. For a laminar two-dimensional thermal boundary layer developing over the heated sensor with an approaching linear velocity profile (Fig. 2) and negligible free convection effect the heat loss from the thermal element can be derived from the thermal boundary layer equation as

$$\frac{q}{\Delta T} = \frac{I^2 R}{\Delta T} = 0.807 \frac{C_{\mathrm{p}}^{1/3}\, k^{2/3}}{L^{1/3}\, \mu^{1/3}} (\rho \tau_{\mathrm{w}})^{1/3} \quad (20)$$

where ρ is the density; k is the thermal conductivity; C_{p} is the specific heat; L is the length of heating element; T is the temperature; μ is the viscosity of the fluid; and τ_{w} is the shear stress. Equation (19) for the ohmic heating of the thermal sensor can be written as

$$\frac{I^2 R}{\Delta T} = A(\rho \tau_{\mathrm{w}})^{1/3} + B \quad (21)$$

where I is the heating current and R is the resistance of the sensor. The term B represents the heat loss from the substrate and depending on the design can be more than the heat loss to the fluid, i. e., the first term of the above equation. The term A is a weak function of temperature. The length of the sensor calculated from the experimentally determined value of A is more than the actual sensor length due to the heat transfer to the fluid from both substrate and the sensor (see Fig. 2). The forced convection heat transfer assumption is limited by the effective length of the sensor. It is also difficult to satisfy the thermal boundary layer to be within the linear velocity profile. Hence, for a turbulent flow the above equation is modified as

$$\frac{I^2 R}{\Delta T} = A_{\mathrm{T}}(\rho \bar{\tau}_{\mathrm{w}})^{1/n} + B_{\mathrm{T}} \quad (22)$$

Here, the constants A_{T}, B_{T} and n should be determined empirically from the calibration procedure. If the resistance of the heating element is held constant and the voltage (E) / current (I) is measured, than the above equation can be rearranged as

$$\tau_{\mathrm{w}} = \left(A_{\mathrm{T,New}}\, E^2 + B_{\mathrm{T,New}}\right)^n \quad (23)$$

Equation (23) between shear stress and the voltage can also be represented as a polynomial function as

$$\tau_{\mathrm{w}} = C_0 + C_1 E + C_2 E^2 + \ldots + C_n E^n \quad (24)$$

One possible experimental arrangement for shear stress calibration is a rotational rig consisting of a rotational disc above a bottom stationary disc (see Fig. 8a). The gap size (δ) between the discs is very small (0.3 mm to 0.45 mm) to maintain a small Reynolds number ($\mathrm{Re_s} = \omega\delta^2/\nu \ll 5$), where ω is the rotating disc angular velocity. For small Reynolds number, the tangential shear stress can be derived as

$$\tau = \mu(\omega r/\delta)\left[1.0 + (1/1050)\mathrm{Re}_{\mathrm{s}}^2 + O(\mathrm{Re}_{\mathrm{s}}^4)\right] \quad (25)$$

During calibration, the shear stress sensor is mounted on the stationary plate at various radial positions with different gap size and rotational speed to achieve wide range of shear stress values for static calibration.

Another possible setup for the static calibration uses a wind tunnel (Fig. 8b). The wind tunnel test section should be sufficiently long to establish fully developed flow. The width over height ratio of the test section also needs to be high, i. e., greater than 30, for the flow to be two dimensional. The shear stress values (τ_{w}) for this configuration is related to the local pressure gradient as

$$\frac{\mathrm{d}P}{\mathrm{d}x} = -\frac{\tau_w}{h} \quad (26)$$

Here, P is the local pressure, x is the streamwise coordinate and h is the half height of the channel. The pressure gradient can be measured by mounting pressure taps along the channel before and after the shear stress sensor location.

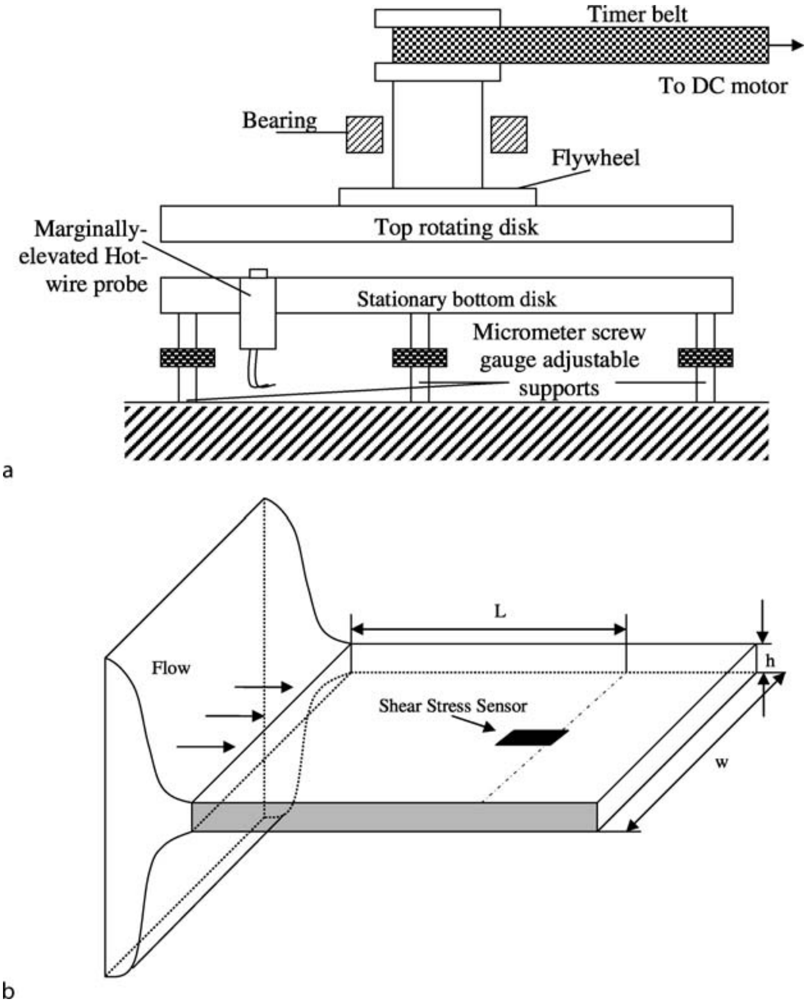

Shear Stress Sensors, Figure 8 Schematic of a static calibration apparatus: (**a**) using a rotating disc and (**b**) long, high aspect ratio smooth channel flow

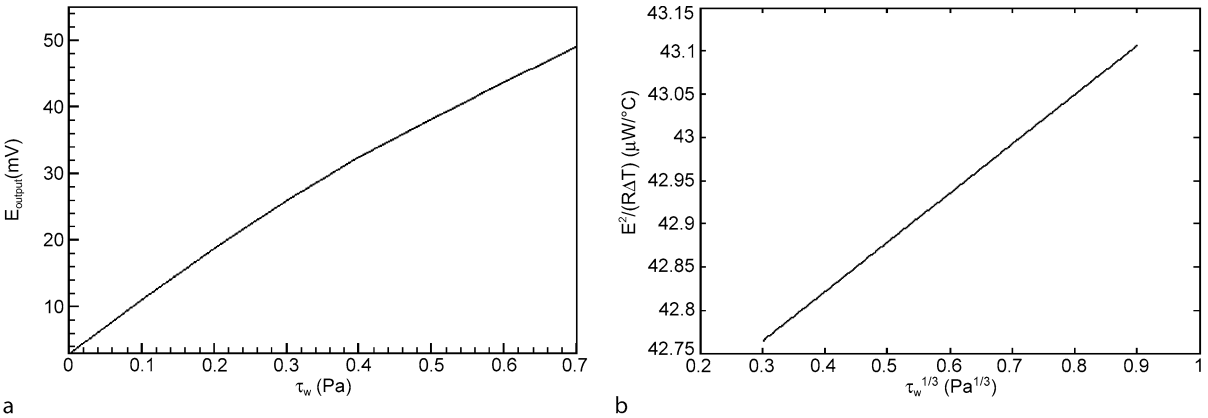

Shear Stress Sensors, Figure 9 Static calibration curve: (**a**) the bridge output (E) versus shear stress (τ_W) and (**b**) the input power versus (shear stress)$^{1/3}$ of a thermal shear stress sensor

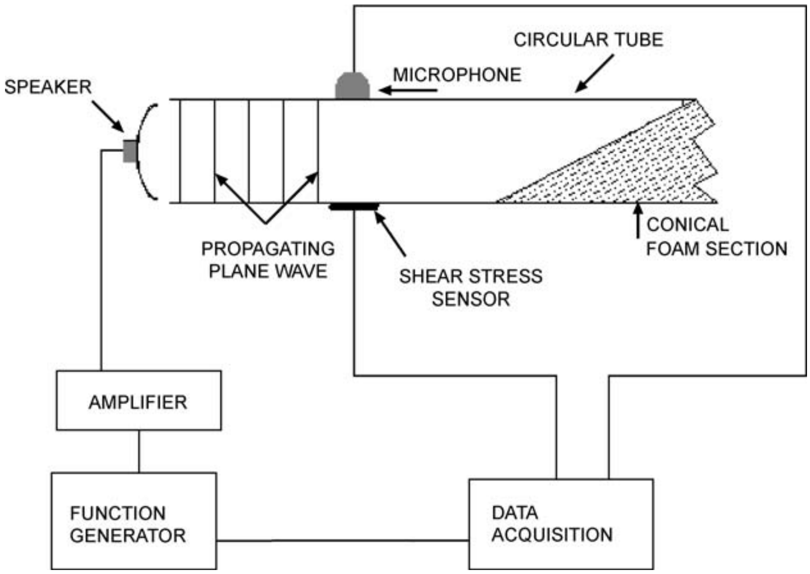

Shear Stress Sensors, Figure 10 The schematic of a dynamic calibration apparatus for the shear stress sensor

Figure 9a shows one representative calibration curve between the Wheatstone bridge output (E) and the shear stress (τ_w) of the shear stress sensor operating in constant temperature mode. The same calibration curve have been re-plotted in Figure 9b using the heating power ($P = E^2/R$) divided by the temperature difference (ΔT) with respect to shear stress to one-third (0.33) power. A linear variation as expected from Eq. (21) is clearly observed. The laminar value of the exponent (0.33) may change due to the restriction by the experimental condition during calibration, i. e., wall presence, mounting location and size of the sensor element. Hence, the exponent value around 0.4 in contrast to the laminar value of 0.33 has been observed in many investigations.

Dynamic Calibration

The shear stress sensor for turbulent flow needs to accurately capture the complete turbulent fluctuation spectrum. Therefore, the shear stress sensor should possess a large bandwidth with flat and minimum frequency–phase relationship. For direct measurement, i. e., floating point sensors, the resonant frequency of the floating element and the fluidic damping determines the usable bandwidth. For the thermal sensor, the thermal inertia of the sensor element and the frequency-dependent heat conduction to the substrate influence the usable bandwidth. It is complicated to analytically predict the frequency response of the thermal sensor. Therefore, dynamic calibration is essential to characterize the frequency response of the sensor.

The Stokes-layer excitation in a cylindrical duct is one of the effective techniques for dynamic calibration of shear stress sensors [8]. The flow inside the duct is driven by an oscillating pressure gradient generated by loud speaker (see Fig. 10). The loud speaker driven by an amplifier generates an acoustic wave. The amplifier receives sinusoidal input from a function generator. The microphone and shear stress sensor are mounted at opposite locations of the tube. The data acquisition system records the signal from the microphone and shear stress sensor.

The solution of the compressible momentum equation provides the relationship between the shear stress and the pressure gradient and the excitation frequency as

$$\tau(z,t) = -\frac{p' e^{j(2\pi f t - kz)}}{c} \sqrt{\frac{j2\pi f \mu}{\rho}} \frac{I_1\left(R\sqrt{j2\pi f/\nu}\right)}{I_0\left(R\sqrt{j2\pi f/\nu}\right)} \tag{27}$$

Here, p' is the magnitude of pressure fluctuation; c is the speed of sound; f is the frequency of acoustic wave; $k = 2\pi f/c$ is the wave number; z is the axial direction; μ is the fluid viscosity; ρ is the density; R is the radius of tube; ν is the kinematic viscosity; and I is the Bessel function. The frequency response function $H(f)$ from Eq. (27) is used to determine the frequency response of the shear stress sensor as

$$H(f) = \frac{V(f)}{\tau(f)} \frac{\delta\tau}{\delta V} \tag{28}$$

Here, $V(f)$ is the sensor voltage, $\tau(f)$ is the shear stress calculated from Eq. (27) as a function of the pressure fluc-

tuation magnitude and $\delta\tau/\delta V$ is the static sensitivity from the static calibration of the shear stress sensor. For an ideal sensor the static and dynamic sensitivity should be equal leading to a normalized frequency transfer function ($H(f)$) of 0 dB at all measurable frequencies.

Uncertainty and Noise

For proper design and practical implementation of shear stress measurement procedure, it is important to be aware of different sources of noise and uncertainty during the measurement. When using shear stress sensor based on MEMS technology, all circuit elements are located on the substrate surface. Hence, the electronics is one of the primary sources for drift or noise during shear stress measurement. The other important contribution to noise is physical sources, i. e., during low flow velocity situations the free convection effect disturbs the signal. The packaging and mounting of the sensor element can generate offset signals which may change in time due to the change in heat dissipation of the sensor element. This influences the frequency response of the shear stress sensor. The MEMS-based shear stress sensor can have the following noise sources: thermal or white noise, shot noise, flicker noise and photon noise. The thermal noise is the movement of electrons due to the finite temperature difference leading to noise in the output voltage or current. Shot noise is due to the flow of charge carriers past different potential barrier sources in the electronic circuits. Flicker noise or $1/f$ noise is the low-frequency noise due to flow of charge carriers in discontinuous medium, i. e., resistors, transistors, thin films, etc. Photon noise is due to the fluctuation in the number of quanta or power reaching the photodiode or CCD element. Photon noise is strongly temperature dependent and can be reduced by effective cooling.

Future Directions for Research

Shear stress measurement plays an important role for characterization and control of both macro- and microscale flows. There are various existing techniques suitable for either steady state or instantaneous nature of the flow. The rapid development of MEMS manufacturing technology has immensely contributed to improvement in spatial and temporal resolution of shear stress sensors. Therefore, turbulent flow control has become feasible for many practical applications. However, the calibration and implementation issues of shear stress measurements are not completely established. Therefore, the implementation procedure for shear stress measurement is problem specific and requires complete understanding of the measurement principle. The existing shear stress measurement technologies have not been implemented over a wide range of microscale flow problems. Therefore, future research should concentrate on critical issues relevant to shear stress measurement in various microflow applications. This will contribute towards development of matured shear stress measurement techniques.

Cross References

► Flow Rate Measurements
► Turbulent Structures

References

1. Hanratty TJ, Campbell JA (1996) Chapter 9: Measurement of wall shear stress. In: Goldstein RJ (ed) Fluid Mechanics Measurements, 2nd edn. CRC. Taylor and Francis, Washington
2. Panigrahi PK, Schroeder A, Kompenhans J (2005) PIV investigation of flow behind surface mounted permeable ribs. Exp Fluids 40:277–300
3. Nguyen N, Wereley ST (2006) Fundamentals and Applications of Microfluidics. Artech House, Norwood/London
4. Xu Y, Jiang F, Newbern S, Huang A, Ho CM (2003) Flexible shear-stress sensor skin and its application to unmanned aerial vehicles. Sens Actuators A 105:321–329
5. Naughton JW, Sheplak M (2002) Modern developments in shear-stress measurement. Progr Aerosp Sci 38:515–570
6. Schober M, Obermeier S, Pirskawetz S, Fernholz HH (2004) A MEMS skin-friction sensor for time resolved measurements in separated flows. Exp Fluids 36:593–599
7. Fujisawa N, Aoyama A, Kosaka S (2003) Measurement of shear stress distribution over a surface by liquid-crystal coating. Meas Sci Technol 14:1655–1661
8. Sheplak M, Padmanabhan A, Schmidt MA, Breuer KS (2001) Dynamic calibration of a shear-stress sensor using Stokes-layer excitation. AIAA J 39(5):819–823
9. Fernholz HH, Janke G, Schober M, Wagner PM, Warnack D (1996) New developments and applications of skin-friction measuring techniques. Meas Sci Technol 7:1396–1409
10. Löfdahl L, Gad-el-Hak M (1999) MEMS-based pressure and shear stress sensors for turbulent flows. Meas Sci Technol 10:665–686

Shockwave

Definition

Large amplitude, non-linear pressure wave produced in supersonic field or flow. The fluid passing through this discontinuity undergoes a finite decrease in velocity accompanied by a marked increase in pressure, density, temperature and entropy.

Cross References

► Shock Wave in Microchannel

Shockwaves in Microchannels

Florin Iancu, Norbert Müller
Michigan State University, East Lansing, MI, USA
ihuin@egr.msu.edu

Synonyms

Pressure wave; Micro-shock tube

Definition

► Shockwaves are large-amplitude, nonlinear pressure waves produced in a supersonic field or flow. The fluid passing through this discontinuity undergoes a finite decrease in velocity accompanied by a marked increase in pressure, density, temperature and entropy.

Although the concept of ► microchannel has been in the field literature for some time now, a clear definition of it has not yet been enunciated. However, it is the general understanding that any channel that has a characteristic dimension is between 1 µm and 1 mm is considered to be a ► microchannel. Most of the microchannels discussed in the literature are manufactured through microfabrication techniques, but not exclusively.

Overview

Since new and more complex microfabrication techniques became available, scientists have been trying to replicate at the microscale technologically more advanced systems and devices that have been available only at the large scale so far. During this process, it has been discovered that the laws of fluid mechanics and fluid dynamics do not necessarily scale linearly with the geometric dimensions. Although in the last ten years many questions have been answered regarding the behavior of fluid flow at the microscale, some phenomena still remain unclear. Among them is the phenomenon of ► shockwave propagation and compressibility effects inside a ► microchannel.

By its nature, the shockwave phenomenon happens in the microscale domain since the shockwave normal width is equal to a few mean free paths (less than a micrometer).

Basic Methodology

Estimates of pressure drops can be made using the traditional theory and correlations. However, accurate prediction of pressure drops in microchannels for non-slip flows is not possible [1]. For better prediction many models have been proposed [2]. Shockwave phenomena in microchannels have been investigated analytically, numerically, and experimental work is under way.

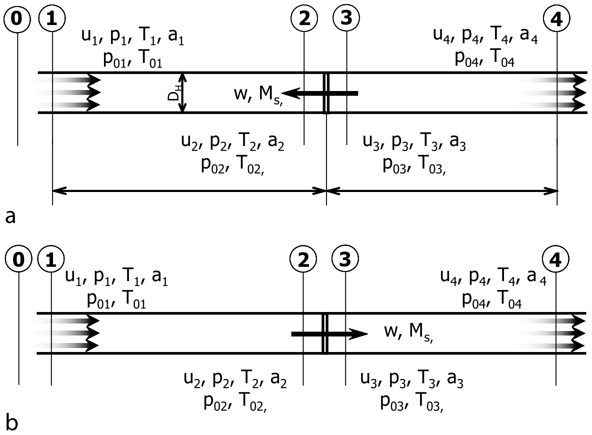

Shockwaves in Microchannels, Figure 1 One-dimensional model of a microchannel: (**a**) with shock traveling in the direction opposite to the flow; (**b**) with shock traveling in the direction of the flow

Knudsen Number

The ► Knudsen number Kn, defined as the ratio between the mean free path of the molecules and the characteristic length of the system, is often used to establish the domain level of the phenomenon and limits in the model application ranges. For $\mathrm{Kn} \gg 1$ the usual continuum modeling is valid. Satisfactory prediction of experimental results can be obtained until $\mathrm{Kn} = 0.3$, but the question is raised as to whether it is possible to further extend the continuum modeling accounting more correctly for surface phenomena like the reflection law, and the Knudsen layer, or whether the validity limit of the continuum approach is reached here [3].

Analytical Modeling

A one-dimensional mathematical model based on basic physical background has been created to investigate the efficiency of shockwave compression in microchannels. The model considers the entropy produced by a single normal shockwave that runs through the channel and by the wall friction due to the gas flow through the channel. Entry losses are also taken into consideration. Only heat transfer is neglected, following a recent study [4] that shows no significant effect of heat transfer on the compression efficiency in silicon microchannels.

Focusing on the phenomenon occurring inside a single channel, the normal shockwave is modeled by gas dynamics for one-dimensional flow [5]. The model has been presented with air as working fluid modeled as an ideal gas, and a friction coefficient that varies along the channel as a function of gas-dynamic conditions. The microchannel geometric characteristics are length ($2L$) and

hydraulic diameter (D_H, equal to 4 times the area divided by the perimeter of a section), shown in Fig. 1a. The model relates the efficiency of the compression process to the velocity, pressure, and temperature of the gas at the entrance of the channel (station 1: u_1, p_1, T_1), the pressure ratio across the shock Π_S, the friction coefficient f, and channel dimensions. In Fig. 1a, a shockwave is shown that moves in the opposite direction to the flow and is positioned in the middle of the channel. It can be shown that a snapshot evaluation at the mid position is a good representation of the overall results and does not affect the accuracy of the model. Friction is considered along the lengths L before and after the shock. The frictional effect is modeled as shear stress at the wall acting on a fluid with uniform properties over the cross-section.

One-Dimensional Flow with Friction

Using equations of one-dimensional compressible flow with friction, and knowing the conditions at station 1, the conditions at station 2, just before the arrival of the shockwave, can be obtained. Temperature and velocity at station 1 determine the speed of sound (Eq. (1)) and the Mach number (Eq. (2)):

$$a = \sqrt{\gamma \cdot R \cdot T} \tag{1}$$

$$\mathrm{M} = \frac{u}{a} \tag{2}$$

The Mach number at station 2 is found, by using the sonic condition as it would develop due to friction, from the state in station 1 through station 2, at the virtual distance from station 1 denoted with L_1^* (Eq. (3)), as can be derived from the momentum equation, expressing the shear stress in terms of friction coefficient and integrating between station 1 and the point where $\mathrm{M} = 1$ [5]:

$$L_1^* = \frac{D}{4 \cdot f}\left[\frac{1-\mathrm{M}_1^2}{\gamma \cdot \mathrm{M}_1^2} + \frac{\gamma+1}{2 \cdot \gamma} \cdot \ln\left(\frac{(\gamma+1)\cdot \mathrm{M}_1^2}{2+(\gamma-1)\cdot \mathrm{M}_1^2}\right)\right] \tag{3}$$

The classical theory of laminar flow relates the friction coefficient to be proportional to the Reynolds number:

$$f = \frac{64}{\mathrm{Re}} \tag{4}$$

The Reynolds number is dependent on density ρ, viscosity μ, velocity u, and hydraulic diameter (Eq. (5)):

$$\mathrm{Re} = \frac{\rho \cdot u \cdot D_H}{\mu} \tag{5}$$

Since the same sonic condition develops from the flow in station 1 and 2, the difference between the two virtual distances to sonic condition equals the distance L between both station 1 and 2:

$$L = L_1^* - L_2^* \tag{6}$$

Applying Eq. (3) to station 2 and substituting L_2^* from the Eq. (6), Eq. (3) can be solved for Mach number M_2. Pressure and temperature at station 2 then can be calculated with the continuity equation in adiabatic conditions, Eqs. (7) and (8), knowing M_2 and all conditions at station 1:

$$p_2 = p_1 \cdot \frac{\mathrm{M}_1}{\mathrm{M}_2} \cdot \sqrt{\frac{2+(\gamma-1)\cdot \mathrm{M}_1^2}{2+(\gamma-1)\cdot \mathrm{M}_2^2}} \tag{7}$$

$$T_2 = T_1 \cdot \frac{2+(\gamma-1)\cdot \mathrm{M}_1^2}{2+(\gamma-1)\cdot \mathrm{M}_2^2} \tag{8}$$

Jump Conditions Across a Moving Shock

Knowing T_2, the speed of sound a_2 (Eq. (1)) and then flow velocity u_2 can be calculated. Assuming that the distance between stations 2 and 3 is negligible, and knowing the pressure ratio across the shock $\Pi_S = p_3/p_2$, conditions at station 3 can be obtained by the normal shock relations (Eqs. (9) and (10)):

$$T_3 = T_2 \cdot \Pi_S \cdot \left(\frac{\frac{\gamma+1}{\gamma-1} + \Pi_S}{1 + \frac{\gamma+1}{\gamma-1} \cdot \Pi_S}\right) \tag{9}$$

From the three basic Euler equations, the Mach number of the shockwave, M_S, can be found:

$$\mathrm{M}_S = \sqrt{\frac{\gamma+1}{2\gamma} \cdot (\Pi_S - 1) + 1} \tag{10}$$

Further, the induced velocity of the flow behind the wave u_p can be calculated:

$$u_p = \frac{a_2}{\gamma} \cdot (\Pi_S - 1) \cdot \sqrt{\frac{\frac{2\gamma}{\gamma+1}}{\frac{\gamma-1}{\gamma+1} + \Pi_S}} \tag{11}$$

The velocity of the flow at station 3 is a vector sum of the initial velocity of the flow and the velocity induced by the moving shockwave:

$$\boldsymbol{u}_3 = \boldsymbol{u}_2 + \boldsymbol{u}_p \tag{12}$$

From station 3 to station 4, the same algorithm is applied as for the flow traveling from station 1 to station 2.

Since this is an unsteady process the total properties behind the shock at station 3 are different from the ones in front of the shock (station 2). The total pressure is calculated using the known properties of the induced mass motion instead of being directly calculated from the equation of state.

The isentropic efficiency of the compression process is defined as temperature difference for an isentropic process versus a real process:

$$\eta_C = \frac{\Delta T_S}{\Delta T} = \frac{\left(\frac{p_4}{p_1}\right)^{\frac{\gamma_{air}-1}{\gamma_{air}}} - 1}{\frac{T_4}{T_1} - 1} \tag{13}$$

Analytical Results

The model described has been applied to compressible air flow with Reynolds numbers in the range of 500 to 1500. These values were obtained using Eq. (5) that is also valid for shockwave propagation in a narrow channel [2]. Further, based on the analysis of gas flow characteristics in silicon microchannels [6], the friction coefficient f has been found to be approximately 0.04 for a Reynolds number of 500, while for Reynolds numbers greater than 1000, the friction coefficient becomes less than 0.005.

A variable friction coefficient is introduced dependent on Reynolds number and therefore indirectly dependent on viscosity and temperature. Using Eq. (13), the efficiency results for various entry temperatures and shock strengths have been calculated. For the reason that for a laminar flow at microscale the friction coefficient does not depend linearly on the Reynolds number [6], a second set of efficiencies for the same range of inlet temperatures has been presented using the experimentally obtained dependence of the friction coefficient on the Reynolds number. Both sets of efficiency results are represented in Fig. 2. The efficiencies obtained with the experimentally determined friction coefficient are about 10% higher than those obtained using the theoretical friction coefficient. For each pressure ratio across the shock, an optimum entry temperature can be found that results in the highest shockwave compression efficiency. Another observation that can be made is that the values of efficiency vary only a little with entry temperature, justifying the use of a constant friction coefficient determined for the inlet temperature. This effect is caused by the competing effects of the temperature in Eq. (3): higher temperature leads to lower Mach number for the same inlet velocity, but lower Reynolds number, thus higher friction coefficient. While the length/diameter ratio is an important parameter in shock tube design, its effect on the shock compression efficiency is not very significant over a wider range. However, at lower pressure ratios its effect is more considerable. For a shock strength $\Pi_S = 1.8$ the variation is only 3.3% for a diameter from $D_H = 30\,\mu m$ up to $100\,\mu m$ and a 1 mm channel length. Efficiency results are plotted in Fig. 3. The left graphs present the results versus length/diameter ratio with shock pressure ratio as parameter, while the graph on the right side is like a side view with the length/diameter ratio as parameter. On the right side the solid line connects the optimum pressure ratios for maximum efficiency for each length/diameter ratio. While in the application of the above described procedure the influence of heat transfer has been found negligible, under the presumption that shockwave motion at low Reynolds numbers is governed by convection as well as viscosity, another one-dimensional model that utilizes the Reynolds analogy for heat and momentum transfer could be applied to the phenomenon of shock and detonation attenuation in narrow channels [7].

Numerical Modeling and Simulation

Numerical Model

With the goal of simulating as best as possible the real-life conditions in a wave rotor channel (Fig. 4), a two-dimensional numerical model has been presented [8]. The channel modeled is 1 mm long and 76 μm wide and has a larger inlet duct (port) and opens into a larger outlet port. The mesh size in channels and inlet and outlet ports has been based on the results of a grid sensitivity study. A tetrahedral mesh is used with a 2 μm cell size for the channel and paved 10 μm cells for the inflow and outflow ports that sequence the flow through the channel. Air treated as a compressible ideal gas is used for modeling the flow.

Computational Fluid Dynamics (CFD) Results

The data trend of the above presented analytical study has been verified by computational fluid dynamics (CFD) analysis. Moreover, some microscale-specific effects could be seen: for the initial part of the process, the pressure drop is confined over a short distance (between stations 2 and 3 in Fig. 5a); as the shockwave travels further from the left to the right, the pressure gradient dissipates more and more continuously over a longer range. Instead of a well-defined shockwave, a set of compression waves can then be seen distributed over more than a half of the length of the channel (Fig. 5b). This effect has already been noted in experiments with microscale shock tubes [9], originating from the stronger influence of the viscous forces at low Reynolds numbers. In the den-

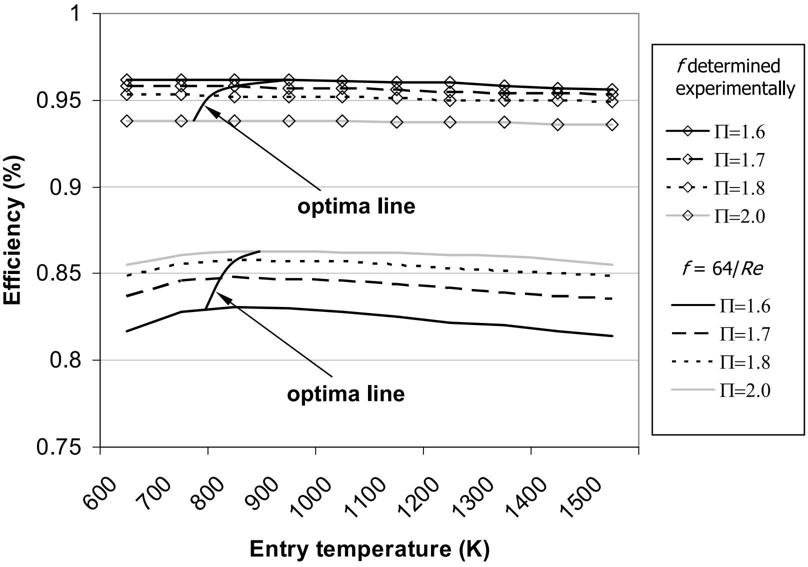

Shockwaves in Microchannels, Figure 2 Efficiency of shockwave compression process as a function of entry temperature for different shock strengths, and for a shock traveling in the opposite direction to the flow. Results obtained with analytical one-dimensional code

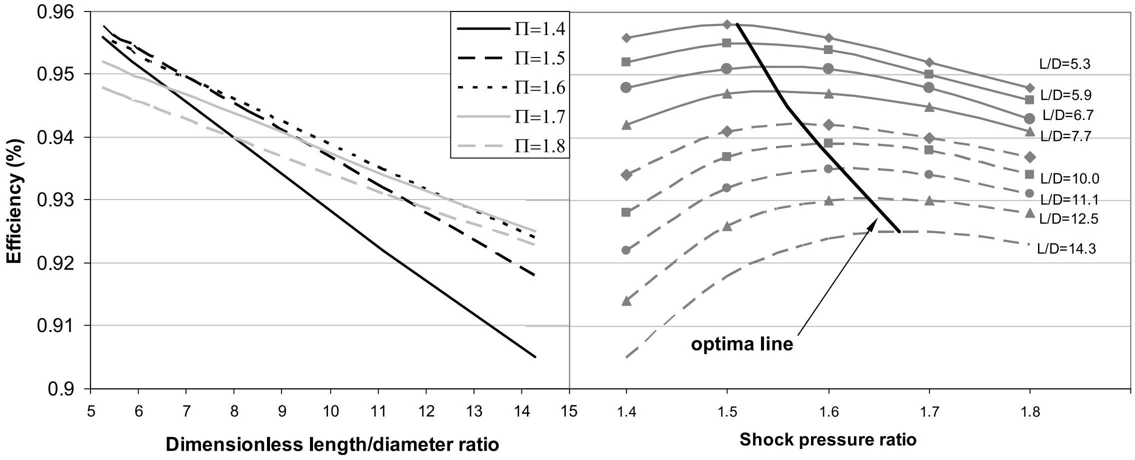

Shockwaves in Microchannels, Figure 3 Efficiency of shockwave compression process as function of microchannel length/diameter ratio for different shock strengths, and for a shock traveling in the direction of the flow. Results obtained with analytical one-dimensional code

sity contour plot (Fig. 6), the existence of the boundary layer can be seen clearly, behind the shockwave as soon as it has traveled about 20% of the channel length. Many more CFD simulations at the microscale exist and the numerical reproduction of the behavior of pressure-driven flows in microchannels has been obtained often [2, 10]. Some discrepancies have been found between numerical solutions of the Navier–Stokes equations and experimental data obtained in viscosity-dominated shock tube investigations. It was noticed that even using fine grid cells of a few micrometers, the solution of the Navier–Stokes equations still does not match experimental data of shockwave reflection transition over a wedge [2]. It has been pointed out that the solution of shockwave motion at low Reynolds numbers requires the finding of a two-dimensional unsteady solution of the Navier–Stokes equations and doubts are raised that the inclusion of transport phenomena as perturbations to a simple shock-tube flow would be adequate for a reliable flow description.

Numerical simulation might become a more efficient and economic way to analyze shock and flow phenomena at the microscale [2]. However, there is still a great need of experimental results to verify and support all the theoret-

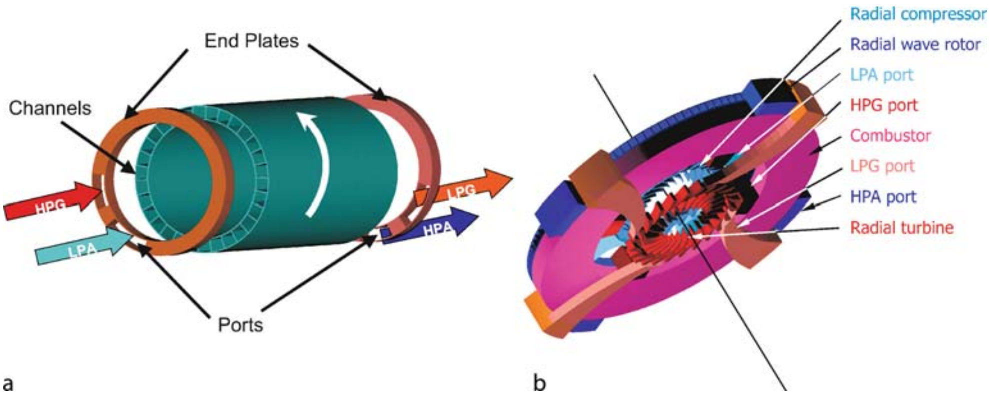

Shockwaves in Microchannels, Figure 4 (**a**) Active components of conventional axial wave rotor. (**b**) Radial ultra-micro-wave rotor used to enhance a microfabricated gas turbine

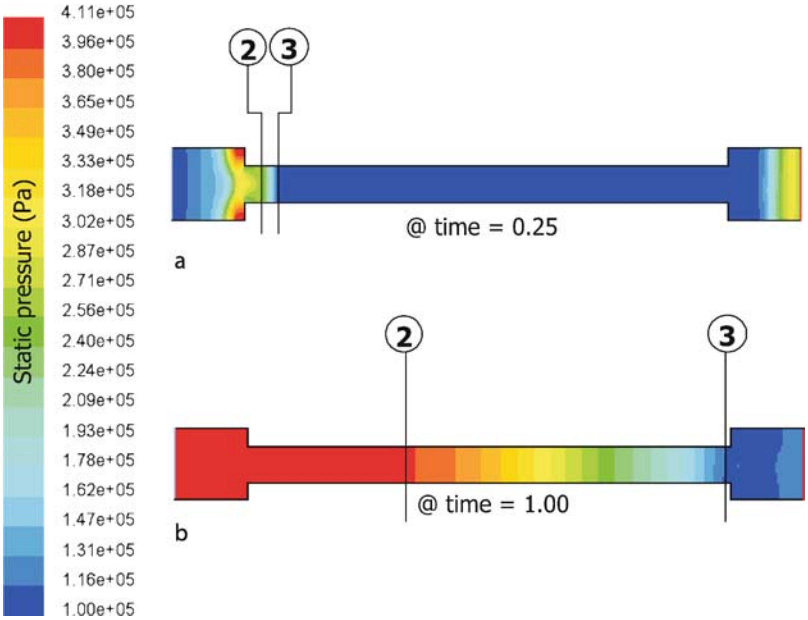

Shockwaves in Microchannels, Figure 5 Static pressure inside a microchannel at two different time steps. Time = 1 is when a pressure wave reached the end of the channel. Flow moving from left to right

ical assumptions made in CFD and to establish reliable numerical models and schemes [2, 10].

Experimental Approach

Although the accuracy of present experiments is still not high enough to fully validate numerical models and solution schemes [2], more experimental investigations are needed in order to better understand the physics of shockwaves at the microscale. A good experiment will focus on trying to visualize the shock front, but a difficult task, besides obtaining good clarity, is recording the images. Although the geometric dimensions are scaled down, the shock velocities remain in the same high range; thus, the duration of shock travel is of the order of a microsecond for a channel length of 1 mm.

Despite the behavior of shockwave motion in large shock tubes at relatively high Reynolds numbers being extensively investigated in the 1950s and 1960s [2], little work has been done for low Reynolds number flows, especially at small scales. The experimental investigation of shock propagation in microchannels could provide valuable validation information on viscosity-dominated compressible flows. Two-dimensionality of the flow in channels is favorable for any validation effort. However, no shock visualization in microchannels has been published. Nevertheless, using the

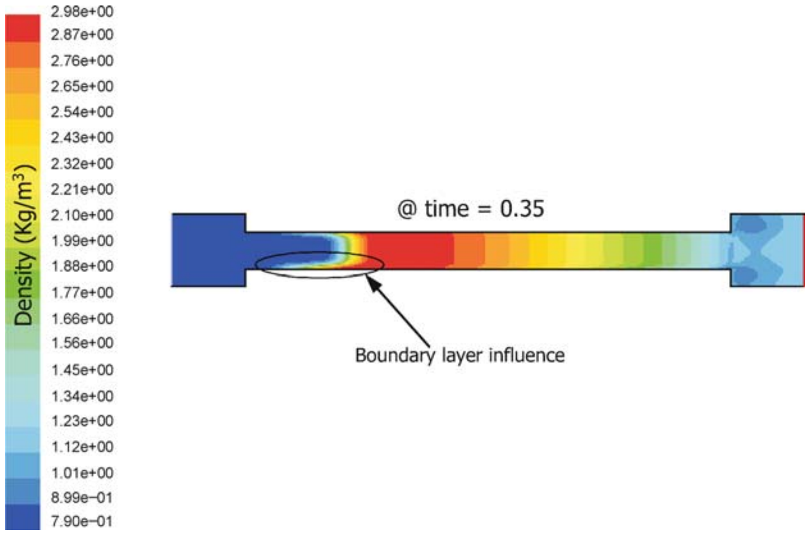

Shockwaves in Microchannels, Figure 6 Density contours inside a microchannel. Time = 1 is when a pressure wave reached the end of the channel. Flow moving from left to right

Schlieren method for flow visualization to record the shock propagation has been successful down to a channel size of 3 mm × 3 mm cross-section and 42 mm length [11]. Investigations for microchannels are under way.

Single-Channel Experiment

Shockwave Visualization on 3 mm Wide Channels

At the University of Tokyo, the Schlieren method and a high-speed camera have been used for capturing images of the flow of a traveling shockwave in channels of 3 mm × 3 mm cross-section and 42 mm and 168 mm length. The channels were closed at one end and high-pressure air (250 kPa) was supplied at the other end by means of rotating ports. The effect of the transient opening was neglected during preliminary calculations and it was observed that it does not affect the shock propagation during the experimental investigations. Shockwave propagation speed has been reported as 300–400 m/s in both tubes. Interestingly, no boundary layer effects on the shock propagation or shockwave dissipation were observed. The wall friction effect seemed not to play an important role in the shockwave behavior [11].

Microchannel Experiments in Preparation for 90–720 μm Wide Channels

At Michigan State University a single-channel experiment has been developed to investigate the wave phenomenon. A set of similar channels have been designed in order to obtain more information on what the characteristic dimension is at which the shockwave behavior starts to deviate from macroscale theory. The channels have the same length/width ratio and same height; the length and width are varied (90 × 750 μm^2, 180 × 1500 μm^2, 360 × 3000 μm^2, 720 × 6000 μm^2), while the height is uniformly 360 mm. The channels are etched in a silicon wafer and closed on top with glass. The access ports are etched on the bottom side of the silicon wafer. Figure 7 shows photos of the silicon/glass microfabricated die. On the top side, the channels and the flow plenums can be observed, and on the bottom side, the access holes and the alignment marks can be seen. The quality of the geometry resulting from the microfabrication technique is impressive: even the smallest channel (90 μm in width) has crisp edges and a well-defined shape. Figure 8 shows SEM images of the four channels. In a first experiment with these micro-shock tubes, the channels are connected via access ports to stainless steel tubing (1.02 mm outer diameter) to a nitrogen supply tank. A quick release valve releases the nitrogen through the microchannel. Since the silicon wafer surface is highly reflective, reflection laser interferometry is used to capture the passing of the shockwave.

Microchannel Experiments in Preparation for 10 μm

A similar experiment is currently being designed at Sherbrooke University [12]. The goal is to build and test a true shock tube with two cavities filled with gases at different pressures, divided by a breakable membrane. The aspect ratio of the channel is 100 and a pressure ratio of 2 is planned for a Reynolds number of 100. These conditions could be achieved in a 5 mm diameter/500 mm long tube

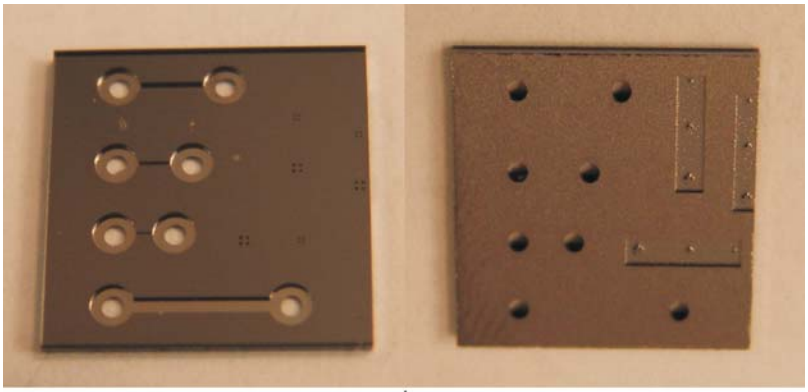

Shockwaves in Microchannels, Figure 7 Silicon microchannels: (**a**) top view; (**b**) bottom view

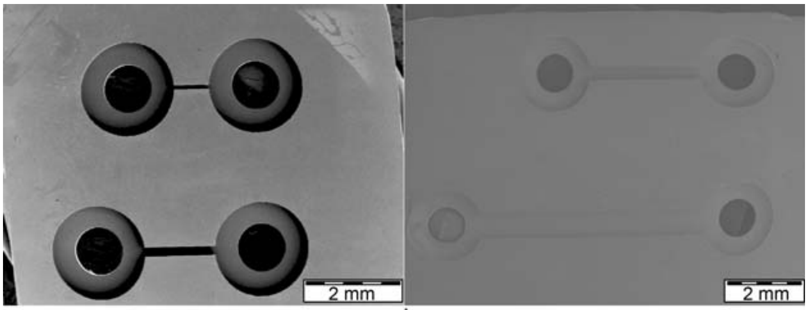

Shockwaves in Microchannels, Figure 8 Different size channels visualized with SEM: (**a**) 90 μm and 180 μm wide channels; (**b**) 360 μm and 720 μm wide channels

with pressures of 1 mbar and 2 mbar, respectively. But the low pressures typically exclude the possibility for flow visualization or measurement. Therefore a more favorable solution is planned that will create the same hydrodynamic flow, using a micro-shock tube with a hydraulic diameter of 10 μm, operating at pressures close to atmospheric conditions.

The tube is created with a squared cross-section, 10 μm wide. The driver and driven section have equal lengths. The driver and driven sections are separated by a membrane, and the test section is pre-filled with the test gas during fabrication. The top side of the tube is made of a plate comprising direct-sensing piezoelectric gauges, used for timing the arrival of pressure waves.

Key Research Findings

Microscale Flow Phenomena

The overall conclusion is that while the currently available experimental data suggest the presence of microscale phenomena, they do not unequivocally identify the effects [1, 13]. In general it is found that the boundary layer effects are dominant at and below the microscale resulting in rarefaction effects in gaseous flow. However, the no-slip boundary condition appears to hold true less and less with smaller scale. The slip flow effect is seen to result in less frictional pressure drop than the continuum model predicts. Further it is widely pointed out that sudden increases in pressure (due to a shockwave) dissipate gradually when propagating through a microchannel due to high hydraulic resistance.

Compressibility and Rarefaction Effect

With the dominant occurrence of boundary layer effects in microchannel flow, in gaseous flows considerable decrease in density is observed with increasing flow length due to viscous dissipation [14]. This is also referred to as the rarefaction effect. Compressibility and rarefaction effects have been studied in three-dimensional gas flow with Reynolds number varying from 0.0001 to 1.2 and pressure ratio varying from 1.5 to 5.0, with the Knudsen number varying from 0.001 to 0.06 [3]. It has been found that the

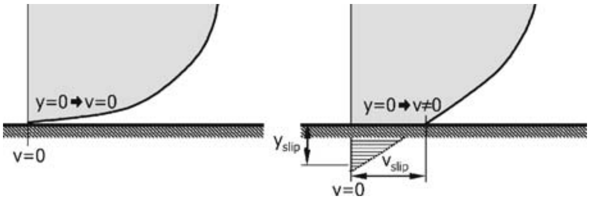

Shockwaves in Microchannels, Figure 9 Non-slip versus slip-flow wall velocity

pressure drop for compressible flows exhibits an unusual nonlinear behavior as compared to that for incompressible flows. Especially at high pressure ratio (or Reynolds number) the compressibility effect becomes dominant although the Mach number may still be very small. So typically Knudsen number increases from inlet to outlet for compressible microchannel flow.

Isothermal Effect

At the microscale the time scales associated with heat loss mechanisms reduce dramatically. However, the characteristic time scales for heat release, governed by the deflagration process, remain fairly independent of scale [9]. In long, non-insulated microchannels, an isothermal flow assumption has been found accurate for Mach numbers $\mathrm{M} \ll 1/\sqrt{\gamma}$, where γ is the specific heat ratio [14]. Values of laminar Nusselt number increase with the cross-sectional aspect ratio and the surface roughness [15].

Slip Flow

With scale in particular, changes in fluid–surface interactions, such as the wetting ability of the fluid, can affect the ability of the fluid to exchange momentum with the surface at the atomic scale, resulting in a slip velocity v_{slip} at the solid wall as shown in Fig. 9 [16]. The slip length y_{Slip} gives the imaginary location behind the wall where non-slip condition with zero flow speed $v = 0$ would be found. Slip flow has been reported for both liquid and gaseous flow. Especially at $\mathrm{Kn} < 0.1$, the effect of slip flow has been seen resulting in reduced pressure loss gradient and hence increased mass flow rate. Deviations from Poiseuille flow predictions are not related to turbulence when Re is too low but to deviations from the no-slip boundary conditions. Increase in the mass flow for given inlet and outlet pressures for microchannel flows has been based on a perturbation expansion of the Navier–Stokes equations with a first-order correction of wall slip [14]. More factors regarding non-continuum effect, compressibility effect, and surface effects are presented in [17].

Friction Factor

Discrepancy between the conventional theory and the microchannel measurements of friction factor f in gaseous flow has been attributed to compressibility [6]. In general it appears that $f\mathrm{Re}$ for compressible slip flow is less than that for the incompressible case [3]. In a comprehensive study of results of microscale single-phase internal flows [1], it has been found that the only definitive conclusion that can be reached from the currently available data is that gaseous slip flow data indicate an approximate 60% reduction in f compared to macroscale theory at the same Re (while for laminar non-slip water flow f appears to be approximately 20% higher than the theoretical predictions). The finding for compressible slip flow seems to be supported by a simple analytical correlation with the factor $c \approx 0.6 \pm 0.05$ [3]:

$$\frac{(f\mathrm{Re})_{\mathrm{slip}}}{(f\mathrm{Re})_{\mathrm{non-slip}}} = \frac{D_{\mathrm{h}}}{D_{\mathrm{h}} + c} \tag{14}$$

The currently available experimental data for other types of flows are inconclusive, as they appear both above and below the theoretical predictions (although data for each researcher are consistently either greater or less than theoretical values). In part, these differences may be attributed to roughness of the channels, to lack of well-controlled surface structures, and to uncertainty in the determination of channel dimensions. Some researchers estimate the entrance effects in determining the microchannel friction factor, while, much better, the measurements should be taken within the microchannel near the channel entrance and exit. Further, preliminarily it has been concluded that, regarding non-slip microchannel flows, f appears to increase with surface roughness and this effect seems to intensify with higher surface roughness.

For $\mathrm{Re} < 700$, global pressure drop has been shown to be proportional to Re. For $\mathrm{Re} > 700$, it deviates from the linear relationship with the deviation dependent on Re. Also it has been found that f increases with the cross-sectional aspect ratio and the surface roughness [15].

Critical Reynolds Number

There is an ongoing debate regarding the critical Reynolds number $\mathrm{R_{cr}}$ for microfluidics at which the transition from laminar to turbulent flow starts. The determination of $\mathrm{R_{cr}}$ depends very much on the method used. $\mathrm{R_{cr}}$ varies widely from 300 to 2200 with it being mostly between 1500 and 1800 [1, 13].

Entry Lengths and Boundary Layers

It is the case that most flow investigations at the microscale happen in the laminar flow regime with developing boundary layer (combined entry lengths). As for macroscale cases, the velocity entry length L_{E} is often simply calculated by

$$\frac{L_{\mathrm{E}}}{D_h} \approx 0.06\mathrm{Re} \tag{15}$$

However, also larger factors of 0.08 and 0.09 [9] have been found for microchannels. The thermal entry length L_{T} may be calculated by

$$\frac{L_{\mathrm{T}}}{D_h} \approx 0.05\mathrm{RePr} \tag{16}$$

where Pr is the Prandtl number, a measure of diffusivity.
When investigating the boundary layer thicknesses, the Euler equations lead to specific solutions. The thermal boundary layer thickness is

$$\delta_{\mathrm{T}}(x) = 3.6\sqrt{\frac{\alpha x}{\mathrm{u}_\infty}} \tag{17}$$

where x is the coordinate along the channel and u_∞ is the velocity of the free stream.
The Reynolds analogy between the flow field and the thermal field provides the relation between the velocity and thermal boundary layer thickness:

$$\frac{\delta_{\mathrm{T}}}{\delta} = 0.975\sqrt[3]{\mathrm{Pr}} \tag{18}$$

Shockwave Phenomena at the Microscale

Dominant viscous and wall effects appear to influence considerably shockwave behavior at the microscale. Sudden increase in pressure (due to a shockwave) vanishes gradually in time due to hydraulic resistance [18]. So, it has been observed that, subsequent to the arrival of the shocks, the pressure increases continuously which is not conventional shock tube behavior [8, 9]. Also the decaying amplitudes of the shocks indicate that dissipation plays an important role. Therefore when waves are generated and propagated into ducts of small dimensions, diffusive transport phenomena, commonly ignored at conventional scales, can no longer be neglected. Viscous stresses at the boundaries lead to the deformation of the wave fronts, and heat conduction with the wall no longer allows the flow to remain adiabatic; at certain scales, molecular diffusion and adsorption may also lead to important effects.
It has been reported that for a given wave Mach number at small scales, the resulting particle velocities are lower but the pressures are higher [9]. Also, it has been shown that at small scales, the weak wave solution is no longer sonic and isentropic but is isothermal and can be subsonic.
Further, a model has been introduced that predicts via molecular diffusion phenomena an isothermal bow at small scales and that the minimum wave velocity can be subsonic. A parameterization of the shear stresses and heat flux at the wall has led to new jump conditions [9].
Experiments with a miniature shock tube using low pressures to simulate the effects of small scale have shown qualitative agreement with the proposed model. The effects of scale are even more pronounced than what has been predicted by the model. Experimental and numerical investigations for incident shock Mach number of $\mathrm{M} = 1.2$ have shown significant viscous effects for channel heights below 4 mm even at atmospheric pressure. That shockwaves propagate more slowly at low pressures in a narrow channel has been confirmed, but they may propagate faster than in a wide channel because compression waves initiated from the entrance of the channel can strengthen the shockwave [2].

Micro-Shockwave Applications

Micro-Wave Rotors

The wave rotor is a pressure exchanger that uses the concept of direct energy transfer between fluids by waves. A basic wave rotor consists of a rotating drum with straight channels arranged around its axis. The drum lies between two end plates, each of which has a few ports or manifolds controlling the fluid flow through the channels. Figure 4 presents a schematic axial wave rotor drum and its end plates and inclusion in a microfabricated gas turbine. In the process of recent turbomachinery miniaturization it has been shown that a decrease of the overall thermal efficiency and output, and increase of losses are severe. While the wave rotor efficiency is based on the efficiency of the shockwave compression inside each channel, the influence of external losses can be minimal since the wave rotor itself is the only moving part and its rotation is only for the flow control. External losses are leakage, windage, friction in the bearings of the rotor, and if microfabricated losses due to sharp bends in the flow path to the rotor since rounded corners are difficult to obtain in the direction of etching. While all these losses also occur in turbomachinery, they can be lower in a wave rotor, since the compression process is only controlled but not determined by the rotational speed of the rotor. Therefore high efficiency can be obtained even at relative low rotational speed and relatively low flow speed, which implies less frictional losses as it becomes very important at small scale. It has been shown numerically that while the efficiency of a conven-

tional radial compressor drops to about 50% when scaled down to millimeter size, the efficiency of shockwave compression has values around 70%. Two effects support this favorable outcome: shockwave entropy production is independent of scale and wave rotors can work with relatively low flow speeds (while the compression is realized by shockwaves that travel at much higher speed than the flow speed).

The results of the previously described analysis show that the efficiency depends not only on pressure gain across the shockwave traveling through the wave rotor channel, but also on the friction coefficient for the channel geometry. According to the model, shorter wave rotor channels with larger diameter allow a higher compression efficiency of the wave rotor. The temperature at which the compression process is initiated also has a considerable influence: higher temperatures yield higher efficiencies. Analytical and numerical results suggest that a shockwave compression efficiency of 70–80% can be achieved in the channels. If the inlet temperature is high enough (about 1500 K), the efficiency is predicted to be even higher, up to 90%. Moreover, the wave rotor, due to its geometry, is ideal for microfabrication processes. Its mainly two-dimensional shape is easy to construct at the microscale, where most of the fabrication techniques rely on etching and deposition [4].

Shock Tube as Vaccine Delivery System

An unique form of powder delivery system, a biolistic system, has been developed [19]. This novel technology accelerates microparticles by a gas flow behind a traveling shockwave, so that they can attain sufficient momentum to penetrate the skin and thus achieve a pharmacological effect. One of the most recent developments is a mouse biolistic system, used in immunological studies. These studies require powdered vaccine to be delivered into the epidermis of the mouse with a narrow and highly controllable velocity distribution and a uniform spatial distribution. The preliminary results demonstrate the overall capability of a newly designed supersonic nozzle to deliver the particles to the skin targets with a more uniform velocity and spatial distribution. CFD has been utilized to characterize the complete operation of a prototype mouse biolistic system.

Micronozzles

The Mach number near the downstream position of a micronozzle's throat is lower than that in a conventional nozzle. In the divergent region of the micronozzle, there is a supersonic area instead of the shockwave that usually occurs in conventional-scale nozzles. Results of numerical simulations also show that the position of the sonic point moves away from the throat towards the outlet with a decrease in the size of the nozzle. This particular behavior is attributed to the higher viscous dissipation in micronozzles as compared to that in conventional-scale nozzles [20].

Future Directions for Research

Recent medical and industrial applications of shockwaves necessitate a better understanding of shockwave motion at low Reynolds numbers: for example, shock motion in very small tubes ($r < 1$ mm) and micrometer-size particles moving at a supersonic speed [2]. Along with this comes a clear need for additional experimental investigations over a wider Re range using microchannels with well-characterized dimensions and surface roughness and well-designed experimental methods in order to understand microscale single-phase internal fluid flow [1]. To enhance the accuracy, flow visualization may focus on a local region instead of the whole test section, and more sensitive and precise pressure transducers for measuring weak shockwaves at low initial pressures are necessary [2]. Wave rotors are a promising technology that uses unsteady waves in an instant self-cooled dynamic pressure exchange between fluids. For high-pressure, high-temperature topping cycles, it results in an engine overall pressure ratio and temperature increase which in turn generates higher efficiency and lower specific fuel consumption. Further applications are pressure wave-driven pumps. Most advanced embodiments are wave discs engines that do not need any other rotating parts beside the wave disc self. They appear to be superior in simplicity and power density [21].

Cross References

- ► Micro and Nanoscale Gas Dynamics
- ► Microscale Flow Visualization
- ► Supersonic Micro-Nozzels
- ► Microturbines
- ► Micro-wave rotor
- ► Pressure-Driven Single Phase Gas Flows

References

1. Papautsky I, Ameel T, Frazier AB (2001) A Review of Laminar Single-Phase Flow in Microchannels. ASME International Mechanical Engineering Congress and Exposition, New York
2. Sun M, Ogawa T, Takayama K (2001) Shock Propagation in Narrow Channels. ISSW23, Fort Worth, Texas
3. Jain V, Lin CX (2006) Numerical Modeling of Three-Dimensional Compressible Gas Flow in Microchannels. J Micromech Microeng 16:292–302
4. Iancu F (2005) Integration of a Wave Rotor to an Ultra-Micro Gas Turbine (UμGT). Michigan State University, East Lansing

5. Anderson JD (2003) Modern Compressible Flow With Historical Perspective. McGraw-Hill, New York
6. Ying-Tao D, Zhao-Hui Y, Meng-Yu S (2002) Gas Flow Characteristics in Straight Silicon Microchannels. Chin Phys 11(9):869–875
7. Thomas GO, Brown CJ, Teodorczyk A (2000) Shock and Detonation Attenuation in Narrow Channels. Experiments in Fluids. Springer, Berlin
8. Iancu F, Müller M (2006) Efficiency of Shock Wave Compression in a Microchannel. J Microfluid Nanofluid 2:50–63
9. Brouillette M (2003) Shock Waves at Micro Scale. Shock Waves 13:3–12
10. Colin S (2005) Rarefaction and Compressibility Effects on Steady and Transient Gas Flows in Microchannels. J Microfluid Nanofluid 1:268–279
11. Okamoto K, Nagashima T, Yamaguchi K (2006) Propagating Shock Waves in a Narrow Tube from the Viewpoint of Ultra Micro Wave Rotor Design in 11th International Symposium on Unsteady Aerodynamics, Aeroacoustics and Aeroelasticity of Turbomachines, 4–8 Sept 2006, Moscow, Russia, pp 421–433
12. Mirshekari G, Brouillette M (2006) Towards a Microfabricated Shock Tube. In: 25th International Symposium on Shock Waves. Bangalore, India
13. Hetsroni G, Mosyak A, Pogrebnyak E, Yarin LP (2005) Fluid Flow in Micro-channels. Int J Heat Mass Transf 48:1982–1998
14. Arkilic EB, Schmidt MA, Breuer KS (1997) Gaseous Slip Flow in Long Microchannels. J Microelectromech Syst 6(2):167–178
15. Hao PF, He F, Zhu KQ (2005) Flow Characteristics in a Trapezoidal Silicon Microchannel. J Micromech Microeng 15:1362–1368
16. Choi CH, Westin JA, Breuer KS (2003) Apparent Slip Flows in Hydrophilic and Hydrophobic Microchannels. Phys Fluids 15(10):2897–2902
17. Takuto A, Soo KM, Hiroshi I, Kenjiro S (2000) An Experimental Investigation of Gaseous Flow Characteristics in Microchannels. In: International Conference on Heat Transfer and Transport Phenomena in Microscale, Banff, Canada
18. De Bruyker D, Puers R (2001) Experimental Characterization of the Reference Channel of a Differential Pressure Sensor Using Pressure Shock Waves. J Micromech Microeng 11:390–396
19. Liu Y, Truong NK, Kendall MAF (2004) Numerical Studies of Contoured Shock Tube for Murine Powdered Vaccine Delivery System. In: 15th Australasian Fluid Mechanics Conference, Sydney, Australia
20. Hao PF, Ying-Tao D, Zhao-Hui Y, He F (2005) Size Effect on Gas Flow in Micro Nozzles. J Micromech Microeng 15:2069–2073
21. Piechna J (2006) Feasibility Study of the Wave Disk Micro-Engine Operation. J Micromech Microeng 16:S270–S281

Shunt Capacitance

Synonyms

Low-frequency capacitance; DC capacitance

Definition

The capacitance associated with the low-frequency response of a system all the way down to direct current (DC).

Cross References

► Piezoelectric Microdispenser

Signal Attenuation

► Frequency Response

Silicon Dioxide Growth

► Oxidation (of Silicon)

Silicon Etching

► Anisotropic Etching
► Silicon Micromachining

Silicon Micromachining

Jianmin Miao
Micromachines Centre, School of Mechanical and Aerospace Engineering, Nanyang Technological University, Singapore, Singapore
mjmmiao@ntu.edu.sg

Synonyms

Anisotropic silicon etching; Deep reactive ion silicon etching; Electrochemical etching; Isotropic silicon etching; Selective silicon etching; Silicon etching; Surface micromachining

Definition

Silicon micromachining concerns a process that involves the removal of silicon materials using wet chemical or dry plasma process in order to create 3-D silicon or non-silicon microstructures for making functional devices such as micro-sensors, micro-actuators, biochips, etc.

Overview

Silicon is a well-known single crystalline semiconductor material, which is widely used in integrated circuits (ICs). Silicon possesses excellent mechanical properties, which surpass stainless steel in yield strength and hardness with good mechanical stability. Silicon also has a high piezoresistance effect, whose resistivity changes when mechanical loads or stresses are applied to it. This makes silicon

a good candidate for various mechanical sensor applications. By combining micromachining technologies, its outstanding properties have made silicon a successful material not only for integrated circuits, but also for Micro-Electro-Mechanical Systems (MEMS), micro-fluidic components, optical devices, and other applications.

In general, silicon micromachining technologies can be classified as follows: wet bulk-micromachining, reactive ion etching (RIE), deep reactive ion etching (DRIE), surface micromachining, and laser micromachining. During the micromachining process, only the surface area, which will be etched away, is exposed to the etchants, such as wet chemicals or gases, while the rest of the silicon surface is protected by the so-called etching masking layer.

Silicon has a diamond cubic crystal structure. The Miller indices of the main crystallographic planes of silicon are (100), (110) and (111), respectively. In the wet bulk-micromachining, there are two silicon etching methods: isotropic (direction-independent) and anisotropic (direction-dependent) etching. Wet chemical etching solutions are used in this bulk silicon micromachining technology.

In the reactive ion etching, silicon is isotropically etched in plasma gases. Its silicon etch rate is relatively low and orientation-independent.

The deep reactive ion etching technology, also called Bosch process, uses the concept of alternate etch and passivation steps to achieve high aspect ratio (depth to width ratio of microchannel) silicon deep micromachining. In this process, silicon can be deeply micromachined, even through the whole wafer of few hundreds micrometers with aspect ratio as high as 30 to 1, without considering the wafer orientation.

Basic Methodology

Wet Silicon Bulk-Micromachining

This micromachining technique has been used for more than two decades and is the most popular fabrication technology for sensors such as pressure sensors and accelerometers [1]. In this bulk-micromachining, chemical etching solutions are used to shape the microstructures by the removal of a large amount of single crystalline silicon substrate. Thin films, acting either as etching mask materials or microstructure materials, are deposited/grown and patterned on the silicon substrate. KOH (Potassium Hydroxide), EDP (Ethylenediamine Pyrocatechol) or TMAH (Tetramethyl Ammonium Hydroxide) are commonly used as chemical etching solution for anisotropic micromachining of silicon materials, while the NHA ($HF-HNO_3-CH_3COOH$) solution performs the isotropic etching of silicon wafers. Thin films, such as SiO_2 and Si_3N_4 with a thickness ranging from few tens nanometers to few micrometers, are the common materials serving as etching mask layers, which can also be used as structure materials for sensors or actuators after silicon bulk-micromachining. The dielectric materials, SiO_2 and Si_3N_4, can be deposited either by low pressure chemical vapor deposition (LPCVD) or plasma-enhanced chemical vapor deposition (PECVD). Additionally, SiO_2 thin film can be also grown by thermal oxidation on the silicon substrate.

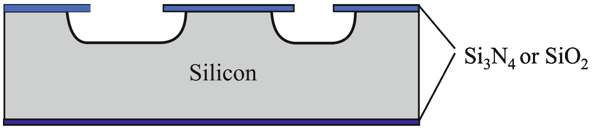

Silicon Micromachining, Figure 1 Schematic of cross sectional view of isotropically etched silicon microchannels using wet chemical etchants of NHA

Isotropic etchants etch in all crystallographic directions at the same rate; they usually are acidic, such as NHA, and lead to rounded isotropic features in single crystalline silicon as shown in Fig. 1. The basic chemical reaction equation is described as follows:

$$
\begin{aligned}
&Si + HNO_3 + 6HF \\
&\rightarrow H_2SiF_6 + HNO_2 + H_2O + H_2 \text{ (bubbles)}
\end{aligned}
$$

The etch rate can be as high as $5\,\mu m\,min^{-1}$ at room temperature, and is very temperature-dependent. At 50°C, the etch rate is increased to about $50\,\mu m\,min^{-1}$ [2].

Anisotropic etchants shape desired microstructures in single crystalline silicon material by etching much faster in one direction than the others. ► Anisotropic etching results in geometric shapes bounded by the slowest etching and perfectly defined crystallographic planes. By using KOH chemical etching solution, the etch rate in the <100> orientation is much higher than that in the <111> direction, up to 400:1. If holes, membranes, groove-type microchannels, pits, etc., have to be etched in silicon, then wafers are taken with surface orientation (100) and (110), depending on the required shape of the etched structures. Figure 2 shows some etch shapes in these two wafers. Parts of the wafers are covered with an etch mask, and the exposed areas are etched. For wafers of <100> surface orientation, etching proceeds along (100) planes, which intersects the surface along the mask edges. If the mask opening is a square with a side that is small compared to the etching depth, then a pyramidal pit is formed, which is defined by four (111) planes, i. e. it will virtually stop. The angle between the <100> and <111> directions is 54.74 degrees.

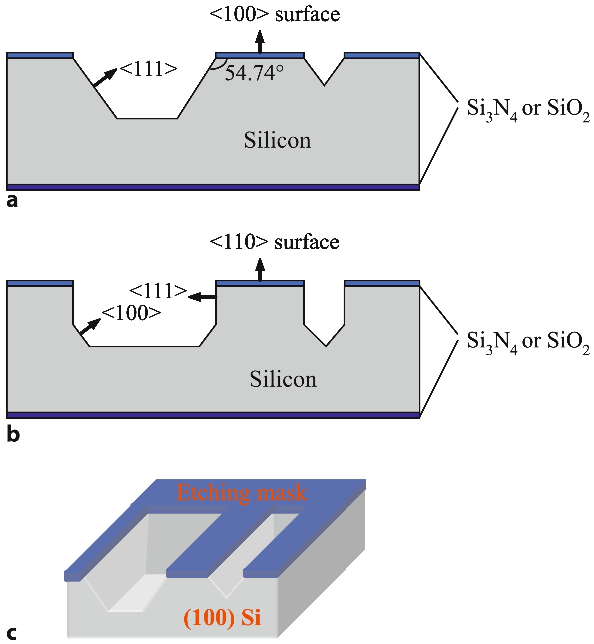

Silicon Micromachining, Figure 2 Schematic of cross sectional view of anisotropically etched microchannels (**a**) in (100) silicon, (**b**) in (110) and (**c**) of 3-D aerial view of anisotropically etched microchannels in (100) silicon using wet chemical etchants of KOH, EDP or TMAH

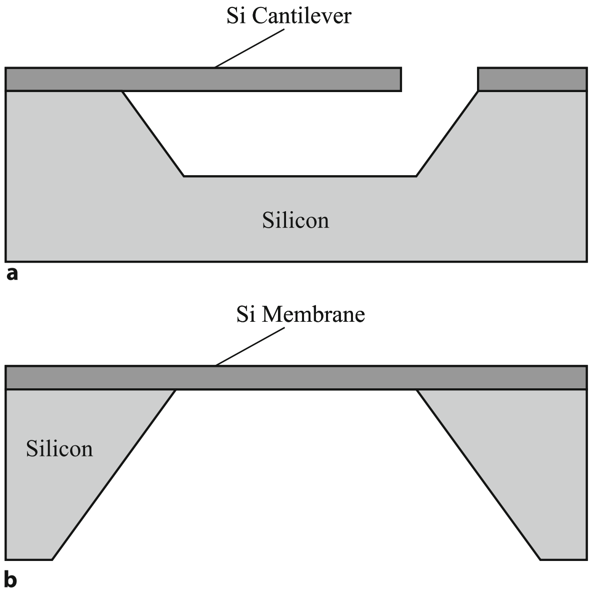

Silicon Micromachining, Figure 3 Schematic of cross sectional view of highly boron-doped silicon (**a**) cantilever, and (**b**) membrane. The anisotropic etching stops at the highly boron-doped (100) silicon layer by using wet chemical etchants of KOH, EDP or TMAH

In <110> wafers, the (111) planes are vertical, and deep trenches with high aspect ratio can be etched since silicon in the <111> direction will not be etched.

The commonly used anisotropic etchants are KOH, EDP and TMAH. KOH added with water is the most popular silicon anisotropic etchant. At 80 °C with 50 wt% KOH, the etch rate of (100) silicon can achieve 1.4 $\mu m\,min^{-1}$ with smooth silicon etching surface. The etching selectivity between (100) and (111) silicon is up to 400:1. However, the etching selectivity between Si and SiO_2 is not very good in KOH, as it etches SiO_2 too fast. So, SiO_2 is not a good choice as etching mask of silicon in KOH. The best candidate as etching mask is Si_3N_4. One disadvantage of KOH is its incompatibility with IC fabrication processes. Therefore, for MEMS with integrated circuits, the IC fabricated steps will be processed first and followed by the wet bulk-micromachining in KOH to create MEMS microstructures.

EDP etching solution doesn't contain sodium or potassium and therefore, it is IC compatible. EDP has also very high etching selectivity of 5000:1 between Si and SiO_2, which is a good etching mask for silicon etching. The etch rate can reach 1 $\mu m\,min^{-1}$ in EDP, however its etching selectivity of 35 to 1 between (100) and (111) silicon is relatively low. Furthermore, EDP contains pyrocatechol, which is described as a corrosive toxic.

TMAH is more compatible with CMOS IC processes than KOH and also neither toxic nor harmful. The etch rate of (100) silicon in TMAH can achieve about 0.7 $\mu m\,min^{-1}$, but its etching selectivity of (100)/(111) silicon is quite low, which is between 12.5 and 50.

For some applications, especially for the microfluidic devices, the etched surface quality of micromachined microchannels is very important. In general, isotropic etching generates smooth etched surface. However, anisotropic etchants leave rough etched surface. A highly concentrated KOH is preferred to obtain a smooth surface. In some cases, a post polishing process after KOH etching can be adopted by using slight isotropic etching to obtain a smooth surface.

If silicon is highly doped, particularly with boron, then silicon will be etched very slowly by the previously mentioned wet chemical etchants such as KOH, EDP or TMAH. One can use ion-implanting or diffusing boron into silicon to form a thin etch-stop layer. Since non highly-doped silicon will be etched very fast, this thin etch-stop layer will stay as a free-standing membrane, bridge or cantilever, depending on its shape patterning, as illustrated in Fig. 3. Such dopant-dependent selective etching techniques have led to the development of pressure sensors, accelerometers and microphones [3] with great commercial success.

The most appropriate technique to make low-doped, single crystalline silicon membrane-type microstructures with

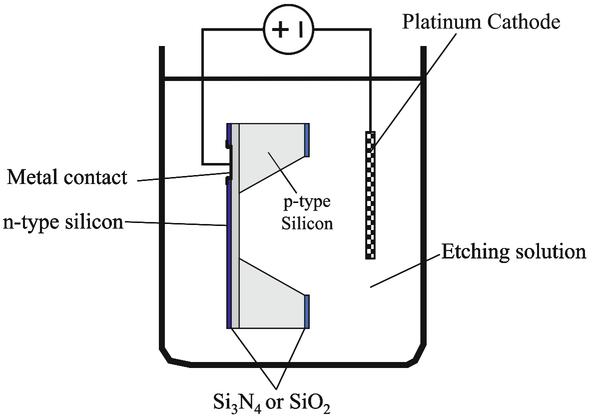

Silicon Micromachining, Figure 4 Schematic drawing of experimental set-up for electrochemical etching of p-type (100) silicon. The etching stops at p-type and n-type silicon interface

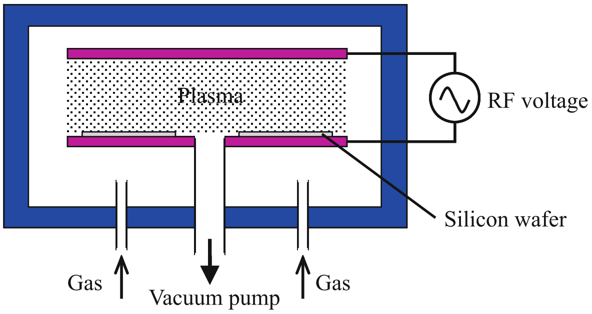

Silicon Micromachining, Figure 5 Schematic drawing of a typical reactive ion etching (RIE) system

well-controlled dimension and thickness is the electrochemical etch-stop on a diffusion or an epitaxial layer as shown in Fig. 4. In this silicon micromachining technique, a positive voltage is applied to one n-type side of a p-n junction of a wafer in an etch bath of a strong alkaline solution such as EDP or KOH. A platinum cathode is connected to the negative voltage and immersed in the etching solution. The etching proceeds as normal wet chemical etching until the exposed side of the p-n junction is completely etched away, which means that the etching stops exactly on the n-type silicon layer to release the diaphragm. In this case, only a low-doped layer is sufficient for the etch stop. Compared to the heavily-doped layer produced by purely chemical etching, silicon membranes micromachined by the electrochemical etching have much less mechanical stress.

Reactive Ion Etching of Silicon

In microelectronic fabrication processes, plasma etching is used to create the patterns of silicon-based thin films (silicon dioxide, silicon nitride, polysilicon). This etch process is performed in the vacuum chamber. By adding etch gases excited by radio frequency (RF) power, plasma is generated in the chamber, where silicon wafers are located. The exposed silicon surface is reacted with plasma gases and then removed layer by layer by this so-called reactive ion etching (RIE) technique. The schematic diagram of the RIE system is illustrated in Fig. 5. Since there is no wet chemical etching solution to be involved, this process is also called dry etching process. Assisted by the energetic plasma ions, fluorine gases, such as SF_6, CHF_3 and CF_4, are the etching gases for silicon-based thin films of SiO_2, Si_3N_4 and polysilicon, which are to be removed or patterned to form the desired shapes of microstructures.

By adding small amount of O_2 gas, the etch rate can be accelerated. In general, in this approach, the etch rate is relatively small, and in the range of few nanometers to tens nanometers per minute. The RIE process is not applicable for bulk material micromachining and therefore, it is suitable only to etch thin films with thickness of few micrometers. However, RIE is a suitable process to etch shallow microchannels in silicon substrate with good etch depth control.

Silicon Surface Micromachining

In this technique, thin layers, such as polycrystalline silicon, SiO_2 and Si_3N_4, will be deposited on the silicon wafer, which serves as a supporting substrate and may contain integrated circuits. The silicon substrate is protected by the etch-resistant film, for example thermal silicon dioxide or LPCVD silicon nitride, grown or deposited on the silicon substrate. A sacrificial layer of low temperature oxide (LTO), phosphosilicate glass (PSG) or borophosphosilicate glass (BPSG) is then deposited and followed by the deposition of LPCVD polysilicon, which is used as microstructures, typically for comb-drive structures, and normally patterned by RIE or DRIE technology [4].

In this approach, the bulk silicon substrate is not etched away, but only the sacrificial layer between the silicon substrate and the polysilicon microstructures is removed by lateral under-etching using the selective wet etchant of HF or BOE. Such etching solutions do not have any etching effect on the polysilicon film. Figure 6 illustrates the process steps to fabricate a polysilicon cantilever.

The surface micromachining technique is a CMOS-compatible process and has some advantages over the bulk-micromachining one. The most popular microstructure is the so-called comb-drive structures as shown in Fig. 7. Several commercially available sensors with integrated circuit on chip have been developed by using

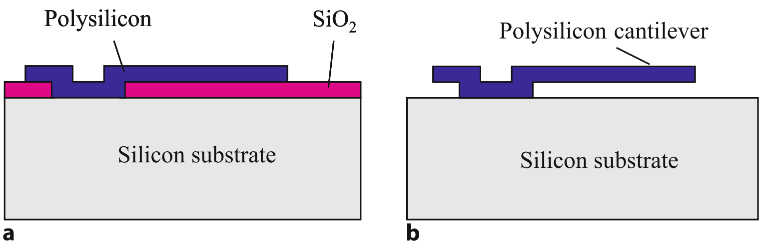

Silicon Micromachining, Figure 6 Fabrication steps of a polysilicon cantilever using surface micromachining. (**a**) Deposition of SiO_2 on silicon substrate, followed by polysilicon, whose shape is etched by DRIE or RIE, and (**b**) generation of polysilicon cantilever after removal of the sacrificial SiO_2

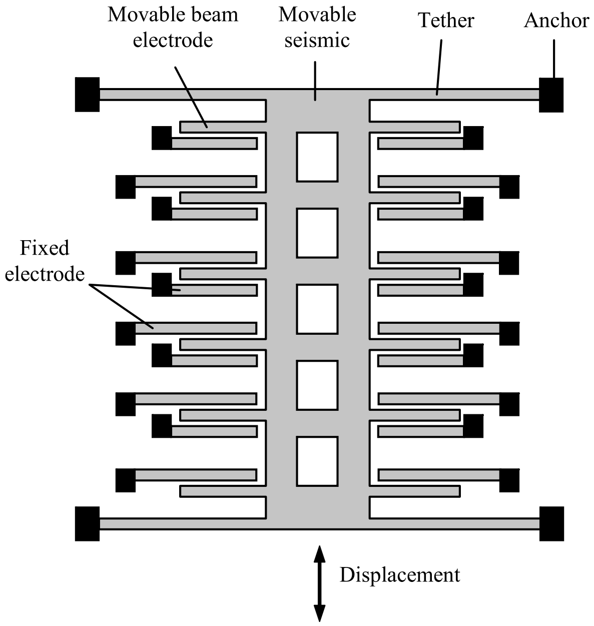

Silicon Micromachining, Figure 7 Schematic plan view of a MEMS device with comb drive structure

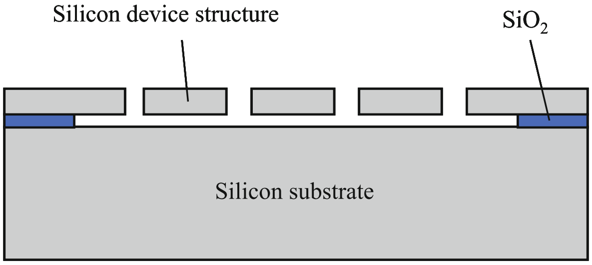

Silicon Micromachining, Figure 8 Illustration of the comb-drive structure in SOI (silicon-on-insulator) wafer fabricated using surface micromachining

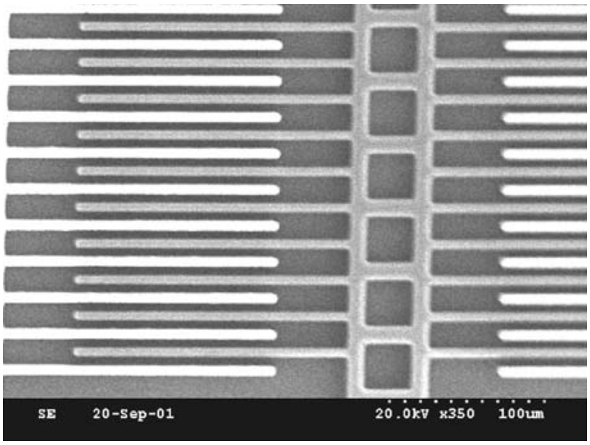

Silicon Micromachining, Figure 9 Scanning electron microscope (SEM) photograph of comb-drive structure in SOI (silicon-on-insulator) wafer fabricated using DRIE and surface micromachining

this technique such as accelerometers, gyroscopes, microphones, etc.

Instead of deposition of different thin films, silicon-on-insulator (SOI) micromachining may surpass the poly-Si surface micromachining technology for fabricating high performance devices. Figure 8 shows the process steps to fabricate a comb drive structure using SOI wafer. The single crystalline silicon device layer, whose thickness ranges from few to 100 μm, can be obtained by epi-silicon or fusion-bonding on a thin SiO_2 insulating layer. The top silicon device layer can be micromachined by RIE for thin layer and then followed by wet sacrificial etching of the buried SiO_2 layer by BOE for the structure release. Microstructures made from these single crystalline Si layers result in more reproducible and reliable sensors and other MEMS devices. Figure 9 presents a fabricated comb drive structure based on SOI surface micromachining.

Deep Reactive Ion Etching of Silicon

Microchannels and holes can be micromachined using wet chemical etching. However, as geometries of micro-device components get smaller, the requirement to etch silicon microchannels with vertical profile becomes important. An increase in aspect ratio for microstructures (for example microchannel) is desirable because more devices can be made from the same size of silicon substrate, and also lead to enhanced device characteristics.

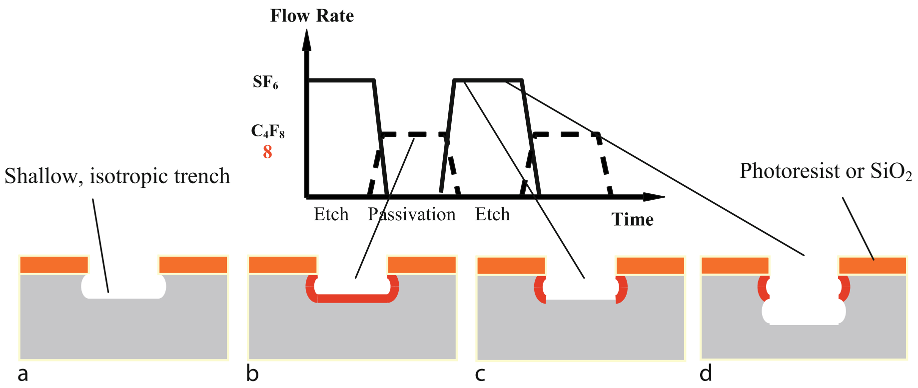

Silicon Micromachining, Figure 10 Illustrations of deep reactive ion etching process by time-multiplexing scheme. (**a**) Silicon is isotropically etched using SF_6 etching gas, (**b**) Polymer is deposited on the trench sidewall and bottom using C_4F_8, (**c**) At the beginning of following etch cycle, the bottom polymer is removed by etching gas ions, (**d**) In the remaining etching cycle, silicon is then further isotropically etched using SF_6 etching gas, forming the scallop sidewall

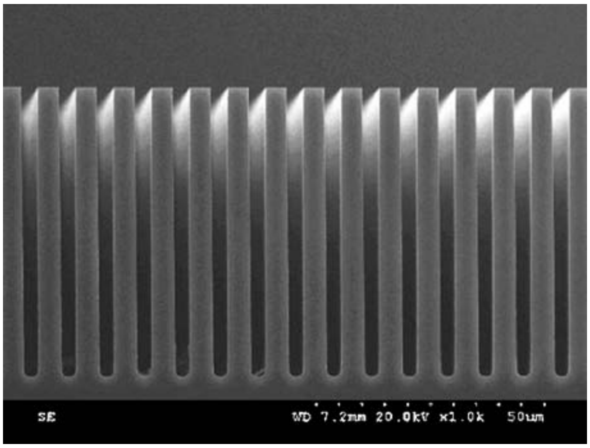

Silicon Micromachining, Figure 11 Scanning electron microscope (SEM) photograph illustrating high aspect ratio and vertical silicon trenches etched by DRIE

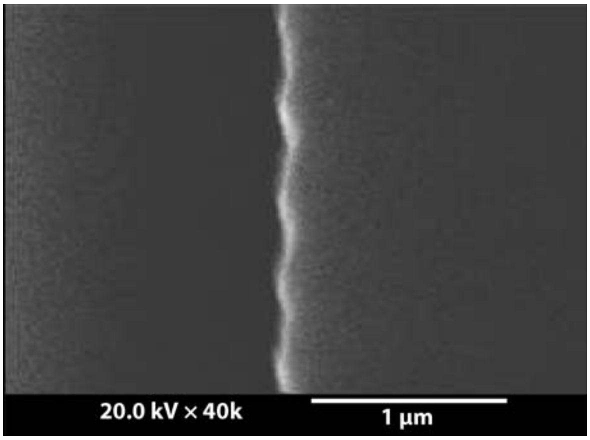

Silicon Micromachining, Figure 12 Scanning electron microscope (SEM) photograph illustrating the DRIE etched silicon with sidewall scallops of 50 nm

Laermer and Schilp of Robert Bosch GmbH originally invented a fluorine-based chemistry process [5], which maintains verticality (anisotropy), by using the concept of alternate etch and passivation steps, which is also called the time-multiplexed deep etching (TMDE) [6].

The TMDE technique utilizes an etching cycle flowing only SF_6 (steps b and d in Fig. 10), which is similar to the normal reactive ion etching process, and then switching to a sidewall passivating cycle using only C_4F_8 (step c in Fig. 10). During the subsequent etching cycle, the passivating film is preferentially removed only from the bottom of the trenches due to vertical ion bombardment, while preventing etching of the sidewalls, which are covered by the passivating layer.

To achieve a high etch rate, a high power inductively coupled plasma (ICP) source is used in the DRIE system. The etch rate can now reach up to $50\,\mu m\,min^{-1}$. The etching process is carried out at room temperature. Photoresist and SiO_2 can be used as etch mask with silicon etching selectivity up to 150:1 and 400:1, respectively. Compared to the wet chemical micromachining of silicon, the DRIE process is direction-independent. Any planar shapes of microstructures can be created while the wet anisotropic etching can only etch rectangle holes on (100) plane.

Key Research Findings

The aspect ratio of the microtrenches is defined as the ratio of the trench depth to the trench width. DRIE can easily reach an aspect ratio of 30. With special recipe and high plasma power, the highest aspect ratio can reach as high as 100 [7]. The smallest feature size is dependent of the patterning capability. Using the normal optical lithogra-

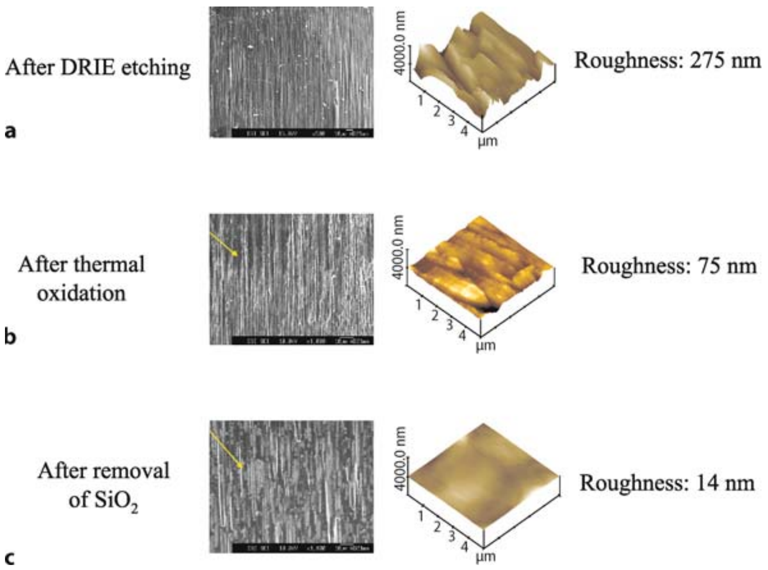

Silicon Micromachining, Figure 13 Scanning electron microscope (SEM) photographs and atomic force microscope (AFM) measurement results showing the improved surface roughness of DRIE etched silicon sidewall by thermal oxidation process, (**a**) after DRIE, (**b**) after thermal oxidation, and (**c**) after removal of oxide layer

phy, 2 µm high aspect ratio silicon beams can be deeply micromachined with almost vertical angle as shown in Fig. 11. Associated with the DRIE process, the etch rate is feature-size dependent, which leads to the RIE-lag effect. Smaller feature size results in a lower etch rate. Due to the nature of the time-multiplexing of etch-passivation process, rough wave-shaped features (called scallops) appear on the etched sidewall. The roughness is about 50 nm as observed in Fig. 12. However, if the etch depth is more than 200 µm, the sidewall is much rougher due to the micromasking effect of the passivation layer of polymer. The rough sidewall surface can be smoothed by the thermal oxidation and oxide removal as indicated in Fig. 13. Silicon material is not bio-compatible. The microchannels, which are micromachined by DRIE, RIE or wet chemical etching, can be coated with silicon oxide by the thermal oxidation process as shown in Fig. 14. For bio-chip applications [8], using silicon is not a cost-effective solution. However, one can use micromachined silicon structures as micro-molds for the polymer, PDMS or silicone replications. In this case, the sidewall of the small trenches needs to be coated with a special thin layer for easy demolding of microstructures [9].

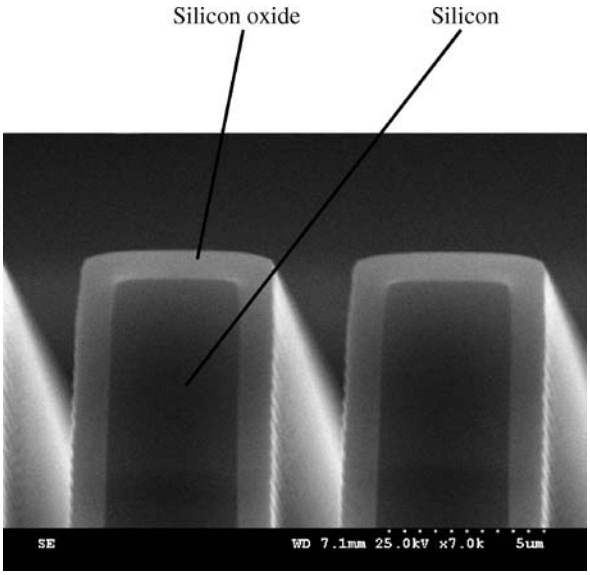

Silicon Micromachining, Figure 14 Cross sectional scanning electron microscope (SEM) of silicon microbeams coated with thermally grown SiO_2

Future Directions for Research

Silicon micromachining technology is important in the fabrication of micro- and nanofluidic chips, MEMS/NEMS and other miniaturized devices [10]. Deep reactive ion etching opens new research opportunities for high aspect ratio silicon-based micro- and nanostructures for various applications. The etch rate needs to be increased to reduce the process time and costs. Further study should be focused on smoothing rough sidewalls of DRIE etched silicon microchannels in order to reduce the fluidic resistance. Ultra high aspect ratio micromachining technology needs to be further developed to fabricate sili-

con nanostructures. Furthermore, a new challenge will be on how to use surface micromachining, which is a compatible process with integrated circuits, for the integrated micro- and nanofluidic applications.

Cross References

- ▶ Anisotropic Etching
- ▶ Anodic Bonding
- ▶ Bulk Micromachining
- ▶ Fabrication of 3-D Microfluidic Structures
- ▶ Heat Transfer in Microchannel Flows
- ▶ Isotropic Etching
- ▶ Lab-on-a-Chip (General Philosophy)
- ▶ Laser Based Micromachining
- ▶ Magnetic Pumps
- ▶ Mechanical Nanosensors
- ▶ Membrane Actuation for Micropumps
- ▶ MEMS-Based Biosensor
- ▶ Microactuators
- ▶ Microfabrication Techniques
- ▶ Microfilters
- ▶ Micromolding
- ▶ Microneedles – Applications & Devices
- ▶ Supersonic Micro-Nozzles
- ▶ Nanochannel Fabrication
- ▶ NEMS-Based Biosensors
- ▶ Oxidation (of Silicon)
- ▶ Photolithography
- ▶ Plasma Etching
- ▶ Powder Blasting
- ▶ Reactive Ion Etching (RIE)
- ▶ Wafer Bonding

References

1. Petersen KE (1982) Silicon as a Mechanical Material. Proc IEEE 70:420–457
2. Schwartz B, Robbins H (1961) Chemical Etching of Silicon-III: A Temperature Study in the Acid System. J Electrochemical Soc 108:365–372
3. Sessler GM (1996) Silicon Microphones. J Audio Eng Soc 44:16–22
4. Howe RT, Muller RS (1982) Polycrystalline Silicon Micromechanical Beams. Spring Meeting of the Electrochemical Society, Montreal 184–185
5. Laemer F, Schilp A (1996) Method of Anisotropically Etching Silicon Robert Bosch GmbH: U.S. Patent 5,501,893.
6. Ayón A, Braff R, Lin CC, Sawin HH, Schmidt MA (1999) Characterization of a Time Multiplexed Inductively Coupled Plasma Etcher. J Electrochemical Soc 146(1):339–349
7. Marty F, Saadany B, Bourouina T, Mita Y, Shibata T (2005) High Aspect Ratio Nano-structures (HARNS) for Photonic MEMS Based on Vertical DBR Architecture. Digest of Technical Papers – International Conference on Solid State Sensors and Actuators and Microsystems Transducers '05, Seoul 1 384-387
8. Chen PJ, Shih CY, Tai YC (2006) Design, fabrication and characterization of monolithic embedded parylene microchannels in silicon substrate. Lab Chip 6:803–810
9. Gao J, Yeo LP, Chan-Park MB, Miao J, Yan Y, Sun J, Lam YC, Yue CY (2006) Anti-stick post-passivation of high aspect ratio silicon molds fabricated by deep reactive ion etching. J Microelectromech Syst 15:84–93
10. Madou MJ (2002) Fundamentals of Microfabrication: The Science of Miniaturization. CRC Press LLC, Boca Raton

Simulating Migration of Polymer Chains, Methods

GREG WALKER
Department of Mechanical Engineering, Vanderbilt University, Nashville, TN, USA
greg.walker@vanderbilt.edu

Synonyms

Macromolecular transport; Active particle flows; Brownian dynamics

Definitions

Polymer chains are long flexible molecules usually associated with organic molecules such as DNA. Their transport is important to many medical screening applications and can be described using Monte Carlo or molecular dynamics approaches.

Overview

The motion of large molecules in microfluidic flows is important because the trajectories of particles in shear flows do not always follow the local flow field. Therefore, a knowledge of the fluid dynamics is not sufficient to completely describe the motion of the particles. When a suspended particle does not track the flow, the particle is said to be active as opposed to passive. The dynamics of active particles are particularly interesting in microfluidic devices because the molecules of polymer chains can approach – and even exceed – the characteristic lengths of the device. Consequently, the deviations between the particle/molecular motion and the fluid motion can be significant.

While active particle dynamics can address the motion of any suspended particle in a fluid, microfluidic researchers are usually interested in polymer chains because these structures in general do not follow the fluid flow, have a high degree of flexibility, and model important biological subsystems such as DNA and many types of proteins. If we want to track or manipulate different polymer chains in

a microfluidic system, we need to understand their dynamics relative to the fluid flow. However, not only will the bulk motion deviate from what the fluid is doing, but also their conformation or shape can change, which alters the transport properties. In other words, as polymer chains travel in a fluid system, the inherent flexibility of the chains allow them to bunch up, stretch out or tumble in the flow. As the shape of the chain changes, the fluid forces imposed on the chain will also change. As a result, the motion of a flexible chain will vary even if the flow field remains constant. For microfluidic systems designed to sequence or hybridize DNA, for example, the conformation can be as important as the trajectory of bulk motion of the molecule.

Basic Methodology

The adjective *macromolecular* is often used to describe transport of molecules in systems as opposed to transport within a molecule. This distinction can be important because some of the same methods can be used to treat both systems. Depending on the size of the system, two general methods could be used to describe molecular motion in a fluid.

1. Molecular dynamics is a fundamental approach that requires only the knowledge of forces between individual atoms. This approach is useful only for the smallest microfluidic systems because modern computational architectures can only handle a few million atoms and a single nanoliter of water contains over 10^{16} atoms.
2. Brownian dynamics approximates a molecule as a structure with limited degrees of freedom and with continuum forces. This approach is useful for multi-scale simulations, which are characteristic of the vast majority of microfluidic systems. With this approach we no longer have to simulate each individual atom, but approximate the force due to a large group of atoms.

Molecular Dynamics

Molecular motion can theoretically be described using molecular dynamics. In this context, molecular dynamics describes the motion of a molecule in a fluid by accurately characterizing the force between any two atoms in the system including the molecules of the surrounding fluid. All forces in the system are summed and Newton's law is applied to each atom to deduce its individual motion. The motion of the molecule is deduced from the motion of its constituent atoms. Because of its fundamental nature, a molecular dynamics approach is often considered ab initio or "from first principles", meaning that there are virtually no fitting parameters required to obtain a physical solution. Nevertheless, the force between atoms, or ►inter-atomic potential, arises from a variety of chemical interactions (Van der Walls' force, chemical bonding, electrostatic) and in general, is difficult to characterize. (Discussion of the different potential fields and their application is beyond the scope of this article, but it should be noted that inter-atomic potentials often contain approximations and non-physical fitting parameters, so the ab initio designation is not always appropriate.)

Applications for molecular dynamics in microfluidic systems include, for example, protein folding in solution, transport of amino acids in ion channels, and locally driven electro-osmotic flows with rigid particles. However, these applications do not involve the bulk motion of a fluid and are extremely small, specialized systems. In general, the systems that microfluidic researchers consider are multi-scale in that they require knowledge of the bulk fluid motion, far-field boundary conditions, interactions with other molecules, walls and fluid structures, and other experimental conditions. Consequently, the molecular dynamics approach is rarely feasible or even necessary for multi-scale systems. Instead, researchers and analysts rely on ►coarse-graining techniques to reduce the degrees of freedom, where tractable solutions are more accessible.

Coarse-Grained Models

By coarse-graining, the molecular system is discretized and treated as a bead/spring system or bead/rod system. In the case of the bead/spring system, the molecule is treated as a series of beads with mass and size connected by springs. In the case of the bead/rod model, the molecule is treated a series of massless beads connected by rigid rods. The bead/spring system is simpler, but can allow the molecule to cross, which is unphysical, and is susceptible to computationally unstable solutions. The bead/rod model is mathematically and computationally more difficult, but the motion is often more realistic. In either case, the discretization or the number of beads used to model the chain is somewhat arbitrary but is chosen so that the behavior of the chain in a flow matches observations of the motion of actual chains. In the case of DNA, each base pair could be treated as a bead, but even this level of coarse-graining is usually far too fine to yield reasonable computational times and unnecessary to achieve accurate results. Instead, most simulations use anywhere from 5 to 20 sections depending on the complexity of the flow and resulting motion of the molecule that needs to be captured. Besides the reduction in the problem size, another advantage of coarse-graining is that the forces on the beads or rods can be described by continuum mechanics instead of requiring inter-atomic potentials. The forces common to most simulations include the following.

Drag

Drag forces arise from the difference between a bead or rod's velocity $\dot{\boldsymbol{r}}_i$ and the local velocity field of the fluid $\boldsymbol{u}_i$, with the difference scaled by the drag coefficient ζ, giving $F_D = -\zeta(\dot{\boldsymbol{r}}_i, -\boldsymbol{u}_i)$.
The drag coefficient depends on the size of the bead. In the case of rods, the local flow field may not be uniform across the rod, which gives rise to moments on the object as well. Because the motion of a rod involves an additional angular acceleration, the computations are often more involved.

Internal

The internal forces for coarse-grained models can be considered elastic (bead/spring) or rigid (bead/rod). Regardless of the method, the force connecting adjacent beads does not represent inter-atomic forces, but merely constricts the distance between adjacent beads. In general, the effect of a shear flow is to stretch the molecule, so an attractive force is applied to keep the molecule intact. For the spring-like model, several non-linear forms of for the attractive force have been proposed. For more information about the types and physical basis for the mathematical form of these forces, the reader is referred to [1, 2]. Although the rigid model (bead-rod chains) introduces an added level of complexity due to constraints on the motion, the results obtained using the bead-rod model are more accurate for a fewer number of beads. Furthermore, for more complex situations such as electric field induced motion and obstacle navigation, the bead/rod formalism is often considered more robust.

Electrostatic

A myriad of conditions could give rise to non-uniform charge distributions in the fluid. For example, electroosmotic flows or solutions of electrolytes are often used to manipulate microfluidic flows. In these situations, the macromolecule may be subject to Coulomb forces. There is no general expression to account for these forces, but they will depend on the location and strength of the charge distribution in the fluid as well as along the molecule.

Image

The force of the wall is modeled as a steep potential near a physical barrier. The force is called an image potential because the magnitude is derived from a phantom particle that is placed on the perpendicular to the wall and the particle near the wall. The phantom particle is exactly the same as the particle being repulsed, and the repulsive force is the force between two neighboring particles (instead of the wall). This approach allows one to consider variations in forces that arise from the particles without having to treat the wall differently.

Brownian

All other forces are essentially continuum forces, i. e. they would be present for a large-scale strand of beads and are not specific to molecules. The Brownian force, on the other hand, is only present for very small objects. This force is the result of individual atoms and other molecules in the flow bumping into the macromolecule to change its conformation. In the continuum limit, enough momentum exchange occurs in all directions so that the net force is zero. For small objects, the net force is some non-zero randomly oriented force that goes to zero over long times. However, in some non-equilibrium situations such as near walls, the Brownian force can be non-uniform.

Hydrodynamic

Objects in the wake regions of other objects are known to experience different flow characteristics compared to the bulk motion of fluid. Therefore, some beads in a macromolecule do not sample the bulk fluid, but a modified version of the bulk fluid because of the proximity of other beads in the flow. A great deal of research has gone into developing techniques and approximations to attempt to include this effect with varying degrees of success. The difficulty lies in the attempt to invent a general solution to a problem that is dependent on geometry, discretization of the molecule and flow characteristics. Discussion of these details are beyond the scope of this article. Instead the reader is referred to [3].

Other External

Many other forces could conceivably be important in macromolecule flows. For example,

1. magnetic forces could arise when dealing with magnetized particles in conjunction with macromolecules, which is often done in drug delivery and targeting.
2. Gravitational forces may be important if transport occurs in a centrifuge.
3. Many experiments also track macromolecules with fluorescent dyes. If the dye molecule is of the order of the transported molecule, then the dye can introduce additional drag.
4. Hybridization of DNA can provide a force at the ends of the macromolecules that tether the molecule to a surface.
5. Van der Waals forces can arise between polar objects.

Once the forces acting on the molecule are known, two approaches can be used to solve for the dynamics behav-

ior of the particles. Boltzmann-based models (also called Fokker–Planck systems) can predict average quantities through calculation of a distribution function.

$$\begin{aligned}\frac{\partial f}{\partial t} &= \sum_i \left(m_1^{-1} p_1 \frac{\partial f}{\partial r_i} + F_j \frac{\partial f}{\partial p_i} \right) \\ &= \sum_i \sum_j \frac{\partial}{\partial p_i} \zeta_{ij} \left(m_j^{-1} p_j f + kT \frac{\partial f}{\partial p_j} \right).\end{aligned} \tag{1}$$

Moments of f result in an average displacement field. This approach has largely been supplanted by non-averaging techniques because of molecular individualism [3]. In other words, instead of calculating average displacements, the behavior of individual molecules are of more interest in modern macromolecule transport.

To determine specific molecular motions, the Langevin approach is relatively straightforward and involves integrating Newton's second law,

$$\sum_i F_{ij} = m_j \boldsymbol{a}_j = m_j \frac{\mathrm{d}^2 x_j}{\mathrm{d}t^2}\,, \tag{2}$$

over time to calculate the displacement (motion) of each bead. In equation 1, i indexes each force acting on a bead and j indexes the beads in the simulation. Tractable solutions to this motion are only possible when time is discretized into tiny steps. Over each time step, the forces and acceleration are assumed constant. The integration scheme varies with the discretization of the molecule and type and magnitude of the forcing functions that are present. However, most generally applicable schemes are second-order accurate and involve some leap-frog technique where velocities are calculated at the half-time step. The two primary difficulties are including the Brownian force and the hydrodynamic interactions because these two forces are not independent of the solution resulting in a non-linear system of equations. If we assume that the momentum relaxation is much faster than the position relaxation of the Brownian particles, then the resulting equations can be simplified with a diffusion tensor that represents the influence of the Brownian force on average displacement [1].

$$\langle \Delta r_i \rangle = \sum_j \left(\frac{\partial \mathrm{D}_{ij}^0}{\partial r_j} + \frac{\mathrm{D}_{ij}^0}{kT} F_j^0 \right) t\,, \tag{3}$$

where the summation index spans the particles in three-dimensional space. In the foregoing expression, time is assumed to be greater than the momentum relaxation, i. e. $t \gg \tau^0 = m\mathrm{D}/kT$. The Oseen tensor is often used for D_{ij} [2], but appropriate expression of this diffusion component is the subject of a great deal of research.

The prediction of molecular motion is only as good as the effective forces that act between beads or rods. In the case of rigid rods connected by rotating joints, Kramer's bead chain rod system is the prevailing model. In this approach, the total length of the polymer is fixed, which may not be physically realistic in many cases. Yet, this model prevents the molecular strand from crossing itself, which is also physically unrealistic. The displacement of the beads is usually predicted from an optimization using the inter-bead distance as an internal constraint. For the bead-spring models, several different forms of inter-bead potentials have been used. The simplest model has a linear spring between each bead. This model tends to allow too much displacement, so an inverse Langevin model is used to stiffen the spring for larger displacements, which can be approximated as

$$F_j = \frac{Gr_i}{1 - (\frac{r}{r_0})^2} \tag{4}$$

where G is the spring constant and r_0 is the relaxed molecule length. For DNA molecules, a worm-like chain model has proven remarkably successful, which has several forms that can be useful.

Key Research Findings

Research in macromolecular transport using Brownian dynamics is either fundamental in that a parameterized class of fluid flow conditions is considered, or a particular experiment is modeled with well-known geometric and fluid conditions.

In the study of molecular transport and conformation in simple flows, results suggest that the motion is not very simple. Many polymers have fairly complex shapes when in a quiescent fluid. They can be coiled, straight, curved or a combination of different shapes as seen in Fig 1. This tendency is important when discussing transport in a ▶ shear flow. Both simulations and experiments produce molecular shapes described as coils, dumbbell, linked, half dumbbell, straight and folded, all in a single longitudinal shear flow. Moreover, for varying flow parameters, the shape can transition between the different forms, and the transition is unpredictable. Similarly, in linear shear flows, the motion can be characterized as longitudinal (perpendicular to the shear direction), tumbling, or globular. Transition between flows can occur without changing flow parameters. The transition rate, however, is usually governed by the strength of the shear.

S

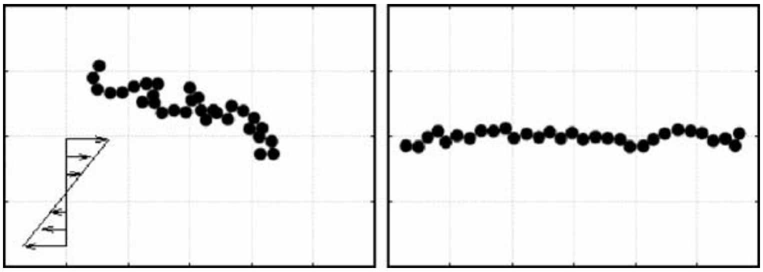

Simulating Migration of Polymer Chains, Methods, Figure 1 Conformation of a 30-bead chain in a linear shear flow at different times. The chain shown will exhibit a periodic tumbling motion if observed for long periods of time

These results suggest that control of a single polymer chain in a flow is difficult because of the unpredictability of any specific molecule. However, we are usually interested in the motion of a large number of molecules in a micro-fluidic system. Therefore, statistics are collected on a single molecule given a variety of initial conditions, for example. Then predictions about the average behavior of certain types of molecules in certain types of flows can be made.

The non-dimensional Weissenberg number ($\mathrm{Wi} = \dot{\gamma}\lambda$) is defined as the product of fluid strain rate ($\dot{\gamma}$) and the longest relaxation time of the polymer chain (λ). This number provides an approximation to the ratio of ability of the flow to stretch the polymer chain divided by the tendency of the chain to resist stretching. For large Wi, the flow generally results in stretching of the molecule; for small Wi, the molecule's conformation is dominated by Brownian motion.

Other studies of polymer transport focus on how long molecules behave in a complex flow in the presence of obstacles. For example, one group has examined how DNA migrates through a field of posts where the strands straddle the obstacle. Simulations of this type are useful to help predict the resident time of DNA in a particular region. This might be important to researchers who are using micro-fluidic chambers to produce chemical reactions with DNA, for example.

Future Directions for Research

Two research direction emerge from existing studies and needs in the community. (1) Fundamental studies focus on the physics governing the relationship between the forces acting on the beads. (2) Applied studies focus on how molecules behave in different systems.

In terms of fundamental studies, modeling of polymer chains is still in its infancy. Although there are plenty of instances where experiments and simulation converge, there is no general purpose, all-encompassing simulation approach that works universally. The primary difficulty arises from resolving the relative strengths of each force acting on the molecule. In isolation, each force can be described mathematically with a good deal of rigor. However, the relative magnitude of each force relies on difficult to characterize free parameters. Therefore, simulations still rely on experiments to provide data for accurate simulations. A first-principles simulation is simply not possible yet. Consequently, much of the current research is devoted to refining the force models to include more physics in simulations.

In terms of applied studies, different configurations are constantly being addressed to help analyze specific experimental studies and to help provide ranges for the free parameters associated with the forces.

To address both of these concerns, the following areas are suggested as immediate research areas where substantial contributions can be made.

Complex Flows

Most fundamental simulations examine simple flow situations such as elongation and linear shear flows. These flows appear in many micro-fluidic structures, and include a wide range of effects that molecules might experience. In addition, the flow solution is simple and can be reliably produced in the lab. Therefore, there is continued need to investigate these configurations. However, these simple flows do not represent all situations seen in modern micro-fluidic devices. For example, stagnation point flow into a stationary wall, flow around corners and flow mixing are all complex phenomena that affect polymer chain transport and conformation.

Overlap Models

Although the bead spring model appears adequate for many situations, more complex flows can cause interaction of a molecule with itself. For bead-spring models, this can be treated by introducing strong, short-range potentials. Because of the large gradients, however, simula-

tions are prone to exaggerated motion when non-adjacent beads approach each other. The bead-rod model attempts to account for the interaction by preventing the coarse-grained model of the chain from crossing itself. This approach can be relatively complex and a universally agreed upon approach has not been established.

Wall Interaction

Typically a wall is modeled with an image potential. In this case, a virtual particle that is located at the mirror location to the real particle provides an interaction potential. As such there is often an artificial buffer that prevents the bead from contacting the wall and migration away from surfaces is possible. Even though these interaction potentials have a short range, they can be strong to prevent beads from penetrating walls. As a result, time stepping becomes crucial, and too large of a time step can result in physically unrealistic motion. New methods to treat this artifact are needed to provide transport in confined channels.

DNA Hybridization

In the case of DNA transport, the researcher is often interested in hybridization, which is a reaction that changes the characteristics of the chain or causes additional forces. Motion in the presence of interaction particles is complex and has not received much attention.

Cross References

- ► AC Electro-Osmotic Flow
- ► Brownian Motion and Diffusion
- ► Dielectrophoretic Motion of Particles and Cells
- ► Dissipative Particle Dynamics
- ► Electrokinetic Flow and Ion Transport in Nanochannels
- ► Electroosmotic Flow (DC)
- ► Multiscale Modeling and Numerical Simulations
- ► Molecular Dynamics Simulation Method
- ► Polymer Synthesis Within Microfluidic Reactor
- ► Van der Waals Interaction Forces

References

1. Ermak DL, McCammon JA (1978) Brownian dynamics with hydrodynamics interactions. J Chem Phys 69(4):1352–1360
2. Yamakawa H (1971) Modern Theory of Polymer Solutions. Harper and Row, New York
3. de Gennes PG (1997) Polymer Physics: Molecular Individualism. Science 276(5321):1999–2000
4. Marko JF, Siggia ED (1995) Stretching DNA. Macromol 28(26):8759–8770
5. Hur JS, Shaqfeh ESG, Babcock HB, Chu S (2002) Dynamics and Configurational Fluctuations of single DNA Molecules in Linear Mixed Flows. Phys Rev E 66(011915)
6. Schroeder CM, Shaqfeh ESG, Chu S (2004) Effect of Hydrodynamic Interactions on DNA Dynamics in Extensional Flow: Simulation and Single Molecule Experiment. Macromolecules 37:9242–9256

Single Cell Analysis in Microfluidic Devices

Luc Charon[2], Aaron R. Wheeler[1], Lothar Lilge[2]

[1] Department of Chemistry, University of Toronto, Toronto, ON, Canada

[2] Department of Medical Biophysics, University of Toronto, Toronto, ON, Canada

awheeler@chem.utoronto.ca

Synonyms

Analysis of individual cell contents

Definition

►Chemical cytometry is a class of highly sensitive analytical techniques for the analysis of the chemical contents of single cells. These techniques enable the detection and identification of cell constituents including oligonucleotides, small molecules, and proteins, as well as providing means to monitor the effects of biochemical and enzymatic reactions.

►Capillary electrophoresis is an analytical technique used to separate chemicals in solution as a function of their charge and size. Samples are injected into a capillary, a high electric field is applied, and the analytes migrate to the end of the column, where they are detected.

S

Overview

The cell is a complex biochemical factory, capable of proliferation, differentiation and communication. The cell also interacts with its microenvironment, comprised of other cells, tissue matrix and interstitial vascular, lymphatic and non-biological compartments. Yet most of what is known about the correlation between behavior, function and genotype of biological cells comes from *average* measurements of cell populations. While useful, these studies are unfortunately incapable of assessing the response and interaction of individual cells within a heterogeneous population. As an illustration, a recent study [1] of hormone-induced maturation of unfertilized eggs (oocytes) as a function of enzyme activation was evaluated both based on populations and individual cells. The population data suggested a *graded* relationship between

the hormone (progesterone) concentration and enzyme activation while the single cell data revealed a sharp *all-or-nothing* switch. The single cell analysis approach can in fact provide not only complementary information but rather reveal the actual functional interaction of biomolecules thus assisting in understanding complex biological systems on the cellular and tissue structural basis. This kind of biological insight is required to understand complex systems such as tissues, organs and even complete organisms. While it is obvious that this type of work is useful, single cell studies are much more complicated and time-consuming than their population counterparts; in fact, single cell analyses push the boundaries of conventional techniques.

Several single cell analysis techniques have been developed, which may be classified in terms of information content (# of elements capable of being studied simultaneously) and throughput (# of cells studied in a given time) – this is illustrated in Fig. 1. The simplest and most widely used forms of single cell analysis are fluorescence microscopy and flow cytometry. In microscopy, fluorescence from small molecule reporters, immunochemical labels, or transfected fluorescent proteins within cells is observed with subcellular localization. While this technique enables the measurement of time-dependent changes in response to stimuli of individual cells as well as cell-cell interaction studies, it is an inherently low-throughput method if used with high magnification. Conversely, flow cytometry is a high-throughput technique that can be used to analyze up to several tens of thousands of cells per second but is limited in the type of assays for which it can be used and does not provide subcellular resolution. Multiple wavelength analysis schemes have been developed, but the number of parameters which can be measured simultaneously is intrinsically limited by the finite spectral bandwidth of the detectors and the increasing complexity of using multiple fluorophores, excitation sources, and/or detectors. These two techniques therefore are classified in the region of low information content space in Fig. 1.

In order to achieve a more comprehensive analysis of individual cells, methods that incorporate chemical separations have been developed to increase the number of parameters capable of being studied simultaneously. These techniques, termed *chemical cytometry* by Dovichi and coworkers [2] are used to detect and identify various components of single cells such as oligonucleotides, small molecules and proteins, as well as to monitor enzyme activity. Capillary electrophoresis (CE), laser-induced fluorescence (LIF), and electrochemistry are the tools which are used in chemical cytometry; this chapter deals with capillary electrophoresis implemented in microfluidic devices.

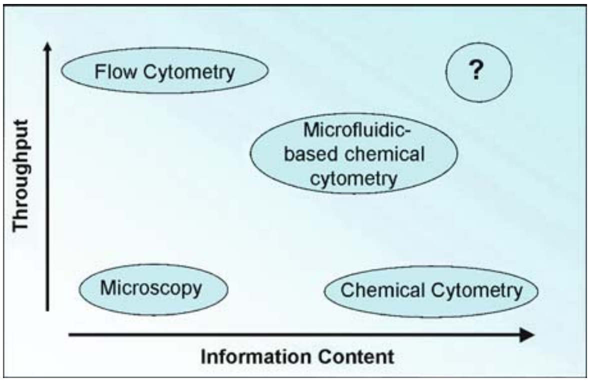

Single Cell Analysis in Microfluidic Devices, Figure 1 Chart comparing single cell bioanalytical techniques in terms of information content and throughput

CE-based chemical cytometry can be used to evaluate many cell constituents simultaneously, and is thus, as shown in Fig. 1, categorized as a high information content technique. This comes at a cost, however, as the cell injection schemes and use of a single capillary makes the technique extremely low-throughput. Ideally, the contents of hundreds of cells could be individually analyzed for statistical evaluation of the heterogeneity of a population; in practice, however, the arduous and time-consuming nature of chemical cytometry typically limits it to a few cells (i. e., < 10) per analysis.

In recent years, microfluidics has become a popular technology for applications in the life sciences. The continued development of new microfabrication techniques has permitted the integration and scaling down of several bioanalytical procedures into a single device, from which emerged the concept of Lab-on-a-Chip or micro total analysis system (μTAS). Microfluidic devices have several advantages over conventional bioanalytical techniques: low reagent and power consumption, low cost, and the potential for mass production and massively parallel scale analysis. As illustrated in Fig. 1, the application of microfluidics to chemical cytometry may result in a solution to the low-throughput problem of capillary-based chemical cytometry techniques, forming a new class of methods with high-throughput and information content. Several good reviews have been recently published covering the potential of microfluidics for applications involving cells [3, 4]. Microfluidics has been applied to microscopy, flow cytometry, and chemical cytometry, among others. As microscopy and flow cytometry are discussed in detail in other chapters in the *Encylopedia* (► flow cytometer lab-on-chip devices, ► detection using confocal microscopy), we focus here on chemical cytometry. In what follows, we discuss the state-of-the-field and

challenges remaining to be solved in the areas of fabrication, cell selection/transportation, cell lysis/treatment, and analysis, from the standpoint of microfluidic method development for high-throughput chemical cytometry.

Basic Methodology

Fabrication Considerations

There are many well-established microfabrication techniques which can be used to construct microfluidic devices (▶ microfabrication techniques). Each has strengths and weaknesses, but the choice of fabrication technique ultimately depends on cost, availability of the facility, and most importantly, on compatibility with the desired application. This is especially important for chemical cytometry, where the fabrication process must be versatile enough to form devices capable of implementing the many necessary functions. Key considerations for fabrication of chemical cytometry include material, integration, and macro-to-micro interface.

Material

The materials used for the fabrication of most microfluidic chips include glass, silicon, quartz, and plastics (▶ materials used in microfluidic devices) In addition to cost and optical, electrical and physical properties, careful consideration must be given to the surface chemistry of the material (▶ methods for surface modifications). In fact, surface chemistry plays a major role in chemical cytometry, as protein adsorption to the channel walls can degrade the separation performance and make the electroosmotic flow unreproducible.

Integration of Multiple Components

The functionality and versatility of microfluidic devices for chemical cytometry requires the combination of several cell manipulation, processing, and analysis steps. These techniques, discussed in detail in the next section, rely on device components such as microstructures, optical windows, electrodes, embedded waveguides, and valves and pumps; each of which must be miniaturized and integrated on a single microfluidic platform (please refer to the following chapters ▶ fabrication of 3D microfluidic structures, ▶ on-chip waveguide, ▶ pneumatic valves, ▶ thermomechanical valves, ▶ thermopneumatic valves). Integrating multiple components on a single device dramatically increases the complexity of the final product and introduces compatibility problems in the various integrated functions. For example, surfaces designed to promote or prevent cell adhesion (for cell manipulation) are often different than surfaces best suited for electrophoretic separations. These engineering challenges are a bottleneck in the development of multifunctional microfluidic devices and must be addressed for the development of high-throughput chemical cytometry.

Macro-to-Micro Interface

A key concern for all microfluidic devices is the macro-to-micro interface. The complexity of the interface depends on the number of integrated functions (see ▶ packaging (including wire bonding)).

Cell Manipulation and Transportation

One of the most critical steps in single cell analysis is selection of predetermined individual cells and transportation through the device (▶ techniques for manipulating cells, ▶ microfluidic sample manipulation). The manipulation and transport techniques used for chemical cytometry should be multiplexed, have the potential for automation, and, depending on the assay, should have minimal biological or chemical impact on the cell(s) to be transported. Techniques fitting this description include cell sorting and integrated flow cytometry (▶ cell sorting, optophoresis for cell sorting, ▶ flow cytometer lab-on-chip devices). Several micromanipulation techniques based on mechanical, electrical and optical means have been developed for cell-based assays in microfluidic devices.

Mechanical Manipulation

While micromanipulators and micropipettes are routinely used for in vitro fertilization studies, they are bulky, suffer from low throughput and are not amenable to integration with a sealed microfluidic device. Other mechanical manipulation techniques include microfilters, dams, and *sandbag* structures. We note that these techniques are often used to capture, dock or sort many cells simultaneously without specificity and thus are limited in their use for single cell analysis where selecting a particular cell is a key goal.

Electrical Manipulation

The electric charge or polarity of cells (and cell contents) may also be used for manipulation and transportation within microfluidic devices. In contrast to mechanical methods, the use of electric field based approaches such as electrokinetics and dielectrophoresis are well-suited for microfluidics as they permit flexibility, controllability, automation and high-throughput capability. We note, however, that these kinds of techniques can produce undesired biological stress such as protein migration and clustering within the cells and in high fields, cells may

even lyse (i. e., die). For more information, please refer to the following *Encyclopedia* chapters: ► dielectrophoretic motions of particles and cells, ► electrokinetic motion of cells and non-conductive particles, ► AC dielectrophoresis Lab-on-a-Chip devices.

Optical Manipulation

Optical micromanipulation techniques use lasers to apply piconewton forces on micron sized particles, and have been demonstrated to be useful for cell transportation in microchannels. One of the most popular optical techniques is ► optical *trapping* (or optical/laser tweezers), which is implemented by focusing a laser to a diffraction-limited spot by a high numerical aperture (N.A.) microscope objective. Although optical trapping can be used to select particular cells accurately, its slow translational speeds (20 – 30 μm/sec) [5] makes it a low-throughput cell manipulation technique. We note that some have used diffractive optical elements (DOEs) and spatial light modulators to create multiple *optical traps* simultaneously, thus improving throughput [6]. These techniques are described further in ► optical tweezers for manipulating cells and particles. Another alternative in optical manipulation is laser-guided direct writing, in which a weakly collimated or converging beam pushes cells to desired locations [7]. This technique has been used to transport cells at 88 μm/s over several millimeters. A similar transportation technique was developed using evanescent waves from integrated waveguides to manipulate micron size particles [8]. While these two techniques suffer from lack of cell selectivity, they could potentially be automated to increase throughput in chemical cytometry by strategically positioning the integrated waveguides within the microfluidic device.

Cell Lysis/Treatment

In conventional population cell-based assays, sample preparation involves several steps, including lysis, filtration of non-solubilized cellular material, labeling of the analytes of interest, and sample purification. However, to prevent dilution of the extremely small samples in single cell analysis, filtration and purification are not typically integrated in chemical cytometry methods. This section briefly describes the various cell lysis techniques which have been implemented in microfluidics; for more detail, please see ► on-chip cell lysis.

In CE-based chemical cytometry, the quality of the information is ultimately determined by the manner in which the cells are lysed and their contents injected into the capillary. The technique employed to perform this task must be carefully designed to enable high quality, reproducible electrophoretic separations. Dilution of the contents of the cell prior to application of the electric field must be reduced to maximize sensitivity and resolution of the separated analytes. Lysis should occur in a manner such that the biochemical contents of the cell are not altered, for example, by the activity of proteases that are usually kept partitioned away from free cellular proteins. The technique must also address capillary clogging issues which result from the presence of insoluble cell debris. Finally, the lysis technique must be able to function in parallel for high-throughput applications. There are three categories of cell lysis techniques: electrical, mechanical and chemical lysis.

Electrical Lysis

When a large electric field is applied across a cell, the transmembrane potential is disrupted and pores are formed on the surface of the membrane. This phenomenon is called ► electroporation and is often used for gene transfection. As conventionally implemented, the process is reversible, and when the electric field is terminated, the pores close. The phenomenon can also be used to cause permanent disruption of the membrane, effectively lysing the cell. There have been several reports on the use of electrical lysis techniques in microfluidic devices [9–11]. Of particular interest, fast lysis of individual cells (∼ 33 ms) by electrical pulses for chemical cytometry was demonstrated in a microfluidic platform [12]. These extremely rapid lysis methods which minimize unwanted effects of slow lysis (that may bias the results) make these techniques favorable for protein analysis when compared to chemical lysis techniques. One drawback of electrical lysis is that much of the cell membrane, subcellular structures and the nucleus may remain intact and thus can clog the channe or adhere to the surface, affecting the separation and limiting the capacity for re-use.

Mechanical Lysis

Typical lysis techniques based on mechanical forces such as sonication and bead milling are not amenable for integration in a microfluidic device; however, in recent work, cells were lysed in microchannels by mechanical shearing on nanostructured filter-like *nano-knives* [13]. This method had the additional advantage of aiding subsequent analysis steps by filtering out cellular debris thus preventing clogging and sample fouling.

Chemical Lysis

The most common macro-scale cell lysis methods make use of chemical agents; as a result, several research groups have used similar techniques to lyse cells in microfluidic

devices [14–16]. While detergents such as sodium dodecyl sulfate (SDS) permit a greater number of proteins to be analyzed due to the capacity to solubilize membrane proteins and lipids, chemical lysis reaction times are relatively slow (tens of seconds). Therefore, this technique may not be ideal for applications in which desired biological events take place on time scales of seconds or less (e. g., metabolite concentrations can change by a factor of 10 within 1 s [17]) or when diffusion of the cellular content within the microfluidic chip structure can not be suppressed.

Analysis

While an array of analytical techniques has been developed to study various aspects of cells (please see ▶ cell assays in microfluidics), this chapter is focused on chemical cytometry. As mentioned above, chemical cytometry refers to methods in which intracellular constituents of a single cell are analyzed by means of a chemical separation. Such methods typically employ capillary electrophoresis for separations, combined with laser induced fluorescence (LIF) or amperometry for detection. We refer readers to other chapters for detailed descriptions of other methods used to evaluate contents of cells (▶ patch–clamp measurements on-chip, ▶ mass spectrometry on chip device).

In capillary-based chemical cytometry, a cell is injected into a capillary, where it is lysed, and then its contents are separated by electrophoresis. The separating contents are detected at or near the end of the capillary, as the analytes migrate past the detection zone. Microfluidic devices are well-suited to replace capillaries for chemical cytometry. The channel dimensions (5 – 100 μm) and planar geometry allow for very efficient dissipation of Joule heat produced from large electric field gradients. The capacity to apply high fields (e. g., 500 – 1000 V/cm) dramatically reduces separation time and minimizes band diffusion. Most importantly, the small channel dimensions can handle injection volumes ranging from nanoliters to hundreds of femtoliters [18], and thus results in minimal dilution of sample.

The level of expression of protein species within a single cell ranges between several millions to under 10 copies, requiring that extremely sensitive detection techniques be employed. LIF is particularly well suited for this task as it is capable of achieving mass concentration detection limits of a few tens of molecules and even single-molecule detection [19]. Amperometry has also been used frequently due to its high sensitivity. A more detailed look at these two techniques can be found elsewhere (▶ fluorescence measurements, ▶ amperometric techniques).

Key Research Findings

Over the past few years, several groups have attempted to integrate all of the critical processes for chemical cytometry on a single mirofluidic plattform. Various combinations of cell manipulation, cell lysis, and analysis strategies were used to obtain high content information with the goal of maintaining analysis in a high-throughput format. Some methods were optimized for analysis of small molecules and proteins, while others were developed for genetic assays, evaluating DNA or RNA content.

Protein or Small Molecule Analysis

Fang and coworkers [9] developed a glass microfluidic chemical cytometry device with a simple cross-shaped channel design. Derivatized glutathione (GSH) in single human erythrocyte cells was separated and detected by LIF. Cells were transported from the reservoir to the T-junction by hydrodynamic flow, which was controlled by adjusting the amount of liquid in the four reservoirs; fine positioning was performed by applying a series of voltages to *dock* the cell. Once positioned, each cell was electrokinetically lysed. This technique yielded a throughput of approximately 15 cells/h.

Hellmich et al. [20] designed a PDMS device comprising a cross-junction integrated with other micro-scale features as shown in Fig. 2a. GFP-transfected insect cells were selected and transported to the intersection using optical tweezers. After positioning, the cells were lysed with SDS; the microstructures acted as a physical cell trap, preventing the cell from moving away during the process. After each cell was lysed, fluorescently labeled contents (amino acids and proteins) were separated by electrophoresis and detected with LIF.

McClain et al. [12] also developed a microfluidic device that integrated cell handling, lysis and electrophoresis, as shown in Fig. 2b. The device was evaluated with T-cells loaded with fluorogenic dyes which were separated and detected by LIF. Cell transport and lysis were accomplished using electric fields. In order to reduce Joule heating, lysis was effected by superimposing AC fields on the DC fields used for separations. This technique enabled separation to be maintained throughout the process; lysis was completed within 33 ms and a throughput of 7 – 12 cells/min was achieved with a separation efficiency ranging from 2300 to 4000 theoretical plates.

As an alternative to using AC fields, to prevent excessive Joule heating, Wang et al. [21] designed a microfluidic device with channels having variable cross-sections which modulated the local electric field strengths. Chinese hamster ovary cells labeled with calcein AM were used to

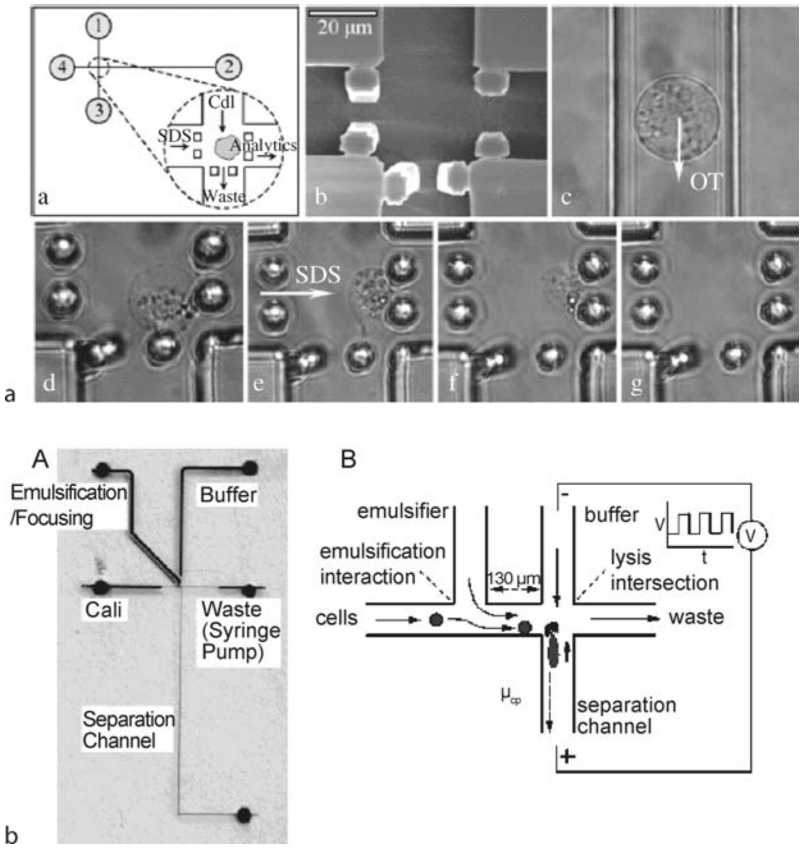

Single Cell Analysis in Microfluidic Devices, Figure 2 (**a**) PDMS single-cell microfluidic device with T-junction and integrated cell trap, formed from micron-sized posts. The cell is transported with optical tweezers (OT) to the intersection, followed by the delivery of the surfactant, SDS, to lyse the cell. (Image reproduced from [20].) (**b**) Design for high-throughput chemical cytometry; this method uses a combination of AC and DC electric fields for cell lysis and electrophoresis. (Image reproduced from [12])

test the device. The cells were driven to the T-junction by hydrodynamic flow generated by a syringe pump. Once at the junction, the cells were lysed and the contents were separated by electrophoresis and detected.

To increase throughput and eliminate sample cross-contamination, which is common when analyzing cells sequentially, Munce et al. [22] developed a microfluidic device with four parallel CE channels. Calcein-labeled acute myloid leukemia cells were selected and transported with optical tweezers to injector structures at the entrance of each channel, as shown in Fig. 3a. Once loaded, the cells were lysed by the combined action of an applied electric field and the reduction in channel cross-section (Fig. 3b). The injector design also enabled stepwise lysis of the cell, shown in Fig. 3c, where only the cyctoplasmic material (containing calcein AM in green) was injected into the capillary while the nucleus (stained blue with Hoechst 33342) remained in the injector structure. This selective lysis is especially useful to separate the cytoplasm from the nucleus and finally the membrane particularly if protein signalling is the focus of the application. The injector structures also prevented extracellular debris from entering the channels. Once loaded in the capillary, the analytes were separated and detected with LIF. The throughput was estimated to be 24 cells/h; however, this could be increased with additional separation channels.

Wu et al. [23] designed a PDMS microfluidic device for chemical cytometry, consisting of integrated valves which formed a reaction chamber and a picopipette for reagent delivery. The system, depicted in Fig. 4a, allows for individual cells to first be isolated in a closed chamber, and then be combined with an aliquot of lysis and fluoresecent derivatization reagents, delivered by the picopipette. After lysis and derivatization, the valves are opened and voltage is applied to separate the derivatized amino acids. Figure 4b shows an electropherogram collected from a single Jurkat T cell compared to one generated from a population of cells with off-column lysis and derivatization. With the pneumatic valves, 70-picoliter reaction chamber, and

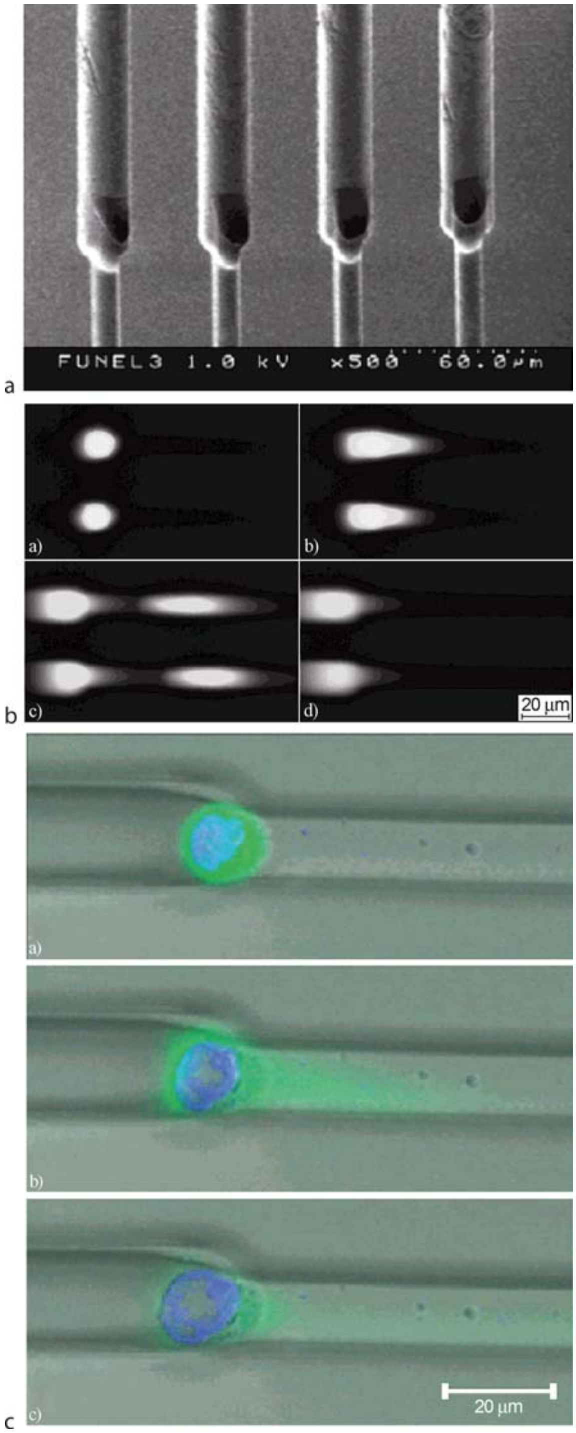

Single Cell Analysis in Microfluidic Devices, Figure 3 (**a**) Four parallel laser-etched injector structures in PMMA. (**b**) Sequence of fluorescent images of two calcein-labeled AML cells being lysed and injected into 2 separation channels. (**c**) Stepwise lysis of an AML cell. The cytoplasmic material (labeled in green) is loaded into the electrophoresis channel while the nucleus (labeled in blue) remains in the injector structure. (Images reproduced from [22])

picopipette, this device simultaneously addresses the problems of fluid control and reagent delivery without affecting sample dilution. This system could also be implemented in parallel to increase throughput.

As an alternative to LIF, Xia et al. [24] used amperometry to detect the contents of single wheat callus cells. In this work, cells were transported electrokinetically to a double T-junction, and docked, after which they were lysed by a DC electric field. Ascorbic acid and other analytes were separated by electrophoresis and detected by means of an amperometric detector.

DNA Analysis

A study of doxorubicin-induced apoptosis (programmed cell death) in individual cardiomyoctes was performed using a microfluidic device created by Horky and coworkers [25]. Apoptotic DNA fragments from individual cells were electrophoretically separated and detected by LIF. The device consisted of a simple cross channel design; cells were injected into the device and transported by pressure-driven flow by application of a vacuum. Cell lysis was achieved by activating an electric field across the T-junction, which was filled with a 2% solution of linear polyacrylamide.

Quake and coworkers [16] developed a PDMS microfluidic device (shown in Fig. 4c) for nucleic acid purification from a small number of bacterial or mammalian cells. This multilayer device contained fluidic channels and a system of membrane-actuated pneumatic valves and pumps, which enabled precise control of buffers, lysis agents and cell solution, and also allowed for parallel processing. Bacterial cells, dilution buffer and lysis buffer are first introduced into the chip and then transferred into the rotary mixer. Once mixed, the lysate is flushed over a DNA affinity column and drained. The DNA is recovered from the chip with an elution buffer for further analysis. We note that this is the only microfluidic chemical cytometry device to use a separation method other than solution-phase electrophoresis (i. e., solid phase extraction).

Future Directions for Research

This chapter has outlined the challenges inherent in chemical cytometry, i. e., the separation and detection of the contents of a single cell. Microfluidics is a promising technology in the goal of developing high-throughput chemical cytometry techniques, which require robust and repeatable means for cell transportation, lysis and analysis applied in parallel (or very rapidly in series). The current methods have established proof-of-principle; however, much work remains to be done, especially related to scaling up for parallel analysis.

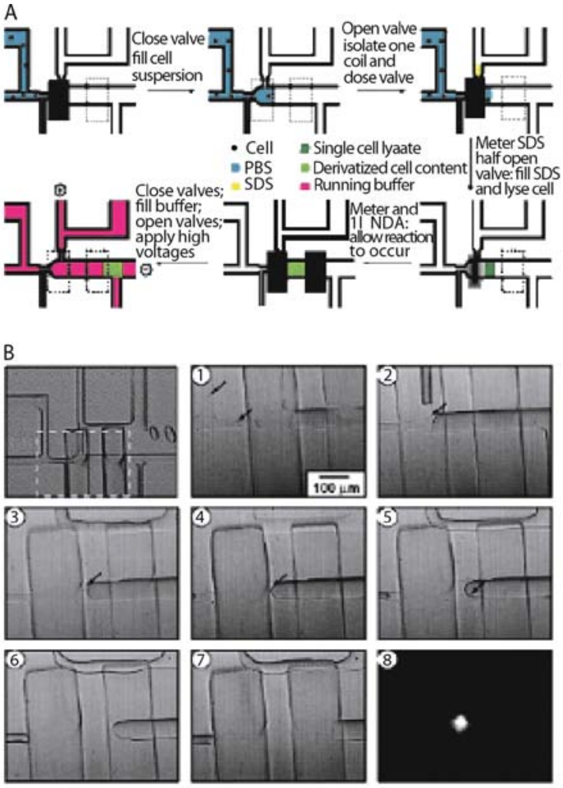
A
Close valve fill cell suspension
Open valve isolate one coil and dose valve
Cell
PBS
SDS
Single cell lyaate
Derivatized cell content
Running buffer
Meter SDS half open valve: fill SDS and lyse cell
Close valves; fill buffer; open valves; apply high voltages
Meter and 1:1 NDA: allow reaction to occur
B
100 µm

a

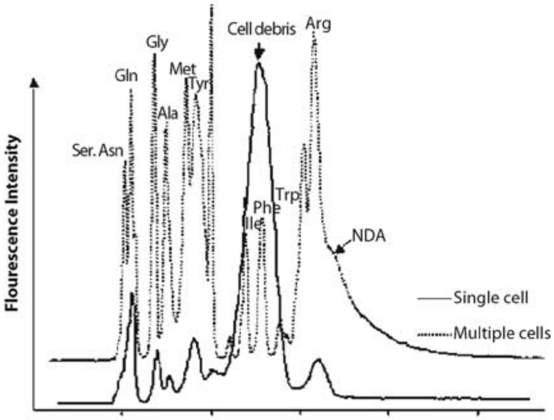
Flourescence Intensity
Ser. Asn
Gln
Gly
Ala
Met
Tyr
Cell debris
Arg
Phe
Ile
Trp
NDA
Single cell
Multiple cells

b

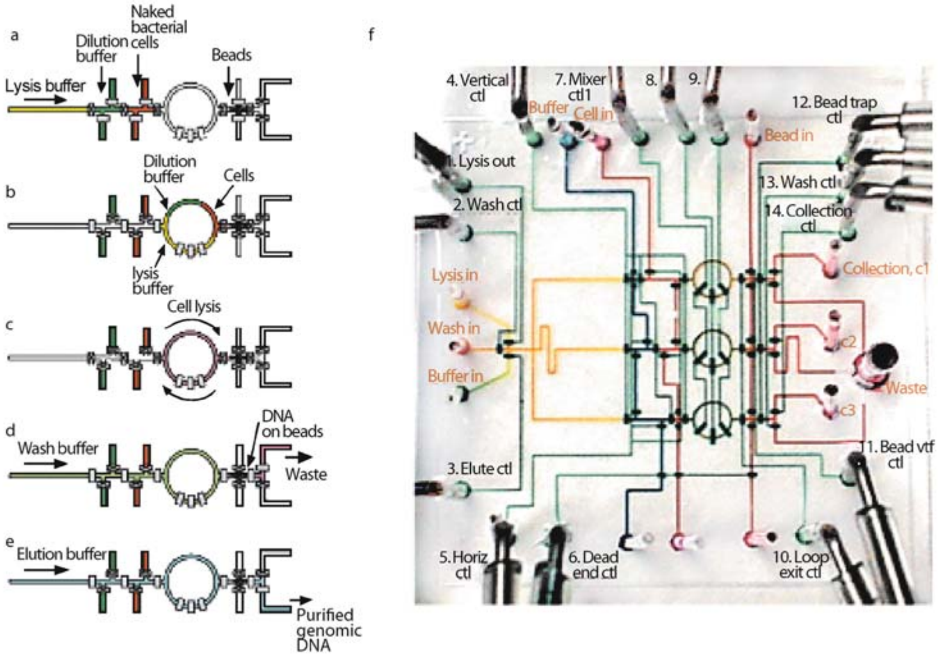
a
Naked bacterial cells
Dilution buffer
Beads
Lysis buffer
b
Dilution buffer
Cells
lysis buffer
c
Cell lysis
d
DNA on beads
Wash buffer
Waste
e
Elution buffer
Purified genomic DNA
f
4. Vertical ctl
7. Mixer ctl1
8.
9.
12. Bead trap ctl
Buffer
Cell in
Bead in
1. Lysis out
2. Wash ctl
13. Wash ctl
14. Collection ctl
Lysis in
Collection, c1
Wash in
c2
Buffer in
Waste
c3
11. Bead vtf ctl
3. Elute ctl
5. Horiz ctl
6. Dead end ctl
10. Loop exit ctl

c

Single Cell Analysis in Microfluidic Devices, Figure 4 (**a**) 70-picoliter reaction chamber chemical for cytometry comprising a 3-state valve, a 2-state valve and a picopipette. The sequence illustrates the isolation and lysis of a single cell, as well as fluorescent derivatization of amino acids in the lysate. (**b**) Electropherogram collected from a single Jurkat T cell (solid line) generated in the microfludidic reaction chamber compared to one generated from a population of cells with off-column derivatization (doted line). (Images in (a) and (b) reproduced from [23].) (**c**) Multilayered PDMS microfluidic device with integrated pneumatic valves and pumps. The sequence illustrates the steps for cell isolation, lysis in a rotary mixer, and DNA purification and harvesting. (Image reproduced from [16]) ◄

Cross References

- ► Flow Cytometer Lab-on-Chip Devices
- ► Detection Using Confocal Microscopy
- ► Microfabrication Techniques
- ► Materials Used in Microfluidic Devices
- ► Methods for Surface Modifications
- ► Fabrication of 3D Microfluidic Structures
- ► On-Chip Waveguide
- ► Pneumatic Valves
- ► Thermomechanical Valves
- ► Thermopneumatic Vavles
- ► Packaging (Including Wire Bonding)
- ► Techniques for Manipulating Cells
- ► Microfluidic Sample Manipulation
- ► Cell Sorting
- ► Dielectrophoretic Motions of Particles and Cells
- ► Electrokinetic Motion of Cells and Non-Conductive Particles
- ► AC Dielectrophoresis Lab-on-a-Chip Devices
- ► Optical Tweezers for Manipulating Cells and Particles
- ► On-Chip Cell Lysis
- ► Cell Assays in Microfluidics
- ► Patch-Clamp Measurements On-Chip
- ► Mass Spectrometry On Chip Devices
- ► Fluorescence Measurements
- ► Amperometric Techniques
- ► Chemical Cytometry

References

1. Ferrell JE, Machleder EM (1998) The Biochemical Basis of an All-or-None Cell Fate Switch in Xenopus Oocytes. Science 280:895–898
2. Dovichi NJ, Hu S (2003) Chemical cytometry. Curr Opin Chem Bio 7:603–608
3. El-Ali J, Sorger PK, Jensen KF (2006) Cells on chips. Nature 442:403–411
4. Yi CQ, Li CW, Ji SL, Yang MS (2006) Microfluidics technology for manipulation and analysis of biological cells. Anal Chim Acta 560:1–23
5. Grover SC, Skirtach AG, Gauthier RC, Grover CP (2001) Automated single-cell sorting system based on optical trapping. J Biomed Opt 6:14–22
6. Ferrari E, Emiliani V, Cojoc D, Garbin V, Zahid M, Durieux C, Coppey-Moisan M, Di Fabrizio E (2005) Biological samples micro-manipulation by means of optical tweezers. Microelectron Eng 78–79:575–581
7. Odde DJ, Renn MJ (2000) Laser-guided direct writing of living cells. Biotechnol Bioeng 67:312–318
8. Gaugiran S, Getin S, Fedeli JM, Colas G, Fuchs A, Chatelain F, Derouard J (2005) Optical manipulation of microparticles and cells on silicon nitride waveguides. Opt Express 13:6956–6963
9. Gao J, Yin XF, Fang ZL (2004) Integration of single cell injection, cell lysis, separation and detection of intracellular constituents on a microfluidic chip. Lab Chip 4:47–52
10. Lee SW, Tai YC (1999) A micro cell lysis device. Sens Actuatores A 73:74–79
11. Lu H, Schmidt MA, Jensen KF (2005) A microfluidic electroporation device for cell lysis. Lab Chip 5:23–29
12. McClain MA, Culbertson CT, Jacobson SC, Allbritton NL, Sims CE, Ramsey JM (2003) Microfluidic devices for the high-throughput chemical analysis of cells. Anal Chem 75:5646–5655
13. Di Carlo D, Jeong KH, Lee LP (2003) Reagentless mechanical cell lysis by nanoscale barbs in microchannels for sample preparation. Lab Chip 3:287–291
14. Irimia D, Tompkins RG, Toner M (2004) Single-cell chemical lysis in picoliter-scale closed volumes using a microfabricated device. Anal Chem 76:6137–6143
15. Wheeler AR, Throndset W, Whelan RJ, Leach AM, Zare RN, Liau YH, Farrell K, Manger I, Daridon A (2003) Microfluidic Device for Single Cell Analysis. Anal Chem 75:3581–3586
16. Hong JW, Studer V, Hang G, Anderson WF, Quake SR (2004) A nanoliter-scale nucleic acid processor with parallel architecture. Nat Biotechno 22:435–439
17. Berridge MJ (1993) Inositol Trisphosphate and Calcium Signaling. Nature 361:315–325
18. Swanek FD, Ferris SS, Ewing AG (1997) Capillary Electrophoresis for the Analysis of Single Cells. In: Electrochemical, Mass Spectrometric and Radiochemical Detection Handbook of Capillary Electrophoresis, pp 495–521
19. Johnson ME, Landers JP (2004) Fundamentals and practice for ultrasensitive laser-induced fluorescence detection in microanalytical systems. Electrophoresis 25:3513–3527
20. Hellmich W, Pelargus C, Leffhalm K, Ros A, Anselmetti D (2005) Single cell manipulation, analytics, and label-free protein detection in microfluidic devices for systems nanobiology. Electrophoresis 26:3689–3696
21. Wang HY, Lu C (2006) Electroporation of mammalian cells in a microfluidic channel with geometric variation. Anal Chem 78:5158–5164
22. Munce NR, Li JZ, Herman PR, Lilge L (2004) Microfabricated system for parallel single-cell capillary electrophoresis. Anal Chem 76:4983–4989
23. Wu HK, Wheeler A, Zare RN (2004) Chemical cytometry on a picoliter-scale integrated microfluidic chip. P Natl Acad Sci USA 101:12809–12813
24. Xia FQ, Jin WR, Yin XF, Fang ZL (2005) Single-cell analysis by electrochemical detection with a microfluidic device. J Chromatogr A 1063:227–233
25. Kleparnik K, Horky M (2003) Detection of DNA fragmentation in a single apoptotic cardiomyocyte by electrophoresis on a microfluidic device. Electrophoresis 24:3778–3783

S

Single Cell Impedance Spectroscopy

► Impedance Measurements of Cells

Single Crystal

Definition

Description of the ordered nature of the atoms in a material. In a single-crystal material, there is only one atomic structure of the crystal.

Cross References

► Fabrication of Self-Assembled Catalytic Nanostructures

Single-Phase Convective Flows in Microchannels

► Convective Heat Transfer in Microchannels

Single-Phase Forced Convection in Microchannels

► Convective Heat Transfer in Microchannels

Single-Phase Gaseous Flow

YILDIZ BAYAZITOGLU
Rice University, Houston, TX, USA
bayaz@rice.edu

Synonyms

Gaseous flow; Slip boundary; Transition flow; Molecular flow

Definition

When gases are at low pressures, or are flowing in small geometries, the interaction of the gas molecules with the wall becomes as frequent as intermolecular collisions. This type of flow is known as rarefied gas flow. Typically, macrochannel boundary conditions, gas velocity and temperature that are applied to fluid flow and heat transfer equations are equivalent to the corresponding wall values. In contrast, these conditions do not hold for rarefied gas flow in microchannels. The Knudsen number (Kn) is used to represent the rarefaction effects. It is the ratio of the molecular mean free path to the characteristic dimension of the flow (i. e., the channel hydraulic diameter). The mean free path is defined as the average distance traveled by a molecule before colliding with another molecule. As Kn takes higher values, due to a higher molecular mean free path by reduced pressure or a smaller flow dimension, rarefaction effects become more significant. Kn is an important parameter to explain the surface effects in gaseous flows in microchannels in determining the pressure drop and the heat transfer coefficient. The continuum flow assumption will only be valid when $Kn < 10^{-3}$. As Kn increases, the flow enters the slip flow regime ($10^{-3} < Kn < 10^{-1}$), transition flow regime ($10^{-1} < Kn < 10$) and eventually the free-molecular flow regime ($Kn > 10$). These four regimes are illustrated in Fig. 1.

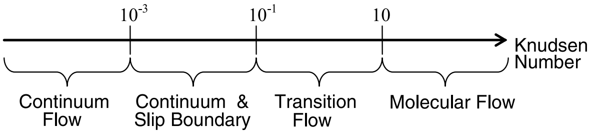

Single-Phase Gaseous Flow, Figure 1 Flow regimes identified by the Knudsen number

Overview

Gaseous flow in micro- and minichannels has been extensively investigated, and it is very important in microdevice development and design. Although several contradictory results have been published related to pressure drop and heat transfer coefficients, a few experiments were also performed to verify the theoretical results and some arguments are also made to explain those discrepancies.

Continuum Regime

The velocity, density, pressure and other properties of a fluid are all defined at every point in space and time and the solutions of fluid flow in the continuum regime are obtained by using the Navier–Stokes equations. For incompressible flow with constant properties we have the following.

Conservation of mass:

$$\frac{\partial \rho}{\partial t} + \nabla \cdot (\rho \boldsymbol{v}) = 0 \tag{1}$$

Conservation of linear momentum:

$$\rho \left(\frac{\partial \boldsymbol{v}}{\partial t} + \boldsymbol{v} \cdot \nabla \boldsymbol{v} \right) = \rho g - \nabla p + \mu \nabla^2 v \tag{2}$$

Conservation of energy:

$$\rho c\left(\frac{\partial T}{\partial t}+\boldsymbol{v}\cdot\nabla T\right)=k\nabla^2 T+\Phi \tag{3}$$

where $\boldsymbol{v}, t, p, T, \mu, k, c, g$ and ρ are velocity, time, pressure, temperature, viscosity, thermal conductivity, specific heat, gravity and density respectively.

The fluid velocity and temperature in this regime are equivalent to the corresponding wall conditions. The boundary layer approximations for a two-dimensional fluid flow in Cartesian coordinates (x, y) are given as

$$u \gg v\,, \qquad \frac{\partial u}{\partial y} \gg \frac{\partial u}{\partial x}, \frac{\partial v}{\partial x}, \frac{\partial v}{\partial y} \tag{4a}$$

$$\frac{\partial T}{\partial y} \gg \frac{\partial T}{\partial x} \tag{4b}$$

The Nusselt number (Nu) for laminar, fully developed flow is constant and independent of the Reynolds number (Re), the Prandtl number (Pr) and the axial location of the channel.

Slip Flow Regime

The current standing on the study of gaseous slip flow in microchannels stipulates that, although the continuum assumption is no longer valid within the slip region, Navier–Stokes equations are still applicable with some boundary modifications. The continuum model will apply at the core of the flow and a modified molecular/continuum boundary condition at the boundaries. That is, the Navier–Stokes equations are applicable except in the layer next to the surface. The commonly used slip boundary conditions are called Maxwellian boundary conditions. Since they are first order in accuracy, other extended boundary conditions are proposed in [1]. In the Knudsen layer, the layer one mean free path away from the boundary, the Maxwellian velocity slip boundary condition approximates the true gas velocity at the boundary by the velocity that the molecules would have if a linear velocity gradient existed, as shown in Fig. 2. In other words, the magnitude of the slip is calculated from the velocity gradient evaluated at $y = \lambda$.

The first-order approximation to the velocity slip within the Knudsen layer is given by

$$u_{\mathrm{s}} = \frac{2-F_{\mathrm{m}}}{F_{\mathrm{m}}}\lambda\frac{\mathrm{d}u}{\mathrm{d}y} \tag{5}$$

Another characteristic of rarefied gas flow is that there is a finite difference between the fluid temperature at the wall and the wall temperature. The temperature jump is first proposed to be

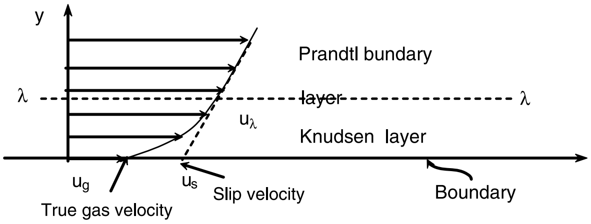

Single-Phase Gaseous Flow, Figure 2 Schematic of the first-order slip velocity approximation

$$T_{\mathrm{s}} - T_{\mathrm{w}} = c_{\mathrm{jump}}\frac{\partial T}{\partial y} \tag{6}$$

The thermal accommodation coefficient is defined as

$$F_{\mathrm{T}} = \frac{Q_{\mathrm{i}}-Q_{\mathrm{r}}}{Q_{\mathrm{i}}-Q_{\mathrm{w}}}$$

where Q_{i} is the energy of the impinging stream, Q_{r} is the energy carried by the reflected molecules and Q_{w} is the energy of the molecules leaving the surface at the wall temperature. F_{T} can be defined as the fraction of molecules reflected by the wall that accommodated their energy to the wall temperature. Let us assume that the temperature of the approaching molecules is T_{s}. The energy difference of these molecules can be written as the summation of the kinetic energy, internal energy and contribution of the incoming molecules to the conduction minus the energy of the outgoing molecules at the wall temperature as

$$Q_{\mathrm{i}} - Q_{\mathrm{w}} = \frac{c_{\mathrm{v}}\left(T_{\mathrm{s}}-T_{\mathrm{w}}\right)(\gamma+1)P}{2\sqrt{2\pi RT}} + \frac{1}{2}k\frac{\partial T}{\partial y} \tag{7}$$

where $R = c_{\mathrm{p}} - c_{\mathrm{v}}$ and $\gamma = c_{\mathrm{p}}/c_{\mathrm{v}}$.

The net energy carried to the surface, $Q_{\mathrm{i}} - Q_{\mathrm{r}}$, is equal to the heat flux at the wall

$$Q_{\mathrm{i}} - Q_{\mathrm{r}} = k\frac{\partial T}{\partial y}\,. \tag{8}$$

Therefore the temperature jump in Eq. (7) is derived to be [2]

$$T_{\mathrm{s}} - T_{\mathrm{w}} = \frac{2-F_T}{F_T}\,\frac{2\gamma}{\gamma+1}\,\frac{\lambda}{\mathrm{Pr}}\,\frac{\partial T}{\partial y} \tag{9}$$

Equation (9) gives the first-order approximation to the temperature jump, and it is assumed that the temperature gradient at the wall is the same as that at $y = \lambda$. The same

S

approach is applied to obtain the second-order velocity slip equation [1]. This results in

$$\theta_s - \theta_w = \frac{2 - F_T}{F_T} \frac{2\gamma}{\gamma + 1} \frac{\mathrm{Kn}}{\mathrm{Pr}\,(1 - a\mathrm{Kn})} \left(\frac{\partial \theta}{\partial \eta} \right)_0 \tag{10}$$

where $\theta = T/T_{\text{reference}}$ and a is a variable.

The gaseous flow heat transfer problem in the slip flow region is solved both analytically and numerically. Larrode et al. [2] solved the problem for micro-circular tubes with constant wall temperatures. Beskok et al. [3] presented computational results in the slip flow region for Knudsen number less than 0.3. Yu and Ameel [4] studied laminar, fully developed slip flow forced convection heat transfer in rectangular microchannels by applying a modified generalized integral transform. The compressibility effects in the slip flow were included in [5, 6] and the results agreed with previous experimental results. It was found that compressibility is significant for high Re and rarefaction is significant for low Re. Exact, analytical solutions for flows in circular, rectangular and parallel plate microchannels were given by Tunc and Bayazitoglu [7, 8]. The neglected frictional heating effects in low-velocity gaseous flows of macrochannel flows are found to be significant for microchannel flows. Bayazitoglu and Kakac [9] reviewed the flow regimes, and Bayazitoglu et al. [10] reviewed mathematical solutions to gaseous slip flows.

Slip Flow Nusselt Number for Different Geometries

The steady-state heat convection between two parallel plates and in circular, rectangular and annular channels with uniform heat flux and uniform temperature boundary conditions including the viscous heat generation for thermally developing and fully developed conditions are solved. Both constant wall temperature and constant heat flux boundary conditions are considered. The velocity and the temperature distributions are derived from the momentum and energy equations by using the proper slip flow boundary conditions. To have a better understanding of the viscous heating effects, the following parameter to combine the effects of the Brinkman number (Br) and the Graetz number (Gz) is used:

$$\frac{\mathrm{Br}}{\mathrm{Gz}} = \frac{\nu u_m}{c_p \left(T_0 - T_s\right)} \frac{L}{D^2} \tag{11}$$

Using the integral transform method, Yu and Ameel [4] solved for Nu for flow in a rectangular microchannel subject to the constant temperature and slip flow boundary conditions. They did not include viscous dissipation in the work, but they included variable thermal accommodation coefficients. Similar to [7], they concluded that Kn, Pr, aspect ratio, velocity slip and temperature jump can all cause Nu to deviate from the conventional value. Overall it is found that the heat transfer coefficient is strongly influenced by variation of Kn.

Transition and Free-Molecular Flow Regime

As the flow enters the transition flow regime and continues into the free-molecular flow regime, Kn becomes significant enough that the molecular approach has to be utilized. Thus, the Boltzmann equation

$$\frac{\partial f}{\partial t} + v_i \frac{\partial f}{\partial x_i} + F_i \frac{\partial f}{\partial \xi_i} = Q\,(f,f) \tag{12}$$

should be considered to fulfill the atomic level of studies of the gaseous flows in the transition regime. The Boltzmann equation denotes v_i as the velocity, F_i as the forcing function and f as the particle velocity distribution function in space, while $Q(f,f)$ describes the intermolecular collisions. The density can be obtained by integrating f over time and space. The integration of the product of the density and the velocity will provide the mass velocity. The Maxwellian distribution is the simplest distribution as it is the zeroth-order approximation of the Boltzmann equation.

The Boltzmann equation is solved by the particulate methods, molecular dynamics (MD), the direct simulation Monte Carlo (DSMC) method or by deriving higher order fluid dynamics approximations beyond Navier–Stokes, which are the Burnett equations. The Burnett equation

$$f = f^{(0)} + \mathrm{Kn} f^{(1)} + \mathrm{Kn} f^{(2)} + \cdots \tag{13}$$

is the first three terms of the Champan–Enskog equation. The simplified Boltzmann equation can be solved using the lattice Boltzmann method (LBM) for the distributed function on a regular lattice. Being a deterministic approach, the MD method simulation may require a very large domain for gaseous flows while the DSMC is a stochastic approach and is simulated more efficiently for gaseous flows. When $\mathrm{Kn} = 0.06 - 1.1$, the flow is called transition flow and the continuum assumption becomes invalid; the DSMC method also requires a large number of particles, which makes it expensive in terms of computational time and memory requirements.

Another mechanism that may affect the velocity profile in a microchannel is thermal creep. It is a molecular transport phenomenon that occurs when two isopressure containers at different temperatures are connected by a channel whose diameter is close to the gaseous mean free path. Under this condition, gaseous molecules start to flow from the cooler

container to the hotter container. Thus, a positive temperature gradient along the flow direction tends to increase the mass flow rate while a negative temperature gradient tends to reduce the mass flow rate. The inclusion of the thermal creep effect in the slip boundary condition is given in by the following formula:

$$u_s = \frac{2 - F_m}{F_m} \mathrm{Kn} \frac{\partial u}{\partial \eta} + \frac{3}{2\pi} (\gamma - 1)\, \mathrm{Kn}^2 \mathrm{Re} \frac{\partial \theta}{\partial \zeta} \tag{14}$$

The large surface-to-volume ratio in microchannels tends to enhance several factors that are neglected in macroscale flow and heat transfer, such as surface friction, compressibility, surface roughness, viscosity, channel surface geometry, surface electrostatic charges, axial wall heat conduction and measurement errors. Certainly more experimental measurements would be necessary to resolve the various discrepancies.

Cross References

► Gas Flow in Nanochannels
► Heat Transfer in Microchannel Flows
► Lattice Boltzmann Method (LBM)
► Microchannel
► Molecular Dynamics

References

1. Bayazitoglu Y, Tunc G (2002) Extended Slip Boundary Conditions for Microscale Heat Transfer. AIAA J Thermophys Heat Transf 16(3):472–475
2. Larrode FE, Housiadas C, Drossinos Y (2000) Slip Flow Heat Transfer in Circular Tubes, Int J Heat Mass Transf 43:2669–2680
3. Beskok A, Karniadakis GE, Trimmer W, (1996) Rarefaction and compressibility effects in gas microflows. J Fluid Eng 118:448–456
4. Yu SP, Ameel TA (2001) Slip-flow heat transfer in rectangular microchannels. Int J Heat Mass Transf 44(22):4225–4235
5. Asako Y, Pi T, Turner SE, Faghri M (2003) Effect of compressibility on gaseous flows in micro-channels. Int J Heat Mass Transf 46:3041–3050
6. Chen CS (2004) Numerical method for predicting three-dimensional steady compressible flow in long microchannels. J Micromech Microeng 14:1091–1100
7. Tunc G, Bayazitoglu Y (2001) Heat Transfer in Microtubes with Viscous Dissipation. Int J Heat Mass Transf 44:2395–2403
8. Tunc G, Bayazitoglu Y (2002) Heat Transfer in Rectangular Microchannels. Int J Heat Mass Transf 45:765–773
9. Bayazitoglu Y, Kakac S (2005) Flow regimes in microchannel single-phase gaseous fluid flow. In: Kakac S, Vasiliev L, Bayazitoglu Y, Yener Y (eds) Microscale Heat Transfer – Fundamentals and Applications. Kluwer Academic, Amsterdam
10. Bayazitoglu Y, Tunc G, Wilson K, Tjahjono I (2005) Convective Heat Transfer for Single-Phase Gases in Microchannel Slip Flow: Analytical Solutions. In: Kakac S, Vasiliev L, Bayazitoglu Y, Yener Y (eds) Microscale Heat Transfer – Fundamentals and Applications. Kluwer Academic, Amsterdam

Slip Boundary

► Single-Phase Gaseous Flow

Slip Flow Regime

► Gas Flow in Nanochannels

Slip Velocity

Definition

Non-zero velocity of a fluid at a solid-fluid interface in situations when the no-slip boundary condition is not necessarily applicable. Generally not well characterized or understood for microfluidic devices.

Cross References

► Surface-Directed Capillary Flow Systems

Slope Method

► Electrical Current Monitoring Methods

Slug Flow

► Taylor Flow in Microchannels

S

Smart Skin

► Flexible Shear Stress Sensor

Smoluchowski Equation

Definition

The Smoluchowski equation is used to relate average flow (v_{av}) velocity to electric field strength (E_z) in electroosmotic flows. Under the conditions of a thin double layer or a large channel height (i. e a plug-like or constant velocity profile), it can be expressed as follows:

$$v_{av} = \frac{(\varepsilon_0 \varepsilon_r)\zeta}{\mu} E_z\,, \tag{1}$$

where ε_0 and ε_r are the electrical permittivity of a vacuum and the relative dielectric constant, respectively. Zeta potential is represented by ζ, and μ is the solution viscosity. The proportionality constant $(\varepsilon\zeta/\mu)$ is often referred to as the electroosmotic mobility.

Cross References

► Temperature Effects on the Zeta Potential

Smoothing Function

► Kernel Function

SNP on Chip – Micro- and Nanofluidics for Single Nucleotide Polymorphism Discrimination

David Erickson
Sibley School of Mechanical and Aerospace Engineering, Cornell University, Ithaca, NY, USA
de54@cornell.edu

Synonyms

Nucleic acid detection

Definition

Single Nucleotide Polymorphisms (SNPs) are single base pair differences in individuals where the less common variant occurs in only a small portion of the total population. Detection of these SNPs is proving to be a useful technique for the diagnosis of a variety of genetic diseases and disorders. In this article microfluidics based techniques for SNP discrimination are explored.

Overview

Single Nucleotide Polymorphisms

Single Nucleotide Polymorphisms (SNPs) are single base pair differences in DNA amongst individuals where the less common variant occurs in at least 1% of the total population [1]. The decoding of the human genome has given us access to more than 3 million SNPs (roughly 1 every 100 – 300 bases) and opened up exciting new capabilities for associating individual SNPs, haplotypes and linkage disequilibrium with disease states and pharmacological responses. The first of these associations represents the simplest of cases, where the SNP alleles are the actual sequence variants that result in differences in gene function (by inducing sequence errors in the expressed protein or the exons it contains) or regulation (as a result of the SNP occurring within a promoter region). In general however the vast majority of SNPs fall into one of the latter two categories in that they do not contribute directly to disease states, but can serve as genetic markers that can be used to find functional SNPs as a result of associations between the two. In such cases many SNPs (in exons, introns and other non coding regions) may all be associated with a disease state or phenotype though only a single one may have a direct effect.

To make good use of SNPs for finding genes related to disease and studying their function, for genotyping them in many individuals, for finding their frequencies in pooled samples and for discerning haplotypes, better and cheaper technological methods are needed for discovering SNPs. At present the technology is not yet cheap enough for studies that would genotype thousands of individuals for hundreds of thousands of SNPs across the genome in order to see which variants are most closely associated with a disease phenotype [2]. The purpose of this article will be to introduce some of the ways micro- and nanofluidic technology is making progress towards addressing this issue. The first *Basic Methodology* section will introduce some of the existing chip based techniques for interrogating SNPs with a focus on surface phase hybridization techniques as being the most commercially viable. The *Key Research Directions* section will then describe how these techniques are being implements in microfluidic formats. In the final section a discussion regarding how these technologies can or should be extended to handle future analytical needs will be provided.

Basic Methodology

Techniques for SNP Screening

All allele-specific SNP discrimination techniques suitable for high throughput genetic analysis can be categorized as either being either primer extension, oligonucleotide ligation, invasive cleavage or hybridization based [3]. There are numerous variants on the primer extension technique however all are based on the ability of DNA polymerase to incorporate specific deoxyribonucleotides that are complementary to the sequence of the template DNA [4]. An entire class of techniques based on electrophoretic separation have also been developed and include: heteroduplex analysis (HA), single-strand conformation polymorphism (SSCP), denaturing gradient gel electrophoresis (DGGE), temperature gradient gel electrophoresis (TGGE), allele-specific PCR amplification and ligase chain reaction/ligase detection reaction (LCR/LDR).

Next generation SNP discrimination techniques should…

1. Have high throughput capabilities, enabling multiplexing of both interrogated SNPs and (less importantly) patient samples on the same device.
2. Minimize the total amount of time and handling required to perform a multiplexed reaction.
3. Enable either disposability or reusability functionality.
4. Be sufficiently sensitive to so as to work with raw, unamplified samples.

SNP on Chip – Micro- and Nanofluidics for Single Nucleotide Polymorphism Discrimination, Figure 1 Requirements for next generation Single Nucleotide Polymorphism Screening Technologies. A technique which meets the above requirements is required to perform the large scale population screening studies

Of all these, the technique that has shown the most commercial promise has been surface phase DNA microarray technologies, involving large-scale DNA sequence detection based on hybridization between complementary DNA sequences on a solid support. In recent years a number of DNA microarray and DNA chip type devices have been developed and commercialized (examples include LabCard by ACLARA Bio Sciences, GeneChip by Affymetrix, NanoChip by Nanogen). Such devices enable parallel DNA or RNA analysis to be carried out in a format that typically includes some functional microfluidic technology which serves to increase the rate at which targets are delivered to the region of interest (either by increasing the probability of target-surface collisions through physical confinement near the probesite or direct electro-active attraction). Though broadly useful to study a number of different target: probe binding systems, such chips are commonly used gene expression analysis or Single Nucleotide Polymorphism (SNP) discrimination applications.

Such high throughput DNA microarray technologies can simplify SNP analysis, but most methods require several hours for hybridization (due to diffusion-limited reaction kinetics) and complicated washing steps demanding strict temperature and buffer salt-content control. In addition, microarray hybridization and washing manipulation is conducted on centimeter-scale glass substrates thereby requiring that large quantities of DNA target sample be used. While numerous techniques have been identified for amplifying the signal, recently even to the point where SNP identification can be performed without the need for target amplification (via PCR), such processes require complex and, often, expensive labeling steps. The main difficulty with such devices however relates to the infrastructure/sensitivity tradeoff whereby either a large expensive tabletop optical apparatus (often con focal) is used to perform ultra-sensitive detection or a smaller footprint (though still relatively large) laser scanner is used to perform much more rapid analysis however the detection sensitivity is significantly lower. Such post-reaction scanning systems typically also lack the ability to monitor reaction kinetics. Based on these limitations the requirements outlined in Fig. 1 are proposed as requirements for next generation SNP discrimination techniques. These conditions will be revisited in the *Future Directions* section of this article.

Key Research Findings

As mentioned above, this section will review the state of the art in microfluidics based SNP discrimination with the goal of providing as broad of an overview of the existing technology as possible. As this review by necessity is somewhat cursory, it will be followed up with a more detailed description of a particular *electrokinetically based* on-chip SNP discrimination technique. The overall thrust of this section will be to determine to what degree exiting microfluidic technology can be used to address the next generation needs described in Fig. 1.

State of the Art in Integrated Microfluidic Devices for Single Nucleotide Polymorphism Discrimination

As described throughout this encyclopedia, microfluidic (Lab-on-a-Chip) technologies enable processing small liquid volumes in a rapid and controlled manner which has proven especially useful for analysis in life sciences. In the early 2000's several researcher groups began to investigate the integration of multiple microfluidic-based technologies into single microscale platforms with the goal of developing integrated technologies for performing nucleic acid analysis. Designs included paramagnetic or glass bead based devices, poly(methylmethacrylate) (PMMA) chips exploiting universal zip code arrays and polycarbonate (PC) chips designed to be credit card sized all of which proved successful in accelerating and automating detection of hybridization events (see Erickson and Li [5] for a more comprehensive review of these devices).

Commonly, a necessity for obtaining maximum discrimination between fully matched target: probe complexes

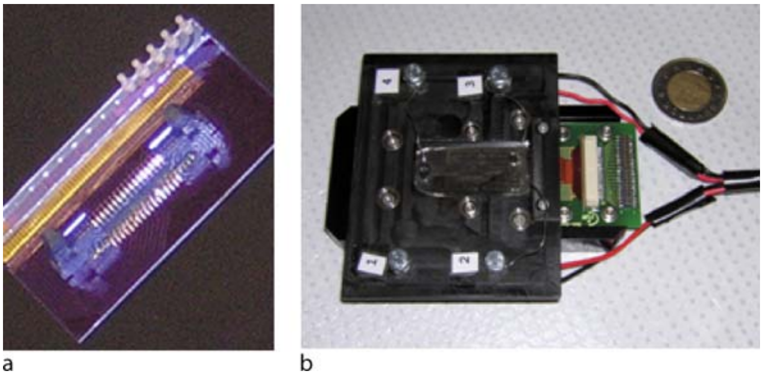

SNP on Chip – Micro- and Nanofluidics for Single Nucleotide Polymorphism Discrimination, Figure 2 Integrated Microfluidic Devices for (**a**) Parallel Polymerase Chain Reaction and (**b**) DNA hybridization (from [5])

and those containing a single-base base pair mismatch in a microfluidic chip is accurate control of the thermal conditions at the reaction site (whether it be in solution or at a surface). This has been largely accomplished through the integration of external heaters and thermal sensors (e. g. RTDs) on chip thereby adding an additional level of device complexity to that required for simple hybridization detection. Figure 2 illustrates recently developed devices for PCR (Fig. 2a) and surface phase DNA hybridization (Fig. 2b) which incorporate such functionality. PCR amplification was one of the first on-chip applications which required this type of control. In what were some of the first prominent examples Kopp, deMello and Manz [6] used a copper heating block for continuous-flow PCR in a microfluidic channel, while others such as Lao et al. [7] used high thermal conductivity silicon-based devices to achieve precise temperature control and rapid cooling in cycling based device. As for devices specifically devices for SNP detection, Buch et al. [8] reported a TGGE method based on the presence of a controllable temperature gradient on a polymer microfluidic chip. Platforms for high-throughput on-chip temperature gradient assays were also developed by Mao et al. [9] who demonstrated discrimination of fully complementary DNA strands from those containing a single T–G or C–A mismatch. This was also done using SYBR Green I intercalating dye and was reported for parallel and combinatorial measurements. As described above these devices required the incorporation of temperature control units, external heaters and thermal sensors on the microfluidic chips making it possible to control and rapidly change the temperature in order to produce spatial temperature gradients. In a recent work, Blazej et al. [10] developed what they terms a *microfabricated bioprocessor* which integrated all three steps involved in Sanger sequencing (namely thermal cycling, sample purification, and capillary electrophoresis). Using this device they demonstrated a 99% read accuracy over 556 bases. The device presented in that work represents one of the most integrated microfluidic systems developed at time of publication incorporating such elements as pneumatic microvalves and electrokinetic flow control elements and low dispersion turns in addition to thermal control and monitoring elements. Of note is that in the majority of these devices, hydrodynamic pumping techniques have been relied upon for performing the majority of the primary transport operations (the exception of course being those which rely on an electrophoresis step).

Electrokinetically Based Single Nucleotide Polymorphism Discrimination

On the length scales relevant to microfluidic devices, fluid flow and species transport can be accomplished using numerous different techniques, a few of which include: traditional pressure driven (pneumatic) flow, electrokinetic transport, buoancy, magnetohydrodynamics, capillarity, electrowetting and thermocapillarity (see Stone et al. [11] for a comprehensive overview). While electrokinetic means can greatly simplify species transport in microfluidic systems (see the section ▶electroosmotic flow), an effect commonly considered a significant drawback is the internal heat generation caused by current flow through the buffer solution. To maintain uniform and controlled system temperatures required for SNP discrimination, devices must have the ability to rapidly reject this heat to the surroundings. This problem is enhanced as a result of the recent shift towards low cost polymeric microfluidic systems (which will be discussed in greater detail in the final section) fabricated from such low thermal conductivity polymeric materials as poly(dimethsiloxane) (PDMS) and poly(methylmethacrylate) (PMMA) as opposed to tra-

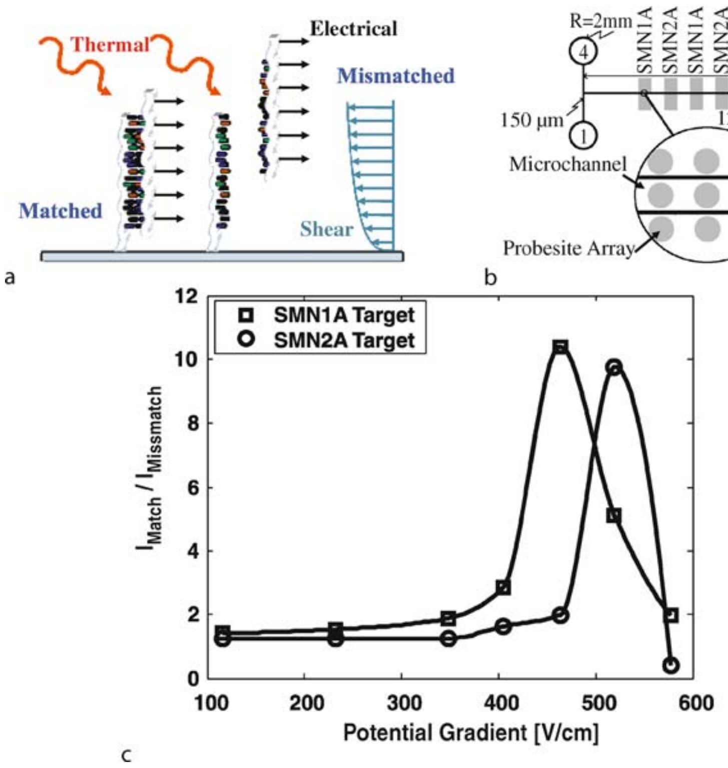

SNP on Chip – Micro- and Nanofluidics for Single Nucleotide Polymorphism Discrimination, Figure 3 Electrokinetically based SNP discrimination technique (**a**) Schematic describing electrokinetically based SNP discrimination technique applying an electrokinetic driving potential allows for precise manipulation of the thermal (through Joule heating), shear (through electroosmotic flow) and electrical (through electrophoresis) forces enabling the SNP to be discriminated. (**b**) H-type channel structure probesite layout for electrokinetically-based single nucleotide polymorphism discrimination. Four regions were robotically spotted onto the chip each with 8 individual probesites shown as SMN1 and SMN2 in the figure. For the purposes of this work the same probes were used for each spot in the individual regions for DNA hybridization chip. Input ports labeled as (1) sample port, (2) waste port, (3) buffer port and (4) auxiliary port. (**c**) Optimal discrimination for both SMN1A and SMN2A target. Data points show ratio of average intensity over the matched probesite to the average intensity of the mismatched probesite. Peak represents point where ratio of match intensity to mismatch intensity is greatest

ditional materials such as glass or silicon. The primary attractiveness of these materials is that they tend to involve simpler and significantly less expensive manufacturing techniques while still being amenable to surface modification and probe functionalization. The low thermal conductivities inherent in these materials (0.18 W/mK for PDMS which is an order of magnitude lower than that of glass) retards the rejection of internally generated heat during electroosmosis.

As mentioned above we have recently developed a novel on-chip electrokinetically-based microfluidic technique for SNP discrimination (see Erickson et al. [12] for details). The traditional advantages in terms of flow and sample handling afforded by electrokinetic transport described in the electroosmotic flow section of the article were extended to include thermal control through on-line manipulation of the Joule heating conditions. Precise control of the thermal, shear and electrical conditions at the probe sites were shown to enable discrimination of single-base-mismatch SNP sample targets on the chip by exploiting differences in denaturation energetics. This technique is expanded on in this article as it uniquely demonstrates how detailed understanding of fluid dynamics and thermal transport on the micro- and nanoscales can be exploited to control reaction specificity without the need for incorporating additional device functionality.

A schematic of the discrimination technique is shown in Fig. 3. As can be seen under standard conditions (or at low applied voltage) both the fully matched hybrid and that with a single base pair mismatch remain hybridized making discrimination difficult. Applying an electrokinetic driving potential allows for manipulation of the thermal (through Joule heating), shear (through electroosmotic flow) and electrical (through electrophoresis) forces above the microarray. To demonstrate the clinical utility of the technique, the detection of single base pair mutations in

the survival motor neuron gene, associated with the childhood disease Spinal Muscular Atrophy, was performed. Specifically the technique was applied to the detection of the common C→T mutation in the SMN1 gene resulting in what is known as SMN2 (and is found in all SMA patients). Such mutations lead to the loss of alphamotor neurons and subsequently the wasting of voluntary muscles.

To determine the optimal conditions for SNP discrimination, a series of incrementally increasing voltages were applied during the discrimination step, ranging from 100 V/cm to 600 V/cm within the hybridization array. Figure 3c compares the florescence intensity of the matched probe sites with that of the mismatched probe sites for both SMN1A and SMN2A targets. While the intensity ratios remained constant at lower voltages, a clear optimum in the discrimination existed for each different target:probe complex, at 460 V/cm and 525 V/cm, respectively. The difference in the optimal potential gradient between these two cases can be attributed to the slightly larger change in the thermodynamic stability associated with the SMN1A:SMN2 hybrid.

Future Directions for Research

In the preceding two sections an overview of microfluidics based SNP discrimination technology has been presented and thus when defining future directions for research it makes sense to compare these devices with each of the needs as expressed in Fig. 1. Continuing the theme from above here we focus more on technology development rather than clinical applications (for more details on the latter of these readers are referred to Motsinger et al. [13].

The first condition for next generation technology outlined in Fig. 1 relates to the development of highly multiplexed devices that enable simultaneous screening of multiple samples against multiple SNPs. While most of the surface phase binding based chips described above have generally targeted a small number of specific SNPs for demonstrative purposes, the extension to the kind of parallelity used in microarray formats is relatively easy. This is as a result of the numerous microfluidic technologies have been developed for dispersing samples over relatively large interrogation areas and the well developed detection/scoring infrastructure. Devices which rely on what have classically been more serial technologies (e. g. capillary electrophoresis) can have many analytical advantages over binding assays (such as enabling Sanger-type sequencing as discussed above) but are likely to face parallelity roadblocks in the future unless more cost-effective multiplexing technologies can be developed.

The second requirement for next generation technologies pertains to minimizing the time and handling required to perform a complete assay. Great advances have been made along these lines in the past 2 – 3 years largely thanks to the development of multi-layer soft lithography [14]. This technology has enabled the incorporation of pneumatic pumps, valves and other flow control elements on chip with relative ease. Given that, much of the effort in the field is therefore directed towards pushing the analytical technology upstream towards processing real patient samples or at least minimizing the number of manual processing steps. Almost inevitably however incorporation of additional on-chip functionality increases the final cost-per-chip and thus a trade off has to be made between how much manual processing the customer is willing to tolerate in order to keep total device costs down. In a research environment, where tests are likely to be conducted by a technician or graduate student with a relatively sophisticated level of expertise, this tolerance level is likely to be relatively high. For point of care applications the requirements are much more stringent.

The third condition relates to disposability or reusability of devices. In general disposability is so ingrained in the medical community that even if washing technologies were developed to the point that the potential for cross contamination could be effectively eliminated, it seems unlikely that reusable devices are likely to have a significant commercial impact. As alluded to above this suggests that development efforts should be focused on polymer devices, where device fabrication can be done using relatively simple and inexpensive casting or hot embossing techniques. This simplification of the fabrication steps tends to conflict with the requirements mentioned above for the basic thermal control (that facilitates SNP discrimination) let alone some of the desired additional upstream functionality. Since fabrication technology is reasonably well developed, research directed towards the development of techniques that can perform the desired analytical operations without the need for additional on-chip functionality (such as the electrokinetic SNP discrimination technique described above) is certainly warranted.

Most of the existing technologies discussed above require some sort of upstream PCR amplification step to bring the target concentration up to detectable levels. This step requires additional time, more functionality to be incorporated onto a chip and limits the degree of multiplexing. For the reasons discussed above therefore it would be desirable if this step could be eliminated in favor of sensor systems which have sufficient sensitivity and specificity to detect relatively minute quantities of a target in its unamplified state. Achieving this task in a multiplexed format requires research that takes an overall systems view

of device development looking at the coupling of sensitivity, specificity, transport and repeatability in the context of a whole device, as opposed to a component view as is commonly done at present.

Cross References

► DNA hybridization

References

1. Brooks L (2003) Single Nucleotide Polymorphisms. In: Kwok P (ed) SNPs: Why do we care? Humana Press, Totowa, NJ
2. Risch N, Merikangas K (1996) The future of genetic studies of complex human diseases. Science 273(5281):1516–1517
3. Kwok PY (2001) Methods for genotyping single nucleotide polymorphisms. Annu Rev Genomics Hum Genet 2:235–258
4. Sobrino B, Brion M, Carracedo A (2005) SNPs in forensic genetics: a review on SNP typing methodologies. Forensic Sci Int 154(2–3):181–194
5. Erickson D, Li DQ (2004) Integrated microfluidic devices. Anal Chim Acta 507(1):11–26
6. Kopp MU, de Mello AJ, Manz A (1998) Chemical amplification: Continuous-flow PCR on a chip. Science 280(5366):1046–1048
7. Lao AIK, Lee TMH, Hsing IM, Ip NY (2000) Precise temperature control of microfluidic chamber for gas and liquid phase reactions. Sens Actuators Phys 84(1–2):11–17
8. Buch JS, Kimball C, Rosenberger F, Highsmith WE, DeVoe DL, Lee CS (2004) DNA mutation detection in a polymer microfluidic network using temperature gradient gel electrophoresis. Anal Chem 76(4):874–881
9. Mao HB, Holden MA, You M, Cremer PS (2002) Reusable platforms for high-throughput on-chip temperature gradient assays. Anal Chem 74(19):5071–5075
10. Blazej RG, Kumaresan P, Mathies RA (2006) Microfabricated bioprocessor for integrated nanoliter-scale Sanger DNA sequencing. Proc Natl Acad Sci USA 103(19):7240–7245
11. Stone HA, Stroock AD, Ajdari A (2004) Engineering flows in small devices: Microfluidics toward a lab-on-a-chip. Annu Rev Fluid Mech 36:381–411
12. Erickson D, Liu XZ, Venditti R, Li DQ, Krull UJ (2005) Electrokinetically based approach for single-nucleotide polymorphism discrimination using a microfluidic device. Anal Chem 77(13):4000–4007
13. Motsinger AA, D Ritchie M, Dobrin SE (2006) Clinical applications of whole-genome association studies: future applications at the bedside. Expert Rev Mol Diagn 6(4):551–565
14. Unger MA, Chou HP, Thorsen T, Scherer A, Quake SR (2000) Monolithic microfabricated valves and pumps by multilayer soft lithography. Science 288(5463):113–116

Soda-Lime Glass

Synonyms

Sodium glass; Sodium silicate glass

Definition

Soda-lime glass is the kind of glass which is most widely used for various purposes. Soda-lime glass is a multicomponent mixture of SiO2 (72.8%), Na_2O (13.7%), CaO (8.8%), MgO (4.0%) and small amounts of Fe_2O_3 (0.12%) and Al_2O_3 (0.1%). Adding sodium carbonate lowers the melting point of the glass, thus lowering the energy required to heat it, but also making it soluble in water. Calcium carbonate or calcium oxide are added to counter this.

Cross References

► Bulk Micromachining

Sodium Glass

► Soda-Lime Glass

Sodium Silicate Glass

► Soda-Lime Glass

Sol–Gel Technique

DOMINIC S. PETERSON
Chemistry Division, Los Alamos National Laboratory, Los Alamos, NM, USA
DominicP@lanl.gov

Definition

The sol–gel synthetic technique is used to fabricate a porous structure composed of transition metal alkoxides. These structures most commonly utilize a siloxane (Si – O) to form the backbone structure. The synthesis of these sol–gels involves a hydrolysis of a silicone monomer followed by the condensation of the silica into a porous structure with a 3-dimensional networked structure. The physical structures of these sol–gels can be tailored to produce structures with a wide range of useful properties and the chemical surface chemistry can be modified to produce various surface interactions.

Overview

Sol–gel chemistry is a versatile tool that can be used to produce organic and inorganic hybrid materials that have properties that can be difficult to obtain from only inorganic or organic synthetic approaches. The synthetic approach involves the polycondensation of sol–gel active molecules to form a macromolecular network structure.

S

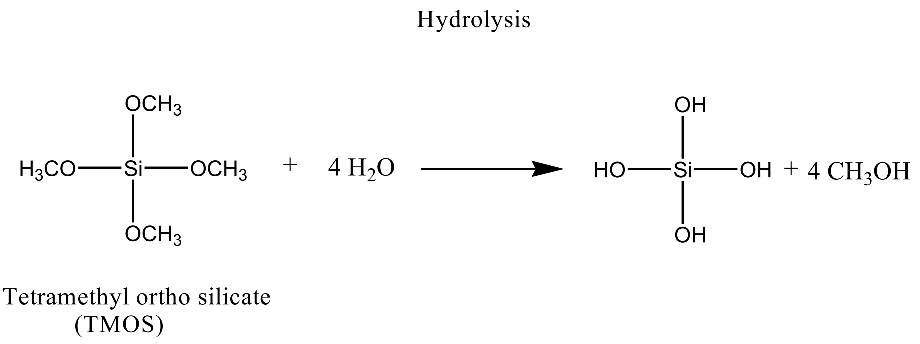

Sol–Gel Technique, Figure 1 Hydrolysis of tetramethyl ortho silicate to silanol

Basic Methodology

The synthesis of a sol–gel follows three primary steps [1]. First, the transition metal monomers are hydrolyzed to form a tetrahydroxy alkoxide. Because most sol–gels are formed from silica monomers the remainder of the discussion will focus on silica sol–gels. The hydrolysis step for silica sol–gels typically involves the use of either tetramethyl ortho silicate (TMOS) or tetraethyl ortho silicate (TEOS). The side product of the reaction is the corresponding alcohol (Fig. 1).

Once the tetrahydroxy silane has been formed, the silica will condense to form larger silica molecules and oligiomers (Fig. 2). This formation of the sol (or small colloidal silica particles) can be controlled to produce particles that have a particular size or size distribution.

Once the sol has been formed, they will cross-link to form a gel structure. This formation of a gel from the sol gives the materials the name sol–gel (Fig. 3). This crosslinking is achieved through a poly-condensation step. This step is the same as the condensation step, except that is results in a structure that is highly crosslinked. The size and amount of cross linking is dependant on the pH of the system and also the presence (and amount of) any other alkyl groups in the silica monomers ($-\mathrm{Si}-\mathrm{OR}$). It should also be noted that a wide range of chemical functionalities can be incorporated into the eventual sol–gel by the use of monomers that have useful alkyl groups incorporated into the structure. Alternatively, it is possible to modify the sol–gel after it has been formed by the condensation of a functional silane onto the sol–gel surface.

The relative rates of reaction between the hydrolysis, condensation, and polycondensation directly affect the type and quality of sol–gel produced. For instance, in base catalyzed sol–gel synthesis, the rate of the hydrolysis reaction is much slower than the polycondensation step, which tends to form a polymeric structure that is highly branched with relatively large particles. In contrast, in acid-catalyzed sol–gel synthesis the rate of the hydrolysis reaction is much faster than the polycondensation step, which favors the formation of linear polymers. This also tends to form much smaller particles that the gel is composed of, which results in materials with much higher porosities and higher surface areas than is formed with sol–gels formed in base-catalyzed reactions. Therefore acid-catalyzed synthesis tends to produce materials that have properties that are preferable for microfluidic applications.

Another process that is essential to the properties of the sol–gel produced is aging. When the gel that is formed is maintained in liquid its structure and properties continue to change after the gel has been formed. There are three processes that continue to change the properties of the sol–gel during aging. These include polycondensation, syneresis, and coarsening. Polycondensation reactions continue to occur within the gel as long as silanol groups are close enough to one another to react with one another. This continues to increase the connectivity within the gel network. Syneresis is the shrinkage of the gel and the expulsion of liquid from the pores of the gel. This shrinkage is attributed to the formation of new bridging siloxane bonds through condensation, which causes the gel to contract. The amount of shrinkage will increase with higher concentrations of silica in the gel and at higher temperatures. Coarsening is the decrease in surface area through dissolution and reprecipitation of dissolved material within the gel network. Due to the solution microenvironment, this precipitation of material is irreversible. The overall aging process is affected by several parameters including time, pH, temperature, and inclusion of organic solvents in the gel system. Through the control of the aging process it is possible to produce sol–gels with specific porous structure including the particular surface area that is needed for specific applications.

The preparation of sol–gels is a simple and straightforward process. Because the precursor sol has a low viscosity, it

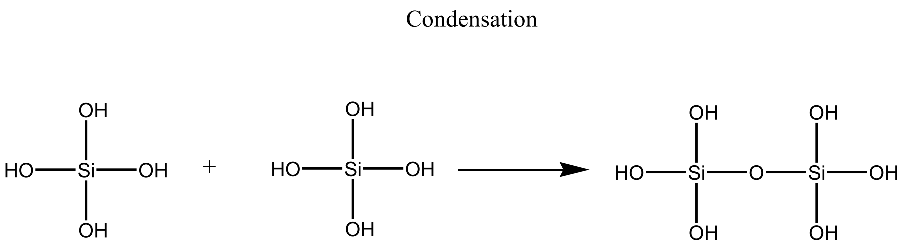

Sol–Gel Technique, Figure 2 Condensation of two silanols into a dimer

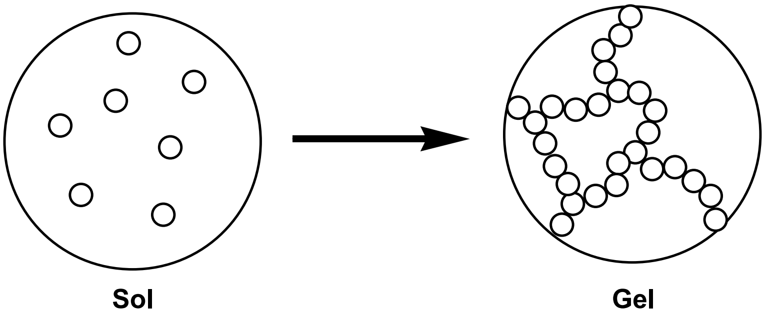

Sol–Gel Technique, Figure 3 Schematic of conversion of the sol into a gel structure

is easy to place it into any mold (including a microfluidic channel) and then form the gel. The primary limitation on the mold is that it needs to avoid adhesion of the sol solution, and it must not lead to the formation of bubbles during filling or during the gelation process.

Key Research Findings

In the past decade there has been intense interest in the use of sol–gels for use in microfluidic and nanofluidic applications. The most widespread use of sol–gels in microfluidic systems has been for capillary electrochromatography (CEC). CEC is a separation technique in which an electrical potential is applied across a capillary (containing a packing material) and the ionic functionalities generates bulk flow through the capillary through electroosmosis. The separation of non-ionic analytes can then be achieved as the analytes will partition between the mobile phase and the packing stationary phase. Sol–gels have provided an excellent method to make CEC columns, as they are simple to prepare within the capillary and they easily crosslink with the silica surfaces of the capillary, thus immobilizing them. Furthermore, in addition to using functionalized silica monomers in the preparation of a CEC sol–gel column, it is also possible to modify the silica surface with functionalized siloxanes. This enables the column to have higher thermal and solvent stability. The sol–gel process for preparing CEC columns enables the surface chemistry to be controlled and the selectivity of the column to separate different compounds can be adjusted for specific applications.

There are two types of preparation that are used to make CEC columns [2]. The first approach involves fully filling the capillary with the sol–gel solution. This method produces a sol–gel that fully fills the capillary, and thus produces the maximum amount of surface area for separation processes. However, fully filling the column with a sol–gel leads to a higher rate of bubble formation under the high voltage conditions utilized for CEC separations. The preparation of filled CEC sol–gel columns involves pre-treating the capillary, preparing the sol and filling the capillary with the sol-solution. After this, the gel step is performed and the sol–gel is formed in situ. After the sol–gel is formed there is typically a rinsing step that is used to remove un-reacted sol and to fill the column with a solution that is more suitable for electrophoretic operations. The other approach to sol–gel columns is the preparation of open tubular columns in which the sol–gel is coated on the interior surface of the capillary. The greatest difficulty in preparing open tubular is in preparing sol–gel coatings which are relatively thick, stable, reliable, and reproducible. There have been many examples of sol–gel CEC columns, and they have been shown to enable separations that have high efficiency and are quite reproducible.

The preparation of open tubular CEC sol–gel columns first involves the pre-treatment of the capillary and the prepa-

ration of the sol. The gel step for open tubular columns is allowed to proceed for only a short period of time (i. e. 20 min). This short time allows the gel to begin to form, typically silanol containing groups will began to react with other silanols in the immediate vicinity. This includes the sol reacting with the silanol groups at the surface of the silica capillary. When the non-reacted sol is rinsed out of the capillary all of the sol–gel that is not covalently attached to the wall of the capillary will be rinsed out. This will leave a layer of the sol–gel on the interior of the capillary.

While the use of sol–gels in capillaries has been extensive, their use in microchannels on chips has been more limited, due to the difficulty of fabricating sol–gels within the chip materials. The primary difficulty is in preparing the sol–gel in the region of the chip that it is needed, while excluding it from the areas where it is not needed. One method that has been introduced to fabricate the sol–gel in a particular area of a chip is to use a photoinitiation step to cause the gelation to form in a specific area [3]. This process first involves preparing a sol from a siloxane containing an organic monomer, such as a methacrylate. Once the sol had been prepared it was placed into a UV transparent capillary or chip. The organic functionalities on the sol was then reacted utilizing a UV active initiator under a UV lamp, which causes the sol to become crosslinked through the organic functional linker. Because this reaction is activated using light it is possible to cause the sol to polymerize only in a specific region of interest. The unreacted sol is then rinsed out of the channel. This approach allows the sol–gel to be placed into a very specific portion of the chip or capillary with no residual sol–gel remaining in other portions of the channel. The primary disadvantage to this approach is that it requires that the sol–gel that is fabricated be imparted with very specific organic functionalities in order to enable the photopolymerization step to proceed with high efficiency.

Another approach that has been used to introduce a sol–gel functionality into a microchip has been to either imbed the sol–gel into the microchip or to coat a microchip channel with a sol–gel. The method to imbed sol–gel functionality into a chip involved to preparing a PDMS chip with silica nanoparticles homogeneously distributed throughout the PDMS [4]. This approach produced a chip that was more hydrophilic than normal PDMS. In addition, when these chips were used for capillary electrophoresis analysis, the electroosmotic flow was much higher than in other PDMS chips.

Another application to which sol–gels have been applied is in assays involving various biocatalytic reactions. It has been demonstrated several times that proteins can be easily immobilized within a sol–gel and then used for a variety of applications. Once the proteins are incorporated into the sol–gel structure they still retain their enzymatic activity. This enables a wide array of enzymatic reactors to be prepared including oxidases, lipases, and proteases. Enzymes and even whole cells can be incorporated into the gels to enable flow-through reactors to be simply constructed. The incorporation of proteins into a sol–gels can also be combined with CEC separations to enable the separation of enantiomers.

Sol–gels with encapsulated enzymes have been demonstrated for high throughput screening of catalytic activity [5]. This involved fabricating an array of sol–gel microstructures on a glass slide. This was accomplished by using a PDMS template and then synthesizing the sol–gel with the active enzyme on top of the glass slide. The enzyme kinetics of the encapsulated proteins can then be studied in detail by changing the concentrations of substrate and inhibitor and using different temperatures. This enables rapid detailed analysis of the behavior of the enzyme. The activity of the immobilized enzyme was similar to the free enzyme, which demonstrates that the activity is maintained even in the sol–gel matrix. Each microwell requires only 50 μg of enzyme. These assays have been demonstrated with dozens of enzymes, which further demonstrates the robustness of the method.

In addition to microwell bioreactors for screening of enzymatic activity, enzymes have also been encapsulated into sol–gels for flow-through systems. For instance, trypsin has been fabricated into a sol–gel on a microchip to form a device that performs both digestion and separation on the same device [6]. Because of the proteolytic activity of the trypsin, proteins that are passed through the device are digested into consistuent peptide fragments. The amount of trypsin that was incorporated into the sol–gel was varied between 0.1% and 10% depending on the size of the analyte that needed to be digested and thus the amount of activity that was needed to adequately digest the sample. For sample introduction the driving force for introducing the analyte to the bioreactor was electroosmotic flow. Once the protein was digested it was then separated using the same electrophoretic forces that are used to introduce the protein to the bioreactor. Because the protein will be digested into fragments of different sizes, the different fragments (which are charged) will migrate at different speeds and be separated in the microchip. The overall time that was required for the digestion of the protein and the subsequent separation is much faster than other methods have been.

Protein encapsulation has also been used to prepare sol–gel columns for CEC separations [7]. This involved incorporating a proteins that has a chiral center such as bovine serum albumin or ovomucoid. Because these proteins have a chiral center it is possible to use the hybrid

protein/sol–gel column to separate enantiomers. In these separations, the amount of protein that was encapsulated was critically important in resolving the enantiomers, and protein concentrations generally needed to be above 5%. Even at these levels, the total amount of protein loaded was in the range of tens of micrograms.

Pre-concentration of analytes is another application that sol–gel materials have been applied to. Pre-concentration steps are critical in microfluidic analytical systems because the small volumes used require that the concentration be relatively high to allow analytes to be detected. The pre-concentration step typically involves loading the analyte onto the sol–gel in one solvent or solution. The analytes are later released from the sol–gel utilizing another solvent in which the analyte is more soluble than the sol–gel. A wide variety of functional interactions can be utilized to pre-concentrate an analyte. These can include ion-exchange, hydrophobic, and hydrophilic interactions. One major difficulty of these types of pre-concentrators is that it is very difficult to change solvents from one to the other in a microfluidic system. Also, the loading and release solvents must be miscible, which limits the solvents that may be used for pre-concentration operations. An example of sol–gels being used for pre-concentration is in the enrichment of DNA [8]. This process involves first adsorption of the DNA onto the silica in the presence of a salt. The containments are then washed off using an alcohol/water solution, and finally the DNA is eluted utilizing a buffer solution. The DNA that is eluted is suitable for further PCR amplification, which adds to the utility of the process.

Sol–gels can also be used for more than one application at the same time. For instance, it has been shown that a sol–gel column can be produced that enables both pre-concentration and separation of amino acids [9]. The column was prepared with a quaternary ammonium functionality, which gives the sol–gel a positive charge. This unique functionality in the sol–gel enabled amino acids to be preconcentrated and separated on the column with high enrichment and efficiency. Furthermore, the use of a positively charged surface for the silica surface enables the electroosmotic flow to be reversed to that which is normally observed in silica capillaries. This enables specialized separations to be performed on the sol–gel CEC column compared to that which would be normally achievable.

Future Directions for Research

Sol–gel technology is a very mature technique with a wide variety of methods that are known and are widely used. However, there are many opportunities that still exist to expand the sol–gel technique to microfluidic applications. One of the most important areas of future research involve developing microfluidic systems that incorporate multiple functionalities. For instance, a device for proteomic determinations may involve a sol–gel bioreactor to digest proteins, a sol–gel pre-concentrator to enrich the peptide fragments, and a CEC separation phase to separate the peptides prior to detection. Incorporating multiple functionalities will require several additional difficulties to be overcome. In addition to placing the sol–gel in a specific portion of a microchip it will be necessary to prepare multiple columns on a chip without adversely affecting the structure or functionality of the other sol–gel devices on the chip. This may be accomplished by using multiple interconnected channels and placing each sol–gel into its channel individually. It may also require some careful selection of the sol–gels to be prepared so that the preparation can be achieved while not disturbing the other devices. The other area that is ripe for further research is to utilize sol–gels for other functional devices in microfluidics. This could involve making electrokinetic pumps from sol–gels, which would involve fabricating sol–gels with high ionic loading so that a current can be used to cause the sol–gel to act as a pump with no moving parts. It has been demonstrated that a variety of biological proteins can be easily encapsulated into sol–gels. This should be expanded so that other functionalities can be included in microfluidic devices. Other pre-concentration approaches could also be fabricated using sol–gels. Pre-concentration will be a critically important step in microfluidics since the concentrations required for detection is relatively large. It should be possible to make pre-concentrators that would release the anaytes in response to other stimuli, such as heat or light, which would simplify the injection of the analytes into the system.

Cross References

- ▶ Bead-Based Microfluidic Platform
- ▶ Capillary Filling
- ▶ Chromatographic Chip Devices
- ▶ Electrokinetic Flow in Porous Media
- ▶ Lab-on-Chip Devices for Chemical Analysis
- ▶ Lab-on-Chip Devices for Separation Based Detection
- ▶ Liquid Chromatography
- ▶ Microfluidic Systems for High-Throughput Screening
- ▶ Stationary Phases in Microchannels

References

1. Hench LL (1998) Sol–Gel Silica. Noyes Publications, Westwood
2. Malik A (2002) Advances in sol–gel based columns for capillary electrochromatography: Sol–gel open-tubular columns. Electrophoresis 23:3973–3992

3. Dulay MT, Quirino JP, Bennett BD, Kato M, Zare RN (2001) Photopolymerized Sol–Gel Monoliths for Capillary Electrochromatography. Anal Chem 73:3921–3926
4. Roman GT, Hiaus T, Bass KJ, Seelhammer TG, Culbertson CT (2005) Sol–Gel Modified Poly(dimethylsiloxane) Microfluidic Devices with High Electroosmotic Mobilities and Hydrophilic Channel Wall Characteristics. Anal Chem 77:1414–1422
5. Park CB, Clark DS (2002) Sol–gel encapsulated enzyme arrays for high-throughput screening of biocatalytic activity. Biotechnol Bioeng 78:229–235
6. Kato KS, Kato M, Toyo'Oka T (2003) Creation of an On-Chip Enzyme Reactor by Encapsulating Trypsin in Sol–Gel on a Plastic Microchip. Anal Chem 75:388–293
7. Kato M, Kumiko SK, Matsumoto N, Toyo'oka T (2002) A Protein-Encapsulation Technique by the Sol–Gel Method for the Preparation of Monolithic Columns for Capillary Electrochromatography. Anal Chem 74:1915–1921
8. Wolfe KA, Breadmore MC, Ferrance JP, Power ME, Conroy JF, Norris PM, Landers JP (2002) Toward a microchip-based solid-phase extraction method for isolation of nucleic acids. Electrophoresis 23:727–733
9. Li W, Fries DF, Alli A, Malik A (2004) Positively Charged Sol–Gel Coatings for On-Line Preconcentration of Amino Acids in Capillary Electrophoresis. Anal Chem 76:218–227

Solid Phase Extraction

► Lab-on-a-Chip Devices for Sample Extractions

Solutal Marangoni

► Marangoni Convection

Solution Reservoirs on Chips

Definition

The solution reservoirs on chips are small vials connected to the ends of the microchannels and can store buffer or sample solutions.

Cross References

► Techniques for Transferring Samples to Chips

Soret

Definition

The *Soret coefficient* is the ratio of the thermal diffusion coefficient and the normal diffusion coefficient; it is a measure for the degree of separation of the species in ► thermophoresis.

Soret Effect

► Thermophoresis

Space Charge

Synonyms

Non-equilibrium diffuse charge; Non-equilibrium electrical double layer

Definition

Space charge refers to the extended diffuse charge in an electric double layer, which is passing a super-limiting current.

Cross References

► Electrical Double Layers
► Electroosmosis of the Second Kind
► Electrophoresis of the Second Kind
► Nonlinear Electrokinetic Phenomena
► Super-Limiting Current

Specific Impulse

Definition

The impulse delivered by a propulsion system per unit of propellant consumed; the quantity can be described either per unit mass or unit weight of propellant. It is a measure of the efficiency of the propulsion system.

Spectral Analysis

► Spectral Methods
► Spectrophotometric Analysis

Spectral Approximation

► Spectral Methods

Spectral Methods

SANGMO KANG, YONG KWEON SUH
Mechanical Engineering, Dong-A University, Busan, Republic of Korea
kangsm@dau.ac.kr

Synonyms

Spectral analysis; Spectral approximation

Definition

Spectral methods are a class of techniques used in applied mathematics and scientific computing to numerically solve certain differential equations using the method of weighted residuals. In spectral methods, the solution is approximated as an expansion in terms of spectral basis functions. Here, the basis functions are infinitely differentiable *global* (non-local) functions defined over a whole domain, e.g. trigonometric functions, Chebyshev polynomials, Legendre polynomials and so on, making the spectral methods different from the finite-element and finite-difference methods. Spectral methods have an excellent property of very high spatial accuracy for well-behaved problems and, thus, they are appropriate for the numerical simulation of accurately predicting flows with a broad range of dynamically significant scales of motion.

Overview

Spectral methods are used to numerically solve boundary value, eigen-value and time-dependent problems and these methods involve a completely different approach from finite-element and finite-difference methods. In spectral methods, instead of representing a function by its values at grid points, one would approximate the function by a series expansion in terms of spectral basis functions as follows (in the case of one-dimensional problem):

$$u(x) \approx u_N(x) = \sum_{n=0}^{N} a_n \phi_n(x) , \tag{1}$$

where $u(x)$ and $u_N(x)$ denote respectively a function and its approximation, and $\phi_n(x)$ and a_n respectively the nth basis function and its corresponding coefficient. N is the degree of the series expansion. The basis functions are infinitely differentiable non-local functions defined over a whole domain. In addition, they should have a lot of appropriate properties, such as easy computation, rapid convergence and completeness (A basis set is said to be *complete* for a given class of functions if all the functions within the class can be represented to arbitrary high accuracy as a sum of a sufficiently large number of basis functions) [1]. The typical examples are the trigonometric functions and Chebyshev and Legendre polynomials. The trigonometric functions, or Fourier series, are used for the periodic boundary conditions, whereas the Chebyshev and Legendre polynomials are used for the Dirichlet conditions. It means that the coefficient, a_n, influences the function, $u_N(x)$, and its derivative, $du_N(x)/dx$, over a whole domain and, thus, spectral methods are completely *global*. Note that finite-element and finite-difference methods are local because the function value at a grid point has influence only near that point.

When the spectral series (1) is substituted into the differential equation

$$Lu(x) \equiv f(x) , \tag{2}$$

where L is the differential operator, the result is the so-called residual function defined as;

$$R(x; a_0, a_1, \ldots, a_N) \equiv Lu_N(x) - f(x) . \tag{3}$$

Since the residual function, $R(x; a_n)$, is identically equal to zero for the exact solution, the ultimate goal in spectral methods is to choose the spectral coefficients, a_n $(n = 0, 1, \ldots, N)$, so that the residual function is minimized. The different kinds of spectral methods differ mainly in the minimization strategies.

The basis functions, $\phi_n(x)(n = 0, 1, \ldots, N)$, should be already determined such that each of them satisfies the corresponding boundary condition. Here, the application of the *method of weighted residuals* [2] determines the coefficients, a_n, by imposing the $(N + 1)$ conditions

$$(w_i, R[x; a_0, a_1, \ldots, a_N]) = 0 , \quad i = 0, 1, \ldots, N \tag{4}$$

for some suitable test functions, $w_i(x)$. The inner product for any two functions, $u(x)$ and $v(x)$, is defined as

$$(u, v) \equiv \int_{\Omega} \rho(x)u(x)v(x)\,dx \tag{5}$$

for a given non-negative weight function, $\rho(x)$, where Ω denotes the whole domain.

There are two basic types of spectral methods: *pseudospectral* methods and *Galerkin* methods. In pseudospectral methods, or spectral collocation methods, the test function is given as

$$w_i(x) \equiv \delta(x - x_i) , \tag{6}$$

where x_i is each collocation point and $\delta(x)$ the Dirac delta-function (1 for $x = 0$ and 0 otherwise). The substitution of Eq. (6) into Eq. (4) results in the algebraic equations

$$R(x_i; a_0, a_1, \ldots, a_N) = Lu_N(x_i) - f(x_i) = 0 , \quad i = 0, 1, \ldots, N \tag{7}$$

at the collocation points.

S

In the Galerkin method, on the other hand, the test function is given as

$$w_i(x) \equiv \phi_i(x) . \tag{8}$$

This choice of test function is successful because any well-chosen set of basis functions would have all the properties desired by weighting functions, including linear independence and completeness. The main difference between pseudospectral and Galerkin methods is as follows. In pseudospectral methods, some of the calculations are carried out in terms of the spectral coefficients, a_n, and some in terms of the values of $u(x)$ at certain grid points, whereas, in Galerkin methods, all the computations are carried out in terms of the spectral coefficients, a_n.

Micro and nanoflows involve a relatively broad range of dynamically significant scales of motion. Thus, highly accurate numerical methods are required for exactly capturing these dynamics. High spatial accuracy is achieved by spectral methods, which thus may be very effective in simulating micro and nanoflows. However, most micro and nanoflows involve complex wall-bounded geometries, that is the flow geometry is complex or particular regions need to be resolved. Note that spectral methods cannot be readily applied to such cases without any special treatment.

Spectral domain-decomposition methods are suggested as an efficient way of resolving the limitation of conventional spectral methods. The basic idea behind the methods is to partition the whole domain into several subdomains, and then to simultaneously solve the differential equations in each subdomain and appropriate matching conditions on each interface. These methods have very attractive features, such as rapid convergence, geometric flexibility, and suitability to parallel implementation. Thus, they are appropriate when particular regions need to be resolved or when flows in complex geometries are to be simulated.

In general, two classes of spectral domain-decomposition methods have been proposed in the literature: *patching* methods and *variational* methods. The difference is in the way how the interface conditions are imposed. To solve second-order partial differential equations as an example, the interface condition is typically enforced by requiring that the solution and its first normal derivative be continuous on each interface. In patching methods, the continuity conditions on each interface are discretized by enforcing them at selected points, and thus are satisfied exactly by any approximation. In variational methods, on the other hand, the continuity conditions are enforced implicitly or variationally with differential equations at all points, including all the subdomains and interfaces.

Patching methods are based on spectral collocation methods first developed by Orzag [4]. They are useful in exploiting the efficiency of spectral collocation methods. On the other hand, the spectral element methods first developed by Patera [5] are a kind of variational methods. These methods are a high-order weighted residual technique that combines the accuracy and rapid convergence of spectral methods with the generality and geometric flexibility of finite-element methods.

Basic Methodology

Pseudospectral and Galerkin Methods

In order to simply explain the basic principle behind spectral methods, consider one-dimensional linear Helmholtz equation as an example:

$$Lu(x) = -\frac{d^2u(x)}{dx^2} + \lambda u(x) = f(x) \quad \text{in } \Omega , \tag{9}$$

where λ is a non-negative constant. The same basic principle can be readily extended to more complex differential equations and more-dimensional problems.

The function, $u(x)$, in Eq. (9) can be approximately written as a series expansion in terms of spectral basis functions, $\phi_n(x)$, as in Eq. (1). When the spectral series (1) is substituted into Eq. (9), the resultant residual function can be written as

$$\begin{aligned} R(x; a_0, a_1, \ldots, a_N) &= Lu_N(x) - f(x) \\ &= \left(-\frac{d^2u_N}{dx^2} + \lambda u_N\right) - f . \end{aligned} \tag{10}$$

Since the residual is zero if $u_N(x)$ is the exact solution of Eq. (9), it follows that the goal of all numerical methods is to choose the undetermined coefficients, a_n, so as to make $R(x; a_n)$ as small as possible. The different kinds of spectral methods differ mainly in the minimization strategies. There are two basic types of spectral methods: pseudospectral methods and Galerkin methods.

In pseudospectral methods, the following $(N+1)$ algebraic equations are derived from Eq. (7):

$$\begin{aligned} &R(x_i; a_0, a_1, \ldots, a_N) = Lu_N(x_i) - f(x_i) \\ &= \left(-\frac{d^2u_N(x_i)}{dx^2} + \lambda u_N(x_i)\right) - f(x_i) = 0 , \\ &i = 0, 1, \ldots, N . \end{aligned} \tag{11}$$

In other words, pseudospectral methods define the 'minimization' of the residuals as 'zero at a set of $(N+1)$ collocation points, x_i'.

In the special case where the differential operator, L, is linear, Eq. (11) converts the differential Eq. (9) into the following linear matrix problem:

$$\bar{L}\bar{a} = \bar{f}\,, \tag{12}$$

where the elements of the matrices are

$$\begin{aligned} \bar{L})_{in} &= L[\phi_n(x_i)] = \left(-\frac{\mathrm{d}^2\phi_n(x_i)}{\mathrm{d}x^2} + \lambda\phi_n(x_i)\right), \\ \bar{a})_n &= a_n\,, \\ \bar{f})_i &= f(x_i)\,. \end{aligned} \tag{13}$$

Thus the inth element of the matrix, $\bar{L})_{in}$, is the approximate value of the differential operator, L, of the nth basis function (where n is the column index) evaluated at the ith collocation point (where i is the row index). If L is a nonlinear operator, on the other hand, then the algebraic Eqs. (11) are nonlinear, too. In such a case, they should be solved by iteration methods such as the Newton–Raphson method.

The alternatives to pseudospectral methods are Galerkin methods. Galerkin methods distribute the residual so that the expansion of the residual function as a series of the basis functions, $\phi_n(x)$, contains no component with respect to the test function, $\phi_i(x)$ $(i = 0, 1, \ldots, N)$. The combination of Eqs. (4) and (8) gives the following $(N+1)$ algebraic equations:

$$\begin{aligned} &(\phi_i, R\,[x; a_0, a_1, \ldots, a_N]) \\ &\quad = \int_\Omega \rho(x)\phi_i(x)\left(-\frac{\mathrm{d}^2u_N(x)}{\mathrm{d}x^2} + \lambda u_N(x) - f(x)\right)\mathrm{d}x \\ &\quad = 0\,, \\ &\quad i = 0, 1, \ldots, N\,. \end{aligned} \tag{14}$$

In the special case where L is a linear operator, Galerkin methods give the linear matrix problem

$$\tilde{L}\tilde{a} = \tilde{f}\,, \tag{15}$$

where the elements of the matrices are

$$\begin{aligned} \tilde{L})_{in} &= (\phi_i, L\phi_n) \\ &= \int_\Omega \rho(x)\phi_i(x)\left(-\frac{\mathrm{d}^2\phi_n(x)}{\mathrm{d}x^2} + \lambda\phi_n(x)\right)\mathrm{d}x\,, \\ \tilde{a})_n &= a_n\,, \\ \tilde{f})_i &= (\phi_i, f) = \int_\Omega \rho(x)\phi_i(x)f(x)\,\mathrm{d}x\,. \end{aligned} \tag{16}$$

In some cases, the orthogonality of the spectral basis-function set may be important because the coefficients of the expansion of an arbitrary function, $u(x)$, in terms of an orthogonal basis function set are given as

$$u(x) = \sum_{n=0}^{\infty} u_n(x)\phi_n(x)\,, \quad u_n = (u, \phi_n)/(\phi_n, \phi_n)\,. \tag{17}$$

If L is a nonlinear operator, then the algebraic Eqs. (14) are nonlinear, too.

Pseudospectral and Galerkin methods are very different in appearance. However, pseudospectral methods are efficient only if the collocation points are distributed so that the residual is not merely zero at the collocation points themselves but also very small everywhere in between. It turns out that, for all the canonical basis sets, the optimum choice of collocation points is to employ the Gaussian quadrature points which are used to evaluate the integral inner product associated with the basis set [1, 3]. From this, one could show that Galerkin and pseudospectral methods are equivalent if the integrals are evaluated by $(N+1)$-point Gaussian quadrature.

To summarize, pseudospectral algorithms are easier to program. On the other hand, Galerkin methods are more accurate for small N and are easier to understand and manipulate for theoretical purposes such as perturbation theory. Perhaps Galerkin methods are more robust for difficult problems. For numerical purposes, however, there is not much to choose between them [1].

S

Choice of Basis Function Set (Fourier Series and Chebyshev Polynomials)

When the solution has spatially periodic boundary conditions, one uses the following Fourier series as a basis func-

tion set:

$$u(x) = a_0 + \sum_{n=1}^{\infty} a_n \cos(nx) + \sum_{n=1}^{\infty} b_n \sin(nx)\,,$$
$$x \in [-\pi, \pi]\,,$$
$$a_0 = \frac{1}{2\pi}\int_{-\pi}^{\pi} u(x)\,\mathrm{d}x\,, \tag{18}$$
$$a_n = \frac{1}{\pi}\int_{-\pi}^{\pi} u(x)\cos(nx)\,\mathrm{d}x\,,$$
$$b_n = \frac{1}{\pi}\int_{-\pi}^{\pi} u(x)\sin(nx)\,\mathrm{d}x\,.$$

Since each Fourier term is individually periodic with a period 2π, the solution, $u(x)$, automatically satisfies the periodic conditions, independent of the spectral coefficients, a_n and b_n.

On the other hand, if the domain is finite, but the function is not periodic, for example $u(\pm 1) = 0$, the Chebyshev polynomials are best. The Chebyshev polynomials of degree n are defined as

$$T_n(x) = \cos[n \arccos(x)]\,. \tag{19}$$

It can also be calculated directly via the following three-term recurrence relation:

$$T_0(x) \equiv 1\,,$$
$$T_1(x) \equiv x\,, \tag{20}$$
$$T_{n+1}(x) = 2xT_n(x) - T_{n-1}(x), \quad n \geq 1\,.$$

To impose the Dirichlet boundary conditions, $u(\pm 1) = 0$, one defines the spectral basis functions to be linear combinations of the Chebyshev polynomials, which vanish at the boundaries, such as

$$\phi_{2n}(x) = T_{2n}(x) - 1\,,$$
$$\phi_{2n+1}(x) = T_{2n+1}(x) - x\,, \quad n = 1, 2, \ldots \tag{21}$$

The fact that $\phi_n(\pm 1) = 0$ for each n follows from the trigonometric definition of the Chebyshev polynomials, which implies $T_n(\pm 1) = (\pm 1)^n$.

There are many exceptions: the basis set can be generally determined by the flow geometry and boundary conditions. Therefore, the interested readers may refer to the literature for more details.

Spectral Domain-Decomposition Methods

Most of spectral methods have been developed paying attention to simple geometries and, thus, one would suffer from many difficulties in applying them to more complex geometries. Recently, there have been a number of developments on the use of spectral schemes in more complex geometries, for example the advent of spectral domain-decomposition methods. The basic idea behind these methods is to partition the whole domain into several subdomains, and then to simultaneously solve differential equations in each subdomain and appropriate matching conditions on each interface. In general, two classes of spectral domain-decomposition methods have been proposed in the literature: patching methods and variational methods.

In order to simply explain the basic principle of patching and variational methods, consider one-dimensional linear Helmholtz equation subject to zero Dirichlet boundary condition as follows:

$$Lu(x) = -\frac{\mathrm{d}^2 u(x)}{\mathrm{d}x^2} + \lambda u(x) = f(x) \qquad \text{in } \Omega \tag{22}$$
$$u(x) = 0 \qquad \text{on } \partial\Omega \tag{23}$$

where $\partial\Omega$ is the boundary of the whole domain.

Patching Methods

Patching methods [1, 3], first developed by Orzag [4], are useful in exploiting the efficiency of spectral collocation methods. Suppose that the whole domain, Ω, is decomposed into M subdomains, Ω_s $(s = 1, \ldots, M)$. N_s denotes the degree of polynomials used to approximate $u(x)$ in the sth subdomain, and $N \equiv N_1 + N_2 + \ldots + N_M$ is the total number of degrees of plynomials in the whole domain. The numerical solution is denoted by $u^N(x)$, while $u_s(x)$ indicates the *restriction* of the numerical solution to the sth subdomain.

In patching methods, the Helmholtz equation and the corresponding boundary condition are satisfied in each subdomain as follows:

$$Lu_s(x_i^s) - f(x_i^s) = \left(-\frac{\mathrm{d}^2 u_s(x_i^s)}{\mathrm{d}x^2} + \lambda u_s(x_i^s)\right)$$
$$- f(x_i^s) = 0 \quad \text{in } \Omega_s\,,$$
$$i = 0, 1, \ldots, N_s\,, \quad s = 1, 2, \ldots, M \tag{24}$$
$$u_s = 0 \quad \text{on } \partial\Omega \cap \Omega_s\,. \tag{25}$$

On the other hand, the solution and its first normal derivative should be continuous across the interface:

$$u_s = u_{s+1} \quad \text{on } \Gamma_s\,, \tag{26}$$

$$\frac{\mathrm{d}u_s}{\mathrm{d}x} = \frac{\mathrm{d}u_{s+1}}{\mathrm{d}x} \quad \text{on } \Gamma_s\,, \tag{27}$$

where Γ_s $[s = 1, 2, \ldots, (M-1)]$ denotes the interface between two adjacent subdomains, $\Gamma_s = \Omega_s \cap \Omega_{s+1}$. If the order of a certain differential equation is d (≥ 2), the solution and all the normal derivatives less than d should be continuous across the interface.

To summarize, in patching methods, the algebraic equations (24) are solved, together with the boundary condition (25), in each subdomain and simultaneously the interface matching conditions (26) and (27) are satisfied on each interface. The same principle can be readily extended to more-dimensional problems.

Variational Methods

Variational methods [3] are a class of high-order weighted residual techniques that combines the high spatial accuracy and rapid convergence of spectral methods with the generality and geometric flexibility of finite-element methods. Consider a variational method on Ω for one-dimensional Helmholtz Eq. (22). A variational formulation of this problem is that $u(x)$ should be the solution to

$$\int_\Omega \left(-\frac{\mathrm{d}^2 u(x)}{\mathrm{d}x^2} + \lambda u(x) \right) \phi_i(x)\,\mathrm{d}x = \int_\Omega f(x)\phi_i(x)\,\mathrm{d}x\,. \tag{28}$$

Equation (28) can be converted into another form, using integration-by-parts and zero natural boundary condition:

$$\int_\Omega \left(\frac{\mathrm{d}u(x)}{\mathrm{d}x}\frac{\mathrm{d}\phi_i(x)}{\mathrm{d}x} + \lambda u(x)\phi_i(x) \right) \mathrm{d}x = \int_\Omega f(x)\phi_i(x)\,\mathrm{d}x\,, \tag{29}$$

where $\phi_i(x)$ is the trial (or test) function which vanishes on $\partial\Omega$ and which is integrable over Ω together with its first derivative. In addition, it is a continuous function of piecewise polynomials defined on the decomposition of the whole domain, Ω. The solution to the Eq. (29) is approximated by a function $u^N(x)$ satisfying

$$\sum_{s=1}^{M} \int_{\Omega_s} \left(\frac{\mathrm{d}u_s^N}{\mathrm{d}x}\frac{\mathrm{d}\phi_i}{\mathrm{d}x} + \lambda u_s^N \phi_i \right) \mathrm{d}x = \sum_{s=1}^{M} \langle f, \phi_i \rangle_s\,. \tag{30}$$

For each s, $\langle f, \phi_i \rangle_s$ is a convenient approximation of the integral, $\int_{\Omega_s} f\phi_i\,\mathrm{d}x$. Equation (30) is a variational formulation with trial and test functions which are continuous across the interface (element boundary).

Key Research Findings

Since micro and nanoflows involve very low Reynolds numbers, the convection effects may be neglected in simple geometries. However, in complex geometries with abrupt turns the effects are substantial [6] and, thus, more accurate and efficient numerical schemes such as spectral methods may be necessary in handling such flows. Up to now, there have been a vast number of numerical studies on micro and nanofluidics. Therefore, few conspicuous numerical studies using spectral methods have been performed, except Karniadakis' research group.

Karniadakis and Beskok [6] developed a code *μFlow* with implementation of spectral element methods. They employed both the Navier–Stokes (incompressible and compressible) and energy equations in order to compute the relative effects of compressibility and rarefaction in gas micro flow simulations. In addition, they also considered the velocity slip, temperature jump, and thermal creeping boundary conditions in the code *μFlow*. The spatial discretization of *μFlow* was based on spectral element methods, which are similar to the *hp* version of finite-element methods. A typical mesh for simulation of flow in a rough micro channel with different types of roughness is shown in Fig. 1. The two-dimensional domain is broken up into elements, similar to finite elements, but each element employs high-order interpolants based on Legendre polynomials. The N points that determine the interpolant correspond to the maxima locations of the Legendre polynomials and the end-points. For smooth solutions, the spatial discretization error decays exponentially to zero (spectral or p-convergence). This means that if we dou-

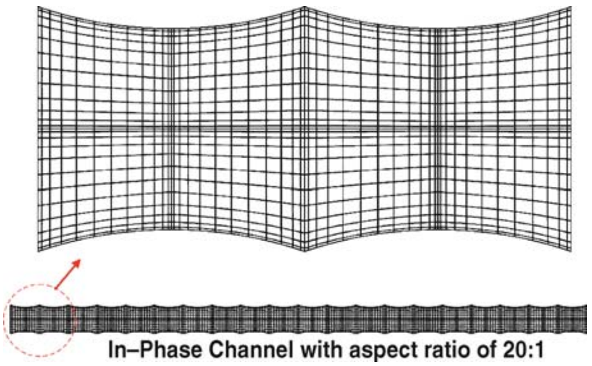

Spectral Methods, Figure 1 A typical mesh in a rough micro channel for the spectral element method [6]

S

ble N, the error would decay by two orders of magnitude. This is a much faster decay than in standard second-order methods which yield an error reduction by a factor of only four. In MEMS simulations, spectral element methods can be used efficiently by exploiting the dual path of convergence allowed by the method. For example, in regions of geometric complexity, a finite element-like discretization (low N and small size elements) can be employed, whereas in regions of homogeneous geometry with steep gradients, a spectral-like discretization (high N and large size elements) can be employed. In particular, the boundary conditions for MEMS flows, either for gases (Knudsen effects) or liquids (electrokinetic effects), can be resolved very accurately.

Future Directions for Research

Spectral methods have been a promising tool for simulating micro and nanoflows as well as macro flows because they have excellent properties of high spatial accuracy and rapid convergence. Therefore, they can capture a broad range of dynamically significant scales of motion very effectively.

Up to now, a vast number of studies on micro and nanofluidics have been performed based on the theoretical, numerical and experimental approaches. For the numerical analysis, however, finite-volume or finite-difference schemes have been mostly used. In the future, spectral methods will contribute more to the studies on micro and nanoflucids that require numerical methods with high spatial accuracy, for example electrokinetic and capillary effects.

Cross References

► Finite Volume and Finite Difference Methods for Modeling and Simulation

References

1. Boyd JP (2001) Chebyshev and Fourier Spectral Methods. Dover, New York
2. Finlayson BA (1973) The Method of Weighted Residuals and Variational Principles. Academic, New York
3. Canuto C, Hussaini MY, Quarteroni A, Zang TA (1988) Spectral Methods in Fluid Dynamics. Springer, Berlin
4. Orszag SA (1980) Spectral methods for problems in complex geometries. J Comput Phys 37:70–92
5. Patera A (1984) The spectral element method for fluid dynamics: laminar flow in a channel expansion. J Comput Phys 54:468–488
6. Karniadakis GE, Beskok A (2002) Micro flows: fundamentals in simulation. Springer, New York

Spectral Response

► Spectral Responsivity

Spectral Responsivity

Synonyms

Spectral response

Definition

The spectral responsivity refers to the electrical signal generated by a photodetector when irradiated with a known radiant flux of a specific wavelength.

Cross References

► Lab-on-a-Chip Device for Chemical Analysis

Spectrophotometer

► Photometer

Spectrophotometric Analysis

Synonyms

Spectrophotometry; Spectrophotometric measurement; Spectral analysis

Definition

The spectrophotometric analysis is the study of the interaction of electromagnetic radiation with chemical compounds. This analytical technique can be used to determine the structure of a new compound, identify a specific compound, determine the activity of a specific enzyme and determine the concentration and/or amount of a particular compound in body fluids samples. It is the one of the most commonly used analytical techniques for body fluids analysis in clinical diagnosis.

Spectrophotometric analysis by optical absorption is based on the absorption of electromagnetic radiation that is proportional to the amount of the element, ion, compound or molecule being analyzed in the sample. Absorbance detection is covered under a separate title.

Cross References

► Lab-on-a-Chip Devices for Chemical Analysis

► Lab-on-Chip Devices for Protein Analysis

Spectrophotometric Measurement

► Spectrophotometric Analysis

Spectrophotometry

► Spectrophotometric Analysis

Spectroscopy

► Photometer

Speed of Sound

Definition

The speed at which an infinitesimal pressure perturbation propagates in a quiescent medium.

Cross References

► Supersonic Micro-Nozzles

Spinning-Disk Confocal Microscopy

► Confocal Microscopy, Detection

Spinodal Decomposition

► Demixing

Spiral Microchannel Flow

► Curved Microchannel Flow

Spontaneous Electrowetting

► Electrowetting, Applications

Spontaneous Polarization

Definition

A polarization that exists within a material in the absence of the application of an external field. Requires non-enantiomorphic polar symmetry. Usually used in the context of electric fields and electrical polarization. Materials that exhibit spontaneous polarization and are piezoelectric are able to retain a ionic polarization and therefore said to be ferroelectric.

Cross References

► Non-Centrosymmetric
► Ferroelectric
► Piezoelectric

SPR

► Surface Plasmon Resonance Sensors

SPRT

► Resistance Temperature Detectors

Sputter Etching

Synonyms

Physical etching

Definition

A purely physical process caused by surface bombardment with high-energy ions, anisotropic etching; also with poor selectivity, high surface damage, and low etching rates.

Cross References

► Anisotropic Etching
► Isotropic Etching
► Reactive Ion Etching (RIE)
► Plasma Etching
► Silicon Micromachining

Sputtering for Film Deposition

ALEXANDER ILES, NICOLE PAMME
Department of Chemistry, The University of Hull,
Hull, UK
n.pamme@hull.ac.uk

Synonyms

Physical vapor deposition; Cathode sputtering; Impact evaporation

Definition

The verb *to sputter* originates from *sputare* (latin, to emit saliva with noise). Sputtering is the ejection of atoms from a surface following bombardment by suitably energetic atomic particles. Typically, these bombarding particles are ions generated by an electrical discharge in a low pressure gas. This process can be utilized as a thin film deposition technique by allowing atoms sputtered from a target to impinge on a substrate. The process is widely used to deposit films less than one micrometer thick for microelectronic component fabrication, the formation of optical coatings and the production of decorative parts.

Overview

The process of sputtering was first reported by W. R. Grove in 1852. He observed the formation of metallic deposits on the inner wall of a glass discharge tube during an investigation into the electrical conductivity of gases using direct current (DC) glow discharges. This observation has led to the development of an extremely versatile thin film deposition technique that is utilized in numerous different fields. A vast range of different materials can be deposited using sputtering, including: pure metals, alloys, semiconductors and insulators. The deposition process can also be used for the formation of films with novel properties in terms of stoichiometry and crystalline orientation. In addition to deposition, sputtering can also be used for etching, surface cleaning and for surface layer analysis.

Sputtering has been used for many years to produce the chromium coated ▶ photomasks that are often used in the production of glass microdevices. Recently, sputtering has become a common technique for the deposition of thin films in microfluidic and nanofluidic devices. For most applications, it is used as a convenient means for the production of patterned electrodes. However, as will be shown below, sputtering can be used to achieve far more than this. In the not so distant future it is likely that the enormous versatility of this technique will be exploited for the fabrication of miniaturized fluidic devices with greatly enhanced functionality that would be difficult or impossible to produce by other means.

The sputtering process is governed by a range of different parameters. These parameters can be manipulated to alter the properties of the deposited film. In DC sputtering systems, the maximum energy (E) of the atoms ejected from the target is determined by the applied voltage. Accelerating a singly charged ion through a potential difference of 1 V imparts a kinetic energy of 1 eV to the ion. For a given voltage atoms are sputtered from the target with a broad distribution of energies. The sputtered atoms impinge on the substrate with maximal energies that are typically 100 times greater than those achieved during film deposition by evaporation. The applied voltage also governs a parameter called the ▶ sputter yield (S), which is the number of target atoms removed divided by the number of incident ions. For applied voltages below a certain threshold value, the ions have insufficient energy to overcome the surface binding energy (U_0) of the target material and so atoms are not ejected. This threshold level usually occurs between 0 and 100 eV. For ion energies between 100 eV and 1000 eV, atoms are ejected from the target and the *sputter yield* increases with increasing applied voltage. For ion energies within this range, the *sputter yield* can be estimated by assuming energy transfer occurs by binary collisions:

$$S = \frac{3\alpha}{4\pi^2} \cdot \frac{4m_\mathrm{i} \cdot m_\mathrm{t}}{(m_\mathrm{i} + m_\mathrm{t})^2} \cdot \frac{E}{U_0} \quad (1)$$

where m_i and m_t are the masses of the incident ion and the target atom, respectively; α is a function of the ratio $m_\mathrm{t}/m_\mathrm{i}$. This increases from 0.17 for $m_\mathrm{t}/m_\mathrm{i} = 0.1$ to 0.28 for $m_\mathrm{t}/m_\mathrm{i} = 1$ to 1.4 for $m_\mathrm{t}/m_\mathrm{i} = 10$.

For ion energies greater than 1000 eV, the probability of ions being implanted into the surface of the target becomes significant. The *sputter yield* no longer increases linearly with increasing ion energy. Eventually, the *sputter yield* becomes almost constant and at very high energies it begins to fall as ▶ ion implantation becomes the dominant process. As a consequence of this, in DC systems, applied voltages between 100 V and 1000 V are most widely used for the sputter deposition of thin films.

The rate of sputtering is determined primarily by the sputter current density. For most systems, this is generally between 0.1 and 10 mA/cm^2. Increasing the current density increases the rate of deposition. However, a faster rate of arrival of material on the surface of the substrate means that there is less time for the occurrence of processes such as surface diffusion and agglomeration on existing growth sites or nucleation with other growth sites.

The rate of sputtering and the properties of the deposited film are also significantly influenced by the sputter gas type and pressure. In most instances, it is not desirable for the sputter gas to react with the target and so noble gases tend to be used. Xenon and Krypton have larger atomic masses than Argon and generally give higher *sputter yields*. However, Argon is most often used as it is cheaper and more readily available.

The gas pressure dictates the average distance the sputtered atoms travel before they interact with gas atoms. This is called the mean free path (λ) and it is inversely proportional to the gas pressure. A short mean free path means that the sputtered atoms will be subjected to many collisions with gas atoms before being deposited on the substrate. This can affect the porosity of the deposited film and also its crystallinity and surface morphology. Hence, it is often desirable to sputter at low pressure, so that λ is as large as possible. For simple DC gas discharge systems (Fig. 1), relatively high pressures are used, typically 30 to 120 mTorr. This is because it is difficult to maintain the gas discharge at lower pressures. DC ► magnetron systems (Fig. 2) can be operated at lower pressures (10^{-5} to 10^{-3} Torr) since the magnetic fields around the target increase the number of collisions between electrons and neutral sputter gas atoms. Sometimes, a reactive gas such as oxygen or nitrogen is added to the sputter gas, so that oxide or nitride films can be deposited.

Not surprisingly, different target materials sputter at different rates. Periodicity is observed when *sputter yields* are plotted against target atomic number. This is related to the surface binding energy (U_0) of the target materials. For the transition metals, *sputter yields* increase between Ti and Cu; then decrease sharply. *Sputter yields* increase again between Zr and Ag before decreasing to another minimum at Hf. Yields increase once more, reaching another maximum at Au. Hence, Cu, Ag and Au are the transition metals that sputter most readily. The orientation and crystal structure of the target relative to the incident sputter ions can also affect the *sputter yield* and the angular distribution of sputtered atoms. *Sputter yields* tend to increase with increasing angle of incidence reaching a maximum between 60° and 80° from the target normal. For larger angles of incidence, the *sputter yield* decreases rapidly. At the optimal angle of incidence, the target atoms are sputtered predominantly in the forward direction with the maximum of their distribution occurring between 10 and 30° from the target normal. If the target is made of a monocrystalline material, then the angular dependence and *sputter yield* will vary according to the orientation of the crystallographic planes relative to the angle of incidence. This is because the surface binding energy (U_0) varies slightly in accordance with the ► anisotropy of the crystal structure.

Different metals sputter at different rates. However, when an alloy target is sputtered, the deposited film develops the same composition as the target material, as long as the target temperature is below that required for thermal diffusion. This is because the faster ejection of one element leads to the enrichment of the target's surface with elements that have lower sputter rates. Hence, differences in sputter rates are counteracted and the deposited film obtains the same stoichiometry as the target.

DC systems cannot be used to sputter insulating targets. This is because an electrical discharge in such a system would result in the charging up of the target. Therefore, radio frequency (RF) excitation is used to sputter insulating targets. RF excitation reverses the surface polarity of the target typically at a rate of 13 MHz, and this prevents the target from becoming charged.

The distance between the target and the substrate dictates the mean number of collisions that occur once the sputtered atoms leave the target and travel through the sputter gas to the substrate. Varying this distance can influence the porosity, crystallinity and surface morphology of the deposited film.

Film adhesion is strongly dependent on the cleanliness of the substrate, the chemical nature of the substrate relative to the film and the surface morphology of the substrate. Surface contaminants may increase or decrease adhesion, depending on how they influence the adsorption energy of the deposited material. Often it is desirable to have a very clean surface and so sputter cleaning of the substrate is performed prior to film deposition. Certain metals do not adhere well to substrates such as glass. Adhesion can be improved by increasing the kinetic energy of the incident atoms or by increasing the number of nucleation sites on the substrate. Alternatively, an adhesion layer could be applied to the substrate prior to deposition. For example, chromium is frequently used as an adhesion layer for the deposition of gold onto glass.

During sputtering, the substrate is bombarded by a wide range of species. Some of these species are charged. Hence the properties of the deposited film can be influenced by applying a ► bias voltage to the substrate. This is typically between ±100 V and it is used to repel or attract electrons or ions. Substrate biasing can exert a great influence on the physical and electrical properties of the deposited film, including: dielectric constant, porosity, surface morphology, hardness and etch resistance. The polarity and magnitude of the optimal *bias voltage* will depend on the target and substrate materials and the desired properties of the deposited film.

As with most vacuum deposition techniques, film growth on the substrate occurs according to the sequence: atom arrival and physical adsorption, migration on the surface

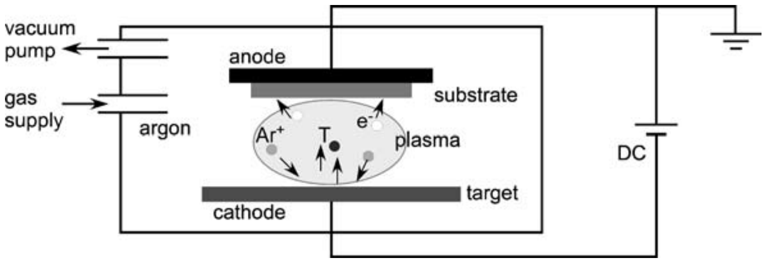

Sputtering for Film Deposition, Figure 1 Schematic of a DC sputtering system

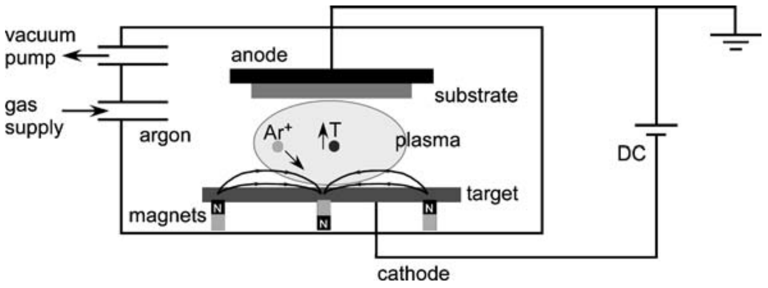

Sputtering for Film Deposition, Figure 2 Schematic of a DC *magnetron*; a magnetic field is generated by an assembly of magnets beneath the target. This lead to the confinement of electrons in the immediate vicinity of the target

Sputtering for Film Deposition, Table 1 Advantages and Disadvantages for film deposition using sputtering.

Advantages of Sputtering	Disadvantages of Sputtering
– no melting of target material required – deposited film has same stoichiometry as target material – sputtering does not require evaporation, can sputter materials with high evaporation temperature – versatility (type of materials, instrumental parameters) – formation of novel materials possible – long target lifetime – simple DC systems can be built easily from primitive materials	– vacuum required – many variables to optimize, complexity to produce high quality films – dedicated instruments are expensive and require cleanroom facilities – contamination (increased porosity, pinholes, gas incorporation into film) – often slower than other methods

or re-evaporation, formation of atom pairs, nucleation of islands, island growth, coalescence and finally continuous film formation. Clearly, the temperature and crystallinity of the substrate will have a significant effect on the growth behavior of the film. Higher substrate temperatures impart higher mobilities to the atoms on the surface. This leads to larger grain sizes and smoother films. Hence, in many sputtering systems, the substrate is placed on a heated stage. However, the sputtering process itself can lead to significant substrate heating. Excessive heating is undesirable and so substrate cooling may be necessary. The use of polycrystalline substrates will generally lead to the formation of a polycrystalline film. However, if a monocrystalline substrate is used at a suitable temperature, then it is possible to form an ► epitaxial film. Substrates may also be chosen with specific crystallographic orientations so that deposited films acquire particular orientations.

The advantages and disadvantages of sputtering for film deposition are summarized in Table 1.

Basic Methodology

The simplest of sputtering systems is the DC gas discharge diode as shown in Fig. 1. This apparatus consists of a vacuum chamber containing two planar electrodes. One electrode is the cathode, to which the target is connected. This is usually water cooled to prevent it from over-heating. The substrate to be sputtered is placed onto the other electrode, which forms the anode. This may also be water cooled if necessary.

Prior to sputtering, the chamber is evacuated to remove as much oxygen and moisture as is possible. The level of vacuum that is achieved will depend on the effectiveness of the pumping system and the desired quality of the

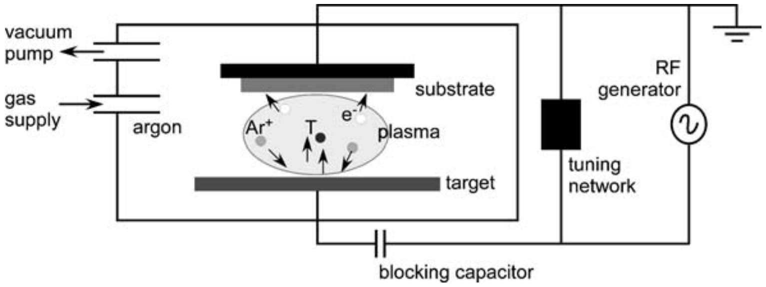

Sputtering for Film Deposition, Figure 3 The principle of a radio frequency (RF) sputtering system

sputtered film. For high quality film production, the pre-sputtering vacuum should be in the region of 10^{-7} Torr. Once this has been achieved, sputter gas (typically Argon) is admitted to the chamber to raise the pressure to between 30 and 120 mTorr. A high voltage is applied to the electrodes and an electrical gas discharge is initiated. Generally, a constant current power supply is used so that the sputter current can be adequately controlled. The spacing between the target and the substrate is usually set at about 10 cm and the sputter current is adjusted to deposit a film at a suitable rate. Deposition rates are usually between 10 and 200 nm per minute, although this will vary significantly depending on the target material.

The main advantage of DC diode sputtering systems is that they can be extremely simple and can be constructed at low cost using readily available components [1] However, the quality of the films deposited with such systems is relatively poor. This is mainly due to the high operating pressure that must be used to maintain the electrical discharge. A widely used technique to lower the sputter gas pressure is to utilize magnetic fields to confine the electrical discharge to the region around the target (Fig. 2). Sputtering systems that utilize assemblies of magnets around the target are referred to as DC *magnetrons*. With these systems, the sputter gas pressure can be as low as 10^{-5} Torr and very high quality films can be produced at deposition rates that match those obtained by ►evaporation deposition techniques.

Unfortunately it is difficult to use DC systems and DC *magnetron* systems to sputter magnetic materials or insulators. For such targets, it is more common to use radiofrequency (RF) excitation to ionize the gas in the sputtering chamber (Fig. 3). A circuit is employed to match the ►impedance of the power supply to the *impedance* of the sputtering chamber. A blocking capacitor is placed in series with the target so that it is negatively biased during excitation. The sputter gas pressure is typically 1 mTorr. RF sputtering systems can also be fitted with magnet assemblies; such systems are referred to as RF ►magnetrons. A major disadvantage of RF sputtering is that substrate heating is more problematic than with DC *magnetron* systems.

Generally, sputtering systems are fitted with a shutter so that the target can be sputter cleaned before deposition. Other refinements include facilities for substrate biasing and for substrate sputter cleaning. Some sputtering systems are fitted with multiple targets so that different materials can be sputtered simultaneously or sequentially without breaking the vacuum.

For micro- and nanofluidic devices, sputtering is usually performed after channel fabrication. Areas that do not require sputter coating are masked off using a lift-off layer. This could be a specially fabricated photoresist layer, or it could just be the chromium mask left over from the channel etching step. The structured substrate is placed into the sputtering chamber where it is sputtered with the desired material. Then it is removed and the lift-off layer dissolved, leaving sputtered material in the appropriate areas. Subsequently the structure is bonded to a sealing layer so that the channel structure is enclosed.

Key Research Findings

Sputtering is a standard process in materials science and it has required fairly minor adaptation for its use in fluidic device fabrication. Hence, few papers specifically deal with sputtering for microfluidics, most authors mention sputtering as a technique employed in a rather brief manner. A non-exhaustive overview of different sputtering applications is given in Table 2. Many more metals, alloys, semiconductors and insulators can be sputtered than are listed in this table; however, they are beyond the scope of this article.

Sputtering is an excellent method for producing photolithographic mask blanks and for fabricating integrated electrodes, heating elements, sensors and catalysts. Sputtering can also be used to deposit sacrificial layers for nanochannel fabrication or for channel surface treatment

Sputtering for Film Deposition, Table 2 Selected examples of sputtering as used for the fabrication of mircrofluidic and nanofluidic devices. (n.s. = not specified)

Metal	Substrate	Adhesion Layer	Layer thickness	Application	Reference
Pt	silicon	Ti	20 nm Ti, 20 nm Pt	catalysis	[2]
	Pyrex glass	Ti	20 nm Ti, 200 nm Pt	microelectrodes, *impedance* sensor	[3]
	PDMS	Ti	30 nm Ti, 320 nm Pt	microelectrodes	[4]
Au	glass	Ti	50 nm Ti and Au	thiol binding, SPR sensor	[5]
	borofloat glass	Cr, Ti	100 nm Au	temperature sensor	[6]
	PMMA	none	40 nm Au	current collector	[7]
Al	Pyrex	none	300 nm	microheater	[8]
	Pyrex	none	200 nm	heater and electrodes	[9]
	Polymer	none	100 nm	masking layer	[10]
Cr	fused silica	none	1 μm	masking layer	[11]
Ta	glass	n.s.	n.s.	to enable *anodic bonding*	[12]
Pt, Pd, Ru	glass	Cr	n.s.	catalysis	[1]
$Tb_{40}Fe_{60}$, $Fe_{50}Co_{50}$	Silicon and Molybdenum	none	(7 nm, 9 nm) × 100	GMR sensors	[13]
SLBTLO on Pt	glass	Cr	30 nm Cr, 120 nm Pt, 100 nm sensing layer	pH sensing electrodes	[14]
ITO and Ag	Pyrex glass	none	100 nm	microheater	[15]
TiNi	Silicon	none	3 μm	micropump, shape memory effect	[16]
C (graphite)	Silicon	none	1 – 7 μm	*diamond like carbon (DLC)* films as microchannel material	[17]

and modification. In addition to this, when microstructures are subjected to scanning electron microscopy (SEM) analysis, sputtering is often used to deposit a conducting layer prior to examination to prevent the structure from charging up when it is exposed to the electron beam.

Chromium is the most widely sputtered material for ►photomask fabrication. It sputters easily and it adheres well to glass. This high level of adhesion can be attributed to its ability to form a metal suboxide interface layer on glass. The exposed surface of the chromium is often oxidized to reduce its reflectivity. Aluminium is also sometimes used as a mask material, although it is more difficult to sputter and is has a higher reflectivity than oxidized Cr. This can be problematic for *photomask* applications.

On-chip electrodes have been fabricated from a number of metals including Al, Pt, Au, Indium Tin oxide (ITO)-Ag and Cu. Sometimes these electrodes have been used as low thermal mass integrated heating elements. The great versatility of sputtering is ideal for the creation of integrated on-chip sensors. These sensors range from simple thermocouples to pH sensors and even to multilayer oxide materials for giant magneto-resistance (GMR) sensors.

Sputtering has been used to incorporate a number of catalytic metals into microreactor devices. Examples include: Pt, Zr, Mo, Pd, Ru, Rh or alloys such as Pt-Ru. It is a convenient fabrication technique, although some researchers argue that the active surface area of the deposited catalyst is unsatisfactory. For many metals this problem can be overcome by sputtering using an oxygen-rich sputter gas rather than Ar alone. This produces a porous oxide deposit with a high surface area that can be reduced back to the metallic form after bonding. Alternatively, the catalytic metal can be co-sputtered with aluminium. The aluminium acts as an adhesion promoter and also forms an intermetallic oxide with the metal catalyst when the device is bonded. This method creates a robust and highly active catalyst.

Channel surface passification or modification can also be performed using sputtering. Examples include the deposition of SiO_2, SiC or even ►diamond like carbon (DLC). In addition to this, sputter deposited Ta has been used to promote ►anodic bonding for device fabrication.

Many sputtered metals do not adhere particularly well to typical device substrate materials such as silicon, glass and polymers. For example, noble metals such as Au can only rely on van der Waal's forces for adhesion and these forces

are relatively weak. Metals such as Cr, Al and Ti readily form a suboxide interface layer on glass and so they are often used as adhesion layers.

There is extensive knowledge of sputtering on Si and glass substrates that is available from the microelectronics and the electro-optics industries. Far less is known about sputtering onto more delicate substrates such as the polymers used for fluidic chip fabrication. Polymers are much more sensitive than glass and silicon to high temperatures and to being bombarded by charged particles and atoms. Conditions must be carefully optimized and the polymer substrate may even have to be protected by a layer of aluminium deposited by evaporation prior to sputtering. Great care must be taken when sputtering onto flexible polymers such as polydimethylsiloxane (PDMS), since bending may lead to cracking of the deposited film. This can be avoided by placing the polymer substrate onto a glass wafer or another rigid material. The adhesion of certain films to PDMS can be problematic. It has been found that ► plasma oxidation is sometimes helpful in improving film adhesion.

Sputtering is usually undertaken before the fluidic device is bonded and it is necessary to ensure that the deposited film does not interfere with the ► chip bonding process. This can be done by using a lift-off layer in the regions that must be clear of sputtered material. *Chip bonding* can have detrimental effects on the deposited film and this must be taken into account, especially where the device must be heated to a high temperature. After bonding, it is generally the case that catalysts deposited by sputtering must be activated before they can be used. This is often achieved by heating under a reducing atmosphere.

Future Directions for Research

Relatively few researchers in the field of micro- and nanofluidics have investigated the application of sputtering to their work. Hence, the potential of sputtering in device fabrication has been far from fully explored. In the future it is highly likely that sputtering techniques will play an important role in blurring the distinctions between electronic and fluidic devices. This will be driven by the desire to produce ever more sophisticated integrated devices with pumps, valves, electrodes, sensors, amplifiers and processors all placed on a single chip. The immense versatility of sputtering will lead to its use in the fabrication of devices with novel, nanostructured, multi-component materials. An infinite variety of composite nanomaterials can be deposited using sputtering. These materials can be engineered by: sputter etching of surfaces, sputtering using reactive sputter gases, sputtering with multicomponent targets (in combination or alternately to produce layers), by using angular dependence sputtering and by using oriented crystal substrates. Such materials will have extremely interesting catalytic and magneto-electro-optical properties and they will be utilized in many different areas of fluidics research. As can be seen from this brief introductory article, the combination of sputtering with micro- and nanofluidics is at a relatively primitive stage of development. Far more remains to be discovered.

Cross References

- ► Anisotropy
- ► Anodic Bonding
- ► Bias Voltage
- ► Chip Bonding
- ► Diamond Like Carbon (DLC)
- ► Epitaxial
- ► Evaporation Deposition
- ► Impedance
- ► Ion Implantation
- ► Magnetron
- ► Photomask
- ► Plasma Oxidation
- ► Sputter Yield
- ► Torr

References

1. Iles A, Wootton RCR, Habgood M, et al (2005) Proceedings of microTAS Conference. In: K. Jensen (ed) Kluwer Academic Publishers
2. Cui TH, Fang J, Zheng AP, et al. (2000) Sensors and Actuators B-Chemical 71:228–231
3. Hong JG, Yoon DS, Kim SK, et al (2005) Lab on a Chip 5:270–279
4. Al Mamun NH, Dutta P (2006) J Microlithograp Microfab Microsys 5
5. Kurita R, Yokota Y, Sato Y, et al (2006) Anal Chem 78:5525–5531
6. Easley CJ, Legendre LA, Roper MG, et al (2005) Anal Chem 77:1038–1045
7. Chan SH, Nguyen NT, Xia ZT, et al (2005) J Micromech Microeng 15:231–236
8. Östman P, Marttila SJ, Kotiaho T, et al (2004) Anal Chem 76:6659–6664
9. Shin WC, Besser RS (2006) J Micromech Microeng 16:731–741
10. Holland A, Cher C, Rosengarten G, et al (2006) Smart Mat Struct 15:S104–S111
11. Steingoetter I, Fouckhardt H (2005) J Micromech Microeng 15:2130–2135
12. Kawamura Y, Ogura N, Yahata T, et al (2005) J Chem Eng Japan 38:854–858
13. Ludwig A, Quandt E (2000) J App Phys 87:4691–4695
14. Lin CF, Lee GB, Wang CH, et al (2006) Biosens Bioelectr 21:1468–1475
15. Yen TH, Shoji M, Takemura F, et al (2006) Intern J Heat Mass Transfer 49:3884–3894

16. Benard WL, Kahn H, Heuer AH, et al (1998) J Microelectromech Syst 7:245–251
17. Mousinho AP, Mansano RD, Massi M, et al (2003) Diamond Related Materials 12:1041–1044
18. Wasa K, Hayakawa S (1992) Handbook of Sputter Deposition Technology, Principles, Technology and Applications. Noyes Publications, New Jersey
19. Stuart RV (1983) Vacuum Technology, Thin Films and Sputtering – An Introduction. Academic Press, New York

Sputter Yield

Definition

The number of sputtered atoms from a given target per incident ion.

Cross References

► Sputtering for Film Deposition

Stability

Synonyms

Numerical stability

Definition

Stability is a desirable property of dynamic systems in general and numerical algorithms in particular. The precise definition of stability depends on the context, but it is generally related to the accuracy of the algorithm. It is sometimes observed that different ways of doing a single calculation yield different results as they have different levels of numerical stability. A numerical algorithm is called robust if it has good numerical stability.

In the context of ►Numerical Solution of Boltzmann Equationnumerical solution of partial differential equations, stability ensures that round-off and other errors in the calculation are not amplified to cause the calculation to blow up. An algorithm for solving an evolutionary (e. g., a time-dependent) ►partial differential equation is stable if the numerical solution at a fixed time remains bounded as the time step-size goes to zero. An important theorem in mathematics, the so-called Lax equivalence theorem, states that an algorithm converges if it is consistent and stable.

Cross References

► Meshless Methods
► Volume and Finite Difference Method for Modeling and Simulation

Stack Actuator

► Multilayer Piezoelectric Actuator

Stagnation Conditions

Definition

For a compressible flow, this is the thermodynamic state that would exist if a flow were brought to rest isentropically. In practice, this would correspond to the thermodynamic state of a very low-speed flow entering the nozzle inlet from an upstream combustion chamber or a pressurized reservoir. For this reason, stagnation conditions are also sometimes referred to as 'chamber' or 'reservoir' conditions.

Cross References

► Supersonic Micro-Nozzles

Standard Deviation

Definition

The standard deviation describes the statistical spread of a bunch of random values to their arithmetic mean. It can be calculated with the root mean square of the values from their arithmetical mean.

Static Electrowetting

► Electrowetting, Applications

Stationary Phases in Microchannels

Anup K. Singh
Sandia National Laboratories, Livermore, CA, USA
aksingh@sandia.gov

Synonyms

Photopatterned materials; Cast-in-place polymeric media; In situ polymerized materials; Polymer monoliths; Cross-linked gels; Hydrogels

Definition

A stationary phase is a solid material, thin film, or gel that remains motionless relative to the flow of buffer, ions, or current in a microchannel during michrochip chromatography, electrochromatography, or electrophoresis.

Overview

Chromatographic separations frequently rely upon interactions between analytes in a flowing liquid or gas stream (or *mobile phase*), and a solid surface which remains motionless. In traditional forms of chromatography, the motionless solid surface, or *stationary phase*, might be porous particles of a polar material like silica (a *normal phase* chromatographic support), hydrophobically modified or coated silica (a *reversed phase* chromatographic support), or a thin polysiloxane film on the inner lumen of a capillary (for capillary gas chromatography).

These common forms of stationary phase are sometimes employed for miniaturized versions of chromatographic separations on microfluidic devices, although achieving uniform packing of porous particles in a planar chip can be difficult, typically requiring some form of on-chip frit. Furthermore, localizing particles to a single portion of a multifunctional device is challenging, requiring some form of on-chip valving or other strategy to isolate the chromatography column from the rest of the chip.

An alternative strategy which is sometimes employed is to fabricate a polymeric stationary phase *in situ*, often combined with photopatterning to localize the stationary phase in a particular region of the chip. As an example, phase separation polymerization using a variety of acrylate monomers, along with a photointiator, crosslinker, and porogenic solvent, can be used to define porous polymer monoliths within microchannels. In this approach, the monomers are initially soluble in the porogenic solvent, but as polymerization proceeds, the growing chains have decreased solubility, and eventually phase-separate or precipitate. Surface properties and pore size can be tailored by choice of monomer and solvent, with possibilities for hydrophobic, polar, or charged surfaces, and microscale or nanoscale pores. Polymerization can be initiated by flood illumination through a photomask, or using shaped laser light to localize monoliths to certain regions of the chip, with well-defined boundaries. Porous polymer monoliths created in this fashion have been used for on-chip liquid chromatography and electrochromatography of proteins, peptides, and other biomolecules, and are suitable for interfacing with mass spectrometry.

The term *stationary phase* can also be applied to a variety of crosslinked gels or hydrogels that can be fabricated within microchannels to act as sieving media for electrophoresis. Polyacrylamide gel is a typical stationary phase for electrophoretic separations, and has been used for sieving separations of native proteins and immunocomplexes, SDS-denatured proteins, and single- and double-stranded DNA. Sieving electrophoresis, particularly for DNA, is also frequently performed using semi-dilute solutions of non-crosslinked polymers. Crosslinked gels, like porous polymer monoliths, can be photpatterned *in situ* and localized to certain regions of the device with good spatial resolution, which can be an important advantage in complex, integrated microfluidic devices.

Cross References

► Liquid Chromatography
► Electrophoresis
► Photopatterning

References

1. Fintschenko Y, Kirby BJ, Hasselbrink EF, Singh AK, Shepodd TJ (2003) In: Svec F, Tennikova TB, Deyl Z (eds) Monolithic Materials: Preparation, Properties and Applications. Elsevier, Amsterdam, pp. 659-686
2. Ro KW, Nayalk R, Knapp DR (2006) Electrophoresis 27:3547–3558
3. Throckmorton DJ, Shepodd TJ, Singh AK (2002) Anal Chem 74:784–789
4. Herr AE, Hatch AV, Throckmorton DJ, Tran HM, Brennan JS, Giannobile WV, Singh AK (2007) Proceedings of the National Academy of Sciences of the United States of America 104:5268–5273

Statistical Sampling Method

► Monte Carlo Method

Steady Streaming

► Acoustic Streaming

Stem Cell Isolation

► Microfluidics for Stem Cell Therapy

Stem Cell Reprogramming

► Microfluidics for Stem Cell Therapy

Stem Cell Tissue Engineering

► Microfluidics for Stem Cell Therapy

Stereolithography

► Microsterolithography

Stokes Approximation

Definition

A simplifying approximation often made in fluid mechanics where the terms arising due to the inertia of fluid elements is neglected. This is justified if the Reynolds number is small, a situation that arises for example in the slow flow of viscous liquids such as when pouring honey over toast.

Cross References

Cross References

► Electrokinetic Flow and Ion Transport in Nanochannels

Stokes Shift

Definition

For fluorescent molecules that are illuminated by incident light, the shift in wavelength of the fluoresced light relative to the absorption wavelength is referred to as Stokes shift.

Cross References

► Fluorescent Thermometry

Stotz–Wien Effect

Synonyms

Nonlinear electrophoresis; Field-dependent electrophoretic mobility

Definition

The Stotz–Wien effect refers to dependence of the electrophoretic mobility of a charged polarizable particle on the field strength due to induced-charge electro-osmotic flow.

Cross References

► Aperiodic Electrophoresis
► Electrical Double Layers
► Electrokinetic Motion of Heterogeneous Particles
► Electrokinetic Motion of Polarizable Particles
► Electroosmotic Flow (DC)
► AC Electro-Osmotic Flow
► Electrophoresis
► Induced-Charge Electro-Osmosis
► Induced-Charge Electrophoresis
► Nonlinear Electrokinetic Phenomena

Streaming Current

Definition

A forced ionic liquid flow generated by a pressure gradient in a microchannel induces an electrostatic field whereas the current induced by the displacement of the heterogeneous charges in the flow is called the streaming current.

Cross References

► Streaming Current and Electroviscosity

Streaming Current and Electroviscosity

David Brutin
IUSTI Laboratory, Poytech'Marseille, Marseille, France
david.brutin@polytech.univ-mrs.fr

Synonym

Electroviscous effects

Definition

A forced ionic liquid flow generated by a pressure gradient in a microchannel induces an electrostatic field, and the current induced by the displacement of the heterogeneous charges in the flow is called the ► streaming current. Due to the electric neutrality of the fluid inside the microchannel, a conduction current, I_C, appears to equilibrate the ► streaming current, I_S. The physical and electrical properties of the fluid such as density, viscosity, electrical conductivity and permeability are influenced by concentrations of cations and anions. A forced ionic liquid flow with a surface potential induces a charge accumulation near the surface. Due to the concentration of charges the fluid viscosity near the surface is modified locally. This phenomenon of a change in apparent viscosity due to the

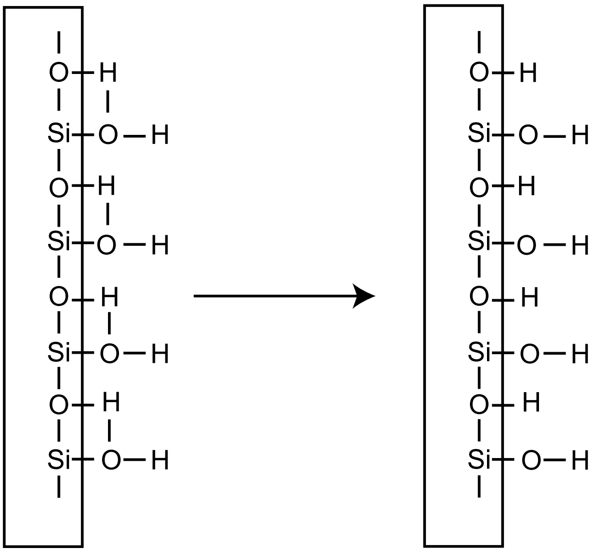

Streaming Current and Electroviscosity, Figure 1 Hydration and ionization of a fused silica surface by H_2O

presence of charges in an electrical field with a Lorentz force is also called ► electroviscosity.

Chemical and Physical Principles

Calculation of Streaming Current

► Streaming current and ► electroviscosity can only appear with an ionic fluid and a microchannel with a nonconductive inner surface such as fused silica. The surface charging mechanism with a liquid can have several origins [1]. One is the ionization and dissociation of a chemical group and another is ion adsorption, also called ion binding, on a surface which has a low charge or no charge initially. Whatever the wall charging mechanism, the final surface charge must be equilibrated by opposite sign charges accumulated in the fluid near the surface. The capacity of the wall to store charges is a function of its dielectric permittivity. For the purpose of this entry, the surface material is assumed to be fused silica (SiO_2). Water molecules hydrate the silica surface to create groups on the surface (Fig. 1). The physical mechanisms involved are the protonation and de-protonation of the SiO groups after hydration. The mechanism depends on the H^+ concentration given by the pH:

$$\mathrm{Si-O^-} + \mathrm{H^+} \longleftrightarrow \mathrm{Si-OH}\,, \tag{1a}$$

$$\mathrm{Si-OH} + \mathrm{H^+} \longleftrightarrow \mathrm{Si-OH_2^+}\,. \tag{1b}$$

If a pressure gradient is imposed on the fluid, a flow which contains charges appears and thus generates an electrostatic field due to the charge displacement. The electrostatic potential that is derived from this field is called the streaming potential. Without a pressure gradient, the fluid can be moved using an electrical field; hence an electro-osmotic flow appears. The fluid velocity profile which develops without the electric double layer (EDL) effect is parabolic; the velocity at the center of the microtube is maximum and null on the microtube surface. The charges in the fluid of opposite sign to that of the surface accumulate near the silica surface (SiO_2) and thus are transported at a lower speed than other charges far from the surface. These ion concentration laws are obtained by solving the Poisson–Boltzmann (PB) equation. Due to this differential transport phenomenon, an electric disequilibrium appears between the entrance and exit of the microtube in order to keep the total charge density constant. A current called a conduction current appears to counter the transport of charges by the fluid (streaming current). Without surface charges, no charge gradient appears in the cross-section; thus neither a streaming nor a conductive current appears. Considering that the Lorentz force (Eq. (2a)) applies on each charge, the balance between positive and negative charge is null at the center of the microtube and thus the resulting force is null. However, this disequilibrium induces a non-zero Lorentz force which has a maximum near the surface. This force decreases far from the surface as the excess charge density $\varrho(r)$ decreases. The fluid potential $\phi(r, z)$, written according to Eq. (2b), is a superposition of two potentials: the surface one $\psi(r)$ due to the EDL on the r-axis and the streaming one on the z-axis due to the differential transport phenomena of charges in the streaming field E_Z.

$$\boldsymbol{F}(r) = \varrho(r) E_Z \boldsymbol{e}_Z \tag{2a}$$

$$\phi(r, z) = \phi_0(r, z) - E_Z * z + \psi(r) \tag{2b}$$

$$E_Z = -\frac{\partial \phi(r, z)}{\partial z} \tag{2c}$$

The surface potential generates the charge gradient along the radius of the microtube according to an exponential law, whereas the streaming field induces a potential gradient along the microtube on the z-axis. As soon as ions are positioned radially, the pressure gradient induces a displacement on z. The total Lorentz force is thus on z. Its orientation is always in the direction of the flow. This phenomenon, in opposition to the fluid flow, occurs whatever the surface charge sign, as presented below:

- If the surface is negatively charged, positive charges are attracted near the surface of the microtube and thus a leak of these charges appears in the diffusive layer. The conduction current which characterizes the electron displacement is directed from the microtube

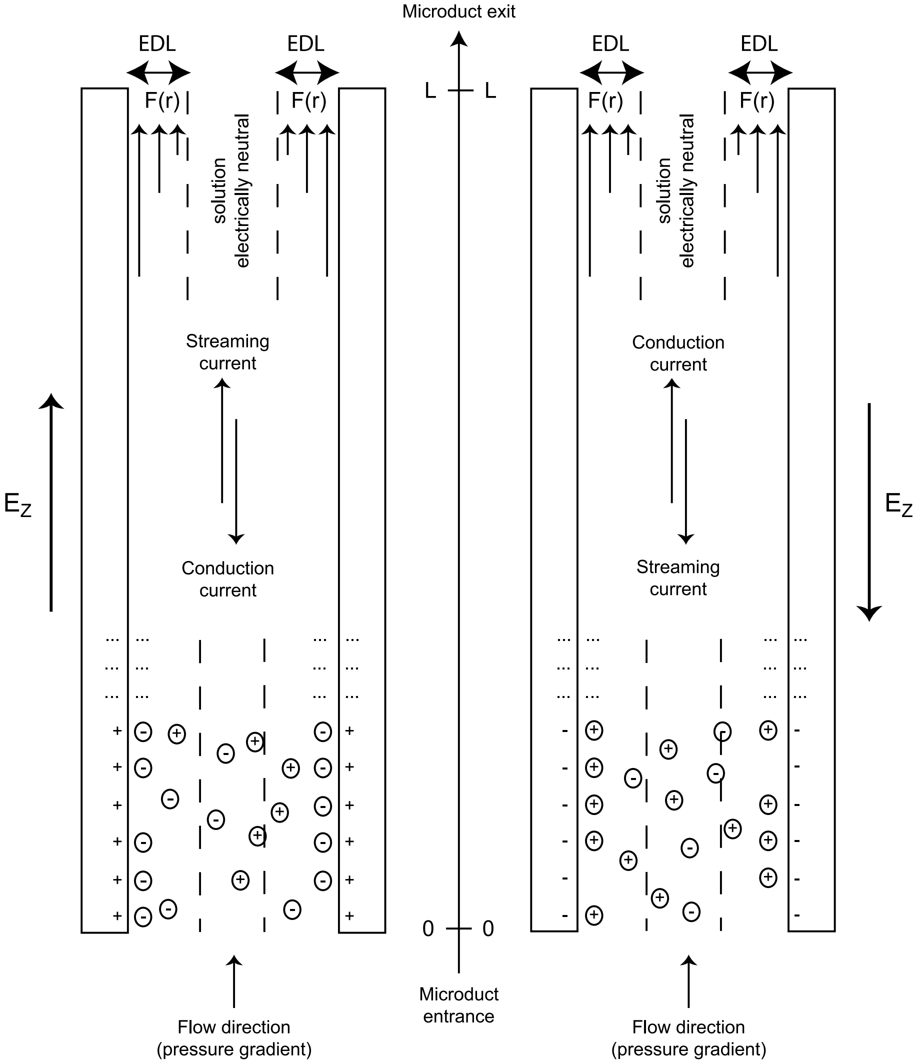

Streaming Current and Electroviscosity, Figure 2 Fluid charge distributions, electrostatic field orientations, force orientations and intensities for positive and negative surface charges

entrance to the exit in the direction opposite to that of the electrical field. The local force $F(r)$ which is based on the excess charge density (here positive charges: $+$e) is applied on a field E_Z oriented following $-\boldsymbol{e}_Z$ (from the exit to the entrance). $F(r)$ is therefore oriented along $-\boldsymbol{e}_Z$ and acts in opposition to the flow.

- If the surface is positively charged, negative charges are attracted near the surface of the microtube and thus a leak of these charges appears in the diffusive layer. The conduction current which characterizes the electron displacement is in the direction opposite to that of the electrical field from the microtube exit to the entrance. The local force $F(r)$ which is based on the excess charge density (here negative charges: $-$e) is applied on a field E_Z oriented along $\boldsymbol{e}_Z$ (from the entrance to the exit). $F(r)$ is therefore oriented parallel to $-\boldsymbol{e}_Z$ and also acts in the direction opposite to that of the flow.

The formulation used in this entry is based on the EDL theory detailed by Israelachvili [1]. The surface potential used for further calculations is denoted by ψ_0. The compact layer near the surface has a thickness of only a few atoms (about 1 nm) whereas the diffusive layer can reach 1 μm. The interfacial potential between these layers is called the zeta potential (ζ). In further computations we assume $\zeta \sim \psi_0$. Assuming a negatively charged surface, which is the case corresponding to our material, positive charges are attracted to the surface and there is a leak of negative charges. To calculate the local density of ions and co-ions, we need to make the chemical potential (μ_C)

balance on each species using the equations given below, where z is the ion valence, k_B the Boltzmann constant, T the average fluid temperature and e the proton charge:

$$\mu_C^i = ze\psi + k_B T \log n^i \,, \tag{3a}$$

$$n^i(r) = n_0 \exp\left(-i\frac{ze\Psi(r)}{k_B T}\right) . \tag{3b}$$

Considering that this potential is conserved, the chemical potential can be written for a radius and at the microtube center where the electrostatic potential is null: $\psi_{r=0} = 0$ where the fluid charge density is the bulk density (n_0). The ion concentration is given by

$$\varrho(r) = [n^+(r) - n^-(r)]ze \,, \tag{4a}$$

$$\varrho(r) = -2n_0 ze \sinh\frac{ze\Psi(r)}{k_B T} . \tag{4b}$$

where n^+ and n^- are respectively the positive and negative ion concentrations. The excess charge density is expressed as a function of the electrostatic potential.

The Poisson equation gives the relationship between the electrostatic potential $\psi(r)$ and the charge density $\varrho(r)$. In a circular geometry, the relation is

$$\frac{1}{r}\frac{\mathrm{d}}{\mathrm{d}r}\left(r\frac{\mathrm{d}\Psi(r)}{\mathrm{d}r}\right) = -\frac{4\pi}{\varepsilon\varepsilon_0}\varrho(r) \,, \tag{5a}$$

$$\frac{1}{\bar{r}}\frac{\mathrm{d}}{\mathrm{d}\bar{r}}\left(\bar{r}\frac{\mathrm{d}\bar{\Psi}(\bar{r})}{\mathrm{d}\bar{r}}\right) = -\frac{4\pi n_0 e^2 R^2}{\varepsilon\varepsilon_0 k_B T}\bar{\rho}(\bar{r}) . \tag{5b}$$

For further calculations we define nondimensional parameters such as $\bar{r}$, $\bar{\varrho}(\bar{r})$, $\bar{\Psi}(\bar{r})$:

$$\bar{r} = \frac{r}{R} \,, \tag{6a}$$

$$\bar{\varrho} = \frac{\varrho}{n_0 e} \,, \tag{6b}$$

$$\bar{\Psi} = \frac{e\Psi}{k_B T} \tag{6c}$$

$$\bar{\rho}(\bar{r}) = -2\sinh\bar{\Psi}(\bar{r}) \tag{7}$$

When Eq. (7) is included in Eq. (5b), the PB equation is obtained. κ is the electrokinetic length (usually called the Debye–Hückel length). The definition of δ depends on the geometry studied because whatever the geometry $\kappa = \delta R$ constitutes the right term of the equation before $\sinh(\bar{\Psi}(\bar{r}))$. In the literature, δ in planar geometry differs slightly from δ in circular geometry: $\delta_{circ} = \sqrt{4\pi}\,\delta_{plan}$. The boundary conditions for this nonlinear ordinary differential equation of second order are given below:

$$\frac{1}{\bar{r}}\frac{\mathrm{d}}{\mathrm{d}\bar{r}}\left(\bar{r}\frac{\mathrm{d}\bar{\Psi}(\bar{r})}{\mathrm{d}\bar{r}}\right) = \kappa^2\sinh\bar{\Psi}(\bar{r}) \,, \tag{8a}$$

$$\kappa = \delta R = \sqrt{\frac{8\pi n_0 z^2 e^2}{\varepsilon\varepsilon_0 k_B T}}R \,, \tag{8b}$$

$$\bar{r} = 0 \quad\Rightarrow\quad \frac{\mathrm{d}\bar{\Psi}(\bar{r})}{\mathrm{d}r} = 0 \,, \tag{8c}$$

$$\bar{r} = 1 \quad\Rightarrow\quad \bar{\Psi}(1) = \bar{\psi}_0 = \frac{e\psi_0}{k_B T} . \tag{8d}$$

The surface potential is related to the surface charge density through the charge balance, also known as the Grahame equation:

$$\sum_i \varrho_{0i} = \sum_i \varrho_{\infty i} + \frac{\sigma^2}{2\varepsilon\varepsilon_0 kT} \tag{9}$$

where σ is the charge density in $\mathrm{Cm^{-2}}$. ϱ is the volumic density of charges in $\mathrm{m^{-3}}$. Physically, the surface charge is constant for a given fluid while the surface potential is thereby a function of the charge fluid density. The glass–water surface potential is negative [2]. This is due to the H_3O^+ ion adsorption from the water dissociation. The authors performed measurements for glass surfaces with KCl solutions and show for a 3×10^{-3} M solution a surface charge of $-0.8\,\mu\mathrm{C\,cm^{-2}}$. For a higher pH of, say, 8.5, the measured surface charge reaches $-1.75\,\mu\mathrm{C\,cm^{-2}}$.

For example, with a 1 : 1 electrolytic solution ($z = 1$) with a concentration varying from 10^{-4} to $1\,\mathrm{mol\,l^{-1}}$ and a low surface charge of $0.2\,\mu\mathrm{C\,cm^{-2}}$, we obtain the relation between the surface charge and the surface potential function of the ion concentrations (C):

$$\sigma = \sqrt{8\varepsilon\varepsilon_0 k_B T\left(1000\left[\frac{C}{2}\right]\right)N_a}\sinh\frac{e\psi_0}{2k_B T} \tag{10}$$

where N_a is the Avogadro number, ε the relative fluid permittivity and ε_0 the absolute fluid permittivity.

To solve the PB equation we consider two zones in the microtube. Thus the hyperbolic sinus function is dissociated into two functions:

$$\bar{\Psi}(\bar{r}) \ll 1 \quad\Rightarrow\quad \sinh\left(\bar{\Psi}(\bar{r})\right) \approx \bar{\Psi}(\bar{r}) \,, \tag{11a}$$

$$\bar{\Psi}(\bar{r}) \gg 1 \quad\Rightarrow\quad \sinh\left(\bar{\Psi}(\bar{r})\right) \approx \frac{1}{2}e^{\bar{\Psi}(\bar{r})} . \tag{11b}$$

S

Equation (11a) is used for the central zone of the microtube for low potentials ($\psi_0 < 25$ mV or $\bar{\Psi}(1) < 1$) whereas Eq. (11b) is used for the zone near the surface with high surface potentials ($\psi_0 > 25$ mV or $\bar{\Psi}(1) > 1$).

Thus we build a potential function consisting of two branches matched at $\bar{r} = \beta$. Both functions are written $\bar{\Psi}_1(\bar{r})$ for $\bar{r} < \beta$ and $\bar{\Psi}_2(\bar{r})$ for $\bar{r} > \beta$. The matching condition is required for the function and their first derivate equality at $\bar{r} = \beta$. The boundary conditions for the potential function are given below:

$$\left[\frac{\mathrm{d}\bar{\Psi}_1(\bar{r})}{\mathrm{d}\bar{r}}\right]_{\bar{r}=\beta} = \left[\frac{\mathrm{d}\bar{\Psi}_2(\bar{r})}{\mathrm{d}\bar{r}}\right]_{\bar{r}=\beta} \tag{12a}$$

$$\bar{\Psi}_1(\beta) = \bar{\Psi}_2(\beta) \tag{12b}$$

$$\bar{r} = 0 \quad \Rightarrow \quad \frac{\mathrm{d}\bar{\Psi}_1(\bar{r})}{\mathrm{d}\bar{r}} = 0 \tag{12c}$$

$$\bar{r} = 1 \quad \Rightarrow \quad \bar{\Psi}_2(1) = \bar{\psi}_0 \tag{12d}$$

The continuity condition on the first derivative is used to access β which cannot be obtained analytically. At this stage it is necessary to solve the problem using a mathematical solver. The method for the solution of the ordinary differential equation is given by Levine et al. [3].

The momentum balance equation is applied for our situation with a volumic force due to the heterogeneous presence of charge excess. The geometry considered is a one-dimensional circular one with an incompressible liquid flow on the z-axis:

$$\frac{\mu}{r}\frac{\mathrm{d}}{\mathrm{d}r}\left(r\frac{\mathrm{d}U_Z(r)}{\mathrm{d}r}\right) - \frac{\mathrm{d}P}{\mathrm{d}z} + F_Z = 0 \tag{13}$$

For the sake of simplicity we use the following notations. F_Z is expressed as a function of the excess charge density ($\varrho(r)$) and E_Z is the electrostatic field given by $E_Z = E_S/L$, where E_S is the electrical field:

$$P_Z = \frac{\mathrm{d}P}{\mathrm{d}z} \tag{14a}$$

$$F_Z = E_Z\varrho(r) \tag{14b}$$

$$\bar{U} = \frac{U_Z}{U_0} \tag{14c}$$

Thus we obtain the following ordinary differential equation to solve

$$\frac{1}{\bar{r}}\frac{\mathrm{d}}{\mathrm{d}\bar{r}}\left(\bar{r}\frac{\mathrm{d}\bar{U}(\bar{r})}{\mathrm{d}\bar{r}}\right) + K_1 - \frac{K_2\bar{E}_S}{\kappa^2}\frac{1}{\bar{r}}\frac{\mathrm{d}}{\mathrm{d}\bar{r}}\left(\bar{r}\frac{\mathrm{d}\bar{\Psi}(\bar{r})}{\mathrm{d}\bar{r}}\right) = 0 \tag{15a}$$

where K_1, K_2 and E_S are defined as

$$K_1 = \frac{P_Z R^2}{\mu U_0} \tag{15b}$$

$$K_2 = \frac{2n_0 e\xi R^2}{\mu U_0 L} \tag{15c}$$

$$\bar{E}_S = \frac{E_S}{\xi} \tag{15d}$$

K_1 is the classical force ratio between pressure and the viscous forces. With a difference of one coefficient, K_1 is the classical definition of the Poiseuille number.

Without the presence of the EDL, it is possible to relate K_1 to the wall shear stress by creating a force balance on the perimeter of the microtube. Thus we obtain the relation between the classical Poiseuille number (Po) and K_1 which is $K_1 = \mathrm{Po}/8$. With the EDL, an additional term must be accounted for. This is the first space integration of the EDL force in the cross-section:

$$P_Z = \frac{4\tau_W}{D} \tag{16}$$

Equation (15a) is transformed into

$$\frac{1}{\bar{r}}\frac{\mathrm{d}}{\mathrm{d}\bar{r}}\left(\bar{r}\frac{\mathrm{d}}{\mathrm{d}\bar{r}}\left(\bar{U} - \frac{K_2\bar{E}_S}{\kappa^2}\bar{\Psi}\right)\right) + K_1 = 0 \tag{17a}$$

then spatially integrated twice to obtain $\bar{U}(\bar{r})$ given by

$$\bar{U}(r) = \frac{K_1}{4}(1 - r^2) - \frac{K_2\bar{\xi}\bar{E}_S}{\kappa^2}\left(1 - \frac{\bar{\Psi}(r)}{\bar{\xi}}\right) \tag{17b}$$

The velocity profile is a function of the electrostatic potential function. For information, the reference velocity profile is given by

$$\bar{U}_{\mathrm{ref}}(\bar{r}) = 2(1 - \bar{r}^2) \tag{17c}$$

and will be used in the following sections for comparison. The electrostatic potential is solved as a function of $\bar{r}$ for both differential Eqs. (18a) and (18b) in the two separated zones:

$$\frac{1}{\bar{r}}\frac{\mathrm{d}}{\mathrm{d}\bar{r}}\left(\bar{r}\frac{\mathrm{d}\bar{\Psi}_1(\bar{r})}{\mathrm{d}\bar{r}}\right) = \kappa^2\bar{\Psi}_1(\bar{r}) \quad \forall\bar{r} \in [0, \beta] \tag{18a}$$

$$\frac{1}{\bar{r}}\frac{\mathrm{d}}{\mathrm{d}\bar{r}}\left(\bar{r}\frac{\mathrm{d}\bar{\Psi}_2(\bar{r})}{\mathrm{d}\bar{r}}\right) = \frac{\kappa^2}{2}e^{\bar{\Psi}_2(\bar{r})} \quad \forall\bar{r} \in [\beta, 1] \tag{18b}$$

The solution of Eq. (18a) can easily be obtained and is given below, where Bessel I_0 is the modified Bessel function of the first kind zero order:

$$\bar{\Psi}_1(\bar{r}) = \frac{\text{Bessel}\, I_0(\kappa\bar{r})}{\text{Bessel}\, I_0(\beta\kappa)} \tag{19}$$

The validity range for the integration of Eq. (18a) is the microtube cross-section ($\bar{r} \in [0, 1]$) and thus we obtain the solution for the assumption of low potentials (< 25 mV). This solution is called LP for 'low potentials':

$$\bar{\Psi}(\bar{r})_{\text{LP}} = \bar{\psi}_0 \frac{\text{Bessel}\, I_0(\kappa\bar{r})}{\text{Bessel}\, I_0(\kappa)} \tag{20}$$

It will be compared with the full solution for high potentials (HP) in the following sections.
According Levine et al. [3] in the case $P < 0$ the solution of Eq. (18b) is given by

$$\bar{\Psi}_2(\bar{r}) = \ln\left(\frac{-P}{\kappa^2\bar{r}^2\cos^2(Q + \frac{1}{2}\sqrt{-P}\ln\bar{r})}\right) \tag{21a}$$

where

$$P = \left[2 + \beta\kappa\frac{\text{Bessel}\, I(1, \beta\kappa)}{\text{Bessel}\, I(0, \beta\kappa)}\right]^2 - e^1\beta^2\kappa^2 \tag{21b}$$

and

$$Q = \cos^{-1}\left(\sqrt{\frac{-P}{e^{\psi_0}\kappa^2}}\right) \tag{21c}$$

The electrostatic potential variation is solved for both zones as defined by

$$\bar{\Psi}(\bar{r})_{\text{HP}} = \begin{cases} \bar{\Psi}_1(\bar{r}) = \dfrac{\text{Bessel}\, I_0(\kappa\bar{r})}{\text{Bessel}\, I_0(\beta\kappa)} \\ \quad \text{if } \bar{r} \in [0, \beta] \\ \bar{\Psi}_2(\bar{r}) = \ln\left(\dfrac{-P}{\kappa^2\bar{r}^2\cos^2(Q + \frac{1}{2}\sqrt{-P}\ln\bar{r})}\right) \\ \quad \text{if } \bar{r} \in [\beta, 1] \end{cases} \tag{22}$$

Thus it is possible to obtain the velocity profile as given by

$$\bar{U}(\bar{r})_{\text{HP}} = \begin{cases} \bar{U}_1(\bar{r}) = \dfrac{K_1}{4}(1 - \bar{r}^2) \\ \qquad - \dfrac{K_2\bar{\psi}^2\bar{E}_{\text{S}}}{\kappa^2}\left(1 - \dfrac{\bar{\Psi}_1(\bar{r})}{\bar{\psi}_0}\right) \\ \quad \text{if } \bar{r} \in [0, \beta] \\ \bar{U}_2(\bar{r}) = \dfrac{K_1}{4}(1 - \bar{r}^2) \\ \qquad - \dfrac{K_2\bar{\psi}^2\bar{E}_{\text{S}}}{\kappa^2}\left(1 - \dfrac{\bar{\Psi}_2(\bar{r})}{\bar{\psi}_0}\right) \\ \quad \text{if } \bar{r} \in [\beta, 1] \end{cases} \tag{23}$$

Now we need to determine $\bar{E}_{\text{S}}$ from the electrical charge balance inside the microtube.
A forced ionic liquid flow generated by a pressure gradient induces an electrostatic field E_{S}. The current induced by the charge displacement in the flow is called the electrostatic current I_{S}; its expression is

$$I_{\text{S}} = 2\pi \int_0^R U(r)\varrho(r) r\, \text{d}r \tag{24a}$$

After a classical nondimensioning of the governing equations on $U(r)$ and $\varrho(r)$, the expression of $\bar{I}_{\text{S}}$ is

$$\bar{I}_{\text{S}} = \frac{I_{\text{S}}}{U_0 R^2 n_0 e} = -4\pi \int_0^1 \bar{U}(\bar{r})\bar{\Psi}(\bar{r})\bar{r}\, \text{d}\bar{r} \tag{24b}$$

Applying the electric neutrality of the fluid inside the microtube, a conduction current (I_{C}) occurs in order to equilibrate the streaming current due to the charge displacement. The following equation gives the expression of the conduction current:

$$\begin{aligned} I_{\text{C}} &= \int_0^R 2\pi rme[n_+(r) + n_-(r)]\frac{E_{\text{S}}}{L}\, \text{d}r \\ &= \frac{E_{\text{S}}\lambda_0}{L}\int_0^R 2\pi r \cosh\bar{\Psi}(r)\, \text{d}r \end{aligned} \tag{25}$$

where λ_0 is the electrical fluid conductivity which can be calculated using

$$\lambda_0 = \text{F}^2 \sum z_i^2 \nu_i c_i \tag{26}$$

where ν_i is the ion mobility, c_i is the ion concentration, z_i is the charge and F is the Faraday constant.

Using a nondimensional form with Eq. (27c), we obtain Eq. (27a) where Σ_1 is a pure numerical integration:

$$\bar{I}_{\mathrm{C}} = \frac{I_{\mathrm{C}}}{\lambda_0 R \psi_0} = 2\pi \bar{E}_{\mathrm{S}} \bar{L} \Sigma_1 \tag{27a}$$

$$\Sigma_1 = \int_0^1 \bar{r} \cosh \bar{\Psi}(\bar{r})\, \mathrm{d}\bar{r} \tag{27b}$$

$$\bar{L} = \frac{L}{R} \tag{27c}$$

Using Eq. (28), the balance is written for both currents:

$$I_{\mathrm{S}} + I_{\mathrm{C}} = 0 \tag{28}$$

Thus we obtain $\bar{E}_{\mathrm{S}}$ which is given by

$$\bar{E}_{\mathrm{S}} = 2\frac{K_3}{\Sigma_1} \int_0^1 \bar{r}\bar{U}(\bar{r})\bar{\Psi}(\bar{r})\, \mathrm{d}\bar{r} = \frac{K_1 \Sigma_3}{\frac{2\Sigma_1}{K_3} + \frac{4K_2\bar{\psi}_0\Sigma_4}{\kappa^2}} \tag{29}$$

where K_3 is given by

$$K_3 = \frac{n_0 e L U_0}{\lambda_0 \psi_0} \tag{30}$$

and

$$\Sigma_3 = \int_0^1 \bar{r}(1-\bar{r}^2)\bar{\Psi}(\bar{r}) \tag{31}$$

$$\Sigma_4 = \int_0^1 \bar{r}\left(1 - \frac{\bar{\Psi}(\bar{r})}{\bar{\psi}_0}\right)\bar{\Psi}(\bar{r}) \tag{32}$$

Using the nondimensional electrostatic potential expression in the velocity profile expression, we obtain the Poiseuille number expression. K_3 is the nondimensional ratio between the convection current and the conduction current.

Electroviscosity

Theory

The net effect of the charge forces close to the wall is a diminished flow in the main flow axis. The fluid appears to exhibit an enhanced viscosity if its flow rate is compared with the flow without the EDL effects. This increase in apparent viscosity of a fluid is the ▶electroviscous effect [4–6].

To calculate ▶electroviscosity, we first define the volumic flow rate using

$$Q_{\mathrm{V}} = \int_0^R U(r) 2\pi r\, \mathrm{d}r \tag{33}$$

To use the previous results of the fluid velocity profile, we require a nondimensional form of the volumic flow rate:

$$Q_{\mathrm{V}} = 2\pi R^2 U_0 \int_0^1 \bar{r}\bar{U}(\bar{r})\, \mathrm{d}\bar{r} \tag{34}$$

The expression of the fluid velocity has already been calculated in the previous section (Eq. (23)). For calculation purposes, we use the following writing simplification ($i = 1$ if $\bar{r} < \beta$, $i = 2$ if $\bar{r} > \beta$):

$$\bar{U}_i(\bar{r}) = \frac{K_1}{4}(1-\bar{r}^2) - \frac{K_2\bar{\psi}_0\bar{E}_{\mathrm{S}}}{\kappa^2}\left(1 - \frac{\bar{\Psi}_i(\bar{r})}{\bar{\psi}_0}\right) \tag{35}$$

By replacing the fluid velocity expression, we extract the expression of the volumic flow rate:

$$Q_{\mathrm{V}} = 2\pi R^2 U_0 \left[\frac{K_1}{24} - \frac{K_2\bar{\psi}_0\bar{E}_{\mathrm{S}}}{\kappa^2}\int_0^1 \bar{r}\left(1 - \frac{\bar{\Psi}_i(\bar{r})}{\bar{\psi}_0}\right)\right] \tag{36}$$

The expressions of K_1 and K_2 (Eqs. (15b) and (15c)) are introduced into Eq. (36) to reveal the fluid viscosity:

$$Q_{\mathrm{V}} = \frac{\pi R^4}{12\mu}P_{\mathrm{Z}} - \frac{4\pi R^4 n_0 e \xi \bar{\psi}_0 \bar{E}_{\mathrm{S}}}{\mu L \kappa^2}\int_0^1 \bar{r}\left(1 - \frac{\bar{\Psi}_i(\bar{r})}{\bar{\psi}_0}\right) \tag{37}$$

The apparent fluid viscosity (μ_{a}) can be deduced by assuming the classical relation between volumic flow rate and pressure drop:

$$Q_{\mathrm{V}} = \frac{\pi R^4}{12\mu_{\mathrm{a}}}P_{\mathrm{Z}} \tag{38}$$

$$\frac{\mu_{\mathrm{a}}}{\mu} = \frac{1}{1 - \frac{32\bar{E}_{\mathrm{S}}(\bar{\psi}_0)^2\varepsilon\varepsilon_0}{\pi R^2 P_Z L}\int_0^1 \bar{r}\left(1 - \frac{\bar{\Psi}_i(\bar{r})}{\bar{\psi}_0}\right)} \tag{39}$$

Volumic flow rates which are identical are identified and enable us to find the ▶electroviscosity.

Equation (39) gives the ▶electroviscosity in a microtube with an inner charged surface at the potential ψ_0. The reduced forward volumic flow rate observed experimentally is interpreted as an increased apparent viscosity. Using the expressions of K_1, K_2, E_{S} and K_3 (respectively Eqs. (15b), (15c), (29) and (30)) it is possible to evidence that μ_{a}/μ is a function of neither the average fluid velocity (U_0) nor the pressure gradient (P_Z) but only a function of the microtube diameter and the electrokinetic parameters. The case of two parallel plates has been studied by Mala et al. [6] and will not be presented here. The ▶electroviscosity equation obtained differs slightly from Eq. (39) due to the geometry.

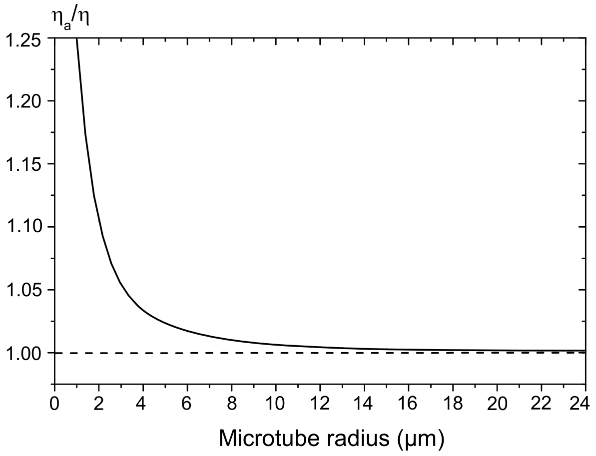

Streaming Current and Electroviscosity, Figure 3 Electroviscosity as a function of microtube radius for a pure deionized water flow with an electrical surface potential of 57 mV

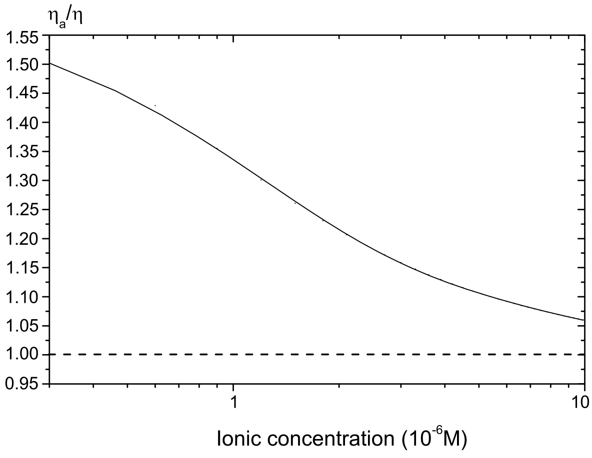

Streaming Current and Electroviscosity, Figure 4 Electroviscosity as a function of fluid ionic concentration in a microtube with a diameter of 1 μm and an electrical surface potential of 40 mV

Example

Let us consider a capillary tube with a radius ranging from 1 to 24 μm, which corresponds to commercial fused silica microtubes used in gas chromatography. The fluid is pure deionized water with a total ionic concentration of 2×10^{-7} M and consequently an electrical conductivity of 4.1×10^{-7} S m^{-1}. The inner capillary surface is slightly charged at 50 μC m^{-2}, with a 1 : 1 electrolytic solution ($z = 1$). We obtain the relation between the surface charge and the surface potential function of the ion concentrations with Eq. (10). The surface potential (ψ_0) which is calculated by deduction is 57 mV.

Figure 3 presents the variation of the ►electroviscosity for a fluid flow of pure deionized water in a microtube with a radius ranging from 1 to 24 μm. The increase in ►electroviscosity in a microtube is not perceptible for diameters above 15 μm. Below 15 μm the increase becomes perceptible with a maximum of 25% for a microtube with a diameter of 2 μm. The model previously described and the mathematical assumptions are correct since the radius of the microtube is greater than the electrokinetic distance, which is about 1 μm for pure water. Experiments with microtubes smaller than the electrokinetic distance have not as yet been reported in the literature.

Figure 4 presents the variation of the ►electroviscosity for a KCl solution with an ionic concentration ranging from 3×10^{-7} to 10^{-5} M. As the ionic concentration increases, the electrokinetic distance ($1/\delta$) decreases according to Eq. (8b). The surface potential is constant at 40 mV and the diameter of the microtube is 1 μm. The largest electrokinetic distance is about 0.2 μm for the lowest ionic concentration based on two kinds of ions: K^+ and Cl^- for a total number charge (n_0). The ►electroviscosity is almost the classical fluid viscosity for solution concentrations higher than 10^{-5} M. For lower concentrations up to 3×10^{-7} M the apparent viscosity increases to reach +50% for a 3×10^{-7} M concentration, which is close to the ion concentration of pure water (total ion concentration of 2×10^{-7} M with H_3O^+ and OH^-).

Key Research Findings

The experimentally observed differences in the literature for fluid flow in microchannels can have many explanations. Some deviations can be rapidly explained by the use of microducts which have not been well calibrated. The four main effects proposed to explain these observed deviations are: the micropolar fluids theory, electrokinetic effects, heat viscosity dissipation and the wall continuity condition. Among all these effects electrokinetic flow has been more widely investigated in the literature; ion interaction with water is of great importance in biological and chemical applications for MEMS technology.

Electroviscous effects on fluid flow for ionic fluids in microchannels have been evidenced over the last decade experimentally [7–9] and are still a subject of widespread theoretical research [4, 10]. Ren et al. [5] found experimentally significant electroviscous effects for dilute solutions flowing through microchannels with hydraulic diameters of 14.1, 28.2 and 40.5 μm. They elaborated a model for a microchannel between two plates which considers the deficit of counterions and the surplus of co-ions outside the EDL. They obtain a nonzero electrical potential gradient and a net charge density near the middle plane of the microchannel. The highest fluid velocity and the transport

S

of the net charge at the center of the microchannel result in a higher streaming potential.

Cross References

- ► Electroosmotic Flow (DC)
- ► AC Electro-Osmotic Flow
- ► Electrokinetic/Hydrodynamic Flow Instability
- ► Nonlinear Electrokinetic Phenomena
- ► Surface Conductivity Measurement
- ► Temperature Effects on the Zeta Potential
- ► Zeta Potential Measurement

References

1. Israelachvili JN (1991) Intermolecular and Surface Forces. Academic Press, London
2. Schweiss R, Welzel PB, Werner C, Knoll W (2001) Interfacial charge of organic thin films characterized by streaming potential and streaming current measurements. Colloids Surf 195:97–102
3. Levine S, Marriott JR, Neale G, Epstein N (1975) Theory of electrokinetic flow in fine cylindrical capillaries at high zeta-potentials. J Colloid Interface Sci 52(1):136–149
4. Bowen WR, Jenner F (1995) Electroviscous effects in charged capillaries. J Colloid Interface Sci 173:388–395
5. Ren CL, Li D (2004) Electroviscous effects on pressure-driven flow of dilute electrolyte solutions in small microchannels. J Colloid Inferface Sci 274:319–330
6. Mala GM, Li D, Dale JD (1997) Heat transfer and fluid flow in microchannels. Int J Heat Mass Transf 40(13):3079–3088
7. Ren L, Qu W, Li D (2001) Interfacial electrokinetic effects on liquid flow in microchannels. Int J Heat Mass Transf 44:3125–3134
8. Brutin D, Topin F, Tadrist L (2003) A transient method for the liquid laminar flow friction factor in microtubes. AIChE J – Fluid Mech Transp Phenom 49(11):2759–2767
9. Brutin D, Tadrist L (2003) Experimental friction factor of a liquid flow in microtubes. Phys Fluids 15(3):653–661
10. Vainshtein P, Gutfinger C (2002) On electroviscous effects in microchannels. J Micromech Microeng 12(2):252–256

Streaming Dielectrophoresis

- ► DC Dielectrophoresis in Lab-on-a-Chip Devices

Stroke

Synonyms

Throw

Definition

In an actuator that produces linear translation, *stroke* refers to the maximum amplitude of the motion.

Cross References

- ► Membrane Actuation for Micropumps
- ► Microactuators
- ► Peristaltic Pumps
- ► Positive Displacement Pump

Stroke Volume

Definition

In a positive displacement pump a moving boundary changes the volume of a pump chamber. The *stroke volume* is the difference between the maximum and minimum chamber volumes.

Cross References

- ► Compression Ratio
- ► Dead Volume
- ► Electromagnetic Valves
- ► Electrostatic Valves
- ► Magnetic Pumps
- ► Membrane Actuation for Micropumps
- ► Microactuators
- ► Peristaltic Pumps
- ► Piezoelectric Valves
- ► Pneumatic Valves
- ► Positive Displacement Pump
- ► Thermomechanical Valves
- ► Thermopneumatic Valves

Subcooled Flow Boiling

Definition

Boiling process at the wall while the mean bulk enthalpy of flow is below the saturation enthalpy corresponding to the local pressure.

Cross References

- ► Bubble Dynamics in Microchannels

Subdynamic Regime

Definition

Laminar fluid flow regime in which inertial effects become negligible compared with frictional damping.
This regime exists at very low values of the Reynolds number, usually below $\mathrm{Re} \simeq 10$. In the true subdynamic

regime the character of the flow ceases to depend on the Reynolds number, the flowfield becomes self-similar. Microfluidic devices are rarely if at all employed in the subsonic regime – usually the inertial effects remain noticeable in them. The regime, however, served as a useful reference asymptotic state.

Superfast Electrophoresis

► Electrophoresis of the Second Kind

Super-Limiting Current

Definition

A super-limiting current in an electrolyte is an ionic current large enough to exceed diffusion limitation, which depletes the bulk salt concentration and leads to the formation of extended space charge.

Cross References

► Electrical Double Layers
► Electroosmosis of the Second Kind
► Electrophoresis of the Second Kind
► Nonlinear Electrokinetic Phenomena
► Space Charge

Superparamagnetism

Definition

Superparamagnetism characterizes materials that have susceptibility typical of ferromagnetism and a reversible magnetization like paramagnetic matter.

Cross References

► Magnetic Field-Based Lab-on-Chip Devices

Supersonic Micro-Nozzles

William F. Louisos, Darren L. Hitt
Mechanical Engineering Program, School of Engineering,
University of Vermont, Burlington, VT, USA
darren.hitt@uvm.edu

Synonyms

MEMS-nozzle; Microthruster; MEMS-thruster

Definition

The fundamental purpose of any nozzle is the acceleration of a flow field via the conversion of available pressure and/or internal energy into kinetic energy. For compressible fluids (gases), it is possible accelerate to the flow from subsonic to sonic speeds – and ultimately supersonic speeds – with sufficiently high inlet pressure ratios. Supersonic nozzles typically consist of three distinct regions: a subsonic converging portion at the inlet, followed by a 'throat' where the cross-sectional area is minimum, and finally a supersonic diverging section ('expander'). Micronozzles are uniquely defined by their small length scales (throat diameters typically below 100 μm) and the low Reynolds numbers of the flow ($Re < 1000$).

Overview

Perhaps the most frequent engineering application of nozzles is in propulsion systems for aircraft or spacecraft; however, other important applications exist as well (e. g., spray nozzles and fluid atomization). Initial acceleration of a flow at subsonic speeds occurs in the convergent section and, for sufficiently high pressure ratios and nozzle area contraction, it is possible to accelerate a flow to sonic conditions at the nozzle throat. The addition of a divergent section downstream of the throat enables further acceleration of the flow through supersonic expansion (i. e., a *de Laval* nozzle). It is the ability of the convergent–divergent nozzle to fully and efficiently extract pressure/internal energy from a low speed inlet flow and produce supersonic exit velocities that make it such a vital component in high-speed aerospace propulsion. In the present article, we shall restrict our focus to supersonic nozzle behavior within the context of propulsion physics and engineering.

In most aerospace propulsion applications, the combination of high speeds and moderate-to-large length scales result in very high Reynolds numbers – sufficiently large that viscous effects can be largely ignored and inviscid analyses employed as a first approximation. However, the importance of viscous effects in supersonic flows is emerging in light of recent trends within the aerospace community linked to the design of next-generation miniaturized spacecraft. Most commonly known as 'nano-sats' (The names 'micro-sats' and more recently 'pico-sats' are also used, and to a certain degree, they can be regarded as interchangeable with nano-sat. At present there exists no formalism to distinguish the specific mass range that defines a micro/nano/pico-sat other than being successfully smaller than each other), these spacecraft will feature masses < 20 kg and be capable of operating in distributed networks ('formation flying') and performing mission objectives not currently achievable with traditional satel-

S

lite architectures. Over the past decade, numerous and diverse micropropulsion initiatives for nano-sats have been undertaken by governments, industry, and academia throughout the world. The various approaches, all of which tend to have their unique benefits, have included both liquid/solid chemical propellants and electric propulsion concepts; many of these options require supersonic micro-nozzles as an integral part of the design. For the interested reader, a comprehensive survey of current micropropulsion concepts is given by Mueller [1].

As a result of the dramatically reduced size, nano-sats require miniaturized propulsion systems to provide the extremely low levels of thrust/impulse necessary for orbital maneuvering and precise station-keeping. With the characteristic length scales being considered for these new propulsion systems being on the order of microns to millimeters, the corresponding Reynolds numbers within the supersonic nozzles are $\mathrm{Re} \sim 10^2 - 10^3$ and hence viscous effects can no longer be ignored. The scenario of low Reynolds number, supersonic flow represents a *very unusual flow regime*, and one that has not been extensively examined in the fluid dynamics literature. In this regime, there is the usual thermo-fluidic complexity of a supersonic flow superimposed with subsonic viscous boundary layers extending from solid surfaces. At these low Reynolds numbers the viscous layer can occupy a sizable fraction of the divergent nozzle cross-section and, as a consequence, substantially impact the performance of the nozzle (e. g. thrust production). Aside from viscous forces, other important effects such as heat transfer and flow rarefaction may also be present on the micro-scale. The former becomes a concern as the thermal mass of the flow is reduced and the surface area-to-volume ratio increases on the micro-scale. The latter introduces additional complications since gas kinetic (non-continuum) effects begin to emerge as the characteristic length scales begin to approach molecular mean free paths.

In this article, we provide an overview of the various engineering issues and challenges surrounding the modeling, design and fabrication of micro-propulsion systems and supersonic micro-nozzles in particular. From this, it is our hope and intent that the reader will develop an appreciation for the unique aspects of supersonic nozzle behavior on the micro-scale.

Basic Methodology

Design Considerations and Specifications

Micro-Electro-Mechanical Systems (MEMS) techniques offer great potential in satisfying future mission requirements for the next generation of small scale spacecraft being designed by the aerospace community. Owing to the substantially reduced size, nano-sats have unique propulsion requirements, including extremely low thrust levels and/or extremely low minimum impulse requirements for orbital maneuvers and attitude control. Nanosatellites will be launched from Earth in a consolidated manner via a single rocket. Once in orbit, they will be subsequently deployed and operate in a distributed network performing simultaneous, multi-point observations and communication. The Magnetospheric Constellation (MagCon) is an example of one mission currently being designed by the NASA Goddard Space Flight Center (GSFC) that will utilize the unique characteristics of nano-satellites to monitor the Earth's magnetosphere. This type of space mission is not feasible with traditional satellite architectures. Nano-satellite technology demands highly accurate and extremely precise control of the spacecraft to maintain pattern formation. The primary method of attitude control is spin axis precession. In order to correct for perturbations such as solar radiation pressure or gravitational non-uniformities, the propulsion system must operate by firing low thrust, precise, and controlled impulse 'bits'. As a result of the spacecraft's reduced size and mass, the ability to perform spin axis precession and very small station-keeping maneuvers will require the development of radically new propulsion systems.

Supersonic Micro-Nozzles, Table 1 Design parameters for the NASA/GSFC MEMS-based monopropellant supersonic micro-nozzle.

Design Parameter	Value/Range
Target Thrust Level	$10 - 500\ \mu\mathrm{N}$
Maximum Specific Impulse	180 sec
Specific Impulse Efficiency	80%
Steady State Inlet Pressure	250 kPa
Mass Flow Rate	~ 0.015 kg/sec
Throat Area	$9000\ \mu\mathrm{m}^2$
Expansion Ratio	6.22
Inlet Mach No.	0.05
Exit Mach No.	$2.5 - 3.0$
Reynolds Number	< 1000
Impulse Bit	$1 - 100\ \mu\mathrm{N}$ sec

As an illustrative example, NASA/GSFC has designed a prototype monopropellant micro-thruster, shown in Fig. 1, for the purpose of nano-satellite attitude control and station keeping maneuvers [2]. The supersonic micro-nozzle has been outlined in the figure for clarity. A listing of target design specifications for this prototype is given in Table 1. The NASA/GSFC prototype is based on catalytic decomposition of a liquid monopropellant; specifically

hydrogen peroxide H_2O_2 or hydrazine N_2H_4. Chemical-based propulsion schemes, on the whole, are attractive in several regards: they feature relatively high energy densities and efficiencies; the propellants can be stored at low pressures thus alleviating leakage concerns; and they offer the ability to throttle and control the rate of thrust production via transient operation.

Quasi-1D Flow Approximation and Analysis

A supersonic micro-nozzle consists of a micro-machined channel with a varying cross-sectional area $A(x)$, where the $+x$-direction coincides with the flow direction within the channel. Under the 'quasi-one-dimensional' (quasi-1D) flow approximation, all flow variables are assumed to vary only with the streamwise position x (and time if the flow field is unsteady). Variations across a given cross-section are considered negligible. Such an approximation is valid provided that the *rate of area variation* $\mathrm{d}A/\mathrm{d}x$ *is sufficiently small*. The quasi-1D model is, of course, only an approximation of an actual 3D flow; however, it greatly simplifies analyses and often yields surprisingly good results in predicting basic nozzle behavior. An overview of the quasi-1D nozzle model and its limitations can be found in most gas dynamics references (e. g., [3]).

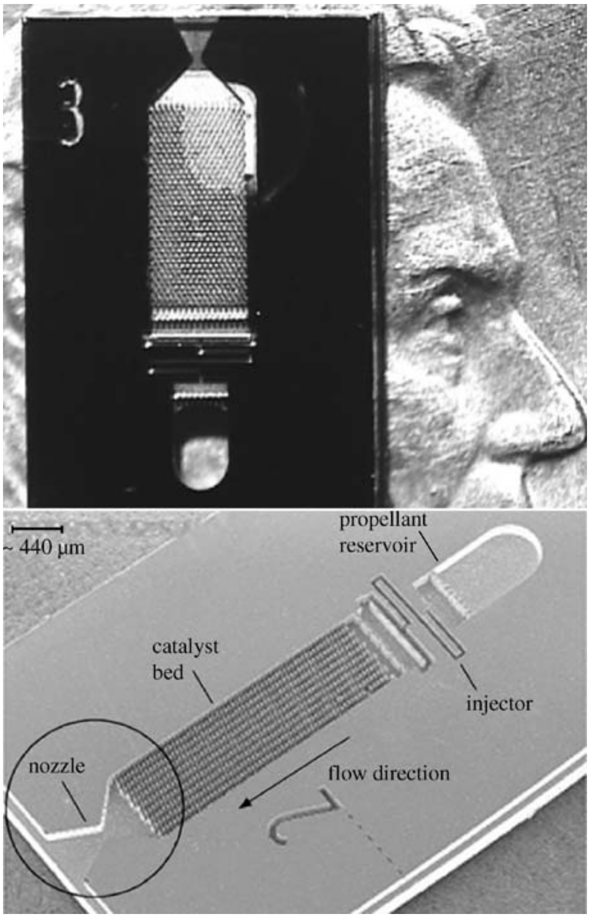

Supersonic Micro-Nozzles, Figure 1 (Top) A photograph of the NASA/GSFC MEMS-based micro-thruster etched into a silicon wafer and placed on top of a US penny for purposes of scale. (Bottom) A Scanning Electron Microscopy (SEM) image of the NASA/GSFC micro-thruster with the converging-diverging supersonic micro-nozzle outlined for clarity. See [2] for details

The governing equations for the flow are obtained by one-dimensional approximations of conservation laws for mass, momentum and energy. Often the additional assumptions of inviscid, adiabatic flow are invoked and, as a consequence, the flow is regarded as isentropic throughout. From the conservation laws, one may derive an important relation between the cross-sectional area, the velocity and the local Mach number:

$$\frac{\mathrm{d}A}{A} = \left(\mathrm{M}^2 - 1\right)\frac{\mathrm{d}u}{u} \tag{1}$$

Here $\mathrm{M} = u/a$ is the Mach number and a is the isentropic speed of sound defined by

$$a^2 = \gamma RT \tag{2}$$

where T is the static temperature, R is the gas constant, and $\gamma = C_\mathrm{p}/C_\mathrm{v}$ is the ratio of the specific heats.

The area-velocity relation provides important insight regarding the behavior of a quasi-1D compressible flow in a channel of varying cross section. It states that for a subsonic flow ($\mathrm{M} < 1$) to increase velocity, a decrease in cross-sectional area is required. This is an intuitive and familiar result similar to incompressible flow theory. In contrast, acceleration of a supersonic flow ($\mathrm{M} > 1$), requires an increase in area: a counter-intuitive result when viewed from an incompressible flow perspective. This relation also indicates that sonic velocity ($\mathrm{M} = 1$) can only occur at a nozzle throat where the area is a minimum. It thus follows for a gas to expand from subsonic to supersonic velocities, it must flow through a convergent–divergent channel arrangement.

An alternative and extremely useful form of the area-velocity relation (1) can be derived for isentropic flow which relates the local Mach number to the local area,

$$\left(\frac{A}{A_*}\right)^2 = \frac{1}{\mathrm{M}^2}\left[\frac{2}{\gamma+1}\left(1 + \frac{\gamma-1}{2}\mathrm{M}^2\right)\right]^{\frac{\gamma+1}{\gamma-1}} \tag{3}$$

where A_* is the area of the nozzle throat where sonic conditions exist. For a prescribed nozzle profile $A(x)$, this 'area-Mach relation' yields the corresponding variation in

the Mach number along flow direction. Further, for isentropic flow, it can be shown that the local thermodynamic properties (T, p, ρ) may be uniquely determined by the local Mach number according to the following:

$$\frac{T_0}{T} = 1 + \frac{\gamma - 1}{2}\mathrm{M}^2 \tag{4}$$

$$\frac{p_0}{p} = \left(1 + \frac{\gamma - 1}{2}\mathrm{M}^2\right)^{\frac{\gamma}{\gamma-1}} \tag{5}$$

$$\frac{\rho_0}{\rho} = \left(1 + \frac{\gamma - 1}{2}\mathrm{M}^2\right)^{\frac{1}{\gamma-1}} \tag{6}$$

Here, the subscript "0" indicates the stagnation conditions $(\mathrm{M} \to 0)$ corresponding to a specific flow state. In practice, these are the conditions of the gaseous products of chemical decomposition or combustion that exist upstream of the nozzle inlet and, therefore, may be regarded as known states for the purposes of the nozzle modeling.

In summary, for a prescribed nozzle profile $A(x)$ and inlet conditions, the area-Mach relation (3) and isentropic flow relations (4)–(6) are sufficient to completely determine the nozzle flow field under the quasi-1D model.

Thrust and Impulse

The ultimate deliverable for a supersonic nozzle in a propulsion application is the production of thrust and impulse. A control volume analysis of the nozzle indicates that the thrust produced at any moment in time can be approximated by the exit conditions according to

$$\boldsymbol{F} = \int_{A_{\mathrm{exit}}} \rho \boldsymbol{u} \left(\boldsymbol{u} \cdot \boldsymbol{n}\right) \mathrm{d}A \approx \dot{m}\boldsymbol{V}_{\mathrm{exit}} \tag{7}$$

where $\dot{m} = \rho_{\mathrm{exit}} V_{\mathrm{exit}} A_{\mathrm{exit}}$ is the mass flow rate through the nozzle and $\boldsymbol{V}_{\mathrm{exit}}$ is the average velocity at the nozzle exit plane. For transient operation, the total impulse during a single firing cycle of the thruster is given by

$$\boldsymbol{I} = \int_0^{t_\mathrm{b}} \boldsymbol{F}\,\mathrm{d}t \tag{8}$$

where t_b is the total burn time or thrust duration of a single micro-nozzle firing. Under the quasi-1D approximation, all force generated is necessarily in the axial direction (i.e., thrust). In actual 2D or 3D flows, this will generally not be the case and there will be performance reductions resulting from transverse velocity components at the exit. Thus, exit flow alignment is yet another consideration that is part of the overall supersonic nozzle design.

Continuum vs. Rarefied Flows

The preceding discussion has implicitly assumed that the flow conditions are such that the continuum assumption remains valid within the micro-nozzle. The usual metric cited in arguing for (or against) the continuum assumption is the *Knudsen number* Kn, defined by $\mathrm{Kn} = \Lambda / L$ where Λ is the mean free path of the fluid particle and L is a characteristic length scale. For converging-diverging nozzles the throat dimension is commonly chosen as the characteristic length scale. An alternative version of the Knudsen number which is of particular use in investigating supersonic flows is given by

$$\mathrm{Kn} = \sqrt{\frac{\gamma\pi}{2}}\frac{\mathrm{M}}{\mathrm{Re}}\,.$$

While $\mathrm{Kn} \to 0$ is the formal requirement for a continuum flow, in practical terms gas flows for which Kn remains below a threshold value can be safely regarded as being within a continuum regime. The exact value of Kn at which rarefaction effects begin to appear remains a matter of some controversy and generally depends upon the specifics of the flow under consideration; however, $\mathrm{Kn} \sim 0.01 - 0.1$ is a representative range of values. At these and higher Kn numbers, the breakdown in the continuum assumption is first manifested at the boundaries with the appearance of velocity and (if applicable) thermal 'slip' wherein a discontinuity occurs between the flow and the solid boundary where they interact. Mathematically, these modified boundary conditions take the form:

$$u_{\mathrm{slip}} = \mathrm{Kn}\frac{\partial u}{\partial n} \qquad T - T_{\mathrm{wall}} = \mathrm{Kn}\frac{\partial T}{\partial n}$$

The flow within a typical converging/diverging supersonic micro-nozzle – and its plume – may span a wide range of Knudsen numbers encompassing continuum flow, highly rarefied flows and all intermediate states in between. A key determinant, however, rests with the value of the ambient back-pressure at the nozzle exit. For cases where there is very low back-pressures (e.g., low Earth orbit or space) a significant portion of the flow field may be influenced by rarefaction effects. Conversely, at more modest back-pressures (e.g., atmospheric operation) it may be that the flow field can safely be regarded as remaining within the continuum regime.

In most high-altitude or space applications, the nozzle flow will be under-expanded and the external plume will experience the greatest flow rarefaction. Depending on the circumstances, the rarefaction can be quite severe, extending beyond the slip regime and bordering on the free molecular regime. In such cases, modeling efforts require the use

of gas kinetic schemes such as Direct Simulation Monte Carlo (DSMC) or even Molecular Dynamics (MD). The discussion of these methods are beyond the scope of this article and the interested reader is encouraged to refer to the classic monograph by G. Bird [4]. It is important to note that, for supersonic flow, the level of accuracy required in the modeling of the plume region is really a 'matter of interest'. For example, if the interest lies in the chemical signatures of exhaust plumes or perhaps the interaction of the plume with a spacecraft's solid surfaces, then flow rarefaction cannot be ignored. On the other hand, if thrust production by the nozzle is the key item of interest, then the specifics of the supersonic plume are of no real import.

It is possible that the supersonic portion of the micro-nozzle may also experience some degree of rarefaction, depending on the specifics of the flow. However, the extent of the rarefaction is usually minor and, if needed, can be reasonably managed by augmenting a continuum model with slip boundary conditions to yield more precise estimates of thrust production.

Micro-Nozzle Geometry

Area Ratios and Physical Nozzle Dimensions

The driving constraint of a micro-nozzle design is the target thrust level, which is determined by the nozzle exit conditions (velocity, thermodynamic state, and area) as given by Eq. (7). It is important to note that there is not a unique flow state for a specific thrust, and thus other design constraints or conditions must be imposed in order to determine a specific solution. Such considerations might include: the ambient back-pressure at the nozzle exit, the maximum allowable size of the nozzle, or the maximum mass flow rate $\dot{m}$ that the system can deliver. For micro-nozzles that are components of miniaturized propulsion systems, size may be the overriding concern and hence the exit area may provide the necessary additional constraint. Once the desired nozzle exit conditions have been identified, the nozzle area expansion ratio (A/A_*) is fixed by the area-Mach relation (3); moreover, the values of all the remaining thermodynamic variables $(T/T_0,\ p/p_0,\ \rho/\rho_0)$ are fixed by the isentropic flow relations (4)–(6). Note that the state of the gaseous products of decomposition or combustion upstream of the nozzle inlet establishes the stagnation values T_0, p_0, and ρ_0.

As an illustrative example, the NASA/GSFC micro-nozzle described in [2] is designed to produce a thrust level in the range of $10-500\,\mu$N. This prototype featured a throat dimension of $90\,\mu$m and an exit area expansion ratio $A_{exit}/A_* \sim 6$ which produce an exit Mach number of ~ 3.4.

Nozzle Profile and 3D Effects

The idealized nozzle profile $A(x)$ is one which provides the required area expansion ratios for supersonic flow and, concurrently, aligns the flow in the axial direction at the nozzle exit. This flow alignment minimizes losses in thrust production associated with unwanted transverse velocity components. The traditional 'bell-shape' contoured nozzle accomplishes this task while maintaining isentropic flow conditions throughout the nozzle. Note that the profile of the isentropic bell nozzle cannot be obtained by quasi-1D theory. Rather, it is determined through the solution of expansion and compression wave propagation in the supersonic portion of the nozzle – typically this is done using the method of characteristics (e. g., [3]). While a bell-shape profile may be the ideal case, linear nozzles are also commonly used in thruster propulsion systems. A linear nozzle features a supersonic section with a fixed expansion rate $\mathrm{d}A/\mathrm{d}x$ characterized by a divergence angle θ. Linear nozzle designs are attractive primarily for their geometric simplicity and the associated advantages in the fabrication process. This has proven to be an important consideration for micro-scale fabrication of nozzles over the past decade; however, microfabrication techniques continue to improve and the likely future trend will be a return to the more efficient bell-shape nozzles.

Regardless of the profile, one key difference between micro-nozzles and their macro-scale counterparts is their inherent 3D nature. Owing to the method of microfabrication (see below) the nozzles are ducts with rectangular cross-sections. Conversely, all macro-scale nozzles are conical in nature and thus the flows are 2D aximsymmetric. The 3D nature of the flow can have substantial effects on the supersonic nozzle performance on the micro-scale.

Microfabrication Techniques

Many MEMS-based micro-nozzles are created from 2D planar patterns which are transferred to a substrate material (typically Si) via a photolithographic masking process. The nozzle is fabricated within the substrate by selectively removing the substrate material from unmasked regions; commonly this is accomplished via reactive ion etching (RIE) or 'deep' reactive ion etching techniques. Whereas the RIE method is acceptable for etching depths on the order of $10\,\mu$m, the DRIE method enables etching depths in excess of $100\,\mu$m. Chemical wet etching is also possible, but is becoming less common because of its inherent limitations compared to RIE techniques. An alternative approach, and one which is becoming more widely available, is the use of 'focused ion beams' (FIB) to mill out the pattern on the substrate. Regardless of the method, high precision is required in the fabrication

process to ensure proper geometry is produced, including smooth nozzle walls. The nozzle is typically sealed by bonding a cover surface (e. g., Pyrex to provide optical access) to the substrate. Often anodic bonding is used to produce a permanent bond which can withstand a wide range of operating temperatures. To date, there has been little effort experimentally to provide for thermal insulation of the nozzle within the substrate. This may be an important area for future work given the potential significance of heat transfer during nozzle operation, as will be described later.

Key Research Findings

Steady Flow

Much of the current research is focused on examining the interaction of viscous forces and nozzle geometry in an effort to better understand and quantify performance characteristics. The majority of the research literature has dealt with 2D steady-state flow conditions. Given the experimental challenges associated with micro-scale supersonic flow interrogation, virtually all analyses have been computational in nature. While some experimental works have also been reported, most of these have reported only thrust measurements without corresponding flow field data.

Within the aerospace literature, Bayt and Breuer [5] were among the first to examine micro-nozzle flow and to identify the key role that viscous effects can play. In short, the low Reynolds numbers of these flows permit the growth of relatively thick viscous layers within the nozzle expander – these layers can occupy a significant portion of the nozzle exit, effectively restricting the flow and reducing thrust production. In an effort to mitigate the growth of viscous layers, propulsion researchers have considered increasing the expansion angle of the diverging section of the nozzle; however, as will be shown, doing so introduces geometric losses linked to increased non-axial exit velocity components.

The results that to follow are based on numerical simulations of the operation of the NASA/GSFC microthruster system described in [2]. While the data is somewhat case specific, the findings and issues that arise are germane to most micro-scale nozzles. Numerical models of monopropellant based supersonic flows have been developed for varying micro-nozzle geometries including linear and bell shaped expander sections. For the linear micro-nozzles, which will be of primary focus, expander half-angles have been examined within the range of $\theta = 10° - 50°$ (Fig. 2). For the present analysis, adiabatic nozzle walls are assumed. The supersonic flow field is characterized by Reynolds numbers typically less than 1000.

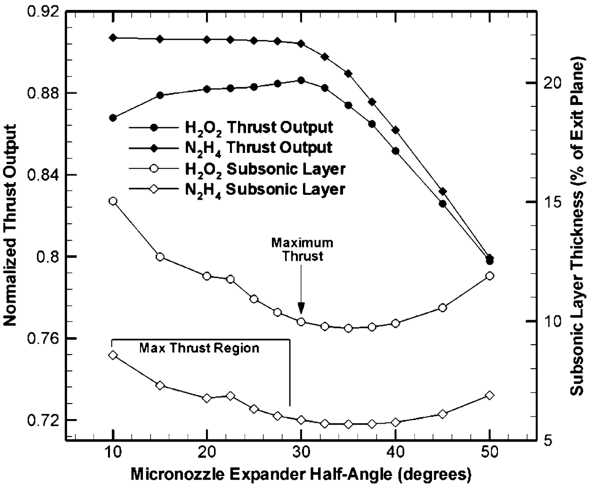

Supersonic Micro-Nozzles, Figure 2 Performance results for the NASA/GSFC supersonic microthruster nozzle with decomposed H_2O_2 and decomposed N_2H_4 as the working monopropellants. Thrust production, as shown on the left axis, has been normalized by the theoretical quasi-1D inviscid value. The percentage of the micro-nozzle exit plane occupied by the viscous subsonic layer is also shown on the right axis for both monopropellants of interest. Results are shown for expander half-angles ranging from 10° to 50°. Note that the expander angle exhibiting the maximum thrust production does not directly coincide with the minimum subsonic layer thickness. This is a direct result of the competing effects of viscous forces and micro-nozzle geometry. The optimum expander angle is the result of this trade-off

Referring to Fig. 2, a rapid and drastic reduction in thrust output is observed as the expander half-angle is increased above 30°. This is a direct consequence of expander geometry. For large expander angles, the flow follows the walls in the expander and thus a sizeable component of the velocity vector exits the nozzle in the transverse direction. This results in a significant reduction of axial momentum flux and a corresponding decline in thruster performance.

For small expander angles, transverse velocity components due to expander geometry are reduced, but at the expense of increased nozzle length in order to maintain the desired area expansion ratio. As the expander angle is decreased below 30°, viscous forces acting over the lengthened expander section begin to dominate nozzle performance. The subsonic layer acts to restrict the flow and reduce the effective exit area. Because the viscous boundary layer at the exit plane is subsonic, the ambient back-pressure conditions can communicate with the flow upstream within the nozzle expander near the walls. As a result, the flow inside the expander will respond in order to match ambient backpressure. The flow exiting the micro-nozzle is inherently underexpanded in a space environment and, as such, premature flow turning occurs via an

expansion fan originating within the nozzle. Thus, a portion of the exit momentum is vectored into the transverse direction which results in a further reduction in micro-nozzle performance. These factors combine to represent a performance trade-off between viscous and geometric effects as described further in Louisos and Hitt [6].

To provide additional insight into the nature of the viscous effects, the subsonic boundary layer in the nozzle expander can be examined. Fig. 3 shows the viscous subsonic boundary layer in the 30° expander half-angle for both decomposed H_2O_2 and decomposed N_2H_4. Forming at the throat, the viscous subsonic layer grows as the axial distance progresses towards the exit. The subsonic layer thickness also scales with the fluid viscosity, as is evident for the two different monopropellants shown in Fig. 3. The steady-state subsonic layer thickness at the nozzle exit has been quantified as a function of expander half-angle in Fig. 2. As the expander angle is decreased, the subsonic layer grows to occupy a larger percentage of the nozzle exit area, up to 15% for decomposed H_2O_2 and up to 8.5% for decomposed N_2H_4. For cases of smaller expansion angles, the corresponding length of the expander increases allowing the subsonic layer to grow as the flow moves further downstream. This scenario is directly responsible for the reduction in performance of the micro-nozzle at small divergence angles. For larger expander angles, the subsonic layer thickness again increases proportionally. Here the flow is forced to turn sharply at the throat as it enters the micro-nozzle expander section. The high speed bulk flow is unable to turn efficiently and a thick subsonic layer results near the wall boundary. However, owing to the low Reynolds number regime, no flow separation is observed.

It is clear that the interplay between viscous effects and micro-nozzle geometry is complex and must be fully understood for the efficient design of high-performance MEMS-based nozzles. In summary, with the flow conditions specified for the micro-thruster nozzle, trade-offs between the size of the subsonic layer and geometric losses due to non-axial flow components result in an optimal linear expander half-angle of approximately 30° with decomposed H_2O_2 as the monopropellant. This value is significantly larger ($2\times$) than half-angles of around 15° typically used in macro-scale conical thrusters [7]. While the N_2H_4 monopropellant thruster does not exhibit a distinct maximum thrust output corresponding to an optimal geometry, it is clear that the most effective half-angle is in the range of 25° and less.

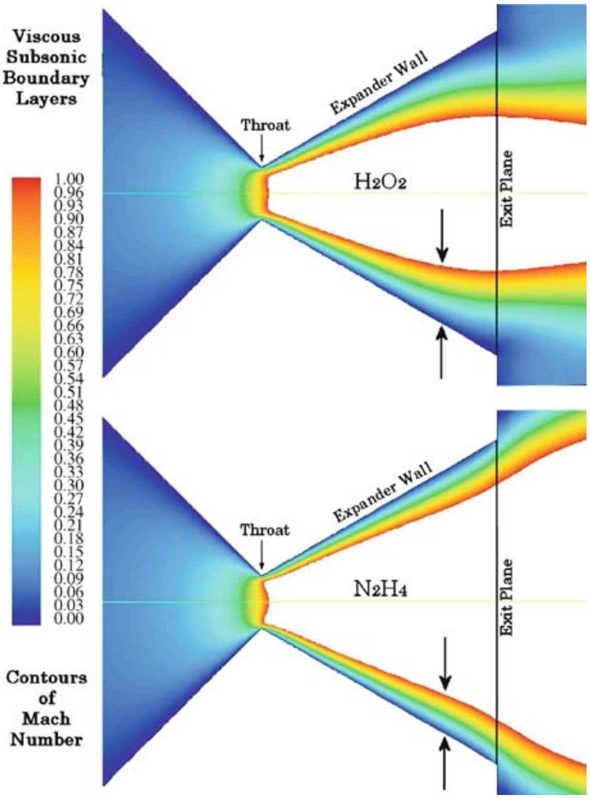

Supersonic Micro-Nozzles, Figure 3 Visualization of the viscous subsonic boundary layer in the 30° half-angle micro-nozzle expander section as shown by Mach contours < 1.0 for both decomposed H_2O_2 (top) and decomposed N_2H_4 (bottom) at an inlet to exit pressure ratio of 10 : 1 across the micro-nozzle. Note that the size of the H_2O_2 subsonic layer is larger compared to the N_2H_4 subsonic layer owing to the fact that decomposed H_2O_2 has approximately a 38% greater viscosity over the operating temperature range within the micro-nozzle

S

Transient Flow

Supersonic micro-nozzles are intended to provide station keeping and attitude control for nano-sats. This is accomplished through the application of discrete impulse 'bits' resulting from the transient firing of the micro-thruster. The ability to precisely predict and control the impulse bit delivered during a firing is evidently of great importance from an operations standpoint. The thruster firing for a chemical-based system essentially involves three phases: start-up, a period of steady-state operation, and finally a shut-down sequence. Currently, typical micro-valve actuation of the propellant flow is on the order of milliseconds. Because of viscous effects on the micro-scale, the use of inviscid theory in determining flow actuation and micro-nozzle performance can lead to innaccurate predictions. This may be present in the form of 'residual' thrust and impulse resulting from the viscous impact on nozzle response. There has been little in the literature on transient operations. Here we describe results for a simulated firing of the NASA/GSFC micro-nozzle prototype.

Transient micro-nozzle simulations have been performed with divergence half angles ranging from $10-50°$ with decomposed H_2O_2 as the gas.

For a typical microthruster firing, the micro-valve is initially closed and there is no flow through the nozzle. As the valve opens, a pressure gradient is established across the nozzle and the corresponding mass flow through the nozzle begins to generate thrust. Initially the pressure ratio is small and the flow at the exit is over-expanded and thus free boundary shock reflection is observed in the exhaust plume. With elapsed time the micro-valve continues to open and the pressure gradient across the nozzle increases as does thrust production. The size of the exhaust plume increases in tandem. As the micro-valve opens to its maximum position the flow transitions from over-expanded through perfectly-expanded and finally to under-expanded flow at steady-state; at this point a sizable expansion fan develops at the nozzle exit. This sequence is then repeated, in reverse order, during the shut-down process of the micro-nozzle duty cycle. The flow field evolution at selected time steps is shown in Fig. 4. A single typical thruster firing, which includes start-up, steady-state, and shut-down occurs on the order of a few milliseconds.

Numerical simulations of transient micro-nozzle flows have shown a lag in thrust production and performance response during the start-up sequence of the duty cycle [8]. For the reduced pressure gradient across the nozzle during start-up, viscous effects dominate and the flow throughout the entire expander section is subsonic. As the pressure gradient increases with time, the flow locally attains supersonic velocities in a region extending downstream from the throat, but then decelerates to subsonic speeds by the nozzle exit. This is seen in Fig. 5 which shows the extent of the viscous subsonic layer in the expander section at various times during the start-up process. As the micro-valve continues to open and larger pressure gradients are established, the flow is able to overcome viscous forces and establish wide-spread supersonic conditions in the expander section.

A finite time 'lag' is observed during the start-up which results from viscous effects. The lag in thrust production during start-up is most pronounced in the 10° and 50° expander half-angles owing to the fact that these geometries feature for the largest subsonic layers. It is interesting to note that the flow does *not* exhibit a lag in response to micro-valve closure during the shut-down sequence of the micro-nozzle [8]. Owing to the fact that viscous effects tend to reduce flow through frictional forces, the shut-down process is in fact facilitated by the existence of the subsonic layer. As the pressure ratio across the micro-nozzle is reduced during shut-down, the subsonic layer grows into the bulk of the flow field and thus promotes the reduction of thrust output. In this sense, viscous forces aid the shut-down sequence through dissipation.

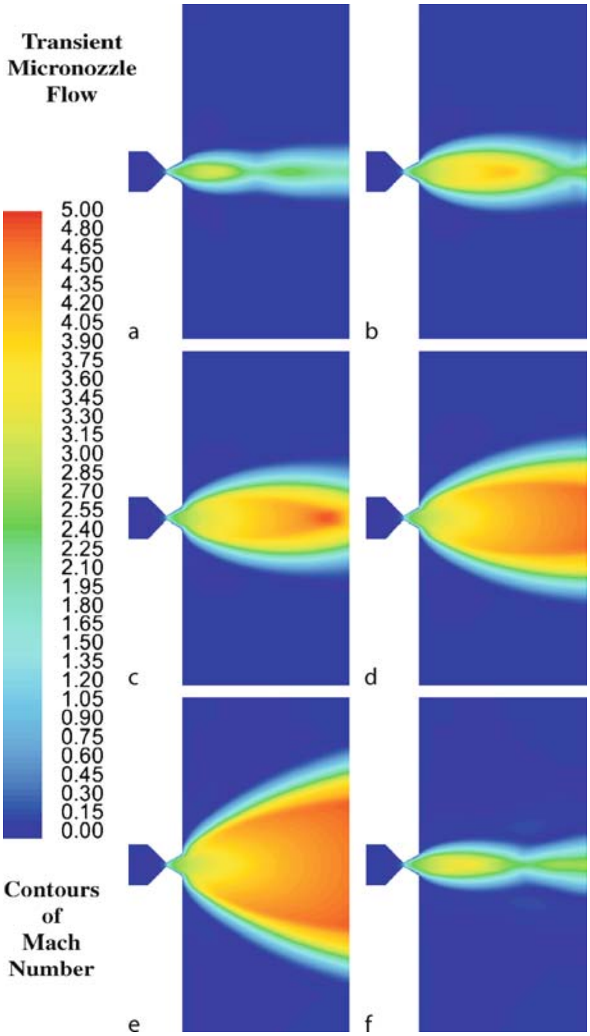

Supersonic Micro-Nozzles, Figure 4 The evolution in time of the micro-nozzle flow field as shown by Mach number contours for the 30° expander half-angle during transient operation of the microthruster. As the pressure ratio across the micro-nozzle increases during start-up, the exhaust plume grows in size and the flow transitions from over-expanded through perfectly expanded flow to under-expanded conditions. A typical microthruster firing is on the order of milli-seconds and the simulation depicted here has a total actuation time of 1.7 ms. The results normalized by the actuation time are characterized as follows; (**a**) $t^* = 0.16$ over-expanded start-up, (**b**) $t^* = 0.176$ over-expanded start-up, (**c**) $t^* = 0.188$ perfectly expanded start-up flow, (**d**) $t^* = 0.206$ under-expanded start-up, (**e**) $t^* = 0.5$ steady-state under-expanded, and (**f**) $t^* = 0.82$ over-expanded shut-down flow. As expected, free boundary shock reflection occurs in the case of over-expanded flow while an expansion fan can be seen near the exit of the micro-nozzle for under-expanded flow

The transient results can be summarized by examining the total impulse over one duty cycle for a single micro-nozzle

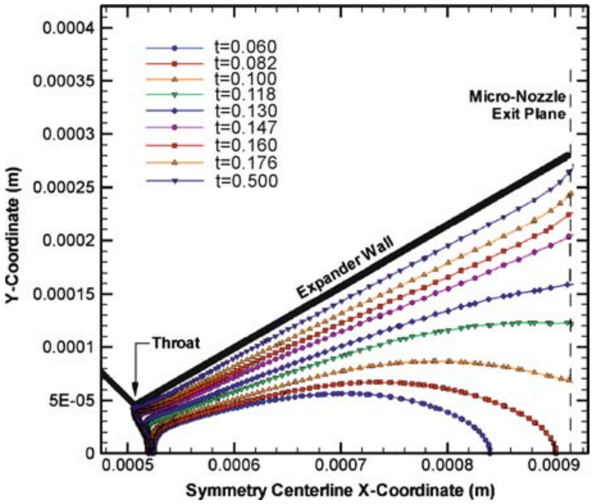

Supersonic Micro-Nozzles, Figure 5 Shown in the figure are transient sonic lines (M = 1) which indicate the maximum extent of the viscous subsonic layers from the micro-nozzle wall during the start-up sequence of the micro-nozzle. The time t has been normalized by the total actuation cycle time of 1.7 ms. Note that for $t < 0.082$ the flow is initially supersonic in the vicinity of the throat before viscous forces impede the flow and thus cause it to revert back to entirely subsonic conditions at the nozzle exit

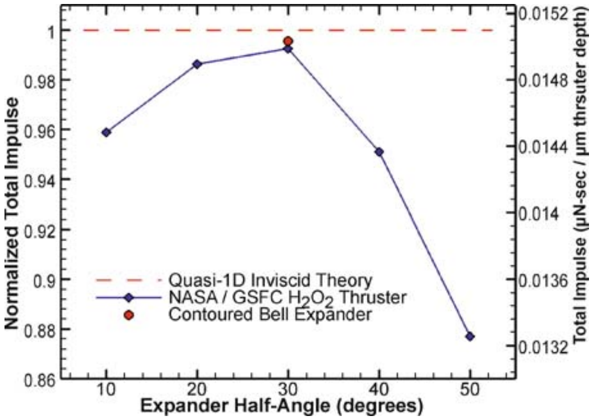

Supersonic Micro-Nozzles, Figure 6 A plot of the total impulse generated during a single actuation cycle for a range of expander half-angles as compared to quasi-one-dimensional inviscid theory. Maximum total impulse occurs at a micro-nozzle half-angle of 30°. For expander half-angles < 30°, viscous effects are responsible for the reduction in performance while at larger expander angles, performance decreases as a result of significant transverse velocity components at the micro-nozzle exit. The bell contoured expander here initially has a 30° half-angle in the vicinity of the throat and the contoured walls align the flow along the nozzle axis. As anticipated, the contoured expander outperforms the linear nozzle owing to the straightening of the flow and lack of transverse velocity associated with the bell profile

firing. The results are shown in Fig. 6; also shown are the results from quasi-1D inviscid theory for comparison purposes. As expected, the total impulse from the simulations is less than that predicted by inviscid theory – this difference can be directly attributed to the integrated effect of viscous and geometrical losses incurred during the transient process. The 'optimal' angle for a linear micro-nozzle in the transient case is seen to be the same as for the steady-state operation.

Heat Transfer Effects

Micro-nozzles are typically fabricated into much larger, thermally-conducting substrates. In an operational setting, these substrates will be thermally linked with the remainder of the spacecraft and will experience major temperature variations over a single orbit due to alternating day/night conditions. It is thus expected that significant heat transfer is possible between the micro-nozzle and the substrate and, in turn, may impact the flow. As a first approximation, one may argue that the substrate can be regarded as a thermal sink (or source) of constant temperature for the nozzle flow. This argument is based on a comparison of the relative thermal masses of the flow and a typical substrate; indeed, a lumped capacitance analysis of the NASA/GSFC micro-nozzle indicates that only a 5% temperature increase would be realized within the substrate under a typical firing sequence involving a 'cold' nozzle.

From a modeling perspective, then, a reasonable first-approximation of heat transfer effects is the imposition of isothermal boundary conditions on the micro-nozzle walls. The particular wall temperature would reflect the thermal state of the spacecraft as a whole based on its orbital location with respect to the Sun. To demonstrate the effect of heat transfer, we present findings obtained from numerical simulations of the NASA/GSFC linear micro-nozzle for expansion angles of 15° and 30° and isothermal wall temperatures ranging from 50 K to 1000 K. The thrust production (normalized with respect to quasi-1D inviscid theory) as a function of isothermal wall temperature is shown in Fig. 7. For comparison, the adiabatic results are also given. Cases with heat loss are seen to outperform comparable simulations with adiabatic walls. From a performance standpoint, as the wall temperature is increased the thrust output decreases and the subsonic layer grows non-linearly. A large subsonic layer has already been shown to greatly reduce micro-nozzle performance.

The observed effects of heat transfer on the flow in micro-nozzles is readily explained as follows. From compressible *Rayleigh flow* it is known that removing heat from a supersonic flow acts to accelerate the flow. At steady-state, the bulk of the flow in the micro-nozzle expander is super-

S

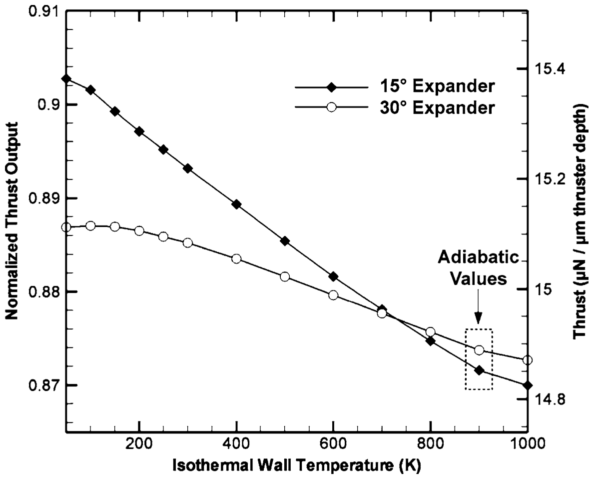

Supersonic Micro-Nozzles, Figure 7 Steady-state micro-nozzle performance including heat transfer through an isothermal wall. A reduced wall temperature is used to model heat losses from the flow field into the silicon micro-nozzle substrate acting as a thermal sink. As heat is removed from the expander, the supersonic flow is further accelerated, subsonic layer size is reduced, and performance as measured by thrust output increases. Note that the adiabatic results nearly coincide with the 900 K isothermal wall values as indicated

sonic and thus heat transfer acts to further accelerate the supersonic flow. Concurrently, as the flow is cooled, the exit density ρ increases. The overall effect is an increase in thrust. Heat extraction from the flow into the substrate increases performance from the subsonic layer point of view as well. For low nozzle wall temperatures, the local sonic velocity is diminished and the near-wall Mach number increases. This phenomena is the force driving the reduction in subsonic layer size for micro-nozzle flows with heat removal. In fact, with sufficient heat extraction from the flow, the subsonic layer can be reduced to the point where the competing effects of viscous forces and nozzle geometry cause the optimum expander half-angle to be shifted from 30° to a more traditional expander half-angle of 15°. This is demonstrated in Fig. 7 for isothermal wall temperatures less than ~ 700 K.

Non-Continuum Effects

Alexeenko et al. [9, 10] have performed non-continuum Direct Simulation Monte Carlo (DSMC) analyses of milli-/micro-nozzle flows in order to examine the influence of rarefaction effects on performance. The DSMC method is a statistical approach to the solution of the Boltzmann equation, the governing equation for rarefied gasdynamics. Their work has found that for Knudsen numbers of $\mathrm{Kn} \sim 0.1$, gas-surface interactions have a strong influence on the flow in both the converging and diverging sections of the nozzle. Owing to the fabrication process of MEMS devices, the surfaces have a significant degree of roughness at the molecular scale and thus result in inelastic diffusive collisons of a molecule with the surface. As such, a large portion of the flow remains subsonic along the nozzle expander walls. This causes an overall reduced Mach number at the nozzle exit and decreased thrust production. Comparisons have also been made between predicted velocity fields obtained by DSMC and Navier–Stokes continuum models for a supersonic converging-diverging micro-nozzle [9]. It was observed that the two solutions exhibit strong agreement within the micro-nozzle and that differences between the two methods were confined to the vicinity of the exhaust plume, specifically the corners of the nozzle exit. This is due to the rapid expansion of the gas and high flow rarefaction that is difficult to capture by continuum methods. Minor differences were reported in the size of the subsonic layers in the expander section owing to the difference in the wall boundary conditions (i. e., no-slip vs. slip). However, comparison of the velocity distributions along the nozzle centerline region shows only a small difference between the two methods.

Rarefied analyses of thermal coupling between the micro-nozzle with the surrounding substrate have also been reported [10]. In this work, steady low Reynolds number gas flows were again modeled by the DSMC approach and the substrate transient thermal response was governed by the heat conduction equation. It was shown that propulsive efficiencies of the micro-nozzle decreased with higher nozzle wall temperatures and vice versa. These results are in agreement with the continuum-based heat transfer results previously discussed.

Future Directions for Research

We close this article with a brief discussion concerning future research opportunities and needs for supersonic micro-nozzle flow within the context of micro-propulsion applications. In some instances preliminary work has been reported in various forms within the aerospace literature, however comprehensive and detailed studies have not yet appeared.

Conjugate Heat Transfer in Prototype Devices

As described previously, heat transfer from the micro-nozzle to its surroundings can have a significant impact on the supersonic flow within. Most of the studies to date, however, have been based on models featuring simplified and somewhat artificial thermal boundary conditions rather than a full conjugate heat transfer analysis with the domain surrounding the micro-nozzle. This shortcom-

ing is a consequence of incomplete knowledge of actual nano-sat propulsion system configurations, geometries and operating conditions. As experimental prototype nano-sats and propulsion systems begin to appear in greater numbers – and the design configurations and typical operating conditions start to take shape – more detailed heat transfer analyses will be warranted. Indeed, the solution of the conjugate heat transfer problem will be an important part in future design optimization process for supersonic micro-nozzles.

Three-Dimensional Geometric Effects

Much of the modeling efforts to date have focused on 2D planar geometries, owing largely to the 2D nature of patterning associated MEMS-based fabrication procedures. To a lesser degree, 2D modeling has also been invoked as a simplification to reduce computational resources required for numerical simulations. In reality, MEMS-based supersonic nozzles will have rectangular cross sections as a result of reactive ion etching or milling performed in the fabrication process. Further, the depth dimension may be substantially smaller than the nozzle width at the exit plane. One could posit that viscous boundary layer growth from the upper and lower boundaries of the nozzle will be of equal, if not greater, significance than the boundary layers studied in the 2D simulations. The presence of the upper and the lower boundaries also provides substantial, additional surface areas for heat loss from the nozzle flow and thus the consequences may well be more severe than those previously discussed in 2D models. In all, it is clear that there is a very real need for the pursuit of 3D models for the supersonic micro-nozzle flow. It is, however, also important to note that the additional computational resources required for full 3D simulations will be significant, particularly in cases of transient flows and flows with rarefaction.

Multiphase Flow

One unique aspect of supersonic micro-nozzles is the potential for the occurrence of multiphase flow, particularly in the expansion section. There are two primary mechanisms by which a liquid phase could be present within the flow. The first scenario would involve sufficiently high levels of heat loss through the nozzle walls resulting in gas condensation near the solid boundaries; this situation would most likely occur in the supersonic expansion section of the nozzle. The probable impact of condensation would be a reduction in thrust and micro-nozzle performance. A second scenario involves a multi-phase inlet that could be the result, for example, of incomplete chemical decomposition (catalysis) of a monopropellant or incomplete combustion of bi-propellants upstream of the nozzle (e. g., Hitt et al. [2]). Such problems could arise in chemical monopropulsion, for example, over time with degradation/fouling of catalysts in micro-reactors. In this case, the multiphase subsonic flow would likely affect the critical conditions required for sonic conditions to occur at the nozzle throat. Regardless of the particular scenario, there is a definite need for modeling efforts in this area – be it analytical, computational or both – to provide predictive capabilities for micro-nozzles under these multiphasic conditions.

Rarefaction Effects for Realistic Gases

Much of the micro-nozzle literature dealing with rarefied flows has focused on so-called 'cold gas' propulsion mechanisms. A cold-gas system features a single, inert gas (typically N_2) as a propellant and, consequently, offers a great modeling simplification for gas kinetic simulations utilizing DSMC or MD approaches. The fact that all molecules are identical within the flow simplifies the treatment of molecular collisions; in contrast, for multi-gas flows the treatment of collisions between molecules of different sizes and number densities becomes considerably more complicated. In practice, many propulsion schemes feature gas mixtures (e. g., decomposed H_2O_2 or decomposed N_2H_4 monopropellant schemes) and as such, there remains a significant void in the micro-nozzle literature concerning the effects of flow rarefaction in these cases.

Cross References

► Microfabrication Techniques
► Microrockets
► Reactive Ion Etching (RIE)

References

1. Mueller J (2000) Thruster options for microspacecraft: a review and evaluation of the state-of-the art and emerging technologies. In: Micci M, Ketsdever A (eds) Micropropulsion for Small Spacecraft – Progress in Astronautics and Aeronautics, vol 187. AIAA, Reston, VA
2. Hitt DL, Zakrzwski CM, Thomas MK (2001) MEMS-Based Satellite Micropropulsion Via Catalyzed Hydrogen Peroxide Decomposition. J Smart Mater Struct 10:1163–1175
3. Anderson JD (2003) Modern Compressible Flow with Historical Perspective, 3rd edn. McGraw–Hill, Boston, MA
4. Bird GA (1994) Molecular Gas Dynamics and the Direct Simulation of Gas Flows. Oxford University Press, Oxford
5. Bayt RL, Breuer KS (2001) System design and performance of hot and cold supersonic micro-jets. AIAA Paper 2001–0721
6. Louisos WF, Hitt DL (2005) Optimal Expander Angle for Viscous Supersonic Flow in 2-D Micro-Nozzles. AIAA Paper 2005–5032

7. Humble RW, Henry GN, Larson WJ (1995) Space Propulsion Analysis and Design. McGraw–Hill, New York
8. Louisos WF, Hitt DL (2006) Viscous Effects in Supersonic Micro-Nozzle Flows: Transient Analysis. AIAA Paper 2006–2874
9. Alexeenko AA, Levin DA, Gimelshein SF, Collins RJ (2002) Numerical Modeling of Axisymmetric and Three-Dimensional Flows in Microelectromechanical systems. AIAA J 40(5):897–904
10. Alexeenko AA, Levin DA, Fedosov DA, Gimelshein SF (2005) Performance Analysis of Microthrusters Based on Coupled Thermal-Fluid Modeling and Simulation. J Propuls Power 21(1):95–101

Surface Acoustic Waves

► Flow by Surface Acoustic Waves
► Transport of Droplets by Acoustics

Surface Capturing

► Numerical Techniques for Free Surface Flows: Interface Capturing and Interface Tracking

Surface Change

► Surface Modification, Methods

Surface-Charge Patterning Techniques

Winky L. W. Hau
IMTEK, University of Freiburg, Freiburg, Germany
winky.hau@imtek.de

Synonyms

Surface chemistry technique; Polyelectrolyte patterning technique; Electro-osmosis with patterned surface charge

Definition

The surface-charge patterning technique is a surface chemistry process to make both positively charged and negatively charged patterns on a glass/silicon dioxide surface.

Overview

In microfluidic systems, liquid flow control is very challenging because of the large flow resistance. As such, electro-osmotic flow (EOF), a surface-driven flow phenomenon, is an alternative to pressure-driven flow (PDF), in order to overcome the flow resistance problem. Since the velocity of EOF depends on the surface charge of the channel wall, the surface-charge patterning technique has thus been developed to control liquid flow in a very confined space.

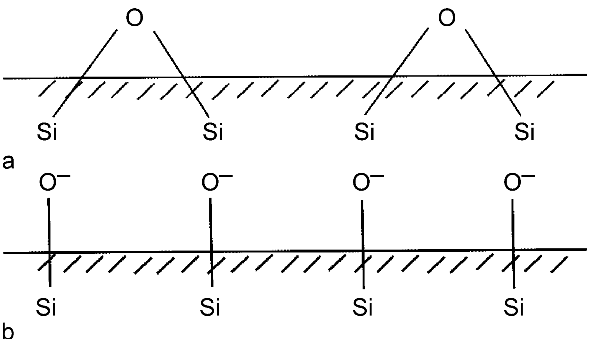

Surface-Charge Patterning Techniques, Figure 1 (**a**) Schematic chemical structure of a glass (or silicon dioxide) surface. (**b**) Glass surface carries negative charges in contact with aqueous solution

Surface Chemistry

Glass (or silicon dioxide) naturally carries negative charges on its surface. When a glass surface is in contact with an aqueous solution, ionization occurs in the surface chemical group [1], leaving the chemical group with negative charges (Fig. 1). However, the surface charge density of such a natural process is low.

The surface-charge patterning technique can be considered as a two-step process. Firstly, the negative charges on the glass surface are enhanced by chemical processing with alkali and acid. The purpose is not only to make a negatively charged surface but also to prepare for the second step. In the second step, part of the glass surface, i. e. the pre-designed pattern, is masked by a very thin polymer coating or polymer structure. Then the whole glass surface is submerged in or flooded with a positively charged polymer solution called a polyelectrolyte. Owing to the glass surface and the polyelectrolyte having opposite charges, the polyelectrolyte is bound to the glass surface by electrostatic force, forming a thin polymer coating of the order of nanometers in thickness, as illustrated in Fig. 2. This binding process is termed an electrostatic self-assembly (ESA) process [2].

The positively charged patterning process in the second step can be accomplished by soft-lithography or photolithography. There exist several variations in soft-lithography but the principles are the same – to mask the pre-designed pattern on the glass surface [3, 4]. To illustrate the general idea, one soft-lithography technique which makes use of molding is presented, followed by a discussion of the photolithography technique.

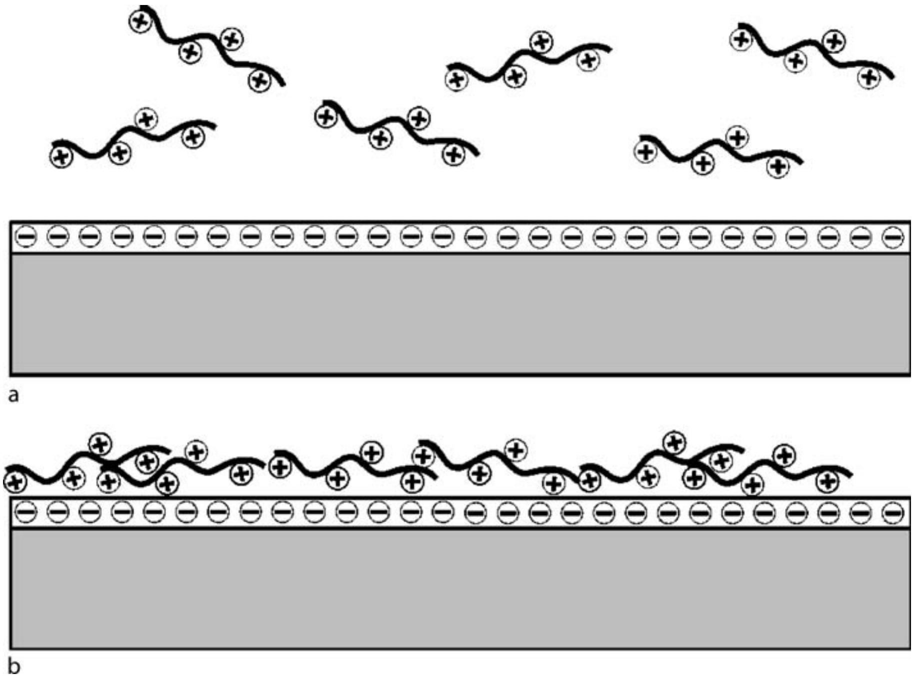

Surface-Charge Patterning Techniques, Figure 2 Electrostatic self-assembly (ESA) process. (**a**) A glass substrate with negative charges on its surface is submerged in a positively charged polymer solution. (**b**) The polymer binds to the glass surface due to electrostatic attraction

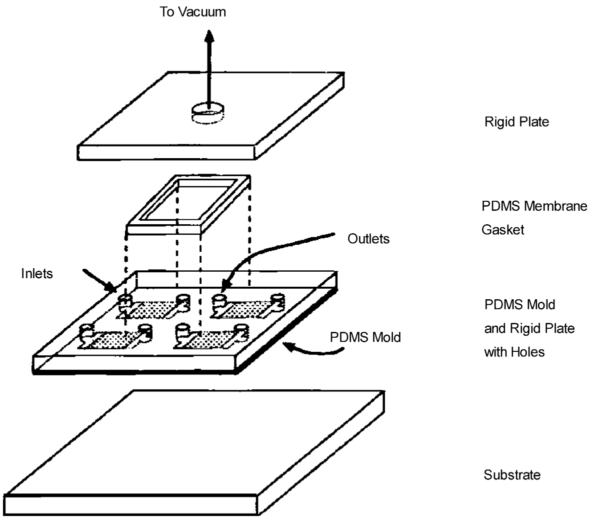

Surface-Charge Patterning Techniques, Figure 3 Schematics of the setup for micromolding that creates polymer surface-charge pattern on a glass surface

Soft-Lithography with Micromolding

The mold used is made of a thin polydimethylsiloxane (PDMS) membrane attached to a rigid plate of glass as shown in Fig. 3 [4]. The plate has holes to introduce the polymer solution and to connect to vacuum. The valve to vacuum is closed while the polymer solution is applied at several inlets. The ESA process takes place on the glass surface when the capillaries are filled with the polymer solution. Finally, the vacuum is released and the mold is removed. As a result, a polymer which has the same pattern as the mold is obtained.

Photolithography with Lift-Off

Photolithography is a standard patterning technique in the fabrication process of integrated circuits (ICs) in the semiconductor industry. In fact, many silicon-based microfluidic devices are fabricated by photolithography. Photolithography is combined with the lift-off technique to make surface-charge patterns [5]. A photoresist (PR), a UV-curable polymer used in photolithography, is patterned on a glass substrate which is submerged in a polymer solution, as shown in Fig. 4a. The ESA process takes place (Fig. 4b). The unnecessary polymer is lifted off by removing the PR underneath. Finally, a pre-designed pattern containing both positive and negative charges is obtained.

Application in Microfluidics

The surface-charge patterning technique combined with EOF is, in principle, able to create numerous flow patterns

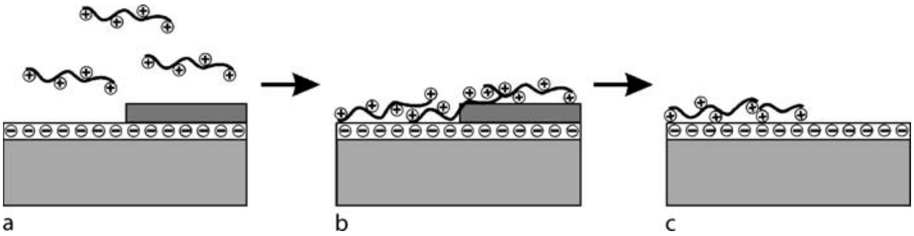

Surface-Charge Patterning Techniques, Figure 4 Schematics of surface-charge patterning by the photolithography method. (**a**) A glass substrate with patterned photoresist is submerged in a polymer solution. (**b**) ESA takes place. (**c**) The unnecessary polymer is lifted off by removing the photoresist underneath, leaving the desired surface-charge pattern

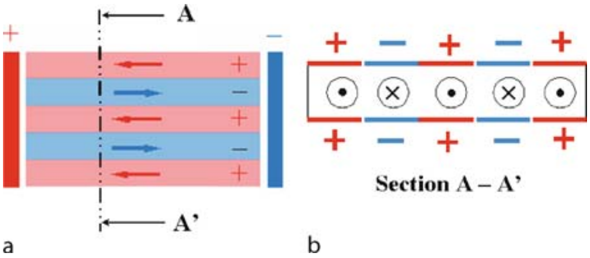

Surface-Charge Patterning Techniques, Figure 5 (**a**) Schematic plan view of longitudinal (i. e. parallel to the electric field set up by the electrodes at both ends) surface-charge patterns in a microchannel which generates bi-directional shear flow. (**b**) A cross-section A–A' of the microchannel showing symmetric patterns on top and bottom of the channel walls

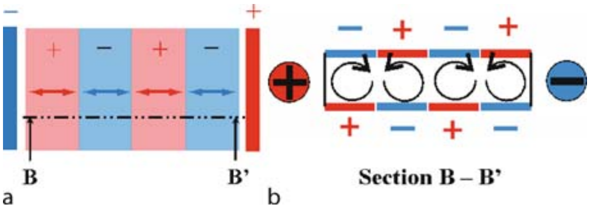

Surface-Charge Patterning Techniques, Figure 6 (**a**) Schematic plan view of transverse (i. e. perpendicular to the electric field set up by the electrodes at both ends) surface charge patterns in a microchannel which generates out-of-plane vortices. (**b**) A cross-section B–B' of the microchannel showing asymmetric patterns on top and bottom of the channel walls

at the microscale. In experiments, several simple flow patterns have been demonstrated, namely bi-directional shear flow (Fig. 5) [5, 6], out-of-plane vortex (Fig. 6) [6, 7] and in-plane vortex (Fig. 7) [8]. These basic flows are studied so that more complex flows can be understood and designed. A promising application is continuous mixing between two liquids or particle-laden liquids because liquid flow at the microscale is always laminar which does not favor mixing. It has already been demonstrated that the mixing efficiency can be significantly enhanced

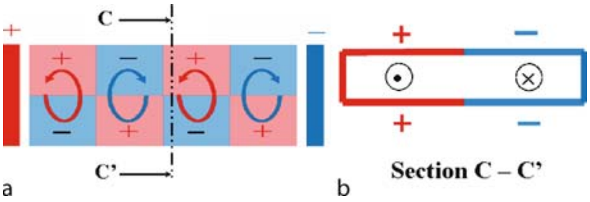

Surface-Charge Patterning Techniques, Figure 7 (**a**) Schematic plan view of chessboard-like surface charge patterns in a microchannel which generates in-plane vortices. (**b**) A cross-section C–C' of the microchannel showing symmetric patterns on top and bottom of the channel walls

by EOF in a surface-charge patterned microchannel [9, 10].

Cross References

- ► Electroosmotic Flow (DC)
- ► AC Electro-Osmotic Flow
- ► Liquid–Liquid Stratified Flow in Microchannels
- ► Photolithography
- ► Photoresist SU-8
- ► Photoresist Reflow
- ► Self-Assembly Fabrication

References

1. Hunter RJ (2001) Foundations of Colloid Science. Oxford Univ Press, New York
2. Whitesides GM, Grzybowski B (2002) Self-Assembly at All Scales. Science 295(5564):2418
3. Liu Y, Fanguy JC, Bledsoe JM, Henry CS (2000) Dynamic Coating Using Polyelectrolyte Multilayers for Chemical Control of Electroosmotic Flow in Capillary Electrophoresis Microchips. Anal Chem 72(24):5939–5944
4. Jeon NL, Choi IS, Xu B, Whitesides GM (1999) Large-Area Patterning by Vacuum-Assisted Micromolding, Adv Mater 11(11):946–950
5. Hau WLW, Trau DW, Sucher NJ, Wong M, Zohar Y (2003) Surface-chemistry technology for microfluidics, J Micromech Microeng 13:272–278

6. Stroock AD, Weck M, Chiu DT, Huck WTS, Kenis PJA, Ismagilov RF, Whitesides GM (2000) Patterning Electro-osmotic Flow with Patterned Surface Charge, Phys Rev Lett 84(15):3314–3317
7. Hau WLW, Trau DW, Sucher NJ, Wong M, Zohar Y (2002) Micro flow patterns on demand using surface-chemistry technology. In: Proceeding of MEMS 2002, Las Vegas, NV, 20–24 Jan 2002
8. Lee LM, Hau WLW, Lee YK, Zohar (2006) In-plane vortex flow in microchannels generated by electroosmosis with patterned surface charge. J Micromech Microeng 16(1):17–26
9. Biddiss E, Erickson D, Li D (2004) Heterogeneous Surface Charge Enhanced Micromixing for Electrokinetic Flows. Anal Chem 76:3208–3213
10. Hau WLW, Leung PK, Lee LM, Lee YK, Zohar Y (2005) Electrokinetically-Driven Micro Mixer with a Novel Surface-Charge Pattern. In: Proc IEEE Robio 2005, Hong Kong, Macau, 29 Jun–3 Jul 2005

Surface Chemistry Technique

► Surface-Charge Patterning Techniques

Surface Conductance

► Surface Conductivity
► Surface Conductivity Measurement

Surface Conductivity

Synonyms

Surface conductance; Surface electric conductance

Definition

The surface conduction is the excess electric conduction tangential to a charged surface, and originates from the excess counterions' concentrations in the electrical double layer region near the solid-liquid interface. The corresponding electric conductivity is called the surface conductivity, λ_s, that is considered as the electric conductivity of a sheet of material of negligible thickness, with a unit $\Omega^{-1}m^{-1}$. Specific surface conductivity values are of the order $10^{-9} \sim 10^{-8}$ for water in glass capillaries.

Cross References

► Electrical Double Layers
► Zeta Potential Measurements
► Electroosmotic Flow (DC)
► Streaming Current and Electroviscosity
► Surface Conductivity Measurement

Surface Conductivity Measurement

Dongqing Li
Department of Mechanical Engineering,
Vanderbilt University, Nashville, TN, USA
dongqing.li@vanderbilt.edu

Synonyms

Surface conductance; Surface electric conductance

Definition

The surface conduction is the excess electric conduction tangential to a charged surface, and originates from the excess counterions' concentrations in the electrical double layer region near the solid-liquid interface. The corresponding electric conductivity is called the ► surface conductivity, λ_s, that is considered as the electric conductivity of a sheet of material of negligible thickness, with a unit $\Omega^{-1}m^{-1}$. Specific surface conductivity values are of the order $10^{-9} \sim 10^{-8}$ for water in glass capillaries.

Overview

Generally, surface conductivity usually is referred to the electrical conductivity through a thin liquid layer near the solid-liquid interface where there is a net charge accumulation due to the charged solid-liquid interface. Zeta potential is considered as an electrokinetic potential at the shear plane near a solid-liquid interface where the liquid velocity is zero. The zeta potential and the surface conductivity are very important interfacial electrokinetic properties to a huge number of natural phenomena, such as electrode kinetics, electrocatalysis, corrosion, adsorption, crystal growth, colloid stability and flow characteristics of colloidal suspensions and electrolyte solutions through porous media and microchannels. In electro-osmotic flow or pressure-driven flow through fine capillary tubes, the zeta potential and the surface conduction will critically influence the velocity or flow rate. In many cases, knowing the surface conductivity is a must in order to evaluate the zeta potential and other electrokinetic properties correctly. Measurement of the surface conductivity, therefore, is important in the studies of electrokinetic phenomena. Two methods to measure the surface conductivity, one involving pressure-driven flow, and the other electroosmotic flow, will be reviewed in this entry.

It is well-known that most solid surfaces carry electrostatic charges, i.e. an electrical surface potential. If the liquid contains a certain amount of ions (for instance, an electrolyte solution or a liquid with impurities), the electro-

S

static charges on the solid surface will attract the counterions in the liquid. The rearrangement of the charges on the solid surface and the balancing charges in the liquid is called the electrical double layer (EDL) [1–3]. Immediately next to the solid surface, there is a layer of ions which are strongly attracted to the solid surface and are immobile. This layer is called the compact layer, normally about several Angstroms thick. From the compact layer to the uniform bulk liquid, the net charge density gradually reduces to zero. Ions in this region are affected less by the electrostatic interaction and are mobile. This region is called the diffuse layer of the EDL. The thickness of the diffuse layer is dependent on the bulk ionic concentration and electrical properties of the liquid, usually ranging from several nanometers for high ionic concentration solutions up to several microns for pure water and pure organic liquids. The boundary between the compact layer and the diffuse layer is usually referred to as the shear plane. The electrical potential at the solid-liquid surface is difficult to measure directly. The electrical potential at the shear plane is called the zeta potential, ς, and can be measured experimentally [1–3]. In practice, the zeta potential is used as an approximation to the potential at the solid-liquid interface. The ion and electrical potential distributions in the electrical double layer can be determined by solving the Poisson–Boltzmann equation [1–3]. According to the theory of electrostatics, the relationship between the electrical potential ψ and the local net charge density per unit volume ρ_e at any point in the solution is described by the Poisson equation:

$$\nabla^2 \psi = -\frac{\rho_e}{\varepsilon} \tag{1}$$

where ε is the dielectric constant of the solution. Assuming the equilibrium Boltzmann distribution equation is applicable, which implies uniform dielectric constant, the number concentration of the type-i ion in a symmetric electrolyte solution is of the form

$$n_i = n_{io} \exp\left(-\frac{z_i e \psi}{k_B T}\right) \tag{2}$$

where n_{io} and z_i are the bulk ionic concentration and the valence of type-i ions, respectively, e is the charge of a proton, k_B is the Boltzmann constant, and T is the absolute temperature. The net volume charge density ρ_e is proportional to the concentration difference between symmetric cations and anions, via.

$$\rho_e = ze(n_+ - n_-) = -2zen_o \sinh\left(\frac{ze\psi}{k_B T}\right) \tag{3}$$

Substituting Eq. (3) into the Poisson equation leads to the well-known Poisson–Boltzmann equation.

$$\nabla^2 \psi = \frac{2zen_o}{\varepsilon} \sinh\left(\frac{ze\psi}{k_B T}\right) \tag{4}$$

When a liquid is forced through a capillary under an applied hydrostatic pressure, the ions in the diffuse layer (mobile part) of the EDL are carried towards the downstream end, resulting in an electrical current in the pressure-driven flow direction. This current due to the transport of charges by the liquid flow is called the streaming current. Corresponding to this streaming current, there is an electrokinetic potential called the streaming potential. This flow induced streaming potential is a potential difference that builds up along the capillary. This streaming potential acts to drive the ions in the diffuse layer of the EDL to move in the direction opposite to the streaming current, i. e., opposite to the pressure-driven flow direction. The action of the streaming potential will generate an electrical current called the conduction current. The conduction current will produce a liquid flow in the opposite direction to the pressure driven flow. The overall result is a reduced flow rate in the pressure drop direction.

The zeta potential can be determined from the measured pressure drop and the measured streaming potential along a single capillary tube. In absence of an applied electric field, when a liquid is forced through a channel under hydrostatic pressure, the excess counter-ions in the diffuse layer of the EDL are carried by the liquid to flow to the downstream, forming an electrical current, i. e., the streaming current. The streaming current is given by

$$I_s = \int_{A_c} v \rho_e \, dA_c \tag{5}$$

where A_c is the cross-section of the capillary, v is the local velocity of the liquid, and ρ_e is the local net charge density. For a liquid flowing through a cylindrical capillary tube of radius R at a steady state, the liquid local velocity $v(r)$ is given by the solution of the Poiseuille equation:

$$v(r) = \frac{\Delta P \left(R^2 - r^2\right)}{4\eta L} \tag{6}$$

where r is the radial variable measured from the central of the capillary, ΔP is the pressure drop along the capillary, η is the viscosity of the liquid, and L is the length of the capillary. The local net charge density $\rho_e(r)$ in Eq. (5) can be replaced by the Poisson equation, Eq. (1). Realizing that local net charge density $\rho_e(r)$ is not zero only in the EDL, i. e., only in a thin region near the channel wall, and that the EDL potential at the channel wall is approximated to

be the zeta potential ζ, one can show that the streaming current is given by:

$$I_s = -\frac{\varepsilon\zeta}{\eta}\pi R^2\frac{\Delta P}{L} \quad (7)$$

As explained above, the streaming potential generates a conduction current in the reversed direction. For a cylindrical capillary, the conduction current is given by:

$$I_c = \frac{\pi R^2 \lambda_b E_s}{L} \quad (8)$$

where λ_b is the bulk liquid electrical conductivity, and E_s is the streaming potential. At a steady state, the net electrical current should be zero, i. e., $I_s + I_c = 0$. Using this condition, one obtains the following:

$$\frac{E_s}{\Delta P} = \frac{\varepsilon\zeta}{\eta\lambda_b} \quad (9)$$

As seen from Eq. (9), by measuring the streaming potential and the pressure drop, and knowing the liquid properties, the zeta potential can be determined.

Generally, for a given solid-liquid system at a given temperature, the zeta potential is considered as a constant, this is because the nature of the material, its surface charge, and the nature and the concentration of the electrolyte determine the electrokinetic potential. However, early studies found that zeta potential determined from Eq. (9) depends on the size of the capillary tubes for the same solid material (the capillary wall) and the same liquid (with the same electrolyte concentration). This problem was solved later by considering the surface conduction, i. e., the electrical conduction through a thin layer at solid-liquid interface. Generally, the surface conduction is the excess conduction tangential to a charged surface, and originates from the excess counterions' concentrations in the EDL region near the solid-liquid interface [4]. Particularly in the cases of low bulk ionic concentrations, the surface conduction will have a significant contribution to the total conduction current through the capillary tube. Usually, the surface conductivity, λ_s, is considered as the conductivity of a sheet of material of negligible thickness, with a unit $\Omega^{-1}\mathrm{m}^{-1}$. Specific surface conductivity values are of the order $10^{-9} \sim 10^{-8}\Omega^{-1}\mathrm{m}^{-1}$ for water in glass capillaries. The surface conductivity is expected to have a significant effect on the zeta potential in capillaries smaller than 1 mm in diameter at concentrations below 1×10^{-3} M.

Briggs [5] suggested a simple procedure to correct Eq. (9). This method requires the measurement of the actual electrical resistance of the liquid in the capillary, R_{exp}, and the comparison of this value with calculated electrical resistance at high concentration, R_{cal}, where the surface conduction is expected to be negligible. The modified Eq. (9) becomes:

$$\frac{E_s}{\Delta P} = \frac{\varepsilon\zeta}{\eta\lambda_b}\frac{R_{exp}}{R_{cal}} \quad (10)$$

Briggs' method does not give explicit information on surface conduction. Two modern methods of determining the zeta potential and the surface conductivity will be summarized below.

Basic Methodology

Streaming Potential Method

Theory

Rutgers [6] was first to rigorously consider the *surface conductance* effect on the zeta potential and solved the problem of zeta potential dependence on capillary size. By considering the *surface conductance*, the conduction current for a cylindrical capillary is given by:

$$I_c = \frac{\pi R^2 E_s \lambda_b}{L} + \frac{2\pi R E_s \lambda_s}{L} \quad (11)$$

In the above equation, the first term accounts for the conduction through bulk liquid, and the second term accounts for the surface conduction. Using Eq. (7) and Eq. (11), and the steady state condition, $I_s + I_c = 0$, we have:

$$\frac{E_s}{\Delta P} = \frac{\varepsilon\zeta}{\eta(\lambda_b + 2\lambda_s/R)} \quad (12)$$

Realize $\varepsilon = \varepsilon_r\varepsilon_0$, where ε_r and ε_0 are the dielectric constant of the liquid and the permittivity of vacuum, respectively, the above equation can be rearranged into the following form:

$$\frac{\varepsilon_r\varepsilon_0\Delta P}{\eta\lambda_b E_s} = \frac{1}{\zeta} + \left(\frac{2\lambda_s}{\zeta\lambda_b}\right)\frac{1}{R} \quad (13)$$

For a given solid-liquid system, ε_r, η, λ_b, and ζ are constant. Equation (13) clearly shows that the term $\varepsilon_r\varepsilon_0\Delta P/\eta\lambda_b E_s$ is a linear function of $1/R$. If we plot $\varepsilon_r\varepsilon_0\Delta P/\eta\lambda_b E_s$ vs. $1/R$, as shown in Fig. 1, the intersection of the line given by Eq. (13) with the vertical axis is $1/\zeta$, and the slope of this line is $(2\lambda_s/\zeta\lambda_b)$. This implies that if one measures the pressure drop and the streaming potential of the same solid (capillary wall)-liquid system for different capillary radii, and plot the data according to Eq. (13), the zeta potential ζ and the surface conductivity λ_s can be determined from the intercept and the slope of the line.

S

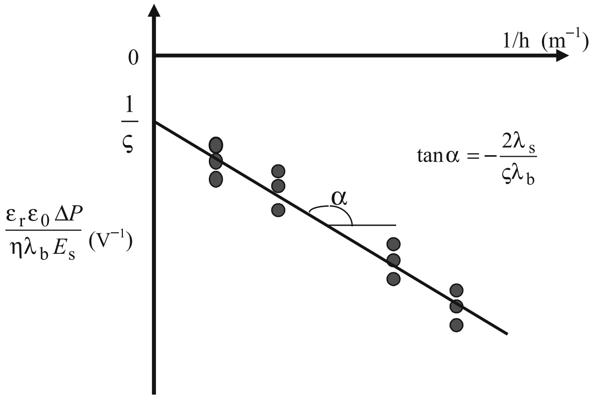

Surface Conductivity Measurement, Figure 1 The linear relationship of $\varepsilon_r\varepsilon_0\Delta P/\eta\lambda_b E_s$ versus $1/h$ for a slit capillary (or $1/R$ for a cylindrical capillary) by using Eq. (14) (or Eq. (13)) to determine the Zeta potential and the surface conductivity by the streaming potential method

In additional to cylindrical capillary tubes, another type of capillary with a simple cross-section shape is the slit capillary, i. e., a channel formed between two parallel plates. For an electrolyte solution flowing through a slit capillary, it can be shown that, in analogy to Eq. (13),

$$\frac{\varepsilon_r\varepsilon_0\Delta P}{\eta\lambda_b E_s} = \frac{1}{\varsigma} + \left(\frac{2\lambda_s}{\varsigma\lambda_b}\right)\frac{1}{h} \tag{14}$$

where h is the height of the slit channel.

Experimental

The key in the streaming potential method is to measure the streaming potential and pressure drop of the same solid-liquid system for different capillary radii. Figure 2 illustrates an experimental setup for such measurements [3, 7]. The capillary used in the test may be a single capillary tube or a bundle of capillary tubes of the same dimensions, or a slit channel formed between two parallel plates. The capillary tube is placed in a two-part symmetrical Plexiglas assembly to form a test cell as shown in Fig. 2. For a given capillary tube and a given electrolyte solution, the precision pump is set to maintain a constant flow rate. The pressure drop across the capillary tube is monitored and recorded by a differential pressure transducer (±0.5% FS accuracy, Validyne Eng. Corp.) and a computer data acquisition system. The flow was considered to have reached a steady state when the readings of the pressure drop do not change any more. Such a constant pressure drop value corresponds to the ΔP in Eq. (13) or (14). At this steady state, two electrodes (e. g., Ag/AgCl electrodes, Sensortechnik Meinsberg GmbH) and a high resistance electrometer (Keithley Instruments Inc.) are used to measure the streaming potential. The streaming potential measured at this steady state corresponds to the E_s in Eq. (13) or (14). It should be emphasized that such a streaming potential measurement should not last more than 60 or 100 s (depending on the electrolyte concentration and the flow rate) to avoid the polarization of the electrodes. In addition to the problem of electrode polarization, it should also be noted that there are no two identical electrodes due to the material and the manufacturing process. Therefore, in order to obtain more reliable and repeatable results, under the same flow rate, the flow is switched in an opposite direction after the previous streaming potential measurement. When the flow reaches the steady state again, the above described pressure drop and streaming potential measurement are repeated. Usually, for one flow rate, the operation described above should be repeated several times to ensure the repeatability and good average values of the pressure drop and the streaming potential. It is recommended to repeat the above measurements for several different flow rates.

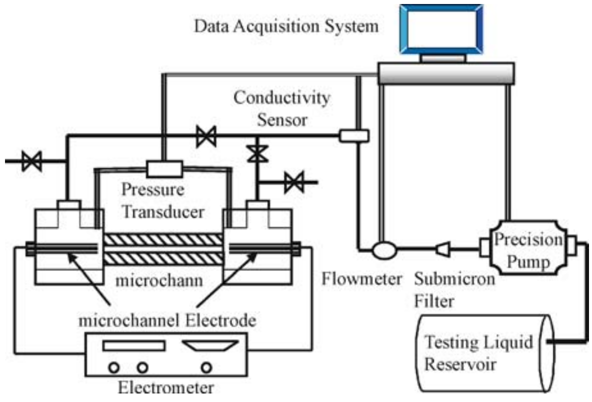

Surface Conductivity Measurement, Figure 2 Schematic of an experimental setup used for measurements of the streaming potential and the pressure across a capillary tube or a microchannel

As explained previously, in order to determine the zeta potential and the surface conductivity by using Eq. (13) or (14), one must measure the pressure drop and the streaming potential of the same solid-liquid pair for different capillary sizes. Therefore, the above-described measurements should be conducted for cylindrical capillary tubes with different radii or slit channels with different heights. Finally, by plotting $\varepsilon_r\varepsilon_0\Delta P/\eta\lambda_b E_s$ vs. $1/R$ (or $1/h$) as illustrated in Fig. 1, one can determine the zeta potential and the surface conductivity from the intercept and the slope of the best-fitted line to the experimental data points.

As an example, the results of glass surface-NaCl solution systems are re-plotted here [7] in Figs. 3 and 4. The measurements were done by using a slit channel formed by

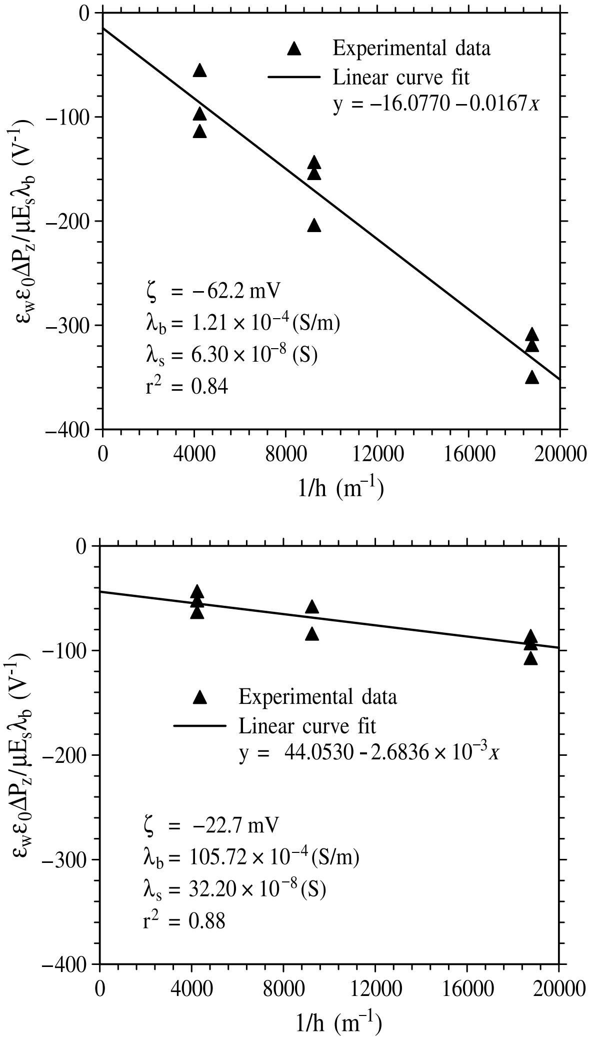

Surface Conductivity Measurement, Figure 3 Experimental data for glass surface with (**a**) De-ionized Ultra-filtered water, and (**b**) 10^{-3} M aqueous NaCl solution

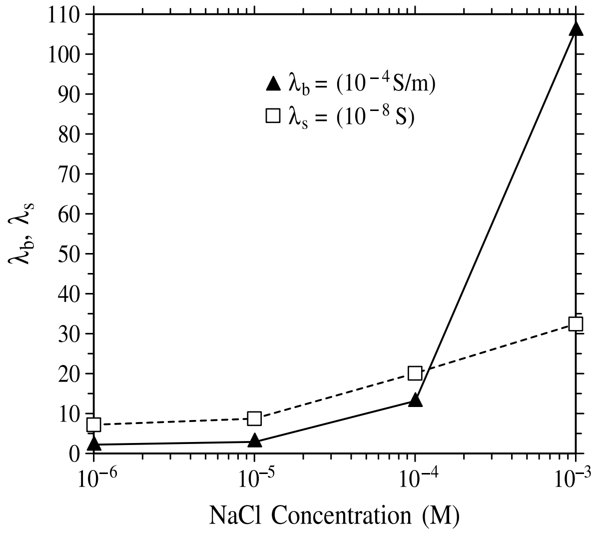

Surface Conductivity Measurement, Figure 4 Variation of the bulk conductivity and the surface conductivity with NaCl concentration

two parallel glass plates separated by two strips of a plastic shim of uniform thickness [7]. In Fig. 3, each data point represents an average value of several measurements as described above for the same channel height. For a given channel height the three data points represent the measurements for three different flow rates. Figure 4 shows the measured zeta potential and the surface conductivity as functions of the NaCl concentration. This method can also be used to study the effects of temperature, pH, different electrolytes and surfactants on zeta potential and surface conductivity.

It should be pointed out that Eq. (13) or (14) is derived on the basis of Eq. (6) (or the equivalent form for a slit channel), the solution of the classical Poiseuille equation. The Poiseuille equation, however, does not consider any EDL or electrokinetic (e. g., electro-viscous) effect on the liquid flow. For small capillaries, the electro-viscous effects on flow may be significant and have to be considered [3]. The Eq. (13) or (14) is no longer valid for small capillaries and may cause a significant error when used to evaluate the zeta potential and the surface conductivity [10]. Since the electro-viscous effect on flow is negligible for flow through a capillary with a hydraulic diameter larger than 50 μm, it is recommended that above-described method should be used with capillary tubes of a hydraulic diameter larger than 50 μm.

S

Electro-Osmosis Current Method

Within the diffuse layer of the EDL, the local net charge density, ρ_e, is not zero. If an electric field is applied such that it is tangential to the EDL, an electrical body force is exerted on the ions in the diffuse layer of the EDL. The ions will move under the influence of the applied electrical field to form a conduction current, pulling the liquid with them and resulting in an electro-osmotic flow. The liquid movement is carried through to the rest (beyond the EDL region) of the liquid in the channel by viscous force. This electrokinetic process is called electro-osmosis. The effect of the electrical force to generate the flow is dependent on the local net charge density within the liquid, which in turn is dependent on the electric double layer field and hence the zeta potential, ζ. On the other hand, the surface conduction will influence the bulk liquid's share of the applied electrical field and hence will influence the electro-osmotic flow. Therefore, electro-osmosis also depends on

both the zeta potential and the surface conductivity. The following will describe a method of determining both the zeta potential and the surface conductivity by measuring the electrical current in electro-osmotic flow through a capillary [8–10].

Zeta potential

Consider an electro-osmotic flow of an aqueous solution in a cylindrical capillary tube with a radius R as a fully-developed, one-dimensional flow at steady state. The momentum equation for such a case is given by [3]

$$-\eta \frac{1}{r}\frac{\mathrm{d}}{\mathrm{d}r}\left(r\frac{\mathrm{d}u}{\mathrm{d}r}\right) = E_x \rho_\mathrm{e} \tag{15a}$$

Where r is the radial variable. The corresponding boundary conditions are:

$$r = 0: \quad \frac{\mathrm{d}u}{\mathrm{d}r} = 0; \qquad r = R: \quad u = 0 \tag{15b}$$

where u is the liquid velocity, η is the viscosity, E_x is the applied electrical potential gradient, and ρ_e is the local net charge density. In order to solve the above flow equation, the local net charge density $\rho_\mathrm{e}(r)$ must be known. The local net charge density $\rho_\mathrm{e}(r)$ can be determined by the Boltzmann equation:

$$\rho_\mathrm{e}(r) = ze(n_+ - n_-) = -2zen_0 \sinh\left(\frac{ze\psi(r)}{k_\mathrm{B}T}\right) \tag{3}$$

The EDL potential $\psi(r)$ can be determined by the solving the well-known Poisson–Boltzmann equation for cylindrical capillary:

$$\frac{1}{r}\frac{\mathrm{d}}{\mathrm{d}r}\left(r\frac{\mathrm{d}\psi}{\mathrm{d}r}\right) = \frac{2zen_0}{\varepsilon_\mathrm{r}\varepsilon_0}\sinh\left(\frac{ze\psi}{k_\mathrm{B}T}\right) \tag{16a}$$

with the following boundary conditions:

$$r = 0: \quad \psi = 0; \qquad r = R: \quad \psi = \varsigma \tag{16b}$$

Once the EDL potential $\psi(r)$ is known, the local net charge density $\rho_\mathrm{e}(r)$ is determined according to Eq. (3). Finally, the equation of motion, Eq. (15a), can be solved numerically to find the velocity $u(r)$. The average velocity can then be determined as follows:

$$u_\mathrm{av} = \frac{1}{A_\mathrm{cross}}\int_0^R u(r)\,\mathrm{d}A_\mathrm{cross} = \frac{2}{R^2}\int_0^R u(r)\cdot r\cdot \mathrm{d}r \tag{17}$$

where A_cross is the cross-section area of the capillary tube.

It should be realized from the above procedure that the velocity $u(r)$ and hence the average velocity u_av are implicit functions of the zeta potential, ζ (in the boundary condition, Eq. (16b)). If the average velocity can be measured directly, the zeta potential ζ can be determined by solving Eq. (17) by using an iterative technique. In this process, an initial guessing value of the zeta potential, ζ_guess, may be obtained by invoking the Debye–Huckel approximation, as described below.

The Debye–Huckel approximation assumes that the value of ψ is small ($\psi \leq 25$ mV) or the following approximation can be made:

$$\sinh\frac{ze\psi}{k_\mathrm{B}T} \approx \frac{ze\psi}{k_\mathrm{B}T} \tag{18}$$

If the above approximation can be made, the following exact solutions for the local net charge density distribution and the velocity profile can be obtained analytically:

$$\rho_\mathrm{DH}(r) = \zeta\frac{I_0(\kappa r)}{I_0(\kappa R)} \tag{19}$$

$$u_\mathrm{DH}(r) = \frac{\varepsilon_\mathrm{r}\varepsilon_0 E_x \zeta}{\eta}\left(1 - \frac{I_0(\kappa r)}{I_0(\kappa R)}\right) \tag{20}$$

where I_0 is the zero-order modified Bessel function of the first kind; and κ is the so-called Debye–Huckel parameter, defined by:

$$\kappa = \left(\frac{2z^2e^2n_0}{\varepsilon_\mathrm{r}\varepsilon_0 k_\mathrm{B}T}\right)^{1/2} \tag{21}$$

As shown in Eq. (17), the average velocity can be found by integrating the local velocity over the cross-section area of the capillary tube. Thus, with the Debye–Huckel assumption, ζ_DH can be expressed as an explicit function of the radius through the average velocity equation, such that if the average velocity is known, then the initial guess for the zeta potential ζ can be determined as

$$\varsigma_\mathrm{guess} = \varsigma_\mathrm{DH} = \frac{u_\mathrm{av}R^2\eta}{2\varepsilon\varepsilon_0 E_x}\left[\int_0^R r\left(1 - \frac{I_0(\kappa r)}{I_0(\kappa R)}\right)dr\right]^{-1} \tag{22}$$

Using this ζ_DH value as the initial guess for ζ_guess in Eq. (17) to calculate u_av, and comparing the result to the known (measured) value of u_av, a new ζ_guess is obtained. This procedure can be continued until the calculated and the known values of u_av converge.

Evaluation of the Specific Surface Conductivity

When considering the transport of an electrolyte solution, one must consider the motion of mobile ionic species in addition to the considerations of traditional fluid mechanics. The transport of ions in a capillary results in an electrical current. In electro-osmotic flow, the total current is a result of three physical processes:

1. the bulk conductivity of the electrolyte solution, resulting in a conduction current, $I_{\text{cond,bulk}}$;
2. the surface conductivity, resulting in a secondary conduction current, $I_{\text{cond,surf}}$; and,
3. the electro-osmotic flow, resulting in a convection current, I_{conv}.

Generally, the convection current is several orders of magnitude smaller than the other two components of the current. Neglecting the contribution of I_{conv} results in the following equation for the total current, I_{total}:

$$I_{\text{total}} = I_{\text{cond,bulk}} + I_{\text{cond,surf}} = \lambda_b A_{\text{cross}} \boldsymbol{E} + L_{\text{surface}} \lambda_s \boldsymbol{E} \tag{23}$$

For the case of a cylindrical capillary with an electrical field $\boldsymbol{E}$ applied in the axial direction only, I_{total} is given by:

$$I_{\text{total}} = \pi R^2 \lambda_b E_x + 2\pi R \lambda_s E_x \tag{24}$$

In general, the surface conductivity λ_s is unknown. Since the radius of the capillary tube, R, and the bulk liquid conductivity, λ_b, can be measured accurately, they can be treated as known, and E_x is applied electrical field strength and is known. Since the total current I_{total} can be measured, the above equation can be rearranged to solve for the surface conductivity, λ_s, such that:

$$\lambda_s = \frac{I_{\text{total}} - \lambda_b \pi R^2 E_x}{2\pi R E_x} \tag{25}$$

As seen from Eq. (25), by measuring the total current during a steady electro-osmotic flow, the bulk conductivity, the applied electrical field and the capillary size, the surface conductivity can be determined. Generally, this is a relatively simple method with a reasonable accuracy.

The above equation should be modified to account for the changes in ionic concentration within the double layer near the wall. The variation in ionic concentration is accounted for in the conduction current component by using the following equation:

$$I_{\text{cond,bulk}} = \int_A \lambda_b E_x \cosh \psi(r)\, dA \tag{26}$$

Thus, Eq. (25) becomes:

$$\lambda_s = \frac{I_{\text{total}} - \int_A \lambda_b E_x \cosh \psi(r)\, dA}{2\pi R E_x} \tag{27}$$

If ζ is known, the electrical field potential $\psi(r)$ can be determined by solving the Poisson–Boltzmann equation. The surface conductivity λ_s, therefore, can be determined by using the measured I_{total} and Eq. (27).

Experimental

The experimental set-up [8, 9] shown in Fig 5a can be used to measure the average velocity by monitoring the current in electro-osmosis. In the experiment, the reservoir 2 will be filled with an electrolyte solution at a desired concentration. The capillary tube and reservoir 1 will be filled with the same electrolyte solution at a concentration lower than the concentration in reservoir 2. For example, the capillary tube and reservoir 1 are filled with an electrolyte solution at a concentration that is 95% of the concentration in reservoir 2. Immediately after connecting the two reservoirs by the capillary tube, a voltage difference between the two reservoirs is applied by setting reservoir 1 at ground potential and reservoir 2 to a high voltage power supply unit (CZE1000R, Spellman, NY) via Platinum electrodes.

The applied electrical field results in an electro-osmotic flow in the capillary tube. During electro-osmosis, the higher-concentration electrolyte solution from reservoir 2 gradually displaces the lower-concentration electrolyte solution in the capillary tube (it can the opposite way depending on the polarity of the applied electrical field). As a result, the overall electrical resistance of the liquid and hence the current in the capillary tube changes, as illustrated in Fig. 5a. An L-DAS8 data acquisition chip (Kieffley) was used to record the voltage (kV) and current (μA) as a function of time (s). Once the lower-concentration solution in the tube is completely replaced by the higher-concentration solution from reservoir 2, the current will reach a maximum and constant value. The measured time for the current to reach such a plateau value is the time required for the solution from reservoir to travel through the entire capillary tube. The average velocity of the liquid flow can then be calculated by using:

$$u_{\text{av,exp}} = \frac{L}{\Delta t} \tag{28}$$

where L is the length of the capillary and Δt is the time required for the higher-concentration electrolyte solution to completely displace the lower-concentration electrolyte solution from the capillary tube.

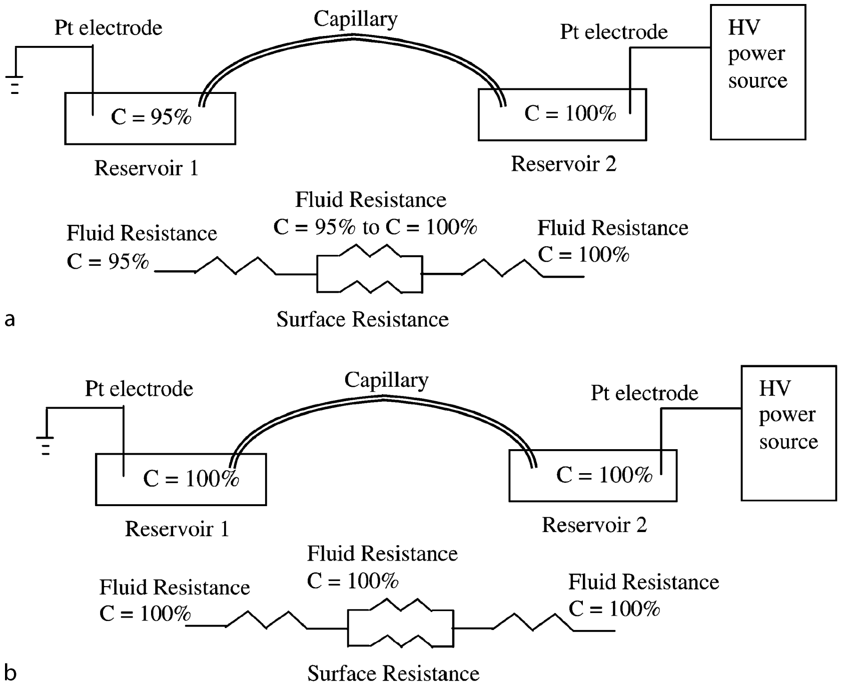

Surface Conductivity Measurement, Figure 5 Schematic diagram illustrating experimental set-up and varying resistances (**a**) for measuring the current variation and the complete displacement time of a two-concentration system; (**b**) for measuring the total current of a single concentration system

For the purpose of evaluating the specific surface conductivity, a second set of measurements using a similar set-up [8, 9], as shown in Fig. 5b, may be used to measure the total current, I_{total} during electro-osmosis. In these cases, reservoir 1, reservoir 2 and the capillary tube will be filled with an electrolyte solution of the same concentration.

Key Research Findings

Generally, the value of specific surface conductivity depends on the molecules of the solid surface, the surface charge, and the electrokinetic properties of the liquid (e. g., type of ions, valance, the ionic concentration, pH). Typical values of specific surface conductivity are of the order $10^{-9} \sim 10^{-8}$ for water in glass capillaries.

The electroosmotic current method described in the above sections was used to evaluate the zeta potential and the surface conductivity for Polyamide coated silica capillary tubes with KCl solutions [8]. In the experiments, polyamide coated silica capillary tubes of various diameters (Polymicro Technologies Inc., Phoenix, AZ) were cut to 10 cm. lengths and connected to the reservoirs. The electrolyte solution was prepared by using KCl (Anachemia Science, Quebec) and deionized ultra filtered (DIUF) water (Fisher Scientific, Ontario). The amount of KCl was measured by using a precision scale (Mettler). The bulk liquid conductivity of the prepared solutions was measured using a high precision conductivity meter (Mettler Toledo). In the experiments, each measurement was repeated at least three times for a given set of conditions. All experiments were conducted at room temperature (22 °C).

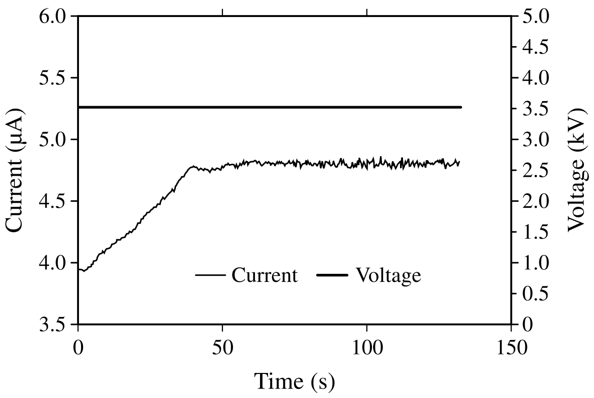

Surface Conductivity Measurement, Figure 6 A typical result of current versus time for Set-up A. For the specific case of: capillary diameter $D = 100\,\mu\text{m}$, $E_x = 3500\,\text{V}/10\,\text{cm}$. KCl concentration in Reservoir 1 is $C_{95\%} = 0.95 \times 10^{-4}$ M. KCl concentration in Reservoir 2 is $C_{100\%} = 10^{-4}$ M

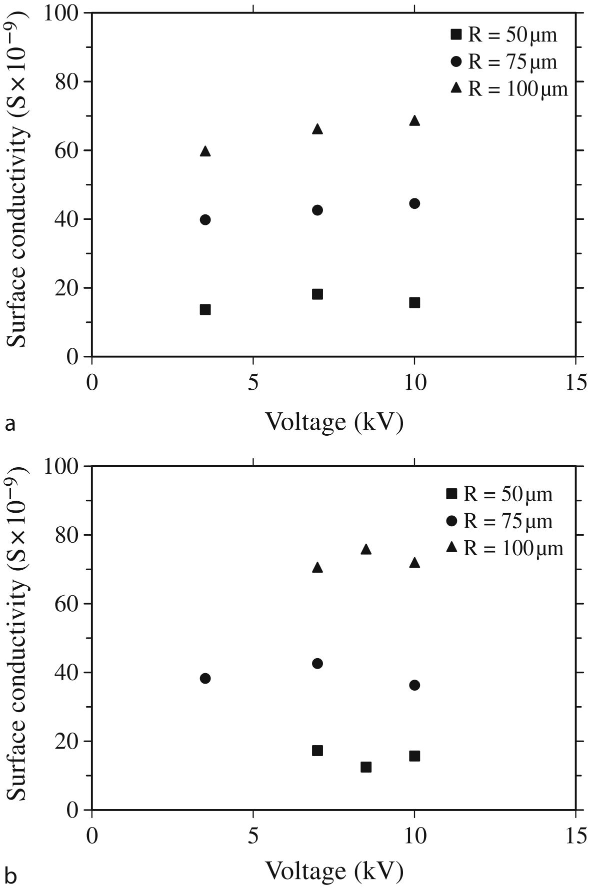

Surface Conductivity Measurement, Figure 7 Specific surface conductivity, λ_s versus the applied voltage and the capillary diameter, for a 10 cm long capillary tube, for: (**a**) $C = 10^{-4}$ M KCl; (**b**) $C = 10^{-3}$ M KCl

Figure 6 shows a typical variation of current versus time for a KCl solution with a 100 µm diameter silica glass capillary and an applied electrical field of 350 V/cm. The concentration in reservoir 2 is $C_{100\%} = 10^{-4}$ M, and the concentration in reservoir 1 is $C_{95\%} = 0.95 \times 10^{-4}$ M . Linear regression was used to smooth the experimental data and determine Δt. The current increases with time as the higher concentration ($C_{100\%}$) electrolyte solution displaces the lower concentration ($C_{95\%}$) electrolyte solution in the capillary. The increase in current continues until the capillary is completely filled with the $C_{100\%}$ electrolyte solution, at which time the current reaches a steady value, which continues until the applied voltage is removed.

The average velocity of the liquid during electro-osmosis is determined by Eq. (28). Using the measured average velocity data, the method described earlier can be used to calculate the zeta potential ζ. The measured total current for single-concentration systems is required to determine the specific surface conductivity λ_s according to Eq. (25). In a more rigorous treatment, using the measured total current and the determined zeta potential, the specific surface conductivity λ_s can be calculated by using Eq. (27). Figs. 7a and b are plots of λ_s versus the applied voltage and the capillary size for the two KCl concentrations, $C = 10^{-3}$ M and $C = 10^{-4}$ M, respectively. From the results, there is clearly a relationship between the size of the capillary and the specific surface conductivity. Comparing the λ_s values between Fig. 7a and b, λ_s appears to have no significant dependence on the ionic concentration. This may be understood as the K^+ and Cl^- are not the potential determining ions in this system and are not adsorbed on the solid surface.

Future Directions for Research

Surface conductance is important in micro- and nano-scale flow and transport processes, especially when the channel size is small and the ionic concentration of the bulk solutions (bulk liquid conductivity) is low. More experimental data of surface conductivity are needed for various liquid-microchannel systems. With the rapid development of nanofluidics, it is highly desirable to develop new theoretical models, experimental methods and the experimental data for surface conductance of nanochannels.

Cross References

► Electrical Double Layers
► Zeta Potential Measurements
► Electroosmotic Flow (DC)
► Streaming Current and Electroviscosity
► Surface Conductivity

S

References

1. Hunter RJ (1981) Charge and Potential distribution at Interfaces. In: Hunter RJ Zeta Potential in Colloid Science: Principle and Applications. Academic, London, pp 11–55
2. Lyklema J (1995) Electric Double Layers. In: Lyklema J Solid-Liquid Interfaces. Fundamentals of Interface and Colloid Science, vol 2. Academic, London, pp 3.2–3.232
3. Li D (2004) Electrokinetics in Microfluidics. Academic, London
4. Lyklema J (1995) Electrokinetics and Related Phenomena. In: Lyklema J Solid-Liquid Interfaces. Fundamentals of Interface and Colloid Science, vol 2. Academic, London, pp 4.31–4.36
5. Briggs DK (1928) The determination of the ζ-potential on cellulose – A method. J Phys Chem 32:641
6. Rutgers AJ (1940) Streaming potentials and surface conductance. Trans Faraday Soc 36:69
7. Gu Y, Li D (2000) The Zeta Potential of Glass Surface in Contact with Aqueous Solutions. J Colloid Interface Sci 226:328–339
8. Arulanandam S, Li D (2000) Evaluation of Zeta Potential and Surface Conductance by Measuring Electro-Osmotic Current. J Colloid Interface Sci 225:421–428

9. Ren L, Escobedo C, Li D (2002) A New Method of Evaluating the Average Electro-Osmotic Velocity in Microchannels. J Colloid Interface Sci 250:238–242
10. Sze A, Erickson D, Ren L, Li D (2003) Zeta-Potential Measurement Using Smoluchowski Equation and the Slope of Current-Time Relationship in Electroosmotic Flow. J Colloid Interface Sci 261:402–410

Further Reading

- Hunter RJ (1981) Charge and Potential distribution at Interfaces. In: Hunter RJ Zeta Potential in Colloid Science: Principle and Applications. Academic, London, pp 11–55
- Lyklema J (1995) Electric Double layers. In: Lyklema J (ed) Solid-Liquid Interfaces. Fundamentals of Interface and Colloid Science, vol 2. Academic, London, pp 3.2–3.232

Surface-Directed Capillary Flow Systems

Michael J. Swickrath[1], J. Adin Mann[1], Gary E. Wnek[2]
[1] Department of Chemical Engineering, Case Western Reserve University, Cleveland, OH, USA
[2] Department of Macromolecular Science and Engineering, Case Western Reserve University, Cleveland, OH, USA
michael.swickrath@case.edu

Synonyms

Surface tension-confined confined microfluidics; Wetting on structured substrates; Capillary-based microfluidics; Hydrophobic/hydrophilic microfluidics

Definition

Generating surface tension gradients such as Marangoni stresses or discontinuities in surface energy, either through ►chemical patterning or ►topographical manipulation, facilitates the control of wettability of fluids upon that surface. Surface-directed microfluidics is the exploitation of this phenomenon to encourage fluid transport through capillary interactions upon a surface-modified platform. Consequently, the need for extraneous pumping components is eliminated. These techniques demonstrate a great capacity to automate fluid transport providing alternative manufacturing methods for microfluidic platform development.

Overview

The field of microfluidics promises the capacity to automate sophisticated laboratory analyses into a diminutive platform that can be implemented by a user with minimal analytical experience. Often an analogy is drawn towards the integrated circuit revolution which facilitated the automation of large-scale computation. Similarly, a great deal of optimism exists that microfluidics may have such an impact on chemistry, biology and medicine, resulting in a drastic decrease in the amount of expensive reagent or invasive fluid samples required while enabling higher degrees of throughput and ►parallelization.

Such microfluidic devices have been successfully developed. However, many microfluidic devices require multiple components to implement fluid transport. This article describes alternative platform design to mitigate the aforementioned problems resulting in a fully-autonomous micro-device capable of promoting capillary flow. An example of commercial microfluidic device exploiting capillarity includes the OneTouch® testing strip developed by LifeScan, Inc. The test strip imbibes micro-volumes of blood which is introduced to a blood glucose meter facilitating fast and accurate results. The autonomous nature of this inexpensive microfluidic device is very attractive with regard to point-of-care diagnostics. Furthermore, many more novel platform configurations and fabrication methods are currently being investigated resulting in stand-alone microfluidic systems. Specifically, spontaneous ►surface-directed capillary pumping of fluids with appropriate surface tension and viscosity is enabled by patterning energetic discontinuities or topographical features upon a surface.

However, before *surface-directed microfluidics* can be employed towards solving problems in chemistry, biology and medicine, a thorough understanding of the underlying physics must be established. This task becomes non-trivial as fluidic miniaturization results in dramatic changes to the fundamental physics manifested at small length scales. For example, mass transport within microfluidic devices is a challenge as viscous effects dominate at small length scales rather than inertial effects [1]. Consequently, utilizing scaling arguments through dimensional analysis, the nonlinear terms in the Navier-Stokes equations can be neglected in most microfluidic systems. Although the lack of inertia at small length scales seems to indicate analysis of microfluidic platforms is straightforward, quite the opposite is true. Other non-linear phenomena that may not be as familiar at the macro scale become apparent as surface area to volume ratios increase [1]. In particular, surface ►curvature and three-phase boundaries must be taken into account making the analysis of *surface-directed* flows substantially more difficult.

With regard to *surface-directed microfluidics*, patterning discontinuities in surface energetics results in deformation of the solid-liquid contact line. Such deformations

can either promote or impede capillary break-up. Consequently, discontinuous energetics serves as a mechanism to harness for autonomous fluid transport. Furthermore, other implications arise as a result of the capacity to manipulate interfacial *curvature* at the microscale. As the surface area to volume ratio experienced within microfluidic devices is rather substantial, the overall shape and stability of boundaries and interfaces can be dramatically affected by minute amounts of surface or fluid contaminants. Accordingly, *surface-directed microfluidic* devices warrant proper surface cleaning protocols, storage procedures and reagent preparation to ensure reproducible and reliable device function. Moreover, since reagents may necessarily contain surface-active components, adsorption dynamics may be an important factor in capillary pumping.

The breadth of this article seeks to address a review of fabrication techniques, characterization and analysis of microfluidic devices implementing the *surface-directed* approach. Furthermore, key research findings will be explicated along with aspects of this approach requiring future investigation. As a result, the methodology to implement the *surface-directed* approach will be established along with a suitable record of pertinent literature regarding this novel technique. However, before doing so, a brief diversion into the treatment of fluid physics for systems exhibiting high surface area to volume ratios may lend much insight in developing a robust understanding and appreciation of capillary-driven microfluidic flow.

Surface-Directed Capillary Physics

As previously mentioned, the analysis of microfluidic systems can be rather difficult for a variety of reasons. The direct implementation of the Navier-Stokes equations toward *surface-directed microfluidic* systems requires careful attention when considering the advection of the free surface and the associated curvature of this surface. Consequently, sophisticated computational fluid dynamics software packages are required for a comprehensive three-dimensional analysis of the fluid transport within *surface-directed microfluidic* devices. However, a time-consuming comprehensive analysis may be beyond the requirements of designing and manufacturing functional surface-directed microfluidic platforms. Consequently, empirical approximations and scaling arguments are commonly used in the characterization of microfluidics physics.

One common approach to treating capillary microfluidic phenomena entails equating the fluid volumetric flowrate to a ratio of pressure drop per resistance, R, in a fluid channel as developed by Washburn circa 1921 [2] where A_{cs} represents cross-sectional area of a fluid duct (assumed to be constant) and x represents the time-dependent location of the ► meniscus position.

$$A_{\mathrm{cs}}\frac{\mathrm{d}x}{\mathrm{d}t}=\frac{\Delta P}{R} \tag{1}$$

Considering capillary dynamics, the pressure drop term is often described by the Laplace equation, $\Delta P = 2\gamma H$, where γ represents liquid surface tension and H represents the mean *curvature* of the liquid-gas interface associated with all curves, C_i, passing through the surface. Furthermore, the character of a sufficiently smooth surface is through the invariant from differential geometry, the principal curvature of each curve, k_i. The the radii of curvature are the inverse of each principal curvature, $k_i = 1/r_i$. Considering the maximum and minimum ► radii of curvature at a point on a three-dimensional surface, the mean *curvature* can be calculated explicitly (see appendix for more thorough derivation of the mean *curvature* parameter).

$$H=\frac{1}{2}\left(\frac{1}{r_1}+\frac{1}{r_2}\right) \tag{2}$$

Curvature is usually assumed to follow geometries that can be fit to a circle (or sphere in the three-dimensional case) in the Laplace equation; this is not typically the case but usually results in a decent approximation. Further, for straight paths, r_2 can be considered as infinite and approximations can be made for r_1 [3].

$$r_1=\frac{h}{2\cos\theta_{\mathrm{I}}} \tag{3}$$

In Eq. (3), θ_{I} indicates the contact angle at the three-phase interface.

Moreover, resistance terms exist for common geometries such as rectangular ducts [4].

$$R_{\mathrm{D}}=\frac{12\mu x}{wh^3}\left[1-\frac{h}{w}\left(\frac{192}{\pi^5}\sum_{n=0,1,2}^{\infty}\frac{\tanh\frac{2n+1\pi w}{2h}}{(2n+1)^5}\right)\right]^{-1} \tag{4}$$

Here w represents channel width, h represents channel height and μ represents the viscosity of the fluid. In the case where $w \gg h$, the bracketed term can be neglected while maintaining sufficient accuracy through the approximation.

By substituting Eq. (3) into Eq. (2) and subsequently utilizing modified Eq. (2) and Eq. (4) with the general Washburn equation, one finds that capillary dynamics tend to follow

S

Eq. (5) with a general geometry-dependent characteristic length scale, L [1].

$$x \sim \left(\frac{\gamma L \cos\theta}{\mu} t\right)^{1/2} \tag{5}$$

Consequently, the time-dependent fluid front position in a *surface-directed microfluidic* device tends to be dependent on system geometry, intrinsic fluid properties, fluid-substrate interactions and the square root of time. This dependency has been derived theoretically and observed for a number of capillary-driven microfluidic systems such as the ▶v-groove geometry [5, 6]. Noting that the ratio γ/μ is a characteristic capillary velocity, U_c, enables the rearrangement $x \sim (U_c L \cos\theta t)^{1/2}$. This relation perhaps leads to a more tangible description of fluid specific capillary transport.

Outside of the capillary dynamics approach, scaling arguments and dimensionless analysis can provide valuable insight into fluid physics on the micro-/nanoliter scale. An exhaustive review of these approaches has been conducted for a variety of microfluidic techniques [1]. However, for this article, we will strictly consider scaling metrics and dimensionless numbers pertinent to the *surface-directed* approach.

First, we will consider perhaps the most often applied dimensionless number toward fluid transport, the Reynolds number. The Reynolds number is a measure of inertial to viscous forces [1] and is dependent upon fluid density ρ, and viscosity μ, as well as characteristic velocity U and the characteristic length scale L which can be written as follows.

$$\mathrm{Re} \equiv \frac{\rho L U}{\mu} \tag{6}$$

Characteristic length scales chosen depend on system geometry. For example, diameter is commonly chosen for cylindrical systems while the hydraulic diameter, $D_A = 4A/P$, may be chosen for Cartesian geometries (such as a microfluidic duct) in which A denotes cross-sectional area and P is the perimeter of the cross-section.

As mentioned earlier, the lack of turbulence in microfluidic devices indicates inertial effects are minimal. Consequently, viscous forces dominate. Reynolds numbers characteristic of microfluidic devices are generally on the order of $O(10^{-6})$ to $O(10)$ [1]. Furthermore, the transient time required to achieve this laminar flow goes according to $\tau \sim \rho L^2/\mu$. Consequently, one can see that flow in microfluidic devices tends to be rather devoid of turbulence.

Another relevant number in the analysis of microfluidic devices in general is the Péclet number; which yields the ratio of convective transport to diffusive transport where D represents the diffusion constant of a molecule within a particular fluid.

$$\mathrm{Pe} \equiv \frac{U}{D/L} \tag{7}$$

As already indicated, flow is laminar in microfluidic devices which results in great difficulty in attaining adequate mixing for chemical reaction processes. Scales for the general time ($\tau \sim w^2/D$) and length ($z \sim Uw^2/D$) to achieve mixing in a low Péclet number devices are known considering a channel of width w [1].

An additional dimensionless number particularly important to *surface-directed microfluidics* is the capillary number utilized to measure viscous to interfacial forces.

$$\mathrm{Ca} \equiv \frac{U}{\gamma/\mu} \tag{8}$$

Surface forces tend to be inherently important for capillary-driven microfluidic devices as surface area to volume ratios are rather high and surface tension-induced interfacial *curvature* is significant enough to promote capillary wicking. For chemically patterned devices depending on hydrophobic/hydrophilic confinement in particular, the capillary number must be sufficiently low (i. e. $\mathrm{Ca} \ll 1$) in order to maintain fluid confinement within intricate geometry implying $\Delta P \leqslant \gamma/w$ [1].

The above analyses lend insight into the behavior of fluids within *surface-directed microfluidic* devices. Now that an intuitive framework of the fluid physics within microfluidic platforms has been established, the contemplation of successful platform fabrication techniques and their associated applications is worthy of consideration.

Basic Methodology

Several approaches exist to manufacture *surface-directed microfluidic* platforms. Examples of relevance to this article include the *chemical patterning* of regions exhibiting drastic and abrupt disparity in surface energies and the manipulation of surface topography to influence mean *curvature*. Furthermore, some alternative techniques will be discussed as potential applications to *surface-directed microfluidics* such as thermal actuation and passive gate fabrication with coatings that enable contact angle mediation via photochemical reactions or the presence of water.

Chemical Patterning

The concept of *chemical patterning* generally involves the deposition of hydrophobic 'curbs' upon an other-

wise hydrophilic substrate. Consequently, capillarity can be exploited to promote autonomous fluid transport eliminating the requirement to integrate pumping equipment into the microfluidic platform.

Initial investigations focused on the relationship between fluid morphology and surface energy. Gau et al. investigated the shape instability that liquids undergo when an appropriate amount of liquid is adsorbed on a hydrophobic surface patterned with hydrophilic microstripes [7]. Hydrophilic stripes were deposited via thermal vapor deposition of MgF_2 (stripe thickness $\sim 20\,\text{nm}$) upon hydrophobic silicone rubber or thiolated gold substrates. The patterned surface was then exposed to sufficiently humid air and cooled to force the condensation of liquid upon the surface. The results indicate that initially, water adsorbs forming a structure with a cylindrical cross-section; however, when an adequate amount of water is adsorbed, instability can occur resulting in bulge formation. This instability is quite different from the classical Rayleigh instability; rather it is a bifurcation in two different morphologies of constant mean *curvature* [7]. A linear stability analysis indicates that the cylinder is locally stable so long as the wavelength of the shape deformation λ, exceeds a critical value λ_c, based upon the hydrophilic path width a and advancing contact angle θ.

$$\lambda_c = \left[\frac{\frac{\pi}{2}}{\theta^2 - \left(\frac{\pi}{2}\right)^2}\right]^{1/2} \frac{\theta}{\sin\theta} a \tag{9}$$

Consequently, Gau suggests that it is in fact feasible to build two-dimensional microfluidic devices through *chemical patterning* techniques.

These results were also independently confirmed by other groups [8]. Darhuber et al. developed disparities in hydrophilicity on a [001]-oriented p-type doped silicon wafers coated with a ► self-assembled monolayer of octadecyl-trichlorosilane (OTS). In all of the studies [7, 8], the experimental results were found to be in good agreement with theoretically determined surface morphology through the ► surface evolver software package. The surface evolver software package is an interactive tool to study the equilibrium surface shapes of liquids subject to surface tensions and other energies under various constraints. The surface evolver evolves the surface toward minimal energy by a gradient descent method. The surface evolver software package is a powerful tool for the theoretical investigation of static surface structures of *surface-directed microfluidics* enabling the determination of surface curvature and quantification of the Laplace pressure. Most often, gravity can be neglected in the surface evolver analysis as indicated by the low Bond number experienced in microfluidic devices (i. e. Bo $\ll$ 1). Specifically, the Bond number is a measure of body forces (i. e. gravity) per surface forces (i. e. capillarity) where $\Delta\rho$ indicates

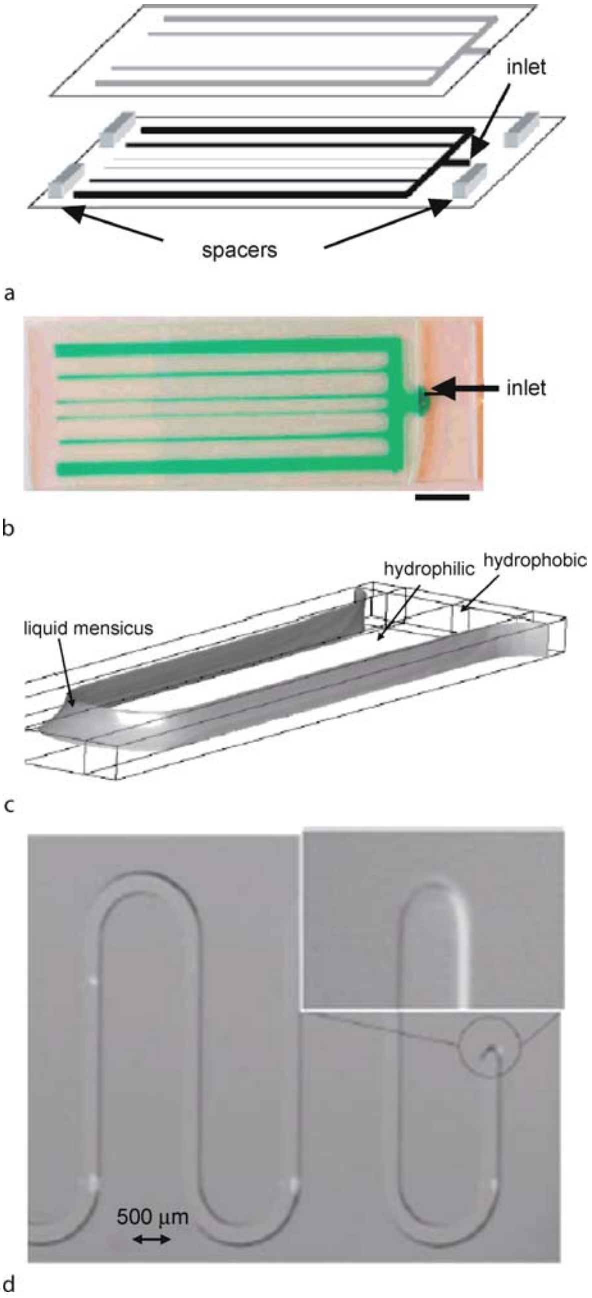

Surface-Directed Capillary Flow Systems, Figure 1 *Surface-directed microfluidic* device fabricated via sol gel processing (**a**) with a demonstration of the configuration of device and (**b**) the implementation of the device with colored fluid for visualization [9]. (**c**) Computational fluid dynamic representation of the fluid front of a device fabricated with a patterned bottom substrate and indiscriminately hydrophobic top substrate. (**d**) The implementation of the device with an unpatterned top substrate [11]

the change in density across a surface, g is the gravitational constant, L is a characteristic length of the capillary cross-section and γ is the surface tension of the fluid.

$$\mathrm{Bo} \equiv \frac{\Delta \rho g L^2}{\gamma} \tag{10}$$

These findings were later extended towards the development of autonomous microfluidic platforms employing *surface-directed* fluid transport. Several studies indicate that microfluidic platforms can be manufactured by chemically patterning substrates in combination with correspondingly patterned (or in some cases unpatterned) lids in a parallel plate arrangement [9–11]. Figure 1 demonstrates the approach utilized to develop such devices. Figures 1a and b demonstrate the configuration of a device fabricated with hydrophobic commodity polymers patterned on both bottom and top substrates with a hydrophilic silica sol gel material [9]. Figure 1c exhibits the fluid front, determined through computational fluid dynamics, of a device (Fig. 1d) where the bottom substrate is composed of a hydrophilic borosilicate wafer patterned with hydrophobic plasma-polymerized hexafluoropropene barriers developed photolithographically. The top substrate in Figs. 1c and d is indiscriminately hydrophobic.

Results from the development of these parallel plate *surface-directed microfluidic* have resulted in optimal device geometry recommendations. The optimal aspect ratio, defined as width per height of the device, has been determined through free energy considerations [3]. To ensure spontaneous capillary flow, the aspect ratio must follow Eq. (11) which indicates that the height of the device b, must always be less than the width of the device a, and the capacity to promote fluid flow is subject to the magnitude of the advancing contact angle of the hydrophilic path. The development of Eq. (11) follows arguments based upon the ▶Laplace pressure drop associated with interfacial *curvature* [3].

$$\frac{b}{a} \leqslant \cos\theta \tag{11}$$

Consequently, as the advancing contact angle increases towards the 90° limit for spontaneous flow, the capacity of the device to promote capillary flow diminishes drastically.

Furthermore, devices have been developed demonstrating reactions and passive valves with *self assembled monolayers* of OTS via either multi-stream laminar flow or photolithography [9, 10]. The pressure sensitive valves were demonstrated with silane solutions and water with trace amounts rhodamine-B for visualization purposes. The maximum pressure experienced based on capillarity was determined for these devices dependent upon device geometry, liquid surface tension γ and the advancing contact angle for the non-polar hydrophobic region θ_N [9, 10].

$$\Delta P_{\mathrm{MAX}} = \frac{2\gamma}{b} \sin\left(\theta_{\mathrm{N}} - \frac{\pi}{2}\right) \tag{12}$$

Furthermore, an application requiring a large interfacial surface area is demonstrated with an acidified gas and phosphate buffer neutralization in the presence of indicator. This investigation also presents conditions for critical width and curve radius that fluid can make under spontaneous flow conditions [10]. Furthermore, through energy minimization considerations, Lam et al. independently derive and demonstrate Eq. (11) is in excellent agreement between theoretical and experimental results [9]. Consequently, Eq. (11) can be derived through an alternative but equally valid approach.

An additional method regarding the fabrication of *surface-directed microfluidic* devices entails chemically pattering plasma polymerized hexafluoropropene coating photolithographically upon a hydrophilic borosilicate wafer [11]. Consequently, such a drastic differential in wettability is established that only one patterned substrate is required and can be coupled with a hydrophobic top substrate. The advantage of this approach is that it eliminates the tedious necessity for proper alignment for top and bottom substrates. The investigators of this approach present a theoretical model to predict fluid front position versus time based upon a conservation of momentum approach and discuss the similarities between their model and an analogous model derived for cylindrical capillaries.

$$\frac{\mathrm{d}^2\left(x^2\right)}{\mathrm{d}t^2} + \frac{12\mu}{\rho a^2}\frac{\mathrm{d}\left(x^2\right)}{\mathrm{d}t} + \frac{2\gamma\left[2a - b\left(\cos\theta_1 + \cos\theta_2\right)\right]}{\rho a b} = 0 \tag{13}$$

In this relation, x denotes the fluid front position as a function of time t, system architecture a and b, and intrinsic material properties including contact angles of the fluid upon the hydrophilic and hydrophobic materials θ_1 and θ_2, respectively. The solution to this second order ordinary differential equation with respect to *meniscus* position squared can be solved relatively easy through numerical techniques. The solution determined by the investigators of this approach is in excellent agreement with experimental results [11]. Furthermore, the investigators demonstrated that confluent monolayers of cells could be cultured in their apparatus and proteins could be selectively adsorbed upon the device surface [11]. Consequently, the *surface-directed* approach may be advantageous for appli-

cations requiring uninhibited gas exchange such as tissue engineering.

Lastly, the *surface-directed* approach is not without limitations. Due to the inherent simplicity associated with these devices, flow control and mixing become an issue. Moreover, paths with bifurcations pose a challenge to flow control as fluid does not discriminate between paths to flow across. Specifically, preferentially controlling which path a particular fluid travels across is difficult, at best. In addition, flow within microfluidic devices tends to be laminar rendering turbulent mixing is difficult to achieve, at best [1]. However, one may be able to overcome this predicament by strategically patterning resistance upon the device surface although this has yet to be employed within a two-dimensional chemically patterned platform.

Although much work still exists before chemically patterned devices provide novel solutions to problems in chemistry, biology and medicine, many of the reports discussed are encouraging regarding the capacity of *surface-directed microfluidic* devices to support autonomous chemical processes.

Topographical Manipulation

An alternative paradigm to facilitating capillary wicking via the *surface-directed* technique includes deliberately manipulating the topography of a device to control interfacial *curvature*. This approach to *surface-directed microfluidics* generally exploits the fact that capillary-based flow can occur where the corners meet as a consequence of the diminishing *radius of curvature* at the intersection [12]. However, for this flow to occur spontaneously, the Concus-Finn condition must be fulfilled considering the advancing contact angle θ, as well as the corner half-angle α [13].

$$\theta < \frac{\pi}{2} - \alpha \tag{14}$$

This technique has been rigorously studied for the determination of equilibrated liquid morphology on structured surfaces such as rectangular channels and in *v-grooves* [5, 6]. In the case of rectangular channels, a map has been constructed enabling the a priori determination of ultimate liquid morphology based upon the contact angle of the substrate and aspect ratio of the duct cross-section [14]. Figure 2 illustrates this morphological dependency on fluid properties and system architecture. The associated syntax addresses features characteristic of each morphological regime. Results were calculated theoretically with the surface evolver software package and were found to be in good agreement with experimental results investigated through AFM [14].

Furthermore, the *v-groove* morphology has been thoroughly investigated and relations for capillary dynamics have been developed [5, 6]. Several alcohols with γ/μ ratios ranging from 46 – 970 cm/s were studied in grooves of varying geometry machined into a copper substrate. Figure 3a illustrates the groove geometry while Fig. 3b demonstrates the experimental platform used to conduct the studies [5, 6]. Two models were developed characterizing the capillary dynamics. The first model considers a hydrodynamic approach where the driving force is a result of pressure drop across a curved interface. The second model depends strictly upon the total interfacial energy change while neglecting the shape of the curved interface. In both cases, flow was demonstrated to always follow a relation of the following form where $K(\alpha, \theta)$ is a geometric parameter dependent on system geometry and contact angle.

$$x = K(\alpha, \theta)\, h_0 \frac{\gamma}{\mu} t^{1/2} \tag{15}$$

The results of these analyses demonstrate that the three-phase contact line location follows the square root of time. Coumarin fluorescent dye was utilized in small quantities to develop sufficient contrast of the three-phase line under UV irradiation for the comparison of experimental data to the models. The investigators of this approach conclude that exhaustive solutions to the capillary flow model can be realized; however, approximations via Eq. (15) can be employed for sufficiently accurate predictive models [5, 6].

As demonstrated through the referenced literature, *topographical manipulation* provides the capacity to induce capillary wicking through interfacial *curvature* modulation. As a result, one can exploit techniques such as photolithography, chemical etching and even three-dimensional machining to produce features promoting *curvature* management. Consequently, the approach of *topographical manipulation* is yet another straightforward but viable technique to produce *surface-directed* fluid transport.

Flow Modulation Techniques

As already established in previous sections, the *surface-directed* approach to microfluidic system fabrication produces autonomously functioning devices with little rigor associated regarding implementation. This is a direct implication of the fact that the driving force for flow exploits capillary interactions producing spontaneous capillary flow. However, an unwanted artifact resulting from the inherent simplicity of these devices is that flow modu-

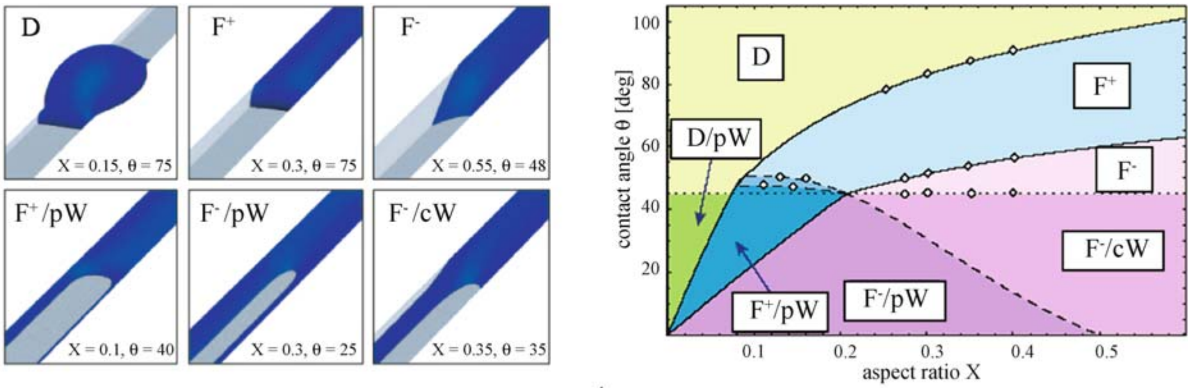

a b

Surface-Directed Capillary Flow Systems, Figure 2 Demonstration of equilibrated liquid structure based on system geometry and advancing contact angle. Characteristic features include droplet (D), filament (F), pinned-wedges (pW) and corner-wedges (cW). The $+/-$ signs indicate whether the ►Laplace pressure associated with each morphology is positive or negative, respectively [14]

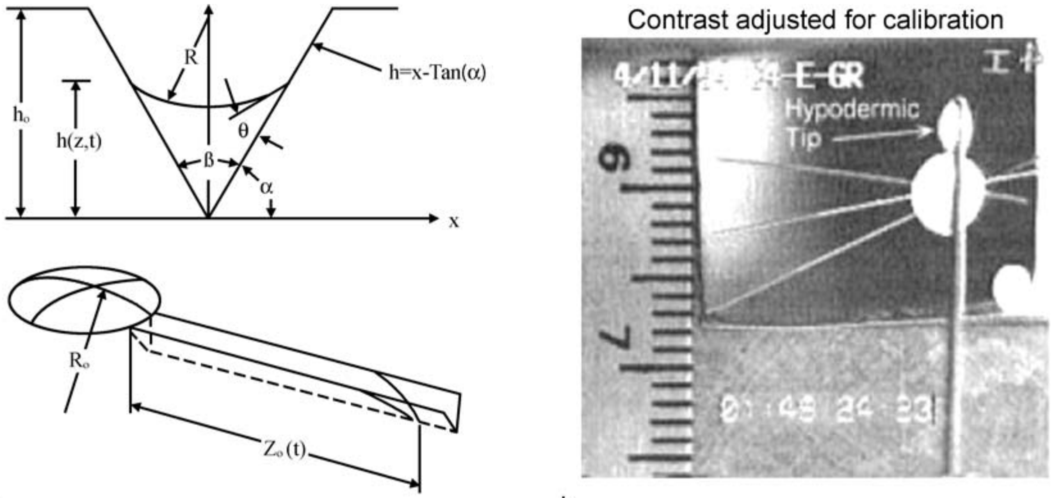

a b

Surface-Directed Capillary Flow Systems, Figure 3 Illustration of *v-groove* experiments (**a**) with the demonstration of system architecture and (**b**) the experimental platform utilized in the study [6]

lation is particularly difficult. This drawback is especially hindering for systems requiring the controlled introduction and the selective guidance of fluids across intricate geometry. This section intends to introduce several techniques that have been or could be employed to guide fluids in specific directions.

One such mechanism to control flow directionality or rate includes manipulating ►thermocapillary shear stresses at the liquid air interface upon a substrate with a temperature gradient to facilitate fluid transport [15]. This technique has been demonstrated through patterning a SiO_2 wafer with hydrophobic strips of octadecyltrichlorosilane and coupling this substrate with a heater array to induce temperature gradients [15]. The driving force for such thermocapillary induced flow is through local heating that can reduce the liquid surface tension producing *thermocapillary shear stress* [15].

$$\tilde{\tau} \cdot \hat{n} = \nabla \gamma = \frac{\partial \gamma}{\partial T} \nabla T \qquad (16)$$

For liquids, $\partial \gamma / \partial T$ is essentially temperature independent indicating that the driving force is ∇T. This affect induces fluid transit from warmer areas to cooler areas of a substrate. Figure 4 demonstrates the capacity to control fluid progression utilizing this technique. As demonstrated, fluid can be directionally guided down required pathways and even across 90° angles. Furthermore, models have

been developed with a lubrication equation approach and found to be in good agreement with the experimental results [15].

Other techniques provide the potential to produce wettability modulation upon chemically patterned substrates. For example, ▶contraphilic polyurethane materials exist exhibiting an 83° contact angle when dry but a 108° contact angle in the presence of water [16]. The proposed mechanism is that amide inter/intramolecular hydrogen bonding occurs in the dry and moderately hydrophilic state while surface-confined amide-water hydrogen bonding releases semifluorinated groups yielding a more hydrophobic surface when wet [16]. This mechanism has been found to be reversible and could potentially serve as method to design passive gates between aqueous and nonaqueous solutions. This material could also be utilized to selectively pattern regions to impede fluid flowrate.

Another example of a coating technique presenting a feasible solution to developing wettability modulation includes employing light sensitive compounds such as spiropyrans. These photoisomerizable compounds can undergo an 11 − 14° reversible decrease in contact angle when light is switched from the visible region to ultraviolet [17]. This photocapillary modulation technique could be utilized to control the *Laplace pressure*, and therefore the flowrate, in a microfluidic channel coated with spiropyran compounds. Consequently, the field of flow modulation in *surface-directed microfluidics* is currently wide-open for investigation. Novel flow control methods are a necessity before integrating complex reaction processes into an on-chip format.

Key Research Findings

As demonstrated within this review, the *surface-directed microfluidics* approach offers a simple method for fabrication and implementation of micro-analytical systems. This burgeoning field offers great opportunity to resolve problems associated with more complicated microfluidic systems. Though this approach is rather new, several findings have already been established which may be of particular importance to investigators initiating research in this field. From a fluid physics perspective, rigorous solutions to the Navier–Stokes equations are not immediately realizable as a consequence of the poor understanding of ▶slip velocities associated with boundary conditions in microfluidic systems. However, alternative approaches towards developing dynamic flow models indicate *meniscus* position progresses according to the square root of time and is dependent upon fluid/substrate properties and system geometry as demonstrated in Eq. (5). Interestingly, Mann et al. [5, 6] found that a dynamic contact angle was not required to fit their experimental data to theoretical predictions. Furthermore, *surface-directed microfluidic* platforms can adequately be characterized as exhibiting low Reynolds, Péclet, capillary and Bond number flow. Subsequently, flow in *surface-directed* devices tends to be rather laminar with transport being dominated by diffusion with surface forces out-competing body forces such as gravity, respectively.

Chemical patterning and *topographical manipulation* techniques have successfully produced autonomous devices for fluid transport. In some cases, reaction processes have been integrated within these devices. However, this field is ripe with opportunity regarding the implementation of *surface-directed* platforms towards developing platforms that conduct reactive and diagnostic analyses. Preliminary diversion into theory has provided some relations that can be utilized for intelligent device optimization; however, a great deal of investigation needs to be addressed before a comprehensive understanding of device function is established.

Surface-directed microfluidic devices are inherently simple. Consequently, flow modulation is a concern. Methods have been employed to gain more control over flow such as mechanical actuation and thermocapillary induction. Moreover, material coatings provide the potential for the development of flowrate impediment and passive gate introduction through contraphilism or light-mediation.

Future Directions for Research

The *surface-directed microfluidics* approach presents a manufacturing methodology involving minimal rigor. Furthermore, *surface-directed* devices are devoid of extraneous mechanical/electrical components which can lead to component malfunction and overall device failure. As a consequence of the inherent simplicity of *surface-directed microfluidic* devices, implementation of the platform is straightforward and requires limited analytical experience. However, before wide-scale deployment of *surface-directed microfluidic* devices can be realized, a more comprehensive understanding of the underlying physics needs to be conducted. Certain phenomena play a larger role in fluid physics as liquid samples approach the nanoliter scale. For example, long-ranged inter-molecular interactions, thermal fluctuations such as capillary waves and the influence of the molecular structure of the fluid all inherit a greater capacity to affect fluid physics as surface area to volume ratios decrease. To realize greater degrees of *parallelization* and high-throughput, a better theoretical framework is a necessity regarding microfluidics as a whole encompassing the

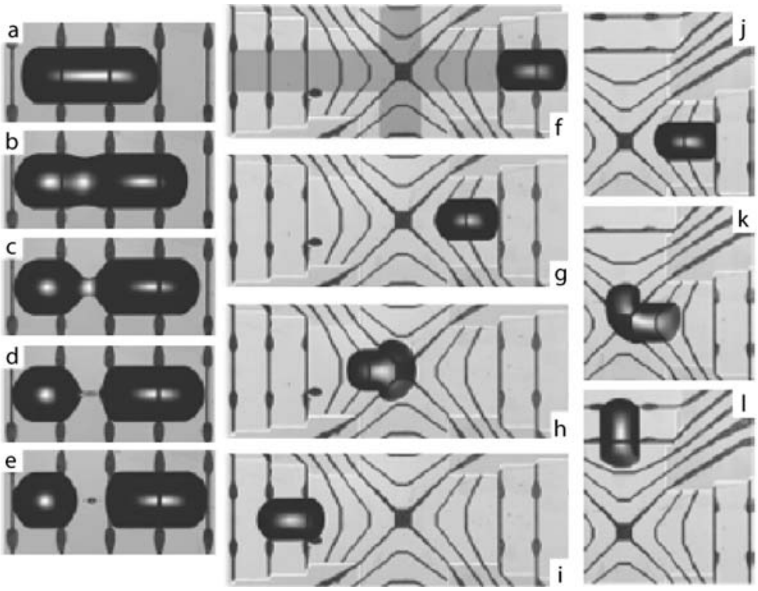

Surface-Directed Capillary Flow Systems, Figure 4 (**a**)–(**e**) Thermal induced division of a drop of dodecane on a selectively wetting strip 1000 μm wide (elapsed time = 8.5 s). (**f**)–(**i**) Dodecane drop propelled through a 1000 μm wide intersection (elapsed time = 104 s). (**j**)–(**l**) Dodecane drop thermally guided across a 90° angle in a 1000 μm wide intersection (elapsed time = 164 s) [15]

surface-directed technique. Lastly, fluid sample pretreatment techniques are of great consideration to ensure reproducible and reliable function of devices as only minimal amounts of contaminants are required to influence capillary dynamics in *surface-directed* devices. A comprehensive literature review exists as a basis for microfluidic sample pretreatment [18]; however, these findings need to be extended to the *surface-directed* approach to enhance platform reliability. Addressing such concerns may expedite the application of the *surface-directed microfluidics* towards current problems in chemistry, biology and medicine.

Cross References

- ► Capillary Filling
- ► Capillary Force Valves
- ► Methods for Surface Modification
- ► Surface Tension Driven Flow
- ► Thermal Capillary
- ► Thermocapillary Pumping
- ► Wetting and Spreading

Appendix

Considering a Monge surface of area A_o in Cartesian coordinates, $\xi\,(t,x,y)$, the change in free energy required to curve this surface with respect to a flat surface with a reference free energy, Ω_0, at a constant composition and temperature is as follows.

$$\Omega - \Omega_0 = \int_{A_o} [p]\,\xi\,(t,x,y)\,\sqrt{a}\,\mathrm{d}x\,\mathrm{d}y + \int_{A_o} \sqrt{a}\,\mathrm{d}x\,\mathrm{d}y \quad \text{(a)}$$

Where $[p]$ is the pressure drop (ΔP) across the interface and the a is a geometrical parameter.

$$a = \sqrt{1 + \left(\frac{\partial \xi}{\partial x}\right)^2 + \left(\frac{\partial \xi}{\partial y}\right)^2} \quad \text{(b)}$$

Considering that the surface $\xi\,(t,x,y)$ is arbitrary and the associated derivatives are small, the free energy function is simplified.

$$\Omega - \Omega_0 = \int_{A_o} [p]\,\xi\,\mathrm{d}x\,\mathrm{d}y + \int_{A_o} \gamma \left[1 + \frac{1}{2}\left(\frac{\partial \xi}{\partial x}\right)^2 + \frac{1}{2}\left(\frac{\partial \xi}{\partial y}\right)^2\right] \mathrm{d}x\,\mathrm{d}y \quad \text{(c)}$$

Let δ be the variational operator and consider that $\xi\,(t,x,y)$ and the derivatives of $\xi\,(t,x,y)$ are equal to zero on the boundary, ∂A_o , over which the variation function is determined. Moreover, it is implicitly assumed that $\delta\,[p] = 0$

and $\delta\gamma = 0$.

$$\delta\Omega = \int_{A_o} [p]\,\delta\xi\,dx\,dy + \int_{A_o} \gamma \left[\frac{\partial \xi}{\partial x}\frac{\partial \delta\xi}{\partial x} + \frac{\partial \xi}{\partial y}\frac{\partial \delta\xi}{\partial y} \right] dx\,dy \tag{d}$$

Utilizing integration by parts on the second integral further simplifies the variation in free energy.

$$\delta\Omega = \int_{A_o} [p]\,\delta\xi\,dx\,dy - \int_{A_o} \gamma \left[\frac{\partial^2 \xi}{\partial x^2} + \frac{\partial^2 \xi}{\partial y^2} \right] \delta\xi\,dx\,dy \tag{e}$$

Because A_o is arbitrary and $\delta\xi$ is small, but an otherwise arbitrary variation, an explicit pressure drop dependence becomes apparent.

$$0 = [p] - \gamma \left[\frac{\partial^2 \xi}{\partial x^2} + \frac{\partial^2 \xi}{\partial y^2} \right] \tag{f}$$

Furthermore, in comparison with the Laplace pressure, $\Delta P = 2\gamma H$, the mean curvature of the Monge surface can be reconstructed leading directly to the result in Eq. (2).

References

1. Squires TM, Quake SR (2005) Microfluidics: Physics at the nanoliter scale. Rev Mod Phys 77:977–1026
2. Washburn EW (1921) The dynamics of capillary flow. Phys Rev 17(3):273–283
3. Zhao B, Moore JS, Beebe DJ (2001) Surface-directed liquid flow inside microchannels. Science 291:1023–1026
4. Constantinescu VN (1995) Steady Parallel Flow of Incompressible Fluids. In: Ling FF (ed) Laminar Viscous Flow. Springer, New York, p 123
5. Mann JA, Romero L, Rye RR, Yost FG (1995) Flow of simple liquids down narrow v-grooves. Phys Rev E 52(4):3967–3972
6. Rye RR, Mann JA, Yost FG (1996) The flow of liquids in surface grooves. Langmuir 12:555–565
7. Gau H, Herminghaus S, Lenz P, Lipowsky R (1999) Liquid morphologies on structured surfaces: from microchannels to microchips. Science 283:46–49
8. Darhuber A, Troian SM, Reisner WW (2001) Dynamics of capillary spreading along hydrophilic microstripes. Phys Rev E 64(3):031603(1–8) http://prola.aps.org/abstract/PRE/v64/i3/e031603
9. Lam P, Wynne KJ, Wnek GE (2002) Surface-tension confined microfluidics. Langmuir 18:948–951
10. Zhao B, Moore JS, Beebe DJ (2002) Principles of surface-directed flow in microfluidics channels. Anal Chem 74:4259–4268
11. Bouaidat S, Hansen O, Bruus H, Berendsen C, Bau-Madsen NK, Thomsen P, Wolff A, Jonsmann J (2005) Surface-directed capillary system; Theory, experiments and applications. Lab Chip 5:827–836
12. Boys CV (1959) Soap Bubbles. Dover, New York
13. Concus P, Finn R (1969) On the behavior of a capillary surface in a wedge. Proc Natl Acad Sci USA 63:292–299
14. Seemann R, Brinkmann M, Kramer EJ, Lange FF, Lipowsky R (2004) Wetting morphologies at microstructured surfaces. Proc Natl Acad Sci 102(6):1848–1852
15. Darhuber AA, Valentino JP, Davis JM, Troian SM, Wagner S (2003) Microfluidic actuation by modulation of surface stresses. App Phys Lett 82(4):657–659
16. Makal U, Wynne KJ (2005) Water induced hydrophobic surface. Langmuir 21:3742–3745
17. Rosario R, Gust D, Garcia AA, Hayes M, Taraci JL, Clement T, Dailey JW, Picraux ST (2004) Lotus effect amplifies light-induced contact angle switching. J Phys Chem B 108:12640–12642
18. Lichtenberg J, de Rooij NF, Verpoorte E (2002) Sample pretreatment of microfabricated devices. Talanta 56:233–266

Surface Electric Conductance

► Surface Conductivity
► Surface Conductivity Measurement

Surface Enhanced Raman Scattering (SERS)

Definition

►SERS is a highly sensitive optical detection technique in which lasers are used to excite vibrational transitions in a molecule adsorbed on a metal nanoparticle surface. As a result of large optical fields, the Raman cross section for a molecule on a surface is enhanced by factors of $10 \times 10^6 - 10 \times 10^{10}$.

Cross References

► Biosensors Using Surface-Enhanced Raman Scattering

Surface Evolver

Definition

An interactive tool to study the equilibrium surface shapes of liquids subject to surface tensions and other energies under various constraints by evolving the surface toward a minimal energy state by a gradient descent method.

Cross References

► Surface-Directed Capillary Flow Systems

S

Surface Features to Enhance Transport

► Roughness Effect on Microscale Transport

Surface Forces

► Disjoining Pressure

Surface Lipid Translocation

► Microfluidics for Studies of Apoptosis

Surface Micromachining

► Silicon Micromachining

Surface Modification, Methods

Sushanta K. Mitra, Auro Ashish Saha
Department of Mechanical Engineering, Indian Institute of Technology Bombay, Mumbai, India
skmitra@me.iitb.ac.in

Synonyms

Surface change; Surface transformation; Surface treatment

Definition

Surface chemistry is of great importance in micro/nano-fluidic devices, especially in the case of miniaturized and integrated systems, owing to the high surface-area-to-volume ratio. Surface properties play a vital role in a number of microfluidic devices through hydrophobic and electrostatic interactions. Protein and cell adhesion at surfaces can occur because of hydrophobic and electrostatic interactions, which is undesirable in bioanalytical applications. Control of surface properties is thus an indispensable prerequisite in microfluidic systems. The approach generally adopted is to modify the surface chemistry of the device to make it more useful for various applications.

Overview

Microfluidic devices have been fabricated from a wide range of materials, such as silicon, fused silica, borosilicate glass, elastomers (poly(dimethylsiloxane) (PDMS)), resins (SU-8), and thermoplastics (poly(methylmethacrylate) (PMMA), polystyrene, polycarbonate (PC), cyclic olefin copolymer, and poly(ethylene terephthalate glycol) (PETG)). The fabrication of glass- or silicon-based devices relies on established technologies such as those of microelectronics and is often considered to be time-consuming and very expensive. Glass, in particular fused silica, is a very attractive material for microfluidic chips owing to its excellent optical properties, good insulating properties, and inertness towards a variety of different solvents. Although silicones have been used mostly as soft-tissue substitutes, serious problems have occurred when silicone devices have been implanted for a long time [1]. In contrast, microfluidic devices fabricated from polymer materials have simpler manufacturing procedures and are cheaper. Furthermore, channels with high aspect ratios are much easier to produce from polymer materials than from glass, which is often advantageous for optical detection.

The surfaces of devices often exhibit different wettability characteristics, depending on the manufacturing approach adopted. Surface modification techniques can be used to alter the wettability behavior of microfluidic devices. This difference in wettability can be used to control the flow rate in devices. There are many other benefits of hydrophilic surface treatments, including the ability to increase adhesion and capillary effects [2]. Irrespective of the material used in the device, the primary requirement that a material needs to fulfill is biocompatibility in various applications. Therefore it is also necessary to use surface modification techniques to render materials biocompatible. It is believed that future devices of increasing sophistication will often require programmable surface properties, including control of the spatial distribution of charge and polarity [3].

Conventional polymers do not always possess the combination of desired bulk and surface properties for a specific application. The polymer materials used for microfluidic devices are innately hydrophobic, low-surface-energy materials and thus do not adhere well to other materials brought into contact with them. This necessitates their surface modification/treatment to render them adhesive. This has prompted the development of a variety of polymer modification techniques, with the aim of developing new materials from known and commercially available polymers that have desirable bulk properties (elasticity, thermal stability, permeability, etc.), in conjunction with newly tailored surface properties (adhesion, biocompatibility, optical reflectivity, etc.).

Currently, the methods used for surface modification of polymers are dynamic coating and permanent surface modification [4]. Dynamic coating is considered to be the easiest way to perform surface modification. In this

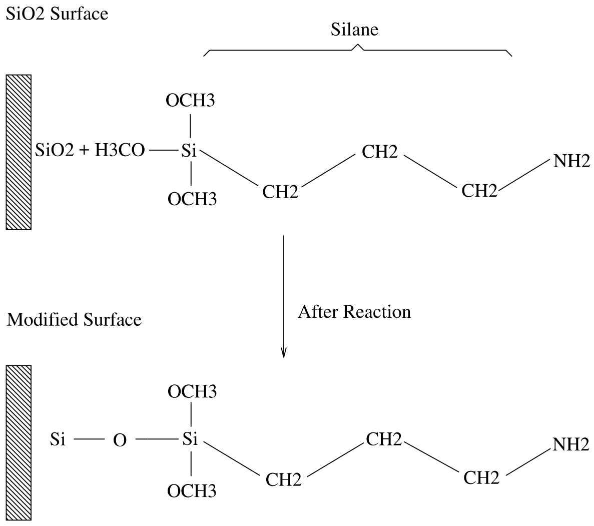

Surface Modification, Methods, Figure 1 Surface modification with 3-aminopropyltrimethoxysilane

coating process, surface-active coating materials or surface modifiers are introduced into the buffer, which is then forced through the channel at a constant speed. The coating materials are strongly adsorbed onto the channel surface via physical interactions. Permanent surface modification involves specific chemical reactions which permanently modify the chemical composition of the surface by the application of high-energy sources such as radiation, flames, coronas, plasmas, electron beams, and ion beams to activate the surface before chemical bonding.

For silicon-based microdevices, most of the surface modification approaches rely on silanization chemistry (Fig. 1), where the silanol groups on the surface are derivatized using various silanes. Silica surfaces must typically be coated to effect permanent changes in their properties [3]. A wide variety of techniques have also been developed around surface functionalization using self-assembling monolayers (SAMs) for coatings on silicon surfaces. Monolayers have been deposited on silica surfaces, primarily using chemicals consisting of a hydrocarbon backbone terminating in a polyfunctional alkoxysilyl moiety. Hydrolysis and condensation of these alkoxy groups attaches the hydrocarbon backbone to the silica surface via a siloxane bond. SAMs have been patterned using UV lithography, microcontact printing, scanned-probe lithography, and electron beam lithography. Polymers including polyethylene glycol, polyacrylamide, and hydroxypropylcellulose have been grafted onto silica surfaces using, primarily, methacrylate-terminated intermediates. Successful polymer films prevent both electrostatic and hydrophobic attractions at the wall by presenting an uncharged polar surface to the fluid [3]. Surface modification of silicon-based devices with polyethylene glycol (PEG) can be performed by physical adsorption, covalent immobilization such as grafting and chemical coupling, or gas phase treatment (plasma treatment or deposition) [5]. Although surface modification efforts have proved successful, however, they do not guarantee conformal coating and long-term stability. As in the case of modified PDMS, the surfaces have shown to slowly recover their original hydrophobicity. It is known that an oxidized PDMS surface recovers its hydrophobicity.

Dynamic coating appears to be especially attractive for plastic microchips, as established surface chemistry such as silanization is often not applicable to polymeric materials. Permanent coatings are often regarded as the most effective way to perform surface modification in order to reduce analyte–wall interactions and to modify electroosmotic flow (EOF). Permanent surface modification is, however, often more laborious in the production process and might, accordingly, be less attractive for disposable devices. Dynamic coating methods are applied not only to control EOF and reduce analyte adsorption but also to make a hydrophobic surface more compatible with a hydrophilic separation medium.

Basic Methodology

The chemical modification of the surfaces of polymers is of increasing importance in many diverse aspects of modern technology, with applications which include solid-phase chemical synthesis related to drug discovery, chemical catalysis, biocompatible medical implants and prostheses, diagnostic devices, and surface-modified fabrics, amongst many others. In biological analysis, it is necessary to make polymer surface properties meet requirements regarding wettability, biocompatibility, and nonspecific adsorption [6]. Introducing biological samples, such as plasma or whole blood, into microsystems needs far more consideration of surface modification compared with working with buffer samples of adjusted pH containing cells in the form of polymeric beads. Blood–material contact most often initiates surface-mediated reactions that lead to cell activation and blood clotting.

A wide array of surface modification techniques, ranging from simple to sophisticated, wet to dry, and vacuum to nonvacuum, are available for a host of polymeric materials. They include plasma surface treatment; laser surface treatment; corona, flame, UV, ozone, UV/ozone, photochemical, photografting, chemical-grafting, and chemical methods of surface modification; and modification of polyamide surfaces by microorganisms [7].

S

The surface modification of PDMS is often found to be difficult because the material is inert. Polymer surface modification is required for applications such as biomedical assays, microfuel cells, and lipid-based immunoassay chips. Many surface modifications have been made to PDMS for electrophoretic separation, but new modifications are being made for emerging applications such as heterogeneous immunoassays and cell-based bioassays. These new modification techniques are powerful because they impart biospecificity to the microchannel surfaces and reduce protein adsorption [8]. To decrease the hydrophobicity of PDMS, low-pressure oxygen plasma, UV/ozone, indirect corona, or oxygen-rich butane gas flame treatment is often used to activate the surface and render it hydrophilic. Oxygen plasmas have been the most popular of these techniques. During plasma treatment, the surface of PDMS is subjected to high-energy species, including electrons, photons, ions, and radicals. The surface is oxidized owing to exposure to the plasma and it becomes oxygen-rich and carbon-lean. However, the surface of oxidized PDMS recovers its hydrophobicity after oxidation in a very short time. The recovery in hydrophobicity is caused by the migration of PDMS chains to the surface. It is believed that continuous storage of oxidized PDMS in water stabilizes electroosmotic flow. High-energy treatments make the surface hydrophilic and thus able to support electroosmotic flow; they also helps in the binding of molded PDMS to flat PDMS or other substrates. However, it should be noted that permanent surface modification techniques cannot be directly applied to rigid polymeric materials, owing to the more challenging microfabrication procedures required for those materials.

Some commercially available protein-inert polymers commonly used in microfluidic applications, all of which require permanent surface modification, are polyacrylamide, poly(N-hydroxyethylacrylamide), poly(N,N′-dimethylacrylamide) (PDMA), polyvinylpyrrolidone (PVP), poly(vinyl alcohol) (PVA), hydroxyethylcellulose (HEC), and hydroxypropylmethylcellulose (HPMC). To permanently attach protein-resistant materials to the channel surface, high-energy sources, special chemistries, or even strong physical adsorption have been employed to introduce reactive functionalities. After activation, protein-resistant polymers can be anchored via UV-initiated free-radical polymerization. Polymeric materials usually do not have good solvent and heat resistance compared with inorganic materials, and hence it is necessary to take precautions during surface treatment to avoid serious damage to the microstructure or alteration of the physical properties of the bulk material.

One successful method for PDMS surface modification is ultraviolet polymer grafting. In this method, PDMS is immersed in an aqueous solution of $NaIO_4$, benzyl alcohol, and a monomer (acrylic acid, acrylamide, dimethyl acrylamide, hydroxyethyl acrylamide, or PEG-monomethoxyacrylate) under uniform exposure to a 200 W mercury lamp. $NaIO_4$ scavenges oxygen in the polymerizing mixture, and benzyl alcohol facilitates chain transfer during polymerization. The graft density increases with the irradiation time and also with the concentration of benzyl alcohol. When individual polymers are compared, the highest graft density is achieved with polyacrylamide, whereas the lowest is obtained with poly(PEG-monomethoxyacrylate) [9].

One of the earliest methods for modification of a PMMA surface for medical applications is based on chemical conversion of the wall rather than on addition of a new layer [9]. The conversion of PMMA consists of reesterification of PMMA with polyfunctional hydroxyl compounds, such as ethylene glycol, glycerol, mannitol, or saccharose. First, the PMMA surface is covered with ethylene glycol or another polyalcohol, which is allowed to diffuse inside the polymer body. Then the surface is treated with hot sulfuric acid to perform reesterification and replace the methanol in PMMA with ethylene glycol. After neutralization with sodium bicarbonate, a hydrophilic, transparent layer is formed on the surface of the PMMA.

Polycarbonate is a thermoplastic material used in many applications, including microchips. The aromatic rings in the polycarbonate structure offer a relatively easy way to modify the PC surface by a direct sulfonation reaction. After cleaning with isopropyl alcohol, the polycarbonate surface is modified by reaction with sulfur trioxide at 50°C for 10 min. Then it is rinsed with water and dried in a stream of nitrogen. The sulfonated PC has shown improvement in both surface wettability and electroosmotic mobility. As an alternative to coating the PC surface forming the wall, UV and excimer laser (at a wavelength of 248 nm) treatment of the PC surface have also been used for surface modification. PETG is another plastic material used for the preparation of microchips. Its surface can be modified easily by NaOH treatment, resulting in ester hydrolysis and the appearance of carboxylic groups on the surface.

Dynamic wall coatings for surface modification can be applied to glass substrates owing to the presence of silanol groups on the channel surface. PDMA can be used simultaneously as a sieving matrix and a wall coating for a glass microchip. Several other polymers, including PEG, PVP, HEC, and epoxy poly(dimethyl acrylamide), are applicable as coatings on a glass chip. Several dynamic coatings can be applied to PDMS chips to make the channel surface more hydrophilic. An n-dodecyl-b-D-maltoside

(DDM) coating minimizes protein adsorption on PDMS surfaces [10]. DDM is an alkyl polyglucoside, which belongs to a family of very mild nonionic surfactants. It adsorbs strongly on hydrophobic surfaces and forms a monolayer. This monolayer coverage causes the surface to become hydrophilic and nonionic, thus reducing the interaction between the protein and the surface. Several dynamic coatings have been tried for modifying PMMA surfaces [9] of microchip channels used with 1-aminopyrene-3,6,8-trisulfonate-labeled oligosaccharides. However, low-molecular-weight compounds, including monoethylamine, diethylamine, and triethylamine, and surfactants, such as sodium dodecyl sulfate, cetyltrimethylammonium bromide, and dodecyltrimethylammmonium chloride, do not adequately suppress the adsorption of analytes on the channel wall. A significant improvement is observed when hydrophilic neutral polymers, including PEG, HEC, HPMC, and methylcellulose are applied to PMMA walls.

The surface properties of many materials may be tailored, for example for adhesion promotion, nonstick properties, or chemical activation, by coating with silanes. From a general point of view, silanization of hydroxyl-terminated substrates is an effective and frequently used procedure for modification of the chemical and physical properties of a substrate, as well as for covalent immobilization of a variety of compounds. Surfaces bearing oxides are well known to be of potential interest for chemical modification with silanes. Silane coatings serve in a number of applications such as protective coatings and adhesion promoters on metal surfaces, adhesives in industrial paints, selectively binding surfaces for tethering biological molecules in biosensor and DNA chip design, scanning probe microscopy (SPM) studies of biomolecules, and chemical force microscopy studies (where they serve as probe-functionalizing agents). Silanes have also been grafted onto plastic and elastomeric microchannels. Silanes have the general formula $RSiX_3$, where R is an organofunctional group, selected according to the desired surface properties, and X is a hydrolyzable group, typically an alkoxy group, which is capable of reacting with the substrate. The silanes are normally hydrolyzed at some stage in the coating process, allowing interaction with the substrate via either hydrogen bonds or covalent bonds.

The surfaces of glasses contain silanol groups. The presence of silanol groups on the surface of a glass microchip makes reaction with silanol the first choice for modification of glass surfaces. In one approach, after the channels have been flushed with NaOH, the channels are first filled with γ-methacryloxypropyltrimethoxysilane in diluted acetic acid and/or acetonitrile for an hour. In a second step, an aqueous solution of acrylamide together with ammonium persulfate and 1,2-bis-(dimethylamino)ethane (TEMED) is then pumped into the channels and polymerized at room temperature. The channels are then flushed with water and dried under vacuum. In another approach, channels in borofloat glass chips are coated with thermally immobilized PVA. A 1% aqueous solution of PVA is repeatedly pumped into the channels, and then the channels are emptied by a nitrogen flow. The chip is flushed with a nitrogen flow at 70°C for 60 min, followed by heating at 160°C for 10 min without any flow.

Chemical modification of microchip surfaces with SAMs has been used to prevent or minimize the deposition of proteins on channels. SAMs are ordered molecular assemblies that are formed spontaneously by the adsorption of a surfactant with a specific affinity of its headgroup to a substrate. Immersing an oxidized silicon wafer in a solution of an organosilicon derivative forms the SAM. The formation of a compact monolayer results in a drastic reduction of the surface wettability.

Measurement Techniques

In order to understand the behavior of surfaces after surface modification, it is essential to examine their surface composition and structure in detail. A large number of techniques are available, and it is often desirable to combine several of these methods. The techniques used to monitor surface properties include scanning electron microscopy (SEM), optical profilometry, atomic force microscopy (AFM), X-ray photoelectron spectroscopy (XPS), infrared (IR) spectroscopy, imaging ellipsometry, and water contact angle measurements.

SEM is a tool for measuring surface topography and morphology. SEM functions by focusing and scanning a relatively high-energy electron beam (usually 15 – 30 keV) on a electrically conducting specimen. The measurement of nonconducting samples is difficult owing to charging effects. Often, the sample preparation step introduces difficulties. Transmission electron microscopy (TEM) or scanning transmission electron microscopy (STEM) can also be employed in surface characterization.

Optical profilometry equipment is used for the measurement of surface texture, which includes features such as roughness, waviness, and lay. The methods of measurement available can be further classified into contact and noncontact methods, and three-dimensional (area) and two-dimensional (profile) procedures.

AFM is a tool for measuring surface topography on a nanometric scale. The principle is similar to that of contact profilometry with a nanometric tip. AFM has made significant contributions to biomaterials research in areas

dealing with structure, properties, dynamics, and manipulation. Interface phenomena such as protein adsorption, conformational changes, and subsequent interactions with cellular components can be observed with AFM. Study of the mechanisms of these phenomena can help in explaining why a particular surface treatment may exhibit performance superior to another.

The X-ray photoelectron spectroscopy (XPS) technique is used to identify chemical species on the surfaces of materials. XPS uses a monochromatic, low-energy X-ray beam. The interaction between the incident beam and the atoms of the material causes emission of photoelectrons from within a few micrometers of the surface. The kinetic energy of the electrons is measured and provides information about the nature and environment of the atoms in the surface.

Infrared-based techniques are used to identify molecules on the surface. IR radiation is used to excite vibrational modes in molecules in the gas phase or adsorbed on a surface. The transmitted or reflected IR spectrum can be analyzed in a spectrometer. Considerable improvement in the sensitivity can be achieved by use of Fourier transform infrared (FTIR) spectroscopy. Attenuated total reflection (the ATR-FTIR method) inside a crystal (Germanium) of high refractive index can be used to further enhance the surface sensitivity (using the evanescent field).

Ellipsometry is a nondestructive, label-free optical method for determining film thicknesses and optical properties. Imaging ellipsometry combines the power of ellipsometry with microscopy, and has an *x*-*y*-resolution of approximately 1 μm. It measures the change in the polarization state of light reflected off the surface of the film. Fast ellipsometry methods, both single-wavelength and multiwavelength, have been used for monitoring film growth in situ, allowing the precise control of film deposition processes.

The contact angles and surface tension are connected via Young's equation, based on the thermodynamic energy balance at a fluid/solid/fluid interface. At any point on the perimeter of a liquid drop on a solid surface, three surface tension components (solid–liquid, solid–vapor, and liquid–vapor) are balanced and control the wetting behavior. Both static and dynamic (advancing/receding) measurements can be performed.

Key Research Findings

Surface modification using vapor-phase deposition is very promising for some biomedical nanodevices and has advantages over liquid-phase deposition, since the vapor phase has the ability to permeate more efficiently into silicon nanochannels. A vapor-phase deposition system described by Bhushan et al. [11] used conformal fluorosilane self-assembled monolayer films on silicon and PDMS surfaces. Different perfluorosilane films were deposited onto three different substrates: piranha-cleaned silicon, oxygen-plasma-treated silicon, and oxygen-plasma-treated PDMS. The films were characterized by means of a contact angle analyzer for hydrophobicity, an ellipsometer for film thickness, and an atomic force microscope for surface roughness. The surfaces modified by the fluorosilane films consistently exhibited dramatically higher water contact angles and lower adhesive forces than did the unmodified silicon surfaces.

A pulsed UV excimer laser [4] has been used to modify the surface chemistry and surface charge of a previously imprinted microchannel in PMMA, without changing the physical dimensions of the channel. This surface modification technique was used to reduce the band-broadening effects that occur owing to electrokinetic flow in bends. The electroosmotic mobility was shown to increase by an average of 4% with UV-modified surfaces compared with nonmodified surfaces without any change in the channel morphology. UV exposure was demonstrated to spatially modify the surface charge and to create the desired electrokinetic flow profiles, without the use of wall coatings or the need to change the channel dimensions.

PDMS surface modification using graft polymerization of 2-hydroxyethyl methacrylate (HEMA) induced by a CO_2 pulsed laser was demonstrated by Khorasani et al. [1]. The CO_2 pulsed laser generated radicals on the PDMS surface, which react with oxygen to form hydrogen peroxide through hydrogen abstraction from the PDMS chains. The PDMS surface was then graft polymerized with the water-soluble HEMA monomer by thermal cleavage of hydroperoxide groups. In vitro assays showed that the addition of poly(HEMA) to hydrophobic PDMS provided a suitable surface for reducing platelet adhesion and allowed activation of the surface, unlike the unmodified sample. It was also observed that the laser-treated samples without any graft polymerization become almost superhydrophobic, with a contact angle of 170°. It was shown that these superhydrophobic PDMS films had higher blood compatibility than the hydrophilic PDMS and the untreated PDMS.

Photopatterned surface modification has been demonstrated by Kirby et al. [3], for the purpose of arbitrary control of the surface charge and hydrophobicity of silica-based microfluidic structures. The microchannels were globally coated with an acrylate-terminated SAM followed by localized polymerization of polyacrylamide, resulting in photopatterning of the surface charge and polarity. The photopatterning technique enabled the researchers to pattern isolated regions in the device. The

performance of the coating was evaluated by performing zeta potential measurements, cell adhesion studies, and micellar electrokinetic chromatography (MEKC) separation. The tests indicated a reduction in cell adhesion and wall charge. The coatings showed good stability under biological pH conditions, but degraded under extreme pH conditions. It was also shown that the SAM coating protocol had only a marginal effect on the electrokinetic performance of silica microchannels.

PEG chains have been added to polymer substrates as a means of minimizing nonspecific protein adsorption, because of their low interfacial energy, nonadhesive properties, and high mobility. A simple method for the deposition of brush-like PEG chains on PMMA microfluidic channel surfaces was reported by Bi et al. [6]. A copolymer of butyl methacrylate (BMA) and poly(ethylene glycol) methyl ether methacrylate (PEGMA) was synthesized to deposit a dense PEG molecular, brush-like coating on the PMMA microchannel surfaces via the anchoring effect of the hydrophobic BMA units. The addition of hydrophilic PEG chains to microchip surfaces overcomes the limitations caused by the hydrophobicity of PMMA. The modified microchannel surfaces showed good wettability, low nonspecific adsorption, and better biocompatibility, and enhanced the electroosmotic mobility compared with the mobility in the native state. The modified surface also showed excellent blood compatibility, with low protein and platelet adhesion.

Recently, a new method has been developed to modify the hydrophobic and hydrophilic nature of silicon surfaces by the use of 5-(4-Hydroxyphenyl)-10,15,20-tetra(p-tolyl)porphyrin self-assembled monolayers [12]. The bare SiO_2 substrate exhibited a contact angle of $33 \pm 2°$, showing the hydrophilic nature of the surface. In the presence of a hydroxyphenylporphyrin SAM, the contact angle was found to increase to up to $75 \pm 3°$, indicating the hydrophobic nature of the surface due to the formation of a self-assembled monolayer on the SiO_2 surface. Hydrophilic surface modification of PDMS using an atmospheric plasma has recently been reported by Hong et al. [2]. PDMS stamps were shown, by measurement of the water contact angle and XPS and AFM analysis, to exhibit surface hydrophilicity after the plasma treatment.

The hydrophilic stability of surface-modified PDMS was described by Bodas et al. [13]. Three different modification processes, namely conventional oxygen plasma treatment, two-step modification using $O_2 + C_2F_6$, and chemical modification using HEMA, were considered in the study. All of the surfaces were characterized using static contact angle measurements and ATR-FTIR spectroscopy. Oxygen plasma modification resulted in hydrophilic stability for about 2 days. The hydrophobic recovery in this case was due to the migration of low-molecular-weight species from the surface to the bulk of PDMS. HEMA modified PDMS showed the lowest contact angle and retained its hydrophilicity for over 10 days. The wettability in this case was attributed to carbonyl groups. The $(O_2 + C_2F_6)$-modified PDMS did not show a much lower contact angle, but its hydrophilic stability was much higher than that of the O_2-plasma-treated sample. This high stability was attributed to stable, hydrophilic CF groups on the surface.

Future Directions for Research

Surface treatments and surface interactions are the challenges ahead for the research community in relation to the development of advanced, sophisticated microfluidic devices. Surface modification techniques need to be optimized for various applications, and particularly for disposable microfluidic devices. PDMS will be a popular material for future microfluidic devices, and some issues associated with most of the currently employed treatments, such as the hydrophobic recovery of PDMS surfaces, need to be adequately addressed.

Cross References

► Hydrophilic/Hydrophobic Patterning
► Plasma Treatment of Nanoparticles for Nanofluids

References

1. Khorasani MT, Mirzadeh H, Sammes PG (1999) Laser surface modification of polymers to improve biocompatibility: HEMA grafted PDMS, in vitro assay – III. Radiat Phys Chem 55:685–689
2. Hong SM, Kim SH, Kim JH, Hyang HI (2006) Hydrophilic surface modification of PDMS using atmospheric RF plasma. J Phys: Conf Ser 34:656–661
3. Kirby BJ, Wheeler AR, Zare RN, Fruetel JA, Shepodd TJ (2003) Programmable modification of cell adhesion and zeta potential in silica microchips. Lab Chip 3:5–10
4. Johnson TJ, Ross D, Gaitan M, Locascio LE (2001) Laser modification of preformed polymer microchannels: application to reduce band broadening around turns subject to electrokinetic flow. Anal Chem 73:3656–3661
5. Kim P, Jeong HE, Khademhosseini A, Suh KY (2006) Fabrication of non biofouling polyethylene glycol micro and nanochannels by ultraviolet assisted irreversible sealing. Lab Chip 6:1432–1437
6. Bi H, Meng S, Li Y, Guo K, Chen Y, Kong J, Yang P, Zhong W, Liu B (2006) Deposition of PEG onto PMMA microchannel surface to minimize nonspecific adsorption. Lab Chip 6:769–775
7. Mittal KL (1996) Polymer surface modification: relevance to adhesion. VSP, Netherlands

8. Makamba H, Kim JH, Lim K, Park N, Hahn JH (2003) Surface modification of poly(dimethylsiloxane) microchannels. Electrophoresis 24:3607–3619
9. Dolnik V (2004) Wall coating for capillary electrophoresis on microchips. Electrophoresis 25:3589–3601
10. Huang B, Wu H, Kim S, Zare RN (2005) Coating of poly(dimethylsiloxane) with n-dodecyl-β-D-maltoside to minimize nonspecific protein adsorption. Lab Chip 5:1005–1007
11. Bhushan B, Hansford D, Lee KK (2006) Surface modification of silicon and polydimethylsiloxane surfaces with vapor-phase-deposited ultrathin fluorosilane films for biomedical nanodevices. J Vac Sci Technol A 24(4):1197–1202
12. Nayak K, Kulkarni PD, Deepu A, Sitaraman VR, Punidha S, Saha AA, Ravikanth M, Mitra SK, Mukherji S, Rao VR (2007) Patterned microfluidic channels using self-assembled hydroxyphenyl porphyrin monolayer. Proceedings of 7th IEEE International Conference on Nanotechnology (in press)
13. Bodas D, Malek CK (2006) Formation of more stable hydrophilic surfaces of PDMS by plasma and chemical treatments. Microelectron Eng 83:1277–1279

Surface Plasmon Resonance Sensors

David Erickson
Sibley School of Mechanical and Aerospace Engineering, Cornell University, Ithaca, New York, USA
de54@cornell.edu

Synonyms

SPR

Definition

Surface plasmons are electromagnetic waves that occur at metal/dielectric interfaces. The conditions for exciting these optical modes are extremely sensitive to the dielectric environment very near this interface. As a result, surface plasmon resonance (SPR) is one of the most commonly exploited label free optical biosensing techniques in use today.

Overview

This article introduces the essentials of surface plasmon resonance biosensing. The *Basic Methodology* section focuses on describing the experimental techniques involved and some of the advantages and disadvantages of the various implementations that are in common use today. In the *Key Research Findings* and *Future Directions for Research* sections, the limitations of the current state of the art in SPR biosensing will be discussed in the context of future analytical needs and the promise of other unlabeled biosensing technologies. For more detailed information, readers are referred to some of the recent reviews of the subject by Homola et al. [1].

Basic Methodology

In this section we introduce the most popular surface plasmon resonance biosensing architectures in use today. In each case the operating principle has been outlined and whenever possible the advantages and disadvantage of the given approach have been discussed both in the context of the competing SPR architectures an other biosensing techniques.

Angular Surface Plasmon Resonance Biosensing

The attenuated total reflection surface plasmon resonance (ATR–SPR), approach using the Kertschmann geometry shown in Fig. 1a, represents the most common SPR configuration in use today. In this arrangement, transversely polarized light is incident on a metal/dielectric interface through a coupling prism. Under most conditions the incident light is nearly completely reflected from the surface and very little loss in optical power is observed at the detector (PMT in Fig. 1a. At a particular angle of incidence, θ_{sp}, a momentum matching condition exists and a certain amount of the incident energy is coupled into a surface plasmon mode resulting in a reduction in the reflected power. The incident angle for this plasmon excitation is described by Eq. (1) below,

$$\sin\theta_{sp} = \frac{1}{n_p}\sqrt{\frac{\varepsilon_m(\lambda)\varepsilon_s}{\varepsilon_m(\lambda)+\varepsilon_s}} \qquad (1)$$

where n_p is the refractive index of the prism, $\varepsilon_m(\lambda)$ is the dielectric constant of the metal film which varies as a function of the excitation wavelength, λ, and ε_s which represents the dielectric constant of the sensing layer (see the inset in Fig. 1a for details of the geometric arrangement). At fixed wavelength, ε_m is constant and thus from Eq. (1) it is apparent that θ_{sp} is only a function of the dielectric constant in the sensing region. The plasmon wave decays exponentially into the sensing layer over a spatial distance on the order of a few hundred nanometers and thus only the near field of the sensing region is probed. In the cases of interest here, this metal/dielectric interface consists of a thin metal film deposited either directly on the prism surface or on a microscope slide that is refractive index matched to the prism. Gold is most often used as it is inert to the atmosphere, can be modified by appropriate surface chemistry to provide active sites for bonding of organic molecules, and exhibits a pronounced surface plasmon effect in the visible and near infrared regions of the electromagnetic spectrum. A subtle variation on the above geom-

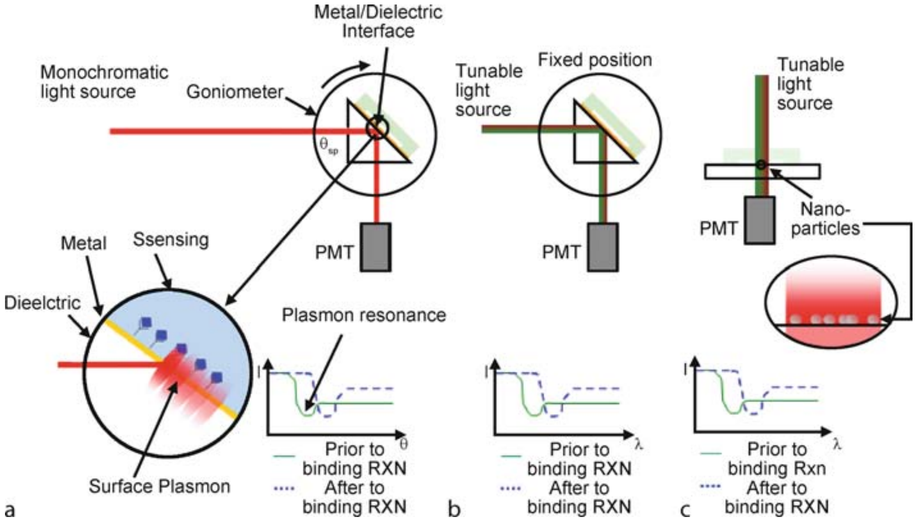

Surface Plasmon Resonance Sensors, Figure 1 Variations on Surface Plasmon Resonance Detection (**a**) Angular SPR (**b**) Spectral SPR and (**c**) Nanoparticle or Local SPR. Details on each of the above techniques is provided in the text

etry uses a grating coupler to excite a plasmon wave at the interface [2].

In a typical biosensing experiment, the metal layer is functionalized with a series of biorecognition agents (referred to as probes herein) specific to a solution phase target of interest. The addition of these probes to the surface increases the average dielectric constant in the near field of the sensing layer and a change in θ_{sp} is observed. Following functionalization a solution which may or may not contain targets specific to the immobilized biorecognition agents is introduced to the surface (for most commercial systems this is done using some form of microfluidic delivery system). Should the solution contain the compliment to the surface probe, a positive binding event will occur and the average dielectric constant in the sensing layer will further increase and another shift in θ_{sp} will be observed.

ATR–SPR has numerous inherent properties that have made it one of the most popular biosensing techniques in use today. The primary advantage is that it represents a *label free* technique in that since the transduction signal is based on changes in local refractive index, the targets do not require tagging (e. g., a florescent label). Because measurements of θ_{sp} can be made dynamically quantitative information on the reaction kinetics, such as the bioaffinity constants, can also be obtained. In addition ATR–SPR also exhibits extremely high sensitivity compared with other biosensing techniques. Most systems have angular resolutions on the order of 10^{-4} degrees and bound mass sensitivities on the order of $\mathrm{ng/cm^2}$ (nanograms per square centimeter) which correspond to average near field refractive index changes on the order of $\Delta n = 10^{-5}$. As a specific example, for many nucleic acid based biomolecular recognition systems an adsorbed mass on the order of $700\,\mathrm{ng/cm^2}$ is required for an SPR shift of 1 degree. A significant disadvantage of SPR, however is that this sensitivity is strongly dependent on the spatial distance of the added mass from the sensor surface. Since the plasmon decays exponentially into the solution phase, bound mass which is farther away from the surface has an increasingly lesser effect on the average refractive index and results in a smaller shift in the SPR angle. This represents a significant limitation on the types of systems which can be investigated through SPR.

Figure 2 demonstrates the use of the angular SPR method for the detection of cancer antigens in human sera as performed in Campagnolo et al. [3]. In this case the patient sera is being screened for the presence of antibodies specific to the NY–ESO–1 which is a cancer/testis antigen expressed in a number of malignant neoplasms (see the above reference for more details). In these experiments a nickel-nitrilotriacedtic (Ni–NTA) surface chemistry is applied to the gold sensor surface to serve as the immobilization chemistry. When His-tagged NY–ESO–1 antigen is flown over the functionalized surface, a change in the SPR angle, $\Delta\theta_{sp}$, on the order of 1.15° is observed. Introduction of the antigen is done through a simple microfluidic flow cell. Note that this is quantified in the figure axis in units of PU or *Pixel Units* which are equivalent to a change of 0.0038° in the SPR angle. After washing with the run buffer $\Delta\theta_{sp}$ reduces to 0.15° (∼

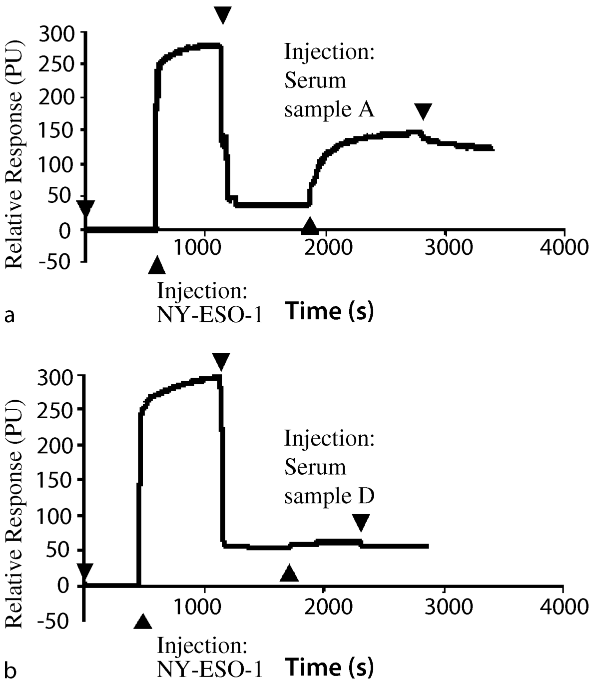

Surface Plasmon Resonance Sensors, Figure 2 SPR sensorgram for the interaction of surface-immobilized His-tagged NY–ESO–1 with (**a**) a serum sample (labeled A) which contains the anti–NY–ESO–1 antibody and (**b**) a serum sample (labeled D) which contains the anti–NY–CO–38 antibody. Both serum samples were dilute 1 : 15 in PBS buffer. Triangles indicate the injection of analyte; inverted triangles indicate the injection of running buffer. Figure and caption reprinted with permission from Campagnolo et al. [3]

40 PU) suggesting that some non-specifically absorbed tumor antigen has been removed from the surface, leaving only the chemically immobilized probes. When Sample A (Fig. 2a) is then flown over the surface, a significant increase in the SPR angle is observed indicating the presence of binding between the immobilized antigen and its compliment and suggesting anti-NY–ESO–1 activity within the patient sample. When Sample D (Fig. 2b) is flown over the surface only a slight change in $\Delta\theta_{sp}$ is observed (due to non-specific adsorption) indicating that the sample does not contain any anti-NY–ESO–1 activity.

Spectral Surface Plasmon Resonance Biosensing

A variation on the above approach, termed spectral SPR (e. g., Otsuki et al. [4]), exploits the wavelength dependence of ε_m to interrogate the surface plasmon coupling conditions. This resonant wavelength condition can be determined from Eq. (1) given a knowledge of the incident angle θ_{sp} and the $\varepsilon_m(\lambda)$ relationship. The apparatus is similar to the angular approach described earlier, the only significant difference being that the experiment is conducted at fixed incident angle and a tunable excitation source is used to sweep over the wavelengths of interest as illustrated in Fig. 1b. Alternatively a broadband excitation source could be used and the spectrum of the reflected light is recorded. Analogous to the angular SPR case, by monitoring the change in the resonant wavelength with time, information on the reaction kinetics and bioaffinity constants can also be obtained.

The spectral technique has two advantages over the traditional angular approach: a simplification of the experimental apparatus for multiplexed SPR imaging and increased inherent sensitivity. As described by Otsuki et al. [4], the spectral approach lends itself to imaging based data collection techniques which are more amenable to high throughput screening applications (this is expanded on in the *Key Research Finding* findings section of this article). The latter of these relates to the relatively weak dependence of ε_m on wavelength as outlined in detail by Homola et al. [5]. Despite these advantages, the angular SPR approach is generally preferred to the spectral approach due to added expense of the tunable illumination source or the added complication of extracting the reflected spectrum.

Local Surface Plasmon Resonance Biosensing

As an alternative to the traditional SPR biosensing approaches, local SPR (LSPR) has recently been developed for surface phase geometries. LSPR surfaces comprise of dielectric substrate with arrays of sub-wavelength scale metallic nanoparticle, nanostructure or nanohole features. Localized surface plasmon resonances occur when light is absorbed or scattered by oscillating electric dipoles within those nanostructures. These standing oscillations represent a slightly different mechanism from the propagating surface plasmon polaritons associated with the architectures discussed above, though the term *plasmon resonance* is commonly used to refer to both. When illuminated these surface arrays exhibit a characteristic change in the transmitted or reflected power at a specific resonant wavelength that is strongly dependent on the local dielectric environment. As such binding events are detected by observing the change in this resonant wavelength using a similar technique to the spectral SPR technique described above. Though the specifics are dependent on the geometric properties of the nanostructure, the relationship between the change in the resonant wavelength and the dielectric constant of the surrounding medium is often reported to be close to linearly proportional to the change in refractive index. The well cited characterization study by Haes et al. [6] provides details of the experimental apparatus and a nanosphere lithography technique

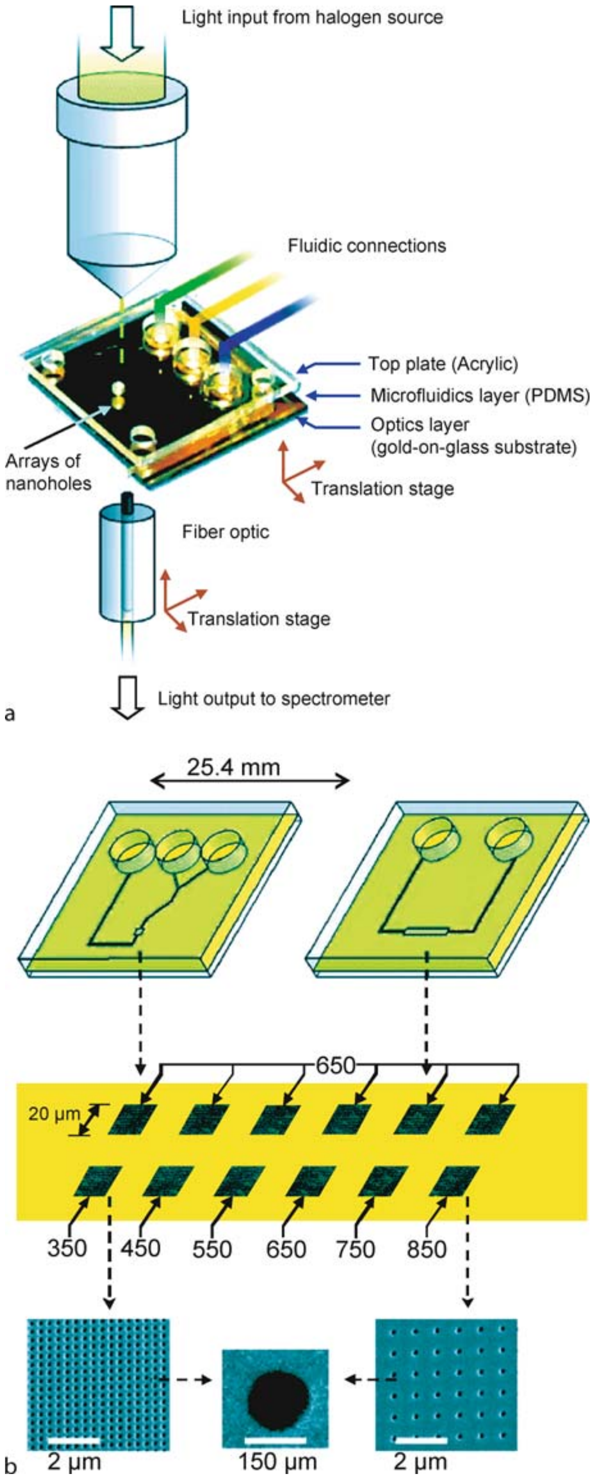

Surface Plasmon Resonance Sensors, Figure 3 (**a**) Schematic of a typical optical configuration and the fluidic connections employed with a transmission mode LSPR device. (**b**) Schematic and images illustrating the architecture of the microfluidic chip with embedded nanohole arrays at relevant centimeter-, micrometer-, and nanometer-length scales. Figure and caption reprinted from De Leebeeck et al. [8]

for surface preparation and functionalization. The sensitivity limits reported in some of the earlier works using this approach were much lower than those for traditional SPR however recently Dahlin et al. [7] described a technique for improving the instrumentation and data analysis techniques for this architecture in the end reporting limits of detection on the order of 100 pg/cm^2. One of the major strengths of the LSPR techniques is that the excitation angle can be normal or near normal to the surface, significantly simplifying the overall setup and facilitating extension to large area two dimensional multiplexing.

As an implementation example of this technique consider the system shown in Fig. 3 which shows a schematic of the optofluidic integration architecture used to couple the microfluidic delivery system with a nanohole array as presented by De Leebeeck et al. [8] . In this case the nanohole array was fabricated in a 100 nm thick gold film on a transparent glass substrate using a focused ion beam milling technique, enabling the creation of feature sizes on the order of 150 nm as shown in Fig. 3b. The plasmonic resonance of each array is governed by the spatial periodicity of the holes. In this experiment, a grouping of nanohole based arrays of varying periodicity constitutes an array of unique SPR sensors. Such a platform could facilitate both a spatial and spectral multiplexed format. The microfluidic chip is fabricated in PDMS using soft lithography and then reversibly bonded to the gold substrate. As shown in Fig. 3a, optical interrogation of the system is accomplished by shining a broadband halogen light source from above and coupling the transmitted light into a fiber spectrometer. In Fig. 4a the transmission spectra obtained with the device through an array of holes with 550 nm periodicity for solutions of varying refractive index are shown. As can be seen the increased refractive index caused by the introduction of the sugar solution cases a red-shift of the transmission spectrum particularly at the $\sim$ 625 nm peak. This is better quantified in Fig. 4b which plots the shift in peak transmission through a 450 nm periodicity nanohole array (which showed three transmission peaks at 604 nm, 644 nm and 674 nm) as a function of the refractive index of the glucose solution. The sensitivity of this device is reported as 333 nm per refractive index unit, or RIU [8].

Solution Phase Nanoparticle LSPR

The final example to consider here is solution phase colloidal nanoparticle LSPR. Such systems comprise of metallic particles (typically spherical, but elongated rods have also been used) dispersed in solution. As with the surface phase LSPR techniques, the nanoparticles are functionalized with a bio-recognition element specific to a target of interest. A sample is then added to the nanoparti-

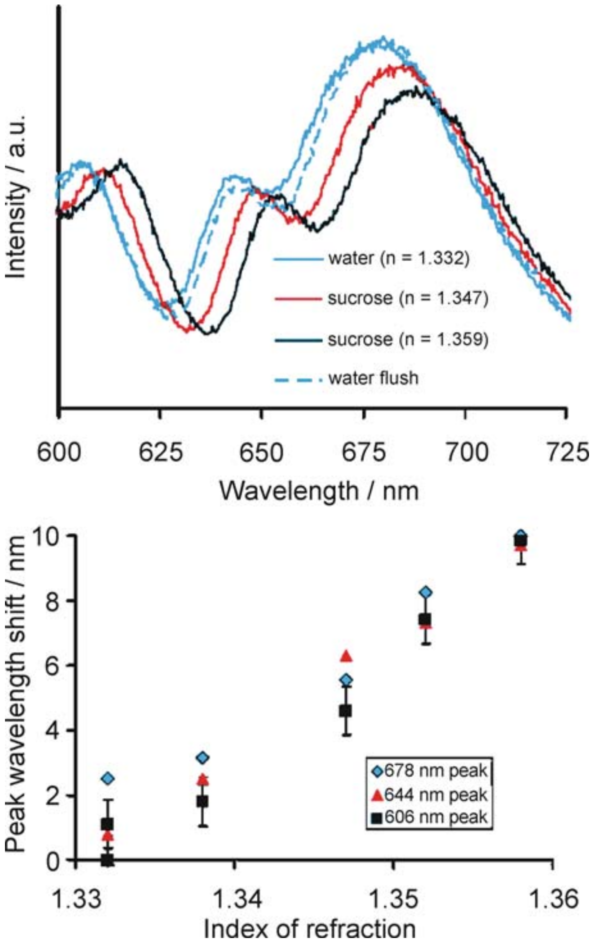

Surface Plasmon Resonance Sensors, Figure 4 Sample sensitivity measurements using solutions of different refractive indices made using the nanohole SPR device shown in Fig. 2. Transmission spectra were obtained through a 450 nm periodicity array for the cases of pure water, sucrose solutions with increasing refractive index, and again for water. (**a**) Sample transmission spectra plotted together. (**b**) The relative redshift in peak wavelength for three SPR peaks (at wavelengths 606, 644, and 674 nm) exhibited by the array as a function of refractive index. Figure and caption reprinted from De Leebeeck et al. [8]

cle solution and the presence of a positive binding event results in a shift in the measured adsorption peak (for measurements done in transmission mode). Solution phase SPR methods have several advantages over surface phase techniques. The most significant of these being the relative ease with which an assay and be prepared and detection feedback received. Since the assay is carried out in solution, the additional effort required to immobilizing the particles or fabricate structures on the surface directly is not required. With regards to feedback, since the wavelength shifts can, in principle, be quite large it is sometimes possible to detect the presence of a binding event with relatively inexpensive spectrographic equipment (in some cases the shift can even be observed by eye). An additional advantage is that time required for solution phase targets to diffuse to its complementary probe is significantly lower (i. e. the diffusion timescale for a target to reach the nearest nanoparticle is much lower than that required to reach the surface) and therefore the overall reaction time is reduced. The most significant disadvantages of solution phase approach is that multiplexing is a challenge, typically only one reaction can be monitored at a time, and that in general relatively large amounts of target are required in order to ensure relatively uniform binding on all nanoparticles.

The theory which ties the observed macroscopic observation of plasmons to electromagnetics involves an expansion of the involved electromagnetic fields into a series of partial waves to obtain,

$$\sigma_{\text{ext}} = \frac{2\pi}{|k|^2} \sum_{L=1}^{\infty} (2L+1) \times \text{Re}(a_L + b_L) \tag{2a}$$

$$\sigma_{\text{scat}} = \frac{2\pi}{|k|^2} \sum_{L=1}^{\infty} (2L+1) \times (|a_L|^2 + |b_L|^2) \tag{2b}$$

where σ_{ext} and σ_{scat} are the extinction and scattering coefficients respectively, k is the wavenumber and a_L and b_L are the coefficients relating a series of Ricatti–Bessel functions involving particle size, medium refractive index, radius and complex dielectric constant of the particle (see Link and El-Sayed [9] for more details). For smaller particles when the dipole oscillations are dominant, Eq. (2a) can be simplified to,

$$\sigma_{\text{ext}} = \frac{9\omega}{c} \varepsilon_{\text{s}}^{3/2} V \left[\frac{\varepsilon_2}{(\varepsilon_1 + 2\varepsilon_{\text{s}})^2 + (\varepsilon_2)^2} \right] \tag{3}$$

where ω is the angular frequency, ε_{s} is the dielectric constant of the sensing medium, V is the volume, and ε_1 and ε_2 are the real and imaginary components of the dielectric constant of the particle (i. e., $\varepsilon_{\text{particle}} = \varepsilon_1 + i\varepsilon_2$) which are typically functions of ω. Given that ε_2 typically shows a much weaker dependence on ω than ε_1, a maximum in the extinction coefficient occurs when the magnitude of the real part of the dielectric constant of the particle (which is negative for a metal) is double that of the surrounding media.

Future Directions for Research

Though numerous label free refractive index based optical biosensor technologies exist, SPR has evolved as likely the

most popular technique for monitoring surface phase binding reactions largely due to its relatively good inherent sensitivity and ease of implementation/use. Since challenges related to reaction specificity and non-specific adsorption are general to all optical biosensors, they will not be discussed in detail here (this is not meant to diminish their importance). Rather we focus here on listing some of the challenges and limitations of the technology itself and outline some of the general trends of current research.

The high sensitivity of many other optical detection technologies relates to the relatively large interaction lengths of the incident excitation field with the sample. As such a large number of binding events are required in order to induce a relatively small overall change in refractive index and rare target identification therefore becomes significantly more difficult. This is to say that while they are very sensitive to bulk measures such as refractive index, the absolute mass sensitivity can be quite poor. In ATR–SPR the reaction site can in principal be as small as the propagation distance of the plasmon wave, which is typically on the order of 20 μm. As reported above most ATR–SPR systems operate with refractive index resolutions on the order of $\Delta n = 10^{-5}$, though values on the order of $\Delta n = 10^{-8}$ have been reported, and limits of detection on the order of ng/cm^2. Given the plasmon propagation distance value listed above a crude estimate for the bulk mass limit of detection for ATR–SPR can be calculated as being on the order of 10 attograms (10×10^{-15} g). The LSPR technologies discussed were largely developed as an attempt to improve on this value since the optical energy is concentrated over a smaller spatial distance, thereby significantly reducing the probed surface area. As such the presence of significantly fewer binding events can have a larger effect on the effective refractive index and by extension the resonance shift. Using single silver nanoparticle Riboh et al. [10] demonstrated wavelengths shifts on the order of 38 nm for adsorption of ~ 100 antibiotin molecules. Extrapolating then it can be argued that, assuming a molecular mass of 150 kDa for antibiotin, the total mass per particle is on the order of 20 zeptograms (2×10^{-17} g). Although the technology for optically probing these ultrasmall systems is reasonably well developed, practical implementation of such low mass limit of detection systems, implies an ability independently functionalize each nanostructure (or at least a small number of them) with different capture agents. One potential way to do this is to increase the spatial distance between nanotructures to the resolution achievable with traditional spotting techniques and then applying a functionalization chemistry specific to the metallic structures and not the base substrate. Increasing this spatial distance however increases the total surface area over which the sample must be delivered. This poses significant reagent delivery techniques in order to ensure that all targets from a sample have the opportunity to be interrogated by each probe site. With traditional transport mechanisms such as diffusive transport or simple microfluidic architectures, the probability of a collision between a given solution phase target and surface bound probe is exceedingly small (for practical time limits). Developing an integrated system which can address this challenge represents a significant challenge.

One limitation of existing SPR devices has been the degree to which the assays could be multiplexed (i. e., with SPR typically only a few reactions are monitored at a time, compared with microarrays where thousands of binding reactions can be monitored in parallel). Relatively recently a number of Commercial SPR biosensor developers have introduced multiplexed versions of their existing platforms (e. g., the Spreeta from Texas Instruments and FlexChip from BIACORE) based on SPR imaging techniques. Of those that which contains the highest degree of parallelity is the FlexCHIP platform. This chip uses a grating coupling mechanisms and a mechanical scanning technique to image as many as 400 reactions over the course of 3 hours (which is still orders of magnitude lower than microarray based assays). In these multiplexed systems however the sensitivity is reduced to that available from a standard microarray (see Usui-Aoki et al. [11]). As such there remains a significant need for the development of platforms which can maintain the extreme sensitivity available from SPR while pushing the limits of parallelity into the 1000 s or tens of 1000 s of binding reactions.

Cross References

► Optofluidics–Applications

References

1. Homola J, Yee SS, Gauglitz G (1999) Surface plasmon resonance sensors: review. Sens Actuators B 54(1–2):3–15
2. Unfricht DW, Colpitts SL, Fernandez SM, Lynes MA (2005) Grating-coupled surface plasmon resonance: A cell and protein microarray platform. Proteomics 5(17):4432–4442
3. Campagnolo C, Meyers KJ, Ryan T, Atkinson RC, Chen YT, Scanlan MJ, Ritter G, Old LJ, Batt CA (2004) Real-Time, label-free monitorine, of tumor antigen and serum antibody interactions. J Biochem Biophys Meth 61(3):283–298
4. Otsuki S, Tamada K, Wakida S (2005) Wavelength-scanning surface plasmon resonance imaging. Appl Opt 44(17):3468–3472
5. Homola J, Koudela I, Yee SS (1999) Surface plasmon resonance sensors based on diffraction gratings and prism couplers: sensitivity comparison. Sens Actuators B 54(1–2):16–24
6. Haes AJ, Van Duyne RP (2002) A nanoscale optical biosensor: Sensitivity and selectivity of an approach based on the localized surface plasmon resonance spectroscopy of triangular silver nanoparticles. J Am Chem Soc 124(35):10596–10604

7. Dahlin AB, Tegenfeldt JO, Hook F (2006) Improving the instrumental resolution of sensors based on localized surface plasmon resonance. Anal Chem 78(13):4416–4423
8. De Leebeeck A, Kumar LKS, de lange V, Sinton D, Gordon R, Brolo AG (2007) On-Chip Surface-Based Detection with Nanohole Arrays. Anal Chem 79(11):4094–4100
9. Link S, El-Sayed MA (2000) Shape and size dependence of radiative, non-radiative and photothermal properties of gold nanocrystals. Int Rev Phys Chem 19(3):409–453
10. Riboh JC, Haes AJ, McFarland AD, Yonzon CR, Van Duyne RP (2003) A nanoscale optical biosensor: Real-time immunoassay in physiological buffer enabled by improved nanoparticle adhesion. J Phys Chem B 107(8):1772–1780
11. Usui-Aoki K, Shimada K, Nagano M, Kawai M, Koga H (2005) A novel approach to protein expression profiling using antibody microarrays combined with surface plasmon resonance technology. Proteomics 5(9):2396–2401

Surface Potential

► Measuring Zeta Potential, Methods
► Zeta Potential Measurement

Surface Roughness Measurement

David Lee Butler
School of Mechanical & Aerospace Engineering,
Nanyang Technological University, Singapore, Singapore
mdlbutler@ntu.edu.sg

Synonyms

Surface topography; Surface texture

Definition

Surface roughness measurement is the measurement of the small-scale variations in the height of a physical surface. This is in contrast to larger scale variations such as form and waviness which are typically part of the geometry of the surface.

Overview

In recent years the importance of surface texture has gained attention in many fields. In particular the surface roughness is an important factor in determining the satisfactory performance of a workpiece in areas as diverse as tribology, surface coatings, microfluidics and biocompatibility.

Surface roughness measurement can be characterized using either quantitative or qualitative methods. Qualitative techniques include optical appearance such as the reflectivity of a surface or the strength of the machining lay as well as dragging a thumbnail across the surface as a crude tactile sensor. Quantitative analysis has evolved from simple two-dimensional profilometry to more advanced three-dimensional area analysis where information regarding surface structure can be easily obtained.

The two-dimensional quantitative approach has been in existence since the early 1930s when the need to better understand the manufacturing process necessitated the desire to characterize the surface. More recently, with the advances in computing and data storage, three-dimensional quantitative analysis has gained popularity. Three-dimensional measurement is more suited for non-contact measurement techniques due to the speed of data acquisition.

Basic Methodology

In order to quantify a surface profile, it is essential to remove the unnecessary wavelength components as well as establish a datum from which the parameters can be calculated.

Cut-Off and Filtering

Typically, a surface consists of many wavelengths all superimposed on each other. The wavelengths are generally classified into three groups, form, waviness and roughness, with the last mentioned being the shortest wavelengths and the first mentioned being the longest. To separate the waviness and form from the roughness, a cut-off filter is employed. Depending on which information is to be retained it is possible to select from high- or low-pass filters as well as a band-pass filter which extracts surface data within a specified bandwidth. The selection of cut-off length is laid down in international standards [1, 2].

A number of filter types have been used over the years, each having its own unique frequency response. The oldest standard filter is the 2RC filter and consists of two sets of a resistor and capacitor in series; however, it is subject to large errors when the surface profile direction changes abruptly. It has now been replaced with digital filters which no longer have to rely on physical components. The most common digital filters are the phase-correct 2RC filter and the Gaussian filter – the latter applies a weighting function to the surface data to establish the profile mean line.

Once the surface data have been filtered and the mean line (or plane in the case of three-dimensional measurements) has been determined it is possible to quantify the surface features. Figure 1 shows a ground surface separated into the roughness and waviness components after applying a Gaussian filter and a 0.8 mm cut-off length.

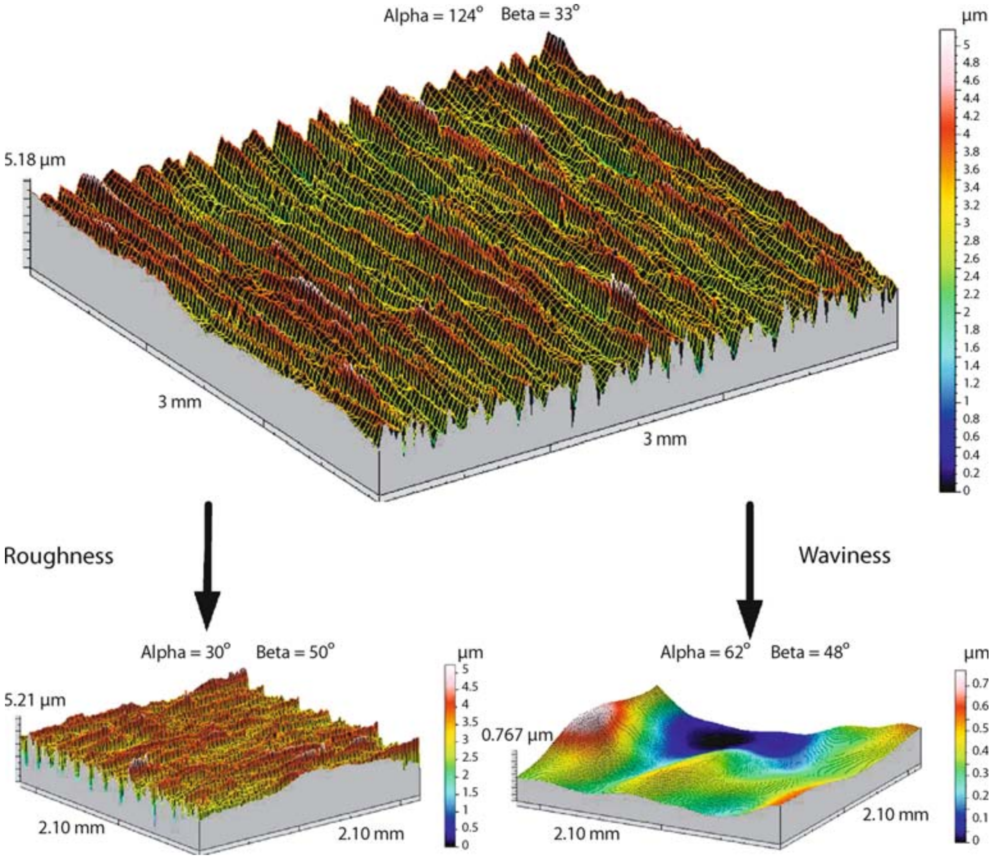

Surface Roughness Measurement, Figure 1 A ground surface being separated into its respective roughness and waviness components after application of a Gaussian filter and a 0.8 mm cut-off length, note the loss of area due to the filtering window

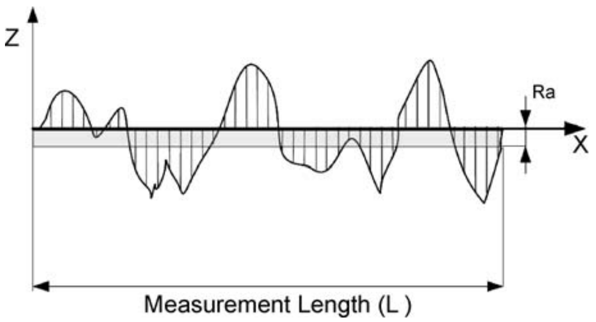

Surface Roughness Measurement, Figure 2 The graphical definition of R_a where the absolute height variations from the mean line are summed

The oldest and most commonly used surface parameter is the average roughness (R_a) which is also known as arithmetic average (AA) and centre line average (CLA) and more mathematically as the arithmetical mean deviation of the profile. The average roughness is the area between the roughness profile and its mean line, or the integral of the absolute value of the roughness profile height over the evaluation length, as shown in Fig. 2 and defined in Eq. (1):

$$R_a = \frac{1}{L}\int_0^L \left|Z(x)\right| \mathrm{d}x \quad (1)$$

However, the main limitation of R_a is that it provides no information about the surface shape; for example, a surface with a regular triangular wave profile could have the same R_a value as a random surface. Over the years, a considerable array of parameters has been developed to provide greater insight into the surface and its function. These parameters are typically grouped depending on what surface attribute they are concerned with such as height or spatial features or a combination of both (hybrid). An additional group which is derived from the amplitude distribution function of the profile provides information regarding the surface shape and its sharpness.

Table 1 provides a list of some of the more commonly used surface parameters with the appropriate standards as reference. The *R* prefix is used for parameters based on the roughness component of the surface while *P* refers to the original unfiltered profile and *W* is the waviness component.

For areal parameters, the main difference is that the reference datum is based on a mean plane and all parameters are calculated from that. The prefix *S* is used to denote these parameters and to distinguish them from the *R*, *P* and *W* prefixes used for profile measurement. A number of the areal parameters are direct three-dimensional equivalents of their profile counterparts such as $S_q(R_q)$ and $S_{ku}(R_{ku})$ while others take advantage of the structural information available to determine the texture direction of the surface and the strength of the surface lay.

Although the application of a single parameter for surface roughness can be used to indicate a change in a manufacturing process, it is not sufficiently discriminating to pinpoint where the changes in the process have occurred. Using an array of simple parameters rather than just one may still not provide the level of discrimination required. With the development of random process analysis, new capabilities arose with the use of autocorrelation and power spectra functions. These are functions rather than numbers such as the average roughness (R_a) of the profile and so can reveal more of the underlying statistics of the surface. The autocorrelation function is particularly useful for looking at random surfaces and the power spectrum is more useful for looking at periodic surfaces. The autocorrelation function is obtained by simply plotting the correlation coefficient between the surface profile and the same profile shifted in space by a set amount. The power spectrum is the Fourier transform of this.

Instrumentation

The earliest ways of measuring surfaces were by using the thumbnail as a tactile sensor or the eyes. Both techniques are highly effective but are completely subjective. Demand for quantitative results led to the development of two distinct branches of instrumentation, one following the tactile approach the other mimicking the eyes.

Both techniques evolved to measure different surface features. Optical methods looked for lateral structure, namely spatial information, whereas contact methods examined heights in the plane perpendicular to the surface. More recently, optical techniques have been developed which can provide height information as well. A more general form of categorization would be to classify the instruments as either contact or non-contact. The lateral and vertical resolutions of the various contact and non-contact techniques are shown in Fig. 3.

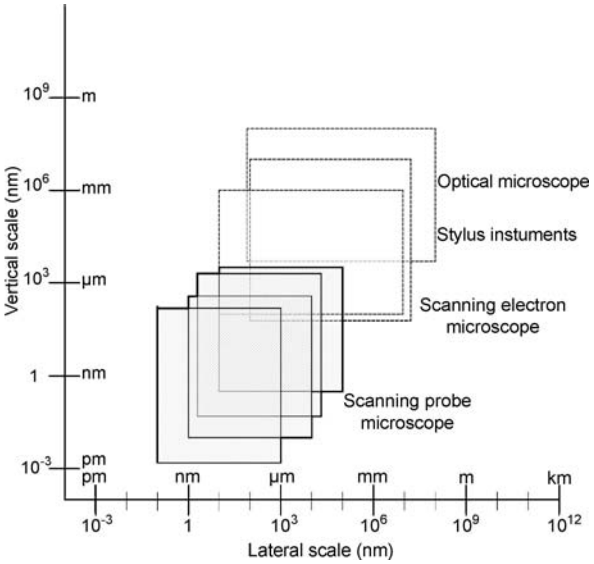

Surface Roughness Measurement, Figure 3 Lateral and vertical measurement ranges of various microscopes

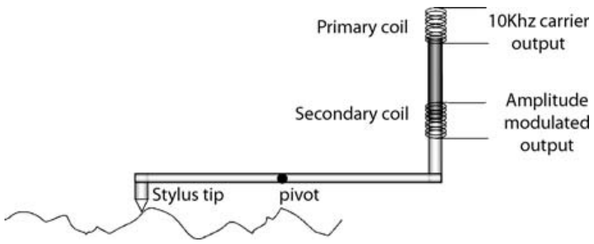

Surface Roughness Measurement, Figure 4 Schematic of an inductance transducer-based stylus

Contact Instruments

The contact method involves the dragging of a diamond stylus whose tip dimension is such that it can penetrate the detailed geometry of the surface. The stylus is mounted onto an arm with a transducer at the other end as shown in Fig. 4. Any change in height of the stylus due to the surface features corresponds to a change in the signal detected and amplified by the transducer and the subsequent electronics. The most common type of transducer is based on the inductance principle and offers a large range-to-resolution as well as being of robust construction.

The main limitation of the stylus approach is the need for contact to be made between the probe and the surface which deems it unsuitable for soft materials and where contamination may be an issue. The actual tip dimensions

Surface Roughness Measurement, Table 1 Common 2D surface parameters

Parameter	Name	Standards	Related
	Height Parameters		
Ra	Roughness average (Ra)	1, 2	Pa, Wa
Rq	Root mean square (RMS) roughness	1, 2	Pq, Wq
Rt	Maximum height of the profile	1, 2	Pt, Wt
Rpm	Average maximum profile peak height	1	
Rz	Average maximum height of the profile	1, 2	Pz, Wz, Rtm
Rc	Mean height of profile irregularities	2	Pc, Wc
Rz(iso)	Roughness height	2	
Wt, W	Waviness weight	1, 2	Rt, Pt
	Spacing Parameters		
Sm, RSm	Mean spacing of profile irregularities	1, 2	PSm, WSm
Pc	Peak count (peak density)	1	
HSC	High spot count		
	Hybrid Parameters		
Δa	Average absolute slope	1, 2	$P\Delta a$, $W\Delta a$
Δq	Root mean square (RMS) slope	1, 2	$P\Delta q$, $W\Delta q$
	Amplitude Distribution Function Parameters		
Rsk, Sk	Skewness	1, 2	Psk, Wsk
Rku	Kurtosis	1, 2	Pku, Wku

also act as mechanical filter removing features smaller than the tip radius from the measurements.

Non-Contact Instrumentation

A wide range of techniques can be used to capture the surface roughness of a component using non-contact methods. Some of the more common instruments used to capture topographic data include confocal microscopy, laser triangulation, focus detection and optical interferometry. A relatively recent branch of microscopy known as scanning probe microscopy (SPM) yields over 20 other instruments which are defined based on what probe–surface interaction they are monitoring. The SPM family is described in more detail elsewhere in this book and will be briefly mentioned in this article.

Confocal Laser Scanning Microscopy

Confocal laser scanning microscopy is a valuable tool for obtaining high-resolution surface images as well as enabling three-dimensional reconstruction of the surface. In contrast to a conventional optical microscope which floods the entire specimen with light, confocal microscopy relies on point illumination. A pinhole in an optically conjugate plane in front of the detector ensures that out-of-focus information is eliminated and thus only light within the focal plane is detected resulting in a much higher quality image. As only one point is illuminated at a time in confocal microscopy, two- or three-dimensional imaging requires scanning over a regular raster (i. e. a rectangular pattern of parallel scanning lines) in the specimen. The thickness of the focal plane is defined mostly by the square of the numerical aperture of the objective lens, and also by the optical properties of the specimen and the ambient index of refraction. This technique has found widespread use for biological and semiconductor applications.

Focus Detection System

The optical focus system or optical profilometer system is based on the dynamic focusing principle of a confocal microscope. These systems work on the detection of the focus position of reflected light from the surface. Any change in the focus position of the light relates to a change in the surface height and by refocusing the lens it is possible to determine the height value. It is widely used in applications where surface damage is an issue for concern.

Optical Interferometry

Optical interferometers work on the principle of exposing the surface to be characterized to monochromatic or white light and observing the interference fringes pro-

duced using an optical flat tilted through a small angle. The fringe patterns are produced by splitting the light beam and the interference patterns are produced due to interference between reflections from the tilted optical flat and the surface to be measured. The fringe patterns are analyzed by a computer program incorporating the appropriate algorithms to give an unfiltered representation of the surface. The data may be statistically processed and filtered to provide parametric values.

Laser Triangulation

The principle of laser triangulation is essentially the measurement of range by location of three points forming a triangle. A laser spot is focused onto the sample surface, and as the surface height changes, the position of the reflected beam onto a position-sensitive detector is also shifted. This shift in the reflected beam can, using the triangulation principle, be related back to the surface height deviation.
As with most optical-based systems, a number of limitations exist which include the need for the specimen to possess some degree of reflectivity, a limitation on the maximum surface slope which can be detected and the effect of surface color change on the fidelity of the data.

Scanning Probe Microscopy

Scanning probe microscopy is a branch of microscopy that forms images using a physical probe that scans the surface of the specimen. An image is obtained by mechanically moving the probe in a raster scan of the specimen, line by line, and recording the interaction between the probe and the surface as a function of the position. A wide range of interactions can be observed depending on which phenomenon is being observed; they include atomic force, tunnel current, magnetic force and electrostatic force.

Future Directions for Research

Current research in surface roughness measurement is directed at both the hardware and the software. Established filtering techniques such as Gaussian filtering do not satisfy all applications and research is currently being undertaken to develop filters based on the wavelet principle. Instrumentation is currently being developed to overcome the limitations of current contact and non-contact techniques such as, for example, measuring the sidewalls of a microchannel. This has led to the development of more specialized probes which can sense topographic changes in more than one direction at the same time.

Cross References

► Roughness Effect on Microscale Transport
► Scanning Electron Microscopy (SEM)
► Surface Modification
► Scanning Probe Microscopy

References

1. B46.1 (2002) Surface Texture, Surface Roughness, Waviness and Lay, ASME, USA
2. ISO 4287 (1997) Geometrical Product Specifications (GPS) – Surface texture: Profile method – Terms, definitions and surface texture parameters
3. Whitehouse DJ (1994) Handbook of Surface Metrology. Taylor Francis, Institute of Physics Publishing, London

Surface Tension, Capillarity and Contact Angle

KAMRAN MOHSENI
Department of Aerospace Engineering Sciences,
University of Colorado, Boulder, CO, USA
mohseni@colorado.edu

Overview

Surface tension is important in daily life and many engineering applications. Surface tension plays a major role in many applications such as washing and cleaning procedures, in lubricants such as those used in automobiles and cosmetics, and the formation of rain drops. It is even the phenomenon that allows the water-strider to walk on water. This introductory review presents some of the basic concepts associated with surface tension and capillarity. First, we consider the mechanical and thermodynamic definition of surface tension. This is followed by capillarity, contact angle, governing interface equations, relevant nondimensional numbers with surface tension effects, capillarity rise, temperature and surfactant effects of surface tension, and dynamic contact angles. Techniques for measuring surface tension and contact angle then follow. Controlling the wettability of a surface is then presented in order to create surfaces with superhydrophobic properties. Example applications of surface tension and capillarity are briefly presented at the end.

Chemical and Physical Principles

Surface Tension

Surface tension, often represented by σ or γ, is a property of liquids arising from an imbalance in molecular cohesive forces at the surface of the liquid (see Fig. 1). The attractive forces between molecules of a liquid are often stronger than forces between the liquid molecules and the surrounding gas or another immiscible liquid. In the bulk of a liquid each molecule is pulled equally, on average,

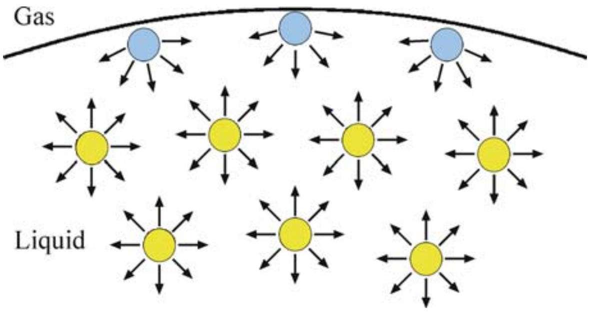

Surface Tension, Capillarity and Contact Angle, Figure 1 Adhesive and cohesive forces on molecules of a liquid close to an interface and away from it

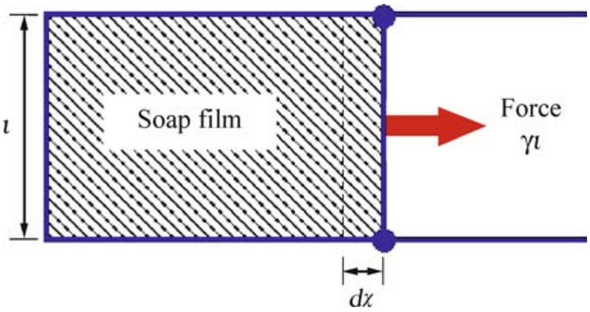

Surface Tension, Capillarity and Contact Angle, Figure 2 Surface tension can be considered as the work required for creating a unit surface area. In this case, the work is equal to $\gamma\delta S$ for a force equal to γl and moving a distance dx. The increment in surface area is $\delta S = l\,\mathrm{d}x$

in all directions by neighboring liquid molecules, resulting in a net zero force. However, the situation is different at the surface of the liquid where the liquid molecules are pulled more effectively by other liquid molecules, resulting in a net inward force. As a result of higher molecular attraction between the molecules of the same liquid than the attraction to molecules of another fluid, the surface of the liquid tends to contract inward. This net inward force can be mechanically modeled by assuming an apparent elastic surface under tension. In this case, the force per unit length along the interface between the two immiscible fluids is called surface tension. Surface tension can also be interpreted as the storage of energy at the surface of a liquid: energy per unit area. Therefore, γ is the work required to create a unit area of interface (see Fig. 2). This is a more thermodynamic definition for surface tension. In this case, in order to increase the surface area of a liquid by δS, an amount of work equal to $\gamma\delta S$ is required. The SI units for surface tension are N/m (force per length) or J/m^2 (energy per area).

Water at 20° has a surface tension of 72.9 mN/m in contact with air compared with 35 mN/m for SAE 30 oil and

Surface Tension, Capillarity and Contact Angle, Table 1 Surface tension values for some common liquids at 20 °C

Interface	Surface tension (mN/m)
Water–air	72.9
Mercury–air	486.5
Methanol–air	22.5
Ethanol–air	22.4
Benzene–air	28.9
Water–Mercury	415
SAE 30 oil–air	35
Soap solution–air	25
Glycerin–air	63
Blood–air	58

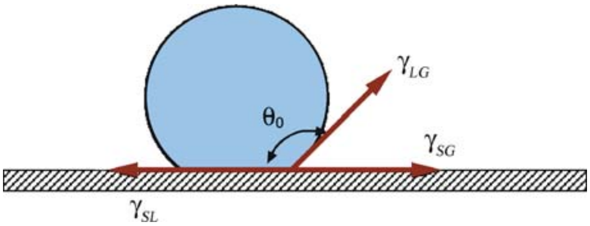

Surface Tension, Capillarity and Contact Angle, Figure 3 A droplet on a hydrophobic surface. The static contact angle, θ_0, is set by the balance of surface tension forces in the horizontal direction

486.5 mN/m for mercury. Surface tension values of common liquids are listed in Table 1.

Contact Point and Line

The line that delimits the wetted portion of a surface by a liquid is called the contact line. In two-dimensional flows the contact line reduces to a point (see Fig. 3). For a static droplet, the angle of the interface between the liquid and the solid surface is called the static contact angle θ.

Capillarity

Capillary actions or capillarity is a scientific topic concerning the equilibrium shape of interfaces in contact with a solid wall; in particular, in thin tubes or capillaries. For instance, for water in a thin glass tube, the strong hydrogen-bonding interactions between the water molecules and air at the surface of the glass causes the water to climb up in the tube. These new intermolecular interactions must balance the gravity and the weight of the water column. As a result, since the weight of water in a narrow tube is less than that in a thicker one, the water will climb higher in a narrow tube. The

curved free surface of the liquid in a capillary is called the meniscus.

Capillary action has major biological and engineering implications. For example, capillary actions are responsible for providing nutrients and oxygen and removing wastes and carbon dioxide from cells wherever blood flow is available. It is also the mechanism which distributes water and nutrients from plant roots to plant tissue.

Hydrophobic and Hydrophilic Surfaces

The strength of the capillary effect can be quantified by the contact angle. The rise or fall of a liquid in a small-diameter tube inserted into a liquid pool can be determined by the value of the contact angle. The contact angle for water in a glass tube is less than 90° (wetting the wall) and is more than 90° for mercury in a glass tube. In general, a nonwettable surface where the contact angle is greater than 90° is termed hydrophobic. Conversely, a contact angle less than 90° characterizes a wettable or hydrophilic surface. Surfaces with contact angles greater than 150° are called superhydrophobic. This is sometimes referred to as the "lotus effect" after the self-cleaning property of lotus plants. Water droplets roll off the leaves and cannot make them wet.

Key Research Findings

Young's Equation

The contact angle, as seen in Fig. 3, is set by the balance of surface tension forces in the horizontal direction

$$\gamma_{\mathrm{LG}} \cos\theta = \gamma_{\mathrm{SG}} - \gamma_{\mathrm{SL}} \,. \tag{1}$$

This is known as Young's equation where γ_{LG}, γ_{SG}, and γ_{SL} are the surface tension between the liquid and gas, solid and gas, and solid and liquid respectively. Young's angle is a result of thermodynamic equilibrium of the free energy at the contact point. This equation was derived by Young in 1805 shortly before its independent publication by Laplace. The same equation was also derived by Gibbs in 1906 through an energy minimization approach. By using Young's equation one can define a wetting coefficient k as

$$k = \frac{\gamma_{\mathrm{SG}} - \gamma_{\mathrm{SL}}}{\gamma_{\mathrm{LG}}} = \cos\theta \,. \tag{2}$$

Note that k has a value between 1 and -1. For hydrophilic surfaces $0 < k < 1$ or equivalently $0 < \theta < \pi/2$ and the solid is said to be wetted by the liquid. For hydrophobic surfaces $-1 < k < 0$ or $\pi/2 < \theta < \pi$ and the solid is not wetted by the liquid.

Young–Laplace Equation

A curved interface is an indicator of a pressure jump across the interface with higher pressure on the concave side. This can be easily seen in the case of a spherical droplet or bubble. For example consider the free body diagram of a droplet with radius R cut in half, as depicted in Fig. 4. The uniform surface tension along the circumference of the droplet is balanced by the pressure acting on the projected area πR^2. The balance of forces in the horizontal direction results in $(2\pi R)\gamma = (\pi R^2)\Delta P$, or $\Delta P = P_{\mathrm{i}} - P_{\mathrm{o}} = 2\gamma/R$ where P_{i} and P_{o} are the equilibrium pressure inside and outside of the droplet, respectively. In the case of a bubble, one obtains $\Delta P = P_{\mathrm{i}} - P_{\mathrm{o}} = 4\gamma/R$ since there are two layers of surface tensions: one in contact with the outside gas and one in contact with the gas inside the bubble. This simple relation can be extended to any surface with a mean curvature $\kappa = 1/R_1 + 1/R_2$, where R_1 and R_2 are the principal radii of curvature. The resulting equation is known as the Young–Laplace equation

$$\Delta P = \kappa\gamma \,. \tag{3}$$

In the absence of viscous forces, this equation provides a relationship for the change in pressure across a curved interface. It should be noted that pressure jumps across a fluid interface can only sustain normal stress jumps, they do not result in a tangential stress jump. Therefore, tangential surface stresses can only be balanced by viscous stresses associated with fluid motion. Consequently, in the absence of other effects, it is not possible to have a static system in the presence of surface tension gradient. A flow induced by a gradient in the surface tension is called Marangoni flow.

Nondimensional Numbers

Surface tension is a dominant force for liquid handling and actuation at microscales. Surface tension forces scale with a characteristic length scale L as compared with body forces (e. g. gravity) that scale as L^3, and pressure forces that scale as L^2. As a result, modifications of surface tension and other methods with similar scalings are much more effective for microdroplet transport than simple pressure-driven flow.

Consider a fluidic system with surface tension effects. The characteristic scales for length and velocity are L and U. The physical parameters are density ρ, viscosity ν, gravity g, and surface tension γ. By using the Buckingham Π theorem one can obtain three independent nondimensional groups from these six variables. An option for a set of three

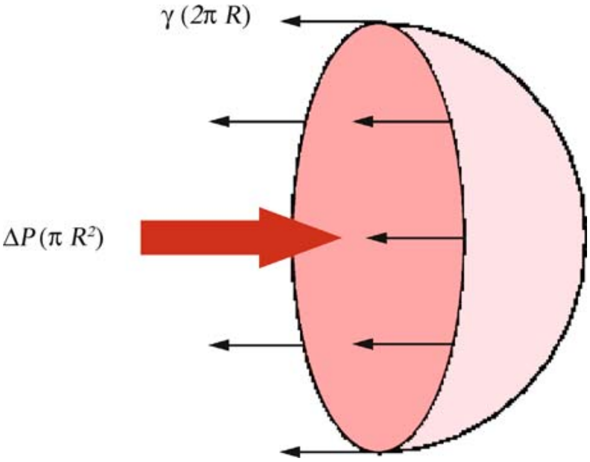

Surface Tension, Capillarity and Contact Angle, Figure 4 Free body diagram of forces on a droplet cut in half

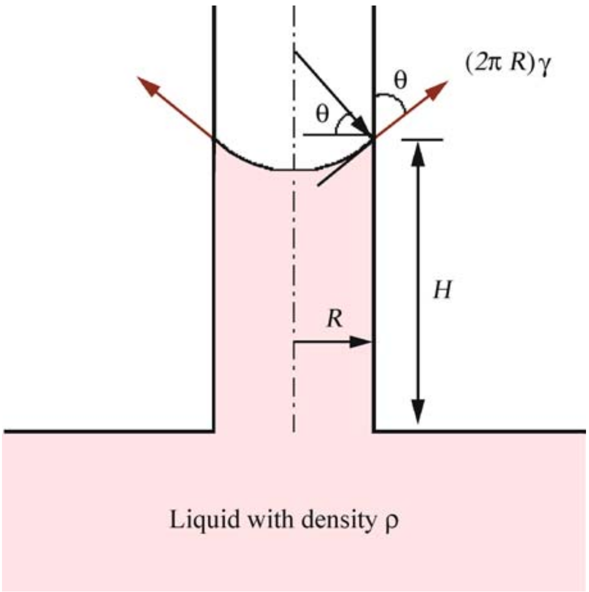

Surface Tension, Capillarity and Contact Angle, Figure 5 Capillary rise in a tube. The weight of the liquid column is supported by the vertical component of surface tension forces on the tube wall

independent nondimensional numbers is

$$\mathrm{Re} = \frac{UL}{\nu} = \frac{\text{inertial forces}}{\text{viscous forces}} \tag{4}$$

$$\mathrm{Bo} = \frac{\rho g L^2}{\gamma} = \frac{\text{gravitational forces}}{\text{surface tension forces}} \tag{5}$$

$$\mathrm{Ca} = \frac{\rho \nu U}{\gamma} = \frac{\text{viscous forces}}{\text{surface tension forces}} \tag{6}$$

where Re is the Reynolds number, Bo is the Bond number, and Ca is the capillary number. The Reynolds number expresses the relative magnitude of inertial forces in the system to viscous forces. Transitions from laminar to turbulent flows are characterized by the Reynolds number. The Bond number is a measure of gravitational forces compared to surface tension forces, while the capillary number determines the ratio of viscous forces to surface tension forces.

Two other relevant nondimensional numbers can be defined as

$$\mathrm{We} = \mathrm{Ca} \times \mathrm{Re} = \frac{\rho U^2 L}{\gamma} = \frac{\text{inertial forces}}{\text{surface tension forces}} \tag{7}$$

$$\mathrm{Fr} = \frac{\mathrm{We}}{\mathrm{Bo}} = \frac{U^2}{gL} = \frac{\text{inertial forces}}{\text{gravitational forces}} \tag{8}$$

The Weber number, We, represents an index of the inertial forces to surface tension forces and it is important in analyzing thin films and the formation of bubbles and droplets. The Bond number is often used when considering static surface tension effects, while the Weber number is more relevant in unsteady and moving systems. The Froude number, Fr, compares inertial and gravitational forces. Note that all the nondimensional numbers involving surface tension are boundary-related phenomena and they enter the governing equations through boundary conditions. On the other hand, the Reynolds number is directly introduced through the Navier–Stokes equations.

S

Capillary Rise

The rise or fall of a liquid interface in a capillary can be easily calculated by writing the balance of forces on a cylindrical column of height H (see Fig. 5). The water at the bottom of the tube, leveled with the free surface of the liquid, is at atmospheric pressure. The hydrostatic pressure drop just below the meniscus is balanced by the vertical component of surface tension at the wall. Therefore, $2\pi R\gamma \cos\theta = \rho g(\pi R^2 H)$. Hence, the capillary rise is given by

$$H = \frac{2\gamma}{\rho g R}\cos\theta = 2\frac{\delta_c^2}{R}\cos\theta \tag{9}$$

where $\delta_c = \sqrt{\gamma/\rho g}$ is the capillary length. For nonwetting liquids $\theta > 90°$ which results in a negative H. The capillary length also express the characteristic length of a meniscus; it is determined by the interplay between the Laplace and the hydrostatic pressure across an interface.

Surface Tension Variation

Surface tension values can be affected by temperature change, addition of impurities or surfactants, and, to a lesser extent, by variation in pressure and surface curvature.

Considering that surface tension is the result of cohesive forces between molecules of the same liquid, it would not be surprising to observe that by increasing the temperature (in an other words, by increasing the random kinetic energy of the liquid molecules), the surface tension is decreased. In fact, at the critical temperature, this kinetic energy is enough to break all the cohesive bonds between the liquid molecules and separate the molecules to form a gas.

The surface tension of many liquids decreases, almost linearly, with increasing temperature. In other words, the quantity $d\gamma/dT$ is negative and almost constant for most pure materials. A well-known relation is the Eötvös rule

$$\gamma = V^{-2/3}k(T_c - T) \tag{10}$$

where V is the molar volume, k is a constant equal to 2.1 erg/K for most liquids, and T_c is the critical temperature. Another relationship suggested by van der Waals and further developed by Guggenheim is

$$\frac{\gamma}{\gamma_0} = \left(1 - \frac{T}{T_c}\right)^n \tag{11}$$

where n is a constant equal to 11/9 for most organic liquids but may be closer to unity for most metals, and γ_0 is another constant that depends on the liquid under consideration. Note that in both equations the surface tension approaches zero at the critical temperature.

The surface tension of a material can also be greatly affected by the presence of impurities, particularly surfactants. Surfactants are surface-active agents that contain hydrophilic polar groups on their heads and hydrophobic groups on their tails. As a result, they are soluble in both water and organic solvents. In general, surfactants reduce the surface tension of a liquid. For example, surface tension of water can be greatly reduced by addition of soap or other detergents. This is used in washing processes in order to enable the liquid to penetrate cavities between fibers for more effective washing. Solutes, depending on their structure, can have different effects on surface tension. For example, sugar has no effect on surface tension of water, while inorganic salts increase surface tension, and alcohols decrease it. Surfactants will only decrease surface tension to a set limit and after that they will have no more effect. This can be explained as follows. The equilibrium value of surface tension can be decreased as the number of surfactant molecules accumulating at the surface increases. This process continues until the surface is completely covered by surfactant molecules. At this point, if the surfactant concentration is further increased the extra surfactant molecules will accumulate within the solution and form aggregates; what are called micelles. The concentration of the surfactant at which the surface is completely occupied by surfactant molecules is called the critical micelle formation concentration.

Dynamic Contact Angles

If a droplet is not in static equilibrium, the contact line might move; so too the dynamic contact angles. Figure 6 shows dynamic contact angles for a droplet moving on a inclined plate. Depending on the direction of the liquid movement, different contact angles may be observed. The contact angle measured when the contact line is in movement by wetting the solid is called the advancing contact angle, θ_A. On the other hand, the contact angle observed when the liquid is withdrawn over a pre-wetted surface is called the receding contact angle, θ_R. The advancing contact angle is always larger than or equal to the receding contact angle.

If the contact angle is a function of the speed of the contact line relative to the solid surface, one needs to consider viscous stress forces among other effects. In fact, the viscous stresses show singular behavior at the contact line [1]. The concept of contact line is a continuum concept. This concept breaks down near the surface and one requires molecular considerations in the vicinity of the contact line.

The difference between the advancing (maximum) and receding (minimum) contact angles is called the contact angle hysteresis. Hysteresis can be used to characterize surface heterogeneity, mobility, and roughness. If the sur-

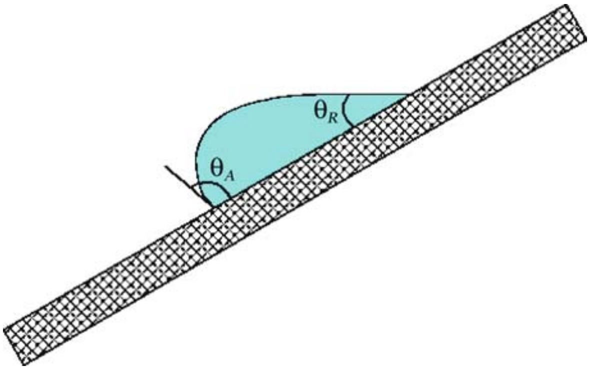

Surface Tension, Capillarity and Contact Angle, Figure 6 A droplet rolling down on an inclined surface. The advancing and receding contact angles are depicted

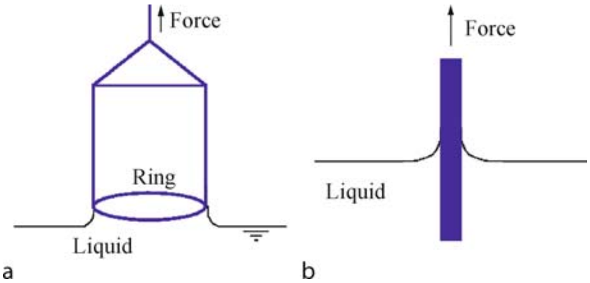

Surface Tension, Capillarity and Contact Angle, Figure 7 Surface tension measurement. (**a**) Du Nouy ring method. (**b**) Wilhelmy plate method

face is not homogeneous, some regions might present a barrier to the movement of the contact line (pinning the contact line) and can be manifested in regions with different contact angles from the surrounding area.

Surface roughness can also generate contact angle hysteresis by actual microscopic variations in the slope of the surface.

Techniques for Measuring Contact Angle and Surface/Interfacial Tension

Correct analysis of capillary and wetting problems requires accurate knowledge of surface tension values and contact angles. In this section we will provide a brief review of methods for measuring surface tension and contact angles. The basic methods for measuring these quantities can be divided into two categories: methods for measuring dynamic quantities and methods for measuring geometrical quantities. Another classification for measuring contact angles of nonporous solids is goniometry and tensiometry. In the goniometry method, the shape of a sessile drop on a solid substrate is analyzed. In the tensiometry method, the interaction forces between a solid in contact with the test liquid are measured.

The Du Nouy Ring Method A ring with perimeter L is immersed in to a liquid and then lifted up. The maximum pull exerted on the ring by the surface tension forces is measured (see Fig. 7a). At the maximum pull the force vector will be exactly parallel to the direction of motion and the contact angle will be zero. The surface tension is then calculated from $\gamma = F_{\mathrm{m}}/L$, where F_{m} is the maximum force during the lift off. A correction for the weight of the volume of liquid lifted beneath the ring could significantly improve the accuracy of this method.

The Wilhelmy Method This is a technique that can be used for both surface/interfacial tension and contact angle measurements (Fig. 7b). To measure the surface tension, a plate with known perimeter P is attached to a balance. The plate is brought into contact with the test liquid and the force due to wetting is measured. The upward force of the surface tension must be equal to the weight of the meniscus measured by the balance. This results in $F = \gamma P \cos\theta$. This equation provides a method to measure the vertical component of surface tension. However, this provides one equation with two parameters: γ and θ. By intensive cleaning or by roughening a platinum plate one could achieve an almost zero contact angle. This results in a single measurement for calculating the surface tension. If the surface tension is known, one can employ the same equation to calculate the contact angle in the same fashion.

Capillary Rise Method In this approach a capillary tube is immersed into the liquid. The surface tension is calculated by measuring the liquid height in the capillary tube via Eq. (9). The capillary rise is also a measure of the vertical component of surface tension.

Tilted Plate Method This is a method for measuring contact angle. In this approach, a plate is immersed in the test liquid until the liquid meniscus becomes horizontal at the point of contact. The contact angle is then equal to the angle of the plate. A tilted plate can also be used for measuring dynamic contact angles. In this case, a plate with a sessile drop on top is slowly tilted until the drop begins to move. At this time, the uphill angle will be the receding contact angle and the downhill angle will be the advancing contact angle. The measurement should be done immediately before the actual droplet motion in order to avoid dynamic effects.

Pendant or Sessile Drop Method The surface tension can be easily measured by analyzing the shape of a drop. This is often done by optical means. Assuming that the drop is axially symmetric and in equilibrium (no viscous and inertial effects) the only effective forces are gravity and surface or interfacial forces. In this case, the Young–Laplace equation relates the shape of the droplet to the pressure jump across the interface. Surface tension is, then, measured by fitting the drop shape to the Young–Laplace equation. Either a pendant or a sessile drop can be used for surface tension measurement. The pendant drop approach is often more accurate than the sessile drop approach since it is easier to satisfy the axisymmetric assumption. Similar techniques can be used for measuring surface tension in a bubble.

Drop Weight Method The drop weight, or Tate's, method is yet another technique for determining surface tension. This approach relies on dripping of a liquid in a gas from a capillary and measuring the combined vol-

umes of the primary and satellite drops that are formed. In this case one can write Tate's law for the weight of the drop

$$\rho g V = 2\pi R \gamma \tag{12}$$

where ρ is liquid density, g is the gravitational acceleration, V is the volume of the drop, and R is the drop radius. By measuring the drop volume and radius one can calculate the surface tension.

Bubble Pressure or Drop Weight Method In this approach, surface tension is calculated from the measurement of pressure inside the bubble or from the weight of the drop when it detaches from an orifice. The gas bubble can be introduced into a liquid through a capillary with known radius. The maximum pressure p_m during this process is recorded and used to calculate the surface tension. At the maximum pressure, the gas bubble radius is the same as the capillary with the gas bubble forming an exact hemisphere. If the hydrostatic pressure is p_0, and the inner radius of the capillary is R, the surface tension is calculated from the equation

$$\gamma = \frac{p_m - p_0}{2} R \tag{13}$$

After the maximum pressure measurement, the bubble radius increases while the pressure drops. The bubble finally detaches from the capillary and rises to the surface.

Superhydrophobicity

Controlling the wettability of a surface is crucial in many industrial applications. Surfaces with water contact angles above 150° are called superhydrophobic. Such surfaces are important because they could have anti-contamination, anti-sticking, and self-cleaning properties. In nature, superhydrophobic surfaces are observed in lotus leaves, cicada orni wings, and water-strider legs. Water droplets easily roll off such surfaces at a small sliding angle and hereby remove contaminants from the surface.
The high contact angle in superhydrophobic surfaces is often called the apparent contact angle since it does not represent the actual contact angle value of the droplet on a flat surface. The superhydrophobic surfaces are usually covered with micro- or nanoscale roughness. As depicted in Fig. 8 the water can penetrate the gap between the spikes on a surface (Wenzel state) or stay in a suspended state above the spikes (Cassie–Baxter state). In either case a higher contact angle is observed than that observed on a flat surface. In the case where the liquid does not enter the roughness, a drop is supported on a patchwork of solid

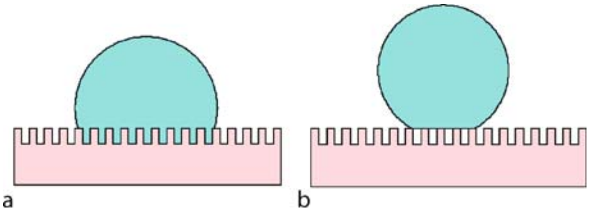

Surface Tension, Capillarity and Contact Angle, Figure 8 Effect of surface structures on wetting behavior. (**a**) Wenzel's model where the liquid penetrates between the structures. (**b**) Cassie–Baxter model where water does not wet the surface between the structures

and gas, which leads to very high contact angles. Furthermore, the gas trapped below the drop homogenizes the solid surface and results in very low contact angle hysteresis. Superhydrophobic windshields are nowadays used for better visibility during rain conditions. The water-repellent coated glass enables windshields to shed rain without the need for windshield wipers. If the spatial scale of the roughness is small compared to the wavelength of light the texture does not affect the optical transparency of the windshield.
In the Wenzel model, the apparent contact angle θ_W is obtained by correcting the Young's contact angle θ with a roughness correction factor r

$$\cos\theta_W = r \frac{\gamma_{SG} - \gamma_{SL}}{\gamma_{LG}} . \tag{14}$$

The roughness factor is defined by the actual surface area divided by the projected surface area. Therefore, for a rough surface $r > 1$. Following Wenzel's equation, surface roughness results in enhancing both hydrophobicity and hydrophilicity depending on the nature of the corresponding flat surface. Therefore, for a truly hydrophobic surface $\theta_W > \theta > 90°$ and for a truly hydrophilic surface $\theta_W < \theta < 90°$. For surface roughness factors greater than 1.7, the droplet will have a hard time to wet all the grooves and the system switches from a Wenzel model to a Cassie–Baxter model. In this case, the droplet is suspended on top of the grooves, where the gas is trapped. The apparent contact angle can be calculated from Cassie's law for a liquid on a composite surface

$$\cos\theta_C = f_1 \cos\theta_1 + f_2 \cos\theta_2 \tag{15}$$

where θ_1 is the Young contact angle for component 1 with surface fraction f_1 and θ_2 is the Young contact angle for component 2 with surface fraction f_2. Note that $f_1 + f_2 = 1$. For a two-component system consisting of an air component with a contact angle of 180° the equation is reduced

to

$$\cos\theta_C = f(\cos\theta + 1) - 1 \quad (16)$$

after dropping the second index. This equation implies that it is possible to create surfaces with very large apparent contact angles if the surface has small f and large true contact angle θ. The lotus effect is based on this principle. Note that for a given surface with a true contact angle θ, the apparent contact angle in the Cassie–Baxter model is a function of f only.

Examples of Applications

Some of the industrial applications of surface/interfacial tension and capillarity are: in soil mechanics where the penetration of liquids into porous rocks are considered; in anti-fog, anti-frost, or anti-stain treatment of glass for enhanced visibility in harsh environments; in the chemical industry for uniform spreading of paints, insecticides, ink, and coloring ingredients; in the construction industry for waterproofing of concrete; and in creating fuel spray in internal combustion engines. In the life sciences, locomotion of insects on water surfaces; the rise of sap in plants; adhesion of parasites on wet surfaces; and wetting of eye (an eye is normally wet while the cornea is by nature hydrophobic). Surface tension is also a dominant force at the microscale. To this end, surface tension and its manipulation play a major role in most microfluidic and Lab-on-a-Chip devices. Capillarity is a significant part of capillary liquid chromatography, capillarity electrophoresis, and flow cytometry. Micropipettes work based on the same principle. Surface tension also plays a significant role in applications where the formation of jets and drops are considered.

Further Reading

Some general references for surface and interfacial phenomenon are the books by Adamson and Gast [2] and Hiemenz and Rajagopalan [3]. An interesting scientific background to molecular and macroscopic properties of soap films and bubbles is provided in [4]. The fluid dynamics, heat transfer, and mass transfer of single bubbles, drops, and particles are covered in [5].

References

1. de Gennes PG (1985) Wetting: Statistics and dynamics. Rev Mod Phys 57(3):827–863
2. Adamson AW, Gast AP (1997) Physical Chemistry of Surfaces, 7th edn. Wiley, New York
3. Hiemenz PC, Rajagopalan R (1997) Principles of Colloid and Surface Chemistry, 3rd edn. Dekker, New York
4. Isenberg C (1992) The science of soap films and soap bubbles. Dover, New York
5. Clift R, Grace JR, Weber ME (2005) Bubbles, drops, and particles. Dover, New York

Surface Tension-Confined Confined Microfluidics

► Surface-Directed Capillary Flow Systems

Surface Tension Driven Filling

► Capillary Filling

Surface Tension Driven Flow

SUMAN CHAKRABORTY
Department of Mechanical Engineering, Indian Institute of Technology, Kharagpur, India
suman@mech.iitkgp.ernet.in

Synonyms

Capillary flow; Wetting phenomenon

Definition

Surface tension driven flow concerns the actuation and control of fluid dynamic transport through a manipulation of the surface tension forces. The manipulation, in principle, can be hydrodynamic, thermal, chemical, electrical or optical in nature. It is also important to mention here that there must be a free surface or a liquid–fluid interface in order to have a surface tension driven flow

Surface tension (γ) is a force per unit length that acts along the interfaces of immiscible phases. For illustration, one may refer to the instance of a liquid–gas interface, the molecules located on which experience a net cohesive force that is directed towards the bulk of the liquid and away from the interface, because of the denser molecular packing in the liquid phase than in the gas phase and a consequent stronger intermolecular force of attraction offered by the liquid molecules. Thus, the interface appears to be in a kind of tension. The interface also must possess necessary energy that overcomes the net attractive force towards the liquid side and allow the interface to sustain. This energy per unit interfacial area is also known as the surface energy.

Overview

It is well known that as the length scale of a system is reduced, surface tension effects become progressively more important, as compared to the other forces that are

S

conventionally dominant over macroscopic length scales. This is primarily because of the fact that the surface tension force scales down only linearly with the length scales whereas most other forces scale down with higher powers of the same. Thus, surface tension, which is a negligibly weak force in the macro domain, may eventually become a dominant force in the micro and nano domains.

From a fluid mechanics viewpoint, the presence of an interface creates a jump in pressure. To appreciate the underlying physical picture from a fundamental viewpoint, let us begin with the thermodynamic description of a liquid droplet in terms of its free energy, as

$$E = \sum_{i \neq j} A_{ij}\gamma_{ij} - \lambda \forall \tag{1}$$

where $\forall$ is the droplet volume and λ is a Lagrange multiplier to enforce a constant volume constraint (physically, λ is equal to the pressure drop across the liquid–vapour interface, thermodynamically consistent with the definition of free energy of a system). Here A_{ij} is the interfacial area that demarcates the phases i and j, with the corresponding surface energy being designated as γ_{ij}. In this article, the subscripts 'l', 's' and 'v' will be employed to represent the liquid, solid and vapour phases, respectively. It can also be noted that if A_{ls} is increased by some amount, A_{sv} is decreased by the same amount. The evaluation of free energy of the droplet, in accordance with Eq. (1), can be best illustrated through the example of a spherical droplet with an equilibrium contact angle θ (refer to Fig. 1 of the article on ▶electrocapillary), for which one can write: $A_{\text{sl}} = \pi R^2 \sin^2\theta$, $A_{\text{lv}} = 2\pi R^2(1-\cos\theta)$, $\forall = \pi R^3\left(\frac{2}{3} - \frac{3}{4}\cos\theta + \frac{\cos 3\theta}{12}\right)$. Thus, for a spherical droplet

$$E = \underbrace{\pi R^2 \sin^2\theta\,(\gamma_{\text{ls}} - \gamma_{\text{sv}}) + \gamma_{\text{lv}} 2\pi R^2(1-\cos\theta)}_{\text{f}} - \lambda\left\{\underbrace{\pi R^3\left(\frac{2}{3} - \frac{3}{4}\cos\theta + \frac{\cos 3\theta}{12}\right)}_{\text{g}} - k\right\} \tag{2}$$

where k is the volume of the droplet. For minimization of E, one must have $\partial E/\partial\theta = 0$ and

$$\frac{\partial E}{\partial R} = 0\,, \quad \text{which implies}$$

$$\frac{\partial f}{\partial \theta}\frac{\partial g}{\partial R} = \frac{\partial f}{\partial R}\frac{\partial g}{\partial \theta}\,. \tag{3}$$

Performing the necessary algebra and simplifying, it follows from Eqs. (3) and (4) that

$$\cos\theta = \frac{\gamma_{\text{sv}} - \gamma_{\text{sl}}}{\gamma_{\text{lv}}}\,. \tag{4}$$

When $0 \leqslant \theta \leqslant 90°$, the liquid is termed as partially wetting, or equivalently, the solid substrate is characterized as hydrophilic. When $\theta > 90°$, the liquid is non-wetting and the substrate is termed as hydrophobic. The case $\theta = 0$, a very special one, represents a theoretically complete wetting. Equation (4), also known as the 'Young's Law', can be interpreted as a balance between the horizontal components of all the forces that act on the 3-phase contact line (refer to Fig. 2 of the article on ▶electrocapillary). The vertical component of this resultant force, on the other hand, is balanced by the normal stress in the rigid solid substrate. Further, substituting the value of $\cos\theta$ from Eq. (4), one may calculate a value of the parameter $\lambda(= \Delta p)$, as

$$\Delta p = \frac{\partial f/\partial\theta}{\partial g/\partial\theta} = \frac{2\gamma_{\text{lv}}}{R}\,. \tag{5}$$

For a droplet of a more general shape, Eq. (5) can be generalized as

$$\Delta p = \gamma_{\text{lv}}\left(\frac{1}{r_1} + \frac{1}{r_2}\right)\,, \tag{6}$$

where r_1 and r_2 are the two principal radii of the curvature of the droplet surface. It is important to note here that the Eqs. (4) and (6) are the two necessary conditions for equilibrium but not sufficient, since in addition, the second variation of E must also be positive for a minimization of the same. In fact, in presence of complex surfaces, certain morphologies may, indeed, result in unstable droplets, even though the necessary conditions of equilibrium are satisfied.

The celebrated Young's equation, as described by (4), is somewhat restricted in nature in a strict sense, since it neglects the bulk internal forces within the droplet that might generate due to gravity, electric field etc. In an effort to generalize the underlying mathematical description, one may note that, for equilibrium of a spherical droplet

$$\mathrm{d}E(R,\theta) = 0\,, \tag{7}$$

which implies

$$\frac{\partial E}{\partial R}\mathrm{d}R + \frac{\partial E}{\partial \theta}\mathrm{d}\theta = 0\,. \tag{7a}$$

Further, since $\forall = \pi R^3\left(\frac{2}{3} - \frac{3}{4}\cos\theta + \frac{\cos 3\theta}{12}\right)$, the condition of $\mathrm{d}\forall = 0$ implies that

$$\mathrm{d}R - Rf_1(\theta)\,\mathrm{d}\theta = 0\,, \tag{8}$$

where

$$f_1(\theta) = \frac{-2\cos^2\frac{\theta}{2}\cot\frac{\theta}{2}}{2+\cot\theta}\,. \tag{8a}$$

Substituting Eq. (8a) in Eq. (7a), one finally gets

$$\frac{\partial E}{\partial R}Rf_1(\theta) + \frac{\partial E}{\partial \theta} = 0\,. \tag{9}$$

Incorporating the effects of gravitational potential energy in the expression for E, one can write

$$E = \underbrace{R^2\left[2\pi\gamma_{\mathrm{lv}}(1-\cos\theta) + \pi\sin^2\theta(\gamma_{\mathrm{ls}} - \gamma_{\mathrm{sv}})\right]}_{\text{contribution from interfacial terms}} + \underbrace{R^4\frac{2\pi}{3}\rho g(3+\cos\theta)\sin^6\left(\frac{\theta}{2}\right)}_{\text{contribution from gravity}}\,. \tag{10}$$

Utilizing the above expression for E in Eq. (9), one can arrive at a more generalized form of the Young equation incorporating gravity effects, as

$$\cos\theta - \frac{\gamma_{\mathrm{sv}} - \gamma_{\mathrm{sl}}}{\gamma_{\mathrm{lv}}} - \frac{\rho g R^2}{\gamma_{\mathrm{lv}}}\left[\frac{\cos\frac{\theta}{3} - \cos 2\theta}{12} - \frac{1}{4}\right] = 0\,. \tag{11}$$

From Eq. (11), following two important observations may be carefully noted:

1. With gravity effects, θ depends on R, unlike the case without gravity.
2. If $\rho g R^2/\gamma_{\mathrm{lv}}$ is small, gravity effects can safely be neglected. This ratio is known as the Bond number (Bo), which essentially compares the square of the system length scale (R) with the square of a characteristic length scale, l_{s}, that depicts the relative contributions of surface tension and gravity influences, as $l_{\mathrm{s}} = \gamma_{\mathrm{lv}}/\rho g$. For Bo $\leqslant 10^{-3}$, gravity effects can safely be neglected, as appropriate to many of the micro-scale transport processes.

The preliminary understanding of pressure jump across a static meniscus with constant surface tension effects (refer to Eq. 6) can be more fundamentally extended to write a generalized expression for the interfacial condition on a mobile phase boundary, as [1]

$$\left[p^{(2)} - p^{(1)} + \gamma\left(\frac{1}{r_1} + \frac{1}{r_2}\right)\right]n_i = \left[\mu^{(2)}\left(\frac{\partial u_i^{(2)}}{\partial x_k} + \frac{\partial u_k^{(2)}}{\partial x_i}\right) - \mu^{(1)}\left(\frac{\partial u_i^{(1)}}{\partial x_k} + \frac{\partial u_k^{(1)}}{\partial x_i}\right)\right] \times n_k - \frac{\partial\gamma}{\partial x_i} \tag{12}$$

where $p^{(1,2)}$, $\mu^{(1,2)}$, $u_i^{(1,2)}$, $u_k^{(1,2)}$ are the pressures, viscosities and velocity components, respectively, in phases 1 and 2, n_i $(i = 1, 2, 3)$ are the components of the unit vector normal to the interfaces and directed into the interior of phase 1, and a summation over the repeated index, k, is assumed. To account for the effects of surface-active elements (surfactants), right hand side of Eq. (12) may be provided with phenomenological source terms of the form

$$-\mu_{\mathrm{s}}\delta_{ik}\frac{\partial^2 u_k^{(s)}}{\partial x_i \partial x_k} \tag{13}$$

where δ_{ik} is the Kronecker delta, $u_k^{(s)}$ are the components of surface motion velocity and μ_{s} is the so-called surface viscosity (a phenomenological constant), which characterizes the dynamical elasticity of the insoluble surface film. In a strict sense, Eq. (13) accounts for the energy dissipation in the surface layer due to irreversibilities associated with the viscous motion of adsorbed particles on the surfaces.

Basic Methodology

Marangoni Effects and Thermocapillary Motion

Fundamental principles associated with surface tension driven flows rely on the motion induced by the variation of surface tension from point to point on a mobile phase boundary, giving rise to tangential strains on the same. According to the boundary condition given by Eq. (12), the presence of tangential strains at the interface is accompanied by fluid motion. Fluid motion induced by the tangential gradients of surface tension is classically known as the Marangoni effect. As an illustration specific to microflow actuations with the aid of thermally-activated surface tension gradients, we consider the steady thermocapillary migration of a gas bubble [2] of fixed volume in a tube of radius a, filled with a liquid of viscosity μ, surface tension γ, density ρ, thermal diffusivity α and temperature coefficient of surface tension $\gamma_{\mathrm{T}} = -\mathrm{d}\gamma/\mathrm{d}T$. Viscosity and the conductivity of the gas are neglected

in comparison to those of the liquid and the length of the bubble is taken to be much larger than the radius of the tube. The temperature gradient imposed on the tube wall is a constant, say β. The variation of interfacial tension as a function of temperature generates a thermocapillary shear stress, inducing the bubble motion at a steady speed towards the hotter region. The liquid is taken to be perfectly wetting. A thin layer of liquid separates the bubble from the tube wall. The three important non-dimensional numbers charecterizing the bubble motion are the Bond number ($\mathrm{Bo} = \rho g a^2/\gamma$), Péclet number ($\mathrm{Pe} = \mathrm{Re}.\mathrm{Pr}$, where Re is the Reynolds number and Pr is the Prandtl number) and capillary number ($\mathrm{Ca} = \mu u_\mathrm{b}/\gamma$), where u_b is the characteristic axial speed of the bubble. For the mathematical analysis, all these non-dimensional numbers are taken to be small. A small Bond number implies that the gravity effects are negligible and the bubble is symmetrically located within the tube. A small Péclet number implies that the advective in the temperature variations are negligible. For small Ca, one can subdivide the flow around the bubble in five different regimes, namely, (I) a section parallel to the wall with constant film thickness (say, b), (II, III) two sections of constant curvature hemispherical caps in the front and in the back, which are connected to the constant film-thickness region through two transient regions at the two ends (IV, V) over which the curvature smoothly varies from zero to a constant value. A small Reynolds number ($\mathrm{Re} = \rho_\mathrm{a} u_\mathrm{b} a/\mu$) assumption allows one to use a lubricating film assumption in the transition regions. With small Capillary numbers, it is also implicit that there are no significant fluid dynamic forces in the regions near the hemispherical caps (since surface tension forces dominate over viscous forces, which in turn dominate over inertia forces for low Reynolds numbers). For the section of the bubble parallel to the wall (section I), one can obtain the maximum velocity at the edge of the thin film of thickness b, analogous to the situation of a shear-driven Couette flow, as

$$U_\mathrm{T} = \frac{\gamma_\mathrm{T}\beta b}{\mu} \tag{14}$$

where the shear stress, τ, is balanced by the Marangoni stress due to temperature gradient (i. e., $\partial\gamma/\partial x = (\partial\gamma/\partial T)(\partial T/\partial x) = -\gamma_\mathrm{T}\beta$). The velocity U_T, however, is unknown, since the film thickness (b) is not known a-priori. In the transition region, the governing equations of fluid flow, in a reference frame fixed with the bubble, can be written as

$$\frac{\partial^2 u}{\partial y^2} = \frac{1}{\mu}\frac{\partial p}{\partial x} \tag{15}$$

subject to the following boundary conditions:

$$u = -U_\mathrm{b} \text{ at } y = 0 \text{ and } \tau = \mu\frac{\partial u}{\partial y} = -\gamma_\mathrm{T}\beta \text{ at } y = h(x) \tag{15a}$$

where u is the liquid velocity in the moving reference frame, x is the axial direction of motion, y is the transverse direction and $h(x)$ is the film thickness. A solution for Eq. (15) can be obtained as

$$u(x, y) = \frac{1}{2\mu}\frac{\partial p}{\partial x}y^2 + \frac{1}{\mu}\left(\frac{\partial\gamma}{\partial x} - \frac{\partial p}{\partial x}h\right)y - U_\mathrm{b}\,. \tag{16}$$

The pressure gradient is related to γ by setting right hand side of Eq. (12) to zero and substituting the expressions of radii of curvature in terms of the geometrical parameters of the surface profile (noting that $\frac{1}{R_1} = \frac{\mathrm{d}^2 h}{\mathrm{d}x^2} / \left[1 + \left(\frac{\mathrm{d}h}{\mathrm{d}x}\right)^2\right]^{\frac{3}{2}}$, where the denominator can be neglected relative to the numerator for small curvature, and $R_2 \to \infty$), one obtains

$$\frac{\partial p}{\partial x} = -\gamma\frac{\mathrm{d}^3 h}{\mathrm{d}x^3}\,. \tag{17}$$

The differential equation for the free surface location can be derived by noting that the flux across any cross section needs to be a constant, which mathematically implies $\int_b^{h(x)} u(x, y)\,\mathrm{d}y = 0$, in the moving reference frame. Also noting that $\frac{\partial p}{\partial x} = 0$ at $y = b$, one can utilize Eq. (16) and (17) to evaluate the above integral and obtain

$$\frac{\gamma}{3\mu}h^3\frac{\mathrm{d}^3 h}{\mathrm{d}x^3} - \frac{\gamma_\mathrm{T}\beta}{2\mu}\left(h^2 - b^2\right) - U_\mathrm{b}(h - b) = 0\,. \tag{18}$$

It is interesting to note that Eq. (18) explicitly takes care of the fact that $h \to b$ when the film becomes flat, or in other words, it takes care of an asymptotic matching of the solution in the constant film-thickness region. For an asymptotic matching with the hemispherical cap, one may use a new set of dimensionless coordinates (refer to Fig. 1)

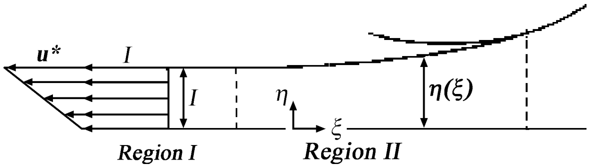

Surface Tension Driven Flow, Figure 1 Dimensionless coordinates for the description of thermocapillary flow around a liquid–vapour meniscus

such that $\eta = h/b$, $\zeta = x/b\,(3\mathrm{Ca})^{-\frac{1}{3}}$. These rescalings cast Eq. (18) in a modified Landau–Levich form, as

$$\eta^3 \frac{\mathrm{d}^3\eta}{\mathrm{d}\zeta^3} - \frac{U^*}{2}\left(\eta^2 - 1\right) - (\eta - 1) = 0 \tag{19}$$

where $U^* = U_\mathrm{T}/U_\mathrm{b} = \gamma_\mathrm{T}\beta b/\mu U_\mathrm{b}$, which is an unknown parameter. However, given a value of U^*, it is possible to integrate Eq. (19) numerically, with specified sets of initial conditions. When η is very close to unity, Eq. (19) can be linearized to obtain

$$\frac{\mathrm{d}^3\eta}{\mathrm{d}\zeta^3} = \left(1 + U^*\right)(\eta - 1) \tag{20}$$

which has the following general solution [2]:

$$\begin{aligned}\eta &= 1 + A\exp\left(\left(1+U^*\right)\zeta\right)\\ &\quad + B\exp\left(-\frac{1}{2}\left(1+U^*\right)\zeta\right)\cos\left(\frac{\sqrt{3}}{2}\left(1+U^*\right)\zeta\right)\\ &\quad + C\exp\left(-\frac{1}{2}\left(1+U^*\right)\zeta\right)\sin\left(\frac{\sqrt{3}}{2}\left(1+U^*\right)\zeta\right)\end{aligned} \tag{21}$$

where A, B and C are constants of integration. The asymptotic behaviour of the solution as $\eta \to \infty$ can be used by applying the perturbation theory over Eq. (21) to yield [2]

$$\begin{aligned}\eta &= \frac{1}{2}C_0\zeta^2 + C_1\zeta + C_2 - \frac{U^*}{C_0}\left(\zeta\ln|\zeta| - \zeta\right)\\ &\quad + \frac{U^{*2}}{2C_0^3}\ln^2|\zeta| + \left(\frac{U^{*3}}{2C_0^3} - \frac{C_1U^*}{C_0^2}\right)\ln|\zeta|\\ &\quad + O\left(\frac{\ln^2|\zeta|}{\zeta}\right).\end{aligned} \tag{22}$$

The coefficients C_0, C_1 and C_2 are determined from the numerical solution for large values of ζ. The constant C_0 (related to the curvature of the end caps) can be determined as the limiting value of the second derivative for large η. When $U^* = 0$, the asymptotic form simplifies to $C_0 = 0.643$ [2]. In general, C_0 is a monotonically increasing function of U^*, as can be obtained numerically. Another matching condition can be obtained by noting that the mean curvature of the caps equals $2/a$ for the leading order approximation for small Ca, which implies

$$h_{\mathrm{xx}} \approx \frac{1}{a}, \text{ or } \frac{(3\mathrm{Ca})^{\frac{2}{3}}}{b}\eta_{\zeta\zeta} \approx \frac{1}{a}. \tag{23}$$

From the above considerations, one gets

$$\eta_{\zeta\zeta} \approx \frac{b}{a(3\mathrm{Ca})^{\frac{2}{3}}}, \text{ or } C_0\left(U^*\right) \approx \frac{b}{a(3\mathrm{Ca})^{\frac{2}{3}}}. \tag{24}$$

Further, from the considerations of global mass balance, one may note that the rate of volume of fluid pumped by the Marangoni stress, Q_1, must be same as the rate of volume displaced by the moving bubble, Q_2. Since $b \ll a$, one can neglect $O(b/a)$ terms and approximate Q_1 as

$$Q_1 = 2\pi\int_{a-b}^{a} U_T(a-r)r\,\mathrm{d}r \approx \frac{-\pi\gamma_T\beta a}{\mu}\frac{b^2}{a^2}. \tag{25}$$

Similarly,

$$Q_2 = \pi U_b(a-b)^2 \approx \pi U_b a^2. \tag{26}$$

Since $Q_1 = -Q_2$, one may write

$$\mathrm{Ca} = \frac{\mu U_b}{\gamma} = \frac{\gamma_T\beta a}{\gamma}\frac{b^2}{a^2}. \tag{27}$$

Equation (27) can be used with Eq. (24) to express $C_0(U^*)$ as a sole function of b/a, in the asymptotic matching condition. With $C_0(U^*)$ already being obtained numerically, the ratio of b/a can therefore be obtained from Eq. (24), for a given value of $\Delta\gamma^* = \Delta\gamma/\gamma = \gamma_\mathrm{T}\beta a/\gamma$ (which is the ratio of the thermocapillary force to the mean surface tension force). The numerical results can be fitted with the following power law expression [2]:

$$\frac{b}{a} = 13.591\Delta\gamma^{*2} \tag{28a}$$

and

$$\mathrm{Ca} = 184.715\Delta\gamma^{*5}. \tag{28b}$$

One can observe from Eq. (28b) that higher temperature gradients may cause the bubble to move faster. The solutions presented above, however, are rather approximate and are valid for vanishingly small Capillary numbers only.

Electrocapillary Flow

Similar to the thermocapillarity (where temperature gradient creates the driving surface tension force), one can also exploit the effects of electrocapillarity or electrowetting, in which electric potentials can be employed to alter the surface tension and thereby cause a fluid motion. Compared to the thermocapillary flows, electrocapillary flows are much more energy efficient, with a much faster speed

S

of operation (speeds more than 100 mm/s have been successfully achieved by electrowetting action, in contrast to a typical speed of only about 1 mm/s in thermocapillary flows). The electrocapillary principles are all based on the fact that the surface tension occurs to be a strong function of the electrical potential acting across an interface. As a consequence, the apparent contact angle, θ, gets modified from its value at zero voltage, θ_0, in the following form:

$$\cos\theta = \cos\theta_0 + \frac{cV^2}{2\gamma_{lv}} \quad (29)$$

where c is the capacitance of the interface per unit area and V is the interface potential. Based on this fundamental principle, one can design various flow actuating mechanisms such as continuous electrowetting (employing liquid metal droplets in a filler liquid and exploiting the electric double layer potential to alter the liquid/liquid interfacial tension), electrowetting (employing liquid droplets in a vapour medium and exploiting the electric double layer potential to alter the solid/liquid interfacial tension), and electrowetting on dielectrics (employing liquid droplets in a vapour medium and exploiting the potential across a dielectric layer to alter the liquid/liquid interfacial tension), the details of which are outlined in the article on ► electrocapillary. It is important to note here that Eq. (29) can be obtained as a generalization of the Young's equation, by noting that there is an additional electrostatic contribution (E_{el}) to the free energy, which, for the case of electrowetting on dielectrics as an example, can be written as

$$E_{el} = -\frac{1}{2}\frac{\varepsilon_d}{d}V^2 A_{sl} \quad (30)$$

where ε_d is the permittivity of the dielectric layer and d is its thickness. For a spherical droplet, $A_{sl} = \pi R^2 \sin^2\theta$. Thus, the total interfacial energy for this case is given as

$$E(R,\theta) = R^2\left[\pi \sin^2\theta\,(\gamma_{ls} - \gamma_{sv}) - \frac{\varepsilon_d V^2}{2d} + 2\pi\gamma_{lv}(1-\cos\theta)\right]. \quad (31)$$

Minimizing $E(R,\theta)$ for a constant droplet volume, one can arrive at the Young-Lippman equation:

$$\cos\theta = \frac{\gamma_{sv} - \gamma_{sl}}{\gamma_{lv}} - \frac{\varepsilon_d V^2}{2\gamma_{lv} d}. \quad (32)$$

It is important to note here that although fairly general, the above analysis is not strictly valid for apolar liquids (for example, silicone oil at the top of a conducting solid substrate). In such cases, the droplet may be modeled as an insulator with a permittivity of ε_l. The electrical energy stored in that case can be estimated as $1/2\varepsilon_l R^3 (V/R)^2 a_{de}(\theta)$, where $a_{de}(\theta)$is a shape factor, which cannot be computed analytically, but can be numerically fitted as [3]

$$a_{de}(\theta) \approx 0.0592 + 0.0012\theta + 0.0022\tan(1.71-\theta). \quad (33)$$

In this situation, a generalized Young equation can be arrived at by applying the energy minimization principle, to obtain

$$\cos\theta - \frac{\gamma_{sv} - \gamma_{sl}}{\gamma_{lv}} + \frac{\varepsilon_l V^2}{2\gamma_{lv} R}\frac{2+\cos\theta}{2\pi\,\sin\theta} \times \left[a_{de}(\theta) f_1(\theta) + \frac{da_{de}}{d\theta}\right] = 0. \quad (33a)$$

Solutal Gradient Originated Surface Tension Driven Flow

Other than due to the imposed gradients of temperature and electrical potential, surface tension gradients can spontaneously originate as a consequence of droplet splitting or coalescence, mixing of samples or chemical reactions. Typically, surface tension gradients generated during the contact of dissimilar liquids are much larger than those obtained as a consequence of thermocapillary variations. Deposition of biological liquids containing surface active elements onto a liquid film with higher γ_{lv} generates Marangoni stresses, which can cause rapid thinning and rupture of films. For an interface containing surface-active molecules, the surface tension is likely to vary with the local concentration, giving rise to a tangential stress, τ, as

$$\tau = \nabla_s \gamma_{lv} = \left(\frac{d\gamma_{lv}}{d\Gamma}\right)\nabla_s \Gamma \quad (34)$$

where $\Gamma(\boldsymbol{x},t)$ is the surfactant surface-concentration, which is governed by the following advection-diffusion equation:

$$\frac{\partial\Gamma}{\partial t} + \nabla_s \bullet (\Gamma \boldsymbol{u}_s) + \Gamma\,(\nabla_s \bullet \boldsymbol{n})\,(\boldsymbol{u}\bullet\boldsymbol{n}) = D_s \nabla_s^2 \Gamma. \quad (35)$$

The flux of the surfactant depends on the tangential component of the surface velocity, $\boldsymbol{u}_s = \left(\underline{\underline{I}} - \boldsymbol{nn}\right).\boldsymbol{u}$, the mean curvature of the interface, $\nabla_s \bullet \boldsymbol{n}$, and the surfactant surface diffusion coefficient, D_s. Soluble surfactants require

the specification of the interfacial adsorption/desorption kinetics relating the surface concentration, Γ, to the bulk concentration, C, for which the governing transport equation is as

$$\frac{\partial C}{\partial t} + \boldsymbol{u} \bullet \nabla C = D_B \nabla^2 C \tag{36}$$

where D_B refers to the bulk diffusion coefficient. Further, for thin film flows on a flat substrate, the variation of liquid thickness is determined from the following equation:

$$\frac{\partial h}{\partial t} - \nabla \bullet \left(\frac{h^3}{3\mu} \nabla p - \frac{h^2}{2\mu} \nabla \gamma_{lv} \right) = 0\,. \tag{37}$$

Equations (35), (36) and (37) can be combined together to depict the dependence of the surface tension on the surfactant concentration and the surface velocity, $\boldsymbol{u}_s = (h\nabla\gamma_{lv}/\mu) - h^2\nabla p/(2\mu)$.

Capillary Spreading

Another variant of the surface tension driven flow that is of potential interest to the microfluidics research community is the capillary spreading phenomenon. Of particular interest can be the spreading of liquids on rough homogeneous substrates or on heterogeneous substrates with hydrophobic and hydrophilic stripes. For smooth homogeneous substrates, the radial advancement of a liquid of volume $\forall$ has been observed by Tanner [4] as

$$r(t) \sim \left(\frac{\gamma}{\mu} \forall^3 t \right)^{\frac{1}{10}} \tag{38}$$

which shows a rather weak dependence on time. However, careful analysis has revealed that a thin precursor film advances at a rate proportional to $\sqrt{t}$, following standard diffusion dynamics.
To illustrate the flow behaviour during capillary spreading in non-smooth surfaces, one may refer to the classical example of liquid spreading in V-shaped microgrooves (see Fig. 2 for the geometrical features of the cross section of the groove). For low Capillary number, the pressure drop across the groove is given by

$$\Delta p = p(x) - p(0) = -\frac{\gamma}{R(x)} \tag{39}$$

where $1/R(x) = \sin(\alpha - \theta)\tan\alpha / h(x,t)$. Following a quasi one-dimensional analysis, the flow rate can be obtained as [5]

$$Q = -\frac{h^4(x,t)}{\mu}\Gamma(\theta,\alpha)\frac{\partial p}{\partial x} \tag{40}$$

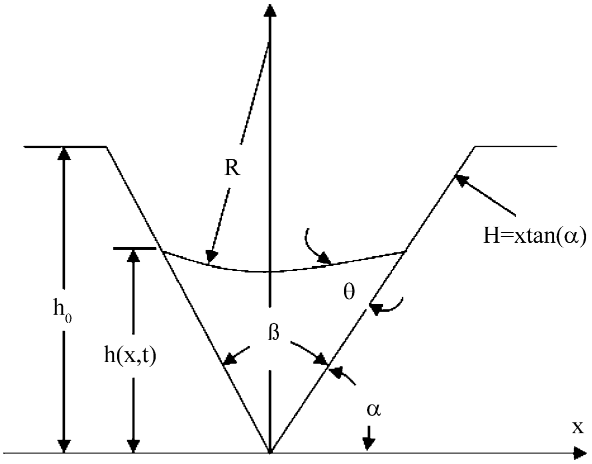

Surface Tension Driven Flow, Figure 2 Geometrical features pertinent to the liquid spreading in a V-microgroove

where

$$\Gamma(\theta,\alpha) \approx \Gamma(\alpha,\alpha) \left[\frac{h_c(\theta,\alpha)}{h_0} \right]^3 \left[\frac{\widehat{A}(\theta,\alpha)}{\cot\alpha} \right]^{\frac{1}{2}}\,. \tag{40a}$$

In Eq. (40a), h_c is the height of the fluid at the middle of the groove, and is given by

$$h_c(\theta,\alpha) = h_0 \left[1 + \cot\alpha \frac{\cos(\alpha-\theta) - 1}{\sin(\alpha-\theta)} \right]\,. \tag{40b}$$

The parameter $\Gamma(\alpha,\alpha)$ can be analytically approximated as

$$\Gamma(\alpha,\alpha) \approx \frac{1}{6} \frac{\cot^3\alpha + 3.4\cot^4\alpha + \cot^5\alpha}{1 + 3.4\cot\alpha + 4\cot^2\alpha + 3.4\cot^3\alpha + \cot^4\alpha}\,. \tag{40c}$$

Also, the function $\widehat{A}(\theta,\alpha)$ in Eq. (40a) is related to the cross sectional area $A(x,t)$ of the liquid inside the groove, as

$$A(x,t) = h^2(x,t)\widehat{A}(\theta(x,t),\alpha) \tag{40d}$$

where

$$\widehat{A}(\theta,\alpha) = \frac{\sin^2(\alpha-\theta)\tan\alpha - (\alpha-\theta) + \sin(\alpha-\theta)\cos(\alpha-\theta)}{\tan^2\alpha\sin^2(\alpha-\theta)}\,. \tag{40e}$$

S

The evolution of the height of the liquid inside the groove is derived from the continuity and the momentum conservation equation as

$$\frac{\partial h^2(x,t)}{\partial t} = \frac{D}{h_0}\frac{\partial}{\partial x}\left[h^2(x,t)\frac{\partial h(x,t)}{\partial x}\right] \tag{41}$$

where D is the diffusion coefficient, given by

$$D = \frac{\gamma h_0}{\mu\kappa(\theta_0,\alpha)} \,. \tag{41a}$$

In Eq. (41a)

$$\kappa(\theta_0,\alpha) = \frac{\Gamma(\theta_0,\alpha)\sin(\alpha-\theta_0)\tan\alpha}{(\theta_0,\alpha)} \,. \tag{41b}$$

It is interesting to note here that the value of D is positive if $\alpha > \theta_0$, which is equivalent to having a concave free surface. For $\alpha < \theta_0$, on the other hand, no capillary wicking takes place. Equation (41) has been solved in the literature [5] under various conditions. In the simple case of $h(0,t) = h_0$, a similarity solution can be attempted with $h(x,t) = h_0\phi(\eta)$, where $\eta = x/\sqrt{Dt}$. An approximate solution, in that case, can be obtained as

$$\phi(\eta) = -\frac{1}{2}\eta_0(\eta-\eta_0) - \frac{1}{2}(\eta-\eta_0)^2 - \frac{1}{108\eta_0}(\eta-\eta_0)^3 + \ldots \tag{42}$$

where η_0 is the location where the solution goes to zero and stays at zero. A major physical consequence of the above analysis is that the diffusion dynamics dominate for the capillary filling of microgrooves, and the leading edge (spreading front) propagates as

$$x_0(t) = \eta_0(\theta_0,\alpha)\sqrt{Dt} \,. \tag{43}$$

Thus, spreading increases with the depth of the groove, since $D \propto h_0$. The similarity solution also implies that free surface of the liquid spreading remains self-similar downstream.

By following an approach analogous to the above, Darhuber et al. [6] studied the dynamics of capillary spreading along hydrophobic microstripes. The smooth surface was processed chemically to create narrow hydrophilic stripes on a hydrophobic background. The equation governing the self-similar solutions, in that case, can be described as

$$\frac{\mathrm{d}}{\mathrm{d}\eta}\left(\phi^3\frac{\mathrm{d}\phi}{\mathrm{d}\eta}\right) + \frac{\eta}{2}\frac{\mathrm{d}\phi}{\mathrm{d}\eta} = 0 \tag{44}$$

where the similarity variables are defined similarly as before. An approximate solution in this case is given by

$$\phi(\eta) \approx \left(1 - \frac{\eta}{\eta_0}\right)^{\frac{1}{3}} \tag{45}$$

where $\eta_0 \approx 0.87$. Thus, the spreading front advances as $x(t) \propto \sqrt{Dt}$, where $D = 64\gamma h_0^3/35\mu w^2$, w being the width of the microstripe. The average streamwise speed, $\bar{u}$, scales as $\bar{u} \sim \gamma w^4/\mu x$.

Surface Tension Driven Flow in Microchannels

Surface tension driven flows not only take place in open conduits such as microgrooves, but are also quite common in capillary tubes and microchannels. In a generic form, one can write the equation of motion describing the capillary advancement as

$$\frac{\mathrm{d}}{\mathrm{d}t}(MV_\mathrm{c}) = \sum F \tag{46}$$

where M is the fluid mass being transported, V_c is the velocity of its centre of mass and $\sum F = F_\text{surface tension} + F_\text{viscous} + F_\text{gravity}$. To illustrate the use of the above equation in simple forms, one may consider the viscous, incompressible and Newtonian flow against the direction of gravity along a long cylindrical capillary of radius r. For this case, one may first assume that $M = \rho\pi r^2 z$, $V_\mathrm{c} = \dot{z}$, $F_\text{surface tension} = 2\pi r\gamma\cos\theta$, $F_\text{viscous} = -8\pi\mu z\dot{z}$(assuming fully developed flow) and $F_\text{gravity} = -\rho g z$, where z is axial displacement of the capillary front. This leads to the following equation of capillary motion

$$\rho[z\ddot{z} + \dot{z}^2] = \frac{2}{r}\gamma\cos\theta - \frac{8}{r^2}\mu z\dot{z} - \rho g z \,. \tag{47}$$

Equation (47) suffers from a fundamental drawback that as $t \to 0$, $M \to 0$ (since $z \to 0$), giving rise to an ill-posed problem with infinite initial acceleration. This ambiguity can be physically resolved by referring to the equation of continuity, based on which it can be inferred that in the onset of the capillary rise, the liquid present in the dipped portion of the capillary and the bulk reservoir to which it is connected also starts moving at the same time. This additional mass of fluid inducted into the motion initially is known as the added mass, m_0. This added mass can be approximated by executing a potential flow analysis for an incoming spherical liquid element of radius r that moves with a velocity $\dot{z}$. Executing this analysis, one can obtain, for a cylindrical tube [7],

$$m_0 \approx \frac{3\rho\pi r^3}{8} \,. \tag{48}$$

The above is equivalent to the introduction of an additional term in the left hand side of Eq. (56), in the form $3\rho r\ddot{z}/8$, which eliminates the prediction of an unrealistic initial burst as $t \to 0^+$.

Equation (47), with the modifications introduced by Eq. (48) physically represents a rather simplified situation. In reality, a number of other complicating factors may be present, resulting in further modifications in the equation of capillary advancement. For example, the capillary walls can adsorb surfactants from the bulk solution, leading to a continuous variation in the surface tension coefficient. The adsorption of the surfactant, Γ_{lv}, can lead to an axial gradient of surface tension, following the Gibbs equation:

$$\gamma = \gamma_0 - \bar{R}T \int_{C=0}^{C(z,t)} \Gamma_{\mathrm{lv}} d \ln C \tag{49}$$

where C is the surface concentration of the surfactant. Phenomenologically, one may carry out an approximate analysis by posing an exponentially decaying time-dependence of the second term appearing in Eq. (49), such that

$$\gamma = \gamma_0 - \Delta\gamma\phi_{\mathrm{B}}(t) \tag{50}$$

where

$$\Delta\gamma = \gamma_0 - \gamma_\infty\,, \quad \phi_{\mathrm{B}}(t) = 1 - \exp(-\beta t)\,. \tag{50a}$$

Here γ_0 is the initial surface tension, γ_∞ is the equilibrium surface tension and β is a relaxation constant. This effect can be introduced in Eq. (47) by first differentiating the same with respect to time, neglecting the terms containing the products $\dot{z}\ddot{z}$ and $z\dddot{z}$ in the quasi-steady limit, to set

$$-\frac{2\beta\Delta\gamma\cos\theta}{r}\exp(-\beta t) = \frac{8\mu}{r^2}[\dot{z}^2 + z\ddot{z}] + \rho g\dot{z}\,. \tag{51}$$

Typical numerical solutions of Eq. (51), following Zhumud et al. [8], are presented in Fig. 3. A maximum occurs in the characteristic displacement curves only when the surface tension relaxation is not as fast as compared to the capillary filling. More simplistic scaling estimates in the capillary rise phenomenon can readily be obtained by noting that within certain limits, the capillary rise represents a quasi-steady process, in which the amount of surfactant adsorbed to the solid/liquid interface per unit time is equal to that transported to the liquid/vapour interface by diffusion, which implies

$$2\pi r\Gamma_{\mathrm{sl}}^m dz \sim \pi r^2 D\frac{C_{\mathrm{b}}}{\sqrt{Dt}}\,\mathrm{d}t \tag{52}$$

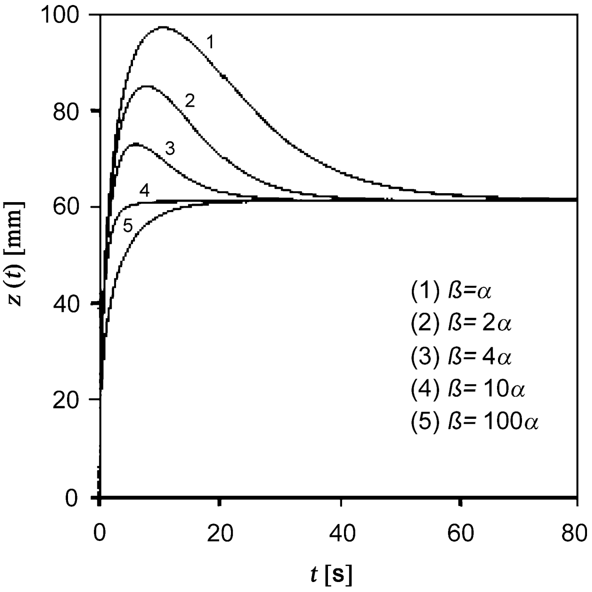

Surface Tension Driven Flow, Figure 3 Simulated capillary rise dynamics for aqueous solutions of surfactants. In the figure, $\alpha = \rho g r^2/8\eta z_{t\to\infty}$. For obtaining the plots, following data are taken: $r = 10^{-4}$ m, $\eta = 10^{-3}$ Pa, $\rho = 10^3$ kg/m^3, $\theta = 0$, $\alpha = 8.3 \times 10^{-2}$ s^{-1}

where Γ_{sl}^m is the adsorption capacity of the monolayer per unit area and C_{b} is the bulk concentration of the surfactant. From Eq. (52), one can obtain

$$z(t) \sim \frac{rC_{\mathrm{b}}}{\Gamma_{\mathrm{sl}}^m}\sqrt{Dt} \tag{53}$$

which physically implies the condition of a diffusion-limited capillary advancement.

The real physical picture of surface tension driven capillary motion appears to be much more complicated than what is depicted by Eq. (47). First of all, the viscous resistance terms need to be modeled more carefully. In reality, as the fluid enters the microchannel, the flow passes through a short entrance region, followed by a fully developed region. A third region, namely the meniscus traction region, also comes into play, because of the influence of the free surface of the meniscus on the flow. This can alter the velocity profiles significantly, and the predicted drag force can appear to be significantly different from that obtained from the considerations of a fully developed Poiseullean velocity profile. These effects have recently been taken into account for analyzing the surfacetension driven flow of blood in microfluidic channels. Details of the underlying physical principles to model the modified viscous drag are presented in the article on ► capillary filling, and are not repeated here for the sake of brevity. Another interesting and important consideration is

S

the modeling of the dynamic evolution of an apparent contact angle, which can effectively represent a gross manifestation of the sub-continuum picture close to the interfaces that cannot be directly resolved in the system-level calculations. It needs to be noted in this context that the capillarity effect within the microchannel essentially implies that a fluid–fluid interface and the fluid–solid interface intersect to form a common line of contact, or a tri-junction. In order to model such moving contact lines appropriately, one needs to first qualitatively assess the physical phenomena influencing the capillarity. In this regard, it has been experimentally shown that points on the interfacial lines arrive at the contact line within a finite time span. Therefore, one must pose an effective slip law that relieves a force singularity condition by ensuring that a finite force is necessary to move the contact lines of a fluid, irrespective of the no-slip boundary conditions classically being applied at the channel walls. In order to mathematically ensure this effect, one needs to pose a condition on the contact angle θ, as a function of velocity of the contact line. In a physical sense, this departure of contact angle from its static equilibrium value is mainly due to viscous bending of the interface near the contact lines. Although exact mathematical quantification of the dynamic evolution of this contact angle may be somewhat involved, experimental studies have revealed that the apparent dynamic contact angle, θ_a, that the liquid forms with the solid surface is closely described by a universal scaling relationship at low speeds, known sometimes as Tanner's law, which can be mathematically stated as

$$\theta_a \sim \mathrm{Ca}^{\frac{1}{3}} \tag{54}$$

where $\mathrm{Ca} = \mu u/\gamma$ is the capillary number, and u is velocity of the contact line. However, in order to quantify the proportionality constant, one must resolve the asymptotic behavior of the thin liquid film in vicinity of the microchannel wall. This thin film region can further be divided into two parts, namely, (a) a lubricating film region followed by (b) a precursor film region as one moves along the direction of wetting. In the precursor film region, one expects the interfacial length scales to approach molecular scales, as intermolecular forces become important. Behind the lubricating film, on the other hand, the length scales are quite large (of the order of r), and a potential challenge remains in devising a quantitative expression for dynamic evolution of θ_a by asymptotic matching from solutions to these regions of widely different length scales. For analysis of the same, one may assume negligible gravitational effects (typically characterized by a low Bond number, $\mathrm{Bo} = \rho g r^2/\gamma$), and viscosity of the gas phase negligible in comparison to that of the liquid phase so that dynamics of the two phases are essentially decoupled. In that situation, the domain of interest can be divided into two regions, namely

- the outer region where the lateral and vertical length scales are both O(1) and
- the inner lubrication region in which the lateral and vertical length scales are $O(\mathrm{Ca}^{\frac{1}{3}})$ and $O(\mathrm{Ca}^{\frac{2}{3}})$, respectively, as capillary and viscous forces balance.

Further division of the inner region may be necessary when the intermolecular forces become important at very thin films. In the lubricating film region, this effect can be incorporated by invoking an extra term of the same dimension as that of pressure in the overall force balance, which can be described as $A/6\pi z^3$, z being the film thickness. This term is known as the ▶disjoining pressure. The parameter A is called the Hamaker's constant (for a further detailing, see the next sub-section), which is negative for wetting fluids. It is important to note here that one needs to be extremely careful in introducing intermolecular forces into a continuum model such as the Navier–Stokes equation. In particular, the surface tension force, which is due to intermolecular forces between the gas and liquid phases, cannot be considered separately from the Van der Waals forces between the gas and the solid phases for very thin films. If one introduces a molecular length scale R_m as $R_m = (|A|/6\pi\gamma)^{\frac{1}{2}}$, or its dimensionless counterpart $\lambda = R_m/r$; the above-mentioned model for lubricating film is valid if its film thickness is much larger than R_m, i. e., $\mathrm{Ca}^{\frac{2}{3}} \gg \lambda$. Since R_m is typically of the order of a few Angstroms, while a typically capillary radius is of the order of 10^{-1} mm, the lower bound on Ca is of the order of 10^{-4}. Beyond this lower bound, the continuum model remains valid for the lubricating film. At relatively larger Ca, the intermolecular forces would turn out to be less effective, so that dependence of Tanner's law on λ becomes progressively weaker. For a significantly large Ca, the meniscus speed may exceed the wetting speed and the meniscus may reverse its curvature as the contact angle passes through 90° . However, the foregoing analysis assumes that such situations do not occur, and accordingly, it remains valid for $\theta < 90°$. An asymptotic matching may accordingly be done between the outer region and the precursor film through the lubricating film at the inner region. At the front of this region, however, intermolecular forces and a vanishingly small film (spread by fast wetting) stipulate a hyperbolic decay of the film thickness towards zero. Accordingly, a universal relationship for dynamic evolution of the contact angle can be obtained as [9]

$$|\tan\theta_a| = 7.48\mathrm{Ca}^{1/3} - 3.28\lambda^{0.04}\mathrm{Ca}^{0.293} \tag{55}$$

It can be noted here that λ is typically of the order of 10^{-8} for wetting fluids flowing through a microcapillary channel having hydraulic radius of the order of 1 mm. Physically, for very low values of Ca, the corresponding correction term appearing in Eq. (55) may become important, where intermolecular forces come significantly into play and $\tan\theta_a$ diverges slightly away from the asymptotic behavior characterized by Eq. (54) towards lower values. Mathematically, Eq. (55) has been derived from a matched asymptotic analysis that matches a static outer region to the precursor adhering the wall, through an intermediate lubricating film. The problem, hence, is characterized by three length scales, namely, the capillary radius, film thickness and molecular length scale (λ). This interconnection is captured by Eq. (55), and the outcome is very much analogous to the slip model obtained by Hoffman [10], which gives the variation of θ_a as a function of slip length as:

$$g(\theta_a) = g(\theta_a(0)) + \mathrm{Ca}\ln\left(\frac{k}{l_s}\right) \tag{56}$$

where the slip length scale is given by: $l_s \sim l_d/\mathrm{Ca}$, l_d being of the order of wall roughness and k being a slip-model dependent constant. Exact for of $g(\theta_a)$ is available in Hoffman [10], which is as

$$g(\theta_a) = \int_0^\theta d\phi\,[f(\phi)]^{-1} \tag{57}$$

where

$$f(\phi) = \frac{2\sin\phi(A+B+C)}{D+E} \tag{57a}$$

where

$$A = q^2\left(\phi^2 - \sin^2\phi\right),$$

$$B = 2q\left[\phi(\pi-\phi) + \sin^2\phi\right],$$

$$C = (\pi-\phi)^2 - \sin^2\phi,$$

$$D = q\left(\phi^2 - \sin^2\phi\right)[(\pi-\phi) + \sin\phi\cos\phi],$$

$$E = (\phi - \sin\phi\cos\phi)\left[(\pi-\phi)^2 - \sin^2\phi\right].$$

In Eq. (57a), q is the ratio of viscosity of the liquid and the vapour. Typical values of the factor k, as reported in the literature [10], can be of the order of 10^{-1} to 10.

Molecular Level Modeling of Wetting Phenomena

The mathematical descriptions outlined in most of our preceding discussions represents a continuum-based picture of the wetting phenomenon and the consequent surface tension driven flow. However, from a more fundamental perspective, these are strongly influenced by the underlying molecular picture; more precisely, through the intermolecular interaction potentials (adhesion and cohesion). One may quantify the net effect of the interaction potentials on the wetting behaviour by considering a liquid film of thickness l on a solid substrate. For strong solid–liquid adhesive interactions, the system can lower its free energy by increasing the distance between the solid–liquid and the liquid–vapour interfaces. This leads to a net repulsion force per unit area between the solid–liquid and the liquid–vapour interfaces, which is called the disjoing pressure, $\Pi(l)$. The disjoing pressure can be related to the effective interface potential, $V(l)$ as per the following relationship:

$$\Pi(l) = -\frac{\mathrm{d}V(l)}{\mathrm{d}l}. \tag{58}$$

The excess free energy of the liquid film, accordingly, can be estimated as

$$E_s(l) = \gamma_{lv} + \gamma_{sl} + V(l). \tag{59}$$

A fundamental estimate of the excess free energy of the liquid film can be provided by the density functional theory, which is based directly on the microscopically specified molecular interactions. In its simplest form, the free energy functional, E_s, can be represented as [11]

$$\begin{aligned} E_S = {} & \underbrace{E_{hc}\left(\{\rho(\mathbf{r})\}, T\right)}_{\text{hard core interactions}} \\ & + \frac{1}{2}\int \underbrace{d^3r d^3r' \tilde{w}\left(|\mathbf{r}-\mathbf{r}'|\right)\left(\rho(\mathbf{r})\rho(\mathbf{r}') - \rho_b^2\right)}_{\text{long range particle-particle interactions}} \\ & + \int \underbrace{d^3r U(\mathbf{r})\rho(\mathbf{r})}_{\text{particle-wall interactions}} \end{aligned} \tag{60}$$

where $\tilde{w}\left(|\mathbf{r}-\mathbf{r}'|\right)$ is the long-ranged part of the particle-particle interaction potential in the liquid phase, ρ_b is the particle-density far from the wall, and $U(\mathbf{r})$ is the interaction potential of a fluid particle with the wall particles. The density profile, $\rho(\mathbf{r})$ can be found by minimizing Eq. (60). Despite being quite straight forward in principle, a execution of this task, however, is rather difficult, owing to the slow decay of parts of the interaction potential. Because of such practical constraints, quantitative predictions based

S

on numerical solutions of the full density functional theory has been rather limited, except for wetting behaviour of simple atoms or molecules (e. g. He) on simple substrates (e. g. Cs) at zero temperature [12]. However, for He, quantum effects also need to be taken into account while formulating the density functional, which takes the following form [12]:

$$E_S = \frac{\hbar^2}{2m} \int \underbrace{d^3 r \left\{ \nabla \left[\rho^{\frac{1}{2}} \right] (\mathbf{r}) \right\}^2}_{\text{quantum kinetic energy}} + \int \underbrace{d^3 r U(\mathbf{r}) \rho(\mathbf{r})}_{\text{particle-wall interactions}} + \underbrace{H_{NL}}_{\text{short range correlations in the liquid}} \tag{61}$$

where the non-local Hamiltonian, H_{NL}, is given by

$$H_{NL} = \frac{1}{2} \int d^3 r d^3 r' \rho(\mathbf{r}) \rho(\mathbf{r}') \tilde{w}(|\mathbf{r} - \mathbf{r}'|) + \frac{c}{2} \int d^3 r \rho(\mathbf{r}) [\bar{\rho}(\mathbf{r})]^{1+\gamma} . \tag{61a}$$

Phenomenologically, H_{NL} accounts for short-range interactions and correlations between the He atoms, and involves a spatially-averaged density, $\bar{\rho}$. One major limitation of expression (61), however, is that it is restricted to $T = 0$, so that it cannot predict the wetting temperature. For wetting of quantum liquids, an alternative approach was introduced by Cheng et al. [12]. As per this consideration, under the assumptions of a sharp interface bounding the wetting layer, the surface free energy of the substrate can be approximated as

$$\gamma_{sl} = \gamma_{sv} + \tilde{\gamma}_{sl} + \rho_b \int_{z_{min}}^{\infty} U(z) dz \tag{62}$$

where $\tilde{\gamma}_{sl}$ is the cost of making the liquid density vanish at the substrate, and is taken to be equal to γ_{lv}. This simple model also assumes the liquid density in the film to be same as the bulk liquid density. The potential is taken as follows:

$$U(z) = \frac{4C_3^3}{27D^2 z^9} - \frac{C_3}{z^3} \tag{63}$$

where C_3 gives the amplitude of the van der Waals interaction between one particle and the substrate, and D is the well-depth of the substrate-adsorbate interaction potential. In addition, if z_{min} is taken to be the minimum of $V(l)$, the wetting transition temperature can be calculated by solving

$$\left(C_3 D^2 \right)^{\frac{1}{3}} = \frac{3.33\gamma(T)}{\rho_l - \rho_v} . \tag{64}$$

It is important to note here that for wetting phenomena, an important contribution to the disjoining pressure arises from the van der Waals interaction ($w(r) \propto 1/r^6$), which includes dipole-dipole, dipole-induced dipole and induced dipole-induced dipole interactions. Performing a volume integral over all the molecules present in the two half-spaces bounding the film, one finds a decay of the form $\Pi(l) \approx A/(6\pi l^3)$, where A is known as the Hamaker constant, which physically gives the amplitude of the interaction. Fundamentally, the Hamaker constant can be calculated in terms of the dielectric properties of the three phases. For example, one can employ a simple approximation by first considering the contribution due to dipolar interactions, given by the zero-frequency permittivities of the respective phases, as [13]

$$A_{\nu=0} = -\frac{3}{4} k_B T \frac{(\varepsilon_1 - \varepsilon_3)(\varepsilon_2 - \varepsilon_3)}{(\varepsilon_1 + \varepsilon_3)(\varepsilon_2 + \varepsilon_3)} \tag{65}$$

where 1(solid) and 2(vapour) denote the phases in the two half-spaces and 3(liquid) is the intermediate phase. For non-zero frequencies, on the other hand, the contribution comes from the relative refractive indices of the three phases, as

$$A_{\nu>0} = -\frac{3h\nu_{UV}}{16\sqrt{2\left(n_1^2 + n_3^2\right)\left(n_2^2 + n_3^2\right)}} \frac{\left(n_1^2 - n_3^3\right)\left(n_2^2 + n_3^2\right)}{\sqrt{\left(n_1^2 + n_3^2\right)} + \sqrt{\left(n_2^2 + n_3^2\right)}} \tag{66}$$

where h is the Planck's constant and ν_{UV} ($\approx 2 \times 10^6$ Hz) is the UV frequency for which the relative refractive indices of the phases become identical (close to unity). In practice, the Hamaker constant is the sum of the two contributions given by Eqs. (65) and (66). Equaion (65) retains the $1/l^2$ dependence for all distances. However, Eq. (66) is subject to retardations, since interactions between dipoles travel only at the speed of light. It also follows from Eq. (66) that for two identical phases1 and 2 separated by a dissimilar phase 3, the net effect is an attractive van der Waals interaction ($A < 0$) between the two interfaces. In typical situations involving surface tension driven flows, the nature of

the contribution given by Eq. (66) is dominated by the relative refractive index difference between the liquid and the solid, since the refractive index of the vapour would generally be close to unity. If the liquid has a refractive index between that of the solid and the vapour, then $A > 0$ and the formation of the wetting layer is preferred (because of an effective repulsion between the interfaces).

A close inter-connection between the molecular and the continuum theories of surface tension driven phenomena can be provided by the equilibrium spreading coefficient, $S = \gamma_{sv} - \gamma_{sl} - \gamma_{lv}$, which physically represents the surface free energy difference between partial and complete wetting. When S is negative, it becomes unfavourable to replace the solid-vapour interface by two others, as pertinent to the partial wetting state. The phenomenological theory of Cahn [14] gives an explicit way to calculate the value of S, from molecular considerations. As per this theory, the surface free energy functional is given as

$$E_s = \underbrace{\phi(\rho_s)}_{\text{wall interaction}} + \int_0^{\infty} \underbrace{\left[\omega(\rho) + c^2/4\left(\frac{d\rho(z)}{dz}\right)^2\right] dz}_{\text{liquid–vapour interaction}} \tag{67}$$

where ω is the grand potential per unit volume, $\rho(z)$ is the density profile as a function of the distance z from the solid surface and $\rho_s = \rho(0)$ is the value of density at the substrate. In principle, Eq. (67) intends to represent a similar physical behaviour as that depicted by Eq. (60), except for the fact that long-ranged interactions are not included in Eq. (67). The wall-interaction term in Eq. (67) is usually expanded to the second order, as

$$\phi(\rho_s) = -h_1\rho_s - g\rho_s^2/2 \tag{67a}$$

where the parameters h_1 and g are referred to as the short-range surface field and the surface enhancement field, respectively. The parameter h_1 describes the preference of the substrate for either the liquid or the vapour, and can be taken proportional to the difference between the substrate–liquid and substrate–vapour interfacial tensions. If $h_1 > 0$, the liquid is preferred at the wall, whereas for $h_1 < 0$, the vapour is preferred. The parameter g (usually a small negative number) is a measure of the 'missing' liquid–liquid interactions due to the fact that a liquid molecule near the wall has a small number of liquid neighbours than the bulk. The grand potential in Eq. (67) can be estimated by employing the classical Landau expansion around the critical point (in units of $k_B T$), in the form of

$$\omega = a_2\rho^2 + a_4\rho^4 \,. \tag{67b}$$

Based on this, the spreading coefficient, S, can be calculated explicitly, as

$$S = c\rho_0/12\left(\left[\kappa^2 + 4(1+\chi)\right]^{\frac{3}{2}} - \left[\kappa^2 + 4(1-\chi)\right]^{\frac{3}{2}}\right) + 3\chi\kappa/4 - 4c\rho_0^3/3 \tag{68}$$

where $\pm\rho_0$ are the bulk densities, $\chi = h_1/c\rho_0^2$ and $\kappa = g/c\rho_0$.

Key Research Findings

Numerous applications of surface tension driven microflows have been presented in the recent literature. Jun and Kim [15] demonstrated the pumping of fluids in microchannels using the movement of a single or multiple vapor bubbles The pumping mechanism required no micromechanical moving components for actuation, and essentially operated by utilizing an asymmetric heating that creates a variation in vapor pressure and surface tension due to the heater-induced temperature gradient along the channel. A heat and mass transfer analysis was performed to model the pumping mechanism and to estimate the pumping capability of the device. Experimental results were also presented to establish the proposition. Chakraborty and Som [16] theoretically determined the rate of heat transfer in a thin evaporating liquid film flowing along the walls of a microchannel under the combined action of surface tension and gravity. Analytical solutions of conservation equations, in both liquid and vapour phases, were obtained in their study. Lee and Kim [17] demonstrated the first microelectromechanical systems (MEMS) device that adopts surface tension as the driving force, by driving a liquid-metal droplet in an electrolyte-filled capillary, by locally modifying the surface tension with electric potential. Certain key issues in practical implementation were identified and investigated, including the problems of material compatibility, electrode polarization, and electrolysis, as well as the micromachining process. Based on these understandings, they demonstrated a liquid micromotor in the form of an electrolyte and liquid-metal droplets rotating along a microchannel loop. Smooth and wear-free rotation of the liquid system was shown at a speed of approximately 40 mm/s, with a driving voltage of only 2.8 V and a little power consumption (10 – 100 W). Chakraborty [18] investigated the breakup of viscous liquid droplets on surface tension modulation during micro-welding metal transfer. This study was motivated by the fact that viscous jets of a molten metal ready to be transferred into the arc welding pools are inherently unstable. From this study, a variation of the time required for droplet formation was obtained as

a function of the surface tension modulation, corresponding to different instability modes. Chan and Yang [19] presented theoretical and experimental studies of the surface-tension-driven, two-immiscible liquid–liquid displacement in a horizontal capillary. A one-dimensional mathematical model was developed to describe the capillary displacement of a fixed liquid column by another liquid that continuously flows into the capillary by surface tension. Experiments for a water column displaced by silicon oil were carried out to examine the underling dynamics in practice. It was found that a faster and longer displacement was achieved for a shorter water column in a larger capillary. Their theoretical predictions agreed well with the experimental results. In a recent study, Chakraborty [20] devised a novel mathematical approach to analyze the surface tension driven flow of blood from a droplet into a microcapillary channel. Special attention was devoted to estimate the effects of variable hydraulic resistance over different flow regimes, influence of suspended RBC particulates on the non-Newtonian flow characteristics and implications of a dynamically-evolving contact angle. These studies have subsequently been extended for capillary transport in presence of electroosmotic effects [21]. There have also been other recent applications on modeling of surface tension driven microflows (for details, please refer to the articles on ► electrocapillary, ► capillary filling and ► droplet dynamics in microchannels), elucidating comprehensive applications of the underlying theory.

Future Directions For Research

Future research in the modeling of surface tension driven flows can be directed towards the development of integrated multi-scale models that can more effectively represent the sub-continuum (essentially, molecular level) level transport features in the framework of continuum based descriptions of the surface tension aided microfluidic transport.

Cross References

- ► Applications Based on Electrowetting
- ► Boundary Slip of Liquids
- ► Bubble Dynamics in Microchannels
- ► Capillary Filling
- ► Chaotic Flow
- ► Compute Mixing Efficiency
- ► Digital Microfluidics
- ► Droplet and Bubble Formation in Microchannels
- ► Droplet Based Lab-on-Chip Devices
- ► Droplet Despensing
- ► Droplet Dynamics in Microchannels
- ► Droplet Evaporation
- ► Droplet Microreactors
- ► Electrocapillary
- ► Electrowetting and Droplets
- ► Transport of Droplets by Acoustics
- ► Transport of Droplets by Thermal Capillarity
- ► Wetting and Spreading

References

1. Levich VG, Krylov VS (1969) Surface-tension-driven phenomena. Ann Rev Fluid Mech 1:293–316
2. Mazouchi A, Homsy GM (2000) Thermocapillary migration of long bubbles in cylindrical capillary tubes. Phys Fluids 12:542–549
3. Shapiro B, Moon H, Garrel RL, Kim C-J (2003) Equilibrium behaviour of sessile drops under surface tension: applied electric fields and material variations. J Appl Phys 93:5794–5811
4. Tanner LH (1979) The spreading of silicone oil drops on horizontal surfaces. J Phys D 12:1473–1484
5. Romero LA, Yost FG (1996) Flow in an open channel capillary. J Fluid Mech 322:109–129
6. Darhuber AA, Troian SM, Reisner WW (2001) Dynamics of capillary spreading along hydrophobic microstripes. Phys Rev E 64(1–8):031603
7. Yih CH (1995) Kinetic-energy mass, momentum mass, and drift mass in steady irrotational subsonic flow. J Fluid Mech 297:29–36
8. Zhumud BV, Tiberg F, Hallstensson K (2000) Dynamics of capillary rise. J Colloid Interface Sci 228:263–269
9. Kalliadasis S, Chang HC (1994) Apparent dynamic contact-angle of an advancing gas-liquid meniscus. Phys Fluids 6:16–23
10. Hoffman RL (1975) A study of the advancing interface I. Interface shape in liquid–gas systems. J Colloid Interface Sci 50:228–235
11. Schick M (1990) Liquids at Interfaces. In: Charvolin JJ, Zinn-Justin J (eds) Liquids at Interfaces, Les Houches Session XLVIII. Elsevier, Amsterdam, pp 415–497
12. Cheng E, Cole M, Dupont-Roc J, Saam W (1993) Novel wetting behaviour in quantum fluids. Rev Mod Phys 65:557–567
13. Israelachvili J (1992) Intermolecular & Surface Forces. Academic, London
14. Cahn J (1977) Critical-point wetting. J Chem Phys 66:3667–3672
15. Jun JK, Kim CJ (1998) Valveless pumping using traversing vapour bubbles in microchannels. J Appl Phys 83:5658–5664
16. Chakraborty S, Som SK (2005) Heat Transfer in an evaporating thin liquid film moving slowly along the walls of an inclined microchannel. Int J Heat Mass Transf 48:2801–2805
17. Lee J, Kim CJ (2000) Surface-tension-driven microactuation based on continuous electrowetting. J Microelectromech Syst 9:171–180
18. Chakraborty S (2005) Analytical investigations on break up of viscous liquid droplets on surface tension modulation during welding metal transfer. Appl Phys Lett 86(1–3):174104
19. Chan WK, Yang C (2005) Surface-tension-driven liquid–liquid displacement in a capillary. J Micromech Microeng 15:1722–1728
20. Chakraborty S (2005) Dynamics of capillary flow of blood into a microfluidic channel. Lab Chip 5:421–430
21. Chakraborty S (2007) Electroosmotically driven capillary transport of typical non-Newtonian bio-fluids in rectangular microchannels. Anal Chim Acta 605:175–184

Surface Texture

► Surface Roughness Measurement

Surface Topography

► Surface Roughness Measurement

Surface Tracking

► Numerical Techniques for Free Surface Flows: Interface Capturing and Interface Tracking

Surface Transformation

► Surface Modification, Methods

Surface Treatment

► Surface Modification, Methods

Suspensions

► Non-Newtonian Fluids in Microfluidics

Switching Etching

► ICP Etching

Synthesis of Biological Molecules in Microfluidics

► Biomolecular Synthesis in Microfluids

Synthesis of Polymer Molecules Using Microfluidics

► Polymer Synthesis within Microfluidic Reactor

Synthetic Jet

► Microsynthetic Jets

Tandem MS

► Mass Spectrometry

Taylor–Aris Dispersion

► Hydrodynamic Dispersion

Taylor Bubble Flow

► Taylor Flow in Microchannels

Taylor Dispersion

► Hydrodynamic Dispersion

Taylor Flow

► Microsegmented Flow

Taylor Flow in Microchannels

PANAGIOTA ANGELI, ASTERIOS GAVRIILIDIS
Department of Chemical Engineering, University College London, London, UK
p.angeli@ucl.ac.uk, a.gavriilidis@ucl.ac.uk

Synonyms

Taylor bubble flow; Bubble train flow; Segmented flow; Slug flow; Plug flow; Elongated bubble flow; Intermittent flow

Definition

Taylor flow is a type of gas–liquid flow pattern that consists of elongated bubbles with equivalent diameter usually many times that of the channel diameter, separated by liquid slugs (Fig. 1). The bubbles adopt a characteristic capsular shape and can either completely or nearly completely fill the channel cross-section where at most a thin liquid film separates them from the channel wall.

Chemical and Physical Principles

Definition of Small Channels

Taylor flow is a dominant pattern during gas–liquid flow in small channels. Channels are generally considered to be small when the surface tension forces dominate the gravitational forces. A measure of the relative importance of the two forces is given by the Bond or Eötvös number (both names are invariably used in the literature)

$$\text{Bo or Eö} = \frac{(\rho_g - \rho) g d^2}{\gamma} \tag{1}$$

where ρ_g and ρ are the gas and liquid densities, respectively, g is the gravitational acceleration, d is the tube diameter and γ is the surface tension. Investigators have suggested different values of the Bo or Eö number below which channels can be considered small, ranging from 0.88 to $(2\pi)^2$. Bretherton [1] has observed that a Taylor bubble no longer rises spontaneously in a water-filled capillary under the effect of gravity for Bo < 3.37 and this value can also be used to define small channels.

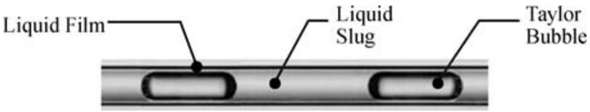

Taylor Flow in Microchannels, Figure 1 Gas–liquid Taylor flow

Flow Patterns

In small channels a number of flow patterns can be observed and the same terminology and classifications as in large channels are commonly used. Because of the dominance of the surface tension forces stratified flow is rarely observed in small channels. In general, bubble flow appears at low gas flowrates. As the gas flowrate increases Taylor bubbles form. With further increase in the gas flowrate annular flow appears with the liquid forming an annulus which wets the wall. At high gas and liquid flowrates, churn flow occurs where there is a liquid film at the wall and the gas flow in the center is interrupted by the frequent appearance of frothy bubbles and slugs.

As the dimensions of the channel reduce, Taylor and annular flows dominate, while patterns specific to small channels appear (such as ring, liquid lump, Yakitori and rivulet flows). These can be considered to be variations of the Taylor and annular regimes. For a review of gas–liquid flow patterns in microchannels see Ghiaasiaan and Abdel-Khalik [2].

Key Research Findings

Flow Patterns in Liquid Slugs

Qualitative sketches of the flow streamlines in the liquid slug ahead of the bubble have been presented by Taylor [3] (see Fig. 2). These were related to the Capillary number, Ca ($Ca = \mu U_b/\gamma$, where μ is the liquid viscosity and U_b is the bubble velocity) and to the dimensionless number m, that gives the relative velocity between the bubble and the liquid

$$m = \frac{U_b - U_{ls}}{U_b} \tag{2}$$

where U_{ls} is the average liquid slug velocity. At high values of Ca, for $m > 0.5$, complete bypass flow was suggested with a single stagnation point at the bubble front. At low values of Ca, for $m < 0.5$ two possible reversal flow patterns were envisaged, one featuring a stagnation ring around the bubble cap (Fig. 2b) and the other featuring a single stagnation point at the bubble cap tip and a second one inside the liquid slug (Fig. 2c).

Although patterns 2a and 2b have been confirmed experimentally and theoretically by many investigators, pattern 2c was observed for the first time in numerical studies [4]. For no inertia and high Ca, a single stagnation point on the bubble tip was seen. As Ca decreased, there was a transition and vortices started to appear at $Ca = 0.69$, as suggested by pattern 2c. A stagnation ring finally developed at $Ca = 0.60$ (pattern 2b). The small range of Ca values, $0.60 < Ca < 0.69$, within which pattern 2c appeared would explain why it had not been observed experimentally before. At the back of the bubble, it was found [5] that as Ca increases from 0.60 to 0.69 the vortex breaks into two regions, a swirl and a recirculating flow separated by a stagnation point, whose sizes diminish as Ca increases.

The analytical model developed by Thulasidas et al. [6], which is suitable for bubble train flow, showed that the transition to complete bypass (pattern 2a) occurs in horizontal flow at $Ca = 0.7$, in upward flow at $Ca = 0.5$ and in downward flow at $Ca = 0.6$.

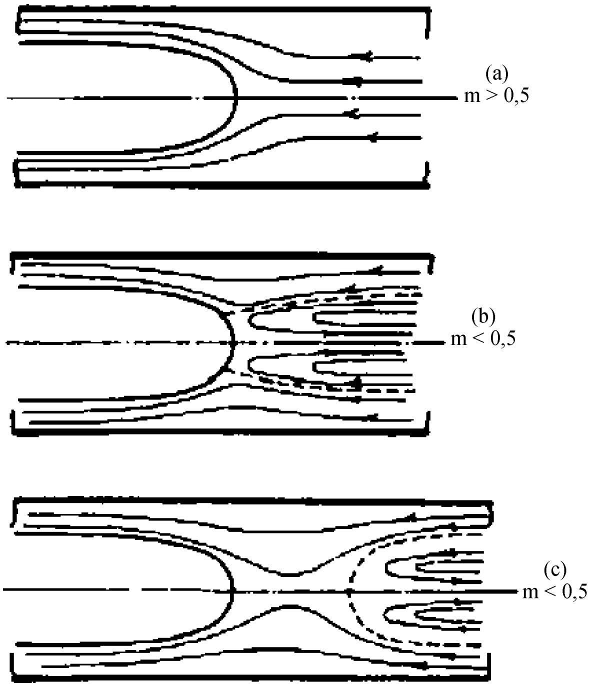

Taylor Flow in Microchannels, Figure 2 Streamlines in the liquid slug in front of the Taylor bubble [3]

Film Thickness and Bubble Shape

The flow of a long bubble in a capillary is a classical problem in fluid mechanics. Bubbles have been used as tracers in capillaries filled with liquid in order to determine liquid velocity. This application led to the discovery that when a wetting viscous liquid is displaced by a gas bubble in a capillary a liquid film is deposited on the wall. Initial experimental findings that the thickness of the film was proportional to $Ca^{1/2}$ were confirmed and extended to $Ca = 10^{-1}$ [3]. In his pioneering approach, Bretherton [1] assumed creeping flow in the liquid and used lubrication theory for the region of the film between the end of the spherical bubble cap and the flat film behind it to calculate the thickness of the film, the pressure drop and

the shape of the bubble. The Taylor bubble was taken to be inviscid with spherical caps. From this analysis it was found that the thickness of the film can be obtained from $\delta/d = 0.66\,\mathrm{Ca}^{2/3}$. This finding should be valid for low values of Ca. Surprisingly, however, the experiments agreed better with the theory for $\mathrm{Ca} > 10^{-3}$, while at lower Ca, where the theory should hold exactly, the thickness of the film was substantially larger than the theoretical values. This discrepancy was later attributed to the presence of surface-active contaminants that are absorbed at the interface. Ratulowski and Chang [7] argued that surface contamination can be correctly assessed only if the surface tension is allowed to vary along the interface. A model was developed that included surfactant transportation at both the interface and in the bulk liquid and showed that an increase in the thickness of the film occurs if the surfactant transport in the bulk is mass transfer limited.

For higher values of Ca ($\mathrm{Ca} > 5 \times 10^{-3}$), numerical studies are required to obtain the shape of the bubble and the thickness of the film. A number of numerical solutions to the problem have been suggested, which also validate Bretherton's approach at very low values of Ca. As the front profile and the thickness of the film of a long Taylor bubble with sufficient separation between the bubbles can be approximated by that of an infinitely long bubble, many early studies, considered semi-infinite bubbles.

In later studies the effect of inertia at increased Reynolds numbers ($\mathrm{Re} = \rho U r/\mu$, where r is the channel radius) was considered. Giavedoni and Saita carried out extensive numerical simulations and analyzed the front [4] of a Taylor bubble for $10^{-5} < \mathrm{Ca} < 10$, $\mathrm{Re} < 70$, and the back [5] of a Taylor bubble for $10^{-3} < \mathrm{Ca} < 1.5$, $\mathrm{Re} < 70$. Because of the development of a constant film thickness it is possible to study the front and rear parts of the bubble independently. The influence of increasing Re on film thickness was found to be weakly non-monotonic where an initial decrease was followed by an increase (see Fig. 3). Later studies at even higher Re confirmed the trend of increasing thickness of the film as Re increased further. For $\mathrm{Ca} < 0.01$, however, inertial forces do not have an effect on film thickness.

Experimentally determined film thickness correlations have been listed by Edvinsson and Irandoust [8]. Based on scaling arguments in a semi-infinite bubble, a correlation was suggested [9] for the film thickness in the visco-capillary regime (where the thickness of the film depends only on Ca) that agreed well with Taylor's data and at very small Ca with Bretherton's model. After fitting it against experimental data the correlation became

$$\frac{\delta}{d} = \frac{0.66\,\mathrm{Ca}^{2/3}}{1 + 2.5\left(1.34\,\mathrm{Ca}^{2/3}\right)} \qquad (3)$$

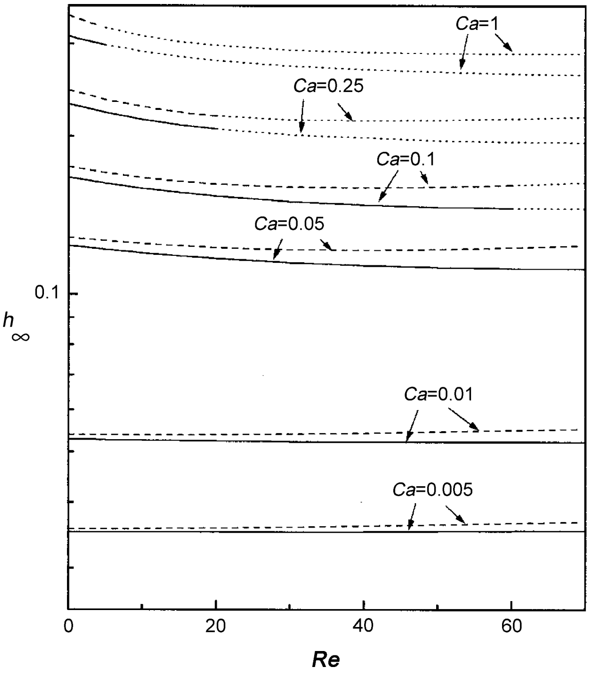

Taylor Flow in Microchannels, Figure 3 Thickness of the film over the half-channel size (h_∞) against Reynolds number for plane flow (dashed lines) and axisymmetric flow (solid lines). Dotted lines represent situations that may not be feasible in practice [4]

At $\mathrm{Ca} > 10^{-3}$ inertial effects become important (visco-inertial regime) and the film thickness becomes larger than the one obtained by Eq. (3). Interestingly, this difference increases as the diameter of the tube increases. In the inertial regime [9]

$$\frac{\delta}{d} \propto \frac{\mathrm{Ca}^{2/3}}{\left(1 + \mathrm{Ca}^{2/3} - \mathrm{We}\right)} \qquad (4)$$

T

The Weber number, We, is defined as $\mathrm{We} = \rho U_b^2 (r-h)/\gamma$, where h is the thickness of the film deposited on the wall. The simulations by Giavedoni and Saita showed that the bubble front tended to adopt the shape of an arc of a circle for decreasing values of Ca. Undulations, which increased with Re, appeared at the back of the bubble. The size of the undulations depended on both Ca and Re and for $\mathrm{Ca} > 0.5$ no undulations were observed. For all the values of Re that were tested the rear of the meniscus was convex at first, became flat as Ca increased and then adopted a concave shape, while as Re increased the change from flat to concave shape appeared at lower values of Ca. The interface at the back of the bubble close to the meniscus tip is an almost perfect hemisphere for $\mathrm{Ca} < 10^{-3}$.

Thulasidas et al. [6] found experimentally that the thickness of the film was almost the same in horizontal and downward flows but was twice as much in upward flows.

Bubble Velocity

Because of the film between the bubble and the wall, the bubble and liquid velocities are not the same. The bubble velocity, U_b, is given by the drift flux model

$$U_\mathrm{b} = CU_\mathrm{ls} + U_0 \tag{5}$$

where C is an experimentally determined coefficient and U_0 is the bubble rise velocity in a stagnant liquid. For very small capillaries the bubble rise velocity is very small or zero (see also the definition of small channels given above). The bubble motion is often characterized by the dimensionless number m (see Eq. (2)). For low values of Ca, $m = 1.0\,\mathrm{Ca}^{1/2}$ which was found to be valid for $\mathrm{Ca} < 10^{-1}$ [3].

Bretherton's [1] analytical approach resulted in the following expression:

$$m = 1.29\,(3\,\mathrm{Ca})^{2/3} \tag{6}$$

Thulasidas et al. [6] compared their and all other available experimental data on relative bubble velocity, m, with the literature correlations. There was a considerable scattering of the experimental data at the lower values of Ca, particularly for $\mathrm{Ca} < 10^{-2}$, while Bretherton's correlation was found to underpredict all the data. The results showed that m reached a limiting value of 0.58 at large values of Ca.

The more recent literature on bubble velocity has been reviewed by Akbar and Ghiaasiaan [10]. They observed that their data and those of others were well predicted by the following correlation, valid for $2 \times 10^{-4} < \mathrm{Ca} < 0.39$:

$$\frac{U_\mathrm{b}}{U_\mathrm{m}} = \frac{1}{1 - 0.61\,\mathrm{Ca}^{0.33}} \tag{7}$$

where U_m is the mixture velocity calculated from the overall gas and liquid flowrates divided by the area of the tube.

Bubble and Slug Length

Various characteristics in Taylor flow (such as pressure drop and mass transfer rate) depend on the bubble and slug sizes. Thulasidas et al. [6] developed a hydrodynamic analytical model for a unit cell (i. e., a bubble and a slug) that allowed the length ratio of bubble to unit cell to be calculated when the superficial gas and liquid velocities, calculated by dividing gas and liquid flowrates, respectively, with the channel cross sectional area, are known. The absolute lengths depend on the dynamics during two-phase contact made at the inlet. Thus, inlet geometry is expected to affect slug and bubble length.

Kreutzer [11] suggested a correlation for the slug length, L_s, based on experimental data in a 200 cpsi monolith reactor

$$\frac{L_\mathrm{S}}{d} = \frac{\varepsilon_\mathrm{l}}{-0.00141 - 1.556\,\varepsilon_\mathrm{l}^2 \ln(\varepsilon_\mathrm{l})} \tag{8}$$

where ε_l is the liquid volume fraction.

Akbar and Ghiaasiaan [10] conducted computational fluid dynamics simulations to model a unit cell (one bubble and two half-liquid slugs) in a capillary of 1 mm diameter. Their numerical results, as well as experimental data from previous investigators, were predicted well by the following equation:

$$\frac{U_\mathrm{m}^{-0.33}}{\sqrt{L_\mathrm{S}}} = 142.6\,\varepsilon_\mathrm{g}^{0.56}\left(\frac{d}{L_\mathrm{UC}}\right)^{0.42}\mathrm{Re}_\mathrm{g}^{-0.252} \tag{9}$$

where U_m is the mixture velocity, L_UC is the unit cell length, η_g is the gas volume fraction and Re_g is the gas-based Reynolds number, $\mathrm{Re}_\mathrm{g} = \rho_\mathrm{g} U_\mathrm{sg} d/\mu_\mathrm{g}$, ρ_g and μ_g are the gas density and viscosity and U_sg is the gas superficial velocity.

Extensive numerical simulations on the formation and channel flow of Taylor bubbles have also been conducted by Qian and Lawal [12] for gas and liquid superficial velocities from 0.01 to 0.25 m/s in a 1 mm capillary, for $0.09 < \varepsilon_\mathrm{g} < 0.91$, $15 < \mathrm{Re} < 1500$, $0.000278 < \mathrm{Ca} < 0.01$. The inlet configuration was varied either by bringing the two separate fluids into the channel through a T-junction or by premixing them. Interestingly, premixing resulted in shorter bubble or slug lengths. The T-inlet orientation and channel sizes, as well as the gas and liquid superficial velocities, affected the lengths. On the other hand, surface tension had only a slight effect while liquid viscosity had almost no influence. Their set of 148 data was correlated to within 10% by the following equation:

$$\frac{L_\mathrm{UC}}{d} = 1.637\,\varepsilon_\mathrm{g}^{-0.893}(1 - \varepsilon_\mathrm{g})^{-1.05}\mathrm{Re}^{-0.075}\mathrm{Ca}^{-0.0687} \tag{10}$$

Bubble and slug lengths can be obtained by multiplying Eq. (10) with the respective phase volume fractions.

Systematic experimental investigations on the effect of the inlet configuration on the bubble size have been carried out by Amador et al. [13]. T- and Y-junctions with different inlet channel dimensions and fluid joining angles were used as well as a co-flow configuration with the gas in the middle and the liquid in the annulus around it. Three bubble formation mechanisms were identified. In some cases bubble pairing was also observed at the inlet. The bubble length was found to depend mainly on the ratio of the

gas to liquid superficial velocities. The size of the gas inlet affected the bubble size but the size of the liquid inlet or the angles at which the fluids joined only had a small effect.
The importance of the gas and liquid flowrates on the size of the bubbles formed in a T-junction, was confirmed by Garstecki et al. [14]. Based on scaling arguments they derived the following expression:

$$L_B/w = 1 - \alpha(Q_g/Q_l) \qquad (11)$$

where L_B is the bubble length, w is the main channel width, α is a fitting parameter of order 1, Q_l and Q_g are the liquid and gas flowrates.

Pressure Drop

Bretherton's analysis also provided an expression for the pressure drop over the entire length of the bubble

$$\Delta P = 7.16\,(3\,\mathrm{Ca})^{2/3}\frac{\gamma}{d} \qquad (12)$$

From numerical simulations Kreutzer [11] derived the pressure drop in a unit cell comprised of a bubble and a slug. At low values of Ca the numerical results were slightly higher than Bretherton's predictions. Simulations indicated that the pressure drop increases with increasing Re and decreasing Ca, while with increasing Ca the effect of inertia on the pressure drop reduces. The extra pressure drop caused by the bubble could be estimated by subtracting the contribution of the liquid flow in the slug from the overall pressure drop. It was found that this extra pressure drop was almost equal to the difference in the interfacial pressure between the tips of the bubble at low Re while at high Re the dramatic increase in the pressure drop over the interface was not reflected in the overall unit cell pressure drop. A strong dependence of the pressure drop on the slug length was found experimentally. Assuming that the overall pressure drop consisted of the pressure drop in the slugs plus a Laplace pressure term caused by the bubbles, the following correlation was suggested for the friction factor, f, in capillaries during Taylor flow. The equation is valid for $2\times10^{-3} < \mathrm{Ca} < 4\times10^{-2}$ and $100 < \mathrm{Re} < 900$:

$$f = \frac{16}{\mathrm{Re}}\left[1 + \alpha_1\frac{d}{L_S}\left(\frac{\mathrm{Re}}{\mathrm{Ca}}\right)^{\frac{1}{3}}\right] \qquad (13)$$

where α_1 was found from the numerical simulations to be 0.07, while a value of 0.17 fitted the experimental data better. The difference was attributed to the presence of impurities. The following equation was proposed for low values of Re:

$$f = \frac{16}{\mathrm{Re}}\left[1 + \frac{d}{L_S}\frac{0.465}{\mathrm{Ca}^{\frac{1}{3}}}\right] \qquad (14)$$

The pressure drop is then found from $\Delta P/L = 2f\rho U_m^2 \varepsilon_l/d$, where L is the channel length.

Non-Circular Channels

In contrast to circular channels there is less information available on Taylor flow in non-circular channels and most of the information that is available refers to square channels. In square channels at $\mathrm{Ca} < 0.1$ the bubble is not axisymmetric and flattens out against the tube walls leaving liquid regions in the corners which are joined by thin flat films at the sides of the channels. As Ca increases the bubble becomes axisymmetric and for high values of Ca the bubble radius reaches an asymptotic minimum value, approximately equal to 0.68 times the square channel half-width [15]. A stagnation ring forms at the bubble surface at low values of Ca, but for $\mathrm{Ca} > 0.54$ the liquid completely bypasses the bubble. In upward and downward flows complete bypass occurs at $\mathrm{Ca} = 0.5$ and $\mathrm{Ca} = 0.57$, respectively [6]. Differences were also observed in the thickness of the film and in m between the upward and downward directions. The bubble relative velocity asymptotically approached a limiting value of $m = 0.6$ at high values of Ca in both the upward and downward flows.

Examples of Applications

One of the first applications of Taylor bubbles was in flow measurements where the bubbles acted as tracers to determine the velocity of the liquid in the capillaries. Later, however, it was recognized that the presence of the film between the bubble and the wall makes the bubble velocity different from the liquid one.

T

Applications of Taylor flow in microchannels stem mainly from the good mass transfer characteristics in this flow regime. In Taylor flow the bulk liquid is separated by the gas bubbles which significantly reduces axial mixing between the liquid slugs. The liquid recirculation within the slugs for the range of Ca encountered in small channels (see Fig. 2) also improves the radial mass/heat transfer. Fast multiphase reactions that can be mass transfer limited can benefit from improved radial mixing. In fact, much of the information on Taylor flow originates from the investigation and characterization of monolithic reactors where the two fluid phases are introduced into the reactor as froth flow and pass through catalyst-coated channels in a Taylor flow pattern. The performance of operations such as liquid chromatography within tubes with absorbing walls and tubular dialysers can be improved if Taylor bubbles are

introduced in the single-phase flow because they reduce backmixing. Even microfiltration efficiencies have been found to improve when Taylor bubbles have been introduced in the liquid medium. This improvement has been attributed to pressure pulsations caused by the alternating passage of slugs and bubbles.

In the past, the low axial mixing properties of Taylor flow were used in automated analyzers, to avoid cross-talking between successive samples. The same concept applies to high throughput screening where Taylor bubbles facilitate the sequential passage of different reactants/samples through a microchannel reactor/analyzer. The enhanced heat and mass transfer rates that are possible in microchannels can enable a kinetically controlled operating regime to be established that would allow evaluation of reaction kinetics.

Investigations on Taylor flow in non-circular channels originated from flows in porous materials, for instance in enhanced oil recovery. They are also relevant to microstructured reactors and to the many monolithic systems which in many cases have non-circular reaction channels.

Cross References

- ► Bubble Dynamics in Microchannels
- ► Pressure Driven Two-Phase Flows

References

1. Bretherton FP (1961) The motion of long bubbles in tubes. J Fluid Mech 10:166–188
2. Ghiaasiaan SM, Abdel-Khalik SI (2001) Two-phase flow in microchannels. Adv Heat Transf 34:145–254
3. Taylor GI (1961) Deposition of a viscous fluid on the wall of a tube. J Fluid Mech 10:161–165
4. Giavedoni MD, Saita FA (1997) The axisymmetric and plane case of a gas phase steadily displacing a Newtonian liquid – A simultaneous solution to the governing equations. Phys Fluid 9(8):2420–2428
5. Giavedoni MD, Saita FA (1999) The rear meniscus of a long bubble steadily displacing a Newtonian liquid in a capillary tube. Phys Fluid 11(4):786–794
6. Thulasidas TC, Abraham MA, Cerro RL (1995) Bubble train flow in capillaries of circular and square cross section. Chem Eng Sci 50(2):183–199
7. Ratulowski J, Chang HC (1990) Marangoni effects of trace impurities on the motion of long gas bubbles in capillaries. J Fluid Mech 210:303–328
8. Edvinsson RK, Irandoust S (1996) Finite-element analysis of Taylor flow. AIChE J 42(7):1815–1823
9. Aussilous P, Quére D (2000) Quick deposition of a fluid on the wall of a tube. Phys Fluid 12(10):2367–2371
10. Akbar MK, Ghiaasiaan SM (2006) Simulation of Taylor flow in capillaries based on the volume-of-fluid technique. Ind Eng Chem Res 45:5396–5403
11. Kreutzer MT (2003) Hydrodynamics of Taylor flow in capillarties and monolith reactors. PhD Thesis, Technical University of Delft, Delft
12. Qian D, Lawal A (2006) Numerical study on gas and liquid slugs for Taylor flow in a T-junction microchannel. Chem Eng Sci 61:7609–7625
13. Amador C, Salman W, Sanguanpiyapan S, Gavriilidis A, Angeli P (2004) Effect of gas/liquid inlet conditions on slug length in Taylor flow. Proceedings 5th International Conference on Multiphase Flow (CD-ROM), Japan
14. Garstecki P, Fuerstman MJ, Stone HA, Whitesides GM (2006) Formation of droplets and bubbles in a microfluidic T-junction – scaling and mechanism of break-up. Lab Chip 6:437–446
15. Kolb WB, Cerro RL (1993) The motion of long bubbles in tubes of square cross-section. Phys Fluid 5(7):1549–1557

TCR

► Temperature Coefficient of Resistance

Temperature Coefficient of Resistance

Synonyms

TCR

Definition

The relative change in the resistance of a substance per unit change in temperature. The units of TCR are K^{-1}, sometimes expressed as %/K.

Temperature Control

- ► Reaction Condition Control
- ► Temperature Gradient Generation and Control

Temperature Control in Microfluidic Systems

Chan Hee Chon, Dongqing Li
Department of Mechanical Engineering,
Vanderbilt University, Nashville, TN, USA
Chanhee.chon@vanderbilt.edu,
dongqing.li@vanderbilt.edu

Synonyms

Temperature control system in microfluidic chips; Integrated temperature control in microfluidic systems; Microfluidic system control modules; Thermal control in microfluidic modules

Definition

Temperature control in microfluidic systems is a way to control the temperature of fluids such as water, chemicals, and biofluids in microfluidic systems or devices by using direct/indirect heating or cooling techniques. The characteristics of the temperature control in microfluidic systems are very small control volume, shorter period of control time, small size of control areas/mass, and small size of control devices.

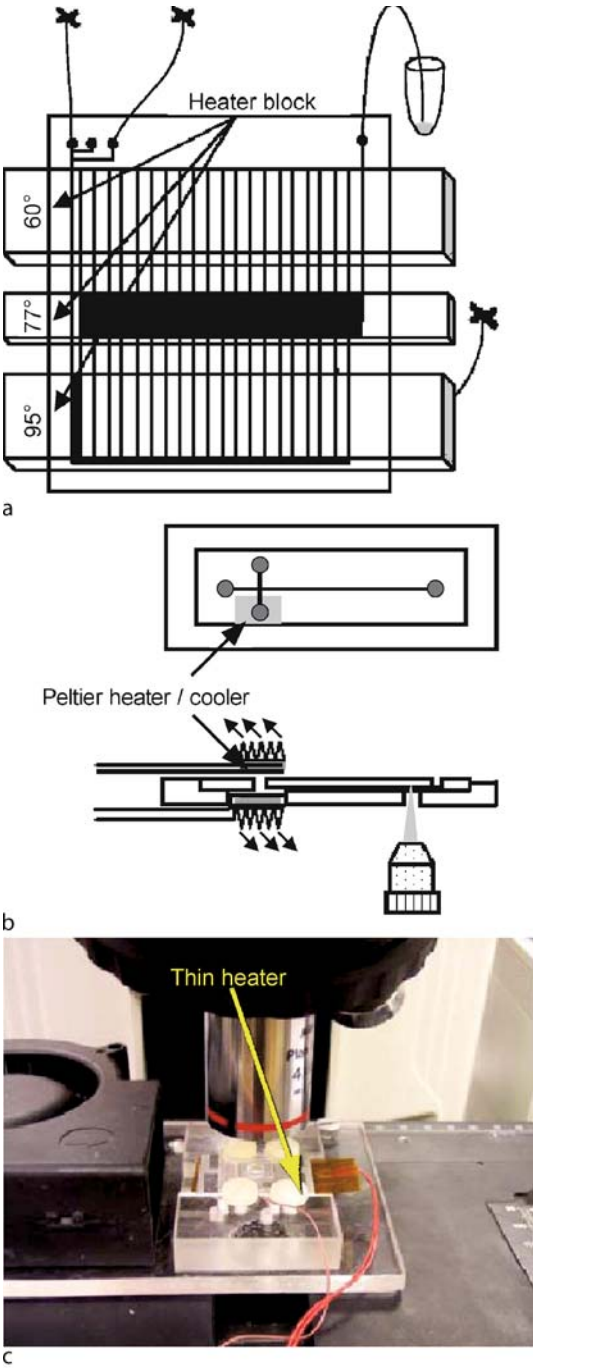

Temperature Control in Microfluidic Systems, Figure 1 Contact external heating methods for microfluidic devices: (**a**) heat exchanger heater [1], (**b**) Peltier thermoelectric heater [2], and (**c**) thin resistive heater [3]

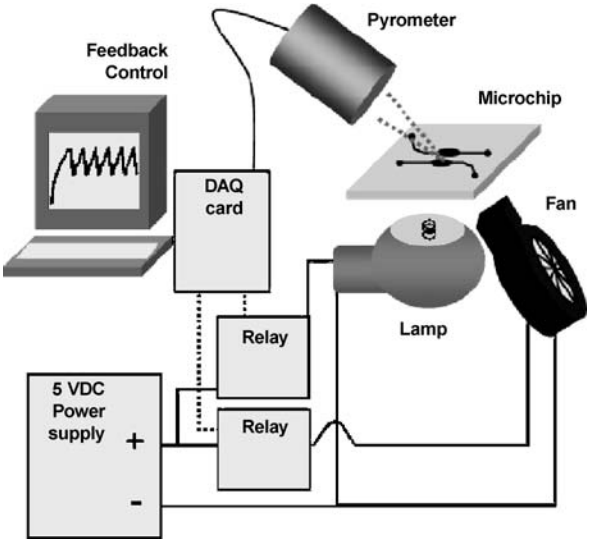

Temperature Control in Microfluidic Systems, Figure 2 Infrared noncontact external heating methods for microfluidic devices [4]

Overview

Due to smaller sample volumes and larger surface-to-volume ratios, the thermal control of microfluidic systems shows many advantages such as small amount of energy, simpler control system, and shorter control time. Precise control and rapid thermal control are also required in certain processes such as the polymerase chain reaction (PCR).

These temperature control techniques for microfluidic devices can be divided into two categories: external temperature control and internal temperature control. External temperature control systems control temperature by using external heating and cooling elements such as a heater and fan and a thermoelectric heater–cooler. Internal temperature control systems achieve heating and cooling with a thermal system embedded in microchannels.

External Heating Technique

The external heating technique relies on heating working fluids in a microchannel with separated heating elements. This is also divided into two types by heat transfer methods: contact and noncontact.

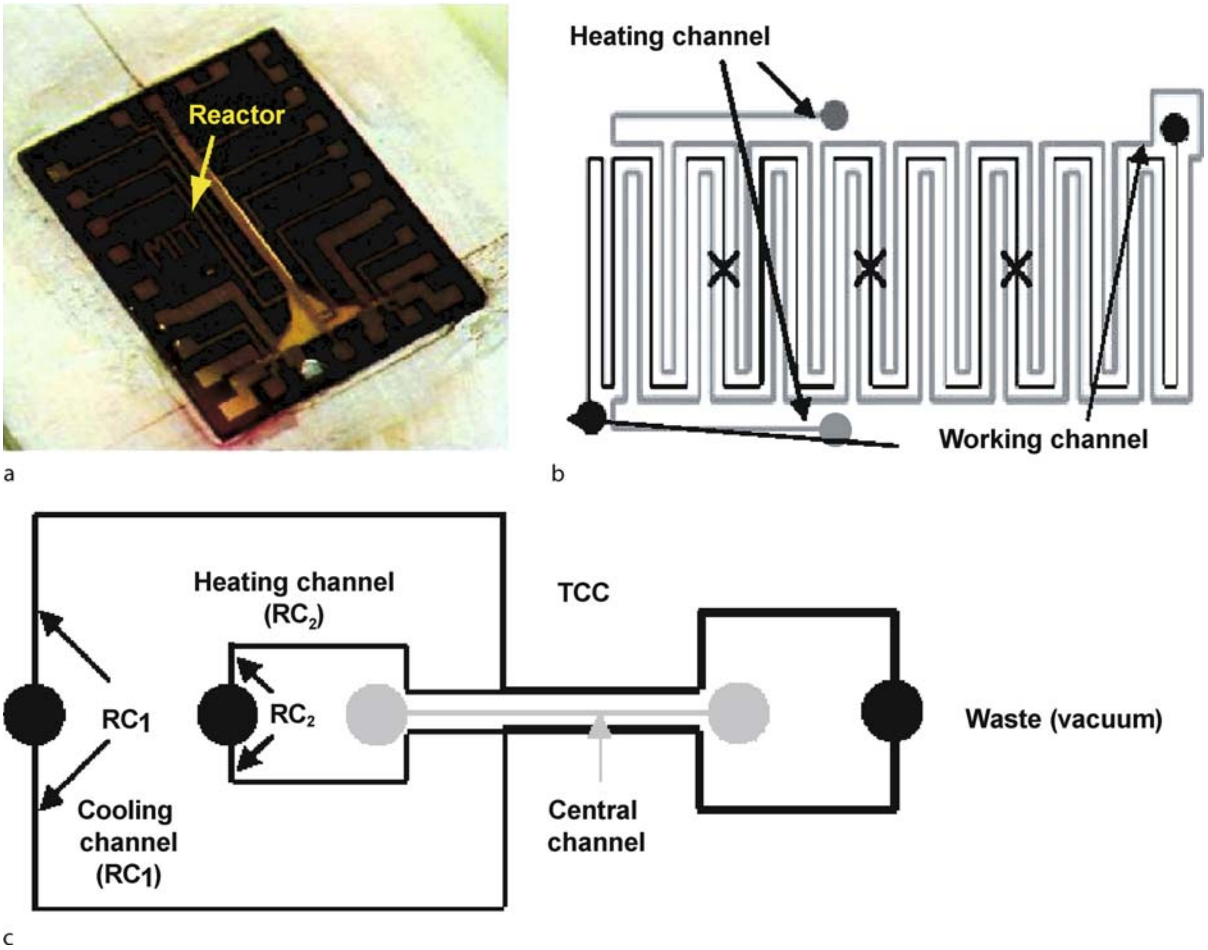

Temperature Control in Microfluidic Systems, Figure 3 Internal heating methods for microfluidic devices: (**a**) micromachined reactor [5], (**b**) Joule heating heater [6], (**c**) endothermic/exothermic heater [7]

In contact-type heating (Fig. 1) one clamps or glues heating elements on the surfaces of channels or containers which contain working fluids and heat is transferred into the fluids by conduction from the heating elements. Heat exchanging [1] by contacting the microsystem to the passively heated or cooled surfaces is widely used to control temperature. However, it is too bulky and limits are involved in integrating a microsystem. The Peltier thermoelectric heater–cooler system [2] is an example of this heating technique. The Peltier heater–cooler is a small solid-state device that functions as a heat pump. It is a sandwich formed by two ceramic plates with an array of small bismuth telluride cubes in between. When a DC current is applied, heat is moved from one side of the device to the other – where it must be removed with a heat sink. The cold side is commonly used to cool an electronic device. If the current is reversed, the device becomes a heater. Another example of contact-type heating involves temperature control by resistive heating elements [3]. Heat is generated when electricity flows in the high-resistance material as in an electric heater.

Noncontact-type heating allows heat transfer by noncontacting methods to fluids such as radiative and ultrasonic heating. Infrared temperature control [4] is a noncontact heating technique, which uses the infrared excitation of a vibration band of water combined with a high-power halogen light bulb and an optical filter (Fig. 2).

Internal Heating Technique

The internal heating technique incorporates heating elements in microfluidic devices to control temperature of fluids. A widely used technique is direct fabrication of a heater or reactor [5] inside of a microchannel or chamber. This requires a microfabricating process to manufacture

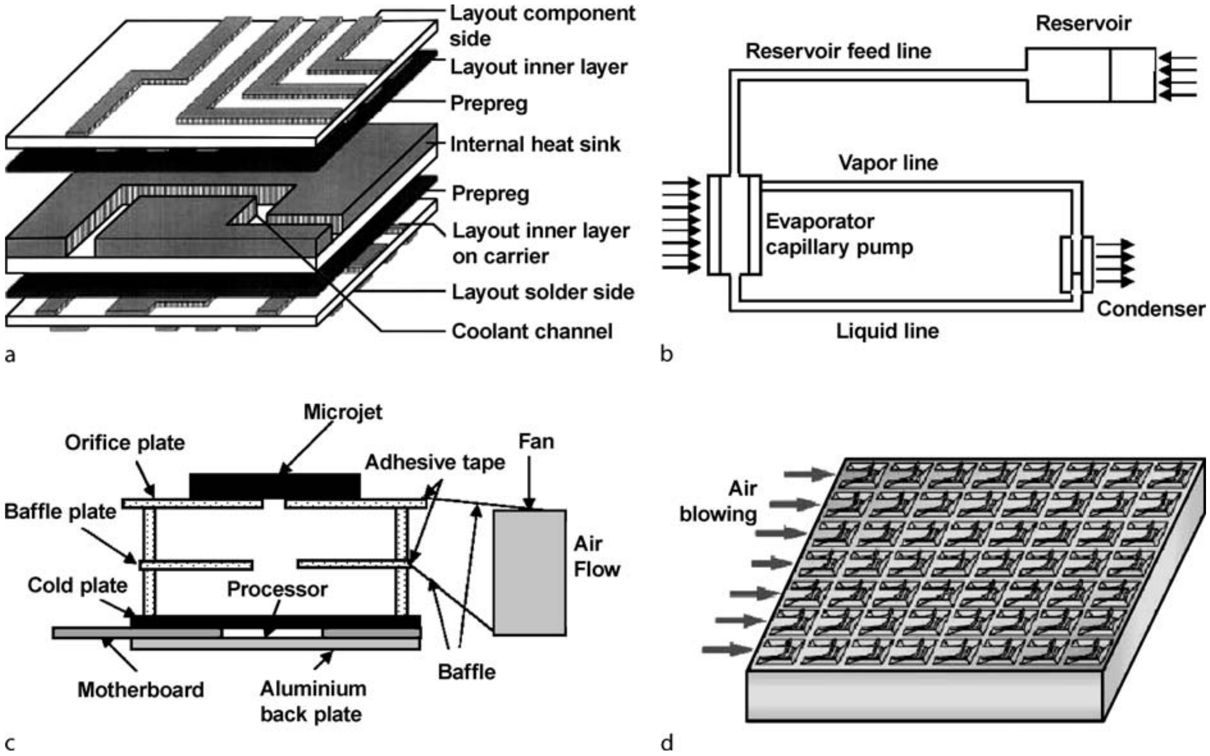

Temperature Control in Microfluidic Systems, Figure 4 Cooling methods for microelectronic or integrated electronic circuits/chips: (**a**) integrated microcooling with microchannels etched on the back of chips [8], (**b**) microcapillary pumped loop cooling [11], (**c**) microjet cooling [12], and (**d**) microfin array cooling [13]

the microheater system to fit in the microscaled container. In electrokinetically driven microflow, naturally generated Joule heating in the channel is used to control the temperature of fluids [6].

Guijt et al. [7] suggested an on-chip heating and cooling technique by using endothermic or exothermic processes in a microchannel to cool or heat solutions within an adjacent sample channel. Chemical or physical processes of solutions in a channel such as evaporation of acetone and exothermic dissolution of H_2O_4 in water are used to cool and heat an adjacent channel (Fig. 3).

Cooling

Currently the most popular cooling method is the externally controlled passive cooling technique using traditional convection heat transfer and heat exchanging techniques such as fins [1], a fan [3], and compressed air for microfluidic device cooling. Integrated cooling techniques for microfluidic devices are very limited such as the Peltier thermoelectric cooler [2] and endothermic cooler [7] mentioned above.

There are several techniques (Fig. 4) for heat removal for microelectronics or integrated circuits or chips not involving microfluidic devices. These techniques may be possible to apply for microfluidic system cooling in the near future. Integrated microcooling flowing water through microchannels etched on the backs or sides of electronic chips is used for heat dissipation in high energy generating electronic components [8]. High-efficiency evaporative heat transfer is applied for heat dissipation of electronic devices: thermosiphons [9], heat pipe cooling [10], and capillary pumped loops [11]. Air-based microelectromechanical devices such as air microjets [12] and microfin arrays [13] also effectively remove heat from microelectronic devices.

Cross References

- ► Electronics Cooling
- ► Heat Transfer in Microchannel Flows
- ► Joule Heating in Electrokinetic Flow: Theoretical Methods
- ► Joule Heating vs. Chip Materials

► Methods for Temperature Measurements
► Micro Heat Pipes
► Microscale Energy Conversion Devices
► PCR Lab-on-Chip Devices
► Temperature Gradient Generation and Control

References

1. Kopp MU, deMello AJ, Manz A (1998) Chemical amplification: Continuous-flow PCR on a chip. Sci 280:1046–1048
2. Khandurian J, McKnight E, Jacobson SC, Waters LC, Foote RS, Ramsey JM (2000) Integrated system for rapid PCR-based DNA analysis in microfluidic device. Anal Chem 72:2995–3000
3. Xiang Q, Xu B, Fu R, Li D (2005) Real Time PCR on Disposable PDMS Chip with a Miniaturized Thermal Cycler. Biomed Microdevices 7:273–279
4. Roper MG, Easley CJ, Legendre LA, Humphrey JAC, Landers JP (2007) Infrared temperature control system for a completely noncontact polymerase chain reaction in microfluidic chips. Anal Chem 79:1294–1300
5. Srinivasan R, Hsing IM, Berger PE, Jensen KF, Firebaugh SL, Schmidt MA, Harold MP, Lerou JJ, Ryley JF (1997) Micromachined reactors for catalytic partial oxidation reactions. AIChEJ 43:3059–3069
6. de Mello AJ, Habgood M, Lancaster NL, Welton T, Woodtton RCR (2004) Precise temperature control in microfluidic devices using Joule heating of ionic liquids. Lab Chip 4:417–419
7. Guijt RM, Dodge A, van Dedem GWK, de Rooij NF, Verpoorte E (2003) Chemical and physical processes for integrated temperature control in microfluidic devices. Lab Chip 3:1–4
8. Schutze J, Ilgen H, Fahrner WR (2001) An integrated micro cooling system for electronic circuits. IEEE Tran Ind Electron 48:281–285
9. Murthy SS, Joshi YK, Nakayama W (2000) Single chamber compact thermosyphons with micro-fabricated components. InterSociety Conf Thermal Pheonemena 321–327
10. Xie H, Ali A, Bhatia R (1998) The use of heat pipes in personal computers. InterSociety Conf Thermal Pheonemena 442–448
11. Pettigrew K, Kirshberg J, Yerkes K, Trebotich D, Liepmann D (2001) Performance of a MEMS based micro capillary pumped loop for chip-level temperature control. IEEE Int Conf MEMS 427–430
12. Campbell JS, Black WZ, Hartley JG (1998) Thermal management of a laptop computer with synthetic air microjets. InterSociety Conf Thermal Pheonemena 43–50
13. Go JS, Kim SJ, Lim G, Yun H, Lee J, Song I, Pak E (2001) Heat transfer enhancement using flow-induced vibration of a microfin array. Sens Actuators A 90:232–239

Temperature Control System in Microfluidic Chips

► Temperature Control in Microfluidic Systems

Temperature Effects on the Zeta Potential

ROBERTO VENDITTI
Department of Mechanical and Industrial Engineering, University of Toronto, Toronto, ON, Canada
roberto.venditti@gmail.com

Definition

The ► zeta potential (ζ) depends on the surface charge that appears at the interface of a liquid:solid pair when the two are brought into direct contact. The zeta potential represents the electrical potential generated as a consequence of this electrical surface charge. The zeta potential is normally treated as being invariant with respect to temperature, but recent experiments have suggested that this is not always accurate. It is important to have a precise estimate of ζ because calculation of ► electroosmotic flow velocity in a microchannel (using the ► Smoluchowski equation) depends directly upon this value.

Overview

When a solid surface is in contact with an aqueous solution, a thin region of nonzero net charge density forms near the interface. The arrangement of the charges at the solid–liquid interface and the balancing counterions in the liquid is usually referred to as the electrical double layer (EDL). There is a thin layer of counterions immediately next to the charged solid surface, called the compact layer. The counterions in the compact layer are immobile due to strong electrostatic attraction. Counterions outside the compact layer are mobile. This part of the EDL is called the diffuse layer. The zeta (ζ) potential is the electrostatic potential at the boundary dividing the compact layer and the diffuse layer [2].

Application of an external electric field along a microchannel exerts a force on the EDL which can be used to drive fluid motion. This method is commonly referred to as electroosmotic flow (EOF). EOF is one of the most popular methods used to induce fluid motion in microfluidic systems (the other being pressure-driven) because it has many advantages, particularly by way of offering precise control over liquid motions.

When measured at elevated temperatures, experimentally-observed EOF velocities of liquids in microchannels are sometimes considerably higher than those predicted analytically using the *Smoluchowski equation* [1, 2],

$$U_{\text{av}} = \left(\frac{\varepsilon_r \varepsilon_0 \zeta}{\mu}\right) E_z \tag{1}$$

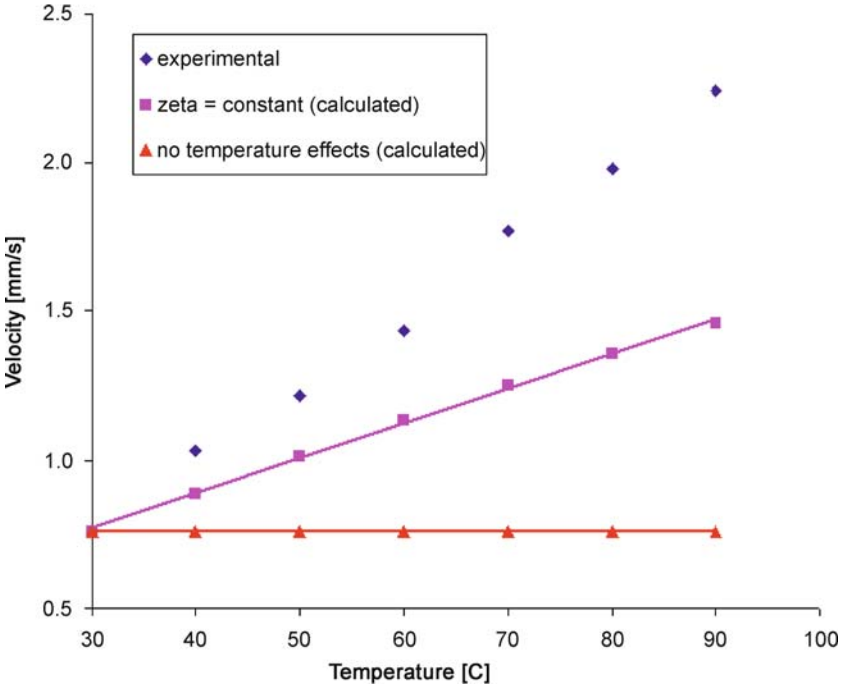

Temperature Effects on the Zeta Potential, Figure 1 Average electroosmotic flow velocity in a 300 μm × 8 μm PDMS : Glass microchannel filled with 10 mM KCl solution under an applied electric field, E_Z, of 15,900 V/m: (◇) experimentally measured velocity, (□) velocity calculated by Eq. 1, with temperature dependence of viscosity and permittivity considered (but not zeta potential) and (△) velocity calculated by Eq. 1, with no temperature dependencies taken into account

where U_{av} is the average channel velocity, μ, ε and ζ are viscosity, permittivity and zeta potential parameters, respectively, and E_z is the applied electric field strength. This equation is used to calculate the fluid velocity in channels driven by electric fields (i. e. ►electroosmotic flow). Adjusting viscosity and permittivity for temperature improves prediction, but can still be insufficient in some cases. An example of this is shown in Fig. 1, and will be explained in more detail shortly.

It has been demonstrated that the difference between measured and calculated EOF velocities can be adequately explained by treating the zeta potential as a temperature-dependent variable [3]. The particular relationship between ζ and temperature varies depending on the combination of buffer solution and microchannel material being used; in some cases there is a strong dependence, while in others the effect is negligible. Treating the zeta potential as a temperature-dependent variable is a relatively new idea in the field of microfluidics; the traditional approach has been to consider ζ constant over all temperatures [4]. It is important to emphasize that this is not a trivial matter; failure to account for the temperature dependence of ζ has been shown to under-predict EOF velocities by as much as 30% at the sort of elevated temperatures (∼ 90°C) that are not at all unusual in microfluidic environments (Fig. 1) [3].

The previously-described situation where in-channel fluid temperatures encountered are significantly above ambient conditions is surprisingly common in microfluidic systems. In particular, ►Joule heating effects can produce elevated temperatures in typical microfluidic channels [4]. The Joule heating phenomenon occurs in electrokinetically-driven microfluidic systems. It describes the heat generated as a result of a liquid's inherent resistance to having an electrical current passed through it. Because EOF is generated using electrical fields, current is always present and Joule heating is inevitable. In some cases the resulting elevated temperatures resulting may be sufficient to change the zeta potential to an extent whereby the effect cannot be ignored. In such cases, ζ should be taken as a temperature-dependent variable. The mathematical function used to describe this relationship should be based upon experimentally-derived results, such as those presented in [3].

The publication authored by Venditti et al. [3] describes the results of an experimental investigation that attempts to characterize the influence of temperature on the zeta potential. The work describes the experimental procedure required to measure and classify the relationship between

T

ζ and temperature for a given liquid : substrate pair. It investigates this relationship for a number of buffer solutions commonly used in the microfluidics community. The influence of buffer concentration on the ζ-temperature curve is investigated. Results are given for both glass and ► poly(dimethylsiloxane) (PDMS) substrates. The consequential effect on calculated EOF velocity is studied and shown to be significant in some cases but negligible in others.

Revil et al. [5] explain that the influence of temperature on the zeta potential is a result of changes in silanol equilibrium, adsorption equilibria, and diffuse double-layer thickness. Their analysis and data is geared towards the geophysical community, but the linear profiles they show describing change in zeta potential with temperature is consistent with [3]. A linear zeta potential-temperature profile is again reported in a more recent paper by Revil et al. [6].

A useful analysis of the effect of temperature on zeta potentials is given by Reppert and Morgan [7]. Their treatment is centred around an analysis of temperature-dependent streaming potentials, which concludes that temperature can have a significant impact on zeta potential. It can be difficult to establish how the data they offered might be applicable in a microfluidic setting, for the same reason that their work is tailored to the geophysical community.

For a thorough review of this topic, see the paper presented by Kirby and Hasselbrink Jr. [8]. This work punctuates the fact that temperature variations can have a significant impact on the zeta potential.

Owing to the vast number of buffer solutions used by the microfluidic community, there are many situations where a researcher might find it impossible to find specific information about the ζ-temperature relationship of the particular reagent being used. In such a case, it is advisable to perform a separate test to evaluate the temperature properties of the solution being used before making any assumptions about whether-or-not the zeta potential can be taken as a constant. The procedure for such an experiment is described in ► Zeta Potential Measurements section to follow.

Basic Methodology

Zeta Potential Measurements

The suggested experimental setup (Fig. 2) and procedure used for zeta potential measurements is identical to that used for the time-interval current-monitoring method of Huang et al. [9]. The procedure used for measuring ζ can be described briefly as follows:

The microchannel and one reservoir are initially filled with the solution to be tested. The other reservoir is filled with a diluted version of the same buffer solution ($\sim$ 95% concentration) and a voltage is applied across the channel. Under the applied electric field, the lower concentration solution gradually replaces the higher-concentration solution. This results in a linearly-decreasing electrical current that ends in a flat plateau (which represents the instant the lower concentration buffer completely fills the microchannel). A schematic illustration of the process is shown in Fig. 3.

The electrical current is arrived at by measuring the voltage drop across a resistor positioned in series with the microchannel as a function of time. The time interval (Δt)

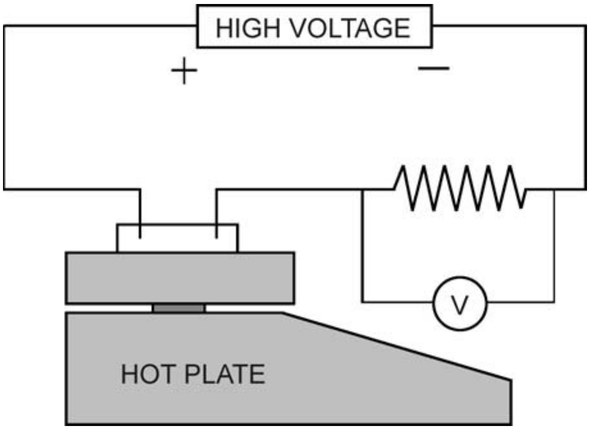

Temperature Effects on the Zeta Potential, Figure 2 Schematic diagram of experimental setup. Microchannel chip placed directly on hotplate surface and Platinum electrodes inserted vertically into reservoirs. Voltage drop measured across a resistor in series with the microchannel was used to calculate current flow in the electrical circuit

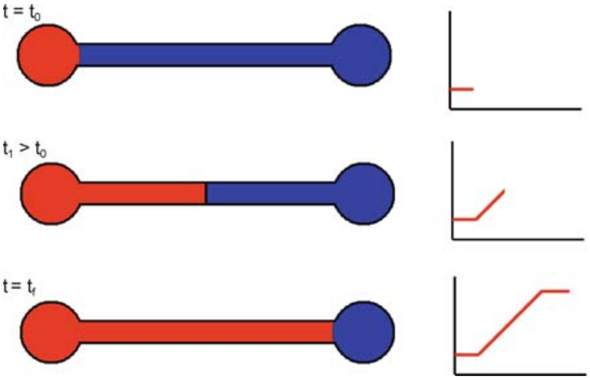

Temperature Effects on the Zeta Potential, Figure 3 Schematic diagram of the current-monitoring method used to measure zeta potential (ζ). As time increases, a higher-concentration buffer displaces a lower-concentration version of the same buffer solution. Consequently, the electrical current passing through the channel increases. ζ can be calculated by using the time required for the displacement process (the sloped portion of the current-time curve) in the Smoluchowski equation

required for the displacement process is measured and used to calculate the average fluid velocity, U_{av}, according to the relationship

$$U_{av} = \frac{L}{\Delta t}\,, \tag{2}$$

where L is the total length of the channel. In turn, this average velocity is used in the ►Smoluchowski equation (Eq. 1), allowing for the calculation of zeta potential by direct substitution.

A possible concern lies in determining the time interval of the displacement process. Depending on the current-time curve obtained, it can be difficult to assess the exact starting and ending points of the fluid-displacement time interval. Any error introduced into this value will affect the calculated EOF velocity (Eq. 2) and ultimately influence the calculated value of ζ (Eq. 1). Care should be taken to minimize this error by using sufficiently long displacement periods (as controlled by the applied voltage) that the reading error (typically ~ 0.5 s) represents an acceptably small portion of total experimental time.

Provided buffer concentrations are sufficiently low, parameters of permittivity and viscosity can be taken to be the same as for pure water [10]. After obtaining the current-time curve, the experiment is run again in the reverse direction. This complete process should be repeated at least once, which provides a total of four separate curves for each data point. Having repeatable results helps minimize the influence of inability to precisely evaluate the start and end points of the displacement curve.

An alternative method that can be used to calculate the value of ζ uses the slope of the current-time curve instead of its duration, as described in [2]. This method can be more accurate then the previously-described option because it avoids needing to take measurement from the beginning and ending regions of the plot. Unfortunately, it requires an accurate measurement of the buffer conductivity which can be inconvenient to obtain for the small volumes used in microfluidic systems.

To allow for temperature-dependent measurements, the fluid temperature in the microchannel must be controlled precisely. One possible method for this is to position the microchannel atop a hotplate that can be used to set and maintain precise channel temperatures. The temperature setting is increased after each experimental run and the procedure is repeated once the hot plate is allowed to reach steady-state. The solution in both reservoirs should be replaced between runs to eliminate any effects of electrochemical changes and concentration increases (due to evaporation).

Special attention must be given to the sizing of the critical elements of the experiment. In particular the resistor value should be carefully-selected to provide a measurable voltage drop for the current draw of the system in use. Using Ohm's law, a 500 kΩ resistor would provide a 1 V signal for every 2 μA of current passing through the circuit. This scenario is typically sufficient for relatively high concentration solutions (~ 1 mM) in moderately-sized microchannels ($D_h \sim 15$ μm). If solution concentration is lowered, or channel size is reduced, resistors of higher value might be required (such as 1 V per 0.5 μA) because the net current through the circuit is smaller.

Caution should also be exercised when deciding upon the channel dimensions to be used for measurement. Larger channels result in a higher electrical current that can be measured more-easily, but the higher current implies that the effect of Joule heating is enhanced. This may lead to a less stable measurement condition. Typically the smallest channel that still provides a voltage that is measurable with available equipment should be used.

Selection of the electric field to be used for experimental measurements also requires some care. In general, the voltage to be used should adhere to three experimental concerns:

- Resultant current should be sufficiently high as to be measured reliably
- but also, resultant current should be sufficiently low that no Joule heating effects are observed (i. e. electrical current stable over a span of at least 60 s).
- Experimental time interval should be long enough that reading error does not adversely effect interpretation of experimental results (typically ~ 30 s displacement time is required).

Running the experiment consecutively in opposite directions helps to eliminate any possible influence of pressure-driven flow. This ensures that measured velocity is due to the driving force of the electric field only and results in a more accurate calculation of the zeta potential. Other steps to be taken to minimize pressure-driven effects include meticulously leveling of the channel prior to experimentation, careful balancing of reservoir heights, and use of small channel heights (resulting in increased flow resistance). Large reservoirs should be used such that any change in fluid elevation caused by fluid flow during experimentation is miniscule.

Key Research Findings

From the perspective of a researcher wanting to implement temperature dependence of ζ into calculations of EOF, specific mathematical relationships are most important. For this purpose, Table 1 [3] summarizes ζ-Temperature

Temperature Effects on the Zeta Potential, Table 1 Summary of measured zeta potential results

Solution		Concentration	$\zeta(30\,°C)$ [mV]	$\zeta = \zeta(T)$[mV, °C]
	(a)	0.1 mM	– 108.2	– 0.06 T – 107.4
	(b)	1 mM	– 92.6	– 0.44 T – 78.2
KCl	(c)		(– 78.2)	(– 0.20 T – 72.8)
	(d)	10 mM	– 56.4	– 0.48 T – 43.8
	(e)		(– 38.4)	(– 0.09 T – 35.5)
1X TBE	(f)	89 mM Tris, 89 mM Boric Acid, 2 mM EDTA	– 52.4	– 0.35 T – 40.0
1X TE	(g)	10 mM Tris, 1 mM EDTA	– 68.2	– 0.01 T – 67.9
$Na_2CO_3/NaHCO_3$	(h)	10 mM	– 92.9	+ 0.02 T – 93.1

Bracketed entries denote PDMS:PDMS microchannels. All other entries represent PDMS:Glass.

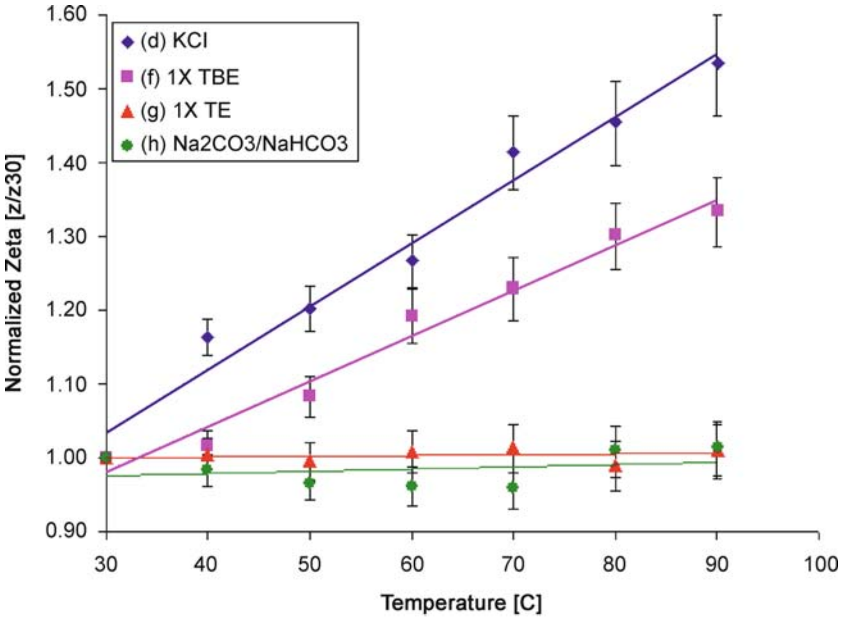

Temperature Effects on the Zeta Potential, Figure 4 Zeta potential measurements as a function of liquid temperature for a number of commonly-used solutions: (◇) 10 mM KCl, (□) 1X TBE, (△) 1X TE , and (○) 10 mM $Na_2CO_3/NaHCO_3$. All values are for PDMS:Glass microchannels and are normalized to the zeta potential measured at 30°C

relationships for a number of solutions that are commonly used by the microfluidics community. The tabulated data compares the temperature dependence for a number of different solutions, including three different concentrations of KCl. Also considered is the influence of the substrate material on the temperature dependence. Both glass and PDMS are examined, as both are highly-relevant to modern microfluidic applications. The data shown in Tab. 1 represents linear fits to experimental data, and are labeled on the other figures shown in this section. Bracketed entries denote PDMS : PDMS microchannels. All other entries represent PDMS : Glass.

Most of the figures present zeta potential values normalized to the value obtained at 30°C. This relative treatment makes it easier to directly compare solution curves that might otherwise be widely separated because of significant differences in the absolute zeta potential values. Error bars were obtained by considering that the greatest source of experimental uncertainty was present in the measurement of the time interval required for one fluid to displace the other during the current-monitoring procedure. It has been estimated that the time interval can be accurately measured within 1.0 s (i. e. ± 0.5 s). Accordingly, this information was used to calculate the range of possible zeta potential values and is reflected in the error bars shown on the figures displaying experimental results.

At this point, Fig. 1 merits further discussion. The experimental curve (◇) displays velocity data obtained by sub-

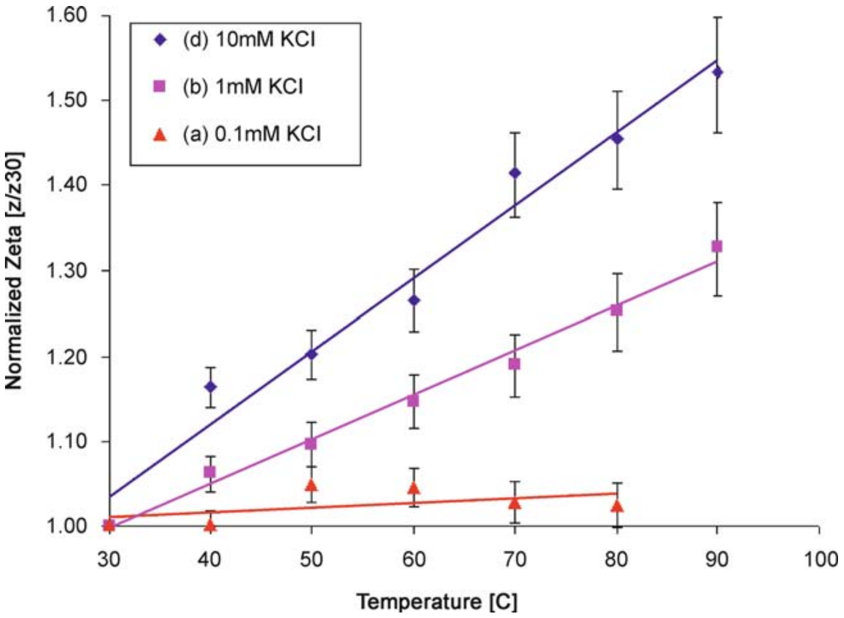

Temperature Effects on the Zeta Potential, Figure 5 Zeta potential measurements as a function of liquid temperature for a various concentrations of KCl solution: (◇) 10 mM KCl,(□) 1 mM KCl , and (△) 0.1 mM. All values are for PDMS : Glass microchannels and are normalized to the zeta potential measured at 30°C

stituting measured displacement time and channel length into Eq. 2. This particular data set shows values measured for a 10 mM KCl solution in a 300 μm × 8 μm PDMS : Glass microchannel under an applied electric field, E_Z, of 15,900 V/m. If no temperature effects are considered on any of the parameters used to calculate channel velocity (Eq. 1), the curve (△) is obtained. As expected, this plot demonstrates no dependence on temperature; it is clearly inadequate for describing the actually observed temperature-dependent velocity (◇). The next level of refinement to this is to make corrections for the known temperature dependence of the viscosity [10] [kg/m − s] (Eq. 3) and relative permittivity [10] (Eq. 4) parameters (temperatures expressed in Kelvin).

$$\mu = 2.761 \times 10^{-6} e^{\frac{1713}{T}} \tag{3}$$

and

$$\varepsilon = 305.7 e^{\frac{-T}{219}}, \tag{4}$$

This plot is represented by the squares (□) in Fig. 1 (note that the value of the zeta potential is held constant at its room-temperature value). This treatment still fails to accurately predict the EOF velocity in the microchannel. For example, at 90°C the EOF velocity predicted by this approach would be 1.5 mm/s, while the actual velocity is 2.2 mm/s; a 32% underestimation! This plot makes it clear that in some cases the typical approach for velocity estimation is insufficient. Since the zeta potential is the only unaltered variable in the ►Smoluchowski equation (Eq. 1), it is assumed that the discrepancy is owing to inaccuracy in this variable. In these cases the zeta potential should be taken to be a temperature-dependant variable rather than a constant.

Following below are results describing the temperature variation of ζ under a number of different circumstances. Specifically, the effect of temperature on the zeta potential of different solutions is considered. Also described is the influence of buffer concentration and the effect that the substrate material may have on the relationship. The temperatures considered vary between 30°C and 90°C. This range was selected because it is believed to encompass the breadth of temperatures that one would expect to encounter in a microfluidic setting. Testing at increments of 10°C allowed for the capture of sufficient detail to provide meaningful conclusions,

T

Buffer Comparison

Figure 4 shows the results from a series of tests conducted to determine whether-or-not temperature had any influence on the zeta potential values of solutions considered important to the microfluidics community. It is surprising to note that the zeta potential of some solu-

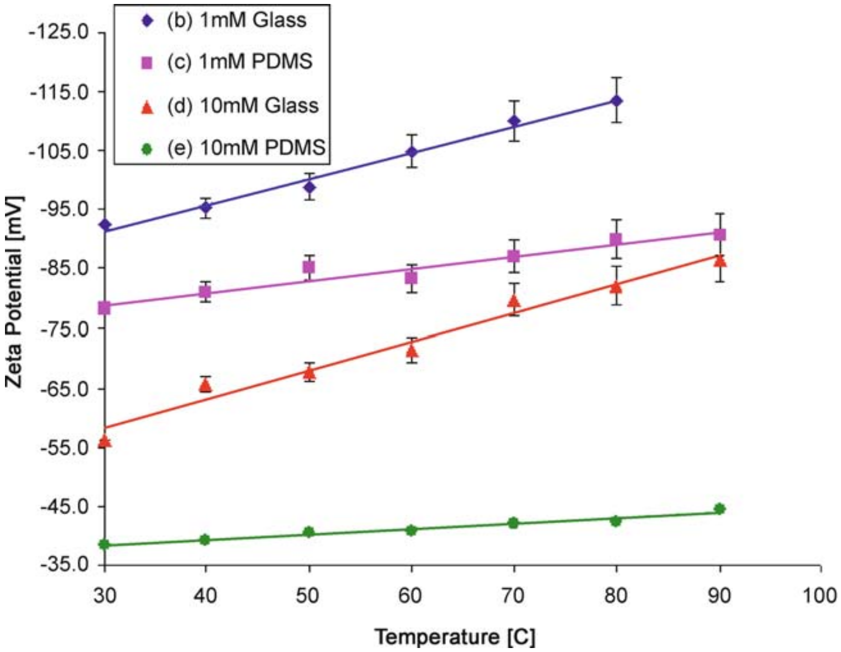

Temperature Effects on the Zeta Potential, Figure 6 Zeta potential measurements as a function of liquid temperature for KCl solution in microchannels of either Glass substrate: (◇) 1 mM, (△) 10 mM, or PDMS substrate: (□) 1 mM, (○) 10 mM

tions is strongly-dependent upon the temperature, while others demonstrate almost no temperature influence. For this reason proper care must be exercised when assuming a constant zeta potential over a relatively large temperature span.

Concentration Effects

The concentration of the solution is also known to influence the temperature dependence of the zeta potential. Consider the following test concentrations of KCl solution: 10 mM, 1 mM, and 0.1 mM. The zeta potential of each of these solutions was measured over the range 30°C to 90°C and the temperature response was noted. The results of the concentration effect analysis are shown in Fig. 5. Results obtained clearly indicate that the zeta potential of higher concentrations (e. g., 10 mM, 1 mM) of KCl solution exhibit a strong dependence on temperature, while the low concentration (e. g., 0.1 mM) KCl shows almost no dependence. Specifically, over the same temperature span ($30-90$°C) the magnitude of the zeta potential increases by 53% in the 10 mM KCl case, 33% in the 1.0 mM case, and almost no change is seen in the 0.1 mM case. Furthermore, the results demonstrate (Table 1) that the magnitude of the zeta potential decreases as the solution concentration increases. This is consistent with the findings of other studies [1, 2, 6]. It seems that the zeta potentials of the systems with lower ionic concentration solutions are less affected by the temperature change than their higher ionic concentration counterparts.

Substrate Effects (Glass vs. PDMS)

The results presented herein are geared towards researchers using PDMS-based microfluidic chips. These devices are fabricated with either a glass or PDMS substrate. It is important to understand the influence that changing the channel substrate material has on the ζ–temperature phenomenon. Results illustrate a marked difference between the two substrate materials for different concentration KCl solutions (Fig. 6).

The observed trend for each substrate material is similar. For both substrates tested the magnitude of the zeta potential increased with solution temperature. Interestingly, the rate of change of zeta potential with temperature in the 10 mM case was much lower for the PDMS substrate than for the glass substrate. This was not seen in the 1 mM case, where the curve slope was similar for both substrates. Additionally, the magnitude of the zeta potential value was lower in the PDMS : PDMS than in the PDMS : Glass channels for both solution concentrations tested (-38.4 mV vs. -56.4 mV, and -78.2 mV vs. -92.6 mV for 10 mM and 1 mM KCl at 30°C, respectively). This result agrees with the trend observed by other groups [8] under similar conditions.

Future Directions for Research

Relatively little work has been done to characterize the effect of temperature on the zeta potential. There is much research that must still be done before we have a complete understanding of this phenomenon. The most immediate need is to conduct ζ-temperature characterization experiments for more buffers (different solutions at varying concentrations). This data will allow researchers to account for this effect in any required EOF calculations. Also required is testing in other materials used to form microchannels; silica capillaries, etched-glass, PMMA and other materials used in the microfluidics community.

A research topic of ever-increasing value is to test this effect at the nanoscale. It would be interesting to know if this phenomenon still exists in nanofluidic environments. If it does, particular relationships should be characterized and quantified.

Ultimately, the most important work still remaining is to offer a proper explanation of the phenomenon itself. Why does the zeta potential vary with temperature in some solutions, but not all? We should be able to predict which buffers will have a temperature dependent zeta potential and which will not vary. A theoretical relationship would prove most useful in avoiding the onerous task of compiling and tabulating a vast array of data covering all of the scenarios that a researcher in this field might encounter.

Cross References

► Electrical Current-Monitoring Methods
► Electrical Double Layers
► Electrokinetic Flow and Ion Transport in Nanochannels
► Electroosmotic Flow (DC)
► Joule Heating in Electokinetic Flow: Theoretical Models
► Joule Heating vs. Chip Materials
► Methods for Measuring Zeta Potential
► Zeta-Potential
► Zeta Potential Measurement

References

1. Hunter RJ (1981) Zeta potential in colloid science: principles and applications. Academic, New York
2. Sze A, Erickson D, Ren L, Li D (2003) Zeta-potential measurement using the smoluchowski equation and the slope of the current-time relationship in electroosmotic flow. J Colloid Interf Sci 261:402–410
3. Venditti R, Xuan X, Li D (2006) Experimental characterization of the temperature dependence of zeta potential and its effects on electroosmotic flow velocity in microchannels. Microfluid Nanofluid 2:493–499
4. Erickson D, Sinton D, Li D (2003) Joule heating and heat transfer in poly(dimethylsiloxane) Microfluidic Systems. Lab Chip 3:141–149
5. Revil A, Pezard PA, Glover PWJ (1999) Streaming potentials in porous media 1. Theory of the zeta potential. J Geophys Res 104(B9):20021–20031
6. Revil A, Hermitte D, Spangenberg E, Cochémé JJ (2002) Electrical properties of zeolitized volcaniclastic materials. J Geophys Res 107(B8):2168
7. Reppert PM, Morgan FD (2003) Temperature-dependent streaming potentials: 1. Theory. J Geophys Res 108(B11 ECV3):1–12
8. Kirby BJ, Hasselbrink Jr. EF (2004) Zeta potential of microfluidic substrates: 1. Theory, experimental techniques, and effects on separations. Electrophoresis 25:187–202 and references cited therein
9. Huang X, Gordon MJ, Zare RN (1988) Current-monitoring method for measuring the electroosmotic flow rate in capillary zone electrophoresis. Anal Chem 60:1837–1838
10. Knox JH, McCormack KA (1994) Temperature effects in capillary electrophoresis. 1. Internal capillary temperature and effect upon performance. Chromatographia 38:207–214

Temperature Gradient Focusing

GONGYUE TANG, CHUN YANG
School of Mechanical and Aerospace Engineering,
Nanyang Technological University, Singapore, Singapore
mcyang@ntu.edu.sg

Synonyms

Thermal gradient focusing

Definition

Temperature gradient focusing was first reported by Ross and Locascio [1]. In principle, with an appropriate buffer having a temperature-dependent ionic conductivity, the application of a temperature gradient creates a gradient in both the electric field and electrophoretic velocities. Charged species can be stationary and concentrated at a unique point where the sum of the bulk and electrophoretic velocities is equal to zero. This means that different species, with differing electrophoretic mobilities, can be focused at spatially distinct points along microchannels or capillaries.

Overview

Separation of charged species can be achieved using capillary electrophoresis (CE), a process that utilizes the different electrical mobilities of dielectric particles/macromolecules under an applied electric field. Due to low reagent and sample consumption and high efficiency, CE has become an effective method for the sep-

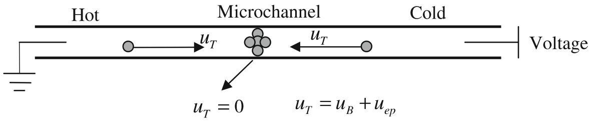

Temperature Gradient Focusing, Figure 1 Schematic illustration of temperature gradient focusing in a microchannel. The microchannel is heated at one end and cooled at the other, producing a temperature gradient in the middle. The sample solute velocity u_T is the summation of two opposite velocities: the electrophoretic velocity, u_{ep} and the bulk liquid velocity, u_B. As both u_{ep} and u are a function of temperature, there exists a unique point along the channel where the sample solute velocity u_T is equal to zero. The sample solute will then move from both directions toward their respective zero-velocity points where the solutes are focused/concentrated

aration of biologically or chemically charged components, such as DNA sequencing in genetic engineering [2].

However, a typical CE-based separation suffers from relatively poor detection limits, particularly when coupled with UV absorbance detection. Consequently, CE has not been widely adopted for the analysis of drug molecules in biological fluids such as serum or urine in which the drug and its metabolites are usually at much lower concentrations than in a laboratory preparation [3, 4]. To address these problems, novel methods are needed to either improve the detection technology or increase the concentration of the sample prior to detection. For CE involving extremely short optical path lengths, the detection technology has been already pushed to its limit, thus methods of concentrating the sample prior to detection appear to be more promising [5].

Although sample extraction methods are often used to preconcentrate samples before analysis by CE, these methods increase analysis time and cost. Transient stacking, sweeping, or isotachophoresis techniques can also be used in conjunction with CE to improve the detection limits. With these types of methods, the sample is concentrated by causing the sample plug to move across a boundary between two buffers with different compositions in a capillary or microchannel. The two buffer compositions are chosen such that the analytes of interest will move more slowly through one buffer than the other. As the sample plug moves from the fast side of the boundary to the slow side, it is compressed and thus concentrated. Concentration enhancements of the order of 100 – 1000-fold are typical [6]. However, these methods are not universally applicable and often require sample pretreatment or extraction to produce a sufficiently clean sample for stacking.

Temperature gradient focusing (TGF) is a newly developed technique for spatially focusing and separating ionic analytes in microchannels or capillaries. With this method, a controlled flow of buffer is applied to the capillary to counterbalance the electrophoretic motion of the analytes. The basic mechanism of TGF is illustrated in Fig. 1. In this case, by applying a temperature gradient along the capillary filled with a buffer with a temperature-dependent ionic conductivity, a nonuniform electric field along the capillary is created. Consequently, the local flow velocity can be adjusted such that the total velocity, u_T (i. e., electrophoretic velocity, u_{ep} + bulk velocity, u) of an analyte is equal to zero at a unique point along the channel. Analytes will then move inward from both directions toward their respective zero-velocity points where the analytes are focused/concentrated.

The major limitation of microchip CE is that it requires long channels for high resolution separations, and long channels are difficult to fit into the small area of a microfluidic chip without introducing dispersion that degrades the resolution. High-resolution TGF does not require long channels; the separation presented in this study only needs relatively short capillaries (about 20 mm in length), with the separation occurring in only 4 mm of the column (a large proportion of the capillary length is required for attachment to the sample and waste reservoirs). High-resolution microfluidic chip-based TGF separations could conceivably be performed in microchannels that are only a few millimeters long, some of which could easily fit into a small, planar chip format [7].

The temperature gradient required for TGF can either be an externally applied temperature gradient or can be generated by Joule heating due to the applied electric field that also drives the focusing [1]. We will emphasize the latter. It is well known that Joule heating results from the inevitable volumetric heating when an electric field is applied across a conducting medium such as an electrolyte. Such heat would lead to an increase in the buffer temperature and develop temperature gradients in the buffer solution along both radial and axial directions of the microchannel [8]. In the following section we will present a comprehensive numerical model that describes the Joule heating-induced TGF.

Basic Methodology

To address the problems in TGF assosciated with Joule heating, computer-aided numerical simulation is needed to solve the coupled governing equations which will be presented below.

Transport of Charged Solutes

As mentioned earlier, the TGF technique is mainly used for electrophoretic concentration and separation of the solutes, and thus the transport of the charged solutes needs to be modeled. For ease of analysis, it is assumed that there is no adsorption of sample solutes onto the capillary

wall and no interaction between the sample solutes and the electrolyte components. In addition, in the vast majority of microfluidic applications, the buffer concentration is many times (100 or more) higher than that of the sample solutes, and hence, the transport equation of the charged solutes can be formulated as [9]

$$\frac{\partial C_s}{\partial t} + \left(\boldsymbol{u} + \boldsymbol{u}_{ep}\right) \cdot \nabla C_s = \nabla \cdot \left[D_s(T) \nabla C_s\right] \quad (1)$$

where $\boldsymbol{u}$ is the bulk liquid velocity (i. e., electroosmotic flow (EOF) velocity of the buffer solution) and will be described in the next section. C_s is the solute concentration and $D_s(T)$ is the temperature-dependent mass diffusivity of the solutes, given by

$$D_s(T) = D_{s0} f_D(T) \quad (2)$$

where D_{s0} is the diffusion coefficient of the solutes at room temperature, and $f_D(T)$ is a function accounting for the temperature dependence of the diffusion coefficient of the sample solutes. The electrophoretic velocity of the solutes $\boldsymbol{u}_{ep}$ can be expressed as

$$\boldsymbol{u}_{ep} = \mu_{ep}(-\nabla\phi) \quad (2a)$$

where ϕ is the applied electrical field potential. μ_{ep} is the electrophoretic mobility of the solutes, and can be written as

$$\mu_{ep} = \mu_{ep0} f_{ep}(T) \quad (2b)$$

where μ_{ep0} is the electrophoretic mobility of the solutes at room temperature and $f_{ep}(T)$ is a function accounting for the temperature dependence of the electrophoretic mobility of the solutes.

Flow Field

Since the TGF utilizes the counterbalancing bulk buffer flow (i. e., EOF) and electrophoretic motion, the flow field should be formulated. Considering the buffer solution to be a Newtonian fluid of uniform and homogeneous composition, the laminar, incompressible flow is governed by the Navier–Stokes equation

$$\rho\left(\frac{\partial \boldsymbol{u}}{\partial t} + \boldsymbol{u} \cdot \nabla \boldsymbol{u}\right) = -\nabla p + \nabla \cdot \left[\mu(T) \nabla \boldsymbol{u}\right] - \rho_e \nabla \Phi \quad (3a)$$

$$\nabla \cdot \boldsymbol{u} = 0 \quad (3b)$$

where $\mu(T)$ is the buffer viscosity, and its dependence on temperature is expressed by $\mu(T) = 2.761 \times 10^{-6} \exp(1713/T)$. ρ and p are the solution density and hydrodynamic pressure, respectively. From Eq. (3a), it can be seen that the evaluation of the momentum equation requires a description of the net charge density, ρ_e, and the total electrical potential, Φ. It is assumed that Φ can be decoupled as the summation of the electrical double layer potential, ψ, and the applied electric potential, ϕ, as expressed in Eq. (4)

$$\Phi = \phi + \psi \quad (4)$$

Electrical Double Layer Potential

When a solid surface is in contact with an electrolyte, the surface usually becomes charged. Due to electrostatic interactions, both anions and cations are preferentially redistributed near the charged surface, leading to the formation of an electric double layer (EDL). According to the theory of electrostatics, the EDL potential distribution, ψ is governed by the Poisson equation, written as [9]

$$\nabla \cdot \left[\varepsilon(T) \nabla \psi\right] = -\frac{\rho_e}{\varepsilon_0} \quad (5)$$

where $\varepsilon(T)$ is the dielectric permittivity of the electrolyte, and its dependence on the temperature is given by $\varepsilon(T) = 305.7 \exp(-T/219)$ [10]. ε_0 is the permittivity of a vacuum.

For a symmetric electrolyte (i. e., both co-ions and counter-ions have the same charge valence, $|\sigma_+| = |\sigma_-| = \sigma$), its ionic concentration distributions for both anions and cations are assumed to follow the Boltzmann distributions [9], and hence the local charge density,ρ_e, is given by

$$\rho_e = \sigma e (n_+ - n_-) = -2\sigma e n_0 \sinh\left(\frac{\sigma e \psi}{k_B T}\right) \quad (6)$$

e is the fundamental charge, T is the absolute temperature, k_b is the Boltzmann constant, and n_0 is the ionic number concentration in the bulk electrolyte solution.

Combining Eqs. (5) and (6), we obtain the well-known Poisson–Boltzmann equation expressed as [9]

$$\nabla \cdot \left[\varepsilon(T) \nabla \psi\right] = \frac{2 n_0 \sigma e}{\varepsilon_0} \sinh\left(\frac{\sigma e \psi}{k_b T}\right) \quad (7)$$

Applied Electrical Potential

According to Probstein [9], the distribution of the applied electric potential, ϕ is governed by the Laplace equation

which is derived on the basis of the law of conservation of current and is written as

$$\nabla \cdot \left[\lambda(T)\nabla\phi\right] = 0 \quad (8)$$

where $\lambda(T)$ is the temperature-dependent electrical conductivity of the electrolyte, and is given by [10].

$$\lambda\,(T) = \lambda_+\,(T)\,\eta_+ + \lambda_-\,(T)\,\eta_- \quad (9a)$$

$$\lambda_+(T) = \lambda_{+0} f_{\lambda+}(T) \quad (9b)$$

$$\lambda_-(T) = \lambda_{-0} f_{\lambda-}(T) \quad (9c)$$

Here [$\lambda_+\,(T)$ and $\lambda_-\,(T)$] and [λ_{+0} and λ_{-0}] are the ionic conductivity of the cations and anions of the electrolyte at temperature T and room temperature, respectively. $f_{\lambda+}(T)$ and $f_{\lambda-}(T)$ are functions accounting for the temperature dependence of the ionic conductivity of the cations and anions, respectively. η_+ and η_- denote the mole concentration of the cations and anions of the electrolyte, respectively.

Joule Heating-Induced Temperature Field

The Joule heating-induced temperature field is governed by the energy equation expressed as

$$\rho c_{\mathrm{p}}\left(\frac{\partial T}{\partial t} + \boldsymbol{u}\cdot\nabla T\right) = k_{\mathrm{l}}\nabla^2 T + \lambda(T)\,(\nabla\phi)^2 \quad (10)$$

where c_{p} and k_{l} are the specific heat and thermal conductivity of the buffer solution, respectively.

In addition, a conjugate heat transfer problem has to be solved to simultaneously account for the heat transfer in the solid channel wall, which is governed by the heat conduction equation expressed as

$$\rho_{\mathrm{s}} c_{\mathrm{ps}}\left(\frac{\partial T}{\partial t}\right) = k_{\mathrm{s}}\nabla^2 T \quad (11)$$

where c_{ps}, ρ_{s}, and k_{s} are the specific heat, density, and thermal conductivity of the microchannel wall, respectively.

Initial and Boundary Conditions

At the initial time, the microchannel is filled with an electrolyte which has the same solute concentration and temperature as the electrolyte in the inlet reservoir. The fluid is assumed to be initially stationary.

A high voltage is then imposed at the inlet reservoir, and the outlet reservoir is grounded. Due to electroosmosis, the electrolyte carrying the solutes of a given concentration is continuously injected from the inlet reservoir at room temperature, and the heated electrolyte is streamed from the microchannel to the outlet reservoir.

At all channel wall surfaces, the no-slip boundary condition is applied to the velocity field (the Navier–Stokes equation), the fixed zeta-potential boundary condition is imposed on the EDL potential field (the Poisson–Boltzmann equation), and the insulation boundary condition is assigned to the applied electric field (the Laplace equation), and the no-mass penetration condition is specified for the solute mass concentration field (the mass transport equation). In addition, the third-kind boundary condition (i. e., the natural convection heat transfer with the surrounding air) is applied to the temperature field at all the outside surfaces of the fabricated channels to simultaneously solve the energy equation for the buffer solution together with the conjugated heat conduction equation for the channel wall.

Key Research Findings

In this section, numerical simulations of the Joule heating-induced temperature field and the sample solute concentration distributions in a microchannel structure with a step change in cross-section (see Fig. 2) will be presented. Because the total current passing through a dielectric channel is constant, the current density in the narrow channel is higher than that in the wide channel. As shown in Eq. (10), the Joule heating is proportional to the second power of the current density, so more heat is generated in the narrow channel. Consequently, the temperature in the narrow channel is higher than that in the wide channel, resulting in the formation of a sharp temperature gradient at the junction. The variations in the

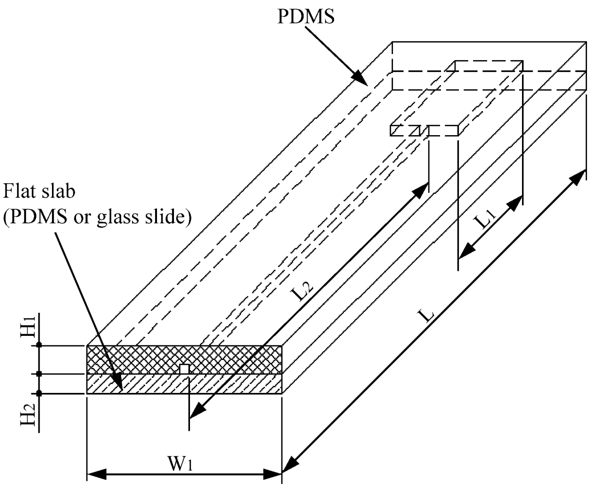

Temperature Gradient Focusing, Figure 2 Schematic diagram of the microchannel with a step change in cross-section

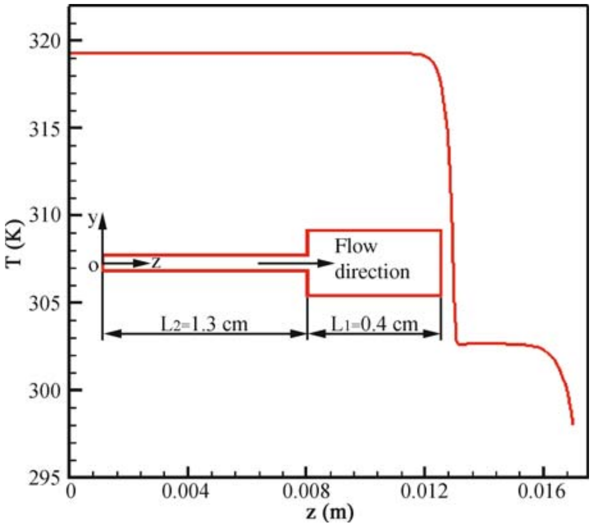

Temperature Gradient Focusing, Figure 3 Temperature variation along the centerline of the microchannel

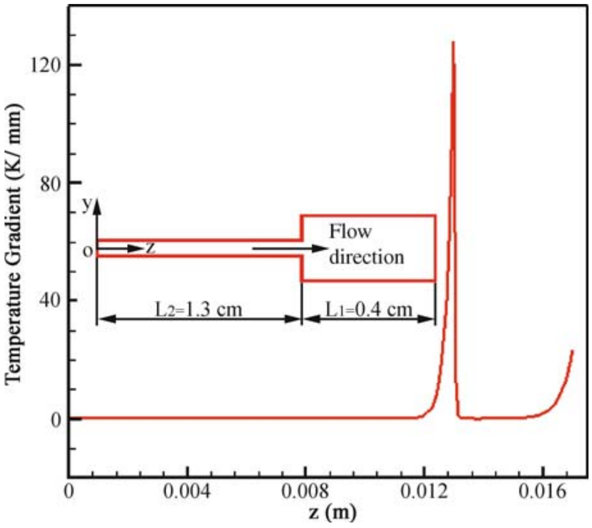

Temperature Gradient Focusing, Figure 4 Temperature gradient variation along the centerline of the microchannel

temperature and temperature gradient along the centerline of the microchannel with a step change in cross-section are shown in Figs. 3 and 4, respectively. The microchannel is made of Polydimethylsiloxane (PDMS) sealed with another PDMS sheet. The parameters used in the simulation are similar to those reported by Ross and Locascio [1], and they are the chip dimensions ($W_1 = 7\,\text{mm}$, $L = 17\,\text{mm}$, $L_1 = 4\,\text{mm}$, $H_1 = H_2 = 2\,\text{mm}$) and the cross-sections for the narrow channel (40 μm × 30 μm) and the wide channel (300 μm × 30 μm) (see Fig. 2). The buffer solution is 20 mM $NaHCO_3$ electrolyte, the average electric field strength is $E_0 = 1000\,\text{V/cm}$, and the air natural-convection cooling mode is selected (i. e., the convection heat transfer coefficient $h = 10\,\text{W/m}^2\text{K}$). Table 1 provides the expressions for the temperature-dependent functions of the solute mass diffusivity ($f_D(T)$), solute electrophoretic mobility ($f_{ep}(T)$), and buffer electrical conductivity ($f_{\lambda+}(T)$ and $f_{\lambda-}(T)$). The numerical predictions presented in Figs. 3 and 4 are consistent with the experimental data [1]. Experimentally, it was recorded that the temperature spanned the range 23 – 39 °C (at room temperature 22 °C, with a maximum gradient of 150 °C/mm. While the numerical simulations show that the temperature varies in the range 28 – 43 °C (the room temperature in the simulation is set at 25 °C), with a maximum gradient of 140 °C/mm. Both the initial and injected sample solute concentrations are 8 μM.

Figure 5 shows the simulated sample solute concentration contours at sequential time of 0 s, 40 s, 90 s, 140 s and 190 s after the electric field has been imposed. Figure 6 displays the quantitative results of the sample solute concentrations varying along the microchannel centerline. As shown in Figs. 5 and 6, the simulations provide reasonable predictions which are consistent with the experimental results [1]. Figure 6 also shows that 190 s after the electric field has been applied, the peak of the sample concentration at the channel centerline reaches 2.8×10^{-3} M which is 350-fold the initial and injected sample concentrations. A similar value was reported by Ross and Locascio [1].

Future Directions for Research

Concentration/separation of sample solutes is one of most important functions in micro- and nanofluidic systems. TGF has proved to be a promising technique that can achieve concentration and separation in microfluidic devices. However, so far very limited experimental and theoretical investigations have been reported. Experimentally, it is highly desirable to develop various microfluidic structures that can be utilized by the TGF technique to concentrate different samples. Furthermore, more

T

Temperature Gradient Focusing, Table 1 Expressions for the temperature-dependent functions of the solute mass diffusivity ($f_D(T)$), solute electrophoretic mobility ($f_{ep}(T)$), and buffer electrical conductivity ($f_{\lambda+}(T)$ and $f_{\lambda-}(T)$)

Properties	Expression	Function
$D_S(T)$	$D_S(T) = D_{S0} f_D(T)$	$f_D(T) = [1 + 0.02(T - T_0)]$
μ_{ep}	$\mu_{ep} = \mu_{ep0} f_{ep}(T)$	$f_{ep}(T) = [1 + 0.04(T - T_0)]$
$\lambda_\pm(T)$	$\lambda_\pm(T) = \lambda_{\pm 0} f_{\lambda\pm}(T)$	$f_{\lambda\pm}(T) = [1 + 0.02(T - T_0)]$

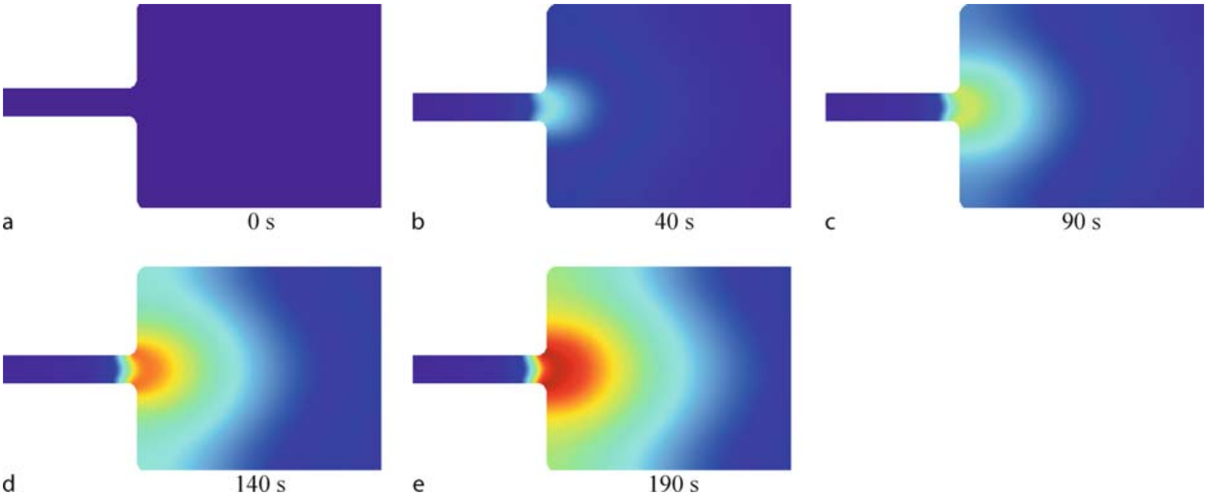

Temperature Gradient Focusing, Figure 5 Sample solute concentration contours near the junction of the narrow and wide microchannels at various times: (**a**) 0 s, (**b**) 40 s, (**c**) 90 s, (**d**) 140 s, and (**e**) 190 s

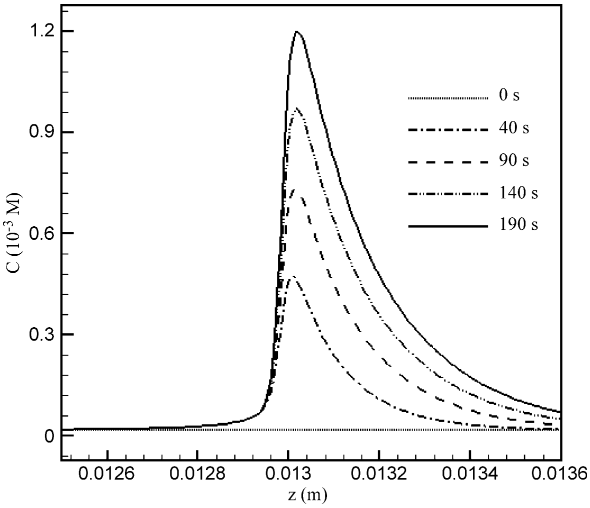

Temperature Gradient Focusing, Figure 6 Distributions of the sample solute concentration along the centerline of the microchannel at various times

experiments should be carried out to characterize the thermo-electrical properties of buffers and samples so as to obtain the temperature-dependent electroosmotic mobility and electrophoretic mobility, as well as buffer conductivity, viscosity and dielectric permittivity for each individual sample and buffer solution. In addition, the development of reliable, accurate, high-resolution, experimental techniques for measuring flow, temperature and sample solute concentration fields in microfluidic channels is needed. Theoretically, the model development of TGF is still in its infancy. The models presented in this study assume the dilute solute sample and linear mass flux–driving forces correlations. However, when the concentrations of the sample solute and the buffer solution are comparable, the aforementioned assumptions break down. Moreover, the channel wall zeta-potential in this situation may become nonconstant. More comprehensive models should be developed to incorporate the solute–buffer and solute–channel wall interactions as well as the heterogeneous distribution of the channel zeta-potentials.

Recent years have seen significant academic interest in nanofluidics. Fundamental research has reached a feverish level. However, no information is available on the demonstration of the TGF in nanofluidic channel structures.

Cross References

- ► Concentration Gradient Generation and Control
- ► Electrothermal Effects
- ► Temperature Control in Microfluidic Systems
- ► Joule Heating in Electrokinetic Flow: Theoretical Methods
- ► Temperature Gradient Generation and Control

References

1. Ross D, Locascio LE (2002) Microfluidic temperature gradient focusing. Anal Chem 74 11:2556–2564
2. Jorgenson JW (1987) Capillary zone electrophoresis: New directions in electrophoretic methods. ACS Symposium Ser 335, Washington DC

3. Scriba GKE (2003) Pharmaceutical and biomedical applications of chiral capillary electrophoresis and capillary electrochromatography: An update. Electrophoresis 24(15):2409–2421
4. Bonato PS (2003) Recent advances in the determination of enantiomeric drugs and their metabolites in biological fluids by capillary electrophoresis-mediated microanalysis. Electrophoresis 24(22–23):4078–4094
5. Ghosal S, Horek J (2005) Mathematical model describing gradient focusing methods for trace analytes. Anal Chem 77(16):5380–5384
6. Urbánek M, Křivánková L, Boček P (2003) Stacking phenomena in electromigration: From basic principles to practical procedures. Electrophoresis 24(3):466–485
7. Balss KM, Vreeland WN, Phinney KW, Ross D (2004) Simultaneous concentration and separation of enantiomers with chiral temperature gradient focusing. Anal Chem 76(24):7243–7249
8. Tang GY, Yan DG, Yang C, Gong HQ, Chai JC, Lam YC (2006) Assessment of Joule heating and its effects on electroosmotic flow and electrophoretic transport of solutes in microfluidic channels. Electrophoresis 27(3):628–639
9. Probstein RF (1994) Physiochemical Hydrodynamics: An Introduction. Wiley, New York
10. Weast R, Astle MJ, Beyer WH (1986) CRC Handbook of Chemistry and Physics. CRC, Boca Raton

Temperature Gradient Generation and Control

Barbaros Cetin, Dongqing Li
Department of Mechanical Engineering,
Vanderbilt University, Nashville, TN, USA
barbaros.cetin@vanderbilt.edu

Synonyms

Temperature control

Definition

In today's microfluidic technology, electrokinetic transport is used to perform many chemical and biological analyses in Lab-on-Chip devices, such as clinical diagnoses, DNA scanning, cell manipulation, cell patterning, and molecular detection. Due to the presence of an electrical potential gradient in electrokinetic transport, Joule heating is a ubiquitous phenomenon which may lead to an increase in the overall temperature and to temperature gradients in the transverse and longitudinal directions inside the channels. These generated temperature gradients and their control are crucial for the performance of the devices.

Overview

Simply, a temperature gradient can be generated by means of two temperature reservoirs at different temperatures at the inlet and the exit of a microchannel. However, in electrokinetic transport, Joule heating results in heat generation which can also result in temperature gradient generation in the longitudinal and transverse directions inside the microchannels due to

- the effect of the temperature reservoirs at the inlet and the exit of the channel (thermal end effects);
- the different thermal boundary conditions at the channel wall (thermostatted and thermostatted region along the channel wall);
- the cross-sectional area change along the channel; and
- the flow of two parallel streams having different molar concentrations.

These temperature gradients also affect the electrical field, flow field, and concentration field via temperature-dependent electrical conductivity, viscosity, and diffusivity. Large temperature gradients inside channels may cause band broadening and dispersion that leads to inefficient and low-quality separation for separation processes [1]. Effective dissipation of the heat generated by Joule heating is critical for reproducible and efficient separations in electrokinetically driven separation systems. These temperature gradients can also be useful for some applications such as isoelectric focusing (IEF) [2–4] and temperature gradient focusing (TGF) [5, 6]. Therefore, generation and control of the temperature generation inside the Lab-on-Chip are very important to enhance and optimize the performance of the device.

Xuan and Li [7] developed an analytical model to study Joule heating effects on electrokinetic transportation in capillary electrophoresis with thermal end effects by considering the temperature-dependent fluid viscosity and electrical conductivity. They derived closed formulas for steady-state temperature field, applied electrical potential field, pressure field, velocity field, and transient concentration field which provide fundamental understanding of effects of the temperature gradients on transport of heat, electricity, momentum, and mass species in capillary electrophoresis. They showed that Joule heating enhances the transport of samples which can provide a reduction in the analysis time for capillary electrophoretic separations. Despite the time reduction benefit, they also showed that Joule heating and thermal end effects increase the sample dispersion which leads to a lower separation efficiency. Xuan and coworkers [8, 9] also studied the same effects with temperature-dependent fluid properties, both numerically [8] and experimentally [9]. They used a caged-fluorescent dye-based visualization technique to measure the EOF velocity profile, and a fluorescence-based thermometry technique to measure the temperature profile inside the channel. They observed concave and convex velocity profiles due to distortion of the plug-like profile

T

because of the induced pressure gradients resulting from the axial temperature gradient.

Non-uniform cooling across the length of the channels can be experienced by some thermostatted portion of the channel either by

1. forced convection of the channel or
2. cooling of the channel by optical infrastructure in the detection region.

This non-uniform dissipation also results in temperature gradients inside the channel. Xuan and Li [10] studied case (1.) and Sinton et al. [11] studied case (2.) for a microcapillary.

Temperature gradients along the channel can also be used to focus different species inside the microchannel. IEF and TGF are the two methods that use this concept for focusing. Temperature generation along the channel is achieved both by using two reservoirs at different temperatures [4, 5] and by using Joule heating by means of the variable cross-sectional area along the channel [2, 3, 5, 6]. Using two parallel flow streams with different molar concentrations also results in non-uniform Joule heating and hence a temperature gradient in the transverse direction as well as the longitudinal direction. Cetin and Li [12] studied the effect of these two streams on the temperature field inside a microchannel for the potential use of this gradient in cell manipulation.

Cross References

► Temperature Control in Microfluidic Systems
► Methods for Temperature Measurements

References

1. Li D (2004) Electrokinetics in Microfluidics. Elsevier Academic Press, Amsterdam
2. Pawliszyn J, Wu J (1993) Ampholyte-free isoelectric focusing of proteins in cone-shaped capillaries. J Microcol 5:397
3. Fang XH, Adams M, Pawliszyn J (1999) A model of thermally generated pH gradients in tapered capillaries. Analyst 124:335
4. Lochmuller CH, Breiner SJ, Ronsick CS (1989) Open-channel isoelectric focusing in thermally engerdered pH gradients. J Chromatography 480:293
5. Ross D, Locascio LE (2002) Microfluidic temperature gradient focusing. Anal Chem 74:2556
6. Kim SM, Sommer GJ, Burns MA, Hasselbrink EF (2006) Low-power concentration and seperation using temperature gradient focusing via Joule heating. Anal Chem 78:8028
7. Xuan X, Li D (2005) Analytical study of Joule heating effects on electrokinetic transportation in capillary electrophoresis. J Chromatography A 1064:227
8. Xuan X, Sinton D, Li D (2004) Thermal end effects on electroosmotic flow in a capillary. Int J Heat Mass Transf 47:3145
9. Xuan X, Xu B, Sinton D, Li D (2004) Electroosmotic flow with Joule heating effects. Lab Chip 4:230
10. Xuan X, Li D (2005) Electrophoresis 26:166
11. Sinton D, Xuan X, Li D (2004) Thermally induced velocity gradients in electroosmotic microchannel flows: the cooling influence of optical infrastructure. Exp Fluid 37:872
12. Cetin B, Li D (2007) Modeling and Simulation of 2D, electroosmotic flow (EOF) in a slit channel with Joule heating effect. Proc 16th Natl Conf Therm Sci, Kayseri, Turkiye 30 May–2 June 2007

Temperature Measurement, Methods

VINAY K. NATRAJAN, KENNETH T. CHRISTENSEN
Department of Mechanical Science and Engineering, University of Illinois, Urbana, IL, USA
ktc@uiuc.edu

Synonyms

Thermometry

Definition

Thermometry is the determination of a medium's temperature as inferred from properties of a probe whose characteristics are highly dependent on temperature.

Overview

There exists a growing demand for the development of advanced diagnostics for high-precision temperature measurements at the microscale. This demand is driven by the ever-increasing use of complex microfluidic devices such as micro-total analysis systems (μ-TAS) and μ-heat exchangers. Lab-on-a-Chip devices, which integrate multiple complex laboratory functions onto a single chip-sized substrate, often require precise temperature control to maximize the productivity of chemical operations like mixing, reactions and separations. Such control becomes especially critical when electrokinetic pumping is used for driving flow through these devices, as the current flowing through the buffer solution can result in significant internal heat generation, a phenomenon known as Joule heating. Since most microfluidic-based MEMS devices utilize very high heat and mass transfer rates, a thorough understanding of their thermal transport characteristics is paramount for optimizing their design for increased performance and reliability.

Several methods exist for measurement of fluid and/or surface temperature at both the macro- and micro-scale; however, the appropriate choice of methodology is tightly coupled to the specific application under consideration. Further, the capabilities of many techniques that are commonly implemented at the macroscale are greatly challenged in microscale applications where one wishes to

not only resolve the local temperature but also *temperature gradients*. Therefore, any technique employed in this regard must not only have satisfactory spatial resolution but also excellent temporal response since dissipation of thermal gradients at the microscale occurs over extremely short time scales owing to high heat-transfer rates and large surface area-to-volume ratios. As such, obtaining accurate measurements of fluid temperature at the microscale is still a topic of intense research interest.

Until recently, temperature measurements in microfluidic systems were limited to measures of bulk fluid temperature at the inlet and outlet of microfluidic sections or simply measurement of the substrate temperature. With regard to local temperature measurements, thermocouple probes provide highly accurate measures of fluid and/or substrate temperature with excellent temporal response. However, thermocouples can often be physically intrusive and generally suffer from poor spatial resolution since most probes have a characteristic size of several microns or more. Alternatively, microfluidic devices can be fabricated with integrated microscale resistance temperature detectors (RTDs's) embedded in the substrate with spatial extents on the order of a few microns [13]. Micro-RTDs overcome the intrusiveness issues of thermocouples; however, their fabrication can be quite complex and RTDs still suffer from poor spatial resolution which limits their ability to resolve local thermal gradients. Further, while RTDs are convenient for monitoring surface temperature, they do not provide a direct measure of fluid temperature.

While local measures of temperature may suffice for some applications, many others require a detailed description of the spatial and/or temporal variations of temperature on a surface or in a fluid. ► Infrared thermography, for example, involves the imaging of the electromagnetic energy radiated by a surface in a specific infrared band which can be directly related to the surface temperature. However, while infrared thermography yields the spatial distribution of temperature on a surface, it does not provide a measure of fluid temperature In contrast, both thermochromic liquid crystals (TLCs) and ► fluorescent thermometry (a specific application of the more general laser-induced fluorescence (LIF) technique) can provide excellent measures of fluid temperature fields. Thermochromic liquid crystals are organic molecules that behave as a liquid but maintain a crystal-like arrangement akin to a solid. For a certain class of TLCs, the molecules align in a helical pattern that reflects a preferred wavelength when under white-light illumination. Since the pitch of the helical arrangement has strong temperature dependence, the wavelength of the reflected light provides a measure of temperature. Therefore, imaging of the light reflected by a suspension of TLCs in a fluid or a surface coating of TLCs can provide a measure of temperature over a given field of view. In fluorescent thermometry, a fluorescent dye whose ► fluorescence intensity is a strong function of temperature is dissolved in a fluid of interest or is coated on a surface of interest. The fluorescent dye is illuminated with incident light which excites the molecules to fluoresce at a different wavelength and this fluoresced light is recorded by a CCD camera. For many dyes, the intensity of the fluoresced light is a strong function of temperature. Therefore, imaging of the fluorescence, in concert with an a priori calibration of the fluorescence intensity with temperature, provides a measure of the temperature over the field of view. Finally, fluid temperature can be inferred by measuring the Brownian diffusion of sub-micron particles suspended in a fluid of interest since this diffusion process is known to be strongly correlated with temperature. While suitable for assessing fluid temperature, measures of Brownian motion cannot provide an estimate of surface temperature since the technique relies upon the free motion of particles suspended in a fluid.

All of the aforementioned methods certainly have many advantages and disadvantages, particularly when implemented at the microscale. Each of these methods is described in detail below and select applications of these methods at the microscale are highlighted.

Basic Methodology

Contact Temperature Sensors

Principle and Implementation

► Contact temperature sensors represent a class of probes used to infer the temperature of a medium through the thermal equilibrium attained between the sensor and the medium when in contact. In particular, changes in the medium temperature yields a corresponding variation of the sensor resistance or output voltage that can be used to infer the temperature difference via an a priori calibration of the sensor output with temperature.

Of the variety of contact sensors that exist for measurement of temperature, thermocouples are amongst the more commonly implemented probes. Temperature measurement by thermocouple is based on the principle that the contact potential generated when two dissimilar metals are in contact varies with temperature. Therefore, by measuring the difference in the contact potential of a measurement junction that forms the probe tip, relative to that of the reference junction, the temperature difference between the junctions is obtained. Thermocouples can be manufactured from many different combinations of metals, depending on the working temperature range, chemical sensitivity of the probe and desired sensitivity and

accuracy. In general, the use of thermocouples is preferred over other contact sensors because of their relatively short response times and low cost. However, the temperature sensitivity of thermocouples can be quite low ($\sim 50\,\mu\mathrm{V}/^\circ\mathrm{C}$ or less) and their accuracy is limited to approximately $\pm 0.5\,^\circ\mathrm{C}$. Further, the spatial resolution of the measurement domain is inherently limited by the physical dimensions of the probe tip that forms the measurement junction, with most thermocouple probes having a characteristic dimension of several microns or more. Therefore, the use of thermocouples for measurements of temperature at the microscale can be quite restrictive.

Resistance temperature detectors (RTDs) are contact-type temperature sensors that are based on the principle that the electrical resistance of metals increases with temperature. Therefore, RTDs are also commonly referred to as positive-temperature-coefficient sensors. Resistance temperature detector elements are typically manufactured from platinum because of the linear variation of its resistance with temperature, high stability and chemical inertness, while nickel and copper represent lower-cost alternatives. In general, while RTDs have a smaller working-temperature range than thermocouples, their increased stability and higher sensitivity ($\sim 0.35\,\mathrm{mV}/^\circ\mathrm{C}$) provide more accurate measurements of temperature (typically $\pm 0.05 - 0.1\,^\circ\mathrm{C}$). In contrast, RTDs have longer response times than thermocouples, which often renders them unsuitable for instantaneous measurements of temperature fluctuations occurring over short time intervals.

Finally, thermistors represent another class of commonly-implemented contact temperature sensors. As the name suggests, thermistors are thermally-sensitive resistors that are manufactured using semiconductor materials or transition metal oxides. The basic principle of their operation is similar to that of an RTD in that the temperature of a medium is estimated via variations in the resistance of the sensing element with temperature. However, unlike RTDs, thermistors are negative-temperature-coefficient sensors and their resistance varies inversely with temperature, often in a non-linear fashion. Although their pronounced non-linearity limits the working temperature range to within $100\,^\circ\mathrm{C}$, thermistors are known to have high temperature sensitivities ($\sim 10\,\mathrm{mV}/^\circ\mathrm{C}$), short response times and provide highly accurate temperature measurements (typically $\pm 0.02 - 0.05\,^\circ\mathrm{C}$).

Infrared Thermography

Principle

►Infrared (IR) thermography is a non-intrusive, two-dimensional technique for the whole-field measurement of surface temperature. An infrared scanning radiometer (IRSR) detects the electromagnetic energy radiated in the IR spectral band by the surface of interest and converts it into an electronic signal. For an object whose surface temperature is T, the monochromatic radiation of intensity E_λ emitted by the surface can be written using Planck's law as

$$E_\lambda = \frac{\epsilon_\lambda C_1}{\lambda^5 (e^{C_2/\lambda T} - 1)}, \tag{1}$$

where C_1 and C_2 are the first and second radiation constants, respectively, λ is the wavelength of the radiation being considered and ϵ_λ is the spectral emissivity coefficient that acts as a correction factor to account for radiation from a real surface ($\epsilon_\lambda = 1$ for a blackbody). Integrating Planck's law over the entire spectrum, from $\lambda = 0$ to $\lambda = \infty$, yields the Stefan–Boltzmann law for the total radiation intensity, E, given by

$$E = \epsilon \sigma T^4, \tag{2}$$

where σ is the Stefan–Boltzmann constant.

In general, most IRSR's are tuned to detect the radiation in a limited bandwidth of the IR spectrum and are therefore classified as long-wave (LW) radiometers or short-wave (SW) radiometers depending upon which window in the IR band is to be detected. For such cases, the radiation intensities detected by the radiometers represent intensity values integrated over the given spectral bandwidth. Temperature is then determined from these intensity values using appropriately modified forms of Eqs. (1) and (2).

Implementation

The two basic components of an IRSR are the optics that form the sensing system and the IR detector. Typically, the characteristics of the optics used in IR systems depends upon whether the incoming radiation is detected in the SW or the LW windows. For the case where the incoming SW infrared radiation is scanned, the radiometer utilizes silicon optics with a coating that has a transmittance peak at a radiation wavelength of about $5\,\mu\mathrm{m}$. Additionally, the detector is manufactured from indium-antimonide and gives a spectral response between $3.5\,\mu\mathrm{m}$ and $5.6\,\mu\mathrm{m}$. Further, a broad-band coating of the SW optics can be used to enhance the relative response of the scanner by shifting the lower limit of the SW window down to $2\,\mu\mathrm{m}$. The use of such a broad-band coating may be favorable for applications such as determining the temperature of semi-transparent objects that makes use of spectral filtering, although these systems are more susceptible to atmospheric losses. On the other hand, radiometers used in the

LW band employ germanium optics that have a peak transmission at 10 µm. The detectors used for LW radiometers are typically manufactured from mercury-cadmium-telluride and give a spectral response between 8 and 12 µm in the far infrared. While the choice of the appropriate spectral-band radiometer depends on several factors, systems operating in the LW region are generally used for higher-accuracy measurements due to relatively low atmospheric absorption. However, SW systems are preferred when the surfaces have higher emissivity factors in the SW window.

The IR detector is a transducer that converts the incoming IR radiation into an electronic signal. The most commonly used detectors are photonic detectors, where the release of electrons is directly governed by photon absorption. While photonic detectors have a very short response time (on the order of microseconds), they suffer from poor spectral response and often require cooling to temperatures well below the ambient to allow for rapid scanning, higher temperature sensitivities and lower noise levels. For most practical applications, the overall performance of an IR imaging system is evaluated using its thermal sensitivity, scan speed, image resolution and the dynamic range of the measurements that can be achieved. Typical operating temperature ranges of IRSRs span from −20 to 800 °C, and can be extended to 2000 °C using appropriate filters (the reader is referred to [1] for the specifications of commercially available IRSRs).

Thermochromic Liquid Crystals

Principle

Thermochromic liquid crystals (TLCs) represent collections of long-chain organic molecules, like cholesterol derivatives, that exhibit liquid characteristics while maintaining a crystal-like order akin to a solid. Of interest from a thermometry point of view is the fact that the optical properties of TLCs strongly depend upon temperature. In particular, the wavelength of light reflected by a TLC is highly correlated with its phase (solid, liquid or intermediate) which is in turn dependent upon its temperature. At low temperatures, TLCs exist in a solid-like crystalline phase and eventually transition through intermediate phases to an isotropic liquid phase with increasing temperature. Two intermediate phases typically exist: the smectic and nematic phases. The smectic phase is achieved by heating the solid, causing the molecules to attain a layered order with their long axes oriented in a preferred direction. Upon further heating, the nematic phase is achieved wherein the layering is destroyed but the preferred orientation remains intact. In this phase, the molecules become asymmetric about their long axis, meaning they can rotate slightly with respect to one another. In this *chiral* state, the nematic phase takes the form of a helical structure wherein its pitch, p, selectively reflects white light with a wavelength on the order of p and transmits all other wavelengths. Further, the pitch of the helical structure is strongly dependent upon temperature. Therefore, the temperature of TLCs can be inferred from the hue of the light that they preferentially reflect when exposed to a white-light source.

Thermochromic liquid crystals in their raw form can provide a nearly continuous coating on a surface or a nearly continuous distribution in a solvent, meaning that the spatial resolution of the measurement is likely governed by the imaging system. Unfortunately, TLCs in this form are prone to degradation due to chemical contamination and exposure to ultraviolet (UV) and oxygen. To alleviate such issues, TLCs are typically manufactured in micro-encapsulated forms wherein the TLCs are encased within polymer shells to form discrete particles ranging in size from approximately one micron to nearly a millimeter. The polymer shell shields the TLC from contamination and most degradation issues; however, the spatial resolution of the measurement will likely be limited by the size of the encapsulated TLC particles. In addition, the thickness of the shell can distort the color reflected by a TLC and variations in shell thickness from particle to particle can produce additional variations in a given experiment. Therefore, the thickness of the polymer shell must be minimized to reduce these adverse influences.

Implementation

The experimental setup for measuring temperature via TLCs is rather simple. In a typical experiment, TLCs are either coated on a surface of interest or suspended in a liquid of interest. A white-light source is employed to illuminate a measurement region and the light reflected by the TLCs is recorded by a color CCD camera. The choice in TLCs is quite dependent upon the temperature range one wishes to resolve because the temperature range over which a TLCs reflectivity varies is a direct function of its specific chemical composition. Since it is important to maintain good contrast in recording the light reflected by the TLCs, it is common for the surface upon which the TLCs are coated or the region behind suspended TLCs to be painted black. Once a color image is acquired, the hue of the reflected light must be related to temperature. However, while this hue is strongly dependent upon temperature through the pitch of the TLC helical structure, it is also tied to other experimental parameters. In particular, the wavelength of the reflected light from a TLC is also dependent upon the angle from which the reflected light

T

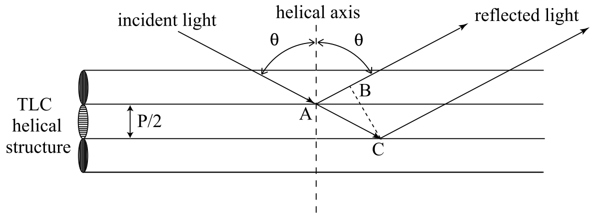

Temperature Measurement, Methods, Figure 1 A schematic illustrating the interaction of TLCs with incident light (Adapted from [2])

is viewed as well as the angle and spectral composition of the incident light. Figure 1 illustrates the interaction of incident light with a repeating TLC helical structure. As discussed in [2], a path difference exists between the light reflected by consecutive helical structures given by

$$\overline{AC} - \overline{AB} = \frac{p}{2\cos\theta}(1 + \cos 2\theta) = p\cos\theta, \quad (3)$$

where θ represents the angle of the incident and reflected light (they are assumed equal for simplicity). Constructive interference will occur when

$$n\lambda = p\cos\theta, \quad (4)$$

where n is a positive integer and λ represents the reflected wavelength. Therefore, the wavelength of the reflected light is dependent upon both the pitch of the helical structure and θ. A careful calibration of the TLCs hue as a function of temperature must be performed to account for these effects. Such a calibration is achieved by placing the TLCs within an environment wherein the temperature of the TLC is known and can be precisely controlled. Images of the light reflected by the TLCs are then acquired at distinct temperature intervals from which a calibration curve relating hue to temperature can be constructed. However, given the strong dependence of the hue on both the viewing angle as well as the characteristics of the incident light, it is strongly recommended that this calibration be performed in situ to properly account for such variabilities.

While TLCs can be quite sensitive to very small temperature variations, the temperature range over which TLCs reflect from red to blue can be quite narrow, typically on the order of 1 K or less. Coupled with a typical temperature uncertainty of 0.1 K, the relative measurement error using TLCs can be larger than 10%. Further TLCs have several drawbacks for use in micro- and nano-scale devices. First, the lower bound on the size of micro-encapsulated TLCs of a few microns can limit their use in microfluidic devices of comparable size when in suspension since they would likely promote blockage. Further, the lower bound in size inherently limits the spatial resolution of the temperature measurement to a few microns. Therefore, TLCs can often be inadequate for resolving strong temperature gradients that can exist in microscale devices.

Fluorescent Thermometry

Principle

►Fluorescence refers to the process by which a fluorophore returns to its ground state through the emission of energy after absorbing a photon of a given energy. During this process, a portion of this energy is lost by the molecule before the emission occurs as it transitions between energy states, meaning that the emission is of a longer wavelength than the energy it initially absorbed. This shift in wavelength of the fluoresced light relative to the absorption wavelength is known as Stokes shift. While the emission of fluoresced light represents one possible path for the molecule to transition back to the ground state, there exist other non-radiative processes by which an excited molecule can return to its ground state. As such, the efficiency of the fluorescence emission by a dye is often quantified by its quantum efficiency

$$\phi = \frac{k_r}{k_r + k_{nr}}, \quad (5)$$

where k_r is the rate of emission of photons via fluorescence and k_{nr} represents the rate at which non-radiative relaxation to the ground state occurs. One key difficulty in exploiting fluorescence to infer temperature is that the fluorophore can sustain significant and irreversible decay of its quantum efficiency due to these non-radiative processes. In particular, repeated exposure to high-intensity incident light increases the probability of this photobleaching effect.

For a dye of concentration C (kg m^{-3}) illuminated with an incident light flux of intensity I_0 (W m^{-3}), the fluorescence energy emitted per unit volume, I (W m^{-3}), is

$$I = I_0 C\phi\epsilon, \quad (6)$$

where ϵ (m^2 kg^{-1}) is the absorption coefficient of the dye. Variations in I with temperature are predominantly attributable to a dye's quantum efficiency, ϕ, which displays some degree of temperature dependence for most organic dyes. While this temperature sensitivity is small for most dyes (typically a fraction of a percent per K), there are other dyes that exhibit significantly stronger temperature dependence, like Rhodhamine B (2.3% K^{-1}). In contrast, ϵ has a very weak temperature dependence, usually of the order of 0.05% K^{-1}. Therefore, by employing a dye whose quantum efficiency is highly-sensitive to temperature variations, the temperature distribution in a fluid

or on a surface can be inferred from intensity variations in the light fluoresced by the dye.

Single-Dye Fluorescence Temperature measurement using a single fluorescent dye is the simplest adaptation of fluorescent thermometry at the microscale. If the intensity of the illuminating light flux, I_0, is assumed constant in both space and time, then the ratio of the emitted fluorescence intensity measured at a temperature T to that measured at a reference temperature T_{ref} for a fixed dye concentration is given by the ratio of the quantum efficiencies of the fluorescent dye at these temperatures:

$$\frac{I}{I_{ref}} = \frac{\phi(T)}{\phi(T_{ref})} = f(T). \quad (7)$$

Therefore, assuming that the variation of the ratio of quantum efficiencies, or equivalently the ratio of the emitted fluorescence intensities, has been properly calibrated as a function of temperature, an estimate of the unknown temperature distribution is arrived at by comparing its fluorescence intensity to that given by the calibration. The spatial resolution of this measurement is defined by the imaging optics while the temporal resolution is defined either by the framing rate of the imaging camera or by the illumination time of the incident light.

Two-Dye Fluorescence As outlined above, the fluorescence intensity measured by single-dye fluorescence depends solely on temperature *only* if the dye concentration and the incident light flux are constant. While maintaining a constant dye concentration is quite simple, sustaining a constant incident light flux is much more difficult since all illumination sources exhibit some degree of spatial and/or temporal variability in their intensity. As such, the measured fluorescence intensity not only embodies temperature variations through ϕ, but also variations in the illuminating intensity through I_0. Therefore, the accuracy of temperature measurements via single-dye fluorescence is strongly dependent on the stability and homogeneity of the illuminating light source. To alleviate such issues, a two-dye methodology has been developed to improve the accuracy of macroscale fluorescent thermometry. In this technique, spatial and/or temporal intensity variations within the illuminating light source are accounted for via a second fluorescent dye whose quantum efficiency exhibits little, or no, temperature dependence. Therefore, while the intensity of the fluoresced light from the temperature-dependent dye embodies both variations in temperature and illuminating intensity, any variations in the fluorescence intensity of the temperature-insensitive dye are directly attributable to variations in the illuminating intensity. As such, one can account for variable illumination intensity by simultaneously imaging the fluoresced light from each dye with separate CCD cameras and normalizing the fluorescence intensity of the emission from the temperature-sensitive dye by that of the temperature-insensitive dye.

Implementation

A schematic of the imaging configuration used for the measurement of temperature via single- and two-dye fluorescence is presented in Fig. 2. Light from an illumination source, like an Nd:YAG laser, Argon-ion laser or a mercury arc lamp, is directed through an epi-fluorescent filter cube and through a microscope objective lens to excite the fluorescent dye molecules in the microfluidic device. The filter cube allows the relatively weak fluorescent signal to pass to a CCD camera while simultaneously blocking the intense illumination wavelength. Given the relatively weak fluorescent signal from the dye, the CCD camera employed must have very low noise levels and a high sensitivity to the emitted wavelength in order to maximize the signal-to-noise ratio of the measurement. In the case of two-dye fluorescence, the emissions of the two dyes must be imaged separately. Such separation is achieved by adding a second camera and additional spectral filters to the aforementioned single-dye optical arrangement (these additions are identified by the dashed bounding box in Fig. 2). In this optical arrangement, both dyes must have similar excitation wavelengths since the same illumination source is typically used to simultaneously excite both dyes. However, the dyes must have different emission spectra so that they can be effectively separated using low- and high-pass spectral filters just upstream of the cameras.

The exact temperature dependence of the chosen dye(s) must be known before the measured intensity fields for single- and two-dye fluorescence can be faithfully converted to temperature fields. This calibration is accomplished by isolating a fixed amount of each chosen dye at known concentration in a well-insulated reservoir whose temperature is both known and precisely controlled. One then maintains the dye solution at a known temperature, begins illuminating the dye solution and acquires an ensemble of images of the light fluoresced by the dye using the same optical configuration outlined above (Fig. 2). The temperature of the dye is then varied slightly and a new ensemble of images is acquired at this new temperature. This procedure is repeated until image ensembles have been acquired at several known temperatures over the range expected in a given experiment. This procedure allows one to construct a calibration curve of intensity ratio (or equivalently quantum-efficiency ratio) versus

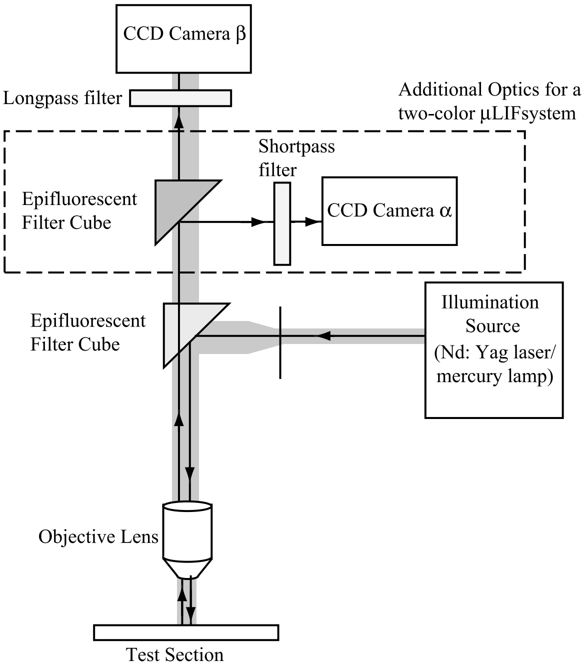

Temperature Measurement, Methods, Figure 2 Representative schematic of the optical configuration for microscale ►fluorescence thermometry. The dashed box outlines the additional optics required for a two-dye fluorescence imaging

temperature. In the context of two-dye fluorescence, the calibration methodology is identical except that one must now assess the temperature dependence of both dyes.

Thermometry via Measures of Brownian Motion

Principle

►Brownian motion refers to the random thermal diffusion of a particle immersed in a fluid of interest due to continual collisions between the particle and the fluid molecules that are in continual, random motion. Such an effect is increasingly prevalent as the characteristic length scale of the particle decreases, meaning micron-size, or smaller, particles immersed in an otherwise quiescent fluid will display measurable diffusion owing to Brownian motion. Einstein [3] was the first to quantify the intensity of this diffusion for a spherical particle subjected to Stokes drag law in terms of the mean-square distance of diffusion defined as

$$\langle r^2 \rangle = 6D\Delta t, \tag{8}$$

where Δt is a time interval much larger than the particle response time and D is the diffusion coefficient given by

$$D = \frac{\kappa T}{6\pi \mu d_p}, \tag{9}$$

where κ is the Boltzmann's constant, T is the fluid temperature, μ is the dynamic viscosity of the fluid and d_p is the particle diameter. Combining Eqs. (8) and (9) gives

$$\langle r^2 \rangle \propto (T\mu^{-1})d_p^{-1}. \tag{10}$$

Therefore, the mean-square diffusion is proportional to the thermodynamic state of the fluid through $T\mu^{-1}$ and inversely proportional to the particle size. For fixed d_p, the mean-square diffusion is entirely defined by the thermal character of the fluid through $T\mu^{-1}$ whose temperature dependence is a function of the phase of the fluid. For a liquid, an increase in T will yield a commensurate decrease in μ, meaning that $T\mu^{-1}$ will always increase with increasing temperature. On the other hand, an increase in temperature of a gas enhances the viscosity μ, meaning that the temperature dependence of $T\mu^{-1}$ is a strong function of the specific properties of the fluid. Nevertheless, while Brownian motion can severely limit the accuracy of particle-based methods for inferring the bulk motion of a fluid at the microscale when sub-micron particles are employed (as is sometimes done in the microscopic particle image velocimetry technique), it can be used quite adeptly to infer the *thermal* character of the fluid.

Implementation

In order to determine the temperature of a fluid via Brownian motion of suspended, sub-micron particles, one must estimate the displacement of the particles owing to this random effect. There are many established methodologies for achieving such estimates, including methods for tracking the motion of single particles (particle-tracking velocimetry) as well as techniques for tracking small groups of particles (particle-image velocimetry, PIV). In both cases, the position of a particle or a group of particles must be documented at two or more times. Tracking of sub-micron particles at the microscale can be accomplished using an epi-fluorescent microscope in concert with an appropriate illumination source and a low-noise CCD camera, very much akin to the experimental arrangement used in single-dye fluorescent thermometry (Fig. 2). It is advantageous to employ fluorescently-labeled particles in conjunction with a filter just upstream of the camera that blocks the illumination wavelength and passes the light fluoresced by the particles. This experimental arrangement ensures optimal signal-to-noise ratios of the particle images. An image of the particle positions in a plane of interest in the fluid is then acquired at some time t_1 followed by a subsequent image at $t_1 + \Delta t$. The time interval, Δt, must be chosen carefully, as an underestimation of Δt will limit the diffusion of the parti-

cles while overestimation can average away the Brownian diffusion effects and can also compromise the fidelity of the tracking algorithm due to loss of particle images due to out-of-plane motion. Once time-delayed images of the particle positions are acquired, the motion of individual particles can then be assessed (particle tracking) or the motion of groups of particles in pre-defined subareas of the field of view can be tracked using statistical methods (as is done in the microscopic PIV method). Specific applications of these methodologies are presented in section *Thermometry via Measures of Brownian motion*.

Key Research Findings

Resistance Temperature Detectors

In general, most contact temperature sensors are designed to provide single-point temperature measurements, although whole-field temperature measurements may be obtained using spatially-distributed arrays of these sensors. While such measurements are fairly simple to conduct at the macroscale, performing similar measurements at the microscale can often be quite complex for several reasons. Typically, most commercially available contact sensors have probe tips whose diameters are at least of the order of a few hundred microns. This size severely constrains the maximum spatial resolution of the measurements that can be attained. Additionally, since the characteristic sizes of these sensors are of the order of the physical dimensions of the microfluidic devices under investigation, these sensors can often be physically intrusive to the flow. Further, limitations on the in-house fabrication technology of microscale temperature sensors not only limits the minimum physical dimension of the sensing element that can be fabricated but can also severely restrict the choice of sensor material. As such, these limitations affect the sensitivity and the accuracy of microscale temperature sensors in comparison to their macroscale counterparts. In particular, while micro-RTDs and micro-thermistors have shown reasonable promise as contact sensors at the microscale, these limitations have stalled development of micro-thermocouples. Watanabe et al. [12] developed a preliminary micro-thermocouple probe for the measurement of cellular thermal responses. The probe was fabricated by thermally tapering a Pyrex glass tube to produce a micropipette tip of diameter 1 μm where a 50 nm thick layer of nickel was deposited. An insulating film of diamond-like carbon (DLC) was then deposited over the nickel layer. Constantan was chosen as the second alloy to form the thermocouple junction and was deposited at the micropipette tip by ion-sputtering following the removal of a small segment of the DLC coating by focused-ion-beam etching. Although the micro-thermocouple fabricated in this manner was in its preliminary stages of validation, the authors noted that the quality of the junction at the probe tip and the decreased signal-to-noise ratio due to the higher thermal conductivity of the culture solution limited the effective sensitivity of the micro-thermocouple probe.

Ryu et al. [11] report the development of a micro-hotwire sensor to monitor the position and speed of advancing liquid fronts in microfluidic channels. A thin film of gold was embedded along the length of the microfluidic channel and used as the sensing element. The resistance of the sensing element as a function of temperature was calibrated and confirmed to be linear. The local fluid temperature was then assessed using this calibration information, from which the speed and position of the advancing liquid front were also determined. The temperature coefficient of the sensing element was measured to be $0.0024\,°C^{-1}$ and its thermal response time was estimated as 4 ms.

A micro-thermistor sensor array was used by Wu et al. [13] to characterize a microscale heat exchanger that utilized a series of impinging jets exiting from micronozzles. The temperature sensor chip consisted of 64 thermistor-type polysilicon sensors, each of which were 4 μm × 4 μm in dimension and were spaced 500 μm apart from one-another to form an 8×8 array in a 4 mm × 4 mm area at the center of the device. The sensors had a nominal resistance of 20 kΩ at room temperature and a temperature resolution of 0.1 °C. A polysilicon heater having a nominal resistance of 55 Ω was fabricated on the backside of the sensor chip in a manner similar to that utilized to fabricate the micro-thermistor array. Using this experimental setup, Wu et al. [13] showed that a 500 μm jet placed 750 μm above the heated surface cooled the chip from over 70 °C to nearly 35 °C.

T

Infrared Thermography

In order to obtain quantitative measurements of temperature using IR thermography, an accurate characterization of the IR system performance and its calibration must be performed prior to conducting the actual experiment. Some of the common sources of error in IR thermography include variability in the surface emissivity of the object, inaccurate mapping of the image coordinates back to the physical coordinates of the object, losses due to radiation and use of external supplementary optics. Additionally, radiation from the background can also introduce large uncertainties in the measurement of surface temperatures. This latter issue is exacerbated at the microscale where the uncertainties due to background radiation can severely limit the resolution of the measure-

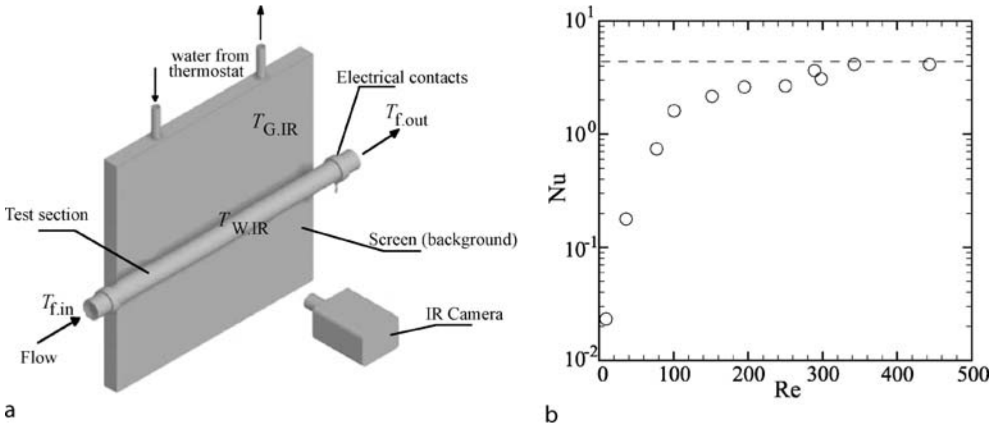

Temperature Measurement, Methods, Figure 3 (**a**) Schematic of the experimental setup used for the IR temperature measurement of a capillary by [5]. (**b**) Variation of the average Nusselt number as a function of Reynolds number (Adapted from [5])

ments. The issue of obtaining accurate surface temperature measurements at the microscale using IR thermography was addressed by Hestroni et al. [5], wherein IR measurements of temperature in a 1.5 mm heated capillary are reported. Hestroni et al. [5] compensated for the background radiation by maintaining the background temperature as close to the measured temperature of the capillary surface as possible via a thermostat (Fig. 3a). A SW radiometer system with a noise-equivalent-temperature-difference of less than 0.07 K at 30 °C and an uncertainty level of 0.1 °C was utilized. Figure 3b presents the variation of average Nusselt number (Nu) with the Reynolds number (Re) of the water flow through the capillary. These results revealed heat-transfer coefficients considerably lower than that predicted theoretically for laminar flow in the range $10 < Re < 100$ through larger-diameter tubes.

Thermochromic Liquid Crystals

Höhmann and Stephan [6] utilized TLCs to study the thermal characteristics of an evaporating liquid meniscus in a capillary-driven heat-transfer device. Of particular interest were the heat-transfer characteristics in a microregion where the liquid–vapor interface approaches the boundary. Höhmann and Stephan [6] constructed a model evaporator wall consisting of a thin layer of non-encapsulated TLCs painted on a plexiglass surface followed by a thin layer of black paint. An electrically-heated metal foil was then placed upon the black surface and the evaporating meniscus was allowed to form along the foil surface. This experimental setup allowed a direct measure of the surface temperature below the evaporating meniscus by illuminating the TLCs with white light through the plexiglass and recording the light reflected by the TLCs with a three-chip CCD camera over a field of view of 640×480 µm. Use of a three-chip CCD camera allowed separate recording of the red, blue and green components of the reflected light. The authors performed a calibration in situ by maintaining a constant surface temperature, independently confirmed using thermocouple sensors at the surface, and acquiring images of the light reflected by the TLCs. This procedure was repeated for temperatures over the range of interest to calibrate the hue of the light reflected by the TLCs with temperature. Figure 4a presents an idealized schematic of the narrowing liquid–vapor interface of an evaporating meniscus and Fig. 4b presents the measured surface-temperature profile beneath the meniscus. The rapid temperature decrease characteristic of the microregion (approximately 50 µm in length) is clearly resolved in the measurement.

Fluorescent Thermometry

Temperature measurement at the microscale by single-dye fluorescence was first accomplished by Ross et al. [10] using RhB as the temperature-dependent fluorescent dye and a mercury arc lamp for illumination. Ross et al. [10] conducted measurements of fluid temperature distributions resulting from Joule heating in a microfluidic circuit (schematic presented in Fig. 5a) due to electrokinetic pumping. Figures 5b–5f present a time series of fluid temperature fields acquired by Ross et al. [10] through a constriction in the microfluidic circuit. These temperature fields clearly highlight the drastic rise in fluid temperature that can occur in the presence of electrokinetic pumping. A spatial resolution of 1 µm and a temporal resolution of 33 ms were reported, yielding temperature uncertain-

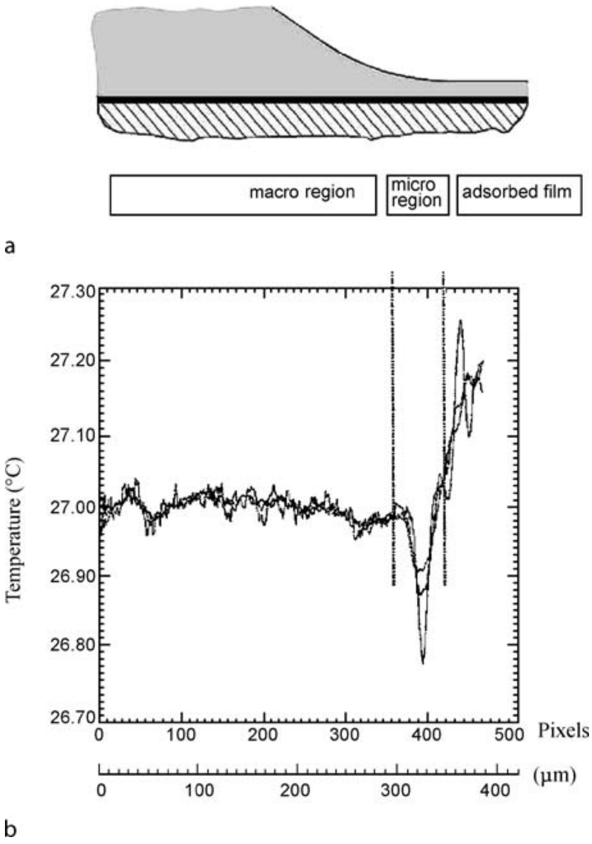

Temperature Measurement, Methods, Figure 4 (**a**) Schematic of the liquid–vapor interface characteristic of an evaporating meniscus. (**b**) Temperature profile along the surface beneath the evaporating meniscus measured with TLCs (Adapted from [6])

ties in the range 2.4 – 3.5 °C with no spatial or temporal averaging. Improved measurement uncertainties (as low as 0.03 °C) were achieved but at a significant cost in spatial and/or temporal resolution. This single-dye methodology was also employed by Erickson et al. [4] to examine Joule heating and heat transfer in electrokinetically-driven flows at the junctions of PDMS and PDMS/glass microfluidic devices. The temperature fields obtained with RhB excited by a mercury illumination source were found to agree with complementary numerical simulations to within ±3 °C. They also reported a repeatability of approximately ±2 °C and a noise level of ±1 °C. Improved noise levels were achieved by applying a Wiener-type filter to their raw image data.

Thermometry via Measures of Brownian Motion

As noted earlier, inferring fluid temperature from the Brownian motion of sub-micron particles suspended in the fluid requires an accurate estimate of the displacement of the particles over a fixed time interval, Δt. Hohreiter et al. [7] used the microscopic PIV technique to estimate the diffusion of groups of particles in pre-defined subareas of the acquired images. In its standard implementation, PIV utilizes time-delayed images of tracer particles to infer the bulk motion of a fluid by correlating subareas of the time-delayed images together. This correlation yields a peak corresponding to the average displacement of the particles in the subarea over the time interval Δt. A displacement vector (or alternatively a velocity vector when the displacement vector is divided by Δt) is then placed at the center of the subarea and the process is repeated throughout the field of view, yielding a velocity field representative of the bulk fluid motion. It is important to note that the spatial resolution of this measurement is exactly defined by the linear dimensions of the chosen subarea. Olsen and Adrian [8] noted that implementing the PIV technique at the microscale with sub-micron particles yields a broadening of the displacement peak computed from the cross-correlation of the time-delayed subareas. Hohreiter et al. [7] exploited this behavior by deriving an expression that relates changes in the cross-sectional area of the correlation peak to $\langle r^2 \rangle$ (the mean-square distance of diffusion due to Brownian motion) and hence the temperature. Hohreiter et al. [7] used this methodology to determine the temperature of a quiescent fluid from the Brownian motion of 700 nm particles suspended in water. Figure 6a presents fluid temperature inferred from the broadening of the correlation peak determined by micro-PIV analysis versus the fluid temperature measured independently with a thermocouple. The average uncertainty is reported as ±3 °C, with the uncertainty increasing slightly with temperature. It should also be noted that since the overall motion of the suspended particles is tracked via the micro-PIV process, this methodology gives one the capability of simultaneously determining *both* the bulk motion as well as the temperature of the fluid when the fluid is in motion. Simultaneous velocity and temperature measurements are particularly important when convective heat-transfer effects are substantial. Park et al. [9] present an alternate methodology for inferring temperature from particle diffusion that involves tracking the three-dimensional motion of *individual* particles using optical serial sectioning microscopy (OSSM). The OSSM technique utilizes a standard epi-fluorescent imaging setup to capture the diffraction patterns of suspended particles from which their positions in a three-dimensional space can be determined (discussion of the OSSM technique is beyond the subject of this contribution; the reader is referred to Park et al. [9] for further details). Therefore, acquisition of time-delayed images of the diffraction patterns of suspended particles enables the

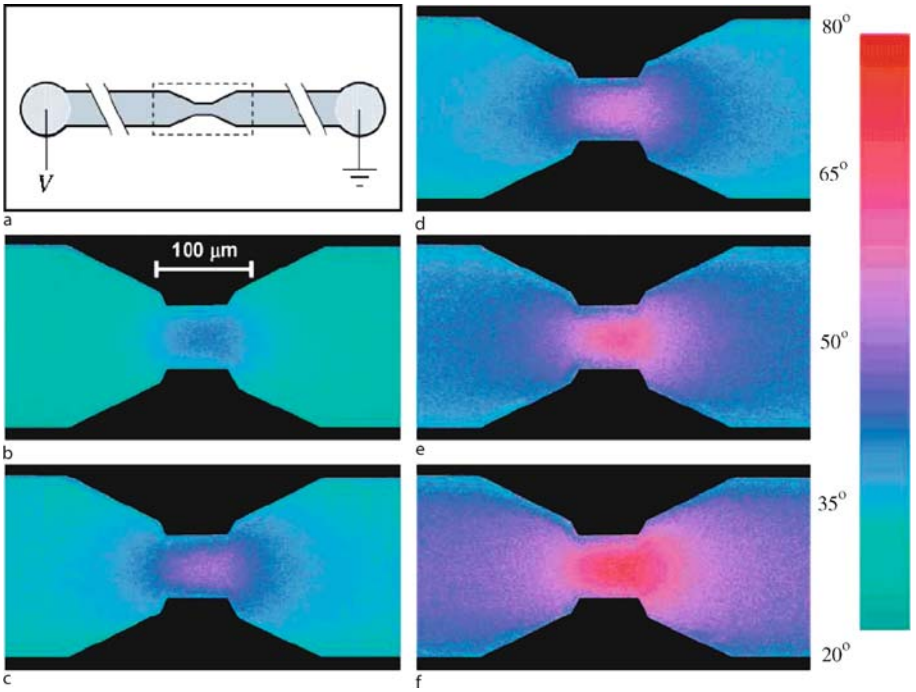

Temperature Measurement, Methods, Figure 5 (**a**) Schematic of a microfluidic circuit through which flow is driven by electrokinetic pumping. (**b**)–(**f**) Temperature fields through a constriction in the microfluidic circuit acquired 0.2, 0.4, 0.6, 1.4 and 3.8 s after the driving voltage was switched on (Adapted from [10])

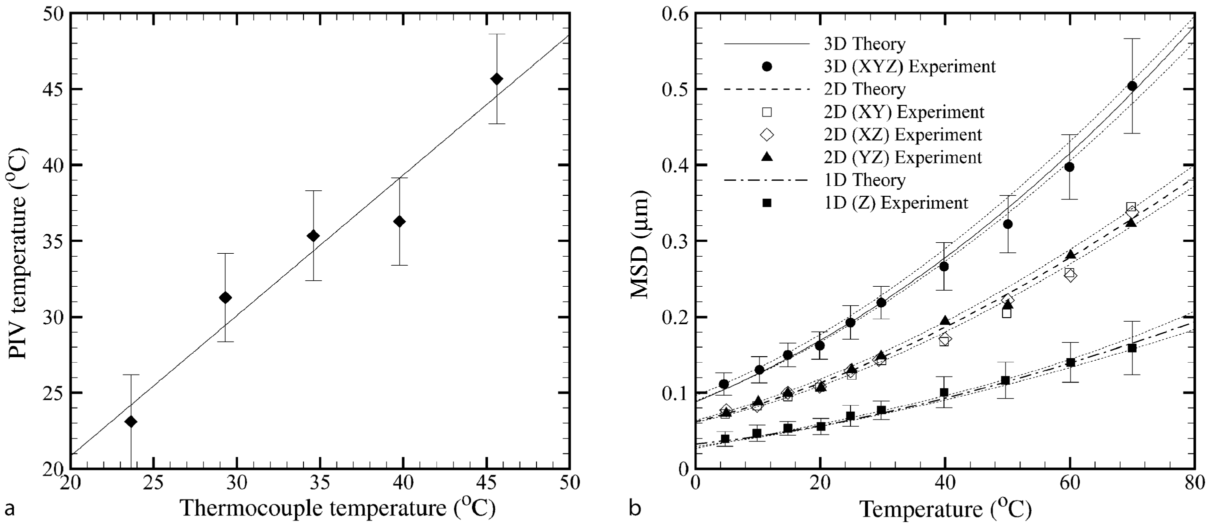

Temperature Measurement, Methods, Figure 6 (**a**) Fluid temperature determined by micro-PIV assessment of Brownian motion versus the actual fluid temperature measured by a thermocouple (Adapted from [7]). (**b**) Mean-square diffusion distances assessed from OSSM tracking on individual particles as a function of temperature (Adapted from [9])

three-dimensional tracking of their motion, specifically their Brownian motion when the fluid is otherwise quiescent. Figure 6b presents $\langle r^2 \rangle$ as a function of temperature for particles tracked using the OSSM technique as reported by Park et al. [9]. The authors tracked the particle motion in one, two and three dimensions and compared the measured diffusion of the particles to theoretical estimates with deviations of 5.54%, 4.26% and 3.19% reported for the one-, two- and three-dimensional measurements.

Future Directions for Research

It is important to note that most of the community's effort in the area of microscale thermometry has focused on adapting established macroscale methods for implementation at the microscale. While significant progress has been made in this regard, the accuracy of these techniques generally suffers when extended to the microscale. In the area of contact sensors, significant work remains in reducing their physical dimensions to a much less intrusive size. Even with such progress, contact sensors will always suffer from the fact that they only yield a local measure of temperature in isolation and can be highly complex when one fabricates arrays to assess spatial distributions of temperature. In contrast, methods like IR thermometry, TLCs and fluorescent thermometry overcome many of the disadvantages of contact sensors because they are ideally suited for measuring spatial distributions of temperature. Still, the accuracy of these methodologies is severely compromised at the microscale compared to their macroscale implementations due to various limitations outlined herein.

It is likely that the research community will need to consider the development of thermometry methods that are specifically tailored to the micro- and nano-scales. One such example is the development of methods relying on the Brownian motion of sub-micron particles to infer fluid temperature. While the current accuracy of this method is still comparable to most adapted macroscale methods, this technique is unique in that it relies upon a defining characteristic of particle motion at these smaller spatial scales. Another promising methodology that is specifically tailored to micro- and nano-scale systems involves the use of ►quantum dots (nanometer-scale semiconductors) as thermal markers. Quantum dots behave similarly to fluorescent dyes in that they can be excited with an illumination source to fluoresce light with rather large Stokes shifts and their fluorescence intensity is strongly dependent upon temperature. In contrast to most dyes, however, quantum dots have exceptional quantum yields (providing a significant improvement in the signal-to-noise ratio) and they do not suffer from photobleaching effects, meaning that their viability as thermal markers is not compromised by continued exposure to illuminating light.

Cross References

► Fluorescence Measurements
► Fluorescent Labeling
► Liquid Crystal Technique for Measuring Temperature
► Methods for Temperature Measurements
► Quantum Dots
► Resistance Temperature Detectors
► Thermocouples

References

1. Carlomagno GM, de Luca L (1989) Infrared thermography in heat transfer. In: Handbook of Flow Visualization Hemisphere, London 531–553
2. Collings PJ, Hird M (1997) Introduction to Liquid Crystals. Taylor and Francis, Oxford
3. Einstein A (1956) Investigations on the Theory of the Brownian Movement. Dover, New York
4. Erickson D, Sinton D, Li D (2003) Joule heating and heat transgfer in poly(dimethylsiloxane) microfluidic systems. Lab Chip 2:141–149
5. Hestroni G, Gurevich M, Mosyak A, Rozenblit R (2003) Surface temperature measurement of a heated capillary tube by means of an infrared technique. Meas Sci Technol 14:807–814
6. Höhmann C, Stephan P (2002) Microscale temperature measurement at an evaporating liquid meniscus. Exp Thermal Fluid Sci 26:157–162
7. Hohreiter V, Wereley ST, Olsen MG, Chung JN (2002) Cross-correlation analysis for temperature measurement. Meas Sci Technol 13:1072–1078
8. Olsen MG, Adrian RJ (2000) Brownian motion and correlation in particle image velocimetry. Optics Laser Technol 32:621–627
9. Park JS, Choi CK, Kihm KD (2005) Temperature measurement for a nanoparticle suspension by detecting the brownian motion using optical serial sectioning microscopy (OSSM). Meas Sci Technol, 16:1418–1429
10. Ross D, Gaitan M, Locascio LE (2001) Temperature measurement in microfluidic systems using a temperature-dependent fluorescent dye. Anal Chem 73:4117–4123
11. Ryu KS, Shaikh K, Goluch E, Liu C (2006) Two-terminal longitudinal hotwire sensor for monitoring the position and speed of advancing liquid fronts in microfluidic channels. Appl Phys Lett 88:104104
12. Watanabe MS, Kakuta N, Mabuchi K, Yamada Y (2005) Micro-thermocouple probe for measurement of cellular thermal responses. In: Proceedings of IEEE-EMBS 27th Annual International Conference 1–4
13. Wu S, Mui J, Tai YC, Ho CM (1999) Micro heat exchanger by using MEMS impinging jets. Proc IEEE MEMS 171–176

Temperature Measurement Using Fluorescence

► Fluorescent Thermometry

Temperature Probes

► Contact Temperature Sensors

Temperature-Sensitive Hydrogels

HEIKO VAN DER LINDEN, JERRY WESTERWEEL
Laboratory for Aero- and Hydrodynamics
Faculty of Mechanical, Maritime and Materials Engineering, TU Delft, Delft, Netherlands
heiko.vanderlinden@tudelft.nl

Synonyms

Thermosensitive hydrogels; Thermally-sensitive hydrogels; Intelligent gels

Definition

Temperature-sensitive hydrogels, which are part of the family of stimulus-sensitive hydrogels, consist of water-filled polymer networks (i. e., gels) that display a temperature-dependent degree of swelling. Temperature-sensitive hydrogels are of interest to microactuation purposes for a number of reasons [1]: their volumetric size changes are large compared to other microactuation principles, hydrogels are soft and resilient, temperature-sensitive hydrogel actuators are operated at conveniently low temperatures and the hydrogel polymer networks can be microfabricated using standard photolithography.

Temperature-sensitive hydrogels can either display a positive temperature response, meaning that the gel material swells with increasing temperature, or a negative temperature response, meaning that the gel material shrinks with increasing temperature.

Chemical and Physical Principles

The amount of swelling of hydrogels is a function of two opposing forces. On one side water molecules moving into the hydrogel cause a swelling force, due to molecular interactions with the polymer molecules in the hydrogel. On the other side, the elastic elongation of the coiled-up polymer molecules in the polymer network results in an *elastic retractive force* opposing the swelling force in the hydrogel.

When water is added to a dry, hydrophilic polymer network (xerogel), a swelling hydrogel is formed. During the swelling process, the swelling forces dominate and the elastic retractive force gradually increases with progressive swelling. When the hydrogel is swollen to a degree that the elastic retractive forces have the same magnitude as the swelling forces, the hydrogel reaches equilibrium swelling. If the conditions of the hydrogel are kept stable, the volume of the hydrogel will remain constant indefinitely.

Stimulus-sensitive hydrogels have the unique property that an external physical parameter, e. g., temperature, pH or ionic strength, has an effect on the swelling forces inside the hydrogel. When the magnitude of the physical parameter is changed, the swelling force increases or decreases. As a result the hydrogel changes its degree of swelling to equilibrate the new swelling force with the elastic retractive force.

The thermal behavior of temperature-sensitive hydrogels is a direct result of the thermosensitivity of the molecular interactions between the polymer network inside the hydrogel and the aqueous solution in and around the hydrogel. In the case of a hydrogel made of poly-[N-isopropylacrylamide] (a hydrogel with a negative temperature response), the efficiency of hydrogen bond formation between the polymer and water molecules decreases at higher temperatures. At temperatures below 22 °C water molecules can form hydrogen bonds efficiently with the amide group in the polymer side chains. As a result of the efficient hydrogen bonding, water molecules move into the polymer network, resulting in the swelling of the hydrogel material. When the temperature of the hydrogel is increased to 42 °C, gradually the hydrogen bonding efficiency decreases to a minimum. This process decreases the interaction energy of the polymer network with water molecules and water moves out of the hydrogel. Macroscopically this process is visible as the shrinking of the hydrogel. Physically the temperature-dependent swelling of temperature-sensitive hydrogels can be expressed through temperature-dependent changes in osmotic pressure differences between the hydrogel and its surrounding solution. A temperature increase results in a reversal in osmotic pressure difference and water exits the hydrogel resulting in shrinking. A temperature decrease results in an increase in osmotic pressure difference and the water enters the hydrogel resulting in swelling.

The temperature-dependent swelling behavior of these hydrogels can be represented in a graph by plotting a dimensional property of the hydrogel (e. g., the thickness or diameter of a hydrogel disc) as a function of the temperature stimulus. The resultant graph for poly-[N-isopropylacrylamide] is shown in Fig. 2.

The polymer network of temperature-sensitive hydrogels is made up of smaller repeating units called monomers. In addition to monomers, so-called crosslinker groups are present in the polymer network. The crosslinker groups form connections between different strands of polymer inside the polymer network. As a result a single giant polymer molecule is formed which is incapable of dissolving.

A commonly used monomer for the fabrication of temperature-sensitive hydrogels is N-isopropylacrylamide. This

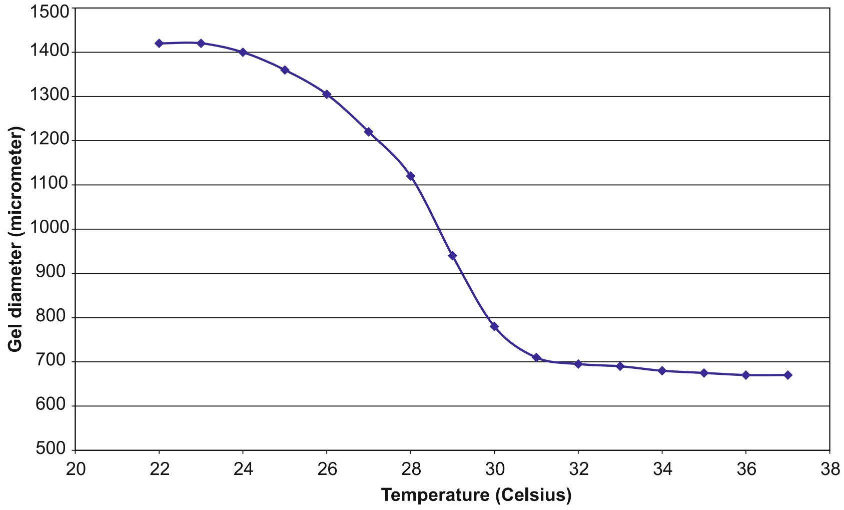

Temperature-Sensitive Hydrogels, Figure 1 Graphical representation of the reversible swelling and shrinking of temperature-sensitive hydrogels. In the swollen state the polymer molecules in the hydrogel are strongly hydrated. The water molecules force the polymer molecules into a swollen state. In the shrunken state, the polymer molecules are attracted to each other due to the elastic retractive force (arrows), resulting in the expulsion of the water molecules

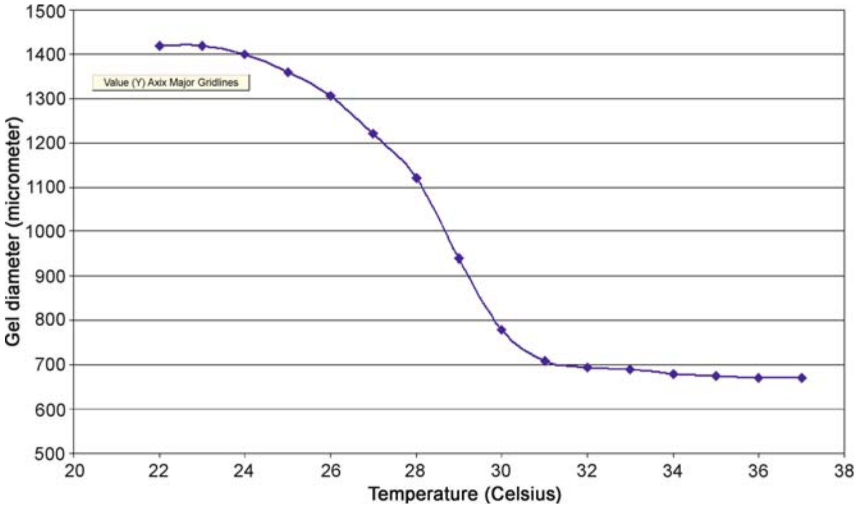

Temperature-Sensitive Hydrogels, Figure 2 Typical temperature response of a temperature-sensitive hydrogel disc made of poly-[N-isopropyl acrylamide]

monomer has the special property that it displays lower critical solution temperature (LCST) behavior and its solubility is a function of temperature. When the temperature of an aqueous N-isopropylacrylamide solution is increased above the LCST, the monomer will crystallize out of the solution. In a temperature-sensitive hydrogel this behavior is visible in the shrinking response of the hydrogel at temperatures above the LCST.

To polymerize NIPAAm into its polymer network (polyNIPAAm), free radicals are needed to initiate the polymerization reaction. Commonly these free radicals are obtained from chemical compounds called initiators. These initiators generate free radicals due to homolytic bond scission inside the initiator molecule. The bond scission can be induced by temperature or light. These initiators are called thermal initiators and photoinitiators respectively.

The swelling force of a temperature-sensitive hydrogel is a strong function of the hydrophilicity of the side groups in the polymer network. If the polymer network contains highly hydrophilic side groups, the resulting hydrogel will swell more compared to a hydrogel with less hydrophilic

side groups. Similarly, the side group hydrophilicity has an effect on the LCST of the temperature-sensitive hydrogel. The composition of the polymer network can be modified by incorporating hydrophobic or hydrophilic comonomers into the polymer network chains. When hydrophobic comonomers are incorporated, the LCST of the hydrogel will move to lower temperature regions. When hydrophilic comonomers are incorporated the opposite effect occurs. Using this method, the temperature region where a temperature-sensitive hydrogel actuator responds can be shifted to higher or lower temperatures [2]. Hence, the response of these actuators can be tailored for a specific need in an application.

Stimulus-sensitive hydrogels, such as pH-sensitive and temperature-sensitive hydrogels can be microfabricated efficiently by photopolymerization [2, 3]. This convenient process allows the use of standard microphotolithography technology (i. e., a mask aligner and photomasks) for the accurate positioning and dimensioning of stimulus-sensitive hydrogel microactuators.

A solution containing the precursors of the hydrogel network (i. e., monomers and crosslinking compounds) and a photoinitiator is deposited onto the substrate where the hydrogels should be fabricated. Using a photomask, selective areas of the precursor solution are irradiated for a sufficient time to allow the polymerization reaction to occur and a polymer network to be formed. After the photopolymerization reaction, the unreacted chemicals are dissolved, by washing the substrate in a suitable solvent. Normally within the period of 10 to 100 s, large numbers of hydrogel actuators can be fabricated with accurately defined dimensions and positions.

Examples of Application

The main focus of research on temperature-sensitive hydrogels as microactuators in microfluidic devices has been on microvalves. Hydrogel actuators have a distinct advantage for microvalve applications since they are very soft and encapsulate dust particles encountered in microfluidic flows. Normally these particles could result in the loss of function of conventional *hard* actuators when these particles get trapped in the actuator. Furthermore, temperature-sensitive hydrogel actuators are controlled by relatively small temperature changes close to ambient temperature (i. e., around 10 K to 20 K). As a result large heating powers are not necessary to control microvalves made out of these materials. Thus affording the possibility of using battery power to control the microvalves. In contrast, most conventional microactuators e. g., piezo or thermal actuators use high voltages or high power to operate.

Stimulus-sensitive hydrogel actuators display a large volume change during swelling and shrinking. Typically this volume change is around 100% to 800% for pH-sensitive hydrogels and 100% to 400% for temperature-sensitive hydrogels. Therefore a small stimulus-sensitive hydrogel actuator can be used to generate a large displacement in a microfluidic device.

Two kinds of temperature-sensitive hydrogel microvalves have been shown in the literature. The first kind of microvalve uses a monolithic piece of hydrogel, which swells and shrinks as a function of temperature to open or close a microchannel. An example of such a microvalve was shown by Yu et al. [4]. Actuation times are relatively short at 3.5 to 5 s and a holding pressure of 1.38 MPa was reported.

A second kind of temperature-sensitive hydrogel microvalve is based on the grafting of thin layers of poly-[N-isopropylacrylamide] on the surface of glass capillaries [5]. The contact angle, and thus the free surface energy, in such a treated capillary is a strong function of the temperature. By changing the temperature of the capillary, the flow of water could be controlled reversibly. The holding pressure of this kind of valve is in the range of 10 MPa.

Future Directions of Research

Because temperature-sensitive hydrogels are still a relatively new material to the field of microfluidics, their full potential in actuation applications has not been reached. It is expected that novel applications will be found where hydrogels replace standard actuators, e. g. electromagnets, but this will only be in cases where the actuation mechanism can be realized in the aqueous environment needed by the hydrogels. Additionally mechanical properties of the temperature-sensitive hydrogel materials have not been thoroughly investigated for microfluidic applications. Therefore it is necessary to both further optimize the characteristics of the actuator material and to come up with a set of design rules to allow the efficient design of temperature-sensitive hydrogel driven microfluidic applications.

Another direction of research could be the use of temperature-sensitive hydrogel thin films to allow fluid control in nanofluidics. Below the LCST these layers will be hydrophilic and above the LCST significantly more hydrophobic. It should be possible to make intelligent hydrophobic patch valves that are switched by temperature.

Cross References

► pH-Sensitive Hydrogel
► Photosensitive Hydrogels

References

1. van der Linden HJ, Herber S, Olthuis W, Bergveld P (2003) Stimulus-sensitive hydrogels and their applications in chemical (micro)analysis. Analyst 128:325–331
2. van der Linden HJ, Olthuis W, Bergveld P (2004) An efficient method for the fabrication of temperature-sensitive hydrogel microactuators. Lab Chip 6:619–624
3. Beebe DJ, Moore JS, Bauer JM, Yu Q, Liu RH, Devadoss C, Jo B-H (2000) Functional hydrogel structures for autonomous flow control inside microfluidic channels. Nature 404:588–590
4. Yu C, Mutlu S, Selvaganapathy P, Mastrangelo CH, Svec F, Frechet JMJ (2003) Flow control valves for analytical microfluidic chips without mechanical parts based on thermally responsive monolithic polymers. Anal Chem 75:1958–1961
5. Idota N, Kikuchi A, Kobayashi J, Sakai K, Okano T (2005) Microfluidic valves comprising nanolayered thermoresponsive polymer-grafted capillaries Adv Mat 17:2723–2727

Temperature Sensitive Resistor

Synonyms

Hot wire; Hot film

Definition

A temperature sensitive resistor has a high enough temperature coefficient of resistance, indicating variation of electrical resistivity with temperature. A temperature sensitive resistor used for the measurement of fluid flow generally takes the form of either hot wire or hot film. When cooled by the surrounding fluid, its electrical resistance would decrease which reflects the flow rate of the fluid.

Cross References

- ► Integrated Microfluidic Systems for Medical Diagnostics
- ► Heat Transfer in Microchannel Flows
- ► Temperature Control in Microfluidic Systems
- ► Resistance Temperature Detectors
- ► Thermocapacitive Flow Sensor
- ► Thermoelectric Flow Sensors
- ► Thermoresistive Flow Sensors
- ► Liquid Crystal Technique for Measuring Temperature
- ► Methods for Temperature Measurements

Temperature Sensors

► Contact Temperature Sensors

Temporal Averaging

Definition

Temporal averaging is an arithmetical averaging of local similar signals at different point of times. It has the background to increase the quality of the measurement signal and decrease the measurement noise. Using temporal averaging in image processing, several pictures (captured within a time period) are averaged. This causes a loss of temporal resolution.

Terminal Velocity

Definition

Peak velocity of an object in a fluid due to gravity force on the object.

Cross References

► Piezoelectric Microdispenser

Test

► Assay

Thermal Anemometer

Synonyms

Micro hot-wire anemometer

Definition

A thermal anemometer typically consists of a heater and one or more surrounding temperature sensors relative to the flow direction. The heater usually works when its self Joule heating is maintained constant. Any fluid flow through the heater will cause a shift in its temperature and thus resistance. By measuring the temperature profile around the heater, the flow rate and direction of the fluid flow can be identified.

Cross References

- ► Fluid Metering
- ► Methods for Flow Rate Measurements
- ► Micro-and Nanoscale Gas Dynamics
- ► Gas Flow in Nanochannels

► Joule Heating vs. Chip Materials
► Thermoresistive Flow Sensors

Thermal Bonding

► Thermal Fusion Bonding

Thermal Bubbles

PING CHENG[1], YI-KUEN LEE[2], PEIGANG DENG[3]
[1] School of Mechanical & Power Engineering, Shanghai Jiaotong University, Shanghai, China
[2] Department of Mechanical Engineering, Hong Kong University of Science and Technology, Hong Kong, China
[3] MEMS Department, China Resources Semiconductor (HK) Co., Ltd., Hong Kong, China
pingcheng@sjtu.edu.cn

Synonyms

Vapor bubbles

Definition

Thermal bubbles are those bubbles generated by heating in a liquid when its temperature exceeds its nucleation temperature.

Overview

In recent years, advances in microelectronic fabrication technology have led to many vapor-bubble actuators, such as thermal inkjet printheads, vapor-bubble micropumps, vapor-bubble perturbators and DNA microarrayers. In all of these microelectromechanical devices, microbubble(s) are generated on a microheater under pulse heating with pulse widths ranging from microseconds to milliseconds.

Thermal Inkjet Printheads

The thermal inkjet printhead is perhaps one of the most successful microelectromechanical systems (MEMS) products to date. The inkjet printhead uses microheaters (about $20 \times 20\,\mu m^2$ to $40 \times 40\,\mu m^2$ in size) under a train of electrical pulses of several microseconds (μs) to periodically generate microbubbles. The microbubble will expel a small droplet of ink through a nozzle at a high frequency to a specified position on a paper to compose the text and graphics. The quality of the printing depends on the thermal properties of the ink, the size of the droplets and droplet velocity, which is closely related to microbubble generation. There are three types of thermal inkjet printheads according to the direction of the ink ejection relative to the direction of vapor-bubble growth. These are: the top-shooter (also called the roof-shooter) with two directions being the same, which has been used in Hewlett-Packard's products [1]; the side-shooter, with the two directions being at right angles to each other, has been used in Canon printers [2]; and the back-shooter, with a droplet being ejected in the opposite direction to bubble growth, was first patented by Bhaskar and Leban [3].

Many improved designs of the top-shooter, side-shooter, and back-shooter types of thermal inkjet printheads have recently been proposed. Lee et al. [4] fabricated a monolithic thermal inkjet printhead, which employed the top-shooter firing mode as shown in Fig. 1. The heater had an area of $40 \times 40\,\mu m^2$. The nozzles, with a diameter of 50 μm, had a resolution of 300 dpi and a nozzle-to-nozzle pitch of 170 μm. Ink ejection up to the operating frequency of 11 kHz with an average ink dot diameter of about 110 μm was achieved under current pulses of 0.3 A and 5 μs.

Baek et al. [5] have adopted two concepts to improve the nozzle density in the top-shooter design. First, the heater was placed on the sidewall of the ink inlet (see Fig. 2) and thus, the area taken by the heater could be minimized. Second, the manifold, the inlet, pressure chamber, and the nozzle were arranged in a line vertically with respect to the substrate. The nozzle density was improved in this new design although it was not easy to fabricate using MEMS technology.

Tseng et al. [6] have introduced a modified back-shooter design, featuring two heaters with different sizes (see Fig. 3). When a current pulse passed through these two heaters connected in series, the smaller heater generated a bubble faster because of higher power dissipation. The bubble formed under the smaller heater, which can work as a virtual chamber neck, blocking the liquid passage as the larger heater started to generate its own bubble.

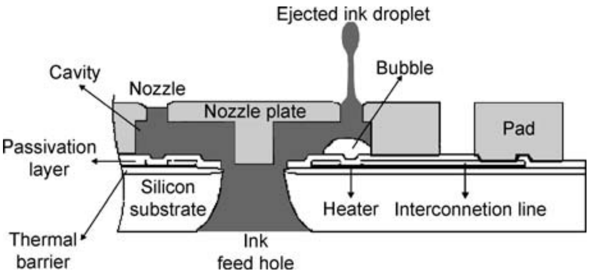

Thermal Bubbles, Figure 1 Cross-sectional view of the monolithic "top-shooter" inkjet printhead [4]

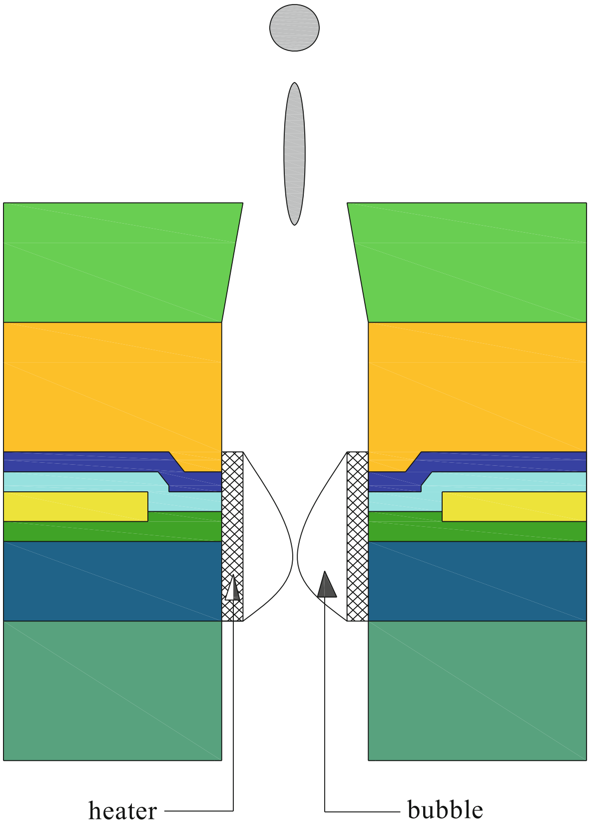

Thermal Bubbles, Figure 2 A “side-shooter” inkjet printhead [5]

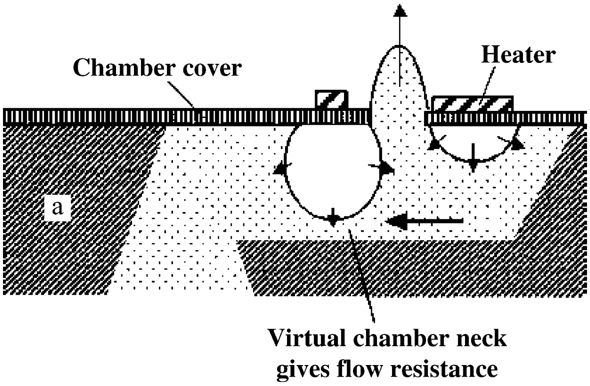

Thermal Bubbles, Figure 3 An improved design of a “back-shooter” thermal inject printhead with two unequally sized heaters. From Tseng et al. [6]

Expansion of the second bubble pushed the ink ejection. As the two bubbles grew and eventually merged, the tail of the ejected droplet was cut off, preventing the formation of a long tail. The operation frequency of the droplet ejection with a 10 μm dimaeter nozzle was around 35 kHz.

Vapor-Bubble Pumps

Geng et al. [7] have designed a novel pumping device based on the periodic generation and collapse of a single vapor-bubble in a tube. The device consisted of two stainless steel tubes with two different diameters (508 μm and 1067 μm, respectively). A divergent passage was connected from the smaller tube to the larger tubes (see Fig. 4). Pulse heating was applied at the narrow end of the divergent channel, where a vapor bubble was periodically generated and collapsed. Because of the difference in the curvature of the bubble at the narrow tube and the large tube, a capillary force was created that drove the bubble toward the larger tube according to the Young–Laplace equation. At a pulse-heating period of 100 – 1000 ms (i. e., a frequency in the range 10 – 1 Hz), the device could develop a head of a few centimeters of water with flow rates in the range of 100 μl/min.

Jun et al. [8] have used the growth and collapse of a single or multiple vapor bubble(s) to displace fluids in microchannels. The pumping action was provided by asymmetric heating along the microchannels that created a variation in vapor pressure and surface tension due to the heater-induced temperature gradient. A pumping device, consisting of a microchannel with a hydraulic diameter of 3.4 μm and 726 μm in length, was fabricated in a silicon wafer. Three heaters were turned on and off sequentially (Fig. 5) to actuate the movement of vapor bubble(s). It was found that the pulse width (in the range 0.25 – 1 s) and power input (in the range 18 – 26 V) determined whether the micropump could operate in single or multiple bubble mode. Experimental results showed that pumping of isopropanol at velocities as high as 160 μm/s with a pressure head of approximately 800 Pa was achieved.

Thermal Bubble Perturbators

Lin [9] has fabricated a polysilicon microheater with nonuniform width ($10 \times 3 \times 0.5\,\mu m^3$ and $5 \times 2 \times 0.5\,\mu m^3$) to generate single microbubbles. This nonuniform microheater can induce highly localized heat source, which can generate a single microbubble periodically at the narrow part of the heater under pulse heating. Using a nonuni-

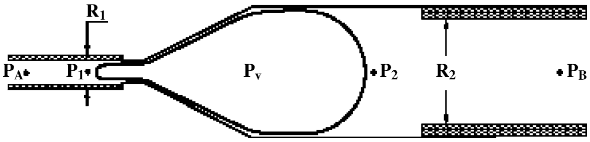

Thermal Bubbles, Figure 4 Sketch of a microbubble pump, from Geng et al. [7]

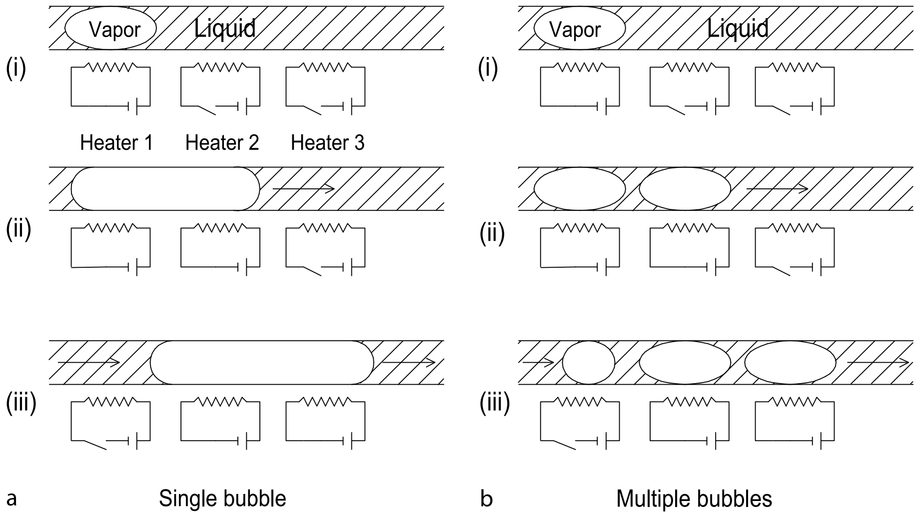

Thermal Bubbles, Figure 5 Vapor-bubble pumps for fluid displacement: (**a**) single bubble; (**b**) multiple bubbles [8]

form width microheater (with the slim part having dimensions of $10 \times 3\,\mu m^2$) under pulse heating in the millisecond range, Deng et al. [10, 11] investigated bubble growth and collapse on the microheater immersed in water as an actuator for mixing and for DNA hybridization enhancement. It was found that when single bubble was generated by pulse heating with the pulse width in the millisecond ranges, the growth and collapse of the bubble was asymmetric, leading to a net perturbation of the local fluid motion [10]. A comparison of molecular beacon-based hybridization assays with and without microbubble agitation revealed that the hybridization time could be effectively shortened by 33% with 10 cycles of microbubble agitation from a 2×1 bubble actuator array, and by 43% with 10 cycles of microbubble agitation from a 2×2 bubble actuator array [11].

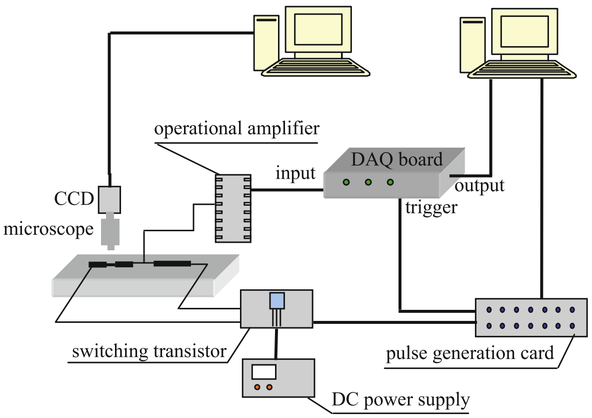

Thermal Bubbles, Figure 6 Schematic diagram of experimental setup [10, 12]

Basic Methodology

The experimental setup for the investigation of microbubble generation and its subsequent dynamics on a microheater under pulse heating is presented in Fig. 6, which shows a test section, a high-speed CCD camera, a microscope, a pulse generation system and a DC power supply. The test section consisted of a nonuniform width platinum microheater submerged in DI water, and the pulse generation system consisted of a control circuit and a switching transistor. Through the microscope and the CCD camera, with its recording process synchronized with the heating process, thermal bubble growth and collapse processes were observed. The platinum microheater was also used as a resistive temperature sensor, and the surface temperature of the microheater versus time was recorded. The temperature inflection point of the surface temperature variation curve can be identified as the nucleation temperature [12].

Key Research Findings

Microbubble Growth and Collapse on a Microfilm Heater

Effects of Pulse Width on Growth and Collapse Periods

The effect of pulse width (in the range 0.015 – 5.0 ms) on the bubble growth and collapse on a nonuniform

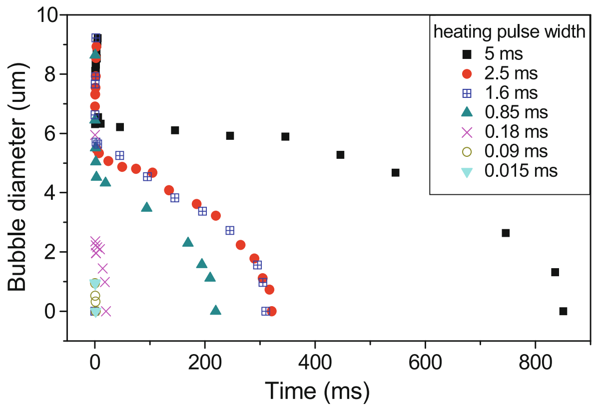

Thermal Bubbles, Figure 7 Effects of pulse width on bubble growth and collapse on a $3 \times 10\,\mu m^2$ microheater at 28.2 mW immersed in DI water [10]

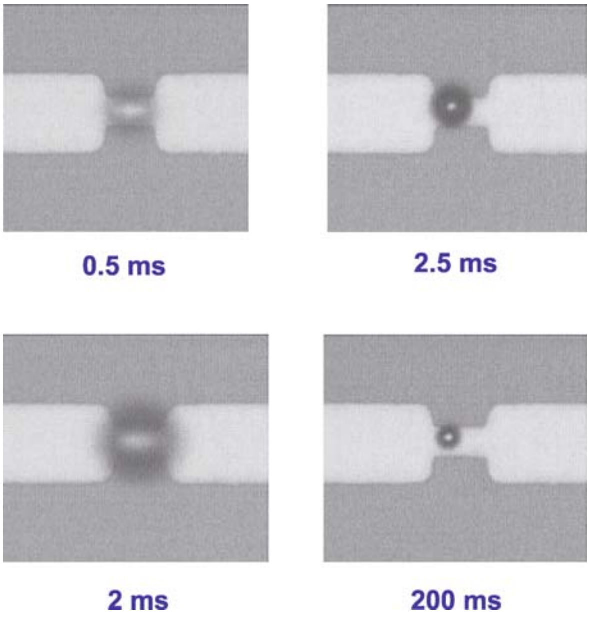

Thermal Bubbles, Figure 8 Microbubble growth and collapse on a microheater at a pulse width of 1.66 ms and a power input of 28.2 mW [10]

width microheater (with the slim part having dimensions of $10 \times 3\,\mu m^2$) at a power input of 28.2 mW immersed in water is presented in Fig. 7. It is shown that the diameter of the bubble undergoes a rapid, initial growth period and after reaching a maximum value, it suddenly drops and then the bubble begins to collapse slowly as a result of the condensation process. For the short pulse widths (e. g., in the range 0.015 – 0.18 ms), a single bubble was barely observable on the surface of the microheater and the growth and collapse of the bubble was almost symmetric. When the duration of the heating pulse was in the millisecond range (0.85 – 5 ms), bubble growth and collapse periods became asymmetric with respect to time.

Asymmetric Growth and Collapse Periods and Perturbation Area

Figure 8 shows time-lapse micrographs about the asymmetric bubble growth and collapse periods on the slim part of the microheater ($10 \times 3\,\mu m^2$) at a pulse width of 1.66 ms under a power input of 28.2 mW [10]. It is shown that the bubble grew during the period 0 – 2 ms and then collapsed in the period 2 – 200 ms. The maximum size of the bubble was about 9.2 µm, which was comparable to the larger dimension of the narrow part of the microheater. To investigate the perturbation area, submicron particles (0.96 µm in diameter) were placed in the DI water near the microheater to trace the movement of the fluid, and the movement of the particles was recorded by a high-speed CCD. At such a pulse width and power input, it was found that the asymmetric growth and collapse periods of the bubble led to a perturbation area of fluid that bwas about six times greater than the maximum diameter of the bubble [10].

Effects of Heater Size on Boiling Patterns

Table 1 lists the sizes of different submicron and micron heaters fabricated by Deng et al. [13] for the investigation of heater size effects on bubble shape, boiling patterns and their growth and collapse periods. A series of tests were carried out for submicron and micron heaters immersed in water at 298 K (room temperature) under a 1.66 ms pulse width. It was found that there was a critical feature size for the heater, 10 µm, for this pulse width. The boiling patterns on heaters with a feature size below or above this critical value were quite different, and they can be classified into two groups as shown in Fig. 9. A single spherical bubble was generated periodically with Group I heaters (a)–(f) with width of the slim part of the heater less than or equal to 10 µm, and an oblate vapor blanket was generated periodically with Group II heaters (g)–(k). The fact that the shape of the bubble and boiling pattern depend on the slim part of the heater can be explained as follows: after the incidence of boiling, the water–vapor interface will try to form a spherical bubble within the thin superheated liquid due to the surface tension effect, which is the dominant force at the microscale level. The spherical vapor bubble stops growing near the outer edge of the thin superheated region because of its contact with the cooled

Thermal Bubbles, Table 1 Dimension of various submicron and micron heaters [13]; The length and width are measured at the slim part of the microheater

Heater ID	Length (μm, ±2%)	Width (μm, ±3%)
(a)	0.5	0.5
(b)	1	0.5
(c)	2	1
(d)	10	3
(e)	10	5
(f)	20	10
(g)	30	10
(h)	30	15
(i)	90	30
(j)	150	50
(k)	200	70

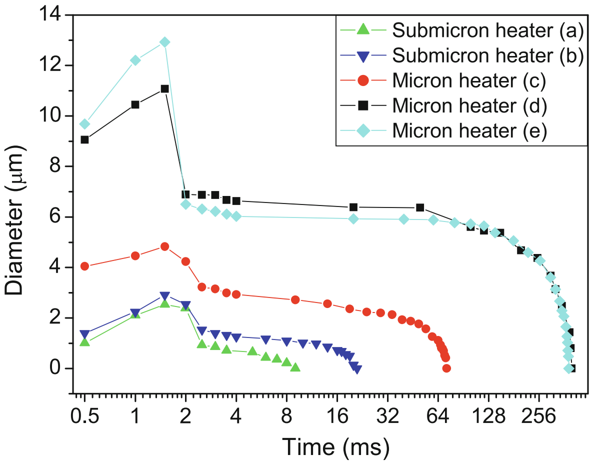

Thermal Bubbles, Figure 10 Semi-logarithmic plot of bubble diameter versus time for spherical bubble growth and collapse on submicron heaters and micron-heaters at a pulse width of 1.66 ms [13]

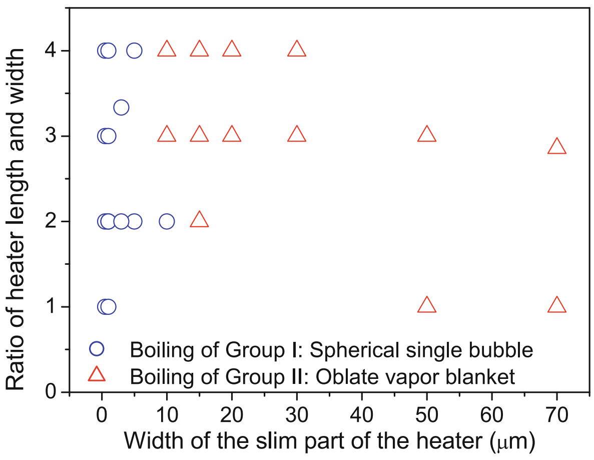

Thermal Bubbles, Figure 9 Map of boiling patterns for various sizes of microheaters [13]

liquid. When the heater has exceeded a certain critical length, the growth of the spherical bubble cannot fit within the thin superheated region, and it grows within the thin superheated region as an elongated bubble on the heater. Because of the larger area of the elongated bubble that is exposed to the outer cooled fluid, the condensation effect is much stronger than the spherical bubble and so it collapses immediately.

Single Spherical Bubble A semi-logarithmic plot of the diameter of spherical bubble as a function of time for the Group I heaters is shown in Fig. 10, which was obtained by using a digital image processing program. The variations in the bubble diameter with time were very similar to each other and a clear bubble growth and collapse process were recorded. In all cases, the spherical bubble growth period was comparable to the width of the heating pulse (1.66 ms). After reaching its maximum size, the bubble began to collapse on the heater surface, and the collapse period, which could last for 10 – 450 ms, was longer than the growth period. The maximum bubble diameter was comparable to the size of the microheater due to the highly localized heating resulting in a superheated zone on the microheater. The bubble lifetime decreased with the heater size due to the shrinking of the superheated zone. Figure 11a shows the growth and collapse of the bubble on a submicron heater having an area of $1 \times 0.5\ \mu m^2$ at a pulse heating power of 1.3 mW and a heat flux of $112.4\ MW/m^2$. Figure 11b shows the growth and collapse of the microbubble on a microheater having an area of $10 \times 5\ \mu m^2$ at a pulse heating power of 38.5 mW and a heat flux of $85.2\ MW/m^2$. Note that in each of these photos, there is a bright circle at the middle of the spherical bubble, indicating a curved spherical vapor–liquid interface.

Film Boiling Oblate vapor blanket or film boiling was found on the surface of the Group II heaters (g)–(k) with the slim part of the heater greater than 10 μm. Figures 12a and 12b show that boiling patterns on the heaters having an area of $150 \times 50\ \mu m^2$ and $200 \times 70\ \mu m^2$, respectively. No single spherical bubble was observed. Instead, an oblate vapor blanket was formed on the heater surface, and it disappeared almost immediately after the pulse heating stopped at 1.66 ms. The light intensity of the vapor layer on the surface of heaters of Group II was fairly uniform, indicating a relatively planar vapor–liquid interface.

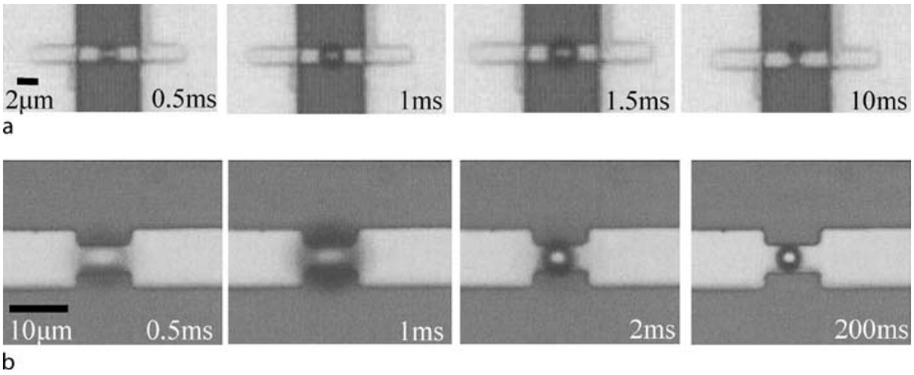

Thermal Bubbles, Figure 11 Spherical bubble generated in water under 1.66 ms pulse heating: (**a**) on submicron heater ($1 \times 0.5\ \mu m^2$) at pulse heating power of 1.3 mW and heat flux at 112.4 MW/m^2; (**b**) on a microheater ($10 \times 5\ \mu m^2$) at 38.5 mW at heat flux of 85.2 MW/m^2 [13]

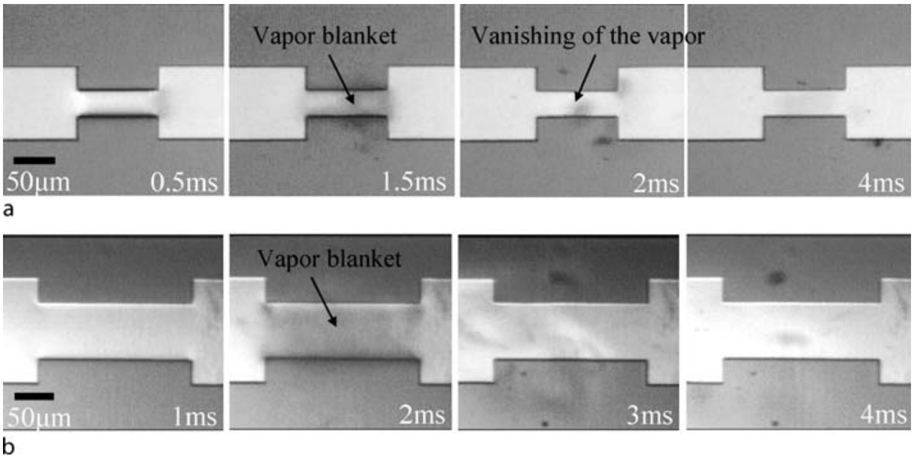

Thermal Bubbles, Figure 12 Oblate vapor blanket on the heater surface (**a**) on a microheater ($90 \times 30\ \mu m^2$) at pulse heating power of 808.2 mW and at a heat flux of 46.3 MW/m^2; (**b**) on a micron heater ($200 \times 70\ \mu m^2$) [13]

Onset of Bubble Nucleation

Effect of Heater Size on Nucleation Temperature and Nucleation Time

Deng et al. [13] experimentally investigated the effects of the size of the heater on the temperature variations of microheaters at a specific pulse width τ of 1.66 ms. The inflection point and temperature discontinuity point of the temporal variations of the surface temperature of the submicron heaters and microheaters were identified as the respective nucleation temperatures. The nucleation temperature and nucleation time for various heaters are presented in Fig. 13. The horizontal axis of this figure is in terms of the featured size of the heater, L_c, which is defined as the square root of the area of the slim part of the heater, i.e., $L_c = (L \times W)^{1/2}$ with W and L being the width and the length of the microheater, respectively. It is shown that the nucleation temperature increases while the nucleation time decreases as L_c decreases. This is because the rate of temperature increase of the heater decreases with the size of the heater.

Microbubble Growth and Collapse and Nucleation Temperature in DNA Solutions

Bubble Growth and Collapse in DNA Solutions

It is known that the viscosity of the single-stranded DNA (ssDNA) solution increases with its concentration [14]. It was found that the overall bubble lifetime in ssDNA solutions decreased distinctly with the increase in the ssDNA concentration [14].

Figure 14 shows the variation of bubble diameter immediately after pulse heating is imposed for the concentrations of 0 µg/µl, 0.1 µg/µl, 1 µg/µl, 6.4 µg/µl, and 10 µg/µl

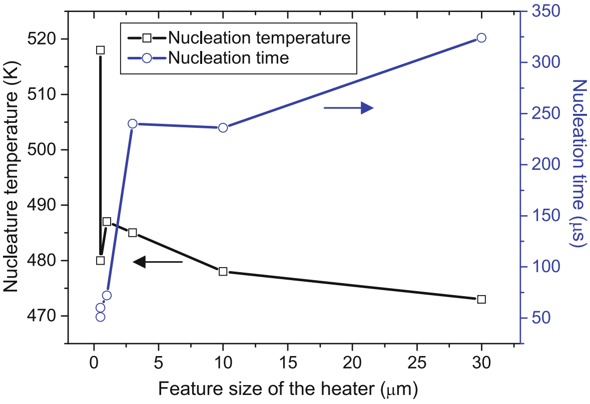

Thermal Bubbles, Figure 13 Effects of heater size on nucleation temperature and nucleation time at $\tau = 1.66$ ms [13]

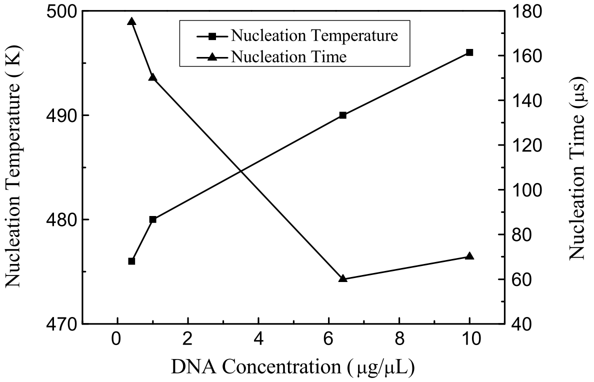

Thermal Bubbles, Figure 15 Effects of concentration on the nucleation temperature and time [12]

ssDNA solutions, respectively [14]. In this figure, the time is normalized by the heating pulse width (1.66 ms) and the bubble diameter is normalized by the characteristic size of the microheater L_c. It is shown that the maximum bubble diameter decreases with the increase of the ssDNA concentration. For both DI water and 0.4 µg/µl ssDNA solution, the largest bubbles were recorded 2 ms after the start of the heating process, implying that the bubble kept on growing even though the heating pulse stopped at 1.66 ms, due to the inertia effect. For the case of 1 µg/µl, the maximum-size bubble was recorded at 1.5 ms, implying that the bubble stopped growing at almost the end of the heating pulse. For high concentrations of 6.4 µg/µl and 10 µg/µl, however, the largest bubbles were both recorded at 0.5 ms, indicating that the bubble growth process was much shorter than that at moderate concentrations, and the bubble stopped growing even though the heater was still operating. From this graph, it can be concluded that high concentrations of the DNA macromolecules in a solution can effectively retard the bubble growth by increasing the dissipation of the kinetic energy of the bubbles. As a result, both the bubble growth period and the recorded maximum bubble diameter are distinctively reduced at high DNA concentrations. For medium and low concentrations (1 µg/µl and 0.4 µg/µl, respectively), the bubble growth period is comparable to the heating pulse width.

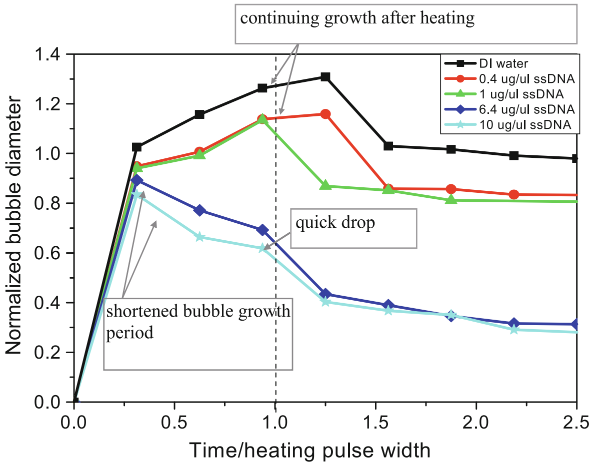

Thermal Bubbles, Figure 14 Variation of microbubble diameter in ssDNA solutions: (**a**) bubble diameter versus time; (**b**) close-up view of bubble initial growth period [11]

Nucleation Temperature and Nucleation Time in DNA Solutions

The effects of DNA concentration on nucleation temperature and nucleation time are presented in Fig. 15. It is shown that the nucleation temperature increases with DNA concentration. This is because higher nucleation work is required for higher DNA concentrations, leading to higher nucleation temperatures. On the other hand, nucleation time decreases with the increases of the DNA concentration. This is because higher power inputs are required for bubble nucleation in higher DNA concentration, resulting in a faster heating rate and therefore a shorter nucleation time.

Future Directions for Research

Although extensive efforts have been focused on fundamental and applied research on microbubble actuators, the demand for high-speed, high-quality printing will be one of the main drivers of the development of the next generation of inkjet printheads using MEMS technology [15]. In

comparison with the other inkjets, such as the piezoelectric type, the bubble actuator-based inkjet has the advantages of a simple fabrication process and high compatibility with the CMOS process. The applications of bubble actuators to microfluidics based biotechnology, such as DNA microarrayer, microcell manipulator/sorter and micro-oligonucleotide synthesizer, are in the early stage of research, and more studies on the behavior of bubble actuators using different biofluids will be needed for design and fabrication of these devices.

Cross References

- ► Bubble Growth and Collapse
- ► Micro Heat Pipes
- ► Nucleation Temperature

References

1. Nielsen NJ (1985) History of the inkjet printhead development – preventing hydraulic crosstalk. Hewlett-Packard J 36:4–10
2. Kobayashi H, Koumura N, Ohno S (1981) Canon Kabushiki Kaisha liquid recording medium. US Patent 4,243,994
3. Bhaskar EV, Leban MA (1989) Integrated thermal inkjet printhead and method of manufacture. US Patent 4,847,630
4. Lee JD, Yoon JB, Kim JK, Chung HJ, Lee CS, Lee HD, Lee HJ, Kim CK, Han CH (1999) A thermal inkjet printhead with monolithically fabricated nozzle plate and self-aligned ink feed hole. J Microelectromech Syst 8:229–236
5. Baek SS, Choi BY, Oh YS (2004) Design of a high-density thermal inkjet using heat transfer from CVD diamond. J Micromech Microeng 14:750–760
6. Tseng FG, Kim CJ, Ho CM (2002) A high-resolution high-frequency monolithic top-shooting microinjector free of satellite drops. Part I. Concept, design, and model. J Microelectromech Syst 11:427–436
7. Geng X, Yuan H, Oguz HN, Prosperetti A (2001) Bubble-based micro pump for electrically conducting liquids. J Micromech Microeng 11:270–276
8. Jun TK, Jin C, Kim CJ (1998) Valveless pumping using traversing vapor bubbles in microchannels. J Appl Phys 83:5658–5664
9. Lin L (1998) Microscale thermal bubble formation: thermophysical phenomena and applications. Microscale Thermophys Eng 2:52–59
10. Deng PG, Lee YK, Cheng P (2003) The growth and collapse of a micro-bubble under pulse heating. Int J Heat Mass Transf 46:4041–4050
11. Deng PG, Lee YK, Cheng P (2006) Two-dimensional micro-bubble actuator array to enhance the efficiency of molecular beacon DNA micro-biosensors. Biosens Bioelectron 21:1443–1450
12. Deng PG, Lee YK, Cheng P (2005) Measurements of micro bubble nucleation temperature in DNA solutions. J Micromech Microeng 15:564–574
13. Deng PG, Lee YK, Cheng P (2006) An experimental study of heater size effect on micro bubble generation. Int J Heat Mass Transf 49:2535–2544
14. Deng PG, Lee YK, Cheng P (2004) Micro bubble dynamics in DNA solutions. J Micromech Microeng 14:693–701
15. Petersen K (2005) A new age for MEMS. 13th International Conference on Solid-State Sensors, Acuators and Microsystems (IEEE Transducers), Seoul, Korea, pp 1–4
16. Okamoto T, Suzuki T, Yamamoto N (2000) Microarray fabrication with covalent attachment of DNA using bubble jet technology. Nat Biotech 18:438–441

Thermal Capacitive Flow Sensor

► Thermocapacitive Flow Sensor

Thermal Conductivity

► Plasma Treatment of Nanoparticles for Nanofluids

Thermal Control in Microfluidic Modules

► Temperature Control in Microfluidic Systems

Thermal Creep Coefficient

Definition

Thermal creep coefficient determines a gas flow induced by a temperature gradient.

Cross References

- ► Gas Flow in Nanochannels
- ► Micro- and Nanoscale Gas Dynamics

Thermal Diffusion

► Thermophoresis

Thermal Flow Sensors

- ► Micro/Nano Anemometers
- ► Micro- and Nanoscale Anemometry: Implication for Biomedical Applications
- ► Pyroelectric Flow Sensors
- ► Thermoelectric Flow Sensors

T

Thermal Fusion Bonding

Synonyms

Fusion bonding; Thermal bonding; Hot press bonding

Definition

Thermal fusion bonding is a process which fuses more than one material or substrate via a thermal cycle. The temperature for performing this process is usually a bit higher than the glass transient temperature (T_g) of the material.

Cross References

► Bulk Micromachining
► Thermal Fusion Bonding

Thermal Gradient Focusing

► Temperature Gradient Focusing

Thermal Lens Effect

► Thermal Lensing, Detection

Thermal Lensing, Detection

Kazuma Mawatari[1], Takehiko Kitamori[2]
[1] Microchemistry Group, Kanagawa Academy of Science and Technology (KAST), Kanagawa, Japan
[2] Department of Applied Chemistry
School of Engineering, The University of Tokyo, Tokyo, Japan
kmawatari@world.odn.ne.jp,
kitamori@icl.t.u-tokyo.ac.jp

Synonyms

Photothermal effect; Thermal lens effect

Definition

Thermal lensing (TL) is one example of a photothermal phenomenon. When an excitation laser is focused into a non-fluorescent sample in a microchannel, the sample absorbs the excitation laser and releases the light energy as heat following non-radiative relaxation. The heat generation induces a temperature distribution which is similar to a Gaussian profile due to the Gaussian intensity distribution of the excitation laser and heat diffusion. Generally, a temperature increase in a liquid decreases the refractive index, and a refractive index distribution working as a concave lens is formed around the focus. This concave lens is a thermally-induced lens and the phenomenon is known as *thermal lensing*. A thermal lens microscope (TLM) utilizes TL effects for ultrasensitive detection of non-fluorescent molecules in microchannels. The TLM features high sensitivity comparable to that obtained by a fluorescence method and, because there are so many more non-fluorescent molecules, much wider applicability. TLM has been successfully applied to various analytical and chemical synthesis applications on microchips combined with general micro-integration methods by micro-unit operations (MUOs) and continuous flow chemical processing (CFCP).

Overview

The basic principle of TLM is illustrated in Fig. 1 [1]. In a TLM, two laser beams are utilized: an excitation laser beam and a probe laser beam. The wavelength of the former is tuned to the light absorption band of the sample and that of the latter is adjusted to avoid the absorption band. The excitation laser is tightly focused into the sample. The diameter of the beam waist is usually around 1 µm. The sample absorbs the excitation beam, and heat is released to the solvent around the molecule, increasing temperature of the solution. The light absorption is linearly dependent on the light intensity distribution which is a Gaussian distribution, and the resultant temperature distribution is sim-

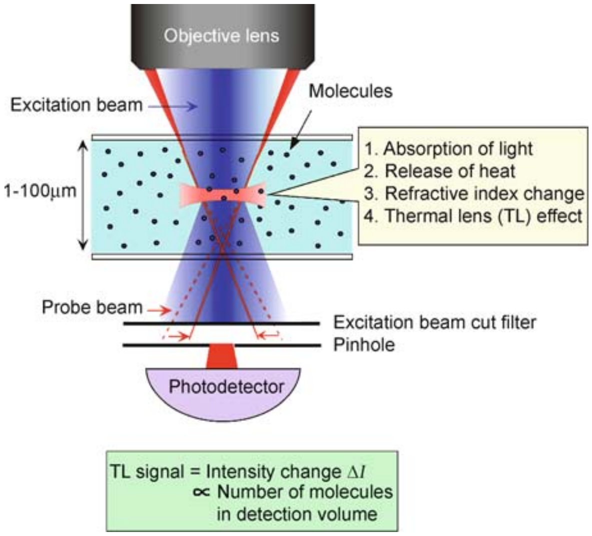

Thermal Lensing, Detection, Figure 1 Basic principle of TLM

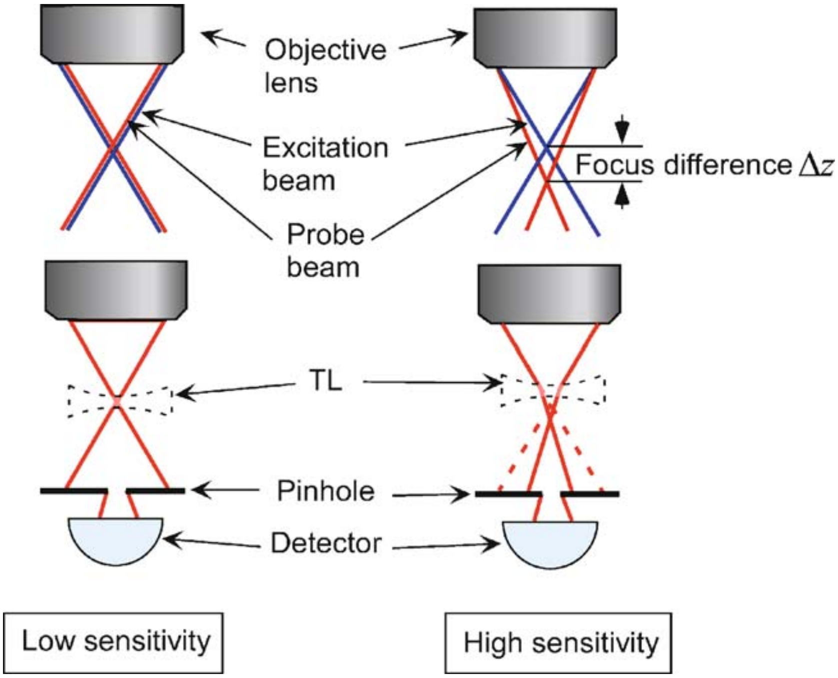

Thermal Lensing, Detection, Figure 2 Illustration of sensitive TL detection by focal length difference Δz: $\Delta z = 0$ (left) and $\Delta z \cong z_C$ (right)

ilar to the intensity distribution. The strength of the lens at thermal equilibrium is expressed as,

$$\frac{1}{f} = \frac{P\varepsilon Cl\,(\mathrm{d}n/\mathrm{d}T)}{\pi J\kappa\omega_0^2} \tag{1}$$

where f is the focal length of the thermal lens near the optical axis, J is the Joule coefficient, κ is the thermal conductivity of the medium (usually solvent in dilute solutions), ω_0 is the radius of the beam waist, P is the power of the excitation beam, ε is the molar absorption coefficient of the sample, C is the concentration of the sample, l is the optical path length of the cell (usually the depth of the cell if the change of the waist ω is ignored) and $\mathrm{d}n/\mathrm{d}T$ is the first derivative of the refractive index, n, of the medium by temperature, T.

For detection of the TL effect, a probe beam is coaxially introduced into the objective lens and focused on the sample. The radius of the spot is also calculated from Eq. (1). When the excitation beam is focused on the sample and the TL effect is induced, the optical path of the probe beam is changed. The change in the optical path is detected by measuring the probe beam intensity through a pinhole. For dilute solutions, the intensity change ΔI is proportional to $1/f$ in Eq. (1) and is defined as a thermal lens signal. The sign of ΔI depends on the TL effect on the probe beam, which is either converging or diverging, and is determined

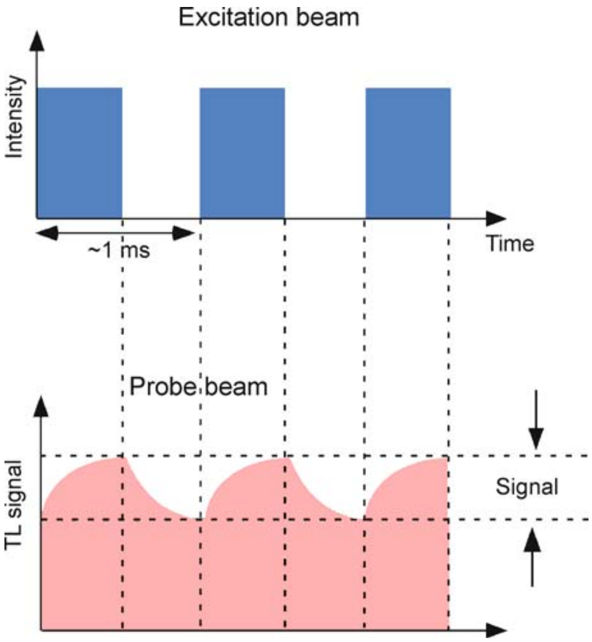

Thermal Lensing, Detection, Figure 3 Signal recovery by intensity modulation of the excitation beam (upper) and synchronous detection of the same frequency component by a lock-in amplifier (bottom)

by the relative focal positions of the probe and excitation beams. When the focus of the probe beam is closer to the

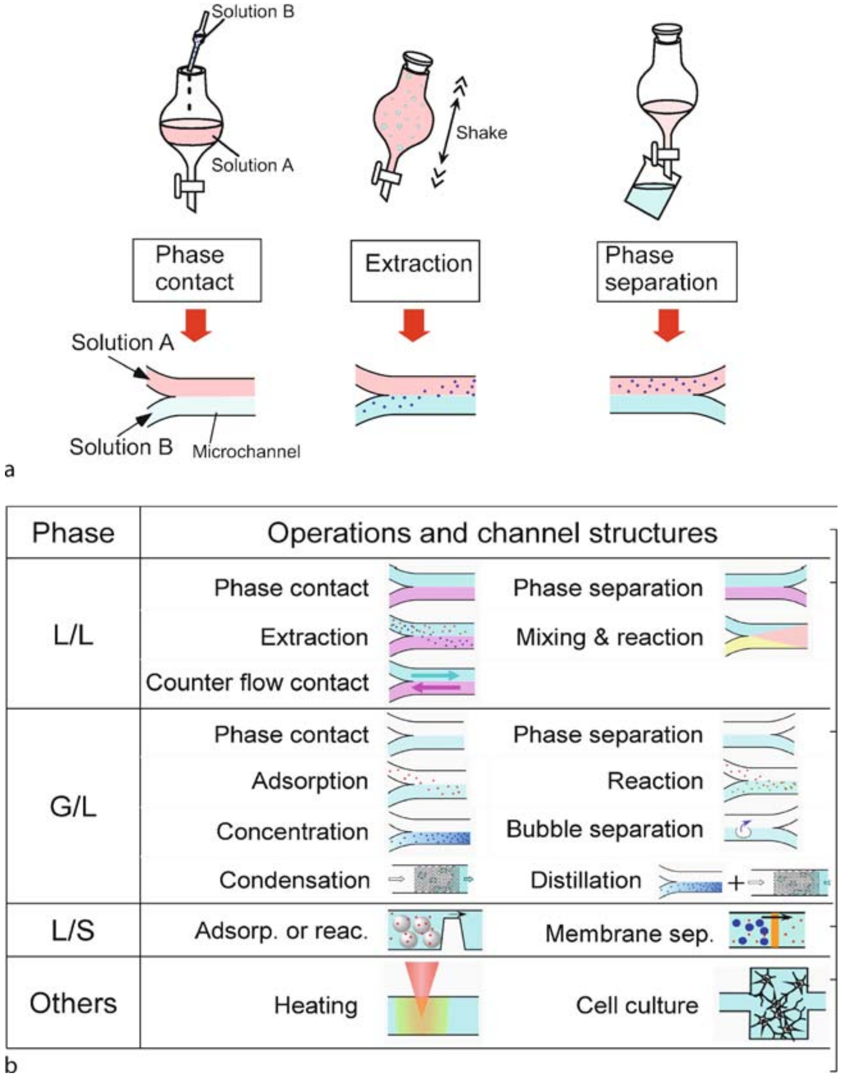

Thermal Lensing, Detection, Figure 4 Realization of micro-unit operations (MUOs): (**a**) example of solvent extraction and (**b**) MUOs developed for various phases

objective lens than that of the excitation beam, the probe beam diverges.

As shown in Eq. (1), the sensitivity of the TL signal depends on chemical and physical properties of the solution. For the chemical properties, the enhancement factor $(\mathrm{d}n/\mathrm{d}T)/\kappa$ is very important. Usually, organic solvents are favorable due to higher $\mathrm{d}n/\mathrm{d}T$ and smaller κ [1]. Water shows the lowest enhancement factor. For example, carbon tetrachloride has an approximately 40 times greater enhancement factor than water.

For the physical properties, the enhancement factor $P/\pi\omega_0^2$ is important. Tightly focusing the excitation beam leads to a strong TL effect; however, it also leads to a large divergence of the excitation beam due to light diffraction and the effective length of the TL contributing to the signal decreases. The detection depth should be experimentally determined.

The most important point to realize sensitive TLM is a focal length difference between the excitation beam and probe beam as shown in Fig. 2. When the focal lengths of the two beams are the same, the probe beam is focused at the center of the TL. In this case, the optical path of the probe beam is not changed, and the signal intensity becomes almost zero. An adequate focal length difference Δz is necessary for realizing optimum sensitivity. The optimum Δz is estimated by

$$\Delta z \cong \sqrt{3} z_{\mathrm{c,pr}} \tag{2}$$

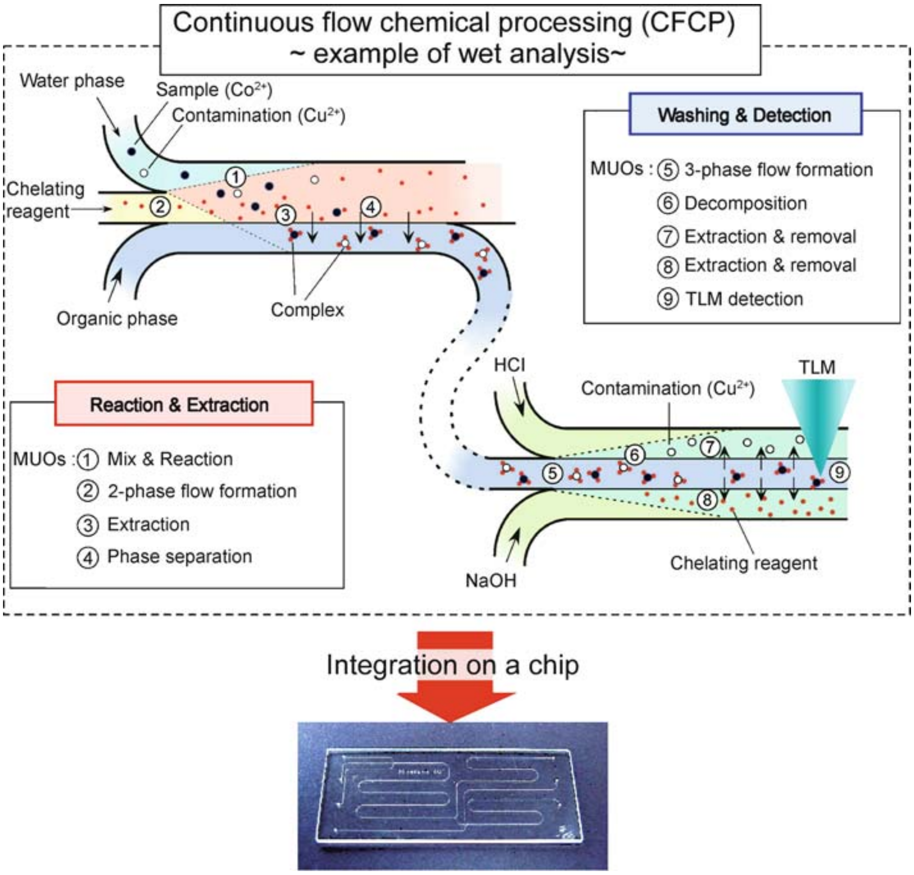

Thermal Lensing, Detection, Figure 5 Concept of continuous flow chemical processing (CFCP) and TLM detection for general micro-integration: an example of wet analysis on a microchip

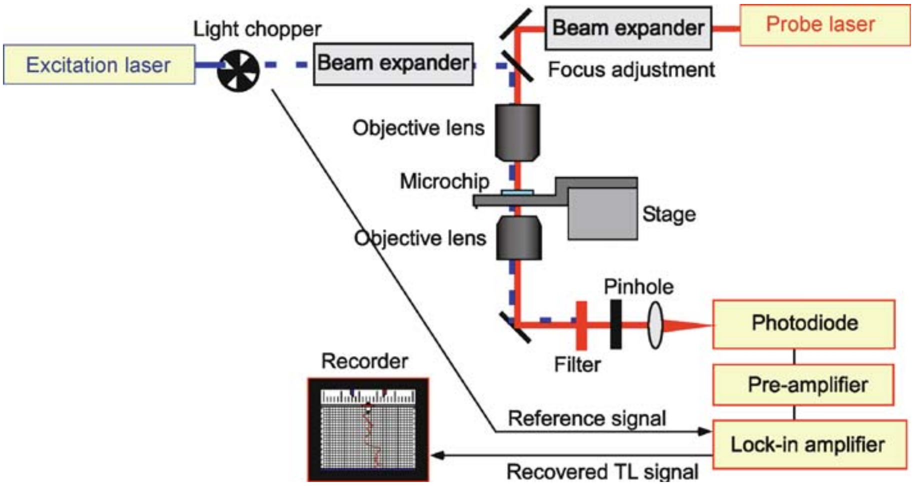

Thermal Lensing, Detection, Figure 6 A typical TLM system

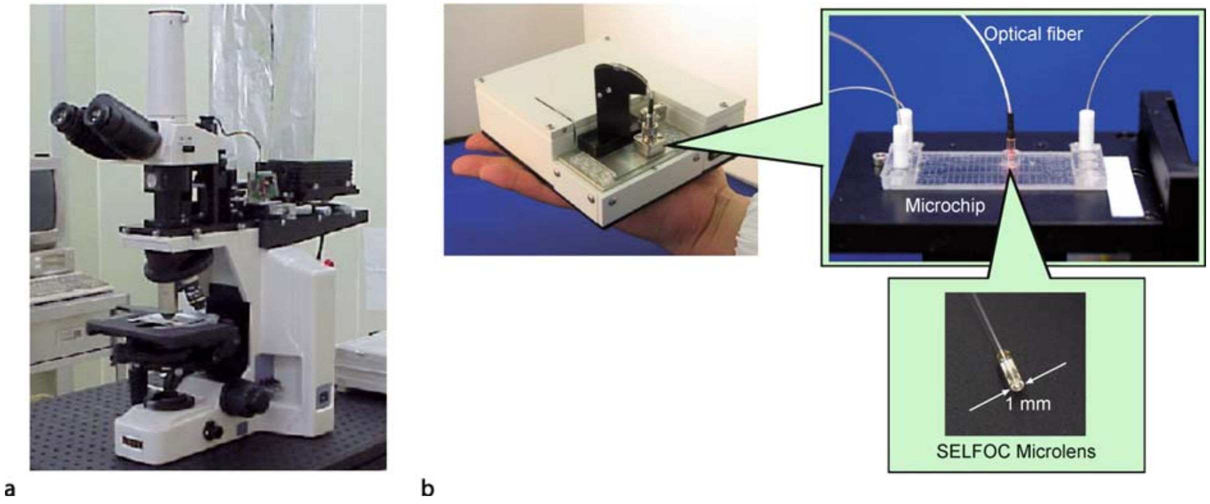

Thermal Lensing, Detection, Figure 7 a) Desktop-sized TLM and b) palmtop-sized TLM

where $z_{c,pr}$ is a confocal distance of the probe beam. However, Eq. (2) assumes that $z_{c,pr}$ is much larger than the TL thickness which is investigated based on Eq. (2). The exact value should be determined by measuring the dependence of the TL intensity onΔz.

Next, the signal processing to recover TL signals from large thermal noises is illustrated because the TL effect is very weak; typically the largest value of ΔT is 10^{-3} degrees and Δn is less than 10^{-7}. The former value is as small as the thermal fluctuation and easily affected by environmental temperature change. In order to recover the true TL signal, the intensity of the excitation beam is modulated at a certain frequency and the synchronous signal of frequency in the probe beam intensity change is detected by a lock-in amplifier. The lock-in amplifier works as an ultra-narrow band pass filter. A typical waveform is illustrated in Fig. 3. Finally, the concept of a general micro-integration method and coupling with the TLM are illustrated. In the 1990's, most microchip-based analytical systems were concerned with genome or protein analysis by electrophoresis with fluorescence detection. However, many other analytical and synthesis applications were expected in general chemistry, organic synthesis, combinatorial chemistry, physical chemistry, and biochemistry that involve complicated chemical processes, organic solvents, neutral species, and non-fluorescent detection. For this purpose, we first realized conventional unit operations on microchips as micro-unit operations (MUOs) utilizing multiphase laminar flow as shown in Fig. 4. These MUOs were connected by continuous flow chemical processing (CFCP) to form a multiphase laminar flow network (Fig. 5), and TLM was utilized for detection of

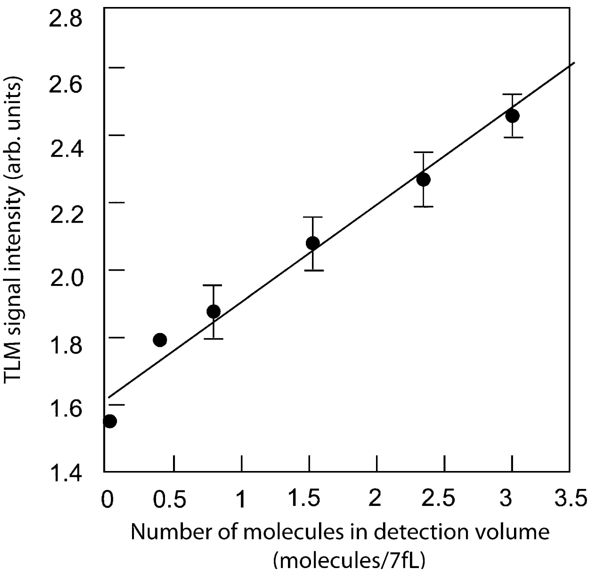

Thermal Lensing, Detection, Figure 8 Performance of TLM for ultrasensitive detection of molecules. The sample was lead(II)-porphyrine complex solution

non-fluorescent molecules. These concepts have opened various analytical and chemical synthesis applications on microchips with wide applicable and sensitive TLM detection.

Basic Methodology

A typical TLM system is illustrated in Fig. 6. The output of the excitation beam is intensity-modulated by a light

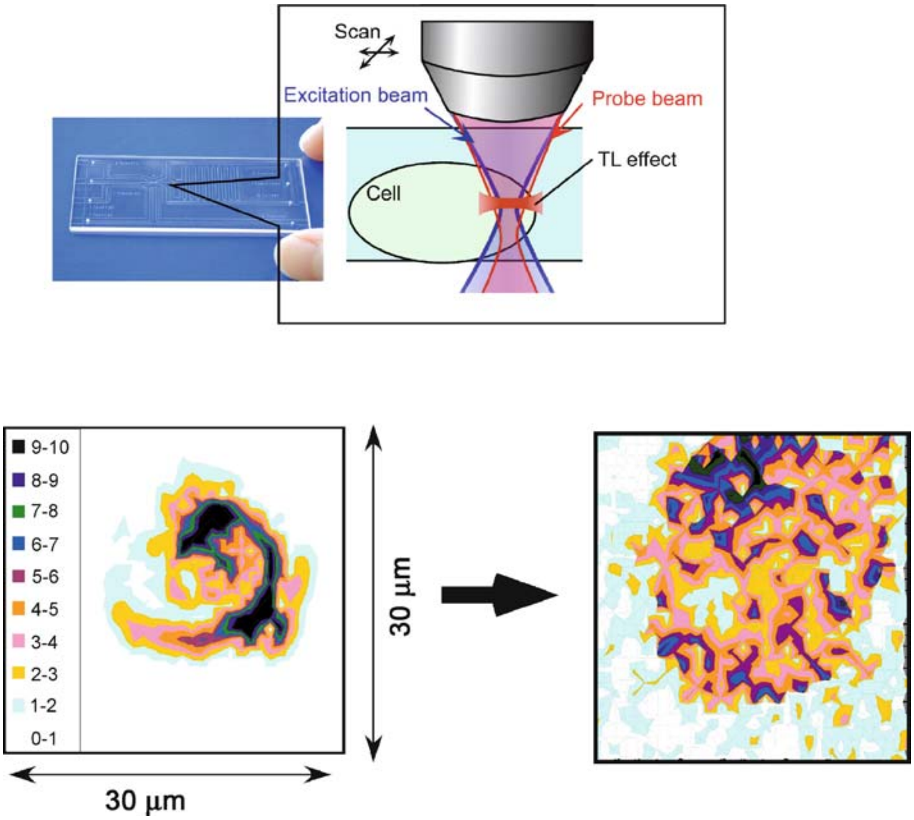

Thermal Lensing, Detection, Figure 9 Single cell imaging by scanning TLM. Cytochrome C was directly measured by scanning the laser beams with a 1 µm increment

chopper. The excitation beam is expanded by a beam-expander to adjust the beam size to the size of the input pupil of an objective lens. Then, the excitation beam is introduced into a microscope through a dichroic mirror and a prism. The probe beam is also expanded by a beam-expander. The distance between the two lenses in the beam expander is adjusted to control the divergence of the probe bam and focal length difference Δz. Then, the probe beam is reflected by the dichroic mirror and introduced into the microscope coaxially with the excitation beam. The objective lens of the microscope focuses the excitation and probe beams into a sample on a microchip. The TL effect is induced in the sample, and the probe beam is converged or diverged due to the TL effect depending on the focal position as described in the previous section. The two transmitted beams are collimated by another objective lens and reflected by a mirror and focused by a third lens. The excitation beam is removed by a filter, and only the probe beam is focused onto the pinhole and collected by a photodiode. The photodiode converts the light intensity of the probe beam to an electronic signal which is amplified by a pre-amplifier. Then, the amplified signal is fed into a lock-in amplifier. The lock-in amplifier extracts synchronous signals in the large background, and the amplitude and phase are measured as TL signals. Available wavelengths range from deep-UV to IR regions.

Desktop- and palmtop-sized TLMs are commercially available (Fig. 7) [2]. In the palm-top TLM, laser-diodes are utilized as excitation and probe beams, and these beams are introduced to a microchannel via a light mixer and a single-mode optical fiber. The palm-top TLM can also be integrated into a system. For example, an allergy analysis system with the palmtop-sized TLM has been reported.

Key Research Findings

Realization of TL detection under a microscope allows ultrasensitive detection of non-fluorescence molecules. An example of dye solution detection in a microchannel is illustrated in Fig. 8 [3]. The microchannel was 150 µm wide and 100 µm deep. The solvent used was benzene and the molar absorption coefficient of the porphyrine complex was $3.2 \times 10^4\ \mathrm{M}^{-1}\mathrm{cm}^{-1}$. The expected value was cal-

Thermal Lensing, Detection, Table 1 Example applications utilizing TLM and microchips [6]

	Analyte	Method
Environmental analysis	Co^{2+}, Cr^{6+}, Fe^{2+}, K^{+}, Na^{+}, Ni^{2+}, PO_4^{2-}, Pesticides, etc.	Solvent extraction
	NH_4, HCHO	Gas/liquid absorption and colorimetric reaction
Clinical diagnosis	s-IgA, INF-.γ, BNP, IgE, CRP, CEA, 17-estradiol, AFP, Amphetamines, Sedatives, Antibiotics, etc.	Immunoassay
	Glucose, HDL, LDL, Albumin, GOT, GPT, ALP, GA , etc.	Enzyme reaction
Bioanalysis	Fe^{2+}, Ascorbic acid, H_2O_2,	Flow injection analysis
	Cytochrome C, TNBS (on a cell)	Direct detection
	NO (released from a cell)	Enzyme reaction
	ApoA1 (released from a cell)	Immunoassay
	DNA, Amino acids	Direct detection
	Arachidonic acid	Direct detection
Food analysis	Prion peptides	Immunoassay
Other	Individual nanoparticles (gold, silver)	Direct detection
	UO_2^{2+}	Solvent extraction
	Dye molecules	Direct detection

culated by multiplying the concentration and the detection volume (7 fL). The signal intensity showed good linear dependence on the expected value. The lower limit of detection was estimated to be 0.32 molecules from the conditions of a signal-to-noise ratio (S/N) of 2 and a signal-to-background ratio (S/B) of 0.1 for an averaging time of several seconds. In comparison with spectrophotometry, more than six orders higher sensitivity in the absolute molecular number is achieved. This ultra-high sensitivity with wide applications for non-fluorescent molecules holds the promise of a powerful tool for various microchip-based analytical or chemical synthesis applications.

TLM can also be utilized for imaging by scanning the laser beams. Figure 9 shows the direct imaging of a single neuron cell by measuring Cytochrome C for monitoring an apoptosis process [4]. In situ imaging of a single cell with almost 1 μm spatial resolution was successfully realized [5]. Many other applications such as in situ immunoassay on biological cells or membranes have also been reported [5].

A summary of example TLM applications coupled with MUOs developed and CFCP is made in

Future Directions for Research

In a previous section, just one example of ultrasensitive concentration determination of non-fluorescent molecules was given. However, the area of micro- and nano-fluidics is rapidly expanding and high degrees of functionality are desired for detection methods.

For these purposes, various functional TLMs have already been realized. For example, sensitive chiral recognition by circular-dichroism TLM (CD-TLM) was reported for synthesis and analysis of drugs on microchips [6]. Other reports have described an electrochemical TLM [7], flow sensing TLM, UV TLM [8], and TLM spectrometer [9].

As important functions for science and technology in micro- and nano-fluidics, three functions are highly desired: individual molecule detection as the ultimate sensitivity, fast (real-time) imaging, and femtosecond time-resolved measurement for investigating molecular dynamics in a nano-space.

The design method of these functional TLMs is also important. The TL effect is usually very complex in the micro- and nano-space and its basic science is still an important issue. Development of a theoretical analysis tool which combines fluidics and optics is desired for this purpose.

Cross References

► Lab-on-Chip Devices for Immunoassay
► Lab-on-Chip (General Philosophy)
► Devices for Sample Extraction

References

1. Bialkowski SE (1996) Photothermal Spectroscopy Methods for Chemical Analysis. Wiley, New York
2. Web site of Institute Microchemical Technology Co., Ltd. http://www.i-mt.co.jp/
3. Tokeshi M, Uchida M, Hibara A, Sawada T, Kitamori T (2001) Determination of subyoctomole amounts of nonfluorescent

molecules using a thermal lens microscope: Subsingle molecule determination. Anal Chem 73:2112
4. Tamaki E, Sato K, Tokeshi M, Sato K, Aihara M, Kitamori T (2002) Single-cell analysis by a scanning thermal lens microscope with a microchip: Direct monitoring of cytochrome c distribution during apoptosis process. Anal Chem 74:1560
5. Kitamori T, Tokeshi M, Sato K, Hibara A (2004) Thermal lens microscopy and microchip chemistry. Anal Chem 76:52A
6. Yamauchi M, Mawatari K, Hibara A, Tokeshi M, Kitamori T (2006) Circular-dichroism thermal lens microscope for sensitive chiral analysis on microchip. Anal Chem 78:2646
7. Kim H-B, Hagino T, Sasaki N, Watanabe N, Kitamori T (2005) Spectrochemical detection using thermal lens microscopy with a glass-substrate microelectrode-microchannel chip. J Electroanal Chem 577:47
8. Hiki S, Mawatari K, Hibara A, Tokeshi M, Kitamori T (2006) UV-excitation thermal lens microscope for non-labeled and ultrasensitive detection of non-fluorescent molecules. Anal Chem 78:2859
9. Tamaki E, Hibara A, Tokeshi M, Kitamori T (2005) Tunable thermal lens spectrometry utilizing microchannel-assisted thermal lens spectrometry. Lab Chip 5:129

Thermally Actuated Mechanical Valves

► Thermomechanical Valves

Thermally Driven Mechanical Valves

► Thermomechanical Valves

Thermally-Sensitive Hydrogels

► Temperature-Sensitive Hydrogels

Thermal Marangoni Effect

► Thermocapillarity

Thermal Mechanical Valves

► Thermomechanical Valves

Thermal Oxidation

► Oxidation (of Silicon)

Thermal Pumping

► Thermocapillary Pumping

Thermal Slip Coefficient

Definition

Thermal slip coefficient determines the tangential velocity of gas near a solid surface due to a longitudinal gradient of surface temperature.

Cross References

► Gas Flow in Nanochannels
► Micro- and Nanoscale Gas Dynamics

Thermistors

► Contact Temperature Sensors

Thermocapacitive Flow Sensor

Hong Jiang[1], Guiren Wang[2]
[1] GraceFlow Technology, Columbia, SC, USA
[2] Department of Mechanical Engineering, University of South Carolina, Columbia, SC, USA
ajiangca2@yahoo.com, wanggu@engr.sc.edu

Synonyms

Thermal capacitive flow sensor

Definition

The thermocapacitive flow sensor is a velocimeter used to measure the rate of fluid flow. In a thermocapacitive flow sensor, there is a heater and sensing capacitor, which has a dielectric material with a temperature-dependent dielectric constant. The heater is located close to the capacitor. If electric power is supplied to the heater, it causes the temperature of the capacitor to rise. The dielectric constant of the capacitor increases with temperature, resulting in an increase in the capacitance. When the fluid flows through the capacitor, the temperature of the capacitor will decrease due to the convective heat transfer from the capacitor to the fluid. Thus the capacitance will also be reduced. Through measuring the capacitive value, the flow velocity can be obtained by a calibration relationship between the flow rate and the capacitance.

Overview

Fluid flow is important not only in almost all engineering fields, but also in micro- and nanofluidic chips. Flow measurements are required to: increase our understanding

of the physicochemical mechanisms of processes; improve the designs of the devices; and enhance the corresponding function of the devices. The measurement of the flow velocity is important in fluid mechanics. There are many conventional advanced velocimetries in fluid mechanics: hot-wire anemometry (HWA), laser Doppler velocimetry (LDV) and particle image velocimetry (PIV) [1]. These methods have been applied in microfluidics to measure the flow velocity in microchannels [2–4]. For microfluidics, there are several other methods to measure flow velocity, these have been reviewed elsewhere [5].

Thermal flow sensors based on convective heat transfer are usually used to measure the flow rate, since a heater can easily be realized by applying electric power to a electric resistor. For instance, HWA, one of the most widely used velocimetries, is a thermal flow sensor.

All thermal flow sensors are based on the convective heat transfer between a flowing fluid and a sensing solid element. Figure 1 shows a simplified case of convective heat transfer which explains the thermal flow sensing principle. A heater heats a solid sensor, which faces the flowing fluid. When power is supplied to the heater, the sensor temperature increases to T_s. As the fluid flows through the solid sensor, there will be a convective heat transfer from the sensor to the fluid. If Q is the heat transfer rate, A_h is the interface area perpendicular to the direction of heat flow between the sensor and the fluid. T_s and T_f are the temperature of the sensor surface and fluid, respectively. The heat transfer can then be described as

$$Q = \mathrm{Nu}\, A_h\, (T_s - T_f) \qquad (1)$$

where Nu $(= \alpha_c L/k_d)$ denotes the Nusselt number, α_c is the convective heat transfer coefficient, L represents the characteristic length for the heat transfer, and k_d is the thermal conductivity of the fluid. Nu normally depends on the flow and material properties and can be described as

$$\mathrm{Nu} = f\nu\, (\mathrm{Re}, \mathrm{Pr}) \ , \qquad (2)$$

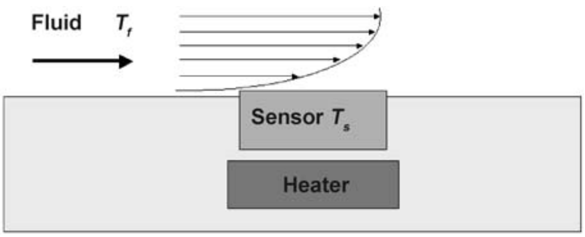

Thermocapacitive Flow Sensor, Figure 1 Simplified case of convective heat transfer

from Eq. (1) and Eq. (2):

$$T_s = \frac{Q}{f\nu\,(\mathrm{Re}, \mathrm{Pr})\, A_h} + T_f = \frac{Q}{f\nu\,(uL/\mu, \mathrm{Pr})\, A_h} + T_f \qquad (3)$$

where Re $(= uL/\nu)$ is the Reynolds number and Pr $(= c_p\mu/k_c)$ denotes the Prandtl number. u, ν, μ, c_p, and k_c are the flow velocity, kinematic viscosity, dynamic viscosity, specific heat, and thermal conductivity of the fluid, respectively [6]. The relationship between Nu and u depends generally on flow (e. g., laminar, turbulent), the geometry of the sensor, the position and the orientation of the sensor to the flow. Nu(Re, Pr) does not have a universal formula. When constant power is applied to the heater, it will cause the temperature T_s to rise. However, when the fluid passes through the sensor, the convective flow will reduce T_s. The higher the flow velocity, the lower the value of T_s. If the fluid temperature, composition, and pressure are constant, the only variable that affects the convective heat transfer or T_s is the flow velocity u. The heater can be an electric resistant. Thus, the flow velocity can be determined by measuring the temperature T_s directly or other variables that are, in turn, related to T_s.

A thermal flow sensor typically consists of a heater and one or more temperature sensors. The heater can operate at either constant heating power or at a constant heating temperature. In thermal microflow sensors, the flow rate is evaluated by measuring the heating power, the temperature of the heater or fluid, and the time of flight of a heat pulse [7].

There are three types of thermal flow sensors that combine the evaluation methods and heater modes: hot-wire (hot-film), calorimetric, and time-of-flight.

- Hot-wire (hot-film) sensors measure the effect of the flowing fluid on a hot body. At a constant heat power, the forced convection causes a decrease in the temperature of the heater.
- Calorimetric sensors measure the asymmetry of a temperature profile round the heater, which is modulated by the fluid flow.
- Time-of-flight type sensors measure the time that it takes for a heat pulse to move a known distance.

In principle, any temperature-dependent property of a solid-state material could be used for temperature measurement. Each of the sensor types can be further categorized, according to their thermal sensing principle as: thermoresistive, thermoelectronic, pyroelectic, thermophilic elements, microresonator structures, or thermocapacitive [7].

In this essay, we focus on the thermocapacitive flow sensor. The advantages of the thermocapacitive flow

sensor are: its low cost arising from batch fabrication; on-chip electronic signal-conditioning circuitry for enhanced performance; low power consumption; low noise due to the metal oxide semiconductor (MOS); and reduced dimensions. Its disadvantages include the fact that it has difficulty measuring velocity distribution in flow fields due to the relatively poor spatial resolution. There are also difficulties with using the thermocapacitive flow sensor in liquids, due to electrical insulation, and in electrokinetic flows, as it could interfere with the flow.

Basic Methodology

The thermocapacitive flow sensor is based on a dielectric material with a temperature-dependent dielectric constant. The sensing module is a capacitor. If the electric power is supplied to a heater that is close to the capacitor, the temperature of the capacitor will increase, causing an increase in the dielectric constant, and thus, an increase in the capacitance of the capacitor. When a fluid flows through the capacitor and if its temperature is lower than that of the capacitor, the temperature of the capacitor will decreases due to the convective heat transfer between the fluid and the capacitor. The temperature of the dielectric material of the capacitor will decrease, resulting in a decrease in the capacity. The higher the flow velocity, the lower the capacity. Therefore there is a relationship between the flow velocity and the capacitance. Like the HWA, with a calibration relationship between the flow velocity and the capacitance, the flow velocity can be calculated by measuring the capacity of the capacitor.

The measurement of flow rate is one of main subjects in experimental fluid mechanics. However, the thermocapacitive flow sensor may have electronic and semiconductor components, such as a capacitor, an n-channel MOS transistor, an oscillation circuit, and microfabrication. Therefore, the thermocapacitive flow sensor is a multidisciplinary tool and some of its electronic and semiconductor components need to be explained.

Components

Capacitor

A parallel-plate capacitor consists of two closely spaced conductive plates. A nonconductive material is termed a dielectric. When the space between the two plates is occupied by a dielectric material, the capacitance is increased by a factor κ that is characteristic of the dielectric and is known as the dielectric constant or dielectric coefficient [8].

$$C = \kappa C_0 = \kappa \left(\frac{A}{d} \right) \tag{4}$$

where C_0 is the original capacitance, A represents the area of the plates, and d is the distance between the surfaces of the two plates. The capacitance C depends on the dielectric constant and the geometrical configuration, but is independent of the voltage on it. Since the dielectric constant κ is dependent on the temperature and frequency, the capacitance C is also a function of the temperature.

N-Channel MOS

Figure 2 illustrates the MOS structure that consists of a semiconductor substrate layer, a middle oxide layer and a top metal layer which acts as the control gate. Most transistors are MOS field-effect transistors (MOSFETs) and the metal gate has mostly been replaced by a polysilicon gate. Although the term insulated gate field effect transistor (IGFET) is sometimes preferred, we will continue to use the term MOS, because it is used in the relevant publication [9]. There are three terminals: D (drain), S (source), and G (gate) in a MOSFET.

The MOS is a voltage sensitive device and operates as the positive gate voltage. This positive potential on the gate causes a polarization of the charges within the oxide insulator as illustrated in Fig. 2. The positive charges (holes) are aligned along the inner surface of the oxide. Consequently, these positive charges attract the negative charges (electrons) from the p-substrate to the area of the oxide. When more electrons are attracted into the n-channel region under the gate oxide than there are holes in the n-channel, that is when the gate voltage is higher than the threshold voltage, the n-channel is created to bridge the two n^+ regions. n^+ regions are so-called in order to emphasize the very large n impurity. If a positive drain voltage is now applied between the D and S terminals, n-channel electrons provide a conducting path between the two n^+ sections and current flows between the source and drain.

A floating gate MOS has one more layer than a MOS. This layer is called the floating gate. It is situated between the control gate and the semiconductor substrate and is surrounded by the oxide insulator (see Fig. 3).

The Sensing Capacitor Module

The sensing module is a capacitor, which has a dielectric layer, whose dielectric constant increases with temperature. In practice the capacitor module can be fabricated

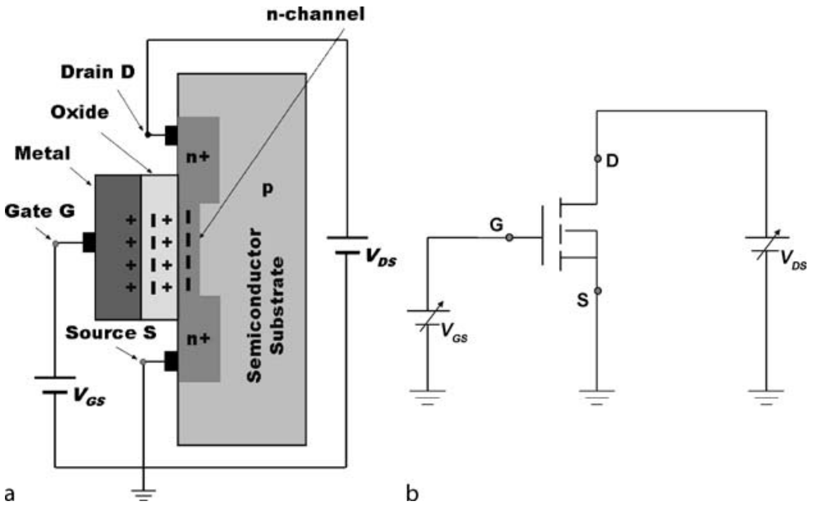

Thermocapacitive Flow Sensor, Figure 2 n-channel MOS structure and wiring. (**a**) n-channel MOS structure; (**b**) diagram showing how the MOS is wired to obtain the current between source and drain

using a MOS-compatible process combined with ethylenediamine pyrocathechol (EDP) groove etching [9, 10] as shown in Fig. 4. The capacitor module consists of multilayers, such as molybdenum for the control gate, a dielectric material Ta_2O_5 [9] or $SrTiO_3$ [10], a polysilicon floating gate, and an oxide insulator. A heating resistor, that can be an electrical resistance, is also included in this module.

Measuring Variables

The sensor operation is based on convective cooling by fluid flow of the sensing capacitor, which is initially heated by a polysilicon microheater which is in close proximity to it. Two variables have been used to measure the flow rate: voltage [9] and oscillation frequency [10].

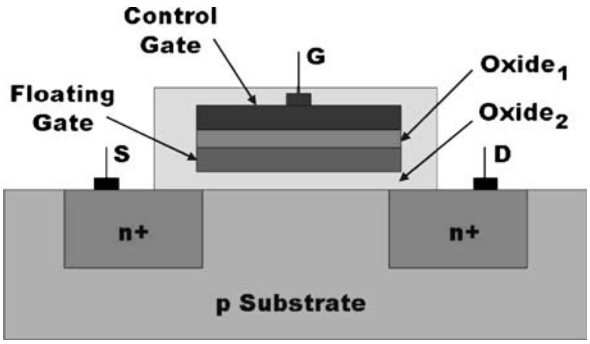

Thermocapacitive Flow Sensor, Figure 3 Structure of a floating gate MOS

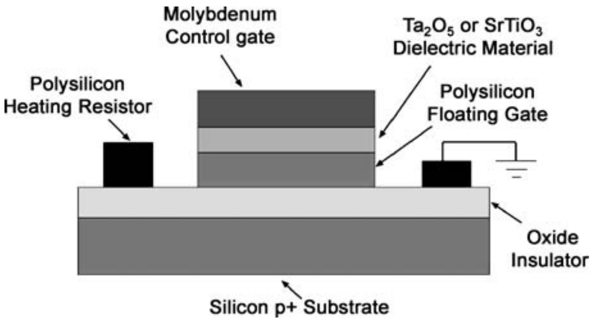

Thermocapacitive Flow Sensor, Figure 4 Sensing capacitor module

MOS Amplified Voltage Output

A schematic of the sensor circuit is shown in Fig. 5 [9]. The sensing capacitor module with a dielectric material (such as Ta_2O_5 or $SrTiO_3$) and a n-channel MOS transistor M_1 together constitute a floating-gate MOS transistor. C is the coupling capacitor between the control gate and the floating gate. For purposes of thermal isolation, the capacitor C and the heating resistor can be located on a cantilever structure, which can be fabricated by bulk micromachining in EDP. The rest of the floating gate MOS was located on the substrate area to avoid heat transfer from the heating element.

The sensor works in the current saturation region where the drain current I_d is nearly independent of the drain–source voltage V_{DS}. The saturation drain current of the floating gate MOS transistor is governed by the follow-

ing equation in simplified form [9]:

$$I_{\mathrm{d}}=\frac{K}{2}\left(\frac{C}{C_{\mathrm{T}}}V_i+W_{\mathrm{B}}V_{\mathrm{B}}-W_{\mathrm{s}}V_{\mathrm{s}}-W_{\mathrm{T}}V_{\mathrm{th}}\right)^2 \quad (5a)$$

Using Eq. (4),

$$I_{\mathrm{d}}=\frac{K}{2}\left(\frac{\kappa C_0}{C_{\mathrm{T}}}V_i+W_{\mathrm{B}}V_{\mathrm{B}}-W_{\mathrm{s}}V_{\mathrm{s}}-W_{\mathrm{T}}V_{\mathrm{th}}\right)^2 \quad (5b)$$

where I_{d} is the drain current, W_{B}, W_{s}, and W_{T} are the coupling ratios which relate to the input voltage V_i, substrate potential V_{B}, source potential V_{s} and threshold voltage V_{th}, respectively. C_{T} is the total capacitance associated with the floating-gate including C. K is the transistor transconductance which relates an output quantity (drain current) to an input quantity (gate–source voltage).

By differentiating I_{d} with respect to κ, where the coupling ratios are a function of C directly, we obtain the expression

$$\frac{\mathrm{d}I_{\mathrm{d}}}{\mathrm{d}\kappa}=\frac{2I_{\mathrm{d}}C_0}{C_{\mathrm{T}}}\left(\sqrt{\frac{I_{\mathrm{d}}^*}{I_{\mathrm{d}}}}-1\right), \quad (6)$$

$$V_0=V_{\mathrm{cc}}-R_{\mathrm{d}}I_{\mathrm{d}} \quad (7)$$

where I_{d}^* is the drain current in the MOS transistor if the control gate voltage V_i is applied directly in the floating gate and V_0 is the output voltage. Since there is a voltage drop on the capacitor, the control gate voltage is higher than the floating gate voltage. Therefore I_{d}^* is larger than I_{d} and $\mathrm{d}I_{\mathrm{d}}/\mathrm{d}\kappa$ is positive. As a result, I_{d} increases with the dielectric constant κ.

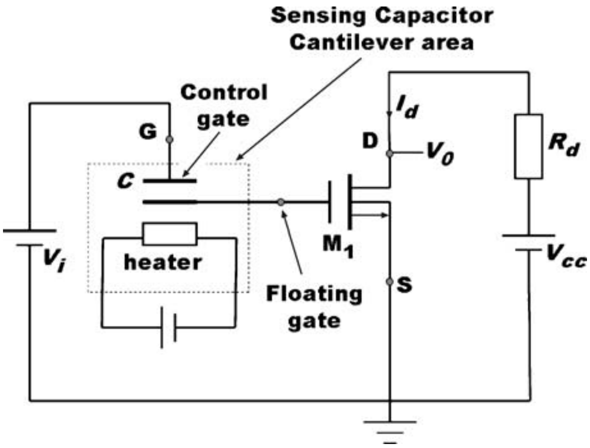

Thermocapacitive Flow Sensor, Figure 5 Circuit schematic of flow sensor measuring capacitor voltage

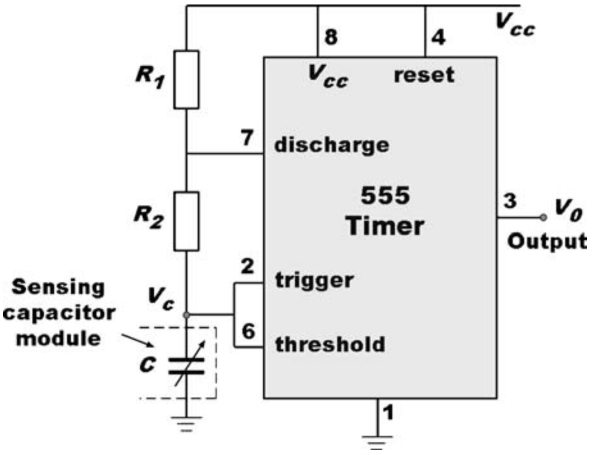

Thermocapacitive Flow Sensor, Figure 6 Circuit of oscillator 555 timer IC chip coupled with sensing capacitor

When power is applied to the heater, the rise in temperature causes the dielectric constant κ in the capacitor to increase, then the drain current increases. When fluid flows through the capacitor convective cooling reduces the temperature, causing κ to decrease, so that the drain current decreases. Therefore the change in the drain current or the output voltage is a measurement of the velocity of the fluid flow.

Frequency Modulated Output

When the sensing capacitor is externally connected to a 555 timer IC chip to form an oscillation circuit as shown in Fig. 6, the oscillation frequency can be used to measure the flow velocity [10]. Here, both inputs of trigger and threshold in 555 timer are connected together. The response of the output voltage V_0 to the input voltage V_{c} on the capacitor is illustrated in Fig. 7.

The lower threshold (V_{TL}) and the upper threshold (V_{TH}) of the 555 timer are internally set at $V_{\mathrm{cc}}/3$ and $2V_{\mathrm{cc}}/3$, respectively. When power is first applied to the circuit, there is no charge in the sensing capacitor and the output V_0 is set high to V_{cc}, since the capacitor voltage V_{c} is below the lower threshold. The sensing capacitor then starts charging through resistors R_1 and R_2 until V_{TH} is reached, which causes the timer to reset and the output V_0 to reduce to a low level. This turns on the internal discharge transistor, which discharges the sensing capacitor through R_2. When V_{c} reaches V_{TL}, the 555 timer output goes high again and the discharge transistor is turned off. The operation is now cyclic, with the sensing capacitor voltage V_{c} oscillating between $V_{\mathrm{cc}}/3$ and $2V_{\mathrm{cc}}/3$.

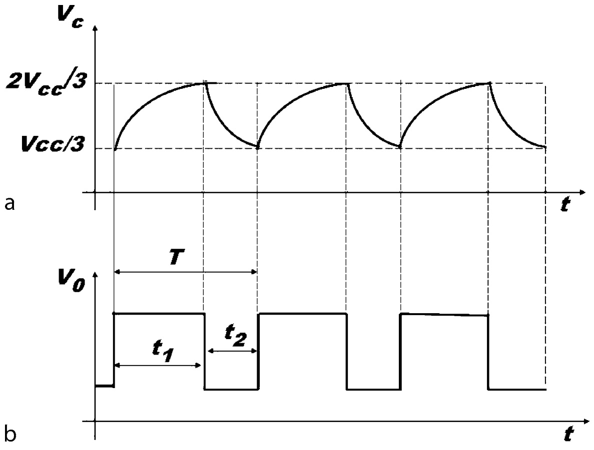

Thermocapacitive Flow Sensor, Figure 7 Response of output voltage V_0 to sensing capacitor voltage V_C. (**a**) Sensing capacitor voltage V_C as input; (**b**) output voltage V_0 from 555 timer

The time interval for charging the capacitor is [10]

$$t_1 = 0.693\,(R_1 + R_2)\,C\,. \tag{8}$$

The time interval for discharging the capacitor is

$$t_2 = 0.693 R_2 C\,. \tag{9}$$

The total period of the oscillation is

$$\begin{aligned} T = t_1 + t_2 &= 0.693\,(R_1 + 2R_2)\,C \\ &= 0.693\kappa\,(R_1 + 2R_2)\,C_0 \end{aligned} \tag{10}$$

and the oscillation frequency is

$$f = \frac{1}{0.693\kappa\,(R_1 + 2R_2)\,C_0}\,. \tag{11}$$

Clearly, the period of oscillation T is proportional to the dielectric constant κ. Because of the positive temperature coefficient of the dielectric constant, there is a proportional increase in the oscillation period, due to the increase in the temperature of the capacitor, when power is applied to the heater. With fluid flowing, the convective cooling of the sensing capacitor surface would reduce its dielectric constant κ again and cause the period to decrease. Hence, the change in the oscillation period or frequency is a measurement of the fluid flow velocity.

Fabrication

The function of the thermocapacitive flow sensor strongly depends on the sensing material and the quality of its fabrication. Two dielectric materials have so far been used for the sensing capacitor: Ta_2O_5 and $SrTiO_3$. The more sensitive the dielectric constant to the temperature, the higher the sensitivity of the sensor for measuring the flow rate. The dielectric constant temperature coefficients of Ta_2O_5 and $SrTiO_3$ are 375 ppm/°C and 2000 ppm/°C, respectively [9, 10]. Therefore the latter is more temperature-sensitive than the former.

The microcapacitor module can be fabricated using microfabrication technology. The MOS process and a slightly modified MOS process followed by the groove-etching technique in EDP have been applied for the microcapacitor module [9, 10]. In order to increase the sensitivity of the sensor, the leakage current, which is the current flowing through the capacitor when a DC voltage is applied to the capacitor, should be kept as low as possible. The leakage current depends on the fabrication process. For instance, when oxygen is used as the sputtering gas for the deposition of the dielectric layer during the fabrication, the leakage current is more than four orders smaller than that when argon is used [10]. The leakage current can be at least six orders smaller than the sensing capacitor charging and discharging current.

If the capacitor module (the capacitor and heater) is thermally isolated from the rest of the active device, the sensitivity can be increased. If the module is built on a cantilever, the thermal isolation can be enhanced. The thermal isolation of the heater element from the rest of the active device can be tested by measuring the MOS transistor current–voltage characteristics and the threshold voltage, with and without power to the heater element. The smaller the difference, the better the thermal isolation.

Key Research Findings

Since the capacitance of the capacitor depends on the dielectric constant, which in turn is related to temperature, Fig. 8 shows the relationship between the normalized capacitance and the temperature for the sensing capacitor, where the capacitance increases with the temperature due to the heating from the heater.

Although capacitance can be used as a measurable variable for flow velocity measurement, in practice, voltage is easier to measure. With the MOS, the voltage signal can be amplified to increase the sensitivity. The relation between the voltage and the flow velocity is shown in Fig. 9. The voltage increases with the flow velocity, since the higher the velocity, the lower the dielectric constant of the capacitor. Since the current I_d decreases with the reduction of the dielectric constant in Eq. (3), the output voltage, based on Eq. (4), will increase.

For the frequency modulated output, the relationship between the oscillating frequency from the timer and flow

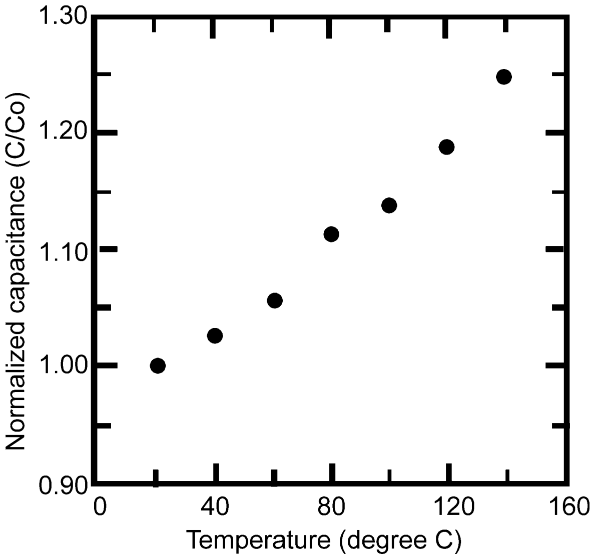

Thermocapacitive Flow Sensor, Figure 8 Normalized capacitance of O_2-sputtered $SrTiO_3$ capacitor as a function of temperature. Reproduced from Sens Actuators A with permission of Elsevier

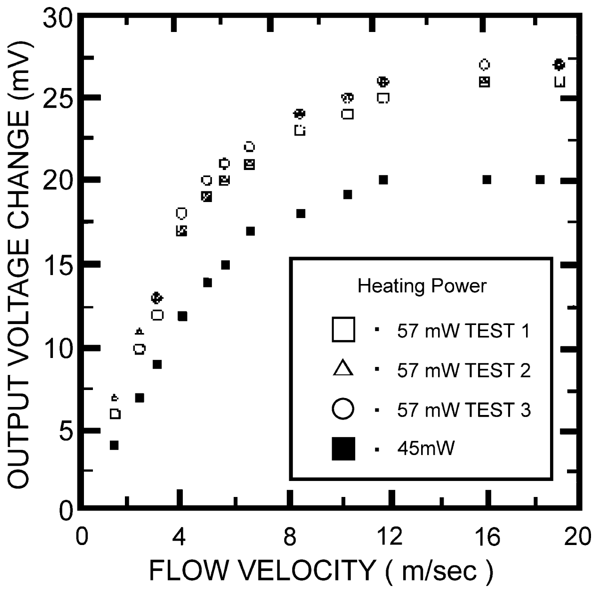

Thermocapacitive Flow Sensor, Figure 9 Relationship between output voltage and gas flow velocity for heater power at 45 mW and 57 mW, respectively. Reproduced from IEEE Electron Device Letters with permission of IEEE

velocity is shown in Fig. 10. The frequency increases with the flow velocity, due to the decrease in the capacitance with the reduction in temperature. At low velocity, the frequency increases linearly with the flow velocity and saturates at a relatively high flow velocity, as shown in Fig. 10. This trend is consistent with theoretical modeling [11], whose result is also shown in Fig. 10.

Figures 9 and 10 show that the sensitivity of the thermocapacitive flow sensor decreases as the flow velocity increases, similar to the case in the HWA and Laser-Induced Fluorescence Photobleaching Anemometer [12]. However, the sensitivity of the thermocapacitive flow sensor increases with heating power, as the higher power will cause a higher temperature difference between the capacitor and fluid, and the change in the flow velocity will cause a larger variation in the temperature, which will cause a larger signal. The sensitivity can be increased by using a large dielectric constant temperature coefficient and a small capacitor.

The response time, which is inversely proportional to the oscillation frequency, determines how fast a sensor can measure the flow velocity, or the frequency band. The higher the heating power, the larger the response time. This is because the higher heating power will generate a larger capacitance, which in turn, will increase the response time. Such a relationship is shown in Fig. 11, where the frequency decreases as the heater power increases.

In practice, a calibration between flow velocity and measuring variables is required before measuring an unknown flow velocity. When calibrating, the fluid temperature,

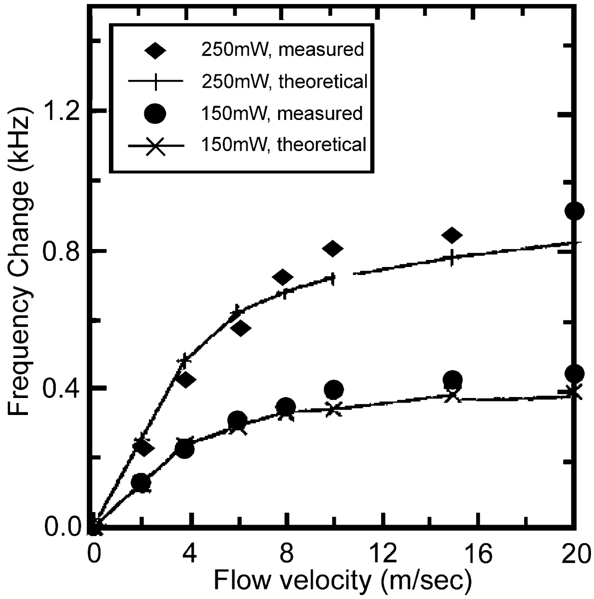

Thermocapacitive Flow Sensor, Figure 10 Relationship between oscillation frequency and gas flow velocity for heater power 150 mW and 250 mW, respectively for both theoretical modeling and experimental measurement. Reproduced from Sens Actuators A with permission from Elsevier

composition, and density should be the same as those to be measured and the fluids are expected to be incompressible.

T

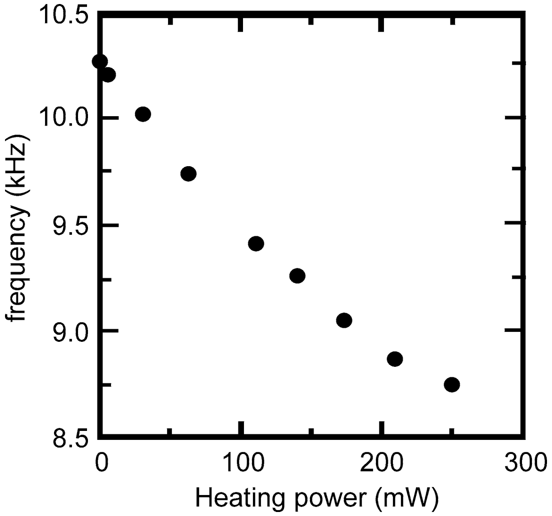

Thermocapacitive Flow Sensor, Figure 11 Oscillation frequency as a function of heater power without gas flow. Reproduced from Sens Actuators A with permission from Elsevier

Future Directions for Research

To date, the thermocapacitive flow sensor has only been demonstrated in the semiconductor field for measuring the gas flow rate. Many microfluidic chips and most BioMEMS chips work with a liquid medium. Possible future work includes applications of the thermocapasitive flow sensor in a liquid medium, where electrical insulation would be required.

Cross References

- ► Velocity Sensors
- ► Thermocapacitive Flow Sensor
- ► Thermoelectric Flow Sensors
- ► Thermoresistive Flow Sensors
- ► Pyroelectric Flow Sensors

References

1. Jensen KD (2004) Flow measurements. J Braz Soc Mech Sci Eng 26:400–419
2. Liu C, Huang JB, Zhu Z, Jiang F, Tung S, Tai YC, Ho CM (1999) A micromachined flow shear-stress sensor based on thermal transfer principles. J Microelectromech Syst 8:90–99
3. Tieu AK, Mackenzie MR, Li EB (1995) Measurements in microscopic flow with a solid-state LDA. Exp Fluids 19:293–294
4. Santiago JG, Wereley ST, Meinhart CD, Beebe DJ, Adrian RJ (1998) A particle image velocimetry system for microfluidics. Exp Fluids 25:316–319
5. Devasenathipathy S, Santiago JG (2003) Electrokinetic flow diagnostics. In: Breuer KS (ed) Micro- and Nano-scale Diagnostic Techniques. Springer, New York, pp 121–165
6. Kreith F (1965) Principles of Heat Transfer, 2nd edn. International Text Book Company, Scranton
7. Kallio P, Kuncova J (2004) Microfluidics. Tekes Technology Review 158
8. Del Toro V (1986) Electrical Engineering Fundamentals, 2nd edn. Prentice Hall, Englewood Cliffs
9. Lin KM, Kwok CY, Huang RS (1996) An integrated thermocapacitive type MOS flow sensor. IEEE Electron Device Lett 17:247–249
10. Kwok CY, Lin KM, Huang RS (1996) A silicon thermocapacitive flow sensor with frequency modulated output. Sens Actuators A 57:35–39
11. Wachutka G, Lenggenhager R, Moser D, Baltes H (1991) Analytical 2D-model of CMOS micromachined gas flow sensors. In: Proceedings of 1991 International Conference on Solid-state Sensors and Actuators, San Francisco, pp 22–25
12. Wang GR (2005) Laser-induced fluorescence photobleaching anemometer for microfluidic devices. Lab Chip 5:450–456

Thermocapillarity

CHARLES N. BAROUD
LadHyX and Departement de Mécanique, Ecole Polytechnique, Palaiseau, France
baroud@ladhyx.polytechnique.fr

Synonyms

Thermocapillary effect; Marangoni effect; Thermal Marangoni effect

Definition

The dependence of surface tension on temperature can lead to the existence of a surface stress imbalance when a liquid interface is subject to variations in temperature. These stresses then lead to fluid motion along the interface. In the low Reynolds number situations typical of microfluidics, this motion along the interface rapidly leads to motion in the bulk of the fluid.

Thermocapillarity, Table 1 Surface tension of water from freezing to boiling

Temperature (°C)	Surface tension (mN m^{-1})
0	75.6
10	75.2
20	72.9
30	71.2
40	69.6
50	68.0
60	66.2
70	64.5
80	62.7
90	60.8
100	58.9

Chemical and Physical Principles

The surface tension between a liquid and another immiscible fluid (liquid or gas) accounts for the free energy associated with the creation of a free surface. It has units of energy per unit area, usually taken as $\mathrm{mJ/cm^2}$. The units can also be expressed as a force per unit length, in $\mathrm{mN/m}$, which accounts for the notion that surface tension is indeed a tension that pulls in the direction tangential to the surface.

Statistical mechanics considerations predict that the surface tension (γ) displays a linear dependence on temperature (T),

$$\frac{\mathrm{d}\gamma}{\mathrm{d}T} = \gamma T < 0\,, \qquad (1)$$

where T is a constant, usually negative. Table 1, adapted from [1], provides the values of the surface tension γ for a water–air interface as a function of temperature. This table shows that the surface tension has a linear evolution with temperature, starting at a finite value and ending at a lower but also finite value. Note that the drop of surface tension to zero at the critical point of boiling corresponds to a discontinuity in the value of γ.

Table 2 is adapted from [2] and provides the values of γ and γT for some commonly used liquids in microfluidics.

Thermocapillary Convection: The Bénard–Marangoni Problem

Consider now a liquid layer with a free surface. If this layer is submitted to local variations of temperature, it follows that the surface tension will also vary which will lead in turn to an imbalance in the surface tension. This uneven pulling on the interface can be expressed as a production of surface stresses and may be written as

$$\sigma = \gamma T \nabla_{\parallel} T\,, \qquad (2)$$

Thermocapillarity, Table 2 Values of surface tension, at a temperature $T = 20\ °\mathrm{C}$, and its dependence on temperature for some commonly used liquids in microfluidics

Liquid	Surface tension γ ($\mathrm{mN\,m^{-1}}$)	γT ($\mathrm{mN\,m^{-1}K^{-1}}$)
Water	72.88	– 0.138
Ethanol	22.75	– 0.086
n-Octane	21.80	– 0.10
Benzene	28.88	– 0.13
Perfluoromethyl cyclohexane (C_7F_{14})	15.70	– 0.10

where σ is the local surface stress and $\nabla_{\parallel}$ denotes the gradient along the interface. This surface stress must be compensated by a flow from the region with low surface tension to the region with high surface tension. Since motion along the interface must be accompanied by motion in the bulk in order to conserve the fluid volume, the thermocapillary phenomenon leads to convective motion in the bulk of the heated fluid.

The early experiments by Bénard (1900), which have been reproduced many times since [3], beautifully demonstrate the presence of thermocapillary flow. The setup consists of a cell which is partially filled with a thin layer of liquid and submitted to a temperature gradient perpendicular to the liquid–air interface, as shown in Fig. 1. If we imagine that the layer of liquid has a small initial undulation, it is reasonable to think that the region close to the upper plate (region (a)) is cooler than the region which is close to the lower plate (region (b)). This leads to a decrease in the surface tension of region (b) compared to region (a), which in turn leads to a flow along the surface from (b) to (a). By conservation of mass, this surface flow must lead to recirculation rolls in the bulk, as seen by the arrows in Fig. 1.

Two scaling laws about thermocapillarity are worth noting. First, it should be noted that the numerical values of γT are relatively small and lead to modest changes in surface tension for large variations in temperature. For this reason, thermocapillary effects are often masked in large-scale systems by bulk phenomena, with the notable exception of microgravity situations. One can show for instance that thermocapillary (Bénard–Marangoni) convection is the dominant convection mechanism only for liquid layers shallower than a few millimeters. For thicker layers of liquid, buoyancy effects grow rapidly and dominate the convective motion.

This corresponds to the often-cited notion of surface phenomena becoming dominant over bulk phenomena at small scales. It may be stated more generally by dimensional arguments: the surface area decreases as the square

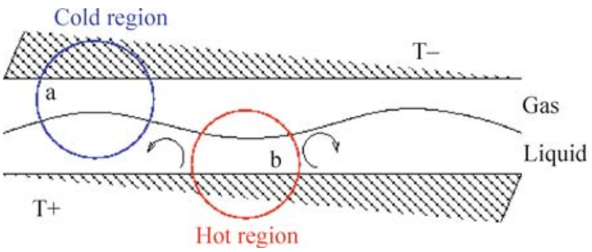

Thermocapillarity, Figure 1 Bénard–Marangoni experiment, demonstrating flow generated on the surface and in the bulk of a thin layer of liquid

of the typical length scale L, while the volume decreases as L^3. As the scale L of the problem decreases, this implies that the bulk phenomena will decrease faster than the surface phenomena and be dominated by them.

The second scaling law concerns the magnitude of the surface stresses. Note that the stresses caused by the variations in temperature (Eq. (2)) do not depend on the value of the temperature but rather on its spatial gradient. This means that the stresses σ may be strong even for modest changes in temperature, if the scale over which they vary is small enough. Microfluidic scales therefore favor surface stresses due to the variations in temperature.

The above two scaling laws both imply that thermocapillary effects may become a dominant driving mechanism for microfluidics. They have led researchers to explore using thermocapillarity to manipulate fluids in microfluidic situations.

The Solutal Marangoni Effect

Surface tension variations can also be produced by adding surfactants on the interface. These surface active materials (e. g. soap) typically consist of a hydrophilic head group and a hydrophobic tail. Therefore, the presence of surfactants in solution is energetically unfavorable and one gains in free energy if the molecules align along the free surface, which is the equilibrium situation. The creation of a layer of surfactant molecules on the interface then lowers the surface tension of the system.

In transient situations, e. g. in the presence of an external flow or during the formation of droplets, the surface density of the surfactant molecules may be inhomogeneous, which again leads to an imbalance in surface tension, similarly to the thermal case. However, in contrast with the thermal case, the relationship between surface tension and surfactant surface concentration (Γ) is highly nonlinear. A classical model for this dependence states that

$$\gamma = \gamma_0 + RT\Gamma_\infty \ln\left(1 - \frac{\Gamma}{\Gamma_\infty}\right) , \quad (3)$$

which predicts a steep decrease in surface tension as the surface concentration approaches a finite value, Γ_∞. The value of Γ_∞ is determined by the finite space occupied by the surfactant molecules, which sets an upper bound on the surface concentration. See the entry on ▶ Marangoni Convection for a more detailed discussion of this topic.

Key Research Findings

Microfluidic applications of thermocapillarity have centered around the use of temperature gradients to manipulate small quantities of fluid. Young et al. [4], in a pioneering use of thermocapillarity, applied a vertical downward temperature gradient to stabilize the position of a gas bubble against buoyancy. In their experiment [4], the air bubble was subjected to differential heating between its upper and lower sides, as shown in Fig. 2. The flow along the surface, from the hot to the cool side, induces a flow of the external fluid around the bubble in the same direction. The bubble, in reaction to this flow, feels a force which pushes it in the opposite direction. It is as if the bubble were swimming up the temperature gradient.

Experimentally, Young et al. [4] showed that air bubbles a few tens of microns in size could thus be suspended in water between the two cylinders of a machinist's micrometer. The maximum force produced, calculated by balancing the buoyancy force, was of the order of 1 µN.

When gravity can be neglected, which is often the case in microfluidics, the main question that has interested researchers has been that of the velocity of propagation of a drop or a fluid layer for a given temperature gra-

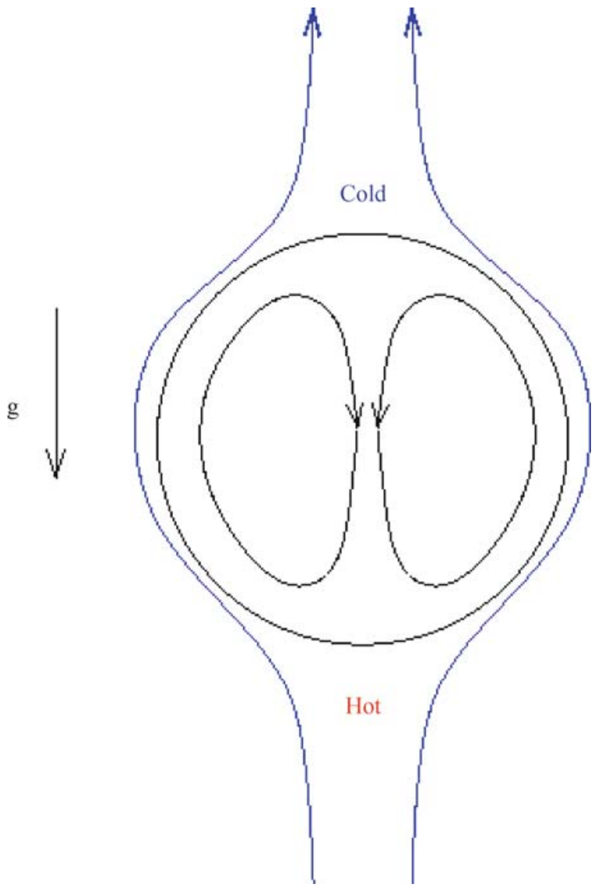

Thermocapillarity, Figure 2 Thermocapillary flow induced by a vertical temperature gradient has been shown to counter the bubble rise due to gravity

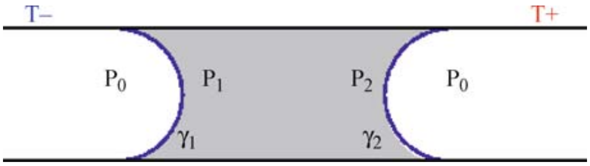

Thermocapillarity, Figure 3 A plug of wetting liquid subjected to a temperature gradient, will experience a preasure gradient pushing it towards the hot side

dient. This velocity is given by a balance between the Marangoni stresses and the viscosity. Two categories of such flows can be distinguished. First, when the fluid is in direct contact with a solid substrate, the contact angle between the wall and the substrate imposes a local pressure drop across the interface, through the Young–Laplace law. Therefore the motion of the fluid is associated with a change in the contact angle as well as the change in surface tension. Second, when the fluid is not in contact with the solid, the change in surface tension is associated with a flow of the external fluid, which in turn imposes surface stresses on the drop, as in the experiments of Young et al. [4].

Fluid in Contact with a Solid Substrate

When the drop is in contact with a solid wall, the simplest case is a liquid plug inside a microchannel, shown schematically in Fig. 2. In this figure, we consider a two-dimensional plug of wetting fluid inside a tube. The pressure outside the plug is assumed to be equilibrated at P_0. Inside the plug, there is a pressure jump due to the Young–Laplace pressure, which states that the pressure P_1 is lower than P_0 by an amount γ_1/R where the radius of curvature R may be considered equal to half of the channel size for a wetting fluid. By the same token, the pressure P_2 may be written as $P_0 - \gamma_2/R$. Since the interface at 1 is considered to be cooler than that at 2 and the surface tension drops with increasing temperature, we find that $P_1 > P_2$ and therefore the plug travels towards the hot side.

This first-order analysis accounts for the direction of travel in the channel but does not yield the speed of propagation. The latter is given by a balance between the surface tension deficit and the viscous effects, both in the bulk and at the advancing and receding interfaces. Furthermore, a complete treatment of the problem must also account for the recirculation inside the drop which acts to transport heat from the hot to the cold sides. However, Sammarco and Burns [5] have found experimentally that plug propagation velocities scale linearly with the applied temperature drop for a variety of liquids.

In the case of an open substrate, meaning that only one wall is in contact with the fluid, the initial observation is that a semi-infinite film of liquid subject to a temperature gradient will spread towards the cooler side of the substrate. This can be understood by referring back to Fig. 1 and noting that fluid is pulled towards the cool region, since the surface tension is higher there. A lubrication analysis yields a speed that is proportional to the thermocapillary stress (σ) and to the layer height (h), and inversely proportional to the fluid viscosity (μ).

However, it should be noted that the motion of the film is also associated with a change in its height and the formation of a rim around the advancing interface. This rim was shown to become unstable and to lead to the formation of a fingering pattern with a wavelength (λ) which scales as $h(3\mathrm{Ca})^{1/3}$, where (h) is the film thickness and $\mathrm{Ca} = \gamma U/\mu$ is the capillary number (U being the advance velocity). It can be shown that the film is stable if the width of the layer is smaller than λ.

The case of an isolated droplet on a solid substrate is more significant for microfluidic applications, where one is typically interested in manipulating small volumes of fluid. The analysis of the drop motion is complicated by several factors compared to the continuous film. First, the freedom to change both the front and rear contact angles can act to move the drop either to the hot or to the cold side. More significantly for experiments, the quality of the surface and the wetting properties play a major role. Experiments on isolated drops require that the drop of fluid partially wets the surface, i. e. yielding a finite contact angle when placed in contact with the solid, in order to avoid the spreading of a film of liquid on the surface. However, surfaces with a finite contact angle tend to exhibit a large amount of hysteresis, which implies that the motion of the drop will be characterized by a stop-start motion unless great care is taken with the cleanliness and smoothness of the surface. Most significantly, contact angle hysteresis leads to the existence of a minimum droplet radius for motion, for a given thermocapillary stress. Above this critical value, the propagation speed increases linearly with the radius and the thermal gradient. A detailed discussion may be found in [6].

Finally, it should be noted that contact angle hysteresis may be reduced by bathing the liquid drop in another liquid. Experiments have shown that a drop of water, immersed in oil, will show a very small amount of hysteresis and may be displaced through localized laser heating [7].

T

Fluid in Suspension away from Walls

The second case is that of a drop of liquid away from any solid walls. In this case, the solid cannot be used to support the production of stresses and the presence of any thermocapillary stress produces a flow in the drop and in the surrounding fluid. This situation also produces a net force on the drop but this situation has been studied much less than that of wall contact. Homsy and his collaborators [8] have studied the migration of a long bubble in a polygonal tube under the effect of a temperature gradient. Although there is always a lubrication film which isolates the bubble from the solid walls, the fluid flow is strongly influenced by the presence of the tube, contrary to the case studied by Young et al. [4]. This allows the modelling to focus on the lubrication film between the bubble and the tube walls and the bubble velocity being computed by conservation of mass. Again, the bubble migration velocity is found to scale linearly with the imposed temperature gradient.

The modelling of an isolated drop involves the calculation of the complete flowfield around the drop in order to determine the forces acting on it. A series of recent papers by Subramanian (and collaborators) [9] have addressed the complete calculations of flow around drops in an infinite medium, taking into account the heat transport, for different ranges in the dimensionless parameters. Solutions for semi-confined geometries, such as those generally encountered in microfluidics, remain generally unavailable although recent work is heading in this direction.

Finally, it should be noted that most experiments with drops involve the presence of surfactants which serve to stabilize droplets and aid in their formation. However, surfactant dynamics and their solubility also vary with temperature. Since the effect of surfactant adsorption can be more dramatic than that of temperature, the surfactant dynamics can greatly modify the effect of temperature gradients. This is the subject of current research.

Examples of Applications

In addition to the transport of fluid, the mixing of the fluid contained inside a droplet is also a major challenge in microfluidics. The flow induced by the thermocapillary forcing has been proposed as a way to mix the contents. This was demonstrated by combining thermocapillary forcing with surface patterning in order to force a liquid layer to flow in an oblique direction with respect to the temperature gradient. The resulting motion of the liquid created recirculation zones which efficiently mix the fluid [6]. Other studies have been undertaken on an isolated drop which is pushed in a carrier fluid. Mixing is achieved in the drop if its motion leads to a breaking of the barriers to mixing, e. g. through a complex cyclical motion. Finally, merging the drops in order to produce chemical reactions by using thermocapillarity has been demonstrated. Droplets in microfluidics are difficult to merge due to the presence of a thin film which becomes harder to displace the thinner it is. This film, known as a lubrication film, prevents drops from approaching each other sufficiently to merge. However, the flow produced by thermocapillary motion has been shown to reduce this film, inducing rapid merging of the drops [10].

Cross References

- ▶ Digital Microfluidics
- ▶ Droplet Based Lab-on-Chip Devices
- ▶ Droplet Dynamics in Microchannel
- ▶ Droplet Evaporation
- ▶ Electrocapillary
- ▶ Electrowetting
- ▶ Marangoni Convection
- ▶ Interfacial Instability
- ▶ Surface Tension Driven Flow
- ▶ Surface Tension, Capillarity and Contact Angle
- ▶ Transport of Droplets by Thermal Capillarity

References

1. Lide DR (2005) CRC Handbook of Chemistry and Physics, 86th edn. CRC, Boca Raton
2. Adamson AW, Gast AP (1997) Physical Chemistry of Surfaces, 6th edn. Wiley, New York
3. Schatz MF, Neitzel GP (2001) Experiments on thermocapillary instabilities. Annu Rev Fluid Mech 33:93–127
4. Young NO, Goldstein JS, Block MJ (1959) The motion of bubbles in a vertical temperature gradient. J Fluid Mech 6:350–356
5. Sammarco TS, Burns MA (1999) Thermocapillary pumping of discrete drops in microfabricated analysis devices. AICHE J 45:350–356
6. Darhuber AA, Troian SM (2005) Principles of microfluidic actuation by modulation of surface stresses. Annu Rev Fluid Mech 37:425–455
7. Kotz KT, Noble KA, Faris GW (2004) Optical microfluidics. Appl Phys Lett 85:2658–2660
8. Lajeunesse E, Homsy GM (2003) Thermocapillary migration of long bubbles in polygonal tubes. II. Experiments. Phys Fluid 15:308–314
9. Barton KD, Subramanian RS (1989) The migration of liquid-drops in a vertical temperature-gradient. J Colloid Interface Sci 133:211–222
10. Baroud CN, Saint Vincent MR, Delville JP (2007) An optical toolbox for total control of droplet microfluidics. Lab Chip 7:1029–1033

Thermocapillary Actuation

▶ Transport of Droplets by Thermal Capillarity

Thermocapillary Convection

► Marangoni Convection

Thermocapillary Effect

► Thermocapillarity

Thermocapillary Pumping

ZHENJUN JIAO, NAM-TRUNG NGUYEN
School of Mechanical and Aerospace Engineering,
Nanyang Technological University, Singapore, Singapore
mntnguyen@ntu.edu.sg

Synonyms

Microplug transport; Microdroplet transport; Thermal pumping; Multiphase pumping

Definition

Thermocapillary pumping (TCP) is a pumping concept based on thermocapillary forces, where a liquid droplet moves through a microchannel or on a planar surface. A temperature gradient leads to a difference of the surface stresses across a liquid droplet and propels it into a cooler region.

Overview

According to the above definition, thermocapillary pumping concept requires an interface between dissimilar continua such as a gas/liquid interface. The molecules of a liquid attract each other due to intermolecular forces. While the molecules inside the bulk liquid experience attractive forces from all directions, the liquid molecules at the gas/liquid interface have neighboring liquid molecules only on the side facing the bulk liquid. The attractive force tends to pull the molecules at the surface into the interior. Thus, the liquid molecules at the interface will rearrange for the minimum surface energy or for the minimum number of molecules at the interface, which also means a minimum surface area. So in the three phase situation, three interfacial forces cause three-phase (solid/liquid/gas) surface tensions. The resultant force caused by these three interfacial forces will decide the final state of a liquid drop. Surface tension σ is considered as the energy required for increasing the surface area of a liquid by a unit area. Surface tension has a unit of J/m^2. Surface tension values of silicone oil in glass capillary are for instance on the order of 10^{-2} to 10^{-1} J/m^2. The surface tension of a liquid depends on the temperature. At a higher temperature, the attracting force and subsequently the surface tension decrease. For a small temperature range, we can assume a linear relation between surface tension and temperature:

$$\sigma_{lg}(T) = \sigma_{lg0} - \gamma(T - T_0) \tag{1}$$

Where σ_{lg} is the surface tension of the gas–liquid interface, γ is a constant, T is the actual temperature, and σ_{lg0} is the surface tension at the reference temperature T_0. The temperature dependency of surface tension is the fundamental concept of thermocapillary pumping.

Thermocapillary pumping offers a simple mechanism for moving drops of liquid within micro-scale channels. The advantage of TCP is its ability to locally control the movement of a single liquid drop rather than a continuous liquid stream. Furthermore, since TCP relies on simple interface heating, devices incorporating TCP can be easily constructed. These advantages make TCP a promising candidate for microfabricated chemical or biological analysis devices that require precisely defined sample volumes and that strive for a simple method for achieving system integration. The above researches have showed us the basic theoretical knowledge of TCP in different aspects which proves that the feasibility of producing TCP [1].

Basic Methodology

The actuation force for a droplet can be achieved by creating a temperature gradient along the direction of the droplet movement. The temperature difference between the two ends of the droplet can cause the different surface tensions, which will finally produce a net force to propel the liquid droplet. Volkoviski first observed that a liquid film tends to spread away from the hotter side of a substrate [2]. Hershey later observed a similar effect, where spatial variation in the film height is determined by the temperature distribution along a thin film [3]. Ludviksson and Lightfoot [4] observed the spontaneous spreading of thin, non volatile films on a vertical wettable substrate subject to a linear temperature change.

Brochard was the first to formulate a theory on the movement of a liquid droplet on a solid with a horizontal thermal gradient [5]. In his paper, reasons of the migration of the droplet under the temperature gradient were determined as the non-uniform surface tension and the different spreading coefficients S which depends on the distance x. The spreading coefficient is negative ($S < 0$) for partial wetting. The advancing velocity of the droplet is deter-

T

mined as:

$$v = C\frac{h_0}{\eta}\left[\frac{\partial}{\partial x}(\sigma_{lg}-\sigma_{sl})+\frac{\partial}{\partial x}(\sigma_{sg}-\sigma_{sl})\frac{dT}{dx} + \frac{1}{2}\frac{\partial\sigma}{\partial T}\frac{dT}{dx}\right] \quad (2)$$

Where h_0 is the thickness of the droplet at the center, σ_{lg}, σ_{sl} and σ_{sg} are the surface tension of the liquid/gas, solid/liquid and solid/gas interfaces, respectively.

Key Research Findings

Brzoska et al. experimentally investigated displacement of liquid droplets in a temperature gradient [6]. This work focused on the different radii of the droplets. The results showed that a droplet only moves if its radius is above a critical radius R_c. The critical radius strongly depends on the contact angle hysteresis, but not on the fluid viscosity. For small liquid droplets and radii above R_c, the velocity of the droplet is proportional to the temperature gradient and inversely proportional to the viscosity η. Ford and Nadim determined the velocity and pressure fields within the droplet which is modeled as an infinitely long strip of finite width and arbitrary height profile under the uniform temperature gradient. And the boundary condition in the vicinity of contact line was highlighted [7].

Sammarco and Burns studied thermocapillary pumping of discrete droplets in micro fabricated analysis devices [8]. The major factor limits the pumping velocity is the contact angle hysteresis. Contact angle hysteresis reduces the temperature induced driving force of TCP, thereby introducing a minimum temperature difference requirement for drop movement. This minimum temperature difference is a function of the hysteresis parameter $(1 - \cos\theta_A/\cos\theta_R)$, where θ_A and θ_R are the contact angles at the advancing and the receding edges of the droplet. The greater the degree of hysteresis, the higher the minimum temperature difference needed to initiate droplet movement. When contact angle hysteresis becomes so large that the droplet may boil before moving. Surface treatment can help to reduce the contact angle hysteresis. Further, converging microchannels can offset the hysteresis and the externally applied pressure. Figure 1 shows a set up for measuring the contact angles of receding and advancing ends. Using the low-pressure air source and submerged in liquid, from the Yong–Laplace equation the contact angle can be determined as:

$$\theta_{A,R} = \frac{1}{\cos\left[d\,(p-\rho g h)\,d/(G\sigma)\right]} \quad (3)$$

while σ is the liquid surface tension, d is the channel diameter and G is a constant specific to channel geometry (G=4 for circular, G=2 for slit-like, and G=2(1 + height/width) for rectangular cross sections).

Besides liquid droplets, bubbles can also be pumped in microfabricated channels. Mazouchi and Homsy investigated the migration of a long bubble in a tube with a prescribed axial temperature gradient [9]. The resulting thermocapillary force moves the bubble toward the hotter region, which is opposite to the liquid droplets. The work focused on the determination the bubble velocity. A simplified model was used. The model ignores the gravity in the horizontal tube, the viscosity and the thermal conductivity of the gas. At small Reynolds numbers and capillary numbers, a theory based on the lubrication approximation and matched expansions was presented to determine the shape and speed of the bubble. The assumption of small capillary numbers and long bubbles allows the division of the domain into five regions depicted in Fig. 2. The long cylindrical region of constant film thickness is connected to two constant curvature caps through two transition regions.

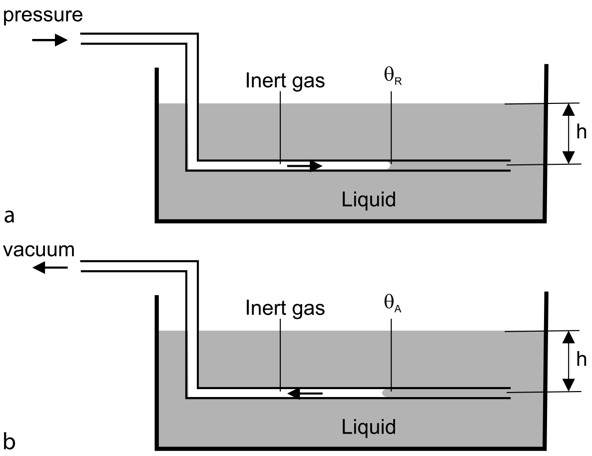

Thermocapillary Pumping, Figure 1 Experimental setup for measuring the receding (**a**) and advancing (**b**) contact angle in a microchannel

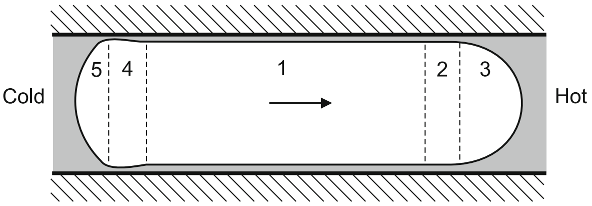

Thermocapillary Pumping, Figure 2 Section of a bubble in a horizontal tube. Five regions are shown: the constant film thickness region (1), two capillary static's regions (3, 5), and two transition regions (2, 4)

Darhuber et al. demonstrated active manipulation of nanoliter droplets on the surface of a glass or silicon substrate by combining chemical surface patterning with electronically addressable microheater arrays [10]. Hydrophilic lanes determine the possible routes for liquid migration, while the activation of a specific heater determines the trajectories. The induced temperature gradients spatially modulate the liquid surface tension by thermocapillary effect; thereby take over the control of the direction, timing, and flow rate of continuous streams or discrete drops. Temperature maps can be programmed to move, split, trap, and mix microscale volumes without mechanically moving parts. Figure 3 shows an example of droplet splitting using thermocapillary forces. The method of fluidic actuation allows direct accessibility to liquid samples for handling and diagnostic purposes and provides an attractive model for the thermocapillary pump.

Yarin et al. studied the movement of liquid droplets consisting of *n*-decane, *n*-undecane, *n*-dodecane, and *n*-hexadecane on a partially wettable cylindrical fiber [11]. When the temperature gradient was created along the fiber, the droplets began to move along the fiber toward the cold region according to the phenomenon related to the thermocapillary motion. Their theoretical results and experimental data agree reasonably well with their theories. The model of the droplet motion reveals its potential importance for a number of applications, particularly for draining filters that coalesces liquid droplets from a gas stream.

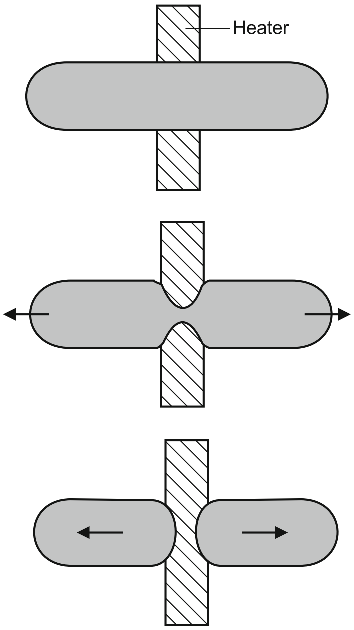

Thermocapillary Pumping, Figure 3 Splitting of a droplet using thermocapillary force. When the heater is turned on, the induced temperature gradient causes the droplet to move away from the heater. As result, the droplet is split at its center

Glockner and Naterer reported a new method of cyclic flow control with an external heat source is developed for thermocapillary pumping of a microdroplet in a closed microchannel [12]. The pumping concept involves a stationary cyclic heat source embedded within an adjoining silicon substrate. Lab on a chip based on thermocapillary pumping can be realized with this concept. The internal and external motions of micro-droplet are examined numerically using the finite-volume method and analytically using slug-flow approximation. The solution of the full Navier–Stokes and energy equations within the droplet were considered. Additionally, temperature boundary conditions for a stationary heat source are applied at the interface between the substrate and its surroundings, rather than along the microchannel wall.

Burns and Masterangelo reported microfabricated structures for integrated DNA analysis based on photolithography silicon micromachining [13]. The thermocapillary pump was able to move discrete nanoliter drops through enclosed channels using only local heating. The same actuation concept can accurately mix, measure, and divide drops by simple electronic control of the heater. In addition, they have constructed thermal-cycling chambers, gel electrophoresis channels, and radio labeled DNA detectors that are compatible with the fabrication process. Since all of the components are made by conventional photolithographic techniques, they can be integrated into a more complex system.

DeBar and Liepmann reported a silicon-based TCP with integrated microheaters [14]. The devices were operated at a variety of heater settings to evaluate their performance over a range of flow rates and pressures. A minimum energy of 140 mW was required from the central heater to generate and maintain the vapor bubble, and the flow rate increased with input energy. The efficiency of the device increased with flow rate, since the overhead to create and maintain the bubble (140 mW) dwarfs the energy expended to generate the temperature gradient (15 – 50 mW). The devices generated a maximum pressure head of 44 Pa, and a maximum flow rate of 9.3 nL/s.

Future Directions for Research

Despites its simplicity in implementation, thermocapillary pumping was not fully exploited in microfluidics research community. Thermocapillary may have a big impact in droplet-based digital microfluidics. Besides droplet transport, thermocapillary force can be used for other droplet manipulation functions such as splitting, merging and dis-

pensing. More research results in this direction can be expected in the near future.

Cross References

► Droplet Dynamics in Microchannels

References

1. Darhuber AA, Troian SM (2005) Principles of microfluidic actuation by modulation of surface stresses. Annu Rev Fluid Mech 37:425–455
2. Volkoviski V (1935) Sur les tourbillons en festons. Compt Rend Acad Sci Paris 200:285–87
3. Hershey AV (1939) Ridges in a liquid surface due to the temperature dependence of surface tension. Phys Rev 56:204
4. Ludviksson V, Lightfoot EN (1971) Dynamics of thin liquid films in the presence of surface- tension gradients. AIChE J 17:1166–1173
5. Brochard F (1989) Motions of droplets on solid surfaces induced by chemical or thermal gradients. Langmuir 5:432–438
6. Brzoska JB, Brochard-Wyart F, Rondelez F (1993) Motions of droplets on hydrophobic model surfaces induced by thermal gradients. Langmuir 9:2220–2224
7. Ford ML, Nadim A (1994) Thermocapillary migration of an attached drop on a solid surface. Phys Fluid 6:3183–3185
8. Sammarco TS, Burns MA (1999) Thermocapillary pumping of discrete drops in microfabricated analysis devices. J AIChE 45:350–366
9. Mazouchi A, Homsy GM (2000) Thermocapillary migration of long bubbles in cylindrical capillary tubes. Phys Fluid 12:542–549
10. Darhuber AA, Valentino JP, Davis JM, Troian SM, Wagner S (2003) Microfluidic actuation by modulation of surface stresses. App Phys Lett 82:657–679
11. Yarin AL, Liu W, Reneker DH (2002) Motion of droplets along thin fibers with temperature gradient. J Appl Phys 91:4751
12. Glockner PS, Naterer GF (2005) Thermocapillary control of microfluidic transport with a stationary cyclic heat source. J Micromech Microeng 15:2216–2229
13. Burns MA, Mastrangelo CH (1996) Microfabricated structures for integrated DNA analysis. Proc Natl Acad Sci 93:5556–5561
14. DeBar MJ, Liepmann D (2002) Fabrication and performance testing of a steady thermocapillary pump with no moving parts. In: Proceedings of the IEEE Micro Electro Mechanical Systems (MEMS 2002), pp 109–112

Thermocapillary Shear Stress

Definition

Shear stress induced by a temperature gradient resulting in directional fluid transport from high to low temperature.

Cross References

► Surface-Directed Capillary Flow Systems

Thermochromic Liquid Crystals

► Liquid Crystal Technique for Measuring Temperature

Thermocouples

Definition

A thermocouple is a measuring device consisting of two different metals or semiconductors, commonly performed as wires, which are connected in one point. Because of the Seebeck-effect an electrical voltage can be measured between the two metals as long as the junction and the free ends of the wires have different temperature levels. The voltage is almost linear with the temperature difference and lies for metals in the range of some micro-volts per Kelvin.

Cross References

► Contact Temperature Sensors
► Thermoelectric Flow Sensors

Thermodiffusion

► Thermophoresis

Thermoelectric Effect

► Peltier Effect

Thermoelectric Flow Sensors

NORBERT KOCKMANN
Laboratory for Design of Microsystems
Department of Microsystems Engineering – IMTEK,
Albert-Ludwig University of Freiburg, Freiburg, Germany
kockmann@imtek.de

Synonyms

Thermoelements; Thermal flow sensors

Definition

Thermoelectric flow sensors indirectly measure the velocity of gases and liquids close to the wall and the volume flow rate in a microchannel. Electrical heating, thermoelectric temperature sensing, appropriate calibration, and

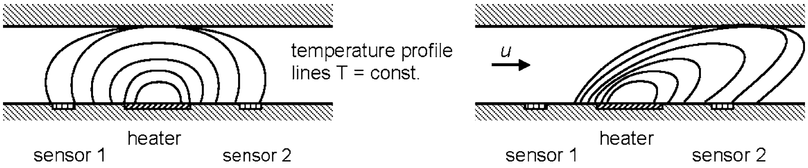

Thermoelectric Flow Sensors, Figure 1 Setup of a thermoelectric flow sensor in a channel consisting of a heater and two temperature sensors upstream and downstream of the heater, method A; *left*: conductive heat transfer with symmetric temperature profile; *right*: convective heat transfer with higher temperature at sensor 2

sensor control are essential for fast, reliable and sensitive measurement.

Overview

Flow measurement using thermoelectric devices and sensors implies the use of heat transfer and temperature measurements in microchannels to determine the near-wall velocity. With appropriate calibration procedures, the mean flow velocity or mass flow rate can be determined by measurements of the local wall temperature. Thermoelectric temperature probes and sensors, also known as thermocouples, rely on the Seebeck effect, where a temperature difference between two metal contacts induces a voltage drop which can be measured. An electrical resistance heater introduces a heat flux into the fluid flow. The temperature is measured either directly at the heater, in its vicinity, or at the wall downstream of the heater. Often, the upstream mean temperature of the fluid flow is also measured to provide a comparison. Thermoelectric flow rate measurement is one of commonest, and for laminar flow one of the most accurate, reliable, and cost-effective measuring techniques.

Basic Methodology

The flow sensor consists mainly of the heating element and temperature sensors, which measure the temperature of the heater or of the fluid before and after the heater. The streaming fluid is mainly heated by resistance heaters. The temperature can be measured either by electrical resistance sensors or by thermocouples. This essay concentrates on the latter method for thermoelectric flow sensors.

Thermoelectric temperature measurement has been established for more than a century, and the sensing devices, including thermocouples, have been miniaturized from the start. Van Herwaarden and Sarro [1] presented thermoelectric flow sensors, which were then adopted in the textbook by Middelhoek and Audet [2]. The basic measuring principle was not changed but was modified and improved by the choice of different materials, geometry, and device design. The basic sensor setup can be classified into two different techniques or methods. In method A, heating of the fluid imposes a temperature profile in the channel or near-wall flow (see Fig. 1), which is measured at certain positions by thermocouples. In method B, fluid flow cools the heater, the temperature or electrical power of which is measured (see Fig. 2). Besides the integral heater temperature, the local temperatures of a heated area can be measured, which allows a direction-sensitive velocimetry (see Fig. 3).

In method A, the temperature downstream of the heater is taken to determine the mean flow velocity in the vicinity of the heater. The general setup is shown in Fig. 1. The geometric setup of the heater and sensors determines the measurement of the fluid flow.

The temperature profile in the microchannel without fluid flow is nearly symmetric, and both sensors are detecting a similar temperature. The fluid flow shifts the temperature profile downwards, and the sensor located downstream measures a higher temperature; the sensor located upstream measures the temperature of the incoming fluid. The temperature distribution has been simulated by Ashauer et al. [3].

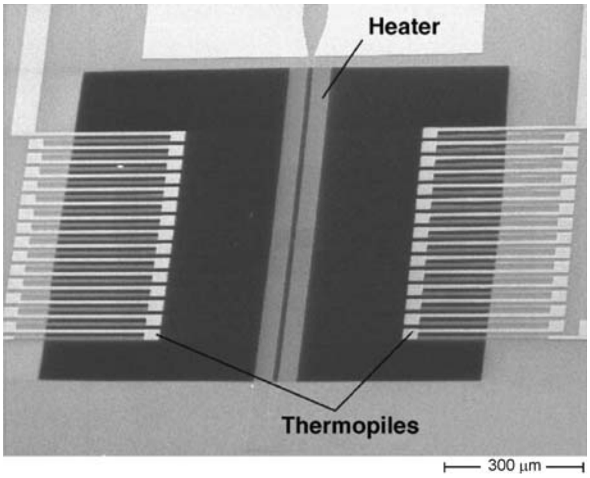

Thermoelectric Flow Sensors, Figure 2 Thermoelectric flow sensor consisting of an electrical heater on a thin membrane with parallel meandering thermoelectric sensors, two thermopiles with 15 thermoelements [4]

T

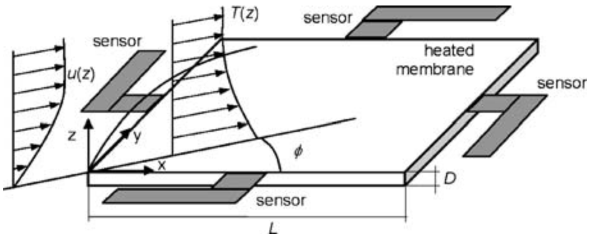

Thermoelectric Flow Sensors, Figure 3 Two-axis flow measurement from convective cooling of the sensor device with connected temperature sensors and direct heating of the membrane, acc. van Oudheusden [7]

The geometric setup of a fabricated device in thin film technology (see Fig. 2) is an example of method B. The heating structure with the adjacent meandering thermopiles to measure the temperature is located on a thin membrane to reduce the heat losses to the wall material. The thermocouples are arranged in a pile (series switching) to increase the sensitivity of the sensor used to measure the temperature difference between the heater and the substrate. A good example of the microstructure device has been given by Buchner et al. [4] (see Fig. 2).
A different scheme with a periodic heater/sensor setup was proposed by Al khalfioui et al. [5] with a more detailed flow measurement. This system is more complex and the effort required to measure the physical domain is correspondingly greater.
Measurement of the flow by a heated membrane with connected thermocouples has been proposed by van Oudheusden [6, 7]. The schematic setup is shown in Fig. 3. Comparing the four measured temperatures allows not only measuring the flow near the wall, but can also determine the angle of attack of the main direction of flow. More details of the analysis have been given by van Oudheusden [7]. The sensor contacts also serve as mechanical hinges and guarantee a good thermal insulation for the heated membrane.
For commercial flow sensors, the in-line setup according to method A with one heater and two sensors, one upstream and one downstream, is the most important and has been commercially realized by sensor suppliers.

Key Research Findings

General Setup

The geometric setup has been explained in the section on basic methodology. The general requirements of the signal processing are now described. The domain of the mechanical signal to be measured is determined by the flow and the velocity profile near the wall and the heating/sensing device. The flow-induced heat transfer (convection) and the parallel heat conduction in the sensor wall/substrate interface determine the measured temperature. Comparison of two or more temperatures indicates the flow and can be transferred into a flow rate, thus giving the complete flow situation. The temperature is measured as a voltage between the hot and cold ends of the thermocouple [6]. With this setup, three complex domains are combined: fluid flow, heat transfer, and thermoelectric energy and signal conversion.
In the following, we will start with the fluid flow and convective heat transfer, followed by the temperature measurement and will then characterize the entire device.

Heat Transfer and Fluid Flow

The electrical power dissipated in the heater spreads into the flowing fluid and the wall or substrate supporting the heater and sensors. In a steady-state situation, the energy balance of the heater/sensor expresses the correlation between the electrical heating power P and the heat dissipated into the substrate Q_S and into the fluid Q_f

$$P = Q_\mathrm{S} + Q_\mathrm{f} = G_\mathrm{S}\,(T_\mathrm{H} - T_\mathrm{S}) + G_\mathrm{f}\,(T_\mathrm{H} - T_\mathrm{f}) \qquad (1)$$

where T_H, T_S, and T_f are the temperature of the heater, the substrate, and the bulk fluid, respectively. The coefficients G_S and G_f indicate the thermal conductivity of the substrate and the convection by the flowing fluid, respectively. Due to the small temperature differences, radiation heat transfer can be neglected in most cases. The flow measurement relies on the variance of G_f with the flow and is measured, for example, by the temperature difference induced by a given electrical power.
As already mentioned, the flow rate can be determined by measuring the temperature of either the heater (method B) or the fluid downstream of the heater (method A). In both cases, the temperature of the fluid upstream of the heater must be known or must be set to the ambient temperature. First, we focus on measuring the fluid temperature downstream of the heater according to method A.
The wall heat transfer from the heater determines the energy used for heating the fluid and increasing its temperature. The location of the temperature sensor influences the measurement and should not be too far downstream from the heater. If the inflowing fluid has the same temperature as the sensor substrate, T_S, and the sensors measure the mean temperature of the fluid, the energy dissipation into the fluid is determined by

$$Q_\mathrm{f} = \dot{m}\,c_\mathrm{p}\,(T_\mathrm{S} - T_\mathrm{f}) \qquad (2)$$

where the mass flow rate $\dot{m} = \rho_\mathrm{f} A_\mathrm{C}\, u$ and c_p is the heat capacity of the fluid. The density of the fluid ρ_f and the

channel cross-section A_C should be known in order to obtain the correct sensing. The mean flow velocity u is determined with the heater power and the measured temperature difference

$$P = Q_S + \rho_f c_p A_C \,(T_S - T_f)\; u \tag{3}$$

where the heat dissipation into the substrate Q_S has to be estimated. The measurement of the fluid temperature downstream is not very accurate, so the fabricated sensor always has to be calibrated.

Convective cooling of an electrical heater and measuring its temperature according to method B avoids some sources of error, like measuring the heated fluid temperature or the unknown amount of heat dissipated into the substrate. For this reason, many sensors are located on a thin membrane or are fabricated on polymers or on other thermal insulations. This minimizes the parasitic heat loss and increases the sensor's accuracy. The convective heat transfer into the fluid Q_f is determined by the heat transfer coefficient α_W at the wall and by the temperature difference.

$$\frac{Q_f}{A_H} = q_f = \alpha_W \,(T_H - T_f) \tag{4}$$

The cooling heat transfer of the electrical heater can be treated like cooling a plate on one side in surface flow. Here, the influence of the surrounding channel walls is neglected for simplicity. With the help of the boundary layer theory, the wall heat transfer is described by the dimensionless heat transfer coefficient, the local Nusselt number Nu [7]

$$\mathrm{Nu} = \frac{\alpha\, x}{\lambda_f} = 0.332\, \mathrm{Pr}^{\frac{1}{3}} \mathrm{Re}^{\frac{1}{2}} \tag{5}$$

which has the dimensionless fluid properties (Prandtl number) $\mathrm{Pr} = \lambda_f / \rho_f\, c_{p,f}$ and dimensionless flow conditions (local Reynolds number) $\mathrm{Re} = u\,x/\nu$. For the entire length of the heater, l_H, the overall $\mathrm{Nu_L}$ number has been given by Welty et al. [8].

$$\mathrm{Nu_L} = \frac{\alpha\, l_H}{\lambda_f} = 0.664\, \mathrm{Pr}^{\frac{1}{3}} \mathrm{Re}^{\frac{1}{2}} \tag{6}$$

Both equations are valid for laminar flow with $\mathrm{Re} = u\,x/\nu < 2 \times 10^5$. The correlation between the flow velocity and the dissipation power and measured temperature difference is given by

$$\begin{aligned}\frac{Q_f}{A_H} &= \frac{\mathrm{Nu}\,\lambda_f}{l_H}\,(T_H - T_f)\\ &= 0.664\,\lambda_f\,\mathrm{Pr}^{\frac{1}{3}} \left(\frac{u}{l_H\,\nu}\right)^{\frac{1}{2}} (T_H - T_f)\end{aligned} \tag{7}$$

where the length coordinate x replaces the heater length, l_H. Arranging the above equations the correlation of the electrical heating power with the flow velocity gives the following equation:

$$\begin{aligned}P &= G_S\,(T_H - T_S)\\ &\quad + 0.664\,\lambda_f\,A_H\,\mathrm{Pr}^{\frac{1}{3}} \left(\frac{u}{l_H\,\nu}\right)^{\frac{1}{2}} \cdot (T_H - T_f)\end{aligned} \tag{8}$$

The detailed analysis of the correlation needs many parameters such as: the heat conductivity of the substrate, the correct fluid properties, and the correct geometry of the sensor. For practical applications, the correlation between the electrical power, the measured temperature difference, and the flow velocity can be reduced to

$$P = \left(c_1 + c_2\sqrt{u}\right)\,\Delta T \tag{9}$$

for laminar flow with $\Delta T = T_H - T_f$ [9]. Both coefficients can be determined by calibration measurements and should not vary with time or flow velocity. However, the fluid properties have to be calibrated to obtain the correct measurements. The operation of the device with different measuring modes is described in the section about the design, fabrication, and operation of the devices.

Temperature Measurement by Thermoelectric Effect

Due to their compactness and standard fabrication technology, the temperature in thermal flow sensors is often measured by thermocouples, which rely on the thermoelectric effect. The thermoelectric effect describes the coupling between the electrical and thermal currents, especially the occurrence of an electrical voltage due to a temperature difference between two material contacts, known as the Seebeck effect. In reverse, an electrical current can produce a heat flux or a cooling of a material contact, known as the Peltier effect. A third effect, the Thomson effect, is also connected with thermoelectricity where an electric current flowing in a temperature gradient can absorb or release heat from or to the ambient [10, 11]. The relation between the first two effects can be described by methods of irreversible thermodynamics and the linear transport theory of Onsager in vector form.

$$\begin{bmatrix} q_{el} \\ q_{th/T} \end{bmatrix} = \begin{bmatrix} \sigma_{el} & L_S \\ L_P & L_q \end{bmatrix} \begin{bmatrix} \Delta U \\ \Delta T \end{bmatrix} \tag{10}$$

The electrical current density q_{el} and the thermal entropy flux q_{th}/T are linked to the driving forces, the temperature gradient ΔT and the potential gradient ΔU with linear coefficients: σ_{el} as the electrical conductivity, L_q for

T

the heat transfer, L_S for the Seebeck effect, and L_P for the Peltier effect.

Solving the first equation for ΔU and substituting the result into the second equation yields

$$-\Delta U = \frac{q_{el}}{\sigma_{el}} + \frac{L_S}{\sigma_{el}} \Delta T \tag{11}$$

$$q_{th} = T \frac{L_P}{\sigma_{el}} q_{el} + T \left(\frac{L_S L_P}{\sigma_{el}} - L_q \right) \Delta T \tag{12}$$

The matrix in Eq. (10) is symmetrical according to the Onsager reciprocity law [11], which means $L_S = L_P$. The linear coefficients can be identified with known material properties

$$\rho_{el} = \frac{1}{\sigma_{el}} \tag{13}$$

$$\lambda_{th} = -T \left(\frac{L_S L_P}{\sigma_{el}} - L_q \right) = -T \left(\frac{2 L_S}{\sigma_{el}} - L_q \right) \tag{14}$$

$$\alpha_{ab} = \frac{L_S}{\sigma_{el}} \tag{15}$$

$$\pi_{ab} = T \frac{L_P}{\sigma_{el}} \tag{16}$$

The thermoelectric temperature measurement employs the Seebeck effect, the voltage between two material pair contacts on a different temperature level without the flow of electrical current ($Q_{el} = 0$). The Seebeck effect can also be described by the correlation

$$\Delta U = (\alpha_a - \alpha_b)\ \Delta T = \alpha_{ab}\ \Delta T \tag{17}$$

where α_{ab} is the Seebeck coefficient for the material pair a – b. The Seebeck coefficient depends on the pair of materials. Certain applications, like sensing or energy conversion, demand certain parameter combinations like heat or electrical conductivity or temperature linearity. For temperature measurement, standardized elements and pairs of materials are used which have good linearity of the material properties, reproducibility, and long-term stability.

A summary of the common standardized thermocouples is given in Table 1. Besides the thermoelectric properties of the Seebeck coefficient, the thermal and electrical conductivities are important for the sensitivity and time response of the thermoelectric flow sensor.

The materials of standardized thermocouples are rarely used in microfabrication, which relies to a large part on CMOS technology. Table 2 lists the metals commonly used in microfabrication. Van Herwaarden [1] and Rowe [11] have also given a summary of microthermocouple materials. Often, the thermoelectric pairs of materials are used for energy conversion from heat to electricity with the help of thermoelectric generators. Here, the so-called figure-of-merit, Z, gives an indication of a good energy conversion and is given by

$$Z = \frac{\alpha_{ab}^2}{\left(\sqrt{\lambda_a \rho_a} + \sqrt{\lambda_b \rho_b}\right)^2} = \frac{\alpha_{ab}^2 \sigma_a}{\lambda_a} \tag{18}$$

The second part of Eq. (18) is often used to characterize the thermoelectric activity of a single material α. This parameter may help to identify sensitive pairs of materials for thermoelectric temperature measurement.

Due to its use in microelectronics, silicon is by far the most common and best understood semiconductor material. It is cheap and a large variety of fabrication processes are available. Consequently, silicon has become a common material for thermoelectric sensors. The material properties of silicon depend heavily on the doping concentration and type as well as on the fabrication process [9].

A comparison of the values in Tables 3 and 4 gives remarkable differences between the bulk material and the deposited film material. Baltes et al. [9] have given the properties of n- and p-doped silicon together with the fabrication process, which also differs over a wide range. The doping concentration determines the thermoelectric properties of silicon over a wide range [12, 13]. For practical

Thermoelectric Flow Sensors, Table 1 Some commercially available thermocouples for temperature measurement (IC 584-1)

Material	Type	Seebeck coefficient (μV/K)	Operating range (°C)
Fe/CuNi	J	51	−200 – 760
NiCr/AlNi	K	41	−200 – 1260
PtRh/Pt	R	6	0 – 1480
Cu/CuNi	T	41	−200 – 370

Thermoelectric Flow Sensors, Table 2 Properties of some metals used in microfabrication at room temperature

Material	Seebeck coefficient α (μV/K)	Thermal conductivity λ (W/mK)	Electrical resistivity ρ (10^{-9} Ωm)
Aluminum (Al)	−1.66	237	26.5
Chromium (Cr)	21.8	93.9	125.0
Copper (Cu)	1.83	401.0	16.78
Titanium (Ti)	9.1	21.9	420.0
Gold (Au)	1.94	318.0	21.14

Thermoelectric Flow Sensors, Table 3 Thermoelectric properties of bulk material

Material	Seebeck coefficient α (μV/K)	Thermal conductivity λ (W/mK)	Electrical conductivity σ (10^4 1/Ωm)
p-$Bi_{0.5}Sb_{1.5}Te_3$	218	0.59	4.0
Bi_2Te_3	210	2.0	7.7
Sb_2Te_3	124	1.3	13.5
Bi	−65	8.3	83
Sb	36	24	238
PbTe	−200	3.5	13.0
Si (n-type)	−450	145	2.9

Thermoelectric Flow Sensors, Table 4 Thermoelectric properties of thin films [9] and other sources

Material	Seebeck coefficient α (μV/K)	Thermal conductivity λ (W/mK)	Electrical conductivity σ (10^4 1/Ωm)
p-$Bi_{0.5}Sb_{1.5}Te_3$	230	1.05	5.8
p-$Bi_{0.87}Sb_{0.13}$	−100	3.1	14.0
Bi	−65	5.2	28.5
Sb	35	13	100.0
PbTe	−170	2.5	5.0
Si (n-poly)	−108 to −520	16 – 29	0.2
Si (p-poly)	190 – 330	19 – 20	n.a.

applications it is very important to characterize the fabrication process and the relevant outcome and to ensure the reproducibility of the properties of the material.

Design, Fabrication, and Operation of Devices

Not only the single sensor components like heater or sensor, but also the interplay of the parts, their integration and the entire device are important for the performance of the sensor. Table 5 gives the general relationship between the film and bulk properties of the sensor and the sensing characteristics.

The more generalized parameters of the thermal conductance, G, and the temperature conductivity, C, are a function of the sensor geometry and the heat and temperature diffusivity. The device parameters and characteristics are determined by the properties such as the thermal conductivity or the Seebeck coefficient of the thermoelectric materials as well as the geometric setup and fabrication method. The main sensor signal output is determined by the number of thermocouples n, the Seebeck coefficient, and the measured or applied temperature differences. With a higher temperature difference, the signal increases with the heat loss. Hence, the sensitivity of the sensor depends mainly on the properties of the thermocouple, and the thermal conductance of the fluid and the substrate. For gas flow measurement and high temperature differences, the emissivities of the heater, thermocouple, and substrate have to be considered.

The necessary power for a clear and noise-free signal can be determined from the noise of the electrical conductivities and the sensitivity of the sensor. The inverse ratio gives the detectivity of the sensor. The time constant of the sensor, which determines the response time to flow changes or the start-up time of the sensor, is a function of the thermal diffusivity of the heater, thermocouple(s), and the substrate, as well as the thermal conductance of the entire device.

In summary, a high Seebeck coefficient and high electric conductivity of the sensor as well as low thermal conductance of the sensor and the substrate provide a sensitive, low energy-consuming sensor with a fast response time. Hence, the figure-of-merit (Eq. (18)) of a thermoelectric flow sensor is a good indicator of quality. However, the heater and sensor are often fabricated in thin-film technology on membranes, glass, or polymer substrates. The material combinations of the devices must also guarantee low thermal stress due to the expansion of heating and

Thermoelectric Flow Sensors, Table 5 Relationship between sensor parameters and film/substrate properties for sensors with n thermocouples, acc. Baltes et al. [14]

Film properties		Sensor parameters
Seebeck coefficient α		Thermoelectric voltage, signal
Thermal conductivity λ		$U = n\left(\alpha_a - \alpha_b\right)\,\Delta T$
Electrical conductivity σ		
Figure of merit $Z = \frac{\alpha_{ab}^2 \sigma_a}{\lambda_a}$		Sensitivity
Emissivity ε		$S = \frac{n(\alpha_a - \alpha_b)}{G(n,\lambda,\varepsilon,\lambda_s,\varepsilon_s)}$
Density ρ		Noise equivalent power
Heat capacity c_p		$\mathrm{NEP} \propto \frac{(R(\sigma))^{1/2}}{S}$
Thermal diffusivity $a = \frac{\lambda}{\rho\, c_p}$	$\Rightarrow$	
Substrate properties		Detectivity
Thermal conductivity λ_s		$D^* \propto \frac{S(F)^{1/2}}{(R(\sigma))^{1/2}}$
Emissivity ε_s		
Density ρ_s		
Heat capacity $c_{p,s}$		Time constant
Thermal diffusivity $a = \frac{\lambda_s}{\rho_s\, c_{p,s}}$		$\tau = \frac{C(a,a_s)}{G(n,\lambda,\varepsilon,\lambda_s,\varepsilon_s)}$

T

Thermoelectric Flow Sensors, Table 6 Material properties for device design, thermal expansion behavior [15]

Material	Specified electrical resistance ρ, 20 °C ($\mu\Omega$cm)	Specified thermal expansion, 0 – 100 °C 10^{-6} (1/K)	Heat conductivity λ_S, 0 – 100 °C (W/mK)
Gold	2.2	14.1	318
Platinum	10.58	9	71.6
Titanium	54	8.9	21.9
Polyimide		30 – 60	0.1 – 0.35
PTFE		100 – 160	0.25
PSU		50 – 60	0.26 – 0.28
PMMA		70 – 77	0.17 – 0.19
Quartz		0.5	1.4 – 1.9
Glass ceramics		13	1.5

cooling. Table 6 gives the thermal and electrical properties of some sensor materials.

Besides the properties and the geometrical setup, the operating mode of the sensor device is important for the application and sensitivity. The heater can be operated in two modes [16]: with constant electrical power or at a constant controlled temperature. With constant electrical heating power, the measurement of the temperature difference ΔT is appropriate for low liquid flow rates or gas flow. No temperature control is necessary for the heater. The heater cannot be overheated when an error occurs. Measuring the heater temperature T_{H} is suitable for liquid flow rates, but the fluid temperature has to be known. With a constant heater temperature, the measurement of the temperature difference ΔT can detect very low liquid flow rates and gas flow. Measuring the heating power is applicable for medium liquid flow rates. Due to the fast signal response, this mode can also be used to investigate the flow behavior. During to the longer operating time, thermal drift of the sensor or time drift of the thermocouple may occur and should be controlled by the routine calibration procedures.

The electrical insulation of the heater and the sensors is not critical when designing gas flow sensors, but has to be considered for liquid flows. In many cases, insulating layers, like metals oxide or polymer films, are deposited on the surface of the electrical conducting layers. Many thermoelectric flow sensor devices have been designed and fabricated for investigation and research purposes, but some are already commercially available. An overview of the existing devices has been given by Dittmann [15], but does not claim to be complete (see Table 7).

Dittmann's [15] estimation of the costs may serve as a reference point. In the fast developing area of sensor technology, costs can change rapidly. Future improvements in fabrication technology and new emerging markets may change the price level of existing sensors or produce new types of thermoelectric flow sensors.

Future Directions for Research

The most important requirements for successful sensors are accuracy, good reliability, and long-term operability at an acceptable price. Many applications may require standard sensors, but tailor-made solutions and integrated devices in Lab-on-a-Chip or microprocess technology application are also urgently needed. A standardization

Thermoelectric Flow Sensors, Table 7 Overview of existing devices [15]

Company, Institute, Sensor	FZK-IMT AMANDA sensor	HSG-IMIT flow sensor	Bosch MFM6	Leister Mflow 20	Sensirion ASF1400	MKS M20	Bronkhorst LiquiFlow L1
Fluids	liquid/gas	liquid/gas	gas	gas	(liquid) gas	gas	liquid
Flow rate (min)	0.1 sccm	0.1 sccm	6 l/min	0.01 sccm	0.01 sccm	0.01 sccm	
Gas Liquid	0.1 μl/min	0.16 μl/min			nl range		1.6 μl/min
Response time	2.5 ms	1 – 3ms	7 ms	>1 ms	150 ms	500 ms	1 – 2s
Temperature difference							
Gas	45 °C	–	150 – 180 °C	–	–	90 – 110 °C	
Liquid	6 °C						>1 °C
Dynamics	1:100	1:100	1:100	1:100	1:40 000	1:100	1:50
Fabrication	AMANDA polymers	silicon	silicon	silicon	silicon	conventional	conventional

of sensing elements and entire devices will help developers and users in many areas. Besides the typical materials, which might already be standardized, like thermocouples or heater materials, the standardization of typical geometries of the heater/sensors and the sensor setup would be very helpful for future developments and applications. The integration of sensing elements into various materials like metals, polymers, glass, or ceramics is very important for the wide application of the flow sensors in chemical or thermally challenging environments. An intelligent three-dimensional setup of the heater and the sensors elements may help to achieve more accurate measurements. For long-term application, an automated calibration procedure is desirable and will give a user-friendly sensor.

Cross References

- ► Chemical Vapor Deposition for Film Deposition
- ► Developing Flows
- ► Electrothermal Effects
- ► Fluid Metering
- ► Heat Transfer in Microchannels Flow
- ► Methods for Flow Rate Measurements
- ► Measurements for Temperature Measurements
- ► Resistance Temperature Detectors
- ► Thermocouples
- ► Thermoresistive Flow Sensors

References

1. van Herwaarden A, Sarro P (1986) Thermal sensors based on the Seebeck effect. Sens Actuators 10:321–346
2. Middelhoek S, Audet SA (1994) Silicon Sensors. Department of Electrical Engineering, Technical University of Delft
3. Ashauer M, Glosch H, Hedrich F, Hey N, Sandmaier H, Lang W (1999) Thermal flow sensors for liquids and gases based on combinations of two principles. Sens Actuators A 73:7–13
4. Buchner R, Sosna C, Maiwald M, Benecke W, Lang W (2006) A high-temperature thermopile fabrication process for thermal flow sensors. Sens Actuators A 130:262–266
5. Al khalfioui M, Michez A, Giani A, Boyer A, Foucaran A (2003) Anemometer based on Seebeck effect. Sens Actuators A 107:36–41
6. van Oudheusden B (1992) Silicon thermal flow sensors. Sens Actuators A 30:5–26
7. van Oudheusden B (1991) The thermal modelling of a flow sensor based on differential convective heat transfer. Sens Actuators A 29:93–106
8. Welty JR, Wicks CE, Wilson RE (1984) Fundamentals of Momentum, Heat, and Mass Transfer, 3rd edn. Wiley, New York
9. Baltes H, Paul O, Brand O (1998) Micromachined thermally based CMOS microsensors. In: Proceedings IEEE86 8:1660–1678
10. Nolas G, Sharp J, Goldsmit H (2001) Thermoelectrics - Basic Principles and New Material Developments. Springer, Berlin, Heidelberg
11. Rowe D (2006) Thermoelectrics Handbook – Macro to Nano. CRC, Boca Raton, Florida
12. Menz W, Mohr J, Paul O (2005) Mikrosystemtechnik für Ingenieure. Wiley-VCH, Weinheim
13. von Arx M (1998) Thermal properties of CMOS thin films. PhD Thesis, ETH, Zürich
14. Baltes H, Moser D, Völklein F (1994) Thermoelectric Mocrosensors and Microsystems. Chap. 2 in Bau H, DeRooij NF, Kloeck B (Eds), Sensors – A Comprehensive Survey. Vol. 7: Mechanical Sensors, VCH, Weinheim, 14–55
15. Dittmann DM (2001) Durchflusssensoren aus Kunststoff für sehr kleine Volumenströme auf der Basis des AMANDA-Verfahrens. Forschungszentrum Karlsruhe, Wissenschaftliche Berichte FZKA 6710
16. Gerlach G, Dötzel W (1997) Grundlagen der Mikrosystemtechnik. Hanser, Munich

Thermoelements

► Thermoelectric Flow Sensors

Thermoforming

► Micromolding

Thermomechanical Valves

Lin Gui, Carolyn Ren
Department of Mechanical and Mechatronics Engineering, University of Waterloo, Waterloo, ON, Canada
c3ren@mecheng1.uwaterloo.ca

Synonyms

Thermal mechanical valves; Thermally actuated mechanical valves; Thermally driven mechanical valves

Definition

A thermomechanical valve is a device that regulates fluid flow (either gas flow, liquid flow or slurry flow) by using an actuator which deforms under different temperatures to open, close, or partially obstruct various channels.

Overview

Since Kilby, the 2000 Nobel Prize winner, proposed the first integrated circuit in 1958, microfabrication has been a very attractive topic in a wide range of research fields. In the late 1970s, influenced by the development of microfabrication technology, microelectromechanical

T

Thermomechanical Valves, Table 1 Materials for the microvalves

	Thermal expansion microvalves		Bimetallic microvalves	Thermally driven SMA microvalves
	Thermal expansion buckling microvalves	SCE microvalves		
Materials	Si, Ni, etc.	Water, paraffin, etc.	PMMA-polymide, $Si-Ni$, $Si-Au$, $Al-Si$, SiO_2-Al, etc.	$Ni-Ti$, $Ni-Ti-Pd$, $Ni-Ti-Cu$, etc.

systems (MEMS) began to flourish in every mechanical field and about 10 years later largely drove the development of microfluidic chips. A typical microfluidic chip is a piece of glass or plastic plate with a network of microchannels, electrodes, and electrical circuits integrated onto it to perform a series of chemical or biomedical diagnoses and analyzes such as: DNA separation, enzymatic analysis, bacterial diagnosis etc. Normally, the volume of liquid that a microfluidic chip deals with is in the range of a nanoliter to a picoliter. The small volume requirement together with other advantages benefiting from miniaturization, such as short analysis time, high throughput, and minimized Joule heating, make such small-scale devices more competitive than their traditional counterparts. There are several commonly used methods to manipulate the liquid in a microfluidic chip including both mechanical and nonmechanical approaches, such as electrokinetic, magnetic, and electrochemical methods. Different approaches will lead to the development of different microvalves, which can be categorized as active or passive valves. Under each of the above category, microvalves can be further classified into mechanical or nonmechanical valves. Typical examples of active mechanical microvalves include, but not limited to, magnetic valves, electric valves, thermal valves, and piezoelectric valves. Active nonmechanical microvalves include phase change valves, bistable valves, and electrochemical valves, etc. Here we will focus on the introduction to thermomechanical microvalves including both active and passive valves, which use heat to conduct mechanical actions.

Generally, the chemical and physical properties of most engineering materials vary with temperature. The only difference lies in the degree to which the property changes with temperature. Among all the properties, the material shape change with temperature has mostly been used for the development of thermomechanical microvalves. The detailed mechanisms of thermomechanical microvalves will be discussed below. Briefly, the deformation of the material shape causes an actuation force, which can be used to induce mechanical actions through actuators. The thermomechanical microactuator is the major component of a thermomechanical microvalve through which thermal energy is converted into mechanical stress. The induced mechanical stress causes the deformation of the material shape of the actuator to close or open a channel. There are two main mechanisms for a thermomechanical actuator to convert thermal energy into mechanical stress: thermal expansion and the shape memory effect. Thermal expansion means that the size of a piece of material expands when its temperature increases and the shape memory effect describes a phenomenon that a piece of material memorizes its original shape and tends to return to it when heated. To control the switch between open and closed, a heater or a cooler is usually also involved in a thermomechanical microvalve. According to the way that the thermal control affects the shape of the microactuator, thermomechanical microvalves can be roughly divided into three categories: thermal expansion microvalves, bimetallic microvalves, and shape memory alloy (SMA) microvalves.

Basic Methodology

Different thermomechanical microvalves use different mechanisms to control the valve although all of them are based on the deformation of the material due to thermal expansion. For example, a thermal expansion microvalve utilizes the thermal expansion of a single material to open or close the flow, a bimetallic microvalve utilizes the thermal expansion difference between two materials which are bond together to open or close the flow, and a thermally driven SMA microvalve utilizes the shape memory effect (a sample of SMA has the capability to regain its original geometry by itself during heating (one-way effect)) to open or close the flow. The detailed methodologies for each category are summarized below.

Thermal Expansion Microvalves

Thermal Expansion

For most materials, when heated, the average amplitude of the atom's vibration within it increases, which increases the distance between the atoms thus causing the material to expand. Early developed thermomechanical microvalves, including bimetallic microvalves, were primarily based on

this principle. In contrast to bimetallic microvalves, only one single-layered beam or membrane is usually involved in a thermal expansion microvalve. Generally, two coefficients are used to depict the thermal expansion in a piece of material: the linear thermal expansion coefficient, α, and the volumetric thermal expansion coefficient, β. These two coefficients relate the change in temperature to the change in the linear and volumetric dimensions of the material, respectively, and are defined as

$$\alpha = \frac{1}{L}\frac{\partial L}{\partial T}\,, \tag{1}$$

$$\beta = \frac{1}{V}\frac{\partial V}{\partial T}\,, \tag{2}$$

where L and V are the length and the volume of the material, respectively, and T is the absolute temperature. For ideal isotropic materials, the linear thermal expansion coefficient is one-third of the volumetric thermal expansion coefficient, i.e., $\alpha = (\beta/3)\,\beta$. For most materials, both coefficients are positive, for example, they expand when heated. Assuming that the linear thermal expansion coefficient is independent of the temperature, the length of the material under zero compressive stress can be simply given as

$$L = L_0\left[1 + \alpha\,(T - T_0)\right]\,, \tag{3}$$

where L_0 is the length of the material at a temperature, T_0.

Beam Buckling

If fixed at its two ends, a straight beam will bend when heated due to thermal expansion. This inflection is usually utilized to design a thermal expansion microvalve actuator and the degree to which the material inflects when heated is key to the valve design. Lin et al. [1] have developed a theoretical model to investigate the buckling under electrothermal buckling conditions. Figure 1a shows a schematic diagram of such a microbeam. The deflection at the center of the beam can be given as

$$h_{\max} = 4\zeta\sqrt{\frac{I}{(\alpha\Delta T - \varepsilon)\,A_c}}\,, \tag{4}$$

where A_c represents the cross-sectional area, I is the inertia moment of the beam, T is the average temperature, ε is the strain of the beam, and ζ is a function of the maximum deflection angle, $\theta_{\max}$, which occurs at one-fourth of the total length, given by

$$\zeta = \sin\frac{\theta_{\max}}{2}\,. \tag{5}$$

There are two important parameters involved in the evaluation of the beam buckling, which are the critical load, P_{cr}, and the critical temperature, T_{cr}. The critical load is the force at which the beam will buckle, given by

$$P_{cr} = \frac{4\pi^2 EI}{L^2}\,, \tag{6}$$

where E is the Young's modulus. If no stress and external pressure differences are loaded on the beam at the temperature, T_0, considering a constant linear thermal expansion coefficient, the theoretical critical temperature for the beam to buckle can be given as

$$T_{cr} = \frac{4\pi^2 I}{\Delta\alpha A_c L^2} + T_0\,, \tag{7}$$

where $\Delta\alpha$ is the difference in the thermal expansion coefficient between the beam and the substrate. Investigations on thermal buckling of eccentric clamped–clamped beams can be found elsewhere [2].

Membrane Buckling

Similar to beam buckling, membrane buckling is another important mechanism for thermal expansion microvalves. To investigate the bending of a membrane when heat is added to it, Fig. 1b illustrates the principle of the thermal buckling of a square membrane. Considering a uniform compression condition cross the membrane (i. e., the compressive stress is constant, $S_x = S_y = S$), the membrane buckles transversally without any additional external load when the compressive stress gradually increases with temperature and exceeds the critical stress, S_{cr}. The critical stress is defined as

$$S_{cr} = 4.38\frac{\delta^2}{l^2}\frac{E}{1-\nu^2}\,, \tag{8}$$

where l and δ are the length (or the width for a square membrane) and the thickness of the membrane, respectively, and ν is Poisson's ratio. After that, a higher temperature will give rise to a larger buckling amplitude. The following equation shows the transversal displacement of the buckled membrane:

$$h(x,y) = \frac{h_{\max}}{4}\left(1+\cos\frac{2\pi}{l}x\right)\left(1+\cos\frac{2\pi}{l}y\right)\,, \tag{9}$$

where $h_{\max} = h\,(0,0)$, is the deflection at the center of the membrane. If no initial deflection is loaded and only the

T

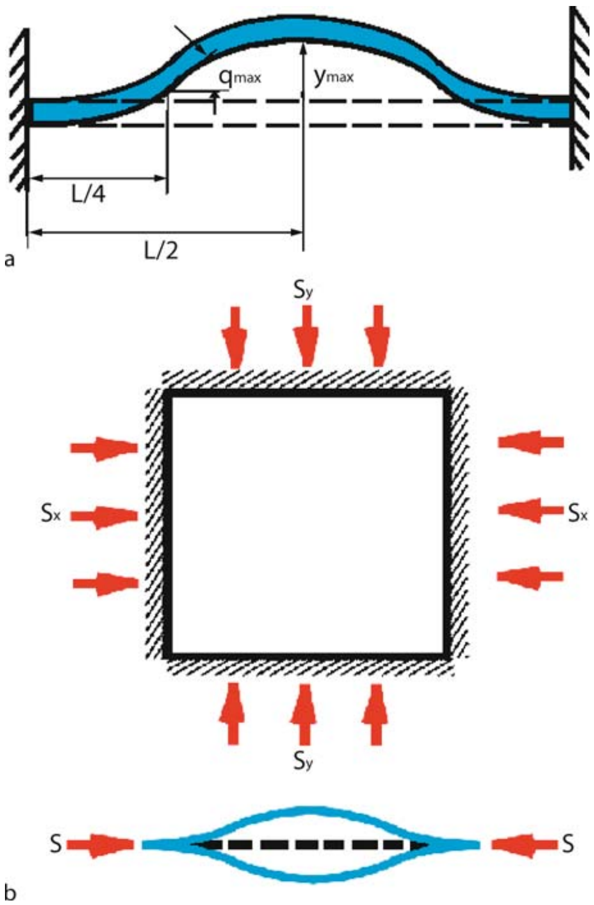

Thermomechanical Valves, Figure 1 (**a**) Schematic diagram of a straight, clamped–clamped beam after buckling; (**b**) illustration of the thermal buckling of a square membrane

first-order buckling of the membrane is considered, $h_{\max}$ can be obtained as

$$h_{\max} = \begin{cases} 0\,, & S \le S_{cr} \\ \pm 2.298\delta\sqrt{\dfrac{S}{S_{cr}} - 1}\,, & S \ge S_{cr}\,. \end{cases} \tag{10}$$

If no stress and external pressure are loaded on the membrane at the temperature, T_0, considering a constant linear thermal expansion coefficient, the theoretical critical temperature for the membrane to buckle can be given as

$$T_{cr} = 4.38 \frac{\delta^2}{l^2\left(1 - \nu^2\right)\Delta\alpha} + T_0\,, \tag{11}$$

where $\Delta\alpha$ is the difference in the thermal expansion coefficient between the membrane and the substrate.

Sealed Capsule Expansion Microvalves

In 1987, Zdeblick and Angell [3] first proposed the concept of the sealed capsule expansion (SCE) valve, which utilized the thermal expansion of a trapped liquid to actuate the valve, instead of the buckling of a beam or membrane. Later, a family of sealed capsule expansion valves trademarked as the *FluistorTM* was developed by Redwood Microsystems. Generally, in a SCE microvalve, there is a small cavity with trapped liquid which has a low boiling point and/or a high expansion coefficient. When the liquid is heated, it expands and closes the valve. When it is cooled, it shrinks and opens the valve.

The cavity can be made of silicon, quartz, or glass substrates or any other appropriate materials. Because of the convenience of silicon micromachining techniques, silicon is commonly used to fabricate the cavity and flexible membrane. Normally a thin-film heating resistor is integrated onto one inner side of the cavity, with a flexible diaphragm wall sealing the opposite inner side of the small cavity. When an electrical current is passed through the resistor, the trapped fluid is heated to evaporate and expand. The expansion causes the flexible wall to flex outward. This outward flex movement is then used to close or open the flow. A SCE microactuator can function as a normally opened microvalve, which opens the channel in its normal de-energized state. At a normal temperature, the flexible wall is in its shrinking stage, which gives a gap between the valve seat and the flexible wall. The valve is in its open stage with the fluid moving through the gap. When the trapped liquid is heated, due to its thermal expansion, the outward-flexing wall comes into contact with the nearby valve seat. Thus the fluid flow is cut off between the input channel and the output channel through the port. A high power can be applied to speed up the closure. Because the cooling is slower than the heating for most thermally driven valves, the following opening is much slower and depends on the thermal conduction and convection in the valves.

Bimetallic Microvalves

Bimetallic Strip

A bimetallic strip was the earliest bimetallic valve structure and was invented by the eighteenth century British clockmaker John Harrison for his third marine timekeeper (H3) to compensate for the error caused by temperature. A bimetallic strip consists of two strips of different metals which have different thermal expansion coefficients. As shown in Fig. 2a, if two strips are bonded together

throughout their length, due to the different degrees of thermal expansion between the two metals, the bimetallic strip will bend to the side with a lower thermal expansion coefficient when heated and to the other side when cooled down. The sideways displacement of the bimetallic strip is much larger than the lengthways change in either of the two metal strips. Thus, a temperature change is converted into a sideways mechanical displacement, which can be used to regulate the flow. For two layers of different thickness, as shown in Fig. 2a, the sideways displacement can

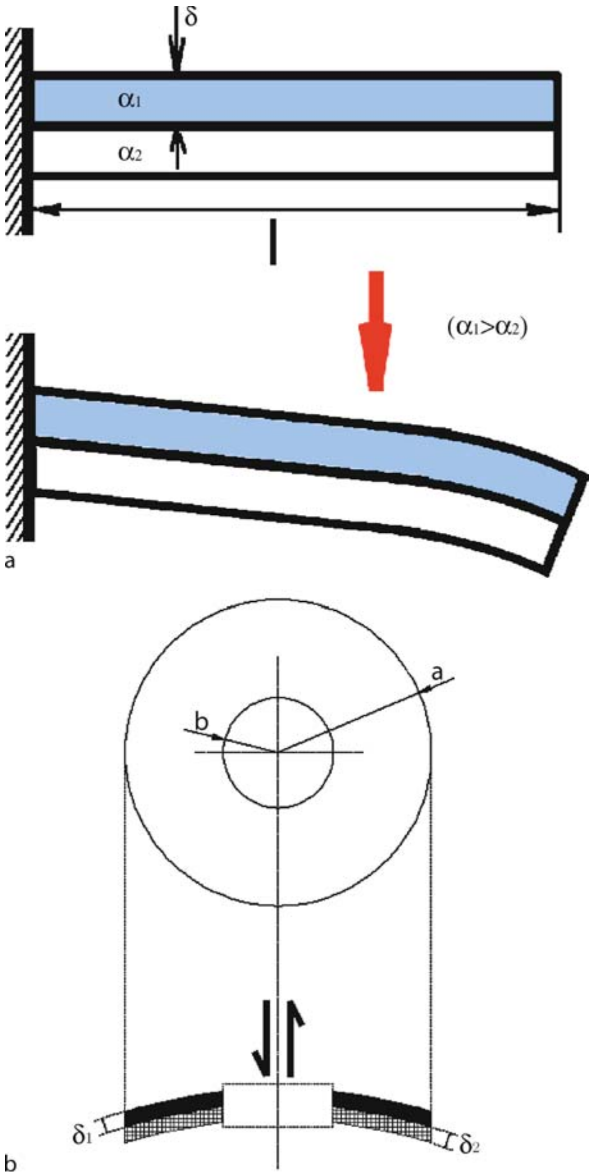

Thermomechanical Valves, Figure 2 (**a**) Cross-section of a bimetallic strip; (**b**) schematic of a circular annular bimetallic membrane

be given as

$$h = \frac{3L^2(\alpha_2 - \alpha_1)\,\Delta T\,(\delta_1 + \delta_2)}{\delta_2^2 K_1}\,, \tag{12}$$

where

$$K_1 = 4 + 6\frac{\delta_1}{\delta_2} + 4\left(\frac{\delta_1}{\delta_2}\right)^2 + \frac{E_1}{E_2}\left(\frac{\delta_1}{\delta_2}\right)^3 + \frac{E_2}{E_1}\frac{\delta_2}{\delta_1}$$

and the subscript, i, represents the ith strip. If the thicknesses of the two layers are equal, i. e., $\delta = \delta_1 = \delta_2$, the sideways displacement can be simplified as

$$h \approx \frac{6L^2(\alpha_2 - \alpha_1)\,\Delta T E_1 E_2}{\delta\left(E_1^2 + E_2^2 + 14E_1E_2\right)}\,. \tag{13}$$

Neglecting the difference between E_1 and E_2, the displacement can be further simplified as

$$h \approx \frac{3}{8\delta}(\alpha_2 - \alpha_1)\,\Delta T L^2\,. \tag{14}$$

Bimetallic Membrane

In addition to bimetallic strips, bimetallic membranes are also commonly used in a microvalve actuator. Figure 2b shows the schematic of a circular annular bimetallic membrane. Similar to a bimetallic strip, a bimetallic membrane consists of two layers of different metal materials which have different thermal expansion coefficients. When heated, due to their different thermal expansions, the center of the membrane bulges vertically to the side with a higher thermal expansion coefficient. As shown in Fig. 2b, for a circular annular bimetallic membrane, if the outer edge is fixed by a wall and the inner edge is guided in the vertical direction by a boss, the displacement at the inner edge can be given as

$$h \approx \frac{3(\alpha_2 - \alpha_1)\,\Delta T\,(\delta_1 + \delta_2)\,(1 + \nu_a K_3/K_2)\,a^2 b^2 \ln\frac{a}{b}}{\delta_2^2 K_4\left(a^2 - b^2\right)}\,, \tag{15}$$

where

$$K_2 = 1 + \frac{E_2\delta_2^3\left(1-\nu_1^2\right)}{E_1\delta_1^3\left(1-\nu_2^2\right)} + \frac{3\left(1-\nu_1^2\right)(1+\delta_2/\delta_1)^2(1+E_1\delta_1/E_2\delta_2)}{(1+E_1\delta_1/E_2\delta_2)^2-(\nu_1+\nu_2E_1\delta_1/E_2\delta_2)^2}, \quad (16)$$

$$K_3 = 1 + \frac{\nu_2E_2\delta_2^3\left(1-\nu_1^2\right)}{\nu_1E_1\delta_1^3\left(1-\nu_2^2\right)} + \frac{3\left(1-\nu_1^2\right)(1+\delta_2/\delta_1)^2(1+\nu_2E_1\delta_1/\nu_1E_2\delta_2)}{(1+E_1\delta_1/E_2\delta_2)^2-(\nu_1+\nu_2E_1\delta_1/E_2\delta_2)^2}, \quad (17)$$

$$K_4 = 4 + 6\frac{\delta_1}{\delta_2} + 4\left(\frac{\delta_1}{\delta_2}\right)^2 + \frac{E_1\delta_1^3(1-\nu_2)}{E_2\delta_2^3(1-\nu_1)} + \frac{E_2\delta_2(1-\nu_1)}{E_1\delta_1(1-\nu_2)}, \quad (18)$$

where a and b are the outer and inner radius of the membrane, respectively. Considering $\delta = \delta_1 = \delta_2$, $E_1 = E_2$, and $\nu = \nu_1 = \nu_2$, the displacement can be simplified as follows:

$$h = \frac{3}{8\delta}(\alpha_2 - \alpha_1)\Delta T(1+\nu)\frac{a^2b^2}{a^2-b^2}\ln\frac{a}{b}. \quad (19)$$

Further numerical and experimental studies on the thermal behavior of other more complex bimetallic membranes can be found elsewhere [4].

Thermally Driven SMA Microvalves

The SMA, known as the memory metal or smart wire, was first discovered in an Ag – Cd alloy in 1932. Due to a crystalline transformation between a high temperature austenite phase and a low temperature martensite phase, when materials with this shape memory property are subject to deformation, they are able to return to their *memorized* original shape after being heated to a temperature above their transformation temperatures. It was not until the early 1960s that SMAs showed their real importance when the Ni – Ti SMA was discovered by Buehler et al. [5]. Compared with other SMAs, Ni – Ti alloys can give a much larger deformation under the same conditions, have good chemical resistance and biocompatibility, and possess superior mechanical properties such as long fatigue life and relatively high ductility. Because of the large deformation occurring under a temperature variation, a SMA is an ideal material for a microactuator, especially for a microvalve.

Shape Memory Effects

In fact, not only alloys have shape memory properties, some polymers, ceramics and even biological systems also possess such properties. For example, bacteriophages can use the shape memory mechanism to enter into host cells. However, to date, only SMAs are widely used in microvalve fabrication. We will focus on the introduction of SMA microvalves.

Different from most normal materials, besides the shape changes resulted from elastic, plastic or thermal contributions, the SMA has three additional shape changes: a one-way effect shape change, a two-way effect shape change, and a pseudoelasticity shape change [6].

- One-way effect: the effect that the material remembers to return to its original shape when heated, but the material needs external loads to make it deform. This thermally driven deformation cycle is the basis for most SMA microvalves.
- Two-way effect: the effect that the material remembers two different shapes: one at low temperatures, and the other at high temperatures. In this situation, external loads are not necessary (intrinsic two-way effect). Normally, a SMA *remembers* its high-temperature shape and immediately *forgets* the low-temperature shape upon heating to recover the high-temperature shape. However, it can be *trained to remember* to leave some reminders of the deformed low-temperature condition in the high-temperature phase.
- Pseudoelasticity: the effect that the material does not need temperature variation to change its shape. It acts like a spring: expanding when added with a load and receding when released from an external load.

Key Research Findings

There have been too many studies and findings on thermomechanical microvalues to list all of them here. Some key research findings about the above-mentioned three cat-

egories of thermomechanical microvalves are briefly discussed here.

Thermal Expansion Microvalves

Thermal Expansion Buckling Microvalves

Figure 3 shows a basic setup of a normally closed thermal expansion microvalve. The main valve components usually include a valve seat, a valve membrane, a thin film polysilicon heater, an upper housing, and a lower housing. Generally, a thin film heater is used to heat the valve membrane. When the membrane is heated, the membrane begins to bulge allowing the flow to pass. A well-designed microvalve can possess a response time of about 10 – 20 ms, which is quite fast for a thermally driven microvalve. Most thermomechanical microvalves are active valves which use external thermal control to change the stage of the valve. A possible passive thermal buckling valve has been proposed [2] as shown in Fig. 4a. In contrast to active valves, passive valves utilize the properties of the fluid itself to control the stage of the valve. As shown in Fig. 4a, a clamped eccentric nickel beam is fabricated over a slot through the substrate. When the temperature is low, the gap between the beam and the seat is small, allowing a small mass of liquid to flow through it. But, if the temperature is high, the beam buckles, allowing a larger flow rate. These eccentric microbeams can potentially be used in the future for thermally adaptive microvalves which can self-regulate the flow. Figure 4b shows possible applications of these thermally adaptive microvalves. It illustrates the schematic of a MEMS skin-cooling scheme which is similar in nature

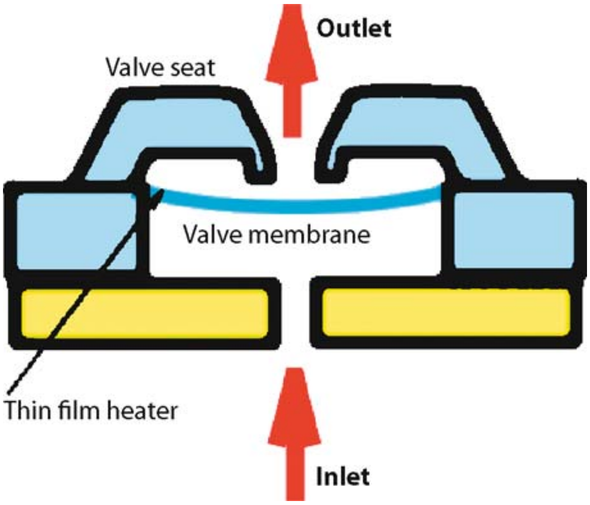

Thermomechanical Valves, Figure 3 A typical normally closed thermal expansion microvalve

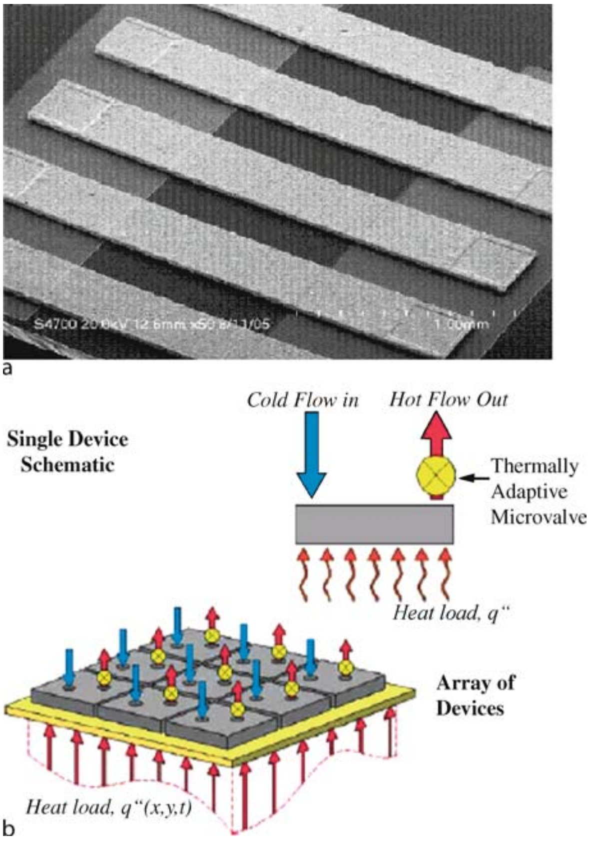

Thermomechanical Valves, Figure 4 A passive thermal buckling valve. (**a**) Photograph of eccentric micro nickel beams; (**b**) application of the valve in MEMS adaptive cooling scheme for both a single device (upper) and an array of devices (bottom)

to the biological phenomenon of perspiration. When the temperature increases, the thermally adaptive microvalve can increase the flow of local cooling fluid, hence automatically enhancing the cooling strength. With this adaptive cooling strategy, the temperature of the surface can be well controlled under a spatially and temporally varying heating load.

SCE Microvalves

Figure 5a shows a schematic of a normally closed SCE microvalve which has been commercialized as the FluistorTM Microvalve of NC-105 by Redwood Microsystems. Different from the normally opened SCE microvalve, this microvalve has a fulcrum point on the flexible diaphragm. In its de-energized state, the body of the actuator falls down on the off-center orifice on the right and closes the flow. When heated, the trapped fluid expands to cause the flexible diaphragm to lever the body of the actuator away from the orifice and allow the flow to pass through. The Fluistor TM NC-105 has been reported to have a leak

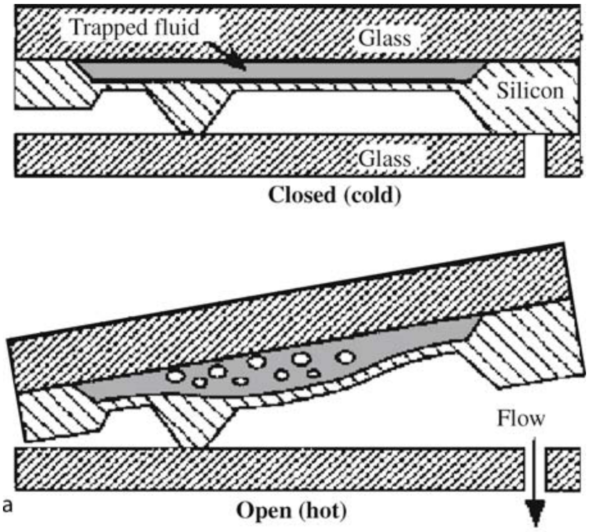

a

b

Thermomechanical Valves, Figure 5 (**a**) Schematic of normally closed sealed capsule microvalve action; (**b**) Fluistor™ NC-1500-T by Redwood Microsystem

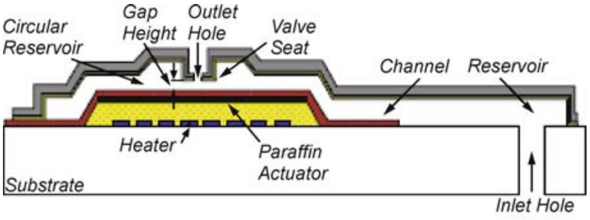

a

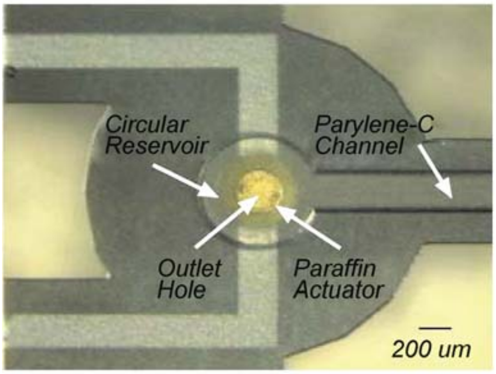

b

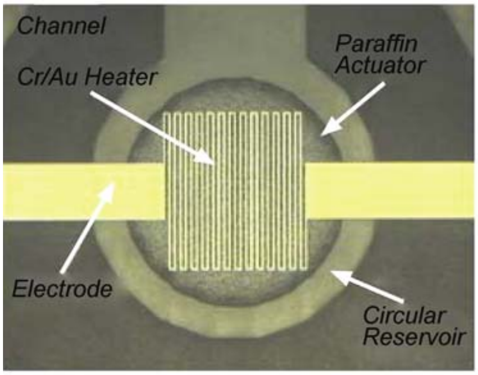

c

Thermomechanical Valves, Figure 6 A paraffin actuated microvalve described in the text. (**a**) Schematic of the cross-section of the microvalve; (**b**) microscope photograph of the microvalve from the top; (**c**) microscope photograph of the microvalve from the bottom

rate of no less than 0.006 ml/min of helium, which is acceptable in many applications. This valve cannot be used to control corrosive fluids, because it uses the flexible diaphragm to directly seal the valve and a very limited range of materials can be used to fabricate the diaphragm. This has since been improved by avoiding the use of the flexible membrane to directly seal the device. Figure 5b shows a typical Redwood Microsystems NC-1500-T normally closed valve, which works at an ambient temperature range of 0 – 55 °C and opens the flow at approximately 56 °C.

Besides the thermal expansion of the fluid and the volumetric expansion of the liquid–gas phase change, the expansion of the solid–liquid phase change can also be used in a SCE valve to actuate the action. Figure 6 shows the microvalve that Carlen and Mastrangelo proposed in 1999 [7]. This SCE microvalve is a normally opened SCE microvalve in which it uses the expansion of the solid–liquid phase change of the paraffin to actuate the switch. Figure 6a shows the schematic cross-section of the microvalve. Because paraffin has a large volumetric expansion upon melting, paraffin melts and expands 10 – 30 % when heated to 65 – 150 °C, and thus causes the flexible membrane to deflect vertically about 3 μm in 20 ms with a power requirement of less than 50 mW. The outward-flexing membrane will then come into good con-

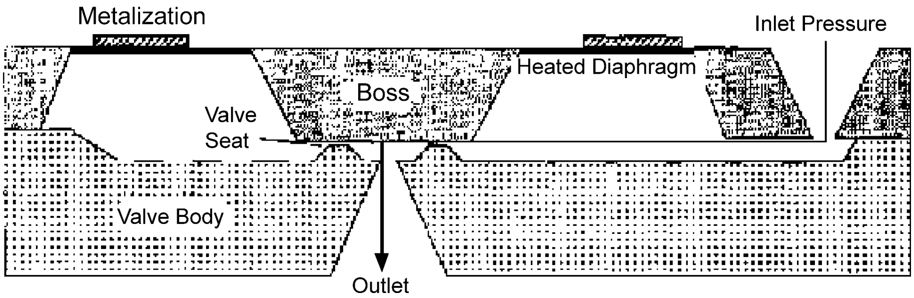

Thermomechanical Valves, Figure 7 Schematic of a normally closed thermal bimorph-actuated valve

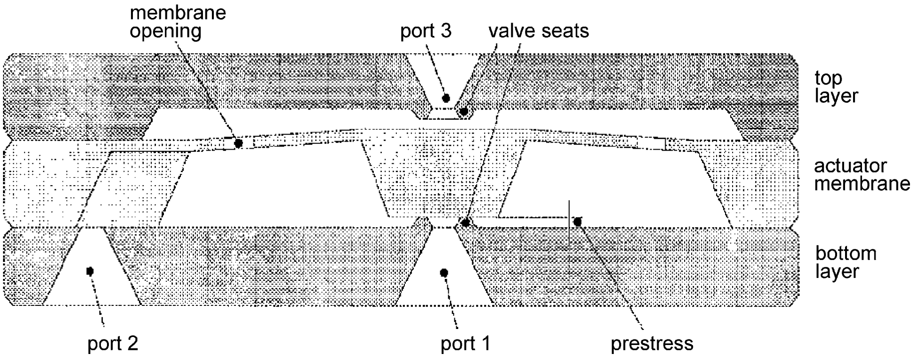

Thermomechanical Valves, Figure 8 Schematic of a bimetallically actuated three-way valve

tact with the outlet hole above and cut off the flow. Figures 6b and 6c show, respectively, the top and bottom view of the SCE microvalve.

Bimetallic Microvalves

Classical Bimetallic Microvalves

In 1991, Jerman proposed a new microactuator based on a bimetallic membrane [8], which was later used to fabricate a normally opened microvalve and a normally closed microvalve. As shown in Fig. 7, a circular annular Al – Si bimetallic membrane with a central boss is used in the microvalve. The bimetallic diaphragm consists of a 5 μm-thick diaphragm of aluminum and a lower 8 μm-thick silicon diaphragm with embedded diffused resistors. In its de-energized state, the central boss seals the valve seat (400 μm × 80 μm) and thus closes the flow. When energized, the resistors heat the Al – Si bimetallic diaphragm making the central boss move up, thus allowing the flow. The displacement of the boss can be changed by altering the electrical power and the temperature of the diaphragm, which can be used to control the flow rate of the valve. The leakage rate of this valve is approximately 0.03 ml/min of nitrogen at a 34.5 kPa input pressure. This microvalve works well under the temperature range of −20 to +85 °C. The response time is about 150 ms, which is quite rapid for a thermally driven microvalve.

Figure 8 shows a similar bimetallic microvalve which was fabricated by Messner et al. [9]. In contrast to the microvalve shown in Fig. 7, it has another port (port 2) which is always open at the edge of the membrane. When the microvalve is de-energized, the center boss seals port 1 thus letting port 2 connect with port 3. When the boss is lifted by the thermally driven metallic membrane, port 1

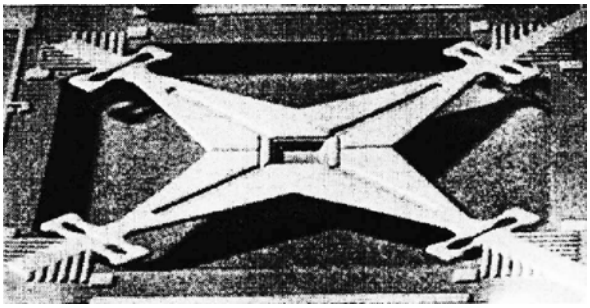

Thermomechanical Valves, Figure 9 A four-leg bimetallic membrane microvalve

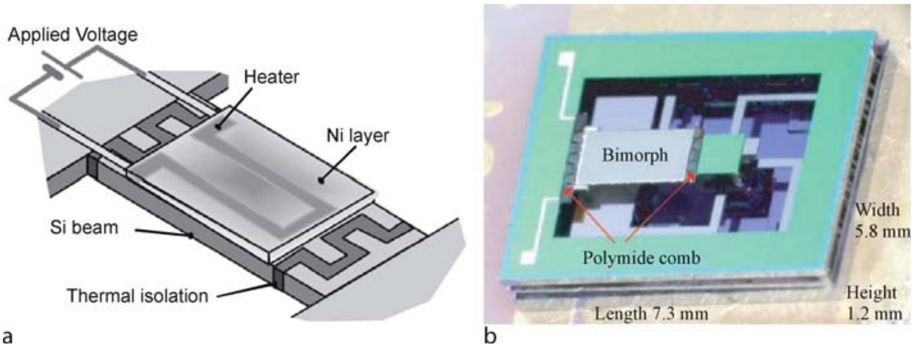

Thermomechanical Valves, Figure 10 A Si – Ni bimorph actuated microvalve with thermal isolation comb regions. (**a**) Thermal isolation comb regions; (**b**) photograph of the microvalve

is released and port 3 is sealed. Port 2 is connected with port 1. This 3-way microvalve is designed to control a differential pressure of 1000 kPa allowing a maximum flow rate of 800 ml/min for dry air at 600 kPa. The electrical power is about 1 W. It works properly in an ambient temperature range of 0 – 50 °C.

Power-Saving Bimetallic Microvalves

To minimize the thermal conduction loss from the membrane, Wang et al. [10] have proposed a new microvalve using a four-leg bimetallic *membrane*. Figure 9 shows their microvalve. In contrast to other bimetallic membrane microvalves, this microvalve has a four-leg Ni – Si bimetallic membrane at the center instead of an annular one. With less conjunction to the substrate this tapered-leg membrane largely decreases the thermal conduction loss, and thus significantly saves on the power required to actuate the valve. It has been reported that the power requirement of this design is 5.3 times less than that of the older design.

Tomonari et al. [11] have used thermal isolation comb regions to minimize the thermal conduction loss from the membrane in their microvalve. As shown in Fig. 10a, they used a Si – Ni bimorph as the microactuator. They fabricated thermal isolation comb regions on either side of the silicon bimorph by etching Si and filling the structure with polyimide resin. Because of the low heat conductivity of the polyimide resin, this structure can effectively protect from heat loss. Figure 10b shows their microvalve.

Other Attempts to Switch the Flow Using Bimetallic Structures

Many other attempts to switch the flow using bimetallic structures have been made. Walters et al. [12]. introduced gate microvalves (cross-flow microvalve or X-microvalve) in 1998. In a gate microvalve, the valve gate moves perpendicular to the flow and static pneumatic force. Figure 11 shows the bimorph-actuated gate microvalves reported by Haasl et al. [13]. The shortcoming of these microvalves is that leakage is unavoidable in the closed state because the limited actuation energy in microsystems does not allow friction between sliding structures.

In 1992, Doring proposed using the bimetallic microcantilever structure to direct a fluid jet. Later, on the basis of this idea, Trah et al. [14] fabricated a micromachined normally closed valve using an Al – Si cantilever, as shown in Fig. 12. When the cantilever is in its de-energized state, the cantilever is slightly bent upwards and directs the fluid to the room above the membrane. Thus, the pressure in the upper room is a little larger than that in the lower room. The pressure difference presses the boss down to the valve seat and seals the valve. When the cantilever is heated and thus bends downwards, the fluid jet also deflects downwards and flows into the lower room to lift up the boss. Thus, the valve opens. The size of the valve is 14.5 mm × 8.5 mm × 1.43 mm. The valve was designed to control a flow rate of 75 ml/min at time constants of about 0.5 ms.

Thermally Driven SMA Microvalves

Microvalves Using Sputtered SMA Thin Films or Rolled Sheets

Thin films and rolled sheets are the most widely used format in microvalve fabrication. Usually a SMA microvalve consists of an upper and a lower housing integrated with a valve seat and fluidic connections, a membrane, a spacer, and a SMA microactuator. The deformation actuated by the SMA thin film pushes or pulls the spacer to seal or open the valve seat, thus to close or allow the liquid to flow through the valve seat.

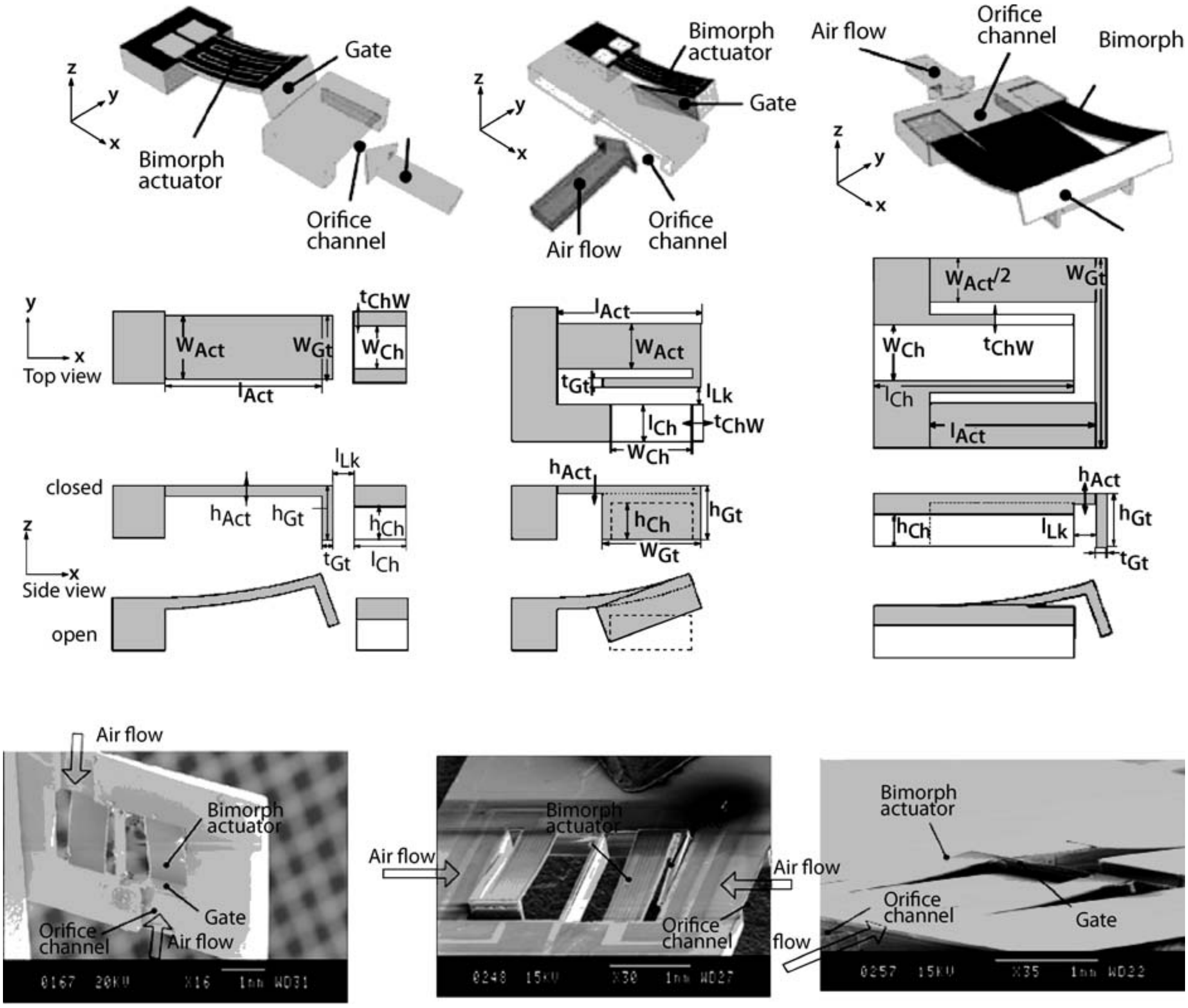

Thermomechanical Valves, Figure 11 Bimetallically actuated gate microvalves

The method of using SMA films to fabricate microvalves can be traced back to Busch and Johnson [15] who successfully fabricated a Ni – Ti film using sputter deposition and crystallization processing techniques and also suggested some microvalve and micromirror structures. Because a Ni – Ti thin film can generate 10 J per cubic centimeter per cycle, it can be used as a heating resistor, which can largely simplify the structure because it avoids the use of additional heaters. They later developed a normally closed SMA microvalve where a Be – Cu spring was used to push a sapphire ball against the silicon over the spacer to close the flow orifice in a de-energized state, as shown in Fig. 13. A thin Ni – Ti SMA film is deposited onto a silicon substrate and is cut into the shape of microribbon by using the photolithography and selective etching techniques. When heated, the Ni – Ti microribbons return to the original undeflected state to move the silicon back from the orifice and thus open the microvalve.

There have been further developments in microvalves using sputtered SMA thin films. The major research efforts have been concentrated on the optimization of the SMA film shape through the simulation of the stress distribution in the film. Figure 14 shows a stress-optimized SMA microdevice designed by Skrobanek et al. [16]. The goal of this practice is to ensure that the stress values in the thin film should be sufficiently high to provide large work outputs, and low enough to avoid fatigue effects. Ikuta et al. [17] have fabricated fluid-driven chips containing multiple pumps and switching valves for the biochemical IC family. The switching valve that they fabricated was driven by a SMA film. Figure 15 shows the operating principle of their switching valve. In contrast to normal valves, this valve has two outlets instead of one. Due

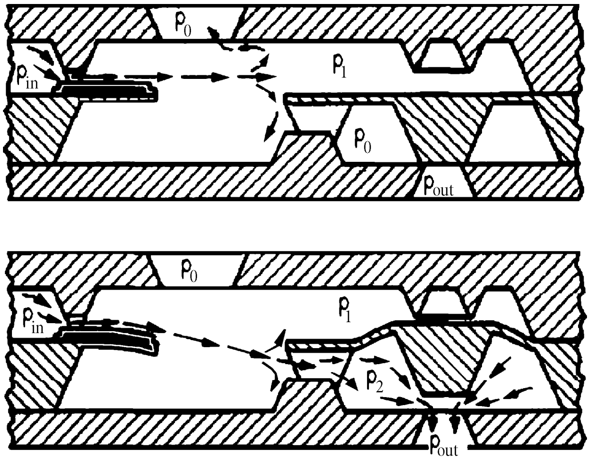

Thermomechanical Valves, Figure 12 Schematic and principle of a hydraulic actuated microvalve

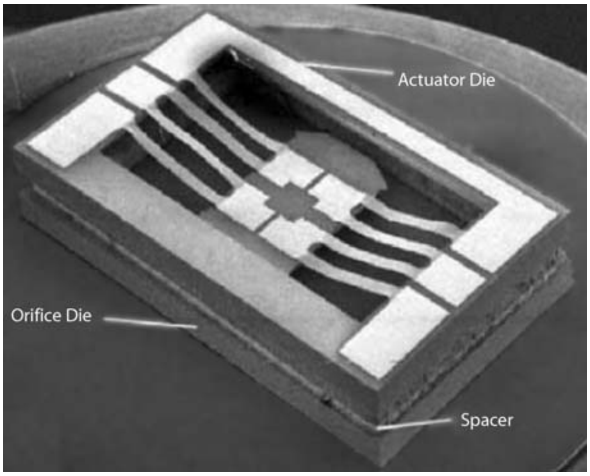

Thermomechanical Valves, Figure 13 SMA microvalve

to the lever action of the silicon rubber, when the SMA actuator pushes the spacer down to seal the right outlet 2, it opens the left outlet 1 automatically. The switching time in the active (heating) phase is 0.5 s and the response time of the opposite way in the passive (cooling) phase is about 2 s. Different Ni – Ti – x alloys were also tried to fabricate such microvalves. The use of Ni – Ti – Pd alloys provides a higher ambient temperature application, and Ni – Ti – Cu alloys provide a higher recoverable stress as compared to Ni – Ti alloys.

Microvalves Using SMA Wires

Micropinch Valves Using SMA Wires SMA wire is commonly used in micropinch valves. A micropinch valve usually consists of a soft tube and a SMA wire. The SMA

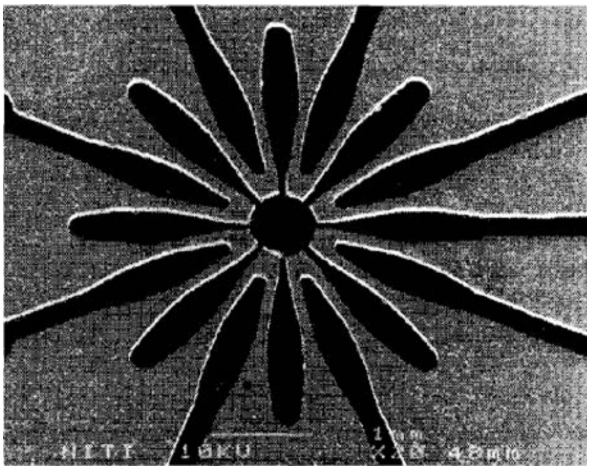

Thermomechanical Valves, Figure 14 Stress-optimized microdevice

wire pinches the tube to close the flow and releases it to open the flow. The first pinch valve using a SMA wire was used in an implantable drug delivery system [18]. A 120 μm-diameter Ni – Ti wire was used to pinch down a silicone rubber tube with an inner diameter of 0.6 mm and an outer diameter of 1 mm. This value is operated with a pressure difference of 200 kPa and can open in less than 1 s with a power consumption of 120 mW.

Later, more normally closed pinch valves were developed. Figure 16 shows another normally closed pinch valve developed by Pemble and Towe [19]. The valve consists of an actuator and silicon tubing. The actuator consists of a 152 μm-diameter Ni – Ti contraction wire in tension with a 584 μm-diameter Ni – Ti superelastic wire. One end of the actuator is fixed to a flat surface using epoxy. In the de-energized state, the actuator tightens the tube and makes it deform to block the flow. When the contraction wire is electrified, Joule heating causes the superelastic cantilever to bend upward. This upward deflection relieves pinch pressure on the tubing thereby allowing the flow. In this pinch valve, the outer diameter of the silicone tubing is 1.2 mm and the inner diameter is 0.64 mm. It operates with a pressure difference of 20.7 kPa and a flowrate of up to 48 ml/min at a current of 420 mA. The valve can be opened in less than 1 s and then closed in less than 2.5 s. The calculated power dissipation has been reported to be 398 mW.

Figure 17 shows a relatively economical micropinch valve fabricated by Piccini and Towe [20]. The system consists of a microbore silicone tube, a Ni – Ti SMA wire, a miniaturized synthetic ruby ball and a thermocouple. All of the components are off-the-shelf components. As shown in Fig. 17, the ruby ball blocks the tubing in a nor-

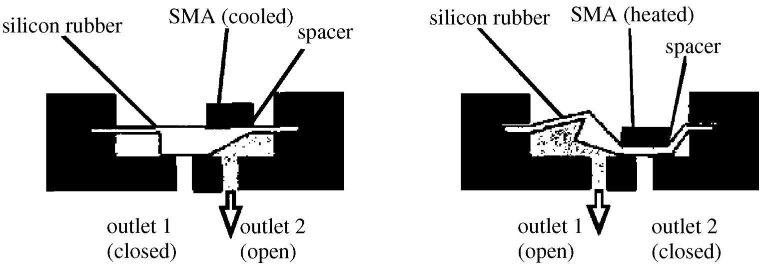

Thermomechanical Valves, Figure 15 Schematic of a SMA switching valve

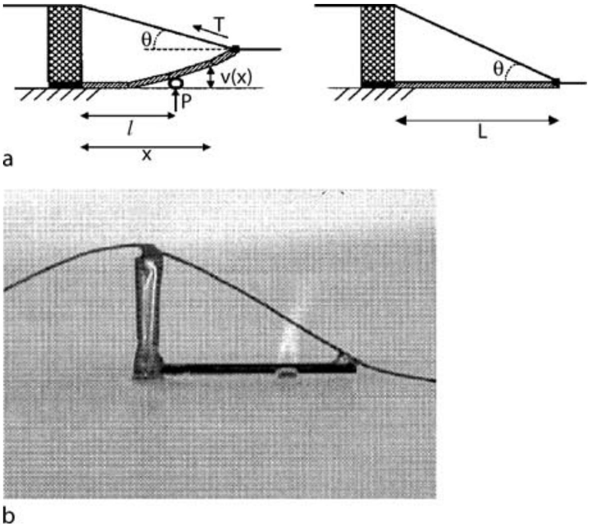

Thermomechanical Valves, Figure 16 SMA pinch valve. (**a**) Schematic of the valve; (**b**) photograph of the valve

mal state. When electrified, due to Joule heating, the SMA wire stretches the microbore silicone tubing away from the ruby ball and the gap between them allows the flow. This microvalve has been reported to have a response time of 2.5 s with a power pulse of 213 mW.

Other Microvalves Using SMA Wires Figure 18 shows another type of gate microvalve using SMA wires [21]. A paddle suspended from a silicon beam is placed on the valve seat. In its de-energized state, the hole in the paddle fits in with the valve seat and allows the flow. When electrified, the SMA wire is heated by Joule heating and bends to push the paddle aside from the valve seat and closes the inlet opening. When the SMA wire cools down, the paddle is pushed back by the silicon beam to allow the flow again.

Future Directions for Research

Various thermomechanical microvalves have been developed with the development of MEMS fabrication technology. Thermomechanical microvalves work by converting thermal energy into mechanical deformation. Compared with other microvalves, such as magnetic microvalves, electrostatic microvalves, and piezoelectric microvalves, thermally driven microvalves have their own advantages such as simplicity of fabrication, controllable deflection (by adjusting the input power), and a relatively large actuation force.

However, thermally driven microvalves also have their drawbacks. First, they have a relatively long response time. Second, because heat dissipation is unavoidable, more attention must be paid when designing a microvalve. In most circumstances, heat dissipation in a thermally driven microvalve is a trade-off. For example, a small heat dissipation helps to obtain a high heating rate to open the valve; while at the same time it also means a low cooling rate to close it. Third, the performance of a thermally driven microvalve is largely affected by the ambient temperature. A thermally driven microvalve usually works within a relatively small temperature range. Fourth, compared to the heating process, the cooling process is relatively difficult to achieve. The cooling process is always the bottleneck in reducing the response time of a thermally driven microvalve. Generally speaking, the response time of a thermally driven microvalve is of the order of a second. Fifth, sometimes due to the large power consumption, a thermally driven microvalve is not appropriate when the energy consumption is limited. Sixth, thermal expansion may cause loosening to the support which may introduce some leakage problems. Seventh, the closing time may not be the same as the opening time. Finally, heating of the fluid may not be appropriate in some MEMS applications because it may introduce some local boiling on the electrode.

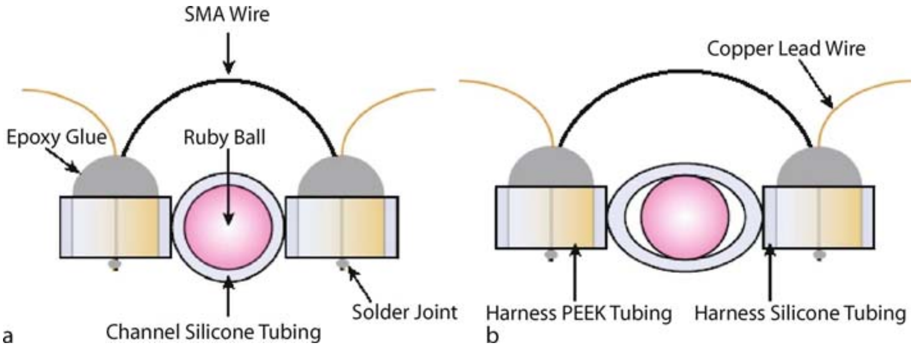

Thermomechanical Valves, Figure 17 SMA pinch microvalve in: (**a**) de-energized close state; (**b**) actuated open state

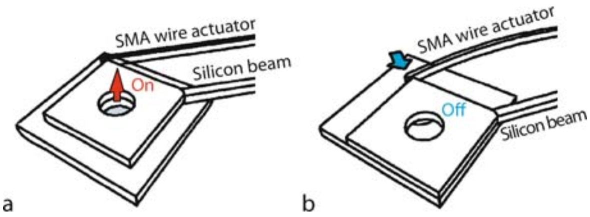

Thermomechanical Valves, Figure 18 A gate microvalve acuated by a SMA wire at (**a**) open position; (**b**) closed position

Overcoming the shortcomings of the thermomechanical microvalves listed above will be the main tasks for future studies in this area. The development of new materials and exploring new methods to make thermomechanical microvalves will also be promising directions.

Cross References

► Thermal Expansion

References

1. Lin L, Chiao C, Luo JJ, Sun TP (1996) Electro, thermal and elastic characterizations of suspended micro beams. The Second International Workshop on Thermal Investigations of ICs and Microstructures, Budapest, pp 219–223
2. McCarthy M, Tiliakos N, Modi V, Frechette LG (2007) Thermal buckling of eccentric microfabricated nickel beams as temperature regulated nonlinear actuators for flow control. Sens Actuators A 34(1):37–46
3. Zdeblick MJ, Angell JB (1987) A microminiature electro-fluidic valve. Proceeedings of the 4th International Conference on Solid-state Sensors and Actuators, pp 827–829
4. Hsu CP, Hsu WY (2000) A two-way membrane-type micro-actuator with continuous deflections. J Micromech Microeng 10:387–394
5. Buehler WJ, Gilfrich JV, Wiley RC (1963) Effect of low temperature phase changes on the mechanical properties of alloy near composition Ti – Ni. J Appl Phys 34:1475
6. Kohl M (2004) Shape Memory Microactuators. Springer, Heidelberg
7. Carlen ET, Mastrangelo CH (2000) Paraffin actuated surface micromachined valves, Micro Electro Mechanical Systems, 2000, MEMS 2000, the Thirteenth Annual International Conference, pp 381–385
8. Jerman JH (1991) Semiconductor microactuator. US Patent 5,069,419, Dec 1991
9. Messner S, Muller M, Burger V, Schaible J, Sandmaier H, Zengerle R (1998) Micro Electro Mechanical Systems, MEMS 98, Proc Eleventh Annual International Workshop, pp 25–29
10. Wang TK, Barth P, Alley R, Baker J, Yates D, Field L, Gordon G, Beatty C, Tully L (1999) Production-ready silicon microvalve. Proc SPIE 3876, pp 227–237
11. Tomonari S, Yoshida H, Kamakura M, Yoshida K, Kawahito K, Saitoh M, Kawada H, Juodkazis S, Misawa H (2003) Efficient microvalve driven by a Si – Ni bimorph. Jpn Soc Appl Phys 42:4593–4597
12. Walters M, Dhuler V, Mahadevan R, Cowen A, Wood R, Hill E, Kao I (1998) A silicon micromachined gate valve. Presented at the 1998 Solid-state Sensors and Actuators Symposium
13. Haasl S, Braun S, Ridgeway AS, Sadoon S (2006) Out-of-plane knife-gate microvalves for controlling large gas flows. J Microelectromec Syst 15:1281–1288
14. Trah HP, Baumann H, Doring C, Goebel H, Grauer T, Mettner M (1993) Micromachined valve with hydraulically actuated membrane subsequent to a thermoelectrically controlled bimorph cantilever. Sens Actuators A 39:169–176
15. Busch JD, Johnson AD (1990) Shape-memory properties in Ni – Ti sputter deposited film. J Appl Phys 68:6224–6228
16. Skrobanek KD, Kohl M, Miyazaki S (1997) Stress-optimised shape memory devices for use in microvalves. J Phys IV 7:597–602
17. Ikuta K, Hasegawa T, Adachi T, Maruo S (2000) Fluid drive chips containing multiple pumps and switching valves for Biochemical IC Family. Proceedings of the IEEE Thirteenth Annual International Conference on Micro Electro Mechanical Systems, pp 739–744
18. Reynaerts D, Peirs J, Brussel H (1997) An implantable drug-delivery system based on shape memory alloy micro-actuation. Sens Actuators A 61:455–462
19. Pemble CM, Towe BC (1999) A miniature shape memory alloy pinch valve. Sens Actuators 77:145–148
20. Piccini ME, Towe BC (2006) A shape memory alloy microvalve with flow sensing. Sens Actuators A 128:344–349

21. Buttgenbach S, Butefisch S, Leester-Schadel M, Wogersien A (2001) Shape memory microactuators. Microsyst Techn 7:165–170

Thermometry

► Temperature Measurement, Methods

Thermophoresis

PETER GEELHOED[1], JERRY WESTERWEEL[1],
SIGNE KJELSTRUP[2], DICK BEDEAUX[2]
[1] Laboratory for Aero- & Hydrodynamics,
Delft University of Technology, Delft, Netherlands
[2] Department of Chemistry, Norwegian University of Science and Technology, Trondheim, Norway
p.f.geelhoed@tudelft.nl, j.westerweel@tudelft.nl

Synonyms

Thermodiffusion; Thermal diffusion; Soret effect; Ludwig–Soret effect

Definitions

Thermophoresis is defined as the migration of a colloidal particle or large molecule in a solution in response to a macroscopic temperature gradient. The inverse effect, i. e., the formation of a temperature gradient as the result of the mixing of different molecular species, is referred to as the *Dufour effect*. The ►Soret coefficient is defined as the ratio of the thermal diffusion coefficient and the normal diffusion coefficient; it is a measure for the degree of separation of the species. These concepts are the same as for a molecular mixture.

Physical Principles

A colloidal particle or large molecule can be driven to move in a gas or a liquid by the application of a non-uniform temperature field. The mass flow rate $\boldsymbol{J}_\mathrm{m}$ of a species or of colloidal particles as the result of a thermal gradient ∇T in a fluid is given in, e. g. [1]:

$$\boldsymbol{J}_\mathrm{m} = -\rho D \nabla c - \rho D_\mathrm{T} c(1-c)\nabla T\,, \tag{1}$$

where ρ is the fluid density, D the diffusion coefficient, D_T the thermal diffusion coefficient, and c the species or particle concentration in terms of mass fraction. The first term on the right hand side is the Fick diffusion law, while the second term describes the migration due to the thermal gradient.

In a stationary state the mass flux vanishes (i. e., $\boldsymbol{J}_\mathrm{m} = 0$), and the Soret coefficient S_T is given by [5]:

$$S_\mathrm{T} \equiv \frac{D_\mathrm{T}}{D} = -\frac{1}{c\,(1-c)}\frac{\nabla c}{\nabla T}\,. \tag{2}$$

Hence, the effectiveness of the separation is given by the Soret coefficient, while the rate of separation is determined by the diffusivity. In general the thermal diffusion coefficient D_T is a function of temperature and concentration, which complicates the description of thermophoresis.
Thermophoresis as defined above occurs in liquids. For molecular mixtures of gases there is a sound theoretical description [5], but a theory has not been formulated satisfactorily for liquids.

Key Research Findings

For gases thermophoresis can be described using Chapman–Enskog theory [5], assuming a Maxwell–Boltzmann distribution for the velocity of the molecules, with corrections. This approach is only valid when the relative temperature change over the molecular free path is small. Using Onsager's theorem the transport equation can be derived from the entropy production, which is described by De Groot [5].
For liquids there does not yet exist a satisfactory theoretical description, despite more than 150 years of research since the first description of thermophoresis by Ludwig [6] and Soret [7]. Theoretical descriptions fail to predict correct values of the Soret coefficient, and sometimes even fail to predict the correct sign. Hence, thermophoresis remains an area of active research, both on a theoretical and practical level. Below follows an overview of approaches applicable to large molecules or colloidal particles in suspension.

Thermophoresis of a Particle with a Thin Diffusive Layer

Ruckenstein [8] proposed that thermophoresis, diffusiophoresis and electrophoresis can be described as the result of a variation of the surface tension (due to a variation in the surface potential; see Fig. 1), so that the motion of a particle is analogous to the Marangoni effect, i. e.:

$$U_\mathrm{T} = -\frac{\varepsilon\varsigma^2}{32\pi\eta}\frac{\mathrm{d}\ln T}{\mathrm{d}z} \equiv -\frac{\ell}{\eta}\frac{\mathrm{d}\gamma}{\mathrm{d}T}\frac{\mathrm{d}T}{\mathrm{d}z}\,, \tag{3}$$

where $\ell = \chi^{-1}$ is the Debye length (i. e., the thickness of the diffusive layer), η the dynamic viscosity of the fluid, ς the surface potential, and $\gamma = \gamma_0 - \frac{1}{8\pi}\varepsilon\chi\varsigma^2$ is the interfacial tension (where the second term on the right is related to the total free energy of formation of the diffusive layer) [8].

T

Thermophoresis, Table 1 Diffusivity and Soret coefficients for different binary liquid mixtures

species	solvent	D [$\times 10^{-12}$ m^2/s]	S_T [K^{-1}]	Ref.
ethanol	water	1280	0.0056	[1]
DNA(27 bp)	water	36	0.013	[2]
DNA (5.6 kbp)	water	3.4	0.14	[2]
30 nm latex particles	water	15	∼2	[3]
490 nm polystyrene particle	water	0.9	∼0.5	[4]

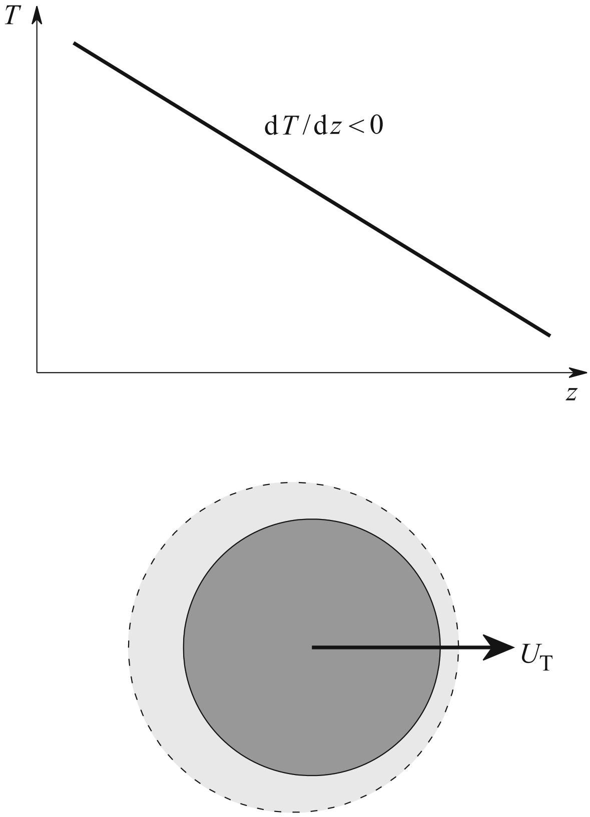

Thermophoresis, Figure 1 The thermophoretic motion of a small particle in a temperature gradient as the result of interfacial tension due to the diffusive layer around the particle; see Ruckenstein [8]

Hydrodynamic Models

Brenner [9] proposes a different description of fluid dynamics. He proposes that $\nabla \boldsymbol{v}$ in Newton's rheological law should not be based on the mass based velocity of the fluid, but on its 'volume velocity.' This is a controversial idea. The adapted Navier–Stokes equations provide a hydrodynamic description of thermophoresis and thermal creep. Bedeaux et al. [13] describe how this alternative approach of the transport equations can be validated experimentally by means of thermophoresis.

It would go too far to derive the complete set of equations here so we suffice with the thermophoretic velocity given by Brenner [9]. The thermophoretic velocity U of a sphere is:

$$U = -\frac{\alpha\beta}{1 + k_p/2k}\nabla T\,, \tag{4}$$

where α is the thermal diffusivity, β the thermal expansion, and k and k_p the thermal conductivity of the solvent and particle respectively.

Solvent Particle Interactions

The entropy of particle solvent interactions plays an important role in thermophoresis. The description by [5] of thermophoresis in gases is based on entropy. In complex fluids the entropy of the interaction between molecules or particles and solvent leads to thermophoretic motion. Schimpf & Semenov [10] consider the slip flow caused by a local pressure gradient set up by the temperature dependent properties of the particle and solvent. They find the same thermal expansion proportionality factor as Brenner [9] who does not consider these interactions.

Change of Sign of Soret Coefficient

The Soret coefficient is not a constant; it may vary due to changes in concentration or temperature. A positive Soret coefficient means a thermophobic particle. The Soret coefficient can change sign as a function of concentration [1] or temperature [3] (see Fig. 2). The inversion temperature for latex particles, which only have electrostatic interactions with water, lies close to the maximum density of the solvent at 4 °C. Iacopini et al. [3] conclude based on empirical findings that the thermal expansivity is the major factor in thermophoresis. They claim that this effect can be added to the Soret coefficient caused by the entropy production of particle solvent interactions. The similarity between the results of Brenner [9] and Schimpf & Semenov [10] suggests that this may be valid. For molecular mixtures, Haase [14], Kempers [15] and Rousseau et al. [16], have given important contributions.

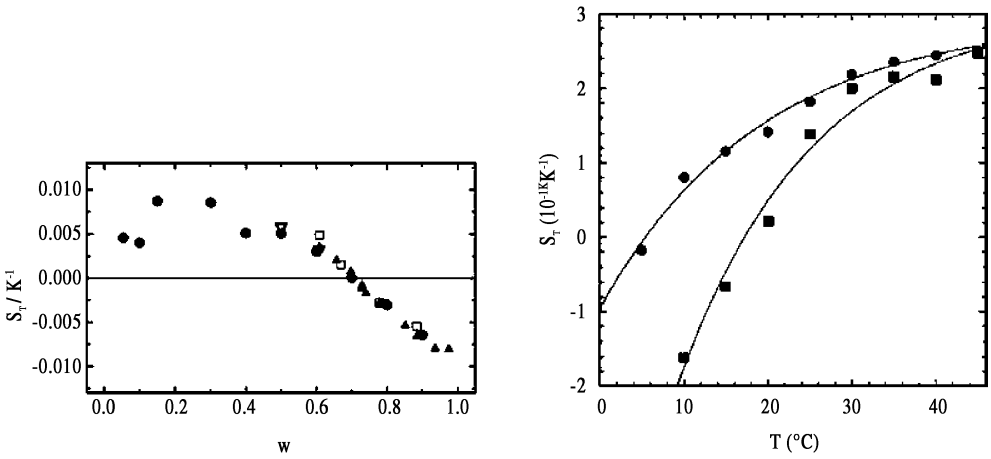

Thermophoresis, Figure 2 Inversion of the Soret coefficient. Left: Soret coefficient measurement of water ethanol mixtures, compiled from results obtained by different groups, which shows an inversion of the Soret coefficient for increasing ethanol weight fraction (from Wiegand [1]). Right: Soret coefficient measurement of latex particles (circles) and pMD31 DNA (squares), which shows an inversion of the Soret coefficient with decreasing temperature (from Iacopini et al. [3])

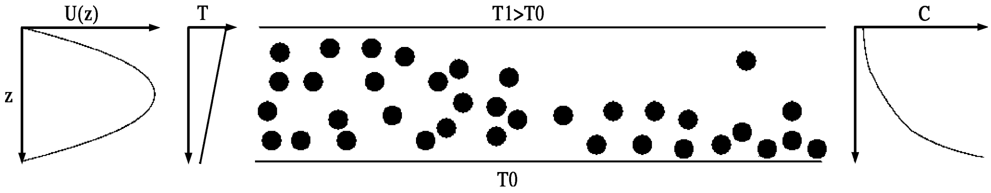

Thermophoresis, Figure 3 Thermophoresis of particles in a microchannel. The top wall has a higher temperature and repulses the particles for thermophobic particles (i. e., a positive Soret coefficient). An exponential concentration profile is established at the channel outlet

Examples of Application

Thermophoresis is applied in industry for the separation of (large) molecules or small particles from their solvent in so-called *thermal field flow fractioning* (TFFF) [11]. A down-scaled version of this process to microscopic scales demonstrated thermophoretic separation on microscopic scales [4, 12]. The advantage of using the very small confinement in a microfluidic device is that the separation times can be reduced, so that thermophoretic separation can be used. Braun & Libchaber [2] use a combination of thermophoresis and convection to concentrate DNA samples. The disadvantage of this approach is that it is a batch process.

As an example we estimate the timescales required to continuously separate a species in a microchannel (see Fig. 3). Consider a two-dimensional channel, e. g., a fluid between two parallel plates separated by a distance h. For low concentrations (i. e., $c \ll 1$) one finds the following stationary solution (i. e., $\boldsymbol{J}_\mathrm{m} = 0$) for the concentration:

$$c = c_0 \exp\left[-S_\mathrm{T}(T - T_0)\right] \qquad (5)$$

where c_0 and T_0 are a reference concentration and temperature respectively. The effectiveness of the separation is essentially given by the Soret coefficient. The time scale τ to reach the steady state is given by:

$$\tau = \frac{h^2}{\pi^2 D} \,. \qquad (6)$$

For a colloidal particle with a diameter d that is suspended in a fluid with a dynamic viscosity η, the diffusion constant is given by:

$$D = \frac{kT}{3\pi \eta d} \,, \qquad (7)$$

where k is the Boltzmann constant ($k = 1.38 \times 10^{-23}$ J/K). A typical particle diffusion coefficient is $D \sim 0.9 \times 10^{-12}\ \mathrm{m}^2/\mathrm{s}$ (e. g., $T \sim 300$ K, $\eta \sim 10^{-3}$Pa s, $d \sim 490$ nm). For a micro-channel (with a typical channel width of $h \sim 10 - 100$ µm) the time scale τ is typically of the order of $10 - 10^3$ seconds. This means that one has to use long microchannels in combination with low flow rates to establish a high separation ratio.

Another advantage of implementing thermophoretic separation at a microscopic scale is that one can reach very large temperature gradients without applying large temperature differences. For example, a 5 K temperature difference over a 50 μm channel implies a temperature gradient of $\sim 10^5$ K/m, while the absolute variation of temperature is limited. This is beneficial in the case of biological samples (cells, proteins, DNA) where large variations in temperature can disintegrate the samples. However, the difficulty lies in establishing and maintaining a temperature difference in a microfluidic device, which is complicated by the high conductivity and small dimensions at small scales. A design of a microfluidic device for thermophoretic separation is given by Geelhoed et al. [4].

Cross References

► Diffusiophoresis
► Electrophoresis

References

1. Wiegand S (2004) Thermal diffusion in liquid mixtures and polymer solutions. J Phys Condens Mat 16:357–379
2. Braun D, Libchaber A (2002) Trapping of DNA by thermophoretic depletion and convection. Phys Rev Lett 89:188103
3. Iacopini S, Rusconi R, Piazza R (2006) The macromolecular tourist. Eur Phys J E 19:59–67
4. Geelhoed PF, Lindken R, Westerweel J (2006) Thermophoretic separation in microfluidics. Chem Eng Res Des 84:370–373
5. de Groot SR (1951) Thermodynamics of Irreversible Processes. NHCP, Amsterdam
6. Ludwig C (1856) Sitz. ber. Akad. Wiss. Wien. Math-Nat wiss Kl 20:539 (cited in Wiegand [1])
7. Soret C Arch (1879) Geneve 3. 48 (cited in Wiegand [1])
8. Ruckenstein E (1981) Can phoretic motions be treated as interfacial tension gradient driven phenomena? J Colloid Interf Sci 83:77–81
9. Brenner H (2005) Navier-Stokes revisited. Physica A 349:60–132
10. Semenov S, Schimpf M (2004) Thermophoresis of dissolved molecules and polymers: Consideration of the temperature-induced macroscopic pressure gradient. Phys Rev E 69:011201
11. Kowalkowski T, Buszewski B, Cantado C, Dondi F (2006) Field-flow fractionation: theory, techniques, applications and the challenges. Cr Rev Anal Chem 36:129–135
12. Edwards TL, Gale BK, Frazier AB (2002) A microfabricated thermal field-flow fractionation system. Anal Chem 74:1211–1216
13. Bedeaux D, Kjelstrup S, Öttinger HC (2006) On a possible difference between the barycentric velocity and the velocity that gives translational momentum in fluids. Physica A 371:177–187
14. Haase R (1990) Thermodynamics of Irreversible Processes. Dover, London
15. Kempers LJTM (2001) A comprehensive thermodynamic theory of the Soret effect in a multicomponent gas, liquid or solid. J Chem Phys 115:6330–6341
16. Rousseau B, Nieto-Draghi C, Bonet Avalos J (2004) The role of the molecular association in the change of the sign of the Soret coefficient in aqueous mixtures Europhy. Lett 67:976–982

Thermopneumatic Membrane Valve

► Thermopneumatic Valve

Thermopneumatic Valve

EUI-HYEOK YANG
Department of Mechanical Engineering, Stevens Institute of Technology, Hoboken, NJ, USA
eyang@stevens.edu

Synonyms

Thermopneumatic membrane valve

Definition

A thermopneumatic valve is a type of micromachined active valve operated by the volumetric thermal expansion of a heated gas or heated liquid in a sealed chamber [1].

Overview

The rapid development of new methods of fabrication and microfluidic components enables the desired control and manipulation of small amounts of fluids. The microvalves in microelectromechanical systems (MEMS) are essential elements of a micro total analysis system. Typically, there are two types of microvalve: one is the passive valve the operation of which is dependent upon its surrounding pressure conditions; the other is the active valve, which can be controlled actively. Active valves are categorized in three major ways: initial working state, control pattern, and actuation principle. Each microvalve has advantages and disadvantages from the viewpoint of power consumption, integration method, response time, operation frequency and voltage, fabrication process, and actuation efficiency. Among the various types of microvalves, thermopneumatic actuation provides a large achievable volume stroke and simple fabrication process relative to other actuation methods for microvalves [1].

A thermopneumatic valve typically consists of a moveable valve diaphragm, a valve seat, and a resistive heater in a sealed cavity. While electrical power is applied to the resistive heater, the initial volume of gas in the sealed chamber expands. Using the volumetric change of the heated gas in the cavity, the diaphragm structure

is deformed and subsequently blocks the fluidic path. Heated effluents (in liquid form) can also be used for thermopneumatic actuation using the phase transition to gas [2, 3]. A thermopneumatic microvalve can be fabricated with rigid materials such as silicon, metal, and glass. The silicon-based valve devices often face issues such as reliability (cycles or time to failure), wear/tear, residual stress, and high production cost. The residual stress is one of the major issues in MEMS devices. As shown in Fig. 1 [4], a corrugated structure can be used for minimizing the process-dependent residual stress of boron-doped silicon film [5]. Its effectiveness is verified experimentally through comparison between the static deflection characteristics of flat and corrugated diaphragms (Fig. 2) [4]. The development of the soft-lithography process [6, 7] allows the rapid prototyping of microfluidics devices. Elastomers possess outstanding mechanical and optical properties, which can provide effective solutions to overcome the limitations of silicon-based microvalves. By choosing elastomers as valve materials, several issues such as valve efficiency, capacity, power consumption, response time, leakage, closing force, biocompatibility, and biochemical compatibility can be addressed. These can also allow the large-format integration of thermopneumatic microvalves with a thin PDMS membrane [8]. For more reliable operation of thermopneumatic microvalves, Parylene C (i. e. gas-impermeable layer) can be deposited on PDMS (i. e. non-porous rubbery elastomer with high gas permeability).

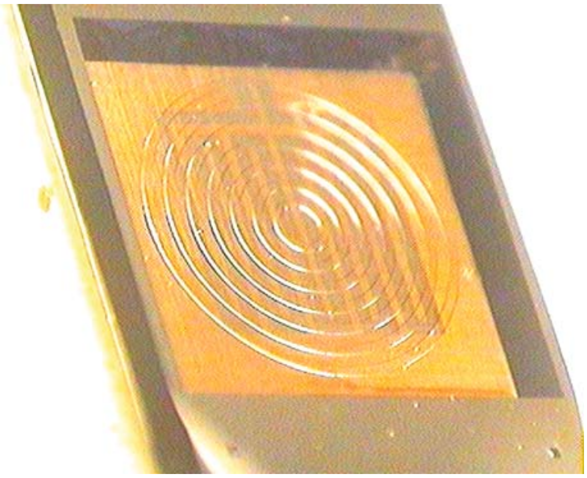

Thermopneumatic Valve, Figure 1 Thermopneumatic actuator consisting of a corrugated p+ silicon diaphragm as the residual stress relaxation structure and a microheater for thermopneumatic actuation [4]

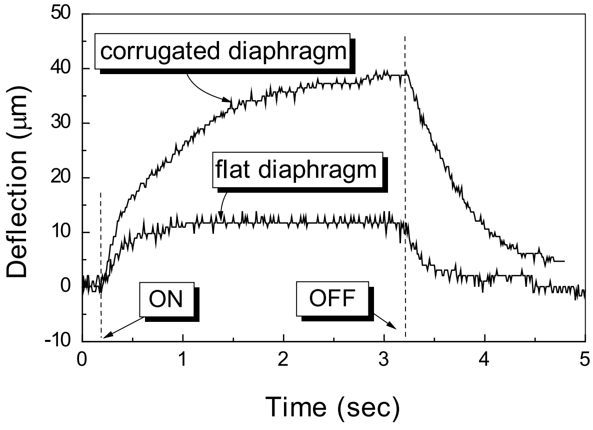

Thermopneumatic Valve, Figure 2 Time response of the static deflection of thermopneumatic actuators with a corrugated and a flat diaphragm [4]

Cross References

► Thermopneumatic Pump

References

1. Oh KW, Ahn CH (2006) A review of microvalves. J Micromech Microeng 16:R13–R39
2. Yang X, Grosjean C, Tai YC, Ho CM (1998) A MEMS Thermopneumatic Silicone Rubber Membrane Valve. Sens Actuators A 64:101–105
3. Sim WY, Yoon HJ, Jeong OC, Yang SS (2003) A phase-change Type Micropump with Aluminum Flap Valves. J Micromech Microeng 13(2):286–294
4. Jeong OC, Yang SS (2000) Fabrication of a Thermopneumatic Microactuator with a Corrugated p+ Silicon Diaphragm, Sens Actuators A 80(1):62–67
5. Yang EH, Yang SS, Yoo SH (1995) A Technique for Quantitative Determination of the Profile of the Residual Stress along the Depth of *p*+ Silicon Films, Appl Phys Lett 67(7):912–914
6. Unger MA, Chou H, Thorsen T, Scherer A, Quake SR (2000) Monolithic Microfabricated Valves and Pumps by Multilayer Soft Lithography. Science 288:113–116
7. McDonald JC, Whitesides GM (2002) Poly(dimethylsiloxane) as a Material for Fabricating Microfluidic Devices. Acc Chem Res 35(7):491–499
8. Baechi D, Buser R, Dual J (2002) A High Density Microchannel Network with Integrated Valves and Photodiodes. Sens Actuators A 95:77–83

T

Thermoresistive Flow Sensors

Jing Liu
Cryogenic Lab, Technical Institute of Physics and Chemistry, Chinese Academy of Sciences, Beijing, China
jliu@cl.cryo.ac.cn

Synonyms

Hot wire; Hot film

Definition

A *thermoresistive flow sensor* refers to the flow measurement element based on monitoring the thermal states of an electrically heated sensor whose dependence on the heat loss represents the flow rates of the surrounding fluid. The thermoresistivity of a sensor reflects its variation in electrical resistivity with temperature. A sensor element should usually have a sufficiently high temperature coefficient of resistance (TCR). Typical sensor materials are platinum, nickel, or polysilicon with a specific TCR in the order $\sim 10^{-3}$ °C. The highest measured resolution for the latest thermoresistive flow sensors has reached the order of $\sim$ nl/min.

Overview

Most commonly used microflow sensors are based on thermal principles [1]. Owing to its superior simplicity, which allows it to be integrated in a MEMS device, the thermoresistive flow sensor has been widely adopted in a variety of practical situations such as: biomedical and home applications, environmental monitoring, process control, microanalysis systems etc. [2, 3]. The dependence on the heat loss between a fine wire or thin film, which serves as the sensor, and the surrounding fluid has traditionally been among the most accepted methods for measuring fluid flow [4]. A thermoresistive flow sensor refers to the flow measurement element based on monitoring the thermal states of an electrically heated sensor immersed in or besides the flowing fluid medium such as a gas or liquid [5]. It usually works when the other physical properties of the fluid such as temperature, composition, density, and pressure are constant, therefore the only variable which affects the heat transfer of the sensor is the flow rate.

A microthermoresistive flow sensor can be composed of a variety of combinations of heat sources and temperature sensors. It typically consists of a heater and one or more temperature sensors [1, 6]. Up to now, thermistor principles, geometries, and sensor materials have been found in a wide variety of combinations from CMOS compatible thermocouples to thermistors with different material compositions and geometries, from bridge structures to membranes [6]. The fluid (a gas or liquid) can either flow over the entire chip or over a controlled area of the chip through an integrated microchannel [2]. The flow rate is estimated by measuring the heating power, heater temperature, fluid temperature, and the time-of-flight of a heat pulse.

The electrical resistance of a thermoresistive flow sensor can be calibrated as a change in the temperature. A linear relation between them is usually adopted, i. e.

$$R(T) = R(T_0)\left[1 + \alpha (T - T_0)\right] \tag{1}$$

where $R(T)$ is the sensor resistance at operating temperature T; $R(T_0)$ is the sensor resistance at the reference temperature T_0; α is the temperature coefficient of resistance, which includes the effects of lead and wire resistance change and may depend on a reference temperature. When an electrical current I_0 is applied on a thermoresistive flow sensor and its self-Joule heating is maintained at a constant level, any fluid flow through the sensor will cause a shift in its temperature and thus resistance R, respectively. As a result, a decrease in the voltage V $(= I_0 R)$ of the sensor will be detected. The aim of the thermoresistive flow sensor is to evaluate such changes caused by variations of the flow rate alone.

The most typical electrical circuits for control and evaluation of a thermoresistive flow sensor are based on the well-known Wheatstone bridge using either the constant-current or the constant-temperature mode, respectively [4]. In a constant-current circuit (see Fig. 1a), resistors R_3 and R_4 at the two arms are much larger than the sensor resistor R_1. Therefore, the electrical current through R_1 is essentially independent of the changes in the sensor resistor R_1. Any flow in the channel cools the hot wire, decreases its resistance as given by Eq. (1), and unbalances the bridge, which then produces an output voltage V. The voltage V is generally small and must be amplified before it is recorded [4]. The values of the TCR α for R_1 and the variable resistor R_2 should be equal in order to eliminate any signal errors due to changes in the ambient temperature. The values of TCR for R_3 and R_4 should also be equal.

A constant-temperature Wheatstone bridge is shown in Fig. 1b. The circuit bridge is balanced in advance under noflow conditions using the variable resistor R_2. Therefore with the flow of the fluid, the hot wire or film is cooled and its resistance decreases and unbalances the bridge. A differential amplifier would then balance the bridge with a feedback voltage [4]. Such electrical output correlates directly with the flow rate.

Traditionally the thermoresistive flow sensor appears as a wire or film embedded inside the flow field. In a microfluidics-related measurement, the microthermal sensor is usually mounted in the wall of a microchannel to avoid disturbing the flow and thus accurately measure the fluid. Due to the highly confined geometry, a complicated MEMS technique has to be adopted for the fabrication of the thermoresistive flow sensor. At present, most of the commercially available sensors are usually inadequate for precise flow control in microfluidics because of their limited sensitivity, large size, high dead volume, and difficulties in interfacing with microfluidic devices [7]. Miniaturization of a sensor in micro- or nanoflow is therefore a necessity, since only a small size will allow for a precise, local and high transient resolution in temperature measure-

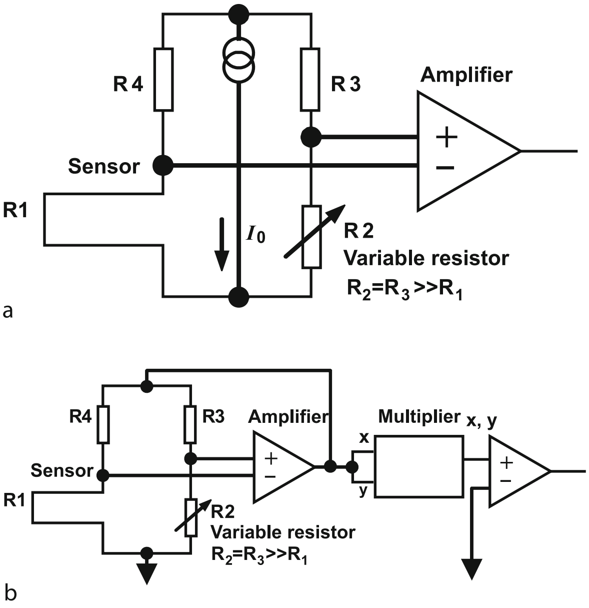

Thermoresistive Flow Sensors, Figure 1 Wheatstone bridge circuit for control and evaluation of hot-wire or hot-film sensor: (**a**) constant-current bridge; (**b**) constant-temperature bridge. Modified from [3]

ment, power reduction, and integration with devices [6]. Overall, the microthermoresistive flow sensor relies heavily on miniaturization and innovation of different well-established thermal macroflow sensing principles. There are three main types of thermal flow sensor which combine the evaluation methods and heater modes: hot-wire (hot-film), calorimetric, and time-of-flight [1]. Each of these sensors types can be further categorized according to their thermal sensing principle as: thermoresistive, thermocapacitive, thermoelectric, thermoelectronic, or pyroelectic. Only the thermoresistive flow sensor will be illustrated in this essay. To interpret the mechanisms of using such sensors to measure the flow parameters, typical principles, and practical design of the device will be considered. Some fundamental issues which will require further investigation are noted.

Basic Methodology

Principle

The operating modes for the microthermoresistive flow sensor are similar to their conventional bulk ones. For traditional research applications, cylindrical sensors which take the form of either a fine wire (typical diameters of 1 – 15 μm) or a cylindrical film (typical diameters of 25 – 150 μm) are the most common. The wire sensor is mainly used for clean air or gas measurement due to its fragility, while hot-film sensors can be used in both liquid and contaminated-gas environments [4]. A major difference between a microthermoresistive flow sensor and its traditional counterpart is that, the former has to be made using micro- or nanofabrication technologies such as bulk micromachining, surface micromachining, epimicromachining, and LIGA-techniques, etc. These new sensors have been able to measure very small flows in the nanoliter and microliter ranges. Depending on the location of the heating and sensing elements, the flow sensors can be either intrusive (lying in the fluid), or nonintrusive (located outside the flow). The intrusive type has many limitations such as disturbing the fluid, easy corrosion or damage, and difficulty in integrating with the channel [4]. Thus, it is more common for nonintrusive thermal sensors to be used in micro- or nanofluidics. The sensors are often embedded in the wall of a microchannel for flow measurement.

The three existing types of thermoresistive flow sensor are generally classified as hot-film, calorimetric, and time-of-flight type, respectively. The basic operating principle of a hot-film flow sensor is based on microconvective heat transfer from a heated thin-film sensing element (also called a heater) to a liquid flowing inside a microchannel [7]. When the sensor (heater) is subjected to a constant current heating, forced convection by the flow causes a decrease in the heater temperature. The flow rate of the fluid can be identified by detecting the effect of the flowing fluid to the sensor. Figure 2a illustrates the geometric design of such an MEMS flow sensor and its operating principle. Here, the heater is built on the wall of the microchannel. By detecting the sensor temperature, one can obtain the liquid flow rate using a precalibrated experimental curve for temperature versus flow rate (see Fig. 2b). In terms of the calorimetric principle, a widely used microthermoresistive flow sensor is the ►thermal anemometer, which typically consists of a middle heater with an upstream and downstream temperature sensors, relative to the flow direction [2]. Such a calorimetric sensor is based on measuring the asymmetry temperature profile around the heater, modulated by the fluid flow [1, 8]. The schematic representation of a calorimetric device and the temperature distribution in the flow direction are shown in Fig. 3. The MEMS flow sensor consists of three electrical resistors which are mounted directly onto the substrate at the bottom of the fluidic channels. The heating element is located in the middle of the flow channel and is symmetrically encircled by two sensor elements. This symmetric arrangement makes the sensor insensitive to fluctuations in the ambient temperature and enables the flow direction to be detected. The resulting temperature gradient is detected by the two ►temperature sensitive resistors. At zero flow rate, no convection exists in the channel and the heat generated will be transmitted by diffusion. As

T

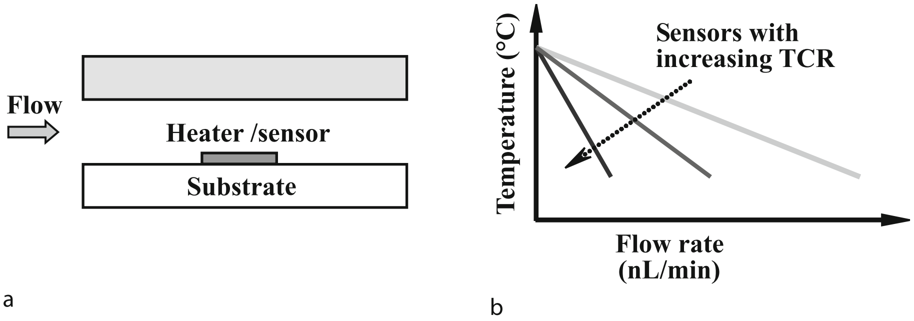

Thermoresistive Flow Sensors, Figure 2 Principle for a single hot-wire or hot-film sensor to measure microchannel flow. (**a**) Sensor configuration; (**b**) Sensor temperature

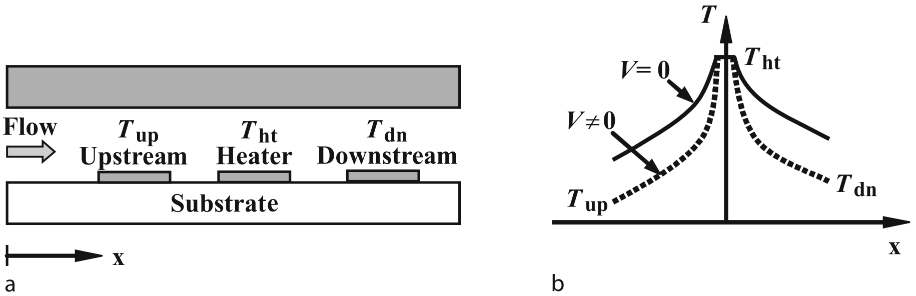

Thermoresistive Flow Sensors, Figure 3 Schematic diagram for calorimetric principle: (**a**) flow microsensors: (**b**) temperature distribution for flow measurements. Modified from [7]

the temperature distribution surrounding the heater is symmetric, no temperature difference is detectable (see Fig. 3). The diffusion can be split into two contributions: the diffusion through the substrate, and that into the fluid via the upstream and downstream directions. Due to heat dissipation, the temperature change is reduced, and may be lower than the detection limit [9]. An increase in the flow velocity shifts the temperature maximum into the direction of the flow. The flow measurement is therefore achieved by the temperature difference between the downstream and upstream sensor microfilaments, whose correlation with the flow rate can also be precalibrated.

The flow measurement principle for the time-of-flight sensor is illustrated in Fig. 4. In this method, the time taken for a heat pulse to pass over a known distance is recorded. The heat pulse generated by an electrical pulse applied to the heater microfilm travels due to the fluid flow and is detected by a sensor microfilm [8, 10]. The time between the heat pulse generation and its detection can then be used for flow estimation (Fig. 4b).

In each of the above thermoresistive flow sensors, the sensor elements are powered by an electrical current like that shown in Fig. 1. The electrical components used for the heater can operate either in a constant heating temperature or in a constant heating current mode depending on whether or not a feedback loop circuit is adopted [1, 2, 5]. The former usually has a fast response. In order to detect the differential voltage, a specific test circuit needs to be manufactured on the device in advance.

Sensitivity of Thermoresistive Flow Sensor

The highest flow measurement resolution for a thermoresistive flow sensor has been in the order of nano- or microliters. To illustrate the basic method of characterizing the sensitivity of a thermoresistive flow sensor, we consider here only a single sensor element for a Lab-on-Chip application, i. e., the hot-film case. For a single thermoresistive element, it utilizes a miniaturized adaption of the anemometric principle. The combination of an established detection principle with the benefits of microtechnology has resulted in a sensor with very high sensitivity [9].

Electrically, the flow-induced output voltage change for the circuit such as shown in Fig. 1a can be written as [7]

$$\Delta V = I_0\left[R(T) - R(T_0)\right] = V_0 \alpha \Delta T \tag{2}$$

where I_0 is the constant current, $V_0 = I_0 R(T_0)$, $\Delta T = T - T_0$.

If the sensitivity (S_V) of a sensor is defined as the ratio between the changes in the sensor output voltage and flow

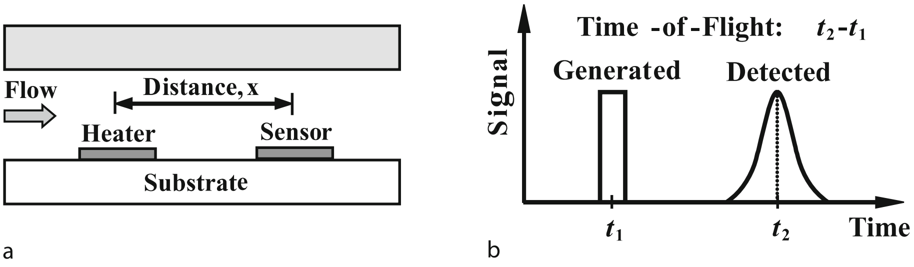

Thermoresistive Flow Sensors, Figure 4 Flow measurement by time of-flight principle. (**a**) Sensor configuration; (**b**) Sensor signal. Modified from [7, 9]

rate (Q), i. e., $S_V = \Delta V/\Delta Q$, one has

$$S_V = V_0 \alpha \frac{\Delta T}{\Delta Q} = V_0 \alpha S_T \tag{3}$$

where $S_T = \Delta T/\Delta Q$, represents the temperature–flow ratio, and is related to the sensor structure design and fluid properties. The sensitivity can be assessed in an average sense by the slope of a straight line fitted to the measurement data. In the microflow measurement, if the temperature variation of the sensor is recorded, the flow rate of the fluid can then be estimated through curve fitting.

Further, S_V may involve an original bias voltage that is not related to the sensor design. Thus, it is more appropriate to normalize the sensitivity by the initial bias signal and define the relative sensitivity as [7]

$$S_{V/V_0} = \frac{\Delta V/V_0}{\Delta Q} = \alpha \frac{\Delta T}{\Delta Q} = \alpha S_T \tag{4}$$

As indicated by Eq. (4), the relative sensitivity is proportional to both the TCR and S_T. It should be noted that the former is related to the sensing material properties and the latter to the sensor configuration design. This suggests that a better resolution can be achieved through an improvement of these two factors.

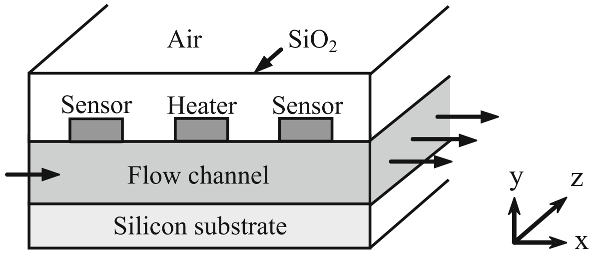

Thermoresistive Flow Sensors, Figure 5 Side view geometry for a typical calorimetric flow sensor with a middle heater and upstream and downstream temperature sensor. Modified from [2]

System Level Modeling

Modeling the electrical, thermal, and fluidic behavior of a microfluidic flow sensor and its surrounding structures will provide comprehensive information on many of the physical and dynamic behaviors of the thermoresistive flow sensors located within microfluidic environments [2]. An accurate device model and simulation offer the designer many advantages such as: reducing the time needed for the development cycle and providing the possibility for device optimization through software instead of iterations on physical devices. This, in turn, helps to reduce the end cost of the device. Here, we will focus on the thermal and fluidic modeling. The electrical effect of the sensor will be attributed to a lumped heat source term which appears in the thermal fluidic models.

Simulation on a flow sensor with its integrated control and signal processing electronics has to simultaneously take into consideration several different domains including the electrical (circuit electronics), heat transfer (thermal phenomena), and fluid flow [2].

As shown in Fig. 5 for the three-dimensional structure of a typical ►thermal anemometer, different types of heat transfer occur in and around the microchip structure [2]. Based on the model developed previously [2], a complete modeling of the thermal state of the flow sensors can be obtained as follows.

Clearly, conduction occurs in the SiO_2 layer, insulating the three flow sensor elements, the flow sensor elements themselves, and the bottom silicon substrate wall of the microchannel. The equations for characterizing the thermal state of these elements can thus be expressed as, respectively, [2]

$$\text{for SiO}_2\text{ layer:}\quad k_{SiO_2} \nabla \cdot (\nabla T) = (\rho c)_{SiO_2} \frac{\partial T}{\partial t} \tag{5}$$

$$\text{for heater:}\quad k_p \nabla \cdot (\nabla T) + \dot{q}_{heat} = (\rho c)_p \frac{\partial T}{\partial t} \tag{6}$$

$$\text{for sensors:}\quad k_{sens} \nabla \cdot (\nabla T) + \dot{q}_{sens} = (\rho c)_{sens} \frac{\partial T}{\partial t} \tag{7}$$

T

$$\text{for silicon substrate:} \quad k_{\mathrm{Si}} \nabla \cdot (\nabla T) = (\rho c)_{\mathrm{Si}} \frac{\partial T}{\partial t} \tag{8}$$

where k_{SiO_2}, k_p, k_{sens}, and k_{Si} are the thermal conductivities of the SiO_2 layer, polysilicon heater, sensor, and silicon substrate, respectively; $\dot{q}_{heat}$ and $\dot{q}_{sens}$ are the Joule heating rates at which energy is generated per unit volume of medium for the electrical heater and sensor, respectively; ρ and c are the density and specific heat for each of the solid materials, respectively.

Forced convection occurs in the microchannel where the liquid flowing through the microchannel carries heat away from the heater location. The liquid flowing through the microchannel is governed by the Navier–Stokes equations. By assuming that the flow includes viscous dissipation, the flow equations can be reduced to

$$k_{\mathrm{f}} \nabla \cdot (\nabla T) + \mu \left(\frac{\partial u}{\partial y}\right)^2 = \rho c_{\mathrm{p}} \left[\frac{\partial T}{\partial t} + u(y) \frac{\partial T}{\partial x}\right] ;$$
$$u(y) = 4u_{\max} \left[\frac{y}{d} - \left(\frac{y}{d}\right)^2\right] \tag{9}$$

where k_f, ρ, c_p, and μ are the thermal conductivity, density, specific heat, and viscosity of the fluid, respectively; u is the velocity of the fluid and u_{max} is the velocity of flow at the center line of the microchannel; d is the gap distance of a microchannel with a rectangular cross-section.

At the top surface of the SiO_2 layer in the device, natural convection and radiation occur due to heat being conducted to the surface of the device from the sensor heater. The boundary equation there can thus be formulated by equating the conduction of heat through and the effective convection on the top surface, i. e.

$$-k_{\mathrm{SiO_2}} \frac{\partial T}{\partial y} = h\,(T - T_\infty) \tag{9}$$

where h is heat transfer coefficient which has included the convection effect and radiation on the device surface, and T_∞ is the temperature in the free stream flow.

A constant temperature is assumed at the entrance of the microchannel bearing in mind that this site is exposed to the ambient temperature, i. e.

$$T\,(x = 0) = T\,(x = L) = T_\infty \tag{10}$$

where L is the length of the microchannel.

To obtain the above equations in a closed form, a series of continuum equations still need to be established. At the interfaces between the heater, sensor, and the surrounding solid material, there is a continuum equation which characterizes the heat conduction at the two sides. A convective heat transfer equation similar to Eq. (9) should be used for the interfaces between a solid surface and the surrounding flowing fluid.

A complete simulation of the above coupled equations and boundary conditions would help to give a complete picture of the detailed working process of the thermoresistive flow sensor including the electrical, thermal, and fluidic phenomena [2]. It would also provide a useful way to optimize the geometry and material of the whole fluidic device.

Device Fabrication

Realization of a flow sensor depends on its specific application. Overall, the spatial and transient resolution and the compatibility of the sensor within the desired device are of major concern [6]. In addition, the protection of the fluids and components demands a reduction in the thermal crossover from the flow sensor. The microflow sensors are usually automatically integrated with the microchannel during the fabrication process. The sensing element should be a resistor that has a resistance with high temperature sensitivity [2, 4, 9]. The heater of the sensor is often fabricated from a platinum or polysilicon resistor and acts as a microheater while the upstream and downstream temperature sensors are made from either polysilicon resistors or thermopiles. Such materials have excellent chemical resistance, biocompatibility, and high TCR [9].

The fabrication of a flow sensor includes making the microchannel and integrated sensor elements. Taking the fabrication of a single heater sensor in a suspended microchannel as an example, the general process involves the following basic sequences (Fig. 6) [7]: Fig. 6a: silicon wafer is often used as substrate. Its surface can be deposited with a thin silicon nitride layer as electrical insulation. A sacrificial PSG layer is then deposited and patterned on top of silicon nitride to define the microchannel geometry. Fig. 6b: Following the above procedure, another silicon nitride layer is deposited above the PSG surface to act as the top wall of the microchannel. After etching the PSG by HF, a microchannel can be formed. Fig. 6c: A polycrystalline silicon layer is deposited on the silicon nitride as the sensor, and then doped by B^+ ion implantation to improve its performance. This is followed by an annealing process. After that the polysilicon is patterned by plasma dry etching to define the sensor geometry. Fig. 6d: The sensors are sealed by uniformly depositing a thin silicon nitride layer. The inlet and outlet are then opened by KOH. Subsequently, contact opening and Al metallization will form connections between the macroworld and the sensing element. Finally, thermal iso-

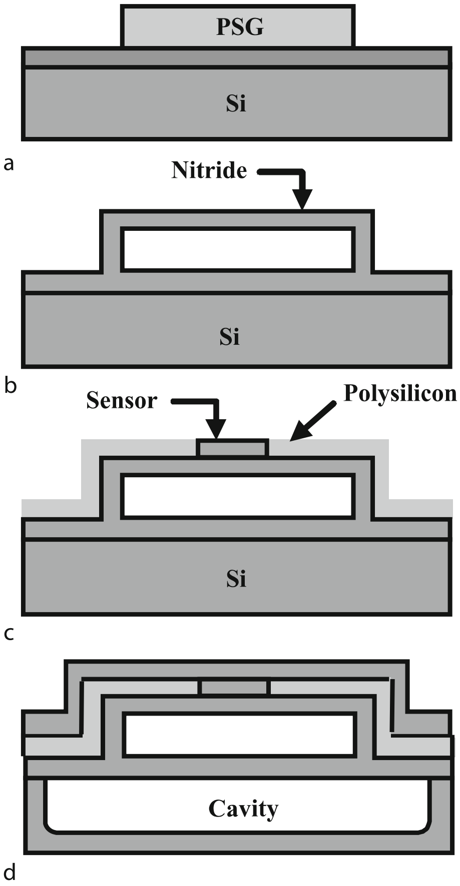

Thermoresistive Flow Sensors, Figure 6 Main process steps for fabrication of MEMS flow sensors. Modified from [6]

lation of the channel is achieved by removing the silicon directly underneath the channel using gas-phase isotropic etching by BrF_3 or XeF_2. In this way, an integrated thermoresistive flow sensor with a microchannel is made. In a practical design, the structure, material and configuration, even the fabrication approaches (see Fig. 6) are subject to change depending on various specific demands.

Key Research Findings

Material matching is a critical issue when making a high quality sensor system. For example, Ni and Pt thin films have often been used as temperature sensing elements on GaAs substrate because of their high temperature coefficients and compatibility with GaAs-based devices and related IC processing steps [11]. But when deposited directly on GaAs, both films exhibit high chemical reactivity and interdiffusion effects on the GaAs interface mainly at elevated temperatures, which can lead to the degradation of their electrical and thermal properties. In order to suppress the interfacial interactions, a thin diffusion barrier layer has to be formed on the GaAs surface before the deposition of the Pt and Ni [11].

Several factors determine the measurement resolution of the microflow sensor [11]. First, the sensitivity of the sensor depends on the heater's TCR. Adoption of an appropriate doping concentration of the polysilicon thin film would improve the measurement resolution. For example, a slightly doped heater increases its resistance and hence reduces inaccuracies arising from the resistance of the leads and wires. Second, *thermoresistive flow sensors* require extremely good thermal isolation to avoid heat conduction in the wall. For the channel in direct contact with the substrate, the heat loss from the heater to the substrate may considerably reduce the sensor's sensitivity to the fluid flow. As a remedy, the microchannel can be suspended from the substrate to improve the thermal isolation. In this way, a flow rate measurement resolution in the nanoliter per minute range is possible [11]. On the other hand, it is also useful to insert a thermal insulation between the substrate and the fluidic channel. Further, to assure a fast response and low power consumption, free-standing microfilms with reduced dimensions and good thermal isolation are also very helpful. They are usually implemented using surface micromachining [8]. Such devices can be applied to both gas and liquid flow measurements and permit dynamical operation with complex heating and possible evaluation of the fluid flow parameters.

The maximum temperature measurement resolution depends on the spatial position of the sensor elements with reference to the distance between the heater and the sensor which can also be optimized. Computational modeling and simulation can provide a predictive capability and the means of evaluating the performance of a new design before hardware fabrication. The effect of varying the geometries of sensors and channel can be tested numerically, with different aspect ratios between them. Further, most fluid properties, which determine the heat transfer process, depend on the working temperature. It should be noted that, some changes to the fluid due to heating may not always be easily compensated. Therefore, accurate thermal flow sensors require both flow calibration and calibration for temperature compensation [4].

Future Directions for Research

Except for the normal microsize sensor devices, which have already been strenuously tested, much smaller *thermoresistive flow sensors* are in urgent need of investigation. However, this may involve a series of new challenges. With the decrease in the flow channel and sensor, conventional flow and heat transport theories may not be valid

to explain the phenomena, due to the multiple physical effects that are involved. Currently, there is still a strong lack of fundamental knowledge on such issues. In particular, the coupled momentum, electrical and heat transfer phenomena in the basic components of the flow sensor and the surrounding fluid and solid components are not well understood. It is possible that if the size becomes smaller, the flow and heat transfer, electrical field, and even mechanical properties such as the expansion effect in such devices may tend to behave differently compared to the behavior of their bulk objects. For example, the inertial force tends to be quite small and the surface effects, the electrical double layer, which were unimportant in the bulk device, will play a dominating role. Friction, electrostatic forces, and viscous effects due to the microfluid and channel may become increasingly important as the devices become smaller. Further, whether or not the specific fluid, usually a biosample, will follow the behavior of Newtonian fluids needs to be clarified experimentally. Additionally, with multispecies such as biological samples or chemical compounds in the micro- or nanofluidics, the thermoresistive flow sensor may encounter difficulty in realizing a high measurement solution and good repeatability. Multiparameter detection in micro- or nanoflows is thus a big challenge.

Overall, a large number of variables determine the measurement resolution of a thermoresistive flow sensor. Among the effects which influence the measurement, sensor material characteristics and liquid flow mode, the channel property, the flow quality, multicomponents, liquid properties and geometry of microchannels all need to be addressed. Previous investigations have provided quite substantial experimental data on the thermoresistive flow sensor. Future study can choose to follow some of the existing technical routes by carefully evaluating the size effects. Clearly, a complete modeling of the various domains in the flow sensor and incorporating the electrical, thermal and fluidic effects into the model are also worth investigating.

Cross References

- ▶ Control of Microfluidics
- ▶ Digital Microfluidics
- ▶ Flow in Channels with 3D Elements
- ▶ Fluid Metering
- ▶ Fluidic Nanosensors
- ▶ Heat Transfer in Microchannel Flows
- ▶ Temperature Control in Microfluidic Systems
- ▶ Implication for Biomedical Applications
- ▶ Methods for Flow Rate Measurements
- ▶ Micro- and Nano-Scale Anemometry: Implication for Biomedical Applications
- ▶ Microfluidic Circuits
- ▶ Temperature Sensitive Resistor
- ▶ Thermal Anemometer
- ▶ Thermoresistive Flow Sensors

References

1. Kallio P, Kuncova J (2004) Microfluidics. Tekes Technol Rev 158/2004:1–33
2. Rasmussena A, Mavriplisa C, Zaghloula ME, Mikulchenkob O, Mayaram K (2001) Simulation and optimization of a microfluidic flow sensor. Sens Actuators A 88:121
3. Xu Y, Chiu CW, Jiang F, Lin Q, Tai YC (2005) A MEMS multisensor chip for flow sensing. Sens Actuators A 121:253
4. Nguyen NT (1999) Thermal mass flow sensor. In: Webster JG (ed) Mechanical Variables Measurement: Solid, Fluid, and Thermal. CRC Press, Boca Raton, Florida
5. Cheremisinoff NP, Cheremisinoff PN (1988) Flow Measurement for Engineers and Scientists, pp 76–113. Dekker, New York
6. Ernst H, Jachimowicz A, Urban GA (2002) High resolution flow characterization in Bio-MEMS. Sens Actuators A 100:54
7. Wu SY, Lin Q, Yuen Y, Tai YC (2001) MEMS flow sensors for nano-fluidic applications. Sens Actuators A 89:152
8. Rodriguesa RJ, Furlan R (2003) Design of microsensor for gases and liquids flow measurements. Microelectron J 34:709
9. Schöler L, Lange B, Seibel K, Schäfer H, Walder M, Friedrich N, Ehrhardt D, Schönfeld F, Zech G, Böhm M (2005) Monolithically integrated micro flow sensor for lab-on-chip applications. Microelectron Eng 164:78–79
10. Rodrigues RJ, Furlan R (2002) Development of a time-of-flight flow microsensor. In: Proceedings of 17th Symposium on Microelectronics Technology and Devices
11. Lalinský T, Držík M, Jakovenko J, Husák M (2005) GaAs thermally based MEMS devices: fabrication techniques, characterization and modeling. In: Leondes CT (ed) MEMS/NEMS Handbook: Techniques and Applications, vol 3. Springer, New York

Thermosensitive Hydrogels

▶ Temperature-Sensitive Hydrogels

Thick Film Lithography

▶ Thick Resist Lithography

Thick-Film Piezoelectric Actuation

▶ Membrane Actuation for Micropumps

Thick Resist Lithography

Clifford L. Henderson
School of Chemical & Biomolecular Engineering,
Georgia Institute of Technology, Atlanta, USA
cliff.henderson@chbe.gatech.edu

Synonyms

Thick film lithography

Definition

Thick film lithography refers to the processes used to make thick films of photoresist, i. e. typically "thick film" is used to refer to films that 5 to 100's of μm (μ) thick, and subsequently produce relief patterns in those films. The *photoresist* is a radiation sensitive material that is applied to a substrate surface, exposed to radiation to create a physiochemical change in the exposed regions, and washed in a developer solution to produce the desired physical relief patterns.

Overview

Lithography in the most general sense refers to methods used for printing on a smooth surface. It has its origins in methods used to print text and artwork onto paper or other suitable materials in the late 1700's. In the context of microfabrication and microsystems today (e. g. integrated circuits, microelectronic devices, microelectromechanical systems, and microfluidic devices), it refers to the processes used to form relief patterns in the photoresist films that are subsequently used in the layer-by-layer fabrication sequences of such micro-scale devices. It is also commonly referred to as microlithography or nanolithography depending on the size scale of features that are being printed. There are many specific types of lithographic processes. It is common to classify them by either:

- the type of external stimuli used to impart pattern definition in the resist (e.g exposure to ultraviolet light, exposure to an electron beam, exposure to x-rays, mechanical force using a mold or template, etc.)
- the type of photoresist being used (e. g. positive tone resist, negative tone resist, diazonapthoquinone-novolac resist, chemically amplified resist, single layer resist, bilayer resist, etc.), or
- the photoresist film thickness range being used (i. e. generally divided into thin film lithography and thick film lithography).

This discussion will be limited to those lithography methods that utilize the application of external radiation (i. e. optical exposure, e-beam exposure, or x-ray exposure) and will not include imprint lithography techniques such as hot embossing. Thick film lithography is generally used to refer to lithographic processes that utilize photoresist film thicknesses greater than 5μ in thickness.

The steps in a basic lithography process are shown schematically in Fig. 1. The first step in the process generally involves cleaning the surface of the substrate on which the lithography is to be performed, and may also involve the application of a surface priming agent. A wide variety of both wet chemical and dry plasma methods for cleaning the substrate surface may be employed. If surface priming of the substrate is performed, it can be done using both vapor phase and liquid phase exposure of the surface to an appropriate priming agent. Surface priming is generally done to improve the adhesion between the photoresist film and the substrate surface so as to prevent problems such as difficulty in wetting the substrate surface during spin coating of the photoresist or delamination of the photoresist film during further processing such as aqueous development. One of the most commonly used surface priming agents for spin coating resists is hexamethyldisilazane (HMDS) which reacts when applied to a surface containing hydroxyl groups (i. e. such as the silanol groups present on native oxide coated silicon wafers) to produce an essentially methyl terminated surface. The organic non-polar nature of this methyl terminated surface generally improves compatability between the surface and the photoresist, which is also typically an organic material of moderate polarity.

Once the substrate surface has been prepared, the photoresist film is applied. Application of the photoresist can be performed using several different methods, with dry film transfer, casting and in -situ polymerization, and spin coating being the most common methods. In dry film transfer, a pre-made solid photoresist film is laminated onto the substrate surface. This type of photoresist film deposition method is relatively common in thick film lithography since spin coating of thick uniform films can be difficult and thick photoresist films respond well to such film transfer methods. Spin coating is the other most common film deposition method and involves depositing the photoresist from solution, i. e. the photoresist solids are dissolved into an organic casting solvent, onto the substrate and subsequently spinning the substrate at moderate to high speeds. The spinning action spreads the solution into a uniform film and also serves to dry the film into a solid form. In cases where the film is spin coated onto the substrate, it is common to then heat the substrate and film in

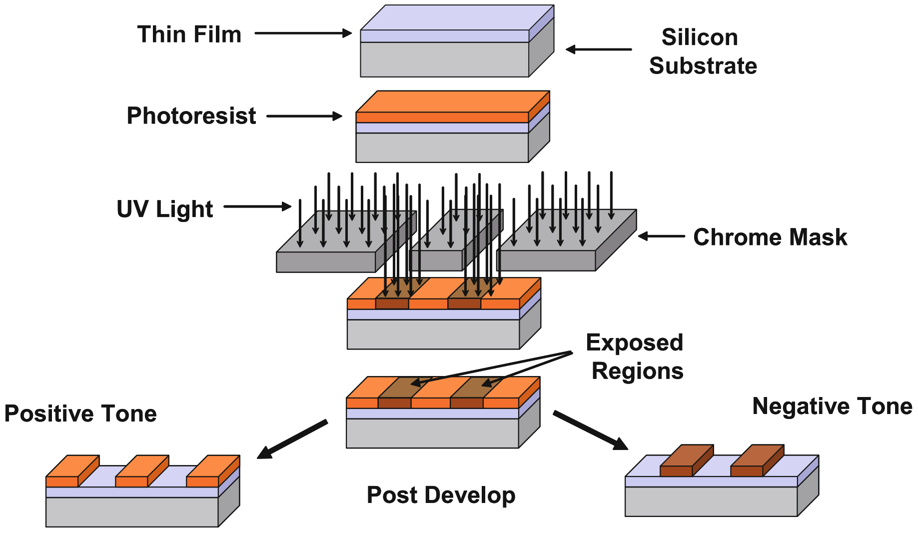

Thick Resist Lithography, Figure 1 Schematic of the basic lithography process. First a resist film is coated onto the substrate of interest that may contain either films to be etched or films that can be used to deposit other materials by techniques such as plating. The resist film is exposed pattern-wise to radiation which results in a physiochemical change in the exposed resist that changes the solubility of the exposed resist in a developing solvent. Treatment of the resist with a developing solvent then leads to either removal of the exposed resist in the case of positive tone photoresists or removal of the unexposed resist in the case of negative tone photoresists

what is referred to as a post-apply bake (PAB). The purpose of this baking step is to further dry the film by evaporating remaining casting solvent in the photoresist film. After application of the film, the next step is to expose the film in a pattern-wise manner to produce a latent chemical image in the film in the shape of the desired final pattern. Depending on the specific type of resist and the type of radiation exposure source used, the type of physiochemical change in the resist film that ultimately leads to development of the desired relief image can vary quite widely. The most common types of thick film lithography are:

- positive tone imaging using ultraviolet exposure of *diazonaphthoquinone-novolac resists*,
- negative tone imaging using ultraviolet or x-ray exposure of cross-linking resists such as *SU-8*, and
- x-ray exposure of positive tone resists such as *poly(methyl methacrylate)* or PMMA. Further attention will be paid to each of these in the following section.

Basic Methodology

Positive Tone Thick Film Lithography using DNQ-Novolac Resists and UV Exposure

In a positive tone resist, the areas that are exposed to the radiation develop away into solvent faster than unexposed areas, resulting in a positive tone image of the mask. The majority of commercial, positive tone, non-chemically amplified resists used today are variations on the well-known, two component, diazonaphthoquinone-novolac resist. (5) Novolac is a name generally given to acid catalyzed phenol-formaldehyde condensation polymers of the type shown in Fig. 2.

Novolac polymers are soluble in a variety of common organic solvents. Resist films are typically cast from organic solutions (propylene glycol monomethyl ether acetate, or PGMEA, is a common solvent) to form isotropic, glassy, thin films. These polymers are also soluble in aqueous alkaline solutions due to the presence of the acidic phenolic functionalities on the polymer backbone. It is this base solubility that is exploited in the development process. In order to print a relief image in a photoresist it must be possible to modify the dissolution rate of the resist upon exposure to radiation. It is not the novolac polymer in DNQ-novolac resists that is sensitive to radiation. Instead, it is the second component of the resist, the diazonaphthoquinone (DNQ), that is responsible for the ability of the resist to change its dissolution behavior upon exposure to radiation. DNQ is often referred to as the photoactive compound (PAC) or sensitizer in the resist, since it is the component which responds to radiation exposure. Thus, the role of the novolac polymer in these resists is to provide the desired physical characteristics of the material, such as good film forming properties and etch resistance to plasma processing, while the DNQ allows the resist to be imaged. Figure. 3 shows a schematic view of the basic mechanism responsible for the function of DNQ-novolac photoresists.

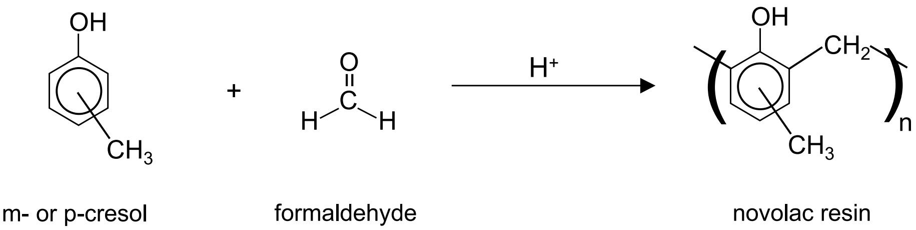

Thick Resist Lithography, Figure 2 Example of the structure of a novolac resin and the commercial production route for the polymer that is typically accomplished via the acid catalyzed polymerization of cresols with formaldehyde

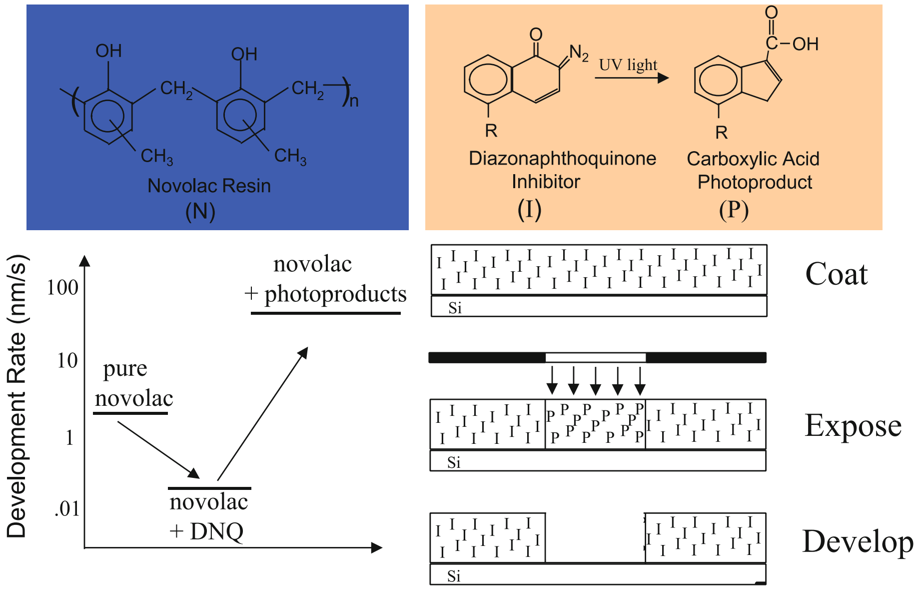

Thick Resist Lithography, Figure 3 Schematic picture of the mechanism by which DNQ-novolac resists function. Addition of DNQ inhibitor (I) to novolac polymer (N) results in a dramatic reduction in the dissolution rate of the polymer in aqueous alkaline developer solutions. Exposure of the DNQ-novolac resist mixture causes a chemical reaction converts the diazonaphthoquinone to a carboxylic acid photoproduct (P), and the presence of this carboxylic acid product in the exposed resist either does not dramatically retard or may in fact accelerate the dissolution of the polymer in aqueous alkaline developers. This differentiation in dissolution rate of the resist upon exposure allows for the formation of relief images in the photoresist after development

The addition of diazonapthoquinones to novolac films leads to a reduction in the dissolution rate of the polymer film in aqueous base relative to the dissolution rate of the pure polymer. This difference in rate can be as large as several orders of magnitude. Diazonaphthoquinone is therefore termed a "dissolution inhibitor" due to its ability to retard the dissolution rate of the novolac film. As shown above, DNQ undergoes a series of reactions upon exposure to radiation to form a carboxylic acid product. This carboxylic acid, unlike the hydrophobic DNQ, is soluble in aqueous base and its presence in the polymer film does not retard the dissolution rate in aqueous base. In fact, the presence of the carboxylic acid often serves to increase the dissolution rate of the novolac several orders of magnitude relative to the pure novolac polymer. It is this change in the dissolution rate of the novolac film due to the reaction of the diazonaphthoquinone with light that allows for the formation of relief images in the resist film. One advantage of DNQ-novolac resists for use in thick film UV lithography is that the resist material becomes more transparent to ultraviolet light, referred to as "bleaching" of the resist, as it is exposed. This bleaching phenomena allows thick resist films to be exposed and developed to produce high aspect ratio patterns relatively easily.

In forming thick resist films using DNQ-novolac resist solutions, solutions containing a high solids content of relatively high molecular weight resist polymers are typically used to provide high solution viscosities that make such thick film formation possible. In general, the relationship between film thickness formed after spin coating (t), spin speed (Ω), polymer concentration (C, typically in grams polymer/ 100 mL of solution), and resist polymer molec-

ular weight ($[\eta]$, as measured by intrinsic viscosity in this case) can be expressed as follows:

$$t = K\frac{C^{\beta}[\eta]^{\gamma}}{\omega^{\alpha}} \quad (1)$$

where K is an overall proportionality constant and *a, b,* and *g* are constants, all of which depend on the particular resist, substrate, and resist processing system used. Once a few experimental data points are collected, for example on the effect of spin speed on resist thickness, Eq. (1) can in general be used to develop a master equation for a resist coating application that can allow for specific resist thickness targets to be achieved. Before applying the resist, the substrate is generally cleaned and may be surface primed as mentioned earlier. In addition, in the case of UV exposure a so-called *anti-reflection coating* (ARC) may also be applied to the substrate. The purpose of such an ARC is to minimize surface reflections during UV exposure of the resist that can lead to undesired exposure variations in the resist, such as the formation of standing waves, that lead to degraded lithographic performance (e. g. the formation of scalloped sidewalls in developed relief images).

Exposure of DNQ-novolac resists is typically done using either I-line 365 nm, G-line 436 nm, or broadband ($\sim$ 350–450 nm) ultraviolet exposure using mercury lamp-based exposure tools. A variety of different types of exposure tools including contact, proximity, and projection exposure tools are used to perform the pattern-wise exposure of such materials. The maximum feature resolution of such exposure tools depends on the tool type, with projection exposure tools exhibiting the highest resolution and proximity tools exhibiting the lowest resolutions. Typical ultraviolet exposure doses for DNQ-novolac resists are on the order of several hundred mJ/cm^2 to several thousand mJ/cm^2 depending on the resist thickness, wavelength used, and formulation. After exposure, DNQ-novolac resists may be subjected to a post-exposure bake (PEB) that is designed to eliminate any significant gradients in DNQ concentration normal to the substrate surface. Such gradients are common in thinner film exposures using near monochromatic exposure sources since standing waves can form in the film during exposure that lead to a sinusoidal-looking concentration profile though the thickness of the resist film. Such oscillating concentration profiles make development of high quality features difficult and lead to scalloped edges in final resist relied profiles. Finally, the resist film is either immersed or sprayed with an aqueous alkaline developer to remove the exposed regions of the resist. Both inorganic alkaline developers (e. g. based on potassium hydroxide or KOH) and organic alkaline developers (e. g. tetramethyl ammonium hydroxide or TMAH) can be used for DNQ-novolac resists.

Positive Tone Thick Film Lithography Using X-ray Exposure

X-ray exposure of samples to fabricate thick film resist structures has developed into an important technique for microfabrication of a wide variety of devices. The use of x-rays to expose thick film resist samples is advantageous for a variety of reasons including:

- a simple printing scheme such as shadow masking (i. e. proximity or contact printing) can be used while still producing high aspect ratio structures with relatively straight sidewalls and
- x-rays have the ability to penetrate and expose the resist film with good uniformity throughout the depth of very thick film samples leading to more uniform structures.

The use of such x-ray exposure techniques is the basis for the so-called *X-ray* LIGA process. LIGA is the German acronym for lithography (LI thographie), Electroplating (G alvanoformung), and Molding (Abformung), which is a microfabrication process that was developed in the late 1970's and early 1980's by a team at the Forschungszentrum Karlsruhe. It was developed to allow the manufacturing of very high aspect ratio parts, in this case nozzles for uranium separation, with lateral precision below one micron. The basic original process involves five key steps steps:

- use of x-ray exposure to produce a high aspect ratio resist structure that can serve as a mold for electroplating,
- electroplating into the resist mold to form a metal master part attached to the substrate,
- removal of the resist layer,
- manufacture of a mold from the metal master part, and
- reproduction of copies of the metal master part by injection molding or other techniques.

Since its invention, this type of LIGA process, and many other variations on it, have been used for fabricating a wide variety of *microelectromechanical systems* (MEMS) and other microdevices.

The original resist used for the LIGA process was thick films of poly(methyl methacrylate) (i. e. PMMA). Because spin coating the very thick layers desired in the original work was not a practical way to obtain thick homogeneous resist films, other alternatives were developed for producing the desired resist layers that were hundreds of microns to millimeters thick. The maximum film thickness reported when spin coating PMMA has been on the order of 150 μ. One technique developed for producing the thick PMMA films desired is the so-called "film casting" process in which:

- PMMA polymer is dissolved in methyl methacrylate monomer to form a very viscous mixture,

- a polymerization initiator and potentially cross-linkers and adhesion modifying compounds are added to the mix,
- the liquid is poured onto the substrate, put into a press configuration where a plate is placed on top of the liquid film and pressed down onto spacer shims located between the substrate and plate (i. e. to control the final film thickness),and
- the material is cured by heating the material or exposing it to ultraviolet light.

One problem with this casting method is the shrinkage that occurs as a result of the polymerization which makes film thickness control somewhat challenging and creates residual stress build-up in the polymer film. This residual stress build-up can be very problematic and can lead to crazing and delamination of the film from the substrate. In order to minimize such problems, very high molecular weight polymers are desired with preference to somewhat networked materials formed through the use of cross-linking agents (e. g. multi-functional acrylate monomers). Furthermore, post-cure annealing steps in which the film and substrate are heated above the glass transition of the polymer can help to reduce residual stress. Another set of techniques that have been used to generate very thick PMMA films involves the lamination of a pre-formed PMMA sheet onto the substrate. In one version of such a process, commonly referred to as a "glueing process", a thin layer ($\sim < 10$ thick) of the polymer-monomer mixture used for the film casting process is spread onto the substrate and the pre-formed PMMA sheet is pressed onto this layer which acts as a glue to stick and bond the sheet to the substrate. The glue layer is then cured to produce a secure bond of the sheet to the substrate. Studies of this technique have shown that the residual stress built up in the glue layer is much lower than that of the film casting technique since the amount of material cured is much smaller. In one final variation of this sheet bonding process, a thin ($\sim 1-2\,\mu$ thick) PMMA layer is first deposited onto the substrate via a method such as spin casting. After the film is cast, a small amount of a good solvent for PMMA is sprayed onto the film and the pre-formed PMMA sheet is pressed onto this solvent rich layer. The presence of solvent results in a melting and fusion of the sheet to the cast film and the process is complete in a few hours as the solvent dries from the thick film.

Upon exposure to x-rays, PMMA undergoes a variety of complex reactions. However, the dominant effect is chain-scission of the polymer which reduces its molecular weight. Figure. 4 shows the effect of x-ray dose on molecular weight for PMMA possessing a relatively high initial molecular weight (i. e. 10^6 g/mol) It is this reduction of molecular weight of the polymer in the exposed areas

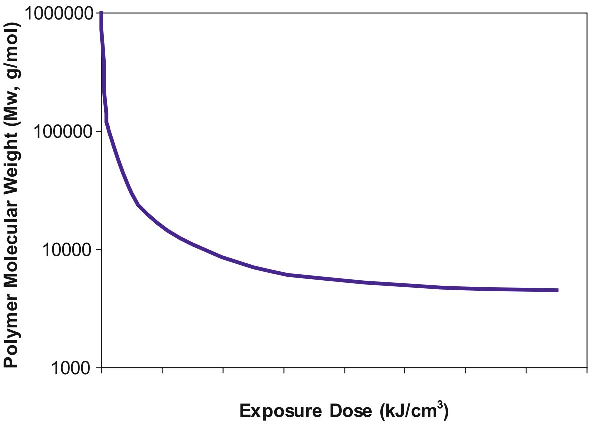

Thick Resist Lithography, Figure 4 Example of the effect of x-ray irradiation on the molecular weight of an initially high molecular weight poly(methyl methacrylate) sample

that is responsible for the increased dissolution rate of the exposed PMMA in developing solvent. As can be seen, there is a point of diminishing returns in terms of using higher exposure energies. This is because as the polymer molecular weight decreases, the chance for cross-linking reactions in the PMMA increases, leading to the fact that at very high doses an equilibrium between chain scission and cross-linking reactions occurs that results in no further change in polymer molecular weight. After exposure, the irradiated regions of the polymer must be selectively remove using a solvent without attacking the unexposed regions. Special multi-component solvent mixtures are commonly used for the development. One example of a solvent developer that has been widely used is a mixture consisting of 20 vol% tetrahydro-1,4-oxazine, 5 vol% 2-aminoethanol, 60 vol% 2-(2-butoxyethoxy)ethanol, and 15 vol% deionized water. The molecular weight cut-off that the developer can dissolve can be adjusted by slight compositional changes to the developer or by simply adjusting the developer temperature. Increasing the developer temperature enables the dissolution of high molecular weight polymer, but temperatures above ~45 °C should be avoided as even very high molecular weight polymer is swollen or dissolved above these temperatures.

Although PMMA is well known for its ability to produce extremely high resolution patterns, it is also known for its relatively low radiation sensitivity. This results in the use of very high radiation doses to pattern the material. Furthermore, in thick resist layers, the absorption of energy by the material can not be ignored and leads to a variation in the energy deposited as a function of depth into the resist film. There is a minimum energy that must be deposited in the bottom of the resist film, otherwise the polymer at

T

the bottom of the film will not undergo sufficient chain scission to develop cleanly and will leave a residue. Likewise, there is a maximum amount of energy that can be deposited into the top of the resist film without resulting in foaming of the resist due to the release of gaseous byproducts during the chain scission process. As a result of these issues, the exposure conditions for PMMA in x-ray thick film lithography must be carefully considered and must take into account the limits for energy deposited into the top and bottom of the resist film.

Negative Tone Thick Film Lithography Using UV and X-ray Exposure of Cross-linking Resists

In the two previous examples, different physiochemical mechanisms were employed to increase the solubility of the exposed resist in developer that led to positive tone image formation. Negative tone imaging can also be performed by invoking physiochemical changes in the resist upon radiation exposure that leads to a decrease in the solubility of the exposed resist in developing solvent. The most popular method for producing such negative tone materials is the use of radiation induced cross-linking reactions in a polymer matrix. Cross-linking of the polymer in general to a reduction of the solubility of the polymer in developing solvent, in a manner that is exactly opposite to that used in x-ray lithography of PMMA. One of the most popular resists for negative tone thick film lithography is SU-8. SU-8 consists basically of a phenolic oligomer that has been functionalized with epoxide groups mixed with a photoacid generator (e. g. an onium salt such as triphenyl sulfonium hexafluoroantimonate). Upon exposure to radiation, the photoacid generator compound produces a strong acid and this acid in turn initiates polymerization of the epoxide groups on the oligomers. This results in heavy cross-linking of the film and a dramatic reduction in its solubility. In addition to providing a mechanism for patterning the resist, the use of the cross-linking reaction produces a very mechanically robust polymer that is often used to directly form structures that are used as a part of the final device being constructed and not simply as a temporary resist mask for other processes such as plating.

Key Research Findings

X-ray based thick film lithography is still the best technique for producing very high aspect ratio structures with little or no variation in part dimensions along the axis normal to the substrate. This ability to produce such high aspect ratio structures with excellent dimensional tolerancing is a result of the very small x-ray wavelength combined with the ability to produce very well collimated x-ray beams using synchrotron sources. Parts that are hundreds of microns to millimeters in thickness with lateral feature resolution well below one micron can easily be formed. However, access to a synchrotron source is required for such x-ray techniques which makes the method impractical for most laboratories or companies. As an alternative, thick film lithography using UV exposure has progressed to the point where it is the dominant over x-ray techniques for MEMS and other thick film fabrication needs. Both positive and negative tone resists are used in such methods, with negative tone materials offering the advantage that they generally have superior mechanical properties that can allow for their permanent use in device structures.

Future Directions for Research

Thick film lithography at this point is a relatively mature technology. While techniques such as x-ray lithography can produce very high aspect ratio structures in very thick resist films, the use of such x-ray techniques is limited by extreme expense of the synchrotron sources needed to produce the well collimated x-ray beams required for such lithography processes. Therefore, work continues to develop much cheaper alternatives based on the use of ultraviolet exposure using both positive and negative tone resists that can produce high aspect ratio structures with high feature resolutions. Such UV exposure methods are now used in so-called UV LIGA in a manner that is analogous to the x-ray LIGA methods discussed earlier. In addition, modern MEMS devices rely on the ability to fabricate released structures, i. e. ones where some part of the device is not in contact with the substrate or some other part of the device. Various sacrificial techniques have been developed in conjunction with thick film lithography to produce these released structures. Development of materials and techniques for the direct use of the resist material as a sacrificial material continues to be of interest. In one example, sacrificial resists based on polynorbornenes and polycarbonates have been developed that can be used for thick film lithography, used to template the deposition of additional materials via plating or other techniques, and finally removed as a sacrificial material by simply heating the resist to a moderate temperature that is capable of transforming the polymer into gaseous products. Using such materials and techniques, microchannels and microfluidic devices have been fabricated with very complex designs in a manner that is compatible with both other microelectronic and MEMS fabrication techniques.

Cross References

► Photoresist SU-8
► Photoresist Reflow

► Photolithography
► SU-8
► LIGA
► Microelectromechanical System (MEMS)

References

1. Friedrich CR, Warrinton R, Bacher W, Bauer W, Coane PJ, Gottert J, Haneman T, Haubelt J, Heckele M, Knitter R, Mohr J, Piotter V, Ritzhaupt-Kleissl H-J, Ruprecht R (1997) High Aspect Ratio Processing, In: Choudhury PR (ed) Handbook of Microlithogr, Micromaching Microfabr, vol 2: Micromachining and Microfabr. SPIE Optical Eng Press, Bellingham, Washington
2. Thompson LF (1994) An Introduction to Lithography. In: Thompson LF, Willson CG, Bowden MJ (ed) Introduction to Microlithogr Second Edition. American Chem Society, Washington DC
3. Willson CG (1994) Organic Resist Materials. In: Thompson LF, Willson CG, Bowden MJ (ed) Introd to Microlithogr Second Edition. American Chem Society, Washington DC
4. Thompson LF (1994) Resist Processing. In: Thompson LF, Willson CG, Bowden MJ (ed) Introd to Microlithography Second Edition. American Chem Society, Washington DC
5. Dammel RR (1993) Diazonaphthoquinone-based Resists. SPIE Optical Engin Press, Bellingham, Washington

Thin-Film Actuation

► Membrane Actuation for Micropumps

Three-Dimensional Electrodes

SHELLEY D. MINTEER
Department of Chemistry, Saint Louis University, St. Louis, Missouri, USA
minteers@slu.edu

Synonyms

3D electrodes; Flow-through electrodes; Porous electrodes

Definition

Three-dimensional electrodes are non-planar electrodes that typically improve the transport of redox species to the electrode surface increasing current density. Some 3-D electrodes are solid, but others are porous or flow-through electrodes whose effective surface area is greater then the geometric surface area on the device.

Overview

One of the common challenges of high sensitivity electrochemical analysis and high power density electrochemical power sources is the need for fabrication of three-dimensional electrodes. Historically, three-dimensional electrodes have been the focus of battery technology for decades and flow-based macroscale three-dimensional electrodes have been used for electrosynthesis [1], electrowining [2], photocatalytic reactors [3], and different types of chemical analysis [4, 5]. The electrodes were fabricated from a number of high surface area and high porosity materials like reticulated vitreous carbon (RVC). Over the last few years, scientists have developed microscale three-dimensional electrodes and have started employing them in microfluidic and nanofluidic devices. These microscale three-dimensional electrodes show promise for improving sensitivity of Lab-on-a-Chip devices and improving control in cell sorting and manipulation.

Basic Methodology

The main principle of employing microscale three-dimensional electrodes is to increase the effective surface area of the electrode to increase current, because amperometric and voltammetric current (i) or electrochemical flux is directly proportional to true electrode area (A).

$$i \propto A$$

Electrochemical current, typically referred to as faradaic current, is a measurement of reaction rate, so the more surface area for reaction, the more product that will be formed and the higher the current. This is illustrated in Fig. 1, which shows the effect of the increase in surface area (via a 3-D electrode) on the number of reactions (turnovers) that can occur at a given point in time. Frequently, the factor by which the current is increased is referred to as the roughness factor, which is the

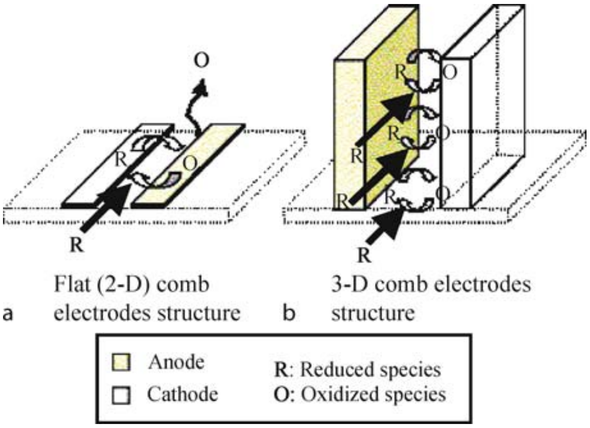

Three-Dimensional Electrodes, Figure 1 Comparison between flat and 3-D electrodes [13], Reproduced with permission from each of the publishers

ratio of the true electrode area to the geometric electrode area, but the concept of the roughness factor gets more complicated with flow-through electrode geometries. However, over the last few years, other purposes for 3-D electrodes have emerged. 3-D electrodes are also useful in the field of dielectrophoresis and electrohydrodynamics.

Dielectrophoresis is sometimes confused with electrophoresis and electroosmosis, but electrophoresis and electroosmosis involve the movement of charged species in a high electric field, but dielectrophoresis is the flow phenomenon by which neutral species can be transported by inducing a spatially non-uniform electric field. There are two types of dielectrophoresis: positive dielectrophoresis and negative dielectrophoresis. In positive dielectrophoresis, sub-micron species move toward high electric field regions, wherein negative dielectrophoresis results in sub-micron species moving toward low electric field regions. Dielectrophoresis is particularly helpful in separating sub-micron species (which cannot easily be separated with traditional filters) and allowing for the deliver of sub-micron species to specific areas of the microchip. It is important to note that all particles can experience dielectrophoretic forces, but the strength of the force predicts the observed dielectrophoretic effect. The strength of the force is dependent on the size and shape of the particle, the electric field gradient, dielectric constant of the solution, and dielectric constant of the particle in the solution. 3-D electrodes allow for a better method for extending the electric field within the solution for improved 3-D control through the solution reservoir and can be designed to have better local control over the dielectrophoretic movement [6].

The final use of 3-D microelectrodes is electrohydrodynamics. Electrohydrodynamic fluid flow is similar to magnetohydrodynamics, but instead is developed by applying a high frequency electric traveling wave, which induces net fluid flow by exerting a force on the charges in the bulk liquid. It is advantageous compared to magnetohydrodyanics or even mechanical pumping, because it is pulseless (continuous) and capable of controllable deliver of very small amounts of fluid, as well as requiring low voltages (around 10V) [7]. Miniaturization of the electrohydrodynamic pump has the advantages of providing the opportunity for bi-directional flow and the ability to more quickly turn the flow on and off.

Key Research Findings

Carbon MEMS (C-MEMS)

Interdigitated arrays of carbon electrodes can be fabricated from pyrolyzing photoresist, as shown in Fig. 2. These electrodes are formed by fabricating a prepatterned photoresist structure using photolithography. The photolithographic process involves coating a surface (typically a silicon wafer) with an organic photoresist (i. e. SU-8) and then exposing the photoresist to UV light through a mask that will define the size, shape, and placement of the carbon electrodes. Then, the photoresist is developed, so that the only remaining structures on the substrate are the UV-crosslinked photoresist structures. The substrate is then pyrolyzed at high temperature ($> 900\,°C$) to form the 3-D carbon electrodes. These electrodes have similar properties to glassy carbon, but with lower oxygen content. They are particularly useful for 3-D electrodes, because they can be fabricated with high aspect ratios (up to 20:1), to tall structures can be fabricated easily and reproducibly. These pyrolyzed photoresist 3-D electrodes have applications in batteries, but they are also applicative to microchip bioanalysis systems. Fischer et al. have used pyrolyzed photoresist to make 3-D electrodes for dual amperometric detection for microchip electrophoresis [8]. However, it is important to note that many electrodes for microchip electrophoresis are 3-D electrodes and can be fabricated from a number of sources including carbon-based screen printing inks, precious metal-based screenprinting inks, carbon fibers, electroplating of metallic electrodes, vapor deposition of metallic electrodes, etc. The choice of material is

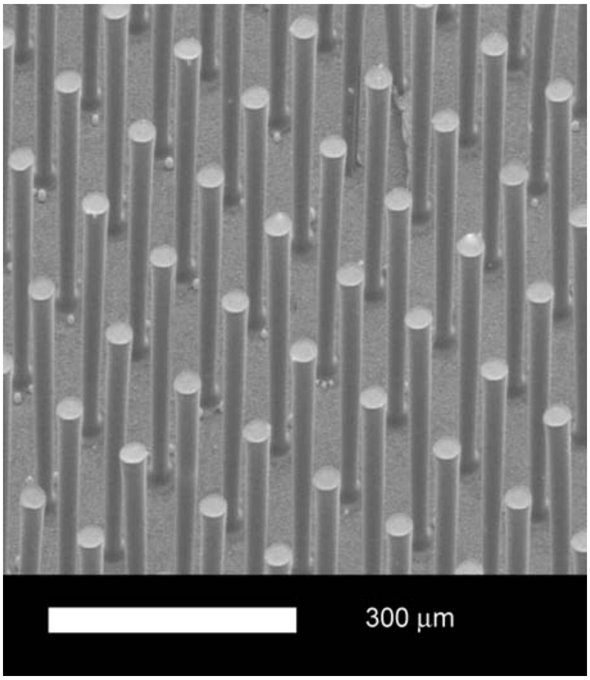

Three-Dimensional Electrodes, Figure 2 Array of carbon microelectrodes produced by pyrolizing photoresist [14], Reproduced with permission from each of the publishers

usually a function of the properties of the analyte being measured and the type of microchip being fabricated. In theory, these same increased surface area electrodes can be used for micro- flow injection analysis and other amperometric biochips. For instance, micromolded screen printing inks can be used to study the release of catecholamines from PC12 cells [9]. Beyond employing 3-D electrodes for electrochemical detection, Park et al. have used the pyrolyzed photoresist 3-D electrodes for dielectrophoretic separation of carbon nanofibers from canola oil, cell sorting (separation of living and dead cells, cancer cells and leukocytes from blood, and even one type of bacteria from another), and engine oil filtering for sub 10 micron particles [6].

Other Fabrication Methods

Although there are a wide variety of methods for fabricating 3-D electrodes, they can be simply characterized as top-down approaches or bottom-up approaches. The top-down approaches typically involve ablating or etching a large structure down to a 3-D micro or nanostructure. This is frequently done to form micro- and nanoscale electrode tips, but is not as frequent in microfluidic and nanofluidic devices as compared to electrodes for scanning electrochemical microscopy (SECM) and other static solution electrochemical devices. Most 3-D electrodes in microfluidic and nanofluidic devices are fabricated from a bottom-up approach (like the C-MEMS discussed above). This can be done for metallic electrodes by sputter coating or vapor depositing metal structures on substrate surfaces (frequently with the help of an adhesion layer, depending on the substrate surface) or by electrodeposition/electroplating through a template. However, there are other fabrication methods including screen printing 3-D electrodes and micromolding with screen printing inks. The process of screenprinting conductive inks is a well developed technology and can be used for fast mass-production of electrodes, but micromolding is a relatively new technology develop by Martin et al. [10] by which a PDMS microfluidic mold is used and the mold is placed over the substrate. Screen printing ink is pulled through the mold and then the mold/ink/substrate are cured and the mold is removed. The result is 3-D carbon electrode with similar properties to a screenprinted 3-D electrode that can be used for amperometric or voltammetric detection and can easily be coupled to microchip electrophoresis. These types of electrodes can also be used in microfluidic biofuel cells, because the micromolding technique can be used to deposit both the electrode and the enzyme immobilization membrane for entrapping the enzyme at the surface of the electrode.

Microfluidic Chambers for Studying Cellular Responses to Electrical Stimulation

In electrochemistry, we normally define 4 types of electrode designs: a single electrode, a dual electrode, an electrode array, and an individually addressable electrode array. The single electrode is used for simple amperometric and voltammetric detection or as the anode or cathode in a battery or fuel cell. The single electrode can be used in either a 2-electrode or 3-electrode electrochemical cell. The 2-electrode electrochemical cell is the typical battery design with a single electrode and a counter electrode, which we can consider a cathode and an anode. The 3-electrode electochemical cell contains the single electrode (frequently referred to as the working electrode or sensing electrode), a counter electrode for completing the circuit, and a reference electrode in a feedback circuit to ensure the proper applied potential. The dual electrode system is used for dual detection systems in either a 3-electrode or 4-electrode electrochemical cell. The 3-electrode cell contains the two working electrodes and a single counter electrode, whereas the 4-electrode cell contains the dual working electrodes, a counter electrode, and a reference electrode.

Electrode arrays are different from single electrodes, because frequently the electrodes are so close together that the electric field and concentration gradient at one electrode can affect the other electrode. There are two types of electrode arrays: a simple electrode array and an individually addressable electrode array. The simple electrode array contains a series of small micro- or nano-scale electrodes that are all connected together (similar to a group of electrodes wired in series), so that the potential (voltage) that is applied is the same for all electrodes. This type of electrode is used to increase the current density of system, but is not helpful for dielectrophoresis or 3-D detection or stimulation, whereas a individually addressable electrode array has a group of electrodes, but a different potential (voltage) can be applied to each electrode and the current can be measured for just that electrode. The individually addressable electrode array is a relatively new technology, but is crucially important in detection schemes for complex systems and the ability to control transport on the microscale.

Three-dimensional microelectrode arrays can also be used for stimulation of cell versus separation or detection. Klauke et al. developed a microchip device for studying cellular responses to electrical stimulation of myocytes. A polydimethylsiloxane (PDMS)-based microchip was fabricated that include an array of three-dimensional gold microelectrodes for stimulation of mycotes cultured on the surface of the chamber. Measurement of action potential,

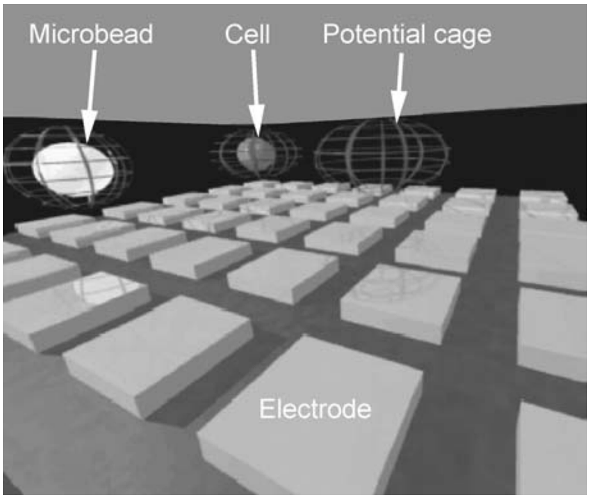

Three-Dimensional Electrodes, Figure 3 Schematic of biochip for dielectrophoresis-based cell separation and trapping [15], Reproduced with permission from each of the publishers

intracellular calcium concentration and cell shortening can be performed in-situ within this device [11].

3-D Electrodes for Cell Manipulation

Three-dimensional electrodes on microchip devices have also been used for cell manipulation via dielectrophoresis. Dielectrophoresis can be used to move neutral particles (like cells) by inducing a spatially non-uniform electric field, which will either force the particle to low or high potentials. Microchips have been fabricated with 102,400 addressable electrodes of 20 micron x 20 micron [12]. A schematic of the microchip is shown in Fig. 3. Varying potentials were applied to the electrode to move cells and trap them into regions for optical detection [12]. This is off particular interest for single cell detection and also for the separation of different types of cell (cancer vs. normal, etc.). However, this type of device requires a complicated individually addressable electrode array instead of just an electrode array, because the non-uniform electrode fields must be controlled precisely to move the cell to the proper place on the chip and then to trap the cell. This particular technology and the control circuitry allowed for the software controlled movement of 10,000 living cells simultaneously [12], which is a significant advancement in both the capacity of the chip, but also the logic, circuitry, and software to be able to handle the increased capacity.

Future Directions for Research

These type of 3-D electrodes on microchips could also be used for a wider variety of biomethods, including electroporation, drug delivery, and electrostimulated cell culturing. 3-D electrodes will also have applicability in laminar flow-based fuel cells and biofuel cells due to the increase in roughness factor. 3-D electrode for dielectrophoresis also have applicability to nanoliter or sub-nanoliter liquid dispensing.

Cross References

- ► AC Dielectrophoresis Lab-on-Chip Devices
- ► Amperometric Techniques
- ► Electrokinetic Motion of Cells and Nonpolarizable Particles
- ► DC Dielectrophoresis Lab-on-Chip Devices
- ► Dielectrophoresis
- ► Dielectrophoretic Motion of Particles and Cells
- ► Droplet Dispensing
- ► Electrochemical Techniques
- ► Electrophoresis
- ► Microfluidic Fuel Cells
- ► Photoresist SU-8
- ► Photoresist Reflow
- ► Techniques for Manipulating Cells

References

1. Chai D, Genders D, Weinberg N, Zappi G, Bernasconi E, Lee J, Roletto J, Sogli L, Walker D, Martin C, Menon V, Zelenay P, Zhang H (2002) Ceftibuten: Development of a commercial process based on cephalosporin C. Part IV. Pilot-plant scale electrochemical reduction of 3-acetoxymethyl-7(R)-glutaroylaminoceph-3-em-4-carboxylic acid 1(S)-oxide. Organic Process Res Dev 6: 178–183
2. Reyes Cruz V, Oropeza MT, Gonzalez I, Ponce-de-Leon C (2002) Electrochemical recovery of silver from cyanide leaching solutions. J Appl Electrochem 32: 473–479
3. An T, Zhang W, Xiao X, Sheng G, Fu J, Zhu X (2004) Photoelectrocatalytic degradation of quinoline with a novel three-dimensional electrode packed bed catalytic reactor. J Photochem and Photobio A 161: 233–242
4. Armalis S, Kubiliene E (2000) Stripping potentiometry signal enhancement using mercury film-coated reticulated vitreous carbon working electrode. Analy Chim Acta 423: 287–291
5. Price A, Bartley S, Male S, Cooley G (1999) A novel approach to utility scale energy storage. Power Eng J 13: 122–129
6. Park BY, Madou MJ (2005) 3-D electrode designs for flow-through dielectrophoretic systems. Electrophoresis 26: 3745–3757
7. Felten M, Geggier P, Jager M, Duschl C (2006) Controlling electrohydrodynamic pumping in microchannels through defined temperature fields. Phys Fluid 18: 051707–1 - 051707–4
8. Fischer DJ, Vandaveer WR, Grigsby RJ, Lunte SM (2005) Pyrolyzed photoresist carbon electrodes for microchip electrophoresis with dual-electrode amperometric detection. Electroanal 17: 1153– 1159
9. Li MW, Spence DM, Martin RS (2005) A microchip-based system for immobilizing PC12 cells and amperometrically detecting catecholamines released after stimulation with calcium. Electroanal 17: 1171–1180

10. Kovarik ML, Torrence NJ, Spence DM, Martin RS (2004) Fabrication of carbon microelectrodes with a micromolding technique and their use in microchip-based flow analyses. Analyst 129: 400–405
11. Klauke N, Smith GL, Cooper JM (2003) Stimulation of isolated ventricular myocytes within an open architecture microarray. IEEE Transact Biomed Eng 52: 531–538
12. Manaresi N, Romani A, Medoro G, Altomare L, Leonardi A, Tartagni M, Guerrieri R (2003) A CMOS chip for individual cell manipulation and detection. IEEE J Solid-State Circuits 38: 2297–2305
13. Honda N, Inaba M, Katagiri T, Shoji S, Sato H, Homma T, Osaka T, Saito M, Mizuno J, Wada Y (2005) High efficiency electrochemical immunosensors using 3D comb electrodes. Biosens Bioelectronics 20 2306–2309
14. Chemical Reviews 2004 104 4463–4492
15. Manaresi N, Romani A, Medoro G, Altomare L, Leonardi A, Tartagni M, Guerrieri R (2003) A CMOS chip for individual cell manipulation and detection. IEEE J Solid-State Circuits 38 2297–2305

Three-Dimensional Patterning

► Fabrication of 3D Microfluidic Structures

Threshold Filter

Definition

With a threshold filter binary images can be created. A threshold of a defined intensity value is set and all pixel intensity values above this threshold are 1 while the others are 0. If only pixel values are set to 0 whose original intensity value is smaller than the threshold, a ► background subtraction can be done. This is often done to divide objects from background.

Throat

Definition

This is the location of the minimum cross-sectional area in the converging/diverging nozzle where sonic flow conditions exist (unity Mach number).

Cross References

► Supersonic Micro-Nozzles

Throw

► Stroke

Time-Dependent Density Functional Theory (TDFT)

► Dynamic Density Functional Theory (DDFT)

Time-of-Flight Filter

Synonyms

Time-of-flight mass spectrometer; TOF-MS

Definition

A mass filter that separates ions according to their time of flight through a fixed distance, following their acceleration through a common potential. Requires a pulsed ion source, fast electronics and sufficient flight path for ion separation.

Cross References

► Mass Spectrometry

Time of Flight Ion Mobility Spectrometry

► Miniaturized Ion Mobility Spectrometry

Time-of-Flight Mass Spectrometer

► Time-of-Flight Filter

Time-Gated Fluorescence Detection

Synonyms

Fluorescence detection

Definition

Time-gated fluorescence detection is used to monitor the fluorescence of a sample as a function of time after excitation by a flash or pulse of light. Steady-state intensity measurements of emitted fluorescence are taken over a period of time following pulsed excitation. Time resolution is optically gated, whereby a short laser pulse acts as a gate for the detection of emitted fluorescence and only fluorescence that arrives at the detector at the same time as the gate pulse is collected. In time-gated detection systems, the detector is turned on after excitation and the fluorescence intensity generated is integrated. This method is useful for long lifetime probes.

Cross References

- ► Biosensors Using Laser
- ► Fluorescent Labeling

Time-Multiplexed Deep Etching

Synonyms

Time-multiplexed plasma etching

Definition

Time-multiplexed deep etching (TMDE) is a special deep reactive ion etching (DRIE) process, and has been commonly applied in inductively coupled plasma (ICP) etching system for anisotropic etching and 3-D microstructure fabrication.

In TMDE, the process conducts the cycling of etching and passivation steps. In each cycle, plasma processing gases are flowed independently one at a time during operation which is known as the Bosch process patented by Robert Bosch GmbH of Germany in the mid-1990s. The etching step forms a shallow isotropic trench in a substrate (typically silicon). The passivation step forms a protective film on all surfaces of the substrate. In the subsequent etching step, ion bombardment promotes the preferential removal of the passivation film on the horizontal surface and further attack the substrate chemically and physically, allowing the profile to evolve in a highly anisotropic structure. In a typical configuration,SF_6 is the etching gas andC_4F_8 is the deposition gas for sidewall passivation. In TMDE processing, gas flow rates, etching durations and working powers in each step can be varied to produce designed 3-D microtructures with the well-controlled sidewall profiles.

Cross References

- ► Fabrication of 3-D Microfluidic Structures
- ► Microfabrication Techniques
- ► Plasma Etching
- ► Reactive Ion Etching (RIE)

Time-Multiplexed Plasma Etching

- ► Time-Multiplexed Deep Etching

TIRF

Synonyms

Total Internal Reflection Fluorescence (Microscopy); TIRM; TIRFM

Definition

Total internal reflection fluorescence microscopy (TIRFM), or simply TIRF, is the application of fluorescence imaging to evanescent wave microscopy. The material of interest is tagged with fluorescent material that emits light at wavelengths greater than the excitation photons from the evanescent field, which additionally improves the detectability of the evanescent wave microscopy technique.

Cross References

- ► Evanescent Wave Illumination
- ► Evanescent Wave Microscopy
- ► Fluorescence Measurements
- ► Fluorescence Labeling
- ► Quantum Dots

TIRFM

- ► Evanescent Wave Illumination
- ► Evanescent Wave Microscopy
- ► TIRF

TIRM

- ► Evanescent Wave Illumination
- ► Evanescent Wave Microscopy
- ► TIRF

TIRV

- ► Total Internal Reflection Velocimetry

T-Junction

- ► Flow Bifurcation in Microchannel

TLCs

► Liquid Crystal Technique for Measuring Temperature

TOF-MS

► Time-of-Flight Filter

Topographical Manipulation

Definition

Three-dimensional management of the landscape of a microfluidic platform utilized to influence curvature to induce capillary flow.

Cross References

► Surface-Directed Capillary Flow Systems

Torr

Definition

A unit of pressure, 1 Torr = 133.322 Pa.

Cross References

► Sputtering for Film Deposition

Total Internal Reflection Fluorescence (Microscopy)

► Evanescent Wave Illumination
► Evanescent Wave Microscopy
► TIRF

Total Internal Reflection Velocimetry

Synonyms

TIRV

Definition

Total internal reflection velocimetry combines evanescent wave microscopy with established mirco- and nano-scale velocimetry techniques. Particle image velocimetry or particle tracking velocimetry are used to infer fluid velocities from tracer particle displacements in two or three dimensions within the penetration depth of the evanescent field.

Cross References

► Micro-PIV-Based Diffusometry
► Brownian Motion and Diffusion
► Brownian Motion
► Evanescent Wave Microscopy
► Quantum Dots

Tracers

Definition

Tracers for flow visualization (PIT/► PIV measurement technique) are used as particles and seeded into fluids. It is important that the tracers are able to follow the flow properly. Smaller particles follow the flow very good but offer worse reflective properties than bigger particles. For PIT TLCs are used as tracer particles. They show indirectly the temperature of the flow within a certain temperature range.

Transesterification

Synonyms

Definition

Transesterification is the process of exchanging the alkoxy group of an ester compound by another alcohol.

Cross References

► Biomolecular Synthesis in Microfluidics
► Lab-on-a-Chip Devices for Chemical Analysis
► Microfluidics for Bio- and Chemical Reactions

Transferring Samples to Chips, Techniques

Gang Chen, Xiaohong Chen
School of Pharmacy, Fudan University, Shanghai, China

Synonyms

Sampling; Microfluidic chip; World-to-chip interface

T

Definition

Techniques for transferring samples to microfluidic chips are of crucial importance because they open the microchip to the macroworld. ►Sample introduction is the beginning of the process of microfluidic analysis on chips. Various techniques for transferring samples in the form of liquid, gas or aerosol to an on-chip liquid environment have been reported for biochemical and environmental analysis.

Overview

Microsystems based on microfluidic chips, are of considerable recent interest owing to their high degree of integration, portability, minimal solvent/reagent consumption, high performance and speed. The dramatic downscaling and integration of chemical assays hold considerable promise for faster and simpler on-site monitoring and decentralized clinical testing and make these analytical microsystems particularly attractive for biological, environmental, and industrial analysis. As with other analysis systems, techniques for transferring samples to microfluidic chips are one of the most important steps for microfluidic analysis on chips. Sample introduction is an important component of these systems and is an essential process for making chip electrophoresis a widely applicable analytical technique. A major obstacle to the realization of such real-life applications has been the introduction of the sample into such microchip devices.

Samples are usually introduced into a microfluidic chip via ►solution reservoirs on chips that are simply storage units for the reagents and samples used within the manifold. Several types of reservoirs have been reported as fabrication techniques have progressed. Effenhauser et al. [1] have developed a simple method that has been commonly used. A blank glass plate (typically 1 mm in depth) was thermally bonded onto the etched chip containing the microstructure, in order to seal the system. Holes were then drilled into this top plate to provide access points to the microchannels. Plastic pipette tips were inserted into these holes to act as reservoirs and to hold the electrodes.

Transferring samples to chips requires the introduction of a reproducible sample into a flowing carrier stream of a manifold without any disturbance to the carrier stream. The system is more versatile if the reproducible volume range that can be introduced is wider. An ideal sample-induction system performs this as a convenient and fast operation so as to provide a high sampling rate. Conventional flow-injection analysis (FIA) injectors (e. g., rotary/slide valve injectors) cannot be used successfully in a microfluidic environment because of the demands of injecting very small volumes. However, some methods for transferring samples based on electrokinetic mobility (electrophoretic mobility or electroosmotic flow), miniaturized valves and hydrodynamic pressure methods employed in micro-FIA system have been adapted to be compatible with the microchip system. Many of the sample-transfer techniques used in the microfluidic chip system were initially adapted from techniques employed in conventional FIA and capillary electrophoresis (CE). Various techniques for transferring samples in the form of liquid, gas or aerosol to an on-chip liquid environment have been reported for biochemical and environmental analysis within the last decade.

Basic Methodology

Samples were usually transferred to the microfluidic system by electrokinetic injection and ►pressure injection. ►Electrokinetic sample introduction is most commonly used for transferring samples to chips. This can be attributed to factors such as the simplicity in achieving electroosmotic flow (EOF), i. e., no moving parts and minimal backpressure effects. The EOF in the microchannel acts as a pump and can easily be controlled by outside high voltages. The two commonly employed injection modes for microfluidic chips are time-based and discrete volume-based injection. In the case of the time-based (or gated injection), the amount of sample introduced into the carrier stream can be controlled by adjusting the injection time.

Figure 1 illustrates the time-based floating injection. The running buffer (Fig. 1b) and unused (Fig. 1c) reservoirs were filled with running buffer solution, while the sample reservoir (Fig. 1a) was filled with a sample mixture. The detection reservoir (Fig. 1d) was filled with the running buffer solution. A high voltage was applied to the sample reservoir to facilitate the filling of the injection channel, while the detection reservoir was grounded and all the other reservoirs remained floating. The sample solution was loaded into the separation channel by applying an injection voltage to the sample reservoir for several seconds, while the detection reservoir was grounded and other

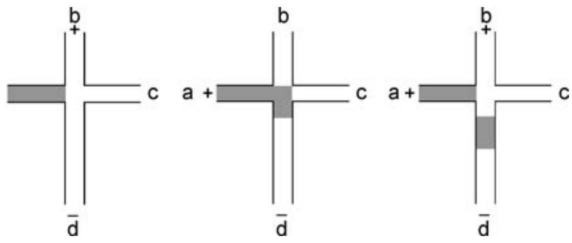

Transferring Samples to Chips, Techniques, Figure 1 Operation processes of time-based floating injection. (**a**) sample reservoir, (**b**) running buffer reservoir, (**c**) unused reservoir, (**d**) detection reservoir

reservoirs floated. The separation was usually performed by applying a separation voltage to the running buffer reservoir (Fig. 1b) with the detection reservoir grounded and other reservoirs floating. This technique is characterized by ease of control and variation of injected volume and is suitable for continuous and sequential injection for on-line measurements. This approach to sample introduction may suffer from uncontrolled dispersion, resulting in irreproducible injection volumes. The electrokinetic biasing of the sample is another major problem of this method. The injected sample may not be representative of the whole sample. Time-based injections involve applying an electric field to move the sample continuously at a known flow rate, for a given period of time into the reaction or separation channels.

The volume-based sample introduction can be further classified into floating and pinched modes. The volume-based floating injection method applies a high voltage across the sample line only, leaving all the other channels and reservoirs floating. The high voltage is applied to the sample channel (ac) (see Figs. 2a – 2c) to pump the sample solution by EOF to fill the intersections. However, no voltage is applied between reservoirs (b) and (d) so that leakage and migration of the sample solution into the separation channel during injection will occur, resulting in uncontrollable injection volumes. This floating sample introduction technique is quite simple since it only requires one high voltage. When the sample zone passes across the intersection, the sample will migrate toward both (b) and (d) due to the diffusion and eddy effects. Separation can be carried out by switching the electric field to run in the direction of (b) and (d). The sample plug in the intersection will move towards (d) and is separated in the separation channel. To prevent leakage and diffusion of the sample solution, a *pinched* injection method has been developed while an electric field is applied to every channel within the microfluidic chip system. Typically, an electric field (ac) is applied across the sample channel as shown in Fig. 2d, thus moving the sample to fill the intersection. Meanwhile, a lower positive potential will be applied to all the other reservoirs to keep the sample solutions pinched so as to reduce, or preferably eliminate, leakage from the sample into the side channels (see Fig. 2d). And then, the electric field is re-directed so that (d) in Fig. 2d is grounded, with all the other channels positive relative to (d) in Fig. 2d for separation. Jacobson et al. [2] have demonstrated that an improvement in RSD values from 2.7% to 1.7% for a 90-pl injection volume could be obtained using the pinched method compared to that achieved using the floating method. The much higher reproducibility of pinched injection than time-based injection and the minimization of the diffusion/leakage at the intersections offer great promise for microfluidic chips.

Pressure injection is another important technique for transferring samples to microfluidic chips. ►Positive pressure or suction (vacuum) pressure is used to generate a pressure difference to the reservoir on the chips and drives the sample solution into the microchannel. The main advantage of pressure injection over the electrokinetic injection mentioned above is the lack of electric discrimination resulting from the different ion mobilities. But it is unsuitable for gel-filled capillaries. Due to the low dimensions of the micochannels in chips, pumping mechanisms usually lead to high backpressure and the conventional parabolic flow, resulting in band broadening and the dilution of the sample. The amount of sample transferred to the chips has to be calculated, considering the sample viscosity, injection time, and pressure differential. The precision of the injection is difficult to control because the atmospheric conditions and elevation affect the pressure differences and the amount of samples being transferred.

Samples are usually manually loaded into the sample reservoir using standard pipettors and their replacement requires extensive washing. Such manual or automated sample removal limits the sampling rate and is incompatible with the high performance of microchip devices.

T

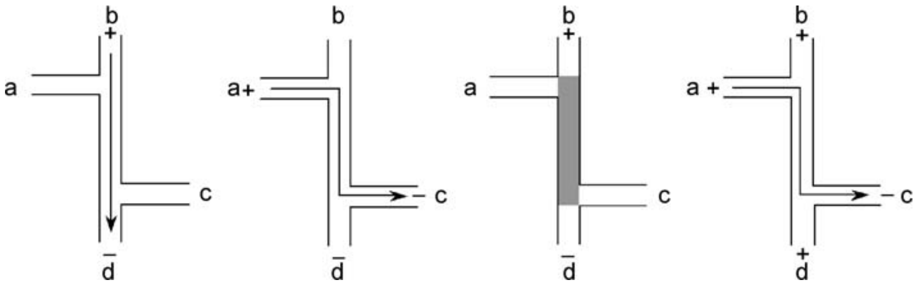

Transferring Samples to Chips, Techniques, Figure 2 Operation processes of (**a–c**) volume-based floating injection and (**d**) pinched injection: (**a**) sample reservoir, (**b**) running buffer reservoir, (**c**) unused reservoir, (**d**) detection reservoir

Efficient assays of real-world samples will require the incorporation of a continuous sampling capability (from the external environment) or rapid sampling of multiple discrete samples. Such ability to continuously introduce real samples into micrometer channels would make *Lab-on-a-Chip* devices compatible with real-life applications. Despite various approaches proposed recently for transferring samples to microchips, the "world-to-chip" interface remains a major barrier for real-life applications of microchip devices.

Key Research Findings

Fang et al. [3] have developed a high-throughput continuous sample-transfer interface for microfluidic chip-based capillary electrophoresis systems. A world-to-chip interface has been fabricated based on a novel flow-through sampling reservoir with a guided overflow design. The flow-through reservoir was fabricated on a glass microchip of crossed-channel design used for CE separations. The 20-μl sample reservoir was produced from a plastic pipette tip and fixed at one end of the sampling channel. Sample change was performed by pumping samples, sandwiched between air segments, through the flow-through reservoir, introduced from an access hole on the bottom side of the chip. A filter paper wrapped tightly around the reservoir guided the overflowing sample solution into a plastic trough surrounding the reservoir and then to waste. The feasibility and performance of the novel system was demonstrated by the determination of arginine, glycine, phenylalanine, and glutamic acid, by continuously introducing a train of different samples through the system without electrical interruption. Maximum throughputs of 80/h were achieved with $<4.1\,\%$ carryover and precisions of 1.5% for arginine and 2.6 % RSD for glycine ($n = 11$) when employing a separation channel of 4 cm (2-cm effective separation length) and a separation voltage of 1.4 kV. The sampling system was tested by continuous monitoring of the derivatization of amino acids over a period of 4 h, involving 166 analytical cycles. There was an outstanding overall precision of 4.8 % RSD ($n = 166$).

Solignac and Gijs [4] have presented a simple capillary electrophoresis microsystem in which the sample is injected hydrodynamically using a pressure pulse. This approach can transfer a sample solution without electric bias, in contrast to a classical electrokinetic injection, in which the magnitude of the electric field in the sample reservoir in combination with variations in electrophoretic mobility can lead to a biased injection. The sample can be loaded using a well controlled and variable pressure pulse ($0.1-1.0$ s) generated by the mechanical actuation of a flexible membrane placed on the sample reservoir of the chip. A fluorescein/calcein-containing borate-tris-hydroxymethylaminoethane (TRIS) sample solution has been taken as a model system for CE analysis. The separation results using pressure pulse injection clearly demonstrate the advantages of this approach. In addition to the reduced bias due to the absence of an electrode in the sample well, this method allows the injection of variable plug volumes by simply changing the pulse length. Figure 3 is a schematic diagram of the cylindrical reservoir used for the pulsed pressure injection. It is identical to a reservoir used with electrodes for electrokinetic pumping, but contains no electrode and is covered by a PDMS membrane that is applied on the top of the reservoir after filling it, but is not firmly bonded to it. This membrane is mechanically actuated with an electromagnet fixed on a linear translation stage. The actuator exerts a mechanical deformation of the membrane (as illustrated in Fig. 3), and provokes a momentary pressure rise within the reservoir. The PDMS membrane provides a good seal with the sample reservoir under pressure. When the membrane is deflected, the pressurized air pushes the liquid in the injection channel. The injection involves small quantities of liquid. The volume flushed into the injection channel is below 0.2 μl, as compared to the 36-μl sample reservoir volume. The pressure is released when the actuator returns to its initial position (after a variable time of $0.1-1.0$ s) using the backforce of a spring. They purposely used a flexible membrane to avoid or strongly reduce "backsucking" from the injection channel.

Most of the sample-transfer methods for microfluidic chips described above have been used to either inject discrete samples into a separation lane on a microchip or perform repeated injections of a single sample. Between

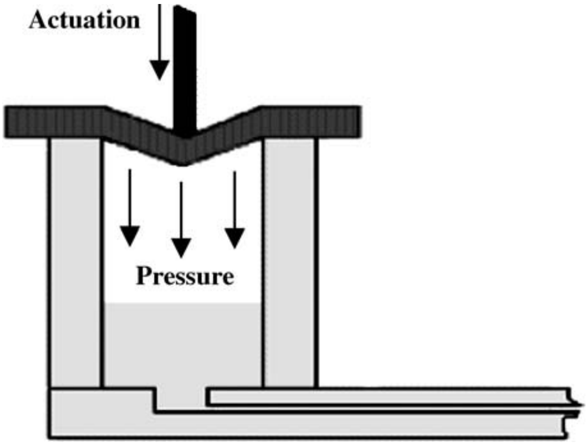

Transferring Samples to Chips, Techniques, Figure 3 Schematic view of the mechanical actuation of the PDMS membrane on the sample reservoir for a pressure pulse injection. (Reproduced with permission from [4])

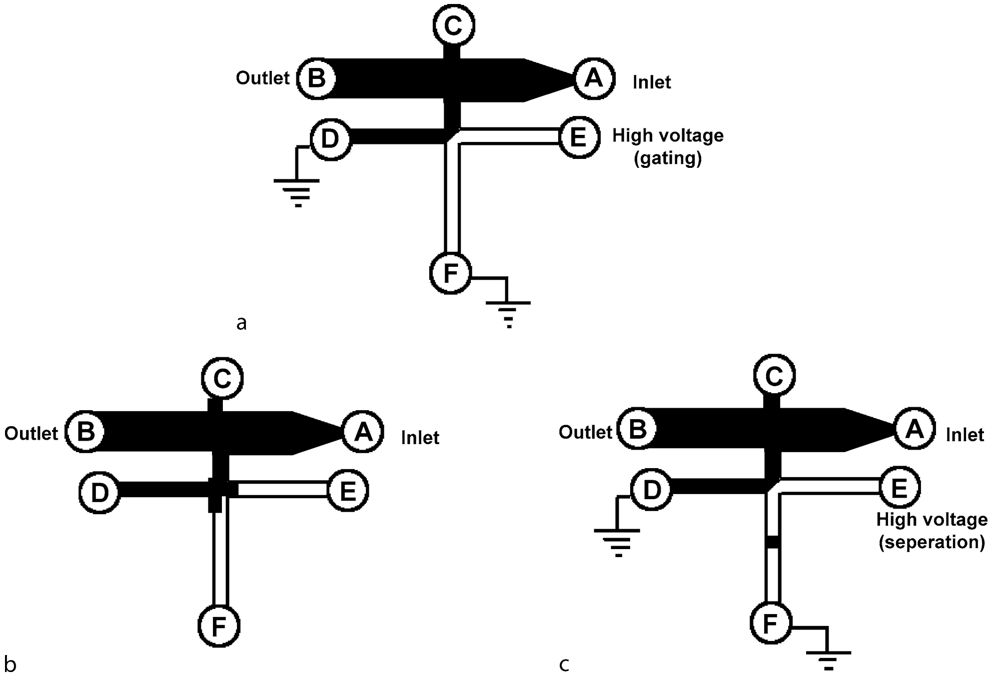

Transferring Samples to Chips, Techniques, Figure 4 A novel flow-through sampling design for continuous sampling on an electrophoresis-based microchip, in which electrical voltages are applied to the electrophoretic channels to control sample loading for separation and detection as well as to inhibit sample leakage. (Reproduced with permission from [5])

analyses of different samples, the reservoirs and channels have often been washed manually and new samples have been placed in the sample reservoirs. This has hindered the realization of high throughput even when very fast separations are achieved on microchips. An attempt must be made to match the amount of time it takes to load the samples into the chip with the high-efficiency characteristic of these microchip devices. Various methods have been developed to transfer samples from the macroworld to a microchip in order to improve the separation throughput and achieve continuous analysis. Chen et al. [5] have proposed a method for the operation of a flow-through sampling chip and its application for immuno-separation, as well as its integration with a wash/elution bed for protein purification, concentration, and detection. This novel device used hydrodynamic pressure to drive the sample flow, and a gating voltage was applied to the electrophoretic channel on the microchip to control the sample loading for the separation and to inhibit sample leakage. Figure 4 illustrates the voltage-switching scheme for this sampling microchip. A high positive voltage, regarded as the gating voltage, was applied to reservoir E while reservoirs D and F were grounded (Fig. 4 (a)). Under this voltage scheme, the inlet flow was split at the first intersection and then directed to reservoir D through the second intersection. For sample loading (Fig. 4 (b)), reservoirs D–F were floating for a specified period that determined the amount of sample transferred to the separation channel. For sample separation (Fig. 4 (c)), reservoirs D and F were immediately grounded and the separation voltage was applied to reservoir E to initiate the electrophoretic separation. Use of this device requires optimization of the gating voltage as a function of the hydrodynamic flow rate. The function of the flow-through sampling microchip has been demonstrated by separation of Cy5-labeled bovine serum albumin (Cy5-BSA) and its antibody complex.

Wang et al. [6] have fabricated a novel dual-injection electrophoretic poly(methylmethacrylate) (PMMA) microchip. It consists of two crosses on both sides of the chip and one separation channel. Anions and cations can be injected electrokinetically from both crosses to the separation channel and then be simultaneously separated and detected. A movable contactless conductivity detector was put along the separation channel between the two crosses to detect the ions. The feasibility, utility, and advantage of this new system has been demonstrated by injecting, separating, and detecting ammonium, methyl ammonium, sodium, chloride, nitrate, and perchlorate (six ionic explosives) simultaneously. This versatile chip can also be used to separate anions or cations alone. The simultaneous detection of anionic and cationic explosives and nerve agent degradation products by the newly designed

chip has also been demonstrated. The attractive properties of the dual-injection chip will find a wide range of other applications in the life sciences, environmental analysis, etc. Figure 5 shows the electropherograms for a mixture solution containing 2 mM ammonium (a), 1 mM methyl ammonium (b), 1 mM sodium (c), 1 mM chloride (d), 1 mM nitrate (e), and 1 mM perchlorate (f) introduced by cathodic injection (A), anodic injection (B), and dual injection (C). As shown in Fig. 5C, six ions were baseline separated by the dual-injection chip after the simultaneous injection. Electropherograms A and B correspond to the detection of the anions alone (via cathodic injection) and of the cations alone (via anodic injection), respectively. In this case, the injection method was changed from the dual-injection described above. It can be seen that the profiles of the single-injection electropherograms of the anions and cations, shown in Fig. 5 (A and B, respectively), are comparable to the corresponding peaks in the combined dual cathodic/anodic injection response (C). Such a microchip layout is therefore very versatile as it offers three operation modes (i. e., anode, cathode, and dual detection corresponding to measurements of the cations, anions, and both, respectively). The change between these modes can be carried out by simply switching the high voltages.

Chen et al. [7] have developed a new CE system based on a PMMA electrophoretic microchip with an easy sample-introduction interface. One side of the PMMA chip was sharpened to fabricate a sharp inlet tip, allowing rapid and reproducible sample introduction into CE microchip devices coupled to contactless conductivity detection. The new microfluidic interface relies on the use of a sharp sample-inlet tip placed alternately in the sample and buffer vials. This design facilitates the electrokinetic introduction of discrete samples directly into the separation microchannel without the use of injection crosses and allows rapid replacement of different samples. One side of the microchip was cut to leave a separation channel (Fig. 6 (see (d)). The hole (b) near the detection point could accommodate the pipette tip (k), allowing the solution connection between the separation channel (d) and the buffer reservoir (j). A 0.8-mm diameter hole (e) was drilled beside the sharp tip to accommodate the Pt high-voltage electrode (f). Figure 6c shows a photograph of the final PMMA microchip with a sharp inlet tip. The sample solution was introduced into the channel by applying the desired potential between the *sample* vial (i) and the buffer reservoir (j) for 2 s. Subsequently, the inlet tip (Fig. 6 (see (h)) was immersed into the running buffer vial (Fig. 6 (see (g)) and the separation voltage was applied between points (g) and (j) in Fig. 6. The high voltage was commonly applied for 2 s after placing the inlet tip in the sample or buffer vials and was disconnected for 3 s before removing the tip from the corresponding vial. The high voltage was disconnected during sample or running buffer change. The solutions in the vials (Fig. 6 (see (g) and (i)) were retained by the surface tension although the orientation of the vial mouths was horizontal. The new sharp-chip design facilitates the analysis of multiple discrete samples through a simplified electrokinetic introduction of highly reproducible sample zones (Fig. 6). Such introduction is carried out directly in the separation channel (without an injection cross) by alternate placement of the inlet tip in vials containing the sample or buffer solutions. This sample introduction results in the insertion of highly reproducible sample plugs and allows rapid replacement of different samples with no apparent carry carry-over because PMMA is hydrophobic. In the case of high concentration samples, the unwanted sample carry-over can be minimized by immersing the inlet tip (Fig. 6 (see (h)) in

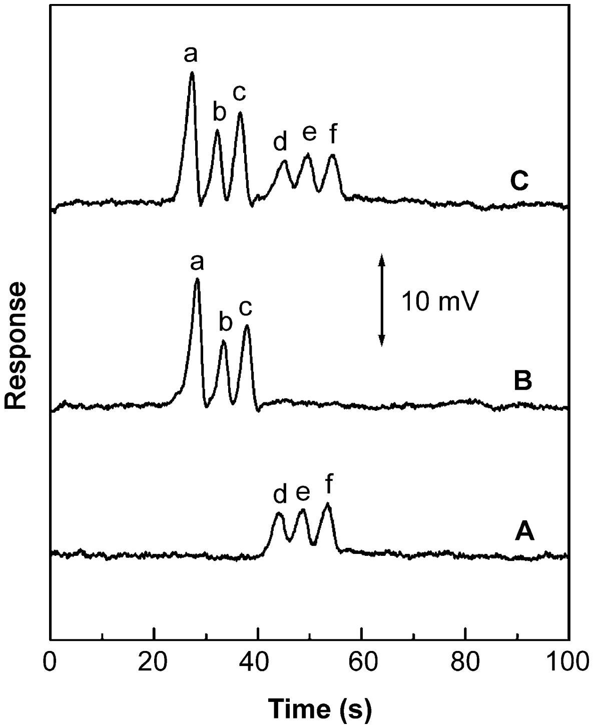

Transferring Samples to Chips, Techniques, Figure 5 Electropherograms for a mixture solution containing 2 mM ammonium (a), 1 mM methyl ammonium (b), 1 mM sodium (c), 1 mM chloride (d), 1 mM nitrate (e), and 1 mM perchlorate (f) introduced by cathodic injection (A), anodic injection (B), and dual injection (C). Operation conditions: separation voltage, +1000 V; injection voltage, +500 V; injection time, 1s; running buffer, 20 mM MES-20 mM His (pH 6.1); sinus waveform with frequency of 200 kHz and a peak-to-peak voltage of 10 V. (Reproduced with permission from [6])

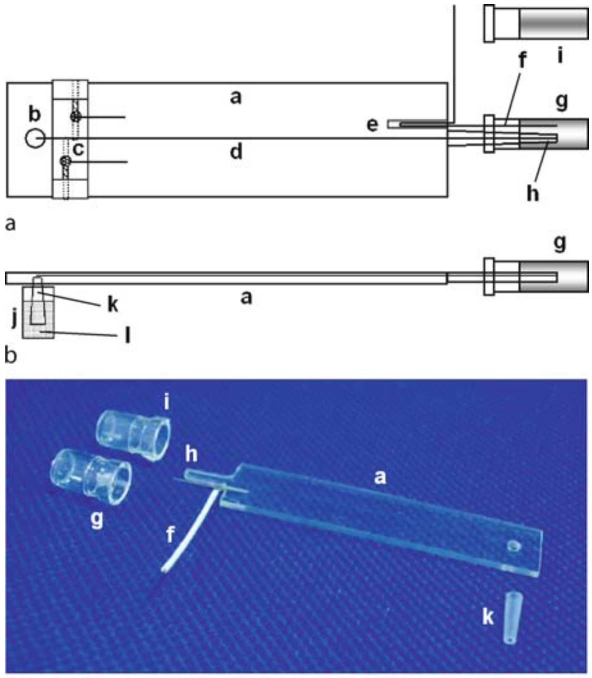

Transferring Samples to Chips, Techniques, Figure 6 (**a**) Top, and (**b**) side view of a PMMA electrophoresis microchip with a sharp-tip inlet (h) and a movable electrode system (c) for the contactless conductivity detection and (**c**) a photograph of the final PMMA microchip with a sharp inlet tip. (a) PMMA chip, (b) hole linked to the buffer solution, (c) movable electrode system, (d) separation channel, (e) hole for the high-voltage power electrode, (f) platinum wire high-voltage electrode, (g) buffer vial, (h) sharp inlet tip, (i) sample solutions vial, (j) buffer reservoir, (k) pipette tip for buffer reservoir, (l) buffer solution. (Reproduced with permission from [6])

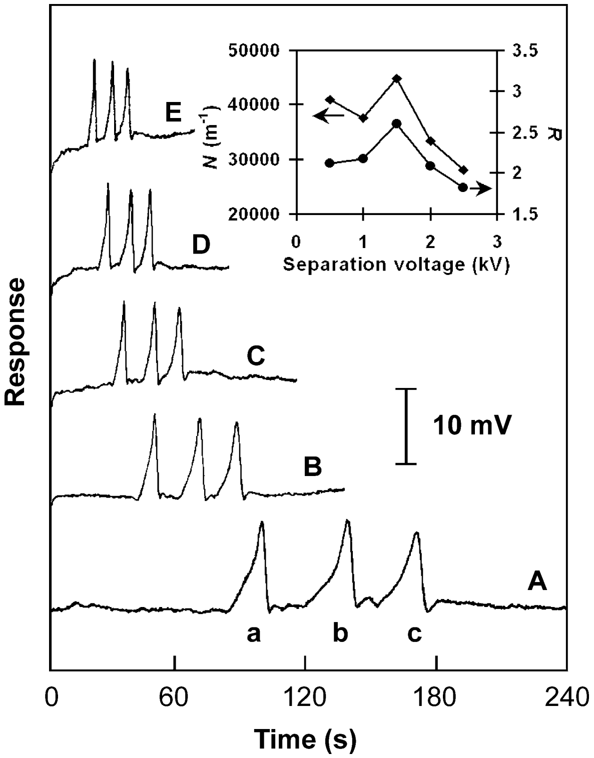

Transferring Samples to Chips, Techniques, Figure 7 Electropherograms for a mixtures containing 1mM potassium (a), 1mM sodium (b), and 1mM lithium (c) at the separation of voltages of (A) +500, (B) +1000, (C) +1500, (D) +2000, and (E) +2500V. Also shown (in the inset) are the resulting plots of the dependence of the plate numbers (*N*) of (c) and the resolution (*R*) between (a) and (b) upon the separation voltage. Operation conditions: injection voltage, +1000V; injection time, 2s; running buffer, 20mM boric acid-20mM TRIS (pH 8.0); sinus waveform with a frequency of 200kHz and a peak-to-peak voltage of 5V; electrode distance, 0.8mm; electrode width, 0.8mm. (Reproduced with permission from [6])

a cleaning vial containing the running buffer for 1 – 2 s before placing the tip in the buffer vial (Fig. 6 (see (g)) for the electrophoretic separation. Figure 7 shows the electropherograms for a mixtures containing 1 mM potassium (a), 1 mM sodium (b), and 1 mM lithium (c) at the separation of voltages of (A) +500, (B) +1000, (C) +1500, (D) +2000, and (E) +2500 V by using the sharp tip microchip. As expected, increasing the separation voltage from +500 to +2500 V (A-E) dramatically decreases the migration time, from 99.6 to 21.1 s, from 140.4 to 29.1 s, and from 174.5 to 36.2 s for potassium (a), sodium (b), and lithium (c), respectively. The inset of Fig. 7 shows the effects of the separation voltage upon the plate number (N/m^{-1}) of lithium (c) and the resolution (R) between potassium (a) and sodium (b). The plots for both N and R versus the separation voltage have the similar profiles. Upon raising the separation voltage between +1000 and +2500 V, N and R increase to the maximum values of 44,814 m^{-1} and 2.6 (at +1500) and decrease gradually to 28,005 m^{-1} and 1.8, respectively. Despite the higher separation voltage, flat baselines and low noise levels are maintained even at high separation voltages. Such behavior indicates an effective isolation from the high separation voltage.

Takabayashi et al. [8] have described the development of a microchip for the detection of nitrogen dioxide (NO_2, a gaseous chemical pollutant) in air. A quartz glass microchip has been fabricated for handling the following three functions: gas absorption, chemical reaction, and fluorescence detection. Channels constructed in the microchip were covered with porous glass plates, allowing nitrogen dioxide to penetrate into the triethanolamine (TEA) flowing within the microchannel beneath. The nitrogen dioxide was then mixed with TEA and reacted with a fluorescence reagent in the chemical reaction chamber in the microchip. The reacted solution was then allowed to flow into the fluorescence detection area to be excited by an ultraviolet light-emitting diode, and the flu-

orescence was detected using a photomultiplier tube. Preliminary studies with standardized test solutions revealed quantitative measurements of nitrite ion (NO_2^-), which corresponded to atmospheric nitrogen dioxide in the range of 10 – 80 ppb.

Kobayashi et al. [9] have developed an efficient system for tri-phase reactions using a microchannel reactor. They conducted hydrogenation reactions that proceeded smoothly to afford the desired products quantitatively within 2 min for a variety of substrates. The hydrogen gas was transferred to the microfluidic channel by pressure and was allowed to interact with the liquid substrates and the solid catalyst. They could achieve an effective interaction between hydrogen, substrates, and a palladium catalyst using the extremely large interfacial areas and the short path required for molecular diffusion in the very narrow channel space. This concept could be extended to other multiphase reactions that use gas-phase reagents such as oxygen and carbon dioxide.

Recently, a glass microimpinger on microchip for gas phase sampling of hydrogen cyanide has been designed and fabricated by Tipple et al. [10]. A microimpinger consisting of a gas sample inlet, gas delivery arms, and an extraction reservoir was fabricated using standard glass microfabrication techniques to extract dilute hydrogen cyanide vapor from a gas delivery system using a basic aqueous trapping buffer. A Teflon membrane was used to contain the liquid sample in the extraction reservoir. The extraction efficiency for sampling the hydrogen cyanide was monitored by forming a fluorescent cyanide isoindole in the reaction of cyanide with naphthalene-2,3-dicarboxaldehyde and taurine. It has been demonstrated that a microfabricated and miniaturized glass impinger could be used as a gas-sampling device on a Lab-on-a-Chip platform. This glass microimpinger relies on the vacuum sampling of gaseous analytes through an extraction solution, much like a traditional impinger. The feasibility and operability of this microimpinger was characterized with regards to hydrogen cyanide vapor sampling. Figure 8 shows the top and side views of the glass microimpinger design. The width and length of the arms extending from the gas sample inlet into the extraction reservoir (Fig. 8 (b)) were 250 μm and 3.5 mm, respectively. These channels were 20 μm deep. The length and width of the gas sample inlet were 6.2 and 3.1 mm, respectively. The small squares shown in the gas sample inlet ($353 \times 353\,\mu m^2$) were intentionally placed in this region to both aid in the further mixing of the diluted cyanide vapor and to provide structural stability to the region during the bonding process. The diameter of the extraction reservoir was 2.10 mm. This diameter and the thickness of the cover plate (5.5 mm) created a reservoir with a total volume of approximately 20 μl.

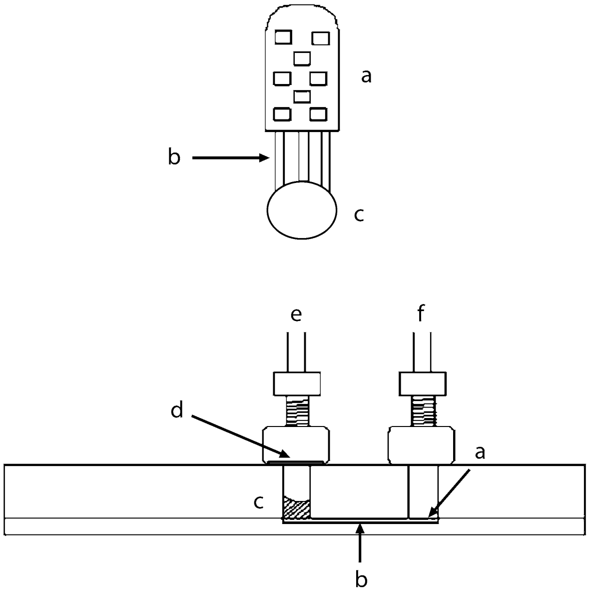

Transferring Samples to Chips, Techniques, Figure 8 Schematic illustration of the glass microimpinger used in these studies. The upper drawing shows a top view layout of: (a) the gas sample inlet, (b) the impinger arms, and (c) the extraction reservoir. The lower drawing shows the side view and the placement of: (d) the Teflon membrane, and the tubing connections (e) for the vacuum pump, and (f) from the gas delivery system. (Reproduced with permission from [10])

Future Directions for Research

Techniques for transferring samples to microchips play a key role in the microchip-based system. Future directions for sample introduction will focus on the automation of the sample transfer to the microchips, the development of the world-to-chip interface for real-life applications, the integration of the sample pre-treatment unit and sample-introduction interfaces, the direct introduction of ► gaseous samples, and various designs for sample introduction. With the rapid development of microfluidic chips, it is highly desirable to develop new theoretical models, experimental methods, and new experimental devices for transferring samples to chips.

Cross References

- ► Active Mixer
- ► Biosample Preparation Lab-on-a-Chip Devices
- ► Control of Microfluidics
- ► Electrokinetic Sample Injection
- ► Lab-on-Chip Devices for Sample Extraction

► Microfluidic Sample Manipulation
► Pressure-based Sample Injection
► Sample Introduction

References

1. Effenhauser CS, Manz A, Widmer HM (1993) Glass chips for high-speed capillary electrophoresis separations with submicrometer plate heights. Anal Chem 65:2637–2642
2. Jacobson SC, Hergenroder R, Koutny LB, Warmack RJ, Ramsey JM (1994) Effects of injection schemes and column geometry on the performance of microchip electrophoresis devices. Anal Chem 66:1107–1113
3. Fang Q, Xu GM, Fang ZL (2002) A high-throughput continuous sample introduction interface for microfluidic chip-based capillary electrophoresis systems. Anal Chem 74:1223–1231
4. Solignac D, Gijs MAM (2003) Pressure pulse injection: a powerful alternative to electrokinetic sample loading in electrophoresis microchips. Anal Chem 75:1652–1657
5. Chen SH, Y LH, Wang LY, Lin CC, Lee GB (2002) Flow-through sampling for electrophoresis-based microchips and their applications for protein analysis. Anal Chem 74:5146–5153
6. Wang J, Chen G, Muck A, Collins GE (2003) Electrophoretic microchip with dual-opposite injection for simultaneous measurements of anions and cations. Electrophoresis 24:3728–3734
7. Chen Y, Yang PY, Li JH, Chen D, Chen G (2006) Electrophoresis microchips with sharp inlet tips, for contactless conductivity detection, fabricated by in-situ surface polymerization. Anal Bioanal Chem 384:683–691
8. Takabayashi Y, Uemoto M, Aoki K, Odake T, Korenaga T (2006) Development and optimization of a lab-on-a-chip device for the measurement of trace nitrogen dioxide gas in the atmosphere. Analyst 131:573–578
9. Kobayashi J, Mori Y, Okamoto K, Akiyama R, Ueno M, Kitamori T, Kobayashi S (2004) A microfluidic device for conducting gas–liquid–olid hydrogenation reactions. Science 304:1305–1308
10. Tipple CA, Smith M, Collins GE (2005) Development of a microfabricated impinger for on-chip gas phase sampling. Ana Chim Acta 551:9–14

Transitional Microchannels

Cross References

► Boiling and Evaporation in Microchannels

Transitional Nanochannels

Definition

Channels with the smallest passage dimension D between 1 μm and 0.1 μm.

Cross References

► Boiling and Evaporation in Microchannels

Transitional Regime

► Gas Flow in Nanochannels

Transition Flow

► Single-Phase Gaseous Flow

Transition in Microchannels

► Turbulence in Microchannels

Transition to Turbulence in Microchannels

Satish G. Kandlikar
Mechanical Engineering Department, Rochester Institute of Technology, Rochester, NY, USA
sgkeme@rit.edu

Synonyms

Laminar to turbulent flow transition; Critical Reynolds number

Definition

Transition from laminar to turbulent flow is identified by a departure from the laminar flow velocity profile, and the presence of time-varying velocity component in the flow, especially near the wall. The wall shear stress becomes higher following the departure from the laminar flow. The transition occurs over a range of Reynolds number, and is dependent on the local wall and flow conditions. Microchannels are defined as channels with the minimum channel dimension in the range from 1 – 200 μm [1].

Overview

Transition to turbulence is the result of localized flow instabilities. As the Reynolds number increases, these instabilities are set in at the wall. The instabilities are also created as a result of the wall roughness or specific structural features present on the wall, such as grooves, ridges and other roughness elements. At Reynolds numbers below the transition value, the instabilities generated are overcome by the flow inertia, and the *relaminarization* process causes the flow to revert back to laminar flow [2]. At higher Reynolds numbers, the instabilities near the wall are propagated into the flow and transition to turbulent

flow occurs. The transition has been linked to the Reynolds number based on the average shear stress Re_τ, [3]:

$$\mathrm{Re}_\tau = \frac{H/2}{\upsilon}\sqrt{\frac{\tau_{\mathrm{w,av}}}{\rho}} > 40 - 60 \qquad (1)$$

Where H is the channel height (the smaller dimension in a rectangular channel), $\tau_{\mathrm{w,av}}$ the average wall shear stress, υ the kinematic viscosity, and ρ the density of the fluid. In internal flows, the laminar to turbulent transition in abrupt entrance rectangular ducts was found to occur at a transition Reynolds number $\mathrm{Re_t} = 2200$ for an aspect ratio $\alpha_c = 1$ (square ducts), to $\mathrm{Re_t} = 2500$ for flow between parallel planes with $\alpha_c = 0$ [4]. For intermediate channel aspect ratios, a linear interpolation is recommended. For circular tubes, $\mathrm{Re_t} = 2300$ is suggested. These transition Reynolds number values are obtained from experimental observations in smooth channels in macroscale applications of 3 mm or larger hydraulic diameters. Their applicability to microchannel flows is still an open question.

Basic Methodology

The transition to turbulence is generally identified by conducting experiments to measure local pressure variation along the length of a tube and estimating the local friction factor value. The local friction factor is then used as an indicator of the type of the flow. Transition from laminar to turbulent flow is identified by noting the departure from the laminar flow friction factor values. As the transition sets in, the friction factor increases above the laminar flow value. Care needs to be taken in ascertaining that the entrance region effects are accounted for properly.

Key Research Findings

Although a number of researchers in 1990s have suggested that the transition to turbulence occurs at lower Reynolds numbers, some of the recent experiments conducted under careful conditions [5–7] have shown that for smooth microchannels, the transition Reynolds number remains the same as for the macroscale channels.

The transitions observed at lower Reynolds numbers are due to the presence of roughness on the wall surface. In order to study the effect of roughness on transition to turbulence, a systematic experimental study was conducted by Kandlikar et al. [7]. A test fixture was developed with 10 mm wide channels, and an adjustable gap to allow for different channel sizes. The two side walls were removable, and different surface features could be machined on them. For smooth channels, the transition was noted to occur between $\mathrm{Re_t} = 2300$ and $\mathrm{Re_t} = 2500$.

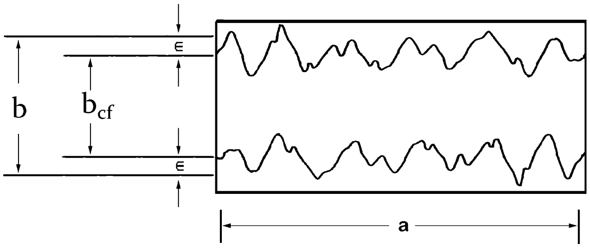

Transition to Turbulence in Microchannels, Figure 1 Geometry of a rough rectangular channel

Different roughness features were introduced by machining ridges onto the walls. As the relative roughness ($= \varepsilon/\mathrm{D_{h,cf}}$) increased, the transition was observed to occur at lower Reynolds numbers. The hydraulic diameter $\mathrm{D_{h,cf}}$ was based on the constricted flow dimensions (representing the free flow area in the channel). Thus for a rectangular channel, shown in Fig. 1, with the long walls having a roughness height of ε, the constricted channel height b_{cf} is expressed in terms of the maximum height of the channel from the base of one wall to the base of the other wall, b, by the following equation:

$$b_{\mathrm{cf}} = b - 2\varepsilon \qquad (2)$$

Figure 2 shows the variation of the transition Reynolds number as a function of $\varepsilon/\mathrm{D_{h,cf}}$. It is observed that for $\varepsilon/\mathrm{D_{h,cf}} = 0.1$, or 10%, the transition Reynolds number is estimated to be as low 700 [7, 10].

The representation of surface roughness itself is an important subject. Taylor et al. [8] provide a detailed descrip-

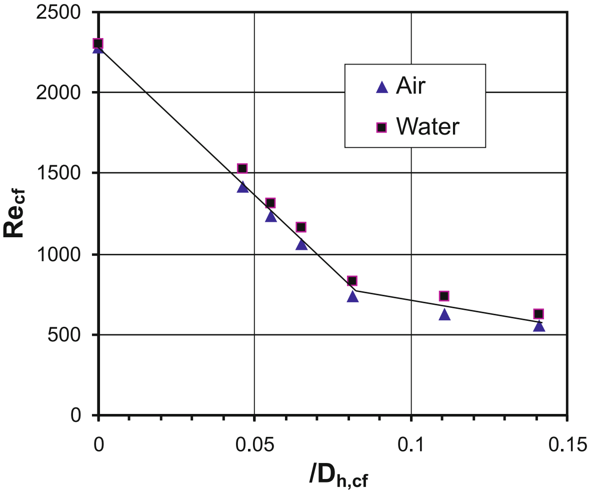

Transition to Turbulence in Microchannels, Figure 2 Variation of transition Reynolds number with relative roughness based on constricted flow diameter, adapted from [7, 10]

tion of various roughness parameters used to represent the roughness of a surface forming the walls of a channel. The traditional roughness parameter Ra was shown to be inadequate as two surfaces with very different surface features, such as ridge heights and pitches, may yield the same Ra, but their fluid flow performance is entirely different. Further details of the specific roughness parameter can be found in [8] and [9].

Future Directions for Research

Since the channel dimensions in a microchannels are less than 200 μm, a roughness height of only several micrometers results in a relative roughness that is sufficient to cause a departure from the flow in smooth channels. The turbulent flow may be desirable in microchannels to enhance the transport processes, such as heat transfer or mass transfer at the wall. It is therefore possible to design microchannels that can effectively use the higher thermal performance characteristics in the turbulent flow. It is essential to keep a watch on the resulting pressure drop. In general, suitable header design will be able to provide a pressure drop that is within an allowable limit.

Mixing in microchannels in another major application where the transition to turbulent flows can be utilized for enhanced mixing possible in turbulent flows. The roughness elements then act to destabilize the flow and induce local instabilities. The localized transition to turbulence will enhance the mixing, and relaminarization process downstream will provide the laminar flow with its lower friction factor and associated lower pressure drop penalties.

Cross References

- ► Developing Flows
- ► Microfluidic Mixing
- ► Pressure Driven Single Phase Liquid Flows
- ► Roughness Effect on Microscale Transport
- ► Turbulence in Microchannels

References

1. Kandlikar SG, Grande WJ (2003) Evolution of Microchannel Flow Passages – Thermohydraulic Performance and Fabrication Technology. Heat Transf Eng 24(1):3–17
2. Narasimha R, Sreenivasan KR (1979) Relaminarization of Fluid Flows. Advances App Mech 19:221–309
3. Mikic BB, Kapat J, Ratnathicam J (1992) Transition to Turbulence in Systems with Eddy Promoters: Implication for the Question of Transition. Phys Fluids A 4(8):1854–1855
4. Hartnett JP, Koh JCY, McComas ST (1962) A Comparison of Predicted and Measured Friction Factors for Turbulent Flow Through Rectangular Ducts. J Heat Transf 84:82–88
5. Baviere R, Ayela F, Le Person S, Favre-Marinet M (2004) An Experimental Study of Water Flow in Smooth and Rough Rectangular Microchannels, Paper No. ICMM2004-2338, Second International Conference on Microchannels and Minichannels. Rochester, NY, USA pp 221–228
6. Bucci A, Celata GP, Cumo M, Serra E, Zummo G (2004) Water single-phase fluid flow and heat transfer in capillary tubes. Paper No. ICMM2004-2406, Second International Conference on Microchannels and Minichannels, Rochester, NY, USA, pp 221–228
7. Kandlikar SG, Schmitt D, Carrano AL, Taylor JB (2005) Characterization of Surface Roughness Effects on Pressure Drop in Single-phase Flow in Minichannels. Phys Fluids 17(10):100606
8. Taylor JB, Carrano AL, Kandlikar SG (2006) Characterization of the effect of surface roughness and texture on fluid flow – past, present and future. Int J Therm Sciences 45(10):962–968
9. Kandlikar SG, Garimella S, Li D, Colin S, King MR (2005) Flow Boiling in Microchannels and Minichannels. In: Heat Transfer and Fluid Flow in Minichannels and Microchannels. Elsevier, London
10. Brackbill TP, Kandlikar SG (2007) Effect of Sawtooth Roughness on Pressure Drop and Turbulent Transition in Microchannels. To appear in Heat Transf Eng

Translocation of Phosphatidylserine

► Microfluidics for Studies of Apoptosis

Transmission-Line Model

Synonyms

Continuous model; Distributed parameter model

Definition

Models arising from the transmission of energy along a finite distance, traditionally associated with electrical transmission cables, but applicable to energy transfer through materials via acoustics, electromagnetics, or electromechanical means.

Cross References

► Piezoelectric Microdispenser

Transmittance

Definition

Transmission is the term used to describe the process by which incident radiant flux leaves a surface or medium from a side other than the incident side, usually the opposite one. The transmittance is the ratio of the radiant flux after it has traversed a surface or medium to its incident flux, often expressed in percentage.

Cross References

► Lab-on-a-Chip Device for Chemical Analysis

Transport of Droplets by Acoustics

ALI NADIM, JAMES D. STERLING
Keck Graduate Institute, Claremont, CA, USA
nadim@kgi.edu

Synonyms

Acoustic droplet ejection; Acoustic levitation of droplets; Droplet transport by surface acoustic waves; Radiation pressure; Surface acoustic waves; Acoustic particle concentration; Droplet manipulation; Drop on demand

Definition

Transport of droplets by acoustics refers to the use of acoustic or ultrasonic waves in fluids or on solid surfaces to generate, manipulate, position or transport liquid droplets, ranging from picoliters to microliters in volume, surrounded by a gas or immiscible liquid phase and/or attached to a solid surface.

Overview

Acoustic waves in liquids can give rise to so-called radiation pressure forces that can in turn drive acoustic streaming flows, deform fluid–fluid interfaces to generate droplets, or exert levitation forces on suspended drops or particles. This contribution reviews three technologically relevant examples of these effects: acoustic droplet ejection, droplet transport along a solid surface using surface acoustic waves, and acoustic levitation of droplets.

Acoustic droplet ejection refers to the process whereby a focused acoustic beam directed toward a liquid–air interface can cause the ejection of discrete droplets of the liquid. Use of surface acoustic waves (SAW) on a solid upon which sessile droplets are attached can cause the migration of those droplets along the solid surface. Finally, standing acoustic waves in flow channels can be used to exert levitation forces on suspended droplets or particles in the channel, causing them to concentrate along a line, which can be applied to sheathless focusing in flow cytometry.

In order to understand the physical underpinnings of the above processes and to be able to model them mathematically, we begin by providing an overview of the relevant concepts from fluid dynamics and acoustics. This is followed by a separate discussion of each of the above applications.

Basic Methodology

In this section, the equations governing acoustic waves in fluids and surface waves in solids are described and concepts from nonlinear acoustics such as radiation pressure and acoustic streaming are reviewed in order to provide an appropriate framework for modeling and simulation of droplet transport by acoustics.

Governing Equations

The equations that govern acoustic waves in an ideal (inviscid) fluid consist of the conservation of mass and linear momentum equations

$$\frac{\partial \rho}{\partial t} + \nabla \cdot (\rho \boldsymbol{v}) = 0\,, \tag{1}$$

$$\frac{\partial (\rho \boldsymbol{v})}{\partial t} + \nabla \cdot (\rho \boldsymbol{v}\boldsymbol{v}) = -\nabla p\,, \tag{2}$$

in which $\rho(\boldsymbol{x}, t)$, $p(\boldsymbol{x}, t)$ and $\boldsymbol{v}(\boldsymbol{x}, t)$ are the density, pressure and velocity fields, respectively, t is time and $\boldsymbol{x}$ is the position vector. In addition, an equation of state (EOS) that relates the pressure and density fields is needed. Since it is usually the case that the fluid remains isentropic during small-amplitude sound propagation, an adiabatic equation of state is generally assumed, in the form [1]:

$$p - p_0 = Q_0 \left[\left(\frac{\rho}{\rho_0} \right)^{\gamma} - 1 \right], \tag{3}$$

where p_0 and ρ_0 are the base pressure and density, respectively, $Q_0 = \rho_0 c_0^2 / \gamma$ and c_0 is the small-signal speed of sound. In an ideal gas, γ is the ratio of the constant-pressure to constant-volume specific heat capacities and $c_0 = \sqrt{\gamma p_0/\rho_0}$, for which Eq. (3) reduces to $p/p_0 = (\rho/\rho_0)^{\gamma}$. For liquids, γ is an empirical parameter and Eq. (3) is known as the Tait equation. For water, $\gamma \approx 7$ and $Q_0 \approx 3000$ bars [1].

Linear Acoustics

Linearization of Eqs. (1)–(3) can be effected by writing the density, pressure and velocity fields as:

$$\rho - \rho_0 = \rho_1 + \rho_2 + \cdots \tag{4}$$

$$p - p_0 = p_1 + p_2 + \cdots \tag{5}$$

$$\boldsymbol{v} = \boldsymbol{v}_1 + \boldsymbol{v}_2 + \cdots \tag{6}$$

in which quantities with subscript '1' are the leading-order perturbations from the base state (referred to as the 'acoustic' fields), with quantities having subscript '2' or higher being successively smaller. Note that it is assumed that the

fluid in the base state is quiescent, so the leading term in the velocity field is due to the linear acoustic signal.

Substitution of expansions (4)–(6) into the governing conservation equations and the EOS and retention of leading terms results in the equations of linear acoustics in the form:

$$\frac{\partial \rho_1}{\partial t} + \rho_0 \nabla \cdot \boldsymbol{v}_1 = 0\,, \tag{7}$$

$$\rho_0 \frac{\partial \boldsymbol{v}_1}{\partial t} + \nabla p_1 = \boldsymbol{0}\,, \tag{8}$$

$$p_1 = c_0^2\, \rho_1\,. \tag{9}$$

Upon taking the partial time derivative of Eq. (7), subtracting the divergence of Eq. (8) from the result and making use of the linearized equation of state (9), the acoustic pressure field is seen to satisfy the linear wave equation:

$$\frac{\partial^2 p_1}{\partial t^2} = c_0^2 \nabla^2 p_1\,. \tag{10}$$

Indeed, the same equation is also satisfied by the density field ρ_1, the velocity field $\boldsymbol{v}_1$ and the velocity potential ϕ_1. The latter may be introduced by noting that for irrotational flows where $\nabla \times \boldsymbol{v} = \boldsymbol{0}$, the velocity derives from a potential: $\boldsymbol{v} = \nabla\phi$.

In the framework of linear acoustics, one can also derive an equation for conservation of *acoustic energy* which involves quadratic terms in the primary acoustic disturbances. That equation is given by [2]:

$$\frac{\partial w}{\partial t} + \nabla \cdot \boldsymbol{I} = 0\,, \tag{11}$$

where the acoustic energy density w and the acoustic intensity vector $\boldsymbol{I}$ are given by

$$w = \frac{p_1^2}{2\rho_0 c_0^2} + \frac{\rho_0 \boldsymbol{v}_1^2}{2}\,, \quad \boldsymbol{I} = p_1 \boldsymbol{v}_1\,, \tag{12}$$

in which $\boldsymbol{v}_1^2 = \boldsymbol{v}_1 \cdot \boldsymbol{v}_1$.

Plane Waves

Starting with the equations of linear acoustics, useful relationships among the variables can be obtained for the case of so-called plane waves [2] propagating in infinite space in a particular direction. If the unit vector in the direction of plane wave propagation is denoted by $\hat{\boldsymbol{n}}$, with the acoustic pressure field of the plane wave given by

$$p_1(\boldsymbol{x}, t) = f(t - \hat{\boldsymbol{n}} \cdot \boldsymbol{x}/c_0)\,, \tag{13}$$

the acoustic velocity and density fields would then be given by [2]:

$$\boldsymbol{v}_1 = \hat{\boldsymbol{n}} \frac{p_1}{\rho_0 c_0}\,, \quad \rho_1 = \frac{p_1}{c_0^2}\,. \tag{14}$$

Note that f can be an arbitrary function of its scalar argument and the above would satisfy the equations of linear acoustics. For instance, for propagation along the x-direction in a Cartesian coordinate system, right-going pressure waves of the form $p_1 = f(x - c_0 t)$ produce a velocity of the form $\boldsymbol{v}_1 = \hat{\boldsymbol{i}}\, p_1/(\rho_0 c_0)$, whereas left-going pressure waves of the form $p_1 = g(x + c_0 t)$ lead to the velocity $\boldsymbol{v}_1 = -\hat{\boldsymbol{i}} p_1/(\rho_0 c_0)$. Here, $\hat{\boldsymbol{i}}$ is the unit vector in the increasing x direction. This becomes an important distinction when the problem of reflection and transmission of a wave across an interface between two media is considered. It is also seen that the product of fluid density and sound speed, $\rho_0 c_0$, provides the proportionality between pressure and speed. This combination occurs frequently in acoustics and is known as the *acoustic impedance*.

The acoustic energy density and intensity vector for a plane wave are given by

$$w = \rho_0 \boldsymbol{v}_1^2 = \frac{p_1^2}{\rho_0 c_0^2}\,, \quad \boldsymbol{I} = \hat{\boldsymbol{n}} \frac{p_1^2}{\rho_0 c_0} = \hat{\boldsymbol{n}}\, c_0 w\,. \tag{15}$$

Radiation Pressure

Acoustic waves in fluids are often characterized by time-periodic oscillations of a given radian frequency $\omega = 2\pi f$ (with f the frequency in cycles per unit time) at any given point in space. As such, time-averages over one period of the oscillation $T = 2\pi/\omega = f^{-1}$ of linear quantities are zero, whereas averages of quadratic quantities over time produce non-zero means. Denoting the time-average over one period by $\langle\cdot\rangle$ and applying this operator to the original momentum conservation equation (2) yields [1]:

$$\nabla \cdot \Pi = \boldsymbol{0}\,, \tag{16}$$

where Π is the acoustic radiation stress tensor

$$\Pi = -\langle p\rangle\, \boldsymbol{\delta} - \langle \rho \boldsymbol{v}\boldsymbol{v}\rangle \approx -\langle p - p_0\rangle\, \boldsymbol{\delta} - \rho_0 \langle \boldsymbol{v}\boldsymbol{v}\rangle\,. \tag{17}$$

To arrive at these results, we have noted that the time-average of the leading partial time-derivative in Eq. (2) is zero and that, since the velocity field is already a first-order quantity (with the base state being one of zero flow), the acoustic stress is correct to second order as written on the far right-hand side of Eq. (17). Here, $\boldsymbol{\delta}$

T

denotes the unit isotropic tensor of rank two whose components in a Cartesian system are given by the Kronecker delta symbol δ_{ij}. That is, in component form, $\Pi_{ij} = -\langle p - p_0 \rangle \delta_{ij} - \rho_0 \langle v_i v_j \rangle$.

The quantity $\langle p - p_0 \rangle$ in Eq. (17) is the *mean excess pressure* and in general, it is nonzero for finite amplitude waves. It is also an *Eulerian* quantity since the time-averaging is being performed at a fixed position in space. Wang and Lee [1] provide a succinct derivation for the value of this Eulerian mean excess pressure, correct to second order but expressed in terms of first-order quantities, in the form:

$$\left\langle p^{\mathrm{E}} - p \right\rangle = \frac{1}{2\rho_0 c_0^2} \left\langle p_1^2 \right\rangle - \frac{1}{2}\rho_0 \left\langle v_1^2 \right\rangle + C$$
$$= \langle V \rangle - \langle K \rangle + C\,. \tag{18}$$

The superscript 'E' is affixed to pressure as a reminder of its Eulerian nature, and $\langle V \rangle = \langle p_1^2 \rangle / 2\rho_0 c_0^2$ and $\langle K \rangle = \rho_0 \langle v_1^2 \rangle / 2$ are the time-averaged potential and kinetic energy densities, respectively. Constant C is independent of both space and time; in linear acoustics it is zero, but at second order, it is sometimes needed to satisfy a constraint such as constancy of total mass or the condition of having no perturbation at infinity.

One can also calculate a *Lagrangian* mean excess pressure by time-averaging the pressure of a material fluid particle which oscillates in space during the passage of the acoustic wave. That pressure, designated by superscript 'L', can be shown to take the form [1]:

$$\left\langle p^{\mathrm{L}} - p \right\rangle = \langle V \rangle + \langle K \rangle + C = \langle w \rangle + C\,, \tag{19}$$

where the acoustic energy density w is defined in Eq. (12).

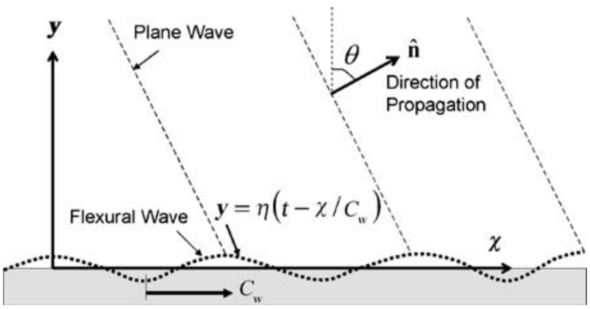

Transport of Droplets by Acoustics, Figure 1 Schematic representation of launching of plane waves in a fluid by small-amplitude traveling flexural waves on a wall. The flexural wave speed c_{W} must be supersonic with respect to the speed of sound c_0 in the fluid for such plane waves to be generated. If the flexural wave is subsonic, the disturbance dies out exponentially with y

Wang and Lee [1] define the so-called Langevin and Rayleigh radiation pressures, respectively, as the mean excess pressures that either depend upon the sound wave only (i. e., with $C = 0$), or on the sound wave together with a constraint which determines the constant C that contributes to the pressure. The concept of the radiation pressure enables the calculation of forces acting upon material surfaces, such as an interface between two fluids or the surface of a particle or a drop in a sound field. Strictly speaking, one should use the acoustic radiation stress tensor Π to calculate such forces. However, in many situations, such as when the surface is rigid or when the velocity at a surface is normal to that surface, it is convenient to use the radiation pressure rather than the full stress.

Sound Radiated by Traveling Flexural Waves

Following Pierce [2] and referring to Fig. 1, consider an infinite plane wall situated at $y = 0$, the region above which (i. e., $y > 0$) is occupied by a fluid with sound speed c_0. Suppose that the wall is undergoing small-amplitude transverse vibrations in the form of a traveling wave that propagates in the positive x-direction, parallel to the wall. In other words, suppose the normal displacement of points on the wall to be of the form $\eta(x, t) = \eta(t - x/c_{\mathrm{W}})$, where c_{W} is the speed of the flexural wave along the wall. The normal velocity of points on the wall is thus given by $v_{\mathrm{W}}(t - x/c_{\mathrm{W}}) = \partial\eta/\partial t$. We consider the limit when $|v_{\mathrm{W}}| \ll c_0$.

The nature of the acoustic disturbance generated in the fluid depends critically upon whether the flexural wave speed is subsonic ($c_{\mathrm{W}} < c_0$) or supersonic ($c_{\mathrm{W}} > c_0$) with respect to the sound speed in the fluid. In the subsonic case, the disturbance in the fluid (generated by constant-frequency excitation of the wall) dies out exponentially with distance y from the surface. On the other hand, when the flexural waves are supersonic relative to the fluid sound speed, plane waves are launched in the fluid at some angle relative with the wall or the vertical. To see this, consider a plane pressure wave in the fluid that propagates in the direction of a unit normal $\hat{\boldsymbol{n}}$. The pressure field for such a wave is taken to be of the form given by Eq. (13), $p_1(\boldsymbol{x}, t) = f(t - \hat{\boldsymbol{n}} \cdot \boldsymbol{x}/c_0)$, satisfying the linear wave equation. The fluid velocity field is therefore given by Eq. (14). Let θ denote the angle between the direction of propagation $\hat{\boldsymbol{n}}$ and the y-axis, as identified in Fig. 1, so that unit vector $\hat{\boldsymbol{n}}$ can be expressed as $\hat{\boldsymbol{n}} = \sin(\theta)\hat{\boldsymbol{i}} + \cos(\theta)\hat{\boldsymbol{j}}$, with $\hat{\boldsymbol{i}}$ and $\hat{\boldsymbol{j}}$ the unit vectors parallel to the x- and y-axes. The y-component of the fluid velocity at the wall is thus given by $\hat{\boldsymbol{j}} \cdot \boldsymbol{v}_1 \Big|_{y=0} = \cos(\theta)(\rho_0 c_0)^{-1} f(t - \sin(\theta)x/c_0)$. This must match the wall velocity that is given by $v_{\mathrm{W}}(t - x/c_{\mathrm{W}})$. One

thus finds the relationships:

$$\sin(\theta) = \frac{c_0}{c_w}\,, \quad f(t) = \frac{\rho_0 c_0}{\cos(\theta)} \boldsymbol{v}_w(t)\,, \tag{20}$$

valid in the supersonic regime $c_w > c_0$. That is, the sine of the propagation angle of the plane waves relative to the vertical direction is given by the ratio of the fluid sound speed to the speed of the flexural waves, and the amplitude and functional form of the pressure of the plane waves in the fluid are determined by the functional form of the transverse velocity of the material points on the wall.

The intensity vector of the radiated plane wave in the fluid, which is a measure of the acoustic energy flux carried by the waves, is given by

$$\boldsymbol{I} = \hat{\boldsymbol{n}} \frac{\rho_0 c_0}{\cos^2(\theta)} \left[\boldsymbol{v}_w(t - \hat{\boldsymbol{n}} \cdot \boldsymbol{x}/c_0)\right]^2 . \tag{21}$$

Note that if c_w decreases toward c_0, θ tends to $\frac{\pi}{2}$ and the direction of propagation becomes parallel to the wall. In that limit, $\cos(\theta) \to 0$ and the radiated acoustic power tends to infinity. This limit cannot be realized because generation of such acoustic waves in the fluid will rapidly deplete the vibrational energy of any such flexural waves [2].

Key Research Findings

We now apply the fundamental concepts outlined above to three specific examples that are relevant to the topic of droplet transport by acoustics; namely, acoustic droplet ejection, droplet transport along a solid surface using surface acoustic waves, and acoustic levitation of droplets.

Acoustic Droplet Ejection

When a focused acoustic beam is directed toward a liquid–air interface from the liquid side, it can cause the ejection of discrete droplets of the liquid that can then be captured by or deposited onto other surfaces. This is shown schematically in Fig. 2. This acoustic droplet ejection (ADE) method and multiple patents based thereupon are the technological basis for the company Labcyte Inc. (Sunnyvale, CA) which uses it for dispensing and liquid handling directed at high-throughput applications [4]. A variety of liquid solvents, containing DNA, proteins, or live cells can be dispensed without loss of activity, at varying volumes ranging from picoliters to microliters.

To model this process, it is instructive to consider first the reflection of a plane wave from a fluid-fluid interface at normal incidence. To this end, we follow a procedure similar to Lighthill [3] who treats the general problem of transmission of waves through junctions. Suppose the interface between the fluids is located at $x = 0$, with the fluid on the left having properties ρ_0 and c_0, while the one on the right has properties $\hat{\rho}_0$ and $\hat{c}_0$. We will affix a caret to quantities that pertain to the fluid on the right. Consider an incident (i. e., right-going) pressure wave in the left fluid given by $p_{1i} = f(t - x/c_0)$. The reflected wave will be a left-going wave of the form $p_{1r} = g(t + x/c_0)$, with the total pressure wave in fluid 1 being the sum of the incident and reflected waves: $p_1 = f(t - x/c_0) + g(t + x/c_0)$. The transmitted wave in the right fluid will be a right-going wave given by $\hat{p}_1 = h(t - x/\hat{c}_0)$. Using the plane-wave relations, the x-velocities in the two fluids are then given by $v_1 = (\rho_0 c_0)^{-1}[f(t - x/c_0) - g(t + x/c_0)]$ and $\hat{v}_1 = (\hat{\rho}_0 \hat{c}_0)^{-1} h(t - x/\hat{c}_0)$. On equating the pressure and velocities at the interface $x = 0$ we find:

$$f(t) + g(t) = h(t) \tag{22}$$

$$(\rho_0 c_0)^{-1}[f(t) - g(t)] = (\hat{\rho}_0 \hat{c}_0)^{-1} h(t)\,. \tag{23}$$

Equations (22) and (23) can be solved for the waveforms of the reflected and transmitted waves, $g(t)$ and $h(t)$, in terms of the waveform of the incident wave $f(t)$ and the ratio $Z = \hat{\rho}_0 \hat{c}_0 / \rho_0 c_0$ of the impedances of the two fluids. The result is that:

$$g(t) = \frac{Z - 1}{Z + 1} f(t)\,, \quad h(t) = \frac{2Z}{Z + 1} f(t)\,. \tag{24}$$

Lighthill [3] points out that for plane wave transmission in channels and tubes, one should actually account for the cross-sectional area change at junctions as well. That is, rather than equating the velocities of the two fluids at junctions, the volumetric flow rates should be equated. For infinite plane waves, our treatment is accurate. If the two fluids have equal impedances so that $Z = 1$, there is no reflected wave ($g(t) = 0$) and the transmitted wave is identical to the incident wave ($h(t) = f(t)$). On the other hand, if the impedance in the right fluid is much less than that

T

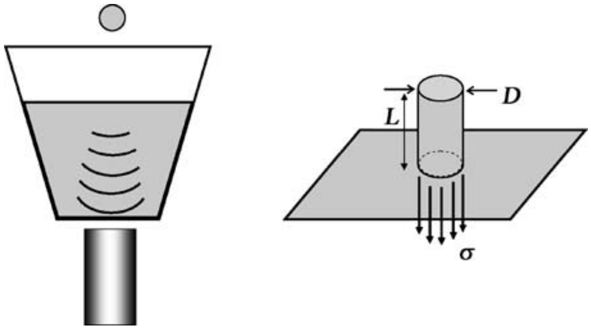

Transport of Droplets by Acoustics, Figure 2 Acoustic droplet ejection

of the left fluid, so that $Z \approx 0$, there will be no transmitted wave ($h(t) \approx 0$) and the reflected waveform is given by $g(t) \approx -f(t)$. This corresponds to the case of waves in water reflecting from a water–air interface, since air has a much lower density and sound-speed (and therefore impedance) than water. Such an interface is often referred to as a pressure–release surface [2] since the pressure at such a perfectly-reflecting interface turns out to be zero.

Now suppose that the incident wave is actually of the form

$$p_{1i} = \mathrm{Re}\left\{A\, e^{i(kx-\omega t)}\right\} , \tag{25}$$

corresponding to a sinusoidal wave of radian frequency ω and wavenumber k (or wavelength $\lambda = 2\pi/k$), with complex amplitude A. Note that the wavenumber and frequency are related by $\omega/k = c_0$. Here Re denotes the real part of its complex argument. Upon incidence on a pressure-release surface, the reflected wave is thus given by

$$p_{1r} = -\,\mathrm{Re}\left\{Ae^{i(-kx-\omega t)}\right\} , \tag{26}$$

which, when added to the incident wave, produces a standing wave of the form:

$$p_1 = 2|A| \cos(\omega t) \sin(kx) , \tag{27}$$

to within an arbitrary shift of the time axis. The corresponding density and velocity fields are then given by

$$\rho_1 = \frac{2|A|}{c_0^2} \cos(\omega t) \sin(kx) , \tag{28}$$

$$\boldsymbol{v}_1 = \frac{-2|A|}{\rho_0 c_0} \sin(\omega t) \cos(kx)\hat{\boldsymbol{i}} , \tag{29}$$

and the time-averaged acoustic energy density turns out to be

$$\langle w \rangle = \frac{|A|^2}{\rho_0 c_0^2} . \tag{30}$$

The Langevin radiation pressure on the interface, given by Eq. (19) with $C = 0$, is therefore also given by

$$\left\langle p^{\mathrm{L}} - p_0 \right\rangle = \frac{|A|^2}{\rho_0 c_0^2} . \tag{31}$$

Wang and Lee [1] provide the corresponding results for a plane wave incident on an interface separating fluids whose impedance ratio is Z, as defined above. The difference in the Lagrangian mean excess pressure across the interface is then

$$\left\langle p^{\mathrm{L}} - \hat{p}^{\mathrm{L}} \right\rangle = \frac{|A|^2}{\rho_0 c_0^2} \frac{(1 + Z^2 - 2nZ)}{(1 + Z)^2} . \tag{32}$$

Here $n = c_0/\hat{c}_0$ is the ratio of the wave speeds in the two media. They also provide more general expressions for the case of sound *beams* (rather than plane waves) that are approximated by a one-term Fourier–Bessel series, having both a radial and an axial wave number. The radiation pressure difference (32) at the interface is said to explain the *acoustic fountain* effect where the directed sound beam creates a liquid jet.

Starting with the radiation pressure of a focused acoustic beam at an interface, Elrod et al. [5] have used useful scaling arguments to characterize the acoustic droplet ejection process as a function of pulse energy and frequency. Their model of the ejection considers an initial expulsion of a roughly cylindrical volume of fluid (as depicted on the right side of Fig. 2) due to the impulse (or momentum) imparted to the interface by the focused acoustic beam. The beam is assumed to be on for a time T which is long compared to the period of the wave, $1/f$, but short compared to the time-scale for the dynamics of the liquid. Focused beams are characterized by the diameter D of the focal spot and axial length L which measures the depth of focus. For an acoustic lens with an F-number of roughly unity, both D and L scale with the wavelength $\lambda = c_0/f$ of the sound wave. Not surprisingly, the diameter of the drop that is finally ejected also scales linearly with the wavelength λ or the reciprocal of the frequency: $D \propto c_0/f$. These same length scales D and L are used to estimate the volume of the cylinder of fluid that is expelled. The volume therefore scales with the cube of the wavelength, or $(c_0/f)^3$. The impulse M delivered to that volume is proportional to the product of the radiation pressure, given by Eq. (31), with the cross-sectional area of the beam, and the time-duration of the pulse, T:

$$M \propto \frac{|A|^2 T\lambda^2}{\rho_0 c_0^2} = \langle w \rangle\, T\lambda^2 = \frac{\left\langle \hat{\boldsymbol{n}} \cdot \boldsymbol{I} \right\rangle T\lambda^2}{c_0} \propto \frac{E}{c_0} . \tag{33}$$

Here, as in [5], we have identified the incident energy pulse E as the product of the acoustic intensity (see Eq. (15)) with the pulse duration and cross-sectional area. This represents the total energy delivered by the beam while it is on. Equating the impulse to the initial momentum of the ejected cylinder, one finds the scaling for the

initial velocity

$$U_{\text{init}} \propto \frac{M}{\rho_0 \lambda^3} \propto \frac{Ef^3}{\rho_0 c_0^4} . \tag{34}$$

The initial velocity of the jet appears to scale linearly with the total pulse energy and with the third power of the acoustic frequency.

As the liquid column is ejected with the above initial velocity due to the impulse delivered by the sound beam, it is continually acted upon by the surface tension σ of the liquid which pulls it downward toward the main liquid bath with a force given by the product of σ with the circumference of the circular cross section of the cylinder $\pi D \propto \lambda$ (see Fig. 2). This constant force decelerates the column until it comes to rest at time

$$t_{\text{rise}} \propto \frac{Ef}{c_0^2 \sigma} , \tag{35}$$

having reached the height

$$h_{\text{rise}} \propto \frac{E^2 f^4}{\rho_0 c_0^6 \sigma} . \tag{36}$$

Whether or not a drop can pinch off during this time depends upon the time-scale for the growth of Rayleigh-Plateau instability on a liquid column, which is given by

$$t_{\text{RP}} \propto \left(\frac{\rho_0 \lambda^3}{\sigma} \right)^{\frac{1}{2}} = \left(\frac{\rho_0 c_0^3}{\sigma f^3} \right)^{\frac{1}{2}} , \tag{37}$$

exhibiting a frequency dependence of $f^{-3/2}$. If the pinch-off time is less than the rise time, a drop can be ejected from the column due to the development of the Rayleigh instability before it returns to the main liquid bath below by the pulling action of surface tension.

Elrod et al. [5] have provided most of the above scaling laws, but have not made use of the fact that a threshold energy for droplet ejection can be obtained by requiring that

$$t_{\text{RP}} < t_{\text{rise}} , \tag{38}$$

so that the drop pinch-off due to Rayleigh-Plateau instability can occur prior to the column returning to the bath. The threshold energy is thus found to be:

$$E > \frac{\rho_0^{\frac{1}{2}} c_0^{\frac{7}{2}} \sigma^{\frac{1}{2}}}{f^{\frac{5}{2}}} . \tag{39}$$

The $f^{-5/2}$ frequency dependence is consistent with experimental observations reported in [5] for which a least-squares fit provides a dependence of the form $f^{-2.3\pm0.2}$. Typical magnitudes for water droplet ejection using a 5 MHz focused beam include a drop of approximately one wavelength in diameter ($\lambda \approx 300\,\mu$m) and a threshold energy in the range of tens of microjoules [5]. Interestingly, most of the energy in the wave is reflected as the interfacial and kinetic energies of the resulting drop are in the nanojoule range [5]. The characteristic time (37) for the Rayleigh instability to lead to droplet pinch-off is hundreds of microseconds, whereas the acoustic pulse used to generated the droplet lasts approximately 20 microseconds, in accordance with the view that the effect of the acoustic beam can be modeled as delivering an initial impulse to the liquid.

A more recent study of droplet ejection from small micromachined nozzles is provided in [6]. The acoustic droplet ejection method has found applications in photoresist deposition and matrix-assisted laser desorption ionization (MALDI) analysis [4], among others.

Droplet Transport by Surface Acoustic Waves

A recent application of acoustics to droplet transport has been through the use of surface acoustic waves (SAW) to move sessile droplets attached to a solid surface [7–9]. The physical basis for this process has been described in simple terms as follows. When a SAW propagating along a surface encounters a liquid drop, as depicted in Fig. 3, by the mechanism described earlier where flexural waves on a solid launch acoustic waves in the surrounding fluid, they launch plane waves at an angle given by Eq. (20) on the side of the liquid drop that they first encounter. The SAW and the corresponding acoustic waves that they generate in the drop diminish rapidly as one moves away from the leading edge of the drop. The acoustic field thus generated within the drop produces a radiation pressure distribution on the drop interface that tends to deform the drop and modify the contact angles at the leading and trailing edges of the drop. Also, mediated by an effect known as acoustic streaming, an internal flow field is generated within the

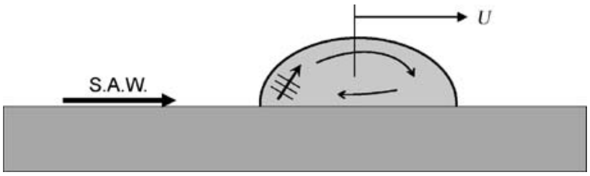

Transport of Droplets by Acoustics, Figure 3 Droplet transport by surface acoustic waves

T

drop that leads to its translational motion parallel to the direction of the original SAW. Typical droplet volumes that are actuated by this effect are tens of nanoliters, although smaller volumes (tens of picoliters) can be left behind on appropriately patterned surfaces as the larger drops move along.

In references [7–9] that describe this phenomenon, the SAW is generated on a piezoelectric substrate with interdigital gold transducers. Typical values of the SAW frequencies and wavelengths are in 100 s of MHz and 10 s of μm, respectively, with the surface wave velocity c_{w} in the range 3000 – 4000 m/s. The amplitude of the waves is said to be in the nanometer range. An order of magnitude analysis can be used to estimate characteristic values of the wave amplitudes that can be established in the droplet. Using an SAW velocity of $c_{\mathrm{w}} = 3000\,\mathrm{m/s}$ and frequency of $f = 100\,\mathrm{MHz}$ provides an SAW wavelength of 30 microns. If we take the amplitude of the wave to be $\varepsilon = 1$ nanometer, the amplitude of the plane pressure waves that get launched in the liquid is estimated to be

$$\frac{2\pi f \varepsilon \rho_0 c_0}{\sqrt{1-(c_0/c_{\mathrm{w}})^2}} \approx 10^6\,\mathrm{Pa}$$

or about 10 atmospheres. The energy density w of such waves (cf. Eqs. (12) and (15)) is approximately $500\,\mathrm{J/m^3}$ or 500 Pa, however. Based on Eq. (19), this is also the approximate magnitude of the radiation pressure that would act upon the droplet interface.

Although a detailed analysis of the flow field within the sessile drops has not been carried out, the coupling between the SAW and the liquid via the oblique plane waves that are launched in the liquid is thought to give rise to acoustic streaming within the droplets or other bulk liquids that are in contact with the solid surface [7–9]. Acoustic streaming refers to nonzero time-averaged bulk flows that result in fluids under the influence of primarily time-periodic acoustic waves [10]. Since time-periodic quantities arising form linear acoustic disturbances have a zero mean, acoustic streaming, like the radiation pressure effect, is based upon nonzero averages of quadratically nonlinear terms. One also needs to include viscous effects in the description. Thus, the divergence of the viscous stress, $\nabla \cdot \tau$, is first added to the right-hand side of the conservation of momentum equation (2). Here, $\tau = \mu[\frac{1}{2}(\nabla \boldsymbol{v} + \nabla \boldsymbol{v}^{\dagger}) - \frac{1}{3}\boldsymbol{\delta}(\nabla \cdot \boldsymbol{v})] + \kappa \boldsymbol{\delta}(\nabla \cdot \boldsymbol{v})$, with μ the shear viscosity of the fluid and κ its dilatational or bulk viscosity. Upon time-averaging the resulting momentum equation and ignoring the dilatational terms that contain $\nabla \cdot \boldsymbol{v}$, one obtains the analog of Stokes equations for the time-averaged quantities, but with an effective body force term, in the form [10]:

$$\nabla \langle p \rangle - \mu \nabla^2 \langle \boldsymbol{v} \rangle = F_e \,. \tag{40}$$

Since acoustic fields p_1 and $\boldsymbol{v}_1$ generally have zero time-averages, the averaged quantities appearing in Eq. (40) could be regarded as being the averages of p_2 and $\boldsymbol{v}_2$ in the series expansions (5) and (6). The effective force, however, involves averages of quadratically nonlinear terms in the first-order quantities, namely

$$F_e = -\nabla \cdot \langle \rho \boldsymbol{v} \boldsymbol{v} \rangle \approx -\nabla \cdot \langle \rho_0 \boldsymbol{v}_1 \boldsymbol{v}_1 \rangle \,. \tag{41}$$

Thus, to analyze acoustic streaming, one must first solve the equations of linear acoustics to obtain the first-order fields. This is followed by the calculation of the effective body force (41) and the solution of the Stokes equation (40) for the time-averaged streaming flow, driven by the effective force. Guttenberg et al. [7] have carried out such an analysis to investigate pumping in a capillary gap driven by SAW.

Acoustic Levitation

In a standing pressure wave characterized by time-periodic acoustic pressure and velocity fields $p_1(\boldsymbol{x}, t)$ and $\boldsymbol{v}_1(\boldsymbol{x}, t)$, consider a spherical droplet of radius R (small compared to the acoustic wavelength) to be located at a given position in space. Upon calculating the scattered acoustic field in the vicinity of the droplet and the resulting radiation pressure acting on its interface, a net force is found to be acting on the drop, obtained via integration of the product of the radiation pressure and the inward-pointing unit normal vector on the entire drop surface. A convenient way to express this acoustic levitation force, F, is in terms of the negative gradient of a potential energy function U, i. e., $F = -\nabla U$, with the potential energy field given by

$$U = 2\pi R^3 \left[\frac{g_1}{3\rho_0 c_0^2} \left\langle p_1^2 \right\rangle - \frac{g_2 \rho_0}{2} \langle \boldsymbol{v}_1 \cdot \boldsymbol{v}_1 \rangle \right] . \tag{42}$$

This result, which is due to Gor'kov (1962), is reviewed in [1] and [11]. The angular brackets denote the time-averages of their arguments at a fixed position in space and dimensionless functions g_1 and g_2 are related to the ratios of the properties of the droplet phase and those of the external fluid. In particular, with $\Lambda = \hat{\rho}_0/\rho_0$ and $\Sigma = \hat{c}_0/c_0$ respectively representing the density ratio and sound speed ratio of the droplet phase (identified with a caret) to the external fluid, these functions are given by

$$g_1 = 1 - \frac{1}{\Lambda \Sigma^2} \tag{43}$$

$$g_2 = \frac{2(\Lambda - 1)}{2\Lambda + 1} . \tag{44}$$

For instance, if in the absence of the droplet, there exists a standing pressure wave of the form: $p_1 = A\sin(kz)\cos(\omega t)$, for which a pressure node is located at $z = 0$, when the droplet center is located at $z = Z$, it experiences the force:

$$F_z(Z) = -\frac{\pi A^2 k R^3}{\rho_0 c_0^2}\left[\frac{g_1}{3} + \frac{g_2}{2}\right]\sin(2kZ) . \tag{45}$$

This force can drive the droplet toward the nodes or the antinodes of the standing wave, depending upon the sign of the factor $g_1/3 + g_2/2$ which in turn depends on the properties of the two fluids. When that factor is positive, the droplets move toward the nodes.

As an application of this effect, a number of recent papers [12–14] have demonstrated and analyzed the potential for concentrating aerosol droplets in cylindrical cavities and for sheathless focusing of particles in a flow cell for subsequent interrogation and sorting. The concentrators are constructed from piezoelectric materials or consist of flow cells that are gel-coupled to piezoelectric transducers and driven at or near resonance modes. Slight modifications to the cavity geometry have been found to have significant impact on the precise positioning of the particles or droplets. The modeling efforts in this area generally require determination of the radiation potential U for the given channel/cavity geometry and investigating the effects of symmetry-breaking changes to the geometry on the radiation potential in order to predict the degree of localization of the particles. The application to sheathless focusing [13] is particularly promising for the development of Lab-on-Chip flow cytometry systems.

Future Directions for Research

There are a number of open problems that can be treated using the modeling principles that have been summarized above. For instance, in the problem of transport of sessile droplets by surface acoustic waves, a detailed understanding of the internal flow within the droplet has not yet emerged. Nor are there simple scaling laws that design engineers can use to predict the speed of droplet motion as a function of the surface wave characteristics and droplet size and physical properties. In acoustic droplet ejection, one can anticipate more detailed computational studies of the droplet pinch-off process using boundary integral methods, initiated in [5], and more sophisticated numerical techniques for multiphase flow systems with interfaces, e. g., the level-set method [15]. The same techniques can also be applied to the problem of acoustic levitation of droplets in order to gain a better understanding of the deformed shapes of levitated droplets [16] or their shape mode oscillations.

Cross References

- ▶ Acoustic Streaming
- ▶ Boundary Element Method and its Application to the Modelling of MEMS Devices
- ▶ Digital Microfluidics
- ▶ Droplet Based Lab-on-Chip Devices
- ▶ Droplet Dispensing
- ▶ Flow Cytometer Lab-on-Chip Devices
- ▶ Flows Driven by Surface Acoustic Waves
- ▶ Interface Capturing Schemes for Free-Surface Flows
- ▶ Interface Tracking Schemes for Free-Surface Flows
- ▶ Interfacial Instability
- ▶ Microfluidic Mixing
- ▶ Supersonic Micro-Nozzles
- ▶ Piezoelectric Microdispenser
- ▶ Surface Tension, Capillarity and Contact Angle
- ▶ Ultrasonic Machining
- ▶ Ultrasonic Pumps

References

1. Wang TG, Lee CP (1998) Radiation Pressure and Acoustic Levitation. In: Hamilton MF, Blackstock DT (eds) Nonlinear Acoustics. Academic, San Diego, pp 177–205
2. Pierce AD (1989) Acoustics: An Introduction to Its Physical Principles and Applications. Acoustical Society of America, Woodbury
3. Lighthill J (1978) Waves in Fluids. Cambridge University Press, Cambridge
4. Papen R, Ellson RN, Olechno J (2004) Sound Effects. Am Lab 36(24):26–30
5. Elrod SA, Hadimioglu B, Khuri-Yakub BT, Rawson EG, Richley E, Quate CF, Mansour NN, Lundgren TS (1989) Nozzleless Droplet Formation with Focused Acoustic Beams. J Appl Phys 65:3441–3447
6. Meacham JM, Varady MJ, Degertekin FL, Fedorov AG (2005) Droplet Formation and Ejection from a Micromachined Ultrasonic Droplet Generator: Visualization and Scaling. Phys Fluids 17:100605
7. Guttenberg Z, Rathgeber A, Keller S, Radler JO, Wixforth A, Kostur M, Schindler M, Talkner P (2004) Flow Profiling of a Surface-Acoustic-Wave Nanopump. Phys Rev E 70:056311
8. Strobl CJ, von Guttenberg Z, Wixforth A (2004) Nano- and Pico-Dispensing of Fluids on Planar Substrates Using SAW. IEEE Trans Ultrasonics Ferroel Freq Control 51:1432–1436
9. Wixforth A, Strobl C, Gauer C, Toegl A, Scriba J, von Guttenberg Z (2004) Acoustic Manipulation of Small Droplets. Anal Bioanal Chem 379:982–991
10. Nyborg WL (1998) Acoustic Streaming. In: Hamilton MF, Blackstock DT (eds) Nonlinear Acoustics. Academic, San Diego, pp 177–205

T

11. Marston PL, Thiessen DB (2004) Manipulation of Fluid Objects with Acoustic Radiation Pressure. Ann NY Acad Sci 1027:414–434
12. Kaduchak G, Sinha DN, Lizon D (2002) Novel Cylindrical, Air-Coupled Acoustic Levitation/Concentration Devices. Rev Sci Instr 73:1332–1336
13. Goddard G, Martin JC, Graves SW, Kaduchak G (2006) Ultrasonic Particle-Concentration for Sheathless Focusing of Particles for Analysis in a Flow Cytometer. Cytometry Part A 69:66–74
14. Kogan S, Kaduchak G, Sinha DN (2004) Acoustic Concentration of Particles in Piezoelectric Tubes: Theoretical Modeling of the Effect of Cavity Shape and Symmetry Breaking. J Acoust Soc Am 116:1967–1974
15. Zheng XM, Lowengrub J, Anderson A, Cristini V (2005) Adaptive Unstructured Volume Remeshing, II: Application to Two- and Three-dimensional Level-Set Simulations of Multiphase Flow. J Comput Phys 208:626–650
16. Yarin AL, Pfaffenlehner M, Tropea C (1998) On the Acoustic Levitation of Droplets. J Fluid Mech 356:65–91

Transport of Droplets by Thermal Capillarity

NAM-TRUNG NGUYEN, ZHENJUN JIAO, XIAOYANG HUANG
School of Mechanical and Aerospace Engineering, Nanyang Technological University, Singapore, Singapore
mntnguyen@ntu.edu.sg

Synonyms

Thermocapillary actuation

Definition

Transport of droplets by thermal capillarity is an actuation concept utilizing thermocapillary forces. A temperature gradient across a liquid droplet leads to a difference in surface tensions at both ends of the droplet. The surface tension difference drives the liquid droplet toward the cooler place.

Overview

Droplet-based microfluidics promises a number of applications for chemical analysis and synthesis. Generally, droplet transport can be achieved by manipulating a droplet's surface tension. Electrowetting or electrocapillarity is a common method for transport, where electrostatic force changes the contact angles and propels a droplet. Thermocapillarity utilizes the temperature dependency of interfacial tension for transporting a droplet. Temperature field on a solid substrate generated by heaters leads to a temperature gradient across a droplet and consequently a surface tension difference across the two ends of the droplet. The imbalance of surface tension makes the droplet move toward a cooler place. Transport of droplets by thermal capillarity is a coupled problem between heat transfer in a solid substrate and the surface tension-driven motion based on Newton's second law.

Basic Methodology

Transport of a Liquid Droplet in a Transient Temperature Field

Figure 1 shows a basic model of the motion of a liquid droplet inside a capillary and under a transient temperature field. At a relatively low heater temperature, the heat radiation can be neglected. The energy equation for heat transport in the capillary wall can be formulated with heat conduction and free convection as

$$\frac{\mathrm{d}T}{\mathrm{d}t} = \alpha \frac{\mathrm{d}^2 T}{\mathrm{d}x^2} - \frac{2hR_\mathrm{o}}{\rho c \left(R_\mathrm{o}^2 - R_\mathrm{i}^2\right)} T \tag{1}$$

where T is the temperature difference between the capillary temperature and the ambient temperature, and α, ρ and c are the thermal diffusivity, the density and the specific heat capacity of the capillary material. R_o and R_i are the outer and inner radii of the capillary as depicted in Fig. 1. The transient boundary conditions of the temperature field are

$$t = 0: \quad T(x) = 0$$

$$t > 0: \quad \begin{cases} x = 0\,, & \left.\dfrac{\mathrm{d}T}{\mathrm{d}x}\right|_{x=0} = -\dfrac{q''}{k} \\ x = L_\mathrm{c}\,, & T = 0 \end{cases}$$

where L_c, q'', k, R_o and R_i are the length of the capillary, the heat flux, the heat conductivity of the capillary's material and the outer and the inner radii of the capillary, respectively. Using the dimensionless variables

$$T^* = \frac{T}{q'' L_\mathrm{c} k}\,, \quad x^* = \frac{x}{L_\mathrm{c}}\,, \quad t^* = \frac{t}{L_\mathrm{c}^2 \alpha}$$

and the dimensionless parameter

$$\beta = \sqrt{\frac{2hR_o L_\mathrm{c}^2}{k\left(R_\mathrm{o}^2 - R_\mathrm{i}^2\right)}}$$

leads to the dimensionless form of Eq. (1):

$$\frac{\partial T^*}{\partial t^*} = \frac{\partial^2 T^*}{\partial x^{*2}} - \beta T^* \tag{2}$$

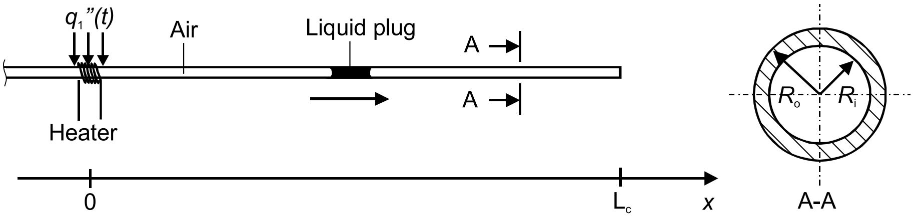

Transport of Droplets by Thermal Capillarity, Figure 1 Model of thermocapillary effect of a liquid droplet in a transient temperature field

as well as the dimensionless boundary conditions:

$$t^* = 0: \quad T^*\left(x^*\right) = 0$$

$$t^* > 0: \quad \begin{cases} x^* = 0, & \dfrac{\partial T^*}{\partial x^*} = -1 \\ x^* = 1, & T^* = 0 \end{cases}$$

Using separation of variables and Fourier series transformation, the solution of the partial differential Eq. (2) is

$$T^* = \frac{1}{\beta}\left[\frac{\sinh(\beta)}{\cosh(\beta)}\cosh\left(\beta x^*\right) - \sinh\left(\beta x^*\right)\right] + \sum_{n=1}^{\infty} D_n \exp\left\{-\left[\left(n-\tfrac{1}{2}\right)^2\pi^2 + \beta^2\right]t^*\right\} \times \cos\left[\left(n-\tfrac{1}{2}\right)\pi x^*\right]$$

$$\frac{\partial T^*}{\partial x^*} = \left[\frac{\sinh(\beta)}{\cosh(\beta)}\sinh\left(\beta x^*\right) - \cosh\left(\beta x^*\right)\right] - \sum_{n=1}^{\infty}\left(n-\tfrac{1}{2}\right)D_n \times \exp\left\{-\left[\left(n-\tfrac{1}{2}\right)^2\pi^2 + \beta^2\right]t^*\right\} \times \sin\left[(n-\frac{1}{2})\pi x^*\right]$$

$$D_n = 2\int_0^1 \left\{-\frac{1}{\beta}\left[\frac{\sinh(\beta)}{\cosh(\beta)}\cosh\left(\beta x^*\right) - \sinh\left(\beta x^*\right)\right]\right\} \times \cos\left[\left(n-\frac{1}{2}\right)\pi x^*\right] \mathrm{d}x^* \tag{3}$$

Figure 2 depicts the analytical transient behavior of the dimensionless temperature distribution along the capillary. The circles represent the position of the droplet in this space–time coordinate system. The liquid droplet is predicted to accelerate first and then slow down when it moves out of the temperature field.

The surface tension is a function of the temperature, which in turn is a function of the position x if a weak thermal interaction between the droplet and the capillary can be assumed:

$$\sigma_{\mathrm{lg}}(T) = f\left[T(x)\right] = g(x) = \sigma_{\mathrm{lg}}(x) \tag{4}$$

The simplest model for the friction between the liquid droplet and the capillary wall is the Hagen–Poiseuille model:

$$\frac{\mathrm{d}p}{\mathrm{d}x} = \frac{8\mu}{R^2}\frac{\mathrm{d}x}{\mathrm{d}t}$$

where $R = R_\mathrm{i}$ is the radius of the droplet and μ is the dynamic viscosity of the liquid. The governing equation for the movement of the liquid drop is

$$\rho\pi R_\mathrm{o}^2 L\frac{\mathrm{d}u}{\mathrm{d}t} = -8\pi\mu L u + 2\pi R_\mathrm{o}\left[\sigma_{\mathrm{lg}}(x)\cos\theta_\mathrm{r} - \sigma_{\mathrm{lg}}(x+L)\cos\theta_\mathrm{a}\right] = 0 \tag{5}$$

where L, θ_r and θ_a are the length and the contact angles at the receding and advancing ends of the liquid droplet,

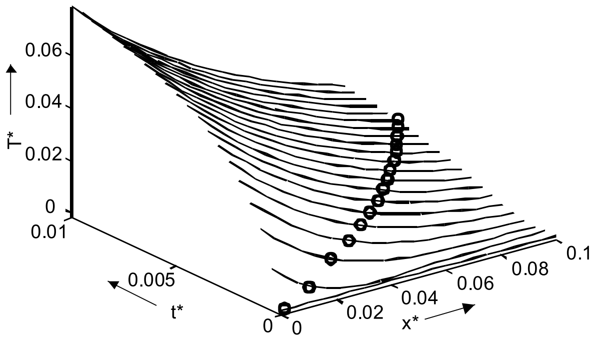

Transport of Droplets by Thermal Capillarity, Figure 2 Graphical representation of the dimensionless transient temperature distribution along the capillary. The circles are the corresponding droplet position in this field

T

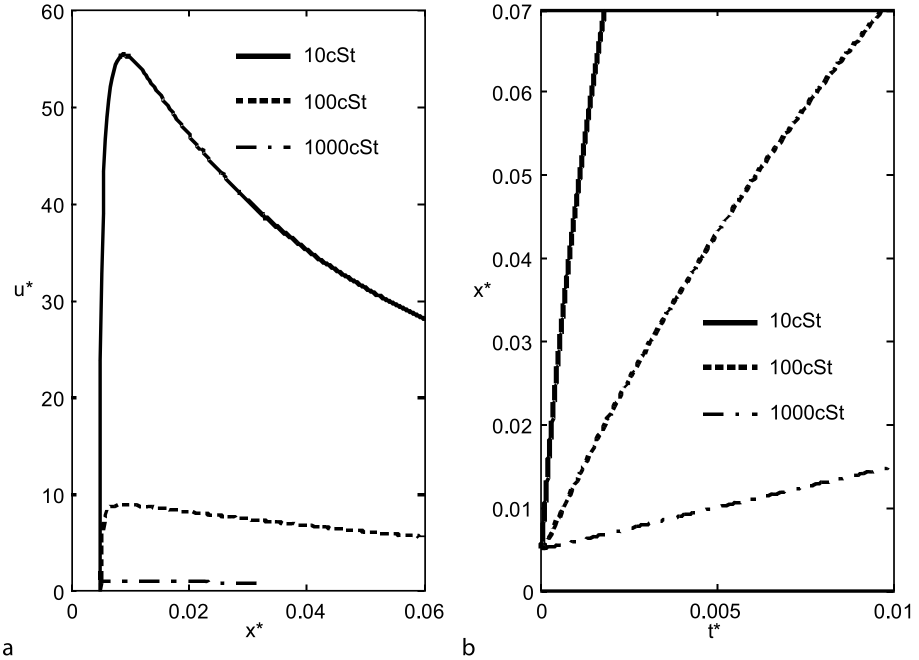

Transport of Droplets by Thermal Capillarity, Figure 3 Position and velocity of the droplet versus time

respectively. Introducing the velocity $u = \mathrm{d}x/\mathrm{d}t$, rearranging Eq. (5) and introducing the kinetic viscosity $\nu = \mu/\rho$, the governing equation of the droplet's motion is

$$\frac{\mathrm{d}u}{\mathrm{d}t} + \frac{8\nu}{R^2}u + \frac{2}{\rho RL}\left[\sigma_{\mathrm{lg}}(x+L)\cos\theta_{\mathrm{a}} - \sigma_{\mathrm{lg}}(x)\cos\theta_{\mathrm{r}}\right] = 0 \tag{6}$$

For a small temperature range, the surface tension can be assumed as a linear function of the temperature:

$$\sigma_{\mathrm{lg}}(T) = \sigma_{\mathrm{lg}0} - \gamma\,(T - T_0)$$

Finally, the velocity of the droplet is determined as

$$u = \frac{B}{A}\left[1 - \exp(-At)\right] \tag{7}$$

with

$$A = \frac{8\nu}{R_{\mathrm{o}}^2}$$

$$B = \frac{2}{\rho R^0 L}\left[\sigma_{\mathrm{lg}}(x+L)\cos\theta_{\mathrm{a}} - \sigma_{\mathrm{lg}}(x)\cos\theta_{\mathrm{r}}\right]$$

Because $L \ll L_{\mathrm{c}}$, the same contact angles at the two ends of the droplet can be assumed. Normalizing the spatial variable, the time and the velocity by L_{c}, L_{c}^2/α and α/L_{c}, respectively, results in the dimensionless velocity:

$$\begin{aligned} u^* &= \frac{B^*}{A^*}\left[1 - e^{-A^* t^*}\right] \\ A^* &= \frac{8\nu}{R_{\mathrm{o}}^{*2}\alpha} \\ B^* &= \frac{2L^3 q''}{\rho R_{\mathrm{o}}^* k\alpha^2}\gamma\cos(\theta)\frac{\mathrm{d}T^*}{\mathrm{d}x^*} \end{aligned} \tag{8}$$

where the asterisk denotes the dimensionless variables. Note that the above dimensionless velocity is the ratio between the droplet velocity and the characteristic spreading velocity of heat in the capillary. Figure 3 shows the position and velocity of the droplet versus time with different liquid viscosities. From the analytical results, it is clear that liquids with lower viscosities can travel much further than those with higher viscosities. As expected from the results of the temperature field, the liquid droplet first accelerates, and then slows down. The acceleration period is determined by A^* in Eq. (8) or the ratio between the kinematic viscosity (momentum diffusivity) of the liquid and the thermal diffusivity of the capillary material. The stabilizing period is determined by B^* or the heat transfer in the capillary wall as modeled in Eq. (8). The less viscous droplet will initially accelerate faster and reach a higher velocity. The velocity then decreases until

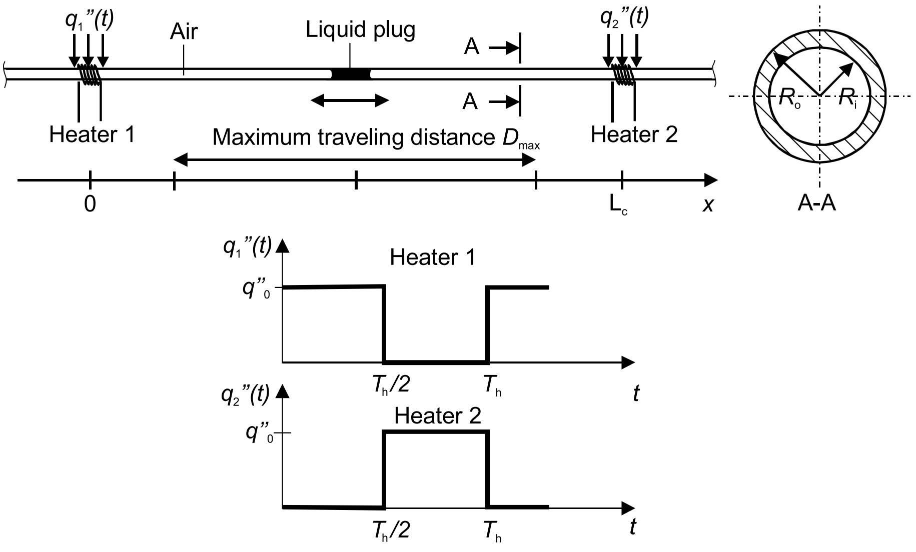

Transport of Droplets by Thermal Capillarity, Figure 4 Model of thermocapillary effect of a liquid droplet in a periodic temperature field

the droplet stops when it moves out of the temperature field. A smaller dimensionless capillary radius R_o^* leads to a higher value of B^* , and consequently to a higher velocity.

Transport of a Liquid Droplet in a Periodic Temperature Field

Figure 4 shows a model of a liquid droplet inside a capillary and under a periodic temperature field. At a relatively low heater temperature, heat radiation can be neglected. The energy equation for heat transport in the capillary wall formulated with heat conduction and free convection remains the same as in the case of a transient temperature field (Eq. (1)), but the periodic boundary conditions are now

$$\left.\frac{\mathrm{d}T}{\mathrm{d}x}\right|_{x=0} = -\frac{q_1''}{k} = -\frac{q''}{k} f_1(t)$$

$$\left.\frac{\mathrm{d}T}{\mathrm{d}x}\right|_{x=L} = -\frac{q_2''}{k} = -\frac{q''}{k} f_2(t)$$

The functions f_1 and f_2 are depicted in Fig. 4. We can also introduce the dimensionless variables

$$T^* = T\frac{k}{q''L_c}, \quad t^* = \frac{t}{T_h}, \quad x^* = \frac{x}{L_c}$$

Eq. (1) then has the dimensionless form

$$\eta \frac{\mathrm{d}T^*}{\mathrm{d}t^*} = \frac{\mathrm{d}^2 T^*}{\mathrm{d}x^{*}2} - \beta^2 T^* \qquad (9)$$

with

$$\eta = \frac{L_c^2}{\alpha T_h}$$

$$\beta = \sqrt{\frac{2hL_c^2 R_o}{\alpha\rho c\left(R_o^2 - R_i^2\right)}}$$

and the dimensionless boundary conditions

$$\left.\frac{\mathrm{d}T^*}{\mathrm{d}x^*}\right|_{x^*=0} = -f_1\left(t^*\right)$$

$$\left.\frac{\mathrm{d}T^*}{\mathrm{d}x^*}\right|_{x^*=1} = f_2\left(t^*\right)$$

The dimensionless temperature field can then be determined as

$$T^* = \sum_{n=-\infty}^{\infty} \left\{ \frac{F_{2n}\mathrm{e}^{\lambda_n} - F_{1n}}{\lambda_n\left(\mathrm{e}^{2\lambda_n} - 1\right)} e^{\lambda_n x^*} + \left[\frac{F_{2n}\mathrm{e}^{\lambda_n} - F_{1n}}{\lambda_n\left(\mathrm{e}^{2\lambda_n} - 1\right)} - \frac{F_{1n}}{\lambda_n}\right] e^{-\lambda_n x^*} \right\} e^{\mathrm{i}2\pi n t^*}$$

$$T(x,t) = \frac{q''L_c}{k}\,\mathrm{Re}\left(T^*\right) \qquad (10)$$

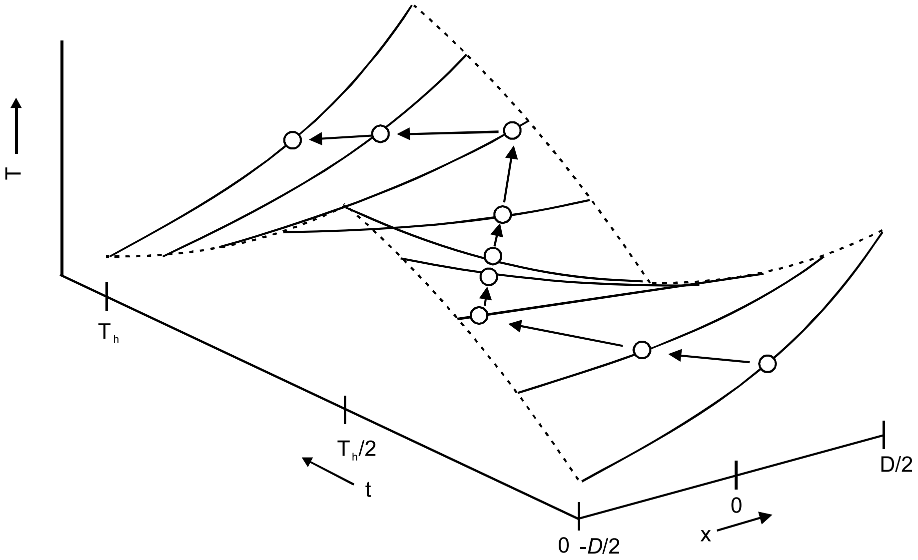

Transport of Droplets by Thermal Capillarity, Figure 5 Graphical representation of the dimensionless periodic temperature distribution along the capillary. The circles are the corresponding droplet position in this field

where Re represents the real part of a complex number and

$$n = 0 \quad \begin{cases} F_{10} = \int_0^1 f_1\left(t^*\right)\,\mathrm{d}t^* = -0.5 \\ F_{20} = -F_{10} \end{cases}$$

$$n \neq 0 \quad \begin{cases} F_{1n} = \dfrac{\mathrm{i}}{2\pi n}\left[1-(-1)^n\right] \\ F_{2n} = F_{1n} \end{cases}$$

Figure 5 depicts the three-dimensional dimensionless temperature difference. Because of the relatively large thermal capacitance of the capillary, a longer heating period T_h results in a better temperature gradient. If the period is too short, both heaters will contribute to an almost uniform temperature distribution.

The motion of the liquid droplet under this periodic temperature field can be obtained in the same manner as previously in the transient case. According to the result, the damping force acting on the droplet is proportional to its viscosity. The higher the viscosity, the smaller is the maximum peak-to-peak traveling distance. A low-viscosity droplet responds quickly to the change of the temperature gradient and causes an initial overshoot in velocity. At a higher viscosity, the response is damped and the velocity curve will have a typical exponential form. Figure 6 depicts the typical dynamic behavior of a droplet at different viscosities.

Key Research Findings

Droplet Motion in a Transient Temperature Field

Figure 7 depicts the measurement results of position and velocity of droplets with different viscosities. The experimental results agree relatively well with the theoretical results shown in Fig. 3. The droplet first accelerates in a short time, but most of the distance is traveled in this period. Initially, the temperature at the heater rises quickly, but temperature spreading along the capillary needs more time. Thus, the initial acceleration is controlled by the heat flux, while the later motion depends on the spreading process of the temperature. During this process, the liquid droplet moves to the cooler region because of the initially high velocity. In this region, the temperature gradient decreases significantly leading to a slowing down of the motion.

Periodic Fields

Figure 8 shows the experimental results of the droplet position and velocity in a periodic temperature field at different switching frequencies. In this case, the experimental results agree relatively well with the theoretical prediction in Fig. 6. Based on both experimental and theoretical data, the dynamic behavior of the droplet is determined by a number of parameters such as viscosity, drop length and switching frequency. In general, the droplet motion can follow the temperature change at low switching frequencies. However, the maximum traveling distance decreases at higher frequencies.

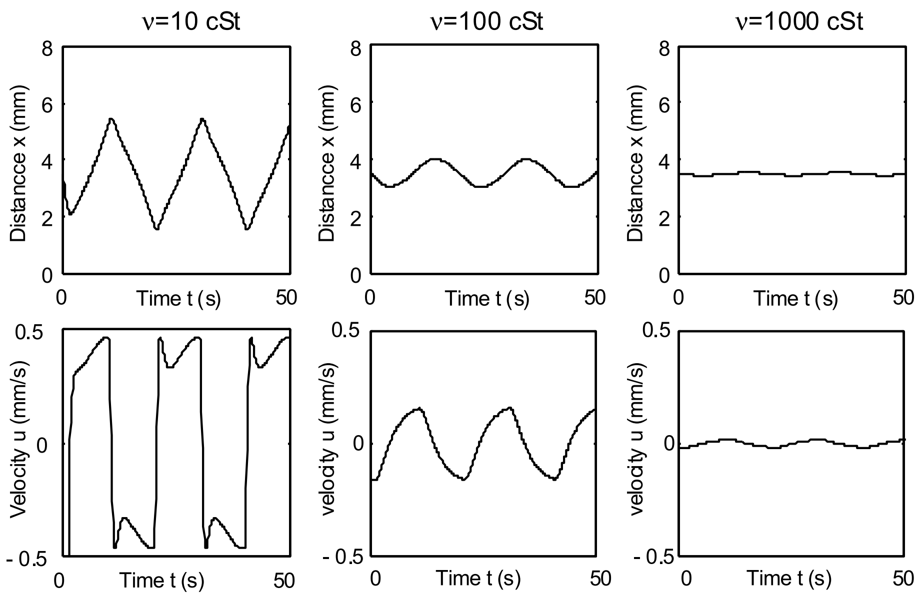

Transport of Droplets by Thermal Capillarity, Figure 6 Position and velocity of the droplet versus time at different viscosities

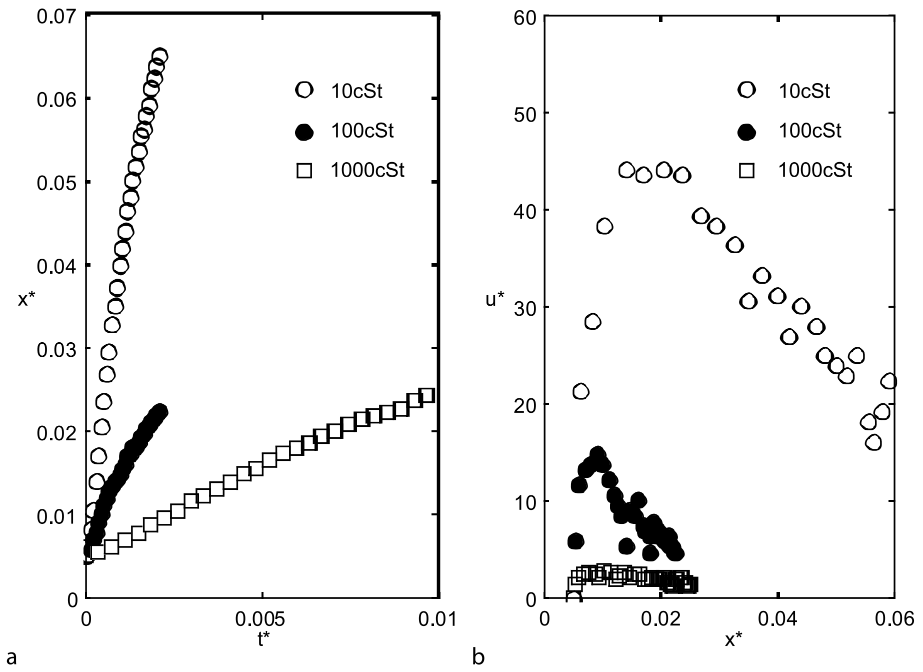

Transport of Droplets by Thermal Capillarity, Figure 7 Measured position versus time and velocity versus position of a droplet in a transient field with different viscosities

A lower liquid viscosity causes a larger traveling distance.

Future Directions for Research

Thermal capillarity is suitable for manipulating liquid droplets in microchannels. Thermocapillary pumps work with the same concept. Theoretical and experimental results show that the droplet motion can be controlled by viscosity, droplet length and the temperature field itself. Using more heaters in an array will allow a more complex droplet motion. In the models presented here the same contact angles at receding and advancing ends were

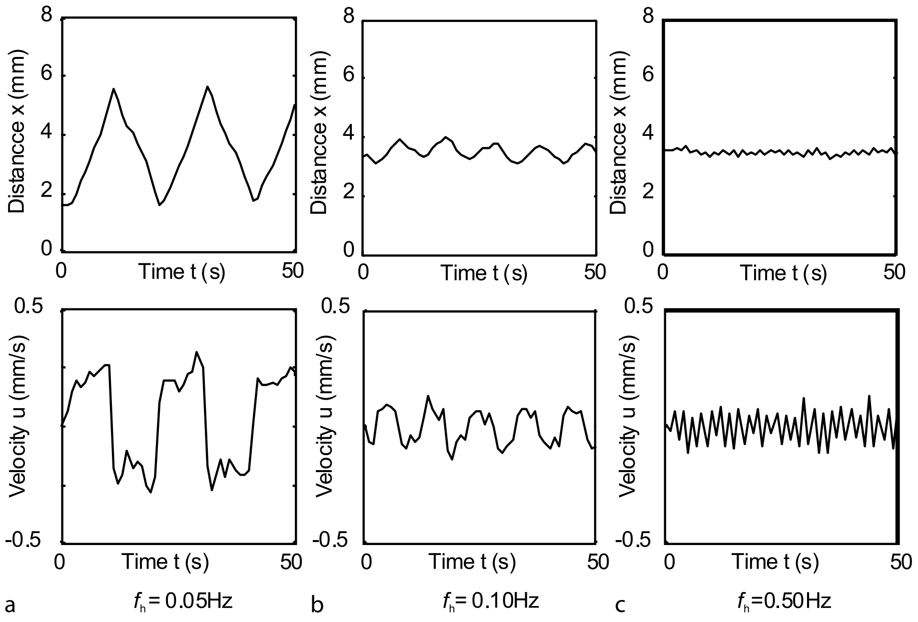

Transport of Droplets by Thermal Capillarity, Figure 8 Measured position and velocity of the droplet at different switching frequencies

assumed. But this is not the case in reality. The contact angles depend on the temperature and the droplet velocity, which directly affect the motion. Consideration of thermal expansion of the liquid, heat transfer inside the droplet and the capillary wall thickness may lead to further interesting findings.

Cross References

► Thermocapillarity
► Thermocapillary Pumping

References

1. Nguyen NT, Huang XY (2005) Thermocapillary effect of a liquid droplet in transient temperature field. Jpn J Appl Phys 44:1139–1142
2. Nguyen NT, Huang XY (2005) Erratum: Thermocapillary effect of a liquid droplet in transient temperature fields. Jpn J Appl Phys 45:6058
3. Jiao Z, Nguyen NT, Huang XY, Ang YZ (2006) Reciprocating thermocapillary droplet motion in an externally heated capillary. Microfluid Nanofluid 3:39–46

Transverse Electrophoresis

► Electrokinetic Motion of Heterogeneous Particles

Trapping Dielectrophoresis

► DC Dielectrophoresis in Lab-on-a-Chip Devices

Traveling-Wave Electro-Osmosis

► AC Electro-Osmotic Flow

Traveling-Wave Pump

Definition

A device for fluidic rectification using a series of nozzles located along a channel for issuing short *puffs* of flow which travel through the channel.

In fluidic pumps, the supplied alternating fluid flow is converted into a mostly one-way (and ideally non-return) output flow. One possibility how to do it is generating a series of travelling waves in a channel by alternating outflows and suction in a series of nozzles arranged along a channel. Each travelling wave drags along another fluid which does not necessarily enter the nozzles. In a more sophisticated versions, the outflow from the nozzles utilizes the Coanda effect of flow attachment to a curved wall.

Cross References

► Valve-Less Rectification Pumps
► Fluidic Pumping
► Fluidic Rectification

Turbulence

► Chaotic Flows

Turbulence Control (Microflap, Microballoon, Microsynthetic Jet)

PRADIPTA KUMAR PANIGRAHI
Department of Mechanical Engineering, IIT Kanpur, Kanpur, UP, India
panig@iitk.ac.in

Synonyms

Flow control; Turbulent shear stress; Mixing enhancement

Definition

A flow field is broadly classified as laminar or turbulent. Pressure, velocity and temperature information are used to characterize a flow field. In turbulent flows, these flow variables are random functions of space and time. The coherent and random flow structures/vortices and interactions between them influence the overall behavior of the turbulent flow field. The location of the wall surface, Reynolds number, Mach number, buoyancy force due to temperature and concentration gradients etc. influence the turbulent flow field characteristics. The nature of flow field also depends on the convective or absolute instability mechanism leading to turbulent flow.

The flow control is a mechanism by which the flow field is manipulated to obtain required behavior in comparison to the natural uncontrolled case. The flow control is broadly classified as: (a) passive control, where no auxiliary power source is required and (b) active control, where there is expenditure of energy. In passive control, parameters like geometry, compliance, temperature and porosity etc. are varied. Boundary oscillation, acoustic waves, blowing, suction etc. are used for active control. The active control schemes use actuators for manipulating the flow behavior. The size of these actuators depends on the nature of the flow. When the Reynolds number is increased, the required size of the actuator is reduced. The availability of MEMS fabrication technique has contributed towards small scale actuators development.

Overview

The industrial applications of turbulent flow control, the design requirements of actuators and the various classification schemes of actuators are discussed in the following sections.

Industrial Applications

The turbulent flow control finds application in various industrial applications: drag reduction, lift enhancement, mixing and or heat transfer enhancement, flow induced noise suppression etc. Reduction in drag of aircraft and underwater body leads to reduced fuel cost and volume. Enhanced heat transfer is desired for heat exchangers and electronic packaging while enhanced mixing is desired in combustors. The reduction in boundary layer noise due to pressure fluctuations helps in operation of under water sonar. To achieve these end results, the flow control techniques aim to control either the transition (delay or advance) or separation (suppression or enhancement) in a wall bounded flow. For an example, when the boundary layer is turbulent on an aircraft wing, the resistance to separation is enhanced and more lift can be attained by operating at higher angle of attack. On the other hand, the skin friction drag for a laminar boundary layer is smaller than that of turbulent boundary layer and therefore the delay in transition leads to lower skin friction drag and flow induced noise.

Implementation Strategy

The turbulent flow control can be implemented through different control schemes [1]. They are: predetermined open-loop control, reactive feed forward open loop control and reactive feedback closed loop control. The physical arrangement of sensors and actuators depend on the nature of control schemes and flow characteristics. The criteria for selection of appropriate actuators have been discussed in next section. It should be noted that the actuators require parasitic power supply for its operation. This fact should be taken into consideration for overall performance analysis of actuators.

Turbulent flow control schemes assume the significant role played by coherent large scale structures or vortices. These structures are responsible for more than 50% turbulence productions. The growth of large coherent structures leads to mixing enhancement. Similarly, the annihilation of large scale structures to small scale structures lead to lower drag. These coherent structures are generated or amplified due to the flow instability and gets convected from the upstream to the downstream locations. The boundary conditions imposed by the actuators located in-between the upstream

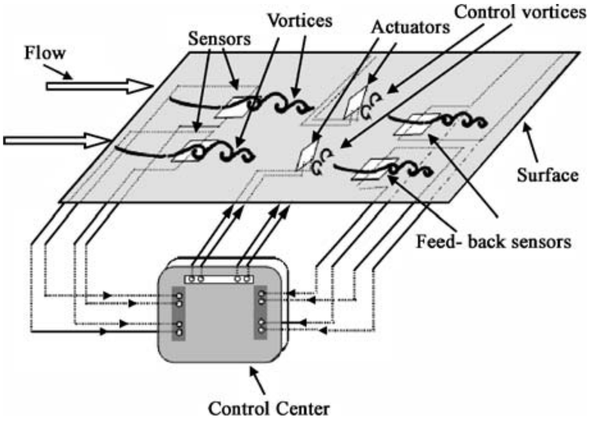

Turbulence Control (Microflap, Microballoon, Microsynthetic Jet), Figure 1 A schematic of flow control arrangement

and downstream locations modify the approaching turbulent structures. One possible turbulent flow control implementation scheme is shown in Fig. 1. The physical system on which the flow control scheme is implemented can be subdivided into three subsystems: (a) flow sensors, which characterize the upstream coherent structures, (b) actuators, which modify the wall boundary conditions experienced by the approaching coherent structures and (c) control sensors, which establishes the coherent structures evolution between upstream and downstream locations and the effect of actuations.

The control sensors are used for verification of control objectives. When, the objective is to reduce drag, the control signal is the shear stress. Similarly, for reduction of pressure fluctuations, the control sensors provide the rms value of pressure fluctuations. For implementation of the control scheme, the relationship/transfer function between the upstream sensors and control sensors is established. Similarly, the transfer function between the actuator properties and the control sensors is obtained. These two transfer functions are used to obtain the actuator state for optimal control.

Actuator Requirements

Due to chaotic nature, the turbulent flow is high dimensional in nature. Therefore, the implementation of turbulent flow control schemes for practical applications is challenging. However, the form and structures in a turbulent flow can be diagnosed and control of turbulent flow is realizable by suitable actuation. It is difficult to specify the requirement of an ideal actuator for turbulent flow control. The ideal characteristics of an actuator for turbulent flow control can be described based on the following guidelines.

- Turbulent flow is quite sensitive to the surface roughness. The actuator should not introduce additional roughness to the surface of the device. It should not have parasitic effect on the flow when the actuator is switched off.
- The frequency to be introduced by the actuators should match with the spatial and temporal frequencies present in the turbulent flow. The high Reynolds number flow has spatial and temporal frequency of the order of microns and kHz respectively. Therefore, MEMS based actuators are ideal for turbulent flow control due to their smaller physical dimension and lower inertia.
- Strength is the other requirement of actuator for maintaining the integrity against the load from the fluid forces.
- During implementation of distributed control with multiple actuators for optimal turbulent flow control, the behavior of the actuators should be uniform for all actuators.

The earlier flow control studies using blowing and suction have shown that the velocity due to the movement of the actuator should be of the order of friction velocity u_τ. For blowing based flow control, the flow blows through the boundary layer when the jet velocity is higher and the control is not effective for boundary layer control. The other observation is that when the size of the actuator is higher than the turbulent length scale ($l = \nu/u_\tau$, where ν is the kinematic viscosity and u_τ is the friction velocity), the surface roughness effect becomes predominant. The size of the actuator is usually about ten times the characteristics turbulent length scale. The operating frequency of the actuator is set based on two criteria:

- The actuator frequency is matched with the instability frequency of the flow and this approach is traditionally successful for separation control;
- The actuator frequency is set higher than the unstable frequency of the flow and the frequency content from the actuator is damped.

Here the actuator acts like a constant flux source without any fluctuations content. This mode acts on the main flow and is effective in turbulent boundary layer control for drag reduction.

Actuator Classification

The actuators can be broadly classified based on their principle of operation as: thermal actuators, electro hydrodynamic actuators, magneto hydrodynamic actuators, momentum injection actuators and moving surface actuators.

Thermal actuators are surface mounted electrical resistor, which injects heat into the near wall flow. The heating of

the working fluid influences the instability of the flow in different ways depending on whether the working field is gas or liquid. The injected heat reduces the fluid density when the working fluid is gas leading to generation of buoyant force. When the working fluid is liquid, there is a decrease in fluid viscosity due to increase in temperature influencing the generation of Tollmien–Schlichting waves. The drawback of these actuators is the low frequency response due to the parasitic heat loss to the solid on which it is mounted and high power consumption.

For an electrically conducting fluid (water or ionized gas), the electrical field can induce motions due to the movement of charged ions or the body forces can be generated due to the interactions between magnetic and electric fields. These options are used in electro hydrodynamic and magneto hydrodynamic actuators. The drawbacks of these actuators are the high voltage requirement and significant loss due to the thermal effect. The micro-fabrication procedure of these types of actuators is not yet established.

The momentum injection actuators act like a source of momentum to the flow. One popular approach in this category is blowing. The other popular actuator in this category which does not require any fluid supply is the synthetic jet. The moving surface actuators provide motion of the wall beneath the flow. These actuators inject momentum to the flow by modification of the surface boundary condition. They introduce localized boundary layer disturbances. Flap actuator and balloon actuator belong to the moving surface actuators. The fabrication procedure of microsynthetic jet, microballoon and microflap actuators is established in literature. The practical applications of these actuators have been demonstrated. The present study discusses the details of these three actuators i. e. microsynthetic jet, microballoon and microflap. Other special MEMS based actuators are electrokinetic actuator, microbubble actuator, microvalve actuator and micropolymer actuator.

Basic Methodology

The physical configuration and the micro-fabrication procedure of microsynthetic jet, microballoon and microflap actuators are discussed in this section.

Micro Synthetic Jet

Configuration

The schematic of synthetic jet is shown in Fig. 2. It consists of a cavity open to the flow through a slit or orifice. The bottom wall of the cavity is driven by a moving surface, which can be either a piston or a vibrating membrane. The vibration of the membrane can be achieved using electrostatic

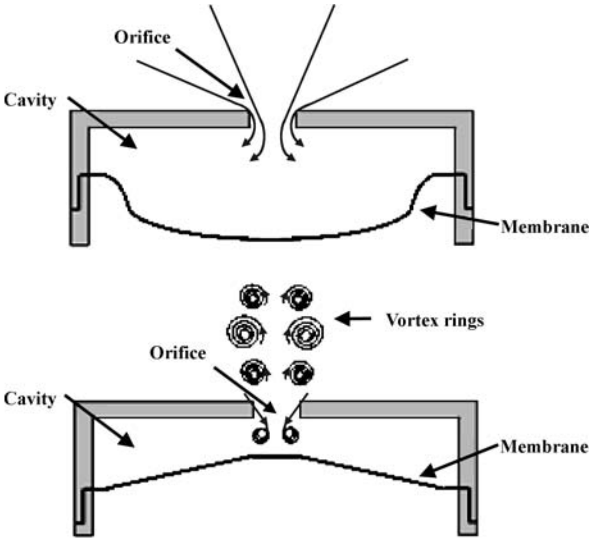

Turbulence Control (Microflap, Microballoon, Microsynthetic Jet), Figure 2 Schematic of synthetic actuator with (top) ingestion and (bottom) expulsion phase

actuation, piezo-ceramic material and differential thermal expansion of the electrode material with silicon layer underneath. When the membrane or piston moves inward of the cavity, fluid is pushed out of the cavity and when the membrane or piston moves back, the fluid is sucked into the cavity. The nature of flow through the slit opening depends on; (a) the frequency of membrane oscillation, (b) the amplitude of the membrane displacement, (c) the size of the orifice and (d) the geometry of the orifice. When the movement of the membrane or piston is small the flow through the slit is reversible during ingestion and expulsion phase. Above an amplitude threshold, the flow through the slit generates acoustic or pressure wave similar to a loud speaker. With subsequent increase in the membrane or piston displacement above a threshold, the outflow separates at the exit corner and a vortex ring moving away from the orifice is formed (see Fig. 2). The jet flow from the orifice draws fluid from the adjacent surroundings contrary to the uniform inward flow during the ingestion phase. Hence, the jet provides a net point source of momentum to the flow. The synthetic jet has zero net mass flux contrary to a normal jet. It imparts a net momentum to the flow without adding any net mass to the system. There is no need of reservoir or piping system for the operation of a synthetic jet. Temporal frequency of the order of 4 kHz can be achieved for a microsynthetic jet. The spatial resolution of the microsynthetic jet depends on the orifice diameter which is of the order of 500 μm. However, the combination of the oscillating membrane size and the substrate increase the overall dimension of the microsynthetic jet limiting the capability of distributed control using multiple actuators.

T

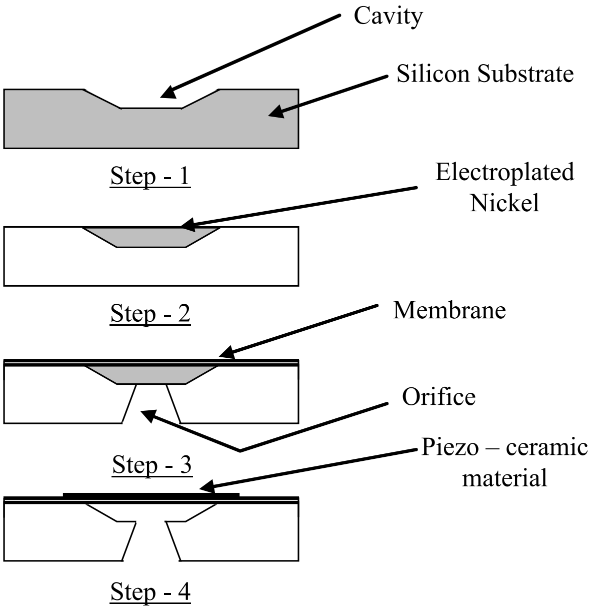

Turbulence Control (Microflap, Microballoon, Microsynthetic Jet), Figure 3 A possible fabrication procedure of μ-synthetic Jet

Fabrication

A possible procedure for synthetic jet fabrication has been shown in Fig. 3. The first step in the fabrication process is the wet etching of the silicon wafer using KOH to form a cavity. The cavity is filled with electroplated Nickel in the second step. A polyimide membrane is deposited over the silicon wafer using spin coating in the third step. The back side of the silicon substrate is etched using KOH to obtain the orifice hole. The orifice hole extends till the filled Nickel inside the cavity and the Nickel material is also etched away. The piezo-ceramic material is deposited on top of the membrane for actuation. In case of electrostatic based actuation, aluminum electrode is deposited on the membrane. The disadvantage of the KOH based wet etching is the limited possible control over the size and shape of the orifice. To have superior control on the dimensional and shape accuracy, dry reactive etching is preferable.

Micro Balloon

Configuration

The schematic of a micro-balloon actuator is shown in Fig. 4.

This consists of Silicone rubber with manifold underneath for pressurized air actuation. The actuation takes place by the deformed shape of the silicone rubber, which is a function of the actuator pressure. The compression and decompression is achieved by a solenoid valve with external compressed air supply. Each micro-balloon consists of about 120 μm thick silicon membrane over two/three holes on a silicone chip. The bottom of Fig. 4 shows the shape and deflection of a balloon actuator at two different pressure levels. The advantage of these actuators is that they can support very large force (> 100 mN) and actuation length (> 1 mm). A micro-balloon can be operated for about 11,000 cycles of inflation and deflation and is robust against harsh environment. The disadvantage of micro-balloon actuators is the low-step response. The other disadvantage is the plastic deformation of the membrane due to stretching at high load. The actuation can be based on micro coil, piezoelectric, electrostatic and electromagnetic principle.

Fabrication

A possible fabrication procedure of the micro-balloon actuator has been shown in Fig. 5. In first step of the fabrication, silicon nitride is deposited using LPCVD (Low Pressure Chemical Vapor Deposition) technique at both sides of the silicon wafer. The back side of the wafer is patterned using reactive ion etching. In the second step, the cavities are etched using KOH based wet etching procedure. In the third step, Parylene-C is deposited on the front side and patterned using oxygen plasma. Parylene-C is used here to act as an intermediate layer between the silicon rubber and the sacrificial materials during the fabrication process. This is required as the sacrificial materials as oxide, silicon, photo-resist and etchants are incompatible with silicone membrane. Before removing the photo-resist, the front side of the wafer is roughened using SF_6/O_2 plasma. The photo-resist is removed and silicone rubber is spin coated on the front side of the wafer in the fourth step. In the fifth step, silcone nitride and Parylene-C are removed from the back side of the wafer using SF_6/O_2 plasma followed by O_2 plasma etching. In the last step, pressurized compressed air is sent through the cavity to release the membrane.

Micro Flap

Configuration

The schematic of flap actuator is shown in Fig. 6. The actuator surface is supported at one end as cantilever support and the actuation takes place due to the external applied force at the other end. The disadvantage of micro coil, piezoelectric and electrostatic actuation is the large voltage requirement. Thus, the devices heat up leading to increase in temperature of the substrate with parasitic heat loss to the fluid. Magnetic

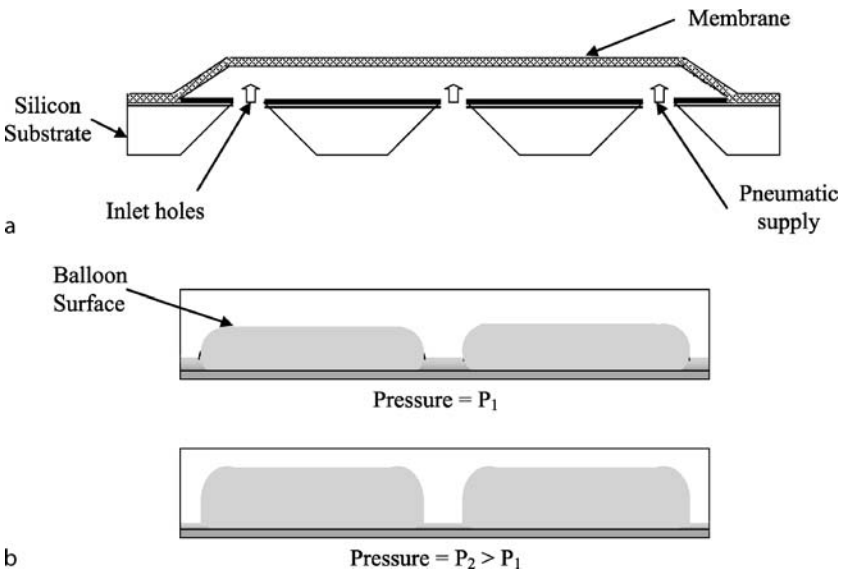

Turbulence Control (Microflap, Microballoon, Microsynthetic Jet), Figure 4 (**a**) Schematic of a balloon actuator and (**b**) the picture of a deformed balloon actuator at two different pressure levels

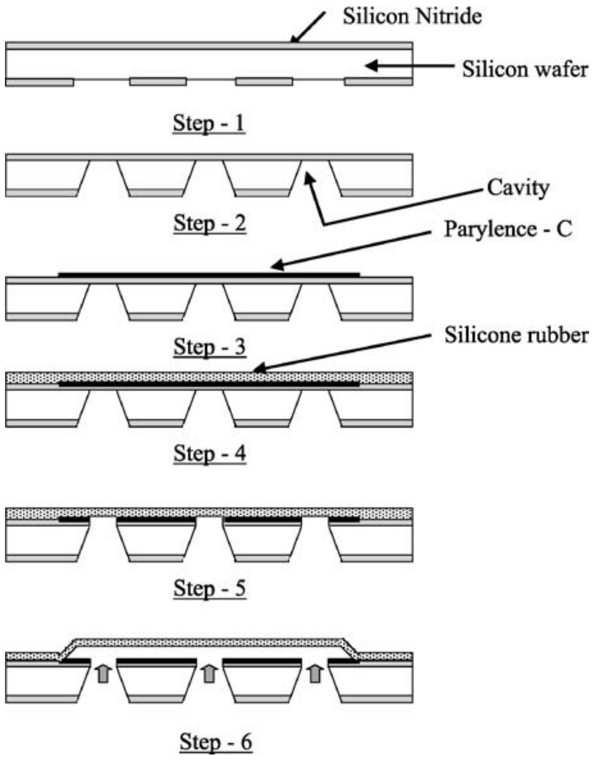

Turbulence Control (Microflap, Microballoon, Microsynthetic Jet), Figure 5 Fabrication procedure of a micro balloon actuator

actuation can achieve large force (order of hundreds μN) and large displacement (tens-hundreds of μm). The actuator consists of suspended magnetic piece supported by cantilever beams. The benefit of magnetic actuation is that magnetic field can be applied externally without any required electrical connections for voltage supply.

Silicon, silicon nitride, silicon elastomer and polymer etc. have been used as flap/membrane materials in literature One mode of operation is the application of current through the coil over electromagnet consisting of thin film coil with current passing through it. The other mode of operation is using a flap fabricated from a permanent magnet (permalloy) and actuated by an external magnetic field. During the rest mode, no magnetic field is applied and the membrane is flushed with the wall. When external magnetic field is applied by using either a permanent magnet or electro magnet, the flaps on the membrane surface are magnetized and a torque is generated due to the interaction between the internal and external magnetic field (see Fig. 6, bottom). The application of torque on the cantilever leads to deflection of the membrane/flap. The strength of the external magnetic field controls the deflection of the flap membrane. The frequency of the voltage supply to the electromagnet can be controlled for dynamic actuation.

Fabrication

The fabrication procedure of a magnetic flap actuator is shown in Fig. 7. The details on the fabrication procedure can be found in Liu et al. [4]. In the first step, phosphosilicate glass sacrificial thin film is deposited on top of the silicon substrate. This thin film is patterned to form mesas on which the actuator will be deposited. The mesas help in

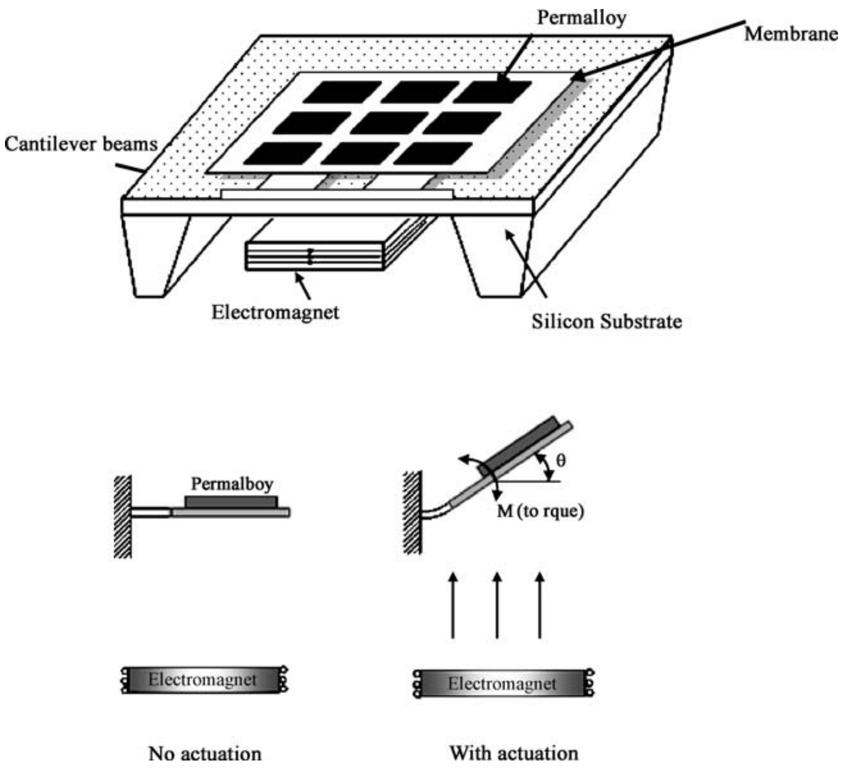

Turbulence Control (Microflap, Microballoon, Microsynthetic Jet), Figure 6 Schematic of a magnetic flap actuator

limiting the possible undercut during the etching process. The photoresist layer is removed and the wafer is annealed in nitrogen at 1000°C for one hour. Subsequently, a layer of LPCVD polycrystalline silicon is coated on which thin phosphosilicate glass layer is deposited for doping purpose. Annealing at 950°C in nitrogen for one hour is carried out next for stress relieving and doping. Conductive seed layer (200 Å thick cromium and 1800 Å thick copper) is thermally evaporated in step 2. The permalloy (80% nickel and 20% iron) piece is electroplated in the third step. During electroplating, the wafer is affixed to the cathode and a pure Ni piece acts as anode. An external magnet is applied with the field lines being parallel to the wafer substrate. This establishes the easy axis of the permalloy parallel to the length of the cantilever beams. In step 4, the photoresist material is removed. The exposed seed layer material is than etched away. For etching copper, etchant (water : acetic acid : hydrogen peroxide) is used. For cromium etching, etchant (water : HCL = 10 : 1) is used. In the final fifth step, HF etching is used for about 20 minutes to release the actuators. The sacrificial layer is removed by etching and there is little effect on polysilicon. The permalloy sustains no structural and chemical damage.

Key Research Findings

The operational characteristics and salient examples of microsynthetic jet, microballoon and microflap applications have been discussed in the following sections.

Micro Synthetic Jet Characteristics

Different non-dimensional numbers and their critical value characterize the operation of a microsynthetic jet. Reynolds number and Stokes number are used to describe the viscous and unsteady effects respectively. The Reynolds number (Re) is defined based on the maximum jet velocity, U at the exit of the orifice and orifice diameter (d) as (see Fig. 2):

$$\mathrm{Re} = \frac{Ud}{\nu} \tag{1}$$

where, ν is the kinematic viscosity of the fluid. When the jet Reynolds number is less than a critical value of about 50, the flow is reversible. For this case, the flow is identical during suction and blowing phase. When the Reynolds number exceeds the critical Reynolds number, the jet separates from the orifice edge. The Stokes number (Stk) is

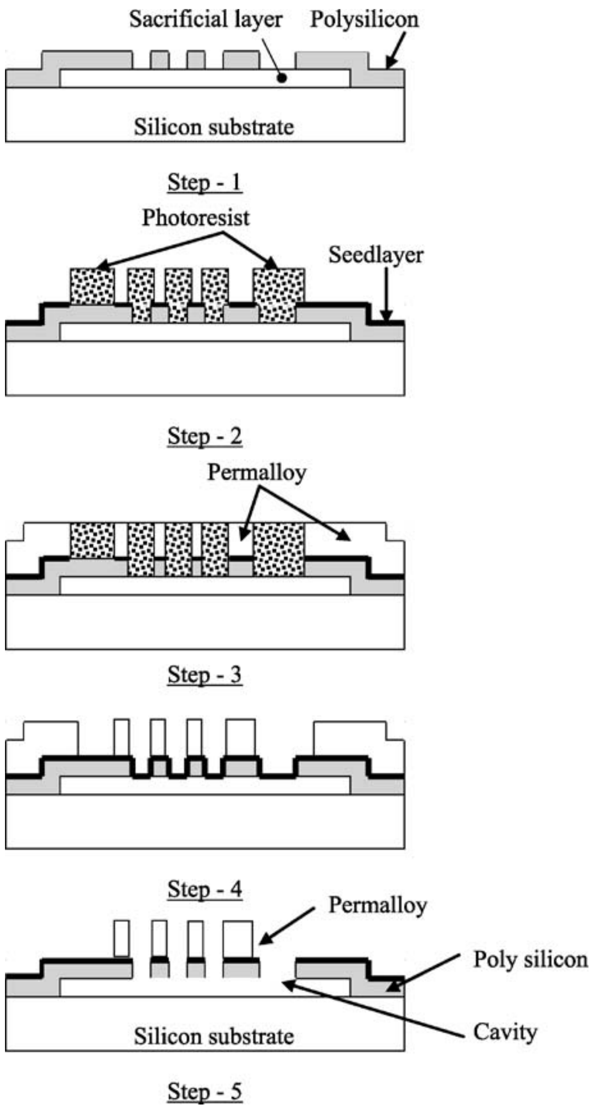

Turbulence Control (Microflap, Microballoon, Microsynthetic Jet), Figure 7 Fabrication procedure of a magnetic flap actuator

defined as:

$$\mathrm{Stk} = \sqrt{\frac{\omega d^2}{\nu}} = \sqrt{\frac{d^2}{\delta_v^2}} \tag{2}$$

where, ω is the oscillation frequency of membrane and δ_v is the thickness of the unsteady boundary layer. Stokes number is the ratio between the orifice diameter and the thickness of the boundary layer at the exit of the orifice. When Stk is large, the viscous effect is not significant. When Stk is small, the viscous effect dominates and the exit velocity from the orifice reduces. This phenomenon is known as *viscous choking*. The increase in orifice size minimizes the viscous effect; but there is a simultaneous reduction in the exit velocity due to large flow area. Hence, a compromise solution is essential for the design of the micro-synthetic jet. The ratio between the square of the Stokes number and Reynolds number is known as Strouhal number (St):

$$\mathrm{St} = \frac{\omega d}{U} \tag{3}$$

The high value of Strouhal number indicates that the number of membrane cycle is higher than the frequency of fluid element passage through the orifice. The low Strouhal number value indicates similar actuation cycle of the actuator and the fluid element. Low Strouhal number indicates higher strength of the jet with low viscous losses. The *stroke ratio* which is defined as the ratio of the expelled stroke (L) to the diameter of the orifice (d) is also used to characterize the vortex ring formation of a synthetic jet. At higher stroke ratio (L/d), the vortex ring formed is disconnected from the trailing jet and at lower stroke ratio only single vortex ring is formed. The transition between these two cases is known as *formation number* and is usually within the range of 3.6 – 4.5.

The stroke ratio $L/d = U/(\omega d)$ is equal to the inverse of the Strouhal number. However, the limitation of stroke ratio definition is the assumption of slug-velocity profile. Holman et al. [2] discussed the formation criteria of synthetic jet based on both numerical simulation and experiment. They observed that vortex ring needs to withstand the suction velocity during ingestion stroke which is a function of the vortex strength. From dimensional reasoning, they proposed the following criterion for jet formation:

$$\frac{\mathrm{Re}}{\mathrm{Stk}^2} = \frac{1}{\mathrm{St}} > K \tag{4}$$

The above equation indicates that vortex escapes when the Strouhal number is less than a critical value. The constant K is a function of orifice geometry, the aspect ratio of the orifice, the shape of the exit edge i. e. sharp or rounded. The constant (K) is approximately equal to 1.0 and 0.16 for two-dimensional and axisymmetric synthetic jet respectively. Figure 8 shows the vorticity distribution during the ingestion and expulsion phase of a synthetic jet. The no-jet case corresponds to the K value less than 1.0 and the jet formation case corresponds to K value greater than 1.0 for a two-dimensional synthetic jet. For the jet formation case, the separated vortex ring is not dragged into the cavity during the ingestion stroke leading to a net momentum transport to the flow. Figure 8 compares the Reynolds number versus Stokes number relationship between the jet and no-jet formation case from both experimental and theoretical data (Holman et al. [2]). The small discrepancy between

T

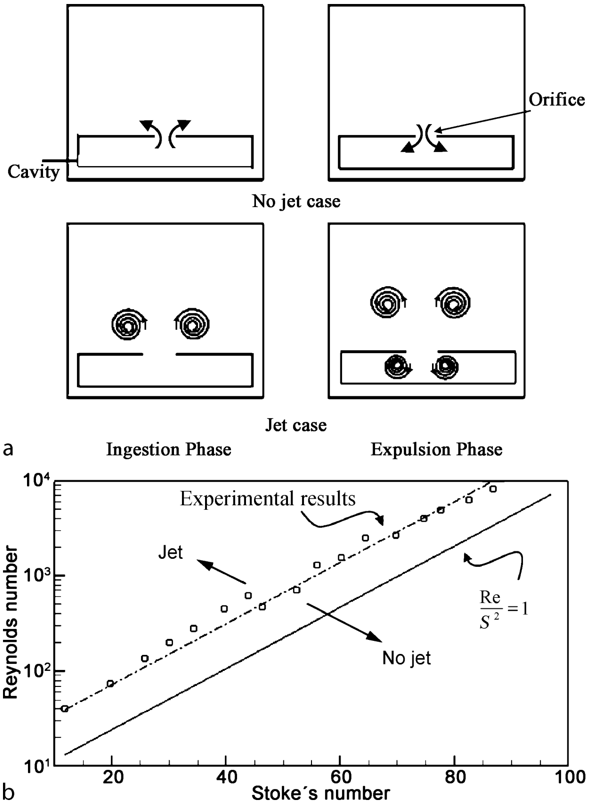

Turbulence Control (Microflap, Microballoon, Microsynthetic Jet), Figure 8 (**a**) Vorticity plots for synthetic Jet during no formation (top) and formation (bottom) cases. (**b**) Reynolds number ($U_0 d/\gamma$) versus Stokes number ($\sqrt{\omega}d^2/\gamma$) of synthetic Jet, for no and formation cases

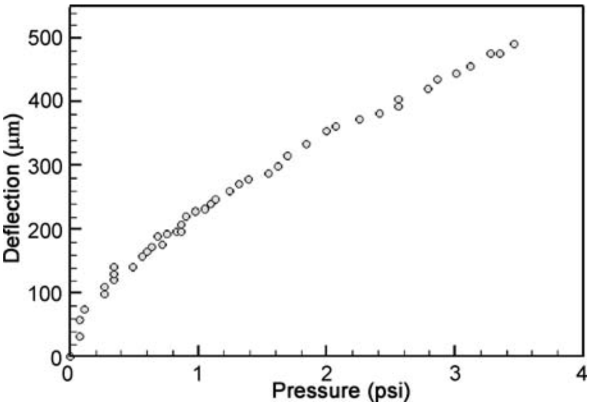

Turbulence Control (Microflap, Microballoon, Microsynthetic Jet), Figure 9 Deflection versus actuation pressure of a balloon actuator

the two is attributed to the orifice geometry or curvature effect.

Lee et al. [8] presented the effectiveness of micro-synthetic jet for modification of turbulent boundary layer under adverse gradient. They showed significant mixing enhancement of the boundary layer when the forcing frequency is closer to the natural instability frequency. The boundary layer modification is more sensitive to forcing frequency compared to the forcing amplitude. The near wall mean velocity and turbulence intensity are significantly enhanced due to the operation of the synthetic jet. The synthetic jet needs to have sufficient velocity output and strong longitudinal vortices for effective flow control.

Micro Balloon Characteristics

The deflection of a micro balloon actuator depends on the actuation air pressure. Figure 9 shows the deflection versus pressure relationship of a silicone based balloon actuator. It shows the direct relationship between the applied pressure and the deflection. The plastic deformation of the balloon and the effect due to cyclic variation is used to decide the operating range of the micro balloon. Tung et al. [6] investigated the compressible flow separation control of a three-dimensional wing section using micro-balloon actuators. A glass plenum was used for supply of compressed air to the balloons. An initial pressure was applied for overcoming the stiction of the diaphragm to the substrate. The balloon deflection of about 1.2 mm was obtained during the testing experiment. The actuation pressure was varied between 4.5 to 7.5 psig depending on the Mach number of the flow. The micro-balloon actuator was shown to be successful in control of separation characteristics. A large pressure recovery was observed during the activation of the micro-balloon actuator. However, the shear stress sensors showed reduction in lift to drag ratio due to the micro-balloon actuation indicating the necessity of proper optimization of control technique. The micro-balloon was shown to be robust demonstrating its ability for high speed flow control applications.

Micro Flap Characteristics

Liu et al. [4] investigated the effect of micro-flap actuator on a delta wing airfoil. The flap was 400 µm long and 100 µm wide. The calibration of the flap actuator was carried out in still air. An electromagnet was used to provide uniform external magnetic field. The magnetic field intensity was measured using Gauss meter. The angular displacement with respect to the magnetic field intensity is shown in Fig. 10. Large angular deflections (about 60 deg) and vertical deflections (about 1 – 2 mm) was demonstrated. It shows the asymptotic variation of flap displacement angle with respect to the magnetic filed

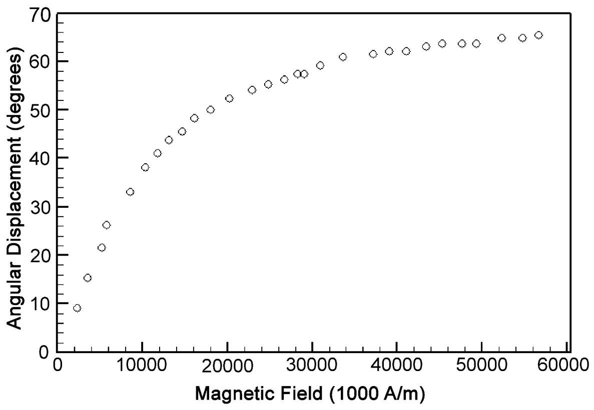

Turbulence Control (Microflap, Microballoon, Microsynthetic Jet), Figure 10 Angular displacement versus magnetic field strength of a flap actuator

intensity. Arrays of flaps positioned near the leading edge of delta wing showed generation of rolling moment by flap actuation. The effect of actuator location on the rolling moment of the delta wing was investigated from the force balance. Clear effect on rolling moment as a function of the actuator location was observed. The flow visualization images showed the vortical structures generated by the actuator.

Future Directions for Research

The micro actuators have shown success in various flow control applications. The detailed criteria for characterization of successful synthetic jet formation are evolving. There are limited data on the synthetic jet formation constant as function of the geometric parameters of the synthetic jet. The universality of jet formation constant needs to be verified for variety of synthetic jet geometries. The size, strength and trajectory of the vortices from synthetic jet need to be characterized from more detailed measurements and analysis. The effect of multiple synthetic jets, the pitch between neighbouring jets and the relative phase difference need to be investigated with respect to the nature of control vortices formation. The efficacies of flap actuators have been demonstrated in axisymmetric jet control and delta wing manoeuvring applications. The micro balloon actuators have shown its receptiveness to boundary layer control over delta wing with limited success on drag reduction. The integration and implementation of appropriate electronics with the micro actuator have not received adequate attention. The integration of microelectronics and micro-actuators with optimal control strategy will improve the performance of turbulent flow control applications. The uniformity in characterization and fabrication procedure of the micro actuators will facilitate their widespread research and industrial applications in future. The efficacy of these micro actuators for micro fluidics applications needs to be further explored.

Cross References

► Shear Stress Sensors
► Flow Structures
► Fabrication of 3D Microfluidic Structures

References

1. Gad-el-Hak M (2000) Flow Control, Passive, Active and Reactive Flow Management. Cambridge Univ Press, Cambridge
2. Holman R, Utturkar Y, Mittal R, Smith BL, Cattafesta L (2005) Formation criterion for synthetic jets. AIAA J 43:2110–2116
3. Huang A, Lew J, Xu Y, Tai YC, Ho CM (2004) Microsensors and actuators for microfluidic control. IEEE Sens J 4:494–502
4. Liu C, Tsao T, Lee GB, Leu TS, Yong WY, Tai YC, Ho CM (1999) Out-of-plane magnetic actuators with electroplated permalloy for fluid dynamics control. Sens Actuators 78:190–197
5. Khoo M, Liu C (2001) Micro magnetic silicone elastomer membrane actuator. Sens Actuators 89:259–266
6. Tung S, Maines B, Jiang F, Tsao T (2004) Development of a MEMS-based control system for compressible flow separation. J Microelectromech Syst 13:91–99
7. Rathnasingham R, Breuer K (2003) Active control of turbulent boundary layers. J Fluid Mech 495:209–233
8. Lee C, Hong G, Ha QP, Mallinson SG (2003) A piezoelectrically actuated micro synthetic jet for active flow control. Sens Actuators A108:168–174

Turbulence in Microchannels

Michael G. Olsen
Department of Mechanical Engineering,
Iowa State University, Ames, IA, USA
mgolsen@iastate.edu

T

Synonyms

Transition in microchannels; Friction factor in microchannels; Pressure drop in microchannels

Definition

Fluid flows can be generally described as being either laminar or turbulent. As opposed to laminar flows, in which the fluid moves in smooth layers (or laminae), turbulent flows are characterized by chaotic motion of fluid elements and seemingly random fluctuations in instantaneous velocities. One result of the chaotic fluid motion in turbulent flows is a tremendous increase in heat and mass transfer compared to laminar flows.

Overview

The governing equations for viscous fluid flow are conservation of mass (or continuity) and the Navier–Stokes equations (conservation of momentum or Newton's Second Law applied to a fluid). For steady-state, incompressible flow, these equations can be written as

$$\nabla \cdot \boldsymbol{u} = 0 \tag{1}$$

$$\rho\,(\boldsymbol{u} \cdot \nabla)\,\boldsymbol{u} = -\nabla p + \mu \nabla^2 \boldsymbol{u} \tag{2}$$

where $\boldsymbol{u}$ is the velocity, ρ is the fluid density, p is the pressure, and μ is the fluid viscosity. By introducing a characteristic length, L, a characteristic velocity, U, and a characteristic pressure, p_0, Eqs. (1) and (2) can be rendered dimensionless, resulting in

$$\nabla \cdot \boldsymbol{u}^* = 0 \tag{3}$$

$$\rho^* \left(\boldsymbol{u}^* \cdot \nabla\right) \boldsymbol{u}^* = -\mathrm{Eu}\nabla p^* + \frac{1}{\mathrm{Re}} \nabla^2 \boldsymbol{u}^* \tag{4}$$

where $()^*$ indicates a dimensionless quantity, $\mathrm{Eu} = p_0/(\rho U^2)$ is the Euler number, and $\mathrm{Re} = (\rho U L)/\mu$ is the Reynolds number.

The Reynolds number is the most important dimensionless parameter in fluid dynamics. Physically, the Reynolds number represents the ratio of inertial forces to viscous forces, and thus quantifies the effects of viscosity in the flow. In a pipe or channel flow, the characteristic velocity is typically taken as the mean velocity, and the characteristic length is typically taken as the pipe diameter or channel width.

In turbulent flows, Re is important because it can be used to determine when the flow transitions from laminar to turbulent flow and also when the flow achieves a fully turbulent state. For macroscale pipe and channel flows, transition to turbulence can occur in the range $1800 < \mathrm{Re} < 2300$, depending of flow conditions, and the flow becomes fully turbulent at a Reynolds number of approximately 4000. As will be shown later in this chapter, whether flows in microchannels agree with this macroscale behavior has long been a topic of debate, as some researchers have reported transitional Reynolds numbers in microchannel flows far lower than the $1800-2300$ reported for macroscale flows. However, recent studies using newly developed experimental techniques and also careful reexamination of the results of some of the earlier studies strongly suggest that microchannel flows do indeed exhibit transitional behavior similar to that observed in macroscale flows.

In designing systems involving pipes or channels, one important consideration is the pressure drop due to fluid friction for a pipe or channel, as this determines the pumping power required to force fluid through the conduit. The pressure drop, Δp, due to fluid friction with the pipe or channel walls can be found using

$$\Delta p = f \rho \frac{\ell}{D_\mathrm{h}} \frac{U^2}{2} \tag{5}$$

where ℓ is the pipe or channel length, D_h is the hydraulic diameter (calculated using $D_\mathrm{h} = \frac{4A}{P_W}$, where A is the cross-sectional area and P_W is the wetted perimeter), U is the mean velocity, and f is the Darcy friction factor. For laminar flow, f is purely a function of the Reynolds number, such that

$$f = \frac{64}{\mathrm{Re}} \tag{6}$$

For turbulent flows, the friction factor is a function of both the Reynolds number and the relative roughness, $\frac{\varepsilon}{D_\mathrm{H}}$, where ε is the root mean square roughness of the pipe or channel walls. For turbulent flows, the friction factor is found experimentally. The experimentally measured values for friction factor as a function of Re and $\frac{\varepsilon}{D_\mathrm{H}}$ are compiled in the Moody chart [1]. Whether the macroscale correlations for friction factor compiled in the Moody chart apply to microchannel flows has also been a point of contention, as numerous researchers have suggested that the behavior of flows in microchannels may deviate from these well established results. However, a close reexamination of previous experimental studies as well as the results of recent experimental investigations suggests that microchannel flows do, indeed, exhibit frictional behavior similar to that observed at the macroscale. This assertion will be addressed in greater detail later in this chapter.

In analyzing turbulent flows, it is often convenient to decompose the instantaneous velocity components and the pressure into mean and fluctuation components, such that

$$u = \langle u \rangle + u', \qquad v = \langle v \rangle + v',$$
$$w = \langle w \rangle + w', \qquad p = \langle p \rangle + p'$$

where $\langle\rangle$ denotes an ensemble average. Introducing these quantities into the Navier–Stokes equations and taking the ensemble average yields the Reynolds-averaged Navier–

Stokes (RANS) equations, which are

$$\rho\left(\langle u\rangle\frac{d\langle u\rangle}{dx}+\langle v\rangle\frac{d\langle u\rangle}{dy}+\langle w\rangle\frac{d\langle u\rangle}{dz}\right)=-\frac{\partial\langle p\rangle}{\partial x}+\mu\nabla^2\langle u\rangle-\rho\left(\frac{\partial\langle u'u'\rangle}{\partial x}+\frac{\partial\langle u'v'\rangle}{\partial y}+\frac{\partial\langle u'w'\rangle}{\partial z}\right)$$
$$\rho\left(\langle u\rangle\frac{d\langle v\rangle}{dx}+\langle v\rangle\frac{d\langle v\rangle}{dy}+\langle w\rangle\frac{d\langle v\rangle}{dz}\right)=-\frac{\partial\langle p\rangle}{\partial y}+\mu\nabla^2\langle v\rangle-\rho\left(\frac{\partial\langle u'v'\rangle}{\partial x}+\frac{\partial\langle v'v'\rangle}{\partial y}+\frac{\partial\langle v'w'\rangle}{\partial z}\right)$$
$$\rho\left(\langle u\rangle\frac{d\langle w\rangle}{dx}+\langle v\rangle\frac{d\langle w\rangle}{dy}+\langle w\rangle\frac{d\langle w\rangle}{dz}\right)=-\frac{\partial\langle p\rangle}{\partial z}+\mu\nabla^2\langle w\rangle-\rho\left(\frac{\partial\langle u'w'\rangle}{\partial x}+\frac{\partial\langle v'w'\rangle}{\partial y}+\frac{\partial\langle w'w'\rangle}{\partial z}\right) \tag{7}$$

The terms of the form $\langle u'_i u'_j\rangle$ are called the Reynolds stresses. The RANS equations do not consist of a closed set of equations (there are more unknowns than equations), so if the RANS equations are to be solved, the Reynolds stress terms must be modeled somehow. Typically, this modeling is based on experimental measurements. The application of models developed for macroscale flows to turbulent microchannel flows is dependent on the Reynolds stresses being similar for both cases. Recent experimental evidence suggests a strong similarity between turbulence statistics measured in turbulent microchannel flows and turbulence statistics measured in turbulent pipe and channel flows. Thus, the evidence suggests that turbulent models and codes developed to study macroscale turbulent pipe and channel flow should be applicable to the study of turbulent microchannel flows.

While the fluctuating velocities in turbulent channel flow may seem to imply random motion in the fluid, in actuality, turbulent channel flows (and turbulent flows in general) do contain underlying structure. One characteristic of turbulent flows is the presence of large- and small-scale turbulent eddies. One way to describe these turbulent structures of the flow is to measure spatial correlations of velocity fluctuations and to define characteristic length scales of the turbulent structures.

The normalized spatial correlation of the fluctuating velocity component u'_i with the fluctuating velocity component u'_j is defined as

$$R_{u'_i u'_j}(\Delta\boldsymbol{x};\boldsymbol{x})=\frac{u'_i(\boldsymbol{x})\,u'_j(\boldsymbol{x}+\Delta\boldsymbol{x})}{\sqrt{\langle u'^2_i(\boldsymbol{x})\rangle}\sqrt{\langle u'^2_j(\boldsymbol{x})\rangle}}$$

Where $\boldsymbol{x}$ is some location in the flowfield, and $\Delta\boldsymbol{x}$ is a displacement vector from location $\boldsymbol{x}$. If the turbulent velocity field was truly random, then $R_{u'_i u'_j}(\Delta\boldsymbol{x};\boldsymbol{x})$ would be equal to zero for all $\Delta\boldsymbol{x}\neq 0$. However, in a turbulent flow, $R_{u'_i u'_j}(\Delta\boldsymbol{x};\boldsymbol{x})$ is not equal to zero, signifying the existence of underlying structure in the turbulent flow. The properties of $R_{u'_i u'_j}(\Delta\boldsymbol{x};\boldsymbol{x})$ can be used to discern some characteristics about this underlying flow structure.

For example, $R_{u'_i u'_j}(\Delta\boldsymbol{x};\boldsymbol{x})$ can be used to define characteristic length scales for the underlying turbulent structures. $R_{u'_i u'_i}(\Delta\boldsymbol{x};\boldsymbol{x})$ has the property of being equal to 1 at $\Delta\boldsymbol{x}=0$ and approaching zero as $\Delta\boldsymbol{x}\to\infty$. The integral length scale for a turbulent flow is defined as

$$L_i=\int_0^\infty R_{u'_i u'_i}(\Delta\boldsymbol{x};\boldsymbol{x})\,d\Delta\boldsymbol{x}$$

One way to compare the turbulent structures present in microchannel flows with the turbulent structures present in turbulent macroscale pipe and channel flows is to compare the integral length scales for each. As will be shown in the next section, the integral length scales of turbulent microchannel flows agree well with the integral length scales for their macroscale counterparts, suggesting that turbulent microchannel flows and large-scale pipe and channel flows are structurally similar.

In summary, even though the characteristic length scales of turbulent flows in microchannels are several orders of magnitudes smaller than their counterparts in macroscale pipes and channels, experimental evidence suggests the flows are statistically and structurally similar. As such, long established correlations for pressure drop in pipes and channels, and computational tools available for the study of turbulent pipe and channel flows should be equally applicable to turbulent microchannel flows.

T

Key Research Findings

Transition to Turbulence

In early studies of flow in microchannels, the onset of transition to turbulence was inferred from measurements of bulk properties of the flow, such as pressure drop or heat transfer rate. The behavior of the friction factor or Nusselt number undergoes a drastic change when the flow transitions to turbulence, and thus an observation of such a behavioral change can be indicative of the onset of turbulent flow.

Many of these early studies of flow in microchannels suggested transition to turbulence occurring at lower Reynolds numbers than those observed at the macroscale. For example, Wu and Little [2] measured friction factors and Nus-

selt numbers of gas flow through etched microchannels with D_H ranging from 45 μm to 83 μm, and their results suggested an early onset of transition occurring at around Re = 350. Similarly, Pent et al. [3] measured the friction factors and Nusselt numbers of flow through stainless steel microchannels of various diameters and aspect ratios and observed behavior consistent with transitional Reynolds numbers ranging from 200 – 700. Evidence of early transition to turbulence was also suggested by other experimental studies, too numerous to list individually here.

One common conclusion of many of these early studies was that the relatively high surface roughness of the microchannels investigated was a major factor in the observed behavior. However, this explanation is unsatisfying because there have also been researchers whose results on transition similarly derived from friction factor and Nusselt number data agreed well with macroscale behavior for microchannels with the same magnitude of relative roughness as the researchers mentioned previously. For example, in experiments on microchannels with hydraulic diameters ranging from 112 μm to 210 μm and aspect ratios from 1.0 to 1.5, Hegab et al. [4] reported transition for Re over 2000. Similarly, Qu and Mudawar [5] found no evidence of early transition in a series of micro heat sink experiments with Reynolds numbers as high as 1672. Transitional Reynolds numbers consistent those at the macroscale have also been observed by numerous other researchers.

In an attempt to clarify the seemingly contradictory results on transition in microchannels presented by various researchers, Hetsroni et al. [6] reexamined the results of previous researchers, with a particular emphasis on determining possible sources of the anamoulous results found in some studies. They determined that the anamoulous results reported by some researchers were due to either improperly defined experiments, heating of the fluid due to viscous dissipation resulting in a change in fluid viscosity, or due to measurement error. After examining the extensive body of experimental studies on transition in microchannels, they concluded that the vast preponderance of evidence reveals that the transitional behavior of flow in microchannels shows no differences with macroscale flow.

The recent development of microscopic particle image velocimetry (microPIV) [7] has provided researchers with the capability of measuring instantaneous velocity fields in microchannels, and hence provided an additional tool for investigating transition in microchannels. Because microPIV can be used to directly observe features of the velocity field in the microchannel, data collected using this technique provide a more direct indication of transition than pressure drop measurements where the transitional behavior must be inferred. In the first study of transition using microPIV, Sharp and Adrian [8] measured velocities in round microtubes with diameters between 50 μm and 247 μm. Using an increase in the root-mean-square velocity fluctuations along the centerline of the microtube as an indication of transition to turbulence, Sharp and Adrian observed transition between $1800 < \mathrm{Re} < 2300$, and thus concluded that early transition did not occur.

Li and Olsen used microPIV to measure velocity fields in microchannels for Reynolds numbers ranging from 272 to close to 3000 in two sets of experiments. In the first set of experiments [9], Li and Olsen measured velocity fields in square cross-section microchannels with hydraulic diameters ranging from 200 μm to 640 μm, and in the second set of experiments [10], they repeated these measurements for microchannels with hydraulic diameters equal to 480 μm and aspect ratios ranging from 0.97 to 5.69. In both sets of experiments, they observed transition in the same range of Reynolds numbers as Sharp and Adrian, indicating transitional behavior in agreement with classical macroscale results.

To summarize, although the transitional behavior of microchannel flows has been a point of significant debate due to conflicting results reported by numerous investigators, a close reexamination of the previous studies and the recent addition of microchannel velocity measurements using microPIV have strongly suggested that microchannel flows exhibit the same transitional behavior as has been observed in macroscale pipes and channels.

Friction Factor in Turbulent Microchannel Flow

Whether the friction factor for flow in microchannels agreed or disagreed with classical macroscale results was also long a point of confusion due to conflicting experimental results. Several of the early studies of flow in microchannels, including those of Wu and Little [2], measured friction factors that were significantly greater than well accepted macroscale results. However, numerous other researchers, including Qu and Mudawar [5] reported good agreement between microscale and macroscale friction factors. The study of Judy et al. [11] is particularly of interest due to its breadth. Judy et al. measured friction pressure drop of fluid flow in microtubes and microchannels with hydraulic diameters between 15 μm and 150 μm for three different fluids (water, methanol, and isopropanol), two different tube materials (and hence two different surface roughnesses), and two different tube cross-sectional geometries (circular and square), and found no significant deviation from macroscale viscous flow theory.

Hetsroni et al. [6] also reexamined previous studies of friction factor in microchannels and drew the same conclusions that they did for transition in microchannels. They found that the anamoulous results reported in some studies could be explained by the same factors that contributed to the observation of anamoulous transitional behavior. Indeed, in the only study performed to date combining both microPIV and extensive pressure drop measurements, Sharp and Adrian [8] found that transition as measured by microPIV agreed well transition as inferred from friction factor data, and also found that their measured friction factors agreed well with macroscale results. As with transition to turbulence, the experimental evidence on friction factors in turbulent microchannel flow shows that microscale flow exhibits the same behavior as macroscale flows.

Turbulence Statistics and Large-Scale Structures

The studies referenced up to this point indicate that the bulk characteristics of turbulent microchannel flow, specifically the onset of transition and the frictional pressure drop, tend to agree well with classical results for macroscale pipe and channel flow. However, the question remains as to whether the microscale turbulence is statistically and structurally similar to turbulence at the macroscale.

The development of microPIV as a microfluidics research tool has made it possible to measure statistical quantities such as velocity fluctuations and Reynolds stresses. Moreover, since microPIV provides instantaneous *velocity field* data, spatial correlations of velocity fluctuations can be measured, yielding insights into the underlying large scale structures in turbulent microchannel flow. However, obtaining reliable microPIV data in turbulent microscale flows is inherently difficult, and thus, to the author's knowledge, at the present time only two research groups have been successful in obtaining *whole-field* turbulence data for turbulent flow in microchannels. The major research findings of these studies are summarized below.

Velocity Fluctuations and Reynolds Stresses

Li and Olsen [9, 10] were the first researchers to measure profiles of velocity fluctuations in turbulent microchannel flow. They measured streamwise and transverse velocity fluctuations and Reynolds shear stresses for a range of Reynolds numbers spanning the laminar through fully-turbulent regime. They found good agreement between their measured fluctuations and Reynolds shear stresses and values reported for macroscale turbulent duct flow.

Natrajan et al. [12] collected velocity fluctuation and Reynolds shear stress data for turbulent flow in round microtubes for Re = 4500 (well within the fully-turbulent flow regime), and compared their experimental results with the results of a direct numerical simulation of turbulent pipe flow at a comparable Reynolds number. The comparison of these results is shown in Fig. 1, with the solid lines representing the DNS results and symbols representing the microPIV results. The agreement for the streamwise velocity fluctuations is nearly exact, while the transverse fluctuations and Reynolds shear stress agree to within 10% with the DNS results (this slight discrepancy in transverse velocity fluctuations is due to limitations in PIV itself and not due to any physical differences between micro- and macro-scale turbulence. See Liu et al. [13] for similar results obtained in comparing macroscale PIV data to DNS results).

Taken as a whole, the studies of Li and Olsen and Natrajan et al. encompass flow in round microtubes, square microchannels, and rectangular microchannels with aspect ratios as high as 5.69. They suggest that, with regards to pointwise turbulent statistics, turbulent flow in microchannels over an array of microchannel geometries agree well with pointwise statistics in similar macroscale geometries.

Large-Scale Structures and Velocity Correlations

The previously mentioned microPIV studies suggest that the turbulence in microchannels is *statistically* similar to flow in macroscale pipes and channels, but it is also important to consider if the microscale flows are *structurally* similar to macroscale flows. One way to determine this is to measure the characteristics of the large-scale turbulent structures in turbulent microchannel flow and compare these to turbulent macroscale flow.

Figure 2 is an instantaneous velocity field in a 536 μm diameter microtube at Re = 4500. Large-scale turbulent eddies are clearly visible throughout the velocity field, and a comparison to a velocity field obtained in a macroscale pipe would show many similarities. However, such comparisons are qualitative only, and a true quantitative comparison can only be made by statistically comparing the large-scale structures, as can be done by calculating spatial correlations and turbulent length scales.

Li and Olsen [14] were the first to perform such calculations. They calculated spatial correlations from ensembles of instantaneous velocities fields for flows in square microchannels and defined turbulent length scales in the streamwise and transverse directions as the distance it takes normalized spatial correlations of streamwise velocity correlations to drop to 0.5. These correlation lengths in the streamwise and transverse directions were called Lx_{uu} and Ly_{uu}, respectively. A comparison of these microchannel correlation lengths normal-

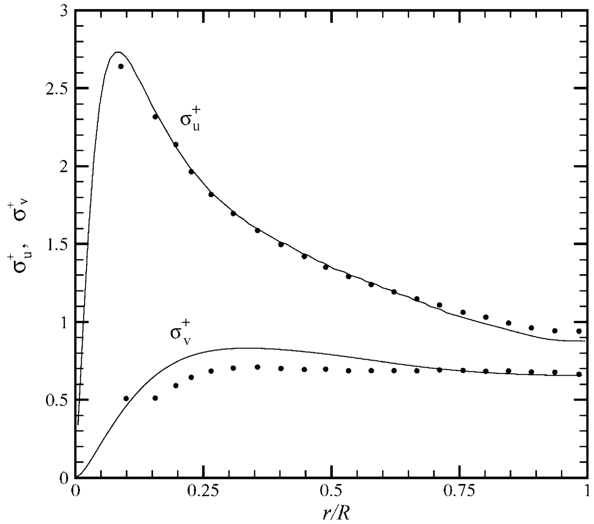

a

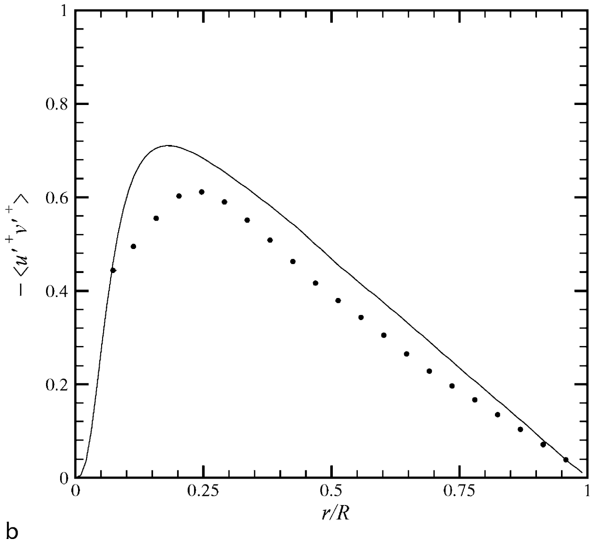

b

Turbulence in Microchannels, Figure 1 (**a**) Rms velocity fluctuations and (**b**) Reynolds shear stress as measured by microPIV for turbulent flow in a 536 μm diameter glass microtube

ized by microchannel width, W, and correlation lengths for macroscale channels [15] are shown in Table 1. Excellent agreement was observed between the microscale and macroscale results. Natrajan et al. [12] also calculated spatial correlations from their microPIV data for turbulent microtube flow and also found excellent agreement between their results and spatial correlations for turbulent pipe flow.

While at the present time, these two studies are the only measurements of spatial correlations and turbulent length scales for microscale flows, the agreement observed in these measurements compared to large-scale pipe and channel flows suggest that the turbulence in microchannels and microtubes is structurally similar to the turbulence observed in similar macroscale flows.

Turbulence in Microchannels, Table 1 A comparison of turbulent length scales for turbulent microchannel and macroscale channel flows

Study	Channel Dimension	Re	$2Lx_{uu}/W$	$2Ly_{uu}/W$	Lx_{uu}/Ly_{uu}
Li and Olsen [14]	325 μm	2853	0.38	0.20	1.90
Li and Olsen [14]	490 μm	3489	0.34	0.17	2.00
Li and Olsen [14]	640 μm	3333	0.30	0.16	1.88
Clark [15]	25 mm	3460	0.37	0.20	1.85
Clark [15]	25 mm	8300	0.29	0.16	1.93

Summary of Key Research Findings

Although for many years there were some questions about whether turbulent microchannel flows exhibited behavior similar to macroscale flows, recent experiments using new experimental techniques and a reexamination of data collected in previous studies suggest that, at least for microchannels as small as 50 μm in diameter, these questions are unfounded. Turbulent microchannel flow exhibits the same transitional behavior, displays similar frictional loss characteristics, and is statistically and structurally similar to macroscale pipe and channel flow.

Directions of Future Research

The number of studies utilizing microPIV in microchannels has to this point been very limited. Moreover, thus far this small number of studies has been limited to microchannels with hydraulic diameters greater than 200 μm. While these studies strongly suggest that microchannel turbulence is statistically and structurally similar to macroscale pipe and channel turbulence, a truly definitive answer cannot be arrived at until these two studies are supplement by additional studies for smaller hydraulic diameter microchannels.

Moreover, there must be some lower limit of microchannel hydraulic diameter beyond which the fluid behavior begins to deviate from behavior observed at the macroscale. At some point, the characteristic length scale of the flow will become so small that the continuum hypothesis must break down. However, the mean free path of molecules in liquid flows in microchannels is on the order of nanometers, and

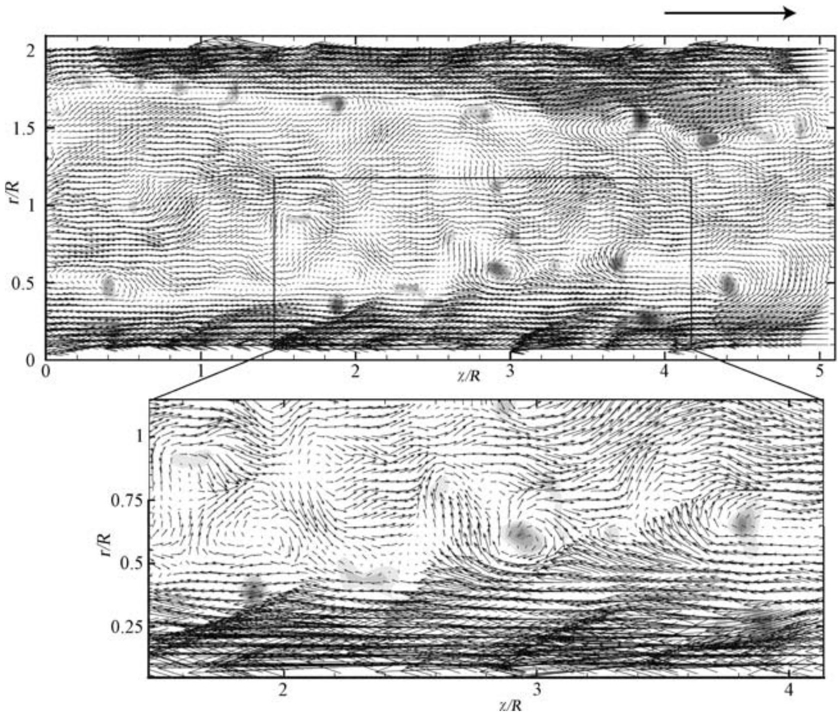

Turbulence in Microchannels, Figure 2 An instantaneous velocity field as measured by microPIV for Re = 4500 flow in a 536 μm diameter glass microtube. A convective velocity of 91% of the centerline velocity has been subtracted to help visualize turbulent structures

thus, this lower limit is likely to be significantly smaller than 1 μm. Experiments will have to be performed to determine what this lower limit is, and also to determine the characteristics of flow in this regime.

Cross References

► Heat Transfer in Microchannel Flows
► Micro-PIV-Based Diffusometry
► Pressure Driven Single Phase Gas Flows
► Pressure Driven Single Phase Liquid Flows
► Transition to Turbulence in Microchannels

References

1. Moody LF (1944) Friction factors for pipe flow. Transactions of the ASME 66:671–684
2. Wu PY, Little WA (1983) Measurement of friction factor for flow of gases in very fine channels used for micro-miniature Joule-Thompson refrigerators, Cryogenics 23:273–277
3. Peng XF, Peterson GP, Wang BX (1994) Frictional flow characteristics of water flowing through rectangular microchannels. Exp Heat Transf 7:249–264
4. Hegab HE, Bari A, Ameel TA (2002) Friction and convection studies of R-134a in microchannels within the transition and turbulent flow regimes. Exp Heat Transf 15:245–259
5. Qu W, Mudawar I (2002) Experimental and numerical study of pressure drop and heat transfer in a single-phase micro-channel heat sink. Int J Heat Mass Transf 45:2549–2565
6. Hetsroni G, Mosyak A, Pogrebnyak E, Yarin LP (2005) Fluid flow in microchannels Int J Heat Mass Transf 48:1982–1998
7. Santiago JG, Wereley ST, Meinhart CD, Beebe DJ, Adrian RJ (1998) A particle image velocimetry system for microfluidics. Exp Fluids 25:316–319
8. Sharp KV, Adrian RJ (2004) Transition from laminar to turbulent flow in liquid filled microtubes. Exp Fluids 36:741–747
9. Li H, Olsen MG (2006) MicroPIV measurements of turbulent flow in square microchannels with hydraulic diameters from 200 μm to 640 μm. Int J Heat Fluid Flow 27:123–134
10. Li H, Olsen MG (2006) Aspect ratio effects on turbulent and transitional flow in rectangular microchannels as measured with microPIV. J Fluids Eng 128:305–315
11. Judy J, Maynes D, Webb BW (2002) Characterization of frictional pressure drop for liquid flows through microchannels. Int J Heat Mass Transf 45:3477–3489
12. Natrajan VK, Yamaguchi E, Christensen KT (2007) Statistical and structural similarities between micro- and macroscale wall turbulence. Microfluid Nanofluid 3:89–100
13. Liu ZC, Adrian RJ, Hanratty TJ (1991) High resolution measurement of turbulent structure in a channel with particle image velocimetry. Exp Fluids 10:301–312
14. Li H, Olsen MG (2006) Examination of large-scale structure in turbulent microchannel flow. Exp Fluids 40:733–743
15. Clark W (1970) Measurement of two-point correlations in a pipe flow using laser anemometer. Ph.D. Thesis. University of Virginia

T

Turbulent Flows

► Chaotic Flows

Turbulent Shear Stress

► Turbulence Control (Microflap, Microballoon, Microsynthetic Jet)

Two-Faced Particle

► Janus Particle

Two-Fluid Stratified Flow

► Liquid–Liquid Stratified Flow in Microchannels

Two Phase Flow

Definition

Two phase flow is the flow of two immiscible fluids in the same micro- or nanofluidic conduits, the fluids can be of different chemical compositions – liquid/liquid, or in different physical states – gas/liquid.

Cross References

► Pressure-driven Two Phase Flows

Two-Phase Flow Driven by Pressure

► Pressure-Driven Two Phase Flows

Ultra High-Throughput Screening System

► Microfluidic Systems for High-Throughput Screening

Ultrasonic Concentration

► Particle Manipulation Using Ultrasonic Fields

Ultrasonic Machining

ZHEMIN WU, DONGQING LI
Department of Mechanical Engineering, Vanderbilt University, Nashville, TN, USA
zhemin.wu@vanderbilt.edu

Synonyms

Ultrasonic material removal

Definition

Removal of materials using an axially oscillating tool at ultrasonic frequency (about 20,000 Hz) with a fine abrasive of silicon carbide, aluminum oxide, or boron carbide carried by a liquid between tool and work piece.

Overview

Ultrasonic vibrations are used in various engineering applications such as cleaning, welding and machining. Ultrasonic machining (USM) is the removal of materials by abrasive bombardment and crushing in which a soft flat-ended tool is made to vibrate at a frequency of about 20,000 hertz and amplitude of 0.001 – 0.003 inch. During the vibration, bunches of hard abrasive particles are continuously fed into the machining zone, between the tool and the work piece. The particles give either direct action on the surface of work piece or cavitation erosion caused by rapid changes in pressure inside the fluid, resulting in the material removal to form the required structure [1–3]. The dimensions of the work piece are determined by the size of the abrasive particles. Micro-ultrasonic machining (μUSM) can be realized by using submicron particles. The USM process is able to machine any material, but is more efficient on brittle materials. The abrasive particles have to be harder than the work piece material.

Ultrasonic machining is mostly used for producing small details in hard materials such as glass, precious stones, ceramics and composites. Many USM applications are involved in drilling where a tool penetrates into the work piece to produce either a through or blind hole of the required dimensions [4]. By applying fine abrasive grains (0.2 μm diamond particles), the technique was successfully utilized to produce micro holes as small as 5 μm in diameter with 37 μm in depth, in glass and silicon [5]. By combining USM and other machining techniques such as wire electro-discharge grinding (WEDG) and electro-discharge machining (EDM), the fabrication of complete 3D microstructure within one total manufacturing process becomes possible, e. g. a 3D micro center-pin bearing air turbine developed by Sun, et al. [6]. Recently, the technique was further extended to the nanometer scale by using ultrasonic actuation with an Atomic Force Microscope tip, which can induce structural surface and subsurface modifications at Highly Oriented Pyrolytic Graphite and thus facilitate the patterning of nanoscale surface features [7].

There are variations on the basic USM techniques. Rotary ultrasonic machining (RUM) [8, 9] is the technique involving the vibration of a small grinding toll, which is excited and simultaneously rotated. The technique permits increase in machining speed and decrease in machining forces, a useful condition for machining with fragile tools. The same advantages of smaller forces can be obtained by applying ultrasonic vibrations to a surgical tool in various medical applications. Examples include ultrasonic assistance dental cutting, brain tumors removal and artery surgeries [9, 10].

Cross References

► Biosensors Using Atomic Force Microscopes
► Bulk Micromaching

► Particle Manipulation Using Ultrasonic Fields
► Integrated Micro Devices for Biological Applications
► Microfabrication Techniques
► Microturbines

References

1. Kainth GS, Nandy A, Singh K (1979) On the mechanics of material removal in ultrasonic machining. Int J Mach Tool Des Res 19:33
2. Nair EV, Ghosh A (1985) A fundamental approach to the study of the mechanics of ultrasonic machining. Int J Prod Res 23:731
3. Soundararajan V, Radakrishnan V (1986) An experimental investigation on the basic mechanisms involved in ultrasonic machining. Int J Mach Tool Des Res 26:307
4. Graff KF (1975) Macrosonics in industry: 5. Ultrasonic machining. Ultrasonics 13:103
5. Egashira K, Masuzawa T (1999) Microultrasonic Machining by the Application of Workpiece Vibration. Ann CIRP 48:131
6. Sun XQ, Masuzawa T, Fujino M (1996) Micro ultrasonic machining and its applications in MEMS. Sens Actuators A 57:159
7. Cuberes MT (2007) Ultrasonic Machining at the Nanometer Scale. J Phys: Conference Series 61:219
8. Komarajah M, Manan MA, Narasimha PR, Victor S (1988) Investigation of surface roughness and accuracy in ultrasonic machining. Precis Eng 10:59
9. McGeough J (2002) Micromaching of Engineering Materials. Marcel Dekker Inc., New York
10. Drobinski G, Brisset D, Philippe F, Kremer D, Laurian C, Montalescot G, Thomas MD (1993) Effects of Ultrasound Energy on Total Peripheral Artery Occlusions: Initial Angiographic and Angioscopic Results. J Interv Cardiol 6:157

Ultrasonic Material Removal

► Ultrasonic Machining

Ultrasonic Particle Manipulation

► Particle Manipulation Using Ultrasonic Fields

Ultrasonic Pumps

Barbaros Cetin, Dongqing Li
Department of Mechanical Engineering,
Vanderbilt University, Nashville, TN, USA
barbaros.cetin@vanderbilt.edu

Synonyms

Acoustic streaming pumps

Definition

Ultrasonic pumps are pumps that use acoustic streaming to create a fluid motion inside microchannels. Acoustic streaming is the time-averaged flow induced by an ultrasonic wave (periodic pressure oscillation). Attenuation of the acoustic energy (via reflection and other distortion) generates a body force within the fluid and converts acoustic energy into kinetic energy of the fluid [1].

Overview

Ultrasonic pumps are very useful for microscale applications due to their simplicity, robustness and scaling advantages. Moreover, they are insensitive to the chemical state of the fluid and the wall material unlike electroosmotic and magnetic pumps. By using acoustic streaming as a pumping mechanism, noncontact fluid control is achievable since no contact is needed between the acoustic source and the fluid; and no valves are required [2].

Acoustic streaming flow fields depend on acoustic beam characteristics, fluid properties and the presence and the geometry of solid boundaries or particles. Depending on these factors, laminar, transitional or turbulent flow with jets and vortices can be generated. Acoustic streaming is proportional to the sound pressure level of the acoustic beam and the square of the frequency of the acoustic wave [1]. However, excessive heating – since most of the acoustic energy becomes heat – and bubble formation set an upper limit for high intensities [2].

An ultrasonic transducer is an integrated component of acoustic pumps. The transducers that generate ultrasonic energy with megahertz frequency for ultrasonic pumps make use of the piezoelectric (PZT) effect. A PZT layer is the vital component of the ultrasonic transducer and provides the oscillatory motion that ultimately produces the acoustic beam.

Rife et al. [3] developed a fluidic pumping circuit powered by an acoustic frequency of 50 MHz, and generated fluid flow with velocities of the order of mm/s. They used ultrasonic PZT transducers for their pump to generate the acoustic waves. The intensity of the waves was low enough to produce negligible heating; however, even if the heating could be tolerated, dielectric breakdown in the PZT thin film limited the maximum intensity. They also discussed bubble formation, and concluded that for frequencies above a few megahertz, the technique was safe to use for degassed liquids without any cavitation problem.

Nguyen and White [4] presented a numerical study of a flexural plate wave (FPW) micropump. Their simulated device consisted of a channel with a thin PZT membrane, whose thickness was $1-3\ \mu m$ attached to a bottom wall. This membrane generated a high-intensity acous-

tic filed in the vicinity of the fluid inducing the motion of a fast-moving layer near the membrane. They investigated the pumping performance with different parameters such as the wave amplitude, channel height and back pressure. They concluded that micropumps with a height of a few micrometers had a good performance due to their high flow rate and high hydraulic impedance against back pressure.

Cross References

- ► Electrical Pumps
- ► Magnetic Pumps
- ► Thermocapillary Pumping

References

1. Martin SE (2001) Parametric Analysis of Acoustic Streaming Pumps Utilizing Planar Ultrasonic Acoustic Beams. Ms. Thesis, Vanderbilt University
2. Minor KT (2002) Acoustic Streaming Micropumps. Ms. Thesis, Vanderbilt University
3. Rife JC, Bell MI, Horwitz JS, Kabler MN, Auyeung RCY, Kim WJ (2000) Sens Actuators 868:135–140
4. Nguyen NT, White RM (1999) Sens Actuators 77:229–236

Ultrasonic Separation

► Particle Manipulation Using Ultrasonic Fields

Unbalanced AC field

Synonyms

Aperiodic AC field

Definition

A periodic alternating-current (AC) electric field is called unbalanced, if its first moment has zero time average ($\langle E\rangle = 0$), but at least one of its higher moments does not (e. g. $\langle E^3\rangle \neq 0$).

Cross References

- ► Aperiodic Electrophoresis
- ► Electrokinetic Motion of Polarizable Particles
- ► Nonlinear Electrokinetic Phenomena

Unimorph

Definition

A structure composed of one active layers and one or more passive layers. Typically the active layers work through either thermal expansion, hygrothermal expansion, or piezoelectric expansion via an externally-applied electrical field. Such devices are asymmetric about their neutral axis, and so may generate axial stretching or contraction along with bending.

Cross References

- ► Bimorph
- ► Piezoelectric Valves

Unit Impulse Function

► Dirac Delta Function

Unmanned Rotorcraft

► Microrotorcraft

Unmixing

► Demixing

U

UV-LIGA

► LIGA-Like Techniques

Valve

► pH-Sensitive Hydrogel

Valveless Pumps

► Peristaltic Pumps

Valve-Less Rectification Pumps

VÁCLAV TESAŘ
Department of Thermodynamics, Institute
of Thermomechanics, Academy of Sciences of the Czech
Republic, Prague, Czech Republic
tesar@it.cas.cz

Synonyms

No-moving-part pumps

Definition

The term, despite its common and frequent use, is actually a misnomer. The fluidic pumps so described in fact do have valves and it is the arrangement and configuration of these valves which is their most interesting aspect. What are absent are the mechanical moving or deformed components in the valves. The valves are there to rectify the alternating flow generated, as in the more conventional pumps, by an actuator performing reciprocating motions and displacing the pumped fluid from the displacement cavity. The actuators are usually driven by an electric input.

In the "valve-less" version, the mechanical blockage of the flow in the *closed* state of the valve is replaced by a dynamic, inertial effect which is to be overcome by the fluid. This never suffices for stopping the flow completely. The rectification – conversion to one-directional movement – is therefore inherently less efficient than with the mechanofluidic counterparts. In microfluidics, there is a distinct continuing trend towards a smaller size and this – together with typically higher viscosity often pumped biological fluids – leads to lower Reynolds numbers. Since one of the interpretations of Reynolds number presents it as the ratio of inertial to viscous friction force acting on a fluid, this trend also contributes to the efficiency being generally indifferent or downright poor. This, however, is not of much significance in most microfluidic applications. The selling point of the "valve-less" pumps is their excellent suitability for micromanufacturing – no need for expensive assembly operations – long life, not endangered by breakage of springs or by moving components getting stuck, and suitability for operation at high working frequencies [1–3, 12].

Basic Methodology

The Grätz Bridge Circuit

Usual present-day pumps in microfluidics are of the simplest configuration corresponding to Fig. 1. The actuator, represented in Fig. 1 symbolically by the traditional crankshaft-connecting rod-piston mechanism, generates the alternating flow, rectified by two one-way valves. During the first half of the cycle, the liquid is sucked into the displacement cavity through the upstream or suction valve. No fluid comes back into the cavity from the output, because the return flow is prevented by the upstream or delivery valve, which is oriented so that in this phase of the cycle it is in its *closed* state. Its state changes into the *open* in the subsequent half of the cycle when it allows the liquid, displaced by the actuator, to flow to the output terminal. Obviously, the output flow is intermittent, available only during one half of each operating period. The output flow pulsation is an obvious disadvantage.

In applications where the pulsation can cause problems – and also in those aiming at a higher efficiency – it is advisable to use, according to Fig. 2, the full-wave, Grätz bridge rectifier. Its name is explained in Fig. 3. It needs to be supplied by two-phase alternating input flow, carried in two channels. Generating it is usually no problem since the to-and-fro motion of the front side of the mechanical actuator

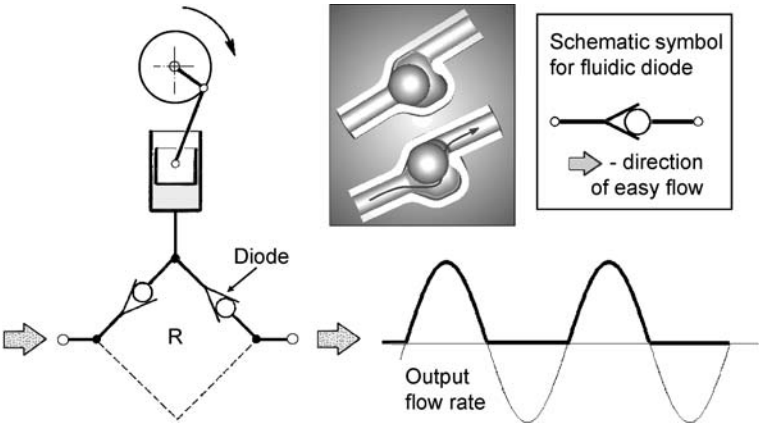

Valve-Less Rectification Pumps, Figure 1 Schematic representation of a single-action reciprocating pump. The alternating flow, shown symbolically as generated by a piston and crankshaft mechanism, is rectified by two fluidic diode valves. Their schematic symbol is derived from one of the oldest rectifying valve versions with a moving ball

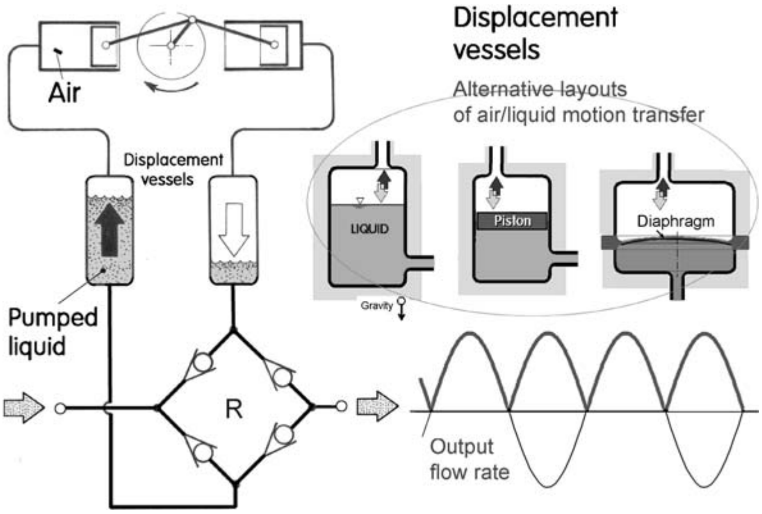

Valve-Less Rectification Pumps, Figure 2 Schematic representation of the double-acting two-phase reciprocating pump. Two alternating flows, mutually shifted by π radians, are rectified by four fluidic diodes connected into the Grätz full-wave bridge. Also shown is one of the advantages of energy transfer by the alternating flow: the possibility of using different fluids (here gas and liquid) in different parts of the fluidic system

(symbolized in the drawing by the piston) means availability of a motion of the same amplitude with the opposite phase on its reverse side. The second phase may be also used differently, according to Fig. 4, to increase the generated output pressure. This is welcome in situations where the pump has to drive a high-dissipance load.

In the "valve-less" pumps, the mechanofluidic one-way valves are replaced by fluidic diodes. A diode is a device exhibiting different hydrodynamic properties for different directions of the flow. The effect is characterized by diodity – the ratio of dissipances

$$\boldsymbol{D} = \frac{Q_{\text{return}}}{Q_{\text{forward}}}, \tag{1}$$

in the return and forwards flow directions. Diodity is usually evaluated in steady regimes, where it is generally found to increase with Reynolds number

$$\text{Re} = \frac{wd}{\boldsymbol{\nu}}, \tag{2}$$

where w [m/s] is the characteristic velocity, d [m] the characteristic length dimension of the device and $\boldsymbol{\nu}$ [m^2/s] is fluid viscosity. In unsteady regimes, the relation between the inertial and friction forces is different. The former increase in importance with increasing operating frequency f [Hz] of the alternating input flow. This is characteristically chosen higher as the size of the pump

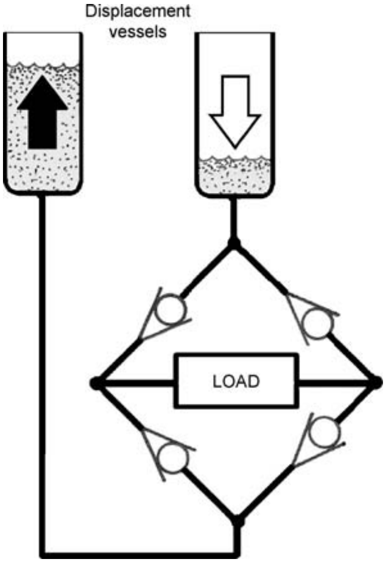

Valve-Less Rectification Pumps, Figure 3 The reason why the Grätz circuit is called a "bridge": the load with one-way fluid flow is bridging the gap between the two parallel systems of diodes

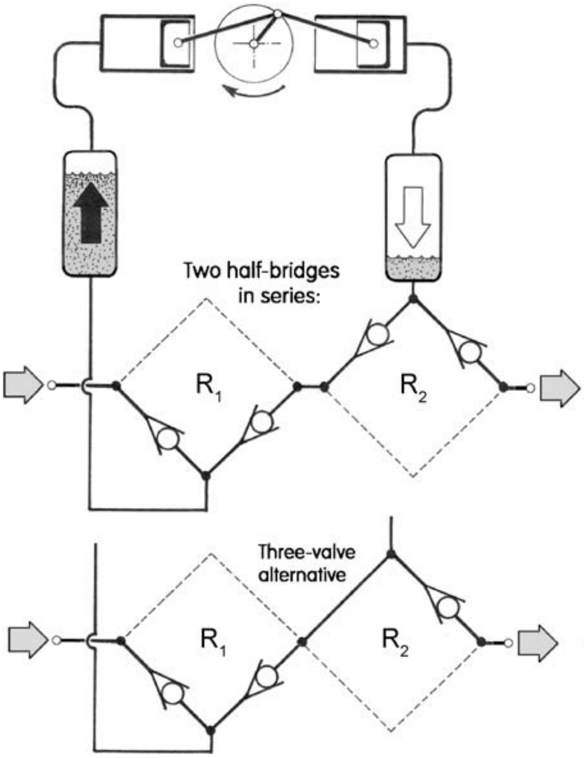

Valve-Less Rectification Pumps, Figure 4 The double-acting, two-phase driving does not necessarily mean the use of the Grätz full-wave bridge. As shown here, the two phases may be used in half-bridges connected in series. The pulsation of the output flow is not suppressed, but the rectifier generates a higher output pressure

decreases. Rather than Reynolds number, the proper characterization criterion in these cases is the Stokes number

$$\mathrm{Sk} = \frac{f\,d^2}{\nu}\,. \tag{3}$$

Of the two-terminal fluidic diodes, the highest rectifying effect is offered by ▶vortex diodes (Figs. 5 and 6). In the *return* flow direction, the flow is opposed by the centrifugal action of rotation in the vortex chamber. The rectification is due to there being essentially no rotation with the central fluid entry into the vortex chamber in the *forward* flow regime. Diodity values as high as about $\boldsymbol{D} = 20$ have been achieved – not, however, with the simple version shown in Fig. 6. This can achieve, depending on its geometry, usually values of about $\boldsymbol{D} = 4$. The versions developed for really high performance are of more complex design, typically with a large number of inlets on the periphery of the vortex chamber, necessary for symmetry of the vortex motion. The inlets and the outlets have to be carefully shaped, the latter as diffusers. Use of vortex diodes in microfluidic pumps is limited by two factors. First, considering the structure of the full-wave bridge in Fig. 5, it is obvious that it is difficult or even impossible to accommodate into the typical planar configuration on a substrate plate the exits leading at right angles from the vortex chamber. Even more problems arise with the complex structure of the inlets in the high-performance versions. The second factor is the relatively poor frequency range. It takes a relatively long time to start up the rotation after the onset of the reverse *closed* state. This counters the modern trend towards operation at a high frequency with small-volume displacement cavities.

More suitable for microfabrication, because of their planar layout, are the Tesla diode (Fig. 7) and the various versions of the labyrinth diodes, in particular the one shown in Fig. 9. Experience with the former type, patented in 1920 by the inventor N. Tesla, has been unfortunately somewhat disappointing. An improved version, the Tesser valve, is described in [4]. To improve the effective overall diodity, these devices are usually designed in multi-stage arrangements – the downstream stages in the Tesla diode actually benefiting from the jet-deflection phenomenon of the stage located upstream. The diodity $\boldsymbol{D}$ is, however, rarely larger than 1.2 to 1.6.

Better performance and, because of the short and simple path, high-frequency range are characteristic of the ▶venturi diode, consisting of a nozzle and a diffuser placed in series. Under various other names [5], it is currently among the most popular among the no-moving-part rectifiers (Figs. 10 and 11). An application of the use of a two-Venturi rectifier circuit in a flow control actuator for gen-

V

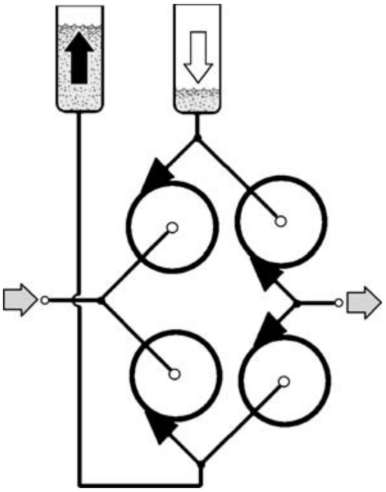

Valve-Less Rectification Pumps, Figure 5 Rectification by vortex diodes – in the double-acting two-phase Grätz full-wave bridge. The advantage is the absence of the moving parts; disadvantages are the slow start-up of diodes and necessity of complex spatial layout

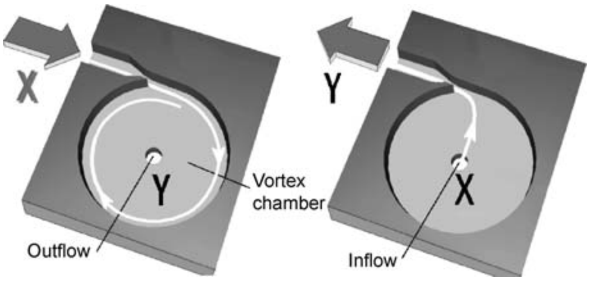

Valve-Less Rectification Pumps, Figure 6 A simple version of the vortex diode. At left is the *closed* state with rotation in the vortex chamber; at right is the easy flow, *open* state with radial forward flow. High-performance diodes have several tangential inlets into the chamber, resulting in symmetric character of the flow – but lead to an even more difficult spatial layout of the rectifier circuit

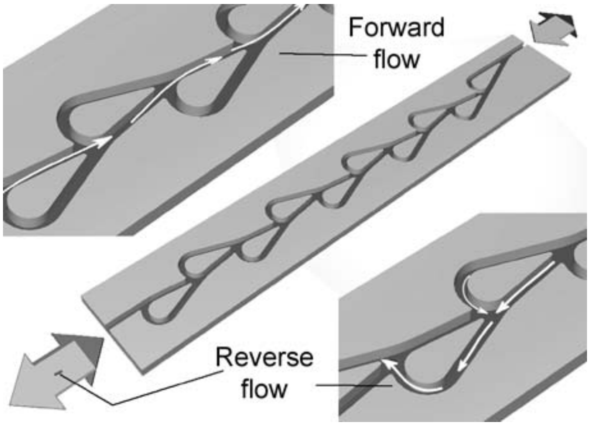

Valve-Less Rectification Pumps, Figure 7 The Tesla diode, one of the earliest no-moving-part devices. As shown here, it is usually used in a multi-stage layout. Diodity is very much worse than with vortex diodes

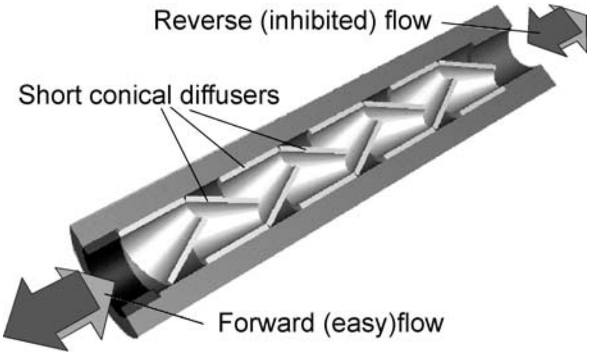

Valve-Less Rectification Pumps, Figure 8 A typical example of the labyrinth diode, here built using short conical tubes

eration of hybrid synthetic jets [6] is an example of a use of the rectifier circuits other than in simple pumps.

Jet-Type Rectifiers

Rectification based on properties of a fluid jet is a very old technique but used to be mostly applied in devices of little importance, such as aquarium ventilators, coolers or humidifiers, where the dominant requirement was low cost. Sometimes the decisive factor for their use was the fact that inertia of moving parts in mechanofluidic diodes prevents them from operation at the frequency of AC mains (also wear of contacting moving components would be too rapid at this frequency). Typically, descriptions in the literature are missing as the designers (and usually inventors) did not consider the solution of this peripheral problem in the main pumping design task worthy of publication. Probably the first reference in the literature is from 1957, when Dauphinne described in a short note the use of the *loudspeaker wind* for a simple closed-circuit cooling. He used a standard loudspeaker provided with a front plate having a central orifice forming a simple displacement vessel with a nozzle. The flow generated and used for cooling would nowadays be called the *synthetic jet*. Better documented use of the jet-type rectifier – in a pump for moving molten salts – was described by Walkden and co-workers (e. g. [7]). Their rectifier was developed from a standard jet pump (Fig. 12a). A very similar jet-pump rectifier was later tested by the present author [8]. To obtain the full-wave rectification, Walkden provided the jet pump with two primary nozzles in parallel, each supplied with one phase of the alternating two-phase flow. An even more important improvement was replacing the two nozzles by diffusers (Fig. 12b). This led to better efficiency

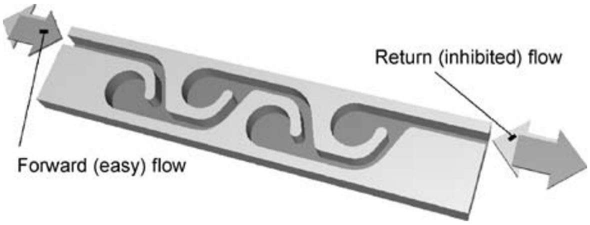

Valve-Less Rectification Pumps, Figure 9 Planar labyrinth diode, more suitable for micromanufacturing: again a multi-stage version

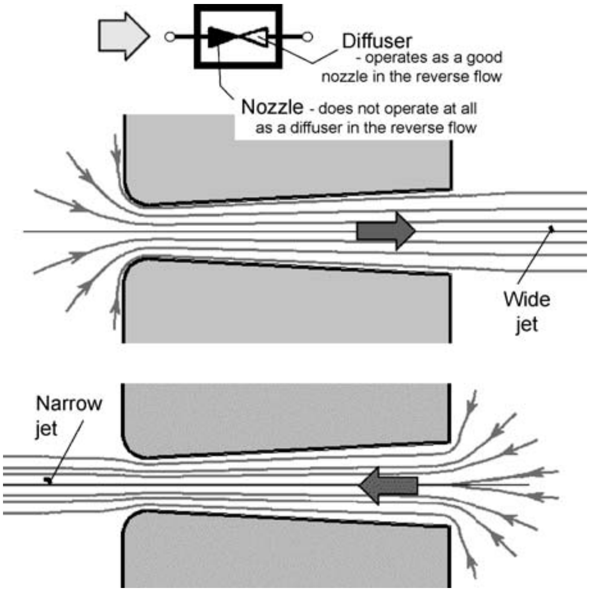

Valve-Less Rectification Pumps, Figure 10 Rectification effect in the Venturi (convergent–divergent) diode is based on the larger energetic loss by dissipating kinetic energy of the narrower jet

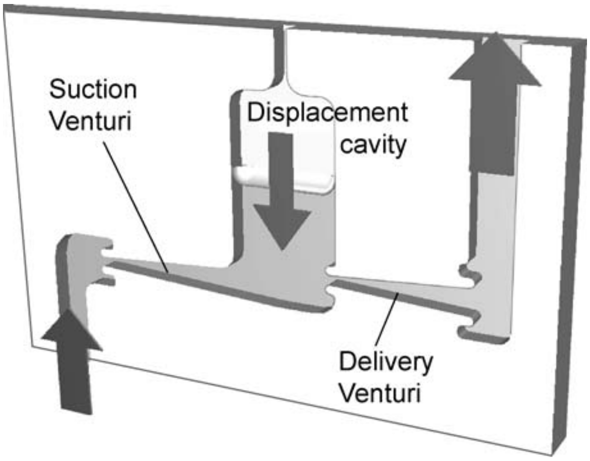

Valve-Less Rectification Pumps, Figure 11 Single-action pump with the Venturi diode rectifier. This is currently the most common type of "valve-less" pumps used in microfluidics

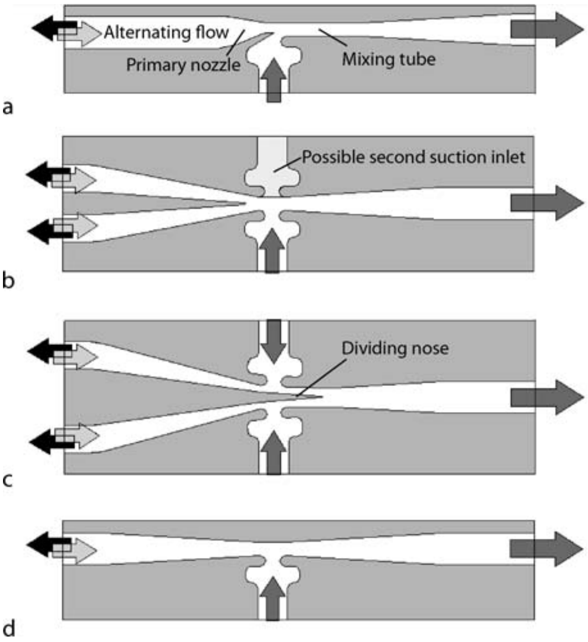

Valve-Less Rectification Pumps, Figure 12 Survey of the jet-type diodes. (**a**) A standard jet pump may exhibit a reasonable rectification effect. (**b**) The Walkden two-phase full-wave rectifier was developed from a jet pump with two parallel "primary nozzles", actually better performing when shaped as diffusers. (**c**) Tippetts' analysis of the long-nosed symmetric Walkden rectifier found it actually consists of three three-terminal devices. (**d**) The three-terminal Venturi, sometimes known as RFD device

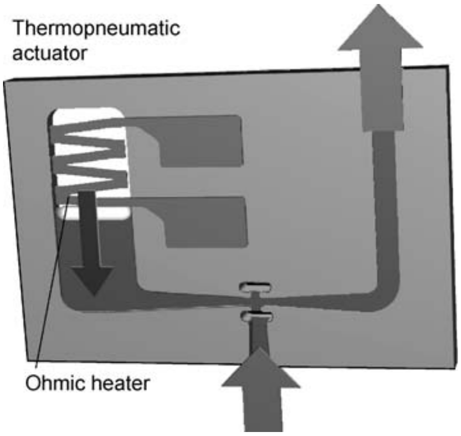

Valve-Less Rectification Pumps, Figure 13 A simple single-action pump with the three-terminal Venturi rectifier. Less known than the version from Fig. 11, it can exhibit higher rectification efficiency. The alternating flow is generated by expansion of gas heated electrically by the resistance heater

V

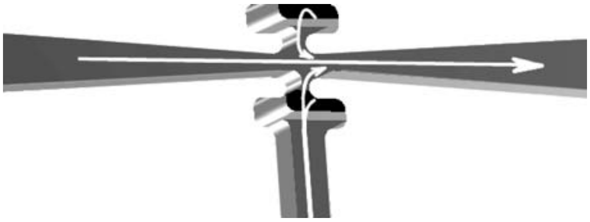

Valve-Less Rectification Pumps, Figure 14 Operation of the three-terminal Venturi rectifier. Fluid from the suction pipe of the pump enters the rectifier due to the jet-pumping effect of entrainment into the jet, which appears in both flow halves of the operating cycle

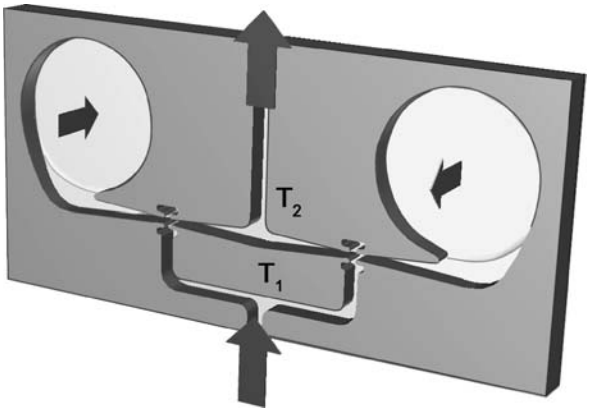

Valve-Less Rectification Pumps, Figure 15 The double-action full-wave pump with two three-terminal Venturi rectifiers. Alternating flow is generated by deformation of round diaphragms

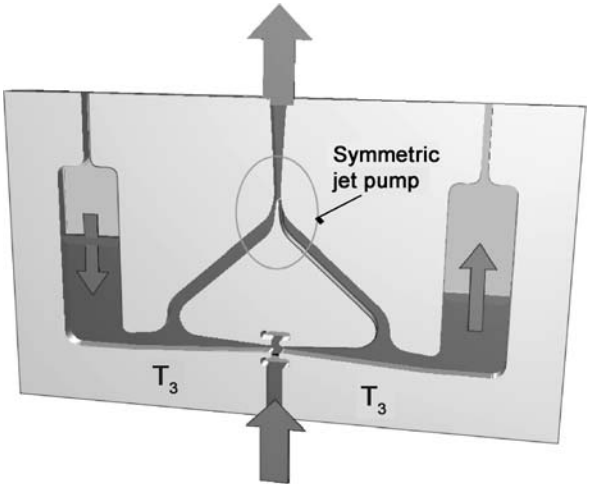

Valve-Less Rectification Pumps, Figure 16 The Tippetts version of the double-action pump with the single three-terminal Venturi rectifier and a symmetric jet pump in the opposite vertex of the Grätz bridge

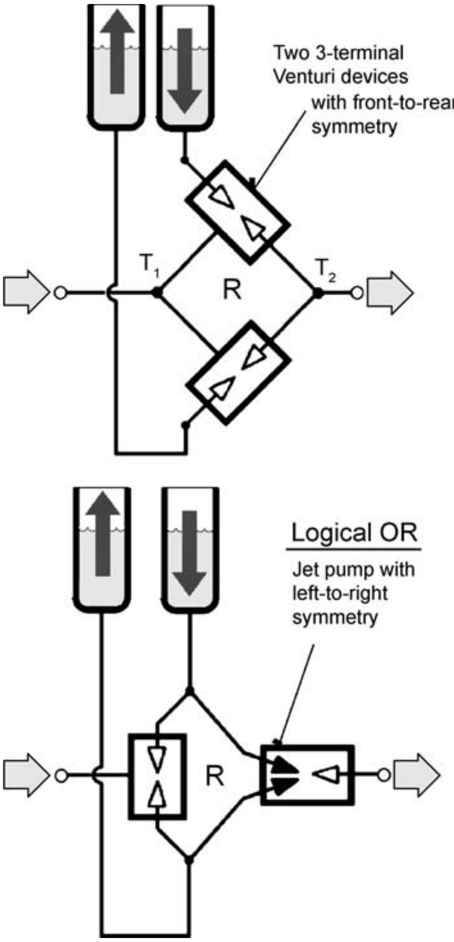

Valve-Less Rectification Pumps, Figure 17 Schematic fluidic circuit diagrams of the two pumps from Fig. 15 (left) and Fig. 16 (right)

due to the absence of flow separation from the walls in the reverse flow direction. Analysis of the Walkden rectifiers led Tippetts [9] to discovering the importance of the three-terminal device shown in Fig. 12d as a member of version C of the variant of Walkden's rectifier shown in Fig. 12 – and the proposal (also in [9]) to use this device alone in a reciprocating jet pump (Fig. 13). The return flow from the load during a part of the cycle was acknowledged as inevitable – and actually made use of by arranging the rectifier device (Fig. 14) so that the jets are formed in both flow directions and the pumped fluid is sucked in from the input inlet due to the entrainment effect of the jets.

Though also using the same two diffusers as the now standard design of Fig. 11, the pump according to Fig. 13, less well known, has more effective rectification. Tippetts himself went on later to extend this principle to the full-wave two-phase operation. He did not follow the more obvious additive layout of Fig. 15, presented also schematically in the left half of Fig. 17. Instead, he placed the rectifier devices into the other vertices of the Grätz bridge, where

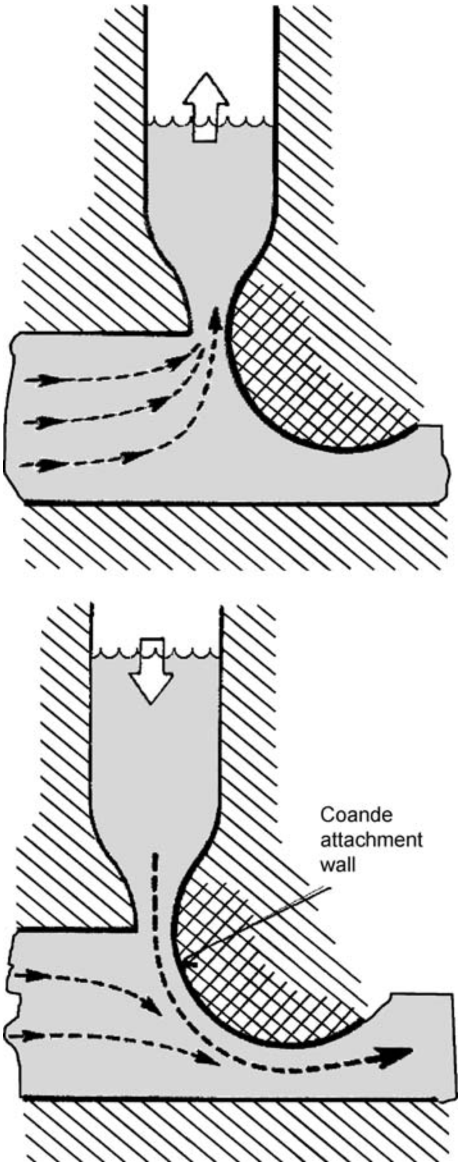

Valve-Less Rectification Pumps, Figure 18 Operating principle of the jet-type rectifier with the *forward flow diverting* by the Coanda effect. The original version with a nozzle at the inlet into the displacement cavity [10]

the single direction of the output flow made possible the replacement of the upstream three-terminal device by the symmetric jet-pump OR logical element.

Traveling Wave Pump

Essentially also a jet-type rectification, this is an alternative that features several important improvements [11]. One of them is the use of the Coanda effect attachment to a curved wall. This wall is positioned so that it turns the direction of the forward flow coming from the dis-

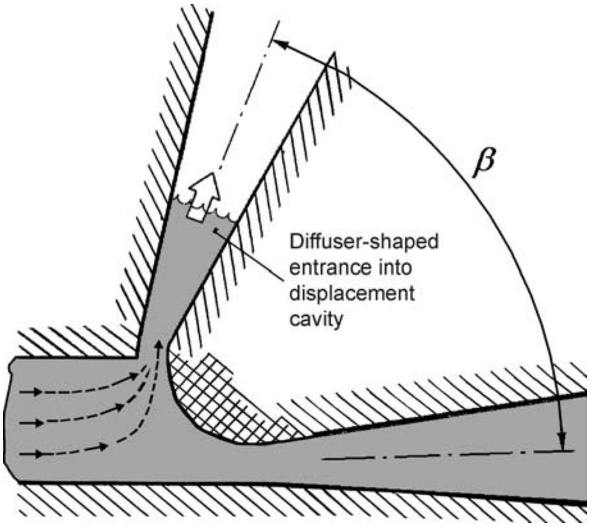

Valve-Less Rectification Pumps, Figure 19 Later improvement of the principle from Fig. 18. Energetic loss associated with inflow into the displacement cavity is reduced by the inlet being shaped as a diffuser. The small angle β (compared with the full 80°in Fig. 14) is made possible by the change of the jet direction due to the Coanda effect attachment to the curved wall

placement cavity. The general direction of the main flow through this rectifier is straight and a considerable proportion of the pumped liquid actually continues in the straight direction without ever entering the displacement cavity. A recently tested version (Fig. 22) uses the principle from Fig. 18, with a number of displacement cavities arranged along the channel length. The entrances into the cavities are placed at a streamwise pitch which corresponds to the distance traveled from one displacement cavity to the following one by the attached Coanda jet during one half of the period. As a result of this timing, the outflows from the cavities form a traveling wave passing through the channel. With proper adjustment of operating frequency it is possible to enter the resonant regime in which the efficiency reaches very high values. Little has been done so far with the improved version of Fig. 19, with angular position of the inlets into the displacement cavities ($\beta < \pi$; in fact $\beta < \frac{\pi}{2}$ (Fig. 19) decreasing the hydraulic losses associated with flow direction change.

Other Principles

To round off the list, the peristaltic pumps should be mentioned. They use a multi-phase multi-stage arrangement similar to that of Fig. 20, but in their common form they are based on much less effective rectification elements.

Finally, a useful rectification has been also demonstrated based on temperature dependence of viscosity. Ohmic

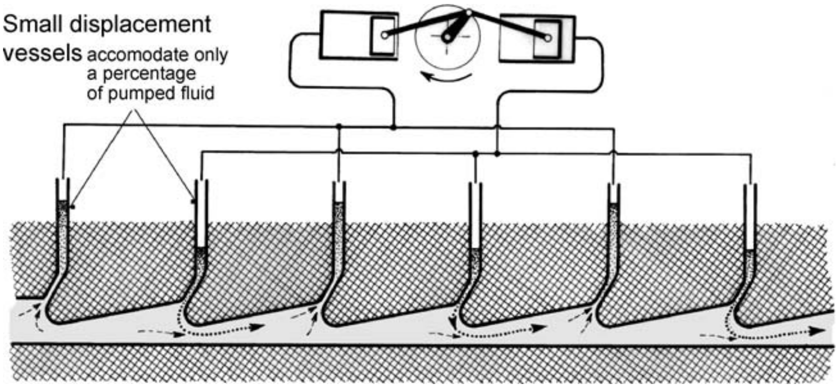

Valve-Less Rectification Pumps, Figure 20 The principle of the traveling-wave pump, two-phase, three-stage rectifier based on the principle from Fig. 19. A substantial proportion of the pumped liquid does not enter the displacement cavities – instead, it is dragged along with the wave

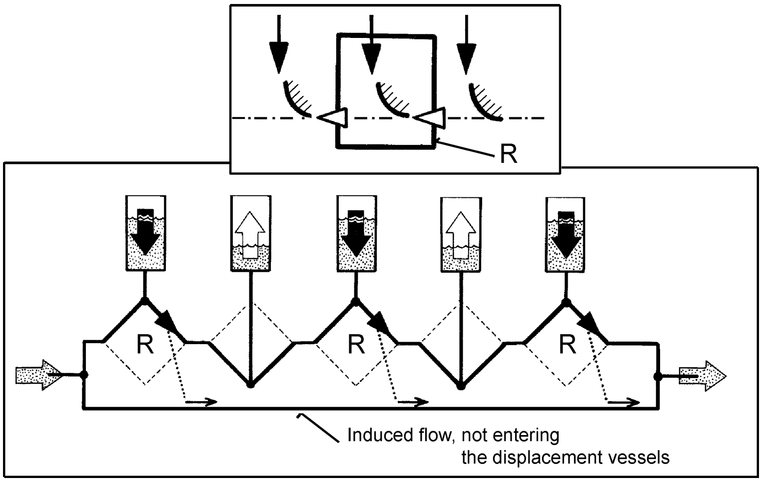

Valve-Less Rectification Pumps, Figure 21 Schematic representation of the working principle (above) and the relation to the Grätz half-bridge principle

heating of the delivery channels synchronized with the flow from the displacement cavity is used with liquids which decrease their viscosity in response to the heating. In a similar design, the electric heating of the liquid is so intense that it leads to boiling – generation of bubbles in the channel resisting the flow by surface tension.

Key Research Findings

Existing designs of microfluidic pumps with operation based on valve-less rectification demonstrate the practical applicability of no-moving-part flow generation and control principles [12]. The absence of moving components makes these pumps attractive for applications stressing the aspects of high reliability, long life and absence of any maintenance. They are also more suitable for micromanufacturing techniques, such as etching, than the pumps with return flow control by mechanical moving components. On the other hand, without the moving components the return flow in the valves is never suppressed completely. As a result, the valve-less pumps are considerably less efficient and therefore suitable for those applications where efficiency of pumping is not of primary importance.

Since the suppression of the return flow in the valve-less pump is based on inertial effects in flowing pumped fluid, the efficiency of the pump decreases with decreasing Reynolds number. This is a serious factor, since the general trend of operating at progressively smaller Reynolds numbers is typical for modern microfluidics [12]. To oppose this effect, it is found useful to employ in a microfluidic system with several circuits, a central pump for driving the flow in all these circuits rather than distributed driving by a separate pump in each circuit. For the central pump, this means a larger size and larger handled flow rates so that the Reynolds number is not so low.

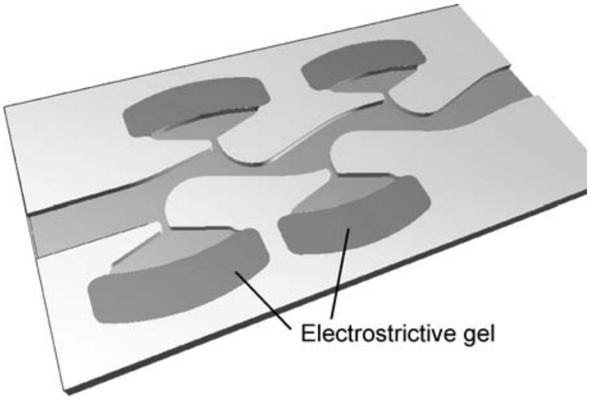

Valve-Less Rectification Pumps, Figure 22 An example of a micropump using the principle from Fig. 18 and generation of the flow wave by alternative suction into the nozzles on both sides of the channel. Nozzles belonging to on phase are on the same side of the channel. Alternating flow is generated by displacement due to volume of a liquid crystal gel exposed to an electrostatic field

Future Directions for Research

The use of the attractive properties of valve-less pumps being limited by the generally poor efficiency, further development concentrates on research aimed at obtaining a higher efficiency of the rectification, especially at low Reynolds number flows. Besides development of new rectification principles with better properties, higher efficiency is obtainable by operating at a higher frequency and therefore higher values of the Stokes number (Eq. (3)). However, this way towards a better performance is not applicable for all operating principles; it is not suitable for those flow mechanisms characterized by long flow paths. From this point of view, it seems advisable to direct future research to the jet-type rectification principles.

Cross References

- ► Electroosmotic Pumps
- ► Fluidic Rectification
- ► Electroosmotic Pumps
- ► Magnetic Pumps
- ► Microfluidic Circuits
- ► Particle Manipulation Using Ultrasonic Fields
- ► Peristaltic Pumps
- ► Piezoelectric Valves
- ► Pneumatic Valves
- ► Pressure-Driven Two-Phase Flows
- ► Rotary Peristaltic Pumps
- ► Thermomechanical Valves
- ► Thermopnuematic Valves
- ► Ultrasonic Pumps

References

1. Zimmerman WBJ (ed) (2006) Microfluidics: History, Theory, and Aplications. CISM courses and lectures No. 466, Springer-Verlag, Wien, New York
2. Laser DJ, Santiago JG (2004) A review of micropumps. J Micromech Microeng 14:R35
3. Nguyen NT, Wereley ST (2006) Fundamentals and Applications of Microfluidics. Chapter 6: Microfluidics for Internal Flow Conrol: Microvalves. Chapter 7: Microfluidics for Internal Flow Control: Micropumps
4. Forster FK, Williams BE (2002) Parametric design of fixed-geometry microvalves – the Tesser valve. In: Proceedings of IMECE. ASME, New Orleans, November 2002
5. Trávníček Z, Tesař V, Wang AB (2005) Enhancement of synthetic jets by means of an integrated valve-less pump. Sens Actuat A (Physical) 125:50
6. Trávníček Z, Vít T, Tesař V (2006) Hybrid synthetic jets as the non-zero-net-mass-flux synthetic jets. Phys Fluid (accepted for publication)
7. Stutely JR, Walkden AJ (1968) Improvements in or relating to pumps. UK Patent 1.132,442, Oct 1968
8. Tesař V (1983) Fluidic Jet-Type Rectifier: Experimental Study of Generated Output Pressure. J Fluid Control / Fluidics Q 14(4):13
9. Tippes JR, Swithenbank J (1974) Fluidic flow control devices and pumping systems. US Patent 4,021,146, 30 Oct 1974
10. Tesař V (1976) Čerpadlo nebo dmychadlo, zejména pro dopravu obtížně čerpatelných tekutin (Pump or blower, particularly for transport of difficult-to-pump fluids). Czechoslovak Certificate of Authorship Nr. 192 082
11. Tesař V (1981) Alternáló légárammal mükodtetett folyadék szivattyu (Fluidic Pump Driven by Alternating Air Flow). In: Proceedings of Pneu-Hidro kollokvium, Gépipari Tudományos egyesület, Györ, Hungary, September 1981
12. Tesař V (2007) Pressure-Driven Microfluidics. Artech House, Boston-London

Van-der-Waals Attraction

Definition

The weak attraction felt by molecules when they are several molecular diameters apart: responsible for condensation and solidification of a gas when the temperature is reduced.

V

Cross References

- ► Electrokinetic Flow and Ion Transport in Nanochannels

Vapor Bubbles

- ► Thermal Bubbles

Vaporization

► Droplet Evaporation

Velocimetry

Synonyms

Flow profiling

Definition

Velocimetry is the measurement of fluid velocity. In the context of microfluidics and nanofluidics, velocimetry involves the determination of the velocity field in small scale internal flows. Most commonly, velocimetry involves optical tracking of a fluid marker. In such cases the terms flow visualization and velocimetry are used interchangeably. A variety of velocimetry methods have been developed for small scale flows. Visualization based methods can be divided into particle-based techniques, such as micro-particle image velocimetry, and scalar-based techniques, such as molecular tagging. Non-visualization based velocimetry methods have also been developed, such as electrochemical velocimetry where fluid velocity is determined via generation of a redox species.

Cross References

► Visualization Based on Molecular Tagging Methods
► Microscale Flow Visualization
► Micro-PIV-Based Diffusometry
► Fluid Metering Methods for Flow Rate Measurements
► Flow Rate Measurement, Methods

Velocity Distribution Function

Definition

Velocity distribution function is defined so that the quantity $f(t, \boldsymbol{r}, \boldsymbol{v})\,\mathrm{d}\boldsymbol{r}\,\mathrm{d}\boldsymbol{v}$ is the number of particles in the phase volume $\mathrm{d}\boldsymbol{r}\,\mathrm{d}\boldsymbol{v}$ near the point $(\boldsymbol{r}, \boldsymbol{v})$ at the time t.

Cross References

► Gas Flow in Nanochannels
► Heat Transfer in Microchannel Flows
► Supersonic Micro-Nozzles
► Micro- and Nanoscale Gas Dynamics
► Lattice Poisson-Boltzmann Method, Analysis of Electroosmotic Microfluidics

Velocity Sensors

AHMAD YUSAIRI BANI HASHIM,
DHARMALINGAM SUGUMAR
Faculty of Manufacturing Engineering, Universiti Teknikal Malaysia Melaka, Melaka, Malaysia
yusairi@utem.edu.my

Synonyms

Flow sensors; Flow meters

Definition

Flow velocity in microchannels can be measured by means of flow sensors. The basic principle of measuring flow velocity is by monitoring the flight time of particles or elements in the moving fluid after heat impulses are injected. The time taken for the particles or elements to move between two predetermined points is called the flight time. In addition, some principles in heat transfer and fluid dynamics are also applied to give precise estimation of flow conditions. Flow velocity is obtainable from flow rate. The flight time unit is second (s), the flow velocity unit is micrometer per second (μm/s) and the flow rate unit is microliter per minute (μl/min). The units for flow velocity and flow rate can sometimes be of nano- and picoscale order of magnitude.

Overview

Fluid (gas, liquid) systems such as natural gas supply or water supply use flow meters, the devices that can be used to estimate the amount of fluid supplied. They are also found in automotive applications in engine control and emission and in fuel flow and consumption, and in biomedical instrumentation [1]. A trend over the last decade has been to develop biochemical sensors that are very small in size. Typical measuring parameters are the temperature, the electrolyte conductivity, the flow rate, the liquid level and the concentration of ions, gases and enzymes. Among these sensors are the flow sensors, the devices that detect physical quantities of fluid flow such as the flow velocity. It was then expected that there were potential applications of these sensors for microanalysis technologies and systems that include analytical chemistry, biotechnology, medicine, environment monitoring, space investigations and industrial process control [2].
A miniature fluid system usually handles transportation of fluids filled with particles and/or biomacromolecules such as protein solution or cell lysate. This system, also called a microfluidic system, works with a flow rate of the order

Velocity Sensors, Table 1 Notations and symbols

Notation	Symbol	Notation	Symbol	Notation	Symbol
Coordinates	x, y, z	Density	ρ	Kinematic viscosity	υ
Velocity components	u, v, w	Stress	τ	Reynolds number	Re
Time	t	Pressure	p	Prandtl number	Pr
Total energy	E_T	Heat flux	Q, q	Heat density	Φ
Nusselt number	Nu	Heat transfer coefficient	α, h	Power	P
Thermal conductivity coefficient	λ, k	Specific heat coefficient	c_p	Volume	V
Temperature	T	Heat conductance	G	Incoming fluid temperature	T_∞

of pl/s to nl/s and where its microchannels have diameters less that a millimeter. Due to the small flow rate required by the system, it depends on micropumping to provide the fluid flow. A micropump, a device that produces a small-scale fluid flow, uses electrical or mechanical stimulus to drive the flow [3]. An example of a pump used in micropumping is the syringe pump. Current trends are to develop microfluidic systems for precise control of gas and liquid flows. The designs typically consist of integrated microfluidic components such as pumps, valves and sensors [4].

Basic Methodology

In this section, the fundamental principles of fluid flow and heat transfer are introduced. Additionally, two representative approaches in flow velocity measurement using pulse modality flow sensors and calorimetric-type gas flow sensors are discussed. There are a number of notations found in the text: Table 1 lists the notations and their respective symbols. Moreover, the articles found in the cross-references list are useful for further understanding of the topics discussed here.

Fluid Flow

In the early 1800s the Navier–Stokes equations were independently derived by G. G. Stokes and M. Navier [5]. These are a set of equations that describe the motion of a fluid. It consists of a time-dependent continuity equation for conservation of mass, three time-dependent conservation of momentum equations and a time-dependent conservation of energy equation. The flow condition can be estimated using these equations.
The continuity equation for conservation of mass where the amount of mass remains constant is

$$\frac{\partial \rho}{\partial t} + \frac{\partial(\rho u)}{\partial x} + \frac{\partial(\rho v)}{\partial y} + \frac{\partial(\rho w)}{\partial z} = 0 \tag{1}$$

The following equations give the x, y, z momentums for conservation of momentums respectively where the amount of momentum remains constant:

$$\frac{\partial(\rho u)}{\partial t} + \frac{\partial\left(\rho u^2\right)}{\partial x} + \frac{\partial(\rho uv)}{\partial y} + \frac{\partial(\rho uw)}{\partial z} = -\frac{\partial \rho}{\partial x} + \frac{1}{\mathrm{Re}}\left(\frac{\partial \tau_{xx}}{\partial x} + \frac{\partial \tau_{xy}}{\partial y} + \frac{\partial \tau_{xz}}{\partial z}\right) \tag{2}$$

$$\frac{\partial(\rho v)}{\partial t} + \frac{\partial(\rho uv)}{\partial x} + \frac{\partial\left(\rho v^2\right)}{\partial y} + \frac{\partial(\rho vw)}{\partial z} = -\frac{\partial \rho}{\partial y} + \frac{1}{\mathrm{Re}}\left(\frac{\partial \tau_{xy}}{\partial x} + \frac{\partial \tau_{yy}}{\partial y} + \frac{\partial \tau_{yz}}{\partial z}\right) \tag{3}$$

$$\frac{\partial(\rho w)}{\partial t} + \frac{\partial(\rho uw)}{\partial x} + \frac{\partial(\rho vw)}{\partial y} + \frac{\partial\left(\rho w^2\right)}{\partial z} = -\frac{\partial \rho}{\partial z} + \frac{1}{\mathrm{Re}}\left(\frac{\partial \tau_{xz}}{\partial x} + \frac{\partial \tau_{yz}}{\partial y} + \frac{\partial \tau_{zz}}{\partial z}\right) \tag{4}$$

The energy equation where the amount of energy remains constant is

$$\begin{aligned}\frac{\partial(E_T)}{\partial t} &+ \frac{\partial(uE_T)}{\partial x} + \frac{\partial(vE_T)}{\partial y} + \frac{\partial(wE_T)}{\partial z} \\ &= -\frac{\partial(up)}{\partial x} - \frac{\partial(vp)}{\partial y} - \frac{\partial(wp)}{\partial z} \\ &- \frac{1}{\mathrm{Re\,Pr}}\left(\frac{\partial q_x}{\partial x} + \frac{\partial q_y}{\partial y} + \frac{\partial q_z}{\partial z}\right) \\ &+ \frac{1}{\mathrm{Re}}\left(\frac{\partial}{\partial x}\left(u\tau_{xx} + v\tau_{xy} + w\tau_{xz}\right)\right. \\ &+ \frac{\partial}{\partial y}\left(u\tau_{xy} + v\tau_{yy} + w\tau_{yz}\right) \\ &\left.+ \frac{\partial}{\partial z}\left(u\tau_{xz} + v\tau_{yz} + w\tau_{zz}\right)\right)\end{aligned} \tag{5}$$

Heat Transfer

The passage of thermal energy from a hot to a cold body is called heat transfer in thermal physics. It can occur through conduction, transfer of heat through matter; convection, transfer of heat through moving liquids and gases; and radiation, transfer of heat through electromagnetic radiation emitted from the surface of an object which is due to the object's temperature [6]. However, radiation heat transfer usage in microfluidic flow sensors has not been found. In 1822, Joseph Fourier proposed a conduction process as in Eq. (6); in 1701, Isaac Newton suggested a convective process as in Eq. (7):

$$q = -k\frac{\mathrm{d}T}{\mathrm{d}x} \tag{6}$$

$$q = \bar{h}\left(T_{\mathrm{body}} - T_{\infty}\right) \tag{7}$$

Representative Approaches in Flow Velocity Measurement

The sensor output signal of pulse modality flow sensors is strongly tied to the relationship between sensing element temperature and flow rate as well to the relationship between sensing element resistivity and temperature [7]. Further explanation of its functionality is discussed in the next section. In steady state, the input heat transfer is balanced by power dissipation:

$$P = Q_{\mathrm{conduction}} + Q_{\mathrm{convection}} \tag{8}$$

The amount of heat transferred to the fluid is proportional to the temperature difference between the hot sensing element and the fluid temperature:

$$Q_{\mathrm{convection}} = G_{\mathrm{convection}}\left(T_{\mathrm{s}} - T_{\mathrm{f}}\right) \tag{9}$$

Equation (10) is the surface heat flux per unit area. Considering laminar flow and the decreasing thermal boundary layer with increasing velocity, the heat transfer increases in relation with the flow velocity.

$$Q'_{\mathrm{convection}} = 0.332\lambda\left(T_{\mathrm{s}} - T_{\mathrm{f}}\right)\left(\sqrt[3]{\mathrm{Pr}}\right)\sqrt{\frac{v}{x\upsilon}} \tag{10}$$

Calorimetric-type gas flow sensors analyze the temperature distribution built up in the environment around a central heater element [2]. Further explanation of its functionality is discussed in the next section. Using thermal electric circuits, thermal behavior of the sensor's structure is determined. A number of resistors and capacitors are used in the circuit to function as heat transfer agents. Equation (11) is modeled for convective resistance, and Eq. (12) for thermal capacitance where A is the heater area. The flow velocity can be obtained from Eq. (12).

$$R_{\mathrm{convection}} = \frac{1}{\alpha A} \tag{11}$$

$$R_{\mathrm{capacitance}} = \frac{1}{\rho c_{\mathrm{p}} A v} \tag{12}$$

Key Research Findings

In this section, the operating principles of selected gas velocity sensors and liquid velocity sensors are explained.

Gas Velocity Sensors

Calorimetric Sensors. The calorimetric type of gas flow sensors analyze the temperature distribution built up in the environment around a central heater element [2]. A photograph of a novel calorimetric sensor design is shown in Fig. 1, while Fig. 2 depicts the general idea behind the concept of calorimetric-type gas flow sensors. Figure 2 shows a single channel with two sensing elements, the temperature resistors, attached upstream and downstream of the direction of flow. These elements confirm the direction of flow that can be in two possible directions.

In between the elements is the central heater that heats up the gas as it passes by. This arrangement allows gas velocity to be measured. The thermal conduction, convection and laminar flow condition of the gas are used for gas velocity determination. Figure 3 shows a typical output of this sensor. It depicts the simulated temperature values of the upstream and downstream resistors for different heater temperatures using nitrogen gas. It can be seen that the temperature difference between the upstream and downstream resistors increases with the flow velocity. The sensor is said to be useful in measuring explosive gas mixture concentrations.

C-MOS Compatible Silicon Gas Flow Sensors. The top view of a novel C-MOS compatible silicon gas flow sensor is exhibited in Fig. 4. The dimension (D) is the width of the porous silicon isolation area. Its function is to measure gas flow velocity applying the principle of heat transfer [1]. The sensor is fabricated using porous silicon. It consists of two thermopiles which have two series of aluminum/p-type polysilicon thermocouples. Thermocouples are types of temperature sensor that convert thermal potential difference into electric potential difference [8].

The heater and the thermopiles are placed on a thick porous silicon layer. There are numbered pads on the top surface of the sensor. Input electric current is introduced to the heater through certain pads to generate heat. Another

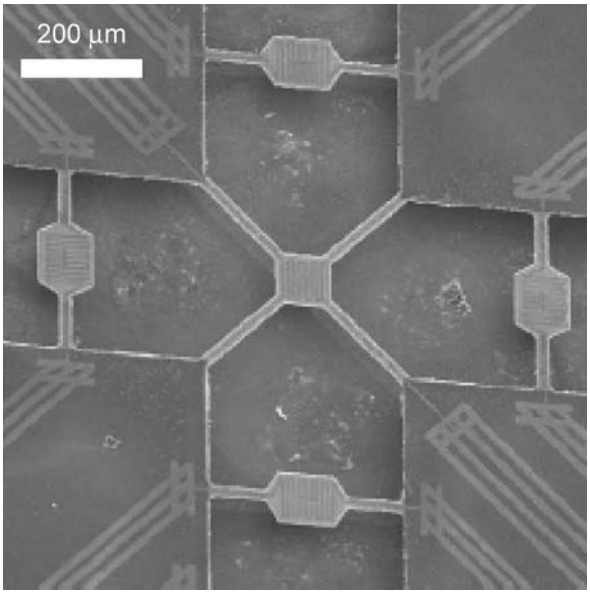

Velocity Sensors, Figure 1 View of a micromachined sensor structure developed for direction-dependent flow detection. Image taken using a scanning electron microscope [2]

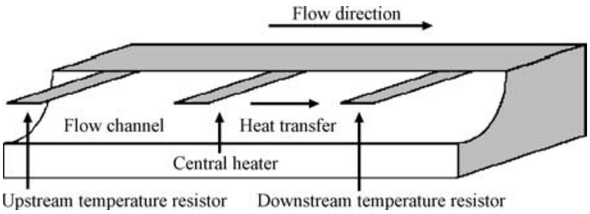

Velocity Sensors, Figure 2 Schematic of a one-dimensional calorimetric mass flow meter. The inhomogenous temperature distribution developing around the central heater characteristically represents the flow velocity [2]

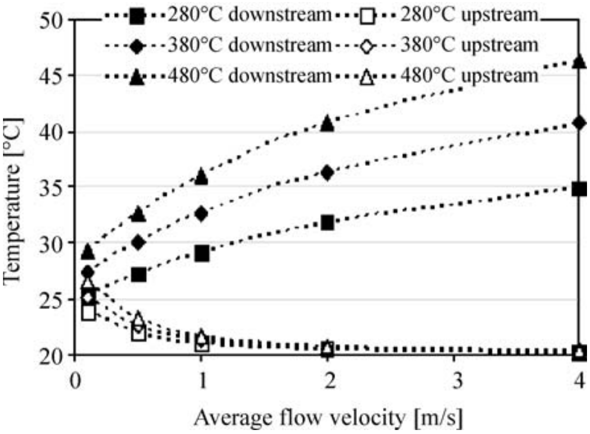

Velocity Sensors, Figure 3 Simulated gas temperature versus flow velocity at the position of platinum resistors. Nitrogen gas was used in this simulation [2]

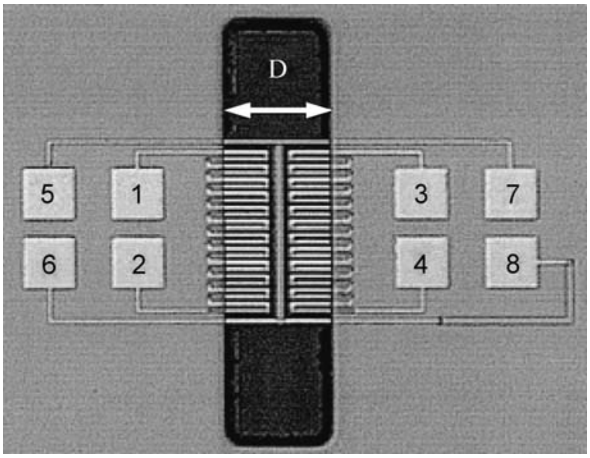

Velocity Sensors, Figure 4 Top view of a flow sensor [1]

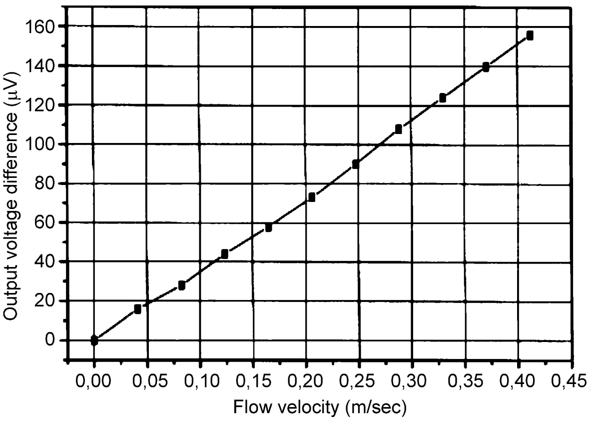

Velocity Sensors, Figure 5 Thermopile difference as a function of flow velocity [1]

option is through pads that have compensation resistors whose characteristics resemble those of the heater. Figure 5 shows the sensor's typical output. It describes the thermopiles' output voltage difference as a function of gas flow velocity. This output is a result of an experiment where nitrogen gas flow in the range of 0 to 1000 standard cubic centimeters per minute at room temperature was introduced.

Carbon Nanotube (CNT)-based Microelectromechanical Systems (MEMS) Flow Sensors. CNT-based MEMS flow sensors can be used to detect air flow inside a poly(methyl methacrylate) (PMMA) microfluidic chamber [9]. Figure 6 shows the sensor's system prototype. The system applies the principle of heat transfer by electrical current heating, flow resistance dependency and current–voltage characteristics to measure gas flow velocities.

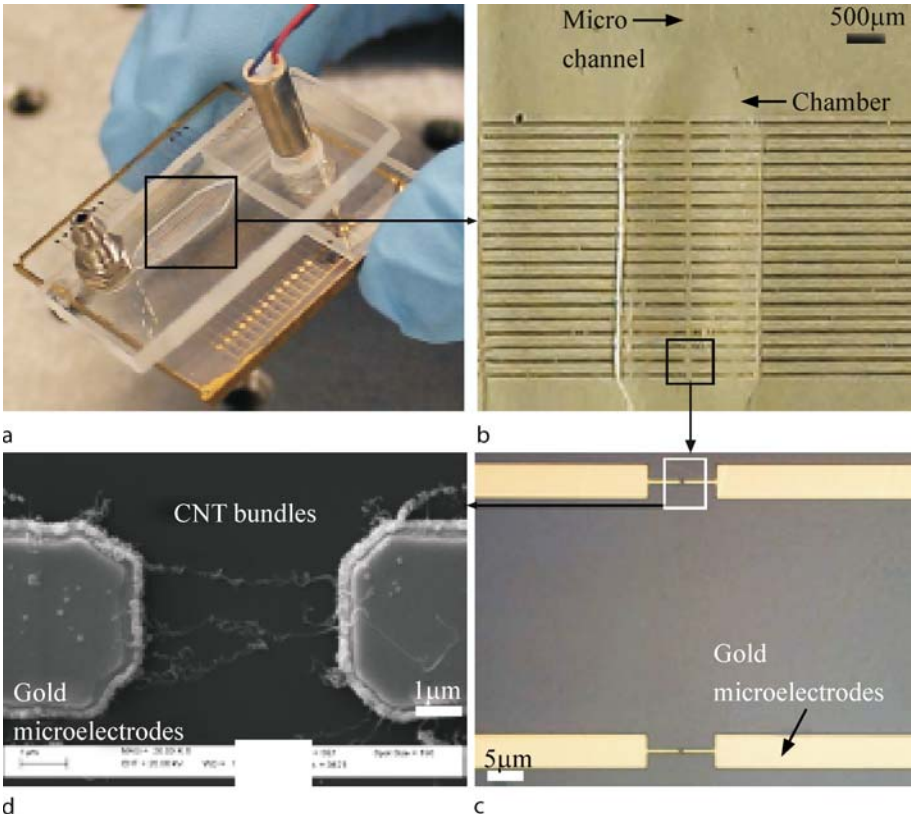

Velocity Sensors, Figure 6 (**a**) Photograph of a flow sensor chip with multi-walled carbon nanotube (MWNT) sensing element; (**b**) optical microscope image showing an array of MWNT sensors inside a PMMA chamber; (**c**) optical microscope image showing two pairs of microelectrodes with CNT bundles; (**d**) scanning electron microscope image showing the formation of MWNTs (~ 5 μm in length) between gold microelectrodes [9]

Figure 7 exhibits a typical result produced by the sensor. In this experiment, a constant current mode circuit is used to generate heat in the sensor with different overheat ratios. As a result, the thermal heat transfer mechanisms across the sensor affect the flow sensitivity. The air flow is supplied using a vortex micropump, a device that produces fluid flow in microliter and nanoliter volumes [8]. The sensor is claimed to have potential for biocompatible and low-cost sensing applications.

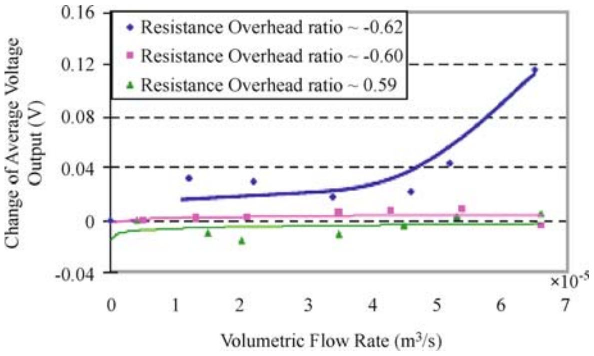

Velocity Sensors, Figure 7 Output voltage variations with different ait flow supplied by an air compressor. Three curves represent three different overheat ratios for the same sensor [9]

Liquid Velocity Sensors

Ion-Sensitive Field-Effect Transistor (ISFET)-based Flow Velocity Sensor. The ISFET-based flow velocity sensor functions as a flow direction and diffusion coefficient detection device [10]. It senses the velocity of liquid through detection of ions. The sensor is shown in Fig. 8. It shows a chemical sensor-actuator system having one ion generator and one detector. The generator–detector pair detects ions that are electrochemically generated. Positive potential applied to the generator electrode results the electrochemical reaction in water solution generating hydrogen ions (H^+). Likewise, hydroxyl ions (OH^-) are generated when a negative potential is applied to the generator electrode. These ions are called the chemical tracers.

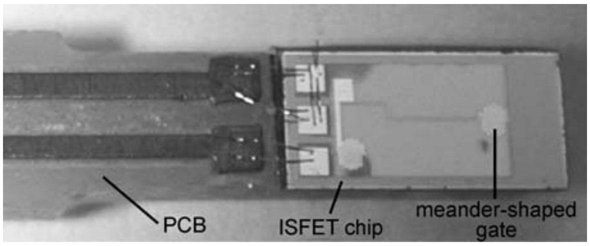

Velocity Sensors, Figure 8 Photograph of a flow sensor with a single ISFET placed onto a printed circuit board before encapsulation [10]

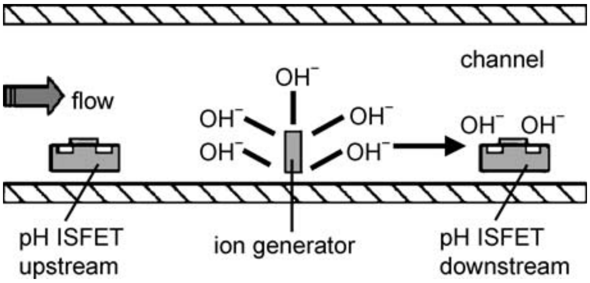

Velocity Sensors, Figure 9 Schematic of a sensor. The corresponding electrochemical reactions for H^+ and OH^- ion generation through the electrolysis of water solution are shown

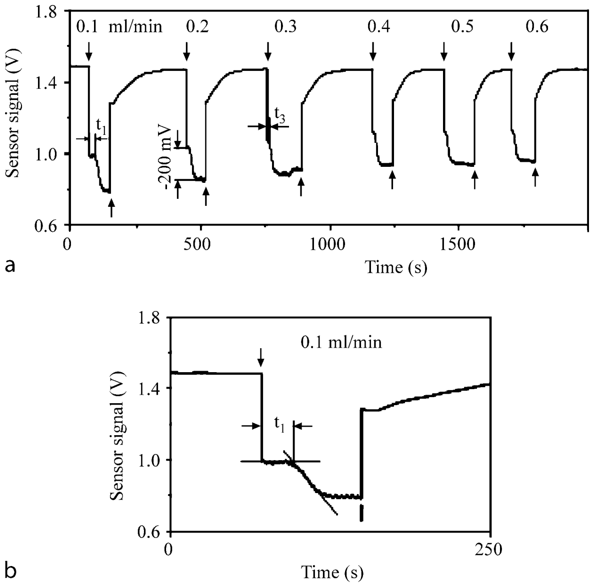

Velocity Sensors, Figure 10 Typical output signal of an ISFET-based flow velocity sensor at different flow rates from 0.1 to 0.6 ml/min (**a**) and determination of the time of flight (**b**). In this experiment, OH^- ions were generated by a constant current of 30 μA to reach a constant sensor signal. The arrows mark the time of the beginning (arrows downwards) and the end of generation (arrows upwards). The time of flight (t_1) is that needed for the generated OH^- ions to reach the ISFET gate region [10]

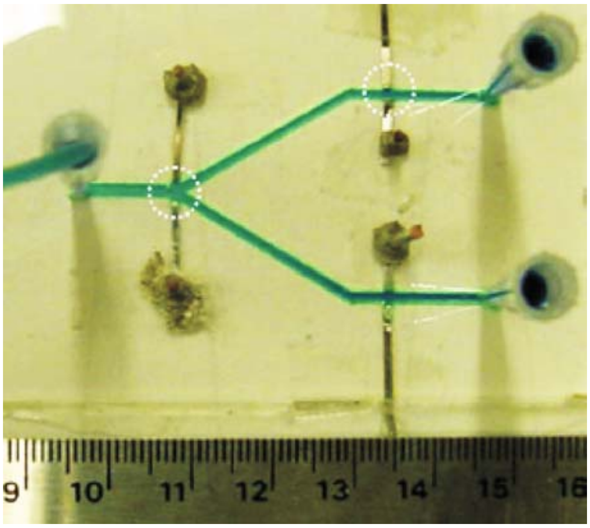

Velocity Sensors, Figure 11 Image of a milliscale prototype. The dotted circles show the separator (left) and analyzer (right) regions. The prototype was made with two analyzers, one on each arm, but only one was used at a time. Ruler scale is in centimeters [3]

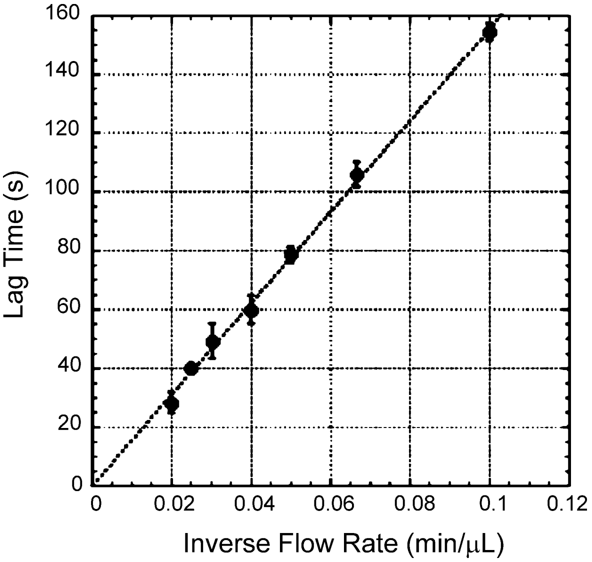

Velocity Sensors, Figure 12 Calibration of a LAPS meter. Lag time was calculated for bovine serum albumin solutions pumped at 10 – 50 μl/min. The lag time was found to be inversely proportional to the flow rate [3]

Figure 9 shows the flow of water solution passing by the ion generator. The ions generated here are then transported until they are detected upon reaching the downstream ISFET. Fluid velocity is measured by the time difference between detection and generation of the ions. The time difference is called the flight time and is inversely proportional to the mean velocity. Knowing the fluid velocity

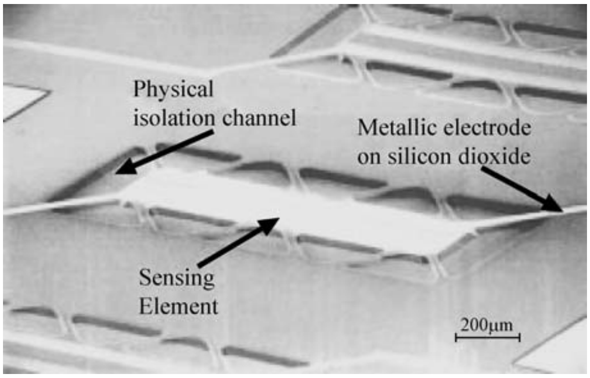

Velocity Sensors, Figure 13 Scanning electron micrograph of the top of a linear array of three fabricated flow sensors [7]

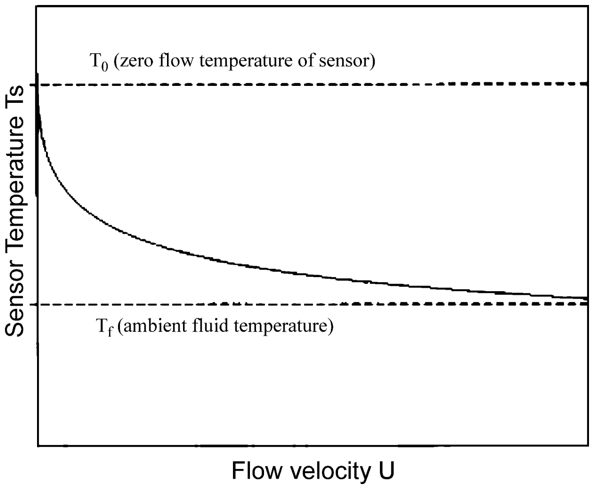

Velocity Sensors, Figure 14 Theoretical sensor temperature T_S versus fluid (water) velocity U, beginning at temperature T_0 and asymptotically approaching final ambient temperature T_f [7]

given that the relevant dimensions of the channel are also known, the flow rate can be determined as well. ISFET is said to have a fast response so it can be used to measure flow velocity in an operating range of μm/s to m/s. Figure 10 exhibits a typical output signal of an ISFET-based flow velocity sensor. It explains how the time of flight is determined. This output is obtained from an experiment where a constant electrical current of 30 μA is applied that generates hydroxyl ions. The arrow that points downwards marks the beginning of the flight time; where it ends is marked by the arrow pointing upwards.

Lag-After-Pulse-Separation (LAPS) Meter. The LAPS meter is a flow meter that measures flow rates of suspensions laden with protein or other charged macromolecules or particles [3]. The sensor prototype is shown in Fig. 11. The sensor system has a channel that branches into two subchannels. The subchannels merge again to allow the flow to continue. There is a pair of electrodes attached at the main channel (as shown in the left dotted circle in Fig. 11) called the separator. When the separator is not supplied with direct-current voltage the particles will move with the fluid. This produces a uniform flow in the main channel as well as in the two subchannels. However, when a finite-duration pulse of direct-current voltage is applied to the separator, the fluid with particles is forced to flow towards one of the subchannels.

There is also a pair of electrodes attached at each subchannels (as shown in the right dotted circle in Fig. 11) called the analyzer. The time taken for the pulse traveling downstream to reach the analyzer location is related to the inverse of the flow rates. The analyzer monitors particle concentration by measuring electric charge values. The pulse's arrival time at the analyzer is considered only when the electric charge reaches its defined maximum value. Figure 12 shows a typical output of the LAPS meter. It shows a graph where bovine serum albumin solution in deionized water is tested with a flow rate of 10–50 μl/min. The lag time is plotted against the inverse flow rate. It is found that the lag time is inversely proportional to the flow rate. Also, the time delay between the event and the detection is inversely proportional to the velocity.

Pulse Modality Flow Sensors. Pulse modality flow sensors measure liquid flow through the integrated channel sidewall using a pulse modality [7]. Figure 13 shows an image of the sensor taken using a scanning electron microscope, a device that produces high-resolution images of a sample surface [8]. It clearly shows the sensing element, the channel and the electrode.

The sensor applies the principle of heat transfer where its output signal is tied to the relationship between sensing element temperature and flow rate, between sensing element resistivity and temperature. Figure 14 shows the relationship between sensing element temperature and flow velocity. This sensor is claimed to produce fast and highly sensitive signals for regulation of microflow in the range 0.01–10 ml/min.

Future Directions for Research

Microfluidic velocity sensors are based on very sensitive structures and materials. Their sensor systems are developed using complicated fabrication technology, sophisticated measuring apparatus and at high production cost [10]. These are issues that require immediate attention

because their commercialization is problematic. Microfluidic systems will achieve their full potential if micropumping operates at an optimum level where flow rate must be measurable and controllable based on the needs of the system. For an application that delivers protein to a microbioreactor at a precise rate using this miropumping operation then some feedback controls would be necessary to ensure that process disruption did not affect the delivery rate [3]. It is highly desirable for microfluidic systems to have necessary feedback controls to produce accurate flow rates.

Cross References

- ► Developing Flows
- ► Electric Current Monitoring Methods
- ► Fluid Metering
- ► Heat Transfer in Microchannel Flows
- ► MEMS-Based Biosensor
- ► Methods for Flow Rate Measurements

References

1. Kaltsas G, Nassiopoulou AG (1999) Novel C-MOS compatible monolithic silicon gas flow sensor with porous silicon thermal isolation. Sens Act 76:133–138
2. Fürjes P, Légrádi G, Dücsó C, Aszódi A, Bársony I (2004) Thermal characterisation of a direction dependent flow sensor. Sens Act A 115:417–423
3. Sengupta S, Ziaie B, Barocas VH (2004) Lag-after-pulsed-separation microfluidic flowmeter for biomacromolecular solutions. Sens Act B 99:25–29
4. Kohl M, Liu Y, Dittmann D (2004) A polymer-based microfluidic controller. 17th IEEE Int Conf Micro Electro Mechanic Sys :288–291
5. Navier-Stokes Equations: 3-dimensional-unsteady. Glenn Research Center. National Aeronautics and Space Administration. http://www.grc.nasa.gov/WWW/K-12/airplane/nseqs.html
6. Lienhard IV JH, Lienhard V JH (2006) A Heat Transfer Textbook, 3rd ed. Phlogiston Press, Cambridge, Massachusetts
7. Okulan N, Henderson HT, Ahn CH (2000) A pulsed mode micromachined flow sensor with temperature drift compensation. IEEE Transact Electron Devices 47(2):340–347
8. Wikipedia: The Free Encyclopedia. http://en.wikipedia.org/wiki/Microfluidics
9. Fung CKM, Sin MLY, Lei TKF, Chow WWY, Lai KWC, Li WJ (2005) Flow rate measurement inside polymer microfluidic systems using carbon nanotube sensors. Sensors 2005 IEEE Oct-Nov: 541–544
10. Poghossian A, Berndsen L, Schöning MJ (2003) Chemical sensor as physical sensor: ISFET-based flow-velocity, flow-direction and diffusion-coefficient sensor. Sens Act B 95:384–390

Venturi Diode

Definition

A version of a no-moving-part fluidic diode consisting of two series-connected components: a flow contraction upstream and a diffuser immediately downstream.
A successful type of a fluidic diode particularly suited for operation at quite high operating frequencies. Its operation may be explained by considering the difference in the widths or diameters of the issuing jets in the two opposing flow direction. The difference is due to the flow separation from the walls of the contraction which lacks the diffuser property of keeping the flow attached.

Cross References

- ► Fluidic Diodes
- ► Valve-Less Rectification Pumps
- ► Fluidic Rectification

V-Groove

Definition

Groove with a wedge-shaped cross section (i.e. V-shaped) machined into a plate utilized to manipulate the mean curvature of a fluid within the groove.

Cross References

- ► Surface-Directed Capillary Flow Systems

Viscoelastic

- ► Viscoelasticity

Viscoelasticity

Hiong Yap Gan, Yee Cheong LAM
Division of Manufacturing Engineering School
of Mechanical and Aerospace Engineering, Nanyang
Technological University, Singapore, Singapore
ganh0002@ntu.edu.sg

Synonyms

Non-Newtonian; Viscoelastic; Relaxation;
Shear; Extensional

Definition

Subjected to an applied force, an elastic solid instantaneously deforms. The deformation is fully recovered with the removal of the force. In contrast, the deformation of a viscous fluid increases with time when a force is applied. With the removal of the force, a viscous fluid ceases to deform further, but any prior deformation remains. A viscoelastic material exhibits both elasticity and ▶ viscosity. Subjected to an applied force, it deforms and its deformation increases with time, i. e., it creeps. When the force is removed, only partial deformation is recovered instantaneously. It recovers more, but not all, of its deformation as time progresses. Depending on the time scale of interest, a viscoelastic material could behave solid-like or fluid-like or a combination of both.

Chemical and Physical Principles

Sir Isaac Newton proposed the law of viscosity in 1687 [1]. Subsequently, the analogous supposition, giving the modern form to the Newton hypothesis, was formulated by Navier and then by Stokes. Liquid with flow properties obeying the Newton hypothesis is called a Newton–Stokes liquid, or a Newtonian liquid. In a simple Newtonian shear flow, the shear stress is linearly proportional to the deformation rate,

$$\tau = \mu\dot{\gamma} \tag{1}$$

where τ is the shear stress and $\dot{\gamma} = \mathrm{d}\gamma/\mathrm{d}t$ is the shear rate or rate of shear deformation. The Newtonian viscosity, μ, is constant for a given temperature and is independent of shear rate or stress. Thus, a plot of shear stress versus shear rate at a given temperature is a straight line with a constant slope.

Another model describing the mechanical properties of materials originated in the seventeen century is Hooke's law for a linear elastic solid [1],

$$\sigma = E\varepsilon \tag{2}$$

where ε, σ and E are the strain, the stress and the elastic modulus, respectively.

Newton's law is satisfactory for describing the flow of simple liquids and gases with molecular weights less than $M_{\mathrm{wt}} \leq 1000\,\mathrm{g/mol}$ [2]. However, it is not adequate to describe the behaviors of polymer melts and simple liquids with the addition of high molecular weight macromolecules (polymers). For a given temperature, μ is no longer constant but depends on the flow conditions such as the shear rate $\dot{\gamma}(t)$ or the shear stress $\tau(t)$. Any fluid that does not obey the Newtonian relationship is termed as a non-Newtonian fluid.

The first person who paid attention to the effect of *viscoelasticity* was C. A. Coulomb in 1784 [1]. He showed that the damping in torsional oscillations of wires is caused by the viscoelasticity of the materials. Subsequently, it has been shown that fluids can also exhibit viscoelastic behavior, which has now been comprehensively documented over the last three decades. Some excellent references are *Viscoelastic Properties of Polymers* by Ferry [3], *The Dynamics of Polymeric Liquids* by Bird et al. [2] and *Rheological Phenomenon in Focus* by Boger and Walters [4].

Viscoelastic Behavior

Creep-and-recovery and stress relaxation experiments are the simple methods to illustrate viscoelasticity.

Creep and Recovery Tests

When a Newtonian fluid is stretched by a stress at $t = t_0$, as shown in Fig. 1a(1), the strain $\varepsilon(t)$ will increase linearly with time, see Fig. 1a(2). If the stress is removed at $t = t_{\mathrm{s}}$, the strain $\varepsilon(t)$ will remain at the level reached at $t = t_{\mathrm{s}}$, i. e., $\varepsilon(t_{\mathrm{s}})$.

When a Hookean solid is stretched, the strain $\varepsilon(t)$ will instantly increases proportionally to the stress to $\varepsilon(t_0)$, see Fig. 1a(3). $\varepsilon(t)$ will remain constant until the stress is removed at $t = t_{\mathrm{s}}$, at which time all the strain is recovered and $\varepsilon(t_{\mathrm{s}}) = 0$.

For a viscoelastic material under a constant applied stress, the strain $\varepsilon(t)$ shows a delay in response to the applied stress, see Fig. 1a(4). When the load is removed at $t = t_{\mathrm{s}}$ a viscoelastic liquid will recover partially its deformation at $t = t_{\mathrm{s}}$ over a period of time. Some deformation remains permanently. In contrast, for a viscoelastic solid, on load removal, the deformation recovery over time is relatively faster, and almost all the deformation may be recovered over a sufficiently long period of time.

Stress Relaxation Test

Figure 1b(1) shows at time $t = t_0$ a material is subjected to a strain step, and with the strain remains at this value for a prolong period of time. For a Newtonian fluid, the stress, $\tau(t)$, will increase suddenly with the sudden and step increase in strain. However, $\tau(t)$ will instantly drops to zero, see Fig. 1b(2). Thus, an immediate and complete stress relaxation occurs.

For a Hookean solid, the stress $\tau(t)$ remains constant after strain step at $t = t_0$, i. e., no stress relaxation occurs.

After the application of a strain step at $t = t_0$, both viscoelastic liquid and solid show a non-linear delay in stress relaxation as a function of their viscoelastic properties, see

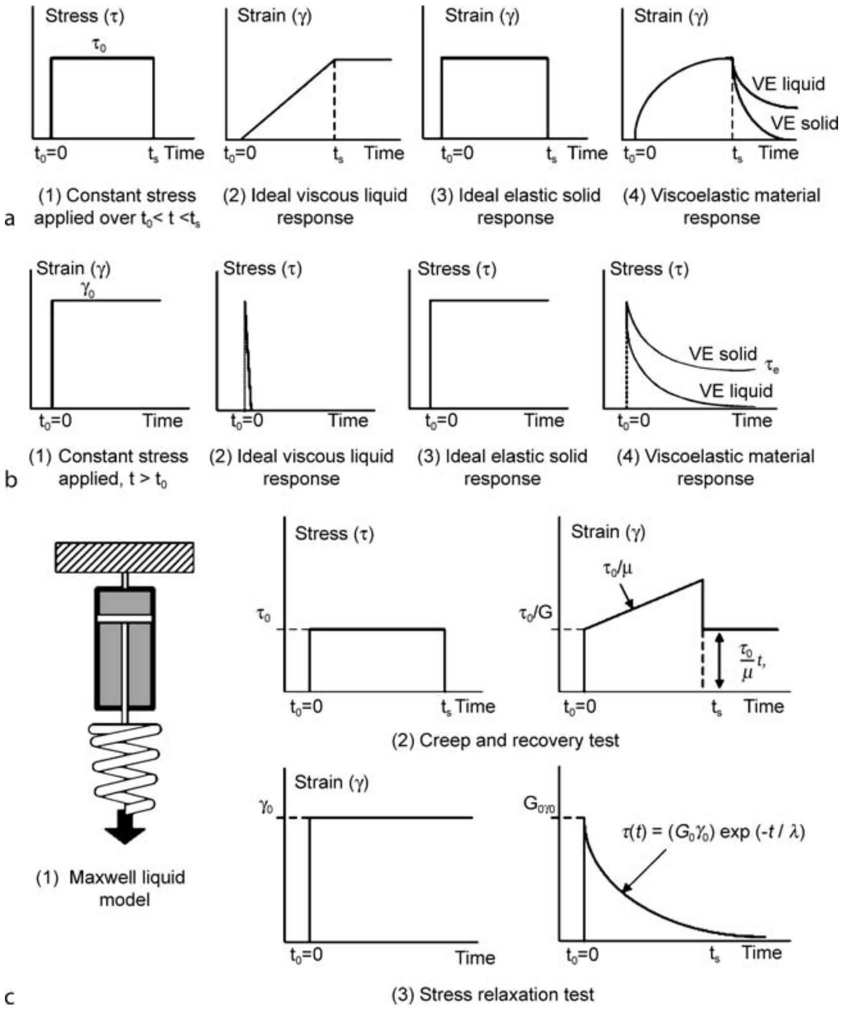

Viscoelasticity, Figure 1 (**a**) Creep and recovery tests: (1) stress step (2) response of an ideal viscous liquid (3) response of an ideal elastic solid (4) response of two different viscoelastic materials, both are showing delayed recovery of deformation. (**b**) Stress relaxation tests: (1) strain step (2) ideal viscous liquid relaxation curve (3) ideal elastic solid relaxation curve (4) Stress relation curves of two viscoelastic materials, both are showing delayed relaxation. (**c**) (1) Schematic of Maxwell liquid model an its response to (2) creep recovery test and (3) stress relaxation test

Fig. 1b(4). For a viscoelastic liquid, a delayed but complete stress relaxation takes place if the period of observation is sufficiently long. However, for a viscoelastic solid, a delayed and partial stress relaxation takes place even after a long period of observation.

Mathematical Model for Viscoelastic Fluid Behavior

It is rather complex to describe viscoelastic behaviors mathematically. We will only focus here the simple, but representative Maxwell model for viscoelastic liquids. A mechanical analogue of a Maxwell liquid model is obtained by a serial combination of a spring and a dashpot, see Fig. 1c(1). If the individual strain rates of the spring and the dashpot respectively are $\dot{\varepsilon}_{\text{solid}}$ and $\dot{\varepsilon}_{\text{liquid}}$, then the total strain rate $\dot{\varepsilon}$ is given by the sum of these two components:

$$\dot{\varepsilon} = \dot{\varepsilon}_{\text{fluid}} + \dot{\varepsilon}_{\text{solid}}$$

$$\Rightarrow \quad \dot{\varepsilon} = \frac{\tau}{\mu} + \frac{\dot{\tau}}{G} \tag{3}$$

where G is the shear modulus.

Incorporating the Hooke's law of elasticity and Newton's law of viscosity with Eq. (3), the stress-strain relationship can be expressed as

$$\mu\dot{\varepsilon} = \tau + \lambda\dot{\tau} \tag{4}$$

where $\dot{\tau}$ is the time derivative of τ, $\lambda = \mu/G$ is the relaxation time. From Eq.(4), if a constant stress is applied to a Maxwell-model fluid, the strain rate will be constant and the strain will increase indefinitely, the so called creep phenomenon, see Fig 1c(2). If instead, a constant strain is applied to the fluid, the stress will decay as $\exp(-t/\lambda)$, the so called stress relaxation, see Fig. 1c(3). An important feature of the Maxwell model is its predominantly fluid-like response, see Fig. 1c. However, comparing Fig. 1c(2) and 1c(3) to Fig 1a(2) and 1a(4) respectively, it can be observed that the Maxell model is only an approximation to a viscoelastic liquid.

There are other models based on springs and dashpots such as the simple Kelvin–Voigt model for viscoelastic solid and the Burgers model. Reader is referred to [1–5] for details. Other elementary models are the dumbbell, bead-spring representations, network and kinetic theories. However, the most notable limitation of all these models is their restriction to small strain and strain rates [2, 3].

Viscoelastic Fluid Behaviors

Polymeric solutions are inherently viscoelastic due to their long molecular chains. Dilute polymeric solutions will be of interests for microfluidic and nanofluidic applications, due to their ease of implementation. Since the polymer coils in a dilute solution are isolated and independent in their molecular movements, their viscoelastic behavior can be explained by the deformation of the individual coil or molecule in the stream [2, 3]. As a result, the viscoelasticity of polymer solutions is generally attributed to the deformation of polymer chains and the consequent generation of unequal normal stresses.

Steady Shear Flows

For a one-dimensional steady shear flow of a fluid between two planes, the velocities of an infinitesimal element of fluid in the y- and z-directions are zero. The velocity in the x-direction is a function of y only. Note that in addition to the shear stress τ_{yx} (refer to τ subsequently) there are three normal stresses denoted by τ_{xx}, τ_{yy}, τ_{zz} within the sheared fluid. Weissenberg in 1947 [6] was the first to observe that the shearing motion of a viscoelastic fluid gives rise to unequal normal stresses, known as Weissenberg effects. Since the pressure in a non-Newtonian fluid cannot be defined, and as the normal stress differences [2, 3], $\tau_{xx} - \tau_{yy} = N_1$ and $\tau_{yy} - \tau_{zz} = N_2$, are more readily measured than the individual stresses, it is therefore customary to express N_1 and N_2 together with the shear stress τ as functions of the shear rate $\dot{\gamma}_{yx}$ to describe the viscoelastic behavior of a material in a simple shear flow.

The first and second normal stress differences N_1 and N_2can be expressed in terms of two coefficients, ψ_1 and ψ_2, defined as follows:

$$\psi_1 = \frac{N_1}{\gamma_{yx}^2} \quad \text{and} \quad \psi_2 = \frac{N_2}{\gamma_{yx}^2} \tag{5}$$

It is common that the first normal stress difference N_1 is higher than the shear stress τ. The ratio of N_1 to τ is often taken as a measure of how elastic a liquid is; specifically (N_1/τ) is referred as the recoverable shear.

Elongational Flow

Three main types of elongational flow are uniaxial, biaxial and planar. Although resistance to flow can be referred to loosely as an elongational or extensional viscosity (which further depends upon the type of elongational flow), this parameter generally is not constant.

For simplicity, consider the behavior of an incompressible fluid element which is being elongated at a constant strain rate $\dot{\varepsilon}$ in the x-direction (uniaxial extensional flow). For an incompressible fluid, the volume of the element must remain constant and therefore it must contract in both the y- and z-directions at the rate of $(\dot{\varepsilon}/2)$ for a system symmetrical in these directions. The three components of the velocity vector $\boldsymbol{V_i}$ are given by:

$$\boldsymbol{V_x} = \dot{\varepsilon}x\,, \quad \boldsymbol{V_y} = -\frac{\dot{\varepsilon}}{2}y\,, \quad \boldsymbol{V_z} = -\frac{\dot{\varepsilon}}{2}z \tag{6}$$

The rate of elongation in the x-direction can be written as:

$$\dot{\varepsilon} = \frac{\partial \boldsymbol{V_x}}{\partial x} \tag{7}$$

In uniaxial extension, the elongational viscosity μ_e can then be defined as:

$$\mu_e = \frac{\tau_{xx} - \tau_{yy}}{\dot{\varepsilon}} \quad \text{or} \quad \frac{\tau_{xx} - \tau_{zz}}{\dot{\varepsilon}} \tag{8}$$

The earliest determinations of elongational viscosity were for the simplest case of uniaxial extension or stretching of a fiber or filament of liquid. Trouton [7], and subsequently many other investigators, found that at low strain (or elongation) rates, the elongational viscosity μ_e was three times the shear viscosity μ. The ratio μ_e/μ is referred to as the Trouton ratio, T_r:

$$T_r = \frac{\mu_e}{\mu} = 3 \tag{9}$$

The value of 3 for Trouton ratio refers specifically to the viscosities in shear and elongation for an incompressible Newtonian fluid.

By analogy, the Trouton ratio for a non-Newtonian fluid, for which T_r is not necessary equal to three, can be defined as:

$$T_r = \frac{\mu_e(\dot{\varepsilon})}{\mu(\dot{\gamma})} \tag{10}$$

Since the Trouton ratio depends on both $\dot{\varepsilon}$ and $\dot{\gamma}$ in Eq. (10), there is some ambiguity in choosing their values. To provide a convenient estimate without this ambiguity, Jones et al. [8] proposed the following definition:

$$T_r = \frac{\mu_e(\dot{\varepsilon})}{\mu(\sqrt{3}\dot{\varepsilon})} \tag{11}$$

i. e., in the denominator, the shear viscosity is evaluated at $\dot{\gamma} = \sqrt{3}\,\dot{\varepsilon}$. They also suggested that for inelastic isotropic fluids, the Trouton ratio is equal to 3 for all values of $\dot{\varepsilon}$ and $\dot{\gamma}$ and any departure from the value of 3 can be ascribed unambiguously to *viscoelasticity*.

A common behavior of polymeric solutions [9–11] and polymer melts [12] is that the Trouton ratio is greater than three at moderate and higher deformation rate. Their typical behaviors are illustrated in Fig. 2, which show that the Trouton ratio can be a function of both strain and strain rate.

Dimensionless Parameters

The relaxation time (λ), which describes the time required for the polymer coil to relax from a deformed state back to its equilibrium configuration, is a key parameter for characterizing a viscoelastic fluid. For a fluid with large λ, the stresses relax slowly and the elastic effects can be observed even at low deformation rates. A fluid with small λ can also exhibit significant elastic effects provided that the deformation rate is high. Clearly, both the fluid characteristic time (the relaxation time) and the flow characteristic time (e. g. the inverse of the deformation rate) are crucial in determining the viscoelastic response of a viscoelastic liquid. For many polymeric liquids, λ lies between 10^{-3} s for dilute solutions and 10^3 s for concentrated solutions.

The relative importance of elasticity in a flow is often described by the Deborah number, De introduced by Reiner [13]. This number may be interpreted as the ratio of the magnitudes of the elastic forces to that of the viscous forces. It is defined as the ratio of a characteristic time (time scale) of the fluid λ to a characteristic time of the flow system t_{flow} [2]

$$\text{De} = \frac{\lambda}{t_{\text{flow}}} \tag{12}$$

The characteristic time of the fluid is often taken to be the largest time constant describing the slowest molecular motions, or else some mean time constant determined by linear viscoelasticity. The characteristic time may also be chosen as a time constant in a constitutive equation. The characteristic time for the flow is usually taken to be the time interval during which a typical fluid element experiences a significant sequence of kinematic events, for example the duration of a characteristic experimental observation. If the flow following a material particle is steady, the characteristic time can be the reciprocal of a characteristic strain rate.

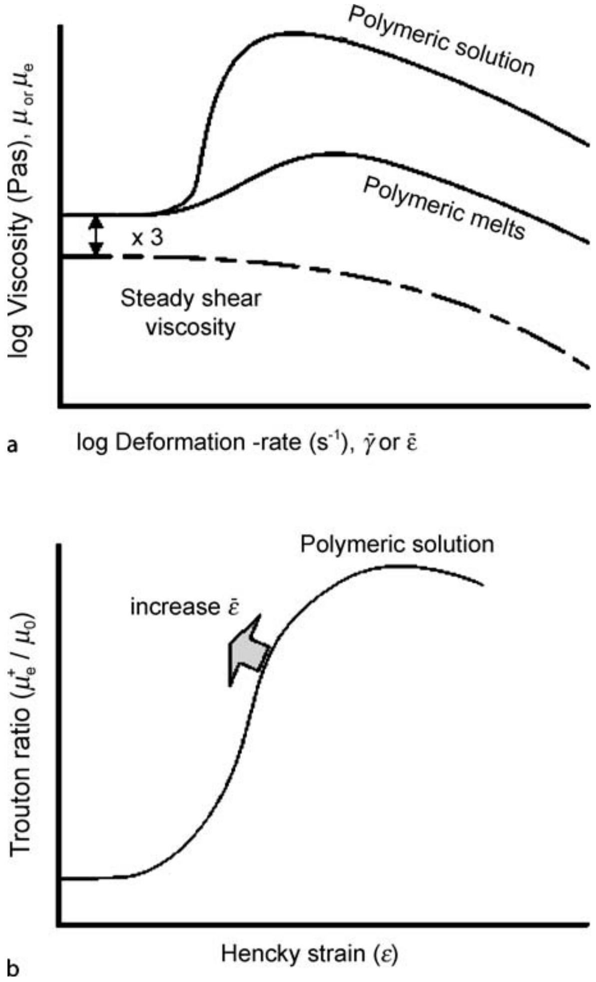

Viscoelasticity, Figure 2 Extensional viscosity curve of polymeric solution and polymer melt. (**a**) Comparison between steady shear and elongation response (**b**) Trouton ratio as a function of total Hencky strain $\varepsilon = \dot{\varepsilon}_0 t$ for polymeric solution

V

Rheological Measurements

Rheological properties of the same polymeric solution measured in shear and elogational flows can be very different as discussed in earlier section. However, a cursory examination of current textbooks on rheology (e. g. Bird et al. [2], Ferry [3], Tanner [14]) shows that shear rheology dominates and research in extensional rheology is comparatively much more recent. The measurements of the shear properties of polymeric fluids are well established and a number of ▶ rheometers are available for both melts and dilute polymeric solutions. Lately, more efforts have been directed in measuring the extensional properties of fluids [8, 9, 15–19].

In practice, the steady shear and oscillatory tests are commonly conducted via rotational rheometers, and the extensional test is widely performed in *liquid filament rheometers* or *capillary breakup extensional rheometers* (CaBER).

Rotational Shear Measurements

Steady Shear Flow Curves Steady shear flow generally is a viscosity measurement on materials undergoing steady and continuous shear. A flow curve, viscosity (μ) versus shear rate ($\dot{\gamma}$), across a wide range of shear rate is often used to design pumps and mixing devices. This method is also used to provide flow behavior which indicates the relationship of shear rate to shear stress between suitable limits. A commonly observed feature of polymeric solutions is the shear thinning characteristic, i. e., the decrease of viscosity with increasing shear rate, which can be determined from this technique. This typical flow curve exhibits two Newtonian plateaus – one at low shear and another at high shear regimes. The shear thinning region lies between the two limiting conditions and may extend over a few decades of shear rate.

However, dynamic measurements, such as the oscillatory tests, are preferred in practice over the steady shear measurements for determining the viscoelastic properties of fluids. This is not only because of the difficulty in determining the first normal stress coefficient accurately, the determination of a fluid's viscosity by steady shear measurement is only a partial characterization of a viscoelastic fluid's properties.

Dynamic Oscillatory Experiments The dynamic rheological properties of a polymeric solution can be determined by small-amplitude oscillation tests [2]. In small amplitude oscillatory measurements, a sinusoidally varying shear stress field is imposed on a fluid and the amplitude of the resulting shear strain and phase angle between the imposed stress and the strain is measured. The test is said to be in the *linear viscoelastic* regime if the strain is linearly proportional to the imposed stress and the response is sinusoidal [1, 5].

In practice, dynamic oscillatory measurements are sensitive probes of molecular structure and interactions, for examples in emulsions and dispersions. Oscillatory measurements probe emulsion structure without destroying it. This is accomplished by applying very small sinusoidal displacements or strains to the emulsion at controlled amplitude and frequency. In general, there are two mechanisms for a material to respond to a deformation:

- elastic energy storage (G', known as storage modulus), and
- viscous dissipation (G'', known as loss modulus).

G', which is proportional to the strain in-phase with the stress, provides information about the elasticity of a material. G'', the loss modulus, is proportional to the stress out-of-phase with the displacement. These parameters are termed the elastic and viscous loss moduli, G' & G'' respectively. The values of the respective stresses measured are divided by the appropriate strains, resulting in the respective moduli. The shapes of the curves for G' and G'' versus the test frequency ω for polymeric solutions are described by Ferry [3]. At low frequency, G' and G' are proportional to ω^2 and ω respectively. As frequency increases, the slope of these curves decreases, as illustrated in Fig. 3.

Qualitatively, the stress created by imposing oscillatory strains will be a function of the amplitude of strain, its frequency, and the properties of the polymeric solution. By applying sufficiently small strains, we can minimize the strain dependency from the material response. Thus, the amplitude of strain is no longer an important consideration, resulting in a *linear viscoelastic* response. Small

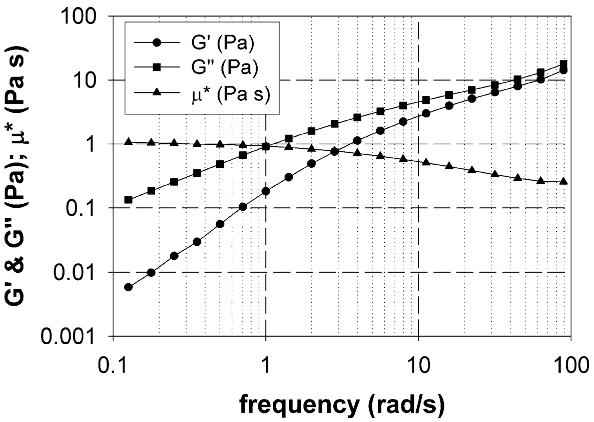

Viscoelasticity, Figure 3 Dynamic test: frequency oscillation sweep. For viscoelastic fluid of 1 wt% poly (ethylene-oxide)(PEO) in 55 wt% glycerol water. Molecular weight of PEO is 2×10^6 g/mol

strain measurements can be important for certain application as they do not adversely affect the structure of the fluid.

These linear viscoelastic dynamic moduli are functions of frequency. For a suspension or an emulsion material at low frequency, elastic stresses relax and viscous stresses dominate with the result that the loss modulus, G'', is higher than the storage modulus, G'. For a dilute solution, G'' is larger than G' over the entire frequency range but they approach each other at higher frequencies as shown in Fig. 3.

The Maxwell relaxation time is commonly evaluated from the first normal stress difference measurement,

$$\lambda_M = \frac{N_1}{2\dot{\gamma}^2\mu_0} \tag{13}$$

However, at zero deformation rate, where the simple fluid theory applies, can be evaluated from the oscillatory data by

$$\lambda_M^0 = \lim_{\dot{\gamma}\to 0}\frac{N_1}{2\dot{\gamma}^2\mu_0} = \lim_{\omega\to 0}\frac{G'}{\omega^2\mu_0} \tag{14}$$

It was shown that for water soluble polymeric solution such as Separan AP30, NP10 and Keltrol with polymer concentration less than approximately 1500, 5000, and 500 ppm, respectively, is independent of polymer concentration [20]. These observations were consistent with the molecular theories such as the Zimm theory, which states that at infinite dilution, the relaxation time is independent of polymer concentration and is given by

$$\lambda_z = 0.423\frac{[\mu]\,\mu_s M_{wt}}{RT} \tag{15}$$

where $[\mu]$ is the intrinsic viscosity [2, 3] and μ_s is the solvent viscosity.

By Cox–Mertz rule, for polymeric solutions at low frequency and shear rate in accordance with the simple fluid theory, the zero shear viscosity can be estimated by [2, 20]

$$\mu_0 = \lim_{\dot{\gamma}\to 0}\mu = \lim_{\omega\to 0}\left|\mu^*\right| = \lim_{\omega\to 0}\left(\frac{G''}{\omega}\right) \tag{16}$$

Key Research Findings

Extensional Rheological Measurement

Elongational or extensional flow of polymeric fluids are experienced in important industry processes, such as food dispersion, paints, adhesives, coating, inkjet printing, enhanced oil recovery, and lubrication. However, extensional properties cannot be determined from shear rheometry experiments.

Filament-stretching has been studied for obtaining extensional properties of polymeric solutions and melts. A comprehensive review of the flow dynamics of filament-stretching is provided by McKinley and Sridhar [9]. Subsequently, *liquid filament rheometers* or *capillary breakup extensional rheometers* (CaBER) has been developed for the characterization of the dynamics of complex fluids undergoing extensional flows.

Technical Aspect of CaBER Measurements

Recently, rheometer for measuring extensional properties is commercially available. It is called the CaBER 1 (the Capillary Breakup Extensional Rheometer). It was designed by the Cambridge Polymer Group and is manufactured by Thermo Haake. The measuring procedure involves the placing of a small quantity of sample fluid between two parallel plates. A fluid filament is formed when the sample fluid is subjected to a rapid extensional step strain, see Fig. 4. The filament evolution as a function of time is dictated by the surface tension and the viscoelastic stresses of the fluid. The surface tension is trying to *pinch off* the filament and the extensional properties of the sample are trying to prevent it. A laser micrometer measures the midpoint diameter of the gradually thinning fluid filament when the upper plate extends to its final position. From the measured data, several elongational rheological properties can be determined such as the extensional viscosity, evolution of the filament diameter as a function of time, the extensional deformation and deformation rate, and the filament break-up time.

In general, the changes of a fluid filament are governed by a balance of forces on the filament. Assuming that a fluid sample is at rest initially, and is subjected to a constant strain rate subsequently. With reference to the mid-diameter (D_{mid}) of the filament and ignoring the very small inertial effects [10], the governing equation can be expressed as

$$\mu_e\dot{\varepsilon}_0 \equiv \langle\tau_{zz} - \tau_{rr}\rangle = \frac{4F_z}{\pi D_{mid}^2} - \frac{2\rho g V_0}{\pi D_{mid}^2} - \frac{2\sigma}{D_{mid}} \tag{17}$$

where ρ and V_0 is the density of the sample fluid and the sample volume respectively. σ is the surface tension of the fluid, which has to be measured separately. g is the gravitational constant. F_z is the tensile force acting on the column ends, and $\langle\tau_{zz} - \tau_{rr}\rangle$ represents the non-Newtonian contribution to the average total normal stress difference over the filament cross section.

Equation (17) is model-dependent and the resulting solution to the differential equation depends on how the polymeric contribution to the stress varies with the rate of deformation. Solutions to this evolution equation have

V

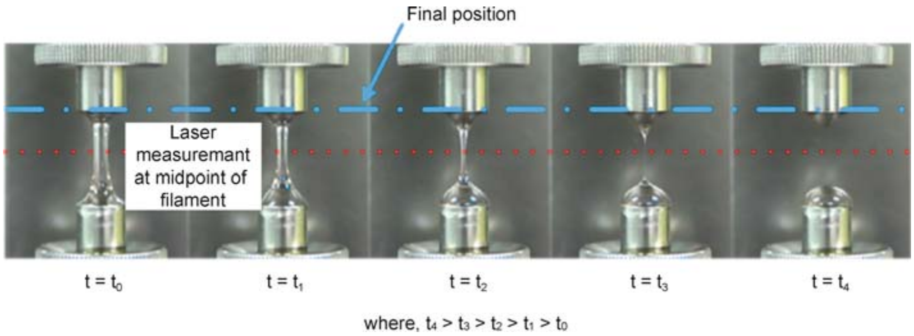

Viscoelasticity, Figure 4 Sequence of a CaBER 1 experiment snapshots

Viscoelasticity, Table 1 Evolution of the mid-filament diameter in a fluid filament undergoing capillary-driven breakup. Note: λ_c is the characteristic relaxation time of the sample, t_c is the filament break-up time and μ_S is the Newtonian viscosity of the solvent

Constitutive Model	Growth of Filament	Inferred Parameters
Newtonian Fluid, $\tau = \mu\dot{\gamma}$	$D_{mid}(t) = 0.142(\sigma/\mu_S)(t_c - t)$	t_c, σ/μ_S
Power Law Fluid, $\tau = K\dot{\gamma}^n$	$D_{mid}(t) = 2^{1-n}(0.142)(\sigma/K)(t_c - t)^n$	t_c, $\sigma/K, n$
Upper Convected Maxwell	$D_{mid}(t) = D_0\left(GD_0/\sigma\right)^{1/3}\exp(-t/3\lambda_c)$	λ_c, G/σ

been found for a number of models [17–19] and are summarized in Table 1.

The Apparent Extensional Viscosity

The evolution of filament diameter is driven by the capillary pressure and resisted by the extensional stress in the fluid. Thus, measurements can also be represented in terms of an apparent extensional viscosity, define as

$$\mu_{app}(\varepsilon) = \langle \tau_{zz} - \tau_{rr} \rangle / \dot{\varepsilon}(t) \qquad (18)$$

where under steady elongation flow, the natural-strain or Hencky strain [9] is given by

$$\varepsilon\,(0, t) = \dot{\varepsilon}_0 t = \ln(L(t)/L_0) = -2\ln(D(t)/D_0) \qquad (19)$$

Hence, the apparent viscosity can be written as,

$$\mu_{app}(\varepsilon) = \frac{\frac{2\sigma}{D_{mid}(t)}}{-\frac{2}{D_{mid}(t)}\frac{dD_{mid}}{dt}} = \frac{\sigma}{\frac{dD_{mid}}{dt}} \qquad (20)$$

Examples of Application

- Inkjet printing cartridge: a micro-entry flow (contraction flow) of a non-Newtonian fluid.
- Micro-injection molding: scaled-down version of injection molding (contraction flow).
- Flow focusing of emulsion: micro-contraction is used to generate emulsion droplet.
- Viscoelastic micro-mixer: elastically induced chaotic flow instabilities through contraction/expansion geometrical configuration in a microchannel.
- Microfluidics rectifier: a channel whose resistance to flow changes based on the direction of the flow.

Cross References

- ▶ Chaotic Mixing
- ▶ Chaotic Mixing Based on Viscoelasticity
- ▶ Droplet Dispensing
- ▶ Droplet Microreactors
- ▶ Microfluidic Mixing
- ▶ Micromolding
- ▶ Micromolding (Injection and Compression Molding)
- ▶ Non-Newtonian Fluids in Microchannel
- ▶ Non-Newtonian Fluids in Microfluidics
- ▶ Viscosity

References

1. Malkin AY, Isayev AI (2006) Rheology: Concepts, Methods & Applications. ChenTec, Toronto
2. Bird RB, Armstrong RC, Hassager O (1987) Dynamics of Polymeric Liquids 1. John Wiley & Sons, New York
3. Ferry JD (1980) Viscoelastic Properties of Polymers. John Wiley & Sons, New York
4. Boger DV, Walters K (1993) Rheological Phenomena in Focus. Elsevier, New York
5. Mezger TG (2006) The Rheology Handbook: For Users of Rotational and Oscillatory Rheometers. Vincentz Network, Germany

6. Weissenberg K (1947) A Continuum Theory of Rheological Phenomena. Nature 159:310–311
7. Trouton FT (1906) On the Viscous Traction and its Relation to that of Viscosity. Proc R Soc A77:426–440
8. Jones DM, Walters K, Williams PR (1987) The Extensional Viscosity of Mobile Polymer Solutions. Rheol Acta 26:20–30
9. McKineley GH, Sridhar T (2002) Filament-Stretching Rheometry of Complex Fluids. Annu Rev Fluid Mech 34:375–415
10. Li L, Larson RG, Sridhar T (2000) Brownian Dynamics Simulation of Dilute Polystyrene Solutions. J Rheol 4:291–322
11. Gupta RK, Nguyen DA, Sridhar T (1991) Extensional Viscosity of Dilute Polystyrene Solutions: Effect of Concentration and Molecular Weight. Phys Fluid 12:1296–1318
12. Cogswell FN (1972) Measuring the Extensional Rheology of Polymer Melts. J Rheol 16:383–403
13. Reiner M (1964) The Deborah Number. Phys Today 17:62
14. Tanner RI (2000) Engineering Rheology. Oxford, Clarendon
15. Tirtaatmadja V, Sridhar T (1993) A Filament Stretching Device for Measurement of Extensional Viscosity. J Rheol 37:1081–1102
16. Sridhar T, Tirtaatmadja V, Nguyen DA, Gupta RK (1991) Measurement of Extensional Viscosity of Polymer Solutions. J Non-Newt Fluid Mech 40:271–280
17. Entov VM, Hinch EJ (1997) Effect of a Spectrum of Relaxation Times on the Capillary Thinning of a Filament of Elastic Liquid. J Non-Newt Fluid Mech 72:31–54
18. Bazilevsky AV, Entov VM, Rozhkov AN (1990) Liquid Filament Microrheometer and Some of its Applications. 3rd Eur Rheol Conf, Elsevier
19. McKinley GH, Tripathi A (2000) How to Extract the Newtonian Viscosity from Capillary Breakup Measurements in a Filament Rheometer. J Rheol 44:653–671
20. Tam KC, Tiu C (1996) Water Soluble Polymers (Rheological Properties). Polymeric Materials Encylopedia. CRC Press, Boca Raton

Viscometer

► Rheometer

Viscosity

Synonyms

Compactness; Plasticity

Definition

Viscosity is a measure of the resistance of a fluid to deform under shear stress. It describes a fluid's internal resistance to flow and may be thought of as the friction forces that act within a moving fluid. Viscosity can also be defined as the ratio of the shear stress to the strain rate.

Cross References

► Micro- and Nano-Scale Anemometry: Implication for Biomedical Applications
► Chaotic Mixing Based on Viscoelasticity
► Droplet Dispensing
► Microfluidic Mixing
► Micromolding
► Micromolding (Injection and Compression Molding)
► Non-Newtonian Fluids in Microchannel
► Non-Newtonian Fluids in Microfluidics
► Viscoelasticity

Viscous Dissipation

Gian Luca Morini
Institute of Physics, DIENCA Università di Bologna, Bologna, Italy
gianluca.morini@mail.ing.unibo.it

Synonyms

Internal friction

Definition

The irreversible process by means of which the work done by a fluid on adjacent layers due to the action of shear forces is transformed into heat is defined as viscous dissipation.

Overview

The equation of continuity and the thermal energy balance on a differential element fixed in a pure flowing fluid can be written as follows:

$$
\begin{aligned}
-\frac{1}{\rho}\frac{\mathrm{D}\rho}{\mathrm{D}t} &= \nabla\cdot\boldsymbol{v} \\
\rho\frac{\mathrm{D}U}{\mathrm{D}t} &= -\nabla\cdot\boldsymbol{q} - p\,(\nabla\cdot\boldsymbol{v}) - \bar{\boldsymbol{\tau}}:\nabla\boldsymbol{v}
\end{aligned}
\tag{1}
$$

in which U is the specific internal energy of the fluid, p the pressure, $\boldsymbol{v}$ the velocity vector, $\boldsymbol{q}$ the heat flux, ρ the fluid density, t the time and $\bar{\boldsymbol{\tau}}$ the viscous tensor.
The second term on the right-hand side of Eq. (1) represents the reversible work done by the fluid against the external pressure field; this term is linked to the compressibility of the fluid and is known in the literature as *flow work*. The third term on the right-hand side of Eq. (1) is linked to the work done by the fluid on adjacent layers due to the action of the shear forces; this work is transformed

V

into heat by means of an irreversible process called *viscous dissipation* in the English language literature and as *internal friction* in the Russian literature.

The effect of the viscous dissipation on heat transfer is significant especially for high-velocity flows, highly viscous flows even at moderate velocities, for fluids with a moderate Prandtl number and moderate velocities with small wall-to-fluid temperature difference or with low wall heat fluxes and flowing through microchannels.

Basic Methodology

Since the internal energy of a real fluid can be related to the temperature and to the fluid specific heat by means of the equation

$$\mathrm{d}U = c_\mathrm{V}\,\mathrm{d}T + \left[T\left(\frac{\partial p}{\partial T}\right)_\mathrm{V} - p\right]\mathrm{d}V \tag{2}$$

one can write the total derivative of the internal energy in terms of the fluid temperature as follows:

$$\frac{\mathrm{D}U}{\mathrm{D}t} = \left[T\left(\frac{\partial p}{\partial T}\right)_\mathrm{V} - p\right]\frac{\mathrm{D}V}{\mathrm{D}t} + c_\mathrm{V}\frac{\mathrm{D}T}{\mathrm{D}t} \tag{3}$$

where V is the specific volume of fluid, T is the absolute fluid temperature and c_V is the specific heat at constant volume.

The continuity equation allows one to write the derivative term of the fluid volume in the form

$$\frac{\mathrm{D}V}{\mathrm{D}t} = \frac{\mathrm{D}}{\mathrm{D}t}\left(\frac{1}{\rho}\right) = -\frac{1}{\rho^2}\frac{\mathrm{D}\rho}{\mathrm{D}t} = \frac{1}{\rho}\left(\nabla\cdot\boldsymbol{v}\right) \tag{4}$$

By combining Eq. (4) with Eq. (3) and the thermal energy balance (Eq. (1)), one obtains

$$\rho c_\mathrm{V}\frac{\mathrm{D}T}{\mathrm{D}t} = -\nabla\cdot\boldsymbol{q} - T\left(\frac{\partial p}{\partial T}\right)_\mathrm{V}\left(\nabla\cdot\boldsymbol{v}\right) - \bar{\boldsymbol{\tau}} : \nabla\boldsymbol{v} \tag{5}$$

in which the energy balance is expressed by means of the fluid temperature and the physical properties of the fluid. In Eq. (5) it is evident that the reversible work done against the pressure field is linked to the fluid compressibility. More explicitly, if one considers the definition of the thermal expansion coefficient (β) and of the volume compressibility (χ)

$$\beta = -\frac{1}{\rho}\left(\frac{\partial\rho}{\partial T}\right)_\mathrm{p} \quad \chi = \frac{1}{\rho}\left(\frac{\partial\rho}{\partial p}\right)_\mathrm{T} \tag{6}$$

the thermal energy equation for viscous flows can be written as follows:

$$\begin{aligned}\rho c_\mathrm{V}\frac{\mathrm{D}T}{\mathrm{D}t} &= -\nabla\cdot\boldsymbol{q} - \frac{\beta}{\chi}T\left(\nabla\cdot\boldsymbol{v}\right) - \bar{\boldsymbol{\tau}} : \nabla\boldsymbol{v}\\ &= -\nabla\cdot\boldsymbol{q} + \frac{\beta}{\chi}T\left[\frac{1}{\rho}\frac{\mathrm{D}\rho}{\mathrm{D}t}\right] - \bar{\boldsymbol{\tau}} : \nabla\boldsymbol{v}\end{aligned} \tag{7}$$

By remembering the following relation between the fluid specific heats:

$$c_\mathrm{p} - c_\mathrm{V} = T\left[\left(\frac{\partial V}{\partial T}\right)_\mathrm{p}\frac{\mathrm{d}p}{\mathrm{d}T} + \left(\frac{\partial p}{\partial T}\right)_\mathrm{V}\frac{\mathrm{d}V}{\mathrm{d}T}\right] \tag{8}$$

the thermal energy equation (Eq. (7)) can be expressed in the following alternative form:

$$\rho c_\mathrm{p}\frac{\mathrm{D}T}{\mathrm{D}t} = -\nabla\cdot\boldsymbol{q} + \beta T\frac{\mathrm{D}p}{\mathrm{D}t} - \bar{\boldsymbol{\tau}} : \nabla\boldsymbol{v} \tag{9}$$

in which the fluid specific heat at constant pressure is involved. Equation (9) is the version of the thermal energy quoted in many textbooks [1, 2]. For Fourier fluids the first term on the right-hand side of Eq. (9) can be expressed in terms of temperature gradient by using the Fourier law:

$$-\nabla\cdot\boldsymbol{q} = \nabla\cdot\left(k\nabla T\right) = k\nabla^2 T \tag{10}$$

where the last equality is obtained only for fluids with a constant thermal conductivity.

It is possible to demonstrate that, if the working fluid is Newtonian, the *viscous dissipation* term can be written as follows (i. e. in Cartesian coordinates):

$$\begin{aligned}\bar{\boldsymbol{\tau}} : \nabla\boldsymbol{v} &= -\mu\Phi\\ &= -\mu\left[-\frac{2}{3}\left(\nabla\cdot\boldsymbol{v}\right)^2 + 2\left(\frac{\partial v_x}{\partial x}\right)^2\right.\\ &\quad + 2\left(\frac{\partial v_y}{\partial y}\right)^2 + 2\left(\frac{\partial v_z}{\partial z}\right)^2 + \left(\frac{\partial v_z}{\partial y} + \frac{\partial v_y}{\partial z}\right)^2\\ &\quad \left. + \left(\frac{\partial v_x}{\partial z} + \frac{\partial v_z}{\partial x}\right)^2 + \left(\frac{\partial v_y}{\partial x} + \frac{\partial v_x}{\partial y}\right)^2\right]\end{aligned} \tag{11}$$

Equation (11) provides evidence that viscous heating can be considered as the sum of two terms:

- the rate of viscous dissipation due to the contribution of the density variation; and
- the rate of viscous dissipation for an incompressible fluid (Φ_inc).

$$\bar{\boldsymbol{\tau}} : \nabla \boldsymbol{v} = -\mu\Phi = -\mu\left[-\frac{2}{3}(\nabla\cdot\boldsymbol{v})^2 + \Phi_{\text{inc}}\right]$$
$$= -\mu\left[-\frac{2}{3}\frac{1}{\rho^2}\left(\frac{\mathrm{D}\rho}{\mathrm{D}t}\right)^2 + \Phi_{\text{inc}}\right] \quad (12)$$

If the fluid density is considered as a function of the pressure and of the temperature ($\rho = \rho(p, T)$), by using the definition of the volume compressibility and of the coefficient of thermal expansion, it is possible to write

$$\frac{\mathrm{d}\rho}{\rho} = -\beta\,\mathrm{d}T + \chi\,\mathrm{d}p \quad (13)$$

For this reason the viscous dissipation term for a real fluid can be written as follows:

$$\bar{\boldsymbol{\tau}} : \nabla \boldsymbol{v} = -\mu\Phi = -\mu\left[-\frac{2}{3}\left(\chi\frac{\mathrm{D}p}{\mathrm{D}t} - \beta\frac{\mathrm{D}T}{\mathrm{D}t}\right)^2 + \Phi_{\text{inc}}\right] \quad (14)$$

Thus, the general expression of the thermal energy equation for a real Newtonian fluid becomes

$$\rho c_{\mathrm{p}}\frac{\mathrm{D}T}{\mathrm{D}t} = -\nabla\cdot\boldsymbol{q} + \beta T\frac{\mathrm{D}p}{\mathrm{D}t} + \mu\left[-\frac{2}{3}\left(\chi\frac{\mathrm{D}p}{\mathrm{D}t} - \beta\frac{\mathrm{D}T}{\mathrm{D}t}\right)^2 + \Phi_{\text{inc}}\right] \quad (15)$$

Table 1 reports the expressions of the viscous dissipation term for an incompressible fluid (Φ_{inc}) with constant properties for different geometry coordinates.

In Table 2 are quoted the values assumed by the volume compressibility and by the coefficient of thermal expansion for a selection of liquids and gases. It is evident that the liquids are in general characterized by very low values of compressibility. On the contrary, it is evident that many liquids have a value of the coefficient of thermal expansion that cannot be considered negligible.

From Eq. (15) it is possible to derive the following particular expressions of the thermal energy equation as a function of the fluid considered:

1. *Ideal gas* ($\beta = 1/T$, $\chi = 1/p$)

$$\rho c_{\mathrm{p}}\frac{\mathrm{D}T}{\mathrm{D}t} = -\nabla\cdot\boldsymbol{q} + \frac{\mathrm{D}p}{\mathrm{D}t} + \mu\left[-\frac{2}{3}\left(\frac{1}{p}\frac{\mathrm{D}p}{\mathrm{D}t} - \frac{1}{T}\frac{\mathrm{D}T}{\mathrm{D}t}\right)^2 + \Phi_{\text{inc}}\right] \quad (16)$$

2. *Incompressible fluid* ($\beta = 0$, $\chi = 0$)

$$\rho c_{\mathrm{p}}\frac{\mathrm{D}T}{\mathrm{D}t} = -\nabla\cdot\boldsymbol{q} + \mu\Phi_{\text{inc}} \quad (17)$$

3. *Real fluid* ($\beta \neq 0$, $\chi = 0$)

$$\rho c_{\mathrm{p}}\frac{\mathrm{D}T}{\mathrm{D}t} = -\nabla\cdot\boldsymbol{q} + \beta T\frac{\mathrm{D}p}{\mathrm{D}t} + \mu\left[-\frac{2}{3}\left(\beta\frac{\mathrm{D}T}{\mathrm{D}t}\right)^2 + \Phi_{\text{inc}}\right] \quad (18)$$

4. *Real fluid* ($\beta = 0$, $\chi \neq 0$)

$$\rho c_{\mathrm{p}}\frac{\mathrm{D}T}{\mathrm{D}t} = -\nabla\cdot\boldsymbol{q} + \mu\left[-\frac{2}{3}\left(\chi\frac{\mathrm{D}p}{\mathrm{D}t}\right)^2 + \Phi_{\text{inc}}\right] \quad (19)$$

As highlighted by Toor [3], observing the typical values of the thermal expansion coefficients and of the volume compressibility of the selection of liquids quoted in Table 2, it is possible to note that in general for liquids small changes in density allow the compressibility contribution to the dissipation function to be neglected so that it is possible to write

$$\Phi \cong \Phi_{\text{inc}} \quad (20)$$

For these reasons the following version of the thermal energy equation can be used with real liquids:

5. *Real liquids* ($\beta \neq 0$, $\chi = 0$)

$$\rho c_{\mathrm{p}}\frac{\mathrm{D}T}{\mathrm{D}t} = -\nabla\cdot\boldsymbol{q} + \beta T\frac{\mathrm{D}p}{\mathrm{D}t} + \mu\Phi_{\text{inc}} \quad (21)$$

V

This version of the thermal energy can be considered appropriate especially for liquids characterized by large values of the thermal expansion coefficient and subject to large pressure gradients; this can be the case for microchannels in which large pressure drops per unit length are ordinary for low hydraulic diameters.

If the thermal energy equation is used in order to study laminar flow forced convection in microchannels, the expression of the thermal energy equation can be simplified.

In this case, the velocity has only one nonzero component, along the axial direction z, and Eq. (15) can be written as

Viscous Dissipation, Table 1 The expressions of the viscous dissipation term for incompressible fluids with constant properties

Coordinates	Φ_{inc}
Rectangular	$2\left(\frac{\partial v_x}{\partial x}\right)^2+2\left(\frac{\partial v_y}{\partial y}\right)^2+2\left(\frac{\partial v_z}{\partial z}\right)^2+\left(\frac{\partial v_z}{\partial y}+\frac{\partial v_y}{\partial z}\right)^2+\left(\frac{\partial v_x}{\partial z}+\frac{\partial v_z}{\partial x}\right)^2+\left(\frac{\partial v_y}{\partial x}+\frac{\partial v_x}{\partial y}\right)^2$
Cylindrical	$2\left(\frac{\partial v_r}{\partial r}\right)^2+2\left(\frac{1}{r}\left(\frac{\partial v_\theta}{\partial \theta}+v_r\right)\right)^2+2\left(\frac{\partial v_z}{\partial z}\right)^2+\left(\frac{\partial v_\theta}{\partial z}+\frac{1}{r}\frac{\partial v_z}{\partial \theta}\right)^2+\left(\frac{\partial v_z}{\partial r}+\frac{\partial v_r}{\partial z}\right)^2+\left(\frac{1}{r}\frac{\partial v_r}{\partial \theta}+r\frac{\partial(v_\theta/r)}{\partial r}\right)^2$
Spherical	$2\left(\frac{\partial v_r}{\partial r}\right)^2+2\left(\frac{1}{r}\left(\frac{\partial v_\theta}{\partial \theta}+v_r\right)\right)^2+2\left(\frac{1}{r\sin\theta}\frac{\partial v_\phi}{\partial \phi}+\frac{v_r}{r}+\frac{v_\theta\cot\theta}{r}\right)^2+\left(r\frac{\partial(v_\theta/r)}{\partial r}+\frac{1}{r}\frac{\partial v_r}{\partial \theta}\right)^2$ $+\left(\frac{1}{r\sin\theta}\frac{\partial v_r}{\partial \phi}+r\frac{\partial(v_\phi/r)}{\partial r}\right)^2+\left(\frac{\sin\theta}{r}\frac{\partial(v_\phi/\sin\theta)}{\partial \theta}+\frac{1}{r\sin\theta}\frac{\partial v_\theta}{\partial \phi}\right)^2$

follows:

$$\rho c_p\left[\frac{\partial T}{\partial t}+v_z\frac{\partial T}{\partial z}\right]=-\nabla\cdot\boldsymbol{q}+\beta T\left[\frac{\partial p}{\partial t}+v_z\frac{\partial p}{\partial z}\right]+\mu\left[-\frac{2}{3}\left(\chi\left[\frac{\partial p}{\partial t}+v_z\frac{\partial p}{\partial z}\right]-\beta\left[\frac{\partial T}{\partial t}+v_z\frac{\partial T}{\partial z}\right]\right)^2+\Phi'_{inc}\right] \quad (22)$$

Some time after the flow has started, the time variation of the temperature approaches zero if the boundary conditions are independent of time. Assuming a steady-state axial pressure distribution and a fully developed velocity field inside the microchannel, the energy equation becomes:

Viscous Dissipation, Table 2 Typical values of the volume compressibility and of the coefficient of thermal expansion for a selection of liquids and gases

	χ ($\times 10^{11}$ Pa^{-1})	β ($\times 10^6$ K^{-1})
Water	45.9	276
Mercury	3.7	181
Glycerin	21	480
Ethyl alcohol	110	1100
Carbon disulfide	93	1190
Polyethylene	–	751
Acetic acid	–	1024
Ether	–	1638
Engine oil (SAE 50)	–	700
Ethylene glycol	–	650
R134a	–	3130
Ammonia	–	2450

6. *Steady-state laminar flow in microchannels (fully developed velocity):*

$$\rho c_p v_z\frac{\partial T}{\partial z}=-\nabla\cdot\boldsymbol{q}+\beta T v_z\frac{\partial p}{\partial z}+\mu\left[-\frac{2}{3}\left(\chi v_z\frac{\partial p}{\partial z}-\beta v_z\frac{\partial T}{\partial z}\right)^2+\Phi'_{inc}\right]\quad \text{(for gases)} \quad (23)$$

$$\rho c_p v_z\frac{\partial T}{\partial z}=-\nabla\cdot\boldsymbol{q}+\beta T v_z\frac{\partial p}{\partial z}+\mu\Phi'_{inc}\quad \text{(for liquids)} \quad (24)$$

where Φ'_{inc} for incompressible laminar flow is given by

$$\Phi'_{inc}=\nabla v_z\cdot\nabla v_z \quad (25)$$

For rectangular and circular geometries the complete expression of Φ'_{inc} is reported in Table 3. It is interesting to observe that, for gases for which Eq. (20) holds, Eqs. (23) and (24) coincide.

In Eq. (24), written for liquids in microchannels, the flow work term is conserved in the energy balance because its role, especially in very fine microchannels, can be important since the pressure gradient along the tube is inversely proportional to the square of the hydraulic diameter of the channel:

$$-\frac{\partial p}{\partial z}=2f\,\mathrm{Re}\frac{\mu W}{D_h^2} \quad (26)$$

Viscous Dissipation, Table 3 The expressions of the dissipation function for fully developed incompressible laminar flow

Coordinates	Φ'_{inc}
Rectangular	$\left(\frac{\partial v_z}{\partial y}\right)^2+\left(\frac{\partial v_z}{\partial x}\right)^2$
Cylindrical	$\left(\frac{\partial v_z}{\partial r}\right)^2$

in which f is the Fanning friction factor, Re is the Reynolds number and W is the average fluid velocity.

By considering Eqs. (24) and (25) it is evident that the flow work term and the viscous dissipation term have opposite signs (negative and positive, respectively). This fact underlines that the viscous dissipation plays the role of a distributed heat source inside the fluid; on the contrary the fluid thermal expansion cools the flow like a distributed heat sink. In a tube, since these two effects are locally proportional to $(\partial v_z/\partial r)^2$ and to v_z respectively, the heat sink prevails in the central region of the channel and the heat source dominates in the wall region. The thermal energy generated mainly near the wall region due to the viscous dissipation is absorbed near the channel central region due to the flow work effect.

In general, it is recommended to use Eqs. (23) and (24) in dimensionless form. To this extent, as suggested by Shah and London [4] and Dryden [5], viscous dissipation effects for internal flows can be captured by introducing the Brinkman number:

$$\mathrm{Br} = \frac{\mu W^2}{k\Delta T_{\mathrm{ref}}} \tag{27}$$

in which ΔT_{ref} indicates a characteristic temperature difference for the specific problem considered (i. e. the difference between the wall temperature and the entrance temperature) and k is the fluid thermal conductivity.

For constant axial wall temperature boundary conditions (T boundary conditions) (see ►convective heat transfer in microchannels) the characteristic temperature difference ΔT_{ref} is defined as the difference between the fluid average bulk temperature and the external temperature.

For constant axial heat flux boundary conditions (H1 boundary conditions) the characteristic temperature difference to use in the definition of the Brinkman number is chosen equal to (q_{w}/k), in which q_{w} is the linear heat flux imposed at the walls of the channels.

When Eqs. (10) and (20) hold and the fluid has constant properties, the momentum and the thermal energy equations for steady-state laminar flow in microchannels with a fully developed velocity profile in dimensionless form become

$$\begin{cases} \nabla^{*2} V_z = -p^* \\ V_z \dfrac{\partial\theta}{\partial z^+} = \nabla^{*2}\theta - 2 f\,\mathrm{Re}\,\mathrm{Br}\,(\beta\Delta T_{\mathrm{ref}})\, V_z\theta + \mathrm{Br}\,\Phi'^{*}_{\mathrm{inc}} \end{cases} \tag{28}$$

in which the following dimensionless quantities are introduced:

$$\begin{aligned} z^+ &= \frac{z}{D_h \mathrm{Re}\,\mathrm{Pr}}\,; & \nabla^* &= D_h\nabla\,; \\ V_z &= \frac{v_z}{W}\,; & p^* &= -\frac{D_h^2}{\mu W}\frac{\partial p}{\partial z}\,; \\ \theta &= \frac{T-T_0}{\Delta T_{\mathrm{ref}}}\,; & \Phi'^{*}_{\mathrm{inc}} &= \nabla^* V_z \cdot \nabla^* V_z \end{aligned} \tag{29}$$

Examples of Application

Let us consider the silicon microchannel heat sink shown in Fig. 1; the microchannels obtained by chemical etching on the silicon wafer are in general closed by a Pyrex glass cover bonded to the substrate or by silicon wafer. A liquid flows through the channels; due to the small size of the microchannels the flow is typically laminar. The microchannels have an axially unchanging cross-section with area equal to Ω and a wetted perimeter equal to Γ. A fixed linear power q_{w} is imposed on the top of the silicon substrate while all the other outside walls can be considered as adiabatic. In silicon heat sinks, owing to the high thermal conductivity of the silicon, the temperature gradient in the silicon substrate is very limited and temperature field in the solid is close to isothermal. When a Pyrex cover is used to close the heat sink, three walls of the microchannel work with a constant temperature; on the contrary, the Pyrex side can be considered adiabatic. In general, the ratio between the thermal conductivity of the silicon and of the liquid assumes very high values, and the same occurs for the ratio between the length and the hydraulic diameter of the microchannel. For these reasons the microchannels can be conveniently studied as "long ducts" under a classical H1 thermal boundary condition with three sides having an imposed uniform temperature and one side (the Pyrex side) as adiabatic (*3bc* version; see ►convective heat transfer in microchannels). Conversely, when a silicon cover is used to close the microchannels, all the boundaries can be considered as isothermal; it is possible to use the H1 thermal boundary condition, with four sides having an imposed uniform temperature (*4bc* version; see ►convective heat transfer in microchannels).

For silicon microchannels produced by chemical etching the shape of the channels depends on a variety of factors such as the crystallographic nature of the silicon used. For example, when a KOH anisotropic etching technique is employed in ⟨100⟩ or ⟨110⟩ silicon, the microchannels have a trapezoidal cross-section (with an apex angle of 54.74° imposed by the crystallographic morphology of the silicon) or a rectangular cross-section respectively. In this analysis, KOH-etched microchannels having trapezoidal,

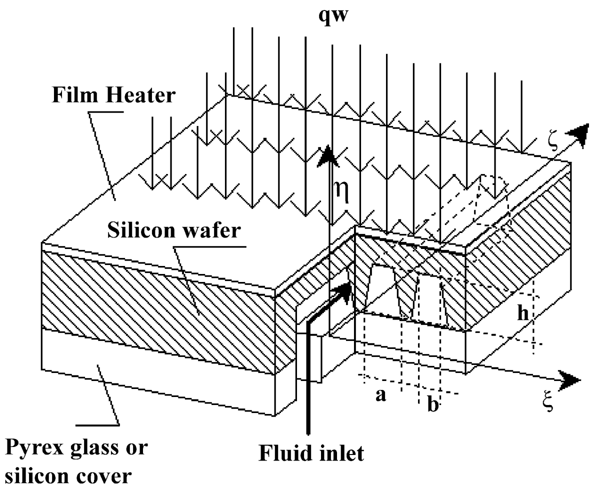

Viscous Dissipation, Figure 1 Schematic of a silicon heat sink

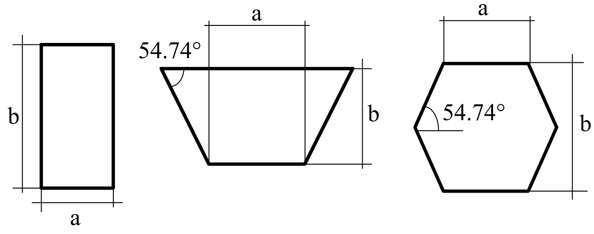

Viscous Dissipation, Figure 2 Rectangular, trapezoidal and double-trapezoidal KOH-etched microchannels

hexagonal (obtained by gluing together two trapezoidal channels) and rectangular cross-sections are considered (see Fig. 2). Each cross-section is characterized by the aspect ratio α defined as the ratio between the height (b) and the minimum width (a) of the channel (see Fig. 2).

By applying Eqs. (28) to model the heat transfer process in the microchannels and considering the flow with constant properties and being thermally and hydrodynamically fully developed, one obtains

$$\begin{cases} \nabla^{*2} V_z = -p^* \\ V_z \dfrac{\partial \theta}{\partial z^+} = \nabla^{*2}\theta + \mathrm{Br}\left[\nabla^* V_z \cdot \nabla^* V_z\right] \end{cases} \tag{30}$$

where the liquid is considered as incompressible ($\beta = 0$) and $\Delta T_{\mathrm{ref}} = q_{\mathrm{w}}/k$ is used in the definition of the dimensionless temperature and the Brinkman number (see ►convective heat transfer in microchannels).

Further simplification can be made by considering that in the fully developed thermal region of a heated duct the temperature profile continues to change axially but the "relative temperature shape" of the profile no longer changes. Resorting to the definition of thermally fully developed region for the H1 boundary condition, it is possible to demonstrate (see ►viscous heating) that

$$\frac{\partial \theta}{\partial z^+} = \frac{\partial \theta_{\mathrm{b}}}{\partial z^+} = \frac{1}{\Omega^*} + 2\mathrm{Br} f\,\mathrm{Re} \tag{31}$$

where Ω^* is the dimensionless area of the cross-section ($\Omega^* = \Omega/D_{\mathrm{h}}^2$) and θ_{b} is the fluid bulk temperature. The momentum balance equation is solved by using the no-slip boundary condition at the wall which means considering negligible any rarefaction effect. The complete set of boundary conditions is thus

$$\begin{cases} V_z|_{\Gamma} = 0 \quad \theta|_{\Gamma} = 0 & \text{(4 version)} \\ V_z|_{\Gamma} = 0 \quad \left.\dfrac{\partial \theta}{\partial n}\right|_{\Gamma_{\mathrm{b}}^*} = 0 \quad \theta|_{\Gamma^* - \Gamma_{\mathrm{b}}^*} = 0 & \text{(3 version)} \end{cases} \tag{32}$$

where Γ_{b}^* is the dimensionless (divided by the hydraulic diameter) length of the adiabatic boundary of the microchannels.

From the dimensionless temperature distribution the value of the fluid bulk temperature can be computed as

$$\theta_{\mathrm{b}} = \frac{1}{\Omega^*} \int_{\Omega^*} V_z \theta \, \mathrm{d}\Omega^* \tag{33}$$

The local Nusselt number along the walls of the microchannels can be calculated as follows:

$$\mathrm{Nu}_{\mathrm{l}} = -\frac{1}{\theta_{\mathrm{b}}} n \cdot \nabla^* \theta \Big|_w \tag{34}$$

where n is the versor normal to the wall.

By averaging the local Nusselt number along the heated perimeter one can obtain the thermally fully developed mean Nusselt number:

$$\mathrm{Nu} = \frac{1}{\Gamma_{\mathrm{h}}^*} \int_{\Gamma_{\mathrm{h}}^*} \mathrm{Nu}_{\mathrm{l}} \, \mathrm{d}\Gamma^* = -\frac{1}{\Gamma_{\mathrm{h}}^* T_{\mathrm{b}}} \int_{\Gamma_{\mathrm{h}}^*} n \cdot \nabla T \, \mathrm{d}\Gamma^* = -\frac{1}{\Gamma_{\mathrm{h}}^* T_{\mathrm{b}}} \tag{35}$$

where Γ_{h}^* is the dimensionless heated perimeter ($\Gamma_{\mathrm{h}}^* = \Gamma^*$ (4bc version), $\Gamma_{\mathrm{h}}^* = \Gamma^* - \Gamma_{\mathrm{b}}^*$ (3bc version)).

The numerical solution of the problem defined by Eqs. (31) and (32) has been presented by Morini and Spiga [6]. In Fig. 3 the trends of the local Nusselt number along the perimeter of two trapezoidal microchannels having aspect ratio α equal to 1 (Fig. 3a) and 0.2 (Fig. 3b) with

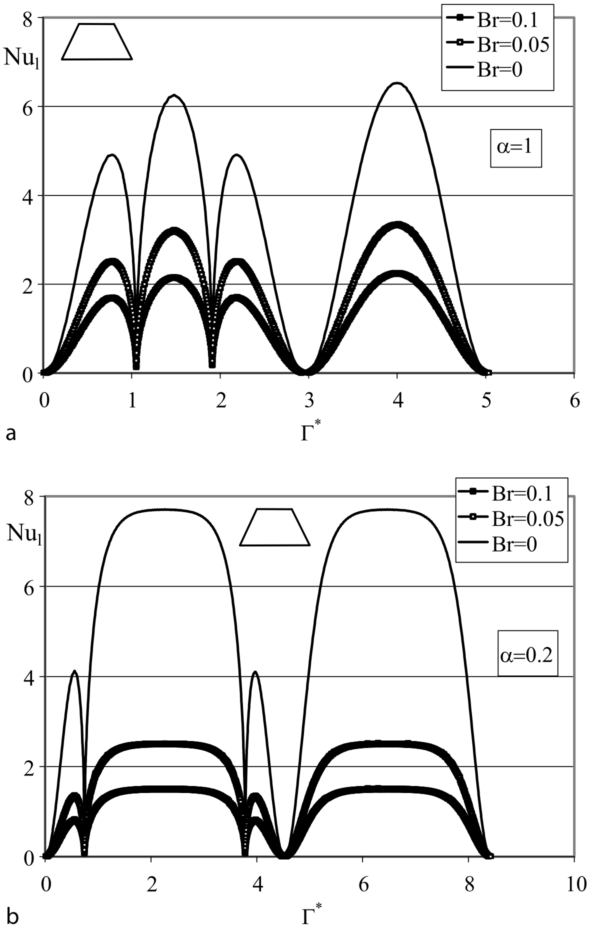

Viscous Dissipation, Figure 3 Local Nusselt number along the perimeter of two trapezoidal microchannels with four heated sides for (**a**) $\alpha = 1$ and (**b**) $\alpha = 0.2$ as a function of the Brinkman number

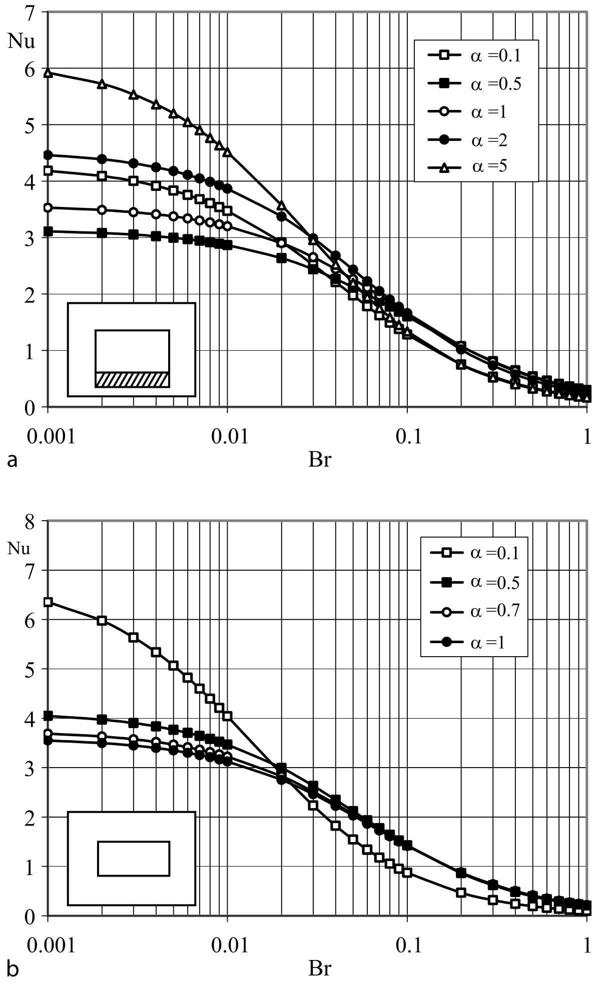

Viscous Dissipation, Figure 4 Average fully developed Nusselt number as a function of the Brinkman number for rectangular silicon microchannels with (**a**) three and (**b**) four sides heated

four heated sides are shown as a function of the Brinkman number. It is evident that the convective heat transfer coefficient presents strong variations along the perimeter of the microchannel; in particular, the value of the local Nusselt number approaches zero near the corners of the channels where the fluid tends to be stagnant. When the aspect ratio decreases the longer sides tend to be characterized by a more uniform value of the local convective heat transfer coefficient. Figure 3 provides evidence for the reduction of the local values of the Nusselt numbers when the Brinkman number increases; when the effect of the viscous forces is significant ($Br > 0.001$) the local Nusselt numbers tend to decrease as an effect of the reduction of the temperature gradients at the walls due to the viscous internal heat production.

The average fully developed Nusselt number for rectangular silicon microchannels is plotted as a function of the Brinkman number in Fig. 4 with three (Fig. 4a) and four (Fig. 4b) sides heated respectively.

Looking at Fig. 4b, it is possible to note that in general the Nusselt number is higher for cross-sections having lower aspect ratios if the viscous dissipation is negligible ($Br < 0.001$). For large Brinkman numbers this rule is reversed; in fact, for large Brinkman numbers the cross-sections with lower aspect ratios exhibit lower Nusselt numbers.

It is possible to demonstrate analytically [7] that the link between the average Nusselt and Brinkman numbers can be expressed by means of a general relationship for circular and non-circular channels:

$$\overline{Nu}_{H1}(Br) = \frac{\overline{Nu}_{H1}}{1 + \sigma Br} \tag{36}$$

where $\overline{Nu}_{H1}$ is the fully developed value of the Nusselt number when $Br = 0$ (the values assumed by $\overline{Nu}_{H1}$ for the most common microchannel cross-sectional geometries are reported in ►convective heat transfer in microchannels) and σ is a parameter depending on the geometry of the channel cross-section (by means of the aspect ratio α) and on the combination of heated and adiabatic sides of the channel.

In Table 4 the values of σ calculated numerically for rectangular, trapezoidal and double-trapezoidal microchannels having three and four sides heated respectively are listed. Using these data and Eq. (36) it is possible to calculate the value assumed by the fully developed Nusselt number as a function of the Brinkman number in KOH-etched silicon microchannels. For the sake of completeness, it can be useful to remember that for circular microtubes with prescribed wall heat flux, the analytical value of σ is equal to $48\pi/11$ and the fully developed average Nusselt number (Nu_0) is equal to $48/11$.

In order to compare the thermal performances of silicon microheat sinks with rectangular or trapezoidal microchannels it is possible to use the *area goodness factor* defined as follows:

$$\frac{j}{f} = \frac{Nu\,Pr^{-1/3}}{f\,Re} \tag{37}$$

This factor was introduced by Shah and London [4] in order to compare different kinds of heat exchangers. From Eq. (37) it is evident that this factor depends only on the Brinkman number for the fully developed laminar flow of a specified fluid.

Since the dimensionless quantities j and f are independent of the scale of the geometry (D_h), the area goodness factor j/f for different microchannels represents the influence of the geometric factors on the pressure losses and the heat transfer.

In Fig. 5 the area goodness factor is shown as a function of the aspect ratio α for rectangular and trapezoidal microchannels with four sides heated. It is evident that the rectangular microchannels give, in general, higher values of the area goodness factor; this fact means that the microheat sinks with rectangular microchannels are more compact than those with trapezoidal microchannels for a fixed value of the heat exchanged because they have a lower flow area.

If the viscous dissipation can be neglected ($Br \approx 0$), when rectangular microchannels are employed very high (deep) or very low (shallow) values of the aspect ratio ensure high values of the area goodness factor. On the contrary, for trapezoidal microchannels the j/f factor is a maximum for low aspect ratio (shallow microchannels).

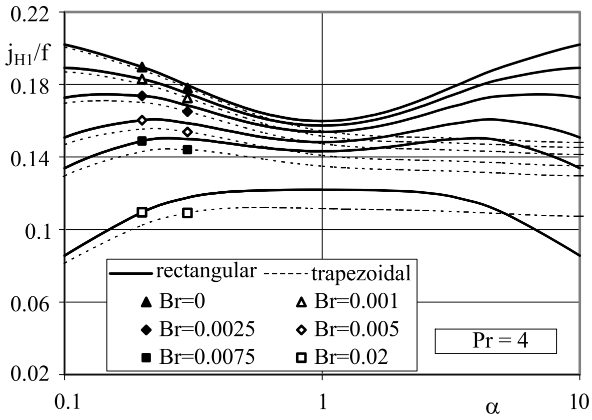

Viscous Dissipation, Figure 5 Area goodness factor j/f as a function of the aspect ratio α for rectangular and trapezoidal microchannels with four sides heated

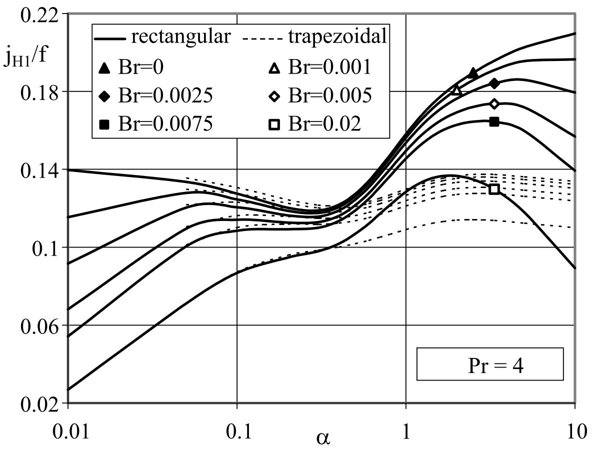

Viscous Dissipation, Figure 6 Area goodness factor j/f as a function of the aspect ratio α for rectangular and trapezoidal microchannels with three sides heated

It is worth noting from Fig. 5 that when α is low the difference between the trapezoidal and rectangular geometry tends to vanish because the cross-section tends to become similar to parallel plates. It is interesting to note that when the Brinkman number increases the area goodness factor reaches the maximum for intermediate values of the aspect ratio; the viscous effects tend to penalize the performances of the microchannel when very shallow and/or very deep.

These conclusions are confirmed by Fig. 6 for microchannels with three sides heated. In this case for $Br = 0$ the j/f factor is a maximum for high values of the aspect ratio when rectangular microchannels are employed. For microheat sinks with trapezoidal microchannels the j/f factor is always lower than for rectangular microchannels but when the aspect ratio decreases this difference tends to vanish. In addition, Fig. 6 highlights that the dependence of the

Viscous Dissipation, Table 4 Coefficients σ for rectangular, trapezoidal and double-trapezoidal KOH-etched microchannels having three or four sides heated

α					
0.05	131.35	136.51		43.98	45.472
0.1	67.98	73.17		23.41	24.863
0.108	–	–	65.46	–	–
0.2	36.57	41.79		13.53	14.866
0.233	–	–	34.04	–	–
0.3	26.39	31.58		10.75	11.844
0.4	21.57	26.68		9.808	10.569
0.5	18.91	23.88		9.605	9.952
0.558	–	–	19.15	–	–
0.6	17.36	22.14		9.75	9.658
0.7	16.42	20.98		10.07	9.52
0.773	–	–	16.62	–	–
0.8	15.89	20.19		10.505	9.476
0.9	15.62	19.62		10.999	9.474
1	15.54	19.22		11.528	9.494
1.042	–	–	15.24	–	–
10/9	15.62	18.9		12.141	9.551
5/4	15.89	18.63		12.935	9.618
1.386	–	–	14.54	–	–
10/7	16.42	18.42		13.971	9.717
5/3	17.36	18.28		15.371	9.848
1.842	–	–	14.30	–	–
2	18.91	18.22		17.353	9.988
2.475	–	–	14.39	–	–
2.5	21.57	18.28		20.357	10.167
3.413	–	–	14.69	–	–
10/3	26.39	18.44		25.449	10.367
5	36.57	18.7		35.817	10.579
7.918	–	–	15.65	–	–
10	67.98	18.99		67.369	10.765
16.078	–	–	16.08	–	–
∞	–	19.15	16.28	–	10.864

j/f factor on the aspect ratio is weak for trapezoidal cross-sections.

Finally, it is important to highlight that the results presented here are valid under the hypothesis of thermophysical properties being independent of temperature. On the contrary the variation with temperature, especially for the fluid viscosity, cannot be ignored in particular for low Reynolds numbers when, for a prescribed wall heat flux, there is a strong temperature rise between the inlet and the outlet of the microchannel. Since the viscosity tends to decrease when the temperature increases, the viscous dissipation effects calculated by using the proposed constant properties model could be overestimated.

Future Directions for Research

The effect of viscous dissipation on convective heat transfer is significant especially for high-velocity flows, highly viscous flows even at moderate velocities, for fluids with a moderate Prandtl number and moderate velocities with small wall-to-fluid temperature difference or with low wall heat fluxes and flowing through microchannels. In this last case, further investigations on the combined effect of the flow work and of the viscous dissipation in microchannels are mandatory by taking into account the temperature variation of the fluid thermophysical properties (especially for the coefficient of thermal expansion and for the viscosity).

Cross References

- ► Viscous Heating
- ► Convective Heat Transfer in Microchannels

References

1. Bird RB, Stewart WE, Lightfoot EN (1960) Transport Phenomena. Wiley, New York
2. Incropera FP, DeWitt DP (1996) Fundamentals of Heat and Mass Transfer. Wiley, New York
3. Toor HL (1956) The Energy Equation for Viscous Flow. Ind Eng Chem 48:922–926
4. Shah RK, London AL (1978) Laminar Flow Forced Convection in Ducts. Adv Heat Transf 14:196
5. Dryden HL, (1936) Aerodynamics of cooling. Aerodyn Theory 6:253
6. Morini GL, Spiga M (2007) The role of the viscous dissipation in heated microchannels. ASME J Heat Transf 129:308–318
7. Morini GL, Spiga M (1999) Nusselt Numbers in Rectangular Ducts with Viscous Dissipation. ASME J Heat Transf 121:1083–1087

Viscous Heating

Gian Luca Morini
DIENCA Università di Bologna, Bologna, Italy
gianluca.morini@mail.ing.unibo.it

Synonyms

Internal friction

Definition

Viscous heating represents the effect of an irreversible process by means of which the work done by a fluid on adjacent layers due to the action of shear forces is transformed into heat.

Overview

In order to study the forced convection of liquids in the laminar regime a common theoretical basis for macro- and microflows can be used; nevertheless, certain effects can be of different importance for microsystems if compared with macrosystems. These effects can be defined as scaling effects with respect to a standard macroanalysis. At the microscale, since different forces have different length dependences, the surface forces (like surface tensions, viscous forces or electrostatic forces) become more important and even dominant as the scale is reduced. Viscous heating, like pressure drop, tends to increase dramatically when the dimensions of microchannels are decreased.

This entry focuses on the role of viscous heating in fluids flowing through microchannels. A criterion will be presented to draw the limit of significance for viscous dissipation effects in microchannel flows. The role of the cross-sectional geometry on viscous dissipation will be highlighted and the minimum Reynolds number for which viscous dissipation effects can no longer be neglected will be calculated as a function of the hydraulic diameter and of the microchannel geometry for different fluids. It will be demonstrated how viscous effects can explain some experimental results on the Poiseuille numbers in microchannels which recently appeared in the open literature.

Basic Methodology

To study laminar flow forced convection in microchannels under the assumptions of steady state axial pressure distribution and fully developed velocity field, the balance of the thermal energy can be written as follows [1] (see ► convective heat transfer in microchannels):

$$\rho c_p v_z \frac{\partial T}{\partial z} = -\nabla \cdot \bar{q} + \beta T v_z \frac{\partial p}{\partial z} + \mu \left[\frac{2}{3} \left(\chi v_z \frac{\partial p}{\partial z} - \beta v_z \frac{\partial T}{\partial z} \right)^2 + \Phi'_{\text{inc}} \right] \quad \text{(for gases)} \tag{1}$$

$$\rho c_p v_z \frac{\partial T}{\partial z} = -\nabla \cdot \bar{q} + \beta T v_z \frac{\partial p}{\partial z} + \mu \Phi'_{\text{inc}} \quad \text{(for liquids)} \tag{2}$$

where Φ'_{inc} for incompressible laminar flows is given by

$$\Phi'_{\text{inc}} = \nabla v_z \cdot \nabla v_z \tag{3}$$

The last term on the right-hand side of Eqs. (1) and (2) represents the work done by the fluid on adjacent layers due to the action of the shear forces (see ► viscous dissipation). This work is entirely transformed into heat by means of an irreversible process and it is responsible for the viscous heating of the fluid.

The integration over the channel cross-section of Eqs. (1) and (2) allows the calculation of the axial distribution of the fluid bulk temperature locally defined as follows:

$$T_b = \frac{1}{W\Omega} \int_{\Omega} v_z T \, \mathrm{d}\Omega \tag{4}$$

in which Ω indicates the area of the channel cross-section and W is the fluid average velocity.

In this entry the effect of the viscous heating in microchannels is highlighted by means of two examples. First of all, a steady-state liquid flow in the laminar regime through a microchannel with an imposed constant linear heat flux

at the walls q'_{w} is considered (H1 boundary condition; see ►convective heat transfer in microchannels). Then, the case of a steady-state liquid flow in the laminar regime through a microchannel with an axially constant outer wall temperature, while the wall heat flux is linearly proportional to the difference between the external temperature and the wall temperature, is considered. This is the case of a microchannel cooled by convection of an external fluid (T3 boundary condition; see ►convective heat transfer in microchannels).

Let us consider the heated microchannel subjected to the H1 boundary condition. By integrating Eq. (2) over the channel cross-sectional area Ω one obtains the following result:

$$D_h^2 \rho c_p W \frac{\mathrm{d}T_b}{\mathrm{d}z} = \frac{q'_{\mathrm{w}}}{\Omega} D_h^2 - 2\mu W^2 f \,\mathrm{Re} \bar{\beta} T_b + 2\mu W^2 f \,\mathrm{Re} \tag{5}$$

where $\bar{\beta}$ is the coefficient of thermal expansion of the fluid calculated at the bulk temperature. The following property of the viscous dissipation term, demonstrated by Morini [2], has been used in order to write Eq. (5):

$$\mu \int_{\Omega} \Phi'_{\mathrm{inc}} \,\mathrm{d}\Omega = 2\mu W^2 f \,\mathrm{Re} \frac{\Omega}{D_h^2} \tag{6}$$

where f is the Fanning friction factor (see ►pressure–driven single-phase liquid flows).

It is interesting to note that, for ideal gases for which $\bar{\beta} = 1/T_b$ the flow work and the viscous dissipation are exactly the same in terms of absolute value and they compensate each to other. For this reason, for ideal gases, the axial variation of the bulk temperature in a channel is independent of viscous heating and flow work even for large values of the Mach number (highly compressible gases).

Equation (6) shows that the viscous dissipation term scales with the internal dimensions of the microchannel. In fact, for a fixed value of the volumetric flow rate ($\dot{V}$) through a microtube with an inner diameter equal to D, the viscous heating generated per unit of length equals the pump power, and it can be written using Eq. (6) as follows:

$$\mu \int_{\Omega} \Phi'_{\mathrm{inc}} \,\mathrm{d}\Omega = \frac{8 f \,\mathrm{Re} \mu \dot{V}^2}{\pi D^4} = \frac{\Delta p \dot{V}}{L} \tag{7}$$

in which Δp is the pressure drop along the microtube and L is the length of the microtube.

By observing Eq. (7) it is evident that the viscous heating and the pressure drop scale with the fourth power of the inner diameter of the channel. This means that viscous heating tends to become very important especially for smaller microchannels.

From the solution of Eq. (5) one can obtain the axial distribution of the bulk temperature along the microchannel. For the H1 boundary condition it is suitable to introduce the following dimensionless quantities (see ►convective heat transfer in microchannels):

$$z^+ = \frac{z}{D_h \mathrm{Re}\,\mathrm{Pr}}; \qquad \Omega^* = \frac{\Omega}{D_h^2}; \qquad \theta_b = k \frac{(T_b - T_{b0})}{q'_{\mathrm{w}}}; \qquad \mathrm{Br} = \frac{\mu W^2}{q'_{\mathrm{w}}} \tag{8}$$

where k is the fluid thermal conductivity and T_{b0} is the value of the bulk temperature at the inlet of the microchannel. Using these dimensionless quantities, Eq. (5) can be written in dimensionless form with the appropriate boundary condition at the entrance:

$$\begin{cases} \dfrac{\mathrm{d}\theta_b}{\mathrm{d}z^+} = \dfrac{1}{\Omega^*} + 2\mathrm{Br} f \,\mathrm{Re} \left[1 - \left(\dfrac{\beta q'_{\mathrm{w}}}{k} \right) \theta_b \right] \\ \theta_b(z^+ = 0) = 0 \end{cases} \tag{9}$$

The analytical solution of this differential problem for a liquid with constant properties is the following:

$$\theta_b(z^+) = \left[\frac{k}{\beta q'_{\mathrm{w}}} \right] \left[1 + \frac{1}{2\Omega^* \mathrm{Br} f \,\mathrm{Re}} \right] \times \left[1 - e^{-2\mathrm{Br} f \,\mathrm{Re} \left(\frac{\beta q'_{\mathrm{w}}}{k} \right) z^+} \right] \tag{10}$$

For an incompressible fluid ($\beta = 0$) the solution of the problem defined by Eq. (9) becomes the following:

$$\theta_b = \frac{1}{\Omega^*} z^+ + 2\mathrm{Br} f \,\mathrm{Re}\, z^+ \tag{11}$$

In the case of a microchannel cooled for convection by an external fluid (T3 boundary condition), the heat flux at the walls can be written as

$$q'_{\mathrm{w}} = -U_{\mathrm{w}} \Gamma \left(T_b - T_{\mathrm{ext}} \right) \tag{12}$$

in which $1/U_w$ is referred to as the wall thermal resistance and Γ the perimeter of the walls.

By combining Eq. (5) with Eq. (12) and introducing the dimensionless quantities

$$z^+ = \frac{z}{D_h \mathrm{Re\,Pr}}; \quad \Omega^* = \frac{\Omega}{D_h^2};$$
$$\Gamma^* = \frac{\Gamma}{D_h}; \quad \theta_b = \frac{(T_b - T_{\mathrm{ext}})}{(T_{b0} - T_{\mathrm{ext}})}; \tag{13}$$
$$R_w = \frac{k}{U_w D_h}; \quad \mathrm{Br} = \frac{\mu W^2}{k\,(T_{b0} - T_{\mathrm{ext}})}$$

where k is the fluid thermal conductivity and R_w is the dimensionless wall thermal resistance, the energy balance equation and its boundary condition in dimensionless form become

$$\begin{cases} \dfrac{\mathrm{d}\theta_b}{\mathrm{d}z^+} = -\dfrac{4}{R_w}\theta_b + 2\mathrm{Br} f\,\mathrm{Re} \\ \qquad \times \left[1 - (T_{b0} - T_{\mathrm{ext}})\,\bar{\beta}\theta_b - T_{\mathrm{ext}}\bar{\beta}\right] \\ \theta_b(z^+ = 0) = 1 \end{cases} \tag{14}$$

The analytical solution of Eq. (14) for a liquid with constant properties is

$$\theta_b(z^+) = \left[1 - \frac{B}{A}\right] e^{-Az^+} + \frac{B}{A}$$
$$\text{with} \quad A = \left[\frac{4}{R_w} + 2\mathrm{Br} f\,\mathrm{Re}\,(T_{b0} - T_{\mathrm{ext}})\,\bar{\beta}\right] \tag{15}$$
$$\text{and} \quad B = 2\mathrm{Br} f\,\mathrm{Re}\left[1 - T_{\mathrm{ext}}\bar{\beta}\right]$$

For an incompressible fluid ($\beta = 0$) the solution of Eq. (14) becomes

$$\theta_b\left(z^+\right) = \left[1 - \frac{\mathrm{Br} f\,\mathrm{Re} R_{\mathrm{w}}}{2}\right] e^{-\frac{4z^+}{R_{\mathrm{w}}}} + \frac{\mathrm{Br} f\,\mathrm{Re} R_{\mathrm{w}}}{2} \tag{16}$$

For an adiabatic microchannel ($R_w = \infty$) in which an incompressible fluid ($\beta = 0$) flows the solution of Eq. (14) becomes

$$\theta_b(z^+) = 2\mathrm{Br} f\,\mathrm{Re}\,z^+ + 1 \tag{17}$$

Examples of Application

The theory developed in the previous section is used to draw the limit of significance of viscous dissipation in heated and adiabatic microchannels.

In particular, in this section a criterion will be stated in order to predict the range of the Brinkman number where the viscous dissipation effect cannot be neglected in the analysis of the fluid flow and heat transfer in microchannels.

Heated Microchannels

If one considers the case of an incompressible liquid flowing through a heated microchannel the axial distribution of the bulk temperature is given by Eq. (11). This equation highlights that the temperature rise along the microchannel is given by two contributions: the heat flux imposed at the walls ($\theta_{b,q}$) and the viscous heating inside the fluid ($\theta_{b,v}$):

$$\theta_b = \frac{1}{\Omega^*} z^+ + 2\mathrm{Br} f\,\mathrm{Re}\,z^+ = \theta_{b,q} + \theta_{b,v} \tag{18}$$

If one considers the ratio between these two contributions, it is possible to demonstrate that this ratio is linked to the Brinkman number and to the Poiseuille number by means of the following relation:

$$\kappa = \frac{\theta_{b,v}}{\theta_{b,q}} = 2\mathrm{Br}\,\Omega^* f\,\mathrm{Re} \tag{19}$$

In order to draw the limit of the significance of the viscous heating in a microchannel, one can impose that this term has to be considered as significant only if this ratio is greater than a fixed value ($\kappa_{\mathrm{lim}} = 1 - 5\%$) [3]; in this manner the following inequality for the Brinkman number can be introduced:

$$\mathrm{Br} > \frac{\kappa_{\mathrm{lim}}}{2\Omega^* f\,\mathrm{Re}} \tag{20}$$

If this inequality holds, the effects of the viscous dissipation cannot be neglected.

For silicon microchannels produced by chemical etching, the shape of the channels depends on a variety of factors such as the crystallographic nature of the silicon used. For example, when an anisotropic KOH etching technique is employed in ⟨100⟩ or ⟨110⟩ silicon, the microchannels have a trapezoidal cross-section (with an apex angle of 54.74° imposed by the crystallographic morphology of the silicon) or a rectangular cross-section respectively. The cross-section is in general characterized by the aspect ratio α defined as the ratio between the height (b) and the minimum width (a) of the channel (see Fig. 1).

For rectangular and trapezoidal channels the dimensionless area of the cross-section is a function of the aspect ratio (α) and of the apex angle (ϕ); it can be expressed as

$$\Omega^* = \frac{\left[1 + \alpha\left(\frac{1}{\tan\phi} + \frac{1}{\sin\phi}\right)\right]^2}{4\alpha^2\left[\frac{1}{\alpha} + \frac{1}{\tan\phi}\right]} \tag{21}$$

In Fig. 2 the maximum value of the Brinkman number for which the viscous dissipation effects can be neglected for

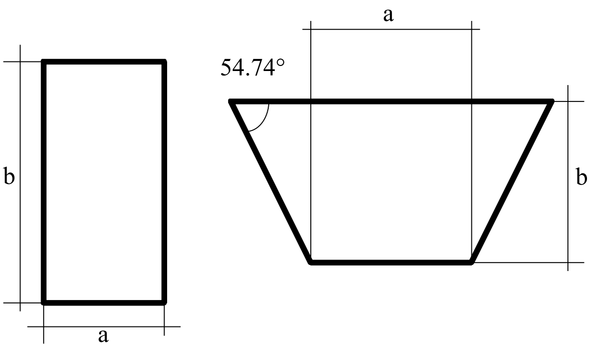

Viscous Heating, Figure 1 Typical cross-section of KOH-etched microchannels

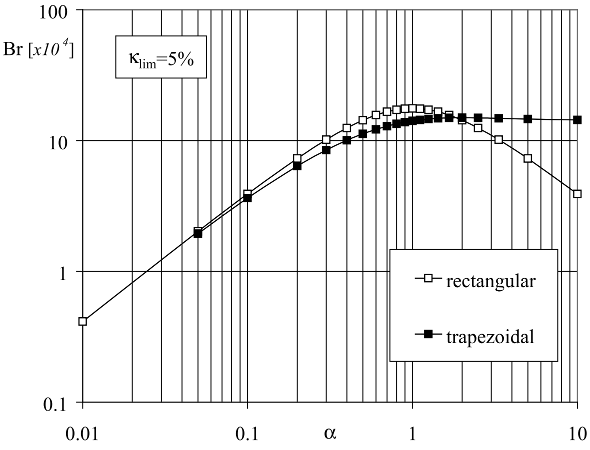

Viscous Heating, Figure 2 Maximum value of the Brinkman number for which viscous dissipation effects can be neglected for trapezoidal ($\phi = 54.74°$) and rectangular ($\phi = 90°$) microchannels as a function of the aspect ratio α

microchannels having trapezoidal ($\phi = 54.74°$) and rectangular ($\phi = 90°$) cross-sections is depicted as a function of the aspect ratio α. A value of κ_{lim} equal to 5% is considered. The results in Fig. 2 show that for shallow microchannels the effects of the viscous dissipation become important for lower Brinkman numbers.

In order to consider the applicability related to microchannels of the proposed criterion, the value of the minimum Reynolds number (linked to the minimum Brinkman number indicated in Eq. (20)) for which κ becomes equal to 5% is computed as a function of the hydraulic diameter for a rectangular microchannel having $\alpha = 3$. In Fig. 3 the minimum Reynolds number is shown for water and isopropanol as working fluids in rectangular and trapezoidal microchannels having an aspect ratio $\alpha = 3$. A constant wall heat flux equal to 90 W/cm^2 is considered. It is evident that the viscous effects are more important for isopropanol than for water because the isopropanol is char-

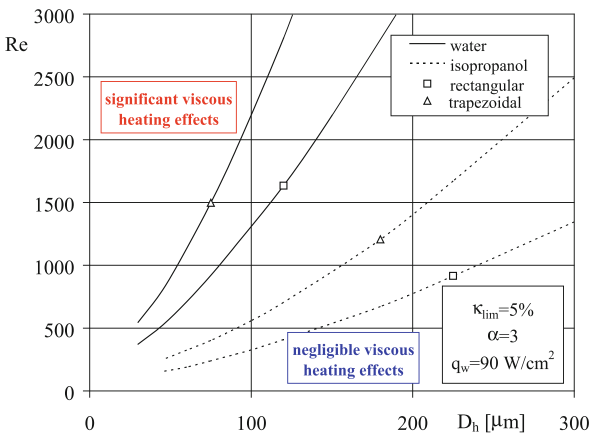

Viscous Heating, Figure 3 Maximum Reynolds numbers for which the effects of viscous dissipation can be neglected in a heated KOH-etched microchannel with imposed wall heat flux q_W

acterized by a lower value of the specific heat at constant pressure as compared to water; as a consequence, the same viscous heating produces a larger temperature rise in isopropanol than in water. In addition, it is interesting to note that for water the viscous effects have to be considered only for microchannels having a hydraulic diameter less than 100 μm; when the hydraulic diameter decreases the minimum Reynolds number decreases and the viscous effects become important even if the Reynolds numbers are low ($\text{Re} < 500$). In Fig. 3 the role of the cross-sectional shape is highlighted; it can be seen that the viscous effects occur earlier in a rectangular microchannel for a fixed value of the hydraulic diameter and aspect ratio. Figure 3 proves that the viscous effects are typical scaling effects. In fact, they are negligible for high values of the hydraulic diameter but become more important when hydraulic diameters less than 100 – 300 μm are considered.

V

Adiabatic Microchannels

For an adiabatic microchannel in which an incompressible liquid flows, the axial temperature rise due to viscous heating can be computed by means of Eq. (17). For a microchannel with a length equal to L, the axial temperature gradient results from Eq. (17) in which the definitions reported in Eq. (13) are used:

$$\frac{\partial T_b}{\partial z} \cong \frac{\Delta T_b}{L} \cong 2\frac{\mu W}{\rho c_p D_h^2} f \,\text{Re} \tag{22}$$

In order to validate this result the experimental data of Celata et al. [4] are used. Celata et al. measured the temperature difference between inlet and outlet of a smooth

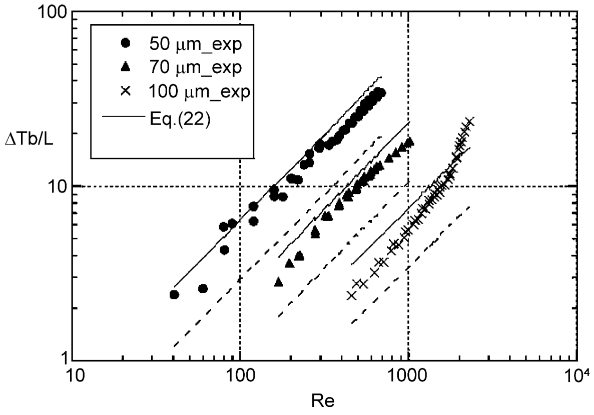

Viscous Heating, Figure 4 Gradient of viscous heating ($\Delta T_b/L$) along adiabatic microtubes versus Reynolds number; comparison of measurements (exp) and the theory for incompressible ($\beta = 0$) laminar flows (Eq. (22))

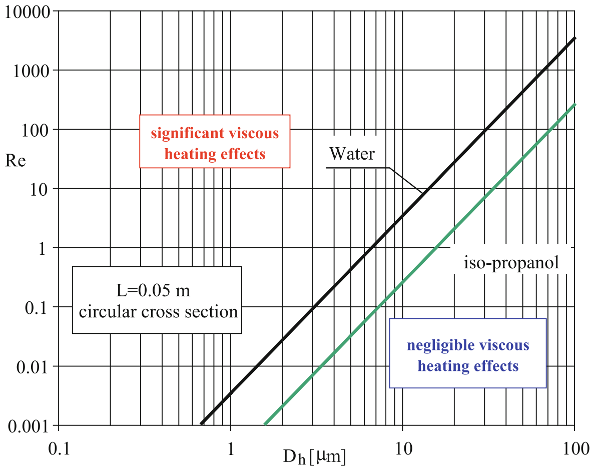

Viscous Heating, Figure 5 Reynolds numbers for which the temperature rise due to viscous heating along an adiabatic circular microchannel 5 cm long is equal to 1 K as a function of the hydraulic diameter

capillary tubes ($f\,\mathrm{Re} = 16$) of fused silica with hydraulic diameters equal to 100, 70 and 50 μm through which water is circulated at different Reynolds numbers in the laminar regime. The comparison between the prediction of Eq. (22) and the experimental data is shown in Fig. 4, and the agreement between the model and the measurements is good. The agreement improves for larger Reynolds numbers and smaller diameters; this fact is due to the smaller temperature rise at lower Reynolds number and larger diameters.

Considering Eq. (22), it is possible to note that, for two different fluids, c and d, and for a fixed value of the Reynolds number, hydraulic diameter and cross-sectional geometry, the temperature gradient ratio is related to the following ratio of the fluid thermophysical properties:

$$\frac{\left(\frac{\mathrm{d}T_b}{\mathrm{d}z}\right)_c}{\left(\frac{\mathrm{d}T_b}{\mathrm{d}z}\right)_d} = \left(\frac{\nu_c}{\nu_d}\right)^2 \left(\frac{c_{pd}}{c_{pc}}\right) \tag{23}$$

The temperature gradient due to the viscous heating is larger for fluids having a large value of kinematic viscosity and a low value of specific heat. For example, for isopropanol and water this ratio is equal to 13.26 at 298 K; for methanol and water this ratio is equal to 2.32 at 298 K. It is interesting to note that for water and air the ratio quoted in Eq. (23) is equal to 10^3 at 298 K; this means that the effects of viscous dissipation could be very strong for air. However, the influence of the compressibility is very important for gases flowing through microchannels and β cannot be neglected; the gas expansion in the flow direction causes a decrease of the temperature, which contrasts the effects of viscous heating.

It is possible to suggest a criterion to establish when viscous dissipation effects cannot be ignored in an adiabatic microchannel. Considering that for water and isopropanol the dynamic viscosity decreases by about 20–25% per 10 K one can assume as reference temperature rise an increase of 1 K of the bulk temperature between the inlet and outlet of a microchannel [2].

When the bulk temperature increase along the microchannel is greater than 1 K the effect of the viscous dissipation cannot be neglected. This means that the following inequality must be satisfied in order to neglect the viscous heating in adiabatic microchannels:

$$\begin{aligned}(T_{be} - T_{b0}) &= (T_{b0} - T_{\mathrm{ext}})\left(\theta_b\left(z_e^+\right) - 1\right)\\ &= 2\frac{Br}{\mathrm{Re\,Pr}}\frac{L}{D_h} f\,\mathrm{Re}\,(T_{b0} - T_{\mathrm{ext}}) < 1\\ \text{with}\quad z_e^+ &= \frac{L}{D_h \mathrm{RePr}}\end{aligned} \tag{24}$$

where L is the microchannel length, T_{be} is the fluid temperature at the exit of the microchannel, θ_b and Br are as defined in Eq. (13).

Equation (24) can be adopted as a criterion to predict the upper limit of significance of viscous dissipation in a microchannel. Equation (24) allows, for a fixed microchannel geometry and hydraulic diameter, the calculation of the values of the Reynolds number for which the temperature rise between inlet and outlet is equal to or greater than 1 K.

Figure 5 shows the Reynolds number for which the temperature rise, between inlet and outlet of a microtube 5 cm long, becomes equal to 1 K as a function of the hydraulic

diameter of the microchannel, for both water and isopropanol flows.

Finally, it must be noted that Eq. (17) can be used to determine experimentally the value assumed by the friction factor in an adiabatic microchannel for incompressible liquids:

$$f = \frac{\mathrm{Pr}}{\mathrm{Br}} \frac{D_h}{L} \left(\theta_b(z_e^+) - 1\right) \tag{25}$$

The friction factor can thus be determined without measuring the pressure drop along the microchannel but by means of temperature and flow rate measurements. This kind of measurement is unsuitable when macrochannels are tested. For this reason Eq. (25) can be considered as an example of the role of scaling effects and to suggest new measurement procedures at the microscale. This relation has been used by Celata et al. [4] in order to determine the friction factor in microchannels. In addition, since Eq. (25) is valid only in the laminar regime, one can use it to individuate the laminar-to-turbulent transition in microchannels. This has been experimentally demonstrated by Celata et al. [4] and Rands et al. [5].

Rearranging Eq. (22) and using the following definition of the Eckert number:

$$\mathrm{Ec} = \frac{W^2}{c_p \Delta T_b} \tag{26}$$

it can be demonstrated that for an incompressible liquid through an adiabatic microchannel the following equation holds in the laminar regime:

$$\frac{\mathrm{Re}\, D_h}{\mathrm{Ec}\, L} = 2 f\, \mathrm{Re} \tag{27}$$

Rands et al. [5] experimentally tested this equation for circular microtubes ($f\,\mathrm{Re} = 16$) having diameters ranging between 16.6 and 32.2 μm and with lengths between 1 and 3 cm.

In Fig. 6 the experimental results obtained by Rands et al. [5] are compared with Eq. (27); it is evident that the comparison between Eq. (27) and the experimental results allows one to individuate the laminar-to-turbulent transition in microchannels without the need to use pressure gauges.

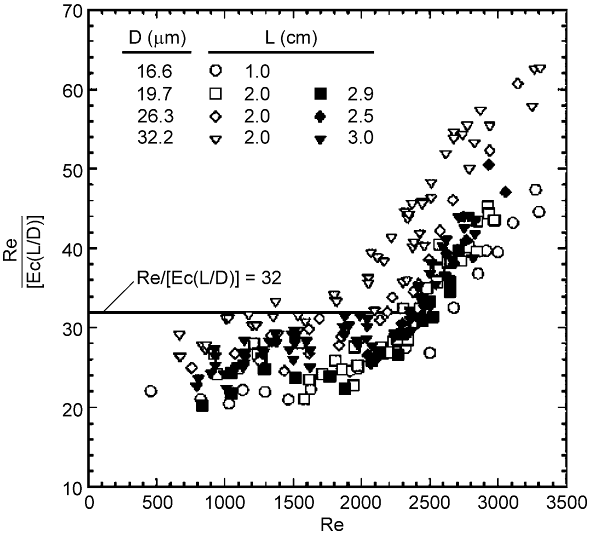

Viscous Heating, Figure 6 Comparison between experimental results of Rands et al. [5] and Eq. (27) for incompressible laminar flows

Future Directions for Research

The effect of the viscous heating of fluids in microchannels is significant especially for hydraulic diameters less than 200 μm. In this case, further investigations on the combined effect of the flow work and of the viscous dissipation in microchannels are mandatory by taking into account the temperature variation of the fluid thermophysical properties (especially the coefficient of thermal expansion and the viscosity).

Cross References

- ► Viscous Dissipation
- ► Convective Heat Transfer in Microchannels
- ► Pressure-Driven Single-Phase Liquid Flows
- ► Pressure-Driven Single-Phase Gas Flows

References

1. Bird RB, Stewart WE, Lightfoot EN (1960) Transport Phenomena. Wiley, NY
2. Morini GL (2005) The Viscous Heating in Liquid Flows in Microchannels. Int J Heat Mass Transf 48:3637–3647
3. Morini GL (2006) Scaling effects for liquid flows in microchannels. Heat Transf Eng 27:64–73
4. Celata GP, Morini GL, Marconi V, McPhail S, Zummo G (2006) Using viscous heating to determine the friction factor in microchannels – An experimental validation. Exp Fluid Therm Sci 30(8):725–731
5. Rands C, Webb BW, Maynes D (2006) Characterization of transition to turbulence in microchannels. Int J Heat Mass Transf 49:2924–2930

V

Viscous Pump

► Microfluidic Rotary Pump

Viscous Slip Coefficient

Definition

Viscous slip coefficient determines the tangential velocity of gas near a solid surface due to a normal gradient of this velocity.

Cross References

- ► Gas Flow in Nanochannels
- ► Supersonic Micro-Nozzles
- ► Micro- and Nanoscale Gas Dynamics

Visualization Based on Molecular Tagging Methods

DAVID SINTON
Department of Mechanical Engineering, University of Victoria, Victoria, BC, Canada
dongqing.li@vanderbilt.edu, dsinton@me.uvic.ca

Synonyms

Flow tagging; Flow profiling; Laser-induced molecular tagging; Laser-induced photochemical anemometry; Photobleached fluorescence; Photo-activated nonintrusive tracking of molecular motion

Definition

In the context of microfluidics and nanofluidics, visualization implies the determination of fluid velocity in small scale internal flows. Visualization requires an optically detectable fluid marker that does not alter the local fluid velocity of interest. A variety of visualization methods have been developed for small scale flows, many of which were derived from methods originally developed for macroscale flows. Molecular tagging describes one class of methods that involve molecules being rendered optically differentiable from the bulk fluid to serve as optically detectable fluid markers. The molecular dimensions of these fluid markers make them well suited to small scale flows. Molecular tagging is commonly achieved by select exposure to light, although the specific photochemical mechanisms vary over the four techniques described here.

Overview

Flow visualization has a long history. A well-known early flow visualization experiment is that of Reynolds in 1883, who studied the transition to turbulence in a pipe flow by observing the transport of an injected dye. Although many flow visualization methods have evolved since, all share a fundamental objective: to alter the fluid such that the fluid transport may be observed, yet not alter the fluid motion. The latter half of this objective is very difficult to achieve in that it requires the method to be totally non-intrusive. Instead, the researcher must either demonstrate that the alterations brought about by the marker are negligible, or be able to model the alterations such that the velocity of the undisturbed flow may be determined.

Visualization has played a central role in the development of the field of microfluidics and associated applications. It is both a natural desire, and highly informative to 'see' what is going on inside these small scale systems. The inherent scale of these systems results in significant deviations from macroscale fluid behavior, most notably due to an increase in the role of surface effects and diffusive transport of mass, momentum and energy. Unique micro- and nanoscale transport phenomena present many opportunities for advanced functionality as exploited by the many applications described in this encyclopedia and elsewhere. The scale of these systems, however, also presents some unique challenges with respect to visualization. Most notably, on the microscale the non-intrusive requirement precludes the use of many techniques commonly applied to macroscale flows, such as hot-wire anemometry and the injection of dye by mechanical means. In addition it is not possible to observe the phenomena without the use of a microscope. Several visualization techniques have, however, been successfully applied to microscale flows. Like much of the research in microfluidics and nanofluidics, many proof-of-concept contributions have appeared in the 1990s, and subsequent advancement has been rapid. Most visualization techniques applied to microstructures may be conveniently divided into two categories: particle based methods and scalar based methods [1].

Particle based visualization methods have been well developed for macroscale flows and popular for many years. In these methods, the motion of the bulk fluid is inferred from that of observed marker particles. Different methods of acquiring and analyzing particle transport data have evolved including, briefly, laser Doppler *velocimetry*, particle streak velocimetry, and particle image velocimetry. The latter includes particle tracking velocimetry and pattern matching velocimetry algorithm methodologies. Although not the focus of this entry, these particle based methods have been successfully applied to microscale flows and highly instrumental in microsystem development. Detailed descriptions of these methods are available in this encyclopedia and elsewhere.

In scalar based visualization methods, the motion of the bulk fluid is inferred from the observed velocity of a con-

served scalar, quite often a dye. Reynolds' historic work fits in this category as do many other visualization methods developed since. The key distinction between scalar and particle based methods is that particle based methods track individual particles whereas scalar based methods track a tagged solute concentration. In the limit where particle sizes approach molecular dimensions, and/or single molecule tracking is involved, this particle/scalar distinction vanishes. Some studies in this regime are discussed under key research findings and future research sections. Commonly employed molecular tagging methods, however, fall under the classification of scalar based visualization. It is the observed transport of a concentration of *tagged* molecules that provides the basis for the determination of fluid velocity.

A schematic illustrating the generic molecular tagging approach is given in Fig. 1. The microchannel, in this case a circular capillary, initially contains a fluid with uniform optical/fluorescent properties. Molecular tagging is most commonly applied to liquid aqueous flows, however, organic solvents and gases have been used as well. In the first step, a portion of the fluid is differentiated from the bulk fluid, or *tagged*, through an interaction with light, commonly from a laser. The specific photochemical mechanisms that facilitate the molecular tagging vary over the four techniques described here, namely: photobleached fluorescence, photochromic reaction, phosphorescence, and caged fluorescence. For the tagging light source, lasers are often employed to achieve a high intensity, wavelength specific, tightly focused light exposure. With the setup shown in the schematic, the molecules are tagged in a cross-sectional volume by a focused sheet of light oriented perpendicular to the channel (this is a common configuration, although point-based molecular tagging has also been demonstrated). The sheet of tagged molecules is deformed into a bowl shape, characteristic of pressure-driven flow in a circular channel. The second, visualization, step involves imaging the transport of the observed scalar and interpreting the results. The visualization is commonly achieved with a microscope system that delivers/gathers light from the microchannel as illustrated in the figure. The transport of the concentration of tagged molecules is imaged through the microscope onto a CCD camera. The resulting image sequence is then processed and analyzed numerically to determine the fluid velocity.

The channel is filled with an aqueous solution containing caged fluorescent dye (which is non-fluorescent). A cross-sectional *sheet* or *band* of the solution is exposed to a brief, intense pulse of ultraviolet light. This exposure breaks the caging groups in the band of fluid and fluorophores are released. These fluorophores are continuously excited by light from the microscope (blue) and the resulting fluorescent emission (green) is imaged through the microscope onto a CCD camera. An image sequence of the transport of the fluorescent band of dye is then analyzed to determine the bulk liquid velocity in the channel.

Flows in micro- and nanochannels are generally laminar and driven electrokinetically, as in electroosmotic flow, by pressure, or by a combination of the two. The pressure source may be external to the microfluidic network, or internally induced via capillary pressure, valving, or nonuniformities arising from electrokinetic effects. Central to electrokinetic effects is the electrical double layer, or EDL, that results from the non-uniform distribution of electrical charges near phase boundaries. Electrokinetically-driven flow, often called electroosmotic flow, results from the response of liquid ions in the electrical double layer to an axially applied electric field. The electric field may be applied via external electrodes in fluid reservoirs, or through embedded electrodes. The nature of electroosmotic flow is compared to that of pressure-driven flow in the image sequences shown in Fig. 2. The images were obtained using a caged fluorescence molecular tagging method (details described later). The transport of the concentration of tagged molecules illustrates the plug-like velocity profile characteristic of electroosmotic flows in microchannels. The velocity profile appears flat because the flow driving force is generated in the electrical double layer which is typically on the order of 10 nm and thus a very thin layer relative to the diameter of the microchannel on the order of 100 μm. In contrast, the transport of tagged molecules in the pressure driven flow reflects the familiar parabolic velocity profile expected from classical theory. Both pressure-driven and electroosmotic flow present unique challenges and advantages with respect to molecular tagging. The plug-like nature of electroosmotic flows, results in reduced dispersion (or blurring) of the tagged solute. This characteristic of electroosmotic flows has long been exploited in the area of capillary electrophoresis. However, the electrophoretic velocity of the tagged solute (if charged) in response to the applied electric field can bias the measurement of the bulk fluid velocity, and must be taken into account. For pressure-driven flow, electrophoretic effects do not play a role assuming there is no externally applied electric field, and streaming potential is not significant. However, the cross-sectional velocity gradients characteristic of pressure-driven flows result in hydrodynamic dispersion or blurring of the tagged solute resulting in a reduced useful lifetime and reduced resolution, particularly near the channel wall.

The processing and interpretation of a sequence of images documenting the observed transport of a tagged solute involves several considerations. In most cases the desired output is the fluid velocity, exhibiting a spatial resolution

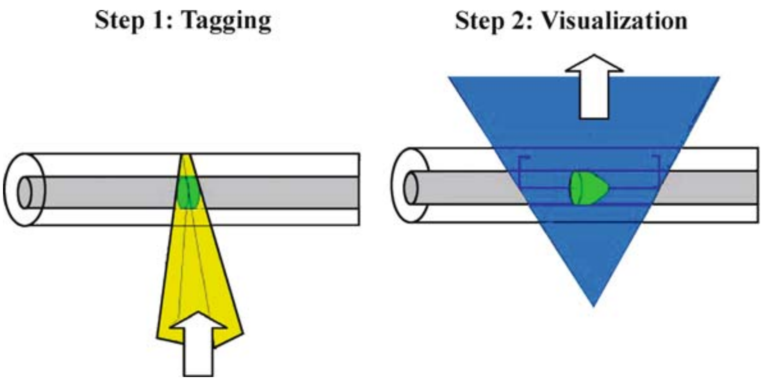

Visualization Based on Molecular Tagging Methods, Figure 1 Schematic illustrating typical molecular tagging methodology as applied to microchannel flow visualization. First, a small cross-stream section of molecules is *tagged* such that they become optically detectable. This step is typically accomplished with intensely focused laser light. Second, the transport of the tagged molecules is recorded, typically using fluorescence video microscopy

as high as possible. Although the fluid velocity is desired, it is the transport of a conserved scalar, the tagged solute concentration that is imaged. This transport, in general, is modeled by the species conservation equation for a dilute solute as follows [2],

$$\frac{\partial c_i}{\partial t} + \boldsymbol{u} \cdot (\nabla c_i) = D_i \nabla^2 c_i + \frac{D_i z_i e}{kT} \nabla \cdot (c_i \nabla \Psi) + R_i \quad (1)$$

where c is the concentration of the tagged solute, $\boldsymbol{u}$ is the bulk fluid velocity, D is the diffusion coefficient, z is the valence charge of the solute, Ψ is the electric potential, R is the rate of generation of the solute, subscript i indicates a quantity specific to the solute species, and other variables/symbols have their usual meanings. For fully developed flow in the x-direction with only an axially applied electric field (i. e., thin electrical double layer limit), Eq. (1) may be recast as,

$$\frac{\partial c_i}{\partial t} + \left(u_x + u_{\text{ph_}x}\right) \cdot (\nabla c_i) = D_i \nabla^2 c_i + R_i \quad (2)$$

where $u_{\text{ph_}x}$ indicates the axial velocity of the solute due to electrophoretic response to the applied field. This velocity is given by,

$$u_{\text{ph_}x} = \frac{D_i z_i e}{kT} \left(-\frac{\partial \Psi}{\partial x} \right) = \nu_{\text{ph}} (E_x) \quad (3)$$

Essentially, Eqs. (1–3) indicate that in addition to bulk fluid velocity, $\boldsymbol{u}$ (which is the desired output), the imaged concentration is also a product of transport by diffusion and electrophoretic motion, and the rate of generation of the tagged molecules. Thus the visualization problem is somewhat the inverse of the conventional computational modeling problem where the evolution of the concentration field is calculated from a known bulk velocity field. In contrast, the bulk velocity field is calculated from the known evolution of the concentration field when interpreting image sequences for visualization purposes. Methods to perform this calculation are discussed in the next section, following a description of four molecular tagging strategies.

Basic Methodology

The basic methodology behind molecular tagging based visualization is illustrated in Fig. 1. In the first step, a portion of the fluid is differentiated from the bulk fluid, or *tagged*, through an interaction with light. In the second step, the transport of the tagged solute concentration is imaged and interpreted to determine the fluid velocity. Provided below are the details of four molecular tagging approaches, and a description of image processing and interpretation procedures.

Photobleached Fluorescence Tagging

Fluorescence is the process by which molecules that are excited by electromagnetic radiation almost immediately emit a photon. It occurs in molecules termed fluorophores, typically polyaromatic hydrocarbons, in a multi-step process. A photon is absorbed by the fluorophore, elevating it to an excited state for a short period (typically 1 – 10 ns) and then the fluorophore releases a photon. The released photon is of lower energy than the absorbed photon due to energy dissipated in the excited state. This energy loss corresponds to a shift in wavelength between the absorbed and emitted light, termed the Stokes shift, and facilitates the filtering out of all excitation light from fluorescence emission and is the basis for fluorescence microscopy. For example, fluorescein dye molecules have an absorption

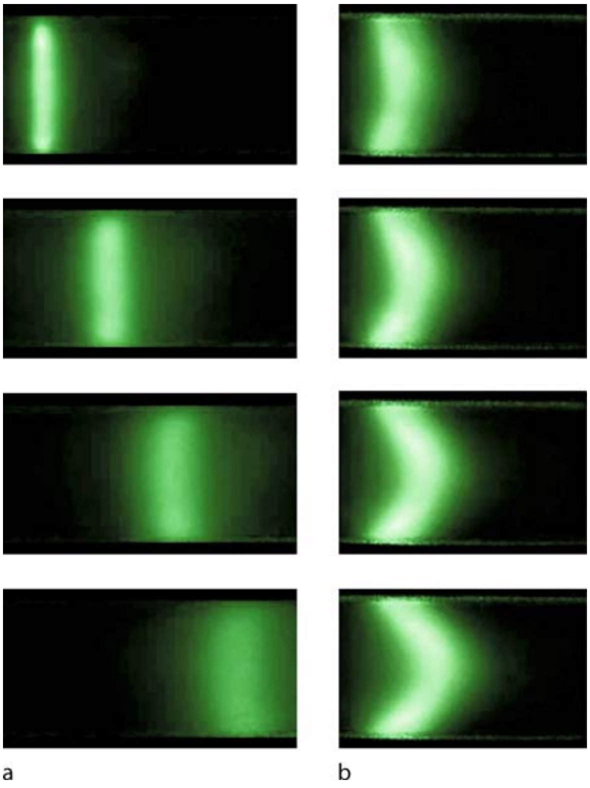

Visualization Based on Molecular Tagging Methods, Figure 2 Visualization of electroosmotic flow (**a**), as compared to pressure-driven flow (**b**), using caged-dye based molecular tagging method. The microchannel was circular in cross-section and 200 μm in diameter. Both the plug-like velocity profile characteristic of electroosmotic flows, and the parabolic velocity profile characteristic of pressure-driven flows are apparent. Adapted from [1] with permission

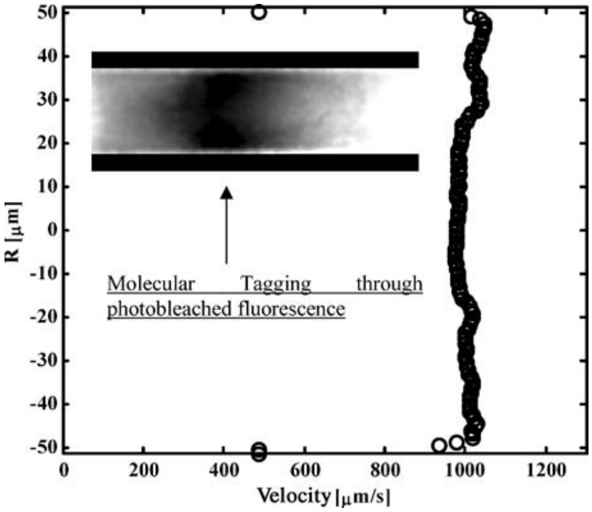

Visualization Based on Molecular Tagging Methods, Figure 3 Photobleached fluorescence based molecular tagging and visualization. A photobleached marker in a microchannel is shown inset of a measured electroosmotic velocity profile. The contrast of the inset image has been adjusted for clarity. (Reprinted from [4])

maximum around $\lambda = 490$ nm and an emission maximum at approximately $\lambda = 513$ nm. Thus if a microfluidic channel is uniformly illuminated with a single-line argon laser at $\lambda = 488$ nm, and a fluorescence microscope filters out all light below $\lambda < 500$ nm, only fluorescent emission from fluorescein molecules will be imaged by the camera. The excited lifetime of fluorescence is too short to facilitate a molecular tagging based visualization strategy (i. e., the flow-wise displacement between excitation and emission would be too small to measure for most flowrates of interest). However, photobleaching of fluorescence does enable molecular tagging based visualization.

Photobleaching of fluorophores is a process by which exposure to excitation light results in chemical alterations rendering the molecule non-fluorescent. Burning out a light bulb is analogous to photobleaching a fluorophore. The rate of photobleaching depends on the photon flux, and photobleaching is typically permanent in aqueous solutions. A common problem in biology experiments, photobleaching can be used to good effect as a molecular tagging strategy. With this tagging method, the fluid is first uniformly seeded with a dilute concentration of fluorescent dye. The molecular tagging step (as shown in Fig. 1) is achieved with a light source close to the absorption maximum of the dye. The intensity and duration of exposure must be sufficient to induce significant local photobleaching. The visualization step involves fluorescence microscopy, where the *tagged* solute is differentiated from the rest of the fluid as it is non-fluorescent. An argon laser is commonly employed in combination with fluorescein dye to achieve the photobleaching [3], however another method employed the reflective optical properties of a gaseous bubble in the microchannel to locally focus flood illumination and achieve local photobleaching without a secondary light source [4]. An image of a photobleached fluorescence tagged flow marker is shown in Fig. 3 along with an electroosmotic velocity profile determined using photobleached fluorescence. The velocity profile exhibits the plug-like shape, characteristic of electroosmotic flows, with resolution extending to 5 μm from each wall.

An advantage of photobleached fluorescence tagging is that visible light and standard, relatively inexpensive, fluorescent dyes can be employed. A disadvantage of this technique is that the signal-to-noise ratio (SNR) that defines image contrast is as much as an order of magnitude [3] lower than caged fluorescence tagging (discussed below). Furthermore, because it is the *unmarked* fluid in the chan-

nel that is fluorescing, out-of-plane velocity gradients can occlude the photobleached section. For this reason, photobleached fluorescence tagging is suited more to electroosmotic flows than to pressure-driven flows.

Photochromic Reaction Tagging

Photochromic reactions induce a change in the absorption spectrum of a solution. This change is observed as a change in the colour of a solution. The tagging process can occur on the order of nanoseconds, however, the colour change, typically from clear to blue, can persist for seconds to minutes. Photochromic reaction tagging is induced by exposure of the solution to ultraviolet light. Although some water-soluble photochromic dyes are now available, many photochromic dyes require the use of organic solvents such as kerosene and ethanol, which limit their usefulness in microfluidic applications that primarily involve aqueous solutions. Another disadvantage of this tagging method is that the image is produced by a change in absorbance which is inherently less sensitive than an image produced by emitted light against a black background as is the case in fluorescence and phosphorescence. None the less, this molecular tagging method has been successfully applied both in macroscale flows and microscale flows.

Phosphorescence Tagging

Phosphorescence is the process by which molecules, excited by electromagnetic radiation, become excited to a higher level and emit energy in the form of light as they return to their unexcited state. The central difference between fluorescence and phosphorescence is the length of time between excitation and emission. Phosphorescence emission lifetimes can be as long as several milliseconds ($\sim$ ms), which is much longer than fluorescence ($\sim$ ns), but much shorter than colour changes in photochromic dyes ($\sim$ s). Thus unlike fluorescence, phosphorescent molecules are suitable for molecular tagging applications where the tracer lifetime ($\sim$ ms) is long enough relative to the flow convection timescale to produce a quantifiable displacement. In other words, phosphorescence itself can be used as a molecular tagging mechanism, without an associated bleaching or caging strategy.

A distinct advantage of phosphorescence based molecular tagging is that only a single light source, that required for excitation, is needed to visualize the flow. Typically a UV laser is used. Traditional phosphorescent molecules suffered from O_2 and H_2O quenching during their excited states, however, so-called phosphorescent supramolecules have been developed more recently that resist quenching. These compounds have been applied to both macro- and microscale flows. For microflows, the emission lifetime on the order of milliseconds restricts their applicability to relatively high-speed microflows. In addition, water-soluble phosphorescent supramolecules require a significant concentration of alcohol ($c \sim 100$ mM or higher) in solution to perform effectively. Thus applicability of this method to study electrokinetic phenomena is limited.

Caged Fluorescence Tagging

Caged fluorescent dyes are fluorophores with additional chemical groups that render the fluorophore nonfluorescent. A caged fluorophore may be *uncaged* by exposure to certain wavelengths of light that break the bonds attaching the caging groups. The original fluorophore is recovered through this process, termed photolysis, and may be tracked indefinitely through fluorescence microscopy. With this tagging method, the fluid is first uniformly seeded with a dilute concentration of caged fluorescent dye. A range of caged dyes are available commercially (Invitrogen Corp.). The molecular tagging step (as illustrated in Fig. 1) is achieved with a light source close to the absorption maximum of the caged dye, (which is distinct from the absorption maximum of the fluorophore) normally in the ultraviolet range ($\lambda < 360$). Once uncaged, the fluorophore requires excitation in the appropriate wavelength range, which is on the order of $\lambda = 490$ nm for fluorescein. Standard fluorescence microscopy equipment is typically sufficient to image the uncaged dye transport. The images shown in Fig. 2 were obtained using fluorescence video microscopy following caged dye based molecular tagging. A schematic of the experimental setup employed is given in Fig. 4. In the case shown, circular cross-section capillaries were used in conjunction with optical immersion oil and an oil immersion objective. The immersion system ensures minimal signal loss and prevents optical distortion due to the capillary wall (the latter is not an issue with chip-based microchannels).

The most critical time scale in caged fluorescence based molecular tagging is the time delay between absorption of the photolysis radiation (untagging light exposure), and a significant release of fluorophore. Several studies have investigated this rate of release. Some fluorescence has been detected only 1 μs [5] after photolysis radiation exposure, more significant release on the order of 10 ms, and gradual increase continuing up to 0.5 s. In general, the time delay is a function of the intensity of the untagging light exposure, the concentration of the caged dye, the sensitivity of the detector employed, and likely other factors including the pH and temperature of the solution. In the context of molecular tagging, this time-delayed release has two ramifications: it imposes a limit on the maxi-

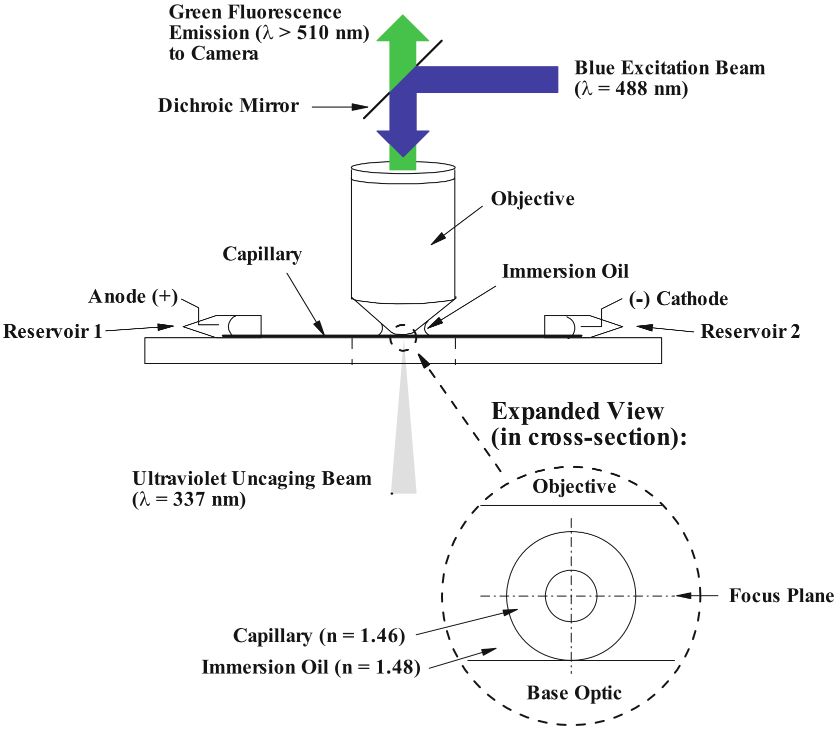

Visualization Based on Molecular Tagging Methods, Figure 4 Schematic of typical experimental setup employed for caged-dye based visualization in capillaries. Optical immersion oil setup ensures minimal signal loss and prevents optical distortion at the capillary wall (the latter is not an issue with chip-based microchannels). Adapted from [6] with permission

mum flow velocity measurable over a given displacement, and the rate of generation term, R, in Eq. (1) becomes finite and thus requires consideration in the image processing/interpretation.

Since uncaged fluorescent dye is detectable at relatively low concentrations, this molecular tagging technique is applicable to electrokinetic flows. Applying caged fluorescence based molecular tagging to electrokinetic flows, however, requires knowledge of the electrophoretic velocity of the dye. As shown in Eq. (2), the observed velocity of the tagged solute is in fact a result of the desired bulk fluid velocity, as well as the electrophoretic velocity if the uncaged dye is charged. In the extreme case where the electrophoretic mobility of the tagged solute is equal to the electroosmotic mobility, the tagged solute will remain stationary regardless of bulk fluid motion. In general however, if the microchannel section of interest is straight and of constant cross-section, the electrophoretic dye velocity may be calculated directly from dye property data and boundary conditions. More involved methods have been developed in order to additionally account for Joule heating induced fluid temperature rise on this calculation [6]. It has also been reported that the adsorption of caged dye onto polymer microchannel walls can alter the surface properties, and thus applicability of caged fluorescence based molecular tagging to electrokinetic flows in polymer based microchannels may be limited.

Caged fluorescence tagging is generally limited to small scale visualization experiments as the cost of caged dyes is relatively high (portions on the order of milligrams are commonly valued on the order of hundreds of US dollars). Another consideration is that the signal strength is generally low (depending on uncaging intensity, untagged volume, dye concentration etc.). Despite some disadvantages however, caged dye based molecular tagging has been relatively popular, and successfully applied in a wide variety of microscale flow visualization efforts. Some of these works are highlighted in the key research findings section here, and a detailed listing is provided elsewhere [1].

V

Determining Velocity from the Image Data

The first step in interpreting the image data is image processing. Image processing is required to both remove any non-uniformities present in the imaging system, and to convert fluorescence or absorbance levels to concentration.

At the minimum this process involves dark-field subtraction and bright-field normalization. Multiple texts on digital image processing are available.

After processing, intensity levels in the image set may be interpreted directly as concentration, and thus the image set forms a sequence of snap-shot solutions to the transport equation described earlier, Eqs. (1–3). The general process of extracting the bulk fluid velocity, $\boldsymbol{u}$, from the species transport equation has been studied extensively and termed Scalar Image Velocimetry (SIV) [7]. A full SIV formulation can be quite involved. For the specific case illustrated in Fig. 1, where a cross-sectional band of molecules are tagged in a straight channel of uniform cross-section, a much simplified SIV technique, such as the one illustrated in Fig. 5, can be effective. In short, the strategy involves choosing axial points of maximum concentration as marker points, and tracking the motion of these marker points over time (i. e., through the image sequence) to determine the cross-stream velocity profile. The axial maximum concentration points are chosen as their axial position is less effected by diffusion and any rate of generation or photobleaching of tagged molecules. As shown in the figure, the axial maximum concentration points form a cross-stream profile at each time-step. The axial displacement of this profile, divided by the time delay between images provides a cross-sectional velocity profile, $\boldsymbol{u}$. Although this method has limitations, it is relatively straightforward to implement computationally and has provided reliable results both for pressure-driven and electroosmotic flows. Some key research findings are summarized in the next section.

Key Research Findings

The limited space available here does not allow for comprehensive review of the multitude of important research contributions, particularly since the late 1990s, in the area of molecular tagging based visualization of small scale flows. For a comprehensive review, the reader is referred to a recent review paper [1] and the references therein. Below, a sampling of some early and influential papers in this area are discussed.

The term molecular tagging velocimetry first became popular in connection to phosphorescence tagging methods [8]. Originally employed in macroscale flow visualization studies [8], so-called phosphorescent supramolecules have since been applied to visualization of relatively fast flows in microtubes.

In 1998, Paul et al. [9] applied caged fluorescence tagging to visualize flows in capillaries. The importance of that contribution is evidenced by a long citation record. This technique has been adapted by several groups, and applied to study flows in microchannel bends, the effect of non-uniform zeta potential, flows in plastic microchannels, Joule heating effects (both on the determination of electrophoretic velocity and on the flow), and many others as described in Ref. [1] and references therein. Shelby and Chiu [5] extended the use of caged fluorescence tagging in microsystems to high speed pressure-driven flows using extremely sensitive single point detection.

Mosier et al. [3] applied photobleached fluorescence tagging to study both electrokinetic and pressure-driven flows in rectangular microchannels. High molecular weight fluorescent conjugates were used to decrease diffusive effects (a diffusion coefficient four orders of magnitude below that of fluorescein). An argon laser was employed to achieve the photobleaching while a fluorescence microscope facilitated the visualization. A niche flow marking technique requiring only flood illumination was later developed using the reflective optical properties of a microchannel-entrapped bubble [4].

Future Directions for Research

The application of molecular tagging based visualization to nanoscale flows is an exciting research direction. The molecular dimensions of these probes make them well suited to these geometries, however, several challenges exist. Most notably, resolving nanoscale features with visible light presents a fundamental challenge due to the inherent wavelength of visible light. Along similar lines it is expected that as nanoscale based flow visualization methods are developed, traditional distinctions between scalar based and particle based methods will vanish. Although nanoscale velocity gradients have not yet been resolved, depth-wise averaging of fluorescence signal over nanoscale depths is one strategy that has been successfully employed recently in nanoscale electrophoresis applications. Another future research avenue is the improvement of molecular tagging probe chemistries and invention of new molecular tagging strategies. A wide variety of probes are produced in response to demand from biological research and molecular probes with improved functionality for visualization purposes may be a useful byproduct of this demand. Lastly, molecular tagging based velocimetry could play an interesting role in the rapidly emerging field of optofluidics, the marriage of optics and fluidics.

Cross References

► Micro-PIV-Based Diffusometry
► Diffusion
► Electrical Current Monitoring Methods

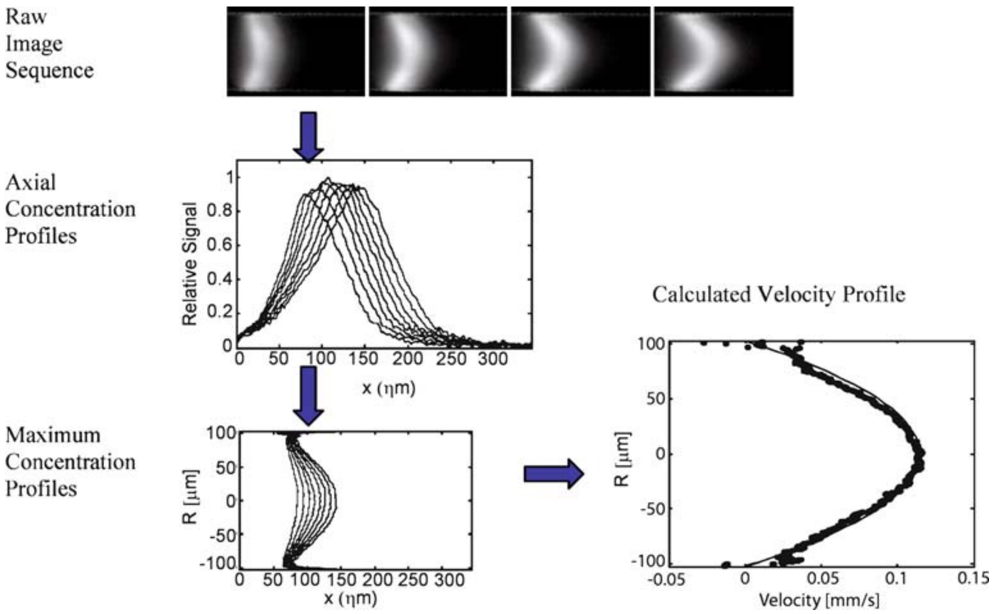

Visualization Based on Molecular Tagging Methods, Figure 5 Compilation illustrating an axial maximum concentration point tracking strategy for determining the bulk fluid velocity from image data. Shown is a much simplified version of general scalar image velocimetry techniques. Adapted from [6] with permission

- ► Electroosmotic Flow (DC)
- ► Electrophoresis
- ► Fluid Metering
- ► Fluorescence Measurements
- ► Fluorescent Labeling
- ► Hydrodynamic Dispersion
- ► Methods for Flow Rate Measurements
- ► Microscale Flow Visualization
- ► Velocimetry

References

1. Sinton D (2004) Microscale Flow Visualization. Microfluid Nanofluid 1:2–21
2. Probstein RF (2003) Physicochemical Hydrodynamics. John Wiley&Sons, NJ
3. Mosier BP, Molho JI, Santiago JG (2002) Photobleaching-fluorescence imaging of microflows. Exp Fluids 33:545–554
4. Sinton D, Erickson D, Li D (2003) Micro-Bubble Lensing Induced Photobleaching (μ-BLIP) with Application to Microflow Visualization. Exp Fluids 35:178–187
5. Shelby JP, Chiu DT (2003) Mapping Fast Flows Over Micrometer-Length Scales Using Flow-Tagging Velocimetry and Single-Molecule Detection. Anal Chem, 75:1387–1392
6. Sinton D, Li D (2003) Electroosmotic Velocity Profiles in Microchannels. Colloids Surf A 222:273–283
7. Dahm WJA, Su LK, Southerland KB (1992) A Scalar Imaging Velocimetry Technique for Fully Resolved Four-dimensional Vector Velocity Field Measurements in Turbulent Flows. Phys Fluid 4(10):2191–2206
8. Gendrich CP, Koochesfahani MM, Nocera DG (1997) Molecular Tagging Velocimetry and Other Novel Applications of a New Phosphorescent Supramolecule. Exp Fluid 23:361–372
9. Paul PH, Garguilo MG, Rakestraw DJ (1998) Imaging of Pressure- and Electrokinetically Driven Flows through Open Capillaries. Anal Chem 70:2459–2467

Voltage Clamp

► Patch Clamp Measurements On-Chip

Volume of Fluid (VOF) Method

► Interface Capturing Schemes for Free-Surface Flows

Volume Illumination

Definition

Volume illumination is an illumination method for image capturing where the whole volume around the focus plane is illuminated. The illumination axis is the same as the camera axis (one-axis-illumination) or the directions of illumination and camera are similar. Volume illumination and illumination with a ► light sheet are used for ► PIV

and PIT measurements. When illuminating the whole volume, the ► measurement depth is defined by the ► depth of field of the optics. The disadvantage of this illumination method is the high background noise when using it in a suspension.

Volume Tracking

► Numerical Techniques for Free Surface Flows: Interface Capturing and Interface Tracking

Vortex Diode

Definition

A type of a no-moving-part fluidic diode the essential part of which is an axisymmetric chamber with tnagential inlet and axial outlet.

A fluidic diode based on the difference in fluid flow between the situations with fluid entering the chamber tangentially a producing there a rotation and with the fluid entering axially, when the rotation is absent. This type of diodes particularly suited for operation at relatively low operating frequencies. because star-up of the rotation in the chamber takes a considerable time.

Cross References

► Fluidic Diodes
► Valve-Less Rectification Pumps
► Fluidic Rectification

Vortex Pair

► Microsynthetic Jets

Vortex Ring

► Microsynthetic Jets

Vortices

► Chaotic Mixing Based on Viscoelasticity

Wafer Bonding

ZHENG CUI
Rutherford Appleton Laboratory, Oxford, UK
z.cui@rl.ac.uk

Synonyms

Direct bonding; Fusion bonding

Definition

Wafer bonding is a process by which two mirror-polished wafers of any materials adhere to each other at room temperature without the application of any macroscopic gluing layer or external force. The bonding is achieved through van der Waals force. Wafer bonding achieved at room temperature is usually relatively weak compared to metallically, covalently or ionically bonded solids. Therefore, for many applications the room temperature bonded wafers have to undergo a heat treatment to strengthen the bonds across the interface.

Overview

It has long been known that mirror-polished surfaces, when in direct contact, adhere to each other by capillary force, or electrostatic force or van der Waals force. In the absence of liquid or electrical charge at the mirror surfaces, the van der Waals force is the primary force to cause adhesion of two mirror-polished surfaces. The van der Waals force is an extremely short-ranged attractive force between two polar molecules. However, the force can be *long ranged* if there are water molecules participating the process, because the hydrogen atoms in water molecules can bridge with other molecules to form *long-ranged* hydrogen bonds instead of direct bonds between the solid atoms [1]. In the example of silicon wafer bonding, most silicon wafers are covered with a thin native oxide (~ 2 nm) or purposely grown thermal oxide which have typically a monolayer or two of water molecules absorbed on OH groups associated with the oxide. At room temperature, silicon wafers may be bonded by relatively weak *hydrogen bridges*. A subsequent heat treatment can turn the weak hydrogen bonds to strong covalent bonds. For a hydrophobic surface where the thin oxide has been removed by dipping into HF, the process is expressed as Eq. (1). For a hydrophilic surface where there is a thin oxide layer, the process is expressed as Eq. (2).

Hydrophobic surface:

$$\mathrm{Si-H+H-Si \Rightarrow Si-Si+H_2} \quad (1)$$

Hydrophilic surface:

$$\mathrm{Si-OH+HO-Si \Rightarrow Si-O-Si+H_2O} \quad (2)$$

In both cases strong covalent bonds are formed after heat treatment. For a hydrophobic surface, the process starts at about 500 °C, while for a hydrophilic surface it is about 120 °C [1]. Typical change of surface energy with heat treatment temperature is shown in Fig. 1. Though they started differently as temperature rises, both hydrophobic and hydrophilic surfaces gain high surface energy at high temperature. The full covalent bond formation is accomplished at temperatures from 800 to 1200 °C. The bonds formed at such temperatures are as strong as those of a crystalline solid.

The first systematic investigation of room temperature adhesion between two optically polished glass plates was done by Lord Rayleigh in 1936. Later, the *anodic bonding* technique was developed for semiconductor wafer bonding with glasses and metals. Direct bonding of silicon wafers was first reported in 1986 [2]. In the same year, silicon wafer bonding with an oxide intermediate layer was also reported, which opened a new route for manufacturing silicon-on-insulator (SOI) wafers [3]. Semiconductor devices built on a SOI substrate were favoured because of their high resistance against the undesirable side effect of radiation-induced electron–hole pairs for application in outer space. The original driving force of *radiation hardness* behind SOI development, however, was dwarfed by

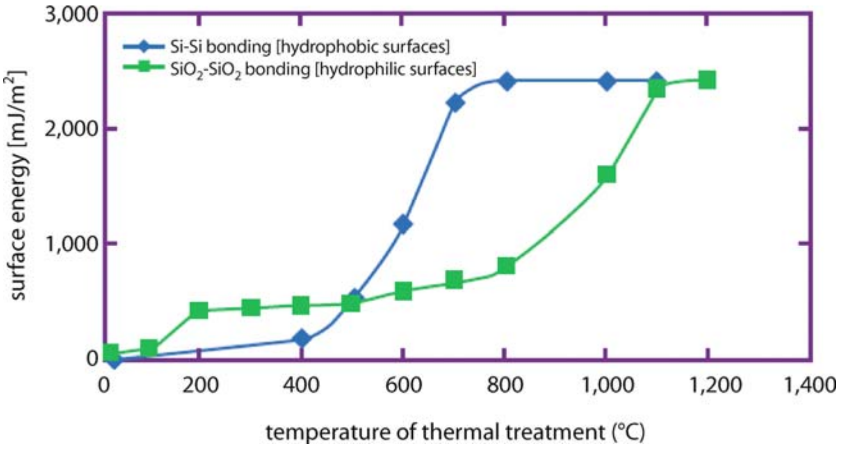

Wafer Bonding, Figure 1 Evolution of surface energy with temperature for hydrophobic and hydrophilic surfaces

its great commercial potential in integrated circuits (IC) manufacturing. ICs built on SOI substrates allow operation at lower voltage and higher packing density, as well as simultaneous use of low and high voltage on one chip. SOI technology has become the mainstream technology for the next generation of ICs [4]. Prior to the advent of silicon direct bonding, SOI wafers were produced by either epitaxial growth of single-crystal silicon on an insulating layer or by the so-called SIMOX process (Separation by IMplanted OXygen), in which high doses of high-energy oxygen ions were implanted into silicon, followed by annealing at a temperature close to the melting point of silicon, resulting in the formation of a buried layer of silicon dioxide below the thin top layer of silicon [5]. The SIMOX technique produces a high density of implantation-induced dislocations in the silicon layer. Both epitaxial growth and SIMOX processes are expensive and of low throughput. Direct silicon wafer bonding has completely changed the way SOI substrates are manufactured.

Another important application of wafer bonding is in microelectromechanical systems or MEMS. Semiconductor wafer bonding is an ideal technique to combine different structures to form functionalised elements in a three-dimensional arrangement. The first application of wafer bonding to build micro-pressure sensors was reported in 1988. Now wafer bonding has been employed in research and production of nearly all types of MEMS, including mechanical, fluidic, power, optical, medical and biological microsystems. Wafer bonding enables combination of silicon with a large variety of dissimilar materials, such as III–V and II–VI compound semiconductors, to build optoelectronic devices. It also enables transfer of MEMS devices onto a fully processed CMOS wafer to realise integration of MEMS with CMOS electronic circuits.

It must be pointed out that direct bonding of silicon wafers is not the only type of wafer bonding, though it represents the largest application of wafer bonding techniques. There are other bonding techniques, apart from *anodic bonding*, that can be considered as wafer bonding, such as eutectic bonding, adhesive bonding and glass frit bonding.

- Eutectic bonding is used when a hermetic or vacuum seal is required, generally for sensors. It uses an intermediate bonding material that forms a eutectic alloy at a specific temperature, such as gold–silicon, gold–tin or lead–silicon. The metal is usually deposited by plating, while the silicon source can be the wafer or chemical vapour deposited. Solid–liquid mixing occurs at temperatures slightly above the eutectic point and high contact force (40 kN) is produced. A hermetic solid seal forms upon cooling.
- Adhesive bonding uses photoresist, spin-on glasses or polymers to deposit a planarising material between two wafers. Such materials can be annealed or UV cured at low temperature to provide a low-stress wafer stack.
- Glass frit bonding uses glass beads (glass frit) suspended in a carrier paste and deposited onto a substrate either in a blanket form or patterned using screen printing. After deposition, the solvents are removed by degassing then heat and pressure are applied to make a hermetic seal.

Although silicon direct bonding has wide applications in MEMS and IC industries, it is not as much used in constructing micro- or nanofluidic systems because of the conductive nature of silicon wafers. Many microfluidic applications require application of an electrical field, such as those utilising *electrophoresis* and *electroosmosis*. For these applications, glass materials are preferred. A glass material permits the use of high voltages, which provides the basis for fast and efficient separation of analytes. Its

transparency allows sensitive and invasive optical detection of samples. Microfluidic applications also tend not to use adhesive or intermediate layers in wafer bonding, because they may clog the microchannels or adversely affect the liquid flow patterns.

Basic Methodology

The success of direct wafer bonding is critically dependent on surface properties and conditions, chemical cleaning process and ambient conditions when the initial room temperature bonding is performed. Particles on the bonding surface will adversely affect the bonding. For example, a particle of 1 μm diameter can generate a void with a diameter of 0.5 mm which is 500 times larger the particle itself. Interfacial bubbles are often generated during the heat treatment step, which is not related to particles. Direct wafer bonding used to be a difficult manufacturing technology and sometimes characterised as *black magic* in the past [1]. Now with better understanding of the fundamental physics and chemistry of the bonding process, the technology has matured and been implemented in high-volume production. The direct wafer bonding involves four basic steps:

1. Preparation of bonding surfaces. The surfaces have to be polished mirror-like, with surface roughness less than 1 nm and thickness variation across a 4-inch wafer less than 2 μm. Normal silicon wafers straight out of the box without any processed structures are of the surface quality for direct bonding. However, if the wafer has been processed a thorough clean is necessary to remove any particulate, organic and metallic contaminations. In the meantime, the cleaning process should not degrade the surface smoothness. Hydrogen peroxide-based RCA wet solutions are commonly used for cleaning, which is also the standard cleaning solution in semiconductor manufacturing. There are two steps in cleaning: the first step is to remove any particles and organics using RCA1 ($NH_4OH : H_2O_2 : H_2O = 1 : 1 : 5$) and the second step is to remove any alkali and heavy metal contaminations using RAC2 ($HCl : H_2O_2 : H_2O = 1 : 1 : 6$) [1]. In addition to cleaning, activating the surface is highly desirable. The surface activation is to create a reactive bonding surface, for example to create the abovementioned hydrogen *bridge* bonds, so that the requirement on surface smoothness can be fairly relaxed. Activation makes the surface either hydrophobic or hydrophilic.
2. Room temperature bonding. After cleaning and activation, the two wafer surfaces are brought into contact in air and at room temperature. With a slight press to push out the thin cushion of air between the wafers, bonding occurs at the pressing area and spreads out rapidly over the entire surface within a few seconds. It must be emphasised that this step should be performed in an environment as clean as possible. Even in a *class 1* cleanroom (one 0.5 μm or larger particle in a cubic foot of air), 100% bonding yield cannot be guaranteed because of the risk of particles falling onto the bonding surface. In order to alleviate the stringent requirement on the cleanroom, special apparatus acting as a micro-cleanroom has been developed to reduce the chance of a particle dropping onto the bonding surface [1].
3. Heat treatment. This step is to convert the van der Waals weak bonds to covalent strong bonds at temperatures from 800 up to 1200 °C. Although the initial change of surface energy is different at low temperature for hydrophobic and hydrophilic surfaces, they all form the covalent bonds in the final stage of heat treatment, as shown in Fig. 1. The time of heat treatment depends on the temperature, ranging from hours to days. High temperature requires less time.
4. Wafer thinning. Although this is not a necessary step, many applications require one of the bonded wafers to be thin, from 100 nm to a few micrometres thick. This is an important step for manufacturing SOI wafers, in which the thin single-crystal silicon layer is called the device layer and the supporting silicon wafer called the handle layer. A number of techniques have been developed for wafer thinning, but the most elegant one is the *smart-cut* process [6]. As shown schematically in Fig. 2, it is based on hydrogen implantation prior to bonding. High-energy hydrogen ions implanted deep into the silicon form a buried layer which leads to cracking and splitting from the silicon wafer during heating to about 500 °C. Therefore, after implantation and bonding the top wafer can be separated from the handle wafer by heating, leaving the thin layer of silicon bonded with the handle wafer. Only a slight polishing to the splitting surface is needed to achieve the equivalent surface of a typical silicon wafer. In this way, the split-off wafer can be used again and again, because each bonding-splitting only loses a fraction of the thickness in the wafer. The smart-cut process has now become a mass production technology for manufacturing SOI wafers.

The bonding strength or surface energy after bonding can be measured by a so-called crack-opening method which is shown schematically in Fig. 3. For bonding of identical wafers ($t_{w1} = t_{w2} = t_w$, $E_1 = E_2 = E$), the surface energy per unit area γ can be expressed as [7]

$$\gamma = \frac{3Et_w^3 t_b^2}{32L^4} \tag{3}$$

W

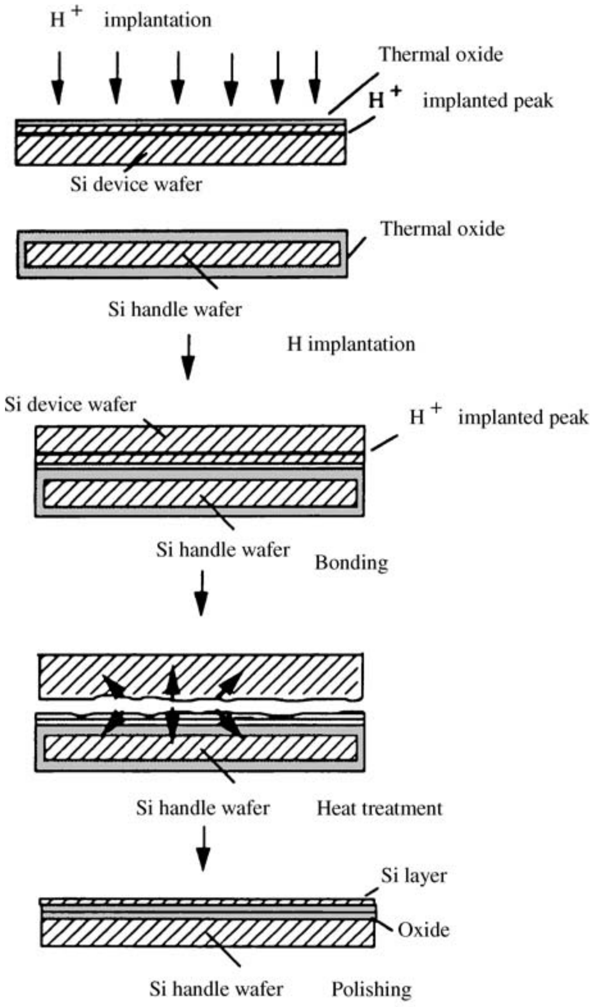

Wafer Bonding, Figure 2 Schematic of the *smart-cut* process for manufacturing SOI wafers

where E is the Young's modulus, t_w is the wafer thickness and L is the crack opening length. The surface energy for room temperature bonding is typically around $100\ mJ/m^2$ for hydrophilic surfaces and around $20\ mJ/m^2$ for hydrophobic surfaces. It becomes one or two orders of magnitude higher after heat treatment, as indicated in Fig. 1. For good-quality bonding, the bonding strength is that of a normal crystalline structure. Bonding uniformity or defects at bonding interface can be inspected by either infrared imaging or scanning acoustic microscopy.

Bonding of glass is also called fusion bonding. The method is more or less the same as silicon wafer bonding [8]. It requires polished surfaces, cleaning in RCA1 and RCA2 solutions. The cleaned and polished surfaces are brought into contact and heated at the temperature nearly to the melting point of glass for 6 to 8 h. For soda-lime microscope glass slides, the thermal fusion temperature is around 630 °C. For quartz substrates, the temperature can be up to 1000 °C. In most cases, a pressure applied to the bonding pair during the thermal fusion process can help to achieve a good bonding. The bonding strength is about 20 – 30 MPa, close to the strength of bulk material [9].

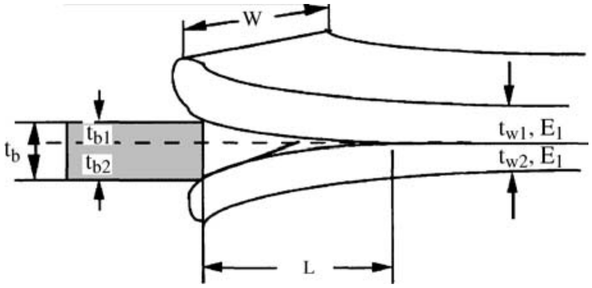

Wafer Bonding, Figure 3 Schematic of the crack-opening method for measuring bonding strength

Key Research Findings

The key development in wafer bonding in recent years is the low-temperature bonding technique. As mentioned above, the typical annealing temperature in silicon wafer bonding is above 800 °C. However, an increasing number of applications require temperature below 500 °C because integration of MEMS devices with a CMOS wafer has a thermal budget below 450 °C. The key to realising low-temperature wafer bonding is to modify the wafer surface: either to increase the number of hydrogen bonds or to generate new types of chemical bonds. Although some techniques utilising various intermediate layers have been developed to facilitate low-temperature bonding, the most simple and effective method is by surface activation using a plasma process. It has been found that a short plasma treatment of a bonding surface (~ 30 s) can lower the bonding temperature to 200 – 500 °C. The exact mechanism of plasma activation is not yet fully understood. For oxygen plasma, it may be due to an increase of oxide layer, combined with a higher porosity of the amorphous layer because of ion bombardment, resulting in an increasing incorporation of additional water molecules [10]. However, wafer surfaces treated in argon and nitrogen plasmas can also undergo low-temperature bonding. Recent studies indicated that the activation effect of semiconductor surfaces is mainly caused by electrons and UV radiation instead of ions. The effect of UV radiation is an additional cleaning of the surfaces by cracking of CH compounds and electrons help to generate surface-active sites, causing bonding of more OH groups [10]. Plasma activation

can also help to lower the temperature for bonding of dissimilar materials.

Future Directions for Research

Wafer direct bonding has become a key technology in semiconductor manufacturing. It offers the freedom in the design of material combination whether they are amorphous, polycrystalline, of different crystalline orientation or lattice constant. The most successful example is mass manufacturing of SOI wafers, which already has had a profound impact in the integrated circuits industry. Applications of wafer bonding in MEMS and microsystems are increasing and the technique is promised to be the key for three-dimensional integration of device structures and full integration with CMOS-based wafers. Such integration will have a significant impact on micro- and nanofluidics development. While it is a constant pursuing goal to further broaden the application of the wafer bonding technique, some basic studies are needed to better understand the mechanism of plasma activation for low-temperature bonding. Further researches are also needed to understand the physical and chemical processes of wafer bonding for materials other than silicon.

Cross References

- ► Anodic Bonding
- ► Packaging (Including Wire Bonding)

References

1. Tong QY, Gosele U (1999) Semiconductor Wafer Bonding Science and Technology. Wiley, New York
2. Shimbo M, Fukukawa K, Fukusa F, Tanzawa K (1986) Silicon-to-silicon direct bonding method. J Appl Phys 60:2987–2989
3. Lasky JB (1986) Wafer bonding for silicon-on-insulator technology. Appl Phys Lett 48:78–80
4. Iyer SS, Auberton-Herve AJ (eds) (2002) Silicon wafer bonding technology for VLSI and MEMS applications. INSEPCT. the IEE, London
5. Izumi K, Doken M, Ariyoshi H (1978) CMOS devices fabricated on buried SiO2 layers formed by oxygen implantation into silicon. Electron Lett 14:593
6. Bruce M (1995) A new silicon on insulator material technology. Electron Lett 31:1201–1202
7. Gosele U, Tong QY, Schumacher A, Krauter G, Reiche M, Plossi A, Kopperschmidt P, Lee TH, Kim WJ (1999) Wafer bonding for microsystem technologies. Sens Actuator 74:161–168
8. Stjernstrom M, Roeraade J (1998) Method for fabrication of microfluidic systems in glass. J Micromech Microeng 8:33–38
9. Sayah A, Solignac D, Cueni T, Gijs MAM (2000) Development of novel low temperature bonding technologies for microchip chemical analysis applications. Sens Actuator A 84:103–108
10. Reiche M (2006) Semiconductor wafer bonding. Phys Stat Sol A 203(4):747–759

Wall Shear Stress

Synonyms

Shear stress

Definition

Wall shear stress is the tangential drag force produced by horizontal movement of the fluid across the surface. It is a function of the velocity gradient of the fluid near the surface. Its magnitude is directly proportional to fluid flow and viscosity and inversely proportional to the cube of the radius.

Cross References

- ► Micro- and Nano-Scale Anemometry: Implication for Biomedical Applications
- ► Pressure

Wang-Chang–Uhlenbeck Equation

► Numerical Solution of Boltzmann Equation

Water Management in Micro DMFCs

Cheng-Chieh Hsieh
Intel Corporation, Chandler, AZ, USA
cheng-chieh.hsieh@intel.com

Synonyms

Direct Methanol Fuel Cell

Definition

A DMFC (Direct Methanol Fuel Cell) converts the chemical energy stored in liquid methanol to usable electrical energy by a direct electrochemical oxidation-reduction reaction.

Overview

In a DMFC, methanol is directly oxidized on the surface of catalytic electrodes at the anode.

$$CH_3OH_{(l)} + H_2O_{(l)} \rightarrow CO_{2(g)} + 6H^+ + 6e^- \qquad (1)$$

The electrons are drawn to an external circuit through conductive backing layers to generate electricity, and the pro-

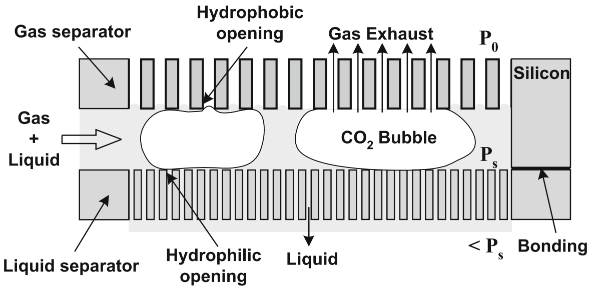

Water Management in Micro DMFCs, Figure 1 Schematic of a passive micro-scale CO_2 degassing system in a DMFC

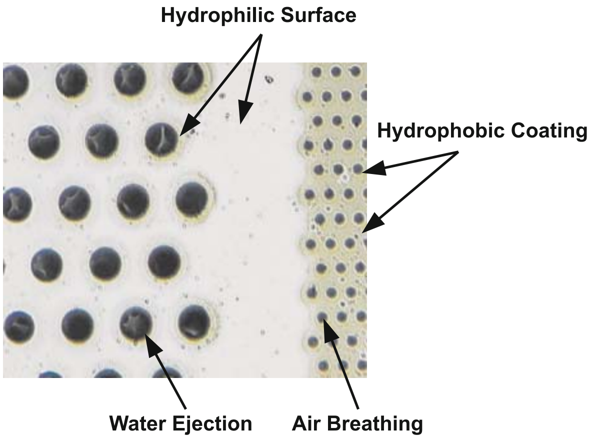

Water Management in Micro DMFCs, Figure 2 Water management at the cathode of a DMFC

tons migrate through a humidified solid electrolyte (Proton Exchange Membrane, PEM) and react with oxygen at the cathode.

$$\tfrac{3}{2}O_{2(g)} + 6H^+ + 6e^- \rightarrow 3H_2O_{(l)} \tag{2}$$

Carbon dioxide (CO_2) evolves on the anode surface in the form of gas bubbles, impeding methanol supply to the catalyst surface. Surface treatment with a selective hydrophobic coating on the backing layer is used to assist CO_2 bubble scrubbing [1]. CO_2 bubbles escaping from the catalyst surface accumulate in the internal fuel circulation loop. The resulting two-phase flow drastically increases the flow resistance of the fuel circulation loop and may totally choke the flow path. A passive CO_2 degassing system, consisting of two parallel plates with an array of etched-through holes, is shown in Fig. 1 [2]. The wettability of the surface of the gas separator is modified by a thin layer of hydrophobic coating to facilitate gas bubble removal from the gas-liquid mixture. The coating also prevents fuel leakage through the openings by forming a meniscus at the mouth of the openings inside the system. The maximum sustainable opening diameter (D_{max}) to avoid liquid leakage can be approximated by the well-known Young–Laplace equation.

$$D_{max} = \frac{4\gamma\cos(180^\circ - \theta)}{P_s - P_0} \tag{3}$$

where γ is the surface tension of the fuel mixture, θ is the contact angle (in degree) of the fuel mixture on the hydrophobic surface, P_s is the system pressure and P_0 is the ambient pressure. The liquid separator, on the other hand, is hydrophilic in order to create an effective passage for the liquid flow.

Water is generated at the cathode. The excessive water may result in flooding, reducing the effective surface area of the cathode available for the reduction reaction and hence, lowering the entire electrochemical reaction rate. The same concept of preferential surface wettability modification used in the passive CO_2 degassing system can be applied to resolve this water management issue. As shown in Fig. 2, a hydrophobic thin film is coated on the area with small openings to allow air (oxygen) "breathing", while the surface of the area with large openings remains hydrophilic to assist water removal from the cathode surface [2]. The water expelled from the cathode through the openings is guided and collected along the hydrophilic surface without cross-covering the area with small. Part of the collected water can then be recycled back to the anode to maintain the electrochemical reaction.

References

1. Scott K, Taama WM, Argyropoulos P (1998) Material Aspects of the Liquid Feed Direct Methanol Fuel Cell. J Appl Electrochem 28:1389–1397
2. Yao SC, Tang X, Hsieh CC, Alyousef Y, Vladimer M, Fedder GK, Amon CH (2006) Micro-Electro-Mechanical-Systems (MEMS)-based Micro-scale Direct Methanol Fuel Cell Development. J Energy 31:636–649

Waveguide Propulsion

► Optofluidics: Optics Enabling Fluidics

Waveguide Trapping

► Optofluidics: Optics Enabling Fluidics

Weak Formulation

Synonyms

Generalized formulation

Definition

A weak formulation is an equation derived from the original (strong) formulation of a physical problem by alleviating the strict differentiability requirements for the unknown function. This is often achieved by lowering the order of partial derivates appearing in the equation for instance using integration-by-parts.
The solution to a weak formulation associated to an ordinary or partial differential equation is called the weak (or generalized) solution. There are many different definitions of weak solution, appropriate for different classes of equations.
Weak solutions are important in engineering because a large number of differential equations which are used to describe real world phenomena do not admit smooth enough solutions. Weak formulations provide a way to solve such problems.

Cross References

- ► Meshless Methods
- ► Volume and Finite Difference Method for Modeling and Simulation

Weber Number

Definition

The dimensionless *Weber number* represents the ratio of disruptive hydrodynamic forces to the stabilizing surface tension force. Hence, the *Weber number* indicates whether the kinetic or the surface tension energy is dominant. For a spherical droplet the *Weber number* can be derived using the kinetic energy compared to the surface energy.
The *Weber number* can be used for two different declarations. On the one hand it describes whether a droplet can leave a nozzle at all due to higher kinetic energy compared to surface energy. On the other hand it can describe whether a droplet has the tendency for splashing when the kinetic energy is released at the impact on a surface.
The higher the *Weber number* the more dominant is the kinetic energy. This means that most of the inserted energy converts into kinetic energy, i. e. an ejected droplet is faster with higher *Weber number*. The lower the *Weber number* the more dominant is the surface tension energy. This means that most of the inserted energy converts into surface tension energy, i. e. a droplet formation is critical or even impossible.
The *Weber number* is the most important dimensionless number characterizing the droplet formation. Therefore, the *Weber number* can be used to distinguish between occurring droplet formation regimes.

Cross References

- ► DNA Micro-arrays
- ► Droplet and Bubble Formation in Microchannels
- ► Electrokinetic Dispensing
- ► Piezoelectric Microdispenser

Weighted Least Square

- ► Least Square

Weights and Measures

- ► Fluid Metering

Wet Chemical Etch

Definition

Wet etching is the process of using liquid reagents of acids, bases or other chemicals to dissolve away unwanted materials such as metals, semiconductor materials or glass.

Cross References

- ► Anisotropic Etching
- ► Bulk Micromachining
- ► Dry Etching
- ► Isotropic Etching
- ► Photolithography
- ► Plasma Etching
- ► Wet Etching

Wet Etching

Definition

Wet etching is a fabrication process of using liquid chemicals or wet etchants (a mixture of acids, base, water and other chemicals) to dissolve the bulk substrate or thin film such as silicon,GaAs,SiC,SiO_2,Si_3N_4 and metals. In

W

microfabrication applications, it is widely used to transfer the designed patterns from an etching mask to the substrate. When the sample is immersed into the etching bath, the etchant only contacts and reacts with the substrate surfaces where are uncovered by the etching mask. The suitable materials for the mask can be polymers or other materials such as photoresist, SU-8,SiO_2 andSi_3N_4, which feature much lower etching rate in the selected etchant in contrast to the substrate material.

Wet etchants fall into two broad categories: isotropic etchants and anisotropic etchants. Isotropic etchants attack the material being etched at the same rate in all directions. Anisotropic etchants attack some single-crystal materials (typically silicon) at different etch rates depending on the crystallographic orientation of the substrate, so there is more control of the shapes being produced.

Wet etching is the most common processing in semiconductor industry and MEMS applications.

Cross References

- ► Fabrication of 3-D Microfluidic Structures
- ► Microfabrication Techniques
- ► Photolithography
- ► Photoresist Reflow
- ► Wet Chemical Etch

Wettability Patterning

► Hydrophilic/Hydrophobic Patterning

Wetting Phenomenon

► Surface Tension Driven Flow

Wetting and Spreading

LESLIE YEO
Micro/Nanophysics Research Laboratory
Department of Mechanical Engineering, Monash University, Clayton, VIC, Australia
leslie.yeo@eng.monash.edu.au

Synonyms

Capillarity

Definition

The wettability of a liquid governs how it spreads over a solid substrate or an immiscible liquid phase and is characterized by a contact angle, which is the angle subtended by the liquid/vapor interface and the solid or immiscible liquid surface. Depending on the surface energy of the substrate, two equilibrium situations can occur upon contact of the liquid and the solid. *Complete wetting* corresponds to the situation when the surface energy of the substrate is high and hence the liquid spreads entirely over (or wets) the solid, thereby forming a film in which case the contact angle is zero. *Partial wetting*, on the other hand, relates to the situation when the surface energy of the substrate is low and hence a finite contact angle is obtained in which case the liquid retains its drop shape which is restricted at the solid surface by a contact line where the solid, liquid and vapor phases meet. The governing principle is the minimization of interfacial energy; in the former case, the interfacial contact between the liquid film and the solid substrate minimizes the free energy of the surface.

Overview

Wetting and spreading, the subject of which is a fundamental pillar of colloid and interface science, are fundamental processes which occur in a wide variety of natural and industrial settings. These processes govern the adhesion between two substances and therefore have significant implications in paint, lubrication, coating, printing and fabric technology as well as in enhanced oil recovery. More recently, there has been renewed interest in the relevance of wetting and spreading in biological and microscale environments. The functional design of biomaterials and biological surfaces requires a thorough understanding of the interrelationships of bio-surfaces and bio-environments. The miniaturization of fluid processes, on the other hand, is associated with an increase in the dominance of surface forces over body forces given that the surface area to volume ratio scales as the inverse of the characteristic system dimension. Thus, at microscale dimensions, surface tension and hence wettability (or capillarity) effects are extremely important considerations in the design of microfluidic devices.

Basic Methodology

Surface Tension and Contact Angle

The relationship between surface tension γ and contact angle θ, formally defined as

$$\theta = \cos^{-1}(\boldsymbol{n}_l \boldsymbol{n}_s) , \tag{1}$$

where $\boldsymbol{n}_l$ and $\boldsymbol{n}_s$ are the outward pointing unit normal vectors from the liquid and solid at the three-phase contact line, respectively, was first established by Thomas Young

in 1805 through a force balance in the plane of the surface at the contact line (Fig. 1):

$$\gamma_{\mathrm{LV}} \cos\theta = \gamma_{\mathrm{SV}} - \gamma_{\mathrm{SL}} , \tag{2}$$

where the subscripts LV, SV and SL denote the liquid-vapor, solid-vapor and solid-liquid phases, respectively. Equation (2) is thus known as *Young's equation*. It should be noted that a force balance also exists in the plane normal to the surface due to the existence of a strain field beneath the contact line to balance the force component $\gamma_{\mathrm{LV}} \sin\theta$. In the case of a liquid lens sitting at the interface of an immiscible liquid, the lens shape is governed by this force balance, the resultant of which is zero (Fig. 2). Equation (2) can also be derived by energy minimization considerations.

The spreading of the drop can be characterized by a spreading coefficient:

$$S = \gamma_{\mathrm{SV}} - \gamma_{\mathrm{SL}} - \gamma_{\mathrm{LV}} . \tag{3}$$

If $S \geqslant 0$, complete spreading occurs in which the drop spontaneously forms a liquid film above the solid substrate, as shown in Fig. 3(a), due to a decrease in the free energy. If $S < 0$, $\theta > 0°$ from Eq. (2) and the drop spreads to an equilibrium shape, constrained by the contact line where the three phases meet; if $\theta < 90°$, the surface is said to be *hydrophilic* (Fig. 3(b)) whereas the surface is said to be *hydrophobic* if $\theta > 90°$ (Fig. 3(c)). Strictly speaking, there is no local minimum in the interfacial energy for $S > 0$ and hence the equilibrium contact angle $\cos\theta$ cannot be defined by Eq. (2). The minimum is defined at $S = 0$, which from Eqs. (2) and (3) gives $\cos\theta = 1$ or $\theta = 0°$, corresponding to the complete wetting case.

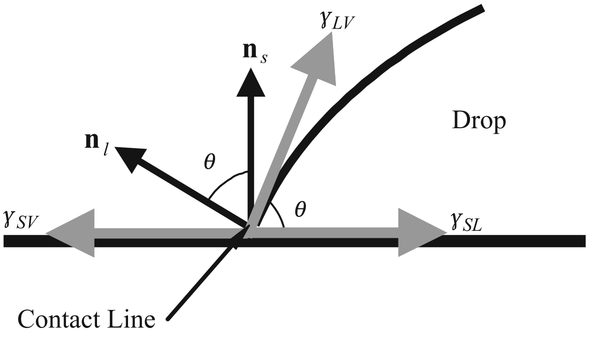

Wetting and Spreading, Figure 1 Force balance at the three-phase contact line where the solid-liquid and vapor phases meet. The outward unit normals protruding from the solid and liquid at the contact line are shown. The angle θ subtending these unit normal vectors or that subtending the interface between the drop and the solid substrate is known as the contact angle

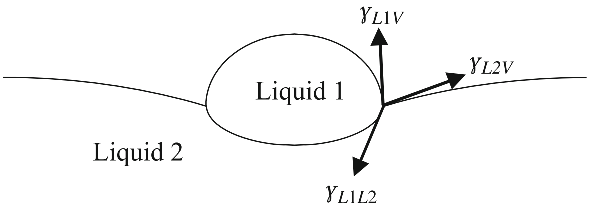

Wetting and Spreading, Figure 2 Force balance at the contact line of a liquid lens sitting above an immiscible liquid

The contact angle is known as a *static* contact angle when the contact line is stationary with respect to the solid substrate. Young's equation in Eq. (2) is therefore a description of the static contact angle. On the other hand, if the contact line is moving relative to the solid, the contact angle, whether it is advancing or receding, is known as a *dynamic* contact angle. The dynamic contact angle varies with the speed at which the contact line advances (or recedes). The upper theoretical limit of the receding contact line speed is therefore the case of complete wetting where the dynamic contact angle approaches 0°. The opposite completely non-wetting limit can be seen when the bulk of the advancing fluid and hence the drop interface overtakes the contact line and hence entrains the fluid being displaced. An example of this is in gravity driven fronts in which the advancing front of the drop forms a nose which rolls over the contact line, as shown in Fig. 4, in which case the dynamic contact angle would approach 180°; in this case, the entrained fluid is therefore the air surrounding the drop. In the extreme completely non-wetting case $\theta = 180°$, a thin submicroscopic film of the displaced phase is entrained beneath the drop therefore causing the complete disappearance of the contact line.

A point should be made here about superhydrophobic surfaces, over which a drop can translate via two states. In a suspended state, the drop sits atop the apex tips of the rough surface; air is entrained beneath the drop and fills the interstices of the rough surfaces between the apex tips. In this state, it has been shown that the velocity of the drop increases with increasing contact angles. Although this may seem contradictory to the classical view above, it is this author's view that the contact line receding speed remains low but the drop itself slides over the entrained air layer due to bulk convection. The increasing bulk drop velocity with increasing contact angles is attributed to the higher center of mass of the drop [1]. For drops in a collapsed state, wherein the liquid fills the interstices of the rough surface, the drop velocity is reduced dramatically each time the contact line reaches a cavity and a stick-slip motion is therefore observed.

W

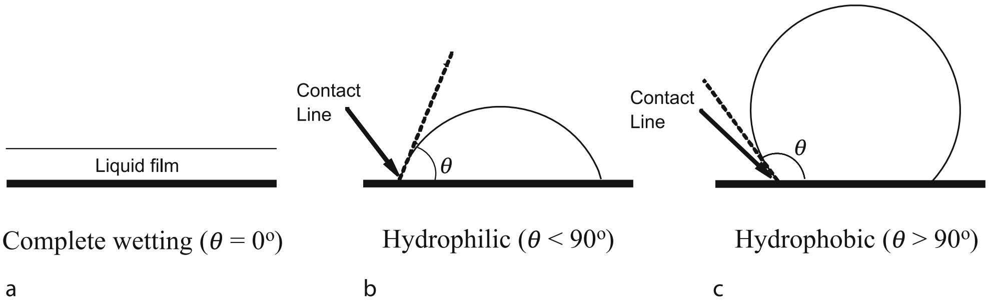

Wetting and Spreading, Figure 3 Equilibrium conditions for a liquid drop in contact with a solid substrate. (**a**) Complete wetting. (**b**) Partial wetting: hydrophilic drop. (**c**) Partial wetting: hydrophobic drop

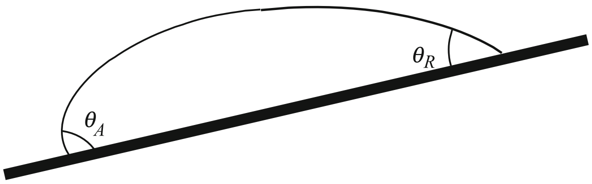

Wetting and Spreading, Figure 4 Schematic depiction of contact angle hysteresis arising when the solid substrate upon which a drop is placed is inclined. At the instance prior to the drop moving down the plane, the contact angle at the advancing front and at the rear are known as the advancing and receding contact angles, respectively

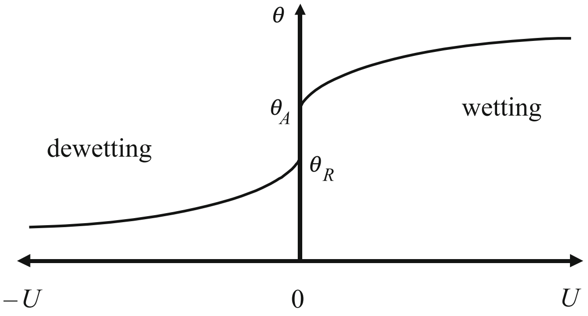

Wetting and Spreading, Figure 5 Contact angle hysteresis arising due to the dependence of the apparent contact angle θ on the contact line velocity *U*

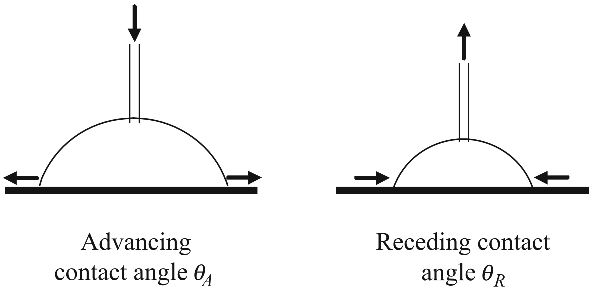

Wetting and Spreading, Figure 6 Measurement of the advancing and receding contact angles by incrementally adding or removing liquid through a thin capillary tube. The measurements are taken just prior to motion of the contact line

The boundary between the static and dynamic conditions also gives rise to contact angle hysteresis, in which the static contact angle when the contact line velocity U is zero is not single-valued (as predicted by Eq. (2)), as shown in Fig. 5, which maps out the velocity dependence of the contact angle. The static contact angle at equilibrium θ appears to be dependent on the history of the drop, i. e., on whether it is on the verge of advancing or receding. The observed contact angle at the front just before the inclined drop in Fig. 4 begins to slide is known as the *advancing* contact angle θ_A whereas that at the rear is known as the *receding* contact angle θ_R. Alternatively, the advancing and receding contact angles can be obtained by measuring the contact angle of a sessile drop just prior to motion when liquid is added or removed from a capillary above the drop to drive it to advance or recede, respectively, as illustrated in Fig. 6. The difference in the advancing and receding angles, i. e., $\theta_A - \theta_R$ (typically 10° or larger), is therefore the contact angle hysteresis, and the equilibrium static contact angle takes any intermediate value in between these limits, i. e., $\theta_R \leqslant \theta \leqslant \theta_A$.

Contact angle hysteresis can be attributed to a departure from the conditions of ideality of the solid, namely, surface roughness, chemical inhomogeneities or contamination, or, the presence of solute (polymers or surfactants) deposits on the surface [2]. Figure 7 shows a plan view illustration of the hysteresis mechanism in which the receding contact line of a drop is locally pinned when the drop moves over a localized surface inheterogeneity which is more hydrophilic than the substrate surface. As a result, there is a distortion of the contact line [3]. If the macroscopic force exerted on the contact line is

$$F = \gamma_{LV} \left(\cos\theta' - \cos\theta\right) , \quad (4)$$

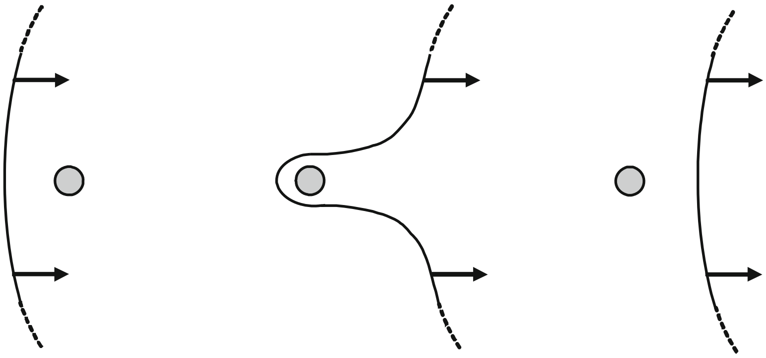

Wetting and Spreading, Figure 7 Plan view illustrating the pinning of the receding contact line due to the presence of a localized surface heterogeneity (represented by the shaded spot) which is more hydrophilic than the substrate. The arrows indicate the direction of the drop motion

where θ' is the contact angle of the drop and θ is the equilibrium contact angle given by Young's equation (Eq. (2)), we note that it is not possible to detach the contact line below a given value of the force and hence the contact line remains pinned for contact angles θ' below that of the equilibrium contact angle θ. In such cases and when evaporation is significant, there arises liquid flow from the bulk of the macroscopic drop in order to replenish the liquid evaporated from the contact line region. If solutes are present in the liquid, these are convected towards the contact line and deposited there, resulting in the formation of concentrated rings along the perimeter of the contact line; an example of this is the ubiquitous coffee-ring stain phenomenon.

A distinction between the *apparent* (or visible) contact angle θ_a and the intrinsic contact angle θ is worthy of mention. The apparent contact angle is a macroscopic extrapolation whereas the intrinsic contact angle is that microscopically subtended from the solid substrate at the contact line, as schematically depicted for a rough surface in Fig. 8. The advancing and receding contact angles due to contact angle hysteresis therefore relate to apparent contact angles. Thus, were the surface ideal, i. e., atomically smooth, clean and homogeneous such that Eq. (2) holds, then the apparent contact angle should coincide with the intrinsic contact angle to describe the equilibrium static contact angle.

Nevertheless, for most practical surfaces, this is not true and hence the intrinsic contact angle is difficult to determine. The surface heterogeneities could very well be the reason why the wetting line moves in a hesitant jerk or shuffling motion, termed as *stick-slip* motion [4]. This could also be attributed to the successive formation and collapse (due to negative disjoining pressure) of the entrained air film beneath the drop. Changes to the apparent contact angle, nevertheless, can be evaluated for rough

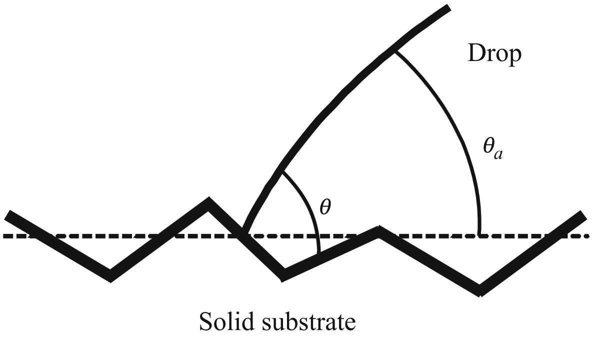

Wetting and Spreading, Figure 8 Schematic depiction of the contact line region on a microscopic level illustrating the distinction between the apparent (macroscopic) contact angle θ_a and the intrinsic (microscopic) contact angle θ due to surface roughness effects on the substrate

surfaces. Consider a small displacement of the contact line dx on a rough but chemically homogeneous surface, as shown in Fig. 9(a). The change in the surface energy per unit length along the contact line dE is then

$$dE = (\gamma_{SL} - \gamma_{SV})\, r dx + \gamma_{LV} \cos\theta^* dx\,, \quad (5)$$

in which r is the surface roughness (assumed to be much smaller than the macroscopic drop length scale) and θ^* denotes the contact angle on the rough surface ($r > 1$).

At equilibrium, the resultant surface forces at the contact line balance and hence the energy is at its minimum, i. e., $dE/dx = 0$. Wenzel's law, derived from this equilibrium condition $dE/dx = 0$ together with Eq. (2) (which can be recovered from Eq. (5) for smooth surfaces where, by definition, $r = 1$), then states

$$\cos\theta^* = r\cos\theta\,, \quad (6)$$

W

wherein θ is the contact angle for smooth surfaces given by Young's equation (Eq. (2)). Since $r > 1$ for rough surfaces, $|\cos\theta^*| > |\cos\theta|$, implying that surface heterogeneities always act to amplify the inherent properties of a surface. In other words, a hydrophilic surface ($\theta < 90°$) will be rendered more hydrophilic ($\theta^* < \theta$) and a hydrophobic surface ($\theta > 90°$) will be rendered more hydrophobic ($\theta^* > \theta$) in the presence of surface roughness.

A similar analysis can be carried out for physically smooth but chemically inhomogeneous surfaces, as depicted in Fig. 9(b), where we allow the surface to comprise of two different materials, each of which is associated with a corresponding contact angle, θ_1 and θ_2. Denoting the fractions along the surface which is composed by each material as f_1 and f_2 (such that $f_1 + f_2 = 1$), assuming f_1 and f_2 are small compared to the area occupied by the entire drop, Eq. (5) now becomes

$$\mathrm{d}E = f_1(\gamma_{SL} - \gamma_{SV})_1\,\mathrm{d}x + f_2(\gamma_{SL} - \gamma_{SV})\,2\mathrm{d}x + \gamma_{LV}\cos\theta^*\mathrm{d}x\,. \tag{7}$$

Energy minimization then requires

$$\cos\theta^* = f_1\cos\theta_1 + f_2\cos\theta_2\,, \tag{8}$$

which is known as the Cassie–Baxter law. In this case, the apparent contact angle due to the chemical inhomogeneous surface is the average of the cosines of the contact angles associated with each chemical that the surface is comprised of, and is hence bounded by the two extremes of these contact angles.

Capillarity

The equilibrium drop shape is related to the surface tension of the drop through its curvature. In other words, the tendency for the drop to assume a curved interfacial shape is due to its surface tension. A consequence of this is the existence of a pressure difference across the interface

$$\Delta p = \gamma_{LV}\kappa\,, \tag{9}$$

with the highest pressure residing on the concave side.

$$\kappa = \frac{1}{R_1} + \frac{1}{R_2}\,, \tag{10}$$

is twice the mean curvature wherein R_1 and R_2 are known as the principal radii of curvature, which is the radii of curvature of the interface along any two orthogonal elements. Equation (9) is known as the *Laplace–Young equation*. For a spherical drop or bubble, $R_1 = R_2 = R$ and hence

$$\Delta p = p_i - p_e = \frac{2\gamma_{LV}}{R}\,, \tag{11}$$

where p_i and p_e are the pressures inside and outside the drop or bubble, respectively.

Capillarity is the phenomena that arises due to the existence of a finite (or even zero) contact angle that a liquid makes with the solid substrate. One example is the height-of-rise of a liquid in an open capillary tube, as shown in Fig. 10. The associated liquid motion due to surface tension is known as *capillary flow*. Assuming the meniscus to be approximately hemispherical with constant radius of curvature $R_1 = R_2 = R/\cos\theta$, where $2R$ is the capillary diameter, the pressure variation across the interface from Eq. (11) is then

$$\Delta p = p_{atm} - p_{liq} = \frac{2\gamma_{LV}\cos\theta}{R}\,, \tag{12}$$

where p_{atm} and p_{liq} are the atmospheric and liquid pressures, respectively. Given that at equilibrium, the hydrostatic head of the liquid capillary $p_{liq} + \rho g H$, where ρ is the liquid density, g the gravitational acceleration and H the equilibrium height of the liquid capillary column, must balance the atmospheric pressure, i. e.,

$$p_{liq} + \rho g H = p_{atm}\,, \tag{13}$$

H can then be obtained by substituting Eq. (12):

$$H = \frac{2\gamma_{LV}\cos\theta}{\rho g R}\,. \tag{14}$$

Equation (14) therefore represents an equilibrium dominant balance between the gravitational and surface tension forces. Thus, given that ρ and $\cos\theta$ are known for a given fluid, the capillary rise can be determined. It is also evident from Eq. (14) that the capillary rise is dependent on the capillary radius. For small capillaries, H can therefore become relatively large. This capillary rise method is therefore very useful and accurate for measuring the surface tension of liquids.

Key Research Findings

Spreading Dynamics

We briefly consider the spreading dynamics of a drop, sufficiently small such that the spreading is not influenced by gravity. We will also assume the substrate to be smooth and homogeneous since surface roughness effects can enhance spreading and even lead to the spontaneous wetting of partially wetting liquids. The interface is also assumed to be

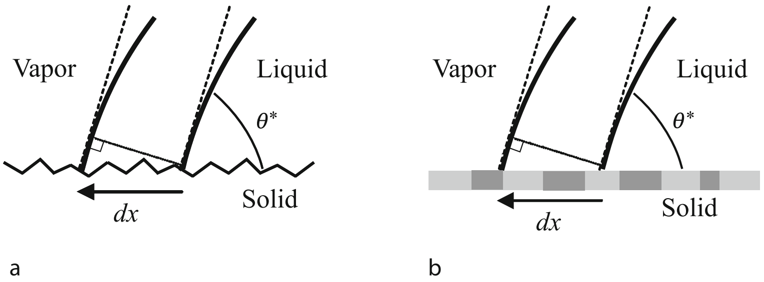

Wetting and Spreading, Figure 9 Contact line region of a drop on a (**a**) physically rough but chemically homogeneous surface, and, (**b**) a physically smooth but chemically inhomogeneous surface consisting of two different surface materials. A small displacement to the contact line $\mathrm{d}x$ is considered in the derivation of Wenzel's law in the case of (**a**) and the Cassie–Baxter law in the case of (**b**)

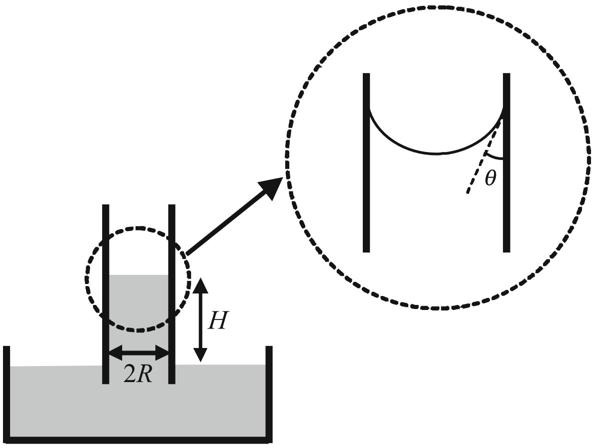

Wetting and Spreading, Figure 10 Schematic depiction of a capillary height-of-rise experiment

clean such that no surface tension gradients are imposed, which could lead to Marangoni stresses; such effects will be discussed subsequently. The experimentally observed spreading data for complete wetting then appears to follow a simple power law relationship given by

$$R(t) \sim t^n \,, \tag{15}$$

where R is the radius of the spreading drop and t denotes time. n has been empirically found to lie between 0.1 and 0.14; it's value has been reported to be dependent on the drop volume, temperature and physical properties as well as the humidity of the ambient phase.

There is also a very specific scaling for the macroscopic dynamic contact angle θ. This was first observed by Hoffman [5], who investigated the variation in the contact angle of an advancing meniscus front in a capillary tube subject to different fluid driving velocities, as well as Tanner [6], who observed similar behavior for drops spreading on a horizontal substrate. In both cases, it was observed that for small Ca,

$$\theta \sim \mathrm{Ca}^{\frac{1}{3}} \,, \tag{16}$$

where

$$\mathrm{Ca} \equiv \frac{\mu U}{\gamma} \,, \tag{17}$$

is the capillary number with $U(t) = \mathrm{d}R(t)/\mathrm{d}t$ being the speed of the contact line in the above, μ is the viscosity. The universal law given by Eq. (16) has since been corroborated by many investigators.

Kalliadasis and Chang [7] considered the behavior of the asymptotic region between the bulk macroscopic drop and a thin film ahead of the drop in which liquid from the perfectly wetting drop drains into due to the negative disjoining and capillary pressures, as shown in Fig. 11. This thin film, known as the precursor film, has both been observed experimentally [8] and is also used as a convenient means of removing mathematical difficulties near the contact line region where continuum theory breaks down; a discussion of this will be carried out below. In this asymptotic region between the bulk drop, of characteristic length scale L, and the precursor film region, of characteristic length scale $\hat{L}$, viscous and capillary forces dominate.

Thus, assuming the film in this region to be thin such that the lubrication approximation holds, the spreading dynamics of the drop in the limit $\hat{L}/L \ll 1$ and the local quasi-steady limit with respect to a moving coordinate frame translating at a constant dimensionless speed given by Ca, is governed by the Bretherton [9] equation:

$$3\,\mathrm{Ca}\frac{\partial h}{\partial x} = \frac{\partial}{\partial x}\left(h^3\frac{\partial^3 h}{\partial x^3}\right) , \tag{18}$$

where h is the dimensionless film height, scaled by the characteristic height of the macroscopic drop H. In the

W

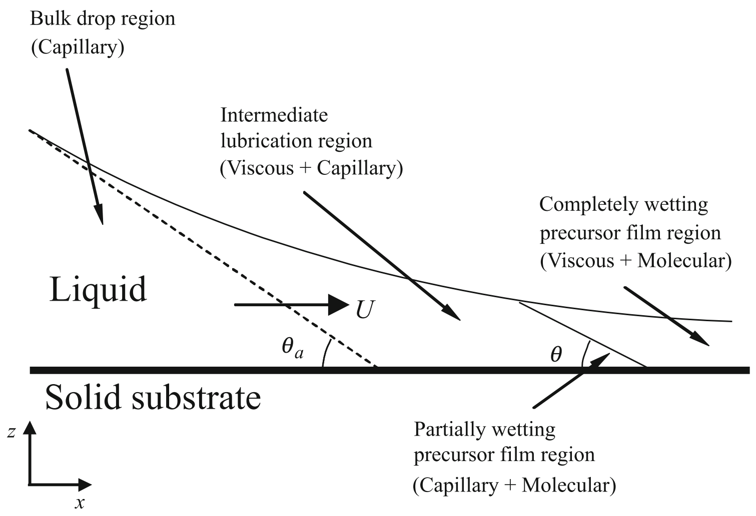

Wetting and Spreading, Figure 11 Contact line region of a spreading drop ahead of which a thin front running precursor film exists. The intermediate asymptotic region where viscous and capillary forces dominate is shown. After Kalliadasis and Chang [7]

above, the axial and vertical coordinates, x and z are scaled by L and H, respectively. Kalliadasis and Chang [7] then showed that the film height, upon redimensionalization, assumes the following weak logarithmic behavior as it asymptotes away from the contact line:

$$h \sim -x\,\mathrm{Ca}^{\frac{1}{3}} \left(9 \log \frac{\hat{L}}{L}\right)^{\frac{1}{3}} . \tag{19}$$

A dynamic contact angle condition can then be written for the macroscopic spreading drop:

$$\tan\theta \sim -\frac{\partial h}{\partial x} \sim \left(-9 \log \frac{\hat{L}}{L}\right)^{\frac{1}{3}} \mathrm{Ca}^{\frac{1}{3}} , \tag{20}$$

showing that the local quasi-steady spreading of a partially or completely wetting liquid drop at constant speed Ca driven by viscous and capillary forces always gives rise to an interfacial shape that scales consistently with the universal law given in Eq. (16). Equation (20) suggests that away from the static equilibrium limit, a partially wetting drop behaves, albeit quite surprisingly, like a complete wetting drop, consistent with the experimental findings for sufficiently large Ca [7].

It is now possible to insert this dynamic contact angle condition back into the spreading relationship in Eq. (15) to obtain an explicit power law for the spreading dynamics of a drop lying on a horizontal substrate [7]. If the drop can be assumed to be thin, then the axisymmetric Laplace–Young equation in the lubrication limit reads

$$\frac{\partial}{\partial r}\left[\frac{1}{r}\frac{\partial}{\partial r}\left(r\frac{\partial h}{\partial r}\right)\right] = 0 . \tag{21}$$

The following boundary conditions apply

$$\frac{\partial h}{\partial r}(r=0) = 0 , \quad h(r=R) = 0 , \quad \text{and,}$$
$$\frac{\partial h}{\partial r}(r=R) = -\tan\theta . \tag{22}$$

In addition, we impose conservation of the drop volume V:

$$\int_0^R hr\,\mathrm{d}r = \frac{V}{2\pi} . \tag{23}$$

Integrating Eq. (21) twice subject to the boundary conditions above then yields

$$h(r) = \frac{2V}{\pi R^2}\left[1 - \left(\frac{r}{R}\right)^2\right] . \tag{24}$$

Substitution of the dynamic contact angle condition in Eq. (20) then gives

$$\frac{\partial h}{\partial r}(r=R) = -\frac{4V}{\pi R^3} = \left(9 \log \frac{\hat{L}}{L}\right)^{\frac{1}{3}} \mathrm{Ca}^{\frac{1}{3}} . \tag{25}$$

Since the dimensionless advancing speed of the contact line can be written as $\mathrm{d}R/\mathrm{d}t = 3\,\mathrm{Ca}$, where time is scaled

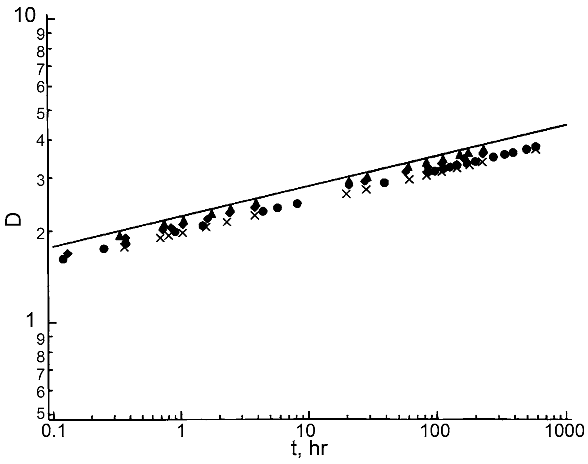

Wetting and Spreading, Figure 12 Collapse of the poly(dimethylsiloxane) drop spreading data of Ausserré et al. [8] with the dimensional form of the universal law given by integration of Eq. (26), which is denoted by *D*. Reproduced with permission from [8]

by $\mu L/\gamma$ and the radius by $V^{1/3}$, it then follows that

$$\frac{\partial R}{\partial t} = -\frac{512V}{3\log\left(\hat{L}/L\right)R^9}\,, \tag{26}$$

and hence

$$R \sim t^{\frac{1}{10}}\,, \tag{27}$$

consistent with the dynamic spreading law of Eq. (15). The collapse of the experimental data of [8] for the spreading of poly(dimethylsiloxane) drops of various volumes on a silicon substrate is shown in Fig. 12 [7]. On the other hand, for large drops where gravity would play an influence, the drop radius would spread as $R \sim t^{1/8}$ instead.

Stress Singularity

In addition to the challenges in the treatment of free surfaces, dynamic spreading models encounter a significant conceptual difficulty due to the breakdown of continuum hydrodynamics at the contact line when the sharp continuum interface is extrapolated to molecular scales to define the contact angle. At these microscopic scales, such geometric conceptualizations such as an interface and the contact angle becomes ambiguous. Moreover, the enforcement of the slip-free and tangential stress continuity on the smooth solid substrate at the three-phase contact line gives rise to a stress singularity [4]. In other words, a logarithmically infinite force is required to advance the contact line, which is not observed experimentally [10]. This locally unbounded force is not the result of a kinematic incompatibility between the no-slip condition on the substrate and the existence of an advancing drop interface that is impenetrable by both sides of the fluid [11]. Instead, Dussan and Davis [11] suggest that the stress singularity is a dynamic consequence of the multi-valued velocity field at the contact line.

Various models have been proposed to overcome this difficulty. Early models allowed the continuum theory to define the contact angle up to a molecular cut-off. One approach is to allow for a finite slip velocity such that the stress singularity, whilst not removed altogether, becomes a logarithmic singularity that is at least integrable [12, 13]. Another approach that we have discussed above is to assume that a thin precursor film precoats the substrate [14]. Alternatively, given that wetting is driven by molecular forces at the inner region of the contact line, the disjoining pressure arising from long-range intermolecular interactions can be introduced to account for a negative pressure that sucks liquid from the bulk into the precursor film.

Nevertheless, it has been shown that the same asymptotic behavior of the inner region away from the contact line given by the universal solution of Eq. (19) is recovered regardless of which model above is adopted to remove the contact line stress singularity in both partially or completely wetting fluids [15]. In fact, the dimensionless length scale $\hat{L}/L$ can be shown to be equal to the precursor film thickness b, i. e.,

$$\frac{\hat{L}}{L} \sim \frac{b}{H}\,, \tag{28}$$

if the precursor film is adopted, the Hamaker constant α, i. e.,

$$\frac{\hat{L}}{L} \sim \frac{1}{L}\left(\frac{|\alpha|}{6\pi\gamma}\right)^{\frac{1}{2}}\,, \tag{29}$$

if the disjoining pressure is used, and, the slip coefficient $\lambda_i = \lambda h^i$, i. e.,

$$\frac{\hat{L}}{L} \sim \lambda_i^{\frac{1}{(1+i)}}\,, \tag{30}$$

if a slip model is employed; λ is the film thickness dependent slip length, the dependence of which is given by the exponent i $(=0, 1)$ and corresponds to the different slip models historically used [16].

To leading order, the intermolecular forces are shown to be solely determined by the apparent dynamic contact angle and independent of slip. The precursor film is also shown to be reasonable approximation to account for intermolecular effects although both the precursor film and slip

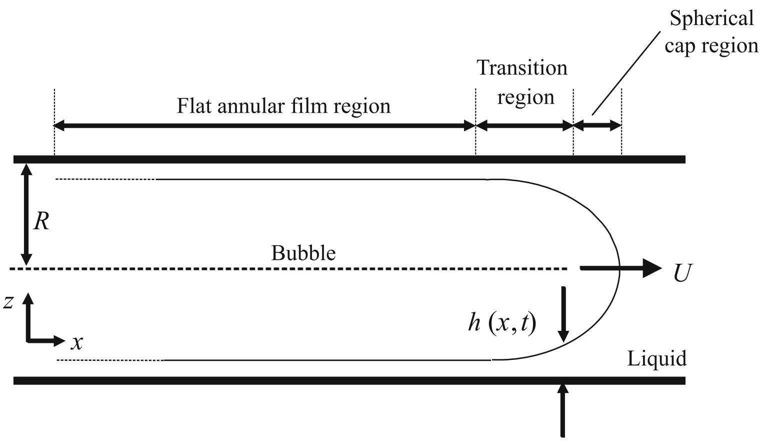

Wetting and Spreading, Figure 13 Schematic depiction of a bubble translating within a long capillary tube

models, while mathematically convenient for handling the problem of stress singularity, do not appear to contribute to the dynamic contact angle condition. In any case, imposing one or the other does not lead to significant error due to the weak dependence of the coefficient $-9\log(\hat{L}/L)$ on the asymptotic behavior of the bulk drop region [15].

Capillary Driven Spreading

We have already observed an example of capillary-driven spreading in the capillary rise experiment described above. Another example of capillarity is that of bubble transport in capillary tubes [9]. Scaling arguments for this problem, illustrated in Fig. 13, are discussed by Chang [17]. To leading order, the pressure drop at the front and rear spherical caps are given by Eq. (11) and thus the axial curvature is $1/R$, where R is the radius of curvature of the bubble cap. In the short intermediate transition region of length L_0 between the spherical cap and annular film regions, the azimuthal curvature gradient, which scales as H_0/R^2L_0 given that the azimuthal curvature is $1/(R-h)$, is negligible compared to the axial curvature gradient, which scales as H_0/L_0^3 since the axial curvature is $\mathrm{d}^2h/\mathrm{d}x^2$ (that $L_0 \ll R$ will be explicitly shown below in Eq. (33)); h is the liquid film thickness with a characteristic length scale in the transition region of H_0 and x is the axial coordinate. Asymptotic matching between the transition and cap regions then gives rise to a balance between the axial and azimuthal curvatures:

$$\frac{H_0}{L_0^2} \sim \frac{1}{R} \,. \tag{31}$$

A balance between viscous and capillary forces requires

$$\frac{\mu U}{H_0^2} \sim \frac{\mathrm{d}p}{\mathrm{d}x} \sim \frac{\gamma}{RL_0} \,, \tag{32}$$

where U is the speed of the bubble. It then follows from Eqs. (31) and (32), with the dimensionless speed Ca defined by Eq. (17), that

$$H_0 \sim R\,\mathrm{Ca}^{\frac{2}{3}} \,, \text{ and} \,, \quad L_0 \sim R\,\mathrm{Ca}^{\frac{1}{3}} \,, \tag{33}$$

as long as $\mathrm{Ca} \ll 1$.
To render the problem quasi-steady, a moving coordinate frame is adopted such that the bubble translates at speed Ca. In the thin annular film region, application of the lubrication approximation to a balance between viscous and capillary forces then yields the following dimensionless equation for the film thickness h [17]:

$$h^3 \frac{\mathrm{d}^3 h}{\mathrm{d}x^3} = h - 1 \,, \tag{34}$$

where h is scaled by the characteristic height of the film H_0 and x by $H_0(3\,\mathrm{Ca})^{-1/3}$. Equation (29) describes the asymptotic behavior in the transition regions for both the front spherical cap as $x \to \infty$ and the rear spherical cap as $x \to -\infty$. Since a quadratically increasing film height is expected, we allow

$$h = A^{\pm}x^2 + B^{\pm}x + C^{\pm} \,, \tag{35}$$

where A, B and C are constants in which the + subscript denotes that pertaining to the front cap and the − subscript pertains to the rear cap. These can be obtained by numerical integration of Eq. (34) starting from the flat film where $\mathrm{d}h/\mathrm{d}x = \mathrm{d}^2h/\mathrm{d}x^2 = 0$, noting that B can be set to zero by arbitrarily shifting the origin. It is then possible to match the curvature $\mathrm{d}^2h/\mathrm{d}x^2$ of the asymptotic solution in Eq. (35) to the outer spherical cap solutions, which to

leading order, are static solutions of the Laplace–Young equation. Chang [17] showed that this leads to

$$\frac{H_0}{R} = 0.643\,(3\,\mathrm{Ca})^{\frac{2}{3}}\ , \tag{36}$$

which is an estimate of the film thickness to leading order. Similar scalings can also be observed in coating flows wherein solid substrates are coated with a thin and uniform liquid film.

Marangoni and Thermocapillary Driven Spreading

In our discussion above, we had assumed that the interface is clean and isothermal. However, surface impurities and non-uniform temperatures can alter the local surface tension, thus giving rise to surface tension gradients that generate additional interfacial stresses, the so-called Marangoni stresses [18]. Marangoni stresses can, in turn, alter the macroscopic spreading behavior significantly and introduce instabilities at the spreading front. Troian et al. [14] have shown that a capillary ridge appears at the advancing front which is the target of viscous instabilities that lead to a fingering phenomenon. Away from the spreading front, instabilities arising from surfactant concentration or thermal non-uniformities can also give rise to dewetting and hence the formation of dry-spots upon rupture of the liquid film [19, 20].

Future Directions for Research

Despite considerable advances in the investigations carried out on wetting and spreading phenomena over several decades, a complete fundamental understanding is still elusive, particularly at the contact line where significant conceptual and mathematical difficulties arise. Although it has been seen above that the weak logarithmic asymptotic behavior in the contact line region suggests that an intimate knowledge of the microscopic conditions is not required to accurately model the macroscopic spreading behavior, the local microscopic wetting behavior may still be important in many physical systems, and particularly so where nanochannel wetting and transport at molecular scales, are concerned. As such, there is a further need to verify and successively refine our current understanding concerning microscopic wetting dynamics.

This is now possible due to advances in computer processing, which has previously limited the scope of molecular dynamics (MD) simulations in microscopically modeling local dynamic wetting behavior. By integrating the laws of motion governing individual molecular particles and taking into account intermolecular interactions, it is possible to resolve the velocity fields which then provide a mechanism for slippage of liquid molecules over the solid. In addition, dynamic contact angle conditions can be inferred and appear to be dependent on the interaction potentials between the liquid and solid molecules. Nevertheless, MD simulations are still confined to small length scales and continue to be limited to short times. As such, it is envisaged that multi-scale spatial and time averaging techniques will allow a unified coupling between continuum and molecular theories to provide a more complete description for modeling wetting behavior. A description of such multiscale models is given in Karniadakis et al. [21]. MD simulations involving equilibrium statistical mechanics or weak deviations from equilibrium (for example, by means of density-functional theories), can therefore replace the disjoining pressure in molecular theories to explicitly account for intermolecular interactions in an intermediary step in asymptotic matching with continuum hydrodynamic models in the long scale limit.

Cross References

- ▶ Applications Based on Electrowetting
- ▶ Bubble Dynamics in Microchannel
- ▶ Capillary Filling
- ▶ Digital Microfluidics
- ▶ Droplet and Bubble Formation in Microchannels
- ▶ Droplet Based Lab-on-a-Chip Devices
- ▶ Droplet Dispensing
- ▶ Droplet Dynamics in Microchannel
- ▶ Electrocapillary
- ▶ Electrowetting
- ▶ Electrowetting and Droplets
- ▶ Interfacial Electrokinetic Flow
- ▶ Surface Tension Driven Flow
- ▶ Surface Tension, Capillarity and Contact Angle
- ▶ Thermal Capillary
- ▶ Thermocapillary Pumping

W

References

1. Dupuis A, Yeomans JM (2006) Dynamics of sliding drops on superhydrophobic surfaces. Europhys Lett 75:105–111
2. de Gennes PG (1985) Wetting: statics and dynamics. Rev Modern Phys 57:827–863
3. Nadkarni GD, Garoff S (1992) An investigation of microscopic aspects of contact angle hysteresis: Pinning of the contact line on a single defect. Europhys Lett 20:523–528
4. Huh C, Scriven LE (1971) Hydrodynamic model of steady movement of a solid/liquid/fluid contact line. J Colloid Interface Sci 35:85–101
5. Hoffman RL (1975) A study of the advancing interface. I. Interface shape in liquid–gas systems. J Colloid Interface Sci 50:228–241

6. Tanner LH (1979) The spreading of silicone oil drops on horizontal surfaces. J Phys D: Appl Phys 12:1473–1484
7. Kalliadasis S, Chang H-C (1996) Dynamics of liquid spreading on solid surfaces. Ind Eng Chemistry Res 35:2860–2874
8. Ausserré D, Picard AM, Léger L (1986) Existence and role of the precursor film in the spreading of polymer liquids. Phys Rev Lett 57:2671–2674
9. Bretherton FP (1961) The motion of long bubbles in tubes. J Fluid Mech 10:166–188
10. Kistler SF (1993) Hydrodynamics of wetting. In: Berg JC (ed) Wettability. Marcel-Dekker, New York
11. Dussan V EB, Davis SH (1974) On the motion of a fluid-fluid interface along a solid surface. J Fluid Mech 65:71–96
12. Hocking LM (1977) A moving fluid interface. Part 2. The removal of the force singularity by a slip flow. J Fluid Mech 79:209–229
13. Dussan V EB (1979) On the spreading of liquids on solid surfaces: Static and dynamic contact lines. Ann Rev Fluid Mech 11:371–400
14. Troian SM, Herbolzheimer E, Safran SA, Joanny JF (1989) Fingering instabilities of driven spreading films. Europhys Lett 10:25–30
15. Yeo LY, Chang H-C (2006) Electrowetting films on parallel line electrodes. Phys Rev E 73:011605
16. Haley PJ, Miksis MJ (1991) The effect of the contact line on droplet spreading. J Fluid Mech 223:57–81
17. Chang H-C (2002) Bubble/Drop transport in microchannels. In: Gad-el Hak M (ed) The MEMS Handbook. CRC Press, Boca Raton
18. Edwards DA, Brenner H, Wasan DT (1991) Interfacial transport processes and rheology. Butterworth-Heinemann, London
19. Warner MRE, Craster RV, Matar OK (2002) Dewetting of ultrathin surfactant-covered films. Phys Fluids 14:4040–4054
20. Yeo LY, Craster RV, Matar OK (2003) Marangoni instability of a thin liquid film resting on a locally heated horizontal wall. Phys Rev E 67:056315
21. Karniadakis G, Beskok A, Aluru N (2005) Microflows and Nanoflows. Springer, New York

Wetting on Structured Substrates

► Surface-Directed Capillary Flow Systems

Wien Filter

► Crossed Field Filter

World-to-Chip Interface

► Transferring Samples to Chips, Techniques

X-Ray Diffraction (XRD)

Definition

Material characterization technique used to determine the crystalline quality, chemical composition, and physical properties of a material. A Cu source is used to generate X-rays, which are then scattered off of a sample and collected by a detector. The full-width at half-maximum (FWHM) value of the scattered X-ray beam can be used as a measure of the materials crystalline perfection.

Cross References

► Fabrication of Self-Assembled Catalytic Nanostructures

Zeta-Potential

Definition

The zeta potential ζ is a measure of the electrical charge developed when a solid surface is brought into contact with an aqueous solution. More specifically, when a solid surface is brought into contact with an aqueous solution an electrical charge is generated at the interface. As a result, local free ions in the solution tend to rearrange themselves such that a thin region of non-zero net charge density exists near the interface. The arrangement of the charges at the solid–liquid interface and the balancing counterions in the liquid is usually referred to as the electrical double layer (EDL). There is a thin layer of counterions immediately next to the charged solid surface, called the compact layer. The counterions in the compact layer are immobile due to the strong electrostatic attraction. Counterions outside the compact layer are mobile. This part of the EDL is called the diffuse layer. The zeta potential is the electrostatic potential at the boundary dividing the compact layer and the diffuse layer.

Cross References

► Temperature Effects on the Zeta Potential
► Measuring Zeta Potential, Methods

Zeta Potential Measurement

Tom Glawdel, Carolyn Ren
Department of Mechanical
and Mechatronics Engineering, University of Waterloo,
Waterloo, ON, Canada
tglawdel@engmail.uwaterloo.ca

Synonyms

Electrokinetic potential; Surface potential

Definition

►Zeta potential is defined as the electrical potential at the shear plane of the electric double layer. Measurement techniques are based on indirect readings obtained during electrokinetic experiments. Typically, the magnitude of the zeta potential varies between $0 - 200$ mV where both negative and positive values are possible depending on the electrochemistry of the solid-liquid interface.

Overview

►Zeta potential refers to the electrokinetic potential at the shear surface of the electric double layer. Along with surface conductance, zeta potential is an important parameter in the study and modeling of a variety of electrokinetic phenomena relevant to microfluidics and Lab-on-a-Chip devices. The zeta potential of a solid-liquid interface depends on a number of factors including the ion concentration, ion valence, pH level and temperature of the solution. For this reason each solid-liquid interface has its own unique zeta potential that must be measured. Zeta potential measurements are based on indirect readings using one of the following electrokinetic phenomena: electro-osmotic flow, electrophoresis and streaming potential. In terms of microfluidics, electro-osmotic and streaming potential techniques are used in the study of microchannels and capillaries while electrophoresis based methods are used to study charged particles such as fluorescent beads, DNA and proteins.

This document is organized in the following manner: first, a brief introduction to the electric double layer and its significance to electrokinetic phenomenon. Second, the principles behind zeta potential measurements based on the three types of electrokinetic phenomenon are discussed, with special attention to the advantages and disadvantages of each method. Finally, a few key research results for each of the methods are presented. The purpose of this entry is to provide the reader with a brief introduction to the fundamentals of zeta potential measurements, for a more detailed description of zeta potential measurements, electric double layer and electrokinetic phenomenon the reader

should consult the various texts that discuss these topics in depth [1–4].

Basic Methodology

Electric Double Layer and Zeta Potential

In most cases, when a solid surface comes in contact with an aqueous solution an electric charge develops at the interface. The surface charge influences the nearby ions creating a non-uniform electric charge distribution near the interface known as the electric double layer (EDL) [1–4]. Several mechanisms cause this effect including ionization, ion adsorption and ion dissolution.

The earliest theoretical study on the structure of the EDL was performed by Helmholtz (1879) who proposed that the charged interface is surrounded by two condensed planes of oppositely charged ions. In actual fact, thermal forces tend to spread out the ions creating a diffuse region around the interface. Gouy (1910) and Chapman (1913) independently tackled this problem by applying the kinetic molecular theory to the diffuse region of ions. In their model, the electric potential and charge distributions are described using the well-known Poisson–Boltzman equation of statistical physics. Although the model is based on statistical grounds, it produces accurate results when the surface potential is low or the electrolyte concentration is not too high. The major defect of the Gouy–Chapman model is that the ions are treated as point charges; however, in reality ions have a finite size that limits the distance they can approach a surface. Stern (1924) resolved this issue and proposed a new model that divides the EDL into an inner compact layer and an outer diffuse layer. Inside the compact layer the size of the ions is considered while in the diffuse layer the Gouy–Chapman model is still applied.

As shown in Fig. 1, the Stern layer is approximately one ion radius thick and is defined by the solid surface and the Stern plane. Counterions in the Stern layer experience strong electrostatic forces and are essentially immobilized against the surface. Ions located outside the Stern plane experience a weaker electrostatic attraction and form the mobile diffuse layer of the EDL. The boundary separating these two regions is defined as the shear plane. In the diffuse layer, competing electrostatic and thermal forces creates a non-zero concentration of ions that is a maximum at the surface and decreases gradually with distance until it reaches equilibrium with the bulk concentration. The thickness of the diffuse layer is often characterized by the Debye length λ_d which can vary from several nanometers to micrometers depending on the concentration and properties of the solution.

The double layer acts to neutralize the surface charge creating an electrokinetic potential distribution between the

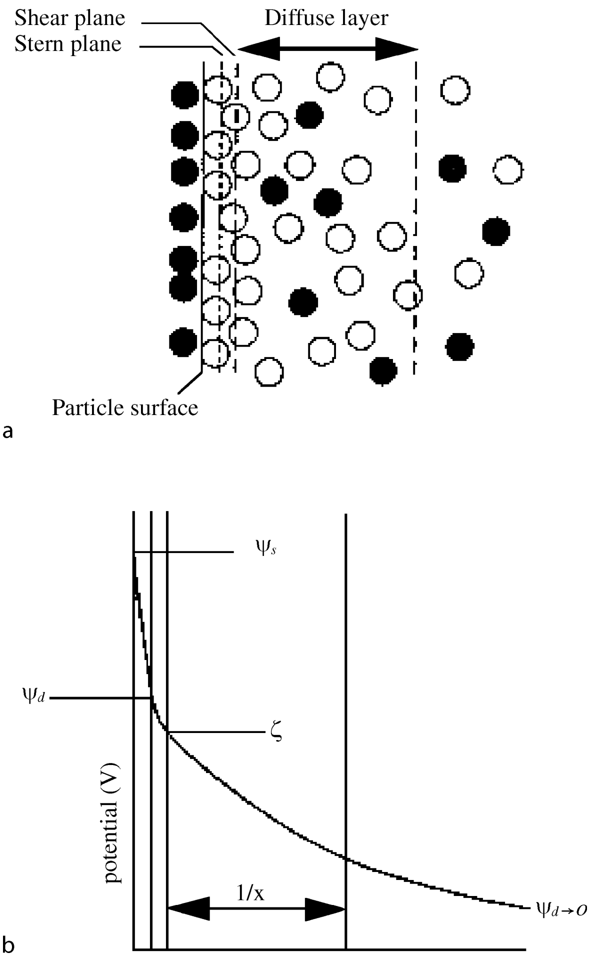

Zeta Potential Measurement, Figure 1 Schematic representation of the electric double layer using Gouy–Chapman–Stern model [3]

interface and the solution. This voltage difference is on the order of millivolts and is refereed to as the surface potential ψ_s. Through the Stern layer the electric potential varies almost linearly to the Stern plane potential ψ_d and then decreases gradually in the diffuse layer until it reaches zero far away from the surface. The electric potential at the shear plane is known as the electrokinetic potential or zeta potential (ζ). Because the zeta potential is located at the fluid flow boundary it is an important parameter for analyzing a variety of electrokinetic phenomenon.

It should be noted that the surface potential and the zeta potential do not always have the same sign [3]. If adsorbed polyvalent or surface active counterions are present the zeta potential may decrease or increase substantially. Thus the zeta potential measurements can not always be extrapolated to determine the surface potential.

In the EDL, the electric potential and net charge density are described by the Poisson–Boltzman equation [1–4].

The Poisson equation describes the electric field within a dielectric medium:

$$\nabla \cdot (\nabla \psi) = \frac{-\rho_e}{\varepsilon_r \varepsilon_0} \quad (1)$$

where ε_0 and ε_r are the dielectric permittivity of a vacuum ($\varepsilon_0 = 8.854 \times 10^{-12}$ C/Vm) and the relative dielectric permittivity of the solution. The net charge density, ρ_e, is the sum of negative and positive ions ($\rho_e = \sum_i z_i e n_i$). Assuming that the Boltzmann distribution is valid, the ionic concentration in the EDL is given by:

$$n_i = n_0 \exp\left(\frac{-z_i e \psi}{k_b T}\right) \quad (2)$$

where n_i is the specific number of the ith ion, n_0 is the number of ions in the bulk solution, z is the valence of the ion, e is the charge of an electron, k_b is Boltzmann's constant and T is the absolute temperature. Combining Eqs. (1, 2) leads to the Poisson–Boltzman equation:

$$\nabla \cdot (\nabla \psi) = \frac{-\sum_i^N z_i e n_0 \exp\left(\frac{-z_i e \psi}{k_b T}\right)}{\varepsilon_r \varepsilon_0} \quad (3)$$

For the special case of a symmetric electrolyte solution ($z : z = 1 : 1$) the Poisson–Boltzman equation reduces to:

$$\nabla \cdot (\nabla \psi) = \frac{2 n_0 z e}{\varepsilon_r \varepsilon_0} \sinh\left(\frac{z e \psi}{k_b T}\right) \quad (4)$$

Applying the non-dimensionalized parameters ($\Psi = ze\psi/kT,\ X = x/L$) to Eq. (4), yields

$$\nabla \cdot (\nabla \Psi) = \kappa^2 L^2 \sinh(\Psi) \quad (5)$$

where κ is the Debye–Hückel parameter and is given by $\kappa = (2z^2 e^2 n_0 / \varepsilon_r \varepsilon_0 k_b T)^{1/2}$. As stated previously, the EDL thickness is characterized by the Debye length ($\lambda_d = 1/\kappa$). For most microfluidic applications involving microchannels the appropriate boundary conditions for solving Eq. (4) are $\psi = \zeta$ at the shear plane and the assumption that $\psi \to 0$ as $x \to \infty$. However, this is not the case for nanochannels where over-lapping boundary layers invalidate the assumption of uniform bulk properties far from the wall. Numerical techniques are usually employed to calculate the electric potential and charge distribution from Eq. (3). Analytical solutions are possible for a few cases where simplified assumptions are justified.

Electrokinetic phenomena arise when the mobile layer of the EDL interacts with an externally applied electric field resulting in relative motion between the solid and liquid phases. There are three types of electrokinetic phenomena relevant to microfluidics: electro-osmotic flow, streaming potential and electrophoresis. In all of these cases, the zeta potential is a key parameter that defines either the fluid flow or particle motion. Since it is not possible to probe the zeta potential directly, measurements are based on indirect readings obtained from electrokinetic experiments. The following discussion focuses on modern methods of measuring the zeta potential using electro-osmotic flow, electrophoresis and streaming potential.

Electro-Osmotic Flow

When an electric field is applied tangentially to the EDL, the mobile ions in the diffuse layer begin to migrate towards the appropriate electrode. Through viscous drag, the motion of the ions causes the surrounding liquid to move generating electro-osmotic flow. The movement also generates an electric current. Since the applied electric field is tangential to the surface, the resulting ion migration does not affect the charge density in the EDL. Thus the body force ($\boldsymbol{F}_b = \rho_e \boldsymbol{E}$) experienced by the fluid is limited to the diffuse layer. Note that it is the external field, $\boldsymbol{E}$, that drives the fluid and not the internal field within the EDL.
The resulting velocity profile is *plug* like, where the velocity is zero at the wall (no-slip condition) and rises to a uniform velocity in the bulk. Since the EDL thickness is very small (~ 30 nm) compared to microchannel (~ 50 μm), to an observer it appears as if the fluid *slips* by the surface. The velocity at the edge of the EDL is given by the classic Helmholtz-Smoluchowski equation:

$$u_{HS} = -\frac{\varepsilon_0 \varepsilon_r \zeta E_x}{\eta} \quad (6)$$

where E_x is the tangential electric field and ζ is the zeta potential. Usually the group of terms, $\varepsilon_0 \varepsilon_r \zeta / \eta$, are combined together into a proportionality constant called the electro-osmotic mobility (μ_{eo}) of the solid-liquid interface. Since the velocity only varies in the EDL, the total flow rate is approximated by $Q = u_{HS} A_c$, where A_c is the cross-sectional area of the microchannel. Thus it is possible to determine the zeta potential by measuring the fluid velocity or volume flow rate under electro-osmotic flow.

Volume Method

One of the earliest methods for determining the zeta potential was to measure the volumetric flow rate of a liquid transported in a capillary under electro-osmotic flow. This method seems simple in principal; however, the small flow rates typical of electro-osmotic flow (~ nl/min) make it

difficult to obtain accurate measurements. Normally the flow rate is determined by following the progression of a meniscus or bubble in an adjoining capillary which in it self produces a variety of errors [2].

Direct Visualization Methods

Several variations of micro flow visualization have been developed for microfluidic applications such as particle-based flow velocimetry and scalar-based flow velocimetry [5]. In terms of the zeta potential measurement, these visualization techniques such as micro-PIV are used to measure the velocity profile and flow rate under electro-osmotic flow. Once the velocity is known the zeta potential can be calculated from Eq. (6). The main advantage of using a flow visualization technique is that the electro-osmotic velocity can be measured directly and in real time. In general, the small amount of particles or dye used has a negligible effect on the electro-osmotic flow being measured. The only significant disadvantage of this technique is that the extent and cost of the hardware may be prohibitive.

Current-Monitoring Methods

Recently a method has been developed to determine the average flow velocity by measuring the electric current in a microchannel under electro-osmotic flow [6, 7]. The experimental set up is shown in Fig. 2, and consists of a microchannel, a high voltage power supply and a data acquisition system. The microchannel and reservoir 2 are initially filled with an electrolyte solution that has a slightly different concentration than reservoir 1 ($c_1 - c_2 = 5\%$). The concentration difference must be small so that the zeta potential and ionic concentrations are nearly uniform throughout the microchannel.

Immediately after the two solutions are in contact, the high voltage power supply is turned on to induce electro-osmotic flow. As the fluid in reservoir 1 displaces the existing fluid in the microchannel the electric current draw changes. Initially the current is constant and then changes linearly until it reaches another plateau once the initial fluid is completely replaced. The time required for the displacement represents the time required for the solution to travel through the channel length, which can be used to determine the average electro-osmotic velocity:

$$u_{\text{ave}} = \frac{L}{\Delta t} \tag{7}$$

where L is the length of the channel and the zeta potential can be calculated from Eq. (6). The major problem associated with this method is the ambiguity surrounding the

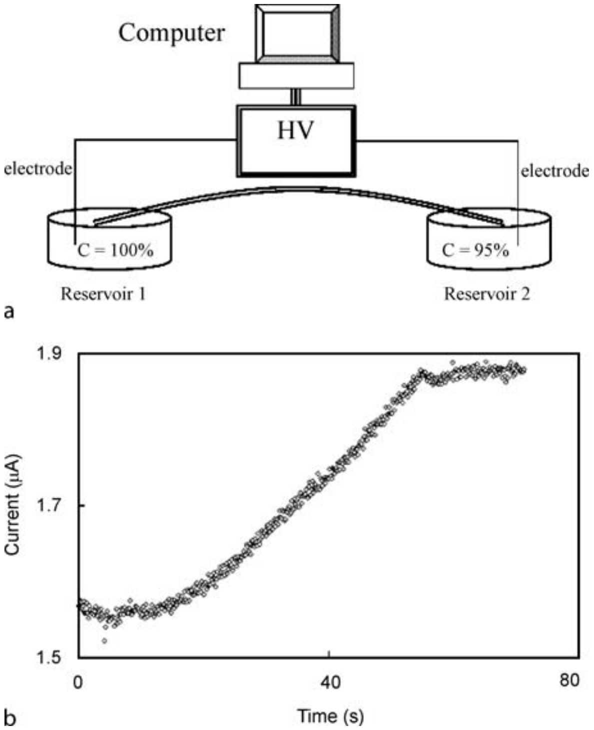

Zeta Potential Measurement, Figure 2 Schematic of the experimental setup for the current-monitoring technique (*a*) and a typical current time plot (*b*) [7]

displacement time. Small current fluctuations and gradual transitions at the beginning and end of the displacement process may cause errors in measuring Δt.

To solve this problem, an improved method was developed to determine the zeta potential by using the slope of the current-time relationship [7]. The slope of the current-time relationship is given as:

$$\text{slope} = \frac{\Delta I}{\Delta t} \tag{8}$$

Under electro-osmotic flow the current in the channel is composed of three parts: 1. the bulk conductivity current, $I_{\text{cond,bulk}}$, the surface conduction current, $I_{\text{cond,surf}}$, and the convection current created by the fluid motion, $I_{\text{cond,conv}}$. Typically, the convection current is several orders of magnitude smaller than the other currents and is neglected. Therefore, the total current is given as:

$$I_{\text{total}} = I_{\text{cond,bulk}} + I_{\text{cond,surf}} = \lambda_b A_c E_x + \lambda_s P_w E_x \tag{9}$$

where λ_b is the bulk conductivity of the fluid, λ_s is the surface conductivity, A_c is the cross-sectional area of the channel, P_w is the wetted perimeter and E_x is the

applied electric field. Substituting Eq. (9) and assuming that $\Delta\lambda_s = 0$, Eq. (8) reduces to:

$$\text{slope} = u_{\text{ave}} \frac{E_x A_c (\lambda_{b2} - \lambda_{b1})}{L} \quad (10)$$

The above expression can then be rearranged to solve for u_{ave} and then substituted into Eq. (6) to calculate the zeta potential. In addition, the surface conductivity can be measured using this method. In this case, the reservoirs are filled with the same fluid and the total current is measured. The surface conductivity is calculated from Eq. (9) assuming that the bulk conductivity is already known.

The disadvantages of the current monitoring technique are that

- the electro-osmotic flow is measured indirectly through the current draw,
- the method assumes constant zeta potential between the two fluids,
- the difference in conductivity must be large enough so that the current change is measurable, and
- there is a lack of spatial and temporal resolution since the zeta potential represents an average value.

The advantage of using this method is in its simplicity, current-time measurements can be performed quickly and with relatively little infrastructure compared to other methods.

It should be noted that there are several additional sources of error for electro-osmotic based measurements. Joule heating must be controlled or temperature fluctuations may cause significant changes in zeta potential, viscosity and other fluid properties. Another source for error is undesired pressure driven flow caused by small head and meniscus (Laplace pressure) differences at the reservoirs. In fact, even modest differences ($\sim$ 5 mm of head) can lead to pressure driven flow rates comparable to the electro-osmotic flow being studied. Also electrolysis occurring at the electrodes may create a pH gradient along the channel creating significant errors in the zeta potential measurement. On the other hand, electro-osmotic flow and electro-osmotic pumping are common methods of transporting fluids in microfluidic devices. Therefore, zeta potential measurements based on electro-osmotic flow provide the most accurate representation of on-chip operating conditions.

Electrophoresis

Electrophoresis refers to the movement of a charged surface relative to a stationary liquid. For instances, under an applied electric field a negatively charged particle will migrate towards the positive electrode (anode).

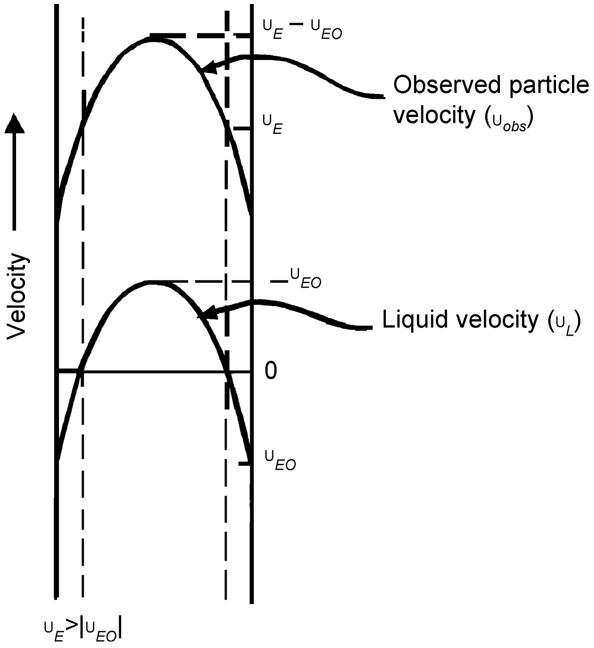

Zeta Potential Measurement, Figure 3 Stationary level, fluid velocity and particle velocity distribution in an electrophoresis cell [1]

For spherical particles the velocity is given as [1]:

$$u_E = \mu_{ep} \boldsymbol{E} \quad (11)$$

where μ_{ep} is called the electrophoretic mobility of the particle. The electrophoretic mobility is related to the zeta potential through:

$$\mu_{ep} = \frac{2\varepsilon_0\varepsilon_r\zeta}{3\eta} f_1(\kappa a) \quad (12)$$

where a is the radius of the particle, η is the viscosity of the liquid, κ is the Debye–Hückel parameter and $f_1(\kappa a)$ is a correcting function that depends on the shape of the particle. Therefore the zeta potential can be calculated from Eq. (12) if the electrophoretic mobility is known.

The most popular method of measuring electrophoretic mobility is micro-electrophoresis. In micro-electrophoresis, particles are placed in a closed capillary with electrodes at either end. When an electric field is applied the particles migrate towards the electrode and their velocities are measured. Because the capillary walls are charged the applied electric field will also induce an electro-osmotic flow. However, since the capillary is closed a back pressure creates a net zero flow in the tube (see Fig. 3). The particle velocity is a combination of the electrophoretic motion and the fluid flow. To obtain the true electrophoretic mobility the particles must be tracked along the stationary layer where the fluid velocity is zero.

Z

For a circular capillary the liquid velocity across the tube is given by the electro-osmotic flow and the back pressure flow:

$$u = u_{EO} + u_{BP} \tag{13}$$

For a pressure driven flow the velocity profile is given by the solution of the Poiseuille equation ($u_{BP} = -c(a^2 - r^2)$), where c is a constant. The value of c is determined by realizing that the net flow in the capillary is zero, $c = 2u_{EOF}/a^2$. The velocity profile is then given by:

$$\frac{u}{u_{EOF}} = 2\frac{r^2}{a^2} - 1 \tag{14}$$

The stationary level is determined by setting u to zero so that $r_{stat} = a/\sqrt{2}$. The same procedure repeated for a plane cell results in $y_{stat} = a(1 - 1/\sqrt{2})$. Since the velocity varies significantly across the capillary, locating the stationary level is critical for obtaining accurate results.

Early methods of measuring the particle velocities involved manually tracking them along a reference grid using a microscope. This process was tedious and not very accurate since only a few particles could be tracked at a time. Modern devices use a variety of measurement techniques to increase the accuracy and throughput of the procedure. Current devices use laser Doppler velocimetry (LDV) and phase analysis light scattering (PALS) to measure particle velocity. New developments focus on suppressing electro-osmotic flow through surface modifications of the capillary or by using oscillating electric fields to take advantage of time scale differences between electrophoresis and electro-osmotic flow. It should be noted that electrophoresis is also used as a method of separating charged particles such as proteins and DNA in a variety of biomedical applications. A few examples include gel electrophoresis, isoelectric focusing and capillary zone electrophoresis.

Streaming Potential

If an electrolyte solution is forced through a microchannel under pressure driven flow, charges in the EDL move downstream resulting in an electric current called the streaming current:

$$\boldsymbol{I}_s = \int_v \boldsymbol{u}\rho_e \, dv \tag{15}$$

where $\boldsymbol{I}_s$ is the streaming current, $\boldsymbol{u}$ is the velocity and ρ_e is the net charge density. The accumulation of these charges creates a potential difference across the channel known as the streaming potential. This potential, in turn, drives the conduction current in the opposite direction of the streaming current. The conduction current is the sum of the bulk and surface conduction:

$$\boldsymbol{I}_c = A_c \boldsymbol{E}_s \lambda_b + P_w \boldsymbol{E}_s \lambda_s \tag{16}$$

where $\boldsymbol{I}_c$ is the conduction current, A_c is the cross-sectional area, $\vec{E}_s$ is the streaming potential electric field, P_w is the wetting perimeter, λ_b and λ_s are the bulk and surface conductivities, respectively. At steady state, $\boldsymbol{I}_c + \boldsymbol{I}_s = 0$ and the general relationship between the streaming potential and *zeta potential* can be derived as:

$$\frac{\boldsymbol{E}_s}{\Delta P} = \frac{\varepsilon_0 \varepsilon_r \zeta}{\eta(\lambda_b + f\lambda_s)} \tag{17}$$

where ΔP is the pressure difference, f is a shape factor for the channel and is given as the ratio of the wetted perimeter to the cross-sectional area ($f = P_w/A_c$). One can see that Eq. (17) provides a basis for calculating the zeta potential and surface conductance if the pressure drop and streaming potential are measured. By rearranging Eq. (17) a more convenient form of the streaming potential equation appears:

$$\frac{\Delta P \varepsilon_0 \varepsilon_r}{\eta \boldsymbol{E}_s \lambda_b} = \frac{1}{\zeta} + \left(\frac{2\lambda_s}{\zeta \lambda_b}\right) f \tag{18}$$

For a physical system λ_s and ζ should remain constant. Eq. (18) shows that there is a linear relationship between the streaming potential measurement and the form factor as shown in Fig. 4. The zeta potential is calculated from the intercept and the surface conductivity from the slope. Therefore, unless the surface conduction is neglected at least two measurements are required to determine the zeta potential and surface conductivity. For practical purposes multiple streaming potential experiments are performed for different form factors to increase the accuracy of the measurements.

A typical experimental apparatus consists of a capillary connected to a pump through a pipe network and a series of transducers strategically placed to measure the pressure drop, flow rate, streaming potential and conductivity. The piping network is designed so that the flow direction can be reversed in the microchannel. Particular attention is required in the preparation and assembly of the apparatus. The potential must be measured with a high impedance electrometer so that the streaming current and therefore the flow in the microchannel are not disturbed. Also, it is important to use electrodes that respond reversibly to current flows (eg. Ag/AgCl).

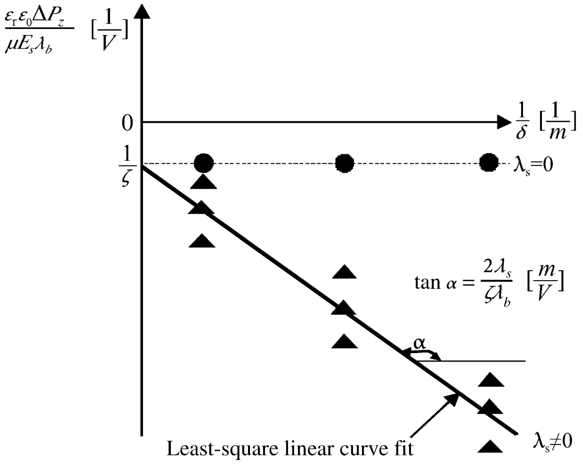

Zeta Potential Measurement, Figure 4 Plot of the relationship between streaming potential, surface conductance and zeta potential used in the streaming potential method [8]

To prevent the electrodes from polarization streaming potential measurements must not exceed 1 – 2 minutes before the flow should be reversed and measurements taken again. By reversing the flow any errors caused by the asymmetry of the electrode system are also reduced. For a given gap height this procedure should be repeated for several different flow rates. Consequently, in order to obtain an accurate streaming potential plot a number of experiments (~ 20) must be performed.

It is important to emphasize the need to measure the surface conductance as well as the zeta potential. If the surface conductance is neglected in Eq. (18) the zeta potential can be severely underestimated. It should also be noted that the equations derived above neglect electrokinetic effects on the flow by assuming a Poiseuille type flow through the microchannel. In actuality the streaming potential creates a reverse electro-osmotic flow in the channel that decreases the overall flow rate. The decreased velocity creates the appearance of an increased fluid viscosity and is known as the electroviscous effect. Generally this effect is prevalent in microchannels less than 50 μm.

Key Research Findings

Sanders et al. applied the micro-electrophoresis technique to measure the zeta potential of finely ground glass slides as a function of pH [9]. The results show that for glass particles suspended in a 0.1 M NaCl the zeta potential varies from −20 mV for a pH of 3 to −75 mV for a pH of 10 demonstrating the importance of pH on zeta potential. One problem that arises with this method is whether the zeta potential measured using finely crushed particles corresponds to the zeta potential of the uncrushed solid-liquid interface. The act of grinding may alter the zeta potential of the original material and is still a topic of debate.

Oddy and Santiago used micro-PIV techniques to study small particles in AC and DC electro-osmotic flow [10]. Independent measurements of the particle motion in the two fields can be correlated to determine the electrophoretic mobility of the particle and electro-osmotic mobility of the solid-liquid interface. The electrophoretic mobility of the fluorescent polystyrene particles was found to be -3.76 ± 0.05 μm cm/Vs and the zeta potential of the glass/water interface for a pH of 7 was -115 ± 10 mV.

Gu and Li [8] used the streaming potential method to study the effects of surface conductance, pH, ionic concentrations and surfactants on zeta potential using the streaming potential technique. A glass slit microchannel was used as the capillary which has a form factor of $f = 1/\delta$, where δ is the gap height. As an example, the streaming potential plot obtained for deionized ultrafiltered (DIUF) water is shown in Fig. 5. Each data point represents the average of 18 readings for a given flow rate and for each gap height three flow rates were studied. Ideally for a given gap height the results for different flow rates should be almost identical. The discrepancy is attributed to the fact that the measured streaming potential $\boldsymbol{E}_S$ is not exactly proportional to the pressure drop ΔP as specified in Eq. (18). A least-square linear curve fit of the data determines the zeta potential and surface conduction. In particular, the zeta potential for a glass-water interface was determined to be -62.2 mV and -22.7 mV for an electrolyte solution of 1×10^{-3} M NaCl solution. In addition, for glass/water the zeta potential var-

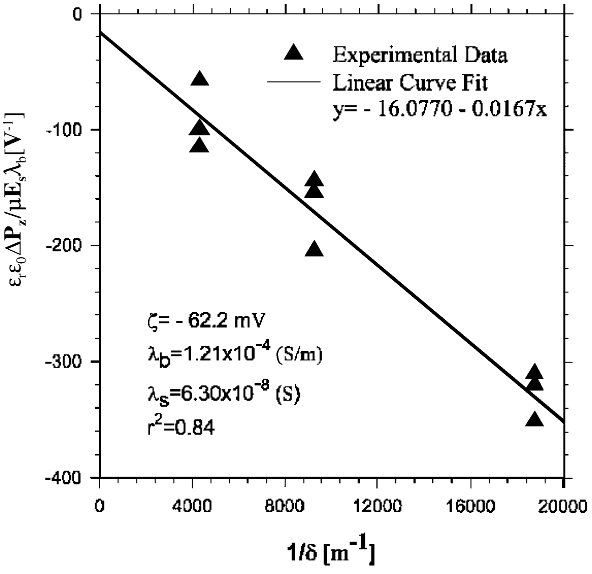

Zeta Potential Measurement, Figure 5 Experimental data from streaming potential measurements for glass/DIUF water in a slit microchannel [8]

Z

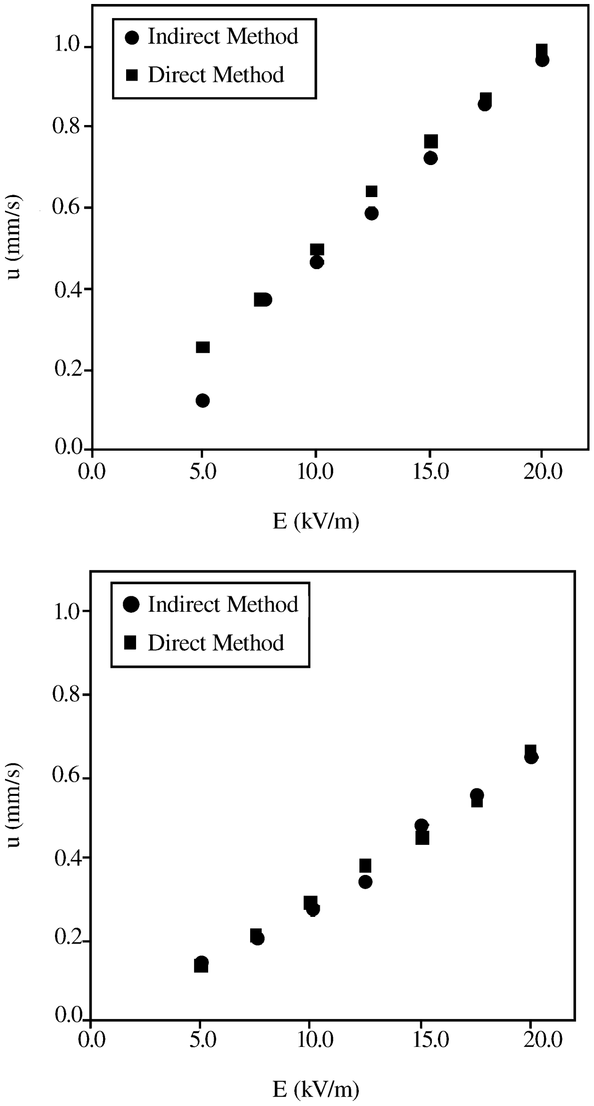

Zeta Potential Measurement, Figure 6 Plot of the electro-osmotic velocity as a function of the applied electric field for two buffers (*a*) 1xTAE and (*b*) 1xTBE. Results for both the direct flow visualization method and the current-monitoring method are shown [6]

ied from −40 mV for a pH of 3 to −80 mV for a pH of 10. Sinton et al. [6] utilized both the direct visualization method and current monitoring technique to measure the zeta potential for two buffer solutions commonly used in biochemistry. The direct method employed caged fluorescent dye that upon exposure to an intense ultraviolet light uncages and fluoresces. The fluorescent dye is then tracked through a series of images that are analyzed to determine the velocity field. Electro-osmotic velocity measurements for the two methods are shown in Fig. 6. The results from both methods are in excellent agreement indicating that the simpler current-monitoring method produces accurate measurements.

Future Directions for Research

Zeta potential is a fundamental parameter for modelling and characterizing electrokinetic flows in a variety of microfluidics and Lab-on-a-Chip devices. Because the zeta potential depends on so many factors (pH, concentration, liquid, surface etc.) more measurements are required for a variety of surface-liquid combinations; particularly, biological and biochemical fluids. Since measurements can vary greatly between methods and experiments, multiple tests should be employed to accurately determine the zeta potential. In addition, measurements performed using multiple techniques can be corroborated which will reduce errors between results. The ultimate goal is to develop an accurate database of zeta potential measurements for various solid-liquid interfaces, however this will most likely require the development of new theoretical models and experimental methods to increase the accuracy and throughput of current devices.

Cross References

► Electric Double Layers
► Electric Double Layer Interaction
► Electroosmotic Flow (DC)
► AC Electro-Osmotic Flow
► Electrophoresis
► Electrical Current Monitoring Methods
► Methods for Measuring Zeta
► Inter-Atomic Potential
► Lennard–Jones Potential
► Microscale Flow Visualization
► Surface Conductivity Measurement
► Electrokinetic Flow and Ion Transport in Nanochannels
► Temperature Effects on the Zeta Potential
► Measuring Zeta Potential, Methods

References

1. Probstein RF (1994) Physiochemical Hydrodynamics. An Introduction. New York, John Wiley & Sons, Inc.
2. Hunter RJ (1981) Zeta potential in colloid science: principles and applications. Academic Press, London
3. Masiliyah JH (1994) Electrokinetic Transport Phenomena. AOSTRA, Edmonton
4. Hunter RJ (2001) Foundations of Colloid Science. Oxford University Press, Oxford
5. Sinton D (2004) Microscale flow visualization. Microfluid Nanofluid 1:2–21
6. Sinton D, Escobedo C, Ren L, Li D (2002) Direct and Indirect Electro-osmotic Flow Velocity Measurements in Microchannels. J Colloid Interface Sci 254:184–189

7. Sze A, Erickson D, Ren L, Li D (2003) Zeta-Potential Measurement Using Smoluchowski Equation and the Slope of Current-Time Relationship in Electro-osmotic Flow. J Colloid Interface Sci 261, 402-410
8. Gu Y, Li D (2000) The ζ-Potential of Glass Surface in Contact with Aqueous Solutions. J Colloid Interface Sci 226:328–339
9. Sanders RS, Chow RS, Masilyah JH (1995) Deposition of Bitumen and Asphaltene-Stabilizing Emulsions in an Impinging Jet Cell. J Colloid Interface Sci 174:230–245
10. Oddy MH, Santiago JG (2004) A method for determining electrophoretic and electro-osmotic mobilities using AC and DC electric field displacements. J Colloid Interface Sci 269:192–204

Zinc Oxide

► Piezoelectric Materials for Microfluidics

Entry List

Essays are shown in blue

Absolute Pressure 1
Absorption 1
AC Dielectrophoresis Lab-on-Chip Devices 1
AC Electrokinetics 8
AC Electro-Osmosis (ACEO) 8
AC Electro-Osmotic Flow 8
Acoustic Droplet Ejection 14
Acoustic Levitation of Droplets 14
Acoustic Particle Concentration 14
Acoustics Based Biosensors 15
Acoustic Separation 25
Acoustic Streaming 25
Acoustic Streaming Pumps 33
Acoustic Waves 33
AC Pumping of Liquids 33
Active Mixer 33
Active Mixing 38
Active Particle Flows 38
Advanced Silicon Etching (ASE) 38
AFM 39
AFM Biosensors 39
Aggregation of Nanoparticles 39
Aging 39
AlN 39
Amperometric Detection 39
Amperometric Techniques 39
Amphoteric Ion Exchange Membrane 47
Analysis/Design 47
Analysis of Individual Cell Contents 47
Analyte 47
Analytical Method 47
Analytical Modeling 47
Anion 47
Anion Exchange Membrane 47
Anisotropic Etching 47
Anisotropic Silicon Etching 49
Anisotropic Silicon Micromachining 49
Anisotropy 49
ANN 50
Anode 50
Anodic Bonding 50
Anthrax 54
Antibody 55
Antigen 55
Aperiodic AC Field 55
Aperiodic Electrophoresis 55
Apoptosis 55
Apparent Slip 55
ARDE 55
Arnoldi Algorithm 55
Arnoldi-Based Macromodeling 55
Arnoldi-Based Model Order Reduction 55
Artificial Atom 55
Artificial Muscle Materials 56
Artificial Neural Networks 56
Aspect Ratio Dependent Etching 56
Assay 56
Assembly of Nanoparticles Into Controlled Nanostructures 56
Atomic Force Microscope (AFM) 56
Atomistic Computer Simulation 56
Atomistic Deposition 56
Atwood Number 56
Background Subtraction 57
Backpressure 57
Band Broadening 57
Bead Based Assays 57
Bead Based Microfluidic Platforms 57
Behavioral Model 65
Bias Voltage 65
Bifurcating Microchannel 65
Bimorph 65
Biocatalytic Fuel Cell 65
Biochip 65
Biochip Printing 66
Bioengineering 66
Biofuel Cell 66
Biognosis 66
Bioimmobilization 66
Bio-Inspired Design 66
Biological Sensors 66
Biomedical Microdevices 66

Bio-MicroElectroMechanical Systems (BioMEMS) 67
Biomicrofluidics 67
Biomimesis 67
Biomimetics 67
Biomimicry 67
Biomolecular Adsorption in Microfluidics 68
Biomolecular Synthesis in Microfluids 76
Biomolecule Detection 84
Bionics 84
Biophysics 84
Bioprinting on Chip 84
Biorecognition 96
Biosafety 96
Biosample Preparation by Lab-on-a-Chip Devices 96
Biosecurity 106
Biosensor 106
Biosensors Using Atomic Force Microscopes 106
Biosensors Using Infrared Imaging 114
Biosensors Using Lasers 114
Biosensors Using Magnetics 119
Biosensors Using Scanning Force Microscope 120
Biosensors Using Surface-Enhanced Raman Scattering 120
Biotechnology 127
Bioterrorism 127
Biothreat 127
Biotransducer 127
Bipolar Membrane 127
Bistability 127
Blending 128
Block Copolymerization 128
Block Heteropolymerization 128
Blood Analysis 128
Blood–Plasma Separators 128
Boiling and Evaporation in Microchannels 128
Boltzmann Equation 131
Boltzmann's Constant 131
Bonding of Non-Metallic Inorganic Surfaces and Polymers 131
Bosch Process 131
Boundary Condition at Interface 131
Boundary Element Method 131
Boundary Element Method and its Applications to the Modeling of MEMS Devices 132
Boundary Integral Approaches 140
Boundary Slip of Liquids 140
Bragg Diffraction Equation or Bragg's Law 147
Bridging Instability 148
Brownian Diffusion 148
Brownian Dynamics 148
Brownian Motion 148
Brownian Noise 148
Bubble Actuated Microfluidic Switch 148
Bubble Dynamics in Microchannels 161
Bubble Formation 163
Bubble Growth 163
Bubble Jet 163
Bubble Train Flow 163
Bulk Materials 163
Bulk Micromachining 164
Bulk Micromachining of Silicon 173
Buried Channel Waveguides 173
Calcium Titanium Oxide 175
Cantilever 175
Cantilever Biosensors 175
Capacitance Cytometry 175
Capacitance Method 175
Capacitive Sensing 176
Capillarity 176
Capillarity-Driven Stop Valve and Sample Injection Switch 176
Capillary-Based Microfluidics 176
Capillary Electrochromatography 176
Capillary Electrochromatography–Electrospray Ionization–Mass Spectrometry: An Integrated Electrokinetic Analytical Technique 177
Capillary Electrophoresis 185
Capillary Electrophoretic Separation 185
Capillary Filling 185
Capillary Flow 192
Capillary Force Valves 192
Capillary Magnetophoresis 196
Capillary Reactor 196
Capillary Valves 196
Capillary Zone Electrophoresis 196
Caspase Activation 196
Cast-in-Place Polymeric Media 196
Catalyst Testing 196
Cataphoresis 196
Cathode 196
Cathode Sputtering 196
Cation 197
Cation Exchange Membrane 197
Cavitation 197
Cavitation in Microdomains 197
Cavity Resonance 201
C-Axis 201
CCD-Camera 202
CEC 202
CEC–ESI–MS 202
Cell Adhesion 202
Cell Adhesion and Detachment 202
Cell Analysis/Testing in Microfluidic Devices 208

Cell Array 208
Cell Arraying 208
Cell Assays 208
Cell Assays/Analysis/Testing on-Chip 208
Cell Assays in Microfluidics 209
Cell-Attached (Single-Channel) Voltage Clamp 216
Cell Attachment 216
Cell-Based High-Throughput Assays 216
Cell Binding 216
Cell Capture 216
Cell Culture (2D and 3D) on Chip 217
Cell Culture on a Chip 223
Cell Disruption 223
Cell Fractionation 223
Cell Handling 223
Cell Membrane Changes 223
Cell Patterning on Chip 223
Cell Positioning 224
Cell Release 224
Cell Separation 224
Cell Sorting 224
Cell and Tissue Culture 234
Cellular Microenvironments 234
Centrifugal Flow 234
Centrifugal Microfluidics 234
Ceramics 245
Changes of Caspase Activity 245
Chaotic 246
Chaotic Flows 246
Chaotic Mixing Based on Viscoelasticity 248
Charge Coupled Device (CCD) Camera 254
Chemical Bond 254
Chemical Cytometry 254
Chemical Etching 254
Chemical Patterning 255
Chemical Vapor Deposition for Film Deposition 255
Chemical Volatilization 260
Chemiluminescence 260
Chemiphoresis 260
Chip-Based Systems 260
Chip Bonding 260
Chip Electrospray Mass Spectrometry 260
Chip Thermocyclers 260
Chiral Nematic 260
Cholesteric 260
Chromatographic Chip Devices 260
Chromatography 264
Closed-Loop 264
Closing Pressure 264
Clusters 265
CMOS-Camera 265
CMUTs 265
Coarse-Grained Particle Methods 265
Coarse-Graining 265
Co-Ions 265
Cold Light Sources 265
Colloidal Forces 265
Color Cameras 265
Color Temperature 265
Combinatorial Library 265
Combined Pressure-Driven Flow and Electroosmotic Flow 266
Compactness 274
Compact Support 274
Complex Fluids 274
Composite Nanoparticles 274
Compression Molding 274
Compression Ratio 274
Computational Domain 275
Computational Fluid Dynamics (CFD) 275
Computational Region 275
Concentration Control 275
Concentration Gradient Generation and Control 275
Condensation in Microchannels 285
Conductivity Detection 291
Confined Bubble Growth 291
Confocal Microscope 291
Confocal Microscopy, Detection 291
Constricted Flow Dimensions 296
Contact Line 296
Contact Temperature Sensors 296
Continuous Model 296
Contraphilic 296
Control 296
Controlled-Potential Instrumentation 296
Controlled System 297
Control of Micro-Flows 297
Control of Micro-Fluidics 297
Control Theory 304
Control Volume Based Finite Difference Method 304
Control Volume Method 304
Convective Dispersion 304
Convective Heat Transfer in Microchannels 304
Conventional Sized Channels 322
Core-Shell Nanoparticles 322
Counterions 322
Coupling Microfluidic Devices to Mass Spectrometers 322
Covalent Bonding 322
Critical Heat Flux (CHF) 322
Critical Reynolds Number 322
Crossed Field Filter 323
Crossed-Field Mass Spectrometer 323
Crosslinked Gels 323

Crystallizaiton 323
Cunningham's Correction 323
Cunningham Slip Correction 323
Curie Temperature 323
Curie–Weiss Temperature 323
Current Monitoring Method 323
Current Monitoring Technique 323
Curvature 323
Curved Microchannel Flow 324
CVD 329
Cy3/Cy5-Dye 329
Cytometric Bead Immunoassay 329
DC Capacitance 331
DC Dielectrophoresis in Lab-on-a-Chip Devices 331
Dead Volume 334
Debye-Hückel Approximation 334
Debye Layer 334
Debye Length 335
Deep Lithography 335
Deep Reactive-Ion Etching (DRIE) 335
Deep Reactive Ion Silicon Etching 335
Degree of Mixing 335
De Laval Nozzle 335
Delta Function 335
Demixing 335
DEP 348
Deposition 348
Depth of Field 348
Detection Groove 348
Developing Flows 348
Developing Region 349
Device Substrates 349
Diagnostic Biochip 349
Diamond Like Carbon (DLC) 350
Diamond Nanoparticles 350
Diaphragm Actuation 350
Diaphragm Pump 350
Dielectric Spectroscopy 350
Dielectrophoresis 350
Dielectrophoretic Force 357
Dielectrophoretic Motion of Particles and Cells 357
Differential Ion Mobility Spectrometry 364
Differential Pressure 365
Diffuse Double Layer 365
Diffuse Interface Model 365
Diffusion 365
Diffusion-Based Mixing 365
Diffusiophoresis 365
Digital Microfluidics 370
Dip-Pen Nanolithography 375
Dirac Delta Function 379
Direct Bonding 379
Direct Current Dielectrophoresis (DC-DEP) 379
Discrete Element Analysis 379
Discrete Least Square 379
Discrete Method 379
Discretization 379
Disjoining Pressure 380
Dispensing 385
Dispersed Magnetic Nanoparticles 385
Dissipative Particle Dynamics 385
Distributed Parameter Model 391
DLVO Theory 391
DNA Array 391
DNA Chip 391
DNA Extraction 391
DNA Fragmentation 391
DNA Hybridization 391
DNA Ladders 391
DNA Microarrays 391
Doppler OCT 396
DPN 396
DRIE (Deep Reactive Ion Etching) 396
Drop 397
Drop on Demand 397
Droplet 397
Droplet Based Lab-on-Chip Devices 397
Droplet-Based Microreactor 402
Droplet Break Up 402
Droplet on Demand 402
Droplet Dispensing 402
Droplet Dynamics in Microchannels 411
Droplet Ejection 418
Droplet Evaporation 418
Droplet Flow 423
Droplet Formation 423
Droplet Generation 423
Droplet Generator 423
Droplet Injection 423
Droplet Manipulation 423
Droplet Microfluidics 423
Droplet Micromixer 423
Droplet Microreactor 423
Droplet Motion in Microchannels 427
Droplet Release 428
Droplet Tear-Off 428
Droplet Transport by Surface Acoustic Waves 428
Drug Delivery 428
Dry Chemical Etch 428
Dry Etch 428
Duty Cycle 428
Dynamic Density Functional Theory (DDFT) 428
Dynamic Mixing 433
EDL Potential 435

Effective Coupling Coefficient 435
Einstein Relation 435
Elastomeric Valve 435
Electrets 435
Electrical Current Monitoring Methods 435
Electrical Double Layer Potential 444
Electrical Double Layers 444
Electrical Double Layers Interaction 453
Electrical/Electrochemical Impedance 459
Electric Debye Layer 460
Electric Heating 460
Electric Paper-Like Display 460
Electroactive Materials 460
Electrocapillarity 460
Electrocapillary 460
Electrocapillary Effect 469
Electrochemical Detection 469
Electrochemical Etching 469
Electrochemical Techniques 469
Electrochemiluminescence 474
Electro Chemo Luminescence (ECL) 474
Electrodeless Dielectrophoresis 482
3D Electrodes 482
Electroendosmosis 482
Electrogenerated Chemiluminescence 482
Electrohydrodynamic Dispensing 482
Electrohydrodynamic Focusing 482
Electrohydrodynamic Instability 482
Electrohydrodynamic Mixing 482
Electrokinetic Dispensing 482
Electrokinetic/ElectroHydrodynamic Flow Instability 489
Electrokinetic Flow 496
Electrokinetic Flow and Ion Transport in Nanochannels 496
Electrokinetic Flow in Porous Media 506
Electrokinetic Focusing 516
Electrokinetic Injection 516
Electrokinetic Instability 517
Electrokinetic Mobility 517
Electrokinetic Motion 517
Electrokinetic Motion of Cells and Nonpolarizable Particles 517
Electrokinetic Motion of Heterogeneous Particles 518
Electrokinetic Motion of Polarizable Particles 522
Electrokinetic Potential 529
Electrokinetic Sample Dispensing 529
Electrokinetic Sample Injection 529
Electrokinetic Sample Introduction 536
Electrokinetic Transport 536
Electrokinetic Transport with Biochemical Reactions 536
Electrokinetic Two-Phase Flows 547
Electromagnetically Actuated Pumps 554
Electromagnetophoresis 554
Electromechanical Coupling 554
Electromechanically Coupled Materials 554
Electromigration 554
Electronic Packaging 554
Electronic Paper 554
Electroosmosis 560
Electro-Osmosis with Patterned Surface Charge 560
Electroosmosis in Porous Media 560
Electroosmotic Dispensing 560
Electroosmotic Flow 560
Electroosmotic Flow (DC) 560
Electroosmotic Flow (EOF) 567
Electroosmotic Flow over Heterogeneous Surfaces 567
Electroosmotic Flow Over Non-Uniform Surfaces 574
Electroosmotic Flow in Porous Media 574
Electroosmotic Pump 574
Electropermeabilization 580
Electrophoresis 580
Electrophoresis of the Second Kind 588
Electrophoretic Flow 588
Electrophoretic Mobility 588
Electrophoretic Transport in Nanofluidic Channels 588
Electroporation 592
Electrospray Emitter on-Chip 593
Electrospray Ionization 593
Electrospray Ionization-Mass Spectrometry (ESI-MS) 593
Electrospray Mass Spectrometry 593
Electrostatic Bonding 593
Electrostatic Quadrupole 593
Electrostatic Valves 593
Electrostrictive 595
Electrothermal Effects 595
Electrothermal Flow 599
Electroviscosity 599
Electrowetting 600
Electrowetting, Applications 606
Electrowetting on Dielectric (EWOD) 615
Electrowetting and Droplets 615
Electrowetting on Insulator Coated Electrodes (EICE) 620
Electrowetting on Line Electrodes (ELE) 620
Element Connectivity 620
Element Connectivity Matrix 620

Element-Free Methods 620
Element Model 620
Elongated Bubble Flow 620
Encapsulation 620
Endergonic 620
Endothermic 620
Entrance Flows 621
Entrance Region 621
Enzymatic Bioreactor 630
Enzymatic or Chemical Digestion 630
Enzymatic Fuel Cell 630
Enzymatic Nanolithography 630
Enzyme Assay 630
Enzyme-Assisted Nanolithography 630
Enzyme Based Nanolithography 630
Enzyme Nanolithography 630
Enzymes 636
EOP 636
EO Pump 636
Epitaxial 636
Epitaxial Growth 636
Epitaxy 636
Equivalent Mean Free Path 636
ESI 637
Establishing Flows 637
Establishing Region 637
Etch Directionality 637
Etching Rate Ratio 637
Etching Single Crystalline Materials 637
Etch Profile 637
Etch Selectivity 637
Eulerian Streaming 637
Evanescent Field 637
Evanescent Wave 637
Evanescent Wave Illumination 638
Evanescent Wave Microscopy 638
Evaporation Deposition 644
Explosive Boiling in Microchannels 644
Extensional 644
External Actuators 644
Externalization of Phosphatidylserine 644
Fabrication of 3D Microfluidic Channels 645
Fabrication of 3D Microfluidic Structures 645
Fabrication of Self-Assembled Catalytic Nanostructures 656
Fabry-Perot Optical Filter 662
Feature Size Dependent Etching 663
Feedback 663
Ferroelectric 663
Ferrofluids in Microchannels 664
Fiber Optic Cables 669
Fiber Optics 669
Field Assisted Bonding 669
Field Asymmetric Ion Mobility Spectrometry 669
Field-Dependent Electrophoretic Mobility 669
Field-Effect Flow Control 669
Film Coating 669
Filters 669
Finite Volume and Finite Difference Methods for Modeling and Simulation 669
Flexible Member Pump 679
Flexible Shear Stress Sensor 679
Flip of Phosphatidylserine 680
Flow Bifurcation in Microchannel 680
Flow Boiling Instability 687
Flow Boiling in Microchannels 695
Flow Boiling in Narrow Channels 695
Flow in Channels with 3D Elements 695
Flow Control 696
Flow of Coolants in Micro-Conduits 696
Flow Cytometer Lab-on-Chip Devices 696
Flow Field-Effect Transistor 708
Flow Instabilities 708
Flow and Mass Transport Through Rough Microchannels 708
Flow Measurement 708
Flow Meters 708
Flow in Microchannels with 3D Roughness 708
Flow Patterns 708
Flow Profiling 708
Flow Rate 708
Flow Rate Measurements, Methods 708
Flow Sensors 718
Flow Simulations in Transitional and Rarefied Regimes 718
Flow by Surface Acoustic Waves 718
Flow Tagging 719
Flow-Through Electrodes 719
Fluerics 719
Fluid Dispersion 719
Fluidic Amplification and Oscillation 719
Fluidic Diodes 719
Fluidic Logic 720
Fluidic Multiplexer 720
Fluidic Pressure Sensing 720
Fluidic Pumping 720
Fluidic Rectification 720
Fluidic Sequencing Circuits 720
Fluid Metering 720
Fluid Metrology 730
Fluid Particle Model 730
Fluid Quantification 730
Fluorescence 730
Fluorescence Detection 730

Fluorescence Efficiency 730
Fluorescence Lifetime 730
Fluorescence Measurements 731
Fluorescence Microscopy 737
Fluorescence Resonance Energy Transfer (FRET) 737
Fluorescence Visualization 737
Fluorescence Yield 737
Fluorescent Labeling 737
Fluorescent Microscopy 749
Fluorescent Probes 750
Fluorescent Thermometry 750
Fluorescent Visualization 759
Fluorophores 759
Focused Ion Beam Milling (FIB) 760
Force-Based Biosensors 760
Force Biosensors 760
FOV – Field of View 760
Free Boundary Reflection 760
Free-Flow Magnetophoresis 760
Free Molecular Regime 760
Free-Surface Atomization 760
Free Surface Electrohydrodynamics 760
Free Surface Electrokinetics 760
Free Surface Flow 760
Frequency Response 760
Friction Factor in Microchannels 761
Front Capturing 761
Front Tracking 761
Fuel Cell 761
Full-Width Half-Maximum (FWHM) 761
Fundamentals of Diffusion in Microfluidic Systems 761
Fusion Bonding 768
Gage Pressure 769
Gas Chromatography 769
Gaseous Flow 772
Gaseous Samples 772
Gas Flow 772
Gas Flow in Nanochannels 772
Gas–Surface Scattering Kernel 778
Gate in the Cell Wall 778
Gaussian Filter 778
GC 778
Gene Chip 778
Generalized Boltzmann Equation 778
Generalized Formulation 778
Genosensors 778
Glass 779
Glass-Polymer Bonding 779
Glycosidase 789
Glycoside Hydrolase 789
Gravity Wave 789
Gray-Scale Lithography 789
Gray-Tone Lithography 790
Guard Flows 790
HARMST (High Aspect Ratio Micro-Structure Technology) 791
Head Pressure 791
Heat Absorption 791
Heat Capacity 791
Heating Foil 791
Heat Transfer in Microchannel Flow 791
Helical Microchannel Flow 791
Helmholtz Cavity 791
Hemholtz Resonance 791
Hermann–Mauguin Notation 792
Heterogeneous Membrane 792
High Aspect Ratio Si Etching 792
High Performance Liquid Chromatography (HPLC) 792
High Pressure Liquid Chromatography (HPLC) 792
High-Throughput Chemical Testing 792
High-Throughput Screening (HTS) 792
Homogenization 792
Hot Embossing 792
Hot Film 793
Hot Press Bonding 793
Hot Press Molding 793
Hot Wire 793
Hot Wire Anemometer 793
HSV 793
HSV Color Space 793
HSV / Intensity Images 793
Hybrid Bonding 793
Hybrid Simulation 793
Hydrodynamic Dispersion 793
Hydrogels 801
Hydrogen Bond 801
Hydrogen Passivation 802
Hydrophilic/Hydrophobic Patterning 802
Hydrophobic/Hydrophilic Microfluidics 803
Hydrophobic/Hydrophilic Patterning 803
Hysteresis 803
ICEO 805
ICEP 805
IC Packaging 805
ICP Etching 805
Illuminance 805
Imaging for Biosensors/Biochips/Microchips 805
Immersed Boundary Method 805
Immersed Interface Method 808
Immobilized Enzyme Biosensor 808
Immobilized Enzyme Reactor 808

Immobilized Microfluidic Enzyme Reactor (IMER) 808
Immunoassay 808
Immunochemistry 808
Immunodiffusion 808
Impact Evaporation 808
Impedance 808
Impedance Biosensors 809
Impedance Measurements of Cells 809
Impedimetric Biosensors for Nano- and Microfluidics 811
Impulse Bit 823
Induced-Charge Electro-Osmosis 824
Induced-Charge Electrophoresis 824
Infrared Imaging and Mapping for Biosensors 824
Infrared (IR) Mapping 826
Infrared Radiation 826
Infrared Thermography 826
Injection Molding 826
Injection Slit 826
Inkjet 826
Inkjet Print 827
Inkjet Printing 827
Inkjet Printing in Microfabrication 827
In situ Polymerized Materials 827
Insulating Post Dielectrophoresis 827
Insulator-Based Dielectrophoresis (iDEP) 827
Integrated Actuators 827
Integrated Biochips 828
Integrated Light Confiners 828
Integrated Light Guiding 828
Integrated Light Propagator 828
Integrated Microdevices for Biological Applications 828
Integrated Microdevices for Medical Diagnostics 834
Integrated Microfluidic Devices 840
Integrated Nanoliter System 840
Integrated Temperature Control in Microfluidic Systems 840
Integrated Waveguides 840
Intelligent Gels 840
Inter-Atomic Potential 841
Interdigitated Microelectrode 841
Interface Capturing Schemes for Free-Surface Flows 841
Interfaces between Microfluidics and Mass Spectrometry 849
Interface Tracking 854
Interfacial Electrohydrodynamics 854
Interfacial Electrokinetic Flow 854
Interfacial Flow 866
Interfacial Flow Modelling 866
Interfacial Instability 866
Interfacing Lab-on-a-Chip Platforms with Mass Spectrometers Using MALDI and ESI 871
Intermittent Flow 871
Internal Friction 871
Internal Rarefied Gas Flows 872
International Notation 872
Internucleosomal DNA Fragmentation 872
Interrogation Area 872
Intracellular Ca2+ Concentration Changes 872
Intracellular Ca2+ Fluxes 872
Inversion Symmetry 872
Ion Channel 872
Ion Conductance in Nanochannels 873
Ion Counter 873
Ion Detector 873
Ion Exchange Membranes 873
Ion Implantation 876
Ionization Source 876
Ion Mobility 876
Ion Mobility Spectrometer 876
Ion Source 876
Ion Transport 877
Ion Transport in Nanopores 877
Ion Trap Mass Spectrometer 877
IPRT 877
Irradiance 877
Isentropic Flow 877
Isotropic Etching 877
Isotropic Silicon Etching 884
I-STAT 884
Janus Particle 885
Jet Pumping 885
Jetting 885
Jet-Type Rectifier 885
Joule Heating and Chip Materials 886
Joule Heating Effect 896
Joule Heating in Electrokinetic Flow: Theoretical Models 896
Karhunen–Loève (K–L) Approach 905
Karhunen–Loève (K–L) Decomposition 905
Karhunen–Loève (K–L) Expansion 905
Kelvin–Hemholtz Instability 905
Kernel Function 905
Kinetic Boltzmann Equation 905
Kinetics 906
Kinetic Theory of Gases 906
Knoevenagel Condensation 906
Knudsen Number 906
Lab-Cd 907
Lab-on-a-Chip 907

Lab-on-Chip Devices for Biodefense Applications 907
Lab-on-a-Chip Devices for Chemical Analysis 910
Lab-on-Chip Devices for Immunoassays 927
Lab-on-a-Chip Devices for Particle and Cell Separation 930
Lab-on-Chip Devices for Protein Analysis 940
Lab-on-a-Chip Devices for Sample Extractions 948
Lab-on-Chip Devices for Separation-Based Detection 954
Lab-on-a-Chip (General Philosophy) 962
Lab-on-a-Disk 969
Laboratorial Microsystem 969
Laminar Flow 969
Laminar Flow-Based Fuel Cells 969
Laminar to Turbulent Flow Transition 969
Laplace Pressure 969
Laplace Pressure Drop 970
Laser Ablation 970
Laser-Based Biosensors 973
Laser Based Micromachining 973
Laser Doppler Anemometry 980
Laser Doppler Sensor 980
Laser-Induced Fluorescence (LIF) 980
Laser-Induced Molecular Tagging 980
Laser-Induced Photochemical Anemometry 980
Laser Machining 980
Laser Micromachining 981
Laser Scanning Confocal Microscopy (LSCM) 981
Lattice Boltzmann Equation 981
Lattice Boltzmann Method (LBM) 981
Lattice Poisson–Boltzmann Method, Analysis of Electroosmotic Microfludics 985
LC-LIGA (Low-Cost LIGA) 999
Lead Zirconate Titanate 999
Least Square 999
Lennard-Jones Potential 1000
Level Set Method 1000
LIGA 1000
LIGA-Like Techniques 1003
Ligand 1005
Light Sheet 1005
Linear Peristaltic Pump 1005
Liquid Chromatography 1006
Liquid Crystal Technique for Measuring Temperature 1012
Liquid Extraction 1022
Liquid Handling 1022
Liquid–Liquid Electroosmotic Flow 1022
Liquid–Liquid Stratified Flow in Microchannels 1022
Liquid Magnet 1031
Liquid–Solid Electrophoretic Flow 1031
Liquid–Vapor Phase Change 1031
Lithography 1031
Local Filtering 1031
Low-Frequency Capacitance 1032
Low-Pass Filtering 1032
Ludwig–Soret Effect 1032
Luminescence 1032
Luminescent Labels 1032
Lumped Analysis 1032
Lumped Capacitance 1032
Mach Number 1033
Macromodel 1033
Macromolecular Transport 1033
Magnetic-Based Biosensors 1033
Magnetic Biosensors 1033
Magnetic Coils 1033
Magnetic Field-Based Lab-on-Chip Devices 1033
Magnetic Field-Based Microfluidic Devices 1040
Magnetic Fields 1040
Magnetic Filter 1040
Magnetic Fluid 1040
Magnetic Mass Spectrometer 1040
Magnetic Microbeads 1040
Magnetic Pumps 1040
Magnetic Split-Flow Thin Fractionation 1043
Magnetic Susceptibility 1043
Magnetohydrodynamic Pumps 1043
Magnetophoresis 1043
Magnetron 1048
Magnets 1048
MALDI 1048
Manipulating Cells, Techniques 1048
Marangoni Convection 1050
Marangoni Effect 1055
Mass Analyser 1055
Mass Filter 1055
Mass Spectrometer 1056
Mass Spectrometry 1056
Mass Spectrometry on a Chip 1057
Materials Used in Microfluidic Devices 1065
Matrix Assisted Laser Desorption/Ionization 1068
Mean Curvature 1068
Mean Filter 1068
Mean Free Path 1068
Measurement Depth 1068
Measurement Standards 1068
Measuring Zeta Potential, Methods 1068
Mechanical Nanodetectors 1076
Mechanical Nanosensors 1076
Median Filters 1078
Medical Imaging 1078
Membrane Actuation for Micropumps 1078

Membraneless Fuel Cells 1082
Membrane Pump 1082
Membrane Reactor 1082
Memory 1082
Memory Effect 1083
MEMS Actuators 1083
MEMS-Based Biosensor 1083
MEMS Biosensor 1091
MEMS-Nozzle 1091
MEMS Packaging 1091
MEMS-Thruster 1091
Meniscus 1092
Meshfree Methods 1092
Meshless Methods 1092
Mesicopter 1100
Mesomorphic State 1100
Mesoscopic Method 1100
Metalorganic Chemical Vapor Deposition (MOCVD) 1100
MGA 1100
Microactuators 1100
Micro Aerial Vehicles 1103
Microair Vehicle (MAV) 1110
Microarray 1110
Microarray Fabrication 1110
Microbial Fuel Cell 1110
Microbiosensor 1110
Microchannel 1110
Microchannel Flow 1111
Microchannel Glow Discharge 1111
Microchannel Heat Sinks (MCHS) 1111
Microchannel Surface Modification 1111
Microchannel Surface Sterilization 1111
Microchemical Systems 1111
Micro Chemlab 1111
Micro Coolers 1111
Microdialysis 1111
Microdrone 1119
Microdroplet Transport 1119
Micro-Encapsulation 1119
Micro Energy Conversion Devices 1119
Micro Energy Harvesting 1127
Micro Energy Scavenging 1127
Microengines 1127
Microfabricated Coulter Counter 1127
Microfabricated Flow Cytometer 1127
Microfabricated Needles 1128
Microfabrication 1128
3D Microfabrication 1128
Microfabrication of Three-Dimensional Microstructures 1128
Microfilters 1128
Microflaps 1135
Microflow Actuator 1136
Microflow Switch 1136
Microfluidic Analysis System 1136
Microfluidic Assembly 1136
Microfluidic Bioreactors 1147
Microfluidic Cell Culture 1151
Microfluidic Chip 1151
Microfluidic Circuits 1151
Microfluidic Component Assembly 1159
Microfluidic Devices 1159
Microfluidic Devices in Tissue Engineering 1159
Microfluidic Flow Visualization 1169
Microfluidic Fuel Cells 1169
Microfluidic Imaging 1177
Microfluidic Integration 1177
Microfluidic Mixer 1177
Microfluidic Mixing 1177
Microfluidic Optical Devices 1186
Microfluidic Platforms 1187
Microfluidic Reactor for Biomolecular Synthesis 1187
Microfluidic Reactor for Polymer Synthesis 1188
Microfluidic Rotary Pump 1188
Microfluidics 1189
Microfluidic Sample Manipulation 1189
Microfluidics-Based Surface Patterning Tools 1194
Microfluidics for Biochemical and Chemical Reactions 1195
Microfluidics on a CD 1207
Microfluidics and Magnetism 1207
Microfluidics and Nanofluidics 1207
Microfluidics for Stem Cell Therapy 1207
Microfluidics for Studies of Apoptosis 1213
Microfluidic Stem Cell Culture 1220
Microfluidic System Control Modules 1221
Microfluidic Systems 1221
Microfluidic Systems Assembly 1221
Microfluidic Systems for Combinatorial Chemistry 1221
Microfluidic Systems for High-Throughput Screening 1230
Microfluidic Systems Packaging 1243
Microfluidic Systems in Space Science 1243
Micro Fluorescently-Activated Cell Sorting (μFACS) 1244
Micro Fuel Cells 1244
Micro Gas Analyzers 1244
Micro Gas Chromatography 1244
Micro Gas and Liquid Chromatography 1244
Micro Gas Turbine Engines 1244
Micro Gas Turbines 1244

μGC 1244
Microgravity 1244
Micro Heat Engines 1244
Micro-Heat Exchangers 1245
Micro Heat Pipes 1245
Micro Hot-Wire Anemometer 1253
Microhypodermic Needles 1253
Microjets 1253
Micro Laser Doppler Velocimetry (μ-LDV) 1253
Microlayer 1255
Micro-LC 1255
Microlithography 1255
Micromachined Coulter Counter 1255
Micromachined Flow Cytometer 1256
3D Micromachining 1256
Micromixer 1256
Micromixing Chip 1256
Micromolding 1256
Micromolding (Injection and Compression Molding) 1267
Micro/Nano Anemometers 1274
Micro/Nanofluidics 1274
Micro- and Nanoscale Anemometry: Implication for Biomedical Applications 1274
Micro- and Nanoscale Gas Dynamics 1281
Micro- and Nanoscale Gas Fluidics 1287
Microneedles – Applications & Devices 1294
μPEMFC 1300
Micro-PIV-Based Diffusometry 1300
Microplug Transport 1305
Microporous Materials 1306
Microporous Membranes 1306
Micropowder Blasting 1306
Micro Power Generation 1306
Microprojections 1306
Micro Propulsion 1306
Microreaction Technology 1306
Microreactor 1306
Microreactor for Synthesis of Biomolecules 1306
Microrockets 1306
Microrotorcraft 1307
Microscale Cooling Devices 1314
Microscale Flow Visualization 1325
Microscale Needles 1334
Microscopic Lenses 1334
Microsegmented Flow 1335
Micro-Shock Tube 1342
Microslug Flow 1342
Micro Steam Turbines 1342
Microsterolithography 1342
Microstructured Hydrogen Fuel Cells 1351
Microsynthetic Jets 1354
Microsystems 1359
μTAS 1359
Microthermocyclers 1359
Microthrusters 1359
Microtips and Microspikes 1359
Micro Total Analysis System (μTAS) 1359
Microturbines 1359
Microvalve 1368
Micro-Wave Rotor 1368
Millikan's Resistance Factor 1368
Miniature Heat Pipes 1368
Miniature Heat-Removal Devices 1368
Miniature Unmanned Air Vehicle (UAV) 1368
Miniaturized Analysis Systems 1368
Miniaturized Fluorescence-Activated Cell Sorting Devices 1368
Miniaturized Ion Mobility Spectrometry 1368
Miniaturized Systems 1376
Miniaturized Total Analysis System (μ-TAS) 1376
Minichannels 1376
Mixing Effectiveness 1376
Mixing Efficiency 1376
Mixing Enhancement 1376
Mixing Measures 1376
Mixing Performance 1382
Mixing Quality 1382
MLPA 1382
Mn 1382
Model Kinetic Equation 1382
Model Order Reduction (MOR) 1382
Model Reduction 1391
Molecular Beam Epitaxy (MBE) 1391
Molecular-Continuum Simulation 1391
Molecular Dynamics 1391
Molecular Dynamics Simulation Method 1391
Molecular Flow 1398
Molecular Method 1398
Molecular Modeling 1398
Molecular Self-Assembly Fabrication 1398
Monoclonal 1398
Monostability 1398
Monte Carlo Method 1398
Monte Carlo Simulation Method 1401
Morphotropic Phase Boundary 1401
Motional Branch 1401
Motional Circuit 1401
Motional Leg 1401
Motion of a Deformable Drop in Microchannels 1401
MS 1401
MS/MS 1401
Multi-Channel Micro Liquid Dosing System 1401
Multi-Channel Micro Switch Pumping 1401

Multilayer Piezoelectric Actuator 1401
Multiphase Flows 1402
Multiphase Pumping 1402
Multiplexed Time Etching 1402
Multiscale Modeling 1402
Multiscale Modeling and Numerical Simulations 1402
Mw/Mn 1407
Nanoarrays 1409
Nanobiosensors for Nano- and Microfluidics 1409
Nanocatalyst 1409
Nanochannel Fabrication 1409
Nanochannels 1414
Nanochips 1414
Nanoclusters 1414
Nanocrystals 1414
Nanofluid Flow in Microchannels 1414
Nanofluidic Channels 1414
Nanofluidics 1414
Nanofluidics in Carbon Nanotubes 1414
Nanofluidic Single Molecule Detection 1417
Nanofluidic Single Molecule Sensors 1417
Nanofluidic Systems for Single Molecule Detection 1417
Nanofluids 1422
Nanolithography 1422
Nanometer 1422
Nano-Particle Controllable Assembly 1422
Nanoparticles 1437
Nanoparticle Synthesis in Microreactors 1437
Nanophotonic Characterization in a Microfluidic System 1446
Nanopore Conductance 1446
Nanopore Fabrication 1447
Nanopores 1447
Nanorods 1447
Nanoscale Biosensors 1447
Nanoscale Optofluidic Characterization Techniques 1448
Nanoscale Optofluidic Measurement 1456
Nanosensors 1456
Nanostructures 1456
NEMS-Based Biosensors 1456
Neural Network 1456
Nitrides 1457
No-Moving-Part Pumps 1457
No-Moving-Part Valves 1457
Non-Centrosymmetric 1457
Non-Continuous Approaches 1457
Non-Covalent Bonding 1461
Non-Covalent Forces 1461
Non-Covalent Interactions 1461
Non-Directional Etching 1461
Non-Equilibrium Diffuse Charge 1461
Non-Equilibrium Electrical Double Layer 1461
Nonlinear Electrokinetic Phenomena 1461
Nonlinear Electro-Osmosis 1470
Nonlinear Electrophoresis 1470
Nonlinear Electrophoretic Mobility 1470
Non-Metallic Inorganic Materials 1470
Non-Newtonian 1471
Non-Newtonian Fluid 1471
Non-Newtonian Fluids in Microchannel 1471
Non-Newtonian Fluids in Microfluidics 1480
Nucleation 1488
Nucleation and Growth 1488
Nucleic Acid Detection 1488
Nucleus 1488
Number-Average Molecular Weight 1488
Numerical Discretization 1489
Numerical Simulation 1489
Numerical Solution of Boltzmann Equation 1489
Numerical Stability 1494
Numerical Techniques for Free Surface Flows: Interface Capturing and Interface Tracking 1494
Ohmic Heating 1513
Ohnesorge Number 1513
On-Chip Cell Culture 1513
On-Chip Cell Lysis 1513
On-Chip Detection 1515
On-Chip Detection Using Optical Fibers 1515
On-Chip Electrospray 1530
On-Chip Free-Flow Magnetophoresis 1539
On-Chip Laboratory 1539
On Chip Light Confiners 1539
On Chip Light Guiding 1539
On Chip Light Propagator 1539
On-Chip Micro-Optical Detection 1539
On Chip Waveguides 1544
Optical Coherence Imaging 1553
Optical Coherence Tomography and Optical Doppler Tomography 1553
Optical Doppler Tomography (ODT) 1557
Optical Doppler Velocimetry 1557
Optical Lithography 1558
Optical Narrow Passband Filter 1558
Optical Trapping 1558
Optical Traps 1558
Optical Tweezers for Manipulating Cells and Particles 1558
Optofluidics – Applications 1563
Optofluidics – Fluidics Enabling Optics 1567
Optofluidics: Optics Enabling Fluidics 1572

Optofluidics – Techniques for Fabrication and Integration 1578
Ordinary Least Square 1583
Organ Fabrication 1583
Organic Material 1583
Organ or Tissue Augmentation 1584
Orthorhombic Crystal 1584
Over/Under/Perfectly-Expanded Nozzle Flow 1584
Oxidation/Reduction 1584
Oxidation (of Silicon) 1584
Oxide Deposition 1591
Oxide Growth 1591
Oxides 1591
Packaging (and Wire Bonding) 1593
Parallelization 1596
Parallel (Stratified) Flow 1597
Partial Differential Equations (PDEs) 1597
Particle Dynamics Simulation 1597
Particle Image Thermometry 1597
Particle Image Velocimetry (PIV) 1597
Particle Manipulation 1597
Particle Manipulation Using Ultrasonic Fields 1597
Particle Methods 1602
Passive Micromixers 1602
Passive Mixer 1610
Patch Clamp Measurements On-Chip 1610
Patch Clamp Technique 1618
Patch Voltage Clamp Technique 1618
PCR Lab-on-Chip Devices 1618
Peclet Number 1626
Peltier Effect 1626
Perfect Slip 1626
Peristalsis 1626
Peristaltic Pumps 1626
Permeabilization of Cells 1633
Perovskite 1633
Phase-Change Heat Transfer in Microchannels 1633
Phase Field Method 1633
Phase Separation Kinetics 1633
Phase Shift 1634
pH Control Device 1634
Phenol Extraction 1634
Phenotypic Assay 1634
Phenotypic Screening in Microfluidic Devices/on-Chip 1634
Phosphorescence 1634
Photo-Activated Nonintrusive Tracking of Molecular Motion 1634
Photobleached Fluorescence 1634
Photobleaching 1634
Photochemical Decomposition 1634
Photochemical Degradation 1634
Photofluidic Devices 1634
Photofluidics 1634
Photolithography 1635
Photoluminescence 1636
Photomask 1636
Photometer 1636
Photometry 1642
Photo Patterned 1642
Photopatterned Materials 1642
Photoresist Reflow 1642
Photoresist SU-8 1643
Photoresponsive Hydrogels 1643
Photosensitive Hydrogels 1643
Photoswitchable Hydrogels 1647
Photothermal Effect 1647
pH-Sensitive Hydrogel 1647
pH-Sensitive Valve 1649
pH Sensor 1649
Physical-Chemical Etching 1649
Physical Domain 1650
Physical Etching 1650
Physical Region 1650
Physical Vapor Deposition 1650
Picoliter Flow Calibration 1650
Piezoelectric 1653
Piezoelectric Drop-on-Demand 1654
Piezoelectric Ink Jet 1654
Piezoelectric Materials for Microfluidics 1654
Piezoelectric Microdispenser 1662
Piezoelectric Micro/Nanoliter Droplet Dispenser 1672
Piezoelectric Pumps 1672
Piezoelectric Valves 1672
pL 1672
Planar Laser-Induced Fluorescence 1673
Plasma Bonding 1673
Plasma Chromatography 1673
Plasma Etching 1673
Plasma in Microchannel 1684
Plasma Oxidation 1691
Plasma Treatment of Nanoparticles for Nanofluids 1691
Plastic 1700
Plasticity 1700
Platinum Resistance Thermometer 1700
Plug Flow 1700
Pneumatic Valves 1700
Poiseuille Coefficient 1702
Poiseuille Single Phase Gas Flows 1702
Polyclonal 1702
Poly(dimethylsiloxane) (PDMS) 1702
Polydispersity 1702

Polydispersity Index 1703
Polyelectrolyte 1703
Polyelectrolyte Patterning Technique 1703
Polymer 1703
Polymer Casting 1703
Polymer Electrolyte Membrane Fuel Cells 1703
Polymerization Reaction in Microreactor 1703
Polymer Monoliths 1703
Polymer Replication 1703
Polymer Solutions 1703
Polymer Synthesis within Microfluidic Reactor 1703
Poor Man's LIGA 1710
Porous Electrodes 1710
Port Resonance 1710
Positive Displacement Pump 1710
Positive Pressure
or Suction (Vacuum) Pressure 1710
Potassium Hydroxide (KOH) Etching 1710
Powder Blasting 1711
Power MEMS 1714
Precipitate 1714
Precipitation 1714
Precursor Materials 1714
Predecessor Material 1714
Preparatory Separation 1714
Pressure 1714
Pressure-Driven Flow 1714
Pressure-Driven Single Phase Gas Flows 1714
Pressure-Driven Single Phase Liquid Flows 1724
Pressure-Driven Two Phase Flows 1736
Pressure Drop in Microchannels 1743
Pressure Injection 1743
Pressure Measurements, Methods 1743
Pressure Sensors 1745
Pressure Wave 1745
Primitive Model 1745
Probe Microscopy 1745
Programmed Cell Death 1745
Proper Orthogonal Decomposition (POD) Based
MOR 1745
Protein Adsorption 1745
Protein Array 1745
Protein Array and Cell Array 1745
Protein Chip 1746
Protein Microarrays 1746
Protein Profiling 1748
Proteolysis 1748
Proteomics 1749
Proteomics in Microfluidic Devices 1749
Proton Exchange Membrane Fuel Cells 1758
PRT 1758
Pump Head 1758
Pyroelectric 1758
Pyroelectric Flow Sensors 1758
Pyroelectricity 1765
Pyroelectric Sensors 1765
PZT 1765
Q-Dots 1767
Quadrupole Filter 1767
Quadrupole Ion Trap 1767
Quadrupole Mass Spectrometer 1767
Quantum Box 1767
Quantum Dot 1767
Quantum-Dot Quantum Well
(QDQW Nanoparticles) 1769
Quantum Efficiency 1769
Quantum Yield 1769
Quartz 1769
Radiation Pressure 1771
Radical Polymerization 1771
Radiofrequency (RF) Sputtering 1771
Radius of Curvature 1771
Random Method 1771
Rarefaction Parameter 1771
Rarefied Flow 1771
Rarefied Gas Dynamics 1771
Rayleigh Flow 1772
Rayleigh Instability 1772
Rayleigh–Taylor Instability 1772
Reacting Electrokinetic Flow 1772
Reaction Condition Control 1772
Reaction Time Control 1772
Reactive Ion Etching (RIE) 1772
Reflective Index 1781
Regular Least Square 1781
Relative Roughness 1781
Relaxation 1781
Relaxation Time of the Viscoelastic Fluid 1781
Relaxor Ferroelectrics 1781
Replica Molding 1781
Reptation Tube 1782
Residual Stress 1782
Resistance Temperature Detectors 1782
Resistance Thermometers 1790
Resistive Heating 1790
Resonance and Antiresonance Frequencies 1790
Reynolds Number 1790
RGB 1791
Rheological Fluid Flow in Microchannels 1791
Rheology 1791
Rheometer 1791
RIE Lag 1791
Rosensweig Instability 1791
Rotary Peristaltic Pump 1791

Rotating Channel Flow 1791
Rough Channels 1791
Roughness 1791
Roughness Effect on Microscale Transport 1792
RTD 1795
Rutherford Backscattering Spectrometry (RBS) 1795
Sample Handling 1797
Sample Pre-Fractionation 1797
Sample Preparation 1797
Sample Purification 1797
Sample Purification Using Magnetic Particles 1797
Sample Transport 1798
Sampling 1798
Sampling Unit 1798
Sand Blasting 1798
Satellite Droplets 1798
Saturated Flow Boiling 1798
Scanning Electron Microscopy (SEM) 1798
Scanning Probe Measurement 1798
Scanning Probe Microscopy 1799
Scattered Light Intensity 1804
Segmented (Droplet-Based) Flow 1804
Segmented Flow 1804
Selective Silicon Etching 1804
Self-Assembled Monolayer 1805
Self-Assembly 1805
Self-Assembly Fabrication 1805
Self-Diffusion 1806
Semiconductor Nanocrystals 1806
Semiconductor Nanoparticles 1806
Sensing and Actuation 1806
Serpentine Microchannel Flow 1806
SERS 1806
SERS-Based Biosensors 1806
Shear 1806
Shear-Driven Flow 1806
Shear-Driven Micro- and Nanofluidics 1807
Shear Flows 1816
Shear Stress 1816
Shear Stress Sensors 1816
Shockwave 1828
Shockwaves in Microchannels 1829
Shunt Capacitance 1839
Signal Attenuation 1839
Silicon Dioxide Growth 1839
Silicon Etching 1839
Silicon Micromachining 1839
Simulating Migration of Polymer Chains, Methods 1846
Single Cell Analysis in Microfluidic Devices 1851
Single Cell Impedance Spectroscopy 1860
Single Crystal 1860
Single-Phase Convective Flows in Microchannels 1860
Single-Phase Forced Convection in Microchannels 1860
Single-Phase Gaseous Flow 1860
Slip Boundary 1863
Slip Flow Regime 1863
Slip Velocity 1863
Slope Method 1863
Slug Flow 1863
Smart Skin 1863
Smoluchowski Equation 1863
Smoothing Function 1864
SNP on Chip – Micro- and Nanofluidics for Single Nucleotide Polymorphism Discrimination 1864
Soda-Lime Glass 1869
Sodium Glass 1869
Sodium Silicate Glass 1869
Sol–Gel Technique 1869
Solid Phase Extraction 1874
Solutal Marangoni 1874
Solution Reservoirs on Chips 1874
Soret 1874
Soret Effect 1874
Space Charge 1874
Specific Impulse 1874
Spectral Analysis 1874
Spectral Approximation 1874
Spectral Methods 1874
Spectral Response 1880
Spectral Responsivity 1880
Spectrophotometer 1880
Spectrophotometric Analysis 1880
Spectrophotometric Measurement 1881
Spectrophotometry 1881
Spectroscopy 1881
Speed of Sound 1881
Spinning-Disk Confocal Microscopy 1881
Spinodal Decomposition 1881
Spiral Microchannel Flow 1881
Spontaneous Electrowetting 1881
Spontaneous Polarization 1881
SPR 1881
SPRT 1881
Sputter Etching 1881
Sputtering for Film Deposition 1882
Sputter Yield 1888
Stability 1888
Stack Actuator 1888
Stagnation Conditions 1888
Standard Deviation 1888
Static Electrowetting 1888

Stationary Phases in Microchannels 1888
Statistical Sampling Method 1889
Steady Streaming 1889
Stem Cell Isolation 1889
Stem Cell Reprogramming 1889
Stem Cell Tissue Engineering 1890
Stereolithography 1890
Stokes Approximation 1890
Stokes Shift 1890
Stotz–Wien Effect 1890
Streaming Current 1890
Streaming Current and Electroviscosity 1890
Streaming Dielectrophoresis 1898
Stroke 1898
Stroke Volume 1898
Subcooled Flow Boiling 1898
Subdynamic Regime 1898
Superfast Electrophoresis 1899
Super-Limiting Current 1899
Superparamagnetism 1899
Supersonic Micro-Nozzles 1899
Surface Acoustic Waves 1910
Surface Capturing 1910
Surface Change 1910
Surface-Charge Patterning Techniques 1910
Surface Chemistry Technique 1913
Surface Conductance 1913
Surface Conductivity 1913
Surface Conductivity Measurement 1913
Surface-Directed Capillary Flow Systems 1922
Surface Electric Conductance 1931
Surface Enhanced Raman Scattering (SERS) 1931
Surface Evolver 1931
Surface Features to Enhance Transport 1932
Surface Forces 1932
Surface Lipid Translocation 1932
Surface Micromachining 1932
Surface Modification, Methods 1932
Surface Plasmon Resonance Sensors 1938
Surface Potential 1944
Surface Roughness Measurement 1944
Surface Tension, Capillarity and Contact Angle 1948
Surface Tension-Confined Confined Microfluidics 1955
Surface Tension Driven Filling 1955
Surface Tension Driven Flow 1955
Surface Texture 1969
Surface Topography 1969
Surface Tracking 1969
Surface Transformation 1969
Surface Treatment 1969
Suspensions 1969
Switching Etching 1969
Synthesis of Biological Molecules in Microfluidics 1969
Synthesis of Polymer Molecules Using Microfluidics 1969
Synthetic Jet 1969
Tandem MS 1971
Taylor–Aris Dispersion 1971
Taylor Bubble Flow 1971
Taylor Dispersion 1971
Taylor Flow 1971
Taylor Flow in Microchannels 1971
TCR 1976
Temperature Coefficient of Resistance 1976
Temperature Control 1976
Temperature Control in Microfluidic Systems 1976
Temperature Control System in Microfluidic Chips 1980
Temperature Effects on the Zeta Potential 1980
Temperature Gradient Focusing 1987
Temperature Gradient Generation and Control 1993
Temperature Measurement, Methods 1994
Temperature Measurement Using Fluorescence 2005
Temperature Probes 2005
Temperature-Sensitive Hydrogels 2006
Temperature Sensitive Resistor 2009
Temperature Sensors 2009
Temporal Averaging 2009
Terminal Velocity 2009
Test 2009
Thermal Anemometer 2009
Thermal Bonding 2010
Thermal Bubbles 2010
Thermal Capacitive Flow Sensor 2017
Thermal Conductivity 2017
Thermal Control in Microfluidic Modules 2017
Thermal Creep Coefficient 2017
Thermal Diffusion 2017
Thermal Flow Sensors 2017
Thermal Fusion Bonding 2018
Thermal Gradient Focusing 2018
Thermal Lens Effect 2018
Thermal Lensing, Detection 2018
Thermally Actuated Mechanical Valves 2025
Thermally Driven Mechanical Valves 2025
Thermally-Sensitive Hydrogels 2025
Thermal Marangoni Effect 2025
Thermal Mechanical Valves 2025
Thermal Oxidation 2025
Thermal Pumping 2025
Thermal Slip Coefficient 2025
Thermistors 2025

Thermocapacitive Flow Sensor 2025
Thermocapillarity 2032
Thermocapillary Actuation 2036
Thermocapillary Convection 2037
Thermocapillary Effect 2037
Thermocapillary Pumping 2037
Thermocapillary Shear Stress 2040
Thermochromic Liquid Crystals 2040
Thermocouples 2040
Thermodiffusion 2040
Thermoelectric Effect 2040
Thermoelectric Flow Sensors 2040
Thermoelements 2047
Thermoforming 2047
Thermomechanical Valves 2047
Thermometry 2061
Thermophoresis 2061
Thermopneumatic Membrane Valve 2064
Thermopneumatic Valve 2064
Thermoresistive Flow Sensors 2065
Thermosensitive Hydrogels 2072
Thick Film Lithography 2072
Thick-Film Piezoelectric Actuation 2072
Thick Resist Lithography 2073
Thin-Film Actuation 2079
Three-Dimensional Electrodes 2079
Three-Dimensional Patterning 2083
Threshold Filter 2083
Throat 2083
Throw 2083
Time-Dependent Density Functional Theory (TDFT) 2083
Time-of-Flight Filter 2083
Time of Flight Ion Mobility Spectrometry 2083
Time-of-Flight Mass Spectrometer 2083
Time-Gated Fluorescence Detection 2083
Time-Multiplexed Deep Etching 2084
Time-Multiplexed Plasma Etching 2084
TIRF 2084
TIRFM 2084
TIRM 2084
TIRV 2084
T-Junction 2084
TLCs 2085
TOF-MS 2085
Topographical Manipulation 2085
Torr 2085
Total Internal Reflection Fluorescence (Microscopy) 2085
Total Internal Reflection Velocimetry 2085
Tracers 2085
Transesterification 2085
Transferring Samples to Chips, Techniques 2085
Transitional Microchannels 2093
Transitional Nanochannels 2093
Transitional Regime 2093
Transition Flow 2093
Transition in Microchannels 2093
Transition to Turbulence in Microchannels 2093
Translocation of Phosphatidylserine 2095
Transmission-Line Model 2095
Transmittance 2095
Transport of Droplets by Acoustics 2096
Transport of Droplets by Thermal Capillarity 2104
Transverse Electrophoresis 2110
Trapping Dielectrophoresis 2110
Traveling-Wave Electro-Osmosis 2110
Traveling-Wave Pump 2110
Turbulence 2111
Turbulence Control (Microflap, Microballoon, Microsynthetic Jet) 2111
Turbulence in Microchannels 2119
Turbulent Flows 2126
Turbulent Shear Stress 2126
Two-Faced Particle 2126
Two-Fluid Stratified Flow 2126
Two Phase Flow 2126
Two-Phase Flow Driven by Pressure 2126
Ultra High-Throughput Screening System 2127
Ultrasonic Concentration 2127
Ultrasonic Machining 2127
Ultrasonic Material Removal 2128
Ultrasonic Particle Manipulation 2128
Ultrasonic Pumps 2128
Ultrasonic Separation 2129
Unbalanced AC field 2129
Unimorph 2129
Unit Impulse Function 2129
Unmanned Rotorcraft 2129
Unmixing 2129
UV-LIGA 2129
Valve 2131
Valveless Pumps 2131
Valve-Less Rectification Pumps 2131
Van-der-Waals Attraction 2139
Vapor Bubbles 2139
Vaporization 2140
Velocimetry 2140
Velocity Distribution Function 2140
Velocity Sensors 2140
Venturi Diode 2147
V-Groove 2147
Viscoelastic 2147
Viscoelasticity 2147

Viscometer 2155
Viscosity 2155
Viscous Dissipation 2155
Viscous Heating 2164
Viscous Pump 2169
Viscous Slip Coefficient 2170
Visualization Based on Molecular Tagging Methods 2170
Voltage Clamp 2177
Volume of Fluid (VOF) Method 2177
Volume Illumination 2177
Volume Tracking 2178
Vortex Diode 2178
Vortex Pair 2178
Vortex Ring 2178
Vortices 2178
Wafer Bonding 2179
Wall Shear Stress 2183
Wang-Chang–Uhlenbeck Equation 2183
Water Management in Micro DMFCs 2183
Waveguide Propulsion 2184
Waveguide Trapping 2184
Weak Formulation 2185
Weber Number 2185
Weighted Least Square 2185
Weights and Measures 2185
Wet Chemical Etch 2185
Wet Etching 2185
Wettability Patterning 2186
Wetting Phenomenon 2186
Wetting and Spreading 2186
Wetting on Structured Substrates 2196
Wien Filter 2196
World-to-Chip Interface 2196
X-Ray Diffraction (XRD) 2197
Zeta-Potential 2199
Zeta Potential Measurement 2199
Zinc Oxide 2207